John K. Warren

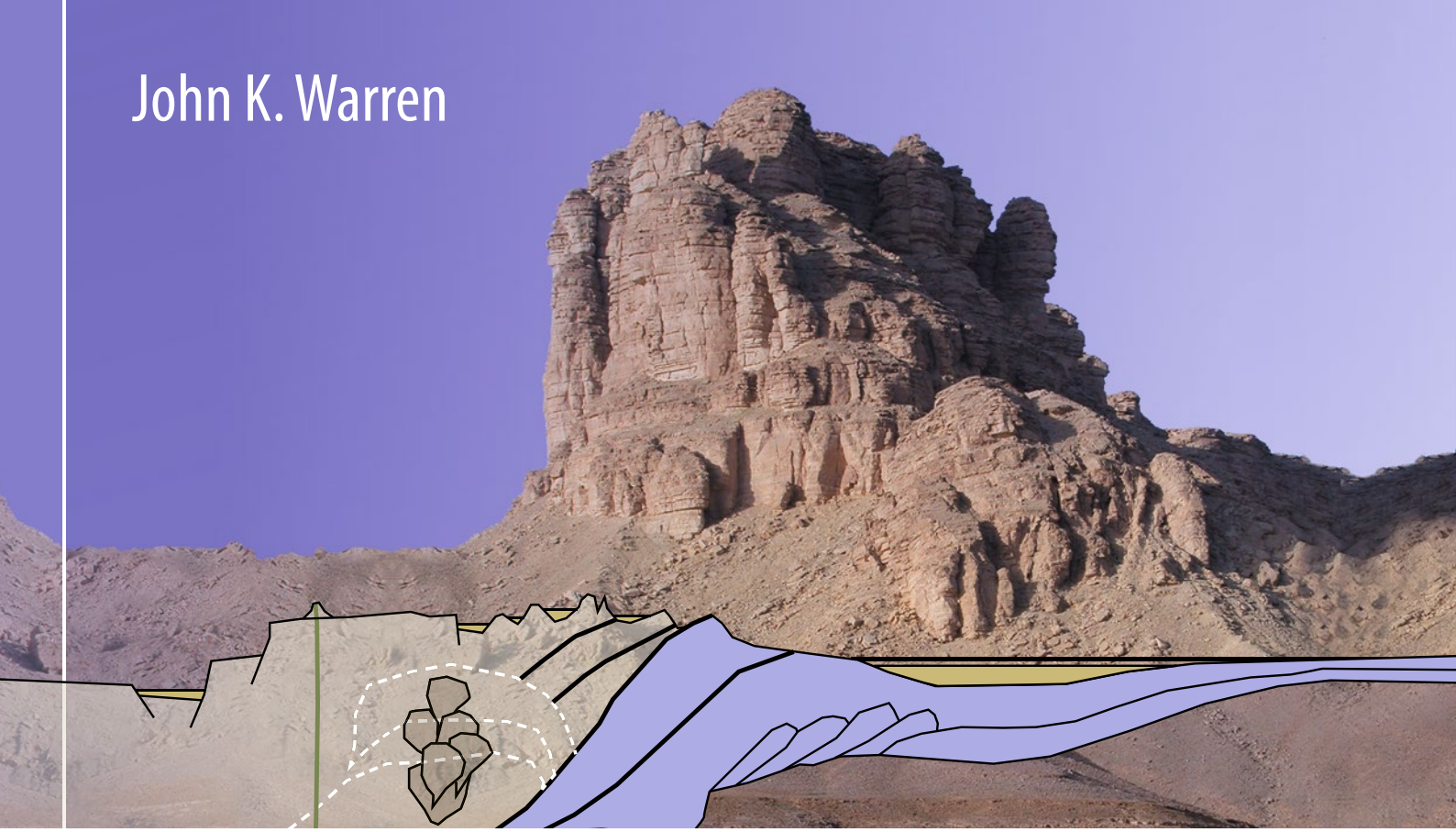

Evaporites

A Geological Compendium

Second Edition

Springer

Evaporites

John K. Warren

Evaporites

A Geological Compendium

Second Edition

Springer

John K. Warren
Department of Geology
Chulalongkorn University
Bangkok
Thailand

ISBN 978-3-319-13511-3 ISBN 978-3-319-13512-0 (eBook)
DOI 10.1007/978-3-319-13512-0

Library of Congress Control Number: 2015959844

Springer Cham Heidelberg New York Dordrecht London
© Springer International Publishing Switzerland 2016
This work is subject to copyright. All rights are reserved by the Publisher, whether the whole or part of the material is concerned, specifically the rights of translation, reprinting, reuse of illustrations, recitation, broadcasting, reproduction on microfilms or in any other physical way, and transmission or information storage and retrieval, electronic adaptation, computer software, or by similar or dissimilar methodology now known or hereafter developed.
The use of general descriptive names, registered names, trademarks, service marks, etc. in this publication does not imply, even in the absence of a specific statement, that such names are exempt from the relevant protective laws and regulations and therefore free for general use.
The publisher, the authors and the editors are safe to assume that the advice and information in this book are believed to be true and accurate at the date of publication. Neither the publisher nor the authors or the editors give a warranty, express or implied, with respect to the material contained herein or for any errors or omissions that may have been made.

Printed on acid-free paper

Springer International Publishing AG Switzerland is part of Springer Science+Business Media (www.springer.com)

For my wife, Jennifer
my sons,
Matthew and Tristan

Eppur si muove
(And yet, it does move)
Galileo Galilei after recanting Copernican beliefs

Preface

So here it is, most of the way through 2015, 8 years after my last effort on this topic, and I am writing yet another preface to yet another edition on evaporites. Once again, my aim is to give you, the reader, a timely overview of our current understanding of all matters evaporitic. That is why the reference list is now the length of a novella and I have added three new chapter topics compared to the 2006 incarnation. And, to massage my ego, I have included the word compendium in the title.

For the first time, the publishers have allowed me to compile an all-colour version, rather than grey-scale. As the use of paper copy for scientific publishing recedes, publishers are finally moving into the digital world, sometimes scratching and screaming. Then again, copyright and intellectual property issues related to information and intellectual property on the internet will be an earner for the legal profession for decades to come. A digital base to any scientific compilation allows a breadth of coverage in the topics and an accessibility to information that is unprecedented, as in all other scientific fields. You can see this evolution in information access in the page lengths in each of my four books on evaporites. The first, in 1989, was a few hundred pages long; the second in 1999, was over 500 pages; the penultimate effort, published in 2006 was over 1,000 pages long; and this current effort runs to more than 1,800 A4 pages.

Yet I now store and access the hi-res digital version of the complete volume, along with numerous other volumes, as a side issue of the use of my smart-phone. On the same device I can link to, search, review and download copies of all related digital information anywhere in the world I can access the net. Needless to say, this is one old-fart scientist who is impressed by this technology. It is a far cry from the 128k Mac that in the mid-1980s I lugged to a house on the coast of Denmark, along with three shipping cases of photocopied references in order to write the first book. On the downside, open internet access has led to a plethora of cacography, prattle and unsubstantiated opinion given as fact.

In this volume I make much more use of online sources, outside the various libraries and subscribed publishing websites. This makes many of the issues and data compilations discussed in this book, both more current and perhaps more relevant but also more readily dated and updatable at the same time. As I sift through much of the unscientific chaff that is presented as fact on the internet, I am very aware of both the strengths and current weaknesses of science conducted on the internet. Outside of the mainstream literature from subscribed publishers and some democratic government bodies, much online material is opinionated and/or uploaded with minimal peer review. As with much educational policy in the Western world these days, the internet approach is by its nature multicultural, largely non-judgemental, non-authoritarian and unfortunately, in terms of science, often phrased in terms of political correctness.

As a rationalist and a non-theist, I welcome the vast increase in freely available knowledge the internet brings. But I worry that logic and rationalism, which underpin all valid science is being lost in many places of education across the developed world. It is swamped in a tsunami of opinionated quasi-superstitious information. In science, not all points of view are equally valid, there are testable hypotheses and then there is opinionated bumpf. One expects the latter from politicians and religious zealots, unfortunately it has entered

matters that should be science-based, such as much of the current climate change discussion, as well as environmental discussions related, for example, to aforesaid climate change, hydrofracing in shale gas exploration, and other low-cost energy-recovery methodologies, as well as the relative merits of vaccinating children and the use of genetically modified crops. It says something about one's intellectual approach to a scientific problem if you tend to use the term skeptic as a pejorative.

Besides the scientific effort involved in writing this book, in order to give the volume broad utility and consistency, a good proportion of the blood, sweat and tears that I put into this volume involved preparing numerous colour illustrations and tables. I hope I have given improved value to the various authors listed, in my converting, compiling and revamping what were mostly their grey-scale and line drawings into Bezier-based colour outputs (all scaled figures with north to top, unless denoted otherwise). For this, thanks also to Saltwork Consultancy Pte Ltd for giving me permission to publish aspects of their evaporite GIS datasets as figures in this volume. In the digital form of this volume, figures should be extractable through any PDF reader and I hope will make a useful teaching and research resource for presentations and writings for anyone interested in matters evaporitic.

I would like to thank the various companies: Chevron Thailand, PDO, PTTEP, SaltWork Consultants Pte Ltd; Shell Brunei, Shell Oman and Statoil, who for the last 20 years have paid my salary allowing me to work as a company-sponsored academic in universities in interesting regions of the world where academic bureaucracy is subjugated to the peoples' thirst for education. So thanks as well, to my host universities of the past two decades: Universiti Brunei Darussalam, Sultan Qaboos University of Oman and Chulalongkorn University, Bangkok. This support has meant my academic teaching for the past 20 years has been based in developing world, in various places where you can be a full-time academic, publish and do research without being involved in the petty bureaucratic politics and political correctness that today plagues the efficiency of most federally and state-funded universities of the Western world.

Most importantly and most completely, my thanks to my wife Jennifer, who even after more than 40 years of marriage still manages to live with her at times abstracted other half.

Bangkok, Thailand John K. Warren

Contents

1 Interpreting Evaporite Textures 1
What is an Evaporite? 1
Solar-Heated Brine Concentration 1
Cryogenic and Other Non-solar Saline Mechanisms 2
Burial and Hydrothermal Salts 5
So, What Exactly Is an Evaporite? 8
Primary Evaporitic Carbonates 12
Carbonate Laminites (Subaqueous?) 13
Strandzone Associations: Microbialites, Pisolites and Tepees 14
Vadose Pisolites, Ooids and Coated Grains 32
Tepees 35
Carbonates: Present and Past 37
Primary Evaporite Salts 39
Gypsum Beds 39
Halite Beds (Chevrons and Crusts) 44
Pedogenic and Wind Reworked Salts 48
Laminites from Settling of Pelagic Salts 54
Salt Reefs, Are They Real? 58
Secondary (Diagenetic) Evaporites 60
Intrasediment Salts 60
Syndepositional Karst in Crusts 62
Shallow Mineralogic Re-equilibration 65
Burial of Sulphate Evaporites 69
Evaporites as Uplift Indicators (Tertiary Evaporites) 74
Fibrous Gypsum and Halite (Satinspar) 76
Anhydrite Rehydration at the Microscale 79
Saline Clay Authigenesis 80
Textural Synthesis 83

2 Depositional Chemistry and Hydrology 85
Quaternary Deserts and Evaporite Assumptions 85
Quaternary Evaporites in a Köppen Climatic Framework 92
Local Variations in Climate 98
Chemical Evolution of Surface and Nearsurface Brines 103
Marine Brines 103
Nonmarine Brines 112
Separating Marine from Nonmarine 120
Back Reactions 121
Marine Aerosols and Continental Gypsum 123
Acid Groundwater in Continental Saline Systems 127

Indicators of Brine Parenthood 132
Bromine Profiles – Parentage or Stability? 132
Sulphur and Oxygen Isotopes 135
Boron Isotopes 138
Chlorine Isotopes 140
Fluid Inclusions and Brine Temperatures 144
Seawater Evolution 147
A Phanerozoic Dilemma: Marine Versus Nonmarine Potash? 147
Precambrian Oceanic Chemistry 153
Precambrian-Cambrian Transition 159
Hydrology Is Depositional Style 162
Active Phreatic/Vadose Regime 162
Hydrologies in Saline Basins 163
Mudflat Aggradation Mirrors Watertable Change 168
Indicators of Fluctuating Watertables 169
Degrading Hydrology and Playa Capture 175
Remote Sensing of Saline Hydrologies 177
Salinity Stratification Controls Texture 185
Brine Stability and Evaporite Textures 188
Brine Reflux Drives Substrate Alteration 190
Can Reflux Really Work? 196
Importance of Hydrographic Isolation 198
Extraterrestrial Hydrologies, "Freeze-Dried" Salts, and the Meaning of Life 201

3 Sabkhas, Saline Mudflats and Pans 207
Introduction 207
What Is a Sabkha? 210
Marine Coastal Sabkhas 211
Carbonate-Hosted Coastal Sabkhas in the Southern Arabian Gulf 212
Siliciclastic-Hosted Coastal Sabkhas, Western and Northern Arabian Gulf 231
Other Coastal Sabkhas 240
Interpretive Limitations of Holocene Sabkha Models 249
Lacustrine Sabkhas and Pans 251
Depositional Characteristics 251
Styles of Continental Sabkhas 256
Salt-Pans (Marshes) and Diapirs 299
Why and Where of Sabkhas & Pans? 301

4 Subaqueous Salts: Salinas and Perennial Lakes 303
Introduction 303
Sea-Margin Subaqueous Salts 305
Coastal Salinas of Australia 305
Coastal Salinas of the Middle East 316
South American Salinas and Dolomite 321
Continental Subaqueous Basins 324
Perennial Saline Lakes 324
Lake Asal, Republic of Djibouti 372
Are Modern Saline Lakes all Shallow? 374

5 Ancient Basins and Stratigraphic Evolution 381
Introduction 381
Linking Present to Past Aridity 382
Varying Extent of Ancient Evaporites 388
Building Blocks of Ancient Salt Beds 393
Evaporites: Broad-Scale Depositional Models 398

Problems in Correlation *Sans* Hydrology 437
Dolomite Aprons in a Drawdown Basin 440
Sequence Stratigraphy in Evaporite Basins? 443
Does Sealevel Control Salt Sequence Boundaries? 446
Icehouse and Greenhouse Eustasy 447
Basinwide Evaporites 451
Basinwide Examples 454
Summary 490

6 Flowing Salt: Halokinesis 491
Introduction 491
Physics of Salt Systems 494
Density, Viscosity, Strength & Buoyancy 494
Thermal Effects 503
Flow Textures and Rates 504
Triggers, Drivers and Outcomes of Salt Flow 510
Diapirs and Extension 512
Diapirism and Differential Loading 514
Sedimentation Rate Controls Diapir Shape 516
Extension, Falling Diapirs and Turtles 518
Falling Diapirs Drive Raft Tectonics 519
Salt as Sheets, Allochthons and Breakouts 521
Inflation, Deflation, Welds and Basal (Subsalt) Shear Zones 524
Near-Diapir Suprasalt Shear (Drag Zones) 534
Welds, Loading Detachments and Growth Faults 536
Fault Families in Allochthons 545
Linking Allochthons at the Basin Scale 548
Compressional Salt Tectonics 551
Shortening with Gravity Gliding 552
Thin-Skinned Fold and Thrust Belts 558
Inverted Salt Basins 563
Mild Shortening in Tectonically Confined Basins 564
Salt Extruding Today? 571
Browne Formation Oldest Known Salt 580
Sediments and Flowing Salt 583
Sedimentation and Evolving Salt Structures 585
Sediments Tied to Salt Basin Evolution 593
Subsalt Sections 600
Caprock Formation (Diagenesis of Salt) 600
Complications of Shale Diapirism 605
Summary 612

7 Salt Dissolution and Pointers to Vanished Evaporites: Karst, Breccia, Nodules and Cement 613
Introduction 613
Evaporite Landforms 618
Local Scale Karst 618
Regional-Scale Karst 624
Salt Dissolution: Solution Breccias and Residues 639
Defining Evaporite Dissolution Breccia 639
Bedded Solution-Collapse Breccias 641
Breccia Extent 645
Diapiric Solution Breccias 650
Diapiric Versus Salt Ablation (Retreat) Breccias 654
Salt-Cored Thrust and Fold Breccias, Rauhwacke and Orogeny 656

Partial Salt Dissolution: Residues of Less-Soluble Salts . . . 665
Focused Rapid Dissolution – Evaporite Clasts . . . 666
Diffuse Dissolution -Markers and Residue Beds . . . 667
Basal Anhydrite, Thailand . . . 672
Caves in Evaporite Karst . . . 674
Gypsum Caves . . . 675
Halite Caves . . . 685
Evaporite Speleothems in Non-evaporite Karstified Host . . . 691
Hazards Tied to Evaporite Karst . . . 692
Problems in the Ripon Area, UK . . . 694
Problems with Miocene gypsum, Spain . . . 697
Gypsum Karst in Mosul, Iraq . . . 699
Coping: Man-made Structures Atop Salts . . . 699
Solving the Problem? . . . 703
Sulphuric Acid Speleogenesis . . . 704
Mineralised Hypogene Breccias . . . 712
Filled Vugs and Nodules . . . 715
Silicified Evaporites . . . 716
Calcitisation and Dedolomitisation . . . 724
Celestite as an Evaporite Indicator? . . . 735
Fluorite as an Indicator? . . . 743
Baryte as an Indicator? . . . 747
Authigenic Anhydrite as a Burial Salt . . . 753
Enigmatic Outlines in Pseudomorphs . . . 758
Summary . . . 760

8 Hypersaline Fluid Evolution During Burial and Uplift . . . 763
Basin-Scale Burial Hydrology . . . 763
Fluids in Subsiding Basins . . . 769
Compactional Fluids . . . 769
Thermobaric-Thermohaline Fluids . . . 770
Deep Flow in Pull-Apart Basins . . . 774
Flow in and Adjacent to Collision Belts . . . 775
Flow in Post-Orogenic Hydrologically-Mature Basins . . . 780
Alteration, Pressure Cells and Salinity-Driven Convection . . . 786
Haloes, Convection and Saltout . . . 786
Evaporites as Pressure Seals . . . 789
Salt-Maintained Overpressure . . . 792
Controlling Unpredicted Pressure Changes . . . 802
Drilling Mud Chemistry in Salt Systems . . . 804
Salt-Generated Underpressure . . . 805
Temperature Anomalies and Brine Flow . . . 806
Fluid Flow in Halokinetic Basins . . . 809
Suprasalt Fluid Flow and Alteration . . . 809
Burial Dewatering of Hydrated Salts . . . 814
Brine-Rock Burial Evolution . . . 818
Brine Chemistry at Depth . . . 819
Effects and Indications of Water-Salt Interactions . . . 824
Crustal Cycling of Brines? . . . 826

9 Halotolerant Life in Feast or Famine: Organic Sources of Hydrocarbons and Fixers of Metals . . . 833
Introduction . . . 833
Evaporitic Source Rocks . . . 837

Halobiota: Adaptations and Bio Markers . . . 853
Metabolic Pathways in Producers and Consumers . . . 854
Light Dwellers and Pigmentation . . . 856
Non-photosynthesizers and Layering . . . 860
Salinity Tolerance . . . 864
Primary Producers (Photosynthesizers) . . . 864
Halobiotal Heterotrophs (Consumers) . . . 873
Cellular Adaptations to Hypersalinity . . . 884
Life in a Layered Microbial Mat? . . . 888
Biomarkers and Microbial Responses to Changing Salinities . . . 890
Do Biomarkers Indicate Hypersalinity? . . . 893
Organic Enrichment . . . 898
Biological Responses to Variably Layered Brines: Cycles of "Feast or Famine" . . . 900
The Where and When of Productivity . . . 912
Life, Brine Seeps and Dissolving Salts . . . 919
Geological and Hydrological Features . . . 919
Life, Fe and Sulphur in Seafloor Brine Lakes . . . 923
Rim Life, CH_4 and H_2S in Seafloor Brine Lakes . . . 930
Hardgrounds, Settings and Stable Isotopes . . . 933
Ancient Saline Seeps . . . 935
Life in the Saline Subsurface . . . 939
Bacterial Sulphate Reduction (BSR) . . . 940
Thermochemical Sulphate Reduction (TSR) . . . 945
H_2S, Natural Gas and Metallogeny . . . 949
Hydrothermal Cracking in Saline Rift Lakes . . . 952
Summary . . . 955

10 Hydrocarbons and Evaporites . . . 959
Introduction . . . 959
Seal Capacity of Evaporites . . . 965
So Why Do Evaporites Seal? . . . 965
Environments Favouring Seal Continuity . . . 968
Reservoirs and Traps . . . 971
Bedded Salt Seals . . . 971
Exploration Paradigms in the Bedded Evaporite Hydrocarbon Association . . . 1025
Halokinetic Salt Traps . . . 1031
Supradiapiric Traps . . . 1032
Tiered Allochthon Plays in the Deepwater Realm . . . 1038
Minibasin Plays . . . 1047
Intrasalt Halokinetic Plays . . . 1049
Subsalt Reservoirs in Compressional Evaporite Provinces . . . 1063
Evaporite Dissolution . . . 1073
Athabasca Tar Sands, Western Canada . . . 1077

11 Potash Resources: Occurrences and Controls . . . 1081
Introduction . . . 1081
Production and Consumption . . . 1085
Ore Extraction Technologies . . . 1088
Conventional Mining . . . 1088
Solution Mining of Potash . . . 1095
Lake Brine Processing and Solution Chemistry . . . 1096
Ore Beneficiation . . . 1096

Quaternary Potash 1100
Playas of the Qaidam Basin 1100
Danakil Depression, Ethiopia 1109
Inland Chotts and Coastal Sabkhas in North Africa 1119
Potash from Brine 1124
Ancient (Pre-Quaternary) Potash 1136
Upper Rhine Graben, France 1136
Khorat Plateau, Thailand 1139
Cretaceous Trans-Atlantic Potash 1145
Moroccan Meseta (Late Triassic) 1148
Permian Potash 1149
German Potash (Z1, Z2 and Z3 Potash) 1149
Z3 – Boulby Potash, UK 1150
New Mexico Potash, USA 1154
Upper Kama Potash Region, Cis-Urals Russia 1156
Canadian Maritimes (Mississippian of Nova Scotia and New Brunswick) 1160
West Canadian Potash (Devonian) 1163
Pripyat Basin (Devonian) Belarus 1168
Other Significant Deposits 1170
So, How Does Mineable Potash Form? 1172
Controls on Potash Quality: Anomalies, Leaching and Problematic Mine Waters 1174
Potash Occurrence and Quality at the Worldscale 1181

12 Non-Potash Salts: Borates, Na-Sulphates, Na-Carbonate, Lithium Salts, Gypsum, Halite and Zolites 1187
Introduction 1187
Borate Salts (Tincals) 1187
Character, History and Processing 1187
Geology of Borates 1192
Evaporitic Borates and the Evolution of Life 1209
Sodium Sulphate Salts (Salt Cake) 1209
Character and History 1209
Canadian Brine Extraction 1216
Karabogazgol Brines, Turkmenistan 1220
Laguna Del Ray Brines, Mexico 1224
Spanish Glauberite Mines 1226
Turkish Deposits 1228
Other Sodium Sulphate Deposits 1231
Sodium Carbonate Salts (Soda ash) 1233
Character and Extraction History 1233
Trona in North America 1238
Natural Soda Ash in China 1242
Trona in the African Rift 1244
$CaSO_4$ and NaCl 1246
Calcium Sulphate (Gypsum) 1246
Rock and Pan Salt (Halite) 1249
Lithium and $CaCl_2$ Brines, Iodine and Bromine 1256
Lithium Brines 1256
$CaCl_2$ Brines and Minerals 1268
Iodine 1273
Bromine 1277
Nitrate Salts (Nitratite and Saltpetre) 1278

Magnesite and Magnesia Salts . . . 1282
Sulphur Salts (Brimstone) . . . 1287
Usage History and Industry Trends . . . 1287
Types of Natural Sulphur Deposits . . . 1289
Biology of Native Sulphur . . . 1290
Occurrences and Textures . . . 1290
Zeolites – Molecular Sieves . . . 1292
Usage and Production . . . 1293
Geological Controls on Saline Zeolitisation . . . 1294
Summary . . . 1300

13 Solution Mining and Salt Cavern Usage . . . 1303
Introduction . . . 1303
The Solution Mining Process . . . 1304
History of Salt Solution Wells . . . 1304
Well and Cavern Design . . . 1306
Solution Well Styles . . . 1309
Techniques in Potash Operations . . . 1310
Lithology Effects Shape . . . 1312
Well Pad Design . . . 1314
Blinding and Phase Chemistry . . . 1316
Phase Chemistry – Trona Solution Mining . . . 1316
Use of Salt Caverns . . . 1318
Energy Liquids & Compressed Air Storage . . . 1318
Waste Disposal . . . 1323
Problems in Salt Solution Mines, Conventional Mines, Well-Bores and Storage Facilities . . . 1325
Case Histories: Caving Brinefields . . . 1326
Case Histories: Caving and Leaking Wells . . . 1343
Case Histories: Storage Cavern Problems . . . 1357
Gas Escape, Explosions and Fires from Cavern Leaks . . . 1359
Recognising and Preventing Potential Cavern Problems . . . 1366
Salt Creep . . . 1366
Salt Falls Versus Roof Collapses . . . 1368
Ground Subsidence . . . 1369
Surface Indicators of Breached Caverns . . . 1370
Monitoring and Minimizing Collapse . . . 1371
Natural or Anthropogenic Subsidence? . . . 1371
So How Stable is a Storage Cavern? . . . 1372
Cavern Plugging . . . 1372
Summary . . . 1374

14 Meta-evaporites . . . 1375
Introduction . . . 1375
World-Scale Tectonism . . . 1379
Many Meta-evaporites are Pre-Neoproterozoic . . . 1381
Protoliths Across the First 2 Billion Years . . . 1384
Metamorphism: Onset and Evolution . . . 1387
Thrust Belts; Dynamic or Regional Metamorphism . . . 1387
Meta-evaporite Mineral Associations . . . 1394
Scapolite and Scapolitization . . . 1394
Albitites and Albitization . . . 1401
Tourmaline and Tourmalinisation . . . 1405
Sodian Phyllosilicates and Talc . . . 1414
Precious Stones as Meta-evaporites . . . 1417
Elevated Magnesium Levels in Metasediments . . . 1428

Meta-evaporite Examples. 1430
Examples in the Greenschist Realm 1430
Examples in the Amphibolite/Granulite Realm 1438
Implications 1468

15 Lower Temperature Metals in an Evaporitic Framework 1469
Introduction 1469
A Little Classification/Exploration Philosophy 1473
Evaporite-Related Metalliferous Brines?. 1474
Modern Basin Brines: Composition 1476
Basinal Brines: Metal Carrying Capacity 1480
Low Temperature Sediment-Hosted Ore Deposits (Evaporite-Related) 1490
Red Sea – Modern Metalliferous Brine Lake Laminite Beds 1491
Stratiform Copper Deposits (Salt-Related) 1498
Stratiform Cu Halokinetic-Salt Associations 1500
Sediment-Hosted Cu in Bedded Evaporite Context 1516
Stratiform Sediment Hosted Pb-Zn Deposits (Salt-Related) 1524
Evaporite Associated MVT Deposits 1525
Evaporite-Associated SedEx Deposits 1563
Arid-Zone Diagenetic Uranium
and Copper Associations 1584
Duricrusts: Yilgarn Australia
and Namibe, Africa 1584
Porphyry Copper, Supergene Enrichment and Aridity 1586
Base Metals, Evaporites and Diagenetic Accumulations: A Summary 1588

16 Magma-Evaporite-Hydrothermal Metal Associations 1591
Introduction 1591
Metal Transport in the High Temperature Saline Realm 1593
Regional Orthomagmatic- Evaporite Interactions 1595
Orthomagmatic Ni-Cu Associations with Evaporites
as a Sulphur Source 1596
Paramagmatic Interactions. 1602
Cooking the Salt: Dykes and Sills in Salt 1602
Molten Salts: Natrocarbonatite and Brine. 1606
Phreatomagmatic Iron-Rich Associations 1609
Korshunovsky (Korshunovskoye) Iron Ore Deposits, Siberia 1609
Paramagmatic Saline Haloes 1610
Iron-Oxide Copper Gold (IOCG) Deposits. 1616
IOCG in an Evaporite/Basinal Brine Milieu 1620
So What Is a IOCG Deposit and Is Mineralisation
Evaporite/Brine Related? 1640
Hydrothermal (Non-evaporitic) Salts and Metalliferous VHMS Deposits 1643
VHMS Deposits in Subduction-Related Island-Arc Settings:
Kuroko-Style Deposits 1646
VHMS Deposits with Thermal Anhydrites at mid Ocean
and Back-Arc Spreading Centres 1650
VHMS Deposits with Hydrothermal Anhydrite at Sediment-Covered
Spreading Centres: Besshi-Style and the Guaymas Basin 1654
Evaporites and Metalliferous Deposits 1656

References 1659

Index 1783

Interpreting Evaporite Textures

1

What is an Evaporite?

I define an evaporite as a salt rock that was originally precipitated from a saturated surface or nearsurface brine in hydrologies driven by solar evaporation (Fig. 1.1a). This simple definition encompasses a wide range of chemically precipitated salts and includes alkali earth carbonates (Table 1.1). Some workers restrict the term evaporite to salts formed at the earth's surface via solar evaporation of hypersaline waters. To underscore the highly reactive nature of evaporites in the sedimentary realm I think of such evaporites as primary, that is, precipitated from a standing body of surface brine and retaining crystallographic evidence of the depositional/hydrological process set where they formed (e.g. bottom-nucleated or current-derived textures). Outside of a few Neogene examples, there are few ancient evaporite beds with textures that are wholly and completely "primary." Most in the subsurface exhibit "secondary" (burial-related) textures, while remnants that have be uplifted back to the surface show "tertiary" (exhumation-related) overprints (Figs. 1.2 and 1.9).

We can contrast the solar-driven set of precipitative processes with other surface and subsurface water-loss mechanisms that can form bodies and beds of mineral salts, with the same chemical compositions as rocks typically called evaporites as listed in Table 1.1. And yet, if applying the term evaporite in its strictest form (i.e., a response to solar-driven evaporation), this second group of mineral salts/sediments are not "true" evaporites; rather, they are mineral salts that crystallized in response to various cryogenic, hydrothermal and burial processes.

Solar-Heated Brine Concentration

In its broadest definition, evaporation is the process by which molecules in a liquid (water) spontaneously become gaseous (water vapour) and escape the liquid state, while evaporites are the resultant mineral precipitates accumulating in and around an increasingly saline residual brine that has reached a state of supersaturation with respect to a particular mineral salt or salts. Water molecules in the liquid phase are in continuous motion and so will collide. As they collide, they transfer energy to each other in varying degrees, based on how they collide. Evaporation, then, is a simple matter of solution kinetics in this milieu of molecular motion and is a response to varying degrees of heat absorption at the molecular scale.

On average, water molecules within a standing at-surface brine lake or in near-surface pore spaces, near a watertable and its associated capillary zone, do not have enough kinetic energy to escape the liquid phase and so cross the surface tension barrier. Otherwise, liquid water would turn to vapour spontaneously, any at-surface liquid phase would spontaneously disappear, while recharge to an underlying watertable would be an impossibility. Every so often, the level of solar energy transfer (heat absorption) at the molecular collision site is sufficient to give a water molecule (near the water-air interface) the heat energy necessary to pass into the vapour phase and so exit the liquid water mass (Fig. 1.1a). That is, for a water molecule to escape into the vapour phase it must absorb heat energy, be located near the liquid surface, be moving in the proper direction and have sufficient energy to overcome liquid phase intermolecular forces and pass through the surface tension interface. As the concentration of the residual brine increases the specific heat capacity decreases and the density increases (Fig. 1.1b, c). Specific heat is a measure of how much heat is required to raise the temperature of the brine by 1 °C.

In the absence of air movement, water vapour so created resides within the region immediately above the air-brine interface, or in the vapour phase in the gaseous portion near the top of the capillary zone, immediately below the land surface and above the watertable. Typically, the rate of evaporation atop a standing brine body, or in the uppermost few centimetres of a sabkha mudflat, increases with increasing temperature and decreases with increasing salinity (Bonython 1966). It also increases with the passage of dry winds over

© Springer International Publishing Switzerland 2016

J.K. Warren, *Evaporites: A Geological Compendium*, DOI 10.1007/978-3-319-13512-0_1

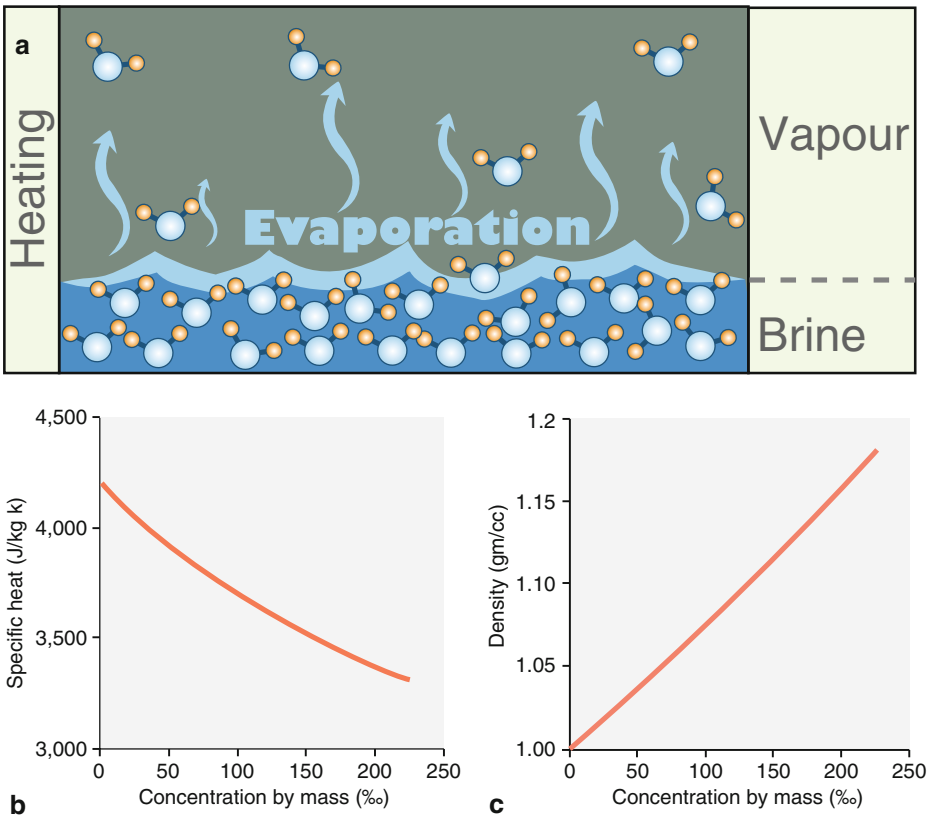

Fig. 1.1 Brine formation by loss of liquid water volume and can occur at any liquid water surface, either at the surface of a standing water body or in a pore. (**a**) Evaporation: the rate of evaporation and consequent rate of brine formation is controlled by rate of molecular passage of H_2O across the vapour – liquid interface. (**b**) Decrease in specific heat with increase in concentration of NaCl solution. (**c**) Increase in density with increase in concentration of NaCl concentration

the brine lake or mudflat as this removes the overlying mass of an otherwise static water vapour cloud. If the water vapour layer is not blown away, it becomes increasingly saturated (humid) and so slows the rate of evaporation, even as the salinity of the underlying water mass increases (Chap. 2). In contrast, if the temperature atop the air-brine interface decreases, the vapour phase can pass back into the liquid phase via condensation. This explains the moisture droplets that form overnight in many saline arid settings and coat rock and salt crust surfaces in the early mornings in most coastal sabkhas. Condensation (not rainfall) explains many of the microkarst runnels that decorate the surfaces in intercrystal vadose contacts of subaerial halite crusts, so obvious in salars in the Andes and in the salt crusts that make up the Devil's Golf Course in Death Valley, California.

Cryogenic and Other Non-solar Saline Mechanisms

In contrast to the formation of evaporite minerals by solar-driven evaporation (heating) of surface and nearsurface waters in hot arid and semi-arid climatic settings, cryogenic brines and associated salts require temperatures at or below the freezing point of the liquid phase. Cryogenic salts, such as hydrohalite, mirabilite, antarcticite and epsomite, can then accumulate. They crystallize in a cold, near-freezing, residual brine as it concentrates via the loss of its liquid phase, which is converting/solidifying to ice (Fig. 1.3a). As brine concentration increases, the freezing temperature deceases (Fig. 1.3b). Hydrohalite is a stable precipitate in a freezing brine only when the water temperature is below 0 °C (Fig. 1.4a).

Hydrohalite ($NaCl{\cdot}2H_2O$) crystals have pseudo-hexagonal cross sections and are found in a number of modern cold saline lakes. Craig et al. (1974) collected hydrohalite from the lake bottom in saline Lake Bonney in Antarctica, where bottom water temperatures vary between +2.0 and −2.0 °C. Nikolaevsky (1938) observed hydrohalite forming in winter in the Baskunchak salt lake, northwest of the Caspian Sea (48°N latitude). It was seen to form on two occasions when formative brine temperatures were between −3 and −23 °C, while in summer halite precipitates. Hydrohalite also occurs in bottom sediments in salt-saturated cryogenic lakes in Saskatchewan, at about 51°N latitude, and has been observed in nearby saline springs sediments of the Northern Great Plains (Last 1989a). Hydrohalite pseudomorphs occur as halite crystals with hexagonal cross sections in cores some 100–140 m deep, in Death Valley, California, indicating NaCl cryogenesis has occurred in the Pleistocene Death Valley Lake from brines with temperatures that were less than 0 °C (Roberts et al. 1997). The climatic significance

Table 1.1 Major evaporite minerals: less saline alkaline earth carbonates or evaporitic carbonates are indicated by **, the remainder are the more saline evaporite salts

Mineral	Formula	Mineral	Formula
Anhydrite	$CaSO_4$	Leonhardtite	$MgSO_4{\cdot}4H_2O$
Antarcticite	$CaCl_2{\cdot}6H_2O$	Leonite	$MgSO_4{\cdot}K_2SO_4{\cdot}4H_2O$
Aphthitalite (glaserite)	$K_2SO_4{\cdot}(Na,K)SO_4$	Loewite	$2MgSO_4{\cdot}2Na_2SO4{\cdot}5H_2O$
Aragonite**	$CaCO_3$	Mg-calcite**	$(Mg_xCa_{1-x})CO_3$
Bassanite	$CaSO_4{\cdot}1/2H_2O$	Magnesite**	$MgCO_3$
Bischofite	$MgCl_2{\cdot}6H_2O$	Meyerhoffite	$Ca_2B_5O_{11}{\cdot}7H_2O$
Bloedite (astrakanite)	$Na_2SO_4{\cdot}MgSO_4{\cdot}4H_2O$	Mirabilite	$Na_2SO_4{\cdot}10H_2O$
Borax (tincal)	$Na_2B_4O_7{\cdot}10H_2O$	Nahcolite	$NaHCO_3$
Boracite	$Mg_3B_7O_{13}{\cdot}Cl$	Natron	$Na_2CO_3{\cdot}10H_2O$
Burkeite	$Na_2CO_3{\cdot}2Na_2SO_4$	Nitratite (soda nitre)	$NaNO_3$
Calcite**	$CaCO_3$	Nitre (salt petre)	KNO_3
Carnallite	$MgCl_2{\cdot}KCl{\cdot}6H_2O$	Pentahydrite	$MgSO_4{\cdot}5H_2O$
Colemanite	$Ca_2B_5O_{11}{\cdot}5H_2O$	Pirssonite	$CaCO_3{\cdot}Na_2CO_3{\cdot}2H_2O$
Darapskite	$NaSO_4{\cdot}NaNO_3{\cdot}H_2O$	Polyhalite	$2CaSO_4{\cdot}MgSO_4{\cdot}K_2SO_4{\cdot}H_2O$
Dolomite**	$Ca_{(1+x)}Mg_{(1-x)}(CO_3)_2$	Proberite	$NaCaB_5O_9{\cdot}5H_2O$
Epsomite	$MgSO_4{\cdot}7H_2O$	Priceite (pandermite)	$CaB_4O_{10}{\cdot}7H_2O$
Ferronatrite	$3NaSO_4{\cdot}Fe_2(SO_4)_3{\cdot}6H_2O$	Rinneite	$FeCl_2{\cdot}NaCl{\cdot}3KCl$
Gaylussite	$CaCO_3{\cdot}Na_2CO_3{\cdot}5H_2O$	Sanderite	$MgSO_4{\cdot}2H_2O$
Glauberite	$CaSO_4{\cdot}Na_2SO_4$	Schoenite (picromerite)	$MgSO_4{\cdot}K_2SO_4{\cdot}6H_2O$
Gypsum	$CaSO_4{\cdot}2H_2O$	Shortite	$2CaCO_3{\cdot}Na_2CO_3$
Halite	NaCl	Sylvite	KCl
Hanksite	$9Na_2SO_4{\cdot}2Na_2CO_3{\cdot}KCl$	Syngenite	$CaSO_4{\cdot}K_2SO_4{\cdot}H_2O$
Hexahydrite	$MgSO_4{\cdot}6H_2O$	Tachyhydrite	$CaCl_2{\cdot}2MgCl_2{\cdot}12H_2O$
Howlite	$H_5Ca_2SiB_5O_{14}$	Thernadite	Na_2SO_4
Ikaite**	$CaCO_3{\cdot}6H_2O$	Thermonatrite	$NaCO_3{\cdot}H_2O$
Inyoite	$Ca_2B_6O_{11}{\cdot}13H_2O$	Tincalconite	$Na_2B_4O_7{\cdot}5H_2O$
Kainite	$4MgSO_4{\cdot}4KCl{\cdot}11H_2O$	Trona	$NaHCO_3{\cdot}Na_2CO_3$
Kernite	$Na_2B_4O_7{\cdot}4H_2O$	Tychite	$2MgCO_3{\cdot}2NaCO_3{\cdot}Na_2SO_4$
Kieserite	$MgSO_4{\cdot}H_2O$	Ulexite	$NaCaB_5O_9{\cdot}5H_2O$
Langbeinite	$2MgSO_4{\cdot}K_2SO_4$	Vanthoffite	$MgSO_4{\cdot}3Na_2SO_4$

Documented dolomite composition ranges from $Ca_{1.16}Mg_{0.84}(CO_3)_2$ to $Ca_{0.96}Mg_{1.04}(CO_3)_2$. Less common evaporite minerals, such as borates, iodates, nitrates and zeolites are not listed here, but are discussed in detail in Chap. 12

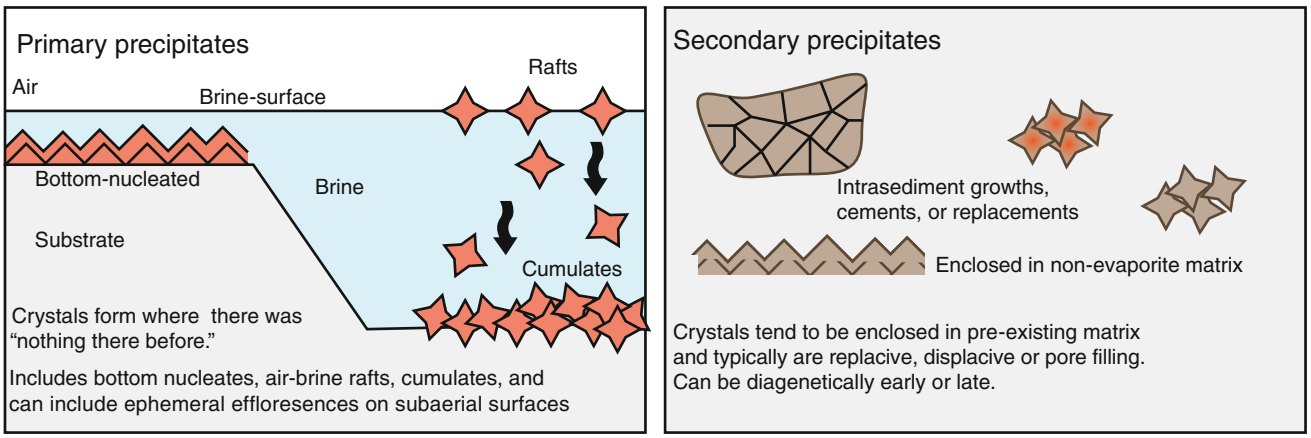

Fig. 1.2 What are primary and secondary precipitates?

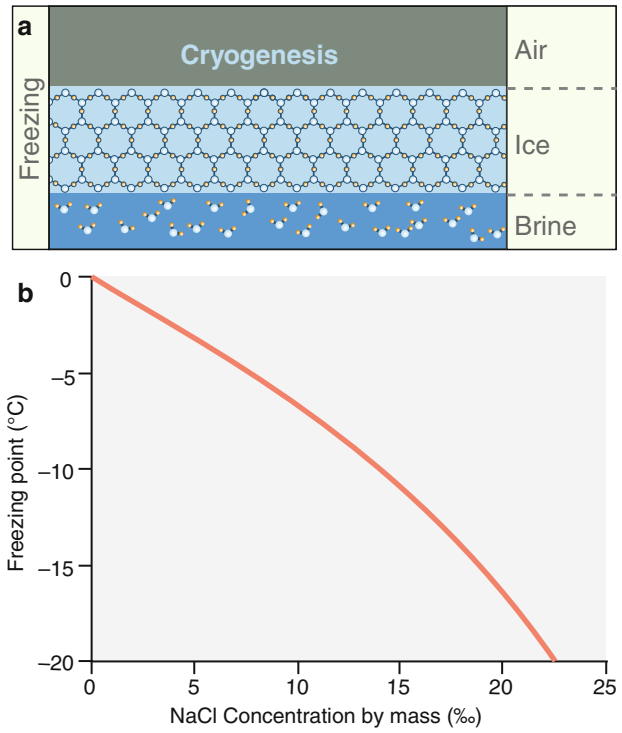

Fig. 1.3 Cryogenesis: (**a**) Brine is formed and concentrated as cations and anions are excluded from the lattice structure of ice (pure water) as it solidifies. (**b**) Brine freezing temperature falls as the NaCl concentration increases

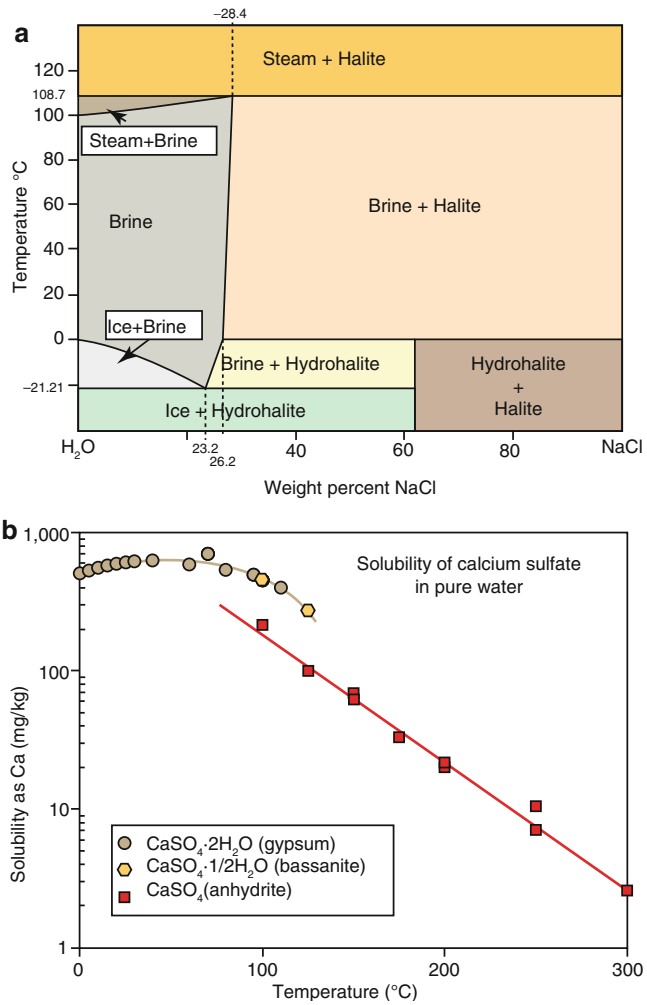

Fig. 1.4 Temperature dependence of (**a**) hydrohalite and, (**b**) $CaSO_4$ (After Cohen 1989)

of such cryogenic salt is discussed in Chap. 2, while economic deposits of cryogenic lacustrine mirabilite are discussed in detail in Chap. 12.

When polar seawaters freeze on Earth, hydrohalite and mirabilite ($Na_2SO_4{\cdot}10H_2O$) precipitate from the residual marine brines and accumulate in ice sheet fissures, or in load-induced fractures in the ice understory wherever an increasingly saline brine sinks into rocks fractures beneath ice sheets. For example, there are numerous mirabilite beds on the ice floes of the Ross Ice Shelf near Black Island. Likewise, there are dense residual saline brines in interstitial waters extracted from deep cores in sediments of McMurdo Sound (Brady and Batts 1981; Frank et al. 2010). It seems that when ice sheets retreat, the at-surface cryogenic salts dissolve in the freshened at-surface hydrology, but the dense hypersaline brines remain behind in deep fissures, held and preserved in the rock fractures (Starinsky and Katz 2003). In the extreme setting of at-surface brine freezing in small saline depressions in the Dry Valleys of Antarctica, a solid form of calcium chloride, antarcticite, grows cryogenically in what is probably the most saline perennial natural water mass in the world (47 % salinity in Don Juan Pond, Antarctica; Horita 2009).

Extraterrestrially, cryogenesis explains sulphate salt phases that typify ice crack fissures crisscrossing the surface of Europa (a moon of Jupiter) and growing seasonally in soils of Mar. Widespread gypsum is also forming via ice ablation in the circumpolar Martian dunefield (McCord et al. 1998; Wentworth et al. 2005; Masse et al. 2012). On Earth, as ground temperatures increase, cryogenic salts tend to deliquesce or convert to their high temperature daughter salts (thenardite, glauberite and halite). Worldwide, in appropriate cold climatic settings, there are also numerous examples of cryogenic hydrated calcite (ikaite-glendonite after $CaCO_3{\cdot}6H_2O$ – see James et al. 2005).

Silica is not normally considered an evaporite salt, but some forms of chert (finely crystalline silica) do accumulate as primary chemical/biochemical precipitates in evaporitic settings. For example, there are hypersaline chert-filled vugs in magnesite crusts in some of the hypersaline alkaline lakes of the Coorong region, Australia (Peterson and Von der Borch 1965) and there are abundant chert co-precipitates (early diagenetic) in Miocene lacustrine beds in the Ebro Basin, Spain (Orti et al. 2007). Then there are thermalitic opal-A cherts associated with hot springs about the edges of

many saline lakes, exemplified by the hot spring precipitates of the East African rift lakes (Owen et al. 2008). These likely-biomediated carbonate and silica terrestrial precipitates crystallize as mineral salts in somewhat saline settings, but unlike other evaporitic mineral salts, these syndepositional calcite and silica cements are not considered a possible variation on an evaporitic theme by the majority of the sedimentological scientific community.

I will leave it up to the purists to decide which of the various "heated" and "freeze-dried" salts, carbonates and silica cements that form at or near the earth's surface, in environments influenced by variations in solar radiation, are "true evaporites."

I am quite happy to call them all variations on the evaporite/mineral salt/brine theme. If not, then the classic thick widespread Quaternary-age cryogenically-formed mirabilites that evolved into the glauberite beds that underlie and typify Karabogaz Gol, and the extensive mirabilite bed in the shallow subsurface of Great Salt Lake, Utah, in two of what are considered by many to be better-known evaporite systems of the Quaternary, are not "true' evaporites. Nor are the mirabilites forming today on the floors and in the mudflats of modern salt lakes across the Canadian Plains.

Burial and Hydrothermal Salts

Substantial volumes of mineral salts, with compositions typically considered evaporite mineralogies, such as anhydrite and even halite, can precipitate in the deep subsurface of the earth in response to heating, cooling, or to increases in pore fluid salinity. None of these process sets, which can typify large parts of the crustal subsurface, are directly solar-driven. Perhaps the resulting mineral precipitates are best classified as hydrothermal or burial salts rather than "true" evaporites. In the sabkha chapter we shall see how retrograde solubility of anhydrite may drive its precipitation as modern sabkha thermalites; the same retrograde precipitation mechanism also drives the formation of burial anhydrites.

The term burial salt is a general descriptor (as defined by Warren 1999, 2006) that encompasses a set of mineral salts created by diagenetic and metamorphic processes that can precipitate mineral salts in the vicinity of a dissolving and altering subsurface salt mass (salt beds, diapirs and allochthons). This is especially so in zones where two brines mix, which premixing had different salinities and chemical constituent proportions. In the sabkha chapter we shall see how retrograde solubility of anhydrite may drive its precipitation as modern sabkha thermalites; the same retrograde precipitation mechanism also drives the formation of burial anhydrites different salinities and chemical constituent proportions. In the subsurface, such burial salts tend to form pore or fracture fills, located wherever the most permeable subsurface conduits were at the time of brine mixing and precipitation. A burial salt is not a true evaporite in that it is not formed by solar evaporation but, the fact that its ionic constituents are typically derived by the dissolution/alteration of a nearby evaporite, means most geologists consider burial salts in sedimentary basins to be evaporites. The precipitative processes driving formation of burial salts are typically heating, cooling or mixing of basinal waters of two salinities, typically derived by the dissolution of subsurface salt masses or relict hypersaline pore brines (see Chap. 2 for detailed discussion of the relevant literature).

The most common burial salt forming within or near a mass of buried evaporites is a sparry poikilotopic anhydrite, as typifies porosity-occluding cements in many reservoir sands in the North Sea (Sullivan et al. 1994). Halite cements can also be burial salts and both minerals are derived by the subsurface flushing of the nearby evaporites, as in carbonate-sliver reservoirs encased in Infracambrian Ara Salt in the South Oman Salt basin (Schoenherr et al. 2009). Timing of the onset of such subsurface dissolution and reprecipitation as burial salts can be late or early (e.g. Schoenherr et al. 2009; McNeil et al. 1998; Kendall 2000).

Hydrothermal salt is a broader descriptor than burial salt and encompasses a higher temperature range for mineral precipitates than the diagenetic realm, Such salts typically formed in heated subsurface fractures or at seafloor vents where hydrothermal waters are escaping, mixing, degassing heating and cooling. Hydrothermal anhydrite crystallizes due to anhydrite's retrograde solubility, whereby $CaSO_4$ becomes less soluble with increasing temperature (Fig. 1.4b). This is why, in the vicinity of active basaltic ridges on the deep seafloor, anhydrite is the dominant component of "white smokers" and is commonplace in other hydrothermal vent mounds; it is also why anhydrite is a major early component of many VHMS seafloor mounds (e.g. TAG Mound where it can constitute more than 50 % of the rock mass; Chap. 16). Hydrothermal anhydrite precipitates in response to the heating of seawater in regions where magmatically-driven hydrothermal fluids are escaping onto the seafloor. In contrast, baryte, another marine hydrothermal precipitate, has prograde solubility and precipitates when an escaping barium-bearing brine is cooled by interacting and mixing with seawater (accordingly the S and Sr isotope signatures in the two precipitates reflect their origins – Paytan and Kastner 2002).

Hovland et al. (2006a, b) and Hovland and Rueslatten (2009) introduced the concept of substantial volumes of hydrothermal halite precipitating from subsurface brines at supercritical temperatures, especially in deeply buried rift-related sedimentary basins. The model relies on heated subsurface waters becoming supercritical and so transforming to a fluid that does not dissolve but precipitates salt (within specific temperature and pressure ranges). A supercritical fluid

is defined as any substance at a temperature and pressure above its critical point; in such a state it can effuse through solids like a gas, and dissolve materials like a liquid. In addition, close to the critical point, small changes in pressure or temperature result in large changes in density. The critical point (CP), also called a critical state, specifies the conditions (temperature, pressure and sometimes composition) at which a phase boundary ceases to exist. Under certain pressure/temperature conditions, supercritical water is unable to dissolve/retain common sea salts in solution (Josephson 1982; Simoneit 1994; Hovland et al. 2006a).

When seawater brines are heated in pressure cells in the laboratory they pass into the supercritical region at a temperature of 405 °C and 300 bar pressure (the CP of seawater). A particulate 'cloud' then forms via the onset of 'shock crystallization' of NaCl and Na_2SO_4 (Fig. 1.5a). The sudden phase transition occurs as the solubility of the previously dissolved salts declines to near-zero, across a temperature range of only a few degrees, and is associated with a substantial lowering of density (Fig. 1.5b). The resulting solids in the "cloud" consist of amorphous microscopic NaCl particles with sizes between 10 and 100 mm. The resultant "salting out" can lead to the precipitation of large volumes of subsurface salts, as well as the ability to carry high volumes of hydrothermal hydrocarbons prior to the onset of supercritical conditions (Josephson 1982; Fig. 1.5c). Supercritical water has enhanced solvent capacity for organic compounds and reduced solvation properties for ionic species due to its loss of aqueous hydrogen bonding (Simoneit 1994).

Hovland et al. (2006a, b) predict that some of the large volumes of deep subsurface salt found in the Red Sea, in the Mediterranean Sea and the Danakil depression, formed via the forced magmatically-driven hydrothermal circulation of seawater down to depths where it became supercritical. This salt, they argue, was precipitated deep under-ground via "shock crystallisation" from a supercritical effusive phase

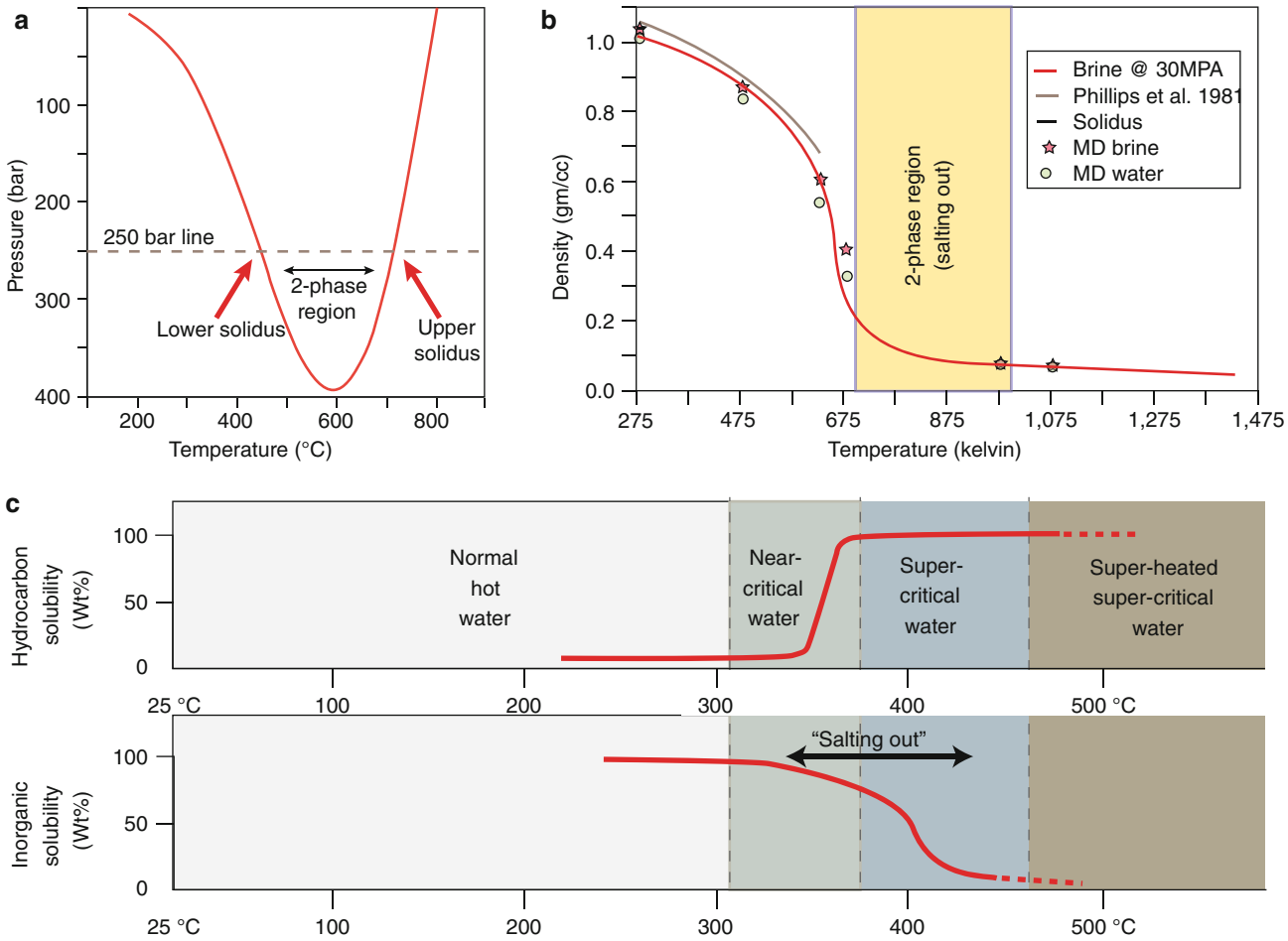

Fig. 1.5 Hydrothermal halite derived from supercritical seawater. (**a**) P-T projection of the monovariant solid-liquid-vapour saturation curve (solidus) for the NaCl-water system. *Arrows* indicate the two points of intersection with the section at 250 bar (defining the lower and upper solidus boundaries). (**b**) Density of water and brine as a function of temperature along the 300 bar isobar. The two-phase region (or "out- salting region") is indicated by the shaded region with onset indicated by a drastic fall in density over a narrow temperature range. (**c**) Ionic and hydrocarbon solubility in heated water at pressures of 200–300 bars (**a**–**b** After Hovland et al. 2006a, b; **c** after Josephson 1982; Simoneit 1994)

and so formed massive accumulations (mostly halite) typically in crustal fractures that facilitated the deep circulation. NaCl then flowed upwards in solution in dense, hot hydrothermal brine plumes, precipitating more solid salt beds upon cooling nearer or on the surface/seafloor. To date, the Hovland et al. model of hydrothermal sourcing for widespread halite from a supercritical brine source (in active magmatic settings) has not been widely accepted by the geological community (Talbot 2008).

Another source of chlorine-rich hydrothermal fluid in the deep subsurface is the recycling of deeply buried sedimentary salt into the greenschist realm and beyond (Yardley and Graham 2002). In the metamorphic realm (T>200 °C) the derived fluids do not precipitate halite, but a series of meta-evaporite indicator minerals (Chap. 14). Lewis and Holness (1996) demonstrated that buried salt bodies, subjected to high pressures and elevated temperatures, can acquire a permeability comparable to that of a sand. This is because the crystalline structure of deeply buried salt (halite) attains dihedral angles between salt crystals of less than 60° and so creates an permeable polyhedral meshwork. Such conditions probably begin at the onset of greenschist P-T conditions, whereby highly saline hot brines form continuous brine stringers around all such altered and recrystallizing salt crystals (Fig. 1.6; Chap. 14). This polyhedral permeability meshwork allows hot dense brines or hydrocarbons to migrate through salt and so ultimately dissolve the salt host, releasing a pulse of sodic- and chloride-rich fluid into the metamorphic realm (Chap. 14). It is why little or no evidence of masses of metamorphosed halite is found in subsurface meta-evaporitic settings where temperatures have exceeded 250–300 °C, even though the melting point of halite is 800 °C. Given the right subsurface conditions these halite-derived metamorphic brines may evolve into supercritical waters.

One of the most visually spectacular examples of hydrothermal precipitation is in the Naica mine, Chihuahua, Mexico (Fig. 1.7a). There several natural caverns, such as Cave of Swords (Cueva de la Espades) and Cave of Crystals (Cueva de los Cristales), which contain giant, faceted, and transparent single crystals of gypsum as long as 11 m (García-Ruiz et al. 2007; Garofalo et al. 2010). Crystals in Cueva de los Cristales are the largest documented gypsum crystals worldwide. These huge crystals grew slowly at very low supersaturation levels from thermal waters near the gypsum-anhydrite boundary. Gypsum is currently precipitating on modern mine walls.

Fluid inclusion analyses show that the giant crystals came from low-salinity solutions at temperatures ≈54 °C, slightly below the temperature at which the solubility of anhydrite equals that of gypsum (Fig. 1.7b). According to García-Ruiz et al. 2007, the sulphur and oxygen isotopic compositions of these gypsum crystals are compatible with growth from solutions resulting from dissolution of anhydrite, which was previously precipitated during late hydrothermal mineralization in a volcanogenic matrix. The chemistry suggests that these megacrystals formed via a self-feeding mechanism, driven by a solution-mediated, anhydrite-gypsum phase transition. Nucleation kinetics calculations based on laboratory data show that this mechanism can account for the formation of these giant crystals, yet only when operating within a very narrow range of temperature of a few degrees, as identified by the fluid inclusion values. According to the paper's authors, these singular conditions create a mineral wonderland, a site of scientific interest, and an extraordinary phenomenon worthy of preservation.

Garofalo et al. (2010), accept the need for a limited temperature range during precipitation, but argue the precipitating solutions were in part meteorically influenced. Their work focused on Cueva de las Espadas. As for most other hypogenic caves, prior to their analytical work they assumed that caves of the Naica region lacked a direct connection with the land surface and so gypsum precipitation would be

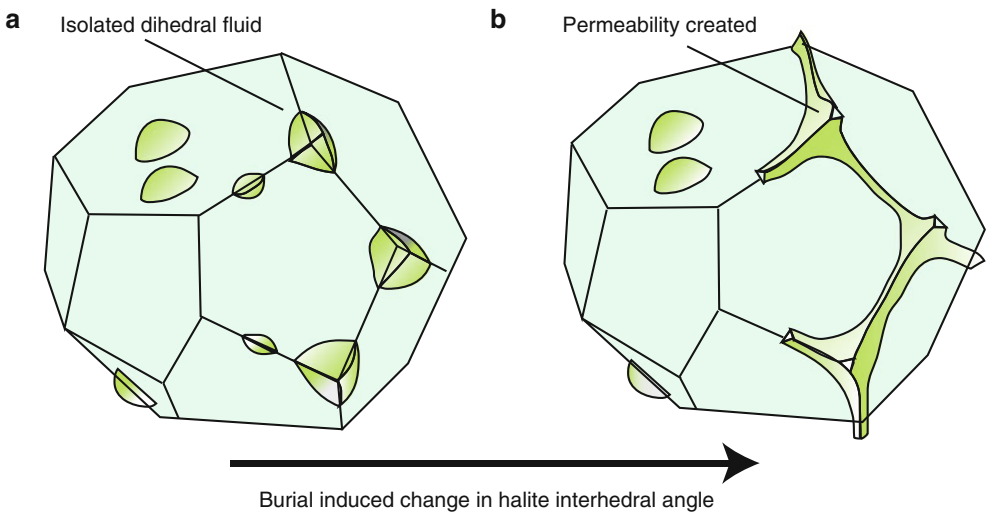

Fig. 1.6 Effect of dihedral angle on pore connectivity in texturally equilibrated monomineralic and isotopic polycrystalline mosaic halite. Shading shows position of dihedral fluid phase within the polyhedral intercrystalline porosity. (**a**) Isolated porosity for dihedral angle >60°. (**b**) Connected polyhedral porosity for dihedral angle <60° (After Lewis and Holness 1996)

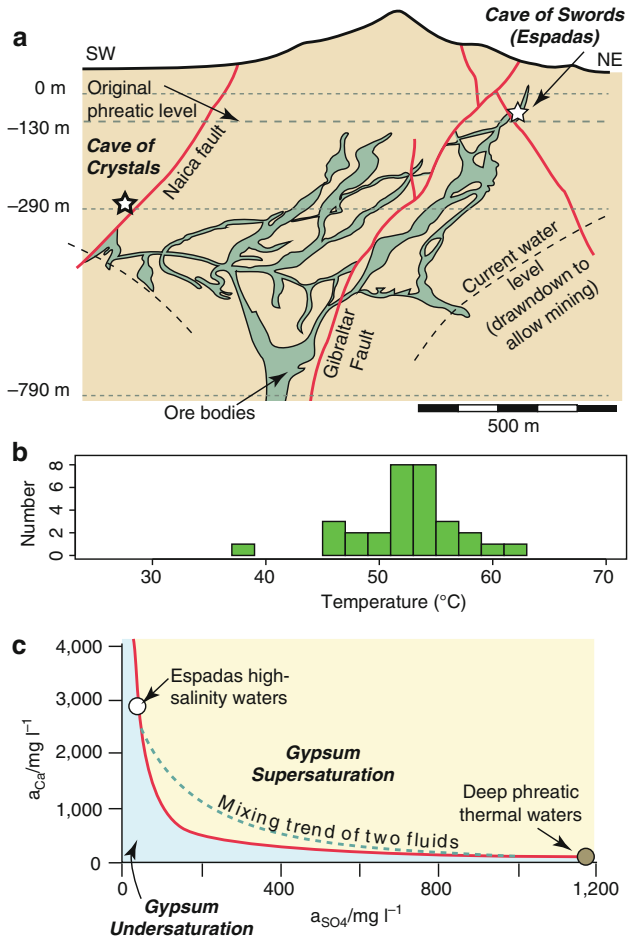

Fig. 1.7 Naica Mine, Mexico. (**a**) Cross section of Naica mine. Mine exploits a hydrothermal Pb-Zn-Ag deposit with irregular manto and pipe morphologies entirely enclosed in subhorizontally dipping carbonates. Cavities of gypsum crystals are located in carbonates close to main and secondary faults. Galleries have been excavated down to –760 m, requiring average pumping rate of 55 m^3/min to depress groundwater to –580 m with respect to phreatic level located at –120 m; Naica and Gibraltar faults act as main drains. (**b**) Homogenization temperatures of 31 fluid inclusions showing actual temperature of growth. (**c**) Solubility of gypsum calculated at 55 °C and 105 Pa and measured activities of shallow and deep cave fluids from fluid inclusion data. Mixing at equilibrium between these two fluids in any proportion generates a fluid with a composition would consistently supersaturated with respect to gypsum, as shown by the position of the mixing curve, indicated by a *dashed line*, in the gypsum supersaturation field (After García-Ruiz et al. 2007; Garofalo et al. 2010)

unrelated to climate variation, Yet, utilising a combination of fluid inclusion and pollen spectra data from cave and mine gypsum, they concluded climatic changes occurring at Naica exerted and influence on fluid composition in the Naica caves, and hence on crystal precipitation and growth.

Microthermometry and LA-ICP-Mass Spectrometry of fluid inclusions in the gypsum indicate that brine source was a shallow, chemically peculiar, saline fluid (up to 7.7 eq. wt.% NaCl) in the Cueva de las Espadas and that it could have formed via evaporation, during an earlier dry and hot climatic period. In contrast, the fluid of the deeper caves (Cristales) was of lower salinity (≈3.5 eq. wt.% NaCl) and chemically homogeneous, and likely was little affected by evaporation processes. Garofalo et al. (2010) propose that mixing of these two fluids, generated at different depths of the Naica drainage basin, determined the stable supersaturation conditions needed for the gigantic gypsum crystals to grow (Fig. 1.7c). The hydraulic communication between Cueva de las Espadas and the other deep Naica caves controlled fluid mixing. Mixing must have taken place during alternating cycles of warm-dry and fresh-wet climatic periods, which are known to have occurred in the region. Pollen grains from 35 ka-old gypsum crystals from the Cave of Crystals indicates a fairly homogenous catchment basin dominated by a mixed broadleaf wet forest. This suggests precipitation during a fresh-wet climatic period, the debate continues.

So, What Exactly Is an Evaporite?

Now that we have discussed some possible complexities in interpretation created by the widespread occurrence of non-solar mineral salts, the remainder of this chapter deals with controls on distribution of "true" sedimentary modern and ancient evaporites (formed at or nearsurface by solar-driven brine concentration). My working definition for an evaporite is, as the name suggests, a sedimentary rock formed at sedimentary surface temperatures (>50–70 °C) and is typically precipitated by solar concentration (heating) of a nearsurface or at-surface brine to where the salinity of residual brine becomes saturated with respect to a particular set of mineral salts, which then drop out of the solution as a series of predictable crystallites, subject to nearsurface and later alteration, replacement and dissolution (Figs. 1.8 and 1.9).

So, what are the basic requirements to form and preserve an evaporite? We need; (1) a surface or nearsurface brine body that is saline enough to precipitate and preserve salt, this typically means an arid to semi-arid climatic setting with a drawdown hydrology capable of maintaining substantial volumes of saltsaturated brine at or near the landsurface, (2) accommodation space in a sedimentary depression that is not completely filled by other sediment, and (3) a burial environment that does not allow sufficient undersaturated porewater throughflow to completely dissolve the buried salts.

Depositional Setting and Texture

Primary evaporites precipitate with distinct textures in a number of hydrologically-contrasted settings, contingent on brine stability and rates of temperature and salinity change in the mother liquor. Primary evaporite textures are direct indicators of the hydrology at the time of precipitation and

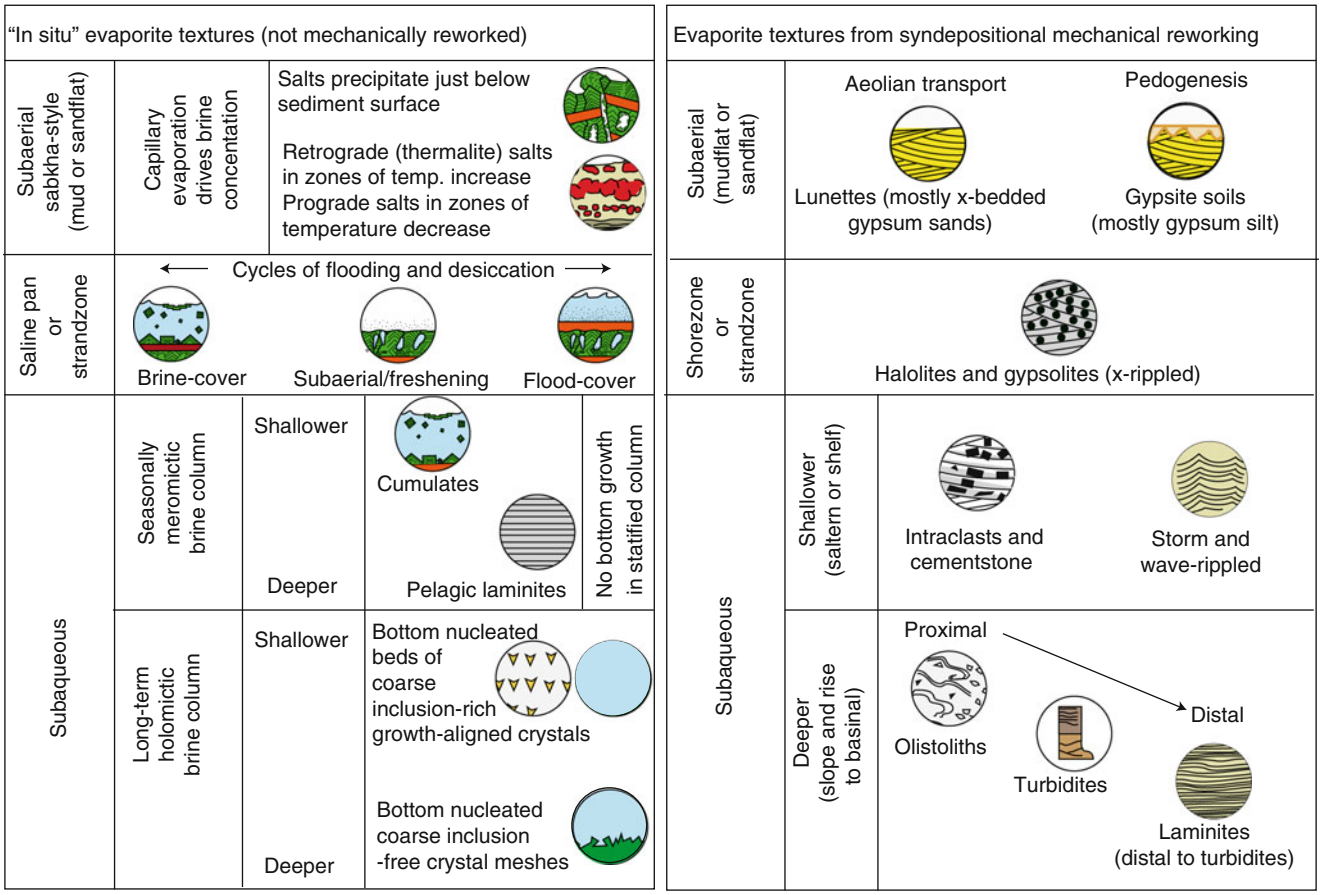

Fig. 1.8 Significance of primary evaporite depositional textures as indicators of brine hydrology

accumulation (Fig. 1.8). Sometimes crystals remain where they precipitate, other times they are mechanically or geochemically reworked, or undergo partial degrees of dissolution and fractional recrystallization.

Crystals may first precipitate at the air-brine interface in rafted crystal clusters that then sink to form cumulate beds, or can be blown to the strandzone (e.g., halite rafts crystallizing at the air-brine interface in Lake Guilietti in Ethiopia). Then again, immediately after they crystallize, precipitates can sink from the uppermost water mass to ultimately collect as pelagic accumulations (cumulates) on the shallow or deep brine floor "rain from heaven" deposits. Seasonal or longer term changes in the chemistry and salinity in the upper water column means many such pelagic deposits are mm-scale laminates made up of mineral doublet or triplet layers. In a holomictic shallow water mass, coarse cm-dm scale crystals can form as bottom-nucleated inclusion-entraining precipitates, typically at the base of a water column that is tens of centimetres to metres deep. Such crystals, be they gypsum swallowtails or halite chevrons, tend to be composed of alternating inclusion-rich and inclusion-poor laminae and micro-laminae, reflecting rapid changes in chemistry or temperature of the overlying shallow holomictic water mass (Fig. 1.8).

If a brine column remains both supersaturated and holomictic to greater depths, then evaporites can accumulate at the deepwater base of a brine column that is hundreds of metres deep. This is the case today in the North Basin of the Dead Sea in the Middle East, where a salt bed, made up of a meshwork of inclusion-free, randomly-aligned cm-scale halite crystals, is accumulating and has been doing so since the North Basin brine column became holomictic in February, 1978. Prior to 1978 and for at least the preceding 400 years the brine column of North Basin (>370 m water depth) was a meromictic density-stratified hypersaline system, with pelagic mm-scale laminites accumulating on the same deep bottom, composed of alternating calcite and aragonite lamina, along with minor cm-scale gypsum crystal clusters or rosettes. The lack of inclusions in the halite mesh on the present-day deep bottom reflects the greater stability of chemical conditions on the bottom. The corollary is that growth-aligned evaporite crystals, rich in entrained inclusions of brine (e.g. chevron halite in Death Valley, California, or carbonate pellets encased in swallowtail gypsum in Marion Lake, Australia) indicate precipitation in much shallower water depths (decimetre to metre depths). That is, inclusion-rich aligned bottom-growth

Fig. 1.9 Classification of evaporite formation in the depositional-diagenetic realms emphasizing ongoing postdepositional evolution of mineralogy and texture

		Type	Precipitation process	Temp (°C)	Hydrological process	
"An evaporite is a rock that was originally precipitated from a saturated surface or near-surface brine by processes driven by solar evaporation"	Remnant primary textures; Seconday texture dominant	"Primary" evaporite	An evaporite salt precipitated via solar evaporation from a brine pool at the earth's surface. Crusts, bottom nucleates & pelagic crystals accumulate on brine pool floor.	0–60 °C	Gravity and density effects at surface or in zone of active phreatic flow (brine reflux	Saturation driven by solar evaporation
		"Secondary" evaporites (include sabkha nodules and the bulk of ancient evaporite beds)	An evaporite salt formed in the shallow subsurface in the zone of active prheatic flow. The concentration process of the brine and the associated gravitational reflux is driven by solar evaporation. May form displacive, replacive or cement textures.			
			A burial diagenetic evaporite phase that replaces earlier evaporite beds. Salt precipitation is driven by fluid mixing or saturation mechanisms driven by burial diagenetic processes. Forms replacive and cement textures.	60–200 °C	Burial effects compactional and thermobaric flow	Brine saturation not driven directly by solar evaporation
		Burial salts	Subsurface precipitation of evaporite as cements and replacements in non-evaporite matrix from a saturated brine derived form the dissolution of adjacent evaporite beds or zones of brine mixing.			
	No primary texture	"Tertiary" evaporites	An evaporite formed by brine saturation related to partial bed dissolution via re-entry into the zone of active phreatic circulation. Often driven by basin uplift and reosion.	0–60 °C	Stagnant to active phreatic flow	
? ?		Hydrothermal salts	Salts (anhydrite – retrograde; halite -supercritical) precipitated by heating of seawater or subsurface brines.	>150 °C	Hydrothermal circulation	

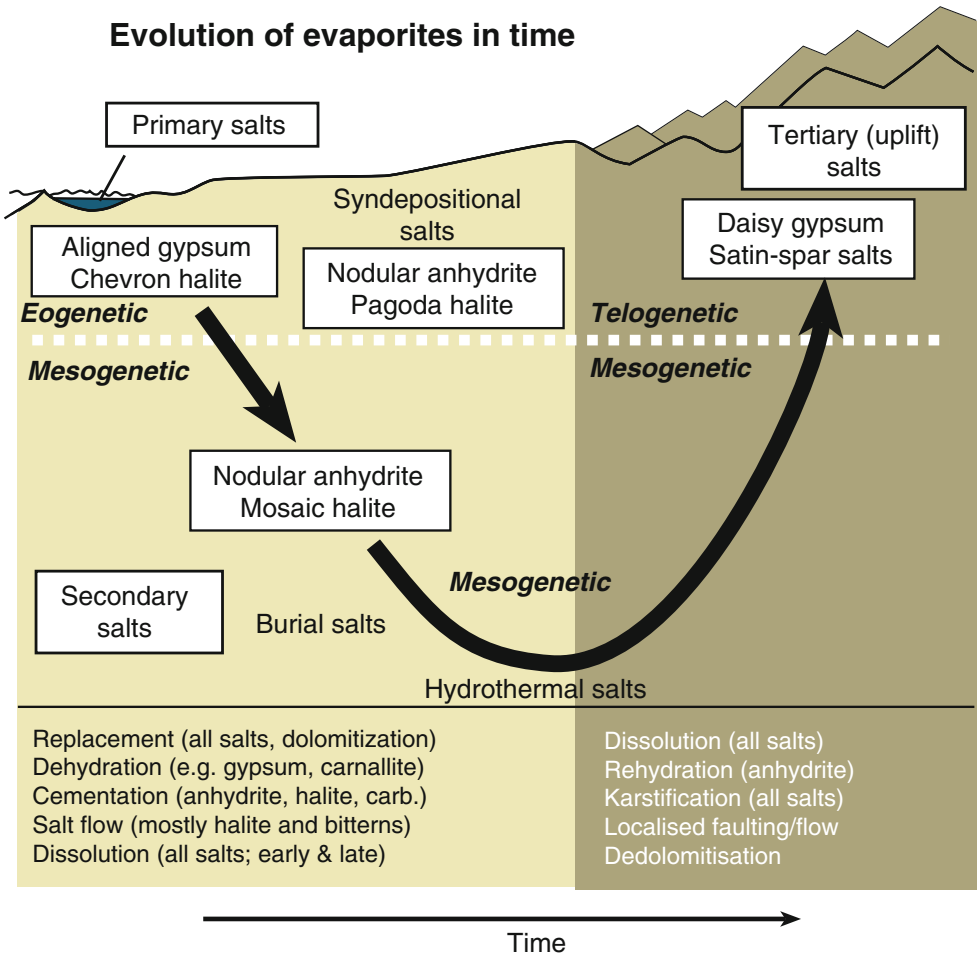

textures form in well-mixed brines that are shallow enough to experience short term changes in saturation and growth rate, coupled to short term changes in water temperature or salinity.

If currents and waves rework the bottom crystals, then ripple structures and dune forms can be the dominant texture in the accumulating evaporite bed. The presence of evaporite equivalents of carbonate ooids, namely gypsolites and halolites, indicate oscillating bottom currents at the time the crystals grew. Brine floor instability, related to seismic events, halokinesis or tectonism, can also lead to the formation of slumps, brine escape and debris flow textures (seismites) in a salt bed deposited at any water depth (El Taki and Pratt 2010). The lowering of suprasalt brine column salinity or the lowering of the regional watertable can create karst cones and breccias in an evaporite bed. For more detail on the significance of the various evaporite textures the reader is referred to (Lowenstein and Hardie 1985; Orti et al. 2010).

Evaporite salts can crystallize as early diagenetic precipitates in the shallow subsurface some mm to cm below the sediment surface, as occurs today in the capillary zones of many marine coastal and continental mudflats and sabkhas (where displacive and poikilotopic crystals, nodules and efflorescent crusts are typical). Some initial crystals precipitates can be dissolved and recycled through the nearsurface sediment column, especially in arid and semi-arid settings, to create pedogenic profiles; as in the gypsite soils atop gypsum lunettes in southern Australia or in the nitrate-rich salt solid of the hyperarid Atacama Desert.

So, as for depositional textural associations in carbonate and siliciclastic sediments, a depositional model based on evaporite textures can encompass a spectrum of formative sites ranging from the pedogenic, to saline mudflats, to shallow and deep subaqueous brine settings. However, because evaporite salts are orders of magnitude more soluble than carbonate or siliciclastic sediments, they require particular postdepositional tectonics and hydrologies in order for large volumes of salts to be buried and textures preserved or no more than partially modified. This high degree of solubility and mobility at the time of precipitation and in their subsequent subsurface evolution is key to understanding deposition and diagenesis in both modern and ancient evaporite settings.

Secondary and Tertiary Evaporites

As soon as an evaporite bed is formed it is subject to alteration, which continues at varying levels of intensity throughout the sedimentary history of the rock (Fig. 1.9). In a Pre-Quaternary, or certainly pre-Neogene evaporite, many textures are secondary; the rock has been diagenetically altered, frequently showing fabrics indicating early recrystallisation and perhaps some later crossflow of basinal waters. Under this definition of a primary versus secondary salt, even the nodules in Holocene mudflats are secondary salts, including those in the various modern mudflats of the Arabian (Persian) Gulf, which is the type area for a sabkha. The nodules are a porewater overprint superimposed on a primary matrix of mud and sand. Ancient bedded anhydrites are typically dominated by secondary textures, although beds may still retain "ghosts" or partial relicts of primary textures such as indistinct laminae or aligned nodules after growth-aligned gypsum. In a halite bed there may be remnant patches of aligned halite chevrons floating in a matrix of mosaic halite spar. Even when evaporite beds are extensively recrystallised, most retain coarse stratiform layering made up of impurities that once defined primary depositional discontinuities.

What distinguishes evaporites, especially NaCl beds, from other types of sediment in the subsurface is their ability to flow via pressure-driven recrystallisation, even as they backreact or dissolve. Even earlier secondary textures can be syndepositional precipitates, formed as cements and replacements, while primary matrix accumulated around them. Early replacement sometimes preserves remnants of the original depositional texture, such as gypsum ghosts in nodular anhydrite or aligned halite chevrons outlined by secondary anhydrite. Nodular anhydrite ghosting of lenticular gypsum was recognised in Permian mudflats in the early 1960s by Kerr and Thomson (1963), they interpreted it as a subaqueous saline pan indicator. Unfortunately, for the next two decades their results were overlooked by workers in the Permian Basin who incorrectly applied supratidal capillary analogs to thick massive subaqueous anhydrite beds.

Early diagenetic overprints and effects of later compactiondriven flow and pressure solution can destroy much of the depositional evidence in an ancient evaporite bed. This means retention of primary crystal textures is at best patchy in both halite and anhydrite beds. Many ancient bedded halites are dominated by coarsely crystalline halite spar. Much of it was deposited in multiple episodes of early diagenetic (syndepositional) cementation, leaving less than 10–15 % of the bed as primary growth-aligned chevrons within a few metres to tens of meters below of the depositional surface. This syndepositional coarse sparry halite formed in multiple dissolution-precipitation events in microkarst pits and was precipitated between successive depositional episodes of chevron halite crust formation (Chap. 3). Other coarsely crystalline halite spar, especially in halokinetic beds, shows pervasive and multiple flow-aligned textures created by pressure-solution. Textures are driven by numerous salt creep and recrystallisation episodes, which occur millennia to millions of years postdeposition, and after hundred to thousands of metres of burial (Chap. 6).

Secondary evaporite textures form in subsurface settings equivalent to the eogenetic[1] and mesogenetic porosity realms, as defined for carbonates by Choquette and Pray (1970). Tertiary evaporite textures tend to form in the telogenetic realm (Fig. 1.9). And, as in carbonate diagenesis, the most pervasive alteration of evaporites is either early in the burial history (eodiagenesis) or it occurs much later during uplift (telo-diagenesis). Both the eogenetic and telogenetic settings are characterised by relatively permeable evaporites and hydrologies capable of high volumes of pore fluid cross-flow. Alteration of a salt mass in the mesogenetic realm consists largely of recrystallisation overprints within a flowing salt mass, but with substantial alteration and dissolution possible about the edge of a bed or a flowing salt mass. In carbonates, the mesogenetic overprint tends to be pervasive throughout the bed (Choquette and Pray 1970). In evaporites units, the pervasive early loss of porosity and permeability in the shallow diagenetic/eogenetic realm means that deep burial (mesogenetic) alteration, prior to halokinesis, tends to be first concentrated about the edges of a buried salt body (see discussion of dissolving salt "block of ice" model in Chaps. 7 and 8). Unlike carbonates and siliciclastics, the core of a subsurface bedded halite unit (nonhalokinetic) can be largely unaffected by fluid flow-driven processes of burial alteration due to its early loss of effective porosity via cementation. Preservation of the unaltered core of the salt unit is why viable Permian halobacteria can be cultured from brine inclusions in remnant chevrons in Permian salt beds from West Texas (Vreeland et al. 2000).

Unlike quartzose and aluminosilicate sediments, buried evaporite beds can flow as ductile masses from the surface down to 8–10 km of burial and even into the metamorphic realm. At the same time their dissolving edges supply ions to adjacent nonevaporitic sediments. Salt flow can be: (a) early diagenetic, coinciding with syndepositional fractionation, reflux or dissolution; (b) later diagenetic, associated with complex burial-stage bed dissolution or reprecipitation and driven by subsurface fluid flow in the zone of free convection below the zone of overpressure; (c) widespread and pervasive, as occurs during halokinesis (salt tectonics); and (d) postdiagenetic and extending well into the metamorphic realm where daughter minerals, such as scapolite and tourmaline, can act as a source of volatiles and lubricants long after the precursor salts have gone.

Exhumed or uplifted evaporite beds also undergo pervasive alteration, dissolution and replacement as they re-enter the zone of active phreatic flow (telogenesis) and regain permeability along internodular nd inter crystalline boundaries. Once again, alteration tends to occur from the edges inward. Soluble components from the altering and dissolving bed can be reprecipitated in adjacent shales as alabastrine and satinspar gypsum or fibrous halite veins. Exhumed evaporite textures are termed tertiary (Fig. 1.9) and are varying combinations of competitive crystal alignment and geopetal void fills. The resulting fabrics can duplicate "primary" crystal alignments, especially when parts of a cavern fill can only be studied at a limited scale, as in core or a mine face. Not recognising a telogenetic overprint typically misidentifies tertiary evaporite textures as primary and so creates interpretive confusion (Chap. 7). This is why interpretations of depositional setting are not reliable if based on observations in an evaporite outcrop where that unit is the remnant of a once more massive and thick primary unit that has passed through the mill of burial and uplift. Adjacent nonevaporitic sandstones, shales and limestones also undergo diagenetic reactions when flushed by evolving pore fluids, but the diagenetic rock/fluid framework is slower to respond and requires years to millennia to overprint an original depositional texture. But, given enough time, the textures of many other sediments evolve during burial, just at much slower rates (Table 1.2).

Primary Evaporitic Carbonates

The simplest subdivision of evaporite minerals is into evaporitic alkaline earth carbonates – aragonite, dolomite, low-Mg calcite and high-Mg calcite – and evaporite salts – gypsum, anhydrite, halite, trona, carnallite, etc. (Table 1.1). Primary evaporitic carbonates tend to form in the initial stages of brine concentration, whereas the other primary evaporite salts are precipitated in the more saline stages of concentration (Chap. 2). Evaporitic carbonates can contain and preserve elevated levels of organic matter that subsequently generate hydrocarbons or act as reductants for base metal sulphides (Chap. 9).

Evaporitic alkaline earth carbonates are the first evaporite minerals to precipitate from a concentrating hypersaline surface water and are usually composed of aragonite, high- and lowMg-calcite, magnesite or even primary dolomite. The essential hydrology of any evaporite depositional setting is that evaporative outflow exceeds inflow. This results in two characteristics of the carbonate depositional system, which hold also for the more saline evaporite salts. First, rapid

[1] In their original definitions Choquette and Pray (1970) focused their studies on carbonate sediments. Throughout this book I have expanded and slightly modified their original definitions (*as noted in italics*). So the modified definitions of eogenetic, mesogenetic and telogenetic are as follows: Eogenetic zone extends from surface of newly deposited sediment (*not just carbonates*) to depths where processes genetically related to surface become ineffective. Telogenetic zone extends from erosion surface to depths at which major surface-related erosional processes become ineffective. Below a subaerial erosion surface, the practical lower limit of telogenesis is at or near watertable (*and the related surface driven zone of phreatic meteoric water movement and includes both unconfined and confined aquifers*). Mesogenetic zone lies below major influences of processes operating at surface. The three terms also apply to time, processes, or features developed in respective zones.

Table 1.2 Characteristics of siliciclastic and carbonate depositional systems

	Siliciclastic: (continental, fluviodeltaic, shelf, submarine)	Carbonate: humid-oceanic/marine tropical/subtropical	Carbonate-evaporite: arid, land-locked subtropical/temperate
Early marine cementation	Rare	Local occurrence	Pervasive (especially in mesohaline platform)
Dolomitisation	Rare	Locally in mixing zones (?)	Pervasive (brine reflux and burial)
Leaching	Uncommon, mostly related to freshwater leaching, rare in burial diagenesis	Common, related to subaerial exposure and karstification	Intensive, related to hypersaline brines
Calcite cementation	Uncommon, locally common (mostly related to burial)	Common	Rare to local occurrence (mostly burial)
Anhydrite-halite	Uncommon	Rare to absent	Common to pervasive
Porosity types	Intergranular	(1) Mouldic, vuggy and chalky microporosity (common) (2) Fracture and intercrystalline porosity (local occurrence)	(1) Intergranular, mouldic, vuggy, and intercrystalline (dolomitic) porosity (very common) (2) Fracture and chalky microporosity (locally common)
Controls on reservoir quality	(1) Stratigraphic position (2) Depositional facies	(1) Stratigraphic position (2) Depositional facies (3) Karst in zones on meteoric influx	(1) Depositional facies (2) Accessibility of sulphate- and chloride-bearing and later corrosive fluids (karstic or deep)
Geometry	Layered	Layered	(1) Carbonate-basinwide evaporite: Massive, irregular, halokinetic (2) Carbonate-saltern-mudflat evaporite: layered
Reservoir distribution	High energy shoreline or channel fills with position related to lowstand, transgressive and highstand system tract	Highstand reef or bank carbonate immediately beneath subaerial unconformity	(1) Carbonate-basinwide evaporite: near faults and fractures where late corrosion is most intensive (2) Carbonate saltern-mudflat evaporite (a) Within grain-supported facies where primary porosity is preserved or mouldic porosity was created through leaching (b) Within coarsely crystalline dolomite (c) Within highly fractured limestone

In part after Sun and Esteban (1994)

changes in water level are possible, especially in the more marginward facies, leading to interlayering of strandzone and subaqueous units. Under such a regime any subaqueously precipitated sediment is liable to subaerial exposure and syndepositional subaerial diagenesis. Second, the solute content, especially the Mg/Ca ratio, of shallow hypersaline water fluctuates as the salinity fluctuates. For example, the Ca content of any freshened water is depleted by the early precipitation of calcite or low-Mg calcite. Subsequent carbonate precipitates drop out of increasingly saline waters that will have a higher Mg/Ca ratio and so saline carbonate precipitates tend to be dominated by high-Mg calcite, aragonite, magnesite, or even dolomite.

Carbonate Laminites (Subaqueous?)

Mm-scale lamination is volumetrically the dominant sedimentary texture in modern and ancient evaporitic carbonates as well as in higher salinity salts, but its origins are varied and complex (Fig. 1.10). Sometimes it is an inorganic cumulate, other times it is biologically structured (biolaminite – see next section). Beds dominated by finely laminated, regular alterations of two or more sediment types are called laminites or rhythmites. Many evaporitic carbonate laminites form couplets or even triplets by the regular superposition of micrite with siliciclastic clay, organic matter or evaporite salts. Such couplets and triplets are frequently referred to as varves, yet are not necessarily "true" varves in that the layers may not define annual couplets.

As an example of a contemporary carbonate laminite, consider deep bottom pelagic sediments deposited prior to 1979 in the Northern Basin in the Dead Sea, Israel (Fig. 4.51). They are made up of alternating light and dark mm laminae that accumulated beneath a density-stratified brine column more than 350 m deep. The whitish laminae are composed of stellate clusters of aragonite needles (5–10 μm diameter), which precipitated each summer at the air-brine interface and then sank. The darker laminae consist of clay minerals, quartz grains, detrital calcite and dolomite that washed in as suspended sediment from the surrounding highlands during occasional storm floods (Garber et al. 1987). Thus laminites in the Dead Sea are not annual layers, but indicate flood events that occur every 3–10 years.

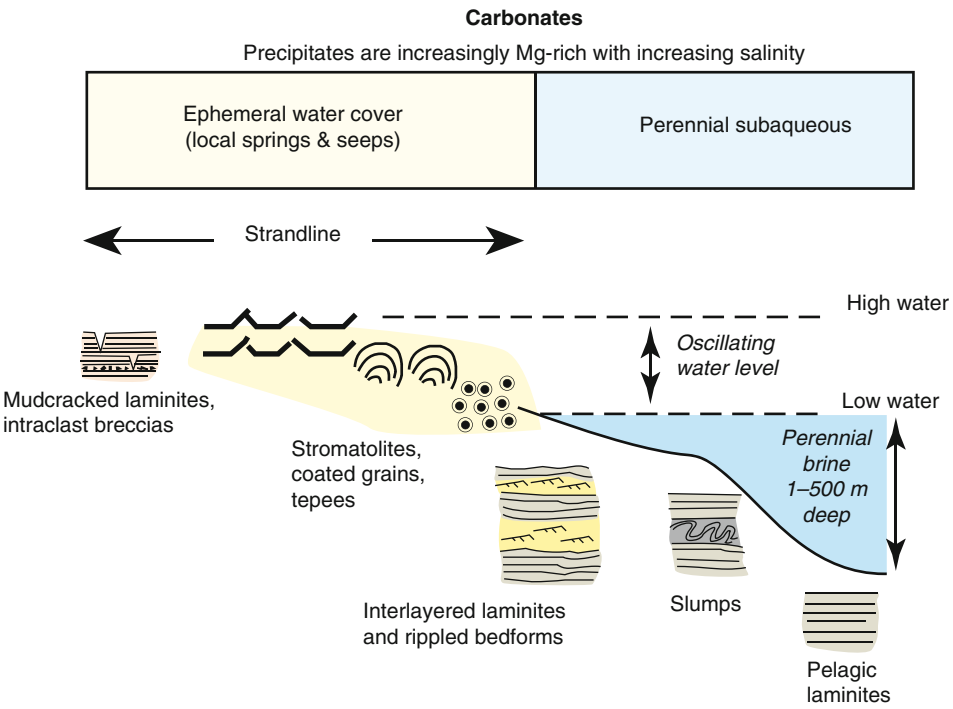

Fig. 1.10 Depositional significance of evaporitic carbonate textures. Note the distinction between subaqueous and strandline (ephemeral water) indicators

Permanent water column stratification, with periodic halotolerant alga blooms at the surface, characterises the current waters of Lake Tanganyika. Deep bottom pelagic laminites (seasonal varves) containing between 7 and 11 % total organic carbon (TOC) accumulate as modern lake bottom sediments where waters are anoxic waters and more than 250 m deep (Cohen 1989). Or consider the shallow lacustrine laminites of the more saline Holocene Coorong Lakes, Australia (Warren 1988, 1990). Coorong laminites make up more than 80 % of the Holocene sediment volume in the Coorong Lakes and are composed of alternating dark-grey organic-rich and light-grey organicpoor laminae. Depending on the salinity of the mother brine, matrix mineralogies range from hydromagnesite to aragonite to Mg-calcite to dolomite and organic levels can be as high as 16 % TOC. As in the Dead Sea, the Coorong laminites formed subaqueously on the floor of a chemically stratified lake. Unlike the 250+ metres depths of the Dead Sea and Lake Tanganyika, Coorong laminites accumulated as microbially entrained pelletal wackestone/mudstones beneath seasonally stratified perennial lake waters, less than 1–5 m deep (Fig. 4.6a, b). Once on the bottom these pellets can be eroded and redeposited as wave-driven bedload, this reworking means the resulting laminite layering is not a varve and can be eroded as it constructs wave ripples.

Laminites can also be preserved under conditions of ephemeral subaerial exposure. Algal-bound laminites (algal mats or biola minites) crosscut by mudcracks characterise the algal channel and strandzone facies in many modern and ancient evaporitic carbonates such as the sabkhas of the Arabian Gulf (Fig. 3.5e). Modern and ancient laterally extensive carbonate laminites, without evidence of subaerial exposure, indicate subaqueous deposition under fluctuating surface water chemistries. They indicate water depths that may have ranged from a few decimetres to hundreds of metres and are not necessarily associated with deepwater conditions or microbial binding (Warren 1985; Kendall 1992). They do indicate a lack of burrowing metazoans in saline carbonate sediments deposited across this wide range of water depths.

Strandzone Associations: Microbialites, Pisolites and Tepees

The strandzone in many evaporitic carbonate systems is characterised by an association of stromatolites, mudcracked cryptalgalaminites (biolaminites), pisolites, ooids, intraclasts, cemented crusts and tepees (Fig. 1.10). Strandzones typify deposition associated with fluctuating shorelines about the edge of a more permanent brine lake or seaway and form in areas of groundwater springs, mudflats and ponds. Rapid fluctuations of strandlines (wet and dry cycles) and associated high rates of capillary crossflow mean this facies association is syndepositionally cemented as it aggrades into stacked layers of intraclast breccia, biolaminites, pisolites and tepees, typically separated by salt beds or their dissolution breccias. Biofilms and mats, in otherwise muddy and granular matrices of any uncemented strandzone sediment, give a leathery depositional strength to this

sediment that encourages the preservation of rip-ups, tears and overfolds due to storm-induced erosion. Biostabilization also tends to encourage the preservation of fenestrae and gas-filled cyanobacterial domes in the surface crusts of many modern strandzones of saltflats and playas.

Microbialites and Stromatolites

Microbialites are "…organosedimentary deposits that have accreted as a result of a benthic microbial community trapping and binding detrital sediment and/or forming the locus of mineral precipitation" (Burne and Moore 1987). They are biogenic structures, the mineralised result of the metabolic activities of microphytic algae, cyanobacteria or archaebacteria (Figs. 1.11, 1.12, and 1.13a; Riding 2000; Brasier 2011). Some possess an internal clotted texture (thrombolites), others are laminar (stromatolites), or combinations with varying degrees of inorganic precipitates and external sediments. Microbialitic structures are commonplace sediments in evaporitic Holocene strandzones (Table 1.3). Textures range from biolaminites (≈cryptal-

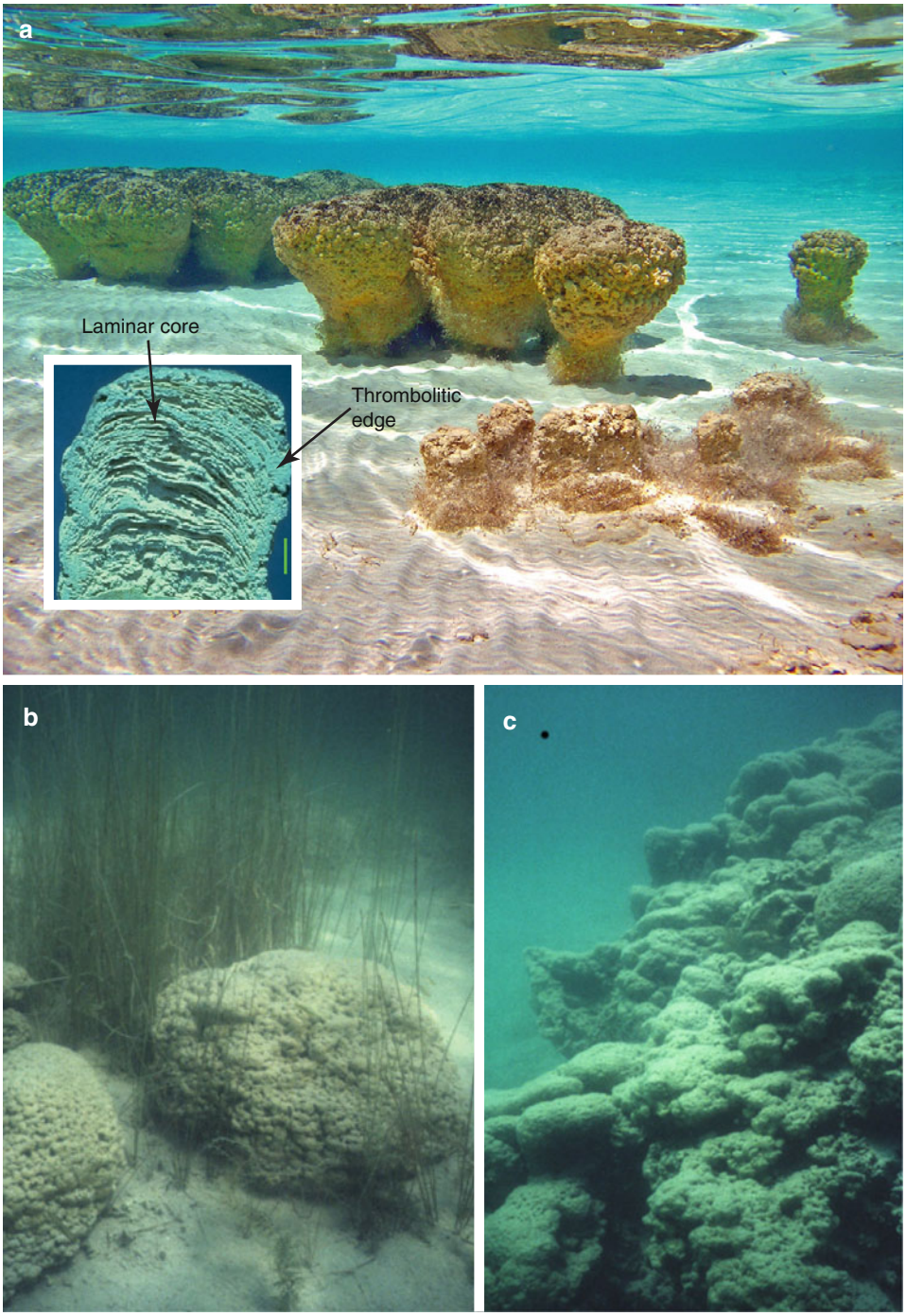

Fig. 1.11 Modern agglutinated stromatolite reefs. (**a**) Intertidal stromatolites in Hamelin Pool, Shark Bay Australia, inset shows layering created by mucilaginous plexi capturing of sand (coarse-grained agglutinated stromatolite (Image courtesy of DiscoverWest). (**b**, **c**) Lacustrine stromatolites from Cuatro Cienegas Pozas, Mexico, Most particles are captured by the mucilage are diatom frustules (Images courtesy of Alan Riggs)

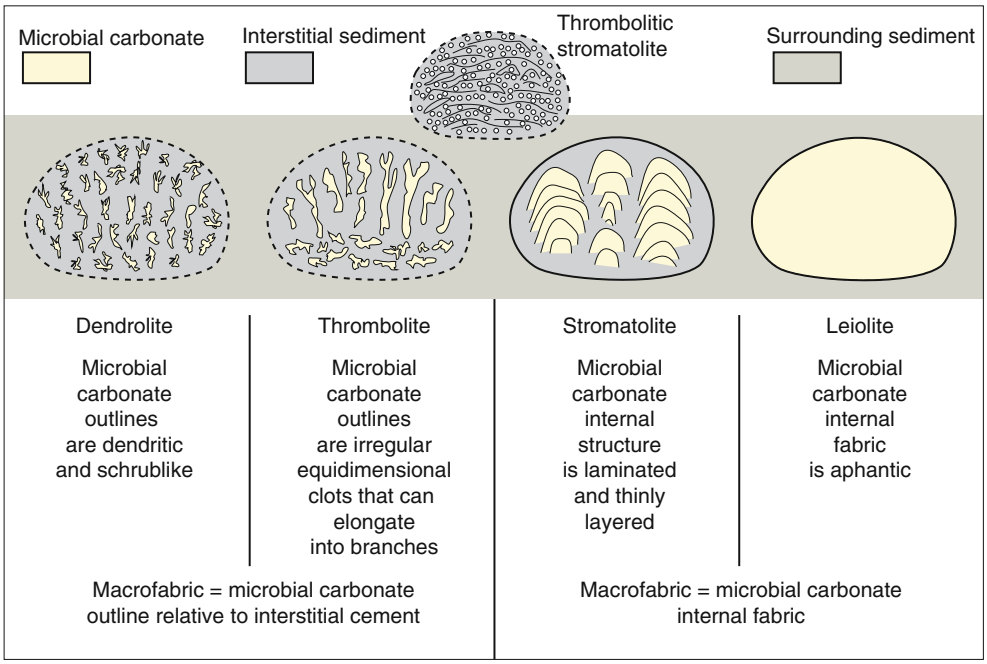

Fig. 1.12 Microbial carbonates defined by macrofabric: leiolite (aphanitic), stromatolite (laminated), thrombolite (clotted), dendrolite (dendritic). Examples show domes and associated sediment. Not to scale (After Riding 2011)

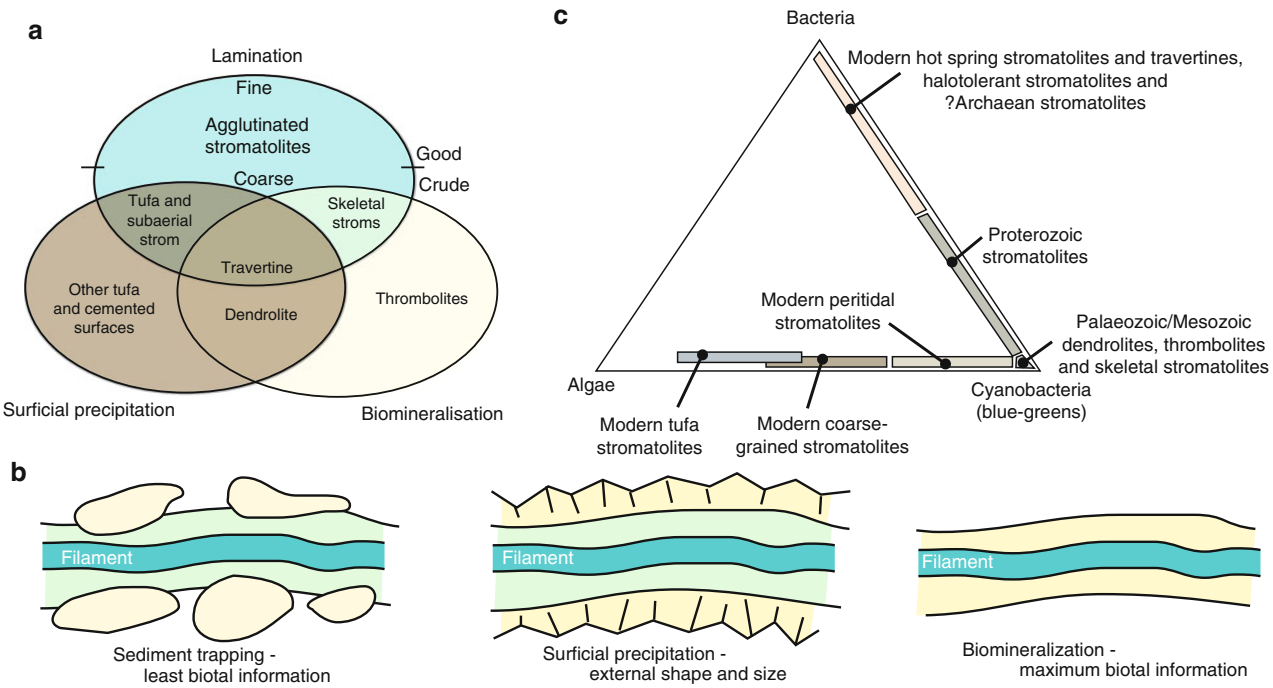

Fig. 1.13 Microbialites. (**a**) Venn classification of microbialites according to dominant constituents and layering. (**b**) Styles of mineral accretion about a trichome. (**c**) Biological components that construct various microbialites and the changes over geological setting and time (After Riding 1991, 2000)

galaminites) and stromatolites (matrix-supported agglutinated microbial reefs) through tufa/travertine (cement-supported) reefs to thrombolites (agglutinated reef). Stromatolites and cyptalgalaminates are the most easily recognised microbialites in ancient evaporitic settings. Quaternary tufas and travertines tend to characterise the humid hydrological stages of saline lakes when water levels tend to be higher and surface water less saline. Such mounds tend to define subaqueous groundwater outflow zones on the lake floor, as in Searles Lake and Mono Lake, California

Table 1.3 Selected examples of well documented Holocene microbialites, stromatolites and thrombolites

Brine style	Location, climate and hydrology	Characteristics	References
Marine (*subsealevel or sea margin lagoon*)			
Open-marine, normal salinity, subtidal	Subtidal and intertidal areas of Highbourne Cay, Lee Stocking Island, Bahamas Köppen: Aw (seafloor)	Coarse-grained agglutinated indurated aragonite and Mg-calcite structures, composed of ooid and skeletal sand; they form in normal marine salinities but stressed intertidal and subtidal environments, exposed to high wave energy and strong tidal currents. Precipitation of aragonitic needles associated with the activity of sulphate- reducing bacteria is a key feature in carbonate precipitation, while periodic sediment cover and erosion controls biotal makeup of stromatolites.	Bowlin et al. (2012), Visscher et al. (2000)
Marine-edge Mesohaline and schizohaline, intertidal to subtidal	Domes with synoptic relief along southern intertidal edge of Hamelin Pool, Shark Bay, West Australia Restricted embayment, limited hydrographic connection due to seagrass banks. Köppen: BSh (restricted sea edge lagoon)	Coarse-grained agglutinated indurated aragonite and Mg-calcite structures, composed of skeletal sand; they form in marine mesohaline (up to 65‰) marine waters, subtidal (thrombolitic) and intertidal, occasionally exposed to high wave energy. Formed by combination of (1) microbial trapping and binding and, (2) microbial precipitation. Both processes are important in the intertidal zone, forming coarse-grained sandy stromatolites. Microbial precipitation is the primary accretionary mechanism in the subtidal zone, forming muddy, micritic thrombolitic stromatolites. Induration is tied to uncoupling of sulphate reduction and carbon fixation in the microbial communities, as in Bahamas. Depositional setting is backed by extensive Holocene coquina beach ridges.	Allen et al. (2009), Reid et al. (2003), Jahnert et al. (2012)
Marine-edge Mesohaline and schizohaline intertidal	Biolaminites, no synoptic relief, on lagoon edge, south of Khor al Bazam, Abu Dhabi. Periodically covered by marine mesohaline lagoon waters Köppen: BWh (restricted sea edge lagoon)	Leathery fine-grained laminar mats composed of aragonitic micrite with Mg-calcite. Form on the protected intertidal and supratidal flats of a highly saline lagoon. From the high-water mark seaward these are: (1) Flat zone; (2) Crinkle zone; (3) Polygonal zone (4) Cinder or warty zone. A diagenetic lenticular gypsum overprint is seen in the more landward hypersaline parts of mat.	Kendall and Skipwith (1968a), Park (1977)
Lacustrine saline (*includes continental interior and coastal marine seepage*)			
Hypersaline marine-seepage lacustrine	Laterally linked mm-laminated lakemargin stromatolites, Marion Lake, coastal region southern Yorke Peninsula, South Australia Marine seepage salina, subsealevel depression (−1.5 m) hydrographic isolation. Mesohaline edge Köppen: Csb (−0.5 m)	A variety of finely laminated, subfossil, indurated aragonitic stromatolites and oncolites occur on a regressive marginal flat surrounding Marion Lake, South Australia. Internal lamination is characterized by an extremely fine sub-millimetric alternation of porous and dense laminae, light-grey and dark-grey, respectively. These microbial forms overlie a substrate of coarse, highly porous, mouldic aragonitic limestone and gypsum. These fine-grained stromatolites retain very well preserved mineralized bacterialike biota.	Von der Borch et al. (1977), Perri and Spadafora (2011), Perri et al. (2012)
Marine coastal interior, mesohaline continental seeps	North and South Stromatolite lakes, Coorong coastal region, South Australia. Schizohaline and mesohaline continental carbonate salinas. Supra-sealevel (+1–2 m). Hydrographic isolation from marine. Köppen: Aw (1 m)	Three morphological forms of subaqueous mm-laminar bio-eroded lake-edge hydromagnesite-aragonite stromatolites in ephemeral mesohaline lakes (25–110‰), No equivalents in the nearby less saline Coorong Lagoon or in other lakes. The three forms are stratiform, globular, and crenulate. Each is built by cyanophytes, the first two by near monospecific mats (respectively *Microcoleus chthonoplastes* and *Schizothrix splendida*) and the third by a variable association dominated by *Schizothrix gracilis* and *Calothrix crustacea*.	Walter et al. (1973), Warren (1990)
Continental interior, mesohaline	Stromatolites and hardgrounds, Lake Manito, Saskatchewan, Canada. Schizohaline and mesohaline continental carbonate-evaporite lake (salinity ≈50‰). Köppen: Dfb (583 m)	The salinity has increased from 10‰ to about 50‰TDS in the last 2,000 years. The associated decrease in water level has exposed large areas of nearshore microbialites. These organogenic domes range in size from several cm to over a meter in relief and can coalesce into large bioherms several meters high. Most of the larger microbialites formed between about 2,300 and 1,000 cal BP, whereas the hardgrounds, cements, and laminated crusts formed about 1,000–500 cal BP. Bacterial dolomite.	Last et al. (2010)

(continued)

Table 1.3 (continued)

Brine style	Location, climate and hydrology	Characteristics	References
Continental interior, mesohaline	Thrombolitic stromatolites, Great Salt Lake Margin, Utah USA Köppen: Cfa (1,283 m) Similar and even larger tufa mounds also typify the now-exposed lake floors of Mono Lake and Searles Lake (Guo and Chafetz 2012)	Holocene aragonite and Mg-calcite stromatolites covered a 280 km ^{2} area when mapped in 1933 when the lake elevation was 1,279.5 m. Bioherms confined to shallow, nearshore areas where wave activity and water circulation was strong. Occur at depths from 5 cm to 3.7 m and formed isolated 20–30-cm-diameter circular mounds to coalesced bioherms 9 m in diameter. Relief above the sediment surface ranged between 15 and 90 cm. In 1933, some 50 % of the bioherm surfaces covered by brown to pink unicellular cyanobacteria *Aphanothece packardii*. The surfaces of these mounds were highly irregular ("nodose"), with many small protuberances. Internally, the mounds were structureless to crudely banded.	Eardley (1938), Halley (1976), Pedone and Folk (1996), Pedone and Dickson (2000)
Continental interior, mesohaline	Laguna Socompa, leathery domal fringe facies in high altitude lake, 3,560 m asl, Andean Puna, Argentina Köppen: ET (3,563 m)	Stromatolites in In small high altitude lake and made up of broad, rounded, low-dome, up to 24 cm high, and 80 cm wide, leathery diatomaceous bioherms, composed of laminated aragonitic muds with bioeroded edges (mound morphology is very similar to North Stromatolite Lake, Coorong region, South Australia).	Farias (2011)
Lacustrine Brackish (*Supra-sealevel Continental, some Marine coastal*)			
Marine coastal interior	Thrombolitic stromatolite edges, Storr's Lake, San Salvador. Suprasealevel (1–2 m) coastal with hydrographic isolation from ocean Köppen: Aw (0–1 m)	Microbialites around the lake margin are made up of alternating stromatolite and thrombolite layers. They are exposed annually above temporary water levels for intervals of many weeks or months. This alternation of exposure and water coverage is triggered by lake-level fluctuations and associated turbidity variability. This mechanism results in a succession of phototrophic-dominated (stromatolites) to heterotrophic dominated communities (thrombolites) as surface communities.	Mann and Nelson (1989)
Marine coastal interior freshwater marsh	Algal pans and marshes, Andros Island, Bahamas Köppen: Aw (0–2 m)	Laminated leathery freshwater cyanobacterial mats in shallow lakes of Andros Island show similarities to ancient hybrid stromatolites, with fine-grained incipiently lithified cyanobacterial mat layers alternating with laminar fenestrae and elongate open voids	Black (1933), Monty (1976)
Marine coastal interior, mesohaline and schizohaline (30–80‰)	Thrombolitic stromatolite edges in Lake Clifton and Lake Thetis, West Australia, and Sleaford Mere, South Australia. Continental carbonate seepage salinas. Supra-sealevel (+1–2 m) coastal with hydrographic isolation from ocean Köppen: Csa (0–1 m)	Lake-margin indurated domes and biscuits with synoptic relief of up to 1 m, periodically exposed and growing in mesohaline to brackish water about lake edges in zones of meteoric spring outflow. Lithified thrombolitic stromatolites comprised mainly of aragonite with patches of living coccoid cyanobacterial mat characterizing their knobbly dome surfaces in the littoral lake area. In contrast a thick flocculent mat composed of phototrophic prokaryotes (principally purple sulphur bacteria) and diatoms accumulates in the central perennial lake basin area. Are distinguished from other nearby coastal salinas by the presence of the flocculent diatomaceous mat and the juxtaposition of this microbial community to the marginal lithified thrombolitic stromatolites.	Burne and Moore (1993), Grey et al. (1990), Warren (1982a), Timms (2009), Burne et al. (2014)
Continental interior, perennial saline lake (depth ≈ 45 m, salinity ≈ 50–90‰)	Tufa mounds and thrombolites, Mono Lake, California Köppen: BSk (1,208 m)	Calcite tufa mounds up to 5 m high and 2–5 m across as lake fringe buildups and also along linear at-surface fault trends. The identification of modern ikaite forming in present day lake waters each winter and its conversion to calcite with spring warming suggests that both Pleistocene and Holocene tufa mounds in the Mono basin originally formed as ikaite in subaqueous spring outflow zones. Similar genesis to Pyramid Lake mounds.	Council and Bennett (1993), Whiticar and Suess (1998)

Table 1.3 (continued)

Brine style	Location, climate and hydrology	Characteristics	References
Continental interior, perennial lake (depth ≈ 30 m, salinity ≈ 9 ‰)	Domal lake-edge and fault seepage trends of digitate stromatolites, thrombolites and tufa Walker Lake, Nevada Köppen: BSk (1,208 m)	Exposed lake terraces and the present shoreline record a sequence of Pleistocene and Holocene stromatolites and tufas. Include modern columnar stromatolites as much as 4 cm high are subcylindrical to club-shaped discrete, and laterally linked at the base with local branching. These digitate stromatolites start as wavy, generalized stromatolites which are vertically transitional to small, laterally linked cabbage heads with laminae which phototropically thicken over the crests.	Osborne et al. (1982), Petryshyn et al. (2012)
Freshwater lacustrine (*perennial*)			
Continental interior, perennial ponds and springs in playa host	Cuatro Cienegas Pozas, system of several hundred springs, pools and streams as fresh to brackish dissolution ponds in a gypsum playa in the high-relief Chihuahuan desert of Coahuila, Northern Mexico Köppen: BSh (726 m)	The freshwater pools of Cuatro Ciénegas exhibit the lowest phosphorus content reported in continental waters. Microbialites (diatomaceous calcitic stromatolites) thrive because nutrient constraints prevent snails and other eukaryotes from effectively grazing microbialites. Key microbial groups include cyanobacteria, aerobic heterotrophic bacteria, sulphate-reducing bacteria, sulphide-oxidizing bacteria and fermentative bacteria. Stromatolites construct offset, horizontally oriented, outwardly projecting ledges dominated by calcifying cyanobacterium *Homoeothrix balearica*, in conjunction with the uncalcified cyanobacterium *Schizothrix lacustris*.	Breitbart et al. (2009), Visscher and Stolz (2005), Winsborough et al. (1994)
Continental interior, perennial ponds and springs in karst cenotes hosted in Cenozoic limestone	Giant Holocene freshwater microbialite domes, Laguna Bacalar, Quintana Roo, Mexico Köppen: Aw (0–1 m)	The 10 km of total length, make this one the world's largest modern freshwater microbialite occurrences. Microbialites include domes, ledges and oncolites. Domal forms can grow to diameters and heights of 3 m. Microbialites are composed of low magnesium calcite, mostly precipitated by metabolic activity of the cyanobacteria, *Homeothrix* and *Leptolyngbya*, and associated diatoms. Photosynthesis removes carbon dioxide and triggers carbonate precipitation.	Gischler et al. (2008)
Continent interior perennial lake	Pavilion Lake, British Columbia, Canada, freshwater lake up to 65 m deep in a steep-walled limestone valley (pH ≈ 8.5) Köppen: Dfc (806 m)	Calcite microbialite tufa mounds, which can display dendrolitic microstructures similar to *Epiphyton* and *Girvanella*. The morphologies vary with depth, with dendritic microstructures best developed in the deeper water (>30 m) mounds indicate that they may be modern analogs for the ancient calcareous structures.	Laval et al. (2000)
Large continental interior perennial lake	Lake Van, Turkey. Third largest closed lake on Earth. (pH up to 9.7) Köppen: Dfb (1,647 m)	Tufa spires, pinnacles and domes up to 40 m tall growing on lake floor. Perennial lake is up to 450 deep Microbial growth is by mats of coccoid cyanobacteria (*Pleurocapsa* group) permineralizing in situ with aragonite and by inorganically precipitated calcite. Lake water are highly alkaline.	Reimer et al. (2009), Kempe et al. (1991)

Köppen climate determinations based on centroid overlays on Köppen base published by Kottek et al. (2006); see Chap. 2 for full discussion of this climate classification

and preserve microbially-mediated textures (Guo and Chafetz 2012). Internally, microbial textures can be stromatolitic (fine planar-undulating to wavy-crenulated lamination), oncolitic (concentrically laminated), thrombolitic (with mesoscale clotted textures, not to be confused with clotted or grumous microfabrics, which occur in both thrombolites or stromatolites) or cryptic without obvious internal structure (Figs. 1.12 and 1.13a; Manzo et al. 2012).

Microbialites are typically classified according to the dominant internal or external microfabrics (Fig. 1.12), but all microbial categories are intergradational (Fig. 1.13a). In addition to domes/mounds, the overall shape of a microbial construct can encompass varying regions made up of columns, layers, and irregular masses (Riding 2011). A complication in applying a consistent classification is that stromatolite, leiolite and macrofabrics are defined by features that can be intergradational within a single buildup (inset in Fig. 1.11a). A stromatolite is internally layered from the mm to cm scale, while a leiolite is internally composed of aphanitic micrite. At the outcrop scale leiolite appears massive or homogenous and lacks internal lamination. In the type area in the Messinian carbonates of the Sorbas Basin, Spain, leiolite domes are always found in association with stromatolites and dendrolites (Braga et al. 1995).

In contrast to the internal structures defining stromatolites and leiolites, thrombolite and dendrolite macrofabrics are defined by the external shape of individual masses of microbial carbonate, such as clots or small shrub-like masses. Thrombolitic stromatolite, typified by external parts of some Shark Bay columns (Fig. 1.11a), can be internally weakly clotted and crudely laminated, while others are laminated. It is essentially an agglutinated composite, in contrast to Neoproterozoic and early Palaeozoic thrombolites with their calcified microbial microfabrics. In the latter, the clots may be prostrate and irregular, and also vertically extended into amalgamated elongate branches (e.g., *Favosamaceria*).

Biology of Stromatolites and Microbial Layers

Stromatolites to some researchers are a specific layered type of microbialite, often defined as laminated organosedimentary structures with positive relief away from a point or limited surface of attachment (Fig. 1.12; Burne and Moore 1987). In this sense stromatolites are equivalent to agglutinated microbial reefs in the terminology of Riding (2002). To others, stromatolites are not necessarily a biological construct. Microbes and biofilms may be present at the time chemical sediments accumulate, but they play a passive role in textural style during the deposition of this type of stromatolite. Researchers with this view of stromatolites like to add the phrase "it may or may not be of biological origin" to any definition of an ancient stromatolite. This distinction becomes important as we shall see in a later discussion of pre-Mesozoic evaporitic stromatolites, but reliably defining the contribution of a biofilm to rock texture in ancient evaporitic carbonates is at times near impossible.

This difficulty is separating biologic from abiogenic constructs is in part a reflection of how a stromatolite grows and accretes and that stromatolite micro- and macrofabrics commonly intergrade with those of dendrolites and thrombolites (Fig. 1.13a). Stromatolite accretion can involve three main processes: microbial precipitation, inorganic precipitation, and grain trapping (Fig. 1.13b). These main types represent respectively lithified microbial mat, sparry crust, and combinations of these are termed "hybrid stromatolites" by Riding (2011) (Fig. 1.14).

Internal layers of most modern marine-edge stromatolites define the successive positions of agglutinating bioplexi (algal/bacterial community), with each accreting layer produced by trapping and binding of sand to mud-sized sediment (Figs. 1.11 and 1.13b) In some settings, agglutination occurs in conjunction with direct carbonate precipitation onto (surficial) or within (biomineralisation) the mucilaginous sheaths of cyanobacterial trichomes. Both precipitative processes are driven by changes in ambient pCO_2 and variations in the intensity of sulphate-reduction (Table 1.3). Modern saline lacustrine stromatolites tend to encompass precipitative biochemical structures, while modern marine-margin stromatolites, such as Shark Bay, tend to be largely agglutinated structures; both possess surface microbial communities that evolve as the stromatolites prograde (Duane and Al-Zamel 1999).

Many coarser-grained stromatolites in the modern marine and marine margin realms, as in Lee stocking Island and Shark Bay, are poorly layered agglutinated forms and are transitional into thrombolitic structures (Fig. 1.11a; Table 1.3). Fine-grained mm-laminated stromatolites tend to form best in or near seepage zones in modern hypersaline lakes, such as Marion Lake in South Australia, Gotomeer in the Nederlands Antilles and the Dead Sea in the Middle East, rather than in the open marine realm (Warren 1982a; Kobluk and Crawford 1990; Druckman 1981). Recent work on the biomineralisation process, as preserved in Marion Lake, South Australia shows that, over time frame of a few thousand years, the biomineralisation in a stromatolite can evolve into the inorganic precipitative.

The internal lamination of subfossil indurated stromatolites (3,780 ± 110 years) in Marion Lake is characterised by a submillimetric alternation of porous and dense laminae (Von der Borch et al. 1977; Warren 1982a – see Chap. 4 for depositional detail). The microfabric of the laminae is ubiquitously composed of a fine (10–20 μm) peloidal texture, with many thinner aphanitic layers. Aggregates of very fine, low-Mg calcite and aragonite constitute both peloidal and aphanitic micrite, which is coated, respectively, by spherulitic and fringing acicular microspar (Perri and Spadafora 2011; Perri et al. 2012). Micrite, with a high organic matter content, is formed of coalescing nanospheres grading into small polyhedrons, probably composed mainly of aragonite, with less calcite, and is enriched in Mg, Sr, Na and S. Bacteria-like microfossils and relics of extracellular polymeric substance (EPS) occur abundantly within this micritic framework. The former consist of empty moulds and mineralised bodies of coccoid forms, whereas EPS relics consist of sheet-like or filamentous structures that appear both mineralised and more often still preserved as a C-enriched dehydrated substance that represents the main organic matter component of the deposit. Acicular crystals, which show a prismatic elongate shape, are composed of Mg-depleted aragonite that lacks fossils or organic relicts. Degrading EPS and micro-organisms appear gradually to be replaced and entombed by the nanospherical precipitates, implying the existence of processes of organomineralisation within an original syn-sedimentary microbial community. Succeeding micron-scale crystals merge to form isolated or connected micritic aggregates (the peloids), followed by the gradual formation of the acicular crystals as purely inorganic precipitates. That is the diagenetic driver for the mineralisation pass from biogenic to abiogenic.

At the worldscale, dominant members of modern microbial plexi range from archaea to eubacteria to cyanobacteria to algae, with the proportions and species changing with

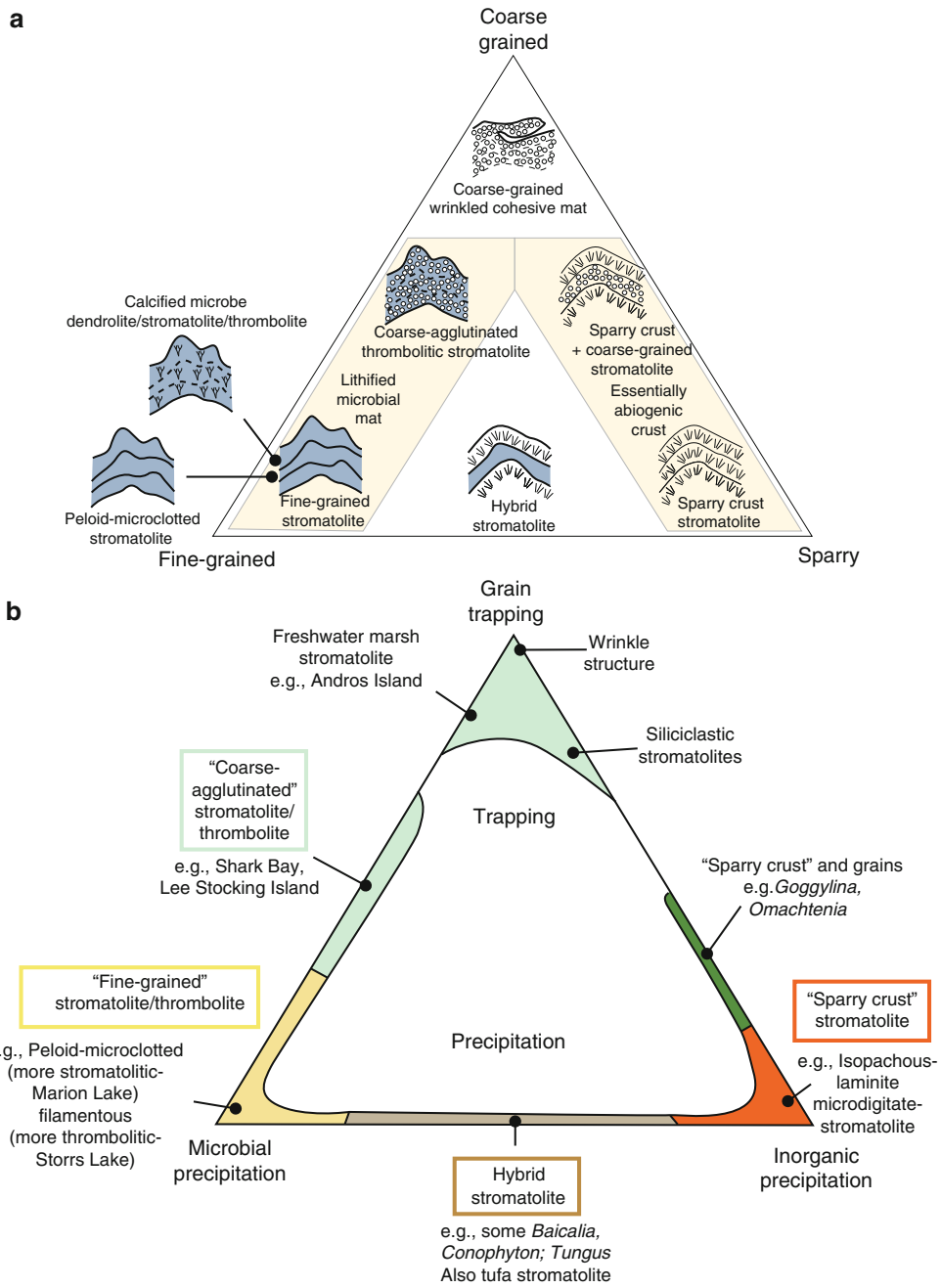

Fig. 1.14 Classification of microbialites (After Riding 2011). (**a**) Classification of stromatolites and thrombolites based on micro/macrofabric. All, except wrinkled cohesive mats, are synsedimentarily lithified by microbial and/or abiogenic processes. Fine-grained varieties include two distinctive types: (i) stromatolites with peloidal-microclotted microfabrics and (ii) dendrolites and thrombolites with abundant filamentous and other calcified microbial microfossils. (**b**) Classification of stromatolitic and thrombolitic carbonates related to grain trapping, and synsedimentary microbial and inorganic precipitation. Principal categories are coarse agglutinated, fine-grained, hybrid and sparry crust. Those dominated by microbial precipitation and/or grain trapping are microbial mats. Sparry crusts are essentially abiogenic precipitates. Hybrid stromatolites are combinations of lithified microbial mat and sparry crust. Fine-grained varieties include filamentous (also termed porostromate, skeletal, and calcimicrobial) which is more thrombolitic and peloidal-microclotted (also termed spongiostromate) which is more stromatolitic. Microbial mats dominated by trapping, but with relatively minor early lithification include freshwater marsh stromatolites and wrinkle marks mainly in siliciclastic sands and silts. For secular distributions see Figs. 1.13c and 1.18

depth in the sediment and salinity of the water column (Chap. 9). The most common biotal constituents of well-preserved stromatolitic bioherms in Phanerozoic evaporitic settings are filamentous and coccoid cyanobacteria, with lesser halobacterias (Figs. 1.13c and 1.14a, b). Species components not only change with water depth and brine salinity but have changed over the course of geological evolution. Modern cyanobacteria typically extrude a mucilaginous sheath that protects the contributing biota from UV radiation. The gooey mucilage also captures sediment particles creating further UV screening, but too thick a sediment layer can cut the necessary exposure to light and so slow photosynthesis. Large amounts of water are held in the mucous sheath and so it also serves as a buffer against osmotic stress in fluctuating salinities.

Modern mesohaline stromatolites exhibit regular occurrences of the halotolerant cyanobacterial species *Microcoleus chthonoplastes*, *Lyngbya* sp., *Entophysalis* sp., *Phormidium* sp. and *Synechococcus* sp. (Gerdes et al. 2000a). *Microcoleus* is one of a number of cosmopolitan cyanobacteria that form ensheathed filamentous cellular bundles in most growing biolaminites. It grows best in the salinity range 80–160‰ but is present as living filaments in salinities as high as 300‰ (Chap. 9). Fibrillar cyanobacteria are able to glide up

and down through nearsurface sediment in order to position themselves in optimal light conditions so that its position below the surface, and the oxygen halo it generates, changes from night to day (Fig. 1.15). This is done by hormogonia, a part of a filament of a photosynthetic cyanobacterium that detaches and grows by cell division into a new filament. Hormogonia are motile and respond phototactically so that, if too much sediment accretes to the mat, or if a deepening brine cover, or the transition from day to night, reduces the light reaching the filaments, they move upwards to where they accumulate on or just below the sediment surface. It is this periodic repositioning that creates the internal laminated structure and phototropic thickening seen in modern stromatolites and algal mats. Left behind in the sediment matrix of an aggrading stromatolite are the abandoned sheaths, immotile filaments, cells and mucilage remnants that, after passing through the decomposer community, become buried organic matter or protokerogen (Fig. 1.15).

Coccoids in modern biolaminites tend to create slime-ensheathed pustules and individual cells grow by binary fission (Gerdes et al. 2000a). *Aphanothece*, *Gloeothece* and *Synechococcus* are three of a number of such coccoid cyanobacteria that make up the other major component of a cyanobacterial plexi. These organisms increase their slime or mucilage content in order to deal with phototoxicity and tend to dominate exposed surfaces of algal mats and stromatolites, as in the algal mats of the Abu Dhabi and Saudi sabkhas (Kendall and Skipwith 1969). Coccoids tend to occur in zones about edges of water-covered biolaminites flourishing on the floors of tidal channels (Chap. 3).

Pleurocapsalian cyanobacteria are a cosmopolitan type of coccoid bacteria, which dominate modern pustular and pinnacle mats. The typical internal structure in a pustule is colonial, with individual nodules showing discontinuous but more or less concentric layers. Slime production is stimulated by an increase in light intensity, salinity or temperature. This creates sediment with a yoghurt-like consistency made up of polysaccharides interwoven with sediment matrix. The slime coat not only protects the coccoids, but also insulates the other species of the mat community from the lethal effects of increasing light, salinity and temperature. Microbial metabolism associated with such slime coats facilitates or even drives the precipitation of primary dolomite in many evaporitic carbonates (van Lith et al. 2002).

It is the alternation between mm-scale layers dominated by the filamentous forms and layers enriched in the coccoids that creates the biolamination of modern marine and marine

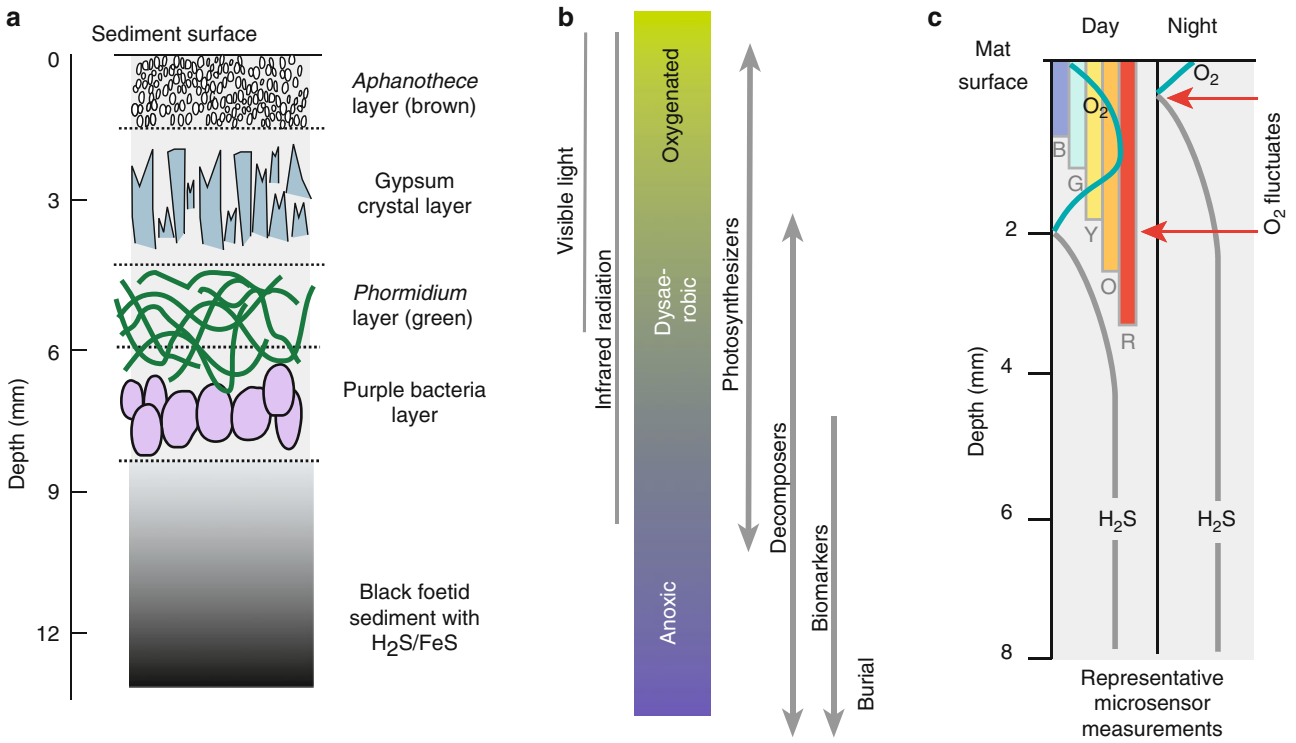

Fig. 1.15 Layering and metabolism in microbial mats. (**a**) Typical microbial community in an evaporitic laminite in a modern coastal salina with salinity in the range 130–200‰ (After Caumette 1993). (**b**) Biogeochemical cycles operating within the mat versus depth. (**c**) Interrelationships between microbes and the oxygen, carbon and sulphur cycles in the uppermost 5–10 mm of a microbial mat. The oxic-anoxic transition shifts lower in the mat in the daytime and higher in the mat at night when photosynthesis has stopped (After Warren 2011 and references therein)

margin stromatolites (Reid et al. 2001; Bowlin et al. 2012). Aggradation in modern marine-edge stromatolite communities represents a dynamic balance between sedimentation and intermittent lithification within the cyanobacterial mat. Periods of rapid sediment accretion, during which stromatolite surfaces are dominated by pioneer communities of gliding filamentous cyanobacteria, alternate with hiatal intervals. Microscale discontinuities in sedimentation are characterized by development of surface films of exopolymer and subsequent heterotrophic bacterial decomposition, which forms thin crusts of microcrystalline carbonate. During prolonged hiatii, climax communities develop, which include endolithic coccoid cyanobacteria. These coccoids modify the sediment micro-environment to create thicker lithified laminae. Subsequence preservation of lithified layers at depth creates the millimetre-scale biolamination that characterises modern and ancient stromatolites.

At the broader scale, successive layers in modern biolaminites can indicate seasonal changes. *Microcoleus*-dominated layers (often associated with diatoms) accumulate in the winter, while coccoid-dominated layers typify the more saline summer growth layers. Alternations of coccoid and filamentous layers in a mat can create lamination, even in the absence of agglutinated sediment. Preservation potential of such organic-only layers is low, unless deposited on the anoxic floor of a perennial stratified brine lake (Chap. 9).

Non-stromatolitic Lacustrine Microbialites

Stromatolites are one part of a much wider group of variably layered microbialites growing in a wide range of saline marine and nonmarine settings (Table 1.3; Riding 2000, 2011; Brasier 2011; Manzo et al. 2012). According to Riding, sediment trapping by filamentous plexi in a modern biolaminite results in an agglutinated stromatolite reef, which is characterised by a particulate microstructure that preserves few, if any, details of the original size, shape or orientation of the biotal plexi responsible for capturing sediment (Fig. 1.13a).

On the other hand, biomineralized deposits, such as thrombolite/tufa/travertine cement reefs described by Riding (2002), retain considerable palaeontological detail about the constituent organisms preserved as skeletal microfossils. Mineralisation is especially important in nonmarine microbialites, as in the lacustrine tufa cement reefs that define the water-covered margins of the less saline high-water stages of many Quaternary salt lakes, as in Great Salt Lake and Walker Lake, USA (Table 1.3). These tufa cement reefs are porous, unbedded or only poorly bedded, and are created by cyanobacteria, algae, grasses, and reeds thriving in brackish to fresh, lake and river waters and groundwater seeps along the landward side of the saline pan or lake edge. Rapid $CaCO_3$ precipitation veneers living plants with cement rinds that would otherwise be masses of soft vegetation (Riding 2000; Pedley et al. 2003; Manzo et al. 2012). Relief on a tufa buildup can be high, with commonplace steep to overhanging, locally cavernous, cemented masses. Tufas tend to occur where inorganic $CaCO_3$ precipitation is enhanced by CO_2 degassing of venting spring waters.

Likewise travertines, which tend to form layered deposits of $CaCO_3$ near the outflow points of groundwater and thermal springs, can preserve details of the contributing microbes. Travertine cement reefs are layered microbialites with dendrolite "shrub" and crystalline fabrics associated with nonskeletal organisms, as in Pavilion Lake, British Columbia (Fig. 1.12; Table 1.3). Deposits tend to form steep-sided mounds, with elevated rimmed pools, normally developed atop and about the mounds (Riding 2002). Smoothly banded crystalline crusts construct horizontal, sloping, vertical or overhanging sheets with pisoids typically developing at the bottom of water-filled pools and polygonal saucers. Folk (1993, 1999) and Chafetz and Folk (1984), along with many others working in travertines, document microbialite microtextures such as spheroidal dolomite, dumb-bell shaped crystals, fine diurnal-layered dendrites and bushes, all of which indicate a strong bacterial contribution to travertine precipitation (Reid et al. 2001). Reeds and grasses can be preserved as moulds within bacterial travertines, but most macroorganisms are excluded by the elevated temperatures and high levels of dissolved minerals (salinity) that typify travertine carbonates. Most travertines are only a few kilometers in lateral extent and, as in tufa cement reefs, subaerial surfaces are common, as are gradations into adjacent marsh and fluvial environments (Manzo et al. 2012; Kosun 2012).

CO_2 degassing, in combination with evaporation and rapid microbial growth, can drive extreme carbon isotope enrichment in the organic matter and co-precipitates in many CO_2 -limited organic-enriched sediments, including evaporitic marls, tufas and travertines (Schouten et al. 2001). Enriched $\delta^{13}C$ values of up to +13‰ in calcite and −10‰ in organic matter were measured in calcite tufas accumulating in well-oxygenated carbonate saturated waters in El Peinado and San Francisco lakes, both high altitude saline lakes in the southern Andean Altiplano, northwestern Argentina (Fig. 1.16). Valero-Garces et al. (1999) argue that the large enrichments of the heavier carbon isotopes in the algally bound sediments indicate nonequilibrium gas-transfer fractionation of the carbon isotopes during CO_2 degassing. Parent waters were derived from thermal springs and subject to subsequent evaporative concentration. In general most ions in lacustrine tufas in volcanic settings ultimately come from geothermal and volcanic CO_2 sources. Physical fractionation, rather than biological enrichment in these settings, may have a greater significance than credited in the commonly accepted biological metabolism arguments typically used to explain carbon isotope records in evaporitic carbonates

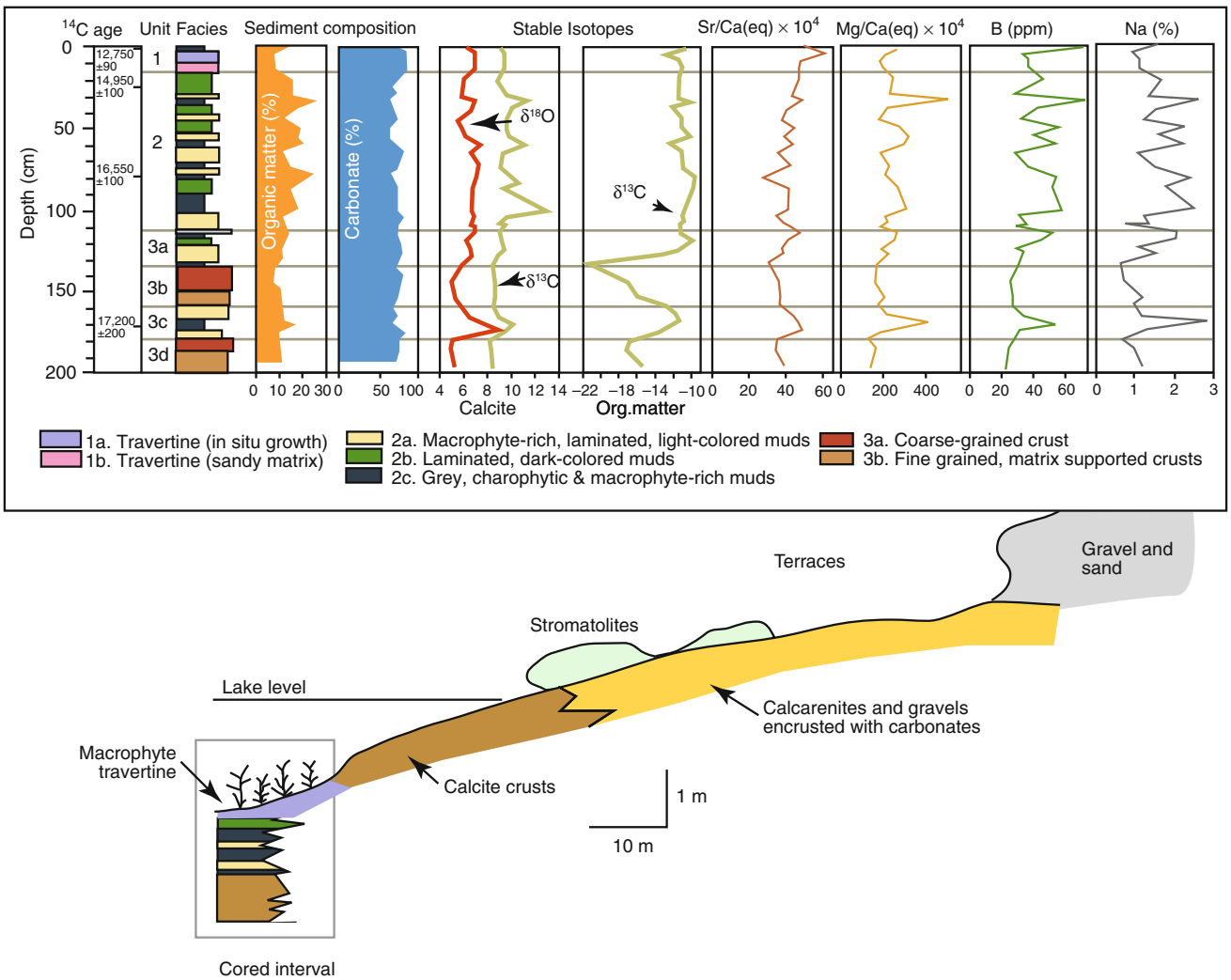

Fig. 1.16 Sedimentary facies, sediment composition, stable isotopes and geochemistry of the Lake El Peinado core, Andean Altiplano. Core was collected in the perennially subaqueous carbonate margin of the lake (After Valero-Garces et al. 1999, 2001). Macrophytes are the current active carbonate binders. Stromatolites today are not active, but grew at an earlier time of more saline water when conditions did not favour macrophytes. Dates are uncorrected AMS 14C ages (years BP). All isotopic measurements are reported as δ values vs. the PDB standard

(see Schouten et al. 2001 for opposing argument). Likewise, the dilution of the isotopic signature by C-14-free CO_2 from volcanogenic sources may hinder accurate C-14 chronologies of lake sedimentation when based on samples of lacustrine organic matter and other aquatic plants.

Microbial plexi can also flourish in a gypsum or siliciclastic host. Meter-sized gypsiferous thrombolites coated by well-developed zonally-differentiated microbial mats have been found growing in the shallow water rim (<1 m deep) of a restricted hypersaline lagoon, Laguna Pirata on the Archipelago Los Roques in Venezuela (Petrash et al. 2012). While within the deeper parts of the same lagoon there are several decimetres of organic-rich material containing gypsum granules and lacking carbonate cementation. The biolithification of the thrombolites is thought to have proceeded as follows: (1) Extracellular polymeric substances (EPS) comprising the microbial mat concentrate Ca^{2+} and other metal cations by adsorption from the hypersaline waters. (2) Some of these bound cations then serve as nucleation sites for primary calcium carbonate precipitation. (3) While carbonate phases are forming in some zones of the mat, in other zones they are being re-dissolved due to the acidity generated through the metabolism of sulphide-oxidizing bacteria. (4) As the dissolved sulphide is oxidized into sulphate, the porewater become saturated with respect to gypsum. (5) As primary gypsum precipitates within the structures, endolithic sulphate-reducing bacteria metabolize the sulphate moiety in the mineral phase, while simultaneously oxidizing the EPS trapped during accretion. (6) As microbial EPS degradation proceeds, the anaerobic oxidation of specific protein fractions

of the EPS matrix leads to increased alkalinity, the partial dissolution of gypsum, supersaturation with respect to calcium carbonate, and ultimately pseudomorphic aragonite replacement; this differs from secondary calcite cements in being enriched in ^{12}C, and depleted in minor and trace metals initially associated with the EPS.

Microbial plexi in a siliciclastic host are typically referred to as wrinkle mats or wrinkle structures and are a common feature in Precambrian sediments. The lack of carbonate minerals and sulphate-reducers makes for a minimum of penecontemporaneous metabolism-related carbonate cementation and they are typically interpreted as dominated by grain trapping processes (Fig. 1.14b). Microbial mats can also occur in a gypsiferous clastic host. This type of saline sedimentary structures, related to mat growth, belong to the group of "mat expansion structures" known as "petees" (Krumbein et al. 1994; Vogel et al. 2009). The name petee is not exclusive as it has also been applied to inorganic pressure expansion ridges and polygons in halite crusts (Bouougri et al. 2007). Petees, as defined by Krumbein et al. (1994) in reference to evaporitic clastic sediment surfaces with biofilms, tend to deform the upper, cohesive part of any gypsum-rich microbial mat into bulges and domes, thus enlarging the mat surface. Sometimes, laterally interacting bulges may be arranged in a polygonal pattern. If petees are filled by combinations of chemical sediment and muds rising up from below, a petee surface may be preserved, such ancient examples have been named "petee ridges" (Schieber 2004; Lokier 2012).

Study of biofilms in the lower portions of gypsum crusts in the gypsum salterns (pre-halite concentrators) at Guerrero Negro has shown they play a role in determining the gypsum saturation state for both the inner regions of precipitation-dominated deposits and biofilm supported surfaces (Vogel et al. 2009) Specifically, biofilms are present where gypsum dissolution has occurred in the interior regions of stacked gypsum bed surfaces. At lower salinities, biofilms apparently facilitated gypsum precipitation within the biofilm-supported surfaces. Both of these processes (dissolution and precipitation) are reflected in fabrics, textures, and mineral morphologies in the crusts. The dissolution zone is important because it becomes a lacunal boundary between the gypsum and the underlying sediment, which is often sulphidic, with much lower gypsum volumes. Significant volumes of gas, containing up to 30 % methane, can occur in sediments beneath gypsum precipitation surfaces in a saltern (Don Bebout, pers. com.). The dissolution zone provides accommodation space for this gas facilitating domal forms and so creating a morphology that may be preserved upon burial (Vogel et al. 2009).

Microbialite Sedimentology in Saline Lakes

Mineralisation associated with biofilm metabolism in hypersaline lacustrine settings is much more important than simple agglutination capture that occurs in many Holocene lacustrine microbialites (Table 1.3). Niches occupied by stromatolites and tufa/travertine cement reefs in saline lacustrine settings circumscribe a much wider range of salinities and water conditions than evidenced by modern marine thrombolites and stromatolites; for example, some modern coastal lacustrine thrombolites in Venezuela are gypsiferous (Petrash et al. 2012). Isopachous biomineralized subaqueous stromatolite reefs, texturally identi cal to their ancient mm-laminated counterparts, still grow in the mesohaline carbonate-saturated seepage waters of some modern marine-fed gypsum lakes (von der Borch et al. 1977; Warren 1982a). The coarse-layered sandy agglutinated forms of Shark Bay and the mud-cracked supratidal algal mudstones of the Abu Dhabi sabkha have fewer ancient evaporitic counterparts.

Similarly, healthy carbonate-precipitating microbialite communities in the upper parts of less-saline carbonate-rich littoral and slope breaks about many prograding lacustrine margins in modern temperate and tropical carbonate lakes, can be used as analogs for microbial growth in the high water stages of some ancient saline basins (Table 1.3; Dean and Fouch 1983). For example, modern thrombolites, tufas and stromatolites occur in littoral waters (10–60 m deep) about the edges of Lake Tanganyika (Cohen and Thouin 1987) and Salda Gölü in Turkey (Braithwaite and Zedef 1996). Near identical fresh to brackish water stromatolites, along with oncoids, travertines and tufas, occur in Plio-Pleistocene sediments of the East African Rift Valley lakes (Casanova 1986). Similar marginward microbial tufa cement reefs (bioherms) reached thicknesses of 7 m, with diameters of 15 m, in the Oligocene Ries Basin (Riding 1979; Arp 1995). Freshwater to mesohaline stromatolites characterise Oligocene lake margins in France (Casanova and Nury 1989) and the 1–10 m deep freshwater-filled evaporite karst pond fills (posas) in a modern gypsiferous playa, Cuatro Cienegas in Coahuila, Mexico (Fig. 1.11b; Minckley 1969; Winsborough et al. 1994). Other examples of ancient lacustrine counterparts include the Tertiary of southern France (Truc 1978) and the Eocene Green River Formation of the USA (Seard et al. 2013).

Widespread mm-laminated fine-grained evaporitic stromatolites tend to accumulate in more saline lacustrine settings, settings where surface brines are waters supersaturated with respect to a carbonate phase, typically aragonite. In these settings the role of biology is less obvious in the laminates. Biofilms of archaea, eubacteria and algae can be passive agglutinators rather than active participants during the formation of domal to massive laminar stromatolites. It is in this group of structures that the phase "may or may not be of biological origin" comes into play. Modern examples of such enigmas include manganiferous aragonitic stromatolites that define the northwestern strandplain margin of the Northern Basin of the Dead Sea (see Druckman 1981 vs. Garber and Friedman 1983). Texturally identical evaporite-associated

biomineralized stromatolites and biolaminites have characterised the mudflat and strandzone margins of saline and alkaline playa lakes and marine evaporite basins throughout much of the Phanerozoic, especially at times or in regions of transition into or out of episodes of basinwide evaporite precipitation.

Mineralogy in most modern saline lacustrine stromatolites is dependent on what carbonate phase is precipitating in the ambient lake water. This is true even when biotal metabolism plays a significant role in driving carbonate precipitation. Stromatolites and microbial bioherms are aragonitic in many modern saline lakes (e.g. Great Salt Lake, Eardley 1938; Marion lake, South Australia, von der Borch et al. 1977) and the precipitation process is often facilitated by the metabolic activities of bacteria. As part of this carbonate saturated spectrum, brine-shrimp egg cases are replaced by aragonite in the growth cavities of modern stromatolites in Great Salt Lake, Utah (Pedone and Folk 1996). Hydromagnesite-aragonite mm-laminated stromatolite domes and mats dominate in the schizohaline ephemeral waters of North and South Stromatolite Lakes in the Coorong region of South Australia (Table 1.3; Chap. 4), while poorly preserved hydromagnesite-magnesite stromatolites characterise many present-day playa surfaces across the Caribou Plateau in Canada (Renaut 1993a). Similar stromatolite domes characterise the highly alkaline (pH>9) fresh to brackish waters of Salda Golu (Lake) in Turkey where lake margin subaqueous stromatolites are composed mostly of hydromagnesite, along with entrapped diatom tests (Fig. 1.17 and Chap. 4; Braithwaite and Zedef 1994, 1996).

At the basin scale, Quaternary calcitic and aragonitic algal tufa and travertine reefs form atop spring vents in groundwater outflow zones, where they can construct substantial spring mounds (Habermehl 1988). Tufa annual growth rates can be impressive in these vent-associated features; Rosen et al. (2004) documented aggradation rates of 30 cm/year in the modern subaqueous tufas of Big Soda Lake in Nevada. In contrast, the annual layers preserved in lacustrine stromatolites are much thinner. When layers in Holocene stromatolites from Walker Lake, Nevada (United States) were dated using high-resolution ^{14}C dating techniques the lamina accretion rate for the 5 cm thick stromatolite layer was low and varied over the period the stromatolite grew from 500 to 3,000 years BP (Petryshyn et al. 2012). At the base of the structure, the laminae formed with a period of 5.6 ± 1.6 years/lamination, in the middle at 1.6–2.8 ± 1.9 years/lamination, and 4.5 ± 0.8 years/lamination at the top of the laminated portion. The predominant 4–6 years periodicity implies that lamination formation is likely more closely related to regional climate forcing (e.g., El Nino-Southern Oscillation) versus the typical diurnal or seasonal changes traditionally assumed for most ancient stromatolites. Some of the impressive thinolitic tufa reef mounds in cool -water temperate and high-altitude saline lakes were originally constructed of an unusual but interesting variety of low temperature calcite called ikaite (Chap. 4). This hexahydrate form of calcite is found today forming ephemeral precipitates in near freezing brines around spring vents of CO_2 -rich waters in Mono Lake and in Quaternary sediments of the Lohanton Basin (Pyramid Lake), Nevada. Similar spectacular tufa mounds occur in groundwater outflow zones on the subaqueous floor of Lake Van, Turkey (Kempe et al. 1991).

Once the water temperature about a spring mound rises above 3–4 °C the ikaite dehydrates to calcite, but the calcite can preserve the characteristic lenticular and twinned outline of its precursor. But a lenticular to lozenge shape in a calcite pseudomorph is easily confused with other evaporite minerals, such as gypsum and gaylussite, which also are readily pseudomorphed by calcite (Chap. 7). Ikaite pseudomorphs can have little to do with an evaporite precursor, and occur in modern marine shelf sediments of the Antarctic and in modern and

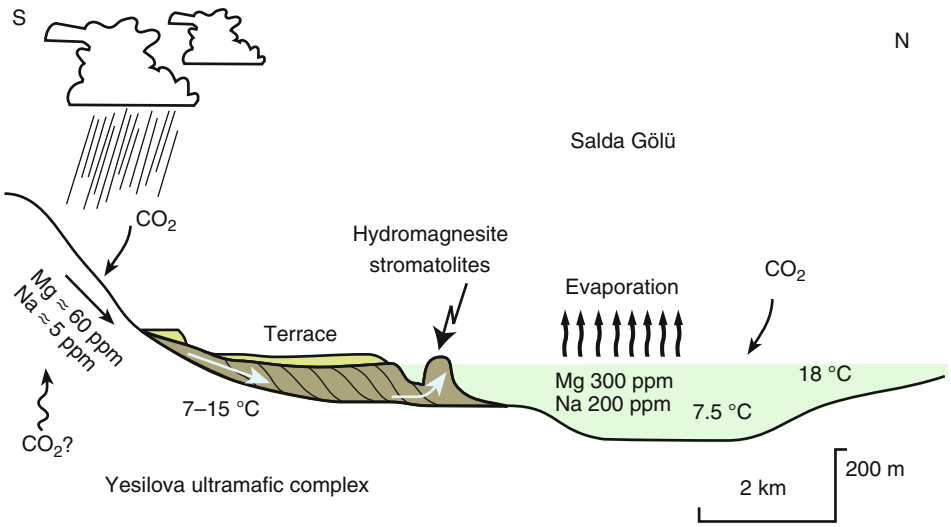

Fig. 1.17 Schematic cross section of Salda Gölü showing hydromagnesite stromatolites growing subaqueously in front of the carbonate tufa terrace (After Russell et al. 1999)

ancient glacial outwash fans from around the world (Shearman and Smith 1985; Larsen 1994; Riccioni et al. 1996).

The perennial, cold, biologically-stressed freshwaters of glacially-fed freshwaters of Lake Untersee in Antarctica provide an interesting setting for conical stromatolite growth (Andersen et al. 2011). Lake Untersee is one of the largest (11.4 km^2) and deepest (>160 m) freshwater lakes in East Antarctica. Located at 71°S the lake has a perennial ice cover, a water column that, with the exception of a small anoxic basin in the southwest of the lake, is well mixed, supersaturated with dissolved oxygen, alkaline (pH 10.4) and exceedingly clear. The floor of the lake is covered with photosynthetic microbial mats to depths of at least 100 m. These mats are primarily composed of filamentous cyanophytes and form two distinct macroscopic structures, one of which – cm-scale cuspate pinnacles dominated by *Leptolyngbya spp*. – is common in other freshwater lake in Antarctica, but the second – laminated, conical stromatolites that rise up to 0.5 m above the lake floor, dominated by *Phormidium spp*. – has not previously been reported in any modern environment, but are analogous to the ancient stromatolite known as *Conophyton*.

The laminae that form the conical stromatolites are 0.2–0.8 mm in thickness consisting of fine glacial clays and organic material; carbon dating implies that laminations may occur on near decadal timescales. The uniformly steep sides (59.6° ± 2.5°) and the regular laminar structure of the cones suggest that they may provide a modern analogue for growth of some of the oldest well-described Archaean stromatolites. Mechanisms underlying the formation of these stromatolites are as yet unclear, but their growth is distinct from that of the cuspate pinnacles. The sympatric occurrence of pinnacles and cones related to microbial communities with distinct cyanobacterial compositions suggest that specific microbial behaviours underpin the morphological differences in the structures across fresh to saline lacustrine settings (Andersen et al. 2011).

Microbialite Sedimentology in Marine Settings

Unlike modern stromatolites and microbialites, which tend to construct significant rock masses in salinity or temperature stressed environments, Precambrian stromatolites were environmentally diverse and abundant across hypersaline, normal marine and nonmarine settings. They first appeared around 3.45 Ga and dominated biogenic sedimentation from 2,800 to 1,000 Ma (Fig. 1.18; Riding 2011). The beginning of their Proterozoic decline and environmental restriction, variously identified at 2,000, 1,000 and 675 Ma, has been attributed to reduced marine cementation or to eukaryote competition. The former was perhaps tied to higher CO_2 concentrations in the atmosphere and higher calcium concentrations in Precambrian oceans compared to oceans of today (Laval et al. 2000), while biogenic competition related to the evolution of shelly exoskeletons and the gastropod radula (Garrett 1970a). The previously enigmatic lack of calcified cyanobacteria filaments in stromatolite-bearing Precambrian sequences is now explained as a likely result of high concentrations of dissolved inorganic carbon in the Precambrian ocean (Arp et al. 2001) or by the postulate that a high proportion of many Archaean stromatolites were the result of inorganic precipitates and the resultant isopachous cement layering (Pope et al. 2000).

Precambrian stromatolites were not confined to the more arid peritidal marine or marginward lacustrine seep situations that characterise most Phanerozoic stromatolites. Such high stress environments (hypersalinity/exposure) tend to exclude many metazoan marine grazers that otherwise browse and destroy algal mats. Modern areas of thick extensive marine-margin stromatolites/cryptalgal laminites are located at the edge of the cropping range of marine grazers. Examples of gastropod restriction include the seaward side of the algal facies of the Arabian Gulf (Kendall and Skipwith 1969), the hypersaline intertidal flats of Shark Bay, Western Australia (Logan 1987) and bio-eroded edges of lacustrine stromatolites in the Coorong Region (Warren 1990).

Various thrombolites and dendrolites, mainly formed by calcified cyanobacteria, became important marine microbialites early in the Palaeozoic and reappeared in the Late Devonian, as marine stromatolite populations declined. Microbial marine carbonates retained their importance through much of the Mesozoic, they became scarcer in marine environments in the Cenozoic, but locally re-emerged as large agglutinated domes, possibly reflecting increased algal involvement in sediment binding and cementation.

There are still a few modern normal-marine settings where metre-scale stromatolites flourish. Holocene columnar stromatolites grow as part of a thrombolite-stromatolite association on the floor of modern tidal channels off Lee Stocking Island, Exuma Cays. These bio-columns show three associations of internal sedimentary structures: (1) prokaryotic stromatolites comprised of alternating layers of coarse-grained ooids and peloids, and fine micrite that are formed exclusively by microbial activity; (2) eukaryotic stromatolites comprised of microbially-induced micritic layers alternating with detrital layers bound and cemented by eukaryotic algae; and (3) thrombolites displaying irregular, clotted fabrics and formed by communities of microbes, algae, and metazoans (Fig. 1.19a; Feldmann and McKenzie 1998).

Onshore in San Salvador in shallow turbid water, beneath the modern mesohaline waters of Storr's Lake, marine-influenced thrombolite layers alternate with stromatolite layers to create mushroom shaped mounds. This alternating layering perhaps reflects changes in salinity and light penetration (Fig. 1.19b; Mann and Nelson 1989). Formation of many modern marine thrombolites has been attributed to

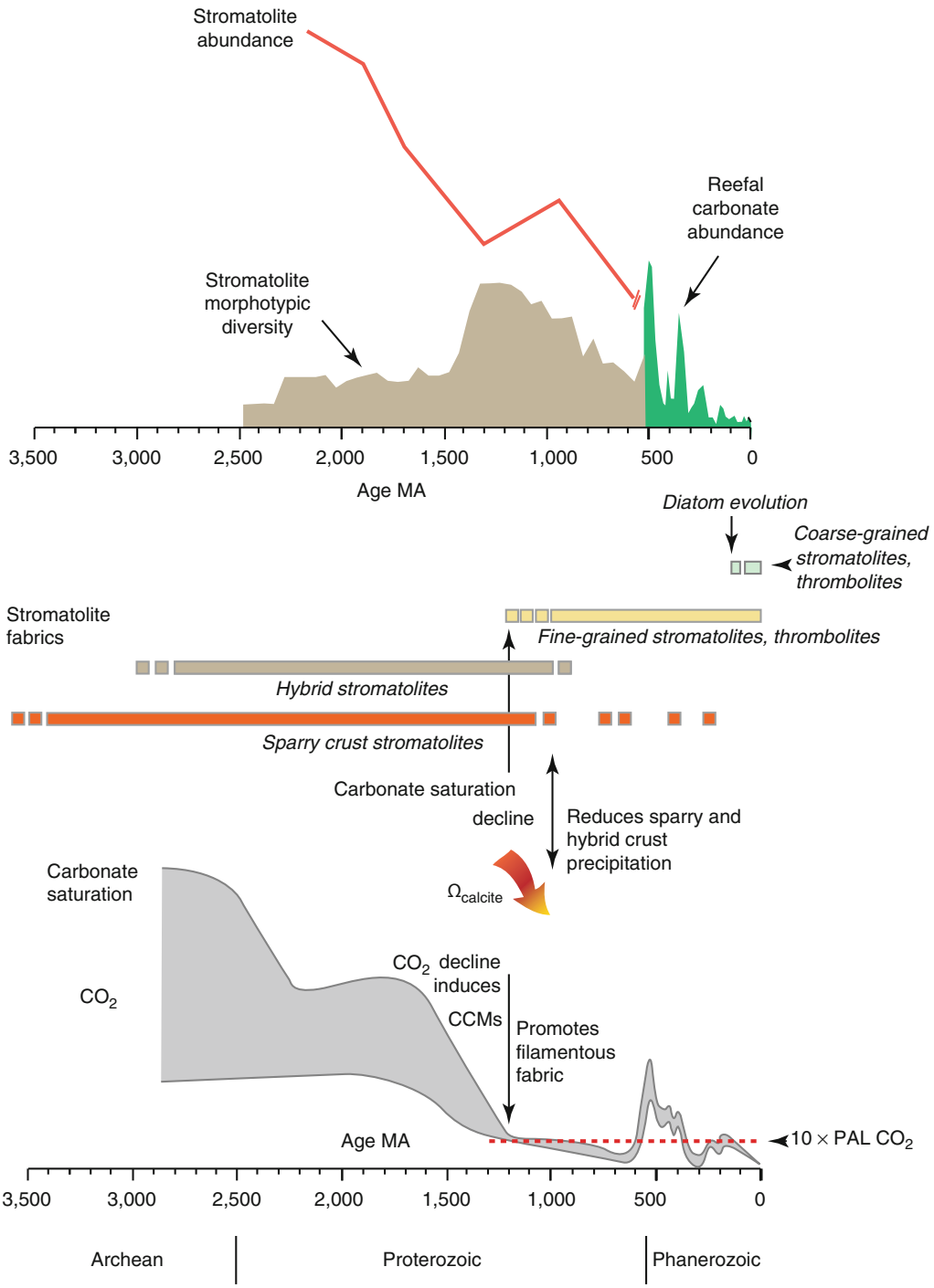

Fig. 1.18 Secular trends and possible controls on microbial carbonate developments across time as compiled by Riding (2011) and references therein. It includes Proterozoic stromatolite abundance (Grotzinger 1990) and morphotypic diversity (Awramik and Sprinkle 1999), together with Phanerozoic reefal microbial carbonate abundance (Kiessling et al. 2003). These suggest overall long-term decline for at least the past 1,000 Ma. Reduction in both Sparry Crust and Hybrid stromatolites 1,000 Ma ago may reflect decline in seawater carbonate saturation (Grotzinger 1990). Stromatolite-like sparry crust occurs sporadically in the Phanerozoic, particularly in evaporite basins (Pope et al. 2000). Increases in thrombolites 1,200–1,000 Ma ago could reflect development of cyanobacterial sheath calcification, reflecting inception of CO_2-concentrating mechanisms (CCMs) as CO_2 levels declined to 10 times present atmospheric level (PAL). Late Neogene inception of coarse agglutinated stromatolites and thrombolite could in part reflect incorporation of diatoms into microbial mats and also generally low values of seawater carbonate saturation

carbonate precipitation driven in large part by sciaphile (dark-loving) bacteria, which flourish under low sedimentation rates, low water energies and higher turbidity, hence the preservation of a clotted fabric and lack of lamination (Dupraz et al. 2009; Dupraz and Strasser 1999; Riding 1991). Phanerozoic marine thrombolites, in contrast, are mostly interpreted as non-laminated microbialites (not stromatolites) constructed by cyanobacteria and are not usually interpreted as sciaphiles.

According to Feldmann and Mckenzie (op. cit.) the contemporaneous formation of prokaryotic stromatolites, eukaryotic stromatolites, and thrombolites under identical conditions within the present marine environment is unlikely. They suggest that the prokaryotic stromatolites in the Lee Stocking bioherms represent microbial forms that began to develop in an environmentally-stressed intertidal setting during the early Holocene flooding of the Great Bahama Bank. In contrast, thrombolites began to form under the present,

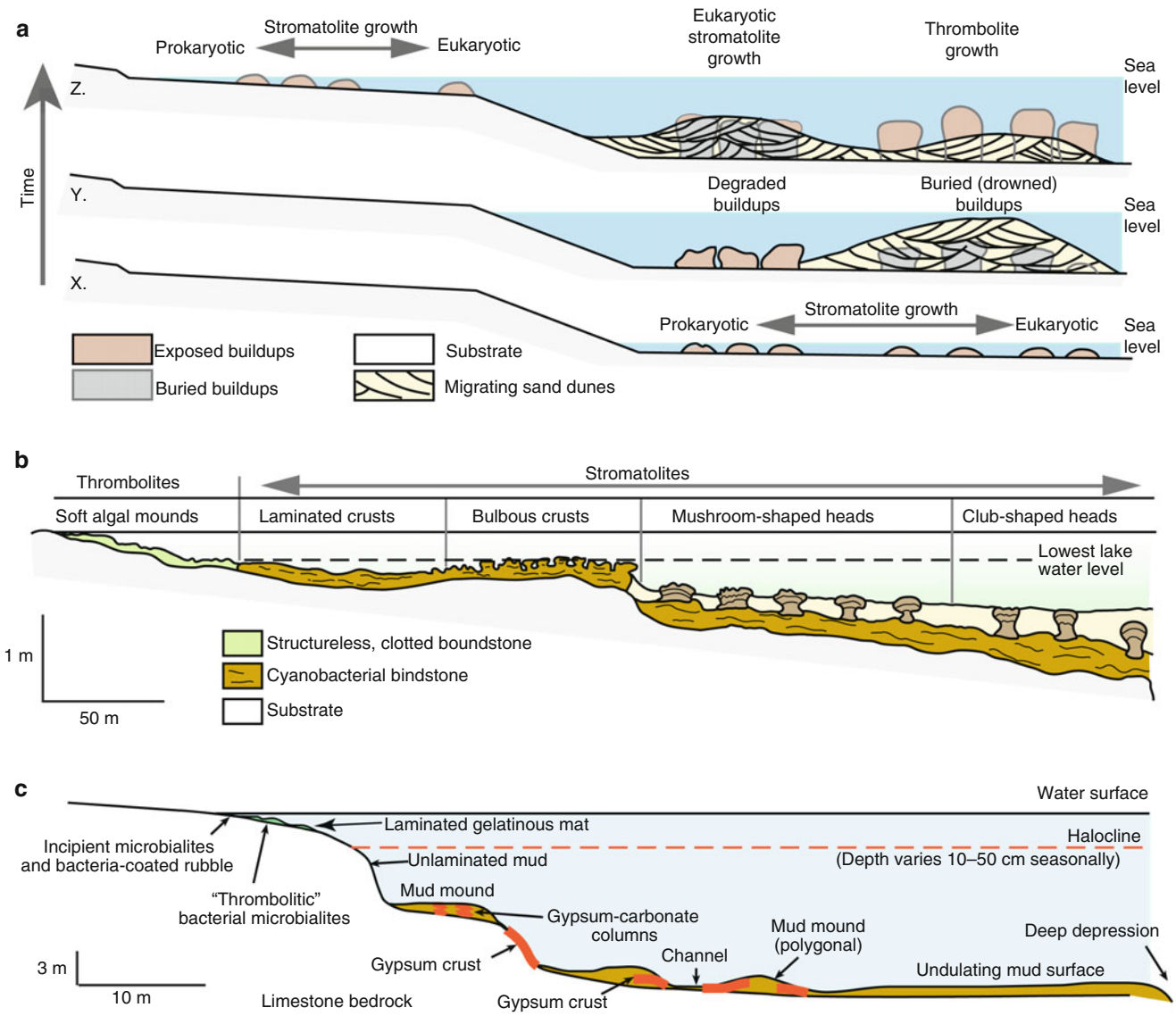

Fig. 1.19 Thrombolites in mesohaline to marine settings. (**a**) Evolution of microbialites during a rise in sea level from time X to time Z in the formation of marine subtidal stromatolites in Lee Stocking Island in the Bahamas (After Feldmann and Mckenzie 1998). (**b**) Distribution of algal/thrombolitic structures in mesohaline aragonite muds of Storr's Lake, San Salvador (After Neumann et al. 1988; Mann and Nelson 1989). (**c**) Thrombolites (aragonitic) passing into gypsiferous mud mounds below the halocline at the southern end of the channel in Gotomeer, Bonaire (After Kobluk and Crawford 1990)

normal-marine subtidal conditions (Fig. 1.19a). The eukaryotic stromatolites represent intermediate forms between prokaryotic stromatolites and thrombolites, with a gradual change from stromatolite to thrombolite reefs tied to rising sealevel. With the deepening, there would have been a decrease in salinity, an increase in energy, and possibly an increase in nutrient supply; all factors that favour thrombolite growth.

Unfortunately, most environmental and depositional models for Phanerozoic stromatolites tend to draw heavily on Holocene peritidal marine-margin analogs, such as Shark Bay, a hypersaline setting where sand grain trapping (agglutination), rather than micrite precipitation, is the dominant mode of sediment accretion. Accordingly, using modern analogs, many sedimentologists assume that well-preserved Phanerozoic stromatolites must have formed in intertidal to supratidal marine settings. As we shall see in Chap. 5, a marine-connected basin is not the best way to model evaporitic carbonates associated with thick evaporites. Microbes living in ancient saline systems constructed a far more diverse and wide ranging biotal association in evaporitic settings than simplistic Shark Bay analogs imply (Chap. 9).

Microbialites Typify Marine to Evaporite and Evaporite to Marine Transitions

Throughout the rock record, Pope et al. (2000) noted that a transition between a carbonate platform or an isolated carbonate buildup and the overlying evaporites is commonly defined by assemblages of stromatolites or interlaminated carbonates and evaporites (Table 1.4). Stromatolites display lamination textures that vary from peloidal and discontinuous on a scale of a millimetre to a few centimetres, to isopachous and continuously laminated on a scale of a centimetre to a few metres. Isopachous lamination may be composed of either: (1) micrite or radial-fibrous calcite, or (2) dolomite. Isopachous laminae are remarkably uniform, varying little in thickness over a given lateral distance, whereas stromatolites formed of peloidal laminae, tend to show marked variations in thickness over an equivalent lateral distance (phototactic thickening). They observe that isopachous textures are uncommon on most open-marine carbonate platforms and apparently developed in transitional carbonate-to-evaporite settings because of basin isolation and drawdown leading to increasing temperature, salinity, and anoxia related to water stratification and saturation with respect to the precipitated carbonate (Table 1.4; Fig. 1.20a). The resulting ecologic restriction created an opportunity for isopachous stromatolite growth.

Stromatolites with isopachous lamination are interpreted to form via in situ precipitation of sea-floor-encrusting calcite and possibly dolomite, whereas the stromatolites composed of peloidal, discontinuous lamination are inferred to have formed by trapping and binding of loose carbonate sediment in microbial mats and can be unrelated to the onset of basinwide evaporite restriction and drawdown. According to Pope et al. (2000), isopachous stromatolites may have accumulated by chemogenic precipitation in the absence of microbial mats, while peloidal stromatolites grew by agglutination in the presence of microbial mats and since the onset

Table 1.4 Selected examples of unique evaporitic carbonate fabrics in basinwide transition facies passing from carbonate through mesohaline to hypersaline deposition

Location	Units	Carbonate fabrics	Composition
Great Slave Lake, Canada, Palaeoproterozoic (1.8–1.9 Ga)	Perthei Grp. (c) Stark Fm. (e)	Tufa, isopachously laminated stromatolite at contact in shallow water; Fibrous marine cements throughout platform	Basinwide evaporite, Halite >> gypsum (no anhydrite)
Oman, Vendian (570–543 Ma)	Buah Fm. (c) Ara Fm. (e)	Fibrous marine cements throughout platform and isolated thrombolitic bioherms; Isopachously laminated stromatolites at contact; tufa-like crusts in carbonates within evaporates	Basinwide evaporite, Halite >> gypsum
Michigan Basin, Silurian (≈400 Ma)	Guelph Fm. (c) Salina Fm. (e)	Fibrous marine cements within pinnacle reefs; Isopachously laminated stromatolites (travertine-like coatings) cap marine reefs; Calcite laminites in interpinnacle reef areas	Basinwide evaporite, Halite >> anhydrite, potash salts
Western North America; Middle Devonian (≈385 Ma)	Winnepegosis (c)	Stromatolites cap marine reefs, fibrous marine cements in reefs and carbonate-evaporite laminites between reefs in deeper-water settings	Basinwide evaporite, Halite >> anhydrite
Sverdrup Basin, Carboniferous, Arctic Canada	Nansen (c) Otto Fiord (e)	Carbonate-evaporite laminites in basinal setting, fibrous marine cements throughout shelf-margin reefs and buildups	Halite ≈ anhydrite
Zechstein Basin, England, Late Permian (≈260 Ma)	Middle Magnesian Limestone (c) Hartlepool Anhydrite (e)	Fibrous marine cements throughout reef complex; Isopachously laminated stromatolites (Crinkly Beds) in bioherm capping marine reef complex; Laminar coatings within bioherm, neptunian dykes and cavities; Laminites in basinal setting between buildups	Basinwide evaporite, Halite >> anhydrite Locally on platform: Anhydrite >> halite
Mediterranean Messinian (Middle Miocene)	Terminal Carbonate Complex (c)	Thinly laminated stromatolites at transition from marine carbonate to evaporite; fibrous marine cements within reefs underlying stromatolites	Basinwide evaporite, Halite >> gypsum
Abu Shaar Complex, Egypt; Messinian (Middle Miocene)	Ruidais Fm. (c) Kareem Fm. (e)	Fibrous marine cements throughout marine reef complex; Thinly laminated stromatolites with fibrous cements on toe of slope; Unique pisoids with distinctive fibrous fabric	Basinwide evaporite, Anhydrite > gypsum > halite

After Pope et al. (2000) and contained references
c carbonate, *e* evaporite

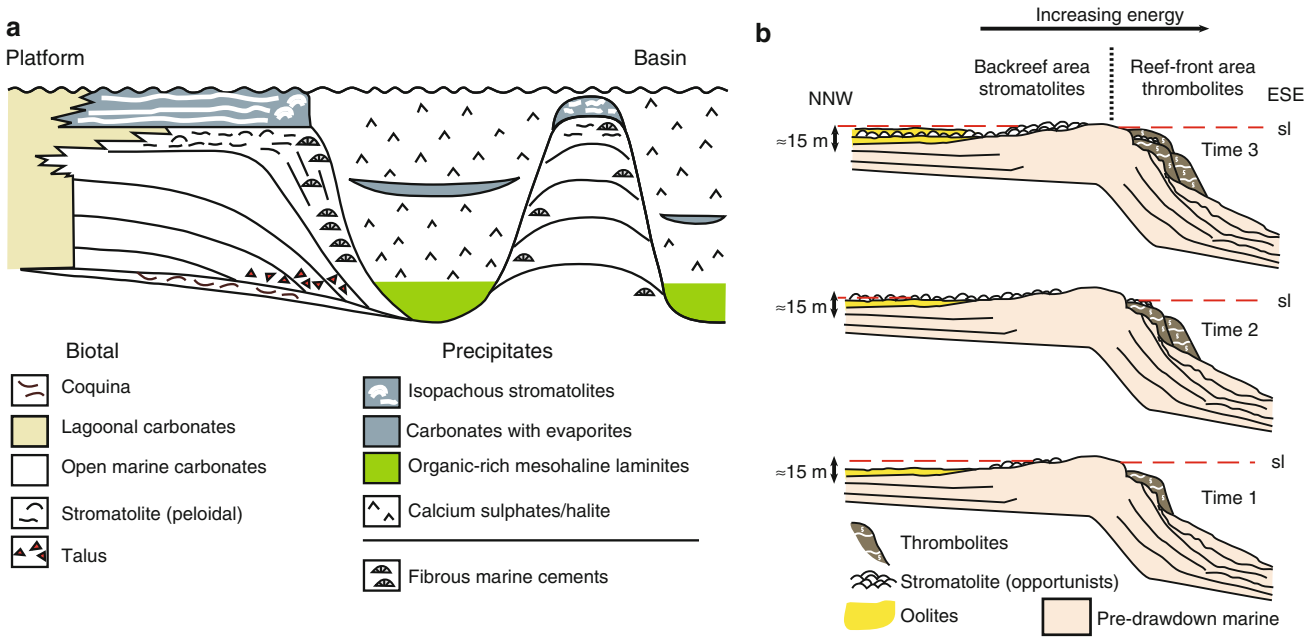

Fig. 1.20 Schematics of marine carbonate to evaporite transitions. (**a**) Typical transitions, showing relative positions in the basin stratigraphy of precipitated isopachous stromatolites and the precipitated carbonate fabrics that typify sediments accumulating mesohaline carbonates immediately prior to complete basin isolation and drawdown that defines the onset of basinwide calcium sulphate and/or halite evaporite deposition (After Pope et al. 2000). (**b**) Platform edge distribution of stromatolites and thrombolites relative to cyclic sea-level changes during the Intra-Messinian flooding event in a marginal Mediterranean sub-basin. (Time 1) Relative high sea-level stand with thrombolite growth in the subtidal zone at the front reef, oolite deposition in the deeper parts of the back-reef area, and stromatolite growth in the intertidal zone of the back-reef area. (Time 2) Relative low sea-level stand promoting thrombolite growth in the basinward migrated subtidal zone at the front reef and opportunist stromatolite growth in the intertidal zone on both the previously deposited ooid sands and thrombolites. (Time 3) Relative high sea-level stand with thrombolites growing over the preceding stromatolites in the subtidal zone at the front reef, opportunist stromatolite growth in the intertidal zone of the back-reef area, and sand deposition in the deeper water of the back-reef area (After Feldmann and McKenzie 1997)

of the Phanerozoic have been largely restricted to environmentally stressed biogenic sediment. The isopachous stromatolites dominated by cementstone textures plot in the sparry stromatolite portion of the classification plot for modern and ancient stromatolites (Fig. 1.14). I would not exclude biofilms from such isopachous stromatolites, it is just that high inorganic precipitation rates, especially in hypersaline settings, can swamp phototactic effects used to interpret ancient biofilms.

Pope et al. (2000) went on to note that when compared to pre-Mesozoic occurrences, stromatolites with thin, isopachous lamination and radial-fibrous textures, though present, are rare to absent in transition facies in Jurassic and younger evaporite basins, such as the Messinian of the Mediterranean region. Instead, the isopachous precipitative facies have been replaced by stromatolites with peloidal, clastic phototropic textures and by mesohaline mudstones with a low-diversity diatomaceous and coccolith biota. These stromatolites are sometimes in terlayered with thrombolites (as in Storr's Lake, Caribbean). They interpret the shift away from chemogenic stromatolites to agglutinated stromatolites as a change in seawater chemistry tied to the evolution of the nannoplankton.

Since the mid-Mesozoic, the accumulation of the biogenic planktonic mudstones beneath deeper ocean waters had three important effects: (1) Increased production of coccolith tests in the world's oceans (chalks) helped extract calcium carbonate from seawater, thus lowering the growth potential for inorganic precipitation of sea-floor-encrusting stromatolites. (2) Settling of both coccoliths and diatoms would have created a sediment flux to the sea floor, which would have served to impede growth of chemically precipitated stromatolites because of ongoing smothering of any growing seafloor crystals. (3) An increase in the Mg/Ca ratio in ocean waters, with consequent effects on the chemistry of marine bittern salts (Chap. 2).

Post-Mesozoic peloidal stromatolites (bio-agglutinates) and thrombolites tend to characterise transitions into and out of episodes of basinwide evaporite deposition. One of the best-preserved transitions of this style of stromatolite/thrombolite occurrence comes from the Late Miocene of SE Spain in cyclic stromatolitic carbonates deposited during and at the termination of the Messinian salinity crisis (Fig. 1.20b; Chap. 5). For example, large microbial carbonate domes (both stromatolites and thrombolites) defined the margins of the Sorbas and Alboran Basin during the uppermost Messinian. They

occur in a unit overlying the Messinian evaporite succession and were deposited in a variety of environments, including strandzones on fan deltas (Martin et al. 1993b; Braga et al. 1995), beaches, and oolitic shoals (Riding et al. 1991).

Their abundance and continuity in the transitional marine setting is comparable in many respects to their omnipresence as transitional forms in the Precambrian. There is, however, an important difference in some parts of the Messinian sequences. Although major unconformities separate normal marine reefs from the carbonates of the "terminal complex complex (TCC)," an impoverished and depauperate, normal-marine biota of Late Miocene corals (*Porites*), coralline algae, serpulids, bivalves, and encrusting foraminifers at times lived alongside the stromatolitic microbes while the TCC was accumulating (Martin et al. 1993b; Braga et al. 1995). The intimate association of stromatolites with a stressed, but stenohaline, marine biota rules out the possibility of continually elevated salinities at the onset of TCC deposition, as suggested by several earlier authors to account for the occurrence and proliferation of widespread microbial structures in the Messinian strata (Esteban 1980; Rouchy and Saint-Martin 1992). The most plausible explanation for this transition into and out of hypersaline into normal marine waters is that microbes acted as opportunistic biota and, for a time, outcompeted other organisms, settling and growing successfully in most of the available and rapidly expanding marine niches (Pope et al. 2000; Feldmann and McKenzie 1997). This happened during the initial stages of marine recolonization of the Mediterranean Sea, after drawdown and deposition of either the lower or upper evaporite sequences.

Thus, the development of microbial structures during the Messinian seems to be related, although indirectly, to the end of each "salinity crisis" and the creation of unoccupied marine ecologic niches as seawater encroached on drawdown unconformities. Earlier but ecologically comparable vacant niche scenarios are found atop Phanerozoic platform carbonates at the onset of basinwide evaporite stages (Table 1.4); examples include the Silurian of Michigan Basin (Sears and Lucia 1979) and the Permian of the Zechstein Basin (Paul 1980). In all these examples an abundance of stromatolites and thrombolites in normal marine environments in the aftermath of a mass extinction of the pre-existing marine benthic biota via drawdown can been explained by the stromatolite and thrombolite communities acting as opportunistic disaster forms taking advantage of vacant ecologic niches (Schubert and Bottjer 1992).

Vadose Pisolites, Ooids and Coated Grains

Fenestral carbonates, sometimes intercalated with grainstones, are frequently interpreted as peritidal sediments (Shinn 1983). Many evaporitic grainstones facies are dominated by coated grains, including oolites, and those with a wave-agitated mechanical genesis are indicated by well preserved crossbed sets. A marine conception is indicated by nuclei of marine shell fragments and intercalation with packstones and wackestones containing marine fossils. More typically in evaporitic settings these metre-thick beds of coated grains lack obvious crossbeds or marine fossils and are intercalated with biolaminites and sharp crosscutting truncation surfaces. Units tend to be inverse graded and coarsen upward into pisolitic rudstones, they are commonly interlayered with evaporite solution breccias (Figs. 1.21 and 1.22a). Pisolitic beds show many textural features, such as bridged coats and polygonal fitting of pisoids, that imply they formed "in situ", under conditions of little or no wave-induced agitation. Individual pisolites, now composed of calcite or dolomite, can show nonconcentric internal truncation surfaces and brick-like crystal terminations indicative of exposure and an aragonite parent (Fig. 1.22b, c; Assereto and Folk 1976).

Pisolite rudstones tend to be caught up in tepee structures or other saline strandzone layers and beds that retain internal

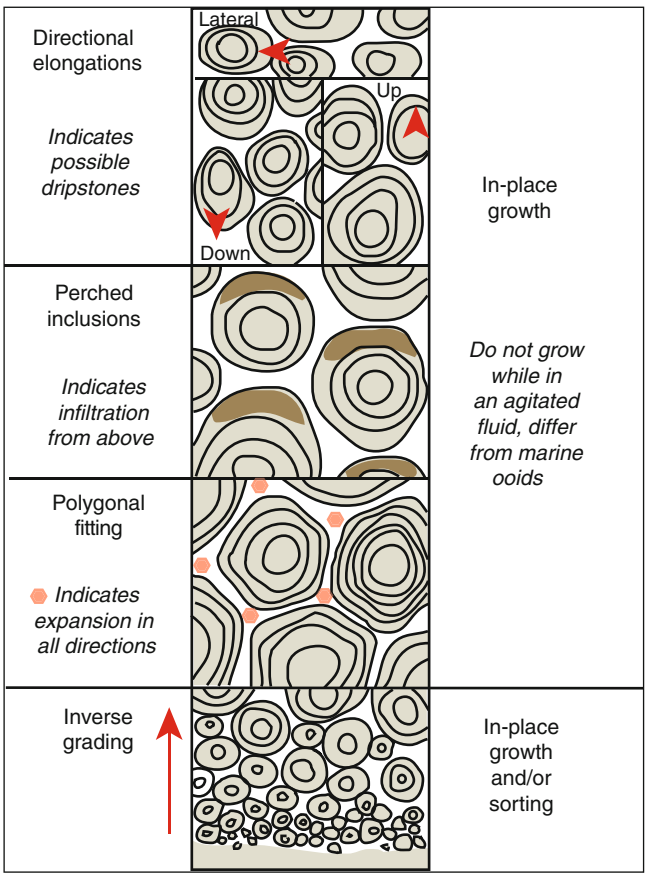

Fig. 1.21 Fabrics of pisoids created by in-place processes. Although all these features have been interpreted as requiring vadose pore conditions, only downward directional elongation (micro-stalactite) require such an interstitial condition (After Esteban and Pray 1983)

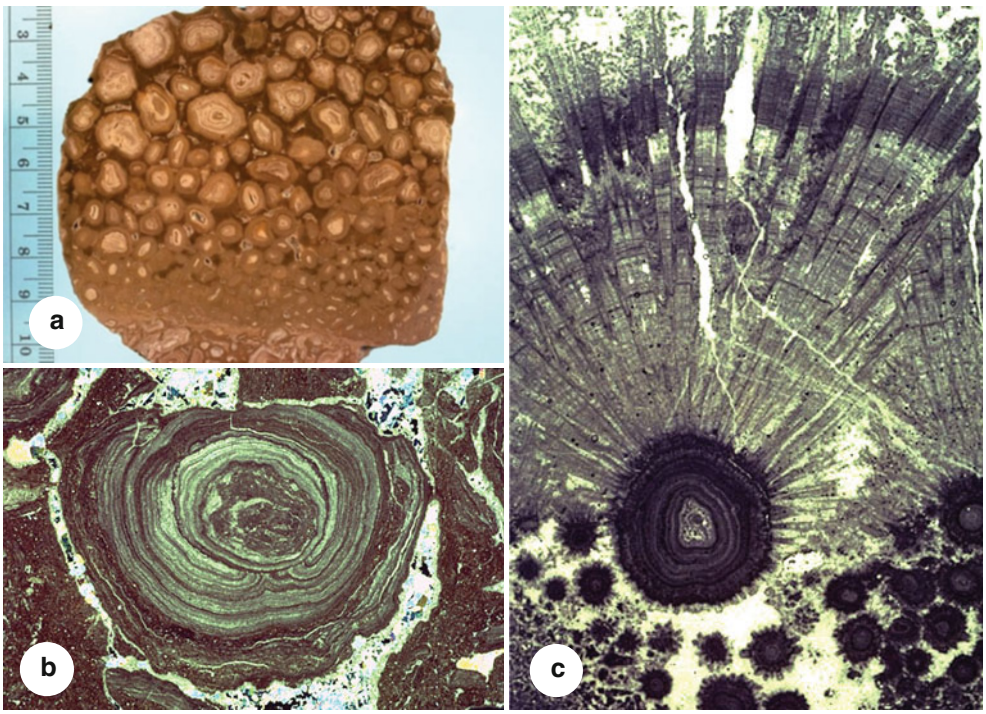

Fig. 1.22 Pisolites from Permian of West Texas. (**a**) Polished slab of pisolitic dolomite from the uppermost Yates Formation. Note reverse grading of grains, and "fitted fabric" in which grains have interlocked boundaries produced by compromise growth of outer coatings. Sample from roadside outcrop at "hairpin turn" on New Mexico Highway 7 in Carlsbad Caverns National Park, Eddy Co., NM. (**b**) Thin-section photomicrograph (cross-polarized light) of a pisoid from the Yates Formation. Note irregular, lumpy, partially concentric coatings; fracturing ("autobrecciation") of micritic- peloidal matrix; and evaporite plugging of remnant intergranular porosity. Sample is from 1,708.1 ft depth in Gulf/Chevron PDB-04 well on Northwestern Shelf of Delaware basin, 30 km ENE of Carlsbad, Eddy Co., NM. Long axis of photo = 14.5 mm. (**c**) Thin-section photomicrograph (plane-polarized light) of a marine-cemented pisolitic dolomite showing transition from pisoid to botryoidal cement crust. Note that the extremely elongate rays of cement which extend from upper surface of the pisoid show squared crystal terminations. This is used as evidence for an originally aragonitic composition for the cement. Sample from 1,739.3 ft depth in Gulf/Chevron PDB04 well on Northwestern Shelf of Delaware basin, 30 km ENE of Carlsbad, Eddy Co., NM. Long axis of photo = 16 mm (Images and descriptions courtesy of P. Scholle)

structures and cements indicative of alternating vadose and phreatic conditions. Such features include; perched inclusions, inverse graded pisolite beds, and pendulous circumgranular cements (Fig. 1.21; Dunham 1972; Esteban and Pray 1983; Handford et al. 1984; Husinec and Read 2006). They indicate a depositional setting that was part of a strandzone, typified by the "to and fro" of the strandline edge of a brine lake or seaway in a zone of groundwater seepage. The associated watertable rose and fell as, pore water conditions alternated between vadose and phreatic.

Pisolite crust cements formed in a strandzone retain infiltrated micrite and pendulous grain underhangs that indicate the sediment spent at least a part of its time above the watertable. The term vadose pisolite is sometimes used to distinguish these evaporitic pisolites from permanently subaqueous isopachous "marine" pisolites or the pedogenically formed calcrete pisolites. The prefix marine is a little misleading when describing isopachous pisolite crusts. Modern examples of isopachous pisolites, along with fitted, pisolith crusts define $CaCO_3$ saturated peripheral marine seepage areas on the strandplain of evaporite-filled coastal lakes in western and southern Australia (Warren 1982a, 1983a; Handford et al. 1984) and the thermal spring-fed margins of large halite-filled continental salars in the Andean Altiplano (Risacher and Eugster 1979; Jones and Renaut 1994). Both settings lack a surface connection to marine waters. The term seepage should perhaps replace the term marine when describing strandzone pisolites.

Ancient pisolites may be marine-fed or continental; all accumulated in $CaCO_3$ saturated waters. Seepage pisolites are part of a sedimentological association where pisolite crusts are forming mainly as accretionary chemogenic particles in areas of cooling, degassing and concentrating resurgent groundwater (in both marine and nonmarine fed hydrologies). Many are coated with microbial communities, which through their photosynthetic activity help drive the process of carbonate supersaturation. Seepage pisolites occur within confined saline groundwater seepage areas that are located on, or adjacent to, extensive carbonate mudflats about saline waterways, even when the waters rarely reach

$CaSO_4$ saturation (Husinec and Read 2006). However, it is emphasised that pisolites (and tepees) are not restricted to marine seepage settings, but also form about the strandzone margins of continental saline lakes and salars.

Esteban and Pray (1983) argue vadose (seepage) pisolites characterise the Permian island shoal and sandflat facies of West Texas (Fig. 1.23). There pisolitic crusts were thicker and most obvious within the central depressions of decametre-diameter saucers in what was an extensive tepee-overprinted megapolygonal terrain. Warren (1983a) argued the same pisolite zones were part of a marine seepage facies about the edge of a widespread saltern/mudflat depression that covered the platform interior and rather that being the high were likely situated behind a sandy island shoal. Nominal "marine" pisolites are characterised by isopachous rim cements, little or no grain fitting and few vadose textures. They are commonplace in normal marine Precambrian carbonates compared with the Phanerozoic marine (Swett and Knoll 1989). Their greater abundance reflects a more carbonate-saturated marine chemistry in Precambrian seas (see below). But, throughout geological time, an isopachous pisolite texture has also been a boiler-plate feature of the carbonate-saturated hypersaline lacustrine realm.

Work by Gerdes et al. (1994) has shown that in addition to "seepage" pisolites other carbon ate grains, such as ooids and peloids, typically thought of as indicators of marine conditions and mechanical agitation, can precipitate *in situ* in $CaCO_3$ -saturated evaporitic settings. They grow within modern microbial mats in hypersaline settings and require no wave-agitated or pelagic phase to precipitate concentric laminar grain coats. Laboratory experiments with unconsolidated muds, and comparisons with fenestral and grainstone textures in evaporitic Guadalupian backreef strata in West Texas by Mazzullo and Birdwell (1989), demonstrated that intense *in situ* hypersaline alteration of fenestral mudstones can create peloidal grainstones. They go on to argue that such diagenetic grainstones may be the precursors of some forms of pisolitic rudstone.

Wave-agitated shore-parallel crossbedded ooid sand belts, very similar to their modern marine look-alikes, can accumulate in a lacustrine strandzone. For example, cross-stratified oolitic lacustrine grainstones and packstones typify wave-agitated strandzone or lake margin sediments of contemporary Great Salt Lake, Utah (Eardley 1938), the Upper Cretaceous to Eocene lacustrine strandzone of Green River Formation of the Uinta Basin, Utah, USA (Williamson and Picard 1974) and the high energy, lake-shoreline carbonates of the Upper Triassic Mercia Mudstone Group of southern Britain (Milroy and Wright 2000). Texturally these hypersaline ooids show a radial texture that contrasts with the more typical tangential structure of modern marine ooids. Eardley (1938) noted that ooid sand bodies in Great Salt Lake are concentrated along relatively narrow, wind-swept coasts, adjacent to steep basement promontories and in waters that are less than 2 m deep (Chap. 4). In contrast, strandzone algal bioherms are typically, although not exclusively, associated with wider, less exposed and more gradually inclined shorelines distal to basement uplands. Work by Halley (1977) on ooids from the Great Salt Lake showed that in an agitated setting radial ooids are structurally weaker than comparable tangential marine ooids (Chap. 4). He argued that a statistically significantly proportion (>1 %) of syndepositionally broken ooids is a reliable indication of radial aragonite ooids associated with hypersaline shorelines (see also, Husinec and Read 2006).

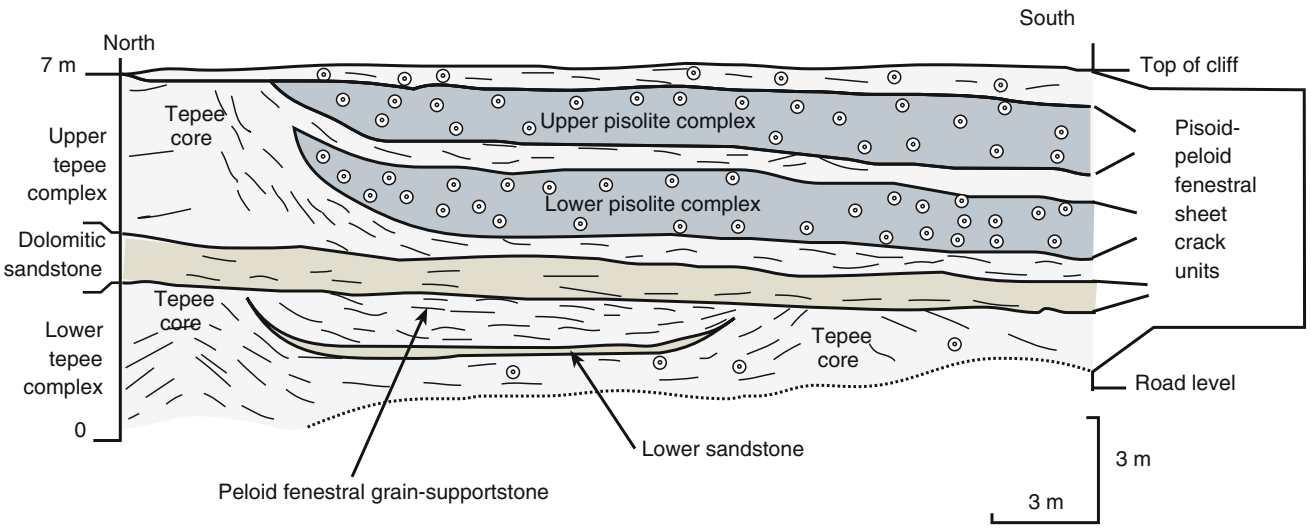

Fig. 1.23 Cross section of a field locality of the Permian Tansill Formation at Hairpin Curve in Guadalupe National Park, West Texas. Note the prominent development of pisolites in intertepee depressions within the upper tepee complex and the erosional surfaces that truncate the tepee complexes (After Esteban and Pray 1983)

Tepees

Tepees are the buckled and broken margins of saucer-like megapolygons in limestone or dolomite crusts that appear as an inverted "V" in vertical two-dimensional exposures (Figs. 1.23 and 1.24a, b; Adams and Frenzel 1950). Tepees are commonplace strandzone features in both modern and ancient settings (Assereto and Kendall 1977; Warren 1982a, b, 1983a; Esteban and Pray 1983; Kendall and Warren 1987; Logan 1987; Kendall 1989; Smoot and Lowenstein 1991; Last 1992; Jones and Renaut 1994; Mutti 1994; Armstrong 1995; lokier and Steuber 2009; Verwer et al. 2009). Some authors have extended the use of the term tepee to pressure ridges in crusts of gypsum or halite. I prefer to restrict usage of the term tepee to overthrust ridges in carbonate crusts and to use the term pressure ridge for overthrust ridges in halite or gypsum crusts. That is, although I use the term tepee non-genetically, I restrict its usage to carbonate crusts and add a prefix to describe its genesis, e.g. groundwater/seepage tepee, seafloor tepee, sabkha tepee, caliche tepee (Kendall and Warren; 1987).

However, not all tepees are tied to sheet expansion via carbonate cements precipitated from supersaturated saline waters, some may be related to microbial growth (Chow and George 2004) and yet others to seismic disturbance and associated thixotropy (Pratt 2002) or saturation in overpressured

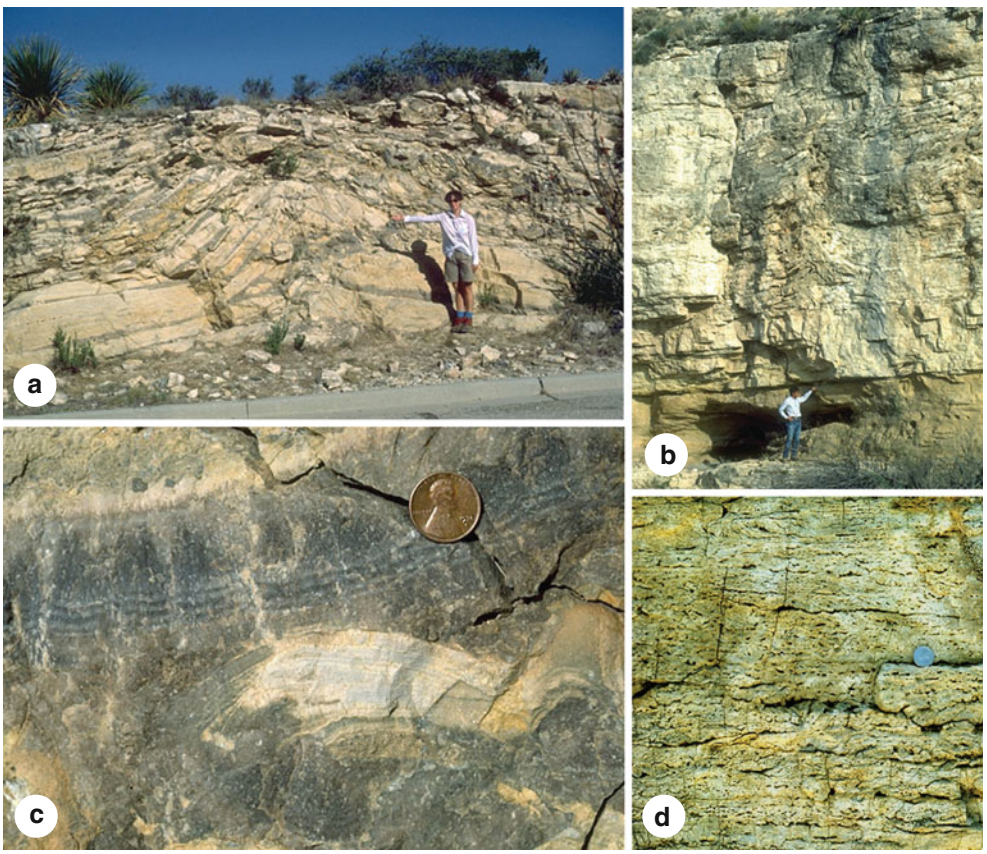

Fig. 1.24 Tepee Structures, Permian Basin, West Texas. (**a**) Tepee structure in Tansill Formation. Note that if the upturned margins of the structure were returned to a horizontal position, they could not be accommodated on a flat bedding plane; this shows that these are expansion polygons. Light yellow layers are dolomitised pisolitic and fenestral sediment; darker, gray layers are zones of sheet spar (aragonitic cement crusts). Interstitial growth of aragonite (in marine or coastal spring settings) was the most likely cause of sediment expansion and buckling. Outcrop at southwest end of parking lot at Carlsbad Caverns visitor's centre, Carlsbad Caverns National Park, Eddy Co., NM. (**b**) Stacked sequence of tepees, associated with fenestral and pisolitic dolomites, in the basal part of the Tansill Formation. A 1.8 m thick sandstone at the base of the exposure (at level of man) has truncated tepee stacks in the underlying Yates Formation and possibly acted as an aquifer for the resurging brines that precipitated these tepees. The sandstone sheets, which thin to a feather edge toward the shelf margin, have been interpreted as sabkha sandflats formed by eolian processes during sea-level lowstands. Roadside outcrop on Dark Canyon road approximately 2 km west of the canyon mouth, Eddy Co., New Mexico. (**c**) Close-up of sheet spar (aragonite cement) crust from within a tepee structure. Note growth of banded cements from top as well as bottom of cavity and incorporation of fragments of matrix sediment. Roadside outcrop at hairpin turn on New Mexico Highway 7 in Carlsbad Caverns National Park, Eddy Co, NM. (**d**) Peloidal and skeletal grainstones with fenestral fabric in the near-back-reef Tansill Formation. These strata were probably deposited on a relatively high-energy mudflat. Outcrop on south side of Dark Canyon, less than 1 km west of the canyon mouth, Eddy Co., NM. Coin is 2.4 cm in diameter (Images and descriptions courtesy of P. Scholle, see http://geoinfo.nmt.edu/staff/scholle/guadalupe.html; accessed May 5, 2014 for more details on this region of New Mexico)

sediments (Gammon et al. 2012). Some workers restrict the use of the term tepee to inorganic overthrust structures (carbonate and salt hosts) and use the term petee to describe overfolded to overthrust ridges in what were originally biogenically-bound surface layers. Petees can occur in layers and crusts composed of both evaporitic carbonates and more saline salts, the ridge crest need not be fractured, but can be a series of polygonally linked folds. See Gavish et al. (1985) for the original definition of petee and Noffke et al. (2003) for a comprehensive discussion of petees and other microbially induced sedimentary structures that are commonplace in evaporitic settings. Microbial petees typically have synoptic relief measured in centimetres, but range up to a metre high in the lagoonal strata of the Devonian Lennard Shelf in the Canning Basin of northwest Australia (Chow and George 2004).

Saline-tepees, along with vadose pisolites are characteristic features of cemented carbonate crusts in areas of a strandplain that experience wetting and drying cycles, $CaCO_3$ -saturated groundwater seepage, fluctuating salinity conditions, and marked diurnal changes in surface and nearsurface temperatures (Fig. 1.24c). Successive episodes of tepee development often stack one bed atop another, with the tepee-overprinted units separated by erosion surfaces, breccias or carbonate-cemented quartz sands (Figs. 1.23 and 1.24d). Pisoids in the Permian strata of West Texas appear to accumulate best within intertepee depressions or saucers (Fig. 1.23; Esteban and Pray 1983). Subsequent expansion episodes, along with local buckling, may rework beds formed in these pisoid-rich depressions into new tepees. When the pace of resurgence was strengthened during times of increased groundwater outflow, tepee crests were capped by domal stromatolites (Warren 1982a; Kendall and Warren 1987).

Many ancient tepee-influenced horizons in saline settings are interbedded with evaporite solution collapse breccias. This characteristic intercalation reflects the to and fro of a brine sheet edge over the strandzone carbonate facies, typically at times when the platform was isolated from a surface connection to the ocean and brine levels were fluctuating in response to the vagaries of evaporitic drawdown (Chap. 5). Some evaporite solution collapse may postdate the depositional hydrology of the cycle that formed the tepee, but, based on modern analogs such as Marion Lake and Lake Macleod, the schizohaline brine hydrology that forms the marginward saline seeps, where tepees flourish, is dominated by pore waters that are undersaturated with respect to halite and gypsum. Resurging groundwaters dissolve nearby evaporite beds as they form the tepee/pisolite beds (Warren 1982a). Because many tepee and seepage pisolite studies are done in the outcrop area of the basin of interest, the significance of thin evaporite residue layers that outcrop as thin layers in a thick stacked sequence is either missed or ignored. Such outcrop features are seen as shortterm exposure surfaces by workers who do not realise these thin residua/breccia bed indicate the former presence of metres to tens of metres-thick evaporite bed. When the unaltered equivalents of these "hiatii" are seen in core they are typically saltern anhydrites. This effect of the telogenetic passage of the platform margin into outcrop should be distinguished from syndepositional evaporite dissolution which can go handin-hand with the formation of stacked and brecciated tepee beds.

The typical result of ongoing early evaporite dissolution (≈eogenetic) is the disturbance or collapse of the tepee-affected strata. Any subsequent prograding of the seepage margin into the edge of an evaporite basin means the tepee zone is cannibalised from below and along its landward margin by its own groundwaters. All that may be preserved as widespread evidence of a prograding tepee hydrology within an ancient platform cycle is a terra rosa profile mixed with remnant breccias composed of fragments of tepee crusts, stromatolite breccias and other residues of the strandplain (Burri et al. 1973; Assereto and Kendall 1977; Bogoch et al. 1994; Mutti 1994).

Evaporite horizons, so typical of sump environments that are located downdip and intercalated with tepee horizons, typically dissolve. Dissolution can very early and effect the depositional landscape or in the mesogenetic or telogenetic realms. These evaporite beds and rarely make it back to the surface as outcrop other than as thin residua horizons. Yet outcrop is where Lidar based studies are done in order to better interpret perceived palaeo-elevations end associated tepee facies inter-relationships, (Verwer et al. 2009). The high probability of syndepositional or early burial evaporite dissolution and its influence of ambient topography is not understood or largely ignored in such studies. So, the tepee--island shoal facies are interpreted as the topographically highest position in the landscape at the time of deposition. Locally, this may be so in regions of strong artesian outflow (as about the pisolitic edges of most drawdown and many endorheic arid lacustrine basins), but much less likely in pisolite zone accumulating in what are interpreted as a open-marine platform edge or ramp setting. These systems, with their inferred surface (hydrographic)[2] connection to the open marine cannot possess the hydrological head required to drive such a pisolite-tepee system (see Chap. 2).

In plan view, tepee ridges define the upturned edges of megapolygonal saucers, typically tens ot metres across (Fig. 1.25). As such they indicate upwelling water-saturated very-shallow watertable conditions where crust volume is

[2]I define brine bodies that are connected to the world's oceans via an at-surface water body as having a hydrographic connection. I do this to contrast the connection hydrology in drawndown water bodies, which require a subsurface or seepage connection. This marine-seepage conduit may be either an open phreatic (no overlying aquitard or aquiclude) or artesian connection.

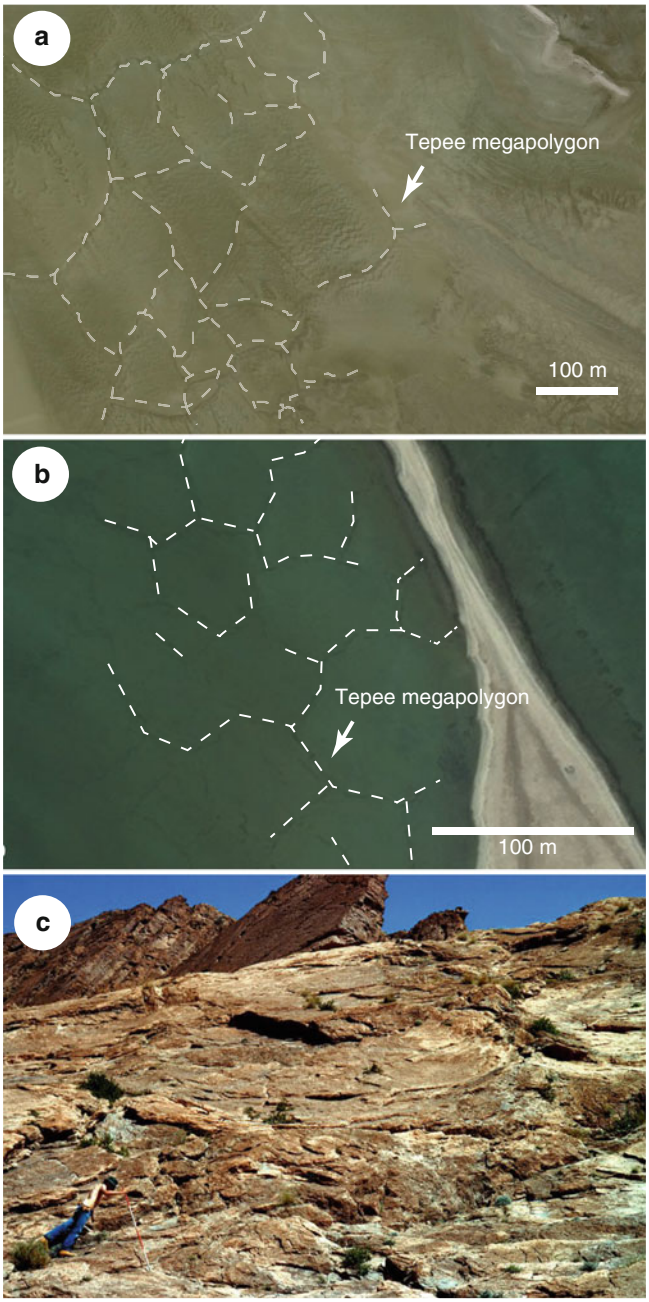

Fig. 1.25 Tepee ridge megapolygons. (**a**) Modern ridge polygons in the water covered lagoon floor at the southern end of Khor Al Bazam, UAE (see Lokier and Steuber 2009). (**b**) Modern ridge polygons in the water covered lagoon floor at Ras Alzabna, near Ra's al Qurayyah at the southern end of Half Moon Bay, Saudi Arabia (see also Fig. 3.17d). (**c**) Tepee megapolygons exposed on a dip surface in Jurassic dolomites in the valley of Todgha, Morocco (see Assereto and Kendall 1977)

being added to form the compressional ridges (Kendall and Warren 1987). This contrasts with the arid hydrological setting where extension-related megapolygonal desiccation features are forming at the same scale. These features are giant, often sediment-filled fissures or open mud cracks that are created by drawdown of the watertable. Such longterm lowering of the watertable can drive formation of huge desiccation polygons and fissures, as are seen today about the edges of the Panamint and Eureka playas, California (Fig. 2.59; Messina et al. 2005). The arid seepage hydrologies inherent to the formation of tepee megapolygons are very different to those required to form desiccation megapolygons and the two should not be confused by the use of the prefix megapolygon when describing either feature.

At a broader scale, the occurrence of a substantial tepee-rich unit in a saline-platform carbonate succession indicates an episode of exposure and watertable drawdown. For example, in the Italian Alps the principal tepee-dominant unit is interpreted as a sequence boundary and forms a regional marker in the highly cyclic Latemar (Triassic) platform interior (Hardie et al. 1986). This 300 m thick tepee facies separates the lower cyclic facies and the upper cyclic facies of the Schlern Formation in the Latemar platform (Christ et al. 2012; Egenhoff et al. 1999; Mutti 1994). It is characterized by 79 tepee zones (0.2–13 m thick) alternating with intervals of thinning-upward, caliche-capped mudstone to packstone cycles. In West Texas the tepee-rich zones of the Late Permian Yates and Tansill formations have been used to pin the highest points in the Permian landscape in what was a laterally-evolving high frequency stratigraphy. For the first time in the history of studies in the Guadalupe Mountains this study quantified the penecontemporaneous nature of downdip high-angle faulting, extension and Permian shelf collapse (Rush and Kerans 2010).

Some authors have suggested a Milankovitch cyclicity may be preserved in thickness variations within the saline platform interior sediments of the Latemar (Hinnov and Goldhammer 1991). If so, the highly altered, overprinted and collapsed origin of at least some of the tepee intervals, probably means individual eustatic parasequences are no longer recognisable within the tepee facies. The predominance of tepees in the Latemar platform also suggests periodic evaporative drawdown in the platform interior. Seepage hydrology needed to form pisolites and tepees implies an exposed and somewhat elevated edge to a platform rim at the time the tepees of the interior were active. In contrast, the thicknesses of the transgressive systems tracts (subtidal successions) also preserved in the platform interior indicate flooding and are more likely to retain finer-scale eustatically/climatically distinctive thicknesses.

Carbonates: Present and Past

Phanerozoic evaporitic carbonates accumulate in $CaCO_3$ -saturated waters. Consequent aragonite/dolomite muds and cements are distinctive and readily separated from open marine shelly carbonate shelf textures. The separation between marine and hypersaline settings is much less

distinctive in Proterozoic or older strata. In fact, the best modern textural analogs for many Precambrian marine carbonates are to be found in Holocene evaporitic carbonates and not in modern normal marine carbonates. The dichotomy reflects two major events in earth history: (1) the evolution of an increasingly bicarbonate-depleted and sulphate-enriched ocean by the Proterozoic, and (2) the rise of a shelly marine macrofauna at the Cambrian-Precambrian boundary.

During much of the Precambrian, $CaCO_3$ was extracted from seawater by a combination of inorganic and microbial processes, the same two sets of processes that dominate in modern evaporitic carbonate settings. Archaean carbonate sediments entrain numerous and prolific giant botryoids of aragonite that can be up to 1 m in radius, as well as widespread Mg-calcite precipitates (Grotzinger and Read 1983; Grotzinger and Kasting 1993; Grotzinger and Knoll 1995; Sumner and Grotzinger 2004; Reitner and Thiel 2011). These beds sometimes formed cementstone sheets several metres thick, with strike lengths of more than 100 km, with no modern counterparts in normal marine carbonates (Figs. 1.18 and 1.26).

By the Palaeoproterozoic, marine carbonates entrained less spectacular masses of aragonite and calcite, although cementstone crusts and microdigitate stromatolites in tidal flats remained a characteristic style of carbonate platform aggradation, as did the widespread presence of molar-tooth structures in the Mesoproterozoic (Shields 2002). In contrast, the late Meso- through Neoproterozoic carbonate sedimentation saw a progressive decline in the precipitation of massive widespread carbonate cements and an increase in widespread precipitation of micritic whitings. Throughout the Precambrian, periodic high-energy events ripped up and transported fragments of these cementstone crusts and whiting beds to redeposit them as intercalated intraclast conglomerates and breccias. The secular decrease in the volume of seafloor precipitates reflects a change in the chemical state of the ocean. The much lower sulphate concentrations and much higher bicarbonate to calcium ratios reflect the elevated levels of CO_2 in the Archaean atmosphere and its long-term decrease since then (Fig. 1.18; Chap. 2; Grotzinger and Kasting 1993; Riding 2011; Bose et al. 2012).

The change in the earth's atmosphere and ocean chemistry from the Archaean to the present is reflected in the evolving nature of microbialites (Fig. 1.18; Grotzinger and Knoll 1999; Riding and Liang 2005). During the Archaean and early Proterozoic, when CO_2 levels were much higher than today, stromatolites formed by "in situ" precipitation of laminae and conoform stromatolites were commonplace. But younger Proterozoic marine stromatolites grew largely through the accretion of carbonate sediments, mostly through the physical process of microbial trapping and binding (agglutination). Conoform stromatolites had by then largely disappeared from the world's oceans (Sumner and Grotzinger 1996) and today are found only as tufas in hypersaline lakes

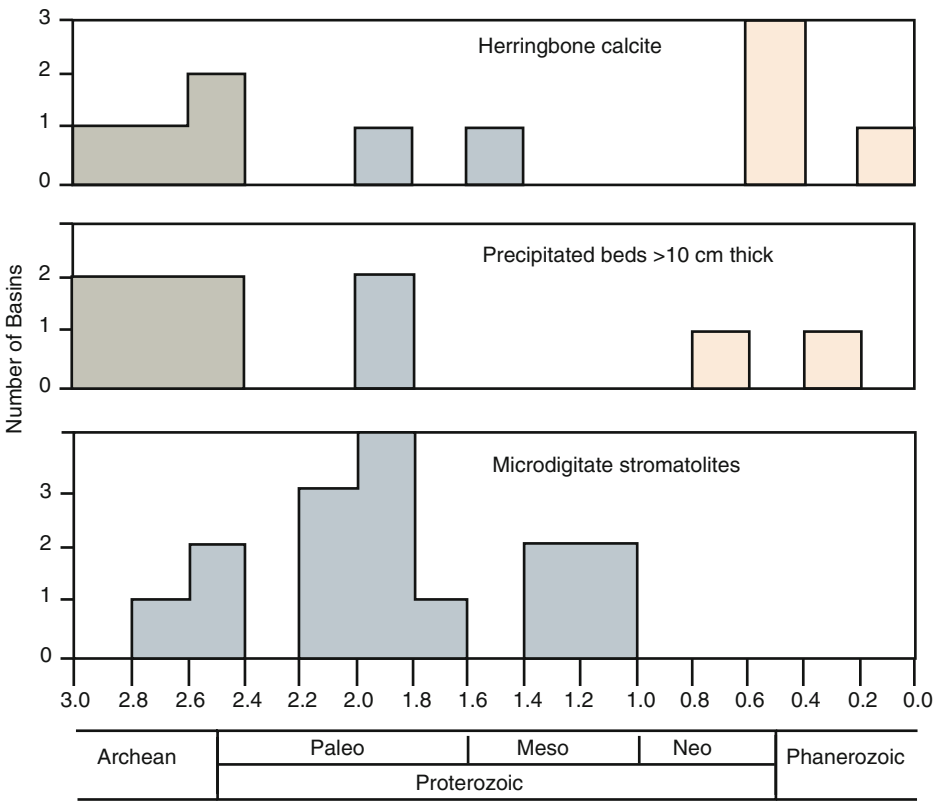

Fig. 1.26 Carbonate precipitation from seawater through time. *Brown fill* represents basins where the textures are abundant across a range depositional settings. *Grey fill* represents basins where the textures are present in a limited number of depositional settings. *Pink fill* indicates textures and minor components with limited extents (After Sumner and Grotzinger 1996)

(Warren 1982a). Marine abundance data across the Phanerozoic Eon show that microbial carbonates episodically declined during the past 545 Myr, from a peak 500 Myr ago (Riding and Liang 2005). The Phanerozoic abundance trend is generally the inverse to that of marine metazoan taxonomic diversity, supporting the view that metazoan competition has progressively limited the formation of microbial carbonates. The Precambrian evolution of the ocean saturation state, and the passage at various times into marine cementstones, was paralleled by times when marine tepees were more commonplace, as in the Marinoan cap carbonates of the Neoproterozoic when marine cold-seep tepees were common (Fig. 1.26; Corsetti and Lorentz 2006; Gammon et al. 2005). Carbonate supersaturation in Archaean seawater has led some to question the biogenicity of the 3.43 Ga isopachous stro matolites at North Pole, Australia – historically interpreted as the world's oldest biological fossils (Grotzinger and Rothman 1996 vs Allwood et al. 2007).

The dramatic rise of a skeleton-secreting and sediment ingesting macrofauna at the beginning of the Phanerozoic changed the nature of marine shelf sedimentation. The proportion of chemically precipitated open-marine mud and cement decreased and new sedimentary particles, such as abundant shell fragments, faecal pellets and biologically derived muds, came to dominate the marine carbonate realm. The formation of widespread cementstone sheets on the seafloor had ceased several hundred million years before the rise of the shelly macrofauna. It was only in widespread hypersaline settings that carbonate supersaturation persisted throughout the Phanerozoic, such as the Permian cementstones that crop out along the edge of the Delaware Basin, Texas. In such settings, isopachous stromatolites and other halotolerant microbialites continued to flourish in the absence of bioturbation and gastropod grazing.

Primary Evaporite Salts

Evaporite salts are deposited in a brine pan or seaway after the brine has precipitated the alkaline earth carbonates. The salts, dominantly $CaSO_4$ or halite, show a range of crystal textures that indicate relative stability, depth and permanence of the precipitating brine (Fig. 1.27a). Variations in key interpretive textures occur in a framework of stratified (meromictic) and non-stratified (holomictic) brine column hydrologies that will be discussed in detail in Chap. 2 (Fig. 1.27b).

Simple monomineralic carbonate, sulphate or halite layers and laminae, as well as beds composed of complex interlayered mixtures, dominate subaqueous deposits of many saline lakes and seaways. Laminae created by chemical settling are a typical subaqueous stratification style at the onset of primary salt accumulation. Some laminae outline underlying crystal morphologies, others are flat-planar and can be correlated for long distances across the basin. Biolaminae, including microbial bedding and accretionary tufa and travertine deposits described previously, are common intercalations and indicate less saline intervals in the same brine body. Mechanically reworked laminae (ripples, dunes and slumps) are less common in subaqueous evaporites than in their carbonate or siliciclastic counterparts. This is due to the predominance of chemical sedimentary processes operating in the brine bodies at the salt precipitating stage whereby early crystal precipitates interlock and cement as they evolve into growth-aligned crystals.

Widespread layers or crusts composed of cm-dm sized aligned bottom-nucleated crystals are one of the most widely recognised shoalwater textures. Depending on the salinity of the precipitating brine this bottom-nucleated unit is typically composed of halite chevrons or aligned gypsum crystals. Beneath deeper waters, crystals may accumulate on the bottom as a silt-sized "rain from heaven" pelagic deposit or as a mass of coarsely crystalline monomineralogic bottom meshworks (Fig. 1.27a). A range of slope deposits, dominated by reworked shoal water crystals, typifies the subaqueous region separating the shallow from the basinal (Chap. 5).

Over time, decimetre-to-metre thick evaporite beds can stack one atop the other to form evaporite units that can be hundreds of metres thick. When conditions are suitable, huge thicknesses of shoalwater evaporite can accumulate in very short time frames. For example, a more than 1-km-thick sequence of interbedded halite and clay has accumulated in less than 10,000 years in the Danakil Depression of the Ethiopian rift (Chap. 11). No other type of sediment, carbonate or siliciclastic, can aggrade as rapidly as a subaqueous evaporite bed (Warren 1991).

Gypsum Beds

A few thousand years ago subaqueous crystals of gypsum, up to 1 m tall, grew in stable bottom waters of shallow (<10 m deep) Holocene brine pans of southern Yorke Peninsula, South Australia (Chap. 4; Warren 1982b). The crystals coalesced into crusts and beds dominated by swallowtail and palmate gypsum crystals. Similar giant growth-aligned subaqueous gypsum with single crystals up to several metres tall have been documented in the Middle Miocene (Badenian) evaporites in the Carpathians (Babel 2007) and the various Late Miocene Messinian sub-basins of the Mediterranean (Lugli et al. 2010). Growth cycles in these subaqueous gypsum deposits range from mm couplets to decametre beds to brining cycles that are tens of metres thick (Fig. 1.28a, b).

Large aligned gypsum crystals that make up the bottom-grown beds typically entrain curved growth faces interspersed among parallel-sided prisms. Very few natural

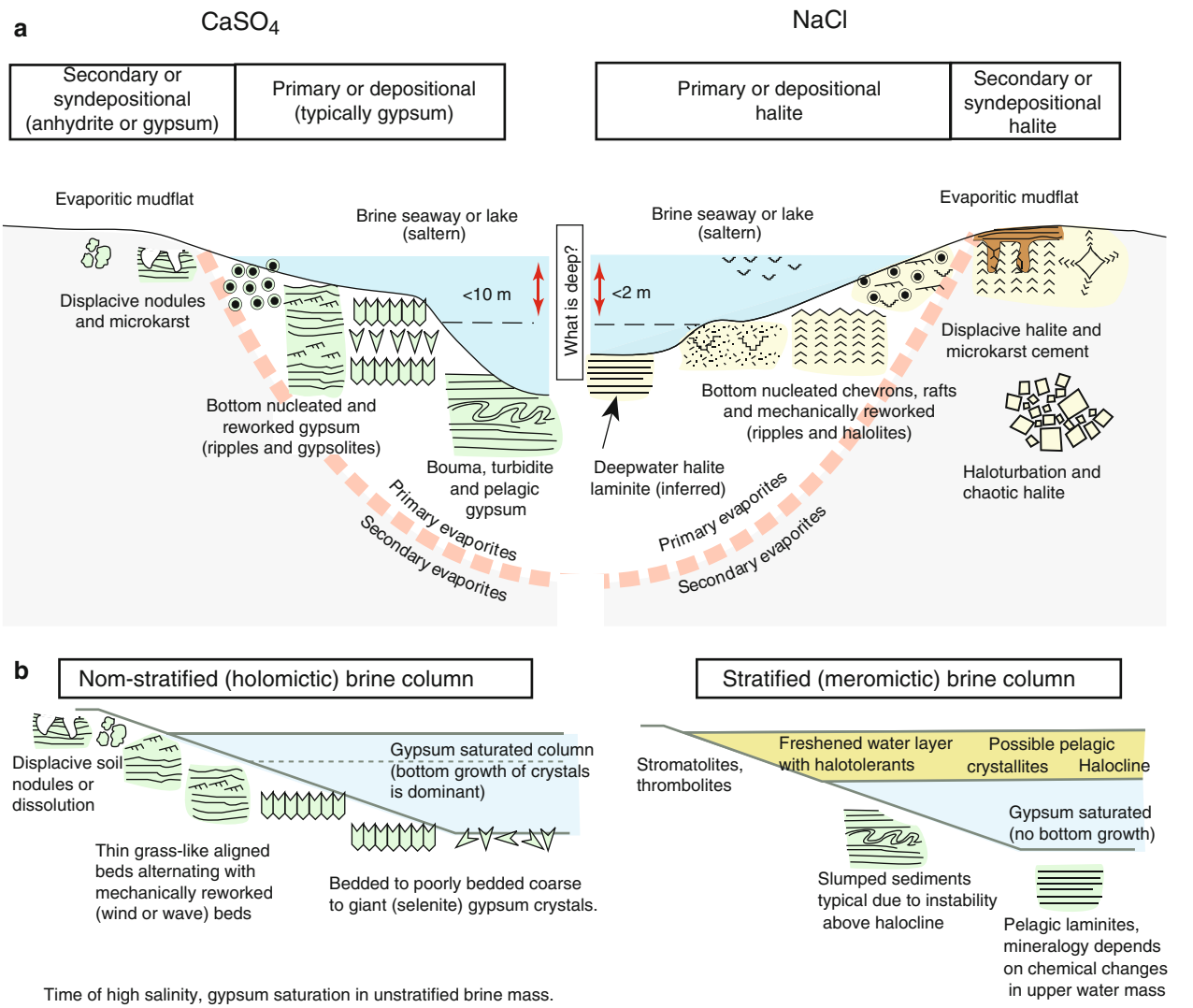

Fig. 1.27 Signatures of primary evaporite textures and syndepositional secondary evaporites for $CaSO_4$ and NaCl salts. (**a**) Depositional spectrum for both gypsum and halite. Secondary textures related to burial are discussed later in this chapter. (**b**) Hydrological end members (non-stratified and stratified waters) and the gypsum textures that illustrate this hydrology

gypsum beds are made up of growth-aligned crystals that first formed as aggregates of upward-oriented simple twins. That is, natural crusts and bed of growth oriented gypsums are not conjoins of the simple prisms shown in Fig. 1.29a. In fact, the crystal forms illustrated in Fig. 1.29a, and given in many mineralogy texts as typical gypsum morphologies, are the least common forms of sedimentary gypsum in beds accumulating in natural subaqueous systems.

Where a curved face encapsulates a crystal, a single lenticular crystal forms (Fig. 1.29b). The term "bird-beak" gypsum is sometimes used to describe its distinctive lenticular shape. The characteristic hooked termination can be used with pseudomorphs to help separate gypsum from the truncated lenticular "axe-head and keg barrel" forms of diagenetic anhydrite. Individual lenticular gypsum crystals range from sand-size to boulder-size. Lenticular sand-sized forms make up the uppermost lake sediments and the gypsum lunettes about the saltflat edges of many coastal and continental salt lakes in Australia (Chap. 4; Warren 1982b). Holocene lenticular gypsum crystals are intimately associated with algal

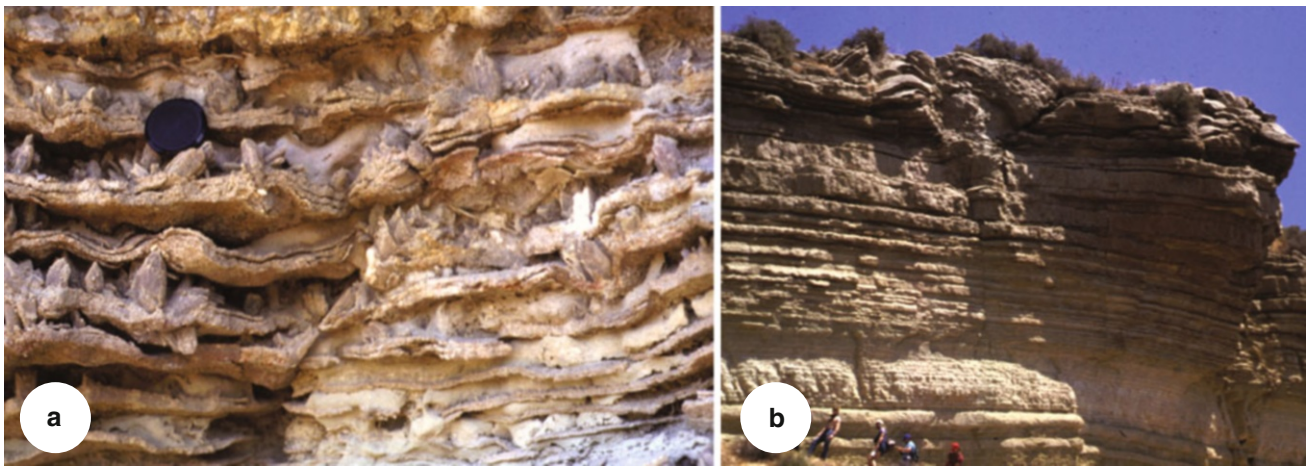

Fig. 1.28 Subaqueous gypsum from the late Miocene of Sicily. (**a**) Stacks of layers of aligned cm-scale gypsum crystals, each layer indicates growth competition from a marly gypsarenite base (lens cap for scale). (**b**) Metre-scale layers showing a larger subaqueous growth cycle from a finely laminated marly base through coarsely-bedded aligned gypsum to a series of domal mounds capping the cycle (people for scale)

sediments in marine-seepage-fed Ras el Shetan mudflats in the Gulf of Aqaba, Egypt (Aref 1998a).

Bedded gypsum growing on the shallow bottom of a perennially subaqueous lake or seaway typically precipitates as masses of large parallel-sided megacrystals that show varying levels of expression of the curved faced (Fig. 1.29c). Individual growth-aligned crystals are decimetres to metres long in gypsum beds in marine seepage fed Holocene salina such as Marion Lake and Lake Asal, while ancient counterparts in the Middle Miocene of the Carpathians can be up to several metres long and variations in their crystal form can be used to define differing styles of brine stability and associated crystal growth (Fig. 1.27b; Babel 2007).

Varying degrees of face curvature lead to the growth of distinctive gypsum twins with acute (narrow) to obtuse (wide) angles along the twin plane. Doug Shearman described this form of overlapping curvature along the twin plane as "arms of Siva" gypsum. Strong vertical development of the upper half of some twins creates beds of upward aligned gypsum crystals showing strong curvature of the intercrystalline faces. Such forms are sometimes called palmate gypsum. Some purists would argue that most of these natural forms of growth-aligned gypsum are not true twins (Babel 1990). The varying degrees of curvature entrained in the crystal generate changes in the apparent twin angle, even in a single crystal. This breaks the rule of constancy of twin angle, leading some to refer to them as pseudo-twins (e.g. Schreiber 1988). Whatever the crystallographic semantics, these large aligned crystals only grow on the gypsum-saturated bottoms of shallow subaqueous brine lakes and seaways.

The reason why the curved face comes to dominate some gypsum crystals (e.g. lensoidal crystals and displacive rosettes) is not well understood. On the basis of a number of laboratory-based growth experiments using brine columns separated by gel growth media, Cody and Cody (1988) argued the lenticular shape of displacive gypsum (intrasediment sediment growth) reflects influence of temperature and the presence of humic compounds in the parent brine (Fig. 1.30). Two temperature dependent trends were obvious in the precipitates. At low temperatures the hemipyramidal habit, dominated by the {111} faces dominate. At higher temperatures the lenticular {$\bar{1}$03} is obvious in all crystals. They concluded that elongate prisms grow best at low temperatures and in the absence of habit-modifying organics.

They found that the modifying influence of temperature on morphology was swamped by the presence of low levels of organics in all the growth experiments. With increasing polytannate concentrations (analog for terrestrial humics), crystals become less elongate and penetration twinning along the {100} develops. This is followed by secondary complex nucleation near twin faces as rosette and rosette-like aggregates form (aka desert roses). The changes in morphology are interpreted as the result of a high degree of adsorption of organic compounds on the $\bar{1}$03 and $\bar{1}$11 faces that inhibits their growth and consequently minimizing growth parallel to the crystallographic c-axis (Cody 1976). This absorption is thought to reflect the peculiar surface structure of the face, which unlike the other faces of gypsum is almost entirely composed of Ca^{++} ions and these Ca^{++} ions bond readily with organics Aref (1998a). In the subaqueous gypsum pools and sabkhas or Guerrero Negro, Mexico, Vogel et al. (2009, 2010) describe equant and distorted gypsum crystal morphologies that were unique to biofilm-supported samples.

Warren (1982b) found that masses of sand-sized lenticular gypsum crystals dominate in near surface beds, deposited

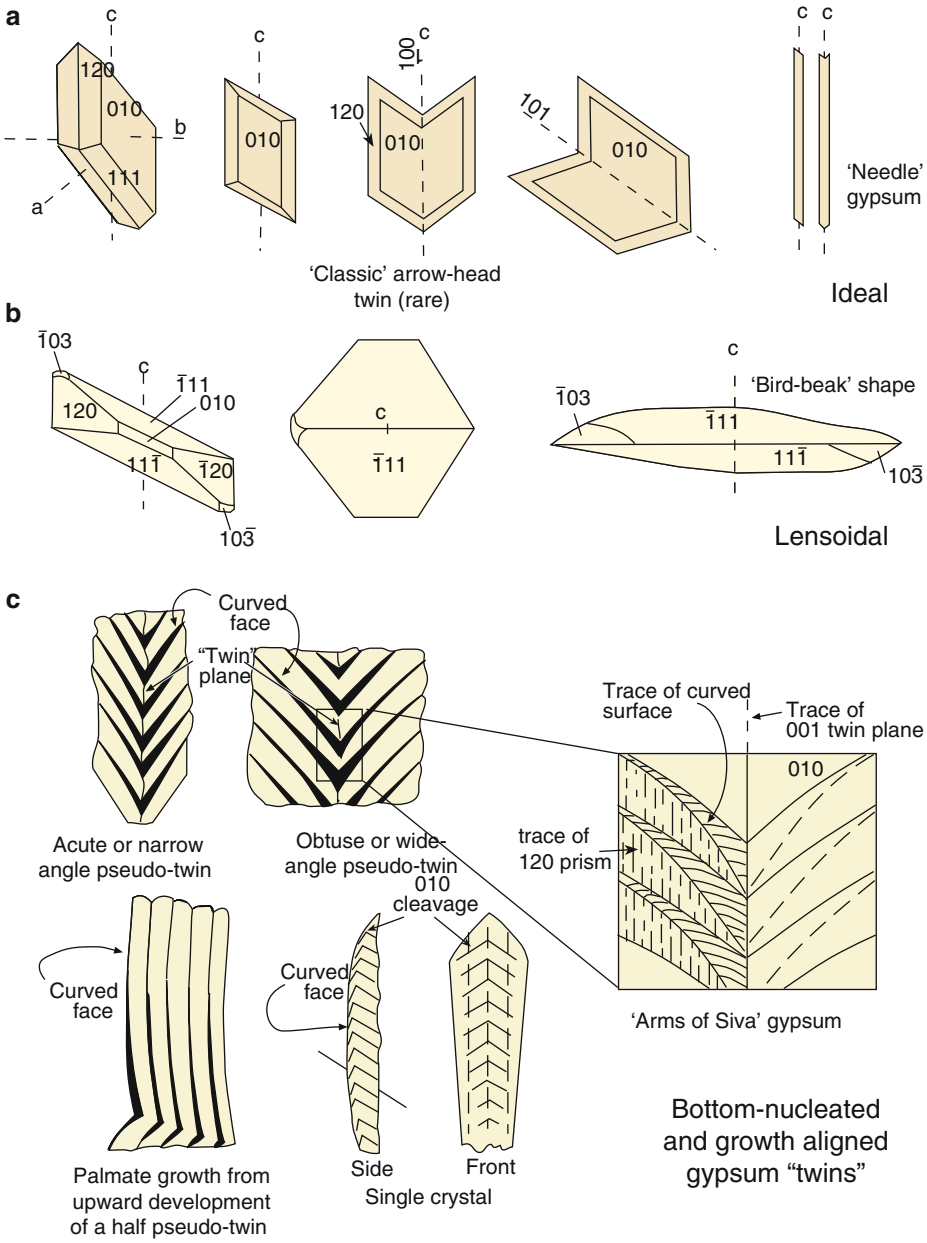

Fig. 1.29 Gypsum. (**a**) Prismatic forms of gypsum parallel to (010) with *arrow head* twins along (100) or (101) and extreme acicular forms of prism and twin on the right. (**b**) Lenticular form of gypsum. Note how the lenticular form (*on right*) is dominated by the curved faces that are much less important on a typical prism as seen in the side and top views of a crystal (*on left*). (**c**) Various forms of typical subaqueous "zig-zag" gypsum growth as described in text (After Shearman 1978; Orti Cabo and Shearman 1977; Rouchy et al. 1994)

in seasonally vadose settings across numerous coastal salinas in southern Australia. He argued the lenticular shape tends to form best in the upper seasonally vadose parts of the brine pan fill, where crystals are subject to periodic short-term dissolution and regeneration. The pristine parallel-sided gypsarenite prisms that constitute the underlying thick beds of gypsarenite or growth-aligned laminar selenite were not present at this upper level in the lake stratigraphy. However, the vadose gypsum in these salinas grows in surface and near-surface pore waters that are more influenced by surface runoff from nearby vegetation-covered calcareous dunes and so entrain higher tannic acid levels.

Growth-aligned coarse-grained gypsum beds form in Holocene coastal lakes of Southern Australia, beneath the waters of perennial subaqueous brine pans that are density stratified for more than 6–8 months of the annual depositional cycle. In the early stages of infill of the salina, the perennial bottom brine was always saturated with respect to gypsum (Fig. 1.27b). Salinity conditions were stable and allowed the upper euhedral surface of the aggrading crystal bed to preserve the upper outlines of crystals in each growth stage. If gypsum precipitating today in Lake Inneston, South Australia, is indicative of the subaqueous growth style, then throughout much of their growth, any large upward facing gypsum crystals are covered by a microbial mat or film that captures aragonite pellets and can be considered a type of gypsum stromatolite (Chap. 4). Similar subaqueous gypsum mounds, coated with cyanobacteria, line the southern end of

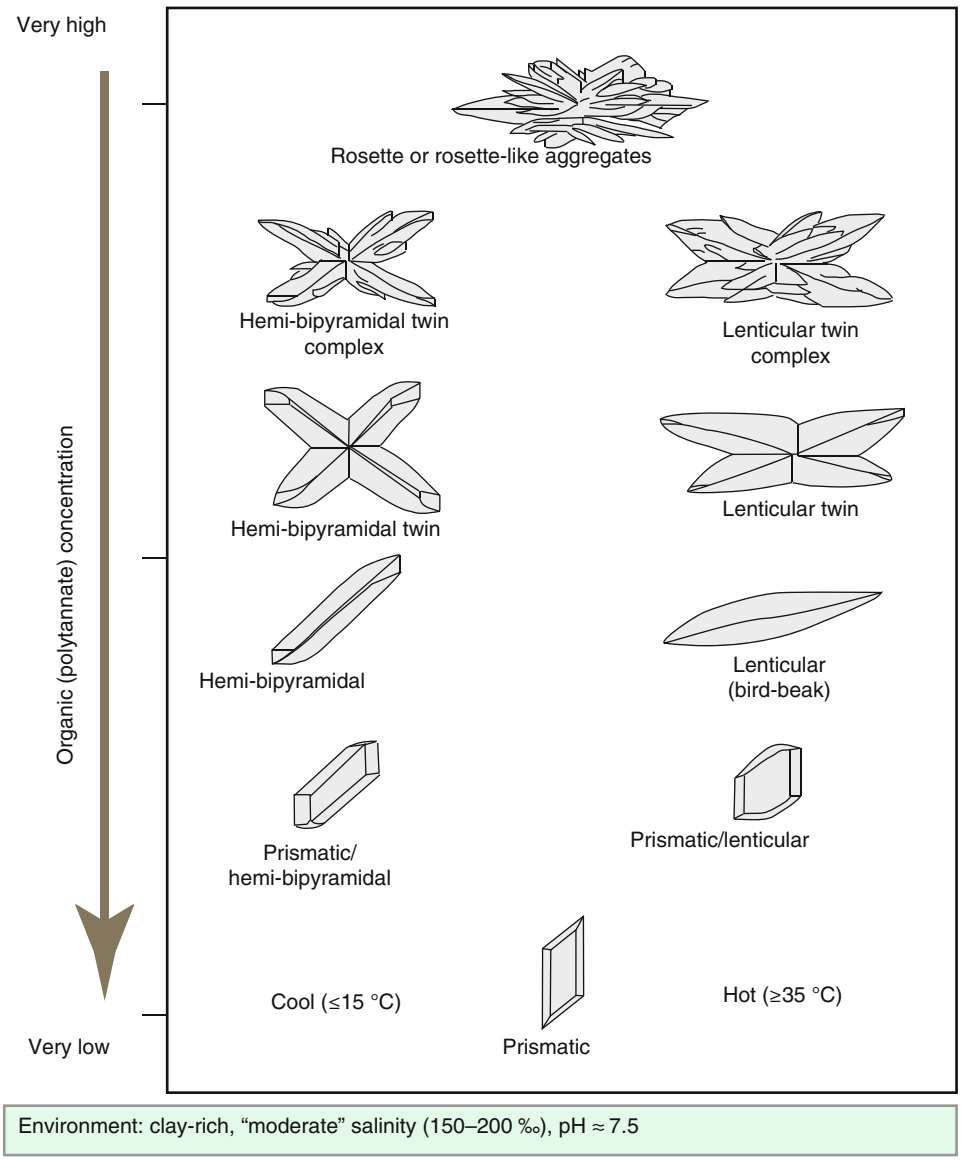

Fig. 1.30 Laboratory based changes in gypsum growing in a muddy (bentonite) sediment matrix at moderate salinity and neutral pH in environments characterized by increasing temperatures and dissolved polytannate concentrations. Polytannate is considered to be an analog for terrestrial humic material. c-axis vertical in all examples (After Cody and Cody 1988)

the brine channel leading into Gotomeer in the Nederlands Antilles and pass into laminated aragonitic microbialites beneath shallower waters along the channel edge (Fig. 1.19c; Kobluk and Crawford 1990).

Beds of growth-aligned crystal beds about the edges of the Danakil Depression, Ethiopia, define an earlier Holocene-Late Pleistocene perennial lake level that was a few metres higher and somewhat fresher than the current saline halite pan level (Fig. 1.31). About the saline lacustrine edge these subaqueous beds alternate with pedogenic beds dominated by nodular gypsum.

Rapid widespread bottom growth of aligned-gypsum occurs when stratification of the brine column is lost via seasonal concentration of any upper fresher surface water body. When it reaches the same salinity as the dense gypsum-saturated bottom waters the two waters mix (Fig. 1.27b). Once this happens the whole water column is supersaturated

Fig. 1.31 Stack beds of alternating growth-aligned gypsum (thickest bed 30 cm) and marly gypsum in the Late Pleistocene-early Holocene gypsum-fringe in the Danakil Depression, Ethiopia

with respect to gypsum and crystal bottom growth begins anew on a metres-deep brine pool floor. As the aggrading euhedral gypsum bed surface encloses $CaCO_3$ impurities, it encapsulates and preserves smooth to ir regular laminae within the bed, so creating textures indicative of brine column stability and oxygenation (Chap. 2).

Aragonite pellets that mantle the re-entrant laminae in the salina gypsum are a combination of a pelagic "rain from heaven" and faecal pellets excreted by a grazing biota cropping the biofilm that covers the gypsum. In the Australian coastal seep salinas, metazoan life flourishes during the freshened salina stage when a less saline surface water body (≈50 cm thick) floats atop the lower brine mass (from spring to early summer). Pellets in Lake Inneston and Deep Lake salinas signify the feeding activities of ubiquitous ostracods and the Southern Hemisphere brine shrimp (*Parartemia zietziana*). When salinities in the surface waters are suitable, this halotolerant pelagic biota spreads through surface waters over the whole brine lake (Chap. 9). When surface salinities later increase to levels that can no longer support a metazoan population, mass mortality occurs. Soon after, the upper and lower brine masses equilibrate/mix and lakewide gypsum precipitation begins again. Even so, small living populations of brine shrimp and ostracods remain in refugia about seawater-fed seeps in the inflow zones supply the tepee and mound-spring dominated salina strandzones.

Over millennia, the depositional surface of the salinas aggraded as successive gypsum layers infilled the centre of the brine lake depression (Warren 1982b). As the top of the salina gypsum bed aggraded, it reached a level where even the dense bottom water mass was seasonally freshened. Then the perennial bottom waters, as well as surface waters, were undersaturated with respect to gypsum for a number of months each year. At that time the upper gypsum surface dissolved each winter to form a flat planation surface. Now the seasonal growth of the aggrading bed surface enclosed $CaCO_3$ pellets laying atop this dissolution surface to form a flat mm-laminated gypsum bed (see Chaps. 2 and 4 for more detail on this typical brine column hydrology).

Halite Beds (Chevrons and Crusts)

Crystals in halite crusts first precipitated on the floors of shallow hypersaline brine pools as upward-growing chevrons, cubes and cornet-shaped crystals (Fig. 1.32a, b). Chevron structures, which preserve the outlines of successive crystal growth edges, are defined by layers of enclosed brine inclusions. Remnants of aligned chevrons are the most commonplace primary texture preserved in ancient halites. Abundant inclusions impart a cloudy or milky appearance to layers rich in chevron crystals. Even without a hand-lens,

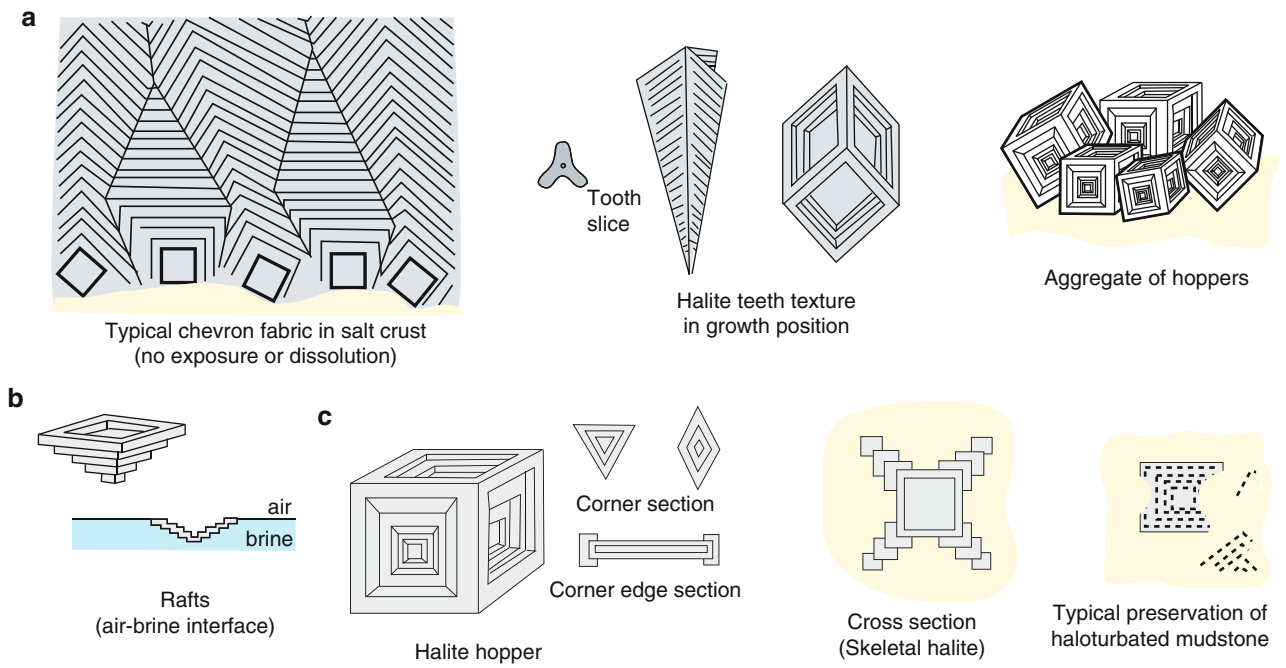

Fig. 1.32 Halite. (**a**) Growth-aligned forms of subaqueous halite and typical chevron growth fabric outlined by inclusions in the crystals. Those crystallite cubes with upward-aligned edges, rather than faces, come to dominate the growth fabric as a series of merged chevron crystals. Other bottom growth forms include upward-growing halite teeth and aggregates of hoppers on the bottom that were created by overgrowths on sunken rafts. (**b**) Halite raft growth, where crystals hang from the air-brine interface. (**c**) Various forms of skeletal or intrasediment halite hoppers. Notice how the outline of the halite shape or its pseudomorph can vary from rectangular to triangular depending on the plane of intersection of the viewing horizon with the crystal hopper (In part after Shearman 1970; Rouchy et al. 1994)

this is a feature that can be used in ancient counterparts to distinguish primary halite from clear or spar-like crystals of secondary or diagenetic halite. Milky inclusion-rich crystals can accumulate as successive layers of growth-aligned prisms or can form as syntaxial overgrowths on floundered rafts and other cumulate crystals that have settled to the pan floor.

As for all isotropic crystals growing in crowded conditions, the crystal edges of halite cubes that point upward into the brine grow more rapidly than crystals with upward-pointing crystal faces. The upward pointing "V's" of the edges quickly dominate and so creates an aligned chevron texture that characterises many subaqueous halite crusts (Fig. 1.33a). Less common are thin crusts and beds composed of upward-facing cornets and plates. There the crystals grew by the upward aggradation of the horizontally aligned faces, and perhaps indicate less crowded conditions of bottom growth (Handford 1990, 1991).

Such halite crystals accumulations form the lower parts of halite beds up to 5 m thick in Lake Macleod, Western Australia where the beds are composed of stacked decametre-thick crusts dominated by bottom-nucleated aligned chevrons. Brine sheets that precipitated the halite were always less than a few metres deep and usually less than 0.5 m deep (Logan 1987). Similar units of stacked crusts, but with obvious truncation surfaces and pervasive capillary overprints, characterise saline pans in Salar Uyuni and other pans worldwide (Fig. 3.43; Bobst et al. 2001). Patchy remnants of chevron halite crusts, deposited in shallow to ephemeral brines, are also preserved in ancient thick halite beds such as the Ordovician-Silurian Mallowa Salt of the Canning Basin (Cathro et al. 1992) and the Permian San Andres Formation of West Texas (Hovorka 1987).

However, there is a sampling bias when Holocene halite pan textures are used as direct deposit-frequency analogs for ancient bedded evaporites. This is related to three factors; (1) Access, (2) Rapidity of subaqueous fill and, (3) Scaling of modern analogs to ancient depositional systems. This true for all evaporite mineralogies and textures, not just halite, we shall discuss analogue scaling problems in detail in Chap. 5. For now let's just consider the implications of access and rapidity of fill. Most of our observations of primary textures forming in natural halite deposits that have been made in the last 100 years comes from areas adjacent to where there was easy foot ot vehicular access. So, we have excellent studies of pan and capillary halites forming in a number of modern salars and playa lakes in South and North America, respectively (e.g. Bobst et al. 2001). We also have well documented examples of halite pan textures in coastal saline pans and anthropogenic saltworks in Mexico and elsewhere (Shearman 1970).

The problem is that these samplings of halite tend to be from areas where we can get out of a vehicle, walk a short distance into the saline system and sample. This creates an immediate sampling bias in that we tend not to sample textures forming in permanently somewhat deeper brine-covered areas, which are highly uncomfortable to access. So, in Holocene studies we tend to sample halites from areas subject to cycles of flooding and drying. We do have drill core samples of some subaqueous versus capillary textures in South American salars, but the key question is how relevant is an endorheic 2,000-m plus-elevation continental lake hydrology to the hydrologies in ancient subsealevel marine-fed megahalite basins for which there are no modern same scale analogs (Warren 2010). In addition, active permanently brine-covered areas where subaqueous halite deposition is

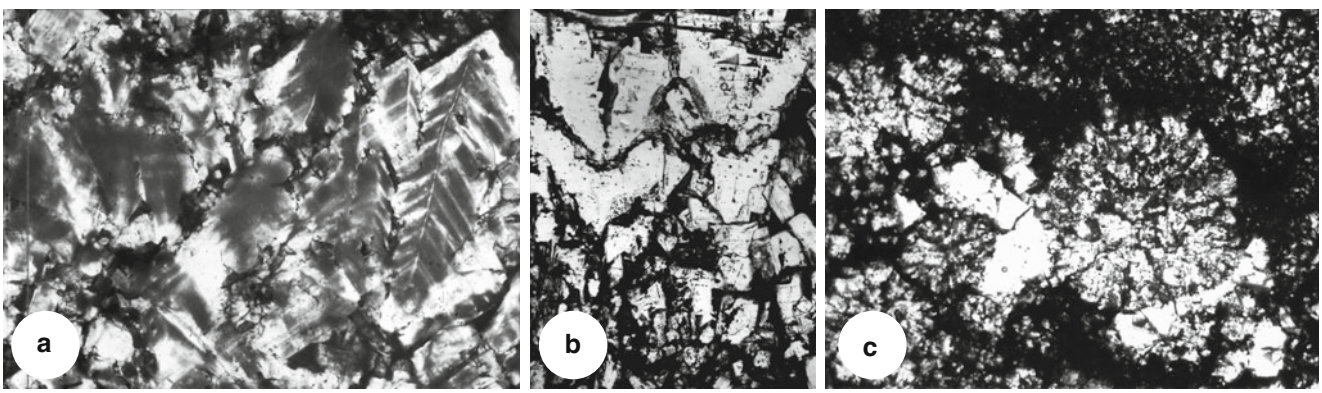

Fig. 1.33 Subaqueous halite (**a**) Thin section photomicrograph of halite from perennial saline lake interval, Death Valley core, depth of 8.1 m. Halite chevrons with dense fluid inclusion banding (dark) and vertical, competitive growth fabrics. Horizontal field of view is 4 mm. (**b**) Thin section photomicrograph of halite from perennial saline lake interval, Death Valley core, depth of 15.8 m. Bottom-grown halite crystals with vertical growth fabric. Note that halite crystals widen upward and contain faint fluid inclusion banding. Some mud (dark patches) is trapped within or between crystals. Horizontal field of view is 4 mm. (**c**) Thin section photomicrograph of halite from perennial saline lake interval, Death Valley core, depth of 8.6 m. Halite pisoids, 2–5 mm in diameter and with faint radial fabric, from the upper shallow saline lake interval. Note mud drape (*black*) and fine-grained halite cumulates above the largest pisoid. Horizontal field of view is 10 mm (Images and descriptions courtesy of Tim Lowenstein)

occurring beneath brines more than a few tens of centimetres deep are relatively rare on the world's surface of today. The best documented current example of a deeper water halite setting comes from samples recovered in piston cores released into the present day deep floor of the Northern Basin of the Dead Sea where halite is accumulating at the base of a 350 m+ brine column. This deep-brine halite started to form in February 1979 when the Dead Sea brine mass changed from perennially stratified to holomictic (Chap. 4).

A paucity of relevant analogs is related to the fact that the present is a limited key to the past in terms of evaporite deposition (the scaling problem) and that when deeper subaqueous halite systems are active in the Holocene they very rapidly aggrade from a permanently subaqueous brine saturated setting to the current hydrological equilibrium surface which is typified by alternating episodes of wetting and drying (Warren 2010).

This limitation in access and rapidity of fill is seen in the most recent episode of halite infill in a large evaporite basin we have available for study, namely the Late Quaternary salt fill in the Danakil Depression, Ethiopia. Cores in halite down to 200 m below the current pan surface show an abundance of pristine primary subaqueous textures (Fig. 1.34a–d). But the system today is in near hydrological equilibrium and

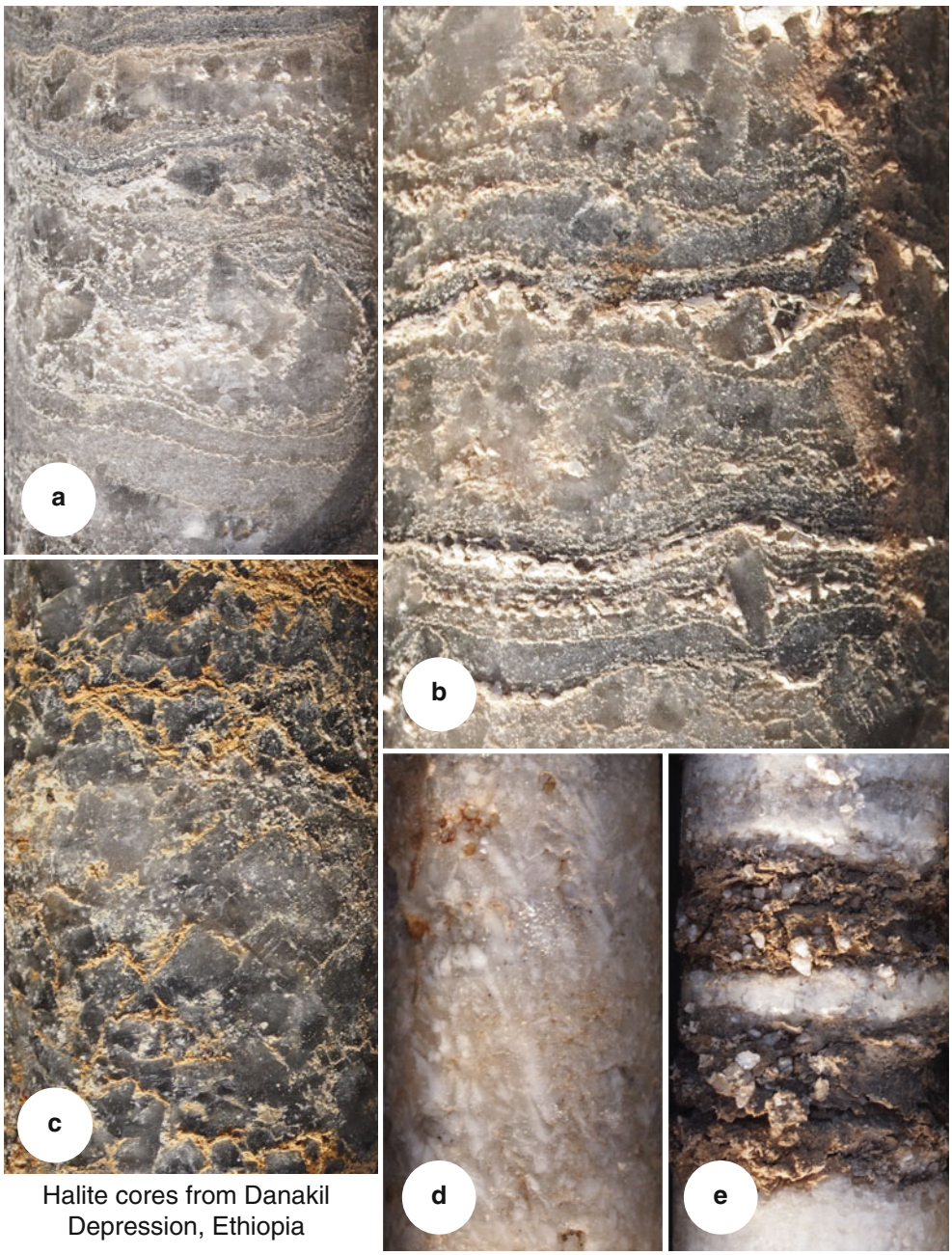

Fig. 1.34 Cores sampling various Pleistocene halite textures in the Danakil Depression, Ethiopia. (**a**, **b**) Primary growth-aligned inclusion-rich halite indicating a periodically stratified shallow subaqueous halite seaway/lake with aligned halites subject to periodic freshening and $CaSO_4$ mantling – similar $CaSO_4$ -encased textures probably misinterpreted as syndepositional brine-reflux secondary by Hovorka (1992) in the Permian of West Texas. (**c**) Stable holomictic pond textures with $CaSO_4$ drapes on upward aligned chevrons. (**d**) growth-aligned milky halite in stacked halite crusts. (**e**) Halite crust alternating with clay influxes (subaqueous settling for clay floods as no obvious capillary textures in salt crusts)

tends to accumulate halite crusts textures interlayered with clays (Fig. 1.34e). Yet in terms of total halite fill these clayey textures are much less important than the subaqueous textures, which dominate the Late Quaternary halite/potash fill in the evaporite sumps across this part of the Afar Depression (Chap. 11).

Capillary and freshwater flood textures forming across the current Danakil surface are similar to what is documented at the surface in Death Valley, Guerrero Negro and the South American salars. Such systems tend to show a strong secondary overprint related to flooding and drying cycles creating evaporite units deposited from markedly schizohaline surface and nearsurface pore waters, which cause the lake surface in areas of such halite nuclei facies to currently aggrade at rates up to 3 cm per year (Fig. 1.35a; Ruch et al. 2012). Most current depositional surfaces in a natural (non-anthropogenic) salt pan setting tend to be near the hydrological equilibrium stage in the basin's fill history and this surface is what we can access for samples of halite texture. But it is a biased sample and as such tends to be unrepresentative of textures in the greater volume of halite fill. This volumetric unrepresentativeness is due the rapid way in which subaqueous basins fill to the equilibrium level, as we shall see in the various proportions of subaqueous versus capillary fill in Holocene marine-fed deposits documented in Chap. 4.

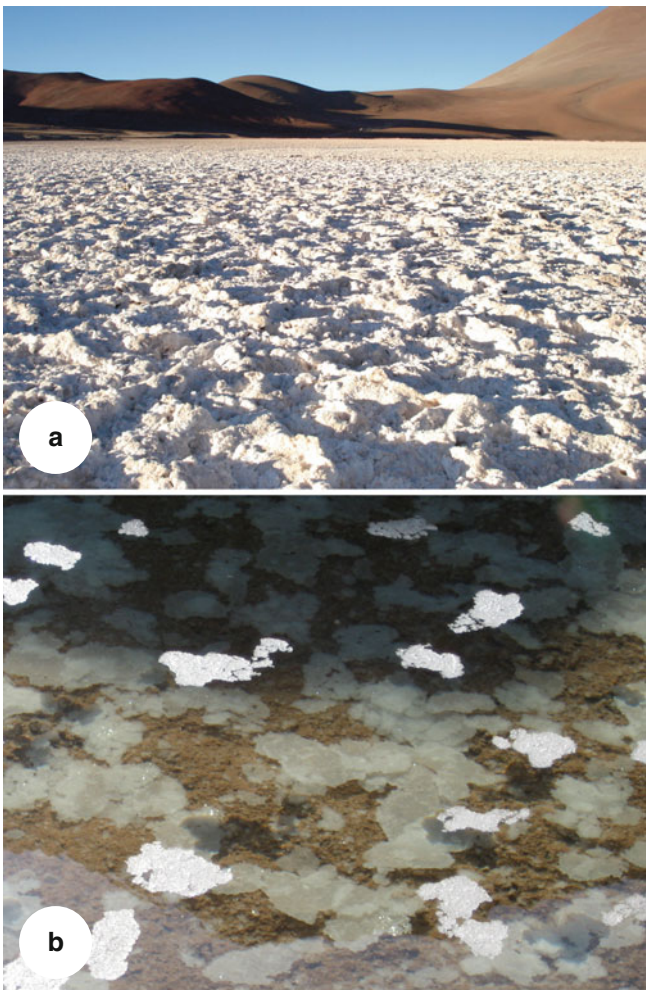

Fig. 1.35 Modern halite textures. (**a**) Halite nucleus (capillary halite) in Salar de Agua Amarga, Andes (photo courtesy of Tom Carpenter). (**b**) Halite rafts (up to 35 cm across) floating on brine pool surface with foundered raft beginning to stack up as "cumulate" layer on bottom of a pond, Kum region, Iran

In extremely hypersaline brines the precipitation behaviour of halite and the resulting textures can respond to elevated cell densities in halobacteria (Gerdes et al. 2000a, b). Proteinaceous compounds coating the surface of the growing halites encourage the growth of dendritic crystals rather than chevrons. Crystals forming in organic-enriched brines contain more and larger brine inclusions than crystals growing at the same salinities from sterile brines. Cells are smaller and much more numerous in the organic-enriched brines and the cells are thought to create templates for halite nucleites.

Halite Cumulates, Rafts and Coated Grains

Crystallites grow in the uppermost part of a standing body of brine where water is rapidly lost by evaporation and salinities are at their highest (Fig. 1.1a). Silt and sand-sized crystals settling to the bottom of the brine pool then form layers and beds of cumulate crystals ("salt and pepper" halite and massive gypsi-siltites). Periodic influxes of freshened surface waters, followed by evaporative concentration, can produce mm-scale lamina in bottom cumulates. Such "rain-from-heaven" laminites are typically composed of alternating carbonate-sulphate and sulphate-halite couplets and triplets.

When surface water salinities are suitable and surface waters are undisturbed by wind and waves, crystals can continue to grow as rafts held by surface tension at the air-brine interface (Figs. 1.32b and 1.35b). Rafts float and grow until the crystal mass becomes so heavy that it exceeds the holding ability of the interfacial surface tension and sinks to the bottom. Halite rafts in quiescent waters can be centimetres to decimetres across before they sink to the bottom. Eventually, increasing wind and wave action breaks up the rafts, usually while rafts are out in the brine lake and still well away from the strandzone. These remnants then sink to mix with the smaller crystals and so make up part of the texture of the cumulate beds of the brine lake floor. Later, when the lake shallows and further desiccates, these cumulate beds are covered by crusts and beds of bottom-nucleated chevron halite or swallowtail gypsum. This upward transition from cumulates to crusts is commonplace in modern crusts.

Rafts and other cumulate crystals in very shallow to ephemeral brine pans may be blown across the brine surface or carried by bottom currents into the strandzone to accumulate as subaerially exposed masses of strandzone crystals.

Such deposits characterise surface carnallite/halite shores about the brine pan edge of Lake Qarhan in China and trona cumulates about the edges of Lake Natron and Lake Magadi (Chaps. 11 and 12). Whenever the adjacent lake water body freshens and expands, the dissolution of the strandzone salts generates dense brine plumes that cement underlying sediment (Casas et al. 1992; Hovorka 1992; Schubel and Lowenstein 1997).

Ancient cumulate crystal beds, when not quickly covered by bottom-nucleated crusts, were sometimes mechanically reworked by storm and wave-induced bottom currents into crossbeds and ripples. This tended to happen on the bottoms of ancient perennial brine seaways and lakes that were above wavebase and covered by brines that were less than 5–10 m deep (Fig. 1.27). In even shallower nearshore positions, which were subject to higher wave-energies, fine-grained cumulate crystals formed the nuclei to concentric ooids composed of gypsum and halite (gypsolite and halolite respectively). Today, such coated grain textures are precipitating immediately basinward of the strandzone of Lake Asal in the African Rift Valley, Tuz Golu in Turkey, and along the southern end in the Dead Sea (Tekin et al. 2007; Castanier et al. 1992, 1999), they are also preserved in perennial brine halites in Death Valley California (Fig. 1.32c). Both Tekin et al. (2007) and Perthuisot and Castanier (2000) have argued that the process of halolite formation is bacterially (biofilm) mediated. The significance of bacterial activity in precipitating evaporitic oolites is widely debated. It is much like the unresolved debate on the importance of bacteria in marine ooid formation that has gone on for decades amongst carbonate sedimentologists.

At the broader scale, Lopez-Cortes et al. (1994) and Gerdes et al. (2000b) have argued that elevated cell densities of halophilic microorganisms in a hypersaline brine can change the crystal growth rate and crystal habit of the precipitating halite. Salt crystals deposited from brines with such dense microbial communities generally contain more and larger fluid inclusions than crystals formed in sterile salt solutions (Norton and Grant 1988). They suggested that the halophilic cells may serve as templates for halite formation, resulting in a larger number of cubic crystals of smaller size than those formed in sterile control solutions. The proteinaceous envelope, called an S-layer, of the archaeal cells may serve as template in the nucleation of halite crystal formation, thereby modifying the halite crystal structure (see Chap. 9).

Pedogenic and Wind Reworked Salts

Many arid to semi-arid desert soils are gypsiferous in areas surrounding the perennial saline lakes, the brine pan depressions and their dune margins. Where gypsum dominates the pedogenic profiles, the soils are typically described as gypcretes, gypsites, gypsicretes, *croûte de nappe* or *croûte gypseuse zonée*. Currently, something like 2×10^6 km^2 of gypsum-entraining soils cover the world landscape (Nettleton 1991). Gypsum crusts have been reported from all the continents, including Antarctica (El-Sayed 1993). They typify soils in arid areas where mean monthly evaporation exceeds mean monthly precipitation, Watson (1985) notes a close association of gypsum soils with areas receiving less than 250 mm annual rainfall.

Use of the term gypcrete often has a connotation of gypsum being the dominant hardpan cement, while the term gypsite implies a finegrained (silt-sized) powdery soil. According to Aref (2003) gypsum crusts and soils are surficial and penesurficial accumulations that have the following specifications: (1) a minimum thickness of 0.1 m; (2) a minimum gypsum content of about 15 % by weight; and (3) a gypsum content at least 5 % greater than the underlying rocks. If the soil contains less than 15 % gypsum it is classified as a gypsiferous soil. Watson (1985) also grouped the consolidated gypsum, together with weakly cemented and powdery gypsum accumulations, under the term gypsum crust.

Four mechanisms or processes precipitate most gypsum soils and crusts worldwide: (1) In-situ pedogenic weathering of existing gypsiferous or volcanogenic (ash) parent material; (2) eolian or fluvial transport of gypsum or SO_4-rich sediment; (3) an oceanic aerosol source, creating in sulphate-enriched rainfall that evaporatively concentrates within the regolith (4) in-situ oxidation of sulphide minerals. The first two sources are direct evaporite associations, while the third is typically associated with salt lakes, sabkhas and playas in semi-arid or desert settings within 500–1,000 km of the coast. Many gypsic soil horizons are combinations of both pedogenically precipitated and detrital wind- reworked gypsum.

Soils with gypsic horizons form in various parent materials such as alluvium, eolian sediments and weathered geologic formations, many in regions of pre-existing gypsiferous sediments (Taimeh 1992). For example, differentiated gypsum soils 0.5–1.5 m thick, largely formed by capillary evaporation, cover much of the area east of the Fayum depression (chott) in the north central part of Egypt (Fig. 1.36; Aref 2003). These pedogenic gypsum crusts only cap Middle Eocene carbonate rocks that are interbedded with thick gypsiferous shale beds and the soils are mostly a result of the hydrological reworking of this Eocene source. The soils show a three-part layering from top to bottom of: (1) massive powdery gypsite/gypcrete, (2) massive indurated gypcrete, and (3) massive mottled gypcrete. All layers are composed of variable amounts of microcrystalline gypsite, fine to coarse lenticular gypsum, as well as porphyroblastic, prismatic and fibrous gypsum. Precipitation of the various types of gypsum is driven by capillary evaporation of $CaSO_4$ -enriched meteoric waters, so most of the gypsum occurs as vadose surficial crusts dominated by displacive gypsum growth. In the lower

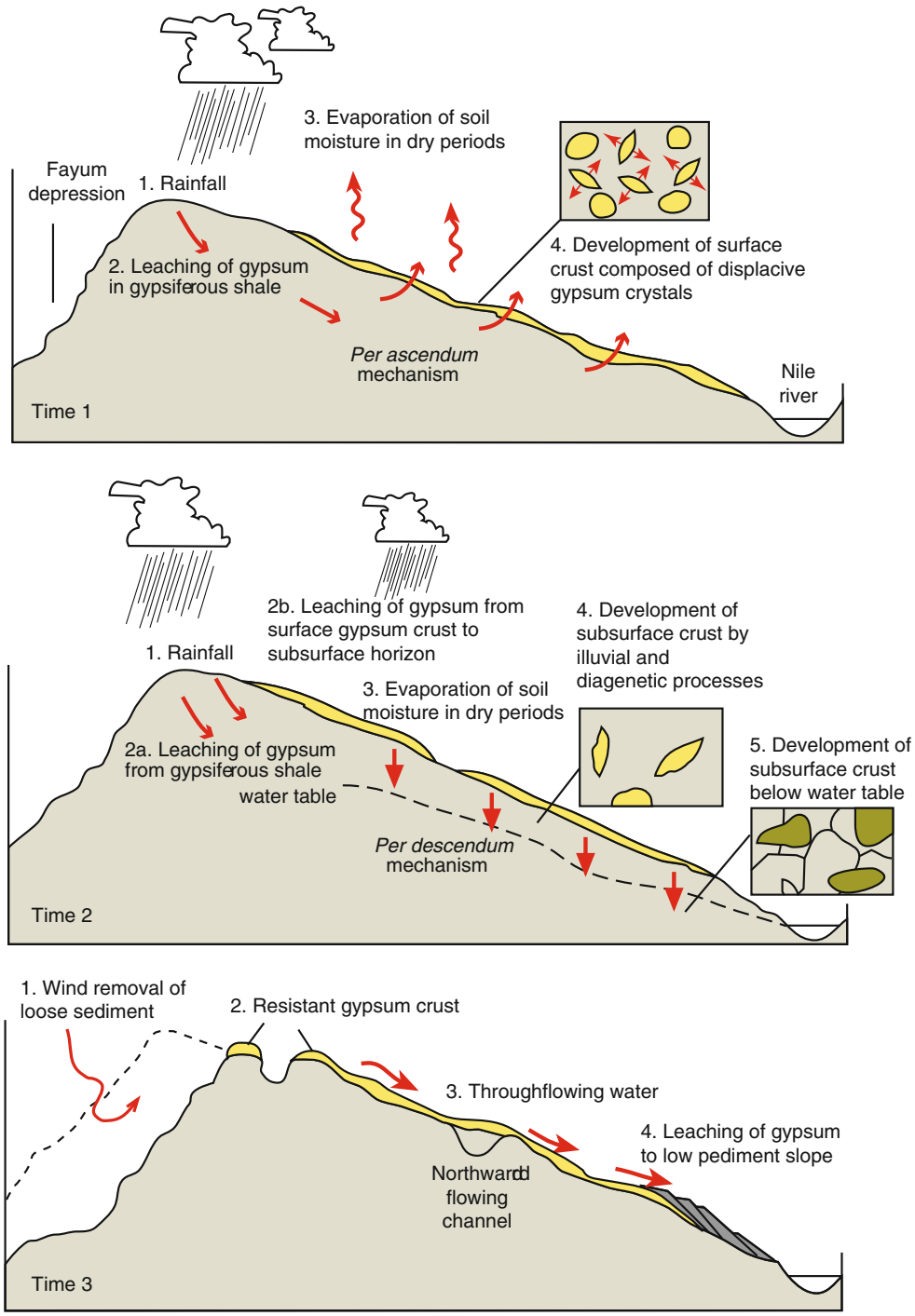

Fig. 1.36 Formation of pedogenic gypsum crusts at the eastern side of the Fayum depression Egypt (After Aref 2003). During dry periods, the gypsum-rich meteoric waters are drawn to the surface by capillarity (*per ascensum*), which leads to gypsum crystallization and crust accretion on the lower slope. During a subsequent wetter period, the surface gypsum crust is partially dissolved by meteoric water that moves downward (*per descendum*) and is mixed with laterally moving gypsum-rich meteoric water from the gypsiferous beds, which leads to deposition of subsurface gypsic crust. During subsequent weathering of the landscape the gypsum crusts can preserve residual landforms from subsequent erosion and weathering

vadose zone, gypsum accumulates by illuviation, interspersed with hydromorphic (sparry) accretion when watertable levels are higher (Aref 2003). The resulting gypsum carapace, although susceptible to dissolution, tends to preserve the residual landforms from severe erosion or weathering and so form gypsum-capped mesas.

Elsewhere, marine aerosols are focused into playa sinks and then reworked by eolian processes, as in much of the Namibian Desert and in soils about the arid salt lakes areas of southwestern and southeastern Australia. Other evaporite salts, with their inherently higher solubilities, tend to dissolve too rapidly in most vadose situations to form soil crusts and so do not form thick preservable accumulations in most of the world's deserts. Impressive exceptions to this generalisation can be found in the hyperarid Atacama Desert of South America. There

pedogenic accumulations of nitrates and iodates, along with halite and gypsum, are accumulating in the desert regolith; and have been doing so since the mid Miocene, when uplift of the Andes first created desert conditions (Chap. 12). For the same reason, namely hyperaridity in the Atacama, small parabolic dunes of halite (0.7–1.3 m in width and length) are today blowing across the saline pan floor of Salar de Uyuni (Svendsen 2003).

Pedogenic gypsum horizons can sometimes stack to substantial thicknesses. This is especially so in arid, subsiding groundwater-basins where ancient evaporite beds exposed by diapirism or uplift about the basin edge are being recycled by karstification. For example, there is a 25 m thick gypcrete hosted in Miocene alluvial fan sediments in the Calama Basin of northern Chile. The gypcrete is a single horizon in the alluvial bajada and it surrounds an ancient endorheic basin. It formed in the Miocene, via stacking of gypsum-cemented soil horizons (Hartley and May 1998). It was probably preserved, despite its high susceptibility to meteoric recycling, by its 9.5 Ma carapace of ignimbrite. This relatively impervious volcaniclastic ashfall isolated it from downward-percolating meteoric waters.

Gypsum dunes, stabilised by gypsite-soil caps, form wind-reworked vadose deposits around the margins of many Holocene and Quaternary brine lakes throughout the world (Table 1.5). For example, gypsum dunes line the salt pan edges of undisturbed continental salt lakes and coastal salinas in southern and western Australia. Lesser accumulations of eolian gypsum can create nabkha fields about the salt pan edge (Fig. 3.19d). Today all lakes are in the penultimate stages of their Holocene brine pan fill; hydrologies are characterised by ephemeral surface waters interspersed with long periods of deflation. In the coastal zone these are the same pans that precipitated large bottom-aligned gypsum crystals in the earlier perennial brine stages of their Holocene infill. But now, with the aggradation of the gypsum fill to near sealevel elevations, the lake surface is at hydro logical equilibrium with current sealevel and can aggrade no further (Warren 1982b). Surface brine sheets in these flood settings come to saturation quickly and all have dried up by late spring. Rapid multiple nucleation of gypsum crystallites takes place across the floor of the brine

Table 1.5 Some of the arid to semi-arid regions where gypsum dune fields (and lunettes) are associated with the deflation of saline lake (playa) sediment

Locality (Köppen)	Style	Reference
Bonneville Salt Flats, Utah (BSk)	Small gypsum dune field along the edge of an active continental sabkha (Bonneville Salt Flat) formed atop a now deflated perennial saline lake, Made up of two shore parallel dune ridges up to 9 m (30 ft high).	Jones (1953), Eardley (1962)
White Sands dune field, Tularosa Basin, New Mexico (BSk)	Dunefield area of 500 km^2 is one of largest gypsum dunefields in the world and consists of a core of crescentic dunes flanked to the north, east and south by fields of parabolic dunes. Gypsum dunes created by active deflation of gypsiferous sediments of Pleistocene Lake Otero around 7,000 years BP.	Langford (2003), Kocurek et al. (2007), Szynkiewicz et al. (2010), Chavdarian and Sumner (2011)
Salt Flat Playa, Guadalupe dune field, Trans-Pecos Basin, Texas and New Mexico (BWk)	Gypsum dunes cover an area ≈100 km^2 and are primarily parabolic in morphology, and reach up to 15 m in height. Occur along the edges of an active continental sabkha at the western foot of Guadalupe Peak, forming atop a former perennial saline lake. Gypsum is deflated from a former large perennial gypsum lake, Lake King, that occupied the closed Trans-Pecos basin during the late Pleistocene.	Hussain and Warren (1989), Wilkins and Currey (1999), Szynkiewicz et al. (2010)
Estancia dune field, Estancia Basin, New Mexico (BSk)	Gypsum dunes cover 120 km^2. Isolated domal bedforms and crescentic ridges occur in the centre of the basin and are derived from the initial deflationary events. Numerous lunettes on margins of isolated deflationary basins were initiated during the last deflationary event. Dunes sands contain about 60–70 % gypsum, within a loose matrix of clay and minor carbonates. Deflation of the gypsum from the former perennial Lake Estancia began with the passage into dryer conditions around 7,000 years BP.	Allen and Anderson (2000), Szynkiewicz et al. (2010)
Laguna Ojo de Liebre area of Baja California (BWh)	Gypsum dunes along the mudflat edges of coastal lagoons.	Kinsman (1969), Holser et al. (1981)
Cuatrociénegas dune field; Cuatrociénegas Basin, Coahuila, Northern Mexico (BSh)	Overall the saline lacustrine environment of Laguna Grande appears to have remained relatively stable through the late Pleistocene and increased in aridity during the Holocene, with associated deflation and gypsum dune formation. Dunes are near pure gypsum in some areas	Forti et al. (2004), Minckley (1969, 1992), Minckley and Cole (1968)
Continental playas or salt lakes of inland Australia (BSk)	Gypsum lunettes in most salt lakes located in zones of continental seepage outflow in the interior of Australia including; Lake Eyre, Lake Frome, Lake Fowler, Lake Malata-Greenly, Lake Amadeus, Cooke Plains, Prungle Lakes, Lake Lefroy and Lake Cowan. Other less saline pans are lined by lunettes of pelleted clay or sand. Dune forms are typically parabolic (lunette) and tied too downwind edge of lake, tend to not coalesce into large dune fields.	Bowler (1983), Chen et al. (1990), Dutkiewicz et al. (2002), Magee (1991), Zheng et al. (2002)

Table 1.5 (continued)

Locality (Köppen)	Style	Reference
Salinas of coastal western and Southern Australia (Csb)	Gypsum dunes formed by late Holocene deflation of lacustrine gypsarenites in a marine seepage lake that is currently filled to within a few cm of sea level (e.g. Lake Macdonnell, Marion Lake, Streaky Bay Lakes, Hutt Lagoon). Dune forms are typically parabolic, some are tied to downwind edge of lake, others still blowing across lake. Tend to not coalesce into large dune fields.	Arakel (1980), Warren (1982b)
Dunes in chotts in South-central Tunisia (BWh)	Small gypsum dunes (≈70 % gypsum) are derived by the subaerial break-up and deflation of older gypsum crusts that cover much of the seepage areas in the chott depressions (as in Chott Fedjaj and Chott el Djerid). This is followed by eolian gypsum transport, deposition and possible recementation into a new crust.	Mainguet and Jacqueminet (1984), White and Drake (1993)

Köppen climate zones are explained in Chap. 2

sheet as beds of sand-sized gypsum (gypsarenite) accumulate, only to be subject to later desiccation and deflation into lunettes that line the edges of the saline depressions.

Thus, each summer, as undisturbed coastal and inland salinas exsiccate, the watertable falls and the upper part of any newly formed gypsarenite layer leaves the capillary zone and is blown into dunes that line the margins of the lake (lunettes). Capillary zone deflation forms the characteristic truncation or Stokes surfaces in regions sourcing eolian sediments worldwide (Table 2.15). When dune growth ceases, a stabilised and vegetated gypsum dune is subject to the ongoing set of pedogenic processes that form gypsite and gypcrete carapaces. Gypsum rhizoliths and bioturbation structures, as well as bioturbated gypsum soils (gypsites) form atop eolian crossbeds (Fig. 4.6g). Both the gypsite soils and the fresh lake flats develop polygonal crack networks similar to the features describe from desiccated dunefields in White Sands, New Mexico (Chavdarian and Sumner 2011). In regions where the watertable is relatively shallow, such cracks are not typical V-shaped mud cracks created by simple drying, rather they form via ongoing cycles of capillary evaporation and gypsum cementation.

Gypsum and pelleted clay dunes (lunettes) line the edges of many salt lakes and playas in southeastern, southern and southwestern Australia; Prungle Lakes and Lake Fowler (gypsum lunettes), Lake Tyrell (clay lunette) and Lake Mungo (quartz sand lunette; Fig. 1.37; Table 1.5). These lunettes are relicts from the Late Pleistocene deflationary period, when the lacustrine hydrology changed from perennial water-filled lakes to desiccated mudflats. Likewise, there are gypsum dunes in deflationary depressions in Salt Flat Playa and the Bonneville/Great Salt Lake region of Utah (Table 1.5). Internal sedimentary structures in many of these lake-edge gypsum dunes or lunettes show tabular cross beds with consistent bedform orientation. Many lack abundant trough or festoon cross beds, suggesting consistent wind directions (Fig. 1.38a; Jones 1953; Bowler 1973, 1983). Grain constituents clearly indicate deflation of former lake sediments, which were mostly vadose prior to deflation and passage into the dunes (Fig. 1.38b).

Gypsum dunes are part of a much broader lake-edge eolian sandflat association with the lakes often supplying large volumes of eolian quartzose sediment into adjacent sand seas or ergs (Chap. 2). Dunes described as 'lunettes' have a characteristic crescentic shape, other lake edge dunes may show more linear or longitudinal outlines (Fig. 1.37; Bowler 1973, 1986). Lunette sediments range in composition from quartz-rich, sandy clay, through gypseous clay to nearly pure gypsum. Pure quartz dunes formed under lake-full conditions and are distinct from that of the clay and gypsum-rich varieties, which formed by flocculation and deflation from adjacent subaerially exposed lake floors. In arid to semi-arid zones throughout the Quaternary the interplay between salinity of lake waters and groundwater levels is critical in lunette growth and the mineralogy of the lunette (Bowler, *op cit*).

Although body fossils are rare in most evaporite beds, many gypsum soils, some subaqueous beds, and associated redbeds which are deposited in and about fluctuating to ephemeral saline water bodies, can preserve abundant trace fossils that, in addition to track and trails, also include rhizoliths and other pedotubules (Chap. 9). Burrows and trackways tend to be more abundant when the pans and playa waters are freshened and ponded, and typified by halotolerant insects and crustacea burrows and feeding traces, along with bird tracks in the Tertiary and desert dinosaur tracks in the Pre-Tertiary (Melchor et al. 2012; Konrad et al. 2010; Minter et al. 2007; Gibert and Ekdale 1999; Brogley et al. 1998). There are even 5,000 year old human footprints preserved in dolomitic carbonate "soupstones" about the edges of coastal salinas in Fowlers Bay, central southern Australia (Belperio and Fotheringham 1990). Rhizoliths in a gypsiferous lacustrine system, tend to indicate periodic wetting/freshening followed by subaerial exposure and colonisation by terrestrial plants with roots growing in the gypsiferous sediments. These plants, if they can tap sufficient fresh-brackish water, can grow into substantial structures. Halite beds tend to be too saline to host plant-root systems and are typified by microbial traces of the shallow soil biota.

Rodríguez-Aranda and Calvo (1998) identified six associations of trace fossils in subaerially exposed evaporitic

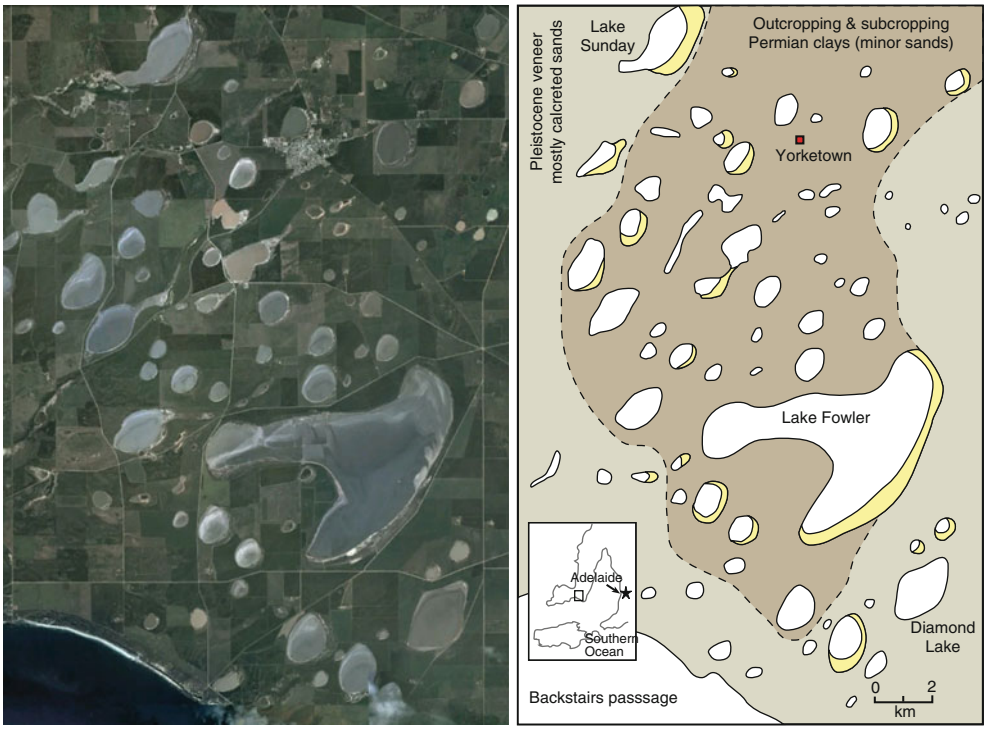

Fig. 1.37 Late Pleistocene lunettes in saline pans (salt lakes) in semi-arid southern Australia near the town of Yorketown showing gypsum lunettes at the edges of some of the wind-oriented lakes at the southeastern end of Yorke Peninsula. The largest is a gypsum lunette some 2 km long 100 m wide and 30 m thick at the southeastern strandline of Lake Fowler, the large T-shaped lake with a long axis ≈6 km (see Warren 1982b for description of gypsum in the lunette). It was extensively quarried in the early part of last century. Larger gypsum dunes (lunettes) are shaded yellow in the geological map (Google image)

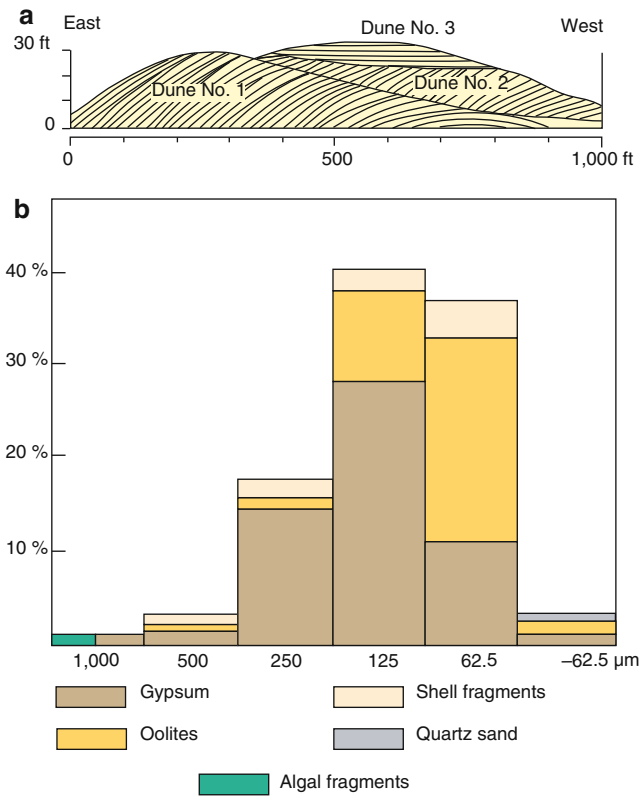

Fig. 1.38 Eolian gypsum in the Bonneville saltflats, Utah. (**a**) Cross section through the dune complex near Knolls, Utah. (**b**) Grain size distribution and mineralogy of the sands showing it is the result of deflation of sediments laid down in highstand conditions in the Bonneville/Great Salt Lake Basin (After Jones 1953; Eardley 1962). See Chap. 4 for a discussion of Great Salt Lake

sediments of the continental Tertiary basins of Spain: (1) networks of small rhizoliths; (2) large rhizoliths; (3) tangle-patterned small burrows; (4) isolated large burrows; (5) L-shaped traces; and (6) vertebrate tracks (Fig. 1.39a). The rhizoliths occur both in the marginal areas of hypersaline lakes and across lakes characterised by ephemeral but moderately high salinity waters (Fig. 1.39b). In either setting, pedoturbation indicates colonization by grasses and bushes and so indicates vadose conditions at the sediment surface that were tied to a drying of the lake and a lowering of the watertable.

According to Rodríguez-Aranda and Calvo (1998) burrowing invertebrates were especially active in those Spanish evaporite lakes where gypsum was the main mineral phase, not the more saline salts. They define a separate, sometimes pedogenic, facies in these lakes they called a "bioturbated gypsum deposit." It is typified by tangle-patterned small burrows and minor isolated large burrows; they are interpreted as burrows of insect larvae, probably chironomids, coleopterans and annelids. Similar organisms typify modern lake environments with water concentrations averaging 100–150 g/l, they flourish in lake areas subject to frequent drying and terrestrial encroachment (Chap. 9).

What is interesting about the bioturbation of these Miocene gypsum lakes in Spain is that the mm-scale layers rich in faecal pellets and associated with this bioturbation can be composed of gypsum and not the aragonite typically seen in Holocene coastal salinas (Fig. 1.39b). For example, the gypsum-pellet-rich Libros Gypsum was deposited in the

a

Type	1	2	3	4	5	6
Geometry	undulate shafts and tunnels (branching)	network of shafts and tunnels	tangle -patterned vertical, oblique and horizontal small burrows	vertical, oblique and horizontal small burrows	L-shaped combined shaft and tunnel	footprints and casts (varied shapes)
Size	d = 0.5–3 mm l = 1–7 cm	d = 0.5–2 cm l = 5–30 cm	d = 0.5–5 mm l = < 5 cm	d = 0.5–3 cm l = >20 cm	d = 0.5–3 cm l = 3–7 cm branch	a few centimentres
Infill	passive: mottled clay and carbonate	passive: clay, gypsum mosaics carbonate	-backfilling lenticular gypsum -diagenetic chert gypsum mosaics	-backfilling lenticular gypsum -diagenetic chert gypsum mosaics	passive: mosaic of gypsum cement	passive: marl gypsum
Facies	-mudstone -marl -dolostone -(gypsum)	-mudstone -marl -lenticular gypsum	-lenticular gypsum -carbonate with intrasedimentary gypsum	-gypsiferous carbonate -lenticular gypsum	-gypsiferous mudstone and marl	-marl -gypsum
Ethological Significance	root penetration	root penetration	feeding/dwelling structures	feeding/dwelling structures	dwelling structures	crawling traces
Organisms	grass root systems	bush root systems	insect larvae (Chironomids?)	-larvae and adult insects -annelids?	invertebrates (arthropods, beetles)	vertebrates (mammals, birds ...)
Palaeo-environment	mudflat (anhydrite) and carbonate ponds	mudflat (gypsum) and desiccated gypsiferous lakes	inland lakes of moderately high salinity (gypsum)	gypsiferous lakes (marginal dilution episodes)	mudflat and marginal gypsiferous lakes	marginal lake and desiccated lakes
Sketches	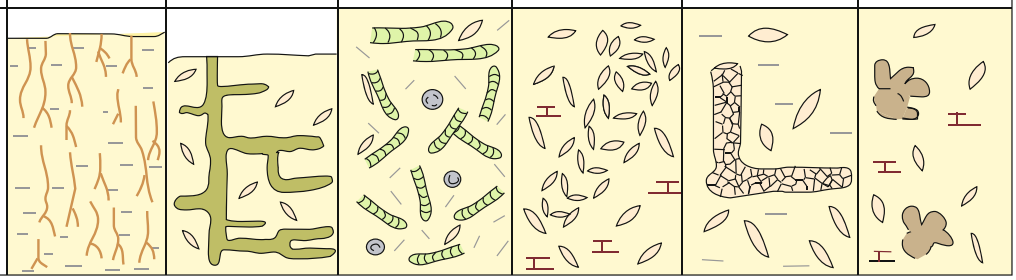					

b

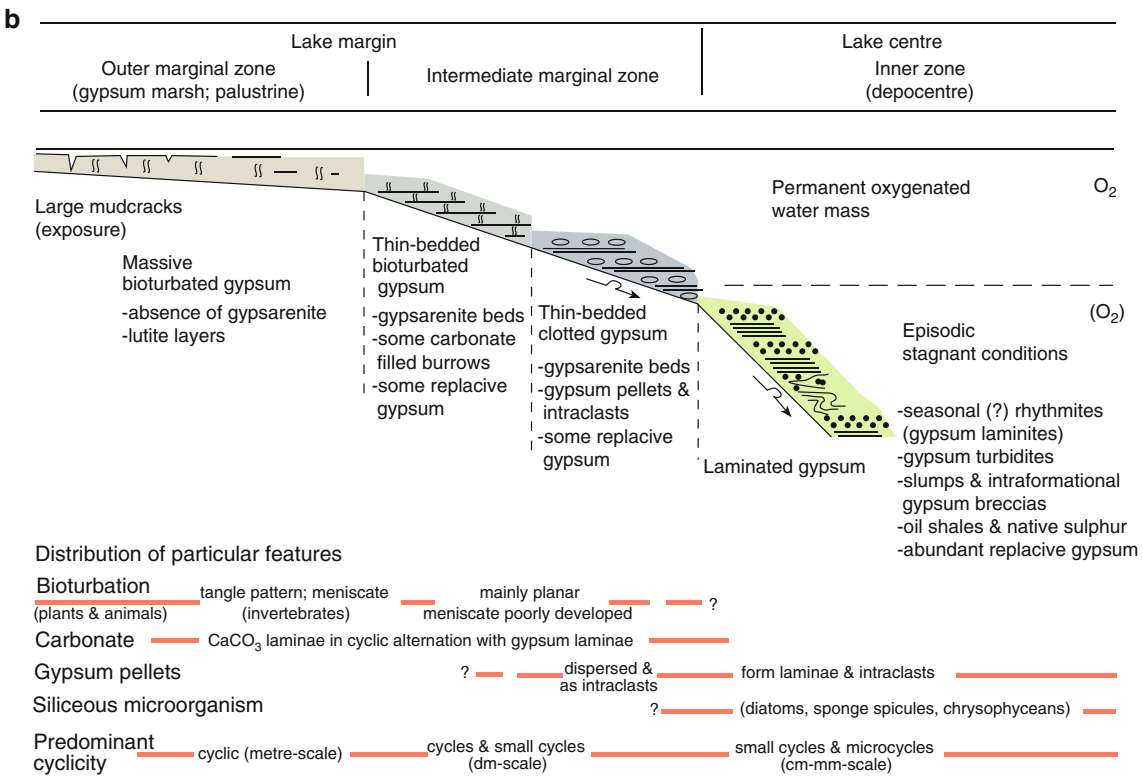

Fig. 1.39 Summary of trace fossil and rhizolith types in continental evaporite beds in Spanish Miocene Lacustrine Basins. (**a**) Spectrum of bioturbation structures, mostly from plants and animals in the lake margin facies (After Rodríguez-Aranda and Calvo 1998). (**b**) Distribution of bioturbation structures in relation to lacustrine gypsum textures and water depths (After Orti et al. 2003)

southern Teruel Basin (NE Spain) during the Miocene (Orti et al. 2003). It accumulated in a deep saline lake in which the water stratification became unstable with progressive shoaling. In the basin depocentre, a continuum of lacustrine evaporite lithofacies was influenced by the activity of organisms. Rhythmites, composed of laminae of pelletal gypsum and laminae of very fine lenticular gypsum crystals mixed with siliceous microorganisms, formed in addition to gypsum turbidites, intraformational gypsum breccias and slump structures.

The pelletal laminae originated from the faecal activity of animals (crustaceans?) ingesting gypsum crystallites in the lake water during episodes of maximum evaporation, whereas the laminae of very fine lenticular gypsum mixed with microorganisms accumulated during episodes of relative dilution. In the wide marginal zones of the basin, the Libros Gypsum unit consists of massive to thin-bedded bioturbated gypsum and thin-bedded clotted gypsum, which formed in intermediate to very shallow (palustrine) water depths. The bioturbated gypsum lithofacies were produced by the action of diverse organisms, presumably worms and coleopterans, and chironomid larvae to a lesser extent; the massive lithofacies precipitated in very shallow water; and the thin-bedded lithofacies formed in shallow to deeper settings. The thin-bedded clotted gypsum is a relatively deep facies that may have diverse origins (e.g. bioturbation, compaction, disruption of soft sediments and early diagenesis). There is a well-developed metre-scale cyclicity in the marginal lake sequences, which is not observed in the inner lake deposits. This suggests a depth change in the various lacustrine subenvironments is needed to record cyclic evaporitic processes. The isotopic composition of the pelletal gypsum indicates early sulphate-reducing bacterial activity in the bottom of the lake (Orti et al. 2003).

Biological metabolism drives substantial fluctuations in pedogenic pore pressures and salinity in gypsiferous and magnesitic soils in many lake margins and vegetated areas of coastal sabkhas. This is especially so in the immediate vicinity of plant roots, where evapotranspiration can precipitate $CaSO_4$ nodules around the plant roots. Such anhydrite and gypsum nodules are growing centripetally about halophyte roots in the modern gypsiferous supratidal sabkha succession of the Al-Khiran sabkha of Kuwait (Gunatilaka et al. 1980) and in the current lacustrine margin facies of the Danakil depression (Fig. 1.40). Anhydrite nodules in pedogenic horizons in the bedded Miocene magnesites of the lacustrine Calatayud Basin in Spain evolved into vertically aligned textures that today resemble gypsum ghosts (Sanz-Rubio et al. 1999). Early stages of this nodule growth were associated with typical pedogenic features such as rhizoliths and clotted to peloidal textures. The consequent anhydrite nodules, which replaced dissolving gypsum during very shallow burial, developed a strong vertical orientation as

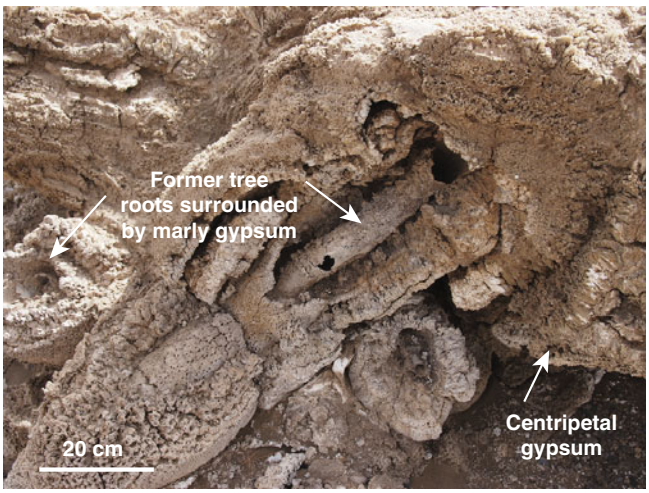

Fig. 1.40 Marly gypsiferous tufa (rhizoconcentionary core), surrounded by centripetal gypsum crystals in saline spring zone on southwestern edge of Danakil depression, Ethiopia

nodules precipitated along what were mostly vertical soil fissures. It is this nodular texture, mimicking a ped structure, that still dominates most clayey soils in the region. Much of the soil fissuring reflects expansion and contraction driven by root metabolism and a changing soil moisture profile.

Laminites from Settling of Pelagic Salts

At the other end of the mechanically-reworked evaporite spectrum from lunettes and soils are the continuously subaqueous basin-centre "rain-from-heaven" accumulations, typically composed of laminar couplets of sand- and silt-sized evaporite crystals. Crystals now on the deep bottom were originally precipitated at the air-brine interface or within the upper few metres below the brine surface (Fig. 1.27b). Less often, pelagic crystals may have precipitated at the mixing interface in a stratified brine (Raup 1982). The resulting finely-layered and laminated bottom cumulates typify many ancient "deepwater" evaporite-laminites. Such deposits tend to occur in basinal positions located well away from the evaporite platform margin.

In some ancient basinal settings, such as in the Castile Formation, which is a widespread Permian laminite in West Texas, water depths in the drawndown seaway bottom were probably sub-wavebase and the sediment-brine interface lay beneath anoxic gypsum-saturated bottom waters. Repetitive layering in laminites is resolvable at two scales; (1) at the scale of individual 1.5–2.0 mm laminar couplets of calcite and anhydrite with calcite making up about 6 % of a typical couplet, and (2) at the coarser scale of millennial brining upward parasequences ≈4 m thick (Figs. 1.41a and 1.42a). The mm-couplets in the Castile are remarkably regular in

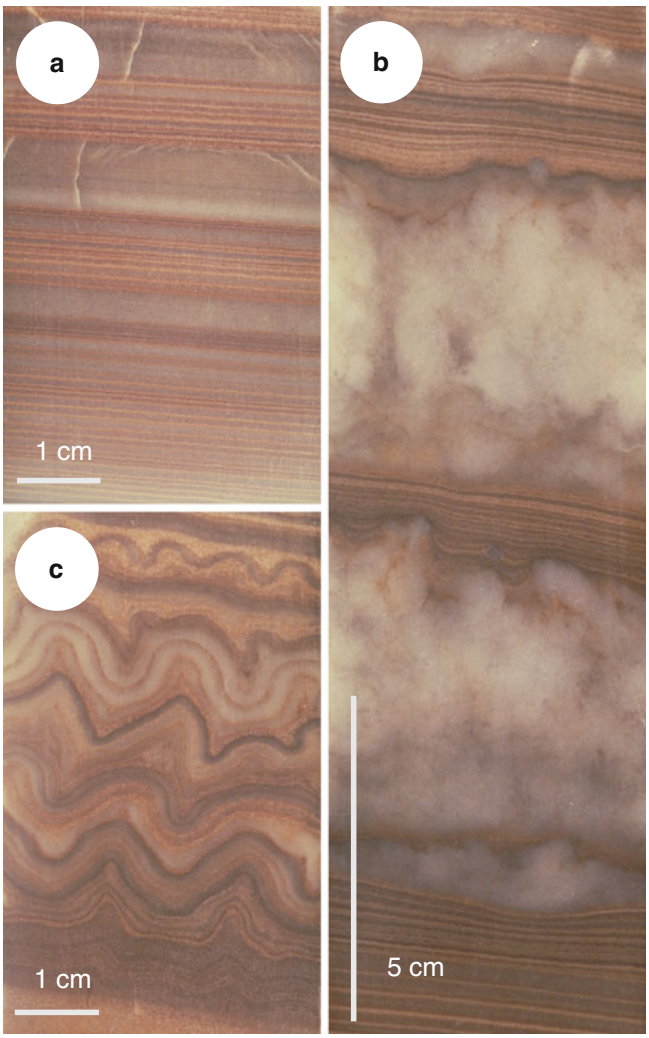

Fig. 1.41 Typical textures in cores from Castile formation, New Mexico. (**a**) Fine mm scale laminae of alternating calcite and anhydrite. (**b**) Beds of gypsum ghosts hosted in laminites. (**c**) Folded laminites possibly related to slumping into cavities created by dissolution of intra-Castile halite beds (Images courtesy of Sue Hovorka)

thickness, and are commonly repeated thousands of times vertically, without interruption in the textural style (Kirkland et al. 2000). The evaporitic sediments that formed these anhydrite-calcite couplets were pelagic cumulates. Crystallites formed at the brine surface or in the upper part of the brine column and "rained" onto the basin floor. Thickness variations of anhydrite laminae in parts of cores dominated by alternating laminae of calcite and anhydrite have been correlated from well to well over distances of up to 113 km (Anderson et al. 1972; Dean and Anderson 1982). Many laminar groupings can be correlated throughout the entire basin to within a fraction of a millimetre (Kirkland et al. 2000).

Spacing variations indicate cyclicity due to Milankovitch fluctuations in solar intensity and so are often interpreted as true varves (Dean and Anderson 1982). If so, it means the broader scale brining upward cycles were deposited in something like 1,800–3,000 years per cycle, with an average of 2,700 years and something like 175,000 years to deposit the Castile Formation (Kirkland et al. 2000). A cycle typically begins with couplets of calcite-anhydrite in which the anhydrite lamina are thin, and calcite may form as much as 80–99 wt% of the couplet. Above the basal carbonate-rich portion, anhydrite laminae increase in thickness, forming the calcite-banded anhydrite typical of the bulk of the Castile where calcite constitutes 10–15 wt% (Fig. 1.42a). Upward within a cycle, anhydrite laminae become thicker, with calcite laminae constituting about 5 wt%. Farther upward within these thick anhydrite laminae are nodules of anhydrite.

But some beds in the Castile Fm., typically up to 1 m thick, are made up of nodular anhydrite mosaics and, like the laminite sections, can be correlated across the basin (Fig. 1.41b; Leslie et al. 1997). Sporadically associated with these beds of nodular mosaic anhydrite are centimetre-size, anhydrite pseudomorphs perhaps after upward-growing gypsum crystals (Fig. 1.42b; Hovorka 1989). These aligned bottom textures suggest that at times the basin was not as "deep" as many have postulated from the laterally extensive laminites. Leslie et al. (1997) argue they represent time intervals when the basin brines became sufficiently shallow (<40–50 m) to allow supersaturated surface brines to come into contact with the basin floor (Kendall and Harwood 1989). Alternatively, and in my mind offering a more hydrologically feasible option, is that the aligned gypsum "ghosts" indicate times when the whole brine column was increasingly drawdown and associated with the loss of the upper freshened water mass (via evaporation without significant refreshing inflow). The brine column became holomictic, so facilitating an episode of basinwide gypsum bottom-growth. In either scenario, gypsum-supersaturated brines on the basin floor drove aligned crystal growth and also precipitated displacive lenticular gypsum in the upper few decimetres of the aggrading sediment column. In about one in ten cycles, nodular mosaic anhydrite is overlain by anhydrite-banded halite where the halite is coarsely crystalline and recrystallised. Although the contact with the halite is abrupt, deposition was regular and uninterrupted and perhaps tied to even more intense drawdown episodes that first changed the depositional style from laminites to bottom-nucleated gypsum (Chap. 5).

Leslie et al. (1996) interpreted some of the abundant structureless interbeds of coarse nodular mosaic anhydrite, which are up to 10 m thick in Castile Formation cores from the Union 4 University 37 borehole, as resedimented beds and not aligned nodules after bottom-growth gypsum (Fig. 1.42b). Based on what we now know about the modern Dead Sea sediments (Chap. 4), they may also be the altered remnants of a former bed made up of a massive inclusion-free gypsum meshwork deposited on the floor of the Castile Basin when the overlying brine column was still deep, but

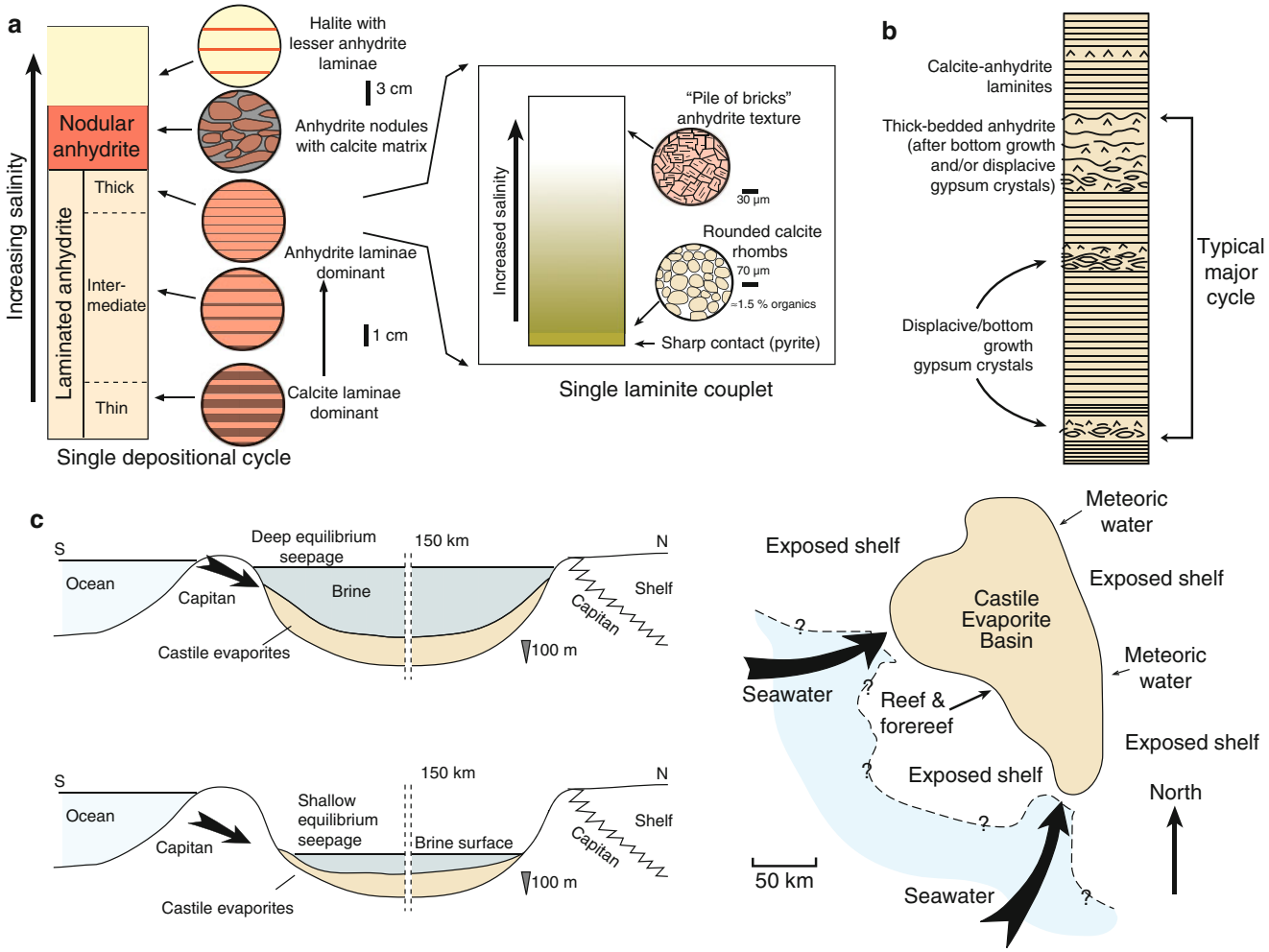

Fig. 1.42 Castile Formation, Delaware Basin, West Texas. (**a**) Representative section of a millennial cycle in the Permian Castile Formation of West Texas with a typical thickness of 1.4 m. Inset shows a typical calcite-anhydrite couplet with typical thickness of 1.5–2.0 mm (After Kirkland et al. 2000). (**b**) Typical sedimentary cycle within the Anhydrite 1 Member, it is capped by thick-bedded anhydrite after displacive and bottom-growth gypsum. Laminae at the base of most cycles are thinner with less anhydrite and more calcite. This cycle is overlain by a layer of laminated anhydrite with less calcite. The top of the Anhydrite 1 Member (which is made up of 5 cycles) is overlain by the Halite 1 Member (After Leslie et al. 1997). (**c**) Alternate models for Castile deposition, both based on a closed-basin, deep-marine-brine model. Brine drawdown either came to drawdown-seepage equilibrium when the brine depth was hundreds of metres or when the brine depth was tens of metres. Seawater seeped into the isolated basin along one or more segments of the reef front. These seepage areas were possibly most active near location of the what were former open marine surface channels through which seawater had entered the Delaware Basin during Guadalupian time (In part after Kirkland et al. 2000)

holomictic. Whatever their origin, these intervals do not exhibit the mm-scale laminae that typify the majority of the Castile anhydrite. Leslie et al. (op. cit.) argued the nodular beds were reworked from a sulphate platform that defined the eastern margin of the Delaware Basin. They noted that thick turbiditic units are less common nearer the centre of the basin, as seen in cores from the PDB-03 research well, where laminites dominate.

Differences in the interpretation of brine depth during deposition of the Castile remain unresolved, especially in some wells where there is evidence of later structuration and folding of lamina, related to collapse-driven filling of accommodation space created by exhumation and dissolution of halite intrabeds (Fig. 1.41c; Chap. 7). However, most agree that the stacked laminites intervals in the Castile Formation accumulated in brines somewhat deeper than the adjacent sulphate platform and that when the laminites formed the water body was density stratified (Fig. 1.42c; Hovorka et al. 2007).

In my mind, it was a hydrology much like that of the Dead Sea prior to 1979. The most significant difference was that there is a detrital supply of calcite to the Dead Sea laminites, while in the Castile basin there was no fluvial- or wadi-supplied detritus, only minor eolian transport of siliciclastics to the basin centre. The Castile evaporites accumulated on the deep subaqueous floor of drawndown carbonate-hosted marine seepage depression. There was no periodic flood of

sand sized detritus and so the bottom sediments are direct indicators of the salinity state of the surface water mass.

Slumped and current-reworked deepwater anhydrite laminites and turbidites have been recognised in slope and rise areas near platform margins in many other ancient evaporites, e.g. Zechstein basinal evaporites in NW Europe (Schlager and Bolz 1977), the Triassic lacustrine slope deposits of Northern Chile (Bell 1997) and the Middle Miocene (Belayim Formation) evaporites of the Red Sea Rift (Rouchy et al. 1995a, b). These deepwater reworked sequences are defined by entrained turbidite textures and Bouma cycles sandwiched in anhydritic mm-laminites. The source for the reworked anhydrite was either clastic $CaSO_4$ crystals eroded from the adjacent, but much shallower, platforms or from the sinking of "pelagic" salts. Deepwater sequences are discussed again in the basin focus of Chap. 5.

Deepwater ancient halites are rarely documented, even less so than in anhydrite-dominated basins, perhaps because beds composed of pure cumulate halite are more liable to recrystallisation and flow. By analogy to ancient anhydrite laminites "deep" water halite, historically has been thought to be thin bedded and intercalated with anhydritic laminites, but documented examples are not forthcoming. Primary textures that are patchily preserved and recognised in most ancient bedded halite are aligned chevrons. The likely deep brine texture, based on comparisons with "deep water" halite accumulating on the bottom of the modern Dead Sea, is a massive meshwork of poorly-aligned clear coarsely-crystalline halite prisms, far different from the commonly accepted notion of a "deep water laminite" as listed in Schreiber and El Tabakh (2000).

One of the few documented examples of an ancient "deep water" halite mass flow comes from the lower Miocene Vorotyshcha Suite in the Ukrainian part of the Carpathian foreland basin (Peryt and Kovalevich 1997). These halite breccias have traditionally been interpreted as tectonically deformed units related to the overthrust nappes of the Carpathians. Most clasts in the breccia consist of intrabasinal sandstone, marlstone, halite, and anhydrite, but exotic clasts consisting of rocks that are characteristic of the Carpathian flysch rocks are also present. Breccia beds are intercalated with salt layers containing chevron crystals and cubic hopper crystals, and some layers are composed of detrital salt. These salt layers rarely display graded bedding or cross-lamination, and continue over great distances. There are also slump structures associated with the bedded salts, where "deep water" halite breccias are interlayered with beds of potash. Deposition versus deformation is an ongoing debate in the interpretation of these sediments.

Can Growth-Aligned Evaporite Crystals, Interlayered with Laminites, Be Deep?

Textural interlayering of beds of cm-scale nodules with beds of laminites, like those of the Castile Fm., underline a broader interpretation problem in our current notions of what constitutes a deepwater evaporite signature. Can layers of coarse bottom crystals, intercalated with laminites, ever have accumulated on the bottom of a deepwater brine lake or seaway? The high degree of supersaturation required for primary crystal growth means that brine depths are generally shallow during crust growth in all modern examples. Maximum brine depths are measured in metres atop gypsum laminites in modern coastal salinas and decimetres to centimetres for halite crusts in saline pans. Halite chevrons and aligned laminated gypsum prisms retain intracrystal evidence of successive growth pulses as either thin layers of less saline salts or varying densities of entrained brine inclusions. This style of microlaminated intracrystal layering reflects changes in crystal precipitation rates induced by short-term changes (daily to monthly) in salinity on the subaqueous floor of the shallow to ephemeral brine pan (Warren 1982b; Handford 1991).

One inference made from modern evaporite textures is that laminated beds separating "in situ" bottom-growth-aligned crystals do not necessarily form in deep (>2 m) water in the salinas of Australia, the Red Sea and Sicily (Chap. 4). This has had significant implications in water depth interpretations of the Castile and other "deep water" laminite formations. Bottom brines in deep stratified brine columns are probably too dense and too stable to change with the rapidity required to form the mm-scale intracrystal discontinuities or layers seen in modern coarsely crystalline beds. Hence, laminated bottom-nucleated coarsely-crystalline growth-aligned textures do not form widespread bottom precipitates in modern deeper water settings (Chap. 4).

Rather, the bottom waters of a deep stratified brine system reach saturation and accumulate coarse salts only if the total brine column is at saturation all the way up to the air brine interface. This deposits monomineralic deep bottom beds made up of meshworks of poorly-oriented coarse crystal meshworks like those forming halite beds on the present-day deep bottom of the holomictic Dead Sea and the mirabilite beds on the bottoms of decametre deep saline lakes in western Canada (Fig. 1.43). Typically, they are interlayered with pelagic laminites formed when the brine column was stratified.

Thus, a modern analogy doesn't exclude a notion of deepwater halite or gypsum laminates interlayered with coarsely crystalline deepwater beds. But it does exclude the notion of coarsely crystalline beds (be they halite or gypsum) entraining regular discontinuities or fine mm-scale intrabed layers in growth-aligned crystal crusts. Otherwise one must ask, what mechanism could act over the floor of an ancient brine seaway, which was up to hundreds of metres deep and hundreds of kilometres across, to rapidly displace or cool dense halite- or gypsum-saturated bottom waters with short-lived pulses of less-dense freshened or cooler water, which would then pulse the rate of bottom crystal growth?

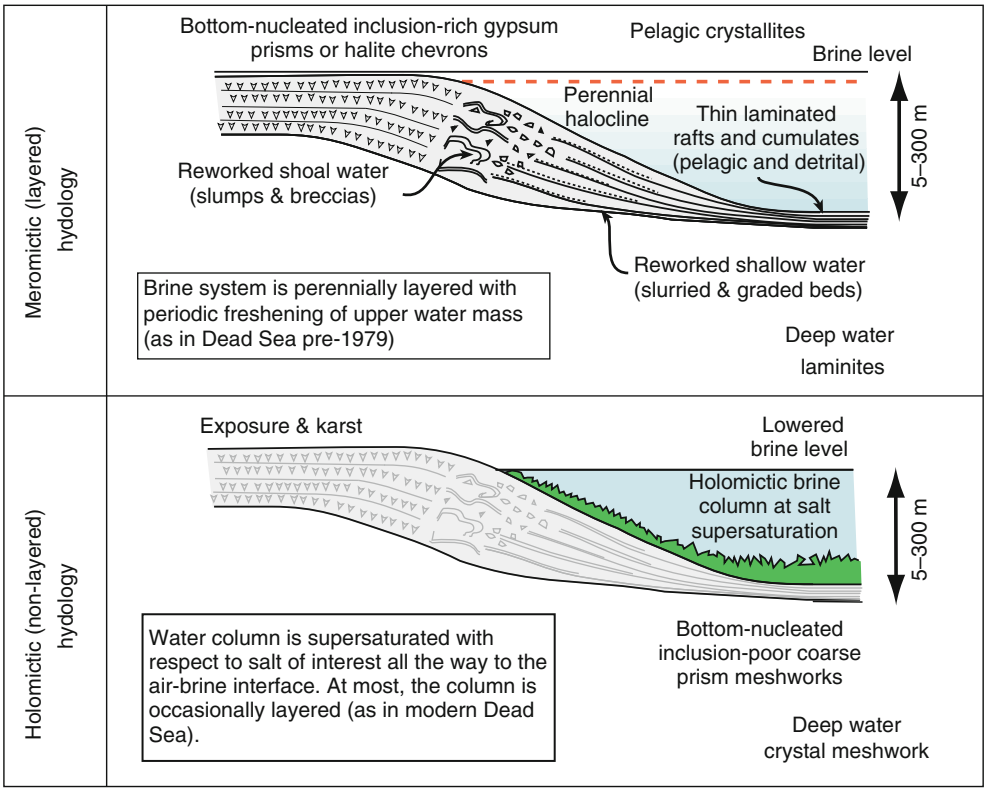

Fig. 1.43 Inclusion-free bottom-nucleated coarse crystal mesh textures can form in deep water when the water mass is holomictic, pelagic laminites form when the brine column is density stratified (meromictic)

Freshened water will always float atop a dense brine. The volume of less dense water required to displace and dilute a brine column hundreds of metres deep, or the time required for complete mixing to the bottom, excludes a deepwater "in situ" origin for fine layering in coarsely crystalline bottom-nucleated fabrics. But it does not prevent "rain from heaven" carbonate laminates accumulating in deep brines (Fig. 1.43), as happened in the Dead Sea when it was a stratified water mass for at least 400 years prior to February 1979 (Chap. 4).

As more studies are completed on modern deepwater evaporites, it is increasingly obvious that laminated beds alternating with coarse crystal beds can be a typical signature of a deep subwave-base evaporite. But the coarse beds sandwiched in among laminite layers do not show evidence of inclusion-rich layers outlining ghosts of growth-aligned swallowtail gypsum or beds of chevron halite. Brine saturations cannot change rapidly enough for these textures to form at the base of deep brine column. If the anhydrite nodules in the Castile and other deepwater evaporites are after coarse gypsum then they were deep bottom crystal meshworks that indicate times of holomictic brines in a hydrographically isolated seaway. Then, when the brine column returned to more typical meromictic (density stratified) conditions, it became a seaway where laminites accumulated on the deep sea floor. This explains the correlatable lamina spacings over distances of more than 100 km in Castile Fm. laminite beds.

As in many evaporite interpretation quandaries, part of the problem lies in the pervasive diagenetic overprinting of primary gypsum texture by a mosaic of overprints that were driven by ongoing compaction and flow. The other part of the interpretation quandary lies in the observation that the present icehouse climate mode limits the range of modern marine-fed evaporite basins available for study (Chap. 5). If a crystal crust is growing near a deepwater hydrothermal spring, there is also the possibility of pulsing crystal growth in the bottom waters due to temperature fluctuations or changes in the rate and saturation of the spring outflow. This last scenario is not volumetrically important in terms of widespread beds of ancient growth-aligned evaporite textures.

Salt Reefs, Are They Real?

Halite in modern pans and salinas typically constructs beds made up of stacked subaqueous crusts, which may locally entrain recrystallised cumulates and have been periodically subaerial. Beds tend to be dominated by flat layers with synoptic relief of no more than decimetres related to the formation of pressure ridges. However, mushroom-shaped halite buildups or reefs, with steep near vertical sides and a relief measured in metres, are currently forming in artificial solar ponds on the southern margin of the Dead Sea (Chap. 11). Halite reefs began to form in the 1970s and 1980s, after

dykes were built to enclose most of the southern basin of the Dead Sea (>200 km^2) and so create two sets of solar evaporation ponds on either side of the Truce Line Channel (Talbot et al. 1996). At that time the reefs were attributed to salting-out via common-ion mixing between natural Dead Sea brines and end-brines from the first potash plant (Chap. 2). However, tens of thousands of new salt reefs continued to grow in the enclosed salt ponds long after the pans were re-engineered and end-brines from both plants were channelled directly back to the depths of the northern Dead Sea basin (Charrach 1986; Ram et al. 1988).

The reefs grow in metres-deep perennial halite saturated brine pans as large isolated vegetable-like shapes that merge to form networks of polygonal salt walls (Fig. 1.44; Talbot et al. 1996). The walls subdivide large salt concentrator ponds into thousands of small compartments that resist brine throughflow. This is contrary to the engineer's plan of large subaqueous pans filled with brines that were easily homogenized by wind. Instead of following a designed flow path of homogenisation and downstream fractionation, brines in the compartments between the halite reef walls stratify, ultimately allowing unrecoverable carnallite precipitation in depressions between the walls.

In the inter-reef polygons is an evaporatively-maintained supersaturated 10-cm-thick surficial layer floating atop brines that are halite saturated all the way down to a cumulate covered floor (Fig. 1.44). Epitaxial halite overgrowths expand along the supersaturated uppermost brine layer and the salt reefs develop botryoidal overhangs. Salt projections can merge into a hollow platform, roofing over a cell of encased brine. Reefs and their overhangs prolong the crystallization season in the halite-saturated pans by breaking up the continuity of brine throughflow to the carnallite pans. Depositionally, they replace the planned cumulates with brine compartments walled by expanding overhangs. Salt-crusted shallows on bridged-over reef platforms and around the pan strandlines are typically made up of thin flat salt beds with vertical palisade and chevron textures that characterise ephemeral brine pans everywhere (Fig. 1.44).

In the 1980s, in order to destabilise the problematic salt reefs, brine levels in the compartments were allowed to draw down by lowering the rate of supply of pumped brine. But, rather than diminishing the evaporation area available for reef growth, the damp emergent salt reefs seemed to act as giant transpirative pumps. This further accelerated salt crystallization rates in the remaining brine compartments, which

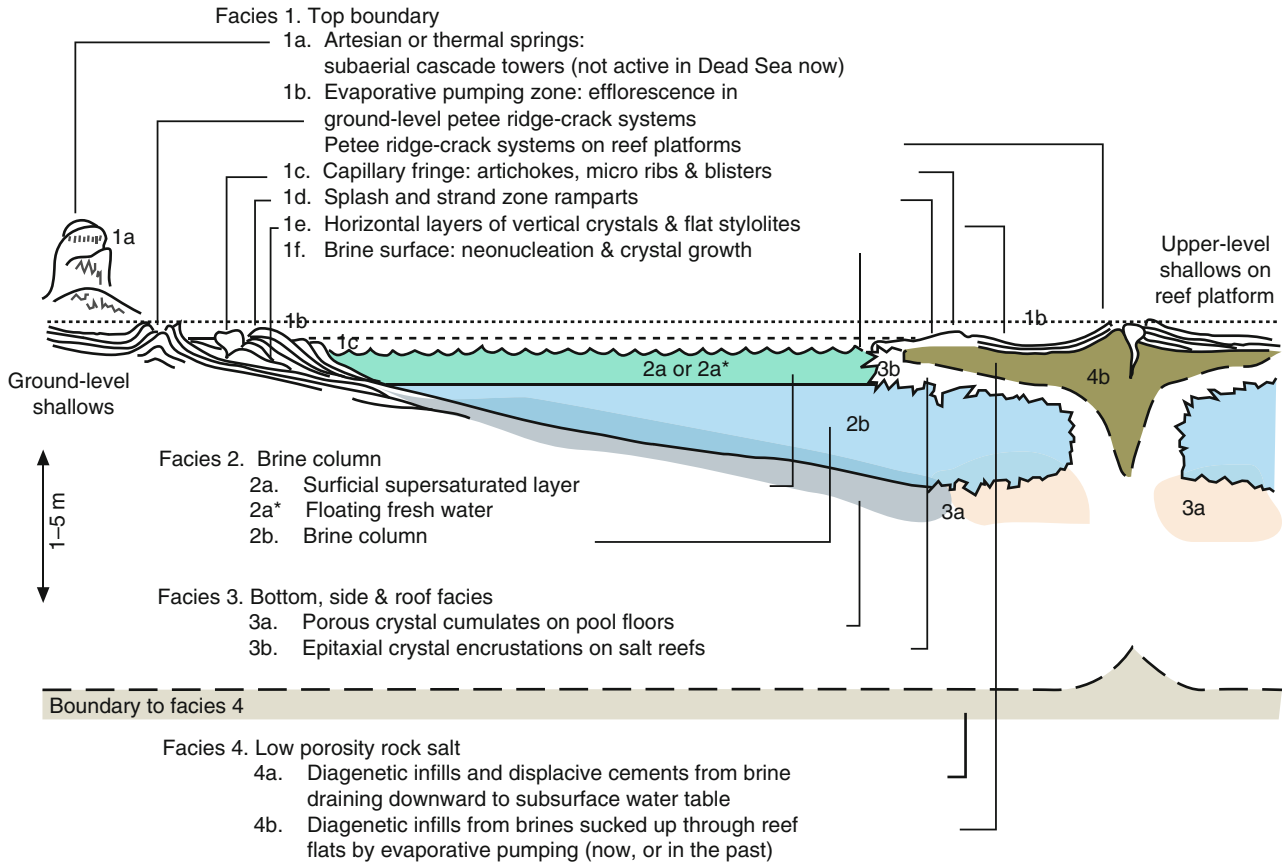

Fig. 1.44 Subdivision of the mushroom-shaped salt reefs of the southern Dead Sea is related to the permanency and salinity of stratification in the perennial pond brines in the inter-reef areas (After Talbot et al. 1996)

continued to reconfigure the evaporation ponds into smaller and smaller areas. Even today the problem is not solved and once an inter-reef area is isolated from brine throughflow, waters caught up in reef-walled depressions concentrate to bittern saturation. Bottom-nucleated carnallite drops out before reaching the target crystallizer pans. Thus, pervasive salt reefs lessen the volume of suitable brine product reaching the final fractionation pans. The solution to this problem is not subtle, reefs in both the Israeli and Jordanian saltworks are periodically removed by a combination of dredging and blasting.

The densest halite reef complex occurs in a broad band that crosses both the Israeli and the Jordanian salt ponds (and their pre-enclosure depth contours), despite each suite of ponds being different distances from the northern basin (Fig. 11.25b). The most vigorous salt reefs within this band nucleated on an old road incorporated into the Jordanian ponds. The natural end of salt reef formation is probably when shallow brines on hollow reef platforms become ephemeral on solid salt flats. But if pans in the saltworks are allowed to evolve and fill to this stage, they are no longer suitable brine concentrators for the continuous feed bittern crystallisers further down the fractionation string.

Reefs seem to evolve from cracks along pressure-ridged salt crusts, and once supersaturated surface brine layers form, grow rapidly outward and upward via epitaxis. Compared to natural saline pans, brine depths in the pans of the Dead Sea saltworks are maintained at artificially deep levels by pumping Dead Sea brine into the pans. Zones of new salt reefs grow alongside recently flooded pan shores and quickly become unrecognizable as former pressure ridges once the brines deepen. Salt reefs are not seen in modern natural brine pans and salars as the water depths where stacked salt crusts accumulate are always too shallow or ephemeral for pervasive reef growth. Talbot et al. (1996) argued epitaxis in supersaturated surface brine layers helps account for the rapid deposition of modern thick beds in the Dead Sea prior to the building of the salt works. He argues that similar structures probably formed in marine-fed regions of pure salt accumulation on the floors of ancient rifts that periodically opened to the ocean.

Domal gypsum reefs occur in modern salinas and in the Messinian of the Sorbas Basin, Spain (Fig. 4.6d), but as yet no ancient halite reefs have been documented. They should be distinguishable as being outlined by botryoidal layers of nonvertically-aligned chevron crystals, which would tend to follow a megapolygonal pattern between saucers of recrystallised cumulates. Part of the problem of recognition lies in the scale of outcrop exposure needed to recognise such a salt reef. Bedded gypsum outcrops entraining reefs and domes are commonplace, but nonhalokinetic ancient halite never makes it to the surface. Halite reef textures would be next to impossible to document in cores, but should be visible in mine walls in the same way that ancient halite megapolygon and pressure ridges are, but would easily be misinterpreted as mesoscale syndepositional karst features. Another part of the problem is a lack of expectation of halite reef structures, which are not a commonly listed texture in sedimentology textbooks. And yet another problem is that rapid infill means metres-deep perennial halite-saturated brine bodies are not found in modern salt lakes, only in anthropogenic ponds as in Israel and in quarried coastal pans in Saudi Arabia (Fig. 3.17). But, as will be seen in Chap. 5, there are many ancient saline seaways where salt reefs were possible in halite-saturated brine bodies with depths measured in metres to tens of metres.

Secondary (Diagenetic) Evaporites

Most ancient evaporites show strong evidence of secondary or diagenetic textural overprints. Providing brine is saturated with respect to a particular evaporite mineral it has the potential to precipitate that mineral. This potential exists both at the surface and in the subsurface. So far, we have discussed the primary processes of evaporite precipitation in the context of single-phase primary evaporite crystals deposited on the floor, or about the margins, of brine pans, lakes, salterns or saline seaways. However, evaporites also precipitate as intrasediment crystal growths and replacements, or as cements in pre-existing evaporite and nonevaporite hosts.

Processes of secondary evaporite formation are reflected in crystals and textures that indicate displacive growth, recrystallisation, back reactions and replacement. Such events indicate a superimposed brine chemistry that differs in terms of chemical composition, or salinity, or temperature from the brine chemistry that formed the primary or pre-existing evaporitic sediments (see Chap. 2).

Intrasediment Salts

The well-studied nodular anhydrites and gypsums of the Abu Dhabi sabkha in the Arabian Gulf are probably the most widely recognised examples of syndepositional intrasediment evaporites (Fig. 3.5). The nodules form displacively and replacively from concentrated pore fluids in the capillary and upper phreatic zones beneath the sabkha surface (Fig. 1.45a). In the type area these intrasediment crystal growths precipitate in a matrix of upper intertidal and supratidal sediments. But in addition to anhydrite capillary salts, gypsum and halite also precipitate displacively in numerous continental and pedogenic settings. Salts and their crusts may come and go, driven by the vagaries of groundwater resurgence, surface flooding and reconcentration, so that all that may be left as indicators of their former presence are

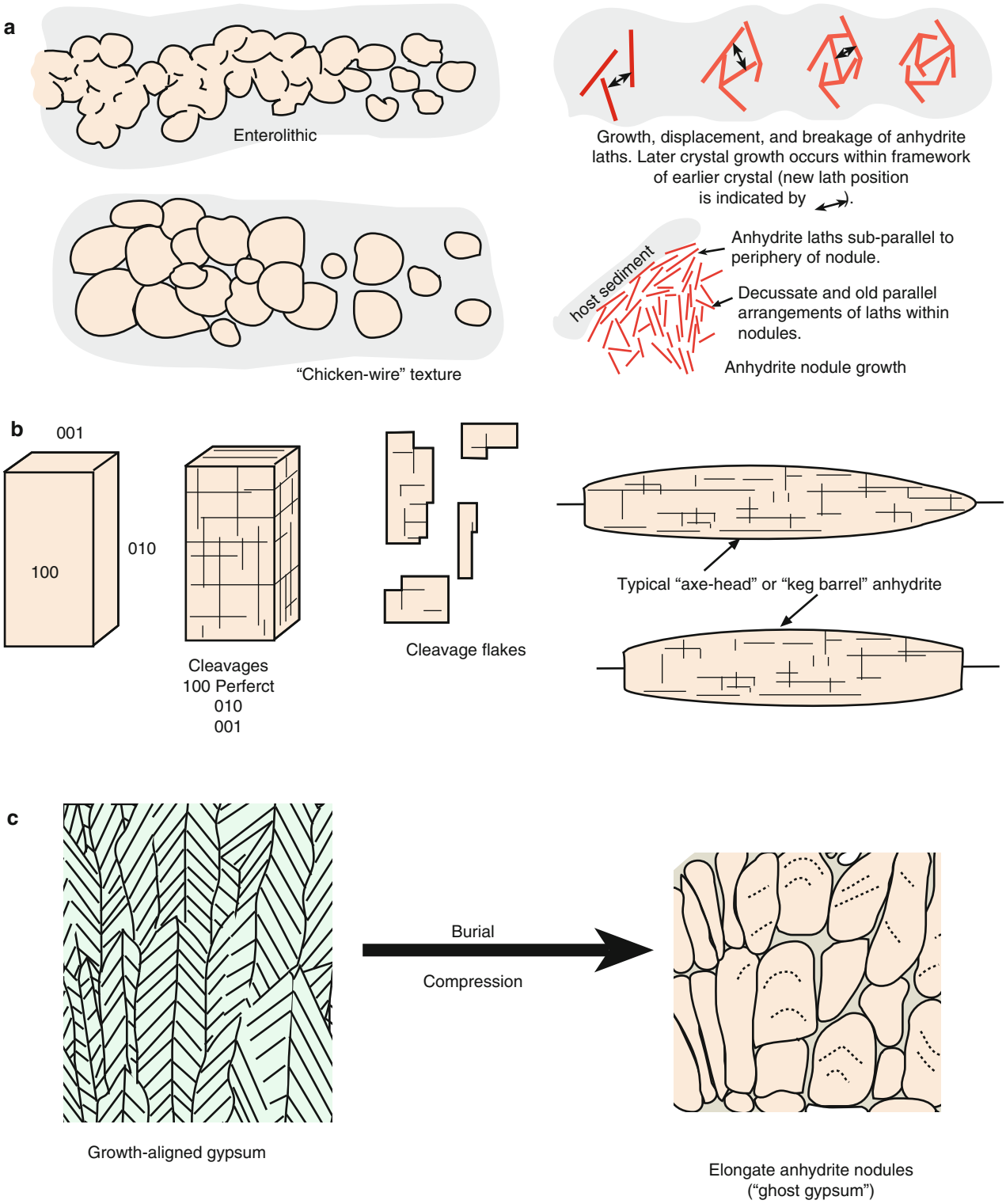

Fig. 1.45 Anhydrite characteristics. (**a**) Anhydrite nodule growth into chicken wire and enterolithic anhydrite. Also shows how successive new anhydrite laths break and rotate earlier formed laths. The end result is a nodule with a margin composed of laths aligned subparallel to the its edge. Many nodule interiors preserve clusters of subparallel laths showing large nodules grow by accretion of smaller nodules. (**b**) Crystallographic characteristics of anhydrite laths showing well developed orthorhombic cleavage. Large isolated anhydrite spar crystals in mudstones sometimes have a lenticular form. It or its pseudomorphs can be distinguished from lenticular gypsum by a typical "axe-head" and "beer-keg morphology" with well developed cleavages at one or both ends of the lens. (**c**) Preservation of gypsum ghosts as elongate anhydrite nodules created during burial (After Shearman and Fuller 1969; Warren and Kendall 1985)

highly disturbed sediments with a few halite or gypsum pseudomorphs.

The amount and variety of intrasediment salt is highly variable. Some mudstones contain scattered crystals and nodules that make up less than 1 % of the rock volume. Others are made up of approximately equal volumes of host matrix and evaporite salts, while yet others are characterised by layers composed almost entirely of intrasediment salts. The thickness of the layer over which intrasediment salts can precipitate is controlled by the style of brine supply. If the salts are precipitating by capillary evaporation beneath a subaerially exposed mudflat then the thickness is controlled by the pore throat size of the host sediment. Capillary zones can be metres thick in fine clays, while they are only centimetres thick in sands. If the intrasediment salts are precipitating by the downward percolation of dense cooling brines from a subaqueous water body then the thickness is dependent on the rate of diffusion or reflux into the underlying clay. Handford (1991) estimates intrasediment halite can precipitate in brine-saturated soft muds down to depths of 1–2 m below the sediment-brine interface.

Sabkha Nodules and Crystals

As gypsum and anhydrite nodules grow and coalesce in highly saturated pore waters of the capillary zone, they form enterolithic, contorted fold (ptygmatic) and chickenwire textures, which typify the supratidal portion of a coastal sabkha sequence. New laths of anhydrite form between older laths as such anhydrite nodules grow "from the inside out" (Shearman and Fuller 1969). Successive laths crystallise, displace, rotate and perhaps break the older laths, while the expanding nodule pushes aside the adjacent host matrix. Figure 1.45a illustrates this process and the position of each successive new lath is indicated by a double-ended arrow in the figure. The end result of this "inside-out" growth is a near pure anhydrite nodule, with laths about the edge of the nodule rotated into a subparallel alignment to the nodule margin. Many nodules are constructed of a number of subsets of this subparallel arrangement, implying large nodules grow by accretion of smaller nodules.

Capillary halite crystals typically show an incomplete development of the cube face, and in soft muds with supersaturated pore brines there is intense development of the cube edges at the expense of the cube faces to create dendritic or pagoda-like morphologies. Rapid crystal growth often entrains some of the mud matrix within the halite, usually parallel to the cube faces. Such rapid growth is thought to indicate a rapidly attained and high degree of supersaturation with respect to halite (Arthurton 1973; Southgate 1982) or perhaps growth in organic-rich brines (Gerdes et al. 2000a, b).

Displacive halite grows by capillary evaporation of supersaturated pore waters in soft brine-soaked mudflat or sabkha sediments (Fig. 1.32c). Such hoppers are found growing in carbonate muds along the western shore of the Dead Sea (Gornitz and Schreiber 1981). Similar halite crystals are found actively growing as much as metres below the surface of present day mudflats in Bristol Dry Lake in California (Handford 1991). Growing about the edges of the same lake are unusual capillary pavements of growth-aligned seepage gypsum (Rosen and Warren 1990). Dendritic or pagoda forms of halite cannot easily grow in deeper burial environments where rates of salinity fluctuation and kinetics of reactions are much slower. The surrounding matrix is more likely to be indurated, so secondary crystals formed at depth tend to be fracture or mould fills.

Syndepositional Karst in Crusts

Crusts and beds dominated by primary subaqueous textures (chevrons and palmate/zig-zag structures) can be partially dissolved by more dilute surface brines or by subaerial exposure. Freshening can be via a rise in the brine-pool level associated with rainfall and sheetflooding, by seawater flooding, or by morning dew dissolution associated with the complete drying of the brine pan. The resultant dilution creates a truncating dissolution surface that crosscuts crystal faces in both subaerial and freshened subaqueous settings (Fig. 1.46). In a subaerially exposed halite crust numerous cm-dm-scale vertical to subhorizontal karst cavities typically form beneath an upper crystal-truncating exposure surface. Cavities subsequently fill with clear evaporite cement sometimes atop a cavity-lining rind of detrital mud and clay (Fig. 3.33). In chevron halite beds these cavities are often filled with a clear inclusion-poor halite spar cement. Void infill is often related to the depositional event that precipitated an immediately overlying chevron halite or swallowtail gypsum layer (Handford 1991; Warren 1982a). Using bromine signatures, Cathro et al. (1992) found the Silurian brines that precipitated the cloudy primary halite in the Mallowa Salt of the Canning Basin were indistinguishable from the signatures in the secondary spar-like halite that filled voids in the primary halite, implying an early origin from the same depositional/syndepositional brine. This is a depositional signature still preserved in these beds more than 400 million years later.

Intensity and frequency of dissolution overprints in salt crusts are largely determined by brine depth, frequency of dilute water floods and the permanency of the brine body. Most modern and ancient halite salt pan crusts preserve evidence of syndepositional dissolution in the form of dissolution surfaces and halite-spar-filled cavities. Lowenstein and Hardie (1985) emphasised that the presence of such features in a halite bed is the unequivocal signature of ephemeral surface waters. The texture reflects dissolution events that accompany subaerial exposure of any salt crust and the periodic flooding of the halite pan by fresh to brackish meteoric

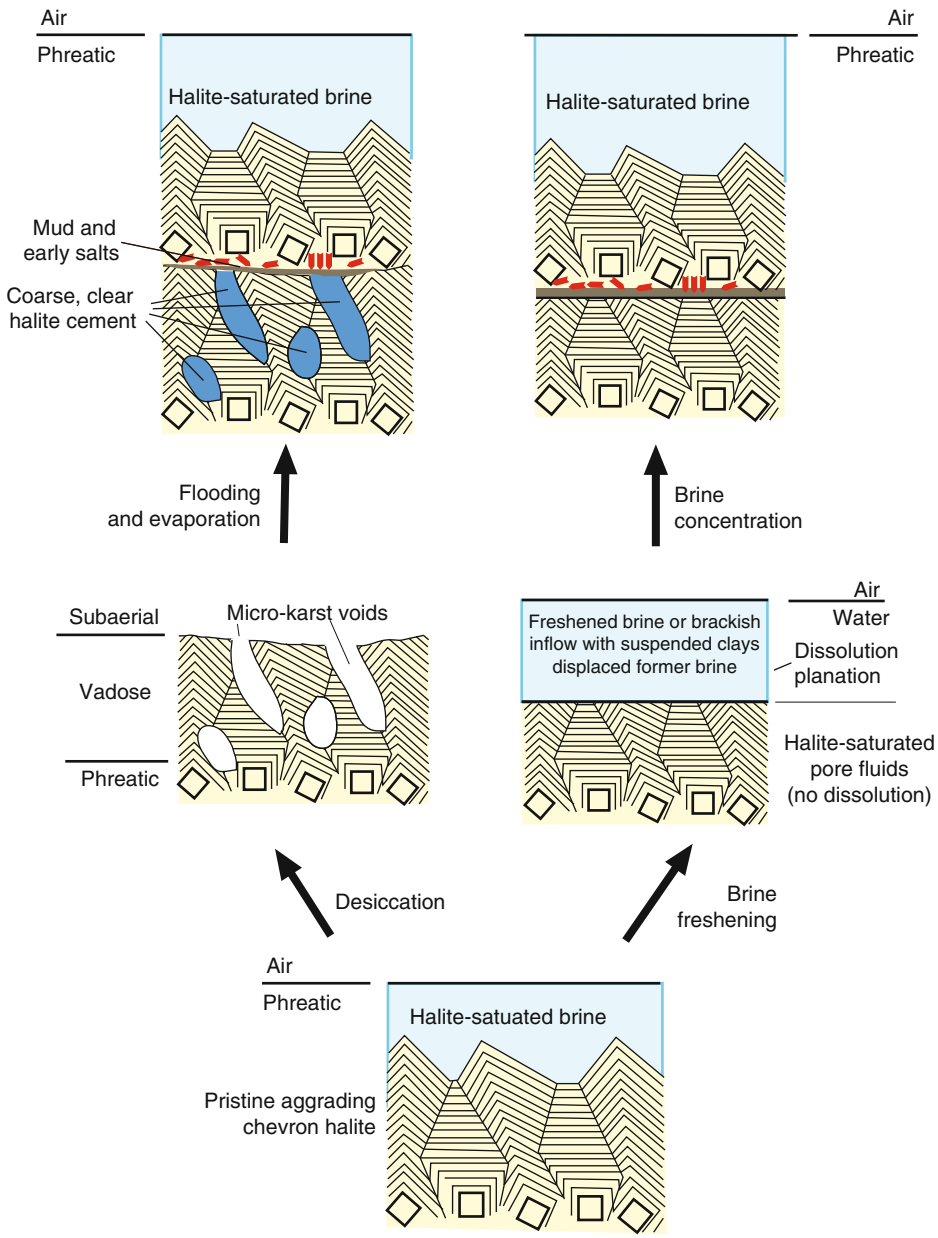

Fig. 1.46 Syndepositional overprints on chevron halite. The textural evolution illustrated on the left shows the formation of vadose microkarst, while that on the right illustrates the effect of bottom freshening on the floor of a perennial brine pool and the formation of a planation surface with no vadose karst development

water (Fig. 3.33). Dissolution cavities are less likely to occur in bottom-nucleated beds deposited in evaporite basins covered by deeper perennial brine bodies. Freshened inflow waters tend to float atop the denser halite-saturated brine body at least until its density equalises that of the underlying brine. If brine freshening does occur in a perennial brine situation then a planation surface without vadose cavities is the likely result (Fig. 1.46).

Nearsurface Crystal and Crust Dissolution

The following section focuses on small-scale syndepositional features indicative of the groundwater cycling of salt crystals and crusts, Chap. 7 looks broader and deeper in a discussion of dissolution mechanisms creating "the salt that was."

Coming and Going of Salt Crusts

Salt crusts and isolated crystals on many modern saline mudflats are ephemeral; they are not preserved in the final sediment matrix, yet their growth and subsequent dissolution on or within nearsurface sediments can alter sedimentary structures and textures to such an extent that it is difficult to identify the original texture. Areas dominated by this set of processes occupy large schizohaline areas of modern salt flats in SE Arabia such as Sabkhat Rumadan in Saudi Arabia, Sabkhat Matti and the At Taf coastal region, both in the Emirate of Abu Dhabi, and the Umm as Samim region in Oman (Goodall et al. 2000; Lokier 2012).

These salt flats are affected by varying combinations of tidal-marine, alluvial and eolian depositional processes and

the resulting sediments include both clastic- and carbonate-dominated successions. The efflorescent and precipitated salt crusts in these areas can be grouped into two main types: (1) thick crusts, with high relief (>10 cm) and a polygonal or blocky morphology; or (2) thin crusts, with low relief (<10 cm) and a polygonal or blister-like appearance. The thin crusts may assume the surface morphology of underlying features, such as ripples or biogenic mats (petees).

A variety of small-scale textures resulting from the interaction of detrital sediments with the salt crusts were observed by Goodall et al. (2000), they include: pustular growths, hair-like spikes and irregular wrinkles. Evolution of crusts over time creates a variety of distinctive sedimentary fabrics by salt-growth sediment deformation, salt-solution sediment collapse, sediment aggradation and compound mixtures of these processes. Preservation ranges from completely preserved crusts to highly disturbed siliciclastics where only suggestions of former salt crusts remain (haloturbation).

When a subaerial sabkha surface is marked by a salt crust with pressure ridges, the lee side of a ridge acts as a trap to cross-drifting sands that become enmeshed and cemented by further salt growth. Eolian-dominated sabkhas accrete via a set of processes that begin with a sandstorm, followed by a new salt ridge episode, followed by another sandstorm (Fig. 1.47a). The resulting sediment is an irregularly layered sandy mud, disturbed by ongoing intrasediment salt and carbonate growth and solution (Fryberger et al. 1984; Goodall et al. 2000). In other words haloturbation, rather than obvious crust preservation, is the dominant texture in many eolian sabkhas.

Salt-crust processes can produce features that may be confused with eolian adhesion structures. For example, distinctive wavy-laminated facies in the Lower Triassic Ormskirk Sandstone Formation in the Morecambe Field of the Irish Sea Basin had previously been interpreted as the product of fluvial sheetfloods modified by soft-sediment deformation and bioturbation. Close inspection of laminations in core revealed many of the same sedimentary fabrics seen in Sabkha Matti (Goodall et al. 2000). This facies is the product of salt growth on eolian sediment and is not of fluvial origin.

Lenticular Mudcracks

Evaporites growing in association with drying muddy sediments and eolian sands can also produce mudcracks that may be confused with syneresis cracks. There are numerous mud cracks in irregular arrays and often showing lenticular outlines in the Orcadian (Devonian) laminites of Scotland. They are considered one of the type examples of syneresis cracking and were used as evidence that these sediments were

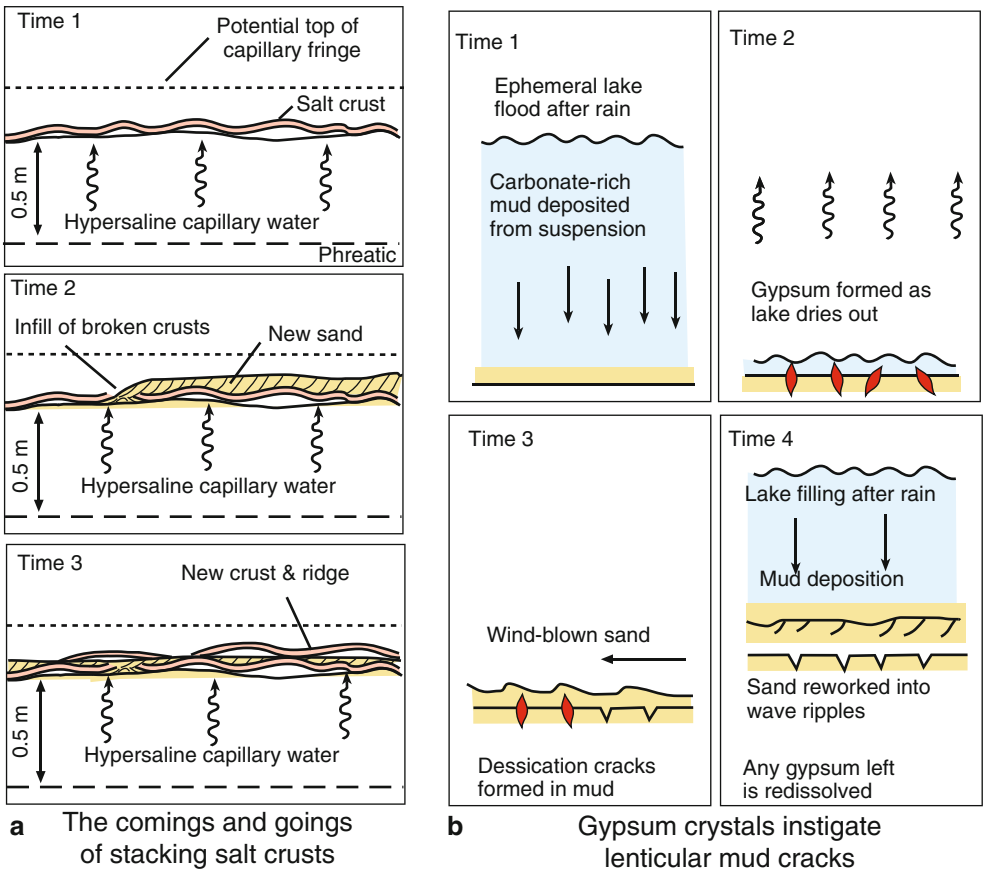

Fig. 1.47 Residual evaporite textures indicating syndepositional precipitation and dissolution. (**a**) Salt crust accretion mechanism. (Time 1) Development of salt crust at top of capillary zone. (Time 2) Covering of crust by windblown sand. (Time 3) Incorporation of crust and salt cover by capillary wicking, portions of the old crust may dissolve and collapse (After Fryberger et al. 1984). (**b**) Instigation of lenticular mud cracks (syneresis mimics) by early gypsum growth and dissolution in an ephemeral mudflat/saline pan (After Astin and Rogers 1991)

deposited in a shallow (<30 m) lacustrine environment. Yet, lenticular shaped features seem to initiate many of the mudcracks. Rather than a subaqueous origin, these mudcracks are equally characteristic of the incipient stages of subaerial shrinkage with what appear to be gypsum pseudomorphs in some of the straight cracks (Astin and Rogers 1991).

Cracks are abundant and irregularly clustered because early gypsum crystals acted as nuclei for cracking and controlled crack morphology (Fig. 1.47b). The majority of the lenticular cracked surfaces formed as the ephemeral lakes waters dried up and deposited lenticular or bird-beak gypsum. The crystals were modified to varying degrees before being covered by wind blown sand laminae and buried. Subsequently the gypsum, along with minor halite, dissolved to leave the characteristic cracks in the lake sediments. In a review of other documented examples of subaqueous syneresis cracks, Astin and Rogers (op. cit.) argue that many can be reinterpreted as the result of gypsum instigation, followed by desiccating cracks centred on the crystals and then burial. They go on to conclude that syneresis cracks, although well documented in the laboratory, are rare and insignificant in nature and that evaporites growing in mudcracks are commonplace. For example, King had noted carnallite-filled mudcracks in the salt clays of the Permian Salado Fm., West Texas, as early as 1946.

Haloturbated and Chaotic Halite

Percolation of capillary waters periodically saturated and undersaturated with a particular evaporite salt can also create textural havoc in a nonsalt matrix. For example, displacement halite grows via capillary evaporation during the supersaturated phase of pore flushing of the saline mudflat facies surrounding many brine pans. The growth of this halite disturbs and rotates primary mechanical structures in the original sediment matrix (laminae, ripples, mudcracks, etc.). But with each flooding of the brine pan there is a freshening of surface waters and nearsurface pore fluids, driven by sheet flood runoff followed by seepage down to a depressed watertable. Near surface pore waters become undersaturated with respect to halite and the displacement halite dissolves. Sediment matrix then collapses into the voids so formed, further disrupting any primary structures in the sediment matrix. As the pore fluids are again concentrated by capillary evaporation, intrasediment halite and gypsum begin to grow once more, further displacing and disrupting existing textures. This process of alternate wetting and drying with the associated destruction of primary stratification in the matrix is known as haloturbation (Smith 1971). If the sediment is preserved with halite still present, it is termed chaotic halite. If the halite is completely dissolved, all that may be left is a haloturbated massive mudstone.

Because it is largely a syndepositional process that occurs prior to induction of the clayey matrix, one of the effects of haloturbation is to create highly deformed intraclasts within the haloturbated or chaotic-halite bed. Powers and Holt (2000) use the term "smeared intraclasts" to describe this form of salt-related mudflat texture. It can be used to recognise a hypersaline capillary mudflat unit, even if the original displacive salt is leached. Smeared intraclasts are typically 2–5 cm across, are made up of the same lithology as the surround matrix and show distorted or smeared internal thin beds or laminae (Fig. 1.48). The facies transition layered and undisturbed mudflat to haloturbated mudflat to chaotic halite indicates increasing proximity to a perennial saltpan (Chap. 3).

Shallow Mineralogic Re-equilibration

Dense saturated bottom brines percolating down through a shallowly buried primary evaporite unit can create diagenetic havoc within the original texture. For example, saturated bottom brines percolating through a buried cumulate halite

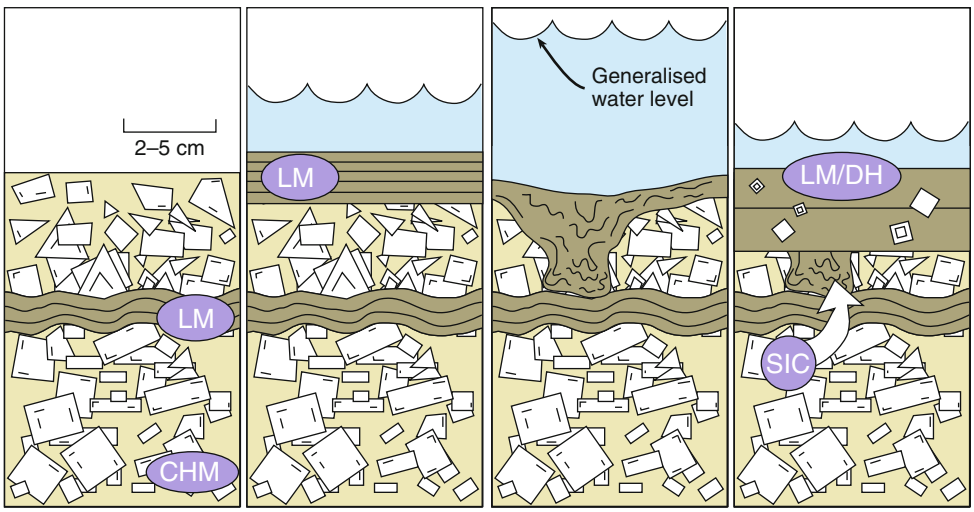

Fig. 1.48 Evolution of smeared intraclasts by collapse of lacustrine mudstone into void space created by dissolution of halite crystals during the freshened stage of a wet-dry cycle in an evaporitic mudflat. *LM* lacustrine mudstone, *CHM* chaotic halite mudstone, *SIC* smeared intraclast, *DH* displacive halite (After Powers and Holt 2000)

deposit can convert it into a tightly-cemented coarsely-crystalline halite mosaic retaining little evidence of the primary texture (Smoot and Lowenstein 1991; Cathro et al. 1992). Dense halite-saturated brines flushing down through shallowly buried subaqueous gypsum beds that are dominated by bottom-nucleated gypsum crystals can set up diagenetic conditions where the gypsum is replaced by halite/anhydrite pseudomorphs of the original aligned gypsum. In Permian evaporites of West Texas the replacement mimics the crystal shapes in beds composed of bottom-nucleated gypsum precursor, as well replacing internal layering within crystals. This tends to happen early and be driven by reflux of halite-saturated brines into gypsum beds. Ambient high temperatures and salinities mean much of the finer grained gypsum matrix has already converted to nodular anhydrite. Reflux in ancient brine platforms drove a process of gypsum dissolution and halite replacement a few metres beneath the brine-covered sediment surface in ancient brine seaways (Figs. 1.49 and 2.64; Hovorka 1992).

In a similar fashion, changes in the near surface hydrology within the modern saline mudflats of Salt Flat playa in West Texas, have "sabkha-ized" a subaqueous laminated lacustrine gypsum bed (Hussain and Warren 1989). The process was driven by the superposition of a Holocene capillary hydrology onto subaqueous gypsiferous laminites originally laid down in a Pleistocene salt lake. This capillary zone overprint precipitated nodular displacive gypsum within a matrix of laminated gyp-sum/dolomite. The change in hydrology indicates a change in climate from more humid Late Pleistocene to more arid Holocene conditions. It also set up shallow subsurface pore chemistries, whereby lenticular gypsum crystals were pseudomorphed and replaced by halite spar.

Owing to the mixing of waters of two salinities, reflux dolomitisation beneath a platform evaporite can take place concomitantly with $CaCO_3$ dissolution (Sun 1992). Relative rate of limestone solution compared to dolomite growth is a likely control on porosity levels during the later stages of the reflux dolomitisation process (Sun 1995). If the rate of dolomite growth keeps pace with the rate of $CaCO_3$ dissolution, then the mimetic replacement of micrite matrix and micritised grains occurs with little change in porosity levels, as in many ancient evaporitic peritidal dolomites. If the rate of reflux dissolution exceeds the rate of dolomite replacement, as in open marine platform carbonates beneath the seaward edge of a platform evaporite, then there is large scale skeletal aragonite dissolution, along with an increase in effective porosity in the dolomitised interval compared to precursor limestone. During shallow subsurface brine reflux in the Permian in the Palo Duro Basin, Texas, the flow of such refluxing waters dissolved marine carbonate to form anhydrite-filled moulds (Bein and Land 1983), while in the Levelland-Slaughter interval it enhanced reservoir porosity (Fig. 10.27; Elliott and Warren 1989).

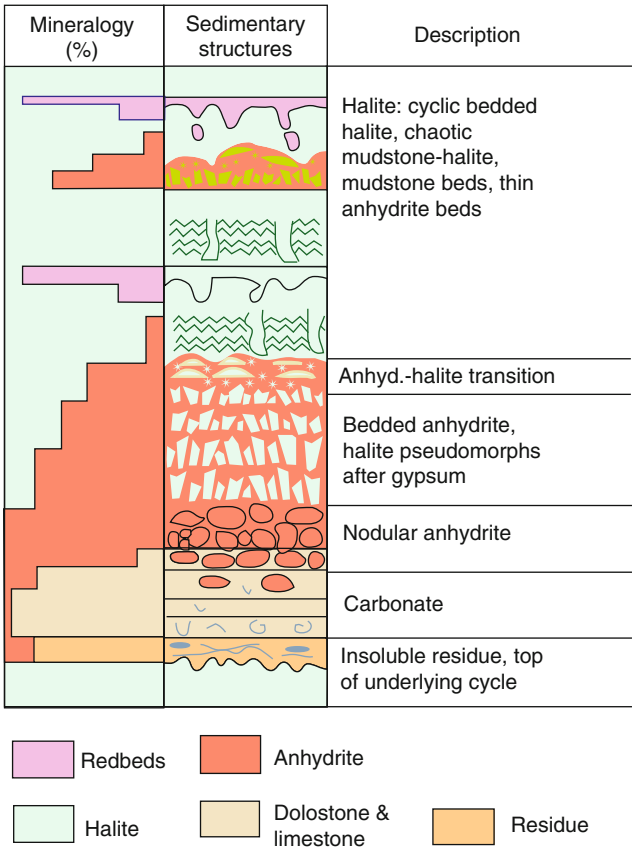

Fig. 1.49 Typical depositional cycle in the Permian evaporites of the Texas Panhandle where gypsum (rather than anhydrite) was the dominant sulphate precipitated, even at salinities near halite saturation. Large gypsum crystals grew vertically on floors of brine pools, surrounded by a matrix of autochthonous trans-ported gypsum sand and silt. Most or all of the primary gypsum was altered to anhydrite or leached and replaced by halite in the very shallow (<2 m) burial environment under the influence of halite-saturated diagenetic brines (After Hovorka 1992)

Porosity Loss

Syndepositional alteration, cementation and porosity loss, in a halite bed continues into the shallow subsurface until the bed can no longer support fluid flushing. This occurs once all effective porosity is occluded by compaction and secondary evaporite cementation. In halite-dominated continental sequences this loss of effective porosity is typically early and shallow (Fig. 1.50). Casas and Lowenstein (1989) showed that Quaternary halite layers only 10 m below the land surface have typical porosities of <10 % and that layers at depths below 45 m are tightly cemented without visible porosity. By 100 m of burial, almost all the halite units were tight and impervious. Diagenetic porosity occlusion by surface-driven hydrology in these halite beds was essentially over. No further porosity change can occur until beds start to dissolve deep in the mesogenetic realm or even in the metamorphic realm as the dihedral intercrystalline angle of halite begins to change as the beds approach greenschist conditions (Lewis and Holness 1996).

From a few hundred metres burial until it reaches the zone of metamorphism, a halite unit maintains permeabilities that are measured in no more than microdarcies or nanodarcies. Thus halite beds and allochthonous sheets provide a highly effective seal to sediments beneath. To move closer to the surface, trapped basinal fluids must either flow laterally around such a salt barrier or dissolve it. If the trapped pore fluids are hydrocarbons then no dissolution can occur as halite is virtually insoluble in gas and oil. Retention of pore fluids below a salt barrier means porosity in the host sediment is maintained to a much greater depth and that sediments below a salt barrier in an actively subsiding basin are typically overpressured.

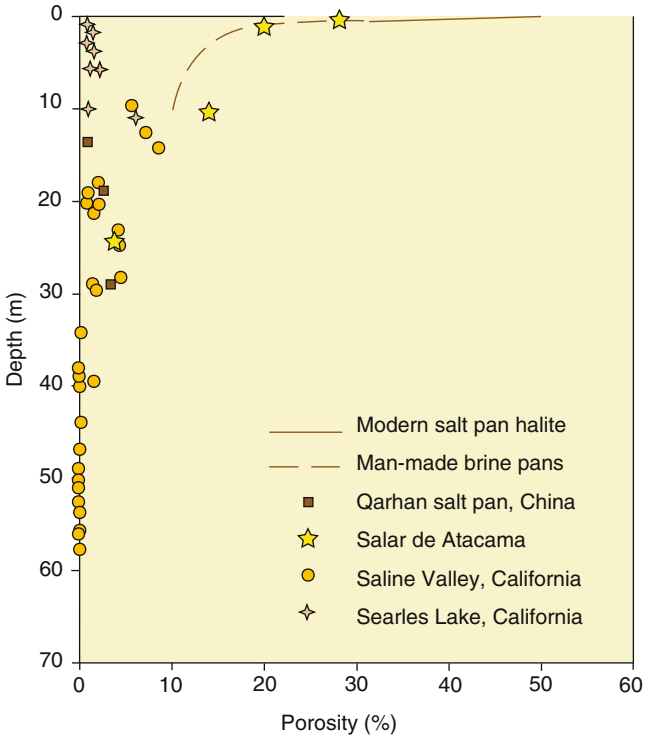

Fig. 1.50 Porosity in Quaternary halite beds versus depth (After Casas and Lowenstein 1989). All effective porosity is lost by 70 m burial

The pervasive early loss of porosity from more than 50 % near the surface to zero by 100 m burial also has important implications for textural and geochemical studies of ancient bedded halite. Casas and Lowenstein (1989) showed that this porosity loss was entirely due to early post depositional diagenetic cementation by clear halite. Other mechanisms of porosity loss by chemical or mechanical compaction were dismissed for lack of evidence. There were no strained or broken crystals, pressure solution boundaries nor stylolites, and patches of chevrons preserved in among the mosaic halite spar were all undeformed.

Many Phanerozoic halite beds that have not undergone halokinetic deformation also contain patches of relict depositional and early diagenetic textures, which have remained unchanged for hundreds of millions of years. For example, the Ordovician-Silurian Mallowa Salt (formerly Carribuddy Formation) in the Canning Basin, West Australia, retains aligned halite chevrons crosscut by syndepositional karst and an overprint of coarse mosaic recrystallised halite (Fig. 1.51a; Cathro et al. 1992). Such textures are thought to be syndepositional, yet are not dominated by large volumes of pristine chevron halite. Rather, they preserve evidence of early porosity loss brought on by numerous syndepositional cycles of dissolution and recementation. Lowenstein and Hardie (1985) showed that patchy remnants of chevrons and cornets in a dominantly coarse-grained mosaic of halite spar are not necessarily a burial fabric. All "mature" saltpan halites have this fabric within tens of metres of the depositional surface.

The mechanisms that allow a shallow brine to become super-saturated with respect to halite and to precipitate intercrystal-line cements/replacements are still not well understood. One possible mechanism is brine mixing. When compositionally distinct brines mix in the subsurface a new

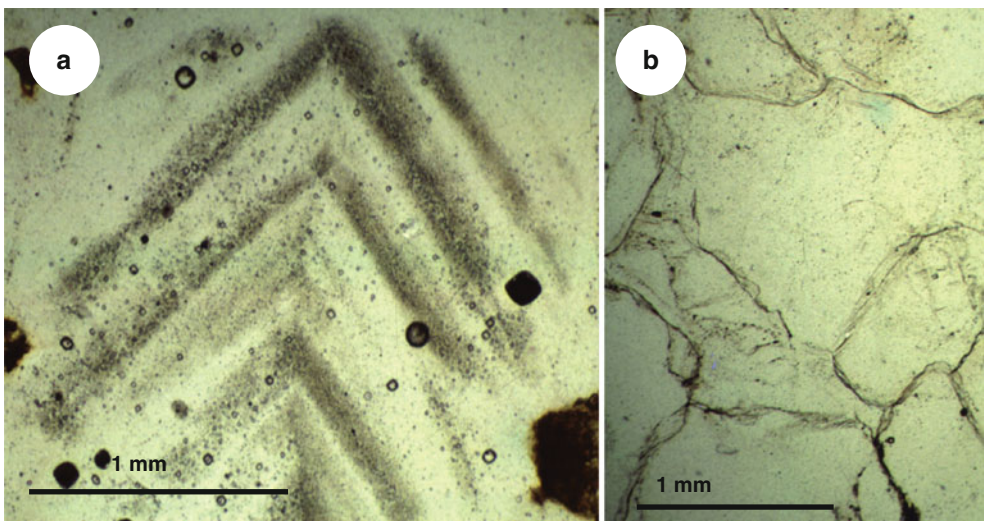

Fig. 1.51 Halite textures in the Silurian Mallowa Salt, Canning Basin. (**a**) Preserved halite chevron in growth position with erosionally truncated crest implying periodic bottom freshening and hence fairly shallow brine. (**b**) Recrystallised mosaic halite, an enigmatic texture that dominated most of the crust textures in the unit (After Cathro et al. 1992)

halite-saturated brine may result. This is the case when $MgCl_2$ brines are mixed with $CaCl_2$ -rich brines (Raup 1970). Casas and Lowenstein (1989) have questioned whether this is the dominant mechanism that forms pervasive halite cements in most shallowly buried playa sediments. Rather, they suggest a simple temperature drop is the dominant control. Brines in halite-forming surface waters can be heated to temperatures in excess of 60–70 °C, while groundwater brines typically have temperatures of 15–30 °C. They suggest that the cooling associated with the downward reflux of a surface water is all that is required to saturate a brine and so precipitate widespread halite cements.

Deeper Burial – Mosaic Halite?

Formation of pervasive mosaic halite spar early in the burial history of a salt bed creates a problem in recognising those parts of a halite unit that have been subjected to later burial recrystallisation as a deeper burial environment is also thought to form mosaic halite spar. Diagenetic textures in most ancient bedded halite units are dominated by sutured mosaic textures, where grain boundaries suture in the same fashion as neomorphic pseudosparite in calcite (Spencer and Lowenstein 1990). Individual crystals display curved boundaries that tend to meet at triple junctions with angles approaching 120°, and interstitial impurities concentrate along the crystal boundaries (Fig. 1.51b).

Mosaic texture is comparable to the polygonal equigranular mosaic texture that forms in annealing metals, where cooling grains tend to optimise their size, shape and orientation in order to minimise energy. The same mosaic texture can also be found in a soap foam as bubble boundaries with 120° triple junctions. The exact mechanism that controls the formation of mosaic textures in halite is still not well understood. It forms either early during brine reflux cementation or later during burial driven compaction and pressure-solution recrystallisation. During burial, flowing halite can create a pervasive overprint whereby pressure solution and recrystallisation moves fluid inclusions to new crystal edges. Crystals tend to flatten in the direction of maximum stress and this flattening can be used to distinguish salt that has flowed from other forms of mosaic halite (Fig. 6.16a; Rahimpour-Bonab and Kalantarzadeh 2005).

Limpid Dolomite in Mosaic Halite

The term limpid dolomite is describes a crystal form of dolomite composed of clear sparry rhombs, which in thin section appears largely free of internal impurities. As such it is a nongenetic term, limpid dolomites can form in a range of environments ranging from mixing zones to refluxing brines moving through recently deposited halite beds (Warren 2000a). Limpid dolomite in mosaic halite was documented as a late, ordered, stoichiometric, euhedral to subhedral set of dolomite crystals along the contact between bedded halites and interbedded mudstones in the platform evaporites of the Clear Fork and San Andres formations of the Palo Duro Basin, Texas (Fig. 1.52; Naiman et al. 1983; Gao et al. 1990). There it is interpreted as an outcome of focused burial diagenesis in a halite-mudstone succession. In these Permian examples, the limpid dolomite is characterised by a low Sr content and depleted $\delta^{13}C$ and $\delta^{18}O$ signatures (Fig. 1.52a). This C-O plot field is interpreted as indicating meteoric or structural waters held in adjacent deeply buried mudstones, and acting as the source of ions for the limpid dolomite that typifies the mudstone-halite contact.

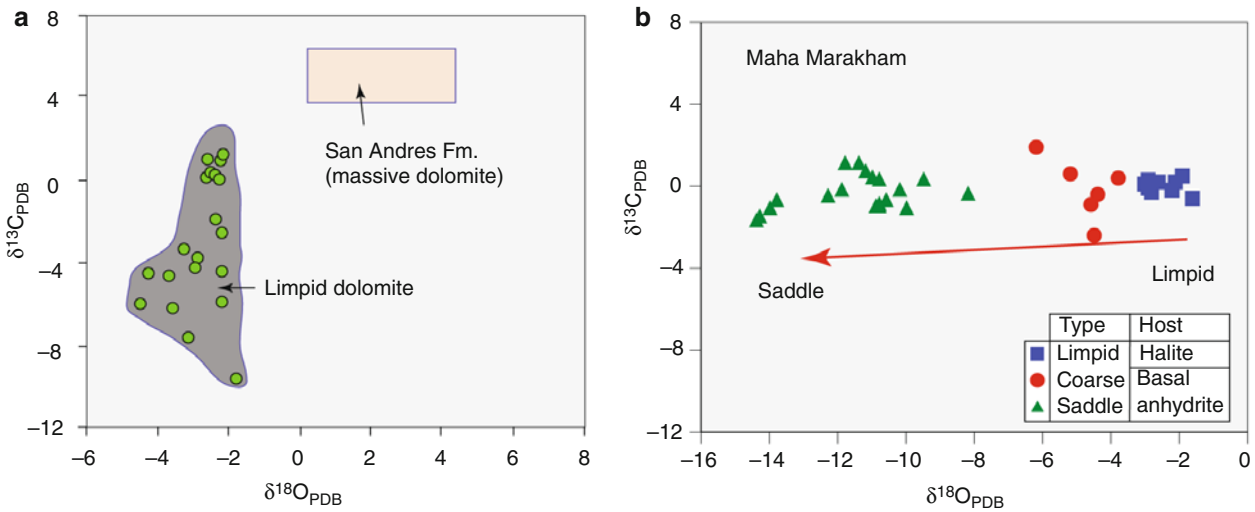

Fig. 1.52 Limpid dolomite in Mosaic halite, (**a**) In halite of San Andres Fm. Palo Duro Basin. Limpid dolomites are depleted in carbon-13 and oxygen-18, compared to typical isotopic signatures in the massive (reflux) dolomite of the San Andres Fm (After Gao et al. 1990). (**b**) Limpid dolomite in a halite host and its isotopic evolution and recrystallization when subject to an ongoing crossflow of escaping basinal waters at the base of the Cretaceous Maha Sarakham evaporites (Replotted form El Tabakh et al. 2003)

According to Gao et al. (1990) limpid dolomite in the San Andres is not the product of reflux brines, which created the pervasive massive mimetic dolomite in the interlayered San Andres platform carbonates. Limpid dolomite in the San Andres crystallised locally under favourable sulphate-reduction conditions during burial compaction and salt dissolution. Compaction mixed the waters, released from the dewatering mudstones, with brines derived by the dissolution or recrystallisation of adjacent impervious halite beds. Limpid dolomite spar precipitated along halite-shale contacts where escaping shale waters caused the halite to dissolve and recrystallize as mosaic spar.

The mode of dolomite formation from escaping structural waters, as indicated by the isotopic cluster in Fig. 1.52a, is part of a larger set of evaporite-focussed fluid flow processes that precipitate sparry or limpid burial dolomites at the contact between a dissolving salt bed and crossflowing basinal waters. The broader context of limpid dolomite is illustrated by the dissolving lower contact of the halite mass that is the Cretaceous Maha Sarakham Fm. of NE Thailand (Fig. 1.52b; El Tabakh et al. 2003). Limpid crystals of dolomite occur in the polyhedral sutures of mosaic halite that has undergone varying intensities of salt flow. In addition to the halite-hosted occurrences, there are two other forms of limpid dolomite crystals, which occur in the Basal anhydrite (a diagenetic unit discussed in Chap. 7) that defines the dissolving underside of the salt mass. These forms of limpid dolomite (coarse and saddle) show increasingly negative oxygen values, related to ongoing dolomite crystal growth in an anhydrite host, while flushed by warmer escaping basinal fluids (Fig. 1.52b). The burial evolution is also seen in the $^{87}Sr/^{86}Sr$ evolution of the various dolomites.

Burial of Sulphate Evaporites

Due to water release, gypsum and other bedded evaporite units made up of hydrated salts with entrained structural water show an inherently more complicated textural response to burial than the simple mosaic overprint of halite beds (Fig. 1.53; Warren 1991). Gypsum releases structural water as it converts with burial to nodular mosaic anhydrite. Carnallite ($KCl{\cdot}MgCl_2{\cdot}6H_2O$) releases Mg and water as it converts to sylvite (KCl) by incongruent dissolution associ-

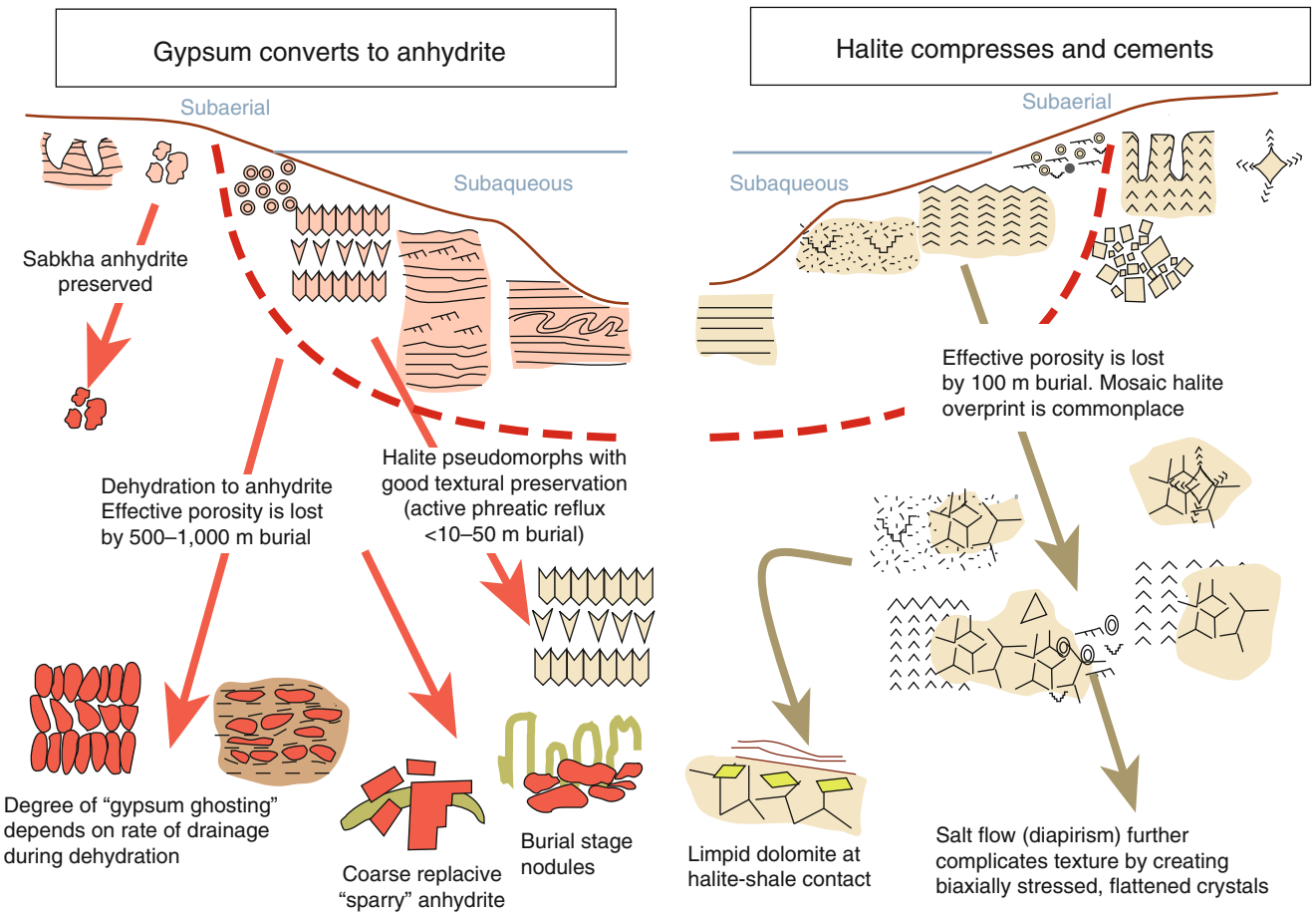

Fig. 1.53 Evaporite diagenesis showing evolution of burial-related secondary evaporite textures (includes burial salts)

ated with burial diagenesis or phreatic flushing by meteoric waters. Loss of structural water during burial dehydration means syndepositional textures in the converting bed are modified by this flush of escaping water.

The following discussion focuses on the conversion of a gypsum unit into anhydrite (anhydritisation) within the same mass of solid $CaSO_4$. There is an associated set of diagenetic fluid processes related to this conversion, namely the escape of $CaSO_4$ -saturated waters that can create sparry anhydrite burial cements in adjacent non-evaporite units. This set of subsurface processes is mentioned again later in this chapter, but textures and outcomes will be discussed in more detail in Chaps. 2 and 8. There is an additional set of anhydritisation processes where the precursor being converted to anhydrite is not gypsum, but a limestone or a dolomite. This set of processes and outcomes is also discussed in detail in later chapters.

Nodular Anhydrite and Water Loss

Gypsum, rather than anhydrite, is the most common form of sedimentary $CaSO_4$ at earth surface temperatures. Intense solar heating in very arid regions can dehydrate gypsum to form bassanite/anhydrite at the surface. Bassanite is also the precursor to gypsum in many depositional settings (Van Driessche et al. 2012). Natural gypsum forms via a three-stage process: (i) homogeneous precipitation of nanocrystalline hemihydrate bassanite crystallites below its predicted solubility, followed by (ii) self-assembly of bassanite into elongated aggregates co-oriented along their c axis, and then (iii) transformation into dihydrate gypsum.

Gypsum can convert to anhydrite in the capillary zones of sabkhas and evaporitic mudflats where gypsum is bathed in highly saline NaCl brines. But thick anhydrite beds deposited in ancient saline giants were first laid down as gypsum on the subaqueous floors of perennial brine lakes and seaways, as were most nodules and capillary layers in ancient mudflats. Prior to anhydritisation, beds of primary saltern gypsum extended across tens of thousands of square kilometres. Such beds compacted and converted by burial dehydration to nodular anhydrite during early burial, so releasing large volumes of structural water (Warren 1991).

As gypsum is buried and ambient temperature rises above 50–60 °C, it converts to nodular anhydrite. The depth of transformation is between a few metres to more than a kilometre. The exact depth in any region will depend on lithostatic pressure, local geothermal gradient and pore brine salinity. For example, in Miocene Lower Fars evaporites of the United Arab Emirates, with its relatively saline pore brines, the conversion depth ranges from 60 to 245 m across a zone some 10 m thick (Billo 1986). In the Salton Sea region with its high geothermal gradients, the conversion from gypsum to anhydrite occurs at 80–105 °C and at depths of less than 200–250 m (Osborn 1989). Similar anhydrite conversion was noted at 150–200 m depth in cores from the Pleistocene evaporites in nearby Bristol Dry Lake, California; but here the isotopic evidence suggests sulphate-reducing bacteria also play a role in the conversion (Fig. 1.54; Rosen and Warren 1990).

If the nearsurface pore-fluid salinity approaches halite saturation, the conversion from gypsum to anhydrite can occur at shallower depths and much lower temperatures ≈35–45 °C. Such temperatures occur as shallow as 1–2 m below the depositional surface of a halite-saturated brine pool where sediments reside in the zone of active phreatic flow or brine reflux. At such depths the buried gypsum bed retains well-developed intercrystalline porosity and inherently high permeabilities. This facilitates the leaching of the gypsum crystals and their infill by clear halite spar, which pseudomorphs the various forms of the precursor gypsum (e.g. Fig. 1.49).

With less saline brines in the pores of a buried $CaSO_4$ bed, the conversion of gypsum to anhydrite may not occur until burial depths of hundreds of metres (Fig. 8.37). By such

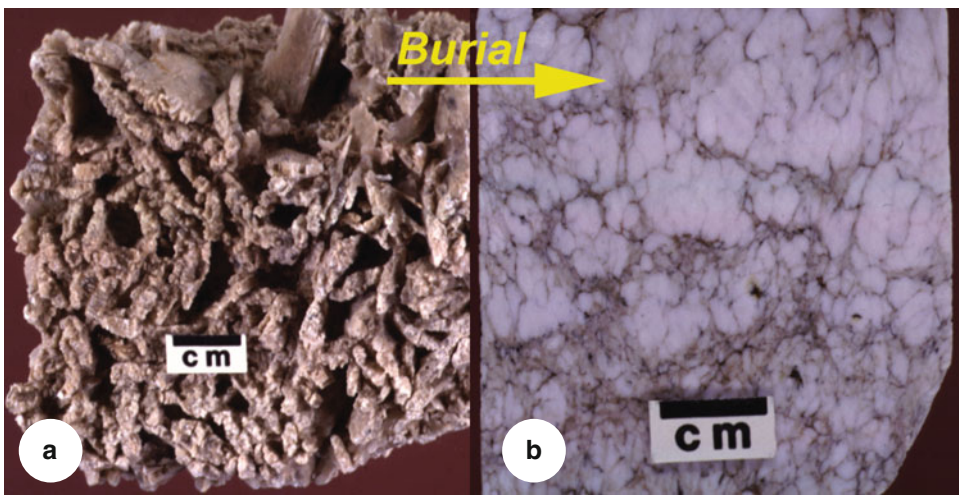

Fig. 1.54 Gypsum converts to burial anhydrite in Bristol Dry Lake, California. (**a**) Lenticular gypsum meshwork from a lake floor sediment sample a metre below the lake surface. (**b**) Nodular anhydrite still retaining the outline of the gypsum precursor. Sample from a lake core some 140 m below the lake surface

depths, natural compaction has greatly depleted intercrystalline porosity in the gypsum bed. Release of water from already compressed and cemented gypsum will create 40 % water-filled porosity in an otherwise impervious anhydrite unit. Over the long term this water is not retained but escapes into the subjacent sediments. A likely effect within the converting $CaSO_4$ bed is a decrease in its inherent strength; and in compressive situations, an increased ability to act as a lubricating horizon or décollement, even if no halite is present. If the water cannot drain freely from the dewatering gypsum, the bed may convert to a quicksand-like consistency. This explains some of the intense deformation and enterolithic textures with flow orientations that are commonplace even in flat-lying and otherwise undeformed ancient bedded anhydrites.

As it converts, the more deeply buried and compressed $CaSO_4$ unit loses almost all of its original texture. Rare indistinct elongate, and partially flow-aligned, nodular "ghosts" may be all that remain of the primary bottom-nucleated textures in many ancient anhydrite beds (Fig. 1.45c). Loss of water of crystallisation also affects units subjacent to the dehydrating gypsum/anhydrite. The escaping water is saturated with respect to $CaSO_4$, but undersaturated with respect to other evaporite minerals, including any nearby carbonates, as well as halite and the bittern salts. The onset of anhydritisation will be effected by the salinity and temperature of pore waters and the volume of pore water throughflow.

Such a complex anhydritisation history is well documented in the varying onset of anhydritisation in calcium sulphate sediments of the Middle Miocene Badenian evaporite basin in the Polish Carpathians. Three distinct, now anhydritised, facies associations record a range of depositional environments from nearshore to deeper basinal settings (Fig. 1.55; Kasprzyk 2003). Coarsely crystalline platform sulphates were deposited in subaerial and shallow-marine environments (shoreline and inner platform-lagoon system) mainly as autochthonous selenitic gypsum. These were reworked and redistributed into deeper waters (outer platform-lagoon, slope and the proximal basin floor system) to form resedimented facies composed mostly of allochthonous clastic gypsum and minor anhydrite. In contrast small gypsum prisms tend to accumulate in water characterised by rapidly fluctuating bottom brine conditions. The prisms were often mechanically reworked into rippled and ooid-like accumulations or captured in algal mats. These laminites were deposited in brine depths ranging down to hundreds of metres, but most accumulate in shallow brines less than a metre or two deep or as pelagics in the deeper part of the basin. It is the rapid salinity fluctuations associated with very shallow waters that favour rapid crystallite formation and multiple nucleation.

Subsequent anhydritization was superimposed on depositional gypsum facies. It was the result of interactions between concentrated seawater, meteoric runoff and highly saline, residual pore fluids. And so two different anhydrite styles overprinted the original Badenian sulphates (Kasprzyk 2003): (1) synsedimentary anhydritisation of gypsum deposits driven by highly concentrated brines and elevated temperatures (mostly in the lower member), (2) successive phases of anhydrite formation (syndepositional de novo growth, early diagenetic to late diagenetic replacement of former gypsum) during progressive burial (mostly took place in the upper member). In the basin the anhydrite started to grow in a fine-grained bottom host under very early, probably synsedimentary conditions and formed a displacive micronodular laminated lithofacies. Likewise the onset of anhydritisation was very early in clastic gypsum of the strandline. It formed abundant displacive anhydrite with intense synsedimentary deformation structures related to nodule growth. This environment was subject to early exposure, high temperatures and high salinities. Later, a deeper burial anhydrite phase spread through the coarsely crystalline gypsum of the shelf. This created replacive nodular anhydrite in sediment hosts so that primary crystal textures are well preserved.

Porosity loss in these units is essentially complete by burial depths of 500 m. After this, these anhydrous units, like halite at even shallower depths, are essentially impervious and act as aquitards and pressure seals to any crossflow of pore water, hydrocarbons or metals. Evaporite salt beds below 500–1,000 m typically respond to further burial by flowage and edge-focused dissolution.

In a variation on the same theme of burial alteration of gypsum (bioturbated bedded) are meganodules of secondary gypsum (after anhydrite) that former in buried Miocene gypsum in the Ebro Basin, Spain (OrtÍ et al. 2012). These outcropping and sub-cropping meganodules and masses are mostly made of crystalline and alabastrine gypsum, which has replaced the original burial anhydrite (relic anhydite is still present in the meganodules, but not in the host gypsum beds). The isotopic composition (11.1–17.4‰ for $\delta^{18}O_{SMOW}$; 10.7–15.3‰ for $\delta^{34}S_{CDT}$) of secondary gypsum in this meganodular facies indicates that the precursor anhydrite derived from in situ replacement of an initial primary gypsum. Anhydritisation was a result of ascending circulation of deep regional fluid flows through the Miocene gypsum units near the basin margins (Fig. 1.56) as primary gypsum was partly altered to anhydrite within burial conditions from shallow to moderate depths (from some metres to a few hundred metres?). At such depths, the temperatures and solute contents of these regional flows exceeded those of the ground water today. These palaeoflows became anhydritizing solutions and partly altered the subsiding gypsum units before they became totally transformed by deep burial anhydritization. The characteristics of the meganodular anhydritization (for example, size and geometry of the meganodules and irregular masses, spatial arrangement, relations with the associated lithologies and the depositional cycles, presence of an enterolithic vein complex and palaeogeographic

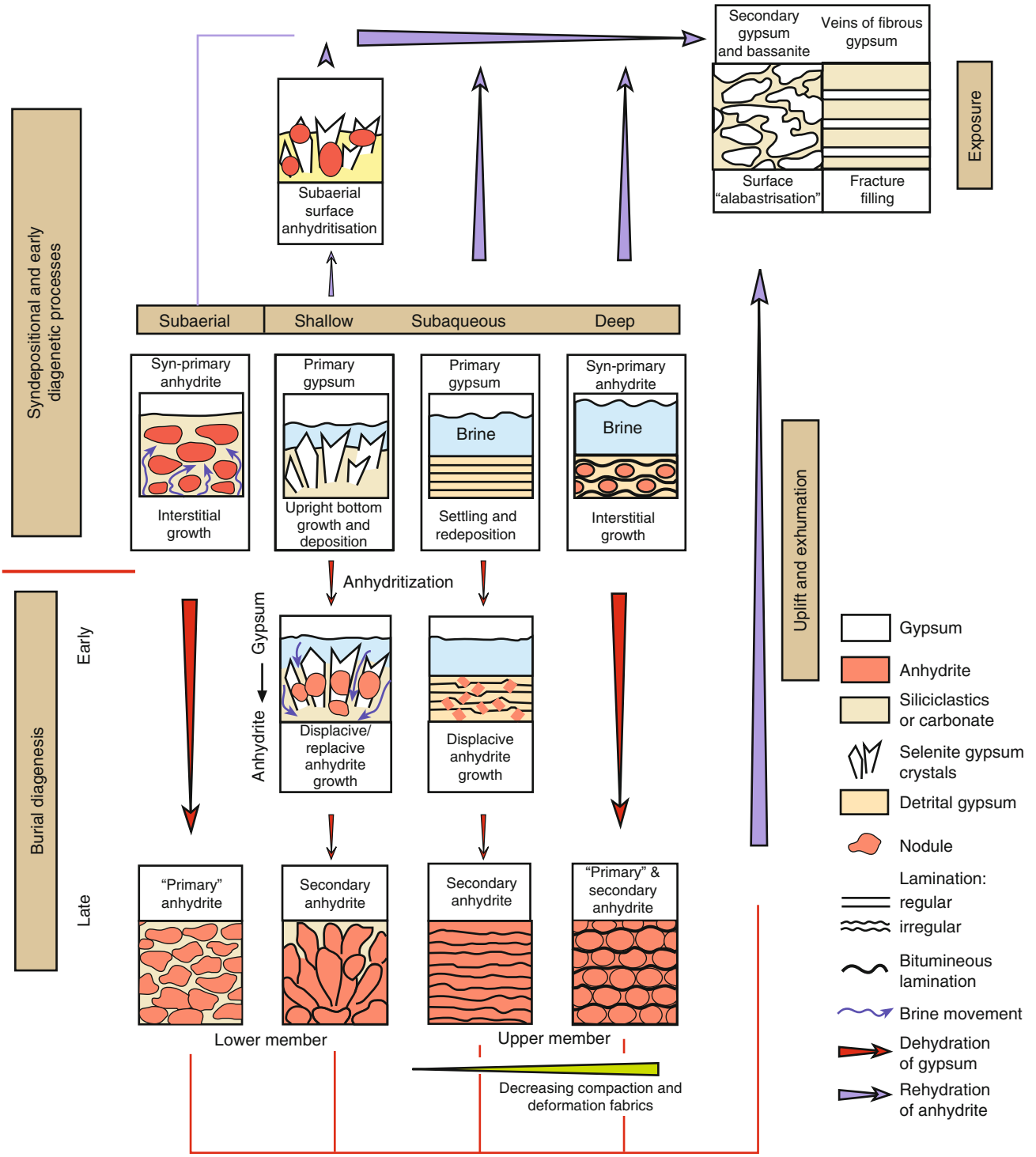

Fig. 1.55 Sulphate textural evolution is clearly seen in Middle Miocene sulphates in the Carpathians (After Kasprzyk 2003). Platform sulphates were deposited in subaerial (sabkha) and shallow-marine environments (shoreline and inner platform-lagoon), mainly as autochthonous coarse-grained aligned (selenitic) gypsum. This platform sediment was reworked and redistributed into deeper waters (outer platform-lagoon, slope and the proximal basin floor system) to form resedimented facies composed mostly of allochthonous clastic gypsum and minor anhydrite. Burial and the conversion to anhydrite subjected these sulphates (mostly gypsum) to two different hydrological styles: (1) synsedimentary anhydritisation of gypsum deposits by highly concentrated brines or elevated temperatures in surficial to shallow-burial environments (mostly in the lower member of these Badenian sulphates), and (2) successive phases of anhydrite formation (syndepositional de novo growth, early diagenetic to late diagenetic replacement of former gypsum), which occurred during progressive burial (mostly in the upper member). Finally, the succession was uplifted and re-entered the active meteoric realm where various fibrous and alabastrine textures formed

distribution) are different to sabkha anhydrites or sparry anhydrites formed under or under deeper burial conditions. The most distinctive feature is the large size of the meganodules (up to 5 m across) and the fact that nodules are devoid of internal textural zoning. In combination, both features suggest anhydrite growth was slow and continuous, which is consistent with the circulation of deep regional aquifers acting as anhydritizing flows. The process affected the subsiding, marginal gypsum units, prior to their complete lithification (Fig. 1.56).

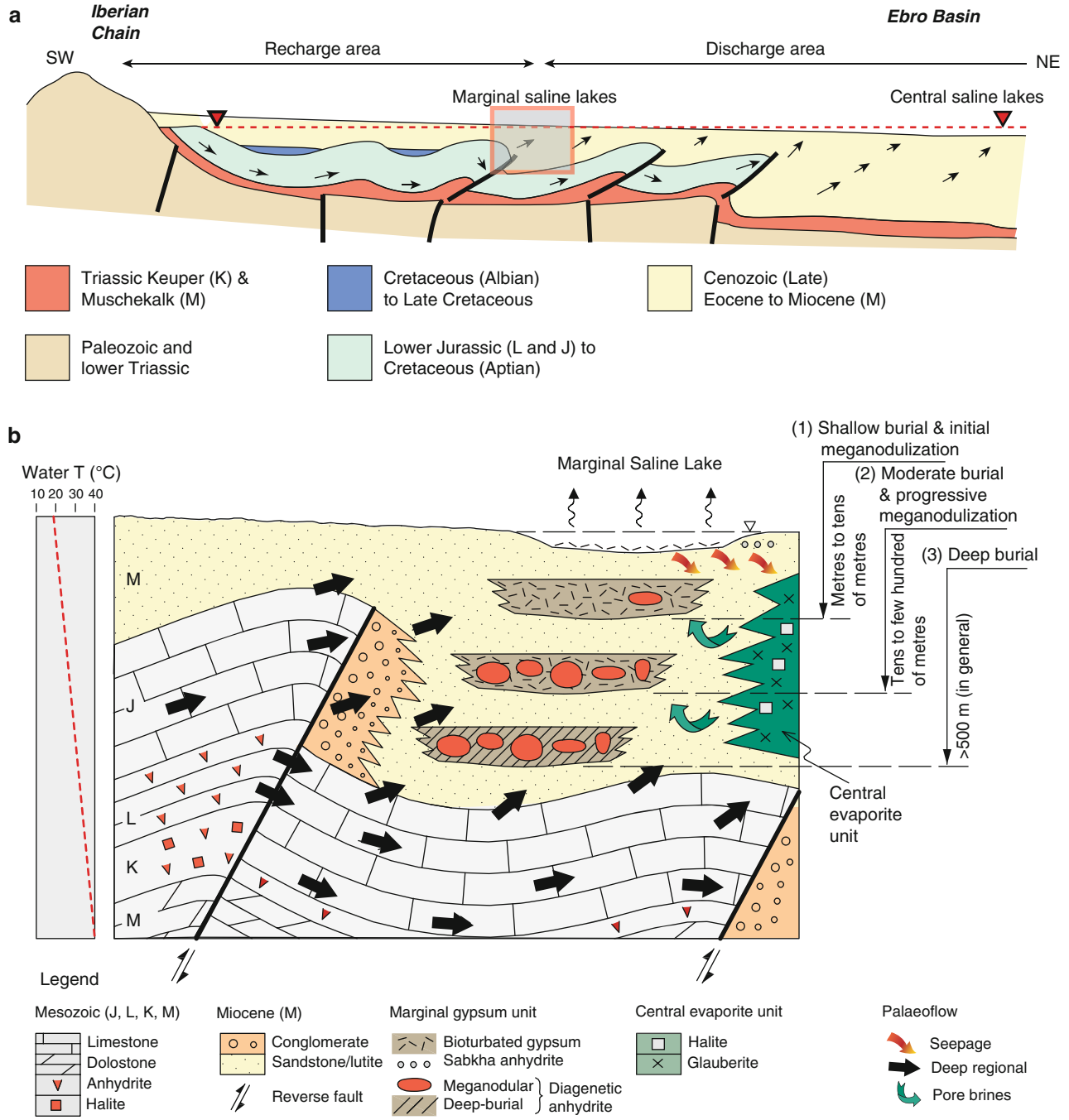

Fig. 1.56 Meganodular anhydritization in the marginal gypsum units of the Ebro Basin during the Miocene (After Ortí et al. 2012). (**a**) Geological cross-section normal to the basin margin at the end of the Miocene (before partial erosion of the basin-fill), Illustrating the palaeohydrological discharge and the downslope transition from marginal saline lakes to perennial saline lakes in the basin sump. (**b**) The process (growth of displacive/replacive meganodules and irregular masses of anhydrite) occurs progressively during shallow to moderate burial (Stages 1 and 2). Under deeper burial conditions the preserved primary gypsum hosting the anhydritized portions is also converted to anhydrite (Stage 3). The anticline structures roughly correspond to those represented in *shaded box* in Fig. 1.56a

One of the most impressive examples of the possible retention of the primary gypsum mineralogy comes from the Lower Cretaceous Ferry Lake Anhydrite in the Mississippi Interior Salt Basin, USA (Amadi et al. 2012). The gypsum remains as cores of anhydrite nodules at depths of more than 3,900 m or 13,000 ft. The gypsum retention is perhaps related no fluid access due to early and ongoing encasement in evaporites, as argued by Amadi et al. (2012). In my mind, if this is the mechanism, we should see similar widespread gypsum retention in the cores of other salt-sealed anhydite nodules and we do not. Another possibility is that anhydrite rehydration has occurred in the core trays in storage, as the documented examples are from decades old wells. Another perhaps more likely possibility is that the gypsum is the result of thermal sulphate reduction waters and the subsequent mesogenetic dehydration of the gypsum (that is, the gypsum formed as a type of burial salt and is not primary).

Burial Salts: Nodules and Stylolites

Subsurface sulphate-rich waters derived from deeply buried dissolving evaporites can precipitate anhydrite nodules in adjacent nonevaporitic strata. Such nodules are a form of burial salt fed by saline compactional and thermobaric waters and are a distinct style from anhydrites formed as part of the burial related conversion of gypsum to anhydrite discussed earlier. Superficially these nodules can resemble those of a sabkha anhydrite, but there are a number of distinguishing features (Machel 1993, 2013; Machel and Burton 1991; Warren 1991). Most obvious is that the burial nodules precipitate in porosity zones that are not depositionally defined. They can occur within or adjacent to faults, or within open marine shelf carbonates, which are not intertidal/supratidal units. They often occur within, or juxtaposed to, dark, bituminous argillaceous seams and pockets, or within zones of anastomose bituminous veinlets and carbonaceous haloes, all of which are the result of pressure solution and stylolitisation. They typically replace the host rock and can crosscut stylolite boundaries in the carbonate matrix. Thus, they enclose material generated during burial diagenesis, such as authigenic pyrite and saddle dolomite, and show little evidence of mechanical compaction. They are often associated with coarsely crystalline, late-stage poikilotopic and pore-filling anhydrite spar cements.

In a study of burial anhydrites in the Devonian Nisku carbonate, Canada, Machel (2013) concluded that most anhydrites (more than 90 %) are replacive and that they are syn or postdate dolomitisation. The six textural types he defines did not form at the same time, some were early burial, some later and some formed during or after oil migration in the Late Cretaceous to Early Tertiary.

Stylolites hosted in a limestone or dolomite matrix are widely recognised pressure solution features thought to indicate burial depths in excess of 0.5–1.0 km (Bathurst 1980). Stylolites in evaporite beds are not common and may not necessarily form by such deep burial. Some have argued that anhydrite and halite cannot exist at the pressure necessary to form stylolites without pervasive recrystallisation. But stylolite horizons do occur in the Gorleben Zechstein salt dome in the Bänderanhydrit located near the top of the Zechstein Hauptanhydrit (Bäuerle et al. 2000). Intra-evaporite stylolites were also noted by Peryt et al. (1993) in the Werra Anhydrit (Zechstein 1) of western Poland and by El Tabakh et al. (1998a) in the Basal Anhydrite of the Cretaceous Maha Sarakham of Thailand. The latter can be related to differential salt solution during burial flushing (Fig. 7.45).

Bäuerle et al. (2000) tied the pressure-solution seams in the Hauptanhydrit to the presence of thin magnesite-clay interlayers and distinguished five principal stylolite morphologies (Fig. 1.57a). The orientation of the sutured seams is generally bedding-parallel with the stylolite axes vertical to the bedding surface. Some seams have been deformed by salt flow and the anhydrite beds with bedding parallel stylolites are now steeply inclined to the horizontal. There is no relation between stylolite formation and pressures created by the modern salt dome crest. Solution rates of up to 26 % were calculated by measuring maximum stylolite amplitudes in core.

The bedding-parallel occurrence of the Hauptanhydrit stylolites, in combination with the observation that the stylolite seams are crosscut by anhydrite pseudomorphs after gypsum, argues that the stylolites formed before the dehydration of gypsum to anhydrite was complete. The lower parts of the Hauptanhydrit were excluded from the stylolitisation process as they had already been converted to anhydrite by ascending compaction fluids of the underlying Zechstein 2 Salt (Fig. 1.57b; Bäurle et al. 2000). Porosity and permeability loss that is an integral part of the conversion process prevents the formation of stylolites once any interval had converted to anhydrite. The transition depth in the Zechstein was around 125 m. Pervasive dehydration of gypsum to anhydrite in the Hauptanhydrit was probably complete before the end of Zechstein sedimentation. The arguments of Bäurle et al. (2000) imply that the formation of stylolites occurs in gypsum, not anhydrite, and is a relatively shallow burial process (≈100–150 m).

Evaporites as Uplift Indicators (Tertiary Evaporites)

At the other extreme of the burial cycle is the conversion of exhumed and uplifted evaporite beds entering the telogenetic realm. Most common is the conversion of anhydrite into diagenetically regenerated gypsum (Fig. 1.58). Uplifted halite beds first undergo differential dissolution to leave behind layers of residual nodular anhydrite, which are then dissolved by ongoing meteoric flushing. Two commonplace

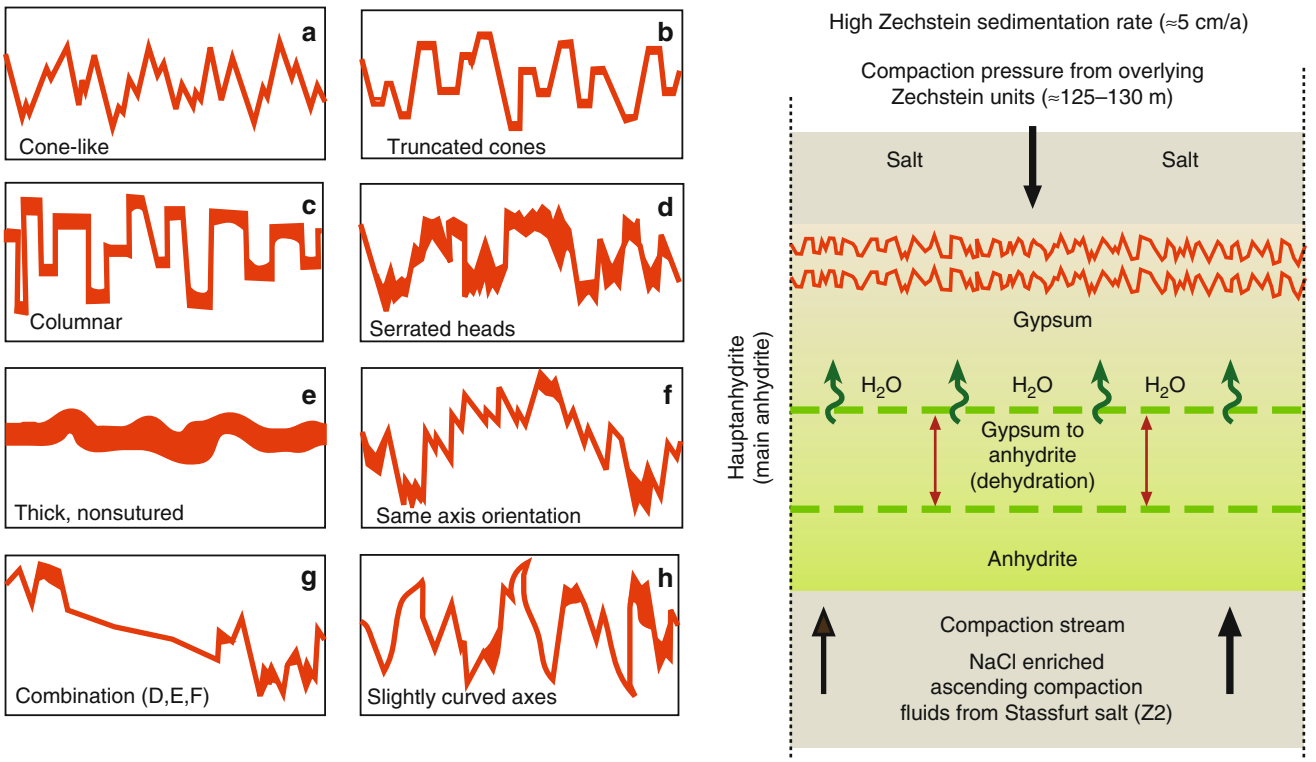

Fig. 1.57 Stylolites in anhydrite beds. (**a**) Types of stylolite seams or sutures hosted in the Hauptanhydrit (Zechstein) of the Gorleben salt dome, Germany. (**b**) Model for the development of stylolites in the upper part of the Hauptanhydrit during deposition of the younger Zechstein beds. Stylolitisation is restricted to a gypsum matrix (pre-anhydritisation) and occurred less than 150 m below the sedimentation surface (After Bäuerle et al. 2000)

gypsum fabrics are the result of exhumation: coarse porphyroblastic gypsum and fine-grained alabastrine gypsum (Holliday 1970; Warren et al. 1990; Arzaghi et al. 2012; OrtÍ et al. 2012). Porphyroblastic gypsum rosettes, especially in the lower parts of the telogenetic realm, can retain dispersed relics of the precursor anhydrite in the core of the nodule. The radiate crystal texture means it is sometimes described as gypsum "daisies" or "daisywheel gypsum." Crystal forms are coarse, up to two cm across, and can be euhedral or anhedral, thin and acicular or thick and stubby (Fig. 1.58). Porphyroblasts typically aggregate into cm-scale layers, rosettes or blebs with acicular gypsum rinds.

Daisy gypsum is a response to rehydration under the relatively homogenous conditions of uplift hydrology in a massive nodular anhydrite unit entering the lowermost parts of the telogenetic zone. Rates of fluid crossflow are low, so chemical dissolution is slow and dissolution fronts tend to be focused about the bed contacts between aquifers and the anhydrite (gypsum is not stable at such depths). As an anhydrite bed is uplifted into the telogenetic zone it once again comes into contact with low salinity, low temperature waters. In many uplift situations there is also an artesian flow system established so that both karstification and rehydration to gypsum tends to at first be focused on the edge of the bed where satinspar gypsum tends to dominate. As rehydration to gypsum becomes more pervasive within a bed, it tends to penetrate first along the impurity-rich more permeable edges of anhydrite nodules. Sparry aligned gypsum crystals grow toward the centre of the nodules to form daisy-wheel gypsum (Warren et al. 1990). As the rehydration proceeds through the bed, some of the gypsum then dissolves to give greater access to undersaturated waters to the gypsum bed to create caverns. Because of the destructive nature of porphyroblastic overprinting, interpreting original depositional environment is next to impossible in nearsurface and outcropping $CaSO_4$ units, they are composed almost entirely of diagenetically regenerated gypsum.

Alabaster is the other form of telogenetic gypsum and is created where anhydrite pervasively rewaters to gypsum in the zone of active phreatic flow. Individual gypsum grains are typically less than 50 μm, with grain boundaries that range from poorly defined to equidimensional granuloblastic. The change from porphyroblastic to alabastrine may be depth-related (Warren et al. 1990). Porphyroblastic gypsum defines the re-emergence of nodular anhydrite from the stagnant phreatic into the deep portion of the zone of active phreatic flow. Alabastrine gypsum forms in the zone of more diffuse active phreatic flow. This re-emergence is also associated with the formation of gypsum karst and the formation of evaporite-dissolution breccias (Chap. 7).

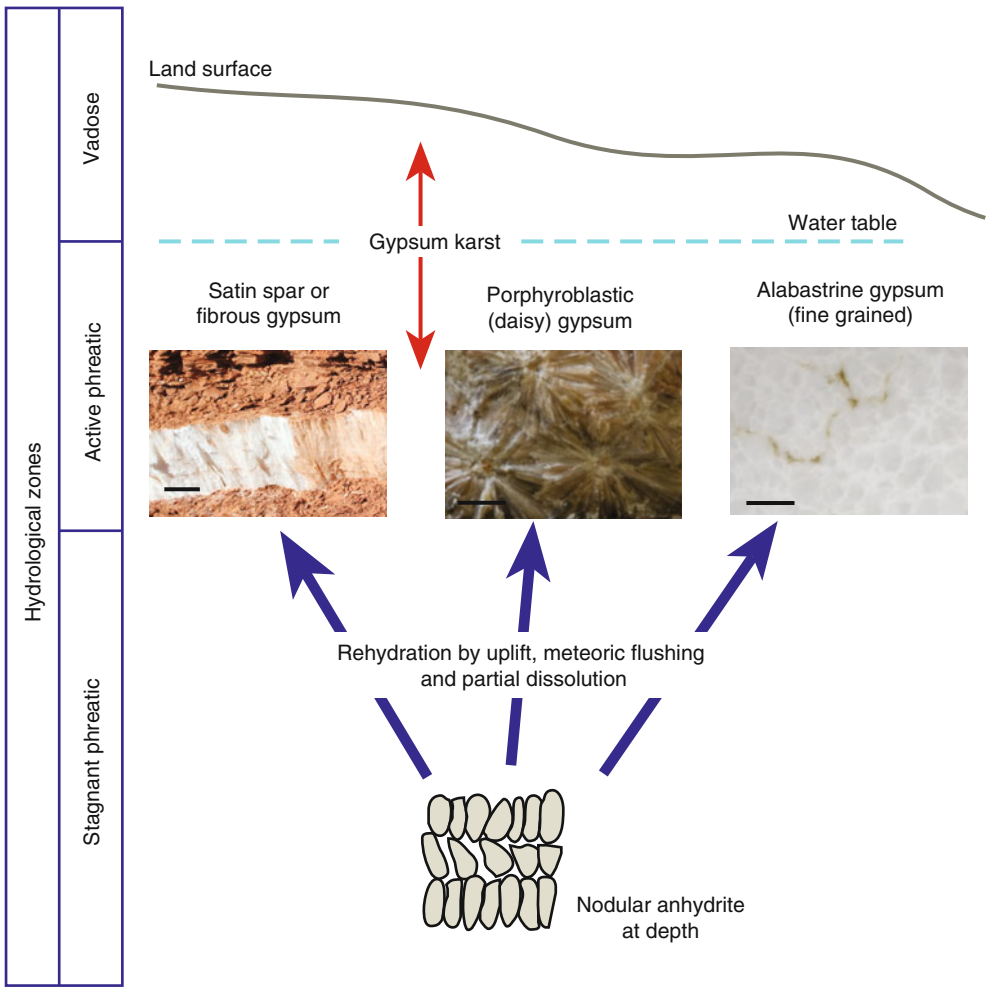

Fig. 1.58 Rehydration fabrics in calcium sulphate from uplift, meteoric flushing and dissolution. Scale bar is 1 cm long. These textures are the tertiary evaporites of Fig. 1.9

Excess amounts of trace elements, especially strontium and boron, are released from some bedded anhydrites as they reconvert to gypsum. The released elements may precipitate in the regenerating alabastrine gypsum as celestite or boron-bearing minerals, such as proberite, ulexite, tyreskite and priceite.

Fibrous Gypsum and Halite (Satinspar)

Veins and fractures filled with fibrous satinspar $CaSO_4$ (typically gypsum) or halite are widespread in the mudstones and shales adjacent to bedded evaporite units undergoing dissolution. Fractures may be subhorizontal and lie roughly parallel to the contact with the bedded evaporite unit or may form as conjugates. The fractures form and fill with fibrous cements in response to stresses set up in the bed by the formation of nearby stratiform cavities (Fig. 1.59). The fracture filling is usually zoned and made up of two or more parallel layers of either fibrous $CaSO_4$ or fibrous halite. Fracture-fill crystals are oriented with their long axes perpendicular to the fracture walls. Coarse calcite crystals can occasionally fill the centre of the fracture. Most fracture fills are monomineralic and gypsum is the dominant mineral in most nearsurface fracture systems. Internal fracture zonation is pronounced and reflects episodic and ongoing opening and filling of the fractures. Some fibrous fills are sigmoidally deformed showing fracture fill was ongoing as adjacent blocks slid and rotated in response to changes in nearby dissolution cavities (El Tabakh et al. 1998b).

Fibrous halite and satinspar formation are linked to fracture and cavity formation in active hydrological systems. Fractures filled with satinspar are linked to uplift and either the generation of open fractures induced by subsidence associated with salt dissolution and uplift (Fig. 1.60; Gustavson et al. 1994) or to hydraulic fracturing associated with the conversion of anhydrite to gypsum (Cosgrove 2001; Philipp 2008). Thus fracture-filling satin-spar may be a passive process in open fractures or a more active process with fractures forced open by overpressured $CaSO_4$ -saturated artesian waters.

Superimposed on these processes may be the force of crystallisation of gypsum. Shearman et al. (1972) suggested that displacive satinspar veining is a feature of anhydrite

hydration, which may have been due to hydrofracturing by overpressured confined groundwater as exhumed anhydrite reconverted to gypsum. Shearman et al. (1972) pointed out that if all the calcium sulphate is retained within the system, the hydration of anhydrite to gypsum should result in an increase in volume of 63 %. They noted that in many secondary gypsum rocks, former anhydrite is replaced on a volume-for-volume basis, and the additional volume of gypsum appears as fibrous or satinspar veins that cut the associated rock. Gypsum grew in the water-filled fractures, whenever the overburden was supported by pressurised water.

Fig. 1.59 Meshwork of satinspar gypsum veins created by dissolution of an adjacent anhydrite bed in the Permian of eastern Saudi Arabia (car key for scale)

Progressive sediment fracturing (hydrofracturing?) is thought to be a response to unroofing. Unloading and release of overburden weight drives the formation of near surface fractures parallel to the earth's surface. Fibrous halite and satinspar $CaSO_4$ are commonly associated with, but not exclusive to, zones of exhuming evaporites (Fig. 1.58). It is not known if satinspar-filled fractures can also form at greater depths (1000s of metres) in mesogenetic realms associated with overpressuring and compactional or thermobaric waters.

Cosgrove (2001) and Philipp (2008) describe networks of satinspar-filled hydraulic fractures preserved only in the exhumed evaporite horizons of the Mercia Mudstones of the Bristol Channel Basin of southwest England. Like Shearman et al. (op. cit.), they conclude satinspar preservation relates to

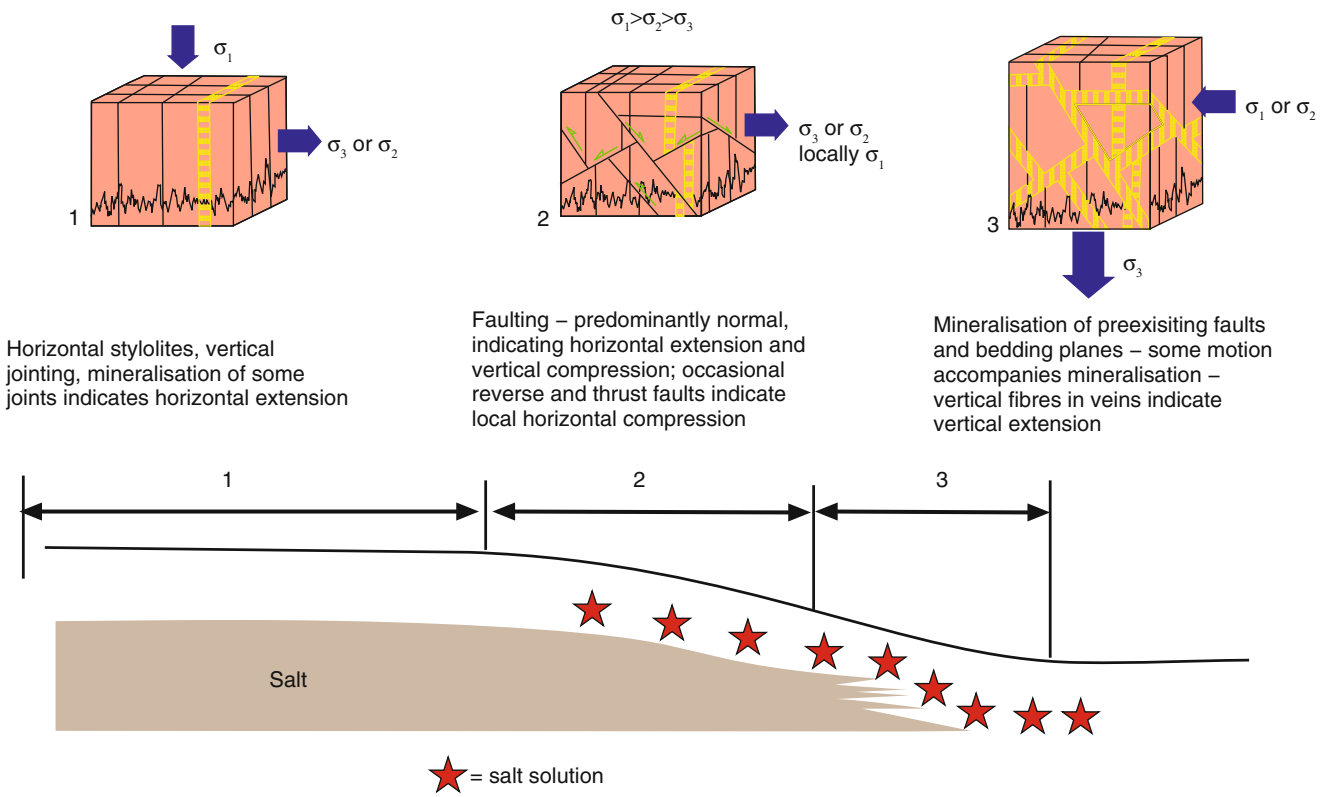

Fig. 1.60 Conceptual model of deformation above salt dissolution zone showing structural sequence and proposed location relative to dissolution front. Stage 1 occurs prior to salt dissolution and is characterised by jointing resulting from normal burial. Late stage 1 and stage 2 occur as salt dissolution begins. Early stage 2 is characterised by a few vertical gypsum veins with horizontal fibres. Later stage 2 is characterised by normal faults and uncommon reverse faults. In stage 2 layer parallel extension results from the onset of dissolution and subsidence. Stage 3 is characterised by gypsum veining of bedding planes and faults. In stage 3 vertical extension results from widespread dissolution and collapse of underlying evaporites (After Gustavson et al. 1994)

the volume changes associated with the hydration of anhydrite to gypsum, which occurred as the rock mass was exhumed and the relatively low temperature and pressure conditions necessary for the formation of gypsum were encountered (e.g., Jowett et al. 1993; Philipp 2008). Hydration in the Mercia Mudstones occurred during the tectonic inversion of the basin as basin sediments experienced tectonic compression during Tertiary exhumation. This caused an increase in fluid pressure and facilitated the formation of hydraulic fractures that then fill with satinspar. Cosgrove goes on to argue that hydraulic fractures also formed in the muddy evaporite-free horizons. But the fractures reclosed and healed as soon as the fluids had passed through them and pressure had dropped as the appropriate brine required for their preservation as satinspar veins was not present within the nonevaporite sections.

The mechanism of creating satinspar filled fractures, as documented by Gustavson et al. (1994), is a much more passive process. They note that most satinspar veins occur in highly fractured or brecciated strata that overlie or are associated with exhumed bedded halite, anhydrite and gypsum. There are often saline springs in the vicinity of a satinspar occurrence indicating active halite dissolution. In this scenario satinspar is a response to several hydrologically driven processes (Fig. 1.60). Cavernous porosity is created as halite is dissolved by crossflows of low salinity active-phreatic waters down to depths of 200–750 m. Extensional fractures form in the strata above these dissolution zones and anhydrite is rehydrated to gypsum either via a dissolution-precipitation interface or though a bassanite intermediary (Holliday 1970). The deeply circulated groundwater is now saturated with respect to gypsum and any further anhydrite hydration results in supersaturation. Excess $CaSO_4$ now carried in solution by groundwaters flowing out of the dissolution zones precipitates gypsum in open high permeability fractures created during overburden collapse.

It may well be that the satinspar and the associated fracturing are a response to both active and passive modes of formation. Perhaps active hydrofracturing, as envisaged by Shearman et al. (1972), is more significant in driving satinspar fracture fill at greater depths where the dissolving evaporites and adjacent beds are still relatively tight and are first entering the telogenetic realm (via the zone of stagnant phreatic circulation). As exhumation and dissolution continues the fracture and fill process evolves into a more passive set of collapse induced features. This occurs once beds are shallower and have become more permeable. They have moved into the zone of active phreatic circulation and are closer to the landsurface (see Chap. 7 for more hydrological detail on the effects of telogenetic alteration).

Isotopically, the effects of dissolution and brine recycling in fracture-filling fibrous gypsum cements of various ages in a formations burial evolution can define the sequential evolution of the unit (Fig. 1.61; Moragas et al. 2013). The upper Burdigalian Vilobí Gypsum Unit, located in the Vallès Penedès half-graben (NE Spain), consists of a 60-m thick succession of laminated-to-banded secondary and primary gypsum variably affected by Neogene extension in the western part of Mediterranean Sea. Tertiary extensional events are recorded in the evaporitic unit as six fracture sets (faults

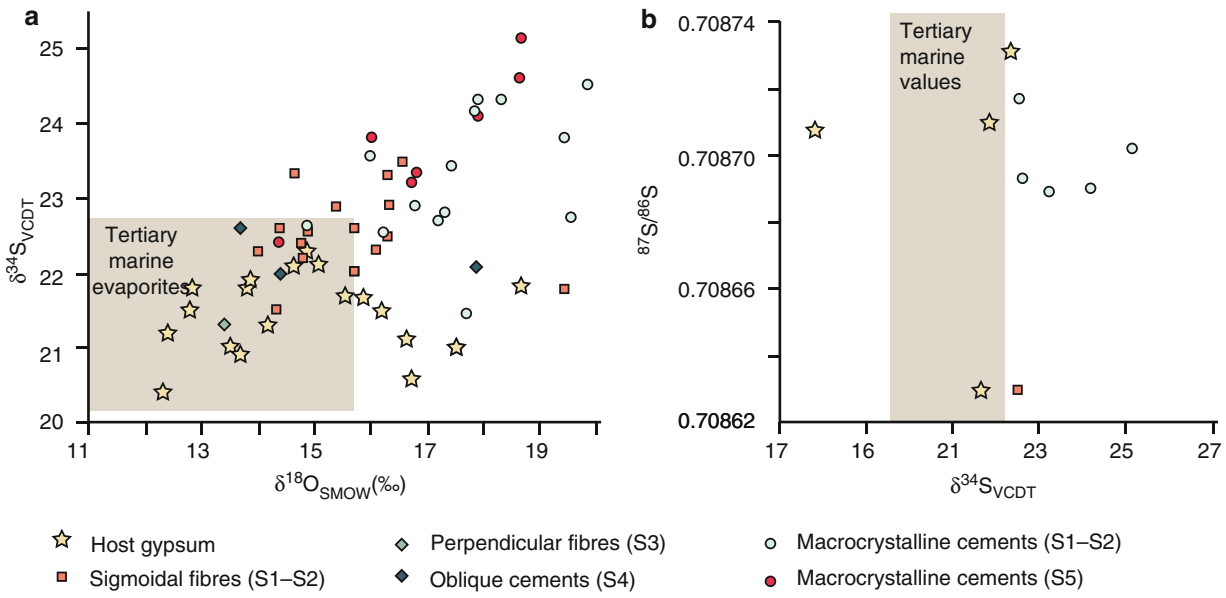

Fig. 1.61 Vilobi Gypsum, Spain. (**a**) $\delta^{34}S$ versus $\delta^{18}O$ cross-plot for both host gypsum rocks and various gypsum vein and fracture fills (S1–S5). (**b**) $\delta^{34}S$ versus $^{87}Sr/^{86}Sr$ cross-plot for host gypsum, sigmoidal fibres and macrocrystalline cement samples. *Shaded areas* indicate plot fields for Tertiary marine evaporites (After Moragas et al. 2013)

and joints), which can be linked with basin-scale deformation stages utilising fracture cement fills. All fractures are totally or partially infilled by four types of gypsum precipitates showing diverse textures and microstructures. Combined structural, petrological and isotopic study of the unit establishes a chronology of fracture formation and infilling, from oldest to youngest as: (i) S1 and S2 normal faults sets with formation and precipitation of sigmoidal gypsum fibres; (ii) S3 joint sets with perpendicular fibres; (iii) S4 inverse fault sets, infilled by oblique gypsum fibres and associated with deformation of the previous fillings; and (iv) S5 and S6 joint sets tied to later dissolution processes and infilled by macrocrystalline gypsum cements. The fractures provided ongoing pathways for focused fluid circulation within the Vilobí Unit. The oxygen, sulphur and strontium isotope compositions of the original host rock and the various precipitates in the fractures imply ongoing convective recycling processes across the host-sulphates to the fracture infillings, as recorded by a general enrichment trend toward heavier S–O isotopes, from the oldest precipitates (sigmoidal fibres) to the youngest (macrocrystalline cements) and to the preservation of the strontium signals in the various infillings (Fig. 1.61).

Anhydrite Rehydration at the Microscale

At the microscale a range of related $CaSO_4$ textures indicate a common set of nearsurface diagenetic (telogenetic) mechanisms and processes, which through multiple dissolution and reprecipitation cycles create ever increasing proportions of purer gypsum and every decreasing amounts of residual anhydrite. Anhydrite at outcrop, where it constitutes more than 5–10 % of the calcium sulphate in a sample, is typically present as scattered, variably-etched, oriented to non-oriented prismatic crystals and laths that are surrounded by more coarsely crystalline poikiloblastic gypsum (Fig. 1.62a–c). No uplifted outcrop is ever composed of pure anhydrite and typically calcium sulphate outcrops with anhydrite present are dominated by gypsum as either finely crystalline alabaster or coarsely crystalline (selenitic gypsum).

Coarsely crystalline (selenitic) gypsum: Outcrop samples with the higher proportions of relic anhydrite typically have anhydrite present as felted aligned to less-aligned masses of lathes encased in coarsely crystalline gypsum and typically adjacent to other coarser gypsum crystals that contain few to minor anhydrite relics (Fig. 1.62a–c). In the literature these larger gypsum crystals are termed porphyroblasts and the texture is typically described as poikiloblastic (Holliday 1970; Artieda 2013). This coarsely crystalline texture, dominated by transparent crystals, is also described as selenitic. Coarsely -crystalline gypsum tends to show open porosity between crystals (intercrystal-line polyhedral porosity; Fig. 1.62a, b). It typically has relatively inclusion-free gypsum pore linings adjacent to the open pores implying a possible mesoscale replacement front is involved in its formation. That is, porosity is created by dissolution of its precursor (gypsum + anhydrite) is followed by precipitation of gypsum in the resulting pore space. This gives the appearance of a clear gypsum rim to some crystals but it is actually a dissolution front moving through the crystal and precipitating pure gypsum (Fig. 1.62c).

Alabastrine gypsum: Alabastrine gypsum tends to contain lesser amounts of anhydrite in gypsum crystal than selenitic gypsum, typically in the range 0–2 %. Gypsum textures tend toward equigranular and interlocking, with growth-sutured crystal edges (Fig. 1.62d). This texture is often described in the literature as granoblastic (Holliday 1970). Granoblastic textures indicate grain boundary equilibration in the solid state. This texture is also seen in metamorphic rocks, such as when limestone converts to marble. It consists of an isotropic aggregate of polygonal grains of more or less similar size, perhaps within an order of magnitude. Samples of alabastrine equigranular gypsum tend to lack significant amounts of polyhedral porosity. Rather the gypsum crystals form an interlocking meshwork, sometimes with local preferred directions of crystal growth elongation. Compared to relic anhydrite crystals in the coarser (selenitic) gypsum the anhydrite residuals in equigranular granoblastic gypsum tend to show more evidence of etching (Fig. 1.62e, f).

Satin-spar gypsum: This style of gypsum is made up of growth-aligned, fibrous elongate crystals that infill veins or fractures (Fig. 1.62g, h). Most satin spar samples lack significant amounts of inter crystalline porosity, although some veins do show geopetal accumulations of anhydrite or dolomite on the lower sides of the fractures. Such geopetalled fractures were likely created via fractional dissolution of precursor $CaSO_4$, leaving behind a residuum of less soluble materials (anhydrite, dolomite).

The relative timing of porphyroblastic versus alabastrine gyp-sum during telogenesis is difficult to determine. A review of the literature suggests porphyroblastic gypsum tends to precede alabastrine gypsum in the uplift realm (when associated with anhydrite telogenesis) and that satin spar forms in fractures created by the dissolution and volume loss associated with meteoric flushing and uplift of a former anhydrite bed (Holliday 1970; Gustavson et al. 1994; Warren et al. 1990). But alabaster and selenitic textures can be intimately intermixed at outcrop and differences in gypsum style may be more related to the degree of gypsum supersaturation during anhydrite dissolution. In this scenario porphyroblastic gypsum is favoured by sluggish water crossflows, slower crystal growth rates and less saturated pore fluids (with respect to gypsum), while granoblastic gypsum is favour by supersaturation, multiple crystallisation nuclei, faster crystal growth rates and Ostwald crystal ripening.

The growth of granoblastic and porphyroblastic textures from an anhydrite precursor, which in turn was often formed

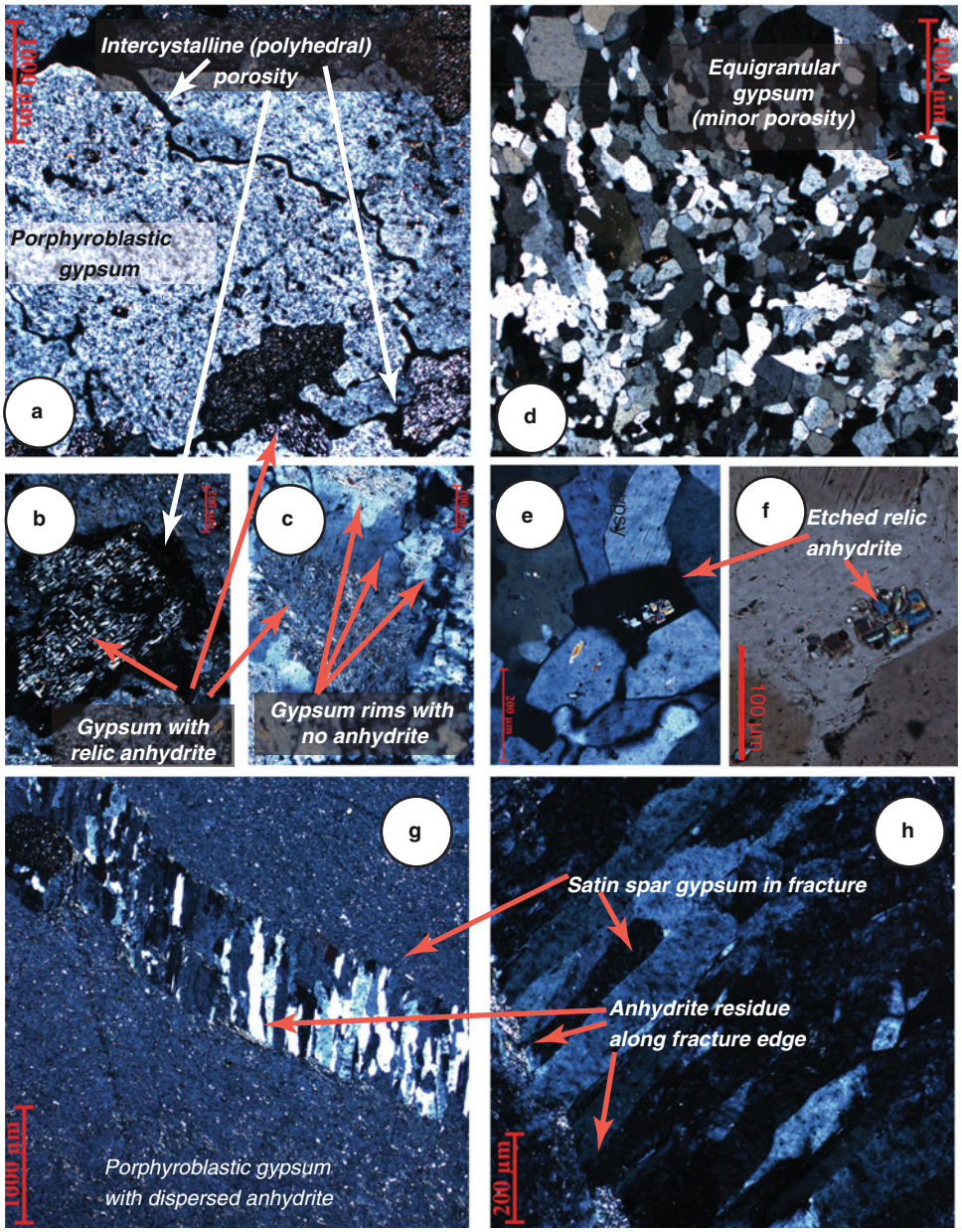

Fig. 1.62 Gypsification microtextures, all photomicrographs are taken in polarised light. (**a**) Porphyroblastic coarsely crystalline (selenitic gypsum with intercrystalline porosity (partially polyhedral). (**b**) Gypsum porphyroblast (in extinction) showing a felted anhydrite relic which it encloses. (**c**) Gypsum porphyroblast with relic gypsum adjacent to newly precipitated rinds with polyhedral contact between the rinds. (**d**) Equigranular (granoblastic) gypsum. (**e**) Equigranular (granoblastic) gypsum enclosing etched anhydrite. (**f**) Close up of etched anhydrite in (e). (**g**) Satin-spar gypsum infilling vein/fracture in porphyroblastic gypsum, with anhydrite residue along lower vein margin. (**h**) Close-up of vein margin (All samples from Laurent Gindre and come from Namibian anhydrite/gypsum residual/caps to the Cretaceous Loeme Fm., see Gindre-Chanu et al. 2014 for detail)

by fractionated removal of halite (see Chap. 7), means that all the textures seen at the micro and mesoscale in gypsum outcrops are indicative of telogenetic processes. There is little or no possibility of these uplifted-related reprecipitation and recrystallisation $CaSO_4$ textures preserving primary depositional relics.

Saline Clay Authigenesis

So far we have focused on the formation and alteration of the various evaporite salts, but the same evolving saline hydrologies can also drive the formation and alteration of clays (Table 1.6). Many authigenic clay minerals formed in hypersaline settings are enriched in magnesium (Fisher 1988), but authigenic clays do not make up the greater volumes of clay in modern or ancient salt lakes. Most of the clays in salt lakes and playas are detrital and reflect compositions of older argillaceous formations in the palaeodrainage areas. Illite, kaolinite, chlorite, dioctahedral smectite and a number of mixed-layers clays are commonplace detrital clay minerals in saline formations (Calvo et al. 1999). Widespread flocculation of clays is an effective sedimenter of suspended clay wherever freshwater runoff and streams flood an area of standing saline water. Thus the composition of initial clay sediments in a playa largely reflects that of the minerals carried as suspended load into the lacustrine depression.

The magnitude of detrital clastic input is thought to be a significant factor in the relative volume of authigenic clay. Regions with rapid deposition of clays, tied to high detrital inputs, tend to be areas where the authigenic clay component is swamped by the high detrital input. Clay authigenesis in evaporitic basins is favoured in marginal playa areas where rates of detrital clay input are low (Fig. 1.63). This encompasses interdunal depressions, peripheral sandflats and muddy carbonate flats. In these low sedimentation areas the transformation of precursor clays is more effective, driven by episode surface inflow and groundwater discharge (Calvo et al. 1999). Highly reactive nearsurface and surface conditions are favoured by inherently large variations in pore water salinity, pH and pCO_2 levels.

Clay authigenesis in many saline depressions is driven by pedogenesis, especially in the marginal areas where sedimentation rates are low and subaerial exposure dominates at the sedimentation surface. Below the surface episodic wet-dry cycles means neoformed clays are the byproduct of complex reactions between Na and Mg-rich interstitial brines and detrital silicates. Pedogenic processes account for the formation of widespread lake margin palygorskite and sepiolite, typically in association with the creation of calcretes, dolocretes and silcretes. In cases where palygorskite dominates the soil profile, they are sometimes described as palycretes. Zeolites can also form from saline groundwaters in saline lake-margin pedogenic settings (Fig. 12.71). Artesian and phreatic groundwater discharge through springs into the lake margin areas also plays a significant role in the formation of

Table 1.6 Main authigenic clay minerals occurring in continental evaporitic environments

	Structural formula	Mg/Si	Al/Si
Saponite	$(Ca, Na)_{0.3}(Mg{\cdot}Fe)_3(Si,Al)_4O_{10}(OH)_2(OH)_2{\cdot}4H_2O$	0.76–0.87	0.07–0.18
Kerolite	$Mg_3Si_4O_{10}(OH)_2{\cdot}H_2O$	0.75	0.0
Stevensite	$Na_{0.15}Mg_3Si_4O_{10}(OH)_4$	0.75	0.0
Hectorite	$Na_{0.3}(Mg,Li)_3Si_4O_{10}(F{\cdot}OH)_2$	0.67	0.0
Sepiolite	$Mg_4Si_6O_{15}(OH)_2{\cdot}6H_2O$	0.67	0.0
Palygorskite	$(Mg{\cdot}Al)_2Si_4O_{10}(OH){\cdot}4H_2O$	0.17–0.49	0.02–0.31

After Calvo et al. (1999)

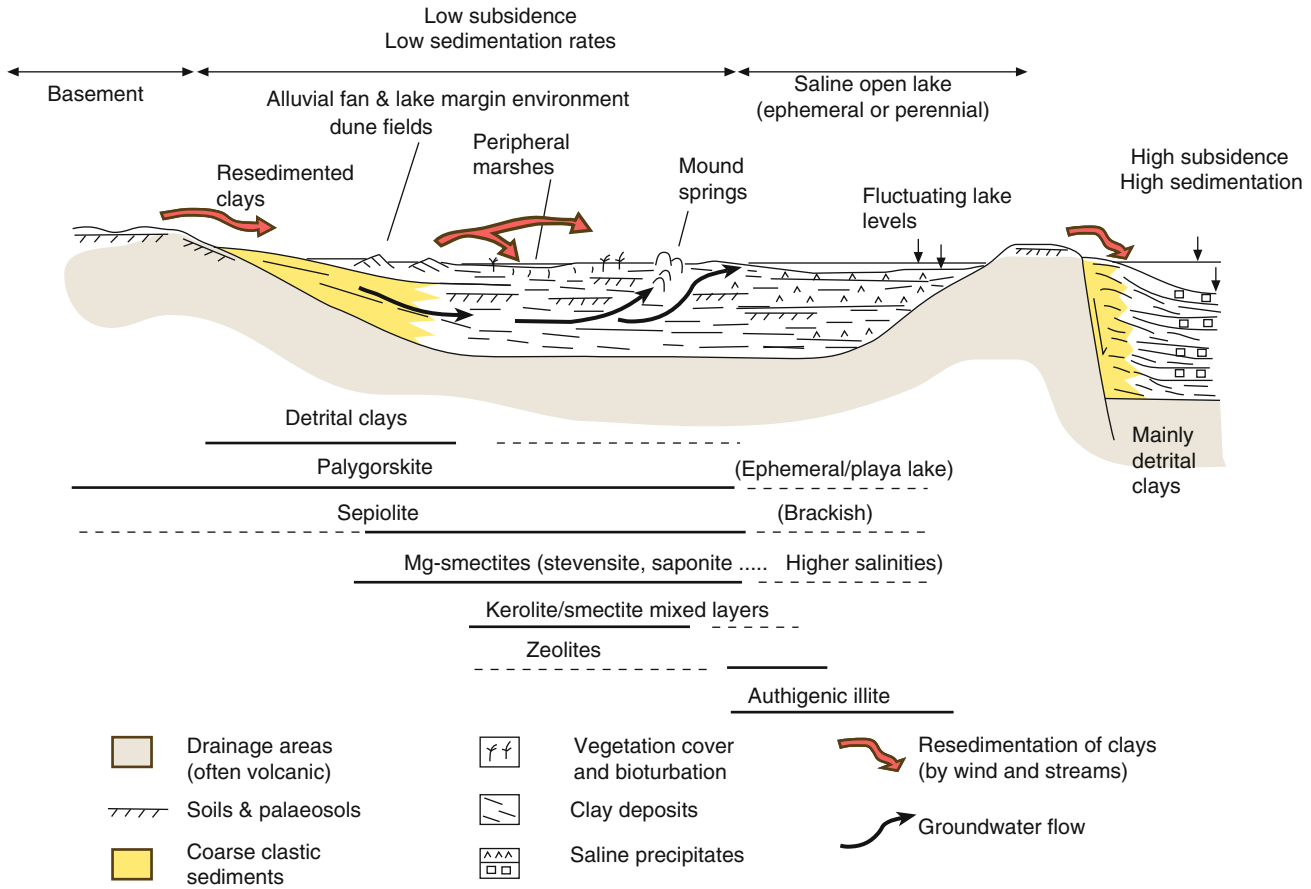

Fig. 1.63 Commonly observed distribution of authigenic clays in saline continental environments, emphasising the differences between basins undergoing slow versus rapid subsidence. Authigenic clays form mostly in saline lake-margin environments. Formation of authigenic clays in open-lake environments is dependent on the degree of schizohalinity (After Calvo et al. 1999)

other authigenic clays, as in saline lakes at the foot of Mt Kilimanjaro, in Tanzania and Kenya (Hay et al. 1995).

Hypersaline brines in modern, marine-edge evaporite basins can also enhance clay authigenesis even in settings where thermal and saline stresses keep both organic and inorganic carbon concentrations in the sediments unusually low relative to coastal marine environments with lower salinities (Martini et al. 2002). This is the case in Salina Ometepec where sediment pore waters exhibit little microbial sulphate reduction, and dissolved inorganic C contents are also very low. Instead of carbonate alteration (dolomitisation) in the Mg brine, authigenic K-rich Mg-smectite (saponite) formation is occurring, driven by the concurrent processes of brine concentration, selective dissolution of K- and Mg-bearing salts, and dissolution of detrital aluminosilicates. Salina Ometepec pore waters at a depth of 1 m have $^{87}Sr/^{86}Sr$ ratios that require input of Sr that is less radiogenic than that of Gulf of California seawater. This Sr is likely derived from weathering and leaching of detrital aluminosilicates from nearby volcaniclastic sources. Although rare in Holocene successions, similar Mg-rich authigenic clay assemblages are well documented in Palaeozoic evaporite basins (Bodine 1983; Janks et al. 1992; Andreason 1992).

Once precipitated in an evaporite basin, authigenic clays can be retransported further out into the saline depression and in more humid climatic stages may even end up on the floor of freshwater lakes (Fig. 1.63). This situation is seen in lacustrine sequences from the Miocene formations of the Madrid Basin (Bellanca et al. 1992) where significant amounts of palygorskite and sepiolite occur as either mud chips or clay aggregates in the basal part of a fresher water lacustrine unit. Eolian transport of saltating clay pellets or dust suspensions may also contribute to the transport of authigenic clays from marginal to more central areas. This sometimes leads to problems of interpretation of detrital versus authigenic in ancient lacustrine successions subject to oscillations in climate, especially when detrital clays are partially or fully inherited from arid soils.

Sepiolite, interstratified Mg-Smectite and palygorskite form authigenic phases in the Quaternary sediments of the Double Lakes Formation, Texas (Webster and Jones 1994). The dominance of each of these minerals in separate horizons represents evaporative shifts in salinity at the time they precipitated. Sepiolite is thought to indicate a brackish lake, while Mg-smectite indicates more saline conditions. Palygorskite is interpreted as a saline pore water precipitate in the arid soils of the playa stage. Likewise Jones (1986) interpreted authigenic Mg-smectites (e.g. stevensite) as requiring higher salinity than sepiolite. Mg-silicates also define saline lake clays in Great Salt Lake (Spencer 1983) and some Bolivian salars (Badaut and Risacher 1983). In Bolivia, the authigenic Mg-smectite replaces the biogenic silica in diatom frustules and requires a pH in excess of 8.2. Authigenic stevensite occurs in unconsolidated muds underlying saline crusts in the interdunal depressions of northern Lake Chad and as small aragonite-associated oolites on the lake floor (Gac 1980; Darragi and Tardy 1987). Similar stevensite oolites have been found in the Eocene Green River lacustrine basin. Stevensite is also an early authigenic phase in the modern carbonate thrombolites in the hyposaline Lake Clifton, Australia (Burne et al. 2014). Authigenic sepiolite associated with calcite, gypsum and dolomite occurs about the margin of Saline Valley Playa, California and the edges of saline pans in the Kalahari of southern Africa (Hardie 1968; Kautz and Porada 1976). Palygorskite, sepiolite and authigenic smectite are commonplace precipitates in calcretes of groundwater discharge playas in inland Australia (Arakel et al. 1990).

Clearly, palygorskite and sepiolite (both two-chain structure fibrous clays) occur worldwide as authigenic phases in the soils and palaeosols of arid and semi-arid regions, but the mode of precipitation is still not well understood (Singer 1979). Both minerals are common in environments with elevated levels of magnesium and silica. Hence they form in alkaline lakes and caliche, as well as in deep sea sediments and hydrothermal alteration products; Folk and Rasbury (2007) argue there may also be a microbial association to their formation, at least in some Texan caliches. Jones (1986) concluded sepiolite in the calcic soils of southwest Nevada required percolation of high salinity groundwaters. Magnesium and silica solutes were sup-plied by the weathering of nearby pyroclastics and carbonates. Sepiolite has replaced magnesite pebbles, from the edges in, during freshened highstand intervals in Miocene Lake Eskisehir in Turkey (Ece 1998). Palygorskite in calcic soils is thought to be the result of incongruent dissolution of pre-existing clays (Jones and Galán 1988). Fibrous clays degrade when climate becomes more humid and alter to smectite. Paquet and Millot (1972) conclude that the transformation takes place when mean rainfall exceeds 300 mm and Calvo et al. (1999) suggested the transformation can be used as a palaeoclimatic indicator.

Alunite ($KAl_3(SO_4)_2(OH)_6$) is a common clay product in acid saline lacustrine settings, but can also form diagenetically in regions where sulphate reduction is occurring. It is thought to be derived by the reaction of clay minerals with sulphuric acid created by oxidation of sulphides or H_2S at a redox boundary. It is a common product where clays are present in zones of sulphate reduction and examples have been documented in the Middle Miocene gypsums of the Gulf of Suez (Rouchy et al. 1995a, b) and the Upper Miocene gypsums of the Lorca Basin in Spain (Rouchy et al. 1998).

Even the smectite to illite transformation, which is used as an indicator of diagenetic intensity and clay transformations occurring at higher temperatures may be influenced by salinity. This makes illite crystallinity a less reliable indicator

of diagenetic stage in environments with saline pore fluids (Honty et al. 2004). Turner and Fishman (1991) found illite-smectite mixed layer clays having a range of expandabilities in altered tuff beds in a Jurassic lake in the Morrison Formation (Eastern Colorado Plateau, USA). The observed clays did not experience deep burial, and did not undergo hydrothermal alteration. The illite content generally increases from the lake margin (100–70 % smectite) to the lake centre (30–0 % smectite) and follows a lateral hydrogeochemical gradient, which was characterized by increasing salinity and alkalinity (Fig. 12.74). It seems that in a saline depositional setting, solution chemistry is a principal factor controlling the smectite to illite proportion. Illite-smectite can form from smectite at low temperatures in several ways (see Honty et al. 2004), but forms best in saline environments subject to wetting and drying cycles, which is a hydrology exemplified in salt lakes and playas. In the presence of K^+ ions, alternating wetting and drying leads to irreversible fixation of K and the formation of illite layers. Illite-smectite clays forming at elevated pH may not even require wetting and drying cycles.

Textural Synthesis

Evaporitic settings can accumulate evaporitic carbonates as well as more saline salts dominated by gypsum and halite beds. Evaporitic carbonates accumulate across the whole range of brine depths from ephemeral to shallow perennial to deep. Carbonate laminites tend to dominate in the deeper brine areas, while a whole range of textures and features, including laminites, form in the shallow and strandzone settings. Strandzone regions are often characterised by pisolites and algal structures of various types, ranging from cryptalgalaminites to stromatolites and tufas. The ephemeral water and groundwater seepage systems that characterise strandzones facilitate the cementation and ongoing growth of carbonate crusts. Over time, these marginward carbonate crusts can grow and deform into overthrust V-shaped carbonate ridges called tepees.

The typical evaporite accumulating on the floor of a stable shallow brine pool or a shallow epeiric shelf is composed of upward or growth-aligned crystals. Depending on the stability, salinity, and permanence of the overlying bottom brine, various mineralogical and dissolution surfaces can be superimposed on the upward growing prisms. When the overlying brine column is not subject to marked salinity fluctuations, then pristine crystal outlines are made up of stacked halite chevrons or zig-zag gypsums, with varying degrees of face curvature. When the overlying brine column is deep and holomictic then beds composed of coarse inclusion-free meshworks can form.

When an overlying perennial but shallow brine body mixes and freshens, subaqueous crystal truncation surfaces can form. Similar surfaces can form where the brine body dries up. Desiccation-related dissolution surfaces are distinguished from subaqueous truncation surfaces by an inherent abundance of vadose, karst and geopetal features. These three are all features that form during complete drying and falling of the watertable into the evaporite bed.

But evaporites do not just form on the bottom of a brine lake or seaway. They can also form where porewaters attain supersaturation in a pre-existing nonevaporite matrix (secondary evaporites). Probably the best-documented textures of this type are sabkha nodules composed of anhydrite and gypsum in the supratidal sediments of the Arabian Gulf. Large crystals of displacive halite form in a similar fashion beneath the mudflats of the Arabian Gulf, where the capillary pore fluids are at halite supersaturation. Dense brines, created during the formation of primary and early secondary salts, can sink into the underlying sediments where they can facilitate backreaction and alteration processes in the now buried evaporite beds.

At greater depths of burial, evaporite salts can reprecipitate as pore-filling cements and burial salts. Many primary and early secondary textures are overprinted at this stage by dewatering and recrystallisation processes associated with compactional dewatering and thermobaric alteration. Brines created by the subsurface dissolution of evaporites may also reprecipitate as burial salts in nearby nonevaporite beds.

If evaporites beds survive the rigours of deeper burial, they can be uplifted and re-enter the active phreatic zone where they are once again subject to dissolution and recrystallisation. Satinspar fractures and alabastrine textures are common indicators of this style of alteration. Such evaporites can be classified as tertiary evaporites. All of the textural and re-equilibration processes outlined in this chapter reflect the ongoing evolution of the brines that bathe the beds throughout their formation, burial and dissolution. Brine hydrology and its evolution is the fundamental control on evaporites. For example, work by Aleali et al. (2013), on the range of depositional and burial textures preserved in anhydritic core has integrated the various types of textures in the Triassic Kangan Formation of the Persian Gulf (South Pars Gas Field) into an inter-related textural classification, tied to the hosting depositional setting. Such an approach should find application in other anhydritic successions. In the next chapter we look at how brine evolution controls evaporites from the time they precipitated until the time they are completely dissolved.

Depositional Chemistry and Hydrology

2

In Chap. 1, an evaporite is defined as a salt rock originally precipitated from a saturated surface or nearsurface brine by hydrologies driven by solar evaporation. There is no assumption as to the origin of the parent brine; it may be marine (thalassic), nonmarine (athalassic) or a hybrid. By implication, there is a need for aridity and for water loss to exceed inflow. This means deposition and diagenesis in evaporites is more climate dependent than in either siliciclastic or carbonate sediments; reaction rates and reversibility are an order of magnitude faster. Suites of precipitated salts follow the geochemical make-up of the parent brine, while primary textures indicate hydrological stability and energy levels of the time of precipitation.

All evaporite salts are ionic salts, containing the major ions Na, Ca, Mg, K, Cl, SO_4, CO_3 in varying proportions along with other less common ionic constituents, such as B, Ba, Sr, Br and I and varying amounts of structural water (Table 1.1). The mineralogy and order of precipitates in any brine pool is controlled by the ionic make up of the parent brine. This, in turn, reflects the chemical composition of lithologies contributing dissolved ions to the parent water on its way to the site of precipitation. Because of consistent ionic proportions in seawater worldwide, the modern marine evaporite series is predictable and tied to increasing salinity. With nonmarine brines, proportions vary according to source terrain and levels of hydrothermal input. Hence, the proportions of minerals and sequence of precipitation is more variable. In addition, we now know that the ionic proportions in seawater were not constant through time and that the modern evaporite series is not necessarily a one-for-one analogue for past marine-fed precipitates.

Quaternary Deserts and Evaporite Assumptions

Modern continental evaporites typically accumulate within groundwater discharge regions in semi-arid to hyperarid deserts[1] (Fig. 2.1a; Table 2.1). Marine-fed coastal evaporites can occur at the oceanic edge of the same deserts, typically in coastal depressions fed by marine seeps or by rising groundwaters along coast-parallel mudflats. Evaporites also form lake precipitates and efflorescences in cold polar deserts in Antarctica, but the volumes of salt in these cryogenic regions pale to insignificance compared to arid settings closer to the equator. Brine freezing and mixing (cryogenesis), rather than direct solar concentration, plays a much more important role in the crystallisation of most cold climate salts, not just in Antarctica but also in the interior plains of Russia and Canada and high alpine deserts of the Andes and Tibet (Carlson et al. 1990; Marion et al. 1999).

Salt-accumulating continental depressions typically define the discharge areas of endorheic (internal drainage) basins; these are areas where more water is leaving the via evaporation than entering as rainfall, snowmelt, surface, or subsurface inflow (Table 2.1). They are found in: (1) tectonic basins, which include fault-defined intermontane basins and intracratonic structural sags, (2) interdune or inter-draa depressions

[1]Semi-arid deserts have a mean annual precipitation of between 250 and 500 mm. Arid deserts have less than 250 mm of annual rainfall. Extremely arid or hyperarid deserts have at least 12 consecutive months without rainfall. Worldwide, some 4 % of the earth surface is hyperarid, 15 % arid, and 23 % semi-arid.

© Springer International Publishing Switzerland 2016
J.K. Warren, *Evaporites: A Geological Compendium*, DOI 10.1007/978-3-319-13512-0_2

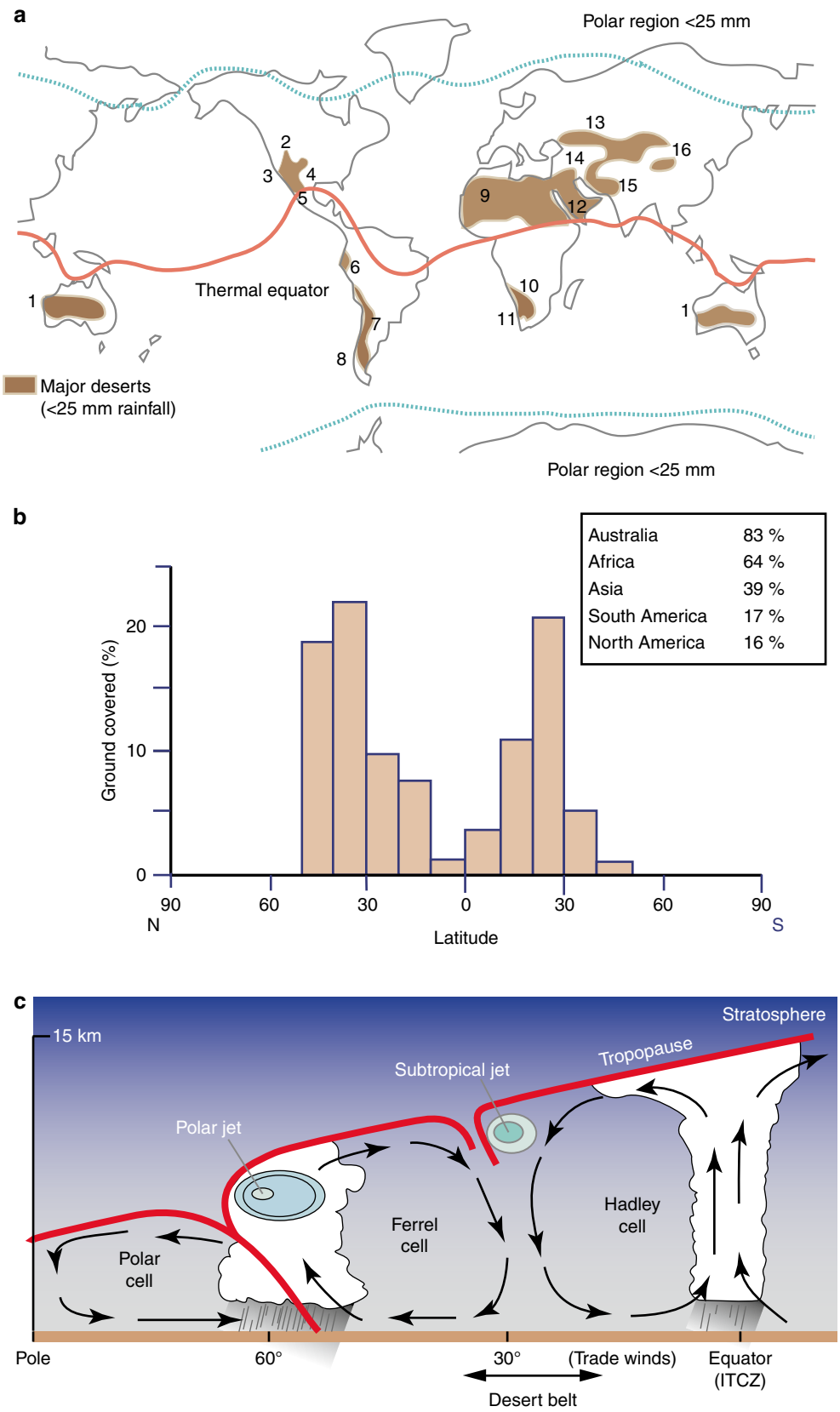

Fig. 2.1 (**a**) World distribution of modern deserts as determined by plotting areas with less than 250 mm annual precipitation. *1*. Australian, *2*. Great Basin, *3*. Mojave (Sonoran), *4*. Chihuahuan, *5*. Baja California, *6*. Peruvian, *7*. Atacama (Chilean), *8*. Patagonian, *9*. Sahara, *10*. Namibian, *11*. Kalahari, *12*. Arabian, *13*. Turkestan, *14*. Iranian, *15*. Thar, *16*. Gobi. Also shows polar regions with less than 25 cm precipitation. Thermal equator joins the points on each line of longitude with the highest annual average temperature (**b**) Latitudinal distribution of the world's modern deserts. Inset gives proportion of each continent that is arid or semiarid. (**c**) Longitudinal cross section through the earth's atmosphere showing major circulation cells, including jet streams. *ITCZ* intertropical convergence zone. Belts of cool dry descending air at 30° N and S of the equator create the main arid zones of the world

about the edges of sand seas or ergs, (3) wind-deflation hollows, (4) abandoned fluvial valleys (5) bolide-impact or volcanic craters, or (6) interior drainage depressions created by a combination of the preceding. The greatest volumes of desert salts today accumulate within arid to hyperarid depressions in continental rifts, compressional sags and transforms.

Climate drives evaporite deposition in modern deserts at scales ranging from broad latitudinal belts (100 s km) down to microclimatic niches (cms; Table 2.2). At the broadest scale, evaporites that occur in deserts are the result of large-scale atmospheric circulation. Modern deserts cover more than 25 % of the world's landsurface, mostly within two belts lying 15–45° north and south of the equator (Fig. 2.1b).

Global-scale atmospheric circulation is driven by varying intensities of solar irradiation, which is most intense directly above the equator and lessens toward the poles (Fig. 2.1c). Hence, the equatorial belt experiences greater insolation than the adjacent temperate latitudes. Equatorial air warms as it rises, creating a tropical belt of low pressure. As it rises it cools, losing most of the water vapour as rainfall to the tropical jungles and rainforests below. This now moisture-depleted air moves up and away from the equator and further cools and compresses. Finally, it sinks back to the earth's surface at around 30° latitude north and south of the equator. The cool descending dry air is reheated as it returns to the lower atmosphere, garnering an enhanced potential to absorb moisture (Fig. 2.1c).

Table 2.1 Quaternary examples of evaporite accumulations in various deserts

	Region	Location and setting	Notable evaporite features
Africa	East	Continental	Continental evaporites. In addition to large volumes of halite and $CaSO_4$, potash salts and trona are important salts in particular lakes with mineral evolution dependent on inflow chemistry.
		Danakil Depression, Lake Magadi, Lake Natron, Lake Kivu, Lake Tanganyika, Lake Turkana, Lake Urmia	
	North	Continental	Sodium carbonate is the dominant primary mineral in Lake Chad, while sodium sulphate and sodium chloride occur in subordinate amounts. Potassium and magnesium salts occur in near negligible amounts.
		Saharan ergs, Lake Chad, chotts of northern Africa	
		Coastal	Coastal sabkhas and salinas dominated by gypsum and anhydrite, along with halite and sometimes small volumes of potash, as in modern chotts and sabkhas of Tunisia.
		Coastal sabkhas and salinas of Algeria, Tunisia Libya, Morocco, the Nile delta and the Red Sea	
	Southern	Continental	Thousands of small wind-aligned salt pans, often with downwind lunettes, dot the arid landsurface. They form preferentially on a clayey substrate that is made up of the Ecca and Dwyka Shales in South Africa, the Karoo in Namibia and the Kalahari Beds in Botswana.
		Pretoria, Otjiwalundo and other salt pans, interdunal sabkhas of Namibia	
	Middle East	Continental	Dead Sea naturally accumulates pan halite in the shallow southern basin, along with carbonate laminites and massive halite in the deepwater northern basin.
		Rub al Khali ergs, Dead Sea evaporites	
		Coastal	Nodular calcium sulphate with minor halite in classic coastal sabkha successions of Abu Dhabi, Saudi Arabia and Kuwait.
		Coastal sabkhas and salinas of the Arabian Gulf	
Antarctica		Continental	Cryogenic evaporites (brine freezing). Aragonite in the Taylor Valley and the Vestfold Hills. Sulphate minerals predominant in the Wright Valley. Halite and mirabilite are widespread. Trona and thermonatrite in the East Taylor Valley, and soda nitre, bloedite, and darapskite in the Wright Valley. Antarcticite ($CaCl_2 \cdot 6H_2O$) in Don Juan Pond.
		Lake Bonney, Taylor Valley; Lake Vanda, Wright Valley, Organic Lake, Deep Lake and Ekho Lake in the Vestfold Hills.	
Asia	Central	Continental	Potash salts (especially carnallite) are accumulating as karstic fills in bedded halite in perennial lakes and playas of the Qaidam Basin. Other lakes in with a range of other salts. Borates occur in Lake Inder. Sodium sulphate (cryogenic) dominant in Korabogazgol.
		Qaidam Basin, Gulf of Kara Bogaz, Lake Inder	
	Southern	Continental	Iranian playas show complex facies interactions with rising salt diapirs with localised potash and even tachyhydrite present. Turkish lakes are accumulating large volumes of magnesium carbonate and dolomite.
		Iranian playas; Van Golü, Salda Golü and Tuz Golü, Turkey; Didwana Lake and other playas of Thar desert	
		Coastal	Gypsum and halite sabkhas, widespread fluidization textures from earthquakes.
		Coastal sabkhas of Ranns of Kutch, India	

(continued)

Table 2.1 (continued)

	Region	Location and setting	Notable evaporite features
Australia	Eastern	Continental	Continental salt lakes (playas), some with gypsum/clay lunettes that rim brine pans; others, especially in volcanic maars, are characterised by Mg-rich carbonate sediments and crusts.
		Lake Tyrell, Lake George, Maar Lakes, Lake Victoria	
	Central	Continental	Continental salt lakes (playas), typically with gypsum lunettes that rim the various brine pans. Many lunettes were more active in the Late Pleistocene. Many pans form as groundwater sumps in paleochannels. Salt crusts are now largely recycling through the lakes, with no massive accumulations.
		Lake Amadeus (Karinga Creek lakes), Lake Eyre, Lake Frome, Lake Torrens Simpson and Victoria deserts	There are fresher artesian aquifers beneath many of the larger continental lakes. Mostly halite and gypsum accumulate in the lakes, minor thernadite/mirabilite accumulating as ephemeral salts in the Karinga Creek area.
		Coastal	Coastal lakes or salinas are classic Holocene areas for coarse-grained bottom growth and reworked gypsum beds up to 10–15 m thick, pisolite seepage pavements, modern tepees, mm-laminated domal stromatolites.
		Marion Lake complex, Lake Macdonnell, Streaky Bay Lakes, Fisherman Point sabkhas	
	Western	Continental	Continental playa lakes within elongate and sinuous Tertiary palaeodrainages on the Yilgarn Craton. Evaporitic fill in the lakes is up to 10 m thick and mostly gypsum with lesser halite. Wind and wave-driven currents rework sediments that are then deflated by the wind to be redeposited in marginal gypsum dunes (lunettes).
		Lake Lefroy, Lake Cowan, Lake Dundas, Lake Ballard, Lake Carey, Lake Raeside	
		Coastal	Coastal lakes or salinas with gypsum and halite in beds up to 10–15 m thick in Lake McLeod.
		Lake Mcleod, Hutt Lagoon, Leeman Lagoon	
Europe	Spain	Continental	Glauberite and other sodium sulphates accumulating in modern playas.
		Playas of Los Monegros and Bajo Aragon, Laguna de Tirez in La Mancha	
Americas	Central Canada	Continental	Salt pan and perennial subaqueous evaporites (mostly cryogenic) containing mirabilite, thenardite, and bloedite. Some lakes, such as Freefight and Deadmoose, are accumulating salts in perennial "deep" waters (10–30 m), as well as bacteriogenic carbonates.
		Ceylon Lake, Freefight Lake, Deadmoose Lake, Little Manitou Lake and many other saline lakes and playas on the Great Plain of central Canada	
	Northern USA	Continental	Salt pans containing sodium sulphate salts, as in Central Canada.
		Saline lakes and interdunal sabkhas, Nebraska and North Dakota. Draas of the southwest USA	
	Southern USA	Continental	Pleistocene continental lacustrine accumulations of mostly gypsum ± halite, now deflated and overprinted by Holocene sabkha signatures.
		Salt Flat playa, West Texas; playas in Rio Grande Rift	
		Coastal	Coastal mudflats with displacive gypsum.
		Laguna Madre	
	Western USA	Continental (Basin and Range) Death Valley, Saline Valley, Deep Springs lake, Searles Lake, Bristol Dry Lake, Great Salt Lake, Owens Lake, Salton Sea	Quaternary continental lakes with diverse range of salts including thick halites, lesser anhydrite, trona, glauberite and other salts depending on chemistry of inflow waters. Holocene is a time of saline mudflats, at other times in the Pleistocene the depressions lay beneath the waters of saline/brackish (glacial) lakes.
	South Americas	Continental	Large volumes of continental evaporites accumulated within the central Andes during Neogene uplift of the Altiplano-Puna plateau with associated development of the Andean volcanic arc. Halite and gypsum are dominant minerals, along with local and economically important borates, nitrates and potash salts.
		Salar de Atacama, Salar Uyuni, Salar Coipasa, Pastos Grandes, Laguna Salinas, Salar de Pintados	
		Coastal	Large volumes of marine-fed estuarine evaporites in a drowned river valley.
		Bocana de Virrilá, Peru	

Table 2.2 Causes of modern deserts

		High pressure belts	Continentality	Adiabatic or rain shadow	Upwelling (cool sea surface)
		Beneath the descending limbs of Hadley cells (centred 20–30° north and south of the equator) or under stagnant air masses.	Regions within the continental interior. Locations isolated by distance from moisture sources, principally the oceans.	Regions located in the lee of topographic barriers where airmass subsides as it warms and dries and flows inland.	Amount of moisture evaporated from the ocean surface is less, so yielding drier air when sea air moves overland and warms.
Australia	Sturt's Stony	X	X	X	
	Victoria	X	X		
	Gibson	X	X	X	
	Simpson	X	X	X	
	Great Sandy	X	X		
Asia	Gobi		X		
	Taklamakan		X		
	Thar	X			
	Iranian	X	X	X	
	Turkestan		X		
	Arabian	X			
Africa	Somali-Chalbi	X			
	Kalahari	X			
	Namib	X			X
	Karoo	X		X	
	Sahara	X			X
South America	Patagonian			X	
	Monte	X			
	Atacama-Sechura	X			X
North America	Chihuahuan	X			
	Sonoran	X			
	Mojave	X		X	
	Great Basin			X	
Polar	Antarctica	X			
	Arctic	X			

See Fig. 2.1a for locations, typically more than one factor drives desertification

Belts of aridity sit beneath cold dry descending air masses of the Hadley Cells, which define high-pressure belts known as the subtropical Trade-Wind Belts or Horse Latitudes. The trade winds form the equatorward limb of the Hadley circulation in each hemisphere Such areas are seldom subjected to moisture-bearing disturbances or pressure depressions (lows), either from the Intertropical Convergence Zone (ITCZ) of the tropics or from the belt of mid-latitude depressions associated with the circumpolar westerlies. The trade winds that blow across these zones are evaporating winds, and, because of the trade-wind inversion, they tend to be areas of atmospheric subsidence and stability. That is, subtropical high-pressure belts are the major cause of aridity, though deserts are not always continuous around the earth at 30 N. For instance, the Asian monsoon supplies large quantities of rain over northern India, and elsewhere the high-pressure cells are disrupted into a series of local cells, notably over the oceans, where air moving clockwise around the equatorial side of the cell brings moisture-laden air to the eastern margins of the continents.

The earth-scale distribution of Holocene desert belts reflects broad-scale atmospheric dynamics. When icecaps expand the atmospheric circulation belts are pushed and compressed toward the equator and they have done so numerous times in glacial maxima of the current icehouse climate mode. Equatorward compression increases the intensity of atmospheric circulation and alters the latitudinal distribution of climate belts. This has a marked effect on climate in Quaternary deserts, so that almost all modern continental playas in the Horse Latitudes have experienced numerous water-full versus dry stages in the last few hundred thousand years, what follows are examples from different continents to underline this fluctuation.

Strontium-isotopic composition of preserved gypsum in Lake Frome, a large discharge playa in South Australia, records periods of high rainfall at 3–6, 12–15, and >17 Ka,

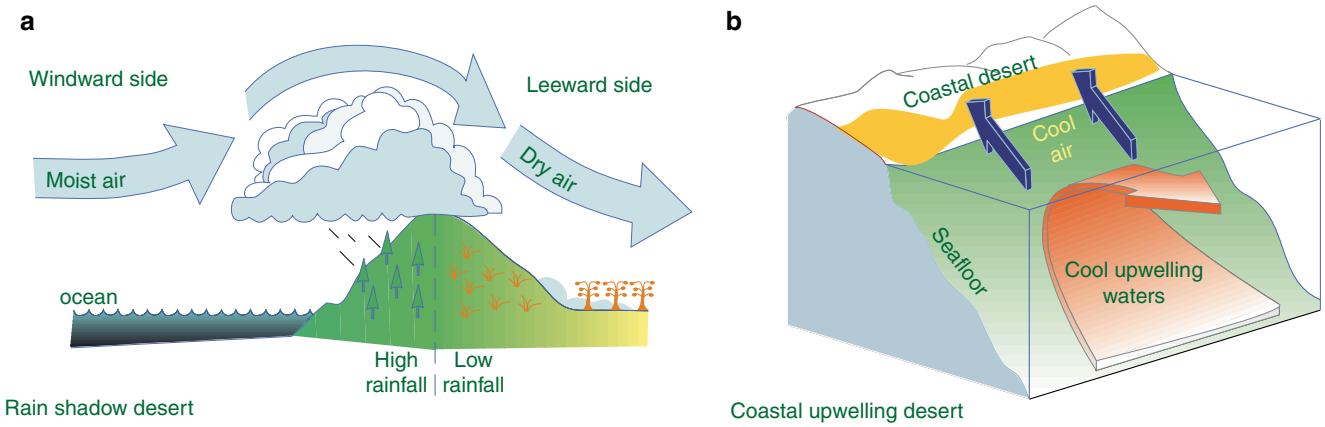

Fig. 2.2 Local controls on deserts. (**a**) Adiabatic or rain shadow desert where rain tends to fall on the seaward side of the mountains. (**b**) Coastal deserts form in response to cool upwelling ocean waters and the cool dry onshore winds warming as they pass overland (After Warren 2008)

and drier periods at ≈10 and ≈17 Ka (Ullman and Collerson 1994). In the last interglacial (early in oxygen isotope stage 5) a nearby and much enlarged Lake Eyre maintained a perennial freshened water body up to 25 m deep (Magee et al. 1995; Cohen et al. 2012). Subsequently, as climate deteriorated into glacial mode, there were a number of dry periods separating successively less effective wet phases, culminating in the deposition of a substantial halite salt crust around the time of the last glacial maximum. Lake Eyre only attained its present saline mudflat/ephemeral playa status some 3–4 Ka. The drying trend over the last hundred thousand years in Lake Eyre corresponds to a longterm lessening of monsoon intensity in the northern part of Australia, which is the main source area for waters flowing into the lake depression.

In Death Valley, USA, there were dry mudflats, characterised by abundant glauberite, gypsum and minor calcite from 0–10 to 60–100 Ka (Li et al. 1997). In contrast, the wet period from 10 to 60 Ka was typified by halite and mud layers, with relatively abundant calcite. This wetter period encompasses sediments deposited 10–35 Ka, when Death Valley contained a perennial halite lake. These millenial-scale oscillations define a predominately Na–Ca spring-fed inflow hydrology during dry climatic periods and increased volumes of bicarbonate-rich river waters in the wetter periods.

Likewise sediments of the inland sabkhat of the Tayma playa (Saudi Arabia) illustrate a change from a relatively humid Holocene period (10–8 ka) to the hyperarid conditions of today (Ginau et al. 2012). During the humid period, a perennial lake defined the playa depression with a characteristic suite of carbonate-dominant sediment, including ostracod valves and foraminifer shells, all adapted to salinity fluctuations. At the same time, phases of lake contraction and high salinity were responsible for the formation of open water evaporitic carbonates, such as aragonite needles, ooids and magnesite in the surrounding mudflats (much as in the Coorong region and in Great Salt Lake, Utah). Dilution occurred during rain events and the flooding of the playa is indicated by clastic layers in the lake sediments, which were often deposited in graded fining-upward sequences indicative of sheet flooding. With time, lake sedimentation became increasingly arid and sabkharized. Today, the lake hydrology is dominated by the precipitation of capillary salts in varying combinations of halite, gypsum, anhydrite and bassanite.

Saline playas and midlatitude deserts of central Asia and central Australia are in part a product of their isolation from the nearest ocean. Continentality is the term that describes the geographic isolation of a desert by its large distance from the ocean. It explains why the highly continental Takla Makan Desert of central China is a hyperarid desert at 50°N latitude, well north of the world's subtropical high pressure belts. Another factor helping form this type of desert is the rain shadow effect.

Rain shadow deserts, also known as adiabatic deserts, form where air masses move up and over mountain ranges (Fig. 2.2a). As air rises over a mountain range it cools, moisture develops into clouds and falls as rain on the side of the mountain range facing into the prevailing wind. Subsiding air on the other side of the range is dry and its moisture-bearing capacity increases further as it sinks and warms. For example, the deserts of Patagonia lie on the lee side of the Andes, while the deserts of Nevada and Utah are in the rain shadow of the Sierra Nevada. The Dasht-i-Lut in Iran is in the rain shadow of the Alborz and Zagros Mountains and its maximum surface temperatures at 70.7 °C (measured in sand) make it one of the hottest deserts in the world. Adiabatic deserts can also be found behind the Himalayas, the Ethiopian uplands and Eastern Highlands of Australia. Extreme examples include the Dead Sea rift and the Afar depression, both areas are subsealevel depressions surrounded by high mountain ranges of the rift rim. Rain shadow effects increase where the region inland of the mountains lacks relief.

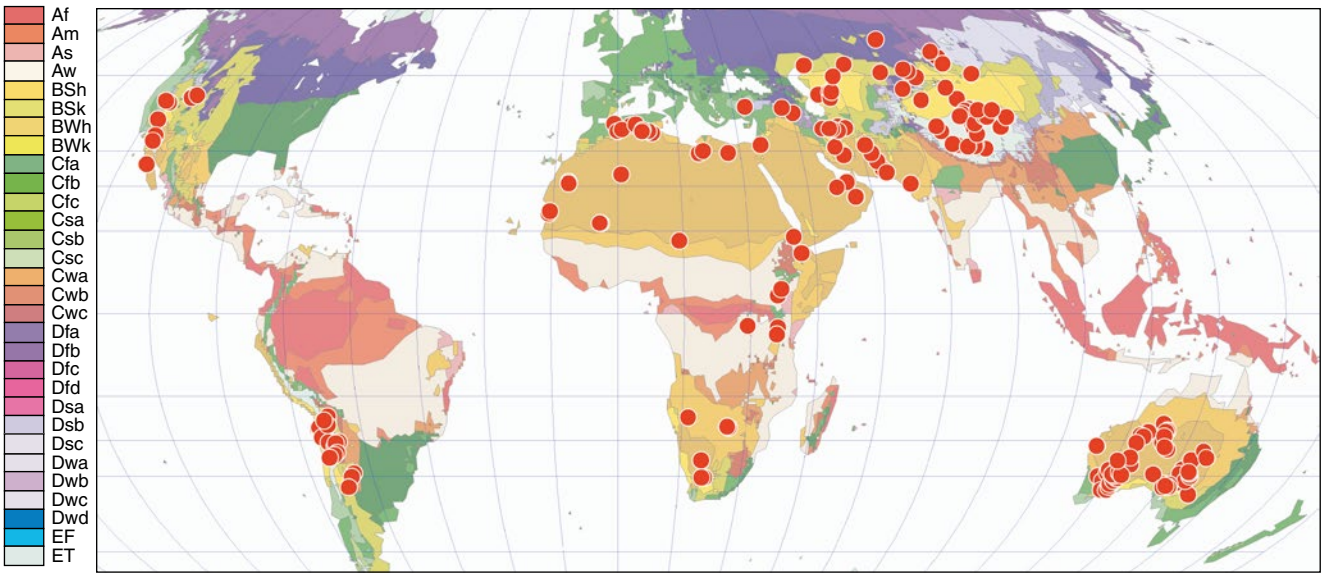

Fig. 2.3 Quaternary evaporites with areas >250 km^2 and climate setting. Centroids plotted on the earth surface where an evaporite depositional setting (sabkha, salina, playa, saline lake, saline soil) extends across an area of more than 250 km^2. This plot set is overlain on a Köppen climate base (After Kottek et al. 2006). *Main Climates*: *A* tropical, *B* arid, *C* warm temperate, *D* snow, *E* polar. *Precipitation*: *W* desert, *S* steppe, *f* fully humid, *s* summer dry, *w* winter dry, *m* monsoonal. *Temperature*: *h* hot arid, *k* cold arid, *a* hot summer, *b* warm summer, *c* cool summer, d extremely continental, *F* polar frost, *T* polar tundra

Rainshadow deserts and bedded evaporites are often part of a longer term tectonic association between sedimentation and climate in both extensional and compressional settings and are a climatic response independent of whether the earth is in greenhouse or icehouse climate mode (Hay 1996). Over millions of years, the rifting of continental blocks involves broad upwarping, followed by subsidence of a central valley and uplift of marginal shoulders. The result is an evolving regional climate-sediment association that is repeated many times in the Phanerozoic: first a vapour-trapping arch with centripetal fluvial drainage forms. This is followed by a rift valley, first with fresh-water lakes, culminating in an arid subsealevel evaporitic rift bordered by mountains intercepting incoming precipitation (adiabatic desert).

Convergence tectonics also affect climate at the broad scale. A rising mountain range is a barrier to atmospheric circulation, especially if perpendicular to the incoming circulation. The uplift of the Tibetan Plateau in the Late Tertiary created an easterly subtropical jet stream, which now flows from Tibet across the Arabian Peninsula toward Somalia. This stream of cool dry air accentuated the existing aridity and created an adiabatic desert that lies almost on the Equator (Fig. 2.3). In the past both extensional sag and compressional tectonism have helped induce hyperaridity atop large subsea-level seepage depressions, which were capable of accumulating thick halite and gypsum successions (Fig. 5.32).

Upwelling ocean waters off continental landmasses in the trade wind belts favour coastal deserts. Cold upwelling ocean water creates a belt of coast-parallel cool water. And, as evaporation is a function of heating, cold offshore oceans provide less moisture and less cloud to the adjacent land. The cool air above creates relatively dry onshore winds. As this colder air moves across the land it is heated, so developing an increased capacity to absorb rather than shed moisture (Fig. 2.2b). Offshore, these cool strips of water are frequently engulfed in winter sea fogs, created by a blanket of warmer air atop cold seawater. Such cold upwelling ocean currents account for the deserts of Baja California and the Namib of southwest Africa (Benguela Current). The Peru Current, as it upwells along the west coast of South America, helps maintain hyperaridity in the Atacama Desert of Chile, which receives around 1 mm of rain every 5–20 years making it the driest desert in the world.

Fog, rather than rain, is the main supplier of moisture to coastal deserts in such areas and it also moderates the coastal air temperature. An array of unusual desert plants and animals have evolved behaviours and physical adaptations to make maximum use of this foggy water. For example, in the early morning some Namibian desert insects with water-capturing fluted carapaces stand on the coastal dunes with sails-high to collect condensation from foggy onshore morning breezes.

The present western edges of most tropical or Trade Wind deserts are washed by cool ocean currents driven by large scale ocean gyres, which rotate anticlockwise in the Southern Hemisphere and clockwise in the Northern Hemisphere. Throughout much of the Phanerozoic, coastal deserts in

ancient trade wind belts, indicated by eolian dunes and evaporites, have characterised the western sides of continents in the horse latitudes (Hay 1996).

Quaternary Evaporites in a Köppen Climatic Framework

In much of the geological literature, Quaternary evaporite occurrences are stated as being directly related to the distribution of the world's hot arid deserts, and in a general way this is true but, as Warren (2010) showed, it is an oversimplification. Hot arid desert does not necessarily equate to laterally extensive bedded evaporite occurrences; there must also be a significant long term brine source, it may be meteoric, marine, a hybrid and perhaps fed brines from dissolution of earlier formed salts in the drainage basin (including diapiric salt).

There are different ways of defining a desert and by implication its associated evaporites. One accepted approach is to define a desert as a land area receiving less that 250 mm of annual precipitation. Using this definition some 26.2 % of the world's landsurface is desert. But, in terms of evaporite distribution and their economics, this climatic generalization of evaporites related to annual rainfall conceals three significant hydrological truisms needed to accumulate thick sequences of bedded salts (Warren 2010): (1) For any substantial volume of evaporite to precipitate and be preserved, there must be a sufficient volume of cations and anions in the inflow waters to allow thick sequences of salts to form; (2) The depositional setting and its climate must be located within a longer term basin hydrology that favours preservation of the bedded salt, so it may pass into the burial realm, and/or it must favour the ongoing creation of a suitable saline brine feed to a solar-evaporation fed chemical sump. (3) There must be a negative water balance with the potential for more water to leave the system than enter. The significance of these simple hydrological statements and the consequences, as to where bedded evaporites accumulate, is lost in the generalization that "evaporites form in the world's deserts."

For evaporite studies it is preferable to define and plot saline hydrologies within a climatic framework where deserts are given the same hydrological consideration that is required for evaporite salts to form. That is, a desert is an area of land where annual precipitation is less than potential evapotranspiration. This definition of a desert is the one used by Köppen (1900). With slight modifications, his climatological scheme is still in widespread use today to breakout the various climatic zones across the world's landsurface (Kottek et al. 2006). Using a Köppen climate base, Fig. 2.3 plots worldwide occurrences of modern saline depositional systems with areas greater than 250 km^2. Table 2.3 compares characteristics of some of the larger Quaternary bedded evaporite settings in marine edge and continental interiors. These regions contain evaporite salts accumulating in saline soils, sabkhas, salinas, saline lakes, playas and salt flats, with textural forms ranging from; isolated crystals and nodules in a terrigenous matrix, to salt crusts, to stacked beds of salts more than 10 m thick. The majority of the saline areas are in arid areas, as defined by Köppen (Zone B), but not all such areas of widespread salts are in deserts (as defined by Köppen) and not all are in hot climates.

Before we get further into a discussion of climatic associations across modern continental and marine-fed evaporite occurrences, a few words are needed to explain the groups and subgroups that make up the Köppen climate classification (see Kottek et al. 2006 for more detail). In terms of evaporite occurrences, the most important is Köppen Group B (arid or semiarid); it defines climate areas on the continents where annual precipitation is less than potential evapotranspiration. Group B climates cover 12.2 % of the world's land surface, much less than the 26.2 % desert area when defined purely by rainfall (Fig. 2.4). Group B is further divided into desert (BW) zones, where annual precipitation is low, and steppe or semiarid (BS) areas where precipitation is somewhat higher relative to evapotranspiration. Kottek et al. 2006, discusses the equations used to define these and other Köppen climate boundaries and how the climate data plot, shown in Fig. 2.3, is generated.

A third letter is added to a Köppen classification of deserts to indicate temperature, for example, h indicates hot and k indicates cold in the BW group. Definitions vary on what is the actual thermal boundary between h and k; in the classification followed in this book Köppen's original separation of average annual temperature being more or less than 18 °C is used. Common practice in the USA today is to assign k if there is one month or more in a year when the average monthly temperature is below zero (°C).

Group A encompasses tropical (megathermal) climates, it is assigned to regions that have year-round monthly temperature averages above 18 °C. The tropics are further subdivided in Af for rainforest, Am for monsoonal, while seasonally variable tropical climates are called savannah. As denotes a tropical savannah zone with a dry summer, and Aw indicates tropical savannah with a dry winter. The savannah group encompasses most tropical setting where bedded evaporites can occur (e.g., Aw characterizes many saline African rift lakes and salt pans on the leeward of some oceanic islands, such as Inagua in the Caribbean, while an As climate typifies the climate over anthropogenic salt pans near Macau in central Brazil (see Chap. 11 for discussion of anthropogenic coastal salt factories).

Group C is the temperate (mesothermal) climate group and includes the dry summer subtropical or Mediterranean climate (Csa, Csb) zones showing marked seasonal separation between hotter drier summers and cooler wetter winters. This climate setting facilitates seasonal salt harvesting in many solar salt farms and pans about the Mediterranean and southeastern Australia (Chap. 11). There is also a humid sub-

Table 2.3 Area, elevation (with respect to msl) and climate in selected natural endorheic saline depressions in marine-margin versus continental-interior positions, with and without salt diapirs in the drainage

Name	Country	Köppen	Area (km^2)	Elev. (m)	Diapirs
Marine margin					
Lake Macleod	Australia	BWh	2,067	−0.6	No
Lake Macdonnell	Australia	BSk	108	−0.5	No
Lake Asal	Djibouti	BWh	54	−155	No
Dallol saline pan	Ethiopia	BWh	344	−115	Yes
Sabkhat Maradah	Libya	BWh	473	−0.5	No
Oje de Liebr	Mexico	BWh	373	−0.1	No
Abu Dhabi Sabkha	UAE	BWh	1,655	0.1	No
Continental interior					
Lake Eyre	Australia	BWh	8,528	−15	No
Salar de Uyuni	Bolivia	BWk	9,654	3,650	Yes
Sua Pan (Makgadikgadi Pans)	Botswana	BSh	3,307	888	No
Salar de Atacama	Chile	BWk	3,065	2,250	Yes
Chagannur Salt Lake	China	BSk	15	968	No
Dabuxum Lake	China	BWk	9	2,681	Yes
Zabuye Salt Lake	China	ET	251	4,426	No
Wadi Natrun	Egypt	BWh	20	−23	No
Gavkhoni Playa	Iran	BWk	477	1,450	Yes
Lake Magadi	Kenya	Aw	111	643	No
Issyk Kul	Kyrgystan	BSk	6,235	1,619	No
Dead Sea	Middle East	BSh	1,023	−415	Yes
Sabkha Matti	Middle East	BWh	2,954	30	No
Umm Al Sammim mudflat	Oman	BWh	2,969	81	Yes
Chott el Djerid (Jerid)	Tunisia	BWh	5,728	14	Yes
Death Valley Badwater Pan	USA	BWh	54	−75	No
Salton Sea	USA	BWh	929	−74	No
Great Salt Lake	USA	Cfa	4,998	1,280	No
Large bodies of saline water					
Aral Sea (Sea of Islands)	Kazakhstan	BWk	58,178	40	No
Kara-Bogaz-Gol (water filled)	Turkmenistan	BSk	17,528	−30.5	No
Kara-Bogaz-Gol (remnant)	Turkmenistan	BSk	919	−29	No

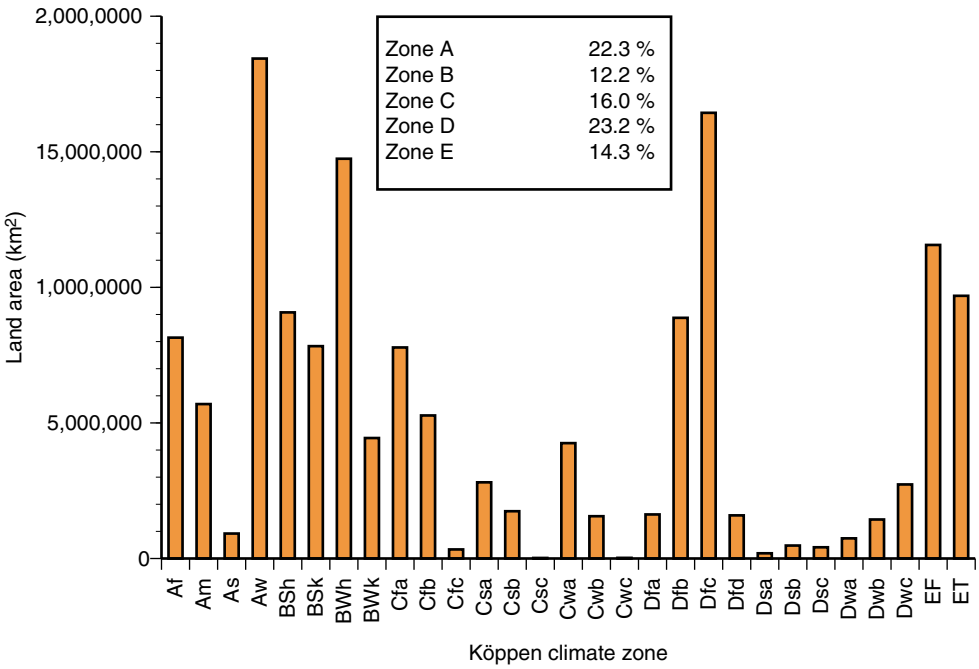

Fig. 2.4 Land areas of the various Köppen climate zones (Extracted and plotted from Kottek et al. 2006). The earth's total land area is 148,940,000 km^2

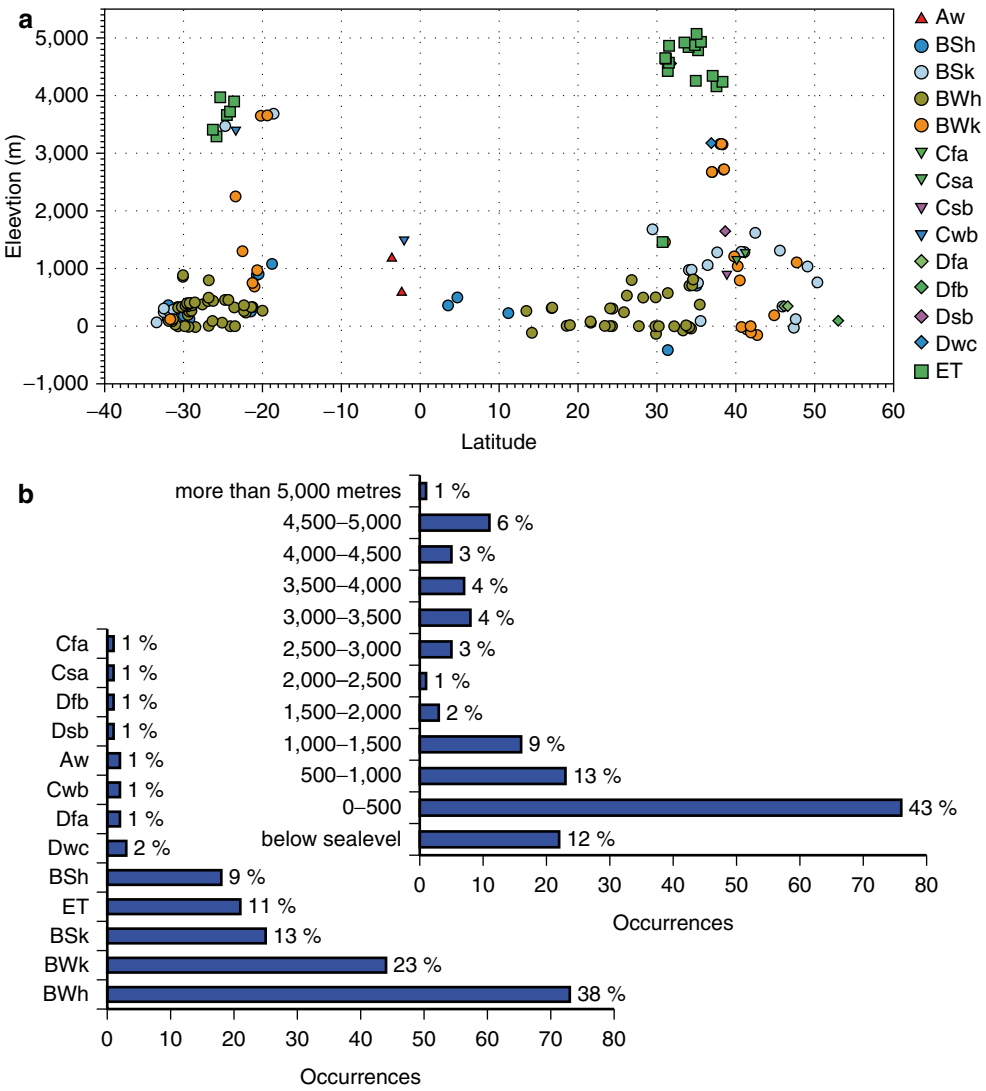

Fig. 2.5 Large saline areas (>250 km^2) on the earth's landsurface in terms of Köppen climate zones. (**a**) Plot of locations in terms of climate versus latitude and elevation. (**b**) Count of occurrences (>250 km^2) as bar charts showing percentage occurrences in climate zone and elevation ranges (metres sea level)

tropical group (Cfa and Cwa) that tends to occupy temperate continental interiors. Maritime or oceanic temperate climate zones (Cfb, Cwb, Cfc) have milder summers and winters; they tend to occur on western sides of continents, polewards of the Mediterranean climate zones of the world (Fig. 2.3). Then there are the temperate climate zones with dry winters and cool summers (Cwb) and the Maritime subarctic climates (Cfc), typically located poleward to the maritime temperate zones. Group D encompasses continental climate regimes, sometimes called the snow climates, which tend be located within continents and subject to greater temperature extremes compared to the maritime zones. They are subdivided into continental regions with hot summers (Dfa, Dwa, Dsa), continental regions with warm summers, also called hemiboreal (Dfb, Dwb, Dsb) and a third grouping that is subarctic or boreal (Taiga) and termed Dfc, Dwc and Dsc. Cryogenic evaporites are not uncommon in regions covered by this D climatic group.

Finally, there are the polar climates of Group E, characterized year round by monthly average temperatures below 10 °C. Group E is further divided into icecap or frost climate (EF) and tundra (ET) which includes alpine or high-altitude climates and encompasses many natural accumulations of borate and low temperature sodium sulphate salts and along with lithium brines in the adiabatic high-altitude deserts of the Andes and the Himalayas (Chap. 11). Above 4,000 m most of these saline ET accumulations are relatively small deposits (<10 km^2).

Continental-Interior Settings

When >250 km^2 evaporite occurrences are plotted against latitude, climate and elevation, the range of large (>250 km^2)

saline systems in the world's landscape is seen to be more climatically diverse than just evaporite occurrences within hot arid deserts (BWh), although such associations do constitute some 38 % of occurrences (Fig. 2.5a; Table 2.3). Cold arid deserts (BWk) host 23 % of large saline occurrences, making a combined total of 61 % for large evaporite accumulation (area >250 km^2) occurrences in modern arid deserts (BW group), while the arid steppes (BSh and BSk) host another 22 %. In total the world's arid climatic zones host 83 % of today's larger evaporite occurrences (Fig. 2.5b).

This leaves another substantial, but not widely recognized, climate zone where Quaternary evaporites accumulate, this is the polar tundra (ET), an environment where some 11 % of large evaporite areas occur. It is typified by arid high altitude belts, mostly in the Horse Latitudes, not in polar positions. As a depositional type it is typified by the lakes and pans of the high plateaus of the Andes (Altiplano) and the Himalayas (Tibetan Plateau). In this zone H_2O may be commonplace, but is there mostly as ice, and cryogenic salts are commonplace. The remaining region (some 6 % of the total of large saline occurrences) is a group defined by continental interior snow climates (group D), some with hot dry summers or dry winters favouring the possible accumulation of cryogenic salts.

Another interesting aspect of the Quaternary salt distribution seen in the latitude plot (Fig. 2.5a) is that in the Northern Hemisphere the occurrence of large evaporite systems within arid deserts and steppe climates (BW and BS settings) extends much further south toward the equator and much further poleward (from 5 to 55°N) than the narrower range of large evaporite occurrences and associated climates in the southern hemisphere. In large part this is a response to world-scale adiabatic effects associated with the growth of the Himalayas. This Cenozoic mountain range diverts world-scale atmospheric air flows from a more north-south trajectory, usually associated with Hadley Cell circulation. For example, the Kunlun Mountains, formed some 5.3 Ma, prevented moisture from the Indian Monsoon reaching much of the adjacent Tibet Plateau. Its adiabatic rain shadow creates the Taklamakan desert, the second largest active sand desert in the world (BWk).

The uplift of the Himalayas also created a dry easterly jet stream, moving arid cool air across the Tibet Plateau, around the northern side of the Himalayas, and then equatorward across the Arabian Peninsula toward Somalia where it descends and gains heat. This stream of cool southward-flowing dry air warms as it moves across the Eastern Mediterranean land areas and so accentuates existing aridity. It helps create an adiabatic desert zone that extends across Arabia and northern Africa almost to the Equator (Figs. 2.1a and 2.5a).

In the southern hemisphere, the uplift of the Andes has formed high intermontane depressions and the associated adiabatic aridity has created Salar de Atacama (with a sediment fill composed of more that 900 m of interlayered salt and clay) and Salar de Uyuni (with more than 120 m of interbedded salt and clay infill) with areas of 3,064 km^2 and 9,654 km^2 respectively. These are the two largest examples of Quaternary bedded halite accumulation, worldwide. Yet neither resides in hot arid desert settings (BWh), both are located in cold arid deserts (BWk) and in actively subsiding, high altitude (>2,500 m) intermontane (high relief) endorheic depressions.

Worldwide, distribution of most larger (>250 km^2) Quaternary evaporite settings in hot arid (BWh) desert settings is tied either to endorheic river terminations along desert margins, especially adjacent to mountain belts (e.g., circum Saharan chotts, playas and sabkhas adjacent to Atlas mountains – Fig. 2.6 and the southern Africa pans), or to ancient inherited paleodrainage depressions (as in the majority of the interior salt lakes of Australia – Fig. 2.3). Another BWh evaporite association is along the termination outflow rims of deep artesian systems, as in Lake Eyre North, Australia (8,528 km^2, with an ephemeral halite crust up to 2 m thick in its southern portion). Similar deeply-circulating meteoric hydrologies explain the distribution of chotts in the BWh zone of NE Africa. Unlike Atacama and Uyuni in the Andes, none of these BWh artesian systems are accumulating stacked decametre-thick salt beds. Rather, the most extensive style of BWh salt in meteoric-fed artesian outflow zones is as dispersed crystals of gypsum and halite in a terrigenous redbed matrix or as visually impressive large ephemeral saline flats and pans covered by metre-scale salt crusts that dissolve and reform with the occasional decadal freshwater flood (Chap. 3). Sediments of such continental groundwater outflow zones are typically reworked by eolian processes and, due to a lack of long term watertable stability, the longterm sediment fill is matrix-rich and evaporite-poor, with the Quaternary sediment column typified by episodes of deflation, driven by 10,000–100,000 year cycles of glacial-interglacial climate changes.

It seems that to form and preserve laterally-extensive decametre-thick stacked beds of halite in a Quaternary timeframework requires an actively subsiding tectonic depression in a cooler high-altitude continental desert, where temperatures and evaporation rates are lower than in BWh settings, allowing brine to pond and remain at or near the surface for longer periods (Fig. 2.7). But perhaps more importantly all of the larger regions of the Quaternary world, where thick stacked bedded (not dispersed) evaporites are accumulating, are located in continental regions with drainage hinterlands where dissolution of older halokinetic

Fig. 2.6 Köppen climate zones across North Africa showing centripetal distribution of saline lakes and chotts (*small blue areas*) about the perimeter of the Saharan Desert (mostly BWh). Clearly show the importance of a fluvial (*blue lines*) or groundwater supply to create an area of saline lake/salt deposits. That is, no brine at or near landsurface means no evaporites can form. For detail on Köppen climate refer to Fig. 2.3. The resolution in this image is better suited to the digital version of this book (Output overlays courtesy of SaltWork Database Version 1.6)

marine-fed salt masses are actively supplying substantial volumes of brine to the near surface hydrology. This halokinetic-supplied set of deposits includes, Salar de Uyuni and Salar de Atacama in the Andean Altiplano, the Kavir salt lakes of Iran, the Qaidam depression of China and the Dead Sea (Table 2.3).

Marine-Margin Settings

Thick sequences of stacked Quaternary evaporite beds with a marine brine feed are far less common and far smaller than meteoric/halokinetic continental evaporite occurrences. Relatively few marine-fed evaporite regions exist today with areas in excess of 250 km^2 (Table 2.3). The largest deposit of this group is Lake Macleod on the west coast of Australia, with an area of 2,067 km^2 and containing a 10 m-thick Holocene gypsum/halite bed. It hosts a saltworks producing some 1,500,000 t/year from lake brines in a BWh setting (Chap. 11). A smaller marine seepage example, with a similar Quaternary coastal carbonate dune-hosted seepage hydrology, is Lake Macdonnell near the head of the Great Australia Bight. It has an area of 451 km^2, a 10 m-thick fill of Holocene bedded gypsum and is located in a milder BSk setting, compared to Lake Macleod. Even so, annually, the Lake Macdonnell operation is quarrying more than 1.4 Mt of Holocene coarsely-crystalline near-pure gypsum and producing more that 35,000 t of salt via by pan evaporation of lake brines. Interestingly, when the climatic settings of Holocene coastal salinas of southern and western Australia are compared, all of which show similar interdunal depression seepage hydrologies, it is clear that gypsum forms from marine brines in BSk and lower precipitation regions Csb, settings. Halite dominates the marine-fed fills in BWh coastal settings, while Coorong-style meteoric-fed carbonates dominate in similar interdunal coastal seepage depressions in the more the humid Csb settings of the Coorong region (Chap. 4)

One of the most visually impressive marine seep systems in the world is Lake Asal, immediately inland of the coast of Djibouti, with an area of only 54 km^2 it is much smaller than the 250 km^2 cutoff used for this discussion. It is located in a BWh climate, similar to that of the Danakil depression, contains subaqueous textured gypsum and pan halites, and lies at the bottom of a hydrographically-isolated basalt-floored depression with a brine lake surface some 115 m below sea-level (see Chap. 4 for geological detail). This difference in elevation between the sea and the lake floor drives a marine seep hydrology, so that seawater-derived groundwater escapes as springs along the lake margin. Most of the cations and anions in the seawater feed, that ultimately accumulate as salts in the subsealevel Asal sump, move lakeward via gravitational seepage along fractures in the a basaltic ridge aquifer separating the Red Sea from the brine lake, in what is an actively extending continental rift that will shortly become and arm of the Red Sea.

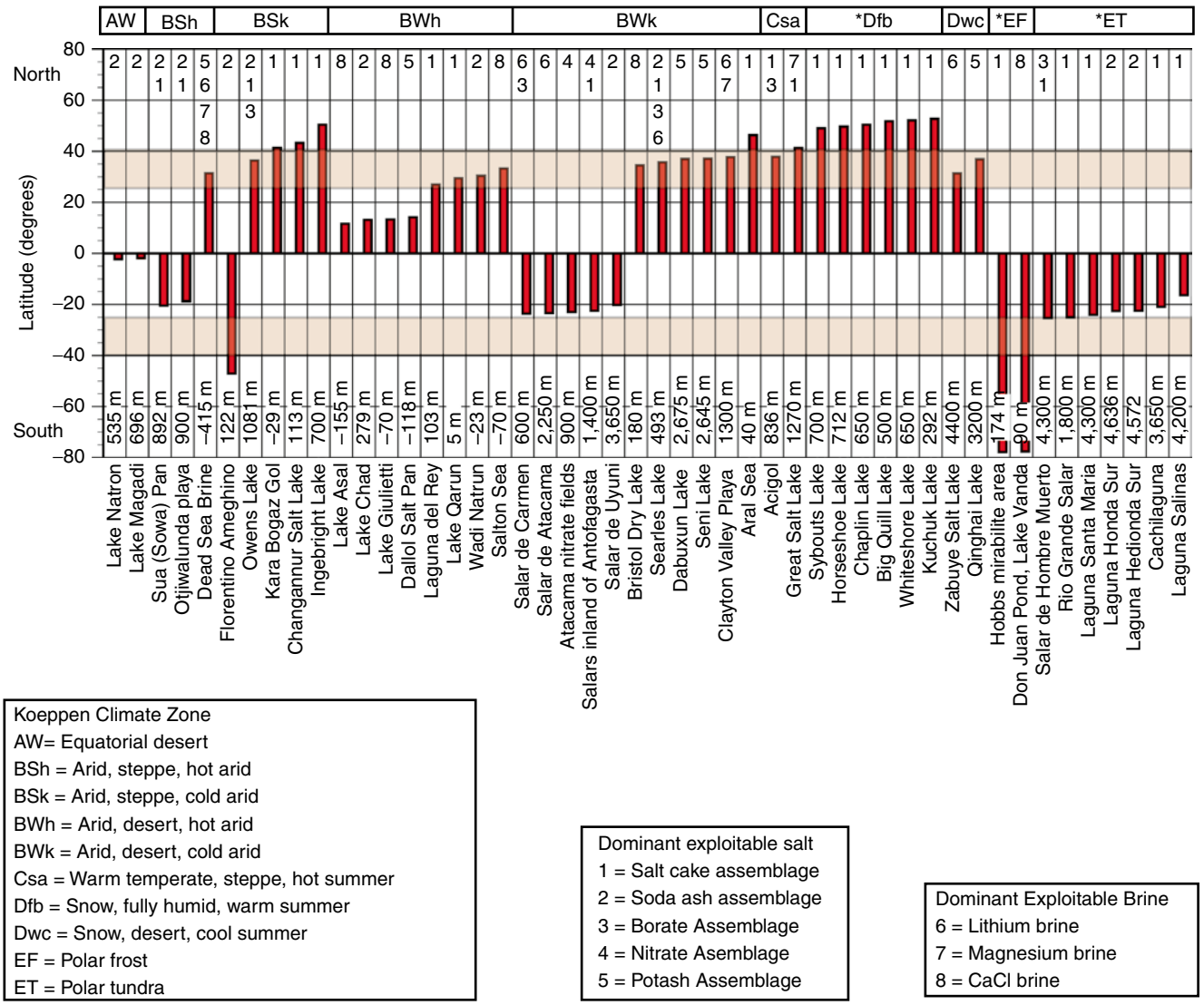

Fig. 2.7 Quaternary continental lacustrine saline deposits plotted against their latitude and Köppen climate zone (see Fig. 2.3). The brown shade indicates "horse latitude" belts situated some 25–40° north and south of the equator. Exploited or exploitable commodities are listed as a set of numeric keys for each deposit, in some lakes the exploited deposits underlie or form about the margins of the current lake/playa and indicate earlier (Pleistocene) or marginward increases in salinity (see Chaps. 11 and 12 for details). Asterisk indicates settings where cryogenic salts dominate the natural precipitates, i.e., saline lakes within the D and E climate settings (After Warren 2010)

That there are very few large marine-fed bedded Quaternary evaporite systems is illustrated by summing the total area of large active continental-fed evaporite areas (>250 km^2) listed in Fig. 2.3, which gives a total surface area worldwide in excess of 360,000 km^2. In contrast, the total area of large modern marine-fed systems, at slightly less 10,000 km^2, is more than an order of magnitude smaller. This low value for large coastal marine-fed evaporite occurrences is in part because many classic coastal sabkhas, with characteristic dispersed evaporites in their supratidal sediments and long considered to be archetypal marine-fed groundwater evaporite system, are now seen as mostly continental brine-fed hydrologies.

For example, the modern Abu Dhabi sabkha system (1,658 km^2; BWh) has been shown by Wood et al. (2005), to be a continental groundwater outflow area, where most of ions precipitating as salts in the supratidal zone are supplied by upwelling of deeply-circulated meteoric waters, not seawater flooding (Chap. 3). Similar continental hydrologies resurging into the coastal zone supply much of the salt accumulating in the suprasealevel sabkhas near Khobar in Saudi Arabia (BWh), Rann of Kutch in India (28,000 km^2, BWh), Sabkha Matti (2,955 km^2, BWh) in the Emirates, and Sabkha de Ndrhamcha (634 km^2, BWh) in Mauritania. And yet today all of these large sabkha occurrences are located just inland of modern coastal zones and so without hydrological knowl-

edge are easily interpreted as marine. This distinction between a water budget and a salt supply budget emphasizes a general observation in Holocene evaporite systems that, in order to define the main fluid carrier for the salt volume in any supratidal part of an evaporitic depression, it is important to understand and quantify the nature of the groundwater feed, be it by marine or nonmarine, in both continental-interior and marine-margin settings. It also means that surface runoff and seawater washovers, while at times visually impressive, typically do not supply the greater volume of preserved salts in a coastal sabkha system.

Due to the highly impervious nature of muddy sabkha sediment, an occasional seawater storm flood into a coastal margin mudflat does not mean the pooled seawater ever penetrates the underlying sabkha. Most of its solute load is deposited as an ephemeral surface crust of halite that is a few centimetres thick atop the sabkha muds (Wood et al. 2005). Based on Wood's and other hydrological studies of modern coastal sabkhas in BWh settings (see Chap. 3) it seems that the salt supply to most modern coastal sabkha depressions is still not at hydrological equilibrium with the present sealevel, which was reached at the beginning of the Holocene some 6,000–8,000 years ago. That is, modern zones of continental groundwater outflow along an arid coast have watertables that are up to a metre of two above sealevel and a strongly influenced by the resurgence of seaward-flowing deeply circulating, continental groundwaters (it is axiomatic that surface runoff and local meteoric recharge tend to be limited in BWh settings). In this situation resurging waters in the sabkha tend to have a dominantly continental ionic supply for their preserved salts.

Lastly, in terms of the climatic and hydrological prerequisites for the accumulations of thick bedded Holocene salt deposits, one must recognize that marine-margin sabkha mudflats do not have the same geohydrology as a near-coastal, hydrographically-isolated seepage-fed sub-sealevel salina depression. A BWh or BSk near-coastal salina is slowly but continually resupplied ions via springs fed by the effusion of seawater, moving under a gravity drive (evaporative drawdown), through an aquifer that is the barrier separating the salina depression from the adjacent ocean. Until the depositional surface reaches hydrological equilibrium, it draws continually on the near limitless supply of ions in the adjacent salty reservoir that is the world's ocean. Salts growing displacively in the supratidal parts of a sabkha cannot call on a drawdown hydrology and can only be supplied marine salts from salt spray as it is blown inland or from waters washed over the sabkha by the occasional storm driven wash-over and breakout (Warren and Kendall 1985).

So, if we based our ideas of where ancient evaporites formed on a strictly uniformitarian approach using Quaternary analogs, then the study of where bedded salts have formed best in the world over the last two million years leads to a conclusion that they are not marine fed. Rather, thick bedded salts form best in tectonically active, subsiding hypersaline groundwater sumps located in cold arid deserts. These depressions are hydrographically closed, with the purer, most voluminous, examples of 100 m-thick evaporite successions located in tectonically active piggy-back depressions with lake floors and hydrologies that are more than 2,000 m above sea level. Their hydrologies are endorheic and strongly influenced by deeply circulating meteoric waters. In addition, the best examples of thick stacked bedded salts are supplied ions via the dissolution of older marine halokinetic salts in the surrounding drainage basin.

Yet, anyone working in ancient evaporites knows from simple arguments of salt volumetrics versus brine sources, and the nature of the enclosing sediments, that they are part of a dominantly marine basin fill. All the larger examples of ancient evaporites are interbedded with or immediately underlain or overlain by marine sediments, with chemistries and mineralogies that can be directly related to the concentration of seawater. They occur in ancient continent margin or intracratonic subsealevel tectonic depressions, which were supplied large volumes of saline waters via seepage of seawater into hydrographically isolated depressions. Such deposits are known as saline giants, megahalites and megasulphates, all with areas well in excess of 10,000 km^2 (Warren 2010). These marine-associated systems have no same-scale Quaternary analogs. We shall return to the tectonic and hydrologic significance of this schism between marine and nonmarine evaporites in Chap. 5.

Local Variations in Climate

At finer climatic scales within a groundwater sump in a desert depression, local variations in effective evaporation rates influence salinity of a brine body, or pore waters in nearby mudflats/sandflats. This in turn influences mineralogy and the preservation potential of precipitated salts. Water vapour pressure over a free-standing brine decreases with increasing salinity and increases with increasing temperature (Fig. 2.8a; Bonython 1966; Calder and Neal 1984). Saturated water vapour pressure over any salt solution is always lower than the vapour pressure of pure water at a given temperature. This is due to the binding of water molecules into hydration sheaths about the various charged ions dissolved in the brine. As the concentration of a surface brine increases, the water vapour pressure decreases in the overlying air mass, reaching its lowest value when the brine is saturated (Kinsman 1976). At very high salinities the pressure difference between the brine and the air immediately above the brine can become so small that evaporation effectively shuts down and the higher salinities necessary to precipitate the bittern salts may not be reached (Fig. 2.8b; Laborde 1983).

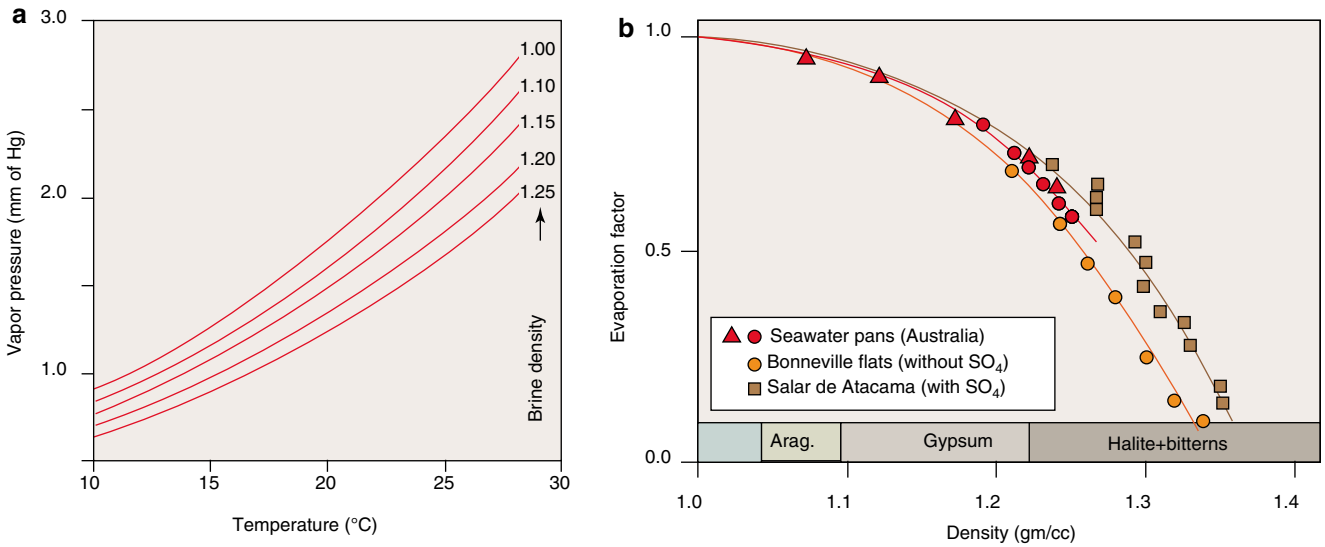

Fig. 2.8 Factors influencing evaporation rates from brine surfaces. (**a**) Salinity (brine density versus vapour pressure above a standing brine replotted from Bonython 1966). (**b**) Evaporation factor (freshwater is 1) decreases as salinity/density of the brine increases. Evaporation factor is applied to measured pan evaporation to attain a more realistic estimate. For example, a seawater brine with a salinity around 200 ‰ has an actual evaporation rate that is only 85 % (0.85) of the measured pan evaporation rate (After Myers and Bonython 1958; Laborde 1983)

Aerodynamically, the evaporation rate of a surface brine is the product of wind velocity and the difference in water vapour pressure between the main air mass and the air above the surface of the evaporating brine. Complete humidity-induced shutdowns of evaporite precipitation are rare as the air above an evaporating brine body is usually in continual motion, driven by adiabatic, catabaric and onshore breezes. Salinity of a freestanding brine is a function of wind speed, surface roughness and atmospheric stability in the air above the brine (Fig. 2.8a; Myers and Bonython 1958; Bonython 1966).

Elevated above-brine humidity and limited lateral extent (tens of kilometres) create a natural buffer to evaporation above modern coastal lakes or sabkhas. Lower salinity evaporite minerals, gypsum and halite, are the dominant precipitates in modern coastal lakes beneath humid marine air, such as the coastal pans of the Saudi Gulf coast and the coastal salinas of southern and western Australia. Gypsum with minor anhydrite is the dominant salt in both the capillary zone and the phreatic zone of most modern arid coastal hydrologies such as the sabkhas of Abu Dhabi (Kinsman 1976). Any efflorescences or crusts of bittern salts do not last long, and are recycled or washed away by occasional rainstorms and sheet floods.

The potential for humidity-induced evaporitic shutdown will have an interesting effect on the currently falling water level of the Dead Sea basin. Asmar and Ergenzinger (1999) conclude that the actual evaporation rate of the surface brines in the Dead Sea will become zero at a salinity of 483–486 g/l. As water loss can then no longer be driven by evaporation, the currently falling Dead Sea level should stabilise when currently increasing salinities reach this level (Fig. 2.9a). The evaporation rate data were calculated using a modified Penman method and were fitted as a function of salinity, where salinity (S) is in g/l and evaporation rate (E) is in mm/year. The relationship is $E = 1{,}826.1 - 1.6405S + 0.0116S^2 - 3 \times 10^{-5}S^3$ Asmar and Ergenzinger emphasize that this equation is an estimate and should be used with caution.

Intrabasin variations in temperature and effective evaporation influence the volume and mineralogy of precipitated sediments and there is often a feedback between these various factors. For example, there is a decrease in the efficiency of capillary evaporation wherever a white salt crust covers the surface of a saline mudflat. The decrease is not just related to a humidity increase in the air above the mudflat, but also to the increased albedo (reflectance) created by the white surface of the salt crust. The amount of short-wave radiation absorbed by any soil surface is largely a function of its albedo (a measure of the amount of light reflected). It varies from 0.2 (20 %) for a water saturated soil surface to 0.75 (75 %) for a salt-encrusted surface (Malek et al. 1990). A salt-encrusted mudflat on a clear calm sunny day makes use of only a quarter of the incoming energy (drives evaporation) compared to a damp crust-free seepage mudflat. For the same reason, sediment below a white salt crust will stay moister for longer in the absence of ongoing inflow/seepage.

To quantify the effects of salt crust formation on evaporation rate, Newson and Fahey (2003) conducted a series of laboratory evaporation experiments using artificial soils saturated by water with various NaCl contents ranging from freshwater to concentrations of 23 % (mass salt/mass solution).

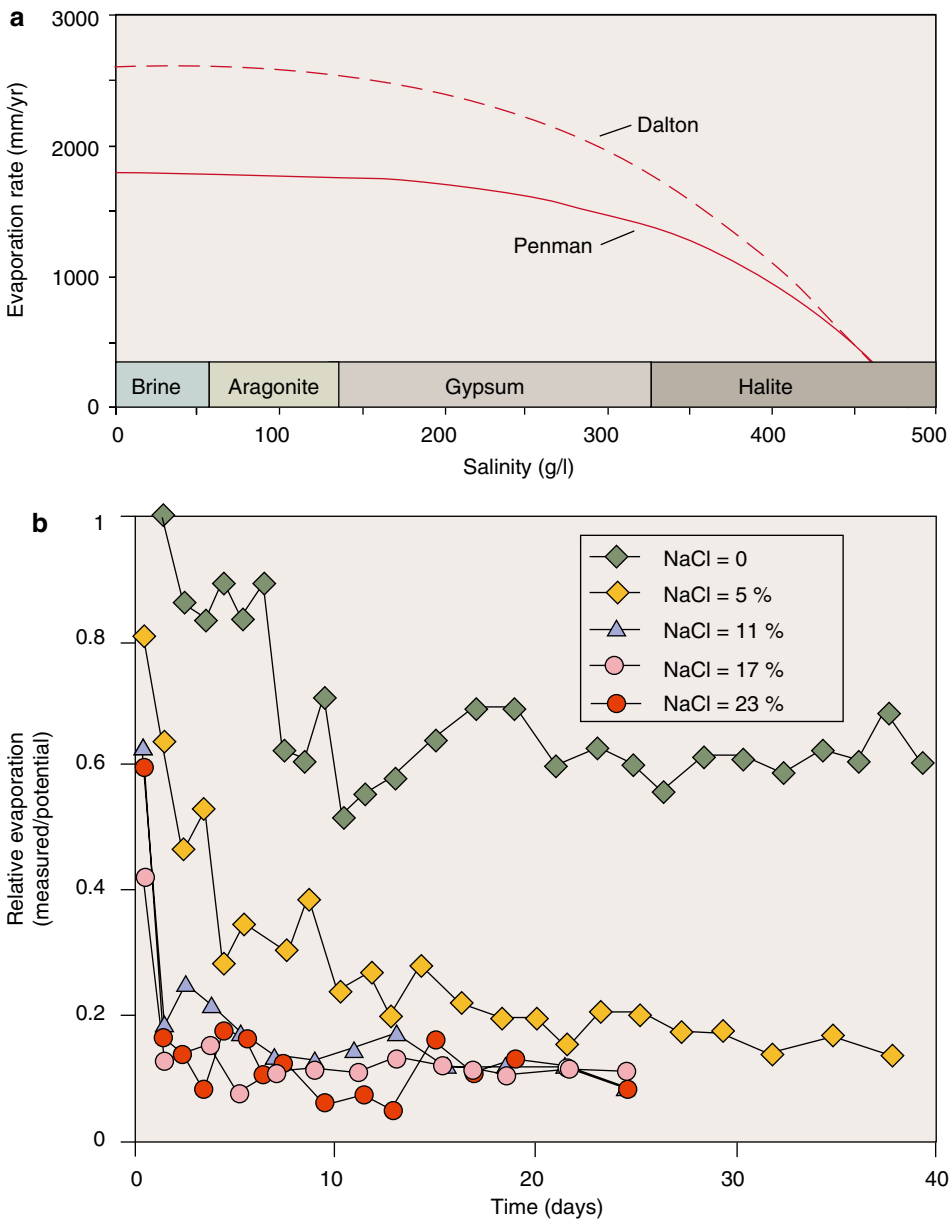

Fig. 2.9 Evaporation and salinity. (**a**) Effect of salinity on evaporation rates in the Dead Sea using the predictive formulae of Penman or Dalton (After Asmar and Ergenzinger 1999). (**b**) Effect of salt crust formation on the relative evaporation (measured evaporation rate/potential pan evaporation) with waters of variable concentration lying beneath the subaerial crust (After Newson and Fahey 2003)

Their aim was to develop an understanding of salt crust formation in order to increase the efficiency of desiccation in mine tailing dams and so improve remediation efficiency. But their results are pertinent to the hydrology of any salt-crusted mudflat. Relative evaporation (ratio of actual to pan evaporation) for the freshwater system fell to about 0.6 after about 10 days, and then remained near constant (this indicates capillary equilibrium with fresh water in pores = no salt crust). However, for all other experimental runs using saline water of varying initial concentrations, the relative evaporation ratio was much lower, and once the salt crusts had formed consistently reached values around 0.1–0.2 of potential freshwater evaporation rates (Fig. 2.9b). For the high concentration pore waters the reduction occurred almost immediately, and somewhat more slowly for the starting solution with the lowest NaCl concentration (C = 5 %). Their results indicate that even a moderate amount of salinity in any feed brine in a semi-arid to arid setting will quickly form a salt crust that severely reduces the relative evaporation rate above the crust.

Their experimental data compares well with observations made for salt-encrusted surfaces on playas and salt lakes around the world. Natural salt encrusted mudflats typically display relative evaporations of the order of 0.03–0.2, for potential evaporation rates of 1.5–3.5 m/year (Malek et al. 1990). For example, the measured effective evaporation rates above salt-free mudflats in Lake Frome, Australia range from 90 to 230 mm/year and average 170 mm/year (Allison and Barnes 1985). In areas in the same lake covered by white salt crusts the effective evaporation rate falls to 5–30 mm/year (equivalent to relative evaporation of 0.03–0.18; Ullman 1995).

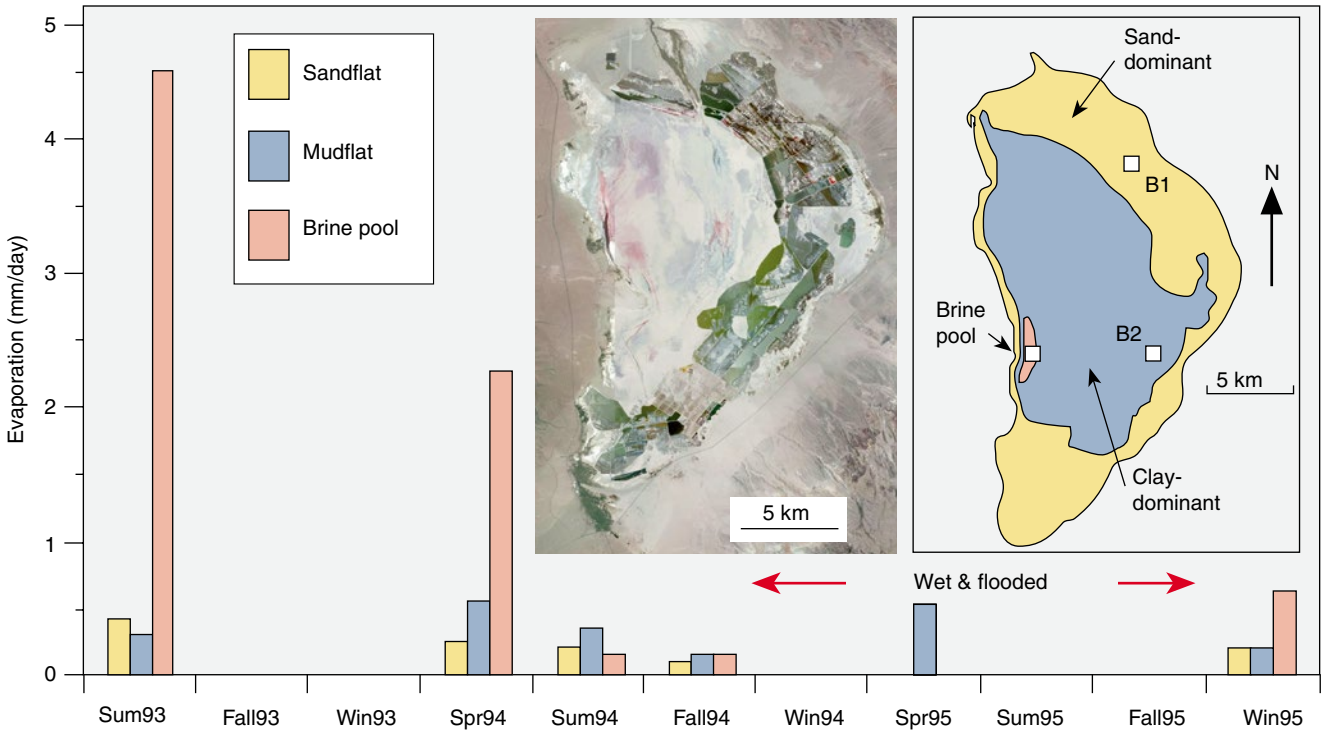

Fig. 2.10 Seasonally measured evaporation from the three dominant types of surface sediment in Owens Lake, California. Squares in the inset map show monitored sites (After Tyler et al. 1997)

Newly formed salt crusts are porous, variably buckled layers (pressure ridges and petees) that lack direct contact with the underlying sediment over at least 50 % of the crust base (Newson and Fahey 2003). Air-filled cavities reduce areas beneath the crust where capillary moisture can be transferred in a liquid phase through the salt crust to the air during evaporation. Coupled with this, the high porosity and broader pore throats in newly-formed salt crust, drastically reduces the rate of capillary rise of water compared to a clay or mud and so further reduces the liquid phase continuity to the crust/air interface. Once a crust forms, the only widespread effective mechanism for moisture transfer from the underlying mud to the overlying air mass is by diffusion in the vapour phase. This means mechanisms involved in reduction of the effective evaporation rate from any salt-encrusted mudflat are varying combinations of; (1) an increase in albedo, (2) resistance to moisture transfer and, (3) a decrease in the saturation vapour pressure of the pore fluid.

In a brine pool-entraining modern playa there is substantial cross-playa variation in effective evaporation rate depending on sediment type, proximity of the watertable to the landsurface, the presence or absence of salt crusts and the permanence of surface brine sheets. An excellent set of data illustrating this complexity was collected during 1993–1996 in Owens Lake, California using monitored lysimeters and evaporation pans (Fig. 2.10; Tyler et al. 1997). Measurements were not made during the period autumn (fall) 1994 to winter 1995 due to playa-wide flooding that marked the end of a long drought period. Rain preceded each summer and autumn measurement period in 1993 and 1994 by at least 15 days and was not significant (1 mm or less). Spring measurements may have been influenced by prior rainfall, with 3 mm falling 1 day before the 1994 measurements and 19 mm falling 21 days before the 1995 measurements.

Figure 2.10 plots the averaged daily evaporation rate as a function of season of measurement from the three study areas in Owens Lake (sandflat, mudflat and free surface brine; Tyler et al. 1997). Evaporation from the sandflat appears to steadily decline from initial measurements in summer 1993 to autumn (fall) 94 and may reflect the prolonged drought and subsequent decline of the watertable in this area. In contrast, evaporation from the salt-crusted mudflat shows similar summer rates in 1993 and 1994. The insensitivity to drought in these saline clayey soils may be related to the continued high water contents maintained by capillary rise to elevations well above the watertable. The mudflat site also shows highest evaporation rates during spring periods (0.5 mm day^{-1}), when near-surface soil moisture is at its highest level. During these periods, the overlying salt crust is less desiccated and so may also maintain better hydraulic contact with the underlying sediments.

Malek et al. (1990) postulated that loss of hydraulic contact between lake sediment and an overlying salt crust impedes capillary evaporation loss by effectively forming the equivalent to

a mulch layer over the clayey substrate. During both spring measurement periods in Owens Lake, no decline in evaporation rate was observed throughout the period of measurement, suggesting that rain before the measurement dates had little influence on the evaporation rates. Winter evaporation rates were slightly higher than those recorded during the autumn months, although they are similar. The winter measurement period was characterized by warmer than average daytime temperatures, which may have slightly increased the evaporation rates. However, wind conditions were uncharacteristically calm, with maximum daily wind speeds rarely exceeding 1 m s^{-1}, which may have reduced the evaporative flux.

Rates measured in the brine pool in spring 1994 were below those in the previous summer, owing to lower temperatures and decreased net radiation (Tyler et al. 1997). However, evaporation in the brine pool area in the following summer and autumn of 94 were much lower than expected for a free-standing saline water body. The dramatic reduction in evaporation in 1994 was due to a thin (less than 2 mm) floating crust of halite rafts that covered the entire extent of the brine pool. Both periods of measurements in the brine pool were characterized by calm conditions, which allowed the crust to remain intact and effectively cut off evaporation. Winter evaporation rates over the raft-covered brine pool averaged 0.6 mm day^{-1}, almost an order of magnitude below that measured during the raft-free summer of 1993. Rafted crusts are a part of the evaporation setting of most halite-saturated brine pools/sheets and are another reason why brine sheets remain for extended periods in some salt lakes. Surface water sheets in nearby less saline raft-free lakes tend to dry much more quickly. Rafts generally break up and sink or are washed to the lake shore during windy periods.

Yearly estimates of groundwater evaporation from the three dominant surface areas in Owens Lake (sandflat, mudflat, brine pool) were calculated by Tyler et al. (1997) using the data shown in Fig. 2.10. Yearly average evaporation was taken as the arithmetic average of the four seasonal rates for each area. For both the sandflat and mudflat areas, autumn rates were well below those measured in the spring, implying that evaporation is more strongly controlled by groundwater conditions rather than potential evaporation rates above the sedimentation surface. Groundwater levels tend to decline in late summer and autumn, owing to evaporative demand, and therefore it is conceivable that winter rates, when the water-table is nearer the lake floor, may actually exceed autumn rates. The coincidence of a prolonged drought (1993 to fall 1994) with the main measurement period appears to have affected evaporative flux in both the sandflat area and the brine pool. Consecutive summer measurement of evaporation at both these sites showed a considerable decrease owing to drought conditions. For this reason, summer evaporation rates from 1993 were considered more representative and used to estimate the yearly evaporation from the sandflat to produce a more representative average annual evaporation. At the brine pool site, autumn rates were assumed to be equal to those measured in spring 1994, when open raft-free water was extensive. Using this approach, the seasonally adjusted annual evaporation rate from the sand-dominated areas was $\approx 88 \pm 22$ mm $year^{-1}$. Clay–salt crust-dominated (sabkha) regions in Owens Lake have an evaporation rate $\approx 104 \pm 26$ mm $year^{-1}$. Yearly evaporation from the brine pool surface was $\approx 872 \pm 218$ mm $year^{-1}$ although this is substantially less whenever a cover of salt rafts floats at the air-brine interface. The crust lowers the actual evaporation rate so much that the halite-precipitating brine pool remains as a perennial feature in the lake's sump (Groeneveld et al. 2010).

In a similar study Kampf et al. (2005) estimated the level of evaporation in across the central halite nucleus of Salar de Atacama, Chile. They found measured values of net all-wave radiation were highest at vegetated and rough halite crust sites and lowest over smooth, highly reflective salt crusts (greater albedo). Over most of the Salar de Atacama, net radiation was dissipated by means of soil and sensible heat fluxes.[2] Dry salt crusts tended to heat and cool very quickly, whereas soil heating and cooling occurred more gradually at wetter vegetated sites. Sensible heating was strongly linked to wind patterns, with highest sensible heat fluxes occurring on summer days with strong afternoon winds. Very little energy available at the land surface was used to evaporate water. Eddy covariance measurements could only constrain evaporation rates to within 0.1 mm/day, and some measured evaporation rates in the halite nucleus were less than this margin of uncertainty (Fig. 2.11). Evaporation rates ranged from 0.1 to 1.1 mm/day in smooth salt crusts around the margin of the salar and from 0.4 to 2.8 mm/day in vegetated areas. No evaporation was detected from the rugged halite salt crust (halite nucleus) that covers the interior of the salar, even though the depth to groundwater across this zone is less than 1 m in this area. These crusts therefore represent a previously unrecorded end member condition in a hypersaline groundwater sump in which the salt crusts form a practically impermeable barrier to evaporation (Fig. 2.11). The significance of this hydrology to the various textures seen in the crusts is discussed further in Chap. 3.

The combination of all local climatic effects, as discussed in this section, helps explains why high salinities needed to precipitate primary bittern salts are unlikely in most modern marine-fed and continental interior hypersaline settings. To produce and accumulate primary bittern salts, like carnallite, sylvite and kieserite, to where they constitute a bed rather than an efflorescent crust, requires a degree of aridity so extreme that it is difficult to envision it forming in the relatively humid climatic coastal conditions in any modern

[2]Sensible heat flux is the heat energy is transferred from the Earth's surface to the atmosphere by conduction and convection.

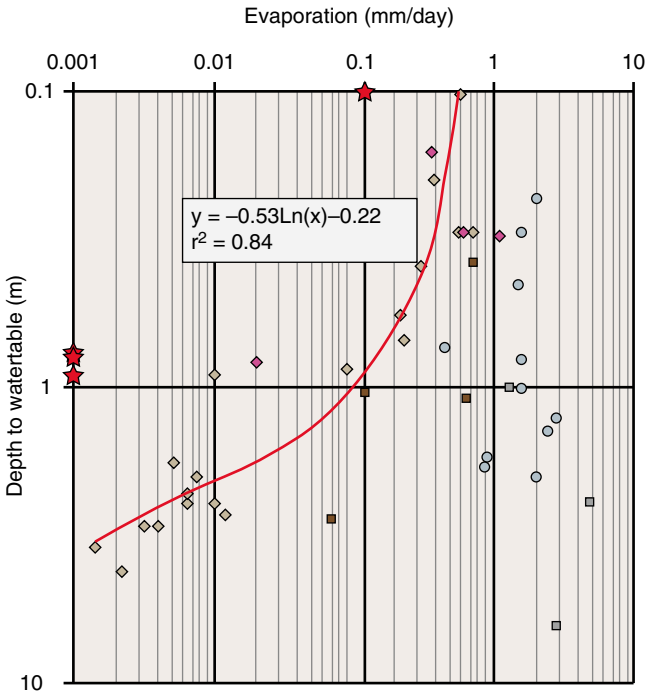

Fig. 2.11 Evaporation vs. depth to watertable for Salar de Atacama, Chile, compared with measurements at other salt flats and from bare soils (After Kampf et al. 2005). *Diamonds* and *red circles* represent playas or salt flats and saline lakes; *squares* represent vegetated areas, *grey circles* represent bare agricultural soils. *Red stars* represent data from Salar de Atacama, *stars* are plotted along 0.001 mm/day axis to conform to the logarithmic scale, but were actually were so low as to be not measurable. Likewise, the *star* plotted as point on 0.1 m depth axis (logarithmic scale) actually corresponds to 0 m depth (watertable at surface). The *red line* represents a logarithmic fit (with equation) for the playa data

marine-fed arid setting and even contemporary continental instances are rare. Carnallitite is a precipitate in saltwork pans of the Dead Sea where it is the end result of anthropogenic management of fractionated brines (Fig. 11.25). The only substantial natural Holocene potash accumulation in the world today is a syndepositional karst fill in bedded halites of the Qaidam Basin of western China, located some 1,500 km from the nearest ocean. Even there, the potash ultimately comes from reworked basinal brines that flush subcropping Plio-Miocene potash evaporites (Chap. 11). One must go to pre-Quaternary megahalite settings to understand how a widespread potash bed can accumulate with a lateral extent measured in tens to hundreds of kilometres and thicknesses measured in metres (Chaps. 5 and 11).

Chemical Evolution of Surface and Nearsurface Brines

Until recently, most geologists assumed ancient marine evaporites were precipitated from seawater brines with chemical make-ups very similar to that of today. Now, there is a growing body of evidence that the ionic make-up of Phanerozoic seawater has varied to where magnesium sulphate was not always a dominant bittern precipitate. In modern seawater bitterns, it is. As well, varying intensities of evaporite dissolution, dolomite precipitation and hydrothermal flushing contributed varying ionic proportions to the brine feed of ancient salt systems (Hardie 1984, 1991). This leads to a dilemma in deciding what is marine, what is nonmarine and what is a hybrid brine, based on mineralogical suites found in ancient bedded evaporites.

Marine Brines

Today the chemical make-up and the proportions of the major ions in seawater are near constant in all the world's oceans. Seawater is dominated by Na and Cl, with lesser amounts of SO_4, Mg, Ca, K, CO_3 and HCO_3. Using the brine classification of Eugster and Hardie (1978), modern seawater is a Na–(Mg)–Cl–(SO_4) water, with a density of 1.03 g/cc and a salinity of 35 ± 2‰. When seawater evaporates, a predictable suite of primary evaporite salts crystallise from increasingly concentrated hypersaline waters (Fig. 2.12; Table 2.4). The sequence of marine precipitates was first documented by Usiglio (1849), while later work by Carpenter (1978) and McCaffrey et al. (1987) focused on the details of the evolving chemistry of the residual bitterns as the various supersaline salts precipitate (Fig. 2.12a).

As seawater concentrates, the first mineral to precipitate is $CaCO_3$, usually as aragonite. This begins in mesohaline waters where the brine reaches twice the concentration of seawater (40–60‰) and achieves a density ≈1.10 g/cc. As the brine continues to concentrate and approaches four to five times the concentration of seawater, that is 130–160‰, gypsum precipitates from penesaline waters with densities around 1.13 g/cc (Figs. 2.12b and 2.13a, b). At 10–12 times the original seawater concentration (340–360‰) and densities around 1.22 g/cc, halite drops out of supersaline marine waters. After halite, the bittern salts (potassium or magnesium sulphates/chlorides) precipitate from supersaline waters at concentrations that are more than 70–90 times that of the original seawater. Carnallite and epsomite are the dominant bittern precipitates from modern marine brines (Fig. 2.12c). Brine density by this stage of concentration is in excess of 1.30 g/cc and brine viscosity and feel approach that of olive oil (Fig. 2.13b).

Modern coastal lagoonal systems do not naturally attain high salinities until the surface (hydrographic) connection to the ocean is lost and they evolve into marine-seepage groundwater sinks (Fig. 4.8). Brines then evolve into mesohaline to penesaline waters with seawater-like (thalassic) ionic proportions (Table 2.5).

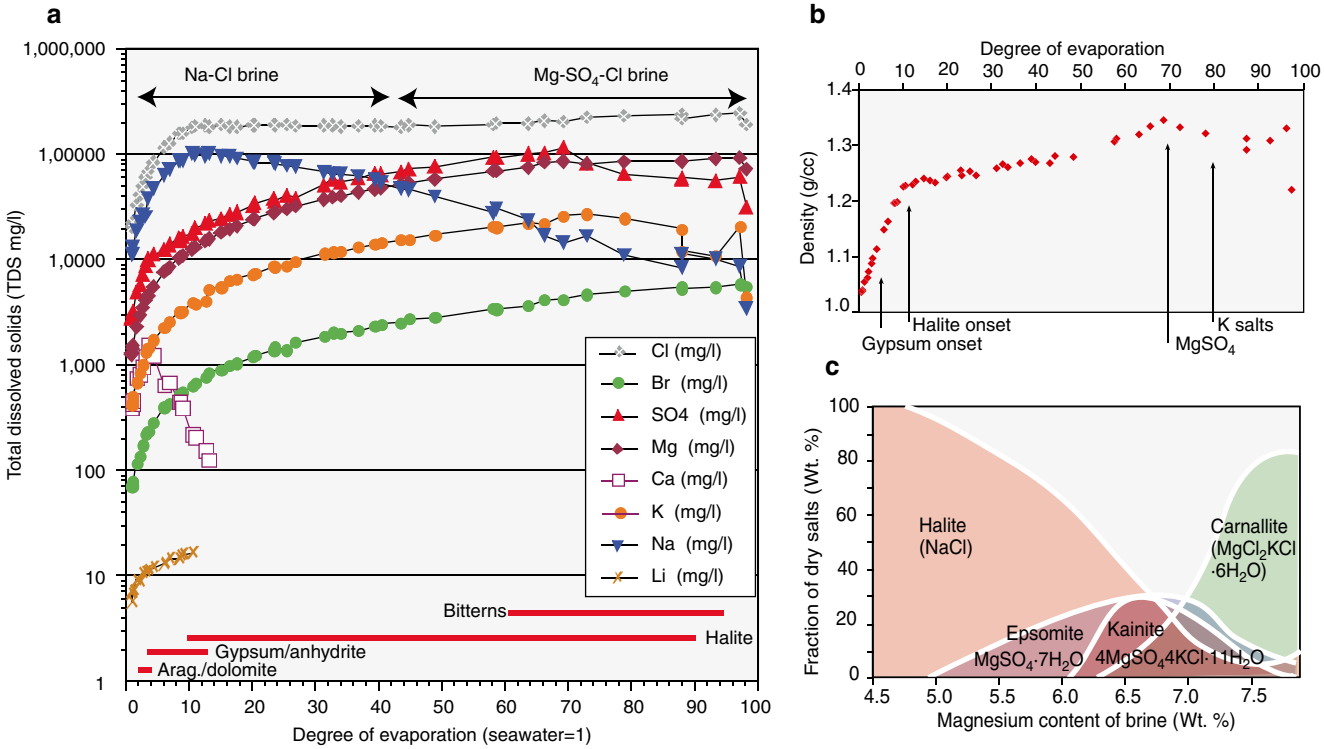

Fig. 2.12 Marine hydrogeochemistry. (**a**) Changes in ionic proportions due to sequential precipitation of aragonite, gypsum, halite and bittern salts as modern seawater is evaporated to 100 times its original concentration (in part After McCaffrey et al. 1987). (**b**) Evaporation pathway of modern seawater showing how density increases and the proportions of various ions in solution change as the brine concentration increases (Recompiled from data in appendices in McCaffrey et al. 1987). (**c**) Sequential precipitation of potash bitterns from modern seawater plotted against increasing Mg content in bittern (After Garrett 1970a)

Table 2.4 Salinity based classification of mineral paragenesis and brine properties based on concentrated seawater

	Brine stage	Mineral precipitate	Salinity (‰)	Degree evap.	Water loss (%)	Density (g/cc)
Sea	Normal marine or euhaline	Skeletal carbonate	35–37	1×	0	1.040
Hypersaline	Mesohaline or vitahaline	Alkaline earth carbonates	3–40	1–4×	0–75	1.040–1.100
	Penesaline	$CaSO_4$ (gypsum/anhydrite) $CaSO_4 \pm$ Halite	140–250 250–350	4–7 7–11×	75–85 85–90	1.10–1.214 1.214–1.126
	Supersaline	Halite (NaCl) Bittern salts (K-Mg salts)	>350 Extreme and variable	>11× >60×	>90 ≈99	>1.126 >1.290

Hypersaline is defined as >35‰. Biologists working in saline waters use a somewhat different classification of; fresh water (less than 1‰), subsaline (1–3‰), hyposaline (3–20‰), mesosaline (20–50‰), and hypersaline (greater than 50‰). Geohydrologists tend to refer to fresh water as less than 1‰, brackish water as 1–10‰, saline water as 10–100‰, and brine as greater than 100‰

Ongoing evaporation of seawater produces two types of high density, high viscosity brine: Na-Cl brines and Mg-Cl-SO_4 brines. Na-Cl brines dominate in the salinity range 35–330‰. Brines become progressively dominated by Mg-Cl-SO_4 at higher salinities, indicating preferential removal of Na by halite precipitation. At first, Mg is the dominant cation in the bittern brines, but as the various $MgSO_4$ bitterns crystallise its place is taken by K. Chlorine remains the dominant anion throughout the evaporation sequence (Fig. 2.12a).

Much of the field and laboratory work done on evaporating water has been done in closed conditions. Usiglio (1849) simply took a container of seawater and monitored its progress as he evaporated it to complete dryness. McCaffrey et al. (1987) studied the evolution of seawater in a series of man-made salt ponds in the Bahamas and supplemented this with laboratory work at higher salinities and densities not found in the ponds, as did Laborde (1983). Ideally, after depositing gypsum and halite, supersaline seawater evaporated to complete dryness

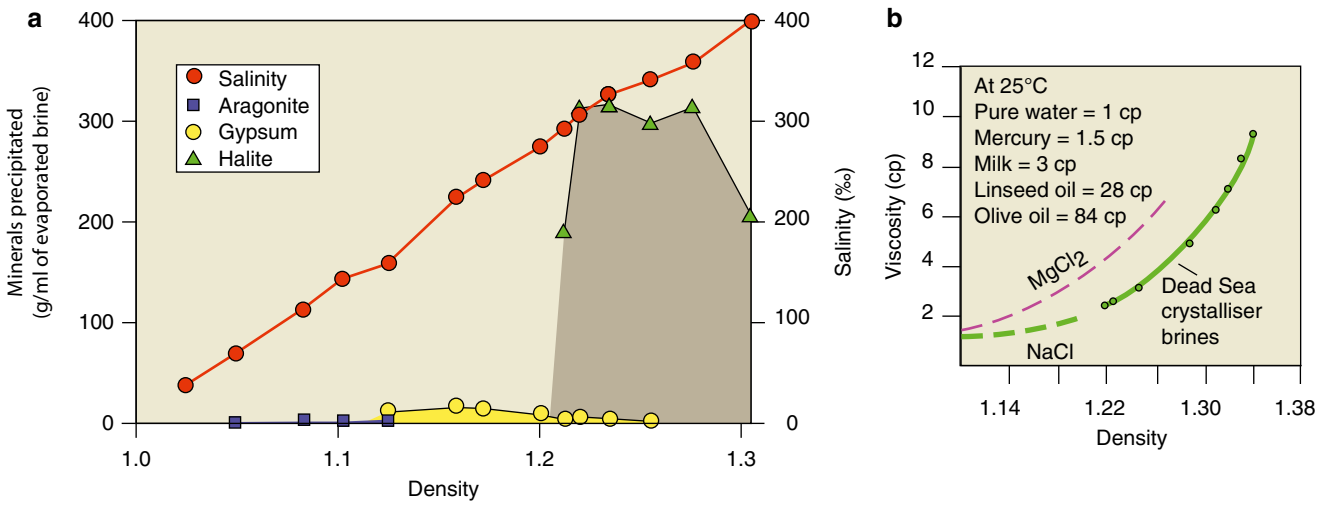

Fig. 2.13 Brine evolution. (**a**) Pre-bittern mineral precipitation sequence in a concentrating marine brine (Replotted from Table 1 in Briggs 1958). (**b**) Viscosity increases with brine concentration (Replotted from Karcz and Zak 1987)

Table 2.5 Examples of the hydrogeochemical make-up of some marine-fed brine systems, salinity is expressed in‰ and ions in mmol/kg (see Chaps. 3 and 4 for discussion of the geology of marine-fed systems)

Locality	Salinity (%)	Na	Mg	Ca	K	Cl	SO_4	HCO_3	Br
Solar Lake, Sinai	70	890	99	21	19	1,040	53	3	2
	146	1,815	205	47	30	2,189	37	4	–
Ras Mohammad, Sinai	244	3,394	391	12	72	3,903	147	3	5
Bardawil Coastal, Sinai	140	1,857	197	8	43	2,146	31	0.8	4
		4,219	712	28	143	4,625	232	5.8	11
Bardawil Inland, Sinai	140	1,666	193	31	3	1,775	3	0.3	2
		4,035	1,088	693	92	5,124	129	3.5	11
Christmas Island ponds	21	279	27	7	5	331	19	–	–
	247	1,893	213	17	34	3,490	48		–
Lake Hayward, Australia	214	3,053	90	23	52	3,569	106	–	–
Mangrove Lake, Caribbean	32	–	–	9	–	480	24	3	–
Seawater (average)	35	468	53	10	10	546	28	2	1
River water (average)	0.11	0.31	0.15	0.37	0.04	0.23	0.12	0.89	–

deposits a predictable suite of Mg and K sulphate minerals, with the majority of the salt volume dominated by halite (Fig. 2.13a; Usiglio 1849). The most problematic endgame in this evolving marine brine system is predicting what will be the bittern salt sequence (Fig. 2.12c). This is especially obvious when one tries to compare the suite of bittern salts seen in ancient marine evaporites to modern bittern; there are obvious discrepancies related to brine leakage, backreaction and evolving Phanerozoic seawater chemistries. As we shall see in the following discussion, these problems can be addressed at varying levels of chemical, hydrological and chronological complexity. In the end, many of the discrepancies can be related to the simple statement, "In nature, there is no such thing as a totally closed, static system."

Chemical Composition and Phase Chemistry

One of the first to attempt to deal with the chemical discrepancies between a modern seawater precipitation suite and the

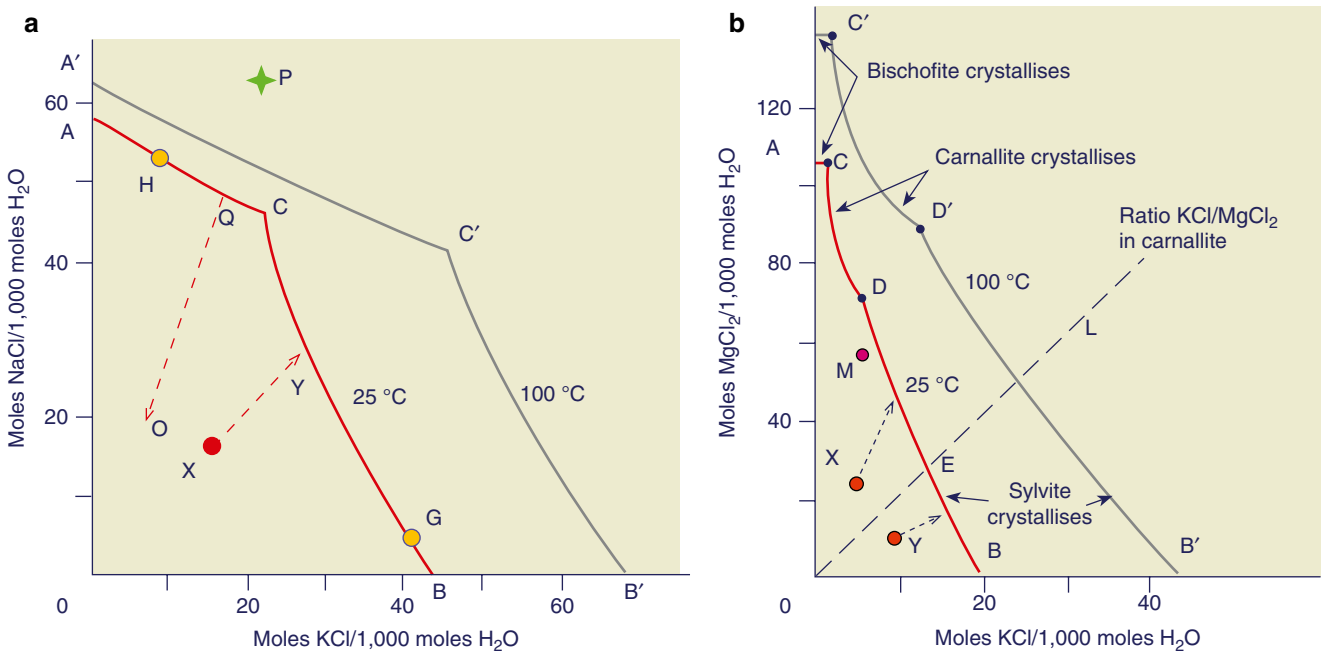

Fig. 2.14 Van't Hoff plots. (**a**) Crystallisation of solutions containing NaCl and KCl at 25° and 100 °C. (**b**) Crystallisation of solutions containing $MgCl_2$ and KCl at 25° and 100 °C

bittern suite, as seen in the Permian Zechstein salts of the Stassfurt β, was Van't Hoff, a nineteenth century German chemist. He reasoned that the best way to study evaporites was to start with a simple solution of two salts and add components one by one, studying the behaviour of the various mixtures at each stage of the experiment. From this work he formulated a series of rules of behaviour for salts in concentrated brines.

- If two salts are in solution, precipitation depends on the relative solubilities of the salts and their concentrations.
- If two salts have a common ion, the solubility of each in a solution of the other is less than in pure water.
- If two salts do not have a common ion, the solubility of each in the other is greater than in pure water.
- Solubility is markedly influenced by increases in temperature, much less so by pressure.

When studying bittern evolution the phase diagrams Van't Hoff developed experimentally are still useful today. Consider a KCl-NaCl system at 25 °C and 100 °C, this is an example of a salt pairs with a common ion (Fig. 2.14a; Borchert and Muir 1964). Points A and B represent solubilities in pure water at 25 °C. Points G and H represent the solubilities in 1:10 NaCl-KCl solution and 10:1 NaCl-KCl solutions, respectively. Point C represents the point at which the mixture is saturated with respect to both NaCl and KCl salts. Any point below line ACB is undersaturated at 25 °C, above it is saturated with the solid salt. Let's now consider the effects of crystallisation and dissolution in this simple system. With concentration, a solution of composition X moves away from the origin until reaching the line ACB at Y, where KCl precipitates (Fig. 2.14a). The ratio of NaCl/KCl increases as the solution composition moves along line Y-C (less water, less KCl in brine as NaCl increases). At C, both salts precipitate until dryness. With dissolution, a mixed salt of composition F remains solid until sufficient water has been added to begin its dissolution. At that point both KCl and NaCl begin to dissolve (point C). When all KCl has dissolved some NaCl remains and the composition shifts along C-Q as NaCl continues to dissolve. At Q the final NaCl dissolves and continued dilution moves the composition of the solution toward the origin along line Q-O.

Figure 2.14b is the Van't Hoff plot of the KCl-$MgCl_2$ system, an example of a salt pair with a common ion forming a double salt. In addition to the two end members (bischofite and sylvite) it has an intermediate double salt $KCl{\cdot}MgCl_2{\cdot}6H_2O$ (carnallite). Points A and B represent saturation with $MgCl_2{\cdot}6H_2O$ (bischofite) and KCl (sylvite) respectively. The dashed line 0-L shows the ratio of KCl to MgCl in carnallite. When a dilute solution of composition X is evaporated its composition shifts directly away from the origin until encountering line ACB. At the intersection point sylvite begins to crystallize and continues to crystallize as the composition of the solution shifts along line B-D, well below the composition of the double salt. Only when the solution has reached composition D does carnallite appear. At this point the composition of the solution remains fixed as carnallite

crystallizes, both directly out of solution and by partial reaction of dissolved ions with some of the previously precipitated KCl. The resulting solid is a mixture of carnallite and sylvite.

Or with a more KCl-rich initial solution of composition Y, as it concentrates it moves away from the origin until it intersects line ACB where sylvite once again begins to crystallize. It continues to crystallize as the composition of the solution moves up along B-D. At D, carnallite begins to crystallize as the sylvite is used up. If evaporation continues, the composition of the solution now moves along line D-C until it reaches point C, where bischofite crystallizes, along with carnallite. The composition of the solution now remains constant until evaporation is complete.

We can also use this Van' Hoff plot to visualise how carnallite dissolves in this simple system. We begin with carnallite, which has an initial composition D. Since this solution is much richer in $MgCl_2$ it is preferentially dissolved (it lies to the left of the dashed line EL) Once all the carnallite has dissolved, the net result is a solid residue of KCl (sylvite) (incongruent dissolution). Further solution of the residual will move composition of the solution down along line D-B. When it reaches E, the last of the sylvite is dissolved, and further dilution shifts the composition along line E-0 (origin).

So, we can describe the section of the saturation line B-D as the 'sylvite region', since here KCl alone is in equilibrium with saturated solutions; CD is the 'carnallite region', and CA the 'bischofite region'. Point C represents the composition of a saturated solution in equilibrium with both bischofite and carnallite, point D the composition in equilibrium with both carnallite and sylvite. Note that point D differs from point C in that during evaporation it can be approached from only one side, the KCl side, whereas C can be approached from either the carnallite or bischofite side. In other words the bittern precipitation sequence sylvite followed by carnallite, carnallite followed by a bischofite-carnallite mixture, or bischofite followed by a bischofite-carnallite mixture are possible, but never carnallite followed by sylvite.

If two salt pairs do not have a common ion they form a reciprocal salt pair such as a KCl-$MgSO_4$ system. In an evolved seawater brine it is possible to have four end members plus any number of intermediate double salts. Rather than depicting such a system as this on a simple Van't Hoff binary plot, it becomes necessary to use a ternary diagram. A ternary plot of reciprocal salts is handy, as fixing the relative concentration of three of the four ions also fixes the fourth, providing the system is at equilibrium. This is the basis for seawater ionic reconstructions in many micro-inclusion studies in halite. The most commonly used type of ternary plot in evaporite bittern studies is a Jänecke Diagram (Fig. 2.15). In many respects it is analogous to the ternary diagrams used in igneous and metamorphic petrology where plotting of two components fixes the relative proportion of the third component and it is very useful in the interpretation of brine inclusion chemistry (Zimmermann 2001).

Evaporation on a Jänecke plot is represented by the reciprocal salt pair $MgCl_2$-K_2SO_4. The solution remains saturated with NaCl at all times and thus this ubiquitous component can be ignored.

The corners of the diagram are represented by:

- Mg^{2+} = 100 % bischofite ($MgCl_2 \cdot 6H_2O$)
- K_2^{2+} = 100 % sylvite (KCl)
- SO_4^{2-} = 100 % thenardite (Na_2SO_4)

Points along the triangle edges are pure salts with only two end members:

- c = carnallite $KCl.MgCl_2 \cdot 6H_2O$
- ks = kieserite $MgSO_4 \cdot H_2O$
- hx = hexahydrite $MgSO_4 \cdot 6H_2O$
- bl = bloedite $Na_2Mg(SO_4)_2 \cdot 4H_2O$
- gl = glaserite $K_3\ Na(SO_4)_2$
- e = epsomite $MgSO_4 \cdot 7H_2O$

Points within the triangle contain end members such as:

- k = kainite $KMgClSO_4 \cdot 11/4H_2O$
- p c = picromerite $K_2Mg(SO_4)_2 \cdot 6H_2O$

If the bulk composition lies within the field, the fields represent the composition of the first salt to precipitate. However, the point representing the actual salt composition often lies outside the field where the ideal salt would precipitate. This is analogous to the previous binary Van't Hoff plots in which point F (carnallite composition) lay far outside the "carnallite region."

In the evaporation of seawater, the average seawater composition is represented by point A on Fig. 2.15. This point lies in the bloedite field. Thus, bloedite is the first bittern mineral to crystallize. As bloedite crystallizes the composition moves away from point A along a line, which is a projection of the bloedite compositional point projected through point A. At B (seen in the expanded part of the plot) there are two possible pathways:

(i) If bloedite has settled out and does not react further, epsomite begins to crystallize and the composition of the salt solution migrates across the epsomite field to point C, the path of migration from point B to C is a projection through B to the epsomite point on the triangle edge. Or (ii) if bloedite is free to backreact with the solution, then crystallisation takes a different path. The composition of the solution shifts along line B-D with bloedite being consumed as epsomite forms. At D, the last of the bloedite

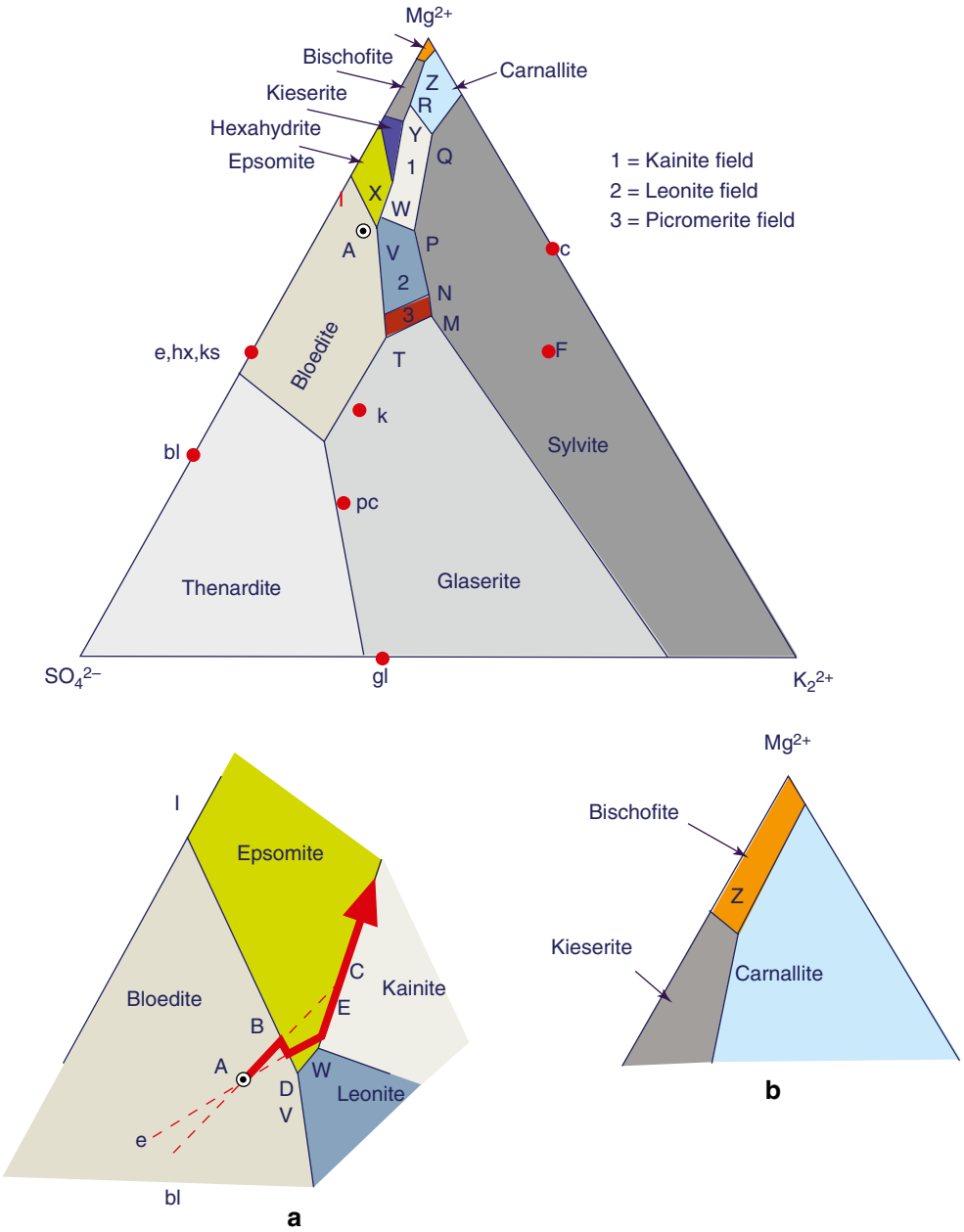

Fig. 2.15 Jänecke diagram for system $NaCl{\cdot}MgCl_2{\cdot}Na_2SO_4{\cdot}H_2O$ at 25 °C. Salt points: *c* carnallite, *bl* bloedite, *gl* glaserite, *e* epsomite, *hx* hexahydrite, *ks* kieserite, *k* kainite, *pc* picromerite. Point A defines the composition of seawater. (**a**) enlargement near I to show part of the crystallisation path of seawater; (**b**) shows detail of the Mg corner

disappears. At this point the composition of the solution is free to migrate through the epsomite field to point E, which is a projection from the epsomite compositional point at the edge of the triangle through D.

At either point C or E kainite begins to crystallize with epsomite (two-phase boundary) and the composition of the solution moves along the kainite – epsomite boundary. At X, epsomite becomes unstable with respect to hexahydrite. It reacts in the same way, consuming earlier precipitates or not, depending on how isolated precipitates are from the evolving brine. With further evaporation the composition of the solution moves along the kainite-hexahydrite boundary and both crystallize simultaneously. At Y, hexahydrite becomes unstable with respect to kieserite. At R, kainite becomes unstable with respect to carnallite. Thus, we have kainite and kieserite remaining when we leave point R. If concentration continues (we are now well into the bittern field) we move to Z, where we reach a three-phase boundary. Bischofite begins to crystallize with carnallite and kieserite. The solution remains at this point until dryness.

If equilibrium is maintained so that earlier salts are reabsorbed (backreacted) during ongoing crystallisation, the final product should be only three salts (bischofite, carnallite and kieserite), plus halite, plus small amounts of some calcium salts. If equilibrium had not been maintained other salts

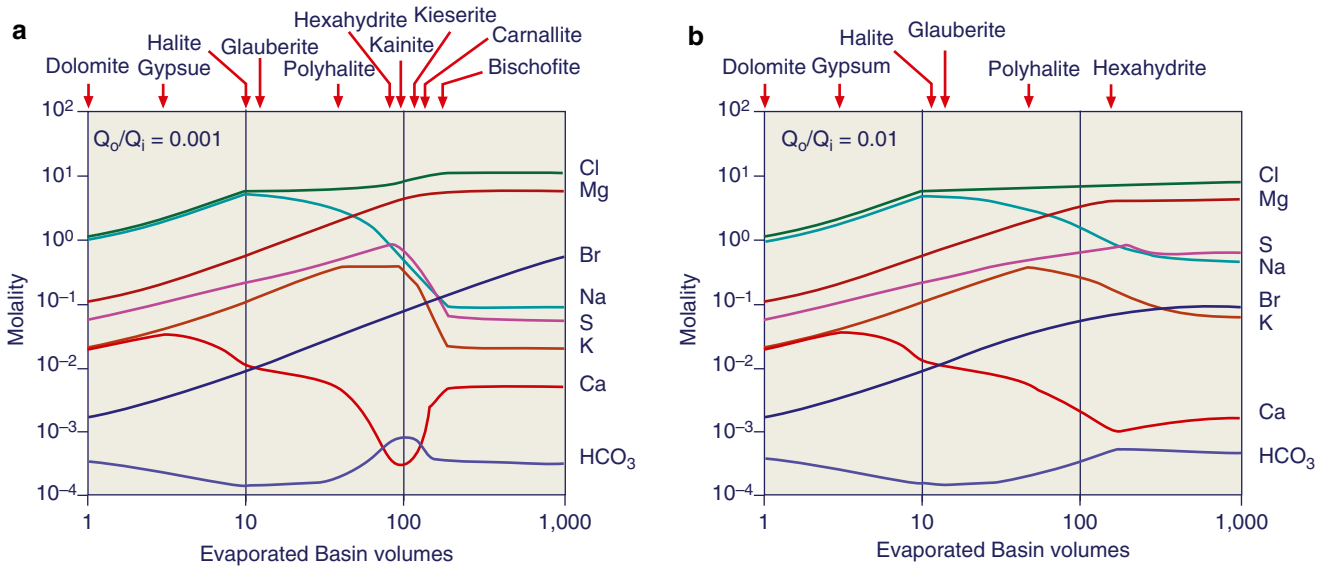

Fig. 2.16 Effects of varying levels of basin leakage on ionic proportions and the precipitated mineral suite with a seawater parent brine and measured as a function of the number of evaporated basin volumes (After Sanford and Wood 1991). (**a**) Leakage ratio of 0.001 (≈ closed basin) shows bittern precipitation. (**b**) Leakage ratio of 0.01, the system never reaches the upper end of the bittern field

could be present, but they should be layered in a vertical sequence predicted by the crystallisation path.

The problem with all this nineteenth-century laboratory-based bittern phase chemistry is that the prediction rarely matched the reality. For example, polyhalite is an abundant component in the Stassfurt Salt of the Permian Zechstein. This was the salt bed that formed the test case for much of Van Hoff's and Jänecke's work, yet polyhalite did not appear in Jänecke's plot. One reason for its absence is our inability to precipitate polyhalite from seawater in the laboratory at earth surface temperatures. Little was known about the stability of polyhalite. Where we do find it in the Holocene is as a replacement of gypsum in zones of mixing between marine brines and continental groundwaters (as in the shallow subsurface of the Ojo de Liebre saltflats, Baja California, Mexico, Pierre 1985). According to the marine brine evolution predicted by the Jänecke plot of seawater, kainite should be absent, or present only in the lower portion of the Stassfurt Salt. Yet, in reality it occurs near the top of the Stassfurt bed and is the dominant primary marine bittern in the Danakil, Ethiopia. Unusual salts, such as loeweite, picromerite, vanthoffite and langbeinite, should not be present at all, yet they are not uncommon in the Stassfurt. A sylvite-kieserite assemblage is forbidden by the phase diagram, but is present in the Stassfurt.

In order to explain some of these problems Van't Hoff suggested that the temperature at the time of salt formation in the Zechstein Basin was as high as 83 °C. This explained some of the unusual mineralogies and the sylvite-kieserite association. If the temperature drops to 55 °C near the end of the deposition, it allows kainite to be present near the top of the Stassfurt. Geologists found his suggestion of temperatures close to boiling in surface evaporite environments, cooling to 55 °C at the end of a cycle, a little unlikely. Jänecke proposed that the high temperatures suggested by Van't Hoff were diagenetic and had developed during burial (Borchert and Muir 1964). He proposed that the problematic polyhalite had formed by secondary alteration as calcium-bearing brines reacted with kainite (addition of calcium, subtraction of chlorine) and that most sylvite formed by incongruent solution of carnallite (loss of magnesium). The more unusual salts, he argued, represented high temperature burial metamorphism. Harvie et al. (1980) recalculated the order of onset for the marine bittern salts in the Zechstein as: glauberite, polyhalite, epsomite, hexahydrite, kieserite, carnallite, bischofite (Fig. 2.16a). They concluded that the type of bittern salt and the salinity at which it precipitates varied according to temperature and levels of impurities in the residual brines.

In reality, hydrology of the system is more significant than idealised chemistry in controlling bittern evolution. Brine leakage, mixing with freshened recharge about the basin's margin and the influence of humid air layers lingering above the brine body mean a standing body of modern seawater-derived brine liquor rarely moves to the bittern stage in a single primary desiccation cycle. Sanford and Wood (1991) modelled the changes in fluid composition and the sequence of primary salts that would precipitate under a leaky brine hydrology where bottom brine slowly discharges through underlying sediments (leakage via brine reflux). They found that the leakage ratio (ratio of water outflow to inflow) has a profound effect on both the evaporite mineral

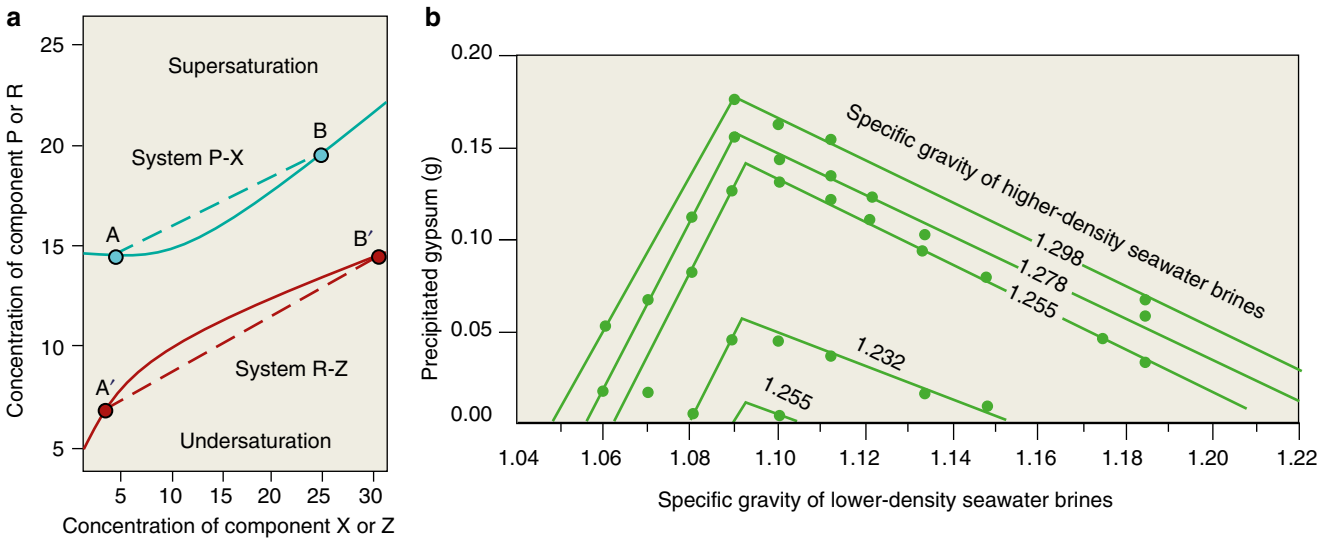

Fig. 2.17 Brine mixing. (**a**) Schematic showing effects of brine mixing on supersaturation in two styles of saturation curves – component system P-X and component system R-Z. Solid lines shows equilibrium saturation curve for their respective systems, while the dashed lines are the mixing lines. When solutions A and B mix in system P-X, the resulting solution is supersaturated and liable to precipitate. When solutions A′ and B′ mix, the resulting solution is undersaturated and liable to drive dissolution of the component of interest. (**b**) Amount of gypsum (in grams) precipitated by mixing of 50 ml each of two seawater brines in various concentrations at 25 °C (After Raup 1982)

suites precipitated and the thickness (or volume) of a deposit (Fig. 2.16). A system with a leakage ratio of 0.001 (that is, a 1× volume of water escapes from the basin for every 1,000× volumes of inflow), the resulting salt evolution sequence is near identical to that of a completely closed system, as first documented by Usiglio (1849). However, with leakier systems there are significant reductions in the maximum salinities that the surface brines can attain and it is increasingly difficult to reach salinities sufficient to precipitate upper-end bittern salts. With a leakage ratio of 0.01 the final brine composition, reached after about 600 basin volumes have evaporated, has higher Na, K and SO_4 compositions and the four most soluble salts, kainite, kieserite, carnallite and bischofite, are not present (Fig. 2.16b). This is reflected in the geological reality that textures in most natural bittern salts, such as carnallite and sylvite, indicate near surface brine cooling or back reactions drive their crystallisation.

There is another problem with much chemical/mineralogic modelling of ancient salts. It is predicated on an assumption that the major ion proportions of seawater do not change with time. But were the ionic proportions of Phanerozoic seawater constant? Ionic proportions and the precipitation order of ancient seawater bitterns may have changed according to variations in the flux rates of river inflow relative to flux rates through mid-ocean ridges or the volumes of magnesium carbonate accumulating in the world's oceans (i.e., the "zip and split" of supercontinents) may have changed through time. Variations in either mechanism would have changed the proportions of major ions in seawater (Fig. 2.45).

Brine Mixing Drives Precipitation or Dissolution

Van't Hoff's work also showed that salts can precipitate at a brine interface. All that is needed is mixing of waters of two saturation states with respect to the mineral of interest (Fig. 2.17a). When two waters that are saturated with a particular phase are mixed, the resulting solution may be undersaturated or supersaturated with respect to that particular phase (two salt problem discussed earlier). The saturation state during mixing depends on the solubility curve of the mineral phase of interest and the parameter of interest (ion concentration, temperature, salinity, etc.). The only requirement is that the solubility curve for that particular component is nonlinear. Raup (1970, 1982) in a number of experiments showed how halite and gypsum can be precipitated by the mixing of two seawater brines of differing salinity and densities. Figure 2.17b plots experimental results for the mixing of various low and high-density seawater brines and the resulting amount of gypsum precipitated (Raup 1982). A similar plot can be drawn for the mixing of more saline seawater brines, where halite is the precipitate (Raup 1970). For similar reasons, gypsum can precipitate in mixing zones in coastal aquifers when seawater first intrudes and displaces freshwater (Gomis-Yagues et al. 2000).

Mixing brines with different temperatures or salinities can be an important salting mechanism in the calcium sulphate (gypsum/anhydrite) salt system as it follows a nonlinear solubility trend, as does the halite-$MgCl_2$ bittern system (Raup 1970, 1982). Figure 2.18a shows the solubility curves

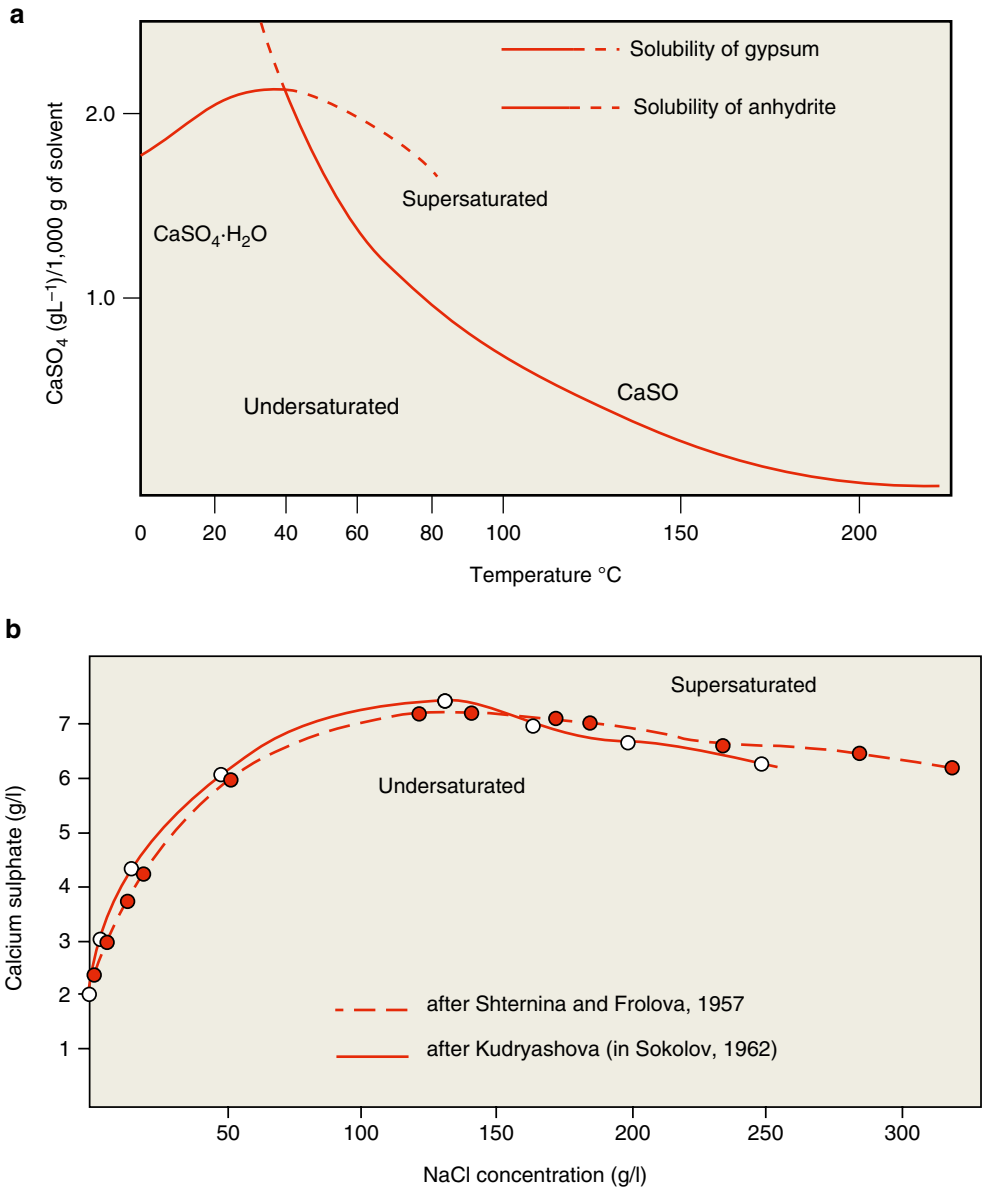

Fig. 2.18 Calcium sulphate solubility. (**a**) Idealised gypsum and anhydrite solubility with respect to temperature (After Zverev 1967). (**b**) Anhydrite solubility first increases then decreases slightly with respect to increasing NaCl content at temperatures of >100 °C (After Hryniv and Peryt 2003)

of gypsum and anhydrite with respect to increasing temperature in pure water. For gypsum, it clearly shows that when two gypsum-saturated waters of different temperature mix then the resulting solution is undersaturated and gypsum tends to dissolve. It also shows that gypsum follows a prograde solubility curve, whereby in the temperature range where gypsum is the stable $CaSO_4$ phase (<40 °C) it is increasingly soluble with increasing temperature. In contrast, at higher temperatures (>40–50 °C) anhydrite and gypsum follow a retrograde solubility curve whereby they are less soluble with increasing temperature. Thus, when two anhydrite-saturated waters of different temperatures mix the result is supersaturated brine with a propensity to precipitate anhydrite. This helps to explain why anhydrite is a commonplace hydrothermal precipitate in many mid-oceanic ridges and smoker chimneys (see Chap. 16). On land, beneath the surface of the Abu Dhabi sabkha, the heating of desert waters rising through the capillary zone to temperatures above 30 °C drives the precipitation of $CaSO_4$ (Fig. 3.15; "thermalites").

Anhydritic systems drive complex diagenetic effects when $CaSO_4$-saturated brines are diluted via dispersion into adjacent less saline waters (Fig. 2.18b). This happens in brine reflux systems where dense $CaSO_4$-saturated brine plumes, derived at the surface at halite saturation, sink into, and interact with less saline brines held in underlying or adjacent anhydritic carbonates. If temperature remains near constant the tendency in this zone of dispersion or mixing is to dissolve anhydrite cements, creating vugular porosity in the interval below or adjacent to a thick salt sequence. If temperature decreases and the brine plume cools, with little change in ionic proportions due to mixing, then the tendency is to precipitate anhydrite. It is not a simple system, with temperature

and mixing processes pulling the brine chemistry in opposite directions. It is of economic interest as brine reflux in ancient evaporitic carbonate platforms created diagenetic conditions suitable for the formation of potential hydrocarbon reservoirs via extensive dolomitisation (Fig. 10.29).

Later in the history of a calcium sulphate bed, during its uplift and dissolution (telogenesis), the mixing of sulphate-enriched waters with waters in adjacent aquifers drives dedolomitisation. This is a process that can also create extensive karst in the absence of soil-derived carbonic acid and is doing so today in the Lake Banyoles region of northeast Spain (Bischoff et al. 1994). Lake Banyoles is a karst lake fed by sublacustrine springs, where dedolomitisation-driven karstic collapse drives ongoing subsidence in the immediate vicinity of the lake. The lake lies within the outcrop area of the middle Eocene Banyoles Fm.; a marine marl and mudstone that is organic-rich and pyritiferous. The marls are underlain by the 200–300 m thick massive gypsum of the Eocene Beuda Formation, which is in turn underlain by the 100–200 m thick dolostones of the Perafita Fm.

Gypsum dissolution drives the local precipitation of calcite, both in the lake and in the aquifer (dedolomitisation), thus consuming ions released by dissolving dolomite and facilitating further dissolution in the aquifer (see Chap. 7 for details).

$$\mathrm{MgCa(CO_3)_2 + CaSO_4 \cdot 2H_2O \rightarrow 2CaCO_3 + Mg^{2+} + SO4^{2-} + 2H_2O}$$

Lake waters reflect this process; they are dominated by Mg-Ca and SO_4-HCO_3 and are supersaturated with calcite, which is actively accumulating in lake sediments at a rate of 38 $mg \cdot cm^{-2} \cdot year^{-1}$. Modelling of the regional hydrology based on the chemistry of lake and aquifer waters, along with measures of the annual water flow through the lake, shows that artesian waters create $\approx$9,500 m^3 of subsurface void space per year, enough to create the present karst depression of Lake Banyoles in 1,800 years (Bischoff et al. 1994). One could argue that gypsum dissolution alone can account for 55 % of the lake volume. However, when coupled with the ionic removal from the dedolomitisation process, gypsum solubility is enhanced by a factor of 1.56, as presumably is the rate of dissolution. Bischoff et al. (1994) go on to argue that gypsum-driven dedolomitisation may be responsible for extensive limestone karst in other exhumed $CaSO_4$ terrains in semiarid to arid settings, heretofore attributed solely to soil-generated carbonic acid.

Nonmarine Brines

Unlike marine-derived brines, evaporating continental waters do not draw on the near isochemical reservoir of an ocean. A more diverse, less predictable, suite of evaporite minerals precipitates during evaporation of continental waters. In nonmarine settings, rivers and groundwaters are the source of most of the ions that are ultimately deposited as evaporite salts. In a closed hydrological system the composition of nonmarine brines depends on the lithologies that are leached in the drainage basin surrounding a salt lake (Eugster and Hardie 1978; Eugster 1980a). Flow through limestone aquifers in hydrologically-closed basins produces inflow waters rich in Ca and HCO_3, dolomite dissolution generates Mg, igneous and metamorphic matrices yield silica-rich Ca–Na–HCO_3 waters. Pyritic shales and other sulphide-rich sediments will contribute sulphate ions, whereas basic and ultrabasic rocks tend to produce alkaline Mg–HCO_3 waters.

In all, Eugster and Hardie (1978) distinguished five major water types in what they termed "hydrologically closed" continental evaporite basins (Fig. 2.19; Table 2.6):

1. Ca–Mg–Na–(K)–Cl
2. Na–(Ca)–SO_4–Cl
3. Mg–Na–(Ca)–SO_4–Cl
4. Na–CO_3–Cl
5. Na–CO_3–SO_4–Cl waters

As any one of these waters concentrates within a particular evaporite basin, it deposits a characteristic suite of evaporite minerals. First precipitates are the alkaline earth carbonates: low-magnesian calcite, high-magnesian calcite, aragonite, and dolomite. The mineralogy of this initial precipitate depends on the Mg/Ca ratio of the parent brine. The subsequent evaporation pathway of a basin brine is determined by the proportions of calcium, magnesium, and bicarbonate ions in the brackish inflow waters. It sets up geochemical divides early in the evolution of a lake brine, these divides define the subsequent geochemical and mineralogical evolution of a lake basin.

If the lake waters are enriched in HCO_3 compared to Mg and Ca (i.e., $HCO_3 \gg Ca + Mg$), then the brine follows path I (Fig. 2.19). Ca and Mg are depleted during the initial precipitation of alkaline earth carbonates, leaving excess HCO_3 in the brine. As HCO_3 is the next most abundant ion in these waters it combines with Na in the next stage of concentration. Sodium carbonate minerals, such as trona, natron and nahcolite, precipitate. Little or no gypsum can form from pathway-I brines as Ca is completely used up during the preceding alkaline earth carbonate stage. In contrast, during the evaporation of modern seawater, all the HCO_3 is depleted in the initial alkaline earth precipitates (mostly as aragonite and Mg-calcite). The excess Ca then combines with SO_4 to form gypsum. It is chemically impossible for sodium carbonate to form by evaporation of modern seawater. The assumption that the proportions of calcium to bicarbonate in seawater have not changed much in the last 600–800 Ma implies that trona salts or their pseudomorphs

Brine type	Saline mineral	
Ca-Mg-Na-(K)-Cl	Antarcticite	$CaCl_2 \cdot 6H_2O$
	Bischofite	$MgCl_2 \cdot 6H_2O$
	Carnallite	$MgCl_2 \cdot KCl \cdot 6H_2O$
	Halite	NaCl
	Sylvite	KCl
Na-(Ca)-SO_4-Cl	Tachyhydrite	$CaCl_2 \cdot 2MgCl_2 \cdot 12H_2O$
	Glauberite	$CaSO_4 \cdot Na_2SO_4$
	Gypsum	$CaSO_4 \cdot 2H_2O$
	Halite	NaCl
	Mirabilite	$Na_2SO_4 \cdot 10H_2O$
	Thenardite	Na_2SO_4
Mg-Na-(Ca)-SO_4-Cl	Bischofite	$MgCl_2 \cdot 6H_2O$
	Bloedite	$Na_2SO_4 \cdot MgSO_4 \cdot 4H_2O$
	Epsomite	$MgSO_4 \cdot 7H_2O$
	Glauberite	$CaSO_4 \cdot Na_2SO_4$
	Gypsum	$CaSO_4 \cdot 2H_2O$
	Halite	NaCl
	Hexahydrite	$MgSO_4 \cdot 6H_2O$
	Kieserite	$MgSO_4 \cdot H_2O$
	Mirabilite	$Na_2SO_4 \cdot 10H_2O$
	Thernadite	Na_2SO_4
Na-CO_3-Cl	Halite	NaCl
	Nahcolite	$NaHCO_3$
	Natron	$Na_2CO_3 \cdot 10H_2O$
	Thermonatrite	$NaCO_3 \cdot H_2O$
	Trona	$NaHCO_3 \cdot Na_2CO_3$
Na-CO_3-SO_4-Cl	Burkeite	$Na_2CO_3 \cdot 2Na_2SO_4$
	Halite	NaCl
	Mirabilite	$Na_2SO_4 \cdot 10H_2O$
	Nahcolite	$NaHCO_3$
	Natron	$Na_2CO_3 \cdot 10H_2O$
	Thernadite	Na_2SO_4
	Thermonatrite	$NaCO_3 \cdot H_2O$

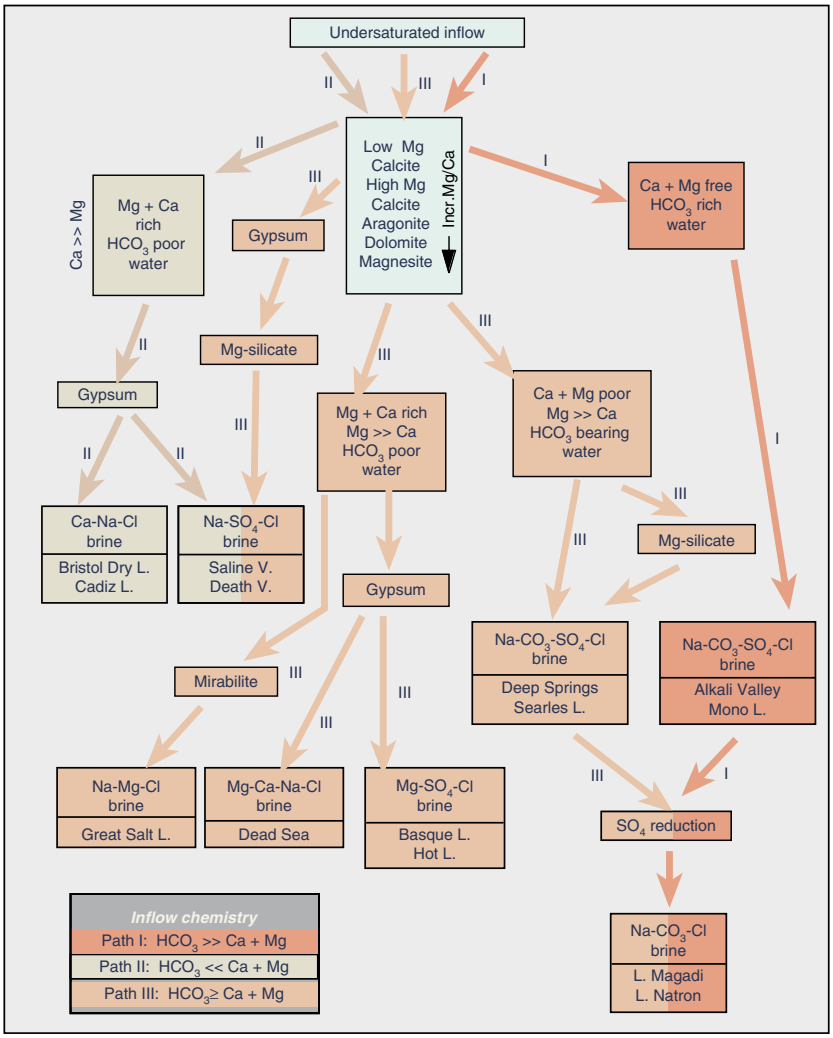

Fig. 2.19 Hydrologic classification and brine evolution pathways of concentrating nonmarine waters and a listing of major evaporite minerals associated with the different brine types (After Eugster and Hardie 1978). *L* lake, *V* valley

Table 2.6 Mineral occurrences and parent brines

Brine composition and source	Major saline minerals	Key minerals
Na-K-CO_3 -Cl-SO_4 Non-marine waters or possibly early Archaean seawater	Alkaline earth carbonates, mirabilite, thenardite, trona, nahcolite, natron, thermonatrite, shortite, halite.	Na_2CO_3 minerals
Na-K-Mg-SO_4 -Cl Seawater, non-marine water or hybrids	Alkaline earth carbonates, gypsum, anhydrite, mirabilite, thenardite, glauberite, polyhalite, epsomite, bloedite, kainite, halite, carnallite, sylvite, bischofite.	$MgSO_4$ and Na_2SO_4 minerals
Na-K-Mg-Ca-Cl Non-marine waters (hydrothermal and basinal brines or seawater with different ionic proportions from today)	Alkaline earth carbonates, gypsum, anhydrite, sylvite, carnallite, bischofite, tachyhydrite, antarcticite.	$KCl \pm CaCl_2$ minerals in the absence of Na_2SO_4 and $MgSO_4$ minerals

After Hardie (1991)

indicate nonmarine settings throughout the Phanerozoic and much of the Neoproterozoic.

If initial inflow waters have $(Ca+Mg) \gg HCO_3$ then, after the initial evaporitic carbonate precipitates, the brines become enriched in the alkaline earths but depleted in HCO_3 and CO_3. If the relative volume of HCO_3 is low, little carbonate can precipitate with further concentration. Brine evolution follows path II, whereby excess alkaline earths (Ca, Mg) left after depletion of carbonate combine with sulphate ions to precipitate large volumes of sulphates (gypsum and/or

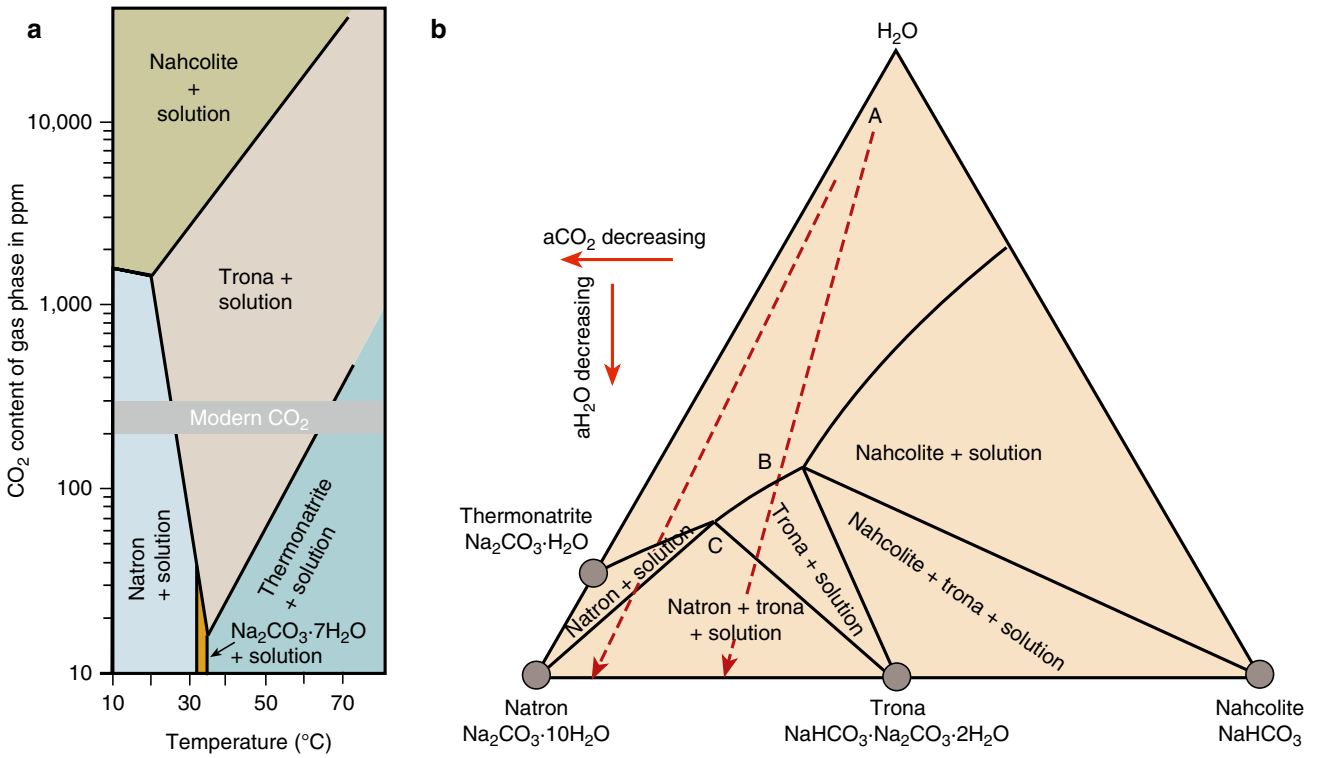

Fig. 2.20 Phase chemistry of sodium carbonate salts. (**a**) Sodium carbonate phases in equilibrium with a saturated solution as a function of CO_2 content of the gas phase and temperature. CO_2 content of today's atmosphere is plotted as a grey band (in part after Eugster 1971a). (**b**) Phase diagram for the sodium carbonate, sodium bicarbonate, water system at 25 °C. Trona saturation occurs at **b** where the brine trajectory *arrow* passes into boundary of trona stability field (After Eugster 1971a)

epsomite). Path II precipitates a suite of continental salts and bitterns similar to that derived from modern seawater. If the ratio of $(Ca+Mg)/HCO_3$ is near unity (path III) carbonate precipitation can be extensive and voluminous. As Ca is progressively removed there is a progressive increase in the Mg/Ca ratio of the residual brine until large volumes of high-Mg calcites, dolomites and even magnesites precipitate.

But such theoretical separations can be difficult to determine in continental lacustrine systems where there is a mixture of groundwater sources and carbonate detrital inputs. For example, across the northern Great Plains of western Canada, there are literally millions of lakes and wetlands of variable salinities and hydrologies (Last and Last 2012). Although typically characterized as a saline, Na-SO_4 system, in fact the wide range of water chemistries exhibited by the lakes results in an unusually large diversity of sediment composition. About 30 species of carbonate minerals have been reported from the modern and Holocene sediment in about 50 lacustrine basins in the region. The ubiquity of detrital calcite and dolomite in most is a legacy of the carbonate bedrock and a carbonate-rich glacial sediment feed to the lakes. Elevated salinities of the lakes, together with high alkalinities, productivity, and pH values, act in concert to create thermodynamically saturated or supersaturated conditions with respect to many carbonate minerals. The most common non-detrital components are Mg-calcite, aragonite and non-stoichiometric dolomite. Many of the basins whose brines have very high Mg/Ca ratios also contain hydromagnesite, magnesite, and nesquehonite. This suggests that extended periods of high salinity and elevated Mg/Ca and alkalinity levels persisted in the basin before climatic and hydrologic changes brought about less saline conditions during the late Holocene. Although not common, sodium carbonates, including trona, natron and nahcolite, also occur in some of these hypersaline lakes. So far, the often-difficult task of distinguishing endogenic lacustrine carbonates from allogenic and authigenic minerals in the lakes has limited the use of carbonate stratigraphy in deciphering the hydrological evolution of region (Last and Last 2012).

Trona-Nahcolite-Shortite Chemistry (Path I Brine)

Clearly, path I brines cannot be derived by solar evaporation of waters with the ionic proportions of modern seawater. An occurrence of primary trona or its pseudomorphs in Phanerozoic evaporites is evidence of a nonmarine brine with an excess of bicarbonate (Fig. 2.20). The three better-known trona deposits in the world are the Pleistocene and

Holocene sediments of Lake Magadi, Searles Lake and the Eocene Green River Formation (Chap. 12). All regions show the appropriate bicarbonate excess in their inflow waters that differentiates them from seawater brine. But, as we shall see later in this chapter, there is increasing evidence that early Archaean marine evaporites are most likely represented in the rock record by silica replacements of widespread nahcolite or trona, as well as halite. So, it's worth considering in more detail what is the phase chemistry of a sodium bicarbonate system.

By definition, there must always be an excess concentration of bicarbonate ions in an inflow water to force it into a path I composition (Fig. 2.19). This means trona-forming brine is always an alkaline solution, typically with a pH above 9, and so is seen in all modern soda lake waters[3] (Eugster 1971a, b; Eugster and Jones 1978). Alkalinity is the result of the required solution's inherent chemistry. Trona cannot form in acidic waters, it is a matter of basic chemistry. Any carbonate ion in any aqueous solution tends to bump into and react with whatever ionic species are around. When there is not much free hydrogen around, carbonate in effect steals a hydrogen ion from a water molecule, leaving a hydroxyl ion behind and so, *ipso facto*, produces an alkaline solution. Because sodium is usually the dominant cation in the world's saline lakes, some make an anionic distinction in their classification, referring to lakes containing predominantly sulphate as bitter lakes and those containing predominantly carbonate as alkaline or soda lakes.

A number of conditions must be present to create natural Path I brines and so produce trona beds: (1) an underfilled tectonic basin in which downwarping exceeds the rate of sedimentation, (2) a closed hydrographic basin in which evaporation exceeds outflow, (3) evolution of solutes in the lake waters that lead to high Na/(Ca + Mg) and ($HCO_3 + CO_3$)/(SO_4 + Cl) ratios, that is alkaline brines, (4) a more-or-less permanent body of nutrient-rich water, (5) a warm climate favouring high primary productivity by microbes and algae, and (6) a high rate of bacterial sulphate reduction. Given the presence of these requisite conditions, varying intensity of photosynthesis, temperature and changes in the amount or volume of degassing spring waters then control the CO_2 content of the sodium bicarbonate precipitating brines and hence the mineralogy of the sodium bicarbonate precipitates (Fig. 2.20a).

Trona evaporites in Lake Magadi accumulate as the surface brine is losing (degassing) a substantial portion of its CO_2 to the atmosphere. As that happens the increasingly concentrated brine follows a path similar to the dashed line moving away from point A (Fig. 2.20b; Eugster 1970, Eugster 1980a, b). Trona precipitation then occurs at ambient equilibrium (point B). Natron rather than trona is likely to form when ambient temperature is below 25 °C (left hand dashed line). Once native trona deposition in Lake Magadi has begun, the CO_2 resupply from the atmosphere is too slow to allow ongoing equilibrium between atmospheric CO_2 levels and levels of CO_2 in the brine. The deposition of the later salts, along with the observed HCO_3 depletion in increasingly saline brines (levels not buffered by CO_2), suggested to Hardie (op. cit.) that fractional crystallisation likely controls trona deposition in Lake Magadi. Thermonatrite/halite can sometimes precipitate in the later stages of evaporative concentration in Lake Magadi. At higher temperatures, earlier formed natron and trona can be replaced by thermonatrite.

Kinetic effects, especially those governing equilibration between dissolved and atmospheric CO_2, are extremely important in determining the final mineralogy of sodium carbonate precipitates (Eugster 1970; Whittig et al. 1982). Evaporative concentrations under conditions of equilibrium with atmospheric CO_2 at 25 °C follow path AB in Fig. 2.20b and at B, trona begins to crystallize. Crystallisation of trona, together with further evaporation, results in the solution composition moving towards C, i.e., it causes a decrease in the HCO_3/CO_3 ratio because this ratio in trona is greater than that in the solution. However, if equilibrium with atmospheric CO_2 is maintained, this ratio should be buffered, and only trona is produced because addition of atmospheric CO_2 stabilizes (buffers) the HCO_3/CO_3 ratio via the following reaction:

$$CO_3^- + H_2O + CO_2 = 2HCO_3^-$$

Under conditions where atmospheric disequilibrium is promoted, i.e., where the HCO_3/CO_3 ratio is not buffered, path BC is followed, producing thermonatrite and trona at C. The removal of HCO_3 along path BC under these conditions also causes a marked rise in the pH (alkalinity), as the solution compensates for HCO_3 removal by the reaction,

$$CO_3^- + H_2O = HCO_3^- + OH^-$$

In spite of this compensation, the HCO_3/CO_3 ratio in lake Magadi brines falls well below that of atmospheric equilibrium, especially in nutrient-rich waters with a flourishing photosynthesising microbial community (Fig. 2.20a).

[3]The term "soda lake" defines a class of saline lakes with water/brine chemistries having an excess in total alkalinity ($\approx [HCO_{3-}] + 2[CO_3^{2}]$, i.e., the sum of the charges of the bicarbonate ion plus carbonate ion) is in excess over the charges of the alkaline earth ions, magnesium and calcium: $[HCO_3^-] + 2[CO_2^-] > 2[Mg^{2+}] + 2[Ca^{2+}]$ when such lake waters concentrate the high CO_2 level causes a rise in pH and eventually, if evaporation proceeds, various sodium carbonate minerals precipitate. The largest soda lake in the world is Lake Van in Turkey. Many soda lakes are located on or near plate tectonic boundaries within continental land masses (rifts and collision zones). About a third of the soda lakes in the world are located in a high-altitude collision belt, stretching from Tibet, through Qinghai Province to the Inner Mongolia Autonomous Region. Precipitation of salts in most of these soda lakes is cryogenically driven.

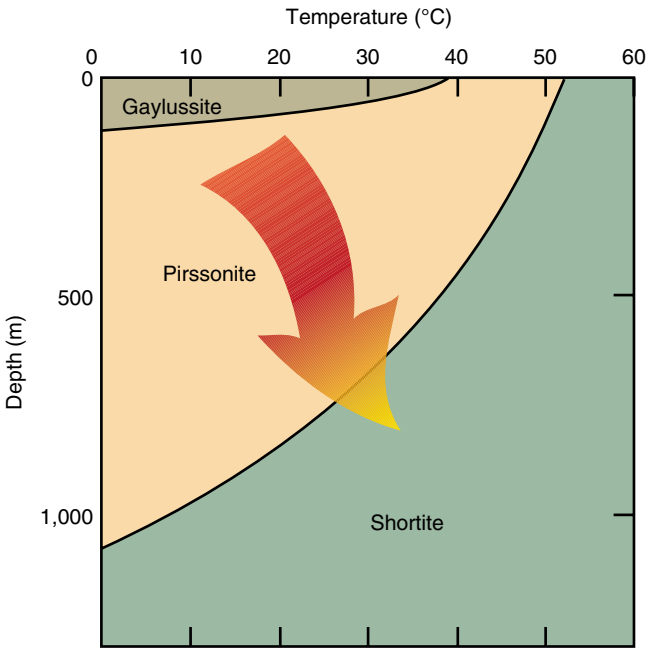

Fig. 2.21 Stability of gaylussite, pirssonite and shortite with inferred burial depth/temperature (°C). The temperature for the gaylussite/pirssonite transition is ≈ 40 °C. The illustrated pirssonite–shortite boundary temperature of 52 °C is the lower temperature stability limit of shortite (Jagniecki et al. 2013)

The grey shaded interval in Fig. 2.20a shows the range of CO_2 values typically present in brines in equilibrium with present-day atmospheric CO_2. Trona is the stable phase in the 25–60 °C temperature range typical of most modern surface brines in modern soda lakes where sodium bicarbonate minerals are precipitating. CO_2 values were higher (10–200 times; Kaufman and Xiao 2003) in the Archaean atmosphere (as were CH_4 levels), favouring the widespread co-occurrence of nahcolite with trona along with halite, not gypsum, in marine evaporites of the time (Fig. 2.49).

Shortite does not form at earth surface temperatures, but its occurrence can also be used to track burial temperature. Based on experimental work, Bradley and Eugster (1969) concluded the reaction, whereby pirssonite converts to shortite:

$$Na_2Ca(CO_3)_2 \cdot 2H_2O + CaCO_3 = Na_2Ca_2(CO_3)_2 + \text{brine}$$

only occurs at temperatures around 100 °C ± 25 °C at 2 kbar pressure. The precursor to pirssonite is gaylussite and the conversion occurs around 40 °C at normal surface conditions (Fig. 2.21) Subsequent experiments on shortite stability by Jagniecki et al. (2013) found that shortite forms via the above reaction at a temperature of 55 °C at standard conditions and in presence of an NaCl brine its temperature stability field is slightly lower (≈52 °C). It seems the temperature at which shortite forms from a pirssonite precursor does not vary significantly with brine chemistry or aH_2O. These results suggest that shortite is not found in modern saline lake environments because the surface temperatures are too low, but also explains why it is a common diagenetic/burial product in path 1 brine settings.

For example, shortite is abundant in the Wilkins Peak Member (WPM) of the Eocene Green River Formation, Green River Basin, Wyoming, USA (≈78 Mt/km^2), where it occurs as diagenetic displacive crystals, fracture fills, and pseudomorphous replacements of a precursor Na-Ca-carbonate (Jagniecki et al. 2013). The large area over which shortite occurs in the WPM indicates that saline type 1 pore fluids once existed in the buried lacustrine sediments, and thus, at times, large Na-CO_3-rich saline alkaline lakes or laterally extensive saline groundwaters existed in the Green River Basin during WPM time with extents greater than those outlined by trona beds, which are also economic (Chap. 12). The thermal stability of shortite, together with vitrinite reflectance data and inferred regional geothermal gradients, establish that the shortite-bearing intervals of the WPM were buried to maximum depths of ≈ 1,000 m in the Green River Basin, and since experienced ≈ 800 m of erosional exhumation (Jagniecki et al. 2013).

Are Continental Salt Lakes Hydrologically Closed?

Hydrogeochemical studies do not always draw the distinction between hydrographic closure (endorheic basin) and hydrological closure (no leakage). The former situation is commonplace in evaporite basins, while the latter is rare. Studies of the nonmarine hydrogeochemistry of low-relief desert terranes detailed in this section show that varying degrees of brine leakage, rather than hydrological closure, characterise large-scale endorheic lakes and playas located well into the continental interior. Even in modern near-coastal settings the hydrology tends to be open and leaky rather than a closed cumulative systems. For example, evolved path III continental brines, in combination with varying degrees of brine leakage, explain the diversity of evaporitic carbonate mineralogies in the lakes of the Coorong, South Australia (Warren 2000a). Individual lakes, less than 1 km apart and with sediment surfaces above sea-level, are filled with up to 6 m of Holocene carbonate and show mineralogies that range from low Mg-calcite to high Mg-calcite to calcian dolomite to magnesian dolomite ± magnesite to aragonite ± hydro-magnesite to aragonite + gypsum (Fig. 4.5). Calcites and calcian dolomites tend to dominate in lakes with lower average annual salinities, while the magnesian carbonate phases, along with aragonite/gypsum, tend to dominate lakes with higher average salinities (Warren 1990). During the desiccated stage of the late summer, halite-$MgSO_4$ efflorescences form atop carbonate mudflats in many

Table 2.7 Major ion composition of waters (ppm) in various Australian playas, all showing Na-Cl dominance and seawater-like ionic proportions

	TDS	pH	HCO_3	Cl	SO_4	Na	K	Ca	Mg	Br
Lake Eyre North, SA	36,800	–	87	21,400	1,100	13,800	35	300	42	–
Lake Eyre South, SA	25,500	–	100	14,300	1,300	9,100	–	600	100	–
Lake Frome, SA	305,900	–	104	173,400	14,100	116,219	366	570	1,030	151
Lake Torrens, SA	301,000	–	–	185,000	7,000	103,000	700	600	4,300	–
Lake Greenly, SA	207,400	7.47	124	109,700	3,500	84,810	1,299	1,170	6,600	314
Lake Malata, SA	224,300	7.49	196	137,200	3,600	71,620	1,609	970	8,690	407
Lake Tyrell, NSW	232,300	–	105	131,000	15,500	77,159	660	510	7,100	347
Lake Amadeus, NT	217,200	7.62	9	118,000	1,440	77,060	2,530	612	2,680	–
Spring Lake, NT	358,000	6.65	72	143,000	55,000	90,000	5,500	250	14,700	–
Glauberite Lake, NT	361,200	6.80	1,102	185,550	31,700	107,000	3,800	39	11,700	369
Palaeochannel, WA	238,800	7.20	50	110,000	18,000	98,000	2,400	430	9,800	–
Seawater	35,700	8.20	140	19,350	2,710	10,760	390	410	1,290	67

After Dutkiewicz et al. (2000), Jacobson et al. (1989) and references therein

Coorong lakes, but are flushed from the system by winter rains. Mineral variation in the Coorong lakes illustrates the importance of relative rates of brine loss (residence time and leakage) in controlling mineralogy in this hydrologically-open continental system. Average brine residence times in the different lakes ultimately control mineralogic assemblage. Those lakes with leakier basements allow a more rapid throughflush of waters and so show lower longterm salinities and so accumulate less saline precipitates.

Yet in the literature, many of our ideas on the nature and evolution of continental evaporite brines and the resulting salts are based on hydrochemical analysis of high topography, "closed-basin" (effectively non-leaking), rain shadow lacustrine systems such as the Basin and Range province of the southwest USA and the continental lakes of the African Rift system. Uplifted bedrock lithologies surrounding these lakes tend to contain abundant labiles in their tectonically-active high-relief catchments. Bedrock alteration with rapid weathering is a major contributing factor to variations in ionic proportions of the final lake brine (Fig. 2.19). In contrast, saline groundwaters in playas and salt lakes of low-relief tectonically-stable deeply leached regions such as the interiors of Australia and southern Africa tend to have salt lakes with seawater-like Na-Cl dominated brines (Type II or thalassic brines). Many Australian playas are hydrologically open; the outcropping parts of mixed local and deeply circulating regional discharge systems (Chap. 3). Aridity and deeply weathered soil profiles have characterised these areas since the early to mid Tertiary. Ionic proportions and chemical constituents of surface waters and brines vary little, even across regions of variable bedrock lithologies (Table 2.7). Gypsum, with lesser volumes of halite, are common precipitates in some, and all lake floors show varying degrees of brine leakage.

Jankowski and Jacobson (1989, 1990) and Jacobson and Jankowski (1989) showed that in such deeply weathered and leached systems the amount of rainfall in a given part of a catchment area is a more important determinant of the chemical composition of the final playa brine, rather than bedrock lithology. In the Lake Amadeus – Spring Lake region of central Australia, higher rainfall regions of the catchment generate playa inflow waters that are bicarbonate-dominated, while lighter rainfall regions generate chloride-dominated inflow waters. Differences in brine chemistry can be related to the rate of cycling of pedogenic carbonate within the catchment profile, not to differences in basement lithology. More carbonate is dissolved in the nearsurface when rainfall is relatively high, and so contributes a greater proportion to the brine composition. Higher rainfall regions also flush greater volumes of water through the same profile in a given time and so are characterised by shorter residence periods per given water volume for rock/fluid interaction. In low rainfall regions chloride tends to remain mobile in the catchment profile, while bicarbonate is more likely to remain fixed as carbonate minerals in the soil profile (Fig. 2.22).

The buildup of more soluble salts as pedogenic residuals in low rainfall regions can be impressive. Salt-rich soil profiles near Lake Eyre, South Australia sit atop a widespread flat-lying and deeply weathered pyritic Cretaceous Bulldog Shale. Deep leaching has created a pedogenic unit of epsomite, with a thickness measured in metres and an area measured in thousands of square kilometres (Lock 1986). Pedogenic nitrates in the hyperarid Atacama Desert have a similar pedogenesis (Fig. 12.62).

Hydrological leakage varies over time through a brine-covered lake floor situated in the lowest parts of an endorheic basin and does so in response to climate changes driving rising and falling watertables. Variation occurs across time frames of hundreds to thousands of years, and periodic deflation is typically part of the sedimentary history of these playas. Variations can create regional disconformities in the upper few metres of lacustrine sediment. This hydrological

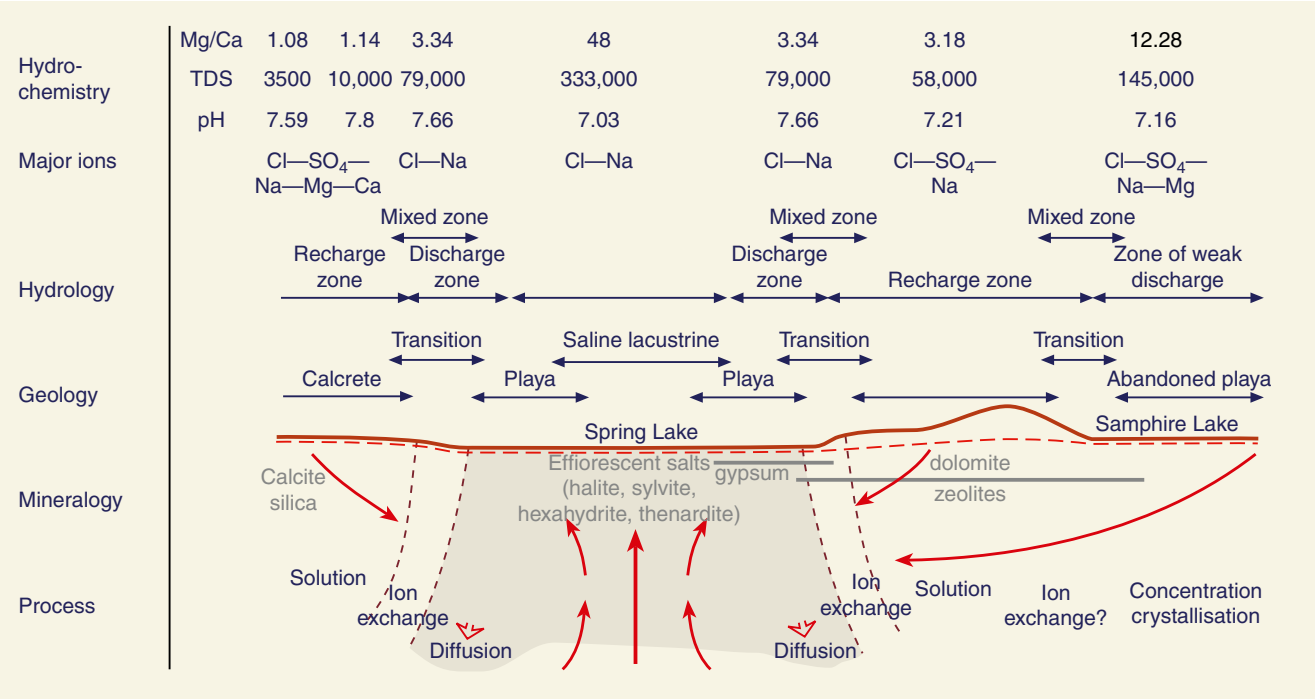

Fig. 2.22 Schematic of hydrochemical processes in a groundwater discharge playa complex, Spring Lake, Curtin Springs, Central Australia (After Jacobson et al. 1989). See also Fig. 2.54

regime begs the question, how useful are the major ions proportions in the present surface waters in understanding the mineralogical evolution of the preserved lake precipitates? In other words, how valid is the assumption, typically made in "closed lake" settings, that the chemistry of the concentrating surface waters gives an understanding of the hydrogeochemical parentage of the preserved sediments?

Studies by Dutkiewicz et al. (2000) underline the significance of varying rates of phreatic leakage (both upwelling and downwelling/reflux) in controlling the mineralogy of lacustrine sediments in more hydrologically open playas. Using a steady-state isotopic model of lacustrine carbonates they concluded that present-day leakage in the Malata-Greenly playa complex in South Australia is 75–90 % of regional inflow. Mineralogy of nearsurface sediment beneath all the lakes in the Greenly-Malata system is relatively simple, dominated by alternating layers of chemically-precipitated gypsarenite and carbonate muds, which are either dolomites or calcites, all with relatively minor amounts of transported calcareous sand (Fig. 2.23a; Dutkiewicz and von der Borch 1995). Under present conditions of high leakage, only low magnesian calcite precipitates are preserved along with gypsum. Compared to more arid times in the past when dolomite accumulated, current lake waters experience somewhat reduced effects of evaporation, gas and vapour exchange and, consequently, reduced isotopic and chemical enrichment.

Using regional groundwater values, Dutkiewicz et al. (2000) calculate that any precipitated carbonate in a salt lake in the region will be calcite, which becomes increasingly Mg-rich as brine concentration continues, until the brine reaches a chemistry favourable for dolomitisation. Thus dolomite intervals preserved in the cores, but not forming in the present climate, probably reflect more arid climate or times of slower leakage of brine from the lake. Their modelling predictions are confirmed by isotopic measurements over the length of a 2.5 m core taken in the dolomitised carbonates of the lake complex, where the $\delta^{18}O$ and $\delta^{13}C$ of the lacustrine carbonates show excursions on the order of 5‰ (Fig. 2.23a).

At one end of the hydrological spectrum are past times of throughflow-dominated leaky conditions, when low-Mg calcite accumulated (with characteristic depleted $\delta^{18}O$ and $\delta^{13}C$ levels). These were times defined by a high watertable, perennial waters and a humid climate (Fig. 2.23b) with relatively short residence times in the pore brines. Then there were times of decreased leakage and higher rates of evaporation. These more arid climatic episodes were characterised by the accumulation of high Mg-calcite/dolomite (relatively enriched in $\delta^{18}O$ and $\delta^{13}C$ (Fig. 2.23a). Dolomite precipitation dominated in Lake Greenly when leakage was reduced to some 55–70 % of present inflow.

Then there is the climatic situation where deflation or a lowering of the regional watertable causes the water level to sink into the lake sediment column to become a watertable. The system is then driven by capillary evaporation, the formation of widespread erosional surfaces (disconformities) and net loss of sediment (via deflation) from the lake. This creates breaks or disconformities in the sedimentation history

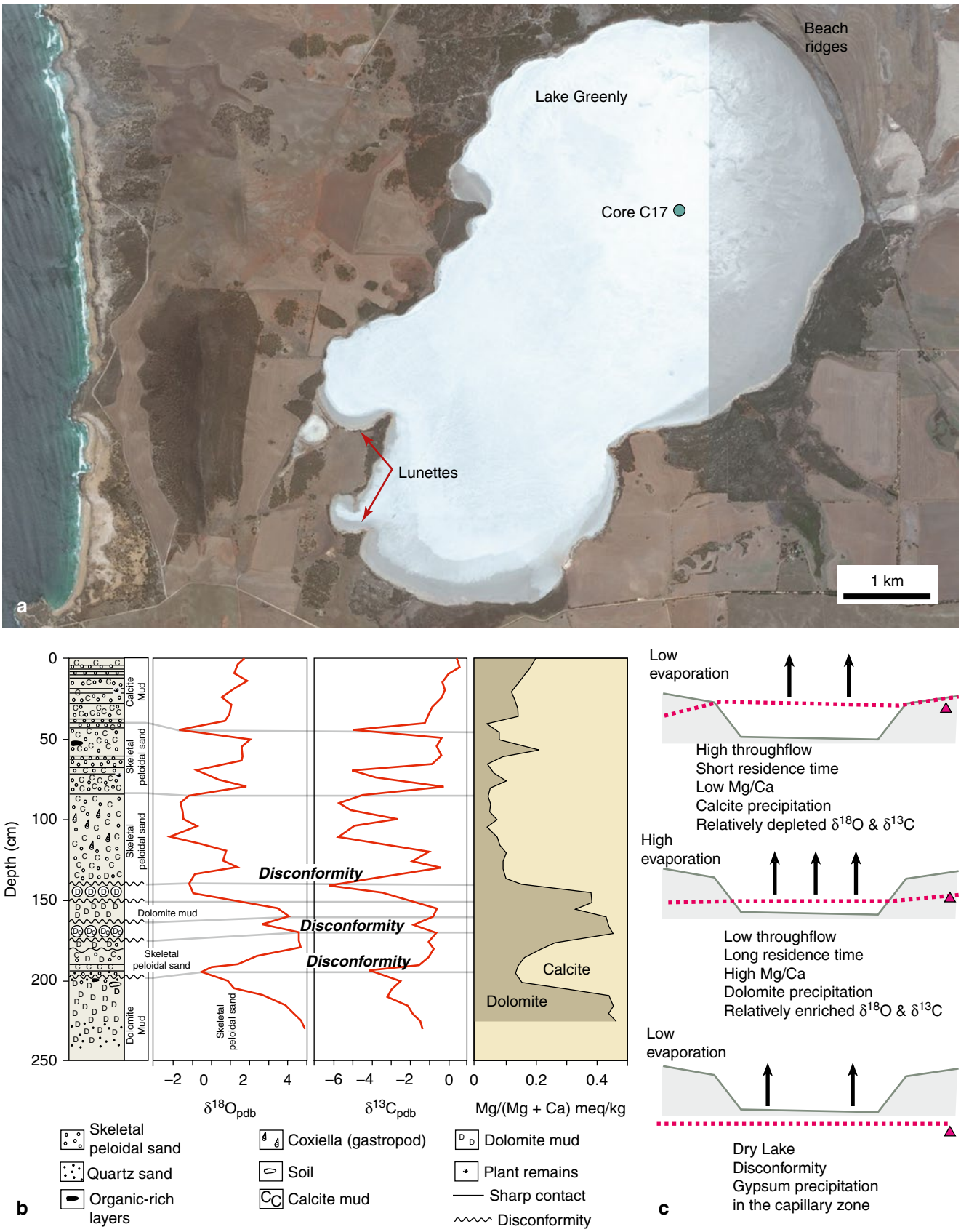

Fig. 2.23 Lake Greenly complex, South Australia. (**a**) Satellite image (Bing® image mounted in MapInfo®). (**b**) Stable isotopes and Mg/(Mg+Ca) ratios plotted against depth and sedimentology of core C17 in Lake Greenly. (**c**) Schematic of the three playa hydrological stages with varying watertables indicated by dashed lines (After Dutkiewicz et al. 2000)

and it can effect both dolomite and calcite successions. It tends to occur more frequently during dolomite depositing episodes, as these were times of greater aridity. Using the modern isotopic signatures of the regional groundwaters as a baseline, signatures in the preserved lake sediments indicate variable, but high, rates of throughflow or leakage throughout the Late Quaternary (55–90 % of today's).

Yet, when mass balance calculations are done using the surface water chemistry in the lake and an assumption that Cl and Br are conservative, there is apparent hydrochemical closure in surface waters of the lake system (ionic proportions indicate <1 % leakage of waters from the lake). Clearly, the surface brine chemistry does not match the leakage history shown by isotopic signatures of the preserved sediments beneath the lake floor (Dutkiewicz et al. 2000). Surface waters reflect the ongoing cycling of a seasonal halite crust, which redissolves each winter. The crust formed during the previous summer under conditions dominated by evaporative discharge into the lake. Circulation of surface waters and the periodic creation of secondary surface brines by halite leaching takes place above a separate widespread mixing zone where older lake brines interact with regional groundwater inflow. Thus the annual solute cycles of surface waters and the halite crusts are decoupled from the subsurface water cycle which are what tends to preserved in the carbonates of the playa sediments (not the uppermost halite level). This decoupling is true of many inland playas across Australia, where reflux and mixing of the lake brines into the regional outflow hydrology prevents the accumulation of thick sequences of bedded gypsum or halite (Fig. 3.59).

Decoupling also explains a general observation that in many Quaternary salt lakes around the world, the relative abundance of preserved authigenic minerals in the sediment column is different from that predicted by conventional solute mass balance calculations using surface brine compositions. Conventional hydrogeochemical mass balance models assume that chloride (and bromine) behave conservatively over long periods of time. Such models of ionic evolution fail to take into account the role of diffusion, deflation and fractional crystallisation/dissolution of salts. That is, not all water exchange in a saline system is closed and so can be tied to a simple relationship between runoff and evaporation; in reality all salt lakes will reflux, seep and leak brine to varying degrees.

This decoupled hydrogeochemistry illustrates a general observation on evaporite deposition, underlined by Sanford and Wood (1991) and Rosen (1994), namely, there are very few truly "closed" hydrological systems in evaporite basins in either marine or nonmarine settings. All natural groundwater systems in salt-accumulating areas leak to varying degrees. Geological evidence for leakage through the floor of an evaporite basin includes the formation of reflux dolomite, the longterm stability of brine plumes beneath lakes that are accumulating thick salt sequences, the loss of halite porosity by 30 m burial, the near surface dissolution of marginward portions of salt beds, the diverse suite of early burial alterations and backreactions, and the formation of burial salts in brine curtains beneath saline depositional systems.

As for seawater bitterns (Fig. 2.12), the geochemical divides defining the evolution of Type I through III nonmarine brines are perhaps more dependent on the ratio of leakage to inflow rather than the lithology of the surrounding basin. Only in high-relief reactive catchments with very low basin floor leak-age (near-closed) hydrologies will surface brine chemistry and crust mineralogy correlate with the suite of minerals and salts accumulating as the lacustrine fill. There the rapid rates of subsidence in the lacustrine sink mean the accumulated salts largely reflect catchment lithologies.

In more hydrologically open systems, with slower rates of lacustrine subsidence and sediment accumulation, the rate of solute input from precipitation and meteoric outflow via pedogenic leakage in the surrounding low-relief deeply weathered and flushed catchment is often more significant in controlling inflow chemistry than the rate of labile bedrock weathering. Hydrogeochemical proportions of ions in waters throughout the continental groundwater profile are then controlled by a combination of rates of leakage and the ionic composition of the precipitation entering the system. Solutes from the shallowest portions of the groundwater profile are recycled through the seasonal formation and dissolution of salt crusts on the lowest parts of the playa floor and so are typically decoupled from the mineralogy in the immediately underlying lacustrine sediments. The proportion of leakage of solutes into the sediment below the cycling crust is controlled by longer term climate change and the interactions between tectonism, subsidence and deflation.

Separating Marine from Nonmarine

Hydrological requirements needed to accumulate large-scale thick salt deposits complicates our ability to separate marine from nonmarine water sources in ancient evaporites. A high degree of isolation or "continentality" is required for stable longterm evaporative drawdown, which is always needed to accumulate a thick sequence of bedded salts (see Chap. 5 for detail). That is, a marine evaporite basin may have been supplied seawater by marine seepage or occasional surface seawater breakthrough via narrow ephemeral surface inlets, but, if the basin is to accumulate thick salt beds, it must be a longterm topographically-isolated regional low. The inherent hydrological requirement of isolation from any continuous surface connection to the ocean means it is by definition a subsealevel basin surrounded by land with a marine-phreatic groundwater feed. The salt accumulating area is

Table 2.8 Examples of diagenetic (secondary) evaporites that form easily below 30 °C

Secondary mineral phase	Syndepositional origin (<30 °C)
Anhydrite $CaSO_4$	Dehydration of early formed gypsum as a_{H2O} of evaporating brine decreases.
Bloedite Na_2 SO_4 $MgSO_4{\cdot}4H_2O$	Back-reaction between previously precipitated epsomite and concentrating brine.
Gaylussite $CaCO_3{\cdot}Na_2CO_3{\cdot}5H_2O$	Back-reaction of evaporating alkaline brine with early formed aragonite or calcite.
Glauberite $CaSO_4{\cdot}Na_2SO_4$	Back-reaction of evaporating Na_2SO_4-brine with early formed gypsum or halite.
Kieserite $MgSO_4{\cdot}H_2O$	Dehydration of early formed hexahydrite as a_{H2O} of evaporating brine decreases.
Polyhalite $2CaSO_4{\cdot}MgSO_4{\cdot}K_2SO_4{\cdot}2H_2O$	Back-reaction of evaporating K-Mg-SO_4 brine with early formed gypsum, anhydrite or glauberite.
Sylvite KCl	Incongruent dissolution of carnallite in undersaturated waters.

After Hardie (1990), Sanchez-Moral et al. (1998)

either surrounded by continental sediments and hydrologies or is a depression within or behind a subaerially exposed carbonate platform. Invariably in some parts of the basin, marine chemistries are overprinted by deeply circulated meteoric waters, thalassic surface waters can be diluted by occasional rainstorms and by the effects of pulses of highly labile volcanic ash. This next section is an attempt to present some of the possible complexities that characterise ancient hybrid (mixed marine/continental) brine systems.

Back Reactions

Backreactions complicate the interpretation of brine parentage in ancient evaporite salt sequences. At the start of the last century they were recognised as significant controls on mineralogy by van Hoff and others (Figs. 2.14 and 2.15). Backreactions can occur both at the sediment-brine interface and within shallow subsurface brine plumes that displace and mix with less dense underlying pore brines. Pseudomorphs and reaction rims are common indicators of this process, as are relict mineral cores encased in the mineral that replaced it. Documented examples include pseudomorphs of halite after subaqueous gypsum, reaction rims of polyhalite and glauberite around earlier gypsum or anhydrite, bloedite after epsomite, relicts of carnallite in secondary sylvite, and pseudomorphs of sylvite plus kieserite after earlier langbeinite (Table 2.8).

Backreaction means relevant bittern chemistry and associated brine evolution is poorly modelled by studying brine evolution in man-made seawater ponds. In such salt works the evolved brines are separated from earlier precipitated mineral species by sluice gates and pumps. The aim of the saltwork engineer is to create harvestable monomineralic or bimineralic salts and brines in the various fractionating pans. Backreaction either does not occur or is kept to a minimum.

Many secondary (replacive and displacive) salts in natural systems, such as sylvite, glauberite and polyhalite, form syndepositionally via interaction between highly evolved near-surface brines and earlier formed minerals (Fig. 2.24; Table 2.8). For example, during the equilibrium evaporation of seawater at 25 °C, glauberite and polyhalite form by

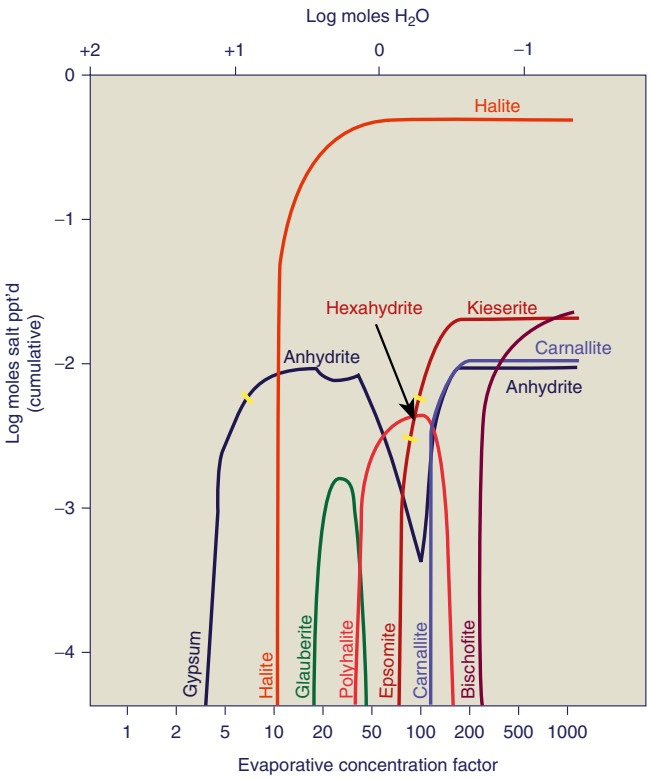

Fig. 2.24 Evaporative concentration of modern seawater simulated using the computer program of Harvie et al. (1980) showing cumulative masses of minerals precipitated and resorbed by backreaction as evaporation proceeds. Initial seawater has a concentration factor of 1, with an initial mass of 1 kg of H_2O (After Hardie 1991)

backreaction of the brine with earlier formed anhydrite and gypsum. Harvie et al. (1980) modelled much of the variability present in the bittern salts of the Permian Zechstein deposits in Germany via a combination of equilibrium batch evaporation interspersed with times of fractionation and backreaction. As seawater concentrates to slightly below halite saturation, anhydrite replaces gypsum.

As evaporation continues, anhydrite is partially replaced by glauberite. Glauberite in turn is replaced by polyhalite and levels of anhydrite are further reduced. These replacements change the residual brine composition so that kainite

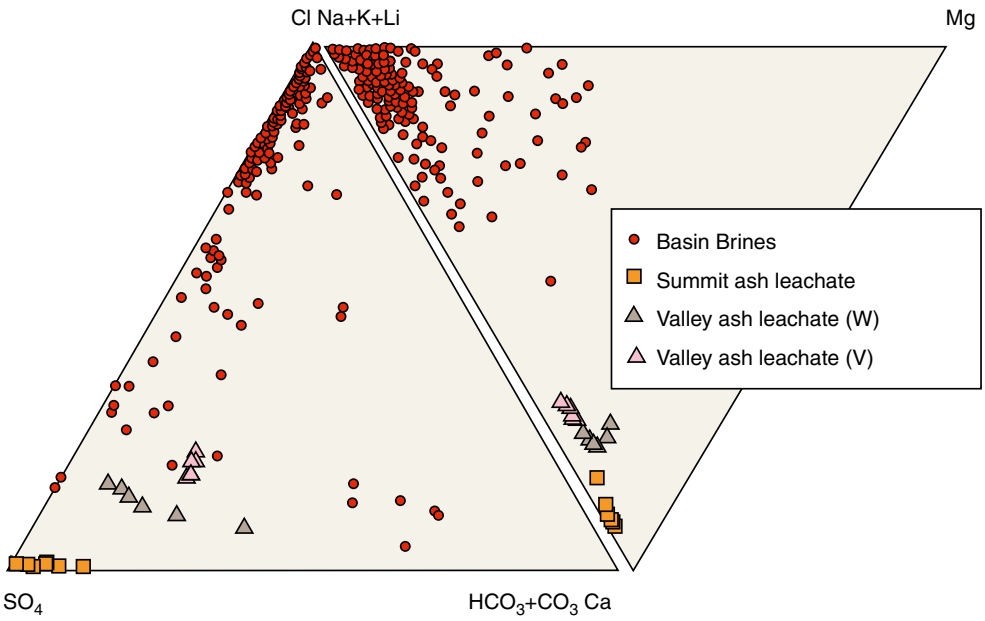

Fig. 2.25 Ionic composition of ash leachate from Lascar volcano summit and Talabre Valley floor (*V* valley floor, *W* valley on west side of volcano) compared with basinal brines of northern Chile (After Risacher and Alonso 2001)

does not supersaturate, a problem that plagued earlier geochemical models of marine-derived potash precipitation in the Zechstein Series. The Harvie et al. (1980) model not only explained the absence of primary kainite in the Zechstein deposits, but also explained the pseudomorphic replacement of gypsum and anhydrite by glauberite or polyhalite and the replacement of glauberite by polyhalite. Previous authors had attributed these replacements in the Stassfurt Salt to burial-stage thermal and solution metamorphism (Borchert and Muir 1964).

Likewise, textures in beds of polyhalite in the Lower Werra Anhydrite (Zechstein – Upper Permian) of northern Poland show they are a very early replacement of anhydrite formed within platform sulphates by diagenetic backreaction with a highly evolved marine brine (Peryt et al. 1998). Formation of polyhalite was preceded by the anhydritisation of the original gypsum. Anhydritisation of primary platform and slope gypsum was an early subsurface alteration driven by syndepositional brine plumes, with ghosts of the primary gypsum texture still visible. Later brines, which were potassium and magnesium rich and nearly saturated with respect to halite, were created by ongoing reflux during more hypersaline conditions on the platform. These more highly evolved brines reacted with anhydrite to precipitate polyhalite along the slopes of the Zdrada Platform. The oxygen and sulphur isotopic compositions of sulphate evaporites indicate that marine solutions were the only source of sulphate ions supplied to the drawndown Zechstein Basin.

Hypersaline groundwaters can also react with adjacent nonevaporite minerals to form indicator clays and authigenic phases. For example, in reactive volcanogenic margins associated with many rift-valley evaporites there are suites of authigenic zeolites and clays (Fig. 12.71). Many formed by the diagenetic reaction of nearsurface saline pore waters with metastable clays derived by weathering and alteration of labile volcanics. The best studied authigenic phases are the sodium silicates, such as magadiite; the borosilicates, such as searlesite; and the zeolites of the alkaline saline lakes, such as clinoptilolite, erionite and analcime. Sepiolite (meerschaum) clays form beds and nodules in saline lake deposits in the Miocene Eskisehir Lake of Turkey. These Mg-rich clays were deposited by direct precipitation out of silica-saturated saline and alkaline lake waters (Ece and Coban 1994). The rather unusual inflow water was derived by the weathering of a Cretaceous ophiolite complex that contained abundant serpentinite and magnesite. Many of the saline lakes in this region of Turkey also contain widespread evaporitic micrites dominated by primary magnesite.

Volcanogenic ash and debris can be a substantial component in the drainage basins of salt lakes and playas in active rift and collision belts. For example, in the Central Andes various volcanic formations overlie Cenozoic evaporites and the longterm meteoric recycling of salts from these labile carapaces into the present endorheic basins is a well-documented process. But, pulsed short term recycling of fractionated ions into the salar hydrology following a volcanic eruption is another widespread, yet less well-documented phenomena (Risacher and Alonso 2001).

During a recent eruption of the Lascar Volcano in northern Chile around 10^9 metric tonnes of air-fall tephra was deposited over the surrounding endorheic basins. Leachate experiments on this ash near the volcano summit and the nearby Talabre Valley produced fluids that were almost pure $CaSO_4$ and near neutral on the summit ashes, while leachates of valley floor ashes were alkaline (pH as

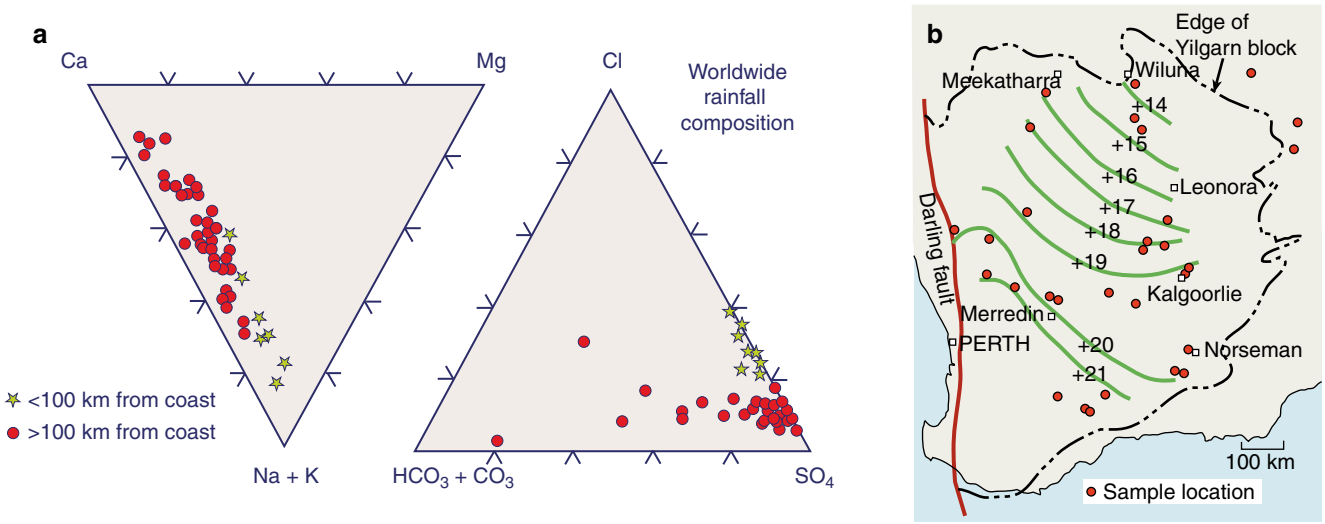

Fig. 2.26 Marine aerosols can supply ions in solution to inland playas and lakes in low relief landscapes. (**a**) Major ion content of worldwide rainfall in relation to distance from coastline, compiled from various sources listed in text. (**b**) Changes in sulphur isotope values (mostly gypsum, occasionally from alunite; After Chivas et al. 1991)

high as 10.5) and more enriched in minor components compared to the $CaSO_4$ leachate of summit ashes (Fig. 2.25; Risacher and Alonso 2001). Sulphur isotope compositions of leached sulphate are consistent with volcanogenic recycling from Tertiary gypsum that underlies the volcanic cordillera. Risacher and Alonso (op.cit.) estimate that 700,000 t of easily soluble $CaSO_4$ were added to nearby endorheic basins by 3 days of eruption. The high pH of the valley floor leachates indicates hydration of alkali and alkali-earth metal-oxides via pyrolysis of vegetation during ash fall. Efflorescent salts encrusted on plants and dissolution of volcanic glass also provided some of the minor leachate components.

The almost pure $CaSO_4$ composition of summit leach waters is compositionally distinct from any present inflow waters in the central Andes. Addition of volcanogenically cycled $CaSO_4$ may explain some of the differences between the observed brine compositions and those predicted by computed simulations of the evaporation series based on the chemistry of longer-term inflows. Rapid recycling of sedimentary gypsum and short-term pulses of salts from labile ashfall is probably not restricted to Lascar volcano. The recycling of ancient salts, and possibly the pyrolysis of vegetation, may have been crucial processes in controlling the ionic proportions of closed basins during episodes of intense volcanic activity in the Tertiary. Some of the anomalies in salt mineralogies in ancient salts may reflect pulses of volcanism rather than variations in short term climate or the degree of leakage. Lascar brine chemistry is an example of a decoupled hydrogeochemical brine system where short term brine chemistries are decoupled from longterm chemistries in the drainage basin.

Marine Aerosols and Continental Gypsum

Brine sources in ancient settings are usually inferred by a study of the regional palaeogeography and a definition of drawdown, seepage and hydrothermal brine supply using outcrop or seismic interpretation. Seepage drawdown or periodic storm floods are thought to be the predominant mechanisms for supplying substantial volumes of marine ions to larger ancient basins. But aerosols are a viable ionic supply mechanism in the hydrochemistry of modern continental arid-zone systems up to a thousand kilometres from the coast. There is even a modern aerosol-defined marine versus nonmarine salt-line in the saline depressions of the Vestfold Hills of Antarctica (Gore et al. 1996).

Aerosols

Modern aerosol supply routes are best seen in isotopic signatures of the resulting salt, but this leads to a circular argument if marine aerosols are invoked as brine sources for ancient evaporites in continental settings (i.e., I assume a portion of the input is marine therefore a proportion is marine), underpinning once more the numerous difficulties involved in separating marine and nonmarine brine sources for ancient salts.

Aerosalts from salt spray can supply substantial quantities of ions to precipitative hydrologies in modern continental salt lake depressions located hundreds of kilometres from the continental margin (Fig. 2.26a). For example, the Murray Basin, in southeast Australia, contains a 500 m thick sequence of Palaeocene to Recent sediments deposited in fluvial to marine settings (Jones et al. 1994). The upper 100 m in the central part of the basin now entrains large vol-

umes of subsurface brines with salinities in excess of 100,000 mg/l. These brines feed many of the discharge playas in the region. They are type II brines with major solute compositions and proportions very much like that of evaporated marine waters (thalassic groundwater). Their isotopic composition, however, is that of evaporated meteoric water. This led Jones et al. (1994) to the conclusion that the brines have been derived by the longterm accumulation of salt from marine aerosols, mixed with continental waters. The marine salts are blown into the basin either as dry salt suspensions or arrived as rainfall. Evapotranspiration in this semi-arid basin greatly exceeds rainfall and so solutes accumulate as brackish near surface waters. These shallow waters are further concentrated via capillary evaporation before escaping into saline discharge lakes. Regionally, the shallow groundwater flow regime is sluggish and not capable of dispelling these brines, so they infiltrate and accumulate above a regional aquitard.

Likewise, the $\delta^{34}S$ values of gypsum accumulating in modern playa lakes in the ancient landscape of southwestern Australia show little relationship with underlying bedrock types or the $\delta^{34}S$ values of any nearby bedrock sulphur (Chivas et al. 1991). Analysis of $\delta^{34}S$ from surficial lacustrine and pedogenic gypsum on a regional scale, in both Western Australia (Yilgarn Block) and South Australia, shows distance-related dispersal patterns over distances of 500–1,000 km from the coast. The highest values (≈21‰) occur near coastlines decreasing to $\delta^{34}S$ values of≈ 14‰ further inland (Fig. 2.26b). Marine sulphate is the dominant source of sulphur to the lakes investigated, with the proportion decreasing from approximately 100 % near coastlines to around 55 % further inland. For tens of kilometres inland of the modern coast, one can argue for a seepage origin of gypsum in many subsealevel lows (salinas) with active seawater seeps and appropriate drawdown surfaces. Further inland the gypsum in the various salt lakes reside in depressions that intersect a regional continental watertable. This watertable is metres or more above sealevel and it slopes seaward, so phreatic seawater seepage is not viable, yet the gypsum still has a marine isotope signature.

In some of the more interior Australian salt lakes, there can be a significant weathered bedrock component to the ionic components in the salt lake waters, especially where the bedrock contains abundant soluble sulphur and high levels of iron. Lake Cadibarrawirracanna (inland South Australia), for example, receives approximately 10 % of its sulphur from weathering of the pyritic Bulldog Shale (Cretaceous); brine in nearby Lake Amadeus receives up to one-third of its sulphate from leaching of evaporites from the Neoproterozoic Bitter Springs Formation.

Like much of arid inland Australia situated up to a thousand kilometres from the coast, the Namib Desert, which hosts one of Africa's most extensive accumulations of modern pedogenic and playa gypsum, is largely supplied by a variable combination of regolith runoff and marine aerosols (Fig. 2.27a; Eckardt and Spiro 1999; Eckardt et al. 2001). An extensive pedogenic gypsum accumulation forms a 50–70 km wide band parallel to the shore in the Central Namib Desert between the Kuiseb and Omaruru rivers. $\delta^{34}S$ analysis of calcium sulphate in this belt and the associated brines, along with an analysis of the brine chemistry shows marine aerosols are a major ion contributor to the gypsum budget (Fig. 2.27b). Marine aerosol sulphates are stored within widespread terrestrial gypsum deposits on the hyperarid gravel plain and are traceable as groundwater precipitates, including gypsum, in near coastal sabkhas and inland playas.

$\delta^{34}S$ values for the gypsum crusts are between +13.0 and +18.8‰, with lower values ($\delta^{34}S$ = +3.1–3.4‰) in crusts near local bedrock sulphur sources, which are typically metal sulphide bodies. These Damaran bedrock sulphides show a wide $\delta^{34}S$ range from −4.1 to +13.8‰ but are significant sulphur sources only on a local scale. Dissolved sulphate in playa, sabkha, spring, borehole and ephemeral river waters have an overall $\delta^{34}S$ range between +9.8 and +20.8‰ but, unlike Australia, do not show a systematic geographical trend tied to distance from the coast. Even so, marine aerosols are the only viable supply mechanism for pedogenic sulphate over such a large arid near coastal area. Further south, in the Holocene Yzerfontein and Zwartwater pans of South Africa, which are some 15 km from the coast, Mauger and Compton (2011) use a combination of stable isotope and radiogenic Sr data to illustrate that marine aerosols are the dominant source of Ca in the bacteriogenic dolomites currently forming in the pans.

Atmospheric sulphates in the Namib are carried landward as marine aerosols, with a large proportion ultimately derived from decomposition of the dimethyl sulphide of phytoplankton. The plankton are an integral part of high levels of primary production driven by the upwelling of the cool Benguela current, the same oceanic system that creates the onshore aridity. The Central Namib Desert lies onshore from the thickest organic-rich sediment accumulations on the Namibian Shelf (Fig. 2.27). This suggests that some of the sulphate component in Namib gypsum is derived from marine H_2S during the anaerobic decomposition of this organic-rich sediment. The gas is probably carried into the desert by frequent advective fogs. Sea salt, decompositional marine biogenic and local bedrock sulphide sources, once invoked as the main sulphate source in these widespread gypsum accumulations in the Namib Desert, cannot account for the volumes of calcium sulphate unless the substantial dimethyl sulphide from plankton is also included in the sulphur supply cycle (Eckardt and Spiro 1999).

That is, most of the marine aerosol that drives extensive onshore gypsum accumulation is a mixture of marine sources

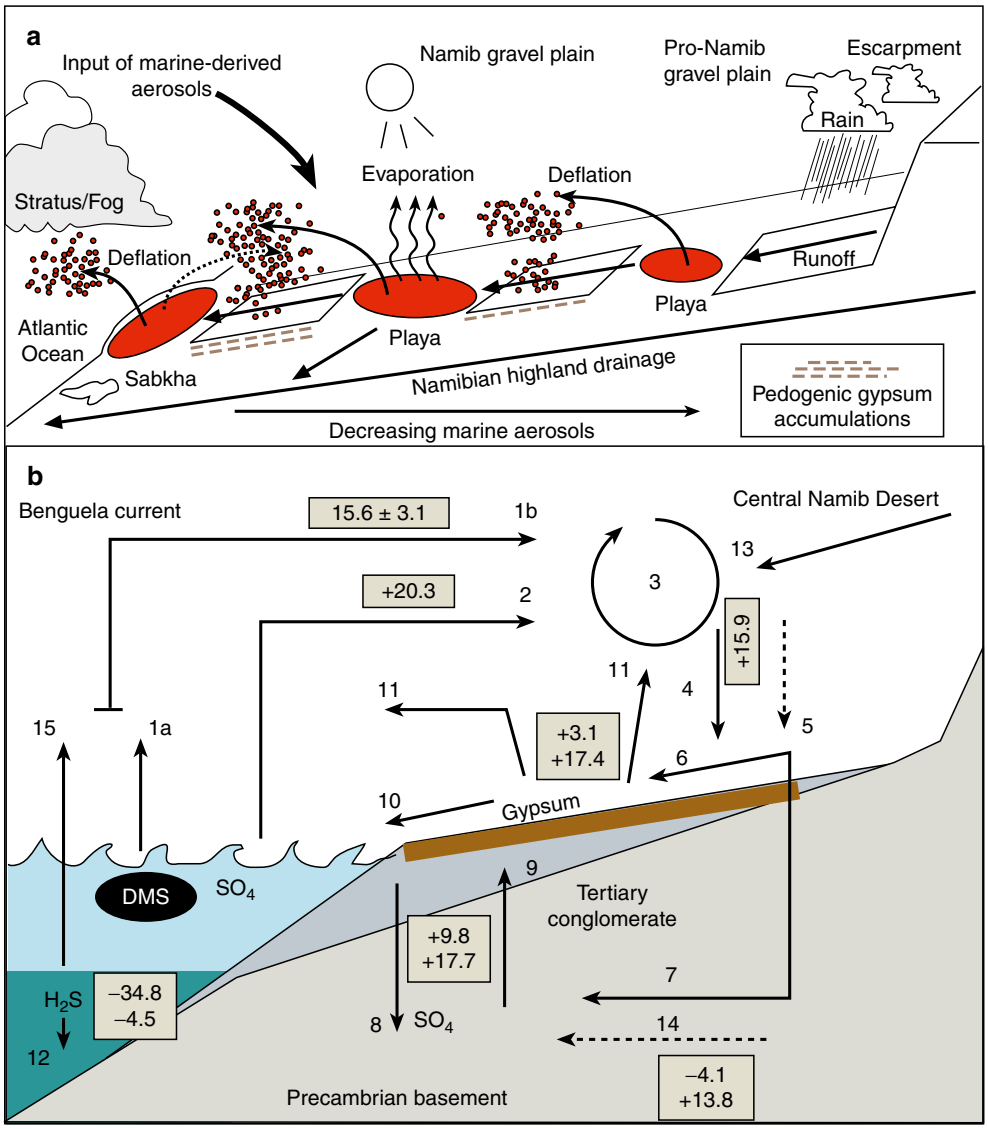

Fig. 2.27 Pedogenic gypsum and the origin of sulphate in waters and sediments of the Namib Desert. (**a**) Model of pedogenic gypsum formation for the Namib Desert where marine-derived dry aerosols are dissolved and mobilized through moisture provided by fog and rain water. Primary gypsum formation takes places in playas and is subjected to eolian and fluvial dispersal. Pedogenic gypsum accumulations increase towards the coast as the volume of marine supplied aerosol increases. (**b**) Schematic representation of hydrogeochemical sulphur cycle along the Atlantic – Namib Desert interface (After Eckardt and Spiro 1999). *Solid arrows* show sulphur pathways, potential sulphur pathways are indicated by dashed arrows. Range of $\delta^{34}S$ composition is indicated in boxed numbers. *1a* dimethyl sulphide (DMS) released from phytoplankton, *1b* Non-sea-(NSS) sulphur, *2* SO_4 release in sea spray, *3* mixing of aerosols in the atmosphere, *4* dry aerosol deposition, *5* – wet aerosol deposition, *6* runoff and gypsum formation, *7* infiltration and groundwater flow, *8* capillary rise and gypsum precipitation, *9* gypsum dissolution and infiltration, *10* gypsum dissolution and runoff, *11* eolian gypsum dust dispersal, *12* in situ sulphide and sulphate formation in Benguela sediments, *13* subcontinental dust input, *14* sulphide oxidation by groundwater, *15* H_2S release to atmosphere (After Eckardt et al. 2001)

of sea spray and atmospheric non-sea-salt (NSS) sulphate, largely supplied by oxidation of biogenic sulphur compounds – dimethyl sulphide, CH_3SCH_3 (DMS). Many organisms, including plankton and seaweeds, rid their bodies of sulphur (a biochemical waste product) by attaching it to various methyl compounds. They do the same with mercury, antimony and arsenic and other toxins. Such compounds are much more volatile than the original and so readily escape from cellular cytoplasm. Hence, a substantial portion of the sulphur isotope signature of pedogenic gypsum in the Namibian Desert reflects a biogenic marine source for the sulphur. The Benguela Current has been a major upwelling system dating back to the Late Miocene (10 Ma) and is likely to have generated DMS for a significant amount of that time (Fig. 2.27a).

Likewise, much of the gypsum in Atacama Desert soils below 1,200 m and within 90 km of the coast receive a portion of their sulphate from coastal fogs locally known as

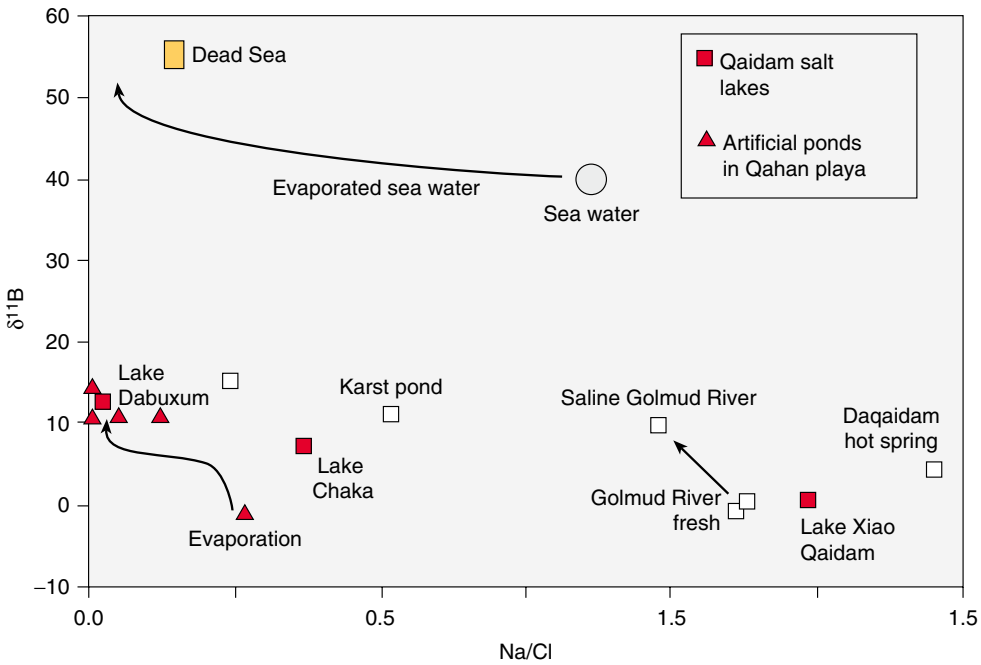

Fig. 2.28 Boron isotopic and Na/Cl ratios of waters and brines in the Qaidam Basin, China (After Vengosh et al. 1995). See Fig. 11.10 for locations

camanchaca. Soils within 50 km of the Pacific Coast and below 800 m elevation, receive 50 % of their calcium and sulphur from marine aerosols (Rech et al. 2003). Interestingly, in this hyperarid region the $\delta^{13}C_{PDB}$ values in the moister area are as negative as −7.2‰ in the soil carbonates, reflecting the metabolic activities of the soil biota, especially in coastal fog oases. In contrast $\delta^{13}C_{PDB}$ values in the drier higher elevation regions, below the puna rainfall belt, have positive values up to 7.2‰, indicating mostly abiogenic precipitation of the soil carbonates (Quade et al. 2007). This same coastal fog system sources much of the economic accumulations of sodium nitrates in the coast-parallel Atacama soils (Böhlke et al. 1997; Chap. 11)

Evaporite Bedrock

Difficulties in distinguishing marine versus nonmarine sources are further complicated by ongoing dissolution of older exhumed evaporites, which can act as chemical feeds into purely continental hydrographically-closed basins. In areas too continental for significant contributions from marine aerosols, this can still create marine-like signatures in the ionic proportions (Na-K-Mg-SO_4 -Cl brines). For example, carnallite-sylvite-halite is a modern lake precipitate in Qaidam Basin, northern Qinghai-Xizang on the Tibet Plateau, China (Fig. 11.10). This basin lies within a large, tectonically active region that is totally isolated from the effects of the ocean and is filled with Neogene clastics and evaporites. Its modern at-surface discharge playas are subject to intense evaporation and are characterised by ephemeral hypersaline brines as well as halite, potash and borate crusts and layers.

The chemical composition and Na/Cl ratios of the dissolved solutes in the modern brines and waters in the salt lakes of Qaidam Basin reveals three main sources (Vengosh et al. 1995): (1) Inflow of hot springs enriched in sodium, sulphate and boron. Evaporation of these waters leads to a high Na/Cl ratio (>1), a Na-Cl-SO_4 brine and an evaporite mineral assemblage of halite-mirabilite-borate (e.g., Lakes Daqaidam and Xiaoqaidam). (2) Inflow surface river waters, which are modified by preferential dissolution of older halite and potassium and magnesium salts. Evaporation of such waters creates Na-(Mg)-Cl brines with low Na/Cl (<1) and low Br/Cl, Li/Cl and B/Cl ratios. (3) Ca-Cl subsurface brines with chemistries controlled by both salt dissolution and dolomitisation processes. Evaporation and salt crystallisation from mixtures of brines (2) and (3) leads to a "marine-like" Na-Mg-Cl brine with Na/Cl ratios $\ll 1$. Although more than 1,000 km from the nearest ocean the precipitated sequence of salts in these lakes is similar to that predicted for progressive evaporation of seawater. Lake Dabuxum and Qarhan playa today contain halite-sylvite-carnallite-bischofite successions.

The lower $\delta^{11}B$ values of the Qaidam basin brines and halites compared to seawater ($\delta^{11}B \approx 40$‰) indicate that the boron within these salt lakes is nonmarine (Fig. 2.28; Vengosh et al. 1995). The $\delta^{11}B$ values of the dilute inflow waters to the Qaidam Basin range from −0.7 to +10.9‰, while brines in the various salt lakes range from +0.5 to +15.0‰ (Vengosh et al. 1995). Both groups overlap and are similar to those of associated granitic rocks ($\delta^{11}B = -2.12$ to +3.7‰) and hence indicate the nonmarine origin of these fluids.

In contrast to the Qaidam playas, the boron isotopic composition of brines, groundwaters and sediments of modern inland salt lakes located nearer the coast across southern

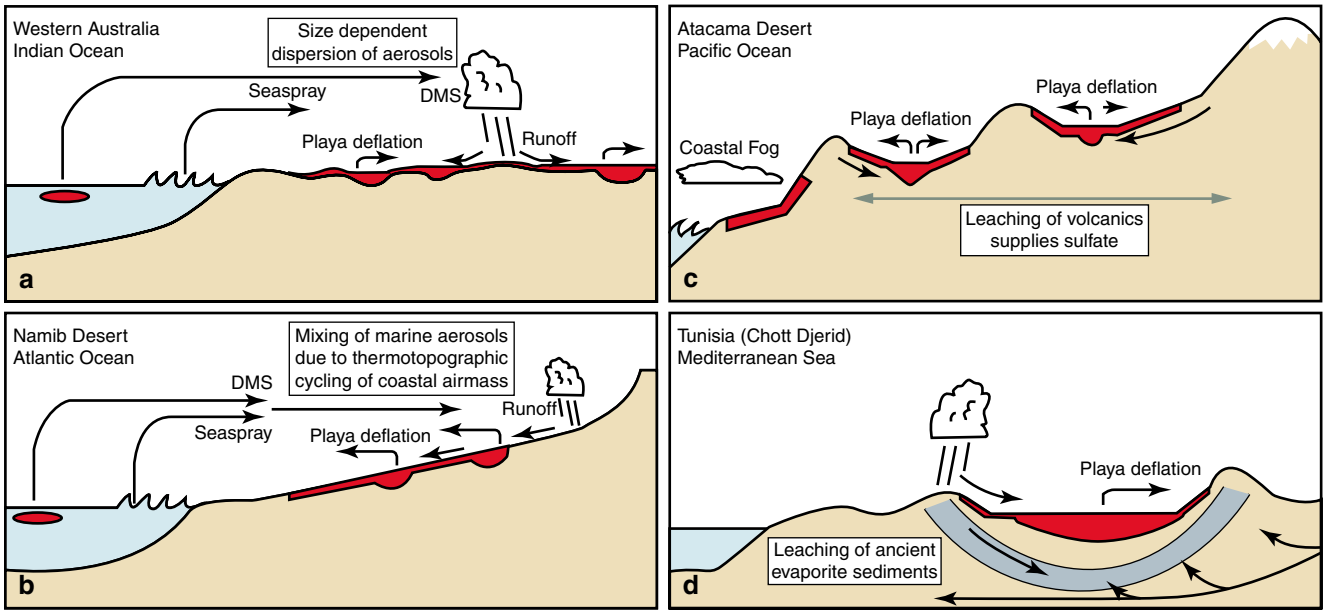

Fig. 2.29 Various atmospheric and groundwater transport mechanisms supplying sulphate to modern continental saline lakes and pedogenic gypcretes in; (**a**) Southwestern Australia, (**b**) Namibian Desert, (**c**) Atacama Desert, (**d**) Chott Djerid. (After Drake et al. 2004)

Australia have a marine component, probably from aerosols (Vengosh et al. 1991). $\delta^{11}B$ values of brines in these salt lakes are 25–48‰, with values up to 54–59‰ in volcanic maar lakes in the higher rainfall areas near coastal region of southeastern Australia. Modern seawater has a $\delta^{11}B$ of 39‰ (Fig. 2.28).

Across much of northern Tunisia, centred on the Chott Djerid region, there is an extensive gypcrete bed up to 7 m thick and sometimes covered by later eolian and fluvial clastics. It is probably the most aerially extensive gypsum bed in northern Africa (Drake 1997; Drake et al. 2004). Sulphur isotope analysis ($\delta^{34}S$) of bedrock samples, groundwater, playa brines, playa sediments, and gypsiferous crusts indicate the ultimate source of sulphate now residing in this regional gypsum unit was not marine aerosols, but weathering and leaching of the subcropping Triassic, Cretaceous, Eocene and Mio-Pliocene marine salts. That is, Drake et al. (2004) conclude that recycling of ancient $CaSO_4$ is the source of the sulphate in the modern groundwater that ultimately deposits the modern playa sediments and crusts of northern Tunisia. The low $\delta^{34}S$ values found in Eocene and Mio-Pliocene gypsum imply that this groundwater recycling of sulphate has been going on for much of the Tertiary. When Tunisian bedrock sources are compared with transport and precipitative processes actively forming continental lacustrine and pedogenic gypsums in Australia, the Atacama and Namibia, it is obvious that, although the source of the sulphur varies from bedrock reworking to marine and local aerosols to eolian reworking, the final pedogenic textures in all areas are derived from a similar set of capillary and eolian precipitative processes (Fig. 2.29).

In summary, the occurrence of modern continental evaporites, especially sulphates, exhibiting largely marine-like (thalassic) brine ionic chemistries and isotopic signatures, is in part due to marine aerosol input and in part due to regionally open or leaky meteoric hydrologies. Mineralogies of preserved evaporitic sediments in low relief depressions on stable cratons can be largely uncoupled from the surface lake chemistries and salt crusts. A leaky hydrology, in a landscape dominated by deep weathering, deep regionally circulating groundwaters, with variable reflux intensity (leakage) can drive the evolution of seawater-like ionic proportions in the subsurface pore waters. It is common set of processes to many modern, low-latitude, tectonically stable desert areas and differs from the less aerially extensive but better documented, highly-endorheic hydrologies of the Basin and Range and East African rift valleys. Perhaps the hydrologically open setting is the more relevant hydrochemical analogue for the continental hydrologies of ancient interior redbed deserts of ancient continents. If so, models based on assumptions of evaporite mineralogies in desert redbeds as being indicators of various "closed basin" hydrologies are largely irrelevant. If so, it makes the hydrochemical distinction between marine and nonmarine evaporites in the geological record even more difficult.

Acid Groundwater in Continental Saline Systems

Many playas atop the deeply weathered ancient regolith in central and southern Australia have elevated iron and sulphur

contents. Salt lakes with more elongate shapes outline Tertiary palaeovalley fills in palimpsest landforms that were created under a different climate than that of today (Fig. 11.34; Clarke 1994). From the mid-Eocene, the climate in Australia became progressively drier until, by the Miocene, much of central Australia was dominated by perennial alkaline lakes (Alley 1998). The subtropical style of weathering that prevailed in the Early Eocene slowly changed with the passage into the Neogene, resulting in the development of a more arid siliceous and ferruginous regolith. The present elevated iron and sulphur levels in the modern Australian landscape ("the Red Centre") were derived, to a large extent, from earlier deep weathering profiles and even today these relicts of a more tropical time are still cycling through the now-arid Australian regolith. Passage into drier conditions allowed the buildup of minerals such as alunite and gypsum in the weathered profiles. The resulting low relief, gently undulating landsurfaces formed partial etchplains with topography controlled largely by the elevation of the paleoweathering front and associated erosional topography of an incised Tertiary-age palaeodrainage and duricrusts. Hilltops may today be composed of fresher rock, while valley slopes, pediments and pediplains are typically composed of fresh to saprolitic rock, along with residual ferricretes that form low mesas.

Palaeodrainage fills can locally be more than 100–200 m thick, with many palaeodrainage networks currently occupied by elongate playa lakes, often with lunette margins and separated by wide areas of desert soils and dune sands. Formation of the weathered regolith largely predated the incision of the palaeodrainage which, in its deepest parts, has cut through to fresh rock (Clarke 1994). Older relict saprolite in the current landscape dates back to the Late Permian-Middle Jurassic. Stripping of this regolith occurred in the Middle Jurassic-Early Eocene during the formation of the seaward-sloping palaeodrainage system. For example, about 400 m of material was denuded from the Yilgarn Craton, to infill the Perth, Eucla and Great Australian Bight Basins. Ongoing deep weathering occurred concurrently with erosion as increasing aridity led to disorganization of the drainage to form numerous chains of lakes, which by the Pliocene had evolved into saline lakes. Some of these palaeovalleys today contain economic capillary uranium (calcrete) deposits.

The great age of the Australia landscape and the buildup of remobilised iron in the modern regolith has led to natural acid brine systems feeding into many inland playas such as Lake Tyrell in Victoria and Lake Yaninee in South Australia. The salt lakes are recharge depressions, which supply free-convecting dense saline brine (Na-Cl-SO_4 reflux brines) to their underlying aquifers.

For example, Lake Tyrell, with an area of 185 km^2, is the largest of three salt lakes in the Tyrell Basin, a structural downwarp located some 10 km east of the N-S trending Tyrell Fault in the riverine plain of the Murray river in semi-arid northwestern Victoria (Fig. 2.30; Macumber 1992). It is a well-studied example of a lunette-fringed lake where deflation plays a major role in controlling morphology and sediment thickness. It evolved into a dry lake some 32 ka, but is today water-covered for up to 3 months in the winter and early spring (Teller et al. 1982). Despite ongoing deflation, up to 5 m of lacustrine sediment is found in the lake centre and consists of varying proportions of clay, silt and sand, covered by an ephemeral halite crust up to 30 cm thick. The lakebeds are underlain by the Parilla Sand, a regional sulphate-rich aquifer.

Lake Tyrell is part of the outcropping expression of a regional oxidised acidic groundwater mass with characteristically low pH of 2–4 and salinities between 35 and 115‰ (Petrides et al. 2006). In contrast to the regional acidic system, the reflux brine plume beneath the lake is neutral (pH ≈ 7) but with salinities around 240‰. Direct rainfall in the winter months provides the bulk of the surface water currently entering the lake, whereas regional discharge and evaporation of westward-flowing Parilla groundwaters contributes most of the salt load. Faulting to the west of the lake uplifts the Parilla Sand aquifer and effectively closes the basin to ongoing throughflow or outward seepage and augments groundwater discharge by halving the saturated thickness of the aquifer. An additional groundwater divide separates the shallower parts of the hydrology of Lake Tyrell from that of Lake Wahpool (Fig. 2.30).

As the regional Fe and S-rich acidic groundwaters resurge into the spring zone about the saline lake edge they precipitate varying proportions of characteristic lacustrine mineral suites made up of varying proportions of alunite, jarosite, halite, gypsum, opaline silica and iron oxyhydroxides. All these mineral phases are rich in Al, Fe and SO_4 giving the oxidised portions of the spring-zone sediments a classic "red bed" appearance (McArthur et al. 1989, 1991; Long et al. 1992a, b; Alpers et al. 1992; Macumber 1992; Benison and Goldstein 2002).

Hemley et al. (1969) showed by experiment that a high H_2SO_4 concentration is needed to form alunite ($KAl_3(SO_4)_2(OH)_6$) and jarosite ($KFe_3\ (SO_4)_2\ (OH)_6$) in any low pH lacustrine environment. Associated acid minerals in the alunite–jarosite family include; natroalunite, alunogen, jurbanite, basaluminite, and rostite (all in the system Al_2O_3-SO4-H_2O), along with natrojarosite, schwertmannite, halotrichite, melanterite, and copiapite (all in the system Fe_2O_3-SO_4-H_2O; Nordstrom 1982a, b; Van Breemen 1982; Bigham and Nordstrom 2000). Once formed in acid settings, these acid minerals may undergo further reactions, breaking down into more stable forms of iron oxides (i.e., goethite or hematite; Bigham and Nordstrom 2000), sulphates (i.e., gypsum or anhydrite; Van Breemen 1982), and aluminosilicates (i.e., microcline or albite; Long et al. 1992a).

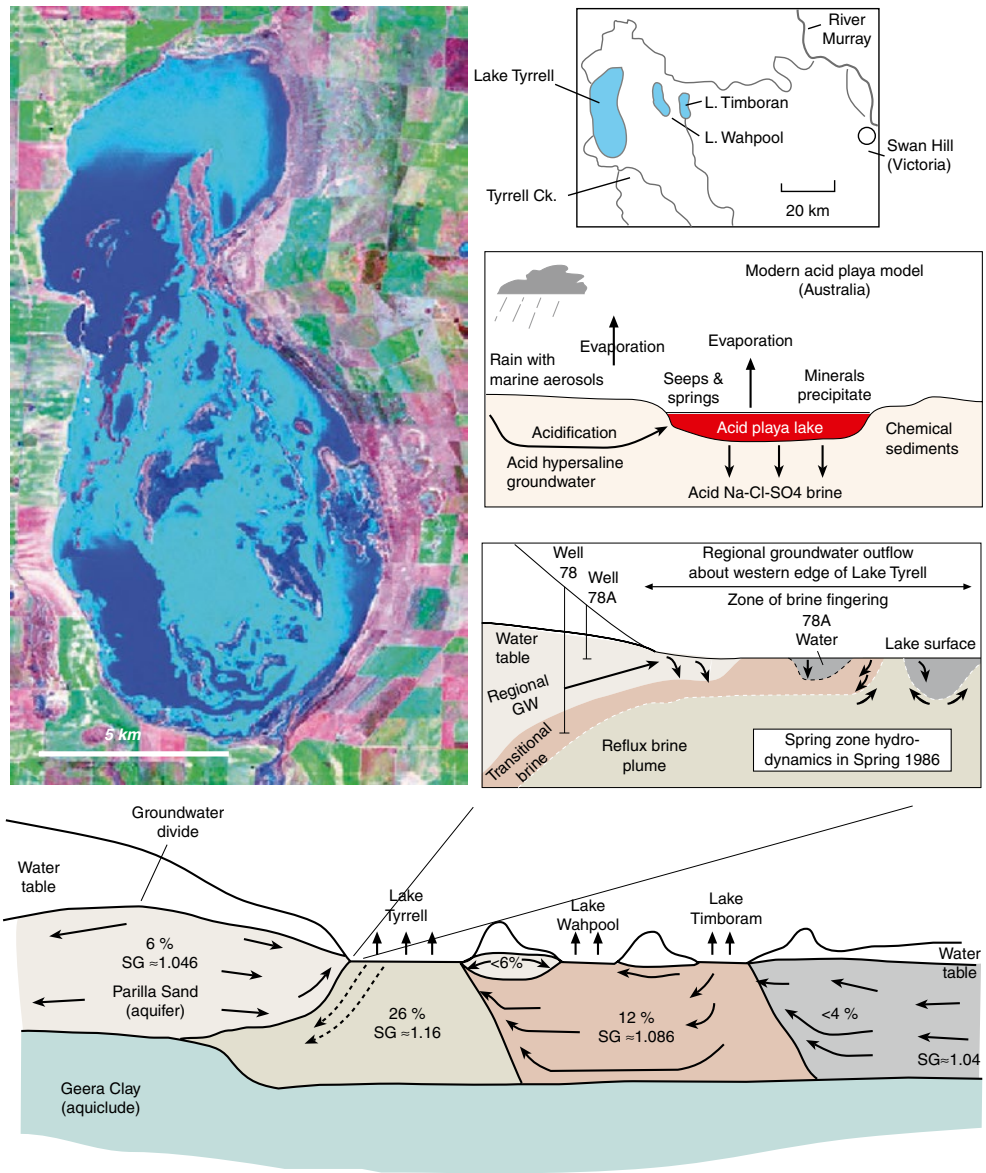

Fig. 2.30 Acid lake formation based on modern natural acid lake and groundwater systems centred on Lake Tyrell in southern Australia (After Macumber 1992; Lyons et al. 1995). These redbed siliciclastic sediments of the Parilla sand aquifer host sulphuric-acid rich saline lakes and groundwaters (pHs of 2–4) which precipitate alunite, jarosite, halite, gypsum, opaline silica, and possibly iron oxyhydroxides. Acidification may occur in the groundwater by processes such as oxidation of pyrite, ferrolysis, and microbial reduction of iron oxyhydroxides. Brine fingering typifies the mixing zone between regional groundwater outflow and the brine reflux prism beneath Lake Tyrell (Landsat image courtesy of NASA)

What make Lake Tyrell sediments interesting is that these lacustrine redbeds indicate the influence of groundwaters carrying elevated levels of sulphuric acid (the pH in the modern groundwater systems of SE Australia is typically in the range 2–4) interacting with the neutral hypersaline waters of the lake itself. These regional naturally acid waters of the regolith are very different brines to the alkaline waters of well documented continental soda lakes and the marine-fed groundwaters of coastal salinas. Acid groundwaters in arid to semi-arid Australia indicate a landscape that has undergone a transition from tropical to arid conditions, perhaps related in part to Australia's northward drift, but more controlled by climate deterioration created by the transition from greenhouse to icehouse climate mode (Chap. 5).

The spring seep region in the Lake Tyrell outflow zone was one of the first wet playas documented with sinking brine plume fingers in the axial saucers of polygons of convective upwelling groundwater across the zone of phreatic mixing about the lake edge (Fig. 2.30; Lyons et al. 1995). As upwelling regional groundwater reaches the Lake Tyrell depression, it evaporates and concentrates and so becomes denser. It then sinks to mix into the regional groundwater crossflow atop the Geera Clay aquiclude. Rather than sinking as a homogenous front these descending waters sink as denser brine fingers surrounded by upward flowing polygonal cells of fresher resurging groundwater that continually resupply the evaporating water surface (Fig. 2.30). This convective counterflow creates large variations in fluid composition in short horizontal distances. Migration of the fingers over time creates numerous laterally migrating redox and salinity interfaces where diagenetic minerals can backreact and precipitate. This patchy diagenesis further complicates simple models for the distribution

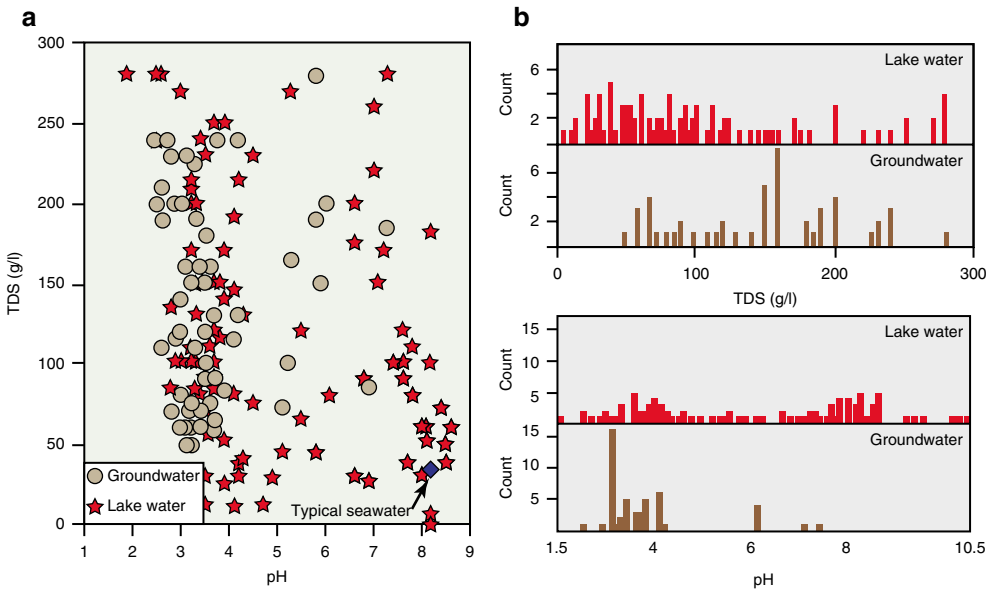

Fig. 2.31 Field pH and salinity (total dissolved solids (TDS) in g/L) data for all West Australian lake and groundwaters (After Bowen and Benison 2009). (**a**) Range of all pH and salinity. Value of typical seawater included. (**b**) Histograms showing the count of all measured lake waters and groundwaters with various salinity and pH values, respectively

of the original "red-bed" precipitates and explains the complex counterplays of salinity indicators seen in ancient spring-seep strandzones (Chap. 1).

Based upon theoretical and experimental evidence, Wooding (1960) and Tyler and Wooding (1991) postulated that near the evaporating water surface, the downward movement of dense brine is confined to fingers or plumes of dense fluids, surrounded by an upward flow of fresher water supplying the evaporating surface. Similar convective polygons can also occur in freestanding zones of mixing near the strandzone edges of coastal salinas and saltworks. Tyler and Wooding (1991) showed that the conditions necessary for the onset of fingered polygonal convection beneath an evaporative wet playa surface are characterized by a modified Rayleigh number, R_c of the form:

$$Rc = \left(kg\Delta\rho\tilde{n}\right)/\left(\mu\varepsilon\right)$$

where k is the intrinsic permeability (in cm^2), $\Delta\rho$ is the difference in density between the evaporated brine and the regional groundwater (in g/cc), μ is the dynamic viscosity, ε is the evaporation rate and g is the acceleration due to gravity.

For a playa groundwater system to exhibit brine fingering, Tyler and Wooding (1991) and Ferguson et al. (1992) suggested that the Rayleigh criteria (R_c) must be around ten or higher. Controlling factors leading to brine instability and convective fingering are sediment permeability, density contrast between the brine and regional groundwater outflow, and the evaporation rate. Using typical playa parameters of $\Delta\rho = 0.3\ g \cdot cm^{-3}$ and $\varepsilon = 30\ cm \cdot year^{-1}$, then the sediment permeability must be $10^{-9}\ cm^2$ (100 md) or higher for the playa groundwater system to begin to convect as polygonally distributed circulation cells. This level of permeability lies between that of unconsolidated clay and sand in the lake sediments, suggesting that spring zones in sandy or permeable carbonate sediments, such as those typically found near playa and marine strandzone margins, are likely to exhibit brine fingering and laterally migrating redox and salinity interfaces. Perhaps some of the megapolygonal patterns seen in domal stromatolites and tepees about the strandzone of Marion lake and other modern coastal salinas are the result of stable convective polygons in a resurgent brine hydrology (Fig. 4.6b, c).

Acid regolith/playa systems dominate also the ephemeral lake hydrologies in paleochannels of the Yilgarn Craton, West Australia (Figs. 2.31 and 2.32; Bowen and Benison 2009; Jagniecki and Benison 2010; Benison and Bowen 2013). Approximately 40 % of the lakes sampled and 84 % of the measured groundwaters in West Australia are extremely acidic (pH <4) with some pHs as low as 1.7. The salinity of lake waters and groundwaters ranges from relatively rare freshwater to common saline water and brine with total dissolved solids >28 %. The fluids are typically Na-Cl to Na-Mg-Cl-SO_4 brines with variable yet locally high amounts of Ca, K, Al, Fe, Si, and Br, especially in more acid waters (Fig. 2.31). The acid brine fluid compositions are unusual in terms of comparison with seawater and most other continental groundwater compositions. For example, in some fluids the amount of Al≫Ca, the amount of Br>K, and comparison of total S to values suggest the presence of uncommon S-bearing species.

Trends in $\delta^{18}O$ and $\delta^{2}H$ illustrate a separation between surface lake water and shallow groundwaters (as in Lake Malata, Eyre Peninsula), and indicate the strong contribution of evaporatively evolved meteoric waters to the lakes. The chemical and isotopic compositions of these fluids indicate a spatially and temporally dynamic, yet regionally consistent, history of brine evolution that is fundamentally different from most other terrestrial closed basin brines. Most importantly, like Lake Tyrell, the West Australian saline lake brines do not evolve from surface evaporation of dilute inflow waters, but rather are fed by highly evolved regionally acid saline groundwaters. This is also true for two small acid

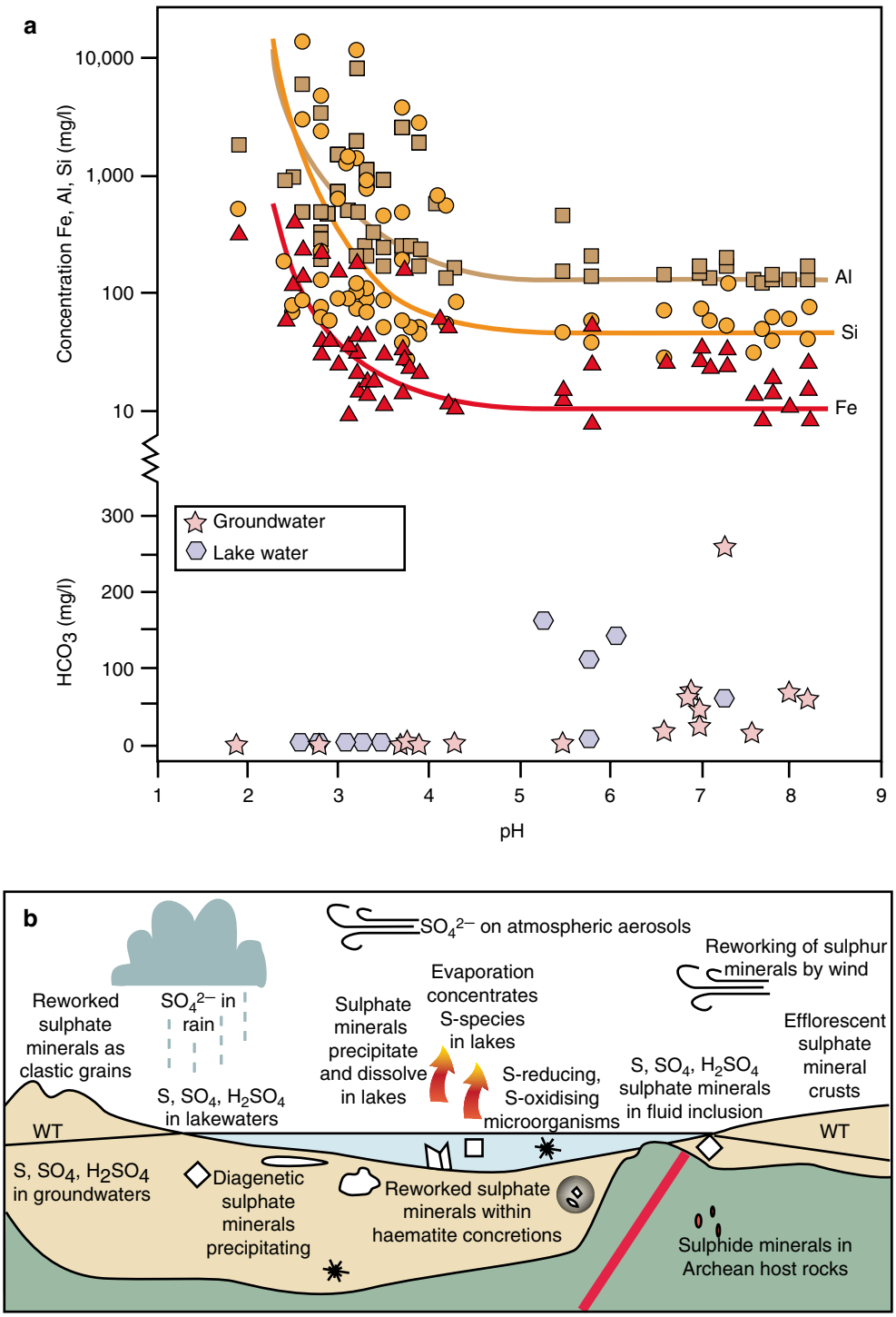

Fig. 2.32 Acid saline lake water chemistry, Yilgarn, Australia. (**a**) Relative concentrations of Fe, Al, and Si in West Australian lake waters and groundwaters versus pH, all three ions increase in concentration with decreasing pH Lower portion shows HCO_3 concentrations in both lake waters and groundwaters tend to increase in more alkaline waters (After Bowen and Benison 2009). (**b**) Schematic of Western Australian acid saline lake system, showing multiple products and processes driving sulphur cycling (After Benison and Bowen 2013)

saline salars in the High Andes of Chile – the Gorbea (3,950 msl) and Ignorado (4,250 m) salars. There the acidity is a direct reflection of the active hydrothermal alteration driven by the andesitic volcanism and the high sulphur content that typifies the region (Risacher et al. 2002). This acidity is localised (2 out of 84 lakes sampled) and is nothing like the more sedimentologically relevant climatic transition that created the acidity in the modern saline waters of southwestern and southeastern Australia.

Rainwaters, which have previously been suggested as a source of sea spray aerosol SO_4 to the lake systems, yielded 7–8 ppm SO_4. Sulphur isotope analysis shows that $\delta^{34}S$ for lake waters is 17.0–19.1‰, for groundwaters is 17.0–18.6‰, for gypsum is 20.2–20.4‰, and for alunite is 18.9‰. These values are consistent with a combination of S sources and sinks. Sulphur cycling processes include sulphide oxidation, evapoconcentration, mineral precipitation, mineral dissolution, and bacterial reduction and oxidation. Field, petro-

graphic, and molecular analyses of microorganisms in these acid saline environments suggest that some are S-oxidizing and S-reducing bacteria. Sulphur-bearing minerals in the area include both sulphides and sulphates (Fig. 2.32b). Sulphides, including pyrite, have been observed in veins and disseminated in surface exposures and shallow cores of Archaean igneous and metamorphic host rocks, as well as in overlying sediments. Sedimentary sulphate minerals include gypsum, bassanite, anhydrite, and rozenite that grow directly from lake waters, and gypsum, anhydrite, jarosite, natrojarosite, alunite, basaluminite, hydrobasaluminite, langbeinite, and rozenite that grow diagenetically from shallow groundwaters.

These sedimentary minerals are subjected to physical reworking and chemical dissolution and re-precipitation. Sulphur cycling among the lithosphere, hydrosphere, biosphere, and atmosphere in acid saline environments is dynamic. Driving forces are rock weathering, weather, and climate, which ultimately influence the water chemistry. Flooding, evapoconcentration and desiccation cycles accelerate short-term local and regional sulphur cycling. The combination of low pH, highly saline waters, and dynamic changes in environment make sulphur arguably the most important element in these environments (Fig. 2.32b; Benison and Bowen 2013).

Similar climate-controlled acid hydrologies probably characterised the continental interior of the USA in the Permian in saline redbeds of both the Opeche Shale and Nippewalla Group halites. Although large volume terrestrial analogs for these deposits are not widespread in the Quaternary, Benison and Goldstein, (2002) argue acidic saline deposits are commonplace in the rock record, whenever continental conditions were saline and subject to transitions from tropical humid to arid. If so they are largely unrecognised. That paper, along with Jagniecki and Benison (2010), propose the following as criteria for wider recognition of ancient acid saline lakes and arid-zone groundwater deposits: (1) high HSO_4 in fluid inclusions in depositional and early diagenetic often red-hued halite (or other evaporite minerals); (2) elevated concentrations of Al, as well as Fe and Si, in the same fluid inclusions; (3) identified remains of acidophilic bacteria or other acidophilic microbes; (4) acid minerals such as alunite or jarosite (or, more likely, the diagenetic products of acid minerals, such as gypsum or anhydrite); (5) presence of continental red beds; and (6) lack of widespread carbonate minerals. They go on to argue that many ancient red bedhosted evaporite saline-pan and saline-lake deposits, which lack widespread bedded carbonates, are likely arid-zone outputs from ancient acidic hydrologies, not just on Earth, but also on Mars (Benison 2006).

Indicators of Brine Parenthood

Chemical and isotopic studies of various evaporite salts have been used for more than four decades in an attempt to define brine parentage. Bromine concentration and chlorine isotopes values have been used in this way to separate marine from nonmarine evaporite source brines, but are perhaps better indicators of salinities and stabilities of the parent brine. Sulphur isotopes can be used to indicate parentage, while the boron isotopic signature from brine inclusions in chevron halite is perhaps the best currently used tool for separating a marine from a nonmarine brine source. The lack of fractionation even with alteration and the creation of new indicator minerals well into the metamorphic realm means a boron isotopic signature in meta-evaporitic tourmalinites is still a reliable separator (Peng et al. 1998). Brine inclusions in unaltered sedimentary halites are also useful indicators of both temperature and salinity, especially when microanalytic techniques are used to interpret the original brine chemistry. In the last two decades the microanalysis of brine inclusions in marine halites has led to paradigm shifts in our notion of the ionic stability of Phanerozoic seawater.

Bromine Profiles – Parentage or Stability?

Trace element concentrations in halite and other salts can sometimes help support an interpretation of a marine origin of the mother brine, especially if microanalytic techniques are used to determine fluid inclusion contents within the salts of interest and the sampled crystals retain primary sedimentary textures, such as bottom-aligned chevrons in halite. Bromine is fourth in anion abundance in seawater anions after Cl, SO_4 and HCO_3 (0.0671 g/1,000 g seawater). With an ionic radius of 1.96 Å it easily substitutes for chlorine (1.81 Å) in the halite crystal lattice as well as in the other chloride salts. Numerous experiments and case studies have found halite's Br-concentration increases in tandem with the bromide concentration of the parent brine, its level in a halite crystal also increases with increases in parent brine temperature and in the speed of crystallisation (Table 2.9; Wardlaw and Schwerdtner 1966; Raup and Hite 1978; Küster et al. 2009).

Fixation of Br in the halite lattice is also dependent on the level of other ionic species present in the solution. Cl is strongly preferentially partitioned over Br into Na, K and Mg halogen salts during their precipitation and Br preferentially remains behind in solution (Fig. 2.12). Br content decreases with increasing $MgCl_2$ content in the mother brine and with any increase in the degree of secondary recrystallisation (Dean 1978). Its conservative behaviour in marine brines means that it has commonly been used as a salinity indicator in ancient halites and other chloride minerals.

The distribution of bromine between a halite crystal and the coexisting solution is described by its partition coefficient (D):

$$D = \left(Br_{mineral}/Cl_{mineral}\right)/\left(Br_{solution}/Cl_{solution}\right)$$

During initial evaporation of seawater, both Br and Cl increase in concentration in the residual brine, and the Br/Cl content of these waters does not vary (Fig. 2.12). When halite saturation is reached, Cl is preferentially removed over Br from the brine. A small fraction of the Br is also partitioned out into the halite,

Table 2.9 Some examples of the use of Br content to interpret depositional setting of the halite

Unit	Location	Observation	Reference
Sedom Fm halite, Pliocene, Sedom diapir	Dead Sea, Israel	Br contents in inclusion in chevron halite crystals (52–191 ppm) are within the range of halite precipitated from marine water, and the highest value (191 ppm) occurs in a general upward increasing, but fluctuating, salting-upward trend is close to those expected for halite associated with potash salts	García-Veigas et al. (2009)
Halokinetic halite of the Upper Red Formation, Middle to Late Miocene	Iran	High bromide content in halites sampled suggests their marine origin (BR ranges up to 226 ppm used to suggest salinities sufficient to precipitate primary marine sylvite were never reached and to confirm the absence of the extensive meteoric alteration or subsequent bromine depletions.	Rahimpour-Bonab and Kalantarzadeh (2005)
Zaragoza Gypsum, Lower Miocene, Ebro Basin	Spain	Br contents in halites with primary textures (hoppers and chevrons) were below the standard for lowest marine Br concentration (<13 ppm). Tis and inclusion microchemistry are interpreted as indicating non-marine halite precipitation or recycling of marine halite in nonmarine waters. Also imply that conditions for co-precipitation of halite and glauberite, or for precipitation of Na-sulphates (mirabilite, thenardite) were never fulfilled in the saline lake system of the Ebro basin at this time	Salvany et al. (2007)
Rot Halite, Lower Triassic in Rockensussra 2/83 borehole	Northern Germany	Br content in fluid inclusions in chevron halite is 78–107 ppm, indicating a marine origin of the halite. Brines of primary gas-liquid inclusions are thus representative samples of trapped evaporate water and they may be used for the reconstruction of the composition of Early Triassic seawater.	Kovalevych et al. (2009)
Z2 in Upper Permian Zechstein of Polish Basin	SW Poland	Br content in halite (49–77 ppm) associated with sylvite daughter crystals in chevron halite indicated that these salts had a marine origin with recycling of earlier salts and were deposited at an elevated temperature, from concentrated seawater with a high potassium content, that favoured precipitation of primary sylvite.	Vovnyuk and Czapowski (2007)
PZ2 and PZ3 in Upper Permian Zechstein of Polish Basin	Poland	Combined use of bromine concentration in halite, isotopic composition of anhydrite, and major-ion composition of brine inclusions in primary halite crystals used to interpret episodes of overturn in Zechstein brine mass	Garcia-Veigas et al. (2011a)
Zechstein 2 rock salts in the Southern Permian Basin, Upper Permian	Germany	Br profile of the bedded and layered salt is characterized by a continuous upward increase in the bromide contents from base to top, indicating progressive evaporation of seawater. This same profile shape is retained in halokinetic salt layers in the studied salt diapirs. Br contents can be redistributed and homogenised via recrystallization processes of halokinesis.	Küster et al. (2009)
Ara Salt and carbonate stringers, Neoproterozoic to Earliest Cambrian, South Oman salt basin	Oman	Br geochemistry revealed significantly higher bromine contents (up to 280 ppm) in the early halite compared with the late halite (173 ppm). The distribution patterns and the (high) bromine contents of early halite are consistent with precipitation caused by seepage reflux of highly saturated brines in carbonate stringers during deposition of the overlying rock salt interval.	Schoenherr et al. (2009)
Early Cambrian Salt Basins of Siberia	Russia	Br content is 60–280 ppm in Usolye halite, 58–203 ppm in Belsk rock salt, and 60–261 ppm in Angara rock salt. Value ranges imply a primary marine source for these halites, a lack of meteoric dilution or subsequent mobilisation indicative of pervasive recrystallization.	Petrychenko et al. (2005)

but most remains behind in the brine. As saturation with the bitterns (K-Mg-Cl) salts is reached, the slope of the Br-Cl curve flattens out as these minerals discriminate somewhat less in terms of Br incorporation (higher partition coefficients).

In earlier studies Br content of ancient rock salt was used to separate marine from nonmarine precipitates (Dean 1978; Holser 1979; Wilgus and Holser 1984). Fresh seawater contains around 65 ppm bromine and reaches 500 ppm by the onset of halite precipitation (Fig. 2.12). Halite from a normal marine feed purportedly contains 50–100 ppm bromide and it should increase up to a maximum of around 270 ppm at the onset of bittern precipitation (Valyashko 1956, p. 578; Herrmann et al. 1973). Halite that has been recrystallised in a second cycle of solution and reprecipitation in a brine of lower Br content than the original brine should have a bromide content of 20 ppm or less, especially if the recycling waters were nonmarine. But variations in salinity and the dilution by shallow to ephemeral residual brines, along with ongoing halite recrystallisation and backreaction, all influence the final Br content of any halite crystal in both marine and nonmarine settings (Fig. 2.33a). Hardie (1984) discussed the limitations of using whole rock Br content as a depositional indicator and clearly showed the possible confusion that results if Br levels in wholerock halite samples are used in an attempt to separate marine from nonmarine halite.

Even if Br content of halite is not always a reliable indicator of the source of the mother brine, perhaps it can tell us something about brine stability at the time a salt was precipitated. Figure 2.33b plots bromide profiles from halites in two saline giants, the Paradox and the Prairie evaporites where values change in a predictable upsection fashion. Increasing upward trends indicate an increase in average annual brine salinity, while decreases indicate freshening (shown by arrows in Fig. 2.33b). The trend to very high values

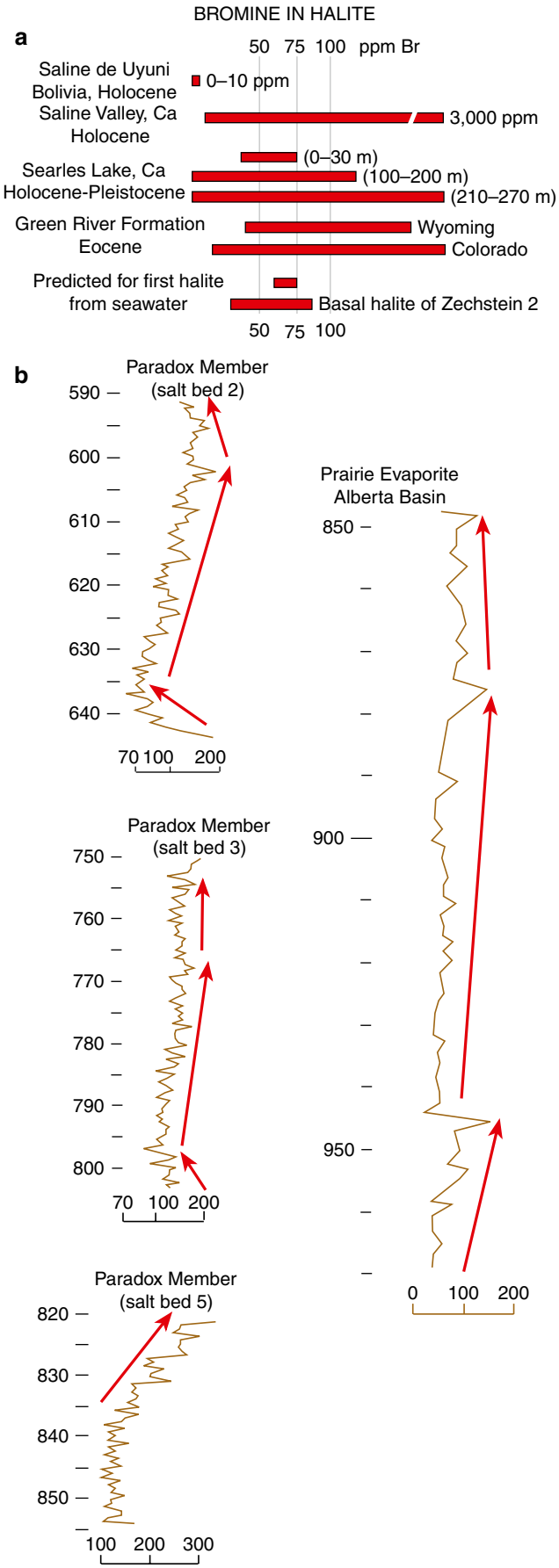

(Br >250 ppm) near the upper part of salt member 5 of the Hermosa Formation in the Paradox occurs beneath a potash bed and indicates higher salinities needed for the precipitation and preservation of bittern salts. The upward trends for the Prairie evaporite, although sampled at a somewhat coarser spacing than the Hermosa, show similar brining upward profiles beneath potash beds. In a similar fashion Bein et al. (1991) used Br variations in brine inclusions in halite to define a southerly brine source for Permian San Andres halite in the Palo Duro Basin, Texas.

Halokinesis drives pervasive halite recrystallisation and migration of primary fluid inclusions to the polyhedral boundaries of newly formed flow-aligned crystals (Chap. 6). Recognition of this pervasive alteration in crystal textures has led some authors to question the reliability of Br profiles as depositional indicators in halokinetic salt (Bornemann et al. 2000). In a study of Zechstein salt in variably flow-overprinted profiles, Küster et al. (2009) found characteristic trends in depositional bromide profile were generally preserved in both the bedded and the more intensely deformed domal salt layers. However, they also concluded that ongoing pervasive deformation and recrystallisation will ultimately homogenise Br profiles in intensively deformed salt. They went on to argue that preservation of the characteristic depositional salting upward trend in the bromide profiles, in all salt dome layering they studied, indicates that large-scale brecciation, folding processes or circulating bromide-rich fluids played only a minor role during the formation of the salt domes.

The relative bromine content with respect to chlorine in a saline aquifer in the vicinity of dissolving salt structures has been used to define the parentage of the saline pore fluid. Figure 2.34 illustrates the Br/Cl content of produced water in the vicinity of a salt structure in offshore Louisiana (Steen et al. 2011). Most of the produced waters plot well below the typical bromine trajectory of evaporated modern seawater (McCaffrey et al. 1987). The Br depletion indicates elevated concentrations of chloride in the pore fluids, it is likely produced by the dissolution of halite rather than by evaporation of marine waters.

Contents of most other trace elements in marine evaporite salts are typically very low and not diagnostic of brine source. Iodine has very low partition coefficients in halite, sylvite, carnallite and the other bitterns, so they contain very little iodine. Its relatively large ionic radius impedes its replacement of chlorine ions in the respective lattices, so any residual liquor (marine or nonmarine) is strongly enriched. Iodate salts form pedogenic phases in the hyperarid Atacama

Fig. 2.33 Bromide in halite. (**a**) Bromine levels in halite in marine and nonmarine settings clearly showing that Br levels have a degree of spread that does not support the assumption that nonmarine or recycled halite will always show values less than first cycle precipitates (in part after Hardie 1984). (**b**) Br profiles from the Paradox Member, Hermosa Formation in the Paradox Basin and the Prairie Evaporite in the Alberta Basin. All wells drawn to the same depth scale (After Holser 1966, 1979)

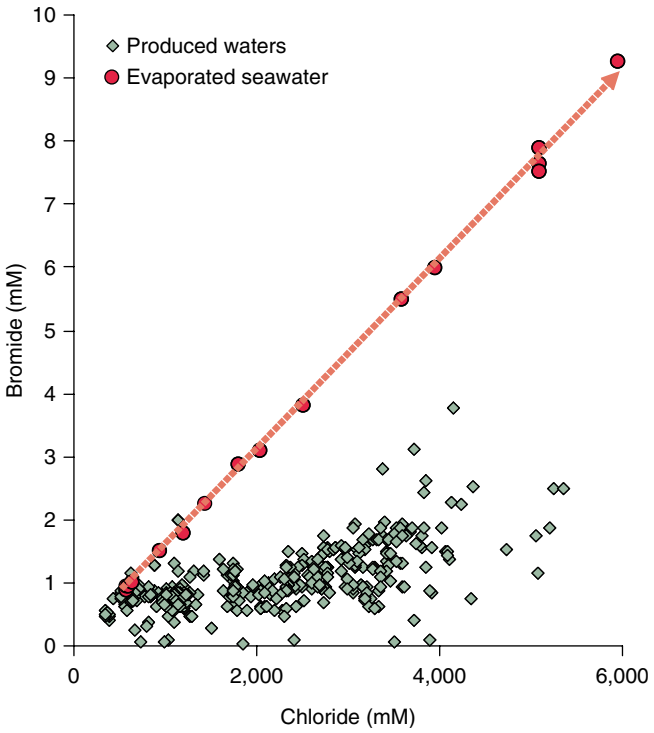

Fig. 2.34 Dissolved bromide–chloride relations for produced waters from the reservoirs in the vicinity of a dissolving salt structure in offshore Louisiana. Most waters plot well below the trend for evaporated seawater (McCaffrey et al. 1987), reflecting elevated concentrations of chloride produced by the dissolution of halite rather than by evaporation of marine waters. The extremely low Br/Cl ratios of a few waters may reflect dissolution of low-Br recrystallized halite (After Steen et al. 2011)

desert (Chap. 11). Fluorine minerals occur principally in sulphate deposits and salt clays that possibly have been influenced by hydrothermal inflows, although some Russian authors have argued for a marine evaporite association (Fig. 7.92). There is no published data on fluorine behaviour during seawater concentration. However, if fluorine concentrates at the same rate as Cl during evaporation, then seawater should have a fluorine concentration around 10 mg/l at the onset of halite saturation. Rubidium and ammonium substitute for potassium in crystal lattices of the bittern chlorides (e.g., sylvite, carnallite). Caesium does not occur in halite, and lithium in water-soluble form is only found in concentrations up to 0.2 ppm. The colouring of halite often feigns higher amounts of heavy metals. Only 2 ppb of trivalent iron can give halite a yellow colour, while a few more parts per billion can turn salt red (Sonnenfeld 1995).

Sulphur and Oxygen Isotopes

Modern seawater sulphate has a homogeneous and well-defined isotopic composition for both sulphur and oxygen:

$$^{34}SSO_4 = +20 \pm 0.5 \quad CDT$$

$$^{18}OSO_4 = +9.5 \pm 0.5 \quad SMOW$$

Likewise, the fractionation of sulphur and oxygen, which occurs during the transition from aqueous to solid state of sulphate is also near constant at earth surface temperatures. For gypsum, the mean values of the isotope enrichment factor are (Pierre 1988):

$$\varepsilon^{34}S_{gypsum-SO4} = 1.65‰$$

and,

$$\varepsilon^{18}O_{gypsum—SO4} = 3.5‰$$

Thus the $\delta^{34}S$ and $\delta^{18}O$ values of sulphate evaporites are directly related to the state of the aqueous sulphate reservoir where precipitation occurred. A plot of ancient marine $CaSO_4$ evaporites shows the sulphur curve for seawater has varied across time from +30‰ in the Cambrian, to around +10‰ in the Permian and the it increased irregularly in to Mesozoic to its present value of +20‰. Oxygen values show much less variability (Fig. 2.35a). Variations are reflected in all major marine evaporites and were most likely controlled by major input or removal of sulphides from the oceanic reservoirs during changes in tectonic activity and weathering rates. Historically, simple removal of oceanic sulphate (increase in evaporite formation) was thought not be accompanied by dramatic isotopic effects.

Rather, variations within the global sulphur cycle were thought to be controlled by a redox balance, which linked to the carbon cycle and the atmospheric oxygen budget. The oxidative part of the global sulphur cycle is governed by continental weathering (especially of marine black shale), riverine transport and evaporite deposition, while the reduced part is controlled by levels of fixation of reduced sulphur-bearing compounds in the sediment column, mostly as pyrite via bacterial sulphate reduction (Fig. 2.35b). The latter process will preferentially remove isotopically light sulphur from seawater and so increase its $\delta^{34}S$ value in the ocean and any subsequent marine evaporite salt.

However more recent work questions aspects of this older sulphur cycle model. As just discussed, variations in $\delta^{34}S_{sulphate}$ across the Phanerozoic are traditionally interpreted to reflect changes in the total amount of sulphur buried in ocean sediments as pyrite—a parameter referred to as f_{pyr} and defined as (Hurtgen 2012);

$$f_{pyr} = \left[\left(\text{pyrite S burial}\right)/\left(\text{pyrite S burial} + \text{evaporite S burial}\right)\right].$$

However, Wortmann and Paytan (2012) conclude that the 5‰ negative $\delta^{34}S_{sulphate}$ shift in ~120-million-year-old rocks was caused by massive seawater sulphate removal, which accompanied large-scale evaporite deposition during the opening of the South Atlantic Ocean (Fig. 2.35). Evaporite formation does not directly cause sulphur isotope fractionation; in their model, the negative $\delta^{34}S_{sulphate}$ shift is driven by lower pyrite burial rates resulting from substantially reduced marine sulphate levels.

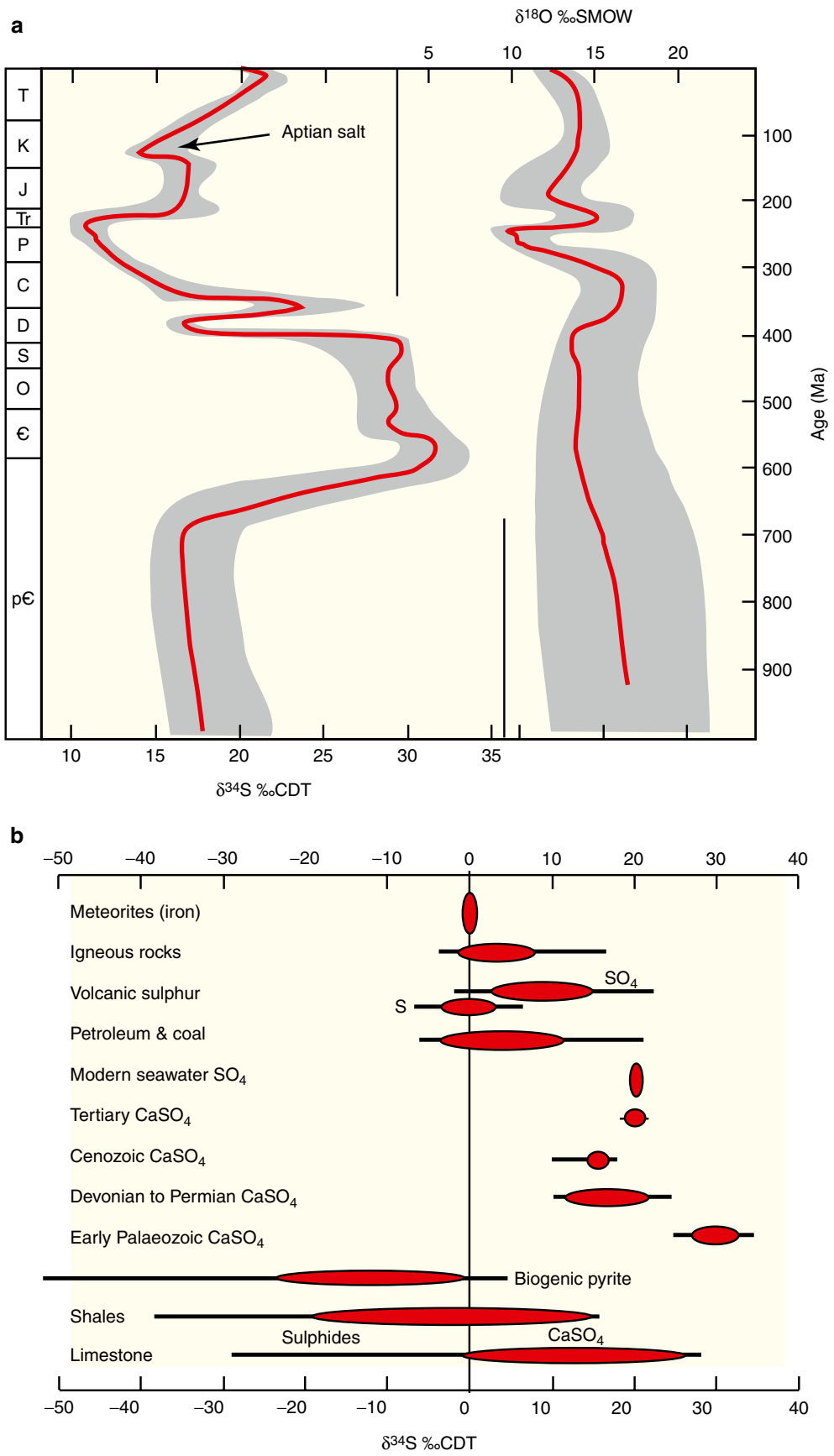

Fig. 2.35 Sulphur and oxygen isotopes. (**a**) Sulphur and oxygen isotope age curves for marine sulphate evaporites. The heavy lines are the best estimates of $\delta^{34}S$ and $\delta^{18}O$ values of calcium sulphate minerals in equilibrium with world ocean sulphate at that time. Shaded areas are estimated uncertainty envelopes of these curves. (**b**) Isotope range of various systems and selected seawater sulphate (After Pierre 1988; Veizer et al. 2000)

The authors attribute a 5‰ positive $\delta^{34}S_{sulphate}$ shift in the world's oceans about 50 Ma ago to an abrupt increase in marine sulphate concentrations as a result of large-scale dissolution of freshly exposed evaporites; they argue that the higher sulphate concentrations in the ocean led to more pyrite burial.

Likewise, Halevy et al. (2012) studied past sulphur fluxes to and from the ocean, but over a longer time-frame (the Phanerozoic). They quantified sulphate evaporite burial rates through time, then scaled these rates to obtain a global estimate of variation in sulphur flux. Their results indicate that sulphate burial rates were higher than previously estimated, but also greatly variable. When Halevy et al. (2012) integrated these improved evaporite burial fluxes with seawater sulphate concentration estimates and sulphur isotope constraints their calculations implied that Phanerozoic f_{pyr} values (f_{pyr}=fraction of sulphur removed from the oceans as pyrite) were ~100 % higher on average than previously recognized. These surprisingly high and constant pyrite burial outputs must have been balanced by equally high and constant inputs of sulphate to the ocean via sulphide oxidation (weathering). These relatively high and constant rates of pyrite weathering and burial over the Phanerozoic, as identified by Halevy et al. (2012), suggest that the consumption and production of oxygen via these processes played a larger role in regulating Phanerozoic atmospheric oxygen levels than previously recognized – perhaps by as much as 50 %.

Both studies recognize the importance of episodic evaporite burial on the sulphur cycle, while Wortmann and Paytan (2012) clearly show that large-scale deposition and dissolution of sulphate evaporites over relatively short geologic time scales can have an enormous impact on marine sulphate concentrations, pyrite burial rates, and the carbon cycle and probably have a more important role than previously recognised in regulating the chemistry of the ocean atmosphere system.

The ^{18}O content in seawater sulphate fluctuates less than sulphur values over geologic time. The isotopic composition of sulphate minerals varied only slightly from the Neoproterozoic to the Palaeozoic decreasing from +17 to +14‰ (Fig. 2.35a). Values then rose during the Devonian to reach +17‰ during the Early Carboniferous (Mississippian). Values then fell to=+10‰ during the Permian, mimicked by a similar decline in sulphur values in the Late Permian to Early Triassic. Since a rise to +15‰ in Early Triassic values of marine sulphate minerals have remained close to +14‰ (add 3.5‰ to mineral determined value to give ambient seawater value). Overall, oxygen values show little correlation with marine sulphate variation and are perhaps controlled by sulphide weathering reactions that contribute sulphate to seawater and the dissolution of sulphate evaporites.

Further discussion on global controls of isotope chemistry lies outside the evaporite focus of this book. What is significant is that, given the now well established sulphur isotope age curve, a comparison of a measured $\delta^{34}S$ value from an anhydrite or gypsum of known geological age to the curve allows an interpretation of a possible marine origin to the salt. A value which differs from the marine signature does not necessarily mean a nonmarine origin, but at the least it does mean diagenetic reworking or, more likely, a groundwater-induced recycling of sulphate ions into a nonmarine saline lake (Pierre 1988). Such oxygen and sulphur isotopic crossplots have been used to establish the continental (nonmarine) origin of the Eocene gypsum of the Paris Basin and the upper Miocene gypsum of the Granada basin, with sulphate derived from weathering of uplifted Mesozoic marine evaporites (Fontes and Letolle 1976; Rouchy and Pierre 1979; Pierre 1982). Sulphur in evaporitic sulphate can come from a number of sources other than reworked marine evaporites, likely isotopic ranges of possible sources are given in Fig. 2.35b.

Crossplots of oxygen with carbon or deuterium isotopes are useful in defining the origin of evaporitic carbonates. If these carbonates are interlayered with gypsum or anhydrite at the mm scale, then their signatures are very useful in determining the origin of the waters precipitating both the carbonates and the sulphates. This was the rationale used by Bellanca and Neri (1986) in a study of the origin of gypsum and associated carbonates in the Messinian of Sicily. The oxygen and hydrogen isotope compositions of crystal water from the laminar gypsum indicate primary precipitation of the sulphate from marine waters concentrated by evaporation (Fig. 2.36a). The isotopic data also show compositional changes due to periodic influx of continental waters into the depositional basin seen by the clustering of the laminar gypsum values along the SMOW concentration-dilution line with a regression coefficient of 0.98. The massive gypsum signature indicates rehydration by meteoric waters (probably modern). Open-marine-water incursions probably led to the deposition of carbonate layers overlying the laminar gypsum. These contain abundant aragonite with textural features and isotopic compositions suggesting precipitation in shallow and quiet marine waters slightly enriched in ^{18}O by evaporation (Fig. 2.36b).

Sulphur is largely resistant to isotopic fractionation during burial alteration and transformation (Worden et al. 1997). Primary marine stratigraphic sulphur isotope variation is preserved in anhydrites of the Permian Khuff Formation, despite subsequent dehydration to anhydrite during burial (≈1,000 m) and initial precipitation as gypsum from Permian and Triassic seawater. Gypsum dehydration to anhydrite did not involve significant isotopic fractionation or diagenetic redistribution of material in the subsurface. At depths greater than 4,300 m, the same sulphur isotope variation across the Permian-Triassic boundary is still present in elemental sulphur and H_2S, both products of the reaction of anhydrite with hydrocarbons via thermochemical sulphate reduction (Fig. 9.65). Clearly, thermochemical sulphate reduction did not lead to isotope fractionation. Worden et al. also argues that significant mass transfer has not occurred in the system, at least in the vicinity of the Permian-Triassic boundary, even though elemental sulphur and H_2S are both fluid phases at depths greater than 4,300 m. Primary differences in sulphur isotopes have been preserved in the rocks and fluids, despite two major diagenetic overprints that converted the sulphur in the original gypsum into elemental sulphur and H_2S by 4,300 m burial and the potentially

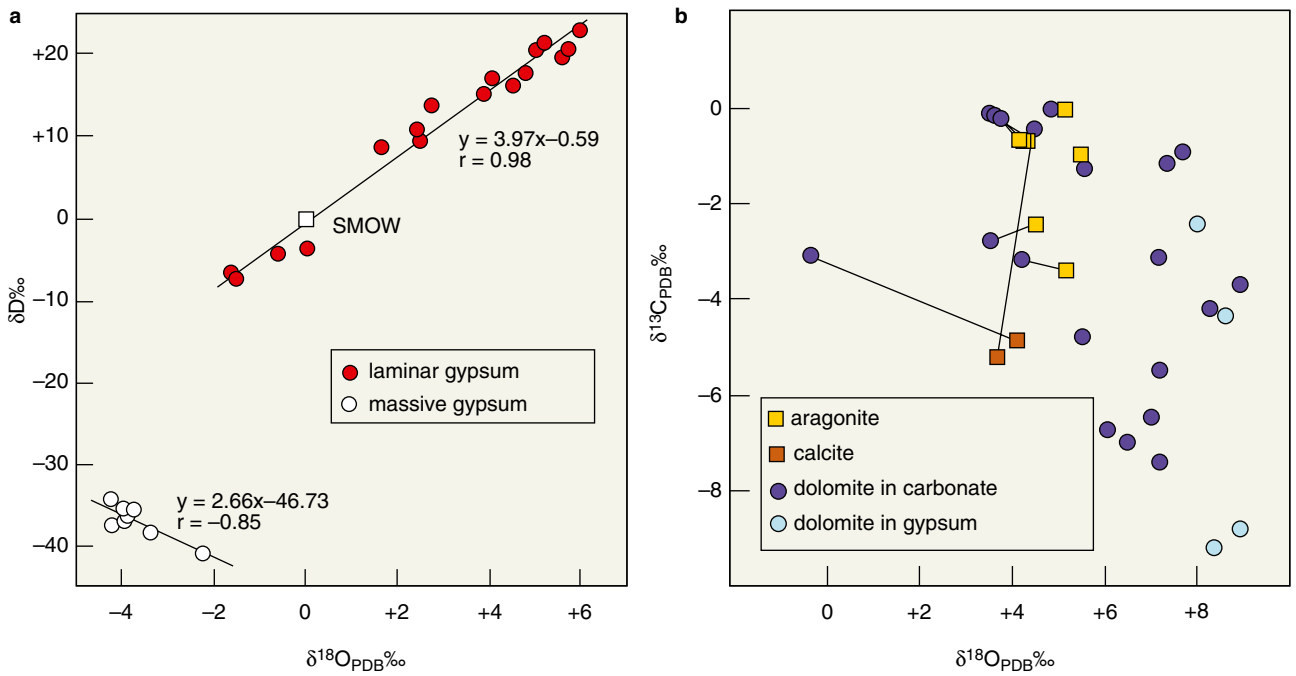

Fig. 2.36 Isotope crossplots in Messinian evaporites, Sicily. (**a**) Isotopic associations (carbon and oxygen) in water of crystallisation. (**b**) Deuterium- carbon relationships in carbonate layers in the same units (After Bellanca and Neri 1986)

mobile nature of some of the reaction products. That is, all reactions must have occurred in situ; there was no significant sulphur isotope fractionation, and only negligible sulphur was added, subtracted, or moved internally within the system.

The resistance to fractionation of sulphur isotopes in subsurface pore waters can also be utilised to determine the origin of saline thermal pore waters. In a study of sulphur isotopic compositions of waters in saline thermal springs, Risacher et al. (2011) came to the interesting conclusion that dissolution of continental sedimentary gypsum from the Tertiary-age Salt Cordillera was the dominant supplier of sulphate (Fig. 2.36). The sulphate in the springs was not supplied by the reworking of volcanic sulphur in this active volcanic terrain. $\delta^{34}S$ values from 3 to 11‰ in continental gypsum and this also encompasses the range of $\delta^{34}S$ in pedogenic gypsum (5–8‰) and in most surface waters (3.4–7.4‰) including salt lakes (Rech et al. 2003). Frutos and Cisternas (2003) found isotope ratios ranging from 1.5 to 10.8‰ in five native sulphur samples. Figure 2.37 presents the sulphur isotope ratio of dissolved sulphate in thermal waters sampled by Risacher et al. (2011) and references therein. The $\delta^{34}S$ of sulphate in northern thermal springs is within the range of salt lakes waters and continental gypsum. In an earlier paper Risacher et al. (2003) showed that salar brines leak through bottom sediments and are recycled in the hydrologic system. Deep circulating thermal waters are dissolving continental gypsum in sedimentary layers below the volcanics associated with the present day salars. The exception to this observation is the sulphur in Tatio springs where Cortecci et al. (2005) proposed a deep-seated source for the sulphate, related to magma degassing (Fig. 2.37).

Boron Isotopes

Boron is a relatively light element in nature, with the atomic number of 5. Boron has two stable isotopes, ^{10}B and ^{11}B, which make up approximately 19.82 and 80.18 % of total boron, respectively. Boron isotope ratios are given in the delta notation with $\delta^{11}B$ (‰) defined as deviation from standard NIST-SRM 951 (Xiao et al. 2013):

$$\delta^{11}B\,(‰) = \left[\left({}^{11}B/{}^{10}B\right)_{sample} \Big/ \left({}^{11}B/{}^{10}B_{NIST-SRM-951} - 1\right)\right] * 1000$$

The large relative mass difference between ^{10}B and ^{11}B leads to significant boron isotopic fractionation in nature. In addition, boron is highly soluble in aqueous environments and has high geochemical reactivity. Thus, $\delta^{11}B$ values in different environments are diverse. In nature, the measured $\delta^{11}B$ values vary between –70 ‰ and +75 ‰. Negative $\delta^{11}B$ values are usual found in nonmarine borate minerals and tourmalines, while positive $\delta^{11}B$ values are found in brines of salt lakes and evaporated seawater. Dead Sea brines, for example, have values from +35 to 60 ‰, while values for the various salts precipitating from the brines are much more negative (Fig. 2.38).

Hence, boron isotope determinations from halite, borate salts, tourmalinites and brines are all capable of distinguishing between marine and nonmarine sources (Fig. 2.38; Xiao et al. 2013; Vengosh et al. 1992; Swihart et al. 1986). Marine evaporite salts are characterised by distinctly higher $\delta^{11}B$ values (+18.2 to +31.7‰) than nonmarine evaporites (–30.1 to +7.0‰; Swihart et al. 1986). The latter span the range typical of the boron isotope signatures of most other rock types (Palmer and

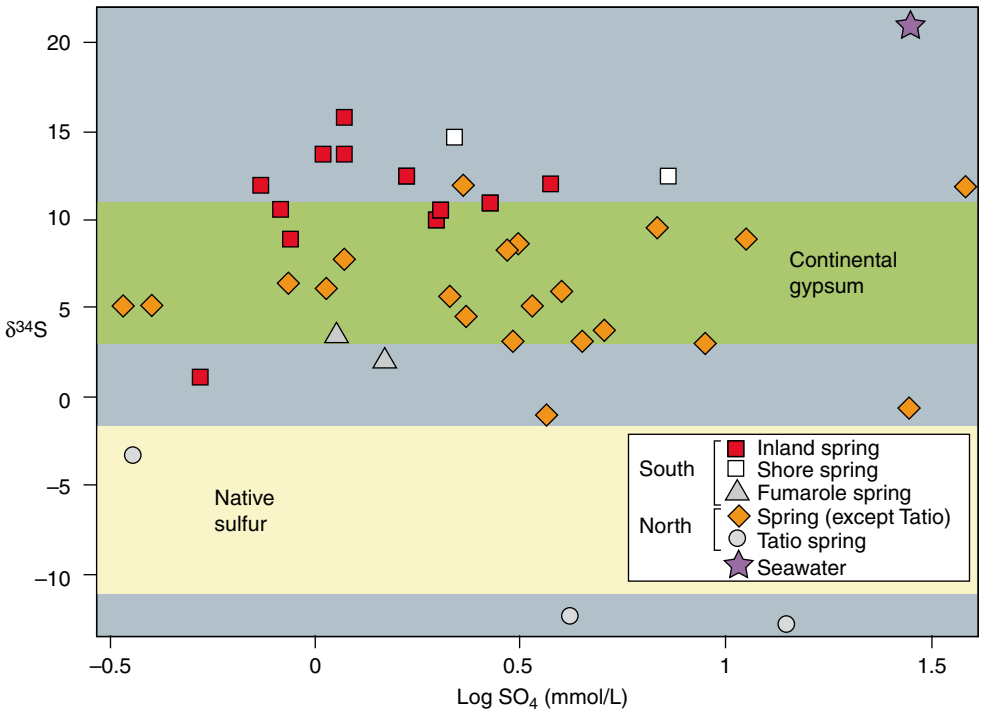

Fig. 2.37 Sulphur isotope ratios in sulphate of Chilean thermal waters, mostly collected from active springs in the salars of northern and southern Chile (After Risacher et al. 2011)

Helvaci 1997). Likewise, there is a clear isotopic separation between marine and nonmarine brines (Fig. 2.39a, c).

The separation reflects the enrichment of the ^{11}B isotope in seawater compared with both oceanic crust and continental crust. Differences are due to the original isotopic fractionation that occurred when boron was extracted from seawater into detrital clays, weathered basalts and carbonate minerals. Continental evaporite brines are derived from the weathering of these various lithologies, while the boron in seawater salts comes straight from the concentration of seawater. Much of the boron signature that is measured when whole rock halites and other salts are analysed comes from the fluid inclusions and not from boron in the lattice structure. The low level of fractionation between the brine and its precipitate at the time of halite deposition means boron isotope analysis can reliably distinguish nonmarine and marine brine parents in modern salts, even in complex multisource systems such as Lake Qaidam (Liu et al. 2000). However, the boron isotope signature of seawater is not a constant (Paris et al. 2010). It has increased by +10‰ over the past 40 my, to its present value of +39.9‰. This is likely in response to more intense continent-continent collision, the Himalayan uplift and an associated increase in erosional input of continental clastics into the world's oceans.

Beyond the halite precipitation field $\delta^{11}B$ values tend to increase with increasing concentration in both brine and the associated bittern precipitates. In all fields the $\delta^{11}B$ values and boron contents are higher in brine than in its precipitated halite suite (Fig. 2.39b; Vengosh et al. 1992). However the boron is not behaving in an absolutely conservative fashion and there is a deficiency of boron in the increasingly saline brines and a concurrent increase in the boron content of the associated salts (Table 2.10; Liu et al. 2000). The highest $\delta^{11}B$ values in the Qaidam Basin are associated with fluids with low B/Li ratios, indicating selective removal of elemental boron and ^{10}B by adsorption onto clay minerals along the flow path into the basin (Table 2.10; Liu et al. 2000). The magnitude of ^{11}B enrichment due to adsorption differs by 15–20‰ from the supply, and thus nonmarine brines are still distinguished from marine-derived evaporitic brines, which have much higher $\delta^{11}B$ signatures in the range +39 to +59‰ (Figs. 2.39a, d).

Palmer and Helvaci (1997) found that the isotopic values of the main borate minerals in the major Turkish borate deposits are largely controlled by their mineralogy and the pH of the brines from which they precipitated. For example, the differences in the $\delta^{11}B$ values of the three main borate minerals at Kirka (colemanite, ulexite and borax) are greater than would be expected if they had precipitated in equilibrium with one another from a solution with the same $\delta^{11}B$ value and pH (Fig. 2.39c). The data are consistent with all three minerals being primary precipitates from a concentrated brine, with colemanite precipitating from a brine of lower pH than ulexite, and borax precipitating from a brine of higher pH than ulexite. The only other Turkish deposit in which there are significant amounts of coexisting primary borate minerals is at Bigadic, which contains coexisting ulexite and colemanite (Fig. 12.6). There the average $\delta^{11}B$ value of ulexite is −6.8‰, this is 3.6‰ higher than that of colemanite −10.4‰ (Fig. 2.39c). This difference suggests that colemanite precipitated at a lower pH than ulexite (Palmer and Helvaci 1995).

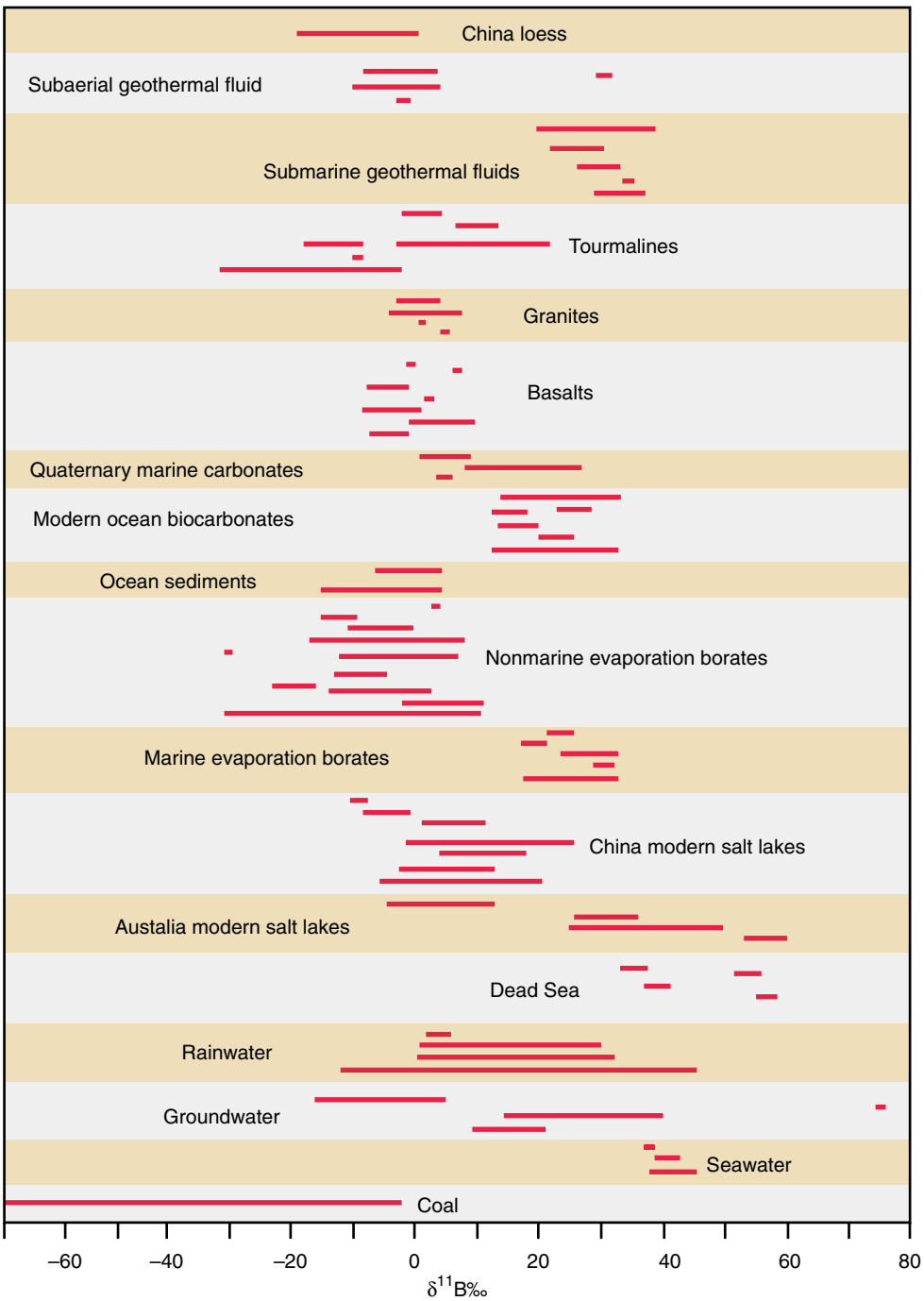

Fig. 2.38 Worldwide ranges of boron isotopes (After Xiao et al. 2013)

Chlorine Isotopes

Unlike the stable isotopes of boron and sulphur, which can be used as indicators of parent brine type, ^{37}Cl interpretation is more problematic due to its inherently low levels of fractionation during evaporation. Prior to the early 1980s, this meant analytical methods lacked the precision needed to detect small variations in chlorine isotopes levels that occur in nature. Measurements have now improved to where even small fractions in natural halites can be reliably and accurately determined (Long et al. 1993). Earlier work also suffered from a poor understanding of evaporitic fractionation mechanism and it was only in the mid 1990s that our understanding of ^{37}Cl determinations evolved into a useful environmental tool in an evaporite basins (Eggenkamp et al. 1995). Ongoing impermeability and a lack of reactivity away from the edge of a halite mass means that depositional isotope values will persist, even in tectonised evaporites or in evaporites that have undergone recrystallisation (Eastoe and Peryt 1999; Eastoe et al. 2007).

Eggenkamp et al. (1995) determined a fractionation of $0.26 \pm 0.07‰$ between halite and a NaCl solution at 25 °C. Halite crystallising from a 0.00‰ NaCl solution will therefore have an initial value of 0.2–0.3‰. Variations in δ

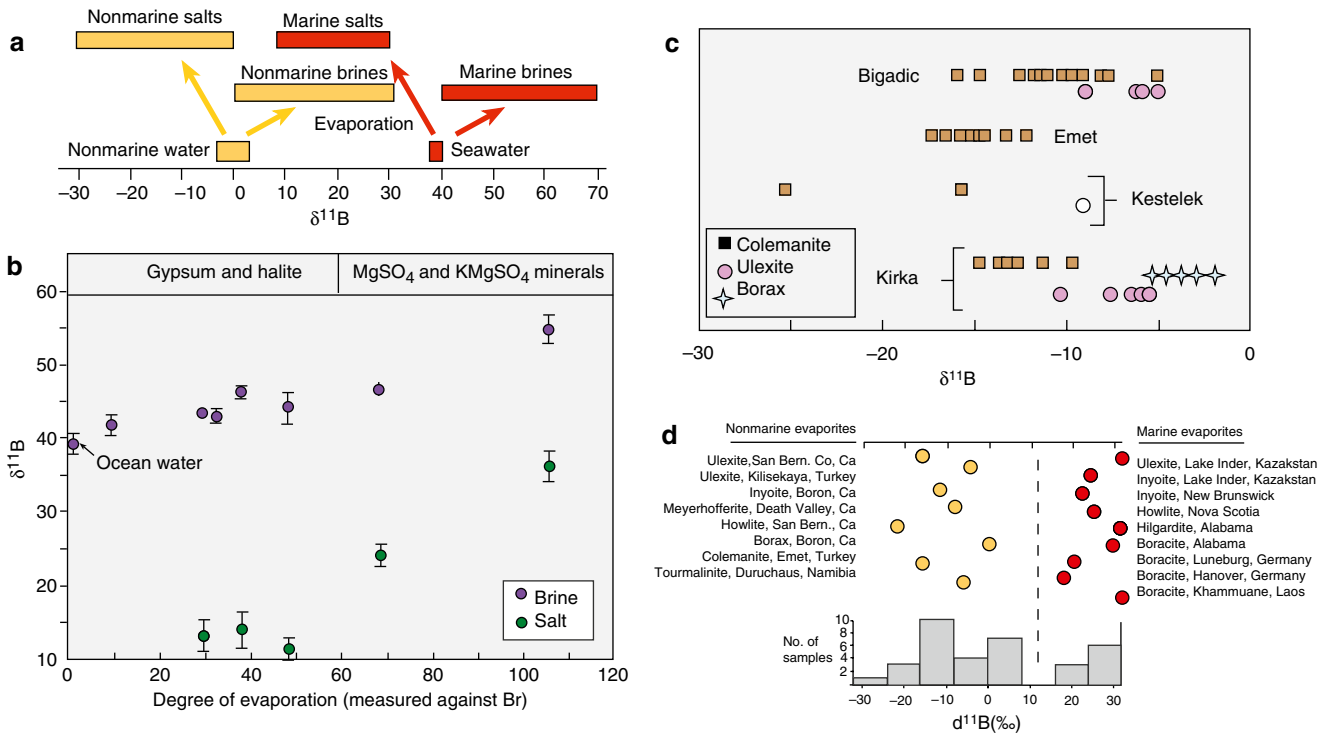

Fig. 2.39 (**a**) Isotopic distribution of boron in evaporatively formed marine and nonmarine brines and salts related to signature of original water source. (**b**) $\delta^{11}B$ values of evaporated seawater (*purple circles*) and co-existing precipitated halite (*green circles*) versus degree of evaporation as calculated from Br values. Note the relative enrichment of ^{11}B in brines relative to salt and the difference in magnitude of enrichment during different stages of evaporation (After Vengosh et al. 1992). (**c**) Ranges of boron isotope values in various minerals in the main Turkish borate deposits- see also Fig. 12.6 (After Palmer and Helvaci 1997). (**d**) Isotopic analysis of evaporitic borates worldwide showing clearly separate fields for marine and nonmarine samples (*dashed line*). The upper part of figure shows analytical determinations from various deposits, the lower part shows a histogram where these values are grouped (After Swihart et al. 1986)

Table 2.10 Boron isotopes in the brines and halite crusts of various salt lakes in the Qaidam Basin, China

Lake name	Constituents in brine				Constituents in halite				
	pH	B (μg/ml)	Na/Ca	$\delta^{11}B$ (‰)	B (μg/g)	$\delta^{11}B$ (‰) Run 1	$\delta^{11}B$ (‰) Run 2	$\delta^{11}B$ (‰) Run 3	$\delta^{11}B$ (‰) Average
Gasikule	7.11	101.6	193.8	17.9	8.0	12.1±0.3	12.5±0.1	–	12.3
Mahai	7.98	162.9	208.3	–4.0	11.6	–4.7±0.2	–5.1±0.1	5.3±0.1	–5.0
Balun	6.50	10.1	12.1	31.4	0.4	25.7±0.3	25.9±0.1	–	25.5
Xiaochaidam	8.14	285.6	167.0	–0.5	13.0	0.4±0.1	0.4±0.1	–	0.4
Dachaidam	7.78	404.3	255.7	5.3	16.0	3.7±0.1	3.7±0.1	–	3.8
Chaikai	7.68	15.4	130.6	9.9	7.4	5.6±0.1	5.6±0.1	6.1±0.1	5.9
Niulang	5.34	53.6	0.7	24.5	3.8	–	–	–	20.0

After Liu et al. (2000)

^{37}Cl in modern seawater are minimal and the oceans appear well mixed, so that a value of 0.00‰ is widely accepted, although the upper current layer in the Bosphorus is unusual as it has a value of 0.4‰ (Eastoe et al. 2007). Halites precipitated from seawater brines show decreasing values from 0.2‰ at the onset of halite precipitation to –0.5‰ by the hexahydrite precipitation stage (Eastoe et al. 1999). Using seawater, Eggenkamp et al. (1995) showed that the $\delta^{37}Cl$ value decreases in the halite stage from 0.0 to –0.45‰. During the subsequent kainite and carnallite stages the fractionation factor is close to unity and the $\delta^{37}Cl$ of the brine is only 0.04‰. In the subsequent bischofite stage the fractionation factor is <1 and $\delta^{37}Cl$ increases during the final stages of evaporation. The $\delta^{37}Cl$ values of precipitates in the halite stage decreases from 0.26 to –0.19‰ (Fig. 2.40). In the kainite stage, the precipitate (a mixture of salts) has a $\delta^{37}Cl$ that decreases to –0.34‰ and then to –0.47‰ in the carnallite stage. However in the last stage, typified by the precipitation of bischofite in the mix, the $\delta^{37}Cl$ value increases from –0.55‰ back into positive values in the very latest stages of evaporation before complete dryness. Error ranges in determinations increases after the end of the halite stage. Because $\delta^{37}Cl$ values decrease monotonically with concentration in the halite stage, it is possible to use $\delta^{37}Cl$ values in unaltered halites (chevron halite) to estimate

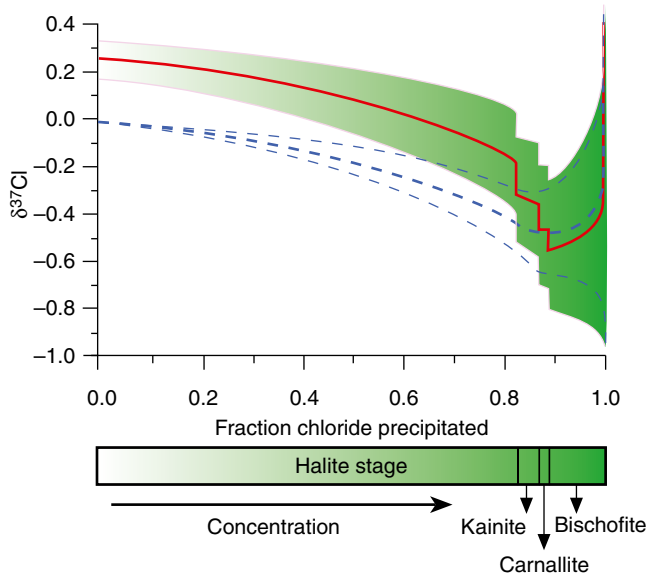

Fig. 2.40 Calculated $\delta^{37}Cl$ values of the precipitate and residual brine during seawater concentration. The *shaded area* indicates the error range for the precipitates (*solid line*), while the area between the *dashed lines* is the error range for the residual brine. Note the discontinuities in the curve for the precipitates (After Eggenkamp et al. 1995)

the concentration stage at the time of precipitation of an ancient halite (palaeosalinity determination). At later bittern stages this methodology is less effective and more subject to ambiguities (Eggenkamp et al. 1995).

That this methodology works is clearly seen in a study of the $\delta^{37}Cl$ signatures of the ZIII interval of the Permian Zechstein salts in the TR-2 well in the Netherlands (Fig. 2.41a). The interval is a combination of halite and bittern stage salts. The halite-dominated interval (Z.III.2a) has a simple salt chemistry with minor amounts of carnallite, bischofite and kieserite. $\delta^{37}Cl$ values tend to decrease upward into the overlying carnallite-kieserite interval at 1,660 m, implying increasing salinities as the unit passes up into the bittern-dominated succession. Samples in the bittern-dominated intervals (Z.III.1b and Z.III.2b) show high levels of carnallite, kieserite and bischofite and values that tend to be toward the lower end of the $\delta^{37}Cl$ value scale, consistent with higher supersaline salinities needed to precipitate these salts, sylvite ore brines show a similar highly negative signature.

Other ancient bedded halites also lie in the marine supersaline range. For example, bedded Permian halites in the Palo Duro basin, situated immediately above and below a halite

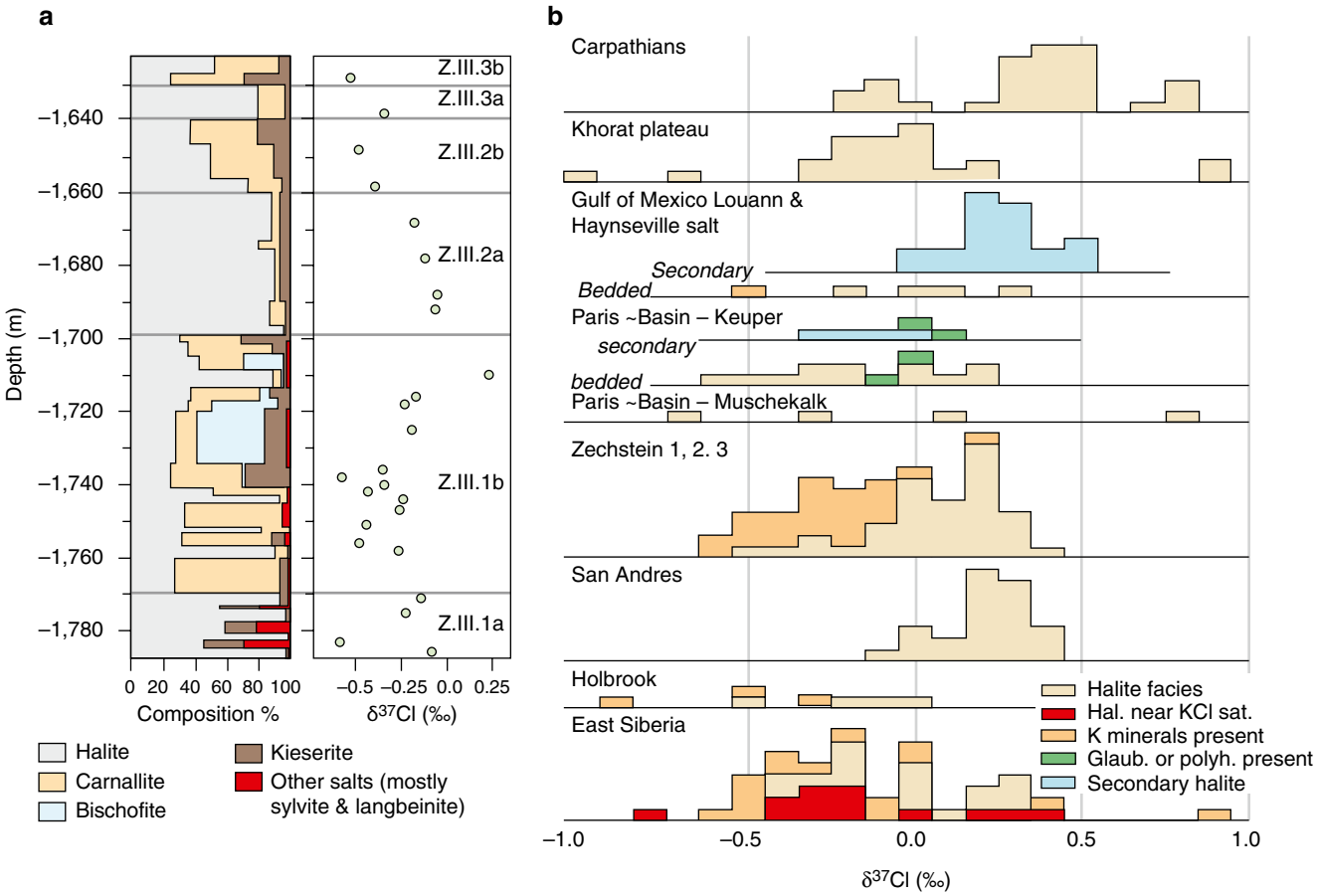

bed preserving chevrons, show primary $\delta^{37}Cl$ values of 0.4 to around 0.0‰ (Fig. 2.41b). Waters driving the recrystallisation cannot have been generated by later meteoric dissolution and recrystallisation. Rather, these recrystallised halites preserve their Permian depositional signatures (Eastoe et al. 1999). This conclusion supports the notion that subsurface salt beds intercalated with remnant chevrons are largely impervious closed systems that dissolve from the edges inward. It means any temperature and salinity values measured in brines in micro-inclusions in the chevron halite will indicate ambient conditions at the time of halite precipitation (e.g., Fig. 2.42). It is also why viable Permian haloarchaea can be cultured from such inclusions (Vreeland et al. 2000).

In contrast, nonmarine chloride contributions to a basinal brine precipitate halite with a more positive $\delta^{37}Cl$ value. Carpathian (Middle Miocene) halokinetic halite has $\delta^{37}Cl$ values greater than 0.4‰, as do some halites in the Gulf of Mexico, the North Sea and the Paris Basin (Fig. 2.41b). Such positive values cannot arise solely from seawater evaporation and require a considerable input of nonmarine chloride, either from a continental meteoric or igneous/hydrothermal source (Eastoe and Peryt 1999).

The contrast between halite with a hydrothermal signature and that preserving original syndepositional values is clear in Jurassic halite in the Gulf Coast Basin (Eastoe et al. 2001, 2007). Halite has a $\delta^{37}Cl$ range of −0.5–0.3‰ in most

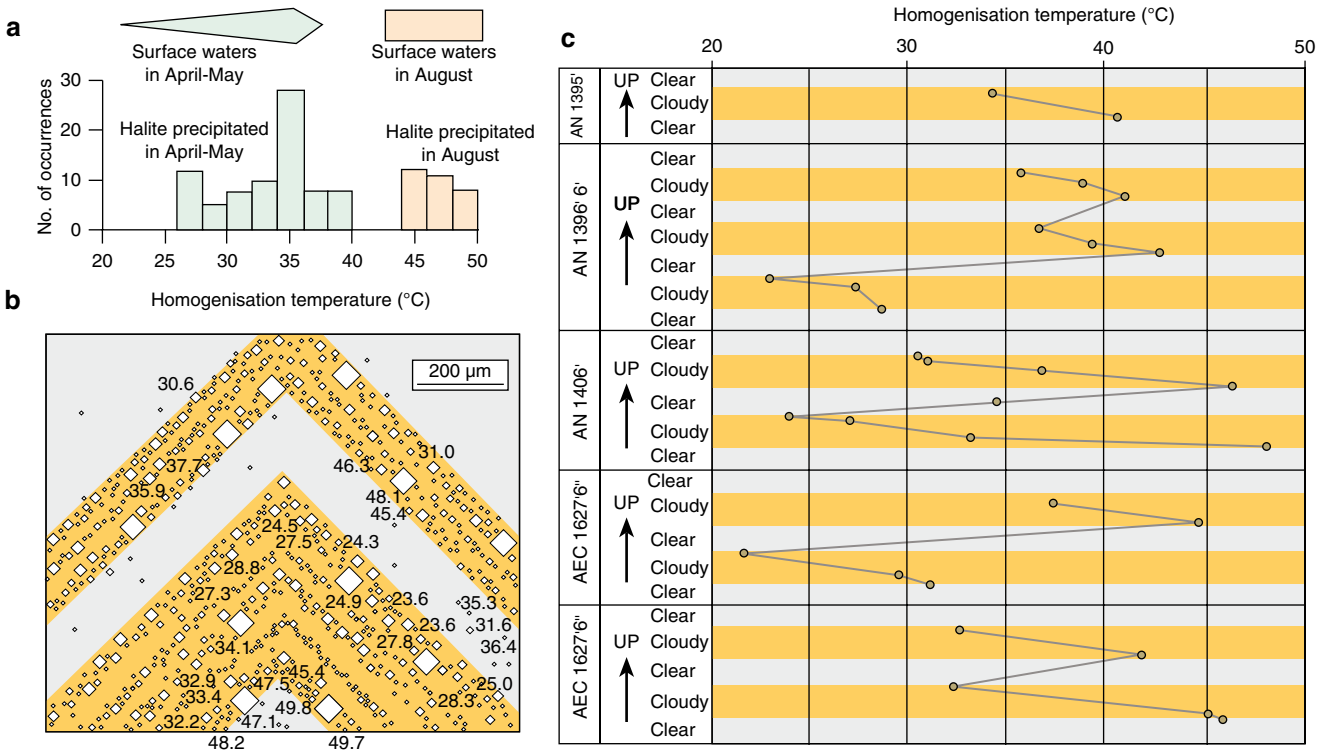

Fig. 2.42 Inclusions in chevron halite. (**a**) Histogram of homogenization temperatures measured by the 'cooling nucleation' method in initially all-liquid primary fluid inclusions from halite in modern pans of Death Valley. Plotted above the *histogram* are the temperature ranges of the brines from which these halite crystals grew (After Roberts and Spencer 1995). (**b**) Representation of chevron bands in a halite crystal from the Anadarko Davis No. 1 core (1,406 ft depth). Note homogenization temperatures in relation to bands; although homogenization temperatures are consistent within individual fluid inclusion assemblages thin, high frequency growth bands, they decrease from base to top of chevrons (After Benison and Goldstein 1999). (**c**) Graphic representation of homogenization temperature trends within and among cloudy, inclusion-rich and clear, inclusion-poor growth bands in five chevron halite crystals from the Nippewalla Group. *Circles* mark average homogenization temperatures within thicker chevron growth bands. Lines connecting *black circles* are extrapolated temperature trends. Upward decrease in homogenization temperatures from base to top of individual cloudy chevron bands probably reflect daily fluctuations in surface water temperatures perhaps related to evening cooling (After Benison and Goldstein 1999)

Fig. 2.41 $\delta^{37}Cl$ isotope as an environmental indicator. (**a**) Isotopic and mineralogic composition of Zechstein III showing that in these marine salts the $\delta^{37}Cl$ isotopic values are typically higher in the halite layers than in carnallite and bischofite layers (After Eggenkamp et al. 1995). (**b**) Isotopic values of selected halites of various ages showing marine values are typically less than 0.4‰ and centred on 0.0‰, with bitterns tending to show more negative values than less saline halite phases, while secondary halite tends to show slightly more positive values (After Eastoe et al. 2007). Secondary salt is diapiric salt in the Gulf of Mexico Basin, and open-space filling salt in the Keuper. *Glaub* glauberite, *polyh* polyhalite

bedded salt and 0.0–0.5‰ in diapiric salt. The values for bedded salt are consistent with a $\delta^{37}Cl$ value of 0.0‰ for Jurassic seawater chloride, as in modern oceans. The slightly higher values for diapiric salt are possibly caused by incongruent solution of halite (Fig. 8.43).

Chloride isotopes in subsurface waters can indicate their provenance and show a $\delta^{37}Cl$ range of −1.9 to 0.7‰ (Eastoe et al. 2001, 2007). Formation waters in the Gulf of Mexico with $\delta^{37}Cl < -0.6$‰ are confined to geopressured Eocene to Miocene strata at depths of 2,500 m or greater. Strongly negative values do not occur in Plio-Pleistocene strata, which retain the values of seawater (connate brines), nor do they occur in Mesozoic strata, which are marine carbonates. It seems that the strongly divergent values come from chloride in waters released from shales undergoing the smectite-illite transformation in the zone of geopressure.

Low $\delta^{37}Cl$ values in such waters are related to low m_{Cl}/m_{Na} (a parameter indicating dewatering) but show no general relationship to Cl/Br ratios (Eastoe et al. 2001). They are consistent with diffusion of chloride from allochthonous brine. Diffusion can generate domains of water with negative $\delta^{37}Cl$ on a scale of hundreds of metres in 10^4–10^6 years, and may also generate positive $\delta^{37}Cl$ chloride in residual source brine. The expulsion of such brines into an evaporite basin may account for most non-0‰ chloride sources in evaporite basins.

The experiments of Eggenkamp et al. (1995; Fig. 2.40) were limited to a single seawater evaporation cycle, but evaporites accumulating in shallow pans in marine and continental settings are subjected to multiple cycles of dissolution and partial reprecipitation before their burial. This can bring about measurable changes in $\delta^{37}Cl$, but also leaves little residual halite within the total halite mass.

Fluid Inclusions and Brine Temperatures

When halite and other salts are precipitated, they can capture and enclose inclusions of ambient brine. Such inclusions form the cloudy lamina that outline milky halite chevron and cornet textures and are used to indicate primary growth orientations of crystals in ancient salt beds (Fig. 1.33). Inclusion-rich bands indicate episodes of rapid growth, while clearer bands indicate slower growth rates (Shlichta 1968; Goldstein 2001).

Chevron banding typically indicates diurnal temperature changes in a shallow brine pan, with rapid growth spurts encouraged by the cooling of brine each evening.

Halite's high solubility and potential for deformation sometimes raises doubts about longterm preservation of the integrity of fluid inclusions. Even ancient halite that still retains abundant growth-aligned textures, if exposed to even moderate heating it may contain fluid inclusions that have leaked. Halite's propensity to flow also means its fluid inclusions are more vulnerable to stretching, leaking, and necking-down compared to most other minerals. But Petrichenko (1979) and Roedder (1984a, b) have shown that even when deformation has occurred, only the outer portions of halite crystals tend to be affected, the centres of crystals typically remain unaltered. Alteration textures in ancient bedded halites with crystals suitable for microinclusion analysis are thus defined by altered, clear, outer rims and unaltered, cloudy, primary inclusion-rich cores that retain meaningful inclusion data (Petrichenko 1979; Roedder 1984a, b). The problems of defining inclusion leakage, coupled with the possibility of bedded and halokinetic salt being used as repository sites for radioactive waste, has generated valuable research on the validity of fluid inclusion data in halite (Chap. 12).

Lowenstein and Spencer (1990) obtained some of the first reliable and consistent estimates of ancient syndepositional brine temperature estimates using solid-liquid homogenization temperatures of sylvite daughter crystals in halite from the Devonian Prairie Formation. They show Devonian brine temperatures were similar to those in Quaternary continental equivalents and that many ancient potash deposits still retained evidence of very early diagenetic features, created by the cooling of syndepositional reflux brines. Since then there have been numerous studies that illustrate the utility of inclusion-based studies of chevron halite (Table 2.11).

Even so, many geologists have maintained a healthy scepticism toward fluid inclusion data derived from evaporites, especially from non-chevron halite (Roedder and Skinner 1968; Kovalevich 1975, 1976; Petrichenko 1979; Roedder and Bassett 1981). Work by Roberts and Spencer (1995) and by Benison and Goldstein (1999) has shown how petrographically controlled microthermometric testing can define and avoid zones of inclusion alteration in ancient halite. If the tests suggested by these authors show that primary fluid inclusions have not been altered since entrapment, then fluid inclusions from the unaltered portions of a salt bed may be considered representative of evaporative parent waters and can even be used to define palaeotemperatures of the mother brine (Fig. 2.42). This is now a widely used approach for determining surface water palaeotemperatures from ancient halites whose fluid inclusions lack daughter crystals (Benison and Goldstein (1999)).

An all-liquid primary inclusion in halite at room temperature indicates mineral growth below approximately 50 °C (Kovalevich 1975; Petrichenko 1979). Vapour bubbles can be nucleated artificially in some all-liquid inclusions by placing samples in a freezing chamber so that homogenization temperatures below 50 °C can be measured. Roberts and Spencer (1995) found that when primary fluid inclusions in newly precipitated halite in ephemeral-lake saltpans in Death Valley, California, were cooled (in order to nucleate vapour bubbles) and homogenization temperature

were measured, the resulting temperature ranges were equivalent to the measured temperatures of the shallow brine sheets from which the halite had precipitated (Fig. 2.42a).

Likewise detailed inclusion analysis, centred on chevrons and cornets in unaltered portions of halite beds in the Permian Nippewalla (uppermost Leonardian – Kungurian) Group of

Table 2.11 Selection of outcomes illustrating the utility of inclusion studies in chevron halite

Unit	Location	Observation	Reference
Sinian Halite, Ediacarian, Neoproterozoic	China	Used to quantify ambient ocean temperatures and influence on multicellular evolution in late Precambrian within a long-term ocean cooling trend from nearly 70 °C at ~3,500 Ma to around 20 °C at ~800 Ma. Showed seawater temperatures when these halites formed were highly similar to tropical Phanerozoic seawater temperature estimates. The authors infer the Proterozoic decline in sea temperatures and the reduction of salinity, along with the sequestration of salt in massive Neoproterozoic halite deposits allowed more dissolved oxygen in oceans, so facilitating evolutionary innovation of complex multicellularity.	Meng et al. (2011)
Hisarkic Fm. borates, Miocene, Emet Basin,	Turkey	Fluid inclusion compositions in halite show that the free-brines in the saline lake corresponded to the Na-K-Cl-SO_4 type remaining very impoverished in Ca and Mg. High K concentrations were present in the final salt-forming brines (borates), which did not reach saturation with respect to K-bearing evaporites.	Garcia-Vegas et al. (2011b)
PZ2 (Stassfurt) halite, Permian, Polish sector European Southern Permian Basin.	Poland	Major ion concentrations in primary fluid inclusions in halite, along with sulphur and oxygen isotopes, show that the change to sulphate-depleted (calcium-rich) brines that occurred during halite deposition of the PZ2 (Stassfurt) cycle is related to the overturn of anoxic sulphidic deep-waters from the Panthalassa stratified superocean and coincides with the Permian-Triassic mass extinction event.	Garcia-Vegas et al. (2011a)
Modern acid and neutral saline lakes, Yilgarn Craton	Western Australia	Acid fluid inclusion freezing/melting behaviours include characteristics that differ from neutral fluid inclusion behaviours, such as lower eutectic temperatures, higher and wider temperature range of hydrohalite rims with a definable fuzzy border and more complex metastable phases.	Jagniecki and Benison (2010)
Salt IV sylvite beds, Oligocene Mulhouse Basin	South France	Small "growth band" scale variations in the K concentration in halite chevrons near potash layers, suggests very sensitive processes within the brine with potential environmental changes (i.e., seasonal variations, day-night temperature fluctuations cycles) leading towards precipitation of a sylvite layer.	Cendón et al. (2010)
Halite from several Cretaceous Basins	Angola, Congo, Brazil, Laos, Thailand	Cretaceous seawater was enriched several fold in Ca^{2+}, depleted in, Na^{+}, and Mg^{2+}, and had lower Na^{+}/Cl^{-}, Mg^{2+}/Ca^{2+}, and Mg^{2+}/K^{+} ratios compared to modern seawater. Elevated Ca^{2+} concentrations, with $Ca^{2+} > SO_4^{2-}$ at the point of gypsum saturation, allowed Cretaceous seawater to evolve into Mg^{2+}–Ca^{2+}–Na^{+}–K^{+}–Cl^{-} brines lacking measurable SO_4^{2-}. Cretaceous (Aptian) seawater has the lowest Mg^{2+}/Ca^{2+} ratios so far documented. Suggests a link between seawater chemistry and midocean ridge hydrothermal brine flux.	Timofeeff et al. (2006)

(continued)

Table 2.11 (continued)

Unit	Location	Observation	Reference
Glauberite-halite Zaragoza Gypsum Fm. (Lower Miocene, Ebro Basin	NE Spain	Geochemical study of halite crystals (bromine contents and fluid inclusion compositions) demonstrates that conditions for co-precipitation of halite and glauberite, or for precipitation of Na-sulphates (mirabilite, thenardite) were never fulfilled in the saline lake system.	Salvany et al. (2007)
Ouldburra Fm., Lower Cambrian, eastern Officer Basin	Australia	Two-phase (gas-liquid) inclusions and poor preservation of chevrons indicate intensive post-depositional recrystallisation. Homogenisation studies suggest that the upper part of the salt-bearing strata was heated to 80 °C, the lower part reached even higher temperatures. This heating was perhaps tied to the Devonian-Carboniferous Alice Springs Orogeny. Chemical composition indicates that parent brines were Ca-rich and SO_4-poor, a composition is similar to that recorded in the Lower Cambrian halite from the East Siberia Basin. Modern seawater is SO_4-rich and Ca-poor.	Kovalevych et al. (2006a)

Table 2.12 Summary of within-bed homogenisation temperatures for Nippewalla Group halite Chevrons

Depth (m)	Number of inclusions	ThAVG (°C)	ThMEDIAN (°C)	ThMAX (°C)	ThMIN (°C)	ThRANGE (°C)
Blaine formation						
587.81	42	29.1	28.6	36.6	16.3	20.3
588.26	24	33.0	33.4	41.2	23.8	17.4
588.44	28	23.2	22.8	36.6	11.4	25.2
592.16	11	24.7	25.8	27.2	20.6	6.6
602.50	57	20.7	18.9	43.0	11.8	31.2
603.58	25	25.8	27.4	39.8	7.2	32.6
Cedar Hills sandstone						
713.94	33	34.8	31.9	56.8	18.4	38.4
715.11	36	35.1	31.3	65.6	21.3	44.3
715.62	16	44.8	44.7	60.0	31.2	28.8
716.58	17	44.7	38.0	73.7	25.2	48.5
Salt plain formation and Harper sandstone equivalent						
773.86	12	40.2	40.9	62.4	22.5	39.9
776.68	32	35.5	32.1	61.5	21.5	40.0
777.29	19	33.8	32.8	52.1	21.7	30.4
779.37	14	36.6	37.1	47.0	22.8	24.2
781.05	27	26.0	23.7	39.0	14.0	25.0

After Zambito and Benison (2013)
Th homogenisation temperature, *AVG* average, *MAX* maximum, *MIN* minimum

Kansas gave cooling-induced homogenisation temperatures representative of the temperature range of the original mother liquor (Fig. 2.42b, c). What was even more interesting was the intimate and consistent relationship between temperature and position in the inclusion rich layer in the chevron bands in this Permian halite (Fig. 2.42b, c). It probably preserves daily temperature changes and shows the propensity of inclusion-rich bands to precipitate when the overlying halite saturated brine cools each evening or with the passage of a cold front.

If the inclusion data in the Nippewalla Group halites are reliable indicators of syndepositional not burial temperatures, then the temperature regime at times was far in excess of any seen in today's deserts (Zambito and Benison 2013). Extremely high temperatures, to 73 °C, are evidenced in the lower Nippewalla Group halite chevrons, as are large diurnal temperature ranges of more than 25–30 °C (Table 2.12). The inclusions suggest conditions were at times more extreme than anywhere on Earth today. In contrast, the

upper Nippewalla Group halites were cooler; maximum temperature was 43 °C and diurnal temperature ranges were smaller, similar to modern extremely hot environments such as Death Valley and the Danakil Depression (Fig. 2.42b, c).

The fact that halite can retain such intimate precipitational detail supports the notion that growth-aligned chevrons are subsurface survivors. This means microanalysis of the chemical make-up of a brine inclusion in an unaltered halite chevron or cornet is indicative of the chemical composition of the water that precipitated the crystals (Timofeeff et al. 2001). This gives an ability to map temporal changes in the ionic proportions of seawater and once again also suggests why Permian halobacteria can be cultured from brine inclusions in Permian salt (Vreeland et al. 2000; Lowenstein et al. 2010).

Seawater Evolution

So far in this chapter three things are clear: (1) it is difficult to separate marine and nonmarine parent brines based on mineralogy; (2) isotopes and micro-inclusions can sometimes separate brine parentage; (3) it is increasingly obvious that the proportions of major ions in seawater are probably not constant across geological time. The significance of various indicators of chemical evolution of seawater over time is now considered in two parts. First, in the Phanerozoic where actual salts are available for sampling and analysis. Second, in the Precambrian, where much of the evidence of brine composition comes from pseudomorphs of evaporite salts.

A Phanerozoic Dilemma: Marine Versus Nonmarine Potash?

Phanerozoic potash evaporites fall into two categories: (1) potash deposits with $MgSO_4$ salts, such as polyhalite, kieserite and kainite; and (2) potash deposits with halite, sylvite and carnallite, and entirely free or very poor in the magnesium-sulphate salts. This latter group makes up more than 60 % of ancient potash deposits (Hardie 1990). The former group may well be marine-derived as they contain the bittern suite predicted by the evaporation and backreaction of modern marine brines, but the latter group must have precipitated from Na-Ca-Mg-K-Cl brines with ionic proportions quite different from that of concentrated modern seawater which have a bittern suite dominated by the $MgSO_4$ salt suite (Fig. 2.12).

$MgSO_4$-depleted potash evaporites have been explained by some as modified marine evaporites thought to result from backreactions during burial diagenesis of normal marine evaporites (Borchert 1977; Dean 1978; Wilson and Long 1993). If so, then they were derived from an ancient seawater source with modern ionic proportions that were altered via; (a) dolomitisation, (b) sulphate reducing bacterial action, (c) mixing of brines with calcium bicarbonate-rich river water, or (d) rock-fluid interaction during deep burial diagenesis.

Alternatively, Hardie (1990) suggested that $MgSO_4$ depleted potash evaporites formed from sulphate-depleted inflow waters seeping into an evaporite basin via springs and faults. Springs were fed either by $CaCl_2$-rich hot hydrothermal brines or by cooling resurging deep basinal brines. Such fault-fed deeply-circulating evaporite brines occur today in springs in the Dead Sea, Qaidam Basin, Salton Sea and the Danakil Depression. The upwelling of the brines in these regions is driven either by thermally induced density instabilities related to magma emplacement, or by the creation of topographic gradients that force deeply-circulated basinal brines to the surface. Ayora et al. (1994) demonstrated that such a continental Ca–Cl system operated during deposition of sylvite and carnallite in the upper Eocene basin of Navarra, southern Pyrenees, Spain (Fig. 8.12).

Thirdly, and more widely accepted as an explanation for Phanerozoic evaporites, is that there is the high likelihood that seawater chemistry has evolved throughout the Phanerozoic and that changing ionic proportions in seawater define whether or not $MgSO_4$ salts were typical marine evaporites. Work by Kovalevich et al. (1998) on inclusions in primary-bedded halite from many evaporite formations of northern Pangaea, and subsequent work using microanalyses of fluid inclusions in numerous chevron halites (Lowenstein et al. 2001, 2003), shows that during the Phanerozoic the chemical composition of marine brines has oscillated between Na-K-Mg-Ca-Cl and Na-K-Mg-Cl-SO_4 types. The former does not precipitate $MgSO_4$ salts when concentrated, the latter does.

The background chemistry of this marine potash dichotomy ($MgSO_4$ -depleted bitterns versus $MgSO_4$ -enriched bitterns) is simple, and can be related to brine evolution observations published by Hardie more than 30 years ago (Hardie 1984).

The chemical makeup of the bittern stages of any marine brine is largely controlled by its chemical constituent proportions in its early stages of concentration. These ionic proportions will control how it passes through the $CaCO_3$ and gypsum divides (Fig. 2.43). That is, a marine brine's evolutionary pathways are determined by the ionic proportion chemistry during the precipitation of relatively insoluble evaporitic carbonates (aragonite, high-magnesium calcite, or low-magnesium calcite) and then by its constituent chemistry as it attains gypsum saturation. These two stages define the $CaCO_3$ and gypsum divides.

The Mg/Ca ratio in any ambient seawater controls whether the first-formed carbonate is aragonite (Mg/Ca >5)

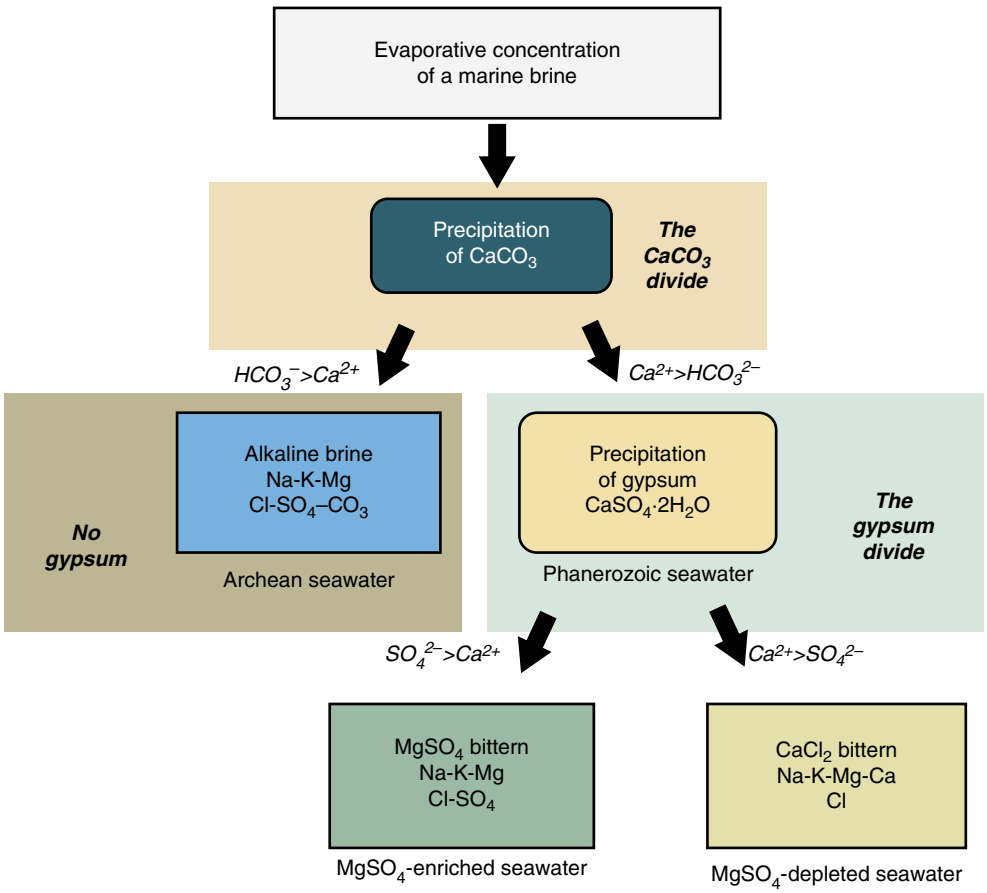

Fig. 2.43 Chemical divides and the evolution of three major brine types (in part after Hardie 1984)

or high-magnesium calcite (2>Mg/Ca>5), or low-Mg calcite (Mg/Ca >2). The latter is not relevant to Phanerozoic seawater. As seawater concentrates and calcium carbonate mineral(s) precipitate, either Ca is used up, or the HCO_3 is used up. If the Ca is used up, an alkaline brine (pH >10) forms, with residual CO_3, along with Na, K, SO_4, and Cl but no remaining Ca. With ongoing concentration this brine chemistry will then form sodium bicarbonate minerals, it cannot form gypsum as all the Ca is already used up. Such a ionic proportion chemistry may have defined oceanic waters in the Archaean but is not relevant to seawater evolution in the Proterozoic and Phanerozoic as gypsum or its pseudomorphs are well documented. At very high concentrations, these brines (aka Type 1 waters) can produce halite and sylvite bitterns but no gypsum or anhydrite (Fig. 2.43).

If, on the other hand, the HCO_3 is used up during the initial formation of evaporitic carbonates, the water will become enriched in Ca and Mg, and a neutral brine, very depleted in carbonate, is formed. The next chemical divide reached by a water depleted in HCO_3 occurs when gypsum precipitates ($CaSO_4.2H_2O$). As gypsum is precipitated, either the Ca in the brine is used up, or the SO_4 in the brine is used up. If the Ca is depleted, a calcium-free brine rich in Na, K, Mg, Cl, and SO_4 will be the final product and the diagnostic bittern minerals will include magnesium sulphate minerals. This is the pathway followed by modern seawater bitterns.

If, however, the sulphate is used up, the final brine will be rich in Na, K, Mg, Ca, and Cl. Such a calcium chloride brine will produce diagnostic potassium chloride and calcium chloride minerals such as sylvite, tachyhydrite, and antarcticite, but no sulphate minerals. Although the theory of chemical divides is important in understanding bittern chemistry, a few problems complicate its direct application to saline-mineral deposition. Problems arise from the thermodynamics, kinetics and hydrodynamics of the precipitation process: (1) whether or not the evolving brine backreacts with previously formed minerals (i.e., whether fractional crystallization prevails or not); and (2) whether or not metastable phases precipitate out of the evolving brine; and (3) Variations of rates of brine loss in a unclosed hydrologies as the basin fills with salts. In natural systems, dense evaporated brines can leak out as dense underflows or as refluxing groundwaters.

A detailed analysis of the ionic make-up of Silurian seawater using micro-inclusion analysis of more than 100 samples of chevron halite from various Silurian deposits around the world was published by Brennan and Lowenstein (2002), and clearly supports the notion that ionic proportions in the

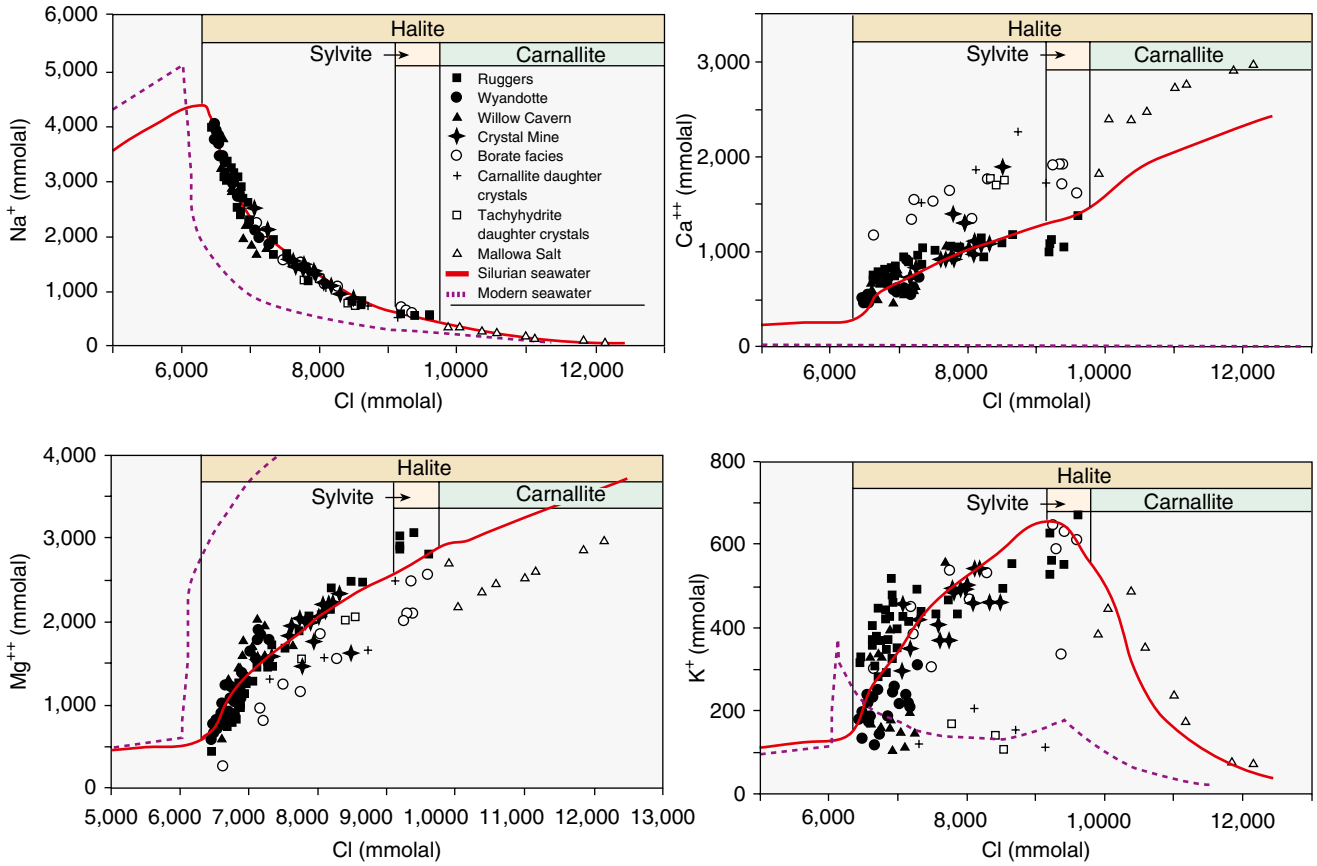

Fig. 2.44 Plots of the major-ion concentrations of the fluid inclusions versus chloride concentrations in Silurian salt with preserved primary structures (After Brennan and Lowenstein 2002). *Closed symbols* represent fluid inclusions from pristine marine halites, *open symbols* represent suspect fluid inclusions from halites associated with potash mineralization or high degrees of evaporation. Only the *closed symbols* were considered for determining Silurian seawater. The evaporation pathway of modern seawater is shown with a *dashed line*, and the best-fit evaporation pathway for the Silurian data is shown with a *solid line*. All the plots show that the evaporation pathways defined by Silurian fluid inclusions are different from the modern seawater pathways. The Silurian fluid inclusions all have an excess of calcium, and no measurable sulphate. Modern seawater evaporated to halite saturation has abundant sulphate, and negligible amounts of calcium. Salts expected to precipitate at given Cl concentrations in evaporated "best-fit" Silurian seawater are indicated along the top of each plot. Sylvite is a primary precipitate from concentrated seawater with these ionic proportions

world's Silurian oceans were different from those of today (Fig. 2.44). Samples were from three formations in the Late Silurian Michigan Basin, the A-1, A-2, and B Evaporites of the Salina Group, and the Early Silurian in the Canning Basin (Australia) in the Mallowa Salt of the Carribuddy Group. The Silurian ocean had lower concentrations of Mg^{2+}, Na^{+}, and SO_4^{2-}, and much higher concentrations of Ca^{2+} relative to the ocean's present-day composition. Furthermore, Silurian seawater had Ca^{2+} in excess of SO_4^{2-}. Bittern stage evaporation of Silurian seawater produced KCl-type potash minerals that lack the $MgSO_4$ -type late stage salts formed during the evaporation of present-day seawater and allowed sylvite as a primary precipitate.

There is now convincing evidence that the chemistry of seawater has varied across the Phanerozoic, what is not so well understood are the processes driving this change (Fig. 2.45). Spencer and Hardie (1990) and Hardie (1996) have argued that the level of Mg in the Phanerozoic oceans has been relatively constant, but changes in the rate of seafloor spreading have changed the levels of Ca in seawater. The postulate was also supported in publications by Lowenstein et al. (2001, 2003). Timing of the increase in the amount of Ca in the world's oceans was synchronous with a decrease in the SO_4 ion concentration, which at times was as much as three times lower than the present concentration of that ion in seawater.

Through its interaction with seawater, ocean crust is a sink for Mg and a source of Ca, predominantly via the formation of smectite, chlorite, and saponite due to alteration of pillow basalts, sheeted dykes, and gabbros (Müller et al. 2013). Additional removal of Mg and Ca occurs during the formation of vein and vesicle-filling carbonate and carbonate-cemented breccias in basalt from low-temperature fluids. Hence changing rates of seafloor spreading likely influenced ionic proportions in the Phanerozoic ocean.

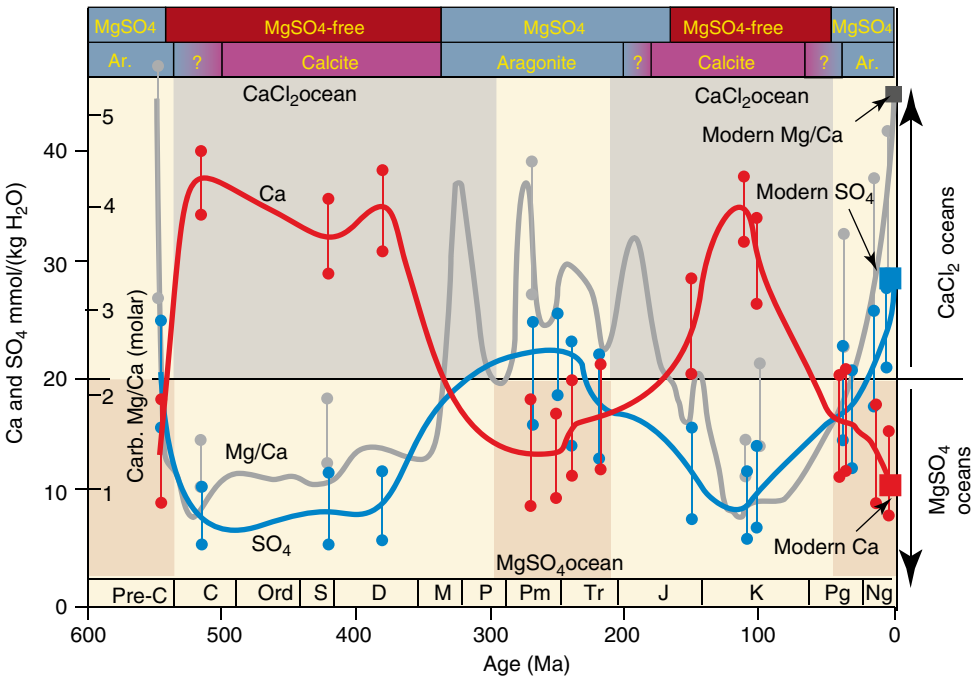

Fig. 2.45 Secular variation in the amounts of Ca and SO_4 in seawater for the last 600 Ma estimated from fluid inclusions in marine halites (*vertical bars*), compared to predicted seawater secular variations. The *horizontal line* around 20 mml/kgH_2O is the approximate divide between $CaCl_2$ and $MgSO_4$ seas. Also plotted are the temporal distributions in the primary mineralogies of Phanerozoic nonskeletal carbonates (calcite and aragonite) and periods of $MgSO_4$-free and $MgSO_4$ bitterns. For Mg/Ca, the grey plot bars are from halite inclusions measurements but the Mg/Ca curve is from marine carbonate data (After Lowenstein et al. 2001, 2003; with Paleozoic $MgSO_4$ boundary change after Holt et al. 2014)

Table 2.13 Predicted composition of seawater (meq l^{-1}) as a function of variations in the ratio of mid-ocean ridge hydrothermal brine flux compared to river water flux into the ocean, and the saline mineral paragenesis of the resulting seawater

Flux ratio	Na	K	Ca	Mg	Cl	SO_4	HCO_3	Order of appearance of saline minerals during evaporative concentration of seawater
0.96	490	3.7	4.8	111	548	59.0	2.7	$CaCO_3$ – gypsum – anhydrite – glauberite – halite – polyhalite – epsomite – hexahydrite – kieserite – kainite – carnallite – bischofite
1.00	470	10.2	20.3	106	548	53.9	0.6	$CaCO_3$ – gypsum – anhydrite – glauberite – halite – polyhalite – epsomite – hexahydrite – kieserite – carnallite – bischofite
1.05	448	17.6	36.2	101	548	53.8	0.6	$CaCO_3$ – gypsum – anhydrite – halite – polyhalite – sylvite – carnallite – kieserite – bischofite
1.10	427	24.3	51.8	97	548	51.4	0.4	$CaCO_3$ – gypsum – anhydrite – halite – sylvite – carnallite – bischofite – tachyhydrite
1.25	376	41.2	91.4	85	548	45.3	0.3	$CaCO_3$ – gypsum – anhydrite – halite – sylvite – carnallite – antarcticite – tachyhydrite

After Spencer and Hardie (1990). Only the first appearance of each mineral is listed (see Fig. 2.24 for backreaction effects)

Simple mixing models show that changes in the flux rate of mid-oceanic hydrothermal brines can generate significant changes in the Mg/Ca, Na/K and SO_4/Cl ratios in seawater (Table 2.13). Such changes of molal ratios in seawater would have generated significant changes in the type and order of potash minerals at the bittern stage. For example, Spencer and Hardie's model predicts that an increase of only 10 % in the flux of mid-ocean ridge hydrothermal brine over today's value would create a marine bittern that would precipitate sylvite and calcium-chloride salts instead of the Mg-sulphate minerals expected during bittern evaporation of modern seawater. This Ca-Cl ocean corresponds to times of "calcite oceans" and contrast with the lower calcium, higher magnesium "aragonite oceans" of the Permo-Triassic and the Neogene (Fig. 2.45; Hardie 1996; Demicco et al. 2005).

Yet many sources have argued, including earlier work by Hardie, that bittern salts lacking $MgSO_4$ components indicate a nonmarine CaCl source. The strong possibility of temporal changes in Phanerozoic seawater chemistry from a $MgSO_4$ to a KCl ocean confuses a mineralogical distinction between marine and nonmarine brine sources. It can be used to argue that many extensive ancient evaporites, such as the Devonian Prairie Evaporite Fm. of Canada and the Cretaceous Maha Sarakham salts of Thailand are in fact marine and formed by the evaporation of a $CaCl_2$ ocean (Timofeeff et al. 2006). A recent paper by Holt et al. (2014), focusing on

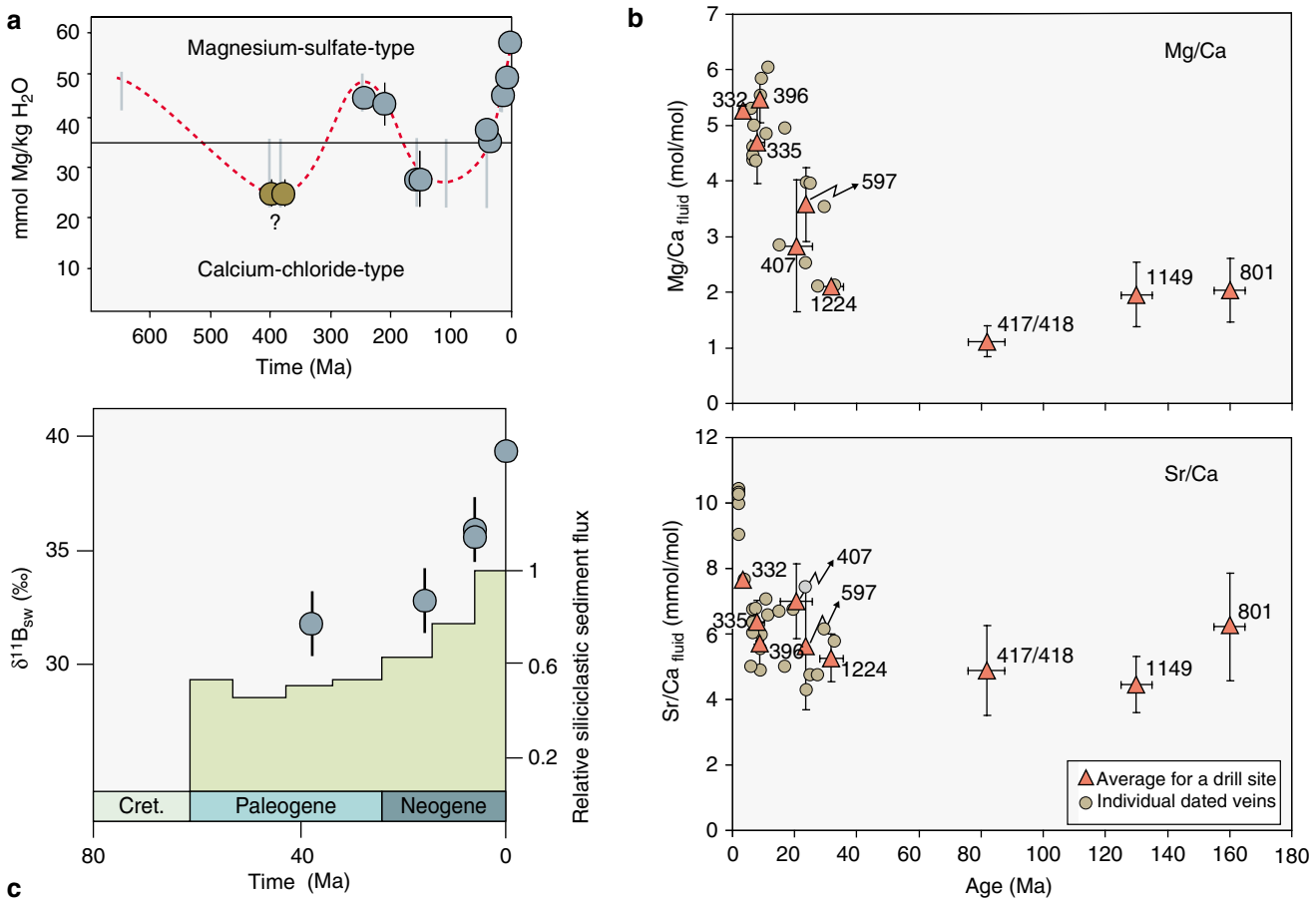

Fig. 2.46 Seawater evolution. (**a**) Secular changes in seawater chemistry based on microanalysis of fluid inclusions in marine halites and tied to levels of shelf dolomite (after Zimmermann 2000a). (**b**) Reconstructed Mg/Ca and Sr/Ca ratios of past seawater, based on calcium carbonate veins from the ocean crust (After Rausch et al. 2013). *Triangles with error bars* are averages for different drill sites. For sites in basement older than 38 Ma, dating of the carbonate veins was not possible and no individual analyses are depicted (**c**) Evolution of boron isotope values in Tertiary-age seawater, based on brine inclusions in chevron halite and plotted against relative siliciclastic input to oceans (After Paris et al. 2010)

chevron halite inclusions from various Carboniferous evaporite basins, further refined the transition from the Paleozoic $CaCl_2$ sea into a $MgSO_4$ -enriched aragonite ocean, so showing $CaCl_2$ oceanic chemistry (and sylvite bitterns) extend even further across the Paleozoic than previously thought (Fig. 2.45).

Holland et al. (1996), while agreeing that there are changes in ionic proportion of Phanerozoic seawater and that halite microinclusions preserve evidence of these changes, recalculated the effects of changing seafloor spreading rates on global seawater chemistry used by Hardie and others. They concluded changes in ionic proportions from such changes in seafloor spreading rate were modest. Instead, they pointed out that the composition of seawater can be seriously affected by secular changes in the proportion of platform carbonate dolomitised during evaporative concentration, without the need to invoke major changes in global seawater composition. In a later paper Holland and Zimmermann (2000), suggest changes in the level of Mg in seawater were such that the molar Mg/Ca ratio of Palaeozoic global seawater (based on dolomite volume) was twice the present value of 5.

Using micro-inclusion studies of halites of varying ages, Zimmermann (2000a, b) has proposed that the evolving chemistry of the Phanerozoic ocean is more indicative of changing volumes of dolomite than it is of changes in the rates of seafloor spreading (Fig. 2.46a). Using halite inclusions she showed that the level of Mg in seawater has increased from ≈ 38 mmol/kg H_2O to 55 mmol/kg H_2O in the past 40 Ma. This increase is accompanied by an equimolar increase in the level of oceanic sulphate. Over the longer time frame of the Palaeozoic to the present the decrease in Mg/Ca ratio corresponds to a shift in the locus of major marine calcium carbonate deposition from Palaeozoic shelves to the deep oceans, a change tied to the evolution of the nannoplankton. Prior to the evolution of foraminifera and coccoliths, some 150 Ma, the amount of calcium carbonate accumulating in the open ocean was minimal. Since then, a

progressively larger portion of calcium carbonate has been deposited on the floor of the deep ocean. Dolomitization of these deepwater carbonates has been minor.

Reasons for the increase in Mg in the past 40 Ma are still not clear. In a study of $CaCO_3$ veins in ocean basement, utilising 10 cored and documented drilled sites, Rausch et al. (2013) found for the period from 165 to 30 Ma the Mg/Ca and the Sr/Ca ratios were relatively constant (1.22–2.03 mol/mol and 4.46–6.62 mmol/mol respectively (Fig. 2.46b). From 30 to 2.3 Ma there was a steady increase in the Mg/Ca ratio by a factor of 3, mimicking the brine inclusion results in chevron halite. The authors suggest that variations in hydrothermal fluxes and riverine input are likely causes driving the seawater compositional changes. They go on to note that additional forcing may be involved in explaining the timing and magnitude of changes. A plausible scenario is intensified carbonate production due to increased alkalinity input to the oceans from silicate weathering, which in turn is a result of subduction-zone recycling of CO_2 from pelagic carbonate formed after the Cretaceous slow-down in ocean crust production rate.

Ayora et al. (2001) called for caution in applying general models of secular changes in seawater chemistry based on assumptions of worldwide sulphate depletion at various times in the past. They reconstructed the chemical evolution of several European Mesozoic and Tertiary marine evaporite basins using mineral associations, primary fluid-inclusion analyses, and numerical simulations of evaporation scenarios. The solute proportion recorded in the fluid inclusions in all basins could be explained using the evaporation of present-day seawater as a major recharge. Sulphate depletion in the brines was responsible for the type of potash deposit formed, namely potassium-magnesium sulphates or sylvite. But this sulphate depletion was due either to dolomitisation or to the addition of a $CaCl_2$-rich solution to the basin. Sulphate depletion occurred in varying intensity in basins of the same age, as well as throughout the evolution of the same basin negating the notion of changes in seafloor spreading. They concluded changes in potash mineralogy and sulphate depletion based on fluid inclusions are not conclusive arguments in favour of secular variations in the composition of the ocean.

Bots et al. (2011) further develop the notion of the importance of sulphate levels in controlling Phanerozoic chemistry. Rather than variations in Mg/Ca ratio in seawater being the prime driver of the aragonite versus calcite ocean chemistries across the Phanerozoic, they conclude sulphate levels are the most important control. They demonstrate that an increase in dissolved SO_4 decreases the Mg/Ca ratio at which calcite is destabilised and aragonite becomes the dominant $CaCO_3$ polymorph. If so, then the Mg/Ca and SO_4 thresholds for formation of calcite seas are mutually dependent and significantly lower than previously estimated.

In a study of boron isotopes in inclusions in chevron halite Paris et al. (2010), mapped out the changes in marine boron isotope compositions over the past 40 Ma (Fig. 2.46c). They propose that the correlation between $\delta^{11}B_{SW}$ and Mg/Ca reflects the influence of riverine fluxes on the Cenozoic evolution of oceanic chemical composition. Himalayan uplift is a major tectonic set of events that probably led to a 2.5 times increase of sediment delivery by rivers to the ocean over the past 40 Ma. They argue that chemical weathering fluxes and mechanical erosion fluxes are coupled so that the formation of the Himalaya favoured chemical weathering and hence CO_2 consumption. The increased siliciclastic flux and associated weathering products led to a concomitant increase in the influx levels of Mg and Ca into the oceans. However the levels of Ca in the world's ocean are largely biologically limited (mostly by calcareous nannoplankton and plankton), so leading to an increase in the Mg/Ca ratio in the Neogene ocean.

As well as changes in Mg/Ca and SO_4, the salinity of the Phanerozoic oceans shows a fluctuating but overall general decrease from the earliest Cambrian to the Present (Fig. 2.47; Hay et al. 2006). The greatest falls in salinity are related to major extractions of NaCl into young ocean (extensional continent-continent proximity) or foreland (compressional continent-continent proximity) ocean basins (Chap. 5). Phanerozoic seas were at their freshest in the Late Cretaceous, some 80 Ma, not today. This is because a substantial part of the Mesozoic salt mass, deposited in the megahalites of the circum-Atlantic and circum-Tethyan basins, has since been recycled back into today's ocean via a combination of dissolution and halokinesis. Periods characterised by marked decreases in salinity (Fig. 2.47) define times of mega-evaporite precipitation, while periods of somewhat more gradual increases in salinity define times when portions of this salt were recycled back into the oceans (Chap. 5).

The last major extractions of salt from the ocean occurred during the late Miocene in the various Mediterranean Messinian basins created by the collision of Eurasia with North Africa. This was shortly after a large-scale extraction of ocean water from the ocean to the ice cap of Antarctica and the deposition of the Middle Miocene (Badenian) Red Sea rift evaporites. Accordingly, salinities in the early Miocene oceans were between 37 and 39‰ compared to the 35‰ of today (Fig. 2.47). The preceding Mesozoic period was a time of generally declining salinity associated with the salt extractions in the opening North Atlantic and Gulf of Mexico (Middle to Late Jurassic) and South Atlantic (Early Cretaceous) and the earliest Cambrian oceans also had some of the highest salinities in the Phanerozoic. Recently, work by Blättler and Higgins (2014) utilising Ca isotopes studies of selected Phanerozoic evaporites has confirmed the dichotomous nature of Phanerozoic ocean chemistry that was previously defined by micro-inclusion studies of chevron halite (Fig. 2.45).

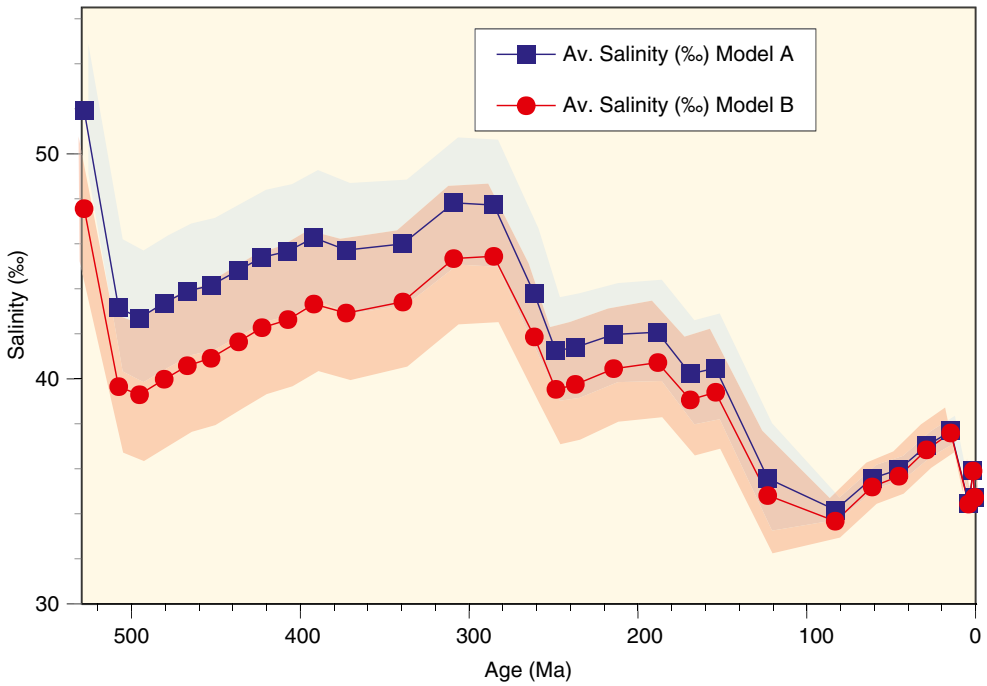

Fig. 2.47 Oceanic salinity changes for the last 500 my (After Hay et al. 2006)

In summary, based on a growing database of worldwide synchronous changes in brine chemistry in fluid inclusions in chevron halite, and Ca isotope variations, most evaporite workers would now agree that there were secular changes in Phanerozoic seawater chemistry and salinity. Ocean chemistries ranged from $MgSO_4$-enriched to $MgSO_4$-depleted oceans, which in turn drove the two potash endmembers (see Chap. 11). What is not yet clear is what is the dominant plate-scale driving mechanism (seafloor spreading versus dolomitisation versus uplift/weathering) that is driving these changes.

Precambrian Oceanic Chemistry

Given that ionic proportions of major ions in seawater and oceanic salinity have changed through the Phanerozoic, forces the question, how constant was the chemistry of the world's oceans since the early Archaean? For example, does the evaporite evidence support the possibility of a primordial reducing atmosphere and/or higher levels of bicarbonate in an ancient ocean?

Some authors postulate that there have been no significant changes in the major ion proportions in seawater for the past 4 Ga (Morse and Mackenzie 1998). Others assert that the Archaean was dominantly a time of little or no atmospheric oxygen and that ocean waters were reducing fluids (Krupp et al. 1994). Yet others propose that the bicarbonate to calcium ratio was so high in Archaean and Palaeoproterozoic seawater compared to today that all the calcium was used up in widespread abiotic marine aragonite and Mg-calcite precipitates (Sumner and Grotzinger 2000). In this case trona or nahcolite are likely marine evaporites in the early Archaean bitterns. Still others have theorised cyclic changes in oceanic chemistry occurred in much of the Precambrian similar to those of the Phanerozoic. Such changes were related to changes in styles and rates of sea floor spreading-hydrothermal circulation in midoceanic ridges (Channer et al. 1997) and the development of tonalitic continents (Knauth 1998).

In the Phanerozoic, seawater was dominantly a Na-K-Mg-Ca-Cl (Ca-rich) type that changed periodically to a Na-K-Mg-Cl-SO_4 (SO_4 -rich) type. Do similar oscillations in ocean chemistry extend back into the Precambrian? Given that the oldest halites are those of the Bitter Springs Formation in the Amadeus Basin and deposited some 840 Ma, we can only extend a halite inclusion based study of ocean chemistry back to that time. Recrystallised halite from the uppermost Neoproterozoic Salt Range Formation (ca. 545 Ma) in Pakistan, contains solitary inclusions indicating SO4-rich brines (Kovalevych et al. 2006b). This supports a similar ocean chemistry derived from primary fluid inclusions from the Neoproterozoic Ara Formation of Oman; that is SO_4-rich seawater existed during latest Neoproterozoic time (ca. 545 Ma). In contrast, Kovalevych et al. (2006b) determined samples of recrystallised halite from the Bitter Springs Formation (840–830 Ma) in Australia contain inclusion brines that are entirely Ca-rich, indicating that basin brines and seawater were Ca-rich during deposition of central Australian evaporites. These combined data, supported by the timing of aragonite and calcite seas, suggest that during the Neoproterozoic, significant oscillations of the chemi-

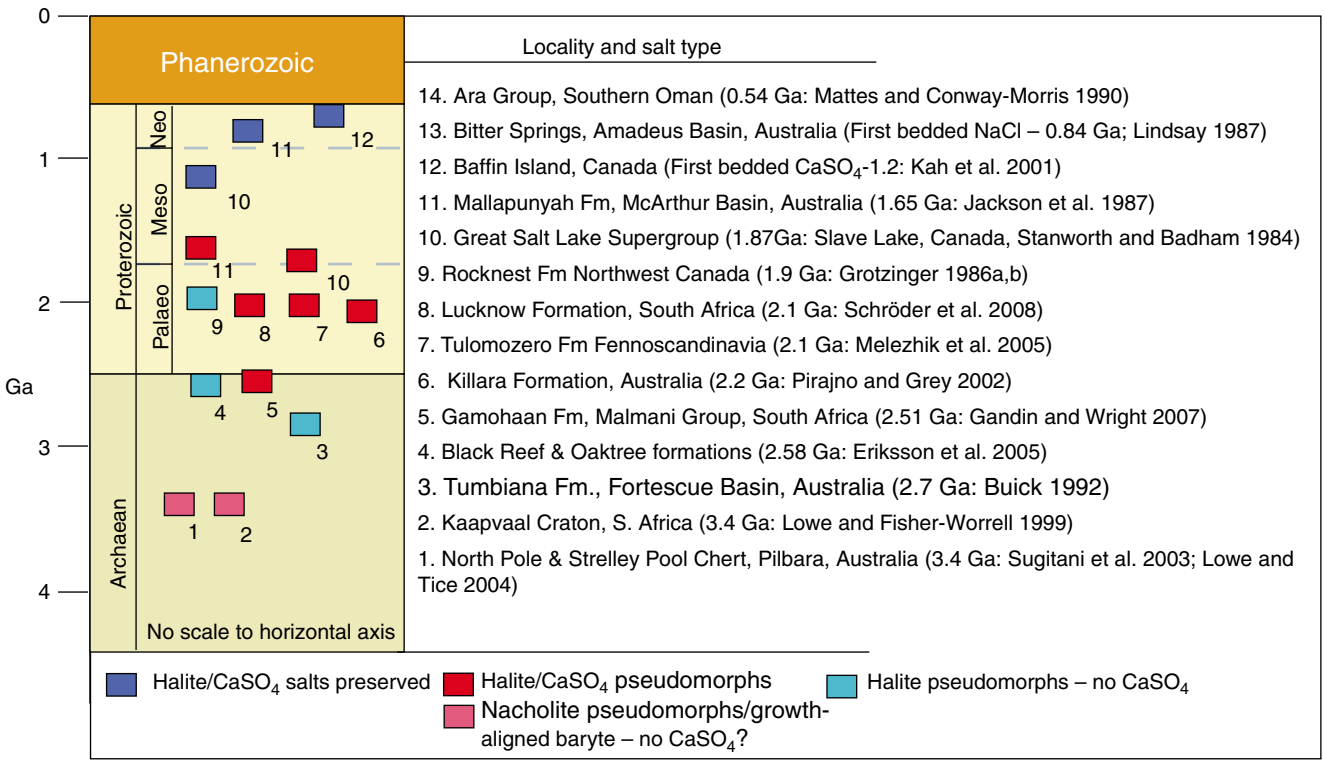

Fig. 2.48 Precambrian evaporite occurrences and mineralogies (compiled from listed sources)

cal composition of marine brines, and seawater, occurred, and were similar to those of the Phanerozoic. It seems that Ca-rich seawater dominated for a substantial period of Late Precambrian time (more than 200 Ma) from 850 Ma, until some 650 Ma, this was replaced by SO_4-rich seawater, returning to Ca-rich seawater at 530 Ma (Fig. 2.45).

The detail for much of the Precambrian is far less than when modelling inclusion chemistries in actual halites. The oldest documented chevron halite is 850 Ma and the oldest bedded anhydrite is 1.2 Ga, beyond that only evaporite pseudomorphs are available to study. So, beyond the 850 Ma record established by halite inclusions, can other Precambrian evaporites especially the calcium sulphates with a record that extends back patchily to the Mesoproterozoic, give indirect clues as to a chemical scenario for the world's paleo-oceans and brine?

Pseudomorphs, especially of halite hoppers, occur in marine rocks as old as Archaean, but are far more common, as are the actual salts, in Proterozoic strata (Fig. 2.48). Halite or its pseudomorphs characterise areas of widespread marine chemical sedimentation from the Archaean to the present. $CaSO_4$ pseudomorph distribution is more enigmatic. In the 1980s and 1990s, the oldest documented $CaSO_4$ pseudomorphs were thought to cm-sized growth-aligned barytes and cherts in 3.45 Ga metasediments in the Pilbara/North Pole region of Western Australia. They were interpreted as replacing primary bottom-nucleated gypsum (Fig. 7.98; Barley et al. 1979; Clemmey and Badham 1982; Lowe 1983; Buick and Dunlop 1990). They occur in volcaniclastics in association with what are possibly the world's oldest stromatolites (Hofmann et al. 1999; Allwood et al. 2007). Similar growth-aligned baryte crystals, which were also interpreted as likely primary gypsum pseudomorphs, occur in the Nondweni greenstones in South Africa, some 3.4 Ga (Wilson and Versfeld 1994).

Sequences in both regions are now completely silicified or barytised. At the time they were first documented, the recognition of what were considered shallow-water Early Archaean gypsum pseudomorphs at North Pole, Pilbara Craton, caused a re-evaluation of models of a totally reducing Archaean atmosphere (Dimroth and Kimberley 1975; Clayton and Thorpe 1982). The presence of free sulphate in surface brines of the Archaean world was thought to imply an at least locally oxygenated hydrosphere. Gypsum precipitating in Archaean ocean waters also meant calcium levels in the ocean waters were in excess of bicarbonate, as is in the modern oceans (Fig. 2.12). The presence of free-standing gypsum on the seafloor is incompatible with any model of the Early Archaean ocean as a "soda lake."

However, in both the Pilbara and the South African sequences there are no actual calcium sulphate evaporites preserved, only growth-aligned crystal textures now preserved as baryte or chert. Textures in baryte ore from Frasnian sediments in Chaudfontaine, Belgium, are near identical to

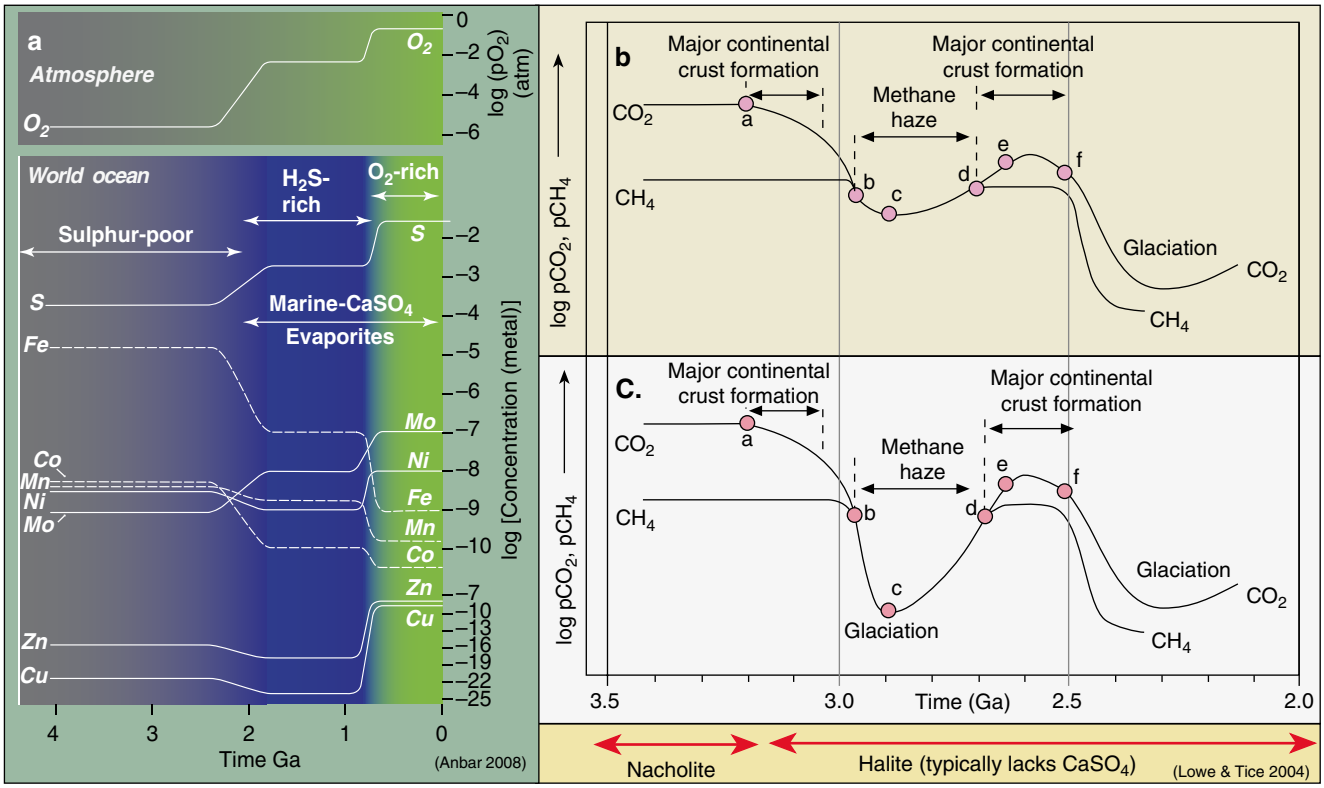

Fig. 2.49 Schematic diagrams showing proposed Earth's oceanic and atmospheric evolution. (**a**) Oxygen, sulphur and metal levels in the world oceans across time. The Archaean ocean was sulphur-poor, an expansion in H_2S-rich oceanic regions occurred around 2.4 billion years, which then gave away to fully oxygenated oceans around 800 Ma ago. That is, marine-derived sulphate evaporites formed both from mother brines that were sourced in H_2S-rich oceans from 2.4 to 0.8 Ga and from O_2-enriched since 0.8 Ga (in part after Anbar 2008) (**b**) and (**c**) pCH_4 and pCO_2 evolution during Archaean and earliest Proterozoic, 3.5–2.2 Ga (After Lowe and Tice 2004). *Diagrams* show atmospheric evolution (**b**) without and (**c**) with glaciation at 2.9 Ga. High surface temperatures, 70 ± 15 °C, were maintained from before 3.5 to at least 3.2 Ga by mixed CO_2 and CH_4 atmospheric greenhouse with $CH_4/CO_2 \ll 1$. Starting ca. 3.2 Ga (point a), enhanced weathering associated with continent formation began to deplete atmospheric CO_2, leading eventually to $CH_4/CO_2 \approx 1$ some. 2.9 Ga (point b) and formation of organic haze, which began to reduce pCH_4 along a path defined by $CH_4/CO_2 \approx 1$. Declining pCO_2 and pCH_4 at 2.9–2.7 Ga resulted in global cooling and possibly glaciation (point c in *lower diagram*). Reduced weathering and continued tectonic recycling 2.7–2.6 Ga led to increasing pCO_2 (line c-d-e), allowing a coupled increase in pCH_4 while maintaining $CH_4/CO_2 \approx 1$. When upper limit of CH_4 production was reached (point d), CH_4/CO_2 became <1 and methane haze formation ceased. Enhanced weathering ca. 2.6 Ga (point e) associated with continent building at 2.7–2.5 Ga once again initiated rapid depletion of atmospheric CO_2 and decline in surface temperatures. Increased O_2 production—associated with latest Archaean spread of oxygenic photosynthetic microbes onto large, shallow-water, continental shelves developed on older (pre–3.0 Ga) blocks of continental crust (point f)—concurrently lowered pCH_4, maintaining CH_4/CO_2 <1 and preventing the formation of organic haze. Oxygen in this period did not approach levels comparable with the Phanerozoic. Widespread glaciation at 2.4–2.2 Ga resulted from decreasing pCO_2 due to weathering and declining pCH_4 due to oxidation

those observed at North Pole, Australia. The Belgian barytes are primary sea-bottom precipitates with no precursor mineral phase (Dejonghe 1990). Some workers in the Pilbara feel that the growth-aligned baryte in this region is also a primary precipitate, formed in the vicinity of hydrothermal vents (Vearncombe et al. 1995; Nijman et al. 1999; Runnegar et al. 2001). As such, it is not secondary after gypsum. A similar hydrothermal discharge model has been developed for aligned barytes in the Barberton Greenstone belt (De Ronde et al. 1994; De Ronde and Ebbesen 1996).

Levels of Archaean sulphate in the world ocean were probably less than a few percent of the current levels and probably remained so until the evolution of an oxygen-producing biota into the Proterozoic (Figs. 2.49a and 2.50; Habicht and Canfield 1996; Kah et al. 2004). Barium sulphate is highly insoluble in modern oxygenated seawater. To carry large volumes of barium or sulphur (as sulphide) in seawater solution to the precipitation site requires anoxic conditions. If the aligned baryte crystals are primary, their formation still requires sulphate to be locally present on the seafloor, at least in the vicinity of the depositional site. A possible source for local sulphate production in the shallow waters that characterised the North Pole site was shortwave ultraviolet photoxidation of volcanic SO_2, indicating an inorganic association (Runnegar et al. 2001). Within barytes in the same 3.47-Ga-old barytes there are microscopic sul-

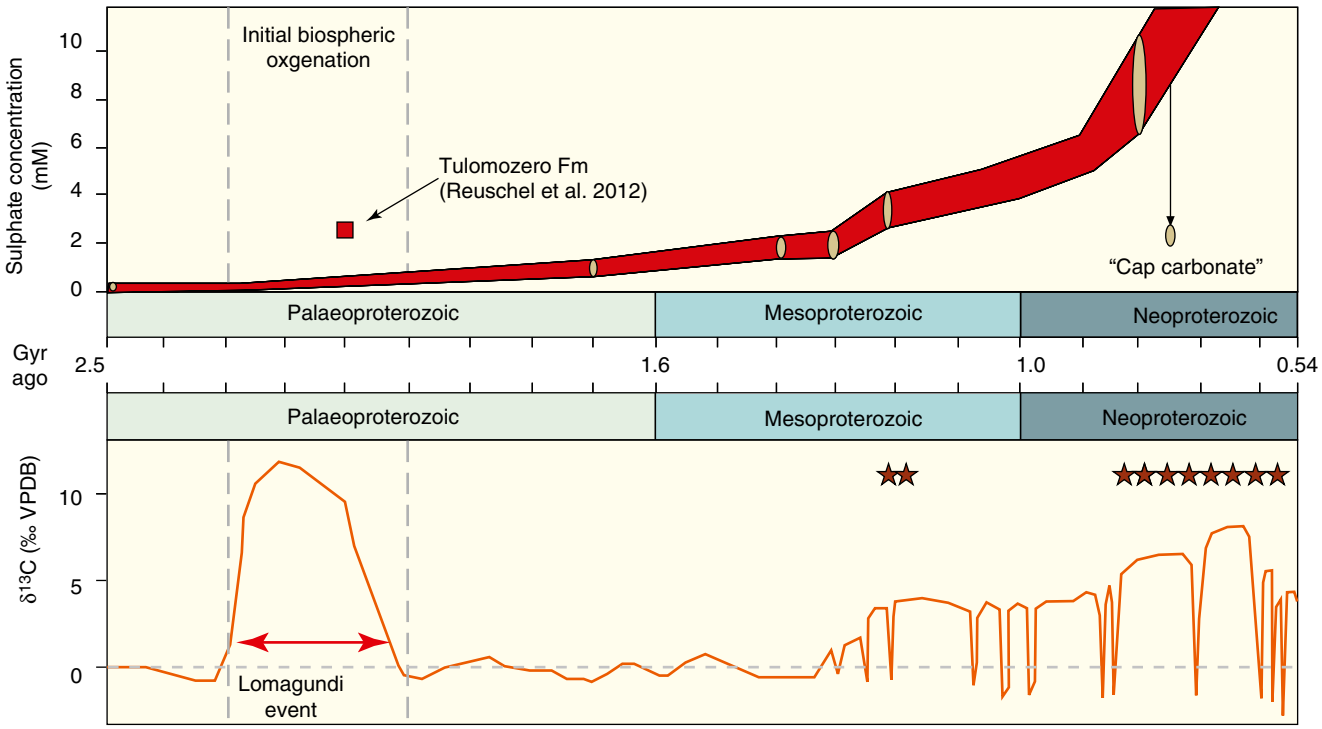

Fig. 2.50 Proterozoic marine sulphate concentrations. Filled ovals mark data determinations (in part after Kah et al. 2004). Marine sulphate concentrations probably remained mostly below 2 mM until about 1.3 Gyr ago (except in the Lomagundi event), rose to, 4.5 mM by 1.2 Gyr ago, and possibly as high as 7–10 mM by the mid-Neoproterozoic, although near-complete reduction of oceanic sulphate may have occurred during Neoproterozoic glacial intervals (*arrow*). Increased sulphate concentrations coincide with changes in marine $\delta^{13}C$ associated with biospheric oxygenation and are marked by the appearance of bedded gypsum (*stars*) in the late Mesoproterozoic and more frequent gypsum deposition in the last two-thirds of the Neoproterozoic

phides. These sulphide inclusions show a $\delta^{34}S$ of 11.6‰, possibly indicating microbial sulphate reduction with H_2 as electron donor (Canfield et al. 2004; Shen et al. 2009).

According to Nijman et al. (1999) the occurrence of the North Pole baryte in sedimentary mounds atop growth faults meant sulphate was locally derived via boiling of escaping hydrothermal vent waters enriched in Ba, Si and sulphide. As these hydrothermal waters vented beneath waters perhaps 50 m deep, they boiled or violently degassed. Consequent mixing with normally stratified seawater, caused instantaneous oxidization of sulphide into sulphate that then, on cooling, combined with the Ba to precipitate as growth-aligned baryte crystals on the seafloor. Conflicting notions (replaced gypsum versus primary baryte) mean that at this stage of our understanding, the bedded baryte evidence cannot be reliably used to support an evaporite paragenesis of gypsum and so infer an Archaean ocean with ionic proportions similar to those of today.

Archaean and Proterozoic distributions of gypsum have been further complicated by the misidentification of primary aragonite splays and pinolitic siderite marbles as gypsum replacements Warren (1999); Chap. 8). When these misidentifications are removed from the record it is obvious that calcium sulphate precipitating directly from Archaean seawater to form widespread beds did not occur, and that precipitation of aragonite as thick crusts on the sea floor was significantly more abundant than during any subsequent time in earth history. In contrast to gypsum, halite pseudomorphs are found throughout the Precambrian (e.g., Boulter and Glover 1986; Fig. 2.48).

Grotzinger and Kasting (1993) argue that high levels of atmospheric CO_2 meant HCO_3/Ca ratios were much higher in the Archaean and the Palaeoproterozoic oceans than today. All the calcium in seawater was deposited as marine cementstones and other alkaline earth precipitates well before bicarbonate was depleted and there was no Ca left over to precipitate as gypsum. The early Archaean ocean was perhaps a Na–Cl–HCO_3 sea, and not the Na–Cl ocean of today (Kempe and Degens 1985; Maisonneuve 1982). This early Archaean hydrosphere had a chemistry similar to that found in modern soda lakes like Lake Magadi and Lake Natron (pathway I brines in Figs. 2.19 and 2.20) and hence the term "soda-lake oceans." This rather different marine brine chemistry would have precipitated halite and trona/nahcolite, not halite/gypsum. It probably meant that if gypsum did ever precipitate from Archaean seawater it did so only in minor amounts well after the onset of halite precipitation. Excessive sodium in the ocean may help explain the ubiquity of stratiform albitites in much of the Archaean. They would have

formed throughout the marine realm as early diagenetic replacements of labile volcaniclastics/zeolites in volcanogenic/greenstone terranes (See Chap. 11, zeolite).

A case for nahcolite ($NaHCO_3$) as a primary evaporite, along with halite, in the 3.42 Ga rocks of the Barberton greenstone belt was documented by Lowe and Fisher-Worrell (Lowe and Worrell 1999). Sugitani et al. (2003) reported silicified nahcolite (the high CO_2 form of sodium carbonate salts; see Fig. 2.20a) in ≈3.2 Ga rocks in the northern part of the Eastern Pilbara block, Western Australia. Coarse, upward-radiating, silicified evaporite crystals in the ca. 3.47–3.46 Ga Strelley Pool Chert (Lowe 1983) show the same habit, geometry, and environmental setting as nahcolite in the Barberton belt and also probably represent silicified $NaHCO_3$ precipitates (Lowe and Tice 2004).

Marine nahcolite in the 3.5–3.2 Ga sedimentary record is thought to be evidence of surface temperatures around 70 ± 15 °C (Figs. 2.20a and 2.49b, c; Lowe and Tice 2004). Contemporary early Archaean nahcolite ($NaHCO_3$) as a primary evaporitic mineral in a very aggressive weathering regime, in the absence of land vegetation, is best explained by a mixed CH_4 and CO_2 atmospheric greenhouse. CH_4/CO_2 ratios were $\ll 1$ and pCO_2 was at least 100–1,000 times the present value, perhaps as high as several bars (Kaufman and Xiao 2003). The formation of large areas of continental crust at 3.2–3.0 Ga, including the Kaapvaal and Pilbara cratons, resulted in the gradual depletion of atmospheric CO_2 through weathering and a lack of marine nahcolite since the early Archaean. By 2.9–2.7 Ga, declining pCO_2 was associated with climatic cooling and siderite-free soils.

Transitory CH_4/CO_2 ratios of ~1 may have resulted in the sporadic formation of organic haze from atmospheric CH_4, and are reflected in one or more isotopic excursions involving global deposition of abnormally ^{13}C-depleted organic carbon in sediments of this age. Surface temperatures of <60 °C after 2.9 Ga may have allowed an increase in the distribution and productivity of oxygenic photosynthetic microbes (and a decrease in sulphur dependent thermophiles). Eventual lowering of newly formed continental blocks by erosion, reduced loss of atmospheric CO_2 due to weathering, and continued longterm tectonic recycling of CO_2 resulted in rising pCO_2 and decreasing CH_4/CO_2 ratios in the later Archaean and eventual re-establishment of a mainly CO_2 greenhouse. Similar events may have been repeated in the latest Archaean and earliest Proterozoic, but gradually rising production of O_2 effectively kept CH_4/CO_2 ratios to $\ll 1$.

By 2.2–2.0 Ga and perhaps as early as 2.5 Ga, reliable examples of pseudomorphs after primary marine-sourced calcium sulphate first appear in the rock record, but aside from the Karelian beds associated with the Lomagundi Event (LE), widespread stratiform sulphate beds of anhydrite do not appear until 1.2 Ga (Figs. 2.48 and 2.49a). Undeniable $CaSO_4$ nodular and lenticular pseudomorphs are widespread in latest NeoArchaean of South Africa and Palaeoproterozoic to Mesoproterozoic sediments of the McArthur Basin, Northern Territory, Australia, and in rocks of Great Slave Lake in northern Canada. For example, in the Malapunyah Formation (1.65 Ga) of the Northern Territory, Australia, the outer portions of numerous decimetre to metre-diameter silicified anhydrite nodules still retain outlines of felted anhydrite laths (pers. obs). The oldest reliable sulphate pseudomorphs after anhydrite and gypsum in Australia come from Palaeoproterozoic cherts in the 2.0–2.2 Ga Bartle Member of the Killara Formation, western Australia (Pirajno and Grey 2002). These cherts locally retain small amounts of anhydrite (verified by XRD, as well as appearing as highly birefringent flecks in thin sections). Other widespread but younger sulphate pseudomorphs occur in the 1.2 Ga Amundsen Basin in the Canadian Arctic Archipelago. Actual $CaSO_4$ beds outcrop in the 1.2 Ga Society Cliff Formation in Baffin and Bylot Islands of the Canadian Archipelago (Kah et al. 2001, 2004). Sulphate evaporite pseudomophs and nodules in all these Neoproterozoic basins are hosted in sedimentary layers up to tens of metres thick and with lateral extents measured in hundreds of square kilometres. All were laid down in shallow marine, coastal, and alluvial environments under an increasingly oxygenated Meso- to Neoproterozoic atmosphere (Jackson et al. 1987; Walker et al., 1977a, b). After passing from the Archaean, by the Mesoproterozoic the hydrosphere contained free sulphate and Ca/HCO_3 ratios were lower, leading to a decrease in molar tooth and other structures indicative of widespread inorganic calcium carbonate saturation in shallow oceanic waters (Fig. 1.26). However, oceanic mother brines for these now-widespread calcium-sulphate evaporites were largely H_2S rich with only moderate levels of oxygen in the atmosphere until some 800 Ma (Fig. 2.49a)

The work of Kah et al. (2004) shows that prior to 2.2 Ga, when oxygen began to accumulate in the Earth's atmosphere, sulphate concentrations in the world's oceans were low, <1 mM and possibly <200 μM (Fig. 2.50). By 0.8 Ga, oxygen and thus sulphate levels had risen significantly. Sulphate levels were between 1.5 and 4.5 mM, or 5–15 % of modern values, for more than a billion years after initial oxygenation of the Earth's biosphere some 2.2–2.4 Ga and mid -ocean depth waters were anoxic for most of that time (Brocks et al. 2005). Marine sulphate concentrations probably remained low, no more than 35 % of modern values, for nearly the entire Proterozoic. A significant rise in biospheric oxygen, and thus oceanic sulphate, may not have occurred until the latest Neoproterozoic (0.54 Ga), just before the Cambrian explosion, when sulphate levels may have reached 20.5 mM, or 75 % of present day levels. This is a time when thick sulphate platforms first characterised the salt basins of Oman, prior to that most actual calcium sulphate is in the form of nodules or relatively thin beds.

In a refinement of the sulphate model, Bekker and Holland (2012) note that free sulphate evaporites and not just its pseudomorphs were present during the Lomagundi Event (2.22–2.06 Ga), and then became relatively scarce once more until some 1.2 Ga. For example, there is a 200 m thick stratigraphic interval of sulphate evaporites of Lomagundi-age, preserved in a shallow-water open-marine siliciclastic and carbonate succession (Lower Jatuli informal group) of Karelia, Russia (Morozov et al. 2010). The Lomagundi Event defines the most extreme and longest lasting isotope excursion of carbon in the world's marine carbonate record. Bedded gypsum pseudomorphs in the Malmani Group some 2.5 Ga (Gandin and Wright 2007) implies that elevated oceanic sulphate levels that typify the Lomagundi Event may have extended a little further back in time, at least locally (Fig. 2.50).

At the same time as the Lomagundi event, the average ferric iron to total iron (expressed as $Fe_2O_3/\Sigma Fe_{|Fe2O3|}$) ratio of shales increased dramatically. At the end of the Lomagundi Event (LE), the first economic sedimentary phosphorites were deposited, and the carbon isotope values of marine carbonates returned to $\approx 0.0‰_{VPDB}$ (Fig. 2.50). Thereafter marine sulphate evaporites and phosphorites again became scarce, while the average $Fe_2O_3/\Sigma Fe_{|Fe2O3|}$ ratio of shales decreased to values intermediate between those of the Archaean and Lomagundiage shales.

In support of this notion of an "oxygen overshoot," sulphur isotope work by Reuschel et al. (2012) on the 2.1 Ga dolomitic Tulomozero Fm, which entrains abundant $CaSO_4$ pseudomorphs, concluded that there was a minimum level of 2.5 mM sulphate in the world ocean at that time (Fig. 2.50).

Bekker and Holland (2012) argue the short appearance of sulphate evaporites in Logamundi and the other associated events can be regarded as a ca. 200 Ma "glitch" in the gradual oxidation of the atmosphere–ocean system. It was driven by a positive feedback between the rise in atmospheric O_2, the oxidation of pyrite in rocks undergoing weathering, a decrease in the pH of soil and ground water, and an increase in the phosphate flux to the oceans. This sequence led to a major increase in the rate of organic matter burial, a rise in atmospheric oxygen, a large increase in the $\delta^{13}C$ value for marine carbonates, the deposition of marine evaporites containing gypsum and anhydrite, and the formation of the first commercially important phosphorites. The end of the LE was probably brought about by the weathering of sediments deposited during the LE.

In yet another proposal of hydrosphere-atmosphere evolution, Huston and Logan (2004) argue that the presence of relatively abundant bedded sulphate deposits before 3.2 Ga (as baryte) and after 1.8 Ga (as $CaSO_4$ salts), and the peak in banded iron formation abundance between 3.2 and 1.8 Ga, and the aqueous geochemistry of sulphur and iron, when taken together suggest that the redox state and the abundances of sulphur and iron in the hydrosphere varied widely during the Archaean and Proterozoic. They propose a layered hydrosphere prior to 3.2 Ga in which sulphate was enriched in an upper oceanic layer, whereas the underlying layer was reduced and sulphur-poor. The sulphate was produced by atmospheric photolytic reactions with volcanic gases in a reducing atmosphere. Mixing of the upper and lower water masses allowed the banded barytes to form prior to 3.2 Ga and created an ocean chemistry where nahcolite was a marine evaporite. Between 3.2 and 2.4 Ga, decreasing volcanogenesis and sulphate reduction removed sulphate from the upper layer, producing broadly uniform, sulphur-poor and iron-rich oceans.

As a result of increasing atmospheric oxygenation around 2.2–2.4 Ga, the flux of sulphate into the hydrosphere by oxidative weathering was greatly enhanced, producing layered oceans, with sulphate-enriched, iron-poor surface waters and reduced, sulphur-poor and iron-rich bottom waters. Gypsum evaporites were increasingly likely as marine precipitates. The rate at which this process proceeded varied between basins depending on the size and local environment of the basin. By 1.8 Ga, the hydrosphere was relatively sulphate-rich and iron-poor throughout. Gypsum was now a widespread marine evaporite. Variations in sulphur and iron abundances suggest that the redox state of the oceans was buffered by iron before 2.4 Ga and by sulphur after 1.6–1.8 Ga.

Gypsum in combination with halite was the marine evaporite association from then until now. Seawater was predominantly a Na-Cl-SO_4 ocean. Neoproterozoic stratiform sulphates along with widespread halokinetic halite, occur in the Bitter Springs Formation of the Amadeus basin, central Australia (0.8 Ga), its equivalents in the Officer Basin, the Callana beds of the Flinders Ranges and the younger Infracambrian salt basins of the Arabian (Persian) Gulf (≈0.545 Ga; Wells 1980; Cooper 1991; Mattes and Conway-Morris 1990; Edgell 1991).

The transition to calcium sulphate textures in evaporite pseudomorphs mirrors a marked change in the style of marine carbonates that began around 2.2–2.3 Ga when herringbone calcite and precipitated carbonate beds become much less common and the precipitation mode shifted from the seafloor to the water column (Fig. 1.26; Saunders and Thomas 1996). The boundary also corresponds to the "rusting" of the oceans when oxygen levels became high enough to precipitate widespread banded iron deposits on the seafloor. Microdigitate stromatolites cross this boundary with little effect, suggesting the marked decrease in dissolved iron exerted little influence on them.

The relative scarcity of actual Pre-Phanerozoic salts, not pseudomorphs, especially in the Archaean has been used by some to argue that conditions were less favourable for

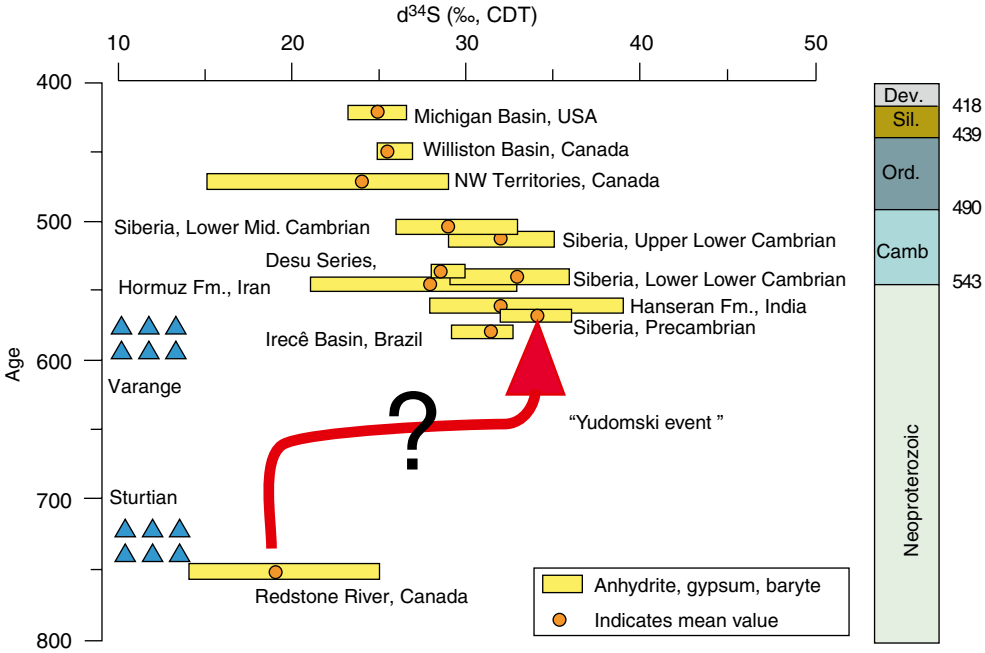

Fig. 2.51 Temporal evolution of $\delta^{34}S$ from marine chemical sediments (anhydrite, gypsum, baryte during the terminal Neoproterozoic and early Palaeozoic. Blue triangles indicate the Sturtian and Varanger glaciations (After Strauss et al. 2001 and references therein)

widespread evaporite deposition in the early Precambrian (Cloud 1972). Others, myself included, feel that the relative scarcity of preserved evaporites in older sequences reflects the greater likelihood of fluid flushing, evaporite dissolution and metasomatism in progressively older rocks. It is likely that oceanic calcium-sulphate evaporites were less common in the Archaean, and that sodium carbonates mixed with halite were dominant evaporite salts in the seawater-fed saline giants in appropriate tectonic seepage depressions of the Early Archaean. But widespread evaporite deposition from sodium-dominated brines did occur throughout the Archaean in large drawdown basins isolated from a surface connection with the ocean. A paucity of preserved bedded evaporite salts in the Precambrian reflects an increased probability of partial or complete evaporite dissolution, remobilization and metasomatism with increasing geological age (see meta-evaporite).

In what is an inclusion study of oldest actual halite, Spear et al. (2014), characterised marine brine chemistry using brine inclusions in the 830 Ma salt of the Browne Formation, Officer Basin, Australia. It seems that concentrations of the major ions in these inclusions, except K^+ and possibly SO_4^{2-}, fall within the known range of Phanerozoic seawaters. This analysis suggests that mid-Neoproterozoic marine sulphate concentrations were lower (≈90 %) than modern values. By the terminal Neoproterozoic, fluid inclusions in halite and evaporite mineralogy from the Browne Formation in Western Australia and the Ara salt in Oman indicate seawater sulphate levels had risen significantly, to 50–80 % of modern concentrations, which parallels increases in atmospheric and oceanic oxygen.

Precambrian-Cambrian Transition

Through much of the Neoproterozoic marine sulphates are preserved as actual chemical precipitates (anhydrite, gypsum, baryte). Their impermeable nature means their isotopic signatures are useful supplements to more widespread marine carbon and sulphide records in defining the transition from the Terminal Neoproterozoic into the early Palaeozoic. Holser (1977, 1984) was the first to address the specific conditions required to produce the rapid rise in $\delta^{34}S$ of seawater sulphate during the terminal Neoproterozoic which he termed the "Yudomski event" after the regional stratigraphy preserved in SE Siberian evaporites. His model of stratification-stagnation and subsequent ventilation of the deep ocean and mixing of different sulphur isotope signatures for dissolved marine sulphate between surface and deep water was reinforced by subsequent workers (Goodfellow and Jonasson 1984; Logan et al. 1995). Recently it has been placed in the contextual framework of a possible "Snowball Earth" and the oxidation of the Ediacaran Ocean (Fig. 2.51; Strauss et al. 2001; Fike et al. 2006). The enrichment in $\delta^{34}S$ signature of chemical sediments across the Precambrian-Cambrian boundary is real, but its ultimate cause is still a matter of debate.

Holser (1977) favoured brine generation and density/salinity stratification of the late Neoproterozoic ocean to explain the "Yudomski event." Alternatively Hoffman et al. (1998), proposed extreme climatic conditions and coverage of the global ocean with sea ice (Snowball Earth) followed by a rapid termination of glacial conditions as a consequence of the build-up of large quantities of volcanogenic CO_2 in the deeper ocean. Subsequent mixing of water masses triggered

the precipitation of large quantities of cap carbonates following the glacial horizons. This scenario (sometimes called "freeze then fry") results in a major reorganisation of the biogeochemistry for the entire water column and is interpreted by some to be documented in the extreme fluctuations of the carbon isotopic composition that occur at that time and likely reflect major changes in the makeup of the world's carbon cycle as we move across the boundary, with related changes in carbonate saturation (Chap. 5).

The Precambrian to Cambrian sulphur cycle, as preserved in marine sulphate evaporites, is intimately linked to the carbon cycle (Holser et al. 1988a, b). This is expressed through a negative correlation of their isotopic compositions i.e., carbonate carbon and sulphate sulphur, reflecting the biological aspects of the exogenic cycle (Figs. 2.35 and 2.51; Strauss et al. 2001). The temporal record of the carbon isotopic composition displays intervals of strongly ^{13}C-enriched values preceding the Neoproterozoic glacials, a decline in $\delta^{13}C$ immediately prior to the glacial horizons, and low $\delta^{13}C$ values in the cap carbonates followed by an evolution back to more ^{13}C-enriched values (Figs. 2.50 and 2.51).

If the Snowball Earth model is real, this may reflect severe changes in primary productivity associated with varying sea ice coverage. Hand in hand with evolving anoxic conditions in the water column under sea ice, heterotrophic recycling of organic matter by sulphate-reducing microbes would have become an important process in the water column, leading to ^{34}S-enriched seawater sulphate. This is clearly documented in the isotopic composition of resulting sedimentary sulphides (e.g., Strauss 1997). Deglaciation and rapid ocean turnover then transferred ^{34}S-enriched water on to the shelf, where marine-fed sulphate evaporites record this isotopic signature.

Next in the geological history of Precambrian seawater, after the "Yudomski event," as preserved in evaporite chemistry, comes what is, at least from an anthropocentric viewpoint, the most significant time in the evolution of life. It is when metazoans evolved mineralised hardparts and there was the concurrent evolution of the phylum Chordata (animals with backbones and our distant ancestors). Comparisons of chemical compositions of primary fluid inclusions in marine halite chevrons from terminal Proterozoic Ara Salt (≈544 Ma) and Early Cambrian (Toyonian) Angarskaya Formation of eastern Siberia (≈515 Ma) indicate that Ca concentrations in seawater increased approximately threefold across the Precambrian-Cambrian boundary and into the Early Cambrian (Fig. 2.52; Brennan et al. 2004). That is, the concentrations of Ca in seawater rose precipitously from the Neoproterozoic to reach a Phanerozoic high in the earliest Cambrian (Peters and Gaines 2012). Much of this increase is attributable to enhanced chemical weathering of continental crust during the Sauk transgression, also known as the "Great Unconformity", which since the time of Darwin has defined the Cambrian-Precambrian boundary.

The timing of this marked increase in Ca in seawater broadly coincides with the Cambrian explosion in life, as well as a brief drop in marine $^{87}Sr/^{86}Sr$ values, and an increase in tectonic activity at mid ocean ridges (see earlier in this chapter for discussion of how midoceanic spreading rates may link to oceanic chemistry). Their coincidence suggests a link between the advent of biocalcification, increased hydrothermal midocean-ridge brine production, and the changed composition of seawater (Fig. 2.52).

Brennan et al. (2004) suggest that the evolution of widespread biomineralization might be a metabolic detoxification process induced by large increases in intracellular Ca^{2+} as identified by increases in Ca levels in halite inclusions. During the Early Cambrian, the ambient oceanic calcium level may have risen to such a degree that cells could no longer effectively exclude or expel Ca^{2+} ions, causing intracellular Ca^{2+} in certain marine organisms to reach toxic levels (Simkiss 1977, 1989; Kempe and Kazmierczak 1994). Furthermore, high phosphate levels in Early Cambrian seawater may have amplified the uptake of Ca^{2+} by organisms (Kempe and Kazmierczak 1994). Opportunistic organisms may have modified their existing cellular waste-removal systems by binding Ca^{2+} as relatively insoluble minerals (calcium carbonate or calcium phosphate).

Yet another factor that favoured the evolution to multicellular life toward the end of the Precambrian was the transition of atmospheric temperatures into more temperate ranges (Fig. 2.53; Meng et al. 2011). Seawater temperatures throughout Earth's history illustrate a long-term cooling trend from nearly 70 °C at ~3,500 Ma to around 20 °C at ≈800 Ma. The terminal Neo proterozoic prior to the "Cambrian explosion" is a key interval in evolutionary history, as complex multicellularity appeared with the advent of the Ediacara fauna. These organisms were likely the first that required higher levels of atmospheric and dissolved marine oxygen for their sustainability. Most modern macroinvertebrates are intolerant of temperatures in excess of 45 °C. Perhaps more importantly, these high seawater temperatures limit the potential of dissolved oxygen, and therefore become an integral part of this evolutionary story.

Most of our understanding of seawater temperature during the terminal Neoproterozoic comes from $^{18}O/^{16}O$ and $^{30}Si/^{28}Si$ ratios a from a limited number of cherts. Isotopic ratio methods for assessing seawater temperatures are inherently indirect and have a wide range. However, maximum homogenization temperatures (T_{hmax}) of primary fluid inclusions in halite are a direct means of assessing brine temperature, and as seen earlier in this chapter have been shown to correlate well with average maximum air temperatures. Some of the oldest chevron halites date to the Neoproterozoic-lower Palaeozoic (≈700–500 Ma), and Ediacaran representatives occur in Sichuan Province, China. Meng et al. (2011) used chevron halite samples from the Changning-2 well, correlative to the Dengying Formation (551–542 Ma), to give a

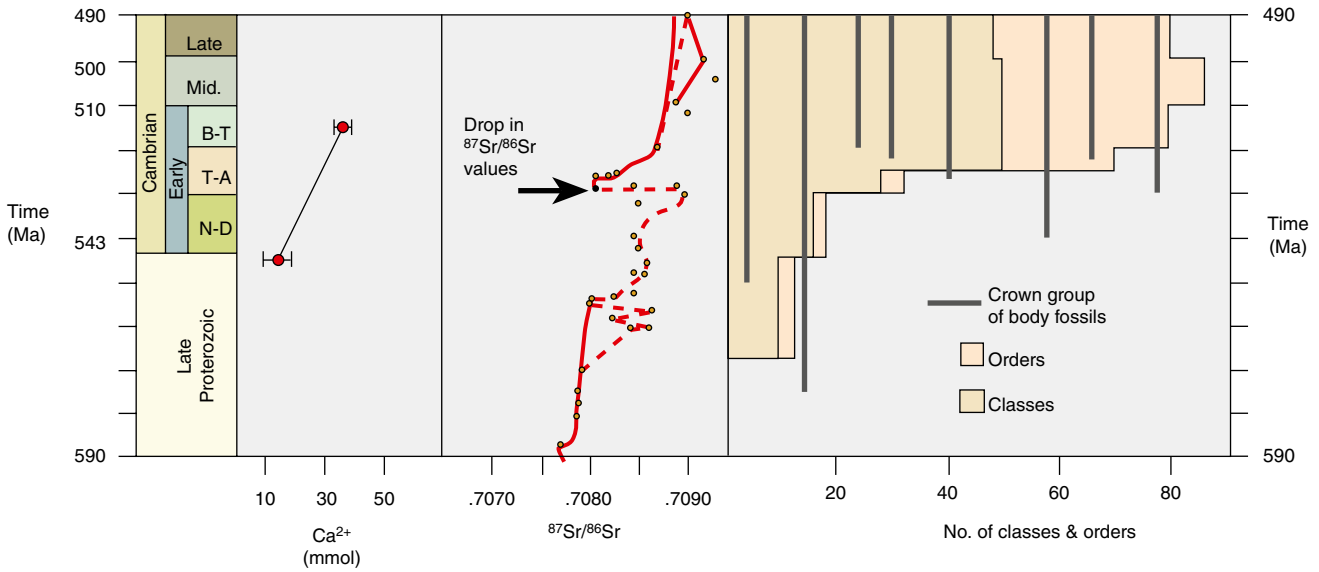

Inferred ion compositions in ancient seawater (chevron halite)

Major Ion	Terminal Prot. (≈ 544 Ma)	Early Cambrian (≈ 515 Ma)	Modern
Na	479	450	485
K	11	9	11
Ca	11 (9.5–18.5)	37 (33.5–40)	11
Mg	52	44	55
Cl	581	605	565
SO_4	20.5 (16–25)	8 (4.5–11)	29
Mg/Ca	≈4	≈1	5

Ca and SO_4 values represent averages of possible end-member concentrations (in parentheses). All concentrations are mmol (millimoles/kg of H_2O)

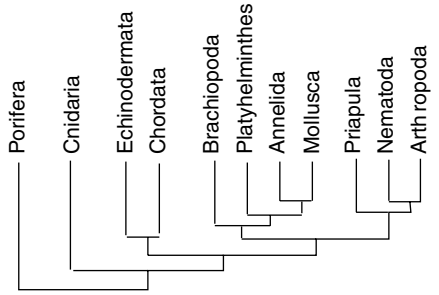

Fig. 2.52 Geological and biological changes in oceanic realm during terminal Proterozoic and Cambrian (After Brennan et al. 2004 and references therein). Stages in Early Cambrian are Nemakit-Daldynian (N-D), Tommotian–Atdabanian (T–A), and Botomian–Toyonian (B–T); Middle (M) and Late (L) Cambrian are also shown. There was dramatic increase in diversity of animal classes and orders starting in Tommotian time. Phylogeny and corresponding crown group first appearances (time line) show diversification of animal clades from the earliest Cambrian. Crown groups are the last common ancestor of all living members of a clade plus all its descendants. Decrease in marine $^{87}Sr/^{86}Sr$ ratios ≈530 Ma during an otherwise increasing trend in $^{87}Sr/^{86}Sr$ ratios likely indicates increase in mid-ocean-ridge spreading rates. Bars indicate possible ranges of oceanic Ca^{2+} determined from inclusions in chevron halite; open circles represent average values with measured ranges shown in parentheses in inset table of computed values of seawater composition for the terminal Proterozoic and Early Cambrian with the composition of modern seawater listed for comparison

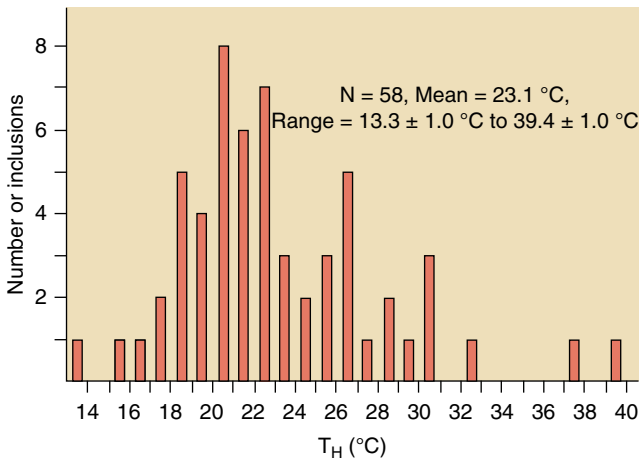

Fig. 2.53 Temperature-frequency distribution of measured homogenization temperatures from inclusions in chevron halite from the Dengying Formation in the Changning well (After Meng et al. 2011)

direct assessment of terminal Neoproterozoic seawater temperature (Fig. 2.53). Their measurements indicate marine-fed brine temperatures similar to those seen in tropical Phanerozoic halites. They argue that the decline in seawater temperatures over the course of the Proterozoic, accompanied by the reduction of seawater salinity with the sequestration of salt in massive halite deposits in the Neoproterozoic, allowed the ocean system to accumulate more dissolved oxygen, and potentially paved the way for the evolutionary innovation of complex multicellularity. These transitions in calcium and O_2 in oceanic chemistry, preserved in halite inclusions, could have been the starting point of the complex process that led to exo- and endo-skeletons (and us!).

Based on the preceding discussion we can state categorically that evaporites and associated isotopic evidence document secular changes in the Earth's atmosphere, hydrosphere and biosphere across the past 4 Ga. In a broader evidential paper

Eriksson et al. 2013 (15 co-authors with Precambrian expertise) noted the following secular changes from the Hadean, across the Precambrian into the Phanerozoic. The documented changes encompassed and were driven by: (1) time related variations in mantle heat, rates of plate drift and of continental crustal growth, the gravitational effects of the Moon, and in rates of weathering, erosion, transport, deposition and diagenesis; (2) a decreasing planetary rotation rate over time; (3) no higher vegetation in the Precambrian, but prolific microbial mats, with the opposite pertaining to the Phanerozoic; (4) the long-term evolution of the hydrosphere-atmosphere-biosphere system. A relatively abrupt and sharp turning point was reached in the Neoarchaean, with spikes in mantle plume flux and tectonothermal activity and possibly concomitant onset of the supercontinent cycle. Substantial and irreversible change occurred subsequently in the Palaeoproterozoic, whereby the dramatic change from reducing to oxidizing volcanic gases ushered in change to an oxic environment, to be followed at ≈2.4–2.3 Ga by the "Great Oxidation Event" (GOE); rise in atmospheric oxygen was accompanied by expansion of oxygenic photosynthesis in the cyanobacteria.

A possible global tectono-thermal slowdown from ≈2.45–2.2 Ga may have separated a preceding plate regime which interacted with a higher energy mantle from a ≈2.2–2.0 Ga Phanerozoic-style plate tectonic regime; the slowdown period also encompassed the first known global-scale glaciation and overlapped with the GOE. While large palaeodeserts emerged from ≈2.0–1.8 Ga, possibly associated with the evolution of the supercontinent cycle, widespread euxinia by 1.85 Ga ushered in the "boring billion" year period. A second time of significant and irreversible change, in the Neoproterozoic, saw a second major oxidation event and several low palaeolatitude Cryogenian (740–630 Ma) glaciations. With the veracity of the "Snowball Earth" model for Neoproterozoic glaciation still under dispute, genesis of Pre-Ediacaran low-palaeolatitude glaciation remains enigmatic. Ediacaran (635–542 Ma) glaciation with a wide palaeolatitudinal range contrasts with the circum-polar nature of Phanerozoic glaciation. The observed change from low latitude to circum-polar glaciation parallels the advent and diversification of the Metazoa and the Neoproterozoic oxygenation (ca. 580 Ma), and was succeeded by the Ediacaran-Cambrian transition which ushered in biomineralization, with all its implications for the chemical sedimentary record.

Hydrology Is Depositional Style

Grains in siliciclastic sediments indicate sediment source or provenance, grains in a carbonate setting indicate biological parentage, mineralogy and textures in an evaporite indicate the nature of the hydrology that created them. During deposition, the hydrologic framework of an evaporite basin consists of surface and near subsurface waters flowing into and out of the areas accumulating salts. It is the upper part of a larger geohydrology made up of several regimes: (1) the active phreatic/vadose, (2) the compactional, (3) the thermobaric, and (4) the active-phreatic-exhumation/uplift regime (Figs. 1.9 and 2.54a). Boundaries are typically indistinct and transitional. The remainder of this chapter concentrates on syndepositional hydrologies of the active phreatic regime, where fluid circulation is driven by solar evaporation and gravity (eogenesis and mesogenesis). Chapter 8 takes this discussion deeper into the subsurface of evaporite basins in thermobaric, compactional and uplift regimes (mesogenesis and telogenesis). In the deep subsurface, where ancient salt masses have spent most of their time, rates of brine flow are slower, alteration events are longer term and driven by a combination of temperature, pressure and density differentials.

Brines and meteoric waters in the zone of active phreatic flow move under the influence of density/salinity or temperature gradients at rates controlled by the permeability of the aquifer. Where areas of strong topographic relief define the basin margin, as in a continental rift valley or in a transtensional basin-and-range setting, unconfined and confined meteoric water typically discharge into the edges of a brine-saturated depression. Further out, beneath the more central and topographically lowest parts of the depression, density-induced brine reflux, and not meteoric throughput, is the dominant process driving shallow subsurface flow (Fig. 2.54a). In a large evaporite drawdown basin, such as in the Mediterranean in the Late Miocene, the level of the discharge zone and the water surface of the perennial brine discharge lake was at times thousands of metres below sea level. Gravity seepage then moved huge volumes of marine/meteoric waters into the depression.

Active Phreatic/Vadose Regime

All primary and syndepositional evaporites first precipitate from brines outcropping at the top of the active phreatic zone or its capillary fringe. This setting is capable of maintaining the density or gravity heads necessary to drive, pond and concentrate large volumes of brines needed to deposit and preserve thick salt beds. An active phreatic flow regime encompasses the zones of seepage outflow, brine ponding, brine reflux and meteoric flow (Fig. 2.54a). The surface of a perennial brine lake or seaway is the outcropping expression of the regional watertable. In the surrounds, where the regional watertable comes near the landsurface, the top of a capillary fringe may be the outcrop expression of the same regional watertable and evaporitic mudflats dominate. Solar evaporation drives water loss at the surface of both settings to form bottom nucleated and pelagic salts in a standing water body and capillary salts in a mudflat. Depressions with

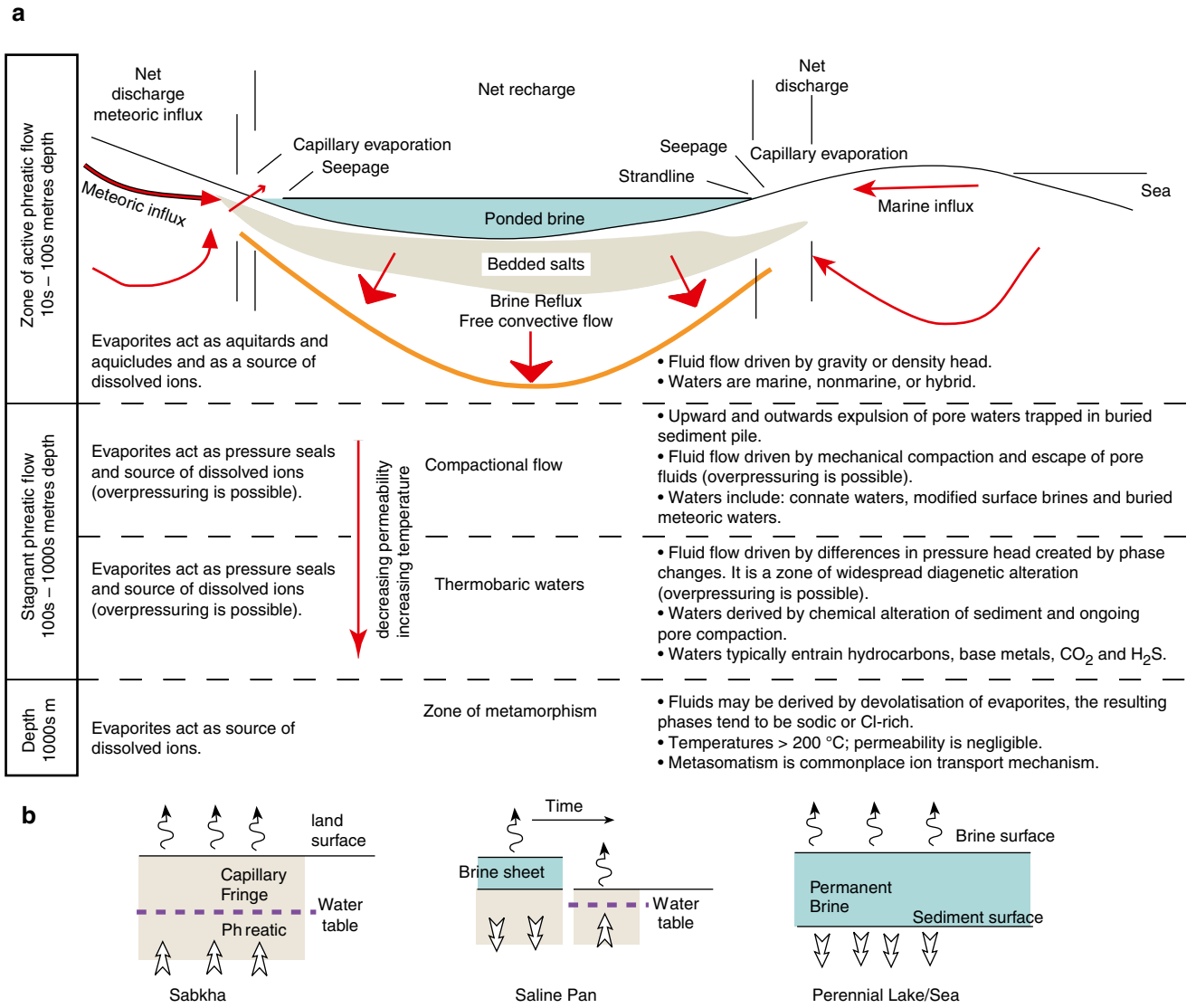

Fig. 2.54 Hydrological regimes and processes in evaporitic systems. (**a**) Depth related mechanisms and processes influencing evaporites. (**b**) Simplified hydrology of the three depositional settings that accumulate evaporites

surface and nearsurface brines in arid settings indicate groundwater discharge zones and their ongoing desiccation creates discharge playas and ancient evaporite seaways. Water lost is replaced by water seeping in from the surrounds creating a replenishment hydrology sometimes described as evaporative drawdown. The replacement water can be continental or marine, and can be supplied via unconfined nearsurface aquifers or via deeply circulating artesian systems.

Hydrologies in Saline Basins

Hydrologies that precipitate salts can be divided into two end members (Fig. 2.54b), (1) a perennial brine lake or seaway (saltern) that at times is density stratified and (2) an evaporitic mudflat (sabkha) with a landsurface defined by deflation at the top of the capillary fringe. A common intermediary stage is an evaporitic mudflat occasionally covered by thin sluggish brine sheets (salt pan). Before discussing the significance of hydrology to evaporitic sedimentation, we first must define some general hydrological principles (Fig. 2.55).

The hydrology of an evaporitic saline mudflat and its landward surrounds (dry mudflat or sandflat) is controlled by the position of the watertable in the sediments (Fig. 2.55a). Pores below the watertable are filled by water of variable salinity and constitute the phreatic or saturated zone where the water volume saturation is total (equals 1 or 100 %). The phreatic zone is the region where gravity-driven groundwaters seep down the potentiometric slope toward discharge

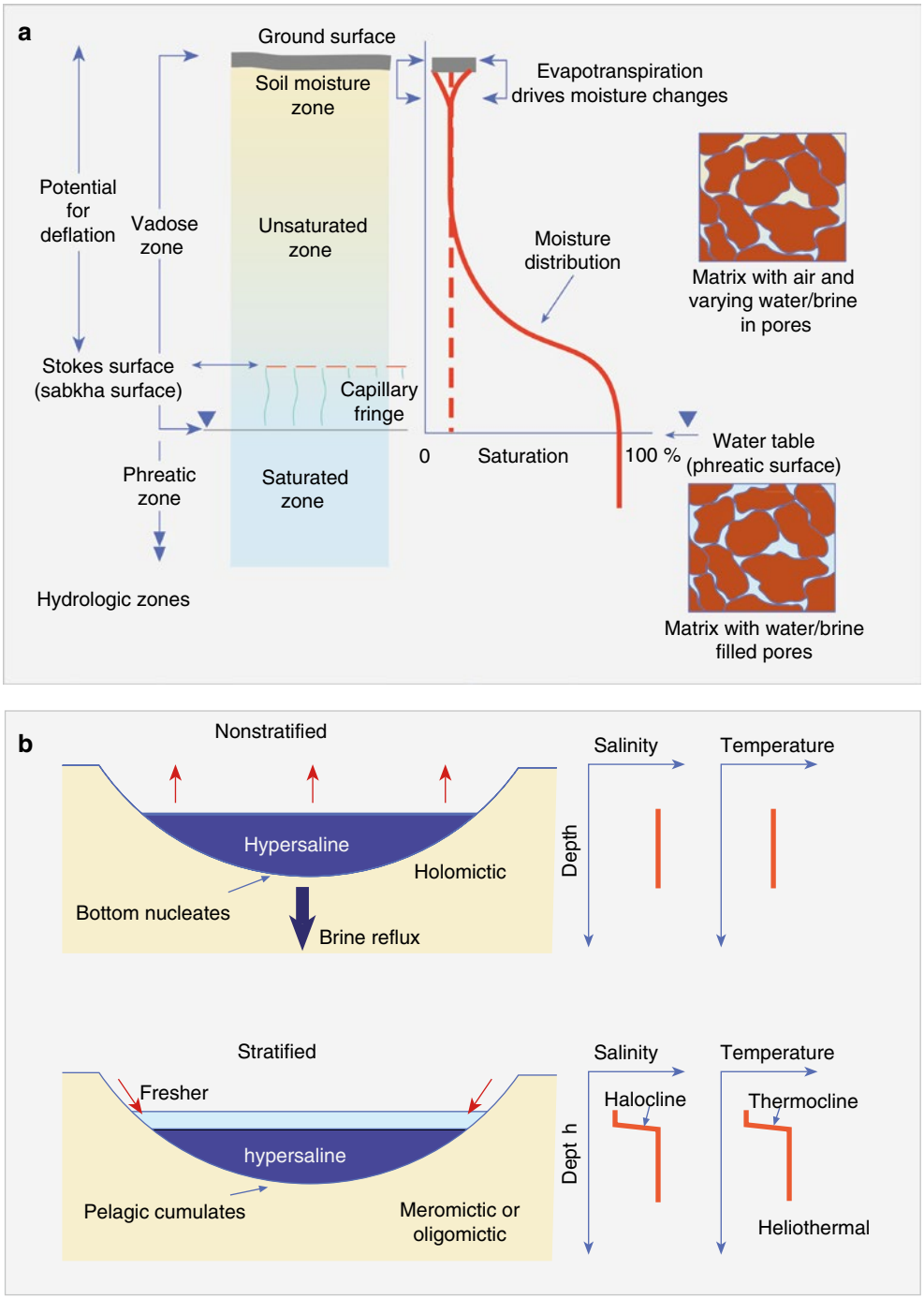

Fig. 2.55 Hydrological classification in saline settings. (**a**) Hydrological zonation in the mudflat and its landward surrounds. (**b**) Water mass zonation in a perennial brine lake or seaway

zones (forced-convection) and dense free-convecting brines, which are created by the evaporation of free surface waters, sink into underlying strata (brine reflux).

Above the watertable is the vadose zone, where pores are filled by a combination of soil air and varying levels of water and brine, water volume saturation is less than one. The vadose zone in dry mudflats or sandflats contains an uppermost interval known as the soil moisture zone where the water content can vary considerably over short time frames. Light rains typically penetrate the soil moisture zone but are not sufficient to saturate the whole vadose zone. Pore water returns to the atmosphere, via evapotranspiration, without ever replenishing the watertable. Fluctuating evapotranspiration levels in this zone vary widely between storms, reflected in variable metabolic activities of the soil biota, variable mean moisture contents, and varying O_2 and CO_2 levels. Pedogenic carbonates and more soluble salts are typically precipitated as surface crusts and near surface cements as a result of these fluctuations. With the next heavy rain the less soluble carbonate precipitates remain, while any more

Table 2.14 Representative thickness of the capillary zone in various host sediments

Sediments	Capillary rise (cm)
Fine silt	750
Coarse silt	300
Very fine sand	100
Fine sand	50
Medium sand	25
Coarse sand	15
Very coarse sand	4
Fine gravel	1.5

soluble salts tend to be flushed back into the subsurface, through a now saturated vadose profile, to re-enter the phreatic water mass.

The process of flushing surface waters to the phreatic zone is known as infiltration. In a homogeneous medium it requires the whole vadose profile to be water saturated. In an inhomogeneous medium, such as a karstic or a fractured and fissured evaporitic landscape, replenishment to the watertable can be more focused. Once the more soluble ions are back in the phreatic mass they continue to flow as dissolved load down the potentiometric gradient and ultimately into the discharge depression where, driven by solar concentration, emerging waters once again can precipitate salts in sabkhas, pans, brine lakes and seaways.

The lower part of the vadose zone beneath a dry mudflat is made up of the capillary fringe (aka tension-saturated or wetting zone). In a saline mudflat the capillary fringe extends all the way to the landsurface. The diameter of pore throats in the capillary zone controls the thickness of the capillary zone; the smaller the throat, the thicker the capillary zone. It is a few mm thick in sands and metres thick in fine clays (Table 2.14). Pores in the capillary fringe are not completely filled with water until its lowermost regions, there 100 % water/brine saturation defines the top of the phreatic zone and the position of the watertable (Fig. 2.55a). Water film and gas phases coexist in the interstitial pore space of much of the capillary zone. The relative humidity of the gas phase (saturated vapour pressure) is, however, equal to the thermodynamic activity of water, and so no evaporative concentration can occur in the capillary zone unless it is very close to the landsurface. Loss of pore water from the capillary fringe in a mudflat typically only occurs in its uppermost few centimetres.

There are some simple principles of soil physics associated with capillary fringes in groundwater discharge zones (sabkhas) that at times have been ignored in sedimentological models of sabkha deposition. First, if the capillary fringe is relatively thick, say 0.5–1.0 m, then host sediments must (by definition) have small pore throats and so must have low permeabilities. A sabkha, by definition, is a zone characterised by the growth of displacive and replacive capillary salts. Salinity of pore water in this capillary fringe is elevated (indicated by the preservation of gypsum, anhydrite, halite etc.). This low permeability means that high rates of transient short-term rapid lateral or vertical flow through a sabkha capillary fringe is impossible. When a sheet flood covers the 0.5–1.0 m thick saline capillary fringe of a sabkha with a sheet of fresher surface water (rainwater or seawater) this water does not begin to infiltrate until its density exceeds that of water in the underlying capillary pores. Then, even when densities do exceed that of the underlying waters, the low permeability of the narrow pore throats means the rate of recharge is slow.

To accumulate salts in the capillary fringe the overall solute-carrying water flow vector over time must be upward, not downward. It also means that almost all of the water in occasional fresher water sheets covering a sabkha are lost to the atmosphere. Low permeabilities mean a sabkha is not capable of maintaining longterm downward reflux flow of water or solute to the phreatic mass. This is true in all evaporitic mudflats. This notion of *per ascendum* rather than *per descendum* hydrologies is correctly accommodated in water flow models for most continental sabkhas and mudflats. This was less so in some sedimentological models of modern marine margin sabkhas, or at least this was so until the last decade when detailed hydrological data sets were collected, and coastal sabkha hydrologies quantified, rather than assumed.

As Wood et al. (2002) has clearly shown in the Abu Dhabi sabkha (Fig. 3.13) and Dutkiewicz et al. (2000) demonstrated in Lake Greenly mudflats and pans (Fig. 2.23), solute flux in the capillary fringe of saline mudflats is largely decoupled from the effects of water cycling in ephemeral sheets of surface water and their salt crusts. Most of the solute load precipitated as salts in a sabkha comes from rising, sometimes deeply circulating groundwater. It does not come from recharge by occasional surface floods atop the sabkha. Floods (marine or meteoric) in a sabkha tend to do little more than redissolve and reprecipitate surface salt crusts and flush the dissolved contents to the sea or the basin pan. Floods of surface waters to a sabkha flat tend to evaporate, not infiltrate. We shall return to this discussion in more detail in Chap. 3, for now we will just note that any secondary salts actively accumulating in a sabkha or evaporitic mudflat at depths of more than a few centimetres below the landsurface are precipitated by physical and chemical changes in ascending, not descending, pore waters.

Quantified hydrological observations in the capillary zone of Owens Lake mudflats by Tyler et al. (1997) underline some other significant general characteristics of the hydrology of evaporitic mudflats (Fig. 2.56):

1. Effective evaporation rates are higher over brine pools than evaporitic mudflats, especially those mudflats covered by a salt crust.

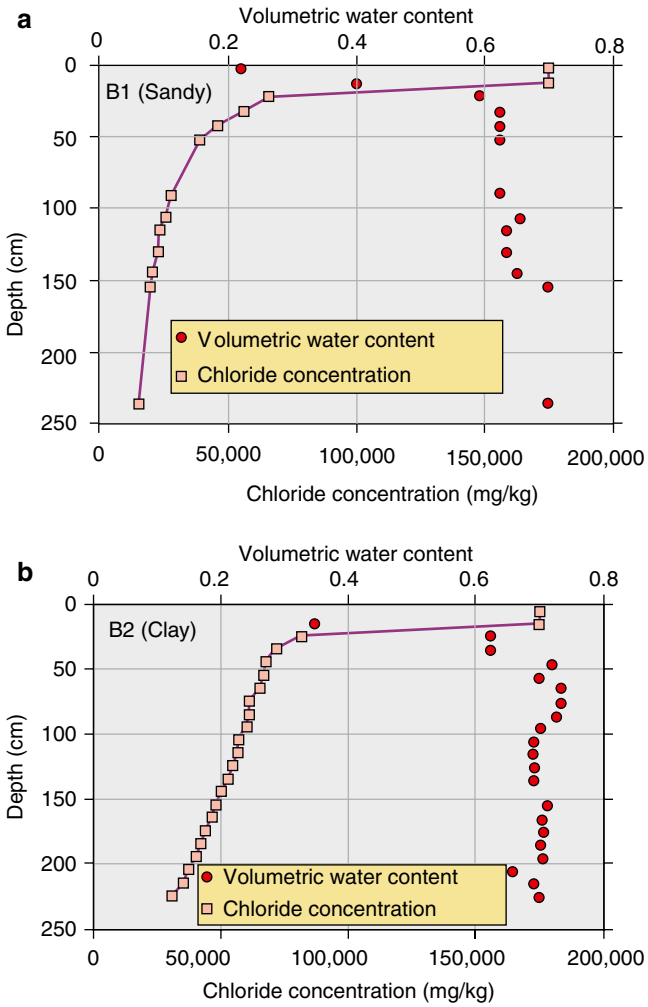

Fig. 2.56 Measured moisture and chloride profiles in the vadose zone of two monitored boreholes in the salt-crusted clay-dominated saline mudflats in Owens Lake, California. Measurements were made in summer of 1994 and 67 days after last recorded rain in the region (After Tyler et al. 1997). A water saturated profile would have a volumetric water content or saturation of 1 or 100 %. See Fig. 2.10 for location, both boreholes are from the saline mudflat sites, one is more clay-rich the other sandier

2. Depth to the watertable in a mudflat is a significant control on the volume of capillary salt precipitated in an evaporitic mudflat or saline pan. That is, much higher volumes of salt accumulate in regions where the saline watertable resides closer to the sediment surface for longer periods of time.
3. Because winter and spring watertables are higher (typically cooler with more precipitation) than summer watertables, the rate of capillary salt accumulation in some mudflats can be greater than in the hottest and driest part of a year, when watertables are lower.

The top of the capillary fringe is the landsurface in those parts of an evaporitic mudflat (sabkha) that are actively accumulating surface salt crusts. Heating of pore waters moves liquid water into vapour that leaks into the atmosphere only in the uppermost few centimetres of the capillary zone, immediately beneath the landsurface. The salinity of the residual brines in this uppermost zone increases to where various salts precipitate (Fig. 2.56). Lost waters are replaced by the rise of capillary waters from below in the process known as capillary rise.

There is another general principal of soil physics in operation here that many sedimentologists working in sabkhas have ignored. To concentrate a brine to where water is lost in large amounts happens largely in the uppermost parts of the capillary fringe, not throughout its whole extent. This is why in every capillary fringe in every discharging sabkha in every modern example, the most saline pore waters (and the most saline salts, sometimes including bitterns) occur in the uppermost portion of the capillary fringe or in the efflorescent crusts at its surface (Fig. 2.56). The underlying capillary waters show upward-increasing salinities, but never attain the salinities of this uppermost few centimetres where salts can evaporatively precipitate (Fig. 2.56).

And yet, from the displacive evaporite textures seen in the capillary fringe of most sabkhas and evaporitic mudflats it is obvious that sabkha salts do not only precipitate as surface and uppermost nearsurface efflorescences and crusts (Figs. 3.6g and 3.7). This leads to the conclusion that preserved calcium sulphate salts in the classic Abu Dhabi sabkha and probably many other sabkhas are a type of retrograde evaporite precipitate known as thermalite salts (Wood et al. 2005). Such salts form passively and displacively in the bulk of the capillary fringe, below the uppermost interval of ephemeral evaporative halite and bitterns. The precipitation mechanism is heating of a rising capillary pore water solution that is dominated by a retrograde phase (anhydrite, gypsum) to temperatures above 25–30 °C (see Chap. 3 for details). Sabkha salts in a capillary zone are "true" evaporites in that the overall precipitation hydrology is driven by solar evaporation, but the local precipitation mechanism in the bulk of the capillary zone is more a response to temperature change than to evaporative concentration.

In contrast, the hydrology that preserves modern bitterns (carnallite) in the bedded halites of Qaidam Basin is not that of a capillary fringe in a sabkha about the lake edge. By definition, sabkha pore waters are rising and heating. Rather, the precipitation mechanism in Qahan salt flats is one of sinking and cooling dense brines precipitating prograde salts, following an episode of halite karstification (Fig. 11.13c). Modern carnallite precipitation is a passive pore filling process that takes place *per descendum*, beneath a freestanding and concentrating holomictic brine sheet, which is feeding a dense descending brine plume (brine reflux). It is a recharge mechanism and not a capillary rise process.

Surface waters within freestanding perennial brine lakes or seaways routinely fluctuate between stratified and

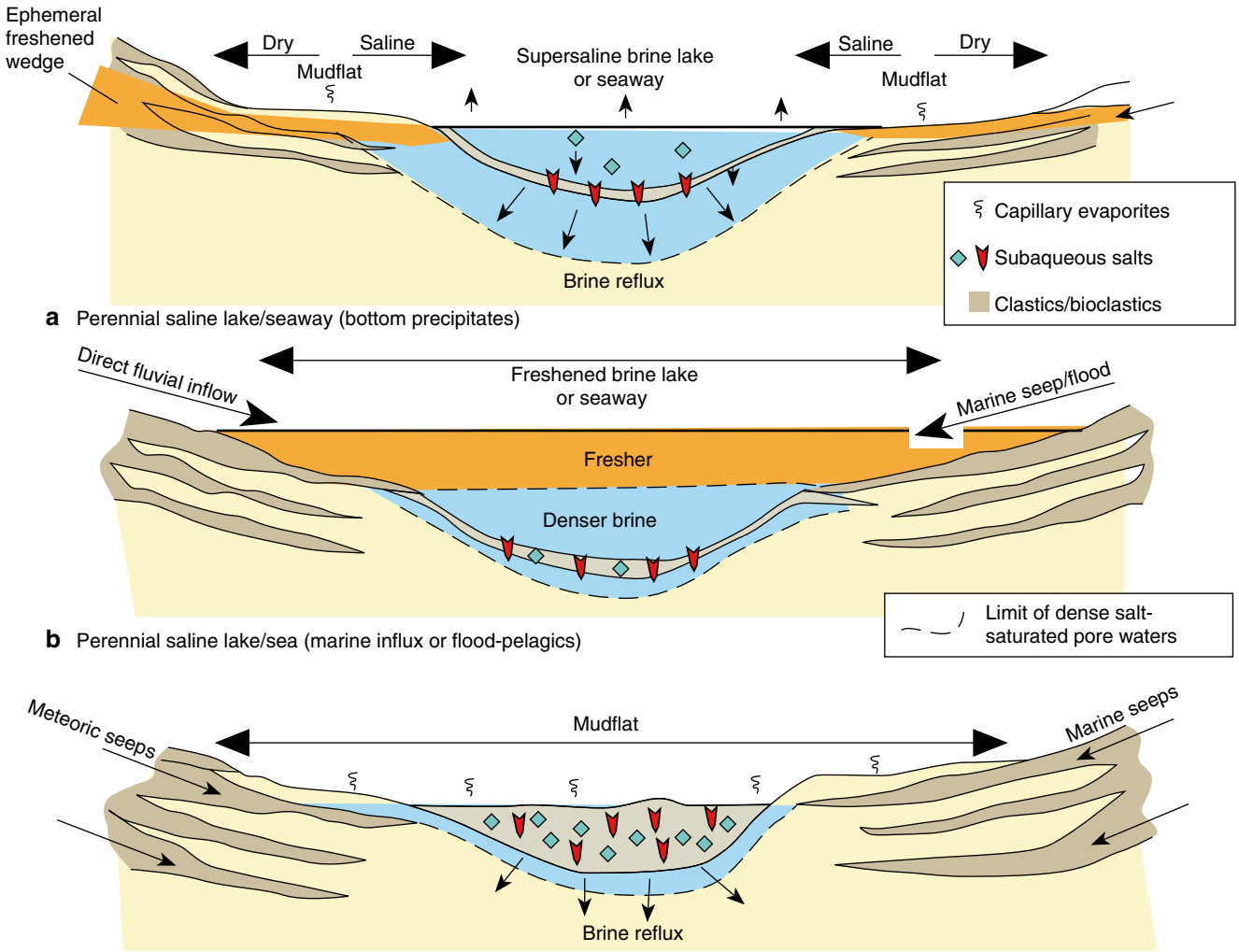

Fig. 2.57 Cross sections showing hydrological stages in the active phreatic zone in an evaporitic seaway or a continental lake. (**a**) Perennial saline lake accumulating widespread subaqueous evaporites from a nonstratified brine body. Capillary evaporation of fresher water lenses about the lake margin. (**b**) Perennial saline lake or water full stage with subaqueous brine lens isolated from solar evaporation processes by a layer of surface water. This shuts down widespread crystallisation in lower brine body and slows brine reflux. (**c**) Playa stage where ongoing evaporite fill, or lowering of regional water level, means the sediment surface is mostly subaerial and in capillary equilibrium with saline lake watertable. This is a classic evaporitic mudflat or sabkha hydrology. No fresh water lens exists until after the next flood event

nonstratified conditions. In the stratified system an upper fresher (less dense) water mass sits atop a more saline (denser) lower water mass (Fig. 2.57b). The narrow zone of transition between the two masses in the brine column is called the halocline. Often a stratified saline lacustrine system is also thermally stratified, with warmer waters in the lower water mass and a zone of transition is called the thermocline. Its position is typically identical in the column to that of the halocline. Thermal stratification with a cool top and a hot base is opposite to that found seasonally in many temperate freshwater lakes and so is sometimes called reverse stratification and also described as heliothermal layering. The term meromictic is used to describe a permanently stratified water mass where surface layers may mix, but the bottom layer does not disappear. The upper water mass that periodically mixes is the mixolimnion, the lower permanent mass is the monimolimnion. Oligomictic is used to describe stratified water masses that mix or homogenise for short irregular periods every few years.

Mixing in a saline water mass is controlled by the evaporation and concentration of the upper water mass until it reaches a density equivalent to the lower water mass. Then mixing or overturn occurs. Substantial density differences between the upper and lower masses in most density stratified systems means diffusive mixing across the halocline is insignificant. A stratified system is a stable system, so that

when a hypersaline water mass is density stratified there is little bottom precipitation of salts. Sedimentation is mainly by a pelagic rain of crystallites, which first formed either in the uppermost part of the upper water mass or by brine mixing at the halocline. Whenever the upper and lower water masses equilibrate and homogenise, bottom nucleation of salts is possible even at the base of deep brine columns, as is occurring in the Dead Sea today (Chap. 4). Whenever a homogenised water mass restratifies, the rate of brine reflux in to sediments below the sediment brine interface slows and ultimately stops, for there is no ongoing mechanism to resupply brines denser than pore waters in the substrate.

Refluxing brine plumes beneath homogenized surface water masses sink and at the same time start to spread laterally toward the basin fringes where they mix with incoming forced-convection waters of the seaway or playa margin. Ultimately plume waters can return to the surface in a diluted form as a component of spring or seep waters or they can be lost to the regional hydrological flow. Reflux-driven convective flow is an effective way of moving salt load through large volumes of basin sediments in modern saline depressions (e.g., Lake Tyrell, Australia: Fig. 2.30) and also explains the distribution of salts, pseudomorphs and dolomites in ancient sediments that underlay or were adjacent to areas accumulating bedded salts.

Mudflat Aggradation Mirrors Watertable Change

Unconfined meteoric and marine groundwaters seeping and discharging into the edges of an evaporitic depression have a potentiometric head defined by the position of the regional watertable. The unconfined meteoric watertable surrounding a modern coastal marine-seepage lake is typically a few centimetres higher than sea level. In a continental saline lake or an ancient drawdown saline giant, the watertable about the basin margin is higher than the brine level within the evaporite-accumulating depression (Fig. 2.57a). Once meteoric/marine groundwater seeps into discharge zones within the salt-accumulating region of the central depression, it comes into contact with more saline and denser surface and pore brines. On average, the throughflowing waters beneath a mudflat or bajada margin are less dense (fresher) than hypersaline waters in the brine-saturated lowermost parts the saline depression. After a heavy rainstorm or a flood, a shallow fresher groundwater layer forms along the strandline edge of the permanent brine lake or seaway as freshwater floats atop a wedge of denser hypersaline pore waters (Fig. 2.57a, b).

Shallow meteoric sheets and groundwater lenses are typically transient mudflat features, so without ongoing recharge, these freshened groundwater outflows within the mudflat dissipate via capillary evaporation and are replenished by more saline pore waters. Alkaline earth carbonates and lower salinity salts can precipitate as surface crusts or nearsurface pedogenic nodules and crystals in the vadose portions of the basin edge. During prolonged dry spells, capillary evaporation continues to lower the saline mudflat watertable until flow directions may be reversed. Brines in aquifers from the basin centre and more deeply circulating region groundwaters begin to seep into the margin to replace the lost capillary fluids. Increasingly saline pore waters in a saline mudflat, mean salts, which crystallised earlier, can now evolve into more saline precipitates via backreaction and replacement (Fig. 2.57c).

With the next inflush of freshened recharge the watertable rises once more in the marginward vadose zone of the saline depression. At the same time a thin sheet of fresh rainwater or seawater can cover the surface of the saline mudflat. This redissolves highly soluble salts of the uppermost capillary zone, along with any of the more soluble surface efflorescences (Fig. 2.57b). A wedge of freshened water now floats above a stable body of dense brine, both atop pore waters of the saline mudflat and atop a dense lower brine mass the central density-stratified perennial brine lake. This blanket of freshened water shuts down evaporation of saturated waters and prevents further accumulation of salts, both in the uppermost parts of the capillary mudflat and in the salt brine covered regions of the perennial lake or seaway. The style of surface sedimentation at this time is sheet flood sands followed by accumulation of suspended load clays.

Then, as the depression begins to dry out, the brine sheet shrinks until it only covers the lowermost parts of the lake depression, the zone of perennial lake waters. Once the saline mudflats are re-exposed, capillary evaporation begins once more. At some point in this desiccation stage, surface water becomes saturated and crystallites formed at brine surface sink through the brine column to the lake/seaway floor (pelagic sedimentation of carbonate and gypsum). Bottom nucleation and intrasediment prograde precipitation of reflux salts beneath a standing brine lake recommence when the rising salinity (density) of the upper water mass comes to equal that of the lower brine mass. The two water bodies then mix and precipitation of bottom salt begins anew (Figs. 2.55a and 2.57b).

Near surface sediments in saline mudflat margins experience the effects of schizohaline pore waters. Salinities in sediments beneath perennial (meromictic) brine-covered depressions tend to be more stable, although a body of freshened surface water comes and goes. Textures in schizohaline salt beds are dominated by ongoing re-equilibration reactions, backreactions, dissolution-reprecipitation and haloturbation, while textures in beds deposited in perennial brine seaways and lakes tend to be more stable and dominated by large growth-oriented crystal beds and brine reflux re-equilibration textures below.

Table 2.15 Some examples of modern capillary deflation surfaces or Stoke's surfaces

Locality	Geological setting of stokes surfaces	References
Arabian Gulf sabkhat, United Arab Emirates	Coastal saltflats prograding into Arabian Gulf	Patterson and Kinsman (1981), Warren (1991)
Jafurah Sand Sea, Saudi Arabia	Interdunal saltflats in sand sea (erg) migrating into the Arabian Gulf	Fryberger et al. (1983, 1984)
Samphire Lake and Spring Lake, Australia	Playa capture and deflation driven by a lowering of the regional watertable	Jacobson and Jankowski (1989)
Guerrerro Negro dune field, Mexico	Coastal barchan dunes migrating landward over lagoonal sediments	Fryberger et al. (1983, 1984)
White Sands dune field, New Mexico, USA	Continental saltflat and gypsum dunes deflated from Lake Lucero	Loope (1984), Langford (2003), Kocurek et al. (2007)
Great Salt Lake desert, Utah, USA	Continental dunes and lacustrine saltflats	Stokes (1968)

As an evaporite basin aggrades toward its hydrological equilibrium level (Fig. 2.57c) the depositional surface aggrades into ephemeral brine sheet (pans) and ultimately mudflats (filled accommodation space). The progression brine lake to a mudflat induces schizohaline textures in the uppermost parts of each shallowing upward hydrological cycle. If there is no rise in regional watertable, the same textural shoaling occurs across the whole discharge zone.

Indicators of Fluctuating Watertables

Because evaporites form by the evaporation of discharging and ponding waters, any longterm water fluctuations in an evaporite basin influence sedimentation style and mineralogy on scales coarser than the stacked gypsum and tepee truncation layers and parasequences described in Chaps. 1, 3 and 4. Longterm aggrading watertables (or regional subsidence) in an evaporite basin enable the capture of formerly vadose sediment by the damp, sticky to wet conditions that characterise the capillary and phreatic zones and so facilitate the preservation of formerly vadose and nonevaporite sediment in the depositional system – sediment that would otherwise be blown away (e.g., Newell 2001). It is aggrading saline watertables that ultimately preserve almost all ancient sabkha, brine lake and dune sediments.

Falling watertables enable entry of vadose conditions into former capillary and phreatic sediments. This leads to the dissolution of salt beds, to eolian deflation and to the formation of residual sediment layers that come to lie at or just above the regional watertable. Episodes of active deflation in the Late Quaternary have periodically fed the extensive quartzose and gypsum sand dunes that abut numerous playas in Australia, Saudi Arabia and the southwest USA. Deflation to the top of the capillary fringe creates the characteristic flat surfaces of many modern playas, sabkhas and interdunal depressions. The hydrological process has been called watertable bevelling as it is tied to the erosional top of the capillary zone (Bowler 1986; Warren and Kendall 1985). The capillary surface erosionally truncating underlying sedimentary structures is termed a Stokes surface.

Stokes Surfaces

Stokes surfaces accompany changes in the base level of erosion/deflation and are commonplace in eolian sand seas or ergs abutting ancient evaporite beds. At the local scale a Stokes surface defines the top of the sedimentation surface in a degrading wet interdunal depression (Table 2.15; Stokes 1968). A succession of such truncation surfaces can be preserved atop a number of depositional cycles as successive packages of sediments aggrade and stack, driven by longterm watertable rise. Changes in watertable level may indicate climatic change or episodic basin floor subsidence. At the regional scale an extensive truncation surface in an ancient desert succession, which passes through various arid lithofacies, is called a super-surface or a super-bounding surface by sequence stratigraphers, but it is really a glorified Stokes surface.

Stokes surfaces create sharp planation surfaces in eolian crossbeds, sometimes outlined by a thin veneer of lag sediment (Fryberger et al. 1983, 1984). Watertable control on their creation is clearly seen in the Umm Said portion of the Qatar coast south of Doha where large transverse and barchan dunes still migrate into the sea (Fig. 2.58a). This eolian-fed progradation of the shoreline and the creation of the associated Stokes surface has been taking place since the early Holocene sea first intersected the sand sheet (Fig. 2.58b, c). The Stokes surface is the surface of uppermost eolian preservation and it migrates seaward as the dunes build out into the Arabian Gulf. In all modern coastal dune successions the Stokes surface is the top of the capillary zone and it approximates sealevel.

Erosion surfaces, defined by the top of the capillary zone also truncate anhydrite nodules or enterolithic folds in the upper parts of the coastal sabkhas of the United Arab Emirates (Fig. 3.5g). In the fine-grained matrices of a sabkha the erosional truncation of an evaporite is typically up to a

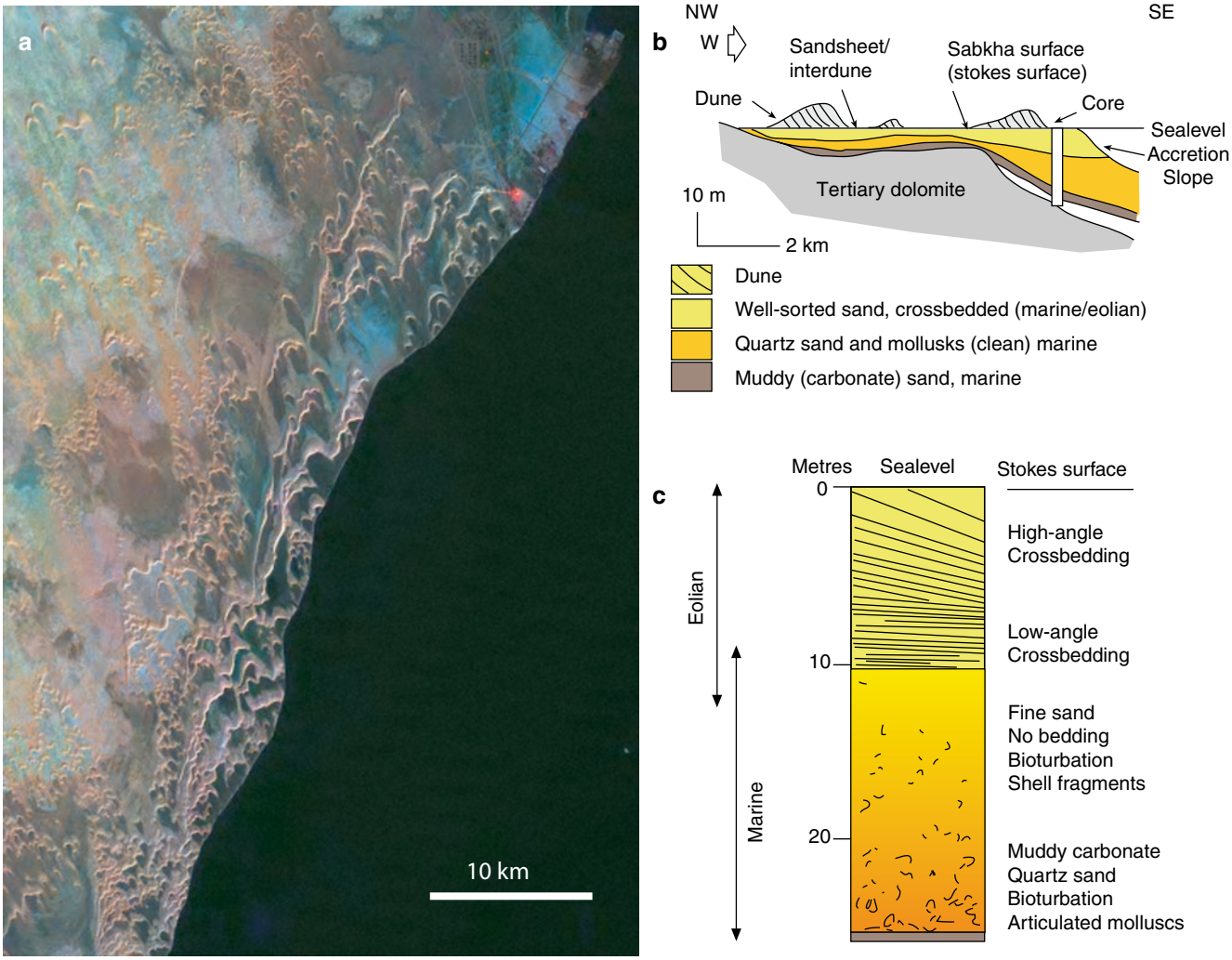

Fig. 2.58 Umm Said Sabkhat, Qatar. (**a**) Transverse and barchan dune moving seaward atop sandflat and coastal sabkha (Image courtesy of NASA). (**b**) Cross section and core from an Umm Said sabkha in coastal Qatar showing how the deflation surface that defines sealevel and the top of modern coastal sabkhas is also a Stokes equilibrium surface (indicates the top of the capillary zone). (**c**) Schematic core taken in position shown in **b**. (**b**, **c** After Shinn 1973)

metre above the watertable. Stokes surfaces are an integral part of the capillary hydrology of a sabkha and are very useful in distinguishing ancient mudflats from subaqueous evaporites (Warren and Kendall 1985).

Aggrading watertables in discharge depressions in sand-rich eolian environments can promote the passive precipitation of pore cements in the uppermost part of the capillary zone. In modern dunes and sandflats these aggrading salt-cemented intervals are sometimes called salcretes, the evaporite equivalent of capillary calcretes. They are made up of passive pore-filling cements (gypsum or halite), not the active displacive nodules and crystals that typify sabkhas. Schenk and Fryberger (1988) noted such massive phreatic-gypsum cemented zones act as a lower limit to any subsequent eolian deflation in the gypsum dunes of the White Sands dune field, New Mexico. They create a cemented near-horizontal base level to erosion, now seen as a widespread Stokes surface in the interdunal corridors. Aggrading salcretes, tied to a rising watertable, can help preserve capillary and eolian sedimentary structures. Salcretes were the main reason why dune topography is preserved in some transgressive settings where ancient ergs are overlain by evaporite beds (e.g., Entrada-Todilto and Rotliegende-Zechstein formations).

Megapolygonal desiccation cracks are another expression of the hydrology associated with a Stokes surface and form in deflating mudflat or playa sediments in conjunction with a regionally falling watertable (Fig. 2.59). Megapolygons can be up to 300 m wide and separated by fissures up to 5 m deep, they characterise the modern surfaces of a number of Basin and Range playas in Oregon,

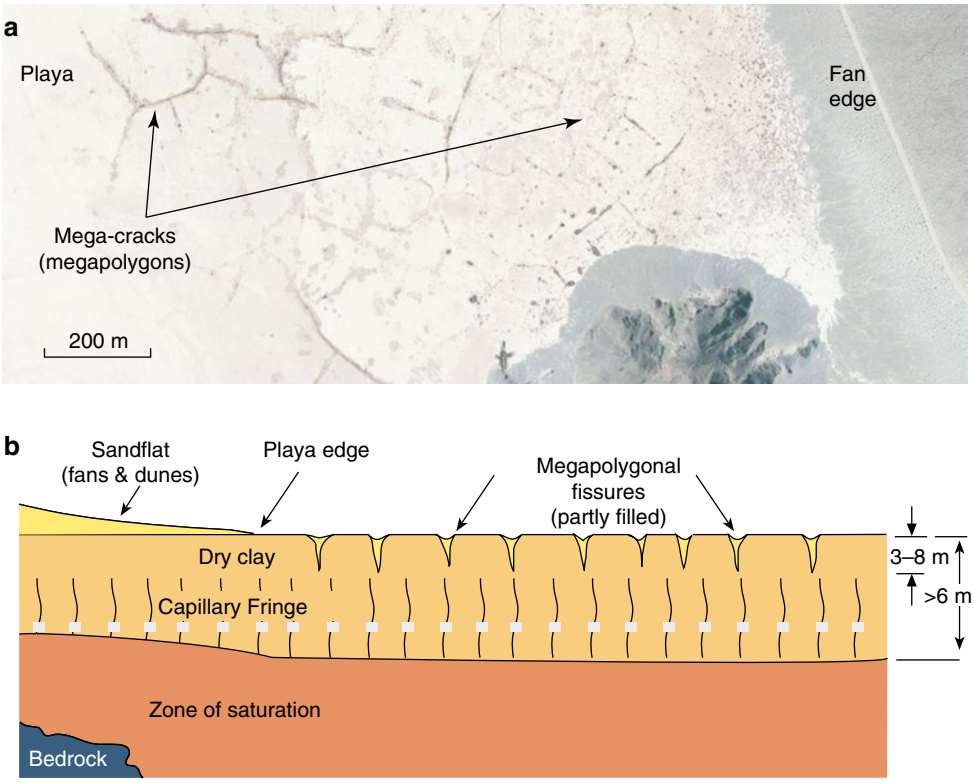

Fig. 2.59 Megapolygonal desiccation cracks. (**a**) Megacracks at the northern end of the Panamint Valley playa. (**b**) Formation and preservation. Vertical section shows megacracks partly filled with sand, captured as it saltated across the deflationary playa surface. Fissures were formed during a lowering of the regional watertable and the associated shrinkage during drying of lacustrine clays (After Neal et al. 1968)

Nevada, California, Arizona and New Mexico (Neal et al. 1968). Fissures are hosted in fine-grained playa sediments rich in clays and carbonate minerals. The fissures, which are up to 1 m wide, are routinely filled or partly filled with wind blown sands (mixture of quartz and gypsum). Individual fissures tend to be discontinuous across the playa surface and often display en-echelon patterns. Antrett et al. (2012) argue that ancient counterparts to these various-scaled megacracks influenced gas production from Permian Rotliegend sediments in northwest Germany, by compartmentalising the reservoir.

Megapolygons are the result of shrinkage in fine-grained lake sediments and indicate water loss following a fall in the piezo-metric head. In some cases the watertable lies 3–20 m below the megapolygonal surface. As pore waters evaporate from the upper part of the newly created vadose zone, tensile stresses accumulate in the muds until they eventually rupture into the polygonal fissure network. Neal et al. (1968) interpret the fissures as indicating vigorous desiccation over a number of years. Some playa fissures may be related to over-exploitation of the local groundwater resources in the last 50–100 years, most indicate the rigorous climatic transformation that occurred during the Pleistocene-Holocene transition. Identical sand-filled fissures, up to 18 cm wide and 5.7 m deep, have been documented in the Pennsylvanian Hermosa Formation of southeastern Utah (Loope and Haverland 1988).

Stokes Surfaces and Palaeohydrology

Recognition of Stokes surfaces, associated interdunal sabkhas and wet mudflats/interdunes has broader scale implications in terms of regional hydrological evolution over time frames measured in thousands of years and to permeability models. Most modern Stokes surfaces either are a coastal groundwater response to progradation since the last rise in sea level some 6,000 years ago, or are a hydrological response related to marked climatic changes in deserts from the Late Pleistocene to the present, usually toward increasing aridity (Table 2.15).

Changes in the level of ancient regional watertables and aggradation of base level (creation of accommodation space) is often preserved in ergs (sand seas) abutting the edges of evaporite basins in the USA and elsewhere (Mountney and Thompson 2002). For example, Havholm and Kocurek (1994) used the presence of regional discontinuities in the erg succession to interpret the depositional history of the Jurassic Page Sandstone of the Colorado Plateau, USA (Fig. 2.60). The Page Sandstone was deposited in a coastal erg where there was a constant rise and fall of the strandzone of the adjacent epeiric seaway. These eolian sediments encompass a number of regional erosion surfaces known as super bounding surfaces or supersurfaces. Sometimes the interdunal portions of these supersurfaces preserve giant (5 m high) stromatolites indicating flooding and longterm at-surface brines in the interdunal corridors (Eisenberg 2003).

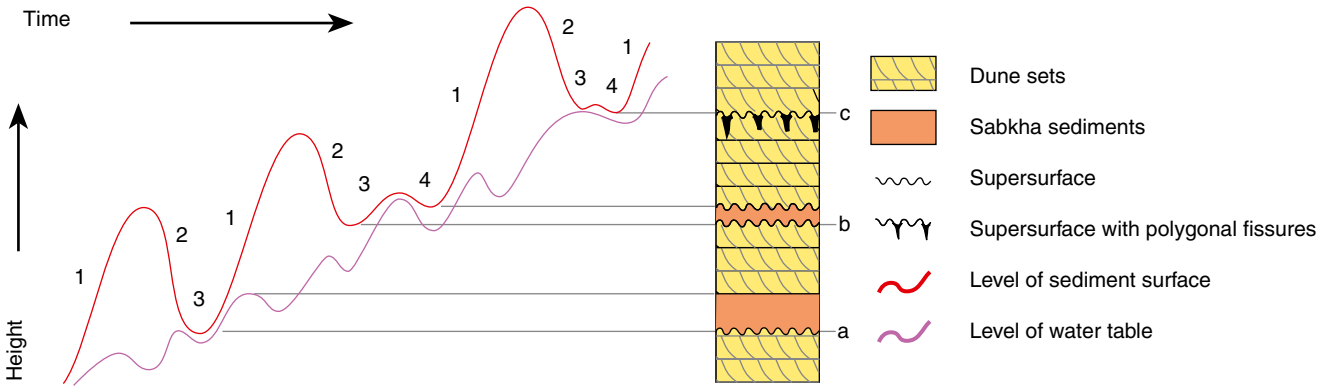

Fig. 2.60 Accommodation space for Jurassic Page Sandstone (30–50 m thick) sedimentation was controlled by interaction during subsidence between deflation (*upper curve*) and changes in the level of the watertable (*lower curve*). Surface a is over-lain by sabkha sediments that were not eroded, surface b is overlain by partly eroded sediments, and surface c is an erosional surface with polygonal fissures. Numbers 1–4 on sedimentation curve indicate type of activity: (*1*) dune accumulation, (*2*) deflation, (*3*) sabkha formation or formation of polygonal fissures, (*4*) deflation of surface features (From Havholm and Kocurek 1994)

Correlation of super-surfaces between outcrops defined inter-relationships between the dune sands and the interlayered sabkha and interdunal successions (Fig. 2.60; Havholm and Kocurek 1994). Sand accumulation in the Page was episodic and punctuated by the formation of supersurfaces tied to substantial lowerings of the regional watertable. This created both Stokes surfaces and megapolygonal fissures. Sabkhas and interdunes aggraded as the watertable rose until sedimentation surfaces sat above the top of the capillary zone. Then vadose sedimentation, typically eolian crossbedded dunes sands, dominated once more. Thus the Page Sandstone is a collection of desert dune-interdune successions preserved in accommodation space created by an overall rise in the watertable (basin subsidence). The smaller scale sequence packaging (dune alternating with wet interdune) reflects periodic rises in the watertable, tied to shorter-term variations in climate, tectonics (subsidence) and changes in the strandline positions of nearby seaways or lakes.

The Jurassic Entrada Formation shows a similar watertable control with its sea-marginal setting, promoting numerous internal truncation surfaces tied to deflation to the top of the capillary fringe (Crabaugh and Kocurek 1993). Sediments deposited in the passage of the Entrada Fm. into the overlying evaporitic Todilto Fm. are unusual for an eolian system. The upper part of the Entrada is characterised by mass flow deposits and preserved eolian dune palaeotopographies beneath sandy subaqueous strata, rather than the more typical erosional top with the eolian unit passing up into continental deposits (Fig. 2.61a; Benan and Kocurek 2000). Preserved dune remnants have relief of up to 35 m and are buried by onlapping, subaqueous, largely structureless sandstones. The latter are derived by mass wasting of the upper portions of the dunes as regional water levels rose. Eolian sands were redeposited as sediment-gravity flows, which infilled depressions between the dunes. Preservation of dune palaeotopography beneath mass-flow deposits argues that flooding of the Entrada dune field was geologically rapid and energetically gentle.

Flooding heralded the onset of a restricted density-stratified brine lake/seaway, which deposited the evaporitic Todilto Formation. This seaway was a marine-seepage fed drawdown depression within what was the lowest part of the erg. This type of seepage encroachment converting the erg to a lake meant there was no transgression of a high-energy marine coastline across the top of the sand sea (Fig. 2.61b). Rather, aggradation of the saline watertable was a relatively gentle process, with preservation of dune topography beneath lacustrine laminites perhaps aided by the formation of ephemeral capillary-fed salcretes. Salcretes precipitate where the capillary zone intersects the eolian landscape in any arid zone transition from an erg to a brine lake. A similar preserved dune palaeotopography, also with ephemeral salcretes, formed atop the Permian Rotliegende/Wiessliegend sands of the North Sea and heralded the onset of evaporite deposition in the saline giant that deposited the Zechstein salts (Glennie and Buller 1983; Glennie and Hurst 2007).

The position of the watertable in many ancient sand seas controlled the depositional style and facies continuity of various windblown sand units (Fig. 2.62). Less permeable lenses of salcrete-cemented, damp and wet interdune strata and interdunal sabkhas exhibit an intertonguing, transitional relationship to the toe-sets of adjacent and overlying eolian dune units (Mountney and Thompson 2002). Intercalation signifies vadose dune migration (eolian cross beds) was contemporaneous with watertable-controlled accumulation in adjacent interdunes. Eolian crossbedding can only form in the vadose zone. Downwind changes in the geometry and facies of the interdune units indicate periodic expansion and contraction of the interdunes in response to changes in the

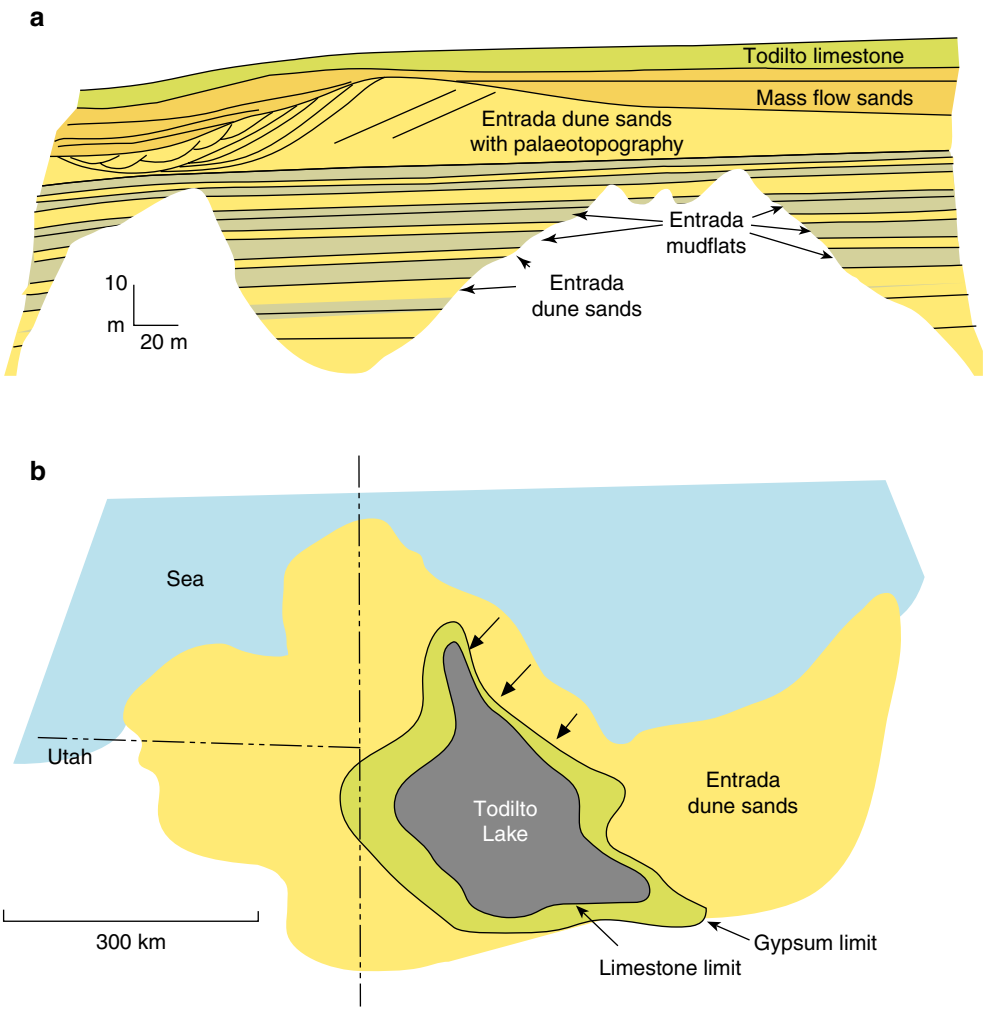

Fig. 2.61 (**a**) Outcrop drawing showing preserved dune palaeorelief with onlapping structureless sandstones and overlying limestones of the Todilto Formation. The Entrada Sandstone underlying the preserved relief consists of interbedded dune sets and evaporitic mudflat (sabkha) deposits (After Benan and Kocurek 2000). (**b**) Approximate Late Callovian–Oxfordian (?) palaeogeography of the four corners area after partial marine transgression of the Entrada. Extent of the Todilto formation shown with concentric limits of limestone and gypsum within the unit, with surrounding eolian units (After Lucas and Anderson 1994)

elevation of the ground-watertable with respect to the land-surface. Changes in geometries and extents of the various vadose, capillary and lacustrine units in an erg are a response to climatic change, subsidence and episodic flooding.

Understanding that hydrology (depth to watertable) creates permeability layering during deposition of ancient dune sand succession adds another level of reality to previous dry erg models for fluid flow in eolian reservoir sands deposited below evaporite seals. Older engineering models guiding hydrocarbon recovery from oil and gas fields from eolian sands below evaporite seals typically assumed that the spectrum of internal flow discontinuities in the eolian sands were largely defined by 1st- through 4th-order bounding surfaces, that is, the primary sedimentary structures control permeability. At the reservoir scale the sands were assumed to respond as largely homogenous flow units during hydrocarbon extraction, with permeability variation tied to grainsize variation. This is after all what is seen in the impressive Quaternary ergs of the Sahara, Arabia and Mongolia.

But these analogs are all purely continental settings, located a long way from the ocean and from any other permanent body of surface water with a hydrology capable of depositing a widespread evaporite seal over the top of the erg.

The reality is that homogenous eolian sand reservoirs are not all that commonly associated with bedded evaporite seals that overlie windblown sediments. Typically, thick homogenous dune sand units are not preserved at or immediately beneath the contact with a encroaching evaporite seal. The encroaching hydrology associated with the passage from an eolian system to an evaporite system simply does not allow widespread vadose conditions during the transition. Rising watertables feed capillary salts that patchily cement the reservoir sands during passage into deposition of an evaporite seal. Reservoir quality in these systems is typically a reflection of intergranular cement intensity (anhydrite or halite) and is not a direct reflection of primary depositional geometries or primary sedimentary structures. By the time an evaporite seal covers a unit dominated by windblown sands any loose sands have already blown on and away into the interior, as is the case in the central Arabian Peninsula, or have been dispersed into the shoreface, as in the southeastern Qatari and northeastern Saudi coastal zones (Fig. 3.68b).

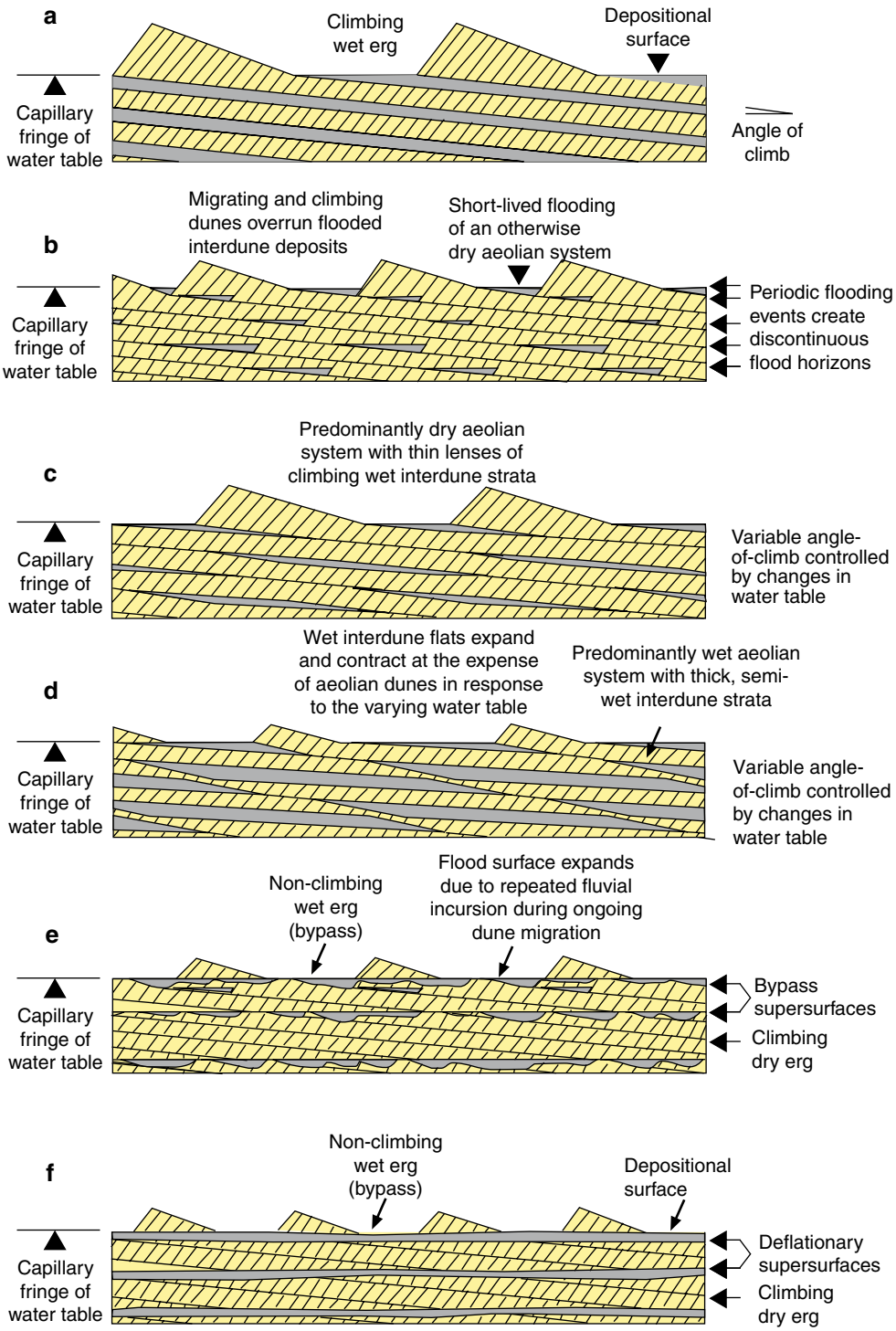

Fig. 2.62 Spectrum of interdune geometries generated by variations in the frequency and magnitude of watertable change, the rate of dune migration and the net eolian sediment budget. (**a**) Entrada Sandstone, (**b**) Navajo Sandstone, (**c**) and (**d**) Helsby Sandstone Formation, (**e**) Cedar Mesa Sandstone, (**f**) White Sands (After Mountney and Thompson 2002 and references therein)

Preserved sandflats about the edges of most aggrading and transgressive evaporite seaways are tied to deflation controlled capillary fringes and aggrading marine watertables. Such a hydrology must deposit evaporite cements wherever the capillary fringe intersects the land surface and reflux cements where brine plumes sink into the underlying sands beneath brine-filled interdunal corridors. In this hydrological setting the sabkhas, mudflats and salcretes that characterise the transition to the seal facies create low permeability cement patches within any underlying eolian sediment sheet. Thick piles of more homogenous vadose crossbedded dune sand that may have once been present in the region prior to the encroachment of the evaporite precipitating hydrology now lie deeper in the succession, and so are of less interest in terms of modelling hydrocarbon production from sediment beneath the evaporite seal.

Reservoir models for flow response in eolian sandflats sealed by evaporites should not assume intraformational continuity in the sands beneath the seal. Instead, a competing model with two end-members is more appropriate. At one end of the depositional spectrum are damp/wet interdune strata in wet eolian sandflats with shallow watertables. At the other end of the depositional spectrum are dry dunes with deep watertables that are flooded by the rapid entry of seawater into the continental depression. Inputs to the model can be quantified by the relative proportion of dry eolian version versus wet interdune structures seen in core or core-calibrated FMI imagery. Scaling of reservoir geometries can be done using analogs for the various styles of watertable encroachment on coastal dunes as seen in modern marine and lacustrine settings (Fig. 3.67).

A climbing dune model (relevant for much of the Entrada Sandstone, in Utah) requires moderate–high sediment supply in balance with a relatively deep watertable. It has a relatively low potential for widespread capillary salcretes and fine-grained interdunal sediments (Fig. 2.62a). The non-climbing dune model at the other end of the hydrological spectrum is characterised by widespread episodes of non-accumulation or hiatii (relevant for climatically controlled supersurfaces as in the coastal zone of modern NE Saudi Arabia, Sabkha Matti in the UAE, the White Sands of New Mexico, the Late Quaternary sandflats surrounding Lake Eyre and their Pre-Khuff counterparts in the subsurface of Saudi Arabia). It requires periodically low rates of sediment supply, high rates of deflation and longterm low rates of creation of watertable controlled preservation space for the sand sheets. It has a much higher potential for large areas of the system to be deflationary, for large areas of the sedimentation surface to intersect the capillary fringe and for the preservation of widespread capillary salcretes (Fig. 2.62f).

Defining which of the various intervening styles of sediment accumulation in the eolian succession under study is important in modelling porosity and permeability extents and in correlating lateral extents of high permeability zones in ancient sand bodies (Mountney and Thompson 2002; Fig. 2.62b–e). Textures indicative of dry or wet eolian systems and interdunal sabkhas are discussed in the next chapter. Wet interdune textures are described in detail by Goodall et al. (2000).

Degrading Hydrology and Playa Capture

Aside from Stokes surfaces, the effects of a degrading (falling) hydrology and associated deflation are seen in sediment and drainage patterns in many Late Quaternary playas, including those in Central Australia located in and around Lake Amadeus and Curtin Springs (Fig. 2.63a; Jacobson et al. 1989). Longterm reduction in groundwater levels associated with increasing aridity at the end of the Pleistocene led to a change in the status of some inland playas from discharge playas to recharge playas (with solution fissures and karst holes) via a process known as playa capture. It occurs when a fall in the level of regional groundwater, perhaps driven by the deflationary deepening of one playa floor leads to the removal of one or more adjacent playas from the discharge level of regional groundwater outflow (Fig. 2.63b; Jacobson and Jankowski 1989). Groundwater head in the Curtin Springs area has decayed over the last several thousand years and so changed the nature of playa sedimentation. A few thousand years ago Samphire Lake was a discharge playa and it still retains thick deposits of groundwater-derived lacustrine gypsum from that time (Fig. 2.63b).

Today the discharge system is no longer active in the lake as the regional watertable lies metres below the playa floor. Samphire Lake has evolved into a vegetation-covered recharge playa and regional discharge is focused into nearby Spring Lake and Glauberite Lake. This has rendered the Samphire Lake surface sediment susceptible to eolian deflation, karstification and vegetation coverage. Over time Glauberite Lake will become the primary focus of groundwater activity in this region and will ultimately form a regional groundwater sump where bedded salts will accumulate.

Falls in local hydrological base level can be driven by changes in climate, uplift or tectonic isolation. It drives local processes such a karstification and carnallite precipitation in bedded halites in the Quaternary playas of Qaidam Basin, China and in Lake Asal, Djibouti. An impressive example of the effects of a local lowering of the saline base level on karst intensity is seen in evaporite-cemented sediments that increasingly exposed about the margins of the Dead Sea in the Middle East. Lake water level has been falling since the 1940s and the rate of fall has accelerated since the 1960s with increasing anthropogenic extraction of fresh water (Figs. 4.45 and 4.46). This fall in water level drags with it the brackish groundwater lens that floats atop dense lake brines about the lake edge (Fig. 2.64a; Salameh and El-Naser 2000; Frumkin et al. 2011). With the encroachment of brackish to fresh pore waters, sediments, which were evaporite-cemented and mineralogically stable when bathed by hypersaline lake brines, become subject to dissolution and collapse. The process of dissolution is especially obvious at the contact between the less permeable Lisan Formation and the overlying salt-cemented gravels. This interface focuses the flow of fresher water at the top of the salt and base of the salt/gravel unit (Fig. 2.64b). The marked fall in the Dead Sea water level in the past few decades has accelerated the rate of sinkhole creation (Nof et al. 2013). The first documented sinkholes along the Dead Sea coast appeared in the 1960s. The occurrence rate has accelerated significantly since then, from less than 50 new sinkholes per year prior to 1999 to more than 380 per year since 2003.

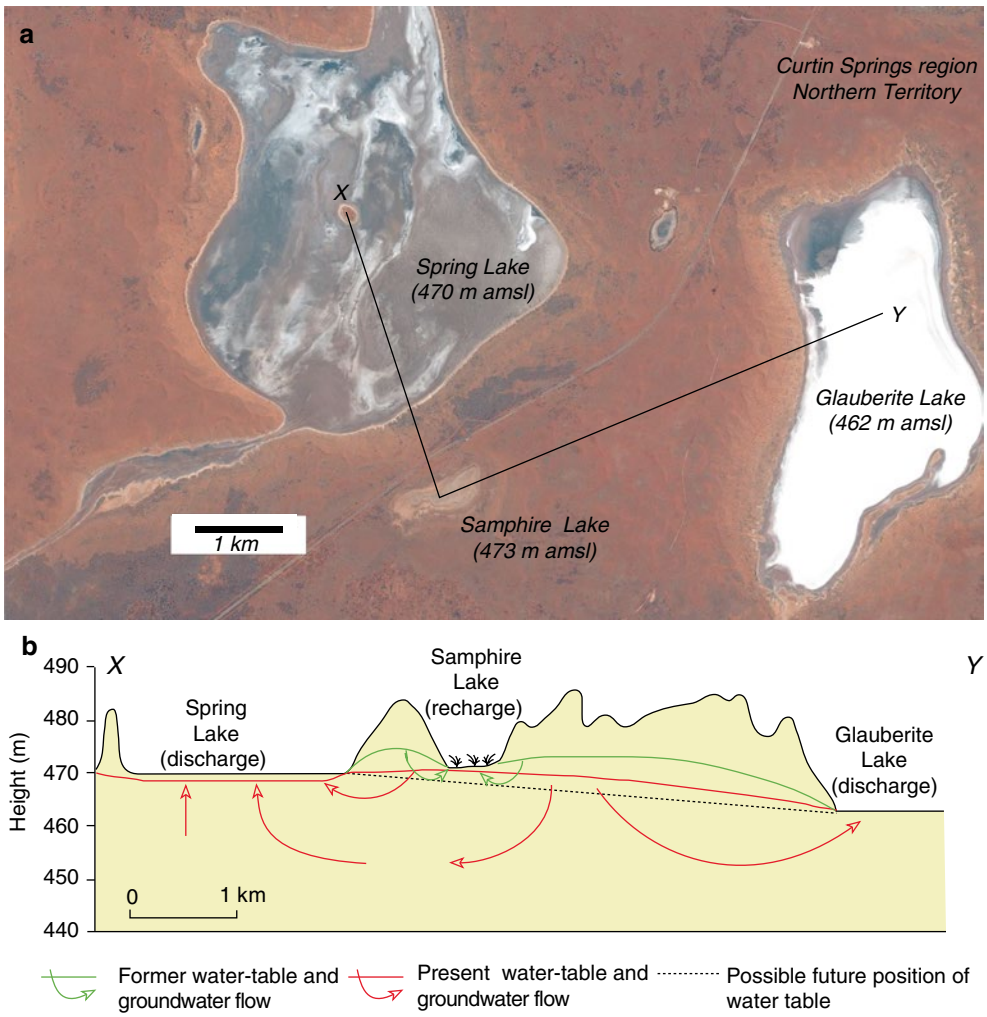

Fig. 2.63 Salt lakes in the Curtin Springs are, Northern Territory. (**a**) Plan view showing elevation above mean sealevel of Spring Lake, Samphire Lake and Glauberite Lake. (**b**) Schematic of playa capture or abandonment via decay of groundwater head. Samphire Lake was once a discharge playa (*green line* indicates former watertable) that was accumulating gypsum, but it was converted to a recharge playa as Glauberite Lake progressively captured the regional groundwater flow system (After Jacobson and Jankowski 1989)

Away from the pervasive collapse dolines tied to the retreating shoreline, other areas of reactivated subsidence in the Dead Sea depression are tied to fault intersections and radial uplift fractures atop and about areas of active diapir uplift in the Lisan Straits (Closson 2005; Closson and Abou Karaki 2009). Groundwater preferentially flows along faults, joints and fractures so that chemical and physical erosion of saline sediments takes place along such weaker zones. Underground voids then appear, creating growing cavities, which come up to the surface after successive roof collapses (Chap. 12). For example, the falling water levels of the Dead Sea lake has created problems for the salt works in the Southern Basin with newly-formed solution collapse structures weakening some of the dykes enclosing the evaporation ponds. Between 2000 and 2002, the Arab Potash Company (APC) lost two salt evaporation ponds due to solution-breaching of dykes resulting in a loss of $70 million. The breached zones show a strong structural control tied to regional lineaments. The southern Dead Sea is by far the most affected by sinkholes and decametric to kilometric subsidence phenomena. In this scenario the sinkholes are the surface manifestations of active neotectonic faults that may serve as conduits for under-saturated groundwater, enabling its access across aquiclude layers.

At first this tectonic hypothesis seems to conflict with models that consider the salt-edge dissolution front as the major site control of sinkhole formation. Recent seismic work by Ezersky and Frumkin (2013) has shown that the thicker shallow buried salt mass largely terminates along the active neotectonic faults that are now covered by recent sediment. That is, the majority of the Dead Sea sinkholes form in a narrow strip (60–100 m wide) along a paleo-shoreline (perhaps 10,500 years old) which was constrained by faults and alluvial fans and this subsurface boundary today determines the edge of the main salt layer dissolution edge. This scenario reconciles the two major competing frameworks (salt edge versus neotectonic lineament) for sinkhole formation in the Dead Sea rim.

At a broader scale, longterm watertable falls in any saline basin drive a redistribution of salt sinks within large isolated drawndown sedimentary basins. Drawdown changes the distribution of marginal versus basin-centre evaporite

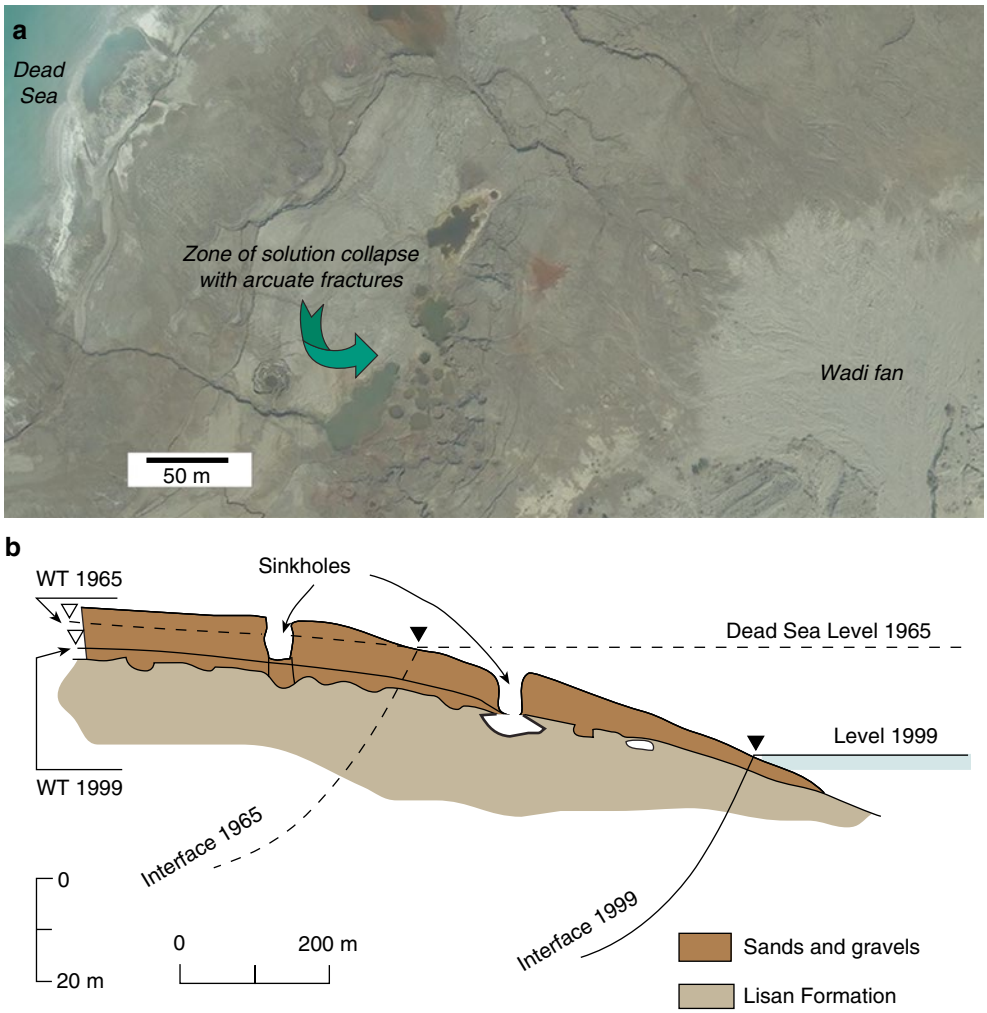

Fig. 2.64 Karstification along the newly exposed margin of the Dead Sea. (**a**) Plan view showing zone of karstic collapse zones near a wadi outflow fan on the eastern margin of the Dead sea (31.333265 N, 35.542658E). (**b**) Collapse process is related to dissolution and removal of salts due to lowering of Dead Sea water level and the associated flow of freshwater along the interface of the sandy gravels and the salty Lisan Formation deposits at the Dead Sea margin. This drives the accompanying cavity, collapse, and sinkhole formation in the at-surface gravel carapace (After Salameh and El-Naser 2000)

accumulations (Fig. 2.64). It can create regional mega-surfaces or unconformities, which are recognisable on seismic sections and can cross continental and marginal marine sequences (e.g., the Messinian M-horizon of the Mediterranean). These surfaces are sometimes described as mega-bounding surfaces by sequence stratigraphers. If they are incorrectly interpreted as eustatically induced contacts, rather than watertable or climatic responses to subaerial exposure in a continental settings, they can greatly complicated any attempt at age fitting a sealevel curve to the seismic sequence stratigraphic signature (Chap. 5).

Remote Sensing of Saline Hydrologies

The preceding discussion shows there are two end member styles in any saline hydrology; (1) Aggrading or accreting systems typified by ongoing accumulations of evaporite beds and an accompanying rise in the saline hydrology/watertable in the depositional sump, (2) Degrading or deflating systems where salts and sediments are being lost by a combination of dissolution and deflations with an accompanying lowering of the watertable. What is interesting is that some of these hydrologies can be identified remotely using satellite monitoring.

This has been accomplished in an investigation of the spatiotemporal evolution of three salars in the Altiplano of the central Andes by defining a deformation time series retrieved from satellite radar interferometry in the time from 2003 to 2008 (Fig. 2.65; Ruch et al. 2012). Located in an arid to hyperarid region, with an average elevation of 3,750 m and annual rainfall less than a centimetre, the Altiplano Puna comprises broad, internally-drained endoreic depocentres with intervening north-south-oriented volcanic mountain ranges, often between 5,000 and 6,000 m elevation, primarily bounded by high-angle reverse faults (Fig. 2.65b, c; Strecker et al. 2007). Sedimentary basins in the Puna-Altiplano contain 3–5 km thick successions composed of varying proportions of continental evaporites, volcanics and clastics. The high elevations of the Altiplano salars mean that in terms of the Köppen climate classification many (including the three salars in this study) reside in the alpine

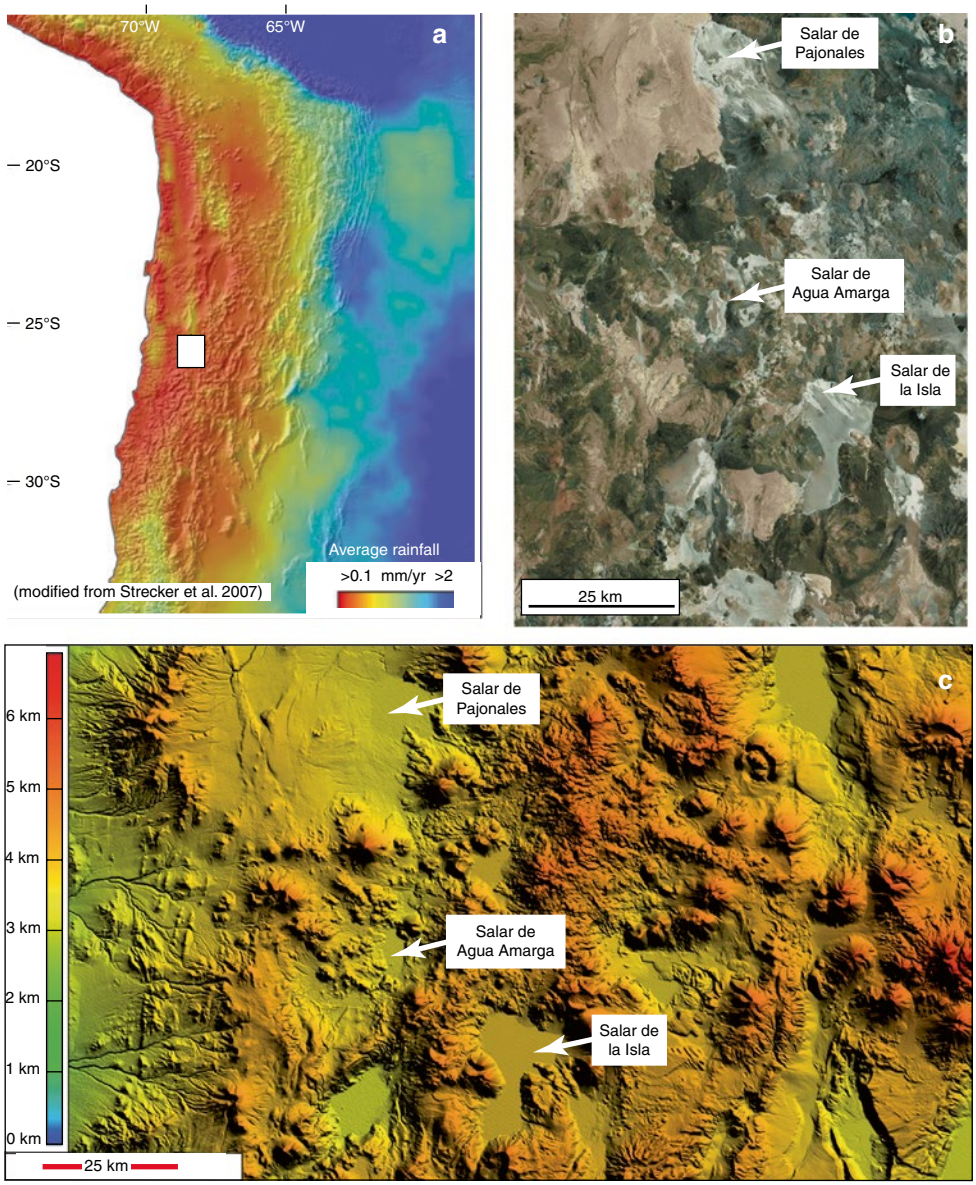

Fig. 2.65 Location, climate and elevation of the salars (After Ruch et al. 2012). (**a**) Topographic map of the central Andes overlain by annual rainfall (Modified from Strecker et al. 2007); the *white rectangle* indicates the position of the salars. (**b**) Image of the South Puna Plateau with salar locations, The *dark area* surrounding the salars are relatively impervious volcanics the *brown regions* are dominated by alluvial sediments (porous). (**c**) DEM overlay showing elevations of the drainage around the three salars. Note that Salar de la Isla is surrounded by volcanogenics in its drainage catchment, Salar de Pajonales lies at the eastern end of a broad bajada (porous), while Salar de Agua Amarga has some alluvials in its drainage basin

tundra (ET) climate belt. Others, such as Salar de Atacama and Salar de Uyuni, lie in the adjacent cold-arid dry winter desert Köppen belts (Bwk).

The Altiplano Puna plateau underwent rapid regional climatic change during the Mid-Holocene period, shifting from vegetated areas subject to frequent rainfall to a more inhospitable desertic environment (Betancourt et al. 2000; Núñez et al. 2002). From 8 to 3 ky BP, in response to the desertification, lake levels decreased and many former perennial lakes desiccated into salars. The term salar (salares) describes salt-encrusted flats formed by the evaporation of at-surface or shallow subsurface groundwater discharge in hydrographically closed (endoreic) desert depressions (Fig. 2.65b, c). A noted earlier, hydrographic closure is not the same as total hydrologic closure; bottom sediments in all modern Andean salars probably leak brine and solutes to varying degrees (with leakage more likely in salars underlain by alluvium rather than lavas and volcanogenics). There is also a strong possibility that the groundwater regime supplying many salars, considered to be surrounded by "fossil" groundwater, are still actively supplying longterm water inflows into the salar sump. The inflow system is driven, at least in part, by the ongoing drainage of groundwater heads and potentiometric surfaces still in a decay-mode response to elevated meteoric inflows from earlier Holocene pluvial periods (Houston and Hart 2004).

The term salar describes a groundwater sump where the sediments are typically subaerial and halite-rich, with intrasediment salt-growth textures driven by capillary evaporation of near-surface hypersaline groundwaters Within a salar, there are a number of typical sedimentary sub-environments tied to inherent hydrological characteristics and responses to

Fig. 2.66 Surface geology. (**a**) Regional view from the northern end of Salar de Agua Amarga showing the white efflorescence-encrusted surface of the marginal facies association and the slightly more elevated, brown irregular surface of the halite nucleus facies association (25°29′43.87″S, 68°49′57.96″W). (**b**) Irregular surface of the halite nucleus facies in Salar de Agua Amarga (25°31′06.16″S, 68°50′50.93″W). (**c**) Flat surface of marginal facies in south of Salar de Agua Amarga, partially covered by frozen brine and passing north across the saline pan into the slightly elevated, dust-cover irregular surface of the halite nucleus facies association. Tom Carpenter (*left*) and Ricardo Jara (*right*) for scale (25°35′12″S and 68°50′40 W). (**d**) Spring-fed channel at the NW end of Salar de la Isla cutting into the halite nucleus facies (25°40′01.33″S, 68°40′55.49″W). (**e**) Tumuli (igloo-structures) in deformed bedded gypsum in a small supra-strandzone embayment at the eastern margin Salar de Agua Amarga (25°32′33.73″S, 68°49′12.69″W) (Ground images are courtesy of Tom Carpenter and Luis Ignacio Silva)

the evaporation of shallow near-surface and surface waters (Ruch et al. 2012). At the broadest scale, the salar sediment system consists of two parts: a halite nucleus and a marginal zone (Fig. 2.66a) with respective proportions varying from one salar to another. Compared to the marginal zone, the halite nucleus surface is typically a zone of somewhat higher elevation in the salar plain compared to the more marginal facies (Fig. 2.66a–c). The salty surface of the halite nucleus facies association is composed of mm-scale sugary inclusion-poor halite crystals and eolian silts. Surfaces of the adjacent marginal facies are varying combinations of silty mudflats, saline pan crusts, brine ponds and salty efflorescences (Fig. 2.66c and Chap. 3). Sheet flood and alluvial processes supply much of the terrigenous mud and silt sediment found in the fringe zone. Spring-fed lakes and brine pools (lagunas) are typically interspersed within the marginal facies

association in most Andean salars (Fig. 2.66d). Evidence of former subaqueous gypsum beds precipitated during higher saline lake levels are indicated by rims of gypsum crusts. These crusts are still subject to ongoing gypsum growth indicated by the tumuli ("igloo") structures that typify outcrops of these older less-saline evaporites (Fig. 2.66e). Table 2.16 summarises the geological and hydrological characteristics of the various facies in the salars.

There is a clear relationship between sediment facies and regions of salar surface accretion versus degradation when SAR surface observation and local geology are compared utilising profiles sampled across the InSAR dataset overlain by optical images acquired by the LANDSAT satellite (Fig. 2.67; Ruch et al. 2012). Band 7 (mid-IR), which is sensitive to soil moisture, provides contrasted information about the ground intensity, often critical to definition of salt-rich areas. Areas with a weaker InSAR uplift signal (see ISLA2, Fig. 2.67a) correspond in LANDSAT to higher ground intensity values (close to white). This geologically matches with the marginal facies, where much of its flat surface is covered by ephemeral white halite (chevron-dominant) crusts. In contrast areas with larger uplift signals (see ISLA1, Fig. 2.67) have lower ground intensity values, these correspond to the halite nucleus regions, where salt typically precipitates by capillarity from shallow groundwater bodies. A ground intensity of zero corresponds to free water, all the light being absorbed and in lower water times defines regions of spring inflow or water-filled solution dolines and pits within the salar.

On the ground it is clear that the nucleus surface is somewhat elevated compared to the lower more-frequently-flooded and dissolved halite pan crusts of the marginal facies. The halite nucleus surface is typically red to grey-red as it retains a hummocky carapace coloured by entrained eolian silt (Fig. 2.66a–c). Profiles across both InSAR velocity maps and LANDSAT ground intensity images show that radar and optic signals have comparable shapes (Fig. 2.67), where the maximum uplift agrees with halite-rich nuclei regions prone to salt accretion. Localized peaks in the ground intensity values that tend to zero correspond to perennial lake locations. The intensity signal in areas prone to subsidence typically correspond to water-saturated grounds.

To analyse the temporal evolution of the salar surface, Ruch et al. (2012) compiled displacement time series on selected areas from 2003 to 2008 (Fig. 2.67d, e). ISLA1 (atop halite nucleus facies) and ISLA2 (atop marginal facies) are both located at the northern end of Salar de la Isla (Fig. 2.67a). The compilations show different cumulative displacements sampled on two clearly-delimited facies zones, with mean values of 2 and 6.5 cm, respectively, implying aggradation of both the marginal facies and the halite nucleus facies in this salar, with aggradation rates greater atop the halite nucleus facies association. Moreover, cyclic displacement changes (mini uplifts) approximately from September to March each year, are best expressed on the halite nucleus at Isla (ISLA1). PAJ1 is located in the northern part of the Salar de Pajonales (Fig. 2.67b) and shows a comparable displacement trend with respect to ISLA2, with a cumulative displacement of 2 cm in almost 5 years. Likewise the AMA profile in Salar de Amarga shows a similar growth profile related to nucleus versus marginal facies, the indicated accretionary rates are less than in Salar de la Isla (Fig. 2.67b).

In contrast, in Salar de Pagonles, the PAJ2 profile, which was collected atop a zone characterised by sedimentary features indicative of local salt dissolution (marginal facies separated by numerous water filled dolines and spring pools and ponds), shows a clear signal subject to a rapid negative displacement along the LOS direction during the first trimester of 2004, for a duration of almost 1 year (Fig. 2.67c). After 2006, the signal follows again a similar ground displacement comparable with areas of PAJ1 and AMA, the latter being located on the Salar de Amarga, 50 km distant, southeast from Pajonales (Fig. 2.67d, e). Clearly, that sediment facies can be related to InSAR-determined surface deformation (velocity profiles and time series analysis), implying an underlying hydrologic/sedimentologic control.

To confirm likely hydrological drivers to the varying rates of ground displacement within and between salars phenomena, the sedimentological and InSAR results were compared to chemical analysis of surface waters, from both water inflow and laguna locations, which were systematically sampled across the Andes in 1991 (Risacher and Fritz 2009). Although there are no pore water samples in the nucleus facies in the salars under study, hydrogeochemistry samples from the salar edges confirm that the salar with the highest ground displacement rate of all salars observed, Salar de la Isla, also contains surface waters with the highest salinity in this section of the central Andes. Its maximum salinity is 330 g/l, significantly more than at Pajonales (247 g/l) and at Agua Amarga (197 g/l), hence, it is more prone to salt precipitation and associated ground displacement, explaining the higher deformation rate observed.

Ruch et al. (2012) show that all salar surfaces they observed are uplifting and at rates directly related to ground compositions. There is a strong intra- and inter-salar association between saline facies distribution and rates of rise or fall of the salar surface. Ground displacement in the salars is directly related to levels of salt precipitation and salt crust thickening at the surface. Salt crust thickening is likely responsible for the revealed ground uplift signal. In this case, based on the stability of InSAR coherence, thickening probably occurs best in zones beneath the upper salt crust levels in the salt nucleus and are driven by capillary evaporation of highly saline brine.

Table 2.16 Summary of geological facies related to hydrology in a South American salar

Major facies association	Halite Nucleus (HN)	Marginal facies (MF) – subaerial portions are covered by thin white ephemeral efflorescent veneer of halite and/or gypsum (in salars with no halite nucleus, such as Pajonales, equivalents (MFE) of this association dominate the whole salar surface)				
Subenvironments	Rugose halite capillary crusts (Subaerial)	Saline pans and mudflats (subaerial most of time)				Moat facies (subaqueous)
Dominant constituent in setting	Halite	Halite	Gypsum	Carbonate	Silty mudflat (terrigenous sediments	Brine pools, channels and lagoons
Hydrologic/ sedimentologic character	Upper zone is up to tens of cm thick, composed of mm scale sugary inclusion-poor halite, with interstitial mud. Worm-eaten appearance of this upper zone is due to periodic dissolution. Remnants of megapolygonal pressure ridges recognisable in less overprinted zones. Below this upper zone the association is metres or more thick and is dominated by large cm-scale interlocking meshworks of halite with minor interstitial mud. Crystals mostly clear (inclusion-free) due to slow shallow diagenetic growth from halite-saturated brines. Some clear crystals grew as cavity fills. This is a polycyclic set of ground water overprints, driven by ongoing capillary evaporation and preserved in the halite textures, so unit retains little or no primary texture.	Zone up to a metre or so thick made up of stacked mostly flat layered salt crusts dominated at deposition by inclusion-rich halite chevrons. Current at-surface crusts show varying development of polygonal and megapolygonal pressure ridges. Initially, this halite precipitates as growth-aligned crystal layers from ephemeral brine sheets. With ongoing desiccation, primary-textured crusts are over printed to varying degrees by capillary salts, efflorescences and karst cavities. Many zones of stacked crusts in the Marginal Facies association are subject to partial to completed is solution in occasional sheet flood events. Dominant formative process is from a desiccating at-surface brine sheet. With time, in a halite-saturated setting, a resurgent hypersaline ground water overprint can alter this unit into a nucleus facies association.	Gypsum crusts have an irregular buckled and blistered surface with locally developed polygonal pressure ridges. Constituent gypsum crystals are mm-scale lenticular to and sugary meshworks. In shallow subsurface can create cross sections of discontinuous bowl shaped, concave upward saucer-shaped layers that are 10s of cm in diameter. This salar gypsum facies association is distinct from supra-strandzone bedded gypsum units (showing coarse selenitic bottom nucleated growth-aligned growth textures) that out crop about some salar margins and formed during earlier, somewhat less saline, hydrological events. This unit can be deformed into tumuli (igloo-like mounds) via ongoing capillary precipitation.	Micritic precipitates (mostly aragonite/ calcite) as cm-scale crusts with varying degrees of induration. Preserved in subsurface as gray-green mud layers.	Subenvironment proportions are variable and include; ephemeral streams, sandsheets, mudflats, eolian dunes, spring-fed vegetated marshes and pools (vegas). Each preserves a characteristic suite of sedimentary structures (crossbeds, conglomerates, caliche, pedotubules, etc.). Silty mudflat sediment scan host lenticular shaped gypsum, fibrous vein gypsum, gypsum cemented thin sandy bands and rare cm scale displacive halite. Also host mm-scale carbonate nodules and rhodoliths.	Variable bottom accumulations and precipitates indicative of ambient salinities. Calcite laminates, tufas and crusts (≈5 cm thick) are typical of fresher/ brackish pools. Gypsum bottom cumulates and aligned cm-scale crystals construct stacked beds away from spring inflow. Rippled surfaces, underlain by carbonates and gravel can form via erosion of surface crusts along the strandzone. Pisolite textures and tepees locally possible, especially in zones of aragonite saturated groundwater resurgence. Ponds typically indicated zones of dissolution of former halite units.
Depth to watertable	Within tens of cm of surface	Within a few cm of the surface	Within a few cm of the surface	Within a few cm of the surface	More than tens of cm to metres below	Crops out as perennial water surface

This classification only considers salars with surface facies dominated by halite, it does not encompass perennial lacustrine gypsiferous, calcitic/terrigenous facies which underlie or are lateral to halite-rich salar facies. These non-halite facies were deposited in humid, less saline periods in the same intermontane lacustrine depression and have modern analogs in some other perennial fresher-water Andean lakes.

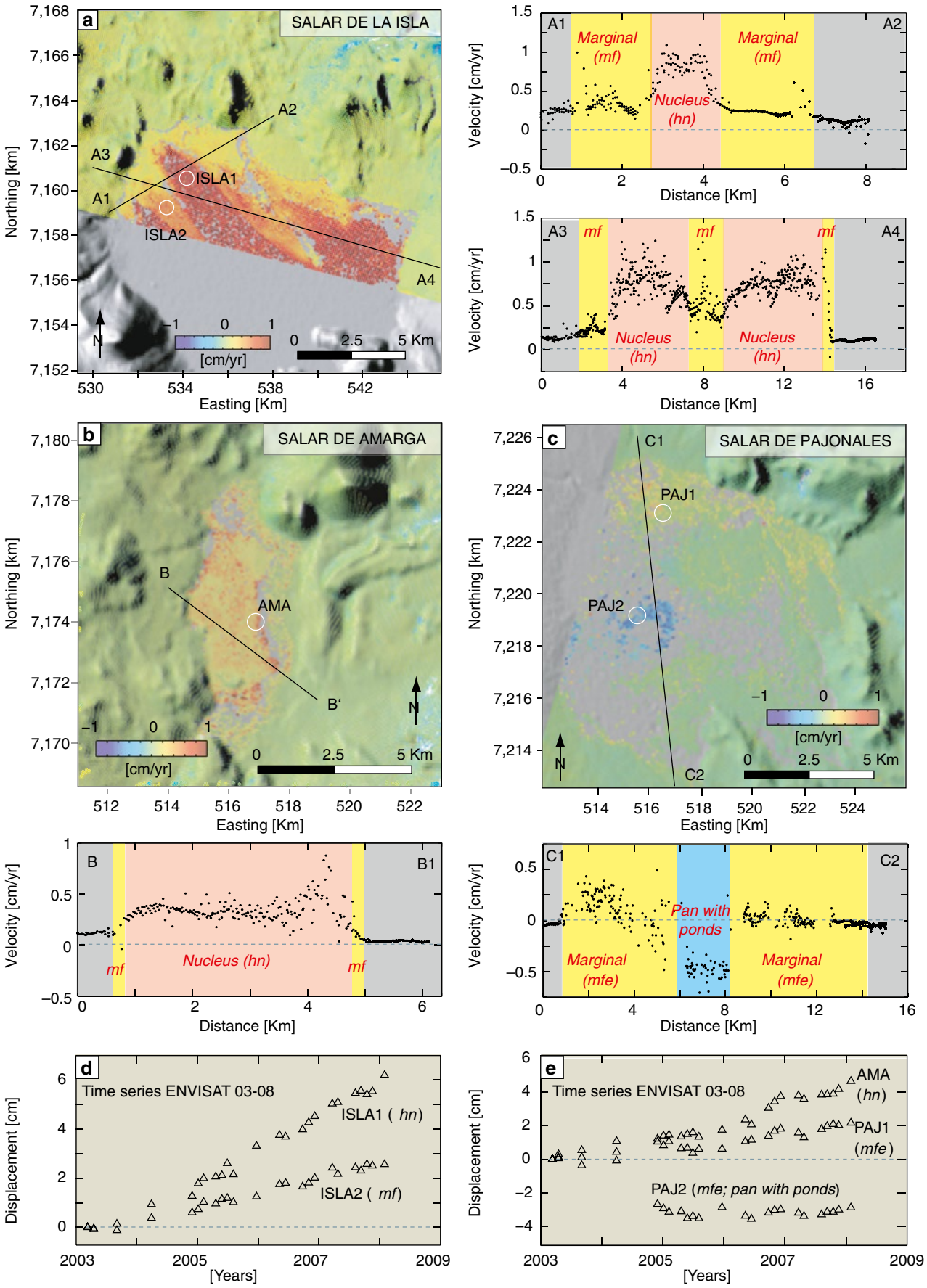
a
SALAR DE LA ISLA
A1
A2
A3
A4
ISLA1
ISLA2
N
−1 0 1
[cm/yr]
0 2.5 5 Km
Northing [km]
Easting [Km]
Velocity [cm/yr]
Distance [Km]
Marginal (mf)
Nucleus (hn)
mf
b
SALAR DE AMARGA
B
B'
AMA
B1
c
SALAR DE PAJONALES
C1
C2
PAJ1
PAJ2
Pan with ponds
Marginal (mfe)
d
Time series ENVISAT 03-08
ISLA1 (hn)
ISLA2 (mf)
Displacement [cm]
[Years]
e
AMA (hn)
PAJ1 (mfe)
PAJ2 (mfe; pan with ponds)

However the observations were taken over a short period of time (about 5 years) in the salars' depositional histories (Fig. 2.67d, e). If a constant ground displacement (aggradation) rate of >1 cm/year (as observed at Salar de la Isla) had continued over a century or more, the ongoing precipitation of halite in the nucleus facies should induce a height differential of around 1 m/century, compared to the aggradation rate of the marginal facies. This is not the case, field observation at Isla and at other salars across the Altiplano indicate that only few tens of centimetres separate the surfaces of the halite nucleus and the margin facies associations, indicating likely variation in the hydrological dynamics in the recent past. Transient strong rain or snowfall events on time scales greater than the few years of observation must influence the heights of differentials across the various salar surfaces (Ortlieb 1995). Alternatively, the regional diminution of the permafrost elevation observed over decades in the Andes (Trombotto and Borzotta 2009; Trombotto 2000; Romanovsky et al. 2007) may have contribute to increase the annual incoming groundwater. In the long-term, this may increase the salar watertable elevation and induce faster salt precipitation in the ground water sumps.

The degree of solute cycling in both the nucleus halite and marginal facies over the longer time frames associated with the halite infill of a drainage sump in an endorheic salar depression, as observed by Ruch et al. (2012) has significant implications in terms of: (1) Recognition of hydrologic stability/climatic variability preserved in the infill beds as variable salt signatures. (2) Identification of regions of likely concentration of particular solute components in salar pore brines, such as lithium and boron (Chap. 12). The fact that salar surfaces are aggrading at different rates, both within and between salars, has direct geohydrologic and indirect long-term climatic implications. (3) Development of remote techniques for recognition of movable nearsurface water in extraterrestial settings (Fig. 2.68).

Earlier studies of South American salars have suggested tectonically or fault-related ground motion can drive elevation changes in the salars (Reutter et al. 2006), while others propose an uplift and subsidence related to unloading, or the reduction of the water column (Bills et al. 1994), while yet others attribute in-salar elevation changes it to climate change and/or ice lens development in elevated saline lakes (Hurlbert and Chang 1988). Historically, all these earlier studies failed to match the hydrological style indicated by the evaporite distribution within the salar to the specific regions where different rates of ground elevation change are occurring. For example, if tectonic uplift was driving changes in elevation across a salar surface, elevation changes would not match the presence or absence and the undulating edges of the halite nucleus in all imaged parts of the salar. Rather, changes would relate to fault position and regional tilting and shifting of the active saline sump within the salar depression. This was not seen in the three studied salars At the millennial scale, tectonic tilting can change the regional salar hydrology, as seen in the changes in the salt sump position being driven by tilting in Salar de Atacama (Bobst et al. 2001; Jordan et al. 2002) but it does not explain the cm/year scale of accretion observed in the imaged salars.

It has been proposed that ice heave in these high elevation BSk and ET climatic locations may have controlled intrasalar elevation changes (Hurlbert and Chang 1988). If so, ice sheets would have to be a dominant feature within the halite nucleus area, where the InSAR analysis shows most of the elevation changes occur. However, the halite nuclei in all Andean salars lack evidence of pervasive intrasediment ice sheets. If an ice sheet ever did form in the halite nucleus area, it could only form atop or very near to the nucleus surface (freezing water is less dense than a halite saturated pore brine). No such feature has ever been documented in any Andean halite nucleus. If any cryogenically precipitated salts ever formed substantial salt masses within a halite nucleus, they would leave behind widespread characteristic mineral fingerprints; such as, cold season hydrohalite, mirabilite, thernardite, glauberite, and epsomite (Warren 2010). None of these cryogenic indicator salts is commonplace in the halite nucleus of any Andean salar.

Another possible alternative to capillary evaporation driving aggradation is a variable distribution of hygroscopic material (i.e., clays or hydroscopic salts) in the salar depression, which may induce local ground swelling and thus ground displacement in response to periodic water influx to the salar system (Gabriel et al. 1989). However the better tie of the InSAR rates to the at-surface expressions of evaporite hydrology (halite nucleus versus margin flat versus salt karst) suggests the relative rates of rise of the various salar evaporite surfaces are more responses to a hydrologically, not hydroscopically, driven set of arid-zone processes. The predominant salt texture present in the halite nucleus is medium to coarsely crystalline halite aggregates and clusters. When halite acts best as a hydroscopic salt it tends to be fine grained with the resulting increased surface area greatly aiding its hydroscopic capacity. Other highly deliquescent salts (such as the calcium chloride salts or the potash salts) are not pres-

Fig. 2.67 Deformation maps acquired by InSAR during the period from 2003 to 2008 on a DEM overlay at (**a**) Salar de la Isla, (**b**) Salar de Agua Amarga and (**c**) salar de Pajonales (Chile). Profiles across the salar surface deformation show a clear transition with the surroundings volcanic basement, indicated by *light grey* at either end of *transect lines*). Also plotted are the facies intercepts along the lines of section (*hn* halite nucleus, *mf* and *mfe* marginal facies and equivalents; ponds = regions of salt karst ponds and lagunas on the surface of Salar de Pajonales). (**d**) Time series plot at Salar de la Isla (ISLA) and (**e**) at Salar de Pajonales (*PAJ*) and Salar de Agua Amarga (*AMA*) (After Ruch et al. 2012)

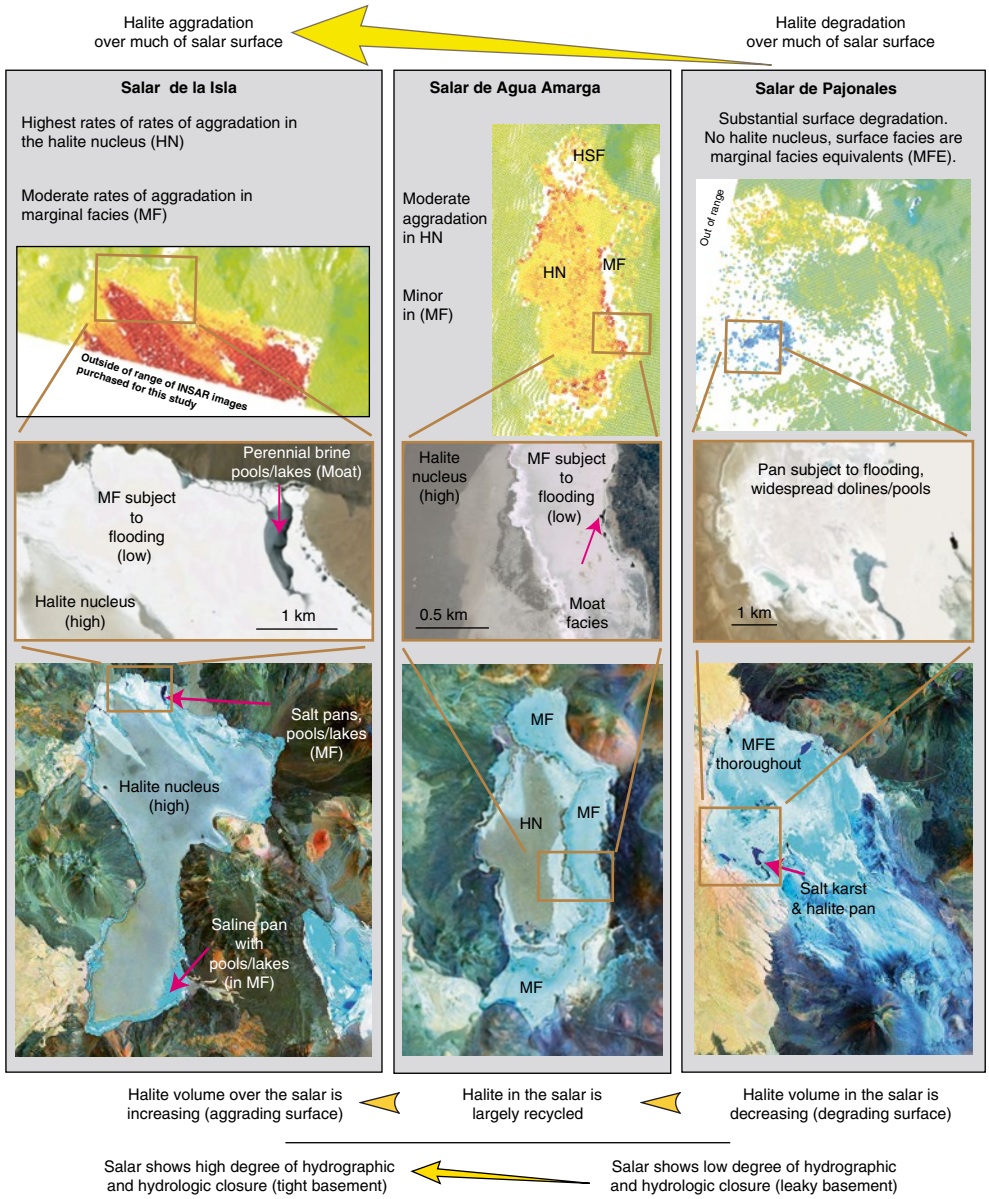

Fig. 2.68 Summary illustrating facies associations and rates of surface deformation in the surface geology are direct responses to the volumes of solute/brine accumulating in the three salar depressions and related to a combination of evaporation and the degree of hydrographic and hydrologic closure that typifies each salar depression

ent in sufficient volumes to explain the elevated rates of aggradation in the nucleus. If hydroscopic clay is the main driver, then the highest rates of aggradation would not be confined to the halite nucleus.

When the three salar settings are compared, the rate of accretion or degradation can be related to the sedimentological, hydrological setting of the three salars (Fig. 2.68). Across the 5-year time frame of the observations, the hydrogeochemical budget in both Salar de la Isla and Salar de Aqua Amarga is positive, with a gain in salt volume over the period of observation. These two salars are clearly acting as sumps for regional groundwater. In contrast, Salar de Pajonales shows a split response in its hydrogeochemical budget. The northern and eastern portions of the salar are groundwater sumps and gaining in salt volume. In contrast, the hydrogeochemical budget in the central and southern end of this salar is negative as soluble sediment material is being lost (the salar surface is lowering). This implies this part of the salar is a region of more open groundwater flux where pore or surface waters carrying the dissolved salt is escaping, possibly related to proximity to the adjacent bajada aquifer. Use of InSAR monitoring of salar surfaces may help define water budgets within and between salar depressions. Drilling through a salar infill and the monitoring of the sedimentological changes in the nature of the recovered core and cuttings can be used to document longterm climatic evolution in the salar depression (e.g., Bobst et al. 2001).

Ions such as lithium and boron tend to be enriched in late-stage magmatic fluids and also become increasingly concentrated in salar pore brines at higher salinities

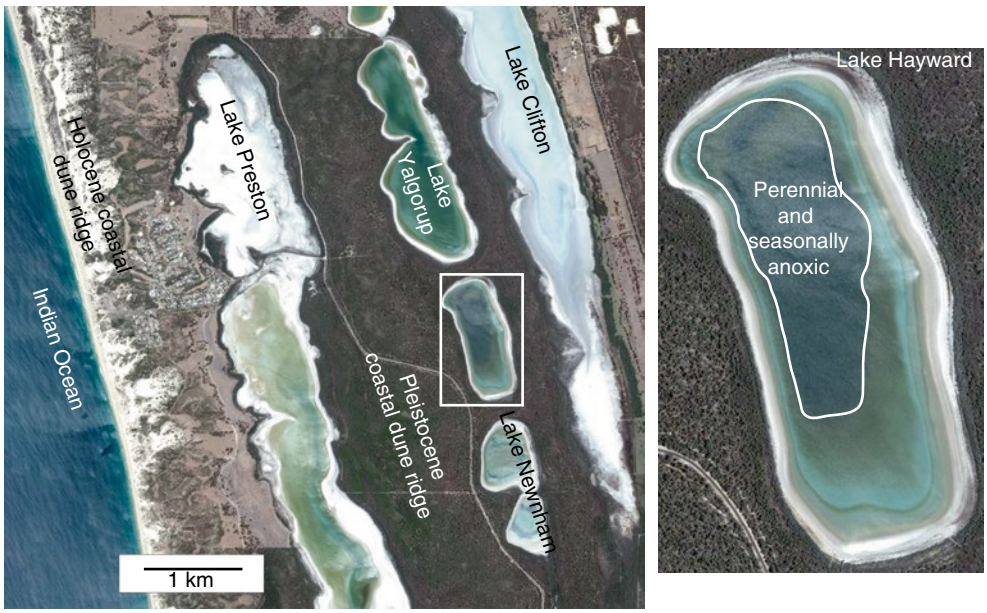

Fig. 2.69 Lake Hayward, West Australia

(Garrett 1998, 2004). Chapter 12 lists and discussed known potential and producing Li and B regions with saline associations worldwide. Interestingly, the two active lithium carbonate brine plants in salars of the Altiplano region (Salar de Atacama and Salar del Hombre Muerto) both produce from brines sources within halite-nucleus dominated sumps and are regionally located in high relief endoreic depressions. Other Andean salars associated with substantial stacked flat-bedded chevron-halite pan fills (equivalent to marginal facies) in high relief endoreic depressions, such as Salar de Uyuni (which is the largest Quaternary halite deposit in the world), have yet to be commercially exploited due to lower concentrations of Li in the salar pore brines. A predominance of stacked beds of the halite nucleus facies association rather than subaqueous sheet crusts, and a predominance of halite nucleus facies associations at the salar surface, probably indicate salars with a longterm hydrology that is more likely to retain high salinity brines over longer time frames. An association with an appropriate source of hydrothermal lithium, either in the drainage hinterland or in springs about the salar margin, indicates a high potential for accumulations of Li and B at economic levels in these nucleus-facies dominated salar pore brines.

Salinity Stratification Controls Texture

The occasional surface input of freshened waters into the central discharge depressions of evaporitic seaways (salterns) or perennial saline lakes tends to create stratified surface water bodies with less-dense lower-salinity waters floating atop more-dense saline bottom brines (Fig. 2.55b). If there are large salinity contrasts between the two water masses, they tend not to mix until their densities equilibrate. The emplacement of a freshwater body atop a lower dense brine slows and stops the concentration process in the lower brine body that drives brine reflux. It can start up again once the freshwater body has concentrated to where it mixes with the underlying brine. This ongoing stop-start mechanism probably explains the finer scale layering seen in the many anhydrite cements and replacement dolomites created by reflux hydrologies.

Brine stratification occurs today in marine-fed coastal salinas in Australia, in perennial saline lakes in the African Rift Valley and in the Dead Sea, Israel (Chap. 4). Lake Hayward, a coastal salina in Western Australia, typifies such a stratified brine system and has ionic proportions in the bottom brines similar to that of seawater. Carbonate muds are accumulating on the microbially bound floor of its small perennial brine pool (2–3 m deep) under a limnology that is density and thermally stratified for much of the year (Figs. 2.69 and 2.70; Rosen et al. 1995). Meteoric inflow creates a well-defined longterm mixolimnion; this upper, less dense and cooler water mass has salinities ranging from 50,000 to 210,000 ppm. It exists from late autumn to early summer (May to February) as it floats atop a lower denser and warmer water mass (monimolimnion) with salinities in the range 150,000–210,000 ppm (Fig. 2.70).

Stratification disappears for a few months each year from mid-summer to mid-to-late-autumn (Fig. 2.70a). During summer the waters of the upper water mass evaporate and concentrate as their bicarbonate content steadily increases. From the onset of stratification in late autumn, across mid winter and on into to early summer the temperature trends of the two water masses are parallel. They form a heliothermic system where the lower water mass is some 15–20 °C hotter

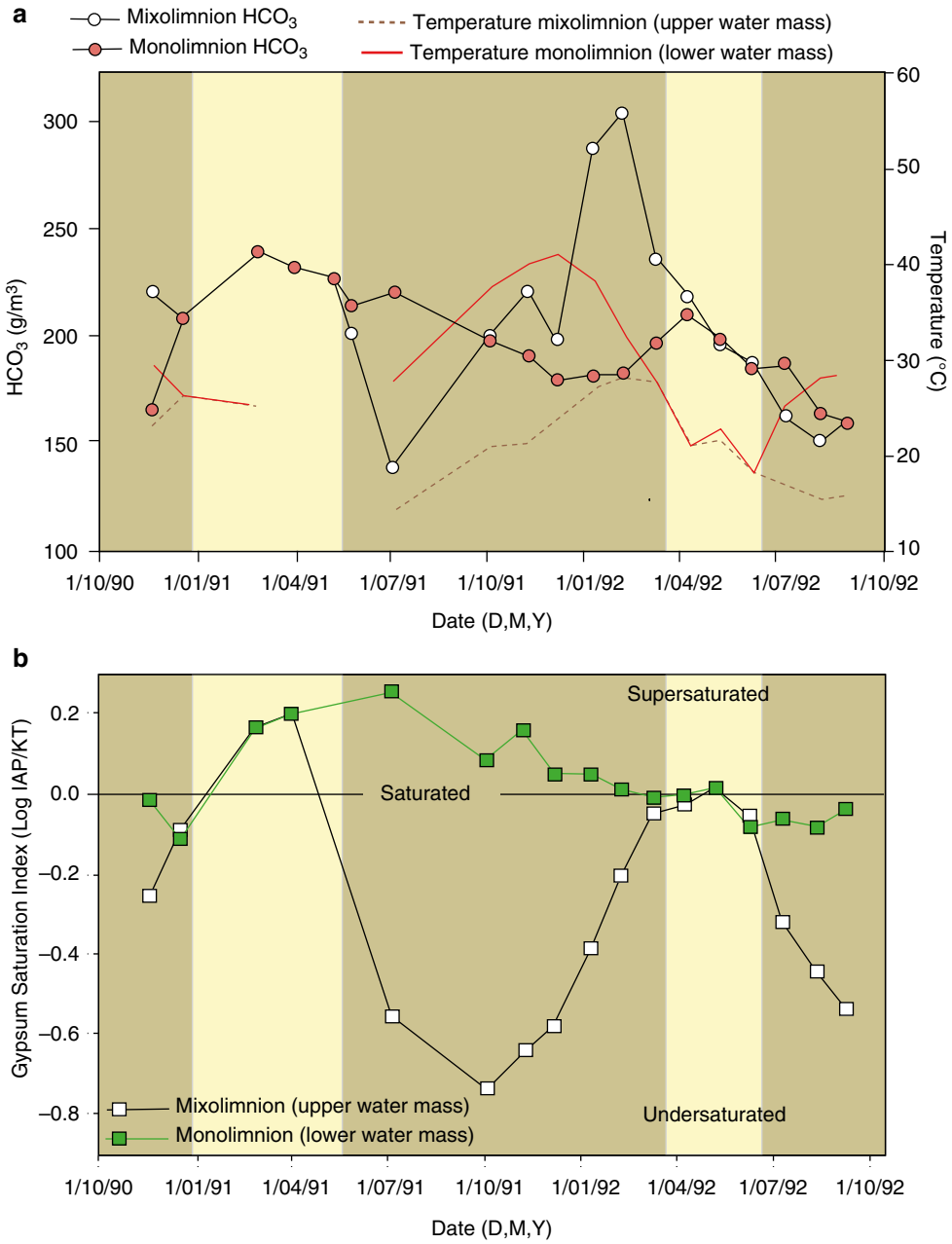

Fig. 2.70 Hydrogeochemistry of Lake Hayward waters, Western Australia. (**a**) Plot of temperature regime in upper (mixolimnion) and lower (monimolimnion) water masses and bicarbonate content. As the lake mixes, the thermal and density stratification disappears. Immediately prior to mixing the bicarbonate concentration decreases suggesting precipitation of calcium carbonate (aragonite) (After Rosen et al. 1995). (**b**) Saturation state with respect to gypsum. The monimolimnion was saturated with respect to gypsum from summer 1991 to autumn 1992 and was again near saturation at the start of summer 1992–1993. The mixolimnion was only saturated when the lake water column was homogeneous (After Rosen et al. 1996)

than the upper water mass. By mid summer (e.g., January 1992) lower water mass begins to cool, while the temperature of the upper water mass continues to rise. Once the temperatures (and densities) of the two water masses equalise they mix as the lake overturns. Waters of the lower water mass (the monimolimnion) now come into contact with the atmosphere once more. While the water masses are stratified, the chemocline and the thermocline are sharply defined across a 10 cm interface with a salinity contrast that may be as much as 135,000–140,000 ppm and a temperature difference of up to 19 °C.

The time of mixing is immediately preceded by a sharp fall in the level of bicarbonate in the mixolimnion, suggesting the precipitation of calcium carbonate (mostly aragonite) occurs in the upper water mass from late summer to autumn (Fig. 2.70a; Rosen et al. 1995). The lower water mass in Lake Hayward was supersaturated with respect to gypsum and anhydrite from late 1990 to February 1992 (Fig. 2.70b; Rosen et al. 1996). When the lake mixed from January 1991 to May 1991 and from March 1992 until early May 1992, the entire water body was at gypsum saturation, but slightly undersaturated with respect to anhydrite. A 'whiting' (a cloudy white appearance to the water body) was observed in the lake in March 92, just at the time of first mixing of the lake. Analysis by scanning electron microscopy (SEM) of the collected filtrate indicated that the 'whiting' was

composed of gypsum and diatom tests, At that time, there was also a thin (10–20 mm) crust of gypsum on the lake floor. After the 'whiting', when the water was unstratified, both the monimolimnion and mixolimnion were near saturation with respect to gypsum.

After mixing, the stratification begins to reform with the next influx of meteoric waters onto the lake surface. In the early stages of setup leading into the longterm stratification it appears stratification is not stable and the water bodies may remix before stable stratification sets in by mid winter (e.g., May–June 1992; Fig. 2.70). Lake Hayward illustrates an aspect of pelagic evaporite precipitation that is probably more generalised in many "deep-water" density-stratified settings. Namely, that evaporite crystals grow on the bottom only when the water column is unstratified. This is so even when the lower water mass is at saturation almost year round (Fig. 2.70b versus Fig. 9.48).

Another well-documented heliothermal brine lake is Solar Lake, a small monomictic hypersaline lake located on the Sinai coast of the Gulf of Aqaba (Cytryn et al. 2000). The lake is separated from the ocean by a narrow sand bar (Fig. 4.12). Water is supplied via seawater seepage through the sand bar and occasional winter precipitation. Brine depth fluctuates between 4 and 6 m, driven by seasonal changes in the intensities of evaporation and the related levels of seawater seepage and brine reflux. High evaporation and aridity in the summer months raises the lake salinity to 200‰. At that time the brine column is completely mixed (holomictic) and the entire water column is oxygenated (Fig. 2.71a). Temperature/salinity vary little throughout the brine column and sulphide/methane concentrations are very low.

By autumn, the water column is stratified with a newly introduced seawater brine (50‰) layer overlying residual, highly saline bottom water (180–200‰). A well-defined density gradient (halocline or pycnocline) now separates an upper oxygenated cooler (16 °C) brine mass (epilimnion) from the lower hotter (45–55 °C) anoxic sulphide-rich brine mass (hypolimnion; Fig. 2.71b). High sulphide concentrations develop in anoxic waters below the halocline from the activities of sulphate-reducing bacteria, both in the water column and in the underlying cyanobacterial mats. Crossing the halocline into the lower brine there is a rapid downward increase in sulphide concentration, which reaches a maximal value of 1,240 μM proximal to the sediment brine contact (Cytryn et al. 2000). At the same time a peak in methane concentration develops directly below the halocline, where a maximum value of 6.5 μM was measured in the December 1997 profile and was in part a reflection of the decomposer activities of the methanogenic haloarchaea (Chap. 9).

As winter passes into spring, a gradual heating and increase in the salinity of the upper water mass degrades the halocline. The data shown in Fig. 2.71c was collected in June 1997 and portray a transitional state between late stratification and the beginning of holomixis. Salinity and temperature gradients across the halocline are more gradual and deeper in the water column than those observed in the December 1997 profile. The deepening halocline allows oxygen to penetrate much deeper than in the earlier stages of stratification, and the chemocline is now located 3.25 m below the water surface. The oxygen concentration in the upper water mass reaches a maximum value of 300 μM at a depth of 1 m below the water surface. These supersaturated values of oxygen imply intense photosynthetic activity at these depths. Below the chemocline, a sharp rise in sulphide concentration occurs, reaching a maximum value of 2,150 μM at the water-sediment interface (Cytryn et al. 2000). Methane concentration increases linearly from the surface and reaches a maximum value of 17 μM adjacent to the lake bottom, implying methane, like the bacterially derived H_2S, is escaping from the sediments. Subsequent increasing evaporation rates further disrupt the stratification and ultimately lead to summer holomixis identical to that in the September 1997 profile.

Thick cyanobacterial mats carpet the Solar Lake sediment surface and contain a highly diverse microbial community of cyanobacteria and haloarchaea. Their metabolic activities, along with the lake's planktonic microbes greatly affect the hydro-geochemistry of the lake waters by exporting oxygen, sulphide, and methane into the brine column. Biological interactions with evaporite sediments and brine columns are discussed in detail in Chaps. 4 and 9.

Although the daily temperature/stratification records of Lake Hayward and Solar Lake are probably the best documented examples of the hydrology of a naturally stratified brine column, both regions have a number of inherent limitations when attempting to use them as direct analogs for the hydrology of ancient stratified brine seaways. Unfortunately, neither are saline enough nor isolated enough from their seawater feeds to accumulate substantial thicknesses of halite. Neither are hydrological analogs for bottom-nucleated salt beds, such as gypsum or halite units that dominate the central portions of ancient evaporite seaways and lakes. They also suffer from the scale limitations that enfeeble all modern marine-associated evaporite analogs (Fig. 5.4). Their small aerial extent ($\leq$0.6 km^2) prohibits a direct hydrological comparison with bedded salt accumulations in ancient saline giants (areas >10^6 km^2). Their centripetal unconfined meteoric inflow hydrologies, driven by winter rains and a lowering of evaporation intensity, means they cannot be directly compared to ancient brine seaways where strandlines moved up to hundreds of kilometres in a wet-dry cycle and where unfractionated meteoric waters or seawaters were insignificant in the freshening process in the subaqueous basin centre.

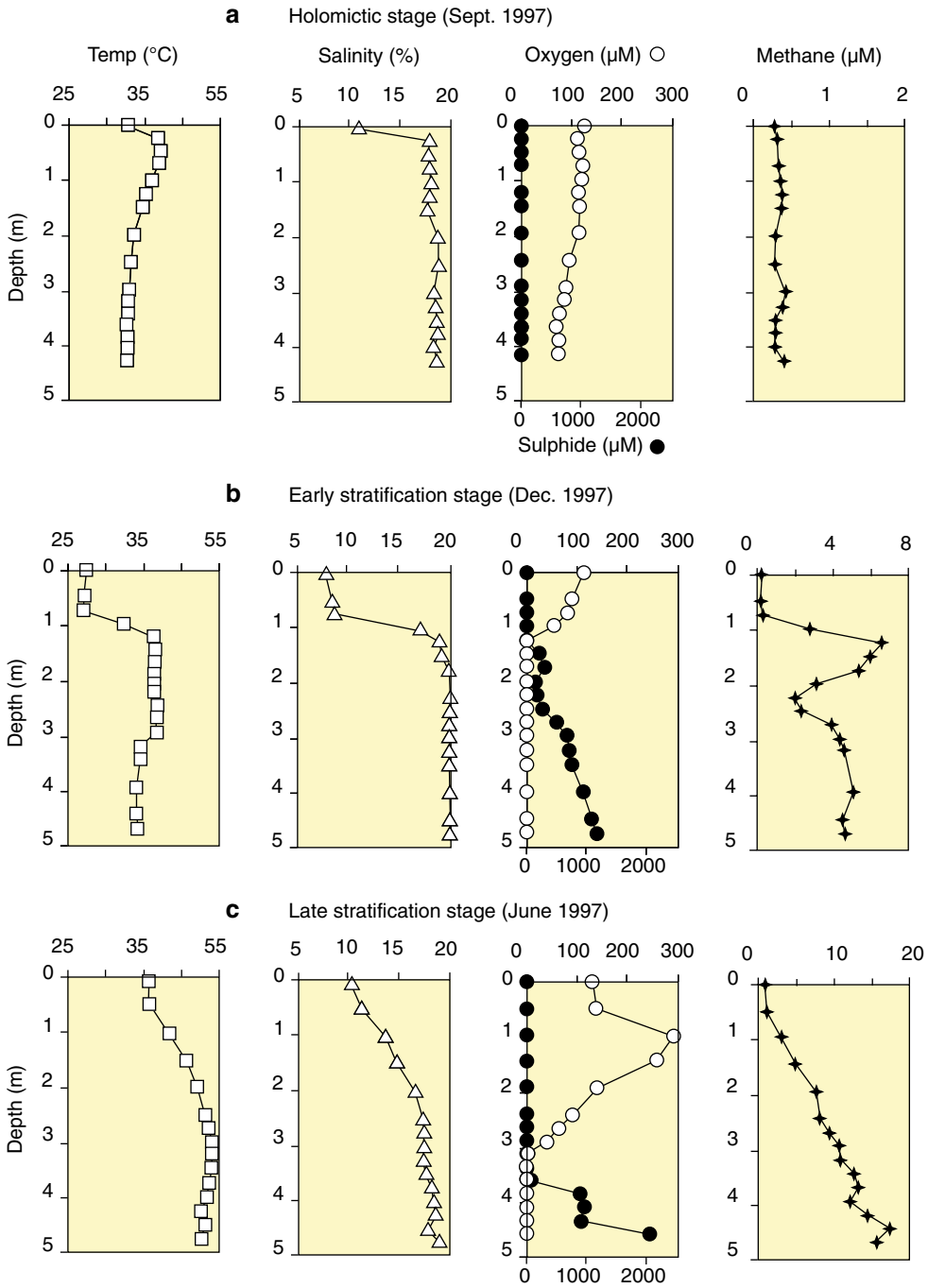

Fig. 2.71 Effects of the seasonal development of heliothermic stratification in Solar Lake, Middle East (After Cytryn et al. 2000). *Open circles* O_2, *filled circles* sulphide

Brine Stability and Evaporite Textures

In ancient evaporitic seaways and lakes the style and permanency of brine stratification is best interpreted from the preserved depositional textures (Lowenstein and Hardie 1985; Warren and Kendall 1985). But there are some physical principles common to modern and ancient brine hydrologies. If a stratified brine column forms above a growing crystallisation surface, solar driven crystal growth of gypsum or halite in the bottom waters first slows then stops (Figs. 2.55b and 2.72). Once a water body is stratified, no solar mechanism is available to further concentrate the bottom waters. Subaqueous crystallisation can only continue in a stratified system in zones of brine mixing or bottom temperature change near subaqueous spring seeps. Once the freshened inflow ceased, ongoing evaporation concentrates the upper brine body until its density matches that of the lower brine body. The two water bodies then mix (holomixis) and crystal growth on the bottom can begin anew (Fig. 2.72). This type of holomictic bottom crystal precipitation, where the crystallisation surface

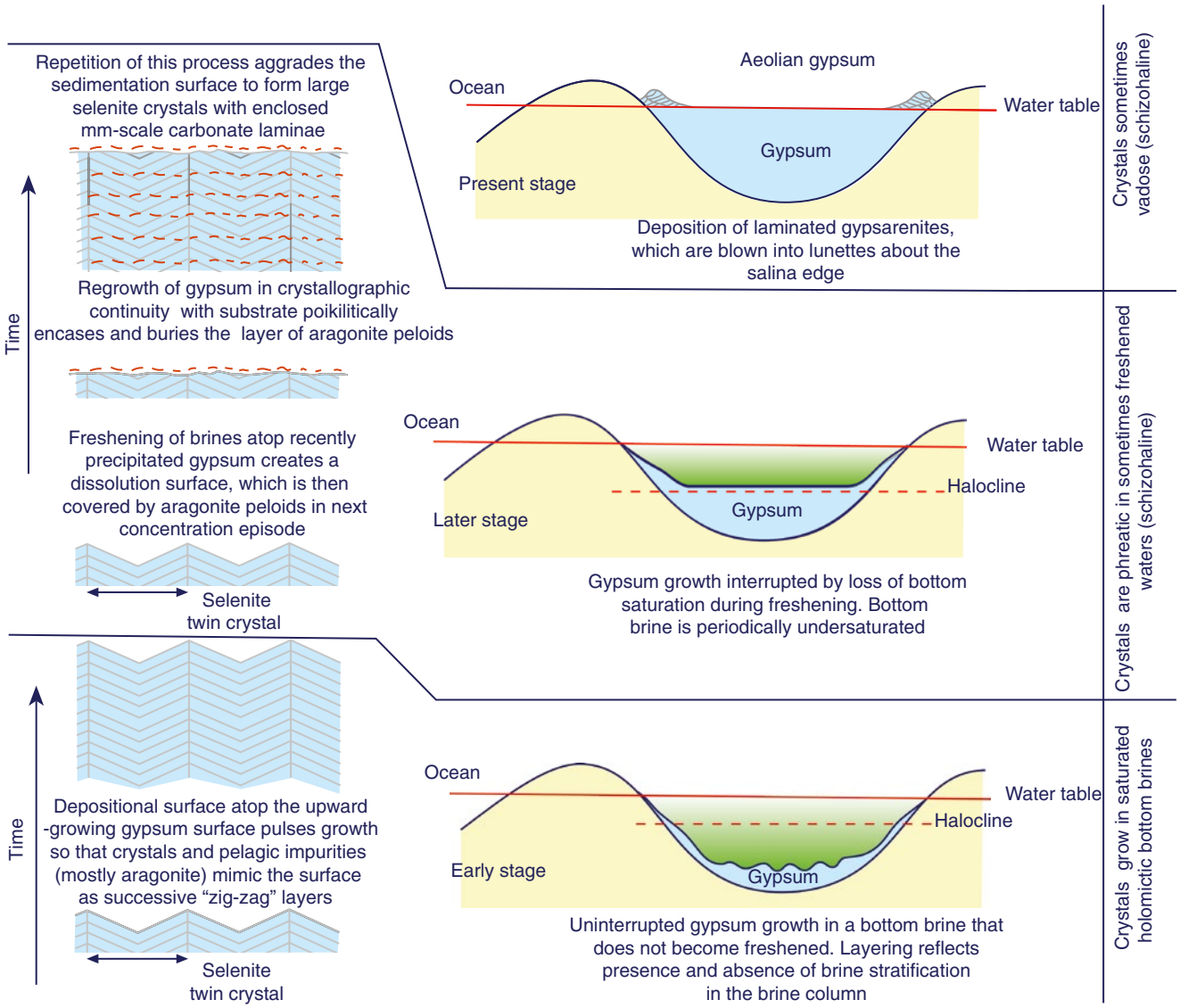

Fig. 2.72 Growth-aligned gypsum shows internal textures are controlled by the gypsum growth surface interacting with the stability and salinity of bottom brines. In the early stage of fill, when the brine lake is deeper, the bottom brines are stable and salinities do not ever decrease to where they become undersaturated with respect to gypsum. "Zig-zag" textures result. When the sediment surface aggrades to where bottom brines freshen, then the periodic dissolution of the upper part of the growth surface dissolves and mm-laminated textures form. The present stage of sediment fill is where the brine lake has been filled to equilibrium with the local watertable, eolian reworking of seasonal gypsarenite precipitates is the dominant mode of deposition (After Warren 1982b)

is never in contact with undersaturated bottom water, deposits layered euhedral growth-aligned crystal beds on the brine floor (e.g., chevron halite or aligned swallowtail gypsum; Fig. 2.72).

If, on the other hand, the freshened upper water body does come into contact with the crystallisation surface of the salt bed then subaqueous horizontal planation surfaces develop. Subhorizontal planation occurs both in saline basins subject to complete desiccation and in those parts of evaporite seaways covered by perennial brine sheets (tens of cm deep) that were subject to periodic freshening. A desiccation stage, followed by a freshened water flood, creates a near horizontal planation surface with intercrystalline karst, which marks a time when the watertable was lowered into the salt bed immediately prior to a subsequent freshening event (Fig. 1.46). In contrast, freshening of perennial bottom brine creates a horizontal planation surface atop the salt bed with little or no intercrystalline karsting (laminated coarse-grained gypsum in Marion Lake; Figs. 2.72, 4.6f).

In both cases the freshened surface water sheet only dissolves the uppermost portion of the salt bed, it does not displace the much denser pore brines that saturated the bulk of the underlying salt bed. A planation surface defines the top of saturated pore brines. Vadose karst in a desiccated salt pan

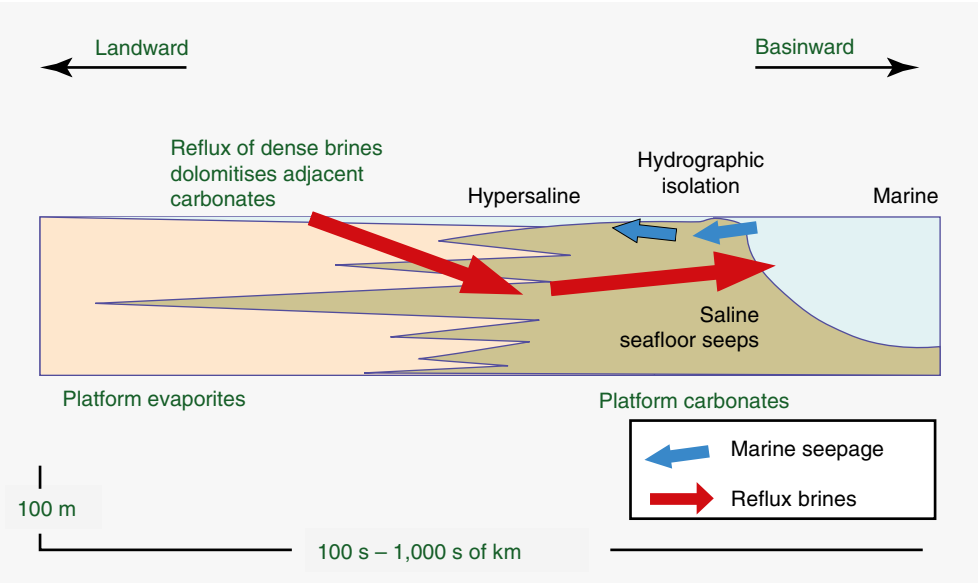

Fig. 2.73 Schematic illustrating the process of brine reflux creating secondary dolomite in a carbonate platform (After Warren 1991)

Table 2.17 Features associated with reflux dolomites

Evaporite unit proximity, geometry and position	Close spatial relationship of dolomite to evaporite sequences that can reasonably be deduced as being subaqueous in origin. Reflux dolomitised units should exhibit dolomitisation gradients, with increasing volumes of dolomite toward the source of refluxing brines. The stratigraphic, tectonic, and eustatic setting of the associated evaporites must be appropriate for the development of a barred base or lagoon.
Textures and hydrological preparation	The dolomitised reflux receptor units must have had high porosity-permeability, and suitable hydrologic continuity at the time of dolomitisation. Reflux dolomite crystal size are generally coarser than those found associated with sabkha sequences, because coarse receptor beds dictate fewer nucleation sites.
Geochemical gradient	While geochemical information relating reflux dolomite to evaporative pore fluids might be lost by recrystallization, gross vertical geochemical gradients, such as increasing Sr, Na trace elements, and stable isotopes enriched in ^{18}O toward the evaporative brine source might be preserved.

After (Moore 2001)

can only extend down to the top of this dense pore brine layer. Below it the pore brines are saturated, above it the waters are undersaturated or nonexistent.

These flat, laterally extensive dissolution surfaces typically truncate the tops of previously growing crystals, be they trona, halite, gypsum or any other bottom nucleating salt (Fig. 2.72). As the freshened water body begins to concentrate it may precipitate a less saline mineral phase, which settles onto the planation surface. It may also be the time when clays, formerly suspended in the floodwaters or blown in by the wind, begin to flocculate and sink through increasingly saline surface waters. As the freshened water body continues to concentrate into salinities that precipitate the dominant salt phase the aggrading crystals that underlie the planation surface can now poikilitically enclose the less saline precipitates (e.g., laminae of aragonite pellets in laminated coarse-grained gypsum; Fig. 2.72).

Brine Reflux Drives Substrate Alteration

Brine reflux occurs when ponded or concentrating holomictic brines atop the floor of an evaporitic seaway or lake become dense enough to displace underlying pore fluids and so percolate into the underlying succession so creating a brine curtain (Fig. 2.73). Descending brines can have chemistries that are supersaturated with different mineral phases to the matrix through which they are flowing and so drive various alteration processes such as dolomitisation, backreactions and pseudomorphing. It may also drive the precipitation of widespread authigenic K-feldspars in siliciclastic hosts at burial depths that are much shallower, and in authigenic stages much earlier than those of equivalent precipitates in non-evaporitic siliciclastics (Sandler et al. 2004).

One of the most widely recognized effects of brine reflux is the formation of dolomite in units underlying and adjacent to a thick evaporite sequence (Table 2.17). When evaporitic

carbonate or gypsum precipitates in hypersaline areas on such platforms, the surface brine densities are in the range 1.1–1.2 g/cc (Fig. 2.12b). Concurrent Mg/Ca ratios of the remaining brines rise compared with their seawater seep feed, and so dense Mg-enriched solutions sink through the underlying platform sediments. They displace connate pore fluids with densities around 1.03 g/cc and slowly seep basinward through underlying platform limestone aquifers. In this way large volumes of Mg-rich brine pass through previously deposited shelf limestones, precipitating dolomite both as a pore fill and as a replacement in the former shelf limestones (Fig. 10.29). The first evaporite-generated brine reflux model for ancient dolomites was by Adams and Rhodes (1960). Their model explained the dolomitisation of the Permian Capitan reef complex of West Texas; whereby backreef, shelf and lagoonal carbonates are intensely dolomitised, while the shelf edge and slope carbonates are not. They envisioned reflux dolomitisation through porous sediments to depths of several hundred metres below the brine source.

By the mid 1960s, seepage reflux dolomitisation as proposed by Adams and Rhodes had gained a large number of proponents working in ancient evaporite-associated dolomites (Hsu and Siegenthaler 1969) but needed, under the dictates of strict geological uniformitarianism prevailing at the time, to be verified in the Holocene (Warren 2000a). In 1965 Deffeyes et al. reported modern Mg-rich brines in a marine spring-fed gypsum salina (Pekelmeer Lagoon) on Bonaire in the Netherlands Antilles in the Southern Caribbean. From the water chemistry, they predicted that concentrated lagoonal brines should be sinking and forming reflux dolomite in underlying sediments. They observed micritic dolomite in Holocene lagoon muds beneath gypsum crusts but, with only a soft-sediment coring device to work with, could not penetrate the cemented Pleistocene base. Outcropping on the opposite end of the island, well away from the present lagoon, they located a dolomite replacing what they interpreted as Pleistocene lime-stone and inferred that this had formed during an earlier episode of brine reflux.

Lucia (1968) subsequently drilled beneath the Pekelmeer Lagoon and found no widespread dolomites in the underlying Pleistocene carbonates. He also found that porewaters were of normal marine salinity in areas where brine was predicted by a seepage reflux model. A thin clayey ash layer of generally low permeability was found forming a hydroseal that separated sediments below with normal salinity from lagoonal sediments with elevated salinity. Thus, reflux dolomitisation was not occurring beneath the lagoon. Springs supplying seawater to the salina were in areas where the ash bed was broken or missing and formed the terminations of flow pathways in the underlying Pleistocene/Pliocene (Murray 1969). For most of the year seawater seeps into the Pekelmeer springs driven by evaporative drawdown. However, during a short period in the late summer, the springs are inactive and the hydrostatic pressure on the landward side is greater than that on the seaward side. Murray concluded that return flow or reflux could occur at such times, but did not appear to do so with sufficient volumes of brine crossflow to form replacement dolomite.

The claim that the Pekelmeer was forming extensive seep-age reflux dolomites beneath an evaporite lagoon was further challenged when Sibley (1980) concluded that the solutions responsible for extensive dolomitisation in Tertiary sediments on Bonaire (dolomites that were earlier used as evidence for reflux dolomite) were probably fresh to brackish meteoric waters mixed with seawater, and were not derived by reflux of the modern Pekelmeer hydrology. Later work by Fouke et al. (1996) on dolomite in the Seroe Domi (Miocene), a unit more than 20 m thick that extends 115 km across the Nederlands Antilles, has reinforced Sibley's conclusions. However, Lucia and Major (1994) continue to argue for a significant input of marine/hypersaline waters during Neogene dolomitisation in the region.

There are, nevertheless, other islands in the tropics where localized brine reflux, associated with hypersaline conditions, is apparently forming local-scale Holocene dolomites. Müller and Teitz (1971) documented brine-reflux dolomite replacing earlier carbonate cement in skeletal grain-stones on the shoreline in Fuerteventura in the Canary Islands. Kocurko (1979) found brine-reflux dolomite a few metres above the high tide line, in the spray-zone pools of the shoreline of San Andres, Columbia. Aharon et al. (1977) described small volumes of reflux dolomite forming in Holocene sediments of Solar Lake. Thin, localized brine-reflux dolomites can also be found about the present-day edges of Ras Mohammed on the Sinai Peninsula (Chap. 3). It seems small-scale examples of brine reflux dolomites exist, but pale in comparison to obvious and extensive reflux dolomites of the past.

Hydrological modelling of ancient reflux systems by Shields and Brady (1995), using very conservative assumptions of brine head and drawdown, show that reflux can explain platform dolomites within geologically realistic time frames of burial (Fig. 2.74). Their flow model used flow lengths varying from 1 to 1,000 km and the relative densities of seawater and brines of two end member compositions (Fig. 2.74a): brine 1 is anhydrite-saturated (density $\rho = 1{,}120$ kg/m^3) and brine 2 is halite-saturated ($\rho = 1{,}200$ kg/m^3). Brine 1 is approximately 9.3 % denser than seawater ($\rho_{seawater} = 1{,}024.5$ kg/m^3), and brine 2 is 17.1 % denser. Using a 100 m tall and 1 m wide flow cell (Fig. 2.74b), brine 1 has approximately 9.3 m more hydraulic head than a comparable column of seawater, while brine 2 has a differential hydraulic head of 17.1 m. Shields and Brady (1995) assume a pure calcite precursor and a final product that is 100 % dolomite with 7 % porosity; this requires 350 kg/m^3 of magnesium. The results (Fig. 2.74c) show that reflux flow could circulate the

a

Flow length (km)	Volume of slice (m^3)	Required Mg (kg)	Required volume (m^3)	
			Brine 1	Brine 2
① 1	1×10^5	3.5×10^6	5.19×10^6	2.59×10^6
② 10	1×10^6	3.5×10^7	5.19×10^7	2.59×10^7
③ 100	1×10^7	3.5×10^8	5.19×10^8	2.59×10^8
④ 1000	1×10^8	3.5×10^9	5.19×10^9	2.59×10^9

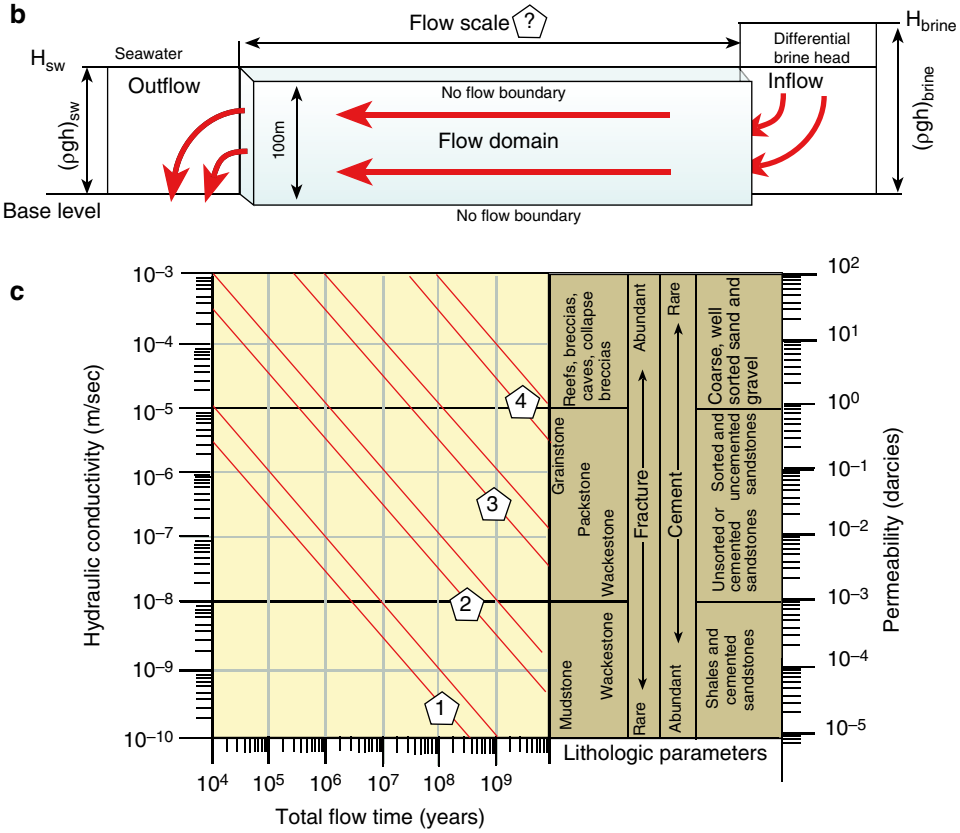

Fig. 2.74 Dimensional analysis of seepage reflux (After Shields and Brady 1995). (**a**) Table of brine properties and amount of Mg required to covert calcite to a dolomite with 7 % porosity. (**b**) Dimension of slice model used in their calculations. Slices are similar except that flow length varies from 1 to 1,000 km. Base level is 100 m in all cases and head drops are 9.3 m for anhydrite saturated brine 1 and 17.1 m for halite saturated brine 2. (**c**) Dimensional analysis of Darcy's Law for a regional brine reflux system with 100 m base level. *Diagram* illustrates the time necessary for the minimum volume of dolomitizing brine to flow through a rectangular slice. All slices are 100 m thick and 1 m wide with varying flow lengths (1–4). It is assumed 350 kg/m^3 of Mg are required to dolomitise the block. The *lower curve* for each flow path represents brine at halite saturation with a Mg exchange efficiency of 47 %. The *upper curve* represents brine at anhydrite saturation with a Mg exchange efficiency of 36 %. Permeability conversions assume an average brine density of 1,160 Kg/m^3 and a viscosity of 8.904×10^{-3} kg/(m/s) and a temperature of 40 °C

Mg necessary to completely dolomitise carbonate platforms with radii of a few tens of km in a few million years. Shelves with shoreline to basin distances of the same order can be completely replaced in a similar period. Larger platforms require more time or that the evaporite recharge areas migrate with time. Carbonate platforms tens to several hundred kilometres across could be dolomitised by such epeiric hydrologies.

The relative abilities of rocks to transmit brine will control where the bulk of the fluid flux occurs within platform limestones of any age. It is unrealistic to think of reflux dolomitisation as a homogenous process uniformly overprinting all platform lime-stones. The inherent permeabilities of the various precursors clearly play an important role in dolomite intensity. The most permeable lithologies beneath the evaporite lagoon will focus the bulk of flow as the brine seeps seaward. Whatever unit acts as the aquifer at the time of reflux will also be the subject of the most intense dolomitisation. High permeability units within flow paths of tens to hundreds of kilometres can channel the volume of necessary brine in time frames ≈1 Ma. Such high permeability units also have the potential to be dolomitised in regions well removed from the brine source.

Jones et al. (2002) has shown that the effects of a single 100,000 year platform evaporite episode can generate a reflux plume that persists for as long as 10 Ma in underlying carbonates before it is once again displaced by geothermally driven brines (Fig. 2.75). They call this long term effect "latent reflux," it documents a hydrological situation where the effects of a sinking reflux brine persist long after the at-surface

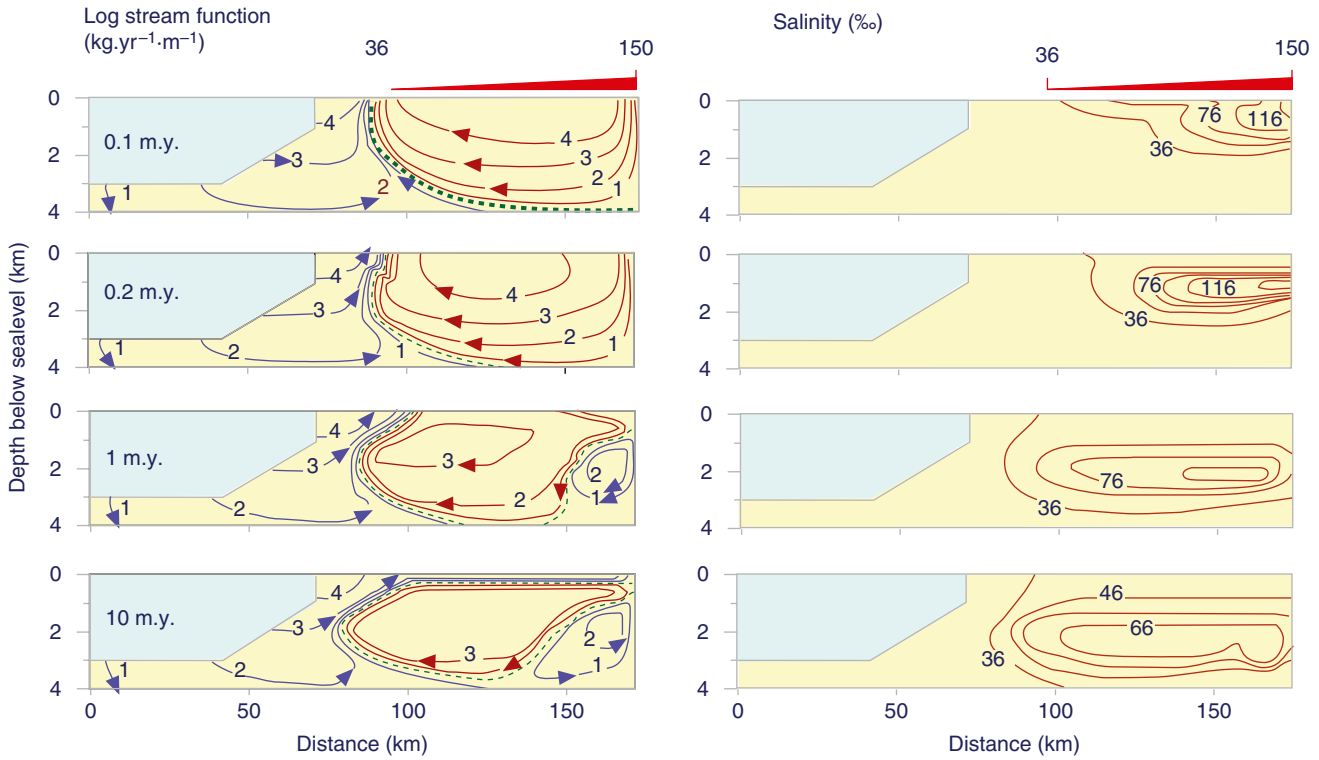

Fig. 2.75 Evolution of groundwater circulation and salinity persists for as much as 10 Ma. after a single reflux event at gypsum saturation which lasted 0.1 Ma. *Dashed line* in the stream-function plots represents interface between geothermal and reflux and latent reflux. Only the upper 4 km of platform is plotted; vertical exaggeration = 9 (After Jones et al. 2002)

brine lake or seaway has disappeared. The modelling utilised a single depositional episode and a surface brine at gypsum saturation (150‰). They went on to note that higher salinity waters and longer episodes of evaporite precipitation would generate more widespread and longer acting brine plumes in the underlying sediments (Jones and Xiao 2005). In this context it is interesting that dolomite is forming today in the slope sediments of southern Australia from marine-derived reflux brines with elevated salinities (Rivers et al. 2012).

Detailed mapping of dolomite distribution across the Permian Capitan shelf, the type area for the brine reflux model, clearly shows reflux works in ancient evaporitic platforms (Melim and Scholle 2002). Dolomite extent is greatest beneath and adjacent to the drawndown lagoon facies. In contrast, dolomite distribution through the Capitan reef and into the forereef outlines the distribution of those brine aquifers that were more active at the time of brine reflux, namely fractures and fore reef debris aprons. Aquifers carrying the descending brines out into the adjacent basin were dolomitised, while tighter aragonite-cemented intervals between aquifers were largely isolated from the flushing brines and so remained undolomitised. Garber et al. (1990) used a similar model of reflux but called upon bittern brines, derived from the very saline Salado Formation, to explain magnesite, not dolomite, distribution in the same basin. They argued that when a brine has a Mg/Ca ratio >40 it will precipitate a magnesite replacement rather than the more commonly observed dolomite. Similar reflux processes, driven by the deposition of Zechstein evaporites, may have precipitated authigenic magnesite cements in siliciclastic dune sands of Rotliegende reservoirs in the North Sea (Purvis 1989).

Reflux dolomitisation in a platform setting can often be distinctive, even in core, as the intensity of total dolomitisation decreases the further down core or laterally one moves from the evaporite-carbonate contact (Fig. 2.76). If not completely re-equilibrated during later burial dolomitisation, the oxygen isotope signatures in platform dolomites formed by reflux typically follow a lightening trend away from the evaporite unit; that is, the further one moves from the contact, the less was the sediment's isotopic signature influenced by the heavier reflux-derived brines. If the sediments are not extensively recrystallised by later burial dolomitisation, trace elements, along with strati-graphic position, can give another clue to a reflux association. In a study of dolomite from Neogene to Permian age, Sass and Bein (1988) found that evaporative dolomites associated with gypsum/anhydrite tend to show 50–57 % $CaCO_3$ and the highest levels of sodium (up to 2,700 ppm). Marine nonevaporitic subtidal dolomites have a similar range of compositions, but sodium concentrations of only 150–350 ppm.

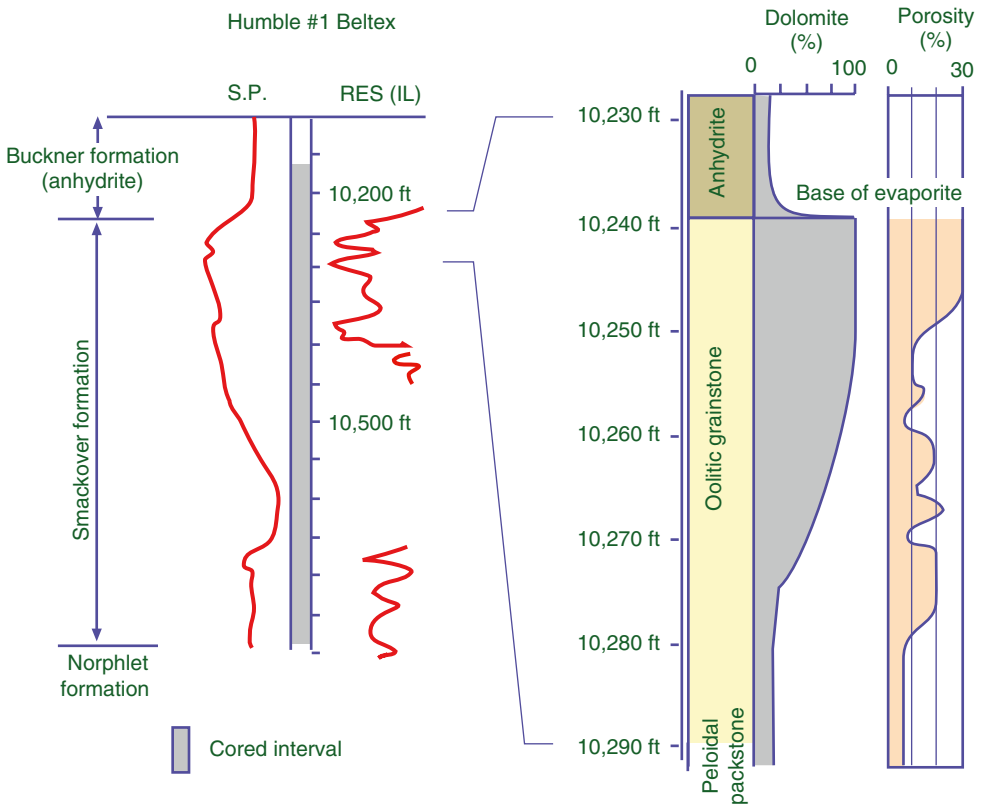

Fig. 2.76 Wireline signature and the interpreted core description of the Humble #1 Beltex Well, Bowie County, Texas. Shows a close relationship between Buckner anhydrite and dolomitisation in the underlying Smackover Formation. Note changes in proportion of dolomite and porosity in terms of proximity to evaporite contact (After Moore et al. 1988)

The present may be the key to the past, but it is simply not a good time to document depositional or diagenetic analogs for ancient platform and basinwide evaporites, nor their associated reflux hydrologies. There are no modern depositional counterparts to most types of ancient marine-platform and basinwide evaporites, hence there are no modern counterparts to brine-reflux dolomites (Chap. 5). Holocene evaporites are accumulating within an "icehouse" climatic phase. The current "icehouse" mode, typified by waxing and waning polar icesheets, has dominated the earth's climate for the last 12 Ma. "Icehouse" times, with their high frequency sealevel oscillations, are not conducive to the formation of thick platform evaporites. In contrast, "greenhouse" time, with their inherent lack of polar ice sheets and low amplitude sealevel changes, favour the formation of platform evaporites and hence widespread reflux dolomitisation of platform carbonates. Basinwide evaporites and their associated dolomites form via tectonic controls on basin isolation that are independent of "icehouse versus greenhouse" sealevel scenarios.

Most brine reflux models published to date utilise a platform evaporite setting typically tied to saltern anhydrites. Examples include: the Cambrian Ouldburra Formation in the Officer Basin, Australia (Kamali et al. 1995); the Devonian Birdbear (Nisku) Formation of Canada (Whittaker and Mountjoy 1996); Pennsylvanian platform carbonates of West Texas (Dickson et al. 2001); the Lower Permian Abo-Tubb (Hartig et al. 2011); Permian San Andres Formation, USA (Leary and Vogt 1986; Ruppel and Cander 1988; Elliott and Warren 1989); the Permian Tansill and Yates Formations of the Central Basin Platform, USA (Andreason 1992; Garber et al. 1990); the Upper Permian Changxing Formation and the Lower Triassic Feixianguan Formation of the NE Sichuan Basin, China (Jiang et al. 2013); the Jurassic Smackover and Haynesville Formations of the Gulf of Mexico (Moore et al. 1988); the Lower Cretaceous Edwards Formation of Texas (Fisher and Rodda 1969) and the Middle Palaeocene Beda Formation, of the Sirt Basin, Libya (Garea and Braithwaite 1996). Hydrological geometries of reflux dolomite associated with drawdown basinwide settings are different and are discussed in Chap. 5 after the various styles of saline giant are presented, while a number of oil field examples are discussed in detail in Chap. 10.

As well as long term effects in underlying carbonates, reflux also has significant syndepositional effects on nearsurface salt beds. Sinking supersaturated brines force backreactions and replacement processes in salt beds immediately beneath an evolving brine body. Hovorka (1992) recognised reflux of halite-saturated brines through gypsum beds as the dominant control in the formation of halite pseudomorphs of subaqueous gypsum (Figs. 1.49 and 2.77). The replacement process is driven by the fact that gypsum precipitation is favoured by low temperatures and low salinities, while anhydrite precipitation is favoured by higher temperatures and higher salinities. At the warm temperatures that typify

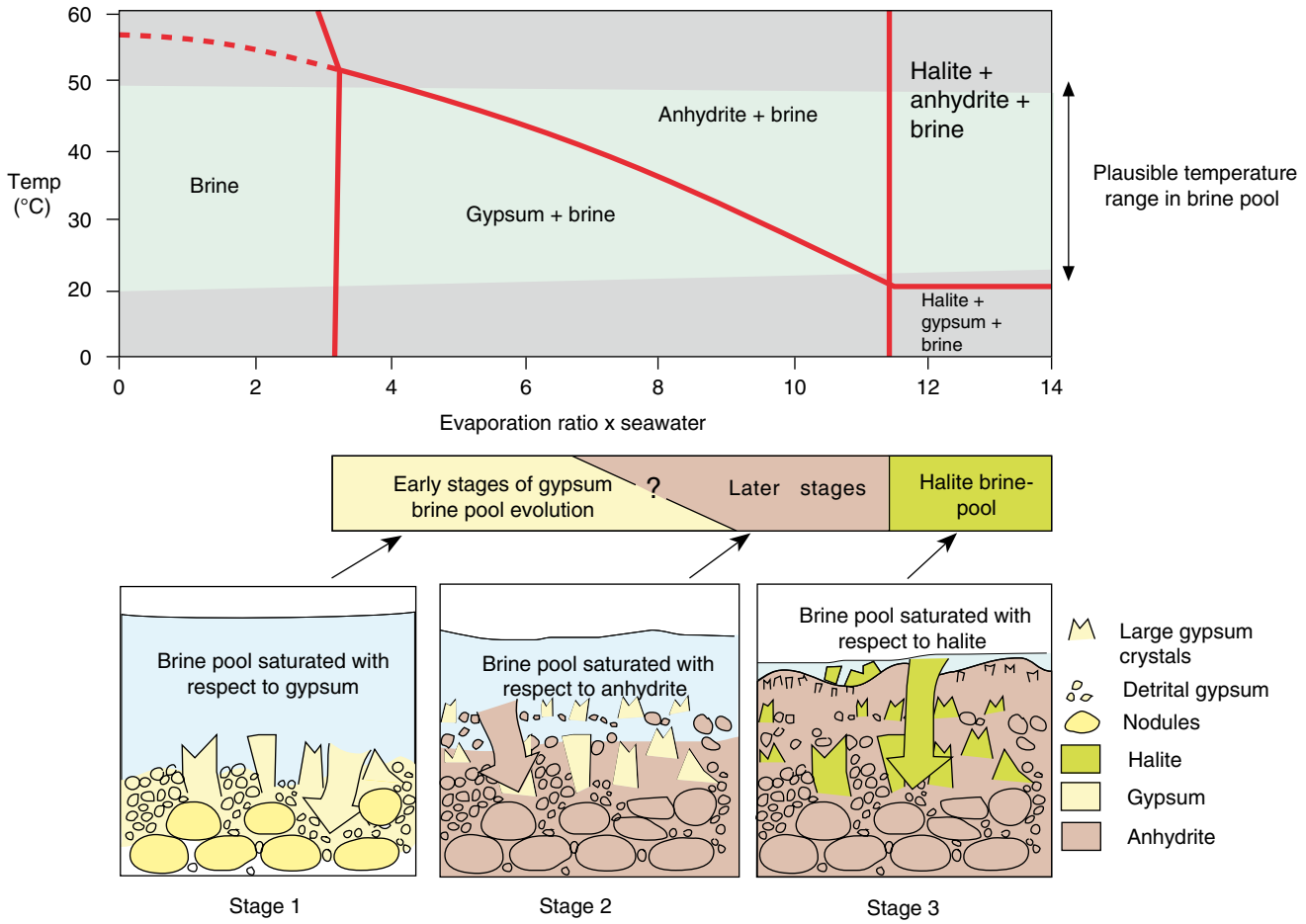

Fig. 2.77 Gypsum replacement by halite during brine reflux. *Upper part* shows phase relationships between gypsum and anhydrite in NaCl brine. *Lower part* shows how the alteration and replacement is dependent on the evolution of the overlying brine supplying waters that are refluxing through the gypsum bed. *Stage 1*: Large gypsum crystals grow vertically from the floor of the brine pool, and gypsarenite accumulates between the crystals. Gypsum is stable in diagenetic fluids concentrated three to approximately six times seawater concentration: alteration to form nodules occurs in shallow subsurface environments. *Stage 2*: As salinity increases from six to ten times seawater concentration, gypsum continues to precipitate metastably, but is dehydrated to thermodynamically stable anhydrite in the shallow diagenetic environment. *Stage 3*: When the brine pool evolves to concentrations about ten times seawater concentration, halite begins to precipitate. Halite-saturated brines introduced into the shallow burial environment dissolve any remaining gypsum and replace it with halite (After Hovorka 1992)

modern low-latitude brine pools (25–50 °C), the gypsum-to-anhydrite transition is predicted to occur somewhere between the initial precipitation of gypsum and initial precipitation of halite. In contrast, brines at halite saturation are undersaturated with respect to gypsum, while saturated with respect to halite. Textural relationships in such settings, where bottom-aligned gypsum is replaced by halite, are shown to be controlled by nearsurface diagenesis and related to brine pool evolution (Hovorka 1992).

During Stage 1 the perennial brine body is four to six times the concentration of seawater and is at gypsum saturation (Fig. 2.77). In stage 2 brines are at the upper end of the calcium sulphate field (6–10× seawater) and are in the anhydrite stability field. Metastable gypsum continues to precipitate on the brine pool floor, but reflux of this brine converts gypsum to nodular anhydrite. By stage 3 the surface brines lie in the halite saturation field (>10–11× seawater) so that halite is precipitating on the floor of the brine pool. The refluxing brine is now undersaturated with respect to gypsum so that it is dissolved in the shallow subsurface and the resulting voids are filled by halite cements. This replacement process is thought to take place in the first few metres of burial, but like reflux dolomite has yet to be documented as more than a localised process in a Holocene gypsum deposit. As thick halite beds are tightly cemented by 100 m of burial, surface-driven brine reflux and associated backreactions in ancient salt beds are most intense in the first few tens of metres of burial.

In a related paper Schreiber and Walker (1992) argue that pseudomorphous replacement of gypsum by halite at the transition between bedded sulphate and chloride documented by Hovorka (op. cit.) in cyclic evaporite sequences of

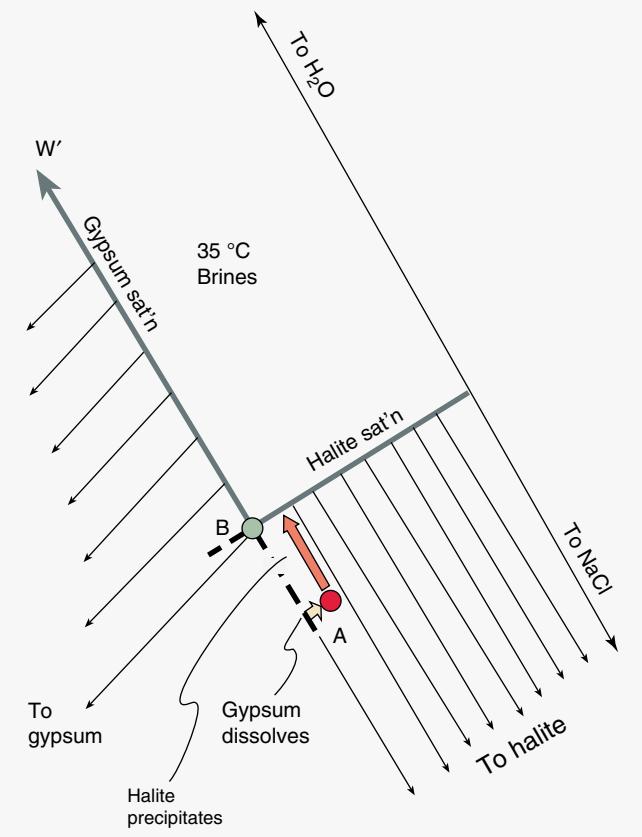

Fig. 2.78 Salient features of the metastable gypsum-halite phase curves at 35 °C (After Schreiber and Walker 1992). A co-saturated brine, as plotted at A from 50 °C when entering the 35 °C environment will be out of equilibrium. Gypsum must dissolve and halite must precipitate in order to move brine A composition to equilibrium at B

Permian age is an early diagenetic reflux process. But they argue it is a thermal disequilibrium process and cannot be directly tied to simultaneous conversion of gypsum to anhydrite (Fig. 2.78). They argue that in solar salt ponds, hot brines at halite saturation are undersaturated in gypsum and oversaturated in halite with respect to the cooler, previously accumulated gypsum substrate. This is what causes the halite to replace gypsum when suitably hot brine is in contact with the substrate. If this is the mechanism driving replacement it too would take place at or very close to the sediment brine interface.

Solar heating of the brines and production of porosity within the gypsum crystals, both of which are key features of the replacement mechanism suggested by Schreiber and Walker (1992), are materially aided by red pigments from halophilic activity (see Chap. 9). If this is the mechanism driving replacement then it cannot be related to the large-scale transition of gypsum to anhydrite (as argued by Hovorka 1992). Diluted brines created by the replacement of gypsum by anhydrite would corrode halite rather than precipitate it. Modern examples of a thermally driven replacement process are rare, perhaps because the appropriate brines are decanted for commercial collection of halite and are not allowed to backreact.

Can Reflux Really Work?

Some have argued that brine reflux cannot be a geologically significant process because we do not see modern marine brines capable of displacing substantial volumes of pore waters at sufficiently rapid rates to drive brine reflux. Rather the deposition of bedded salt creates a "hydroseal" (discussed in Chap. 5). I have just stated and will argue in detail in Chaps. 5 and 10, that marine-fed reflux dolomite is not a widespread process in today's marine platforms but is a significant process in ancient evaporitic settings.

Today's carbonate platforms are characterised by laterally discontinuous buildup geometries. They are a response to high-amplitude high-frequency eustatic signals of the current icehouse climate mode whereby continuous reef rims and shoals do not form. Subsealevel marine seepage inflows into an isolated platform lagoon, and consequent reflux of dense brine is impossible in the hydrologies of icehouse mode carbonate shelves. Likewise, there is nowhere on the world's surface today where large subsealevel marine basin floors are hydrographically isolated from the ocean, so no basinwide evaporites and reflux dolomites are accumulating in modern examples of this setting. But the viability of reflux hydrology and its ability to quickly drive brine descent into underlying strata can be seen in modern continental systems where man has interfered with natural hydrologies and created saline hydrologies in regions where there were none before. This is perhaps our best set of hydrological analogs to characterise modern counterparts of the hydrologies of ancient platform and basinwide evaporite systems.

One of the best examples comes from Owens Lake, California, where the water needs of the City of Los Angeles converted a moderately saline perennial lake (salinity ≈90‰) into a hypersaline pan accumulating bedded halite and trona. Starting in 1913, the streams that fed the Owens River, which in turn fed Owens Lake, were diverted by Los Angeles Department of Water and Power to feed the Los Angeles Aqueduct. The lake level started to drop quickly and by 1924 the lake had completely dried out. Prior to this the lake was saline, but perennial.

In order to study the Quaternary history of the lake, the US Geological Survey collected a 323 m long core from the lake (Bischoff et al. 1993a). The core encompasses the last 800,000 years of basin fill and was analysed for water content, pore water salinity, sulphate and chloride values (Fig. 2.79). Water content, a measure of compaction, varies erratically down the core, generally decreasing from about 60 wt% at the top to about 20 wt% at 240 m (Bischoff et al. 1993a). Below

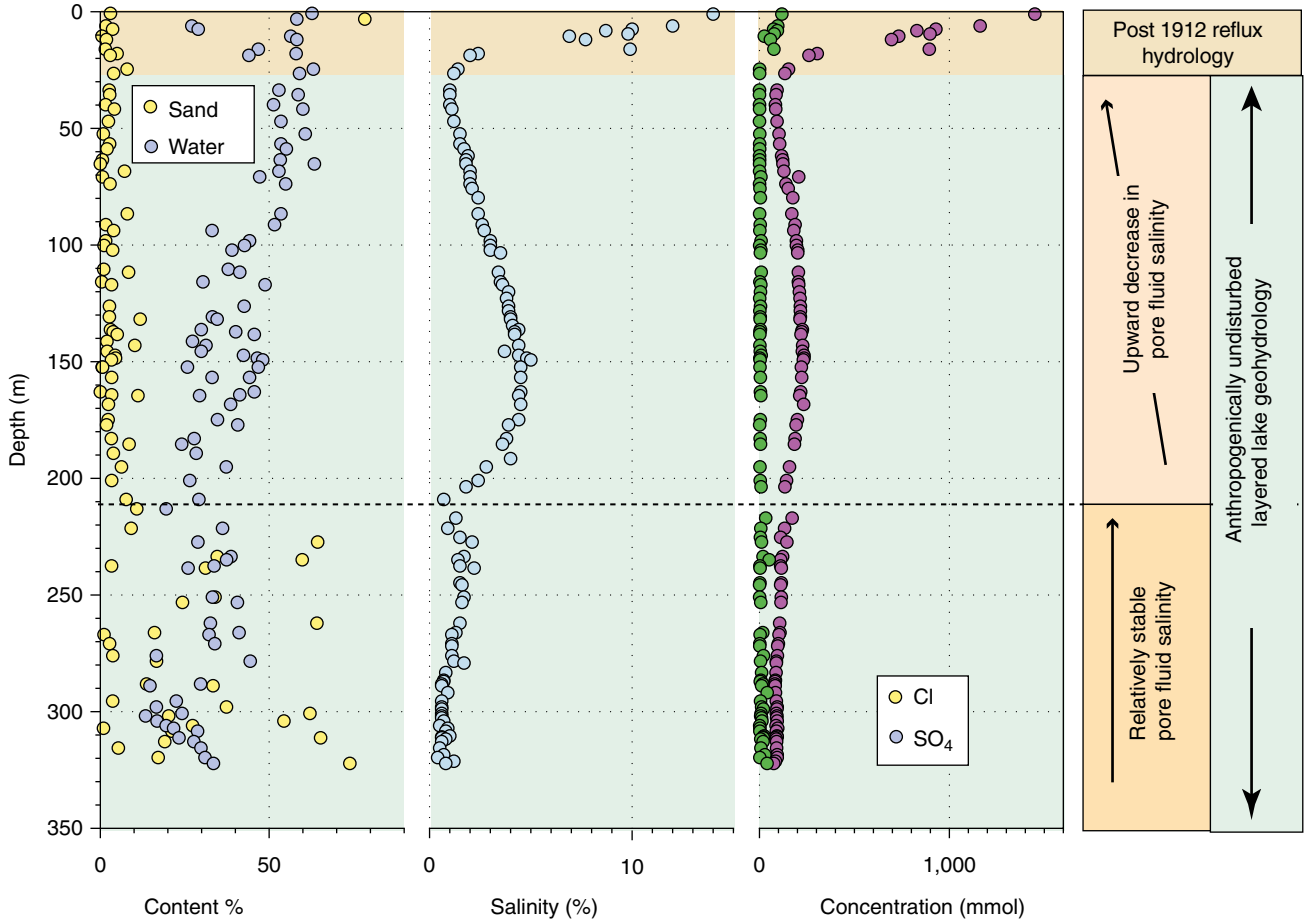

Fig. 2.79 Core OL-92 a 327 m core collected in Owens Lake, California (See also Fig. 2.10). Shows depth plots of sand and water content (%), salinity (%), chloride and sulphate content (mmol) of pore waters squeezed from the core (Replotted from data in Table 1 in Bischoff et al. 1993a)

1,200 m and to the bottom of the core the water content sharply maintains levels of less than 50 % by weight. This zone is characterized by an increasing abundance of sandy units, which are less subject to dewatering-related compression. Salinity varies with depth in a smooth pattern, with a minimum at 30 m, gradually increasing to a single broad maximum at about 150 m depth, and sharply declining thereafter to steady low values at 210 m and below.

The salinity of the modern lake prior to diversion of the Owens River, was about 9 % (Bischoff et al. 1993a). Assuming that similarly elevated salinity characterizes previous interglacial times when Owens Lake was the terminus to the Owens river, and that fresh waters must have characterized the glacial periods of intense overflow, expect about eight salinity oscillations during the past 800 kyr time span of the core. Such cycles are seen in the solid components of the sediments, particularly for carbonate and organic carbon content (Bischoff et al. 1993a) indicating the lake did indeed experience such climate changes. Yet the salinity-depth profile has been drastically smoothed by post-depositional diffusion of dissolved salts. This is not a hydrologically closed system.

Remnant water, a leftover from the last glacial is the likely explanation only for the first salinity minimum seen at 30–40 m depth (Bischoff et al. 1993a). The smooth and gradual increase of salinity in the older sediments below this depth to a maximum at about 150 m is likely the result of diffusional smoothing of waters of older cycles. Diffusion should have had more than sufficient time, therefore, to smooth salinity gradients even lower in the core. The abrupt and erratic decrease of salinity from 150 to 210 m depth, and the erratic and generally low salinities from 210 to the bottom of the hole points to an open throughflow system for the basal pore fluids. The most likely explanation for this pattern is that deeply circulating fresher waters are actively moving through the sandy units below 200 m, diffusionally harvesting solute from the overlying fine-grained sediments in the process. Thus ground water is moving at different velocities in the varyingly permeable sandy units. A diffusional steady state and smoothing of the salinity gradients has not been achieved. This particular depression in the Basin and Range province of the USA, is in the type region for what has been argued are “hydrologically closed” lake systems, clearly is

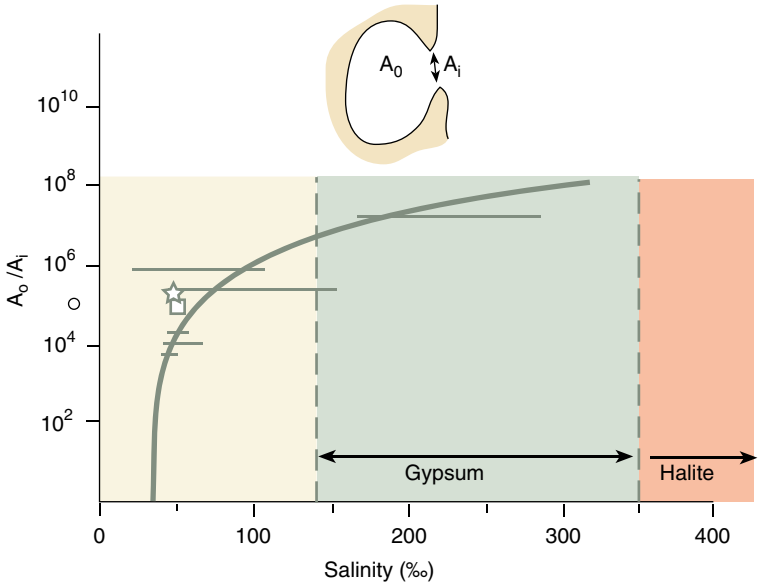

Water/brine body	A_0/A_i
Red Sea □	3×10^4
Arabian (Persian) Gulf ☆	1×10^5
Shark Bay	2×10^4
Laguna Madre	9×10^5
Karaboguz Gol	2×10^7
Danakil Depression	No surface inlet
Lake MacLeod	
Lake MacDonnell	
Hutt Lagoon	
Dead Sea	
Lake Asal	

Fig. 2.80 Relationship between the ratios of the cross-sectional area of a surface inlet (*Ai*) and the surface area of the associated hypersaline basin (*Ao*) plotted against salinity in the basin, with examples from several modern evaporitic depressions. Note that Quaternary examples that are accumulating substantial evaporite beds have no surface connection and are fed either by continental inflow or by marine seepage (Modified from Lucia 1972; Handford 1991)

not. It is leaking waters vertically and laterally at a rate sufficient to smooth any former climatic layering.

But what is most impressive in the lake's hydrology is what has happened in the upper 20 m in the last 80–90 years (Fig. 2.79). The pre-1900 waters of Owens Lake had a salinity less than 9 %, the lake was alkaline and probably had a pH ≈9–10. The extremely high salinity of the top 20 m is not a reflection of the pre-1912 natural lake. Rather, it is a consequence of river diversion and almost complete desiccation of the lake basin since 1924, and the associated downward migration of dense residual-brines (Bischoff et al. 1993a). As the post-1924 lake dried out, Na-carbonate minerals precipitated to form a 1–2 m thick salt bed now covering the lower parts of the lake depression. Residual brines from the salt bed were denser than the underlying 9 % pore water and were also relatively enriched in Cl. Modern brine percolated downward by gravity displacement and ionic diffusion, so that high salinity pore waters now dominate down to about 15–20 m.

Reflux brines derived by the accumulation of 2 m of bedded salt have penetrated some 20 m of relatively fine-grained water-saturated sediment in 80 years. The original now-displaced pore waters had a salinity up to three times that of seawater and so would have been more difficult to displace than seawater brines in an ancient carbonate platform undergoing reflux, which would have had salinities around 3–4 %. Clearly once a holomictic bedded salt system has formed, associated reflux is rapid and ongoing. What is more, the total system leaks water and brine at all levels in the cored hydrology. It possesses an open hydrological base to the lake depression even though the underlying nonevaporite sediments are more than 90 % clay. Reflux rules the upper portions of the hydrology, deeper artesian circulation rules the lower part of the hydrology. It is a small, but temporally impressive, example of the hydrological processes that would be active in ancient drawndown platform or basinwide evaporite settings (Chap. 5).

Importance of Hydrographic Isolation

Modern continental lacustrine evaporites accumulate in underfilled endorheic or hydrographically closed basin hydrologies. Likewise, modern marine-fed evaporite basins like Lake Macleod, Lake Asal and Marion lake require complete hydrographic isolation from the ocean and a subsea-level water surface in order to maintain the required throughput/seepage of brine (Chaps. 3 and 4; Nunn and Harris 2007). In Chap. 5 we shall see that both basinwide and platform evaporites are a response to underfilled marine-seepage hydrologies.

I use the term hydrographic isolation as distinct from the groundwater connection, which dominates in all evaporite-accumulating depressions. Lucia (1972) studied the interrelationship between maximum salinity in a modern evaporite basin and the basin's water balance (water loss versus gain). He showed that for marine-fed halite to precipitate any surface inlet from the ocean must be at least one hundred million times smaller in cross-sectional area than the surface area of the basin; for gypsum it must be at least a million times smaller (Fig. 2.80). That is, any basin accumulating

thick beds of halite effectively lacks a continuous surface connection to the ocean or other standing body of brackish water.

The nature and driving processes that bring about hydrographic isolation are contentious, in the most recent example we have to study, the onset of Messinian salinity crisis in the Mediterranean, most authors would agree it was driven by tectonic uplift creating inflow restriction. The final nail in the coffin that created complete hydrographic isolation was probably eustatic. Possibly, gypsum began to form in the more isolated parts of the circum Mediterranean before the complete cutoff of Atlantic and Tethyan surface inflow, but halite is a response to complete isolation.

In a theoretical consideration of the passage to cutoff in the Mediterranean and loss of exchange with Atlantic waters, Meijer (2012) concluded that the response of Mediterranean basin salinity to strait depth, strait width, and relative thickness of the outflow layer (return of Mediterranean water to the Atlantic) was highly nonlinear. For a strait width on the order of kilometres, an asymptotic rise in basin salinity occurs when the strait depth is on the order of a few tens of metres. Completely blocked outflow takes place when the depth is reduced to metres. The nonlinear nature of the system implies that even a slow gradual reduction in the sill depth leads to an event-like rise in basin salinity. For values of basin salinity approaching gypsum saturation, the response of the basin to changes in the strait depth is significantly delayed in the order of several thousand years. Nunn and Harris (2007) came to similar conclusions in terms of the lack of a need for spillover and the dominance of marine seepage, not hydrographic connection, in the formation of the Aptian salts in the Circum Atlantic and the thick salts of the west Siberian basin.

Maiklem (1971) in a study of evaporative drawdown in the Elk Point Basin of Canada showed that, once it was hydrographically isolated from the ocean, the Devonian Pesqu'ile barrier it did not have sufficient transmissivity to prevent evaporative drawdown, even with permeability of 73 darcies. Kendall (1989) recalculated Maiklem's figures using more realistic values of 0.9–2.7 darcies for permeability in the barrier and concluded that evaporative losses were as much as 200–800 times greater than the rate of supply. Any saline giant precipitating bedded salts is subject to evaporative drawdown and seepage influx of marine-fed phreatic waters. A corollary is that at the time of thick evaporite precipitation there is a correlative unconformity or hiatus forming in the adjacent nonevaporite lithologies that make up the surrounds of the hydrographically isolated depression.

An evaporite basin capable of accumulating thick salt beds is always located in a large isolated depression where at the onset of drawdown more water is being lost by evaporation than entering as seepage inflow and runoff (Nunn and Harris 2007). The water level in the basin is drawn down until the volume of water lost equals the volume of inflow (hydrologic equilibrium). A potentiometric gradient (elevation head) then exists between the level of water in the basin and its surrounds, so that by definition an evaporite basin must be an underfilled basin. Such large deep holes in the landsurface attract not just marine seepage, but also ground and formation water seepage from beneath areas adjacent to the hole. In a drawndown saline-giant basin, with a predominantly marine source, the seawater enters mostly as resurging brines through springs in the basin floor. In a saline lake fed by nonmarine water, the water enters by a combination of occasional storm runoff and rainfall, as well as by groundwater and hydrothermal springs (Chap. 4).

Water ponded in an evaporitic depression must remain at the surface or reside just below the land surface in the realm of capillary evaporation. Otherwise, thick sequences of bedded salt could not accumulate, parent waters would seep away before attaining salinities high enough to precipitate salts. In a hydrological setting where the saline watertable is rising into a previously vadose environment, the first salts typically precipitate as a capillary cement in previously nonevaporitic sediments of the basin floor. This is the typical situation in marine transgressions and it characterises evaporite accumulation in marine-fed Holocene coastal salinas without a hydrographic connection to the ocean. It is also the hydrology of their larger scale counterparts in subsiding rifts and intracratonic sags where rising relative sealevels force a marine-fed seepage hydrology into a previously continental depression. It also characterises Quaternary continental lacustrine transitions from a dry mud-flat or sandflat into a saline pan or perennial saline lake and can be driven by a change to a more humid climate in an arid nonmarine basin.

In a hydrological situation where a previously marine basin becomes a marine-fed depression, the basin waterlevel falls. It is drawdown once the basin-centre or platform lagoon becomes hydrographically isolated from the ocean. Now the water level falls and surface water concentration increases to where dense saline brines begin to sink into the underlying succession. The water level will fall until the volume of water lost from the basin by a combination of evaporation and reflux leakage equals the volume entering by influx seepage of marine and continental waters. Hydrological equilibration in some basins occurs at gypsum saturation, in others at halite saturation. In some basins it occurs when the water level is a water surface and subaqueous evaporites accumulate. In other basins it does not occur until the water level falls below the surface of the sediments and evaporitic mudflat deposition dominates.

Hydrographic isolation drives the formation of marine-fed platform evaporites where a fourth order sealevel fall occurs during a 3rd order rise and it also dominates in basin-wide evaporite deposits formed in soft-collision continent-continent suture belts (Chap. 5). It also occurs in continental

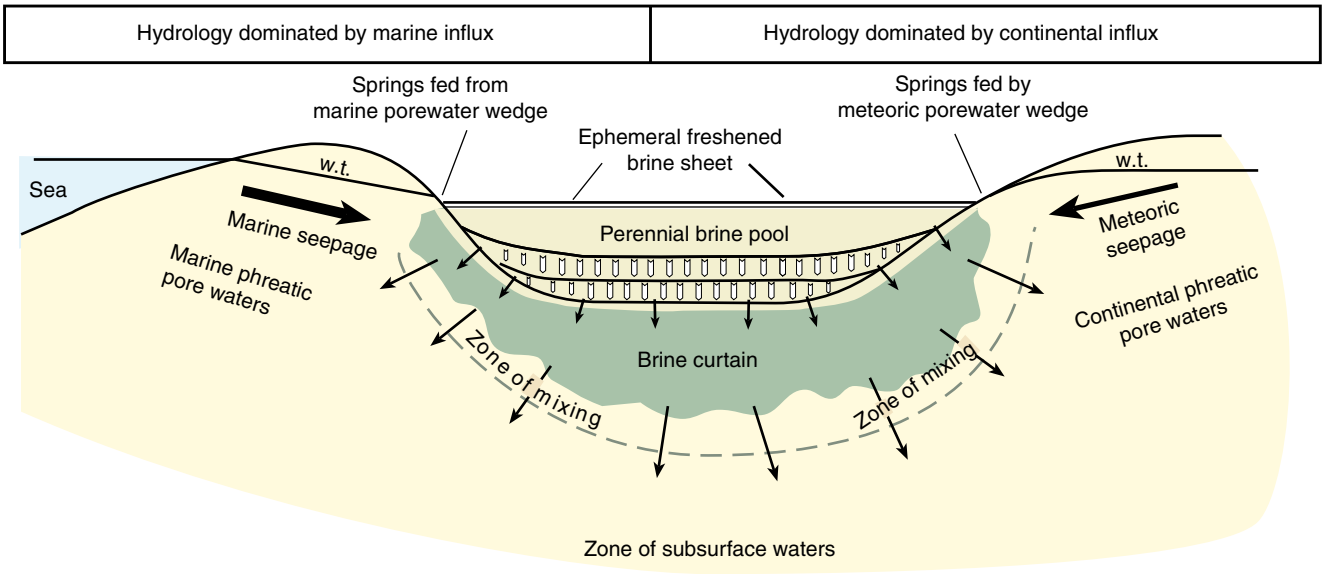

Fig. 2.81 Schematic of a brine curtain in a marine-fed and a meteoric-fed evaporitic setting (V:H ≈ 10:1). Once established the brine curtain is actively maintained by ongoing evaporation and reflux, as well as by the relatively impervious nature of the salt bed (highly effective aquitard). It is difficult to displace the curtain via influx from the margin of less-dense marine or meteoric waters. These tend to float out over the saline watertable atop the denser waters of the curtain and move into the salt-filled depression via groundwater wedges that feed spring seeps about its edges. Short-term high-volume runoff or floods of fresher waters tend to form a floating brine sheet across the brine body, which disappears once it is concentrated to where its salinity and density equals that of the underlying brine body. Focused outflow of confined artesian water can locally displace the brine plume. Longer term fluctuations in the volume of all types of freshened inflow can cause changes in the mineral equilibrium that is depositing salts across the perennial brine covered floor. It can lead either to a freshening or a salinity increase in the waters of the brine curtain. Such longterm changes in flow volume favour dissolution, alteration or backreaction of pre-existing mineral phases, as can complete drying of the brine body, which may follow a longterm lowering of the regional watertable

lakes undergoing a transition from fresher high-waterlevel systems into saline lower-waterlevel lakes. In this purely continental scenario the transition in lake style can be a climatically-driven change from humid to arid, or it can be a tectonically-driven change in the amount of fresh water entering the lake depression (Chap. 4).

In all situations of holomictic subaqueous and salt pan evaporites, the necessary hydrology creates a cone of refluxing brine below the concentrating water mass. This leaky plume of dense brine bathes the accumulating evaporites in saturated and supersaturated water as the plume sinks, spreads and diffuses into the underlying regional hydrology. I call this zone of sinking waters associated with the accumulation of bedded salts the brine curtain (Fig. 2.81). The process is brine reflux, the geometry outlined by salt-saturated pore waters defines the brine curtain. Rates of brine escape or brine residence time within the plume of the brine curtain control many of the backreactions discussed in Chap. 2 (e.g., halite pseudomorphs after subaqueous gypsum – Hovorka 1992; carnallite in Lake Qaidam – Casas 1992; and the mineralogy of the Holocene Coorong Lakes – Warren 1990).

Once the brine curtain (reflux plume) is established and actively cycling hypersaline groundwaters, it is not easily displaced by short-term inflows of less-dense marine or meteoric groundwaters. The curtain creates an autochthonous hydrology of stable hypersaline pore waters where evaporites can continue to accumulate as secondary cements and alteration haloes. It is a plume of dense pore waters with wedgelike margins that force less-saline groundwaters to enter the basin as a series of seeps and springs about the edge of the curtain. Upon burial the evaporite cements associated with the base of the curtain are typically the first part of the evaporite sequence to be dissolved by resurging basinal and compactional waters.

Locally, the brine curtain may be breached atop areas of exceptionally strong upwelling or artesian outflow, which can be situated well out into the salt-saturated parts of the basin.

Where resurging artesian waters break though the brine curtain to the landsurface, as along the fault lines that cut across Lake Frome, they feed prominent lines of spring mounds on the lake floor. In some ancient drawdown basins a localised freshened upflow occurred through zones of exposed pinnacle reefs and were associated with haloes of less saline mineralogies in a sea of halite. Unlike the hydrologies of most ancient basinwide evaporites, the brine curtain in many Quaternary continental lakes in central Australia fades at depths not far below the surface of the lake sediments. In lakes such as Lake Eyre and Lake Amadeus, or the sabkhas of the Abu Dhabi coast, the brine curtain is destroyed

at depths of a few metres by dilution from resurging artesian waters. This brackish to mesohaline upwelling of regional groundwater, coupled with periodic surface floods, continually recycles salts into nearsurface sediments. There they are deflated or washed away, so preventing stacking of thick bedded salts within the playa or sabkha depressions. The only bedded salt to accumulate in such settings is a continually recycling pan crust that is never more than a metre thick. Its hydrogeochemistry is largely decoupled from the mineralogies of the underlying sediments (Chaps. 2 and 3).

Logan (1987) and Kendall (1992) use the term "hydroseal" to describe the lowermost salt layer in any evaporite sequence. They interpret it, and not the formative reflux hydrology, as the fundamental cause of evaporite accumulation and the varying mineralogies in the basin. The notion of a "hydroseal" is not strictly correct, as secondary or capillary salts precipitated in any zone of refluxing brine must be by definition forming in an aquitard and not an aquiclude. It leaks, to varying degrees, across the whole of the salt -covered basin floor. Even when a salt bed becomes cemented it still dissolves from its underside and becomes a supplier of brines to the base of a more deeply buried brine curtain (Chap. 8). As pore waters making up the brine plume slowly seep and sink, they ultimately mix with underlying compactional and basinal crossflows, as well as any more marginward meteoric or marine inflows. This mixing drives diagenetic reactions that include the precipitation of quartz overgrowths and dolomite cements in units located further away from the brine curtain (Ceriani et al. 2002; Morrow et al. 2002).

Thus, the term "seal" is not appropriate to any reflux situation and the notion of the base of an evaporite bed as a total seal, which is not subject to dissolution or alteration, is one of the reasons why the significance of basal anhydrites and other diagenetic deposits, such as some of the Rote/Faule Kupferschiefer ores, were not attributed to an inherent evaporite dissolution hydrology (Chap. 15; Warren 1999, 2000b).

Extraterrestrial Hydrologies, "Freeze-Dried" Salts, and the Meaning of Life

In order to complete this chapter on hydrology and evaporites, with its focus on the interactions between the earth's hydro-sphere, atmosphere and the lithosphere, I would be remiss if I did not include some mention of possible implications for extraterrestrial salts. Are there possible examples of large-scale occurrences of extraterrestial evaporite salts? If so what are the atmospheric implications of extraterrestrial salts, as well as their possible significance as indicators of extraterrestrial life? And lastly, what were the contributions of bolide interactions with earthly evaporites as drivers of extinction events here on Earth?

Partial analogs to the Earth's saline pans and saline lakes may have existed in crater-basins during the early Noachian epoch on the planet Mars (Forsythe and Zimbelman 1995). Evidence includes images of terraced, patterned and channelized ground in crater-basins, which imply ancient ponding of surface water, as well as possible prolonged and evolving erosional base levels. Williams and Zimbelman (1994) argue that White Rock, an enigmatic highly reflective crater interior deposit, measuring 12.5×15 km across, with an eroded thickness of 180–540 m, and a volume of 40 km^3, may be the remnant of a saline lacustrine deposit. They infer the exposed sequence may include deposits similar to those that outline layered rocks and concentric desiccation rings formed during drying of continental salt lakes on earth.

Edgett and Parker (1997), in a discussion of surface imagery of cratered terrain in the Sinus Meridiani region of Mars, recognised a combination of aeolian dunes and polygonally patterned ground. They argued, using a comparison with similar features that form today in saline seepage areas of the present-day Saudi Arabian desert, that Mars once had flowing surface waters and that capillary evaporation hydrologies creating and preserving evaporite sediments in the early history of Mars are a distinct possibility.

Further developing this concept of at-surface waters, Montgomery and Gillespie, 2005 argued that the Martian outflow channels developed via the catastrophic dewatering of evaporite deposits. Layered deposits within Valles Marineris, are interpreted as unconformably underlying Hesperian-age lava flows, which are thought to contain hydrous sulphates. These hydrated salts were heated by an increased geothermal gradient associated with to development of Tharis. Increased temperatures adequate to dehydrate hydrous evaporites would have triggered significant volumetric expansion and catastrophically released tremendous amounts of overpressured water onto the Marian surface.

So, across the last few decades, the discovery on the Martian surface of hydrated salt minerals, including sulphates and chlorides, all interpreted as deriving from the desiccation of preexisting large bodies of water, such as lakes, has been used to conclude there was liquid water activity on the surface of Mars. Consequently, it has reinforced the plausibility of finding relics of life on Mars (Barbieri and Stivaletta 2011). Because evaporites require short-term aqueous processes for their formation, they can trap and preserve over geologic times a biological record made up of halophilic extremophiles—such as microalgae, bacteria, and their remains—that recent research on Earth has shown to be characterized by unexpectedly high biodiversity. Space agencies, such as CNSA, ESA and NASA, have accordingly increased their interests in Earth-bound saline deposits as analogues for the Martian salts.

On the theme of evaporites and water on Mars, and as an alternative to the notion of an early warm wet Mars, Banin

(2002) has proposed a model that attributes the peculiar nature of Mars soil to it being a relatively 'young' weathering product. The model suggests that Mars soil components formed at the microscopic rock/atmosphere interface during recent periods by a process involving chemical neutralization of acidic volcanic aerosols containing soluble S and Cl species. This 'Acid Fog' formation scenario seeks to reconcile conflicting evidence for the presence of very soluble, water-transported sulphate and chloride salt minerals ('evaporites') in the soil with the lack of crystalline secondary iron oxides, clays and carbonates that usually form during weathering in aqueous environments. This emerging new view of Martian hydrology, based on the recent imagery that show water seepage, surface ice-dust interactions and volcanic activity on Mars as recent as the last 10 Ma, adds strength to a model of recently mobile water. A major conclusion from the 'Acid Fog' hypothesis is that the lack of organic matter in Martian soil may be due to low cumulative meteoritic input rather than to exceptionally high oxidizing power of the atmosphere.

Consistent with a non-waterlain theme, Michalski and Niles (2012), in a spectral/morphologic study focused on Valles Marineris, argue that many of the supposedly waterlain layered deposits of Mars are more akin to the layered aeolian-ice deposits with partial analogs in layered ice deposits in Antarctica. They postulate formation of sulphate-rich layered sediments on Mars was governed through time by volcanogenic SO_2 and H_2O emission rates and dust production against a backdrop of obliquity variation under a largely cold and dry climate. That is, layered Martian deposits indicate an atmospheric source, not water transport; volcanogenic acid volatiles were deposited along with snow, ice, and dust during periods of obliquity-driven climate change. If so, intervals when sulphate-bearing layered deposits formed might mirror periods of extremely high volcanic outgassing rates on a planet that was largely cold and dry with no surface water to act as a sink. They do not infer diapir-like associations with the layered sulphates they interpret.

In yet another evaporite-related study of the layered chasma deposits of Mars, Adams et al. 2009 concentrated on the nature of the layering and mineral spectra in Hebes Chasma, a Martian erosional valley located a few degrees north of Valles Marineris. They conclude that the mineralogical spectra (including kieserite), and the erosion/collapse patterns defined by the layering, are indicative of salt diapirism. That is, Hebes Chasma, formed by solution-related saltflow collapse of the Martian megaregolith. Local heating facilitated drainage of ~10 km of brines and so entrained particulates both through fractures in the chasma floor and into a regional aquifer. They argue a mega-regolith, rich in salts and water, is implied by massive, low-gradient allochthonous flows that terminate in deep pits and troughs, marked by emergent diapirs, and by arching of Hebes Mensa. These at-surface dipping structures are consistent with plastic and viscous deformation, but inconsistent with collapse of basalt flows and/or tephra. Spectral measurements confirm that hydrated sulphate salts (including kieserite) are spatially associated with allochthonous flows in the chasma, derived from depth and now indicated by light-toned at-surface deposits. Collapse features and flows are present in many other chasmata in Valles Marineris, suggesting that widespread salt tectonics and dissolution may have shaped the regional landscape, as also interpreted by Montgomery et al. 2009 (Fig. 2.82).

Likewise, Wezel and Baioni (2014) interpret the 1,500 m-thick "Sinus Meridiani complex" as sulphate rich and saltflow-based. It appears to be composed of a superposition of three lithologically similar stratigraphic units, each ending with a residual mesa caprock associated with planation surfaces. The three exposed caprock plains display polygonal fault networks, nodular anydrite/gypsum dykes located along subvertical polygonal fractures, and presumed pipe-like fluid flow structures. Such vertically intrusive fluidized bodies are interpreted as indicative of subsurface evaporite remobilization and injection, which probably occurred near actively rising evaporite diapirs originating from an autochthonous "mother" layer situated underneath the Meridiani region. Renewal of diapirism is inferred to have caused repeated post-depositional cycles of uplift and erosional exhumation during relatively recent times. The differences in interpretation by Adams et al. (2009), Montgomery et al. (2009) Wezel and Baioni (2014) versus Michalski and Niles (2012) are yet to be resolved.

The discovery of halite-siderite-anhydrite-chlorapatite assemblages in interstitial positions in the Nakhla meteorite with halite often being adjacent to or enclosing siderite, strengthens the argument for some form water of Mars (Bridges and Grady 2000). The Nakhla meteorite, recovered in Egypt in 1911, is a fragment of Mars pushed into space by a bolide impact. The nature of the mineral assemblage suggests that its source rocks on Mars were evaporites, which may be common in the craters and flood plains of the Martian southern highlands (Bridges and Grady 1999). Two models can explain the incorporation of evaporitic material into the Nakhla igneous parent. It may have happened as a low-temperature process (<200 °C by crystallisation from an aqueous fluid. An origin at low temperature is compatible with the available experimental data on siderite stability. Alternatively, evaporitic material may have been incorporated into the Nakhla parent while melt was still present and crystallized $\approx$800 °C. The latter model can more readily explain the trace element abundances and also the siderite textures that imply intergrowth with residual interstitial melt. Both high- and low-temperature models are consistent with the presence of sulphate salts (evaporite?) on Mars.

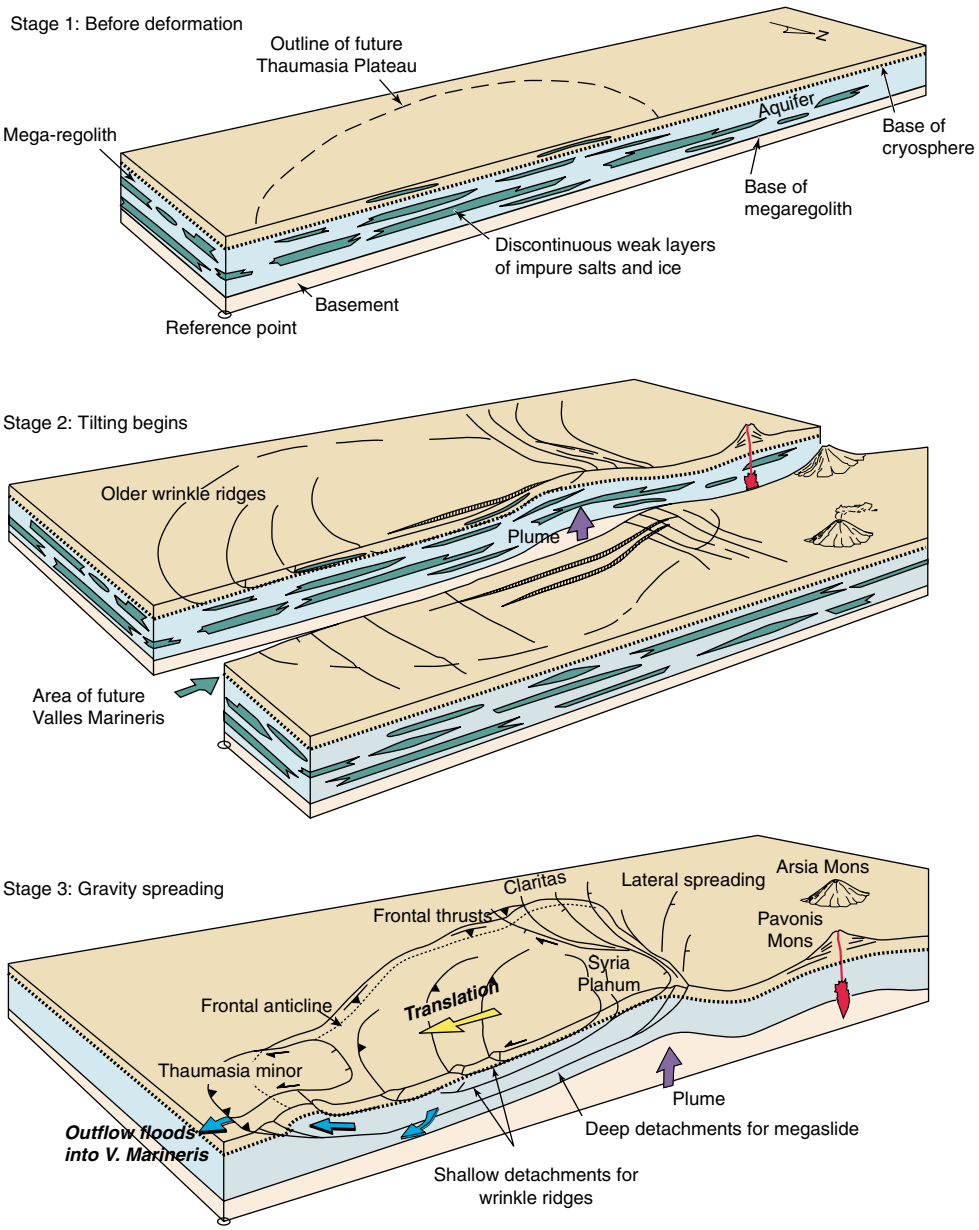

Fig. 2.82 Schematic illustration (not to scale) of the deformation of the Thaumasia Plateau as a "mega-slide" formed by continental-scale salt tectonics (After Montgomery et al. 2009). In *stage 1*, discontinuous layers of salts, ice, and impact breccia accumulate in Noachian time as megaregolith before the growth of Tharsis, perhaps as surface evaporites, or subsurface precipitates during impact-driven generation of the brecciated martian megaregolith. In *stage 2*, the rise of the Tharsis volcanic province and later arching of Syria Planum above a suspected plume increased both the regional heat flux and local topographic slope, loading the region with ash and lava flows and producing radial extension faults that may have penetrated through the regional cryosphere. In *stage 3*, layers of salts, ice, and basaltic debris within the regolith provided multiple detachments for the gravity spreading southeastward, possibly in response to further intrusion under Syria Planum. In addition, the aquifer below the cryosphere found outlets to the surface along the chasmata of Valles Marineris where the basal décollement cuts upward to intersect radial extension cracks projecting from Tharsis. This connection rapidly drained the extensive confined aquifer, which had substantial topographic head within the deforming zone. Drainage then carved the outflow channels

Radar imagery of the surface of Venus has outlined Venusian canali or outflow channels, as well as other associated volcanic deposits (Kargel et al. 1994). Most of these features resemble fluvial landforms much more than they resemble volcanic features on Earth and Mars. Yet surface temperatures on Venus are above 500 °C, and are well above that of the boiling point of water. Some of the canali show meandering habits, crevasse splays and other geomorphic features that are very similar to fluvial channels and flood plains here on Earth. Given the high temperatures on the Venusian surface, these feature must be related to lava landforms, yet they more closely resemble the water-carved outflow channels of Mars and the channelled scablands here on Earth. Likewise, the collapsed terrain at the sources of some Venusian channels resembles chaotic terrain at the meltwater sources of martian outflow channels. There are also Venusian lava deltas with shapes identical to bird's-foot deltas such as the Mississippi delta on Earth.

According to Kargel et al. (1994) these canali features suggest the involvement of an unusual lava and/or extraordinary eruption conditions, which they relate to a carbonatite lava rather than a silicate melt. Venusian nearsurface rocks may contain 4–19 % calcite and anhydrite, this is in part a reflection of the likelihood that Ca-bearing hydrous silicates are unstable on the surface of Venus due to widespread sulphatisation to anhydrite (Zolotov et al. 1997). Unlike silicate lavas, some carbonatites (including carbonate-sulphate-rich liquids) have a more fluid rheology (on earth, carbonatites

can have viscosities that are only 500 times that of water and tend to flow in water-like channels – canali. If these Venusian outflows are carbonatites, they would have a melting point that was only slightly greater than the Venusian surface temperature. Such lavas could flow great distances while retaining high fluidity, significant mechanical erosiveness, and a substantial capacity to transport and deposit entrained sediment.

Such mixtures of crustal salts would melt at temperatures a few tens to a few hundred Kelvins above the Venusian surface temperature; hence, melting may be induced by modest endo-genetic or impact heating (Kargel et al. (1994)). Salts on Venus may play many of the same geologic roles as water and ice do on Mars and Earth. A molten salt (carbonatite) "aquifer" may exist beneath a few hundred metres to several kilometres of solidified salt-rich "permafrost". In this way many geologic features on the Venusian surface can be explained by carbonatite magmatism and impact melting. They include: (1) impact melting of crustal salts to form crater outflows, (2) small, sustained eruptions from molten salt aquifers to create sapping valleys, (3) large, sustained eruptions that form canali and their flood plans, and (4) catastrophic outbursts forming outflow channels and chaotic terrain.

Further out in the solar system on the surface of Europa, a moon of Jupiter, and a celestial body much more distant from the Sun than Mars, there is an even more spectacular and unusual development of salts. Using infrared spectral analysis on images of the cracked and icy surface of Europa, McCord et al. (1998) and Kargel et al. (2000) identified spectra that are best interpreted as hydrated salts dominated by trona and epsomite, rather than clays or other alternate minerals. The salts characterise distorted spectral bands that are only observed in the optically darker areas of Europa. This includes regions along many of the lineaments that crisscross the icy surface.

According to the authors the spectra may represent "evaporite" deposits formed by water, rich in dissolved salts, that reached the surface from a water-rich layer underlying the ice crust. Whether the sub-ice ocean still exists is a matter of speculation. Such a salt precipitating mechanism visualises at-surface freeze drying of the salts. Salts are cryogenically precipitated from liquid water as it escapes via breaches and lineaments to flow and quickly freeze on the extremely cold Europan surface (−160 °C). Such a mechanism means these salts are "freeze-dried" and not true evaporites as defined in Chap. 1. But, as noted by McCord et al., if the spectra are truly those of hydrated salts escaping from a saline liquid ocean beneath the icy cap, then it offers exciting evidence for the possibility of extraterrestrial life on Europa. It suggests that there may be, or once was, active hydrothermal activity on Europa and that water rock interaction has created an ionic solution beneath the icy surface similar to that of the early Archaean bicarbonate ocean. It may well indicate hydrothermal vent conditions on a sub-ice ocean floor similar to those on earth when life first evolved in the early Archaean.

So far, all extraterrestrial evaporites we have discussed (solar or cryogenic) are carried as ions in a water solution; Barnes et al. (2011) and Cordier et al. (2013) note the possibility of a different solute carrier, namely liquid hydrocarbon on Titan. Titan is a moon of Saturn with a surface temperature of −179 °C (Fig. 2.83a). It is the only moon in the solar system with a substantial atmosphere, composed of 98.4 % nitrogen and the other 1.6 % is composed of methane, along with trace amounts of other gases. At that low temperature Titan hosts at-surface lakes of liquid hydrocarbon, mostly methane and ethane. There are other organic molecules in solution in the liquid methane, all derived from ultraviolet photolysis of methane and then carried to and across Titan's surface, dissolved in rain, surface and ground liquids (Fig. 2.83a, b).

The surface temperature is around 92°K and the temperature lapse rate through the troposphere was determined by the Voyager measurements (Fig. 2.83a). A temperature inversion occurs at an altitude of 50 km, allowing the stratospheric temperature to rise to 170° K (−103 °C). The small hydrocarbon molecule composition of the atmosphere, made up principally methane and extended hydrocarbons, is an effective short-wavelength shield with photochemistry inducing the formation of high-molecular-weight hydrocarbons known generally as'tholins'[4] (Fig. 2.83b). A cycle of heating and cooling with convection allows methane to reach its saturated vapour pressure at 1.5 bar to form clouds. The hydrocarbon hydrosphere, called the liposphere (from the Greek lipos meaning 'oil'), here completes the cycle, condensing into lakes and oceans of hydrocarbon, hydrocarbon snow and rain.

Organics in solution can precipitate out of lakes as evaporites when liquid methane pooled on the surface and a methane ocean passes back into the gaseous phase, which dominates in the atmosphere. According to Barnes et al. (2011) these methane lakes are the only known extraterrestrial indicators or an active extant "hydrological"[5] cycle. In the same vein, they note that darkening of Titan's surface

[4]Tholin [after the ancient Greek word θολός (tholós) meaning "not clear"] is a heteropolymer molecule formed by solar ultraviolet irradiation of simple organic compounds such as methane or ethane along with ethylene, acetylene an hydrogen cyanide. Tholins do not form naturally in our modern-day Earth atmosphere, due to the presence of oxygen, but are found in great abundance on the surface of icy bodies in the outer solar system. They usually have a reddish-brown appearance and on the early Archaean or even late Hadean earth may have been the first microbial food for heterotrophic microorganisms before autotrophy evolved.

[5]Barnes et al. (2011) use the word 'hydrological' to refer generally to 'volatilological', i.e., any substance on a planetary surface that undergoes processes physically similar to those of water in the Earth's hydrological cycle passing from a liquid to a gaseous state, and leaving behind solutes. In the case of Titan, the fluids passing from a liquid to a gaseous state are dominated by methane and ethane.

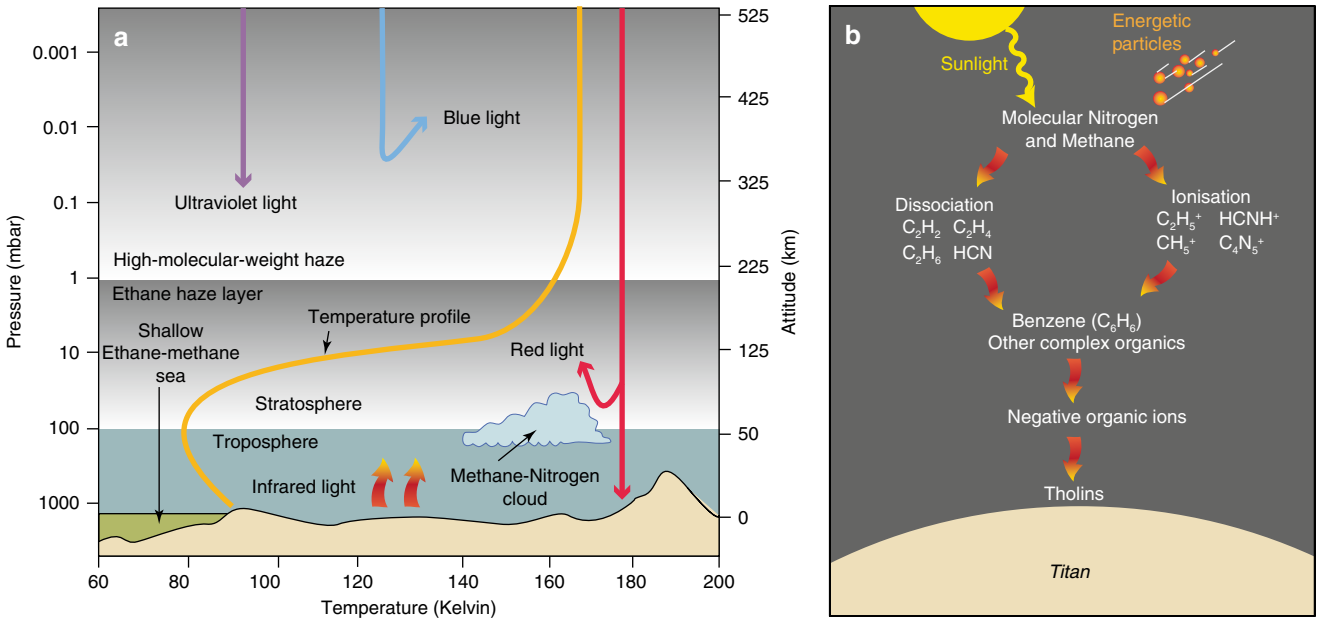

Fig. 2.83 Atmosphere of Titan, (**a**) Stratification and temperature profile. (**b**) Formation of tholins in the atmosphere of Titan (After Barnes et al. 2011)

occurs in the wake of large equatorial storms, empirically demonstrating that rain, composed mostly of liquid methane not water, reaches the surface of Titan. Other monitored surface changes shows that some hydrocarbon lakes appear and disappear with time. For example, near-infrared imaging reveals concentric deposits rimming the south-polar lake Ontario Lacus, much like the layered desiccation patterns found in arid-zone lakes on earth. Multiple images acquired years apart show that south-polar lake Ontario Lacus may be drying up right now. According to Barnes et al. this lake dessication process indicates the formation of evaporite deposits in the floors of dried hydrocarbon lake beds.

Methane and ethane that make up the lakes are nonpolar molecules, hence their solutes and the resulting evaporitic precipitates would be quite different from those of liquid water. Most of these evaporite candidates would be organics and probably be derived from species forming atmospheric haze particles. For example, McKay (1996) shows a solubility upper limit of tholin in liquid methane of 0.03 % by mass, making this a prime candidate for a Titan evaporite. Even this low level of solubility should produce detectable evaporitic deposits, if at least 10 m depth of methane solute were evaporated. Alternatively, more volatile species like CO_2 (McCord et al. 2008) or benzene (Clark et al. 2010), are other evaporite possibilities. Along with the evaporite lakes, vast dune fields are found near Titan's equator, shaped by strong winds blowing east to west. Unlike Earth's sand dunes, Titan's dunes are thought to be composed of organic material that has rained down from its smoggy photochemical skies.

Here on earth evaporites may have played a major role in the end-Cretaceous and end Permian extinction events (Brett 1992; Svensen et al. 2009). At the end of the Cretaceous a large asteroid collided with the earth to create the Chicxulub impact crater in Yucatan, Mexico. This region is underlain by widespread Jurassic anhydrites and their vaporization during the impact added a good deal to the ensuing climatic mayhem. Pope et al. (1994) calculated that $0.4–7.0 \times 10^{17}$ g of sulphur were vaporized by the impact into the anhydrites. A large portion of sulphur was released as SO_2, which, due to the rate-limiting oxidation of SO_2, very slowly converted to aerosol. Their radiative transfer calculations of the effects of this aerosol, when combined with rates of acid production, coagulation and diffusion, show that solar transmission was reduced to 10–20 % of normal for a period of 8–13 years. This reduction in solar transmission produced a climate forcing (cooling) of −300 Wm^2, so producing a decade of freezing and near-freezing temperatures.

The direct modelling of the results of shock vaporisation of anhydrite, when applied to the Chicxulub geology and using bolide diameters of 10 or 20 km across, yield volumes of 0.5×10^{17} g and 2×10^{17} g of degassed sulphur from the impact (Yang and Ahrens 1998). These results add further veracity to the models of Pope et al. (1994). Passage of these volumes of sulphur into the atmosphere (as SO_2 or SO_3) are sufficient to cause global cooling of 10 °C or more. A prolonged impact winter, with a major contribution from the degassing of evaporites, is a major contributing cause to the K/T extinctions.

The end Permian extinction, its tie with the Siberian traps and associated Permian and Cambrian evaporites and volatiles, is detailed in Chap. 16. And who said evaporite studies were esoteric?

Sabkhas, Saline Mudflats and Pans

3

Introduction

This chapter looks at Quaternary depositional styles depositing saline sediments in ephemeral saline waters, focusing on modern evaporitic mudflats (sabkhas) and saline pans. These two settings encompass that part of the hydrological spectrum dominated by capillary and ephemeral at-surface brine hydrologies. Climatically, these settings tend to occur in arid deserts (Köppen zone: BW) in both coastal and continental interior arid settings where saline groundwaters are found with a metre of the landsurface. A saline watertable may sometimes outcrop for a short period and precipitate a layer of pan evaporites with primary textures before drying up once more. With drying the brine surface sinks into the sediment to become a watertable and the evaporite system switches to capillary evaporation with secondary (very early diagenetic) sabkha salts forming in the sediment host. The other modern hydrological setting where salt beds tend to form is that typified by perennial subaqueous brine hydrologies (primary textures) in coastal and continental settings and this will be the focus of the next chapter.

The first sedimentological studies of sabkhas were in the Arabian (Persian) Gulf (e.g. Curtis et al. 1963), but similar arid-zone capillary salts were soon described in sediments along the coast of Baja California, Mexico (Phleger 1969; Shearman 1970), the coast of Sinai (Gavish 1974; Levy 1977a, b), and in various continental playas worldwide (Fig. 3.1; Table 3.1; Moiola and Glover 1965; Surdam and Wolfbauer 1975). Ancient sabkha successions are typically dominated by matrix, with capillary salts occupying less than 30–50 % of a stack of m-scale erosion-capped beds, that also contain biolaminites and microbial peats.

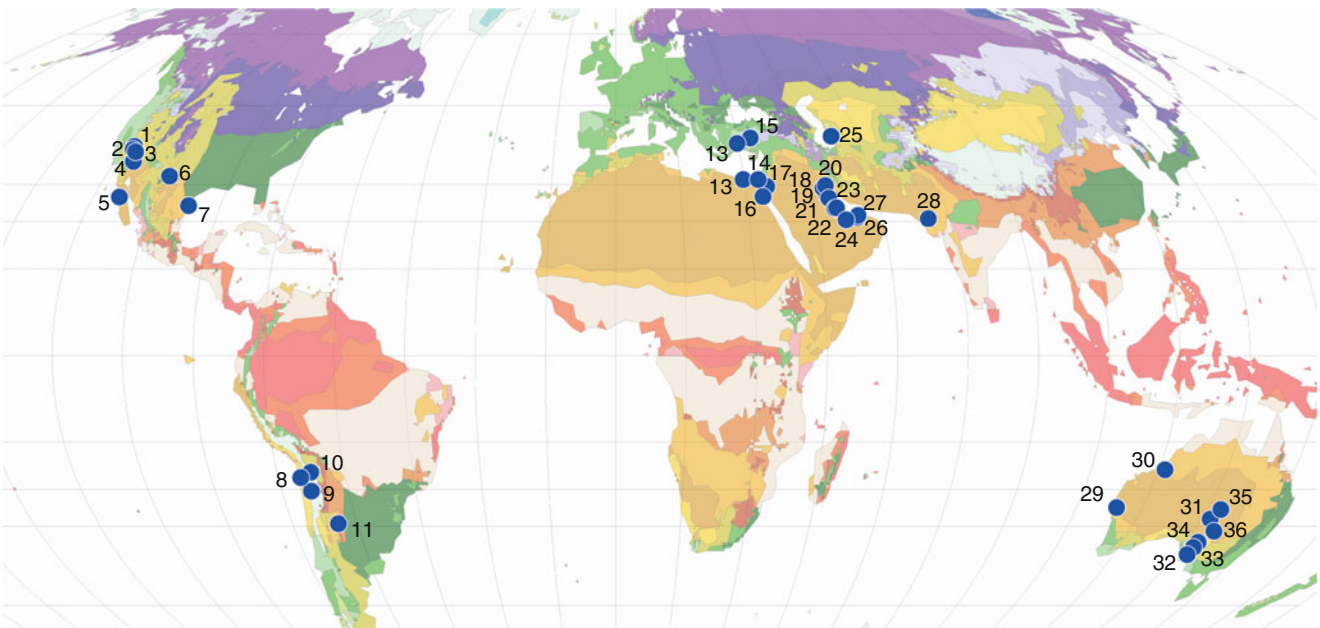

Fig. 3.1 Distribution of selected modern sabkhas and pans plotted on a Köppen climate base, see Table 3.1 for index to locations (numbered west to east) and Fig. 2.3 for Köppen legend. Plots extracted from SaltWork® database Version 1.6

© Springer International Publishing Switzerland 2016

J.K. Warren, *Evaporites: A Geological Compendium*, DOI 10.1007/978-3-319-13512-0_3

Table 3.1 Selected Quaternary sabkhas and pans listed against latitude of occurrence centroid, Köppen zone, area and elevation of feature. Index number cross references the locations on Fig. 3.1. Refer to Fig. 3.2 and text for depositional subdivision

	Style	Latitude	Köppen	Area (km^2)	Elev. (msl)	Index
Marine-edge saline flat						
Guerrero Negro, Baja Mexico	Sabkha	27.895	BWh	373	0.1	5
Laguna Madre mudflats, Texas	Sabkha	26.372	Cfa	106.3	0.1	7
El Hamman Sabkha, Egypt	Sabkha	31.098	BWh	79.3	4	12
El Qaa, Gulf of Suez	Sabkha	28.016	BWh	4.9	0.5	16
Kadmah Bay	Sabkha	29.577	BWh	80.8	0.1	18
Al Khiran sabkha	Sabkha	28.654	BWh	49	0.1	19
Shatt at Arab delta	Sabkha	29.990	BWh	0	0.1	20
Pans near Half Moon Bay, Saudi Arabia	Saline pan	25.948	BWh	22.7	0.1	23
Abu Dhabi Sabkha	Sabkha	24.254	BWh	1,654.8	0.1	26
Shark Bay Mudflats (southern)	Sabkha	–26.468	BSh	21.1	0.1	29
Heads of Spencers & St Vincent gulfs	Sabkha	–32.782	BSk	0	0.1	34
Continental to marine transition						
Sabkha Matti	Sabkha	23.801	BWh	2,954.4	10	24
Ranns of Kutch, India (total area)	Sabkha	24.015	BWh	24,008.1	1	28
Continental playa						
Deep Spring Lake, California	Saline pan	37.273	Csb	4.4	1,497	1
Saline Valley, California	Saline pan	36.702	BWk	4.5	323	2
Death Valley, California	Saline pan	36.252	BWh	30.6	–75	3
Bristol Dry Lake, California	Saline pan	34.464	BWk	200.6	183	4
Salt Flat Playa, west Texas	Sabkha	31.740	BWk	135.3	1,104	6
Salar Grande, Chile	Saline pan	–21.095	BWk	270.7	684	8
Salar de Atacama, Chile	Saline pan	–23.512	BWk	3,064.6	2,250	9
Salar de Uyuni, Bolivia	Saline pan	–20.157	BWk	9,653.9	3,650	10
Salinas de Ambargasta, central Argentina	Saline pan	–29.395	BSh	3,068.4	123	11
Aci Golu, Turkey	Saline pan	37.837	Csa	152.9	836	13
Tuz Golu, Turkey	Saline pan	38.863	Csb	971.5	905	15
Sabkha Yotvata, Israel	Sabkha	29.838	BWh	28	61	17
Lake Eyre, South Australia	Saline pan	–28.567	BWh	8,528.8	–15	31
Lake Fowler, SA	Saline pan	–35.082	Csb	9.8	0	32
Lake Frome, South Australia	Saline pan	–30.760	BWh	2,658.6	–2	36
Umm Ash Shurabyat, Saudi Arabia	Sabkha	25.832	BWh	76.3	0.1	22

Eolian-hosted sabkha						
Bardawil Lagoon sabkha, Egypt	Marine-margin	31.093	BWh	135.9	0.1	14
Al Khawwari Coast, Saudi Arabia	Marine-margin	27.730	BWh	5	0.5	21
Abu Dhabi region (Al Taf Coast) UAE	Marine-margin	24.610	BWh	10	0.5	27
NW Coast, Australia	Marine-margin	−19.722	BWh	5	0.1	30
Tickera region, South Australia	Marine-margin	−33.736	BSk	1.3	2	33
Umm Ash Shurabyat, Saudi Arabia	Continental	25.832	BWh	76.3	0.1	22
Cheleken region Caspian Sea	Continental	39.197	BWk	−10	−30	25
Poolowanna Lakes (Bilpa Plains salt flats)	Continental	−26.810	BWh	445.9	7	35

Often forming in depressions in the sabkha flats, modern saline pans accumulate as metre-scale stacked masses of salt crusts, typically retaining patches of chevron halite and variably overprinted by karst and capillary cements (Table 3.1). Ancient saline pans can stack into relatively pure beds of recrystallised halite with remnant patches preserving aligned chevrons, which are crosscut by syndepositional karst (Chap. 1). In contrast, perennial subaqueous sequences tend to be purer and thicker than sabkhas, dominated by remnants of bottom-nucleated textures and, compared to pans and sabkhas, the salt beds are cross cut by far fewer exposure surfaces.

In the minds of some geologists the recognition of anhydrite nodules is sufficient to classify a core or outcrop as a sabkha. The reality is more complex. For example, in the past 10 years the importance of subsurface diagenetic cements composed of anhydrite nodules within ancient evaporitic platform hosts has been increasingly recognised as indicative of a widespread mesogenetic process (Al-Helal et al. 2012). Such nodules grow poikilotopically and replacively in a burial setting, fed by dense surface brines sinking through restricted marine carbonates. Ensuing textures, when seen in limited exposures or core, are similar to the matrix-dominated nodular textures that typify sabkhas. It is likely that a significant proportion of subsurface successions, previously interpreted as ancient sabkhas, are actually stratabound zones of nodular anhydrite burial cements (Chap. 8). Hence, when making a sabkha interpretation, it is important to look beyond the presence of nodular anhydrite. One must also look at the vertical sequence, the presence of stacked erosion surfaces, lateral equivalents and the hydrological setting in order to make a reliable sabkha interpretation.

What Is a Sabkha?

Sabkha is a transliteration of the Arabic *sebkha* describing a salt flat. In the local terminology of the Arabian Gulf region it describes any area of extensive, barren, salt-encrusted, and periodically flooded, coastal or inland mudflats. Geological usage implies intrasediment evaporite growth beneath a flat geomorphic surface, with single-cycle bed thickness dictated by the vertical extent of the capillary fringe (Warren and Kendall 1985). Modern sabkhas in the Arabian Gulf (sabkhat is the correct form of the Arabic plural) are occasionally covered by ephemeral marine and continental floodwaters that, until recently, were thought to be the major suppliers of ions to underlying salts growing displacively in the sabkha matrix (*per descendum* – ions come from above). We know now that this is not the case and that deeply circulated resurging continental groundwater moving into the strandzone is the major supplier (*per ascendum* – ions come from below) of salts to most sabkhas and many saline pans. The mudflat surface is dry and subaerial for most of the time. It is held in place by capillary moisture, fed from a shallow saline water-table lying a few centimetres to a metre or two below the sediment surface.

Occasionally, the term sabkha is used in a narrow sense to describe anhydritic mudflat sediments deposited in a marine coastal or sea-margin sabkha, exemplified by the Arabian Gulf coastal sabkha. But when sabkha is used to imply "salt flat," it should include both coastal and continental sabkhas and encompass displacive growth of other intrasediment capillary salts like halite or glauberite as well as calcium sulphate. Some coastal sabkhas, such as those along the At Taf coastal strip (formerly known as the Trucial Coast), pass laterally in to continental sabkhas (e.g. Sabkha Matti) without any noticeable change in surface morphology (Kinsman 1969; Goodall et al. 2000). The seaward side of a modern coastal sabkha is characterized by a matrix of marine sediments, while the continental portion is characterised by non-marine sediments and continental groundwaters.

Sometimes, the term playa is used as a geological equivalent to continental sabkha. But, as used in the southwest USA, playa is a much wider ranging depositional descriptor than sabkha. In addition to the salt-crusted evaporitic mudflat (sabkha) a playa encompasses other related settings including, distal alluvial fans, sand flats, saline pans and dune fields as well as abandoned or desiccated shorelines[1]. Continental sabkhas may also be encompassed in local usage of other wider ranging terms such as; chott (northern Africa); vloer/pan (southern Africa), salt lake (Australia), rann (India); nor (Mongolia), takir (Russia), kavir (Iran), salar (Chile) and alkali flat/ salada/dry lake/playa (southwest USA). Terms in local usage may not necessarily identify geomorphologically and geologically identical features. Even the original usage of the term playa does not mean salt flat, rather its Spanish usage covers the terms beach, shore, strand or coast. Its usage first came across into English to describe abandoned beaches or strandlines that can be seen on the margins of many inland salt lakes and saline pans. Likewise the word chott comes via French from the Arabic shatt. As originally used in Tunisia, shatt/chott describes the halophyte-covered portion of a saltflat and contrasts with sabkha, which describe the vegetation-free portion of the saline flat. Using sabkha, playa or chott interchangeably is very poor usage of what is already a poorly defined set of terms (see Briere 2000).

In an attempt to clarify the geological usage of the term sabkha so it can be more easily applied to a particular vertical sequence in ancient evaporitic sediments, I define a sabkha as a ground-water driven sedimentary system indicated by syndepositional intrasediment capillary evaporites, which precipitate in both marine and continental saline mudflats (Warren and Kendall 1985; Warren 1989). The hydrology of precipitation, via capillary evaporation, is the same in both

[1] In the original Spanish, playa means beach or shoreline.

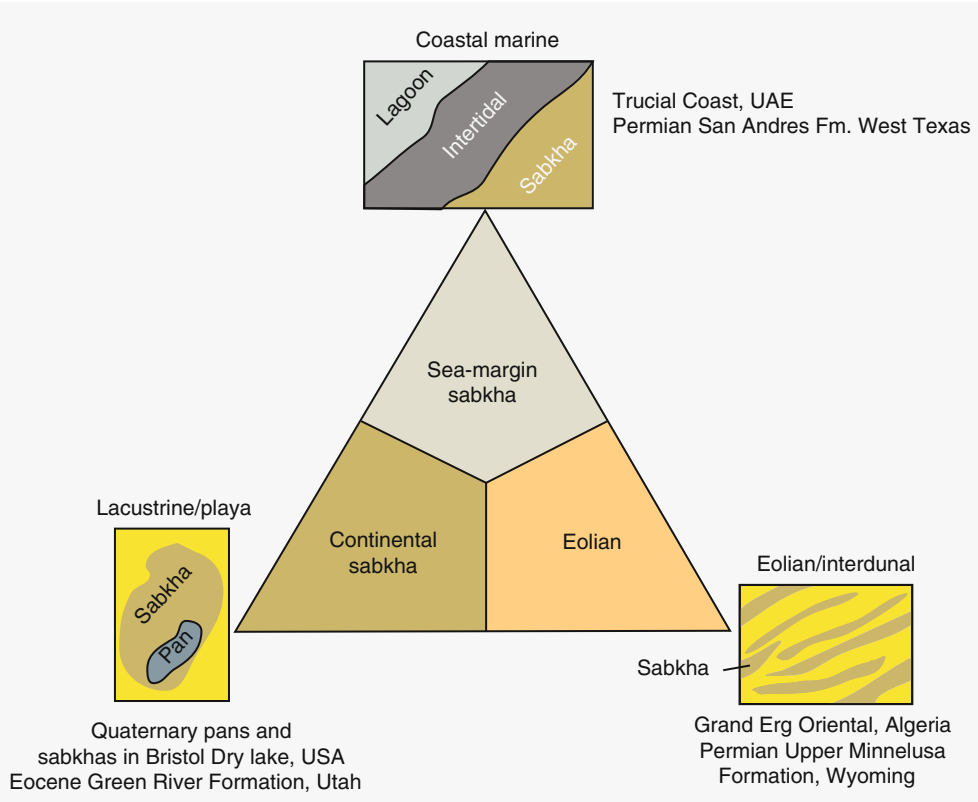

Fig. 3.2 Sabkha classification using regional depositional setting of the matrix material (Modified from Handford 1981a) – see Table 3.1 for examples

marine and continental settings. Even so, the matrix typically shows evidence of its marine or continental pedigree, as can the hydrogeochemistry of the pore waters (Table 3.1). In other words, sabkhas are hydrological settings where resurging groundwaters form displacive and replacive evaporite minerals (gypsum, anhydrite, halite, polyhalite, glauberite, etc.) in the capillary fringe above a saline watertable or in the brine-saturated muds immediately below. By this definition the sabkha sequence or cycle is capped by a deflationary surface, which defines the top of the capillary zone (Stokes surface). The whole capillary sequence is typically made up of more than 50 % non-evaporite matrix (Warren and Kendall 1985). Based on their work in the Qatar coastal sabkhat, and in agreement with the above definition, Jameson et al. (2009, 2010) state;… "A sabkha is a diagenetic overprint, not a depositional system."

The advantage of this definition is its utility in subsurface studies of ancient sediments where it can be applied using sedimentary textures in a single core; the surrounding depositional sequence does not need to be interpreted. The common thread is the growth of intrasediment salts in the capillary zone and in brine-saturated phreatic muds immediately below the watertable, with the whole succession capped by a syndepositional erosion surface. Sabkha hydrology controls the thickness of an evaporite unit, the style of intrasediment crystal (euhedral outlines to nodules) and most importantly generates the characteristic erosional or hydraulic "jack-up" surface that caps a sabkha cycle.

The host matrix, and associated sedimentary structures, in which sabkha salts grow by capillary evaporation, along with the underlying sediments, is the sedimentological basis of most sabkha classification (Fig. 3.2: Handford 1981a; Warren 1991). Matrix in modern and ancient sabkhas is deposited in varying hosts that may grade laterally into each other, namely;

- Marine coastal
- Fluvio-lacustrine
- Eolian

Dominance of one of the three matrix associations gives rise to sea-margin, continental, or eolian sabkhas. Modern coastal sabkhas typically contain gypsum or halite and less often anhydrite, likewise for many inland sabkhas, but these interior settings can also contain more unusual intrasediment salts such as; trona, borax or glauberite.

Marine Coastal Sabkhas

Modern sea-margin sabkhas form as narrow belts along many coastal arid to semi-arid deserts including; the western and southern coasts of the Arabian Gulf, the coast of western and southern Australia, Northern Africa, and the Sinai (Table 3.1; Fig. 3.1). The most complete documentation of modern marine-carbonate sabkhas centres on the southern

coast of the Arabian Gulf (aka Persian Gulf[2]) in the emirate of Abu Dhabi, while siliciclastic sabkhas typify the Saudi Arabian coast between Qatar and Kuwait, and fluvio-deltaic coastal sabkhas are forming atop the Shatt al Arab delta at the northwestern end of the Gulf. Elevated pore water salinities along the various BWh coasts of the Arabian Gulf (aka Persian Gulf), reflect a combination of; frequent winds (mostly blowing from between 315° and 15° – the Shamal), high temperatures (up to 45–50 °C), low precipitation (typically less than 5 cm a year), low fluviatile input (except for the Tigris, Euphrates and Karun rivers in the extreme north of the Gulf) and the restricted silled connection via the Strait of Hormuz between the saline waters of the Arabian Gulf and the normal salinity waters of the Gulf of Oman and the Indian Ocean.

Physiographically, the Arabian Gulf is an almost enclosed sub-rectangular basin that trends northwest-southeast; it is approximately 850 km in length, with a maximum width of 330 km (Fig. 3.3a; Wyn Hughes 1997; Evans 1995, 2010). The basin floor is markedly asymmetrical, forming a ramp that dips gently (35 cm per km) away from the tectonically stable Arabian side (typical depths of 20–40 m), and more steeply (175 cm per km) away from the tectonically active Iranian side (depths of 40 to nearly 100 m). The greatest water depth (100 m) is reached near the entrance to the Gulf at the Straits of Hormuz.

In terms of its regional tectonic setting, the Arabian Gulf is an epicontinental sea within a foreland basin, located between the geologically stable, low-lying, Precambrian Arabian Shield and the high, geologically unstable Tertiary foldbelt of the Zagros Mountains of Iran. The foldbelt is a compressional suture, active since the Early Miocene along the Zagros Thrust Zone and driven by the subduction of the Arabian Plate beneath the Eurasian Plate (Wyn Hughes 1997). The Gulf's bathymetric asymmetry comes from Pliocene to Quaternary tectonic loading on the Iranian side, and tilting of the Arabian Peninsula in the Neogene, during the opening of the Red Sea. The southeastern part of the Arabian Gulf is a very gently sloping ramp. The Qatar Peninsula forms a distinct feature on the near-linear Arabian coastline, and causes anomalous trends in current direction, and possibly of sedimentation, along the southeastern Gulf.

Ramp carbonates, including sabkhas, define the coast along much of the cratonic southern side of the Gulf, while the northern coast is dominated by more-steeply dipping siliciclastic alluvial aprons, passing landward and northward into the Zagros Mountains (Fig. 3.3a). Moving south from the deepest Gulf floor, the bottom changes from deepwater micrites through grainstones and reefs of the Great Pearl Bank into reworked dune and eolianite barrier shorelines into the coastal carbonate sabkhat (the shorelines of the Emirates, Qatar and Saudi Arabia).

Entry of siliciclastic sediment to the present Arabian Gulf is mostly longitudinal via the Shatt Al Arab delta at the northwestern end of the Gulf. The Shatt Al Arab is the confluence of the Tigris, the Euphrates and the Karun rivers. It has constructed a huge wedge of fluviodeltaic sediments, with thin patchy sabkha capstones landward of the shoreline (coasts of Iraq and Kuwait). Siliciclastics enter also from wadis along the northeastern side of the Gulf and from encroaching dunes along parts of the Saudi coast. Eolian transport is driven by the northwesterly Shamal winds (*shamal* is Arabic for northerly) and carries both siliciclastic and carbonate fines well out into gulf waters. Interestingly, detrital dolomite rhombs make up around 15 % of the non-clay component of modern bottom sediments in the northern Arabian Gulf and up to 60 % of the 30–125 μm fraction (Al-Bakri et al. 1984). Morphologically they are near identical to the authigenic sabkha dolomite rhombs that first caused so much interest in sabkhas in the Emirates in the 1960s.

Geologically the Arabian Gulf is unique as it is the only modern example of a modern shallow inland sea in which widespread ramp carbonates are accumulating. This is attributed to its low latitudinal position and relatively clear waters, the result of low terrigenous input, making much of the seafloor suitable to a tropical carbonate-secreting biota (Wyn Hughes 1997). The depth to the base of the photic zone is around 20 m in turbid waters above the muddy sediments along the Abu Dhabi coastline, but increases to 30 m in the clearer deeper waters in the axial parts of the seaway.

Although the Gulf floor is a marine carbonate setting today, 20 ka when sealevel was 120 m below its present level, the whole Gulf was a desiccated basin with active eolian dunes covering much of what is the present seafloor. The Pleistocene-Holocene (Flandrian) transgression covered and reworked much of this dune sand as the gulf waters returned to the present coastline some 7–10 ka. Much of the Holocene marine carbonate section in the southern Gulf is now underlain by these eolian siliciclastics.

Carbonate-Hosted Coastal Sabkhas in the Southern Arabian Gulf

The Arabian Gulf sabkha, centred on Abu Dhabi city, is the eastern part of a sabkha belt known as Sabkhat as Salamíyah that extends along the coast of the United Arab Emirates between Yas Island and Ras Ghanada (Figs. 3.3b and 3.4). Further west, adjoining the eastern base of the Qatar

[2]On almost all maps printed before 1960, and in most modern international treaties, documents and maps, this body of water is known as the "Persian Gulf". This follows similar usage of Persian Gulf by the ancient Greek geographers, Strabo and Ptolemy, who in contrast, used Arabian Gulf to the refer to the Red Sea. With the rise of pan-Arabism and Arab nationalism, the name Arabian Gulf, not the Persian Gulf, become predominant in many Arab countries, initially as an expression of anti-American feeling in the Arab world, because until 1979 and the Iranian Revolution, America supported the of Shah of Iran. Since 1980, the term Arabian Gulf, is increasingly used by many Sunni-dominated Arab Gulf states to counter the rising power of the theocratic (Shia-dominated) Iranian (Persian) Republic.

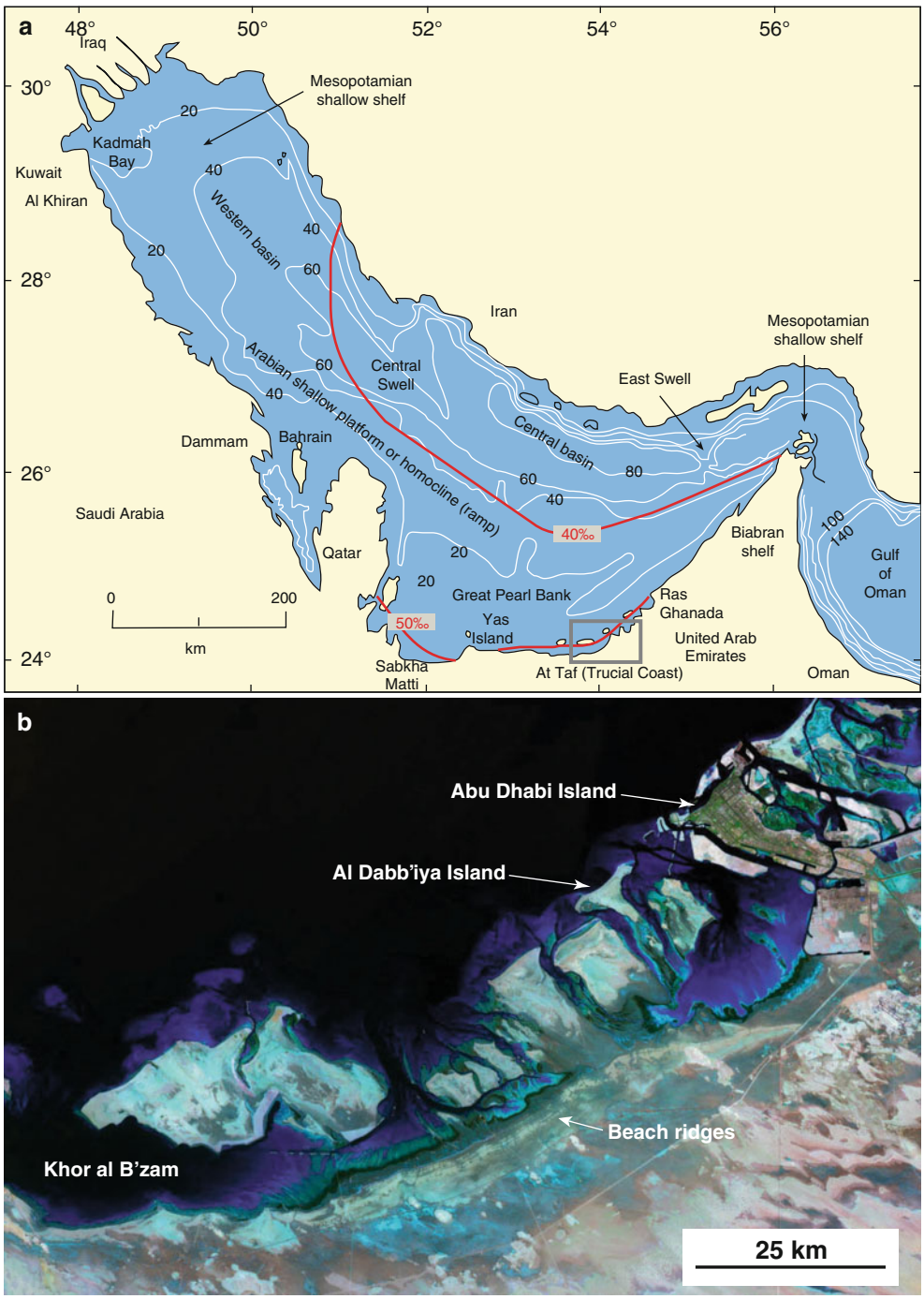

Fig. 3.3 Sabkhas of the Arabian (Persian) Gulf. (**a**) Physiography (m) and salinity (‰) in the Arabian Gulf (After Purser 1973a; Evans 1995; Wyn Hughes 1997). (**b**) General sediment distribution of the Trucial Coast of the United Arab Emirates from the entrance to the Khor al B'azm Lagoon to Abu Dhabi Island, showing the shallow water areas of the lagoon and the oolitic ebb-tidal deltas on the seaward side of the tidal channels between the islands (see Fig. 3.4). The intertidal zone, defined by intertidal algal mats, is clearly visible as zones of dark-coloured sediment. Landward of the intertidal zone is the supratidal zone of the sabkha, which in turn passes into dune sands across the mesa that defines the erosional edge of the Miocene plateau (Landsat image courtesy of NASA)

peninsula is Sabkha Matti, one of the largest tectonically-induced sabkha depressions in the region (see eolian sabkhas). The sabkha-dominated At Taf coastal strip is approximately 320 km (200 miles) long and the coastal sabkha belt is up to 24 km (15 miles) wide; on average it has prograded 1.5 km (1 mile) every 1,000 years. Seaward slopes on the sabkha are low and range from 1:3,000 to 1:4,000, this means whenever water a few centimetres deep arrives on the sabkha, the strandline on the brine sheet will have migrated kilometres.

It was the occurrence of modern nodular anhydrite and dolomite in the sabkhas of Abu Dhabi and Qatar that first attracted the attention of the geological community during the 1960s. The work of Curtis et al. (1963), Illing et al. (1965), Evans et al. (1969), Kinsman (1969), Shearman (1963), Butler (1966, 1969, 1970), and Kendall and Skipwith (1969a, b) provided observational data on which most of our current sabkha models are based. Field-work since the 1960s tended to consider specific sedimentological problems within the sabkha setting, such as hydrological zonation (Patterson 1972; Hsu and Schneider 1973; McKenzie et al. 1980; Patterson and Kinsman 1981), the origin of dolomite (McKenzie 1981; Patterson and Kinsman 1982; Bontognali et al. 2012), or it has reinforced the facies model of earlier

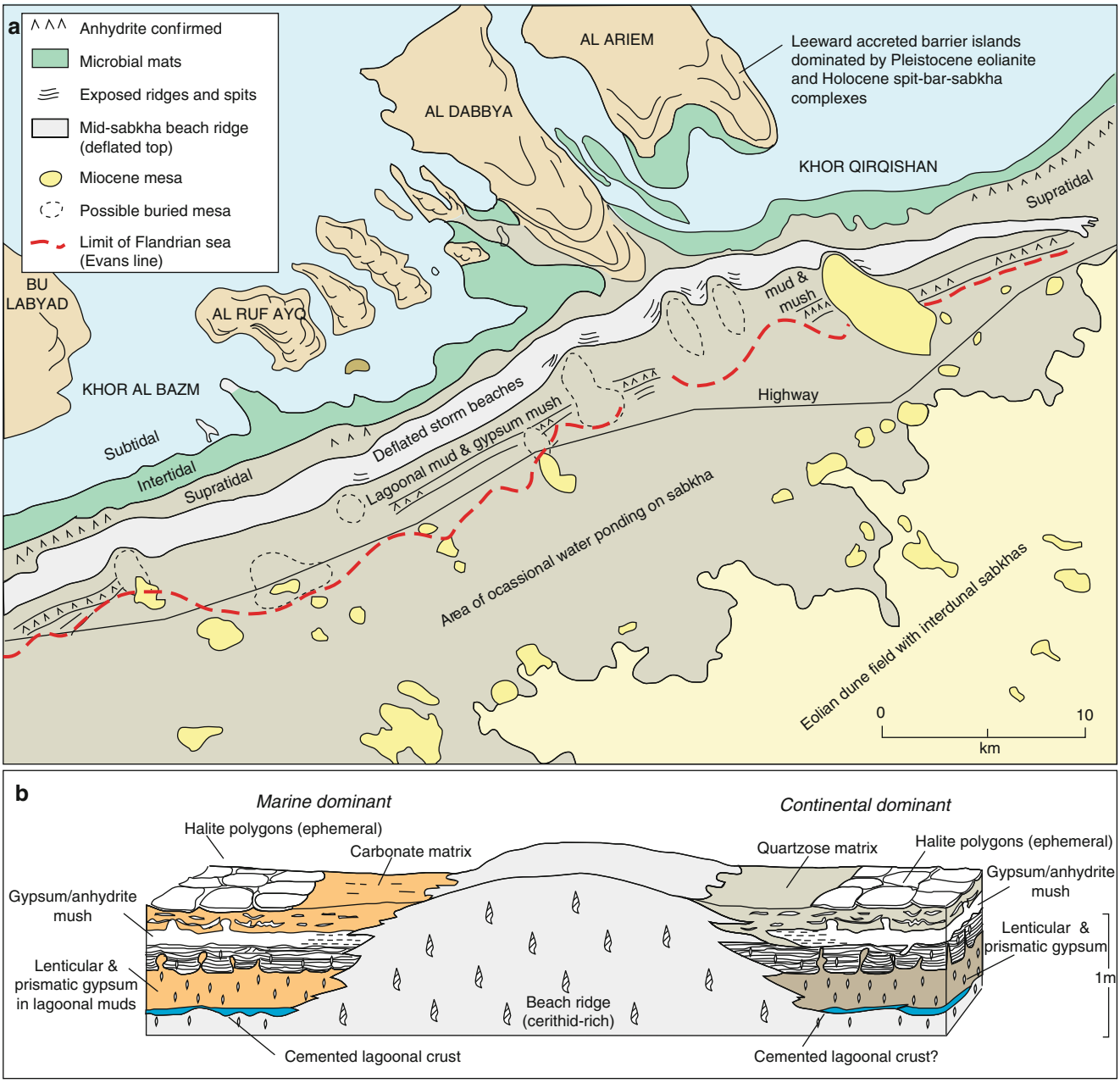

Fig. 3.4 Abu Dhabi sabkha. (**a**) Sabkha facies located to the west of Abu Dhabi showing beach ridges encased in sabkha sediment in the vicinity of Bu Labyad – Al Du'yybaya (After Kirkham 1997). (**b**) Sabkha cross section based on facies present in the vicinity of the beach ridges south of Al Du'yybaya Peninsula and the Mussafah Channel wall (After Warren and Kendall 1985)

workers (Bush 1973; Butler et al. 1982; Kendall and Warren 1988). More recently, Lokier and Steuber (2008, 2009), Lokier (2012) have looked at various polygonal features in the intertidal and supratidal zones. Excellent reviews of the relevant Gulf literature, and some new insights, are given in review papers by Strohmenger et al. 2011; Alsharhan and Kendall (2003), Kirkham (2011), Riegl et al. (2010) and Evans (1995, 2010). Over the past decade or so, the most significant addition to this substantial knowledge base is a drastic revision of our understanding of the dynamics of sabkha hydrology by Wood et al. 2002. It changes our understanding of evaporite capillary salts from one of marine-derived floodwaters to one of solutes precipitated in a Holocene marine matrix, but sourced from resurging basinal waters.

To understand sabkha deposition requires an understanding of the climatic and hydrological factors that create conditions suitable for sabkha progradation into the southern Gulf. The Arabian Gulf is the warmest sea in the world and, like the Red Sea, lies within the most laterally extensive

BWh climate belt in the world (Figs. 2.3 and 3.1). Surface temperatures in the open Gulf range from 20 °C in February to 34 °C in August, with an annual average around 29 °C in waters located offshore from Abu Dhabi. Water temperatures on the open platform in the vicinity of Abu Dhabi Island range from 23 to 34 °C and from 15 to 40 °C in the inner lagoon. Shallow waters in the lagoon can experience daily changes of 10 °C. Air temperatures on the adjacent mudflat can be as low as 5 °C in the winter and as high as 50 °C in summer, with average temperatures ranging from 23 to 33 °C. Sediment surface temperatures on the sabkha are even more variable, with reported values up to 60–80 °C atop dark-coloured microbial mats (Kinsman 1965). Temperatures a few centimetres below the sabkha surface range from 22 to 40 °C. In summer, the sabkha is extremely humid, especially at night, when the humidity reaches 100 %. Salinities in the open Gulf are 3–4‰ above normal open marine salinities. Where coastal islands restrict exchange with the open Gulf, as in the vicinity of Abu Dhabi Island, lagoon salinities range between 54 and 67‰, near double that of the open ocean.

Prevailing onshore winds influence evaporation levels on mud-flats along the southern coast of the Arabian Gulf. In winter the intensity of the onshore winds increases as the Shamal blows seawater and sediment from the lagoon onto the mudflat. At other times offshore winds blow continental dune sand into the back-side of the sabkha. Winter Shamals occur from November through March and tend to follow cold fronts (Riegl et al. 2010). Shamals tend to set in with great abruptness and force, often with wind speeds of 40–50 km/h and gusts up to 100 km/h. Both summer and winter Shamals are known, those in summer being less powerful. This dominant northwest to southeast airflow is a result of orography. Sharply rising mountains lie to the east and north of the Gulf, while gently rising mountains lie to the west and southwest effectively funnelling the low-level airflow. Alsharhan and Kendall (2003) consider the Shamal to be a equally important sedimentological drivers in southern Gulf sedimentation to the Caribbean hurricanes on the Bahamian platform.

The sabkha is furnished with matrix sediment from two sources, carbonates from the lagoon and siliciclastics from the hinterland. Many earlier sabkha models tended to ignore the eolian input, yet some areas of the mainland side of the Abu Dhabi sabkha (e.g. Al Du'yybaya sabkha) have quartz silt and sand as the major matrix material and it is the dominant unconfined aquifer supplying meteoric water to the coastal plain. Rainfall along the sabkha coast averages 70 mm/year and is very irregular, in some years no rainfall is recorded. In the 6-year period from 1958 to 1964 the highest annual reading on the sabkha was 6.73 cm, the lowest 0.33 cm. When rain does fall it can be torrential. Bottomley (1996) notes that in the last 30 years there was at least one 24 h period when more than 200 mm of rain fell on the sabkha. Although infrequent, such desert rains can be torrential, especially in coastal sabkhas near the foot of the Oman Mountains, such as at Rams, where flooded wadis typically carry continental sediments as sheet floods many kilometres into the sabkha (Warren 1991). Rain floodwaters can sometimes cover portions of the sabkha for 1–3 months and so dissolve and recycle surface and nearsurface halite/bittern crusts, as occurred in late 2003 and 2009.

Physiographically, the Abu Dhabi and other sabkhas in the Gulf are characterized by billiard table flatness, a direct reflection of control by capillary wicking, fed from the underlying watertable. The sabkha surface is a Stokes surface (Fig. 3.5a). In general, the watertable control to any sabkha gives them one of the most levelled forms of any arid landscape feature. Below this flat surface the Abu Dhabi sabkha preserves an evaporitic mixed-carbonate-siliciclastic stratigraphy (Evans et al. 1969; Kinsman 1969; Kirkham 1997). Deposition began some 7,000 years ago when a rapid transgression flooded interdunal (eolianite) depressions with a veneer of marine-reworked, predominantly quartzose sediments. About 4,000 years ago the Arabian Gulf shoreline reached its maximum Holocene strandline and the edge of this flooding event is defined by a line of well preserved beach-ridge sediment sometimes called the "Evans line" (Strohmenger et al. 2011) This was followed by pulsed progradation of the sabkha sequence to its present configuration.

Abu Dhabi Facies Associations

The peritidal belt that defines the Abu Dhabi sabkha is divided into three: subtidal, intertidal, and supratidal (Fig. 3.4a). Tidal range is 2–2.5 m along the seaward side of the islands of the southern Gulf, but it can be as little as 1 m in the more restricted lagoonal areas, which are locally known as khors. As the strandzone progrades, the peritidal belts of the lagoon, cyanobacterial mat and sabkha, all located landward of the present barrier island belt, are stacked one atop the other to create an archetypal shallowing-upward sabkha cycle. We will discuss each peritidal belt in detail, but first let's look at a largely ignored part of the southern Arabian Gulf peritidal trilogy, the island shoal and bank facies. This is the unit that protects the muddy lagoons in the vicinity of Abu Dhabi and allows the various coastal sabkhas to form. Facies belts basinward of the island shoal are classic carbonate ramp sediments, while peritidal sediments landward of the island shoal make up the sabkha association.

Island Shoal and Bank Facies

Cemented coastal-beach-dune barriers form the core of a belt of northeast trending carbonate islands that are the easternmost extent of the "Great Pearl Bank" (Wyn Hughes

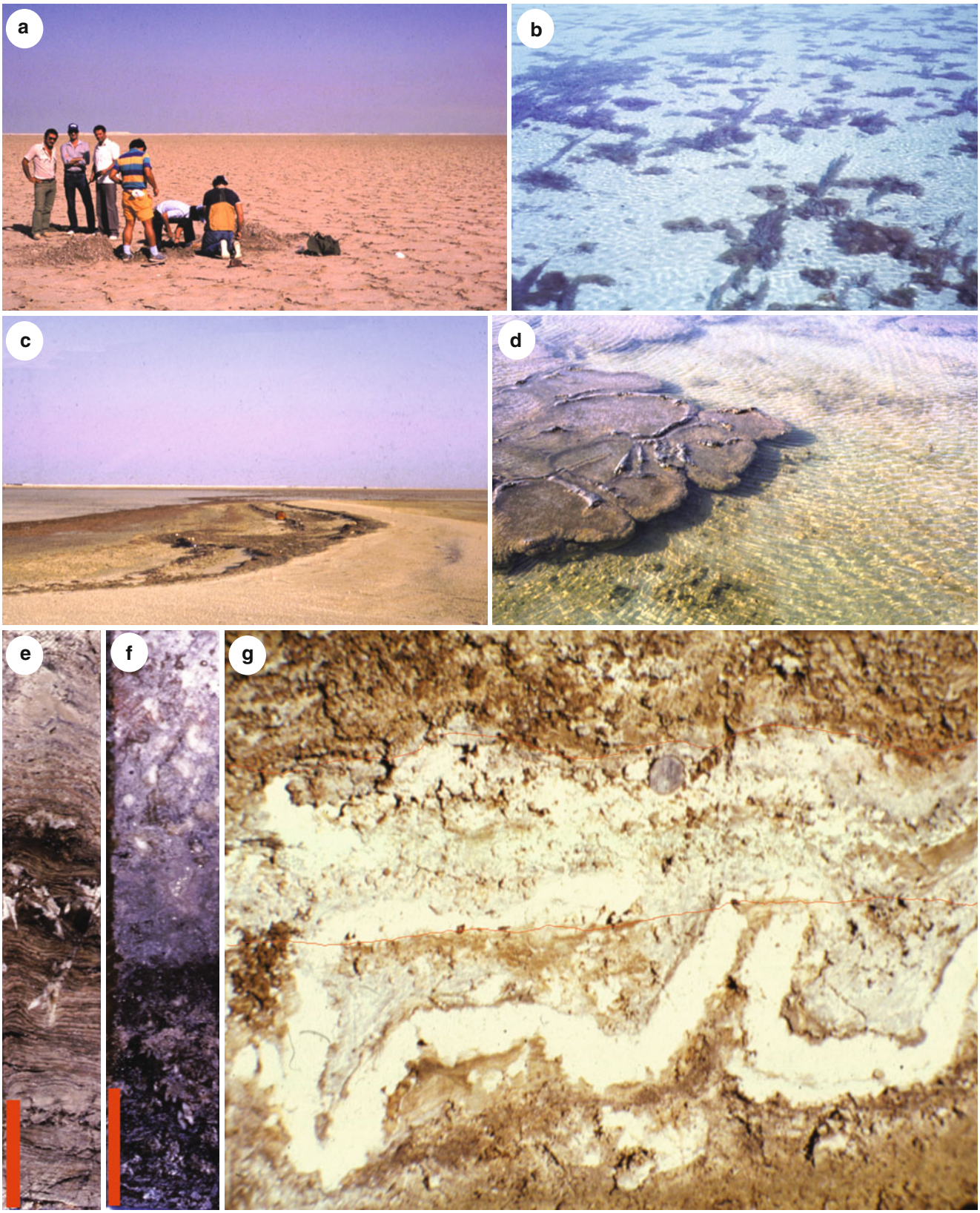

Fig. 3.5 Arabian Gulf sabkha, Abu Dhabi. (**a**) Sabkha surface covered in an ephemeral halite crust; (**b**) Lagoonal sediments of Khor Al B'azm showing peloidal grainstones and packstones with growing clumps of brown algae covered with calcareous epibionts (photo courtesy of Xris Kendall); (**c**) Cuspate, laterally accreting beach ridge on seaward side of Al Du'yybaya sabkha, Abu Dhabi; (**d**) Truncated and grazed edge of laminated polygonal mat at the edge of a tidal pool, southern Khor Al B'azm; (**e**) Core of laminated mat with displacive euhedral gypsum and an overlying unit of supratidal gypsum and anhydrite, sabkha south east of Abu Dhabi City (scale bar = 5 cm); (**f**) Core of cyanobacterial peat (?pustular mat) with lenticular gypsum and an overlying unit of supratidal gypsum and anhydrite, sabkha south east of Abu Dhabi City (scale bar = 5 cm); (**g**) Nodular and enterolithic anhydrite with obvious truncation surface preserved in middle of unit, Al Du'yybaya sabkha

1997). These barriers enclose lagoons or tidal estuarine sequences and in places may directly abut the mainland (Warren 1991). Most of the islands are eolianite-cored shoals, composed of varying proportions of Holocene and Pleistocene ooids, along with skeletal and quartz sands (Teller et al. 2000). Island cores are stationary, fixed in place by carbonate cements, and are separated by active tidal channels up to several kilometres wide and 7–10 m deep (Figs. 3.3b and 3.4a; Purser and Evans 1973; Loreau and Purser 1973). Further up the Gulf coast on the Qatar Peninsula and along parts of the Saudi coast their place is taken by marine-reworked quartzose eolian dune sand shoals, which still have counterparts building directly into the Gulf (see later discussion of eolian sabkhas for details). The coastal barriers and spits along the At Taf coastal strip, which form the depositional frame for the Holocene sabkha, formed in the late Pleistocene via carbonate accretion atop reworked eolian quartzarenites as the desert dunes were inundated during the final phase of Flandrian rise (Purser and Evans 1973; Kirkham 1998; Teller et al. 2000). Up to 9 m of Pleistocene eolian material and 2.7 m of Holocene carbonates overlie Miocene marine carbonates in the vicinity of Abu Dhabi city (Butler et al. 1982). Miocene strata also form mesas and outliers on the landward side of the sabkha (Fig. 3.4a).

Holocene vadose and phreatic cements stabilised the transgressive island shoals at the position of the Pleistocene-Holocene stillstand. Previously, the coastal dune/shoreface had migrated landward in front of the rising late Pleistocene sea. The early Holocene stillstand, in combination with cementation meant the islands evolved into wave-resistive structures fronted by coralgal reefs. This in turn preserved a barrier lagoon, even in the early Holocene when wave-resistive reefs had yet to grow on the seaward side of the now stationary barrier islands. Cemented sands formed a stable substrate for subsequent coralgal reefs and today maintain a relatively fixed focusing grid for wave, longshore and tidal currents.

Island stability in turn maintains the position of numerous active tidal channels as fixed breaches in the cemented eolianite topography. Tidal channels between the islands allow exchange of seawater with the more saline waters of the inner lagoon. The longterm stability of the island shoal facies explains the formation of thick ooid ebb-tidal delta sands on the seaward ends of many channels along the Abu Dhabi coast. Where these ooid sands accumulate above sealevel they are blown into Holocene coastal eolianites, adding volume to the island shoal sediment pile (Fig. 3.3b). If the islands were not cemented stationary structures, then tidal channels and islands would migrate laterally, ebb sands would spread out as much thinner accumulations and form barrier geometries more akin to classic "drumstick" tidal deltas in mesotidal barrier coasts.

Subtidal Facies

Subtidal sedimentation along the Abu Dhabi coastline can be divided into sediments accumulating seaward of the island shoal facies and sediments in the lagoon (Evans 1995):

1. *Open marine sedimentation* occurs along the seaward side of the northeast trending barrier island coast and has largely buried the underlying Pleistocene eolianites and seif dunes (Fig. 3.4a). Seaward terminations of shallow channels draining the lagoon are flanked by tidal ebb deltas composed of oolitic sand. These Holocene lobes form lens-shaped bodies 2–10 km wide and 1–5 m thick. They occur in wave- and tide-agitated areas where ooids are piled into shoals by opposing onshore waves and offshore ebb-tidal currents. The ooid sands (ooid grainstones) are fashioned into various bedforms including break point bars, along with large and small-scale ripples. Skeletal fragments in the shoals indicate a limited macrofauna of molluscs, echinoids and burrowing crustaceans. Broken fragments of this fauna typically form the core or nuclei to individual ooids.

The Gulf lacks many of the algal sediment producers that are found in the Atlantic and Indo-Pacific (like *Halimeda*, *Penicillus*, etc.). Red algae can occur as encrusters primarily associated with other calcareous substrata, such as reef corals, or they can occur in more or less dense growths by themselves (Riegl et al. 2010).

Within the ooid sand pile that define tidal deltas on the seaward end of inter-island channels feeding the lagoons, typical ooid grain size and cortex thickness decreases away from the channel levees. Cemented crusts (aragonite and Mg-calcite) and crust fragments can also be found in the sand pile, much in the same way they occur in the less active portions of Bahamian ooid shoals (Lokier and Steuber 2009). At a water depth of about 2 m on the spillover front of the Abu Dhabi ooid shoals there is an abrupt change into mixed ooid-bioclastic grainstones/packstones. Storms and the wind drive ooid sands onto the island shoal belt and so continue to supply sediment to the barrier islands. High eolian dunes form where active ebb tidal deltas are building out onto the cemented island core. Bedding in these parabolic dunes is inclined landward and retains continental indicators such as occasional rhizoconcretions and insect burrows.

Patch reefs are growing immediately seaward of the Pleistocene-cored islands (island shoal facies) in areas between the ooid shoals. Reefs also extend landward along the sides of some of the more stable open-marine tidal channels, but do not extend far into the more restricted sections of the lagoon. There the waters quickly become too saline for the stenohaline components of the reef to remain healthy (Kinsman 1969) especially during intense temperature and salinity variations induced by Shamal storms (Fig. 3.6; Riegl 2003). Shinn (1976) attributed massive coral die-back in the southern Gulf (Qatar) to a severe Shamal, which caused cooling to 4 °C at sea surface and to 14.1 °C at 18 m

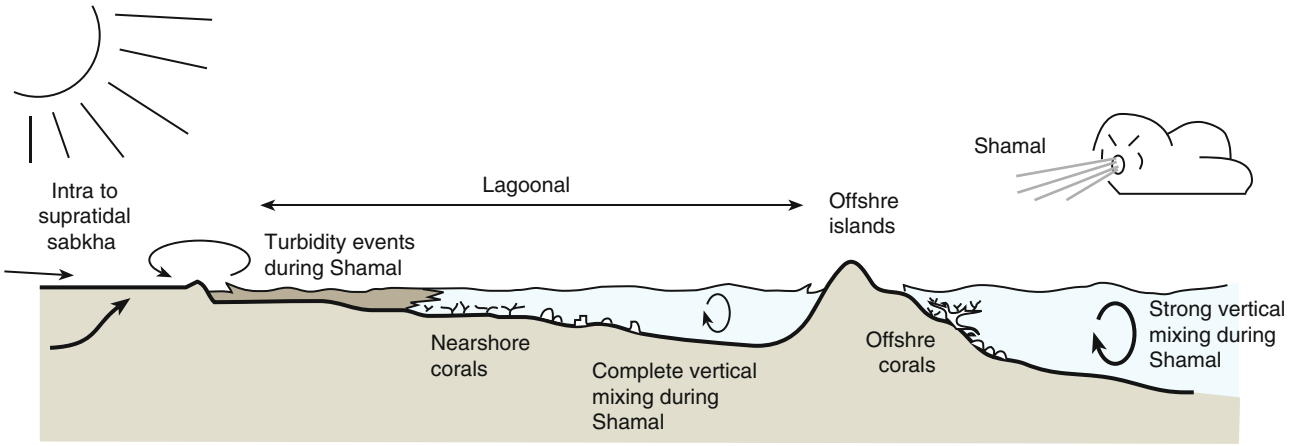

Fig. 3.6 Schematic of hydrodynamics in the near offshore and lagoon/sabkha of the southern Arabian Gulf (After Riegl 2003)

depth. Shamals may generate storm seas of up to 6 m wave height (65 kph winds), driving erosion, turbidity and complete vertical mixing of lagoon waters and partial mixing offshore. Clearly, rapid cooling by Shamals, sometimes coupled with extremely low tides, amplified by negative storm surge, are a significant stress factor causing repeated coral mortality and bleaching throughout the southern Arabian Gulf (Riegl 2003).

Accordingly, when compared to reefs of the open Indian Ocean, the coral fauna of the southern Gulf, even on the open marine side of the islands of the Emirates, is somewhat sparse and restricted but is well adapted to recovery from bleaching events (Burt et al. 2011). Southern Gulf reefs are dominated by genera of *Porites* and *Acropora* along with *Platygyra*, *Cyphastrea*, and *Stylophora, while* binders are dominated by coralline algae (*Lithothamnion*, *Lithophyllum,* and *Goniolithon*.). Regionally, the open marine reefs are dominated by extensive *Acropora* thickets that often extend over many km^2, with a mixed understory assemblage mainly made up of poritids, faviids, siderastreids, and dendrophyliids. In areas of elevated salinity (>45‰), typically in lagoonal habitats, Acropora gives way to Porites dominance.

This is a response to temperature and salinity stresses inherent to the restricted Shamal-prone lagoonal waters of the Arabian Gulf. Salinity and turbidity oscillations mean many of the corals growing along the sides of tidal channels feeding the lagoons appear unhealthy and at times are covered by flourishing coats of green algae, which do better in elevated salinities. Like *Acropora*, echinoids die out in the lagoons although asteroids, and more particularly ophuroids are more salinity tolerant and extend much further into the lagoons.

Seaward of the coral-fronted islands is a broad gently sloping Holocene platform covered by skeletal sands, which pass offshore into progressively deeper and finer-grained carbonate silts and muds of the Gulf centre. This sloping profile is one of our better modern analogs for ancient carbonate ramps (Evans 1995), while the Great Pearl Bank makes and excellent Holocene analogue for Cretaceous rudistid buildups (Wyn Hughes 1997).

2. *Restricted marine (khor) sedimentation* takes place along the landward side of the barrier islands in areas dominated by lagoon and sabkha sediments (Fig. 3.5b). The tidal inlets and khors (*khawrs*) are unique subtidal settings formed behind the grainstones of the island shoals and constitute the protected seaward edge of many sabkhas. They vary in shape and size from large elongate lagoons such as Khor al B'azm and Khor al Baghi (behind Abu Dhabi Island) to the estuarine inlets of Umm Al Qwayn (Warren 1991). Most channels are dendritic (tidal) and lack any permanent surface freshwater inflow on the updip side (Warren 1991). The exceptions are those khors located close to the mountains near the Straits of Hormuz, which can be periodically flushed by meteoric runoff. Today many khors in the Emirates are dredged to form accessible waterways and sheltered harbours. Some deepened channels can now accommodate large dhows and other seagoing vessels, whereas undredged natural tidal channels into the khors are typically less than a metre or two in depth, even at high water.

Tidally- scoured lagoonal channels join the open-marine settings to the restricted-marine lagoons or khors. Channels are floored with skeletal and peloidal sands, which are reworked by tidal and wave action into crossbedded skeletal/peloidal grainstones. Toward their inner parts, in the lagoon proper, the channel floor sediments become sandy muds (peloidal/skeletal packstones and wackestones). Wherever they poke through a thin lag of coarse shell and intraclasts, cemented calcareous eolian sands (eolianite) sometimes crop out on the channels floors.

Extensive shallow-water lagoons, filling with bioturbated packstones and wackestones, occupy the shallower parts of

the khors away from the channels. Because of their higher elevation relative to the lagoonal channel floors, subaqueous areas of khor away from the channel are sometimes described as lagoonal terraces. Terrace sediments entrain a diverse biota made up of many benthic species but relatively few phyla (Kendall and Skipwith 1968b). Molluscan sands and peneroplid foraminifera dominate the more open terrace areas, whereas pelleted carbonate mudstones with a sparse fauna accumulate in the more protected reaches. Cyanobacterial grain coats and biofilms are abundant on the lower-energy terrace sediments and encourage healthy populations of cerithid gastropods, which through their grazing contribute a large proportion of the pellets in the lagoon. Crustaceans and worms also heavily burrow terrace sediments. The somewhat elevated temperatures and salinities on the lagoon floor drive seafloor cementation of these ubiquitous pellets.

In the more marine parts of the terraces various sea grasses and seaweeds (brown algae) form dense carpets on the channel floors, along with healthy epiphyton coats of bryozoans and calcareous algae (Fig. 3.5b). There are four species of seagrass in more open marine parts of the khors and further offshore: *Halodule uninervis, Halophila stipulacea, H. ovalis* and *Syringodium isoetifolium. Halodule uninervis* is the dominant species of seagrass in the southern Gulf and in the UAE is the major food-plant taken by herds of grazing dugongs.

One of the more interesting mega-fossils preserved in the Abu Dhabi sabkha sediments is a cetacean (Stewart et al. 2011). These whale remains (a left and right mandible, scapula, humerus and fragmentary radius and ulna as well as parts of the cranium and rostrum) belong to a humpback whale (*Megaptera cf. novaeangliae*) and were found in excavated edge of the Musaffah Industrial Channel (now backfilled). Sediments encasing the whale bones were age-dated at approximately 5,200 ^{14}C yrs BP and are therefore interpreted to correspond to the late Flandrian sea-level peak, preceding a fall in sea-level which culminated in the supratidal sabkha overprint of the carbonates. Associated with the whale remains is an assemblage of molluscs, foraminifera and ostracods. Together with the inferred presence of sea grass and algae, these facies are interpreted to indicate a very shallow subtidal to intertidal lagoonal environment. Cirripede remains found associated with the skeleton were identified as those of the whale barnacle *Coronula diadema* and hence had their origins with the whale. Significantly, the low species diversity of microfossils associated with the whale remains suggests that higher salinities existed in the mid-Holocene lagoon than are present in its modern counterpart and tied to the onset of continental aridity in Arabia during the mid-Holocene (Stewart et al. 2011).

Due to the saturated state of lagoonal and intertidal waters, isopachous crystalline rinds and micrite crusts, composed of aragonite and Mg-calcite, bind large areas of the lagoon terraces into cemented layers. Ongoing expansion of the layers creates dm-scale tepee structures or megapolygons up to 165 m across, which can also be traced upslope into the base of the intertidal zone and also occur further offshore in fully subaqueous settings (Fig. 1.25a; Shinn 1969; Kendall and Warren 1987; Lokier and Steuber 2009). Tepee-overprinted ridges on the lagoon floor create a stable substrate or holdfast for much of the larger epiflora as well as a healthy population of borers. Seaweeds tend to attach themselves to tepee ridges in preference to the less stable muddy bottom veneer that forms the lagoon bottom away from the tepee crest.

Intertidal Facies (Strandline Sands)

Waves can drive loose terrace sediments shoreward to build narrow sandy beaches and berms of peloidal and skeletal grainstone, typically with landward-directed cross stratification (Figs. 3.3a, b, 3.5c, and 3.7a; Evans 1995; Warren and Kendall 1985). Cerithid gastropods, which populate the more landward parts of most khors, are a major skeletal component of the ridge sands, as are bivalve fragments and benthic forams. In areas more exposed to wave action the beach ridge sediments are coarser, ranging from coarse sands to skeletal gravels (rudstones). Locally, low-relief tidal levees and ridges enclose monospecific mangrove swamps (*Avicennia marina*) where sediments tend to be highly bioturbated muds crosscut by rhizophores. More typically, the narrow beach ridges in a sabkha coast are transitional into the cyanobacterial-dominated intertidal sediments that typify much of the intertidal zone of the inner lagoon (Fig. 3.4a).

I have trenched and cored buried equivalents of these beach ridges within various parts the Abu Dhabi supratidal sabkha succession, they are most obvious in the sabkha to the south and west of the Al Du'yybaya peninsular (Fig. 3.4a). Historically, they have not been well documented as a facies within the Abu Dhabi sabkha as the tops of older ridges landward of the modern strandline are typically deflated and buried beneath a halite crust (Fig. 3.7a). Southeast of Khor al B'azm a line of deflated beach ridges lies behind the currently active area of sabkha sedimentation. It is some 3–4 km inland of the present edge of the lagoon and forms the seaward edge of a 10 km wide belt of older Holocene sabkha sediments (Fig. 3.4). Remnants of an older sequence of beach ridges define the maximum extent of the Flandrian (Holocene) transgression (aka the "Evans Line"), indicating the initiation of the seaward progradation of the Holocene sabkha coastline and the occurrence of supratidal $CaSO_4$ facies. Portions of this ridge system are now buried beneath lagoonal muds. The contact between more oxidised beach-ridge pore waters and the reducing waters of the lagoon muds is typically defined by an iron-stained band of lenticular and prismatic gypsum (Fig. 3.7a).

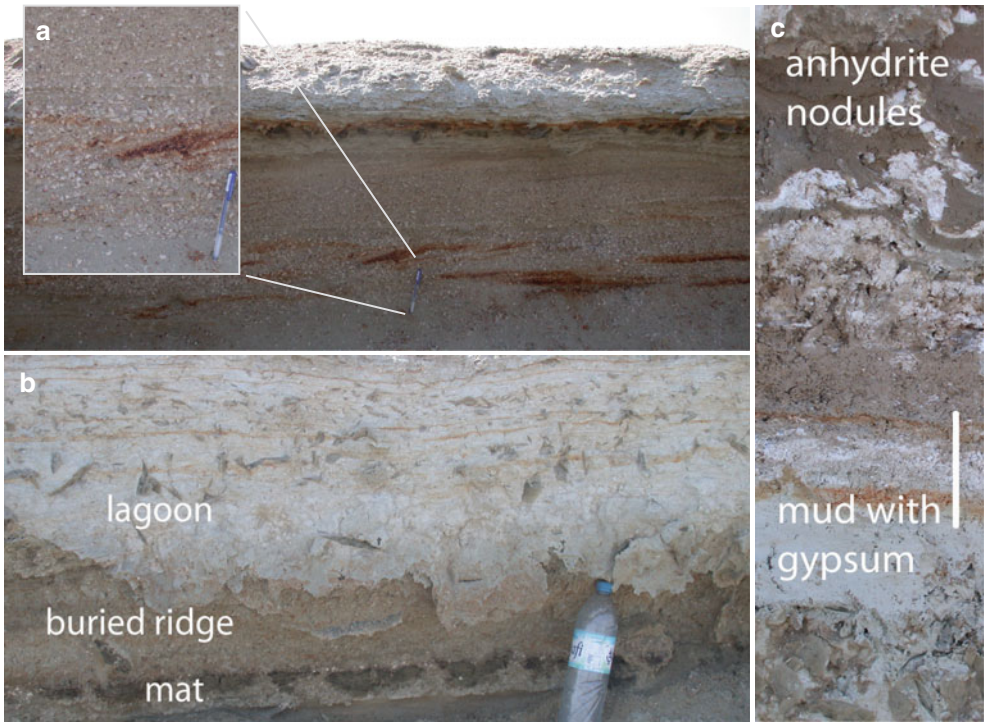

Fig. 3.7 Styles of $CaSO_4$ occurrence exposed in the Mussafah Channel, Abu Dhabi: The trench is actually the wall of a man-made shipping canal cut into the sabkha near the Mussafah Industrial Area. The locality is over 7 km landward of the present-day restricted lagoon and 25 km from the open Arabian Gulf waters. (**a**) Buried beach ridge gastropod rudstone showing landward-directed low-angle accretionary bedding and gypsum at the contact with overlying mud (*inset* shows detail of bedding). (**b**) Buried algal mat (*dark blebs*) overlain by ridge and lagoon sediment, with lenticular gypsum growing in the overlying lagoonal muds. Site is located about 50 m seaward of ridge in (**a**). (**c**) Enterolithic anhydrite in the supratidcal sabkah which is a lateral equivalent of gypsum in 3.6b, the site is located around 200 m northwest of the gypsum in 3.6b. Scale bar is 10 cm long

The presence of Holocene beach ridges along the coast on the seaward side of the present day sabkha supratidal, the presence of older largely buried and deflated Holocene beach ridges in the mid sabkha, and the relicts of early Holocene ridges defining the most landward extent of the Flandrian transgression clearly show Holocene sabkha progradation is not a simple seaward progression of peritidal facies. It is a punctuated and possibly forced regression (Warren and Kendall 1985; Warren 1991; Kirkham 1997; Strohmenger et al. 2011). Similar beach ridges within Holocene sabkhas are described from the northern Emirates by Al-Farraj (2005), from Kuwait by Picha (1978) and from northeast Qatar by Shinn (1973).

Intertidal Facies (Lagoon-Edge Muds)

Away from the active beach ridges, the intertidal zone is divided into upper and lower intertidal facies, although the lower intertidal facies of some workers is equivalent to the lagoonal terrace facies of others. The confusion stems from the presence of a wide cemented flat along the mainland shore of the various khors; a flat that is covered by rippled peloidal sands or muddy sands (peloidal grainstones and packstones) and hosts a dense population of cerithid gastropods. Some authors place this flat in the shallow subtidal as an extension of the lagoonal terrace, while others place the cemented terrace in the lowermost intertidal. The lack of firm definition of its distribution is due to the flat, shallow nature of the southern Gulf sediment surface. This means minor variations in wind direction, speed and the barometric pressure can cause the predicted tides in the khors to remain either "out" or to advance several kilometres further "in" than predicted. Longer term seasonal variations follow a more defined if unusual pattern, with inundation of many otherwise "supratidal" areas, that is large areas of sabkha flat, not occurring until late autumn (post-equinox). Hence, the lateral extent (strandzone) of the intertidal area of sedimentation in the UAE is large, but poorly defined. Even the terms tidal to describe sheets of lagoon water that at times cover more than the uppermost parts of the sabkha "intertidal" is a little misleading as the process driving the sheets further landward is typically the shamal.

Geologically, what defines the muddy intertidal facies is evidence of cyanobacterial (aka algal) mats. Mats first occur as degraded cyanobacterial peats in a transitional 100–200 m-wide zone where the bare lagoonal flats pass landward into a belt of well-preserved laminated mats

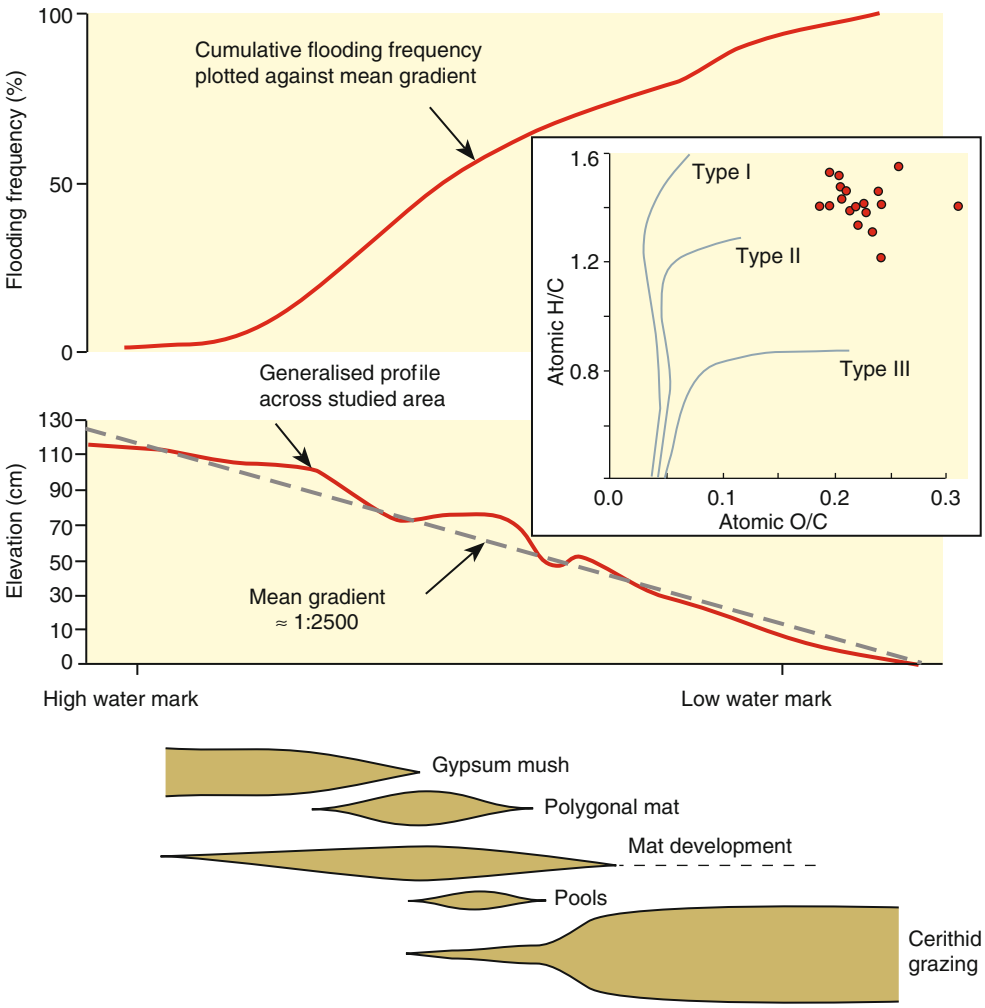

Fig. 3.8 Distribution of cyanobacterial mats in relation to tidal range, flooding frequency and cerithid grazing on the Abu Dhabi coast. *Inset* shows van Krevelen plot of protokerogen type in mat organics (After Park 1977; Alsharhan and Kendall 2003)

(Figs. 3.5e, f and 3.7b; Kendall and Skipwith 1968a; Park 1977). Hence, the lower intertidal is defined by degraded oxidised peats composed of the bioturbated remnants of cyanobacterial mat. The upper intertidal facies is variably defined by laminated microbial mats across an extensive belt up to 1–2 km wide. These biolaminites accumulate in moist intertidal areas where salinities and temperatures are too hostile for cerithid gastropods and the other grazing animals of the lagoon flat (Fig. 3.8). Many mats have sharp edges on their seaward side due to the grazing activities of the cerithids and other salinity-tolerant gastropods (Fig. 3.5d). Sediments in the microbial flat are dominated by mm-laminated mudstones up to 50 cm thick composed of cyanobacterial remnants interlayered with aragonite muds. Periodic exposure means many mats are crosscut by desiccation cracks and are termed polygonal mat. Measured TOC contents of the microbial mats vary between 0.5 and 2.7 %, with hydrogen indices between 510 and 675 in a range of type I-II protokerogens, with a $\delta^{13}C_{PDB}$ range from −8.41 to −10.78‰ (see inset in Fig. 3.8; Kenig et al. 1990; Kenig 2011). The highest TOC contents in the Abu Dhabi sabkha occur in mangrove peats (up to 8.6 %), not in microbial mats. But these mangrove-derived organics contain higher levels of higher plant protokerogen and so would constitute of more gas-prone source of future hydrocarbons.

Most of the literature on the sabkha gives the impression that laminated cyanobacterial mat is the only type of microbial sediment accumulating in the upper intertidal zone. Yet, in almost every area of mat I have visited along the mainland shores of the various khors of the Arabian Gulf, laminated mat tends to occur beneath the floors of shallow channels and pools (waters a few centimetres deep), separated by interchannel areas of rugose or pustular mat. The sedimentary signature of the pustular mat is a poorly layered organic-rich mush or peat, often mixed with patches of lenticular gypsarenite. Thus, the intertidal zone in an ancient equivalent need not be laminated to be microbial in origin.

Many intertidal mats are crosscut by desiccation cracks that contain euhedral or lenticular (diagenetic?) gypsum crystals up to 2 mm long (Figs. 3.5e, f and 3.7b). Gypsum is especially common in areas of pustular mat and along the landward side of the cyanobacterial belt, where it passes into

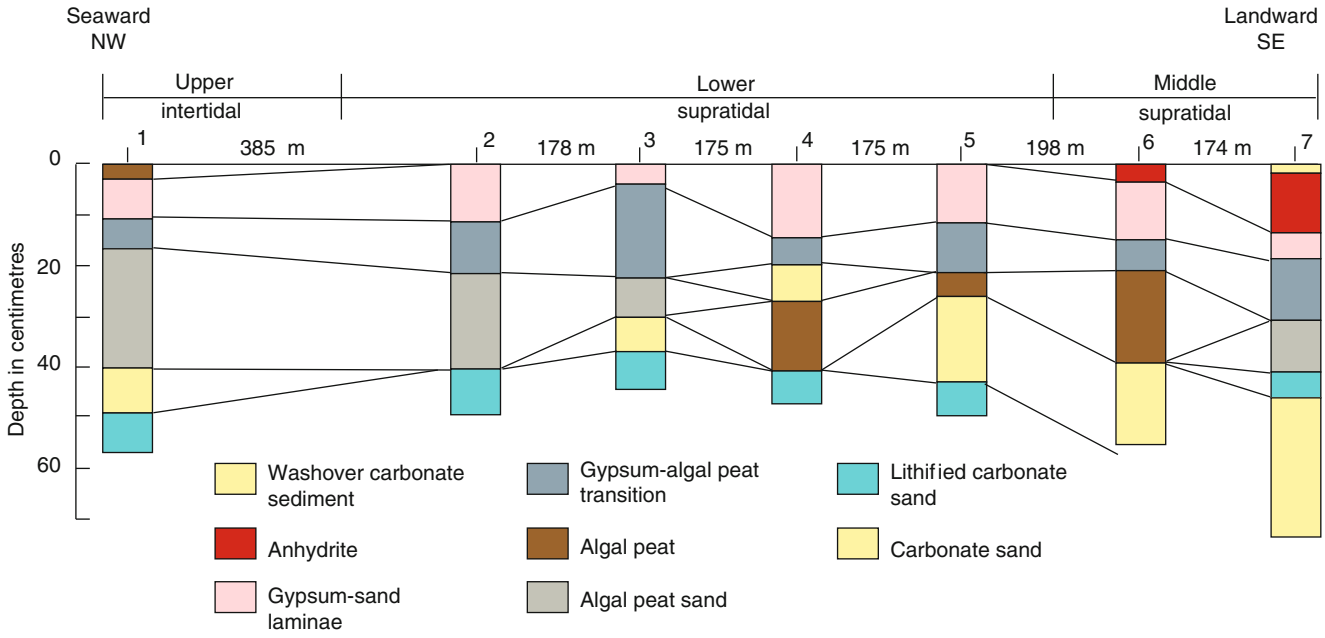

Fig. 3.9 Lithofacies distribution in subsurface across the upper intertidal to middle supratidal along the southern shore of the SW Khor al B'zam south of Al Qanatir Island, western Abu Dhabi (After Alsharhan and Kendall 2003)

the gypsum mush zone. Aragonite, magnesite, and dolomite locally cement surface and shallowly buried sediments of the cyanobacterial flat (Butler et al. 1982).

Arabian Gulf sabkha dolomites were first documented by Wells (1962) and are one of the two or three areas on the world's surface where Holocene dolomites are forming over aerially extensive regions, even if the actual distributions are somewhat thin and patchy (Warren 2000a). Holocene dolomite distribution in the Abu Dhabi sabkha is closely tied to the presence of cyanobacterial mat, suggesting that microbes and sulphate-reduction are involved in the dolomite mineralization process (Bontognali et al. 2010, Bontognali et al. 2012). The 16S rRNA gene sequence of a microbial isolate from the mat revealed a 99.6 % identity (i.e. same species) with *Desulphovibrio brasiliensis*. This is the sulphate-reducing bacterium, previously isolated from Lagoa Vermelha (Brazil), and known for its ability to metabolically precipitate dolomite.

Supratidal Facies

That part of the sabkha landward of the microbial mats and active beach ridges is further subdivided into three subfacies: lower, middle and upper supratidal (Figs. 3.4 and 3.9).

Lower Supratidal Lower supratidal sediment accumulates in a belt just above the high water mark (hwm) in a zone up to 2.5 km wide and flooded perhaps once or twice a month during high spring tides. It is characterized by a mushy gypsum bed, up to 30 cm thick, which passes seaward into cyanobacterial mat. Its lower part is an aragonite mud, crisscrossed by cyanobacterial filaments and isolated gypsum prisms (Fig. 3.4b). The upper part is a near-thixotropic mush of lagoonal mud and small, mostly sand-sized lenticular gypsum, with an occasional 1–1.5 cm long crystal. Much of the mush is thought to grow as displacive gypsum crystals within the capillary zone, from pore waters not saline or hot enough to precipitate anhydrite. If it desiccates, the surface of the mush can alter to white bassanite ($CaSO_4 \cdot 1/2H_2O$), or to anhydrite during longer hotter, dry periods.

Middle Supratidal The middle supratidal is a belt of sediment up to 1.6 km wide covered by lagoonal water at less than monthly intervals. It is characterized by growth of nodular anhydrite or gypsum within the sediment matrix. In the shallow subsurface, well away from the lagoon, there is a lateral transition from gypsum to anhydrite (Fig. 3.9). Subsurface and surface anhydrite nodules can increase in size and number in a landward direction until in some areas they eventually form interlocking polygons. Along the Al Du'yybaya sabkha, pockets of gypsum crystals are mixed with anhydrite nodules and layers, especially on the landward side of this zone, where they are dispersed in a matrix of reworked eolian quartz sand and silt (Wilson et al. 2013). An ephemeral halite crust and thin patches of loose blowing siliciclastic and carbonate sands sometimes cover the middle sabkha surface.

Intrasediment anhydrite tends to grow as nodules above the watertable, while displacive and pore-filling gypsum precipitates in sediments immediately beneath the sabkha watertable (Fig. 3.7c). Crystal growth breaks up and destroys laminar textures in some buried biolaminites (Fig. 3.5e, f). The seaward part of the middle supratidal is also the zone

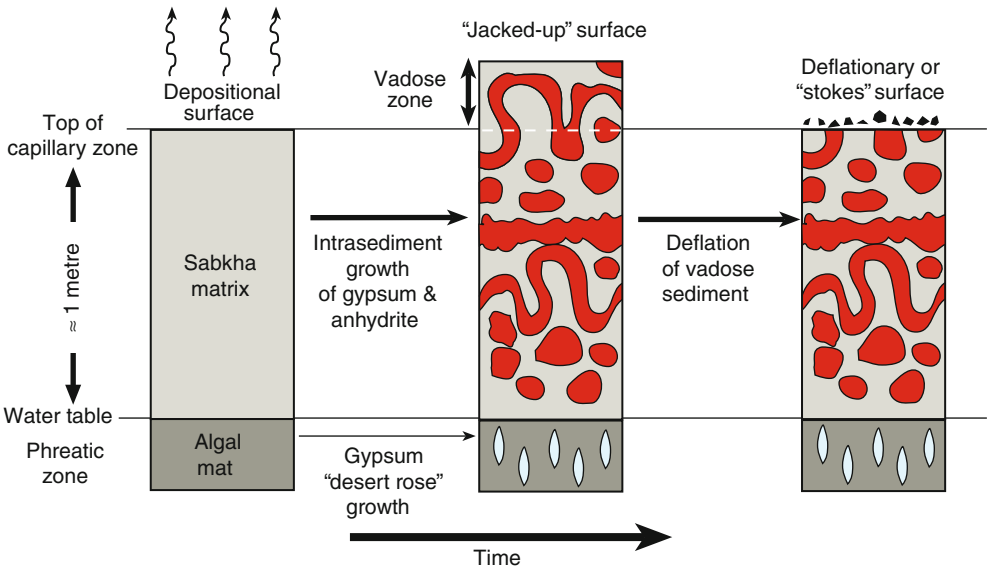

Fig. 3.10 Capillary evaporation in the sabkha precipitates nodules and crystals of gypsum and anhydrite in the capillary zone. This increasing volume lifts the upper part of the sediment column out of the zone of capillary water into the vadose zone where it deflates to leave behind the characteristic erosional surface that caps modern and ancient sabkhas. It is a type of Stokes surface (After Warren 1991)

where dolomite is most common. It grows best as a pore cement in aragonite muds and can replace portions of the lower supratidal and intertidal mud facies (McKenzie et al. 1980; Butler et al. 1982).

Upper Supratidal In the vicinity of Abu Dhabi city the upper supratidal zone is up to 4.8 km wide and is rarely flooded by seawater (less than once every 4–5 years) when there is a fortuitous combination of storm surge and high tide. In this, the most landward zone of the sabkha, the gypsum mush can be completely replaced by coalesced nodules of "chicken-wire" anhydrite to form near pure intervals that are up to 30 cm thick and lie mostly above the watertable, not immediately below the landsurface (Figs. 3.5g and 3.7c). Ongoing growth of irregular anhydrite layers creates "thrust" folds, ptygmatic and enterolithic folds, and diapir-like protuberances. Beneath this zone much of the original cyanobacterial lamination is partially or completely obliterated by the growth of clusters of large prismatic to lenticular gypsum crystals (6–25 cm in diameter, locally known as desert roses). Anhydrite and gypsum also fills the interior of hollow aragonitic shells, especially the former living chambers of cerithid gastropods. Along its most landward extent, the upper supratidal anhydrite layer can contain gypsum after anhydrite, with some nodules constructed of mixtures of both gypsum and anhydrite.

Widespread displacive calcium sulphate growth in the capillary zone sediments raises the sabkha surface out of the capillary zone to form a widespread erosional surface. As the rising sediments enter the vadose zone they dry and are blown away to leave behind the characteristic erosion surface of a sabkha sequence, covered in places by a deflation veneer (Fig. 3.10).

This erosion surface, especially where it truncates enterolithic or ridge anhydrite is one of the most useful indicators of the sabkha hydrology. Like other Stokes surfaces, it defines the top of the capillary fringe (Fig. 3.5g). Its presence in an ancient sabkha clearly distinguishes this style of truncated nodular anhydrite layering as penecontemporaneous and cannot be the result of burial conversion of gypsum to nodular anhydrite.

In times of drought much of the middle and upper sabkha is covered by a pock-marked crust of halite, crosscut by pressure ridges and petees. This crust contains a range of efflorescent bittern and nitrate salts, but is dissolved and the soluble products flushed seaward with the next intense rainstorm or sheet flood. It is an ephemeral crust with a decoupled hydrology much like salt crusts in Australian salt lakes, as described in the previous chapter. Cm-sized displacive halite crystals can grow below these ephemeral salt crusts in the uppermost few centimetres of the upper supratidal sediments, attesting to the infrequency of surface water in this region. The coming and going of the halite crust at the depositional surface of aggrading sections of the Abu Dhabi sabkha strongly influences textures in the remaining "supratidal" sediments (Fig. 1.46a). Although the halite crust is ephemeral there is a strong inheritance in the position of the ridges in the crust each time it reforms; it seems the topography of the underlying sediment surface is the primary controlling factor on halite polygon development. In almost all cases recurrent polygon margins form in association either with low-amplitude mud ridges or with exposed anhydrite mounds (Goodall et al. 2000; Lokier 2012).

Sabkha Hydrology and Hydrogeochemistry

Hydrologically, much historic argument in the Abu Dhabi sabkha has dealt with the ultimate origin of the pore waters precipitating supratidal sulphate, i.e. marine flooding versus continental storm runoff (Fig. 3.11a). Hydrogeochemical

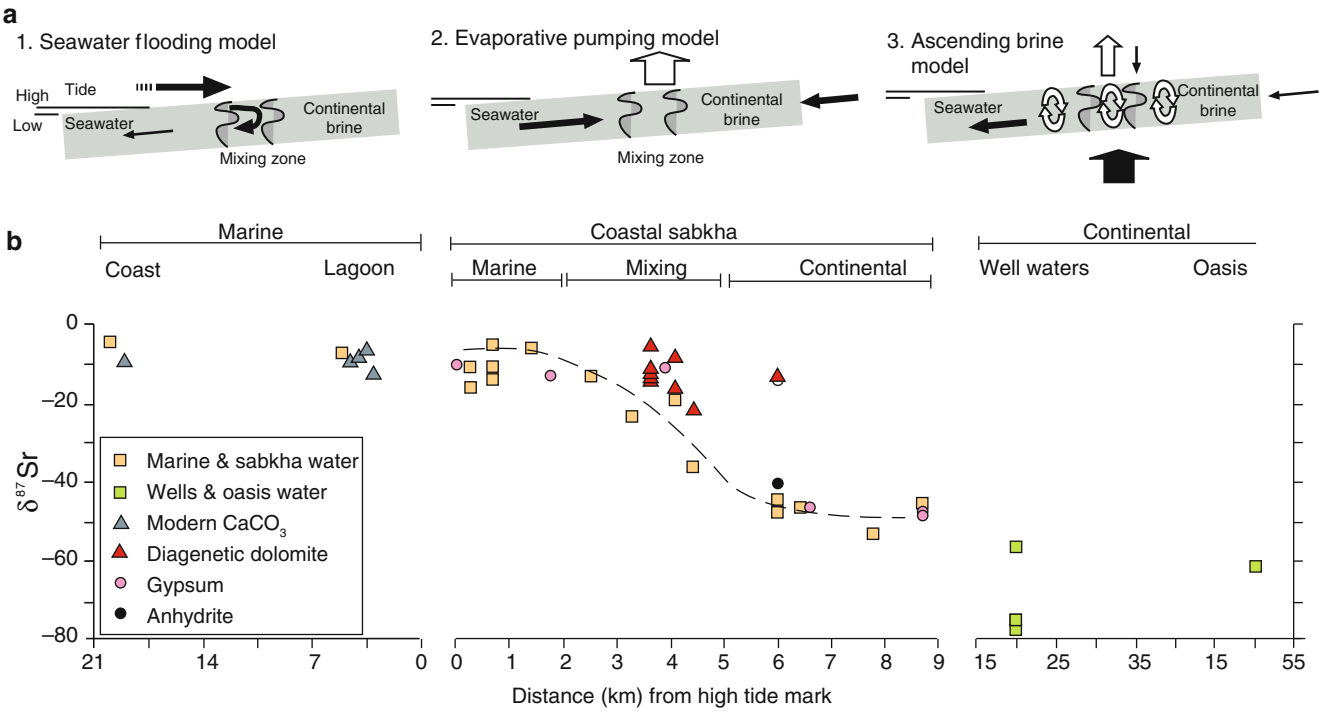

Fig. 3.11 Hydrology of the Abu Dhabi Sabkha. (**a**) Schematic of various models for sources of solutes in the (*1*) seawater-flooding model, (*2*) evaporative-pumping model, and (*3*) ascending-brine model. Open arrows indicate vapour loss, solid arrows represent solutes, and width of arrows indicates relative solute mass (After Wood et al. 2002). (**b**) Analysed $\delta^{87}Sr$ values for water, carbonate and sulphate samples versus distance from the high tide mark. On the basis of these values the sabkha hydrology is divided into marine, mixing and continental zones with the dashed line representing the generalised trend (After Müller et al. 1990)

work in the 1960s and 1970s argued for a largely marine origin of the sabkha brines, which were supplied and replenished by occasional Shamal-driven tidal/storm seawater floods (Kinsman 1969; Butler et al. 1973). The seawater-flooding model was the first to provide a mechanism for cycling ions through capillary sediments and so account for the observed dolomite and calcium sulphate (Fig. 3.11a). An alternate "evaporative-pumping" model was proposed by Hsu and his coworkers (Hsu and Siegenthaler 1969; Hsu and Schneider 1973) and included in the layered seawater flood/upwelling models of McKenzie et al. (1980), which suggested a compartmentalised hydrology made up of aquifers and aquitards and that capillary evaporation from the sabkha induced lateral flow of both seawater and continental groundwater (Fig. 3.11a). All these early models suggested that seawater, either by flood recharge or seepage reflux, was the dominant supplier of ions to the salts precipitating in the coastal plain. Much of the base hydrochemical data for a marine source was ambiguous. And, some measurements such as strontium isotopes suggested the possibility of at least a partial continental source to the ions in the sabkha groundwaters (Fig. 3.11b; Müller et al. 1990). Warren and Kendall (1985) and Warren (1991) noted that much of the matrix hosting the coastal sabkha salts of the Emirates was not marine but was a continental eolian sediment. Warren (op. cit.) also noted that, as the sabkha prograded, pore waters were replaced by continental fluids and that in ancient counterparts marine hydrologies probably only dominated the most lagoonward portions of the coastal sabkha flat.

Much of this earlier work extrapolated longterm hydrological processes over the whole sabkha coast, based on short term observations of the effects of Shamal winds and storm surges covering the sabkha with sheets of water, and on studies of a limited number of shallow trenches and transects. The assumption was that the solutes accumulating in the sabkha were derived and replenished in these occasional marine and wadi sheetfloods. Recent detailed groundwater study of the sabkha has concluded much of this earlier hydrological discussion assuming a marine solute source to the sabkha is largely erroneous or irrelevant (Sanford and Wood 2001; Wood and Sandford 2002; Wood et al. 2002; Wood et al. 2005).

Quantitative hydrological modelling uses longterm (1–2 year) monitoring of changing water levels and chemistries in a continually logged database across the sabkha. It is made up of data from 490 wells drilled to 1–2 m below the sabkha watertable, including a number of piezometer nests (listed as RP wells in Table 3.2) and six deep cased wells to monitor deeper hydrological circulation (listed as GWP wells in Table 3.2). The deep wells were drilled to depths of more

Table 3.2 Well Information from Abu Dhabi sabkha

Well name	Depth (m)	Unit well screened	Depth to water (m)	Conductivity (m/d)	Dissolved solids (g/l)	Density (g/cc)
GWP-287A	121	Tertiary	–20.6	–	118	1.080
GWP-288A	89	Tertiary	–9.5	–	37	1.026
GWP-289	120	Tertiary	–4.6	–	22	1.025
GWP-290	88	Tertiary	–7.7	–	50	1.037
GWP-291A	142	Tertiary	–22	–	96	1.069
GWP-292	120	Tertiary	–13.0	–	146	1.097
GWP-306A	137	Tertiary	–8.3	–	107	1.082
RP-1-2.5	0.8	Sabkha	–	–	275	1.175
RP-1-10	3.0	Sabkha	0.95	0.6	286	1.187
RP-1-36	11.0	Sabkha	0.96	0.6	283	1.184
RP-2-4.5	1.4	Sabkha	0.17	–	104	1.071
RP-2-12	3.7	Sabkha	0.28	–	194	1.132
RP-2-21	6.4	Sabkha	0.19	0.3	214	1.152
RP-3-3	0.9	Sabkha	0.59	–	238	1.197
RP-3-10	3.0	Sabkha	0.59	–	232	1.174
RP-4-3	0.9	Sabkha	0.79	–	237	1.199
RP-5-16	4.9	Sabkha	1.56	1.0	131	1.070
RP-5-35	10.7	Sabkha	0.71	–	140	1.072
RP-6-2.5	0.8	Sabkha	–	–	238	1.178
RP-6-10	3.0	Sabkha	–	1.3	241	1.180
RP-6-16	4.9	Sabkha	–	2.0	240	1.180
RP-6-35	10.7	Sabkha	–	0.4	242	1.183

Minus signs in "depth to water" column indicate water level below landsurface
After Wood and Sanford (2002)

than 100 m into the Tertiary aquifers that underlie the sabkha (Fig. 3.12a, b). These real time measurements, and the resultant realistic hydrologically and geochemically balanced models, show that some 95 % of the solutes precipitated as salts in the capillary zone of a sabkha are derived from ascending deeply-circulating continental brines; only minor amounts of the solutes are derived from rainfall or from lateral groundwater flow entering from nearby areas, including the ocean. Solute load in the capillary salts are largely decoupled from the rainwater cycling in the sabkha as are the salt crusts, which dissolve and reprecipitate with each flood-desiccation cycle. Flood recharge of marine water does not supply ions to the capillary salts of the sabkha, upwelling or ascending continental groundwaters do (Wood and Sandford 2002).

Potential (pan-measured) evaporation rates of fresh surface water on the sabkha are ≈ 3,500 mm/year. But free surface water rates are not the same as actual rates of evaporation of pore waters held in the sabkha capillary zone by pore surface tension (Fig. 2.10). Measured evaporation rates, using a humidity chamber, were around 0.24 mm/day at site 1 and 0.14 mm/day at site 2, with rates of evaporation changing with time of day (Fig. 3.12c, d). These values are 3 % of the pan evaporation rates at both measurement sites and correspond roughly to the mean annual rainfall throughput at both sites (90 mm/year for Abu Dhabi City and 50 mm/year at Sabkha Matti). The estimated rainfall recharge to the sabkha occurs at a rate of 640 m^3/year in the representative volume illustrated in Fig. 3.13. A mean value of 69 mm/year (from humidity chamber values) for evaporation gives a value of 690 m^3/year for the volume of water lost in the sabkha, as shown in Fig. 3.13. This volume of evaporative loss is about 15 times that of upward leakage from the underlying Tertiary aquifer (45 m^3/year), and there is a meteoric-evaporation deficit of ≈ 50 m^3/year. Put simply, the sabkha is taking up Tertiary groundwaters like a sponge.

The humidity chamber measurements also showed that water flux during the night can be reversed at times when the humidity in the air above the sabkha exceeds the activity of water on the surface of the salt crusts, causing night dew and some redissolution of the crusts. Periods of reversal are the times when the sabkha evaporation values are less than zero in Fig. 3.12c.

Ongoing capillary evaporation means water level in the sabkha is typically around 1 m below the sabkha surface (Table 3.2). Pore waters above this level are held in the pore throats by capillary pressure. Measurement of squeezed pore waters shows most salinities in the unsaturated zone are in the gypsum/ anhydrite saturation range, as are waters at and just below the watertable (130–290 mg/l), with brine densities ranging from 1.070 to 1.187. Measured conductivity (permeability) of the sabkha sediment is between 0.3 and

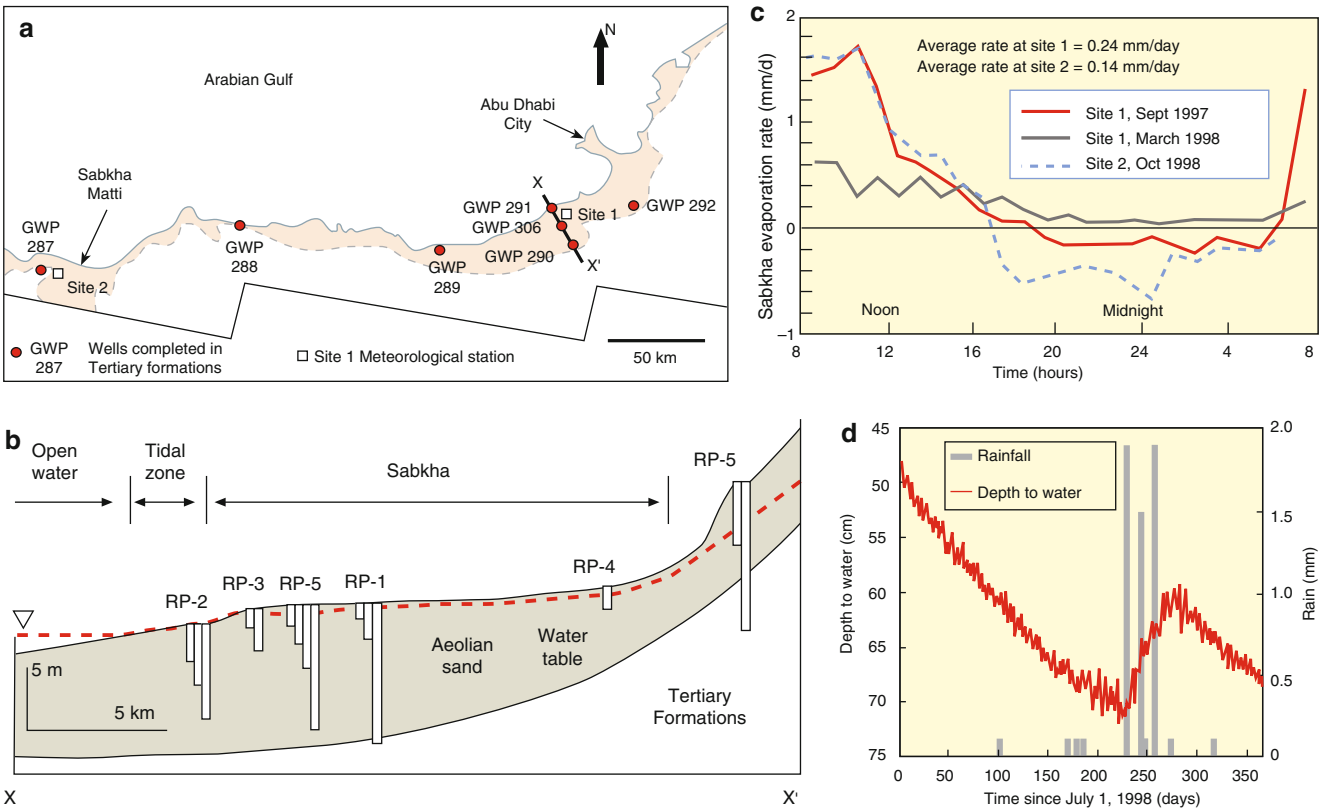

Fig. 3.12 Hydrology of the Abu Dhabi sabkha (from Sanford and Wood 2001; Wood and Sanford 2002; Wood et al. 2002; Wood et al. 2005). (**a**) Localities of selected monitoring wells, transects and sites. (**b**) Measured evaporation rate at sabkha surface using a humidity chamber. (**c**) Geological section showing thickness and piezometer nests along transection X-X'. D) Groundwater level and rainfall over a year (beginning July 1998) at site 2 in Sabkha Matti

2.0 m/day (≈3–10 md), and is relatively uniform across the sabkha. Using a hydraulic conductivity of 1 m/d, and a density-corrected piezometric gradient of 0.0002, results in a lateral flux of between 7 and 8 cm/year (Wood et al. 2002). Dividing the flux by porosity from an average of the measured porosities (0.38) gives a seepage velocity of 18–21 cm/year. This range in itself negates any notion of lateral marine seepage from the lagoon ever being capable of supplying the volumes of solute needed to precipitate the Holocene evaporites of the sabkha coast. These transmissivity calculations show that solute-carrying water simply cannot seep into the sabkha from its sides in sufficient volume to explain the volumes of capillary salts now in the sabkha. Solute-carrying waters must be coming from below.

Between 47,600 and 55,500 years are required for a molecule of a conservative (i.e., nonreactive) solute to traverse the 10 km width of the sabkha in the considered rectilinear volume (Fig. 3.12). If it is assumed that the average residence time is one-half of the total time required for a conservative solute to traverse the full length (10 km) of the rectilinear volume by horizontal flow, the average steady-state residence time of a conservative solute in this sediment volume is ≈26,000 year. Because the calculated residence time is greater than the age of the sabkha-aquifer system, it is clear that steady state for the solute flux has not been achieved. Capillary salts are still accumulating across the sabkha and it is this mechanism that is driving the jack-up and formation of Stokes surfaces.

In terms of the water cycle (not the solute cycle), direct rainfall onto the sabkha and subsequent groundwater recharge to the underlying aquifer accounts for 90 % of the annual water input to the system; the remaining 10 % comes from both lateral and ascending saline groundwater flow (Wood et al. 2002). Less than 1 m^3/year of pore water enters and exits by lateral groundwater flow into a representative rectilinear volume of sabkha aquifer measuring 1 m wide, 10 m deep, and 10 km long (Fig. 3.13a), Some 45 m^3/year enters by upward vertical leakage, 640 m^3/year enters by recharge of rainfall, while 690 m^3/year is lost to evaporation. But, and this is what earlier work had not expected, the water and solutes in the sabkha are largely from different sources; they are decoupled as they are in the playas and salt lakes of Australia (Chap. 2). The bulk of the solute load precipitated in the Abu Dhabi coastal sabkha comes from the resurgence of deeply circulated groundwater returning to the surface in the coastal plain via Tertiary limestone aquifers. Most of the solutes precipitated as capillary salts are not from seawater or from direct rainfall onto the sabkha. Approximately

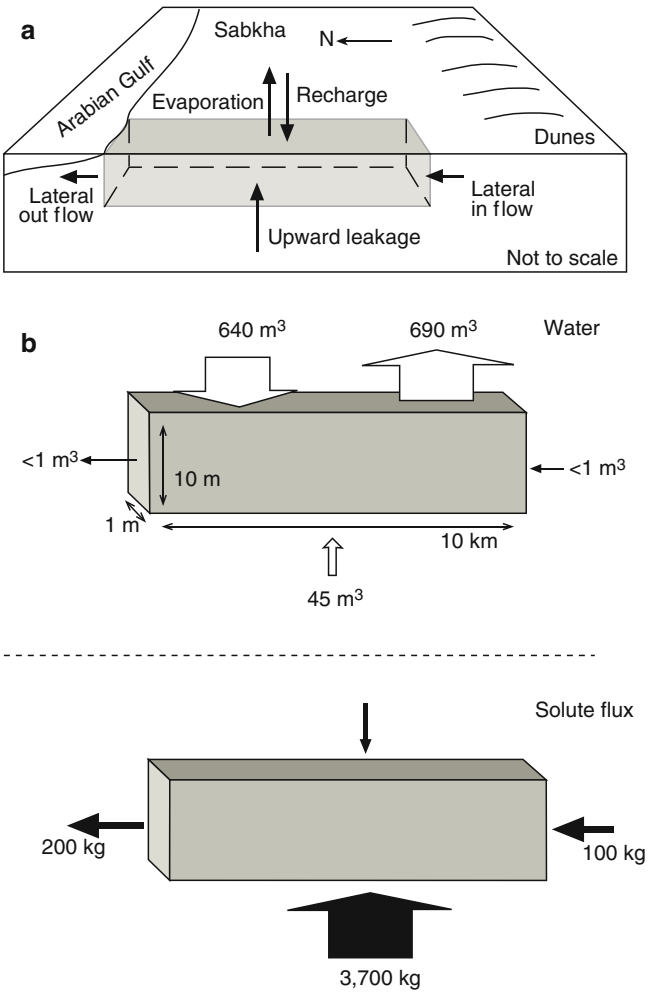

Fig. 3.13 Hydrologic fluxes in the coastal sabkha aquifer of the Abu Dhabi sabkha. (**a**) Schematic of hydrologic processes in the Abu Dhabi sabkha. (**b**) Magnitudes of the various annual water fluxes in a 1 m × 10 m × 10 km control volume (After Wood et al. 2002)

100 kg/year of solute enters from lateral flow; ≈15 kg/year enters by rainfall; and ≈ 3,700 kg/year enters by ascending vertical leakage (Fig. 3.13b). Some 200 kg/year is discharged to the Gulf by lateral flow. Upwelling groundwater originally entered the system in feeder zones in the Oman Mountains some tens to hundreds of kilometres to the east and picked up much of its solute load by water-rock interaction on its way to the coast.

Vertical gradients and hydraulic conductivity suggest that approximately seven pore volumes of water from the underlying Tertiary formations have discharged to the original coastal sabkha-aquifer system in the 7,000 years since deposition of those Holocene formations (Wood et al. 2002). Wood et al. (op. cit.) go on to argue that, if there are no other sources or sinks of solutes, then the concentration of a conservative solute should be approximately seven times the concentration of the input Tertiary brine. Bromine, a conservative element in brines, should have a concentration ratio close to the seven fold predicted by the hydrologic analysis if fed by Tertiary aquifers, and this expectation is realized (Fig. 3.14a).

Loss of halite from the pore water is clearly shown by the low concentration ratios of both sodium and chloride. Sulphate and calcium concentrations are less than seven because of the precipitation of calcite, anhydrite, and gypsum in the unsaturated zone in the sabkha. Magnesium should be generally conservative in this system because there is no significant mass of clay that could act as an ion exchanger or structural sink for the mineral. Magnesium, like bromine, is not being removed by mineral precipitation of chloride bitterns within the aquifer. The current chemical conditions in the majority of the sabkha aquifer do not favour dolomitisation (low concentrations of bicarbonate, low pH, and magnesium/ calcium ratio of ≈ 1:1; Table 3.3; Wood et al. 2002). It means that magnesium in the dolomite observed by previous workers in the sabkha is related to the original volume of trapped seawater and the interaction of these pore waters with microbial metabolisms. Significant masses of magnesium are not lost or gained from sources other than the brine, and the concentration ratio is approximately seven (Fig. 3.14a). Like bromine, it is behaving conservatively.

In solutions without significant concentrations of carbonate species, magnesium hydroxide complexes [$MgOH^+$ and $Mg(OH)_2$] can control the pH (Wood et al. 2002). Observed pH in sabkha brines, which declines with increasing magnesium concentrations is consistent with this hypothesis (Fig. 3.14b). The relative concentrations of calcium and sulphate can also be used to define the source of the solutes. Hydrochemical divides, as conceptualised by Hardie and Eugster 1970, mean that mineral precipitation in a relatively closed system, such as the sabkha, will cause the concentration of one element of a precipitating mineral to approach zero, while the other element or elements will increase in concentration (Fig. 2.19). The initial input concentration of the elements determines which element will be limiting. In the case of seawater, there is a greater equivalent of sulphate compared to calcium; thus, with precipitation of calcite, anhydrite, and gypsum, the thermodynamic activity of calcium will approach zero. In the case of the Tertiary brines and oilfield waters, the average equivalents of calcium are greater than the average equivalents of carbonate and sulphate (Table 3.3). Thus, precipitation of anhydrite and calcite from the concentration of Tertiary brines will result in sulphate and carbonate levels in the brines approaching zero, while calcium increases in concentration. In the Abu Dhabi sabkha system the observed calcium is increasing, and sulphate approaches zero in most cases (Fig. 3.14c), consistent with a Tertiary brine source for the sabkha anhydrite and gypsum. The few analyses in which sulphate is greater than calcium are from the supratidal zone nearest the lagoon. The concentration of sulphate does not go to zero because of hydrated complexes formed with magnesium and calcium;

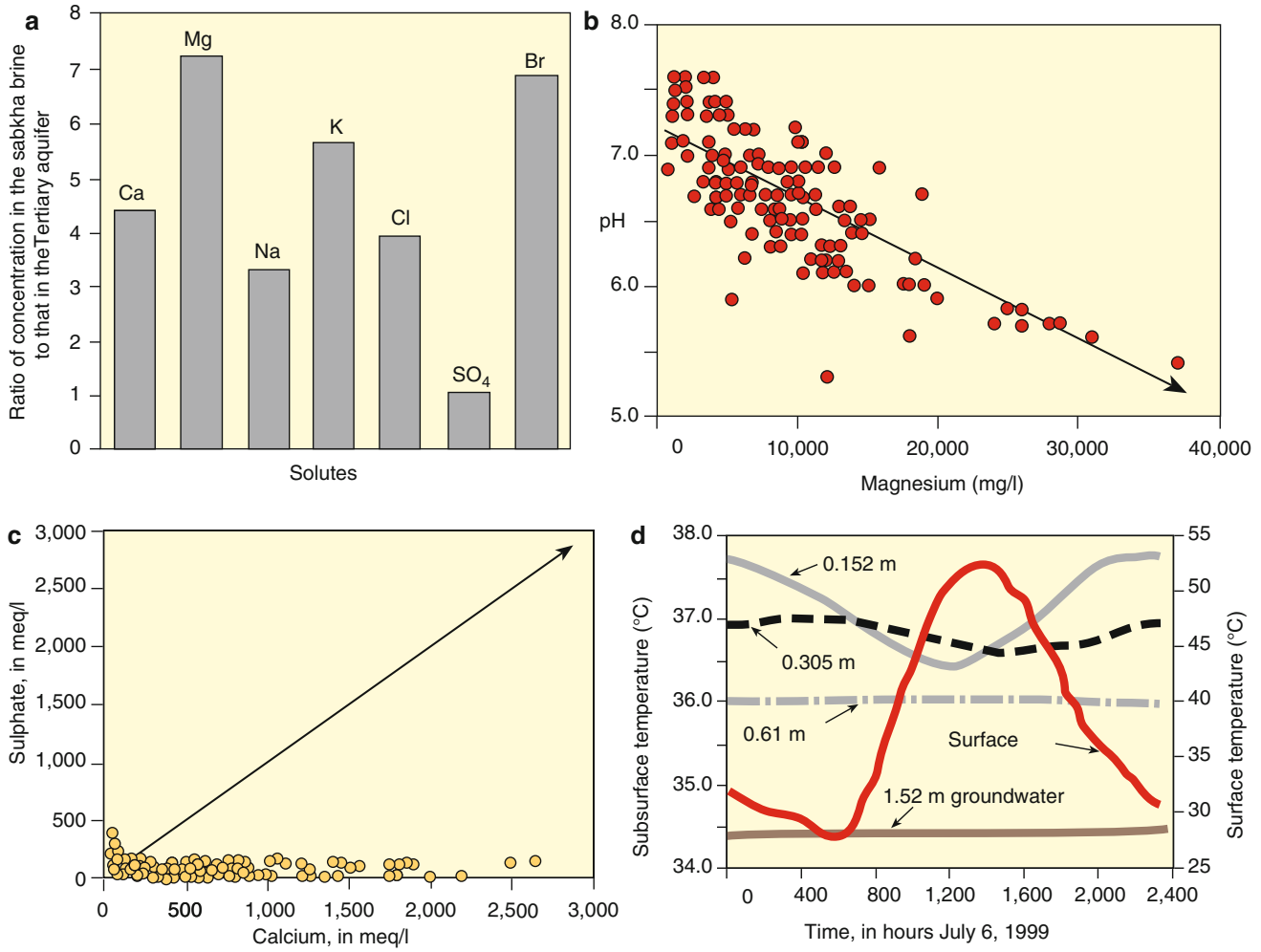

Fig. 3.14 Hydrogeochemistry of pore waters in the Abu Dhabi sabkha (After Wood et al. 2002). (**a**) Concentration factor (ratio of existing concentration in the sabkha-aquifer to input concentration of Tertiary brines) in the sabkha aquifer. (**b**) Decline in pH with increasing magnesium in sabkha aquifer. (**c**) Sulphate as a function of calcium in sabkha-aquifer. (**d**) One day temperature record of the surface, at various depths in the capillary zone, and of groundwater at site 1 in the coastal sabkha of the Emirates of Abu Dhabi

however, the thermodynamic activity does approach zero (Wood et al. 2002).

This interpretation of ionic proportions assumes that no other process, such as bacteriogenic sulphate reduction, is removing sulphate from solution. The regional groundwater system is oxidizing, with dissolved oxygen values between 4 and 5 mg/l, except at the distal edge of the sabkha. Therefore, it is not likely that bacterial sulphate reduction is removing a substantial mass of sulphate to significantly alter the Ca/SO_4 ratio as this bacterial process requires anoxic pore waters.

Periodic intense recharge by rainwater in the coastal plain dissolves halite and other soluble minerals on the sabkha surface, causing the surface and near surface waters to become more dense and sink (reflux) to the bottom of the aquifer where it vertically mixes with less dense ascending basinal brines (Wood et al. 2002). With the next drying cycle solutes are once again returned to the surface by capillary forces (a cycle that is largely decoupled from external solute supply). Thus, the system becomes vertically mixed, but there is essentially no horizontal mixing of seawater with groundwater. In the same way bittern salts are flushed from the uppermost parts of the unsaturated sediment column.

Any observed seawater solutes in the undersaturated zone come from interstitial seawater trapped by the rapid progradation of the sediments into the Arabian Gulf or from marine aerosols, they are not refluxed or laterally mixed marine pore brines as was inferred in the previous hydrological models. For example, Müller et al. (1990) observed a seaward gradient in strontium isotope values perpendicular to the coast, which they attributed to lateral mixing of continental brines and seawater within the sabkha (Fig. 3.11b). Wood et al. (2002) reinterpret the significance of this distribution, noting that the inferred lateral mixing is as readily explained as the function of the number of pore volumes of resurging conti-

Table 3.3 Hydrogeochemistry of source of solutes in Abu Dhabi sabkha; hydrogen and oxygen isotopes in SMOW

Source	Locality	Depth (m)	Date	Ca	Mg	Na	K	Sr	SiO_2	Alk. HCO_3	Cl	SO_4	Br	NO_3	TDS	Density	pH	$\delta^{34}S$	δ^2H (TU)	$\delta^{18}O$
Marine	Arabian Gulf	surface	Apr. 96	625	1,750	13,000	625	13	4.2	152	24,000	3,450	72	2	43,560	1.0290	7.6	–	17.7	2.63
Marine	Arabian Gulf	surface	Apr. 96	625	1,700	13,200	625	13	4.3	140	24,000	3,400	72	1	43,658	1.0291	7.6	–	17.7	2.63
Marine	Khor Bazam	surface	Apr. 96	700	2,150	16,100	750	18	5.0	170	28,500	3,800	89	1	52,150	1.0356	7.9	–	24.6	3.54
RP-5-3	groundwater	10	May 96	2,200	2,000	34,000	600	50	32	41	61,500	5,050	–	40	139,697	1.0719	7.2	15.91	15.3	5.63
Tertiary	GWP-288A	89	Jan. 98	1,450	950	10,500	300	25	36	55	15,700	4,050	11	33	37,076	1.0258	8.0	19.80	−0.2	2.37
Tertiary	GWP-289	119	Jan. 98	1,150	675	5,600	120	23	15	49	10,300	4,000	5	8	21,922	1.0146	7.8	19.84	0.7	2.92
Tertiary	GWP-290A	80	Feb. 98	1,500	850	15,500	450	27	20	50	25,000	5,750	15	22	50,251	1.0389	7.4	17.72	5.9	4.09
Tertiary	GWP-291A	142	Feb. 98	2,200	1,350	31,500	950	40	18	39	55,100	4,650	20	36	95,867	1.0608	7.8	18.42	5.0	4.64
Tertiary	GWP-292	119	Feb. 98	3,600	2,400	48,000	1,500	52	23	34	67,300	3,300	6	33	145,239	1.0971	7.4	17.82	7.5	5.19
Tertiary	GWP-306A	129	Mar. 98	2,750	1,250	34,500	11,00	50	16	64	62,500	4,600	12	50	107,056	1.0820	7.7	–	–	–
Sabkha	Av. (n = 161)	3	97–98	9,280	9,929	84,039	4,156	211	53	49	172,649	4,417	78	2,283	286,415	1.1658	6.7	15.77	27.6	6.5
Rain	Av. (n = 4)	–	95–97	3.73	0.20	0.82	0.52	–	–	47	1.48	2.85	–	–	39	−7.7	–	–	–	
Bu Hasa	Oilfield brine	16,400	Nov. 95	16,400	4,900	60,500	2,100	725	50	180	131,500	500	310	650	217,400	1.415	6.4	–	−2.8	3.19
Ramaitha	Oilfield brine	14,200	Apr. 96	14,200	1,600	57,900	1,350	1,000	22	210	110,000	350	620	1	186,600	1.0289	6.2	–	−5.3	6.47
Jam Yaphour	Oilfield brine	9,700	Apr. 96	9,700	1,200	40,000	600	200	29	142	62,000	200	345	0	114,000	1.0291	6.6	–	7.1	7.12

Sulphur isotope values in PDB
After Wood and Sanford (2002), Wood et al. (2005)

nental brine contributed to a specific area on the sabkha. That is, the distance from the shoreline and the number of pore volumes of Tertiary brine recharged to the sabkha-aquifer system are directly proportional and it is this that controls the Sr isotope values in the Abu Dhabi sabkha, not lateral recharge of seawater. In other words it is not necessary to invoke lateral mixing or transport to obtain the observed strontium isotope distribution.

Wood et al. (op. cit.) go on to note that the area of dolomitisation (as identified by Patterson and Kinsman 1982) is the region closest to the Abu Dhabi shore. This is the zone that retains the largest amount of seawater solutes because it is the area most recently prograded. The mass of dolomite formed on the sabkha is limited to that derived from the magnesium and carbonate concentrations in the initial pore volume of seawater trapped by the prograding sediments. The evaporative geochemical mechanism for regional dolomite formation, as proposed by Patterson and Kinsman (1982) appears to be correct; it is just that there is no ongoing seawater reflux occurring in this dolomitizing system. Arguing that all that is needed is more time to explain extensive dolomite cycles by prograding a set of sabkhas across ancient platforms is not hydrologically viable, syndepositional ancient platform dolomites require a different set of hydrological drives than icehouse sealevel (Chap. 5). In addition, dolomite seeding may require the local presence of organic matter and the appropriate microbial (sulphate-reducing) community.

The hydrological mechanism driving the accumulation of calcium sulphate salts in the sabkha is the rise of deeper circulating groundwater to replace waters lost by evaporation. The process moving capillary waters and their solute load through the unsaturated zone of the sabkha is solar driven and so the calcium sulphate in the sabkha is a true evaporite mineral (Chap. 2). Within this evaporative framework, Wood et al. (2005) argues that brine warming drives calcium-sulphate precipitation in the Abu Dhabi sabkha. That is, gypsum and anhydrite precipitate in the capillary zone because of their retrograde solubility. As well as belonging to the broader family of "true" evaporites, they are also "thermalites." A thermalite is defined by Wood (op. cit.) as a mineral formed by changes in temperature, independent of other processes that alter the thermodynamic properties of the solution. He argues that the capillary zone is critical to the development of the authigenic thermalite salts in any sabkha.

Any capillary fringe is the result of two sets of forces: mutual attraction between water molecules (hydrogen bonding), and molecular attraction between water and the different minerals that form the aquifer. Thus, for any given mineral, the smaller the interstitial pore size, the greater the vertical rise of water (Table 2.14). The zone of capillary rise (also known as the "zone of tension saturation" or the "wetting front") is the saturated zone above the watertable in which the interstitial pore space is completely filled with water, but this water is under less than atmospheric pressure. There can be no evaporation within this zone of tension saturation (no pore water passing into its gas phase) because water completely fills the narrower pore spaces and the atmospheric pressure is negative. If it does not, capillary rise cannot occur. Above the zone of tension saturation in the unsaturated zone is a zone in which the water film and a gas phase coexist in the interstitial pore space. The relative humidity of this gas phase is, however, equal to the thermodynamic activity of water, and no evaporative concentration can occur in this interval as well.

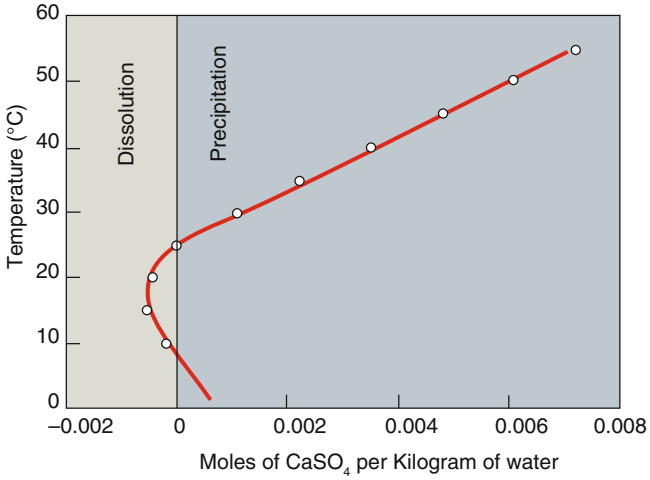

Fig. 3.15 Moles of $CaSO_4$ precipitated per kilogram of water as a function of temperatures for a representative solute sample from the sabkha of the Emirates of Abu Dhabi (After Wood et al. 2005)

The physics of the capillary zone means evaporation in the Abu Dhabi sabkha (or any other sabkha) can only occur at the surface, or in the pore spaces a few cm below, in the interval where the relative humidity of the gas phase is less than the thermodynamic activity of the water. Thus, any minerals precipitated lower in the capillary zone must be thermalites with precipitation driven by the retrograde solubility of calcium sulphate and not by an evaporation driven increase in the salinity of the pore fluids (Fig. 3.15). The notion of thermalites explains the typical occurrence of the bulk of the $CaSO_4$ in the sabkha. Nodules and prisms are most common in the interval about the watertable and toward the base of the capillary fringe, not in the few centimetres immediately below the land-surface. This would be the position of maximum anhydrite growth if evaporation of capillary waters, not their heating, was the dominant process driving $CaSO_4$ precipitation.

Wood (op. cit.) argues this conceptual model of thermalite precipitation applies to mineral deposition in the capillary zones of most coastal sabkhat. Water and solutes are transported upward by capillary forces from the shallow watertable in response to water evaporating at the surface. As water passes into the gas phase and is removed from the uppermost few centimetres it leaves behind evaporatively precipitated salt residues, including bitterns in the uppermost part of the capillary fringe. It is a diverse suite, dominated by halite (NaCl), but encompasses other more saline salts such as carnallite ($KMgCl_3 \cdot 6H_2O$) and antarcticite ($CaCl_2 \cdot 6H_2O$)

as well. Below this uppermost zone, minerals exhibiting retrograde solubility, such as anhydrite ($CaSO_4$), calcite ($CaCO_3$), dolomite ($CaMg(CO_3)_2$), and gypsum ($CaSO_4 \cdot 2H_2O$), are precipitated as thermalites. They are the result of increasing temperature experienced by solute-rich deeply circulated groundwaters as it moves through the capillary zone toward the surface during the summer months.

A representative summer day temperature profile (July 6, 1999) illustrates a positive gradient of approximately 25 °C m^{-1} in the Abu Dhabi sabkha at site 1 (Fig. 3.14d). A reverse thermal gradient (upward cooling) in the winter permits dissolution of some of the previously precipitated retrograde minerals. Because the negative thermal gradient is less in the winter than in the summer with nearly the same water flux, the water does not have the capacity to dissolve all of the mineral mass that was precipitated in the preceding summer. Thus, there is a net accumulation of these retrograde (thermalite) minerals in the capillary zone (Wood et al. 2005). Figure 3.15 illustrates the difference in mass of salts precipitated and dissolved as a function of temperature for anhydrite based on measurements made in the sabkha. It clearly shows the relatively small temperature window in the sabkha (5–25 °C) during which winter dissolution can occur.

Detailed hydrological studies of the coastal sabkhas of the Abu Dhabi region show they are no more than the outcropping expression of outflow zones of regional artesian aquifers. Clearly the ascending brine model of Wood et al. (2002), and his subsequent conclusions of sabkha salts accumulating beneath the halite crust as thermalites, contrast significantly with both the seawater-flooding and evaporative pumping models previously proposed and widely accepted as explaining the source of solutes to the coastal sabkha of the Emirate of Abu Dhabi (Fig. 3.11a). Wood's conclusions show solute cycling in the coastal sabkha setting is decoupled from the water budget and similar to that in continental sabkhas and chotts in many inland deserts with seawater like ionic proportions, as in the Sahara or central Australia (Chap. 2). The phreatic seawater wedge associated with the modern shoreline focuses outflow of deep seepage throughput in the Abu Dhabi coastal sabkha. Sediment matrix in some parts of the sabkha may be marine, but the hydrology and the authigenic overprint (mostly $CaSO_4$) comes largely from ions supplied by a deeply circulating continental aquifer. This new understanding of the large-scale sabkha hydrology has significant implications for the preservation potential of ancient marine-margin sabkhas.

Siliciclastic-Hosted Coastal Sabkhas, Western and Northern Arabian Gulf

An excellent literature base dealing with the sedimentology of the seaward side of the Abu Dhabi sabkhat creates an impression that coastal sabkhas bordering the Arabian Gulf are characterised by capillary salts hosted in marine carbonate matrices. But this is not always the case and many marine-margin capillary salts in the Arabian (Persian) Gulf are hosted in siliciclastics or even in desert loess blown into coastal depressions. Even in the type area, the Abu Dhabi sabkha, at least 50 % of the coastal plain sediments that host capillary evaporites do so in a matrix of mixed carbonate-siliciclastic or pure siliciclastic. Many ancient counterparts to strandzone sabkhas have siliciclastic matrices. Well-documented examples include the Permian sandflats of Europe and much of the Guadalupian lagoonal sediments of the Central Basin Platform in west Texas and New Mexico (Chap. 10). The following section describes some modern coastal sabkhas of the Arabian Gulf with capillary salts growing in mixed siliciclastic/carbonate and pure siliciclastic matrices.

A predominance of siliciclastics in the sabkhas of Kuwait and Saudi Arabia in the northwest of the Gulf versus carbonate in sabkhas along the At Taf coastal strip in the southeast of the Gulf simply reflects sediment transport and coastal dynamics in the Gulf seaway (Fig. 3.3a). The northwestern shore of the Gulf passes from the siliciclastics of the shallow Mesopotamian Shelf to the carbonate shoals of Bahrain, Qatar and the At Taf coastal strip. The northern Gulf is an arid, micro to mesotidal region with tides ranging from 1 to 4 m (Gunatilaka and Mwango 1988). Anticlockwise tidal currents of the northern Gulf and the prevailing northwesterly Shamal winds produce a shore-parallel, largely southeasterly-directed, wind-wave energy system, which supplies a combination of desert sand and loess to this part of the Gulf coastline, with an increasing fluvial contribution toward the northernmost gulf.

From the coast to inland areas along the northwestern Gulf there are three broad depositional environments (Lomando 1999). Along the coast is a near continuous belt of modern mixed carbonate-siliciclastic deposits with a wide range of depositional styles from interdunal to estuarine to barrier coast. To the immediate landward is a discontinuous belt of active and abandoned marine sabkhas, which pass into a broad desert system of continental sabkhas, desert flats, and dune fields. The inland desert system is the flattest area of Kuwait and northern coastal Saudi Arabia and is part of a zone of regional deflation, providing wind-blown sand to the Jafurah Sand Sea and ultimately accumulating in the northern areas of the Rub Al Khali in Saudi Arabia (Fig. 3.63).

Coastal Sabkhas of Eastern Saudi Arabia

Sabkhas of eastern Saudi Arabia are divisible into coastal and inland sabkhat, both are surrounded and underlain by Pleistocene and Holocene dune sands (Fig. 3.16a). Eolian sandflat sediments of the coastal region were documented by Fryberger et al. (1983, 1984) in a study of the Jafurah Sand Sea margin and are discussed in detail toward the end of this chapter. The Eastern Province of Saudi Arabia, south of Dammam, is characterised by a north–south elongated belt

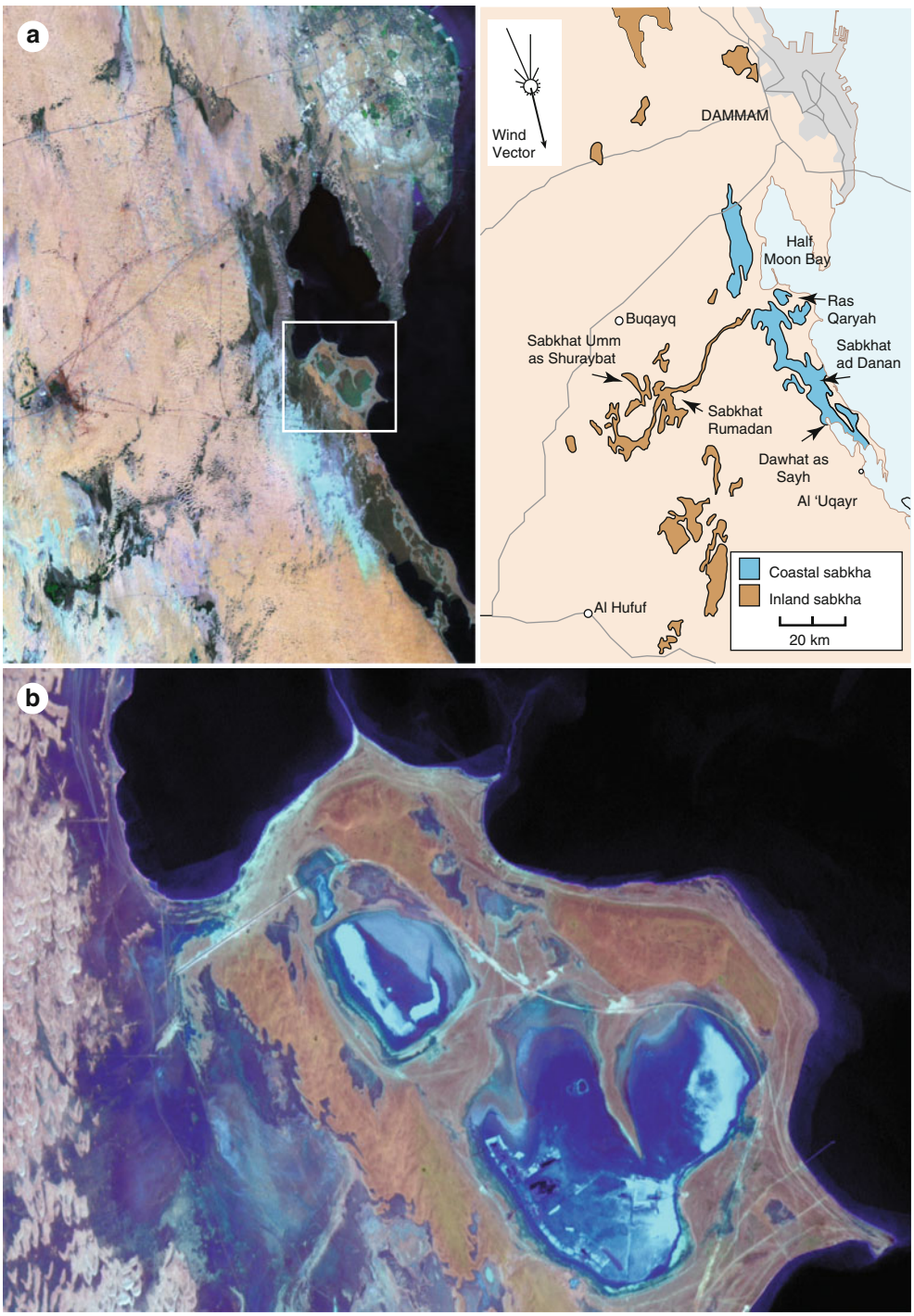

Fig. 3.16 Sabkhas of Saudi Arabia southeast of Dammam. (**a**) Distribution of coastal and interdunal sabkhas in areas of shallow groundwater resurgence along the Dammam coastline. The coastal region defines the modern marine edge of the Jafura sand sea where isolated subsealevel coastal depressions are today filling with capillary salts in a mostly siliciclastic matrix. In the last glacial this sand sea extended well out into the Arabian Gulf (Landsat image courtesy of NASA, wind vector after Fryberger et al. 1984). (**b**) Semi-circular marine seepage sabkhat behind Ras Qaryah and adjacent to the eastern edge of Sabkhat ad Danan

of eolian dune sand, which approaches the coast between Doha Dhalum (Half Moon Bay) and Al-'Uqayr (Fig. 3.16a). To its immediate north are the Tertiary limestone and dolomite highlands that define the outcrop expression of the Dammam dome (cored by a salt diapir). This coastal zone is surrounded by siliciclastic sand sheets, passing upwind into active barchan sand dunes, which are still moving sand into and across the coastal sabkha to create a prograding siliciclastic shoreline. Sand movement is principally towards the south-southeast and sand is driven seaward by the Shamal (Fig. 3.16a). In areas where the watertable approaches the landsurface, sabkha evaporites are growing in sand sheets in both sea-margin coastal sabkhas and in interdunal sabkhas located further inland (Fig. 3.16a, b). At Dahat as Sayh there is a highly restricted saline lagoon at the southern end of the Sabkhat as Danan, with a restricted marine carbonate fauna, somewhat akin to Hamelin Pool, although at a much smaller scale (≈75 km^2; Jones et al. 1978).

The dominant capillary salt is gypsum (Fig. 3.17a–c) in both inland and coastal sabkhas in the Eastern Province on

Fig. 3.17 Coastal sabkhas of the Eastern Province, Saudi Arabia. (**a**) Flat puffy algally-bound (petee) surface of the Sabkhat ad Danan. (**b**) Typical displacement gypsum (desert rose) growing within a half a metre of the sabkha watertable in Sabkhat ad Danan. Crystal is 10 cm across. (**c**) Gypsum lunette showing characteristic eolian cross bedding (outcrop face ≈ 1.5 m high) (**d**) Megapolygonal tepee ridges in marine cemented intertidal lagoon crusts in southern Half Moon Bay (area locally known as "wrong way spit"). (**e**) Pressure ridges in the halite pan facies (lowest point) of the Ras Qaryah sabkha shown in 3.16b in March 2004. The watertable at this time of year is no more than a tens of cm below the sabkha surface. (**f**) Displacive nodular anhydrite growing in the capillary zone in fine detrital clay about the edge of this saline pan facies in the Ras Qaryah sabkha (scale division is in cm)

Saudi Arabia, with small local areas of halite and anhydrite in the most saline parts of both the inland and coastal sabkhas. Some of the large coastal sabkhas, such as Sabkhat ad Danan, have gypsum lunettes along the sabkha edge (Fig. 3.17c). Gypsum is also a widespread pedogenic precipitate in much of the arid landscape of eastern Saudi Arabia. The level of carbonate matrix in the Saudi sabkha increases with proximity to the present coastline with a few wet interdune seeps adjacent to the coast even supporting a healthy mollusc and gastopod population. Coastal margins to the sabkhas show a range of cemented carbonate crusts with some modern lagoonal shorelines showing megapolygons in marine-cemented layers identical to those of the Abu Dhabi lagoonal margin (Fig. 3.17d). The important difference in the sabkha between the two areas is the amount of eolian siliciclastics in the upper intertidal and lower supratidal sediments.

Brine seeps through the sand aquifer to replenish areas depleted via drawdown, driven by capillary evaporation within the lower parts of the sabkha depressions. Gypsum crystals grow in the pore spaces near the watertable, poikilitically enclosing sand grains, to form spectacular crystal clusters or desert roses (Fig. 3.17b). Individual crystals can be up to a metre across, but most are measured in centimetres. The proportion of gypsum in the crystals is more than the porosity of the adjacent loose sand, showing that gypsum is not only growing in the pore spaces, it is also displacing the sand as it grows (Warren 1991).

Gypsum typically grows in a matrix of brown quartz sand and silt, in a capillary zone that can actively precipitate gypsum up to 50 cm above the watertable. Some sabkhas, such as Sabkhat ad Danan are currently deflating so that parts of the surface of the sabkha are paved by isolated prismatic gypsum blades standing up along fracture polygons, while the edge of the adjacent sabkha is lined by a dissected terrain of gypsum lunettes (Fig. 3.17c). Most of the crystals at the surface are weathered white and have split along cleavage planes. Immediately below the sabkha surface the gypsum crystals are still entire. The Stokes surface overprint indicates a fall in the regional watertable or active hydraulic jacking, which moves crystals into the vadose zone. Ongoing deflation may in part be a response to regional uplift driven by the nearby salt diapir-cored Dammam dome, which is currently rising at a rate of 5.5 m per million years (Weijermars 1999). More likely, it indicates the local vagaries of erosion associated with ongoing autocyclic gypsum crystal growth jacking overlying sediment up and out of the capillary zone, where it is subject to intense wind deflation.

In the lowermost parts of the regional sabkha plain there are local depressions a few kilometres across where brines pond and the sediment surface periodically lies below the watertable.

There, marine-seepage fed saltpans are forming and filling with successive crusts of chevron halite, rather than the more typical displacive gypsum of the regional sabkha (Fig. 3.17b, e). Around the high salinity edges of these halite pans are zones of nodular anhydrite rather than the ubiquitous sabkha gypsum (Fig. 3.17f).

Sabkhas of Coastal Kuwait

Modern sea-margin sabkhas in coastal Kuwait are not developed at the same broad scale as those of Abu Dhabi or the Dammam region, but are nonetheless interesting as they illustrate a transition from a fluvio-deltaic to an alluvial fan-fluvial supplied sabkha in Kadmah Bay (aka Kuwait Bay) to a mixed eolian siliciclastic-carbonate matrix sabkha in the Al Khiran region to the south (Fig. 3.3a). Inland, Kuwaiti sabkhas are also widespread in depressions more than 10 km from the coast. Both inland and coastal sabkhas of Kuwait are largely hosted in sheets of reworked medium-grained quartz dune sand, along with variable amounts of eolian reworked authigenic gypsum sand (Al-Hurban and Gharib 2004; Khalaf and Al-Awadhi 2012). Compared to inland sabkhas, the detrital matrices in coastal sabkhas are slightly muddier, contain less gravel and show higher levels of gypsum due to their proximity to marine aerosols and marine seeps (Fig. 3.18).

Sabkhas of Kadmah Bay

To the north of Al Khiran sabkha, the Holocene sediments of Kadmah Bay (Kuwait Bay) represent the western-most limit of the siliciclastic Shatt Al-Arab delta and the southern limit of the alluvial fans of Jal Az-Zor escarpment (Saleh et al. 1999; Al-Sarawi 1988). Most of the sediment matrix in the western part of the Kadmah Bay hypersaline system is deposited at the distal end of large alluvial fans, downdip of the Jal Az-Zor Escarpment (Fig. 3.19a, b). In contrast, sabkha matrix in the northeastern part of the bay is fed substantial volumes of finer-grained sediment by longshore drift of sediment sourced in distributaries of the Shatt el Arab delta sediments. This higher volume of sediment supply means sabkha at the northeastern end of the bay has prograded further into the bay waters (Fig. 3.19a). Today, the bay is about 20 km wide, has a tidal amplitude of almost 2 m and is around two-thirds exposed during very low tide. Although very shallow, the lack of wave energy and the proximity of the muddy Shatt al Arab, means the central bay fill is very muddy and is near impossible to cross on foot at low tide.

Four sedimentary settings define the northwestern Kadmah Bay margin; namely alluvial fans, playas, sabkhas and beaches (Fig. 3.19b; Al-Zamel and Al-Sarawi 1998). Coastal sabkha deposits extend landward to where they interfinger with the distal ends of modern alluvial fans, much

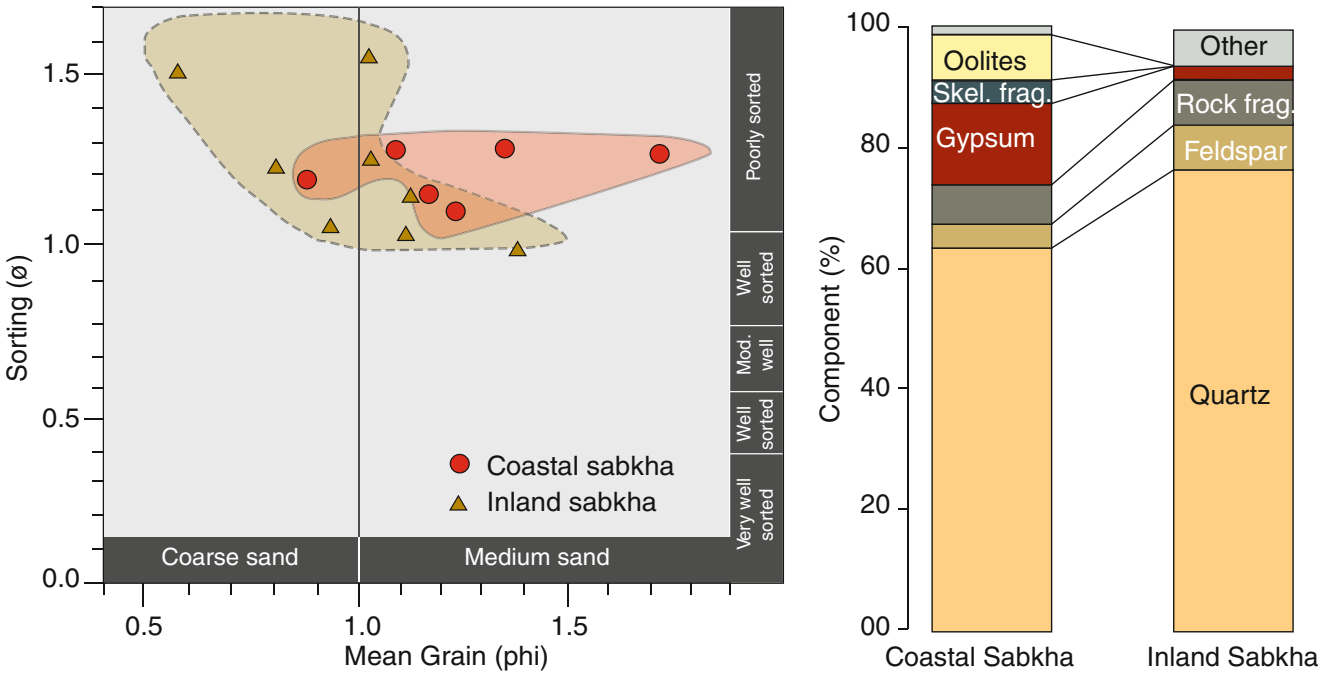

Fig. 3.18 Grain-size and mineralogical comparison between sediments of inland and coastal sabkhas of Kuwait (Replotted from Al-Hurban and Gharib 2004)

like the sabkhas of Ras Al Khaimah at the other end of the Arabian Gulf (Warren 1991). Distal fan sediments are typically plane-laminated sands interlayered with playa lacustrine muds and are often encrusted by a gypcrete carapace. Mid fan sediments are dominated by crossbedded and parallel laminated sands, while proximal fan sediments are poorly sorted imbricated gravels and poorly stratified pebbly sandstones.

Evaporitic Kadmah Bay sabkha sediments can be divided into two subfacies: (1) dark brown silt mixed with very fine sand, rich in prismatic gypsum, gypsum roses and gypsum nodules at the level of the watertable, along with some halite and aragonite and very minor amounts of anhydrite; and (2) light brown silts mixed with local anhydrite nodules in fine sands in the upper parts of the sabkha plain. Gypsiferous sabkhas dominate.

An erosional or deflationary regime now characterizes the sabkha of the coastal plain of Kadmah Bay (Saleh et al. 1999). Maximum marine flooding of the supratidal area is dependent on the coincidence of high water spring and/or storm tides with southeasterly winds and is an uncommon event. This results in a very limited portion of the tidal zone (0.6–0.7 km wide) being subjected to flood recharge during the normal tidal cycles. Away from the immediate bay waters, much of the active Kadmah Bay sabkha is best described as an evaporitic 'wind flat' or sandflat rather than a diurnally flooded carbonate mudflat. The closest comparable modern setting documented in the sedimentological literature is probably the evaporitic mudflat of the Colorado River delta (Shelton et al. 1978). Once again, this is a continental system that just happens to be at the edge of a modern sea and its hydrology is largely continental.

The dominant southeasterly flow of the Shamal wind means coastal sabkhas in Kadmah Bay and on Bubiyan Island are distinct from carbonate-dominated coastal sabkhas further south in the Gulf. The Shamal blows continental sediment south into the bay, so that the sabkhas are the seaward edges of deflation flats with matrices characterized by abundant siliciclastics, not carbonates. The dry windy setting means there is an absence of healthy laminated cyanobacterial mat along much of the intertidal sabkha strandline. It is simply too dry, so laminated cyanobacterial mat is mostly confined to small moister areas on the floor and the immediate vicinity of tidal channels.

However, oncolites can grow in this shallow subtidal to intertidal siliciclastic environment, mostly as syndiagenetic carbonate precipitates (Alshuaibi et al. 2012). The cyanobacterial population in oncolites is closely related to the population found in the subtidal sediments, along with abundant *Dunaliella viridis* (see Chap. 9). The biota forming the binder population are halotolerants, as it is a setting subject to periodically excessive hydraulic energy, extreme salinity (up to 47‰), and high concentrations of organic matter subject to bacterial sulphate reduction and elevated H_2S in the pore fluids.

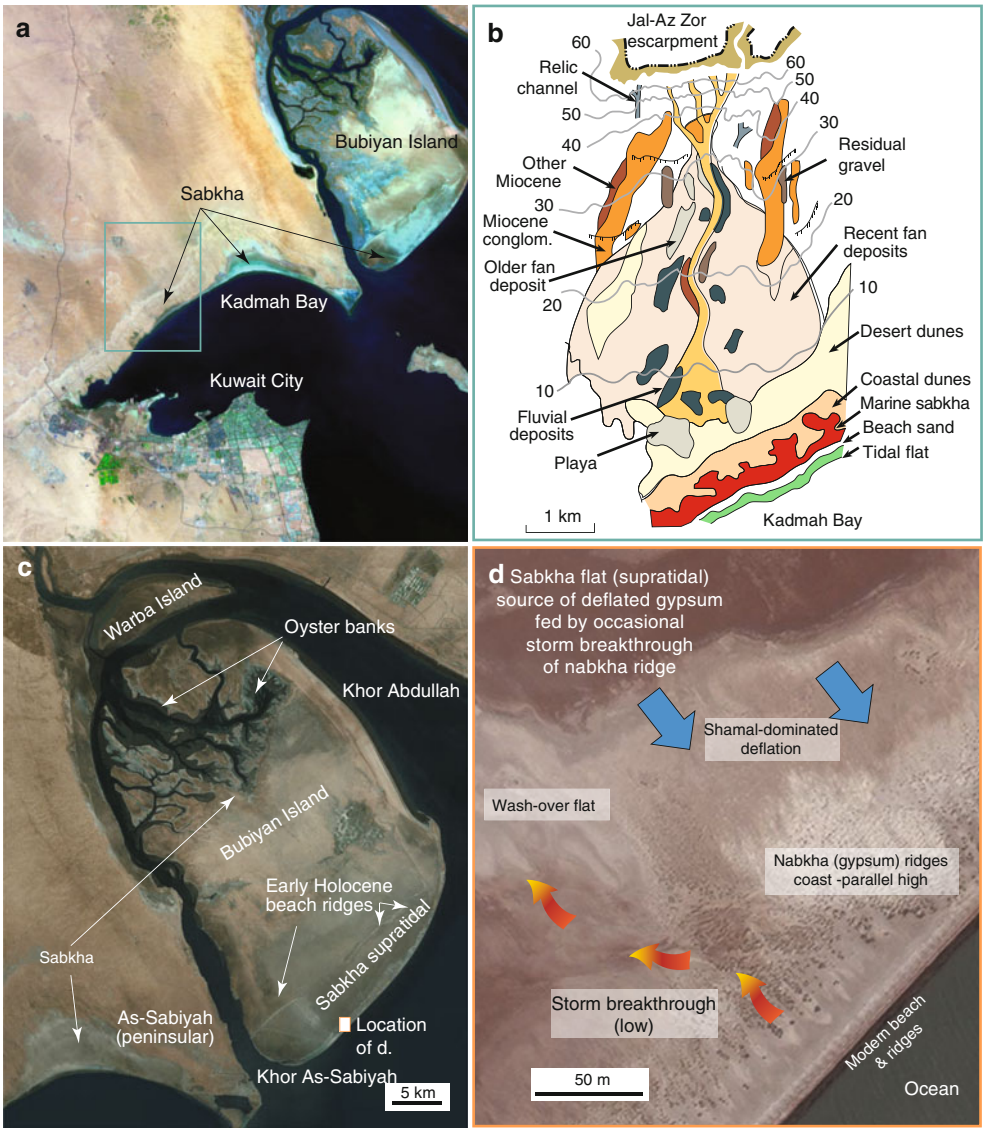

Fig. 3.19 Kadmah or Kuwait Bay (**a**) Shows the development of an extensive but narrow coastal sabkha with a siliciclastic matrix on the northern margin of the bay (Landsat image courtesy of NASA). (**b**) Surface geology of the region where alluvial fans pass south into Kadmah Bay sabkhat, Kuwait (After Al-Sarawi 1988). (**c**) General Holocene geology of Bubiyan Island (After Khalaf and Al-Awadhi 2012). (**d**) Relationship between coastal belt of gypsiferous nabkhas (low lunettes) washover breakouts and the deflationary supratidal sabkha plain

The mud-size fraction in the Kadmah sabkha (≈5 % of sediment volume) is dominated by carbonate minerals, but this carbonate is detritus from weathering carbonate strata to the north, not diagenetic or marine supplied material from the bay to the south (Saleh et al. 1999; Al-Bakri et al. 1984). Much of it is low-Mg calcite washed in from the surrounding plain where capillary calcretes (*gatch*) are commonplace. Similarly, almost all of the dolomite in the northern Arabian Gulf, including that on the floor of Kadmah Bay is detrital and derived either from longshore transport from the Shatt el Arab delta or is blown in by the Shamal as it scours the desert plains of Iraq (Al-Bakri et al. 1984). Numerous primary sheet flood and eolian structures are preserved beneath the prograding supratidal flat, with only minor disruption to these structures caused by local growth of intra-sedimentary gypsum. Gypsum and other capillary salts never dominate mineral proportions in the supratidal zone of Kadmah Bay (Fig. 3.18).

The windblown and deltaic siliciclastic coastline of Kadmah Bay has been prograding into the bay for 3,000 years at a rate of 1.5–2 km per 1,000 years. More landward, the preceding "Early Holocene" transgressive coastal sediments are made up of patchily distributed, autochthonous carbonates (aragonitic oolites, pellets and micrite), similar to the early Holocene beach ridge carbonates of the At Taf coastal strip. The Mid-Holocene transition to a siliciclastic matrix along the north coast of Kadmah Bay indicates the time when longshore currents flooded the northern bay with reworked muddy fluviodeltaics from the prograding Bubiyan channel.

Along the prograding southern coastal zone of Bubiyan Island the Shamal deflates gypsum from the coast-parallel

sabkha belt and so constructs a downwind coast-parallel nabkha belt (Fig. 3.19c, d; Khalaf and Al-Awadhi 2012). A nabkha[3] is defined as a vegetation-stabilised aeolian landform, which usually develops as result of the depositional capture of wind-driven sediments around desert shrubs in arid and semi-arid regions (Cooke et al. 1993). Typically they occur in the vicinity of dune fields where the dominant eolian component is quartz sand and other siliciclastics along with minor gypsum. Khalaf and Al-Awadhi (2012) make the point that the term "gypsiferous" is used for sediments containing gypsum (i.e., gypsum occurs in small amounts), while the term "gypseous" is used for sediments having gypsum as the main component, and go on to note the coastal nabkhas on Bubiyan Island are gypseous with well developed gypsite or gypcrete crusts.

In my opinion, the coast-parallel gypsum nabkhas of Bubiyan Island are an excellent example of a deflationary process set that dominates the sabkha edges in most saline depressions across the world. It is a response to the formation of the Stokes surface that caps all sabkhas (Table 2.15). I have seen similar gypsum nabkha rims to those of Bubiyan Island in the coastal and inland sabkhas in Saudi Arabia and the UAE. Nabkhas also line saline paleochannels and inland saline lakes in Australia and the southwest of the USA and atop the gypsum rim to the Dallol depression in Ethiopia. In all cases they are a response to flooding followed by desiccation and deflation (Fig. 3.19d). On Bubiyan Island the flood occurs via combinations of storm surge and high tides. In the various inland playas the flood is sourced in rainstorms and the resultant sheet flooding of the sabkha/playa depression. Gypseous nabkhas form best on the dominant downwind parts of a saline sump. In cases where substantial volumes of gypsum are deflated from the sump, they can evolve into downwind gypsum dunes or lunettes, as in White Sands in New Mexico, or Lake Eyre and Lake Frome in South Australia (Table 1.5). The distinction between a saline sump with a dispersed downwind gypseous nabkha rim, versus a more lake-edge defined gypseous lunette rim, probably indicates a hydrological contrast in the two depression styles, with nebkhas indicative of a more arid setting.

Al-Khiran Sabkha

To the south, near the Kuwaiti border with Saudi Arabia, Late Pleistocene and Holocene sediments are exposed in and about the sea-margin sabkhas in the Al-Khiran area (Fig. 3.20; Lomando 1999; Duane et al. 2004). The Al-Khiran sabkha is one of three carbonate-hosted lagoonal/coastal sabkha systems, some 120 km^2 in area. The Al Khiran sabkha, the best documented of the three sabkhas has much of its original depositional geometry now disturbed or destroyed by development of a resort city. All three sabkhas lie behind chenier belts of oolitic beach-dune ridges where large parts of the inter-ridge sabkha depressions are no longer subject to marine flooding (Fig. 3.20). In the Al Khiran sabkha the oldest and most landward exposed beach ridge is older than the Flandrian transgression. The four younger, accreted ridges, as mapped by Al-Sarawi et al. (1993), are dated at 6,800, 5,800, 3,000 and 2,000 years BP.

Sabkha flats in the various inter-ridge depressions were formed by sedimentary offlap, driven by the relative fall in sea level since the last Holocene transgressive maximum, approximately 4.5–4.7 ka. Sabkha evaporites (gypsum and anhydrite) in the inter-ridge depressions are hosted by aragonite-rich pellet muds, which also entrain significant amounts of comminuted marine shell material. Thin layers of blowing sand now cover portions of the sabkha to varying thicknesses, depending on depth to the top of the capillary fringe. Some of the anhydrite in the Al Khiran sabkha is unusual compared to the Abu Dhabi sabkha in that it first nucleates in zones of moisture stress around plant roots and so is an evaporitic form of dikaka or rhizoconcretion often related to vegetation-bound nabkhas (Gunatilaka et al. 1980).

At the regional scale, each of the three structurally controlled headlands has major modern shoal complexes several kilometres in length extending from their tips to the northeast along the structural axis of underlying folded successions (Fig. 3.20). Large bars within the shoal complexes are oriented roughly northwest-southeast, parallel to the longshore drift direction. At Ras Al-Qulay'ah, a bar complex extends seaward from the point of the spit, with an overall arcuate shape. Patch reefs grow along the windward northwestern flank of the bathymetric nose. Sediments from the nearshore to beachface are composed of fine- to medium-grained ooids with lesser amounts of quartz sand, intraclasts, and skeletal grains. At Ras Al-Zour (Fig. 3.20), the headland shoal and spit complex has the same overall geometry as Ras Al-Qulay'ah, and has begun to build above sea-level to form a small island. Headland spit extension is likely a response to anticlockwise eddy currents.

Sabkha development at each headland is related to the progressive cutoff of a marine lagoon, which formed in a sag located southeast of the sea-covered anticlinal high, where the carbonate sediment factories are flourishing in the shallows. Longshore transport is driven by the nigh-on coast-parallel direction of the prevailing winds (Shamal). As the entrance to a lagoon is choked, marine inflow becomes more restricted and sabkha evaporites start to precipitate in its marine sediment matrix. Khor Iskander illustrates the open stage of inflow hydrology (Fig. 3.21).

Today, during an annual sediment cycle in the Al Khiran sabkha, modern marine water diurnal inflows are confined to

[3]In original Arabic, nabkha (nebkha) translates as "small sandy hillock".

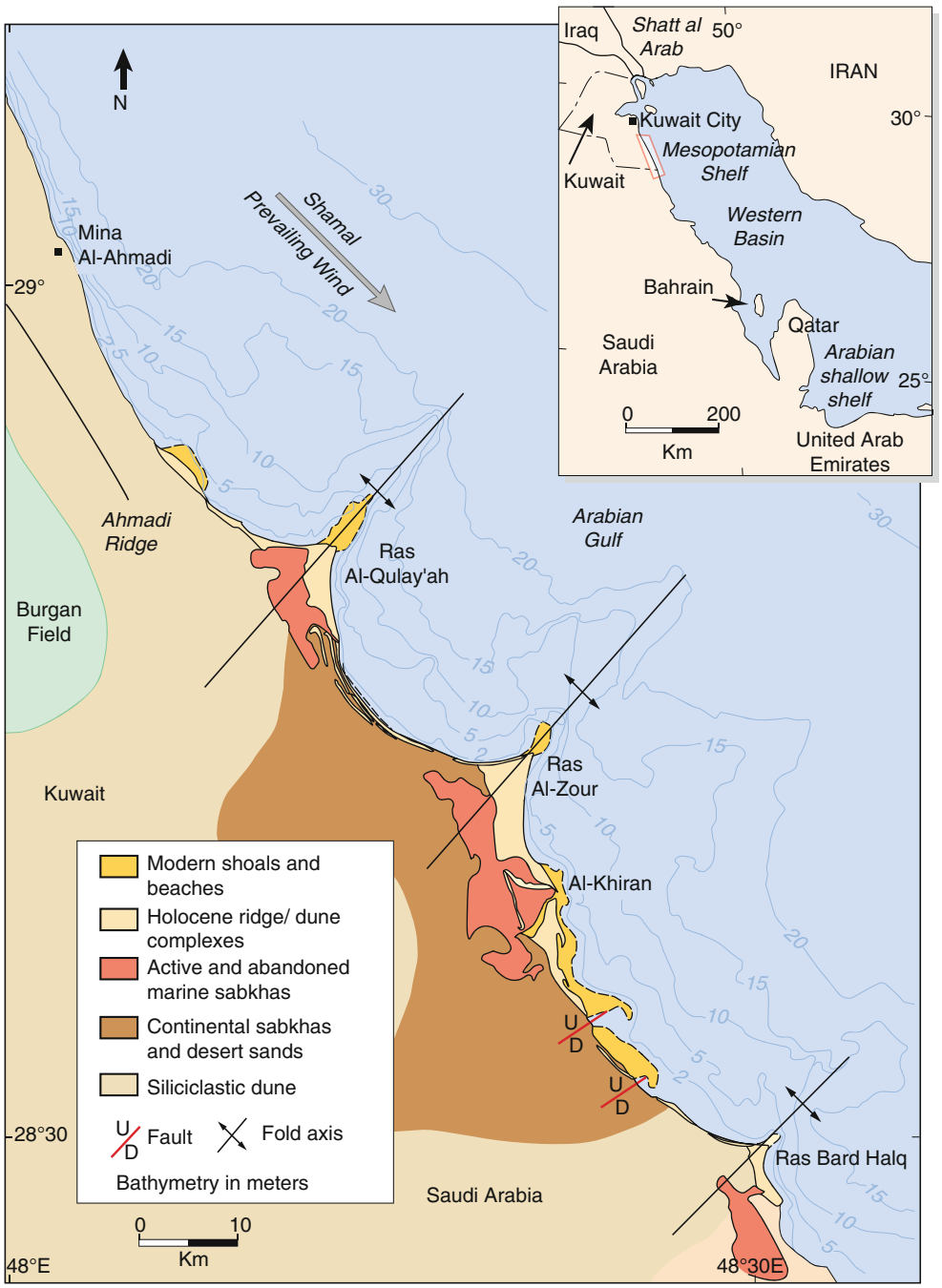

Fig. 3.20 Location map showing the major coastal deposits and offshore bathymetry along the Kuwait- Saudi Arabian coast. Prevailing wind direction (Shamal) is from the northwest. General facies distribution patterns are associated with folds and are repetitive across each of the three-fold related headlands. Siliciclastic dune fields are best developed in the intervening sags between the headland folds while the sabkhas form in the protected lee of the carbonate sediment buildups that typify the three structurally-controlled headlands (After Lomando 1999)

two tidal creeks cutting the Al-Khiran sabkha (Fig. 3.21; Gunatilaka et al. 1987). Occasionally, perhaps a few times in a year, a narrow strip, up to a 100 m wide adjacent to the creeks, is covered by tidal waters, brought there by exceptionally high spring tides and/or storm surges. An absence of significant marine flooding over the rest of the sabkha means much of the current hydrology and pore chemistry is controlled by influxes of continental groundwater. This topographic-continental hydrologic framework is also reflected in the formation of diagenetic continental dolomite in some depressions on the salt flat, as well as the isotopic make-up of the dolomite, which indicates a continental or nonmarine source, with similarities to the Coorong dolomites.

Major ions show a steady evaporative concentration across the sabkha from inland to the coast, with a "high" chloride plateau in the central parts of the marine sabkha similar to the plateau that occurs in the Abu Dhabi sabkha (Robinson and Gunatilaka 1991). Monitoring of groundwater over a 3-year period indicated that: (a) when the water-table depths are <1.2 m, the sabkhas are in a state of depositional equilibrium; (b) watertable fluctuations (due to

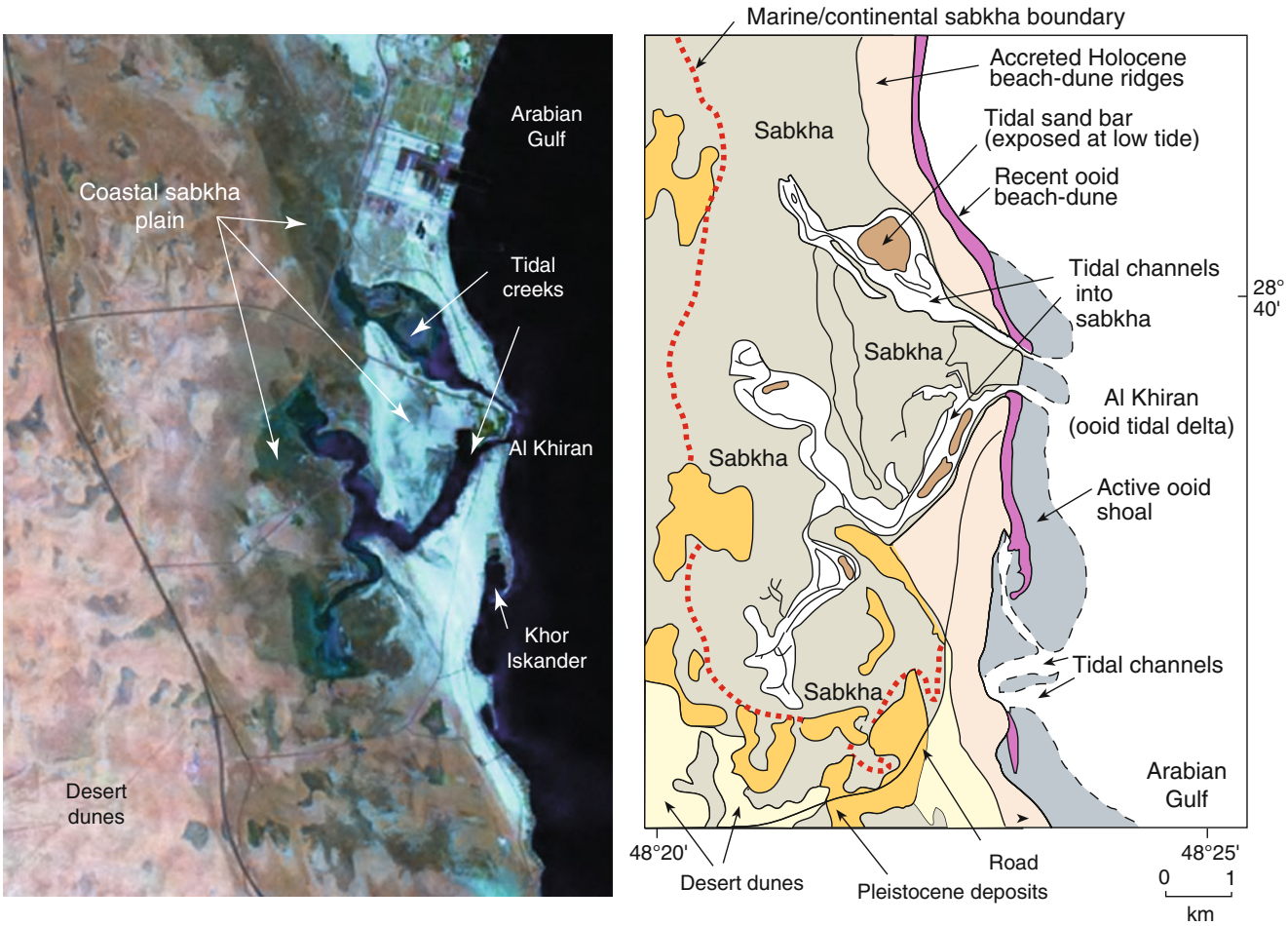

Fig. 3.21 Surface geology of part of the Al-Khiran sabkha, Kuwait, showing the importance of accreted ooid beach ridges in forming the structural framework of the coastal sabkha estuary and the passage into dune sands in the sabkha hinterland. Year 2000 vintage is used as subsequent engineering works have constructed a luxury marina at this site and depositional patterns have been drastically altered (Landsat image courtesy of NASA, surface geology after Gunatilaka et al. 1987)

drawdown or recharge) exceed 0.5 m/year; and (c) calculations based on measured fall in watertable levels, porosities of the sediments, and the volume of anhydrite formed in the sabkha all suggest that over the last 4,700 years, since progradation commenced, only 2–4 cm/year (net) of groundwater is lost from the sabkha surfaces. This is a surprisingly low rate for this arid region and indicates significant replacement by resurging continental groundwaters. This groundwater replenishment maintains longterm stability of the sabkha sequence. Without it, deflation would dominate and most of the older sediment would be planed off to the level of the intertidal/subtidal crust, much like what has occurred on the backside of Kadmah Bay.

Supratidal anhydrite in the Al Khiran sabkha has three distinct morphologies (Gunatilaka 1990): (a) hair-cream anhydrite, which occurs exclusively in association with the halophytic saltbush *Halocnemum strobilaceum*; (b) nodular/laminated cottage cheese anhydrite, which is associated with a bacterial-cyanobacterial mat. This nodular anhydrite forms massive layers up to 4 cm thick with the anhydrite initially pseudomorphing gypsum crystals in the mats. In laminated anhydrites it can form aphanitic layers up to 7 cm thick, made up almost entirely of microcrystalline anhydrite; (c) anhydrite formed by the alteration of prismatic gypsum crystals now exposed in the lowermost parts of some now abandoned and desiccated drainage channels.

With "hair cream" anhydrite, climate and biological influences play a significant role in what is often an annual mineralogical change between gypsum and anhydrite, depending in part on rainfall intensity. On the death of the halophyte, hair-cream anhydrite reverts to microcrystalline alabastrine secondary gypsum and then to a gypcrete. The gypsum-anhydrite transformation is a reversible dissolution-reprecipitation process and there appears to be an intimate relationship between the plant, its "soil water" requirements and the hydrodynamic behaviour of capillary groundwater brines in the vadose zone, which interact to control mineralogy. Compared to "hair cream" anhydrite, type (b) anhydrite

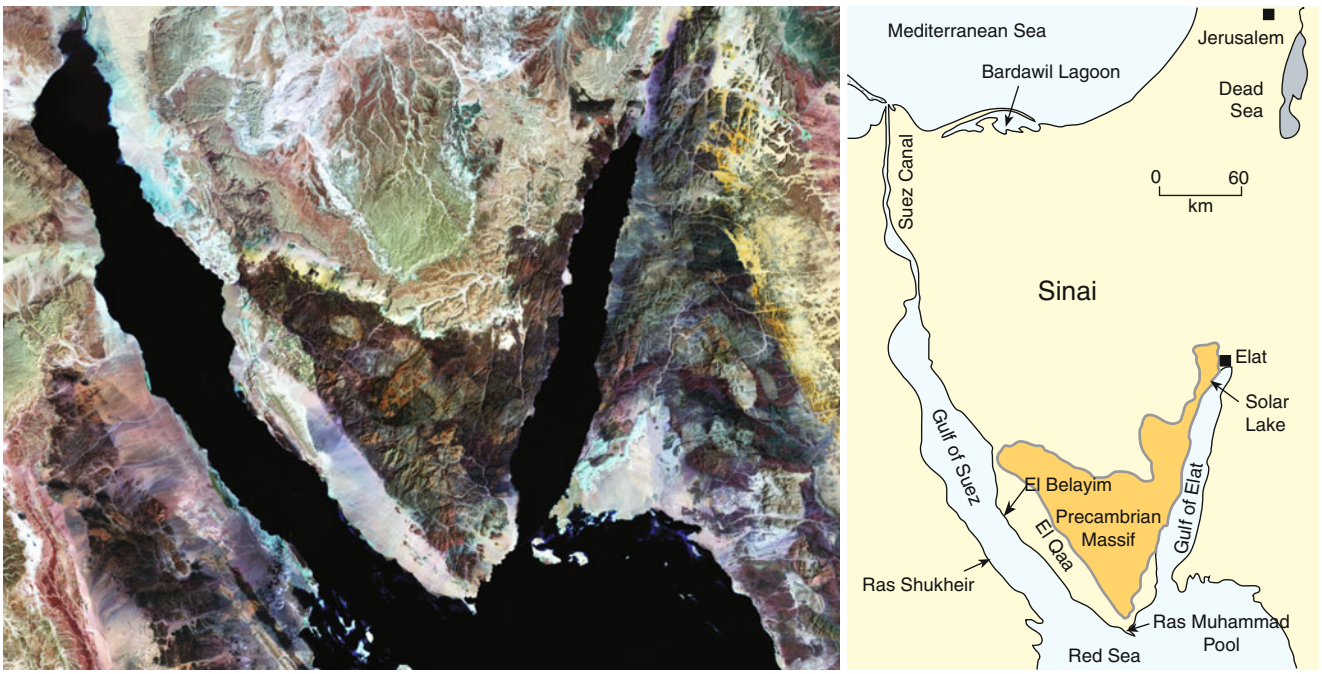

Fig. 3.22 Sinai Peninsula showing distribution of some of the studied Holocene sabkhas and salinas in the Quaternary coastal fringe (Landsat image courtesy of NASA)

is more likely to be preserved as anhydrite, not gypsum, at least into the shallow subsurface above the watertable. Type (c) anhydrite is rare and possibly only forms with complete drying of the channel bottom, it is always susceptible to deflation or rehydration and so has low preservation potential compared to types (a) and (b).

All anhydrite in the Al-Khiran sabkha forms from a gypsum precursor at temperatures >30 °C, with brine chlorinities >4 mol Cl/kg. Al-Khiran is the northernmost occurrence of widespread patches of anhydrite in the coastal belt of the Arabian Gulf (gypsum dominates further north). It also defines a change in lagoonal matrix in the coastal plain to the fluviodeltaic sabkha coast of northern Kuwait and Iraq.

Other Coastal Sabkhas

Outside of the southern coast of the Arabian Gulf there are many other coastal deserts where evaporation of a combination of marine and continental waters precipitates capillary salts in a matrix of marine-reworked sediment.

Gulf of Suez

Sea-margin sabkhas occur along both sides of the Gulf of Suez. Small sabkhas are patchily developed along the seaward edge of the El-Qaa, in a coastal strip that runs from Abu Rudeiz to Ras Muhammad (Fig. 3.22; Gavish 1974, 1980). The El Qaa is a near-flat alluvial plain, mostly composed of alluvial silicate minerals weathered from Precambrian metasediments and granitic massifs to the east. The El Qaa area experiences some of the hottest and driest conditions in the Sinai, yet it lacks substantial accumulations of sabkha anhydrite or other salts. Capillary evaporites where they do occur are mostly scattered patches of interstitial gypsiferous cements within a few hundred metres of the coast (Fig. 3.23). Nowhere in the Sinai coast are sabkha salts as extensive as in the Arabian Gulf sabkha, indicative of a lack of shallow groundwater to source capillary precipitates (Gavish 1974). Gypsiferous capillary cements in marine-reworked siliciclastic matrices, are also patchily developed in a narrow coastal strip on the opposite (African) side of the Gulf of Suez (Keheila et al. 1989). At Ras Shukheir the sabkha is unique in that it is developed atop and around one of the world's few examples of a Late Pleistocene coastal salina, which was once filled with laminated subaqueous gypsum, although now the succession is heavily eroded (Fig. 4.16).

The sabkha fringe to the Gulf of Suez coastal plain typically extends from the marine shoreline to the seaward base of an alluvial fan apron or bajada, which lines a faulted escarpment located up to a kilometre or more in the hinterland. The sabkha itself usually occupies the first few hundred metres immediately landward of the shoreline where the bajada watertable approaches the landsurface in what is typically a fan delta coast (Fig. 3.23a). Matrix sediments are mixtures of clastic fine-sands, derived from alluvials, and marine carbonate washover sands composed of skeletal

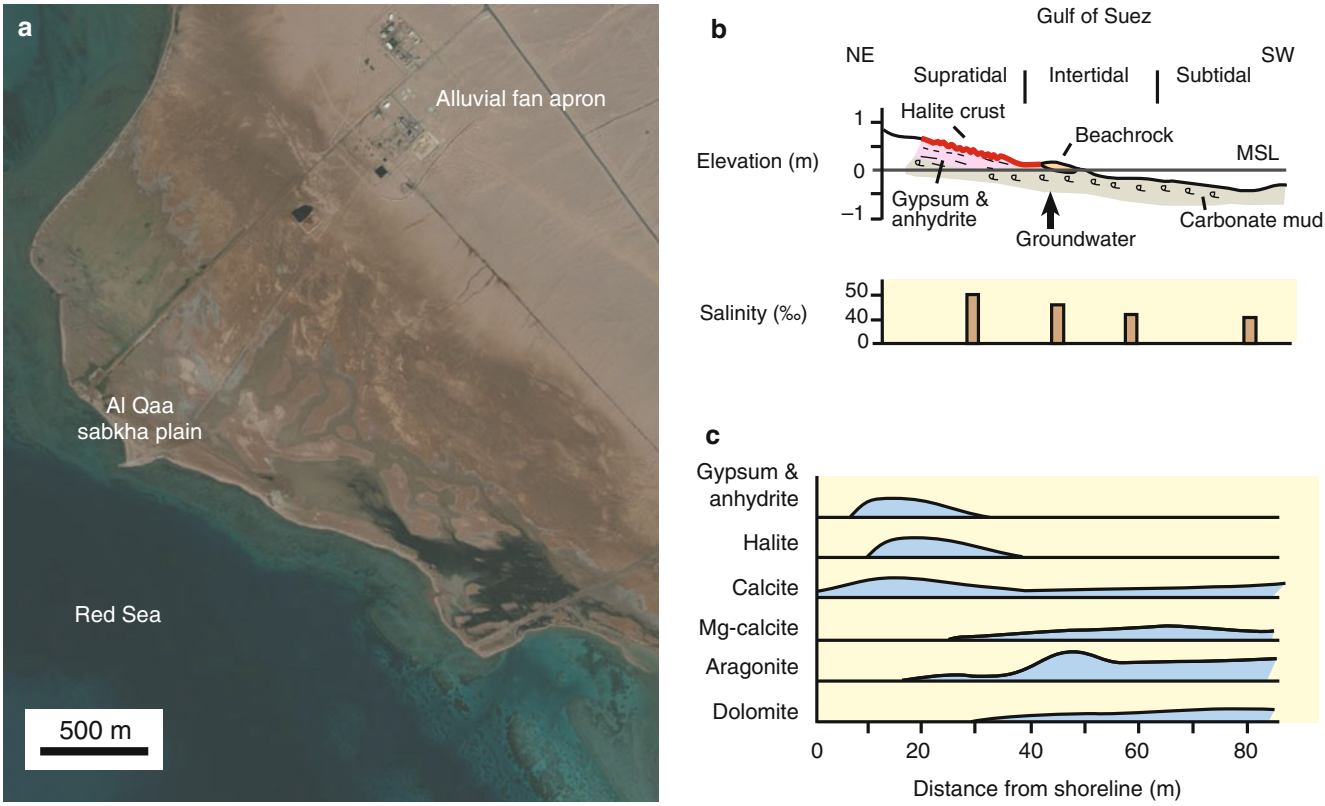

Fig. 3.23 Gulf of Suez sabkhas. (**a**) Geological overview of the Al Qaa region, Red Sea (Bing® image scaled and mounted in MapInfo®). (**b**) Generalised cross section through sabkhas of the coastal zone of the Al Qaa region, Gulf of Suez and typical pore water salinities (After Gavish 1980). (**c**) Idealised distribution of various mineral phases in terms of distance landward from the marine shoreline in Al Qaa region. Gypsum, anhydrite and halite are the main evaporite minerals (After Gavish 1980)

fragments, pellets, ooids, and some intraclasts (Sellwood and Netherwood 1984). Finer-grained marine carbonates typically occupy the seaward side and coarser-grained alluvial clastics occur on the landward side, so that the proportion of carbonate decreases upward in a prograding sabkha cycle. In many places there is an elevated sandy berm or a strip of pebbly beachrock defining the upper limit of the intertidal zone and a sabkha flat is developed behind the berm (Fig. 3.23b). The supratidal zone generally extends a few hundred metres inland, its width being dependent on the regional slope. Further landward the top of the capillary fringe passes below the landsurface. Storm surge waters occasionally cover portions of the supratidal flat and a thin ephemeral crust of pressure-ridged chevron halite may form a cm-thick cap to the sabkha as the surface waters disappear. The crust too disappears in the next flood or rainstorm. Once again, it is highly likely the hydrology of the crust is decoupled from that of the underlying sabkha.

Evaporite mineral distribution in a typical Gulf of Suez sabkha is very similar to the mineral suite in an Arabian Gulf sabkha but the volumes of capillary salts and their lateral extents are far less. Sabkha depositional belts are much narrower due the greater slopes as they occur mostly on the seaward edges of alluvial fan aprons advancing into the Gulf of Suez. Like the Arabian Gulf, the Gulf of Suez sabkhas precipitate evaporites mostly as displacive crystals within the supratidal zone (Fig. 3.23c). Capillary driven concentration precipitates salt in a matrix-rich supratidal evaporite unit, which is no more than 60–80 cm thick – the thickness of the capillary fringe. Most of the gypsum is precipitated as passive pore cements immediately above the watertable. Gavish (1974, 1980) attributes most of the ion supply to landward seepage of seawater, driven by capillary evaporation, as per the model of Hsu and Schneider (1973). The hydrology of the Gulf of Suez sabkhat has not been re-assessed since the work by Wood et al. (2002) on sabkhas of the At Taf coastal strip.

One of the most obvious differences between the Gulf of Suez sabkhas and the Arabian Gulf sabkhas is the distribution of the two calcium sulphate phases (Gavish 1974). In the Gulf of Suez, gypsum is the dominant sabkha mineral in all active parts of the sabkha. Only very minor traces of anhydrite are found and only in the older more elevated portions of the sabkha where it has locally recrystallised or replaced a gypsum precursor.

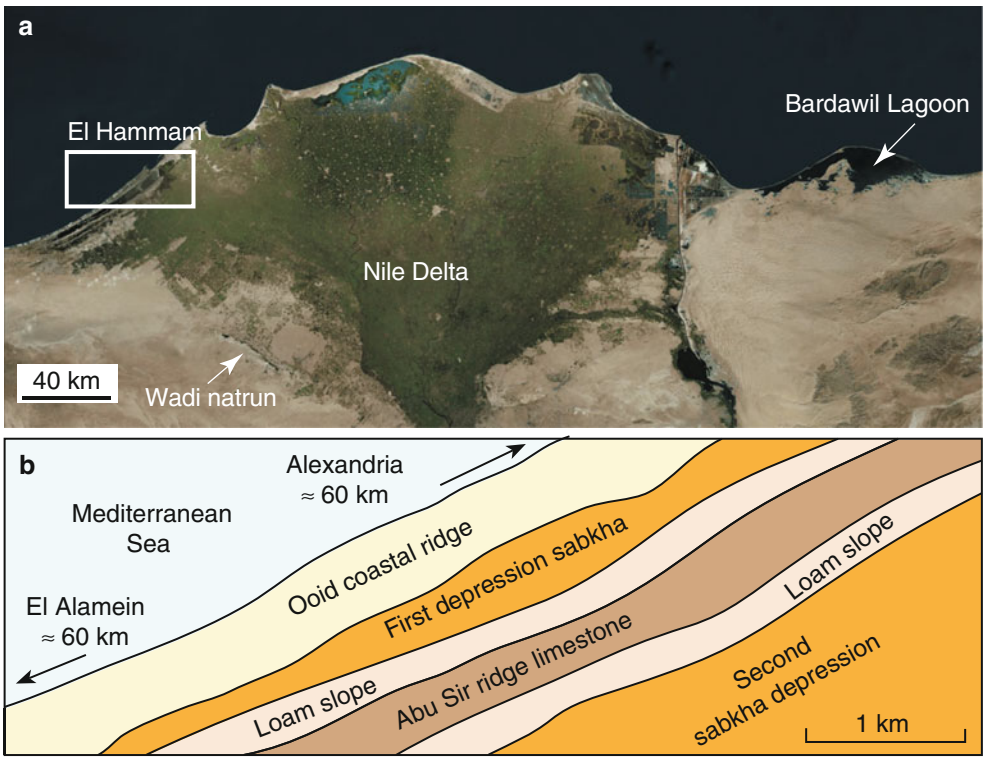

Fig. 3.24 Nile Delta. (**a**) Egyptian coast centred on the Nile Delta. Interdunal coastal sabkhas occur on the eastern end of the vegetated Nile cone (rectangular inset, while Sabkhat Yathal Yam occur on the southern side of Bardawil Lagoon beyond the eastern end of the Nile delta (Bing® Image mounted in Mapinfo®). (**b**) Surface geology of El Hammam sabkhat in interdunal depressions (After West et al. 1979)

Beach-Dune and Fluvial Sabkhat on Deltas

Modern sea-margin settings where large river systems are building deltas into the marine realm in arid settings are areas that set up shallow watertables and so can host local near-coastal sabkha systems. They form where the capillary fringe intersects the land surface and so tend to be preserved either in more protected subsealevel depressions behind coastal beach ridges (Nile Delta) or as fringes to coastal lagoons fed by occasional storm surges and marine floods (Bardawil Lagoon).

Western Nile Delta Coast, Mediterranean, Egypt

Interdunal sabkhas of the Nile delta are forming today along the Mediterranean coast near El Hammam, a region halfway between Alexandria and El Alamein (Fig. 3.24; Bellah and Hassouba 1995). There the coastal zone consists of nine or more Quaternary shore-parallel carbonate beach-dune ridges. All the ridges are cemented with a hard caliche cap, except the most recent dune known as the "coastal ridge." Lagoonal and desert loess sediments fill large swaths of the elongate depressions between the ridges and act as host matrices to the sabkha precipitates.

The first sabkha depression is situated immediately behind the "coastal ridge" of oolitic sand and is more than 8 km long and a few 100 m wide (Fig. 3.24b; Ali and West 1983; West et al. 1979). Displacive nodular gypsum (with minor palygorskite/attapulgite) is growing in the capillary zone of the carbonate-rich desert loess that has filled this most seaward interdunal depression. Landward and to the south, beyond the Abu Sir limestone ridge (Pleistocene), there are other interdunal sabkhas forming about and within various halite-encrusted, cyanobacterial-mat-fringed lakes.

Sediment behind the third ridge back from the coast is very interesting in that it contains a laminated gypsum fill, which is possibly the preserved remnant of a Pleistocene subaqueous deposit (pers. obs). The beds there are extensively quarried and well exposed, but as yet its geology is poorly documented and it is not known if it formed as a marine-fed salina or as a continental chott. The fact that this laminar gypsum fill alternates with thin limestone layers preserving articulated shells of *Cardium sp.* argues perhaps for a marine seepage origin.

All the sabkhas in the inter-ridge depressions are characterised by gypsiferous capillary zone units up to 60 cm thick made up of a combination of lenticular to prismatic gypsum crystals, and small spherical to elliptical nodules 1–4 cm wide composed of silt-sized gypsum. There is no anhydrite growing in the capillary fringe. Matrix sediment is a mostly brown, laminated, very fine quartzose silt and carbonate sand. It was deposited as desert loess and is occasionally reworked by sheet floods shed from the adjacent ridges. Nodules grow most efficiently in Zone III and IV of the inter-ridge sabkha, with more saline pore waters above and less saline waters below (Fig. 3.25). Nodules in zone IV and the uppermost part of Zone II are soft, very friable, uncemented and still maintain high intranodule porosity and permeability. Zones of coalesced nodules can create local upward-bulging enterolithic structures. Nodules made of

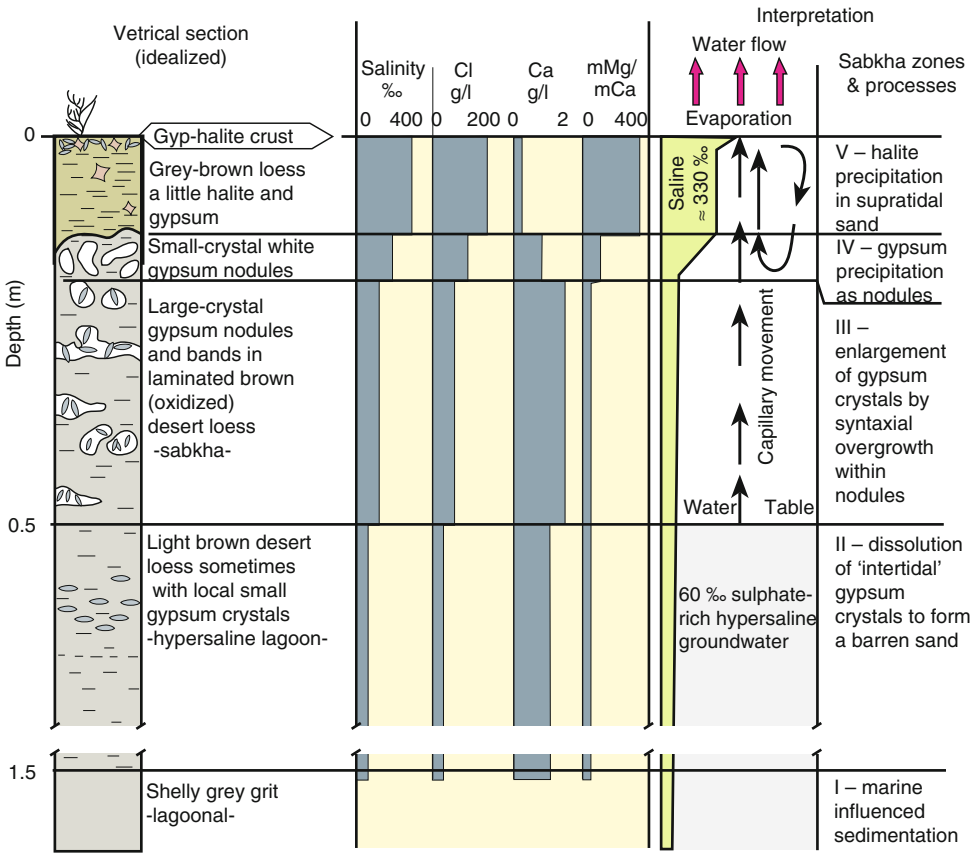

Fig. 3.25 Inter-ridge gypsum sabkhas on the Nile delta, Egypt showing idealised vertical section through the first sabkha depression and the interpreted capillary-driven subsurface evaporation hydrology forming the gypsum nodules that define the sabkha sequence (After West et al. 1979; Ali and West 1983)

Table 3.4 Average compositions of 25 interstitial waters squeezed from evaporitic sediments in the first interdunal corridor, Abu Sir sabkha, Nile coast. Bicarbonate was below the detectable limit in all samples

	No. of samples	Na	K	Mg	Ca	Cl	SO_4	HCO_3	Sr	Salinity (‰)
Zone V	6	77,500	5,200	21,800	100	173,000	49,200	Trace	21	327
Zone IV	4	46,000	3,000	11,100	1,100	66,000	19,700	Trace	45	148
Zone III	6	24,700	1,200	2,500	1,500	54,000	19,300	Trace	42	103
Zone II	9	16,300	600	2,000	1,000	31,000	7,800	Trace	40	59
Seawater	–	10,600	380	1,270	400	18,980	2,650	140	8	34

After Ali and West (1983)

small gypsum crystals typically overlie nodules composed of larger crystals. The relationship between crystal size and distance from the sabkha surface shows that nodules are precipitating in the active capillary zone and do not form by replacement of an anhydrite precursor. As capillary gypsum crystals continue to grow, the nodule expands by pushing aside and deforming adjacent sediment laminae. The fine-grained nature of the hosting loess encourages displacive growth rather than passive interparticle poikilotopic growth. Minor amounts of authigenic calcite and dolomite are also precipitated.

A marine-seepage origin for the gypsum nodules was inferred by Ali and West (1983), based on the seawater-like proportions of the interstitial brines and periodic gypsum saturation in waters of zones III and IV in the waters of the first inter-ridge depression (Fig. 3.25; Table 3.4). But as we saw in Chap. 2 seawater-like proportions in a groundwater do not necessarily mean a seawater origin in continental areas with caliche. Salinities of phreatic groundwaters in Zone II vary from 40 to 80‰, with a mean of 59‰, which is almost twice as concentrated as seawater. Na, Mg and Cl are present in thalassic proportions; Sr is somewhat in excess, as are Ca and SO_4, an association that probably indicates ongoing dissolution of gypsum. Above Zone II, salinities increase upward in zones III and IV. Zone IV, with a predominance of growing gypsum nodules has an average pore water salinity of 148‰ (Fig. 3.25). The uppermost part of the sabkha interval has the highest salinity pore waters, averaging 327‰, a salinity value that is five times that of zone II. Na and Cl maintain their relative proportions, tied to brine concentration in Zones II through V (five-fold increase from Zone II to V). K rises nine-fold over the same interval and Mg about

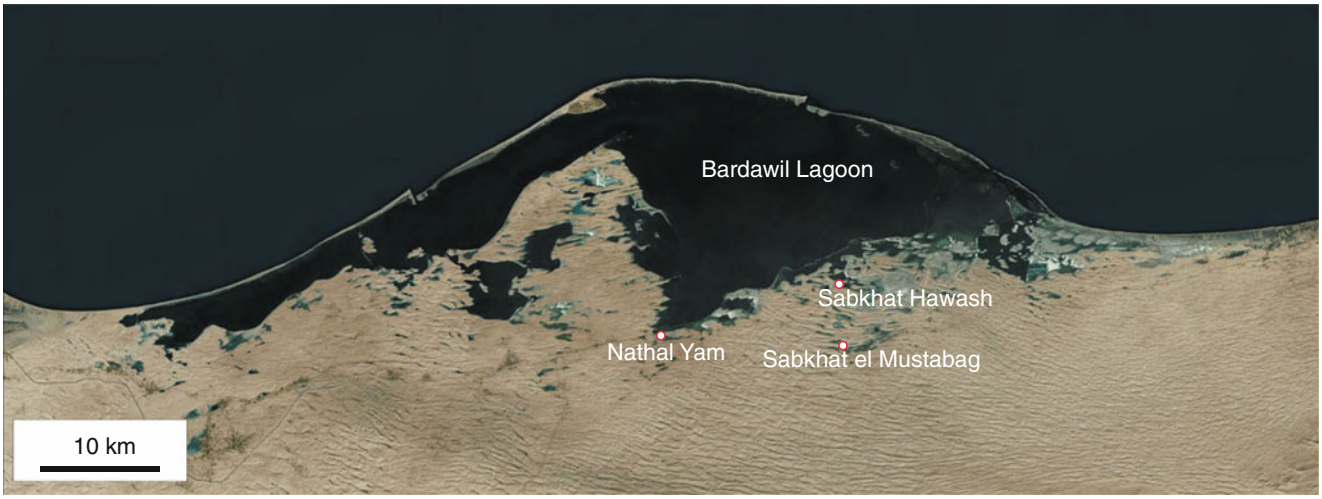

Fig. 3.26 Southern coast of Bardawil lagoon, northern Sinai, Egypt, shows beach-lagoon and interdunal sabkhas within the coastal portion of a sand sea dominated by longitudinal (seif) dunes. Sabkha deposition was a response to a rise in the regional watertable driven by the end-Pleistocene rise in sea level to its present position some 6 ka (Image courtesy of NASA)

eleven-fold. In contrast the Ca content is almost constant in zones II through IV and drops sharply in zone V, showing that gypsum is actively precipitating in zones III and IV. Sr shows a similar trend to Ca, although it does not decrease as sharply in Zone V. SO_4 increases upward to a concentration in Zone V that is a six-fold increase over its levels in the groundwaters of Zone II.

Ali and West (1981) utilised the measured hydrogeochemistry of the interstitial waters to argue for gypsum precipitation by capillary evaporation of thalassic seepage waters via "per ascendum" rather than a "per descendum" model, although at the time they published their work the latter was the prevailing interpretation for a sabkha hydrology.

This series of Egyptian coastal sabkhas is of interest as it is an active sabkha plain in the low-fluvial-supply (desert loess) coastal portion of the prograding Nile delta. It also shows that extremely arid conditions are not a requirement for evaporite nodule growth; it only needs the appropriate seepage hydrology where the capillary fringe intersects the land surface and there is an excess of evaporation over inflow. These sabkhas are actively accumulating gypsum in a region where annual rainfall is ≈ 18 cm.

Once again, like the At Taf sabkha, it demonstrates the lack of preservation potential of any salts precipitated in the seepage hydrology of all modern coastal sabkhas. Once the gypsum nodules are buried into Zone II they are seen to dissolve in rising phreatic brines, which are undersaturated with respect to gypsum (Fig. 3.25). Gypsum is being recycled through the upper parts of a subsiding profile and its preservation potential is low (implications of this typical saltflat hydrology are discussed further later in this chapter).

Eastern Mediterranean Coast of the Nile Delta and Northern Sinai

On the other side of the Nile delta, the northern Sinai coast is bordered for about two-thirds of its length by the Bardawil Lagoon (Figs. 3.24 and 3.26; Levy 1977a, b, 1980). It is a broad marine lagoon with smaller evaporitic sabkha/lagoons in interdunal depressions along its southern coastal interface. The southern part of the Bardawil also defines the coastal desert edge of an extensive sand sea or erg dominated by longitudinal or seif dunes. Regional climate is arid, evaporation rates are high (≈2 m/year) and precipitation is low (≈100 mm/year). Marine-influenced sabkhas on the southern side of the lagoon occur wherever the capillary fringe intersects the landsurface and are of two types: (1) Coastal sabkhas (also called lagoon-beach sabkhas-see Warren 1991), which are at present connected to the lagoon and flooded occasionally by seawater – examples include the inner lagoons and Nahal Yam, and (2) Near-coastal interdunal sabkha depressions, which are now cut off from the lagoon by sand dunes – examples include Sabkhat Mahzin and Sabkhat Hafiordim (Figs. 3.26 and 3.27a). Both types of sabkha formed as a rising marine watertable, created by the Late Pleistocene-Holocene transgression, encroached upon the erg. There is also a third type of sabkha in the region; it is typified by large inland eolian sabkhas such as Sabkhat el Mustabag and Sabkhat Bir Kasiba. This group of sabkhas is carbonate rich and formed under a Late Pleistocene paludal hydrology, which was active at the edges of this desert sand sea in more humid climatic periods. Eolian-lacustrine sabkhas are discussed in more detail toward the end of this chapter.

The largest documented coastal-beach sabkha, Sabkhat Nathal Yam, is about 7 km long and extends about 1 km

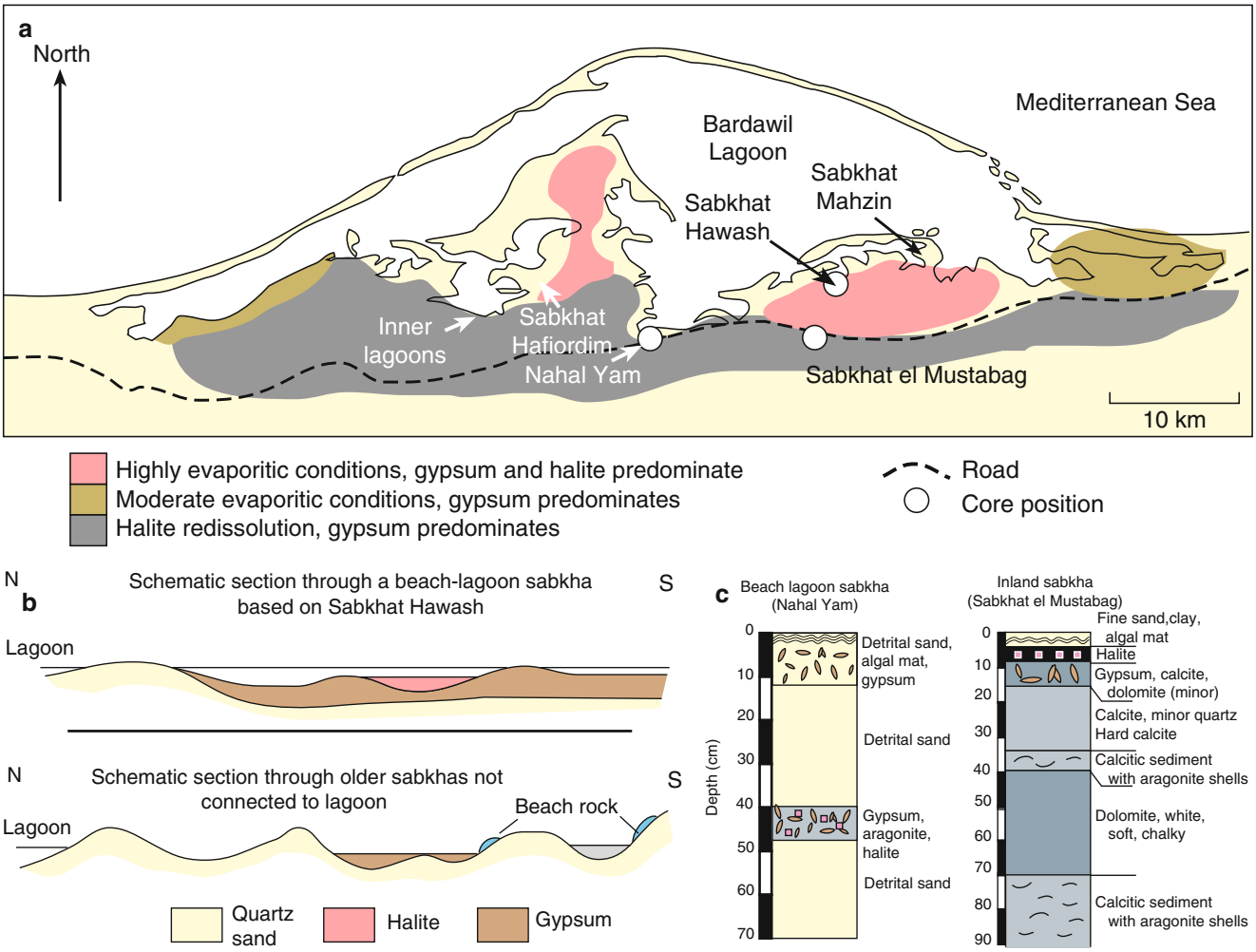

Fig. 3.27 Sabkhas of the Bardawil lagoon, Mediterranean Coast, northern Sinai (After Levy 1977a, b; see Fig. 3.22 for locality). (**a**) Distribution and mineralogy of sabkha salts south of the Bardawil Lagoon. (**b**) Schematic cross section through a beach-lagoon sabkha based on Sabkhat Hawash, showing differences in lateral scale with older inter-ridge sabkhas. (**c**) Composite vertical section in a beach-lagoon sabkha based at Nathal Yam, it is based on cores taken at 20, 500 and 700 m from the beach line

inland. To the south of the lagoon beach sabkhas, coastal interdunal sabkhas extend inland to a distance of about 1–4 km and are accumulating capillary salts from hypersaline capillary water lenses surrounded and underlain by slightly less saline continental phreatic wedges. These "inland" eolian sabkhas tend to be a few kilometres long and less that a kilometre wide (Fig. 3.27a). They define a coast-parallel hydrological transition from marine seepage into continental groundwaters carried in the unconfined aquifers of the regional sand sea or erg.

Both types of sabkha are typified by siliciclastic matrices, with displacive gypsum occurring within supratidal evaporitic units up to 60 cm thick (Figs. 3.27b, c). The intertidal zone in the beach-lagoon sabkha of Nathal Yam is 200–300 m wide and is regularly flooded by tidal waters of the lagoon. The intertidal is characterised by cyanobacterial mats, interlayered with low Mg-calcite muds and containing marine gastropod and lamellibranch shells derived from the lagoon. Lenticular and prismatic gypsum crystals are growing in the cyanobacterial mat layer in the more landward parts of this zone; it is very similar to the gypsum mush zone of the At Taf coastal strip. Landward of the intertidal zone is a 100 m-wide outer flood recharge zone, it experiences no more than an occasional marine flood (a few times a year) during a fortuitous combination of storms and high tide. There, the cyanobacterial mat is covered by a thin layer of detrital quartz sand and otherwise lies atop the same basic sequence of sediments found in the intertidal zone. Landward, still at the southern end, is a 500 m-wide supratidal zone. This area is not currently flooded by lagoon waters, even during storms and defines the interval where the capillary zone intersects the land surface. Under an ephemeral halite crust it hosts displacive gypsum lenses and prisms in a matrix that is otherwise identical to its more seaward counterparts.

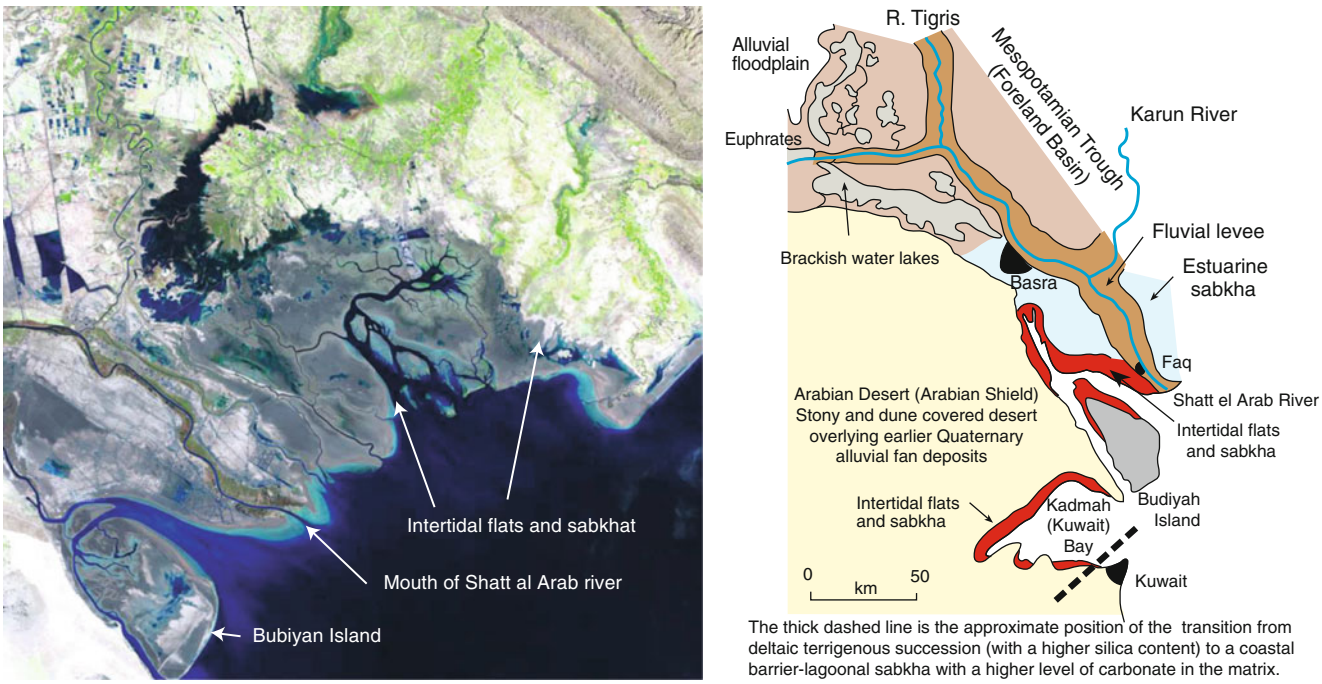

Fig. 3.28 Distribution of fluvial related facies including estuarine sabkha with a siliciclastic matrix along the lower length of the Shatt el Arab River. Note Kuwait Bay in lower centre of geology map (Landsat image courtesy of NASA, surface geology after Evans 1995)

Unconfined continental groundwater, moving north toward the shoreline, periodically seeps into the supratidal zones of all the beach lagoonal and near coast "inland" sabkhas along the southern side of Bardawil Lagoon. Rising water levels occur after heavy winter rains and create ponds of surface water that rapidly evaporate to precipitate thin halite crusts and efflorescences. In fact, most of the present freshened inflow into the supratidal zones both beach-lagoon and coastal interdunal sabkhas comes from a winter groundwater flood from the nearby dunes and not from any influx of storm-derived seawater. This rising watertable dissolves most surface halite crusts, as well as some of the gypsum precipitated in the more isolated parts of all sabkhas in the previous summer. The inherent fractionation explains why ephemeral halite crusts are typically found in depressions located seaward of the gypsum-dominated inland sabkhas.

The calcium sulphate mineral in both styles of near-coastal sabkha is a gypsum pore cement, it is not anhydrite. The groundwater setting is not saline enough, nor hot enough, to favour the preservation of anhydrite. Groundwater floods in the winter means most crystals of capillary gypsum are periodically flushed by meteoric waters and so show internal layering and lenticular shapes indicative of alternating stages of precipitation and dissolution. Mg-calcite, dolomite and halite are minor authigenic components in some near-coastal sabkhas.

Large inland sabkhas, such as Sabkhat el Mustabag, were possibly once connected to the Bardawil Lagoon, although dunes now cut off all the inland sabkha depressions from the sea (Figs. 3.26 and 3.27b). More likely, they formed in the Late Pleistocene in an earlier paludal phase at the seepage edge of the Sinai sand sea, when the seacoast was tens of kilometres further out on the exposed shelf. Soft chalky-white calcian dolomite (layer up to 20–30 cm thick) caps the upper portions of the sediment fill in some of the larger inland sabkhas (Fig. 3.27c). The age of the carbonate precipitates in these older sabkhas is not well constrained. Beneath the dolomitic carapace are well preserved aragonitic gastropod shells, typically embedded in a muddy calcitic groundmass. Radiocarbon dating shows that the dolomite and the underlying unit is older than 35,000 years (Fig. 3.27c). It is a lacustral continental sabkha, possibly deposited in a Pleistocene pluvial, with little tie to the present largely vadose hydrology of the inland sabkhas along the landward edge of the Bardawil coastal prism.

Shatt el Arab Estuarine Sabkha Iraq

The Shatt el Arab delta lies at the northwestern end of the Arabian Gulf, immediately northeast of Kuwait (Kadmah) Bay. It is an area where three rivers (Tigris, Euphrates, Karun) merge to form the Shatt el Arab delta (Fig. 3.28). It is an unusual region in that it is one of a few modern examples of a large modern river delta feeding into an enclosed saline sea and where the amount of eolian sediment in the delta (via the northwesterly Shamal wind) may equal the volume of water-borne fluvial sediment (Evans 1995).

The Shatt el Arab is fed by a broad funnel-shaped estuarine channel with wide levees on either side. Spreading out from the levees are dense surrounding marshes of reed beds (locally known as *ahwar*). The region was drained

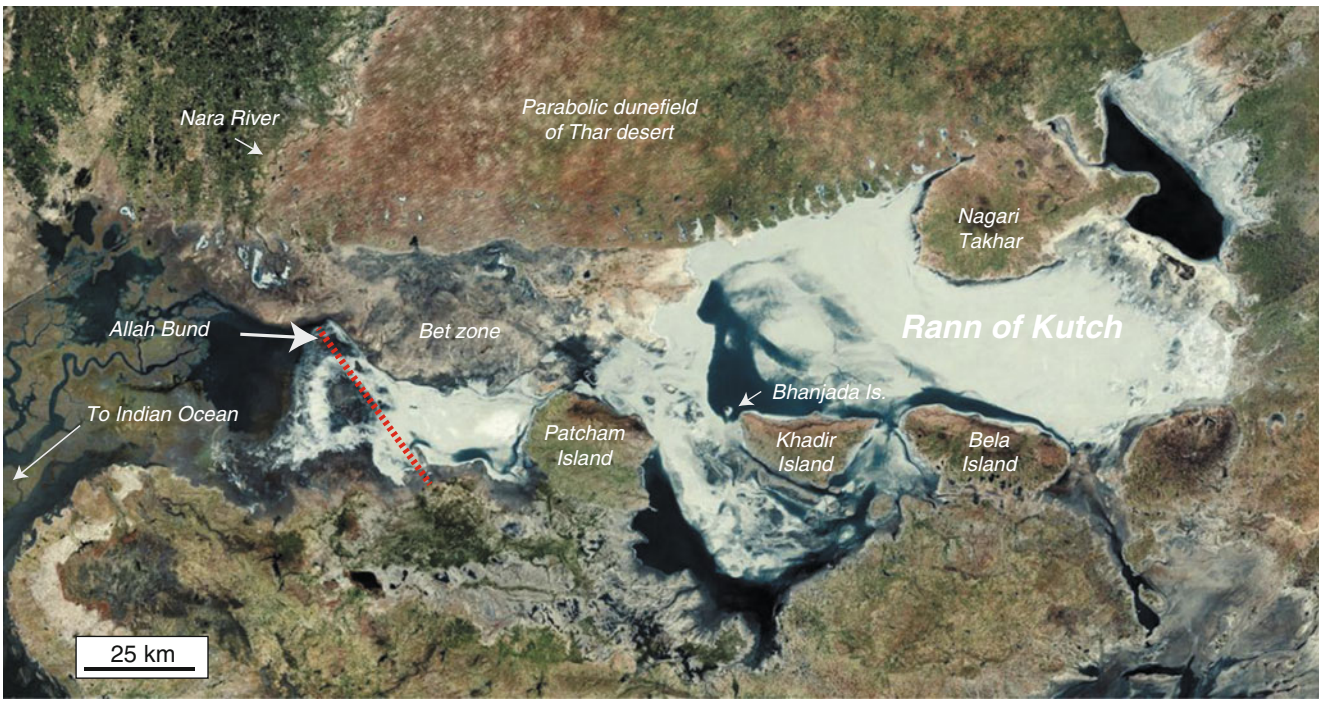

Fig. 3.29 The Rann of Kutch, see text for discussion of noted features

under the genocidal policies of Saddam Hussain, but has now been re-engineered to return the reedbed system to its natural state. These areas are flooded each spring and early summer by waters fed from snowmelt in the river headwaters. Large crevasse splays spread into interchannel areas, which in the lower deltaic plain are dominated by brackish to freshwater lakes and dense surrounding reed-bed marshes (Aqrawi and Evans 1994; Banat et al. 2006). Lakes are floored by bioturbated sandy silts and clayey silts, which preserve abundant meshworks of plant roots and a brackish shelly fauna. Crevasse sediments feeding the lakes are well-stratified sandy silts and muds. At its most seaward extent and across Bubiyan island an extensive plain of estuarine sabkha takes the place of the reedbed.

Matrix in both the sabkha and the ahwar regions is similar. It is rich in detrital carbonates as well as quartz, reflecting the large volumes of outcropping carbonate in the hinterland. What separates the two settings is the lack of higher plants on the estuarine sabkha (instead of root meshworks there are widespread cyanobacterial mats and some local mangroves) and the widespread authigenic precipitation of high-Mg-calcite, calcite, calcian-dolomite, gypsum and perhaps pyrite as capillary salts in the sabkha matrix. Palygorskite is present in the sabkha as both authigenic and allochthonous phases (Aqrawi and Evans 1994).

The extremely low wave energy attacking the front of the Shatt el Arab delta separates it from other arid-zone deltas, such as the Indus, which show similar 2–3 m tidal ranges. Due to this low wave energy (limited fetch), only narrow beaches and small coastal dune systems form along the leading edge of this arid zone delta. Rapid progradation of fines forms widespread saline mudflats and sandbars across much of the seaward part of the delta plain, also dissected by tidal channels along the delta front. Saltpans and gypsiferous sabkhas form behind low relief beach ridges and chenier ridges wherever surface seawater is trapped after very high tides and storm floods. The resulting evaporitic zones are characterised by crusts of halite and capillary precipitates of gypsum. Anhydrite after gypsum occurs in the most exposed and saline portions of this system.

The seaward extent of the evaporite-capped volume of deltaic sediment is not well established, but is significant as the delta lobe probably extends some 100 km from the modern shore (Fig. 3.3a; Evans 1995). Away from the active fluvial-fed portions of the delta lobe, quartzose sands are reworked into a shoalwater complex of elongate tidal bars that passes seaward in prodeltaic marls, which in turn enclose the reef capped Kharg Island off the Iranian coast.

Sabkha sediments, passing updip into dense reed beds, show affinities to similar facies on the Nile Delta. In both, the increasing distance from the active part of the delta explains the change from a quartzose matrix in the delta sabkhas to a more carbonate-rich barrier-lagoon style of sabkha (e.g. Fig. 3.28 – dashed line southeast of Kadmah Bay).

Rann of Kutch

The Great Rann of Kutch (Kachchh) is a marine-influenced evaporitic sump some 300 km long and 80–100 km wide on the margin of the Thar Desert in arid western India (Fig. 3.29; Glennie and Evans 1976; Tyagi et al. 2012). Its intra-plate

position, south of the Himalayan suture, creates a unique arid capillary salt landscape inundated during the monsoon by wind-driven marine storm surges, sourced on its seaward side, and continental fluvial influxes from the landward (Glennie and Evans 1976). The Kutch depression is bound by the Nagar Parker Fault (NPF) on the north and Kachchh Mainland Fault (KMF) on the south. Capillary evaporitic sedimentation in the Great Rann occurs in a siliciclastic matrix with deposition controlled by an interplay between tectonic, continental and marine processes.

Glennie and Evans (1976) concluded that the Great Rann was probably occupied in the Early Holocene by shallow marine gulfs following the rise in sea level after the last glacial epoch, whereas continental sediment influx dominated during the transgressive phase. According to them, the clay mineral matrix assemblages is dominated by illite, kaolinite, chlorite and montmorillonite, with little or no carbonate, suggesting the dominant influence of the Indus River drainage system on the matrix mineralogy. They argued that most of the matrix was derived from the combined Indus and Nara Rivers, which extended southwards towards the present Indus delta, with some of its waters escaping into the Arabian Sea via Kori Creek. There is also the possibility that a former mighty river, called the Saraswati, received water and sediment from the Himalaya and once flowed into the Great Rann of Kutch.

The sabkha-capped Western Great Rann is also known for its tectonic instability, this has created numerous episodes of liquefaction and seismite overprint in the sediments of the Rann as evidenced in the 2001 earthquake (Rastogi 2004; Rajendran et al. 2001). As well as causing severe structural damage, this 7.7 magnitude event killed more than 13,000 people, caused collapse or severe damage to over a million houses and an economic loss in the region of US$10 billion. Paleoseismological investigations in the vicinity of the earlier 1819 Allah Bund earthquake indicate the occurrence of an even older earthquake around 800–1,000 years ago, both relate to the surface expression of a growth anticline atop an active (but hidden) thrust fault (Rajendran and Rajendran 2001).

The various documented seismic effects on sedimentation (summarised in Tyagi et al. 2012) strongly support the notion that the present Rann is the uplifted floor of a former Holocene marine gulf. Studies of the occurrence of raised notches and abraded platforms on the margins of Bela, Khadir and Bhanjada islands, suggests uplift of the Rann Gulf occurred less than 2,000 years ago and that marine ports were once active in what is now the Rann (Chowksey et al. 2010; Khonde et al. 2011). The most recent seismic event driving a substantial rise in portions of the Rann floor was the 1819 Allah Bund (*Dam of God*) earthquake. It created a 6 m tall, 6 km-wide, natural dam across the Puran or Nara River. This NE–SW trending scarp not only dams river inflow, on its seaward side it controls the distribution of modern tidal influence (Fig. 3.29).

Today, interactions of marine and fluvial processes continue essentially unchanged (Glennie and Evans 1976). The annual flooding by the sea, driven by the Southwest Monsoon, still brings fine sediment into the Ranns. The streams draining the borders of the Ranns transport coarser material from the hills during this season and deposit it where they debouch into the Ranns. The finer material is carried further out onto the Ranns to mingle with the marine derived silt and clay. Small waves rework the outwash plains around the edges of the Rann at these high-water stages and sometimes cut cliffs in the outwash plains.

As the water recedes, evaporation proceeds and halite crystallizes out to form the extensive surface crust. The interstitial waters become concentrated and gypsum crystals grow within the sediment. Waters enriched in magnesium ions, as a result of precipitation of other salts, react with the sparse carbonate present in the sediment to form dolomite.

The outwash material is reworked by the wind and some sand, very rich in gypsum, has been blown into low dunes (lunettes) along the edges of the Rann. Some of the crystallized halite and gypsum is blown even further landwards into the Thar (Rajasthan) Desert. Similarly, considerable dust is probably blown back onto the Rann from the surrounding arid areas during times of wind reversal in other seasons (e.g. northeast winds of the ‘Little Monsoon’).

Much of the halite crust is recycled each year via flooding by marine waters and so does not attain any great thickness in the sediment column. Halite layers with thicknesses of 90–120 cm were, however, described by Oldham (1893) from near Sindree. The lenticular gypsum that has grown within the sediment will probably remain and may gradually increase in percentage with time to preserve a displacive salt sabkha signature in the more evaporitic sediments.

Although the total proportion of the Holocene sediment volume in the Rann of Kutch that is made up of capillary gypsum is less than 5–10 % it is an interesting marine-associated evaporitic example for a number of reasons. It has a sedimentary system with tidally-influenced marine clastics as the primary signature in the matrix (mostly tidal flat heterolithics with some tidal channel sands). At the time the matrix of the Rann of Kutch saline flat was deposited there were no evaporite salts. The transition to a capillary evaporite hydrology, came about some 1,000–2,000 years ago, as a diagenetic evolution driven by tectonics and the formation a hydrographic barrier tied to the early stages of the Allah Bund high. This makes it an interesting example of a Holocene marine sabkha created by tectonics, not eustasy. The other question generated by its current sedimentological scenario is how would we recognise an ancient counterpart? The pervasive seismically-induced liquefaction that occurs in the Kutch sediments with each significant seismic event

(every hundred or so years) probably means little or no primary matrix structure (tidal sedimentation) will be preserved in ancient counterparts. What would be preserved is likely a few anhydrite nodules (after gypsum) floating in a relatively structureless or intensely seismite overprinted matrix.

Interpretive Limitations of Holocene Sabkha Models

Capillary salts and surface crusts precipitated in Holocene marine-margin sabkhas and many continental sabkhas have low preservation potential. They precipitate in a hydrological fringe underlain by undersaturated waters and below a land surface subject to periodic freshening and flooding. Whether capillary salts form by cooling (thermalites) or pore brine evaporation is irrelevant in terms of their ultimate preservation potential. To pass into the rock record any sequence must, by definition, subside. As it does so, the sabkha nodules, crystals and crusts at the edge of a body of brine of normal seawater salinity must pass back into waters undersaturated with respect to the minerals precipitated in the capillary fringe. At best, what will be preserved of the original salts in the prevailing hydrology at the edge of a normal marine water body will be partially dissolved remnants of the salts and nodules. More likely, the capillary fringe precipitates will become a thin interval of haloturbation textures and dissolution collapse. If, on the other hand, a sabkha succession sits on the edge of a hypersaline saline pan (as in some modern continental sabkhas) or on the edge of an ancient saltern or seaway, then the capillary salts pass into a saturated brine curtain or into the edge of a reflux plume, and so preservation of the original capillary textures is more likely.

There are other implications of the sabkha signature always forming in a capillary fringe. A typical sediment distribution model for an ancient sabkha, based on the Abu Dhabi Holocene, looks something like that presented in Fig. 3.30. Such models typically do not consider hydrology, bed thickness, lateral extent or structural controls when compiling the sabkha units; they merely use Walther's Law[4] to stack the various peritidal sequences into a vertical

[4]Walther's Law of Facies states that the vertical succession of facies reflects lateral changes in environment. Conversely, it states that when a depositional environment "migrates" laterally, sediments of one depositional environment come to lie on top of another.

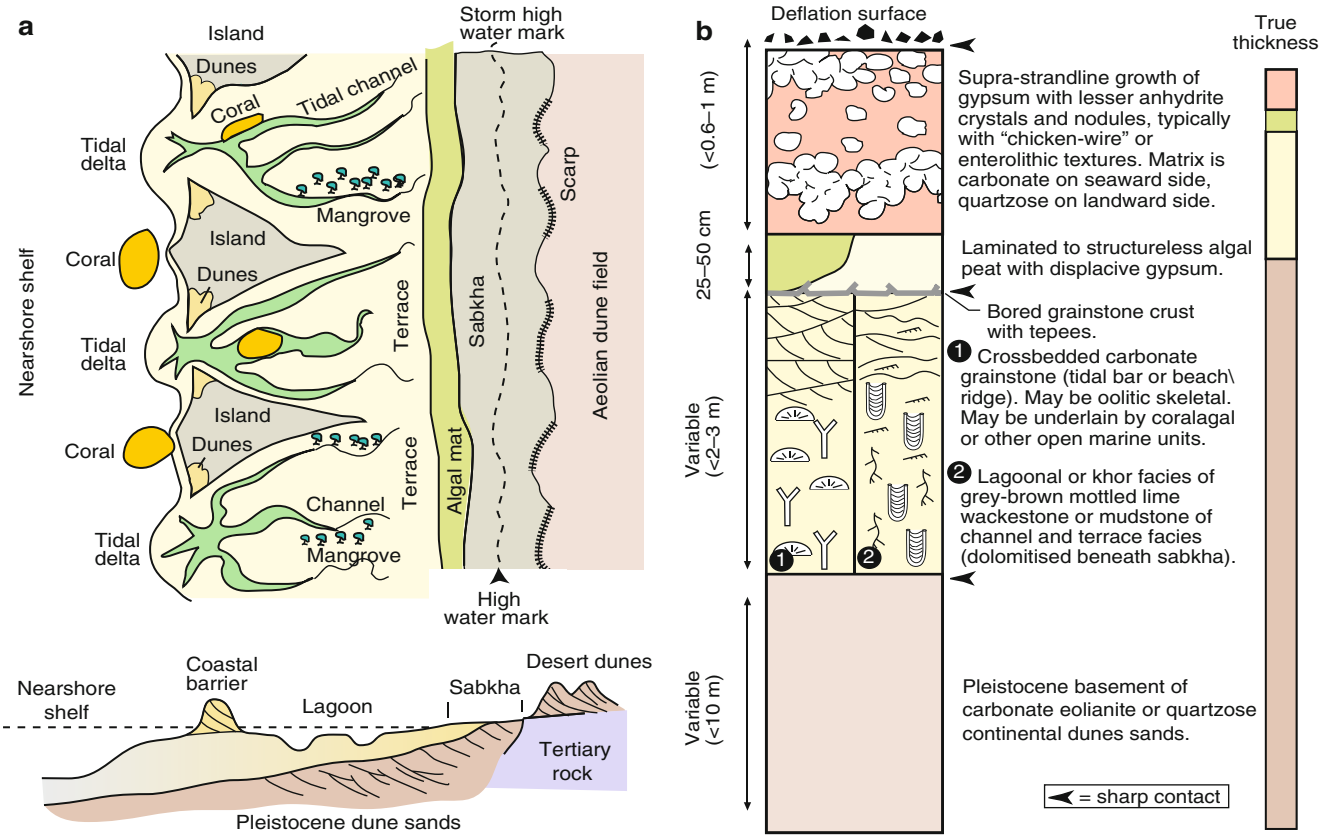

Fig. 3.30 Generalised geological model. (**a**) Based on the distribution of the main carbonate facies belts in Abu Dhabi – Khor al B'azm region (in part after Evans 1995). (**b**) Characteristic vertical succession of sea-margin carbonate sabkha showing typical thickness for each unit, *right column* shows true relative thickness (in part after Warren 1991)

succession. Because of this, the Abu Dhabi sabkha analogy is sometimes used to interpret ancient evaporitic platform successions composed of marine carbonate beds interlayered with nodular anhydrites (platform evaporites), without a full understanding of the implications of the requisite sabkha hydrology.

An Arabian Gulf carbonate-hosted sabkha is part of a prograding Holocene ramp where the total succession is composed of subtidal, intertidal, and supratidal sediments. It is capped by a Stokes surface and typically backed by a siliciclastic sand sheet/dune association. The complete Holocene section is no more than 3 m thick and in the type area centred on the Abu Dhabi region the Holocene sequence is composed predominantly of subtidal lagoonal carbonates. The evaporitic intertidal and supratidal cap is up to a metre thick and always reflects the thickness of the capillary fringe.

Underlying Pleistocene sediments are up to 12 m thick in the vicinity of Abu Dhabi Island; they are permeable Pleistocene dune sands that directly overlie the Miocene carbonate aquifer supplying solutes to the sabkha (Fig. 3.30a). In terms of sediment volume, scaling and perhaps even geometries of accommodated sediment, much of the Abu Dhabi sabkha is best considered to be an eolian sabkha with a watertable closer to the landsurface because of proximity to the ocean (eolian sabkhas are discussed in more detail at the end of this chapter).

In its strictest sense, based on relative unit thicknesses, an Abu Dhabi sabkha should only be used as an analogue for ancient successions made up a transgressive subtidal lagoonal carbonate (1–3 m thick) with a 0.5 m thick matrix-rich cap containing capillary salts, which is in turn capped by an erosional surface (Fig. 3.30b). The whole succession should have been deposited atop a much thicker marine-flooded eolian dune aquifer system (Achauer 1985). In most Holocene-based analogs for ancient evaporite systems, we modify notions of Holocene thickness and stacking to accommodate great changes in scale and thickness needed to typify ancient epeiric settings. Sometimes this is done without considering inherent hydrological limitations and the laws of fluid physics are unknowingly ignored (see Chap. 2 for hydrological details of various saline hydrologies).

For example, many thick, ancient sequences of pure nodular anhydrite have been interpreted as sabkhat deposited under conditions of slowly rising sea level (transgressive systems tract). There are hydrological and preservation restrictions associated with this hypothesis that are not considered in many sabkha reconstructions. The thickness of nodular anhydrite in any supratidal unit is limited by the thickness of the capillary fringe. Any evaporite sediment lying above the top of the capillary zone is blown away or dissolved (Fig. 3.30b). Aside from the preservation issues mentioned earlier, this means that the supratidal evaporite phase in a single sabkha cycle (stillstand) can be no more than 0.5–1 m thick and by definition it is matrix dominated (Warren and Kendall 1985). Matrix must exist before capillary salts can grow. Hence, the inherent difficulty in explaining metres-thick pure nodular anhydrite as a thick sabkha without any encapsulated erosion surfaces. If in an ancient succession a nodular anhydrite is relatively pure and lacks internal erosion surfaces it cannot be a sabkha, it is some sort of subaqueous succession or subsurface replacement front.

The only exception to ancient sabkha sequences being dominated by non-evaporite matrix is when the matrix is composed of mechanically deposited sulphate or halite, perhaps derived by storm or eolian transport from a nearby saltern or saline pan. If such a succession was buried, the result would be a nearly pure sulphate or halite unit composed of sabkha cycles, each 1–2 m thick, interlayered with saltern or saline pan units many metres thick. No modern examples of this style of evaporite deposition exist outside of the stacked saline pan halites in the South American salars discussed in the next part of this chapter. Modern sulphate equivalents are unknown, although they can be commonplace in stacked saltern-dominated marine-fed platform successions such as the Cretaceous Ferry Lake Anhydrite of the Gulf of Mexico and the Permian Werra Anhydrite of the Zechstein (Chap. 5).

The need to stack sabkhas into hypersaline, not marine, groundwaters also means that wherever matrix-rich beds of nodular anhydrite are metres to tens of metres thick with no intrabed erosional surfaces (Stokes surfaces) then the sequence is probably not a sabkha. It may be a reflux-cemented marine platform carbonate, or an interval overprinted by burial cements. In my experience many ancient normal marine platforms overprinted by later patchy diagenetic anhydrite nodules and axe-head anhydrite cements are often misinterpreted as sabkha indicators. In many sequence stratigraphic reconstructions this leads to such intervals being misinterpreted as being formed in times of lowered sealevel. This is especially so in studies by stratigraphers looking for evidence of times of sealevel lowering in platform successions. They tend to ignore the possibility of diagenetic evaporites or the marked differences in eustatic amplitude and frequency that characterise icehouse and greenhouse climate modes (Chap. 5). The presence of a few anhydrite nodules in a core or an FMI image, floating in a matrix of carbonate or siliciclastics, is not sufficient evidence to interpret the sequence as an ancient sabkha.

In the modern sabkha, the evaporites of the sabkha supratidal zone overlie restricted lagoonal sediments; they never overlie open-shelf carbonates. Yet in ancient platform evaporites, many beds of nodular anhydrites have been interpreted as sabkha. Such units typically seal dolomitised open-marine shelf carbonates. Perhaps insufficient time has elapsed in the Holocene for sabkha progradation to form a geologically

realistic sabkha cap atop marine platform carbonates. Or perhaps ancient nodular anhydrite beds were deposited in a subaqueous saltern at a time when the platform was an isolated drawdown lagoon.

In a few millennia in the Abu Dhabi region, and only if the At Taf coastal strip undergoes suitable subsidence, the succession of sabkha evaporites, and its formative hydrology, may prograde over the Holocene carbonates of the oolite shoals and the open shelf. And yet, the modern sabkha progrades across the inshore lagoon in response to the protecting action of the offshore oolite-reef shoal. The barrier islands screen the soft sabkha muds and evaporites from the erosive forces of the open gulf waves and the Shamal storms. Once the sabkha has infilled the lagoon behind this buffer, it is unlikely the sabkha will prograde much further seaward without the deposition of another sand shoal or reef a little further offshore.

Yet the sabkha "Trilogy" used by many to interpret ancient nodular anhydrite is supposedly composed of three laterally continuous facies belts with subtidal overlain by intertidal overlain by supratidal sediments, all merrily marching out into a subsiding basin without a change in facies. In reality, sabkha progradation, using an Arabian Gulf analogue, must be a punctuated process over geologically significant time scales with the original evaporite capillary salts unlikely to be preserved (Warren and Kendall 1985). A sabkha succession cannot be a simple continuous seaward movement of the 'Trilogy", never broken up by coquinas, barrier islands, ooid shoals, beach ridges or reefs.

Lastly, models used to interpret ancient sabkhas typically regard the Arabian Gulf as a carbonate province with the siliciclastic components ignored, or mentioned only in passing. This should not be the case. In almost all coastal areas along the southern Arabian Gulf the most landward portion of the sabkha is a sediment belt 2–6 km wide with gypsiferous evaporites accumulating in an eolian derived siliciclastic matrix. This zone passes seaward into a predominantly carbonate matrix. There are, in fact, numerous modern siliciclastic continental sabkhas both in the Arabian Gulf and elsewhere, all of which show lateral extents more akin to larger scale ancient counterparts than do any modern carbonate-hosted coastal sabkhas (see eolian sabkha section at the end of this chapter).

Lacustrine Sabkhas and Pans

So far this chapter has focused on sabkhas and evaporitic mud-flats in modern sea-margin settings. But at the 10,000-year-scale these are aerially-limited and ephemeral hydrologic systems, tied to the Holocene coastal highstand, with inherently poor preservation potentials. To study sabkhas that can stack to greater thicknesses and have sizes and volumes comparable to some of the smaller ancient evaporite systems we must move to Quaternary continental lacustrine settings in regions of intermontane subsidence and include hydrology of the saline pan in our modelling of preservation potential.

Modern continental sabkhas contribute to salt deposits with thicknesses of more than a hundred metres and areas measured in thousands of square kilometres. Evaporites in continental sabkhas grow by displacive crystal growth in the capillary zone or in immediately underlying brine-saturated muds. Ongoing growth of capillary salts above the watertable pushes the sabkha surface up out of the capillary zone into the vadose zone. This raised and dried continental sediment deflates to create the characteristic erosion/truncation surface. As in models based on modern marine-margin sabkhas, the presence of a Stokes surface is a key feature in recognising an ancient continental sabkha succession. Brine concentration in the saline mudflat is driven by the intensity of capillary evaporation and occurs adjacent to areas of saline pan and even adjacent to perennial subaqueous salt beds. Pans and holomictic brine lakes are needed to generate stable brine plumes or brine reflux curtains that preserve a stacked sequence of salt beds. The presence of a pan or perennial lake next to a sabkha defines the hydrology needed to preserve subsiding sabkha sequences. Their longterm absence is why Quaternary marine-margin sabkhas have little or no preservation potential.

Depositional Characteristics

A continental sabkha is the part of a playa mudflat complex where the capillary fringe intersects the landscape. It sits within a sedimentary transition from the basin margin to the lowest parts of the brine-saturated basin floor (Fig. 3.31; Eugster and Hardie; 1978):

alluvial fan / ephemeral stream / floodplain → sand flat → dry mudflat → saline mudflat → saline pan

The more landward parts of this depositional association are composed of terrigenous alluvial sediments and their reworked eolian residues in the dry sand flat (Fig. 3.32a). The watertable is usually deep within these alluvials and so sediments do not retain the more saline capillary salts, which are the focus of this discussion. They can contain caliche horizons formed by soil moisture fluctuations and perched capillary evaporation. We will come back to these less saline

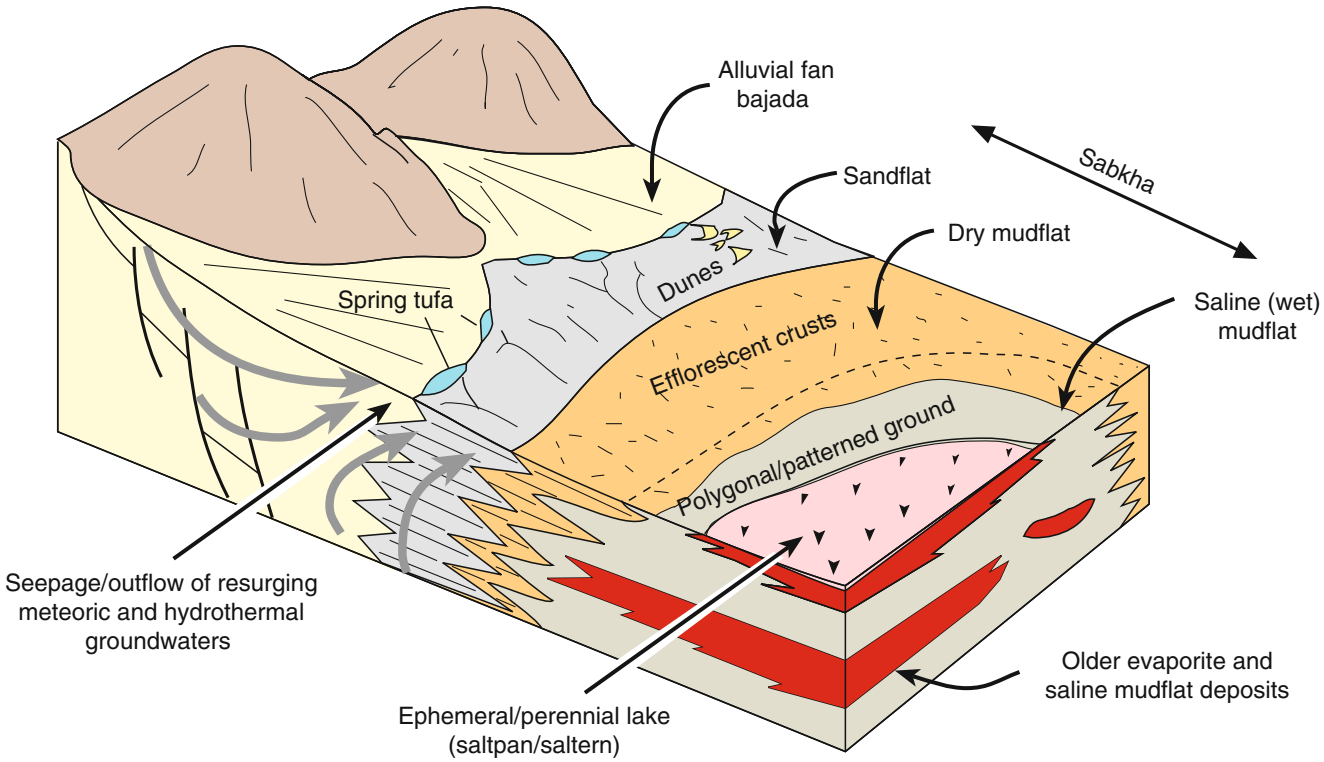

Fig. 3.31 Continental sabkha/playa showing various facies belts and processes of solute supply that include surface runoff, meteoric and hydrothermal groundwaters (in part after Kendall 1992; Eugster and Hardie 1978)

margins settings in our discussion of various specific examples of modern continental sabkhas. For now, we will focus on those parts of the playa system that do preserve substantial volumes of the evaporite salts, namely, the saline mudflat and the outer edge of the saline pan.

Saline Mudflat

The saline mudflat, along with the haloturbated parts of the dry mudflat, define the sabkha belt of a continental sabkha and together make up what is also often called the ephemeral saline lake belt (Figs. 3.31 and 3.32a; Eugster and Hardie 1978). The sabkha passes basinward into beds of the saline pan, which are made up of stacks of predominantly subaqueous and recrystallised salt crusts, and landward into dry mudflats, sandflats and alluvial fans. Additional sedimentary facies may be found within the sabkha tract at any of several positions depending on short and longterm changes in the basin hydrology. They include dunefields and lunettes, which are composed of terrigenous sands, mud pellets, or evaporite grains; travertine springs or tufa mounds; and shoreline/strandline features such as sheet deltas, beach ridges, or spits.

Continental saline mudflats (sabkhas) are extensive vegetation-free flatlands composed of fine-grained sediments with displacive intrasediment precipitates of halite, gypsum and anhydrite or, less often, of more exotic salts such as glauberite, mirabilite and trona. Displacive salts may grow randomly in the capillary fringe as crystals and nodules or be concentrated in dm-thick layers (Fig. 3.32b). Backreactions, periodic freshening and progradation may drive alteration, leaching and replacement of salts in this zone and mineral precipitation is sometimes aided by bacterial processes (Rosen and Warren 1990).

Dry mudflats, with their requirement of a somewhat deeper watertable, typically lie closer to the landward edge of a playa and form the rim to saline mudflats and saline pans. Sediments are mostly fine-grained, characterised by primary structures formed under alternating upper and lower flow regime conditions, such as sand-rich layers deposited by sheetflood, along with palaeosol horizons indicating periods of landscape stability. Dry mudflats do not retain evaporite salts, but may show disrupted to massive textures created by earlier intrasediment evaporite growth and dissolution (haloturbation), related to earlier times of higher watertables. Occurrences of actual salts on modern dry mudflats are limited to puffy surface efflorescences related to humidity fluctuations in the soil moisture zone and are destroyed/dissolved with the next light rain or fog.

A feature common to many dry mudflats is a pervasively cracked surface with crack diameters ranging from centimetres to giant polygons tens of metres across. Giant polygons or megapolygons indicate a longterm drawdown of the

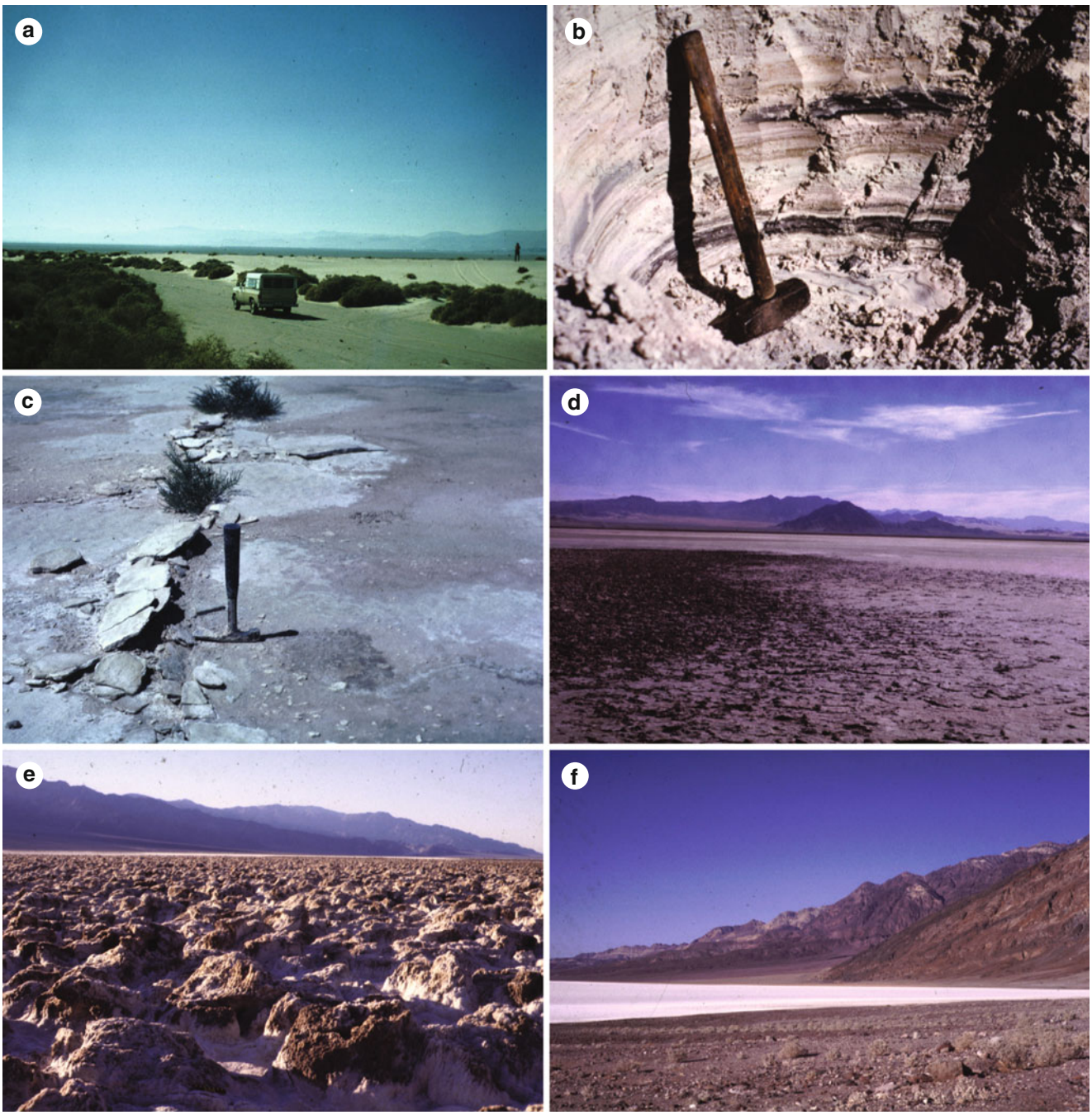

Fig. 3.32 Continental sabkhas. (**a**) Dry mudflat with local eolian dunes and nebkhas on the edge of Owens Lake, California. (**b**) Laminated dolomite-gypsum sediment where capillary gypsum is growing above the water-table, the hosting matrix is made up of former perennial lake sediments with dark organic rich layers, Salt Basin Playa, west Texas. (**c**) Transition between dry mudflat and wet mudflat atop a tepee-overprinted dolomite crust, Salt Basin Playa, west Texas. (**d**) Transition between saline mudflat and saline pan facies, Bristol Dry lake, California. (**e**) Highly etched and disturbed salt crust of completely desiccated saline pan (Devil's golf course; Death Valley). (**f**) Panorama of Death Valley showing juxtaposition of alluvial fan with sabkha/saline pan facies due to steepness of valley walls

regional watertable associated with longer-term climatic change (Fig. 2.59; Neal et al. 1968). Cracks may not be a simple V, but may step across layers, show evidence of multiple stages of growth and be filled by a variety of sediments ranging from sands to muds.

Groundwater Transport and Fractionation in Saline Mud-Flats

Sheet floods in ephemeral lakes are relatively rare, most salts move about the lake flats as soluble load in shallow groundwaters, not as mechanically reworked sediment.

Surface water and groundwater always flows to the lowermost point on the playa surface. Groundwater on this journey can come near or to the playa surface a number of times in zones defined by capillary salts and ephemeral efflorescent crusts. Crusts and salt assemblages in early stages of their formation can contain metastable high salinity salts such as epsomite and thenardite, which can even occur at the surface of the most landward parts of a mudflat. But when subjected to fluctuating humidities or light rains the less stable (more soluble) salts are quickly leached back into the dissolved load of the groundwaters and continue their journey basinward down the potentiometric gradient. Brines derived from the partial dissolution of efflorescent crusts are usually simple chemical solutions dominated by one or two major solute species (e.g., NaCl, Na_2SO_4, Na_2CO_3). The less-soluble mineral fraction is then left behind, in the more landward parts of the saline mudflat where it forms a carbonate crust, such as the dolomitic crusts of Salt Flat Playa, west Texas. There, the ongoing accumulation of capillary carbonate has forced the surface crust to buckle and crack into lacustrine mudflat tepees (Fig. 3.32c; Hussain and Warren 1988).

Farther out into a salt basin, ongoing capillary evaporation precipitates new salts as efflorescences on the lake surface or as intrasediment nodules and the process of fractionation can begin all over again. Ongoing repetition of this process means shallow sabkha groundwaters become increasingly saline as they seep toward the lowest part of the lake floor – so saline that even the more soluble salts become stable and can accumulate as intrasediment precipitates (e.g. displacive halite, glauberite, thenardite). Only the most soluble salts are carried into the lowermost portions of the lake basin, so that crusts deposited in saltpans define mineralogically simple bull's-eye patterns with the most soluble salts accumulating only in the lowermost portions of the ephemeral lake floor. Such concentric or "bull's-eye" fractionation patterns are often assumed for salts making up ancient sabkhas and pans, with the most soluble salts indicating the deepest part of the basin. But this simple pattern can be complicated by periodic near-unidirectional flooding fed from a single inflow channel, as seen today in some of the sabkhas in the salt lakes of central Australia (e.g. the Warburton Channel into Lake Eyre; Fig. 3.55).

Saline Pan

Saline pans in modern continental salt lakes are closely tied to the formation of saline mudflats and dry mudflats (Fig. 3.33; Lowenstein and Hardie 1985). They define zones on the salt lake floor where surface brines pond and concentrate long enough to stack into layers and beds composed of aggrading salt crusts (Fig. 3.33; Stage II). Pans typically form in drainage sinks situated in the lowest parts of the playa surface. A pan is typically surrounded by a saline mudflat and is frequently underlain by older bedded or layered salt units (Figs. 3.31 and 3.32d). In Lake Magadi, for example, the pan is defined by a trona bed 40 m thick, while in Bristol Dry lake the saline pan facies can be found intercalated with saline mudflat facies throughout the 400 m of core recovered from the basin centre.

Pans range in size from small features a few km across to gigantic continental salt sinks as in Salar di Uyuni where the pan area is more than 9,000 km^2 (Rettig et al. 1980). Textures in the stacked salt layers are a combination of subaqueous aligned features (e.g. chevrons and swallowtails) and exposure overprints (e.g. microkarst pits, subhorizontal erosional bevels and salt-filled polygons) that formed each time pan dried and its surface was exposed (Fig. 3.32e). Stacked crusts are usually dominated by halite, but other minerals such as gypsum, mirabilite and trona can be important.

When the pan dries eolian dust is trapped by capillary adhesion on its moist, rough surface or filters down cracks and fissures in the salt crust. Storm waters cover the pan after the next lake flood and the upper part of the salt crust dissolves, while flocculating muds settle onto the solution surface and sink into intercrystalline karst cavities (Fig. 3.33, Stage I; Shearman 1970). Ongoing evaporation then creates a new subaqueous salt crust atop the dissolution surface. The knobbly surface seen on some playa salt crusts is the result of continual precipitation and fretting of a subaerial salt layer, fed brine by "capillary wicking."

The halite in the initial crust is often composed of upward-pointing subaqueous halite chevrons (Fig. 3.33; Stage II). The freshening episodes plane off the upper part of the chevrons as undersaturated waters eat into the crust along the inter-chevron boundaries and form brine-filled pores (Chap. 1). Capillary evaporation and brine reflux then fills the porosity with clear halite cement. Continued dissolution and reprecipitation of halite and other soluble salts in the vadose and capillary portions of the crust can destroy much of the initial aligned chevron texture. The end result of alternating freshening and drying episodes is a bedded stack of salt crusts with pores filled by halite spar, occasional relict zones of aligned chevrons and numerous internal truncation surfaces (Fig. 3.33; Stage III).

At the broader scale, the continual addition of new salt crystals from evaporating pore waters causes an increase in the volume of the surface crust, which, once the pan desiccates, lies at the top of the capillary zone. Thickness of the capillary fringe limits any continued vertical growth of the crust and focuses precipitation into the uppermost parts of the crust, so the crust attempts to expand horizontally. The force of crystallisation creates a biaxial stress in the crust that ultimately forms cracks that grow into overthrust salt polygons or pressure ridges. Freshly exposed thin halite and gypsum crusts in modern pans and sabkhas around the world show this style of polygonal ridging and crestal cracking.

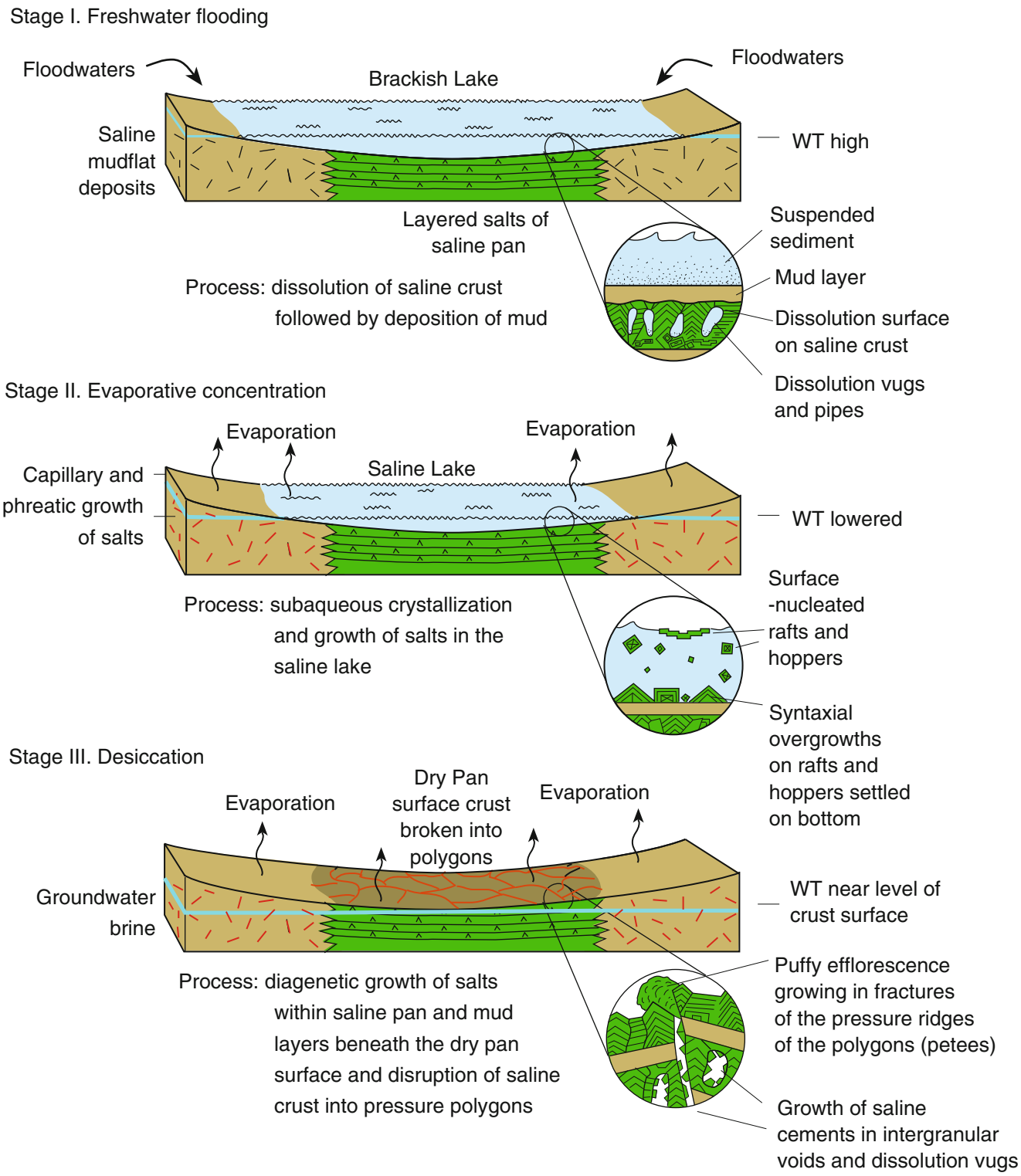

Fig. 3.33 Evolution of a depositional cycle in a saline pan setting (After Lowenstein and Hardie 1985)

But the mechanism creating mature metre-thick pressure-ridged beds is not crust expansion driven solely via the force of crystal growth. There is also the addition of detrital sediment to the crust via infill and cementation in newly formed fissures. Wind-blown detrital sediment fills fissures with successive linings that are cemented into the crust.

Ongoing capillary precipitation means pressure ridges rarely retain the simple inverted V cross section of the infill

formed in the initial break in the salt crust. Ongoing salt growth, fissuring and dissolution, along with infiltration of eolian silt and sand into cracks and fissures, deforms and anneals the crust into a variety of knobs, ridges, and pinnacles with a relief of up to a metre above the adjacent mudflat floor (Fig. 3.32e). Underlying clays often heave up and out through the axis of the megapolygon suture. Ancient counterparts to salt hosted pressure ridges and megapolygons have been recognised in the Messinian salts of Sicily (Lugli et al. 1999) and the Triassic salts of Cheshire, UK (Tucker 1981), where they are used as indicators of times of exposure in thick halite sequences. Fissure fills in these ancient counterparts can cut up to 6 m vertically across stacked halite beds.

Each salt layer in a thick saltpan unit, is in large part derived from the recycling of older salt layers. Layers are separated and crosscut by mud partings composed of detrital material carried in by floodwaters or eolian detritus blowing across the emergent salt surface. The final buried sediment is a thick bedded-salt composed of randomly aligned recrystallised evaporites. Saline pans form relatively pure salt units, which are metres thick, layered, and crosscut by fissures filled with eolian or detrital impurities. This type of bedded salt, which has been subjected to ongoing exposure and capillary evaporation, contains randomly aligned and overprinted crystals precipitated from a brine hydrology characterised by crystallisation, dissolution and recrystallisation. It contrasts with bedded salt deposited in the relatively stable perennial brine hydrologies of a more-or-less continually subaqueous saline lake where, even after burial, the crystals in the stacked crusts still retain a growth-aligned fabric of upward pointing large gypsum crystals, chevron halites, or trona prisms (see perennial lake discussion in the next chapter).

Styles of Continental Sabkhas

Mudflats, sabkhas and saline pans occur as parts of three saline lacustrine settings, with or without a saline pan in the depositional sump (Hardie et al. 1978);

- Alluvial fan–ephemeral saline lake
- Ephemeral stream floodplain–dune field–ephemeral saline lake
- Perennial stream floodplain–perennial saline lake

Settings are not static and changes in tectonics or climate can cause one setting to evolve into another. Texture of the capillary precipitates are similar in all three, but differences in lacustrine hydrology means continental sabkhas are more widespread in ephemeral lake systems than in perennial lake systems, which seem to require steeper sided basins (Table 4.7).

Alluvial Fan–Ephemeral Saline Lake

The alluvial fan–ephemeral saline lake depositional complex typifies fault-bounded, orogenic basins in tectonically-active arid areas. Tectonism generates topography and increased contrast in thermal gradients, so that water volumes seeping into the evaporitic mudflat (continental sabkha) and adjacent saline pan can be quite high, fed predominantly from groundwater and occasional storm runoff. Such arid intermontane lows can be covered by extensive continental sabkhas, with areas of saline pans in the lowermost positions on the playa floor (Fig. 3.31). Modern examples range across various tectonic settings and include intermontane playas in the Basin and Range of North America, salars of the Central Andes, some East African rift valleys, saline valleys at the southern end of the Dead Sea transform, and playas on the Tibetan Plateau and Mongolia. Of the two ephemeral lake settings, this is the one where thick sequences of evaporitic salts are more likely to be preserved due to rapid subsidence. Ancient counterparts of this style of deposit include the saline mudflat and pan facies in the Wilkins Peak Member of the Eocene Green River Formation, Utah, the Tertiary borate deposits of Turkey and Cambrian Lake Parakeelya of the Officer Basin, South Australia (Fischer and Roberts 1991; Helvaci 1995; Southgate et al. 1989). Let us now look in more detail at the geology of few Quaternary examples.

Sabkha Yotvata, Israel

Sabkha Yotvata is a continental sabkha with an aerial extent of 45 km^2; it infills the entire 10 km width of the southern Arava Valley (Fig. 3.34a; Amiel and Friedman 1971). It is located some 45 km north of the Red Sea and 110 km south of the Dead Sea in the Great Rift Valley, the transform depression separating the Jordanian and Palestinian plates. The Yotvata valley floor is only 75 m above sea level. To the east and west the sabkha is bordered by steep-sided valley margins; to the east the valley wall rises up to 1,300 m above the valley floor while to the west it rises up to 600 m. Differences in relief are a response to current movement on the Avrona Fault zone (Sarti et al. 2003). Some 1 km wide and 35 km long, the Avrona Fault extends in a NNE direction from the western margin of the northern coast of the Gulf of Elat across the Avrona Playa and up along the steep eastern side of the Yotvata Playa (Amit et al. 1999). North of the Yotvata Playa it dies and merges with the prominent strike-slip fault that trends north to become the Dead Sea Fault.

Steep valley walls have led to the development of an extensive bajada, which interfingers with the evaporitic sediments of the sabkha. In the valley to the north of the sabkha is an extensive dune field extending some 40 km up the valley. To the south is another smaller dune field, which partially covers the south-ernmost sediments of the sabkha.

Matrix sediments are moved in to the sabkha by sheetfloods and a series of short ephemeral anastomose streams

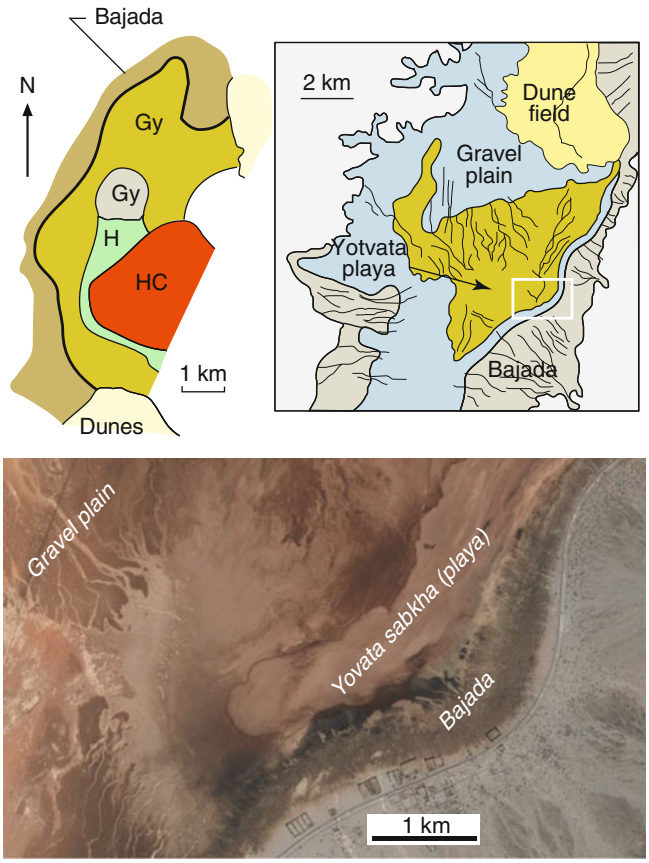

Fig. 3.34 Surficial geology of Sabkha Yotvata, Israel, showing centripetal hydrology created by the bajada rim (Amiel and Friedman 1971; Amit et al. 1999). *Gy* gypsum, *H* halite, *HC* halite crust

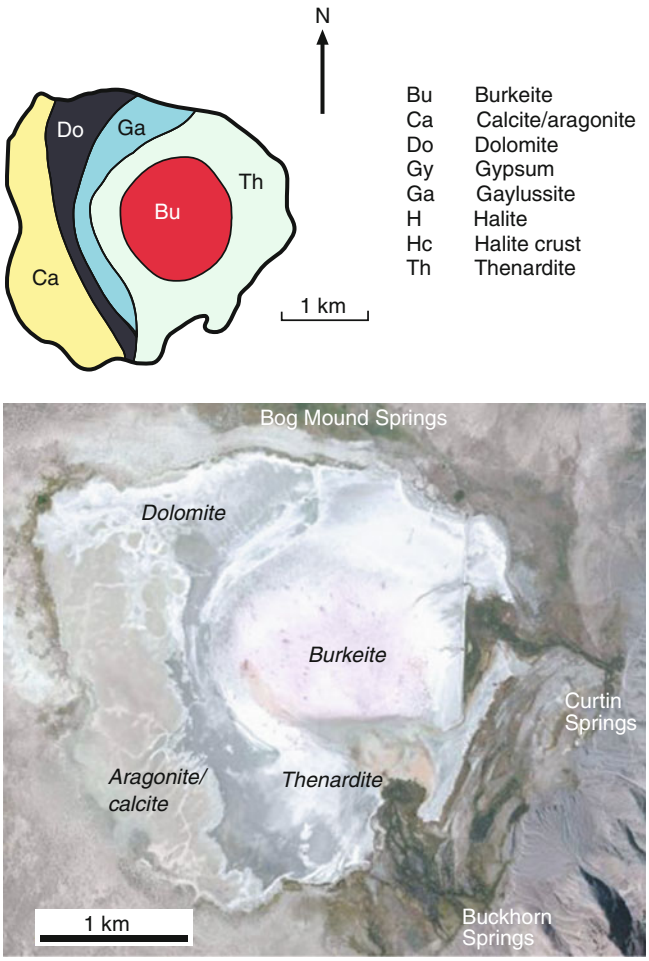

Fig. 3.35 Deep Spring Playa, California (Eugster and Hardie 1978). Note the off-centre bull's-eye pattern in the distribution saline salts indicating nearsurface seepage fractionation and the accumulation of the most saline salts in the lowermost part of the playa floor

(wadis) on the bajada, while fine silts and sands are blown into the sabkha by northerly winds from the dunes. Matrix grain size in the sabkha shows a bull's-eye pattern of distribution with fine to coarse sands and pebbles about the margin and silty to sandy clays in the central sump. North and south the grain-size bull's-eye is complicated by the presence of dune sands. The displacive evaporite salts of the sabkha grow in the capillary and phreatic zones and also follow a bull's-eye pattern related to efflorescent/capillary fractionation of the groundwater; gypsum dominates the periphery and halite the lowermost central portion of the sabkha. The watertable is as deep as 4 m about the bajada periphery and shallower than 1 m beneath the sabkha. Puffy ground and dissected halite crusts form the ephemeral saline pan facies in the lowest part of the valley, whereas displacive nearsurface gypsum grows in the capillary zone of the adjacent saline mudflat.

Basin and Range Playas, USA

Saline lakes with extensive mudflats and smaller areas of saline pans, both surrounded by extensive alluvial aprons (bajada) characterise many of the depressions in the arid zone of the southwestern USA. These saline systems are locally known as playas. Tectonically, the depressions hosting the sabkhas are a response to extension and transform faulting.

Deep Springs Lake, California

Deep Springs Lake is a small 5-km wide playa at an elevation of 1,500 m asl in Deep Springs Valley in eastern California, just east of Owens Valley (Fig. 3.35; Jones 1965). The valley was an eastward draining fresh water-filled lake during the last glaciation (Jones 1965; Meister et al. 2011), but modern Deep Springs Lake only covers an area of 4 km^2. About 1 km^2 of the depression is water saturated and largely water covered throughout the year. The water depth varies in the central sump of the lake between ≈30 cm during the wet season and a few centimetres in the dry season, but its extent is strongly subject to sporadic rainfall in the area. Lake water is constantly supplied from different springs around the lake (Fig. 3.35). Jones (1965) mentioned the inflow of water from

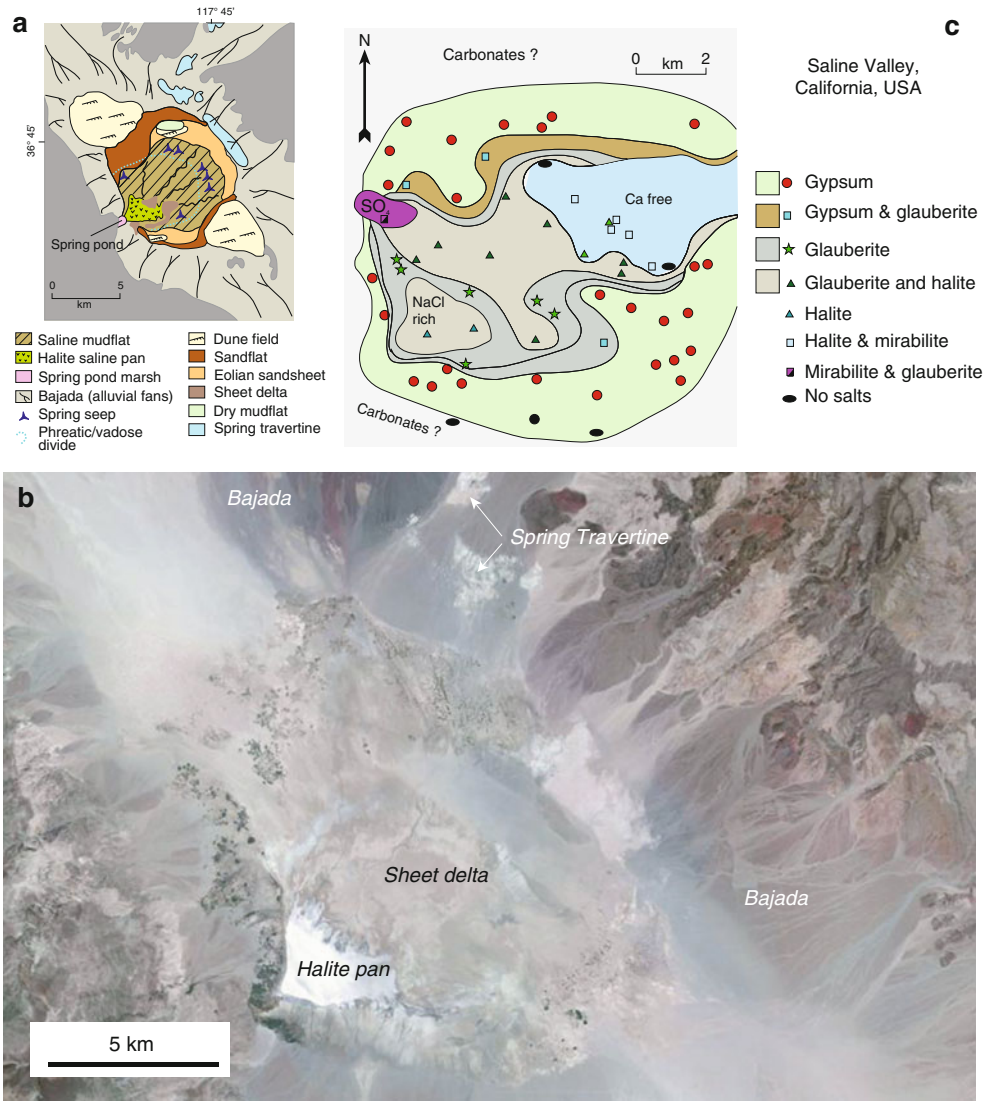

Fig. 3.36 Saline Valley Playa, California. (**a**) Regional sediment distribution (After Hardie et al. 1978). (**b**) Landsat image of the valley showing the off-centre saline sump surrounded by bajada apron. (**c**) Distribution of intrasediment evaporite salts in the saline mudflat (sabkha) part of the playa. The concentric of "bull's-eye" pattern with the more soluble salts in the lowest parts of the area indicates fractionation and progressive concentration of groundwater seepage (After Hardie 1968 and Smoot and Lowenstein 1991)

river drainage; however, today this source is almost completely exhausted due to artificial water collection. The central playa depression is fed by a series of tufa springs with waters that have been in contact with igneous and metasedimentary rocks. The pan in the lowest part of the playa floor is occupied by soluble, mainly Na-rich salts –thenardite, burkeite, trona and halite– deposited as a bedded crust deformed into overthrust pressure ridges.

Dolomite is present across the playa, but elevated levels typify mudflat sediments in the more peripheral, less saline pan areas. Isotopically, there are two types of dolomite; Type A and Type B, very similar to the two types defined in the Coorong lakes of South Australia (Meister et al. 2011; Peterson et al. 1963). Type A precipitates in hypersaline surface brines while Type B is more common in subsurface crusts and cements, under the influence of meteoric waters. The playa is surrounded by the distal sediments of a series of alluvial fans with carbonate-cemented tufa springs at their feet. Volumetrically the capillary and pan salts are a minor portion of the valley-fill, which is dominated by alluvial fan and sand flat (distal fan) facies.

Saline Valley Playa, California

Saline Valley playa is a small continental sabkha-salt pan playa in a fault-bound graben located east of Owens Lake across the Inyo Mountains. Amalgamated alluvial fans (bajada), fed from adjacent mountains, are dominated by debris flow deposits; their slopes are short and steep with little sandflat development around their bases (Hardie 1968; Hardie et al. 1978). In contrast, fans at the NW and SE ends of the depression are more longitudinal to the basin axis and so show lower gradients allowing eolian sand sheets and dunes to accumulate adjacent to wind-reworked fan toes (Fig. 3.36). Pleistocene travertines and active spring mounds mark zones of groundwater seepage.

Sabkhas (saline mudflats) cover a large portion of the basin floor and are dissected by sinuous seepage channels,

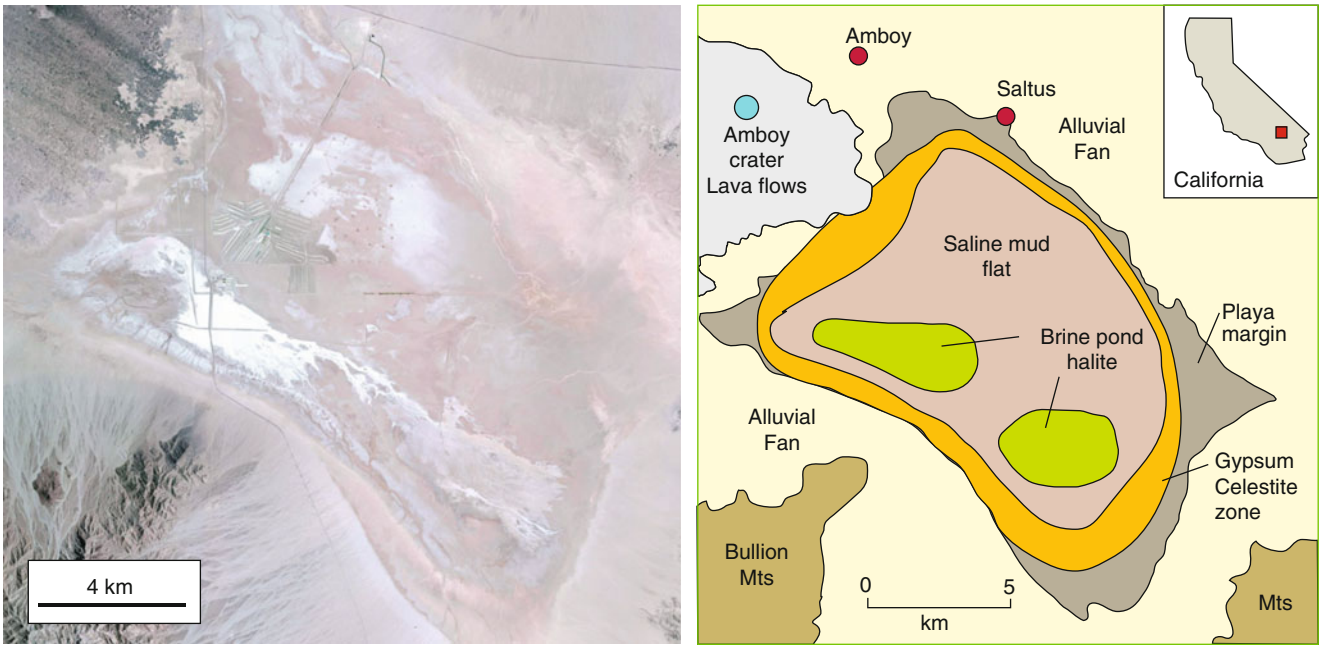

Fig. 3.37 Bristol Dry Lake, California. The continental sabkha facies shows concentric pattern of intrasediment salt growth with an outer gypsum capillary pavement and an inner halite saline mudflat, the halite pan facies is slightly offset from the centre and occurs in the lowest parts of the lake in the southern part of the depression (Bing® image scaled and mounted in MapInfo, surface geology after Rosen and Warren 1990)

while a halite-floored saline pan defines the lowest part of the playa. Pan facies are made up of dm-thick halite beds separated by mud layers with abundant intrasediment crystals of halite, glauberite and thenardite (Fig. 3.36). Glauberite crystals and moulds of mirabilite, now filled with glauberite, are common in the sabkha or saline mudflat. Along the southern zone of the saline mudflat is a belt of layered aligned gypsum that probably formed by intense capillary fringe evaporation like the texturally identical capillary gypsum crusts defining the sabkha edge of Bristol Dry lake (Rosen and Warren 1990). The sulphate-rich northwest corner of the mudflat is tied to ponding and evaporation of seepage waters from a nearby spring.

Bristol Dry Lake, California

At the surface, the Bristol Dry Lake basin in the Basin and Range province of California exhibits what appears to be a slightly off centre bull's-eye distribution of surface and near surface salts (Fig. 3.37; Handford 1982; Rosen 1991). Low-gradient alluvial fans ring the 10-km wide playa, while extensive calcretes and pedogenic calcites, associated with halophyte plants, cement mid-to-distal fan gravels and sands. There is a 62 km^2, ≈2 m thick, roughly circular and level black basaltic lava flow atop the playa surface along the west and northwest edges of the lake depression. It originated at the same time as the Amboy Crater and is likely a Holocene feature. It indicates ongoing hydrothermal circulation, so explaining the $CaCl_2$ brines that typify lake porewaters and the natural, but highly unusual occurrences of antarcticite precipitates in the lake trenches (see Chap. 12).

Basinward of the distal fans, in the playa margin facies, is a centripetal gypsiferous sabkha some 300 m wide where celestite precipitation forms large decimetre-size nodules that can coalesce into metre-size patches. The gypsum unit is characterised by a growth-aligned fabric created by competitive alignment of gypsum prisms in a zone of capillary wicking (Fig. 3.38; Rosen and Warren 1990). Once these gypsum crystals are buried and converted to aligned anhydrite nodules it would be next to impossible to distinguish them from the much more commonplace subaqueous textures. Basinward of the playa margin facies, halite hoppers (up to 0.5 m in diameter) form displacive intrasediment precipitates in brine-saturated muds of the saline mudflat facies. Finally, in the basin-centre depression a 0.2-m thick chevron-halite crust (salt pan) is forming by evaporation of ponded ephemeral waters.

The lateral facies distribution seen at the surface also stacks throughout the entire length of deep cores collected in the playa (Rosen 1991). Saline pan halite beds alternate with halite-saturated siliciclastic muds in a 500-m core from the basin centre. Playa margin cores exhibit alternating beds of playa margin sediments and saline mudflat (sabkha) units for most of their length. Towards the base of the deepest playa-margin core, distal alluvial fan sediments are also present. Rosen (op. cit.) notes that a delicate balance between subsidence and mechanical/chemical deposition of minerals was necessary to maintain a vertically-consistent ephemeral

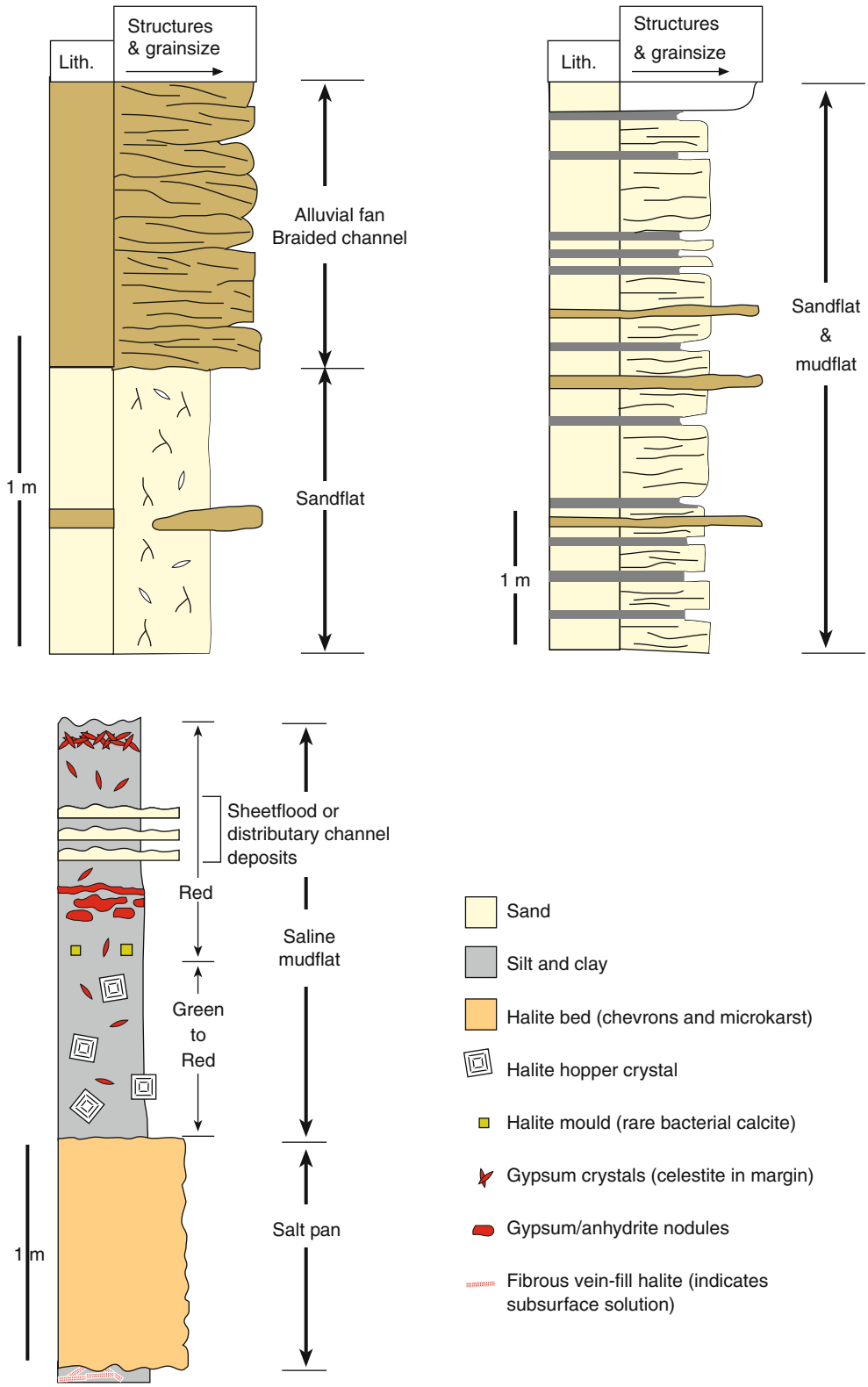

Fig. 3.38 Generalized stratigraphy based on Bristol Dry Lake from the alluvial fan margin into the saltflat saline pan centre (After Handford 1991; Rosen and Warren 1990)

brine environment during the deposition of over 500-m of basin fill.

I would say this is not really an example of some rather unusual delicate balance preserved in the sedimentary signature, so much as it is evidence of a hydrological/deflation forcing mechanism. It is a response to the same Stokes-surface hydrology that drives sedimentation in the sabkha and pan regions of most Quaternary continental playas and sea margin sabkhas. Accommodation space in the Bristol Dry Lake depression is created by subsidence in

a tectonically active region, in what has been a variable but mostly arid climate throughout the basin's Quaternary history. The basin's hydrology dictated the contrast in accumulation styles between the salt rich succession in the basin centre and the coarser siliciclastic dominated basin edge. The volume of sediment accumulating in the basin centre in Bristol Dry Lake can never surpass the ability of the wind to blow any dried sediment out of this depression centre into surrounding areas. That is, the surface of the sedimentation in the basin lowermost parts is maintained by deflation at a position that is always near the watertable. The only types of sediment that can remain in the arid basin centre are in equilibrium with the watertable and the top of the overlying capillary zone. When the watertable was a metre or so below the sedimentation surface, aggrading sediments were held in place by meniscus forces inherent to the capillary fringe and accumulated in saline mudflats as sabkha sediments. When the watertable rose to become a water surface, it created a semipermanent saline brine pan that then deposited and stacked salt pan crusts.

Basin edge sedimentation was not hydrologically forced but built up as volumes of centripetally-supplied sediment accumulated. This is turn facilitated the creation of an aggrading potentiometric head feeding ground and surface waters to the basin centre lows. About the edges of Bristol Dry Lake, where the accumulating clastic sediment is closer to its source, it is coarser grained and less liable to deflation. Clastics are accumulating in sufficient volumes to build facies belts situated well above the regional watertable, hence the accumulations of alluvial fan, dune and sandflat sediments. At times when the subsidence rate exceeds the rate of sediment supply in this area, its hydrology becomes more like that of the basin centre and saline mudflat facies come to dominate over much of the playa floor. Such a hydrologically forced system means that when regions of maximum subsidence in a basin change position, it moves the position of the hydrologically forced sediments into the new lowermost areas on the playa floor. Ultimately, once the rate of subsidence decreases to where the rate of clastic sediment supply exceeds the ability of the wind to deflate, the margin sediments will cover the whole basin and evaporite sedimentation will cease.

Death Valley Playa, California

Death Valley is probably the best known playa of the Basin and Range setting in the USA, yet Death Valley is a very steep sided and unusual lacustrine depression. Its floor is some 24 m below sea level, making it the lowest continental locality in the Western Hemisphere. Its steep sides mean it is likely to become a perennial saline lake with minor changes in climate (Chap. 4). In many areas of Death Valley the coarse-grained debris flows of the alluvial fan directly abut the salt crusts of the sabkha and the saline pan. Sandflats and dry mudflats, so obvious in most Basin and Range playas, are poorly developed or absent in Death Valley. This too reflects the steep valley walls (Fig. 3.32f) and its relatively high watertable in relation to the lake surface. It is a rapidly subsiding saline lacustrine system in which more than 50 % of the Quaternary sediment fill beneath the lowest parts of the lake floor are dominated by saline lake and pan halite rather than matrix-rich evaporitic mudflat (sabkha).

This is clearly seen in a 90-m length of core (DV93-1), which returned an interbedded salt and mud sequence extending back some 200,000 years (Fig. 3.39; Li et al. 1996, 1997; Lowenstein et al. 1999). Minerals intersected in the core include sodium chloride (halite), sulphate minerals (glauberite, gypsum, and thenardite), and carbonate minerals (calcite and dolomite). Glauberite, gypsum, and thenardite occur in mud layers or partings as randomly oriented, mud-incorporative crystals. They are thought to be early diagenetic and to have precipitated from nearsurface ground waters within saline mudflat or sabkha settings. Carbonate minerals calcite and dolomite occur as rhombs to irregularly shaped crystals that are less than 5 μm in diameter. Vertically, there are significant mineral assemblage variations in the core. Abundant glauberite and gypsum, and relatively small amounts of calcite (13–35 % of >1 μm size insoluble fraction) are associated with both sabkha and subordinate saline pan settings. They formed in relatively dry periods from 0 to 10 ka and 60 to 100 ka (0–8 m and 60–90 m depths in the core, respectively). Sabkha sediments (0.25–7 m, 60–78 m, 87–90 m) consist of muddy silts with sand patches and mud cracks and accumulated during long periods of desiccation. They indicate sedimentary accretion via formation and incorporation of efflorescent salt crusts in the accreting sediment matrix. These episodes of sabkha and subordinate saline pan deposition indicate periods when Death Valley was relatively arid and the sedimentation surface was the top of the capillary zone over much of the valley floor, similar to the modern setting.

In contrast, most of the remaining intervals in the core are characterised by sparse $CaSO_4$-bearing minerals and relatively high amounts of calcite (20–50 % of the >1 μm-size insoluble fraction). These are intervals where much of the sediment is halite rather than mud-dominated. It defines a time 10–60 ka (8–60 m) when the basin-floor watertable was above the sedimentation surface for long periods of time, including the 25,000 year wet period when Death Valley contained a perennial halite lake (10–35 ka; 8–18 m) and the 25,000 year period when the floor of Death Valley consisted of saline pan-ephemeral saline lake environments (35–60 ka; 18–60 m; Fig. 3.39). Core intervals through saline pan sediments are composed of interbedded halite, chaotic muddy halite, and mud. The halite contains abundant vertical dissolution pipes, cemented with clear halite, indicating the watertable periodically

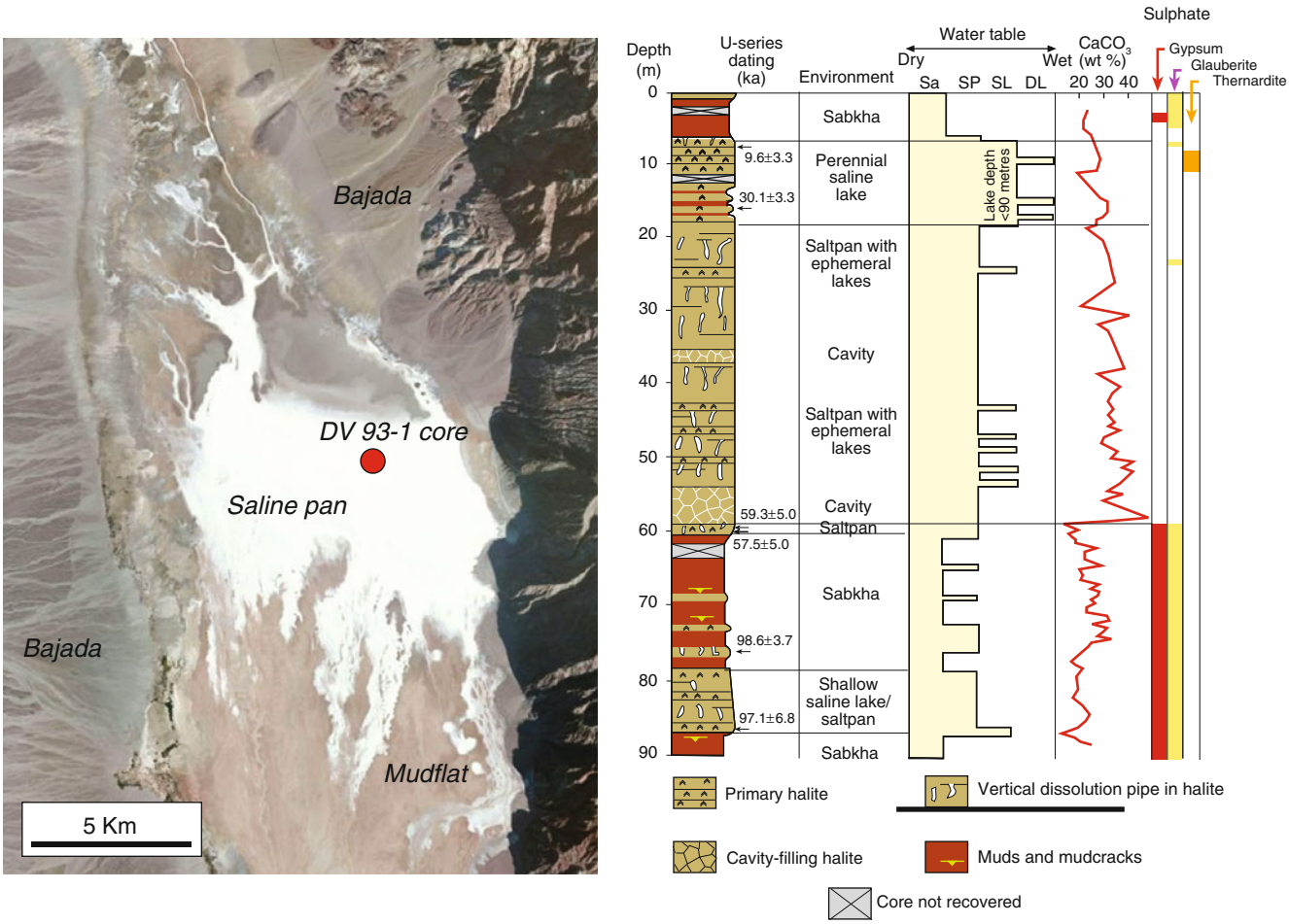

Fig. 3.39 Landsat image of Death Valley, California, showing saline pan in lowest part of sump and the stratigraphic column of upper 90 m of core DV-93-1 from within Death Valley (After Li et al. 1997). Lake levels and watertable fluctuations are shown ranging from driest (sabkha) through saline pan (*SP*) to the wettest lacustrine phases of saline lake (*SL*) and deepest lake (*DL*). The dominant evaporite mineral is halite and the position of the sulphate evaporites in the core, as well as the weight percent $CaCO_3$ in the >1 μm fraction, are also shown

dropped below the surface of the stacking halite crusts. These sediments record repeated flooding by dilute waters, dissolution of subaerially exposed surface salt crusts, deposition of mud from suspension, precipitation of halite during the saline lake phase, and cementation by diagenetic halite (Li et al. 1996). Such deposits document a relatively wet climate with a high ratio of water inflow to evaporation compared to today. Ostracods in mud layers represent the least saline, deepest lake phases when, based on the position of beach deposits in the valley walls, water depths in the deepest part of the lake were as much as 90 m. Halite layers are made of fine-grained cumulates and clear, vertically oriented crystals precipitated during shallower, perennial lake stages. The near complete absence of syndepositional dissolution textures in saline minerals precipitated in the perennial saline lake interval, imply that the accumulating salts were permanently protected from dissolution by an overlying perennially-saline at times holomictic water column (see detailed discussion in Li et al. 1996).

According to Li et al. 1997, the interval with little glauberite and gypsum, and relatively abundant calcite, dated from 10 to 60 ka (8–60 m), corresponds to the last glaciation, i.e., stages 2 and 3 of the marine oxygen isotope record. This was a relatively wet period in Death Valley. The intervals with abundant glauberite and gypsum and relatively low calcite correspond to the Holocene and to stages 4 and 5 of the Quaternary marine record, which were two relatively dry periods in Death Valley. Therefore, mineral assemblages correlate with wet and dry climate cycles in Death Valley (lake versus mudflat), which shows once more that mineral assemblages, depositional style and brine chemistry are all linked to climate changes (Chap. 2).

Salars of South America

The greatest thicknesses and volumes of evaporites currently accumulating anywhere in the world are doing so in the various collision related intermontane depressions and deserts of South America. More than a hundred salt-crusted pans or playas, locally known as salars, characterise

Fig. 3.40 Saline lakes (salars) of the desert belt of South America, shows the proximity of many salars to active rhyolitic/andesitic volcanoes in the Altiplano (refer to Fig. 3.41 for location of individual lakes and salars – Landsat image courtesy of NASA)

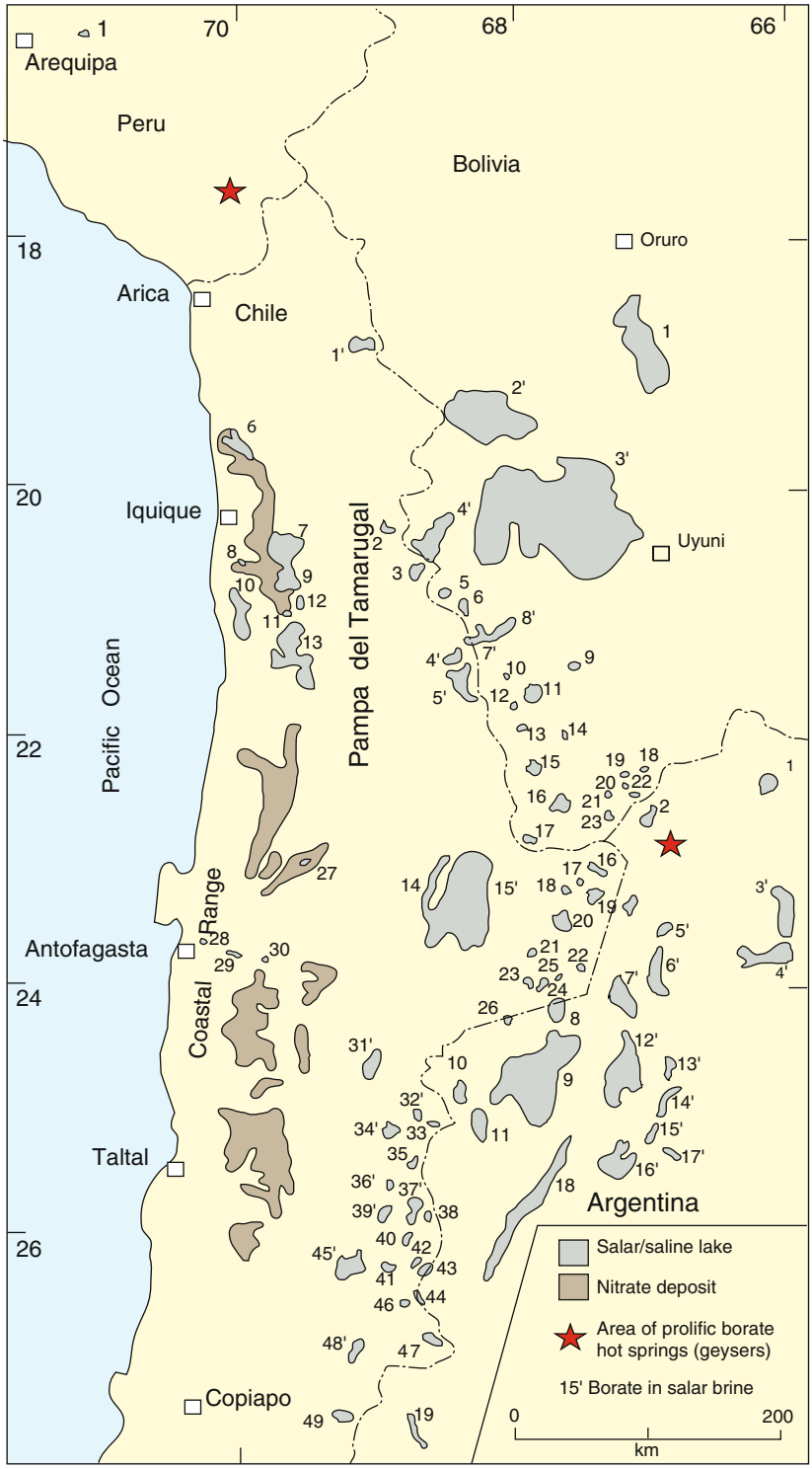

Argentina

1. Laguna Pozuelos	10. Salar de Lluaillaco
2. Laguna Vilama	11. Salar de Rio Grande
3. Laguna Guayatáyoc	12. Salar Pocitos
4. Salinas Grandes	13. Salar de Pastos Grandes
5. Salar Olaroz	14. Salar Centenario
6. Salar de Cauchari	15. Salar Ratones
7. Salar del Rincó n	16. Salar de Hombre Muerto
8. Salar de Incahuasi	17. Salar Diabillos
9. Salar de Arizaro	18. Salar de Antofalla

Bolivia

1. Laguna Poopo	12. Laguna Cachi
2. Salar de Coipasa	13. Laguna Khara
3. Salar de Uyuni	14. Laguna Capiñ a
4. Salar de Empexa	15. Laguna Colorada
5. Salar de la Laguna	16. Salar de Challviri
6. Salar Laguani	17. Laguna Verde
7. Salar de Ollagure	18. Laguna Corante
8. Salar de Chiguana	19. Laguna Mama Khumu
9. Laguna Tarija	20. Laguna Chojllas
10. Laguna Cañ apa	21. Laguna Loromayu
11. Laguna Pastos Grandes	22.Laguna Coruto
	23. Laguna Kalina

Chile

1. Salar de Surire	25. Laguna Tuyacto
2. Salar de Huasco	26. Salar de Pular
3. Salar de Coposa	27. Salar de Pampa Blanca
4. Salar de San Matin	28. Salar de Carmen
5. Salar de Ascotán	29. Salar de Navidad
6. Salar de Obispo	30. Salar de Mar Muerto
7. Salar de Pintados	31. Salar de Punta Negra
8. Salar de Soronal	32. Salar de Aquas Calientes III
9. Salar de Bellavista	33. Laguna Azufrera
10. Salar Grande	34. Salar de Pajonales
11. Salar de Lagunas	35. Salar de Gorbea
12. Salar de Sur Viejo	36. Salar de Agua Amarga
13. Salar de Llamara	37. Salar de la Isla
14. Llano de Paciencia	38. Salar de las Pariñ as
15. Salar de Atacama	39. Salar de Aguilar
16. Salar de Tara	40. Salar Grande II
17. Salar de Aquas Calientes II	41. Salar de Piedra Parada
18. Salar de Pujsa	42. Lagunas Bravas
19. Salar de Quisquiro	43. Laguna Wheelright
20. Salar de Aquas Calientes I	44.Laguna Escondida
21. Laguna Miscanti	45. Salar de Pedernales
22. Salar de Laco	46. Laguna Wheelright
23. Salar de Talar	47. Laguna Verde
24. Salar de Purisunchi	48. Salar de Maricunga
	49. Laguna Negro Francisco

Peru

1. Laguna Salinas

Fig. 3.41 Index of the main salars and salinas and nitrate deposits in the central Andes, South America (After Ericksen 1993)

depressions in the high-relief arid region of the central Andes and constitute salt deposits with areas ranging from more than 9,000 km^2 to less than 1 km^2 (Figs. 3.40 and 3.41). Some have been harvested on a small scale since the mid 19th century for their chloride, nitrate, borate and iodide salts. Huge state-of-the-art brine extraction/processing plants have come to operate in some of these salars in the last two decades and have taken much of the world

market from similar older smaller facilities in North America (Chap. 11).

Salars occur within a tectonically active region of largely interior (endorheic) drainage over an area of more than 400,000 km^2. It extends from the arid to semi-arid deserts of the Andean highland plateau (Altiplano Puna) down to the hyperarid Atacama desert, an area that is so arid that nitrate salts form widespread (and mineable) pedogenic precipitates (Fig. 12.62). Altiplano Puna was uplifted in the Miocene and is characterised by an average elevation greater than 3,000-m and widespread endorheic drainage. Salars of the Puna are either "wet" or "dry" and similar styles of arid deposition have dominated their fills throughout their Neogene histories (Alonso et al. 1991).

Dry salars are characterized by high rates of evaporation and are starved of detrital sediment. Fluvial input is restricted to rare flash floods and groundwater seepage is the dominant source of solutes. Stacked crusts of salar halite are typically in direct contact with basin margin gravels. Desert indicators are abundant in the clastic edge and include, eolian sands, polished clasts, varnished cobble, desert pavements and gypcrete soils. Volcanism, either by ash fall or hydrothermal circulation is the parent to almost all solutes accumulating in the basin. Examples include; Salar de Uyuni, Salar de Atacama, Salar Grande and Salar Arizaro.

In addition to groundwater seepage, wet salars are fed by permanent streams. These salars have perennial brine lakes and evidence of fluvial deposits, especially alluvial fan deposits, is more significant in the fill than in dry salars. Salar fill is typically alternating beds of clastics and evaporites. The slightly wetter (but still arid) environment of deposition is indicated by mud cracks, raindrop prints, bird tracks, ripple marks, desiccation breccias and preserved plant fragments. Modern examples include the Pastos Grande and Hombre Muerto salars.

The hyperaridity of much of this region of South America reflects a confluence of a number of desert-forming conditions. First, it lies in the Horse Latitudes, a region of permanent subtropical highs locally blocking influence of the semi-permanent South Pacific Anticyclone and so limiting the influence of winter storm tracks from the south. Second, offshore upwelling of the cold northward Humbolt current creates an atmospheric temperature inversion (≈1,000 m elevation) that prevents inland penetration of Pacific moisture. And third, the Atacama Desert lies on the western flank of the high Andes and so sits in a rain shadow not subject to tropical/subtropical moisture from the east. The driest part of the Atacama, which is 50 times more arid than Death Valley, California, in effect lies in a "double" rain shadow with the Andes to the east and the Coastal Range to the west (Figs. 3.40 and 3.41).

The region has experienced arid to semi arid climate as far back as the Middle Miocene, when the modern Andes were first uplifted to form a barrier to easterly trade winds. Uplift anchored the South Pacific Anticyclone to the western bend in the South American continent. Uplift of the Andes to its present elevation may have occurred as early as 15–19 Ma, although palaeobotanical evidence suggests the Central Andes were at half their present elevation some 10 Ma (Vandervoot et al. 1995; Gregory-Wodzicki 2000). The Humbolt current has been active since the Early Tertiary, but reached its present intensity either during a major expansion of the Antarctic ice sheet 15 Ma or after the Isthmus of Panama formed some 3.5 Ma (Chap. 5). Onset of Miocene aridity also shut down the meteoric flushing that drove supergene enrichment needed to create the giant porphyry copper deposits of the Southern Atacama (Sillitoe and McKee 1996).

There are four Neogene evaporite domains in the Andean highplain (Fig. 3.42a; Alonso et al. 1991). Deposits change from only travertine in the north, to a mix of travertine, gypsum and minor borate, to completely evolved halite dominated successions in the south, with borate-rich sequences along the eastern Puna. Older halite-rich successions are often caught up in subsequent tectonism and become halokinetic sources to modern salars such as Salar de Uyuni and Salar Atacama. The southward change from travertine to halite is consistent in deposits ranging in age from the Miocene until the present and probably indicates a consistent trend of increasing aridity from north to south since the Andes first arose in the Miocene (Alonso et al. 1991).

Present day rainfall in the Andean Highlands ranges from <50 mm in the vicinity of Salar di Maricunga and nearby areas in Bolivia and Argentina to nearly 300 mm in the area around Lake Titicaca and southern Peru (Fig. 3.44; Ericksen 1993). In contrast, the Atacama Desert lacks an annual rainfall and it may rain as infrequently as once every 10–20 years. Much of the groundwater in the desert is sourced from runoff in the Andean Highlands. Unlike the playas in the southwest of the USA, dry salars are dominated by pan facies rather than mudflats, perhaps reflecting higher relief and lower permeability substrates in this region creating more opportunities for flooding, followed by extended times of brine ponding.

Active continental volcanism is ongoing, with several west-northwest trending volcanic ridges cutting the Puna. This divides the Puna into several stagnant endorheic basins, further subdivided by north–south trending structural blocks creating local sources for alluvial fans and groundwaters. Thus, many of the salars show elevated lithium and boron contents in their surface and interstitial brines, with solutes sourced in abundant highly reactive volcanics, mostly rhyolitic ash-flow tuffs. Ions are redistributed to the salar by runoff and ongoing hydrothermal circulation (Table 3.5; Ericksen 1993). Evaporative concentration of salar brines leads to the depletion of Ca, HCO_3, B_2O_3 and SiO_2, and the enrichment of Li, K and Mg. Ca and SO_4 are removed from

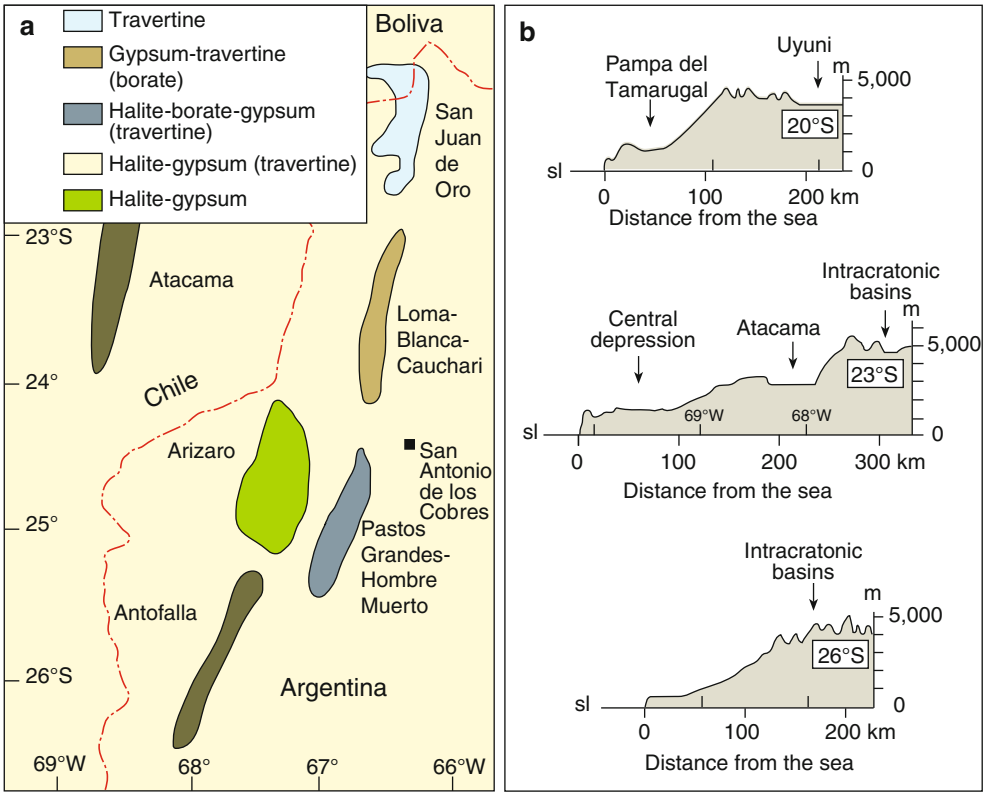

Fig. 3.42 (**a**) Evaporite belt and physiography, Andes, South America. (**a**) Generalized latitudinal distribution of Pliocene-Miocene evaporite belts (After Alonso et al. 1991). (**b**) Physiographic profiles at various southern latitudes across the Andes (After Risacher et al. 2003)

Table 3.5 Chemical analyses of selected brines from salars in the central Andes, South America

Component	Atacama	Uyuni	Hombre Muerto	Del Rincon	Empexa	Ascotan
Cl	189,500	191,800	194,800	191,000	120,000	70,000
SO_4	15,900	13,200	11,100	13,500	34,100	25,000
HCO_3	230	592	n.d.	n.d.	430	2,900
B_2O_3	1,416	1,136	1,455	1,570	702	2,520
Li	1,570	700	914	310	213	186
Na	103,000	94,900	121,900	121,800	67,200	45,000
K	23,600	13,500	9,340	6,260	3,400	3,500
Mg	6,130	11,800	268	2,090	8,480	5,125
Ca	520	461	1,000	480	259	920
TDS	370,000	351,000	340,920	330,000	239,000	153,600

In part after Ericksen (1993)

the concentrating waters as gypsum, while Ca and HCO_3 are removed early in brine evolution as cyanobacterial limestones, ostracode carapaces and inorganic precipitates, mostly travertines (Risacher et al. 2003). Boron precipitates as ulexite (see Chap. 11), while SiO_2 is removed by incorporation into widespread diatom tests in the fresher water lakes and spring pools. The proportions of Li, K and Mg tend to remain constant in a single lake basin, but vary from basin to basin owing to varying proportions of contributing lithologies from one drainage basin to another.

According to Risacher et al. (2003), sea salts and desert dust are blown eastward over the Cordillera, where they can constitute an appreciable fraction of the solute load of very dilute waters feeding the salars (salt content <0.1 g/l). But weathering of volcanic rocks contributes most components to inflow waters with salt content ranging from 0.1 to 0.6 g/l. However, the average salt content of all inflows is much higher, about 3.2 g/l. Chemical composition, Cl/Br ratio, and ^{18}O–^{2}H isotope contents point to the mixing of very dilute meteoric waters with present lake brines for the genesis of most of the saline inflows. Saline lakes and subsurface brines are a steady-state hydrologic regime. The average residence times of conservative brine components ranges from a few years to some thousands of years and indicate permanent leakage of the brines through bottom sediments. The infiltrating brines are recycled in the hydrologic system where

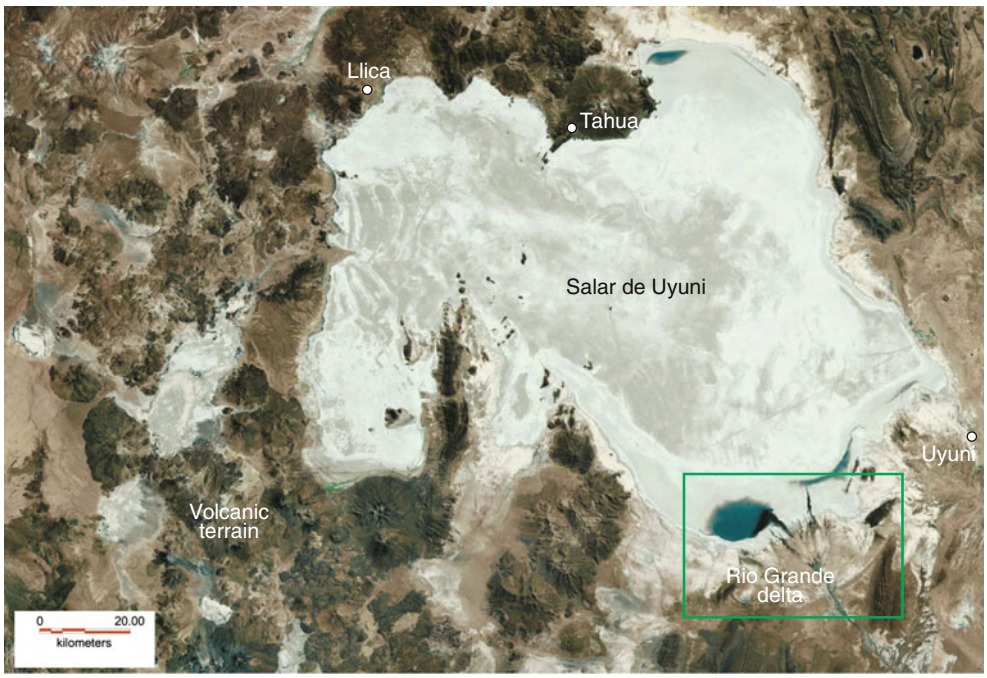

Fig. 3.43 Salar di Uyuni, Central Altiplano, Bolivia, showing salar is dominated by white halite crust with Rio Grande fan delta in southwest (delta region indicated by green rectangle; Bing® image automounted and scaled in MapInfo®)

they mix with dilute meteoric waters. High heat flow is the likely driving force that moves the deep waters in this magmatic arc region. According to Risacher et al. (2003), active Chilean salars cannot be considered as terminal lakes nor, strictly speaking, as truly "closed" basin lakes. They leak (see Chap. 2). Almost all incoming salts ultimately leave the basin and are transported elsewhere. Moreover, the dissolution of fossil salt crusts in some of the active salars also carries away important fluxes of components in percolating brines. In effect, the regionally leaky salar hydrology constitutes a broad scale fractionating system that can accumulate relatively pure salts in each of the large salt basins.

Although there is a longterm north to south trend of increasing salinity, evaporite basins and aridity have migrated eastwards with time, driven by the Miocene evolution of the Andean Range. Consequently, many of the westernmost salars, such as Salar Grande, are presently not regions of internal drainage (Pueyo et al. 2001). Worldwide, this migration of precipitative activity in "piggy-back" salt basins characterises the evolution of many evaporite deposits that accumulate in collision belts. The Central Depression is bounded on the west by the Coastal Range and the Pacific Ocean and to the east by the Andean Pre-Range (Fig. 3.42b). Throughout the Neogene, it acted as a significant drainage basin for pluvial input from the east that flowed into the area without reaching the sea. Its alluvial fan systems reach dimensions of tens of kilometres wide and hundred of metres in thickness. In the more distal parts of the fans, both perennial and ephemeral lakes developed (e.g. Calama-Chiu Chiu, Batea, Quillagua-Soledad, Bellavista-Pintados, Pisagua basins). The topography responsible for this drainage arrangement was generated during the Upper Paleogene, as a result of the Incaic orogenic pulse. From this time to the Pliocene the Central Depression was an endorheic area, and the Coastal Range acted as a barrier to drainage to the sea.

In plan view, sediment patterns in most of the South American salars with salt fills show a central zone, consisting of a relatively thick stack of halite crusts, surrounded by a thin marginal sulphate zone consisting of a variety of sulphate minerals, as well as minor halite and ulexite (Ericksen 1993). The zoning may be symmetrical (bull's-eye pattern) with sulphate surrounding a central halite core, or asymmetrical with the halite zone crowded against one side of the salar. This is the situation in Salar de Atacama where tectonic tilting has displaced the lowest part of the brine sink to the southern end of the playa. Alternating arid and pluvial climatic episodes, since the mid-Miocene, means alternating beds of salt and siliciclastics fill most Andean salars/playas.

Salar de Uyuni, Bolivian Altiplano

The Salar of Uyuni, at an elevation of more than 3,600-m in the central Bolivian Altiplano, is an active ephemeral saline lake (salt-crusted saline pan) where substantial salt thicknesses have accumulated across an area of a little less than 10,000 km^2, making it the world's largest salt-filled saline pan (Figs. 3.43 and 3.44a; Risacher and Fritz 2000). A 121 m deep well, drilled in the central salar, intersected a complex evaporitic sequence made up of 12 saline pan intervals separated by 11 mud layers deposited mostly as saline mudflats or sabkhas (Fig. 3.44b). The thick saline pan beds are composed of stacked salt crusts and alternate with thinner mud units in the lower half of the well. The mud beds show obvi-

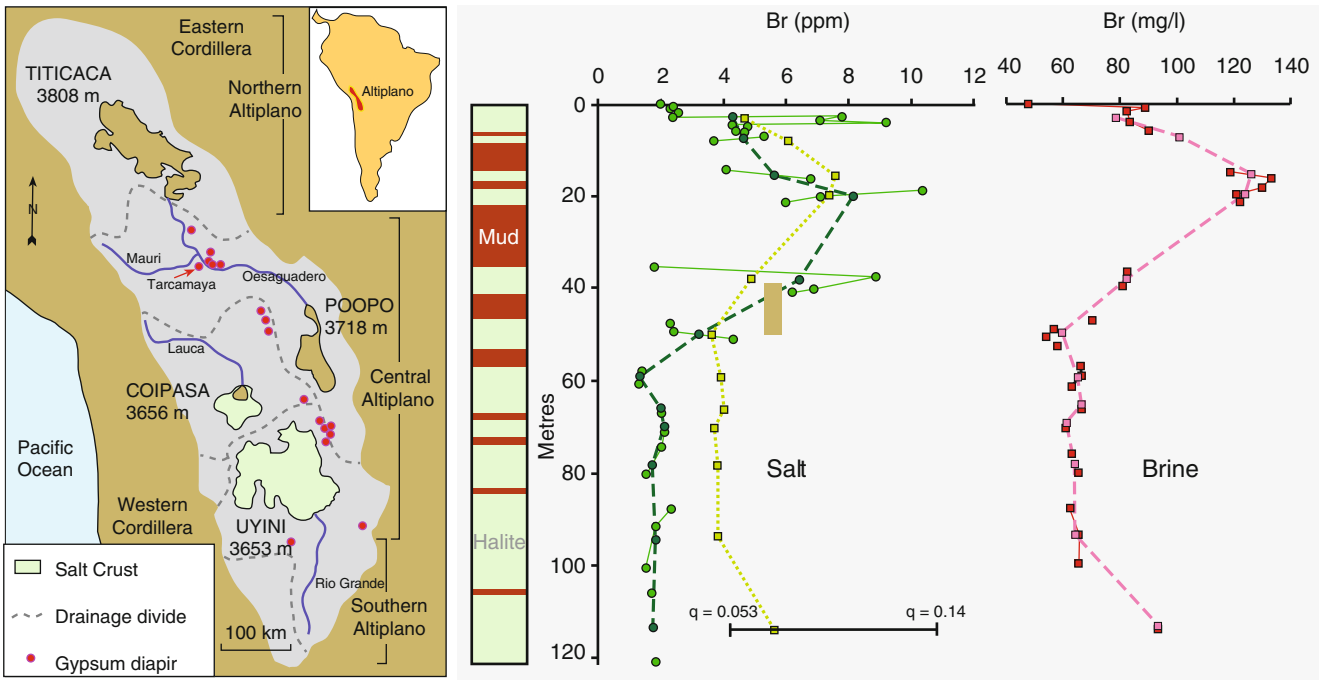

Fig. 3.44 Salar di Uyuni, Andean Altiplano. (**a**) Locality map showing hydrological relations with drainages of other salars and lakes of the Altiplano as well as its proximity to diapirs. The dissolution of diapir salts has sourced much of the salt accumulating in the Salar di Uyuni. (**b**) Lithology and Br profiles from a 121 m well in Salar di Uyuni (After Risacher and Fritz 2000)

ous lacustrine features and thicken upwards as salt beds thin. The well indicates a longterm hydrology where tectonics, as well as climate, controlled the level of the regional watertable.

Bromine contents of the recovered pan halites range from 1.3 to 10.4 mg/kg (Fig. 3.44b). Such low values mean the various halite beds were not precipitated by simple evaporation of meteoric and surface waters. This would be indicated by Br contents of tens of mg/kg in the pan halites (Risacher and Fritz 2000). Rather the brines were created by dissolution of older evaporites, which subcrop in the drainage basin. Halite from one such nearby gypsum-capped diapir has a very low Br content of 2 mg/kg, strongly suggesting that most of the halite deposited at Salar di Uyuni originated from the leaching of similar diapiric salt. The ubiquity of this salt source is indicated by the numerous gypsum-crested diapirs, which still outcrop in the Altiplano (Fig. 3.44a).

The very low and fairly constant Br content (1.6–2.3 mg/kg) of the lower salt beds, along with an abundance of detrital minerals, suggest the deeper and thicker halite beds were deposited as saline pan intervals in ephemeral lakes (Fig. 3.44b). Thereafter, perennial water episodes of increasing duration, flooded the central Altiplano. This change is tied to an increase in the volume of dilute meteoric waters entering the Uyuni drainage basin and in the proportion of mud beds in the salar core. These waters had lower Cl/Br ratios, indicated by an increase in Br to 6–10 mg/l in the pan halite beds between 10 and 40 m depth (Fig. 3.44b). The change may have also coincided with the exhaustion of diapiric halite as a source of ions, perhaps related to a decrease in the intensity of tectonism that was driving diapiric salt to the surface. Paleolake levels in the central Altiplano rose at this time, while those in the northern Altiplano (the Titicaca basin) were simultaneously falling. This reflects progressive fluvial erosion of the threshold between the northern and the central Altiplano, which lowered the levels of the northern lakes and allowed more dilute waters with lower Cl/Br ratio to flood the central Altiplano and so move into Salar di Uyuni. The three uppermost salt crusts show a decrease in bromine content, which may reflect a recent modification to the inflow regime.

The salt of the uppermost saltpan layer began to accumulate around 10,000 years ago and continues today. The halite shows a bromine distribution that is low in the shallow parts of the bed (≈2 mg/l) but unexpectedly increases with depth to values in excess of 8–10 mg/l (Fig. 3.45a, b). This increase is thought to indicate an episode of exposure and recycling of earlier formed marginward salt crust into the current brines (Fig. 3.45c). As the lake dried some 10,000 years ago, the resulting salt crust was initially distributed over a wider area than the crust of the present pan. It covered the topographic surface of the salar depression up to the level of the lake where halite brines first reached saturation (Fig. 3.45c). Ongoing lowering of the Holocene watertable, and the associated dissolution of the higher parts of the salt crust about the more marginward parts of the pan depression recycled ions (including Br) from crusts about the margins of the lake into the brines feeding the lowered

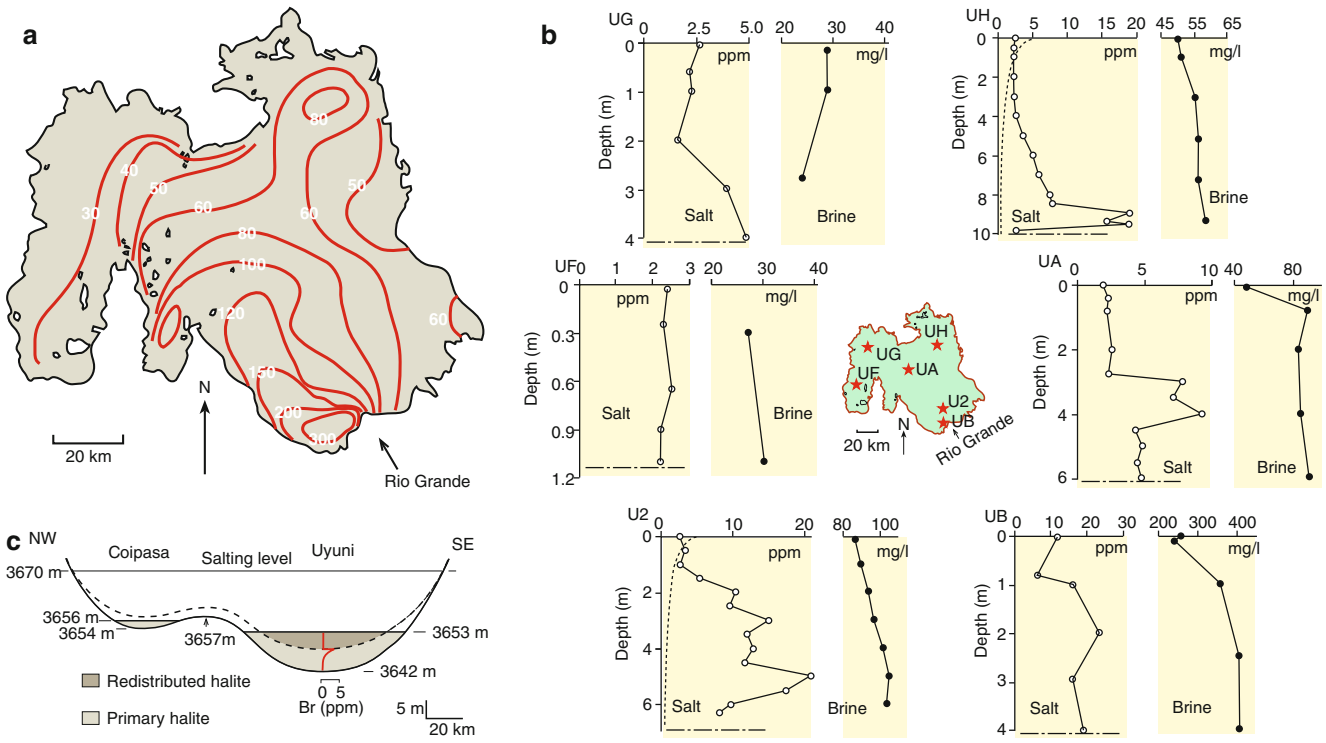

Fig. 3.45 Distribution of Br in shallow saline pan sediments of Salar de Uyuni. (**a**) Distribution of Br in nearsurface brine. (**b**) Br profiles of pan halite and interstitial brines from selected shallow cores. (**c**) Schematic showing how low bromine salt is reworked and redistributed from initial marginward crusts by a lowering of the perennial watertable (After Risacher and Fritz 2000)

brine levels located further toward the salar centre. Ongoing recycling explains the progressively lowered Br contents in successive pan crusts in the more central parts of the salar. Clearly, the increasing aridity and lowered watertable that typifies the current episode of saline pan aggradation has cannibalised earlier versions of itself as ongoing longterm drying of the lake raised marginward crusts above the salar watertable.

Many parts of the lake surface about the lake edge still show evidence of salt dissolution and crust recycling. Circular holes appear in the lake crust, especially about the salar edge; surface expression of the holes can be a few tens of centimetres wide but they are typically underlain by brine-filled swallow holes opening out in to salt cavities that are metres deep and wide. It makes driving on some parts of the salar edge quite hazardous.

The local name for these small holes at the surface is "Eye of the Devil" (*ojo del diablo*). Local karst development about the edge of a bedded salt mass is an early diagenetic overprint common to many modern and ancient saltpans. It is driven by changes in the lake watertable and the encroachment of regions of less saturated water into the margins of the bedded salt. The associated preferential leaching and fractionation drives the syndepositional formation of many potash and borate accumulations (Chaps. 11 and 12).

The main fluvial feed to the salar is from the Rio Grande, which enters the salar depression in its southwestern part. There it has built up a 300-km^2 delta, characterised by a lens of fresher water and sediment that intertongues with the halite crust unit (Fig. 3.46). The delta itself is a complex of silt and clay with local sand lenses indicating fluvial channel fills. Clays are mostly smectite with some illite and minor kaolinite. Overall, the delta prism is characterised by low porosity and permeability (Risacher and Fritz 1991a, b). Paludal muddy lacustrine sediments underlie both the delta prism and the halite crust facies. The contact between the delta wedge and the halite unit is a brine interface and the watertable of the delta prism today lies close to the surface. It converts much of the delta prism situated some distance from the fluvial channels into an evaporitic mudflat, where capillary evaporation is driving fluid flow. This in turn drives a slow circulation in the underlying mixed waters and so precipitates calcite, gypsum and ulexite ($NaCaB_5O_9.8H_2O$) toward the edge of the delta prism (Fig. 3.46). This has created one of the largest borate accumulations in Bolivia where the ulexite interval in the delta prism has an average thickness of 0.1 m over a 120 km^2 area with a water content of 50 % (Risacher and Fritz 1991b). Total boron reserves in this area are estimated to be around 1.6×10^6 t.

The Salar di Uyuni surrounds also preserve evidence of Upper Pleistocene sedimentation, a time when the Central Altiplano of Bolivia was repeatedly flooded by deeper and extensive saline lakes (Rouchy et al. 1996; Baker et al. 2001a). These freshening episodes in the Salar di Uyuni area

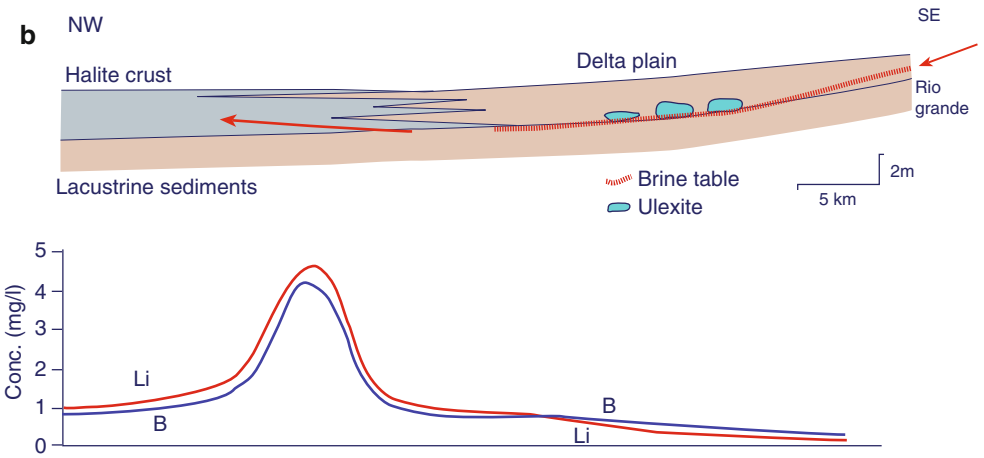

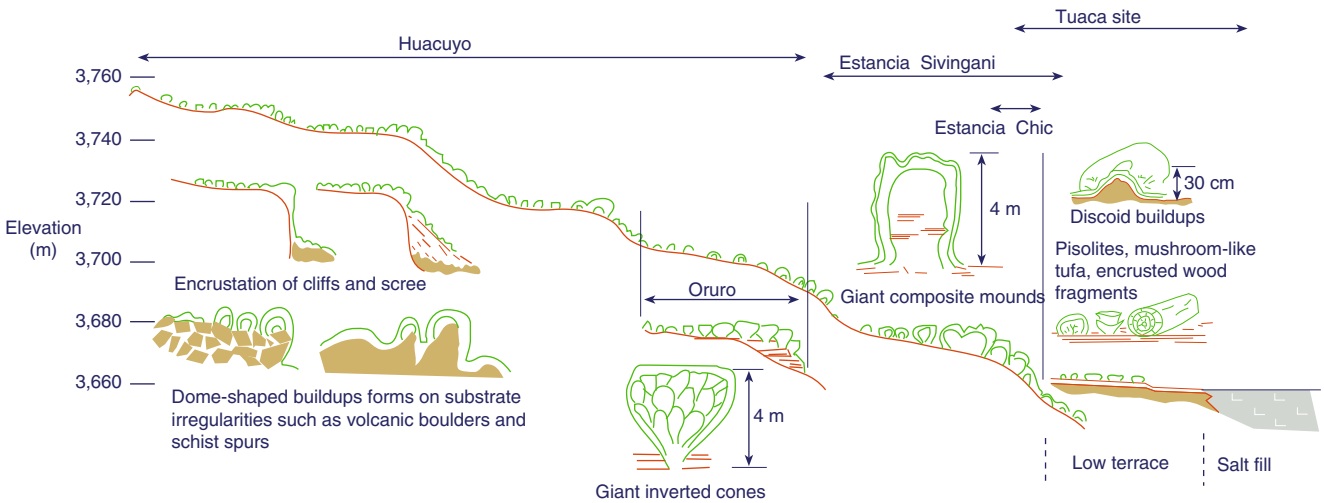

Fig. 3.46 Rio Grande Delta in southern Salar de Uyuni. (**a**) Scaled satellite image downloaded as Bing® image and mounted in MapInfo®. (**b**) Stratigraphic cross section and associated B-Li content of shallow brine in the southwestern portion of Salar di Uyuni in the Rio Grande delta. *Arrows* indicate brine flow, Brine chemistry shows a peak in both B and Li at the chemical interface between halite saturated lake brines and the delta prism, but the ulexite precipitates by capillary evaporation at the brine table interface beneath the delta prism (After Risacher and Fritz 1991a, b). See Fig. 3.43 for location of delta

Fig. 3.47 Schematic of the distribution of various types of algal bioherms within the outcropping as carbonate veneers in the surrounds of Salar di Uyuni. At the time the bioherms were actively accumulating these areas were shoal water portions of a perennial lake (After Rouchy et al. 1996)

are marked by the development of microbial bioherms defining at least three major periods of lacustrine highstand (Fig. 3.47). These calcitic tufas discontinuously cover the 300-km-long and up to 100-km-wide lacustrine slopes and terraces of the surrounds of Uyuni up to an elevation of 100 m above the surface of the modern halite crust. Clearly, Salar di Uyuni was a perennial mega-lake when the bioherms were growing and deepwater diatomaceous siliceous muds were accumulated across the same area where subaerial crusts are accumulating today.

The distribution, size and shape of the bioherms are diverse, reflecting various factors such as the nature and morphology of the substrate and the hydrodynamic conditions that prevailed during bioherm growth (Fig. 3.47; Rouchy et al. 1996). Build-ups on the larger palaeoterraces coalesced to form platform-like carbonate reef mound accumulations. Although the morphologies closely resemble those created by cyanobacterial binding, they were predominantly constructed by other plant communities, largely dominated by green algae. Cyanobacterial communities flourished in association with the plants, but they did not contribute significantly to the architecture of the bioherms; rather they encrusted the plant stems and microbial bushes, or formed thin laminated layers that covered the last stages of build-up growth. Buildups located between 3,660 and 3,680 m elevation show one or more of three growth stages or envelopes: (1) a massive inner core formed before 40 ka during an early Minchin highstand; (2) a large peripheral envelope deposited at about 40 ka (late Minchin) and (3) a thinner outermost crust formed during a late glacial event. Many bioherms show composite growth layering indicating episodes of microbial growth during lake highs separated by times of subaerial exposure and moderate erosion.

Salar de Atacama, Chile

Salar de Atacama is the lowest drainage sink in another endorheic basin in the pre-Andean depression of the Atacama Desert and contains more than a kilometre of interlayered halite and siliciclastics (Jordan et al. 2002; Rech et al. 2002). At an elevation of 2,300 m above sea level with an area of 3,000 km^2, it is the third largest saline pan in the world and an excellent barometer of Pleistocene climate change in the southern hemisphere (Figs. 3.40 and 3.41).

Today the San Pedro River forms an ephemeral stream feed along the western margin of the northern sector of the salar and defines the edge of a saline mudflat dominated by sulphate, carbonate and siliciclastic sediments (Bobst et al. 2001). The mudflat surface is dominated by brown halite-rich crusts and is underlain by silty clays with sand, displacive halite and locally organic-rich mud. A "sulphate marginal zone" dominated by ephemeral streams, eolian dune fields, sand sheets, dry mudflats and spring-fed ponds and marshes, forms the eastern edge of the salar and lies to the east of the saline mudflat (Figs. 3.48 and 3.49a). This northern region captures the majority of the siliciclastics entering Salar de Atacama. In general its watertable is between tens of centimetres and several metres below the deflationary land surface. Uppermost sulphate zone sediments are typically covered by and cemented with efflorescent sugary gypsum and minor halite. When trenched these gypsum crusts form discontinuous bowl-shaped concave-upward layers tens of centimetres in diameter.

In addition, the sulphate-margin flat entrains a number of gypsiferous brine-filled depressions or laguna (Stivaletta 2011). These depressions form separate small brine lakes in the dry season (such as Laguna Cejas, Laguna de la Piedra and Laguna Tebiniquiche), which merge into a connected water mass when the saltflats flood (Fig. 3.48b, c). The water bodies are up to a few metres deep and floored by mamelon-like mounds of halite and gypsum that entrain a halotolerant to halophilic biota.

South of the gypsum flat and its laguna is a thick layer or crust of halite that defines the halite nucleus of modern Salar de Atacama (Bobst et al. 2001). The top 40 cm of this crust is made up of millimetre-scale "sugary" inclusion-poor halite crystals along with interstitial mud. The crystals show a well-developed interlocking polygonal texture. At the broader scale the crust appears "wormy" with numerous subvertical to randomly oriented tubular microkarst voids. The crust surface is broken by metre-scale polygons with typical upturned edges showing up to a metre of relief. Mud typically ponds in the centres of saucers between the megapolygonal salt ridges. This uppermost crust is interpreted as an efflorescent crust formed largely by the capillary evaporation of groundwater brines and contains only a few growth-aligned chevrons.

Below the surficial crust the halites of the saline pan nucleus are massive and mainly composed of cm-sized interlocking crystals separated by mud-filled voids. Most of this halite is clear and inclusion poor indicating slow subsurface growth. Occasional freshwater influx drives dissolution of surface efflorescent halite crusts and creates large voids that then fill with clear cm-scale euhedral halites growing in toward the centre of the void. This dissolution-reprecipitation of halite is an ongoing process with evidence of numerous overprinting episodes destroying most primary chevron structures. Layering is poor to nonexistent.

A deep core (No. 2005) through the halite nucleus facies recovered some 100 m of evaporitic sediment and sampled some 100,000 years of salar sedimentation (Fig. 3.49b; Bobst et al. 2001). Deposition was dominated by arid conditions similar to today, with two significant wetter intervals. From 100 to 62.8 m the core is composed of clear interlocking halite with patches of millimetre-scale sugary halite. These textures are near identical to those forming at the sur-

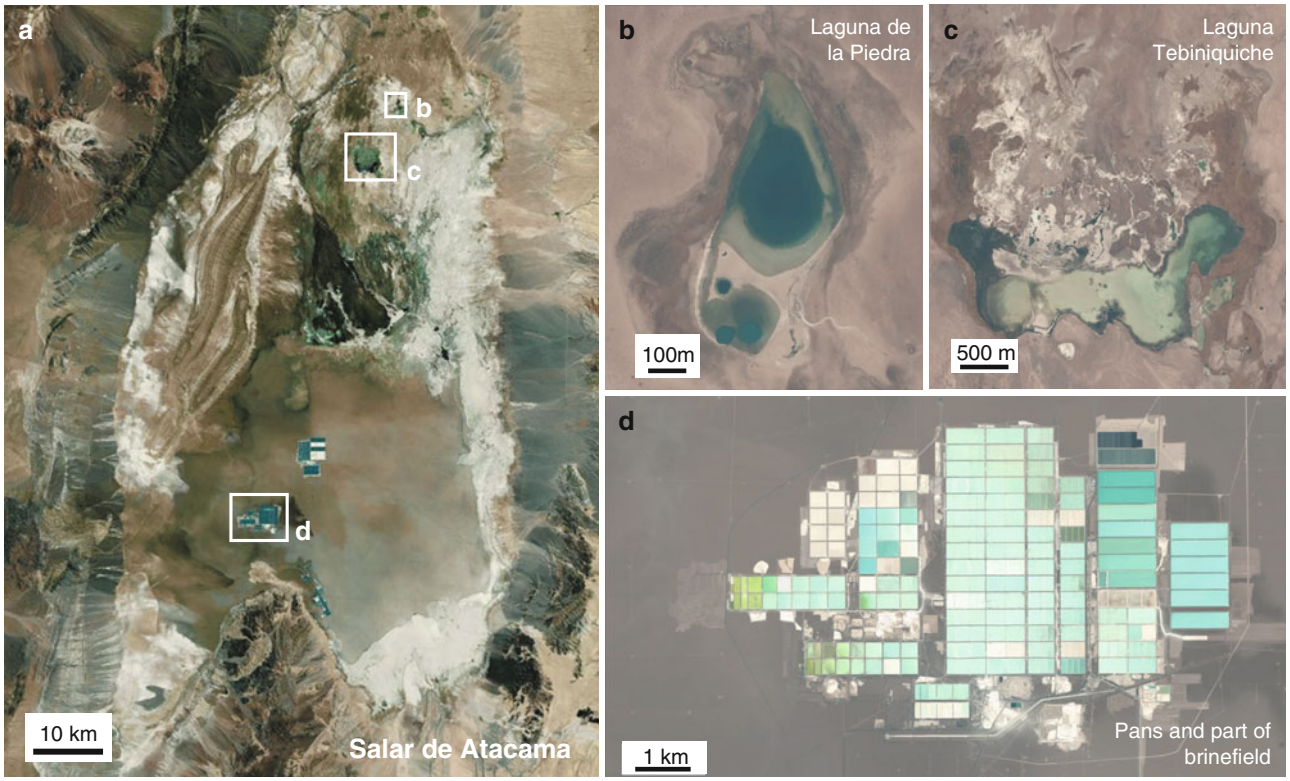

Fig. 3.48 Salar de Atacama, Chile. (**a**) Saline pan facies associated with the influx of the San Pedro River along the northeast side of the salar, the sulphate-rich marginal zone along the east and northeast of the salar and the salt-crusted halite facies dominating the southern portions of the salar. (**b**) Laguna de la Piedra in the Gypsum flat. Shows circular doline features indicating these zones of perennial brine ponding are karst associated. (**c**) Laguna Tebiniquiche, cuspate outline of perennial water body indicates dissolutional karst feature. (**d**) Some of the potash/lithium pans on the halite nucleus as are the brinefield wells and pipelines that feed the pans. See also Fig. 3.49. Image scaled in MapInfo from a Bing® upload

face today and indicate dry mostly subaerial accumulations. From 62.8 to 47.0 m (75.7–60.7 ka) there is a vertical succession passing from mudflat gypsum to mudflat/shallow pond to subaerial halite and mudflat deposits that represent a progressive increase, then a decrease and finally an increase in water supply to Salar de Atacama. This occurred within what were moderately wetter conditions (saline lakes and saline mudflats) than the subaerial conditions of today (Bobst et al. 2001). A similar somewhat wetter interval occurred from 53.4 to 15.3 ka, with the wettest perennial lake interval from 26.7 to 16.5 ka. Short relatively wet periods (chevron halite) also occurred in the Holocene from 11.4 to 10.2 ka and from 6.2 to 3.5 ka. The remaining sections are dominated by halite textures similar to the subaerial dominated capillary fringe conditions of today.

Seismic collected across Salar de Atacama shows a north-northwest–striking fault system that extends for at least 30 km across the salar and can be seen intersecting the lower part of the halite nucleus (Fig. 3.50a; Jordan et al. 2002). In the southern sector of the salar there is at least 700 m of Pliocene–Quaternary down-to-the-east reverse motion across the fault, but locally the salar fault system deforms the lower halite unit into a monocline with 400 m of structural relief (Fig. 3.50a). Rates of displacement throughout the Quaternary have been on the order of 0.1–2.0 mm/year. And yet, despite these large displacements and large displacement rates so obvious in the seismic, no modern topographic scarp exists in the halite nucleus. Seismically-defined stratal geometries and thicknesses reveal variation between former times when there was a topographic scarp at the deformation zone and times, like today, with no topographic expression. The available borehole data suggest that both the times with and without a topographic scarp were likely dominated by halite accumulation adjacent to the salar fault system (Fig. 3.50b).

Jordan et al. (2002) propose that unique sedimentation processes in a groundwater-fed evaporite environment are responsible for the lack of topographic expression of a major fault system that intersects the salt. During desiccated times, groundwater derived from topographically driven flow on the east side of the salar would have been forced upward by a barrier created at the fault zone, enhancing the supply of solutes to the zone immediately east of the fault (Fig. 3.50c). This mechanism generates a higher rate of accumulation of

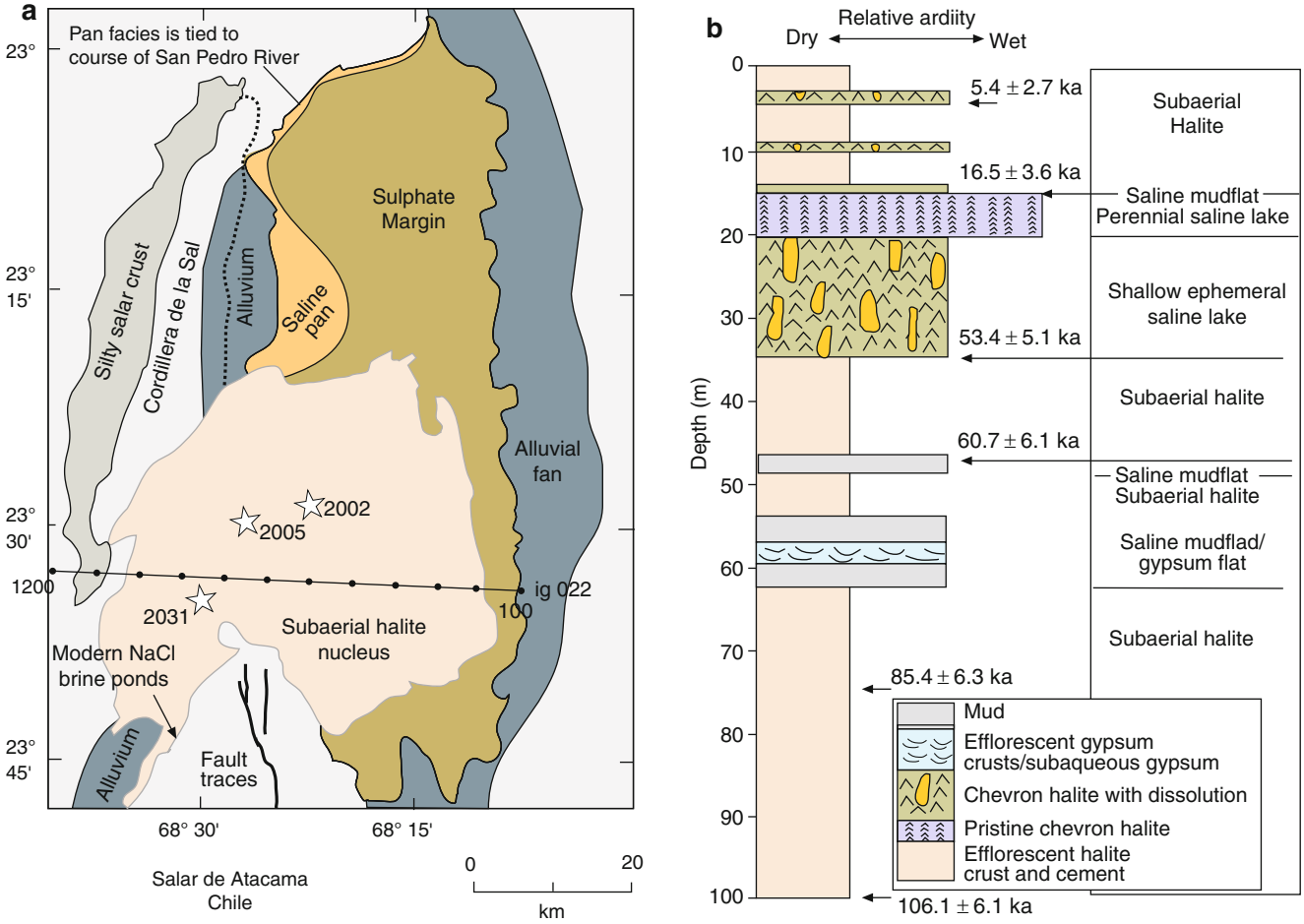

Fig. 3.49 Salar de Atacama, Chile (see Figs. 3.41 and 3.48). (**a**) Surface geology and extent of main salar lithofacies. Also shows onshore position of main salar fault and location of seismic trace ig 022 (with shot point positions). The stars show the position of cores 2002, 2005 and 2031. (**b**) Sedimentology of core 2005 (After Bobst et al. 2001; Jordan et al. 2002)

halite east of the Salar fault system than to its west. The enhanced deposition on the eastern fault block is sufficient to prevent scarp formation during times of moderate displacement by the Salar fault system, though during times of especially high rates of offset, this depositional mechanism was not sufficient to prevent temporary formation of scarps. It is not yet known how common "truly blind" faults are beneath the dry salt pans of other salars, but they are not unique to the Atacama basin. Similar occurrences of blind faults beneath the depositional surface of the ephemeral saline pan facies characterise; Salar de Antofalla and Salar de Hombre Muerto in the Altiplano, along with the Badwater salt flat in Death Valley, California and Great Salt Lake in Utah (Jordan et al. 2002). Like Salar de Atacama, they indicate the rapid deposition/accumulation rates that typify brine-saturated salt accumulating depressions.

Salar Grande, Central Andes of Chile

The Salar Grande is a 45-km-long (N-S axis), 4–5-km-wide, fault-bounded (pull-apart) Neogene forearc evaporitic basin, located in a depression in the Cordillera de la Costa of northern Chile (Fig. 3.51a). The altitude of the Salar Grande salt surface is currently 640–750 m above sealevel and halite deposition is inactive compared with salars to the east (Pueyo et al. 2001). The salar fill is composed almost exclusively of dry massive halite around 100 m thick, with dry salt in the deepest parts more than 160 m thick (Pueyo et al. 2001; Diaz et al. 1999; Ericksen 1993). The salt is very pure, locally 99 % NaCl, with a lakewide average of 95 % over an area of 280 km^2. It has been mined at least since the mid 19th century and today it supplies all of Chile's needs, as well as being exported, mostly to Japan.

Halite is in direct contact with igneous lithologies about the salar edge, while something like 10 m of alluvium separates the bottom of the salt body from its andesitic Mesozoic basement. There is no evidence of a concentric pattern of mineral fractionation in the salar, nor of any significant volume of salts other than halite (Diaz et al. 1999). Only a patchy anhydrite belt, several metres thick, caps portions of the salar edge (Ericksen and Salas 1989). It is made up of

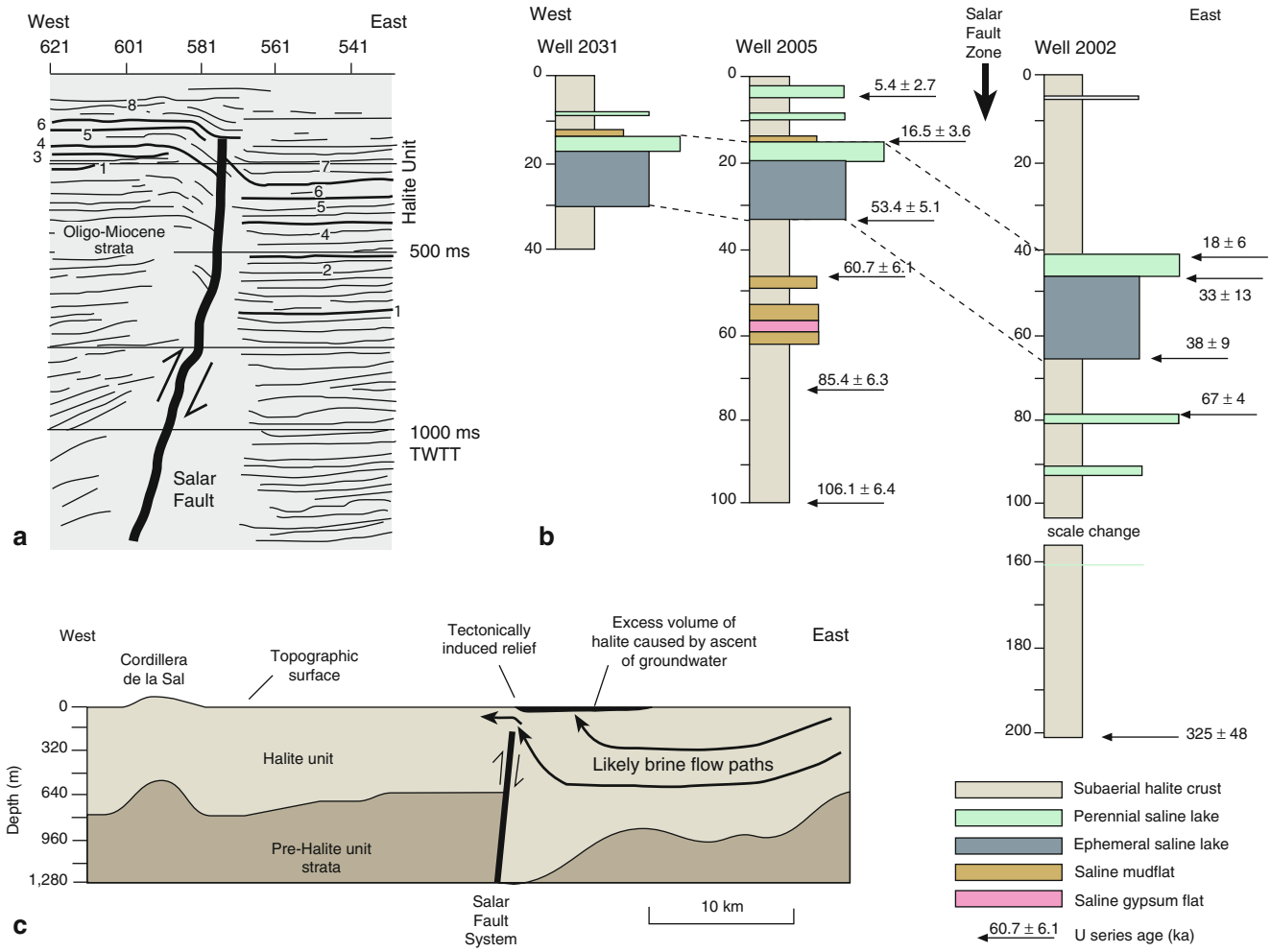

Fig. 3.50 Interactions between the Salar de Atacama fault zone and halite sedimentation (See Fig. 3.49a for location of seismic line and wells; after Jordan et al. 2002). (**a**) Interpreted seismic line ig 022 across the Salar reverse fault showing monoclinal flexure and thickening of beds across the fault. Fault trace dies out before reaching current halite surface. (**b**) Summary of halite facies in sequence 8, documented in SQM cores. Boreholes 2031 and 2005 are located west of the Salar fault system, whereas borehole 2002 is located east of the Salar fault system. U-series dates from boreholes 2005 and 2002 and comparisons of halite depositional environments at the three sites allow temporal correlation among the cores. The top of the perennial saline lake facies, dated as ca. 16.5 ka, is readily identifiable in all three locations. That horizon occurs at similar depths in cores 2005 and 2031, but is vertically displaced ≈ 28 m across the Salar fault system. (**c**) Conceptual model of enhanced halite accumulation east of the Salar fault system, which leads to a horizontal depositional surface across the fault trace. Under the conditions of a desiccated surface environment, halite accumulates because of evaporation of groundwater-fed brines. A drop in permeability at the fault (either due to juxtaposition of lower permeability rocks in the western fault block or due to properties of the fault zone itself) blocks the westward flow of topographically driven groundwater, forcing a high rate of upwelling in the downthrown eastern fault block

saccharoidal $CaSO_4$, which sometimes retains selenite pseudomorphs (dm-diam), as in the SE margin of the salar (Fig. 3.51). This sulphate bed can be traced into the adjacent western Llamara area.

The Neogene depositional history of Salar Grande is closely tied to an adjacent Tertiary lacustrine basin, the Llamara-Quillagua basin to its east (Fig. 3.52a). The Salar Grande basin became hydrologically inactive during the Late Pliocene (Chong Díaz et al. 1999). The present-day, dry, fossil salar consists of thick beds of almost pure halite with scarce sulphate and terrigenous elements (García-Veigas et al. 1996; Chong Díaz et al. 1999). Fogs and occasional rain periodically dissolve the surface halite, down to a maximum of 1 m (Chong Díaz et al. 1999).

During the hydrologically active stage, phreatic waters flowing into the Salar Grande depression from the east (now the Precordillera and Altiplano) were progressively enriched in solutes by interaction with volcanic rocks. These fluids had first drained into the Llamara-Quillagua lacustrine system of the Central Depression to deposit thick sequences of diatomites, carbonates, evaporites and clastic sediments. This lacustrine area eventually filled and dried to where it became a salar filling with anhydrite and halite. During this stage (Late Miocene-Pliocene), the evolved

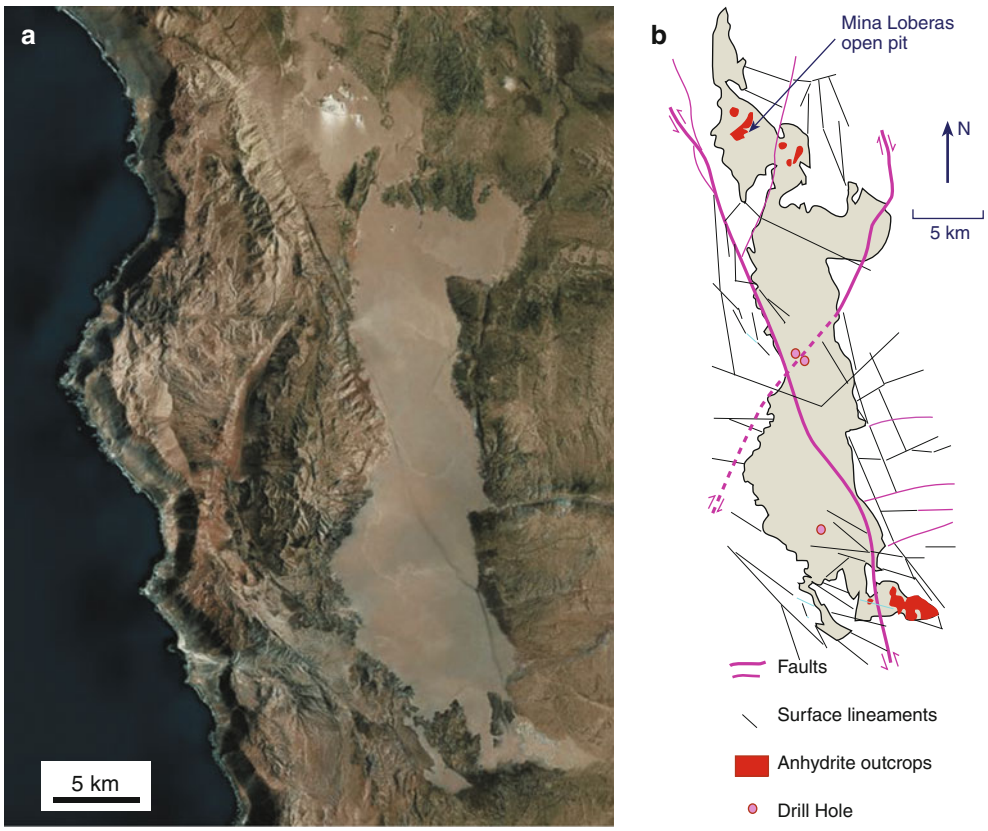

Fig. 3.51 Salar Grande, Northern Chile. (**a**) Satellite image clearly show fault trace cutting across salar floor. (**b**) Geological map shows position of 3 drill holes drilled in the 1920s for potash, which established salt in the central portion of the salt was more than 162 thick and underlain by dry alluvium. Also shows main fault of Atacama fault system trending SE-NW as well as other faults and lineaments in and around the salar (Bing® image mounted and scaled in MapInfo®)

brines of the Llamara-Quillagua area seeped eastwards along structural paths (fractured bedrock?), to reach the Salar Grande basin, which acted as their final sink. Proof of this connection is the anhydrite/selenite bed that overlies the halite in both lakes and links the western Llamara to the southeastern Salar Grande areas via the Montón de Gloria pass (Diaz et al. 1999).

Phreatic brines were subsequently lost from the basin in late Pliocene times when the Loa River canyon reached the sea. This was the beginning of the current exorheic hydrology and the opposite of its previous endorheic hydrology. Drainage into the ocean was reflected in a fall of the regional watertable, the drying of the salt body and the underlying alluvium, and the creation of a hydrologic situation in Salar Grande that still exists today (Ericksen 1993).

Large halite sinkholes, up to 10–20 m deep are best developed on the eastern side of the salar, while others developed along fault lines where they transect and weaken the now dry salt body (Diaz et al. 1999). Some sinkholes are funnel-shaped, while others are cylindrical; all may be connected laterally by a network of caves. Etched profiles in the sinkholes walls indicate they were brine-filled pools prior to the drainage of brine from the salar much like the "eyes of the devil" in Salar di Uyuni.

The regionally extensive Atacama Fault zone, a major tectonic feature in the region, transects the Salar Grande with its position marked on the salt crusted surface by irregular elongate depressions and mounds, low scarps and fractures (Fig. 3.51b). Other active faults, defined by open fracture networks, outline tectonic zones in the adjacent and underlying bedrock. The appearance of the fault trace at the surface of Salar Grande is in marked contrast to Salar de Atacama, which lacks any expression of its active faulting at the surface. That the regional fault intersects the surface of Salar Grande and not the surface of Salar de Atacama shows that the halite accretionary process is today much less active in Salar Grande. Accretion of halite requires a saline watertable within a few decimetres of the lake surface; the watertable of Salar Grande is much deeper.

Dripping fogs (*camanchacos*), in combination with deflation, capillary evaporation and rain, have sculpted a knobbly and pressure-ridged surface to the modern salt crust with relief up to 50–60 cm. At the larger scale some pressure ridges outline megapolygons in the salt with saucer diameters measured in tens to hundreds of metres, as well as smaller polygons measuring several metres between ridges (Ericksen 1993). Ongoing reworking of the upper boundary of the massive salt crust by fog moisture and the incorporation of eolian, detrital and insoluble clays through time has created a dirty brown salar-capping halite crust, up to 1 m thick, atop thicker, drier, purer halite.

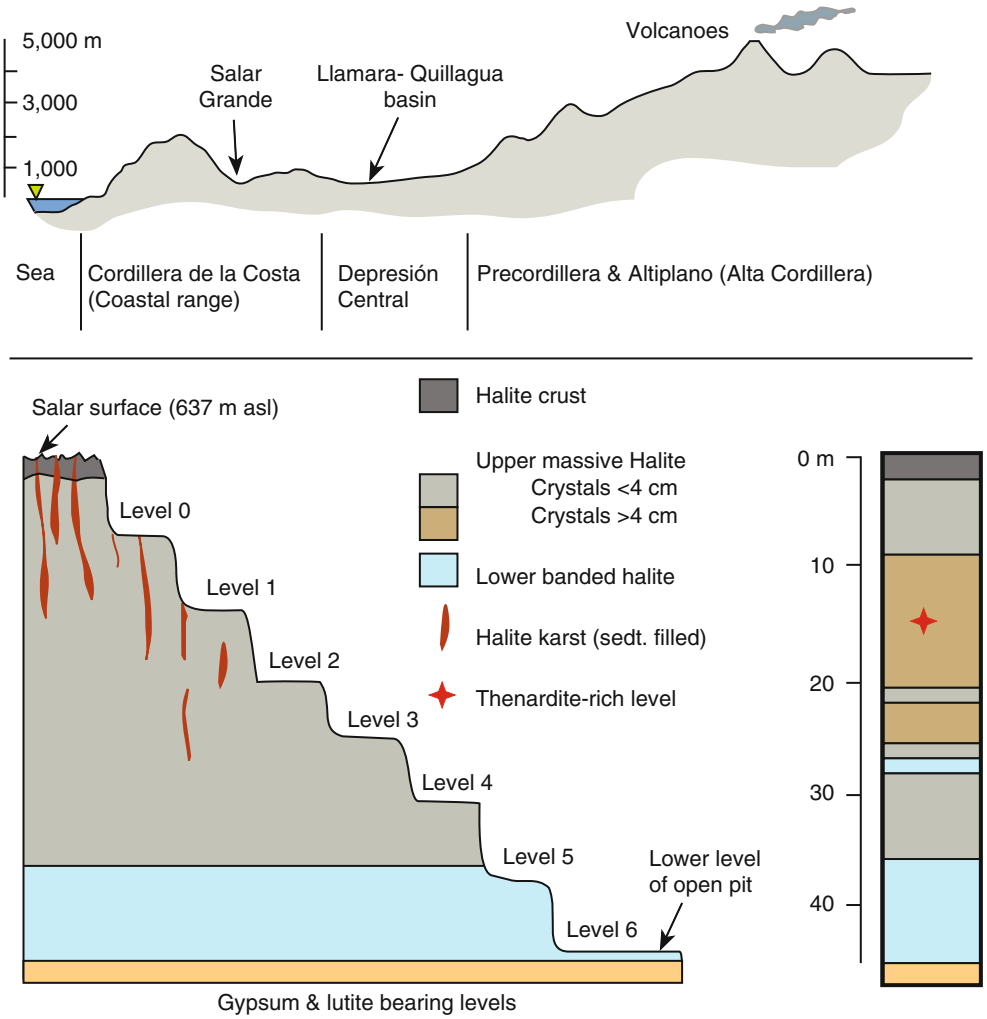

Fig. 3.52 Salar Grande. (**a**) Schematic of main physiographic subdivisions and the relative position of the Llamara-Quillagua Basin. Total section length is about 100 km. (**b**) Section through open pit at Mina Loberas in the northern part of the salar showing stratigraphic arrangement of different lithofacies discussed in text. (After Diaz et al. 1999; Ericksen 1993)

Mining and coring in the northern part of Salar Grande shows the lower 10 m of the salt fill was deposited on the floor of a mostly brine covered saline pan. It is made up of thinly-layered halite composed of cm-mm-sized bands of chevron halite, separated by synsedimentary dissolution surfaces. It is depositionally similar to the shallow saline pan facies of Salar di Uyuni and the saline lake facies of Salar de Atacama (Fig. 3.52b). Minor amounts of sulphate salts (mostly mm-sized glauberite, thenardite and polyhalite) and clay minerals cap each dissolution surface, indicating settle-out and freshening related to periodic flooding of the basin. The overlying Massive Halite was deposited as displacive or intrasediment halite, still in a saline pan but now accumulating in the capillary fringe of a pan that was subject to ongoing desiccation and evaporation, much like the majority of the halite filling Salar de Atacama.

The transition between the Lower Banded Halite and the Upper Massive Halite takes place over an interval several metres thick, which shows alternations of both units. Lower banded halite passes by an increase in crystal size into the Upper Massive Halite, which is made up of two halite crystal classes (<4 cm diam and >4 cm diameter). The random nature of crystal alignment in the massive halite shows its precipitation as multiple overprints of displacive crystal growth from saturated phreatic and capillary waters at a time when the salar surface was mostly subaerial.

Minor thenardite (Na_2SO_4) crystals occur in the Upper Massive Halite at levels 2 and 3 in the Mina Loberas pit where it appears to be an early, perhaps syndepositional, cement between displacive halite crystals (Diaz et al. 1999). Thenardite locally replaces the halite, but typically shows poikilotopic textures with solid inclusions of glauberite, clay and micrite. Polyhalite ($2CaSO_4{\cdot}MgSO_4{\cdot}K_2SO_4{\cdot}H_2O$) is the most abundant sulphate mineral in Salar Grande; it outlines grain boundaries and dissolution surfaces in the Massive Halite.

Pockets of very coarsely crystalline halite (>50 cm diameter) occur in the Massive Halite and in parts of the underlying Banded Halite. They show centripetal or geode-like patterns of halite growth and infill. This very coarse halite is

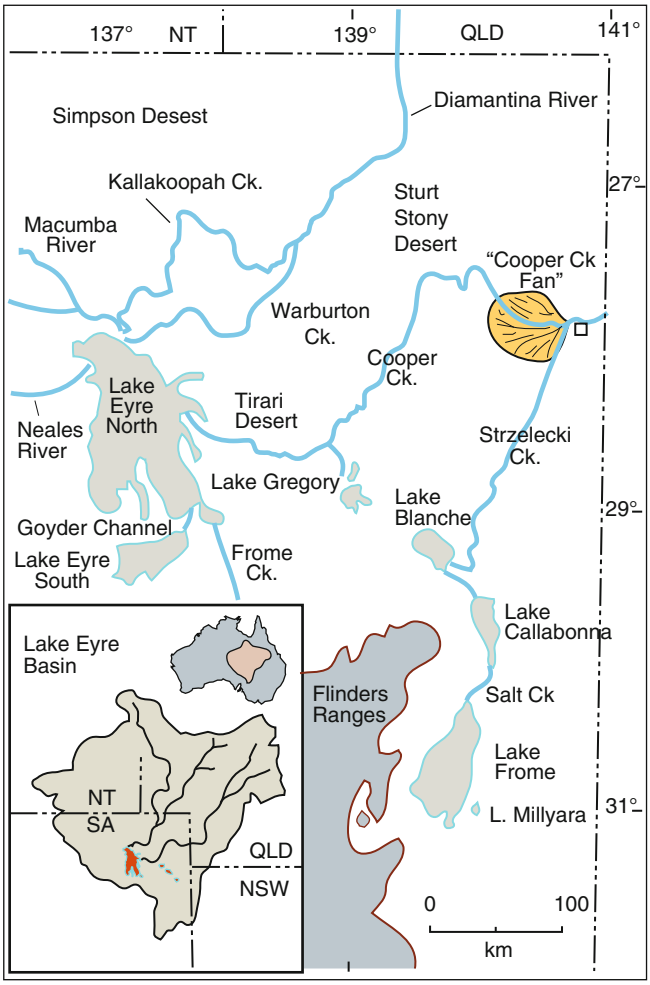

Fig. 3.53 Drainage into and between lakes in the Lake Eyre Basin of South Australia

thought to be an earlier dissolution tube fill precipitated when the watertable was higher. It is a common texture in many other South American salars where it precipitates as halite karst-fill cement in the Ojo de Diablo.

Work on the sedimentology of the halite pans in the South American salars over the last two decades has substantially improved our understanding of the hydrological significance of halite textures. It has added a third group of textures to prior notions of: (1) matrix-dominated displacement halite forming in the capillary fringe of a sabkha sitting in a zone of ascending waters above a less saline phreatic water mass and (2) subaqueous chevrons, overprinted by subaerial microkarst forming in areas of ephemeral waters in saline pans. This third textural style is exemplified by the halite units currently forming in Salar de Atacama and dominating the Massive Halite fill of Salar Grande. It is a form of chaotic displacement halite with little or no non-evaporite matrix and little or no preserved chevron textures. It is porous and forms mostly in the capillary fringe above a groundwater fed halite-saturated brine mass or brine curtain. As it forms it cannibalises itself to such a degree that little or no primary texture is preserved.

Ephemeral Stream Floodplain – Dune Field–Ephemeral Saline Lake

The ephemeral stream floodplain–dune field–ephemeral saline lake complex typifies tectonically-stable low-relief areas usually located within arid-zone subtropical high-pressure belts. Continental saline mudflats (sabkhas) are commonplace in regions of shallow watertables in this lacustrine complex, but low rates of subsidence and high rates of deflation mean evaporites are less likely to be preserved compared to rapidly subsiding alluvial fan–ephemeral saline lake settings. Rather, sediments are composed of varying combinations of saline mud flats or sandflats, with the more saline intervals showing widespread haloturbation, but little or no preserved salts. The latter were recycled as ≈ 1 m thick at-surface crusts, dissolved and reprecipitated after each flood event.

Most of the large ephemeral lakes in this setting occur in regional outflow zones of large artesian hydrologies or regional artesian seeps in low relief terranes. The rise of less saline resurging water inhibits development of a thick brine curtain or reflux plume beneath the pan and the mudflat, a requirement for longterm preservation of salt beds (Chap. 5). Surface inflow is a combination of local storm runoff and long distance ephemeral floods, with intense flood events often spaced years apart. Lake sediments are subject to the vagaries of climatic changes outside the immediate vicinity of the saline lake. These lakes generally lie at the edges of sand seas or ergs. They tend to preserve relatively thin lacustrine sediment piles with numerous truncations that indicate ongoing deflation Wind reworking of vadose lacustrine and fluvial sediment supplies substantial volumes of sediments to these adjacent sand seas.

Ephemeral braided stream floodplains, sheet deltas, dunes and sandflats are the dominant facies in the depositional basin, not bedded evaporites. Lake Eyre (9,500 km^2), Lake Amadeus (1,032 km^2), Lake Frome (2,700 km^2), Lake Gairdner (4,351 km^2), and Lake Torrens (5,745 km^2) in inland Australia are modern well-documented examples of this depositional style (Fig. 3.53; Pell et al. 2000). Major flood events are mostly fed by long distance southward transport from intense monsoonal outbursts in northern Australia.

Likewise, Lake Chad in North Central Africa, another well documented example of this style, is fed via the Chari/Logone river system from monsoon rains that typically fall in June, July and August. The subtropical position of all these examples means vertical sequences retain evidence of Pleistocene fluctuations in monsoonal intensity. Many lake complexes in southern central Australia (Lake Callabonna,

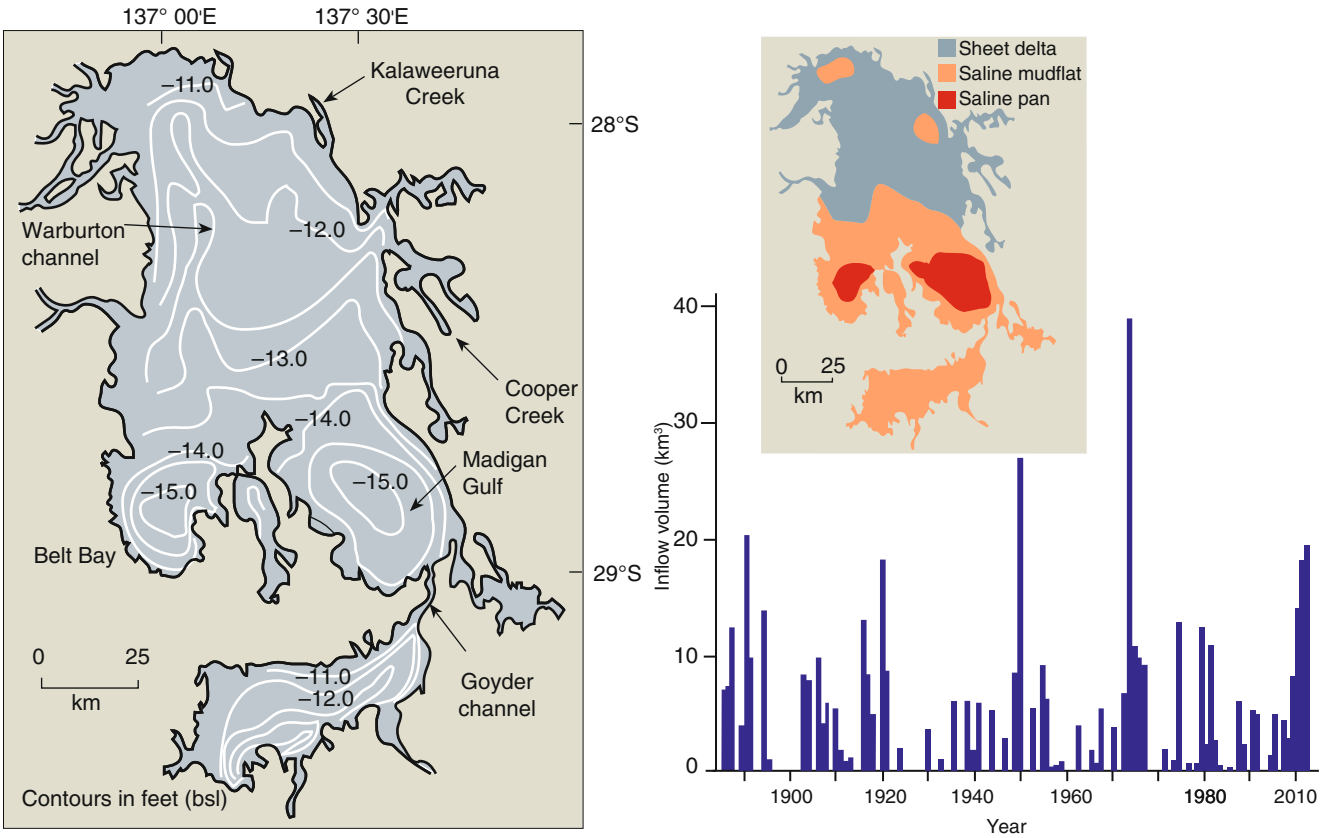

Fig. 3.54 Lake Eyre bathymetry, facies and flooding history compiled from Kotwicki (1986), Kotwicki and Allan (1998) and various references cited in text. Lake floor contours are in metres below sea level. Inflow volumes (1885–2012) replotted from <http://www.k26.com/eyre>, last accessed April 24, 2014

Lake Eyre, Lake Frome, Lake Gairdner, and Lake Torrens) were freshwater to brackish water lakes some 35,000 years ago, yet today are saline mudflats with only short-term episodes of filling. Likewise, Lake Chad has undergone massive fluctuations in size and salinity; at one point during the Pleistocene it extended to the Tibesti Mountains in northwest Chad, at another point it was sufficiently saline to precipitate natron (Eugster and Maglione 1979). Droughts since the 1970s have decreased Lake Chad levels so that it is now extremely shallow and divided into northern and southern pools. This drying is not unusual, the lake has dried up completely a number of times in the last 200 years. What is unusual in the lake's long history is the environmental stress created by too many people attempting to eke out a living in and around the lake.

Ancient counterparts to the ephemeral stream floodplain-dune field-ephemeral saline lake association include portions of the Lower Permian Rotliegende of northern Europe, Permian red beds of the US interior centred on Kansas; the Late Triassic of northwest Europe and the Palaeoproterozoic Whitworth Formation of the Mt Isa Block, Australia (Glennie 1989a, b; Benison and Goldstein 2000; Talbot et al. 1994; Simpson and Eriksson 1993).

Lake Eyre, Australia

Lake Eyre North has an area of some 8,430 km^2 and is 144 km long and 77 km wide. It is joined by the narrow Goyder Channel to Lake Eyre South, which is 64 km long and 24 km wide with an area of 1,260 km^2. The lowest part of Lake Eyre North is the eastern part of Belt Bay with some areas slightly deeper than −15.2 m ahd, making it the lowest point on the Australian continent (Fig. 3.54). The floor of the Lake is very flat with bottom slopes $\approx 2 \times 10^{-5}$, so the definition of the exact location of the deepest point is rather arbitrary. For the same reason, boundaries of its sedimentary facies tend to migrate large distances with little change in the lake water level. In dry times the lower parts of Lake Eyre North in Belt Bay and Madigan Gulf are covered by a bedded halite crust around 0.5 m thick. The 4×10^8 tonnes of salt held in this crust completely dissolves during major floods, so the lake floor actually deepens topographically during a flood (Dulhunty 1977). When the lake is dry, the saline pan crust is surrounded by a saline mudflat facies where gypsum grows displacively in the capillary fringe (Figs. 3.54 and 3.55).

The northern portion of Lake Eyre is where most of its ephemeral streams enter the lake depression. Entry points

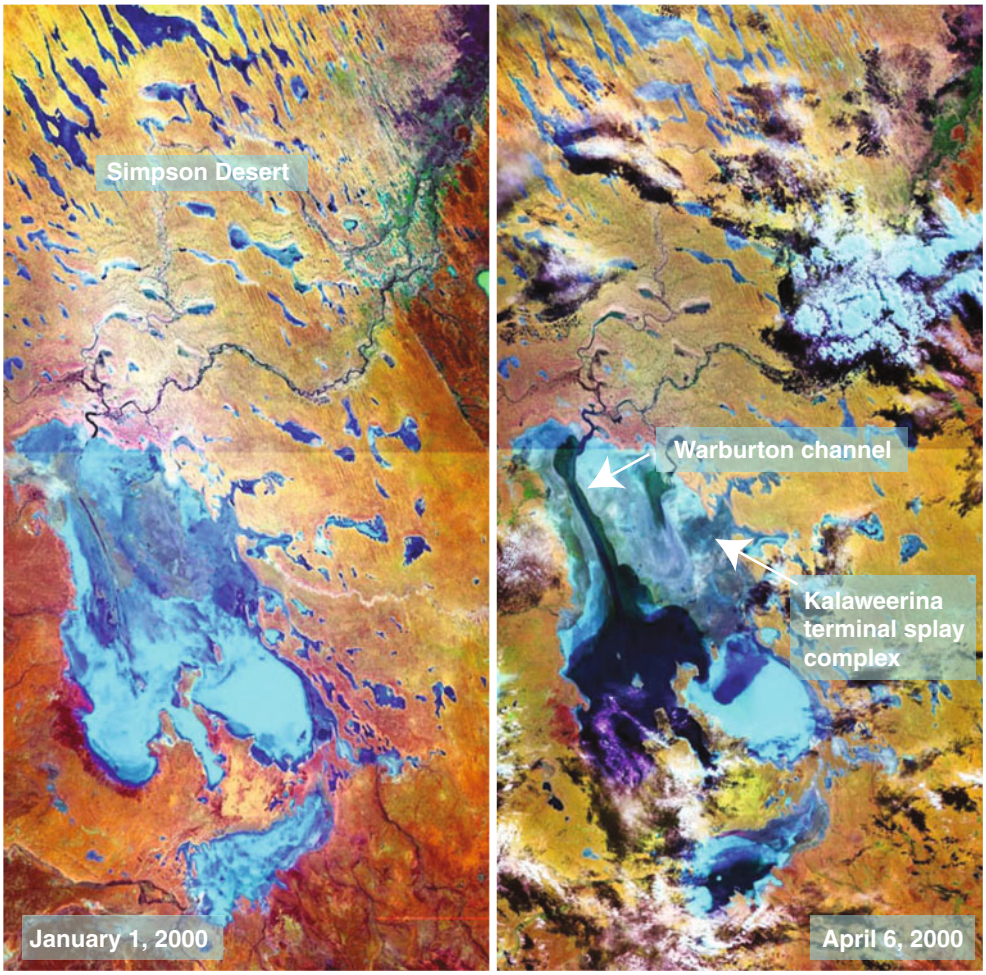

Fig. 3.55 Lake Eyre, South Australia. Image on left taken on January 1, 2000 at a time prior to a major flooding event. Partly cloud-obscured image on right taken on April 6, 2000 after a major monsoon-fed flood influx into lake from northern part of lake. The elongate interdunal sabkhas and pans in the northern part of the image constitute the Kallakoopah Pans. Note the water-filled Warburton Channel transecting the northern lake floor (Landsat 7 satellite images acquired and processed by ACRES)

are defined by a number of low flat amalgamated sheet deltas (aka terminal splay complexes), which are dominated by fine sands and silts.

Sedimentation in these sheet deltas is not the classic fluvial dominated delta topset sand association. Shallow trenches through these terminal splay complexes, such as in the outflow sheet where Kalaweerina Creek exits into Lake Eyre (Fig. 3.55) document paired mud drapes (bundles) on cross-beds, cross-bedding reactivation surfaces, lateral bundle thickness variations, herringbone cross-bedding, flaser, wavy, and lenticular bedding, and desiccation cracks (Ainsworth et al. 2012). Historically, this association of sedimentary structures has been used to indicate marine tidal sediments, yet is forming in Lake Eyre an arid-zone playa, located hundreds of kilometres inland of the ocean. In Lake Eyre these features indicate meteorological tides that are active during the flood stage in the lake and are generated by daily changes in wind direction and velocity, along with weekly to monthly discharge variations in the feeder river/creek system.

Further out in the lake depression the lower part of the coalesced sheet delta facies are cut by low channels, the largest of which is a north–south depression that transects the northern two thirds of the lake and is known locally as the Warburton Channel (Fig. 3.55). When the lakes first floods, these channels quickly drain the floodwaters into the lowest part of the lake and dissolve the salt crust (Fig. 3.54). As more floodwater enter, the lake sump areas expand and these brines are covered by a floating mass of fresher flood water that at peak flood occupies the whole lake depression and sets up stratified water conditions suitable for a mesohaline biotal bloom (Chap. 9).

Lake Eyre is an ephemeral playa-salt lake that lies asymmetrically in the southern portion of one of the largest internal drainage basins in the world (1.14 million km^2) and covers one-sixth of the Australian continent (3.53). Drainage topography is flat, with extensive areas of sandy and stony deserts. There are regions with some relief near the boundaries of the drainage basin, but only 30 % of the area is elevated more than 250 m above sea level. All streams flowing into Lake Eyre are characterised by extreme variations in discharge and flow duration (Fig. 3.54). Mean annual runoff across the basin is 4 km^3, equivalent to a water layer 3.5 mm in depth, the lowest runoff level of any major drainage system in the world. The Lake Eyre Basin is large but dry, its

Table 3.6 Evolution of the Lake Eyre brine chemistry following the 1984 flood event

Date	Salinity	Na	K	Ca	Mg	Cl	SO_4	HCO_3	CO_3
14 Feb, 1984	25,331	9,114	<1	545	53	14,290	1,274	55	0
28 Mar, 1984	40,989	14,620	70	876	150	23,000	2,140	35	7
30 Mar, 1984	42,355	15,150	93	887	143	23,350	2,700	32	0
30 Apr, 1984	49,023	17,520	70	1,050	171	27,220	2,950	42	0
7 May, 1984	51,301	18,400	46	1,040	187	28,300	3,280	48	0
28 May, 1984	57,728	20,640	48	1,240	193	31,880	3,670	57	0
25 Jun, 1984	61,278	21,970	49	1,350	173	34,360	3,310	66	0
21 Jul, 1984	64,969	23,320	92	1,350	236	35,910	4,070	81	0
27 Aug, 1984	71,248	25,500	136	1,450	264	39,640	4,170	88	0
24 Sep, 1984	86,710	31,200	68	1,680	310	48,100	5,290	62	0
28 Oct, 1984	117,797	42,600	111	2,050	451	65,700	6,820	65	0
30 Oct, 1984	120,067	43,800	111	1,820	473	67,500	6,300	68	0
26 Nov, 1984	162,697	60,300	129	1,650	725	93,100	6,720	78	0
17 Dec, 1984	217,350	82,000	208	1,220	874	126,200	6,800	48	0
16 Jan, 1985	272,819	101,300	555	459	2,500	155,600	12,300	105	0

After Kotwicki (1986)
Note the marine-like proportions
Values in ppm

drainage spans a number of climatic zones, including the tropical monsoon system to the north and the mid-latitude westerly circulation belt to the south. Some 5×10^5 km^2 of the drainage basin receives less than 150 mm of rainfall per year (on average). The highest rainfalls, with annual averages around 400 mm, occur in the northern and eastern margins, where rainfall comes from the edge of the monsoon belt.

The northern end of the Lake Eyre catchment lies barely on the periphery of the planetary monsoon system. The Northern Australian monsoon is erratic both in space and time. Recent lake floods are related to La Nina phases of the El Nino-Southern Oscillation (ENSO)[5] and are out of phase with the Pacific Dry Zone rainfall and El Nino events (Kotwicki and Allan 1998). Changes in the intensity of the monsoon have controlled the frequency and permanency of Lake Eyre waters throughout much of the Quaternary (Magee et al. 1995, 2004).

Monsoonal outbursts supply water to the Lake Eyre via its eastern tributaries; Cooper Creek, Diamantina and Georgina rivers systems. This water takes weeks to reach the lake and floods much of its flow path on the way, as it deposits sediment in a unique set of anastomose arid-zone fluvial deposits, known locally as "the Channel Country" (Gibling et al. 1998). Trustworthy data on the filling of Lake Eyre reports flooding in 1938, 1955, 1963, 1968, 1973, 1974, 1975, 1976, 1984, 1989 and 2012 with exceptional floods occurring every 25–30 years (Fig. 3.54; Kotwicki 1986; Kotwicki and Allan 1998). In 1974, in the largest flood on record, water flowed from Lake Eyre North to Lake Eyre South between March and October when an equilibrium level was obtained. More than 39.3 km^3 of surface runoff flowed into the lake at this time, completely dissolving the salt crust. The crust reformed in the following 2 years as more than 39.5 km^3 of water was evaporated (Dulhunty 1977; Kotwicki 1986). Large quantities of salt, estimated at 30 million tons (7.5 % of Lake Eyre North content), were transferred into Lake Eyre South during this event, creating, in its lowest portion, a salt crust up to 29 cm thick for the first time on record (Dulhunty 1977).

As well as the monsoon feed from the north, significant runoff can originate in the desert west of the basin, where it is drained by the Neales and Macumba creeks. The 1984 filling, with a total volume of 10 km^3, was a relatively minor one but if proved that the western tributaries can fill Lake Eyre in a matter of days. During the 1984 flood, maximum water depths were 5.7 m in Lake Eyre North and 3.7 m in Lake Eyre South. Lake Eyre South this time filled first – an event never previously recorded and considered to be extremely unlikely – and overflowed to Lake Eyre North, reversing the usual flood pattern in the lake (Allan et al. 1986).

Monitoring of the chemistry of the lake brines in the 1984 flood shows the conservative behaviour of all the major ions in Lake Eyre with the exception of Ca, which, relative to the other ions, started to deplete after October 1984 and to sulphate, which flattened its still rising concentration rate. This coincides with the onset of gypsum precipitation around October 1984. Its seawater like brine evolution is typical of most inland waters in Australia (Table 3.6 and Chap. 2).

[5]The El Nino – Southern Oscillation (ENSO) is a global climatic phenomenon marked by see-saw shifts in air pressure between the Indo-Australian and eastern regions of the Tropical Pacific. El Nino and La Nina refer to extreme phases in the 2–7 year cycle. During the warm 'El Nino' phase, the Australian seaboard cools, SE trade winds slacken and extended periods of drought are experienced in the Australian interior. In the cool 'La Nina' phase, the seas around Australia warm, the SE trade winds intensify, and widespread rain and flooding occurs.

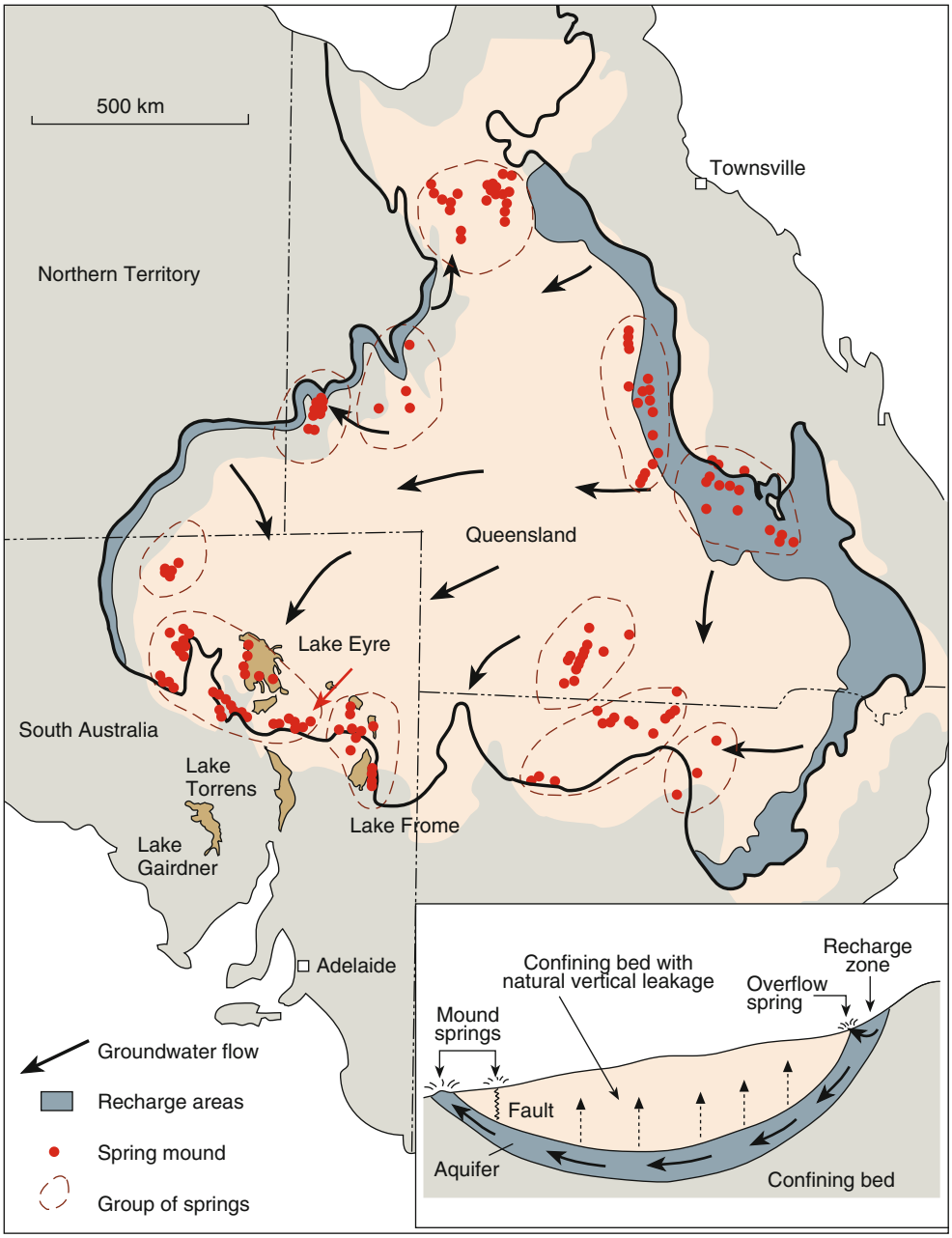

Fig. 3.56 Location of spring mound groups and artesian groundwater flow paths in the Great Artesian Basin, Australia. Shows a high density of mounds in the vicinity of Lake Eyre and Lake Frome (After Habermehl 1982)

In 1989 another western-fed flooding event occurred, coinciding with the filling of Lake Torrens on the other side of the Flinders Ranges. Lake Torrens is the second largest Australian playa after Lake Eyre and in 1989 it filled for the first time since 1878. Short term inflow rates into Lake Eyre during both the 1984 and 1989 flooding events were enormous: for example in 1984 and in 1989 Lake Eyre received some 8 km^3 from western tributaries in three days, which implies discharges of the order of 30,000 m^3/s, or one-sixth that of the Amazon. The 1989 "wet" continued into 1990 when, after some of the most devastating floods of the Channel Country in Australian history, water from the Cooper Creek reached Lake Eyre for the first time since 1974.

As well as the being the regional sink for its surface run-off, Lake Eyre's position also defines the southern outflow or seepage area of the Great Artesian Basin (GAB), which covers an area of 1.7 million km^2 (Fig. 3.56). The GAB consists of several contiguous sedimentary basins with confined aquifers of Triassic, Jurassic and Cretaceous continental quartzose sandstones, underlain by an impervious pre-Jurassic base (Habermehl 1980, 1982, 1996). It forms a large synclinal structure, uplifted and exposed along its eastern margin, leaving the overall basin tilted southwest. Recharge to the GAB occurs primarily along the uplifted eastern margins and also on the western margins where the aquifers are exposed or overlain by sandy sediments. Confined groundwater then

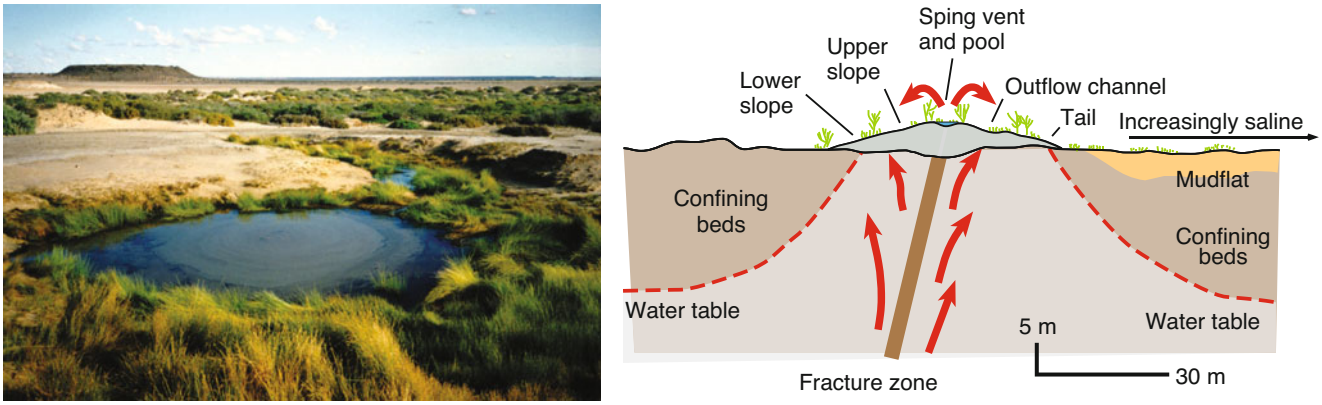

Fig. 3.57 (**a**) Active mound spring in the southern margin of the Great Artesian Basin artesian where water up to 3 million years old returns to the surface. (**b**) Schematic cross section of typical Lake Eyre Basin mound spring

percolates very slowly towards the terminal base level of Lake Eyre and saline lake sumps, reaching the Lake Eyre area after a calculated travel time of up to three million years (Fig. 3.56).

Natural discharge from the GAB comes from two principal processes: (1) diffuse vertical leakage towards the regional watertable and, (2) from focused outflow via 600 springs located in 11 groups along the western and southern boundaries of the Lake Eyre basin (Fig. 3.56). Many spring mounds define linear fault-controlled surface trends. Flow from the mounds totals 0.03 km^3/year and is a minor discharge component of the overall diffuse artesian discharge to the watertable. But it creates distinct carbonate spring mounds with the potential to be preserved (Ponder 1986; Mudd 1998, 2000; Keppel et al. 2011). Measured flows from various springs range from 0.0001 to 0.23 m^3/s totalling around 1 m^3/s. Salinities range from 700 to 800,000 ppm, pH from 7.1 to 8.0 and water temperatures from 30 to 40 °C.

A typical mound consists of a central pool of water, an outer rim of reeds and vegetation, an outflow channel, and successive layers of carbonate (Fig. 3.57). They are constructed of micritic marls, invertebrate remains, microbial thrombolitic tufa, pisolites and micrite-cemented eolian sands and are surrounded by gypsiferous saline mudflats. Spring mounds are especially obvious in the southern part of Lake Eyre (Habermehl, op cit). Active mounds are up to 8 m in height and up to 30 m across. The now extinct Hamilton Hill Spring Mound rises more than 40 m above the surrounding hypersaline playa floor, suggesting that late Pleistocene artesian pressures have been higher (Habermehl, op cit.). Flow rates from Lake Eyre springs are directly proportional to the area of wetland vegetation that the spring supports (Williams and Holmes 1978). Mineralogically, the mound springs are dominantly calcitic and constructed in response to the degassing of emerging Great Artesian groundwaters. Textures are combinations of thrombolitic, microbial and higher plant moulds and linked to the development of extracellular polymeric biofilms (Keppel et al. 2011).

The shores of modern Lake Eyre erode the edges of some now inactive spring mounds and a number of lunette-cored islands within the lake. The southeastern lake coastline, which today consists of eroded dune sand cliffs, is being rapidly cut back, with an erosion rate in the order of 5 m per major flood. The presence of several older strandlines some 0.7, 1.6 and 2.8 m above the 1974 water level, indicate previous unrecorded major flood events. According to Kotwicki (1986), the above levels represent approximate storages of 35, 48 and 67 km^3 respectively. The highest potential available storage in the Lake Eyre depression is more than 200 km^3, i.e. almost seven times greater than the 1974 storage. The terms "full" or "flooded to capacity" should therefore be used cautiously in Lake Eyre in relation to historical flooding events.

The Lake Eyre basin has been an area of lacustral sedimentation since the Mesozoic. The first documented lacustrine sediments are of freshwater Lake Walloon, which occupied central eastern part of the Australian continent some 150 Ma (Middle Jurassic). By the late Cretaceous (85–75 Ma) it had shrunk to become the much smaller 5×10^5 km^2 Lake Winton. By the early Miocene (21 Ma) the freshwater lake had assumed a position closely resembling that of Lake Eyre, it even had an indigenous species of freshwater dolphin. This freshwater system in turn evolved into Lake Dieri, a Pleistocene "greater Lake Eyre or mega-Eyre" which underwent large scale variations in size and salinity from a perennial freshwater lake up to 25 m deep, to a groundwater-controlled playa marked by substantial sediment deflation to enter the Holocene as a dry salt pan subject to occasional flooding (Magee et al. 1995, 2004; Magee and Miller 1998; Cohen et al. 2012). Four Late Pleistocene shorelines have been recognised in those parts of the present Lake Eyre surrounds not located downwind of the depression. They are: a 40 ka shoreline at –10 m AHD (Australian Height Datum),

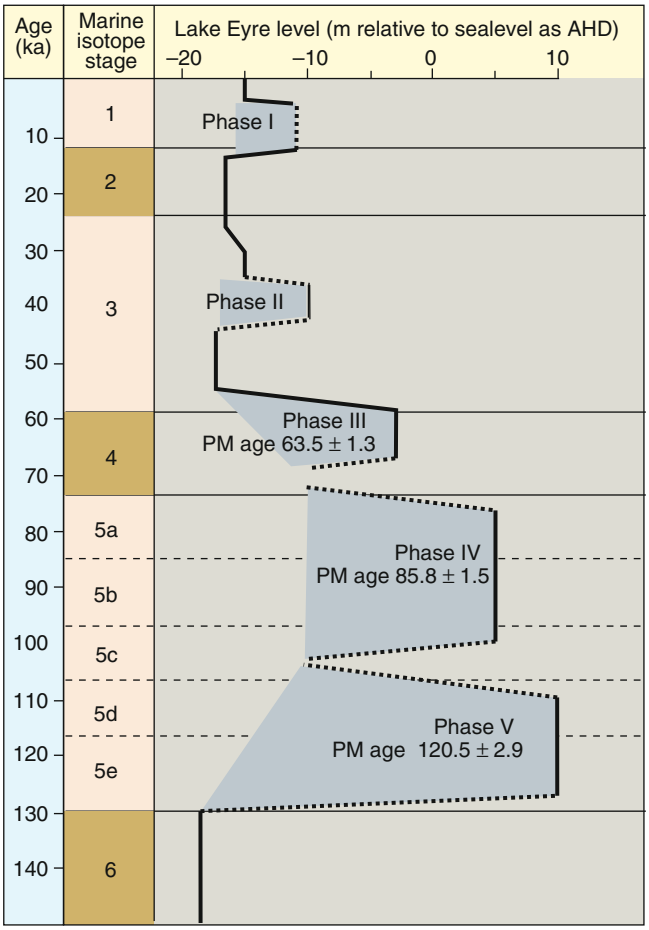

Fig. 3.58 Late Quaternary changes in lake level in Lake Eyre (After Magee et al. 2004)

a 65 ka shoreline at –3.5 m AHD, a 80 ka shoreline at +5 m AHD shoreline and a 125 ka shoreline at +10 m AHD, which corresponds to Stage 5e on the Quaternary eustatic curve (Fig. 3.58; Magee et al. 2004; De Vogel et al. 2004).

Greatest effective aridity in Lake Eyre over the past 150,000 years occurred in marine oxygen isotope stage (MIS) 6, when basin deflation was 4.3 m lower than today (Fig. 3.58). This arid event was followed abruptly by formation of the deepest perennial lake (phase V at +10 m relative to the Australian height datum [AHD—mean sea level]), a level some 10 m above sealevel and some 25 m above the modern playa floor. At least 6 m of finely laminated gypsiferous and calcareous clay were deposited at this time in conditions characterised by salinity stratification and strongly reducing bottom conditions (Magee et al. 2004). At the same meandering inflowing streams deposited thick, lateral-accretion sediments and fluviodeltaic sediment at the stream mouths.

After this acme level, the lake then shallowed and briefly dried at least once, but no evidence is seen of deflation or pedogenesis (Magee et al. 2004); then the lake refilled to +5 m relative to AHD between 100 and 75 ka (Phase IV), when lacustrine deep-water clays, calcareous nearshore and beach sands, and clastic gypsum evaporites were deposited coevally with renewed fluvial aggradation. Fluctuations in lake level and salinity noted by Magee et al. (op cit.) suggest decreasing regularity of inflow and gradual diminution of the monsoon toward the end of Phase IV.

Sediments of Phase IV were pedogenically modified and eventually truncated by deflation when the lake dried at 75–70 ka and disrupted gypsiferous playa sediments were transported downwind. Incision of tributary rivers into previous fluvial and lacustrine sediments, extending down almost to the modern level, documents a transition to significant aridity.

Lacustrine conditions returned at 65–60 ka (phase III), depositing lake sediment and a prominent beach sand, rich in the brackish water gastropod *Coxiellada gilesii* at −3 m relative to AHD; coeval fluvial aggradation and vertical accretion of overbank muds occurred. Though having shallower water and shorter duration than Phases V and IV, Phase III had significantly deeper water and longer duration than the modern ephemeral events and represents the last deep-water perennial lake in the basin and the last influence of moderately effective monsoon precipitation.

A major deflation episode between 60 and 50 ka excavated the present Lake Eyre basin to deposit gypsum- and clay-rich lunettes at a number of sites around the lake edge as well as covering former shorelines on the windward side of the lake. After deflation ceased, a thick secondary gypsum soil profile (gypsite) developed on the dunes early in oxygen-isotope stage 3. Between about 30,000 and 12,000 year. B.P. Lake Eyre was at least as dry as it is today. At many sites a lunette-like, playa-marginal, eolian unit formed from saline mudflat sediments deflated from the playa floor. After 10,000 year B.P. a minor lacustral phase occurred (Phase I) until the modern ephemeral playa regime became established at 3,000–4,000 year B.P.

Given the large volumes of water periodically entering the lake depression, and its long history extending back to the Mesozoic, one would perhaps expect large volumes of salt to have at times accumulated in the lake sediments. Certainly, Lake Eyre (Madigan Gulf) is the only Australian playa to retain buried Pleistocene halite beds (Fig. 3.59; Magee et al. 1995), but both beds are less than a metre thick. The total Pleistocene thickness is only 3 m in this the saltiest part of Lake Eyre North. A lack of preservation/accommodation space, tied to ongoing lake floor deflation, reflects the meteoric/artesian recycling hydrology that also characterises most other large low relief playas of inland Australia (Chap. 2).

Gillespie et al. (1991) interpreted the buried halite in Madigan Gulf as a former salt pan unit, which was partially dissolved during the onset of a minor halite phase in the early Holocene and then preserved by the deposition of the

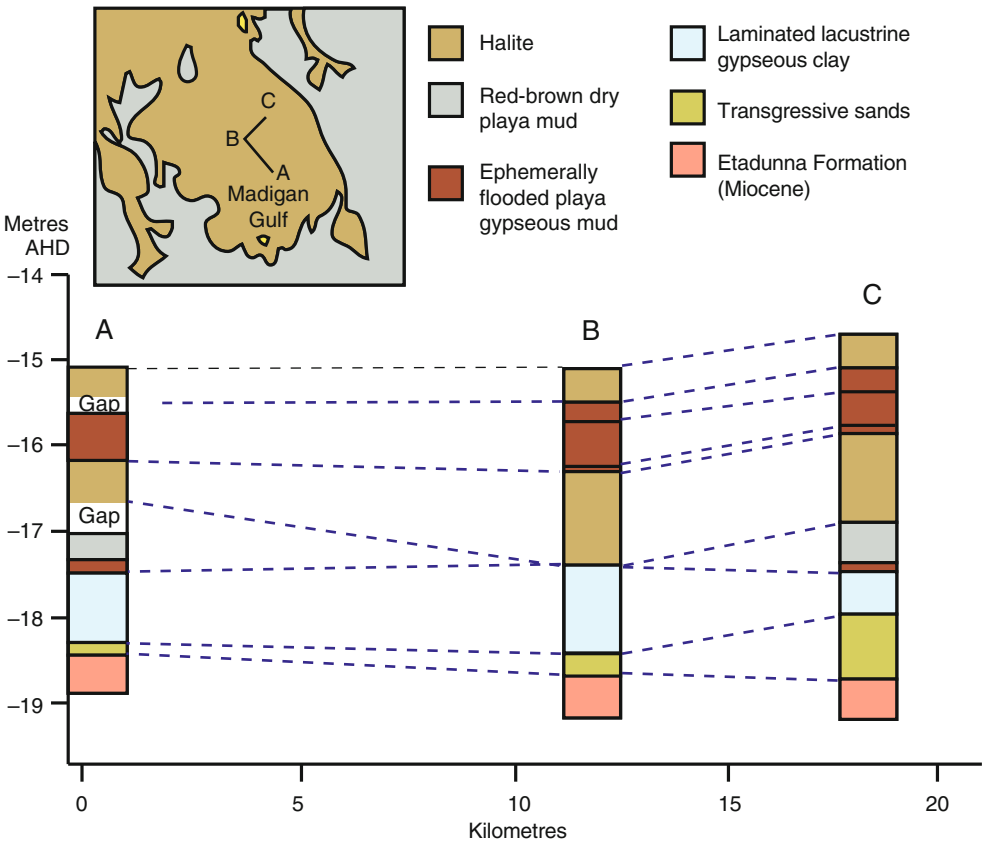

Fig. 3.59 Distribution of buried saline pan halite beds and associated sediments in Madigan Gulf, Lake Eyre North (After Magee et al. 1995)

overlying gypsiferous clays. But with thicknesses of less than a metre for each of the two preserved saline pan beds it is not a geologically significant body of halite. Inherent low relief and artesian hydrologies means the ephemeral stream floodplain – dune field – ephemeral saline lake playas of Australia and elsewhere are unable to accumulate thick sequences of bedded salt in the lowest parts of the drainage basin. It simply blows away. Haloturbation of siliciclastics in continental sabkhas in association with widespread redbed fluvial and eolian deposition is the dominant signature of this style of deposition.

Lake Frome, Australia

Lake Frome, South Australia, is another example of an ephemeral stream floodplain – dune field – ephemeral saline lake complex in the major outflow zone of the Great Artesian Basin (3.53). Lake Frome is approximately 100 km long and 45 km wide with an area of 2,700 km^2 and lies to the south of Lake Eyre (Fig. 3.60). Sediments come mainly from the west via a series of short, relatively steep gradient streams, originating in the Flinders Ranges some 40–50 km away. Overflow waters from Lake Eyre sometimes spill into the north of the lake via Warrawoocara Channel, which also connects lakes Gregory, Blanche and Callabonna. This spillover prevents Lake Eyre water from today rising to a height of more than 12 m above the Australian height datum (AHD).

The lake contains many islands mainly in the south, where the lake floor is at its lowest, some 2 m below mean sea level (Fig. 3.60). These islands are the erosional remnants of earlier now largely deflated Pleistocene sediments and are composed of gypsiferous quartz sands atop a clay surface. Around the edges of the lake there are quartzose spits and bars, beach deposits, and delta fans, as well as Pleistocene transverse and longitudinal desert dunes (Draper and Jensen 1976). As in Lake Eyre, sheet delta fans define the entry points of the larger ephemeral streams and are built by the coalescence of flat lenses of ephemeral stream sediment and dominated by low angle layering. Stream channels are shallow, straight to gently curved features with few point bars. Oxidised organic-rich muds define lowest parts of the channels. Fine-to-coarse sands with minor gravels form the bulk of the sheet delta sediment. Interchannel areas are composed mostly of reworked eolian sands. Marginward evaporitic flats with widespread capillary gypsum form large areas peripheral to, but sometimes, atop the sheet delta sand prisms.

Further out into the lake the channels die out and pass into the sands and muds of the saline mudflat, which dominates the lake basin. The bulk of the mudflat matrix is a quartzose sandy mud or mud with displacive gypsum forming in the capillary fringe and displacive halite in the uppermost 10 cm. Mudflat sediments tend to be massive but can locally show

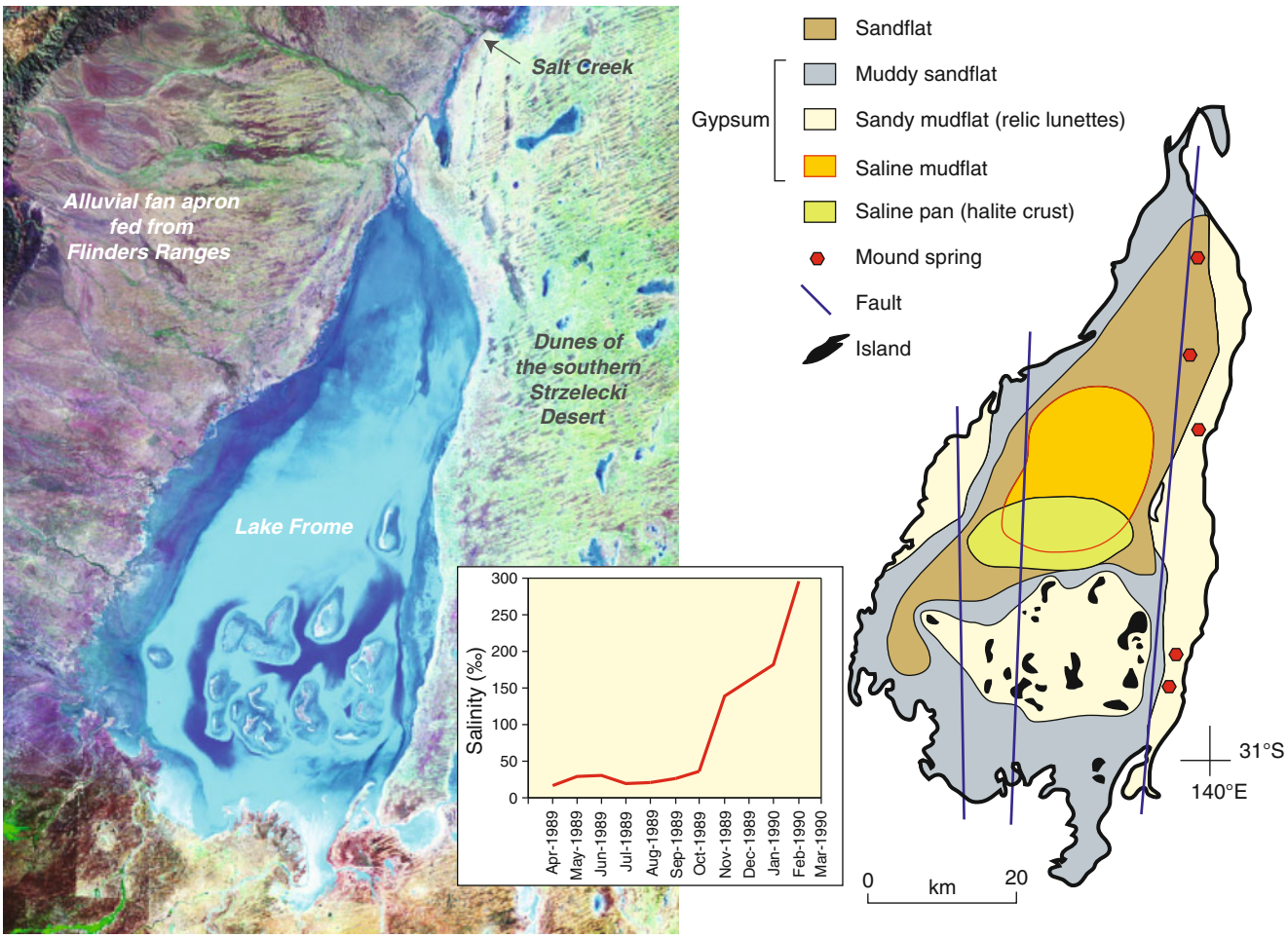

Fig. 3.60 Surface sediments in Lake Frome, South Australia. The Flinders Ranges are visible in the upper northeast corner of Landsat image. Sediments in the lake depression show an off-centre bull's-eye pattern related to the presence of a deflationary high in the southern centre with islands dominated by lunette gypsum. The clastic distribution is also inverted with high proportions of sand in the more central positions of the saline mudflat rather than along the current lake strandline. This unusual matrix position indicates detrital flooding from the north fed by overflow from the Warrawoocara Channel (Salt Creek), which feeds overflow from Lake Eyre into the northern end of the lake. Note also the association of aragonitic spring mounds along the eastern side of the lake with their positions controlled by upwelling along a north–south trending fault. *Inset* shows salinity evolution of surface waters after the April 1989 flood (Landsat Image courtesy of NASA, surface geology in part after Draper and Jensen 1976)

indistinct wispy organic lamination. In the lowest part of the lake floor is the saline pan made up of an ephemeral halite crust up to 20 cm thick and composed of halite rafts and chevrons. The crust completely dissolves during times of flood and is continually underlain by water-saturated muds with large crystals of lenticular and prismatic gypsum.

Like Lake Eyre, the lake also displays large active spring mounds along its eastern side. Mound sediments are made up of varying proportions of detrital sediment and authigenic aragonite, calcite, and dolomite cements forming an microbial tufa bindstone. An apron of gypsite fringes the active mounds. As in Lake Eyre, the mounds indicate fault-focused outflow fed from aquifers of the Great Artesian Basin and line up parallel to the major north–south normal fault system that characterises the area.

The inset in Fig. 3.60 shows the salinity evolution of a brine sheet from April 1989 until complete desiccation 11 months later in March 1990. The rate of salinity change in the brine sheet was climatically controlled. In April 1989 it was a sheet of mesohaline water (<50‰) covering the previously dry lake floor. Much of the salinity in the water sheet soon after flood-ing came from dissolution of the salt crust that had previously occupied the central depression. The brine sheet remained for 6 months through the cool months of winter and spring, with little change in its mesohaline salinity. Then, with passage into the hot summer of the Australian interior, brine sheet salinity rose rapidly. In less than a month it moved from its previous salinity plateau into gypsum saturation and then into the halite saturation field before desiccation 3 months later. By end March-early April,

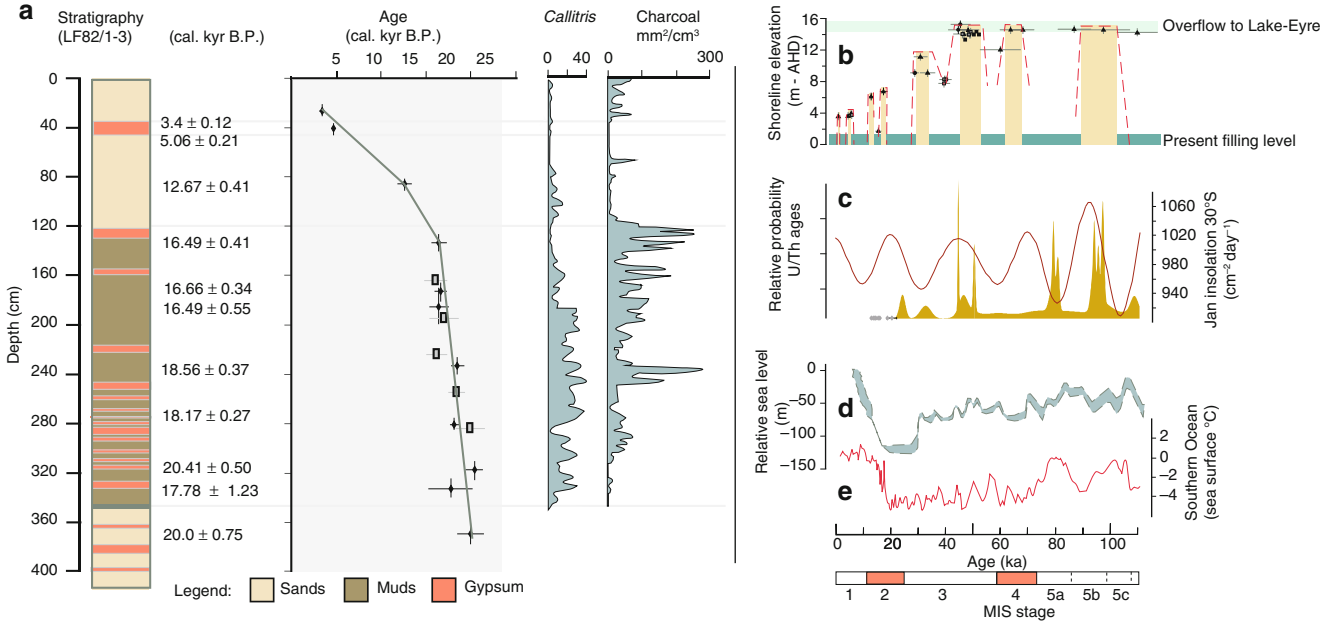

Fig. 3.61 Lake Frome (After Cohen et al. 2011 and references therein). (**a**) Age-depth profile and stratigraphy for core LF82/1–3 with calibrated radiocarbon ages on organic fraction. (**b**) Lake-level phases of Lake Mega-Frome derived from single-grain optically stimulated luminescence (OSL) ages on stratified palaeoshoreline deposits (*solid black triangles*), multigrain thermoluminescence (*solid black circles*), and calibrated accelerator mass spectrometry (AMS). ^{14}C ages on freshwater molluscs (*solid gray squares*; *black solid squares* are beyond calibration) plotted against elevation. Errors for OSL are ±1σ and for calibrated AMS ^{14}C are 2 standard deviation (for AMS ^{14}C calibration, Lake-phase shading: gray bars denote pooled mean estimates ±1σ. *Horizontal gray band* represents elevation of Warrawoocarra sill at 15.4 m AHD (Australian Height Datum) whereby Lake Mega-Frome overtopped to join Lake Eyre. (**c**) Histogram of summed individual $^{230}Th/^{234}U$ age distributions of speleothem ages at Naracoorte Caves and Kelly Hill Caves, Kangaroo Island, normalized to unit area (low analytical errors give sharply defined age distributions). Multicollector – inductively coupled plasma – mass spectrometry Mairs Cave ages are not included in summed distribution due to differing techniques and are plotted on x-axis; January insolation at 30°S (Berger 1992). (**d**) Sealevel curve. (**e**) Stacked sea surface temperature (SST) record for Southern Ocean. MIS—marine isotope stage

1990 (almost a year after the flood) the lake floor had dried out and its 30 cm-thick salt crust had reformed. This style of salinity increase, with a long plateau of mesohaline waters, is important to life in the lake as it allows sufficient time for a halotolerant macro and microfauna to breed and survive into adulthood. Plateaus in salinity evolution can control the intensity of the "feast or famine" response in many saline water bodies worldwide (Chap. 9).

The gypsum-entraining sediments of Lake Frome, like those of Lake Eyre, preserve a high-resolution record of climatic fluctuations over the last 100,000 years (Fig. 3.61; Cohen et al. 2011). Over the past 20,000 years the climate in the drainage basin has become increasingly arid (Fig. 3.61a). The hydrologic feature known as a "mega-lake" stage indicates a former lake water level that was sufficiently high to merge Lakes Frome, Blanche, Callabonna and Gregory. This Lake Mega-Frome was connected for the last time to adjacent Lake Mega-lake Eyre in the high water period 50–47 ka, this defined the largest remaining interconnected system of paleolakes on the Australian continent at that time. The final disconnection and a progressive drop in the level of Lake Mega-Frome indicates a major climate shift to aridification (gypsum beds) that coincided with the arrival of humans and the final demise of the megafauna in the Lake Eyre Basin.

The elevated supply of moisture to the Australian continent at various times across the Quaternary has been inferred to be to a response to an enhanced monsoon. The Lake Frome data provides reliable quantitative evidence for periods of enhanced tropical and enhanced Southern Ocean sources of water that supplied and filled these lakes at different times during the last full glacial cycle.

Mega-Lakes and Mega-Faunas

Interestingly, for much of the Mid to Late Pleistocene especially in glacial periods, the Lake Eyre catchment was savannah grassland, supporting large numbers of marsupial grazers and predators; this was an megafauna-dominated ecosystem and very different to today (Webb 2006, 2009). At various humid times (times of Megalake Eyre and Megalake Frome) the surrounding grasslands and along-drainage forests supported large numbers of *Diprotodon* and other megafauna.

This included giant 3-m tall kangaroos, giant flightless birds such as *Geryonis* (aka "thunder birds") that stood more than 2 m tall and were much heavier and taller than an ostrich or emu. There were also large lizards, including predatory herds of *Megalania prisca*, a species of predatory lizard that when fully grown was up to 7 m in length and so was larger than the modern Komodo dragon. Its main prey was likely the various species of diprotodontids. As well, there were numerous snakes, including 5 m-long pythons (*Wonambi naracoortensis*), and several species of predatory thylacines (marsupial tigers), including the lion-sized *Thylacoleo carnifex*. At the top of the mega-lake food chain were two species of 5–8 m long crocodilian predators, *Crocodilus porosus* and *Palimnarchos pollens*. During lake-full times these crocodilians occupied almost all of the Lake Eyre catchment waterways.

D*iprotodon* species were grassland marsupial grazers that were a widespread inhabitant of the savannah surrounding the megalakes. The diprotodontid group includes the largest marsupial known to ever exist in Australia (some species were rhinoceros-sized) and as a group were the main prey species for the crocodilians. Crush pits on Diprotodon long bones are up to 10 mm in diameter, showing the enormous crush strength of the jaws of these crocodilian predators. Tapir to rhino-sized Diprotodontids were most vulnerable on steep, muddy banks of rivers feeding into perennial mega-lake Eyre and Frome. A 5–8 m crocodile clamping its jaws over the snout of one of these animals and then rolling would have caused massive injury and instant death if the neck was broken by the roll.

Today, in what was the former water covered areas of Lake Callabonna and Lake Blanche the remains of various large-bodied vertebrates, especially *Diprotodon,* are found in wind-eroded muddy mounds that encase or partially expose fossil carcasses. There are thousands of such mud-covered gypsum-cemented mounds littering the exposed lake floors.

According to Webb (2009), the savannah areas of the paleo-Lake Eyre catchment had a low drought threshold with stream and lacustrine standing water drying out long before main feeder channels. Around 80 kyr the Lake Eyre and Lake Frome regions experienced fluctuating widespread aridity with decreasing maximum lake levels. It is likely that, after 80 ka, mega-faunal populations never again reached the same proportions in the Lake Eyre and Lake Frome drainage, although they did survive in the less arid parts of Australia until as recently as 15 ka, before being hunted into extinction. Climate deterioration drove a slow reduction in the population and species variety, commensurate with deepening aridity throughout central Australia. This pattern gained momentum after 65 kyr. River channels probably provided escape corridors and re-entry for animals at these times as they followed fluctuating water levels.

Remnant animal populations focused on shrinking water bodies along main channels but tethering of groups would have occurred as water holes became isolated; Lake Blanche and Lake Gregory were probably the last two water holes of what was once the megalake system (De Vogel et al. 2004). Increasing bouts of aridity brought food shortages and the concentration of dwindling animal populations at reducing riverine refuges. Increased competition at these places followed as plain dwelling animals fell back on major streams with predators experiencing a short-lived abundance of prey. While some animals may have used northern escape routes, the main exit and supply of species probably came not along riverine corridors but through southerly directed corridors into areas of western, southeastern Australia.

Salina de Ambargasta, Central Argentina

Salina de Ambargasta is a saline depression situated in the mid latitudes in central Argentina (29°S, 64°W). Its Köppen climate setting is BSh, a hot arid setting, but some 20 or so kilometres to the east is a milder Mediterranean-style climate (Cwa) in the lowlands, while to the west are the BSk and ET climates of the Andean cooler rain shadow deserts. As such, Ambargasta straddles a transition in hydrological and climatic environments marked by fluvial and cooler perennial lake deposits to the east and the classic volcanic salars and lagunas evaporitic lakes of the Andes highlands to the west.

Because of its hydrological setting, the Ambargasta saline complex can be subdivided into a closed system "sensu-stricto" (area A) and an "open-like system" (Area B) in the north, characterised by seasonal overflow (Fig. 3.62: Zanor et al. 2012). Its geomorphological and sedimentological features also divide the Ambargasta depression into well-defined western, eastern and northern zones, where aeolian processes, groundwater supply and surface inflow, respectively, define distinctive sedimentary environments and typical processes of deposition within what is a single playa depression. The following depositional settings are seen to follow this topographic subdivision: (1) alluvial fan; (2) sandflat; (3) springs; (4) dunes and palaeo-dune field; (5) dry mudflat; (6) capillary mudflat; (7) ephemeral saline lake (includes saline mudflat and salt pan).

The dry mudflat is present at the highest topographical zone, where the groundwater influence is less important and only intermittent ponds are present. In the capillary mudflat, evaporite sedimentation is limited to the development of efflorescences via evaporative capillary pumping. The ephemeral saline lake system, occupies the lowermost topographical region, as is evidenced by the strong asymmetric distribution of the various lagunas in the Ambargasta

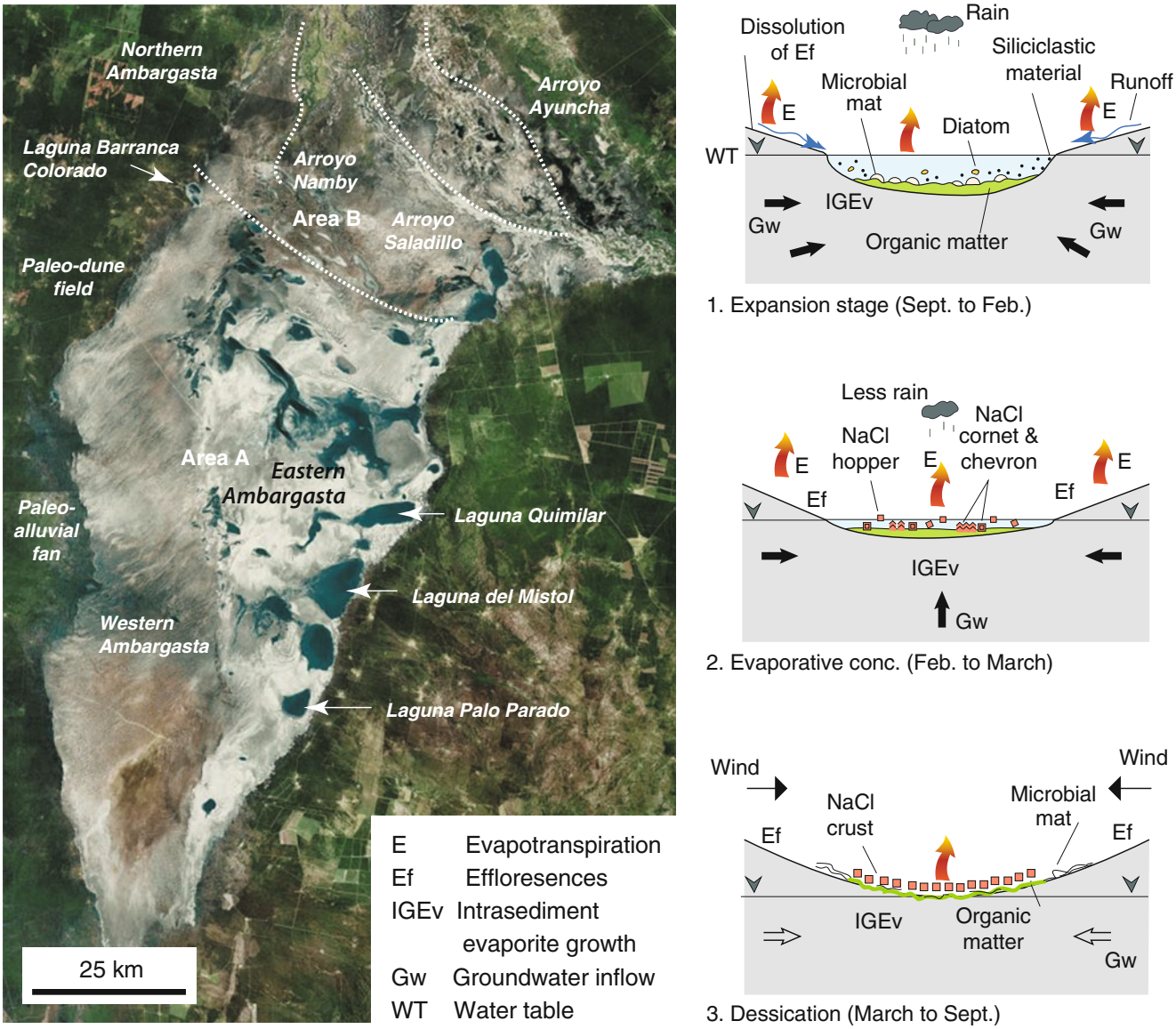

Fig. 3.62 Salina de Ambargasta is made up of Area A, which is a hydrographically closed system and Area B which is a more open hydrology that is drained by Arroyo Saladillo. The boundary between A and B is indicated by a white dashed line. The three geomorphic zones that make up the main topographical levels correspond to western Ambargasta, eastern Ambargasta and northern Ambargasta. Also shown is the seasonal evolution (Stages 1–3) of the salar's hydrology and associated sedimentation systems (After Zanor et al. 2012)

depression. Alternate cycles of lake expansion and contraction in the lagunas and across the depression are responses to inter-annual hydrological variability as well as to seasonal variability (Zanor et al. 2012). Isotopic compositions of surficial and underground waters (^{18}O and ^{2}H) indicate that lake waters become isotopically enriched during summer when evaporation plays a significant role in the saline complex.

Ambagastra's transitional climatic setting means seasonal fluctuations in the hydrological balance throughout the year trigger the flooding and desiccation stages in the lakes and the surrounding depression. After the lakes are flooded by meteoric waters (Stage 1), they begin shrinking due to the intense evaporation during the late austral summer (Stage 2). Whenever the lakes completely dry up, as in the case of Laguna Quimilar, Laguna Mistol, Laguna Palo Parado and Laguna Barranca Colorada, a salt pan forms in the lowest part of the lake area across the austral winter (Stage 3).

In the various Ambargasta salt lakes, the saltpan deposits typically reach no more than 2.5 cm in thickness and are

Table 3.7 Rates of extreme rainfall events that create sheetfloods in the arroyos, ephemeral fans and "channel country" fluvial systems feeding surface waters into saline lakes and pans

Location of event	Date of event	Annual av. (mm)	Storm rainfall (mm/time)
Aozou, Sahara	May, 1934	15	370 mm in 3 days
Tamanrasset, Sahara	Sept., 1950	27	44 mm in 3 h
El Djem, Tunisia	Sept., 1969	275	319 mm in 3 days
Bisra, Algeria	Sept., 1969	148	210 mm in 2 days
Sharja, UAE	1957	107	74 mm in 50 min
Swakopmund, Namibia	1934	15	50 mm
Dead Sea, Middle East	Nov., 1995	90	150 mm in an hour (2.5 mm per minute)
Mt Dare, Australia	March, 1967	126	149 mm in 1 day
Alice Springs, Australia	March, 1988	275	205 mm in 1 day
Innamincka, Australia	Jan., 1974	172	356 mm in 3 days
Balcanoona, Australia	March, 1989	200	341 mm in 2 days
Chicama, Peru	1925	4	394 mm in single storm
Lima, Peru	1925	46	1524 mm (more than 30 times annual)

composed almost exclusively of cubic halite and minor quantities of gypsum, not continuous salt beds. So, instead of forming extensive continuous saltpan layers in the lowest portions of the saline depression, halite precipitates as small crystal bowls of a diameter of 1 m, separated from each other by muddy, relatively halite-free, sediment. Modern and ancient lakes with these mosaic halite distributions were termed "spotted lakes" by Renaut and Long (1989).

Perennial Stream Floodplain–Perennial Saline Lake

Perennial stream floodplain–perennial saline lake depositional complexes, the third saline lacustrine depositional style of Hardie et al. (1978), occur in several high relief tectonic settings and usually lack extensive sabkhas. Any sabkhas that are present tend to be localised muddy embayments about the lake shoreline. Most perennial saline lakes such as the Dead Sea and the Great Salt Lake are characterised by steep slopes surrounding the lake. The steep slope allows saline water to pond in an arid climate and the lack of sabkhas is often the result of the steep basin sides, with the associated lack of an aerially extensive outcropping of the capillary fringe. These perennial lakes are discussed in detail in the next chapter.

Continental Inflow

All the ephemeral saline water systems discussed in this chapter have one very obvious feature in common, that is, all are subject to an unpredictable and variable rate of water inflow. Researchers who have not experienced a heavy desert rainstorm often do not appreciate how much and how quickly moisture can enter the system and move large volumes of poorly consolidated sediment in a desert soil system, which largely lacks a stabilising vegetation carapace. Desert downpours in the drainage hinterland create debris-charged raging torrents in normally dry streambeds, along with crossbedded and rippled sheet sands and vast areas of muddy floodplain. This is especially so when rain falls over barren rock at higher elevations in the drainage. As little as a few millimetres of rain can produce flow in dry desert wadis; the flow tends to emerge suddenly, peak rapidly, but last only a few hours (flash flooding). Less than 100 mm can produce catastrophic floods. In the Tadmait Plateau of the Sahara a rain of approximately 16 mm generated a flood with peak discharge in emergent wadis of about 1,600 m^3/s.

The results can be catastrophic for the people living in these areas. For example, a storm in August 1988 at Khartoum, at the eastern edge of the Sahara, had a daily rainfall of about 200 mm (twice the previous heaviest fall on record in the region). The resulting flash flooding left tens of thousands of homes destroyed and vast areas around the city inundated (Hulme and Trilsbach 1989). An estimated 1.5 million people were made homeless, and there were over 100 deaths and hundreds of injuries. Most of the homeless had nowhere to go; even areas which had not suffered damage were under water and there were few areas dry enough for temporary camps to be erected.

In a day or two such rapid influxes of water can convert a saline pan sump into a lake filled with brackish water and teeming with a halotolerant biota (Chap. 9). Table 3.7 lists extreme rates of rainfall in some of the areas that occasionally can feed huge volumes of surface flow into the saline lake depressions. Once this huge volume of water has moved large volumes of siliciclastic sediment into the lake depression, it dries out within weeks to months and the system then can stay dry for years. With desiccation the newly deposited sediment is subject to the vagaries of deflation and with longer term climatic change and lowering of the regional watertable can evolve into what can be extensive eolian sand and dust sheets.

Eolian-Hosted Sabkhat

So far, this chapter has described and defined sabkha and pan salts hosted in either marine-margin or continental sediments. In both situations the interpretation of ancient counterparts comes from the matrix, not the salts. Put simply, nodular anhydrite accumulating in a marine sabkha is hosted in, and intercalated, with marine (fossiliferous) fine-grained sediment, while continental sabkhas are intercalated with, and hosted in fine-grained nonmarine fluvio-lacustrine matrices. But there is a third sabkha association, that of eolian sabkhas, where nodular anhydrites, gypsums and displacive halites are hosted in muddy eolian matrices (Table 3.1; Fig. 3.2). Eolian-hosted sabkhas can form in either marine margin or continental lacustrine settings. In either setting their depositional proximity to eolian sands means eolian sabkhas tend to be intercalated with potential eolian reservoirs and can form lateral discontinuities (lenses) in the eolian sands (Figs. 2.61 and 2.62). For this reason I have broken out modern occurrences of eolian sabkhas as a separate topic.

I define an eolian-hosted sabkha as being characterised by capillary salts accumulating in any eolian-derived matrix and sitting below a Stokes surface. It may form in interdunal depressions, in sand sheets on the marine or lacustrine edges of ergs, or even in areas of desert loess. By definition, eolian sabkhas, like all sabkhas, require the upper part of the capillary fringe to intersect the landsurface. Fluctuating water levels and watertables will move a sabkha strandline back and forth over the lower parts of an arid drainage so that eolian sabkha sediments are often intercalated with units deposited in either the ephemeral saline pan or in sand sheets. The ratio of siliciclastic matrix to capillary evaporite in an eolian sabkha unit means it can be further classified into: (1) detritally-dominated (wet eolian sabkha) with a capillary succession showing haloturbation but little or no preserved capillary salts (possible hydrocarbon reservoir), and (2) chemically-dominated (saline eolian sabkha) with abundant capillary salts preserved (possible hydrocarbon seal).

Matrix in wet eolian sabkhas has a characteristic association of sedimentary structures associated with ephemeral water and eolian overprints ranging from; subaqueous current and wave ripples, wavy laminae and contorted bedding (wet-surface conditions), through adhesion structures, bioturbation structures, desiccation cracks (damp-surface conditions), megapolygons and Stokes surfaces (falling watertables) to wind-ripple lamination (dry-surface conditions; see Chap. 2; Mountney and Thompson 2002; Goodall et al. 2000). Similar sedimentary structures occur in chemically-dominated eolian sabkhas but they tend to be overprinted and disturbed by pervasive chaotic salts and associated haloturbation.

One of the better modern areas to study the interrelationships between eolian sabkhas and dune systems is the Arabian Peninsula (Fig. 3.63). At least six generations of dunes can be identified on satellite images of the United Arab Emirates and Saudi Arabia (Glennie 1998). Geomorphic relations indicate that older periods of Pleistocene dune formation have been modified by later periods of eolian activity, including modern wind flow patterns. In addition, at least two periods of older eolian sedimentation lie beneath the modern dunes. Some dunes sands have a high content of comminuted marine shells and along with wind-reworked oolites have been cemented into calcareous eolianite, locally known as miliolite. They were sourced in sands blown out of the exposed marine shelf during glacial induced sealevel lows (Fig. 3.63). Thus, the modern eolian sabkhas on the Arabian Peninsula indicate a complex combination of groundwater overprints interlayered into active dunes and palaeodune bedforms. Those dunes cemented into calcareous eolianites (miliolites) tend to be associated with sea margin sabkhas, as in the vicinity of Al Liwa oasis in the UAE, others form in siliciclastic matrices at the edges of ergs in continental interiors, as at Umm as Samim in Oman (Fig. 3.63).

Older literature discussing eolian-hosted sabkhas typically assumes an elongate interdunal geometry, inherited from groundwater-driven infill between the partially preserved topography of the underlying dune ridges (Fig. 3.2; Handford 1981a). But dunes are merely loose sediment blowing around above the watertable, if the dunes blow on, the remaining sediment is held in place by the capillary fringe and so this type of eolian sabkha can stack into a sheet-like geometry. It also means the edges of many active ergs are flat laterally extensive erosional sandflats with deflation limited by the top of the capillary fringe, as in the Tamya sabkha of northwest Saudi Arabia (Ginau et al. 2012). Thus, sheet-like sandflat-hosted styles of eolian sabkha about the edge of a sand sea are likely more commonplace in continental interiors than the more typically cited elongate interdunal sabkha geometries.

Elongate interdunal geometries tend to be most obvious where changing climate or subsidence pushes a rising watertable further into a sand sea. They are typical of low energy desert coastlines preserving lacustrine or Flandrian marine transgressions. In the southern Arabian Gulf the Flandrian event is typically associated with carbonate-rich (miliolite) hosts. Interdunal geometries are typical of rising water levels at lacustrine-dune contacts, for example in Lake Chad or the southeastern coastal portion of Caspian Sea, south of Karabogaz Gol (Fig. 3.64a, b). There rising lake levels in the last 10,000 years and limited fetch in the adjacent lakes push the rising watertable to outcrop in nearby partially reworked dunes. In Lake Chad the rising circum-lake watertable drove the formation of authigenic silicates and sodium bicarbonate salts in the interdunal capillary fringe.

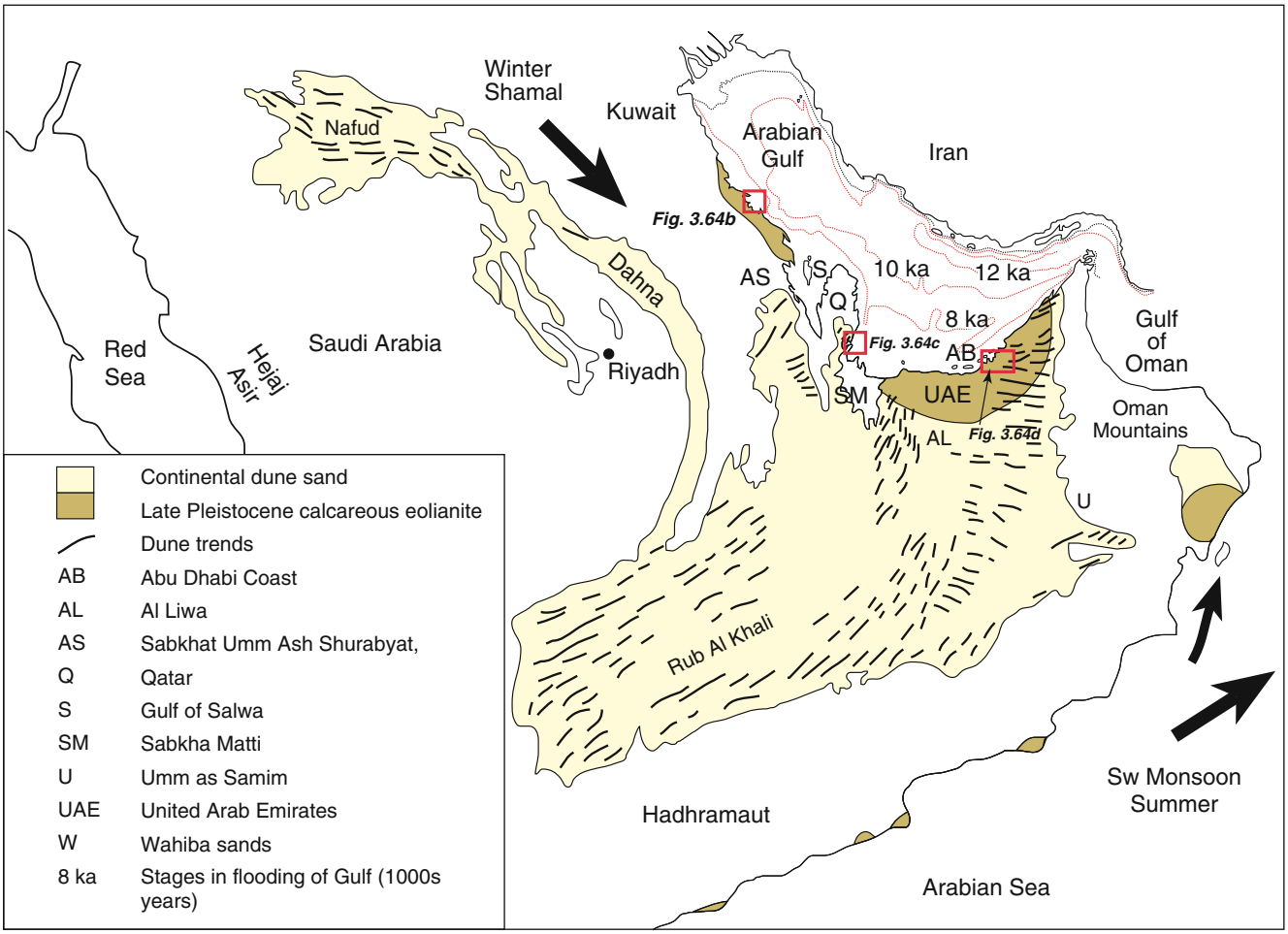

Fig. 3.63 Extent of dunes and orientation of their crests on the Arabian Peninsula and approximate extent of the postglacial marine transgression into the Arabian Gulf basin at 12, 10, and 8 ka (After Glennie 1998; Teller et al. 2000). Dominant modern wind directions are shown by *arrows*. Occurrence of late Pleistocene eolianite (Miliolite) is indicated by a dark brown pattern along coast, especially along southern coast of the Arabian Gulf around the Salwa Gulf and in the United Arab Emirates (*UAE*) where these palaeo-dunes extend as far south as about Liwa Oasis (*AL*), which is just north of the Saudi Arabian border. AB, SM, U and AS show the position of Abu Dhabi coast, Sabkha Matti, Umm as Samim and Sabkhat Umm Ash Shurabyat, all examples that are discussed in this section on eolian sabkhas

Sea-Margin Sabkha Capping Preserved Dune Shape

For an dune geometry to be preserved during a marine transgression requires relatively low energy in the zone of marine encroachment. Otherwise, the encroaching high-energy coastal shoreface will erode and transform the depositional signature to a planar unconformity and largely destroy any sabkha signatures and geometries (Fig. 3.65a). That is, these modern marine interdunal systems tend to occur in coastal zones on the edges of marine gulfs with limited fetch and sediment columns indicating a Pleistocene-Holocene rise in sea level (transgression that defines the end of the last glacial).

Interdraa marine coastal eolian sabkha geometries are obvious along the low energy coast in the region south of Munfah, Saudi Arabia (Fig. 3.64c). There interdunal depressions are dominated by muddy sands with fringes of mm-scale biolaminites and displacive and lenticular gypsum growing at or above the watertable (pers obs). Likewise the landward side of the barrier-lagoon northeast of Abu Dhabi is a somewhat more energetic setting located at the sandflat edge of a large sand sea (erg) in the triangle between Abu Dhabi, Dubai and Al 'Ayn (Figs. 3.63 and 3.64d; Abu-Zeid et al. 2001; Teller et al. 2000; Glennie 1998). Close to the coastal plain these dunes contain a high proportion of marine derived calcareous sand grains (miliolite). The dunes were at their most active in the late Pleistocene glacial maximum when strong winds blew from the west across the Eastern Emirates. Dune surfaces have been subsequently modified by the modern NNW Shamal winds.

At the time they were at their most active the ocean had receded from the Arabian Gulf and the Tigris-Euphrates River reached the sea east of the Strait of Hormuz. Along the At Taf this facilitated transport of exposed shelf sediments

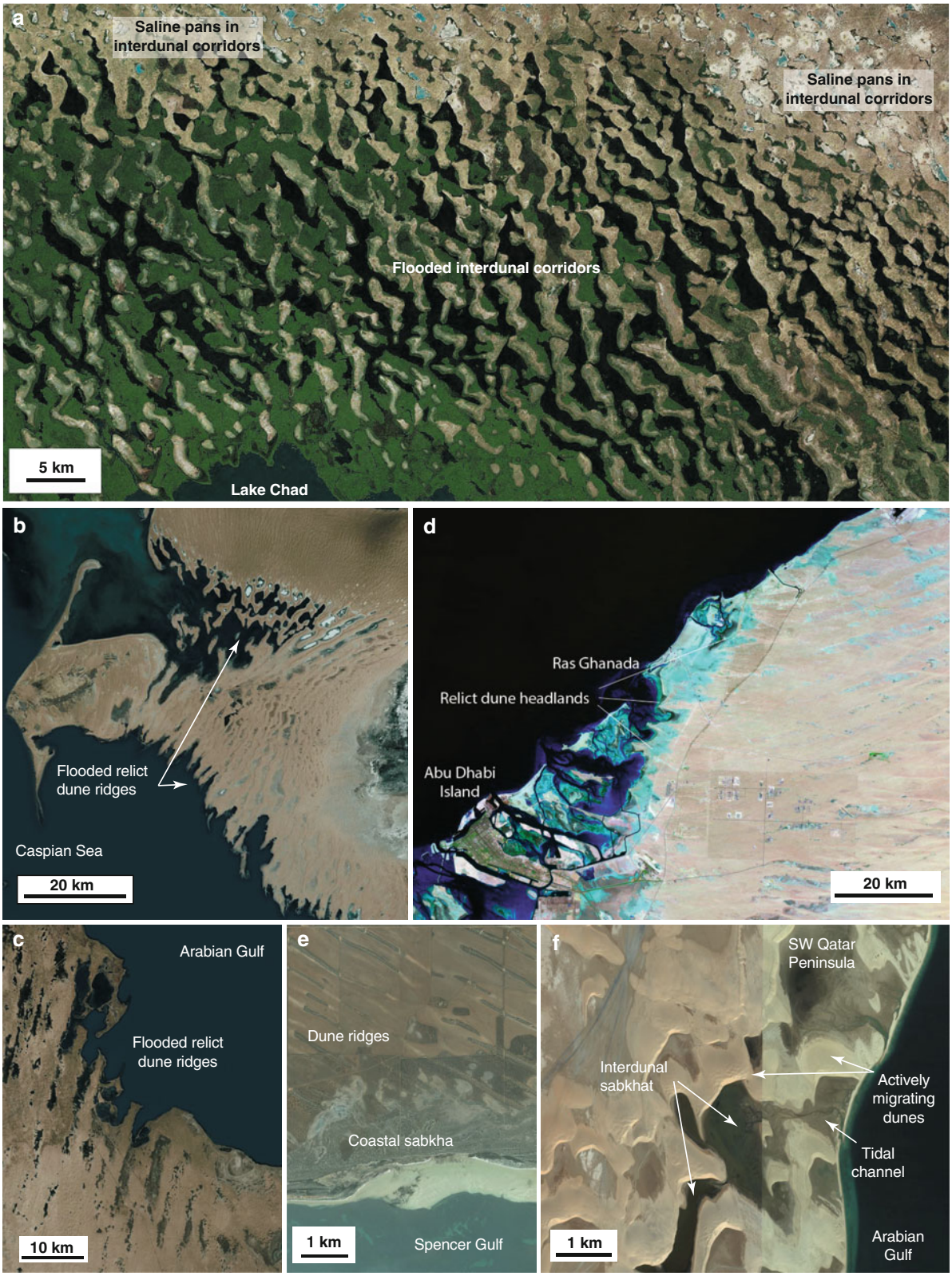

Fig. 3.64 Examples of modern eolian sabkhas created by lacustrine transgression or the Flandrian sea level rise and the encroachment of a groundwater wedge into what were formerly continental interdunal corridors. (**a**) Embayed sabkha pan-lacustrine coastline in the strandzone of north eastern Lake Chad, Chad. (**b**) Embayed sabkha-lacustrine coastline in the coastal zone south of Kora Bogaz Gol, Caspian Sea. (**c**) Embayed interdunal sabkhas in the coast in the Al Khawwari area, south of Munfah, Saudi Arabian coast of the Arabian Gulf. (**d**) Embayed sabkha-lagoonal coastline in the coastal zone between Abu Dhabi and Ras Ghanada, UAE. (**e**) Interdunal seepage sabkhas near Lucky Bay, Spencer Gulf, South Australia. (**f**) Marine-fed interdunal sabkhas in an active Shamal-driven dunefield migrating to the Arabian Gulf in the southeast coastal zone of the Qatari Peninsula (Bing® images mounted and scaled in MapInfo®) See Fig. 3.63 for location of Arabian Gulf examples

into a series of E-W trending seif dunes and draas (Fig. 3.63). Then, between 12 and 6 ka, the sea transgressed more than 1,000 km to fill the formerly subaerial Arabian Gulf and in so doing cut off the supply of eolian sand to the dunes of the At Taf (Trucial Coast). At the same time the rising watertable and the encroachment of the Flandrian seashore converted the present day coastal area from an eolian-dominated system to the Holocene coastal sabkhat documented earlier in this chapter.

Today the lagoon-sabkha system between Abu Dhabi and Ras Ghanada shows broad-scale E-W curvilinear trends that are partially truncated by marine encroachment, so that sabkha-lined dune-cored spits now protrude into the lagoon (Fig. 3.64d). To the south, similar now sabkha-covered dune ridges constitute the core to the elongate trend of the Abu Dhabi and Al Du'yybaya spits. In fact much of the classic sabkha coast of the southern Arabian Gulf shows broad scale thickening patterns in the base of the Holocene section that indicate an initial relatively low energy passive marine encroachment into interdraa depressions that facilitated the partial preservation of the dune form (Warren 1991; Kirkham 1998).

Yet another coastal association of somewhat low-energy marine encroachment onto interdunal ridges is clearly seen on the northwestern coast of Spencer Gulf, South Australia (Fig. 3.64e). In this case the encroachment was more energetic than on the Saudi coast. Many of the coastal sabkhas behind the Lucky Bay shore lie parallel to the coastline in an area immediately in front of relict seif dune ridges. The dunes were last active in the Late Quaternary and subsequently the most seaward quartzose dune sand ridges were reworked into coast-parallel beach ridges. Hence, the most seaward portion of the sabkha flat shows a coast parallel orientation. It changes to a more obvious interdunal orientation a little further back from the coast.

According to Eschner and Kocurek (1988) and Fryberger (1986), the geometry of preservation of an eolian dune system when undergoing transgression and possible encasement by an evaporite seal, is classifiable into inherited, reworked, and/or erosional dune morphologies at the contact with the sabkha evaporite (Fig. 3.65a, b). Reworked dune relief, a preservation style which shows significant destruction of original dune topography, but with remnants preserved, is the most typical situation when an erg experiences marine encroachment or transgression in both the modern and the ancient. Modern examples include relict dunes of coastal Australia and the Arabian Gulf (Fig. 3.64), ancient examples include marine-transgressed parts of the Jurassic Entrada Sandstone of the San Juan basin, and the Pennsylvanian-Permian Minnelusa Formation of Wyoming (Fig. 3.65b; Vincelette and Chittum 1981; Achauer 1982).

Eschner and Kocurek's modelling was done based on Holocene analogs and prior to our current understanding of the hydrological requirements needed to create platform and basinwide evaporite seals. We now know that most laterally extensive marine evaporites are seepage fed systems that form when a basin is hydrographically isolated and that there are no modern same-scale marine analogs for this hydrology (Chap. 5). The corollary is that in any ancient drawdown saline basin filling with subaqueous salts, the system will tend to have strandzones that transgress on adjacent sand seas in the same fashion as occurs in modern lacustrine settings, like Lake Chad and the Caspian Sea, whereby the relief of the dune tends to be preserved (plotfield indicated by rectangular outline in Fig. 3.64c). Transgressing brines in an ancient evaporite basin are an inherently lower-energy system compared to open-ocean facing coastal settings. This is why inherited dune morphologies tend to be preserved below evaporite seals (Weissliegend and Entrada sands beneath Zechstein and Todilto seals, respectively; Figs. 2.61a and 3.65b).

With thicker evaporite seals to the preserved dune morphology, the base of the seal tends to be a sabkha cement, hosted in the dune sands or its reworked equivalent, which in turn passes up into subaqueous evaporitic carbonates and salts of the evaporite proper. Initial cementation in the reworked dune sand carapace is typically due to capillary salts and so is tied to a shallow watertable. Hence, the most intense capillary cementation can be associated with interdunal rather than high dune positions in the landscape. This creates a carbonate/evaporite cemented carapace that is more resistant to erosion than mobile loose sands of the draa crests. Upon transgression, this can create an inverted remnant topography with the cemented carapaces forming higher parts of the beleaguered landscape and corridors of marine embayment preferentially entering and reworking the more easily eroded loose draa sands (Fryberger 1986). Remnants of this style of cementation beneath a platform or basinwide evaporite seal can give strong directionality to permeability and create fluid flow corridors in the upper parts of an eolian reservoir sand beneath the seal.

Whether inherited or somewhat reworked, how much dune relief is preserved in a marine transgression depends on the sand budget of the dunes and the erg, the degree of capillary cementation prior to transgression, and to the level of coastal energy in the transgressive environment (Fig. 3.65b; Eschner and Kocurek 1988; Fryberger 1986). Sand budget refers to the maintenance, gain, or loss of dune sand prior to and during initial transgression. Sand can be conserved and the dune form stabilized by vegetation, early capillary salt cementation, or a wind regime conducive to "sand trapping" by the dune as it is encroached by the sea (Eschner and Kocurek 1988).

Dune building and interdunal cementation can continue during initial transgression by maintenance of sand-drift paths, best accomplished by offshore winds, as seen today along the marine edge of southeastern Qatar (Figs. 2.58 and 3.64e). In contrast, dune forms can be degraded by deflation, a cutoff of the sand supply, and a variety of marine processes as is seen today along the At Taf coastal strip and the

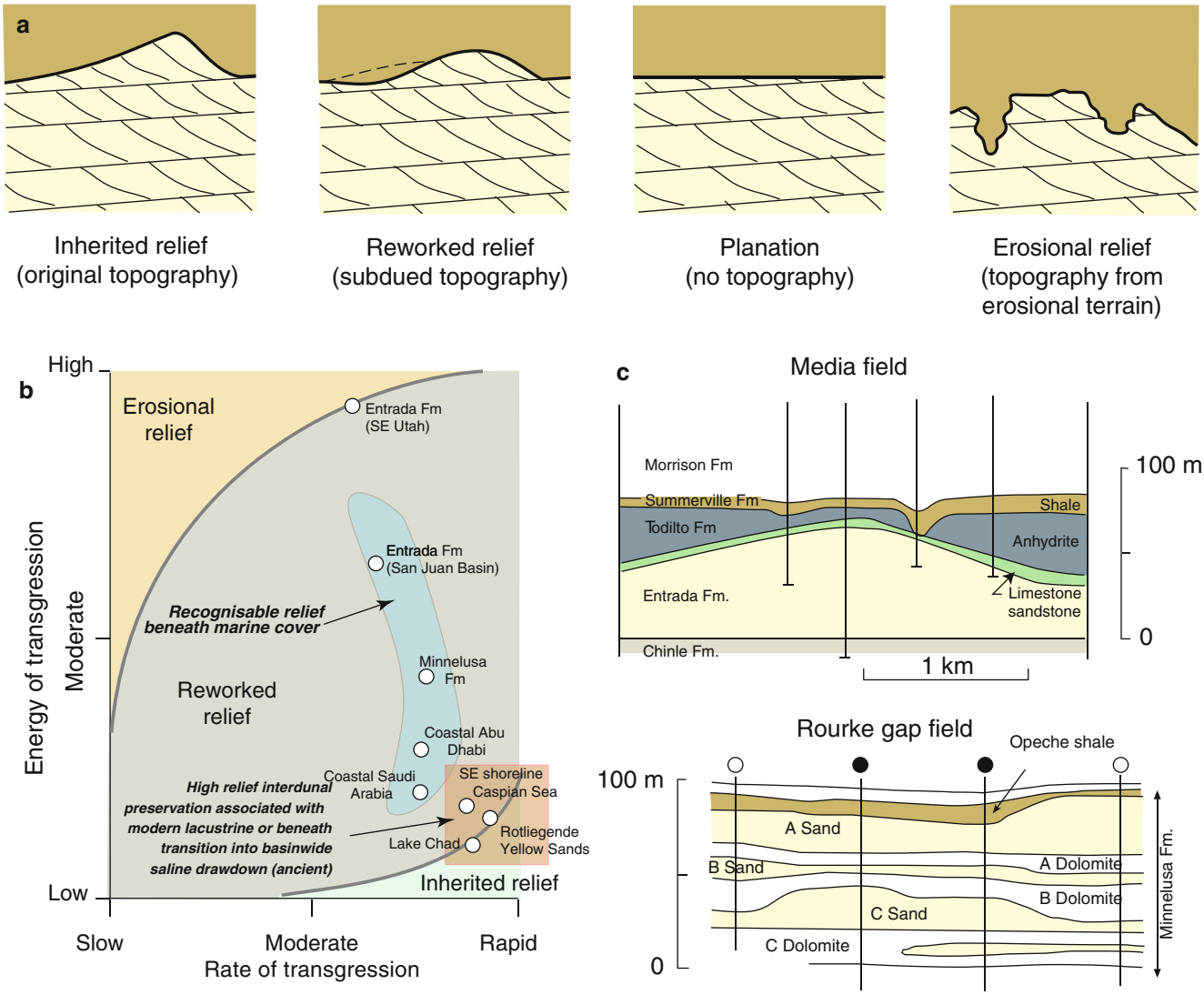

Fig. 3.65 Preservation of marine-margin eolian sabkha geometries. (**a**) Schematic of varying styles dune-sabkha contacts in transgressive marine-margin situations. (**b**) Controls on the preservation of relict dune topography during a marine transgression (**b**, **c**) in part after Eschner and Kocurek 1988). (**c**) Ancient dune-hosted oil field encased by an eolian sabkha seal (After Vincelette and Chittum 1981; Achauer 1982)

northern end of Sabkha Matti. Factors related to the nature of the transgressive environment and ultimate permeability in the reservoir sand include; (1) orientation of the dunes to destructive marine processes, (2) types of processes, (3) energy level, (4) type and rate of sedimentation, and (5) rate of marine encroachment (Eschner and Kocurek 1988).

Preservation of inherited to reworked relief requires that the dunes ridges become stabilized or remain active into the early phases of the transgression. Effects of destructive marine processes are minimized by; (1) resistant, early capillary saline cement in the encroached dunes, (2) an orientation of the dunes such that marine energy is dissipated along a minimum area of the dunes, (3) low-energy, non-wave-dominated transgressive marine environment and (4) rapid transgression that reduces the length of time for reworking, or by high rates of marine or evaporite sedimentation burying dune forms (Fig. 3.65b).

Sheets of Eolian Sabkhat

This style of eolian sabkha is not as widely documented as elongate interdunal sabkhas in modern settings. Yet modern examples characterise numerous continental interior situations where a rising watertable in a deflationary sand sheet creates conditions suitable for the preservation of eolian sabkhas. They tend to be geomorphologically stable areas in that within a yearly sedimentation cycle they experience less erosion or deposition than nearby dunes sheets. In fact, because they lie in a moist hydrological zone below the top of the influence of the shallow watertable, sheets of continental eolian sabkha tend to have much higher preservation

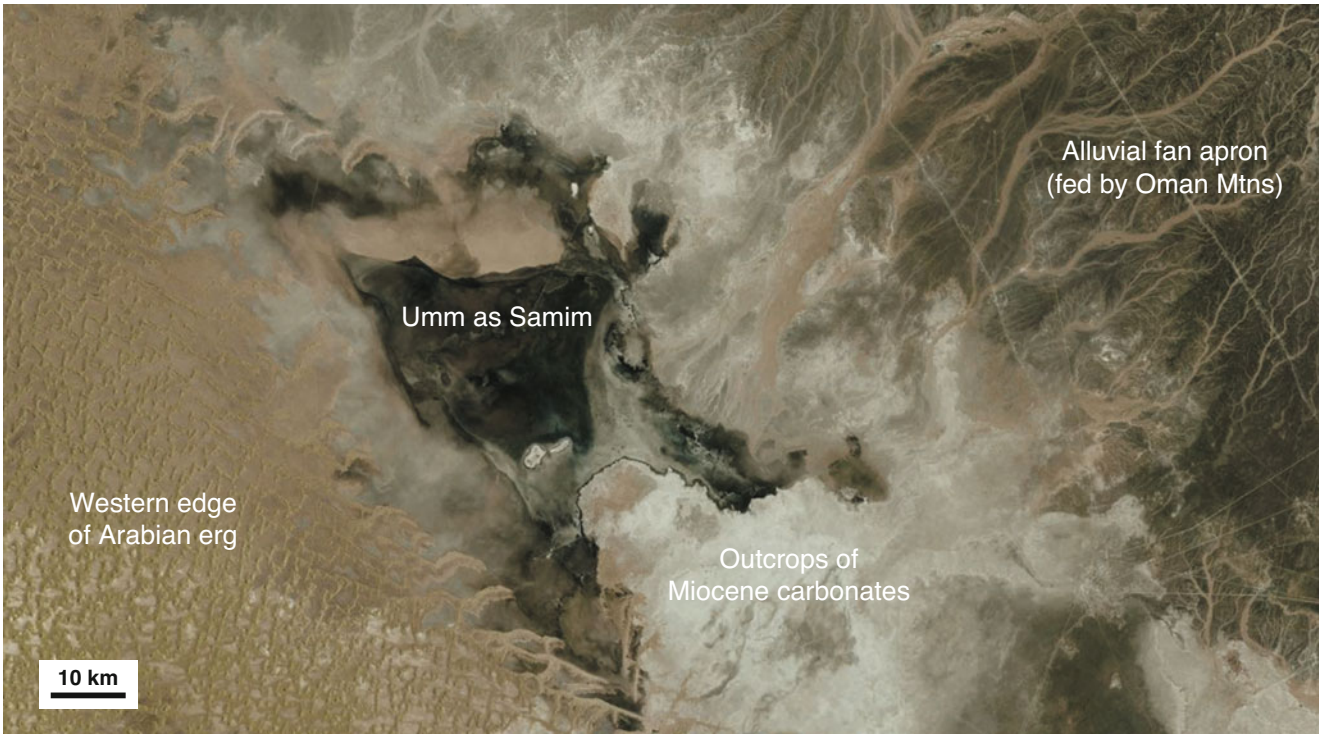

Fig. 3.66 Umm as Samim, occurs in a groundwater sump at the hydrological interface between the alluvial fans of the Oman Mountains to the east and the Arabian Erg to the west. Bing® image mounted and scaled in MapInfo

potential than most of the crossbedded sands of the dunes. The latter sit above the watertable and so have a tendency to blow on through (Fig. 2.62f). Eolian sabkha sheets lie beneath exposed surfaces with high rates of sand cross-drift, a direct result of their saline watertable-induced flat topography and lack of vegetation. That is, in sump regions of shallow desert groundwater the flat bedded eolian sabkha sheets with characteristic capillary salts and Stokes surfaces are preserved more often than cross-bedded eolian sand, which by definition is deposited in a vadose environment and subject to ongoing deflation.

Depending on grain size of sediment in the capillary zone and the time of the year, the surface of a modern eolian sabkha sheet can lie up to a metre above the regional watertable in the driest times of the year. Fluctuations in the regional watertable in ergs can lead to the deflation of gypsiferous inter-draa sabkha and the creation of an eolian gypsum component to the dunes. This is the case in the near coastal region of Saudi Arabia where deflation has formed gypsum lunettes along the deflated pan margin of the gypsum encrusted Sabkhat ad Danan (Fig. 3.16b; Barth and Böer 2002). Similar long term deflation of saline mudflats led to the downwind formation of extensive quartz dune fields as in the Late Pleistocene Chott Rharsa Basin of Tunisia (Blum et al. 1998) and to the growth of Holocene gypsum dunes along the edge of Lake Lucero in White Sands, New Mexico (Langford 2003).

Continental eolian sabkha surfaces can be accretional or deflational, depending on the availability of sand, subsidence rate and whether the watertable is rising or falling. Deflationary eolian sabkhas typically leave behind little more than an evaporite-cemented Stokes surface and so have little preservation potential. Modern deflationary sabkhas are commonplace occurrences at the arid endorheic ends of large areas of monsoon-fed fluvial drainages, as in the Kallakoopah interdunal sabkhas and pans north of Lake Eyre and Lake Frome. Both are examples of the ephemeral stream-dune field-ephemeral saline lake association, discussed earlier in this chapter.

Accretionary eolian sabkha sheets have higher preservation potential and tend to characterise areas where eolian and alluvial sediment is piling up within rising artesian saline groundwater and surface water outflow zones. Such conditions are typically found at the foot of mountain ranges with sands piling up at the base of the fan or in arid continental regions characterised by subsidence (alluvial fan-ephemeral saline lake association). This is the case at Umm as Samim ("Mother of Worries") sabkha in Oman, which is fed sediment from dunes to the west alluvium from the Oman Mountains to the east and groundwater from the limestone aquifers of the Tertiary Umm Er Radhuma Formation to the east and south (Fig. 3.66).

At around 3,000 km^2 in area (55 m elevation, BWh) Umm as Samim is one of the largest sabkhas on the Arabian

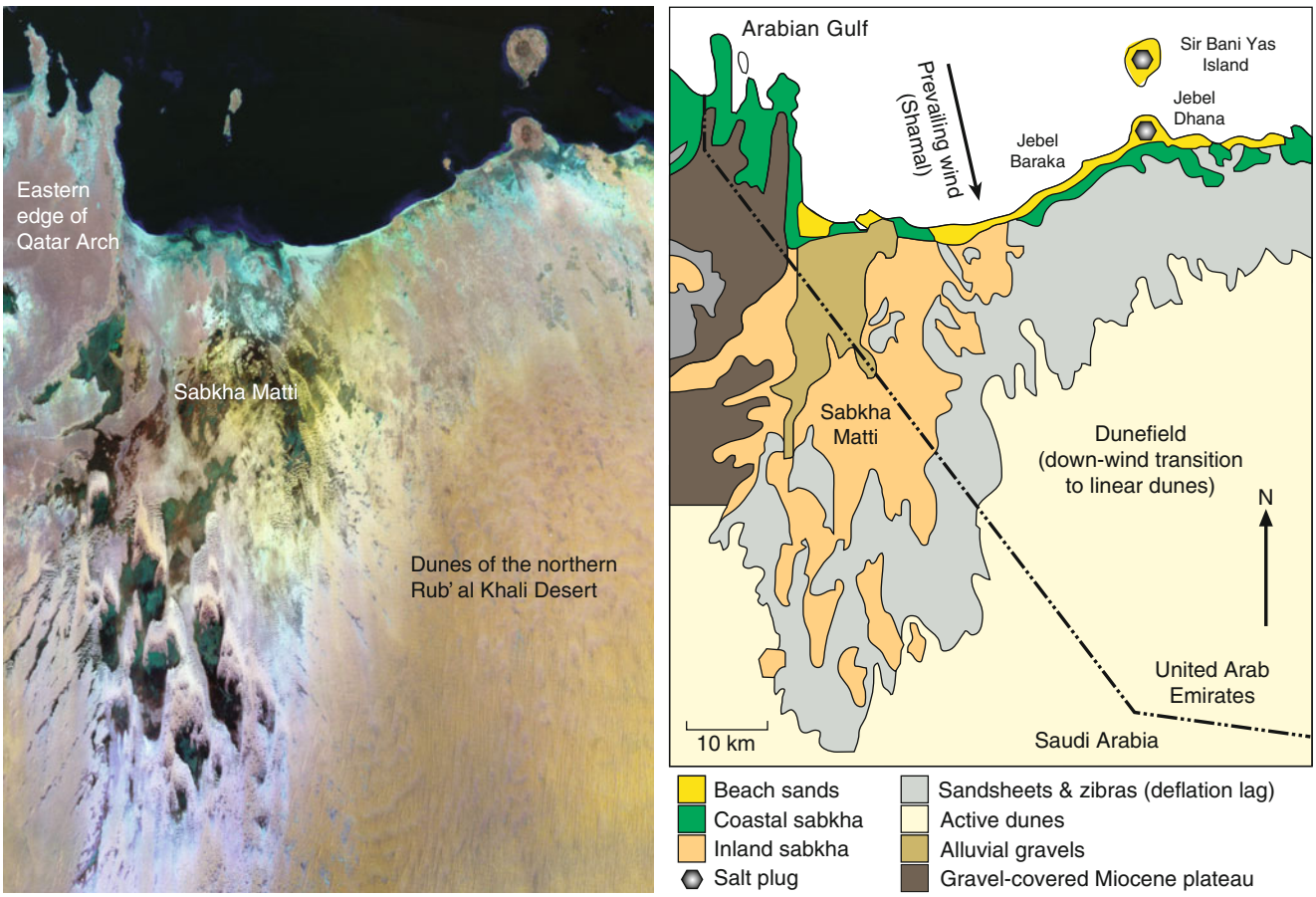

Fig. 3.67 Sedimentary facies in Sabkha Matti, and inland sabkha in the southern central Arabian Gulf (in part after Alsharhan and Kendall 2003; Landsat image courtesy of NASA)

Peninsula. It forms a groundwater sump along the boundary the eastern edge of the Arabian erg and the alluvial fans to the east, with many widyan draining from Al Hajar (Oman Mountains). Wadi Aswad, Wadi Musallim, Wadi Majhul, Wadi Umayri and Wadi Haliban all periodiaclly feed the Umm as Samim sump. Units hosting Holocene capillary salts are typically less than a few metres thick. Today, the water source is dominated by alluvial seeps, but prior to 6,000 years ago it was a much less saline hydrology (Heathcote and King 1998). Then the sump was a perennial lake. The initial closed sabkha depression or playa formed via deflation in the gypsiferous 'Fars Group' sometime prior to 30 ka BP. During the Late Pleistocene, from 30 to 20 ka, this closed depression became a saline lake, and fluvial flow brought in detrital silt and clay. A drier climate prevailed from 20 to 15 ka and the lake changed to a sabkha. Wetter conditions returned towards the end of the Pleistocene, from 15 to 12 ka, and a perennial saline lake was re-established, whereby halite was dissolved but gypsum still remained. In the interval from 12 to 9 ka, sabkha conditions were again established with deposition of displacive gypsum and minor halite in a sandy matrix. During the Early Holocene wet phase, from 10 to 5.5 ka, a saline lake formed again, only to terminate in the arid capillary gypsum/halite conditions from 5.5 ka to the present-day (Heathcote and King 1998).

Likewise, in the region of subsidence that defines Sabkha Matti groundwater sump, capillary salts (gypsum and halite) are growing in inland sabkha zones where shallow water-tables occur across large expanses hosted within deflationary eolian sand sheets (Fig. 3.67; Goodall et al. 2000). Coast-parallel supratidal salt flats of the marine margin sabkha grade southwards into inland flats of the continental eolian sabkha of Sabkha Matti with no distinct break in surface topography. The inland sabkha (BWh), with an area of 2,950 km^2, extends southwards for about 150 km and, in this distance, the land surface rarely rises more than 40–60 m above sea level (Fig. 3.67). There is little information available on rainfall for the inland areas of Sabkhat Matti, but measurements taken on the coast show that average annual rainfall is less than 40 mm and further inland it is less.

Like the Rann of Kutch, Sabkha Matti occupies a former fluvial valley that in the Miocene was a fresh water river system. Goodall (1995) reported OSL/TL ages of 5.9 ± 0.5 and ≈ 208 ka on aeolian sands, and 40 ± 2.7 and 147 ± 12 ka

on fluvial sands that host the sabkha salts of Sabkhat Matti. Today the region of saline mudflats is a groundwater sump to the Qatar Arch and defines the margin to a modern accretionary eolian sabkha sheet and so is adjacent to a set of dry mudflats and sand sheets. This in turn passes downwind into an active sand sea (Rub Al Khali portion of the Arabian Erg) that is ultimately piling up sand at the foot of the Oman Mountains (Fig. 3.63).

Evaporation of occasional ephemeral brine sheets forms and reforms the salt crust, which for most of the year covers large areas of Sabkha Matti. Somewhat thicker salt crusts (1 ± 5 cm), with large megapolygonal pressure ridges characterise the Sabkha Matti surface situated within 5–10 km of the modern coast. Further inland the Sabkha Matti surface is characterised by thinner salt crusts (≈1 cm) and smaller, lower-relief, pressure ridges, along with more numerous blisters and petees interacting with windblown sediments to form characteristic haloturbated structures (Fig. 1.46a; Fryberger et al. 1979; Goodall et al. 2000).

The surface of the sabkha-hosting sand sheet of Sabkha Matti is planed by wind action (Stokes surface). Internally the eolian sabkha sheet consists mostly of low-angle eolian stratification (cm-scale laminae) created by migrating ripples and grainfall that can be altered by ongoing haloturbation. Quartz sand fills the saucers between eroded salt ridges and locally gives the Sabkha Matti surface a "leopard-skin" appearance (Goodall et al. 2000).

This "leopard-skin" terrain is most obvious in the landward sabkha region behind the coastal sabkha. Its slightly reddened appearance is emphasised by a characteristic hummock and hollow relief of up to 1 m (Kirkham 2011). Within 50 cm of the surface, hummocks are typically underlain by concentrations of fibrous halite, gypsum and palygorskite. In some areas selenitic and fibrous gypsum veins protrude onto and crosscut the leopard skin surface. Near the centre of the larger depressions on Sabkha Matti there are artesian gypsum mounds (aka gypsum volcanoes) made up of concentric gypsum cones, some 50–80 cm across, typically with hollow cores to the centripetally aligned crystal rims They are likely artesian features and texturally near-identical to modern gypsum spring mounds that typify the early Holocene margins of the Dallol Depression (pers. obs; Chap. 11).

The end result of ongoing wetting and drying in the sandsheet host is a highly disturbed sheet-like body of sediment entraining a variety of distinctive sedimentary fabrics. Formative processes range across salt-growth sediment deformation, salt-solution sediment collapse, sediment aggradation and compound mixtures of these processes. Salt-crust processes also produce features that may be confused with eolian adhesion structures (Goodall et al. 2000).

Elsewhere in Saudi Arabia, modern accretionary sabkha sheets define groundwater sumps adjacent to zones where eolian dune sediment is accumulating. As in Sabkha Matti and Umm as Samim, these regions tend to be located near zones of alluvial sediment supply (reworked fluvio-lacustrine sediment) and regions where shallow groundwaters abut actively encroaching sand seas, often in association with ephemeral river breakout through the dunes. Unlike Umm as Samim and Sabkha Matti the much smaller Sabkhat Umm Ash Shuraybat (75 km^2; BWh), an hour's drive southwest of Dammam in Saudi Arabia is one of the more accessible areas to study capillary processes in action in dune flats and accretionary eolian sabkhat located at the edge of a sand sea. It defines a zone of aggrading sabkha sedimentation subject to occasional floodwater ponding adjacent to a sand sea and like Samim and Matti it was a region of fresher water ponding in the Late Pleistocene and early Holocene (Figs. 3.16a and 3.68a).

The dunes fields are still active and form a cover to the aggrading outflow zone of a regional artesian aquifer. The dunes also store waters from rare periods of heavy rainfall. Because of this, the watertable intersects the edges of some dunes where oases form. Oases define areas where local fresher water seeps support a halophyte fringe and with evaporation also precipitate the salts of the adjacent sabkha sheet. Spring mounds, cyanobacterial blisters and petees dominate in the seepage zones immediately downstream from the outcropping watertables that define the edge of the dunes (Fig. 3.68b). In places the seepage waters are fresh enough to support a flourishing biota of ostracods and brine shrimp (pers. obs.). Away from the seepage zone the accretionary eolian mudflats (a combination of desert loess and fluvially-supplied sediment) host displacive capillary gypsum, identical in morphology to that described for the coastal sabkhas of Saudi Arabia. Further down the fractionation trend in Sabkhat Umm Ash Shuraybat, the saline waters pond in the lower parts of the depression and have precipitated stacks of saline pan halite crust (Fig. 3.68c). The resulting halite beds are up to 4 m thick and layered at the decametre scale by thin laminae and partings of clay and anhydrite (Collenette and Grainger 1994).

In addition to its currently active eolian sabkha/pan the Umm Ash Shuraybat area preserves evidence of a late Pleistocene-early Holocene river, which flowed into the Gulf but is now largely covered by dunes. Ephemeral streams, which follow remnants of this old channel, still flow into the dunes as periodically water-filled channels before being dammed by the dunes. Ponded water is then lost to the dunes via seepage. Historically, there is no record of the main stream channel breaking through the dunes to the coast in this region, although the satellite imagery suggests this may have happened sometime in the last few thousand years.

Better documented examples of catastrophic breakout of flooded rivers through an erg to the sea can be seen in

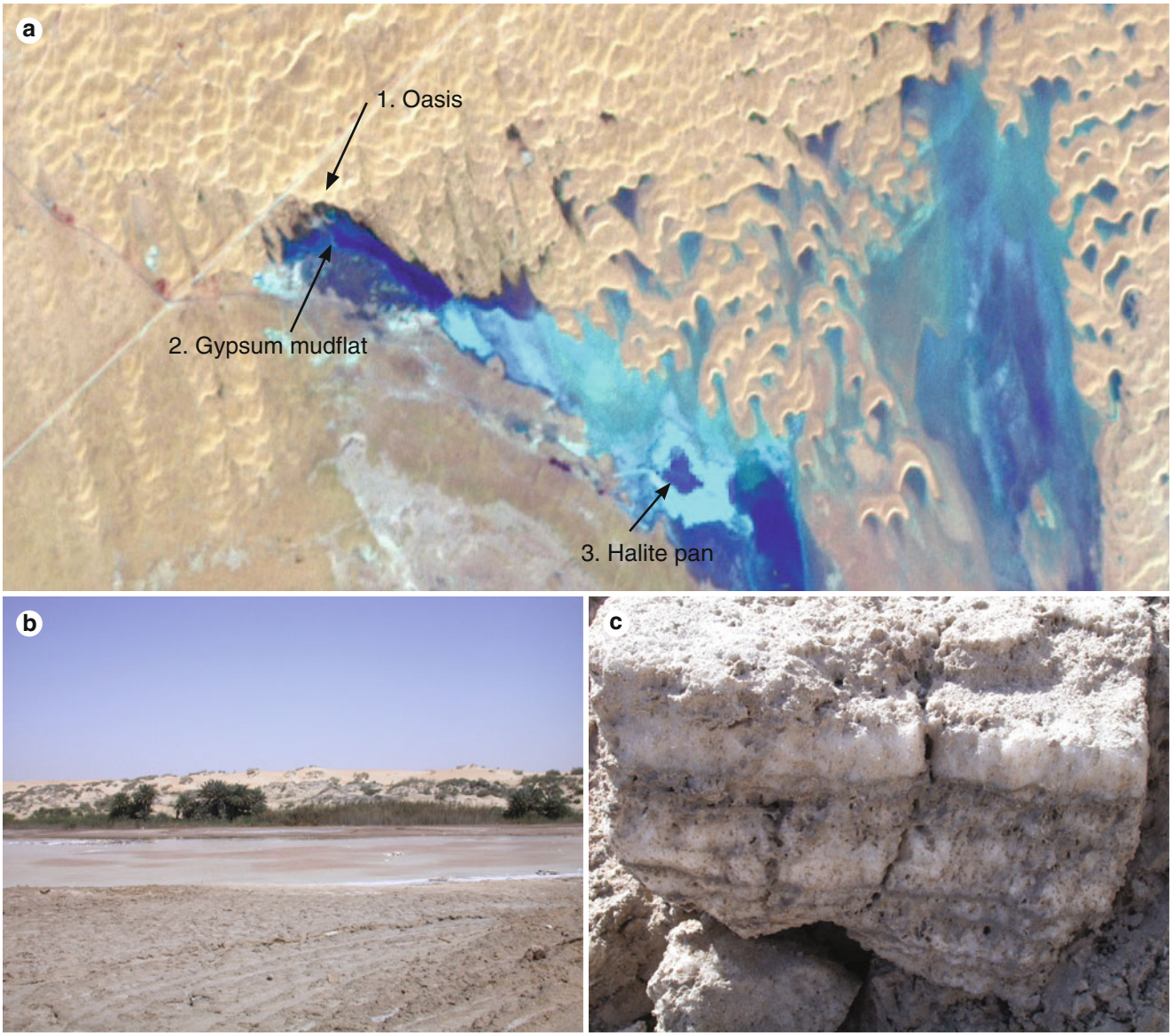

Fig. 3.68 Sabkhat Umm Ash Shurabyat, Saudi Arabia (Fig. 3.16a for location). (**a**) General location of the sabkha at the edge of the dune field clearly shows the position of the intersection between landscape and dune watertable at position 1 where fresh to brackish phreatic water held in the erg seeps into the sand flat margin to create an oasis (position 1 as seen in Fig. 3.67b). (**b**) View from puffy ground atop gypsum mudflat (eolian sabkha) and looking north toward oasis at the edge of the sand sea. (**c**) Stacked saline pan halite facies with eolian silt laminae. Sample was extracted from position 3, each pan halite layer is between 5 and 10 cm thick

Namibian ergs of the Skeleton Coast of southwest Africa (Svendsen et al. 2003). Evidence of periodic flooding, ponding and occasional breakout of a stream channel into any dune field is a number of clayey fluvial lenses in the interdunal corridors, which then act as a host for capillary sabkha salts. Such elongate or interdunal geometries fed by streams and deposited in corridors dominated by interdunal fluvial and carbonate marls (pedogenic), have been documented in the Permian sandstones of Utah and Colorado (Driese 1985) and in Tertiary "oases" in the Namibian desert (Smith and Mason 1998).

It seems that some ancient counterparts of continental eolian sabkha sheets are preserved in regions where little or no crossbedded dune sand is preserved; these sheets do not show the elongate interdunal geometries that much of the literature seems to require for an eolian sabkha interpretation. Rather, they possess a sheet geometry associated with capillary evaporite-cemented and haloturbated muddy sands accumulating in large erosionally-capped flatlands (Figs. 2.62f and 3.65a). Their sheet-like distribution is the sedimentary response to their watertable-capillary zone origins. Such sheet-like eolian sabkha systems typify the flat-topped depo-

sitional geometries of the Permian Yates Formation reservoir sands of west Texas and portions of the reservoir sands of the Rotliegende Formation in the northern Netherlands (Chap. 10). It is also the case for muddy sand sheets in parts of the Lower Triassic Sherwood Sandstone Group of offshore NW England (Cowan 1993; Herries and Cowan 1997) and parts of the Lower Permian Rotliegende Group in the North Sea (Goodall 1995). In the North Sea examples, which are offshore reservoirs for gas, the change in understanding of the origin of these facies from fluvial shoestrings to haloturbated sand sheets has had profound implications in planning for the exploitation of the entrapped gas.

This is not to say all evaporite-cemented intervals in eolian reservoir sands beneath an evaporite seal are preserved eolian sabkha caps. But sabkhas will be a commonplace signature of the transition from a completely isolated continental basin into the outcropping hydrology required for widespread evaporite deposition. The limited fetch of hydrographically isolated evaporite seaways, the widespread capillary cementation in the strandzone and across the basin at the onset of evaporite accumulation, along with the consequent low energy of the transgressing hypersaline water edge, will tend to better preserve dune topography. There will be less high energy coastal reworking of sediment compared to a marine transgression into a sand sea (Fig. 3.65b). Excellent examples are preserved in the transition from the Rotliegende-Weissliegend into Zechstein evaporites in the Permian Basin of NW Europe and in the transition from the Jurassic Entrada into the Todilto evaporites in the San Juan basin of the USA.

In summary, eolian sabkhas are a response to areas of shallow subcropping watertables within or about the edges of continental sand seas (ergs). The matrix for the displacive evaporite growth comes from the sediments of the dunes blown onto the areas of shallow subcropping watertable, or is supplied by fluvial processes periodically cutting through a sand sea. In many cases the geometry of the eolian sabkha is not an elongate shoestring or interdunal trend. Rather the capillary salts accumulate in areas of shallow watertable in aggrading sand/mud sheets. Thus, in the rock record, narrow (1–2 km) elongate interdunal eolian sabkha trends have much lower preservation potential than areas of capillary cementation in eolian sand sheets (>5–10 km wide) accumulating in regions of rising watertables (Chap. 2). A rising watertable can be driven by subsidence, changing climate, or by a rise in the regional hydrological base level driven by sea level rise. In these situations the eolian sabkha is more likely to be deposited as the evaporite-cemented portions of a sand sheet with textures dominated by adhesion ripples and haloturbation rather than by preserved salts. High watertables and high salinities in "wet" or chemically-dominant sabkhas can induce widespread early cementation, which through its retention or dissolution may control lateral variations reservoir quality in ancient counterparts. Episodes of deflation during the aggradation of the eolian sabkha are indicated by "Stokes surfaces," which are often preserved in ancient eolian counterparts (Newell 2001).

Salt-Pans (Marshes) and Diapirs

So far, we have discussed the various pans and sabkhas in a hydrologic framework of endorheic depressions, with the topography doing little more than supply the gradient to an arid groundwater and crating the hydrographic sump. But there are also a few modern deserts where the drainage topography is not passive, rather it is salt-cored and replenished by halokinesis even as the diapiric salt is simultaneously recycled into salt encrusted depressions. Earlier in this chapter in the various South American salars, such as Salar de Uyuni and Salar de Atacama we saw a more passive mode of diapiric supply whereby ions derived from the dissolution of at-surface diapirs supplied significant volumes of ions (along with weathered acid volcanics), to the groundwater as it seeped into saline sumps floored by hardrock basement. But in parts of the Iranian interior, centred on the Kavir and Lut deserts located north of the Zagros Mountains and south of the Alborz Mountains, the role of the diapirs in controlling the drainage and groundwater network is much more active. There the diapirs and their namakiers create the landscape, the drainage patterns and supply ions to various suprasalt groundwater sumps so that recycled diapiric salt (Miocene) accumulates in salt-rich Quaternary playas atop suprasalt rim synclines (Fig. 3.69).

The region is known as the Dasht-e Kavir or great salt desert; it is some 800 km long and 320 km wide, located southeast of the Alborz Mountains in north central Iran. It is a huge saline desert basin with endorheic drainage and named after the large kavirs (salt marshes) that characterise salt-floored depressions in the landscape. The Kavir Buzurg (Great Kavir), some 320 km long and 60 km wide, constitutes the lowest part of the desert depression. It lies in a rain-shadow desert that is almost rainless. Strong surface evaporation in the salt marshes and wet saline mudflats in the lower regions of the kavir sump precipitates stacked crusts of pan and capillary salt with a high proportion of the ions in the crusts coming from the dissolution of nearby diapir crest. The ease of breaking through the surface salt crusts into hot dark saline mush beneath makes travel across the kavirs quite dangerous. The kavir's aridity and hostility means it is almost uninhabited and only partly explored; human settlement is largely restricted to the hills and mountains surrounding the kavir. Extending south from the Dasht-e Kavir is the Dasht-e Lut, which is a more typical sand and stone desert, some 480 km long and 320 km wide. It is dominated by dry mudflats and sandflats with extensive sand dunes and

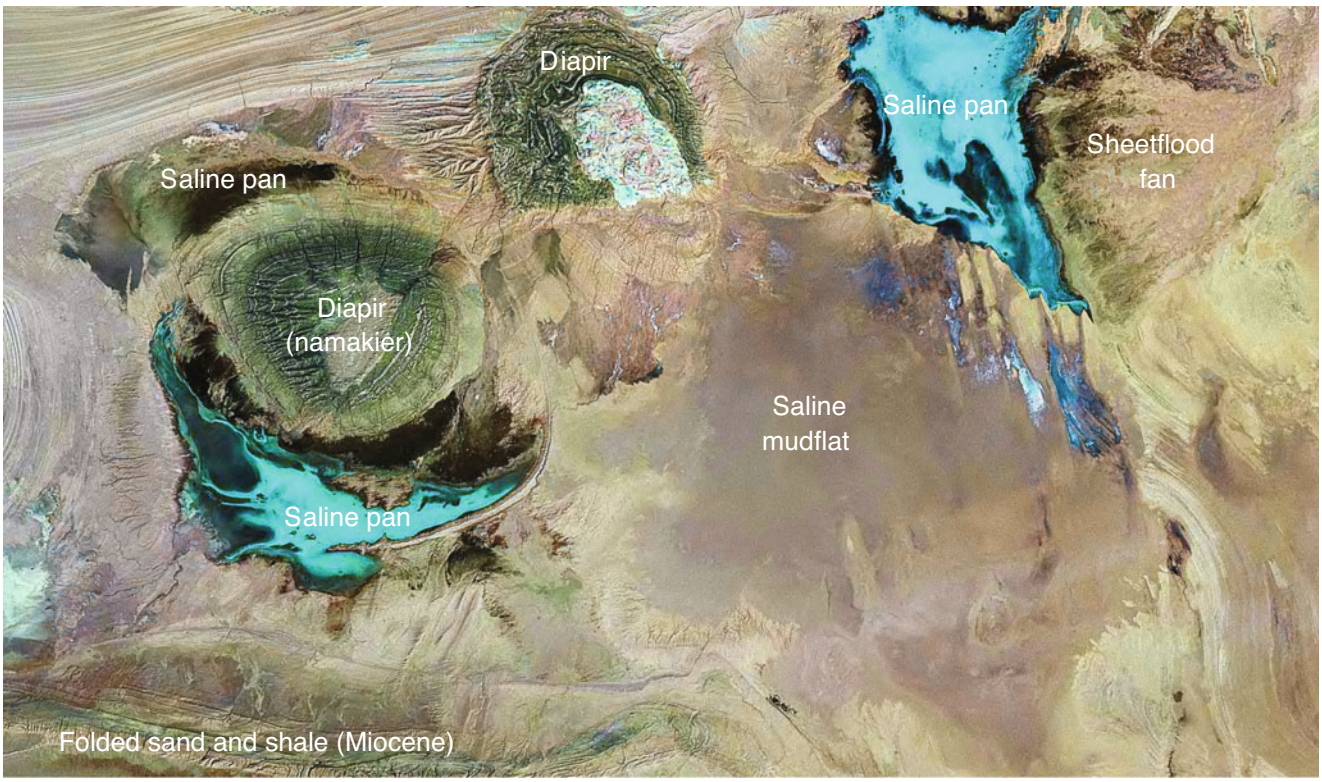

Fig. 3.69 Diapirs composed of Miocene salt pierce the surface of the Great Kavir, Central Plateau of Iran (see also Fig. 6.13). Salt is dissolved from the diapir crest and redeposited in a saline pan facies in the rim synclines created by salt withdrawal adjacent to the diapir crest. (Diapir on the left is diapir No 10 in Jackson et al. 1990; Image courtesy of NASA)

deflationary lag plains. Together the two deserts occupy most of the central Iranian plateau.

Salt in the various active diapirs that have surfaced in the Kavir plateau of Iran is much younger (Lower Oligocene-Miocene) than the Hormuz namakiers of SE Iran (Figs. 6.90 and 6.91). This part of North Central Iran is undergoing north–south shortening between the Alborz mountains in the north and the Zagros mountains in the south (Talbot and Aftabi 2004). Diapirs tend to emerge along releasing bends that have been pulled apart along major dextral transpressive faults in the central plateau of Iran. These structures include the small but mature salt fountain of Kuh-e-namak (mountain of salt in Farsi) near the holy city of Qum. This is probably the salt mountain best known to most Iranians because it dominates the western skyline of Qum, the religious capital of Iran some 140 km SSW of Tehran. It is probably the best described namakier and brief descriptions of Qum Kuh are given in Gansser (1957), Richter-Bernberg (1980), Aghashahi and Zomorodian (1981) and Jackson et al. (1990), with a more detailed analysis by Talbot and Aftabi (2004). Qum Kuh is of economic interest as centimetre to decimetre thick beds of sylvinite (KCl ± NaCl) are interbedded with the halite and repeated by folds in the extrusion.

The shapes of these extrusions of Tertiary salt indicate that they have followed a history similar to that of extrusions of the older Hormuz salt in the Zagros (Fig. 6.87). Gansser (1957) and Jackson et al. (1990) noted that salt deformation in the central Iranian Plateau involves two Tertiary-age salt sequences: a clean white salt at the base of the ductile marls and shales of the Lower Oligocene Lower Red Fm, and a rhythmic sequence of multicoloured salt at the base of the salty marls of the Lower Miocene Upper Red Fm. These two salt sequences are generally separated by limestones of the Qum Formation, which according to Talbot and Aftabi (2004) tend not to surface in emergent salt structures.

Influence of the diapir-induced topography is clearly seen in the position of the various modern saline pan facies, which tend to stack in the lows atop secondary rim synclines adjacent to outcropping salt ridges of the diapir high (Fig. 3.69). The dissolution of this Miocene salt supplies most to the salt accumulating in the depressions. Further away from the diapir crest is the saline mudflat interval, which tend to dominate atop turtle-structure anticlines. Based on the Landsat imagery this mudflat succession is topographically higher than the sump of the saline pan floor, arguing that the zone of maximum salt withdrawal (indicated by maximum subsidence at the landsurface) has migrated progressively closer to the stem from the position of the original primary rim syncline (see Chap. 6 for a discussion of topography associated with diapirs and turtles).

Although as yet poorly documented, the sedimentology of this diapir-cored landscapes offers an excellent modern analogue for syndepositional responses to halokinetic highs such as those that once characterise the salt beds of the Triassic Kueper Fm. in Germany and the Cretaceous Maha Sarakham Fm. of Thailand. (Mohr et al. 2004; Warren 2000c, 2008).

Why and Where of Sabkhas & Pans?

Now that the detail of depositional variability of sabkhas and saline pans has been outlined using documented Quaternary examples, it is useful to go back to examples given in Table 3.1 and Fig. 3.1 and place them in a broad geographic, climatic and latitudinal framework. Figure 3.70a, b plot all the listed examples as climate-coded crossplots of area versus elevation and area versus latitude. Plots of documented sabkhas in their climatic framework lead to the following general conclusions at the world scale.

1. Latitudes tied to Hadley atmospheric cell (15–40°) encompass all of the larger Quaternary sabkhas and pans.
2. Most documented sabkhas, located in BWh climate zones (hot arid deserts), are situated near or below sealevel, including the Rann of Kutch (the largest example). The next most common sabkha climatic grouping is the BWk grouping (hot arid steppe) encompassing a range of areas and elevations
3. With the exception of Tuz Golu in Turkey, all of the sabkhas and pans with areas of more than 200 km are located in hot arid deserts. That is, sabkhas and pans located in desert steppe and Mediterranean climates tend to be smaller.

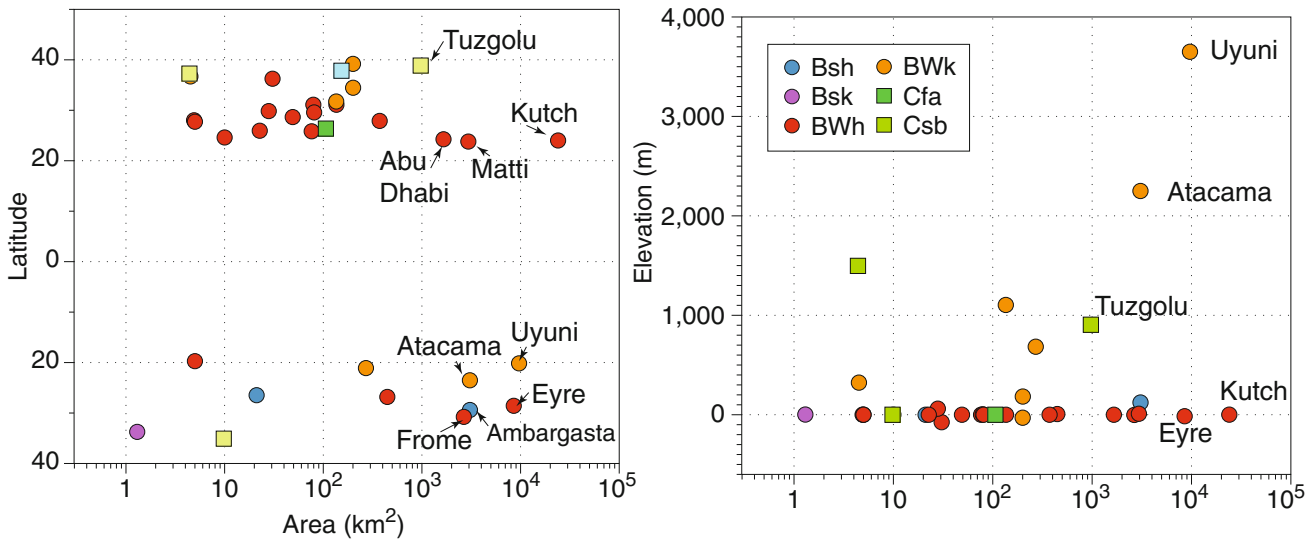

Fig. 3.70 Worldwide compilation of selected sabkhas and saline pans using all examples listed in Table 3.1 and discussed in this chapter. (**a**) Area versus deposit latitude. (**b**) Area versus deposit elevation

Subaqueous Salts: Salinas and Perennial Lakes

4

Introduction

Ancient shoalwater platform (saltern) and deepwater (slope and basin) evaporites are dominantly subaqueous precipitates, and, as for the mudflats and pan settings discussed in the previous chapter, when we seek equivalence in the Quaternary record we find our marine-fed choices are limited both in number and scale (Fig. 4.1; Table 4.1). If we consider all nonmarine and marine saline perennial water masses in modern systems as suitable for discussion in this chapter then, as well examples of larger saline perennial lakes, such as Great Salt Lake and Lake Urmia, we must include the feeder-edge brine pools to some larger saline pans and lakes, such as pools or moat facies to lakes Magadi and Natron, and some centripetal depressions to the Turkish lakes such as in Acigolu. In Chap. 12 subaqueous cryogenic continental examples discussed include Karabogazgol and various mirabilite lakes on the Canadian plains. I also arbitrarily split out of this chapter some examples of the larger continental saline pans with feeder pools. This latter group, including most of the South American salars, were discussed in the preceding chapter. Following a similar reasoning, if the bulk of the Holocene column in a lake is dominated by subaqueous textures, then I include it in this chapter, even though Holocene aggradation has moved uppermost part of the Holocene column into a sabkha setting, as in many modern gypsum-filled coastal salinas in southern and western Australia.

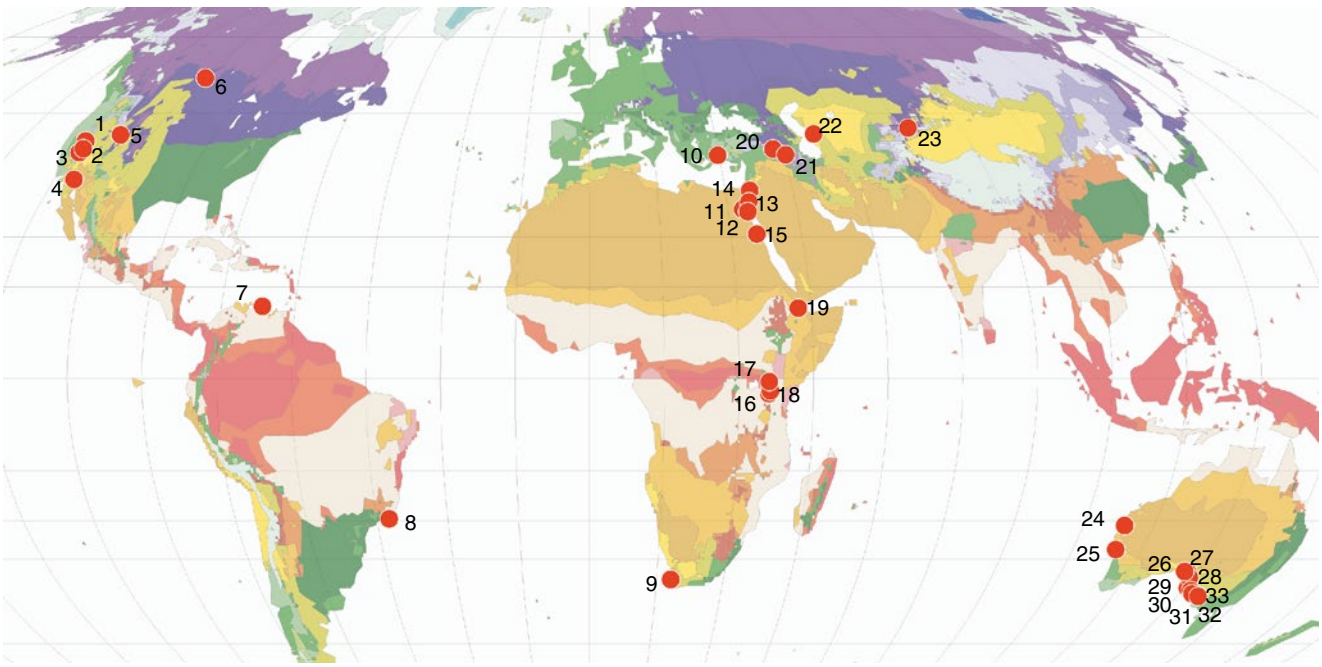

Fig. 4.1 World distribution of selected Quaternary subaqueous evaporite settings. Location index numbers and site detail listed in Table 4.1. Plot is overlain on a Köppen climate base – see Fig. 2.3 for explanation of Köppen legend. (Extracted with permission from SaltWork® database version 1.6)

© Springer International Publishing Switzerland 2016

J.K. Warren, *Evaporites: A Geological Compendium*, DOI 10.1007/978-3-319-13512-0_4

Table 4.1 World distribution of selected Holocene subaqueous settings, see Fig. 4.1 for geographic plot

Index	Location	Dominant hydrology	Köppen	Area (km^2)	Elevation	Water depth (m)	Dominant matrix
1	Pyramid lake	Continental lacustrine	Csa	313	1,161	103.0	Carbonate (calcite ikaite)
2	Mono Lake, California	Continental lacustrine	Csb	212	1,955	45.7	Carbonate (calcite ikaite)
3	Walker Lake	Continental lacustrine	BSk	165.5	1,339	33.0	Carbonate (calcite ikaite)
4	Salton Sea	Continental lacustrine	BWh	929	−74	12.0	Clastic
5	Great Salt Lake, Utah	Continental lacustrine	Cfa	4,998	1,280	10.0	Carbonate (aragonite)
6	Big Quill Lake	Continental lacustrine	Dfb	236.8	517	2.6	Mirabilite
7	Laguna Pirata, Los Roque archipelago	Coastal salina	Aw	0.4	0	1.0	Carbonate
8	Lagoa Vermelha, Brazil	Coastal salina	Aw	1.8	2	1.0	Carbonate (dolomite)
9	Yzerfontein and nearby coastal pans	Coastal salina	Csb	1.3	1	0.5	Carbonate (dolomite)
10	Salda Golu, Turkey	Continental lacustrine	Csa	44.1	945	196.0	Carbonate (hydromagnesite)
11	Ras Shukheir, Gulf of Elat	Coastal salina	BWh	24	0	0.5	Gypsum
12	Ras Muhammad Pool	Coastal salina	BWh	0.1	0.5	0.5	Gypsum
13	Solar Lake, Gulf of Elat	Coastal salina	BWh	0.1	0	5.0	Gypsum
14	Dead Sea, Middle East	Continental lacustrine	BSh	1,023	−415	330.0	Halite
15	Ras Banas, Red Sea coast	Coastal salina	BWh	23.6	0	0.5	Gypsum
16	Lake Natron, Tanzania	Continental lacustrine	Aw	763	583	2.0	Trona
17	Lake Nakuru	Continental lacustrine	Cfb	41.2	1,757	3.0	Carbonate
18	Lake Magadi, Kenya	Continental lacustrine	Aw	110.7	643	2.0	Trona
19	Lake Asal, Djibouti	Coastal salina	BWh	53.6	−155	60.0	Gypsum/halite
20	Lake Van	Continental lacustrine	Csa	3,539.1	1,648	550.0	Carbonate (calcite)
21	Lake Urmia, Iran	Continental lacustrine	BSk	5,014.5	1,280	16.0	Carbonate (aragonite)
22	Kara Bogaz Gol	Continental lacustrine	BSk	17,528.1	−55	3.0	Mirabilite (glauberite)
23	Issky-Kul	Continental lacustrine	BSk	6,234.7	1,619	702	Mirabilite (glauberite)
24	Lake Mcleod	Coastal salina	BWh	2,066.6	−0.6	0.5	Gypsum/halite
25	Hutt Lagoon, WA	Coastal salina	Csa	26	0	0.5	Gypsum
26	Point Fowler Lakes	Coastal salina	BSk	54.7	0	0.5	Gypsum
27	Lake Macdonnell, SA	Coastal salina	BSk	108	0	0.5	Gypsum
28	Streaky Bay Lakes	Coastal salina	Csb	25.2	1	0.5	Gypsum
29	Sleaford Mere, SA	Coastal salina	Csb	6.8	1	2.0	Carbonate (calcite)
30	Marion Lake Complex, SA	Coastal salina	Csb	3.3	−0.5	0.5	Gypsum
31	New Lake, Kangaroo Island, SA	Coastal salina	Csb	0.5	−0.3	0.5	Gypsum
32	Pellet Lake, Coorong interdunal lakes	Coastal salina	Csb	1.2	2	1.0	Carbonate (dol., arag., hydromag.)
33	South Stromatolite lake	Coastal salina	Csb	0.5	2	1.0	Carbonate (hydromag., arag.)

Index of localities in this table run from west to east in Fig. 4.1

As explained in Chap. 5, there are two main reasons for the scale dichotomy between examples of marine-fed Quaternary and ancient marine subaqueous evaporites. First, we live on an icehouse earth, characterised by climate-driven high-amplitude high-frequency changes in sea level. In marine settings this glacially-driven eustatic style forms small-scale coastal ponds and mudflats, with limited preservation potential. Widespread marine seepage-fed platform evaporites that dominate portions of the ancient record simply do not form nor could they be preserved in this hydrology. Periplatform evaporites require the hydrological stability associated with much gentler sea level fluctuations that characterises greenhouse earth climates. Second, there are no sizeable areas on the world's surface today where the appropriate combination of tectonics and climate have hydrographically isolated and desiccated whole ocean basins and so turned them into subsealevel seepage-fed marine basins (these platform and basinwide settings are discussed in Chap. 5).

What we are left with today as depositional analogs for ancient marine subaqueous systems (platform and basinwide) are transient, limited-scale sea-margin settings or somewhat larger high-relief continental saline lakes in closed intermontane basins (Table 4.1). Neither setting approaches the scale nor the subsealevel hydrographically-isolated hydrology that defines most ancient marine-fed systems. To form a permanent body of saline water in the Quaternary, with a lateral extent of more than a few tens of kilometres, with salt beds accumulating to thicknesses of more than a 50 m, today requires a high relief tectonically-active continental closed basin. It needs a landscape and a hydrology characterised by subsidence of the lake floor and the maintenance of a longterm brine or reflux plume (brine curtain) within and beneath the accumulating salt beds (Warren 2010).

Until the 1970s most subaqueous evaporite textures had been documented in ancient halite-rich basins (e.g. Dellwig 1955) and very few examples of Holocene subaqueous gypsum or halite deposition had been published. Then Holocene subaqueous gypsum was documented in sea margin settings in Baja California, the Mediterranean, Southern and Western Australia and the Middle East (von der Haar and Gorsline 1977; Aharon et al. 1977; Schreiber and Kinsman 1975; von der Borch et al. 1977; Arakel 1980). This body of work led to a new understanding of the significance of laminar and bedded textures (both sulphate and halite), so that in the last 30 years many ancient evaporites, previously interpreted as sabkhas, have been re-evaluated and found to be combinations of a number of mostly subaqueous settings. In the last 20 years we have also documented the beginnings of a partial Holocene analogue for ancient deepwater evaporites via the ongoing hydrological transformation of the Dead Sea into a halite-accumulating perennial lake. So, let us now look at some modern examples of subaqueous evaporites, first in small coastal subsealevel (sea-margin) settings then in larger Quaternary lacustrine depressions.

Sea-Margin Subaqueous Salts

Modern subaqueous evaporites are forming today in shallow marine-fed coastal lakes or salinas around the edges of the Mediterranean, the Black Sea, the Red Sea and along the southern and western coast of Australia (Fig. 4.1). All these marine-fed coastal salina systems are subsealevel depressions, all lack a permanent surface connection to the sea (hydrographically isolated) and are supplied most of their solutes via seawater seeps or coastal spray. Within the coastal salina grouping, most of the salinas accumulating carbonate minerals (dolomite, hydromagnesite, aragonite) occur in milder Mediterranean or tropical climates, while the larger deposits of gypsum and halite are found in somewhat warmer arid deserts (Table 4.1)

Coastal Salinas of Australia

Holocene salinas occupy isolated depressions within Quaternary calcareous coastal dunes along the southern and western coasts of Australia (Fig. 4.2). Most depressions are filled, or are filling, with bedded subaqueous evaporites; some are filled with evaporitic carbonates (e.g. Coorong dolomite lakes and Sleaford Mere in Southern Australia, Lakes Clifton and Haywood in southwestern Australia), while others are filled by combinations of carbonate, gypsum and halite (Marion Lake, Lake Macdonnell and Lake Macleod complexes). Solutes in all the salinas are supplied by resurging groundwaters, no salina has a surface connection to the sea if subaqueous evaporites are accumulating. Seawater seepage, plus varying amounts of meteoric water, supply coastal salinas filling with gypsum or halite, while carbonate-filled salinas are largely supplied by resurging continental groundwaters. Winter temperatures typically reach 10–20 °C and rarely fall below freezing, summer air temperatures are often in the 30°s but can climb into the 40°s. The $CaSO_4$ phase in coastal Australia is always gypsum, not anhydrite, temperatures are not high enough, nor the basins saline enough, for anhydrite to be stable. Its lack tempts one to propose that primary sedimentary anhydrite only forms as a capillary salt in hot arid mudflats (thermalites?) and never forms as a subaqueous precipitate at the sediment-brine interface in nonhydrothermal waters.

The three salina styles – carbonate versus gypsum versus halite – can be separated using annual rainfall, an indirect measure of the degree of coastal aridity. Carbonate salinas dominate in the higher rainfall parts of the southeastern coast

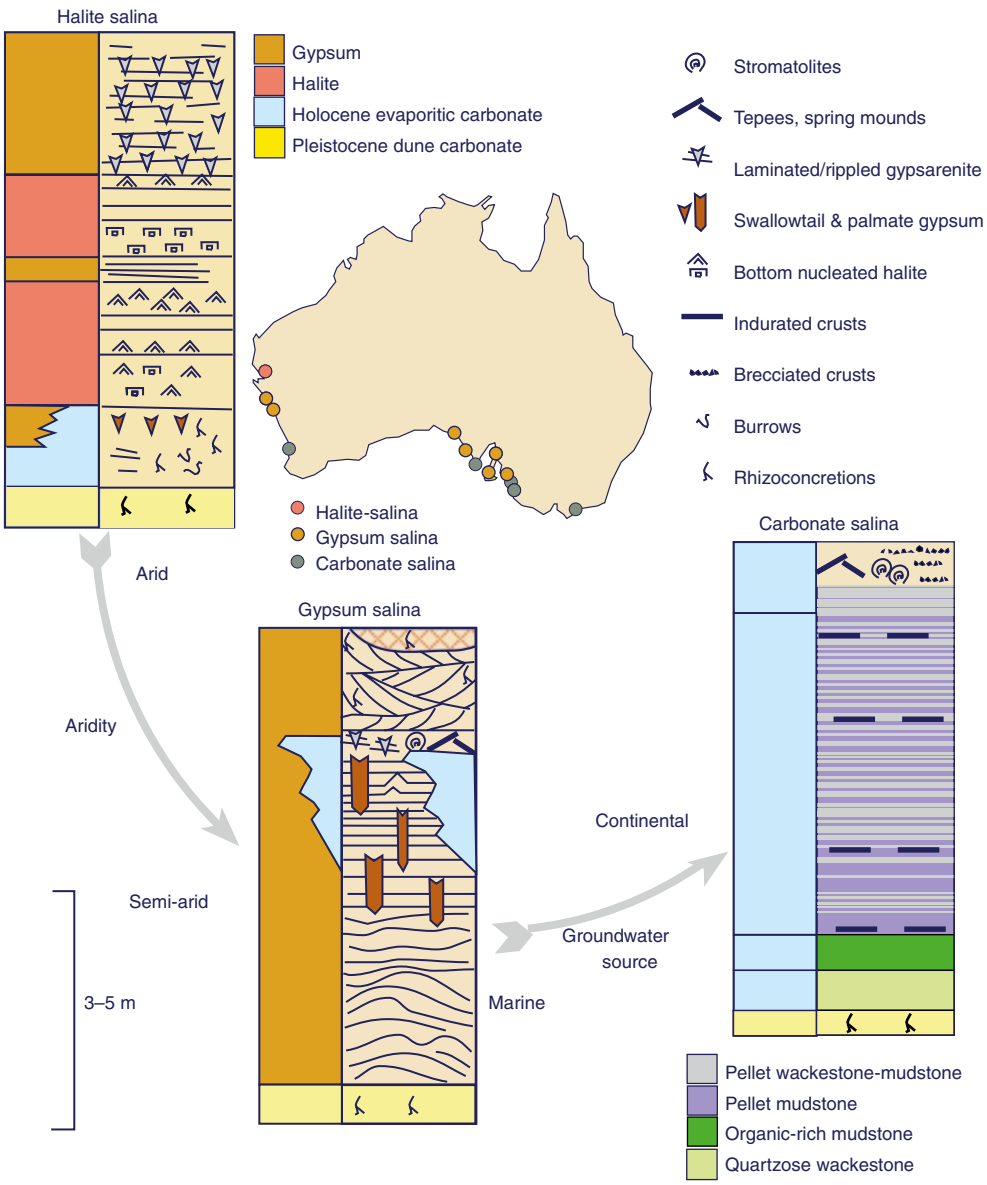

Fig. 4.2 Climatic and groundwater spectrum, textures and mineralogies in the Holocene coastal salinas of southern and western Australia (After Warren 1982a, b, 1990)

of South Australia and the southwestern coast of Western Australia, where annual rainfall is 450–800 mm. Gypsum salinas typically form best along the semi-arid southern Australian coast where annual rainfall is between 300 and 450 mm/year, while the halite-filled salinas such as Lake Macleod form in arid areas of the central western coast of Australia where annual rainfall is less than 300 mm.

Carbonate Salinas

The best documented and most voluminous carbonate fills of Holocene salinas, including some salinas filled with Holocene dolomite, are found in Pleistocene interdunal corridors behind the main Coorong lagoon in South Australia in Csb climate belts (Fig. 4.2). The modern coastal dune ridge (Younghusband Peninsula) and the adjacent Coorong Lagoon are the latest of a number of offlapping highstand beach-dune ridges and lagoons that have typified the slowly uplifting southeastern coastal zone of South Australia since the Pliocene (Fig. 4.4; Schwebel 1983; Warren 1983b). Dolomite and other lacustrine carbonates begin to form in the interdunal sumps, once the lagoons lose a hydrographic connection to the ocean.

There are numerous less well documented examples of Holocene lacustrine carbonates accumulating in coastal salinas in other parts of southern and western Australia, such as Sleaford Mere on Eyre Peninsula, and Lakes Clifton and Haywood in southwest Australia (Fig. 4.2). Actively growing calcite and aragonite tufas dominate the strandlines in these other settings, mostly as indurated reef mounds (thrombolites and tufas). Further out into the tufa-fringed salinas, where water depths can be up to 4–5 m, bottom sediments are laminated ostracodal pellet wackestones and mudstones. Bioherm shapes around the salina edge range from elongate reef terraces to isolated domal and conical mounds, some with *Conophyton*-like shapes. Individual mounds can be 2 m high and extend as reefal terraces for up to 6 km along the

Fig. 4.3 Algal tufas of Sleaford Mere, Southern Eyre Peninsula, Australia. (**a**) Tufa reef mounds define the lake strandline (kangaroo for scale). (**b**) Looking down on the cracked, knobbly and crenulated surface of indurated calcite tufa mounds (coin for scale)

Fig. 4.4 Coorong region in the area centred on the township of Salt Creek, South Australia. Part of the 120 km long barrier island, composed of carbonate sand (Younghusband Peninsula), is visible, backed by the waters of the Coorong Lagoon, which is floored by mm-laminated aragonite muds. Laminated lacustrine carbonates, including dolomites, are accumulating in lakes in isolated interdunal corridors behind the Coorong Lagoon, especially south of Salt Creek – see Fig. 4.5 (Bing® image mounted in MapInfo)

salina strandline (Fig. 4.3; Warren 1982a; Coshell et al. 1998; Konishi et al. 2001). This indurated fringe contrasts with the leathery Holocene cyanobacterial mats and hollow domes that typify most of the Coorong ephemeral lakes.

The Coorong Region was first documented as an area of modern dolomite precipitation by Mawson (1929), but was not studied in any detail until the work of Alderman and Skinner (1957), von der Borch (1965, 1976), von der Borch and Lock (1979), Rosen et al. (1988, 1989), and Warren (1988, 1990), Wacey et al. (2007). Most early work in the region concentrated on salinas that contained dolomite, but there are many salinas, probably the majority, where the fill is dominated by carbonate mineral phases other than dolomite (Warren 1990). Fills include low and high Mg-calcite, magnesite, hydromagnesite, aragonite, and less commonly gypsum (Figs. 4.4 and 4.5). Von der Borch (1976) observed that Holocene dolomite occurs in areas of the coastal plain where rainfall is less than 700 mm, encompassing the area

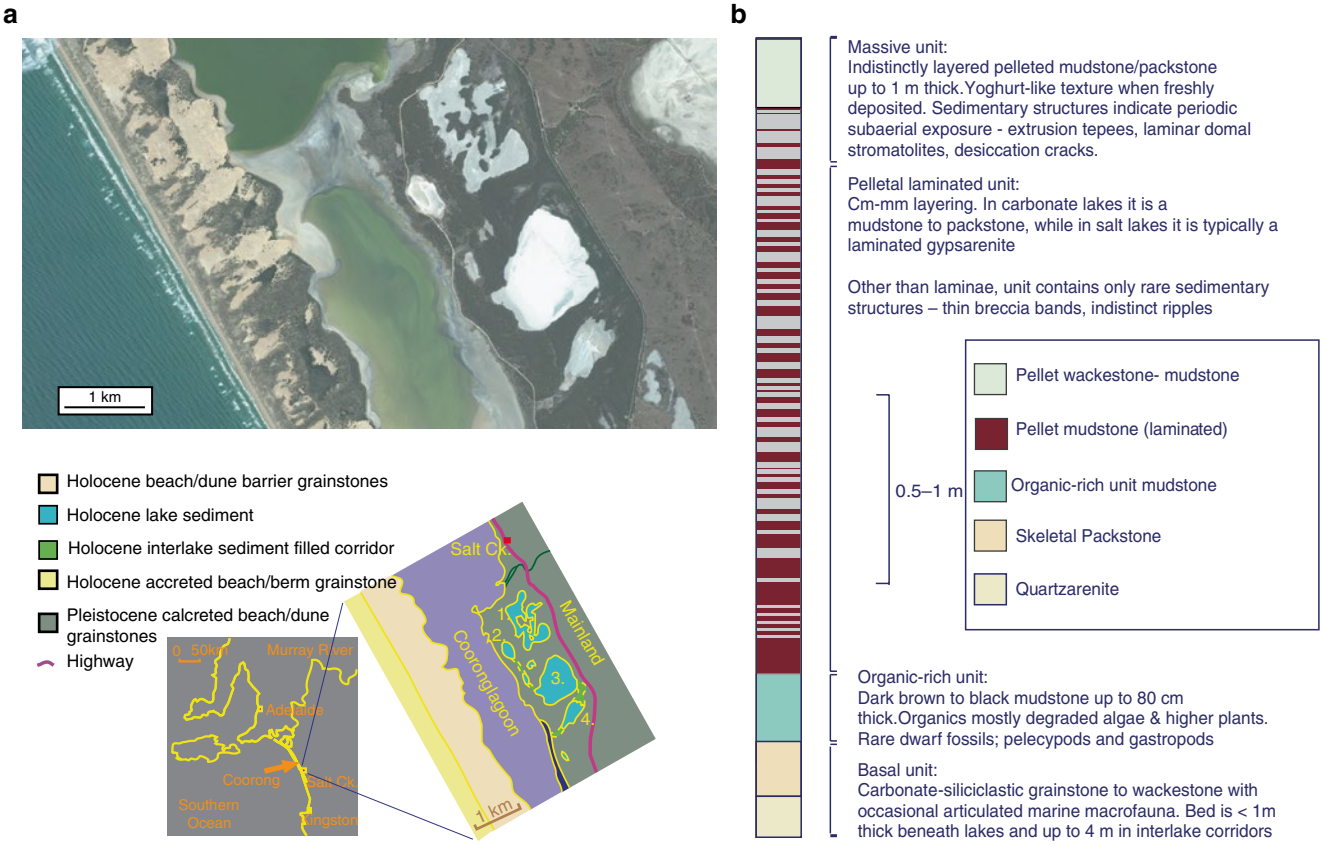

Fig. 4.5 Coorong Lakes, South Australia. (**a**) Locality and map of the Coorong region. Geological plan of the Salt Creek region shows how three of the four major lakes are joined by an interdunal corridor and were connected to the Coorong lagoon earlier in the Holocene. Milne Lake, the best dolomite accumulator in the Coorong coastal plain, never had a surface connection with the Coorong Lagoon. Mineralogies: Lake 1 = Milne Lake (dolomite + magnesite), Lake 2 = Halite Lake (gypsum + aragonite overlain by hydromagnesite + aragonite in massive unit and currently covered by ephemeral halite crust), Lake 3 = Pellet Lake (dolomite + hydromagnesite + aragonite), Lake 4 = North Stromatolite Lake (hydromagnesite + aragonite; minor dolomite in basal unit and about lake edge) (After Warren 1990). (**b**) Typical vertical sequence in Holocene evaporitic lakes of the Coorong coastal plain (After Warren 1990, 2000a)

between Kingston and Salt Creek (Fig. 4.5a). He suggested that south of the 700 mm isohyet, reduced evaporation rates and higher rainfall prevented the concentration of lake waters to salinities where dolomite could precipitate. Regional sampling of lakes across the area tied to climate confirms his postulate and shows that the more magnesian-rich dolomites tend to occur in the more arid northwestern portion of the Coorong coastal plain, centred on lakes in the vicinity of Salt Creek, while Mg-calcite and calcite filled salinas are increasingly common in the cooler moister parts to the southeast (Warren 1988, 1990). More recently, papers detailing the organic constituents of selected Coorong lakes, and their geological significance, have been published (Krull et al. 2009; McKirdy et al. 2010).

Textures in Coorong salinas and pans are largely independent of mineralogy and can be related to salinity, brine depth and permanence (Fig. 4.5b; Warren 1990, 1991). If the salina possessed an early Holocene connection to the marine waters of the Coorong Lagoon, then the lowermost Holocene unit is a marine/estuarine skeletal grainstone/packstone, similar to Holocene units flooring the more saline salinas of the Marion lake Complex and Lake Macleod. If there was no marine connection to the Coorong lagoon then the basal unit is a quartzose packstone to wackestone. These lowermost sediments can contain small percentages of diagenetic calcian dolomite (Rosen et al. 1989). Above the lowermost unit is a variably-developed massive to faintly laminated organic-rich unit. In lakes with an early marine connection the levels of total organic carbon (TOC) in this unit can be as high as 12 %, usually as an oil-prone proto-kerogen. Its formation indicates a seasonally stratified water column where fresh oxygenated water seasonally overlay stagnant marine water, during the transition from a surface connected marine estuary to a totally isolated groundwater-fed salina.

Above this is a mm-laminated unit of pelletal packstone to mudstone, deposited on the floors of perennial, but schizohaline, density-stratified brine lakes, which formed in the Salt Creek region once the estuarine connection to the open

Coorong Lagoon was cut off by beach-ridge accretion at the entrance to the chain of salinas around 6,400 years ago (Fig. 4.5a). The proportion of faecal pellets in the laminated unit is a direct reflection of energy level and organic binding on the subaqueous salina floor. In areas of higher wave energy/bottom currents and little or no algal binding, the sediment is a packstone. Such sediments are more common about the salina edge and in the shallower parts of the more central sediment fill. In areas of lower wave energy in relatively deeper water, or in areas of algal binding, the sediment is a wackestone or at times a mudstone. Muddier sediments are more common in the central parts of a salina. In a few coastal salinas with no early Holocene marine connection, such as Milne Lake, the laminated unit is dominated by magnesian dolomite in a unit up to 5 m thick (Fig. 4.5a). More typically the laminated unit in the Coorong ephemeral lake fill is composed of varying proportions of aragonite, hydromagnesite, magnesian calcite and low magnesian calcite. In one marine-seepage lake (Halite Lake), it is made up of laminated gypsum/aragonite couplets.

Capping the lake sediments is a "massive" unit of poorly layered packstone/mudstone. It is usually less than 60–80 cm thick and shows varying degrees of induration from brecciated crusts about the salina edges to domal leathery stromatolites in some of the more central water covered areas. Domal stromatolites seem to flourish in Coorong salinas filling with a mixture of hydromagnesite and aragonite (Fig. 4.6a). This, the uppermost part of the sediment fill, usually holds the bulk of the evaporative dolomite in the majority of the Coorong carbonate salinas containing dolomite, especially in the vicinity of Salt Creek. But the Massive Unit can also be composed of aragonite, hydromagnesite, magnesian calcite and magnesite. This uppermost unit in the Coorong lake fill stratigraphy contains numerous terrestrial burrows and root traces, as well as mud cracks, extrusion tepees and breccia fragments – all features indicative of at least occasional desiccation and thorough bioturbation (Figs. 4.6b).

Whatever the mineral assemblage, the dominant textural feature in the sediment column of a carbonate salina is lamination passing up section into a more massive unit with evidence of seasonal subaerial exposure of the sedimentation surfaces. Tepee-overprinted carbonate crusts are especially common in the desiccated strandzones of the lake margins (Fig. 4.6b), while domal stromatolites and cyanobacterial are common in areas of more permanent brine cover or saturation, especially in salinas precipitating hydromagnesite and aragonite. Brackish lakes, such as Lake Fellmongery, in the southeastern part of the Coorong coastal plain have well-developed algal tufa fringes, as described earlier, with some tufas first precipitated as monohydrocalcite and quickly altering to calcite. Surfaces of all the carbonate-filled salinas in the Coorong coastal zone are half a metre or more above sea level indicating the current nonmarine supply of waters (as groundwater cannot flow up hill). Some Coorong lakes had a marine seepage connection in their earlier stages of infill (e.g. Halite Lake, with a laminated unit composed of gypsum and aragonite; Fig. 4.5).

Organic content and biomarker stratigraphy in North Stromatolite Lake defines five discrete organic facies, each with a distinctive mineralogy (Fig. 4.7a; McKirdy et al. 2010). The organic-rich unit (6–12 % TOC) may be subdivided into facies 1 (Type I/II kerogen) and 2 (Type II kerogen), whereas the organically-leaner laminated and massive units are distinctly bimodal with respect to organic content, hosting both facies 3 (Type II/III kerogen) and 4 (Type III kerogen). The latter two facies together define an inverse relationship between hydrogen index and TOC content, which is a geochemical signature attributed to differences in the extent of pelletisation of carbonate muds by a diverse halotolerant fauna including brine shrimp, gastropods and ostracods during the shallowing perennial and ephemeral phases of the lake's history. One sample from the basal unit is representative of organic facies 5 (Type IV kerogen).

Aliphatic hydrocarbon distributions in these lacustrine sediments are dominated by C_{20} and C_{25} highly branched isoprenoids; and C_{12} – C_{33} n-alkanes displaying marked odd/even predominance above, and even/odd predominance below, C_{20}. This biomarker assemblage reflects the respective major contributions of bacillariophyceae (diatoms), chlorophyceae (green algae) and eubacteria (including cyanobacteria) to their preserved organic matter. Its passage through the guts of the aforementioned grazers and excretion as faecal pellets has dramatically enhanced the relative abundance of cholest-2-ene, thereby imparting to the pelletised upper sapropel, laminated and massive units a molecular signature indicative of mud ingestion and defecation.

Biomarker work across the sapropel underlines significant distinctions, not generally recognised in sedimentological studies, namely (McKirdy et al. 2010; Edwards et al. 2006): (1) Absence or presence of lamination in a fine-grained lacustrine succession does not necessarily mean that the sediment has or has not been ingested; however the absence or presence cholest-2-ene does. (2) If pellets are deposited as soft aggregations of micrite, then the pelleted texture will be quickly lost during the physical compaction associated with early burial and diagenesis, yet the organic signature of ingestion may remain. (3) In lacustrine associations, high levels of hydrogen-rich Type-1 protokerogen may have accumulated beneath relatively-shallow bottom waters (<5 m deep) that, although meromictic, were not necessarily perennially anoxic. We shall return to the discussion of organics in the Coorong lakes in Chap. 9.

Volumetrically, most salina carbonates in the various Coorong Lakes form by the evaporation of unconfined magnesium-rich continental groundwaters, driven to the

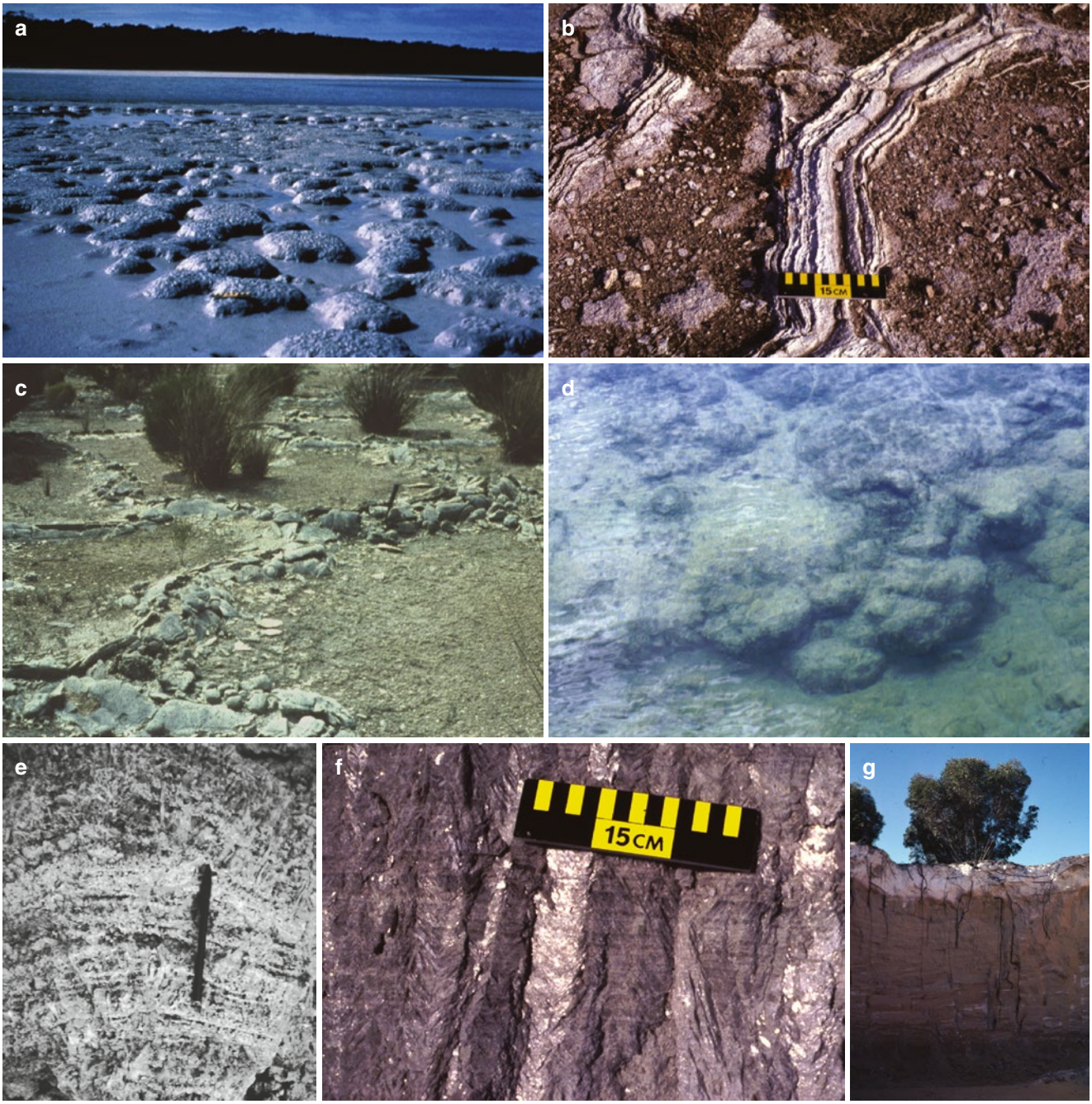

Fig. 4.6 Salina geology. (**a**) Domal stromatolite; North Stromatolite Lake. (**b**) Extrusion tepee; North Stromatolite Lake (**c**) Domal stromatolites capping tepee polygons Marion Lake. (**d**) Actively growing gypsum dome, subaqueous floor Inneston Lake; (**e**) Layered gypsum Dome, New Lake. (**f**) Laminated gypsum, Marion Lake. (**g**) Gypsite soil atop gypsum dune, Cooke Plains

surface along the coastal zone as they float up over a more dense seawater wedge. That most dolomite forms where large volumes of resurging continental waters can evaporate, explains why the thickest Coorong dolomites form adjacent to the present coast. However, mineralogically similar dolomites are also precipitating 20–40 km further inland as thin capping units in fully continental ephemeral lakes. These areas are well away from the seawater wedge, but still in areas where the regional watertable intersects the land surface and continental groundwaters can pond and evaporate.

Dolomites in salinas in the Salt Creek region precipitate as two geochemically and isotopically distinct types (Type-A and -B), typically in association with other carbonate minerals. Type-A dolomite has a slightly heavier oxygen isotope signature than type-B, and is 3–6‰ heavier in ^{13}C (Fig. 4.7b). Type-A dolomite also has distinct unit cell dimensions

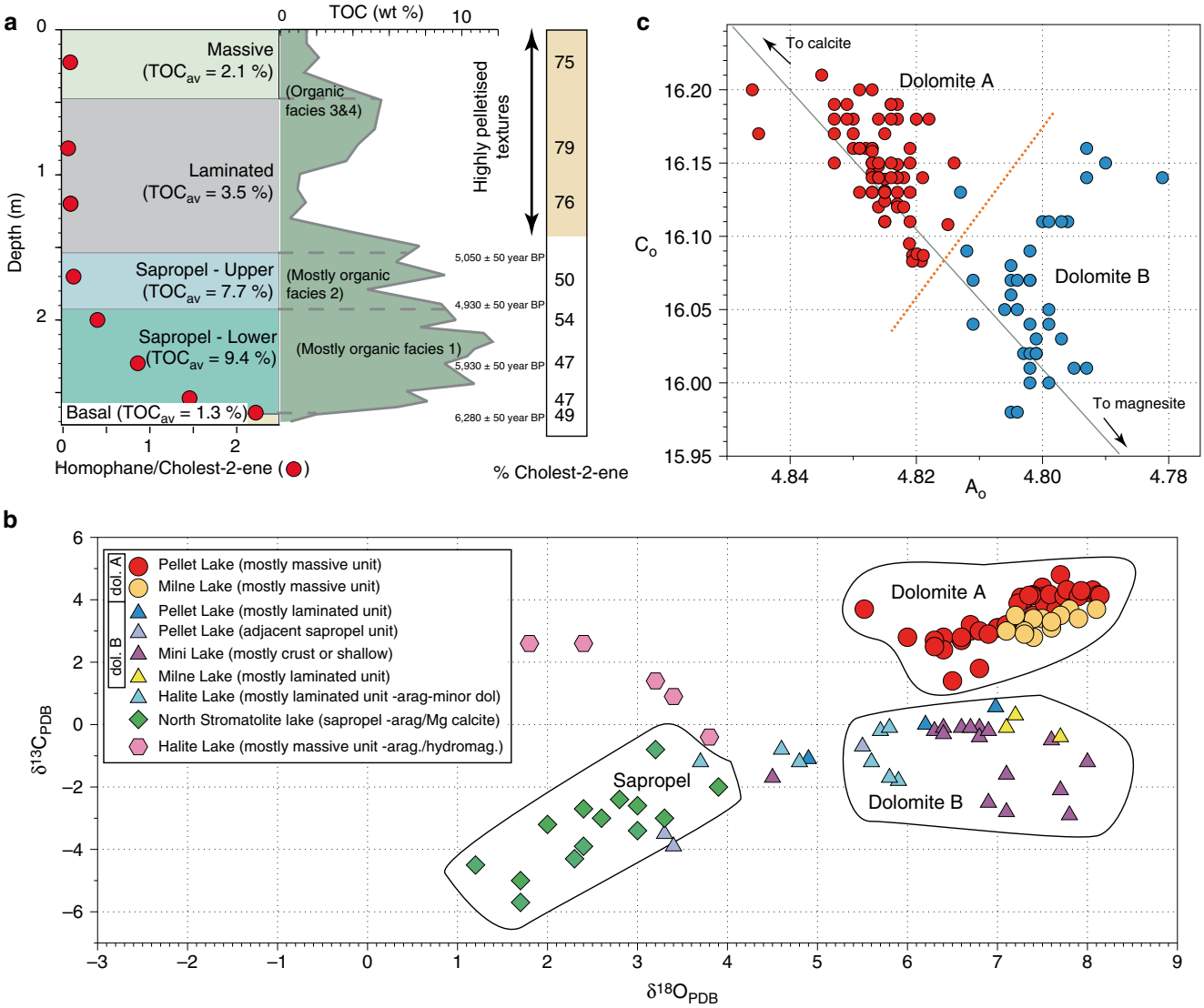

Fig. 4.7 Geochemistry of Coorong dolomites. (**a**) Plot of homohopane/cholest-2-ene ratio versus depth in a core from North Stromatolite Lake recording the up-section addition of faecal cholesterol to the mud by benthic microfauna that grazed on algae and cyanobacteria. The *right-hand panel* highlights a parallel increase in cholest-2-ene as a proportion of the total eukaryotic input of $C_{27}-C_{29}$ Δ^2-sterenes. (**b**) Isotopic signatures of Type A, Type B dolomite and sapropel carbonates across various Coorong Lakes. (**c**) Unit cell parameters of type A and Type B dolomite across various Coorong lakes (In part after McKirdy et al. 2010; Rosen et al. 1989; Warren 1990)

(Fig. 4.7c). It tends to be magnesium-rich with up to 3 mol% excess $MgCO_3$, while type-B is near stoichiometric or calcian-rich. Type-A dolomite typically occurs in association with magnesite and hydromagnesite, Type B with Mg-calcite. Transmission electron microscopy (TEM) shows that Type A dolomites have a heterogeneous microstructure due to closely spaced random defects, while type B dolomites exhibit a more homogeneous microstructure implying excess calcium ions are more evenly distributed throughout the lattice. TEM studies show that the two types of Coorong dolomite are distinct and are not intermixed with other mineral phases; they are primary precipitates, and not replacements and are not transitional (Miser et al. 1987).

Sapropel carbonates are typically mixtures of aragonite and Mg-Calcite, indicative of the somewhat lower ambient salinities when these sediments precipitated (McKirdy et al. 2010). As such sapropel carbonates tend to occupy a distinct isotope plot field compared to type A and B dolomite (Fig. 4.7b). Their somewhat more negative carbon isotope values may indicate a greater organic contribution to the carbonate precipitate in the sapropel. The separation of isotope fields for dolomite A from dolomite B is also largely due to differences in carbon values, with dolomite B tending to have more negative values. Rosen et al. (1989) attributed this to differences in water chemistry (more evaporitic versus more meteoric-influenced feeder brine).

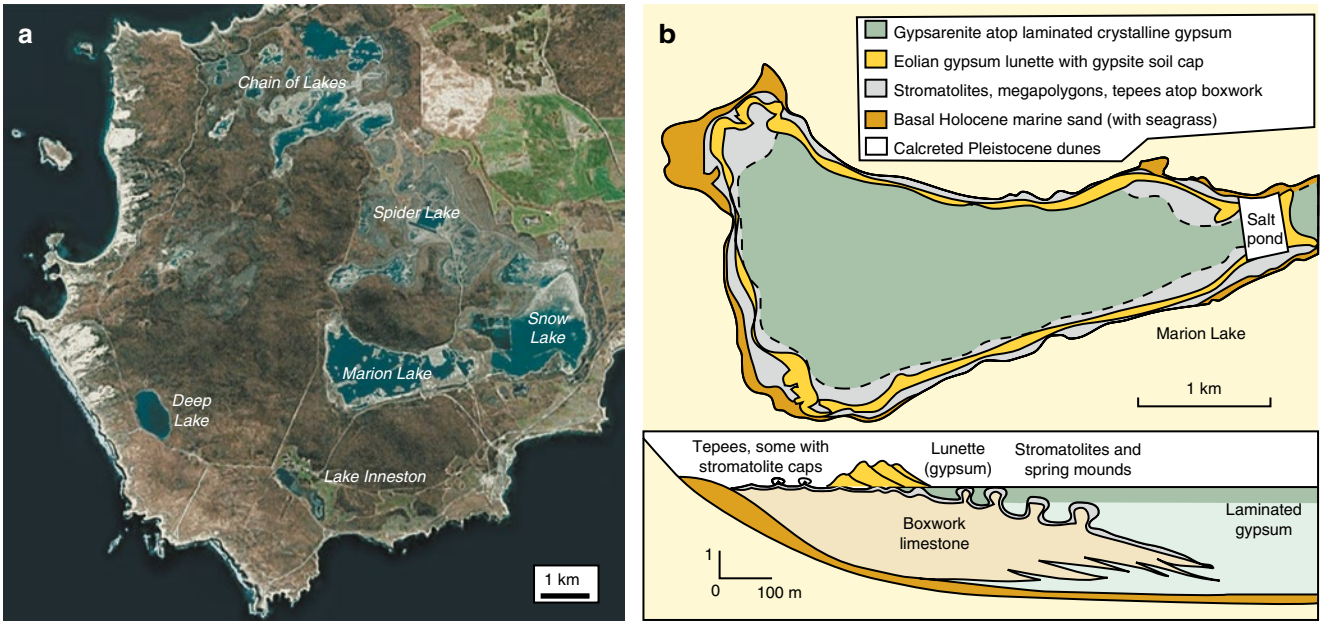

Fig. 4.8 Gypsum salinas. (**a**) Seepage fed coastal salinas of the Marion Lake complex at the southwest tip of Yorke Peninsula, South Australia. (**b**) Surface geology and cross section of Marion Lake are after Warren 1982a, b (Landsat image courtesy of NASA)

In later papers, Wright (1999), Wacey et al. (2007) argued dolomite formation in the Coorong salinas is bacterially mediated, based on a combination of SEM and sulphur isotope observations.

Bacteria can play a role in shaping all isotope signatures. However, neither type A and B dolomites show the negative carbon values typically associated with the bacterial sulphate reduction (BSR) and Coorong dolomite plotfields lie outside the documented sulphate reduction or methanogenic dolomite fields (Fig. 4.18). Wacey et al. (2007) argue this is because bacterially-mediated precipitates in the Coorong lakes incorporate carbon primarily from the inorganic, lakewater reservoir, partially diluted by an organic component. However, it is important that any proposed precipitation process does not oversimplify or overgeneralise a complex set of precipitation mechanisms across a range of evolving carbonate mineralogies. Figure 4.7b clearly shows dolomite mineral phases occupy separate isotope plot fields and so likely involve a range of feeder chemistries. The research on the relative importance of bacteria versus concentration on the formation of Coorong dolomite continues.

Dolomites in Coorong salinas are evaporitic carbonates, once thought to only form in areas free of preserved evaporites (von der Borch and Lock 1979). Yet, Milne Lake, a salina filled with 4 m of laminated dolomite-magnesite, lies less than a kilometre from Halite Lake, a depression filled with 2–3 m of laminated gypsum-aragonite (Fig. 4.5a; Warren 1990). Milne Lake was fed by seaward-flowing continental groundwaters throughout its infill history. Halite Lake, during the gypsum stage of its fill, was fed by landward-flowing marine groundwaters (evaporative drawdown stage). Today Halite Lake is filled to its hydrological equilibrium level; its present depositional surface lies above the level supplied by marine seepage and it no longer accumulates laminated gypsum-aragonite. Above its laminated gypsum-aragonite unit is a 10–50 cm thick capstone bed of pelleted aragonite-hydromagnesite, a mineral association that indicates the current surface hydrology is dominated by a non-marine groundwater feed, but with a distinct isotope plot field (Fig. 4.7b). Other Coorong Lakes in the same climatic zone, but located further inland, and more isolated from resurging marine groundwaters, are completely filled with this aragonite-hydromagnesite association (Fig. 4.5a; North Stromatolite Lake and South Stromatolite Lake).

Gypsum Salinas

Gypsum-filled coastal lakes in southern Australia are located mostly to the west of the Coorong coast (Fig. 4.2) and are best documented in the region of Marion Lake on the southwestern tip of Yorke Peninsula (Fig. 4.8a). Most of these gypsum salinas occur within a Mediterranean-style Csb Köppen climate regime; although the largest of the exploited gypsum salinas, Lake Macdonnell, lies in a BSk climate. Groundwater feeds to these salinas are dominated by seawater, so the current hydrological equilibrium surfaces (Stokes surface) in all the gypsum salinas are still up to 50 cm below sea level. In plan view, surface sediments in a gypsum salina define bull's-eyes, consisting of a carbonate seepage rim and a more central gypsum zone (Fig. 4.8b). Individual gypsum-filled salinas measure up to 20 × 12 km (Lake Macdonnell on

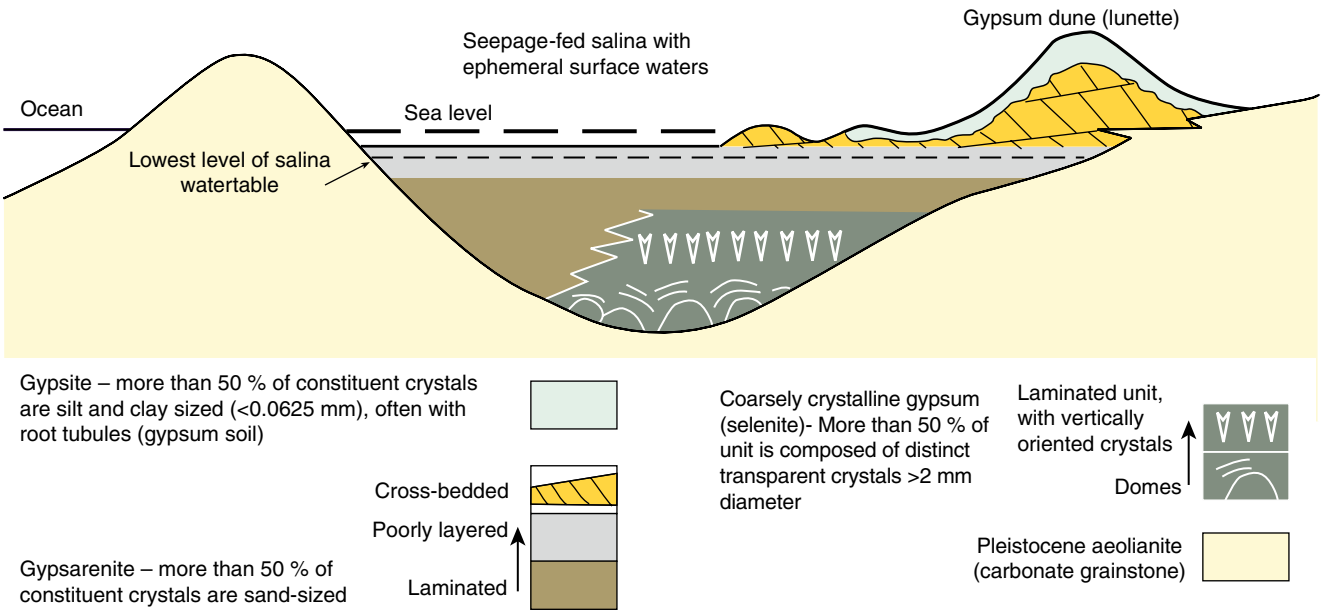

Fig. 4.9 Gypsum facies in South Australian salinas (After Warren 1982b), showing domes overlain by laminites and the eolian reworking of upper portions of the lake sediments into gypsite-capped lunettes. For simplicity, the carbonate rim is not shown (see Fig. 4.8b)

the coast of the Great Australian Bight), with centres filled by laminated gypsum units up to 10 m thick.

A carbonate unit forms a seepage rim about the salina edge and is composed of a boxwork limestone unit (up to 4–5 m thick) overlain by a fenestral limestone sheet or crust, which is typically less than 1 m thick (Fig. 4.8b; Warren 1982a). Boxwork limestone is a diagenetic unit created by the cannibalization of earlier marine-lacustrine carbonates and sulphates by inflowing "fresher," but still saline, marine-derived groundwaters. The "boxwork" contains relict algal structures, evaporite pseudomorphs and other highly altered bedded fabrics in proportions depending on pre-existing sediment types. Some areas of the limestone sheet above the boxwork limestone consist of tepee-overprinted crusts, others of mm-laminated subaqueous stromatolites and algal mats.

Taller stromatolites in Marion Lake grew as current-aligned mm-laminated elongate domes (up to 40 cm relief) in a brine-filled feeder channel, that focused the flow of marine seepage waters into the perennial gypsum lake of the salina centre (Fig. 4.8b). Other smaller domal and encrusting stromatolites define the water-saturated cyanobacterial terrace of the lake strandzone, where indurated biolaminites define areas of very shallow and sometimes ephemeral surface waters (von der Borch et al. 1977; Warren 1982b). Stromatolite domes cap tepee structures in some marine-fed seepage areas (Fig. 4.6c). Like stromatolites, tepee structures are confined to the capping carbonate unit and form an extensive fenestral limestone sheet or capstone, up to 60 cm thick. Tepees form readily in areas of resurging groundwater, where seasonal changes in the groundwater head encourage tepee growth (Warren 1982b). Most of the limestone sheets caught up in the tepee structures are capillary crusts composed of fenestral lime mudstones containing stromatactic-like voids, pisolites, laminar cements, and geopetal internal sediment partially filling pores and vugs. A similar lake-margin recharge hydrology controls the formation of stromatolite-capped tepees in Holocene Lake Walyungup in coastal Western Australia (Coshell et al. 1998; Coshell and Rosen 1994).

Salina gypsum in the central portions of Marion Lake is coarse-grained, porous, bottom nucleated and growth-aligned; it retains intercrystalline porosity of 15–25 %; pore infilling gypsum cement is rare (Figs. 4.6e, f and 4.9). South Australian salinas are one of a few Holocene occurrences where subaqueous gypsum is deposited as widespread units of coarsely crystalline bottom-aligned swallowtail and palmate crystals (Warren 1982a). Worldwide, gypsum in most modern salinas is a layered gypsarenite. The cm-scale gypsum crystals are usually more than 90 % pure and laid down as characteristic shallowing-upward growth-aligned crystal aggregates (Fig. 4.2). At the base of an idealized succession are massive, poorly layered domes of coarsely crystalline palmate and swallow tail crystals (aka selenite; Fig. 4.9). Modern growing examples of this style can be found regrowing on the floors of flooded mined-out salinas such as Lake Inneston (Fig. 4.6d). The elongate gypsum prisms in the early stages of dome growth show little or no preferred orientation, with carbonate pellets and flakes distributed randomly through the gypsum porosity. Active domes on the floor of Lake Inneston are coated by microbial slime and can be considered to be a type of coarsely-layered gypsum stromatolite.

Higher in the sedimentary section, the degree of lamination increases and dome amplitude decreases until domes pass into sub-horizontally layered and laminated units of aligned crystals (Fig. 4.6e). Higher still, individual laminae of pelletal and micritic aragonite appear to crosscut large upwardly-aligned gypsum crystals (Figs. 4.6f and 4.9). Such large crystals at first sight appear secondary and their Miocene equivalents in the Sicilian Basin were once interpreted as secondary gypsum after anhydrite (Ogniben 1957). Studies of identical Holocene gypsum in the South Australian salinas have shown that the crystals (30–50 cm long) are primary, not secondary. They grow with their long axes perpendicular to bedding, an effect of crystal impingement and growth alignment (Fig. 2.72; Warren 1982b).

Gypsum is not only deposited as coarse-grained gypsum (selenite) in South Australian coastal lakes. Some salinas are filled with laminated gypsarenites and are probably as common, if not more common, than those filled with the geologically more interesting coarsely-crystalline gypsum. Laminated gypsarenite fills large interdunal corridors near Streaky Bay and Point Fowler in South Australia and Hutt and Leeman Lagoons in Western Australia (Fig. 4.2).

In salinas with coarse-grained fills, the coarsely-crystalline laminated gypsum (selenite) unit, punctuated by carbonate laminae, is in turn overlain by a mm-laminated, sand-sized gypsarenite accumulation (Fig. 4.9). Parts of the horizontally laminated gypsarenite unit, especially near the salina strandzone, can be reworked into wave-oscillation ripples. Laminated and rippled gypsarenite is in turn overlain by a thin, massive, poorly-bedded gypsarenite unit deposited under seasonally vadose or subaerial conditions and represents accumulation in the salina capillary fringe.

Topping the whole succession is a unit of cross-stratified eolian gypsum and, in areas stabilized by vegetation, a pedogenic cap of gypsite (silt-sized). Throughout coastal and inland Australia, this gypsum soil is a degradational profile that is slowly cannibalising depositionally inactive regions of both lacustrine and eolian gypsum (Fig. 4.6g).

Carbonate laminae in the various gypsum units form by the precipitation and accumulation of aragonite pellets during the spring and early summer (Chap. 9). The pellets come from the faeces of ostracods and brine shrimp, mixed with the micritised remnants of algal tubules. At first the pellets mantle any underlying gypsum and often are captured by a cyanobacterial mat that covers the gypsum. During the ensuing summer and autumn, as the lake maintains its gypsum saturation, the pellets are encased by the upward poikilitic growth of large gypsum crystals (Figs. 2.72 and 4.6e, f).

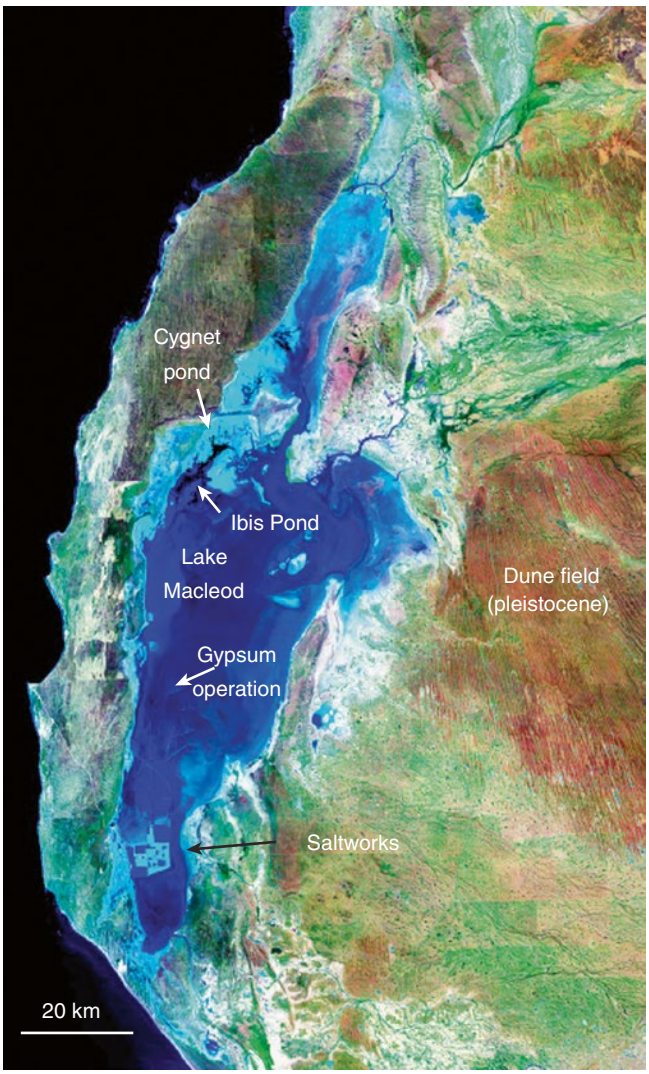

Fig. 4.10 Lake Macleod, Western Australia. It is the largest evaporite-filled coastal salina in the world. Marine-fed brine springs and sheets are visible in the central western and northwestern strandzone, while solar ponds are visible in the south. The interdunal depression only started to accumulate Holocene salts after its surface connection to the ocean at its southern end was cut off by longshore sand drift (Landsat image courtesy of NASA)

Halite Salinas

Lake Macleod is a halite-filled salina some 120 km long and 40 km wide, lying just to the north of Shark Bay (Fig. 4.10; Logan 1987; Handford et al. 1984). Climate is arid, with average rainfall around 230–260 mm and annual potential pan evaporation in excess of 2,600 mm (BWh Köppen Climate zone). The surface of much of Lake Macleod still lies well below sea level indicating evaporative drawdown and a groundwater feed from the nearby Indian Ocean. Some parts of the lake depression, especially near the marine seeps, are still covered with semipermanent water sheets. In its northern part, and across the current lake surface, the lake fill is a Holocene gypsarenite unit; it is as much as 5 m thick along the northern and western (seaward) sides of the lake (Fig. 4.11). To the south and beneath the laminated gypsum unit is a widespread halite bed up to 7 m thick. It is made up of stacked halite crusts, dominated by growth-aligned chevrons and cornets. Brines from this halite unit in the south

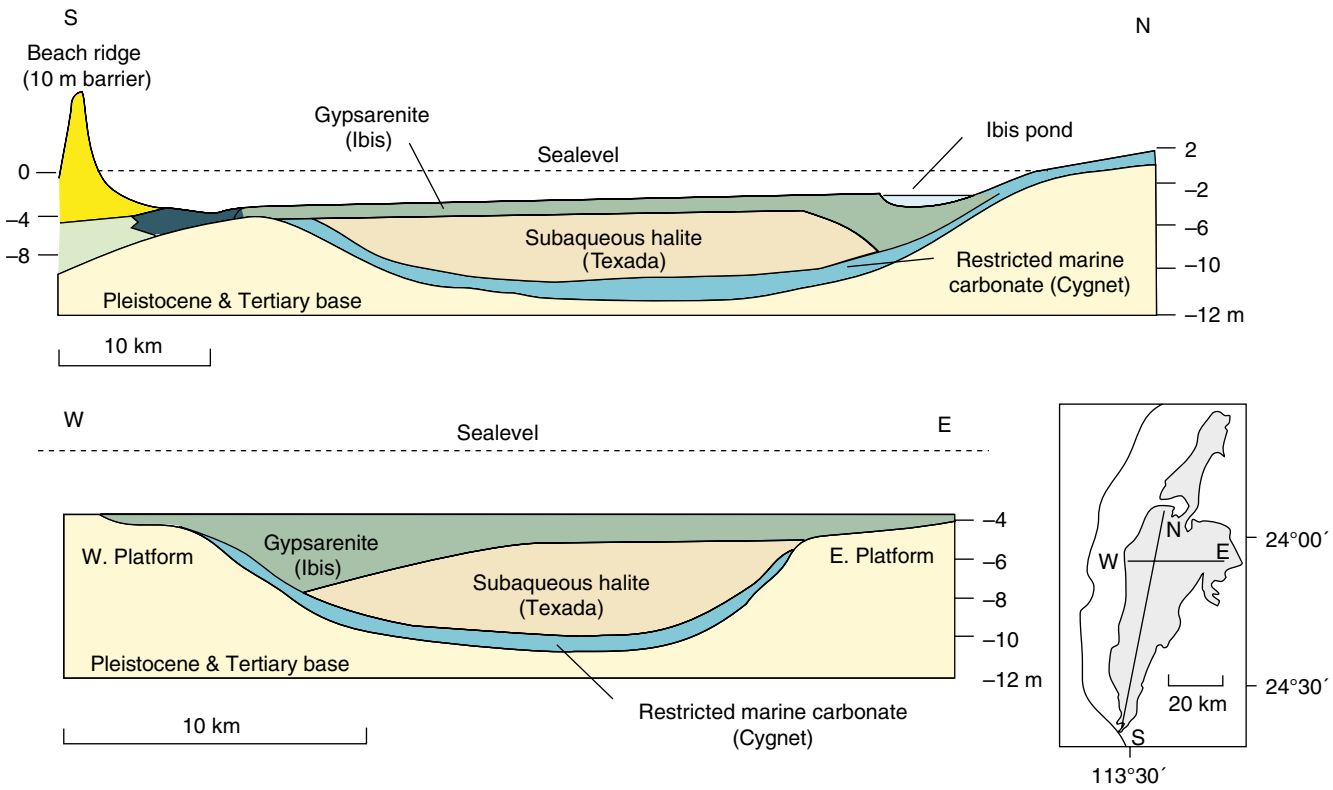

Fig. 4.11 Lake Macleod, Western Australia. Stratigraphic cross sections showing distribution of halite and gypsum as well as the effect of seepage decreasing the salinity so that the gypsum thickness increases toward areas of carbonate seepage defined by Ibis Pond and the western platform (After Logan and Brown 1976)

are pumped into saltwork ponds to produce halite for the chemical industries of southeast Asia. Gypsum was dredged in the central part of the lake and mostly used for wallboard manufacture. Both the gypsum and the halite units overlie a thin unit of Holocene lagoonal carbonate deposited prior to the depression's transition from marine embayment to coastal seepage lake.

Lake Macleod never possessed a surface (hydrographic) connection to the ocean at any time in its salt-accumulating Holocene history. Seawater seeps onto the subsealevel lake floor via a series of marginward carbonate-precipitating spring pavements and beds, fed from fractures and caves in the underlying and surrounding calcareous coastal dune aquifer. As the escaping water exits the dune aquifer it degasses and concentrates to salinities where it precipitates seepage or strandzone carbonates, including aragonite pisolites and tepees, especially about seeps along the eastern and northern edges of the Macleod salina (Handford et al. 1984).

Today, the northern part of the lake is a perennial seepage pond, called Ibis Pond, where the perennial inflow water gathers in ponds that are over a metre deep (Fig. 4.10). When the water first escapes into the pond it has normal to near normal marine salinities and supports a restricted population of halotolerant marine gastropods and small fish. A similar marine biota can be found in marine seepage ponds on the seaward side of gypsum-filled Lake Macdonnell of coastal South Australia. Spring-fed normal marine waters are thought to have supplied the Lake Macleod brine lake for the last 5,000 years, ever since the Australasian Sea rose to a level that was within a metre or two of its present level. At that time a series of laterally accreting beach ridges cut off the lake's southern surface connection to the Indian Ocean (5,100 years ago). Since then, evaporative drawdown has pulled seawater into the lake depression and bedded salts have accumulated.

From 5,300 to 3,800 years ago, seawater seepage flowing out over the lake depression concentrated to halite saturation and deposited some six billion tons known as the Texada Halite, with a remaining brine-filled porosity in the salt beds of around 30 %. As the salina filled with beds of stacked chevron halite, the depositional surface aggraded (fill and spill hydrology – see Chap. 2). Over time, this meant that the groundwater head drawing water into the lake was reduced. At the same time the once perennial brine lake, depositing the halite and the gypsum, began to dry out each year and evolved into a saline pan. Meteoric input became more important in this later stage in the depositional fill, much in the same way it did in the South Australian salinas (Warren 1982a). This meant the salinity of the surface brine sheet was reduced to where gypsum was the stable mineral phase

throughout the brine lake and the Ibis Gypsite[1] unit was deposited across the lake. Local springs fed the lake throughout its Holocene history, so that aragonitic carbonate was deposited adjacent to the springs, while gypsum and halite filled the salina in an asymmetrical fashion away from these water sources (Handford et al. 1984).

Coastal Salinas of the Middle East

In the coastal deserts of the Middle East there are a number of small-scale coastal depressions filling with subaqueous evaporites, mostly aragonite and gypsum. They are flooded by perennial brines and replenished by phreatic seawater drawn into the lakes by evaporative drawdown. Like the Australian salinas, these Holocene fills have low preservation potential and will be largely flushed and dissolved during the next glacial event and its associated sealevel low.

Solar Lake, Gulf of Elat

The Sinai coast of the Gulf of Elat is characterized by steep rifted-margin topography and a clearly defined fringing-reef (Aharon et al. 1977; Gavish 1980). In most areas along the northern part of the Gulf the mountainous granitic and metamorphic massif meets with gulf waters to produce a narrow steep shorezone composed of slump blocks, coarse beachrock plates and narrow reef flats. Locally wadis extend as fan deltas into the gulf to produce wider, flatter coastal plains. Small brine ponds or salinas can develop in sub-sealevel depressions in this narrow coastal plain. Probably the best known of these is Solar Lake, a salina located immediately north of a large fan delta (Wadi Murah), some 18 km south of Elat. It is located in the BWh Köppen Climate zone that typifies the Red Sea, Suez and Elat coasts (Figs. 3.22 and 4.12a).

Solar Lake is a meromictic brine pond, about 140 m long and 65 m wide, with a maximum depth of 5 m. It is separated from the open sea by a porous beach-barrier, some 60 m wide and up to 3 m high, composed of coarse sand and pebbles of igneous and metamorphic rocks, along with abundant molluscan shell debris (Fig. 4.12b). Water is drawn to the pond by evaporative drawdown especially during high tide when the piezometric head is at its maximum. Minor amounts of seawater may also enter the pond by splashing over the barrier during occasional winter storms. Evaporation exceeds inflow each summer, raising the total dissolved solids of the pond brine to 160–180‰ in an unstratified or mixed brine column (May-September). In winter, the combination of lessened evaporation, ongoing inflow of seawater and minor amounts of rainwater combine to create an upper water layer of lower salinity (70–100‰) atop an anaerobic hypersaline hypolimnion (≈180‰) and a corresponding seasonal thermocline separating the two brine masses and making the lake a meromictic system (Fig. 2.71).

The resulting heliothermal layered brines in Solar Lake are typical of many other density-stratified coastal brine lakes. Bottom water temperatures in Solar Lake reach 57 °C in winter and spring, while year-round surface water temperatures range from 20 to 28 °C (Fig. 2.71). During stratification, as the lower brine layer absorbs heat, convection between the two layers is inhibited, and the bottom layer becomes increasingly hot and anoxic, with elevated levels of H_2S. By summer, evaporation and concentration of the upper water body drives a weakening of the density stratification and finally overturn. At that time the water level in the pond is as much as 0.5 m below sea level. With overturn, the water body becomes homogeneous, aerobic, and cools by convective heat loss to a consistent 28 °C (Fig. 2.71).

Sediments accumulating in the pond reflect the style of water supply and the meromictic stratification of pond waters. Down to a bottom depth of 2 m the margins of the pond are covered by thick halotolerant cyanobacterial mats atop carbonate mud. Precipitation of carbonate in the mats is largely driven by the metabolic activities of sulphate-reducing bacteria (Lyons et al. 1984b). Slopes of the pond are composed of a white crust of interlayered bottom-nucleated gypsum crystals and aragonite mud, while the deep pond bottom is covered by black mud and a loose gypsum mush (Fig. 4.12b). There the halobiotial biomass changes to halophilic cyanobacteria with soft flocculent fabrics and an associated increase in the numbers of sulphur-dependent anoxy-photobacteria (Krumbein et al. 1977). Interestingly, the carbonate in these deep bottom mats is dominated by near-perfect hollow microspheres of monohydrocalcite, possibly precipitated in response to bacterial metabolic processes (Krumbein 1975).

A total of about 70 cm of biolaminated sediment has been deposited in 2,400 years about the lake margin. Seasonally exposed portions of the biolaminites are crosscut by well-developed polygonal cracks giving the cyanobacterial mat a "lily-pad" appearance identical to the "lily pad" mats of the Abu Dhabi sabkha and the Ras Muhammad pool. Cracks open to their maximum extent during the late summer and autumn when the lake water level is at its lowest and the mat surface is subaerially exposed. Carbonates in the mat laminae and in the gypsum are composed of aragonite, with lesser Mg-calcite, dolomite and calcite, with dolomite forming as a replacement of the aragonite (Friedman et al. 1973; Aharon et al. 1977). The bulk of the dolomite occurs in gypsiferous sediment and not in the algal mats. The dolomite indicates a throughflow of

[1]Use of the term gypsite by Logan and coworkers to describe a unit that is laminated and dominated by sand-sized gypsum prisms is unfortunate. Outside of the University of Western Australia, the use of the term gypsite follows general sedimentological usage to define a very fine grained silt or mud-sized sediment (pelite, micrite, etc.).

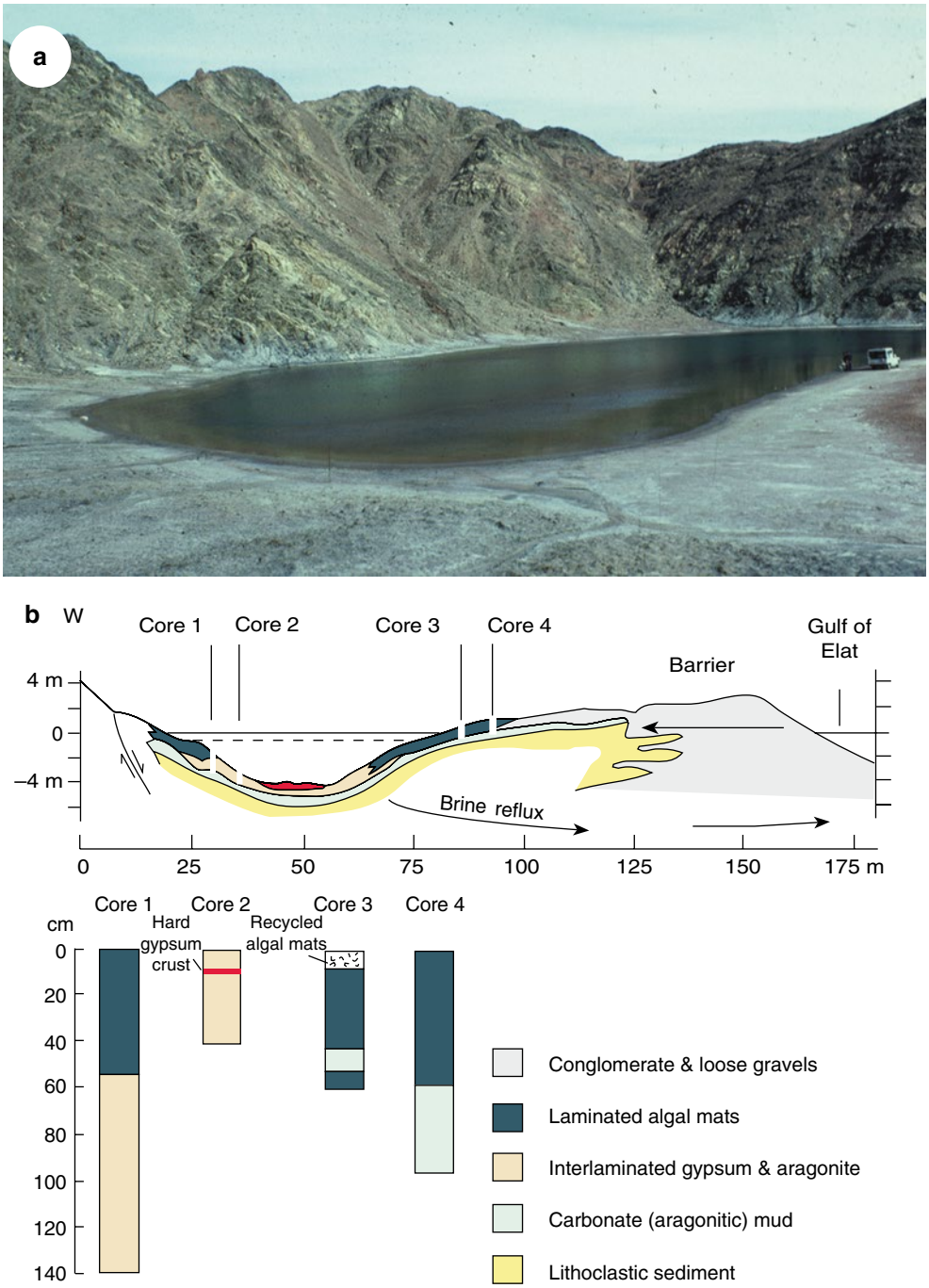

Fig. 4.12 Solar Lake, Gulf of Elat. (**a**) View shows cyanobacterial mats rimming the more central gypsum area. Note the steep-sided surrounds of the Precambrian Massif (Photo courtesy B. Lyons). Vehicle for scale. (**b**) E-W topographic and lithologic cross section based on cored sediments showing peripheral algal facies and a more central gypsum zone (After Aharon et al. 1977)

hot hypersaline brines, with a Mg/Ca ratio increased by the precipitation of gypsum, it is a local-scale brine reflux dolomite, possibly facilitated by bacterial sulphate reduction (Aharon et al. 1977). Beneath the cyanobacterial and gypsum layers of the pond is an earlier muddy aragonite unit with numerous *Cerithium* gastropod shells, indicating less saline deposition during the initial isolation of the pond.

Submersed sediments of Solar Lake are rich in organic carbon, a one metre deep core showed TOC values consistently in the range of 5–20 % (Schidlowski et al. 1985). Lyons et al. (1982) found significant levels of dissolved organic carbon, in the range 119–818 mg/l, in the pores of the same sediments. They concluded this material is not a "photosynthetic exudate," rather it is a build up from the early stages of the organic maturation, a response to early-onset catagenesis driven by high temperatures and high salinities attained in the sediment mass (see thermal maturation and early cracking in Chap. 9).

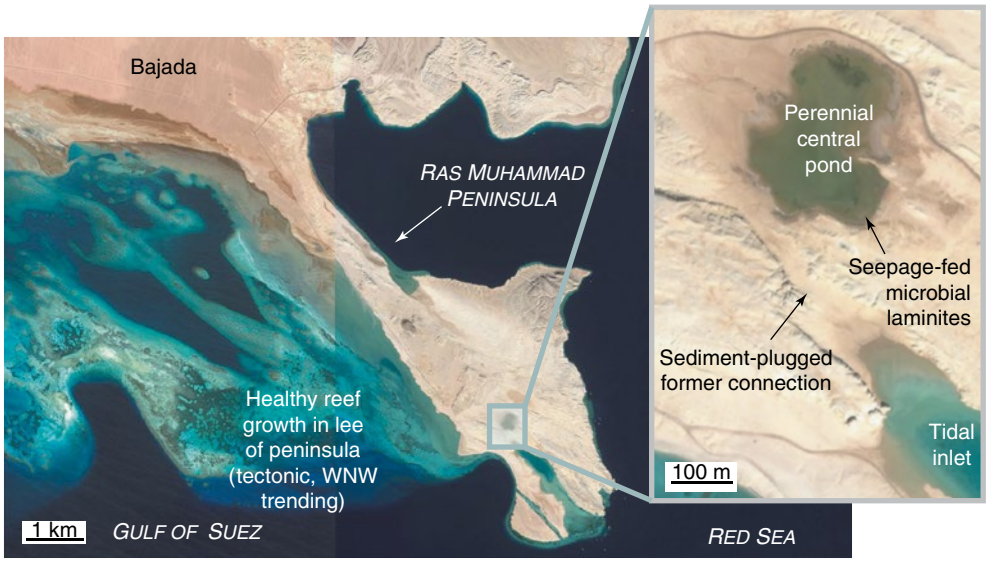

Fig. 4.13 Ras Muhammad pool, Southern Sinai Peninsula, view to the south, clearly shows seepage feed to the salt-encrusted perennial pool, tectonic alignment and its proximity to a seawater seepage source in the nearby tidal inlet (Bing® images scaled in MapInfo)

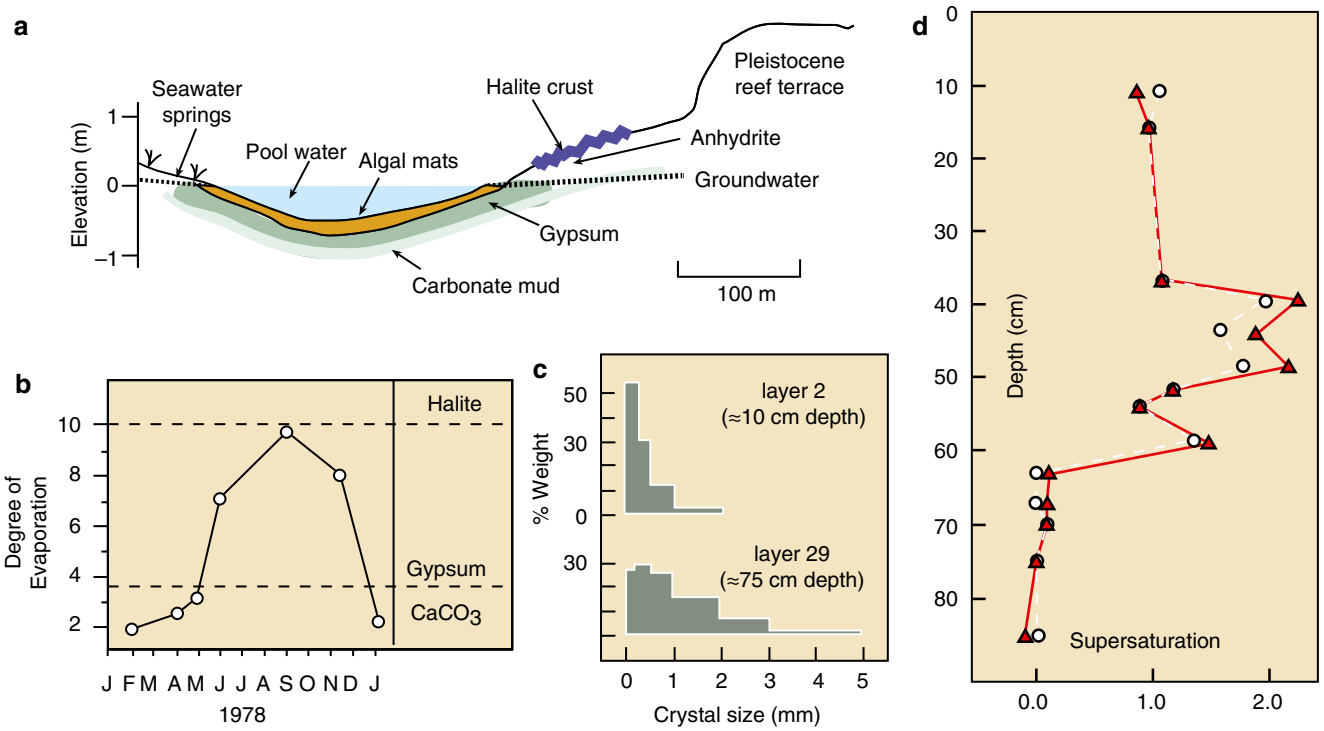

Fig. 4.14 Ras Muhammad pool, southern Sinai Peninsula. (**a**) Generalised cross section through the pool showing asymmetrical sediment distribution controlled by zones of seepage outflow. (**b**) Annual brine concentration cycle of surface waters for 1978 – Seawater is unity on the degree of concentration scale. (**c**) Gypsum crystal size distribution in a shallow and a deep sediment layer. (**d**) Gypsum saturation versus depth, using interstitial waters squeezed from gypsum layers (After Kushnir 1981)

Ras Muhammad Pool, Southern Sinai

At the southernmost tip of the Sinai there is a small peninsula, called Ras Muhammad, constructed by tectonically uplifted Pleistocene reefs (Figs. 3.22 and 4.13; Gavish 1980; Kushnir 1981). At the termination of this spit is a 1 km long tidal inlet with a small perennial brine pool at its end called Ras Muhammad Pool. The pool is an oval feature about 100–170 m in diameter and never more than 50 cm deep. It is separated from the inlet by a porous barrier, some 250 m wide, composed of reef material and carbonate sand (oolitic) that can be blown or washed into the pan. Most of the water in this subsealevel pool enters via a series of seawater springs around the pool's edge (Figs. 4.13 and 4.14a). The proximity of the groundwater source means the pool never dries up,

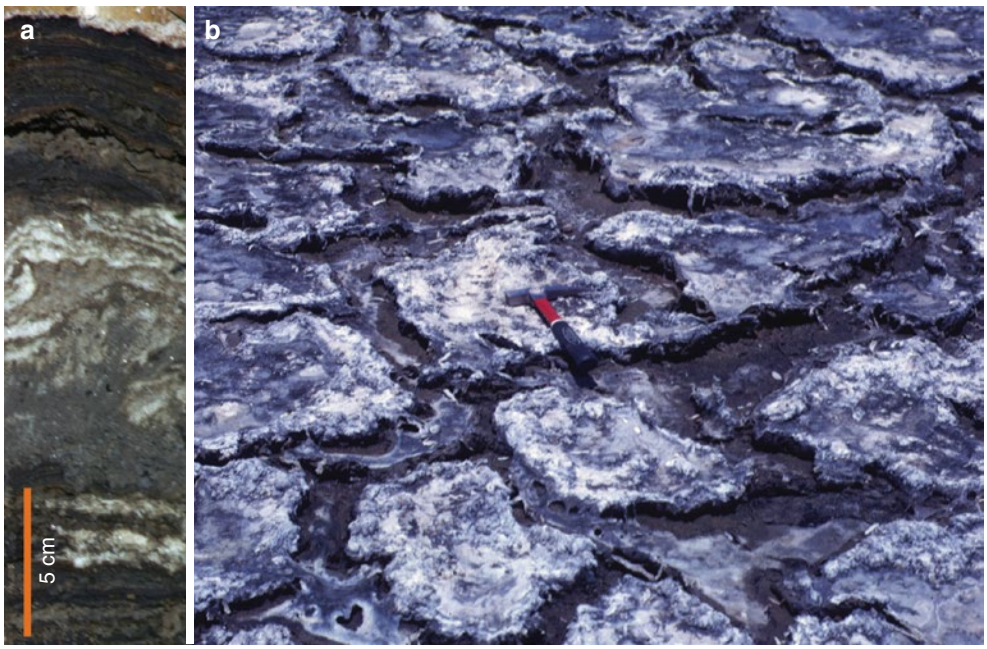

Fig. 4.15 Microbial mats of Ras Muhammad pool. (**a**) Core through irregularly layered mat from the strandzone. (**b**) Polygonal microbial mats ("lily pads"). Mats are seasonally desiccated and underlain by biolaminites and gypsum (geological hammer atop the mat in the *centre* of the image for scale) (Originals courtesy of G. M. Friedman)

although the extent and depth of surface water in the pool varies with the seasons. During summer and fall, the water volume in the pond is reduced by high evaporation levels (BWh; Köppen climate) and salinities in the pond can be more than 300‰. In winter and spring the pond expands and surface water salinities fall to 100‰ (Fig. 4.14b).

Sediments below the perennial pool are composed of alternating layers of gypsum mush and algal mats, there is no primary or diagenetic anhydrite (Fig. 4.15; Kushnir 1981). Thickness of gypsum layers ranges between 0.3 and 6 cm and averages 1.8 cm. Porosity in the gypsum layers ranges between 64 and 69 %. The gypsum in the layers is mainly prismatic (crystals up to 6 mm long) and associated with minor amounts of aragonite, calcite, quartz and feldspar. The gypsum in the upper younger layers (e.g. layer 2) consists mainly of small crystals whereas the deeper older layers (e.g. layer 29) have a broader, coarser size distribution (Fig. 4.14c). Mid-portions of cores taken through the cyanobacterial sediments can contain lenticular and prismatic gypsum crystals that have grown displacively within these biolaminites. The continued growth of gypsum eventually destroys the original lamination, as in the sabkha of Abu Dhabi. Likewise, much of the evidence of the original nearsurface organic binding (cyanobacterial filaments) is destroyed by the activities of heterotrophic decomposers that live below the surface of the mat. The final fabric as revealed in the lower-most layers of the cores taken by Kushnir (about 80 cm deep) is a laminated and disturbed gypsum mush with thin interlaminations of carbonate crusts and ooids with very little identifiable cyanobacterial material (Fig. 4.15a).

Strandzone sediments around the pool edge are cemented by an ephemeral halite crust, while beneath the crust and above the watertable are rare concentrations of anhydrite after gypsum, but salts in these strandzone sediments are dominated by gypsum. Pore fluids become increasing saline below the sediment surface and down to depths of 50–60 cm can be supersaturated with respect to gypsum by upward of a factor of 2 (Fig. 4.14d). High levels of gypsum supersaturation are relieved by the precipitation of gypsum and the growth of coarser prismatic crystals, as is seen in the coarser crystal sizes of layer 29 some 75 cm below the sediment surface (Fig. 4.14c). According to Kushnir (1981) high levels of organics in the supersaturated pore fluids inhibit precipitation of larger gypsum crystals in the uppermost capillary intervals. Alternatively, the coarser gypsum just above the watertable may indicate thermalitic precipitation. It is very likely that the precipitative mechanism for gypsum in the capillary fringe in Ras Muhammad is the same at the nearby Nabq sabkha/pan (Attia 2013) and in the Abu Dhabi upper intertidal section.

Late Pleistocene Salinas, Egyptian Red Sea Coast

Ongoing aridity along the tectonically stable area of the Egyptian coast of the Red Sea (BWh Köppen climate zone), has locally preserved Pleistocene remnants of embayment salinas (khors) that had filled with laminated subaqueous gypsum during the Last Interglacial (Eemian, 5e = 5.5 Marine Isotopic Substage; Plaziat et al. 1995; Orszag-Sperber et al. 2001). Heavily eroded remnants of the sediments in these small gypsum-filled khors, each up to a kilometre across, are scattered along a 400 km long narrow coastal strip, backing on to Precambrian basement, between Ras Shukheir on the Gulf of Elat and Ras Banas on the Red Sea coast (Fig. 3.22). Evaporitic sediment was initially

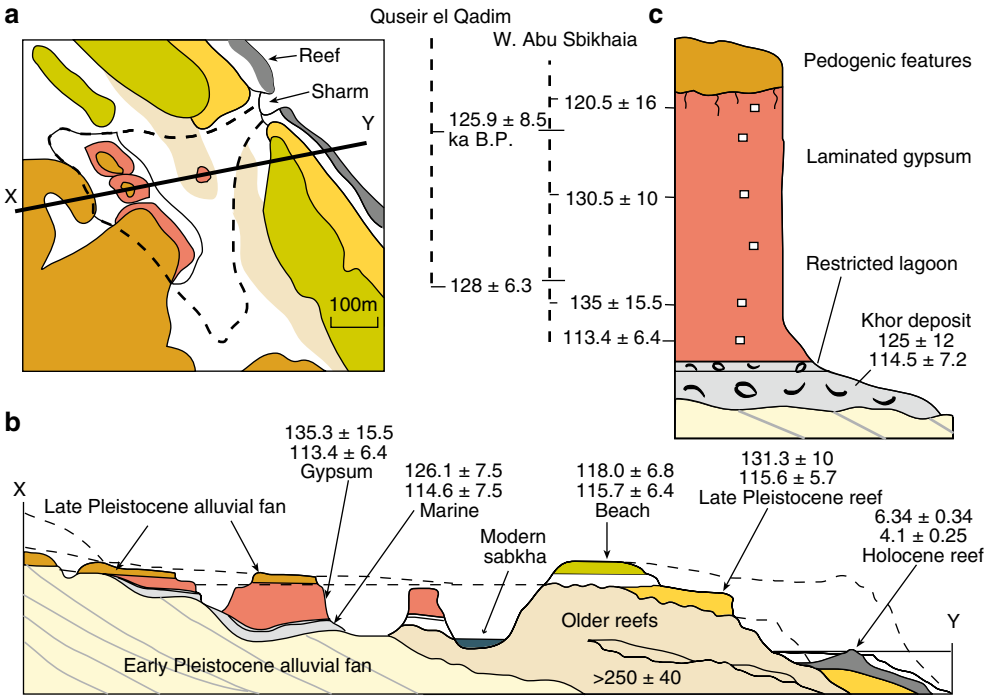

Fig. 4.16 Remnants of a Pleistocene salina, Red Sea coast, Egypt showing the geometry and age distribution of Late Pleistocene units and their Early Pleistocene alluvial fan substrate at Quseir el Qadim (**a** map; **b** cross section), (**c**) vertical section at wadi Abu Sbikhaia. The Late Pleistocene marine khor carbonates give U-Th dates similar to those of the overlying salina gypsum (After Orszag-Sperber et al. 2001)

deposited as shelly and subaqueous laminated gypsum in erosive depressions elongated parallel to the present shore and behind a subcontinuous Late Pleistocene fringing coral reef (Fig. 4.16a, b). The entrenched geometry and the marine to brackish evolution of the pre-evaporite faunas indicate deposition in a hydrographically-isolated depression behind a reef rim. Gypsum precipitation occurred during a brief relative sealevel drop that cut off the surface connection with the Red Sea. Both the reefal and gypsum units are Late Pleistocene, with a consistent set of U/Th dates around 123 ka bp. Ages from reef and gypsum are at times so close that there is no statistical difference between their respective ages in spite of the large number of dates collected by Orszag-Sperber et al. (2001).

This is not a matter of poor precision in dates, but indicates the very rapid rate of gypsum infill, once the khor lost its surface connection to the waters of the Red Sea. Narrow-mouthed embayments along the present coast quickly develop into kharms or khors that with further isolation and closure of the surface connection to the adjacent ocean of the Red Sea could became evaporitic drawdown basins filling with subaqueous gypsum units composed of coarse growth-aligned gypsum crystals up to 5–10 cm long (Plaziat et al. 1995). There is a possible Holocene counterpart to these systems on the Red Sea coast at Ras Shukeir (Aref et al. 1997) but laminar aragonite, rather than gypsum, dominates the fill in all modern kharms (Plaziat et al. 1995).

Textures indicating permanent Late Pleistocene salina waters atop the aggrading gypsum and the mm-laminae of carbonate that interrupted gypsum crystal growth suggest it was very similar in both its marine seepage hydrology and its depositional setting to the salinas of southern Australia and to Lake Asal (Fig. 4.16c). That is, it was an anchialine salina system (littoral saline lake) fed though the reef by permanent seawater seeps.

Tops of the laminated subaqueous gypsum outcrops locally grade up into polygonal gypsum pressure ridges near the top of the gypsum unit implying that the level of free-standing salina waters was about 3 m below the locally derived mean sea level as deduced from the shoreline of the former Late Pleistocene reefal unit (Orszag-Sperber et al. 2001). This reflects the evaporitic drawdown of the salina water level necessary to drive seawater seepage and gypsum precipitation.

Laminated salina gypsum in the Late Pleistocene Red Sea backreef is transitionally overlain by a massive pedogenic gypsum subunit (with root traces, burrows) interpreted by some as an emergent sabkha facies (Aref et al. 1997). It can grade laterally into older alluvial-fan substratum to become sloping gypsum crusts (gypcretes) cementing the gravels. These gypcretes and the sabkha facies clearly differ in process of formation and perhaps solute source from the laminated subaqueous gypsum. Likewise for the gypsum cements in coarse gravelly sand and sandy gravel about the khor edge, which were fed by a combination of marine aerosols and saline continental phreatic waters, seeping slowly seaward (Fig. 4.16b). Capillary rise of phreatic seawater is prevented by the elevation and coarseness of the host-material. Holocene gypcrete crusts throughout the Red Sea coast indicate a combination of marine aerosols and sulphate-rich

continental water leaching halokinetic Miocene gypsum, which outcrops near these Late Pleistocene salina remnants.

Slightly inland from the coast there are similarly textured laminated gypsarenite lenses in small depressions with heights ranging between 17.5 and 110 m above sea level. These are continental not marine fed salinas and are similar to continental salt lakes inland of El Alamein west of the Nile Delta (Fig. 3.24). There sediment fill lacks the basal marine fossiliferous sands that define the basal succession of many Late Pleistocene coastal salinas and watertable heights are so far above sea level that seawater seepage is impossible. Marine aerosol sources are a distinct but as yet untested possibility.

The highly dissected nature of all these 1-km scale examples of Late Pleistocene marine-fed evaporite khors along the Red Sea Coast attests to the low preservation potential of Quaternary coastal salina evaporites worldwide. The high frequency (100,000-year), high amplitude (100 m+) sealevel changes, that are diagnostic of icehouse climate, drive substantial dissolution of marine salts even in the very arid climate of the Red Sea (Chap. 5).

South American Salinas and Dolomite

One of the more interesting accumulations of modern evaporitic carbonate to be documented in the last two decades occur in a series of coastal depressions centred on Lagoa Vermelha, which is a small shallow isolated hypersaline coastal salina east of Rio de Janeiro, Brazil, situated in an Aw Köppen zone (Fig. 4.17a). Its Holocene fill provides the best evidence to date of the likely involvement of particular species of sulphate-reducing bacteria in producing primary dolomite (Vasconcelos and McKenzie 1997; van Lith et al. 2003; Vasconcelos et al. 2006; Delfino et al. 2012). Ca-dolomite is crystallizing within a black aragonitic sludge layer in Lagoa Vermelha muds at or near the sediment-brine interface under anoxic hypersaline conditions (Fig. 4.17b). Bacterial dolomite has also been identified, along with lenticular gypsum in nearby Brejo do Espinho (Delfino et al. 2012).

Although the near coastal setting is similar (compare Figs. 4.17a and 4.4), unlike the Coorong salinas, the source brines for these evaporitic carbonates on Vermelha are thought to be marine or connate groundwaters drawn into the salina by evaporative drawdown. Some marine-fed salinas in the Coorong occupy similar hydrographically-isolated subsealevel depressions (e.g. Halite Lake), but are in a more arid coastal setting and tend to precipitate greater proportions of laminated gypsum-aragonite, not dolomite in salinas with seawater feeds.

Both the initial precipitation and early diagenetic evolution of Lagoa Vermelha dolomites is strongly mediated by microbial activity. In fact, sulphate-reducing bacteria from Lagoa Vermelha samples, cultured in brines at low temperatures from artificial seawater, produced highly ordered dolomite in the laboratory at earth-surface temperatures (Vasconcelos and McKenzie 1997). *Desulphovibrio brasiliensis sp. nov*., a moderate halophilic sulphate-reducing bacterium from Lagoa Vermelha (Brazil) was identified as one of a number of BSR species that are mediating dolomite formation (Warthmann et al. 2005).

Evaporation lowers the lagoon water level in the dry season and drawdown then allows seawater to enter via seepage through the dune barrier. Elevated organic productivity in the lagoon leads to anoxia at the sediment-water interface and the formation of a black organic-rich carbonate sludge on the meromictic salina floor. The highly saline waters have elevated sulphate levels, which in the shallow subsurface provide a sulphur source for bacterial sulphate reduction, as well as elevated magnesium that is precipitated as Mg-calcite and calcian dolomite. Microbial activity in the sludge mediates the precipitation of these primary carbonates. Eventually microbial activity ceases, but the diagenetic precipitation of dolomite continues atop the microbially precipitated crystal substrate.

Vasconcelos et al. (1995) first suggested that sulphate-reducing bacteria in hypersaline waters promote the essential conditions needed for dolomite precipitation. Van Lith et al. (2002), after a detailed study of the hydrochemistry in the lagoons, concluded that elevated salinity and sulphate reduction are the main factors inducing dolomite precipitation in these lagoons (Fig. 4.17c, d). Their detailed measures of water and sediment conditions during an annual cycle (1996–1997) demonstrated that dolomite formed in May–June which was a time of high salinity. High $\delta^{34}S$ of pore water sulphate and high sulphide concentrations correlated with dolomitic horizons, demonstrating the association of bacterial sulphate reduction with dolomite formation.

Dolomite forms year round in another small nearby salina, Brejo do Espinho; perennial precipitation is a direct response to its higher year-long salinity compared to Lagoa Vermelha. High salinity apparently provides the ions and saturation state necessary for dolomite precipitation, while the observation that dolomite formed at times or in zones of decreased sulphate concentrations underlies the likely importance of bacterially-driven sulphate reduction in Brejo do Espinho. Bacterially-driven sulphide oxidation also drives dolomite precipitation in other as yet untested high salinity lakes in the same region (Moreira et al. 2004; Delfino et al. 2012). The precipitation of dolomite in the lab at earth surface conditions using various strains of halotolerant sulphate-reducing bacteria (Van Lith et al. 2003) underlines the fundamental role of microbial metabolism in these and likely many other saline anoxic environments (Chap. 9).

Sulphate ions in the muds form strong ion pairs with Mg^{2+} ions and so are held together in space like a single particle. When sulphate-reducing halotolerant bacteria metabolize

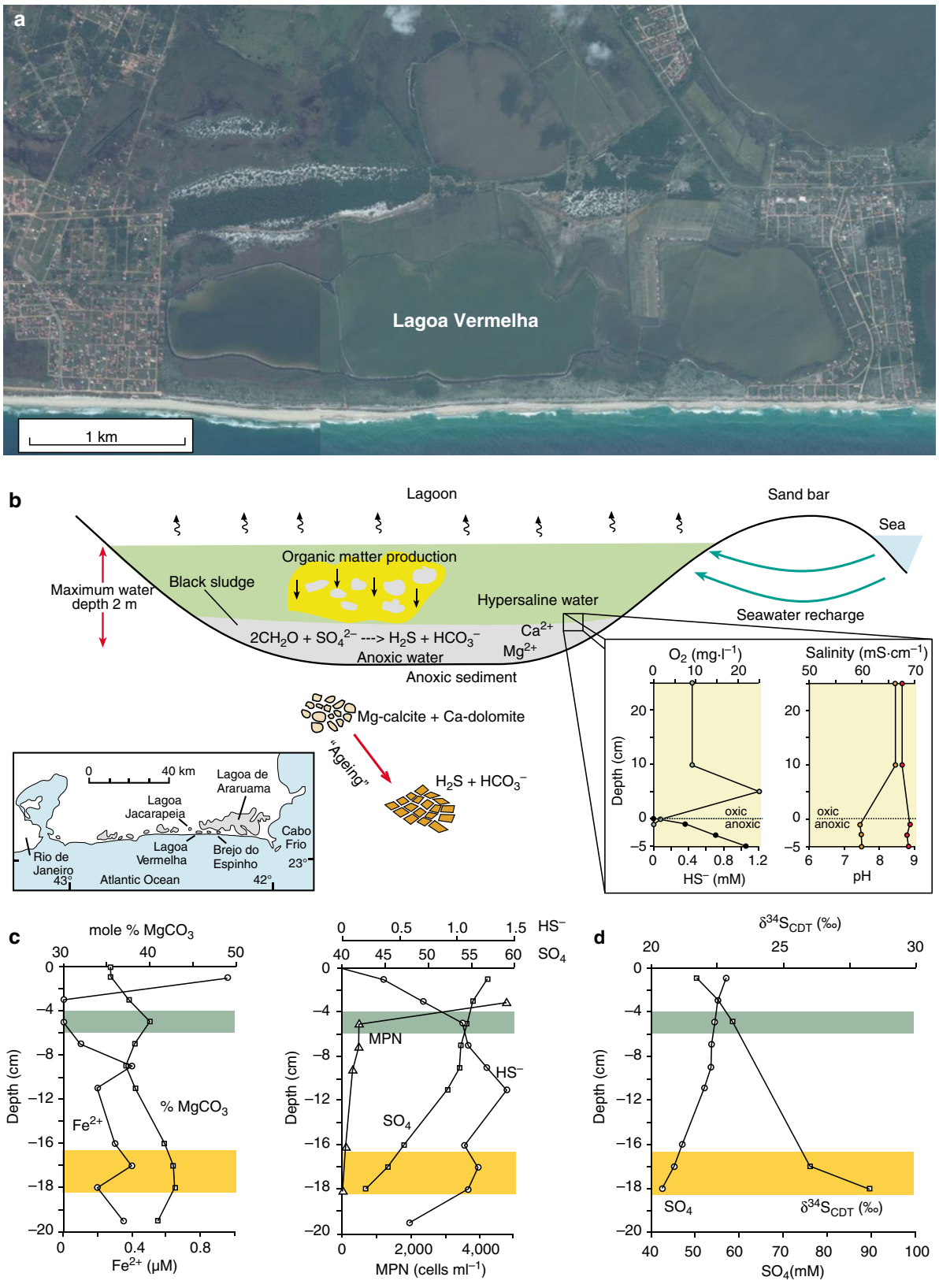

Fig. 4.17 Lagoa Vermelha, Brazil. (**a**) Aerial view of Lagoa Vermelha. (**b**) Schematic of microbial dolomite formation in Lagoa Vermelha and Brejo do Espinho, Brazil. Insets show the location of the salina on the Atlantic Coast and the pore water conditions immediately above and below the sediment brine interface. (**c**) Mol% $MgCO_3$ in carbonate, Fe^{2+}, HS^-, and SO_4^{2-} concentrations, and most probable numbers (*MPN*) of sulphate-reducing bacteria in Lagoa Vermelha sediment from 0 to 24 cm depth. (**d**) Dissolved sulphate concentration in pore waters of Lagoa Vermelha and its sulphur isotopic composition ($\delta^{34}S_{CDT}$). In April 1999 the core illustrated in **c** and **d** was taken and pore water extracted. The *coloured bars* indicate depths with well-developed Ca-dolomite horizons (After Vasconcelos and McKenzie 1997; van Lith et al. 2002)

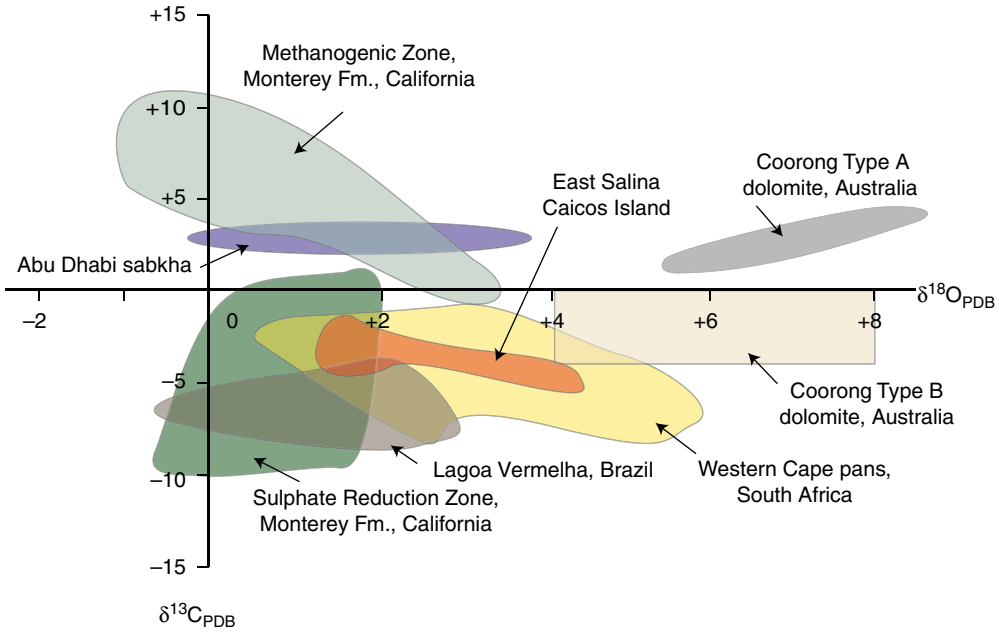

Fig. 4.18 Plot fields of $\delta^{18}O_{PDB}$ versus $\delta^{13}C_{PDB}$ values for Holocene dolomites and associated minerals in various documented sulphate reduction and methanogenesis zones (After Mauger and Compton 2011; Warren 2000a, and references therein)

SO_4 ions, they also metabolise the accompanying Mg^{2+} ions inside their cells. Magnesium is essential for many vital physiological functions in the bacterial cell, and makes up 0.5 % of the cell's dry weight in halotolerant strains. During bacterial metabolism, excess Mg is released together with other byproducts of sulphate reduction, such as bicarbonate ions and hydrogen sulphide (Chap. 9). Saturation with magnesium in microenvironments around the bacterial cell probably creates conditions favourable for preferential precipitation of dolomite, as is observed in lab-based bacterial culture experiments (Van Lith et al. 2003).

Using their understanding of the Lagoa Vermelha dolomite system as their starting point, Vasconcelos and McKenzie (1997) proposed a new actualistic model for dolomite formation that they call the microbial dolomite model (Fig. 4.17b). An anoxic turbid layer at the sediment surface creates a special magnesium-entraining environment where photosynthetically produced organic matter can be microbially recycled by sulphate-reducing bacteria on a submicron scale, with concomitant precipitation of high-Mg calcite and Ca-dolomite. In contrast, to the sulphate-reduction model of Kastner (1984), which required a lack of sulphate, this model requires a continuing supply of sulphate in order for halotolerant sulphate-reducing bacteria to metabolise and so precipitate dolomite (Fig. 4.17b). It seems that living sulphate-reducing bacteria are required to overcome the kinetic problems of penecontemporaneous dolomite formation.

Once dolomite bionucleation has occurred, the Ca-dolomite ages; as is indicated by depth-related trends of larger dolomite crystal size, more negative $\delta^{13}C$ values and increased stoichiometric ordering of the dolomite lattice. Bacteria apparently remain important in shallow burial, as seen by the continued presence of nanobacteria on the surfaces of the "aging" crystals. With time, and deeper in the sedimentary section (70–90 cm), the crystals grow by a layer-by-layer mechanism that creates smoother and euhedral crystals. Apparently, once the dolomite is nucleated, crystals can continue to grow by inorganic processes, but each new layer still appears to be composed of coalesced submicron-size bacterial balls (spheroids). The microbial dolomite model requires an ongoing supply of sulphate to maintain the microbial activity promoting dolomite precipitation. In contrast, it may be that the presence of sulphate in a sterile (bacteria-free) environment may act to inhibit dolomite precipitation as shown in the laboratory experiments of Baker and Kastner (1981) and Morrow and Ricketts (1988).

Wright (1999) and Wacey et al. (2007) present a similar set of microbial arguments and laboratory experiments to explain the ease of dolomite precipitation in some of the carbonate salinas of the Coorong. Likewise, Mauger and Compton (2011) document microbial (BSR) mediated formation of Holocene dolomite in the near-coastal hypersaline pans of western Cape (centred on Yzerfontein), South Africa (Köppen Csb). Isotopically, with the exception of the Coorong, these coastal lagoonal dolomites show similar carbon-oxygen plot fields indicative of bacterial sulphate reduction, while the Abu Dhabi dolomites show the more positive carbon signatures, perhaps associated with archaeal methanogenesis.

Coorong isotope data are perhaps more influenced by evaporative concentration and Raleigh distillation in increasingly saline brines (Fig. 4.18; Rosen et al. 1988, 1989; Warren 1990). When comparing stable isotope values (including sulphur values) from dolomite and non-dolomite lakes in the Salt Creek region of the Coorong, Wacey et al. (2007), found it difficult to interpret the dolomite as unequivocally bacterial based on isotopic analysis, although they

favoured this origin. The evaporative concentration trends noted in earlier work on dolomite type-A by Rosen et al. (1988, 1989) and the two isotopically and crystallographically separate dolomite cluster fields, in Coorong dolomites defined in this work support at least a partial contribution from inorganic concentrative processes, as illustrated in Figs. 4.7 and 4.18. The defining study for the unequivocal bacterial origin of Coorong dolomite is probably yet to be published.

Unfortunately, in the realm of bacterially-mediated dolomite studies, some authors have attempted to draw a dichotomy between bacterial mediation and evaporitic conditions favouring dolomite precipitation, but this is an extreme view. The Brazilian, South African and Coorong pore waters are all settings where sulphate-reducing or methanogenic bacteria flourish. The same settings are also hypersaline, and depending on climate and hydrology their waters capable of precipitating evaporite salts, including nearby gypsum, as in South Africa and the Coorong. This is where the dolomite-mediating microbial community thrives in schizohaline sulphate-entraining salinities that can be seasonally up to four to five times that of seawater. It is a halotolerant community that thrives at the expense of a less halotolerant biota. That is, it is the somewhat elevated salinities in surface and near surface waters that allow appropriate halotolerant sulphate-reducing bacteria to flourish in pore waters that can be marine, nonmarine or hybrid (see Chap. 9). High salinity and halotolerant bacterial mediation of natural primary dolomite are associated, not separated, features in many natural hypersaline waters.

Continental Subaqueous Basins

Examples of subaqueous evaporite deposits discussed so far occur in hydrographically-isolated subsealevel coastal depressions fed solutes via inflows of marine groundwaters. The resulting marine-fed evaporitic sediments accumulate at limited scales (1–20 km across) and limited thicknesses (<10 m). Such deposits have little or no longterm preservation potential within the rapidly migrating shorezone hydrologies that typify today's icehouse eustasy (Warren 1991). To find active examples of thick widespread subaqueous evaporite deposition in Quaternary sediment, we must move to continental lacustrine settings in lake depressions characterised by perennial saline water bodies. This setting corresponds to the third category of Hardie et al.'s (1978) classification of saline lacustrine settings described in Chap. 3; namely the perennial stream floodplain – perennial saline lake. In such a setting Quaternary evaporites have filled lake basins measuring up to a 100 km across with stacked saline beds that can be more than tens of metres thick.

Perennial Saline Lakes

Subaqueous lacustrine beds typically alternate with brine pan and sabkha salt beds in most active continental saline lakes. Changes from one depositional style to another relate to changes in inflow volume and chemistry and often indicate a change in climate, fluvial supply and/or tectonics. Saline perennial lakes and pans typify the topographically lowest part of a endorheic lake basin. Most subaqueous lake sediments are dominated by carbonates and siliciclastics, higher salinity salts are less common. This reflects the hydrology needed to form a permanent saline lake. That is, to maintain a perennial above-surface brine body requires continuous water inflow to the lake depression, either from river inflow or from spring seeps.

The definition of what surface salinity constitutes a modern saline lake varies between the Northern and Southern Hemispheres; Hardie et al. (1978) chose a minimum concentration of 5,000 ppm to define saline lake waters, based on Beadle's (1974) definition of the upper salinity tolerance of freshwater organisms. In contrast, most Australian limnologists use 3,000 ppm to separate freshwater and saline biotas (Geddes et al. 1981).

Regardless of its minimum salinity, a perennial brine lake and its biota is at the mercy of variations in the local climate and inflow intensity. Lake water levels and salinities are subject not only to seasonal changes but to longterm fluctuations in climate and tectonism. In the short term the volume of inflow water increases after a storm or winter snow melt; in the long term a change to a more humid climate increases the volume of water in the lake depression, while a change to more arid conditions decreases the volume of surface water and may convert a perennial saline lake into a saline pan or evaporitic mudflat. Tectonic uplift also affects lake deposition, it can convert what was formerly a hydrologically open basin into an endorheic basin, or vice versa, volcanism and lava flows can do the same. Tectonism can also change the position of the topographically lowest point in the lake and, via uplift in the drainage region-, can change the volumes of surface runoff, groundwater seepage and inflow chemistry.

The chemical make-up of continental lake brines is much more variable compared to the near isochemical seawater reservoir that supplies mostly gypsum and halite to modern coastal salinas (Table 4.2). Proportions of the various ions in perennial saline lake waters are controlled by chemistries of the dilute inflows, which are a combination of rainfall intensity and the lithologies in the drainage area surrounding the lake (Fig. 2.19).

Great Salt Lake, Utah

Great Salt Lake is a perennial water body and has been so for the last 30,000 years. It is the largest saline lake in the United States and one of the largest perennial saline lakes in the

Table 4.2 Varying ionic proportions in selected perennial lake waters, compiled from various references listed in text

	Great Salt Lake, USA North Arm (mg/l)	Lake Van, Turkey (mg/l)	Tuz Golu, Turkey Deep Zone June (mg/l)	Tuz Golu, Turkey Main Zone June (mg/l)	Dead Sea, Middle East, Upper water (mg/l)	Dead Sea, Middle East, Lower water (mg/l)	Lake Asal, Djibouti (ppm)
Na	105,120	7,747	31,500	114,717	38,510	39,700	101,200
K	8,480	508	453	1,458	6,500	7,590	5,161
Mg	10,420	95	1,327	3,963	36,150	42,300	12,500
Ca	420	5–10	478	772	16,380	17,180	2,677
Cl	181,730	5,450	50,875	185,454	196,940	219,250	199,155
SO_4	21,730	2,344	3,485	8,838	580	420	4,320
HCO_3	–	2,191	–	–	–	–	184
CO_3	–	3,331	–	–	–	–	–
TDS	328,110	22,000	–	–	300,000	332,000	
pH	7.3	9.5	8.5	7.3	–	–	7.1
Br	120	–	–	–	4,000	5,270	–
Sr	–	0.70	–	–	–	–	–
Li	50	1.50	–	–	–	–	–
B	40	–	–	–	–	–	–
PO_4	–	0.52	–	–	–	–	–

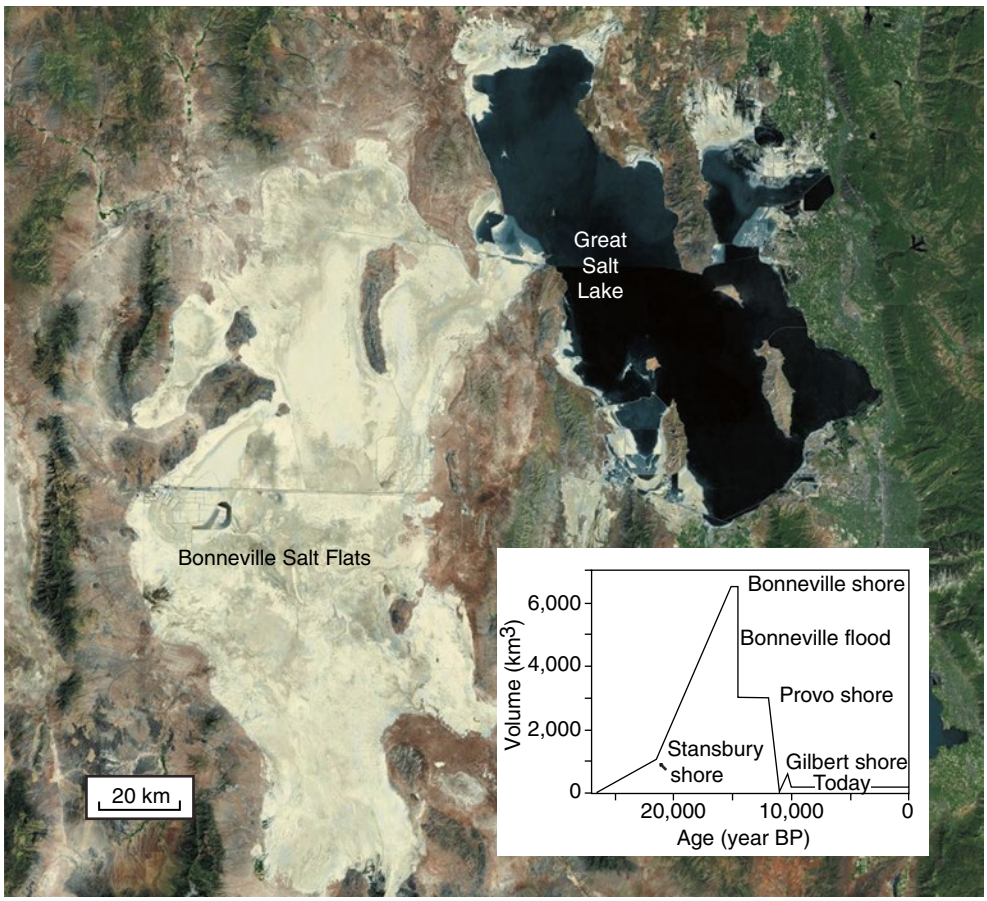

Fig. 4.19 Great Salt Lake and the Bonneville Salt Flat, Utah and the adjacent peaks of the Wasatch Mountains east of the lake depression. A railway causeway that transects the northern arm of the lake is visible, as are solar evaporation ponds. The Lake Bonneville salt flats (*lighter coloured*) lie to the west of the Great Salt Lake. *Inset* shows changes in lake water volumes over the past 25,000 years

world, measuring some 120 km (75 miles) long and 55 km (35 miles) wide, with a water surface elevation that oscillates around 1,280 m (4,200 ft) above sea level (Figs. 4.19 and 4.20). At this elevation the lake brines cover an area of 4,180 km^2 and have a maximum depth of 10 m. In a typical year the water surface fluctuates around 30–60 cm, reaching its highest level in May-July (after snow melt) and dropping to its lowest level in October-November. Since 1847 the water level of Great Salt Lake has varied from a low of 1,277.5 m in 1963 to a high of 1,283.75 m in 1986–87

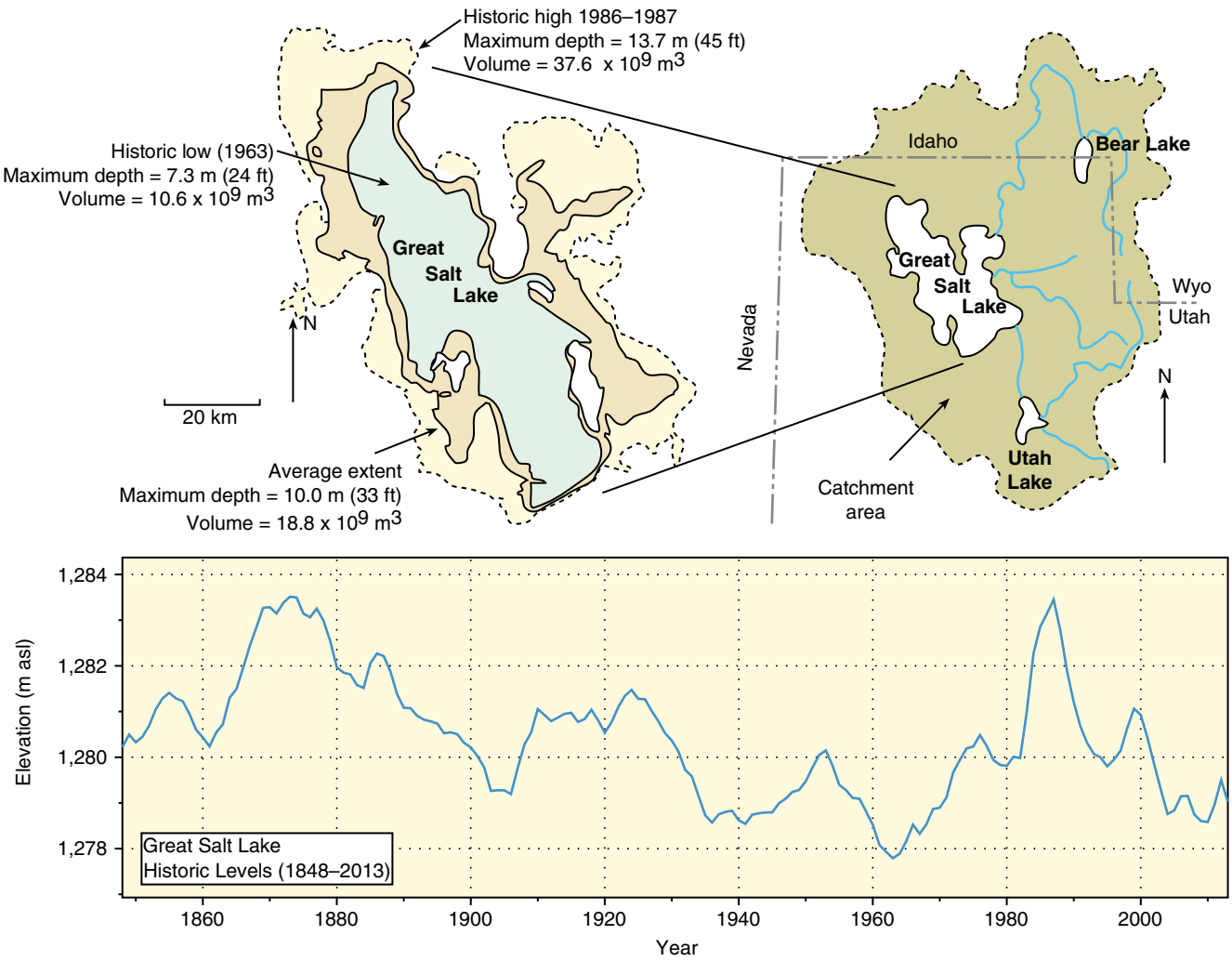

Fig. 4.20 Great Salt Lake, Utah. The lake is subject to large changes in the extent of its perennial water body. The *upper figure* shows the different extent of its highest and lowest levels in historical time. The chart plots yearly changes of lake water level since 1847

(Fig. 4.20). The 3.7-m rise in the level of the Great Salt Lake (Utah, USA) between 1982 and 1986, leading to the record historical high in lake water level, was at least partly related to the record rainfall and snowfall in its catchment during the 1982/3 El Niño (Arnow and Stephens 1990). Because the lake is so shallow and its floor so flat, small changes in water level correspond to large migrations of the strandline.

Great Salt Lake lies in an endorheic basin with no surface outlet. The main rivers entering the lake are the Bear River from the north, the Weber and Ogden Rivers from the east, and the Jordan River from the south (Jones et al. 2009). Together with small volumes of bajada runoff, the rivers supply around two thirds of the water currently entering the lake. Direct precipitation into the lake supplies some 31 %, while ground water supplies the remaining 3 %. The drainage basin of the lake today covers an area of about 57,000 km^2 (21,500 mile^2). Water is lost from the lake mostly through evaporation, with something like 3,500 km^3 of water evaporating annually (Fig. 4.20). When inflow equals evaporation, the level of the lake remains constant. If inflow is greater or less than evaporation, the level of the lake will rise or fall, respectively.

Being situated along the Wasatch Front at the eastern edge of the tectonically active Basin and Range Province, means the size, shape, and location of the Great Salt Lake depression has been a response to variable intensities of subsidence and faulting, overprinted by the intense climatic vagaries of the Late Pleistocene. It currently straddles BSk and Cfa Köppen climate zones. Present-day Great Salt Lake is a remnant of a much larger and fresher water body that was once linked into the Pleistocene Lake Bonneville system, as were Utah Lake, Sevier Lake, and the Bonneville Salt Flats (Fig. 4.21a). Areas of perennial fluvial inflow into Pleistocene Great Salt Lake are defined by classic "bird's-foot" or "Gilbert-style" hanging deltas (Fig. 4.21a). The downcutting of the current hydrology and the presence of Pleistocene shoreline terraces on higher levels of the delta prism suggest

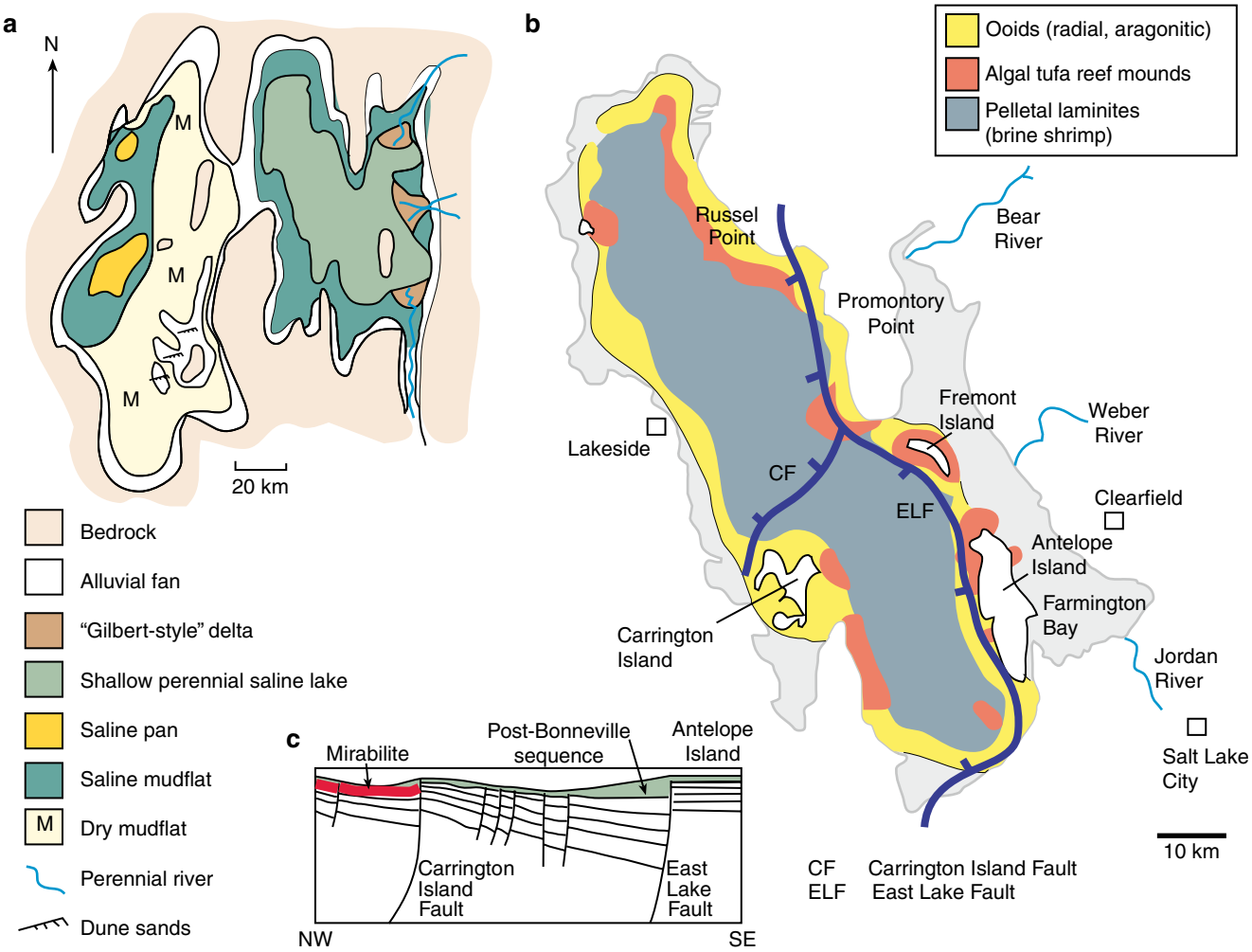

Fig. 4.21 Sediment distribution in Great Salt Lake and surrounds. (**a**) Distribution of depositional settings in the Bonneville/Great Salt Lake basin, Utah. The lake itself is a perennial water body fed by rivers with "bird's-foot" deltas at the older entry points into the lakes. The saline pan facies are halite-rich with lesser glauberite, while the dry and saline mudflats are subaerially exposed parts of the old subaqueous floor of Lake Bonneville. Carbonate mudstones, mostly aragonite pellets, dominate sediments currently accumulating on the subaqueous lake floor (After Smoot and Lowenstein 1991). (**b**) Distribution of algal tufa reefs and ooid sand shoals about the strandzone at the edge of the perennial water body in Great Salt Lake. Positions of the East Lake Fault (*ELF*) and the Carrington Island Fault (*CF*) are shown (After Eardley 1938; Colman et al. 2002). (**c**) Schematic cross section based on seismic lines between Antelope Island and Carrington Island showing the importance of syndepositional faulting in controlling thickness of post Bonneville (<13.5 ka) sedimentary packages (*grey*) and the distribution of the mirabilite bed in the lake (After Colman et al. 2002)

deltas were most active during Pleistocene lake full stages (Lake Bonneville time) when the lake was not accumulating evaporite salts (Spencer et al. 1985a, b; Balch et al. 2005; Jones et al. 2009).

Modern strandzone deposits are mostly shorezone spits and bars, which are dominated by aragonitic ooid and peloidal sands (mostly brine shrimp pellets). Carbonates also precipitate about the lake strandline in spring mounds, algal mounds, and in stromatolites (Fig. 4.21b; Eardley 1938; Halley 1977). Older algal reef mounds are located further out in the lake and are now buried by lake muds; they grew earlier in the Holocene when lake water levels were lower than today (Colman et al. 2002). Oolite shoals today form sand waves that define the lake strandzone (Fig. 4.21b). Individual ooids are aragonite with a radial crystal structure. When and how the individual ooids grew is not well understood, but halobacteria and organic matrices are thought to play a role (Sandberg 1975; Pedone and Folk 1996; Reitner et al. 1997).

Laminated mudstones, in large part composed of the faecal pellets of brine shrimp, are currently accumulating further out in the lake (Eardley 1938). The pellets are a mixture of aragonite and detrital matter, mostly quartz, clays and organics. The brine shrimp *Artemia gracilis* thrives in the lake, it is a filter feeder that flourishes in spring and summer. It supplies a seasonal rain of faecal pellets to the lake bottom and its droppings represent a sampling of the mineral matter

suspended in the water column. This implies aragonite is a seasonal precipitate within the upper part of the meromictic water column (see Chap. 9 for biology and feeding styles of brine shrimp and other halozoa).

Rippled sand lamina alternate with laminar mud in the deeper water deposits of Great Salt Lake, with many deeper beds disrupted by the growth of now-dissolved evaporites (Unit I; Spencer 1983). Remnants of bedded Holocene halite still remain on the deepest parts of the lake floor, preserved by longterm density stratification in the overlying waters. Spencer (1983) recovered euhedral gypsum in the upper 1–2 m of the now water-covered aragonitic sediments of the lake centre. This sediment also shows evidence of haloturbation and pinch-and-swell bedding. Below this is a 1 m-thick bed of finely laminated aragonitic clay and algal mat partings, which passes laterally into bedded mirabilite (Unit II; Spencer 1983). Shallow seismic shows this mirabilite unit is restricted to a fault-controlled depression north of the Carrington Island Fault (Fig. 4.21c). Laminated aragonite is underlain by laminated calcitic clays, interspersed with lamination-poor ostracod-rich horizons. Spencer (1983) interpreted this bed (his Unit III) as the deepest water unit recovered in his coring program. Only one core penetrated below this deeper water unit to recover clays and muds of what may be a subaerial mudflat (Unit IV).

Prior to 32 ka, the basin was an ephemeral pan – saline mudflat system (Unit IV). Since then, Great Salt Lake has mostly been a perennial water body, initially a shallow saline brine lake, then a brackish lake between 25 and 19.5 ka. Between 19.5 and 17.5 ka a fresher, but somewhat restricted, lake occupied the basin with a water surface near or above the Provo level (water was ≈ 195 m deep). Fresh water conditions with a standline near the Bonneville level existed around 17 ka (with waters around 310 m deep). Then 16,800 years ago a sharp drop in lake level occurred as Lake Bonneville was drained suddenly into the Snake River Basin through the Red Rock Pass region in Idaho. This catastrophic drop occurred after the rising waters of Lake Bonneville topped a natural dam formed by coalesced alluvial fans at Red Rock Pass. This flood set up an ongoing crossflow, which rapidly eroded and downcut into the fans, dropping the lake level by 105 m (see inset in Fig. 4.19; O'Connor 1993). The flood from this event was catastrophic, releasing some 4,168 km^3 of water in the first few weeks and lasting about a year. At peak discharge, flow was around one million m^3/s and the incision was some 100 m deep. The resulting scabland swath leading into in the Snake River Basin is some 5 km wide are still visible today. Before the catastrophic draining, Lake Bonneville had a surface area of 51,000 km^2 (on par with Lake Michigan or lake Huron) and was up to 300 m deep.

The lake shrank further around 14,000 years ago as glaciers retreated from North America and the climate became more arid. Between 14 and 8 ka the lake was at extremely low levels and at times was divided into two separate saline basins. For the past 8 ka the lake has fluctuated near its present level. Much of the salt now contained in the Great Salt Lake was originally dissolved solute in the waters of Lake Bonneville. An additional two million tons of dissolved salts now enter the lake each year via river and spring inflow, which carries leachate from the surrounding soils and rocks.

Recent study of a single long core that records the last four glacial/interglacial sequences in the Great Salt Lake Basin has shown that salt/freshwater marshes as documented by Spencer (op cit) were common during interglacials (Fig. 4.22; Balch et al. 2005). Deep freshwater conditions correspond with the maximum global ice volume in Oxygen Isotope Stage 2, and before a maximum in global ice during Oxygen Isotope Stage 6. Immediately following each deep lake period the lake level crashes via rapid desiccation that deposits thick evaporite units.

Fault-accommodated subsidence in the Great Basin has now filled the depression with more than 3,700 m of continental sediment, with most of the sediment carried in by the major rivers. Two currently-active faults underlie Great Salt Lake (Fig. 4.21b, c; Colman et al. 2002). The East Lake Fault passes along the west edge of Antelope and Fremont Islands and on northwards by the west side of Promontory Point. The Carrington Fault extends northeastward from Carrington Island to merge with the East Lake Fault of the southwest tip of Promontory Point.

Most of the current strandzone facies along the eastern side of the lake are tied to the topographic escarpment created by the East Lake fault, many now buried Holocene tufa-reef mounds also sit atop subsidiary faults in the lake. Similar broader-scale fault-controls to Late Pleistocene lacustrine geometries are seen in seismic facies throughout the lake basin. Colman et al. (2002) concluded that the Great Salt Lake basin has been, and continues to be, an area of active extensional tectonics and that tectonics has exerted a major effect on the distribution and type of sediments in the lake. Currently, the East Lake Fault is at least as active as any of those along the Wasatch Front, showing at least three episodes of significant faulting since lake water level fell around 13.5 ka from its Pleistocene high. The upthrown side of the Carrington Fault today forms a sill, with a seismically resolvable tip that is only about 5 m below present lake floor. Fluid flow into the lake along this and other fault planes may explain some of the indurated bioherm mounds and pavement sheets present on the lake floor.

The fall of the lake waters that marked the end of the high Bonneville phase led to the formation of a basin-wide seismic horizon associated with lowered lake levels (Colman et al. 2002). Mapping of this reflector shows that the southern basin comprises a distinct sediment wedge thickening toward the East Lake Fault, a geometry that contrasts, to

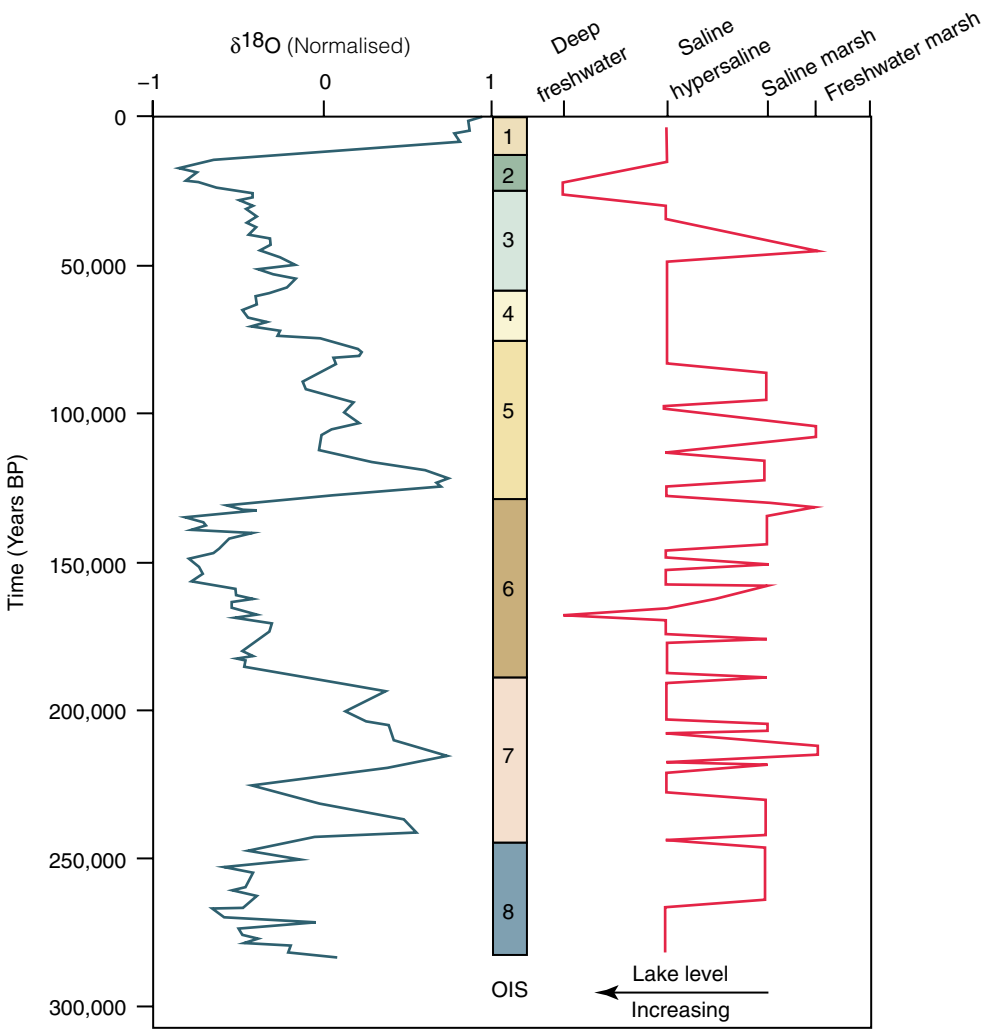

Fig. 4.22 Great Salt Lake, showing water elevation variations and corresponding environments over the last 300,000 years, plotted against Marine Oxygen Isotope stage (*OIS*) with corresponding $\delta^{18}O$ curve (After Balch et al. 2005)

some degree, with the smooth symmetry of the current lake floor (Fig. 4.21c). Seismic facies maps also show the lake level during the early Holocene was considerably lower than today; it was a time when the lake was an intermittently flooded playa and when up to 13 m of post-Provo halite accumulated near the East Lake Fault. At that time small remnant water bodies probably ponded in local lake-floor grabens along the downthrown sides of active fault scarps. Thus fault-controlled tectonics controlled the distribution of the various early Holocene pan evaporites, including the mirabilite/halite beds (Fig. 4.21c).

Within this tectonic framework, Late Quaternary climate change across the Great Basin altered solute proportions in the lake inflows and so influenced mineralogies in the evaporite suites accumulating in low water stages in Great Salt Lake. Spencer (1983) defined three major styles of inflow to the lake system; (1) concentrated Na-Cl dominant spring waters, (2) dilute Ca-HCO_3 river waters, and (3) dilute Ca-HCO_3 precipitation (rainfall and snow melt). During the fresh-water period of the Lake Bonneville and other pluvial times, the inherently higher levels of meteoric discharge to the lake meant inflow chemistries were dominated by calcium bicarbonate waters. Saline stages, as in most of the Holocene, are characterised by lowered meteoric inflow volumes and so fault-fed hydrothermal springs are an increasingly significant solute source. Between 15 and 8 ka the lake waters were cold and relatively depleted in Cl. Mirabilite accumulated in the lowermost parts of the cold, largely subaqueous meromictic lake floor, in a setting much like the subaqueous salts of the modern meromictic saline lakes of the Canadian interior (Fig. 12.19).

Since that time, conditions became drier and warmer, with higher proportions of Cl-rich waters entering the perennial lake. Halite was precipitated prior to mirabilite during hypersaline or droughty episodes in the lake and this mirabilite is still an ephemeral mineral in the pans of the North Arm. Before the lakewide drawdown that ended Lake Bonneville, the dominant lake carbonate was calcite. Since that time a more arid climate has dominated and aragonite is the dominant carbonate precipitate.

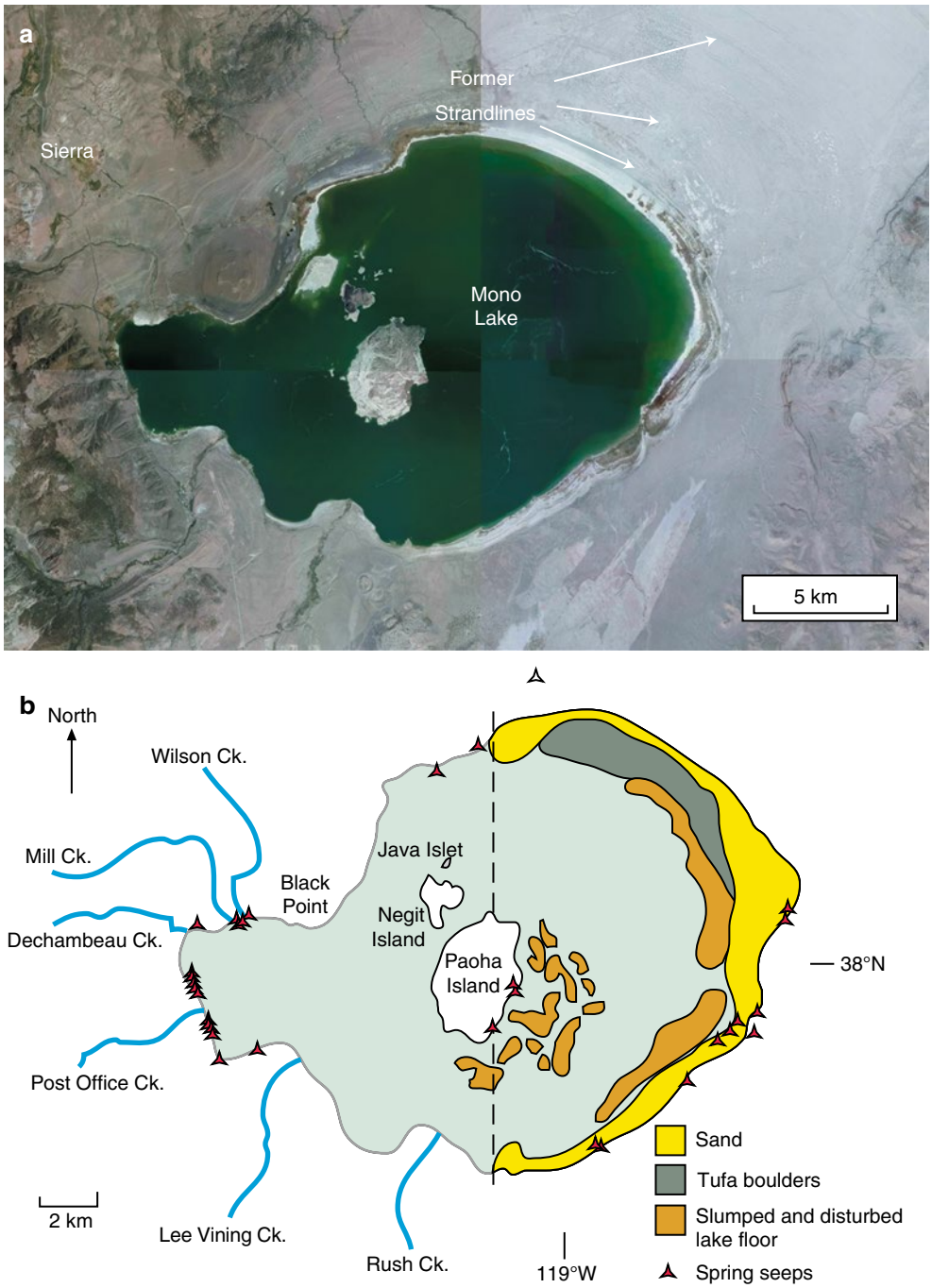

Fig. 4.23 (**a**) Mono Lake, California. Successive strandlines associated with lake shrinkage are visible in the Landsat image, as are the volcanic centres of Paoha Island and the adjacent lake plain to the northwest. High relief drainage source to the west in the Sierra Nevada is clearly seen in the high proportion of creeks entering the western side of the lake (Landsat image courtesy of NASA). (**b**) Geological interpretation of the type of sediment is only published for the eastern half of the lake – extent indicated by dashed line (In part after Benson et al. 2003)

Mono Lake, California

Mono Lake, an endorheic meromictic alkaline saline lake with an average depth of 17 m, in a volcanically active area at the edge of the Sierra Nevadas, California (Fig. 4.23a), which has been accumulating laminated lacustral sediments since 760 ka. Current free surface brine volume is ≈3.2 km^3, surface area is 184 km^2, annual total inflow is around 283.7×10^6 km^3 and current salinity is around 90,000 ppm. It lies in a Csb Köppen climate zone. Major anion content of lake brines is divided almost evenly between chloride, sulphate, and bicarbonate. The high pH (≈9.8) and alkalinity of lake waters leads to high concentrations of volcanic elements that ordinarily have short residence times in lakes (i.e. lanthanides and actinides, including naturally high levels of arsenic in bottom brines; Tomascak et al. 2003). Calcium carbonate (calcite and aragonite) precipitates spontaneously from the lake waters and makes up 3–10 % of the laminite sediment on deeper tufa-free bottoms, the remainder is detrital. Some of the lake bottom laminites are slumped, possibly initiated by ongoing volcanic disturbance

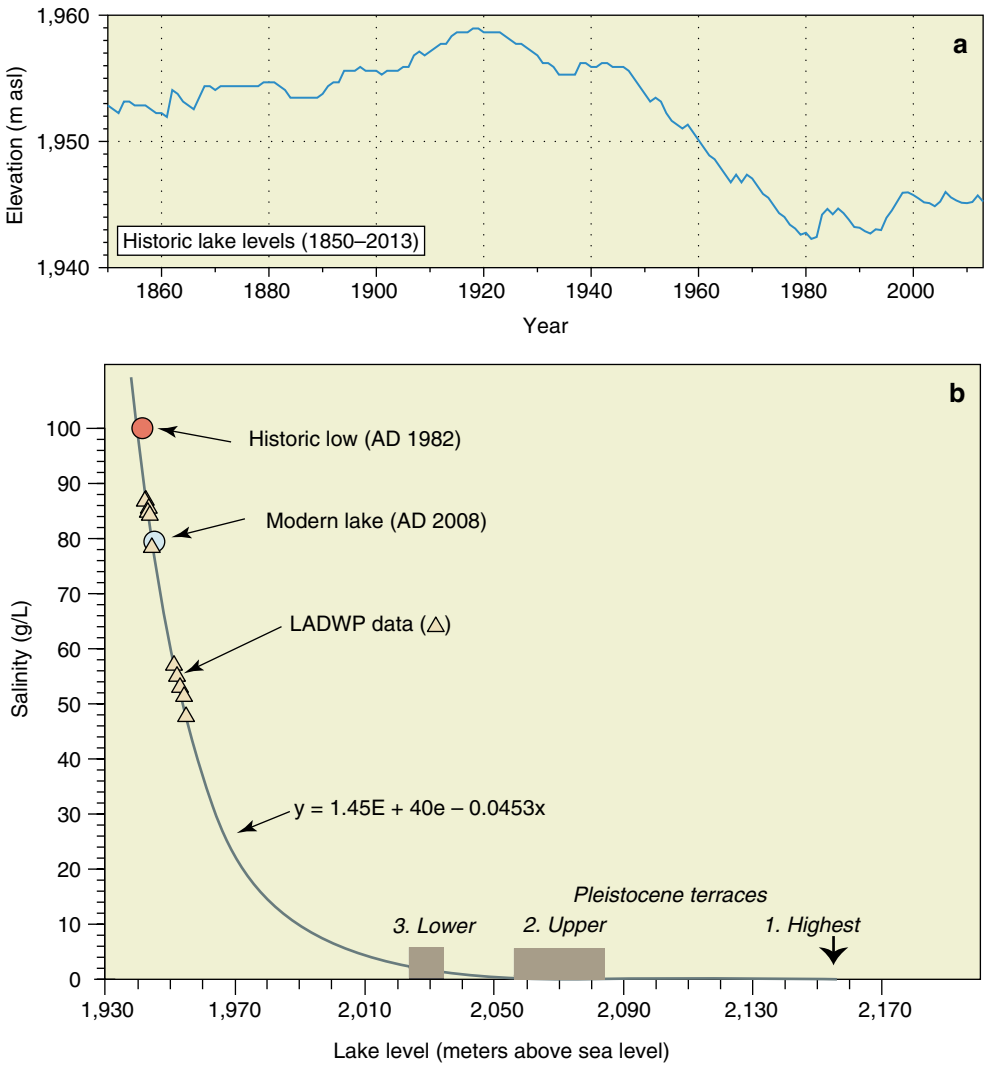

Fig. 4.24 Mono Lake levels (**a**) Historic levels from 1850 to 2010 (Replotted from online data of Mono Lake Preservation Society last accessed on June 3, 2013 at http://www.monolake.org/live/lakelevel/yearly.htm). (**b**) Exponential relationship between Mono lake level and salinity is extrapolated to show very low salinities in the ancient lake levels associated with the Pleistocene terraces that surround the current lake (After Zimmerman et al. 2011)

(Fig. 4.23b; Benson et al. 2003). Calcite accumulates, sometimes with an ikaite precursor, where resurging groundwaters degas on the lake floor and can form spectacular biogenically-bound towers of tufa.

Lake Levels and Conditions

From 1850 until the middle of last century the lake water level rose some 5 m, then the water needs of the City of Los Angeles caused a drastic water fall. In 1941 the State Resources Board diverted the distributaries that fed Mono Lake into the Los Angeles aqueduct. In the 50 years since the diversion, Mono Lake water level dropped more than 10 m, the lake water volume was cut in half, while the alkalinity and salinity of the lake waters doubled (Fig. 4.24). Water levels were as high as 1958 m above sealevel, before the diversion of Mono's tributary streams. Subsequent lower lake levels exposed numerous calcitic tufa mounds and pinnacles on the lake floor and enlarged the portion of the lake floor made up of subaerial saline mudflats.

To prevent further desiccation of the lake, some water from the former distributaries has been rediverted back into Mono Lake, which is now slowly refilling after reaching an all time low of 1,942.2 m asl in 1982 (Fig. 4.24a). The current lake level is 1,944.35 m asl (June, 2015). The projected stabilized lake elevation is 1,948.3 m, but reference to Fig. 4.24 argues this may not be attained in the next few years. Interestingly, the anthropogenic lowering of lake water level in the last half-century and the associated increase in lake salinity is still well within the range of natural fluctuations experienced by Mono Lake in the last 2,000 years (Fig. 4.25a, b). Historic salinity and lake levels measurements can be related, exponentially, Zimmerman et al. (2011) document this relationship (Fig. 4.24b). It clearly shows that as lake levels fall the lake salinity increases. It implies that lake waters were fresh in the Pleistocene at times the various high lake level terraces were formed.

In years with large fresh water inputs the lake may become meromictic. The more usual state of the lake is

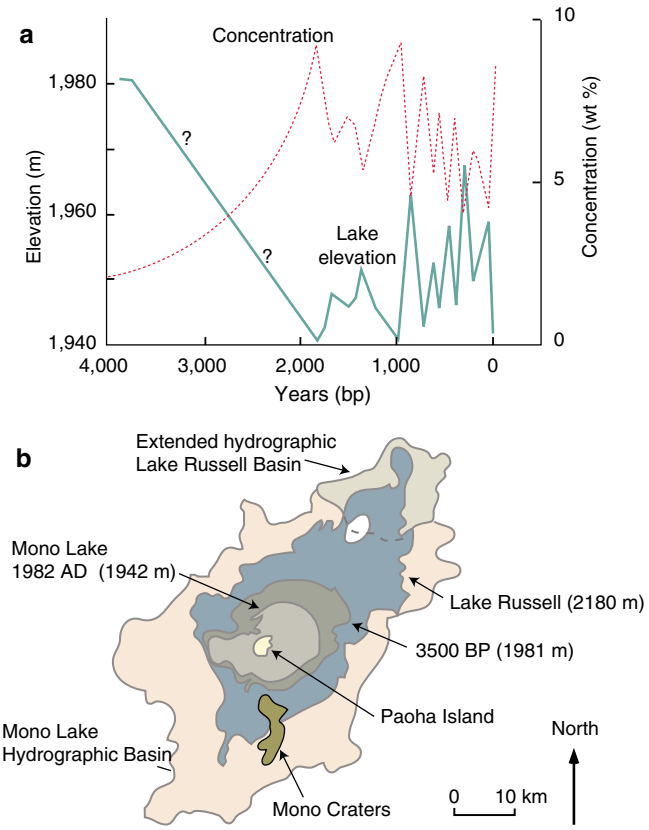

Fig. 4.25 Mono Lake, California. (**a**) Hydrological conditions for the last 4,000 years (After Stine 1990). (**b**) Map outlining different lake areas related to changing water elevations through time (After Rogers and Dreiss 1995a, b)

monomictic (annual mixing). In 1994, an unintentional consequence of lessening drainage water diversions from the Mono basin into the LA aqueduct was the onset of a period of anthropogenically induced "meromixis" (Jellison et al. 1998). Earlier, in 1982 and 1983, the lake had also become meromictic when exceptionally large volumes of freshwater runoff led to a rapid 2.6 m rise in surface elevation of the lake (Jellison and Melack 1993). In 1984 this chemical stratification accounted for a density difference of 1.2–1.5×10^{-2} g/cc between the 2 and 28 m water depths. At the same time the midsummer density difference between 2 and 28 m brine depths that was due to temperature was approximately 0.5×10^{-2} g/cc. Salinities ranged from 77 to 98 g/l across the interface and sodium, chloride, sulphate, and carbonate were the major ions in both the upper and lower water mass.

The lake's second transition from monomixis to meromixis began in 1994–1995 and had ended by 2004. A comparison of density differences between the 2 and 28 m water depths indicate thermal stratification predominated in 1993 and 1994 (monomictic years), while chemical stratification dominated the density differences in 1995, 1996 and 1997 (meromictic years) (Melack and Jellison 1998).

When monomictic, the lake has typically thermally stratified in March and mixed to the bottom by December. Since 2004, the lake has mixed annually with the loss of seasonal thermal stratification as it had in 1993 and early 1994, prior to 8 years of meromixis. During the meromictic conditions in the late 1990s, the absence of holomixis during winter created persistent anoxic conditions beneath the chemocline. This led to the accumulation of ammonium in the monimolimnion, its depletion in the mixolimnion, and low mixolimnetic chlorophyll concentrations in the spring and autumn (lessened photosynthetic activity).

Tufa Mound and Pinnacles

The most visually striking geological features of Mono Lake are its metres-tall tufa columns, which protrude from lake waters and line portions of the lake edge. These mounds and needle-like pinnacles of calcium carbonate frequently define linear trends that are the seepage expression of underlying faults and joints (Fig. 4.26). Soft bottom sediments surround columns and many columns are rooted in massive domal buildups of calcite. Dominant growth orientation is vertical and defines the rapid upward rise of less saline CO_2-rich waters. Branching of lithoid columns is rare and "pseudobranches" easily explained by the collapse of one or two adjacent columns imply much of the precipitation mechanism is via inorganic degassing of groundwater on reaching the lake floor. Microbial biofilms coat active tufa surfaces beneath the lake waters and create characteristic knobbly grumous microtextures in the reef mounds and pinnacles as they capture the precipitated carbonate (Fig. 4.26b).

In today's lake waters calcite and aragonite are the carbonate minerals with long-term stability and they dominate the nonsiliciclastic fraction accumulating in the lake (Benson et al. 2003). But during the colder Tioga glacial period of the Late Wisconsian (12–9 ka), and during the present day winter season, ikaite ($CaCO_3 \bullet 6H_2O$), was the dominant carbonate precipitate (Whiticar and Suess 1998). Ikaite is a metastable cryogenic carbonate and the low temperatures needed for ikaite stability are obvious in winter in Mono Lake. In the winter of 1985 ikaite crystals were visible as coatings on the subaqueous surfaces of active spring seep tufas about the shallow lake edge (*pers obs.*). If these small ikaite crystals were removed from the icy cold winter waters of the lake and held in an ungloved hand, the increase in ambient temperature caused the ikaite to deliquesce, so that in a few minutes it disappeared leaving behind a pool of milky water. Council and Bennett (1993) and Bischoff et al. (1993b) argued that during winter, calcite precipitation in Mono Lake is inhibited by low temperatures and high concentrations of phosphates and organic carbon. The same factors allow metastable ikaite to form. Ikaite decomposes into calcite during the spring warming, occasionally leaving pseudomorphs of the primary precipitate in the calcitic tufa.

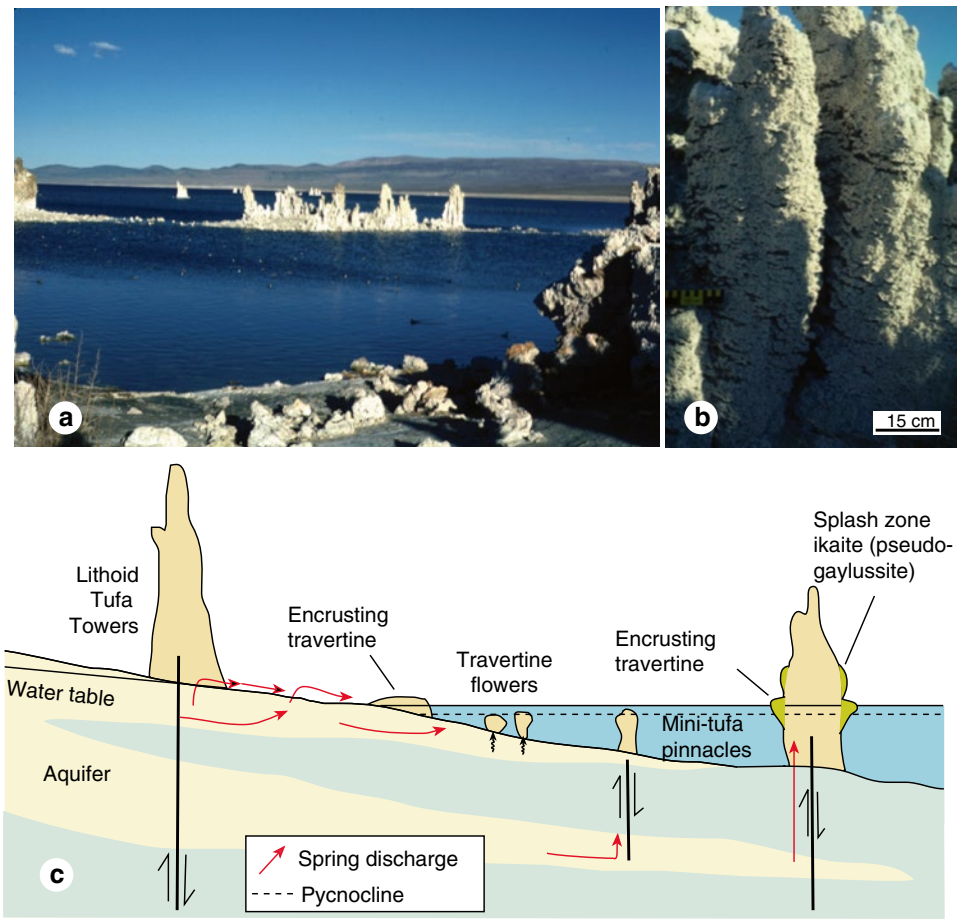

Fig. 4.26 Mono Lake, California. (**a**) Tufa pinnacles forming linear growths on the saline linear ridges in the lake floor in Nov. 1985. (**b**) Close up of algal-bound crenulated pinnacle surface and subhorizontal layering (scale bar is 15 cm long). (**c**) Schematic cross section showing aquifer control on the development of modern tufa mounds on the margin of Mono Lake California (After Council and Bennett 1993)

At a broader scale Council and Bennett (1993) demonstrated a strong hydrological control on the position of many of the larger lithoid tufa mounds. The unconfined aquifer that dominates the western side of the basin is composed of fluviodeltaic sediment and it controls the modern discharge at many points about the current lake shoreline (Fig. 4.26a, c). Currently active diffuse low-flow-rate seeps are dispersed across the strandzone, and extend from ≈200 m above the present lakeshore to around 1 m below the present lake water surface (Fig. 4.23). Diffuse outflows are geologically defined by flat beachrock-like zones of encrusting tufa and tufa flowers, and are most active about the present lake strandline.

Further offshore the aquifer is largely confined by lake muds, so CO_2-saturated groundwaters discharge onto the lake floor via fault and fracture focused conduits. The associated tufa (spring) mounds precipitate along linear trends, tied to positions where faults transect the confining clays. Other older, now exposed and mostly inactive, linear tufa mounds and encrustations define prior times of higher lake water levels and watertables. Modern springs mostly occur along the western side of Mono Lake with waters originating along the Sierra front. They discharge as Ca-HCO_3 waters, which are neutral to slightly acidic and their degassing drives present day tufa precipitation (Fig. 4.24b). In contrast, springs along the eastern shore typically discharge Na-HCO_3 waters, have lower hydraulic heads and are not generally associated with the formation of modern tufa sheets.

The identification of modern ikaite (pseudo-gaylussite) suggests that portions of many Pleistocene and Holocene tufas in the Mono Basin and other cold saline lakes in the Great Basin first precipitated as ikaite (Whiticar and Suess 1998; Shearman et al. 1989). These palaeo-ikaites have long since recrystallised to form their calcitic pseudomorphs (thinolites). Ikaite pseudomorphs are also found in recent and ancient sediments of Polar Regions where they are known as glendonites, or colloquially as "devil's horns". The environmental occurrence of ikaites and their pseudomorphs deem them as potential palaeoclimatic indicators of cold environments including saline lakes. Larger crystals are typically restricted to colder, deeper organic-rich marine sediments or groundwater outflow zones in cold moderately saline evaporitic basins (Buchardt et al. 2001).

Aside from Mono Lake and its spectacular tufa mounds, the other obvious geological feature in the immediate area of the lake is the Mono Craters (Fig. 4.25b). These are the remnants of 24 domes of explosive rhyolite, which erupted

over the last 40,000 years, with the last eruption occurring less than 700 years ago to form Panum Crater (actually a plug-dome volcano) located just above the south shore of Mono Lake. Black Point, Negit Island, and Paoha Island are all recent volcanic features of the lake geomorphology; Paoha Island emerged from the lake waters within the last 350 years. This recent volcanism drives hydrothermal circulation and is still active in the surface and subsurface hydrochemistry of the Mono Lake waters. It supplies elevated levels of sodium and bicarbonate ions compared to chlorine.

High concentrations of inorganic arsenic oxyanions (200 μM), rare earths and sulphate (130 mM) have also been reported (Tomascak et al. 2003; Oremland et al. 2000; Hoeft et al. 2004). Mono Lake water further contains very high levels of dissolved organic carbon (7 mM), although much of it is refractory to microbial mineralization and pulses of labile organic matter are released in spring and fall to the bottom from the breakdown of single- celled algae that inhabit the shallow lake water (Hoeft et al. 2004). Sulphate reduction accounts for 41 % of the mineralization of annual primary production in Mono Lake (Hoeft et al. 2004)

Hydrological and Hydrogeochemical Evolution

Up to 2 km of lacustral and volcanogenic sediments underlie Mono Lake, and saline groundwaters (>18,000 ppm) extend to the bottom of the basin's sediment fill (Rogers and Dreiss 1995a, b). The position of the saline-fresh groundwater interface within the lake basin reflects a balance between a dense saline brine plume or curtain beneath the lake and the force of inflowing fresh groundwaters fed from the Sierras and discharge near the lake's western shore. The rain shadow of the Sierra Nevada to the immediate west of the lake has had a dramatic effect on the asymmetry of surface and groundwater inflow to the lake depression. More than 114 cm of precipitation falls at the Sierra crest, which then supplies waters to the western side of the lake's drainage basin, mostly by surface drainage. Lee Vining Creek, Mill Creek, Rush Creek and Wilson Creek together supply $\approx 1.75 \times 10^{11}$ l/a to the lake (Fig. 4.23b; Tomascak et al. 2003). Less than 13 cm of precipitation falls on the eastern shore of Mono Lake. Altogether surface inflow supplies around 75 % of the lake's water and springs supply the remainder.

The much higher recharge rates for fresh surface and groundwater seepage along the western or Sierra Nevada side of the lake have pushed the saline-fresh water interface basinward of the shorezone beneath that side of the lake. This creates the artesian head that facilitates the formation of the more spectacular linear-trending tufa mounds. In contrast, the brine plume-freshwater interface lies near or directly below the shoreline around much of the rest of the lake. There the saline groundwater discharge zone is just below the playa surface and it contributes to development of saline mudflats and flat sandy beachrock/rubble atop recently exposed former lake beds in an area that lacks significant tufa pinnacles.

Simulations by Rogers and Dreiss (*op cit*) confirm that extensive faulting controls local permeability in the basin fill beneath the lake waters. Faulting increases vertical permeability and leads to focused or channelled regions of outflow and seepage in the lake floor. High permeability zones in the lake substrate on the western side means resurging less-saline groundwater can overcome the opposing force of the saline groundwater density plume and so can issue onto the lake floor where its degassing outflow is marked by linear belts of spectacular tufa precipitation, (Council and Bennett 1993).

In the longer time frame of the Mono Lake's Quaternary hydrology, the redistribution of the basin's solutes between the lake and underlying saline groundwater body is today still driven by late Quaternary lake level changes (Fig. 4.25b; Rogers and Dreiss 1995b). At times of low lake levels in the Late Pleistocene, the higher concentration and density of lake waters caused solute loss via free convection (brine reflux). This probably occurred more rapidly and penetrated deeper into the sediment column along open faults or fractures. At higher lake levels, the shoreline discharge zone moved closer to the basin edge (e.g. the Lake Russell strandline; Fig. 4.25b). The now-unrestrained saline groundwater mass subsided, drawing solutes from the lake waters into the basin sediments. Subsequent falling lake levels again constricted the saline groundwater zone beneath the lake, driving saline water and their solutes back into the lake waters and once again increasing solute content of surface waters. Sediment permeability below the lake is the major control on the solute transfer rate between the lake and its groundwater reservoir. Only the larger, longer-term lake level changes drive saline groundwater movement in the lake margin. Depending on permeability of the basin fill aquifer, the equilibration of the saline groundwater and lake solute content to lake water level requires hundreds to thousands of years. Rogers and Dreiss (1995a, b) suggest that current conditions, where a more saline Mono Lake brine pool (50,000–90,000 ppm) overlies less concentrated groundwater (≈18,000 ppm), reflects the still active impact of late Pleistocene lake high stands. In support of this they note that Mono Lake's historical salinity data have a large scatter, but suggest there was a 5 % decrease in the lake's solute content over the last 50 years of drawdown; they suggest this indicates a diffusive solute flux into lacustrine sediments for this period. Their conclusions are the opposite of the commonly accepted view of Mono Lake drawdown automatically increasing the salinity of the lake waters.

Saline Lakes of Turkey

Turkey, with its active compressional tectonics and semi-arid climate, is ideally situated to form a range of pans and lakes that include permanent ponded bodies of somewhat saline

water in mountainous endorheic depressions. It has some of the largest modern saline lacustrine systems in the Northern Hemisphere in subaqueous settings ranging from perennial water pools about the edges of ephemeral saline mudflat and pan systems like Tuz Golu and Aci Golu (Golu = lake), to large deep bodies of alkaline water, such as Lake Van which have extents comparable to Great Salt Lake and Lake Urmia (Fig. 4.27). As in the Andes, ongoing plate-to-plate compression and associated volcanism throughout the Neogene of Turkey has created rich deposits of exploitable saline minerals, especially borates and zeolites, in the many endorheic Tertiary lacustrine depressions of Turkey (Chap. 11).

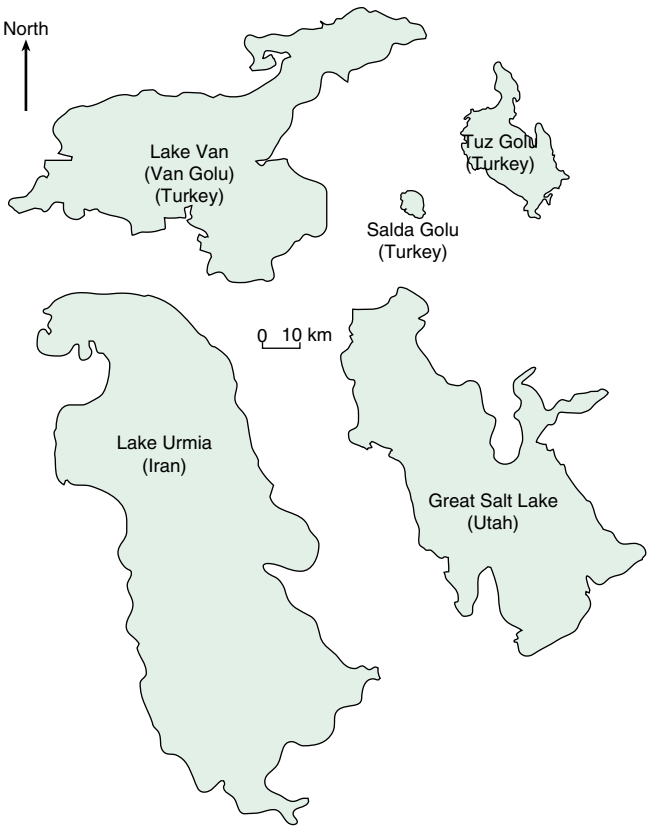

Fig. 4.27 Same scale outlines of the various Turkish Salt lakes compared to Lake Urmia (Iran) and Great Salt Lake (Utah)

Lake Van, Turkey

Van Gölü in eastern Turkey has an area of 3,574 km^2, a maximum water depth of 451 m, a volume of 576 km^3, a catchment of more than 15,000 km^2 and a cored sediment record that extends back for more than 600,000 years (Stockhecke et al. 2014). It is the world's largest soda lake and the fourth largest closed-basin perennial lake in the world (Reimer et al. 2009). It is the largest lake in Turkey and at its widest point it is some 119 km across (Figs. 4.28). The main water mass of the lake lies in its west, where waters are deeper than 400 m. The lake sits in the lower part of a steep-walled, fault-controlled basin, once drained by the Murat River (Fig. 4.28). During the mid Pleistocene, some 200 ka, a lava flow from the Nemrut volcano extended some 60 km across the southwestern end of the basin, blocking westward drainage from the lake via the Murat River and thereby transforming the depression into an endorheic basin.

Climate in the drainage basin is highly continental with hot dry summers and long cold winters (Köppen Climate Dsb). Annual precipitation across the drainage basin is variable and ranges between 400 and 700 mm. Most detrital influx into the lake is in April to June, carried by snowmelt and spring rains. In summer the present day lake waters are thermally stratified and temperatures within the uppermost water column reach as high as 19–20 °C (Fig. 4.29). Below 50 m depth, water temperatures are less than 3 °C and do not change much year round. In winter the shallower northern sections of the lake can freeze over, and the onset of lower

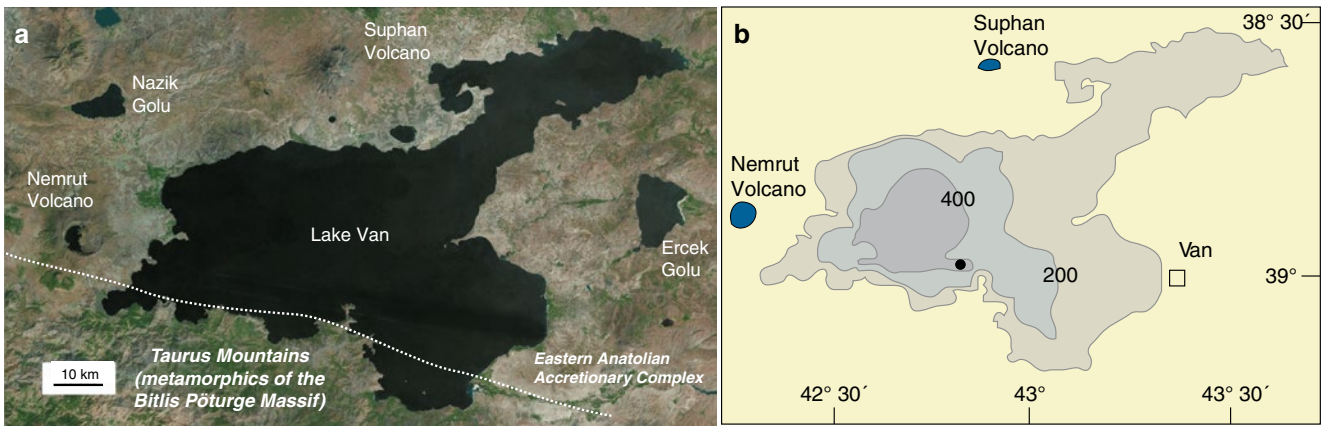

Fig. 4.28 (**a**) Lake Van, eastern Turkey, is the largest perennial saline lake in Turkey and is located at the southern edge of the East Anatolian accretionary complex (*dashed line*). Toward the *top* of the image are the Satak Mountains, Nemrut Lake, the crater lake of an active volcano, that last erupted in the year 1440 lies to the west. Ercek Lake can be seen to the east of Lake Van. To the north of Lake Van is the extinct Suphan Volcano, a circular volcanic maar with an elevation of 4,061 m (Bing® Image mounted in MapInfo®). (**b**) Bathymetry is in metres and the *black circle* indicates the position of piston core K10, with its geology and chronology illustrated in Fig. 4.31

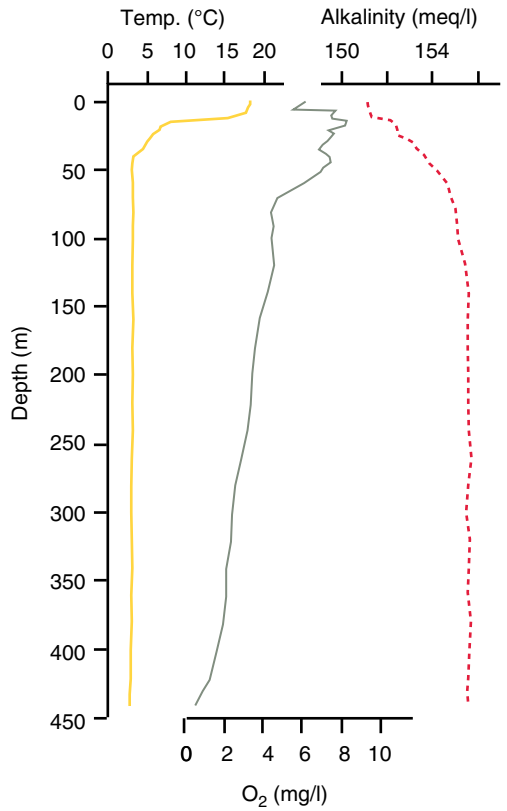

Fig. 4.29 Temperature, oxygen and alkalinity profiles in the Lake Van water column (After Thiel et al. 1997)

surface water temperatures in the autumn drives an annual overturn of the lake waters.

Salinity is 22‰, pH hovers around 9.5 and can be as high as 9.8, making the lake waters highly alkaline (≈153 meq/l; Fig. 4.29). Free oxygen is present throughout the water column, but drops to values <1 mg/l near the lake bottom. Calcium concentrations in the lake waters are low (≈4 mg/l; Thiel et al. 1997) The main cation in the lake waters, sodium, is not only balanced by chloride, but also to a near equivalent extent by high levels of carbonate and bicarbonate ions. As in Mono Lake, the high alkalinity reflects the preponderance of young volcanics in the drainage basin and ongoing hydrothermal circulation.

This high alkalinity in the lake's hydrogeochemistry explains the onset of trona deposition when the lake dried out some 15 ka. Relatively high salinity and very high alkalinity means modern lake waters host a low diversity, largely endemic phytoplankton population, dominated by diatoms and cyanobacteria (primary producers). Copepods and ciliates are the main contributors to the zooplankton.

Today, the lake water level is around 1,648 m asl and fluctuates around 50 cm annually, being lowest during the winter months and rising after the spring thaw to reach its highest level each July (Fig. 4.30a). Lake levels over the last few decades have been rising with some 2 m (2.1 m) of rise from 1944 to 2000 and levels continue to rise today, at an average rate of 3.7 cm/year (Fig. 4.30a; Deniz and Yildiz 2007). The swift rise, especially after 1987, drove a natural environmental disaster in the lake coasts, inundating approximately 5,200 ha of land. Tens of villages together with Van, Tatvan, Ercis, Adilcevaz and Ahlat cities were affected, and thousands of houses, tens of thousands of acres of agricultural lands, highways, the ferry harbour, historical sites, and wetlands in the mouths of streams, shelters of wild birds were damaged. In addition, drinking waters, canalization networks, urban infrastructure systems as well as some parts of Van Airport and many holiday camping areas have been detrimentally effected by the ongoing rise. Millennial lake level changes are also significant. Some 15 ka the lake had dried into a series of saline pans, precipitating sodium carbonate salts and the water level was more than 450 m below that of today (Fig. 4.30b; Landmann et al. 1996; Reimer et al. 2009). A few thousand years earlier, at the height of the last glacial, some 18 ka, the water level in Lake Van was 72 m above its present position (Degens et al. 1984). The rapidity of natural water level change is of the same magnitude as in the Dead Sea Basin (Fig. 4.45).

Lake Van deep bottom sediments were collected by a series of piston cores in 1990 and the results published in Landmann et al. (1996), Thiel et al. (1997) and Reimer et al. (2009). Their work, along with the results of an earlier piston core studies by Kempe and Degens (1978), are summarised in the next few paragraphs and illustrated in Fig. 4.30b. Sediments accumulating on the deeper parts of the Lake Van floor are mainly dark-coloured carbonaceous siliceous carbonate laminites/mudstones, with layering that indicates annual deposition cycles and so are true varves.

Varve counts in various K series cores recovered some 15,000 years of lake history (Fig. 4.30b). Lighter coloured laminae in each varve couplet are dominated by micritic carbonate and opaline silica. Darker laminae are characterised by higher amounts of organic material and high proportions of nonchemical detrital sediment matrix, which was carried into the lake by spring melt waters. Dolomite occurs in various lamina, but is detrital, not authigenic, and comes from eroded Cretaceous dolomites.

Snowmelt and rain peak from April to June and rising river discharge not only increases the lake level by about half a meter, but also delivers most of the clastics to the lake during this time of the year (Fig. 4.30b; Reimer et al. 2009). At the same time, the mass of the dissolved ions is delivered to the lake by the spring-time freshwater spreading over the underlying saltier lake water. While clastics and organodetritus settle directly to the lake bottom, dissolved ions concentrate during summer due to ongoing evaporation. Supersaturation necessary to cause $CaCO_3$-precipitation is surpassed in late summer and autumn when the surface layer starts to mix with the higher saline lake water below. Aragonite and calcite constitute about 35 wt% of the sediment (Landmann et al. 1996). Thus, laminated sediments are

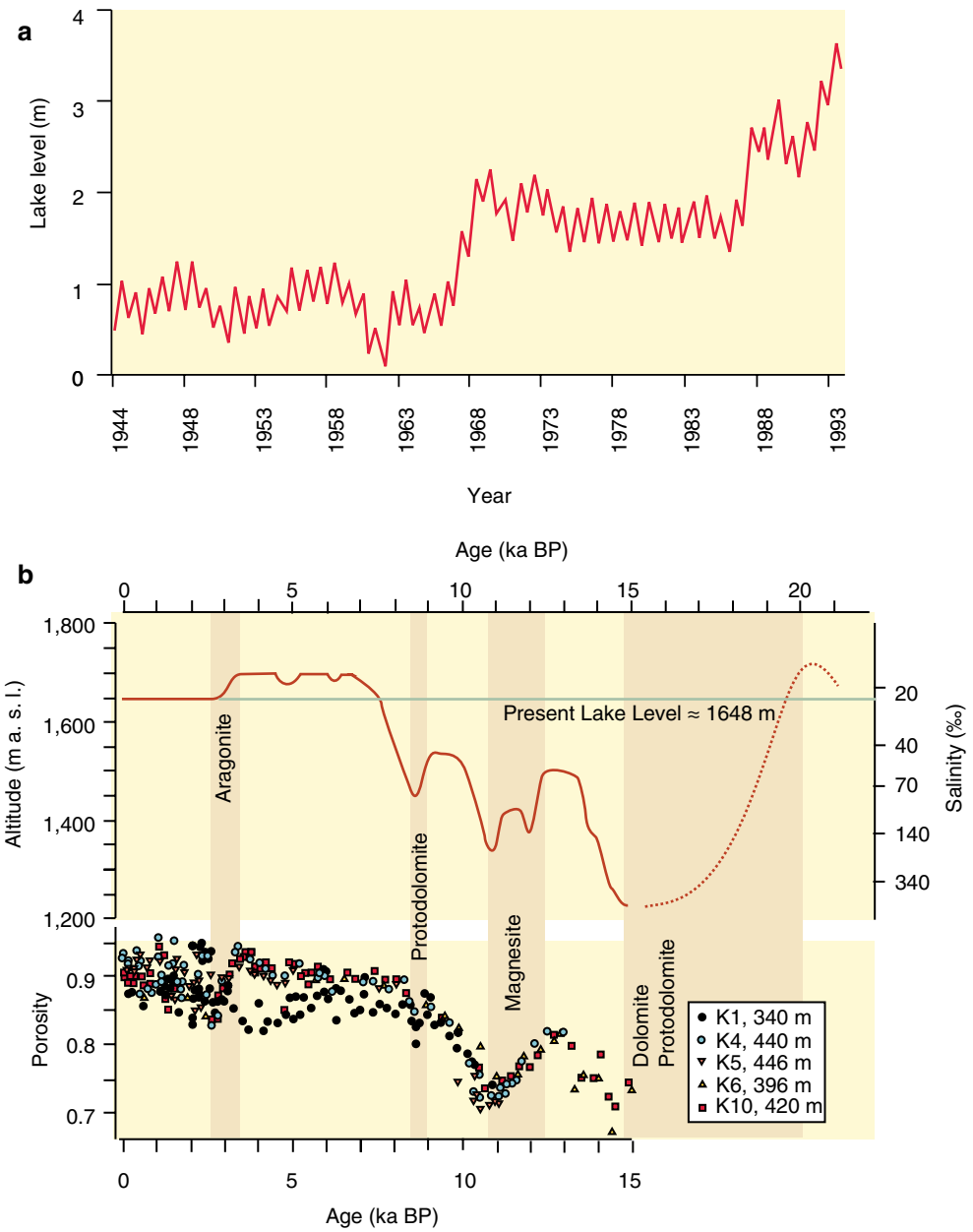

Fig. 4.30 Water levels and mineralogy across time in Lake Van (Vangolu), Turkey. (**a**) Water levels changes in the period 1944–1993 (After Kadioglu et al. 1997). (**b**) Lake level fluctuations of Lake Van in the past 20 ka, salinity and sediment porosity versus age. *Brown shaded* areas define periods in lake history with negative water balance and more evaporitic carbonates. Maximum depth of Lake Van today is 451 m, water depths of the various cores used to calculate porosity curves are given in the legend. Note that the scale of the salinity axis is not linear (After Reimer et al. 2009)

deposited as varves with darker laminae in winter and spring and lighter carbonate dominated bands in late summer and autumn (Kempe and Degens 1978).

Colours in the recovered core are mostly dark and range from dark brown to dark greyish green; they reflect largely anoxic deepwater conditions (Eh of 150 to −280 mV), which have prevailed on the subaqueous lake floor for the last 15 ka. Accordingly, organic contents in the bottom sediments are high, the organics are oil prone, and TOC ranges up to 5–6 % (Thiel et al. 1997). The base of the laminite unit is at around 8.5 m in core K10 and is defined by a sandy layer, thought to indicate the drawdown stage in the deeper parts of the lake, some 15 ka (Fig. 4.31). All piston cores for the lake are water saturated and show porosities that are typical of deepwater micrites, with porosity decreasing with age and depth (Fig. 4.30b).

Material caught in floating sediment traps in the central parts of the lake show that most of the micritic carbonate in the cored laminite was annual, probably precipitated in the evaporative surface layer each summer to fall (Landmann et al. 1996). Aragonite/calcite ratios, determined by X-ray diffraction analysis on core K10, scatter between 2 and 9 in sediments younger than 3,700 year B.P., and from 1 to 4 in older sediments (Fig. 4.30b). The other main chemical component in the sediment traps is opaline silica, largely derived from phytoplanktonic diatom tests.

Because present lake waters are supersaturated with respect to alkaline earth carbonates, carbonate precipitation is most obvious in the lake at positions of calcium input where fresher waters mix with more saline lake waters. This can be at the mouths of rivers, where whitings have been

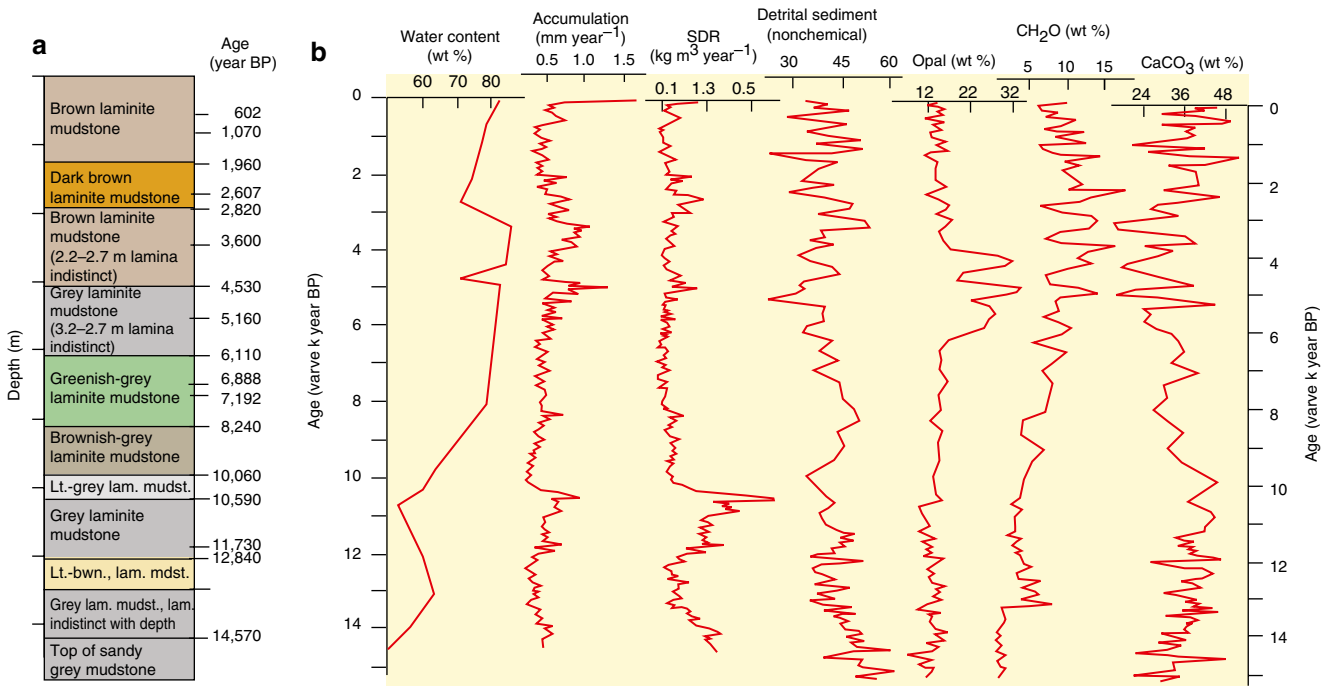

Fig. 4.31 Lake Van Core K10 (see Fig. 4.28 for location. (**a**) Laminite lithology plotted against depth and varve-determined ages. (**b**) Core properties plotted against varve determined time. SDR = rate of sediment deposition. Opal is dominantly from diatom tests and $CaCO_3$ is mostly from aragonite with lesser calcite (After Landmann et al. 1996)

documented, or it can occur on the shallow lake floor down to depths of 120 m, where the degassing of resurging calcium-rich groundwaters escaping into the lake waters creates tufa towers or pinnacles, up to 40 m high. These structures constitute some of the largest active microbial lacustrine buildups in the world today (Kempe et al. 1991). Lake Van does suffer from severe winters, but these aragonite/calcite tufa samples described by Kempe et al. (1991) were collected in the summer. The possibility of primary ikaite was not considered. So, it not known if some of the initial tufa in Lake Van was once ikaite, which then converted to $CaCO_3$. A textural comparison with similar structures in Mono Lake suggests this may be so, especially in older colder stages in the lake history.

The current condition of Vangolu is a useful analogue for the Pleistocene freshwater stages in many of the world's soda lakes that are currently in a hypersaline (trona) stage and for many pre-Quaternary alkaline lakes. It serves as a useful analogue for the laminites of High Magadi Beds of the Lake Magadi and Lake Natron and for the oil shales of the Eocene Green River Fm, USA. More arid episodes in the lake history, when water levels were lower and salinities are higher, are indicated by the presence magnesite and dolomite in the cores (Fig. 4.30b).

Salda Lake, Turkey

Saldagölu is another highly alkaline (pH >9) saline lake in southern Turkey, located in a collision belt at an elevation of 1,139 m asl. It is bowl-shaped and occupies the lowest part of a fluvial and seepage-fed endorheic depression at the foot of the Esler Mountains (Köppen Climate Csa). Lake waters are up to 184 m deep and cover an area of 43.7 km^2 (Fig. 4.32a, b). Lake levels rise about 50–70 cm each spring, but longterm levels are falling and have been doing so for decades exposing widespread beach-rock like terraces and stromatolites of hydromagnesite and aragonite. Inflow waters to Salda Golu are enriched in magnesium and carbonate and when compared to Lake Van are much fresher and are capable of supporting the local livestock (Shirokova et al. 2013).

The lake drainage is rimmed on three sides by serpentinites (ophiolites) and on the fourth by a downfaulted block of Upper Cretaceous limestone. Hazburgite is the dominant country rock, though in places it has been metamorphosed to lizardite ($Mg_3Si_2O_5(OH)_4$) and subsidiary dunite, all Mg-rich phases. All the rivers draining into the lake follow faults, flow across peridotites, and under the lowered water levels of today are losing streams. Waters typically seeping into fan deltas or into the lake surrounds before ever reaching the strandzone of Salda Golu (Russell et al. 1999).

Magnesium concentration averages 60 ppm in wells and cold springs in the lake surrounds, temperatures range up to 12–15 °C and pH lies in the range 8–10 (Braithwaite and Zedef 1996). Sodium levels in the groundwaters of the lake surrounds are low (≈5 ppm) as are most other ions, with the exception of HCO_3. In contrast, lake waters contain 300 ppm of Mg and 200 ppm of Na down to a depth of 80 m, with a pH around 9.1. Mg in the lake has increased by a factor of 6

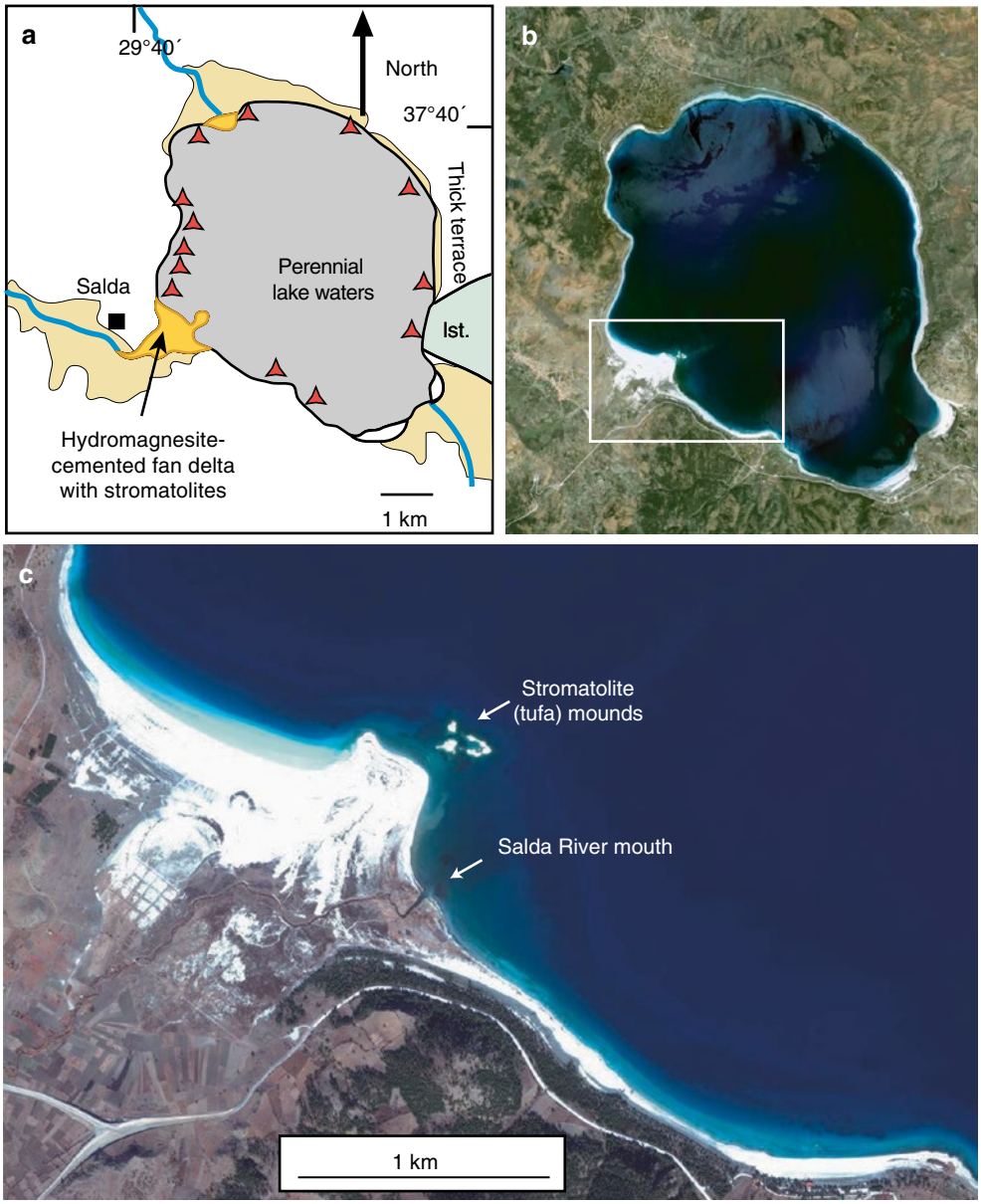

Fig. 4.32 Salda Lake, Turkey. (**a**) General geology of this perennial carbonate precipitating lake, currently accumulating hydromagnesite and aragonite. The lake is best known for the subaqueous stromatolites accumulating basinward of hydromagnesite strandline terraces, with most prolific occurrences indicated by *triangles* (For more detail on the stromatolites see Chap. 1 and Braithwaite and Zedef 1996). (**b**) General view. (**c**) Close up of Salda delta showing stromatolites and position of modern river mouth on the delta wedge

compared to waters in the surrounding aquifers, while Na in lake water is more than 40 times that in the lake surrounds. Obviously, the bulk of the groundwater seeping into the lake edge gathers Mg as it seeps lakeward through older river mouth fan deltas, which contain abundant cobble of metastable Mg-rich ultramafics such as lizardite (Russell et al. 1999). Lakeward seeping groundwater outside the deltas also picks magnesium, relative to Ca, as it cannibalizes the older hydromagnesite-cemented gravelly strandlines/terraces that circumscribe the present lake. Subsequent hydromagnesite precipitation in the lake is probably related to an increase in pH in the lake waters, tied to HCO_3 depletion (CO_2 depletion) as it enters the lake, perhaps indirectly brought about by the metabolic activities of microbialites.

Composite stromatolites, several metres high and composed largely of hydromagnesite, line significant portions of the current lake margin; they are best developed atop the now largely inactive fan deltas of the Salda River (Karakova Dere) in the SSW of the lake and the Yesilova delta in the ESE of the lake (Figs. 1.17 and 4.32c). On the Salda River delta they form three 20 to 100 m^2 partially subaerial mounds, situated ≈50 m offshore and rising ≈10 m from the lake bottom, reaching within 3–4 m of the lake surface (Shirokova et al. 2011). The deepest part of these mounds showed no evidence of stromatolites below 6–10 m water depth. There are other 1–1.5 m^2 stromatolites in other parts of the lake, within 10–20 m of the shoreline (Fig. 4.32b). In contrast to these lithified examples, most submerged pebbles in the littoral of the north side of the lake, are covered with actively forming, non-solidified stromatolites. The mineralised surface of the indurated stromatolites is covered by a layer of green algae, diatoms, and cyanobacteria with oxygen

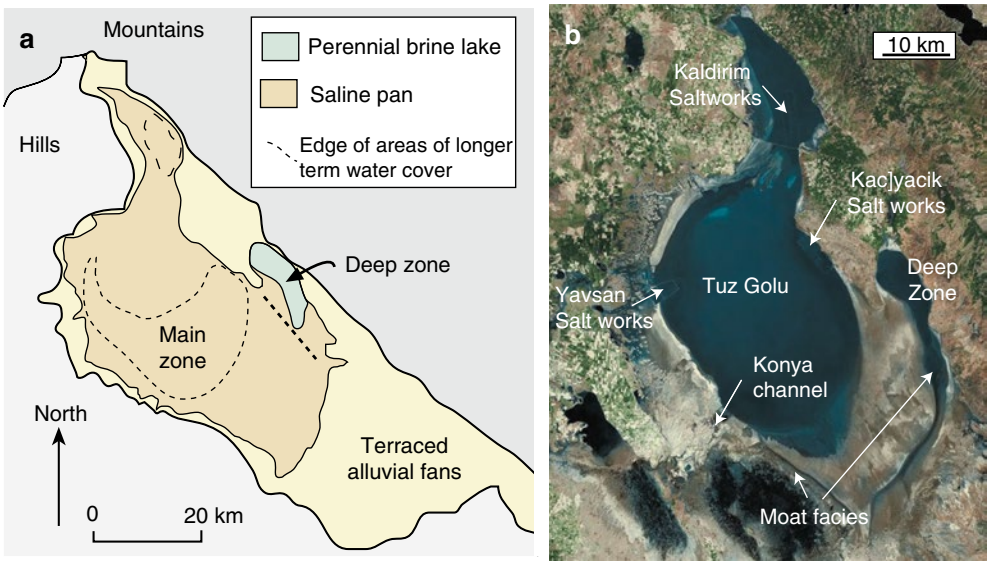

Fig. 4.33 Tuz Golu, Turkey. (**a**) Geological plan view ot the two hydrological zones (**b**) shows a partially desiccated stage in the lake when much of the saline pan is still water covered. The sill separating the main zone from the deep zone is clearly exposed. The man-made Konya drainage channel and its waste plume cutting into the southwestern part of main zone is also visible. The obvious linear separation between the mountains to the northeast and the terraced alluvial plain reflects the transtensional fault-controlled origin of the Acigolu depression (Bing® image mounted in MapInfo®)

bubbles adjacent to the surface of the microbial mats. The general depositional style of the stromatolitic tufa mounds is similar to the tufa mounds of Sleaford Mere.

Most of the detrital sediment currently accumulating along the strandzone between reef mounds is created by the mechanical (wave-driven) breakdown of former carbonate terraces and hydromagnesite microbialites; it is not derived from longshore transport of fluvial sediment (Braithwaite and Zedef 1994, 1996; Russell et al. 1999). Hydromagnesite precipitates, which are now exposed by falling water levels, give the present strandplain its bright white colour. Fine-grained hydromagnesite, reworked from tufa shorelines and from the terraces, is suspended in the water column during storms and is probably redeposited as micritic turbidites alternating with laminites in the deeper part of the lake.

Further landward from the present strandline, the earlier hydromagnesite terraces preserve no obvious stromatolites, but include boulders and blocks of reworked hydromagnesite up to 0.5 m across. Many of these circum-lake terraces appear to be inorganic precipitates that started to form when lake levels were higher. It seems that stromatolitic morphologies do not survive long-term exposure and lithification as they quickly degenerate into a porous, coarse-grained poorly lithified floatstone, with the positions of former microbialites sometimes still recognisable as mounded outlines in intervening muds (Russell et al. 1999). Like the hydromagnesite stromatolites of the Coorong region, stromatolites in Salda Golu have poor preservation potential.

Hydromagnesite precipitation and biofilm coating throughout the current lake is facilitated by the metabolic activities of the flourishing flora of diatoms and cyanobacteria (Shirokova et al. 2013). Biofilms cover the surface of the stromatolites and much of the littoral zone of the current lake. But precipitated crystals do not occur in direct contact with cell surface, implying CO_2 fluctuations may be driving precipitation rather than direct biomineralization. Interestingly, diatoms rather than cyanobacteria dominate the phytoplankton assemblage in the current surface waters of the lake and each year take up all the available silica (Russell et al. 1999). Silica averages 16 ppm in the wells and springs about the lake yet is below detection limit (1 ppm) in the lake surface waters. Opaline diatom tests rapidly dissolve out of the consolidating stromatolites and are rarely found as body fossils in any of the exposed hydromagnesite cliffs about the lake edge, once again a similar situation to that found in the hydromagnesite-aragonite lakes of the Coorong.

Lake Tuz, Turkey (Tuz Gölü)

Lake Tuz (*tuz* = salt; aka Lake Sereflikochisar) has an elevation of 905 m asl and a water full area of 2,600 km^2. After Lake Van, it is the second largest lake in Turkey (Fig. 4.27) and occupies the lowest part of a fault-defined (transtensional) endorheic depression in the arid Central Plateau (straddles Köppen climate zones BSk; Csb). Unlike Vangolu, much of the current lake floor is a salt-crusted saline pan for at least 6 months a year, with a small area of perennial brine along its eastern higher-relief edge.

To the east of the lake lies a mountainous highland of metamorphics dominated by granites and gneisses. Highlands to the north are composed of sandstones and shales, andesitic and basaltic volcanics lie to the northwest, ophiolite hills lie to the west, and rhyolitic tuffs and andesites constitute the lower relief hills to the south and southeast (Aydemir 2008). Flatter areas of the Konya drainage basin between these highlands are covered by gypsiferous lacustrine marls of various Neogene ages (Fig. 4.33).

At some 350 mm/year the area receives the lowest annual precipitation in Turkey, while potential monthly evaporation

Table 4.3 Typical chemistry of waters and brines in saline Turkish lakes with elevated lithium in Tuzgolu

Lake	Locality	T (°C)	pH	Li^+ (mg/l)	Na^+ (mg/l)	K^+ (mg/l)	Mg^{+2} (mg/l)
Acigolu	Lake water (1)	31	8.5	15.0	45,000	1,000	4,100
	Lake water (2)	31	8.5	16.0	47,000	1,000	4,108
	Production pool (1)	33	8.4	14.0	48,000	1,050	4,100
	Production pool (2)	30	8.6	15.0	45,000	1,000	4,100
	Spring water of Gemi village (1)	22	7.4	0.3	59	3.1	60
	Spring water of Gemi village (2)	22	7.5	0.3	58	3.0	60
Saldagolu	Akceme spring (1)	24	9.0	0.3	200	19.0	250
	Akceme spring (2)	25	9.0	0.3	196	19.5	245
Tuzgolu	Lake water of Yavan saltpan (1)	34	6.0	325.0	61,000	12,000	37,500
	Lake water of Yavan saltpan (2)	34	6.0	325.0	62,000	12,100	38,000
	Production pool water of Yavan saltpan (1)	33	6.1	310.0	61,500	12,100	38,000
	Production pool water of Yavan saltpan (2)	33	6.1	318.0	62,000	12,100	38,000

After Helvaci et al. (2003)

ranges between 1,175 and 1,390 mm in a yearly cycle. Natural river inflow to the lake depression totals 88×10^6 m^3/year and comes from three main rivers (Peceneközü, Uluirmak and Insuyu). Each year a discharge from the artificial Konya drain releases around 75×10^6 m^3 of wastewater into the lake.

Maximum brine depth in the lake is 1.5 m, attained in the spring when meltwaters reach the lake from the adjacent highlands. Evaporative evolution of the natural inflow brines shows a continuous trend from Ca-HCO_3 rich spring waters to Na-SO_4-Cl rich brines with considerable variations in ionic proportions in inflow brines related to lithologic variations in the drainage area. There were times in the Late Pleistocene (20–17 and 13 ka) when lake levels were 15 m higher than today and the Tuzgolu depression was filled with permanent water up to 16 m deep (Kashima 2002). Older, but undated, Quaternary shoreline terraces occur some 100 m above the present lake level (Erol 1978). Tuzgolu waters show elevated lithium levels compared to other saline lakes in the region and so constitute a brine of potential economic interest (Table 4.3; Helvaci et al. 2003), although the associated elevated magnesium levels are problematic in terms of current extraction technologies.

Each year, by mid summer most of the lake floor has dried up and only a few small areas retain permanent surface water in spring-fed seep ponds or brackish marshes (aka moat facies). The largest area of pooled perennial brine lies south of the town of Sereflikochisar, in the eastern part of the lake. It has a permanent brine-covered area of 35 km^2 called the "deep zone" and it expands with each snowmelt in the nearby mountains. It is separated from the "main" salt pan, which constitutes much of the rest of the lake surface, by a low salt crusted ridge (Fig. 4.33).

Waters covering the "main" zone are ≈70 cm deep in spring, but dry out in summer to early autumn and leave behind a 1–30 cm thick halite crust over an area of 1,200 ha, which is mined by saltworks on the lake shore (≈750,000 t/year) to provide 55 % of Turkish salt needs. In contrast, waters in the deep zone are permanent, are not halite-saturated and can be as deep as 1.5 m in the spring.

Evaporite mineralogy in the seasonal salt crust in the "main zone", especially in the northern arm studied by Camur and Mutlu (1996), consists of mixtures of halite, gypsum, aragonite and calcite. Unconsolidated evaporitic sediment extends for 1–30 cm below the salt crust and consists of a gypsum-, huntite- and magnesite bearing level, which is up to 25 cm thick, with polyhalite occurring beneath the more central parts of the main zone. This is underlain by a layer up to 35 cm thick composed of gypsum, huntite, magnesite, illite and smectite-bearing sediment. Holocene dolomite was documented in shallow sediment cores collected from the central parts of the main zone (Irion and Mueller 1968) and minor anhydrite was noted along the northern edge of Tuzgolu by Camur and Mutlu (1996). Each summer halite cumulates cover the chevrons of the salt pan crust and coarsely-crystalline lenticular and prismatic gypsum crystals (0.3–4 cm diameter) are commonplace displacive growths (up to 50 % by volume) in the sediment immediately beneath the salt crust. They constitute a "desert rose" unit with a micritic matrix made up of varying proportions of magnesite, huntite and dolomite mixed with siliciclastic detritus.

The interaction of microbialites with the recycling salts in the "main" zone has produced interesting disc-like structures in dried halite known as salt biscuits (Mueller and Irion 1969). Biscuits are 2–7 mm thick crusts, with diameters between 3 and 8 cm. The upper surface tends to be smooth and covered with cumulates of small halite cubes (<2 mm diameter), the lower surface is made up of larger downward-aligned halite crystals up to a centimetre long. Irion and Mueller (1968) concluded that the biscuits are foundered halite rafts with ongoing underside growth fed by ongoing capillary rise after surface waters had receded. Tuzgolu is

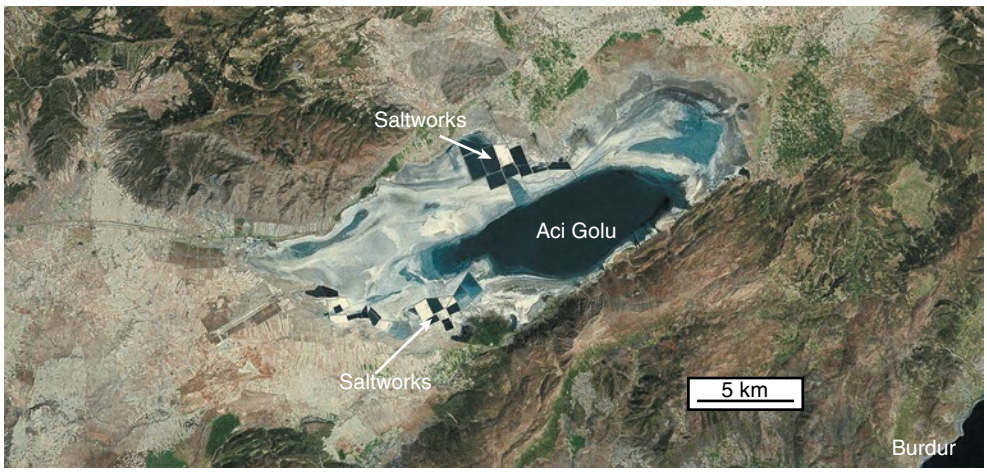

Fig. 4.34 Aci Golu, SW Turkey. Older strandlines are visible in the north of the lake, while an area of shallow perennial brine (aragonite + organics) occupies the more southerly portion of the lake depression. Part of the fresher water Lake Burdur is discernible toward the *bottom right* of the image. Numerous faults and lineaments are visible in the surrounding highlands and obviously control the linear orientation of the southwest lake edge

also a modern halite environment where halite oolites (halolites) are forming (Tekin et al. 2007).

A constant freshened, but unnatural, inflow today reaches Tuzgolu via the 150 km long Konya drainage channel (completed in 1974). It feeds a saline sump that drains agricultural wastewater from the Konya irrigation area to the south. In addition, all untreated sewage from Konya city and several hundred industries are periodically released into this drainage channel. This means that each year agricultural waste exuded from the channel into the lake includes the leached residues of more than 1,105 t of pesticides and 446 t of fertilisers applied to the Konya basin. Industrial waste includes outflows from dairy farms, aluminium and copper plants, leather processing units and a LPG bottling plant. Large amounts of nitrogen, oil, phosphorous, sulphur and organic wastes, as well as heavy metals, including borax, zinc, iron, lead, arsenic, cadmium and mercury today reach the lake depression through the Konya channel. Yet the lake brine is recovered annually for salt manufacture in a number of pans about the lake edge, which supply more than half of the domestic and industrial salt consumed in Turkey (Fig. 4.33). Pumping of industrial and agricultural wastes into salt sumps is an environmental quandary, typical of many developed agricultural and industrial areas in semi arid areas across the world. Only in the last decade have the some of the required hydrological and groundwater studies begun to assess wastewater and salinization effects in such drainage sumps in Australia, Egypt, Israel, Mexico, Turkey and the USA.

Lake Aci, Turkey

Acigolu lies at an altitude of 836 m in the next major intermontane valley to the northeast of Salda Lake (Fig. 4.34). It lies in an endorheic depression in a Csb climate zone, fed via run-off from the Yan and Maymun Mountains, more than 25 karstic springs – some with freshwater marshes, and the Kocacay stream, which enters the lake near Basmakci. Its surface water area varies greatly through the seasons, around 100 km^2 in spring and 35 km^2 in late summer, with a maximum depth around 2 m and salinities in excess of 100 g/l. It is a perennial brine lake surrounded by extensive saline pan and mudflat sediments, with saltworks focused on the production of sodium sulphate (Chap. 12).

Like Tuzgolu, the lake is fed by two distinct water sources, less saline Mg-HCO_3 groundwater from streams and local Na-SO_4 waters from springs mostly along a fault zone that defines the southern side of the lake. Final lake waters are Na-Cl-SO_4 brines with relatively lower lithium levels than Tuzgolu (Table 4.3; Mutlu et al. 1999; Garrett 2004). Differences in composition of the two inflow waters are attributed to different water cycles and different intensities of rock-water interactions. Like Saldagolu, it lies in a Csa climate zone. It is the second most saline lake in Turkey, only Tuz Golu is more saline.

Dry mudflats in Acigolu are composed of gypsum, calcite, dolomite and huntite, together with clastics. In contrast, wet or brine-soaked mudflats remain year round, typically near saline Na-SO_4 springs and are characterised by efflorescences of halite, bloedite; thenardite and/or mirabilite (Mutlu et al. 1999). Laminated to structureless gel-like sediments composed of aragonite and organic matter typify the bottom sediments of areas of perennial lake brines along the fault controlled southwestern margin and are also zones where halobacteria flourish year-round (Mutlu et al. 1999).

Lake Urmia, NW Iran

Lake Urmia, formerly Lake Rezaiyeh[2], is a shallow perennial saline lake in the lowest part of an endorheic depression in Azerbaijan Province of northwest Iran. Surface waters have a current elevation of slightly more than 1,280 m asl and

[2]In the early 1930s, Lake Urmia was called Lake Rezaiyeh after Reza Shah Pahlavi. In the late 1970s, after the Islamic revolution, the Government of Iran reverted to calling the lake by its previous name – Lake Urmia. Lake Urmia's ancient Persian name, however, was *Chichast* (meaning glittering), a reference to the glittering evaporitic salts suspended in the lake water and its shores. In the medieval times the lake came to be known as Lake Kabuda, meaning azure in Persian.

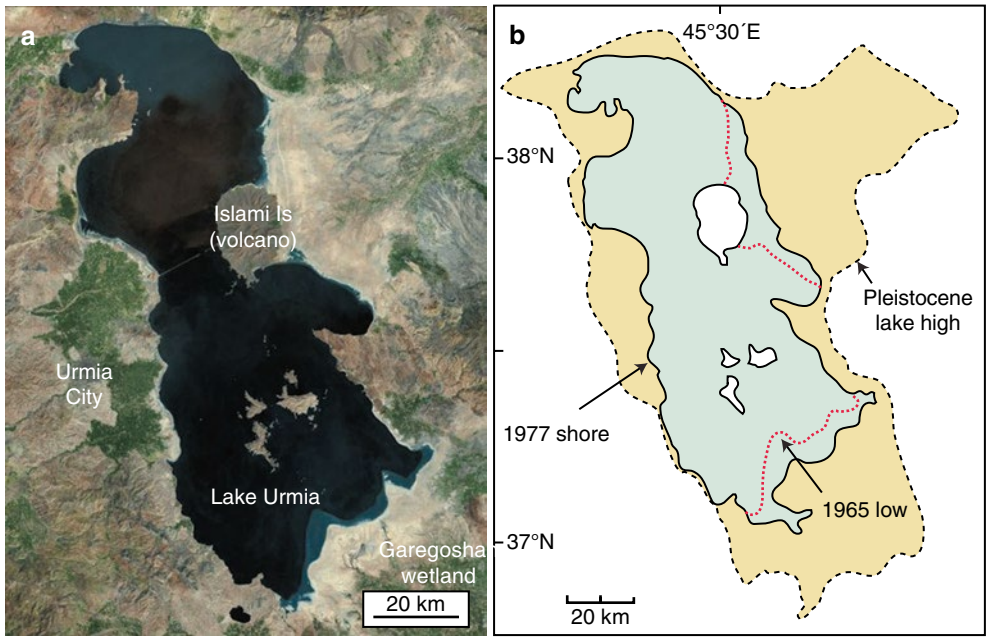

Fig. 4.35 Lake Urmia, Iran. (**a**) General distribution of lake sediments clearly showing the Talkerud alluvial braid plain and fan delta to the northwest of the lake and exposed strandline sediments along parts of the northwest and southeastern shores. (**b**) Varying extent of Lake Urmia, northwest Iran, shows outline of the lake as defined by its 1977 AD water level, as well as the 1965 AD shoreline and the much more extensive freshened lake that formed during the Pleistocene (In part after Kelts and Shahrabi 1986)

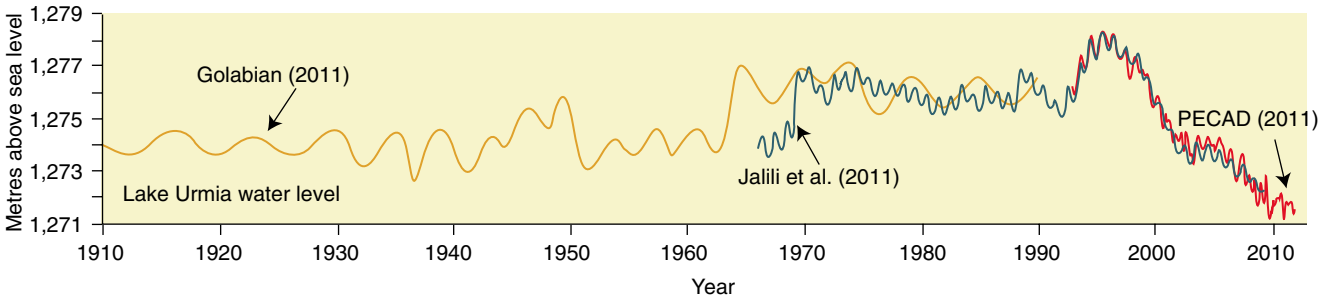

Fig. 4.36 Water levels changes in Lake Urmia, Iran, for the period 1910–2012 (Replotted from altimetry derived from TOPEX/POSEIDON and Jason-1 satellite passes last accessed on March. 4, 2014 at http://na.unep.net)

surface salinities range annually from 80 to 280‰. The lake is some 140 km long and 80 km wide, with an area of 4,700–6,000 km^2. It is the largest lake in Iran and, with a brine volume around 28 km^3, it is also one of the world's largest perennial hypersaline lakes (Figs. 4.27 and 4.35a). Average water depth is around 5 m, which deepens to 8 m in the south, where the maximum water depth is 15 m.

Lake Urmia lies at the bottom of an endorheic basin located further along the same alpine collision suture as the Turkish lakes. It was created as the Turkish and Eurasian plates were squeezed sideways along very active strike-slip fault systems. Palaeozoic metamorphics crop out in the Zagros Mountains to the west of Lake Urmia. Infracambrian sediments lie to the south, while the northern and northeastern lake margins are characterised by outcrops and subcrops of the evaporitic Middle Miocene Fars Formation and underlying marine limestones of the Lower Miocene. Several Miocene salt domes pierce the surface of the lake's drainage basin.

Climatically, the lake lies in a semi-arid, desert steppe environment (Köppen BSk), with precipitation averaging 30 cm per year. The climate is harsh with winter temperatures down to −20 °C and summers up to 40 °C. Surface inflow from the 52,000 km^2 drainage basin is strongly seasonal, driving an annual lake water level fluctuation of up to 1–2 m, especially during the spring melt when the Talkheh and Simineh Rivers discharge around 57 m^3/s into the lake (Fig. 4.35; UNEP 2012). By summer the inflow drops to 1.7–3.7 m^3/s and lake levels fall once more.

Topographically, the surrounding region is either plateau or mountain. Mountains west of the lake have peaks that exceed 3,350 m making that side of the lakeshore somewhat steeper. Salt flats and the fan deltas characterise lake sediments along the southern and western shores. Slight changes in water level can drive drastic migrations of the strandline across the evaporitic mudflats of the lake. In 1970 the lake had a water level of 1,277 m asl, while in 1965 the water level had hovered around 1,274 m; the lake level had risen by 3 m in a decade and the shoreline had migrated some 5–10 km (Fig. 4.35b). From 1996 until 2013, there was a 7 m fall in lake level (Fig. 4.36). This latest fall means the lake's water level has now reached

historical lows, while salinities have attained historical highs of 300–320 g/l (approaching halite saturation). The current scenario of ongoing falling water levels and elevated salinities is likely due to over-extraction from inflow water sources (13 rivers that supply the lake are now dammed and feed stored waters into various irrigation schemes; UNEP 2012). It defines an anthropomorphic hydrological/salinisation evolution that is detrimental to the diversity of the lake biota, much like the anthropogenic pressures that detrimentally effect biodiversity in other modern saline sumps such as the Dead Sea, the Aral Sea, Lake Texcoco and the Coorong Lakes (Gill 1996; Alcocer and Williams 1996). The pressure of a rapidly growing population, currently around of 6.5 million people within the Urmia watershed, will likely force continued diversions and damming of streamflow within the basin, before it reaches Lake Urmia sump.

Lake floor sediments are mostly aragonitic pelletal laminite/mudstones, near identical in appearance, depths of deposition and origin to those of Great Salt Lake, Utah. The Urmia pellets are composed of 80 % aragonite, along with small amounts of quartz and calcite, and rarely dolomite (Eimanifar and Mohebbi 2007). Laminites in both lakes result from seasonal biologically-mediated precipitation of aragonite (Kelts and Shahrabi 1986). When salinity and nutrient levels are suitable, Urmia's stratified surface waters support an abundant summer flora of the green alga *Enteromorpha intestinalis*, along with species of *Dunaliella* and *Tetraselmis*. Blooms can be so intense that in some years the water changes colour to a deep green and light penetration is measured in tens of centimetres. The algal bloom is followed quickly by a bloom of the endemic brine shrimp *Artemia urmiana* (up to 4,000 individuals per litre), which graze the alga. While feeding, the shrimp also ingest particulate aragonite that is precipitating in the lake waters. Thus aragonite in the Urmia laminites occurs both as 10 μm-long euhedral prisms in pelagic muds and as the major constituent in sand-sized brine shrimp faecal pellets. Both types of aragonite are interlaminated with organic-rich laminae in a matrix dominated by terrigenous sediment brought to the lake by spring melt. The aragonite is sometimes sufficiently cemented to form cm-thick crusts on and beneath the lake floor. The precipitation of aragonite, rather than calcite, in the lake reflects the high Mg/Ca ratio of the waters (molar ratio 28:1).

At the northern end of the lake the gypsum bed is now some 1.5 m below exposed laminites, with the latter tied to the same sedimentation style as the current subaqueous lake floor. The gypsum bed was interpreted as a sabkha unit by Kelts and Shahrabi (1986). That is, earlier in the Quaternary, the lake level was lower than today and portions of the lake floor became so saline that gypsum precipitated in a saline playa. Approximate U-Th dates based on aragonite-pellet lamina across a 100-m long piston core, studied by Stevens et al. (2012), places the playa episode at 15–55 ka. In other parts of the lake, partially exposed dolomitic mudflats were probably time equivalents to this now buried gypsum. Oolites shoals formed at the northeast end of the lake but they too are now buried beneath 30 cm of putrid, black organic-rich mud.

The biota and the general spectrum of carbonate sediments found in Lake Urmia are near identical to that of Great Salt Lake, Utah. Like Great Salt Lake, sediments accumulating in the deeper parts of the perennial saline lake are pelletal aragonite laminates. In shallower waters the sediments can construct aragonitic ooid strandzones (as near Gulman Khaneh on the western margin) or cemented crusts/beachrocks, as typifies much of the lake edge.

Lake Natron and Lake Magadi, East Africa

These two lakes are perhaps the most often cited saline alkaline (soda) lakes in the geological literature. Both are groundwater and hydrographic sumps, are small, and lie just south of the equator in the volcanically active eastern branch of the East African Rift (Fig. 4.37a). The rift extends for more than 3,000 km from the Afar Triangle in the north to Mozambique in the south. Lake Natron, the larger of the two lakes, is in northern Tanzania, at latitude 2° 20′ S, and longitude 36° 10′ E; it extends some 55 km N-S and 24 km E-W, with a total surface area of about 950 km^2 (Fig. 4.38). Its northern shore touches the territorial boundary with Kenya. Lake Magadi lies within Kenya slightly to the north of Lake Natron at the bottom of a steep-sided valley, which is the lowest point in the eastern or Gregory Rift Valley (Fig. 4.37a). It extends roughly 20 km N-S and is up to 6 km wide. Both lakes lie at an altitude of some 600 m above sea level and are surrounded by plateaus and active volcanoes reaching to more than 3,000 m asl (Fig. 4.37b). With an area of only 90 km^2, Lake Magadi is one of the most saline, but also one of the smallest, alkaline lake sumps in the Rift Valley.

The eastern Rift Valley stretches from Ethiopia to Tanzania and contains numerous endorheic soda lakes of varying salinity (Fig. 9.38a). Some lakes are fresh, like Lake Naivasha, others are quite saline Na-CO_3-HCO_3 solute systems like Natron and Magadi. Salinities range from 5 % in the more northerly lakes (Bogoria, Nakuru, Elementeria, Sonachi) to around 30 % and halite/trona saturation (Magadi, Little Magadi and Natron) in the south of the valley. The pH of surface waters in all is typically above 9, with values ranging up to 11.5 in the more saline alkaline depressions. Hydrographic closure is provided either by a lake's location in a volcanic crater or by formation of lake depressions in block-faulted lava and volcaniclastic terranes. The Rift Valley is volcanically active, with ongoing outpourings of sodic lavas and numerous hot springs (some boiling) about the edges of many of the modern lakes, indicating active hydrothermal circulation (e.g. Fig. 4.39). Spring outflows are

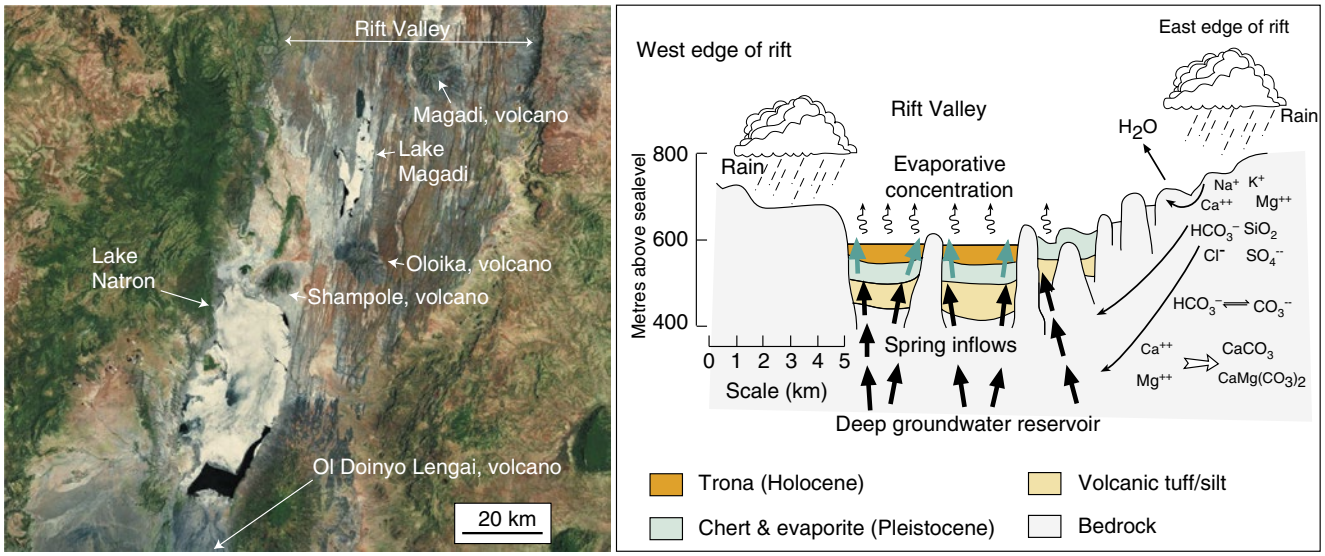

Fig. 4.37 Lake Natron and Lake Magadi, East African Rift. (**a**) Position in the East African (Gregory) rift showing adjacent and underlying volcanogenic basement (Landsat image courtesy of NASA). (**b**) Scaled schematic of the distribution of evaporitic lacustrine sediment in the rift valley based on an east-west transect of Lake Magadi (After Jones et al. 1977)

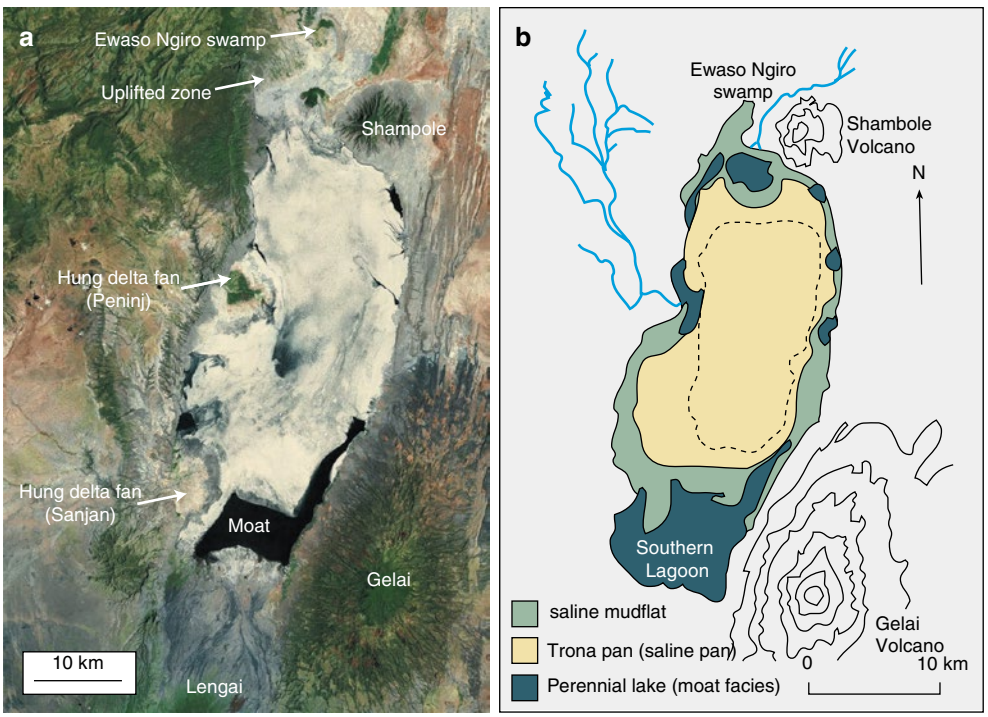

Fig. 4.38 Lake Natron, Kenya. (**a**) Plan view of Lake Natron showing moat facies about the lake edge and the white of the trona/halite pan-crust facies. Ol Doinyo Lengai (aka Mountain of God; 3,188 m asl). (**b**) Geological setting of Lake Natron

typically less saline than the lakes they feed and form biological refugia during times of widespread drought (Chap. 9).

Climate in the lowermost parts of the rift valley in the vicinity of lakes Natron and Magadi is arid, with high temperatures and an adiabatically reduced mean annual rainfall that is typically less than 500 mm in non El Nino years. Most precipitation falls in a single rainy season from March to May (Köppen Aw). Potential evaporation on the rift valley floor exceeds rainfall for most of the year so that the hydrological balance in the drainage region about both lakes is clearly negative. This facilitates the precipitation of aragonite in perennial brine pools (moats) about the lake edges and trona in the more central saline pan areas. Air temperatures around the lake can reach 40 °C in the dry season, while temperatures can be as high as 66–68 °C in dark-coloured mudflat sediment that make up the edge of

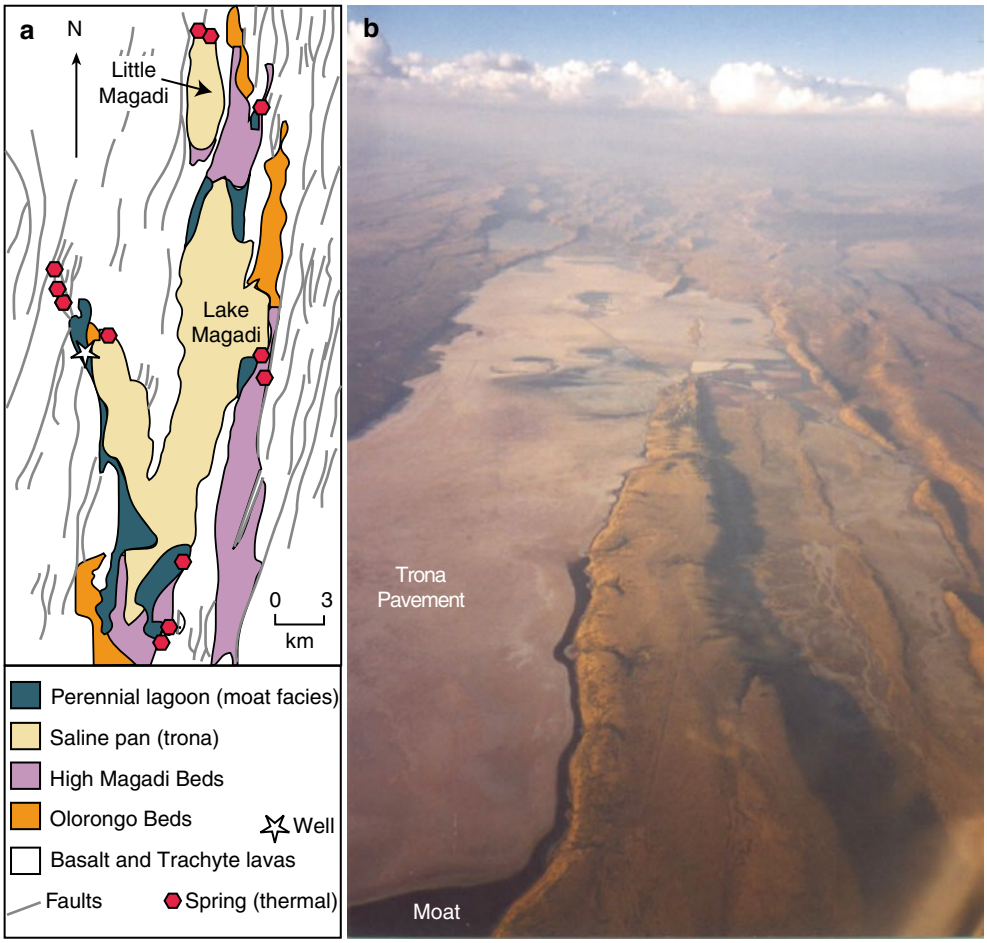

Fig. 4.39 Lake Magadi. (**a**) Geological setting of Lake Magadi. The well position locates the core in the High Magadi beds documented in Fig. 4.40. (**b**) Aerial view looks north and shows dark coloured moat facies of perennial lagoon defining lake edge

the moat facies and in the thin brine sheets in megapolygonal saucers in the trona areas. Pigments in periodic blooms of halobacteria or haloarchaea can turn more saline lake waters pink or red.

Both lakes are surrounded by metamorphosed Precambrian basement rocks. Volcanism began in earnest with the Neogene opening of the rift and continues today, with active volcanoes in the vicinity of both lakes. A general rule for volcanoes of the rift valley near Magadi and Natron is: the younger the volcanism the higher the alkalinity. Ol Doinyo Lengai, which is the youngest volcano in the vicinity of Lake Natron (≈20 km south of the lake), spews forth carbonatite lavas that are molten mixtures of sodium carbonate and calcium carbonate salts.[3] Hydrothermal circulation, associated with the numerous active volcanoes and their feeder faults, supplies hot alkaline brines to the many hot springs situated about the edges of both lakes (Table 4.4). More than 20 warm, saline springs, with temperatures between 32 and 52 °C, and release rates between 30 and 300 l/s, discharge into Lake Natron from scree slopes and hung fan deltas adjacent to the salt pan. There is no perennial stream flow into Lake Magadi, but it too has numerous warm surface springs feeding saline brines to the perennial lagoon portions of the Magadi depression (Figs. 4.37b and 4.39). Eugster (1970) argued that subterranean seepage from nearby Lake Naivasha contributes a solute load equivalent to that carried by all other saline groundwater springs in the Magadi depression.

Other than spring brines, the only other perennial water source to Lake Natron is the Ewaso Ngiro River, which drains into the north end of the lake. Yet today, no bedload sediment carried by the Ewaso Ngiro reaches Lake Natron. It is almost all deposited in an adjacent swamp created when the river was ponded and dammed behind a recently uplifted horst adjacent to the Shambole volcano. River blockage forced the river to dump its traction/suspended load into the waters of the burgeoning Ewaso Ngiro swamp. River water, minus any sediment load, now continually seeps out of the edge of the swamp into a perennial brine pool at the northern end of Lake Natron (Fig. 4.38). The effect of uplift on

[3] South of Lake Natron, within an ephemeral channel of the Engare Sero River, 120 ka hominid footprints are preserved in a tuff bed. It preserves the oldest modern human trackway in East Africa and one of the largest collections of hominid footprints in the world, giving an indication of the size of foraging parties of early modern humans (Richmond et al. 2011; Zimmer et al. 2012).

Table 4.4 Typical chemistry of waters and brines in saline East African rift valley lakes (ion contents in ppm, cited from various sources listed in text

	Ewaso Ngiro River	Hot spring (Natron)	Interstitial brine (Natron)	Surface water (Natron)	Hot spring (Magadi)	Salt pan brine (Magadi)	Moat brine (Magadi)	Surface water (Nakuru)
Na	7.0	12,166	119,500	104,000	7,000	160,930	64,970	7,500
K	2.3	212	1,470	1,700	75	2,230	1,040	220
Ca	6.5	0.5	n.d.	1.5	0.6	<1	<1	225
Mg	3.7	0.0	n.d.	<1	<0.4	<0.5	<0.5	<0.5
SiO2	20	91.0	976	186	36	895	425	200
HCO3	48	14,600	3,230	52,000	13,000	237,900	110,820	12,100
CO3	0	3,490	94,050	162,700				
SO4	2.4	159	2,100	165	52	1,680	1,230	50
F	0.2	154	1,440	n.d.	70	n.d.	n.d.	n.d.
Cl	4.0	4,740	71,750	51,970	3,550	112,000	39,900	2,040
Br	n.d.	114	265	n.d.	n.d.	n.d.	n.d.	n.d.
PO4	0.08	10	70	400	n.d.	175	22	14
B	n.d.	8.6	88	n.d.	n.d.	n.d.	n.d.	n.d.
TDS	77	29,200	294,000	352,000	24,100	340,000	210,000	22,100
pH	7.0	9.2	10.5	>11.5	9.9	>11.5	>11.5	10.5

bedload in Lake Natron implies that mineralogical changes in ancient lacustrine units are not always a response to climatic changes; mineralogy in a lake depression can change due to tectonics.

Brine Chemistry

Interstitial groundwaters and hot spring waters come from parent waters with low levels of alkaline earths Mg and Ca, and high levels of Na, Cl and HCO_3 (Table 4.4). This chemistry is ideal for ongoing trona precipitation at higher salinities (Figs. 2.19 and 2.20). Rain falling in the drainage basin contains normal levels of Ca^{2+} and Mg^{2+} but on the way to the lake depression the same waters flow over and through highly alkaline and reactive volcanics. By the time these same waters flow out onto the lake as springs and seeps they have gathered a four-fold dominance in bicarbonate over the alkaline earths (Ca + Mg). They have already passed the calcium carbonate chemical divide and left behind their calcium and magnesium in various pedogenic and phreatic carbonates to become path I brines (Fig. 2.19).

Chloride in brines in both lakes behaves conservatively, and so its concentration can be used as a brine evolution marker (Eugster 1970). Chlorine levels show an 18,000 fold increase in concentration in the lake brine compared to river and spring inflow. Yet this is not sufficient to precipitate large volumes of halite within the Natron-Magadi depression, nor does the current warm climate favour the accumulation of natron over trona. Trona is the first Na-carbonate mineral to precipitate in equilibrium with concentrating lake brines. Natron could form as a coprecipitate if the surface brine temperature falls below 25 °C (Fig. 2.20). But, such low temperatures do not occur in either Lake Magadi or Lake Natron at the times trona precipitates.

As trona forms, there is a marked decrease in the bicarbonate proportion (relative to chloride) in the increasingly saline lake brine. As the brine continues to concentrate, lesser amounts of trona precipitate and ultimately halite should crystallise. But, the high humidities maintained over the lake brines in the deep valley bottoms of Lake Magadi and Lake Natron mean surface waters can only rarely attain concentrations where halite can precipitate in large volumes (no more than 5–10 % halite is preserved in the trona crusts in either lake). Higher temperatures at the time the various Na-carbonates precipitate from the lake brines means thermo-natrite (not natron) is the other sodium carbonate accumulating in both lakes (Fig. 2.20); only at rare to minor levels in Magadi, but it can locally constitute up to 30 % of the trona pavement in Lake Natron.

Interestingly, the concurrent fluoride increase between inflow and the trona stage of the lake brine is only 7,200 times (compared to 18,000 in chloride in the same waters), indicating its removal as a sodium salt. A lack of Ca in lake brines prevents direct fluorite precipitation in this fluorine-rich hydrothermal province. Accordingly, fluoride concentrations in the interstitial brines of the trona platform can be more than 1,400 ppm. This, and the elevated Na levels in the concentrated lake brines, leads to the precipitation of sodium fluoride salts[4] in the trona crust that include kogarkoite (Na_3SO_4F) and villiaumite (NaF) (Darragi et al. 1983; Eugster 1986). Prior to its documentation in a Lake Natron trona crust, kogarkoite had only been observed in hydrothermal deposits.

[4]Use of fluoride-rich trona (from the East African rift) as a food tenderiser has led to widespread fluorosis (mottled teeth and skeletal fluorosis) in the local population (Vuhahula et al. 2009; Rango et al. 2009).

Holocene Sediments

Spring and ephemeral stream-fed carbonate lagoons form permanent water-filled depressions that line the edges of the trona pan in both lakes. Unlike the more central trona-depositing saline pan, the lagoons never dry up and are sometimes described as a "moat" to the lakes (Figs. 4.38 and 4.39). In Lake Natron, which year-round contains more free-standing water than Magadi, the lagoon water depths during the wet season can be upwards of 10 m. The deeper parts of these perennial brine lakes are floored by black micritic laminites, which are mostly composed of aragonite and dolomite peloids, and can retain up to 16 % TOC. The lagoon floor laminites, nearby pisolites, and cemented crusts of the spring seeps, constitute a carbonate "moat" facies. Although located about the lake edge, the laminated carbonate unit is deposited in waters deeper than the ephemeral brine sheets forming the trona pavement lake centres. Less saline areas near spring seeps in the moat lagoons in both lakes can contain thriving populations of *Tilapia alcalica*, a small fish that survives at temperatures of 39 °C and pH up to 10.5. Away from the spring-freshened areas, the lagoon bottom waters and pore waters in pavements become too saline and too anoxic to support vertebrates and a well-adapted halophilic microbial biota flourishes, including endemic alkaphilic archaea (Chap. 9).

Trona accumulates in the central portions of both lakes as flat pavements composed of stacked saline pan crusts. Some 2,100 km^2 of the northeastern part of Lake Natron is covered by an impure trona bed averaging 1.5 m thick (Fig. 4.38). The Lake Magadi trona pan is some 74 km^2 in area and is 7–50 m thick, known locally as the "Evaporite Series" (Fig. 4.39). It is made up of cm-scale stacked trona-detrital couplets (Baker 1958). Light-coloured trona layers are composed of rosettes and splays of upward pointing, growth-aligned trona crystals. Thin bands of finer trona coloured by dark, mainly windblown dust separate the crust layers from each other. Even as it stacks and dissolves, each layer retains some porosity between interlocking growth-aligned crystal splays.

During the wet season the trona pans in both lakes are covered by shallow brine sheets (<1 m deep) and are subaerially exposed for the remainder of the year. When not covered by lake brines, the modern surface of both the Magadi and Natron trona pans are rock hard and occupy topographically higher positions compared to the water surface of the adjacent perennial lagoons. This "moat" geomorphology provides protection from predators for flocks of flamingoes that, once waters recede from the trona pan, nest in large numbers on the platform, especially in Lake Natron (see flamingo connection in Chap. 9).

Trona saturation is achieved when the shrinking brine sheets are 2–10 cm deep. At that stage the trona prisms grow upward from the pan surface as cm-scale aligned elongate blades and splays. Interlocking of the crystal splays give the accreting trona sheet an inherent strength that allows it to support expansion polygons or pressure ridges, with saucers up to several tens of metres wide and ridges up to a metre high. Ridging is the result of pavement overthrusting, driven by the sideways expansion of trona layers jostling for space in the various growing crystal pavements. The resultant cracking and thrusting of the layers cuts the trona pavement up into a series of overthrust-edged saucers, with small bright pink brine pools in the centre of each polygon; the colour is the result of a haloarchaeal bloom (see Chap. 9).

At the same time the ridges are forming, thin films or rafts float on the surface of the brine sheet. Trona rafts contribute only a minor amount to the total trona volume in the pavement unit, but are important in controlling mineralogy as they slow evaporation and raise the temperature of the underlying brine through a greenhouse effect. Temperatures of 60–65 °C can occur annually within thin brine sheets immediately below the trona rafts and so drive precipitation of thermonatrite (Fig. 2.20). As brine level continues to fall, the upward-growing bottom-nucleated trona splays break through the floating rafts. Prior to complete drying, high winds can break up and flounder the rafts or blow them into heaps about the local strandzones of small brine pools.

Finally, the brine level falls below the surface of the newly formed trona crystal crust and the annual primary depositional cycle is complete. Small volumes of trona continues to crystallise as minor interstitial cements, below the surface of the exposed pan. When the pan surface dries out, the brine level stays very close to the surface of the trona pavement. Even during exceptionally dry years it drops no more than 5 cm into the trona layer. It can be covered by a thin layer of windblown material whenever the surface of the layer is exposed during the dry season.

With the next rainy season the watertable rises as the pan is once again covered by water. Initially, these inflow waters are fresh and undersaturated with respect to the pore waters of the trona pavement. So they float above the top of the dense interstitial brines and any trona crystals poking up into these freshened waters start to dissolve. Last season's crystals are truncated by the influx of freshened waters. During this freshened stage, windblown clays and other detritus on the pavement surface can be retransported by waves. Then the wet-season rains cease and the trona precipitation cycle begins anew. Each season a trona layer 2–5 cm thick forms on the saline pan in both lakes but subsequent seasonal dissolution means the average Holocene accumulation rate for Lake Magadi trona is at most 0.4 cm/year. The much thinner layer of Holocene trona preserved in Lake Natron, implies dissolution levels are even higher compared to Lake Magadi. The annual trona crop in Lake Magadi is around 1.5 million tonnes/year, but the bulk of this crop (≈75 %) is recycled by pan dissolution each wet season. Lake Magadi has been

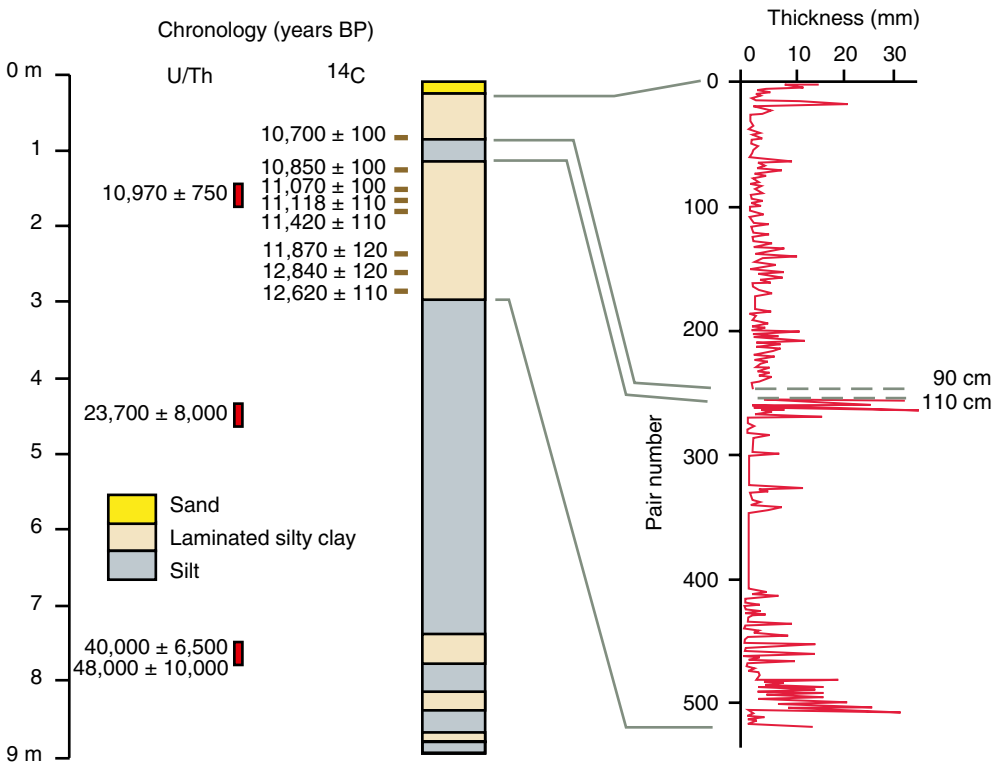

Fig. 4.40 Core in the High Magadi beds, Lake Magadi (See Fig. 4.39a for location; after Damnati and Taieb 1995)

described as an "ephemeral saline lake at the peak of its trona productivity" (Eugster 1980b). Trona in Lake Magadi has been extracted at various times from 1914 until today using dredging barges. Replenishment of trona in the lake is so rapid that at the rates the Magadi trona is mined (230,000 t/year) it is a renewable resource (Fig. 12.41).

Late Pleistocene Sediments

Aside from the Ewaso Ngiro River, two other significant rivers flow toward the shores of Lake Natron, the Peninj and Sanjan (Malambo) Rivers (Fig. 4.38a). Today, these rivers are ephemeral and any surface water sinks into the riverine sediment fans well before it ever reaches the current lake strandline. Some 9,000–10,000 years ago during the last high water stage, these rivers, and the Ewaso Ngiro, deposited fan deltas along the edge of a much fresher and higher Lake Natron. Today, these sediments form "hung" delta lobes on the surrounding landscape located well back from the lake shoreline, some 10–60 m above the present lake level. In earlier lake-full times the flood sands from these highstand deltas probably extended further out into the lake centre and so may now directly underlie the trona-hosting sediments of the lake centre and act as potential aquifers for fresher groundwaters that prevent the accumulation of thick trona units in Lake Natron.

At the time the fan deltas were active Lakes Magadi and Natron were both deeper, larger and fresher water bodies. At such times in the late Pleistocene the two lakes sometimes merged into a single pluvial lake (Hilaire-Marcel et al. 1987). Studies of stromatolites and tufa terraces from various high lake levels in the vicinity of both lakes show that the most recent high lake levels were part of a two-stepped climatic optimum that occurred some 12–11 ka (Williamson et al. 1993; Icole et al. 1990). The first humid period (between 12 and 11 ka) created a lacustrine highstand that topped the 635 m-elevation barrier (msl) separating the Magadi and Natron depressions. Between 11 and 10.7 ka the lake level dropped below the barrier, once again separating the two lakes. A second maximal high stand occurred around 10 ka, possibly once again joining the lakes. Since that time, and throughout the Holocene, the lake levels have been consistently near their present levels and some 60 m below their former highstands.

The High Magadi Beds were deposited as diatomaceous mudstones when lake waters were more than 13–14 m above the present level and relict shorelines from that time are still mappable (Fig. 4.39). Lake sediments of that time are mostly bedded volcanic muds and cherts, typically deposited as lakefloor laminates with abundant fish scales visible on partings. An 8.7 m core taken from this highstand facies in the Flamingo Nursery area on the northern edge of Lake Magadi recovered High Magadi beds that were deposited from 40 to 9 ka (Fig. 4.40; Damnati and Taieb 1995; Williamson et al. 1993). The lower (870–740 cm) and upper (295–6 cm) units in the core consist of laminated silts made up of alternating layers of magadiite (zeolite-rich) and organic-rich muds

(TOC >5 % dry weight). The middle unit (295–740 cm) contains homogenous inorganic clay silts that are unlaminated, suggesting the lake was not stratified at that time. The upper laminated unit was deposited 12–9 ka, the middle unit ≈23 ka, while the lower laminated unit contains sediments as old as 40 ka. Each unit is separated from the other by a thin sand, which is thought to mark a hiatus in chemical sedimentation and to be a flood sand from the feeder deltas and sheet floods.

The laminite episodes in the core indicate times when a relatively deep lake was chemically and thermally stratified. Light laminae in the couplets are in turn comprised of finer-scale micro-couplets. Each light layer is made up of a microlayer rich in detrital elements (quartz and feldspar) and broken diatom frustules that is overlain by a microlayer of magadiite (Damnati and Taieb 1995). The dark lamina in each couplet is composed of a microlayer made up mostly of well preserved diatom frustules, covered by a layer of microspheres (probably microbial) associated with autochthonous organics generated in the lake waters. White laminae indicate a more humid season climate and dark laminae indicate drier climatic conditions in the lake depression. Variations in lamina thickness can be tied to year-to-year variations in monsoonal intensity and to ENSO years. These Pleistocene laminites are very similar to those accumulating in Lake Van today, the general lake hydrologies and their humid settings are probably comparable, although one forms in a transtensional tectonic regime and the other is part of a rift valley fill.

Two hundred kilometres north of Magadi is Lake Bogaria, a shallow, perennial, saline (60–100 g/l total dissolved salts, alkaline, pH: ~10–10.5) lake with Na–HCO_3 –CO_3 waters. Today it is a permanent freshwater lake, that currently receiving more fluvial inflow than either Magadi or Natron. The northern margin of the lake basin is defined by the spill-over point into the drainage for Lake Baringo and is located almost on the equator (Aw). It occupies the lower part of what is locally an asymmetric rift valley with active fan deltas forming along the steeper gradient eastern side of the lake, Gilbert-style deltas and hydrothermal stromatolites typify Holocene deposits on the less steep western side and diatomaceous laminites are accumulating in the deep lake centre (McCall 2010; Scott et al. 2009). Its current sediment styles and hydrologies are likely Holocene counterparts for the Late Pleistocene situation when the High Magadi beds were deposited.

Holocene cores from Lake Bogoria have recovered crystals of trona and nahcolite from 5–10 cm thick beds at depths of a few metres below the current lake surface. In the lowermost unit cored by de Cort et al. (2013) there are four trona layers attributed to drier conditions during the second half of the first millennium AD and in the period equivalent to the Medieval Climate Anomaly, which lasted until the first half of the twelfth century AD. Lake Bogoria hydrology was probably polymictic at that time, its surface level standing significantly lower than today. The overlying sodium carbonate unit displays uniform deposition of nahcolite, interpreted as indicative of a strongly stratified lake where a layer of less saline surface water (near-) permanently covers a hypersaline water mass with high pCO_2. De Cort et al. (2013) propose that this depositional phase reflects a rising lake level related to the transition from dry to more humid climate conditions at the onset of the Little Ice Age. The third, uppermost sodium carbonate unit in Bogoria contains only sporadic magadiite of magadiite and various other sodium carbonate minerals. This, together with low magnetic susceptibility in the core, is interpreted to indicate humid Little Ice Age conditions, with highest lake level and reduced salinity occurring around the late-fifteenth to early-sixteenth century AD. From the late-eighteenth to early-nineteenth century and again in the 1870s, the region experienced two episodes of drought more severe than any other recorded in historical time. The result is interesting in terms of current discussions of anthropogenic climate change and illustrates significant hydrological excursions and climate-driven desiccation events over the past few thousand years that are unrelated to anthropogenic industrial activity.

An important general observation for saline systems, based on the African Rift valley lakes, is that perennial continental lakes in a single sump do not usually deposit bedded evaporites at the same time that they deposit thick fluviodeltaic successions. Nor do all lake sumps along the lower parts of a rift valley accumulate evaporites at the same time. Episodes of fluviodeltaic deposition and thick evaporite deposition are separate in time and space – a restriction inherent in the isolated lake hydrology needed to precipitate evaporites. That is, ancient lacustrine evaporite beds accumulating in separate but adjacent basins are not necessarily time equivalent. And, it is almost impossible to form evaporites when the lake waters are diluted by fresh water carrying siliciclastics into deltas. However, the time intervals resolvable in the siliciclastic-to-evaporite transition in the African Rift Lakes are less than a few thousand years. In pre-Quaternary lacustrine deposits, such as the Eocene Green River Formation, the two sedimentation styles may appear syndepositional and are easily mis-correlated.

Diagenesis – Magadiite and Evaporitic Chert

Pleistocene nodular and bedded chert outcropping in the lake margins in Lake Magadi, Kenya, are thought to form inorganically via early replacement of sodium silicate precursors – magadiite and/or kenyaite. These neoformed sodium silicates (especially magadiite) accumulate in alkaline carbonate-rich hydrogeochemical environments, especially in organic-rich diatomaceous laminites in the freshened stages of soda lakes. Such sodium silicates were first documented in the High Magadi beds (Eugster 1969, 1980b;

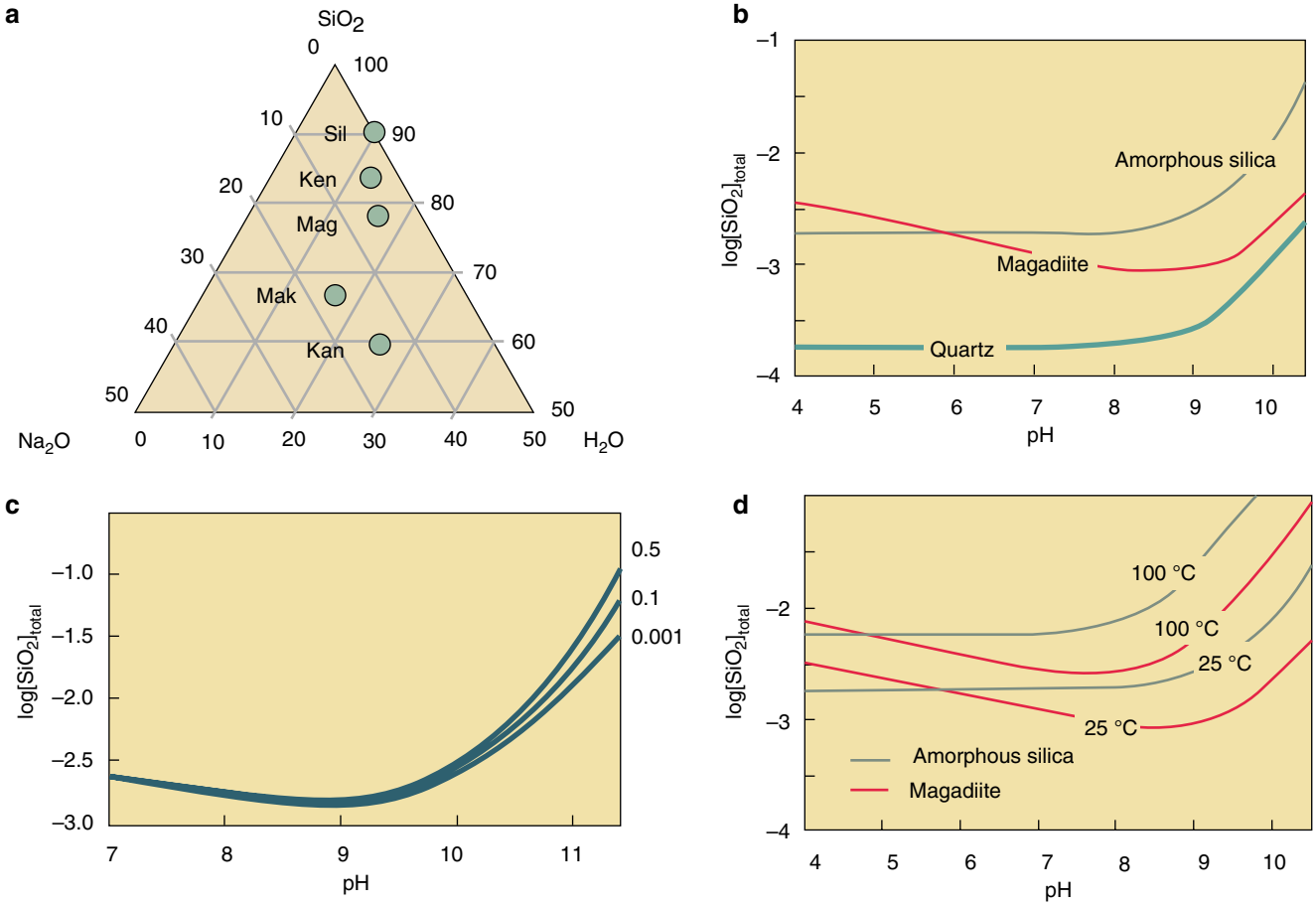

Fig. 4.41 Magadiite chemistry. (**a**) Sodium silicate minerals plotted in the *upper* part of the ternary diagram Na_2O±SiO_2±H_2O showing the position of various hydrous sodium silicates related to varying proportion of the constituent water silica and sodic contents (*Ken* kenyaite, *Kan* kanemite, *Mag* magadiite, *Mak* makatite, *Sil* silhydrite). (**b**) Concentration of $[SiO_2]_{total}$ at equilibrium with magadiite, amorphous (**c**) Concentration of $[SiO_2]_{total}$ at equilibrium with magadiite and amorphous silica at 25 and 100 °C (0.1 mol Na(OH,Cl) L1; I = 0.5). (**d**) Concentration of $[SiO_2]_{total}$ at equilibrium with magadiite as a function of pH at ionic strengths of 0.5, 0.1 and 0.001 at 0.001 mol Na^+ L^{-1}, 25 °C (After Dietzel and Letofsky-Papst 2002)

Baker 1958) and also occur in the High Natron beds. There are three sodium silicates in the High Magadi beds: magadiite – $NaSi_7O_{13}(OH)_3$ .H_2O, kenyaite – $NaSi_{11}$ O_2 $0.5(OH)_3$. H_2O, and makatite – $NaSi_2O_3(OH)_3.H_2O$ (Fig. 4.41a). Of these, only magadiite occurs in substantial quantities, typically as beds, mounds and nodules. Kenyaiite, never occurs as beds, but is not uncommon as nodules in the bedded magadiite laminites of Lake Magadi. Some magadiite nodules have kenyaite at their centres, perhaps implying kenyaite can be created by the weathering of magadiite.

When fresh, magadiite is white, soft, putty-like and easily deformable, but it dehydrates rapidly on exposure to air and hardens irreversibly to a fine-grained cherty aggregate. To date, magadiite has been found only in Quaternary alkaline lacustrine settings. In addition to Lake Magadi, Quaternary magadiite has been found in Lake Bogoria, Lake Kitagata, in Lake Chad in western central Africa, Alkali Valley playa in Wyoming, and Trinity County in California (Sebag et al. 2001; Ma et al. 2011). On a longer time scale, ancient Magadi-type (crocodile skin) chert has been found in many ancient lacustrine basins, in the Jurassic of Wyoming, the Proterozoic Callana Beds of the Adelaide geosyncline in South Australia, and in Precambrian banded iron formations in Western Australia (see also Table 7.13).

The solubility equilibrium curves for silica and amorphous silica are similar, with a marked increase in solubility occurring in more alkaline conditions (pH >9; Fig. 4.41b, c; Dietzel and Letofsky-Papst 2002). In contrast, SiO_2 contents at equilibrium with magadiite show a minimum value at a pH around 8.5 and follow a different dissolution pattern to silica. At low pH the concentration of silica in solution increases, as it does also in alkaline solutions at the other end of the pH spectrum. Thus, the concentration of silica in a solution saturated with respect to magadiite, at constant Na content, is lowest in neutral to slightly alkaline solutions. Below pH 5.9, which is the intersection point of the magadiite and

amorphous silica curves, magadiite exhibits a higher solubility than amorphous silica. Thus, at pH <5.9 magadiite will dissolve, while amorphous silica precipitates (Dietzel and Letofsky-Papst 2002).

Conditions associated with the precipitation of magadiite from lake brines in Lake Chad, and probably most other soda lake occurrences, including Lake Magadi, require fluctuations in alkalinity or mixing interfaces between alkaline and less alkaline groundwaters (Fig. 4.41b–d). Sebag et al. (2001) list the following conditions as typical of most modern magadiite occurrences; (1) Elevated alkalinity, typically in the lake dry season (pH >9) allow dissolution of silica, followed by lowering of alkalinity in the wet season driving precipitation of silica (Fig. 4.41b, c), (2) High concentrations of dissolved silica (up to 2,700 ppm), (3) Incorporation of sodium ions into the silica lattice that precipitates at the time of silica supersaturation (Fig. 4.41d). Depending on the concentration of Na and Si in the brine at the time of precipitation, the various sodium silicate minerals will precipitate (Fig. 4.41).

Bedded magadiite is widespread in High Magadi laminites, it precipitated in the Pleistocene when Lake Magadi was deeper, fresher and density stratified. Most of this magadiite is an authigenic phase precipitated during shallow diagenesis via the interaction of alkaline brines with reactive siliceous materials such as volcanic glass and zeolites (Jones et al. 1967). Even today, hydro–sodium–aluminosilicate gels precipitate about the edge of Lake Magadi where saline spring waters first emerge. With shallow burial the gels convert to analcime, erionite, and magadiite.

Two mechanisms are thought to drive the precipitation of the sodium silicates. One is intense evaporation, so the resulting sodium silicates are intimately associated with evaporite indicators, such as evaporite splays and dissolution breccias with evaporite pseudomorphs and moulds in the magadiite host. The other is the pH decrease that occurs when a brine comes into contact with more diluted or more acidic water as when two stratified water masses with differing chemistries mix (Fig. 4.41b–d). Likewise, although the pH change may be as little as 0.5, a decrease in pH from 10.3 to 9.8 lowers amorphous silica saturation more than 500 ppm (Fig. 7.79). In contrast to the modern occurrences, the pH and dilution changes needed to form the Pleistocene magadiite of the High Magadi laminites were probably related to the annual overturn of the stratified water mass.

Freshly precipitated, magadiite is a soft plastic white paste (Maglione 1980; Ma et al. 2010), and remains so while bathed in alkaline pore brines. However, when exposed to drying and dehydration it quickly loses its plasticity, cracks and shrinks as it irreversibly hardens into chert. Shrinkage (25 % volume change) of the hardening surface creates neoformed chert with a superficial crack network made up of small prisms separated by fissures (Icole and Perinet 1984).

Fig. 4.42 Magadiite chert from Lake Magadi showing cauliflower surface texture, also known as crocodile skin

It gives the surface of any resulting chert a characteristic "crocodile-skin" or cracked appearance (Fig. 4.42). This is a texture used to support an alkaline lacustrine interpretation in ancient counterparts, such as the crocodile cherts in the Eocene Green River Formation (Fig. 4.42). In Phanerozoic hosts, such nodules are readily distinguished from the much more commonplace and nondiagnostic smooth-walled chert nodule, which are widespread in both marine and nonmarine matrices.

Whenever a plastic magadiite horizon in the High Magadi beds is traced from depth (≈1 m) to the surface or from subcrop to outcrop, a conversion from magadiite to surface chert is always seen. In the perimeter sediments of Lake Magadi, Eugster (1969) described what he considered to be an impressive syndepositional result of this transformation, namely shrinkage megapolygons up to 50 m across in a bedded chert host with bounding upturned chert ridges up to 2 m high.

Subsequent work on the same structures by Behr and Röhricht (2000) concluded the megapolygons do not indicate a response to mineralogical transformation, rather they are part of a suite of prelithification structures in soft siliceous lake sediment. The chert megapolygons are a soft sediment response to strong deformation and local-scale diapirism, as are the associated pillow-chert mounds, chert extrusives along dykes and fault ramps, horizontal liquefaction slides with breccias, slumps, petees, flows and shear-structures in the magadiite beds (now all chert at outcrop). Collapse, liquefaction and extrusion of the pre-lithified siliceous matrix were caused by seismotectonic rift activity in the lake basin and it activated fault scarplets and large-scale dyke systems. Seismic activity led to liquefaction and other earthquake-induced intrasediment deformation, especially along fault ramps and on tilted blocks. The textures all

indicate the chert megapolygons are a form of seismite and do not indicate volume changes in the transition from magadiite to chert. After liquefaction and extrusion, the exposed magadiite material solidified via spontaneous crystallisation in an environment that was characterised by highly variable pH and salinity.

Since the work of Eugster in the 1960s, three sets of diagenetic processes are now thought to be responsible for driving the conversion of magadiite to chert in Lake Magadi and other soda lakes:

1. Leaching of sodium by dilute surface runoff during weathering of the High Magadi beds, as evidenced by tracing unweathered beds into outcrop and summarized in the chemical transformation (Eugster 1969);

$$NaSi_7O_{13}(OH)_3 \bullet H_2O + H^+ \rightarrow 7SiO_2 + Na^+ + 5H_2O$$

2. Spontaneous release of sodium driving the conversion of magadiite to chert, whatever the nature of throughflushing solutions and environments. In this process sodium is expelled even in the presence of brines; it does not require the fresh water needed for process 1, and perhaps better explains the occurrence of calcite-filled trona casts in cherts and the presence of chert nodules in unweathered magadiite horizons in Lake Magadi (Hay 1968, 1970).
3. To this inorganic perspective on the transformation to form chert, Behr and Röhricht (2000) added a biological one. Based on their field observations and microbiological studies of the cherts in Lake Magadi region, they argue that inorganic cherts are rare at the type locality of Magadi-style cherts. They go on to note that most of the cherts in the Magadi depression are older than the High Magadi Beds and developed from flat-topped calcareous bioherms of *Pleurocapsa*, *Gloecocapsa*, and other coccoid cyanobacteria, along with thinly bedded filamentous microbial mats, stromatolites, bacterial slimes, diatoms, *Dascladiacea* colonies and other organic matter accumulations. Silicification occurred from a silicasol[5] via opal-A to opal-C with final recrystallisation to a chert of quartzine composition. They conclude that metabolic processes of cyanobacteria controlled the pH of the brine and strongly influenced the dissolution-precipitation mechanism that created the chert (Fig. 7.74).

Dead Sea, Middle East

The Dead Sea water surface defines what is the deepest continental position (−415 m asl) on the earth's current terrestrial surface. It is our only modern example of bedded evaporitic sediments accumulating on the floor of a brine body, where water depths are measured in hundreds of metres. This salt-encrusted depression is 80 km long and 20 km wide, has an area of 810 km^2, is covered by a brine volume of 147 km^3 and occupies the lowest part of a drainage basin with a catchment area of 40,650 km^2 (Fig. 4.43). However, falling water levels in the past few decades mean the permanent water mass now only occupies the northern part of the lake, while saline anthropogenic pans occupy the southern basin so that the current perennial "Sea" is now only some 50 km long. Rainfall in the region is 45–90 mm, evaporation around 1,500 mm, and air temperatures between 11 and 21 °C in winter and 18–40 °C in summer, with a recorded maximum of 51 °C. The subsiding basin is surrounded by mountain ranges to the east and west, producing an orographic rain shadow that further emphasises the aridity of the adjacent desert (Fig. 4.43a).

So, until recently, the basin floor was physiographically divisible into two contiguous and permanent brine-covered water bodies, the Northern and Southern basins, largely separated by a diapir-cored shallow sill, the Lisan Ridge and joined at the Lisan Straits. Top of salt is 100–120 m below the surface in the Lisan Peninsula and a few metres below the surface at Mt. Sedom. The land surface of the Lisan Peninsula is slowly rising and being karstified, at a rise rate of a few mm per year, driven by salt flow (Closson et al. 2007). Widespread at-surface evidence of this rise is swamped by the changing of the depositional and hydrological system, driven by fluctuating lake water levels. Continuing falling water levels since the 1930s means that today the North Basin is the only permanent natural water mass, with waters some 320 m deep (Fig. 4.43b). The Southern Basin is today a saline pan/mudflat, which would be a subaerially exposed plain, except that brine-filled saltworks now cover much of the former Southern Basin lake. Perennial brine sheets are artificially maintained in these pans by continually pumping of brines from the Northern Basin (Fig. 11.25).

The basin floor beneath the waters of the Northern Basin is asymmetric, with the western slopes around 7° and the eastern slopes about 8°. The northern part of the Northern Basin is flatter and smoother than either its eastern or western slopes, and is covered by deltaic clays of the Jordan River outfall (Fig. 4.43a). Away from the northern slope the outflow zones of the various streams and wadis are defined by local clastic aprons or fan deltas, most of which are now "hung" in response to the lowered lake levels (Figs. 4.43b and 4.52a).

Geological Setting

The Dead Sea depression is a large strike–slip basin located within the Dead Sea transform; a plate boundary separating the Arabian plate from the African plate and connecting the divergent plate boundary of the Red Sea to the convergent

[5]Colloid grains in a silicasol are minute (10–20 nm) and so have relatively large specific surface areas, making them highly responsive to changing brine chemistries.

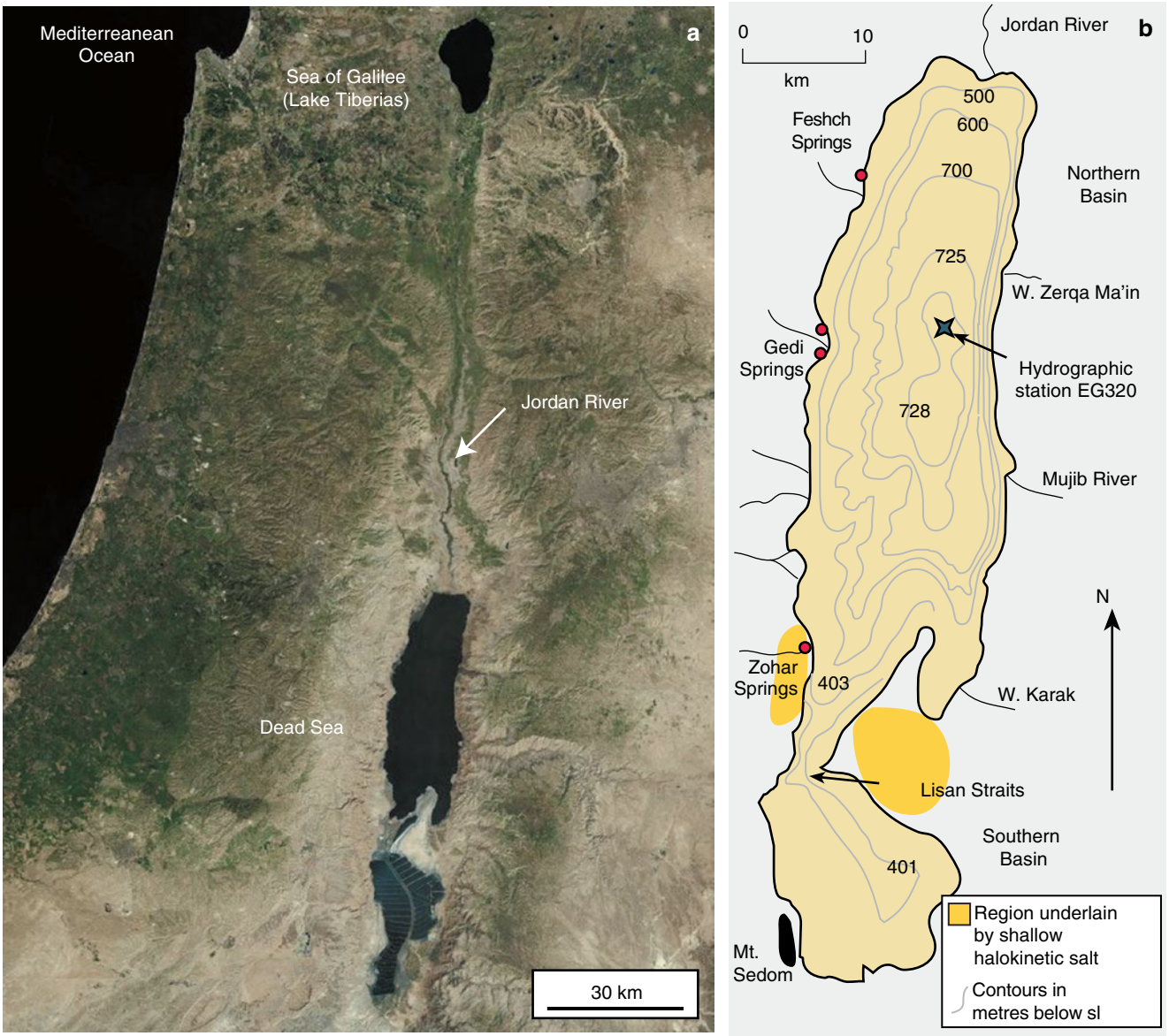

Fig. 4.43 Dead Sea depression, Middle East. (**a**) Dead Sea Valley. Image of the depression in the early 1990s, showing the Dead Sea separated into a deep Northern Basin separated by the Lisan Straits from the Southern Basin with its solar ponds. The Jordan River enters the Dead Sea at its northern end. Sea of Galilee is visible in the northern end of image. (**b**) Bathymetry of lake floor in metres below sea level, the basin shows E-W basin asymmetry with a somewhat steeper eastern margin

plate boundary of the Taurus Mountains in southern Turkey. Since it formed, 105 km of left-lateral horizontal movement has occurred along the transform. In places along the transform where crust is stretched or attenuated, plate stress is accommodated via several rapidly subsiding en-echelon rhomb-shaped grabens separated across west-stepping fault segments. The Dead Sea basin and the Gulf of Elat to its south are the largest of these graben depressions and are separated by the Yotvata Playa basin (Fig. 3.34). The Dead Sea basin fill is 110 km long, 16 km wide and 6–12 km deep and located in the offset between two longitudinal faults, the Arava Fault and the Western Boundary (Jericho) Fault (Fig. 4.44a; Garfunkel et al. 1981; Garfunkel and Ben-Avraham 1996).

Movement began 15 Ma in the Miocene with the opening of the Red Sea and is continuing today at a rate of 5–10 mm/year. The Dead Sea basin floor is more strongly coupled to the western margin (Levantine plate) and is being left behind by the northward moving Arabian plate. Since the Miocene, depocentres in the Dead Sea region have moved 50 km northward along the shear zone (Zak and Freund 1981) to create the offlapping style of sedimentation in the Dead Sea–Arava Valley, with a basin geometry reminiscent of the Ridge Basin in California. Continued extensional movement has

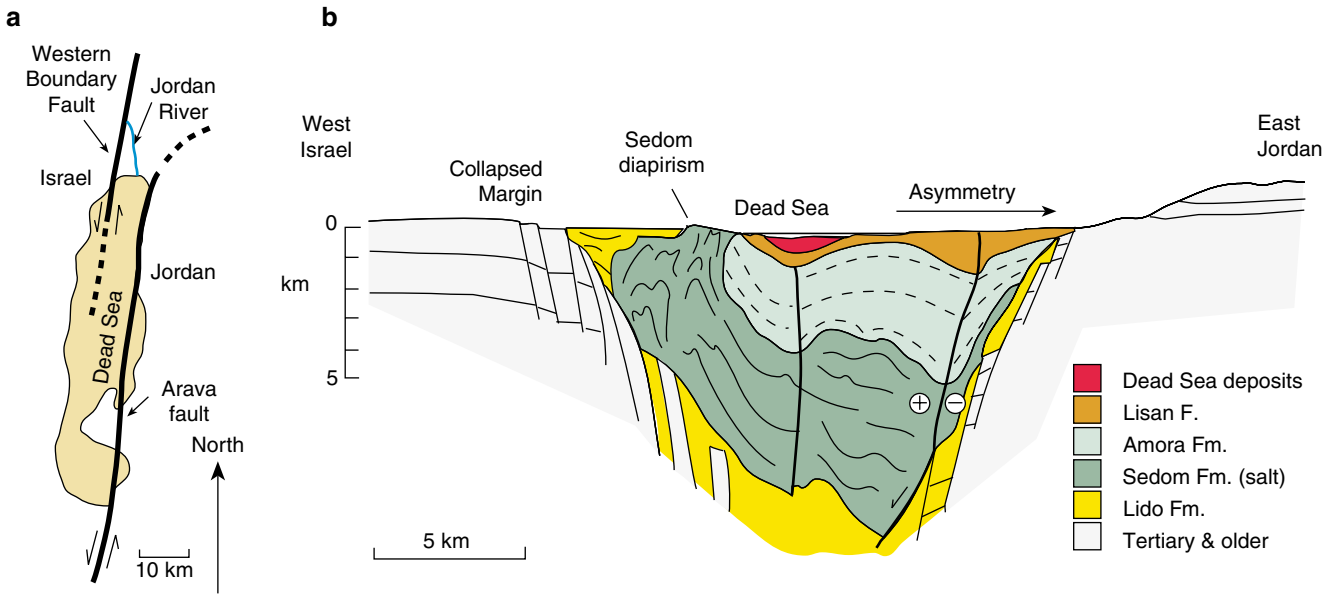

Fig. 4.44 Dead Sea, Middle East. (**a**) Plan view show the location of the Dead Sea depression in relation major transtensional faulting. (**b**) Schematic cross section of lake geology showing the importance of subsidence, in relation to salt tectonics and strike-slip faults as controls on sediment distribution in the depression (In part after Zak and Freund 1980, 1981)

triggered halokinesis in the underlying Miocene evaporites so that diapirs subcrop along the Western Boundary Fault and its offshoots (Figs. 4.43b and 4.44b; Neev and Hall 1979). Salt in these structures is equivalent to the salt in the outcropping Mount Sedom diapir. The Holocene to Miocene fill is 8–10 km thick beneath the Dead Sea, with at least 90 m of Holocene fill beneath the Southern Basin. There have been three stages of deposition since the Miocene inception of the Dead Sea valley (Fig. 4.44b; Garfunkel and Ben-Avraham 1996). The bottom 2–3 km of fill is made up of continental conglomerates of the Hazeva (Lido) Formation. This represents the first stage of basin fill, during which deposition kept pace with subsidence of the rift. It ended in the late Miocene (8–10 Ma) when differential uplift along the transform edges and rapid subsidence of the basin led to a deep topographic trough. During this second stage (4–6 Ma) the trough was invaded by Mediterranean seawater through the Yizre'el Valley to create a highly restricted arm that was periodically cut off from the ocean and deposited the 2–3 km thick halite-rich evaporites of the Sedom Formation (also known as the Usdum Fm.). This 2–3 km-thick section is now halokinetic in the Dead Sea region. In its third stage, the basin was cut off from the Mediterranean seepage to become a closed continental basin. A series of large lakes formed during this time and 3–4 km of fluviatile and lacustrine sediments of the Plio-Pleistocene Amora and Samra-Lisan formations were deposited (Fig. 4.44b). The Pleistocene Amora Fm. in the region of the Dead Sea is a fluvio-lacustrine chalky marl with entrained gypsum, anhydrite, sands, conglomerates and thin halite layers. The overlying Lisan-Samra Fm. was deposited in the last large lake that filled the majority of the Dead Sea-Jordan Rift Valley during the late Pleistocene. It consists mostly of finely layered marls, laminites and chalks with gypsum and aragonite couplets in its more evaporitic portions.

Unlike the marine isotopic signatures of the salts in the Sedom Formation, isotopes in the evaporites of the various Pleistocene sequences indicate their precipitation from lacustral CaCl-rich connate brines. Groundwater inflow chemistries were created by rock-water interactions with an original connate seawater brines, first trapped in sediments of the rift walls in "Sedom time" (Raab et al. 2000). After the final Pliocene disconnection from the sea and a lowering of the lake levels, these residual brines gradually seeped and leached back in to the Sedom basin (García-Veigas et al. 2009). There was never a hydrographic connection of the Dead Sea to the Gulf of Aqaba in the south and all of the Pleistocene salts in the depression come from the evaporation of continental groundwaters, not from ongoing marine-fed seepage. Neogene parts of the intervening rift valley were always above sea level and even today the Arava Valley is characterised by ridges up to 200 m above sea level in the Gulf of Aqaba.

The rapid accumulation of Amora and Samra sediments within a subsiding and extending valley, atop thick bedded evaporites of the Sedom Fm. initiated several salt diapirs along the valley floor, the best known being Mt. Sedom (Fig. 4.44b; Larsen et al. 2002). The Mount Sedom diapir has pierced the surface atop a 200 m-high salt wall. Throughout the Holocene, salt has been rising in Mt. Sedom at a rate of 6–7 mm a^{-1} (Frumkin 1994a).

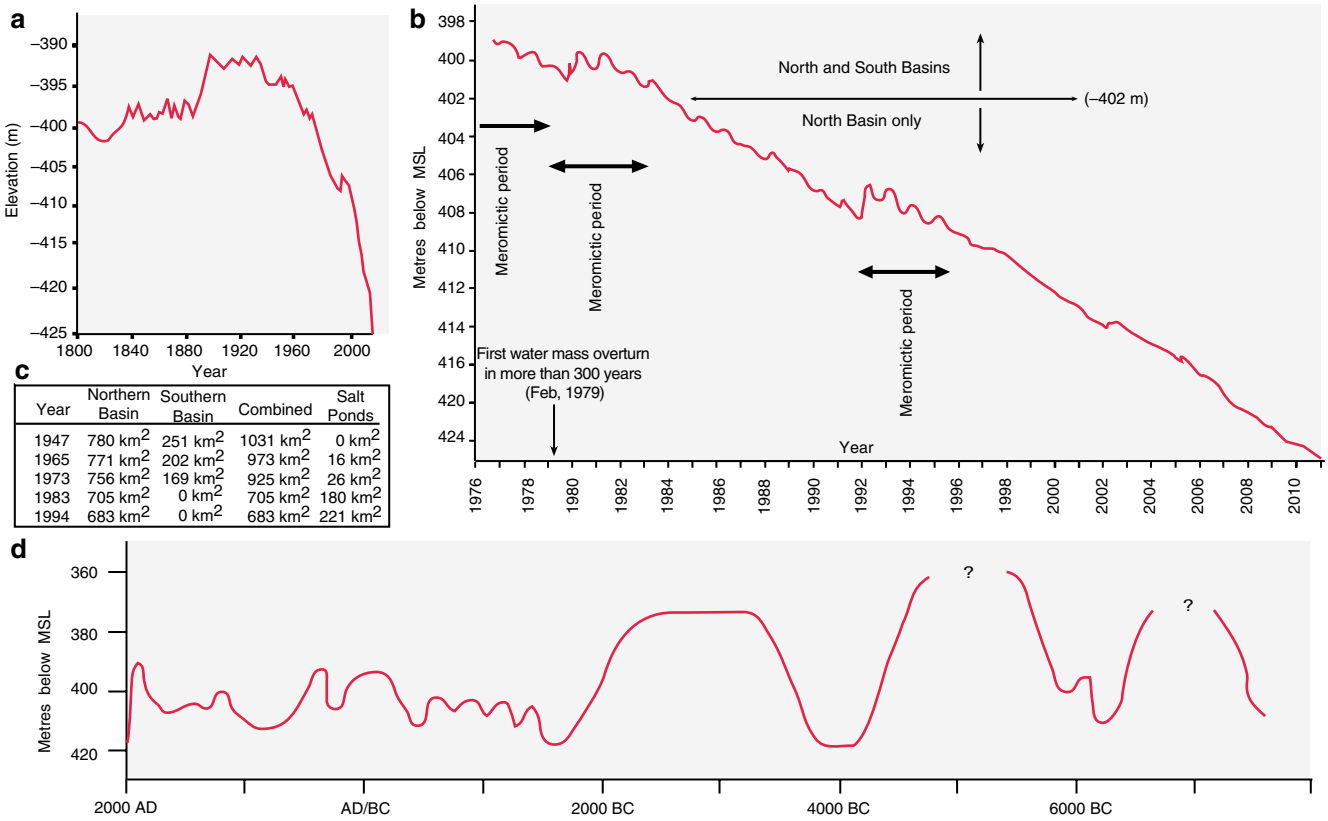

Fig. 4.45 Changes in the Dead Sea water level at various time scales. (**a**) Historical changes in the water level of the Dead Sea brine level since 1800, showing obvious acceleration in rate of fall since the 1960s and the "droughty" or falling trend since 1918. (**b**) Detailed curve for the last four decades showing how rapid rises are tied to "wet" years and the consequent meromictic lake hydrology. (**c**) Variations in the areas of the Northern and Southern Basins and the growing area of anthropogenic salt pans as it relates to changing brine levels. (**d**) Changes in the Dead Sea level for the past 8,000 years (**a**, **c**: Replotted in part from Enzel et al. 2003, **b:** Replotted from Gertman and Hecht 2002, data from http://isramar.ocean.org.il and more recent measures)

Water Level Changes

The highest recorded level of the Dead Sea (–392 m asl) was reached in the 1920s (Fig. 4.45a), since then the lake level has been decreasing and today (2014) is around –427 m asl and still falling. At the beginning of 1978 the falling waters reached a level of –399.6 m asl, which dried out the Lisan Straits and divided the water covered area of the Dead Sea into separate Northern and Southern basins (Fig. 4.45a). Since 1977, the surface level of the Dead Sea has been falling at a rate ≈60 cm/year. The lake water surface reached –410 m (msl) in 1997 and from 1998 to 2002 the lowering rate reached 100 cm/year. Since the 1930s, the trend of water levels in the Dead Sea lake has been falling or "droughty" (Fig. 4.45a). In a "droughty" year the total level rise in winter is smaller than the yearly drop, and in a "rainy" year-larger. For example, in the droughty period 1981–1988, the net level drop in water level in every single year is in the range 70–90 cm year^{-1} (Fig. 4.45b; Anati 1998; Yechieli et al. 1998; Gertman and Hecht 2002). An exactly balanced year, which is the common situation in most of the world's perennial lakes in temperate climates, has never been recorded in the Dead Sea. Dead Sea water level changes underline the general observation that differences in the hydrological balance in a lacustrine setting are the dominant control on the various styles of lake fill and that evaporites only accumulate in underbalanced lacustrine settings (Fig. 5.10).

It seems the rate of fall has been accelerating since the 1960s. This more rapid rate of fall is largely a response to the diversion of river water from the Jordan and Yarmuch Rivers into irrigation projects in Syria, Israel and Jordan. As a result, the inflow of fresh water into the Dead Sea has diminished significantly in the past half century. In the 1950s, the yearly Jordan River input to the Dead Sea was estimated to have been 1,370 million m^3, while present annual inflow is between 250 and 300 million m^3. Moreover, Israel and Jordan are pumping Dead Sea waters from the northern basin into saltworks in the southern Basin, further contributing to the falling water levels. Streams other than the Jordan River supply surface runoff to the Dead Sea and include; Wadi Mujib, which discharges around 83×10^6 m^3, Wadi Karak, which discharges around 18×10^6 m^3; Wadi Hasra, which discharges about 34×10^6 m^3; and the Zerqa Ma'in Springs

Table 4.5 Major inputs to the Dead Sea and their solute compositions

		Flow	Na	K	Mg	Ca	Cl	SO_4	HCO_3	Br
Inflows	Jordan River	400	765	51	276	330	1,630	452	436	2
	Mujib River	42	316	40	108	106	573	279	140	0.3
	Zerqa Ma'in River	25	428	56	29	139	709	198	301	7
	Zohar Spring	?	20,500	2,575	22,500	11,400	119,900	1,551	130	2,950
	Yesha Spring	3	27,800	3,500	18,700	10,300	11,753	1,060	142	2,206
	Rainfall (µg/l)	–	6.5	0.4	2.5	4.6	14	11.4	–	–
Dead Sea waters	Modern surface	–	39,330	6,500	40,450	17,750	212,600	760	290	6,120
	1960, lower water mass	–	38,510	6,500	36,150	16,380	196,940	580	230	4,600
	1960, upper water mass	–	39,700	7,590	42,430	17,180	219,250	420	220	5,270
	1977, northern basin	–	40,100	7,650	44,000	17,200	224,900	450	270	5,300
	Post-halite crystallizer	–	11,800	21,000	81,700	16,300	302,000	>100	>100	5,000

Compiled from data in Asmar and Ergenzinger (2002), Abu-Jaber (1998), Karcz and Zak (1987)
Flow is in 10^6 m^3/year and concentrations in mg/l

which discharge about 23×10^6 m^3. Small intervalley catchments provide an additional 30×10^6 m^3 (Table 4.5, Fig. 4.43b; Abu-Jaber 1998; Salameh and Bannayan 1993).

Until the 1960s, the Jordan River, flowing south from the Sea of Galilee, provided 80 % of the water received by the Dead Sea (Eugster and Hardie 1978). The Sea of Galilee is the largest freshwater lake in Israel. Storm runoff centripetal to the Dead Sea provided around 8 % and spring inflow the remainder. Historically, the bulk of the water and detrital sediment entering the Dead Sea Basin was carried by the Jordan River into the northern end of the lake. However, even before the current drastic lowering of the Jordan's flow to a quarter of previous levels, the bulk of the solutes forming chemical precipitates in the Dead Sea came from saline springs fed by dissolving Miocene salt and not from the Jordan inflow. Annual spring inflow is thought to be around 80 million cubic metres and up to 300 times more saline than the waters of the Jordan River. As in many other evaporite basins, hydrography and solute cycling in the Dead Sea are largely decoupled (Chap. 2).

Given the marked fall in brine level over the last 50 years, Yechieli et al. (1998) addressed the interesting quandary, "Will the Dead Sea ever dry up?" They argue it will not dry up completely as the rate of evaporation will continue to decrease as the salinity of the brine increases. The evaporation rate of fresh water under Dead Sea conditions is about 3.5 m/year, while the evaporation rate of Dead Sea surface waters is about three times lower (Fig. 2.9a). In 1944, when the surface salinity of the Dead Sea was about 280 g/l, the rate of evaporation was 1.7 m/year. By 1960, it decreased to 1.5–1.6 m/year at a salinity of 300 g/l, and in 1979–1980, the evaporation rate was 1.3–1.4 m/year at a salinity of 330 g/l. An extremely low evaporation rate (1.05 m/year) characterised the period 1983–1987. The present rate of evaporation is believed to be ~1.25 m/year (range 1.1–1.4 m/year).

Assuming water inflow remains at present levels, a new equilibrium between evaporation and water input will be reached in about 400 years (Yechieli et al. 1998). The brine surface will then be at –500 m, more than 80 m below the present value. The surface area of the lake will be 526 km^2, and the water volume will have decreased by about one-third from its present level. The remaining brine, in equilibrium with the air of 50 % humidity, will contain about 380 g/l dissolved salts, and have a density of 1.27 kg/l (Krumgalz et al. 2000). Over longer time frames encompassing the Holocene, the current levels of the lake are not unusual, although the rate at which levels are changing may well be (Fig. 4.45c). Similar lake level lows ≈−500 m asl characterised the Dead Sea some 2.5 and 4 ka (Enzel et al. 2003). However, in December 2013, Israel, Jordan and the Palestinian Authority signed an agreement for laying a water pipeline to link the Red Sea with the Dead Sea. The pipeline will be 110 miles long and is estimated to take up to 5 years to complete. It is designed to prevent the ongoing fall of the Dead Sea level and stabilise brine intakes for the salt processing works.

Density Stratification: Holomixis Versus Meromixis

Until 1979 lake waters were meromictic or "permanently stratified" and had been so for 300 years (Stiller and Chung 1984). In the 1950s there was a well-developed permanent pycnocline and thermocline at a depth of 50 m (Fig. 4.46; Neev and Emery 1967). The average temperature of the upper 50 m of the water body was between 16 and 36 °C and density around 1.205 g/cc, while at brine depths greater than 50 m, the temperature was a constant 21.5 °C and the water density was 1.232 g/cc. But in the 1960s and 70s the lessening inflow from the Jordan meant the surface water mass became increasingly saline and the permanent pycnocline deepened. In 1975 the pycnocline was some 100 m below the lake surface and the upper water mass had a density of 1.229 g/cc. In February 1979 the densities of the upper and lower water masses equalised and the lake overturned, whereby the lower water mass mixed with the upper water mass and the lake had become holomictic (Steinhorn 1983).

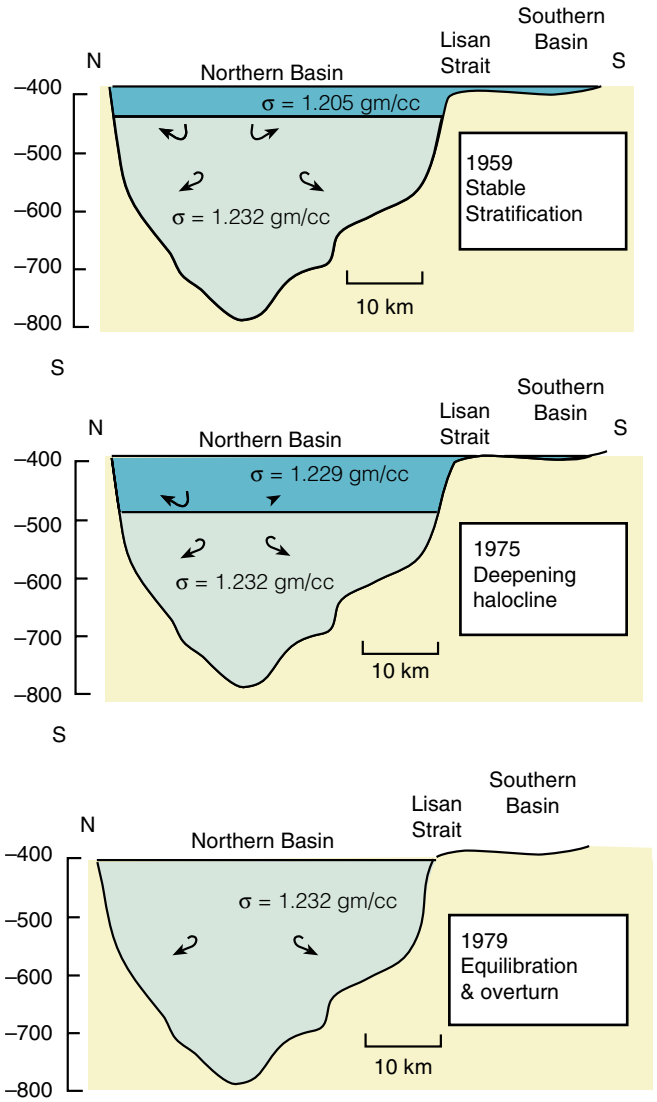

Fig. 4.46 Evolution of Dead Sea stratification in the period 1959–1979 showing the loss of brine stratification via lessening of freshened inflow from Jordan River and entry of brine waste from south. This resulted in increased salinity of surface waters, a deepening of the halocline and final equalisation of densities of the two masses and their overturn in 1979

It was marked by a strong and persistent H_2S smell as bottom waters came into contact with the atmosphere for the first time in centuries. Prior to the 1979 overturn, the lake had been continually stratified (meromictic) since its last holomictic period some 300 years earlier. Overturn has occurred naturally a number of times in the lake's Holocene history and these episodes are marked by beds of massive coarsely-crystalline deepwater halite.

After 1979 the lake entered a new phase in which its hydrological regime see-sawed between holomictic and meromictic regimes, depending on the size of the storm runoff into the lake (Gertman and Hecht 2002; Anati 1998). The Dead Sea level occasionally rises, typically in winter, in an relatively unpredictable fashion driven by short events of varying intensity (storm runoff and sudden floods), and drops via evaporation at a fairly constant rate for the rest of the year (Fig. 4.45b). The first holomictic period, 1979–1980, lasted for 2 months only. It was succeeded by a 4-year meromictic period (1980–1983). The second holomictic period lasted for 9 years (1983–1991; Fig. 4.45b). Then, during an unusually wet winter in 1991–1992, some 1.5×10^9 m^3 of meteoric water entered the lake. This caused the lake level to rise by 2 m and formed a freshened relatively stable upper water mass, which persisted until November, 1995 when stratification collapsed and the lake overturned once more and a new holomictic period began (Anati et al. 1995). Since then, there has not been another well developed meromictic period in the Dead Sea hydrology.

During each meromictic period, the hydrological regime of the Dead Sea is characterized by following long-term trends ultimately leading to holomixis (Gertman and Hecht 2002): the mixolimnion thickens as the depth of the summer thermocline increases from 12–15 to 25–30 m; the quasi-salinity of the upper layer[6], initially around 164 kg/m^3, increases rapidly at a rate of about 16–18 kg/m^3/year; the quasi-salinity of the deep water, initially of about 235 kg/m^3, decreases slowly at a rate of about 0.08–0.10 kg/m^3/year; and the winter minimal temperature of the upper layer, initially of about 16 °C, increases rapidly at a rate of about 2 °C/year. In November 1995, the latest meromictic period of the Dead Sea came to an end.

In other words, even though the meromictic upper water mass persists for years, its physical properties not only change annually, driven by seasonal changes in temperature and evaporation intensity, it also evolves from year to year as it becomes increasingly warmer, more saline and denser until its physical properties equal those of the underlying deep water mass and the lake waters overturn. This evolution can be clearly seen in maps of the time-based evolution of temperature-salinity space (Fig. 4.47a; Anati 1998).

During holomictic periods, as exemplified by the period 1983–1991 and 1996–2013, the hydrological regime of the Dead Sea *in toto* is also characterized by long-term trends (Figs. 4.47b, c and 4.48; Gertman and Hecht 2002; Anati 1998): in 1983–1991 the quasi-salinity of the entire Dead

[6]Solute proportions of the waters of the Dead Sea are relatively rich in calcium, magnesium, potassium and bromine, and relatively poor in sodium, sulphate and carbonate, thus are significantly different from those of modern seawater (Table 4.4). Strictly speaking, in view of the peculiar chemical composition of its waters, the accepted definition of "salinity" based on seawater ionic proportions does not apply to the waters of the Dead Sea and it has been replaced by an "equivalent salinity" based on pycnometry (Anati 1999; Gertman and Hecht 2002) and referred to as "quasi-salinity." Thus, quasi-salinity is defined as the Dead Sea water density anomaly from 1,000 kg/m^3 at an arbitrary reference temperature of 25 °C. For the sake of comparison, a quasi-salinity of 235 kg/m^3 is the equivalent of 280‰.

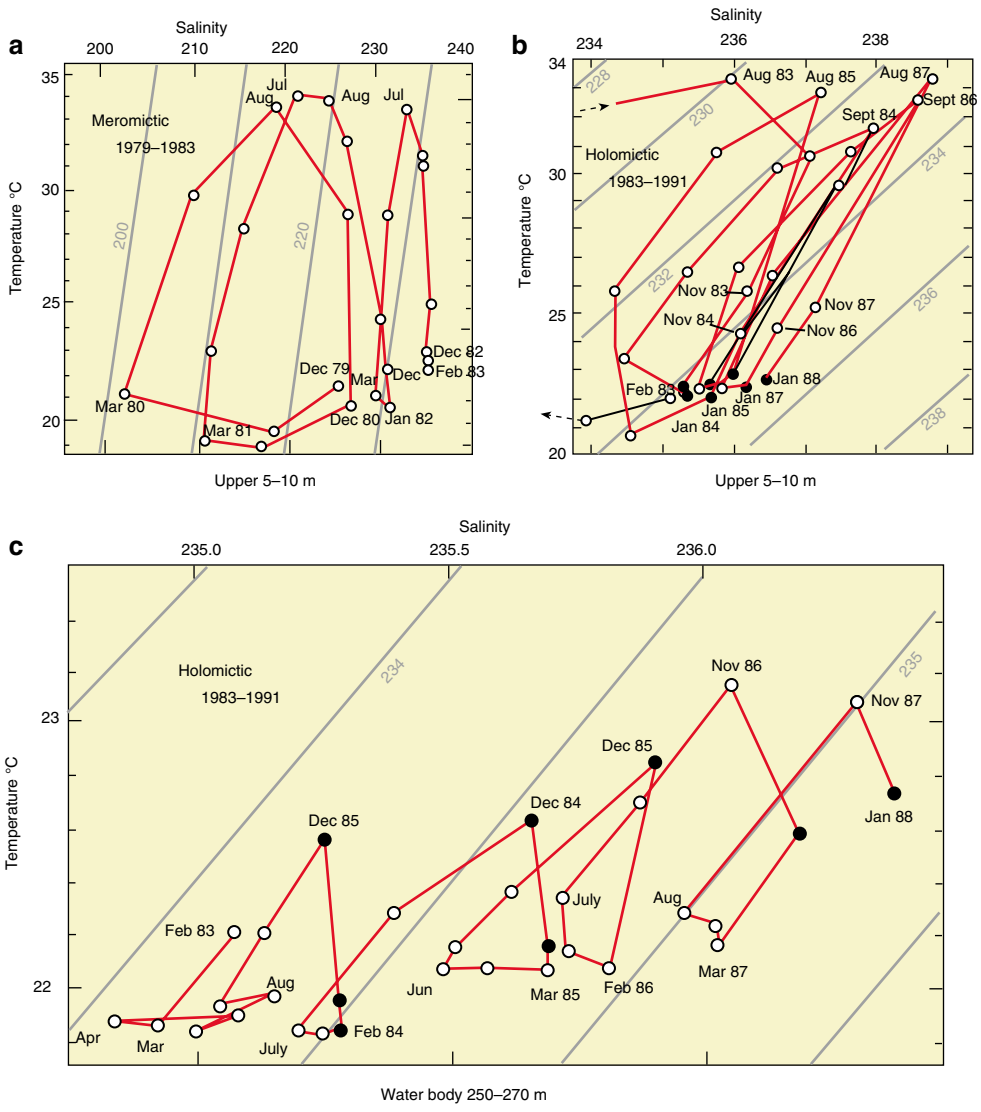

Fig. 4.47 Dead Sea hydrological evolution in temperature-salinity space (T-S diagrams after Anati 1998) (**a**) Upper 5–10 m water trends in the meromictic period 1979–1983. (**b**) Upper 5–10 m water trends in the holomictic period 1983–1991. (**c**) Water trends in lower water mass at 250–270 m depth for much of the holomictic period 1983–1991

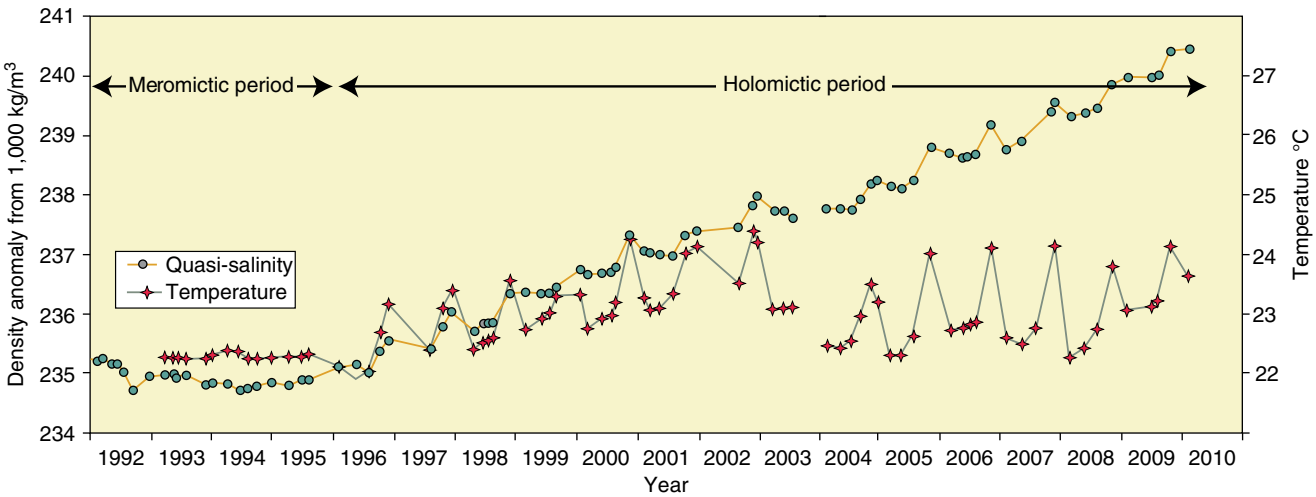

Fig. 4.48 Long-term changes in quasi-salinity and temperature in the deep water body (below 100 m) of the Dead Sea in a meromictic to holomictic period (In part after Gertman and Hecht 2002 and replotted data from http://isramar.ocean.org.il. Last accessed Jan 7, 2013)

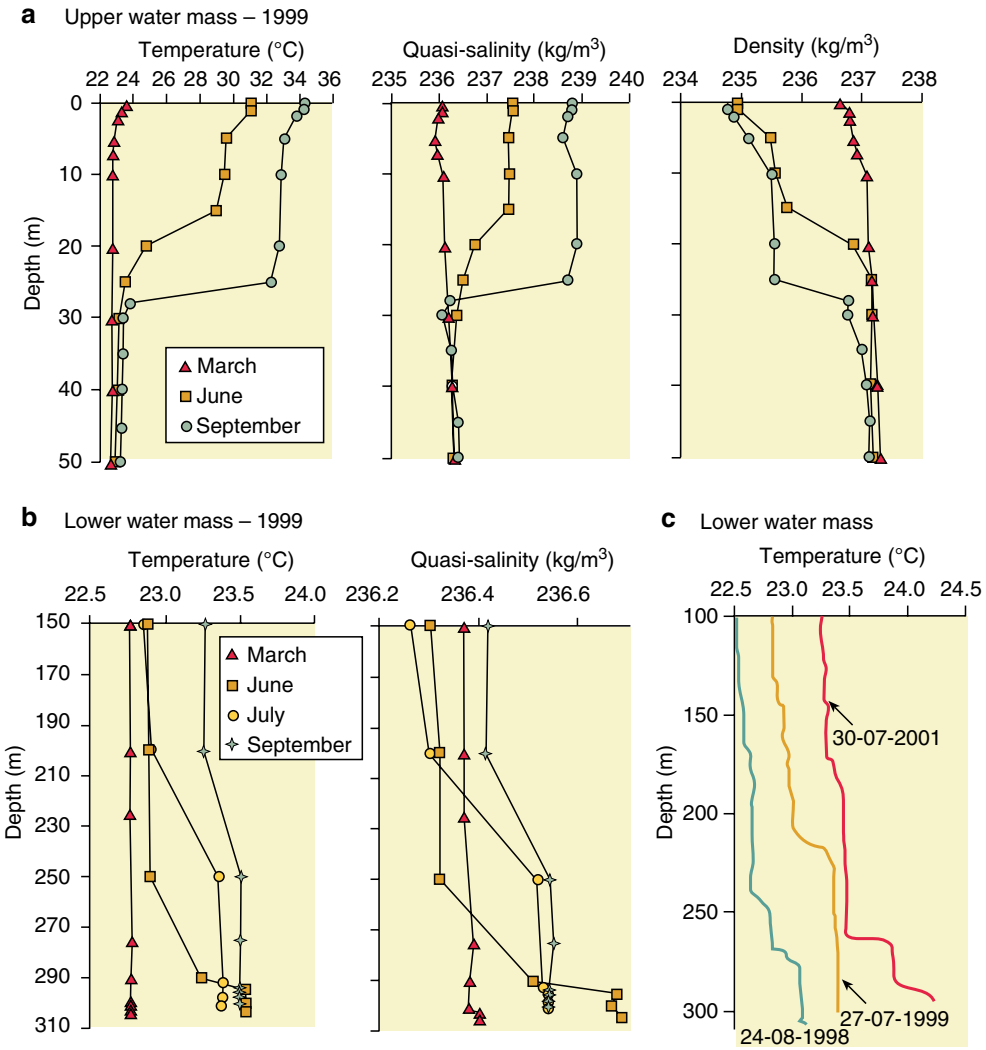

Fig. 4.49 Stratification of the Dead Sea during holomictic years as illustrated by temperature, quasi-salinity and density profiles (After Gertman and Hecht 2002). (**a**) Stratification builds in the upper water mass at a depth of 20–30 m in the summer (June-September) and is destroyed by overturn in the autumn (March). Note the smaller daily increase in temperature and salinity/density in the uppermost 5 m of the water mass due to intense daily evaporation. (**b**) Temperature and salinity anomalies in the lower water column in September 1999. (**c**) Temperature anomalies in the lowermost part of the lower water column. All profiles were measured at site EG320, its location is shown in Fig. 4.43b

Sea increased at a rate of about 0.5 kg/m^3/year, with practically no decrease during the winters; the temperature of the deep water mass increased with a rate of about 0.25 °C/year; and the period of vertical convection of the entire water column, initially about 3 months, increased at a rate of about 1 week/year (Figs. 4.47c and 4.48). Moreover, the temperature and salinity of the bottom layer in the deepest part of the Dead Sea rose by about 0.5–0.6 °C and 0.15–0.25 kg/m^3 during each holomictic summer.

During holomictic years, a stratification builds during the summer months with a thermocline generally located between 15 and 30 m depth (Fig. 4.49a). The density contrast at the base of the upper water mass is large enough to balance an ephemeral destabilising halocline formed daily in the uppermost few metres as a result of intense evaporation. At night the same uppermost waters cool and mix with underlying waters above the major thermocline. This stable thermocline persists throughout the summer and into autumn when the overlying air mass cools, so driving a cooling of the whole upper water mass until temperature and densities equalise and overturn occurs, usually in November. A temporary dilution of the upper water layers may occur due to winter rain floods, but in a holomictic year it is destroyed by summer evaporation, so preventing the year round stratification that characterises the lake in its meromictic stage.

Detailed work on the lower Dead Sea water mass by Gertman and Hecht (2002) shows an additional interesting stratification in the lowermost parts of the lower water mass (Fig. 4.49b, c). Temperature profiles of the bottom layer exhibit a step-like feature indicating advection of saltier, warmer and denser water into the lowermost parts of the Dead Sea. The differences in the size of the steps indicate the changes in the intensity of the advection in this part of the column. There are three possible sources for such waters; (1) End-brines pumped back into the Northern Basin from the Dead Sea Works at the southern end of the Dead Sea, (2) Subsurface hot springs similar to those documented by Niemi et al. (1997), (3) Slope convection of warm saline dense brines from the shallow

edges of the Dead Sea. At this time there has been insufficient monitoring to determine which of the possibilities is the most likely, or if all can contribute to the bottom anomaly.

Deepwater Halite

The transformation of the brine column since 1979 has allowed substantial halite to accumulate on the deepwater floor of the basin for the first time in 300 years. Halite first crystallised in at-surface lake brines in 1979, while massive halite began to crystallise from the entire brine column toward the end of 1982, when ropes suspended in the water would quickly accumulate cm-thick rinds of centripetal halite (Steinhorn and Gat 1983; Stiller and Sigg 1990; Stiller et al. 1998). The mass of halite that precipitated between 1976 and 1992 is estimated to be about $2{,}550 \times 10^6$ tonnes (Gavrieli 1997).

The result of holomictic saturation in the Dead Sea is a layer of coarse crystalline halite accumulating rapidly on the deep lake bottom that today (30 years after it began) is already several tens of centimetres thick. For the period 1983–1989 the estimated annual accumulation rate for halite on the Dead Sea floor was 3–6 cm/year. This new bed of halite defines the end of several hundred years of longterm brine stratification (meromixis) when halite did not precipitate in the hydrologically isolated lower brine mass. Instead a pelagic/detrital carbonate laminite had accumulated (see next section). Previous episodes of nonstratification in the deep brine column (holomixis) are indicated by similar but now buried beds of widespread metre-thick massive halite beneath the lake floor (Levy 1984).

Several crystal morphologies define the halites currently accumulating above and on the deep bottom of the Dead Sea (Gavrieli 1997; Herut et al. 1998); (a) Clear aggregates of sedimentary halite crystals forming interlocked aggregates and massive dm-thick bed on the lake floor that are made up of white to clear crystals up to 1 cm in diameter and typically interbedded with layers composed of fine grained (<1 mm diameter) halite crystals and brown mud, (b) Individual clear idiomorphic cubes up to a cm across floating within brown mud layers and, (c) Large interlocked clear centripetal halite crystals (0.5–2.0 cm long) growing on ropes suspended in the brine column. Much of the halite on the Dead Sea floor consists of intercalations of types a and b, with each constituting around 50 % of the newly formed halite layer. Mud layers entraining halite are thought to indicate wet years in the lake hydrology, such as the period 1992–1993 (Gavrieli 1997).

Finer-grained halite and gypsum layers in shallower waters (<50 m) about the lake edge, particularly in the western and southern parts of the Northern Basin where they cover much of the lake floor and may well indicate the sedimentary response the effects of brine outfall. Prior to 1979 this occurred naturally where dense brine plumes, created in the areas of more intense evaporation about the lake edge sank into the deeper part of the basin (Fig. 4.47c). Anthropogenic outsalting, via mixing between Dead Sea waters and the industrially concentrated end brines pumped into the Northern Basin from the solar operations of the Southern Basin is most obvious in the southern part of the Northern Basin (Fig. 4.50; Epstein et al. 1975; Gavrieli 1997). At 480 g/l these bottom hugging waste brines from potash manufacture are more concentrated than waters of the Northern Basin and have different relative proportions of the major ions. They are depleted in potassium and sodium and are enriched in magnesium and chloride relative to the Dead Sea waters, creating a situation ideal for saltout at the mixing zone between the two waters (Gavrieli 1997; Yechieli et al. 1998). Saltout has probably occurred in the southern part of the Northern Basin for decades, even prior to 1979, and is defined by bottom sediment areas where finer-grained halite occurs as 1–20 cm thick layers interbedded with gypsiferous brown mud. Descending brine plumes probably allowed halite and coarse-grained gypsum to accumulate beneath zones of mixing, even prior to the 1979 turnover, as can be clearly seen in preholomixis maps of bottom sediments (Fig. 4.50).

But mixing-induced saltout does cannot explain all of the halite currently accumulating across the floor of the Northern Basin. Another possible mechanism is the annual cooling of the uppermost brine layer in holomictic years (Gavrieli 1997). Temperatures in summer in the upper water 30 m in holomictic years are ≈34–36 °C, while in winter they are ≈22–24 °C (Fig. 4.49a). Although annual precipitation due to cooling of surface waters creates supersaturated chemistries, no unequivocal halite crystallisation driven by seasonal cooling has been observed in the Dead Sea. Yet, when saturated brines are collected and allowed to cool in the lab, halite precipitation as mm-scale crystals does occur spontaneously (Gavrieli 1997).

Brine mixing and seasonal cooling explain the formation of finer-grained cumulate halites, but do not explain the formation of cm-scale crystal aggregates and layers. Yet such crystals can and do form in the current waters of the Dead Sea, as evidenced by coarse clusters in the current seafloor bed and large crystals hanging off anchor ropes. Gavrieli (1997) argues that these larger crystals in the bottom layers are authigenic and indicate slower ongoing authigenic growth in halite-saturated pore waters and brine columns situated at or just beneath the present day lake floor. Such saturated growth can only be maintained when the lake waters are holomictic. It seems that authigenic growth and recrystallisation is an ongoing process, as is seen in the pervasive recrystallisation and coarse crystalline overprint preserved in the 500 year old Dead Sea halite layer cored by Levy (1984).

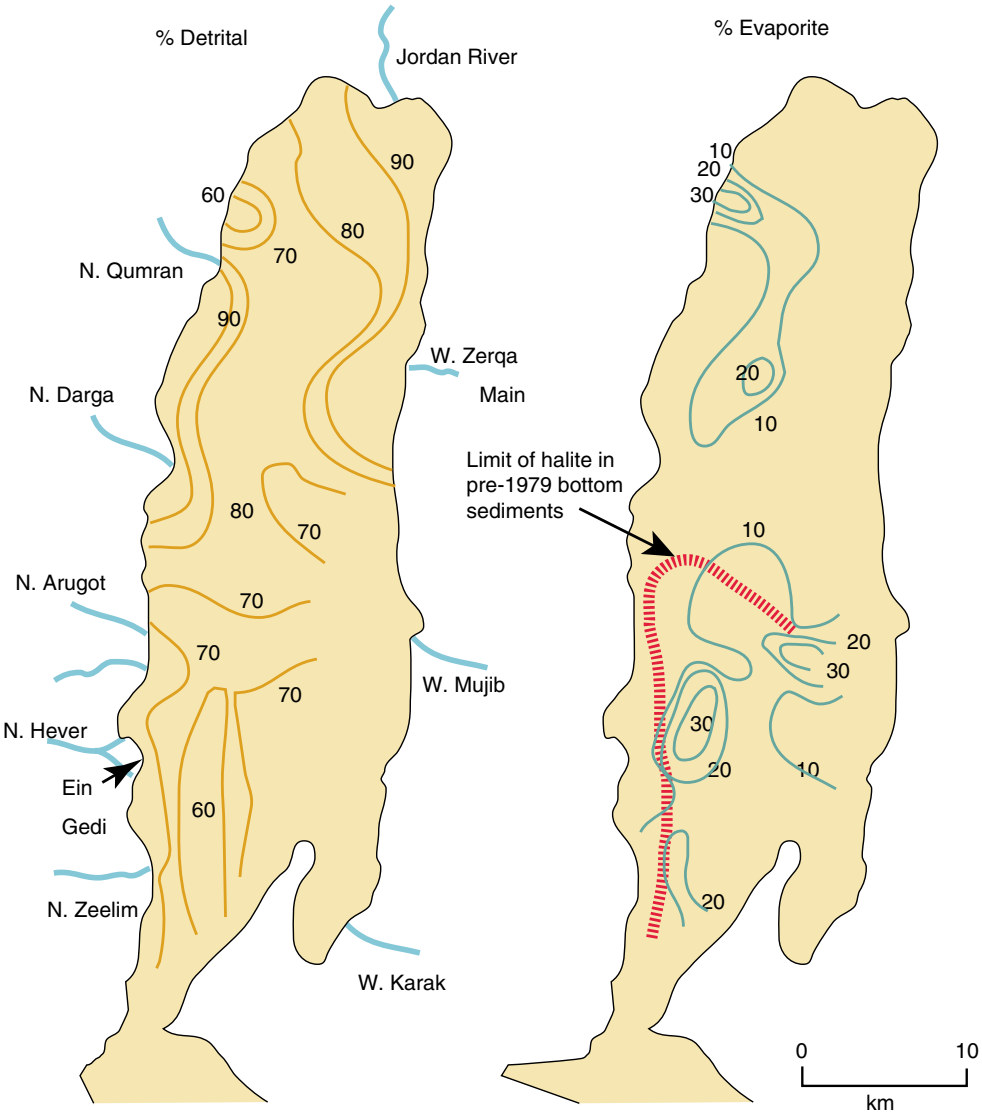

Fig. 4.50 Bottom sediment distribution map of sediment mostly created prior to monomictic halite precipitation in 1979. The eastern or Jordanian parts of the Lake floor was not sampled (In part after Garber et al. 1987)

Interestingly, cores taken 20 years earlier in the 1960s, below water depths of 40 m at the southern end of the Northern Basin, bottomed on a hard halite bed after passing through 10–80 cm of soft carbonate laminite (Neev and Emery 1967). This halite was likely deposited some 300–500 or so years ago during a previous holomictic event. Similarly, four shallow seismic reflectors, obvious in sediments of the deeper part of the Northern Basin, probably mark contacts between carbonate marls and beds of massive rock salt (Ben-Avraham et al. 1993). If the massive cm-scale inclusion-poor randomly-oriented crystals of the halite bed intercalated with finer-grained halite layers that are currently accumulating on the floor of the Dead are similar to textures in this buried deep water halite, then the notion that deepwater halite is solely a silt-sized "rain from heaven" or "salt and pepper" laminite is problematic. But, then again, the uniqueness, the small scale, and the continental transform setting of the Dead Sea, with its steep walls and lack of an extensive evaporite platform means its utility as an direct analogue for ancient marine-fed basinwide evaporites is also somewhat problematic (Chap. 5).

Deep Water Laminites

Prior to overturn in 1979, away from the Jordan River delta, away from wadi aprons and away from the influence of end brine mixing, the deep bottom sediments were mostly carbonate laminites accumulating in water depths ranging from more than a few metres down to the deepest parts of the basin. These laminites are today being covered by coarsely-crystalline halite, but prior to the onset of holomixis in 1979 carbonate laminites were the main sediment accumulating on the deep lake floor. Lamina in the mm-scale light-dark couplets are dominated by two time-separate pelagic components, namely terrigenous detritals and chemical precipitates (Garber 1980; Garber et al. 1987). Light coloured lamina are dominated by chemical precipitates, mostly made up of stellate aragonite clusters precipitated in the upper water mass (Fig. 4.51). Dark-coloured detrital layers in laminites

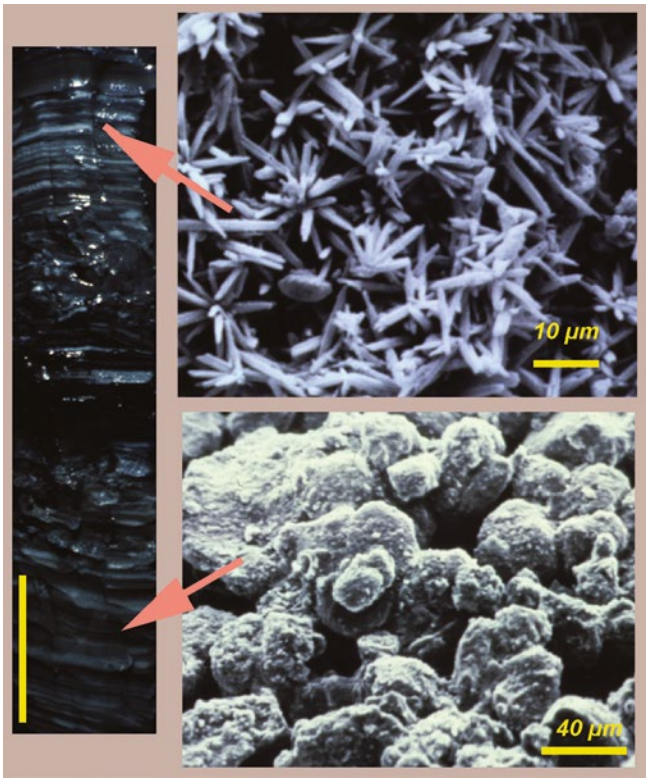

Fig. 4.51 Dead Sea deep water laminites in bottom core collected in Northern Basin in water depths of more than 200 m. It was collected in late 1970s when water mass was still stratified. *Light coloured* laminae are composed of stellate aragonite prisms precipitated as "whitenings", while *dark-coloured* laminae are dominated by detrital calcite. Scale bar on core is 5 cm (Images courtesy of Ray Garber)

contain limestone (calcite) grains, quartz, and silicate clays, along with minor feldspar and dolomite, all allochthonous components carried into the basin as bottom load, suspended load and air-borne detritus. The proportion of terrigenous material in the laminites increases toward the lake shoreline, especially toward river and stream mouths (Fig. 4.50). Illite averages about 40 % of the carbonate-free clay fraction of the laminites, smectite about 32 %, and kaolinite about 28 %. Locally, there are lesser and varying proportions of pelagic gypsum and coarser "in situ" gypsum roses within the carbonate/detrital laminites (Fig. 4.52b).

Whitening events precipitating the aragonite occurred in the surface waters of the Dead Sea every few years prior to 1979. For example, Neev and Emery (1967) sampled two summer "whitenings" of surface waters that occurred in 1959 and determined a gypsum-to-aragonite weight ratio of 3.14. Yet the aragonite in light lamina in the laminites from shallow bottom cores, collected from the seafloor hundreds of metres below the air-brine interface, were almost 100 % $CaCO_3$. They had identified a chemical discrepancy that needed an explanation and attributed the alternation of aragonite in the lighter lamina and calcite in the darker lamina to the activities of sulphate-reducing bacteria acting on pelagic gypsum settling through the anoxic density stratified water column and converting it to bacterial calcite. Elsewhere, sulphate-reducing bacteria are known to destroy organic matter and gypsum, converting them to sulphides, energy, and H_2S with calcite as a byproduct (Fig. 9.65a).

Subsequent isotopic work on the calcite lamina by Garber (1980) showed the calcite was detrital, not bacteriogenic. He also found that the laminites were not annual or "true" varves, only 15–20 lamina couplets had been deposited on the Dead Sea floor in the first 75 years of the last century. More recent work on CO_2 flux in the Dead Sea water during the meromictic period from February 1993 to December 1994 showed that summer whitenings are probably not the major source of aragonite in the laminites (Barkan et al. 2001). Rather aragonite precipitation occurs via mixing (salting out) in the upper water mass after a massive bicarbonate input from winter floods. This notion of precipitation resulting from winter flooding and brine mixing is contrary to the accepted notion of summer precipitation of aragonite in the uppermost surface waters of the historic Lake Lisan, the predecessor of the Dead Sea (see next section). But it better explains the lack of annual varving noted by Garber and means that either the origin of the aragonite laminites in the Lisan Fm should be re-evaluated, or the present Dead Sea should not be considered a direct hydrologic analogue for the somewhat fresher and deeper waters of Lake Lisan.

The dark coloured detrital-dominated mm-scale layers of the Dead Sea laminites lack a pervasive microfossil/diatom component, unlike laminites forming in less saline perennial lakes such as Lake Van. Diatom frustules do accumulate on the lake floor where diatoms flourish in areas of longterm freshened water. Their remains are common only in the detrital-rich prodelta laminites of the northern region of the Dead Sea. There, the Jordan River delta is building out into the lake and carries the remains of diatoms, along with abundant clays and silts. Surface waters over the rest of the Dead Sea are too saline to allow diatoms to live.

Prior to the onset of holomixis, intrasediment gypsum made up of individual crystal disks, constituted around 6 % of the sediment volume in deep basinal laminites. Garber (1980) found gypsum in all cores recovered in the mid 1970s from laminites in lake bottom settings ranging from shallow sea-marginal, through slope to deep basinal settings. Gypsum rarely formed in discrete laminae, small lenticular crystals were mostly disseminated through the terrigenous (dark) layers but larger crystals cut though both light and dark lamina. Garber (op cit.) concluded that gypsum in the deepwater laminites was present even during the studies of Neev and Emery. He argued that finely crystalline sand-sized gypsum was probably the settled-out remnants of gypsum precipitated in the surface waters, either as documented in the whitings by Neev and Emery (1967) or by brine mixing near the contact of the upper and lower water masses. Further gyp-

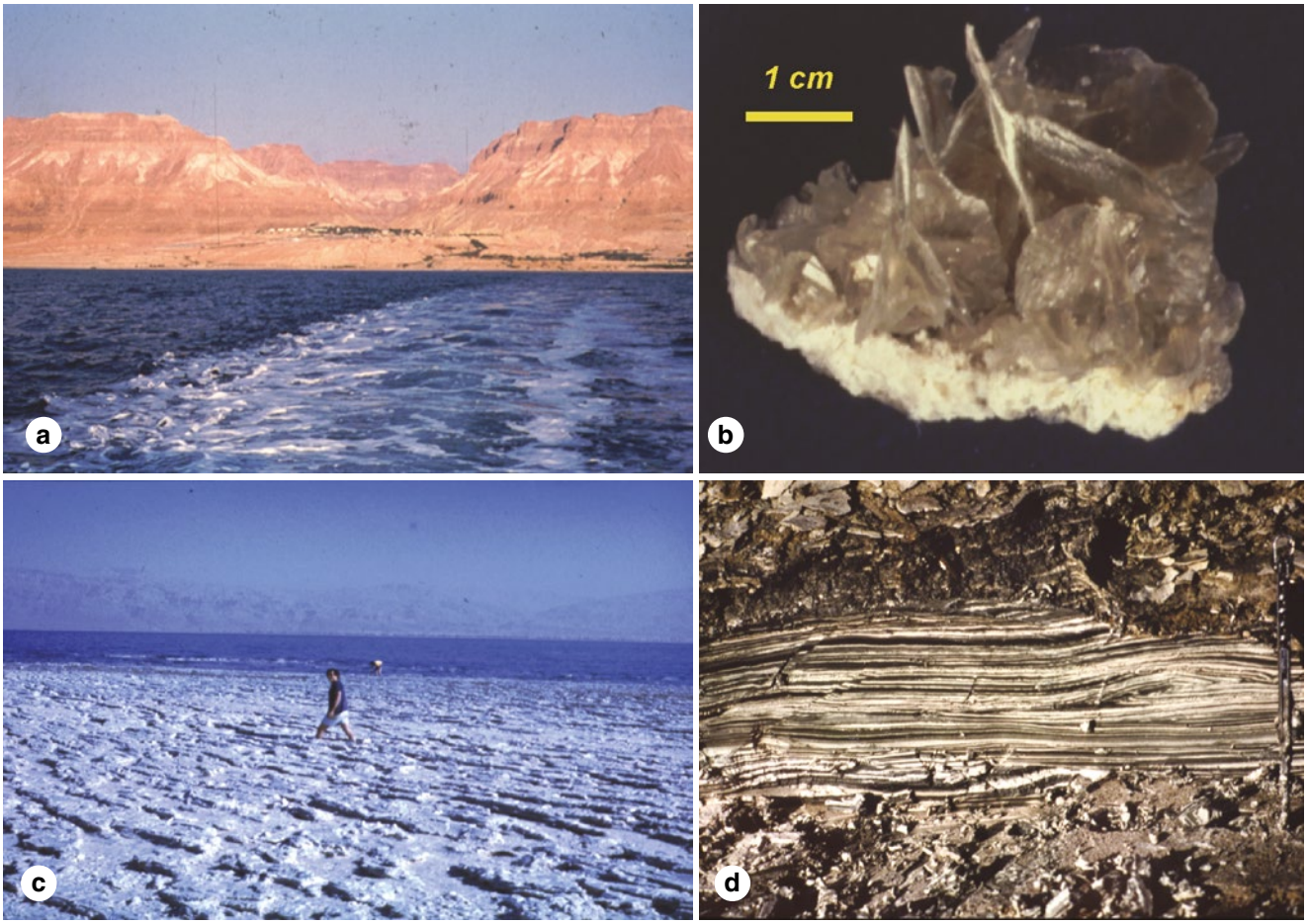

Fig. 4.52 Dead Sea. (**a**) Ein Gedi, village located on a "hanging" fan delta of Late Pleistocene age and is evidence of higher lake levels at that time. (**b**) Intrasediment gypsum rose growing in bottom sediment in brine depths of more than 200 m. Brines may be supplied from brine plumes from dissolving salt diapir crests. (**c**) Exposed unconsolidated laminite muds on the eastern margin of the Dead Sea. (**d**) Trench in muds shown in (**c**); Note the soft sediment deformation in some layers (All photos courtesy of Ray Garber)

sum crystal growth into desert-rose like displacive aggregates in the sediment (Fig. 4.52b) was interpreted to indicate upward brine diffusion through the bottom sediments. Such upwelling brines were perhaps derived by the dissolution of nearby subcropping salt structures.

More recently, Reznik et al. (2009) have addressed the relative paucity of gypsum compared to halite in Dead Sea precipitates. They note that their laboratory experiments and evaluation of historical data show gypsum nucleation and crystal growth kinetics from Dead Sea brine are both slower in comparison with similar brine solutions at a similar degree of supersaturation. Slow kinetics of gypsum precipitation in the Dead Sea brine is mainly attributed to the low solubility of gypsum which is due to the high Ca^{2+}/SO_4^{2-} molar ratio (115), high salinity (≈280 g/kg) and to Na^+ inhibition in the Dad Sea waters (Table 4.5). Their experiments with various clay minerals (montmorillonite, kaolinite) indicate that these minerals do not serve as crystallization seeds. In contrast, calcite and aragonite, which contain traces of gypsum impurities, do prompt precipitation of gypsum but at a considerable slower rate than with pure gypsum.

This implies that transportation inflow of clay minerals, calcite and local crystallization of minerals in the Dead Sea, in times of meromixis and holomixis does not prompt significant heterogeneous precipitation of gypsum. Based on their historical analyses of the Dead Sea, it is clear that over the last decades dominated by holomixis, as inflows to the lake decreased and its salinity increased, gypsum still continuously precipitated from the brine. The increasing salinity and Ca^{2+}/SO_4^{2-} ratio, which results from the precipitation of gypsum, led to even slower kinetics of nucleation and crystal growth, which resulted in an increasing degree of supersaturation with respect to gypsum. Today the amount of gypsum in the bottom sediment is swamped by the high volume of halite. Herut et al. (1998) predict that as the salinity of the Dead Sea brine continues to increase (accompanied by Dead Sea water level decline), the degree of halite supersaturation will increase, but gypsum will also continuously precipitate

at these higher saturations due to progressively slower kinetics.

The relative paucity of bedded evaporitic salts, other than aragonite, during meromixis was the most surprising aspect of the deepwater sediments accumulated in the Dead Sea in the 300 years prior to 1979. Why were more saline salts absent on the bottom when the upper water mass was at gypsum saturation a number of times each summer and the lower water mass was at or near halite supersaturation year round? The answer lay in the permanence of the upper water mass, it prevented chemical change in the lower mass and hence, although the lower waters were supersaturated there was no concentration mechanism to allow it to accumulate salts. Only pelagics made it to the bottom until the brine column mixed and the Dead Sea became a holomictic system in direct contact with the atmosphere. Then large volumes of evaporitic halite could accumulate on the deep basin floor in areas covered by waters hundreds of metres deep. The Dead Sea clearly shows that halite and other salts can accumulate at the base of a brine column several hundred metres deep. But, they do so mostly as coarsely crystalline aggregates, not fine-grained laminites, and can only do so when the whole brine column is a well mixed (holomictic) water mass. When a brine column is permanently stratified, no "in situ" bottom growth occurs. The dominant depositional style is a "rain-from-heaven" made up of less saline precipitates and siliciclastic fines, with chemical precipitates forming either at the mixing zone between the two water masses, or at the air-brine interface.

Basin Margin Sediments

Layers of siliciclastic and calcitic detritus in the deepwater bottom sediments are generally tied to floods and wind borne dust sourced in the highlands about the basin margins. Fan delta lobes about the basin margin indicate positions where streams and wadis drain into a water- filled depression. In the Dead Sea they show two main styles; (1) Currently active deltas that reach down to the present lake shoreline (Fig. 4.53) and, (2) Late Pleistocene fan deltas that are typically smaller in extent than their Holocene counterparts and form "hanging" deltas such as Ein Gedi (Fig. 4.52a; Sneh 1979; Bookman et al. 2004). The more obvious hanging deltas were actively accumulating sediment in Lake Lisan time when lake waters were fresher and lake levels were up to 200 m higher. Sizes of the fan deltas vary, with the Nahal Zeelim delta being the largest of the active deltas located along the western margin of the depression (Sneh 1979). In terms of the morphometry of fan deltas worldwide, Nahal Zeelim is relatively small (≈6 km^2), its slope is steep (2.5°), and its catchment (235 km^2) is quite large for the size of the sediment lobe. Its morphometry reflects its arid setting whereby water supply volume is low and pulsed, with resupply during times of short intense storm floods.

Each delta lobe is made up of several successive fan sequences, with facies changing from dominantly conglomerates at the head of the fan to sands and muds at the foot (Fig. 4.53). In the proximal parts of a Dead Sea fan delta lobe, units of crudely stratified conglomerate alternate with coarse to medium sands that show cut and fill textures, along with abundant trough and planar cross beds. In the sand-dominated medial parts, structures range from unstratified or poorly layered sandy beds, through granule and mud-ball layers, into trough and planar crossbedded sands. Many of the finer sands in this zone preserve ripple cross laminae. Further into the basin, the more distal parts of the fan lobes are composed of interlayered sand/mud facies intercalated with carbonate laminites. Alternations of coarse to medium sand with layers of very fine sand characterise distal fan sediments, as do thin 2–3 cm thick layers of mm-layered aragonitic laminite. Rapid deposition of fan sediments atop water-saturated laminites creates numerous examples of convolute bedding that formed as rapidly deposited sands loaded brine-soaked muds.

In strandzones away from the direct influence of active fan deltas, the grain size of sediments tend to indicate distance of the strandline from the base of the cliffed escarpment, which defines the edge of the present Dead Sea basin. Where the present shoreline of the Dead Sea is a long distance from the fan-lined border escarpment, sediments tend to be muddy laminites, deposited during times of relatively higher water (meromictic) during the last few centuries and including blocks derived by reworking of Lisan marls (Fig. 4.52c, d). In strandlines closer to the escarpment the shores are moderately steep with beaches and bars of sand and gravel reworked from the base of the escarpment, especially where waves are eroding older bajada sediments. Where the shoreline is a cliff at the base of a border escarpment, the sediments tend to be reworked blocks and muddy slumps of Pleistocene Lisan Formation (Neev and Emery 1967). Fluctuations in water levels throughout the Quaternary have created numerous terraces; more than 30 near-horizontal sandy shore terraces and gravel bars have been recognised behind the current lake strandline (Bookman et al. 2004).

The shorezone of the Dead Sea is also of interest in that there may be local accumulations in the shorezone sediments of blocks of asphalt. Similar blocks of floating asphalt have been collected in the Dead Sea waters. The ultimate source of this material is possible seeps from Cretaceous organic-rich shales. Asphalt has been collected from the Dead Sea depression since the time of the ancient Egyptians[7].

[7]The Ancient Egyptians used Dead Sea asphalt in the mummification process. The word "mummy" comes from the Arabic word "*mummiyah*," which means asphalt. Mummiyah also has what are considered by some to be medicinal properties (Nissenbaum et al. 2002).

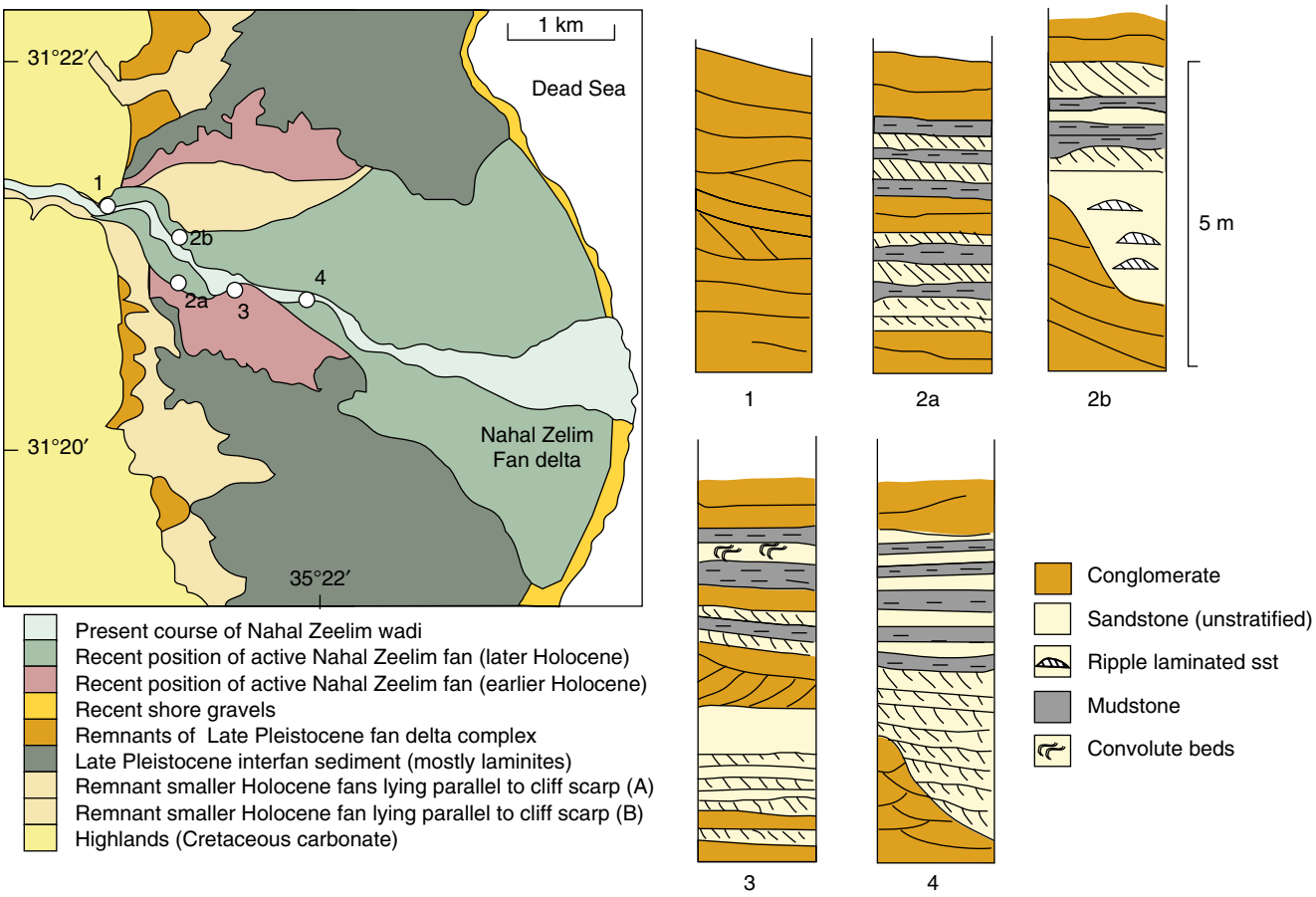

Fig. 4.53 Nahal Zeelim (Tze'elim) fan delta, Dead Sea margin. Map shows multiple overprinted fan delta lobes from avulsion. Lobes of the Holocene delta lie below "hanging" late Pleistocene fan delta sediments deposited when the lake water level was 180 m above its present level. Vertical successions of five measured fan delta sections (*1–4*; localities shown on map) show a fining into the basin trend in average grain size (After Sneh 1979)

The asymmetry of the tectonic setting of the Dead Sea depression is reflected in the granulometry of the fans. The eastern side of the Dead Sea is the more active transform escarpment, so slopes are somewhat steeper and fans are dominated by poorly-sorted debris flows, which often reach all the way to the modern strandline. On the western side of the depression the slopes are not as steep (Fig. 4.43b). Based on comparisons with the rift lakes of Africa, there should be sand aprons created by widespread longshore reworking of fan delta sediments along this western side. But this is not happening in the Dead Sea, any clean sands created by wave action on the western side of the depression are swamped with sheets of muds derived by erosive reworking of Lisan Fm. laminites which blanket the depression. In terms of the Dead Sea's ability to act as a Holocene lacustrine analogue for modelling reservoir sand distributions in ancient evaporite-sealed lacustrine counterparts, it suffers from the same problems as that other deep hole in the ground with evaporites – Death Valley, California. Both depressions are too deep, with sides simply too steep, to allow well-sorted sand bodies to accumulate in substantial volumes about the lake edge.

Much of the exposed margin of the Dead Sea between active fan delta lobes is made up of soft laminites and intercalated indurated beach-rock-like aragonitic crusts. These exposed recent laminites were deposited from meromictic lake waters and were deposited prior to 1979 (Fig. 4.52c, d). Intercalated with the sea margin laminites are gravels and sands reworked from fan sediments and perhaps acting as aquifers or at least zones of high crossflows of waters into the lake margins. Exposed gravels and sands are sometimes cemented into beach rock sheets and have been coated with mm-scale laminated aragonite encrustations and stained with manganese (Garber et al. 1981; Garber and Friedman 1983). Some of these aragonite precipitates are botryoidal, others are encrusting, yet others are oolitic/pisolitic, all are interpreted by Garber as largely inorganic precipitates. They are reminiscent of the microbial, stromatolitic and pisolitic crusts of the South Australian salinas and like them indicate strandzones and seeps in ancient counterparts.

In summary, surface sediment distribution in the Dead Sea region is a combination of Holocene accumulations and palimpsest Lisan Fm. derivatives (Fig. 4.54). Today the lake

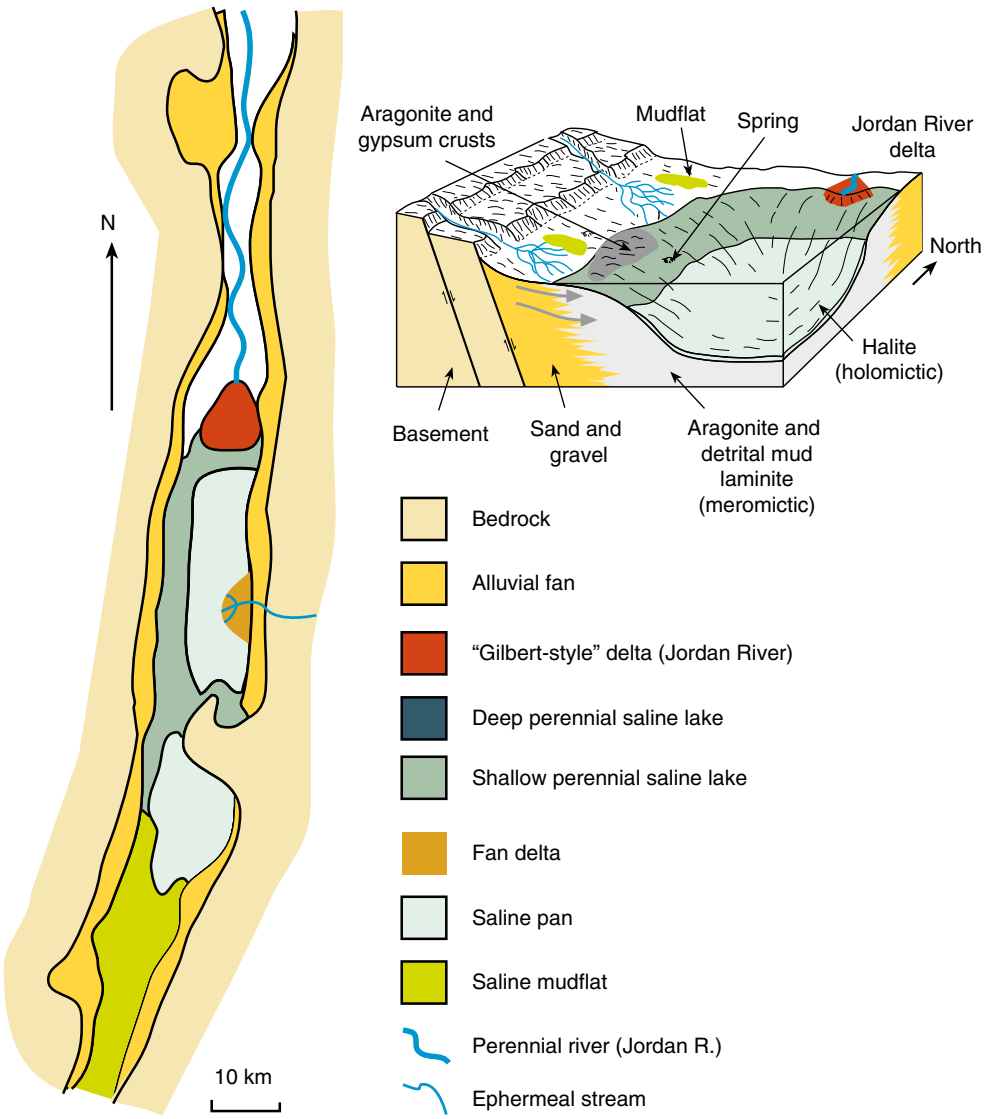

Fig. 4.54 Geology of the Dead Sea basin showing the distribution of the various depositional settings in plan view and as a block diagram of the Northern Dead Sea basin. The River Jordan forms a fluviodeltaic wedge in the northern part of the basin. Active transtension faulting and block rotation has exposed older lake deposits of the Lisan Formation at higher elevations as well as an apron of alluvial fan sediments with a number of "hung" fan deltas tied to older higher water levels in the lake. The saline pan in the southern basin is dominated by halite, artificial pans fed with deep brines have been constructed in this area to produce sylvite and other potash products (see Chap. 11)

is holomictic and a bed of coarsely-crystalline, inclusion-free halite is accumulating on the deep water floor of the lake. At the same time detrital accumulations fed from stream inputs, especially the Jordan River, dominate the northern parts of the lake. In the recent past (pre 1979) the lake was permanently stratified and deposition of carbonate laminite was the dominant depositional style on the deep lake floor. Fluvial input to the fresher surface waters of the lake supplied both the detritals (calcite, aluminosilicate clays and siliciclastics) and drove the mixed water chemistry that created the aragonite rich portions of the laminite couplets. Dust storms also supply detritus to the deep lake bottom.

Lake Lisan, Jordan Valley

Beneath and surrounding the Holocene sediments of the Dead Sea are the sediments of the Quaternary Lisan[8] (70–17 ka) and Damya (17–12 ka) formations (Bartov et al. 2002; Haliva-Cohen et al. 2012). The Lisan Formation forms a blanketing cover throughout the Jordan Valley (Fig. 4.57a). Pleistocene Lake Lisan waters left behind dissected terraces of lacustrine sediment, consisting of laminated marls up to 40 m thick, that extend from Lake Tiberias (Sea of Galilee) in the north to a boundary ridge some 35 km south of the Dead Sea (Fig. 4.55). The highest outcrops of Lisan laminites are found at −180 m asl, but there is morphological evidence for lake waters as high as −150 m or even −130 m asl during Lisan time (Fig. 4.56). During its highstand, Lake Lisan covered several subbasins in the Jordan Valley, it had a maximum area of some 2,000 km^2 and a drainage basin of 40,000 km^2. Pre-Holocene, but post-Lisan, sediments occur in fan delta regions near the current Dead Sea shore and in the vicinity of the city of Damya in Jordan, which is the type area for the Damya Formation.

Mineralogical variations in the Lisan Formation along the Jordan Valley show lake waters varied both in aerial extent and salinity. The lake was permanently stratified for much of

[8] *Lisan* is Arabic for tongue and describes the shape of the Lisan Peninsula where the type section was measured.

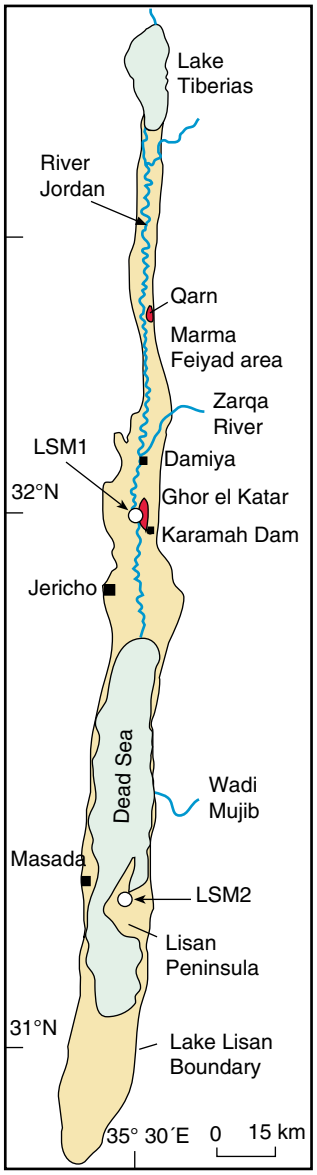

Fig. 4.55 Extent of Pleistocene Lake Lisan in the Dead Sea transform. Positions of sites LSM1 and LSM2 are indicated (see Fig. 4.58 for detail)

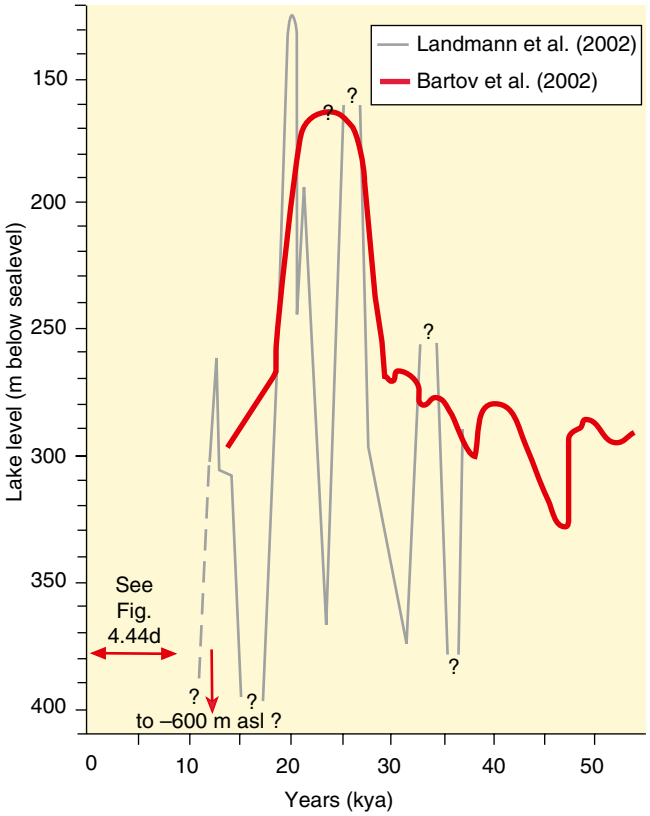

Fig. 4.56 Lake Lisan levels between 15,000 and 50,000 years ago

its history. In its southern part, the sedimentary sequence consists mainly of laminated evaporites, and salinity is thought to have ranged between 100 and 300 g/l and lake water levels were probably lower. At the higher elevations that characterise Lisan outcrops in the north in the Kinarot basin, sediments of the Lisan Formation are very different, and the sequence is mainly diatomite. The change from south to north probably indicates inflow from the north and a freshening of surface waters during the highest stands of the lake. Salinities throughout Lisan time were hypersaline but probably less than those of the present Dead Sea (Fig. 4.56) (Abed and Yaghan 2000).

Landmann et al. (2002) document two styles of couplet in the Lisan laminites; (1) detritus–aragonite (most common), and (2) detritus–aragonite–gypsum. Begin et al. (1974) documented the lithology and biota of the Lisan Formation along the Jordan Valley west of the Jordan River. They subdivided it into a lower Laminated Member and an upper gypsiferous White Cliff Member (Fig. 4.57). Along the Jordan Valley they described three laminite facies; a gypsum facies in the Dead Sea region, and an aragonite facies north of the Dead Sea up to Marma Feiyad and a diatomite facies further north. Later work by Abed and Yaghan (2000) in the vicinity of Ghor el Katar and the nearby Karameh Dam reclassified the Lisan into three members; Lower Laminite, Middle Clay and Upper Laminite with the White Cliffs making up the upper part of the Upper Laminite. The contrast in gypsum content in laminites of the Lisan formation from the Ghor el Katar region (LSM1) compared with those of the Dead Sea region (LSM2) is clearly documented in the detailed mineralogy of two outcrop sections published by Landmann et al. (2002; Figs. 4.55 and 4.58).

The Lower Laminite is made up of thinly interlaminated calcareous silt and aragonite with subordinate sand layers. In the Ghor el Katar area (LSM1) the Lower Laminite is 15 m thick and the aragonite proportion is less than 30 %. The Middle Clay is composed of massive black clays, and is around 9 m thick. The clay matrix is mostly mixed layer illite/smectite with minor kaolinite. No gypsum or other evaporites occur in the Middle Clay and its organic content can be as high as 6 %. The Upper Laminite is once again mostly interlayered aragonite and detrital silt (Fig. 4.58).

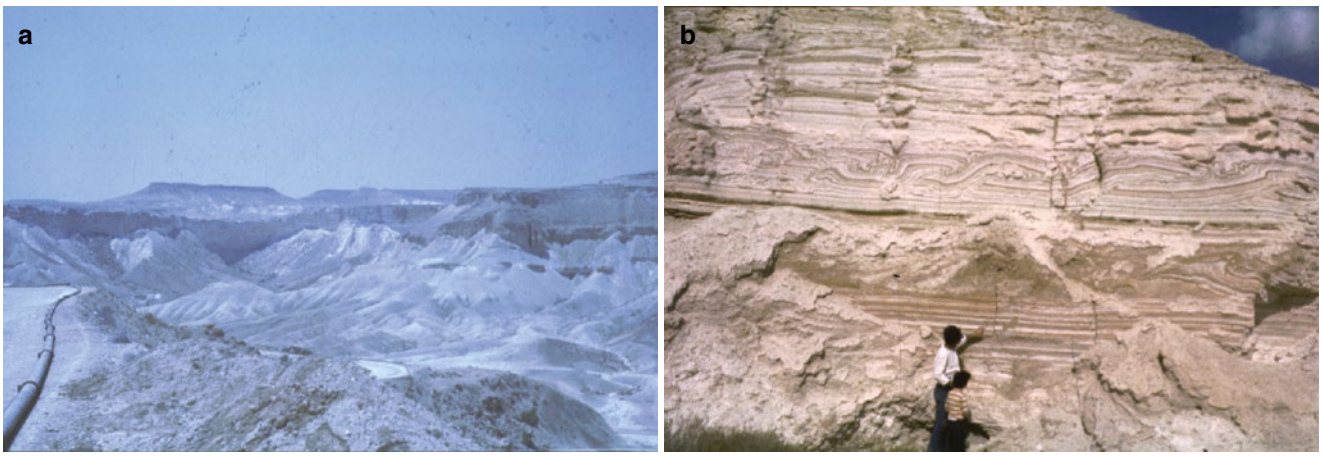

Fig. 4.57 Lisan Formation. (**a**) View of Lisan Formation outcropping along the escarpment of the Dead Sea, (**b**) Syndepositional slump in the Lisan Formation (Images courtesy of Ray Garber)

Thin sand and clay layers are not uncommon in this unit. Its uppermost 5–7 m crops out as a conspicuous white cliff that entrains layers with abundant gypsum. This upper portion in section LSM1 is equivalent to the White Cliff Member of Begin et al. (1974) as documented in section LSM2 (Fig. 4.58). To the south of Ghor el Katar area, the White Cliff unit thickens until it is more than 25 m thick on the Lisan Peninsula (LSM2; Fig. 4.58).

The Lower and Upper Laminated members are composed of very fine, varve-like white and dark laminae. White laminae are usually monomineralic and composed mainly of aragonite needles with diatom frustules. In the White Cliff unit the light-coloured laminae are composed almost entirely of gypsum or mixtures of aragonite and gypsum. Gypsum laminae are dominated by fine lenticular gypsum crystals (0.25–0.50 mm) with their long axes arranged parallel to the bedding. Dark laminae are predominantly detrital mud-sized calcite, the reworked remnants of microfossils, nannofossils and rock fragments. Quartz, dolomite, clay minerals (kaolinite, smectite, illite, and palygorskite), halite, and gypsum also occur in these detrital calcitic layers, much like in the laminites of the present Dead Sea floor.

In the vicinity of the modern Dead Sea the laminae in the Lisan Formation are sometimes crenulated and may contain sulphur concretions. Some layers display sediment slumps and overfolds, water escape structures, growth faults, and other evidence of soft sediment deformation (Fig. 4.57b). Many slumps and other fluidisation features are likely seismites, triggered by the ongoing seismic activity in the basin. That is, within the Dead Sea basin, earthquakes have kicked off multiple episodes of sediment movement, both syndepositionally and in the shallow subsurface (Weidlich and Bernecker 2004). Similar seismic response textures have been documented in the epeiric carbonates and evaporites of the Ordovician Red River Fm., Canada (El Taki and Pratt 2010)

Historically, seismic events preserved in Holocene (post-Lisan Fm) laminites have been given religious significance in the Christian Bible[9], although the actual timing of events has been altered for a more dramatic effect and tied to the crucifixion (Williams et al. 2011)

Some of the non-gypsiferous aragonitic couplets in the Lisan Fm are interpreted as accumulating in lake-waters some 400–600 m deep. But gypsum in some of the Lisan laminites in the White Cliff Member show evidence of much shallower deposition in the form of large vertically aligned gypsum crystals. These giant crystals fit better an earlier model of Lisan Formation deposition by Picard (1943) who described the coarsely crystalline gypsiferous parts of the Lisan Formation as being deposited in a combination of settings, a shallow lake, a large playa, and/or a giant sabkha. The presence or absence

[9]There is the report in the 27th chapter of the Gospel of Matthew in the New Testament that an earthquake was felt in Jerusalem on the day of the crucifixion of Jesus of Nazareth. Williams et al. (2011) tabulated a varved chronology from a late Holocene core from Ein Gedi on the western shore of the Dead Sea between deformed sediments due to a widespread earthquake in 31 BC and deformed sediments due to an early first-century earthquake. Twenty-eight historically documented earthquakes were identified in the 1598-year interval between 140 BC and 1458 AD preserved in the Ein Gedi core. The early first-century seismic event is tentatively assigned a date of 31 AD with an accuracy of ±5 years. Plausible candidates for this event include the earthquake reported in the Gospel of Matthew. That is, there is an earthquake event preserved in the sediments that occurred sometime before or after the crucifixion and it was of sufficient magnitude to be impressed in the popular mind. So, earthquakes were ongoing in the region and one was in effect "borrowed" or time shifted by the author of the Gospel of Matthew. It is highly likely a local earthquake occurred during the time of writing of the Gospel of Matthew and it was "called upon" so as to match the date of the crucifixion. The aforementioned event occurred sometime between 26 and 36 AD and was sufficiently energetic to deform the sediments at Ein Gedi, but not energetic enough to produce a still extant widespread and extra-biblical historical record (unlike the higher magnitude earthquake of 31 BC with its widespread historical documentation).

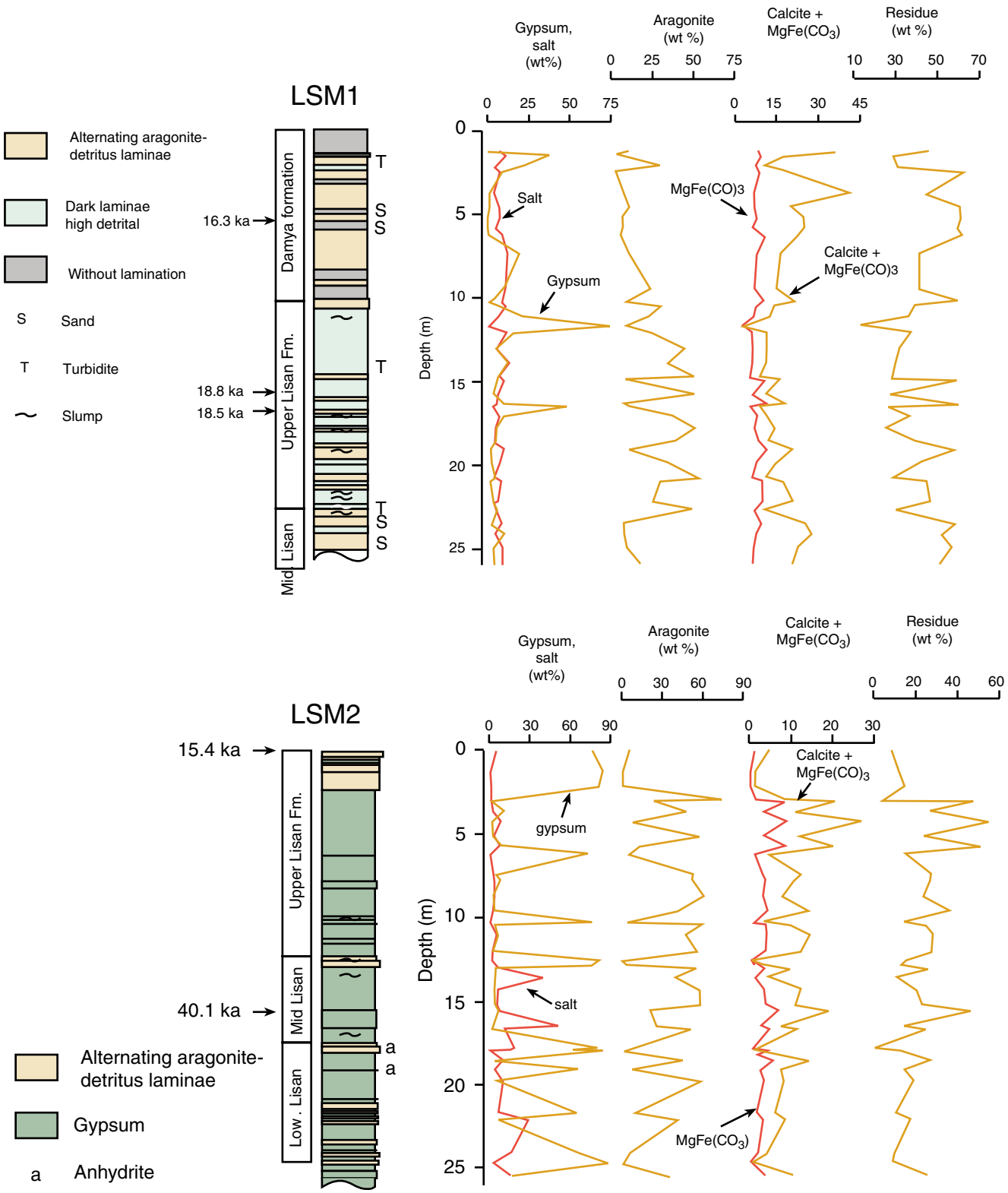

Fig. 4.58 Stratigraphy and mineralogy of the Lisan and Damya formations in the Jordan Valley. Positions of the sections are shown in Fig. 4.55 (After Landmann et al. 2002)

of gypsum perhaps indicates changing water levels in the Lisan Lake so that when bedded and growth-aligned gypsum is commonplace the Lisan water levels were lower.

Overlying the Lisan Formation is up to 14 m of clastics of the Damya Formation (equivalent to the "unnamed unit" of Begin et al. 1974). Damya sediments are mostly clays, silts and sands, some gravels, and no evaporites (Abed and Yaghan 2000). It was deposited in a freshwater to brackish lake stage with a water level of −160 m at the onset of Lake Damya some 15–16 ka. According to Begin et al. (1985), the Lake Damya ended some 10–11 ka with a drop to −700 m asl, a fall in lake level of more than 800 m in a few thousand years (Fig. 4.56). If real, it means the driest period in Lake Lisan's history was immediately preceded by the wettest time in Damya climate. Clearly, waters levels in perennial saline lakes are subject to high frequency, high amplitude changes in water level with rates of change that can be four to eight times greater that marine eustatic changes in an icehouse climatic mode (Chap. 5).

Throughout its Pleistocene history the Dead Sea/Lisan succession preserves evidence of its hydrological state in the dominant mineralogy of the chemical precipitates preserved in the laminites. Aragonite dominance in the lacustrine laminites (Lisan) indicates least saline waters and highest lake water levels. At the other end of the climatic spectrum, halite beds indicate lowest lake levels and highest salinities, while gypsiferous laminites indicate intermediate water levels and salinities in the basin. The other component in the laminites is non-chemical detrital sediment. Interestingly, this detrital input to the laminites and halites is present in all three evaporite styles from evaporitic carbonates to halites, although the rapid aggradation rates in the halite beds make it less obvious as separate laminae. Earlier work assigned much of this non-chemical detritus to a fluvial source (Jordan River and various wadis). However it is becoming increasingly apparent that much of the non-chemical detritus, especially the fines, is windblown and ultimately derived from adjacent deserts, including the Sahara with the greatest influx at times in the past when wind intensities were greatest. It is also obvious that during lake level lows there are sediments accumulating about the lake margins in the various subaerial zones above the water level that are non-aragonitic (as in lower portion of the Holocene Zeelim formation, Fig. 4.59).

Laminites outcropping in the modern margins of the Dead Sea Basin encompass the Samra, Lisan and Zeelim formations (Fig. 4.59; Haliva-Cohen et al. 2012). Mineralogically they can be broken down into two sedimentary facies, based on the presence or absence of aragonite: (1) The *aad* facies, which consists of alternating laminae of primary aragonite and silty detritus material; (2) The *ld* facies, which consists mainly of laminated detritus particles and typically lacks aragonite. The *aad* facies characterizes glacial intervals (e.g. MIS; stages 2 and 4) when lake levels in the basin were high, while the *ld* facies characterizes interglacials (e.g. MIS; stages 1, 5) and warmer glacial intervals (e.g. MIS; stage 3), when lake levels were low and evaporites were probably accumulating at times of holomixis in the adjacent drawndown lake (Fig. 4.59).

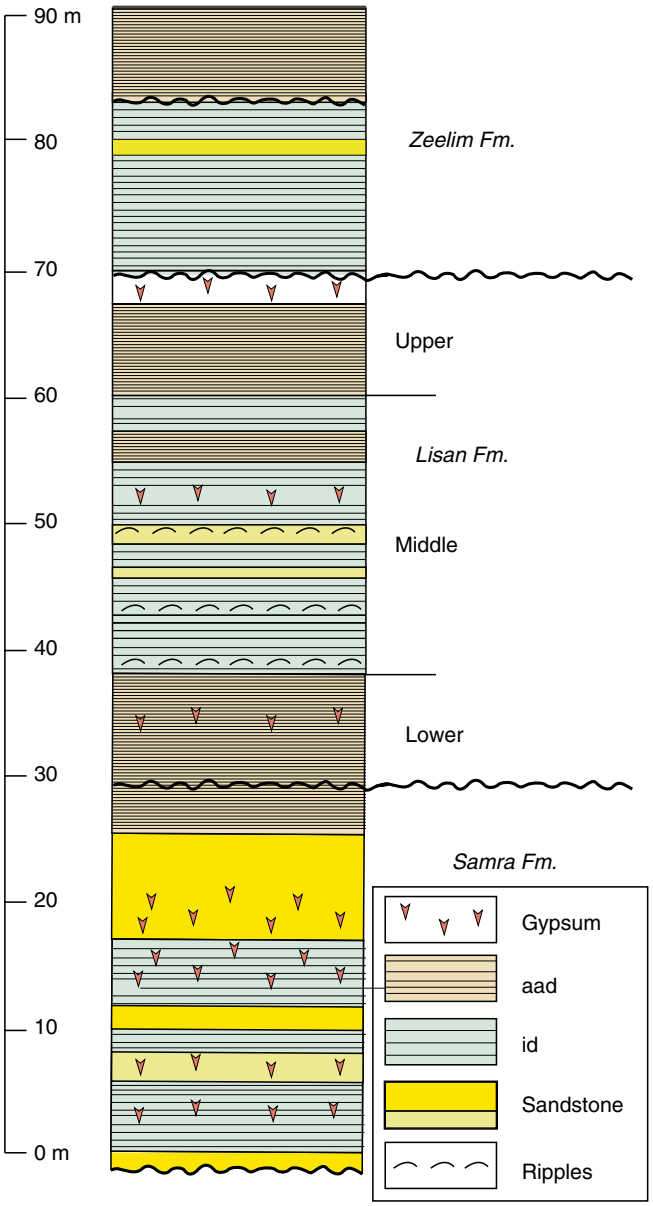

Fig. 4.59 Composite stratigraphic section of upper Samra Fm. (Last Interglacial: late MIS5), Lisan Fm (last glacial, MIS4, 3 and 2) and Zeelim Fm. (Holocene, MIS1). The Samra Fm. comprises mainly sequences of laminated calcitic detritus (the ld facies). The Lisan Fm. is divided to three Members: The Lower and Upper Members are mainly composed of sequences of laminated primary aragonite and silty-detritus (the *aad* facies, Figs. 3 and 5). The Middle Member consists of sequences of both the *aad* and *ld* facies. The lower and middle parts of the Holocene Zeelim Fm. consist mainly of the *ld* facies with more of the *aad* facies in the upper part (past 3,000 years) (After Haliva-Cohen et al. 2012)

The detritus in both *aad* and *ld* facies show similar mineralogies: mainly quartz ± calcite grains, with minor feldspars and clays, but with distinct grain-sizes (8–10 μm and

50–60 μm, respectively). They also show distinct $^{87}Sr/^{86}Sr$ and ƐNd (0.711–0.712 and ≈−7 to −8, versus 0.709–0.710 and ≈−5, respectively). Detrital fines in the *aad* and l*d* comprise desert dust of mixed granitic – basaltic composition that was blown from the Sahara desert and from the Nile delta to the northern Negev desert (loess deposits) and the Judean Mountains bordering the Dead Sea basin, mainly during glacial intervals along with enhanced Mediterranean rain fronts. The *aad* fines imply an enhanced transport of Saharan granitic dust to the vicinity of the lake mainly during glacials. The *ld* fines were recycled from the loess surface cover of the Negev desert mainly during interglacials and warm glacial intervals when lake levels tended to be lower.

Lake Asal, Republic of Djibouti

Lake Asal, with a water surface some 155 m below sea level, is the lowest place in Africa and defines the lowest part of the Afar rift (Fig. 4.60). Asal lake is small (area 52 km^2), endoheic and shallow, with a maximum water depth of 30 m and an average depth of 7.4 m. The Afar depression contains a series of lakes and salt pans at various depths below sea level: Lake Badda (−50 m), Lake Assale (−118 m), Lake Bakili (−120 m), Lake Afrera (−111 m), Lake Acori (−94 m) and the lowest Lake Asal (−155 m). Regionally, the area is extremely arid with average rainfall below 100 mm/year and evaporation of about 5 m/year (Köppen climate – BWh). Locally, in the Asal area, mean annual rainfall in the area is 175–200 mm/year and evaporation exceeds 3.5 m/year. The lake depression lies in the NW-SE oriented Asal – Ghoubbat al Kharab (Ardoukôba) rift extending northeast into the Gulf of Aden.

In the vicinity of Asal, the rift is subaerially exposed over a 12 km distance between Lake Asal and the Red Sea and is part of a tectonic system considered to be one of two examples where an oceanic ridge outcrops; the other being on the island of Iceland. This part of the rift extends southwest into the East African rift and is at the marine-fed end of what is our type example (Afar triangle) of a spreading centre (triple junction) in an arid part of world's rift systems.

Locally, the ridge shows a spreading rate of 30–60 mm/year. Magma-water interaction has produced tuff cones, some of which form islands or are breached by the Red Sea. The most recent lava flows on the ridge are younger than lake sediments deposited 5,300 years ago and thought to have been erupted during the past 3,000 years. The Ardoukôba fissure last erupted in 1978, producing numerous fissure and vent lavas, as well as scattered hornitos and a large spatter ring that marked the climax of the eruption.

Although small, Lake Asal is one of the few modern examples of a marine-fed rift basin that is actively accumulating bedded evaporites. As such, it is the only Quaternary analogue for ancient marine-fed rifts including the numerous Mesozoic evaporitic lacustrine basins that underlie passive margins on either side of the Atlantic (Chap. 5). The lake surround today is completely continental with no surface connection to the ocean. Yet the fact its −155 m asl level has changed little in the last few centuries argues it is fed a steady flow of seawater through the highly fractured 10 km wide volcanic ridge that separates oceanic water at Ghoubbat al Kharab from the hypersaline waters of Lake Asal. It constitutes an excellent example of a drawndown marine seepage basin fed through a volcanic ridge (Fig. 4.60).

Over the longer time frame of the past 10,000 years, lake levels have changed drastically (Fig. 4.60; inset from Gasse and Fontes 1989). Some 10,000 year ago Lake Asal was almost dry in the late Pleistocene. A highstand lake level at 160 m asl existed in the early Holocene, between 8.6 and 6 ka, and the lake at that time drained to the Ghubbet el Kharab, across a shallow sill at an elevation of some 4 m bsl, to the Gulf of Aden, both as surface and subsurface flows (Fig. 4.60). Subsequent to this time span, the lake level dropped considerably to 150 m below sealevel enabling at the first time subsurface seawater infiltration from the sea to the lake across the fractured divide. Since then, the lake water salinity is controlled, mainly, by seawater input and high evaporation, responsible also for Ca-sulfate and halite deposition.

Today, any actively flowing springs, locally called manda, are dotted along the southeastern strandzone of the lake. Their geochemical makeup is very close to seawater proportions (Sanjuan et al. 1990). Outflow zones of some perennial thermal ponds support populations of small halotolerant fish of Family *Cyprinodontidae* (minnows and killifishes). Total marine inflow to the lake is estimated to be of the order of 60–80 m^3 per second, with transit times for waters seeping from the ocean to the lake floor measured in less than tens of years, or at most two centuries (Demange et al. 1971; Fontes et al. 1980). Outflow is focused along shallow narrow fracture networks that cut the volcanic ridge (Mlynarski and Zlotnicki 2001). There are also several hydrothermal springs and many fumaroles still active in the area and it is clear that the subsurface temperatures are still very high below the fracture meshworks carrying cooler seawater inflows to the lake depression making the region a possible candidate or geothermal energy.

Three independent geothermal systems have been identified, so far, namely. Gale le Goma, Fiale and South of Lake (Houssein and Axelsson 2010). Six deep wells have been drilled in the region, the first two in 1975 and the others in 1987–1988. Well A2 was damaged and wells A4 and A5 encountered impermeable yet very hot (340–365 °C) rocks. Wells A1, A2, A3 and A6 produce highly saline (120 g/L TDS) fluids leading to significant mineral scaling. The first two deep wells, Asal-1 had a final depth of 1,154 m and Asal-2, a final depth of 1,554 m. These thermal test holes were drilled at the southwest edge of the geothermal area in a region where there is no direct inflow from the sea. Asal-1 produced 22 kg/s of high salinity water with a measured tem-

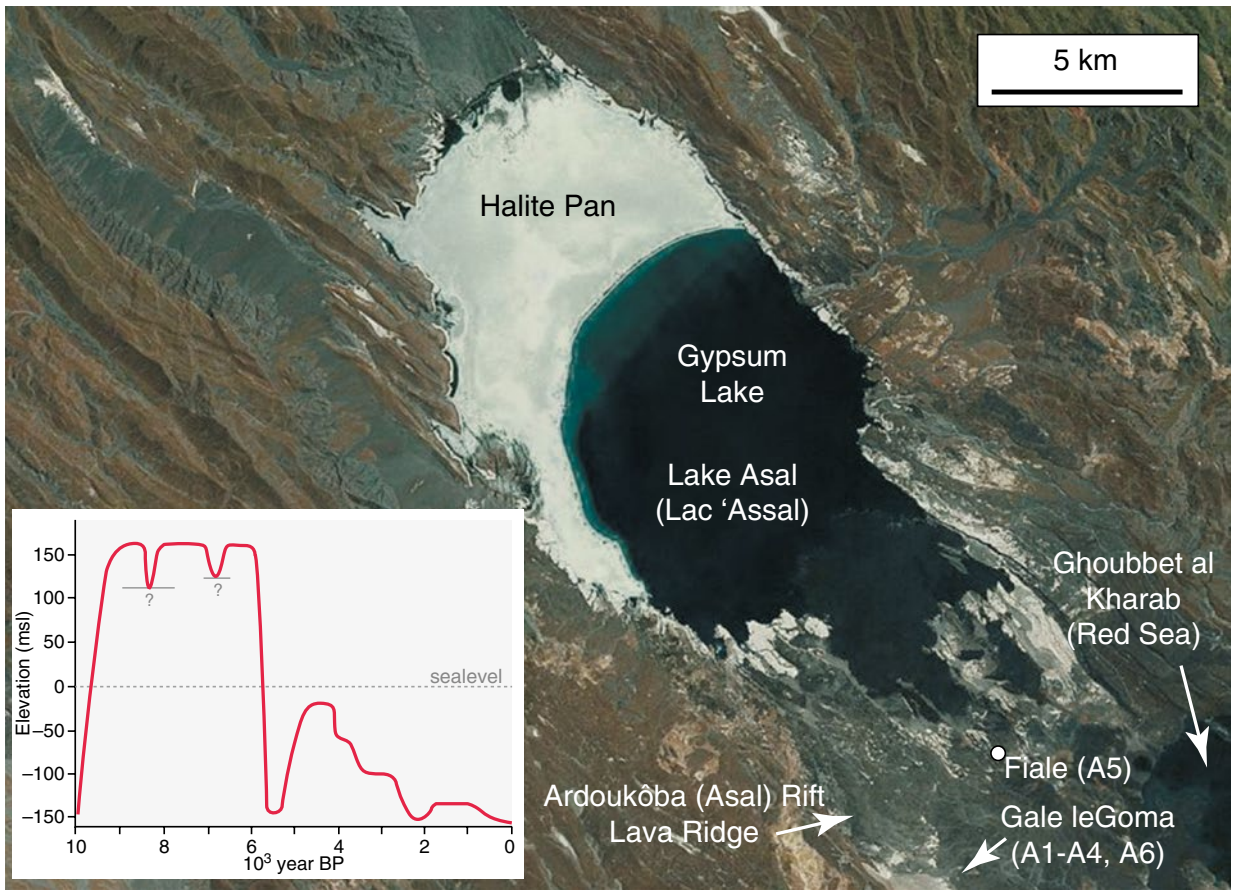

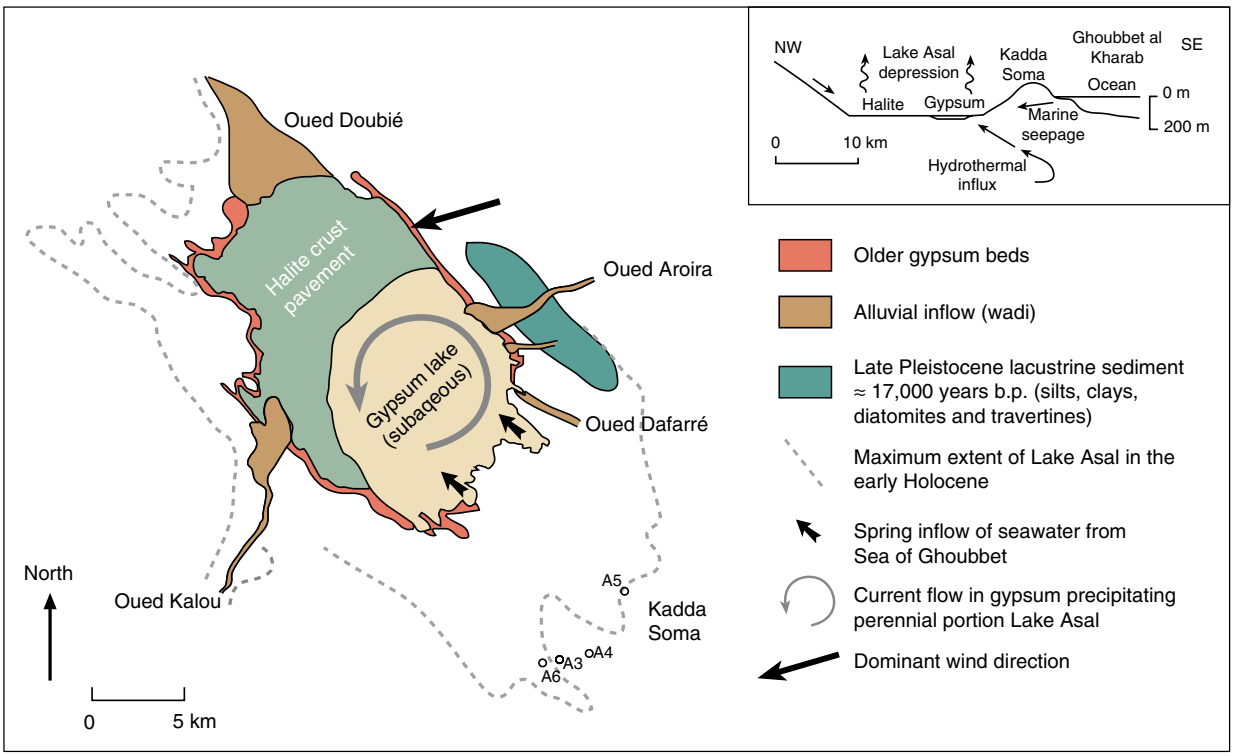

Fig. 4.60 Holocene sediment distribution in Lake Asal, Republic of Djibouti (surface geology after Stieljes 1973). Marine inflow is via fractured basalts of the Kodda Soma. A_{3-6} indicate positions of geothermal test wells – A_1 and A_2 lie further to the southwest. Insets show water levels in past 10,000 years (After Gasse and Fontes 1989) and an idealised cross section from the ocean to the lake depression (Landsat image courtesy of NASA)

perature at 1,040 m of 255 °C prior to flow testing, and 260 °C during a flow test in 1981 (Fig. 4.61). Water produced by Asal-1 had a very high solids concentration (128 g/l) and during the 1981 flow test, rapid incrustation in the casing had plugged the well in less than 3 months. The other well, Asal-2, was plugged inside the casing, possibly by drilling mud, and is no longer producing steam. Well test data from all six wells indicate that the reservoir might be producing from layered fractured and porous zones (Fig. 4.61). The estimated permeability-thickness of the deep Gale le Goma reservoir is in the 3–9 darcy-meter range.

Free-standing lake brines reach salinities of 350‰ and, like their marine spring feeds have seawater like proportions, dominated by Cl, Na, K, SO_4 and Mg. Salts in the perennial standing body of lake brine (up to 40 m deep, mostly 5–7 m deep) are mostly gypsum, which is accumulating with mounded and bottom-nucleated aligned-layer textures identical to those that characterise the South Australian salinas. Gypsum precipitation dominates in this the southeastern part of the lake depression, located next to the seeps that bring seawater to the surface. Fractures also intersect the subaqueous lake floor and seawater can be seen to rise up along fractures cutting the lake bottom. Older layered and mounded gypsum beds crop out around the lake edge to as high as 55 m above the present lake level (Stieljes 1973).

Stacked halite crusts characterise the saline pan facies that covers much of the northeastern part of the lake where it forms a wide (≈60 km^2) and thick (20–80 m) accumulation of pan halite. Prior to 1978 the top of this halite plain lay some 30–80 cm above the typical water surface of the perennial gypsum lake. Then in 1978 renewed volcano-tectonic activity in the region reopened fractures and faults leading to an increased influx of waters from the Ghoubbat al Kharab and a rise of lake waters which partially submerged the top of the salt pan (Ruegg et al. 1979). Once again, as in most other basins accumulating bedded evaporites, the changes in hydrological base level in this depressed pan are in large part driven by tectonics, not marine eustasy (see Chap. 5). The separation between areas of subaqueous gypsum and pan halite clearly shows how two mineral phases cannot accumulate simultaneously in a single holomictic brine lake, but can be adjacent facies controlled by separate hydrologies (salina versus mudflat).

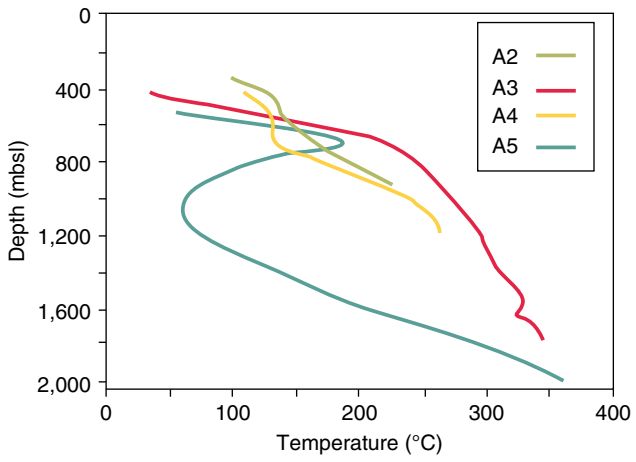

Fig. 4.61 Temperature profiles of Asal wells A2–A5 (After Houssein and Axelsson 2010). Layering indicated by variable geothermal gradients in each well (Locations in Fig. 4.60)

Are Modern Saline Lakes all Shallow?

Table 4.6 shows the relative importance of saline lakes in the total volume of the world's surface waters. There is as much water caught up in the world's saline lakes as there is in stored in freshwater lake systems. Figure 4.62 plots the salt mass held in various saline water bodies, including the Caspian Sea which exceeds all other saline lake examples by an order of magnitude, holding some 70 % of the stored total salt mass listed in Table 4.6. The Caspian Sea has a surface area of 371,000 km^2, not including Karabogazgol, and a volume of 78,200 km^3. However, the relatively low salinity of the Caspian (12‰, some 1/3 of seawater) may preclude it from this compilation of salt masses in non-seawater saline water masses, especially if an additional defining criteria was that the basin must be precipitating salt, making the Dead Sea the largest mass of salt stored in a freestanding non-oceanic brine. Ultimately the Caspian Sea does precipitate a substantial salt mass, via the Karabogazgol depression.

Table 4.7 summarizes the physiographic variety of some of the larger Quaternary perennial brine lakes. The Caspian

Table 4.6 Water volumes in the global water compartments

Hydrological compartment	Volume of water held (1,000 km^3)	Percent
Oceans	1,370,000	97.61
Glaciers, ice, snow	29,000	2.08
Subsurface	4,067	0.295
Freshwater lakes, rivers	126	0.009
Saline lakes	104	0.008
Atmosphere	14	0.001

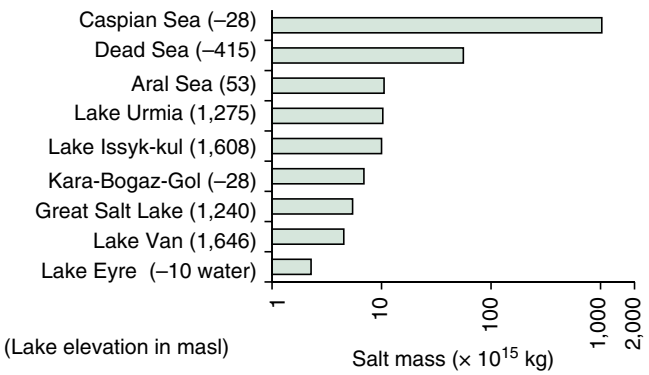

Fig. 4.62 Mass of salt held in selected freestanding lake waters. Note logarithmic scale

Table 4.7 Representative listing of variations in Quaternary evaporite deposits

	Area km^2	Brine surface	Hydrological setting (Brine source)	Tectonic setting	Characteristics
Lake Macleod, Australia (Köppen BWh) (Logan 1987)	2,500	≈1 m below sealevel	Evolved from stratified perennial to ephemeral during sediment infill (marine)	Passive margin	Holocene marine-fed coastal salina with 10 m thick bottom-nucleated salt beds. Stable brine curtain maintains salt beds and marine-fed seepage margin. Salts have filled an interdunal depression to within a metre of ambien t sealevel via seepage of mostly marine-fed groundwater.
Abu Dhabi mudflats (Köppen BWh) (Evans et al. 1969)	≈300	≈1 m above sealevel (asl)	Ephemeral with water cover during marine flood stage (marine)	Ramp in foreland basin	Holocene marine-fed coastal mudflat with 1–2 m thick displacive salts growing in detrital matrix of supratidal and intertidal units. Stable brine curtain is maintained by capillary evaporation and marine seepage.
Dead Sea, Middle East (Köppen BSh) (Ben-Avraham et al. 1999)	1,000	−415 m asl	310 m deep lake hypersaline lake with alternating longterm meromictic and holomictic brine columns (nonmarine)	Continental transform basin	Quaternary fluvial/seepage-fed deep perennial lake. Thick stable brine curtain bathes multiple stacked subaqueous beds. Beds in Northern Basin deposited in deep water, Southern Basin in saline pan/salina settings. Much of the solute is fed to the lake from springs carrying dissolved Miocene (4–6 Ma) evaporites (diapirs also outcrop on lake floor).
Kara-Bogaz-Gol, Turkmenistan (Köppen BSk)	13,000	28 m below sealevel	Endorheic basin joined by a narrow inlet to Caspian Sea (nonmarine)	Intramontane basin in a continent-continent collision belt	In the last 0.5 million years three separate Mg-Na-SO_4-rich salt layers have formed across the gulf, perhaps forming best in glacial episodes when the connection to the Caspian was reduced compared to today, and year round temperatures were much lower. Such glacial conditions favoured a perennial lake to pan mode of cryogenic mirabilite precipitation (Fig. 12.21)
Lake Eyre, Australia (Köppen BWh) (Magee et al. 1995)	9,300	−15 m asl	Ephemeral lake mudflats with up to 6 m of freshwater cover emplaced during occasional storm flood (nonmarine)	Intracratonic sag atop Precambrian rift	Quaternary fluvial-seepage fed, has changed from fresh (100 ka) to the ephemeral salt lake of today, showing the decreasing effect of the monsoonal feed. Upwelling and through flushing of freshened artesian waters beneath the lake destroys the brine curtain and so prevents more than 2–3 m of halite accumulating beneath the lowermost parts of the lake floor
Salar Uyuni, Bolivia (Köppen BWk) (Risacher and Fritz 2000)	10,600	+3,653 m asl	Saline pan with peripheral mudflat (continental/ hydrothermal)	Intramontane basin in a forearc collision belt	Largest salt pan in the world today. A 121 m deep well intersected 12 saline-pan beds separated by 11 lacustrine mud beds, all bathed in a stable brine curtain. Mud layers thicken upwards, while the thickness of the salt beds decreases markedly from the base upward.

See also Tables 4.1 and 3.1

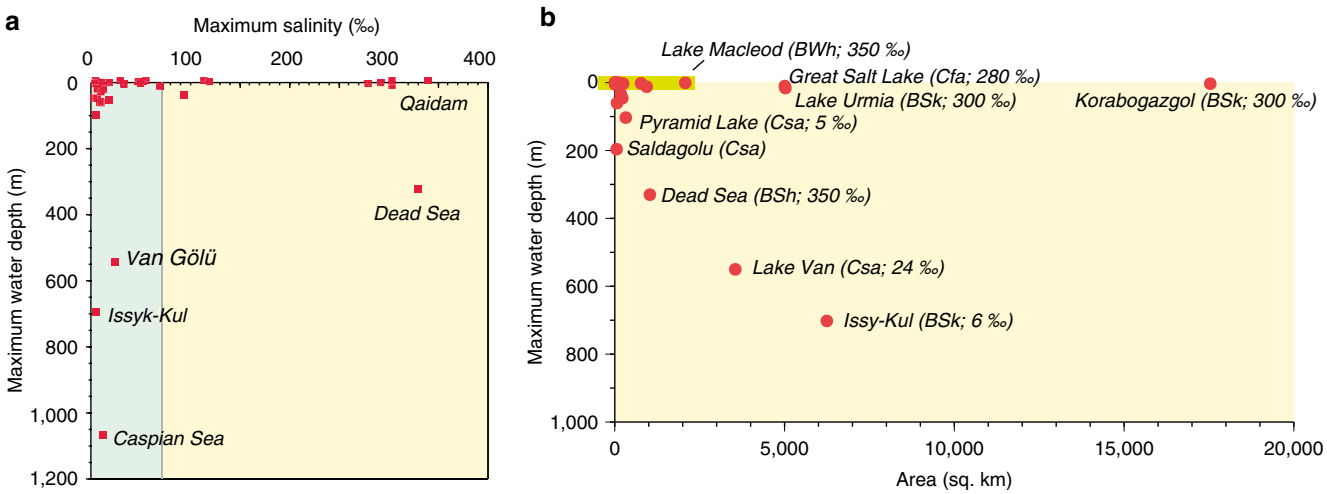

Fig. 4.63 Physiography of saline lakes of the world. (**a**) Plot of maximum salinity of freestanding saline lake waters versus maximum water depth. Note logarithmic scale (see also Table 4.1) (**b**) Plot of maximum brine depth versus brine area (also shown is Köppen climate and maximum salinity reached by most saline brines). Larger saline lakes tend to be less saline and in cooler arid climates. *Green rectangle* encompasses plot field of all Holocene coastal salinas, including the largest – Lake Macleod

and the other perennial saline lakes of western Asia (Karabogazgol, Lake Urmia, Lake Issyk-Kul and Lake Van) are all located in foreland basins created by Neogene collision tectonics and together contribute a high proportion to the world's total volume of saline lake waters. Then again, over 40 % of the listed freshwater volume in Table 4.6 comes from the combined volumes of Lake Baikal and the Great Lakes of the North Americas. Also, most saline water bodies are shallow, so the area of the world's surface covered by saline lakes is probably greater than that covered by freshwater lakes.

In terms of saline lake sediments associated with saline water bodies, the largest contiguous area of Quaternary bedded salt accumulating today is in Salar Uyuni, a continental lake (saline pan/mudflat) with a water level some thousands of metres above sea level. The Dead Sea, with a water surface more than 415 m below sealevel, is our one Holocene example of a substantial deepwater evaporite basin currently accumulating halite. Its inflow is a combination of river and saline spring inflow, with most of the solute content coming from groundwaters flushing nearby Miocene salts. One of our best examples of an active marine-fed perennial saline lake, which is still accumulating bedded shoalwater gypsum and pan halite, is Lake Asal, a rift depression lake with a water surface some 155 m below sea level. In area, it is exceeded by many of the marine seepage-fed Holocene coastal salinas of southern and western Australia. Unlike Lake Asal, the Australian coastal salinas have equilibrated within a metre of the height of their sea level source and are no longer actively accumulating subaqueous bedded salts. Active subsidence in a rift seems to allow a continental lake to maintain permanently subaqueous brines, as is the case in the Dead Sea. After Lake Asal, Death Valley at −86 m asl, is the next deepest hole on the world's surface that is occupied by a saline lacustrine system. In its current form it is a saline pan rather than a perennial halite accumulating lake, but in the Late Pleistocene it was a deep perennial system (Chap. 3). Although well studied, the volume of salts accumulating in Death Valley is relatively minor in terms of the total volume of salt in saline lacustrine settings of the world.

A plot of salinity versus brine depth in the world's perennial saline lakes shows that perennial lakes accumulating salts more saline than calcite/aragonite/dolomite couplets (salinities >70‰) tend to be shallow, river fed and with brines typically less than 10 m deep (Fig. 4.63a). In terms of total salts held in the lake waters, the less saline lakes dominate – Caspian, Aral Sea, Lake Urmia (Fig. 4.63).

The current condition of the Dead Sea is an obvious exception to the general observation that gypsum/halite-accumulating lakes are characterised by shallow to ephemeral surface waters (Fig. 4.63a). The Dead Sea's physiography as a narrow rapidly subsiding basin in the deepest continental position on the world's surface makes it unique amongst the world's modern saline lakes. But the Dead Sea can accumulate halite in its deepest waters only when its longterm density stratification is destroyed (holomixis). The destruction of the halocline is not an annual event, as it is in some of the less saline lakes (e.g. Lake Van), but seems to occur every few hundred years. A plot of lake water area versus depth shows that larger nonmarine-fed saline lakes tend to be located in cooler deserts (Fig. 4.63b; see also the more detailed discussion on climate controls in Chap. 2).

All of the largest active perennial saline water bodies, which are depositing substantial volumes and areas of

Quaternary subaqueous salts over time frames measures longer than 10,000 years, are continental not marine depressions. All the largest perennial saline lakes occur in semi-arid rather than arid to hyperarid climates and all are located in tectonically active and subsiding (underfilled) basins such as in the Andes, the tectonic collision zones of Turkey and Iran, and the Basin and Range of USA (Table 2.3). Tectonism facilitates steep topographic gradients, endorheic closure and subsidence within large intermontane depressions, all three factors seem to be needed in order to form a permanent brine body in Quaternary systems. Milder levels of aridity allow waters to persist above the land surface and do not drive the conversion of the hydrology to sabkhas and evaporitic mudflats that characterise the more arid settings.

Climate and Scale of Quaternary Saline Systems

The other significant factor common to the formation of large perennial saline lakes is longterm climate change. Ephemeral flood-pan lacustrine systems, such as Lake Eyre and Lake Frome in Australia, which today are combinations of saline pans and evaporitic mudflats, were large perennial brackish to freshwater lakes in milder climatic episodes in the Late Pleistocene. These southern hemisphere "mega-lake" phases are tied to a more southerly influence of the monsoonal belt during these times. Even historical flooding events in the central Australian playas are frequently tied to La Nina phases in the El Nino-Southern Oscillations (ENSO). Laminated Pleistocene (10–12 ka) lacustrine sediments from Lake Magadi also preserve evidence of ENSO changes in the variations of laminae thickness (Damnati and Taieb 1995). Changes in Pleistocene climate also explain why many modern playas and pans in the Basin and Range were once perennial lakes; during pluvial episodes of the Late Pleistocene some were even freshwater lakes with waters more than 100 m deep (Smoot and Lowenstein 1991).

Many such Late Pleistocene lakes during their humid or wetstage were huge, are termed megalakes as they had water covered extents that extended far beyond the borders of their current saline residuals. Some 48,000 year ago lakes Mega-Frome and Mega-Eyre were joined to create one of the largest Pleistocene systems of perennial palaeolakes on the Australian continent. When joined the combined lakes had a water covered area of 25,000 km^2 and a volume of 285 km^3 with a water level of +5 m AHD (Cohen et al. 2012). Even larger in the Australian context was the gypsiferous Bungunnia megalake, which occurred in southern Australia in the late Neogene, when it covered an area of more than 50,000 km^2 in the Murray Basin in its brackish phase and a lesser area in its underfilled more evaporitic phase (McLaren and Wallace 2010; McLaren et al. 2012). Another impressive megalake was Lake Chad some 8,000–10,000 years ago when its freshwater-covered area of more than 50,000 km^2 was equivalent to that of the present Caspian Sea. Yet another, even larger, lacustrine system was the Late Pleistocene Kalahari mega-lake, which had an area of more than 66,000 km^2, extending across the current Makgadikgadi (Sua Pan) and adjacent depressions of Africa (Burrough et al. 2009). All these mega lakes occupy what are today desert-margin areas (see Chap. 2) Interestingly, some modern perennial saline lakes, currently in their fresher saline stages (Lake Van and Lake Urmia), experienced times of shrinkage and desiccation in the Late Pleistocene.

To state everything we have discussed so far in its simplest terms: To accumulate bedded salts, you need a large, deep centrally-draining somewhat leaky hole in the ground (a groundwater sump). And, like Goldilocks, such saline systems perform best in a climate that is not "too hot" and not "too cold" and not "too wet" and not "too dry." Variation in climate and tectonics causes these lacustrine systems to expand and contract, they oscillate between less saline water-full and highly saline drawndown stages.

If we use Quaternary examples of evaporite deposition as strict uniformitarian analogs for ancient evaporite deposits then we must conclude that the largest and thickest, laterally extensive salt beds are always continental lacustrine deposits, accumulating in tectonically-induced, rapidly-subsiding intermontane basins and sags. The most voluminous accumulations of pure halite are not in intracratonic sags like megalakes Chad and Eyre, which retain only thin impure evaporite beds, but in more hydrologically focused Quaternary intermontane salar depressions in the Andean Altiplano. There, Uyuni and Atacama are saline pans today, but were perennial aerially-larger saline lakes in the Late Pleistocene. In the largest Andean salar deposits the salt depositional surface is more than 2,000 m above sea level. This is a setting with limited lateral continuity, some tens of kilometres across and, as will shall see in Chap. 5, not relevant to the scale or setting of ancient marine fed sumps, such as those that deposited the Messinian of the Zechstein, salts.

Likewise, note that there are scale, continuity and preservation limitations if we consider as analogs the geological setting and extent of the well documented various Quaternary saline pans and sabkhas that occupy various intermontane depressions, such as in the Southwest USA. Figure 4.64 illustrates the extent of the region to the west of the Bonneville salt flats and Great Salt Lake, which are visible in the upper right side of the figure. Note the 100 km scale bar in this figure, it emphasises the limited extent and thickness of the various thin, laterally-discontinuous 1–10 m thick salt beds that form as veneers in the lower portions the intermontane valley sumps. These salt beds form as the result of evaporation of ponded continental and magmatic brines. It is not an hydrological environment where salt masses hundreds to thousands of meters across and hundreds

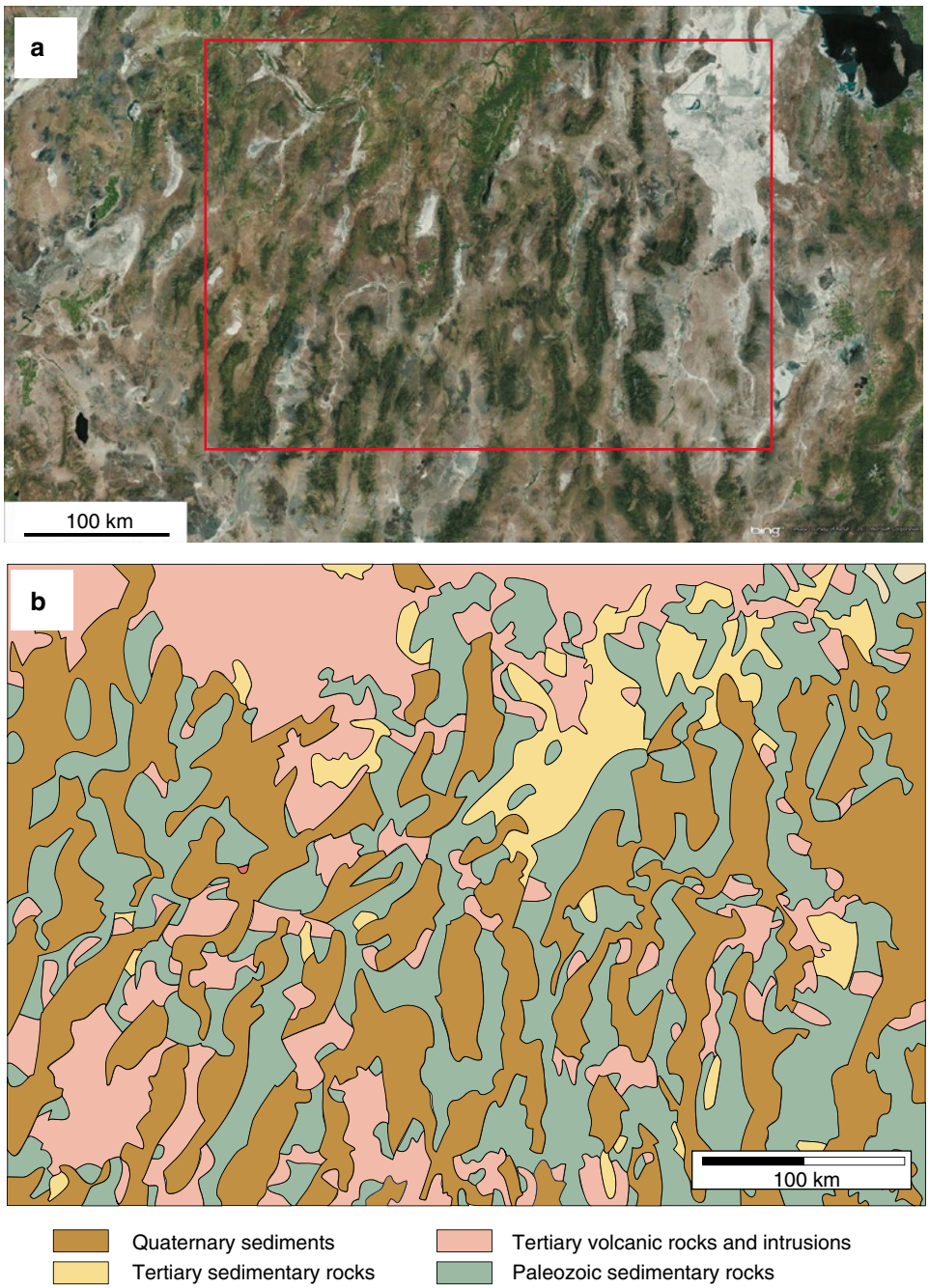

Fig. 4.64 Basin and Range: scale of depositional setting. (**a**) Landsat image (**b**) General geology showing a strong structural grain to the distribution of the various laterally discontinuous Quaternary sediments including thin veneers of saline minerals. *Red rectangle* indicates area of geological map.

of meters thick can form. Such megasalt geobodies require a marine-feed and a subsealevel sump setting to facilitate the ongoing hydrology that facilitates the accumulation of such salt volumes (Chap. 5).

Such marine-seepage fed platform and basinwide evaporite settings do not exist today. But, the next chapter will show that most of the larger examples of ancient evaporites are actually marine-fed precipitates, deposited under eustatic and tectonic conditions for which there are no Quaternary counterparts.

Comparing Quaternary Sabkhas, Pans and Lakes

So, in this and the preceding chapter we looked at some the better documented, hydrologically active, examples of the world's modern evaporite systems. We can now begin to construct an understanding framework needed to test and answer that perennial geological question: Is the present the key to the past? When documented Quaternary saline lakes are climate-sorted and plotted using a similar climate-sorted approach, as was done with saline pans and sabkhas at the end of Chap. 3, a number of similarities and significant dif-

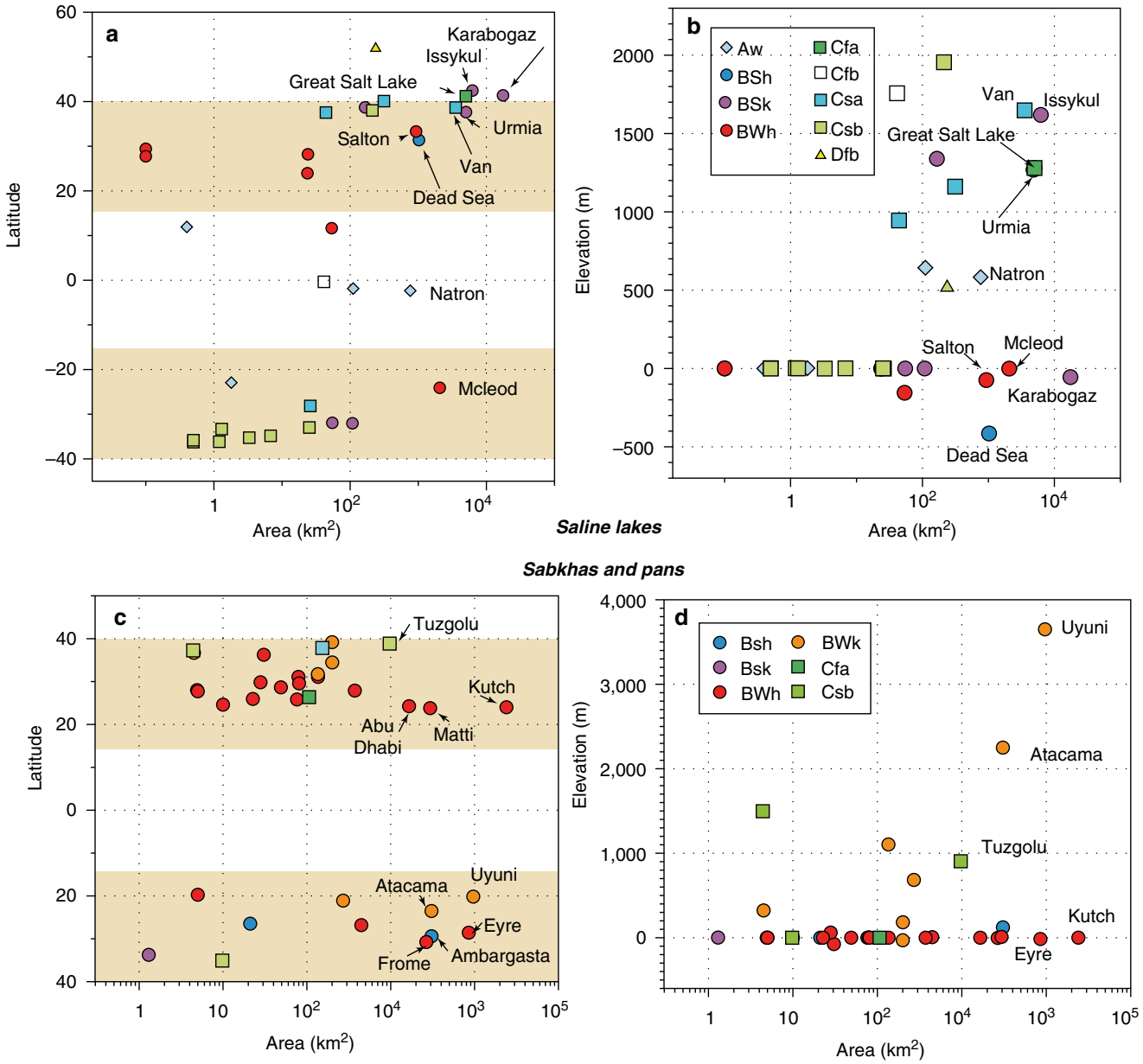

Fig. 4.65 Köppen climate sort plots of area (km^2) versus latitude and elevation (with respect to sealevel = 0 m). (**a**) and (**b**) plot saline perennial lakes, based on Table 4.1. (**c**, **d**) Plot sabkha and saline pan occurrences, based on Table 3.1. *Colour bands* indicate approximate latitudinal positions of descending arms of Hadley Cells (15–40° north and south of equator)

ferences are seen between perennial saline lakes versus sabkha/pans (Fig. 4.65).

1. Many significant perennial saline lakes occur outside the trade wind belts (beyond the influence of Hadley cells). For example, Lake Magadi and Natron occur in adiabatic dry zones within an Aw climate zones, located within a few degrees of the equator. Issykul and some of the Himalayan/Chinese perennial lakes occur as far as 55° north of the equator in cold arid deserts. The distribution of perennial saline lakes is more latitudinally dispersed than sabkhas and pans.
2. Steep intermontane (rain shadow-or adiabatic) arid continental settings encourage the formation of suitable at-surface saline hydrologies need to maintain large perennial saline lakes and pans. The five largest modern saline lakes (Karabogaz, Issykul, Urmia, Great Salt Lake and Van) and the two largest saline pans (Uyuni and Atacama) occur in cool, rather than hot, arid settings.
3. Although transitions from fresher to more saline perennial or pan systems is often a response to climate change, the transitions can also be tectonic or sedimentologic. This was the case with the rapid fall and transition into a saline system that marked the end of Lake Bonneville,

Utah. It seems that megafloods are more typical of saline lakes located in semi-arid regions, where in the Quaternary icehouse earth water levels tend to oscillate between higher and fresher, to lower and more saline (O'Connor and Costa 2004). The associated rapid changes in water head in an intermontane setting are more likely to set up mechanical instabilities in the encasing unconsolidated sediments (overtopping and groundwater sapping).

4. Megafloods can also occur when a rapidly rising sea breaches a previously continental lacustrine depression. A Holocene example of this style of marine megaflood occurred in the Black Sea Basin (as opposed to the much gentler marine seepage-flooding that typifies many Holocene coastal salinas). Some 7,500 years ago the Black Sea was catastrophically flooded by seawater from the rising Mediterranean Sea as it overtopped and eroded a former divide at the present-day Bosporus Strait. Ryan and Pitman (1999) speculate that this event was the folk memory that is the basis for the biblical myth of the worldwide Noah's Flood.
5. The largest saline lake sump known today is Karabogazgol, which formed as a natural concentrative sump to the already somewhat saline waters of the hydrographically-isolated fluvial-fed Caspian Sea. Karabogazgol is accumulating cryogenic salts, not salts formed by solar evaporation in a hot arid desert. Also the greater volumes of preserved and buried salts in Karabogazgol accumulated in cooler glacial periods, not in the warmer interglacials, such as that of today.
6. Because of the importance of relief and lower temperatures in facilitating the ponding of surface water in arid conditions with reduced evaporation rates, the five largest extant saline lakes (Karabogaz, Issykul, Van, Great Salt Lake and Urmia) are not found in BWh climates. Rather hot arid climates favour the formation of sabkhas especially adjacent to a large standing brine mass or ocean. The largest extant saline lake in a BWh setting is Lake Macleod, which is supplied large volumes of seawater via evaporitic drawdown and seepage.
7. Unlike sabkhas, where the majority of the documented BWh deposits occupied at-sealevel positions (Chap. 3), many of the documented at-sealevel Quaternary saline lake coastal deposits occur in milder Mediterranean (C) or arid steppe (BS) climatic settings, with many of the larger perennial saline lakes being continental, not marine-fed, in intermontane settings at elevations well above sealevel.

So, when comparing saline deposit styles in Quaternary sabkha versus subaqueous climatic settings, it seems larger bedded saline lake deposits require somewhat less extreme desert or steppe conditions to form (BWk or BSk). Perennial Quaternary brine lakes seem to form best in cooler arid settings where there is a steep sided topography to the lake sump (the "Goldilocks syndrome"). In contrast, hot arid desert and steppe climates (BWh and BWk) favour the accumulation of sabkhas and pans, especially in sump areas with low relief in the surrounding topography and a relatively shallow watertable. Often in these ephemeral water hydrologies the bulk of the sabkha salts are subject to deflation and thick stacked salt accumulations are rare.

In summary, because modern continental settings lack a hydrology suitable for supplying huge volumes of brine, sufficient to form a megasalt deposit, neither modern sabkhas or salinas are directly relevant to the formation of the hydrologies and eustasies needed to deposit the huge masses of ancient marine-fed subaqueous salts detailed in Chap. 5.

Ancient Basins and Stratigraphic Evolution

5

Introduction

Is the present the key to the past in evaporite studies? It's part of a broader question that has plagued geologists working with salts since the seventeenth century, when Werner's Neptunist postulates explained world geology (including igneous strata) as layered precipitates from cooling oceanic waters. And, like Werner's Scottish antagonists, we are still discussing the merits of strict uniformitarianism. In this chapter I am not questioning the fundamental principle of using present-day process studies to interpret the past. Nor am I questioning the utility of detailed studies of process analogs and the use of physical constants to reliably interpret the past. Let me put it plainly for the creationist community and proponents of "intelligent design," all the geological evidence clearly shows the earth is not 8,000, but more than 4 billion years old. Biological evolution is fact, it interacts with and responds to the physical environment and has been in operation on the earth's surface for at least the past 3.45 billion years. There is no need to invoke the supernatural and sky faeries to explain biological evolution and other earth processes, and there is no geological evidence for a worldwide biblical flood of epic proportions drowning mankind and covering all the land.

What I am questioning is strict actualistic approaches to sedimentological interpretation of evaporites, whether the depositional diversity we see in our current icehouse climate mode and eustasy is sufficiently broad to explain the diversity of ancient evaporites (Table 5.1). If our present climate is the key in terms of all scales of deposition and climate, then why are no marine platform evaporites forming today and why are there no evaporitic seaways? Chapters 3 and 4 show that the largest and thickest Quaternary evaporites are continental lacustrine deposits, not marine-fed systems. We shall shortly see that such lacustrine systems are directly and completely comparable with their ancient lacustrine counterparts in terms of facies, salt thicknesses and lateral extents. But the scale of lacustrine evaporite development, past and present, pales in comparison to some ancient marine-fed saline systems. There are no modern counterparts to such ancient marine-associated systems. Our inability to compare all aspects of evaporite deposition, past and present, reflects a present-day lack of both longterm shallow epeiric seas and of large drawdown basins fed by seawater seeps.

The Hith Anhydrite of the Middle East, the Zechstein salts of Europe and the Messinian evaporites of the Mediterranean have no modern same-scale counterparts. An understanding of the shortcomings inherent in applying strict uniformitarian models is tied to current styles of continent-scale tectonics and icehouse eustasy. Put simply, the rates and amplitudes of seafloor spreading, orogeny and eustasy are not constant across deep time, nor is the climatic system they drive. Widespread marine evaporites require particular tectonic and/or eustatic conditions to accumulate, conditions that are not present on the world's modern surface (Table 5.1). They will be in the future, and they have been many times in the past.

This chapter demonstrates the importance of differences between icehouse and greenhouse climate/eustasy as controls on evaporite style in marine platforms. It shows how particular tectonic and climatic settings are needed to form saline giants in isolated subsealevel drawdown depressions. It also shows how interpretations using sequence stratigraphic marine eustatic frameworks do not work as well in ancient basinwide saline giants as they do in interpreting evaporites laid down on ancient marine platforms. Even on an ancient continental shelf, we need to separate icehouse from greenhouse platforms in order to understand variations in evaporite distribution.

By the end of this chapter, I hope it will be obvious that when trying to predict and model ancient evaporites it is much more useful to consider tectonics and hydrologies of large evaporite basins as the fundamental controls of basin-scale evaporite geometries, mineralogies and bounding surfaces. One should not force marine-seepage-fed drawdown systems into a marine-eustatic icehouse model. Nor should our interpretations be driven by the hydrologically dubious notions of ongoing surface (hydrographic) connections between ocean waters and restricted basins at the time thick salts accumulate (Chap. 2); and yet these assumptions still dominate many interpretations of ancient evaporite basins.

© Springer International Publishing Switzerland 2016

J.K. Warren, *Evaporites: A Geological Compendium*, DOI 10.1007/978-3-319-13512-0_5

Table 5.1 Climatic and depositional contrasts between icehouse and greenhouse earth

	Icehouse	Greenhouse
Age	Icehouse Late Cenozoic, Late Carboniferous to Early Permian, Late Neoproterozoic	Greenhouse Cambrian to Middle Carboniferous, Middle Permian to Early Cenozoic
Tectonic style	Collision, telescoping	Stretching, rifting
Seafloor spreading	Slow	Rapid
Subduction/volcanism	Low	High
Marine margin basins	Narrow shelves, limited short-lived interior seaways with small aerial extent, evaporites mostly in lower latitudes	Wide shallow shelves and large long-lived interior seaways (epeiric seas). Evaporites with broader latitudinal spread
Marine eustasy	High amplitude (≈100 m) change on 100,000 year times scale (4th order). World sealevel is low (caught up in longterm polar ice sheets)	Low amplitude (>5–10 m) change on 100,000 year times scale (4th order). World sealevel is high (no polar ice sheets)
Ocean Basins	Cold, oxygenated, low sealevel, aragonitic ocean, (high Mg/Ca), low $MgSO_4$	Warm, often anoxic, high sealevel, Mg calcite ocean (low Mg/Ca), high $MgSO_4$
High latitude climates	Glaciers, taiga and tundra	Deciduous forest
Mid latitude climate	Deciduous forest, glacial advances and steppe	Tropical wet and stressed forest
Low latitude climate	Rainforest, savanna and desert	Desert
Erosion/weathering	Fast, mechanical	Slow, chemical
Depositional styles of large evaporite basins	Tectonically induced endorheic continental depressions (terrestrial lacustrine; no significant marine-seep platform and basinwide evaporites accumulating at present time; but basinwides can form in suitably isolated icehouse conditions, and did so most recently in the Middle and Late Miocene)	Tectonically and eustatically induced endorheic continental and marine margin depressions (terrestrial lacustrine, marine platform and marine-fed basinwide styles can be widespread whenever suitable combinations of tectonics and eustasy occur)

Linking Present to Past Aridity

In order to understand possible linkages between present and past evaporites, we must first understand geological indications of past and present climate. After all, the preceding chapters clearly show it is ambient climate that drives the accumulation of salts in the deserts, lakes and sea margin systems of today and the same was true in regions of saline giants of the past. Only with a sturdy palaeoclimate understanding can we reliably compare Quaternary to older saline depositional settings. Quaternary and late Neogene climatic systems, characterised by waxing and waning polar ice sheets, define the current "icehouse" climate mode. Today, some 10 % of the world's surface is covered by ice, representing about 80 % of surface freshwater, and a further 20 % is affected by permafrost. Of these ice-covered lands, Antarctica has 86 % by area and Greenland 11 %. In the last glacial maximum (18–20 ka) a staggering 30 % of the earth's surface was covered by ice.

The current icehouse mode evolved during the latter part of the Tertiary period and is characterised by glacially -driven oscillations in sealevel, with amplitudes around 100 m, with repeat frequencies of 100,000 years for the past 780,000 years. Ice sheet oscillations in this very short portion of the earth's history is paced primarily by the ~100,000 year eccentricity cycle of the earth's orbit (Fig. 5.1). Smaller amplitude changes (typically <60 m) dominated prior to this time when these earlier ice sheet fluctuations were paced primarily by the 41,000-year tilt cycle of the earth's axis. Growth and decay of a continental-scale ice sheet in Antarctica caused 50–60-m variations on the 10^6-year scale beginning ~33.5 million years ago. Prior to this time, Earth had been a warm, high-CO_2 "greenhouse" world that was largely ice-free back to 260 million years ago (Figs. 5.2 and 5.3; Miller et al. 2011) Modern marine-fed evaporite distributions, associated with icehouse earth and its older counterparts at the end of the Palaeozoic and the Neoproterozoic, are not the same as that of the "greenhouse" climate mode, which has dominated much of the earth's history (Table 5.1).

Quaternary climate (icehouse), especially in semi-arid to temperate latitudes over the past 500,000 years, is characterised by repeated rapid temperature swings from levels much like those of today (interglacial) to levels many degrees colder. Colder (glacial) times are associated with growth of huge km-thick circumpolar and high latitude/high elevation ice sheets and lowered sealevels. Ocean surface temperatures were up to a few degrees cooler at such times, while sealevels fell more than a hundred metres compared with interglacial highstands. On the land, mountain tree lines shifted to lower positions during glacial periods, grasslands replaced forests, continental ice-and periglacial-driven processes were more widespread and large volumes of dust and sand were blown about by cold, intense winds. There were rapid pulses of sealevel fall during passage into the cooler climatic phases (glacials) of icehouse mode climate, while in the passage to warmer (interglacial) periods the rates of sealevel rise were even more intense over periods measured in hundreds to thousands of years (Fig. 5.1a). There have been more than 15 glacial periods in the last 1.7 million years. It was in the latter part of this icehouse regime of rapid change and climatic stress that *Homo sapiens* first came to be, some 150 ka.

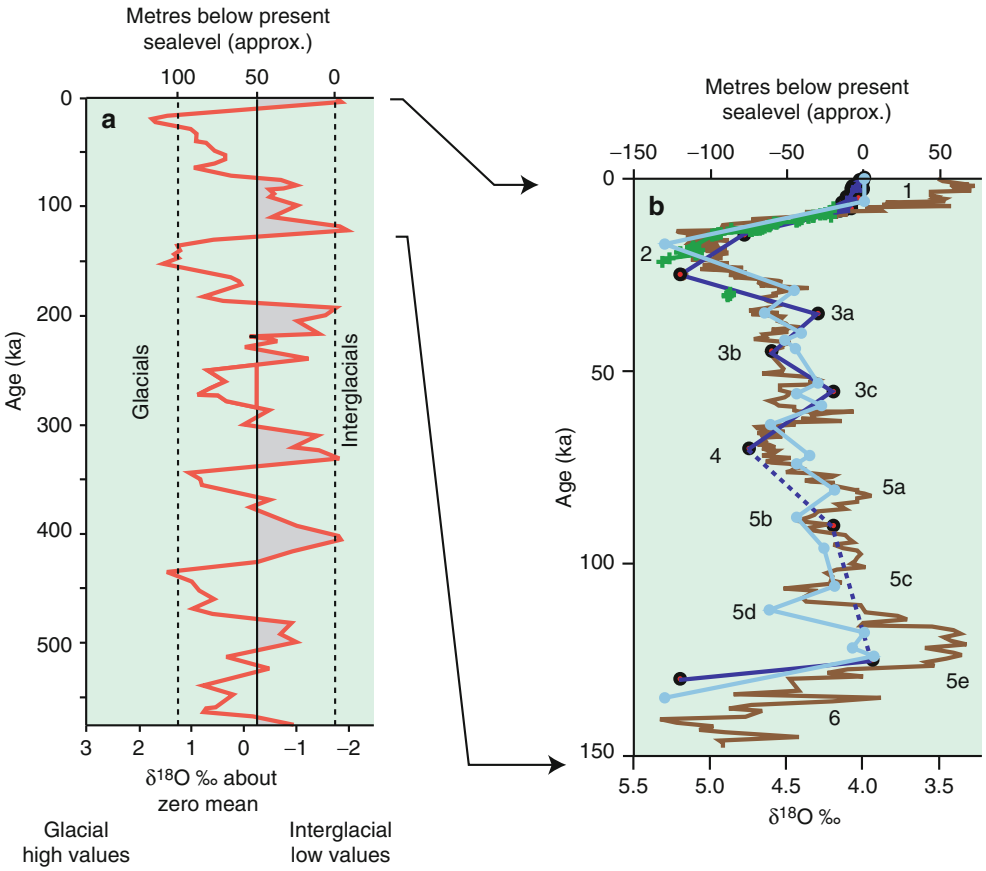

Fig. 5.1 Sea level change through the Late Quaternary. (**a**) Oxygen isotope curve for high latitude seawater for the past 400,000 years based on benthic forams in deep marine sediment cores in the Southern Ocean. Isotope scale is corrected to a zero mean (after Williams et al. 1993). Scale to mean sea level. (**b**) Late Pleistocene sea level (last 150,000 years, from continental margins and $\delta^{18}O$ (eastern Pacific piston core V19-30; Shackleton et al. 1983) record. The mid-Atlantic US margin, *solid blue-edged circles*; Huon Peninsula, Papua New Guinea, *light blue curves and circles*; Barbados, *green*), all show excellent agreement except for the Holocene Chron 1 and Marine Isotope Chron 5e where the prediction of sea level from scaling $\delta^{18}O$ is too high. *ka* thousands of years ago (After Miller et al. 2011; Isotope curve is relative to SMOW)

The 2.5 Ma climatic period known as the Quaternary[1] is the culmination of a slow and uneven climatic progression toward cooler conditions that typified much of the latter part of the Tertiary and a transition from the Cretaceous greenhouse to icehouse earth of today. At the start of the Tertiary, Antarctica was ice-free. Oxygen isotope palaeotemperatures suggest that the nearby southern oceans were quite warm, perhaps 18 °C at the surface, atmospheric CO_2 levels were well above those of today and forests were flourishing even at very high latitudes (Fig. 5.2; Frakes et al. 1992; Williams et al. 1993, p. 21; Zachos et al. 2001; Miller et al. 2011).

The penultimate cooling of the world's oceans, as interpreted from $\delta^{18}O$ data, started during the early Eocene climatic optimum (≈50–52 Ma) when the measured $\delta^{18}O$ reached a minimum for the Cenozoic with equivalent deep ocean temperatures of +12 °C. The Early Eocene (around 55–50 million years ago) is thought to be the warmest climate phase of the last 100 million years and this warmth is usually thought to be caused by unusually high atmospheric CO_2 conditions, possibly four times current levels and a time when nahcolite was a commonplace sodium carbonate evaporite (Huddart and Stott 2010). Melting of seafloor methane hydrates may also played a role in the development of the Eocene climatic maxima.

From ≈50 Ma until the early Oligocene the world's ocean seems to have steadily cooled. The reasons for this cooling and the onset of the current icehouse mode are a topic of ongoing debate. All agree the underlying cause is plate tectonics. Interpretations as to mechanism are split between proponents supporting changing oceanic circulation, driven by a widening Southern Ocean and a closing Tethys as the main driving mechanism, versus those arguing that falling CO_2 levels was the major driver driven[2] by the rising

[1]Prior to 2009 the proposed base of the Pleistocene (Quaternary was at 1.805 Mya, long after the start of the major glaciations of the northern hemisphere. The ICS (International Commission on Stratigraphy) then proposed to abolish use of the name Quaternary altogether, which appeared unacceptable to the International Union for Quaternary Research (INQUA). In 2009, it was decided to make the Quaternary the youngest period of the Cenozoic Era with its base at 2.588 Mya and including the Gelasian stage, which was formerly considered part of the Neogene Period and Pliocene Epoch.

[2]Major climatic cycles are possibly related to plate tectonics; every time the continents are pulled apart huge quantities of volcanic water, carbon dioxide and methane are released into the atmosphere and greenhouse climates prevail on Earth. On the other hand, when continents come together and mountain ranges are created, the mountains are eroded, new soils form and remove CO_2 from the atmosphere, these soils are also eroded and the CO_2 becomes locked in ocean floor sediments. So when atmospheric CO_2 is low, glaciation occurs (as in the Late Ordovician about 440 mya and in the Permo-Carboniferous at about 310–270 mya.)

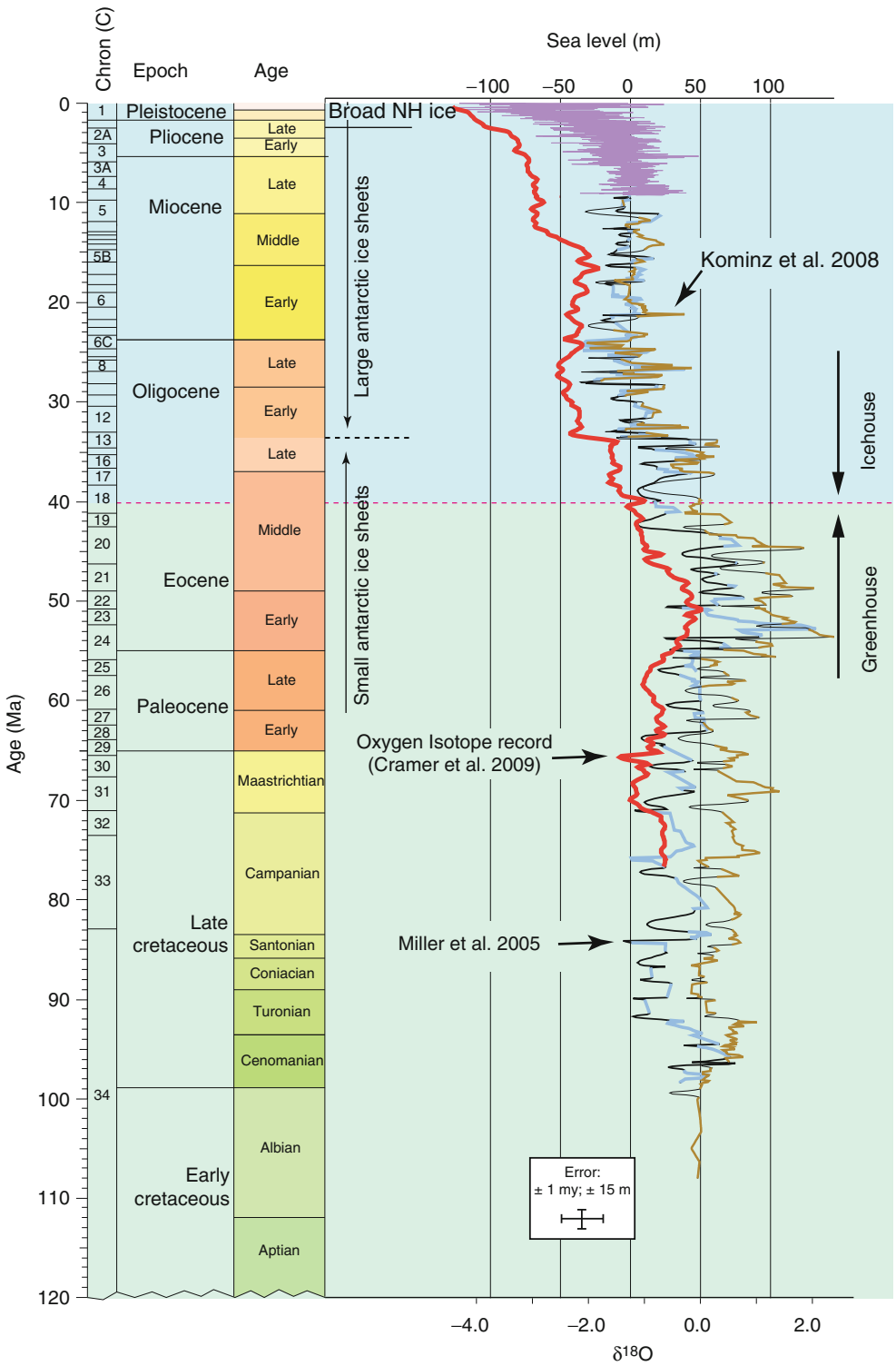

Fig. 5.2 Sea level estimates derived from New Jersey that provide a record of global sea level for the past 100 million years (After Miller et al. 2011; Kominz et al. 2008). The figure also shows the oxygen isotopic world synthesis of Cramer et al. (2009). *NH ice* Northern Hemisphere ice sheets, *Ma* millions of years ago

Himalayas and burial of significant quantities of terrestrial biomass. The post-Cretaceous lessening of oceanic ridge activity may be another contributing factor to gradual Cenozoic cooling.

Around 50 Ma Australia began to drift north, opening the Southern Ocean Seaway and so establishing the beginnings of the Antarctic Circumpolar Current (ACC). From that time the ACC completely encircled the Antarctic continent. It acted as a barrier that prevented warm currents of the lower latitudes ever reaching the Antarctic coast and reduced the transport of "sensible" heat to the higher latitudes, so contributing to the growing polar cold. The tropics were little

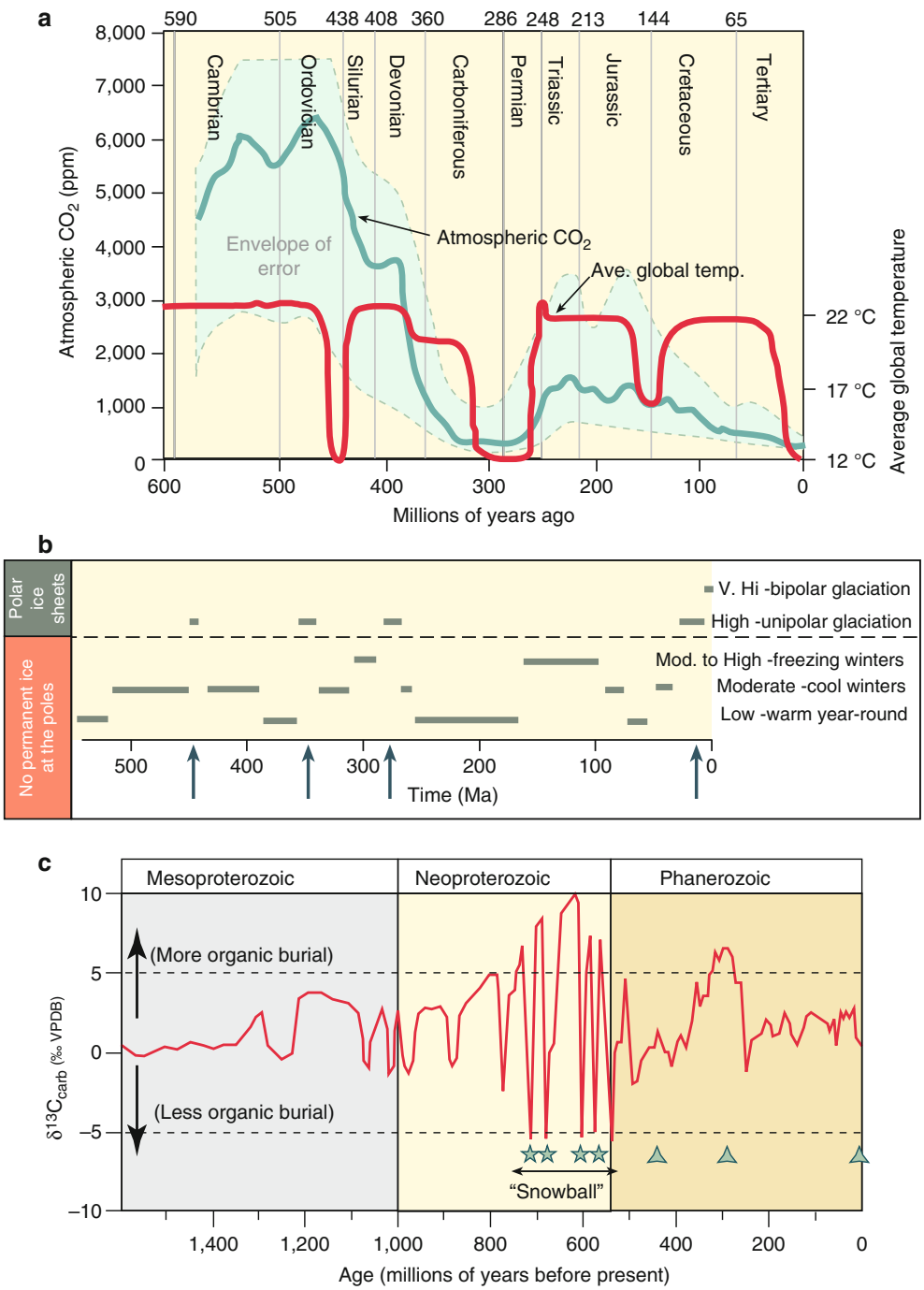

Fig. 5.3 Climate change across geological time. (**a**) Global temperature and atmospheric CO_2 change over time (After Berner 1999). (**b**) Pole to Equator climatic gradient through time, arrows indicate episodes of polar ice (Replotted from data in Boucot and Gray 2001) (**c**) Secular variation in Carbon-13 content of shallow marine carbonates over the last 1,600 million years – see also Fig. 2.33 (After Kah et al. 2001)

effected and so the equator-pole temperature gradient began to increase, invigorating the intensity of worldscale atmospheric circulation.

Throughout the Paleocene and the Eocene it was still possible for the major equatorial ocean currents to encircle the globe, passages were still open between the Americas, between India and Europe, and between Australia and Indo-China. Worldwide climate was still generally warm. A powerful western equatorial drift passed through the open remnants of the Tethyan Ocean and allowed ongoing transfer of tropical heat to the polar regions. Closure of the Tethys, as India approached the Eurasian continent, ended circum-equatorial circulation and forced circulation south of Africa into the temperate zone. This early Eocene event is the first of four major steps that punctuate the longterm history of Cenozoic cooling (McGowran et al. 1992).

But even when the Tethyan connection closed, the initial effect on Antarctica's cool, but not frigid, climate was

relatively minor. As the Eocene progressed, the Southern Ocean continued to widen but the ACC circulation did not develop to its present intensity because of shallow barriers or seafloor baffles between Australia and Antarctica (East Tasman Rise) and in the region of the Drake Passage between South America and Antarctica. Even so, high latitude cooling continued to increase, driven forward by the ongoing widening of the Southern Ocean.

At the end of the Eocene, around 33–34 Ma, there was a major cooling episode (Fig. 5.2; Lawver and Gahagan 2003). High latitude deep water temperatures in the Southern Ocean dropped 4–5 °C, probably indicating the development of freezing conditions at sealevel around Antarctica and the first formation of significant Southern Hemisphere sea ice. Land temperatures over high latitudes in both hemispheres probably dropped by 10 °C. With the opening of the Drake Passage around 32 Ma to water depths greater than 2,000 m, South America completely parted from Antarctica. This enhanced the intensity of the ACC, so producing further cooling and formation of greater volumes of ice on the Antarctic land mass (Lawver and Gahagan 2003). The very rapid cooling of ocean temperatures at the end of the Eocene probably reflects a positive feedback between growing Antarctic ice and an increase in the world's albedo (increased reflection of sunlight).

The continuing widening of the Southern Ocean and the complete floundering of Drake Passage around 25 Ma allowed the ACC to begin to develop to its full intensity, including the set up of cold bottom water circulation, which effectively cut off Antarctica from any warming equatorial influences. By the Miocene, the ACC had attained levels of flow volume comparable to those of the Quaternary (Rack 1993).

Widespread thick ice sheets covered Antarctica by the Middle Miocene and ice sheets moved out onto the continental shelf by the Late Miocene, as indicated by ice-rafted continental debris in deep oceanic sediments around much of Antarctica at that time (Lawver and Gahagan 2003). It heralded the arrival of permanent thick glacial ice at sealevel, a circum-Antarctic condition that persists today. Significant cooling is seen in the oceanic paleotemperature curve at this time. It is still not well understood why it took until the Mid-Miocene for the Antarctic ice to reach extents similar to those of today, long after the development of the ACC in the early Miocene. But the associated effects on equatorial-pole temperature gradients are clear. The resulting strengthened winds intensified Mid-Miocene ocean water circulation, which in turn was associated with increased upwelling and biological activity in many of the world's oceans.

A further global cooling took place in the Late Miocene when world sealevel dropped a further 40–50 m (Kennet 1982). This regression, in association with local tectonic activity, contributed to the isolation of the Mediterranean from the rest of the world's oceans. It perhaps helped deposit huge thicknesses of salt in giant shallow lakes across the lower parts of the former Mediterranean seafloor in the MSC. But this widely accepted correlation of an icesheet-induced major sealevel fall and widespread evaporite deposition in the Mediterranean was questioned by Hodell et al. (2001) who defined a Miocene glacial period that lasted from ≈6.26 to 5.50 Ma. It consisted of 18 glacial-to – interglacial oscillations that were controlled by the 41-kyr cycle of obliquity. Although the intensification of polar glaciation at 6.26 Ma may have contributed to the restriction of the Mediterranean, it preceded the depositional onset of the lower Messinian evaporite unit at 5.96 Ma by some 300 kyr. It seems that the initiation of evaporite accumulation in the Mediterranean evaporite basin, the world's last "saline giant," was largely tectonic and not glacio-eustatic.

However, Pérez-Asensio et al. (2013) argue that although ongoing tectonic uplift had reduced the depth of the Rifian Corridors considerably in the Late Miocene it was not sufficient to account for the complete hydrographic of the corridors. They note that at 5.97 Ma, a global cooling event occurred with an associated glacioeustatic sea-level drop, which they estimated to be ≈60 m (Fig. 5.48). This they infer was sufficient to restrict the uplifting Rifian Corridors and to trigger the onset of hydrographic isolation that created the Messinian.

Whatever the ultimate cause of the Messinian isolation, the volume of oceanic salt deposited in the Mediterranean during the salinity crisis is 40 times that which would be deposited if the present Mediterranean evaporated to complete dryness, illustrating that there was a phreatic inflow of subsurface seawater brines into the drawndown Mediterranean depression. Removal of this volume of salt from the world's oceans lowered the salinity of the open ocean water by 6 %. As less saline seawater freezes at a higher temperature, this in turn fed back into global climate by allowing yet more sea ice to develop in higher latitudes, so further reinforcing high latitude cooling.

After a slight warming in the early Pliocene, conditions cooled still further. As North and South America united across the Panama Isthmus, late Pliocene (around 3 Ma) climatic conditions in the Northern Hemisphere had cooled to where ice-rafted debris was being deposited in deep water sediments of the Northern Atlantic. By 2.4 Ma, soon after the beginning of the Quaternary, permanent moderate-sized ice sheets characterised the high latitude lands of the Northern Hemisphere. This marked the beginning of a climatic phase characterised by the repeated waxing and waning of polar ice sheets in the high latitudes of both the Southern and Northern Hemispheres, further enhancing high amplitude and high frequency changes in sealevel and further intensifying the alternation of warmer (interglacial) and cooler (glacial) climatic episodes.

By the Matuyama magnetic chron (0.78–1.77 Ma) the warm to cool climatic alternations followed a periodicity of 41 ka (Williams et al. 1993). This is equivalent to the repeating cyclicity in the obliquity of the earth's axis in terms of the plane of its ecliptic (21.8–24.4°). From 0.8 Ma the amplitude of climatic fluctuations recorded in marine sediments seems to increase, reflected in the increased sizes of the cold phase ice sheets. The periodicity of climatic fluctuations in this time also appears to increase to a cycling time of 100 ka. This correlates to the eccentricity of the earth's orbit around the sun as it varies from nearly circular to somewhat elliptical. This 100 ka periodicity, with sealevel amplitudes of more than 100 m, is especially dominant in the last 400 ka of world history, but superimposed on this are the 41 ka cycles and 23 ka precession cycles of the earth's equinoxes (Fig. 5.1; Miller et al. 2011).

Rapid climatic change and high amplitude high-frequency glacio-eustatically-driven changes in sealevel are the hallmarks of the Quaternary, and probably most of late Neogene. Relative to the previous 200 million years of climatic history, the climatic/eustatic fluctuations of the Quaternary and the Neogene were unprecedented in terms of their speed and amplitude. For example, the mean annual temperature difference between the last glacial maximum (18 ± 3 ka) and the early Holocene climatic optimum (9 ± 3 ka) is around 10 °C in many temperate land areas of the world (Williams et al. 1993; p. 223). This is roughly equivalent to the inferred longterm drop in temperatures between the early Eocene and early Pliocene in these same regions. The surface of the Southern Ocean cooled by 10–15 °C over this 40 million year period. Temperature drops of a similar magnitude occurred in eastern Australia over the 100,000 year time span that separates the last interglacial from the last glacial maximum in this region. Similar high frequency changes typify the Quaternary in many other parts of the world.

Prior to our present "icehouse" climate mode of the last 30 million years, the last time when there were widespread polar ice sheets, high amplitude-high frequency sealevel fluctuations, and a similar "ice house" climate was the Permo-Carboniferous some 270–315 Ma (Fig. 5.3a, b). Prior to this we must go as far back as the Late Ordovician and then to the Neoproterozoic to see evidence of other worldwide "icehouse" conditions (Fig. 5.3). The late Ordovician glaciation (≈440 Ma) was unusual compared to the icehouse episodes that preceded and postdated it. Major glaciation was apparently confined to South America and Northwest Africa and nowhere else. Timewise, it is also the most contentious of the Phanerozoic icehouses. Brenchley et al. (1994) argue it was restricted to the Hirnantian and was some 0.5–1 m.y. long, rather than the 35 m.y. of earlier estimates. In terms of paleogeography, it probably defines the southern polar position of a uniting Gondwana. It was an Ordovician Antarctica equivalent, not associated with the breakdown of worldscale ocean circulation and it probably had no more than local climatic influence in a overall warming greenhouse world (Drury 1999).

In fact, in the last 600 million years the late Carboniferous to the early Permian (315–270 Ma) was the only time when atmospheric CO_2 and average global temperature were both as low as they are today. Even so, today's bipolar glaciation appears to be a unique icehouse scenario compared to the rest of the Phanerozoic (Fig. 5.3b). The obvious conclusion is that the last 20–30 Ma, and certainly the last 2.5 Ma of the Quaternary experienced climate and eustatic styles that are simply not representative of non-icehouse conditions covering the majority of Phanerozoic time.

Prior to the Phanerozoic, preceding Proterozoic icehouse regimes consist of at least three and maybe up to five glacial pulses between 900 and 550 Ma (Fig. 5.3c), the latter part of this interlude encompasses the notion of a completely ice-covered "snowball earth" (Fig. 2.50; Hoffman 2011; Hoffman et al. 1998; Eriksson et al. 2013). If real, this was a cryogenic system far more intense than the bipolar system of today, with its own unique climatic and sedimentologic implications. Prior to this Neoproterozoic icehouse, there is evidence of earlier worldwide glacial (icehouse) conditions at 2,200 Ma and possibly at 2,500 Ma. If snowball conditions did encompass the Neoproterozoic earth with an ice envelope, and ultimately lead to the Phanerozoic explosion of life, then the only possible "evaporite" salts that could have accumulated in snowball episodes would have been hydrothermal anhydrite in the vicinity of volcanic vents and spreading ridges, or cryogenic hydrohalite precipitates and volumetrically minor slushes of mirabilite and hydrohalite created during the formation of widespread sea ice. Hydrohalite ($NaCl{\cdot}2H_2O$) is the stable form of halite below temperatures of 0.1 °C, it is anhydrous at higher temperatures; hydrohalite has four times the volume of mirabilite in modern sea ice (Richardson 1976). The possibility of preservation of either mineral, other than as isolated pseudomorphs, along with ikaite in glacial meltwater deposits is zero.

The rapid melting of the global icesheets of Snowball Earth and the transition to widespread temperatures as hot as 50 °C during the formation of successive cap dolomites, along with the likely encroachment of shallow epeiric seaways via the return of continental glacial waters to the sea, would have encouraged the formation of widespread platform evaporites in association with the cap carbonates. Widespread megapolygonal tepees and/or salt karst does outcrop in the appropriate stratigraphic position in the Neoproterozoic dolomite capstones in Oman (pers. obs.) and atop the Elatina Shale in the Flinders Ranges of Australia. Defining the worldwide timing of such Neoproterozoic

evaporites and their dissolution residues may be an interesting test of the validity the "freeze and fry" climate conjectured for snowball earth.

Some megapolygons beneath cementstone layers have been interpreted in a very non-uniformitarian fashion by Snowball Earth proponents. The structures are tepee-like, but with unbroken crests and not thought to be true tepees (definition of Kendall and Warren 1987). One hypothesis is that they are mechanically-formed chevron-like wave structures indicative of wave periods of 21–30 s and formed by consistent flow velocities of up to 20 m/s in megawinds blowing across oceans with unlimited fetch (Allen and Hoffman 2005). An alternative hypothesis, by Lamb et al. 2012, agrees that the megapolygons are giant wave ripples but not indicative of mega-winds. Rather they are restricted to episodes of cap carbonate and are a consequence of the unusual mode of carbonate precipitation tied to a global carbon cycle and climate perturbation unprecedented in Earth history (Fig. 2.49).

Clearly, our present icehouse climatic regime does not encompass all climatic and sealevel regimes that have occurred across geological time. The present style of icehouse climate dominates the amplitude and frequency of sealevel changes for the past 20–30 million years. Greenhouse climate and its associated eustasy, which typifies much of earth history, is not tied to icesheet hydrologies and volume changes. Thus we must not assume constancy in glacioeustasy as the dominant control on Phanerozoic or Precambrian sedimentation, especially in biochemical and evaporite sediments. As Charles Dickens once wrote on contemporary time, "It was the best of times, it was the worst of times." In terms of marine evaporite deposition, a lack of "strict uniformitarianism" leads to a paucity of Quaternary analogs for most large marine-fed evaporite deposits.

Varying Extent of Ancient Evaporites

Nowhere in Quaternary depositional systems is there Holocene proof of a desiccated ocean basin, yet in the Late Miocene (Messinian) salinity crisis a series of subsealevel saline depressions on the Mediterranean floor filled the lowest parts of the Mediterranean with 2-km-thick sequences of halite and gypsum in less than 300,000 years (e.g. Balearic Basin; Fig. 5.4). The various Messinian evaporite pods were laid down on the floors of a chain of shallow saline seas that were more than a 1,000 km long, more than 2,000 km across, with brine surfaces more than 2,000 m below ambient sealevel. They formed in the lowermost parts of a hyperarid to semiarid seafloor desert that extended over much of the current extent of the Mediterranean, stretching from Spain to Israel and from northern Italy to Libya (Rouchy and Caruso 2006; Cita 1983; Hsu et al. 1973).

Similarly, there is no Holocene proof of evaporitic brine-reflux dolomitisation and the associated salt seals, simply because there is no Holocene example of a whole carbonate platform being covered by an evaporite deposit. Yet in most ancient evaporite basins, reflux dolomitisation was a widespread and pervasive mechanism that yielded substantial intercrystalline porosity in platform carbonates beneath laterally continuous beds of platform evaporite salts (Chap. 10).

Many thick ancient salt accumulations are underlain or overlain, and sometimes intercalated, with thick widespread marine carbonate beds. A major dilemma facing geologists interpreting such strata is the lack of Quaternary marine counterparts with comparable depositional scale and unit thickness (Figs. 5.4 and 5.5). All thick Quaternary salt deposits are medium-scale accumulations of continental lacustrine evaporites in tectonically active settings (Table 5.2;

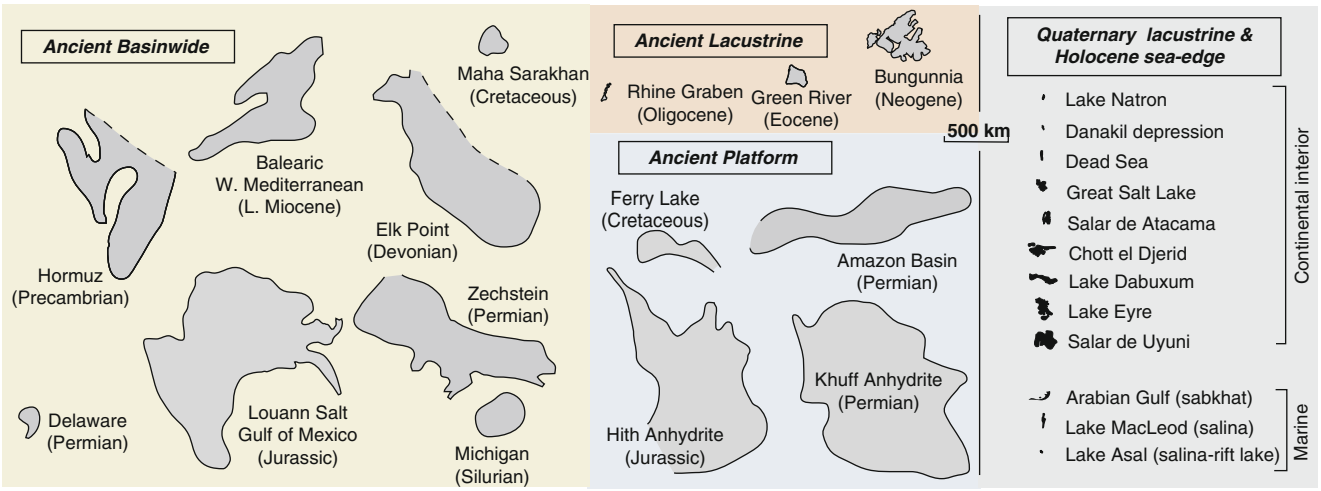

Fig. 5.4 Area contrasts of Quaternary and ancient evaporites

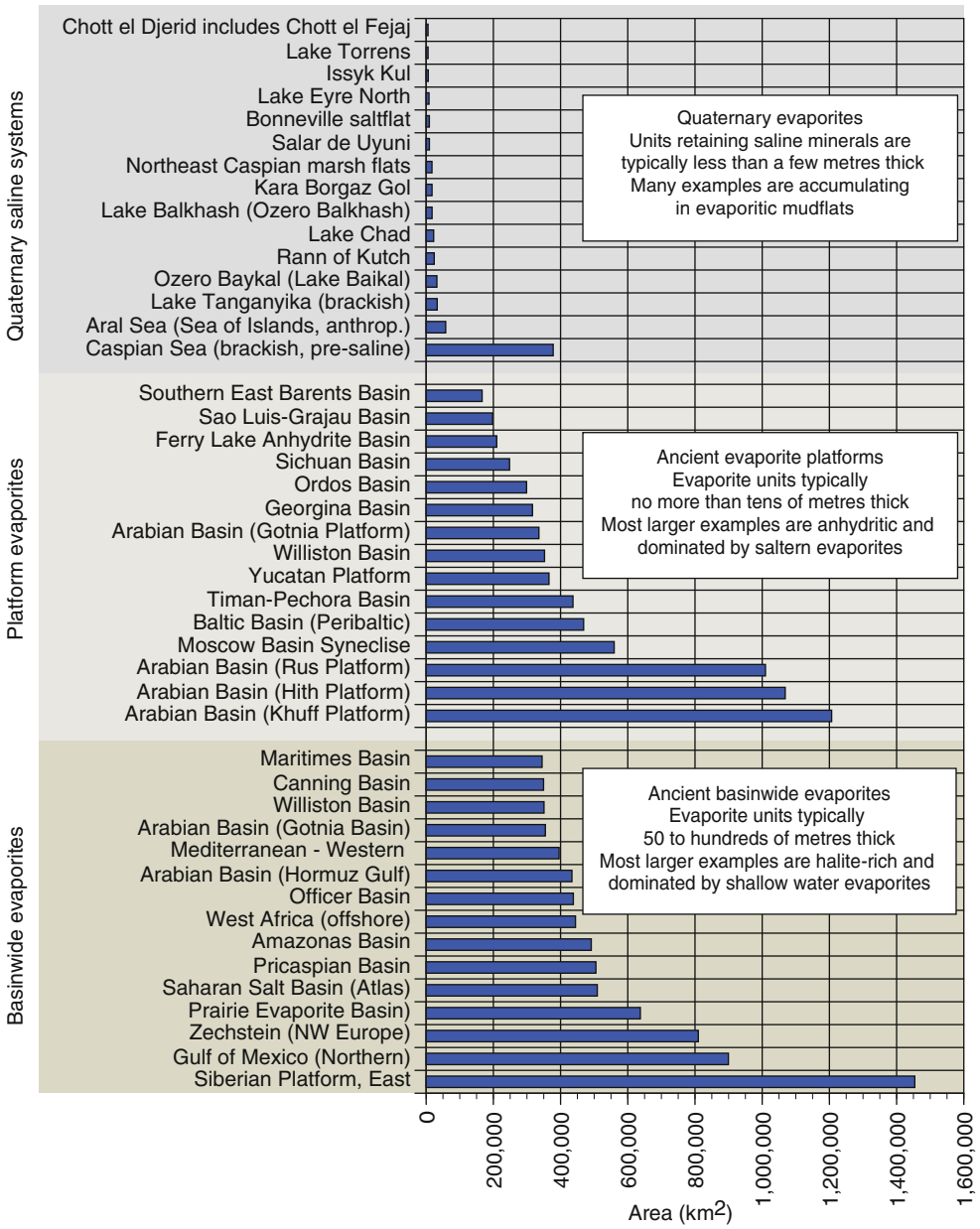

Fig. 5.5 Plots of the areas of each of the 15 largest examples of Quaternary lacustrine, Platform evaporites and basinwide evaporites (Extracted from centroid areas listed in SaltWork version 1.6)

Chaps. 3 and 4). The ancient evaporite record entrains much larger volumes of salts precipitated in platform or basinwide settings tied to a seawater feed (marine-fed evaporites), as well as ancient continental lacustrine deposits (continental evaporites) with similar thicknesses and extents to the Quaternary examples discussed in Chaps. 3 and 4 (Fig. 5.3). Larger examples of modern evaporites are dominantly supra-sealevel nonmarine lacustrine deposits, while ancient evaporites are subsealevel marine-fed systems. Yet, the first-order latitudinal distribution of modern and ancient evaporite basins is similar. That is, the dominant world-scale control on evaporite distribution is climatic and largely the result of the presence of Hadley cells (Figs. 2.1 and 5.6; Edwards et al. 2006).

As we saw in Chap. 2, Hadley cells are a planet-scale atmospheric circulatory response to the varying intensity of solar irradiation from the equator to the poles. Unfortunately, the climate of the Holocene and the Pleistocene (Quaternary) is not well suited to act a baseline for the extent and distribution of arid Phanerozoic climates. The last 8,000–10,000 years is an interglacial and, based on world $\delta^{18}O$ curves in deepsea sediments, is a state typical of some 10 % of the icehouse climate of the past few million years (Fig. 5.1; Hay et al. 1997). The current interglacial, and older counterparts over the past 780 ka, are highstands and times of relative sea-level stability, some tens thousand years long, occurring after rapid 100 m-scale rises from the lowstand of the preceding glacial maximum. The last glacial maxima

Table 5.2 Some representative examples of Quaternary lacustrine deposits, list is sorted by size of the basins and should be compared to Fig. 5.5

	Area (km²)	Locality	Lat. – age	Evaporite style	References
Continental					
Salar de Uyuni	10,600	Bolivia	20.2 Quaternary	Saline-pan to mudflat	Risacher and Fritz (1991b, 2000)
Lake Eyre	9,300	Australia	−28.4 Quaternary	Saline-pan to mudflat	Alley (1998), Magee et al. (1995)
Great Salt Lake	6,000	USA	41.2 Quaternary	Saline-pan to mudflat	Eardley (1938), Spencer et al. (1985a, b)
Qaidam Basin	6,000	China	36.7 Quaternary	Saline-pan to mudflat	Schubel and Lowenstein (1997)
Lake Torrens	5,900	Australia	−31.1 Quaternary	Saline-pan to mudflat	Schmid (1988a, b), Williams et al. (1998)
Lake Urmia	5,800	Iran	37.6 Quaternary	Brine lake	Kelts and Shahrabi (1986)
Chott Djerid	5,000	Tunisia	33.7 Quaternary	Saline-pan to mudflat	Bryant et al. (1994a, b), Gueddari (1984)
Lake Gairdner	4,800	Australia	−31.7 Quaternary	Saline-pan to mudflat	Herdendorf (1984), Johns (1968)
Lake Chad (saline)	4,000	Chad	13.4 Quaternary	Saline-pan to mudflat	Eugster and Maglione (1979), Maglione (1980)
Van Golu, Turkey	3,700	Turkey	38.7 Quaternary	Brine lake	Herdendorf (1984), Kipfer et al. (1994)
Salar de Atacama	3,100	Chile	−23.4 Quaternary	Saline-pan to mudflat	Alonso and Risacher (1996)
Lop Nor	3,100	China	40.5 Quaternary	Saline-pan to mudflat	Herdendorf (1984)
Lake Frome	2,700	Australia	−30.1 Quaternary	Saline-pan to mudflat	Nanson et al. (1998)
Salar de Coipasa	2,200	Bolivia	−19.4 Quaternary	Saline-pan to mudflat	Risacher and Fritz (1991b)
Tuz Golu	1,600	Turkey	38.9 Quaternary	Saline-pan to mudflat	Braithwaite and Zedef (1994, 1996)
Charhan marsh	1,600	China	36.7 Quaternary	Saline-pan to mudflat	Chen and Bowler (1986), Yang et al. (1995)
Chott el Hodna	1,200	Algeria	35.4 Quaternary	Saline-pan to mudflat	Guiraud (1965)
Lake Natron	1,200	Tanzania	−2.3 Quaternary	Saline-pan to mudflat	Gueddari (1984), Manega and Bieda (1987)
Dead Sea	1,000	Israel	31.4 Quaternary	Brine lake	Ben-Avraham et al. (1999), Talbot et al. (1996)
Lake Amadeus	880	Australia	−24.7 Quaternary	Saline-pan to mudflat	Herdendorf (1984), Jacobson (1988)
Kobar Sink, Danakil	400	Ethiopia	14.1 Quaternary	Saline-pan to mudflat	Holwerda and Hutchison (1968)
Lake Magadi	105	Kenya	−1.9 Quaternary	Saline-pan to mudflat	Eugster (1986)
Marine-fed					
Lake Macleod	2,000	Australia	−24.1 Holocene	Coastal salina	Logan (1987)
Arabian sabkhat	500	Emirates	24.3 Holocene	Coastal sabkha	Evans et al. (1969), Warren (1991)
Lake Asal	52	Djibouti	11.7 Holocene	Marine-edge rift lake	Fontes et al. (1980)

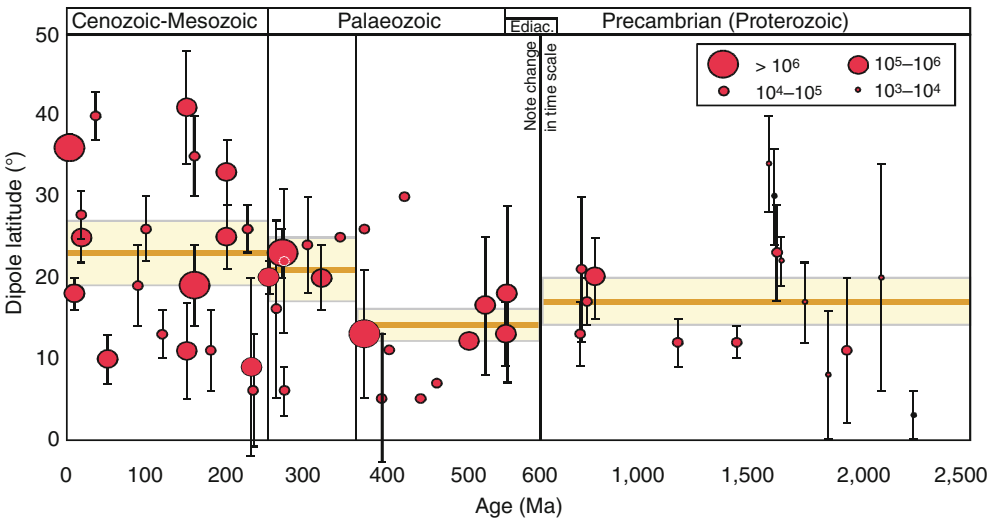

Fig. 5.6 Evaporite palaeomagnetic latitudes through time, individual basin plots are schematically scaled to evaporite volume (*circle sizes* are scaled in km³ as in the *inset*) and shown with 95 % uncertainty limits in palaeolatitude. Volume-weighted means (*solid brown bars*) and 95 % error envelopes (*shaded light yellow*) are broken down into four age intervals. Note the change in time scale at 600 Ma (After Evans 2006)

occurred some 18,000 years ago. The last few million years of intense icehouse-mode climate, is a period of glacial-interglacial alternations when physical geologic processes operate at unusual rates compared to the bulk of the Phanerozoic and when much of the earth's geochemical system is not in a steady state.

Times of expanded ice sheets, with their more intense ice sheet-induced atmospheric circulation cells, are probably the least representative states for the world's Phanerozoic climate. Interglacial periods within icehouse mode, like the Holocene, are perhaps a little closer to the "average" Phanerozoic climate. But today's climate is still a long way

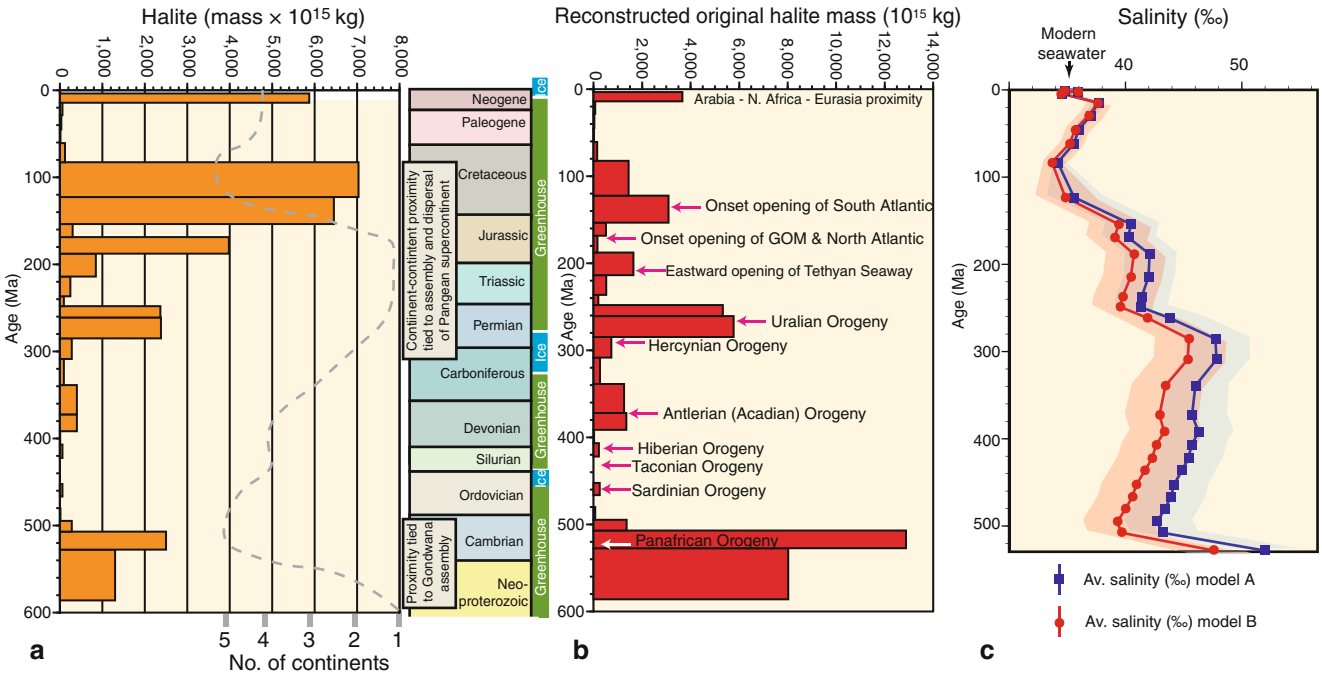

Fig. 5.7 Phanerozoic evaporites in Deep Time (After Warren 2010). (**a**) Mass of Phanerozoic halite currently residing in basin (After Hay et al. 2006; Number of continents curve from Condie 2004). (**b**) Reconstructed mass of recycled Phanerozoic halite lost by combination of erosion and dissolution (After Hay et al. 2006). Time of halite precipitation as influenced by accretion and disintegration (dispersal) of Pangean supercontinent as well as other orogenic and tectonic events is also shown (greenhouse after Fischer 1981; tectonics after Haq and Van Eysinga 1998; Haq and Al-Qahtani 2005). (**c**) Oceanic salinity changes for the last 500 my (After Hay et al. 2006)

from a climate more representative of the bulk of Phanerozoic time, when the polar regions were free of permanent ice and world climate and the eustatic frequencies and amplitudes were in "greenhouse" not "icehouse" mode (Fig. 5.7).

In greenhouse times there are no widespread continental or polar ice sheets and the planet's meridional temperature gradient is much less steep than it is at present (Table 5.1). For the past few million years, since the initiation of permanently grounded Antarctic ice sheets in the Miocene (≈12 Ma) and possibly as long ago as the Eocene (≈33 Ma), the distribution and effects of broad-scale atmospheric circulatory belts (including the Hadley cells) have been modified by the waxing and waning of polar ice. During glacial periods the expanded circum-polar ice sheets act as frigid plateaus, forcing a stronger meridional temperature gradient, so altering significant portions of the world's atmospheric circulation, as well as creating their own ice-cap associated pressure systems.

Whenever ice-caps expand, the Hadley-related circulation belts are pushed and compressed toward the equator; this occurred numerous times during glacial maxima of the current icehouse climate mode. These ice-sheet forced climatic oscillations have a marked effect on sediment styles in Quaternary deserts. Many halite-entraining continental playas and pans have sedimentary records extending back a few hundred thousand years and entrain alternating water-full versus drier stages (e.g. Baker et al. 2001a; Hesse et al. 2004; Yan et al. 1998). In contrast, the world's marine-fed subaqueous[3] deposits are Holocene, with little or no preservation of Pleistocene salts. There is a similar lack of Pleistocene salts preserved in the type area for modern marine-fed evaporitic mudflats, or sabkhas, in the Arabian Gulf (Warren and Kendall 1985; Warren 1991). The largest such Holocene marine deposits fill coastal salinas with halite or gypsum beds up to 10 m thick along the semi-arid western and southern coasts of Australia. These are marine-seepage sumps that can be up to tens of kilometres wide (areas up to 2,500 km^2) with extents and thicknesses much less than contemporary continental evaporite deposits (Fig. 5.4). Even the largest Holocene marine coastal deposits pale in size and volume when compared to ancient marine-fed accumulations (Fig. 5.5), although they are excellent natural environments to study the sedimentary textures of precipitation in relation to brine stability and permanence, and to document early alteration mechanisms.

[3]The term "marine-fed" refers to the dominant source of the inflowing groundwaters at the time the evaporites are deposited, not to the presence of a hydrographic connection to the ocean, which these deposits typically lack.

The largest accumulations of Phanerozoic marine-fed salts are basinwide deposits, which were laid down in hydrographically-isolated subsealevel depressions, created by divergent, convergent and intracratonic (intraplate) tectonics. Their sediment volumes are not evenly distributed across the Phanerozoic and times of widespread salt deposition correspond to falls of salinity in the world's oceans (Fig. 5.7; Hay et al. 2006). That is, the greatest falls in oceanic salinity are related to major extractions of NaCl into young oceans (extensional continent-continent proximity) or foreland ocean basins (compressional continent-continent proximity; Warren 2010).

Phanerozoic seas were at their freshest in the Late Cretaceous some 80 Ma, not today. This is because a substantial part of the Mesozoic salt mass, which was deposited in the megahalites of the circum-Atlantic and circum – Tethyan basins, has since been recycled back into today's ocean via a combination of dissolution and halokinesis. Periods characterised by marked decreases in salinity (Fig. 5.7b) are defined by times of mega-evaporite precipitation, while periods of somewhat more gradual increases in salinity define times when portions of this salt were recycled back into the oceans (compare Fig. 5.7b, c).

The last major extractions of salt from the ocean occurred during the late Miocene in the various Mediterranean Messinian basins created by the collision of Eurasia with North Africa. This occurred shortly after the large-scale extraction of water from the ocean to form the ice cap of Antarctica and the deposition of the Middle Miocene Red Sea rift evaporites. Accordingly, salinities the early Miocene were between 37 and 39‰ compared to the 35‰ of today (Fig. 5.7c). The preceding Mesozoic period was a time of generally declining salinity associated with the salt extractions in the opening North Atlantic and Gulf of Mexico (Middle to Late Jurassic) and South Atlantic (Early Cretaceous).

Across the Phanerozoic, after deposition of the Hormuz/Ara salt successions at the Cambrian-Precambrian boundary, the next major salt extractions occurred during the Carboniferous – Permian and were related to the final accretion of the Pangaea supercontinent[4] (Fig. 5.7). During the intervening Palaeozoic periods there were only a few large extractions of halite from seawater, mostly in intracratonic sag settings. The Hay et al. (2006) model suggests that the Palaeozoic was a time of relatively stable, but slowly increasing, salinity ranging through the upper 40s into the lower 50s (in parts per thousand).

The somewhat elevated Palaeozoic ocean salinities, (c.f. 35‰ today) implies that arid-zone marine-fed evaporites and evaporitic mudflat carbonates perhaps formed more readily from concentrating seawater brines in the early Phanerozoic epeiric seas. That is, for much of the Palaeozoic and part of the Mesozoic, marine-fed evaporation started from a higher base, compared to the less saline oceans and narrower steeper icehouse continental shelves of today (less freeboard). This implies that halite saturation was more easily attained from Palaeozoic ocean waters, and yet the volumes of extracted marine halite were low for most of the Phanerozoic (300–500 mya) (Fig. 5.7). Perhaps conditions were less suitable for world-scale salt extractions at that time due to the more dispersed nature of the major continental plates and the associated paucity of locales of plate-scale continent-continent proximity. Most Palaeozoic megahalites accumulated in epeiric intracratonic sags (distal effects of orogeny) rather than as deposits along a cratonic periphery (see later basinwide and platform evaporite discussion).

When estimates of the volume of salt being recycled back into the oceans are added to volumes of actual salt in the various megahalite beds of the world an interesting picture emerges of actual precipitated salt volumes at various times of enhanced evaporite deposition (Fig. 5.7b; Hay et al. 2006). The greatest volumes of halite still remnant in sedimentary basins are defined by Jurassic and Cretaceous successions. Deposition was largely within the circum-Atlantic salt basins and tied to the early rift to drift transition during the opening of the Neo – Tethys and the northern and the Southern Atlantic. Yet when recycled halite estimates are added, these Mesozoic deposits are lesser volumes compared to the Permian and Neoproterozoic/Cambrian successions, with the greatest volume of salt deposited across the past 600 million years occurring in the various Neoproterozoic-early Cambrian Hormuz and Ara halite deposits of the Middle East (Fig. 5.7). In the Phanerozoic, the period from the Permian through Jurassic generated the greatest volumes of both halite and total evaporites (Fig. 5.7). This corresponds to the time of the assembly and disassembly of the Pangaean supercontinent. A supercontinent is the culmination of a mega-longterm (300–600 million year duration) tectonic pattern of continental accretion and fragmentation, whereby a supercontinent gradually assembles then rifts and drifts apart prior to reassembling (e.g. Veevers 2004). Substantial accumulations of basinwide evaporites are most likely to accumulate on the floors of isolated subsealevel depressions at times of close proximity of drifting landmasses. This occurs both during the building of the supercontinent and then during times of its early disassembly. Ongoing marine drawdown incursions into marine-fed arid-zone subsealevel basins takes place both as a supercontinent assembles (collision and foreland basins) and then as it unzips (rifts and sag basins). Intracratonic evaporite basins, the third setting of substantial ancient salts typically form in the continental interior in zones of distal crustal flexure in response to tectonic interactions at the continent margins (see later).

[4] A widely accepted definition of the term "supercontinent" is that it describes an assembly into a single landmass of all, or nearly all, the Earth's continental blocks (Bradley 2011).

Marine platform evaporites are the other major type of ancient marine-fed salt accumulation. They formed on continental margins throughout much more of Phanerozoic time than basinwide evaporites. They are characterised by bedded units of calcium sulphates (with lesser halite), typically 10–50 m thick and interbedded with marine carbonates. Stacked platform sections with this style of accumulation encompass depositional time frames of ≈1–10 my. Basinwide evaporite fills tend be thicker (>100 m), more halite prone and purer than platform evaporites and to accumulate rapidly across time frames of less than a million years. Platform evaporite occurrences are largely tied to times in earth history when climate was in greenhouse mode. Hence, the wider extents, greater depositional and diagenetic diversity and greater thicknesses of Phanerozoic marine-fed evaporites (Pre-Quaternary) reflects two sets conditions not actively influencing modern marine evaporites:

- *Warmer climates of greenhouse earth* creating wider latitudinal distributions of reefs, shoal-rimmed platforms and epeiric seaways under styles of eustatic fluctuation that were more suited to extensive evaporite deposition in the isolated backreef and lagoon.
- *Set up of the correct tectonic and climatic conditions* for the hydrographic isolation of large subsealevel tracts in a tectonic depression where marine groundwater feed was the dominant source of solutes onto the arid basin floor.

Study of ancient marine evaporite deposits underscores limitations inherent in the strict actualistic application of the Law of Uniformitarianism. Processes and textures of deposition and early diagenesis can be studied in modern settings (as detailed in Chaps. 1, 2, 3 and 4), but current climatic eustatic and tectonic interactions do not encompass all the levels of climatic and tectonic variation that have occurred across deep time.

Building Blocks of Ancient Salt Beds

Whatever an ancient evaporite basin's regional or tectonic setting, the depositional signature can be broken down into three main building blocks: (1) Mudflats (with sabkhas, salinas and saline pans), (2) Salterns and, (3) Deeper water slope/basin deposits (Table 5.3; Fig. 5.8).

Evaporitic mudflats form laterally extensive strata composed of stacked, shoaling-upward, matrix-dominated units (1–5 m thick). The mudflat package is typically widespread and readily correlatable across scales of up to hundreds of kilometres, but individual evaporite beds or layers within the package are not easily traced across the same lateral extent. Salts accumulate as a mosaic of dry and saline mudflats (sabkhas) separated by local brine-filled depressions (salinas/salt pans) in both marine-fed and continental settings. Much of

Table 5.3 Characteristics of depositional systems that define ancient evaporite deposits

	Evaporitic mudflat	Saltern	Slope and basin
Brine depth and stability	Ephemeral shallow brine sheet to subaerial	Longterm brine sheet to permanent shallow seaway	Permanent brine lake or sea deeper than 2–10 m up to hundreds of metres
Dominant evaporative/precipitation mechanism	Capillary evaporation, wind-blown thin brine sheets	Solar concentration of permanent surface brine mass, typically density stratified for at least part of its annual depositional cycle	Solar concentration with laminites in density stratified bodies, massive coarsely crystalline in unstratified brines
Textures	Displacive and replacive capillary salts, chicken wire and nodular textures, skeletal and pagoda halite, chaotic halite, haloturbation, Stokes surfaces, syndepositional micro-karst cements, eolian silt and sand ripples in evaporitic beds	Bottom nucleation, growth-aligned laminar to chevron textures crosscut by dissolution. Mechanically reworked beds with ripples, cross beds, gypsolites/halolites. Syndepositional exposure with water-table drawdown is not common, but does occur	Pelagic settling of cumulates and rafts, dense brine underflows, turbidity cur-rents in density stratified brines. Massive beds of inclusion-free coarsely crystalline bottom growths at the base of unstratified saturated brine bodies
Holocene depositional analogs	Sabkhat, salt pan, salina	Salt pan, salina	Some aspects of deepwater brine lakes (esp. Dead Sea)
Lateral extent and wireline correlation	Whole unit is laterally continuous, but it exhibits strong lateral variability in proportions and distributions of internal salt masses. Tendency to be matrix-rich and show a "spiky" signature in conventional wireline logs. Conventional wireline not calibrated to core can be confused with reflux-generated evaporite cements	Good lateral continuity of whole bed. In a marine shelf this can extend over the whole extent of underlying platform. Good lateral continuity of various internal salt horizons within a saltern unit. Tendency to be evaporite-rich with little matrix and show "blocky" signatures in conventional wireline logs, which can be similar to slope and basin	Good lateral continuity of bed. Internal salt units tend to be laterally continuous in deeper parts of basin and individual layers in laminites can extend for 50–100 km. Slope units tend to show less lateral continuity. Tendency to be matrix-poor. Conventional wireline signature similar to saltern. FMI can be distinctive

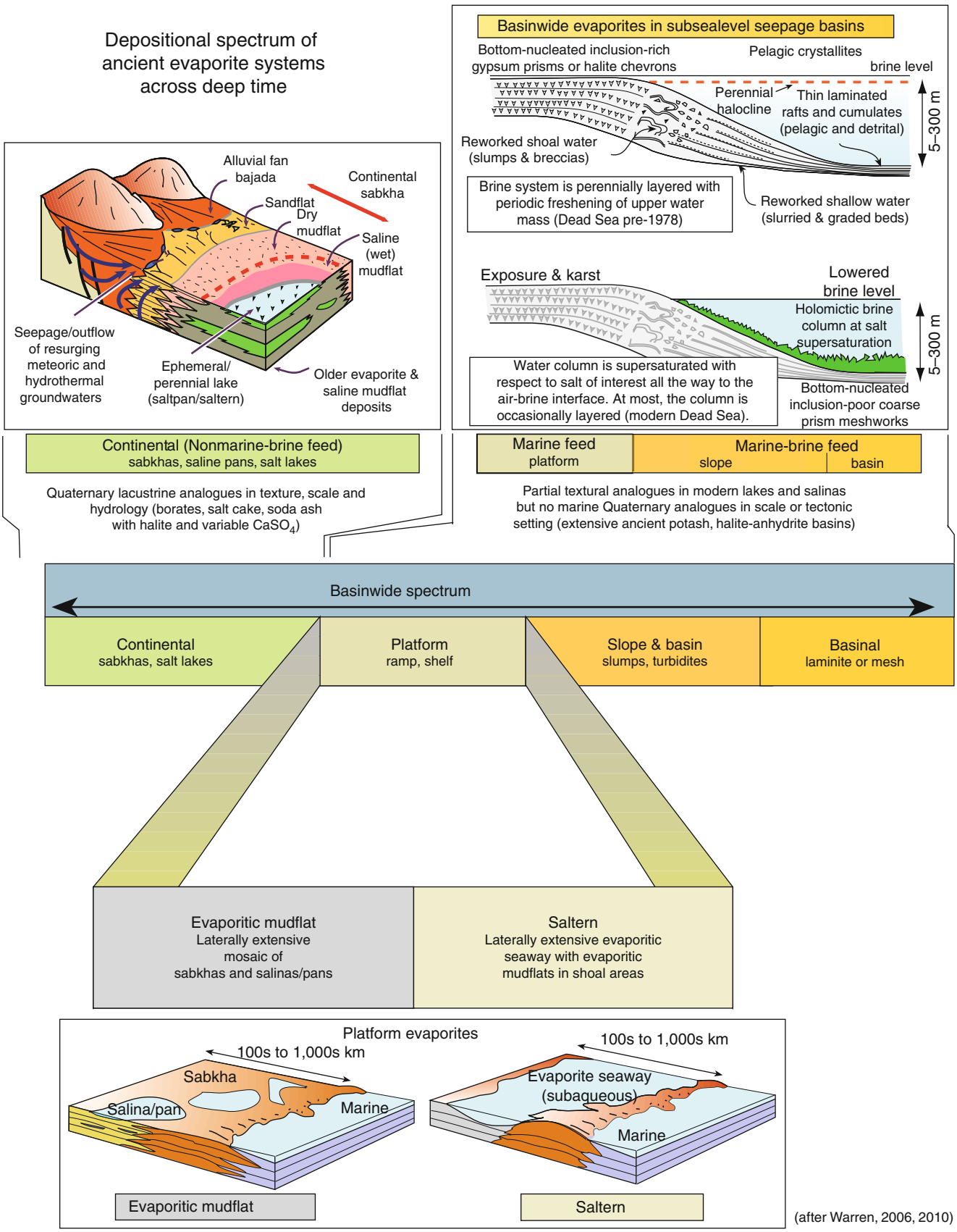

Fig. 5.8 Evaporite depositional settings in the context of time and process (After Warren 2010). Only continental lacustrine settings have same-scale ancient and Quaternary age counterparts

the matrix is deposited by storm-induced sheet floods, feeding sediments and surface waters onto the mudflat, both from the land and from the lake or seaway. Matrix on the "seaward" side tends to be carbonate mud, but typically lacks stenohaline marine fossils. On its "landward" side, beds are often interlayered with eolian or fluvial braidplain/sheetwash sediments (Fig. 5.8).

As stormwaters dry up on an evaporitic mudflat, windblown cm-thick evaporating brine sheets ooze and trickle back and forth atop the very flat mudflat surface. The vast extent of the ancient mudflat, and resulting high humidity in the overlying air, greatly slowed the rate of evaporation so that halite and gypsum were the dominant precipitates. Large parts of these ancient mudflats were sabkhat accumulating displacive and replacive capillary salts. Hence, much of an ancient evaporitic mudflat mosaic is characterised by nodular and enterolithic $CaSO_4$, pseudomorphs after discoidal gypsum, skeletal and chaotic halite.

Thin sheets of brine covered extensive tracts for weeks or months after a storm or flood, depositing thin layers and stringers of pan gypsum or halite a few centimetres thick atop the freshly deposited silts and sands. Later, once the brine sheet had dried up or was blown to another locality on the mudflat, it left be-hind a freshly deposited salt crust exposed to the vagaries of air, sun, wind, haloturbation and diagenesis. Ongoing exposure and deflation of the mudflat surface created Stokes surfaces, drove additional precipitation of intrasediment salts, exposed earlier carbonate crusts, altered gypsum to anhydrite, and meant the partial or complete dissolution of early brine sheet crusts. Throughout, the aggrading mudflat periodically captured influxes of eolian silt blown in from adjacent dry mudflats.

Somewhat longer-term ponding of brine sheets (months to years) occurred within local sumps where small shallow brine lakes (salinas and pans) formed atop the more regionally extensive mudflat. Water bodies were a few to tens of kilometres across and a few dm to metres deep (Fig. 5.8). Resulting salt crusts and subaqueous beds were purer and somewhat thicker (>1–2 m) than time-equivalent intervals of capillary salts accumulating in the subaerial mudflat surrounds. Such purer units are resolvable in the vertical perspective of a conventional wireline log, especially in an image log, but are not readily correlated from well to well due to limited lateral extents of individual pans or groundwater sumps. Overall the matrix-rich evaporite mudflat log is a distinguishable wireline signature. But, if it is not calibrated to core or to an image log, it is readily confused with units of open marine carbonate plugged by evaporite cements precipitated during brine reflux.

The term tidal-flat or peritidal evaporite is inappropriate in describing these gigantic epeiric/continental mudflats as large parts of the mudflat were not ever covered by tidal waters (only storm surges and sheet floods). Yet, Holocene marine-edge terminology is widely used by some sedimentologists in describing ancient evaporitic mudflats. They base its application on textural comparisons with the coastal sabkhas of Abu Dhabi. But as we saw in Chap. 3, nodular and displacive sabkha salts form in capillary settings ranging from continental lacustrine to coastal. Capillary salts, even in the classic sabkha, come mostly from resurging deeply-circulated groundwaters, a transport and emplacement mechanism that is independent of any possible tidal association. Plus, the huge lateral extent of ancient mudflats, typically constituting the edges of huge interior seaways or shallow brine lakes, meant there was little or no tidal exchange with open ocean waters (Hallam 1981; Warren 1991). Strandplain or strandzone evaporite is apropos when describing the vast expanses of ephemeral water edge in ancient evaporitic mudflats.

Examples of evaporitic mudflat-dominated deposits include; the La Manga Formation (Oxfordian), Neuquén Basin, Men-doza, Argentina (Palma et al. 2013); Sequence 4 in the Upper Triassic Argilo-Greseux Inferieur of the Berkine Basin, Algeria (Turner et al. 2001); Jurassic Arab Cycle seals of the Middle East (Lindsay et al. 2006); Permian Minnelusa Formation in Wyoming (Achauer 1982); seal facies in the Permian Basal Seven Rivers Formation in Yates field, West Texas (Warren 1991); northern regions of the Palo Duro Basin during deposition of the Permian Upper San Andres Formation, Texas Panhandle (Hovorka 1987); more landward parts of the Lower Clear Fork Formation of Texas (Handford 1981b); Cambrian Red Heart Dolomite of the Georgina Basin, Australia (Nicolaides 1995); Neoproterozoic of South Gabon (Schisto-Calcaire Subgroup, Nyanga Basin, (Préat et al. 2010); Archaean Wittenoom Dolomite of the Hamersley Group, Western Australia (Kargel et al. 1996).

Saltern describes extensive shallow-subaqueous evaporite beds (5–50 m thick) deposited across hundreds of kilometres in the hypersaline portions of an ancient evaporite lake or seaway (Warren 1991). Deposition took place in both marine-fed and continental settings (Fig. 5.8; Table 5.3). Unlike evaporite mudflats, units tend to lack matrix within the stacks of salt layers that constitute the unit. Internal textures range from aligned crystals layers, or their ghosts, which preserve little evidence of syndepositional exposure through to stacks of salt pan crusts separated by abundant dissolution surfaces.

There are no modern counterparts for salterns in terms of scale or location, unlike the sabkha, pan and salina components of an evaporitic mudflat. Salterns formed in extensive salt-depositing seaways that covered former open marine platform carbonates or accumulated on 100 km+ wide evaporite shelves about the edges of giant deep brine seas (Fig. 5.8). Even so, most saltern texture can be interpreted using analogous textures documented in subaqueous salt beds in Quaternary lakes (Chaps. 1 and 4).

Individual saltern beds were precipitated from perennial brine sheets that were a few tens of centimetres or more deep and were originally accumulations of growth-aligned crystals, rafts, clusters and crusts. Horizontal laminae in calcium sulphate beds were often crosscut or interrupted by aragonite or dolomite layers. Primary sulphate textures were altered and recrystallised syndepositionally or during burial into nodular and coarsely crystalline textures. Primary halite chevron textures tend to be retained as remnants in a variably recrystallised matrix of halite spar. The end result of saltern deposition is a number of superimposed shoaling-upward beds (parasequences) composed of one or two dominant minerals, usually halite or gypsum (now nodular anhydrite).

Smaller crystals were reworked by storms into subaqueous traction deposits characterized by graded and reverse-graded beds, rippled and crossbedded layers, and algal rip-up structures. The graded beds and the rippled layers probably recorded waning storm-flood conditions (Hardie and Eugster 1971). Reverse-graded mechanical beds recorded either episodes of storm surging (increasing energy levels) across the saltern, or episodes of brine dilution that had slowed precipitation, so that coarser crystal overgrowths came to dominate the upper part of the lamina or layer.

Longer term freshening of saltern waters to where salinities were undersaturated with respect to halite or gypsum created cm-dm mudstone to wackestone layers that entrained intraclast breccias, tepees, pisolites, cross beds, cryptalgalaminites, micritic domal stromatolites, often with numerous pellets coming from brine shrimp and ostracodes or other opportunistic halotolerant species. Mud interbeds can also preserve rare vertebrate tracks.

Using the high-resolution outputs from a conventional wireline logs suite (e.g. Neutron, PEF or MSFL), a saltern is typically resolvable into internal beds of relatively pure cyclic salt sets (parasequences). Core and image logs show cycles are typically shoaling (e.g., domes passing up into laminites) with decimetre to metre scale layering that can be traced over significant well-to-well distances (> tens of kilometres). When using conventional wireline profiles for subsurface correlation, the relative purity (>95 % salts), greater thickness of bed cycles and improved lateral continuity gives saltern beds a blocky wireline signature that frequently allows their distinction from the more spiky signal in evaporitic mudflats (Table 5.3). Mapping this distinction can be an important reservoir quality predictor in underlying strata (Fig. 10.45).

Ancient examples of saltern deposits include; D-member of the Miocene Qom Formation, Central Iran (Khalili et al. 2007); Cretaceous Ferry Lake Anhydrite in the northern Gulf of Mexico (Pittman 1985); ramp interior evaporite cycles of the Early Cretaceous of the Caohuila platform (Lehmann et al. 1998); P_1 and P_2 evaporites of the San Andres Formation on the northwest shelf of the Permian Basin; the Lower San Andres Formation of the Texas Panhandle (Elliott and Warren 1989); upper Visean anhydrites of southern Belgium (De Putter et al. 1994); Upper Ordovician halites of the Canning Basin (Kovalevych et al. 2006b); Jurassic Hith Anhydrite of the Middle East (Azer and Peebles 1998); and the Herald Formation in the Ordovician red River Group, Saskatchewan (El Taki and Pratt 2010).

Deepwater evaporites accumulated beneath deeper brines of lacustrine and basinwide evaporite successions and encompass the slope, rise and basin deposits (Fig. 5.8). Fine-grained halite or gypsum laminites accumulated in the central deeper parts of a density-stratified basin, typically intercalated with less saline salt beds, as well as with carbonate or organic laminites. The fine layering reflects change in the saturation states of the surface brines or variations in the rate of sediment supply and grain size from the more marginward slope deposit feeds (Fig. 5.8). These "deepwater" laminites accumulated in two main ways: (1) As "rain from heaven" with crystallites first forming in the upper supersaturated metre or two of the brine column and then settling to the deep brine seafloor, (2) As the distal ends of evaporite turbidites and debris flows that typify the slope and rise in basinwide deepwater settings. Slope deposits accumulate up-dip from the laminites of the basin floor and are mechanically reworked from saltern or mudflat parent. They are characterised by textural associations typical of deeper water in all sedimentary basins and include; turbidite fans, Bouma cycles, slumps and debris flows, sole marks, tool marks, scour and fill, ball and pillow structures. All are relatively high-energy features, intercalated with laminites deposited during times of quiet bottom settle-out.

Studies of basin-centre and slope evaporites in the Permian of the Delaware and Zechstein basins, the Visean evaporites of the Canadian Atlantic, and the Miocene of Red Sea rift in the Yemen Republic, the Messinian of circum-Mediterranean, indicate these ancient deepwater sequences can be interpreted in much the same way that deepwater deposits are interpreted in carbonate and siliciclastic depositional systems (Anderson et al. 1972; Clark 1980a, b; Richter-Bernburg 1986; Schlager and Bolz 1977; Schenk et al. 1994; El Anbaawy et al. 1992; Rouchy et al. 1995a, b; Peryt 2000; Orti et al. 2003; Roveri et al. 2006). The main difference when compared to other deepwater clastics relates to water depth and the relative importance of "rain from heaven" versus resedimented shelf deposits in depositing the fine laminites of the basin centre.

Interpreting actual water depths above the basin floor is more difficult than separating subaqueous and subaerial depositional styles (Warren and Kendall 1985; Warren 1985). A lack of a benthonic microfauna, similar conventional wireline signatures and varying degrees of drawdown during ongoing deposition of thick interlayered coarsely crystalline and laminated evaporite sequences, means water depth deter-

minations are difficult in ancient slope and basin evaporites. Varying intensities of draw-down as evaporites accumulate in a basin centre plays havoc with the assumptions of rates of water-level change that are inherent in estimating water depths in open marine deposits. Unlike marine basins where sealevel tends to fluctuate tens of metres above and below the shelf break, brine surfaces in basins accumulating evaporites in drawndown basin centres can be 2 km or more below sea-level and basinal of the position of what was the shelf break prior to basin isolation. Drawdown of hydrologic baselevel can happen in the space of a few tens of thousands of years, as can the return to a marine baselevel once the basin in fully reconnected to the waters of the open ocean.

The effects on basin sediment of such substantial drawdown over relatively short times are likely substantial. Based on three-dimensional seismic mapping, Bertoni et al. (2013) document a field of pockmarks in the Levant Basin (south-eastern Mediterranean) buried at present depths of ≈4 km. The pockmarks cover an area of ≈1,000 km^2, have diameters as great as 2 km, and erode as much as 200 m into their substrate of deep-water clastic sediments, which immediately predate sediments of the Messinian Salinity Crisis (MSC; 6.2–5.5 Ma). These craters are filled by the basal units of the Messinian evaporites, implying they formed at or close to the time of the earliest major drawdown of Mediterranean sea level. All the pockmarks are developed at a single, regionally correlatable surface, Horizon N, which is observed throughout the Mediterranean to coincide with the onset of the MSC. In the Levant region, this surface formed during erosion and drawdown with a magnitude of 900–1,000 m. Rapid basinal drawdown, and the removal of hydrostatic pres-sure exerted by a kilometre of water, led to a dramatic increase of the shallow subsurface pore-fluid overpressure regime in the mostly fine-grained pre-Messinian sediments. Subsequent pres-sure release then resulted in high flux fluid venting, sediment remobilization, pockmark formation and general near-surface sediment instability. The spatial association of the craters with an underlying canyon suggests that their formation is linked to biogenic methane generation. Their model of drawdown-induced overpressuring and remobilization is likely applicable to many other evaporitic basinwide setting. It offers a novel mechanism for inducing large-scale sediment remobilization of shallow buried depositional systems during the earliest stages of salt basin development.

Using a deep "water full" basin model, Richter-Bernburg (1957) estimates water depths of more than 1,000 m for anhydrite laminites in the centre of the Permian Zechstein basin. Subsequent work by Schreiber (1988) postulates a minimum relief of 100–200 m for the shelf to base-of-slope transition during anhydrite deposition. Warren (1989, 1991) argues that determinations of deep versus shallow in a drawndown basin are difficult, but favours typical water depths of no more than 100–200 m. Kendall (1992) argues deepwater evaporites typically form in water depths greater than 20–40 m; but, like Warren (1985), notes that "deepwater" sulphate laminates can form in brines less than a few metres deep. The mechanism driving resedimentation in "deepwater" salts is also contentious; Schlager and Bolz (1977) favour turbidity currents, while Clark (1980a) favours a control by storm surge instability (Fig. 5.8). Reworked deepwater clastic gypsum textures (uncomplicated by a conversion to burial anhydrite) have been documented in the Messinian gypsum in Apennines of Italy and in cores recovered from canyon fill in the lower Messinian evaporites of offshore Israel (Lugli et al. 2012).

Unlike deepwater $CaSO_4$ laminites and slumps, resedimented ancient halites are not widely recognised and their interpretation in ancient salt beds typically stems from their entrained nonevaporite clasts, rather than from textures in any finely layered halites (Czapowski 1987). One of the better-documented examples of platform halite being redeposited into deeper water is the halite breccias and olistoliths in Middle Miocene evaporite in the Wieliczka and Stebnyk salt mines of Poland (Peryt and Kovalevich 1997). There, the salt breccia is interpreted as a series of subaqueous fans, with redeposition of the originally shallow water halite into deep water, driven by vertical tectonic movements and the northward advance of the Carpathian Nappes, some 13.81 Ma (De Leeuw et al. 2010). Water depths at the time of halite deposition are interpreted to have been between ten and tens of metres deep. Others have interpreted the same mine sequence textures to be halokinetic.

In understanding ancient deepwater evaporites and reliably tying down water depths, a significant problem is that there are only two Holocene settings, both continental lakes, where "deep water salts" are accumulating in waters deeper than 30 m (Dead Sea halite and Canadian mirabilite lakes; Chaps. 4 and 10, respectively). Deepwater sediments in almost all other modern saline lakes are carbonate laminites (pelagites). Modern deepwater analogs accumulate in small steep sided continental depressions, while deepwater ancient evaporites accumulated across the flat deep-brine-covered floors of broad drawndown marine basins, with no modern counterpart. If we take the two Holocene examples as direct analogs they show the following: (1) Massive beds made up of coarsely crystalline meshworks of sodium sulphate salts are accumulating beneath 30 m deep brine columns in small salt lakes in the interior of Canada. (2) Finely-laminated bottom carbonates, alternating with massive crystalline halite beds, are accumulating on the floor of the Northern basin of the Dead Sea (≈300 m deep brine).

Using the current lacustrine textures in the salts of the Dead Sea and Canada as a process analogue we should add another style of deepwater evaporite; namely, beds made up of rapidly deposited, coarsely crystalline, inclusion-free, meshworks of prisms. The prisms accumulate on stable

bottoms and so show little upward crystal orientation with a characteristic lack of inclusion-rich layering in individual prisms. These beds indicate times when the deep brine column was holomictic, stable, and saturated with respect to the salt of interest (Fig. 5.8). From strandzone to deep basin floor, this coarsely crystalline halite is a lakewide time-synchronous holomictic unit.

In contrast, laminites probably indicate periods when deep bottom brines in the centres of many ancient evaporite basins were density-stratified, sediment starved and anoxic, or at best dysaerobic for long periods (Kirkland and Evans 1981; Hite and Anders 1991). The resulting cumulates ("rain from heaven" textures) entrain significant volumes of pelagic organic matter and, with suitable burial, have yielded hydrocarbons or ultimately were converted to graphitic schists. For example, the bottom sediments in the deepwater gypsum of the Gibellina Basin contain up to 7 % TOC, similar elevated levels occur in the mesohaline laminite of the Paradox basin (Chap. 9). At present the organics entrained in the evaporitic carbonates of the Sicilian basins are still thermally immature, while those in the Paradox are mature but mostly locked in placed by pervasive diagenetic salt cements. The evaporite association of many of these deepwater meromictic pelagics means their potential to act as source rocks is limited to a few particular hydrologic settings (Fig. 9.4).

Evaporites: Broad-Scale Depositional Models

Saltern and mudflat beds, along with varying development of slope and basin deposits, occur in three interrelated regional depositional settings (Figs. 5.8 and 5.9):

Platform evaporites: Stratiform beds typically <50 m thick and composed of stacked <1 to 5 m thick parasequences or cycles with a variably present restricted marine carbonate base. Salts were deposited as mixed evaporitic mudflat and saltern evaporites, sometimes with local accumulations of bitterns. Typically they were deposited in hydrographically-isolated subsealevel marine-seepage lagoons (salterns) or evaporitic mudflats. These regions have no same-scale modern counterparts and extended as widespread depositional sheets across large portions of marine platform areas that in passed seaward across some sort of subaerial barrier into open marine sediments (Fig. 5.9a). In marine-margin epeiric settings, such as the Jurassic Arab/Hith and Permian Khuff cycles of the Middle East, these platform evaporites are intercalated with shoalwater marine-influenced carbonate shelf/ramp sediments, which in turn pass basinward across a subaerial sill into open marine carbonates. Landward they pass into arid zone continental siliciclastics or carbonate mudflats. Deposition occurred in pericontinental or intracratonic settings

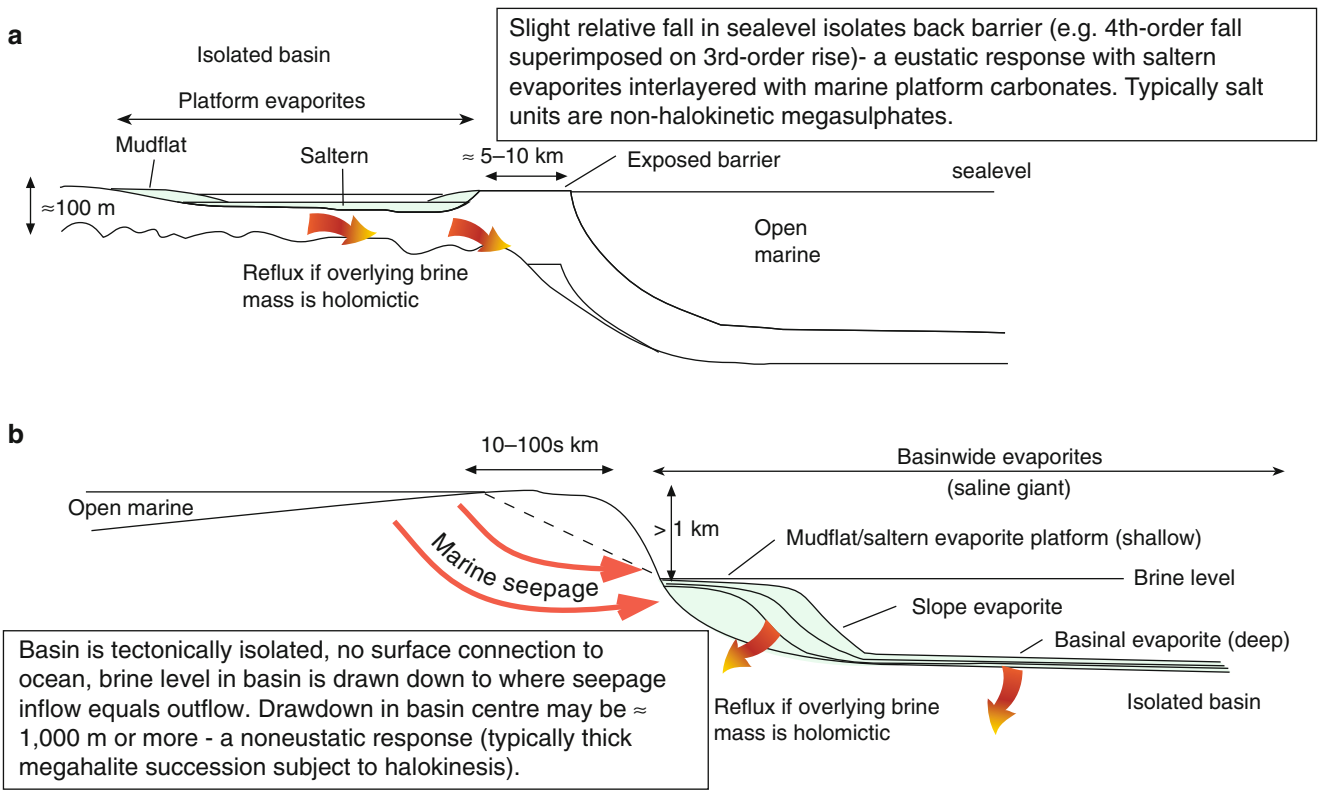

Fig. 5.9 Schematic cross sections of ancient evaporite settings that have no modern analogs. (**a**) Platform evaporites. (**b**) Basinwide evaporites (See text for explanation)

Platform evaporite successions may contain halite beds, especially in intracratonic basinwide settings, but in periplatform settings are typically dominated by 5–40 m thick Ca-sulphate beds intercalated with normal marine platform carbonates (Fig. 5.9a; Table 5.5). The lateral extent of these epeiric platform salts, like the Khuff Anhydrite with its area of 1,206,668 km^2, constitute some of the most aerially extensive evaporite beds ever deposited (Fig. 5.4).

Platform-wide megasulphate beds of Eocene age in the Middle East, centred on Iraq, Kuwait and Saudi Arabia (Rus Fm. and equivalents) are our most recent example of a time when an epeiric carbonate platform succession was covered and interlayered with a widespread combination of saltern and evaporitic mudflat gypsum and anhydrite (Table 5.8). A similar set of bedded platform-carbonate saltern-sulphate interlayers characterises the depositional cycles of Jurassic Arab Fm sediments (especially the Hith Anhydrite) of the Middle East, the Middle Anhydrite Marker (and equivalents) in the Permian Khuff Fm of Saudi Arabia, Qatar and the Emirates. There are numerous other large-scale Ca-sulphate saltern/mudflat examples including the anhydrite portion of depositional cycles in the Cretaceous limestone platforms and atolls of the circum Gulf of Mexico (e.g. Ferry Lake Anhydrite), the Permian back-shoal lagoons of West Texas and New Mexico (e.g. San Andres Fm. and equivalents) and the Cambrian carbonates of the Georgina Basin in Australia (e.g. Red Heart Dolomite and equivalents).

In many cases, especially in older examples, such as the such as the Red Heart Dolomite and Cambrian Cool Creek Fm of Oklahoma, the anhydrite unit has dissolved and all that remains as evidence of a former widespread $CaSO_4$ bed is a dissolution breccia, or dispersed and altered nodules and associated burial salt cements. In some cases these dissolution breccias are now mineralised MVT deposits, as with the San Vicente Mine, Peru and the ore zones in the Cadjebut mine region of the Canning Basin Platform, Australia. In the latter case the ore zones pass laterally into saltern anhydrite beds (Warren and Kempton 1997).

Basinwide evaporites Thick, basinwide units >50–100 m thick of deepwater/shallow water evaporites retain textural evidence of different but synchronous depositional settings, including mudflat, saltern, slope and basin (Figs. 5.8 and 5.9b). When evaporite deposition took place, the whole basin was evaporitic typically saturated with the same mineral phase across large areas of the basin (as when halite today forms decimetre-thick chevron-dominated beds on the saline-pan floors and coarse inclusion-poor crystal meshworks on the deep basin floors of the Dead Sea).

Basinwide successions are typically dominated by thick massive salt beds (more than 100 m thick), which typically are made up of stacked thick halite beds, but can also contain substantial volumes of thick-bedded Ca-sulphate and evaporitic carbonate, as in the intracratonic Delaware and Otto Fiord Basins. Some basinwide systems (mostly marine-fed intracratonic) also entrain the larger accumulations of the world's potash salts, even though our only Quaternary examples of economic potash are continental systems (Chap. 11). Many halite-dominant basinwide beds are also remobilised into various halokinetic geometries owing to the purity and thickness of the deposited halite (Chap. 6).

Basinwide evaporite deposits are the result of a combination of tectonic and hydrological circumstances that are not currently active on the world's surface. They were last active in the Miocene in association with soft-suture collision basins tied to the Alpine-Himalaya orogenic belt and to rift basins developed in the early stages of the Red Sea. They will be active again in the future at sites and times of appropriate plate-plate interaction, when two continental plates are in close proximity and the intervening floor at or near a plate-edge rift or suture is both subsealevel and hydrographically isolated.

Continental playa/lacustrine deposits These are constructed of stratiform salt units, typically with the greater volume of sediment made up of nodular gypsum and displacive halite deposited in widespread evaporitic mudflats and saltpans, rather than in perennial brine lakes (Chap. 4). Total thickness ranges from metres to hundreds of metres, with lateral extents measured in tens to hundreds of kilometres (Fig. 5.4). Such salt beds are separated and often surrounded by deposits of lacustrine muds, alluvial fans, ephemeral streams, sheet floods, eolian sands and redbeds. Typically the salts accumulated in endorheic or highly restricted discharge basins. Basins typically have a shallow watertable in the saline mudflat area and a lowermost depression or sump typified by ephemeral ponded brine pan deposits. Perennial saline lakes formed during more humid periods in the same continental depression or in parts of the saline lake floor located below the regional watertable (moat facies).

Evaporite mineralogies depend on compositions of inflowing waters (Fig. 2.19); suitable settings accumulated thick sequences of trona, glauberite and the nardite as well as more typical sequences of halite and anhydrite. Highwater stage perennial sediments tend to be carbonate-rich or silica-rich (diatomaceous) laminites. Ancient examples include the Eocene Green River Formation of Wyoming and the Permian Pingdiquan Formation of the Junggar Basin, China. Evaporites deposited in suprasealevel lacustrine basin (especially Neogene deposits) have numerous same-scale Quaternary analogs and so are discussed first.

Lacustrine Evaporites

According to the degree of accommodation space, all ancient lacustrine deposits can be subdivided into three types: underfilled, balanced and overfilled (Fig. 5.10; Bohacs et al. 2000, 2003). Accommodation is the space available for sediment

Lake type & lacustrine facies association	Stratigraphy	Lithologies	Sedimentology	Organic matter	Kerogen-hydrocarbon characteristics
Overfilled Fluvial-lacustrine facies association	Maximum progradation: • parasequences related to lateral progradation (relatively stable) • maximum fluvial input	Terrigenous sediment dominant • mudstone, marls • sandstone • coal, coaly shale • coquina (isolated highs in basin)	Physical sedimentation dominant: • ripples, dunes, flat bed • root casts • burrows (infaunal and epifaunal)	• freshwater biota charophytic and aquatic alga OM • low to moderateTOC • terrigenous and algal biomarkers	• mixed type I-III kerogen • both oil and gas generative • very waxy, low sulphur oils
Balanced fill 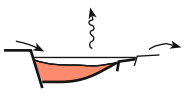 Fluctuating-profundal facies association	Mixed progradation & aggradation 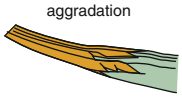 • distinct shoaling cycles common • fluvial input variable	Mixed chemical and terrigenous sediment: • marl, mudstone • siltstone, sandstone • carbonate, grainstone, wackestone, micrite • kerogenite	Physical & biogenic sedimentation: • flat beds, • current,wave and wind ripples • stromatolites, pisolites and oncolites • mudcracks • burrows (epifaunal)	• saline tolerant biota aquatic algal OM minimal land plant • moderate to highTOC • algal biomarkers	• predominantly type I kerogen, type I-III mixtures near flooding surfaces • mostly oil generative • paraffinic but relatively nonwaxy oils, low sulphur
Underfilled Evaporitic facies association	Maximum aggradation minimum progradation 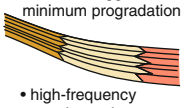 • high-frequency wet-dry cycles • minimum fluvial input • maximum evaporite input	Chemical sediments dominant: • mudstone, kerogenite • evaporite • siltstone, sandstone • grainstone, boundstone wackestone, micrite • flat-pebble conglomerate	Chemical, biogenic & physical sedimentation: • cumulative textures • displacive fabrics • stromatolites, pisolites and oncolites • climbing ripples • flat beds • eolian cross beds	• low diversity halotolerant to halophilic biota • algal-bacterial OM • low TOC in oxidised margins • high to very high TOC oil shale in basin centre • "hypersaline" biomarkers	• type I kerogen • mostly oil generative • paraffinic oils, moderate to high sulphur

Fig. 5.10 Attributes of the three major styles of lacustrine basins (After Bohacs et al. 2000)

accumulation below the basins outlet or spill-point. The type of lake is defined by how much of that space is filled by some combination of sediment + plus water over a particular time span. Hence climate (≈ sediment supply + water depth and permanence) and tectonics/inherited topography (≈ potential accommodation) exert coequal controls on the nature and distribution of the various lacustrine deposits. Changes in climate or tectonic subsidence means ancient lacustrine basin fill can evolve from one lake type to another a number of times in the infill history of the basin (Lambiase 1990).

The fluvial-lacustrine facies association in overfilled (humid) lakes is composed of marlstone, argillaceous coquina and bioclastic grainstone, along with widespread sandstones, carbonaceous mudstones and coals with a freshwater fauna. Beds retain mixtures of aquatic and terrigenous organic matter and most sedimentary textures indicate physical, not biogenic, processes (Fig. 5.10; Bohacs et al. 2000, 2003). A fluctuating-profundal lacustrine facies association is common in balanced lakes and is made up of a complex of interbeds of heterogenous lithologies including; carbonates, siliciclastics, argillaceous and organic rich mudstones, with a fresh to saline water biota, Dominantly aquatic organic matter is found in beds and bedsets, while sedimentary structures are typified by a combination of physical and lesser biogenic features.

Evaporitic lacustrine facies typically accumulate in underfilled basins, with lithologies ranging across clastic sandstone and carbonate grainstones, kerogenites (oil shales) and evaporites. Widespread shoalwater evaporites typically fill the lowermost parts of the basin during the most arid or underfilled times in the lake history. Halophilic organic matter can accumulate in moat facies at that time, or halotolerant organic remains can accumulate across larger parts of the lake floor when water levels are somewhat higher and fresher (Chaps. 4 and 9). Sedimentary structures include both physical and biogenic structures, as well as textures indicating periodic desiccation (mudcracks) and crystallization in fluctuating brine conditions (inclusion-rich cumulate, growth-aligned and displacive textures).

Studies of sizes of modern lakes of all three types, water depths and the character and thickness of ancient counterparts typically do not correlate with measured or inferred climatic humidity (Bohacs et al. 2003). Interestingly, the drainage basins of the world's largest rivers contain no large lakes, only a few relatively small ones (e.g., Amazon, Congo, Orinoco and Mississippi River basins). Ancient lake systems show a similar lack of correlation between lake size, climate and fluvial volumes (Carroll and Bohacs 1999; Bohacs et al. 2003). Of the three types of ancient lakes, the focus for the remainder of this section is on the underfilled or evaporitic lakes. For further discussion of the sedimentology of other two lacustrine associations, the interested reader is referred to the excellent review papers by Bohacs et al. (2000, 2003) and the references therein.

Ancient saline lacustrine deposits range in age from Neogene to Precambrian (Table 5.4). Facies patterns and distributions in saline lakes are different to marine carbonate or siliciclastic-filled basins as; (1) the depositional base level

Table 5.4 Some representative examples of Pre-Quaternary saline lake deposits (underbalanced systems)

Sequence of interest	Basin/setting	Locality	Age	References
Beds of displacive borates	Bigadic, Emet and Kirka basins	Turkey	Neogene	Helvaci et al. (2012), Gurer and Gurer (1999)
Gypsiferous Blanchetown Formation	Palaeolake Bungunnia	Murray Basin, Australia	Neogene	McLaren et al. (2012)
Massive halite of Salar Grande	Cordillera de la Costa forearc	Central Andes, Chile	Neogene	Diaz et al. (1999), García-Veigas et al. (1996)
Bed I and Bed II	Olduvai Gorge, East African Rift	Tanzania	Pliocene	Hover and Ashley (2003), Hay and Kyser (2001)
Furnace Creek Fm. (borate beds)	Extensional half-graben	Death Valley, USA	Pliocene-Miocene	Tanner (2002)
Gypsum as beds and fracture-fills	Sivrihisar/Sultancayir/Cankiri basins	Anatolia, Turkey	Miocene	Orti et al. (1998), Varol et al. (2002)
Lacustrine carbonates	Ries-impact-crater	Southern Germany	Miocene	Arp (1995), Pache et al. (2001)
2.5 km thick lacustrine halite	Hualapai basin	NW Arizona	Miocene	Faulds et al. (1997)
Kirmir Fm.	Beypazari Basin	NW Turkey	Miocene, Middle – Upper	Yagmurlu and Helvaci (1994), Gundogan and Helvaci (2001)
Juncalito Fm.	Puna Plateau – intra-arc basin	NW Argentina	Miocene, Middle – Upper	Kraemer et al. (1999)
Bedded and nodular gypsum (glauberite)	Calatayud Basin	Spain	Miocene, Lower	Aziz et al. (2003), Orti and Rosell (2000)
Bedded and nodular gypsum (glauberite)	Ebro Basin – foreland basin	Spain	Miocene, Lower	Salvany et al. (2007), Arenas et al. (1999)
Creede Fm.	Ancient Lake Creede	Colorado, USA	Oligocene, Upper	Finkelstein et al. (1999)
Potash beds of Couche Inferieure	Mulhouse Basin	Rhine Graben, Europe	Oligocene, Upper	Gely et al. (1993), Orti-Cabo et al. (1985)
Green River Fm.	Uinta and Piceance basins	Utah and Colorado	Eocene	Dyni (1981), Aswasereeleert et al. (2013), Surdam and Wolfbauer (1975)
Bembridge Limestone Fm.	Isle of Wight	Southern England	Eocene, Upper	Armenteros et al. (1997)
Taleh Fm.	Somalia	El Bur Plateau	Eocene, Lower -Middle	Singer et al. (1998)
La Tinaja del Oso (colmanite)	Magdalena extension basin	Mexico	Mid-Tertiary	Mirandagasca et al. (1998)
Uhangri Fm.	Yucheon Group	SW Korea	Cretaceous	Chough et al. (1996), Paik and Kim (1998)
Mmashoro Fm.	Basal Kalahari Group	Botswana	Cretaceous, Upper	Du Plessis and Leroux (1995)
El Molino Fm.	Potosi Basin	Bolivia	Cretaceous, Upper -Tertiary, Lower	Camoin et al. (1997), Rouchy et al. (1993)
Lagoa Feia Fm.	Campos Basin	Brazil	Cretaceous, Lower	Trindade et al. (1995)
Codocedo Limestone Member	Atacama region	Northern Chile	Jurassic, Upper – Cretaceous, Lower	Bell (1989), Bell and Suarez (1993)
Drakensberg Group	Intercalated in Karoo basalts	Southern Namibia	Jurassic, Lower	Stollhoffen et al. (1998)
Kalkrand Fm.	Karoo flood basalt province	Namibia	Jurassic, Lower	Stollhoffen et al. (1998)
Mercia Mudstone Group	North Atlantic rift basins	Southern Britain	Triassic, Upper	Milroy and Wright (2000), Talbot et al. (1994)
Passaic and Lockatong Fms.	North Atlantic rift basins	Southern Britain	Triassic, Upper	El Tabakh et al. (1997, 1998b), Smoot (1991), Redfern et al. (2010)
Blomiden redbeds	Newark Basin	Eastern North America	Triassic, Upper	Hubert and Hyde (1982), Leleu and Hartley (2010)
Buntsandstein	Fundy Basin	Nova Scotia	Triassic, Upper	Clemmensen (1978), Clemmensen et al. (1984)
Pingdiquan Fm.	Helgoland Basin	East Greenland	Triassic, Middle	Carroll et al. (1992), Tang et al. (1997)
Groden Fm.	Junggar Basin	NW China	Permian, Upper	Spötl and Burns (1994)
Opeche Shale	Williston Basin	North Dakota, USA	Permian, Middle	Benison and Goldstein (2000)
Nippewalla Group	Continental interior sag basins	Kansas, USA	Permian, Middle	Zambito and Benison (2013)
Rotliegende sediments	Muhlhausen and Ilfeld basins	Germany	Late Carboniferous-Permian	Paul (1999)
Old Red Sandstone (middle)	Orcadian Basin	Scotland	Devonian, Lower	Clarke and Parnell (1999), Donovan (1993)
Parakeelya Alkali Member	Officer Basin	Australia	Cambrian	Southgate et al. (1989)

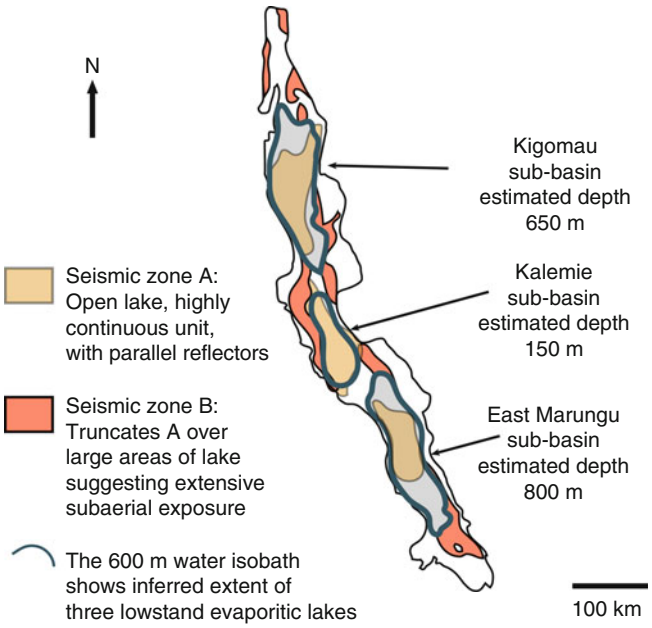

Fig. 5.11 Subdivision of Lake Tanganyika into three separate sub-basins during a mid- to late-Pleistocene lowstand (After Tiercelin and Mondeguer 1991)

changes much more rapidly and frequently in lakes and with much higher amplitudes, (2) salinity is not constant. Water/brine depth and lake salinity can change hundred of metres in less than a few 1,000 years, from a highstand deep perennial fresher lake accumulating deepwater chemical laminites, along with lake-plain and highstand deltas, to a shallow or ephemeral lake made up of small saline pans on broad salt flats and mudflats. In Lake Van, Turkey, there was a change of 600 m in 2,000–3,000 years, Lake Malawi in the East African rift dropped as much as 140 m in just 340 years (Owen et al. 1990) and the lake level in the Dead Sea is currently falling at similar rates. Changes are related to local climate and uplift and, unlike the base level changes in marine eustasy, do not show time synchronous change tied to worldwide climate mode (icehouse versus greenhouse). Facies analyses tied to dated cores in Lake Tanganyika, Africa, show the current lake was made up of three separate saline lakes when water levels were lower in the mid to late Pleistocene (Fig. 5.11). Compared to Lake Tanganyika, Lake Magadi and Salar Uyuni show the opposite effects in terms of timing of late Quaternary high water in that their current salt pan surfaces are some tens of metres below what were the much higher lake water surfaces in the late Pleistocene.

Vertical changes in facies and lithologies are abrupt in many ancient saline lake systems, a reflection of these rapid high amplitude changes in water levels. Large falls in lake water level lead to "hanging" deltas and terraces along with deep incisions through highstand Pleistocene deposits. In arid lowstand lakes, newly exposed lake floor sediments can be overprinted by subaerial weathering and the processes of soil formation. Exposed lake floor laminites can be sabkharized, as is happening today in Salt Flat Playa, West Texas (Hussain and Warren 1989).

Intuitively, many sedimentologists assume that climate is the major control on water depth and salinity in a saline lake basin. That is, larger deeper lakes, with thicker lake sediment packages, should accumulate in wet or humid climatic periods, while drier saline periods should be characterised by saline deposits with lesser aerial extents. But the hydrology of all lake basins, including endorheic basins, is never truly closed and varying degrees of reflux and leakage play significant roles in the final salt distribution (Chap. 2). Concurrent saline lakes in Turkey or the African Rift Valley can range from hypersaline to brackish in intermontane valleys located only a few tens of kilometres apart. Assuming all ancient lakes in an area are arid or humid at the same time is not a valid approach to correlation of salt beds in adjacent saline lake basins (e.g., Bohacs et al. 2003).

Eocene Lake Gosuite, USA

Lacustrine sediments deposited in Eocene Lake Gosiute are preserved in the Green River Formation, which has several members corresponding to major lake high- and low-stands, each of which probably lasted several hundred thousand years or more. Saline lacustrine phases of the Green River Formation, such as the Wilkins Peak Member, have two main modes: (1) Lake high-stands are marked by oil shales (laminated dolomitic kerogenites). (2) Lowstands, when water covered areas of the lake contracted and salinity increased, are indicated by salt beds of saltern/pan trona or halite deposited atop the oil shale layers and stromatolite dominated sediments in the more marginward mudflats (Aswasereelert et al. 2013; Seard et al. 2013; Smith et al. 2008).

Dolomitic mudstones were deposited during lowstands as subaerial evaporitic mudflats across over the dried and exposed lake floor. These strandzone to shoalwater carbonates are made up of structureless to laminated muds, algal dolomudstones algal boundstones, oolitic pisolitic grainstones and ostracode grain-stones, which a comparison to the massive unit in the Holocene Coorong lakes show are mostly ephemeral to strandzone indicators. The various Eocene shallow water microbialite-insect buildups in the Laney Member are considered excellent analogs for the subsalt lacustrine Albian reservoir carbonates in Tupi and other subsalt targets of offshore Brazil and western Africa (Seard et al. 2013).

Sandstone and siltstone line the basin edge and may be present as thin interbeds in the basin-centre kerogenites. Roehler (1993) identified 77 depositional cycles of mudflat/kerogenite in cores from the Wilkins Peak Member. Based on an estimated duration of 1.6 My for the member, he calculated an average period of 21 kyr for the cycles and

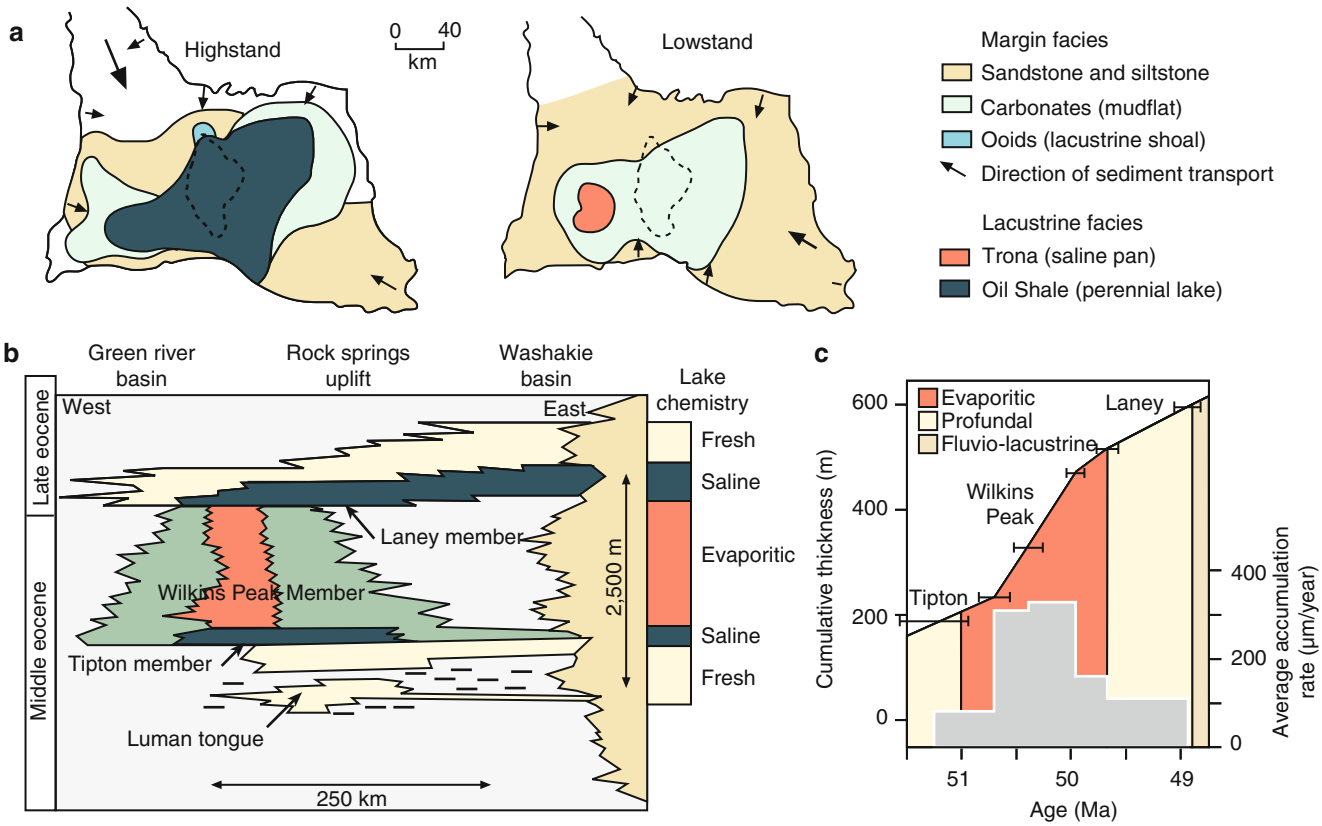

Fig. 5.12 Lithofacies distribution of Eocene Lake Gosuite as preserved in the Green River Formation, Wyoming. (**a**) Wilkins Peak time showing highstand conditions with extensive accumulations of oil shale beneath the salinity-stratified waters of a perennial lake versus lowstand conditions when carbonate mudflats dominated and trona was precipitated beneath very shallow to ephemeral waters of a hypersaline brine lake (After Surdam and Wolfbauer 1975). *Dashed line* outlines the approximate position of the Rock Springs Uplift. (**b**) Schematic E-W cross section showing lateral extents and thicknesses of various lacustrine units (After Bohacs et al. 2000). (**c**) Average sediment-accumulation rates for the Green River Formation based on a reference section in the southern Greater Green River Basin (After Smith et al. 2003, 2008, 2014)

suggested they were probably caused by the earth's precession, which has periodicities of 19 and 23 kyr. Pietras and Carroll (2006) found that tectonism was the primary control on basin fill and that differential accommodation was most pronounced during deposition of the lower Wilkins Peak Member and became progressively less so after that time. Based on their detailed structural and stratigraphic observations, they concluded a period of increased tectonic uplift commenced concurrent with deposition of the evaporitic lower Wilkins Peak Member (underfilled stage).

The oil shales (kerogenites) in the Green River Fm. are composed of mm-scale alternations of amorphous-algal organic matter (kerogen) and slightly thicker laminae of carbonate (mostly dolomite) and clay. TOC content can exceed 25 %. Comparisons to laminites accumulating in the various Quaternary saline lakes detailed in Chap. 4 means most authors now agree the Eocene kerogenites of the Green River Basin indicate highstand conditions (Fig. 5.12). But the definition of "deep" for the water depths accumulating kerogenite varies from author to author. The thickest beds of oil shale tend to occur toward the basin centre and some oil shale intervals are laterally extensive, perhaps indicating deposition at the bottom of a substantial body of perennial lake waters. Toward the basin margin the oil shales change to marlstones, kerogen-rich marlstones and lean oil shales (Hite and Anders 1991). Basin-centre oil shale accumulations can also contain diagenetic dawsonite, halite and nahcolite (Dyni 1981). They may also entrain mud-cracked horizons and solution breccia beds. To interpret the shales, some authors focus on the large lateral extent of the finely-laminated kerogenites and infer deposition at the bottom of a deep stratified water mass with density-stratified permanent waters more than tens of metres deep (Bradley and Eugster 1969; Desborough 1978; Dyni 1981). Others focus on the intercalation of the oil shales with evaporites and subaerial indicators such as mud-cracks, along with the dolomitic nature of the matrix and propose a shallow lake/saline pan depositional model for the widespread kerogenites (Eugster and Surdam 1973; Smoot 1983).

Changes in Lake Gosuite water levels mean the highstand sediments of kerogenite have a somewhat greater areal extent than the salts (Fig. 5.12a), but their deposition on the floor of

a perennial body of water does not mean they also show greater thicknesses. The freshest "lake-full" organic-enriched sediments of the Green River Formation in Wyoming are actually the thinnest and least aerially extensive of the various organic-rich units of the Green River Formation (e.g. Luman Tongue). In contrast, the Tipton and Laney members, which accumulated as varved oil shales beneath more saline meromictic lake waters have greater extents and thicknesses (Fig. 5.12b; Hite and Anders 1991).

Within the saline lake phase, those sediments deposited when the lake was at its driest (the Wilkins Peak Member), were deposited much more rapidly than the perennial saline lake laminites either of the Tipton or Laney members. $^{40}Ar/^{39}Ar$ based accumulation rates of Smith et al. (2003, 2008) are direct measurements of accumulation rates and do not rely on lamina counts being annual varves (Fig. 5.12c). For a reference section near the southern Green River Basin depocentre, they calculated accumulation rates of 88 ± 34 and 104 ± 18 μm/yr for the Tipton and Laney members; both values are consistent with an annual origin for the laminae. A much faster accumulation rate emerges from the Wilkins Peak Member. In the same reference section they calculated a net average rate of 327 ± 85 μm/yr, which is three times as fast as the Tipton or Laney Members.

Their observation of faster accumulation rates for saline phases is in accord with U-series disequilibrium-based results from Quaternary playa-lake evaporites. Ku et al. (1998) found that accumulation rates in a core from Death Valley were much higher for the salt-pan evaporite facies than for perennial lake muds, and Bobst et al. (2001) noted that accumulation rates during dry phases of the Salar de Atacama were up to three times as high as during wet periods (see Chap. 3). Net accumulation rates in these cases range between 0.5 and 1.8 mm/yr, which are up to five to six times faster than deposition of the Wilkins Peak Member. However, higher rates of Wilkins Peak Member evaporite accumulation may have occurred in the basin's subsurface depocentre, which lies to the west of the reference section (Smith et al. 2003).

Evaporitic sediments of Wilkins Peak Member, which accumulated at a time when the lake's waters were at their shallowest (perennial saline lake) and saltiest (pan/mudflat), are stratigraphically the thickest member of the Green River Formation (Smoot 1983; LaClair and Lowenstein 2009). This more saline lacustrine phase separating the kerogenites is enriched in sodium bicarbonate minerals such as trona and nahcolite in layers and is discussed in more detail in Chap. 11.

The alternation of playa and perennial lake modes explains accumulations of hydrogen-prone organics as oil shales in many saline lacustrine systems (Table 9.2). Boyer (1982) argues that hydrogen-rich oil shales in the Green River Basin accumulated beneath an anoxic lower brine layer in a density-stratified meromictic and relatively shallow saline lake. Stratification was created and maintained by ongoing dissolution of under-lying pan evaporites, especially trona/halite. He named this evaporite-induced stratification, ectogenic meromixis. If true, then accumulations of very thick oil shales in the Laney Member of the Bridger-Washakie basins and the Mahogany Bed of the Uinta-Piceance Creek basins are also a likely response to shallow subsurface dissolution of lake evaporites. The lack of similar underlying soluble beds in fresher water lacustrine oil shale basins (as in Honyanchi Fm. of China and the Rundle oil shale of Australia) may help explain why the trona-associated oil shales of the Green River Fm. are unique in their very high oil content. It also explains why virtually the entire Green River fish fauna, world famous for its high quality of tissue preservation, is made up of pelagic freshwater taxa, which flourished in the freshened upper water mass (Grande 1980). The permanent saline anoxic bottom layer was too nasty to support most life, other than well-adapted microbes (see Chap. 9).

Oligo-Miocene Lake, Calatayud Basin, Spain

The Oligocene-Miocene Calatayud basin of Spain is a foreland basin formed by the uplift of the Pyrenean chain to the north and is bounded to the southeast by the Catalonian Coastal Range and the Iberian range to the southwest (Fig. 5.13a). Thick beds of lacustrine salts accumulated in the endorheic lower parts of the basin. These deposits entrain a combination of carbonate and sulphate lacustrine environments, fed by a combination of Pyrenean waters via resurging groundwaters and alluvial systems. Deposits show strong similarities in distribution patterns and textures with the lacustrine evaporites and clastic aprons of the adjacent Ebro Basin (Fig. 8.17; Salvany et al. 2007; Arenas and Pardo 1999).

Miocene climate fluctuated from arid to more humid but, more importantly, the mountains to the North of the lake depression were composed of Triassic evaporites and Mesozoic marine carbonates. As they weathered they supplied ions for the salts accumulating in residual brines within the topographically lowest parts of the lake floor. The nearby Ebro Basin is well known for its economic accumulations of lacustrine glauberite that, as in the Calatayud Basin, largely occur in the central part of the basin (Fig. 12.26). Two distinct lake styles alternated through time: (a) High lake levels associated with a single body of dilute carbonate water, where massive biogenic carbonate facies proliferated. These lakes had wide palustrine vegetated margins, where bioturbated facies dominated the depositional signature. (b) Low lake levels of a playa-lake with extensive development of saline pans and mudflats surrounding a more permanent gypsum-saturated brine body in the lowermost parts of the lake depression.

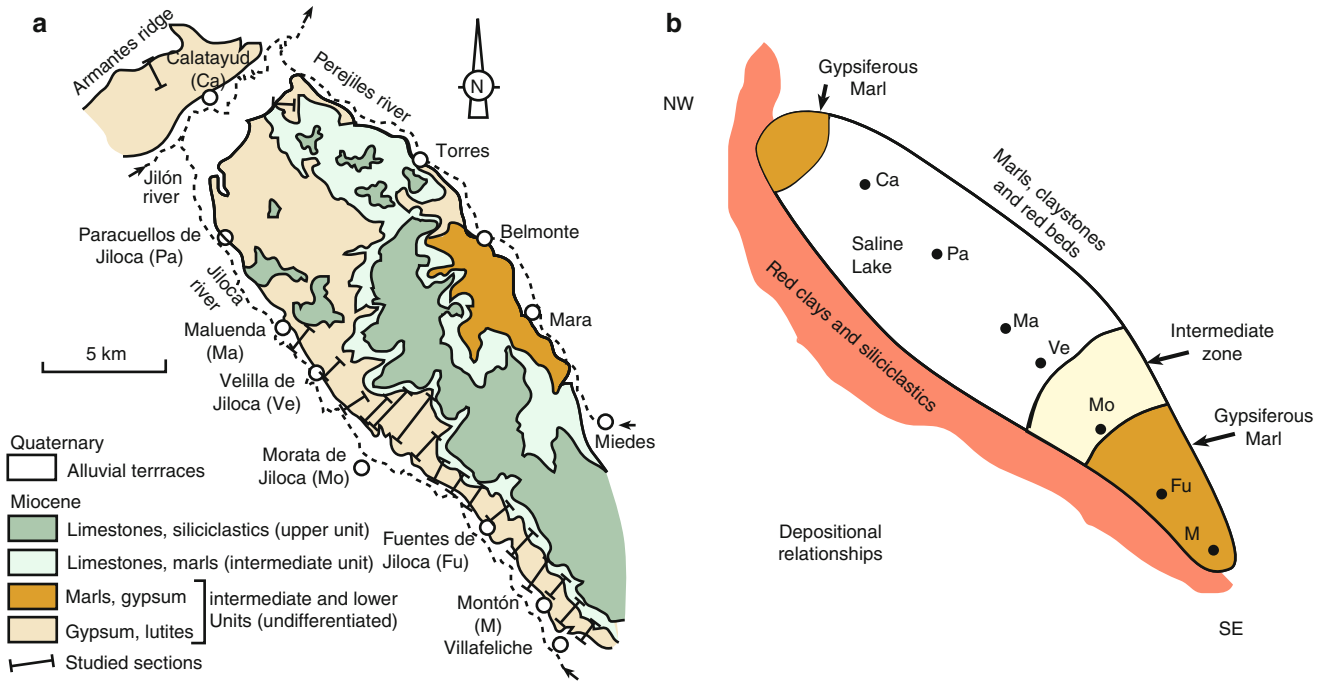

Fig. 5.13 Lacustrine sediment distribution in Cataluyud Basin, Spain. (**a**) Lithologic map showing distribution of Miocene lacustrine sediments in the area between the Armantes Ridge in the northwest, the village of Villafeliche in the SE and the area between the Jiloca and Perejiles rivers. (**b**) Schematic of the same area, showing areal distribution of the main lacustrine subenvironments in the lower evaporite unit (After Orti and Rosell 2000)

In the drawdown or playa stage a subaerial basin floor sloped gently down from a northern marginal mudflat zone to a central saline complex. Gypsum accumulated across the lake depression as both primary beds of mechanically reworked and 'in situ' gypsarenite, as well as early diagenetic precipitates of lenticular anhydrite (Fig. 5.13a). Surface runoff from nearby highlands constructed a bajada along the southern margin of the lake depression. But, transport of the greater volume of solutes into the basin was from the north and largely subsurface, via groundwater flow through an extensive karst systems in the evaporitic Mesozoic limestones that made up the hinterlands. Shallow groundwaters seeping south down the hydrologic gradient supplied increasingly fractionated and saline brines to lakes and pans all the way from the basin margin to the basin centre (Fig. 5.13b; Salvany and Orti 1994; Salvany et al. 1994; Orti and Rosell 2000).

Calcium carbonate and gypsum precipitated in the fan edges and in marginal palustrine marshes and ponds, while substantial beds of dolomite and charophyte residues accumulated over large parts of the lake floor during more humid climatic episodes (Fig. 5.11a). Many of the laminated gypsarenite beds are bioturbated, indicating periodic episodes of freshening and exposure, even as the gypsum was accumulating (Fig. 5.14a; Rodríguez-Aranda and Calvo 1998). Margin mudflats, marshes and ponds acted as preconcentrators for shallow groundwaters seeping slowly toward a central sump. By the time these fractionating brines reached the central drainage low, they were highly concentrated and capable of precipitating thick beds of gypsum, halite and glauberite. Much of the glauberite and polyhalite, along with some of the gypsum, was an early diagenetic interstitial precipitate, created by capillary evaporation of cross-seeping brines. The halite beds were predominantly primary saline pan units, composed of hoppers and chevrons, interbedded with laminated primary gypsum (Fig. 5.14a). The whole Oligocene Miocene lacustrine succession in the Cataluyud Basin is made up of six 100–200 m thick cycles. The lower part of each cycle commences with beds of saline lake salts (including glauberite) that show typical playa mudflat/pan textures and have the greatest lateral extent (Fig. 5.14b; Orti and Rosell 2000; Salvany and Orti 1994; Arenas and Pardo 1999). Saline facies then shrink toward the basin centre as the lakes evolve into a freshened palustrine carbonate-dominant stage. The top of each cycle is dominated fine-grained siliciclastics and alluvial fan sediments, indicating progressive progradation of alluvial fans toward the lake centre. Tops of some cycles are composed entirely of clays and fine-grained clastics. Over time, depocentres of successive cycles shift toward the north, suggesting the ultimate control on the cyclicity and accommodation space creation was tectonic, not climatic.

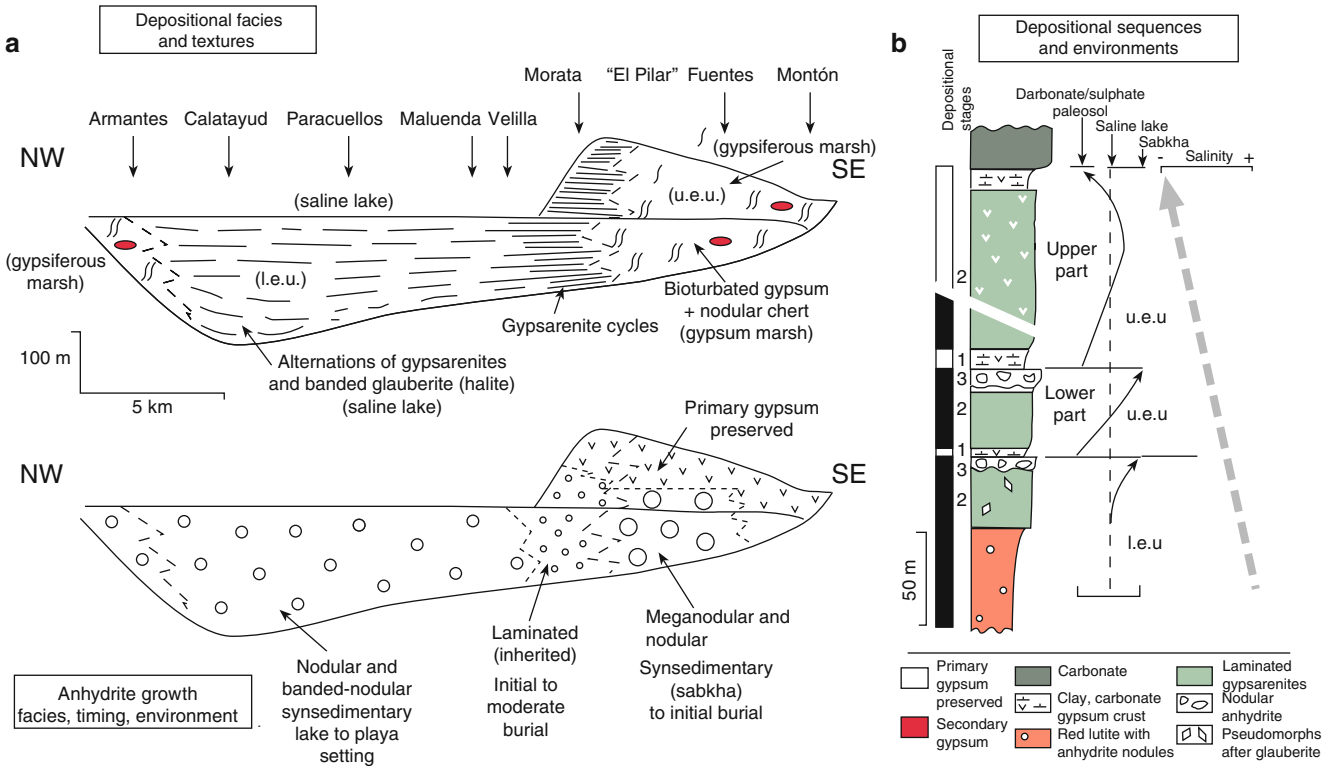

Fig. 5.14 Lacustrine evaporites in the Calatayud Basin, Spain. (**a**) Depositional facies distribution and their differential conversion to anhydrite: *l.e.u.* lower evaporite unit, *u.e.u.* upper evaporite unit (See Fig. 5.13 for location of sections and Fig. 12.26b for depositional style). (**b**) Depositional sequences and evaporite units in the area of the village of Morata. Salinity arrow indicates a decrease in the ionic concentration of the parent brines with time. The lower part of the upper evaporite unit shows a complete depositional cycle with associated salinity increase. Depositional stages: (*1*) dilution stage: gypsiferous-calcareous horizon (carbonate-sulphate palaeosol); (*2*) concentration stage: laminated gypsarenite (saline lake); (*3*) subaerial, hypersaline stage: nodular anhydrite (sabkha) (After Orti and Rosell 2000)

Much of the Miocene evaporitic sediment in the Calatayud Basin today outcrops or subcrops along the southwestern part of the basin, where it is liable to karstification and collapse. Ongoing groundwater crossflow, throughout the late Tertiary period, means primary evaporite textures have been diagenetically overprinted at various times in the burial and uplift history (Orti and Rosell 2000). In the gypsiferous marsh facies, the dominant, massive, bioturbated gypsum was partly replaced very early in the sediment history by synsedimentary chert nodules and siliceous crusts (Fig. 5.14a). In the saline lake facies, replacement of portions of the laminated glauberite by anhydrite also occurred soon after deposition. Multiple episodes of subaerial exposure and pedogenic/capillary alteration are indicated by: (1) pedogenic carbonates (with nodular magnesite) and gypsiferous crusts composed of poikilitic crystals; and (2) nodular anhydrite, which began forming in the capillary zone of a lacustrine sabkha or mudflat and continued to form during ongoing shallow burial. Additionally, a somewhat later pervasive meganodular secondary anhydrite texture overprints much of the laminated lake gypsum, presumably driven by heating of ascending, highly saline groundwaters. Thus anhydritization was controlled by the salinity of the pore solutions, and was ongoing from the onset of deposition to moderate burial to uplift (Orti and Rosell 2000). Anhydite meganodules, the most visually impressive type of anhydrite in these lacustrine sulphate salts, were telogenetically generated via the rise of deeply circulated meteoric waters, as discussed in Chap. 1 (Fig. 1.56; Ortí et al. 2012). The basin's diagenetic history indicates the typical complexity of evaporite textural evolution, even in strata that are undeformed and have undergone no more than shallow burial prior to exhumation.

Permian Lacustrine Redbeds, Kansas

The Permian (uppermost Leonardian-Kungurian) Nippewalla Group of Kansas and the Opeche Shale of North Dakota are part of an extensive redbed succession deposited in an arid continental interior sag basin on the Pangaean megacontinent (Fig. 5.15a; Benison and Goldstein 2000, 2001; Zambito and Benison 2013). Characteristic lithologies comprise bedded pan evaporites, red-bed siliciclastics and grey siliciclastics, all laid down in a series of continental playa depressions (Fig. 5.15b, c). Most evaporite deposition took place in a series of halite-dominated ephemeral saline lakes surrounded by saline and dry mudflats, sandflats and sand dunes. It was an evaporitic environment characterised by acid groundwaters with hydrologies not unlike those of

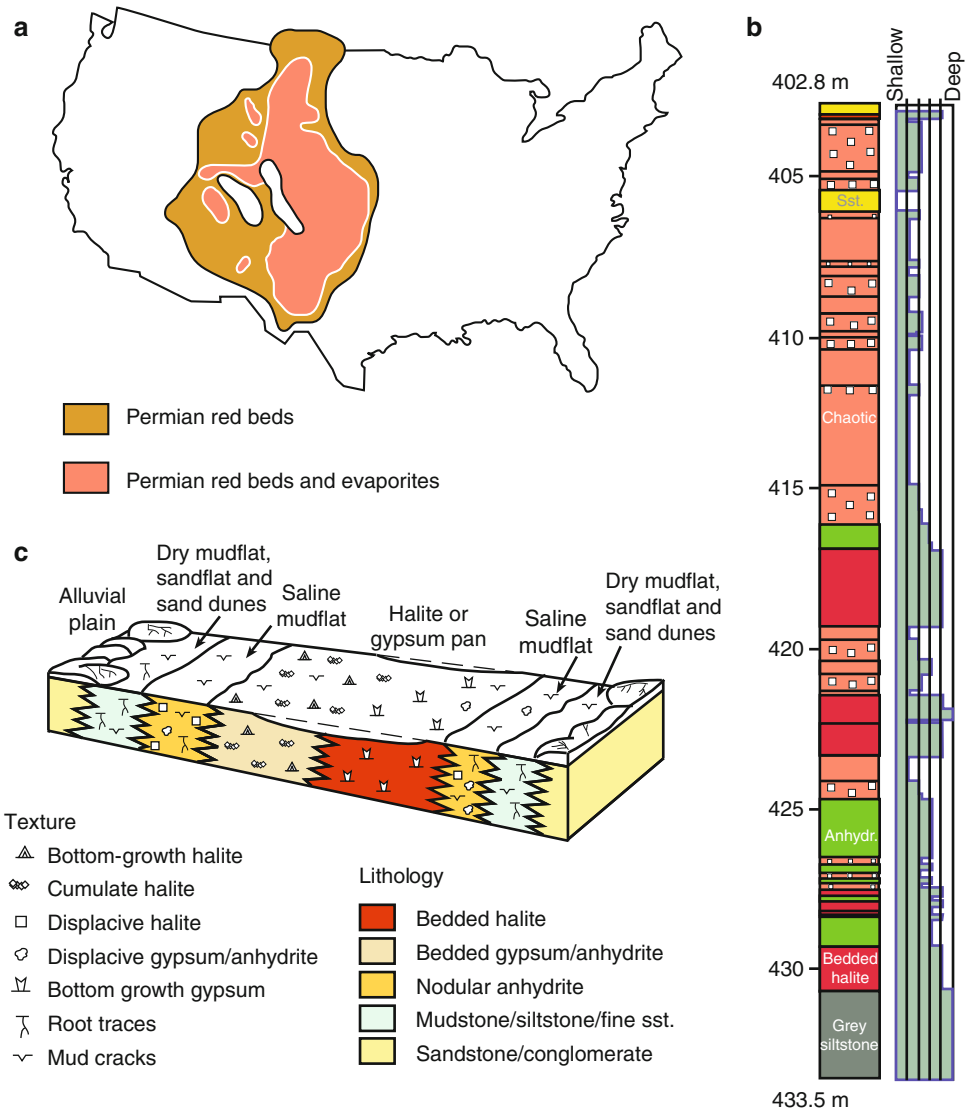

Fig. 5.15 Permian redbeds of interior USA. (**a**) Distribution of Permian red beds and evaporites in the USA. (**b**) Lithological description and relative depths of depositional environments of the Nippewalla Group from the subsurface of western Kansas; Anadarko-Davis No. 1 core, Seward County, Kansas. Deeper probably indicates a wetter climate and so this core seems to represent a transition from a wetter to a drier climate. (**c**) Inland playa associations that controlled sediment patterns in red beds of both the Opeche Shale and Nippewalla Group (After Benison and Goldstein 2000, 2001)

southeastern interior Australia and exemplified by the redbed lacustrine associations forming today in and around Lake Tyrell, Victoria and the salt lake landscape of southwest Western Australia (Bowen and Benison 2009; Benison and Goldstein 2002; Fig. 2.32).

Permian climate alternated between arid, when red siltstones and bedded evaporites dominated the various saline lake centres, and more humid, when grey siltstones and palustral carbonates were widespread. Much of the fine matrix in the ubiquitous Permian redbeds deposited at this time (e.g. Blaine Formation and Flowerpot Shale) is likely eolian dust and silt, rather that waterlain sediment (Sweet et al. 2013). An eolian origin to much of the redbed matrix is indicated by the fine and remarkably uniform grain size, internally massive structure, blanket-like geometry, and common palaeosols.

Bedded evaporites were deposited as saltpan and chaotic halites, or as less widespread bedded units containing calcium sulphate salts. Like the acid drainage basins of Australia, the system lacked widespread carbonates. These evaporite-depositing depressions were surrounded by extensive redbed mudflats and sandflats. Lithologies and sedimentary features indicate lacustrine and eolian deposition, subaerial exposure and palaeosol formation. Grey siliciclastic mudstones represent a freshwater-brackish perennial lake facies and are characterized by planar and convolute laminations, ostracods, peloids and plant material. Water levels were higher and the climate more humid when the grey siltstones were deposited. Bedded anhydrites containing gypsum-crystal pseudomorphs, clastic anhydrite grains, along with grey mud drapes and partings, all suggest deposition in saline lake depressions. Bedded halites consist of chevron and cumulate crystals, dissolution surfaces and pipes, and mudcracked microcrystalline salt crusts. They were deposited in saline pans subject to flooding, evaporative concentration and desiccation. Chaotic halite, composed of

red-bed mudstone and siltstone with displacive halite crystals, formed in saline mudflats surrounding the salt pans. Red-bed mudstone and siltstone with little or no displacive halite, but with abundant ped-cracking, root and plant features were deposited in dry mudflats in areas where water throughputs were less saline and waters were sufficiently fresh to allow halophytes to grow. Red-bed sandstone, composed of well-sorted, well-rounded quartz grains cemented with halite, preserve textures that indicate eolian and rare shallow-water deposition.

Evaporation, desiccation, flooding and wind reworking played significant roles in this environment (Benison and Goldstein, op. cit.). The Nippewalla Group/Opeche Shale siliciclastics and evaporites represent an evolution from a muddy perennial lacustrine system to a nonmarine, acidic saline pan system in the mid-continent of North America. Inclusion data from primary chevrons in the pan halite preserve temperature fluctuations at the seasonal scale and act as first-rate proxies for Permian climate in an arid megadesert created by the formation of Pangaea (Fig. 2.42). To the south, time equivalent evaporitic sediment in the San Andres and Clear Fork formations of the Palo Duro Basin, show an increasing marine influence in the form of intercalated carbonates. There widespread pan halites and bedded gypsums are intercalated with oolitic, restricted-marine platform carbonates, cryptalgalaminites become significant contributors to the sediment volume, and bioturbation from marine burrowers are locally important in some of the carbonate units (Handford 1981b; Hovorka 1987). Halite pseudomorphs after bedded coarse-grained gypsum is an important early diagenetic fabric in some of these sediments.

This passage to more marine-influenced saline pan and saltern salts in the south illustrates a correlation problem common to many ancient evaporites deposited atop cratonic landmasses. Namely, what defines an evaporite bed as marine or marine seepage-fed versus continental lacustrine in what where highly restricted settings where even marine-fed depressions had no surface connection to the ocean. This paradox is discussed in more detail later in this chapter.

Later work on this Nippewalla Group, using a halite core recovered from the Amoco Rebecca K. Bounds well, has further re-fined the climate-temperature significance of brine inclusions in aligned chevrons in bedded halite deposited in what was a continent interior playa system. Extremely high temperatures, to 73 °C, and large diurnal temperature ranges are evidenced in the lower Nippewalla Group, suggesting conditions more extreme than anywhere on Earth today (Fig. 5.16; Zambito and Benison 2013). In contrast, the upper Nippewalla Group was cooler; maximum temperature was 43 °C and diurnal temperature ranges were smaller, though even these conditions are similar to modern extremely hot environments, such as Death Valley, California. Comparison to prior studies suggests that these temperature results may be indicative of regional patterns. In may well be that the huge supercontinent interior deserts of Pangaea at times experienced more extreme temperatures than today, due to the high degree of continentality in such deserts and the fact that the Neogene Earth climate is in icehouse mode.

Other Lacustrine Red Bed Associations

In a number of underfilled lacustrine basins the supply of water may be insufficient to maintain a shallow watertable or a perennial lake in the drainage basin sump. In this situation the basin dries to where much of the sediment is reworked by wind action and little evidence of bedded lacustrine evaporites remains. Much of the basin fill is wind-reworked silt and loess. This is the situation in the present day Lake Eyre drainage basin of Central Australia and was also the case in the Middle to late Triassic across much of northwest Europe (Fig. 5.17; Talbot et al. 1994; Reinhardt and Ricken 2000; Porter and Gallois 2008; Brookfield 2003, 2008). This was when the Mercia Mudstone Group was deposited in Great Britain and the various Kueper lithofacies in Germany. Deposition was dominated by a characteristic assemblage of fine-grained sediment, the most widespread of which is a variably dolomitic red mudstone. It is typically massive and unfossiliferous except for occasional vague horizontal laminae and irregularly distributed wispy sand patches (e.g. Brookfield 2008). Desiccation features are common, as are blocky ped-like weathering patterns. Ainsworth et al. (2012) identified mud drape and other textural features in portions of this formation that indicate sedimentation similar to that seen in the terminal splay complexes, which periodically feed flood-stage sediment into modern Lake Eyre.

Nodular beds of gypsum/anhydrite and celestine are associated with the Mercia mudstone, along with gypsum-filled desiccation cracks and pseudomorphs after displacive halite and suggestions of haloturbation. Locally there are also 10–30 cm thick beds of dolomite and limestone. These thin beds range from micritic mudstones to ooid grainstones and packstones with freshwater algal remains (charophytes and *Botryococcus*). The local freshwater intervals are interpreted as areas of ponded floodwaters brought to the basin by exceptional rains (Talbot et al. 1994). As for the rest of the Mercia lithotypes, they too have their counterparts in times of freshened lacustrine sedimentation tied to flooding of the Quaternary Lake Eyre Basin, Australia and the Lake Chad Basin, Africa (Chap. 3).

Details of other ancient, mostly Neogene, saltpan and perennial lacustrine deposits, where the bedded salts are an exploited resource or a intimately associated with an exploited resource, are discussed in Chap. 11 (borates, lithium, magnesites, nitrates, potash, sodium carbonate, sodium sulphate, zeolites).

Platform Evaporites on Epeiric Shelves

Platform evaporites accumulated in epicontinental (epeiric) or pericontinental settings and constitute the salt layers in many stacked shoaling marine platform cycles, where

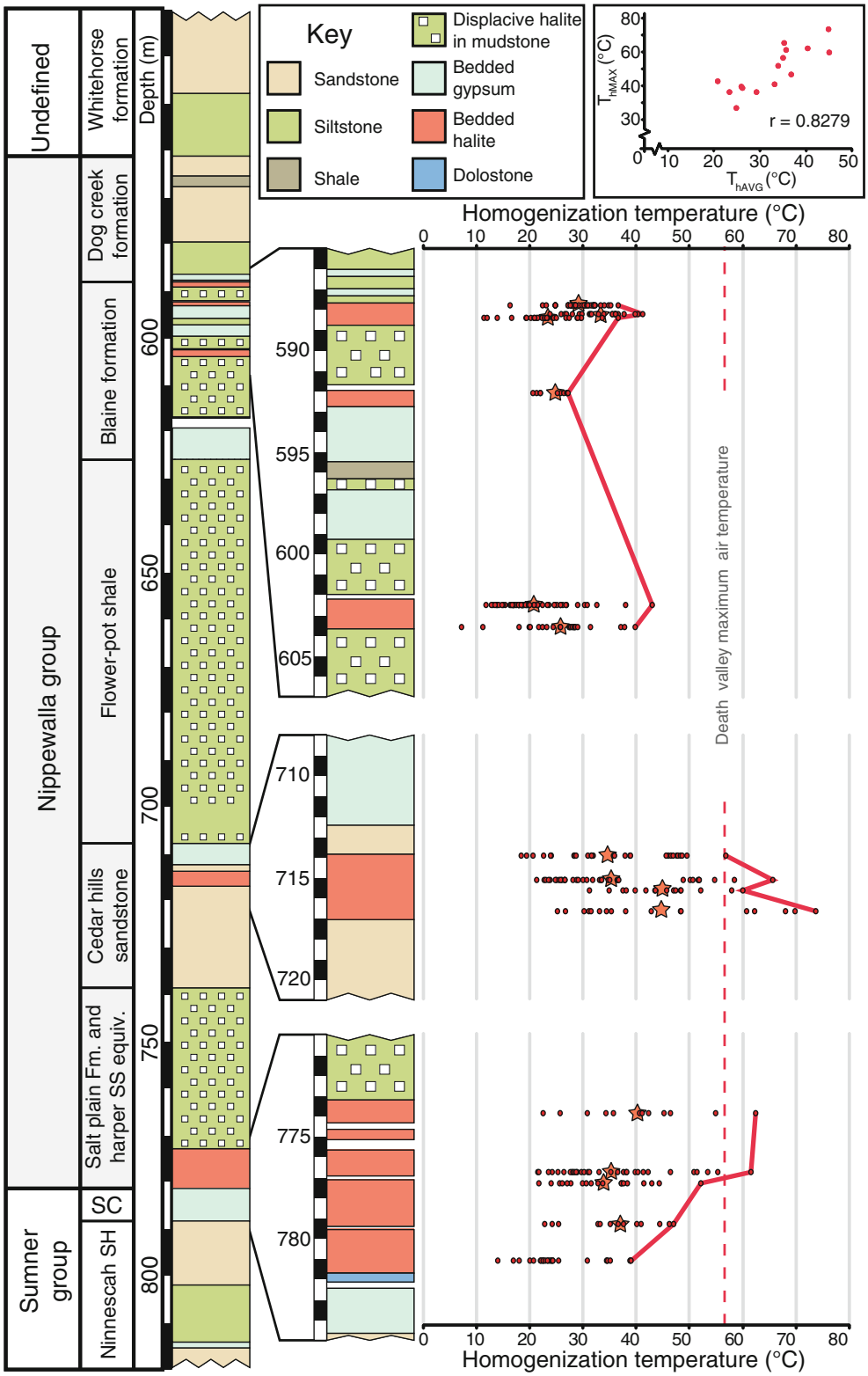

Fig. 5.16 Homogenization temperatures (T_h; *MAX* maximum, *AVG* average) for fluid inclusions within Nippewalla Group halite in the Amoco Rebecca K. Bounds core, Individual values represented by *black-edged red circles. Stars* represent T_{hAVG} for each sampled bed; T_{hMAX} is traced within subgroup units by *solid red line. Thin red dashed line* marks 56.7 °C, the hottest known air temperature measured on Earth (Death Valley, California). *Inset plots* T_{hmax} versus T_{hAVG} for all beds sampled (After Zambito and Benison 2013)

5–10 m thick evaporite units (typically anhydrite with lesser halite) are repeatedly interbedded with open-marine shoal-water carbonates or continental siliciclastics. Epeiric seaways were huge very shallow shelf and interior seas, up to thousands of kilometres across, that typically held waters no more than tens of metres deep and were usually much shallower during the hydrographically-isolated bedded salt phases (Fig. 5.18; Table 5.5). Epeiric seaways occupied large areas of continental interior (intracratonic seaway), while pericontinental (pericontinental seaway) describes situations

where large portions of the continental margin freeboard are covered by seawater. Both styles tend to be commonplace at times when world sealevels were high, as exemplified by greenhouse climate modes. In the world's current icehouse mode, sealevels are low as much of this water is caught up in polar icesheets and continental freeboard is limited. Consequently, there are few Quaternary examples of epeiric seaways and, because the icecap driven eustatic signal is one of high amplitude (120 m) and high frequency (100,000 years). They are all open marine systems: e.g. Gulf of Carpentaria, northern Australia, with its patchy but widespread *Halimeda* mounds, and the Yucatan Shelf of Mexico with its well developed strandline of calcareous eolianite.

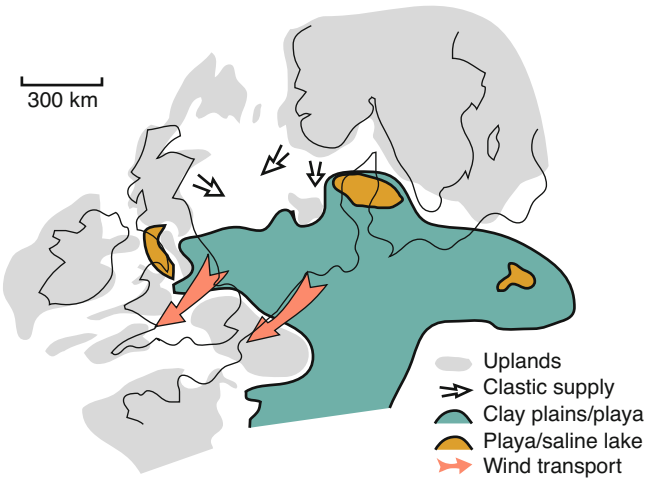

Fig. 5.17 Late Triassic palaeogeography of northwest Europe showing how deposition was predominantly in an endorheic basin and wind was blowing dust from mudflats about large discharge playas (After Talbot et al. 1994)

When an epeiric basin is cut off from a surface connection to the open ocean (hydrographically-isolated), saline deposition occurs either in: (1) Widespread evaporitic mudflats surrounded by desert dunes and wadi plains or, (2) Beneath sluggish, slowly circulating perennial sheets of marine-fed brine (saltern seaways) that cover the lower parts of the basin. These saltern water sheets can become holomictic and attain sufficient salinity to precipitate and stack widespread salts beds into units as much as 5–10 m thick. A region of subaerial evaporitic carbonate mudflats and sandplains, or an older now exposed platform edge shoal, typically separated the brine sheets from the open ocean.

At other times, when the same areas on the epeiric platform had a surface connection to the adjacent ocean (hydrographic connection and sealevel high), they were covered by shallow

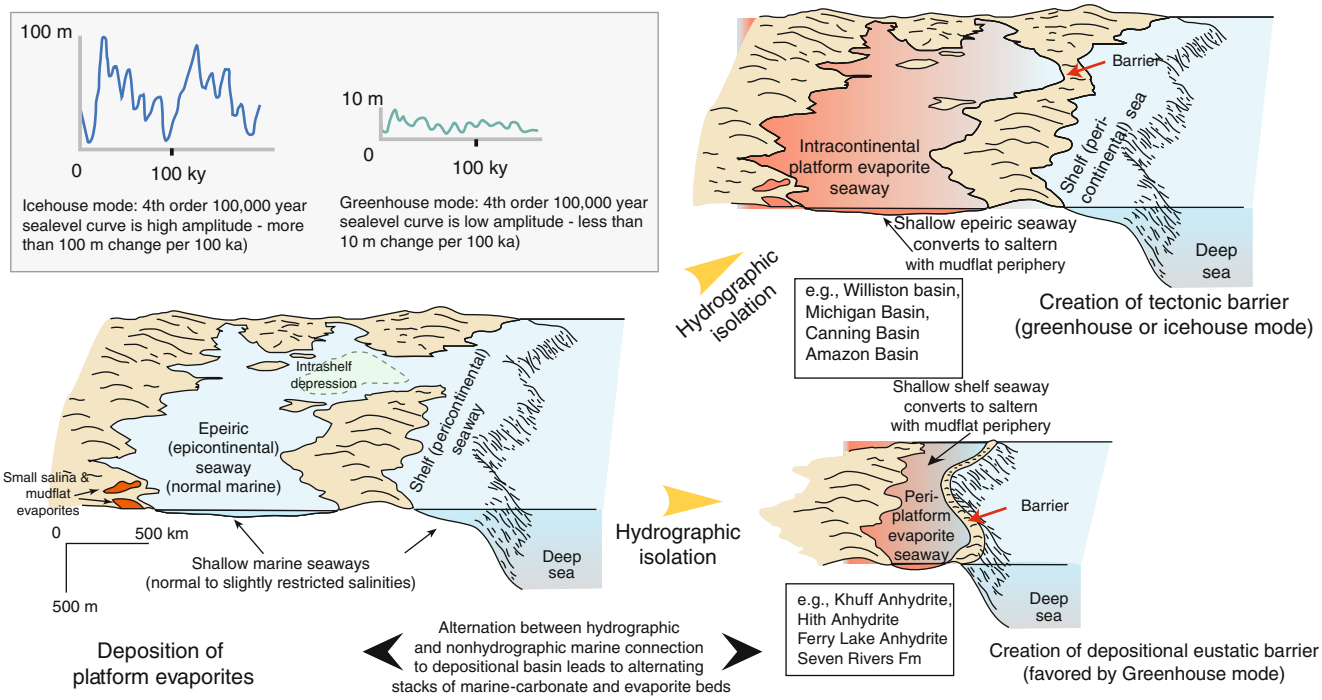

Fig. 5.18 Epeiric (epicontinental) seaways that covered large areas of the continental interior with shallow marine waters are known as intracratonic basins, while epeiric seaways that formed as very wide shelf edges along the continental margin as known as pericontinental seaways. Waters were very shallow over areas that were hundreds to thousands of kilometres across. Neither setting has a modern counterparts; pericontinental seaways that evolve into salterns and or evaporitic mudflats are more typical of marine-margin eustatic styles on the earth in greenhouse climate mode, when the lack of permanent polar icecaps, especially coupled with higher rates of seafloor spreading, meant the continental freeboard was much larger than it is today. Greenhouse meant relatively stable low-amplitude 4th-order sealevel and that there was time to build up a near continuous platform edge shoal. Intracratonic basins tended to go evaporitic with tectonically driven hydrographic isolation, in both greenhouse and icehouse mode. With hydrographic isolation both these restricted marine seaways quickly became salterns or evaporitic mudflat systems (After Warren 2010)

Table 5.5 Selected platform evaporites (dominantly megasulphate systems)

Periplatform evaporite successions	Age	Comments/key references
Ferry Lake Anhydrite, NE Gulf coast, USA	Cretac., Lower	Divided in 9 individual saltern anhydrites that are traceable from southern Mississippi to southern Florida and intercalated with normal marine bioclastic limestones (Pittman 1985; Petty 1995)
Rus Fm., Arabian Basin, Qatar, Saudi Arabia	Eocene, Lower	Has a total thickness of about 100 m, composed of limestones and dolomitic limestones (often argillaceous) passing upward into massive 10 m thick saltern anhydrite (Whittle and Alsharhan 1994; Ziegler 2001; Al-Saad 2003; Steinhauff et al. 2008)
Smackover/ Buckner Fm., N Gulf Coast, USA	Cretac., Lower	Buckner Anhydrite made up of intercalated 2–6 m thick saltern anhydrites and marine limestones. It extends from Florida Panhandle to South Texas (Mann 1988)
Hith Anhydrite, Arabian Basin, Middle East	Jurassic, Upper	Hith anhydrite is a regional seal that extends across much of the Arabian Peninsula and locally reaches 170 m in thickness. It is composed of bluish-gray to alternating bands of blue and white anhydrite with two internal carbonates and separates marine carbonates of underlying Arab Fm from overlying Yamama (unconformable base) (Alsharhan and Kendall 1994; Ziegler 2001)
Middle Anhydrite Marker, Khuff Fm., Middle East	Permian, Upper	Middle Anhydrite can be traced from eastern Saudi Arabia to offshore UAE, and reaches the onshore Fars Province of Iran. This anhydrite is some 12–17 m (20–39 ft) thick and consists of massive saltern anhydrite with minor thin interbeds of dolomite (Alsharhan 2006)
San Andres Fm., Northern Delaware Basin margin, USA	Permian, Upper	Anhydrite occurs as widespread saltern units composed of massive nodular mosaic anhydrite beds up to 5 m thick capping cyclic shoaling variably-dolomitised platform carbonates. Individual anhydrite beds (P1-P5) that can be traced from Palo Duro basin into shelf edge of the Slaughter-Levelland trend (Elliott and Warren 1989)
Cadjebut Fm., Canning Basin margin, Australia	Devonian Middle	Saltern anhydrites up to 5 m thick extend across a Devonian platform embayment pass and pass laterally into the sulphide mineralised ore horizons of the Cadjebut Mine region. Saltern sulphates capped shoaling oncolitic and bioclastic muds that overlie normal marine grainstones and wackestones (Cathro et al. 1992)
Cool Creek Fm., Arbuckle platform, USA	Ordovic., Lower	At least three 1–2 m thick breccias, interpreted to be of solution collapse origin, are present in the Cool Creek and define the presence of former widespread saltern anhydrite units that capped restricted marine stromatolitic carbonate platform sediments (St John and Eby 1978)
Red Heart Dolomite, Georgina Basin, Australia	Cambrian, Lower- Middle	Red Heart Dolomite which extends across much of Central Australia is a completely dolomitised 100 m thick platform carbonate deposited in an evaporitic shallow-water epeiric seaway It is characterized by at least four shallowing-upwards saltern anhydrite-capped cycles. Many of the surface and near-surface anhydrites caps are now leached and represented by collapse breccias (Nicolaides 1995)
Intracratonic Platform evaporite successions	Neoproterozoic to Eocene	North Sahara Basin, Africa; Canning Basin, Australia; Muschelkalk and Paris Basins, SW Germany and Spain; Amazonas Basin, South America; West Siberian Basin, Russia; Michigan Basin and Williston Basin, USA (see also Tables 5.6 and 5.8)

The shallow water textures and intercalated marine carbonates mean many basinwide intracratonic evaporites are also classified as platform evaporites

seawater (e.g. Feng et al., 1998; Fuersich et al., 1995). These waters could concentrate into the mesohaline range, especially in more restricted parts away from areas of marine resupply, but could not reach sufficient concentration to produce bedded salts (Chap. 2). The greater volume of the platform sediments at times of hydrographic connection were muddy marine carbonates, mostly peloid wackestones and mud-stones. Skeletal and peloidal (oolitic) grainstone shoals built up in areas where current energies from waves, or possibly tides along the marine edge, were sufficient to winnow lime mud but not grains. This created sandflat islands or shoals with long axes subparallel to the direction of dominant current transport, and subsequently encased in peloids or muds. These sandy beds constitute the reservoir sands in many mudflat and saltern-sealed epeiric sequences, such as the Arab D and Khuff carbonates in the Middle East (Chap. 10). Repetitive and characteristic shoaling-upward stacks or parasequences accumulated on the platform as the various types of marine sediments aggraded and prograded in this dominantly carbonate milieu. Extensive flat arid areas circumscribing the seawater-covered areas of the open seaway were typically huge evaporitic mudflats. Salinities along the low-relief strandzones of these huge shallow seaways were sufficiently elevated that the only fossil evidence of life was the occasional stromatolite or thrombolite and a mass of flat-laminated microbially-influenced mudstones (cryptalgal laminites).

Marine-fed mudflats and holomictic salterns generated dense seaward-flowing seeps of residual reflux liquor, via a reverse flow hydrology situated below the less dense marine-inflow seep groundwaters. Such dense groundwater brines cycled through and across the underlying platform sediment to create reflux dolomites (Fig. 2.73). The return fluxes were sometimes sufficiently voluminous to supply longterm chemosynthetic seeps in the outflow zones on the open sea floor of the adjacent open marine platform. At times of hydrographic connection, brines escaping from an adjacent mud-

flat into the seaway would become bottom-hugging waters, which trickled and seeped into local brine sumps on the marine platform floor. Ultimately, these denser, bottom waters formed areas characterised by longterm dense anoxic bottom water beneath a column of normal platform seawater. These areas were intraplatform or intrashelf basins that were local, slightly deeper, warmer (heliothermic) depressions on the seaway floor (Chap. 9).

The intrashelf subaqueous sumps could be up to hundreds of kilometres across, but water columns were no more than 10–30 m deep. By the time the mudflat-derived bottom brines finally ponded in the deeper parts of such intraplatform lows, salinities may have been diluted, via diffusive mixing, to where they were no more than a few ‰ higher than normal seawater. This was sufficient to maintain a density/thermal stratification, so that the bottom waters were dysaerobic to anoxic. A number of organic-rich oil-prone carbonate laminites and marls (source rocks) accumulated in these lows, such as the Jurassic Hanifa Formation a significant source rock of the Arabian Platform (Figs. 9.4 and 9.5). At times of hydrographic connection between the epeiric platform and the world's oceans, the platform areas surrounding these intraplatform depressions were shallow and more oxygenated than the depression floor, with largely normal marine salinities and water depths typically less than 10 m. This encouraged the local accumulation of reef mounds and sandy shoals on the highs.

Hydrographic connection between the open ocean and the epeiric seaway could be lost for a number of reasons; a sand shoal buildup at the platform rim, a slight fall in sealevel, or tectonic tilting. Once portions of epeiric or pericontinental seaways lost their hydrographic connection to the open ocean, bedded marine-fed saltern and mudflat evaporites were laid down. This occurred within one of two carbonate platform chassis; either on a *carbonate ramp* or on a *carbonate shelf* (Fig. 5.19). Carbonate ramps have slopes of less than 1°, the wave agitated zone is typically close to the seashore, and there is no high relief shelf break located some distance seaward from shoreline (Ahr 1973, 2008). Slopes in ancient epeiric ramps in greenhouse times and in intracratonic seas were as low as 1 in 50,000, compared to modern ramp gradients of between 1 in 500 and 1 in 2,500 (Fig. 5.19a; Burchette and Wright 1992; Warren 1991). In contrast, carbonate shelves are shallow water, land-coupled platforms with a pronounced break in slope into deeper water (Fig. 5.19b). The break in slope is typically a wave agitated to high-energy feature, it may be composed of a reef rim or a series of mechanically-reworked sand shoals and islands. The slope, seaward of the platform edge, is typically measured in degrees of inclination. In modern reef-rimmed platforms the seaward slope ranges from 30° to vertical.

Rather than the icehouse climate mode of today, periplatform evaporite systems require greenhouse eustasy in order to establish the required seepage hydrology (Warren 2010). Times of greenhouse climate were times when 4th order (100,000 year) sealevel changes were an order of magnitude less than the 100 m sealevel cycles that typify 4th order eustatic cycles in the icehouse-driven world of the last 10–12 million years (inset in Fig. 5.18). There was another Phanerozoic episode of icehouse-dominated eustasy some 300 Ma in the Permo – Carboniferous and another somewhat shorter possible episode some 440 Ma in the Ordovician (Fisher 1981).

During icehouse times the oceanic eustatic response to rapidly waxing and waning polar icesheets is in terms of amplitude excessively high, and time-wise too short, to allow sufficient time for periplatform-margin biogenic buildups to grow into continuous platform-edge barriers. It is the long-term elevated sealevels of greenhouse times, along with their lower fourth order amplitudes (less than 5–10 m of sealevel change every 100,000 years), that allow persistent platform-edge reefs and shoals to form (see inset in Fig. 5.18). With a subsequent slight fall in sealevel, these contiguous platform-edge barriers became subaerial barriers to any hydrographic connection of the back-barrier lagoon to the open ocean. This initiates marine-seepage fed lagoons (salterns) in their hinterland.

Periplatform evaporites tend to megasulphate rather than mega-halite affinities and today act as regional seals to many of the world's oil and gas fields (e.g. Hith Anhydrite, Middle Anhydrite marker of the Khuff Fm and the Ferry Lake Anhydrite; see Chap. 10 for details on various evaporite-sealed oil and gas fields). But in addition to the periplatform settings, there are shallow-water platform evaporite systems in continent-interior (intracratonic) settings. There, laterally extensive sulphate and halite beds are interlayered with units of normal to restricted marine platform carbonates, defining cycles more than 30–60 m thick. Well preserved nonhalokinetic bedded halite in these cycles tends to be part of the depositional succession in this type of platform evaporite. These platform evaporite successions tend to occur in intracratonic sags (typically tied to aulocogens in extensional or distal flexures in compressional settings), as in the Amazonas and Michigan basins (Table 5.5). At the basin scale, such intracratonic halite beds can become halokinetic, but only when later caught in tectonic events such as a zone of continent-to-continent collision.

Unlike periplatform evaporites, where the hydrographic isolation is a eustactically-driven, typically greenhouse, response; the hydrographic isolation needed to create an intracratonic evaporite phase tends to be tectonically induced. Compared to saline giants (megahalites) deposited in rift and collision basins along the continental edge, intracratonic evaporites can be considered a transitional tectonic subset of basinwide evaporite successions. Deposition is related to gentler topographic expression in a intracratonic sag with slow relative subsidence an occasional marine ingress. This encourages stacking of a number of shoalwater saline episodes (up to 5 or more third-order evaporite-carbonate cycles, sometimes spread over tens of millions of years in an intracratonic system). In contrast, typical basinwide evaporite (megahalite and megasulphate) are deposited as thicker salt masses (>100–200 m thick) over shorter active saline

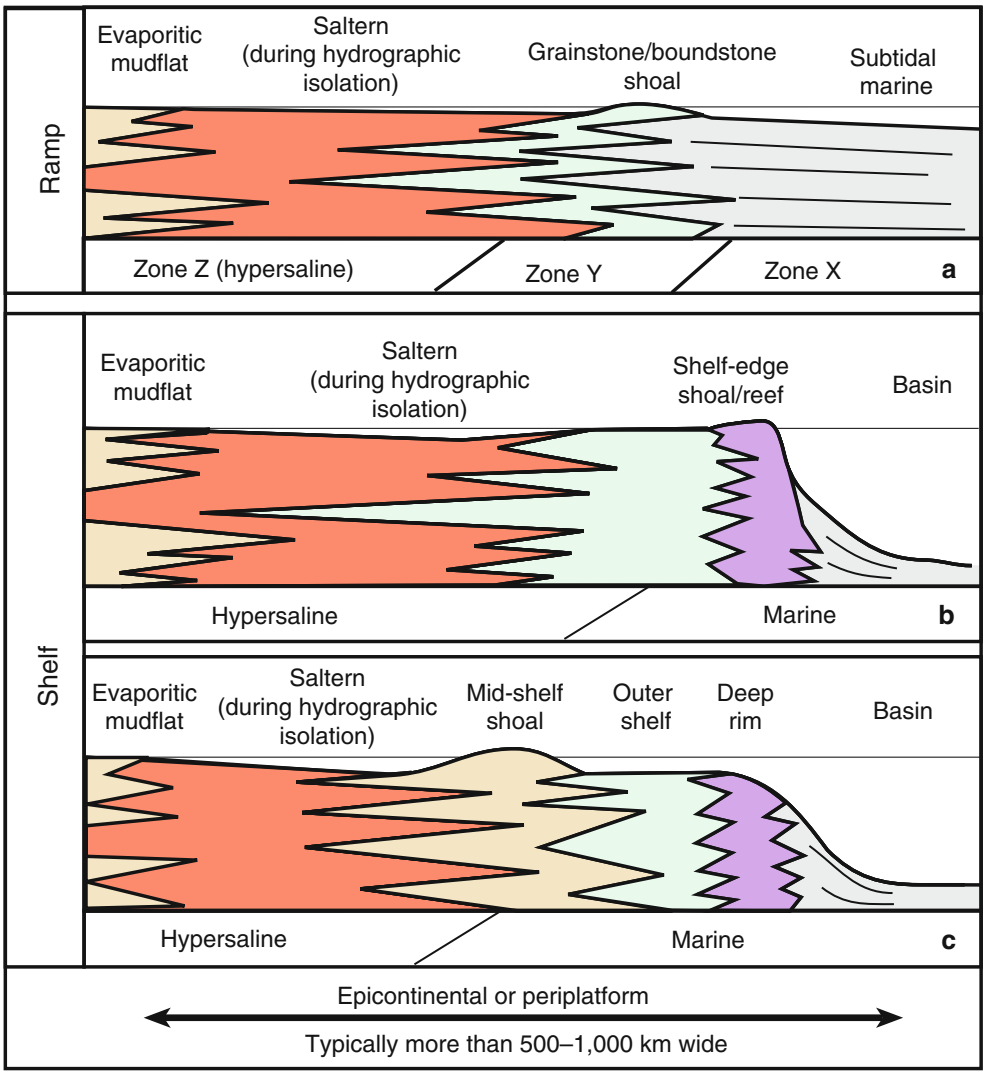

Fig. 5.19 Evaporite depositional styles – ramp and shelf. (**a**) Gently deepening ramp with restriction created by exposed zone Y shoal. (**b**) Rimmed shelf with restriction supplied by exposed reef/shoal that defines the platform margin. (**c**) Rimmed shelf with deep rim and restriction supplied by exposed mid-shelf shoal

basin time frames (forth-order cycles stacking into a thick evaporite sequence over ≈1 million years). These evaporites tend to have higher average sedimentation rates than the underlying or overlying nonevaporite sediments within the incipient marine rift and continent-continent collision basins where they form. The greater thickness of salt and its relatively purity makes these salt masses more susceptible to halokinesis than the intracratonic evaporite units (Chap. 6).

Evaporitic Epeiric Ramps

Ahr's 1973 ramp model envisaged a uniform slope from the shoreline into the basin, later termed a homoclinal ramp by Read (1985). However all modern ramps, and some ancient ramps appear to have a subaqueous slope break in deeper water and are termed distally-steepened ramps. The overall inclination of the slope is still flat (<1–2°) and never approaches that of a carbonate shelf. Modern ramps characterise the tropical arid carbonate coasts of the southern Arabian Gulf, the Gulf of Carpentaria and the more humid Yucatan shelf. All these modern ramps face directly into the open ocean and have never shallowed sufficiently to isolate large portions of their lagoons and so lack widespread salt beds. Minor marine-fed evaporites do accumulate in small volumes as laminites and displacive aggregates in the transitional marine portions of the Arabian and Carpentarian gulfs.

The best-documented example of a modern carbonate ramp, with some evaporite deposition, is the Trucial Coast of the southern Arabian (Persian) Gulf (Purser and Evans 1973). But, it is a poor analogue for any epeiric or pericontinental counterpart as it is not supplied solute from a seawater source, its evaporite belt is supratidal, less than 10–15 km wide, matrix-rich and less than a metre thick (Chap. 3). In the Gulf of Carpentaria, evaporitic conditions some 70 ka produced a decimetre-scale unit made up of repetitive alternations of μm to mm-thick gypsiferous and micritic laminae, with a varve-like appearance. These precipitates are interpreted as primary features, deposited in a shallow lake that retained limited water in its centre (core MD-32; Playa et al. 2007). Elemental and isotope geochemistry of the laminae show a complex evaporitic environment where initially marine waters evaporated with the input of continental waters compensating for evaporative losses.

Unlike most modern arid-zone carbonate ramps, which are tens to a few hundred kilometres wide, ancient hypersaline epeiric ramps were hundreds to thousands of kilometres across and formed huge evaporitic seaways at the edges of continents (pericontinental seaways; Fig. 5.18) or extended as near-land-locked interior seaways that spread out across large areas of various continental cratons (epicontinental seaways and intracratonic basins). The Permian red beds discussed earlier in the lacustrine section are the landward end of one such interior evaporitic lake or seaway (saltern). The world's last development of such a huge interior seaway was in the Eocene in evaporitic platform carbonates of the Middle East (Table 5.5). But these platform evaporites (Radhuma, Rus and Dammam formations) are perhaps better considered as basinwide back-bulge or intracratonic sag salts, deposited in a response to flexural sag and basin isolation behind the migrating forebulge of the Zagros Orogeny (Alavi 2004; Steinhauff et al. 2008). If so, this makes the world's most recent episode of marine periplatform evaporite as old as the Paleocene or the Cretaceous (Table 5.5; Fig. 10.36).

The transition into an icehouse climatic mode in the Eocene, the capture of large volumes of ocean water in oscillating ice caps, and a slowing in the rate of seafloor spreading, meant large evaporite seaways, so conspicuous on the Late Permian and Mesozoic platforms, had disappeared from the face of the earth by the mid Tertiary. A lack of modern analogs means we cannot directly observe the influence that epeiric seaways had on the depositional styles of ramp evaporites. We are forced to scale up sediment patterns in Quaternary coastal evaporites in the knowledge that the high amplitude, high frequency, eustasy of today is not the hydrological or eustatic equivalent of the sea-margin periplatform ramps of greenhouse earth.

Epeiric ramps were first modelled by Shaw (1964) and Irwin (1965), they both concluded that the huge areas of restricted stagnant circulation on the hind parts of these seaways were capable of periodically accumulating extensive beds of evaporites. Irwin's epicontinental-sea model proposed there were three zones of varying hydraulic energy on ancient platform ramps (Fig. 5.19a):

- *Zone X* was a wide low-energy region situated below wavebase on the open-marine side of the platform, so that sediments were mainly bioturbated marine mudstones and wackestones. It was often hundreds of kilometres wide and locally characterized by limited water circulation, with occasional stagnation. Now and then, this led to the deposition of organic-rich laminated sediments.
- *Zone Y* was a narrow, intermediate to high-energy belt beginning where waves first bottomed on the seafloor and extending landward to the limit of any tidal action. Sediments in this zone included sand and grainstone shoals, mud banks, reef mounds and patch reefs. These sediments could build elongate shoals that restricted and at times prevented the surface entry of seawater into the adjacent zone Z.
- *Zone Z* was an extremely shallow, restricted low-energy region on the landward side of zone Y. In arid settings, wherever zone Z was hydrographically isolated from zone X, extensive saltern and mudflat evaporites were deposited. At times when zone Z and zone X had a surface connection through zone Y, the seaward portion of zone Z was covered by restricted-marine mostly muddy sediments with local sandier carbonates. The more distal portions on its continental side were evaporitic mudflats.

Marine wave energy was dissipated some distance basinward from zone Z as it spent itself against the seaward side of the shoals, bars, and reefs of zone Y. Shallow wave-agitated facies of zone Y passed down the slope into deeper-water subtidal open-marine facies of zone X without a rapid change in slope angle. Behind the zone Y shoal, bottom slopes in zone Z were even less than on the open marine ramp and had maximum bottom angles of only a few seconds of arc (≈1:50,000). Thus, huge areas of zone Z were covered by extremely shallow water sheets, much of it only tens of centimetres deep. This is a setting replicated at a much smaller scale in the modern khors of the United Arab Emirates (e.g. Khor al B'azm). During times of widespread evaporite deposition across zone Z there was no hydrographic connection to the ocean and so tidal effects were negligible. Depositional textures were largely akin to those formed in modern saline pans and sabkhas although perennial seaways depositing salterns were a distinct possibility in zones with more relief behind Zone Y.

Zone Z water levels fluctuated most rapidly during intense storms or hurricanes, as sheets of sediment-laden seawater could be washed landward over zone Y into zone Z, or during exceptional episodes of flash-flooding generated by torrential rainstorms in the continental hinterland. Both marine and meteoric influx freshened the surface and nearsurface brines of Zone Z as sheets of water migrated tens of kilometres across the strandplain. At the same time a new pulse of marine or continental clastic sediment matrix was delivered. Evaporite-forming areas in zone Z were up to hundreds of kilometres wide, far wider than any evaporitic area on the modern land surface.

On any evaporitic ramp there was some degree of topographic relief about zone Y, and restriction of water flow across it. When salts were accumulating in Zone Z there were no perennial surface channels connecting it to the waters of Zone X (no longterm hydrographic connection Fig. 5.19). Vertical sequences of evaporites deposited in zone Z were very much dependent on the relative physiography of zone Y. If zone Y was a well developed low-relief shoreline with extensive washover flats behind, then much of zone Z was an evaporitic mudflat; a mosaic of sabkhas and salinas. Or, if zone Y was a higher-relief shoal, it would be backed by a marine seepage-fed evaporite lagoon, and zone Z would consist of saltern evaporites with an increasing proportion of subaerial mudflat indicators (desiccation cracks, karst, erosion features, displacement textures) toward the top of the unit and toward the landward and seaward strandplains.

Units P_1 and P_2 of the San Andres Formation in the northwestern platform of the Permian Basin and the Palo Duro Basin illustrate the saltern-ramp end member (Fig. 10.22; Elliott and Warren 1989). Similar saltern signatures dominated the San Andres and Clear Fork formations in the Palo Duro Basin (Fig. 5.27). Correlatable units of saltern anhydrite or halite in the Palo Duro Basin have areas of more than 26,000 km^2. At times of widespread evaporite deposition on the Palo Duro Basin and the northwestern shelf of West Texas, one could have travelled 50–150 km south and seaward from the strandplain of the brine sheet and never crossed through water that was much more than a few metres deep, nor less saline than gypsum-saturated.

The northern portions of the Lower Clear Fork Formation of the Palo Duro Basin illustrate the evaporitic mudflat-ramp end member where extensive "dirty" halite beds are intercalated with fine-grained siliciclastics (Fig. 5.20a; Handford 1981b, 1991). Deposition took place in an evaporitic mudflat and pan complex that passed further northward into the large continental desert made up of salt pans, wadis and dunes documented by Benison and Goldstein (2001). Southward, the Clear Fork ramp passed from highly continental mudflats into marine-fed saltern deposits and then across the restriction of the Zone Y phylloid buildups into open-marine carbonates of zone X (Fig. 5.20b; Ramage 1987). Deciding where to place a line separating marine from nonmarine brines is near impossible; although it is generally true in this and in most other arid successions passing from the marine into huge interior redbed deserts that the thicker bedded salt accumulations are more likely on the marine side of the system.

Thick evaporitic carbonates and intercalated anhydrites of the Khuff Formation define a huge evaporitic platform (≈255 Ma) in the Arabian Gulf, with an upper section that straddles the Permo-Triassic boundary (Fig. 5.21a; Al-Jallal, 1991, 1995; Dasgupta et al. 2002). In eastern Saudi Arabia, the Khuff Formation is divided into five units or members designated as Khuff A through E. However, throughout the Gulf region the Khuff may comprise as many as eight designated mappable subsurface units or members (KS1-7; Alsharhan 2006; Al-Jallal 1995; Strohmenger et al. 2002). Most of the Khuff Formation is composed of carbonates and evaporites; major siliciclastic facies increase towards the west and toward the base of the sequence, especially in Saudi Arabia (Ehrenberg et al. 2007). As many as six or seven grainy units are capable of acting as hydrocarbon reservoirs and correspond to depositional carbonate-anhydrite cycles where transgressive marine carbonates are capped by regressive anhydrites.

The Khuff Formation thickens from about 260 m in southwestern Saudi Arabia to more than 915 m in the central Rub 'al Khali Basin, 1,220 m in Oman, and 1,520 m in Iran. Typical thickness for the Khuff ranges between 370 and 490 m over most of central and eastern Arabia (Al-Jallal 1995; Strohmenger, et al. 2002; Alsharhan 2006). The basal Khuff section consists mostly of siliciclastics throughout southern Arabia. The "basal Khuff clastics" in Saudi Arabia are made up of shale, carbonaceous shale, limestone streaks, and incised channel-fill sandstones. Individual channel-fill sandstone units of the basal Khuff clastics are as much as 18 m in thickness and can cut deeply into the underlying Unayzah Formation. In the Hazmiyah field of central Saudi Arabia, the reservoir occurs entirely within these channel sandstones in the basal Khuff (Fig. 5.21b; Senalp and Al-Duaiji 1995). The Unayzah and basal Khuff sandstones form the principal reservoirs in central Saudi Arabia and extend north in Kuwait; however, widespread reservoir quality variations occur in

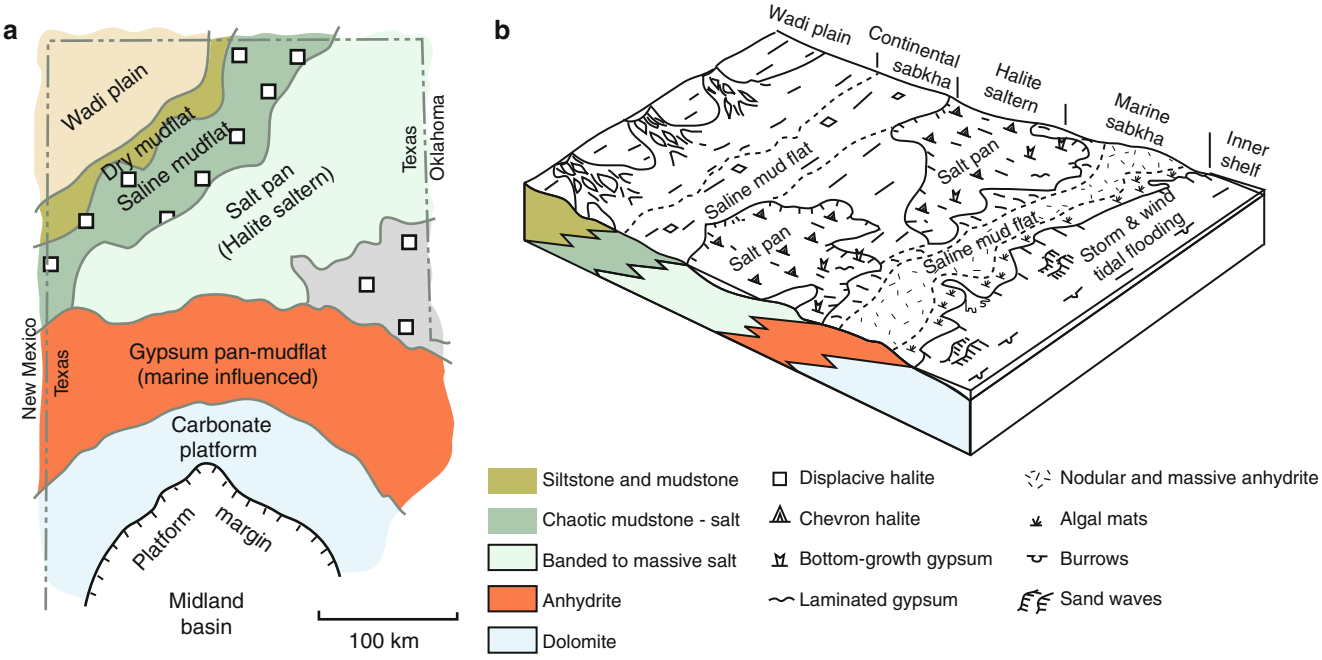

Fig. 5.20 Lithofacies and paleogeography of the early Permian Lower Clear Fork Formation, an evaporitic ramp at the northern end of the Midland Basin in the Texas Panhandle. (**a**) Plan View. (**b**) Schematic of depositional relationships between main evaporitic facies (After Handford 1981b)

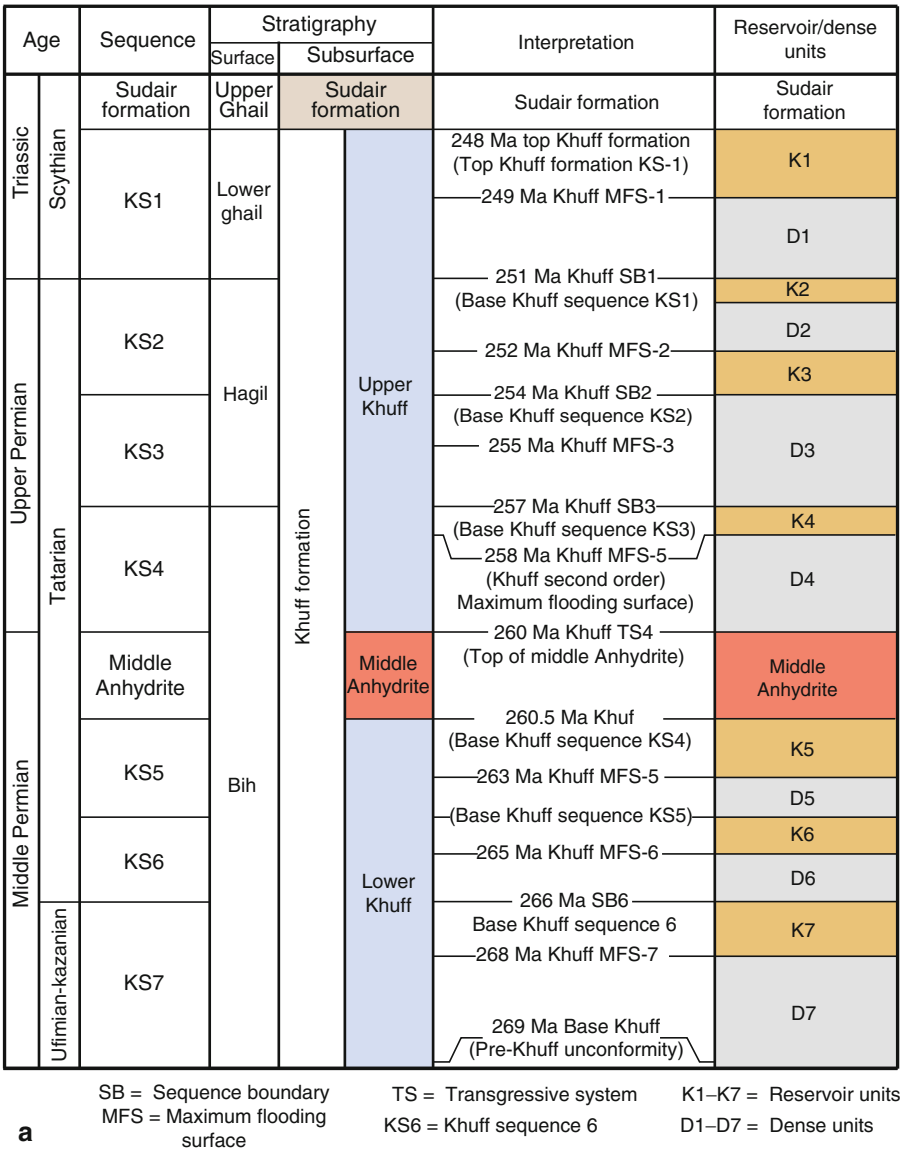

Fig. 5.21 Khuff Formation, Middle East (After Alsharhan 2006). (**a**) Sequences of the Khuff Formation and their equivalents in outcrop of the United Arab Emirates. Age determinations show the Middle Anhydrite was deposited in less than 0.5 million years (260–260.5 Ma). (**b**) Palaeozoic regional cross-section, highlighting sequence stratigraphic framework of the Middle Permian to Early Triassic Formation

these sandstone reservoirs owing to heterogeneous sedimentary facies and variable diagenetic intensity (Aktas and Cocker 1995; Polkowski 1997; Tanoli et al. 2008).

Over most of the rest of Saudi Arabia and west into Oman and the UAE the Khuff is more than a 1 km thick and composed of numerous 2–10 m thick shoaling stacked dolomitised carbonate cycles or parasequences. These Late Permian dolomites are major gas reservoirs along the offshore in the Arabian Gulf north and west of Qatar. In contrast, the regionally extensive anhydrite, shale, and tight (low-permeability) carbonates of the Khuff Formation form the major regional seal for Pre-Khuff hydrocarbon accumulations in central and eastern Saudi Arabia (Al-Jallal 1995; Wender and others 1998; Alsharhan 1993, 2006).

Deposition of this thick carbonate succession was initiated as a ramp in the late Khazanian or early Tatarian and had evolved into a reef-rimmed evaporitic platform by the later Permian to early Triassic (Fig. 5.22). Most of the cycles in the upper part of the Khuff are capable of producing gas and are variably dolomitised oolite-peloid successions that typically grade upward into fine-grained laminites and nodular mudflat/pan anhydrite. Carbonate cycles atop siliciclastics in the lower part of the Khuff tend to be more dominated by coarsening-upward shoreface/shoal cycles with lesser mudflat laminites.

All the Khuff beds and anhydrite saltern marker pass westward via a belt of mixed detrital carbonate and siliciclastics onto the palaeohigh of the Arabian Shield (Fig. 5.21b; Alsharhan 2006). Correlations and definitions of time-equivalence in adjacent wells or outcrops in this belt is problematic due to a lack of appropriate fossils and similarity in wadi/dune depositional styles throughout large passages of Palaeozoic and Mesozoic time in the circum-Arabian Shield area.

The Khuff succession is punctuated by numerous intervals of subaqueous and pan anhydrite (after gypsum) with local development of evaporitic mudflat facies atop shoals (pers. obs.). In the middle of the Khuff succession is a thick saltern sulphate bed called the Middle Anhydrite. It is a regional marker bed originally deposited as a thick sequence of bottom-nucleated subaqueous gypsum. This marker defines a time when the whole of the Khuff platform was converted to a saltern rather than the more typical combinations of evaporitic mudflats and pans (see also Chap. 10).

The Jurassic section atop the Khuff in Saudi Arabia and the Emirates is another evaporitic platform succession. It constitutes the most significant source-reservoir-seal association for hydrocarbons anywhere in the world (see detailed discussion of Hanifa, Arab D and Hith Anhydrite in Chaps. 9 and 10). Both the Arab and the Khuff formations accumulated at different times along the southern shore of the Neo-Tethyean Ocean when sediment accretion atop an original Hercynian horst and block terrain periodically isolated large parts of the platform interior. This led to the

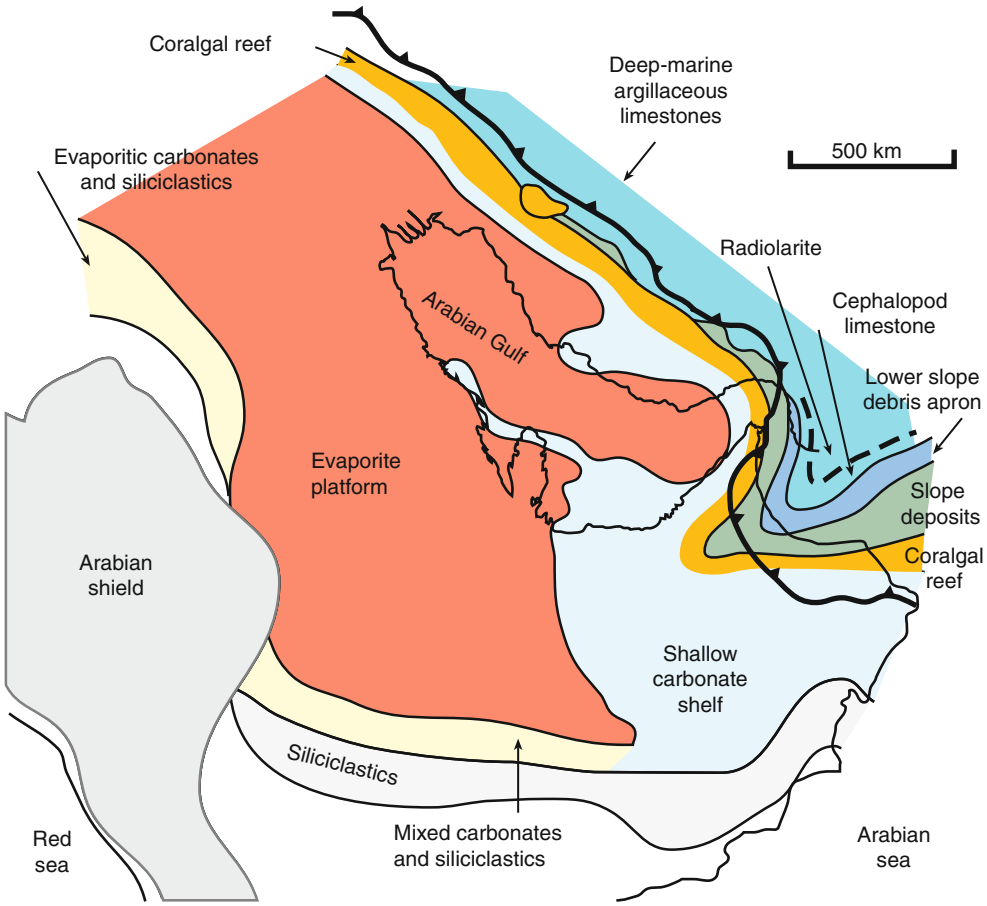

Fig. 5.22 Major facies belts and their interrelationships in the Permian Khuff Formation of the Middle East (After Al-Jallal 1995)

punctuation of the carbonate platform record with evaporite beds throughout much of the Mesozoic.

Regionally, the Mesozoic in the Middle East was a period of tectonic activity centred on the opening and closing of the Tethys. The Late Permian ocean backed onto the huge landmasses of Pangaea and in both opening and closing stages of the supercontinent the ocean created large subsealevel marine margin areas where epeiric carbonate seas formed that were periodically isolated as intracratonic sags and then filled to hydrologic base level with bedded salts. Similar evaporite entraining epeiric carbonate ramps also characterised the Infracambrian of the Middle East, the lower Palaeozoic of North America and Australia, the late Palaeozoic of America and Russia, and the Triassic and Jurassic of Europe (Table 5.5).

Evaporites Atop Rimmed Epeiric Shelves

Ancient rimmed-shelves were shallow-water carbonate platforms with an outer wave-agitated edge marked by biogenically induced buildups or highs and a pronounced increase in slope that was typically a few degrees, less often more than 60°, into deep water (Read 1985). Platform evaporites can be found behind such rims throughout the Phanerozoic (Fig. 5.9a). Subsurface examples of this style of carbonate deposition, as opposed to ramps, are readily identified seismically using obvious clinoforms and reflection discontinuities that define the shelf edge or shelf break. Many modern reef-rimmed shelves are constructed by combinations of coral and coralline algae, but different organisms have occupied the framebuilder niche in the past; stromatolites in the Proterozoic, stromatoporoids in the Devonian and rudistids in the Cretaceous. When Phanerozoic reef occurrences are plotted in time against evaporite volumes there is little or no correlation implying reef-rimmed platforms are not the dominant mechanism driving times of widespread evaporites. It implies tectonic isolation during times of continental make-up or break-up, and not eustasy, created the depressions and the drawdown hydrologies that precipitated the greater volumes of world's ancient evaporites as basinwide not eustatic reef-rimmed platform evaporites (Fig. 5.23).

The platform rim in greenhouse times was continuous to semicontinuous during times of open marine carbonate growth, characterized by high-energy reefs and reef mounds with intervening grainstone shoals and flats. Areas behind platform rims in arid settings are typically made up of seepage-fed evaporitic carbonate flats alternate with salterns and mudflat evaporites or arid zone siliciclastics. Rimmed shelves require biogenic binding and cementation to maintain an elevated biogenic rim, they do not form on siliciclastic platforms, nor can reef flourish if they are connected at the surface to hinterland areas where extensive evaporites are accumulating. Both these scenarios set up inimical seaward-flushing waters; in the former the reef-biota is killed off by detrital plugging, in the latter by elevated salinities.

The degree of restriction in the evaporite-depositing lagoon area behind the platform edge is controlled by the continuity of the rimming shoal. To form a saltern or an evaporitic mudflat in an ancient lagoonal depression requires the rim crest to be at or above sealevel, with any channels cutting across the rim and its sandflat to be choked with sediment (Lucia 1972). This prevents freshening via the free exchange of marine and

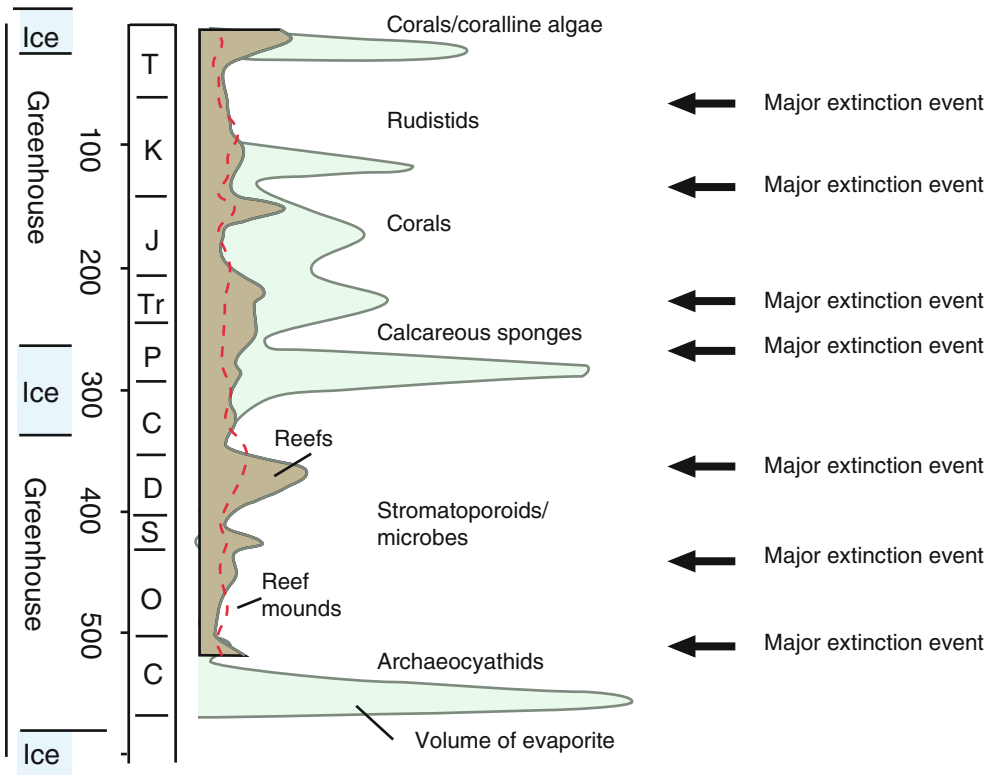

Fig. 5.23 Phanerozoic distribution of reefs (*brown shading*), reef mounds (*dashed line*), major extinctions and the dominant reef formers through time (After Kiessling et al. 1999) versus the worldwide volume of evaporites (After Hite and Anders 1991)

backrim waters. Otherwise, like the carbonate platforms of today, conditions behind the shelf rim or shoal can never become saline enough to deposit widespread evaporites and, at best, restricted marine carbonates are deposited.

Evolution of major reef biota through time does create some interesting variations in the ability of the living reef formers to live proximal to evaporite accumulating areas. Precambrian stromatolitic platform-edge reefs could grow in close to an evaporitic mudflat; some stromatolitic horizons are repeatedly intercalated and even penetrate saltern beds in the Neoproterozoic Ara salt of Oman. Cambrian archeocyathids were much more fragile. For example, in the well-exposed reef outcrops of the Flinders Ranges in South Australia the archeocyathids never occur in close proximity to evaporitic mudflats. There are always debris aprons and unconformities separating bioherms from overlying evaporite dissolution breccias. Stromatoporoids in lagoonal bioherms in the Alberta Basin appear to have better tolerated exposure to mesohaline waters, at least for short periods. But with no modern analogue it is difficult to define why this is so (e.g. were stromatoporoids related more to calcareous sponges or to cyanobacterial plexi?). Phanerozoic corals (rugose, tabulate and scleractinian) consistently show a poor tolerance to salinity change (stenohaline fauna) and living communities were never able to tolerate salinity changes for more than a few hours. Rudists appear to have been more robust in their salinity and temperature tolerances. In core recovered from the subsurface of Texas I have seen small *in situ* buildups forming units adjacent to both oyster bioherms (estuarine) and the less saline portions (mild sabkhas) of ancient evaporitic mudflats. This ability of rudists to survive changed salinity and temperature is probably related to their molluscan pedigree. When conditions became too saline, too hot or too fresh they could retract their filtering apparatus, pull down their opercular caps and wait out the adverse conditions, at least for a day or two. Even today, chemosynthetic molluscs survive in close proximity to deep seafloor brine lakes (Fig. 9.50).

The Cretaceous Ferry Lake Anhydrite formed behind a rimmed rudist platform as a 90 m-thick unit extending from east Texas to Alabama (Fig. 5.24). It is made up of metres-thick alternating units of carbonate and anhydrite deposited in the lagoonal area of a broad, shallow reef/shoal-rimmed carbonate platform. Using wireline signatures, individual sulphate beds can be traced over distances of more than 160 km (Fig. 5.24a; Pittman 1985). Where it subcrops toward its present landward extent the anhydrites have been dissolved by meteoric waters. At the time of deposition they passed further landward into alluvial plain conglomerates and redbeds. Detailed core study in the J. B. Kitchens No. 1 well (Henderson Co, Texas) showed the anhydrite beds are mostly composed of vertical- to near vertical-aligned nodules separated by fine mm-laminated anhydrite (Loucks and Longman 1982). These structures are diagenetic "ghosts" after original bottom-nucleated gypsum. Throughout much of its subsurface extent the wirelines signature of the correlated anhydrites show a clean blocky appearance with neutron-density crossplots indicating high levels of sulphate purity, making it a saltern deposit (Warren 1991). Sabkha mudflat signatures in the anhydrites are rare. The saltern/lagoon was up to 260 km (160 miles) wide and was separated from open marine waters by shelf-margin bank or shoals dominated by rudistid debris of the Glen Rose Formation (Fig. 5.24b). The position of the shoal was possibly controlled by down-to-the-basin faulting. This in turn was controlled by into-the-basin salt flow and associated growth faulting, driven by halokinetic movement of the underlying Jurassic Louann Salt (Chap. 6).

The anhydrite beds are up to 7 m thick and contain thin mudstone layers with entrained anhydrite rip-up clasts. The thicker carbonate beds, which separate the anhydrites, are near-normal marine lagoonal bioclastic/oolitic wackestones indicating times of hydrographic connection through the rim facies to the open ocean. The entrained fauna includes ostracodes and molluscs, several units contain *Orbitulina* and echinoid fragments, indicating that normal marine waters were present either during highstands or in times of storm-induced marine floods. Loucks and Longman's original 1982 interpretation was that the marine carbonate beds were deposited during periodic storm flooding of a restricted carbonate lagoon by marine waters. They also postulated that a single perennial evaporite lagoon was capable of depositing gypsum on its seaward side and halite on its landward side. Given a lack of widespread halite and what we now know about saltern hydrology this surface-connected scenario of marine on one side of a lagoon and halite on the other is somewhat unlikely. To deposit a widespread subaqueous evaporite unit requires total or near total isolation from a surface connection to the ocean in a system where a single perennial brine is at saturation with a single mineral phase (see later hydrological discussion in this chapter). A more likely scenario is that the Ferry Lake Anhydrites were precipitated simultaneously across a gypsum-saturated seaway during times of complete surface isolation from the ocean, and halite was perhaps forming stacked crusts in isolated pan depressions within subaerial mudflats in the most landward parts of the basin (as in Lake Asal today). On the seaward side of the saltern the crests of the rudistid shoals and reefs were subaerially exposed, while the underlying shoal sediment was an unconfined aquifer facilitating the phreatic supply of marine water into the drawdown saltern filled with gypsum-saturated brine sheets up to a few metres deep. Interestingly, the Ferry Lake Anhydrite retains remnants of the actual primary gypsum as gypsum cores encased in secondary anhydrite nodules at depths as great as 3,993 m (13,100 ft; Amadi et al. 2012).

An even more thoroughly documented example of a rimmed evaporitic platform is the Permian margin of the Delaware Basin in West Texas and New Mexico, USA (Fig. 5.25a). The margin is exposed in the Guadalupe Mountains, while its dolomitised, evaporite-sealed, subsurface lagoonal counterparts form the most productive reservoir intervals from the NW shelf into the Central Basin

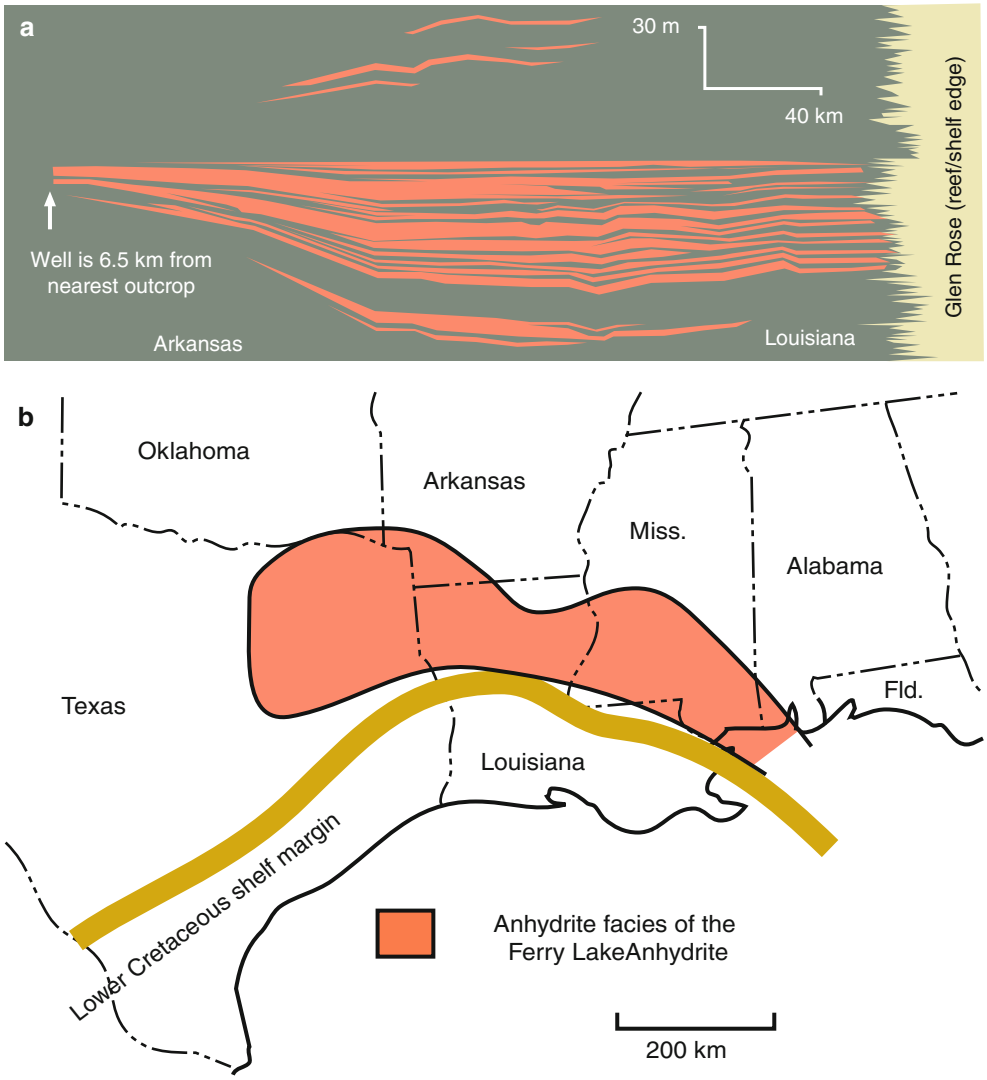

Fig. 5.24 Lower Cretaceous Ferry Lake Anhydrite, northern Gulf of Mexico. (**a**) N-S cross section showing distribution of main anhydrite beds from wireline logs (After Pittman 1985). (**b**) Distribution of anhydrite saltern on the platform behind the rudistid shelf margin shoal (After Loucks and Longman 1982)

Fig. 5.25 Permian reef complex of the Guadalupe Mountains, West Texas. (**a**) Schematic cross section of the Permian carbonate platform based on outcrops in the Guadalupe Mountains of Texas and New Mexico. Note the initial strongly progradational ramp-like profile in the San Andres Formation and its evolution to a reef-rimmed shelf with a well defined slope break, along with a steep shelf margin that was several hundred metres high. The platform interior is dominated by saltern evaporites (*white*) that pass seaward through pisolitic island shoal/strandzone facies into the deep-rim reef of the Capitan Formation (After Kerans et al. 1993; Kerans and Fitchen 1996). The basinward slope of the evaporite sequence is based on the current configuration of the basin margin and probably does not reflect the original slope. It is created by post depositional regional tilting. Map *inset* shows major physiographic provinces of the Permian Basin in West Texas and New Mexico. (**b**) Detailed facies and dolomitisation relationships based on measured sections in the Yates/Tansill Formation showing the position of the shelf crest landward of the reefs of the Capitan limestone (After Mutti and Simo 1993). (**c**) Dolomitisation of the Capitan shelf strata and reef by dense mesohaline fluids that originated in the near back reef evaporitic shelf-lagoon (Hunt et al. 2002). Basinward flow of the dolomitising fluids was along aquifer units within the shelf—the sandstones resting on sequence boundaries. The basinward tilting of the back reef strata between the shelf crest and the Capitan may have helped promote a basinward flow of the dolomitising fluids, but the main hydrological gradient came from natural brine reflux. In areas updip of the faults (*zone 1*, the basinward flow of the dolomitising fluids would have primarily been along aquifers and downward through the reef and forereef (both areas here are extensively dolomitised). The flow of fluids through the forereef followed bedding, and dolomitisation decreases downward through these strata (Melim and Scholle 2002). Further downdip in the cross-section (*zone 2*), much of the basinward flow of the dolomitising fluids would have been captured by the syndepositional faults and related fracture systems that reach high into the platform stratigraphy. Here, the sandstone-dominated fill of the faults and fractures provided vertical conduits for the dense dolomitising fluids through the platform. Capture of the flow of the dolomitising fluids by the fault zones in updip locations (*zone 2*) may have acted to inhibit the extensive dolomitisation of the middle and upper Capitan reef further downdip (*zone 3*). Here, dolomitisation is mostly limited to tepee–pisolite facies. Hunt et al.'s model is a logical extension of that developed by Melim (1991) and they argue dolomitisation was likely a discontinuous process typical of TST and HST times, while fracture-controlled dissolution prevailed during lowstands

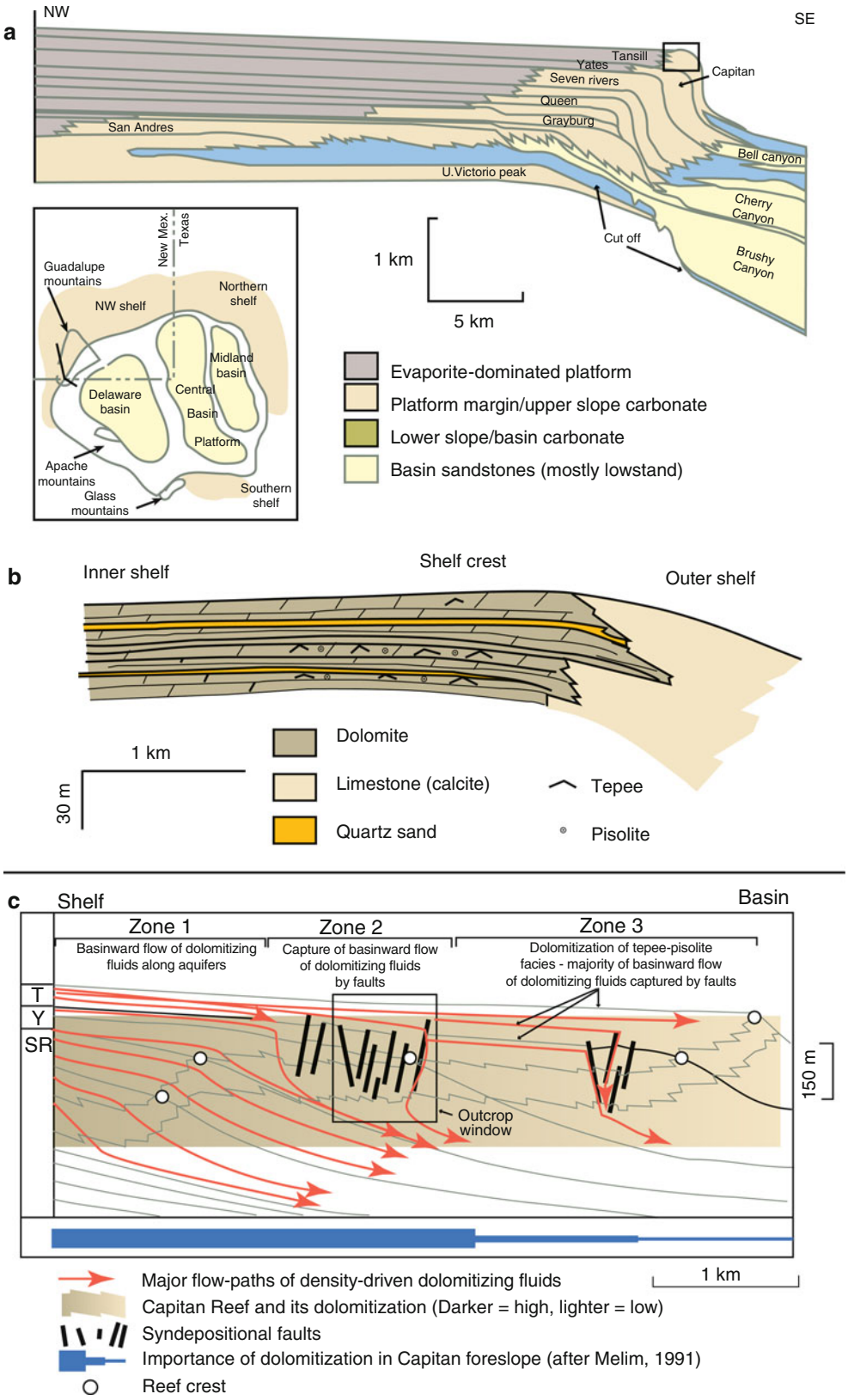
a
NW
SE
Tansill
Yates
Seven rivers
Queen
Grayburg
San Andres
Capitan
Bell canyon
U.Victorio peak
Cherry Canyon
Brushy Canyon
Cut off
1 km
5 km
New Mex.
Texas
Guadalupe mountains
NW shelf
Northern shelf
Midland basin
Delaware basin
Central Basin Platform
Apache mountains
Glass mountains
Southern shelf
Evaporite-dominated platform
Platform margin/upper slope carbonate
Lower slope/basin carbonate
Basin sandstones (mostly lowstand)
b
Inner shelf
Shelf crest
Outer shelf
1 km
30 m
Dolomite
Limestone (calcite)
Quartz sand
Tepee
Pisolite
c
Shelf
Basin
Zone 1
Basinward flow of dolomitizing fluids along aquifers
Zone 2
Capture of basinward flow of dolomitizing fluids by faults
Zone 3
Dolomitization of tepee-pisolite facies - majority of basinward flow of dolomitizing fluids captured by faults
T
Y
SR
Outcrop window
150 m
1 km
Major flow-paths of density-driven dolomitizing fluids
Capitan Reef and its dolomitization (Darker = high, lighter = low)
Syndepositional faults
Importance of dolomitization in Capitan foreslope (after Melim, 1991)
Reef crest

Platform. The Permian Basin of West Texas covers an area of more than 100,000 km^2 and is almost completely encircled by the reef-rim sediments of the Goat Seep and Capitan formations. Some distance landward of the reef is a 13 km wide belt of highly cyclic platform carbonates made up of widely correlatable stacks of dolomite mudstone and wackestone, capped by anhydritic laminites, which Sarg (1981, 2001) interprets as subaqueous. Even further landward are thick belts of saltern evaporites, which have been largely dissolved from their outcrop expressions in the Guadalupe Mountains.

Seaward of the cyclic platform dolomites, in a position somewhat closer to the reef mass proper, is an 0.8–3 km wide belt of carbonate sands and pisolitic rudstones. These were deposited as mostly coarsening-upward, cyclic stacks, which culminate in tepee-overprinted pisolite beds with subaerial exposure or truncation surfaces. These evaporitic carbonates constitute the tepee-overprinted pisolitic strandzone and barrier island shoal facies of the Guadalupe platform (Esteban and Pray 1983) and were described in some detail in Chap. 1. Evaporite-sealed counterparts to the dolomitised pisolitic cycles also constitute high quality subsurface reservoirs (Chap. 10).

During deposition the pisolite facies constituted a series of shoals that are considered by many to have been the topographically highest part of the platform (Esteban and Pray 1983; Mutti and Simo 1993; Rush and Kerans 2010). Located landward of the reef, the island shoal facies distinguishes this style of platform from the more usual reef-rimmed reconstruction, where the reef mass and its sand flat occupy the topographically highest position on the platform profile (Figs. 5.25b and 5.26b). The pisolitic high of the Guadalupe region is the type area for what is called a distally-steepened reef rim or deep reef-rimmed shelf. This platform profile occurs in other shelf margins characterised by platform salterns (Fig. 5.25c). A little further basinward of the pisolites and tepees are the reef masses of the Goat seep and Capitan formations. Separating the pisolitic shoal zone from the reef rim proper was a narrow belt of carbonate wackestones, typified by a low diversity marine fauna.

The basal part of the reef mass is pervasively cemented by cm scale aragonite botryoids (now calcite), which can constitute up to 90 % of the reef matrix. This zone of intense cementation passes upward into prolific biogenic masses of sponges, bryozoa, brachiopods and *Tubiphytes*, all bound by calcareous algae and marine cements. Some of the calcareous algae are coelobites, which flourished in dark aragonite-cemented fractures in the growing reef. The reef mass is largely undolomitised and internally shows no evidence of subaerial exposure, implying aragonite cementation was early and that the reef was never capable of growing to sealevel.

It may well be that the stenohaline biota of the reef rim could never grow to sealevel, nor form closer to the pisolitic shoreline, because of the debilitating effect of increased salinities. Dense brines, created by evaporative drawdown on the landward side of the island shoal, refluxed seaward via sandstone aquifers and growth faults beneath the unconfined marine phreatic lens to seep back to the seafloor just seaward of the basin shoreline to create a facies belt characterised by a low diversity, halotolerant biota. Brines mixed freely with seawater in this near coastal seafloor zone and so were dissipated into the huge reservoir of open ocean water that occupied the Delaware Basin (Fig. 5.26a). If the deep reef rim grew up toward the sea surface it would create greater

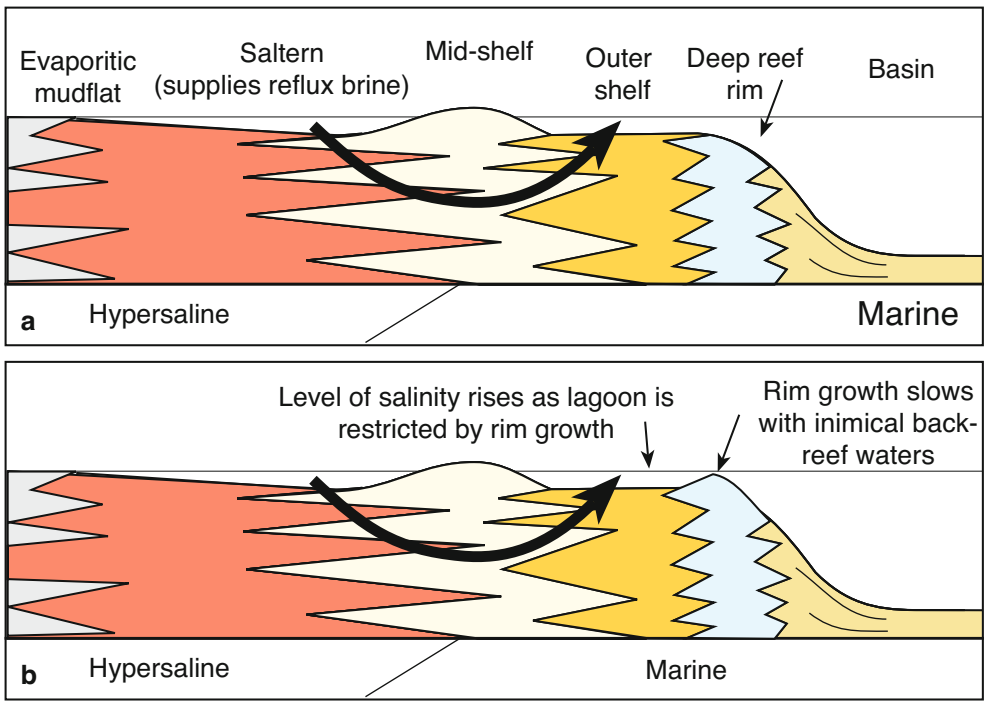

Fig. 5.26 Effect of a deep reef-rim growth in a saltern-backed platform. (**a**) Rim below sealevel (**b**) rim near or at sealevel

restriction immediately behind the reef rim allowing the escaping reflux brines to gather and increase the salinity of the back reef waters. As these more saline waters spilt and washed over the still subaqueous reef rim it would slow the growth of the reef until subsidence allowed freshening of the lagoon once again (Fig. 5.26b). Hence the reef could never grow to approach the sea surface in front of a huge area of widespread evaporites and refluxing dolomitising brines. Whenever it did so, it shot itself in the back before it ever reached the sea surface.

Seaward of the reef rim is a 2 km wide belt of carbonate slope and rise sediments, which also defines the shelf break. It is made up of massive to thinly bedded limestones with intercalated slumps of shelf material, breccias and debris flows (Melim and Scholle 2002). Small downslope buildups are found on the shallower parts of some slopes. Portions of the deepwater carbonate sands and the deeper parts of the shelf margins of the Delaware Basin are dolomitised to lesser degrees than the platform. Even so, the distribution of dolomite in these sediments reflect the influence of widespread evaporite deposition and brine reflux in the hinterland and the more seaward focusing action of syndepositional growth faults (Fig. 5.25c; Hunt et al. 2002).

Further out still, widespread siliciclastic sand sheets dominate the basin floor. These form a channelized deepwater belt at the foot of the carbonate slope in a zone some 6 km wide and up to 35 m thick. The sand sheets were fed from the continental hinterland by reworked desert dune sands, which largely bypassed the shelf margin, via canyons transecting the reef. Some of these basinal channelized sands are unusual, compared to typical deepwater marine sand channels, in that they contain drape muds on the channel floor and a rather homogenous set of sedimentary structures. They are interpreted either as density flows created by bottom-hugging saline brine flows, which originated in the platform salterns (Williamson 1978) or as settle-out muds and silts carried out over the seaway by intense winds from an adjacent sand sea (erg), much in the same way that silt and mud is carried out into the Atlantic off the Saharan coast of north Africa today (Fischer and Sarnthein 1988).

Evaporitic platform sequences have been recognised as far back as the Archaean (Fig. 5.27). For example, a number of impure dolomitic limestone beds in the latest Archaean (≈2.5 Ga) Wittenoom and Carawine dolomites of the Hamersley Group in Western Australia contain features such as mud cracks and evaporite pseudomorphs that indicate shallow water with local evaporitic mudflats (Kargel et al. 1996; Awramik and Buchheim 2009). The depositional system extended across what was possibly the original extent of the Hamesley Basin as defined by Trendall (1983) in his evaporite-basin model for initial banded iron precipitation. Likewise, in the barred platform model for initial iron precipitation, published by Morris (1993), deposition took place in what was interpreted to be a broad carbonate platform passing into deeper marine waters to the south. In either case, during the accumulation of the Wittenoom and Carawine dolomites the depositional setting was a carbonate platform that at times was evaporitic.

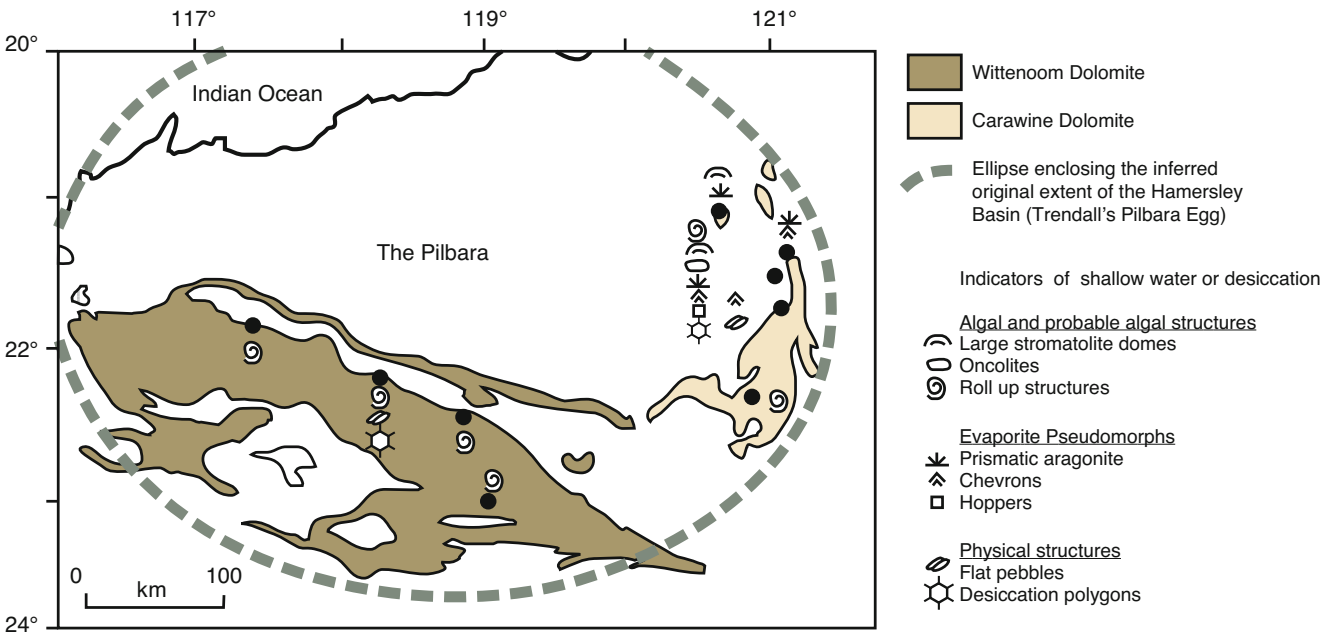

Fig. 5.27 Sketch map showing the distribution of sedimentological features that indicate shallow water and evaporitic conditions in the Archaean Wittenoom and Carawine dolomites in the Pilbara of Western Australia (After Kargel et al. 1996) and used as evidence to indicate that the widespread banded iron ores in this region first precipitated as saline precipitates in a barred marine platform basin

These evaporitic dolomites underlie the world-scale banded iron ores (BIFs) of the Hamersley Basin, deposits that contain 10 % of the world's known iron ore reserves. As in all models of ore deposits of this age, explanations for the formation of the banded iron ores are contentious. Trendall (1983) favours an evaporitic basin to explain the precipitation of the ore, Morris (1985) favours supergene enrichment beneath a Paleoproterozoic weathering surface, Li et al. (1993) favour a hypogene origin, while Powell et al. (1999) argue for synorogenic Paleoproterozoic hydrothermal fluids squeezed northward away from the Ophthalmian foldbelt. Awramik and Buchheim (2009) argue the carbonate-rich layers in the intracratonic BIFs are part of the world's oldest known carbonate-rich lacustrine system, which they call the Meentheena lake system.

Marine Versus Nonmarine Stages in Epeiric Seaways

Correlations across the Clear Fork ramp passing into the siliciclastics of the Opeche Shale or the Khuff Formation anhydrites passing laterally into basin rim continental siliciclastics derived from the Arabian Shield, or Guadalupe salterns passing landward into wadi and dune deposits are all problematic. They underline the everyday problem of reliably tying facies to time horizons in many ancient mixed siliciclastic/evaporite/carbonate platforms. Fossil-lean but extensive areas of saltern evaporites typically backed onto, and were surrounded by, evaporitic mudflats and fossil-lean sand-sheets with numerous internal disconformities that are Stokes surfaces. Reliable correlation of beds across ancient ramps are more difficult; bed layers lack well developed clinoforms, which can be used seismically to define the seaward side of a subsurface carbonate platform. Something as simple as determining whether the platform had a marine or nonmarine brine feed can be problematic in many subsurface salterns. Little if any open-marine carbonate matrix was ever transported into the highly isolated parts of the hinterland, even during intense hurricane events. For much of the time the water conditions in the saltern/lagoon were too saline for most marine or carbonate-secreting organisms with the possible exception of cyanobacteria and halophilic mats. When the base of a saltern evaporite cycle is made up of carbonates, they usually retain some evidence of a marine biota so that it is likely that the overlying salt beds were fed by marine seepage. But, if the intrasalt beds are dominantly mud, with no fossils, what was the precursor depositional setting?

This problem beleaguers depositional interpretations of the Permian (Leonardian) Nippewalla Group of Kansas, a lateral time equivalent succession to the Clear Fork Formation of the Palo Duro Basin. As mentioned earlier, Benison and Goldstein (2001) argue the Nippewalla Group siliciclastics and evaporites represent an evolution from a lacustrine system to a nonmarine, acidic saline pan system in the midcontinent of North America. Most evaporite deposition took place in halite-dominated ephemeral saline lakes surrounded by saline and dry mudflats, sandflats and sand dunes. The key to their continental interpretation comes, not from the textures in the nodular anhydrite or the halite and chaotic halite beds, which are equivocal, but from a volumetrically unimportant grey mudstone facies. This they interpret as a perennial lake deposit akin to the acid redbed lakes in parts of modern Australia. It is a grey siliciclastic mudstone characterized by planar and convolute laminations, ostracodes, peloids and plant material laid down in a freshwater-brackish perennial lake.

More reliable interpretations of a salt bed as marine or nonmarine are usually best done by studying the less saline intrasalt beds. In fact, it is the first feature on the list of four criteria noted by Hardie (1984) as most useful in separating marine and nonmarine evaporites. He listed; (1) sedimentology of the associated nonsaline facies, (2) kinds of fossils, (3) kinds and associations of primary evaporite minerals and, (4) geochemical characteristics of evaporite minerals. Then there is the problem of the volume of brine supply needed to accumulate thick widespread evaporites. As we saw in the hydrological discussions of Chap. 2, continental supra-sealevel meteoric-dominant intramontane hydrologies cannot supply sufficient water volumes or solutes required to form the volumes of salts that typify ancient saline giants or basinwide evaporites.

Basinwide Evaporites

Basinwide evaporites are thick basin-filling evaporite units, often described as "saline giants" or "mega-evaporites." Salt sequences typically extend across large areas of the central parts of a sedimentary basin and contain textural evidence of a variety of depositional settings ranging from deepwater to saltern to mudflat (Figs. 5.9b and 5.28; Table 5.6). Basinwide

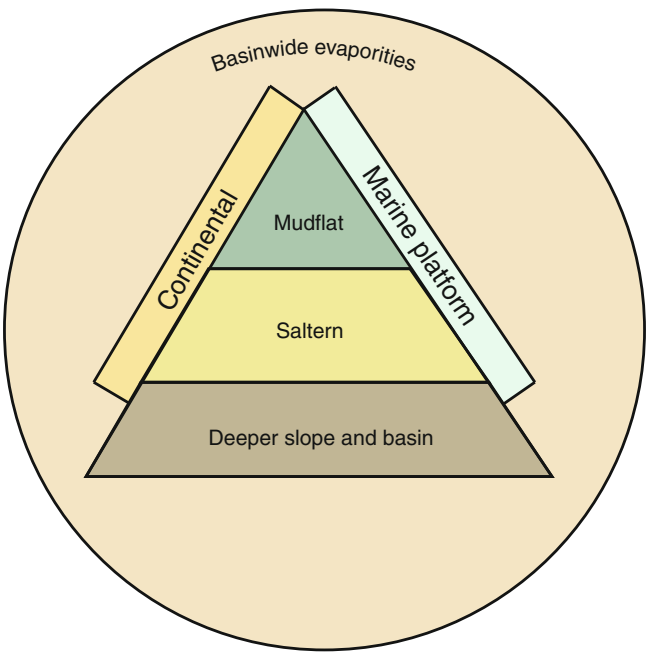

Fig. 5.28 Venn plot showing the diversity of environmental settings possible in basinwide evaporites

Table 5.6 Representative examples of basinwide evaporites (also called saline giants and basin centre evaporites)

Sequence of interest	Basin/setting and location	Age	Basin style	Tectonic event	References
Messinian Evaporites	Lago-Mare ("lake sea"), Mediterranean	Miocene, Upper	Flexure	Convergent foreland Alpine	Krijgsman et al. (1999)
Belayim and Gharib formations	Gulf of Suez – Red Sea, Middle East	Miocene, Middle – Upper	Extension	Red Sea Breakup and the formation of the Red Sea/ Suez Rift	Rouchy et al. (1995a, b), Meshref (1990)
Gachsaran Formation	Mesopotamian Basin, Middle East	Miocene, Middle	Flexure	Convergent foreland Zagros-Taurus	Tucker (1999)
Maha Sarakham Formation	Khorat Basin, Thailand	Cretaceous, Upper	Flexure	Convergent foreland Cretaceous inversion and thrust loading	Utha-Aroon (1993), Booth and Sattayarak (2000)
Todilto Formation	Todilto Basin, New Mexico, USA	Jurassic, Middle	Flexure	Convergent foreland Ancestral Rockies	Benan and Kocurek (2000)
Louann Salt	Gulf of Mexico Basin, Gulf Coast	Jurassic, Middle	Extension	Incipient Gulf of Mexico-Atlantic rift	Land et al. (1988, 1995), Hudec et al. (2013a, b)
Argo Formation & Osprey Evaporites	Scotian Basin, and Grand Banks, Canada	Upper Triassic-Lower Jurassic	Extension	Incipient Atlantic rifting	Holser et al. (1988a)
Northwich Halite	Cheshire Basin, United Kingdom	Triassic	Extension	Incipient Atlantic rifting	Pegrum and Mounteney (1978)
Halite (S1–S4, Lias and Dogger Anhydrite units)	Oued Mya Basin, Algeria, Northern Sahara	Upper Triassic-Lower Jurassic (Liassic)	Extension	Intraplate sag basin atop grabens created by incipient Atlantic and Tethyan rifting	Yahi et al. (2001), Turner et al. (2001)
Saliferous units	Ghadames (Berkine) Basin, Algeria	Triassic, Upper Jurassic, Lower	Extension	Intraplate sag basin atop grabens created by incipient Atlantic and Tethyan rifting	Yahi et al. (2001), Turner et al. (2001)
Argiles d'Argana	Essaouria Basin, Morocco	Triassic, Upper	Flexure	Intraplate sag basin atop grabens created by incipient Atlantic and Tethyan rifting	Hafid (2000), Evans (1978)
Formation Salifere	Saharan Atlas, Algeria	Triassic, Upper	Flexure	Intraplate sag basin; incipient Atlantic and Tethyan rifting	Hardie (1990), Merabet and Popov (1971)
Salina d'Ourgla	Northern Sahara Salt Basin, Algeria	Triassic, Upper	Flexure	Intraplate sag basin; incipient Atlantic and Tethyan rifting	Hardie (1990), Merabet and Popov (1971)
Nikitov, Slavyan, and Kramatov Formations	Dnieper-Donets Basin, Ukraine and Russia	Permian, Lower (Kungurian salt)	Flexure	Post-rift sag reactivated by Uralian Orogeny (Hercynian)	Ulmishek (2001a), Chekunov et al. (1992)
Rotliegende	Dniepr-Donets Basin, Eastern Europe	Permian, Lower	Flexure	Foreland Variscan Orogeny	Kabyshev et al. (1998)
Zechstein Basin, NW Europe	NW European Basin, NW Europe	Permian, Upper	Flexure	Post Variscan Orogeny collapse	Hardie (1990)
Castile Formation	Delaware Basin, West Texas	Permian, Upper	Flexure	Marathon-Ouchita	Kirkland et al. (2000)
Iren Horizon Kungurian evaporites	North Caspian Basin (aka Pri- or Peri-Caspian), Kazakhstan and Russia	Permian, Lower	Flexure	Foreland, Uralian Orogeny. Collision of Russian Platform with the Siberia/ Kazakhstan block	Ulmishek (2001b)
Otto Fiord Formation	Sverdrup Basin, Canadian Arctic Islands	Carboniferous	Extension	Synrift stage of post-Caledonian intracontinental rifting	Balkwill (1978), Stephenson et al. (1992)
Paradox Formation	Paradox Basin, Colorado-Utah USA	Carboniferous, Upper	Flexure	Ancestral Rockies	Barbeau (1999)
Caurauri Formation	Amazonas Basin, South America	Carboniferous, Upper	Flexure	Distal effect of Marathon-Ouchita orogeny	Hardie (1990), Szatmari et al. (1979)
Windsor Group	Magdalen Basin, Eastern Canada	Carboniferous, Lower	Extension	Cabot fault-Belle Isle transtensional system	Langdon and Hall (1994), Lynch and Keller (1998)

(continued)

Table 5.6 (continued)

Sequence of interest	Basin/setting and location	Age	Basin style	Tectonic event	References
Liven Horizon	Dniepr-Donets Basin, Ukraine and Russia	Devonian, Upper Frasnian and Famennian	Extension	Synrift via crustal stretching (passive margin)	Ulmishek (2001a), Ulmishek et al. (1994)
Prairie Evaporite	Elk Point Basin, Western Canada Plains	Devonian, Middle	Flexure	Intracratonic sag; a distal effect of thrust-loaded compression of the western Laurasian plate	Pysklywec and Mitrovica (2000)
Salina Group	Michigan Basin, USA	Silurian, Middle-Upper	Flexure	Intracratonic sag during Taconian thrust loading, sits atop Mesoproterozoic Midcontinent rift basin	Howell and Van der Pluijm (1999)
Mallowa Salt (Carribuddy Formation)	Canning Basin, Northwest Australia	Ord. -Silurian	Extension	Pre-rift to Synrift stage of intracratonic sag	Cathro et al. (1992)
Chandler Formation	Amadeus Basin, Central Australia	Cambrian, Lower	Flexure	Petermann Range Orogeny Gondwana Accretion	Bradshaw (1991)
Lower and upper Usolye Group	Turukhan – Irkutsk Olekmin salt basin, SE Siberian Craton	Late Neoproterozoic (Vendian) early Cambrian	Flexure	Intracratonic Sag-Gondwana assembly	Ulmishek (2001b), Petrychenko et al. (2005)
Hormuz Formation	Arabian Basin, Middle East	Late Neoproterozoic-early Cambrian (550 Ma)	Compression	Collision flexure – Pan African Orogeny; Gondwana Accretion	Edgell (1991, 1996), Husseini (1989)
Ara Salt, Oman	Fahud, Gaba and South Oman Salt Basins, Oman	Late Neoproterozoic-early Cambrian (550 Ma)	Compression	Collision flexure – Pan African Orogeny; Gondwana Accretion	Schröder et al. (2003), Sharland et al. (2001)
Bitter Springs Formation	Amadeus Basin, Central Australia	Early Neoproterozoic (≈800 Ma)	Extension-intracratonic sag	Rift – Rodinia breakup	Lindsay (1987), Southgate (1991)
Callana Formation	Adelaide Geosyncline, South Australia	Early Neoproterozoic (≈800 Ma)	Extension-intracratonic sag	Rift – Rodinia breakup	Powell et al. (1994)
Browne Fm	Officer Basin, West Australia	Early Neoproterozoic (≈800 Ma)	Extension-intracratonic sag	Rift – Rodinia breakup	Apak et al. (2002), Simeonova and Lasky (2005)

In some the former evaporite beds are now represented by laterally extensive solution breccia horizons. This listing is representative, not complete, compare with Fig. 5.30. Also, it does not consider the many examples of meta-evaporites including numerous examples older than Neoproterozoic (see Chap. 14)

evaporites are not accumulating anywhere on the surface of the world today as the necessary interactions between tectonics, hydrology and climate do not exist. Basin-central evaporite is another term to describe this grouping of ancient deposits (Kendall 1992). I prefer the term basinwide as the evaporite sequence can fill the basin centre and then climb out over the old basin margin (e.g. the transition from Castile to Salado formations in the Delaware Basin).

Basinwide evaporites can constitute large proportions of the sediment fill in many ancient evaporitic basins, such as the Delaware Basin of West Texas, the Zechstein Basin of Europe, the Louann Salt Basins in the Gulf of Mexico, the Hormuz Salt Basins in the Arabian Gulf and the Late Miocene Messinian sub-basins in the Mediterranean (Figs. 5.29 and 5.30). The total evaporite fill in such basins is often hundreds to thousands of metres thick and composed of numerous stacked "brining upward" evaporite cycles tens to hundreds of metres thick (e.g. the Z1–Z4 of the Permian Zechstein of northwest Europe). Rather than the anhydrite that dominates the mineralogy of many marine platform evaporites, basinwides typically contain thick halite beds that can source halokinetic structures.

Saltern textures (salt pan and salina) dominate basinwide deposits, although basin and slope deposits can also occur, especially in the early stages of each depositional cycle. Sometimes, especially in the gypsum/anhydrite stages of an evaporite fill the saltern constructs a "platform" area in the basin with deeper water sulphate laminites accumulating in the central part of the basin (Figs. 5.8 and 5.29a). At other times the basin centre had filled and shallowed to where a saltern extended across the entire depositional area of the basin (Fig. 5.29b, c). Stacking of a number of saltern cycles into a thick basinwide sequence indicates the basin did not fill in a single depositional episode, but as a number of

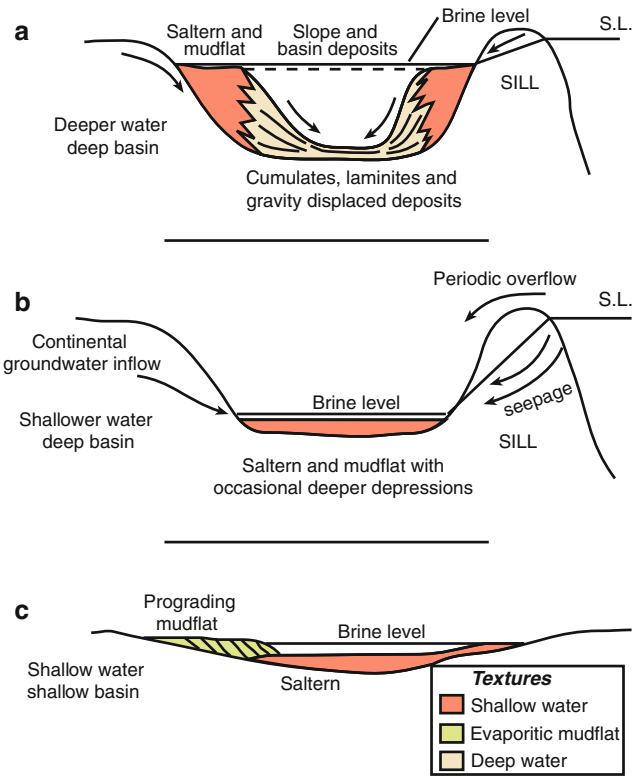

Fig. 5.29 Basinwide evaporite settings as three endmember associations (Modified from Warren 1989; Kendall 1992)

brining-upward and/or shoaling-upward depositional cycles typically composed of even finer scale parasequences. Compared with saltern deposits in marine-margin platform evaporites, the salterns in many basinwide evaporite basins tend to accumulate as much thicker units (>100 m), and bedded salts are not restricted to the shoalwater/lagoonal portions of any underlying carbonate platform. Rather, they tend to cover and encase underlying carbonate reef rims and pinnacles.

Depositional Styles

Basinwide evaporites can be classified into three settings (Fig. 5.29):

- Deeper water–deep basin
- Shallower water–deep basin
- Shallow water–shallow basin

Deeper water–deep basin evaporites have basin centres dominated by "deepwater" evaporites composed mostly of finely laminated salts (mostly sulphates) or coarsely crystalline inclusion-free halite meshworks. Individual laminar groupings in the basin-centre laminites can be correlated over wide areas (Fig. 5.29a). This style of deposition dominates a hydrographically isolated marine-fed basin that reaches hydrologic equilibrium (water inflow = loss) at a time when a relatively-deep water mass still covers the basin centre. The contentious part of this model lies in what water depth defines a deepwater brine in the basin centre, is it 30, 100 or >1,000 m? At times when the basin water column is meromictic, basin slopes are dominated by reworked saltern evaporites deposited as slumps and turbidites, while pelagic laminites dominate the basin centre during times of a stratified brine column (Fig. 5.8). At times when water levels are somewhat lower and the water mass is holomictic then coarsely crystalline evaporites (either gypsum or halite) are deposited across the basin floor (Fig. 5.8).

Seawater flows into the drawdown basin as a perennial seepage; if the basin remains hydrographically isolated, evaporites can fill the basin to a water level just below that of the supplying ocean (Fig. 5.29a). Consequently, the evaporite unit "in toto" is a shallowing upward succession, often composed of smaller shallowing-upward cycles (parasequences). The basin fill starts off dominated by deeper water laminated and resedimented salts that pass up section into shallowwater salterns, pans, mudflats, or continental playas. But it can also preserve coarser crystalline units indicating holomictic but still "deep" episodes in the basin fill.

The Permian Castile Formation and the transition into the overlying Salado Formation in the Delaware Basin in West Texas is a good example of this passage from predominantly deep to predominantly shallow. The basin-centre started off relatively deep with the deposition of the varved sediments of the Castile Formation, and with time filled and shallowed into the shoalwater/playa deposits of the Salado Formation. Any sediments that immediately postdate the evaporites of this overall shallowing sequence will also be shoal water or saline mudflat deposits. This is the case with the shoalwater/mudflat deposits of Rustler Dolomite where it overlies the Salado Formation in the Permian Basin, West Texas. Other examples of deeper water deposition occur in the basin-centre deposits of the north and south Zechstein basins of NW Europe and the deeper parts of the marginal basins in the Messinian of the Italian Apennines.

The *shallower water–deep basin* sequence is dominated by shallow water evaporites deposited as stacked saltern to mudflat cycles in a basin with a hydrological base level hundreds to thousands of metres below sealevel. This type of basin is supplied by evaporative drawdown, pulling seawater into the basin as a series of marginward seeps perhaps interrupted by the occasional refill tied to a marine-fed cataract (Fig. 5.29b). It characterises the more drawndown stages of evaporite deposition in both soft suture collision belts and some intracontinental rift to drift tectonic settings. This style of evaporite fill is often intimately related to the deeper water-deep basin style of deposits and indicates a more arid period in the same depositional basin. That is, its hydrological equilibrium is reached when much shallower waters cover the basin centre and there are many topographically

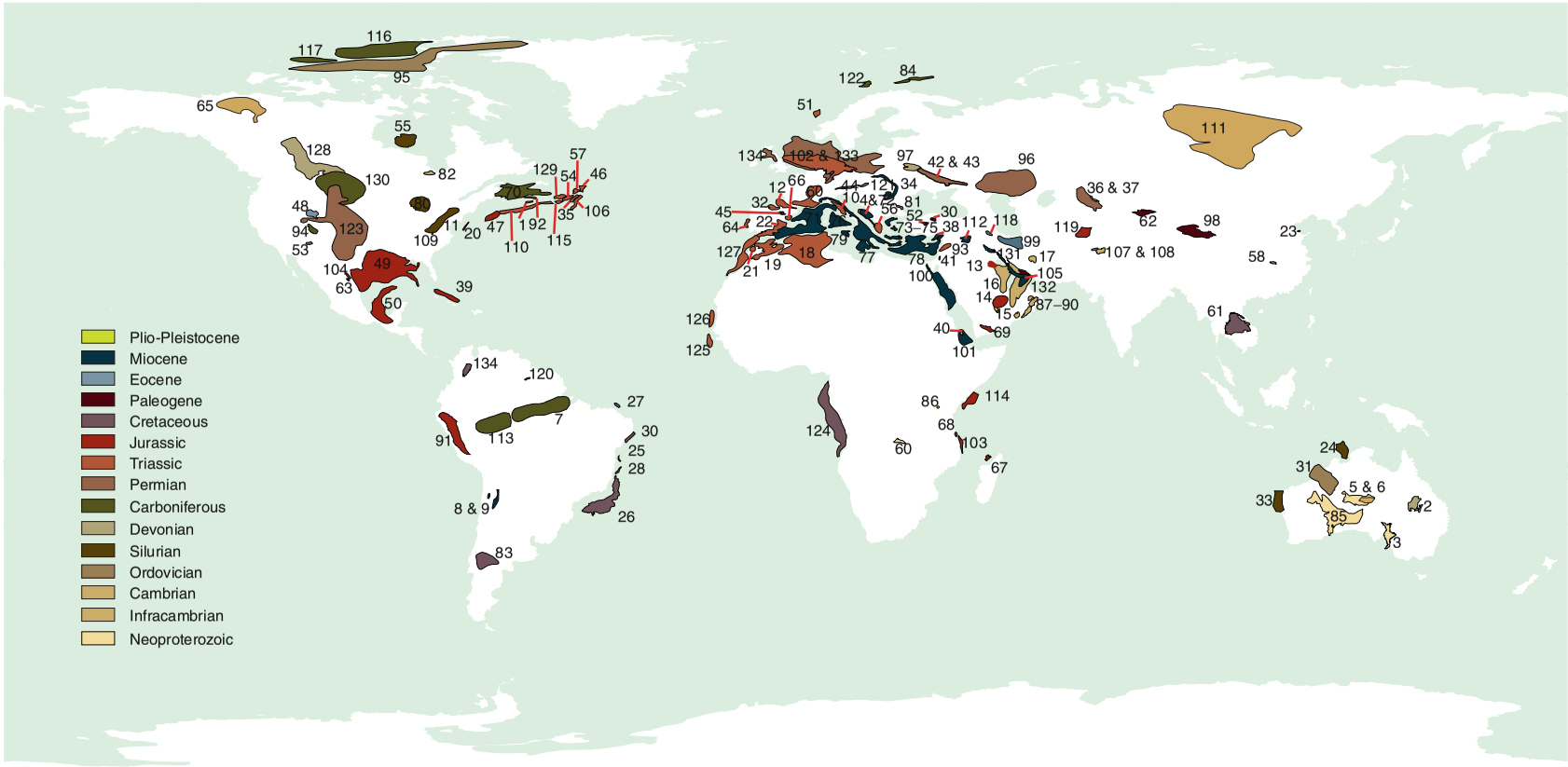

Fig. 5.30 Distribution of halite-entraining basins across deep time (Extracted from SaltWork version 1.6). To make it readable at this output scale this plot does not illustrate most of the calcium sulphate-dominant systems in the Middle East. Basins: *1*. Abenaki (N. Scotian); *2*. Adavale; *3*. Adelaide foldbelt; *4*. Adriatic-Albanian foredeep; *5*. Amadeus Basin; *6*. Amadeus Basin (Chandler); *7*. Amazonas; *8*. Andean; *9*. Andean; *10*. Apennine; *11*. Appalachian; *12*. Aquitaine; *13*. Arabian Basin (Gotnia Salt Basin); *14*. Arabian Basin (Hith Salt Basin); *15*. Arabian Basin (Hormuz central Saudi); *16*. Arabian Basin (Hormuz Gulf region); *17*. Arabian Basin (Hormuz-Kerman region); *18*. Atlas (Algerian – Tunisian); *19*. Atlas (Moroccan); *20*. Baltimore Canyon; *21*. Berrechid; *22*. Betic-Guadalquivir Basin; *23*. Bohai Basin; *24*. Bonaparte (Petrel); *25*. Brazilian Aptian Basin (Camamu); *26*. Brazilian Aptian Basin (Campos-Santos); *27*. Brazilian Aptian Basin (Ceara); *28*. Brazilian Aptian Basin (Cumuruxatiba); *29*. Brazilian Aptian Basin (Sergipe-Alagoas); *30*. Cankiri-Corum; *31*. Canning Basin; *32*. Cantabrian-West Pyrenees; *33*. Carnarvon Basin (Yaringa); *34*. Carpathian foredeep; *35*. Carson Basin (Grand Banks); *36*. Chu-Sarysu (Devonian); *37*. Chu-Sarysu (Permian); *38*. Cicilia-Latakia; *39*. Cuban; *40*. Danakil; *41*. Dead Sea; *42*. Dniepr-Donets; *43*. Dniepr-Donets; *44*. Eastern Alps; *45*. Ebro Basin; *46*. Flemish Pass Basin (Grand Banks); *47*. Georges Bank; *48*. Green River Basin; *49*. Gulf of Mexico (Northern; Gulf coast); *50*. Gulf of Mexico (Southern; Salina-Sigsbee); *51*. Haltenbanken; *52*. Haymana-Polatli; *53*. Holbrook Basin; *54*. Horseshoe Basin (Grand Banks); *55*. Hudson Bay; *56*. Ionian; *57*. Jeanne d'Arc Basin (Grand Banks); *58*. Jianghan Basin; *59*. Jura/Rhodanian; *60*. Katangan; *61*. Khorat Basin; *62*. Kuqa Foreland (Tarim Basin); *63*. La Popa (Monterrey) Basin; *64*. Lusitanian; *65*. Mackenzie Basin; *66*. Maestrat; *67*. Majunga Basin; *68*. Mandawa Basin; *69*. Ma'Rib-Al Jawf/Shabwah (Hadramaut); *70*. Maritimes Basin; *71*. Mediterranean–Western; *72*. Mediterranean–Adriatic; *73*. Mediterranean-Andros Basin; *74*. Mediterranean-Cretean Basin; *75*. Mediterranean – Samothraki basin; *76*. Mediterranean-Tyrrhenian; *77*. Mediterranean-Central; *78*. Mediterranean-Eastern; *79*. Mediterranean-Sicilian; *80*. Michigan Basin; *81*. Moesian; *82*. Moose River Basin; *83*. Neuquen Basin; *84*. Nordkapp Basin; *85*. Officer Basin; *86*. Olduvai depression; *87*. Oman (Fahud Salt Basin); *88*. Oman (Ghaba Salt Basin). *89*. Oman (Ghudun Salt Basin); *90*. Oman (South Oman Salt Basin); *91*. Oriente-Ucayali (Pucara) Basin; *92*. Orpheus Graben; *93*. Palmyra; *94*. Paradox Basin; *95*. Parry Islands Foldbelt; *96*. Pricaspian Basin; *97*. Pripyat Basin; *98*. Qaidam Basin; *99*. Qom-Kalut; *100*. Red Sea (North); *101*. Red Sea (South); *102*. Rot Salt Basin; *103*. Ruvuma Basin; *104*. Sabinas Basin; *105*. Sachun Basin; *106*. Salar Basin (Grand Banks); *107*. Salt Range (Hormuz – Punjab region); *108*. Salt Range (Kohat Plateau); *109*. Saltville (Appalachian); *110*. Scotian Basin; *111*. Siberia, East; *112*. Sirjan Trough; *113*. Solimoes; *114*. Somalia-Kenya; *115*. South Whale Basin (Grand Banks); *116*. Sverdrup Basin (Ellef Ringnes – NW Ellesmere); *117*. Sverdrup Basin (Melville Is); *118*. Tabriz Salt Basin; *119*. Tadjik Basin; *120*. Takutu Salt Basin; *121*. Transylvanian; *122*. Tromso Basin; *123*. USA Midcontinent; *124*. West Africa (Angola-Gabon); *125*. West Africa (Gambia-Guine Bissau); *126*. West Africa (Mauritania-Senegal); *127*. West Africa (Morocco-S. Spain); *128*. Western Canada (Alberta Basin); *129*. Whale Basin (Grand Banks); *130*. Williston Basin; *131*. Zagros (Mesopotamian Basin); *132*. Zagros (Mesopotamian Basin); *133*. Zechstein (NW Europe); *134*. Zechstein (onshore UK); *135*. Zipaquira Basin

deep evaporite basins where deeper fills alternate with shallower fills.

In the collision setting the underlying basin-centre succession is typically a deep marine sediment, often a pelagic carbonate that passes upward across a disconformity or unconformity into alternating stacked saltern and deeper water evaporites. Normal marine pelagics were deposited before the basin depression was hydrographically isolated from the ocean and can return to dominate the basin fill if a hydrographic connection is re-established. The transition from a deeper marine basin to an evaporitic sump can be marked by organic-rich restricted marine-influenced deposits (Chap. 9). Basin margin regions can contain reefal deposits from the preceding marine phase and their higher position in the basins means they are colloquially described as the "bathtub scum rim."

Shallower water-deep basin fills dominate the evaporite fill in many marine-fed rift successions, such as the Aptian South Atlantic Salt Basin. Thick salts precipitated atop an endorheic rift valley floor that was hundreds of metres below sealevel (Szatmari 2000). Unlike the relatively small volumes of marine-fed salts being deposited in today's best example of a shallow water-deep basin marine-fed rift (Lake Asal depression; Fig. 4.60), the volumes of salt deposited in ancient rift sags could be huge. Consider the wedge-shaped body of Upper Aptian salt, it was deposited in the South Atlantic Salt Basin as Africa separated from South America about a rotational pole in NE Brazil (Szatmari 2000; Torsvik et al. 2009). The salt basin was more than 2,000 km long, some 400 km wide at its southern end in the Santos Basin and tapered northward to less than 100 km wide in the Sergipe-Alagoas Basin. Prior to halokinesis, the original salt thickness in the various sub-basins was around 2 km. Most of the salt was deposited as halite in a series of saline lakes/salterns within a pre-existing continental rift depression, with a floor some 2 km below sealevel. Marine flooding ended the depression's isolation from the sea in the late Aptian. It required nearly one million cubic kilometres of water to fill the depression to sealevel, an event that would have caused a geologically instantaneous drop of 3 m in global sealevel (Szatmari 2000).

The *shallower water–shallow basin* association forms under conditions of ongoing subsidence where the rate of evaporite aggradation keeps pace with tectonic subsidence (Fig. 5.29c). The basin depositional setting starts off shallow and remains shallow throughout the deposition of the evaporite sequence. Sedimentary signatures are dominated by interfingering saltern, saline pan and mudflat successions often crosscut by karstic erosional surfaces. There is little or no evidence of deeper water evaporites. Shallow water–shallow basin evaporites are typical of intracratonic sag fills, such as in the Williston Basin in the USA and the Silurian-Ordovician Canning Basin in Australia. Salt beds in intracratonic fills are typically intercalated with shallow-water open-marine carbonates and siliciclastics and tend to form stacked cyclic units with thicknesses between 10 and 100 m, unlike the thick rift and collision successions (>100–1,000 m thick). Using data from one or two wells it can be very difficult to distinguish intracratonic basinwide evaporites from marine-margin platform evaporites. The distinction requires a thorough knowledge of the basin's architecture and tectonic history and is often best resolved using regional seismic and well data. This style of deposition also dominates the later stages of basin infill in what were previously deep hydrographically-isolated evaporite basins, as described in the other two members of this classification (Figs. 5.29 and 5.30).

In reality, codifying basin-filling evaporite successions is never as simple, nor as predictable, as a three-end-member classification suggests. Changes in brine level, subsidence rates or climate, play havoc with a simple tripartite breakdown of evaporite basins. Water depths in an evaporite basin are never constant, they rise and fall in response to intensity of tectonism, climate, sealevel change, playa capture and associated changes in the degree of seepage, evaporation intensity and surface runoff in the inflow zones. Basinwide provinces such as the Mediterranean Basin during the Late Miocene, or the Permian Basins of Texas and northern Europe in the Late Permian, are actually composed of a series of large sub-basins. Each subbasin in an evaporitic province responds in its own fashion, depending on the local topography, tectonics, and climate and the total fill can contain examples of all three end members. Understanding and predicting facies evolution in a basinwide evaporite setting is simplified if the various deposits are placed in their plate tectonic setting using the Wilson Cycle as the first order control on the possibility of hydrographic isolation. Such an evolution must a first be broken down into mega-evaporites formed at a tectonically active continental margin edge and the more tectonically quiescent continental interior (intracratonic).

Tectonic Styles of Basinwide Evaporites Across Time

Throughout earth history, basinwides tend to accumulate in three tectonic settings: (1) Areas of rifting continental plates; (2) Areas of converging continental plates (collision belts); (3) Areas of intracontinental or intraplate sags, which are often the result of farfield plate stress induced by continental orogeny acting on zones of pre-existing crustal weakness such as an old rift belt (aulocogen) or foreland depression (Table 5.6; Warren 2010). Evaporating brines in most basinwide lows tend to be maintained by a continuous inflow of marine groundwaters into tectonic depressions (marine-fed hydrological systems). This hydrology is created in an arid setting wherever tectonically driven subsidence moves the basin floor to sub-sealevel elevations without allowing a surface connection to the open ocean.

Basinwide evaporite styles at continental margins change as continents accrete and suture. For example, the various salt-filled basins, that together make up the Pangaean peak in the salt volume curve, were created mostly by plate tectonic mechanisms within what were tectonically-induced arid to hyperarid climatic zones of the latest Palaeozoic to Mesozoic earth (Fig. 5.7). Volumes of salts caught up in this association dwarf all Quaternary salt volumes. Zharkov (1981) recognized 95 Permian evaporite basins with a total volume of 1.5×10^6 km^3 (37 were halite-dominated and 48 sulphate-dominated). The basinwides that make up the Pangaean peak came into being as the continents collided to construct the Pangaean supercontinent and then as it rifted and sagged during its breakup into a number of smaller continental landmasses.

That is, continent-continent proximity and associated tectonic flexures and downwarps during the accretion of the Pangea supercontinent facilitated the deposition of widespread collision-and intracratonic evaporites. Carboniferous basinwide evaporites were precipitated in the Williston Basin and northern Ellesmere region in North America, in northern Brazil, North Africa, the East-European Platform, and Kazakhstan (Trappe 2000). Early Permian evaporite basins form a broad saline sediment belt along the western Pangaean margin and also in northeastern North America and eastern Greenland, as well as in northern South America (including western Brazil). Large collision-induced salt deposits of the same age are found in central Europe including portions of the East-European Platform and the Urals. The largest Early Permian deposit fills the East European Basin from the Caspian to the Black Sea with some 500×10^3 km^3 of halite and 100×10^3 km^3 of anhydrite (Magaritz 1987). Late Permian Pangean evaporites also include major deposits in the Zechstein Basin of northwestern Europe and the evaporites of West Texas. Together these basins define a broad band of equatorial aridity extending from about 50°N to about 30°S palaeolatitude, with basinwide salt deposition ranging in time and world climate across Carboniferous icehouse to Permian greenhouse.

Permian halite volumes are in their turn dwarfed by those of the Triassic Pangean-breakup, which account for 22 % of all Phanerozoic halite, while Permian and Triassic halite together make up 35 % of the world's halite (Fig. 5.7). During the Early Triassic, evaporite formation intensified as huge sea-edge drawdown rift-to drift basins and continent interior evaporite pans, associated with redbeds, developed in southeastern and western USA, western Canada, northwestern Africa, western and southeastern Europe, central South America, south–central Africa and eastern Greenland (Tables 5.6 and 5.8). Huge evaporite platforms were established in the same time period in northern Arabia, Iraq, Kazakhstan, and northern China. The increased salt volume reflects intensified rift activity in low latitude regions during the Triassic breakup of Pangaea. Extension, followed by cooling and sagging, established a number of large isolated subsealevel rifts and intracratonic sags, which acted as the pre-eminent salt accumulators.

Thus, the profusion of Pangaean basinwide evaporites is allied with three time-plate tectonic associations (Table 5.7; Fig. 5.7): (1) Pennsylvanian to Permian accretion of the Pangaean supercontinent, as mostly marine-fed collision basin evaporites were deposited along the soft collision belt of the irregularly embayed margins of Gondwana, Laurussia and Siberia; (2) Intraplate extensional depressions created during the subsequent Mesozoic breakup of Pangaea into Gondwana/Laurasia; salt beds deposited in these widening marine-fed rift basins, including the continental salts of the Newark Basin (Triassic), the marine salts of the Gulf of Mexico (Jurassic), the Campos Basin (Cretaceous) and the various mostly marine-fed salt basins of offshore west Africa (Evans 1978); and (3) Associated intracratonic sag salt accumulations in basins that typically sit atop the failed arms of earlier more sharply-defined fault-bound rift successions (Youssef 1998) or in the hinterland or foreland of orogenic belts created by farfield stresses driven by interplate collision (Pysklywec and Mitrovica 2000). The intracratonic-sag basins in the Pangaean association are especially obvious in the various Triassic and Jurassic salt basins of Northern Africa, which formed isolated subsealevel marine-fed depressions as Pangaea unzipped along its Tethyan and Atlantic axes.

Large intracratonic sags also typify many other subsea-level isolated marine-seep fed saline giants, precipitated

Table 5.7 Timing of the assembly and disassembly of the Pangean supercontinent

Late Palaeozoic accretion of Pangean supercontinent	Pennsylvanian collision of Laurussia, Kazakhstania and Siberia to form Laurasia (≈280 ma), followed by Permian collision of Laurasia and Gondwana Associated orogenic events Appalachian/Alleghenian orogeny of eastern North America Mauritanide/ Moroccan foldbelt of northwest Africa Hercynian orogeny of southern Europe Marathon/Ouachita orogeny of southern North America Uralian orogeny of Europe-Siberia
Mesozoic breakup of Pangean supercontinent	Breakup of Pangea (into Laurasia and Gondwana): 220–190 Ma: Newark and other rift basins in northeast North America and northwest Africa 175 Ma: Opening of Neo-Tethys 135 Ma: Separation of South America from Africa (opening of south Atlantic)
	Breakup of Gondwana (as it unzips around Antarctica): 165 Ma: Rifting of Africa from Antarctica 125 Ma: Separation of India from Antarctica 100 Ma: Separation of Australia from Antarctica 85 Ma: Separation of New Zealand from Antarctica
	Breakup of Laurasia: 90–50 Ma: Opening of the north Atlantic between North America and Eurasia/Greenland

Table 5.8 Listing of tectonic setting of various halite-entraining basins at the time that thick halite was precipitated

Divergent	Abenaki (N. Scotian), Adelaide foldbelt, Adriatic -Albanian foredeep, Apennine, Aquitaine, Arabian Basin (Gotnia Salt Basin), Arabian Basin (Hith Salt Basin), Atlas (Algerian-Tunisian), Atlas (Moroccan), Baltimore Canyon, Berrechid, Betic-Guadalquivir Basin, Brazilian Aptian Basin (Camamu), *Brazilian Aptian Basin (Campos-Santos), Brazilian Aptian Basin (Ceara), Brazilian Aptian Basin (Cumuruxatiba), *Brazilian Aptian Basin (Sergipe-Alagoas), Cantabrian-West Pyrenees, Carson Basin (Grand Banks), Chu-Sarysu (Devonian), Cuban, Danakil, Dniepr-Donets, Eastern Alps, Flemish Pass Basin (Grand Banks), Georges Bank, Gulf of Mexico (Northern; Gulf coast), *Gulf of Mexico (Southern; Salina-Sigsbee), Haltenbanken, Horseshoe Basin (Grand Banks), Ionian, Jeanne d'Arc Basin (Grand Banks), Jura/Rhodanian, Katangan, La Popa (Monterrey) Basin, Lusitanian, Maestrat, Majunga Basin, Mandawa Basin, Ma'Rib-Al Jawf/Shabwah (Hadramaut), Moesian, Nordkapp Basin, Olduvai depression, Orpheus Graben, Palmyra, Red Sea (North), Red Sea (South), Rot Salt Basin, Ruvuma Basin, Sabinas Basin, Salar Basin (Grand Banks), Scotian Basin, Somalia-Kenya, South Whale Basin (Grand Banks), Tadjik Basin, Takutu Salt Basin, Tromso Basin, *West Africa (Angola-Gabon), West Africa (Gambia-Guine Bissau), West Africa (Mauritania-Senegal), West Africa (Morocco-S. Spain), Whale Basin (Grand Banks), Zechstein (NW Europe), Zechstein (onshore UK)
Convergent	Adavale, Amadeus Basin (Chandler), Andean, Arabian Basin (Hormuz central Saudi), Arabian Basin (Hormuz Gulf region), Arabian Basin (Hormuz-Kerman region) Bohai Basin, Cankiri-Corum, Carpathian foredeep, Chu-Sarysu (Permian), Cicilia-Latakia, Ebro Basin, Green River Basin, Haymana-Polatli, Holbrook Basin, Jianghan Basin, Khorat Basin, Kuqa Foreland (Tarim Basin), Mediterranean-Western, Mediterranean-Adriatic, Mediterranean-Andros Basin, Mediterranean-Cretean Basin, Mediterranean-Samothraki Basin, Mediterranean- Tyrrhenian, Mediterranean-Central, Mediterranean-Eastern, Mediterranean-Sicilian, Neuquen Basin, Oman (Fahud Salt Basin), Oman (Ghaba Salt Basin), Oman (Ghudun Salt Basin), Oman (South Oman Salt Basin), Paradox Basin, Pricaspian Basin, Qaidam Basin, Qom-Kalut, Sachun Basin, Salt Range (Hormuz – Punjab region), Salt Range (Kohat Plateau), Sirjan Trough, Sverdrup Basin (Ellef Ringnes – NW Ellesmere), Sverdrup Basin (Melville Is), Tabriz Salt Basin, Transylvanian, Western Canada (Alberta Basin), Zagros (Mesopotamian Basin), Zipaquira Basin
Intracratonic	Amadeus Basin, Amazonas, Appalachian, Bonaparte (Petrel), Canning Basin, Carnarvon Basin (Yaringa), Hudson Bay, Mackenzie Basin, Maritimes Basin, Michigan Basin, Moose River Basin, Officer Basin, Oriente-Ucayali (Pucara) Basin, Parry Islands Foldbelt, Pripyat Basin, Saltville (Appalachian), Siberia-East, Solimoes, USA Midcontinent, Williston Basin
Transform	Dead Sea

It is based on an interpretation of the synprecipitational setting, so in basins with an ongoing polyphase tectonic history (like the various Zechstein sub-basins of Europe) it is not the same as the salt's current tectonic situation. See Fig. 5.30 for basin age and location, asterisk indicates postrift megahalite deposition

outside of the time of the Pangaean supercontinent (e.g. the Devonian Elk Point Basin, the Palaeozoic Williston Basin, the Silurian Michigan Basin and Ordovician Canning Basin), as do other rift (e.g. Frasnian of Dniepr-Donets of eastern Europe) and collision (Miocene of the alpine Mediterranean and the Zagros foreland) associations (Table 5.8).

Creation and destruction of the Rodinia/Gondwana[5] supercontinent(s) in the Neoproterozoic-Early Cambrian (≈550 Ma) defines earlier, but not as well documented, peaks in the evaporite distribution curve, as shown in Fig. 5.7. Thick layers of preserved rock salt (halite) are widespread in the latest Ediacarian to the Early Cambrian in the Middle East, Pakistan, Siberia and Australia. Indeed, these strata contain some of the world's thickest successions of rock salt (Table 5.6). They include the Hormuz Salt of Iran and the Arabian Gulf, the Ara Salt of Oman (both thought to be latest Ediacarian), the Salt Range salt of Pakistan (Atdabanian-Botoman), and the Usolka and equivalent salts of Siberia (Tommotian-Atdabanian). The assembly of Gondwana took place during the Ediacarian to Early Cambrian. It involved the amalgamation of the separate crustal blocks of Avalonia, Europa, Arabia, Africa, Madagascar, South America, and Antarctica (together forming West Gondwana) and resulted in the compressional Pan-African orogeny, which culminated between 560 and 530 Ma. East Gondwana (India, South China, North China and Australia) collided with West Gondwana along the Mozambique suture between ca. 600 and 550 Ma. The development of thick salts in the Ara Formation, once thought to be rift deposits of Tommotian age, now appear to be foreland basin deposits of late Ediacarian age, tied to the Pan-African orogeny and Gondwana assembly

Even older thick halite beds (early Neoproterozoic) such as the Bitter Springs Fm. in the Amadeus and the halites of the Browne and Madley Fms. in the Officer Basin of Central

[5]Rodinia, is generally regarded as having been assembled near the end of the Mesoproterozoic and disassembled in stages during the Neoproterozoic. Reconstructions of Rodinia are notable for their lack of agreement (Bradley 2011), but published assessments of Rodinia's dates are in general agreement. It was assembled between 1,300 and 950 Ma, lasted from 950 to 850 Ma, and was disassembled from 850 to 600 Ma.

Whether or not the next youngest continental assemblage in deep time–Gondwana– qualifies as a supercontinent depends on the definition of a supercontinent (what does "nearly all" mean as used in the definition of a supercontinent – see footnote 5.4). Gondwana consisted of all the cratons now in South America, Antarctica, Africa, Arabia, India, and Australia, as well as microcontinents in the Appalachian and Paleotethyan realms. Its fit is well constrained because the now-dispersed pieces can be brought together by closing the modern South Atlantic, Indian, and Southern Oceans; this is essentially the southern half of the Pangaea fit. The collisional assembly of Gondwana spans the interval 690 to 530 Ma, and it remained intact as the southern portion of Pangaea until it began to break up around 300 Ma when it was re-established as Gondwana, a separate large landmass south of Laurasia (Table 5.7).

Australia, as well as the widespread dissolution breccia after Callana Fm. halites in the Flinders Ranges and the Duruchaus Fm. in Namibia and its equivalents in the Katangan copper Belt are perhaps related to the breakup some 800–850 Ma of the Mesoproterozoic supercontinent known as Rodinia (or Kanatia). The Centralian and Namibian evaporites are the oldest preserved masses of actual salts, beyond that age only meta-evaporites are preserved, such as those of associated with the Grenvillian Orogeny, which occurred during the accretionary phase of the Rodinian supercontinent (Chap. 13).

Volumes of salt deposited in saline giants can be huge, with individual deposits accumulating over geologically short time frames of no more than a few million years. For example, the deposition of the Jurassic Louann Salt in the Gulf of Mexico some 175 Ma, sequestered approximately 8 % of world-ocean NaCl (Land et al. 1988), while the Messinian evaporites of the Mediterranean were deposited in less than 300,000 years, yet lowered oceanic salinities by 6‰. Unlike platform evaporites, which can be tied to climate and eustasy on greenhouse epeiric platforms, the formation of basinwide deposits is not related to icehouse or greenhouse episodes in earth history. Placing basinwide evaporite occurrences into a plate tectonic framework simplifies the discussion of where suitable worldscale subsea-level marine seepage evaporite depressions can occur. At the plate tectonic scale the world's lithosphere is divisible into a number of major and minor plates, which because their interiors are relatively cool and rigid are mostly tectonically stable. Plate edges, also known as plate margins, are zones where moving plates interact one with another and tend to be tectonically unstable, these are the zones where the largest and thickest basinwide evaporites tend to form.

Plates are composed of variable amounts of continental and attached oceanic lithosphere. They float atop the athenosphere and are carried about on the upper part of its convective cells. In places where the lithosphere in a plate is largely composed of continental siliceous material (sial) it is less dense and tends to float above the geoid (and above sealevel) so constituting the suprasealevel portions of the larger continents. Where the plates are dominated by less dense basaltic material (sima), the surface of the plate tends to lie below the geoid and sealevel, constituting much of plates beneath the deep ocean floor (Fig. 5.31a).

Most of the larger continental blocks have elevations within a few hundred metres of sealevel, while most of the ocean floor lies some 5 km below the seasurface (Fig. 5.31a). The difference in elevation between the continental surfaces and the ocean floors is the result of a number of factors that include; thickness and density contrasts between continental and oceanic crusts, tectonic activity, erosion, sealevel and the ultimate strength of continental rocks, which determines their ability to maintain an unsupported slope above oceanic crust.

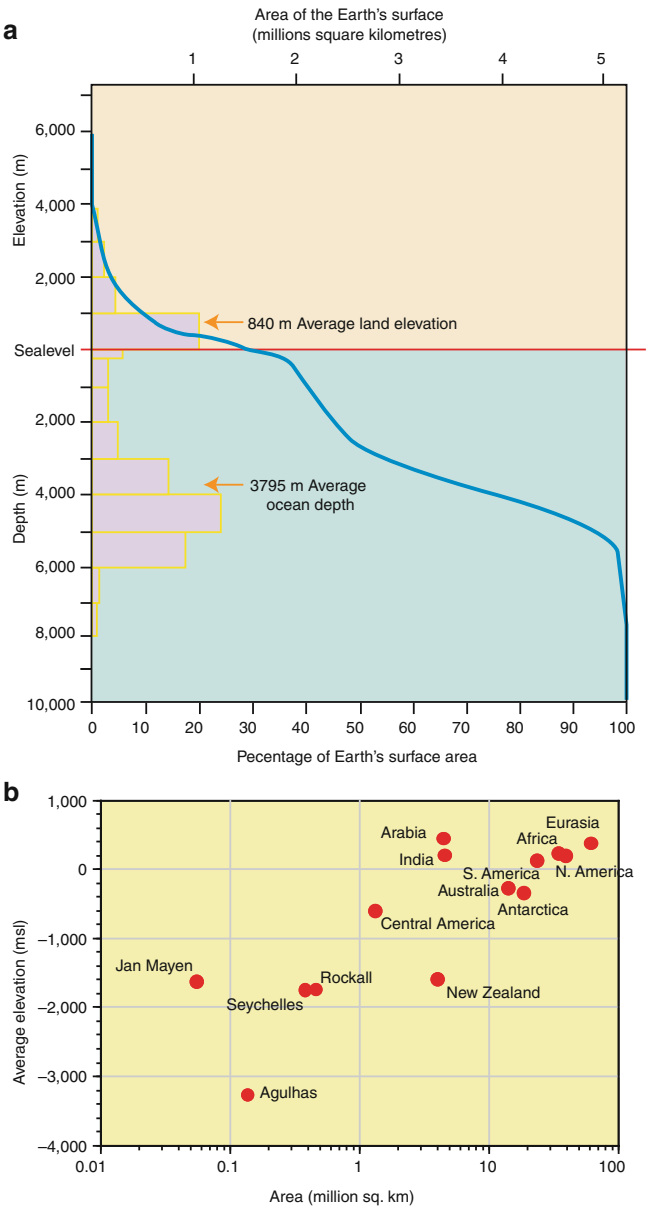

Fig. 5.31 Isostasy. (**a**) Distribution of earth surface elevations. Histogram shows percentage/area of the earth's surface within elevation intervals of 1 km. Cumulative curve (*blue*) shows the percentage of the earth's surface that is above a particular elevation. (**b**) Mean continental heights as a function of areas of continental lithosphere in selected continental and micro-continental blocks (Replotted from data in Cogley 1984)

There is an overall positive correlation between areas of continents and microcontinents and their average elevation relative to sea level (Fig. 5.31b; Cogley 1984; Condie 2004). Small continental fragments, such as Agulhas and Seychelles, lie 2 km or more below sea level. Arabia and India are higher than predicted by the area-height relationship, a feature probably related to their collisional tectonic histories. The height of a continental block relative to sea level depends on the uplift rate and the rates of erosion and subsidence.

Collision between continents resulting in lithosphere thickening is probably the leading cause of continental uplift in response to isostasy. The anomalous heights of India and Arabia undoubtedly reflect the Neogene collision of these microcontinents (Fig. 5.31b).

The six large continental blocks have undergone numerous collisions in the last 2 Ga, each thickening of the lithosphere in collisional zones leads to a greater average continent elevation both in the lead up to and after the collision. Hotspot activity can also elevate continental interiors and portions of the seafloor, it explains the relatively high elevation of the basaltic Jan Mayen Island mass. In both uplift situations any supracrustal depositional system has the potential to pass from submarine to continental. Likewise, in a newly formed continental rift atop an upwelling mantle plume, the depositional system will pass from continental to submarine as the rift widens and underlying crust thins and cools.

It goes beyond the needs of this chapter to delve more deeply into the causes and outcomes of hypsometric analysis, other than to note one self-evident truism and then make a set of simple deductions that must characterise basinwide and platform evaporites. First the truism: Sediments deposited within a continent tend to accumulate above sealevel. This may seem to be a trite statement, but it has substantial implications in terms of hydrological controls on ancient evaporites. We have seen in Chap. 2 how the volumes of solute needed to explain the huge volumes of halite in ancient evaporites must come from seawater (or dissolution-related reworking of older marine evaporites into the landscape drainage). We know that water cannot flow uphill and so such marine-derived evaporite systems must by definition be accumulating in subsealevel depressions. Yet, we also know that evaporites cannot form when a restricted basin has a surface connection to the ocean. Evaporite basins require hydrographic isolation and a surrounding barrier that facilitates marine seepage. Thus, substantial volumes of evaporites can never accumulate in open marine situations (characterised by large distances between continental masses), nor in highly elevated continental situations where there is no huge isochemical solute reservoir to draw upon (seawater cannot flow uphill). We saw earlier how endorheic drainages at suprasealevel elevations in continental settings so allow relative small evaporite deposits to form. These are the borates, salt-cake and soda-ash salts discussed earlier, which have precipitated from the requisite nonmarine mother brines (Chap. 12).

The need for a large volume of seawater, in order to accumulate huge volumes of halite or calcium sulphate in a sedimentary basin, means it can only happen in an arid, subsealevel, hydrographically isolated marine-fed seepage depression. That is, the evaporite basin is isolated from a hydrographic connection to the ocean, yet still remains in a subsealevel position so as to allow seawater seepage. The basin is desiccated and its hypsometric position is passing either from the continental into the marine realm or immediately prior to the passage from the marine to the continental realm. This happens in a continental margin position when two or more continental plates are in close proximity, either as; (1) an opening continental rift causes the floor of a rift valley to pass below sealevel or, (2) in a situation of continent-continent closure as the rising floor of the closing basin is still subsealevel as the hydrographic connection is lost (Fig. 5.32; Table 5.8). The former situation characterised the formation of Miocene halite in the Red Sea, the latter characterised the precipitation of Messinian halite across the floor of the Mediterranean.

Timing and styles of plate-plate interaction are summarised by the Wilson Cycle, which breaks down a plate tectonic cycle into a time of divergence passing to convergence via stages A through H (as shown in inset in Fig. 5.32). Named in honour of J. Tuzo Wilson, the Wilson Cycle encapsulates the notion that as new ocean basins open, via the formation of new seafloor, others must close, driven by the process of subduction and ultimately by continent-continent collision (Wilson 1966).

Compilations of the time-related distribution of ancient marine evaporites shows there are four plate tectonic situations where thick evaporite beds have accumulated at particular times in the past (Fig. 5.9). As illustrated in Fig. 5.32, they are: (1) Areas of rifting where continental plates are beginning to move apart (divergent plates in "rift to drift" transition in Wilson Cycle stages B to early C); (2) Areas where continental plates are coming close to one another (convergent or colliding plates in Wilson Cycle stage F); (3) Areas of intracontinental or intraplate sagging (intracratonic basins), which are often the result of farfield plate stress induced by continental orogeny acting on zones of pre-existing crustal weakness such as an old rift belt (aulocogen) or farfield sags tied to the formation of foreland depressions (intracratonic basins in Wilson Cycle stage A). (4) Thick (km-scale) halite sequences in local regions of rapidly subsiding continental crust in transform or strike-slip settings where the plates are sliding horizontally past one-another (conservative or neutral plate margin).

Only in Wilson stages F (continent-continent collision) through the onset of Stage C (intracratonic through rift through incipient ocean) can continental plate edges be in sufficient proximity to create the hydrographic isolation needed to facilitate marine seepage to a desiccated subsealevel basin floor and so precipitate marine-fed saline giants. The same plate edge interactions likely also drive the gentle continent interior flexures that create intracratonic sags.

Isostatic responses to plate edge and plate interior flexure explains why many regions of basinwide evaporites are underlain by thinned or transitional continental lithosphere,

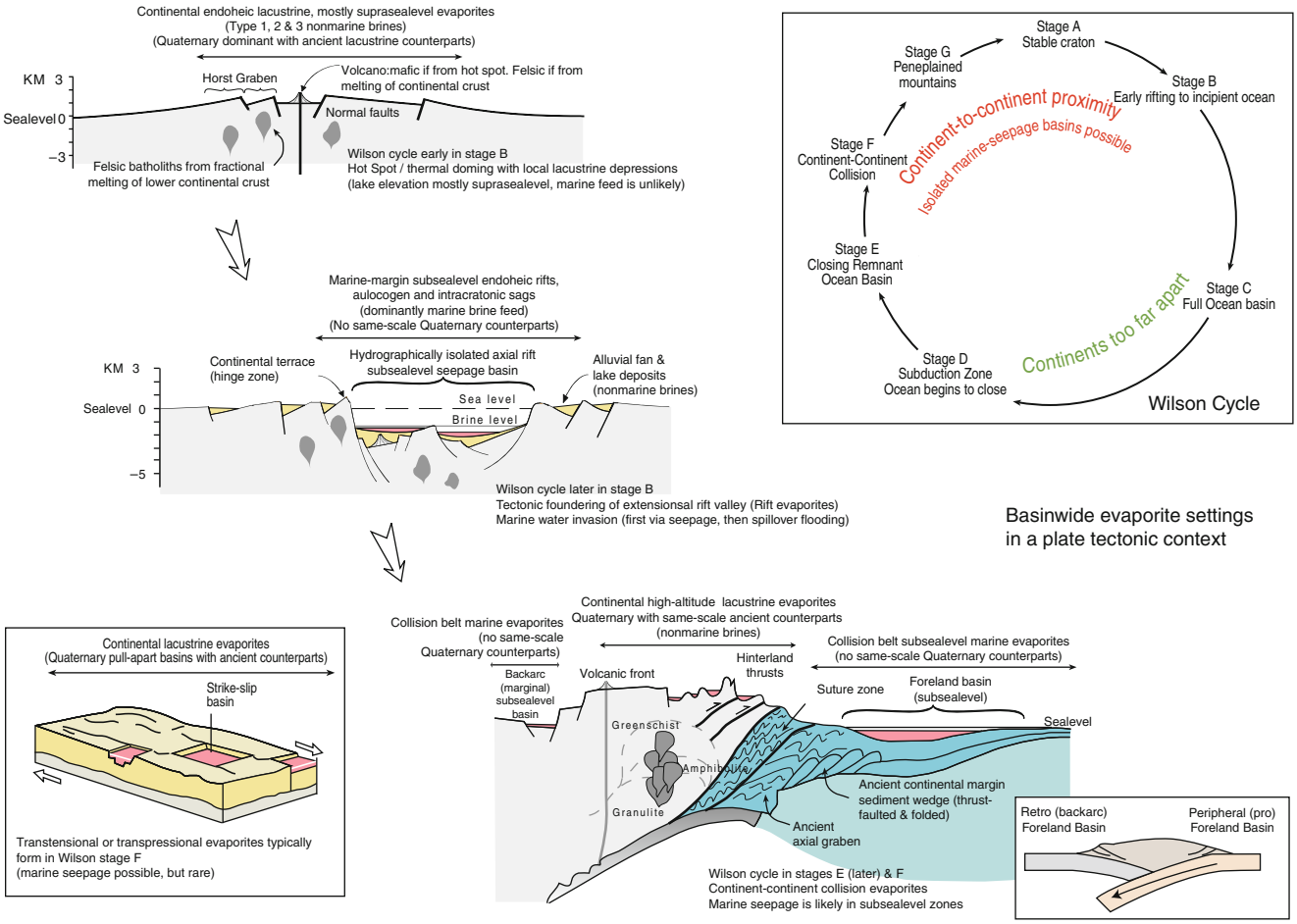

Fig. 5.32 Tectonic and hydrographically isolated (marine endorheic) continent-margin situations where basinwide evaporites tend to accumulate (evaporite beds are shaded *pink*). Positions are largely tied to world-scale times of continent-continent proximity and so can be tied to the various stages of the Wilson Cycle (After Warren 2010)

although in some cases hydrographically isolated parts of the basin floor can be underlain by oceanic crust (e.g. some South Atlantic Aptian salt basins; e.g. Jackson et al. 2000). Stages C, D and E of the Wilson Cycle encapsulate open marine settings where any deposited sediments are situated atop and surrounded by dense ocean lithosphere with a hypsometry that favours ongoing hydrographic connection to the waters of the open ocean, so precluding subsealevel hydrographic isolation, unless the plate was elevated by the effects of local tectonism or migration over a mantle plume (hot spot).

An extensional basinwide evaporite succession typically passes up into marine carbonates as it is deposited in an extensional setting where a widening subsealevel rift opens into a hydrographically-isolated incipient ocean (Fig. 5.32). Evaporite deposition then ceases as the marine basin opens further into a passive margin with its continuous surface connection to waters of the open ocean. The transition from continental interior rift with continental lacustrine brine-fed evaporite mineral and carbonates, to marine-fed rift successions with marine evaporite mineralogies, to open marine passive-margin carbonates is seen in most rift evaporite fills, worldwide (Fig. 5.33).

A compressional basinwide evaporite sequence typically overlies marine sediments and is in its turn overlain by continental sediments. Like epeiric periplatform evaporites, both these ancient tectonically induced marine-fed deposits have no modern same-scale Quaternary analogs. They are the result of a combination of tectonic and climatic processes that are not present on the world's surface today. They have been in the past and they will be again in the future.

Brine inflow to these ancient tectonically-induced evaporitic lows tends to be maintained by continuous seepage of marine groundwaters into the depression (i.e. they are subsealevel marine-fed hydrologies), along with the occasional marine flood of the barrier. This ancient evaporite hydrology is tied to arid climates as these are the zones of the world's ocean surface where there is always the potential to lose more water from the basin than can actually enter via a combination of groundwater seepage and surface floods.

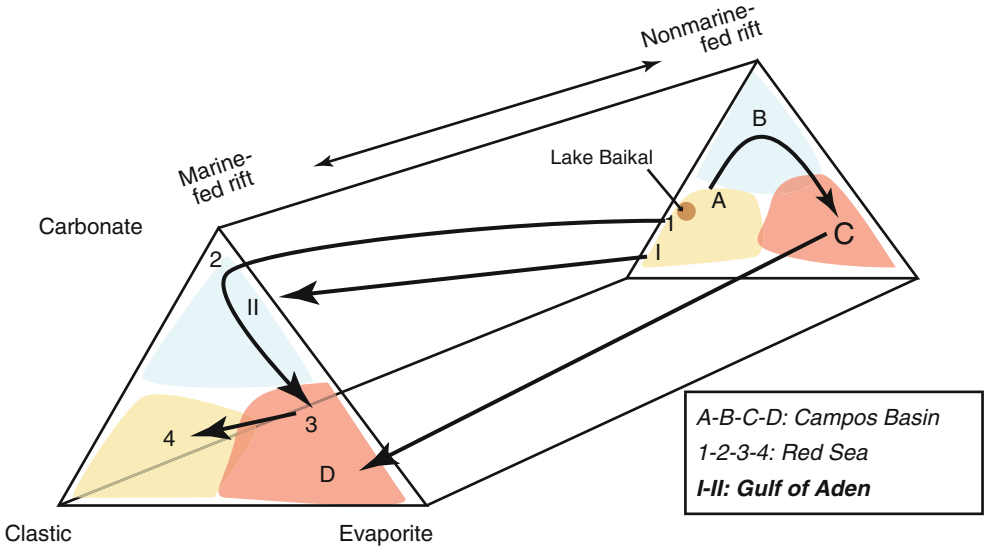

Fig. 5.33 Selected sediment response pathways to an evolving brine feeder hydrology in a opening rift that is passing from nonmarine to marine, a typical evolution in the Wilson Cycle (In part after Bosence 2012)

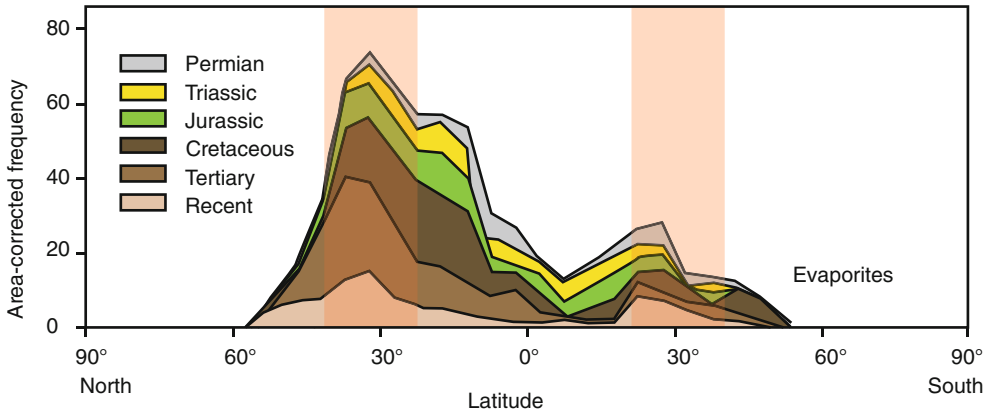

Fig. 5.34 Latitudinal distribution of evaporites from Permian to present (After Ziegler et al. 2003). *Shaded belts* indicate *horse latitudes*. Note, this plot is a count of an evaporite occurrence in each one degree latitude-longitude region; unlike Fig. 5.7, it plots latitude occurrence and is not a plot of evaporite volume. The dominance of northern hemisphere occurrences reflects the dominance of landmasses in the northern hemisphere across the Permian to Recent

Throughout deep time, evaporite sediment occurrence occupied the same two latitudinal belts, known as the Horse Latitudes, which also typifies the majority of occurrences of Holocene evaporites (Fig. 5.34). However, the same plot shows that marine evaporite occurrences in greenhouse earth (Pre-Eocene-Permian) were more latitudinally diverse and more equally distributed over broader latitude ranges

What is more variable is the volume of evaporite sediment deposited in arid latitudes (Fig. 5.7a, b). This is why there are no Quaternary examples of megahalites. Our largest and thickest bedded modern halites are forming in suprasealevel Quaternary collision belts as lacustrine "piggy-back" basins in the salars of South America (Bobst et al. 2001; Jordan et al. 2007). The only Quaternary examples of marine-fed subsealevel rifts are small-scale and include Lake Asal, Djibouti and the late Pleistocene marine-fed halites (with $MgSO_4$ bitterns) in the Danakil depression. Modern inflow waters in the Danakil are continental/hydrothermal and not marine, so the modern bittern precipitates lack $MgSO_4$. Earlier in the Pleistocene, the inflow to the same region was marine/hydrothermal seepage into the widening subsealevel rift, and kainite precipitated.

In the relatively recent geological past the best example of a full-scale rift-associated marine-seepage evaporite is probably the thick Middle Miocene salt layer beneath much of the Red Sea (Bosworth et al. 2005). Other well-studied older examples of rift-associated evaporites include the Mesozoic circum-Atlantic salt basins (Manspeizer 1982; Mohriak et al. 2008).

Evaporites deposited in ancient continental rifts that passed into incipient ocean basins have a sediment fill that can be further subdivided in prerift, synrift and post-rift

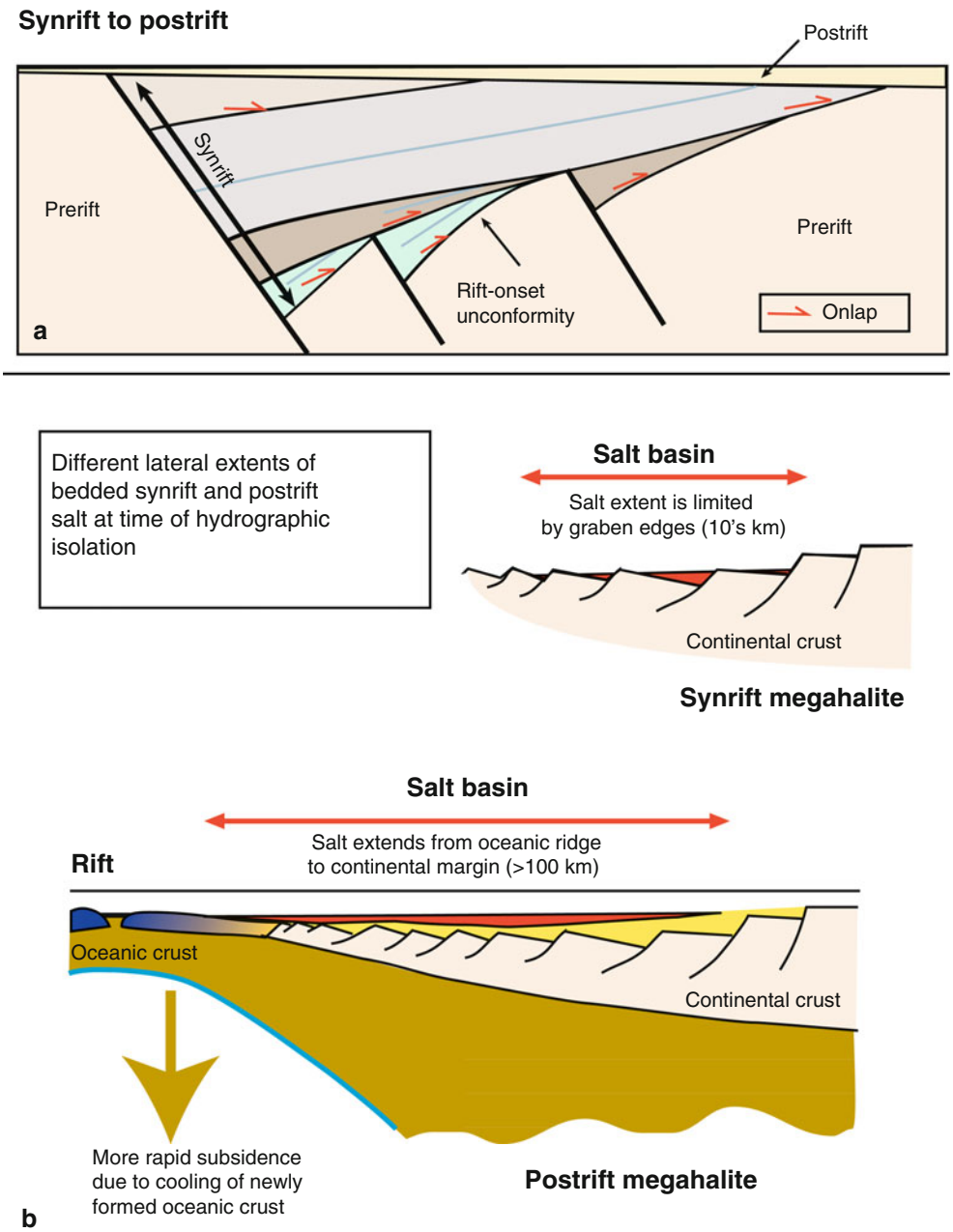

Fig. 5.35 Synrift to postrift associations. (**a**) Stages in rift related sedimentation showing typical characteristics of prerift, synrift and postrift sediment packages. (**b**) Lateral extents of megahalite basins in synrift and post rift settings See also Figs. 6.59 and 6.70

(Fig. 5.35a). Prerift accumulations are lithologies that predate the onset of the extensional faulting that defines the rift. Synrift sediments are deposited in a subsiding zone that thickens toward active normal fault(s) along the rift margin. There is typically a well-defined rift onset unconformity at the lower contact of the synrift with the prerift sediments. The synrift sediment package typically expands over an ever-larger area with time, driven by subsidence related to ongoing normal fault activity. Expansion in the area of synrift sediments is associated with onlap of sedimentation surfaces and is a characteristic feature that is usually recognizable in associated seismic reflectors. Post-rift sediments are deposited when the rift-bounding normal faults are no longer active. These sediments tend to be deposited atop and over the rift graben edges (Fig. 5.35b).

When this classification of pre-rift, synrift and postrift sediment packages is applied to thick salt fills accumulated at divergent plate margins, it seems most megahalites in divergent settings were deposited as synrift packages within well-defined graben profiles, as exemplified by the various Triassic salt basins of the northern Atlantic rim. Permian and Triassic salt basins of Europe and the North Sea are also synrift deposits (Fig. 5.36; Table 5.8).

And yet, a plot of world salt basins at divergent margins shows the largest and thickest halite accumulations (remaining salt) are postrift, not synrift packages (Fig. 5.35b;

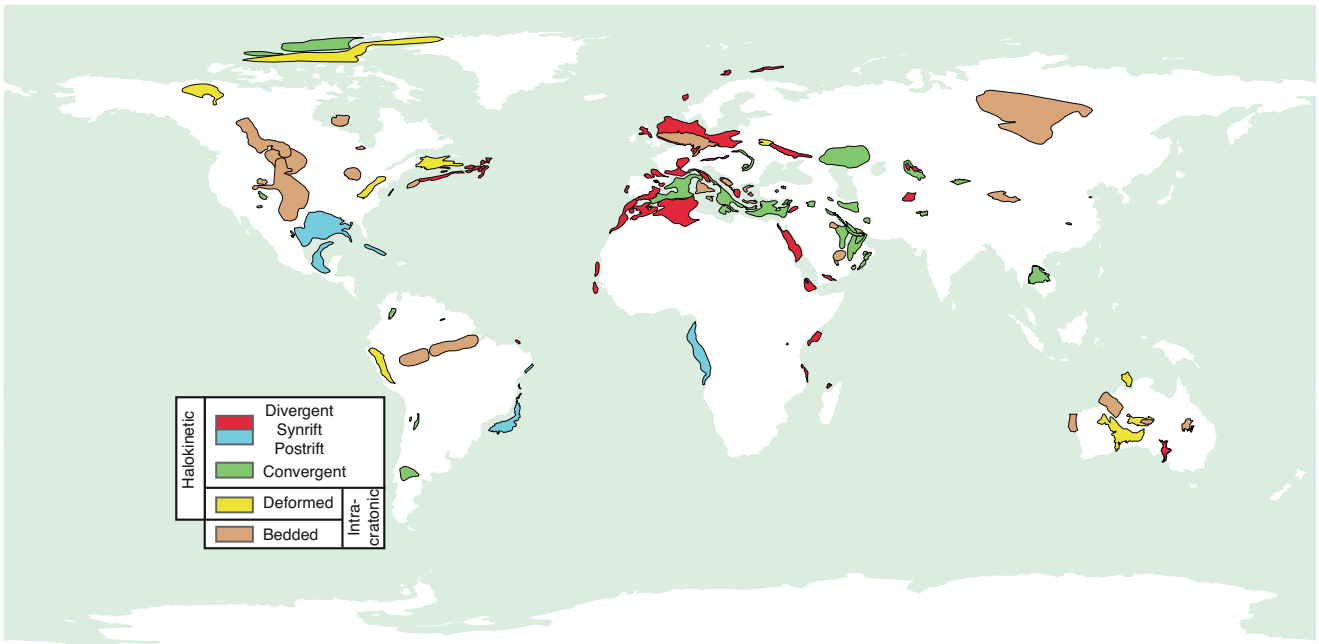

Fig. 5.36 Classification of selected NaCl-dominant basinwide evaporite deposits in terms of tectonic situation, including lacustrine associations (Refer to listed basin key in Fig. 5.30 for basin names)

Table 5.8). They formed in palaeo-Gulf of Mexico and in the South Atlantic Aptian salt basins of Brazil and West Africa. The lateral extent of the salt beds into the synprecipitational basin were not defined by a graben edge atop transitional crust, but in places thick postrift halites were in direct contact with seafloor basalts of the oceanic crust (Salvador 1987; Jackson et al. 2000). It is very likely that the hydrographic barrier that facilitated the hydrology of these subsealevel megahalite basins was also an offset volcanic ridge. It also implies that the northern and southern Jurassic salt masses of the Proto-Gulf of Mexico, and the Brazilian and Angolan Aptian salt masses were never in direct depositional contact, rather, they were separated by a basaltic midoceanic ridge, even as they precipitated. Recently, Huismans and Beaumont (2008) proposed that, compared with earlier one-dimensional depth-dependent models, the post-rift Mesozoic salt basins of the Atlantic are better explained by a model that includes notions of decoupling between upper and lower parts of the lithosphere during stretching, with contrasting wide and narrow extensional styles above and below the decoupling level and progressive focusing of crustal extension toward the rift axis.

Halokinesis in postrift evaporite-floored basins is characterised by well-developed allochthonous salt tiers, strong components of subhorizontal salt translation and secondary minibasin-capped canopy levels (Aptian salt basins of the South Atlantic and the Gulf of Mexico; Davison 2007; Tari et al. 2003; Hudec and Jackson 2007). Stronger vertical aspects of salt flow (c.f. lateral flow), both in extension and compression, characterise synrift basins such as the Permian Zechstein Basins of Europe and the Triassic salt basins of the circum North Atlantic (Warren 2008).

A classification of ancient salt basins, as illustrated as the inset in Fig. 5.36, shows that halite sequences in intracratonic sag basins tend be less subject to halokinesis than halites in rift and collision basins. The NaCl remains as a bedded deposit unless an intracratonic basin is caught up in a subsequent deformation belt, as has affected Neoproterozoic halite in the Amadeus and Officer basins, the Cambrian salts in the Mackenzie Basin and the Silurian salts in the Appalachian basins. The lack of halokinesis prior to later superimposed deformation in intracratonic sag basins is in large part a reflection of their depositional style. As mentioned earlier, halite beds in these basins tend be intercalated with anhydrites and marine platform carbonates. As such, the beds rarely attain the 80–100 m thicknesses of pure salt typically needed for syndepositional salt flow (Chap. 6).

Problems in Correlation *Sans* Hydrology

The need for hydrographic isolation means thick salts are not simultaneous with marine carbonates. Likewise, there are fundamental hydrological problems with the notion that evaporite beds pass laterally below the same sheet of water into contiguous synchronous carbonates and clastic beds. This requires longterm maintenance of subvertical density interfaces in a fluid, which is a physical impossibility. Put

simply, if you ignore the unique hydrology needed to deposit a thick evaporite bed, the correlation will fail. Thick evaporites must correlate to unconformities in their surrounds and subaqueous evaporite deposition in a single brine-filled water body (basin) must be a simultaneous holomictic event.

Shaw (1977) in a landmark paper was one of the first geologists to recognise that the classic silled-basin model, with evaporites accumulating in the basin centre and a restricted surface connection to the ocean defined by growing reefs, is hydrostatically unsound. He went on to demonstrate that in such a scenario deepwater evaporites cannot accumulate. Kendall (1988) further develops this argument by integrating his conclusions with the work of Lucia (1972) to illustrate that when an evaporite basin is depositing widespread salts it must be totally isolated from a surface supply of seawater. Deepwater evaporites are possible in such isolated nonstratified basins (see discussion of the Dead Sea halite in Chap. 4).

Deepwater halite accumulating simultaneously with platform gypsum and basin entry carbonate in a single water mass is not possible, yet it is commonly invoked in models of many ancient evaporite basins. In order to deposit gypsum in a shallow area of a brine body and halite in a deeper area of the same brine body requires an inclined halocline. The required fluid system cannot exist over the longterm in a single brine body. Any body made up of liquids of two different densities cannot support shear. The inclined halocline required by this model will spontaneously collapse in order to regain its gravitational equilibrium. Once it has restratified to a horizontal interface the precipitation of salts in the deeper brine body ceases until the salinities of the upper and lower brine bodies are equalised by the concentration of the upper less saline water body (Chaps. 2 and 4). There never has been and there never will be a brine lake or seaway with a permanently non-horizontal halocline.

In terms of stratigraphy, this means a thick subaqueous bedded halite intersection in one well is an unlikely time correlative of a thick subaqueous anhydrite/gypsum bed in an adjacent well a few kilometres away. The only exception is if they were deposited in nonconnected water bodies in two separate sub-basins or if one or both units were capillary salts not bottom growths. Monomineralogic subaqueous evaporite beds are perhaps one of the few examples of true "layer cake" stratigraphy. Many of the supposed correlations and basin reconstructions in the literature, which propose that a deep subaqueous halite in the basin-centre is time-equivalent to a shallower subaqueous basin marginward anhydrite and to a biologically restricted, but growing, reef carbonate in the seawater inflow area are wrong as they ignore fundamental principles of physics and hydrology. By implication, the geological interpretations and correlations in the same regions will be marked by the nonrecognition of the significance of erosion surfaces, hiatii or dissolution horizons in adjacent wells or in the carbonates or other marine strata that occupy the basin margin. A time of evaporite deposition corresponds to a time of exposure and the creation of a subaerial unconformity in adjacent carbonate sills.

Table 5.9 Typical evaporitic sediment accumulation rates

Mineralogy	Accumulation (cm/ka)
Carbonate bed	50–100
Gypsum/anhydrite bed	1,000
Halite bed	5,000

Kendall (1988) lists five factors that should be addressed when correlating evaporite units or applying the principles of sequence stratigraphy to evaporite basins:

1. *A lack of stratigraphic control;* evaporite depositing areas tend to be populated by halotolerant organisms that have low biostratigraphic potential. This means that biostratigraphic faunal analysis can be used to bracket the evaporite group (using fossils in nonevaporite strata above and below the unit of interest); but intra-evaporite biostratigraphic subdivision is near impossible.
2. *The rapidity of evaporite deposition;* evaporites can accumulate at some of the most rapid sedimentation rates known (Table 5.9; Einsele 2000; Warren 1989). Even if fossils are present in intrasalt units that separate a number of evaporite beds, the very short time required to deposit thick evaporite sequences means the biota are incapable of evolving fast enough to be used for biostratigraphic control of the evaporites.
3. *Complexity of stratigraphic relationships;* stratigraphic relationships between the surrounding nonevaporite lithologies and the evaporites are typically dynamic and problematic. Their hydrology and rapid rate of deposition mean evaporites accumulate so rapidly that lateral correlatives to the evaporite deposit are at best thin, or more typically, are surfaces of erosion or nondeposition.
4. *Early dissolution about basin edge;* A high likelihood of partial to complete subsurface dissolution exists, especially of the more soluble salts, almost from the time the salts accumulate (Fig. 5.37). This means most ancient evaporite deposits show clear evidence of thinning, especially about the edges of a thick evaporite succession where flushing by meteoric and basinal waters is most likely to occur. As we shall see in Chap. 7, a salt bed or halokinetic salt mass shrinks like a block or ice, inwards from its edges. If the evaporite dissolves completely, remnants may be missed (such as layers of insolubles or thin dissolution breccias), and a whole episode of basin history and structural evolution ignored. Even when evaporites remain in the basin, a greater degree of dissolution in zones of freshening about the basin edge means the current distribution of mineralogies may bear no relation to

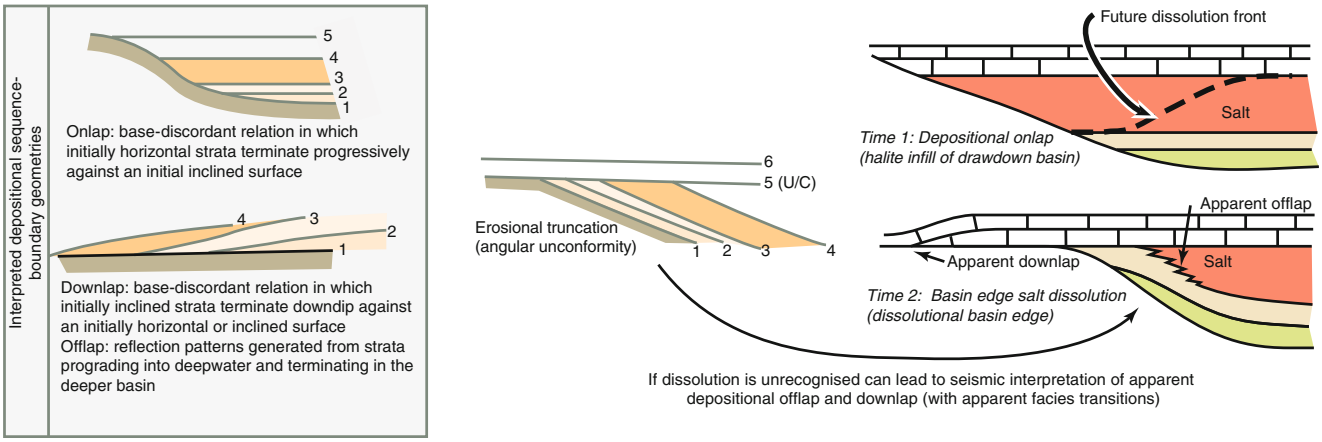

Fig. 5.37 Dissolution of evaporites about the margin of a basin can create an apparent downdip offlapping and updip downlapping stratigraphy from an original depositional onlap situation (In part after Kendall 1988). See also Fig. 5.38

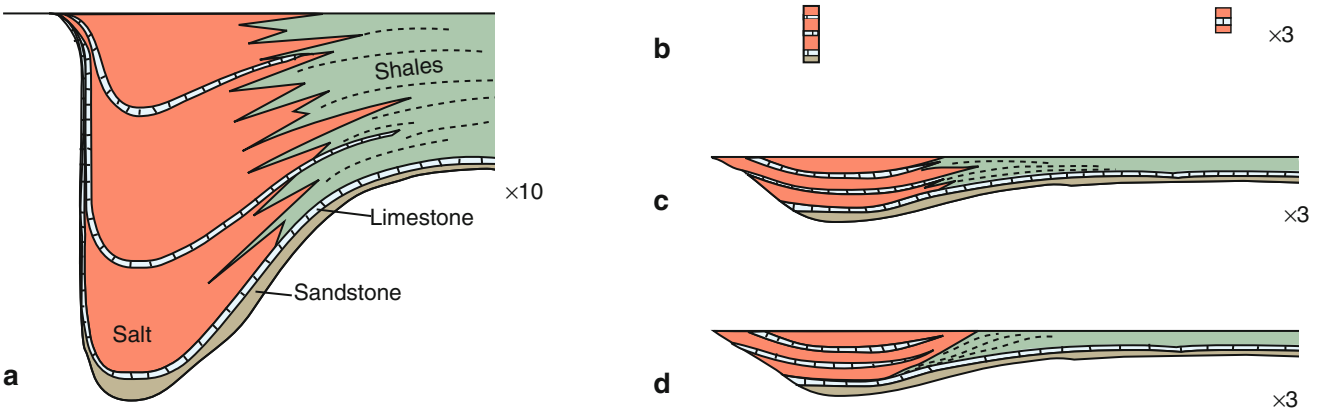

Fig. 5.38 Effect of vertical exaggeration on correlation between thick evaporite sequences and marginal clastics or carbonates (After Busson 1980; Kendall 1988). (**a**) Conventional correlation with significant vertical exaggeration showing lateral equivalency of evaporites and marginward clastics or carbonates. (**b**) Original data drawn with less vertical exaggeration. (**c**) Conventional correlation with less vertical exaggeration (hydrologically unlikely in an evaporite basin accumulating thick salt beds). (**d**) Alternative correlation, which assumes drawdown is require and so there is no equivalency between salt beds and marginward clastics or carbonates (hydrologically likely in drawdown basin). Alternative (**d**) is reasonable to most geologists when not suffering from a psychological need to draw near-horizontal correlation lines. It implies times of thick salt accumulation were distinct from times of carbonate deposition

their original distribution in a basin (Fig. 5.30). Removal of the marginal portion of a halite layer that had overstepped an earlier anhydrite unit will convert an onlapping situation to an apparent offlapping situation in a seismic section in an area without well control. Likewise many apparent "bull's-eye" basins may be the result of marginward dissolution of the more soluble evaporite layers.

5. *Inappropriate scaling*; We tend as a profession to use vertically exaggerated cross sections to make relationships more obvious in what are natural systems with thin beds with low bed thickness relative to width ratios (Fig. 5.38a). Our training in mapping skills makes most geologists reluctant to draw steeply inclined bed-to-bed correlations when more horizontal possibilities are available (Kendall 1988; Busson 1980). A propensity for large vertical exaggeration in basin cross-sections leads to a tendency to draw correlation lines that show transitional facies between the evaporite beds and the surrounding nonevaporites, and to impose age equivalence of evaporites and nonevaporites (Fig. 5.38b, c). But the inherent hydrological constraints required to form a platform or basinwide evaporite fill means salt beds tend to accumulate rapidly in isolated depressions on the land's surface. Times of evaporite deposition correlate to times of isolation and so to times of nondeposition or gaps (unconformities) in adjacent nonevaporite strata. In such situations we should be quite happy to draw inclined correlation lines showing that at the time of evaporite deposition there was little or no deposition taking place in the adjacent nonevaporite strata (Fig. 5.38b, d).

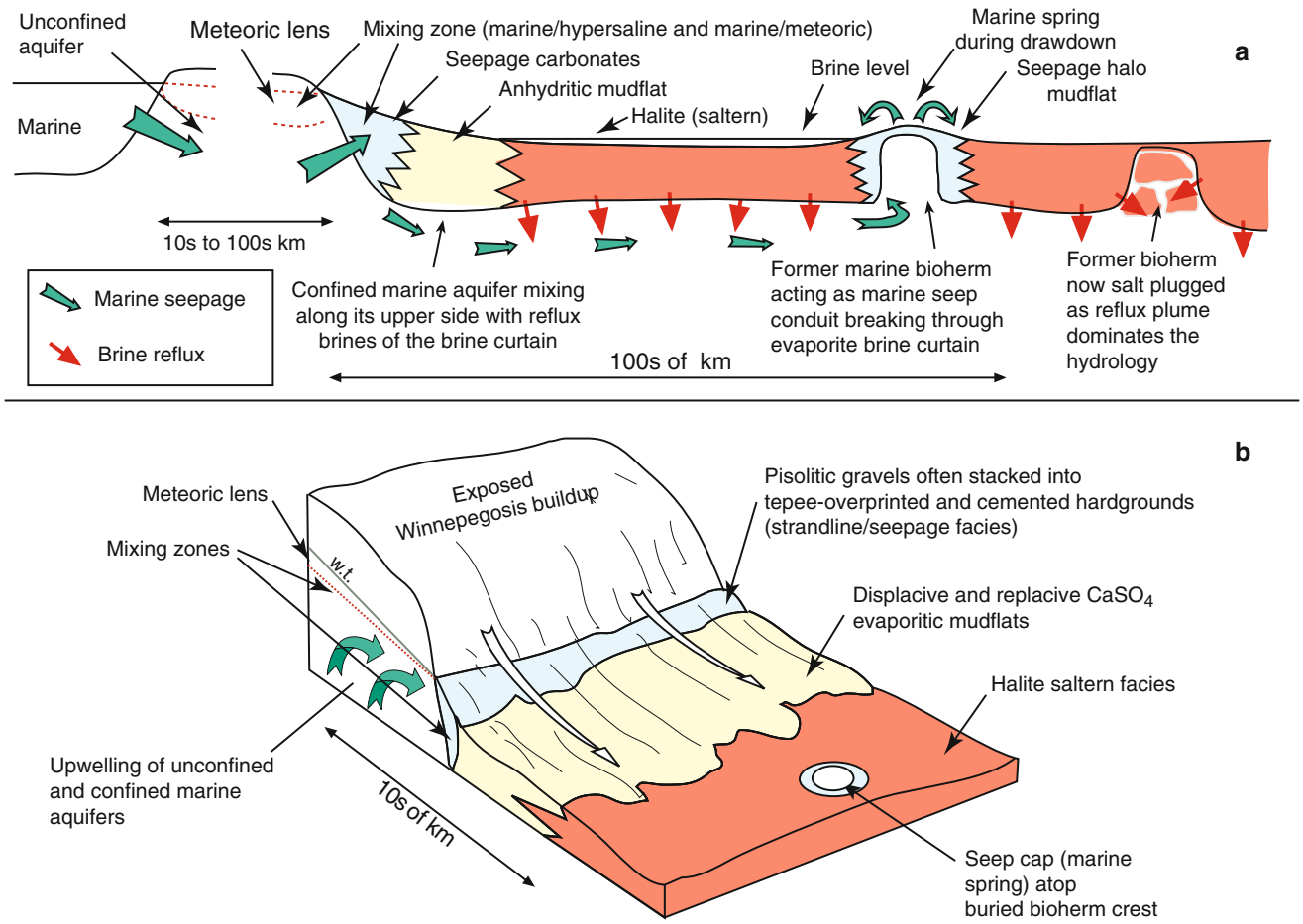

Fig. 5.39 Evaporative drawdown dolomitisation. (**a**) Hydrology of basin showing seepage facies and halite in basin centre. Note the potential for the mixing of seawater seepage with refluxing brines both about the margin of the drawdown basin and beneath the reflux curtain across much of the basin floor. Diagram is not drawn to any consistent lateral scale. (**b**) Close-up of facies pattern associated with seepage outflow zones and the potential positions of marine/meteoric and marine/hypersaline mixing zones (In part after Warren 2000a; Kendall 1989)

Dolomite Aprons in a Drawdown Basin

There is good evidence that much of the finer-grained mimetic dolomite, which is intercalated and dispersed within the main evaporite mass of a basinwide evaporite, has, at least in part, a microbial genesis (Dela Pierre et al. 2012; de Lange and Krijgsman 2010). Such primary dolomite is not discussed further in this section, rather, it focuses on the replacive mesogenetic dolomite in the apron carbonates, beneath and adjacent to the main evaporite body. These dolomites can enhance poroperm levels in these evaporite-sealed carbonates. Requirements of hydrographic isolation for basinwide evaporites have consequences for reflux dolomites. In contrast to well documented reflux dolomite geometries and distribution s in platform evaporite associations, outputs from dolomitising hydrologies in saline giants are a shade more complicated and as well as classic per descendum reflux hydrologies can include aspects of meteoric or brackish waters mixing with dense seawater derived brines (Fig. 5.39; Lu et al. 2002; Li et al. 2013).

Brine plume and seawater seepage inflow phreatic volumes in drawndown basinwide-accumulating depressions are driven by the piezometric head between sealevel and the brine -air interface, which can be hundreds or more metres below sealevel (Fig. 5.7b). With no modern counterpart, one can only infer, not observe, the hydrological and diagenetic character of such basinwide systems by studying the more accessible outcrop examples of platform and basinwide evaporites, as in the Messinian evaporite/dolomite associations of the circum-Mediterranean (Sun 1995; Sun and Esteban 1994; Lu and Meyers 1998), the Permian Zechsteinkalk dolomites associated with basinwide evaporites of NW Europe (Clark 1980a; Peryt and Scholle 1996) and the Devonian basinwide evaporites and associated dolomites of the Keg River- Pine Point Presqu'ile of Canada (Maiklem 1971; Kendall 1989).

Maiklem (1971), Cercone (1988) and Kendall (1989) pointed out the potential for widespread dolomitisation via seawater seepage beneath subaerially exposed carbonate slopes about a drawndown basin mmaiklargin is largely independent of marine eustasy (Fig. 5.39). Drawdown basins have the potential to flush huge volumes of phreatic seawater through the basin edge. As the groundwater heads in such systems are measured not in metres but hundreds of metres, and if one accepts that seawater flushing has the potential to dolomitise marine limestone, then the potential for dolomitisation is huge within carbonate aquifers about the margin of an evaporite drawdown basin. "Mixing" zone dolomites are also likely, but not in a classic seawater-freshwater Ghyben Herzberg interface on the marine side. Rather dolomite will form in rapidly fluctuating and flushed interfaces and outflows in and about the now isolated and exposed carbonate slope and rise shown in Fig. 5.39. The schematic is drawn assuming an unconfined aquifer in the interval separating the marine from the seepage zone. The reality is much more likely to be a combination of confined and unconfined aquifers feeding predominantly seawater into the basin margin. This zone of mixing and seawater spring outflows will move to and fro over the exposed basin edge as the brine level in the basin responds to changes in tectonics and climate.

Outflow points of these predominantly seawater brines develop a characteristic set of pisolitic/tepee cementstone lithologies the strandline/seepage facies described in Chap. 1. Kendall (1992) showed how such a carbonate seepage facies can be used to define hydrologies in the Devonian Keg River Basin where these spring-aprons were mostly located about exposed former shelf slopes and pinnacle reefs (Fig. 5.39b). When part of an inactive pinnacle reef or other aerially exposed bioherm, these permeable carbonates can act as confined aquifer outflow zones capable of breaching the active reflux curtain on the basin floor, much like the modern spring mounds of Lake Eyre and Lake Frome (Fig. 5.39a). Slightly down dip of the seepage facies were evaporitic mudflats dominated by anhydrite and in the lowermost sections of the basin floor were widespread areas of perennial surface brine (the halite seaways of the Keg River Basin). Away from seawater and meteoric discharge seeps, the downward reflux associated with the brine curtain moved Mg-rich waters into underlying sediments driving reflux dolomitisation and evaporite plugging. This water ultimately mixed with deeply circulating seawater seepage fluids and other subsurface waters (Fig. 5.39a).

Such a basinwide hydrology creates both reflux and mixing zone chemistries, which have the potential to dolomitise any limestone host in contact with the outer parts of the brine curtain. Detail of such drawdown mechanisms can be inferred in dolomite distribution within Neogene evaporitic sub-basins of the Mediterranean. For example, Meyers et al. (1997) and Lu and Meyers (1998) have documented pervasive dolomites that cut across intra-Miocene sequence boundaries in the Nijar Platform and also occur in the youngest Messinian reef/oolitic units (Fig. 5.40a). The dolomites do not transect the Miocene-Pliocene unconformity, although they do occur as clasts in overlying basal Pliocene lime grainstones. This constrains the dolomitisation as being latest Miocene and pre-Pliocene, suggesting this widespread dolomitisation occurred within 600,000 years and possibly in less than 200,000 years. It is a excellent indication of the large volumes of phreatic seawater that can be cycled through the rock pores in short times in drawdown hydrologies.

Carbon and oxygen isotopes of Nijar dolomites show marked positive covariation, with most values ranging from +5.4 to −1.2‰ $\delta^{18}O_{PDB}$ and +2.5 to −4.3‰ $\delta^{13}C_{PDB}$ (Fig. 5.40b; Meyers et al. 1997). The highest $\delta^{18}O$ values are heavier than reasonable estimates of Messinian normal-salinity seawater dolomites, suggesting the involvement of evaporative brines in the dolomitisation process. Calculations of covariations of O and C isotopes during water-rock interaction and fluid-fluid mixing argue against recrystallisation of Nijar dolomites, an interpretation also supported by their Ca richness (49–57 mol %). Mixing calculations show that four-fifths of Nijar data are consistent with dolomitisation via mixtures of freshwater and a few tens of per cent of marine-derived evaporative brine, while one-fifth are consistent with mixtures of freshwater and normal-salinity seawater (e.g. covariant isotope curve in Fig. 5.40b) Likewise, modelling of covariations of $^{87}Sr/^{86}Sr$ and Sr/Ca ratios that developed during mixing, further supports involvement of evaporative brine, and suggests that any freshwaters involved in the dolomitisation had low Sr/Ca ratios and relatively high Sr and Ca concentrations. Na, Cl, and SO_4 concentrations in Nijar dolomites (200–1,700 ppm, 300–600 ppm, and 600–6,500 ppm, respectively) also argue for involvement of evaporative brines, and for mixtures of brine with freshwater and/or seawater (Fig. 5.40c).

Meyers et al. (1997) and Lu and Meyers (1998) proposed that most dolomitisation occurred after Messinian reef formation during multiple relative sealevel/brine level changes associated with evaporative drawdown. Marine carbonate deposition of the Nijar shelf occurred during high sealevels, and evaporite deposition during lowered basin water levels associated with evaporative drawdown. During drawdown, basin brines with five to sixfold seawater concentrations (gypsum precipitating) developed on the floor of the Nijar Basin. Brines mixed with freshwater and seawater mainly in a groundwater setting about the basin margin as fluctuating base levels of the brine curtain drove before it a zone of freshened/meteoric water seepages (Fig. 5.40d).

Similar drawdown dolomites can be found in the Zechstein of NW Europe where dolomitised algal-bryozoal reefs, oolites and intertidal to shallow subtidal skeletal grainstones to mudstones occur adjacent to the margin of

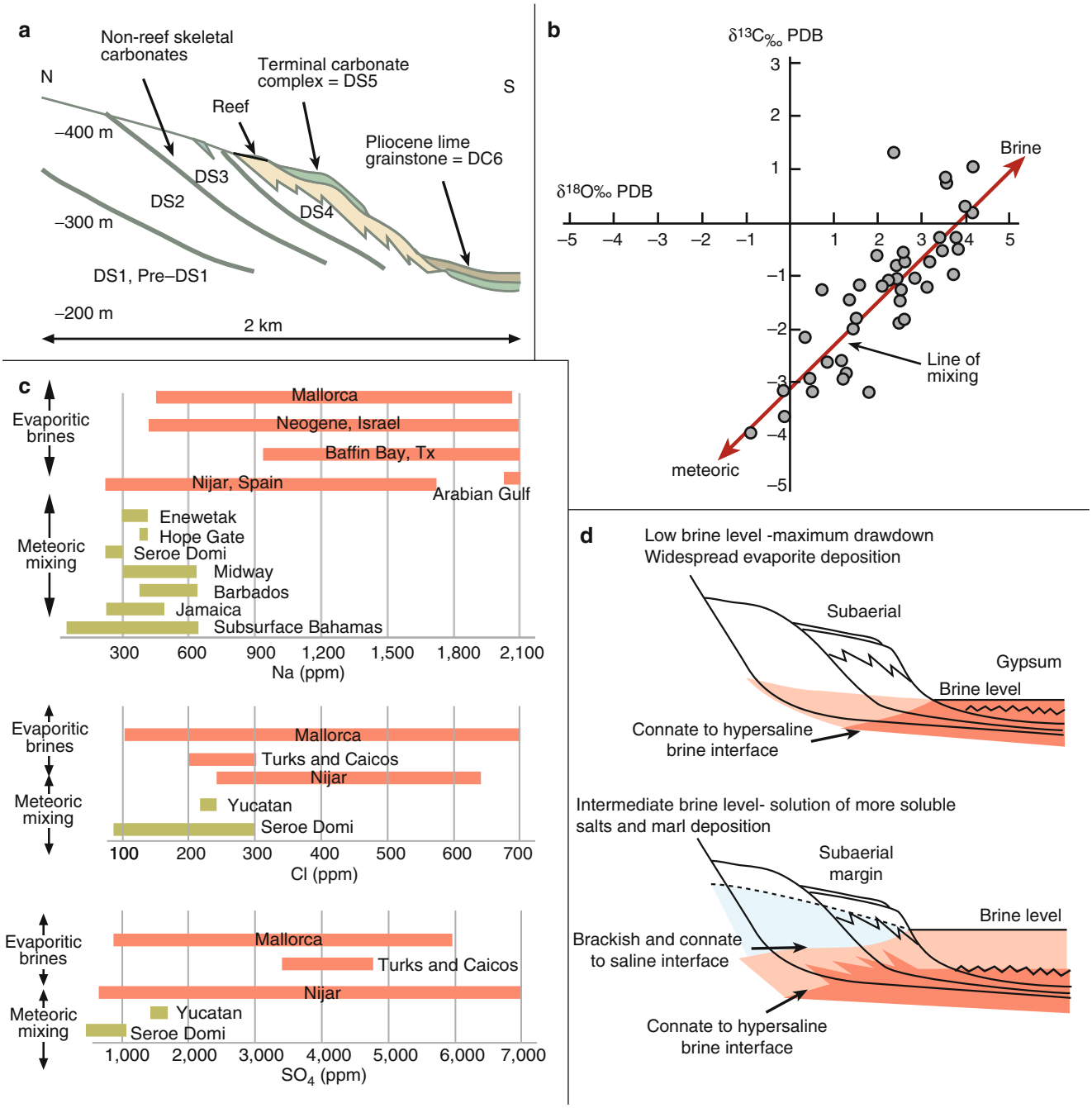

Fig. 5.40 Nijar dolomites in the Messinian of Spain. (**a**) Composite stratigraphic cross section of the Tortonian-Messinian carbonate platform at Nijar. *DS* depositional sequence. (**b**) Oxygen and carbon isotopes of the Nijar dolomites (**c**) Na, Cl and SO_4 contents of Nijar dolomites compared to other Tertiary and modern dolomites formed in mixing zone, seawater and evaporative brines. (**d**) Model of migration of mixing interfaces between hypersaline brine, connate seawater and meteoric brackish waters. Their position within the carbonate margin is controlled by fluctuation in brine level in the basin (After Meyers et al. 1997; Lu and Meyers 1998; Lu et al. 2002)

the Zechstein salts. They are interlayered with the platform portion of basinwide evaporite beds composed of anhydrite and halite (see later in this chapter). Evaporite salts were deposited during the complete isolation and drawdown of the Zechstein Basin. It was at this time of drawdown that reflux dolomites replaced the adjacent and underlying Zechstein limestones (Clark 1980a). At the same time the regression of facies associated with the drawdown of the brine base level caused the encroachment and displacement of formerly marine to hypersaline porewaters by meteoric waters in the dolomites of the Magnesian Limestone (Kaldi and Gidman 1982).

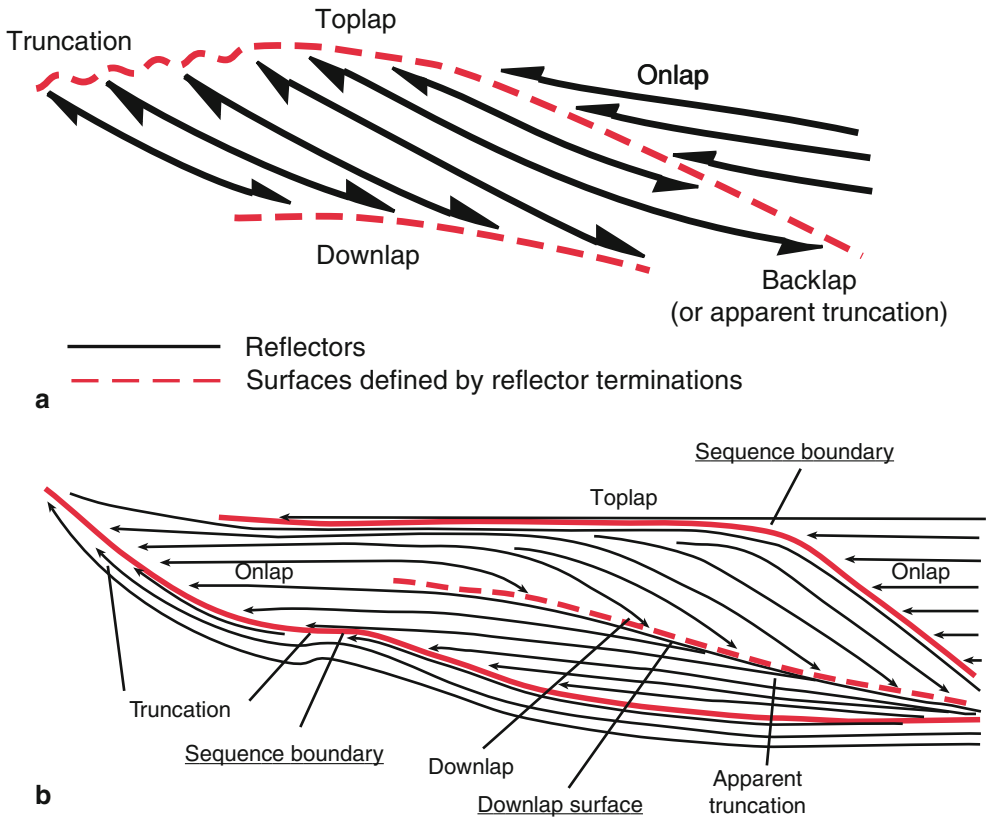

Fig. 5.41 Fundamentals of seismic sequence interpretation. (**a**) Terminology used in defining sequence interpretation of seismic reflectors. (**b**) Sequence boundaries define a depositional package

Sequence Stratigraphy in Evaporite Basins?

Sequence stratigraphy is the study of ancient rock relationships within a chronostratigraphic framework of repetitive, genetically related strata, bound by surfaces of erosion or nondeposition or their correlative conformities (Posamentier and James 1993). Stratigraphic sequences are deposited during a single cycle of relative sealevel change and the rise and subsequent fall of sealevel within the shallow marine setting generates a characteristic sedimentary wedge with a specific geometry and vertical stacking pattern. Sequences are conformable successions constructed by genetically related strata, bound at the top and bottom by unconformities and their correlative conformities (Fig. 5.41; Van Wagoner et al. 1988, 1990; Tucker 1993). Unconformities bounding sedimentary wedges may represent a significant time gap and may die out in more basinward positions where sealevel oscillations do not expose the sedimentation surface.

In classic sequence stratigraphic interpretations of marine sequences, the major control on depositional extent and geometry is assumed to be relative sealevel change, determined by rates of eustatic sealevel[6] variation and tectonic subsidence. Depositional sequences are generated by a single cycle of relative sea-level change, and a complete depositional sequence, bounded by unconformities, consists of, from oldest to youngest, lowstand, transgressive, and highstand components (= systems tracts). This evolution creates the characteristic transgressive-regressive pattern of sedimentary facies within a depositional sequence with the outline of a sigmoidal wedge or prism (Fig. 5.41b); lowstand systems tract (LST), transgressive systems tract (TST) and highstand systems tract (HST). A seismically resolvable depositional sigmoid typically has a thickness of 10–100 m, extends laterally for 10–100's km, and represents a depositional episode of 1–5 million years in duration. According to Haq et al. (1987), it is a response to 3rd order sealevel changes (Table 5.10; Fig. 5.42). Internally, depositional sequences are constructed of sub-seismic-resolution parasequences (metre- to decametre-scale 4th and 5th order depositional cycles). Parasequences are typically bound by local scale unconformities and disconformities are visible in most outcrops and cores.

Chronostratigraphic correlation is an important application of marine sequence stratigraphy. It is tied to the notion that sediment wedges form in response to worldwide sealevel cycles of rise and fall. If so, then seismic geometries can be used to extract a global sealevel cycle chart (aka Vail or Exxon sealevel curves). This then leads to the construction of age models for given stratigraphic successions that

[6]Eustatic change (as opposed to local change) results in a worldwide alteration to the global sea levels due to changes in either the volume of water in the world oceans or net changes in the volume of the ocean basins.

Table 5.10 Orders of sealevel change and likely driving mechanisms (In part after Tucker 1993)

Order	Years	Tectonoeustatic	Rifting and thermal subsidence	Global eustatic	In-plane stress	Glacioeustatic, tectonic, sedimentary	Basinwide evaporites time to deposit 1–2 km of fill
1st	10^8						
2nd	10^7						
3rd	10^6	Seismic sigmoids					
4th	10^5						
5th	10^4	Typical limit of seimic resolution in siliciclastics and carbonates					
6th	10^3	Parasequences					

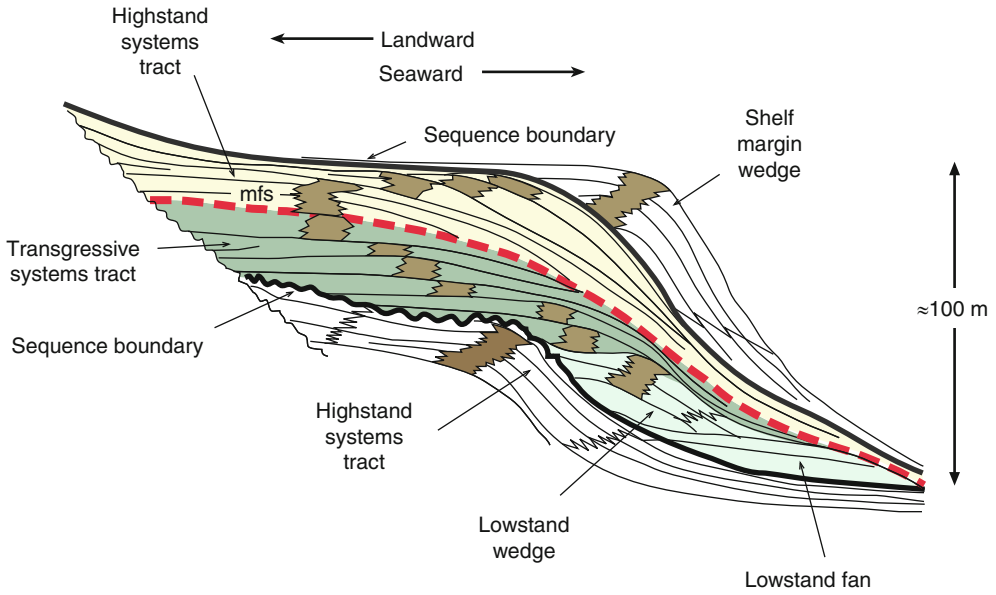

Fig. 5.42 The familiar sigmoidal or "slug" model of a marine carbonate depositional sequence used by sequence stratigraphers with the brown shaded areas representing carbonate shoal/reef sediments. A single depositional sequence consists of lowstand, transgressive and highstand systems tracts (After Van Wagoner et al. 1988 and other sources). A maximum flooding surface (*MFS*) separates a transgressive (retrogradational) from a highstand (progradational) system tract. In terms of associated evaporite deposition each sequence boundary (unconformity) may be time equivalent to a thick sequence of basin-wide evaporite fill, which accumulated further out in the basin (low-stand? but there is no hydrographic connection to ocean). Saltern evaporites tend to accumulate on the platform landward of the reefs within transgressive system tract sediment packages when higher order sea sealevel falls expose reef crests and isolate lagoons from a surface connection to the ocean

are based on the correlation of a local stratigraphic sigmoid to this global sealevel curve (Posamentier and James 1993). Different orders of sealevel change are recognised based on the time interval encapsulated in the sealevel cycle (Table 5.10). The use of sequence stratigraphic principles to construct age-eustatic (chronostratigraphic) models is based on the assumption that stratigraphic successions are a function primarily of eustatic rather than local tectonic fluctuations or that the effect of tectonics can be reliably removed so as to allow sealevel curve fitting.

First and second order changes in world sealevel are a response to changes in the volume of the ocean basins caused by continental dispersal and collision (Figs. 5.43 and 5.44). High rates of seafloor spreading during continental dispersal reduce ocean basin volume, leading to high sealevel. Third order changes have durations of 1–10 m.y. and are typically about 2.5 m.y. in length. The cause of third order cycles is controversial as they are too short to attribute to most world scale tectonic events affecting the volume of the ocean basins, but too long to attribute to glacio-eustatic responses. Other more local tectonic events, such as changes in plate stress and regional tectonism, are of the correct duration, but do not appear to be capable of generating sufficient change in water depth to account for the magnitude of world scale third order cycles. Fourth order (500–200 ky) and fifth order (200–10 ky) cycles are widely documented in marine sediments (outcrop and core based parasequences) in many periods of the Phanerozoic in both shallow marine and pelagic

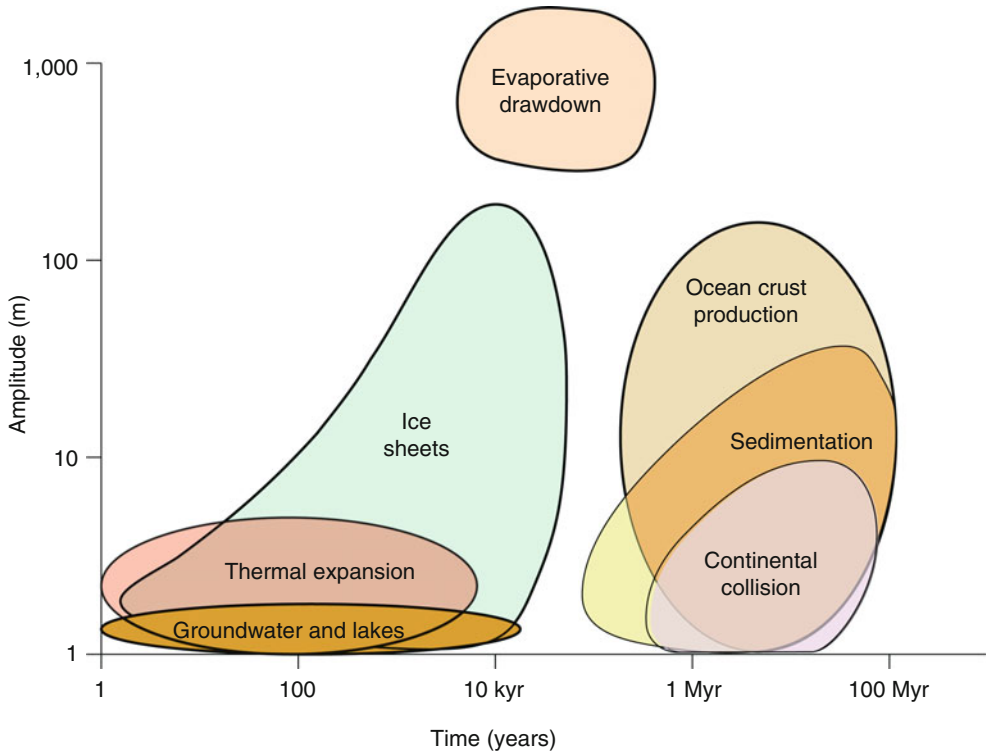

Fig. 5.43 The various geological processes that drive different amplitudes of sealevel change across different time periods (In part after Miller et al. 2011; see also Table 5.10)

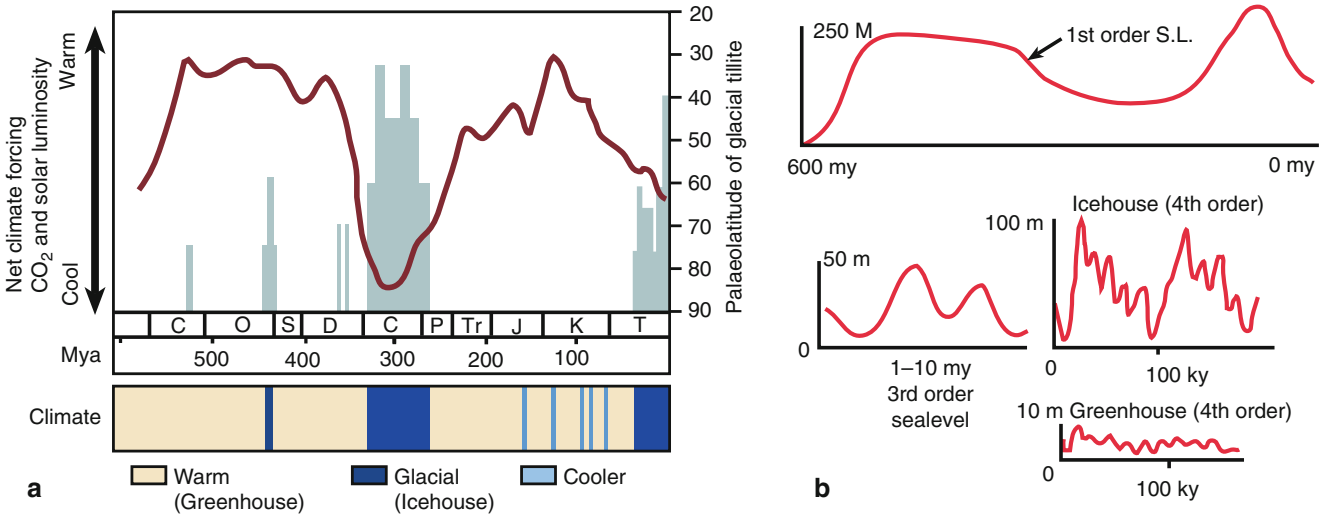

Fig. 5.44 Relationship between icehouse and greenhouse conditions, eustasy and global CO_2. (**a**) Palaeolatitudinal extent of glacial tillite in relation to net forcing of climate due to variations in CO_2 and solar luminosity. Inferred times of general greenhouse, icehouse and short cooler climate periods in Mesozoic (After Royer et al. 2004). (**b**) Eustatic sealevel curves, showing first order Vail sealevel curve in the upper part. Rest of diagram plots typical amplitudes and periodicities of higher order sealevel curves. Third order curves have a 1–10 my periodicity. Schematic 4th order with superimposed 5th order sealevel curves are drawn for icehouse and greenhouse conditions (See text for explanation)

strata. These cycles are possibly the result of changes in global climate driven by cycles in the Earth's orbital parameters and tilt, collectively referred to as Milankovitch Cycles.

There is still much debate in the literature as to controls on the magnitude and frequency of the various sealevel changes that could facilitate a correlation of sedimentation packages worldwide; especially at the third order world scale cycles where seismic and rock based interpretations overlap. At that scale, some authors well versed in outcrop and core study go further and question the reality and the scientific basis for the construction of world scale age correlations based on seismic-based third-order eustatic age curves in almost all sedimentary basins (e.g. Miall 2010).

For evaporites, there is also the additional problem of different depositional rates of water level change inside and outside a hydrographically isolated groundwater sump

(Fig. 5.40). Rates of evaporite deposition, especially in basinwide settings, are an order of magnitude higher than that of marine shelf carbonates or siliciclastics (1–2 km in 300,000–500,000 years are typical). Seismic geometries resolvable in evaporite fills are typically 4th and 5th order, with parasequence sets resolving time frames of the order of a 1,000 years (6th order). Comparing seismic stratigraphies inside and outside a basinwide evaporite basin and attempting, based on the evaporites, to relate the eustatic interpretation to the global curve is difficult if not impossible. We are not resolving depositional evolution at the same time scale (Table 5.10).

More generally accepted than worldwide chronostratigraphic correlation is the application of seismic sequence stratigraphy to lithology prediction based on interpretation of depositional geometries and basin architecture using a combination of seismic, wireline, core and outcrop data (Miall 2010). For example, the favoured sites for major porosity development in carbonate-dominated depositional sequences include large, isolated buildups within the transgressive phase, massive grainstone aprons located immediately landward of the shelf-margin facies within the regressive phase, and karst-affected platform interior facies immediately beneath the sequence-bounding inter-regional unconformities (Fig. 5.39).

There are numerous volumes and papers now published that deal with high resolution sequence stratigraphy of arid zone carbonate shelves and ramps and how they differ from siliciclastic sequences in their response to sealevel changes (Fig. 5.39; Miall 2010; Read et al. 1995; Budd et al. 1995; Loucks and Sarg 1993; Tucker 1993; Posamentier and James 1993; James and Kendall 1992). The details will not be repeated here and the interested reader should refer to these volumes. There are only a few published papers that deal specifically with the sequence stratigraphy of evaporite systems; key papers include, Tucker 1991; Goodall et al. 1992; Strohmenger et al. 1996a, b; Sarg 2001. The results are contentious and most concentrate on the carbonate (marine-connected?) stage of the evaporite basin. This is understandable as it is in these carbonate units that potential hydrocarbon reservoir facies are to be found, often beneath or adjacent to the evaporite seal.

Does Sealevel Control Salt Sequence Boundaries?

When attempting to interpret eustatic effects (global sealevel) in evaporite basins, a requirement of no effective hydrographic connection to the open ocean during times of extensive evaporite accumulation plays havoc with the fundamental marine eustatic paradigms of sequence stratigraphy. Documented brine level changes in lacustrine and marine basinwide settings are ≈1 km in a few thousand years and there is no simple relationship between sealevel changes going on outside the basin and the geometry of the evaporite body in the isolated evaporite-accumulating basin (Fig. 5.43).

All evaporite basins with a marine-seepage feed have a brine level that is below sealevel. It is, after all, drawdown that drives brine influx in ancient marine-fed basins. The relative difference in water level across the isolating barrier may be no more than a few metres, as it was in the platform evaporites of Guadalupian backshoal strata in West Texas, or it may be thousands of metres as it was in the late Miocene salinity crisis in the Mediterranean, the Cretaceous evaporites of the southern Atlantic and the early stages of the Permian salinity crisis in the Zechstein Basin of NW Europe. Brine salinities and the rate of salinity change in a brine-filled depression, as well as the absolute brine level in an isolated basin, are controlled by the local climate, the rate of brine leakage through the underlying brine curtain and the rate of seepage replenishment of the inflow waters and brines about the depression's margin. With most ancient saline giants the creation of a depression capable of accumulating and preserving thick lacustrine and basinwide evaporite fill is a response to tectonics, not eustasy.

Marine-fed platform evaporites must be distinguished from basinwide evaporites if one wishes to apply the marine eustatic concepts. At our present level of understanding we can probably fit marine-margin platform evaporites and some intracratonic saltern fills (epeiric seaways) into a global eustatic context. In the absence of tectonic tilting in these two settings, the precipitation of large volumes of platform salts is largely dependent on marine phreatic seepage through a carbonate barrier. It requires platform isolation brought about by a slight fall in sealevel, perhaps a 4th order fall on a 3rd order rise in greenhouse mode (Fig. 5.7a). The evaporites can fill the depression behind the barrier; but cannot, as they are seepage fed, rise any higher than sealevel and still be active. The isolating barriers in turn have geometries and distributions across the platform that are controlled by sealevel changes (Miall 2010; Read et al. 1995; Loucks and Sarg 1993).

In contrast, tectonically-formed subsealevel basinwide evaporite units, with their much lower hydrological base level, are more problematic in terms of using the effects of sealevel fluctuations to understand and predict evaporite geometries and mineralogies. The problem will remain until the hydrologies of large-scale drawdown systems are better understood. Formation of basinwide evaporite sequences are largely tied to a suitable juxtaposition of tectonics and climate. In such a scenario the decametre sealevel fluctuations on the marine side of the isolating barrier are largely irrelevant to evaporite depositional styles within the lowermost

portions of an isolated basin experiencing a drawdown that is up to 1,500–2,000 m below sealevel. Likewise continental lacustrine evaporites are not directly tied to the world sealevel curve. In both basinwide and continental lacustrine scenarios the application of sequence stratigraphic modelling is most useful in a genetic rather than an age (world sealevel/eustatic) context.

Icehouse and Greenhouse Eustasy

Sequences in seismic stratigraphy are unconformity-bound packages generated by high amplitude sealevel changes, with bounding surfaces typically produced during relative sealevel falls (Tucker 1993). High amplitude sealevel changes producing regional sequence boundaries can occur on several time scales depending on the presence or absence of polar ice caps and glacial tillites (Fig. 5.44a). At times of no polar ice cap (greenhouse earth) the high amplitude changes that produce sealevel oscillations of several tens of metres are a response to second and third order processes, while fourth/fifth order processes produce only metre-scale relative sealevel changes and associated parasequences (Fig. 5.44a). In contrast, when there are polar ice caps (icehouse earth) the high amplitude sealevel changes (typically greater than 100 m) are brought about by fourth/fifth order processes.

The driving force for these high amplitude/high frequency oscillations is change in polar ice volume driven by Milankovitch rhythms (Figs. 5.1 and 5.2). During icehouse times the same longer term second-/third-order fluctuations in sealevel that dominate the greenhouse style still occur, but they now have a lower amplitude and longer period than the glacially driven changes. Thus the glacially-driven eustatic cycles swamp these longer term effects, so that in icehouse times fourth-order sequences are produced and are arranged into sequence sets (Tucker 1993). Greenhouse periods produce third order sequences constructed by fourth-/fifth order parasequences and show a much more prevalent cyclicity in lagoonal parasequences (Fig. 5.44b).

The Neogene sedimentary marine record is an icehouse record, where fourth-order sequences dominate the continental margin as unconformity-bound, relatively thin (5–30 m thick), stratal packages. Other older icehouse intervals include the late Precambrian and the Permo-Carboniferous (Figs. 5.2 and 5.44a). In contrast in greenhouse times (Late Cambrian to Middle Ordovician, Silurian to Early Devonian, Late Permian to Oligocene), marine stratal packages consist of much thicker unconformity-bound sequences (50 m to hundreds of metres thick) deposited as third order cycles made up of fourth-fifth order parasequences that are 1–10 m thick.

Marine-Margin Platform Evaporites

Marine carbonate platform systems show a different set of depositional responses to sealevel change compared with siliciclastics, the differences were not recognised in the early Vail/Exxon models (Fig. 5.45; Miall 2010). The difference is there because almost all marine carbonate is ultimately biogenic. Unlike siliciclastic shelves (Fig. 5.45a–c), carbonate shelves most actively aggrade and then prograde both seaward and landward during times when the continental margin and interior is covered by shallow seas. That is, those most rapidly growing parts of any epicontinental carbonate platform, usually the reef crest and associated grainstone belts, aggrade most rapidly when part of a transgressive systems tract (Fig. 5.45e). In contrast, the marine carbonate platform progrades most rapidly when part of a highstand systems tract and the accommodation space in the platform lagoon is filled (Fig. 5.45f). When part of a lowstand systems tract, the much more restricted area of the "carbonate factory" means little or no growth can take place in either deep or shallow water, karstification of exposed platform sediments dominates at the sequence boundary on the platform (Fig. 5.45d). The lowstand response is very different in carbonate and siliciclastics.

Carbonate sedimentation rates cannot be assumed to be near-constant across a water-covered platform. The variation in unit thickness reflects the strong environmental controls imposed on biogenic sedimentation rates. Thus, changes in geometric stacking patterns in carbonates do not necessarily directly reflect changes in the rates of relative sealevel rise as environmental changes are not always directly linked to changes in sealevel, but may reflect differing rates of deposition due to differing biotal growth rates across the platform (James and Kendall 1992; Hunt and Tucker 1992).

In a marine carbonate system the TST is the time when the maximum growth potential of the carbonate platform is realised and the parts of the open marine platform with the greatest growth potential typically aggrade to sealevel and then begin to prograde both seaward and into the lagoon (Fig. 5.45e). In contrast, evaporite deposition occurs on a marine platform when a back-reef or lagoonal depression is isolated from a surface connection with the sea (Fig. 5.45h). On a ramp, the barrier is usually a buildup of some sort of continuous zone Y shoal, on a rimmed shelf it is typically the reef belt or the associated grainstone/pisolite flat that have built up to sealevel.

Hydrographic isolation across the barrier crest and the onset of thick platform evaporites are usually initiated by a slight fall in sealevel, following a time of vertical aggradation (catch up) in the more rapidly growing parts of the carbonate platform; e.g. a fourth order fall superimposed on a third order rise in greenhouse mode. Thick platform evaporites are most likely to form as part of a transgressive systems

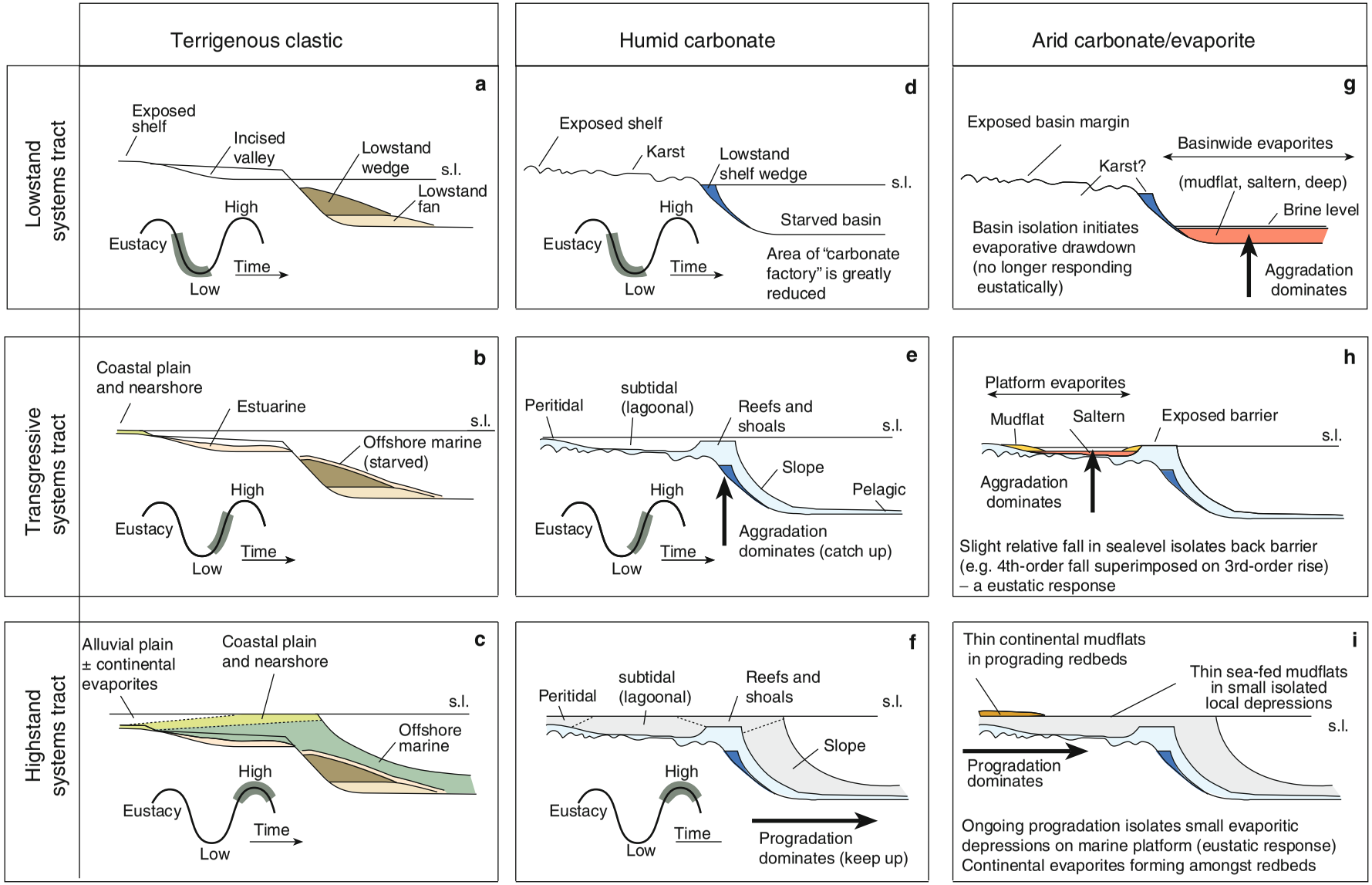

Fig. 5.45 Sequence stratigraphy of siliciclastics, carbonate and evaporite platform sequences (see text for explanation)

tract (third order) in a greenhouse earth. Any slight fall in sealevel will be marked by an unconformity across the topographic high (rim/shoal), which isolates the marine from the evaporite-depositing areas (Fig. 5.45h). Thinner evaporative mudflat (sabkha/salina) units may form as part of a highstand systems tract where ongoing progradation of the shelf (keep up) isolates small depressions further landward (Fig. 5.45i).

When platform evaporites were deposited, the subaerial isolation either of the rim/grainstone buildups on a rimmed shelf or of the zone Y shoal facies on a ramp were responsible for the restriction of the lagoon to the point where evaporites could accumulate (Fig. 2.80; Lucia 1972). Otherwise, like the carbonate shoals and reefs on platforms of today, subaqueous conditions behind the shelf rim or shoal would have never become saline enough to deposit subaqueous evaporites and only thin capillary zone sabkha caps (<1 m thick) could prograde across the landward feather edge of marine lagoon sediments. Prior to hydrographic isolation, normal marine to restricted marine sediments had been accumulating in the lagoon, so that in a vertical profile normal marine bioturbated shelf wackestones and mudstones typically underlie bedded platform evaporites. In sequence stratigraphic terms, episodes when platform evaporites accumulate correlate to karstic exposure surfaces or bounding surfaces on the platform crest. But, as it occurs in greenhouse eustasy, 4th-order sealevel did not fall more than a few metres, so it is a type 2 sequence boundary. In contrast all basinwide deposits are defined by type 1 sequence boundaries (in truth, applying marine seashore terminology to a hydrographically isolated and drawdown basin is probably wrong usage, or at least inappropriate).

Once an evaporite lagoon on the platform is hydrographically isolated from the open ocean, two end members can be deposited behind the rim; either saltern sequences or mudflat-dominated successions (Fig. 5.7). The dominance of one or the other reflects the response of evaporite drawdown hydrology to changes in relative sealevel on the platform. An evaporitic mudflat mosaic forms when there is intense evaporation and relatively slow rates of marine seepage recharge and longterm surface brine cover is relatively rare. Mudflat fills dominate if there is little difference in elevation between the sealevel on the other side of the exposed barrier crest and the floor of evaporitic depression. Sediments of the rim/shoal (oolite/grainstone/pisolite/boundstone) pass directly upward into thin intercalated sabkha/salina units or stacked sabkha cycles and back to shoal facies that make up the base of the next cycle, with no intervening saltern sequences.

Saltern fills tend to dominate evaporites of the lagoon fill when evaporation is less intense and/or there is a greater rate of seepage replenishment through the isolating barrier. Salterns are more common if there is a greater potentiometric head across the barrier between ambient sealevel and the water surface in the lagoon. This tends to occur when the platform lagoon was deeper at the time of its isolation. This happens during a transgression in settings where the rim/shoal aggrades relatively rapidly, while the backshoal platform does not keep pace with the same rise in sealevel. Early shoalwater carbonates deposited on the lagoonal side of the rim are not all that different from those on the seaward side of the rim. This is especially true where the rim is incipiently drowned at the onset of the transgression. While the rim was growing and catching up to a new, higher sealevel the waters in the lagoon could freely exchange with the open ocean and so a diverse open-marine biota flourished within the lagoon.

When a rim reef or shoal catches up to the new higher sealevel and coalesces into an isolating barrier, conditions in the carbonate-accumulating epeiric lagoon become more restricted. As the exchange with open ocean waters is reduced; sediments are now deposited as restricted-marine carbonates. With complete restriction across the rim or shoal, the lagoonal waters become sufficiently saline to deposit evaporites and fill the drawdown lagoon with a shoaling-upward saltern cycle, perhaps capped by a mudflat sequence. The saltern evaporite unit is as thick as the lagoon was deep at the inception of evaporite deposition (Figs. 5.7a and 5.45h).

Such subaqueous saltern beds tend to be widespread across the evaporite lagoon and so are easily correlated from well to well as metre- to decametre-thick clean evaporites. The ten or so subaqueous cycles of the Cretaceous Ferry Lake Anhydrite in the northern Gulf of Mexico region (Fig. 5.24a; Pittman 1985) and the Permian San Andres cycles on the northern margin of the Delaware Basin (Elliott and Warren 1989) are examples of stacked saltern beds, while the base of the Late Permian Seven Rivers Formation atop Yates Field on the Central Basin Platform in West Texas is an example of the stacked mudflat mosaic (Fig. 10.44). The geology and reservoir/seal properties of these platform evaporite units is detailed in Chap. 10.

Unlike bedded carbonates and siliciclastics, the effects of syndepositional and later evaporite dissolution can greatly complicate any attempt at high-resolution stratigraphic interpretation in an evaporitic platform. Dissolution typically occurs as the subsiding platform evaporite passes from an active phreatic hypersaline hydrology into a compactional or thermobaric regime. This creates thin dissolution breccias and residue layers that extend over large portions of the platform (Chap. 7). Such breccias can be confused with subaerial exposure surfaces and humid/temperate phreatic karst. Unless the significance of evaporite dissolution breccias and the timing of dissolution in relation to burial is recognised, whole episodes of platform isolation may be miscorrelated. Many published outcrop-based studies of high-resolution stratigraphy in carbonate-evaporite platforms are problematic because dissolution breccias, which tend to be thin and recessive, are largely unrecognised or, if recognised, misin-

terpreted as marine flooding surfaces. And yet, a 1-m thick breccia may mark the position of a former 100 m thick salt bed. This is especially true in Precambrian platforms where biostratigraphic checks on correlation are not possible.

Clearly, there are significant differences in response geometry and basin position across the three lithologies (siliciclastic/carbonate/evaporite). In a lowstand systems tract there are substantial volumes of terrigenous sediment deposited at the foot-of-slope, but relatively minor carbonate deposition if sealevel is below the shelf break (lowstand shelf wedge). In a hydrographically isolated basinwide setting large volumes of evaporites can accumulate as a lowstand systems tract, but as widespread sheets across the hydrographically-isolated basin floor. In a transgressive systems tract, carbonate sedimentation in a humid setting reaches its highest growth potential. If a transgressive systems tract is also subject to a higher order fall that isolates a seepage depression on the shelf, then thick sequences of platform evaporites can form. In a highstand systems tract only thin mudflat evaporite units can form, while thick sequences of platform clastics and carbonates can accumulate.

Platform Evaporites in a Greenhouse Earth?

The high amplitude rapid to-and-fro of the icehouse seas across Neogene platforms has discouraged the deposition of extensive shallow-water platform evaporites. The most recent time of extensive platform evaporites is perhaps the Eocene in the Middle East, centred on Iraq and Iran or the Paleocene of North Africa (Table 5.5; Rus Fm.). Platform evaporites tend to form under greenhouse earth conditions characterised by lower amplitude sealevel fluctuations and higher world sealevel with marine waters over large parts of the continental masses (epeiric seaways). The high-amplitude high-frequency sealevel changes of icehouse earth encourage local high-relief "catch-up" reefs and banks due to ongoing rapid flooding and exposure of the platform, along with substantial unconformities and pervasive meteoric diagenesis deep in the reefs. Hence icehouse carbonate facies show considerable lateral thickness variations (Read and Horbury 1993). Throughout the Quaternary and the Neogene there has never been sufficient time for shelf-edge periplatform reefs and sand belts to grow and accrete into a single continuous shelf margin facies belt, unlike the periplatform buildups that characterise greenhouse time. Before a continuous periplatform rim can happen, icehouse sealevel falls off the shelf edge every 100,000 years or so (Fig. 5.44).

Thus, platform-edge reefs and shoals typically do not develop into laterally continuous strike-parallel belts under an icehouse scenario. Converting large areas of periplatform lagoons into isolated depressions with marine-seepage hydrologies suitable for precipitating evaporites simply does not happen. The only place where marine-fed isolated seepage depressions can occur in today's icehouse scenario is in narrow sea-marginal highstand bands, as evidenced by numerous small scale sabkhas and salinas along the marine coasts of many arid areas (Chaps. 3 and 4). Shoreline/sealevel repeatedly falls off the platform in icehouse earth mode (>100 m fall; type 1 boundaries) and so any local areas of sea-marginal peritidal or seepage evaporites that may have formed in a highstand are subject to widespread dissolution via vadose flushing, as is seen in the worldwide lack of well preserved Pleistocene marine sabkhat and salinas (Warren 1991). Even in the hyperarid coastal zone of the Red Sea, only small isolated remnants of marine-fed evaporites from the last 100 ka sealevel high remain and none remain from the previous 200 ka high. Thus, modern highstand marine-edge evaporites are small in scale and have little or no long-term preservation potential.

In contrast, the low amplitude low frequency 4th-order sealevel oscillations that characterise epeiric seaways and shelves in greenhouse earth intervals favour the formation of stable, large, highly restricted, at times evaporitic, depressions on the inner shelf portions of many marine platforms (Fig. 5.44b). A lack of permanent polar ice meant sea levels were high and covered more of the craton. Likewise, carbonate-amenable temperatures had wider latitudinal distributions. Carbonate platform rims had growth potentials that could more than keep pace with the low amplitude fourth order sealevel fluctuations. Wide, flat carbonate platforms with huge back-platform lagoons were commonplace (epeiric seas). A slight fall in sealevel meant seepage waters easily ponded in isolated large shallow shelf depressions behind continuous, now subaerially exposed reef or shoal rims. In areas where epeiric seaways covered large inland portions of the continental interior, the formation of a tectonic or shelf rim barrier followed by a fall in sealevel meant that the entire platform interiors and intracratonic sag basins could become evaporitic.

Thus, episodes of stacked platform evaporites tend to favour epeiric and pericontinental seas in greenhouse times as rapidly deposited, but extensive, saltern and mudflat beds precipitated atop marine lagoon sediments (Fig. 5.18). They were part of an overall TST, but only precipitated during short intervals characterised by higher-order low amplitude falls in sealevel. At such times the platform crest was subaerial and much of the platform was brine saturated. Today there are no substantial epeiric seaways and the isolating effects of slight sealevel falls, as well as any possibility of accreting an ongoing laterally continuous carbonate platform rim, are swamped by the overriding influence of rapid, high-amplitude, icesheet-induced 4th order sealevel changes moving across relatively narrow and steeper continental shelves. Conditions suitable for the formation of platform evaporites simply do not exist under today's icehouse eustatic regime.

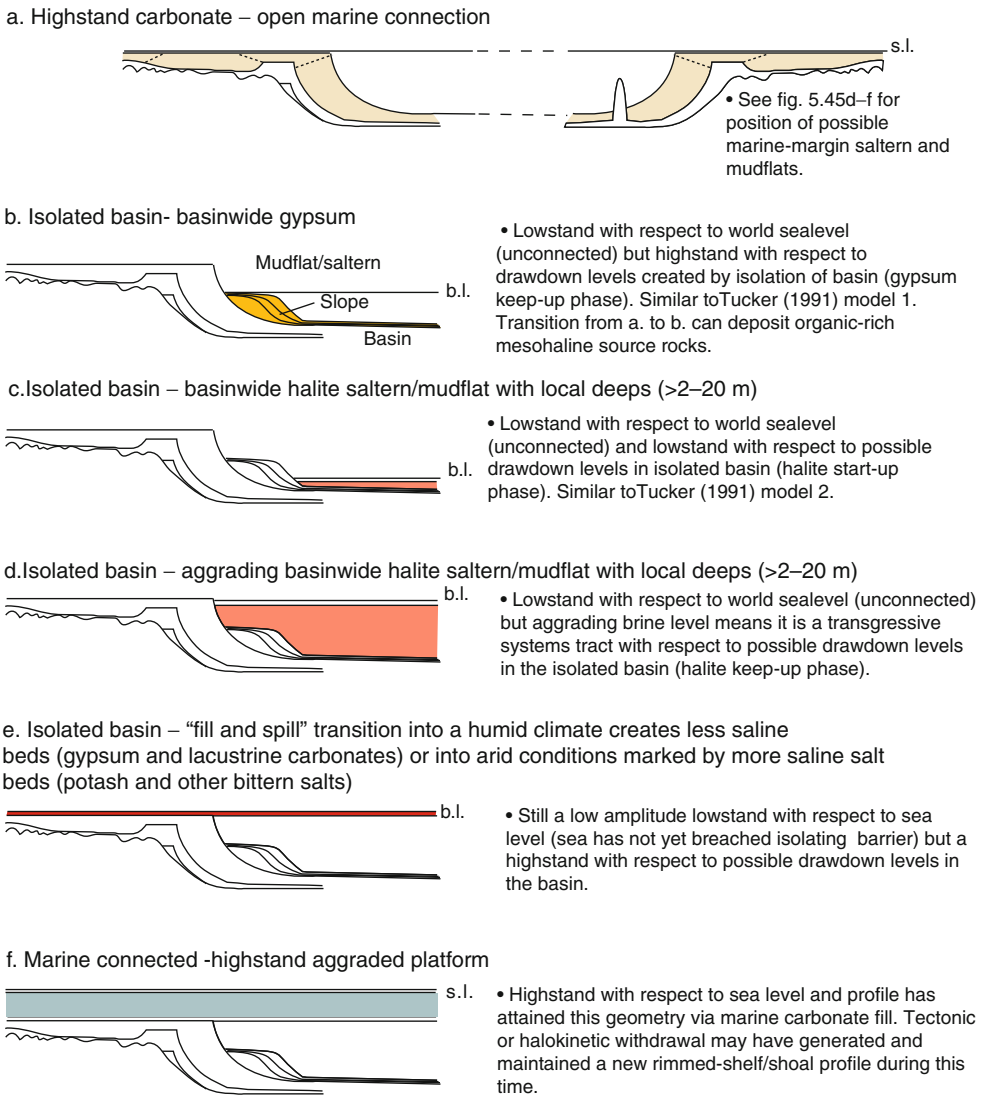

Fig. 5.46 Sequence stratigraphic model for basinwide evaporite deposition in a basin undergoing complete isolation from a surface connection to the world's oceans and subsequent drawdown. See text for detailed discussion of stages **a–f**

Basinwide Evaporites

Thick basin-filling evaporites (more than 500–1,000 m thick and hundreds of kilometres across) accumulated in both greenhouse and icehouse periods. They did so, not because of fluctuations in sealevel, but as a result of tectonic isolation of large parts of the earth's surface from the direct surface influx of the world's ocean waters (hydrographic isolation). Evaporite fills tend to be autocyclic and tectonically induced, although subsequent fluctuations in sealevel may have aided erosional breaching and refilling of the depression by seawater episodes (Table 5.6; Fig. 5.46). Once isolated, changes in sealevel outside the basin rim may change potentiometric head with respect to the free brine surface in the basin and so drive changes in the rate of supply of brine. A relatively high sealevel outside of the basin will create a steeper potentiometric gradient and hence encourage more rapid replenishment of brine and a greater volume of brine seeping through the permeable barriers that separate the brine depression from the open ocean (e.g. Kendall 1992). When relative sealevel is lower, this decreases the potentiometric gradient and slows the rate of brine flow. A fall in sealevel also causes the sea coast to retreat from the isolated depression, which further decreases seawater supply.

But autocyclic mechanisms, including the vagaries of climate, tectonics and adiabatic effects, along with the rate of formation and efficiency of intrabasin brine curtains or hydroseals, all interact to swamp the influence of sealevel changes to the hydrology of the evaporite basin (Chap. 2). For example, the aggradational infill of a tectonic depression by salt beds that create their own underlying aquitard or brine curtain has the same effect as the change in sealevel on potentiometric gradient of the inflow. As the sequence aggrades it decreases the potentiometric gradient and so slows the rate of marine recharge independent of changes in absolute sealevel.

The effect was noted by Warren (1982b) and used to explain the changes in the infill cycle textures in Holocene gypsum-filled salinas in coastal southern Australia. Logan (1987) discusses similar hydrological transitions in controlling vertical sequences and the transition from halite to gypsum with aggradation in Holocene Lake Macleod, Western Australia. Kendall (1989) used such Holocene analogs to interpret the upward transition from anhydrites to carbonates in the Middle Devonian of northern Alberta (Muskeg and Sulphur Point Formations). Previously the transition was interpreted as reflecting a sealevel rise, but Kendall argued it would more likely reflect a transition related to sealevel fall outside of the basin and a decreasing volume of marine inflow into a marine-fed basin with no surface connection to the ocean. His model better explains the terminal nonmarine bed that makes up the overlying Watt Mountain unit.

In summary, unless a rise in sealevel breaches the tectonic sill and converts the basin once more to a restricted mesohaline seaway, decametre-scale sealevel fluctuations outside the isolated evaporite basin exert a relatively minor influence on basinwide hydrology and hence on the detailed stratigraphy of a basinwide evaporite unit. While the basin is isolated much of the fill is autocyclic, it reflects changes in the hydrological base level that have more to do with fluctuations in tectonics and climate as they effect inflow/seepage hydrology. In the larger saline giants, such as the Messinian sequences of the Mediterranean, the Zechstein of NW Europe, and the Late Precambrian-Cambrian Ara Salt in the South Oman Basin, any changes in relative sealevel that occurred outside the drawndown evaporite basin and probably across a barrier that was hundreds of kilometres from the drawndown strandline were largely irrelevant to the style and geometries of evaporite deposition in the basin.

Basinwide Sequence Stratigraphy?

Given our rudimentary understanding of hydrology and isolation in basinwide settings, let us now look at some of the implications in terms of high-resolution stratigraphic analysis in basinwide evaporite deposits. Documented examples are few and far between, and tend to concentrate on patterns in the mesohaline to marine carbonate facies. High-resolution interpretation of any intercalated thick salt beds is more challenging because:

- Outcrop studies of geometries of evaporite units are near useless as most of the evaporite is dissolved well before it approaches the land surface – differential collapse and flow during dissolution means detailed internal relationships and depositional geometries are lost not just at outcrop but also in the shallow subsurface,
- Seismic analysis tied to well data in bedded saline giants is rarely undertaken because very few oil companies wish to characterise the internal stratigraphy of what is an undeniable seal facies,
- Deeply buried thick basinwide salt sequences are routinely subject to flow into diapiric and other structures – this largely destroys the stratigraphic integrity of internal reflectors in halokinetic portions of the basin fill and the onset of this flow can be very early, even synprecipitational (see Chap. 6).

All authors working on basinwide systems (aka basin-centre and saline giants) agree that they are lowstand deposits (Kendall 1988; Strohmenger et al. 1996a, b; Tucker 1991; Warren 1999; Sarg 2001). Kendall (1988) and Warren (1999) attempt to address the principles of sequence stratigraphy in terms of the isolated hydrological framework and the need to precipitate widespread and thick salt sequences. Others consider that basinwides require a reduced connection to the world's oceans, yet others allow intrabasinal marine carbonates to be possible syndepositional sediments with basinwide evaporites. The latter modelling expresses a blissful ignorance of the fundamentals of hydrology and hydrography seen in sediment textures and distributions in all modern evaporite basins.

Tucker (1991) derives two end member models to interpret the evaporite carbonate relationships in saline giants: Model 1, incomplete drawdown with marginal gypsum wedges and basinal laminated gypsum; and Model 2, complete drawdown with halite basin-fills. However, his hydrological constraints are not clearly stated and his hydrological assumption that marginal gypsum wedges typically form in relation to a lowered sealevel without isolation (his Fig. 2) is probably not correct (see Goodall et al. 1992).

Figure 5.46 assimilates some of the concepts of Tucker (1991) as well as the work of Kendall (1988) and my own work. It is a preliminary attempt to place basinwide evaporite geometries and overall basin fills into a sequence stratigraphic context. Unlike Tucker (1991) it is based on the notion that in an isolated basin the drawdown hydrology is largely independent of decametre scale sealevel fluctuations that are going on outside the basin. In my opinion, most of the internal decametre-scale evaporite geometries in a saline giant are autocyclic, while larger scale geometries reflect ongoing interactions between tectonics and climate. Only if and when the basin is connected at the surface to the world's oceans do the geometries of the carbonate units reflect a marine eustatic control and by then basinwide evaporites are not accumulating.

In the time prior to the onset of hydrographic isolation the basin has a surface connection to the world's ocean (Fig. 5.46a). The depositional response at this time is a classic marine carbonate response and the only widespread evaporites that precipitate are typical marine-margin saltern/mudflat evaporites that are intercalated with normal marine platform sediments (see Figs. 5.7a and 5.45 for interpretations of this style). Pinnacle reefs and mud mounds may grow on the shelf foreslope during the marine TST (e.g. right-hand part of Fig. 5.46a). In the basin centre, thin (condensed) pelagic deepwater carbonates and hemipelagic mudrocks will

be deposited, mostly as thin finely-laminated units that pass laterally into slope deposits about the basin edge.

Once sealevel starts to fall below the sill height —either through a eustatic change in sealevel or, more likely, through regional tectonic movement that cuts off the basin from a surface connection with the world's oceans— evaporative drawdown will quickly lower the brine level in the evaporite basin to where it is well below the old carbonate shelf break (Fig. 5.46b). Under an arid climate, water within the now isolated basin will rapidly become hypersaline. Seawater, along with formation, continental, and hydrothermal waters, now seeps into the depression. It enters through permeable, now subaerially exposed, formerly deepwater carbonate slopes and former pinnacle reefs (Fig. 5.46). These outflow zones generate spring and tufa deposits with characteristic textures such as pisolites, tepees, tufas and stromatolites. In the relatively-deep subaqueous basin centre, organic-rich mesohaline carbonate laminites typically mark the onset of basin isolation and continue to form until the basin is hydrographically isolated and equilibrium is reached.

If hydrological equilibrium is reached at gypsum saturation then gypsum has the potential to accumulate across the whole basin. When the water column is meromictic coarsely crystalline zigzag or laminated gypsum dominates the "chemical factory" of the shallow basin edge, while detrital and pelagic laminites accumulate in the basin centre, and possibly inclusion-free crystal clusters as well (Fig. 5.46b). If the basin does not subside greatly as it becomes isolated, the level of this new gypsum wedge (platform) will first form atop old slope carbonates and below the old carbonate shelf break. With respect to sealevel outside the isolated basin this is a lowstand deposit associated with the creation of a karstic type 1 sequence boundary on the old carbonate shelf prism in areas about the basin edge not covered by brine. But, with respect to the subsequent drawdown hydrology of the basin, it is a highstand system tract.

Resedimentation of the saltern/mudflat sediments of the gypsum wedge into deeper density-stratified waters by storms, slope failures, debris flows and turbidity currents will deposit graded beds, slumps and breccias as gypsum slope deposits and fine-grained "rain-from-heaven" gypsum laminites in the basin centre. At times when the brine column is holomictic, coarse-crystalline inclusion-free gypsum can perhaps accumulate across the deeper basin floor (there are no Holocene analogs for deepwater gypsum, but there are for halite and mirabilite).

If this situation of gypsum saturation is hydrologically stable, that is hydrological inflow balances outflow at gypsum-precipitating salinities, and the situation is maintained for time frames $\approx 10^5$ years or more, the whole basin evaporite fill may be composed of gypsum. Such was the case during precipitation of large portions of the Permian Castile Formation of Texas (Chap. 1). Metre-scale sedimentary cycles (parasequences) will be developed within the prograding gypsum wedge reflecting higher-frequency low-amplitude autocyclic brine-level changes within the basin (5th/6th-order $-10^4/10^3$ year cycles).

If hydrological equilibrium is still not maintained in the basin, and brine losses continue to exceed inflows, the brine level will continue to be drawn down and the salinity of the residual brine will increase. Saltern gypsum will begin to precipitate in the basin centre if the brine depth drops below 10–30 m. If a hydrological balance is still not reached and the brine level continues to fall, the brine body next reaches halite saturation (Fig. 5.46c). Based on most Holocene analogs (except the current Dead Sea) water depths at the onset of halite deposition are less than a few tens-of-metres to metres and saltern or pan halite will be deposited across the whole basin floor. If the waters are density stratified then locally there may be deeper-water depressions on the basin floor that fill with fine-grained laminated "salt-and-pepper-textured" deepwater halite cumulates lacking any evidence of subaerial exposure (if Lake Macleod and the artificial halite pans of the southern Dead Sea Basin are used as textural analogs, this requires brine depths of 2 m or more; Warren 1991). If the brine column is holomictic, then beds of coarsely-crystalline randomly-oriented inclusion-free halite meshworks will accumulate, rather than fine-grained halite or gypsum cumulates. This stage of the sedimentation is still a lowstand with respect to sealevel outside the basin, and is now a lowstand systems tract with respect to the basin hydrology and earlier evaporite platform wedges.

Once thick pan halite units begin to accumulate across the basin floor, the degree of permeability loss in salts below the precipitation surface increases drastically, reflecting a near complete loss of porosity in metre-decametre thick halite beds. The brine curtain and its cement aquitard can now support a permanent halite-saturated brine body. This can maintain a near permanent position atop the primary crystallisation surface with only occasional episodes of complete desiccation or flood-induced surface freshening. Thus the halite body begins to aggrade as a series of subaqueous metre-thick autocyclic parasequences, with each metres-thick cycle deposited in time frames of 10^2–10^3 years. The maintenance of this aggrading hydrology allows the basin to fill with predominantly saltern halite (Fig. 5.46d).

With respect to sealevel outside the isolated basin it is still a lowstand system, but in terms of the intrabasin geometries it is a transgressive systems tract. But it is a transgressive systems tract that has no parallel in the marine realm. It is an autocyclic transgression that aggrades as it maintains and grows its own near impervious base soaked in a saturated brine curtain that is maintained by slowly refluxing brines. There is no suitable eustatic term in the classic sequence stratigraphic literature to describe this, as there is no concept of autocyclic transgression where the sedimentation surface creates the stabilising hydrology that in turn facilitates the rise of the sedimentation surface. Tucker (1991) terms this

unit the lowstand basin-fill-halite; I am more comfortable calling it an intrabasinal transgressive systems tract halite.

As the halite fill continues to aggrade it climbs over the old gypsum wedge and, if the basin is subsiding but still isolated, it can also climb over the old gypsum and then the carbonate shelf margin (Fig. 5.46e). As the fill tops an older platform margin it reaches a vast flat karst-etched plain. Before being retained the permanent basin waters must now spread over a much wider area of an older platform top. I call this the "fill and spill" stage of the basin's sedimentation and hydrology. It is still a lowstand systems tract with respect to external sealevel and the marine groundwater feed, but a transgressive systems tract with respect to intrabasin geometries. It is typically a mudflat system, although salterns may still occur. The fill and spill point horizon is often marked by a change in mineralogy, which indicates a change in depositional hydrology.

In a semi-arid system this spill point is often defined by beds of less saline evaporite minerals such as gypsum or lacustrine carbonates. Rainfall and meteoric influx are an increasingly important part of the ponded surface water volume as they spread outside the former less aerially extensive depression. In contrast, if fill and spill occurs in a very arid setting, the effect of meteoric freshening is minimal and as the piezometric head is less than at the onset of evaporite deposition in the drawndown basin. Surface brines are less diluted and the hydrology may pass into bittern saturation so that syndepositional bittern or potash salts are possible precipitates. A hydrological transition to "fill and spill" under a hyperarid scenario explains why the potash cycles in the Salado Formation of the Delaware Basin are largely confined to regions in the vicinity of the old carbonate platform margin (Chap. 11).

Once again the transition is autocyclic and dependent on climate/hydrology within the basin. The system is still a lowstand with respect to sealevel outside the basin. In terms of the intrabasin geometry it is a transgressive systems tract either atop the older HST gypsum wedge or atop the former HST of the older carbonate margin. Tucker (1991) also recognises this TST (his early TST gypsum or TST retrogradational sabkha evaporite lagoons), but he only allows for a $CaSO_4$ mineralogy and he relates it to a surface reconnection with the world's oceans. Unlike Tucker (1991), I feel that this widespread thin unit is deposited subsealevel in a still isolated basin where surface reconnection to the ocean has yet to occur. I also emphasise that this TST is not always gypsum/anhydrite, it can be composed of a multiplicity of mineralogies depending on the degree of climatic restriction in the basin. Kendall (1992; his Fig. 40) also recognises this stage, but he relates the mineralogical transition to less saline minerals to a transgression beyond a hydroseal or basal aquitard, that allows greater volumes of brine to be lost from the system, and so average salinities in the surface brines are lowered. This is a valid concept, but it is not complete as it does not explain why some basins are actually precipitating more hypersaline minerals and bittern salts in the upper parts of the halite basin fill.

Once the basin is reconnected to the open ocean, the formerly exposed carbonate platforms are reflooded and a carbonate TST re-established. In this scenario any subsequent platform evaporite deposits can be considered equivalent to the marine marginal platform evaporites discussed in the preceding section and their internal geometries behind the isolating platform rim or shoal may well once again reflect eustatic controls (Fig. 5.46f). Because the aggraded evaporite surface is a flat plain at the time of marine reflooding, the onset of marine carbonate deposition is typically characterised by ramp deposits. If the carbonate biota also contains appropriate binders and reef formers the profile quickly evolves into a rimmed carbonate shelf. The transition to a rimmed shelf in many ancient basins undergoing regional extension is typically focused by halokinetically induced shallowing of the seafloor driven by flow of the thick underlying halite (Chap. 6).

Basinwide Examples

Four of the better documented areas where high resolution sequence analysis has been attempted on bedded basinwide evaporites are; (1) Gypsum-halite evaporites of Messinian age in the marginal and central basins of the Mediterranean, (2) the basinwide anhydrite-halite evaporites of Permian Zechstein Series in NW Europe, (3) the halite-dominated salt beds of the Silurian Salina Group salt of the Michigan Basin, and (4) the highly halokinetic terrain of the Jurassic Louann Salt in the Gulf of Mexico. We shall start the discussion with the Mediterranean salts as it is a saline giant where much of the $CaSO_4$ is still present as gypsum that retains depositional textures and much of the basin centre halite away from tectonic suture zones is still largely flat bedded. Then we shall discuss Permian and Silurian examples, where the gypsum has altered to anhydrite and in the Zechstein a substantial portion of the halite is halokinetic. In the fourth case example, the Jurassic Louann Salt in the Gulf of Mexico, almost all of the salt has flowed into salt structures with varying internal complexity. We shall look at these structures in the Gulf of Mexico in much more detail in Chaps. 6 and 10. In the current chapter we shall discuss the depositional setting for the Louann Salt in the context of its rift setting and likely stratigraphy. In all cases the interpretations of depositional setting in terms of water depths, and associated correlations between halite, $CaSO_4$ and carbonate beds, are still actively debated.

Messinian Evaporites of the Mediterranean

There are two styles of marine-fed evaporite occurrence in the icehouse world of Messinian evaporite deposition in the Mediterranean. One is characterised by high level, margin-

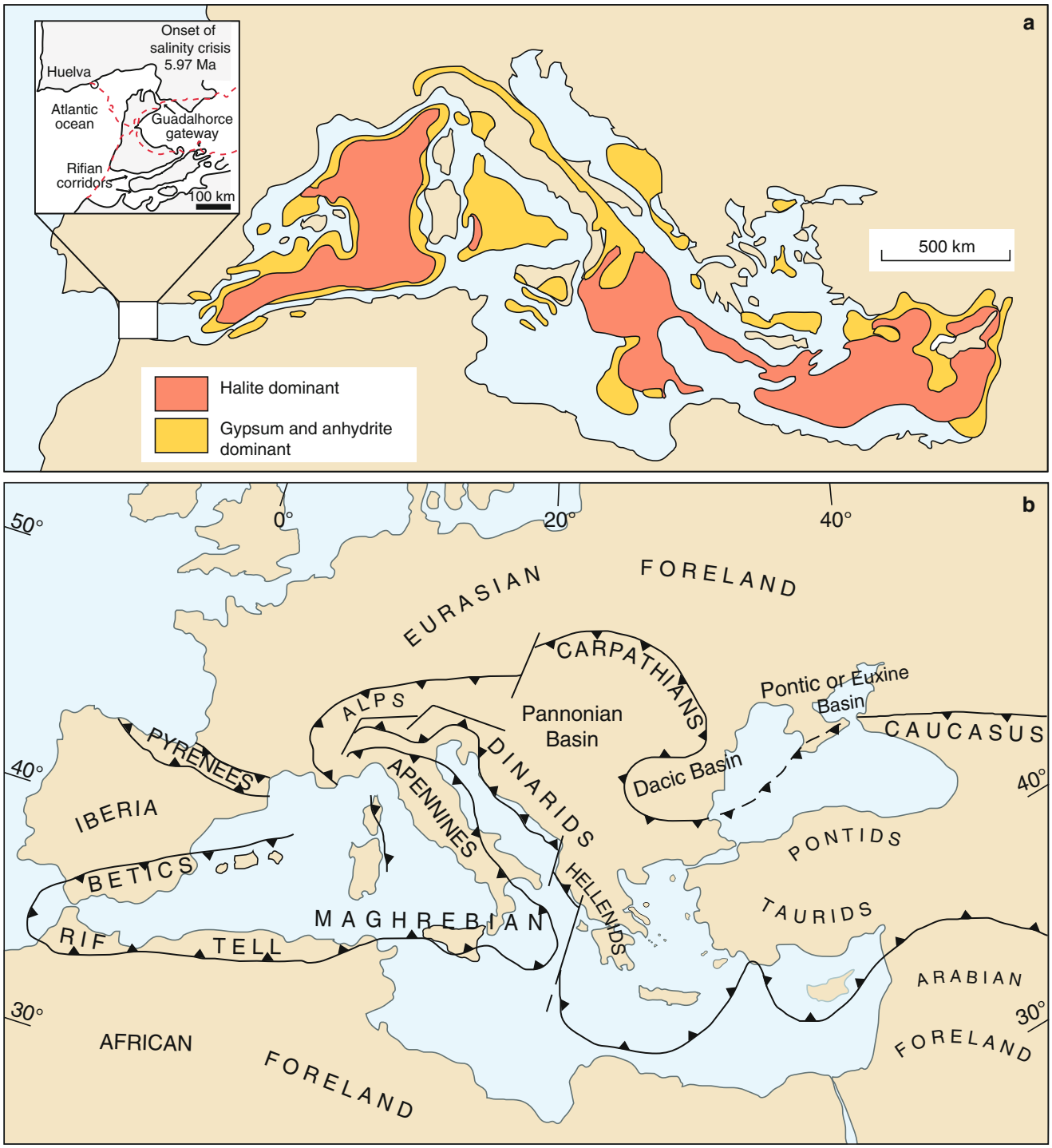

Fig. 5.47 Messinian evaporites and tectonic setting. (**a**) Distribution of basinwide Messinian evaporites, both onshore and offshore. *Inset* shows region of the Gibraltar Straits at the onset of the Messinian salinity crisis from Pérez-Asensio et al. 2013 (*red dashed line* shows approximate position of present-day coastline. (**b**) Tectonic (Alpine) – foreland basin associations in the Mediterranean region

ward circum-Mediterranean deposits, the other by a number of much larger, thicker, basin-centre deposits, which now lie below more than 2,000 m of water and hundreds of metres of Plio-Pleistocene overburden in the deeper parts of the Mediterranean Sea (Hsu et al. 1973). There are excellent onshore exposures in the marginal Messinian basins in Sicily, Spain and Cyprus (Fig. 5.47a). In contrast, in the various sub-basins in the deeper parts of the Mediterranean Sea, where seismic lines show thick sequences of salts were deposited during times of maximum drawdown, there has been little core sampling and so there is little reliable facies interpretation based on rock samples. There is an

increasing amount of high quality offshore seismic now coming into the public realm, especially in the eastern Mediterranean, driven by gas discoveries in the region off the Israeli coast and southwest of Cyprus. What is clear in the distribution of Messinian evaporites across the Mediterranean is the significance of the various suture and thrust belts, both during deposition and in subsequent reworking (compare Fig. 5.47a, b).

DSDP (Deep Sea Drilling Project) wells in the Mediterranean that did manage to recover core in evaporites sampled a possible combination of salt pan halite and sabkha anhydrite, implying the salts accumulated on a basin bottom that was covered with brine lakes, which at times dried up sufficiently to accumulate pan halite (Hsu et al. 1973). For 30 years the notion of pan and sabkha deposition dominated interpretations of basin centre evaporites. While not questioning the hydrographic isolation of the Mediterranean during the Messinian salinity Crisis (MSC), Hardie and Lowenstein (2004) have questioned the notion of basin desiccation and saline pan deposition. Rather, they argue for a sub-wavebase subaqueous origin to much of the evaporite recovered in the DSDP cores. That is, the Mediterranean Basin salt fill contains an as yet unknown, but perhaps substantial, proportion of deeper water halite. Likewise, Krijgsman and Meijer (2008) argue for a deep water setting for the basin centre deposits. They also infer an ongoing surface connection to the world's oceans as these evaporites were deposited.

In the last decade, the interpretation that has come to dominate is that gypsum deposited during initial basin drawdown, prior to the salinity maximum that deposited widespread halite, was laid down in deeper water (Briand 2008). In some regions these gypsum deposits moved downslope via active slumping and gravitational reworking. Undeniable evidence for Mediterranean isolation and widespread water-level drawdown of at least a kilometre comes from seismic and the presence of the "M" reflector. It indicates subaerial exposure about much of the Mediterranean margin and slope during the peak of the Messinian Salinity (Ryan et al. 1970; Montadert et al. 1970).

Basinwide drawdown also deepened the thalwegs of many major rivers draining into the various Late Miocene Mediterranean sumps. Wells in the Nile Delta at the eastern end of the Mediterranean, which are more than 300 m (1,000 ft) deep and enter Messinian strata, do not reach the bottom of Nile canyon (Aal et al. 2000). Said (1993) shows the Messinian incision of the Nile thalweg reached a depth of 170 m at Aswan, 800 m at Assuit and more than 2,500 m immediately north of Cairo. Similar deep Late Miocene channels occur at the western end of the Mediterranean in Libya and Algeria, and the eastern end in offshore Israel and Syria (Griffin 2002). Likewise, the thalweg of the northern end of the Rhone River gorge was cut deeply into its granite basement in the Late Miocene and is now filled with marine sediments.

For the same reason, some of the deepest karst in the world formed in Yugoslavian (Montenegran) and Ukrainian carbonate hosts during this time of maximum drawdown, with a number of caves now more than 900 m deep. The deepest of these Messinian-drawdown induced caves is the Krubera-Vornja cave in the Ukraine, which is now documented to descend for more than 2,191 m below the current landsurface, and well below the current hydrographic level of the Black Sea (Macnamara and Furnell 2009). This is also the deepest cave currently known in the world. Its depth and steeply descending cavern pattern are clearly responses to the drastic hydrological drawdown induced by the MSC (Klimchouk et al. 2008).

Assuming a surface marine connection to the Atlantic immediately prior to the time of evaporite precipitation, Krijgsman et al. (1999, 2002) and De Lange and Krijgsman (2010) argue that the onset of drawdown marking the beginning of the MSC was synchronous over the entire Mediterranean basin, at 5.96 ± 0.02 Ma (Fig. 5.48a). Basin centre drawdown was established between 5.59 and 5.33 Ma, associated with a large fall in Mediterranean water level, followed by circum-Mediterranean erosion (M-marker) and basinwide evaporite deposition 5.59–5.50 Ma. This was followed by deposition (5.50–5.33 Ma) of nonmarine sediments in a large 'Lago-Mare' (Lake Sea) basin immediately prior to surface reconnection with the world's ocean with a complete reconnection in the early Pliocene (Bache et al. 2012; Salé et al. 2012).

Once hydrographically isolated, the cyclic evaporite deposition in the various Messinian marginal basins can be almost entirely related to circum-Mediterranean climate changes driven by obliquity-induced glacio-eustatic sealevel changes. Govers et al. (2009) argue in favour of a dominantly tectonic/isostatic origin and evolution the MSC, although its exact timing of some of its parasequence boundaries may well have been controlled by the ≈40-kyr component of the Earth's eccentricity.

It is now clear that the stratigraphy in marginal basins of the Mediterranean Ridges, Sicily, and other Messinian basins, such as Crete and Cyprus, are defined by mineralogies that evolved separately in a series of rising "piggy-back" highs and foreland basins, created during thrusting-related uplift, which were active in the Messinian and continues today in some areas (Figs. 5.47b and 5.49; Westbrook and Reston 2002; Calon et al. 2005; Roveri et al. 2008). In some marginal basins, as in Spain, changes in the level of drawdown were related to syndepositional transcurrent faulting and rifting altering the degree of connection to the adjacent seaway. It is this association of marginal basins on the highs and basin centre deposits in the lows that typify evaporite distribution in the Mediterranean (Fig. 5.49).

Much of the tectonic drive creating the evaporite fill in the various marginal basins, prior to the main drawdown, was a result of the collision of Africa with Eurasia, which ultimately drove the closure of the surface connection to the

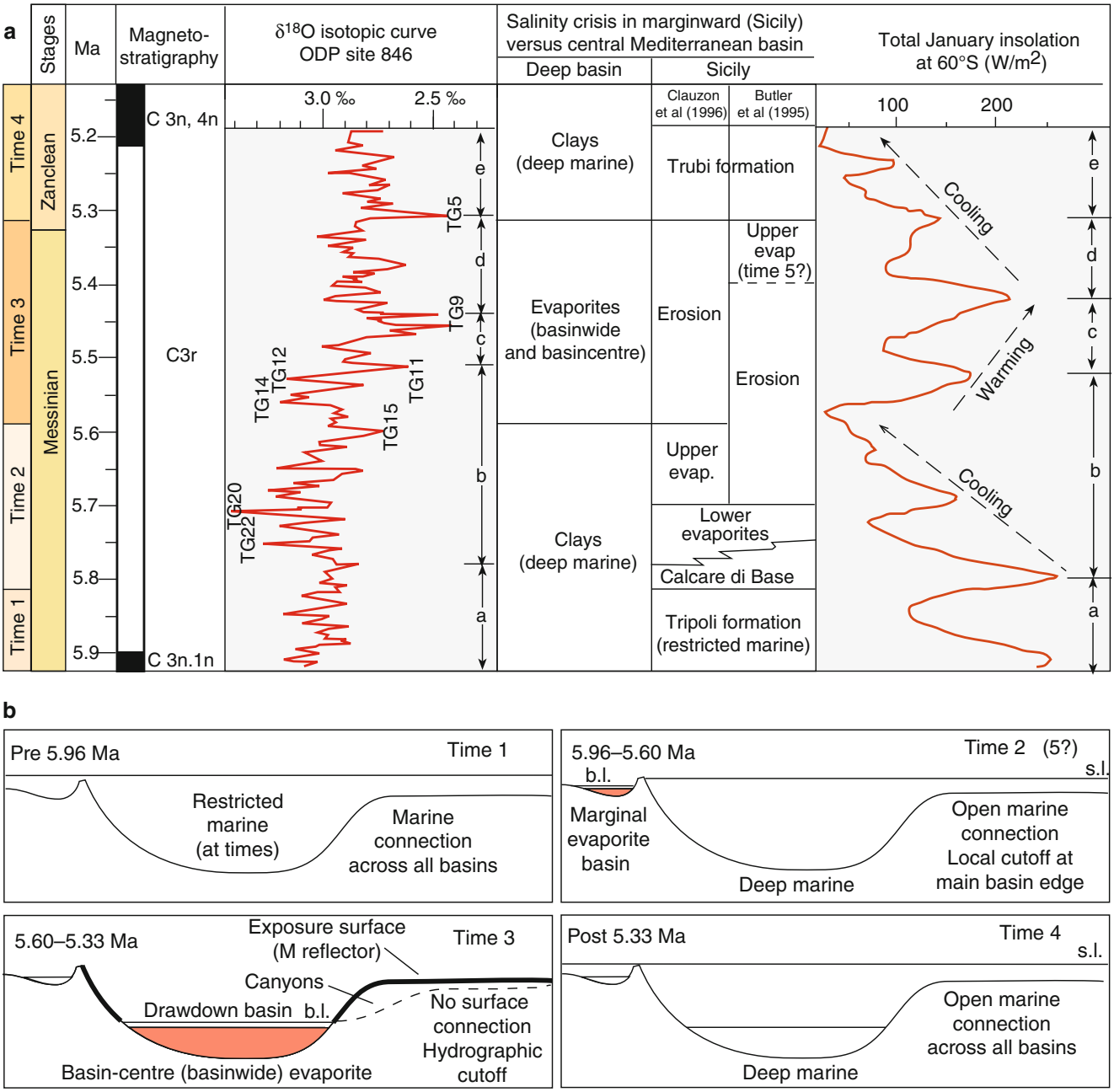

Fig. 5.48 Messinian salinity crisis in the Mediterranean. (**a**) Plot of $\delta^{18}O$ of equatorial Pacific tied to magnetostratigraphy, Messinian stratigraphy and modeled January insolation for that time frame (Modified after Clauzon et al. (1996) and Butler et al. (1995)). Note the difference in interpretation of the upper evaporite in Sicily compared with Fig. 5.60; Briand 2008. (**b**) Schematic times sequence showing mode of formation of marginal and basinwide evaporites in the Mediterranean. Note that the interpretation of Butler et al. (1995) requires a time 5 when the upper evaporites were deposit after the main drawdown

Atlantic and ultimately caused the whole Late Miocene Mediterranean deep basin floor to become a series of isolated and evaporitic marine-fed salterns (Fig. 5.47b; Govers et al. 2009). According to Clauzon et al. (1996) the first major evaporite-depositing episode (5.75–5.60 Ma) took place during a cooling period associated with a weak global sealevel fall that isolated numerous tectonically induced circum-Mediterranean marginal basins in Spain, Libya, Morocco, the Apennines, Sicily, and Cyprus. Isolation of these marginal basins occurred while the adjacent Mediterranean Sea still, at least at times, retained a direct surface connection with the Atlantic (Time 2; Fig. 5.48b). Even so, the evaporite and underlying stratigraphy of Cyprus suggest restriction and isolation of the Mediterranean Sea prior to the MSC was not a single event (Orszag-Sperber et al. 2009). Stratigraphic sections on Cyprus below the Messinian gypsum show a

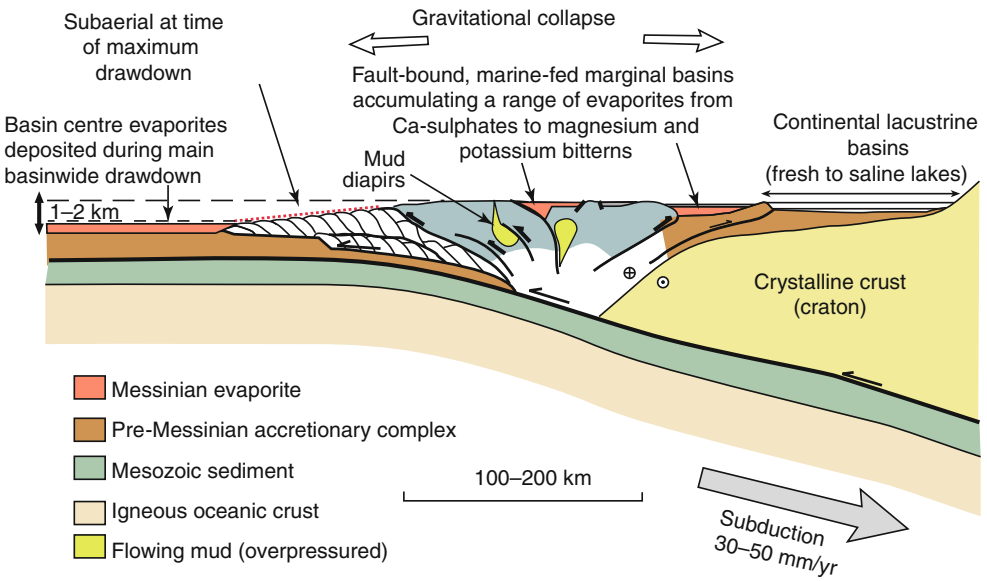

Fig. 5.49 Schematic shows tectonism related distribution of continental, marine margin and basin centre lacustrine evaporites around the time of closure of the Mediterranean basin and the Late Miocene salinity crisis. Schematic is constructed based on geology of the Mediterranean Ridges, Sicily and the Italian Peninsula (In part after Westbrook and Reston 2002)

general evolution of the depositional environment from marine to restricted conditions was emphasized by dates at 7.16, 6.7, and 6.1 Ma. If so, isolation was preceded by a progression of associated events spread over 1 million years.

The notion that restriction and perhaps even the formation of a land bridge between Spain and North Africa occurred sometime prior to the MSC is supported by Late Miocene mammalian biogeography (Gibert et al. 2013). African mammals migrated to Iberia and European mammals migrated to North Africa at the same time and before isolation of the Mediterranean Sea during the Messinian. This two-way African-Iberian mammal dispersal occurred just before 6.2 Ma showing that an ephemeral land corridor existed between the two continents some 250 k.y. before the onset of the MSC at 5.9 Ma, reflecting a tentative initial hydrographic isolation of the Mediterranean Sea from the Atlantic. This land corridor developed after tectonics closed the Betic Seaway at 6.3 Ma and perhaps during the intensification of the latest Miocene glaciation at 6.26 Ma, when water circulation in the Mediterranean became very restricted (Gibert et al. 2013).

When continent-continent collision hydrographically isolated the whole Mediterranean, basinwide or basin-centre evaporites were deposited in a series of giant evaporite subbasins (hundreds to thousands of kilometres across) in regions now located beneath the present deep Mediterranean floor (Time 3; Fig. 5.48b; 5.60–5.33 Ma?). Away from marginal basins and tectonic ridge-associated halokinesis, none of these sump areas outcrop on the Mediterranean seafloor, and only their uppermost portions were sampled by the wells in the DSDP programme (Hsü et al. 1970). At the time halite accumulated in the central sumps there was a huge drop of some 1,500–2,000 m in Mediterranean water level. The various basin-centre sumps were completely isolated from any surface connection with adjacent Atlantic or Tethyan remnants. At the time of the complete isolation of the Mediterranean Basin there was a worldwide warming trend and a likely global sealevel high, but tectonic isolation negated the effects of eustasy within the Mediterranean.

The evaporite phase of many marginal basins in Spain and Italy was typically preceded by cyclic Late Miocene carbonate ramp or reef cycles; which are readily interpreted using the principles of high-resolution carbonate sequence stratigraphy (e.g. in Spain and Italy- Martin et al. 1996; Esteban 1996: in Morocco- Benson et al. 1997; Cunningham et al. 1997). Postreef growth, the typical response of the marginward basins to isolation and the onset of basin drawdown was the accumulation of an evaporitic carbonate rim (aragonite/dolomite) about a drawndown bedded-gypsum saltern, with marine-fed bitterns accumulating in the most isolated portions of these subsealevel depressions. Such a situation outcrops today as the Calcare di Base rim facies circumscribing the bedded salts of the dominantly gypsum saltern fill in the Sicilian Basin. There Calcare Di Base sections more than 50–60 m thick typify the pre-gypsum fill (Fig. 5.50a).

Sorbas and Fortuna basins, Spain: There is still a degree of chrono-stratigraphic confusion in relating the evaporite fills of many of the marginward basins of Spain to the main Mediterranean drawdown event. There is also the problem that some of the Spanish evaporite basins evolved from a continental to a marine feed to their saline hydrologies The Sorbas Basin, Spain, is a good illustration of the chronostratigraphic problem while the Fortuna Basin illustrates an evolution in its saline hydrology from nonmarine to marine.

Depending on the author, the main saltern unit (Yesares gypsum) is considered to be time equivalent to the Lower Evaporite unit of the main Mediterranean drawdown event, or it postdates it or predates it (Fig. 5.50a). The key to where it is positioned in the stratigraphy relates to where the equivalent to the main erosion surface (M-equivalent) is placed. Riding et al. (1999), place a regional erosion surface and

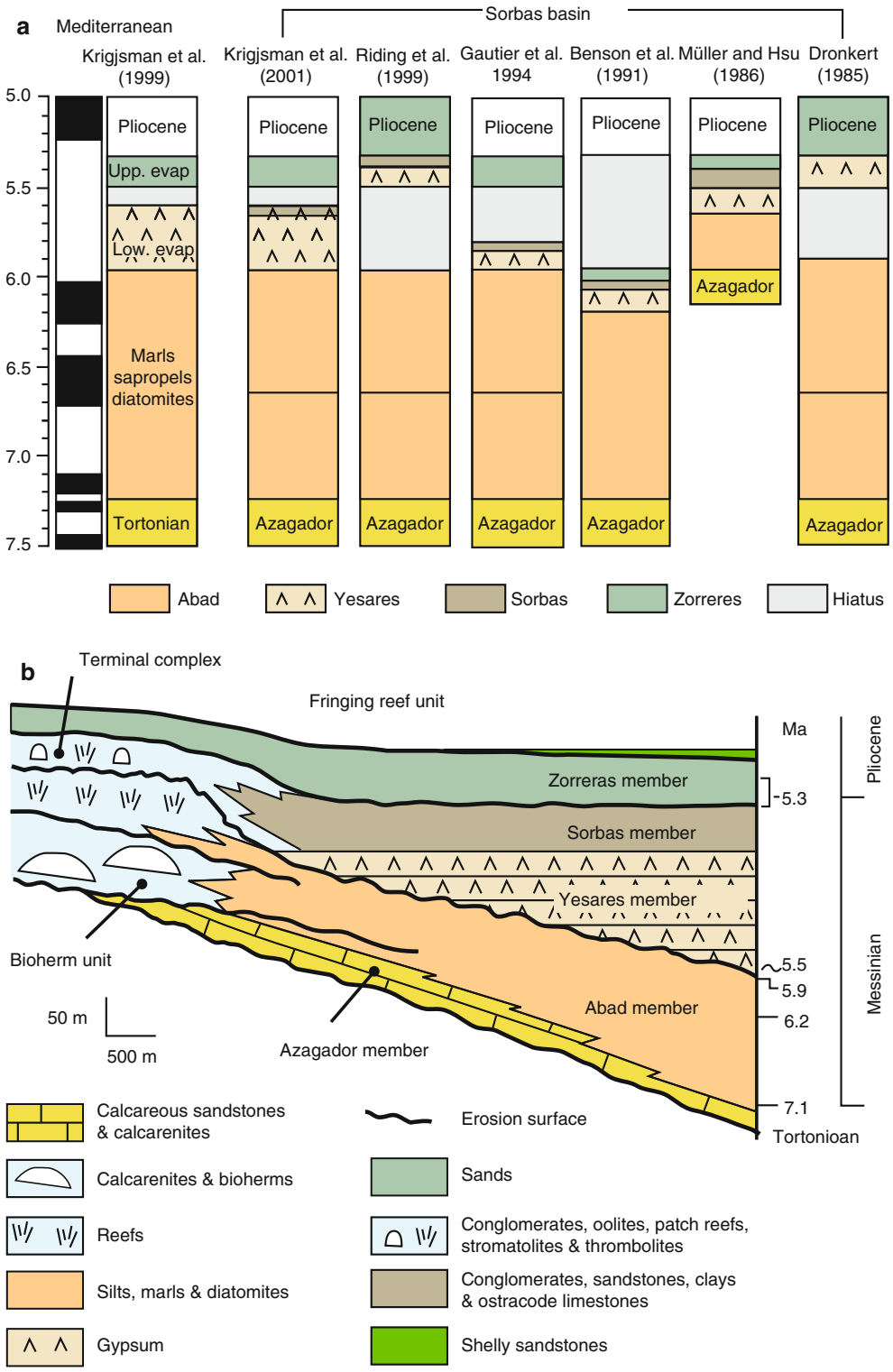

Fig. 5.50 Messinian lithofacies, Sorbas Basin, Spain. (**a**) Overview of different chronostratigraphic models for the marginal Sorbas basin showing the large controversies in timing and duration of the various stratigraphic members in relation to the recently established Messinian Mediterranean astrochronology (Krijgsman et al. 2001). The models of Dronkert (1985) and Riding et al. (1998) are based on a correlation of the Yesares Member to the 'Upper Evaporites' of the Mediterranean. The models of Müller and Hsü (1987) and Gautier et al. (1994) are plotted along with the timing by various cited authors of Yesares Member to the 'Lower Evaporites' and the Zorreras to the 'Upper Evaporites'. (**b**) The Messinian–Pliocene succession in the Sorbas Basin. According to Riding et al. (1998) the "Salinity Crisis" sealevel fall occurred within the interval 5.9–5.5 Ma, and the resulting drawdown-driven erosion surface is below the Yesares Gypsum Member, and atop the Fringing Reef Unit. Note the marginal onlap of the Sorbas–Terminal Complex

unconformity (300,000 years exposure) at the base of the Yesares Formation, making the Yesares equivalent to the Upper Evaporite, while Krijgsman et al. (2001), argue any discontinuities at the base of this unit are not regional but reflect no more than local slumping. The debate continues and is yet to be resolved. Resolution will require application of evaporite textures as indicators of watertable, brine depth and brine stability indicators, as has been done for the Italian basins (Roveri et al. 2003; Dela Pierre et al. 2011).

The Sorbas Basin is one of a number of marginward basins formed in a complex system of transcurrent faults, with both transpressive and transtensional characteristics. Tectonics controlled depositional geometries in the evaporite fill of the marginal basins of the Betic Cordillera of SE Spain, not sea-

level changes outside the hydrographically isolated depression (Fig. 5.53a; Playa et al. 2000; Michalzik 1996). The Spanish Messinian basins are seepage basins and there is no evidence for any cataract-like connection of any of these basins before, during or after the formation of Messinian evaporites.

The most frequently occurring gypsum lithofacies in all the Spanish basins indicate shallow-water depositional environments and textures include: crystalline selenitic gypsum ('grasslike gypsum'), laminated gypsum and crossbedded gypsarenite. Sabkha-type chickenwire alabastrine gypsum is rare in the Spanish sea marginal basins (Michalzik 1996). Evenly-laminated gypsum units interbedded with graded gypsarenites (turbidites), gypsrudites (debrites) and slumps also occur in basins or parts of basins with considerable palaeoslopes. Evidence for early diagenetic overprinting includes the formation of giant gypsum twin crystals, 'super cones' and alabastrine nodular gypsum. The accumulation of Messinian evaporites in SE Spain was likely instigated by a third-order sealevel lowstand that isolated these marginal tectonic basins from the Mediterranean Sea. But all the smaller-scale evaporite units (parasequences) in the various marginal basins, at the scale of shoaling decametre-cycles, are fourth- to sixth-order cyclic and rhythmic responses. They are clearly related to basin dynamics or to autogenetic processes of the local facies (facies dynamics). None are related to high-frequency marine eustasy (Michalzik 1996).

Inland from the marine fed sea-marginal Messinian basins of Spain are large saline lacustrine basins fed both by seawater seeps and continental waters from the Pyrenees with a substantial solute component coming from the dissolution of Triassic sulphate salts. The saline fills of these largely continental depressions started earlier in the Miocene than the sea-marginal marine-fed depressions (Tortonian versus Messinian) with both their surface and groundwater feeds showing a more continental provenance (Fig. 5.51a). For example, Playa et al. (2000) differentiated a number of continental-influenced evaporite units in the inner basins of the Murcia-Alicante region. The more continental saltern gypsum lithofacies have the following characteristics (Fig. 5.51b): (1) Variable strontium contents, with mean values (primary gypsum) between 1,121 and 2,380 ppm; (2) Isotopic compositions of sulphur ($\delta^{34}S$) ranging from those characteristic of the Tertiary marine water (+20.3 to +25.5‰) to those characteristic of the Triassic sulphates (+8.0 to +16.0‰), the latter suggesting recycling of the sulphate anion in meteoric waters; intermediate values (+17.4 to +19.6‰) are attributed to mixed mother brines; and, (3) Strontium ratios ($^{87}Sr/^{86}Sr$) between 0.70804 and 0.70888; these values range from those of the Tertiary marine water to those exceeding the Triassic sulphates, suggesting additional continental contributions (from both dissolving country rocks and hydrothermal solutions). The comparison between the sulphur and strontium isotopic compositions of the sulphates, together with the study of the biota present in the marls associated with the gypsum, distinguishes marine, continental, and mixed units (Playa et al. 2000).

In the marine-fed sea marginal basins of the Eastern Betics, where single evaporite units characterized by selenitic gypsum prevail: (1) the strontium contents are more homogeneous, with mean values (primary gypsum) between 493 and 625 ppm; (2) the isotopic compositions of oxygen ($\delta^{18}O$) and sulphur ($\delta^{34}S$) between +12.2 and +14.8‰, and between +22.0 and +23.5‰, respectively; and (3) the strontium ratios ($^{87}Sr/^{86}Sr$) varying from 0.70890 to 0.70895. The clear separation between properties of the two gypsum-entraining foreland depressions (Fortuna Basin versus San Miguel de salinas Basin) illustrate that, although gypsum deposition occurred in two side-by-side basins, some units on the continental side started to accumulate bedded gypsum earlier than the Messinian and with isotope signatures that reflect a mixed continental-marine parentage (Fig. 5.51c).

The Apennines: Complicating the resolution of any marine eustatic history for evaporite cycles in MSC sediments is ongoing penecontemporaneous tectonism and gravity in moving large blocks and detrital volumes of shallow water evaporites into deeper water settings. Such olistoliths and turbidites characterise many continent-to-continent collision belts and such a gravity slump system controlled the distribution of Messinian sediments about the Riolo anticline in the Italian Apennines and the Lower Evaporites of Sicily (Roveri et al. 2003; Manzi et al. 2005, 2011).

Lateral and vertical facies changes within the underlying deepmarine turbidites of the Marnoso-Arenacea Formation show Messinian evaporite precipitation occurred in a thrust-top basin (Vena del Gesso basin), bound to the north and to the east by the thrust-related Riolo anticline, which had been actively growing since the late Tortonian (Fig. 5.52a). Both gypsum deposition and its subsequent deformation were strongly controlled by evolving palaeobathymetry driven by gravity/thrust tectonics.

Primary growth-aligned gypsum, which outcrops in the Apennines, originally accumulated in a shallow, silled marginal basin (Vena del Gesso basin) that lay to the east of the growing Riolo anticline, while organic-rich shales were deposited in the adjacent deeper and larger foredeep basin to the west (Fig. 5.52b, c). These gypsum deposits underwent severe postdepositional deformation related to large-scale gravitational collapse, tied to regional uplift events. Deformation was also coincident with the end of the evaporitic phase in the marginal thrust-top basin. Along the inner, shallower-dipping limb of the anticline bounding the basin, large-scale, weakly deformed gypsum slabs slid downslope along a detachment surface developed at the contact with the underlying euxinic shales, forming both extensional and compressional features and showing an overall southwestern vergence (Fig. 5.52d).

The identification of a south-southwest–dipping palaeoslope by Roveri et al. (2003) suggested that the initial deformational features affecting the gypsum unit were likely driven by gravity perhaps tied to highs atop active thrust planes (Fig. 5.52). The steeper frontal limb of the anticline

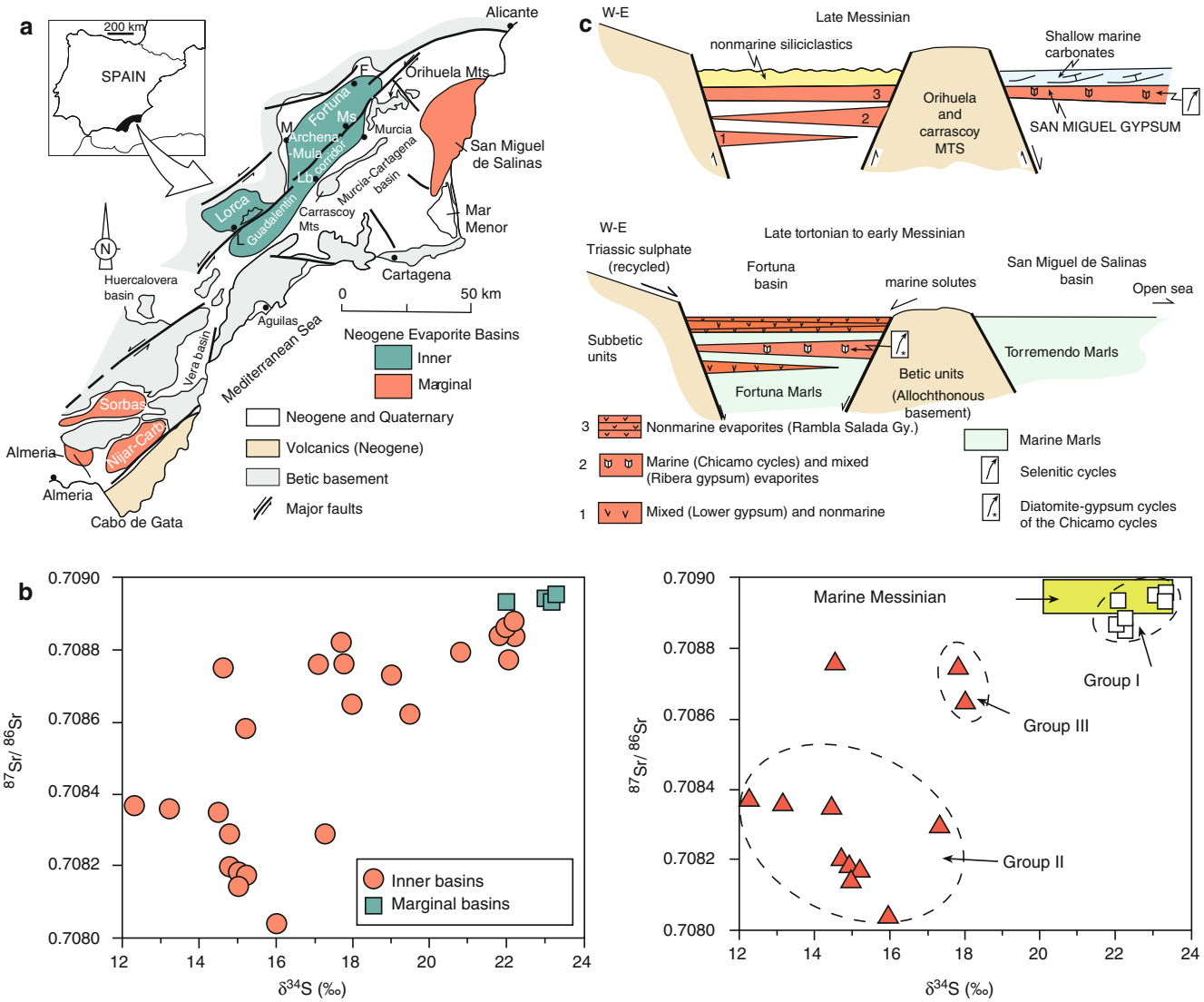

Fig. 5.51 Neogene evaporites, Spain (After Playa et al. 2000). (**a**) Location of the Neogene inner and marginal basins in the Eastern Betics. Towns: *F* Fortuna, *L* Lorca, *Lb* Librilla, *M* Mula, *Ms* Molina de Segura. Ridges: *LT* La Tercia Mts. (**b**) Isotopic composition ($^{87}Sr/^{86}Sr$ ratio, and $\delta^{34}S$) of gypsum lithofacies. Plot on *left* shows primary and secondary gypsum (undifferentiated) samples in the inner and marginal basins. Marine-fed gypsum in the sea-marginal basins shows a much tighter clustering of values reflecting its near isochemical seawater parent. Plot on the *right* shows primary gypsum samples. *Group I*: selenites (aligned coarsely crystalline gypsum of the sea-marginal basins. *Groups II and III*: gypsum lithofacies of the inner more continental basins. The areal distribution of the Messinian marine sulphates from the Mediterranean region is shown shaded in grey. (**c**) Schematic showing the distribution of Neogene evaporite sediments from more continental basins in the west (inner basins such as the Fortuna basin) to the east (sea-marginal basins such as the San Miguel de Salinas basin) in the easternmost part of the Betics (Murcia–Alicante region)

promoted the transformation of gypsum slides into debris flows and turbidite currents that deposited their load in the adjacent deeper basin to the west. This gravitational deformation was sealed by postevaporitic upper Messinian Lago-Mare deposits.

The sedimentary history of the Vena del Gesso basin, as documented by Roveri et al. (2003) and Manzi et al. (2005), suggests that the MSC in the Apennine foredeep was tightly linked to a combination of intra and extrabasinal tectonic processes, not worldwide eustasy. This is now thought to be also true in the Balearic, Tyrrhenian, Sicilian, and Eastern Mediterranean Basins.

By using the Moncucco gypsum quarry in the Torino Hill – Monferrato outcrops of the Tertiary Piedmont Basin, some 50 km to the west of the Apennines, Dela Pierre et al. 2007 further defined Messinian depositional detail. They document the inherent tectonically-driven complexity which overprinted the Messinian stratigraphy prior to Lago Mare deposition (Fig. 5.53). The geology includes episodes of mud diapirism (overpressure) that in part overprints the fragmented Messinian evaporitic section. This section was deformed prior to the deposition of the Lago Mare sediments. Three chaotic units are exposed in the quarry: together, they make up a composite chaotic unit that is

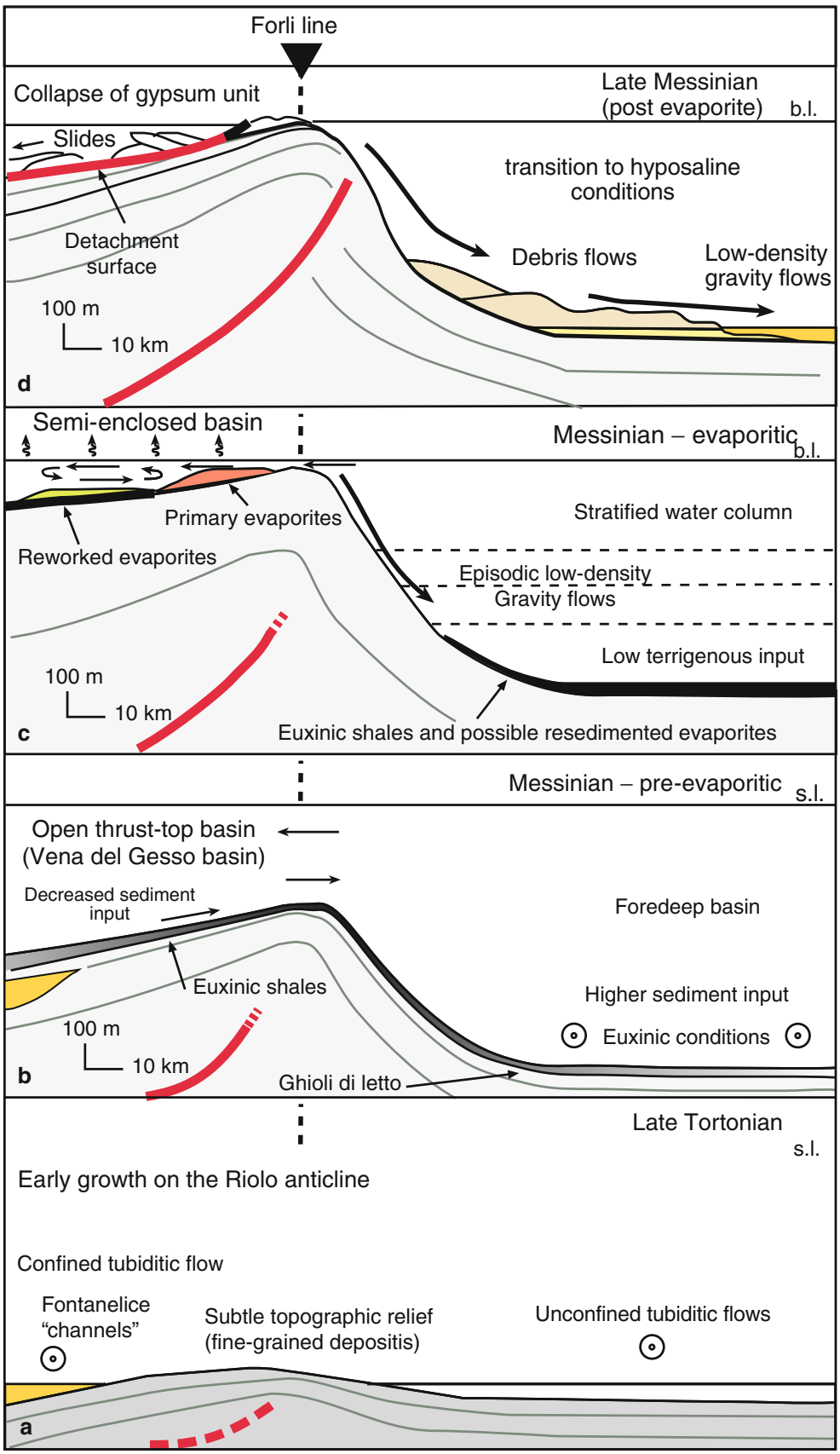

Fig. 5.52 Evolution of the Vena del Gesso basin, Italian Apennines, from the Tortonian to the late Miocene with respect to facies and the evolving thrust basin topography indicated by the Forli Line (After Roveri et al. 2003)

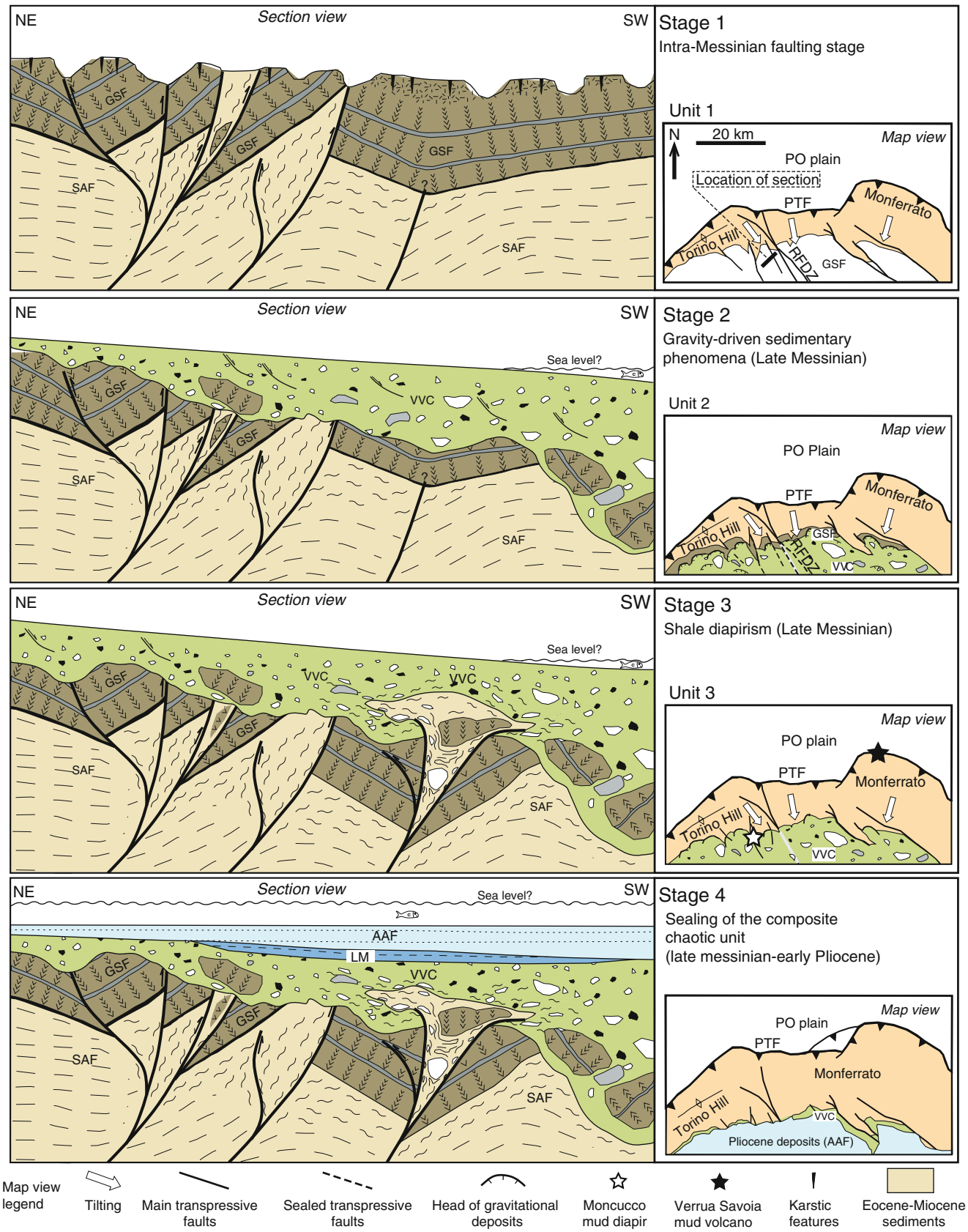

Fig. 5.53 Multistage evolution of the Messinian composite chaotic unit. *SAF* Sant'Agata Fossili marls, *GSF* Gessoso Solfifera Formation, *VVC* Valle Versa chaotic complex, *LM* Lago Mare marls, *AAF* Argille Azzurre Formation, *PTF* Padane thrust front, *RFDZ* Rio Freddo deformation zone (After Dela Pierre et al. 2007)

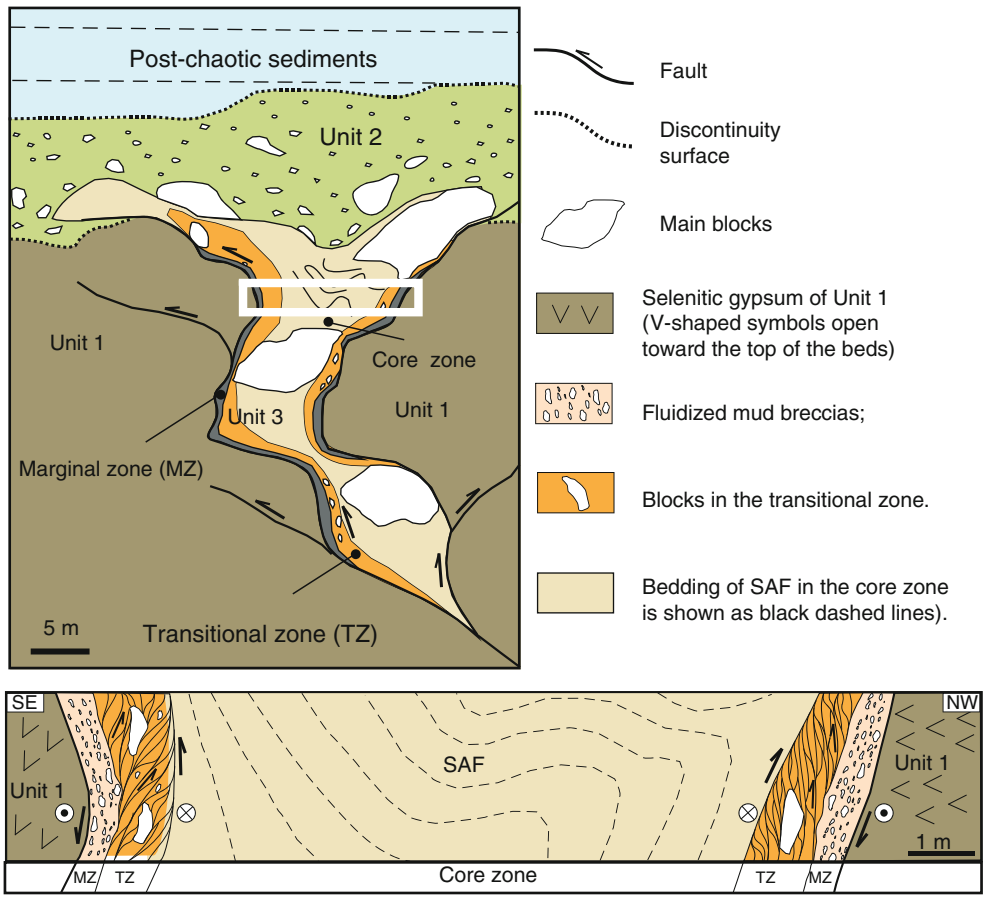

Fig. 5.54 Deformation styles associated with mud diapir emplacement in the faulted and brecciated gypsum of the Lower Evaporite. The intensity of mud deformation (argillokinesis) increases from the muddy folded core of the Sant'Agata Fossili marls (*SAF*) outwards toward the tectonised margins. Opposing senses of shear on the opposite margins of the structure are clearly indicated by the orientation of S-C fabrics in the transitional zones (After Dela Pirre et al. 2007)

unconformably overlain by post-chaotic sediments, including Lago Mare beds (Fig. 5.53). Unit 1 is composed of blocks of primary evaporites that are juxtaposed to marine marls by subvertical transpressive faults and are parallel to the fault surfaces. Unit 2 unconformably overlies Unit 1, and consists of a lenticular sedimentary body containing both angular and rounded blocks, randomly distributed in a fine-grained matrix.

Unit 3 consists of a 10-m-wide body bounded by transpressive faults, and it pierces both Units 1 and 2. It is composed of strongly deformed muddy deposits (argillokinetic textures) that envelop blocks of gypsum and carbonate rocks. Between the core and the margins of unit 3, three zones are defined based on the increasing amount of deformation toward the margins (Fig. 5.54). The distribution, size, and shape of the cemented blocks floating in the matrix are related to differences of velocity gradient of the poorly consolidated Sant'Agata Fossili marls, acting as a viscous fluid as it migrated through a rigid but faulted rock mass. The alignment of long-axis blocks to the scaly cleavage, and their increased clustering toward the external zones are consistent with an increase in velocity gradient toward the marginal contacts (Fig. 5.54).

Bedded post-chaotic sediments unconformably overlie both Units 1 and 2, sealing the main fault systems an indicting the cessation of diapirism. Thus the composite chaotic unit is related to thrust propagation during a regional phase of deformation that occurred pre-Lago Mare deposition.

The current distribution of various beds preserves the result of different evolutionary stages, in each of which a single genetic mechanism prevailed (Fig. 5.53). Tectonic faulting prevailed during stage 1 and was responsible for the formation of a tectonically disrupted assemblage (Unit 1). During stage 2, gravity-driven sedimentary phenomena, related to slope oversteepening triggered by ongoing thrust propagation, resulted in the deposition of Unit 2. Gravity sliding was favoured by the mechanical weakening of sediments caused by tectonic faulting. Over-pressured conditions resulting from the rapid deposition of Unit 2 triggered mud diapirism (Unit 3) so that the Sant'Agata Fossili marls pierced Units 1 and 2. The involvement of methane-rich fluids in the formation of the mud diapir is suggested by the occurrence of blocks of methane-derived carbonates, found not in the quarry, but just outside it (Dela Pierre et al. 2012). Most significantly, the Moncucco study illustrate clearly that thrusting mobilised Messinian evaporites prior to deposition

of the Lago Mare succession, a unit that indicates the end of the MSC and the transition back into marine sedimentation.

Sicily: Historically, much of the stratigraphy used to interpret the history of Messinian sedimentation is based on work done in Sicily, mostly in the Caltanisetta Basin, which is the largest depozone of the Sicilian-Maghrebian foreland basin (Fig. 5.47b; Decima and Wezel 1971). Depocentres that make up Messinian-entrained marginal basins in Sicily, including the Caltanisetta Basin, contain gypsum ± halite, and are located in synclines tied to foreland depressions and underlying thrust structures in the frontal part of the Maghreian chain (Fig. 5.47b). Prior to hydrographic isolation from the Mediterranean seawater, these basins are interpreted as being hydrodynamically linked through the thrust foredeeps to water levels in the adjacent Mediterranean (Fig. 5.55a; Butler et al. 1995). Accordingly, early isolation and drawdown of the Mediterranean base level is marked across the thrust belt by first cycle evaporitic carbonates (Calcare di Base) on the structural highs and evaporites in lows, respectively.

Hence, significant accumulations of halite and potassium salts (up to 1,200 m thick) are restricted to growing thrust synclines in the Sicilian basin. Salts were deposited once the subsealevel depressions were hydrographically isolated from the adjacent Mediterranean. At that time different evaporite signatures were related to different water conditions, reflecting various continental and marine seepage plumes and circulations across various sub-basins (Fig. 5.55a, b; Butler et al. 1995). Thrusting provided accommodation space for evaporite sumps and also controlled the groundwater pathways into the desiccating basins. In similar fashion to Messinian sediments of the northern Apennines, the Sicilian salts form part of a syn-orogenic foreland basin succession that underwent shortening by thrust-related folding soon after deposition (Mazzoli 1994).

Clauzon et al. (1996) group the deposition of the Upper and Lower Evaporites of Sicily into a single period from 5.75 to 5.60 Ma. The initial eustatically-induced marginward isolation was then followed by complete isolation and drawdown of the whole Mediterranean (Fig. 5.51a). In contrast, and although they use only relative time, Butler et al. (1995) recognised a major sequence boundary between the Upper and Lower Evaporites of the Sicilian Basin, also called the First and Second cycles (Fig. 5.55). They interpreted this sequence boundary as corresponding to the major drawdown of the whole Mediterranean and the formation of a major regional unconformity, which now surrounds all these basin-wide deposits (M reflector; see Lofi et al. 2005). They went on to interpret the Upper Evaporite (Second Cycle – mostly saltern gypsum, not halite or bitterns) as being deposited in the isolated marginal seepage basins of Sicily once the Mediterranean was again flooded by seawater entering via a newly re-established surface connection (Fig. 5.51b). The contact with the upper evaporites and the overlying deepwater marine Trubi Formation is a maximum flooding surface in both scenarios.

The tectonic scenario has now been further improved by the recognition of that the major unconformity separating the Upper and Lower evaporites in Sicily actually separates a system that was thrust into its present position from a deeper water setting. It was the work in the Apennines that drew the conflicts in the Sicilian stratigraphy and hydrogeology into focus and ultimately led to a revised stratigraphy incorporating aspects of both regions. The following lists some of the problems in the Messinian sequences of Italy that required solving in the middle of the first decade of the current millennium (Lugli et al. 2008).

1. Deposits traditionally included in the Lower Evaporites are actually clastic sediments that derive from the dismantlement of autochthonous Lower Evaporites.
2. Many of the Lower Evaporites outcrops in Italy are actually large-scale blocks emplaced by extensive mass-waste movements; some of these chaotic complexes were previously interpreted as collapse deposits due to halite dissolution.
3. Some Lower Evaporites outcrops were commonly considered Upper Evaporites and vice-versa.
4. Laminated clastic sulphate sediments were commonly mistaken for primary cumulate deposits and vice-versa.
5. The significance of halite deposition, which actually bears the only unequivocal sign of exposure found within the Messinian evaporites in the Sicilian Basins, has been overlooked, as has its likely tie to the main evaporite drawdown stage in the Mediterranean.
6. The Calcare di Base carbonates commonly show evidence of resedimentation.
7. The Calcare di Base is never found at the base of the Lower Evaporites primary “in situ” selenites.
8. Lateral transitions between carbonate, gypsum or halite primary evaporites cannot be directly observed and must be considered speculation.

These problems led to further study and a revision in the way the various outcrops of Sicily are interpreted. A key question in resolving the stratigraphic conflicts in the Sicilian basins is how does the unit known as the Calcare bi Base, which tends to occupy highs and basin margins, relate to evaporites that tend to occupy the basin (syncline) lows. Historically, the Calcare di Base (CdB) in the Sicilian basins has been interpreted as indicating initial drawdown. It has an isotopic signature that becomes increasingly heavy toward the sites of gypsum and halite precipitation (Fig. 5.56a; Decima et al. 1988). Its “in situ” outcrops have historically been interpreted as dolomitic seepage units with a distribution mostly restricted to highs (edges) of the Sicilian Basin

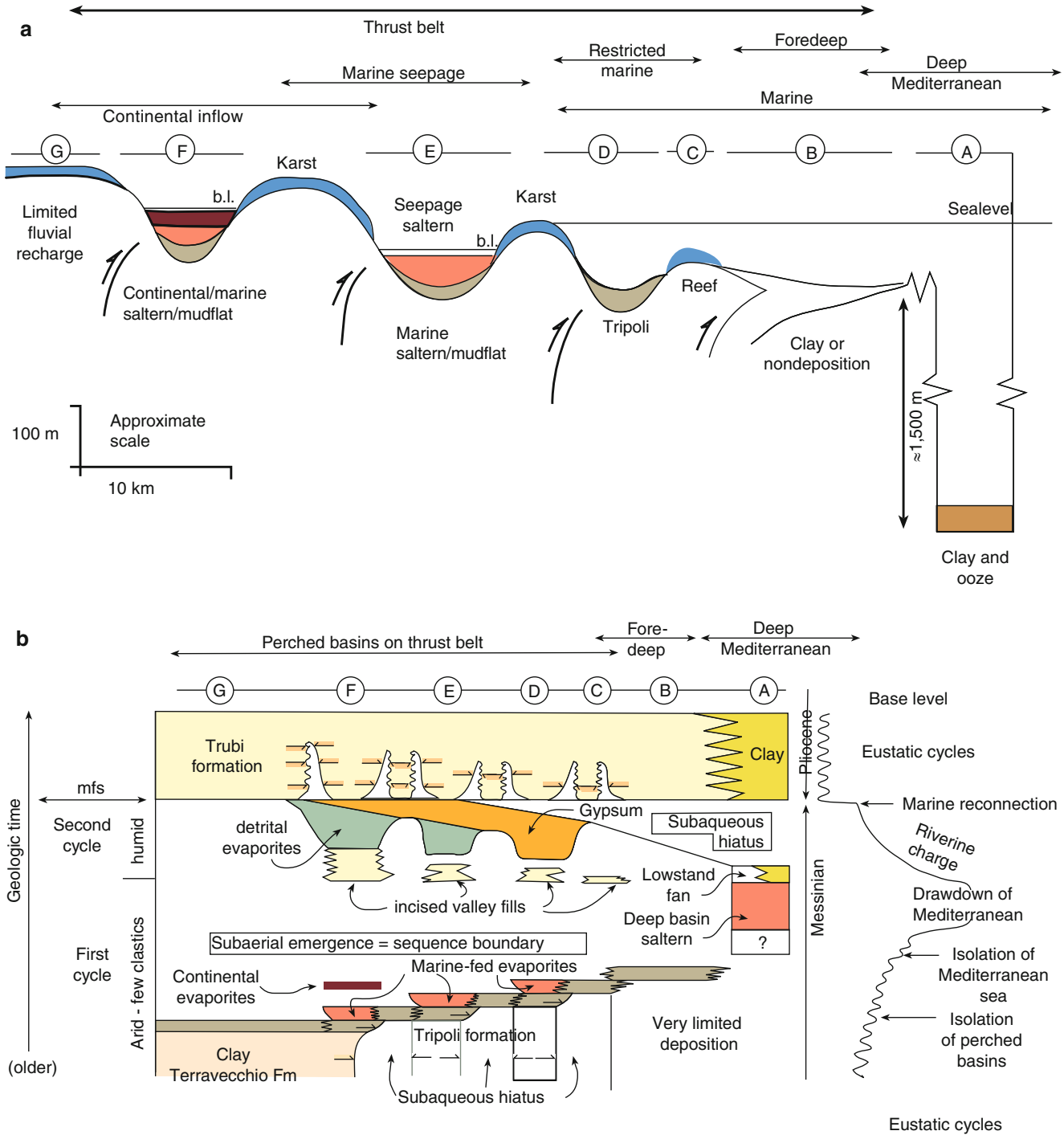

Fig. 5.55 Marginal thrust top evaporites in Sicily (Modified after Butler et al. 1995). (**a**) Sequential model for stratigraphy across different thrust top basins during deposition of the Lower Evaporites. Note the evaporite forming basins are isolated from a surface connection with the Mediterranean, but have a seepage connection. Restricted surface marine circulation facilitates deposition of the Tripoli Formation. Progressive thrusting leads to progressive reduction of import of marine inflow and finally to deposition of potash evaporites under conditions of hyperaridity and predominantly continental recharge. (**b**) A relative chronostratigraphic model for Messinian and Lower Pliocene deposits of Sicily and their correlation with basinwide deposits of the central Mediterranean sub-basins. Note that deposition of basinwide evaporites on the floor of the Mediterranean corresponds to an unconformity (sequence boundary) that separates the Lower and Upper Evaporites

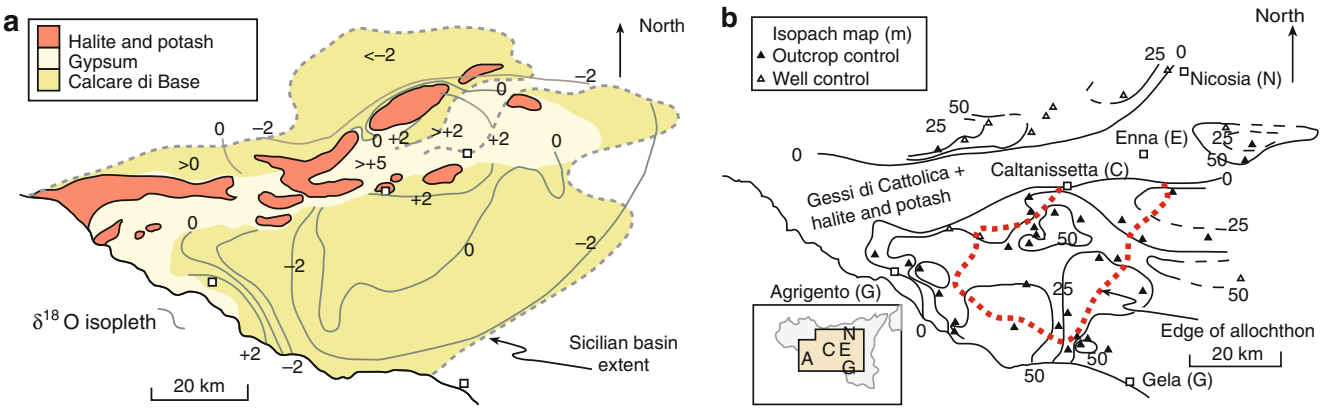

Fig. 5.56 Calcare di Base and equivalents, Caltanisetta Basin. (**a**) Distribution of main mineralogies overlain by oxygen isotope distribution ($\delta^{18}O_{PDB}$ ‰) in the in situ unit showing depletion in parts of Calcare di Base deposited further from areas of contemporaneous salt deposition (gypsum, halite and potash) (**b**) Isopach (in metres) of Calcare di Base and breakdown into an "in situ" unit and an allochthon block that was thrust over the evaporite salts (After Decima et al. 1988)

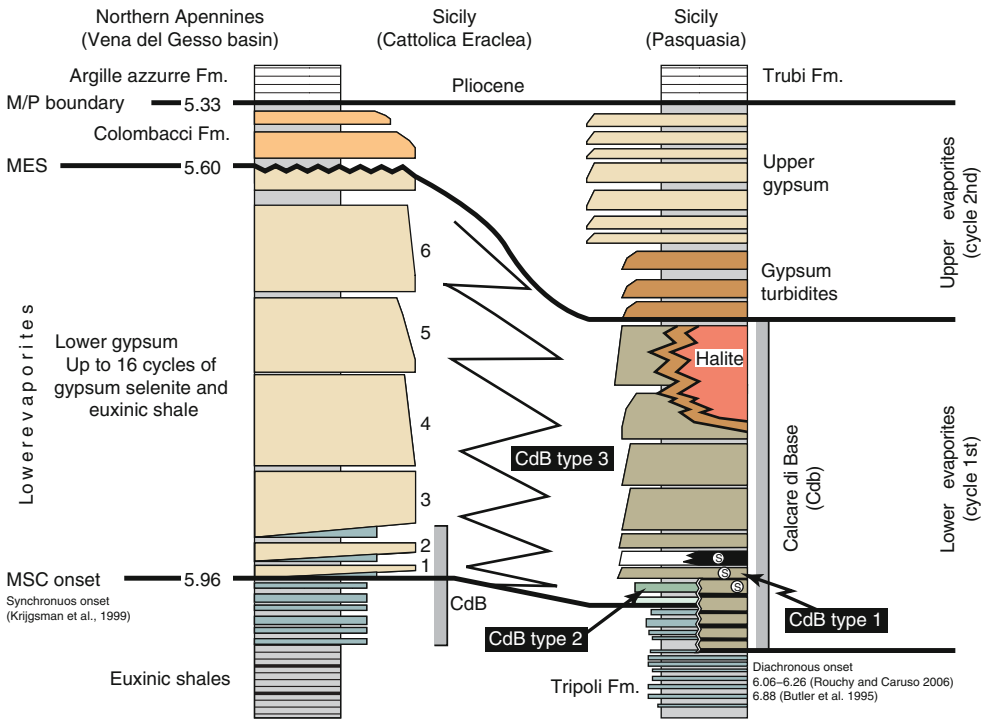

Fig. 5.57 Comparison of the Messinian successions of the Northern Apennines and of Sicily, showing the stratigraphic distribution of "Calcare di Base" (*CdB*). Note the inferred lateral transitions and timings between Lower Gypsum, Calcare di Base, and halite. Abbreviations: *Fm.* Formation, *MES* Messinian erosional surface, *M/P* Miocene–Pliocene, *MSC* Messinian salinity crisis, *S* sulphur-bearing) (After Manzi et al. 2011)

(Fig. 5.56b). More recently these dolomites, or at least that part of the CdB that is stromatolitic, is interpreted as having a microbial genesis (bacterial sulphate reduction; Oliveri et al. 2010). Three different types of carbonate deposits are now known to be included in the unit described as the "Calcare di Base," which is commonly envisaged to record the MSC onset (Fig. 5.57; Manzi et al. 2011): They are: Type 1, which consists of sulphur-bearing limestones, representing the biogenic product of bacterial sulphate reduction after original gypsum; Type 2, which comprises dm-thick, laminated dolomitic limestones interbedded with diatomites, sapropels, and marls found at the top the Tripoli Formation; and Type 3, the most common variety, consists of m-thick, brecciated limestones interbedded with shales and clastic gypsum. Type 3 shows sedimentary features suggesting a clastic origin and deposition from high- to low-density gravity flows; thus, these deposits can be regarded as an end-member of a large variety of evaporite-bearing, gravity-flow deposits, with a dominant carbonate component. They are likely equivalent to the gypsum clastic cycles in the Lower Evaporite in the Apennines.

The new genetic and stratigraphic characterization of the CdB carbonates has strong implications for a better comprehension of Messinian events; the three types of Calcare di

Base (CdB) seem to have formed during different stages of the MSC (Fig. 5.57). Type 2 formed in the first stage (5.96–5.60 Ma), and is the only type that can be regarded as the Lower Gypsum time-equivalent. Type 3 was deposited in the second stage (5.60–5.55 Ma), and its base is associated with a regional-scale hiatus and erosion (Messinian erosional surface). Type 1 formed even later, likely in post-Messinian time, through diagenetic processes affecting resedimented gypsum deposited during the second stage of the MSC. It follows that not all the CdB deposits record the onset of the MSC, as commonly thought. We shall discuss this further after we have looked at Messinian evaporites in the eastern Mediterranean and use this to develop an understanding of the saline hydrology tie to the basins hypsometric evolution.

Cyprus and the Levantine basin: The Latika, Tartus and Levantine basins of the Eastern Mediterranean were covered by widespread Messinian evaporites during the main Messinian Mediterranean drawdown (Fig. 5.58a; Calon et al. 2005; Roberts and Peace 2007; Hübscher et al. 2009). In these eastern Mediterranean deep basins, three distinct seismic units (the Messinian "trilogy") have been identified. This trilogy is observed beneath modern abyssal plains across the Mediterranean from the Gulf of Lions to the Levantine and laterally onlaps the margins (Montadert et al. 1970; Lofi et al. 2005). This onlap geometry is interpreted as a progressive infill of the abyssal plains when subsidence apparently did not compensate the high sedimentation rates (partial fill and spill).

For a long time, the three members of the offshore trilogy were called, respectively; Lower Evaporites, Salt, and Upper Evaporites and considered equivalent to the outcrop stratigraphy. However it is likely that the offshore unit referred to as the Lower Evaporites is mostly non-evaporitic, made up of varying combinations of marine turbidites, slumps and pelagics, typically with evidence of periodic restriction prior to the MSC. Onshore, the unit referred to the Lower Evaporites is just that — evaporitic. To avoid confusing these offshore terms with the stratigraphy of the onshore outcropping Messinian units, Lofi et al. 2005 proposes that we refer to the offshore trilogy as the Lower Unit at the base of the seismic trilogy (LU, which is at least partly turbidite), the Mobile Unit in place of the term Salt (MU, which in seismic typically shows the variably transparent characteristics of halite and in places has experienced plastic deformation), and the Upper Unit at the top of the trilogy (UU, made up of marls and evaporites, and interpreted as being deposited under increasing less saline conditions ≈ Lago Mare).

The basins are located east and southeast of Cyprus and are associated with the collision front between the African and Anatolian plate (Figs. 5.47b and 5.58a). The Pliocene-Quaternary sediment succession is underlain by up to 1-km thick Messinian evaporites. Both thick-skinned plate tectonic and thin-skinned salt tectonics control fluid dynamics and associated mud volcanism in the Latakia and Cyprus Basin as well as along the Troodos Latacia Culmination, which separates both basins.

An end-member model to explain the current distribution of basin-centre Messinian salts was proposed by Hübscher et al. (2009) that also explains the presence of elongated topographic highs and trenches along the Troodos Larnaca Culmination, and south of it. It calls upon gravity gliding of the Messinian evaporites and associated fluid migration (Fig. 5.58b). Thin-skinned extension in the Troodos Larnaca Culmination and boudinage, respectively, facilitate fluid flow through and out of the deforming evaporites. Fluid or mud crossflows dissolve the salt layer and create elongated dissolution and salt withdrawal trenches. Pressurised subsalt mud then intrudes Pliocene-Quaternary sediments atop and between the trenches. Consequently, the overburden is thickened and forms morphological ridges. The small-scale outcrop analogy for this style of argillokinetic deformation may be the Moncucco gypsum quarry (Fig. 5.53).

South of the Troodos Larnaca Culmination in the Tartus Basin, the evaporites and overburden are folded due to thin-skinned shortening of the evaporites. Fluid extrusion out of the evaporites can inferred from discontinuities in the seismic. The outflow caused a volume reduction and collapse of the evaporites. Mud volcanoes and fold anticlines align above deep-rooted transpressional fault systems which are associated with the African-Anatolian collision zone, where the faults acted as conduits for rising fluids. Mud volcanoes emerge in the western part of the same region, where the Cyprus Arc (thrust) strikes almost West–east and the plate collision occurs more frontally, so stress is highest. Fold anticlines evolved further to the east, north of the Aleppo High where the Cyprus Arc runs SW-NE and sinistral strike-slip has been proposed. Particular mud volcanoes and folds had emerged prior to the deposition of the Messinian evaporites. The undisturbed upper Pleistocene sequences, as well as the absence evidence of significant mud outflow on the seafloor, strongly suggest that the main fluid dynamic ceased prior to Quaternary sedimentation.

Further south is the Levantine basin and then the Nile Delta cone, both areas of active hydrocarbon exploration (Fig. 5.59; Cartwright and Jackson 2008). In both regions the current edge to the Messinian salt is not the depositional edge of the salt, rather, as in many basinwide salt masses on passive margins the current salt edge is controlled by gravity sliding and salt withdrawal associated with sediment loading (Chap. 6).

Regional 2D and 3D seismic data from the Levant Basin reveal the updip extensional component of thin-skinned gravity tectonics on this continental margin (Fig. 5.59; Cartwright and Jackson 2008). Because of its youth (5–7 Ma), the earliest stages of deformation of this salt basin are preserved without the severe structural overprinting, typ-

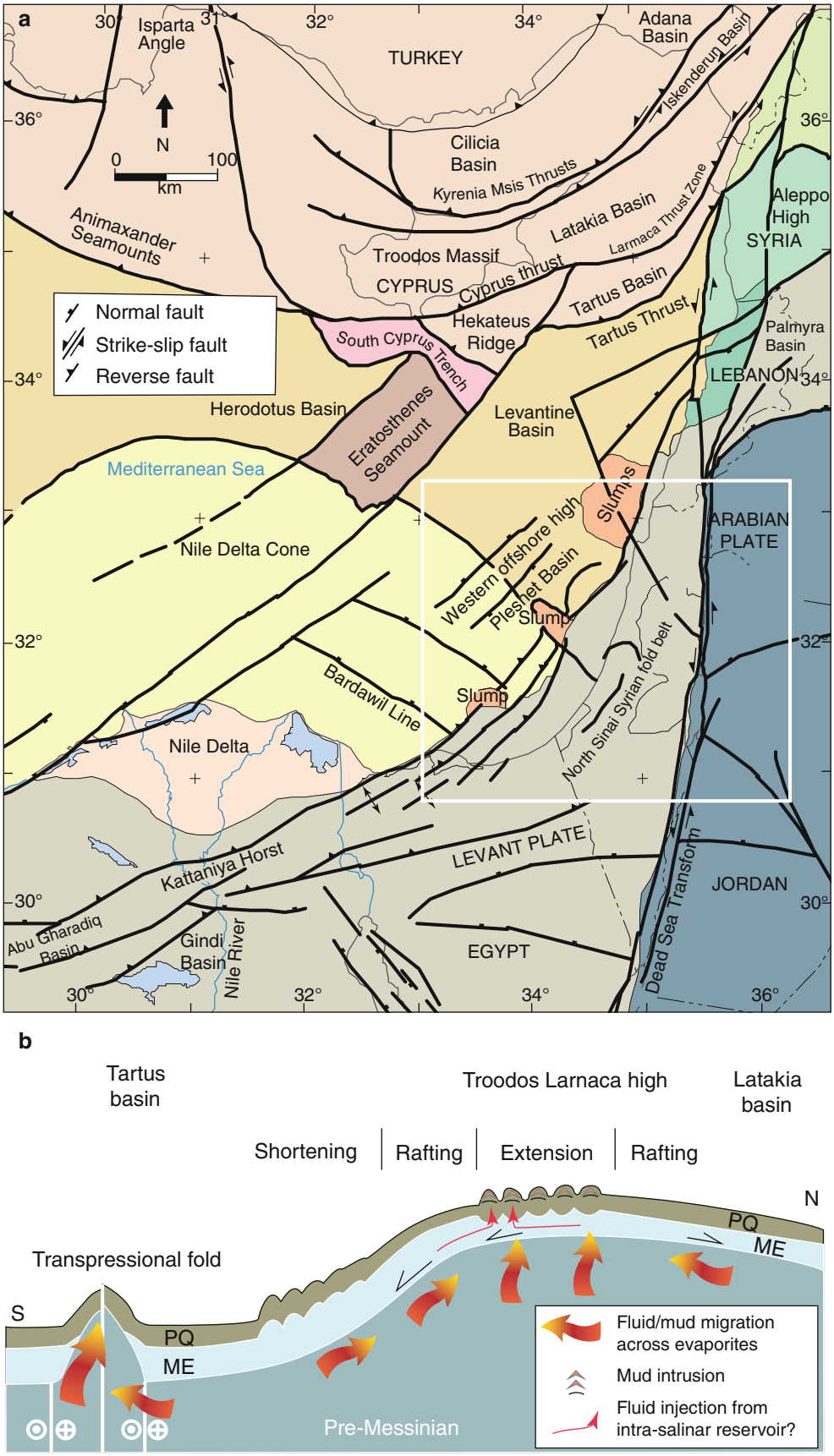

Fig. 5.58 Eastern Mediterranean. (**a**) Tectonic elements in the East Mediterranean Basin. The main elements defining the Levantine Basin include the Nile Delta Cone, Eratosthenes Seamount, the Cyprus/Larnaca Thrust Zone and the coastal margin faults along the Eastern margin of the Basin (After Roberts and Peace 2007). (**b**) Morphostructure along the Troodos Larnaca Culmination driven by salt tectonics. Downslope creeping salt leads to extension or salt boudinage at the culmination itself. Here, fluids flow through or out of the salt and dissolute elongated trenches. Mud intrusions thicken the overburden. Downslope creeping results in compressional folds in the salt and overburden. The thin-skinned tectonics as outlined here superimposes active plate tectonics. In the Cyprus Basin fold anticlines emerged above fault traces of deep-rooted strike-slip fault systems. *ME* Messinian evaporites, *PQ* Pliocene–Quaternary (After Hübscher et al. 2009). The *white rectangular outline* shows the approximate position of Fig. 5.59)

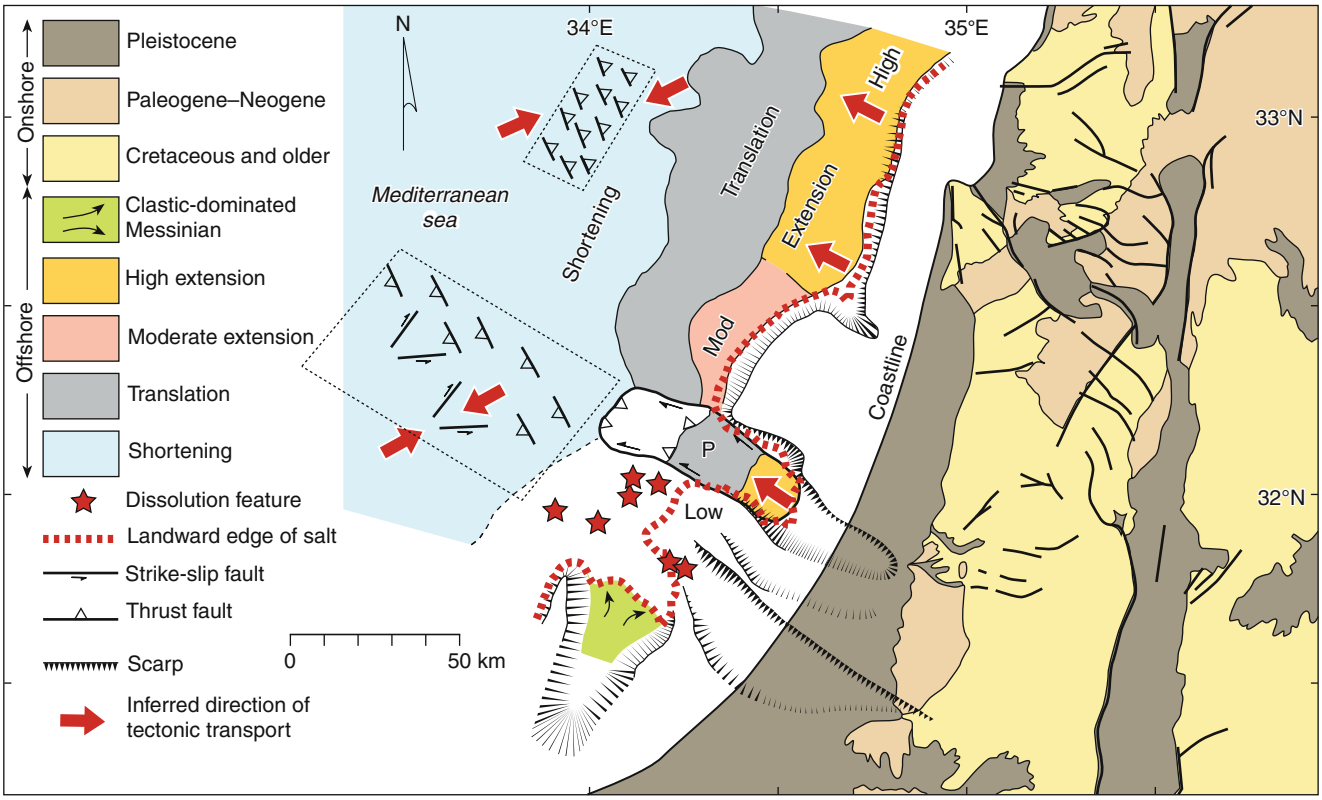

Fig. 5.59 Structural domains and features along the Levant margin. The updip edge of Messinian salt (*red dashes*) correlates closely with the updip limit of extension. The frontal scarp (hachured) also tracks these features in the north but deviates in the south, where it deflects into and merges with major pre-Messinian canyons. P marks the Palmahim submarine landslide. The degree of onshore exhumation is shown by the three geologic units, the ages for which correlate with increasing elevation (After Cartwright and Jackson 2008)

ical in more mature, giant salt-tectonic systems. Extension detaches onto and within Messinian evaporites up to 1,800 m thick. Structural restoration suggests that the Mediterranean drawdown during the Messinian Salinity Crisis was ≈800 m. The 10- to 15-km wide extensional domain tracks the landward pinch-out of the mobile Messinian evaporites against an older Late Miocene scarp. Diachronous extension began in the centre of the margin in the mid-Pliocene, then spread northward in the late Pliocene, then finally southward in the early Pleistocene. Extension continues today on many of the most landward faults. Extensional strain varies greatly along strike from <1 km to as much as 12–15 km. Extension and seaward salt flow thinned the evaporite margin and its overburden. Both processes were triggered by a combination of uplift of the continental shoulder of the Dead Sea Rift and subsidence in the Mediterranean Basin. At least three factors controlled variations in extension: (1) degree of tilting of the salt wedge, related to the interplay of coastal uplift and basin subsidence; (2) presence of pre-Messinian canyons overlain by landward salients of salt; and (3) variations in evaporite facies and the proportion of siliciclastic admixture.

In general, work in the offshore of the eastern Mediterranean has established the following (Briand 2008)

1. There is no evaporite underlying the Anaximander area and at Erathostenes seamount, implying these structures predated the MSC.
2. Layered halite (MU) is the predominant phase found in most of the eastern Mediterranean basin-centre sumps.
3. Gypsum/anhydrite (typical of the Upper Evaporite in marginal basins) is a minor contribution, with only one site where the gypsum contribution seems more important than halite to the Messinian succession (located on the Nile fan with an approximately 1,200 m present-day waterdepth).
4. Mg-Cl salts are a minor but rather variable contribution to deep brine sites on the current seafloor of the Mediterranean. In particular, the Discovery Brine basin in the mid-Ionian Sea, consisting of waters associated with almost pure bischofite, is an extreme case.

When seismic character of halite in the Eastern Mediterranean is compared to that in the western Mediterranean there are some obvious, as yet unexplained, differences (Lofi et al. 2011; Topper and Meijer 2013). In the Western Mediterranean there is a single transparent layer of halite, suggesting negligible amounts of intermixed clastics,

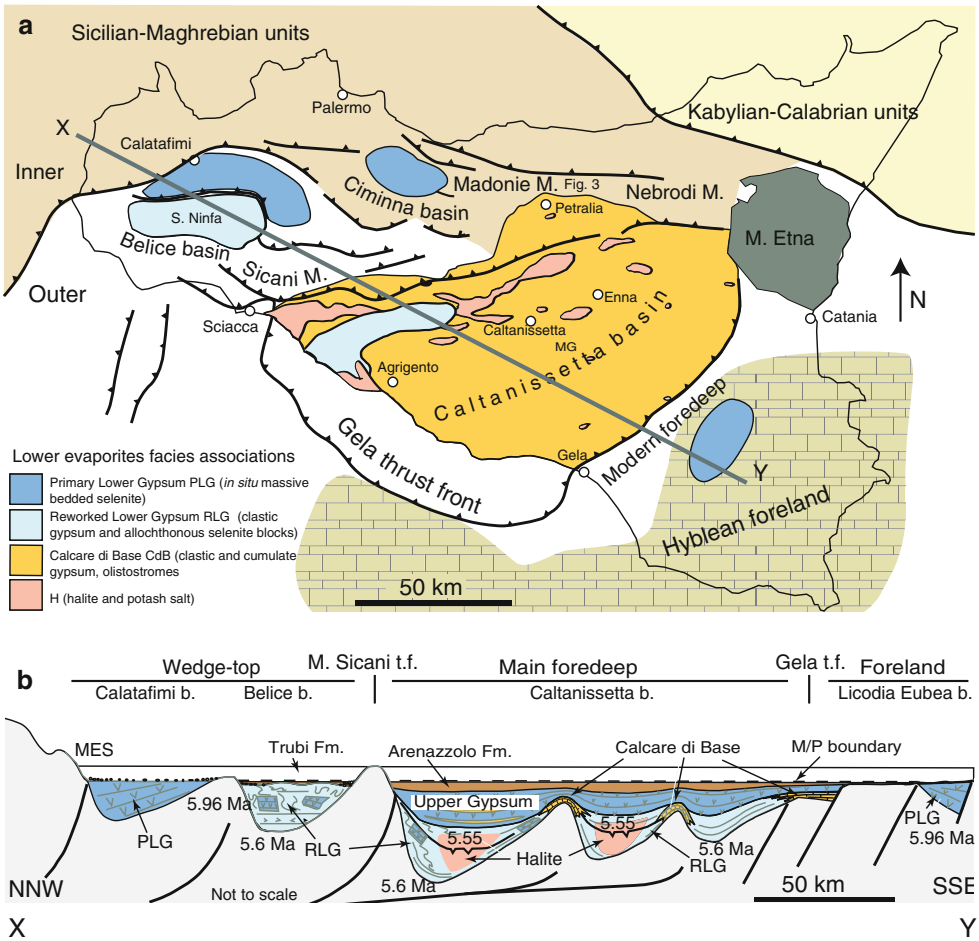

Fig. 5.60 Geology of Sicily with the distribution of the Lower Evaporites (Modified after Roveri et al. 2008; Manzi et al. 2011) (**a**) Distribution of the major geologic units (**b**) Schematic geologic cross section across the Sicilian Basin flattened at the base of the Pliocene showing the upper Messinian deposits (above the Tripoli Formation). *MES* Messinian erosional surface. Also shown are ages of main surfaces in million years

with a maximum thickness of 1,200 m in the Provencal basin. In the Eastern Mediterranean, up to six layers with alternating seismic facies, transparent–nontransparent, add up to a thickness of 2,100 m in the central deep basins. Three packages with alternating transparent– nontransparent halite have been drilled in the Nile delta (Ottes et al. 2008), The oldest (deepest) halite of the three has a more chaotic seismic character and possibly consists of redeposited evaporites, mixed with some clastics. It is assigned a Tortonian age (with an uncertainty of a few Ma). The middle halite unit is the cleanest (most transparent) and has undergone no more than minor deformation. These three halites are considered by Ottes et al. (2008) to be likely time equivalents to condensed anhydrite-rich sections in the up-dip shelfal areas.

A More Realistic Messinian Stratigraphy

A comprehensive integration of as yet undrilled basin-centre evaporites, as studied in seismic across the Mediterranean, and the various basin margin outcrops with their well-preserved stratigraphic detail, is needed if sequence stratigraphic principles are to be tested across this our youngest example of a saline giant.

Since the 1990s, textural studies have shown significant volumes of deeper water evaporites are present in the Apennine, Sicilian and Cypriot outcrops (Roveri et al. 2008). The large-scale, postdepositional gravity collapse of primary evaporitic (mostly gypsum) deposits into the deeper parts of adjacent foreland basins is a widespread feature in the Mediterranean peripheral basins of Italy and Cyprus. Similar but larger scale evidence is seen in seismic across basin edges in the Eastern Mediterranean. Such slumping and collapse has altered original stratigraphic relationships in some places and means the amplitude of any waterlevel fall cannot be easily determined in some marginal basins where beds can be allochthonous. It means the simple bipartite stratigraphic separation, based on Butler et al. (1995), is somewhat more complicated by ongoing "piggy-back" tectonics (Figs. 5.60 and 5.61). Many authors (see Briand 2008) now accept that the Sicilian, and possibly the Cypriot, basins differ from the Spanish marginal basins in that they preserve evidence of the halite unit that was deposited at the time of maximum drawdown of the Mediterranean basins (Time 3 scenario in Fig. 5.48). The halite (and associated potash salts) that subcrop in Sicily is autochthonous. It was thrust

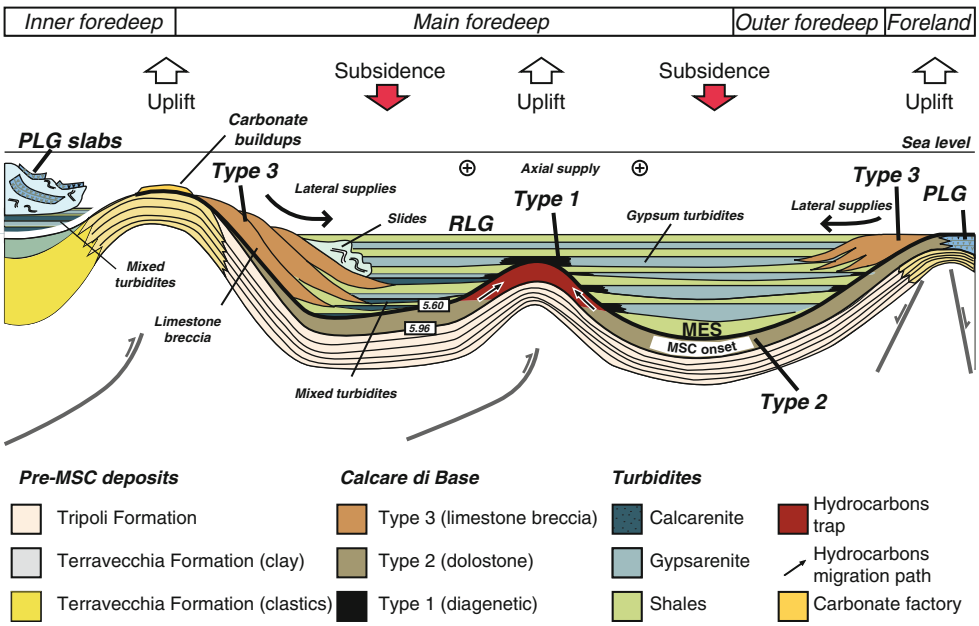

Fig. 5.61 Schematic reconstruction of the Sicilian foredeep during the Messinian salinity crisis (*MSC*) in the Sicilian Basin showing also the distribution of the three Calcare di Base types and their relationship to underlying open marine (*pre MSC*) and overlying retransported units of the lower Gypsum unit (Lower Evaporite; see Fig. 5.57, after Manzi et al. 2011)

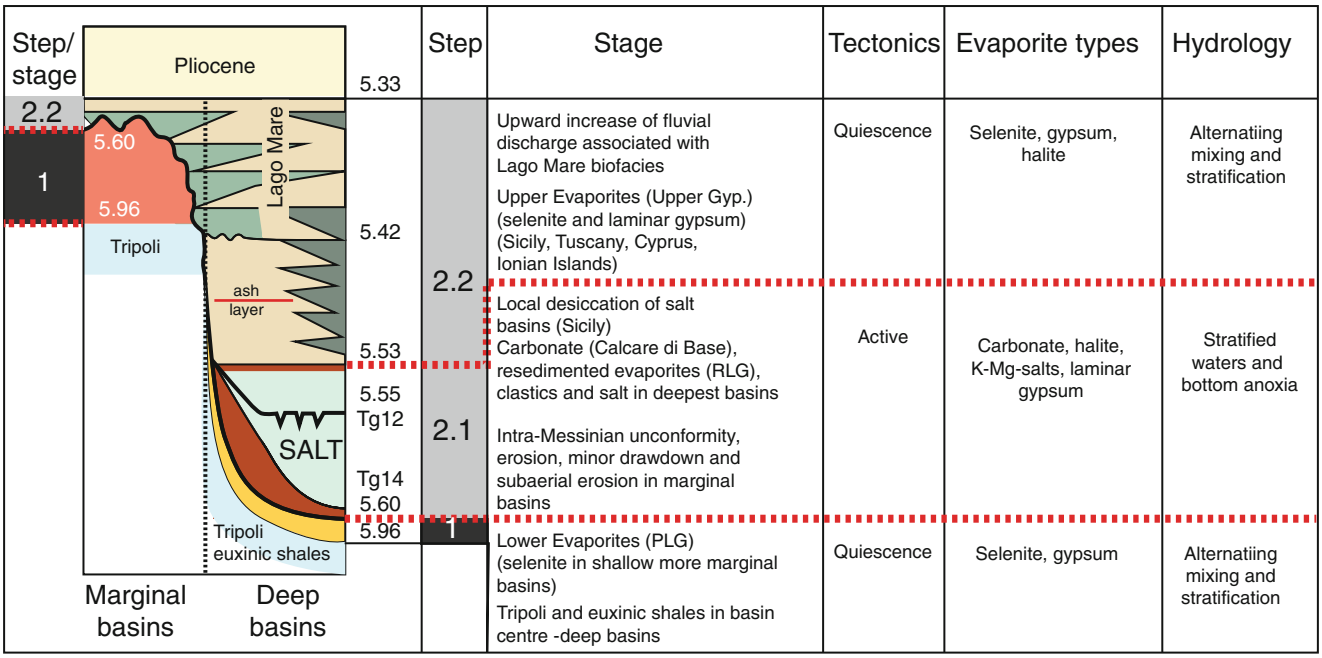

Fig. 5.62 A tentative integrated stratigraphy for the Messinian evaporites of the Mediterranean region (Briand 2008)

into its current elevated position on the isle of Sicily, while gypsum of the marginal basin was gravitationally reworked into deeper water (Figs. 5.60 and 5.61). This autochthonous section is overlain by bedded gypsum of the Upper Evaporite and the Lago Mare.

Accordingly, Roveri et al. (2008) and Manzi et al. (2011) postulate a three stage depositional association in the Sicilian Basins (Fig. 5.60b). The Lower Gypsum of Sicily comprises primary and resedimented evaporites, separated in space and time by the intra-Messinian unconformity. At that time a composite unit including halite, potash (kainite), resedimented gypsum and Calcare di Base equivalents accumulated between 5.6 and 5.55 Ma in the main deep basin shallow-water depocentres. Simultaneously, gypsum in more marginal basin settings was reworked and brecciated; it records the acme of the Messinian Salinity Crisis during a tectonic phase coupled with sea-level falls at glacials TG14-TG12 (Figs. 5.61 and 5.62). These basin-centre deposits post-date *in-situ* primary selenite gypsum, which had precipitated in shallow-water wedge-top and foreland ramp

basins between 5.96 and 5.6 Ma. The revised stratigraphic framework defines a three-stage Messinian Salinity Crisis (MSC) scenario characterized by different primary evaporite associations: selenite in the first and third stages, carbonate, halite and potash salt in the second one that was also associated with hybrid resedimented evaporites. Such a stratigraphy better ties to the offshore record.

Further east in the Mediterranean, in Cyprus, where now outcropping Messinian gypsum units accumulated in a series of semi-isolated tectonically-induced small marginward piggyback basins, the stratigraphic evolution is not dissimilar to the Italian basins. Dominantly, the gypsum deposits formed from landlocked marine-fed brine sheets (gypsum salterns of the Upper Evaporite unit) located not far below ambient sea-level (Robertson et al. 1995). Evaporites in south Cyprus (Maroni Basin) formed in elongate marginal basins between compressional lineaments instigated by Early Miocene thrusting in a tectonic situation similar to that described for Sicily. In the sub-basins of west, southwest and south Cyprus, large scale slumping of saltern gypsum into deeper water formed megarudite debris flows, which are thought to have been triggered by one or several phases of extensional faulting tied to regional thrust tectonics.

The improved, but still tentative, understanding of the tectonic evolution of the tripartite Sicilian section and thrust-related Cypriot counterparts underlines the considerable limitations that still exist in our current understanding of any Mediterranean-wide evaporite stratigraphy. That is, through ongoing studies of circum-Mediterranean Messinian outcrops, we now have a thorough understanding of the sequences and the relative importance of drawdown versus tectonic position in their formation. But, still we can only tentatively relate our detailed outcrop-based understanding to the much thicker, uncored, largely undisturbed, flat-bedded successions of the main drawdown stage, which seismic shows occupy huge areas across the deep Mediterranean seafloor.

What is clear from the basin hydrology required to form gypsum in the marginal basins it that it cannot be time-equivalent to the halites that dominate the drawdown deposits of the basin-centre sumps (Fig. 5.61). While gypsum was accumulating in the marginal basins, euxinic carbonates and clastics, including equivalents to the Tripoli Fm, were accumulating beneath kilometres of water cover atop the deepwater sumps on the Mediterranean floor.

How Did the MSC End?

Lago-Mare (literally "lake-sea") deposits in the Mediterranean typify the transition from the evaporites of the Messinian salinity maxima back into the open marine waters of the Pliocene. According to Orszag-Sperber (2006) the term "Lago-Mare" is now employed unanimously by geologists across the Mediterranean to designate dominately transitional sediments deposited in what were mostly oligo-mesohaline lacustrine settings that ended Messinian time, immediately prior to the Pliocene marine re-flooding.

The Pissouri and Polemi basins of south Cyprus preserve excellent outcrops of late Messinian-Early Pliocene "Lago-Mare" sediments, as do approximately equivalent sediments in the Mediterranean on the edge of the Erathostenes Seamount (Fig. 5.61; Orszag-Sperber et al. 2009). In fact, all the Messinian-Pliocene transitions that define the end of the salinity crisis in the Eastern Mediterranean are marked by a very rapid environmental change, as indicated by sharp variations in lithology, sedimentology, microfaunal assemblages and stable isotope composition (Rouchy et al. 2001).

The most striking feature in the Pissouri Basin is the intercalation between the uppermost gypsum bed and the base of the Zanclean (Early Pliocene) deposits of four main horizons of palaeosols interbedded with carbonates and conglomerates. Palaeosols indicate periods of subaerial exposure in the marginward basins of Cyprus that were long enough to permit pedogenesis during the transition to less evaporitic conditions. The Lago-Mare succession is not indicative of a geologically instantaneous event. Intercalated conglomerates indicate intense erosion of the Troodos Massif and its sedimentary cover. In contrast, shallow oligohaline conditions persisted in the deeper parts of the Mediterranean basin, as indicated at ODP Site 968. Both in the Pissouri Basin of Cyprus and on the flank of the Erathostenes Seamount in the Mediterranean the late Messinian sediments are directly overlain by the lowermost Pliocene sediments deposited in well-oxygenated deep marine conditions (Orszag-Sperber et al. 2009). The drastic change of water depth that typifies the basinwide end to the salinity crisis shows that as in the earlier evaporite stages, water levels of the latest Messinian "Lago-Mare" were still far below that of the world ocean, by at least more than several hundred metres.

Moreover, the study of the Polemi sections shows that oligohaline conditions had already started during the deposition of the Upper Gypsum sub-unit (Fig. 5.61). Typical brackish and fresh water assemblages are present in the last two gypsum layers and inter-gypsum beds on Cyprus (Rouchy et al. 2001). This indicates that freshwater dilution, i.e. passage into the Lago-Mare conditions, resulted from a progressive change of the hydrological budget. It started during deposition of the Upper Evaporites and climaxed after the deposition of the uppermost gypsum layer (passage into the classic Lago-Mare facies). This basinwide evolution is interpreted as being due both to the severance from the marine brine-seep feed and to the increasing contribution of the runoff-precipitation versus marine inputs in the hydrological budget of the Mediterranean. This occurred toward the end of the salinity crisis, immediately prior to the re-establishment of open marine conditions. (In my opinion it reflects a transition into a fill and spill mode of deposition in a relatively humid setting).

The marine refilling at the beginning of the Zanclean and associated with the end of the Mediterranean Lago-Mare is considered to have been very rapid (Orszag-Sperber 2006). For Hsu et al. (1973), the event length of the re-flooding event was evaluated at "probably less than 10,000 years". It was considered as a "catastrophic deluge" by Cita et al. (1978a), with associated instantaneous marine flooding through the Mediterranean basin (Hilgen and Langereis 1988). This has led some envisaging a series of cataracts (mega-Niagara waterfalls) in the vicinity of the Rifian corridors at the western end of the Mediterranean (inset in Fig. 5.47). Blanc-Valleron (2002), who takes into account both the present exchanges of water between the Atlantic Ocean and the Mediterranean Sea and the morphology of the Gibraltar Strait area, estimated that only 36 years were needed "to fill an empty Mediterranean, even when taking into account the evaporation." The velocity of the flow refilling the Mediterranean from the Atlantic through the Gibraltar Strait is evaluated at several tens to more than 100 m s^{-1}, and termed "cataclysmic". But the sedimentological evidence for this spectacular scenario is enigmatic.

Evaporites indicative of the Messinian Salinity Crisis must have resulted from a significant drop of the Mediterranean sea level and associated hydrographic isolation. As outlined above the subsequent reflooding is generally thought to have been very sudden. Offshore seismic evidence from the Gulf of Lions and re-visited onshore data from Italy and Turkey, as interpreted by Bache et al. (2012), offer a new concept of a two-step reflooding of the Mediterranean Basin after the Messinian Salinity Crisis. The refilling rate was first moderate and relatively slow, accompanied by transgressive ravinement, and later on was very rapid, preserving the subaerial Messinian Erosional Surface (M-reflector). The amplitude of the two successive rises of sea level is estimated at ≤500 m for the first rise and 600–900 m for the second rise. Upper Evaporites from the central Mediterranean basins appear to have been deposited principally at the beginning of the first step of reflooding. After the second step, which preceded the Zanclean Global Stratotype Section and Point, successive connections with the Paratethyan Dacic Basin, then the Adriatic foredeep, and finally the Euxinian Basin occurred, as a consequence of the continued global rise in sea level. Marine flooding (transgression) across a complex basin-floor morphology, with sills and sub-basins, led to somewhat diachronous events encompassed in the term "Lago-Mare" succession.

Implications for Eustatic Correlations

If we summarise our current understanding of Late Miocene evaporites in the Mediterranean (Fig. 5.62; Topper and Meijer 2013) then; (1) During the Messinian Salinity Crisis (5.96–5.33 Ma) deposition took place in two distinct settings in the Mediterranean: marginal and deep basins. In (former) marginal basins all around the Mediterranean, Messinian sequences start with up to 16 distinct cycles of gypsum intercalated with marl/carbonates. A duration of ≈360 ka has been calculated for their formation by linking the cycles to precession-driven climate changes. This first phase of the MSC, the so-called Primary Lower Gypsum phase (PLG, 5.96–5.61 Ma), is followed by the second phase of the MSC, the halite phase (5.61–5.55 Ma), which is characterized by widespread erosion of the PLG deposits, redeposition of the eroded gypsum, and formation of a halite unit in deep marginal basins in Sicily, Calabria, and Cyprus and likely across the deep basins of the Mediterranean (Roveri et al. 2008). The third and last phase recognized in marginal basins is the Upper Evaporite phase (5.55–5.33 Ma), which generally consists of non-evaporitic shallow-marine deposits and the mesohaline to brackish water Lago Mare sediments that defines the end of the MSC.

Depending on the author, different Late Miocene-Pliocene intervals are defined in the Mediterranean as indicative of the MSC, with the main differences mainly relating to the way the Messinian event is studied (onshore through fieldwork or offshore using seismic data). The water-level fall in the basin driving evaporite deposition in the more central Mediterranean sumps is estimated to have been at least 1,000–2,000 m. It drove the loss of any surface connection to the world's oceans and the massive erosion of the surrounding continental margins. It created marine seeps and deep karst, as well as large quantities of clastic detrital deposits (including reworked evaporites) before, during, and after widespread marine-fed salt deposition in the deep basin centres (Loncke et al. 2006). Offshore, the top and base of the evaporites can generally be identified on seismic profiles. However, because the deep-basin evaporites themselves have never been sampled by wells, establishing a reliable seismic stratigraphy tie to the onshore is difficult.

What marine geologists tend to call the 'Lower Evaporites' in much of the Mediterranean corresponds to a highly reflective series of probably detrital sediments deposited by slumping processes during the first stage of drawdown (Loncke et al. 2006). In the deep basin, above these layers, acoustically transparent layers characterize locally-mobile evaporites, made essentially of halite. The Upper Evaporites, appearing as layered and reflective packages above these transparent layers, most likely correspond to cyclic alternations of marls and gypsum, as defined by Rouchy and Saint Martin (1992). These beds were possibly deposited in the first stage of transgression marking the end of the MSC. The problem in typing evaporites in the marginal basin to those in the deep basins is that during the maximum intensity of the salinity crisis, erosion was active on the exposed margin and this level shifted in time with the changing water level, leading to various detrital deposits interfingered between salt and the upper evaporites.

The preceding discussion of the inherent, and still not fully resolved, largely tectonically controlled climatic and hydrologic complexities in the Messinian of the Mediterranean is based on more than five decades of detailed scientific work, mostly in exposed marginal basin stratigraphies, where the evaporites are still largely preserved as primary gypsum. With the possible exception of an initial third-order fall in worldwide sealevel cutting off the basin, all these deposits were isolated via active tectonism. Their finer stratigraphic geometries are not reflective of world eustasy but of more local tectonically-induced drawdown, climate variation and autocyclicity.

The crux of the problem in applying the results of detailed Mediterranean Messinian studies to better interpret the internal stratigraphy of other older basinwide evaporites is that the larger more representative volumes of basinwide Mediterranean evaporites are as yet unstudied. They are preserved beneath the present deepwater centres of the various Mediterranean basins. These bedded sections currently lie beneath hundreds of metres of Pliocene and Pleistocene sediment; only halokinetic intervals or dissolved salt edges lie within a few tens of metres of the modern deep seafloor. With the exception of a few DSDP holes that intersected the uppermost few metres of these salts, the internal stratigraphies of these saline giants are largely unsampled and uninterpreted. And yet, we know deposition of a km-thick basinwide salts took place in less than 300,000–400,000 years. By definition, the total package of the Messinian sequence must be a fourth-order sequence (Table 5.8). It implies that internal reflectors layers and cycles seen in seismic sections through thick evaporites, must reflect fifth and sixth order time frames.

Any eustatic curves, based on seismic that encapsulates the very high accumulation rates of basinwide evaporites in large basin-centre positions in the Mediterranean, will outline very high frequency responses. Work on Messinian evaporites implies that ancient basinwide evaporites are also depositional systems with internal responses not related to world sealevel changes. If so, then a comparison of eustatic curves derived from internal geometries of basinwide evaporites with lower order eustatic curves, derived from the worldwide study of various marine carbonate or siliciclastic sequences, is simply not possible. The internal reflectors and responses that we can resolve seismically within a basinwide evaporite unit are responding to water level changes that are far too short-term to be compared with the eustatic information captured in classic Vail or Exxon-style sealevel curves.

We cannot correlate the various eustatic peaks and troughs outlined by the depositional tracts in either open marine carbonates or siliciclastic system to layers in thick evaporite beds, they are responding to different time-based waterlevel amplitudes and climatic frequencies. The highest seismically resolvable frequencies in an open marine sequence are third, and perhaps the occasional fourth, order responses. In basinwide evaporite cycles we are looking at seismically resolvable bounding surfaces that are responses to fifth or sixth order environmental changes.

Outside of the Mediterranean we can see other complications to a notion of world-scale Miocene eustasy controlling basinwide evaporite deposition. Work in the Neogene sediments in the Red Sea and the Gulf of Suez has shown that the concept of maximum regional aridity corresponding to times of maximum evaporite accumulation and minimal clastic accumulation is not that simple (Griffin 1999). Studies of the Miocene/Plio-Pleistocene succession in the Gulf of Suez and the Red Sea have shown that the Messinian sediments (Zeit Formation and equivalents) were deposited at rates greater than other units of the Miocene/Plio-Pleistocene. The Zeit Formation contains a significantly higher clastic content than the underlying evaporitic South Gharib Formation indicating that the Messinian interval in this region, adjacent to the main Mediterranean basin, was a time of high rainfall and high sediment yield rates. This period, named the Zeit Wet Phase, stands in marked contrast to the arid conditions of the preceding Tortonian Stage when halite-bearing South Gharib Formation and its equivalents were precipitated in the Gulf of Suez and Red Sea (Griffin 1999). It suggests that the Zeit Wet Phase was marked by high monsoonal activity and that this wet phase peaked in the late Messinian. This was the time of the lowstand maximum in the Mediterranean. So, using the most recent example we have of a saline giant, the deposition of the 1-km-plus evaporite units in the various Mediterranean basin centre sumps corresponds to a two dimensional bounding surface or centripetal unconformity (M-marker) on the basin margins immediately outside of the evaporite depositing areas. This should be the starting point for any seismic-based correlation of the evaporites (or their subsequent dissolution breccias) with adjacent normal marine sediments. This erosion surface (a major sequence boundary) is millions of years younger than the erosion surface formed when Middle Miocene salts formed in the adjacent Red Sea basin. It underlines that scientific principle well known to Ancient Greek philosophers, namely, “similarity is not equivalence”.

The corollary, when interpreting intrasalt seismic reflectors in any ancient evaporite, is a question; Is it possible to attempt a sequence stratigraphic age comparison between marine sediments and layered non evaporite deposits sandwiched between the various salt beds of a marine-fed saline giant? Unless we clearly define all sequence boundaries and realise that thick beds of evaporites equate with regional unconformities in surrounding sediments, we may be comparing chalk and cheese. Yet some authors have been courageous enough to attempt internal sequence stratigraphy of ancient saline giants based on various eustatic scales. We shall now look at such a set of studies in the Zechstein evaporites.

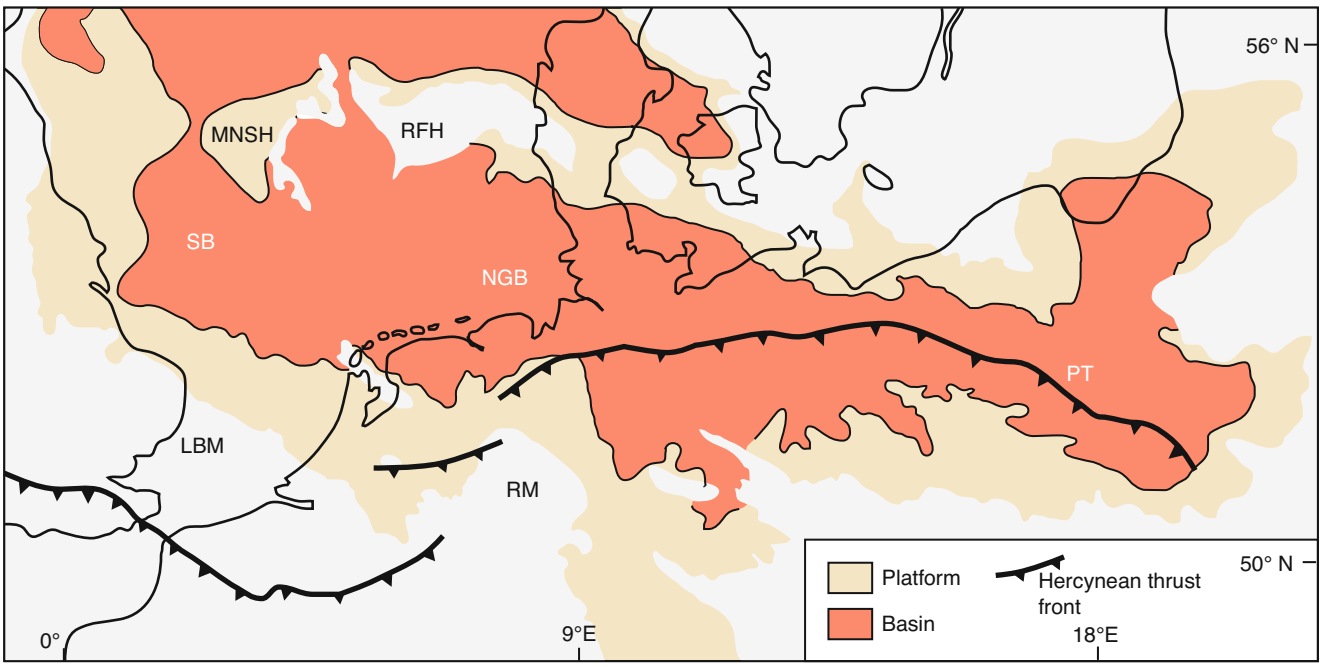

Fig. 5.63 Facies distribution in the southern Zechstein Basin (After Geluk 2000). The basin is bordered to the north by the Mid North Sea High and Ringkøbing-Fyn High and the London-Brabant Massif and Rhenish Massif in the south. The *solid black line* represents the location of the Variscan Thrust Front. *MNSH* Mid North Sea High, *RFH* Ringkøbing-Fyn High, *SB* Silverpit Basin, *LBM* London-Brabant Massif, *RM* Rhenish Massif, *NGB* North German Basin, *PT* Polish Trough

Stratigraphic Evolution in the Zechstein

In the Late Permian greenhouse world an area of approximately 600,000 km^2 in northern Europe was covered by the waters of the epicontinental Zechstein Sea (Fig. 5.63). The sea was relatively shallow; its maximum basin-centre depth is estimated to have been ≈300 m in the early mesohaline stage prior to complete isolation and drawdown (Brongersma-Sanders 1971).

The basin was subdivided into two main east–west oriented basins, called the Northern and Southern Permian Basins, which were separated by a sequence of palaeo–highs, the Mid-North Sea and Ringkøbing-Fyn Highs. Lithostratigraphic similarities between the evaporitic fill of the two basins suggest that the highs did not prevent the free surface exchange of brine between the north and south regions of the Zechstein depression.

During the Late Permian, this part of northern Europe lay at a palaeolatitude of ≈25°N and within the Pangaean supercontinent. This, coupled with the restricted and at times marine-fed seepage supply of seawater from the Boreal Ocean to the North and the Tethys Ocean to the Southeast, resulted in deposition of thick sequences of bedded sulphate and halite evaporites, along with minor volumes of bittern salts. Prior to the onset of marine-fed seepage that typifies the Zechstein Series, the basin accumulated terrigenous desert sediments of the Rotliegende/Wiessliegend Formation, in an arid continental playa/eolian/wadi setting. It was a sub-sealevel depression created by the final stages of the Variscan Orogeny (Carboniferous-Early Permian). During times of increases runoff, a saline ephemeral Rotliegend lake periodically covered wide expanses of the southern Permian basin (Legler et al. 2011). As it dried, waters reached $CaSO_4$ saturation but widespread deposition of halite beds did not occur. The region at that time was characterised by the development of pull-apart rift basins that evolved into passive margins by the Middle Permian-Triassic period.

This time frame encompasses the main stage of basin subsidence and is characterised by aridity and periodic widespread evaporite deposition including Zechstein evaporites in the Late Permian, followed by Muschelkalk salts in the Middle Triassic and Keuper salts in the Late Triassic (Fig. 5.64a). The Mesozoic of NW Europe was also characterised by ongoing metasomatic and hydrothermal activity, as evident from multiphase, cross-cutting, intraformational veinlets. The following Rhaetian through Lower Cretaceous period was marked by intensive faulting, rifting, and the initiation through much of the basin of large-scale halokinesis, sourced in the Zechstein halites.

The Zechstein encompasses the last 5–7 million years of the Permian (Fig. 5.64a; Menning 1995). Most drill intersections and most sequence stratigraphic interpretations have been completed in the southern basin. This is the region associated with onshore hydrocarbons in the Zechstein of the Nederlands and northern Germany and is also a region where

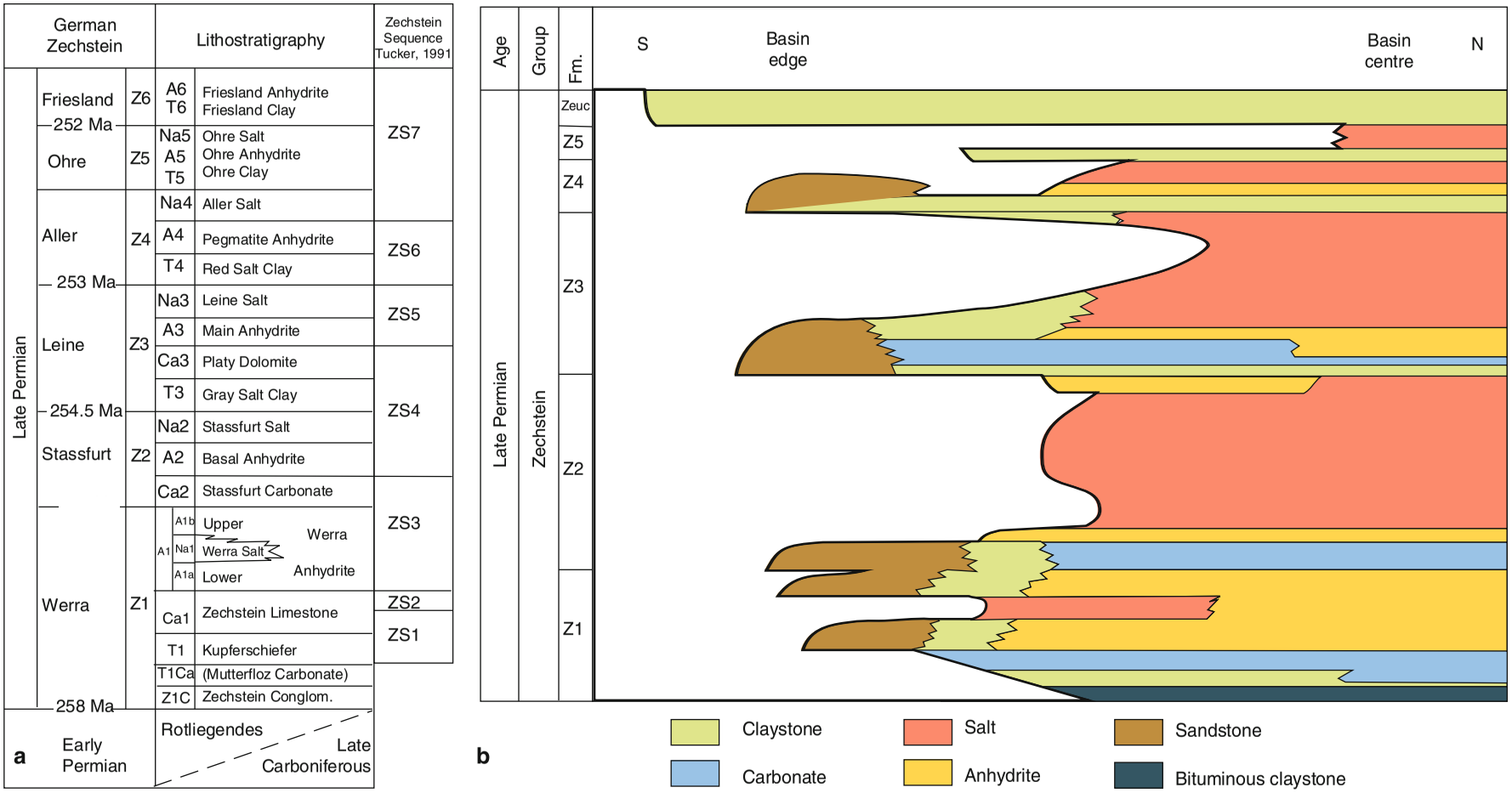

Fig. 5.64 Zechstein Stratigraphy. (**a**) Stratigraphy of the Zechstein Series in Germany (After Strohmenger et al. 1996a, b, and sources therein). Shown are the classic Zechstein cycles (Z1–Z6) and the Zechstein sequences (ZS1–ZS7) as proposed by Tucker (1991). (**b**) Classic lithostratigraphic subdivisions from the basin fringe to the basin centre (After Geluk 2000)

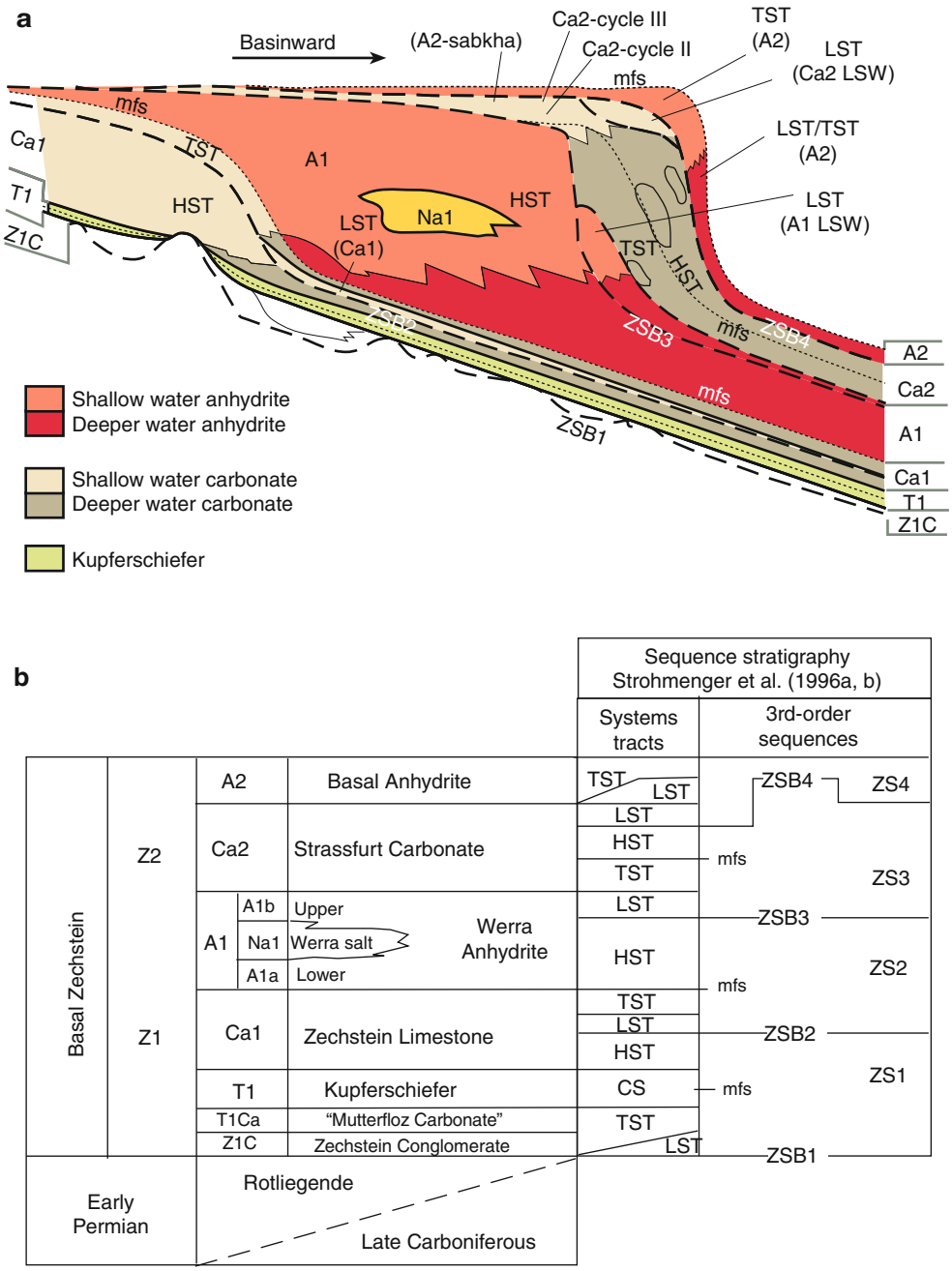

Fig. 5.65 Zechstein evaporites of northwestern Germany (After Strohmenger et al. 1996a, b and sources therein). (**a**) Schematic of basal Zechstein relationships on the southern margin of the Zechstein Basin. (**b**) Lithostratigraphy of basal Zechstein showing classic subdivision (Z1–Z2) and Strohmenger et al. (1996a) subdivision (ZS1–ZS4). *ZSB* Zechstein sequence boundary

halite and potash salts have been mined for centuries (Chaps. 6 and 11). Late Permian fill in the southern Zechstein Basin constitutes a classic basinwide deposit, with circumbasinal transitions from an evaporite platform about the basin edge into a deeper-water centre dominated by laminites (Figs. 5.65 and 5.66b).

Traditionally, the Zechstein Group is divided by its mineralogy into evaporitic cycles that reflect progressive evaporation from less saline to more saline salts. This method defined four main evaporite cycles (Z1–Z4) and rudimentary fifth and sixth cycles (Z1–Z6; Fig. 5.65a). An ideal Zechstein cycle starts with a transgressive nonevaporitic "shale," followed by carbonates and culminates in thick evaporites (mostly halite/anhydrite). Since most of the classic formation boundaries are picked at what are now considered by sequence stratigraphers to be maximum flooding surfaces (at base Z1: Coppershale or Kupferschiefer Member; base Z3: Grey Salt Clay Member; base Z4: Red Salt Clay Member), the lithostratigraphy of the Zechstein Group closely approaches that of units broken out using the concepts of genetic sequence stratigraphy (Fig. 5.64b; Geluk 2000). It means these basal transgressive units (mfs) provide a base for correlation of the main lithostratigraphic units. The lower three Zechstein evaporite cycles (Z1–Z3)

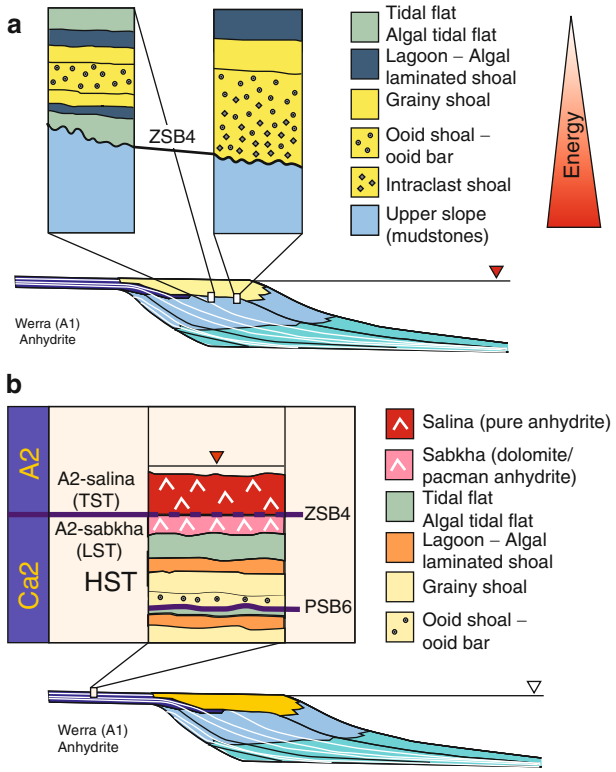

Fig. 5.66 Facies associations in Ca2 carbonate platform, Zechstein Basin, northwest Germany (After Leyrer et al. 2001). (**a**) Slope position (HST of ZS3 to TST of ZS4). (**b**) Platform position (HST of ZS3 to TST of ZS4)

are marine-fed basinwides. They contain evaporitic carbonates in their basal parts that indicate initial precipitation from brines with near normal marine salinities (Taylor 1990; Leyrer et al. 2001). The overlying anhydrites and salts in these cycles reflect the progressive evaporation of marine-fed salterns and deeper water brine lakes. The question is how do these mineralogies relate to changes in relative water depth in the Basin?

Classic transgressive/regressive cycles interpreted in the Z1 and z cycles have been related to glacio-eustatic sealevel fluctuations by Strohmenger et al. (1996a, b) and Leyrer et al. (2001). Earlier, Tucker (1991) published an alternative to the classic Zechstein stratigraphy based on what he interpreted as third order sequences (ZS1–ZS7). In it he correlates evaporites with sealevel lowstands (LSTs) and carbonates with sealevel highstands (TSTs and HSTs). Tucker's approach, in tying evaporites to lowstands, is opposite to that of the classic stratigraphic approach in the basin (pre-sequence stratigraphy) that tied evaporite deposits to highstands, but his approach is more realistic in terms of evaporite hydrology. His classification was criticised firstly by Goodall et al. (1992) on the basis he assumed external sealevel exerted a one-for-one control on evaporite mineralogy and position, and then by Strohmenger et al. (1996a) as his classification did not respect exposure surfaces and stratal geometries.

Strohmenger et al. (1996a, b) and Leyrer et al. (2001) went on to refine a sequence stratigraphic approach for the basal Zechstein (Z1 and Z2) using facies analysis, geometric relationships, stacking patterns and forward modelling based on core and seismic from the subsurface of northern Germany (Fig. 5.66). However, Strohmenger et al. (op. cits.) found that due to the poor quality of internal reflectors in the Zechstein sequence they could not use the usual approach of interpreting the major depositional units from seismic, then establishing a seismic stratigraphic model and then tying well data to seismic. Rather they had to first establish a geological model based on detailed stratigraphic analysis of core and outcrop. Then they developed a sequence stratigraphic framework and then interpreted and forward modelled the intra-Zechstein reflectors. Their analysis (Fig. 5.66) shows that reworked sandstones of the Weissliegend and/or the Zechstein conglomerate (Z1C) record the initial transgression of the Zechstein sea and overlie the Zechstein sequence boundary (ZSB1). Transgressive systems tract (TST) deposits of the first Zechstein sequence (ZS1) are also represented by deeper marine carbonates of the Mutterflöz (T1Ca). The overlying Kupferschiefer is interpreted as a condensed section (CS) indicating maximum flooding (mfs) of the first Zechstein sequence. The bulk of the shallow water Zechstein limestone (Ca1) is interpreted as a highstand systems tract (HST). It is separated from the thin uppermost part of the Zechstein Limestone by a karst horizon corresponding to an erosive sequence boundary (ZSB2).

Correlatable shallow water carbonates (oncolites and stromatolites) indicate lowstand systems tracts (LST) of the second Zechstein sequence (ZS2; Fig. 5.66). The uppermost part of the Zechstein Limestone represents the transgressive systems tract of the second Zechstein sequence (ZS2). According to Strohmenger et al. (1996a, b) there is no indication of a sequence boundary at the top of the Ca-1 platform carbonates (contrasts with Tucker 1991). They argue Ca1 carbonates, in a basinal position, show a deepening upward tendency toward the superimposed deposits of the A1 sulphates. They place the maximum flooding surface (mfs) of the second Zechstein sequence at the top of the Ca1 platform carbonates. The overlying anhydrites of the A-1 sulphate platform (Werra Anhydrite) are interpreted as predominantly highstand systems tract deposits displaying an erosive sequence boundary (ZSB3) at its top. This is in direct contradiction with Tucker (1991) and according to Strohmenger et al. (1996a, b) it is only in the slope and basinal environments that the A1 also represents lowstand wedge deposits of the third Zechstein sequence (ZS3).

In reality, each of the evaporite cycles is made up of a highly complicated stack of parasequences that sequence stratigraphers argue represent higher order sea-level fluctuations. In my opinion, climate-related intrabasinal autocyclicity is a more likely driving mechanism at the scale of the

parasequences. The contradiction underlies the difficulties in sequence stratigraphic analysis of evaporite deposits using models derived from geometries and 3rd order eustatic responses of marine systems. The terms highstand systems tract and lowstand systems tract are largely defined by whether the shelf of the basin that is under consideration is covered by water. There is no concept as yet in the sequence stratigraphic literature that an aggrading evaporite bed causes its overlying brine level to rise (autocyclic hydrologic feedback – the concept of evaporites "fill and spill").

Most Zechstein sequence stratigraphic interpretations of the Zechstein prior to 2000 assume a surface connection to the ocean at all times and that there were direct marine eustatic responses in brine base level. Using the late Miocene sediments of the Mediterranean as a template, we have already discussed the likely errors inherent in this assumption of hydrographic connection to the open ocean. In the marine realm we are talking about eustatic sealevel amplitudes of no more than a 100 or so metres in icehouse periods and less than decametres in greenhouse periods. There is an inherent assumption in classic sequence stratigraphy that in greenhouse and icehouse times the prime locus of sedimentation is near a marine shoreline, either on the shelf or just basinward of the shelf break (Type 2 and Type 1 boundaries). In an evaporite basin that is undergoing drawdown we are discussing an initial hydrographic isolation (mesohaline carbonates are considered to indicate the mfs by most sequence stratigraphers) quickly followed by a water level fall of more than 500–1,000 m and the onset of widespread evaporite precipitation. Any strandline in the system will likely have migrated hundreds of kilometres and be situated well out on the old continental slope at the onset of evaporite accumulation. These drawdown unconformities are likely correlate to salt deposition in basin sumps. Clearly, marine eustatic models do not apply. At hydrologic equilibrium (inflow = loss) the whole marine highstand shelf and slope, as well as part of the basin floor, is exposed. Water levels even in the deepest parts of the basin are mostly less than a few tens of metres and no more than 100 or 200 m. In this scenario the locus of maximum deposition is not tied to sediment supply from outside the basin (siliciclastics) or to any need for shallow waters atop a carbonate platform. The maximum locus of evaporite deposition is in the lowest part of the isolated depression in many drawdown basins with no surface connection to the ocean. This area is assumed to be deep water by sequence stratigraphers, but textures from the salts accumulating there are typically saltern or salt pan with local deeper water cumulates.

Defining the stratigraphic significance of sequence boundaries, such as the ZSB2, are more problematic in such hydrographically isolated drawdown scenario (Fig. 5.65). Strohmenger argues that the Ca1 carbonates, in basinal position, show a deepening upward tendency toward the superimposed deposits of the A1 sulphates. What he is observing is a gradational transition. The term deepening is probably too categorical in this scenario. If the basin is isolated so that thick gypsum/anhydrite can accumulate, then the brine level in the basin must be lowered with respect to the old shelf. The A1 profile above the ZSB2 sequence boundary is most likely subaqueous throughout, and is a "brining upward" profile. The sequence does not deepen upward, it is continuously subaqueous but brines upward as the regional water level is lowered. That is, the average annual salinity of the brine body is increasing up section and ongoing lowering of the brine level does not stop until an effective brine curtain/inflow equilibrium is established. The brine level is not reflecting marine eustasy but a hydrological/climatic balance.

Stacking patterns laid down in such scenarios are not well understood, but should not be forced to fit the classic paradigms of marine sequence stratigraphy. We are looking at an evaporite system that probably was at any time deeper or shallower depending on the vagaries of climate and tectonics and largely independent of eustasy. For example all we can say in terms of the A1-sulphates is that at no time during the deposition of the sulphate phase was the water deeper than a few hundred metres and probably was mostly less than tens of metres deep (Warren 1989; Kendall 1992). During the preceding carbonate platform phase the water body was obviously less saline and probably deeper on average than during sulphate deposition and tended toward meromictic rather then holomictic conditions.

Even in the carbonate horizons separating the main evaporite phases, thought by many to be marine, the drastic changes in intrabasinal base level create problems in creating a reliable sequence stratigraphic interpretation if interpreters have assumed a hydrographically connected sealevel in the basin. The Zechstein 2 Carbonate (Ca2) overlies the A1-Sulphate (Werra Anhydrite) and according to Strohmenger et al. (1996a, b) and Leyrer et al. (2001) encompasses transgressive systems tract as well as highstand systems tract deposits of Zechstein sequence ZS3. The maximum flooding of the Ca2 is correlated with the flooding of the A1-sulphate platform. Therefore, Ca2-platform carbonates (Main Dolomite) are dominated by shallow-water highstand deposits of the third Zechstein sequence (ZS3). Deposits of the Ca2 transgressive systems tract are coated-grain and composite-grain packstones/grainstones that contain reworked anhydrite clasts of the underlying Al. Leyrer et al. (2001) clearly demonstrate that the depositional facies, and hence the porosity distribution of the gas-bearing Ca-2 carbonates in the subsurface of northern Germany, are in large part controlled by high energy positions that reflect a shallow "sea" superimposed on the underlying evaporite topography. This topography was created prior to evaporitic carbonate

deposition by saltern to basin transitions in the underlying Werra (A1) Anhydrite.

An upper contact of the Ca2 carbonate is defined by the transition of shallow-water Ca2 carbonates into the overlying anhydrites of the A2 (Strohmenger et al. 1996a, b; Leyrer et al. 2001). The stratigraphic limit between the Ca2 and A2 is highly arbitrary and conventionally drawn in wells by the last up-section occurrence of bedded dolomite, but is gradational. Carbonates near the contact show typical Ca2 facies (e.g. algal-laminated coated-grain and composite-grain wackestones/packstones and algal bindstones) and are often intercalated with bedded anhydrites of the A2 (Fig. 5.66). Furthermore, according to Strohmenger et al. (op. cit.), the platform anhydrites of the A2 at this contact can display ghost structures of Ca2 facies. Leyrer (pers comm.) appropriately describes this as "Pacman" anhydrite, although it is perhaps more widely known as anhydritization. It indicates that the lower part of the A2 can be interpreted as sabkha/pan deposits (A2-sabkha) cannibalising the Ca2 carbonate and indicating the emergence of the Ca2 platform at the end of Ca2 time (Fig. 5.66b). Alternately, the widespread evaporites within and replacing A2 carbonates could be a form of reflux-driven cementation/replacement created during deposition of the overlying saltern anhydrite. In my opinion this contact is perhaps tied to the time when the ooid/grainstone shoal along the basin edge became sufficiently well developed to isolate the platform lagoon and so it converted to an evaporitic mudflat or saltern.

According to Strohmenger et al. (1996a, b) the fourth sequence boundary of the Basal Zechstein (ZSB4) occurs not on top of the Ca2 shallow-water carbonates, but somewhere within the A2-platform deposits, once again in contrast to the model of Tucker 1991. The lower part of the A2 (anhydritised or Pacman-style Ca2 facies) is interpreted as the time equivalent of shallow-water Ca2 carbonates that overlie deeper-marine upper slope carbonates in a basinward position, corresponding to the lowstand systems tract (lowstand wedge) of the fourth Zechstein sequence (ZS4; Fig. 5.66a). The uppermost part of the A2 (pure salina-type anhydrites on top of pacman anhydrites showing ghost structures of Ca2-platform facies) is thought to represent the transgressive systems tract of the fourth Zechstein sequence (ZS4; Fig. 5.66b). The relatively thick anhydrite accumulations of the A2 (approx. 100 m), which occur basinward of the Ca2 slope, are thought to represent both lowstand systems tract as well as transgressive systems tract deposits of the fourth Zechstein sequence (ZS4).

According to Strohmenger et al. (1996a, b) the basinward progradation of the third-order Basal Zechstein depositional sequences is forced by the tectono-eustatic, first- and second-order sealevel lowstand of the latest Permian. The cyclicity observed within the different systems tracts are thought to be caused by higher order sealevel fluctuations with durations of 0.08–0.5 Ma (fourth-order cycles), 0.03–0.08 Ma (fifth-order cycles) or 0.01–0.03 Ma (sixth-order cycles) and related to orbitally controlled Milankovitch cycles (Leyrer et al. 2001). Strohmenger et al. (1996a, b) go on to argue that the 0.1 and/or 0.4 Ma Milankovitch cycles indicate to high-amplitude sealevel fluctuations throughout the Late Permian. They draw analogies to small-scale sequences as described from the Yates Formation (United States, Permian Basin) by Borer and Harris (1991) and from the Wegener Halvø Formation (Jameson Land Basin, East Greenland) by Scholle et al. (1993).

In my opinion, there is a problem in comparing eustatic sealevel models, derived from platform evaporites of the Permian of Greenland and West Texas, to the basinwide drawndown platform evaporites of the Zechstein. Work by Strohmenger et al. (1996a, b), and Steinhoff and Strohmenger (1999) provide excellent core-based facies breakdowns of the evaporite stratigraphy and mapping of water level changes and hence predictors of porosity in units such as the Ca-2 carbonates, which are the major onshore gas reservoir in northern Germany (Leyrer et al. 2001). Where I have a problem is accepting the leap of faith in applying marine-derived Vail-curve age models (timing of cycle orders) to the brine level fluctuations that controlled the shelf to basin geometries of the Basal Zechstein. This approach ignores the need for complete lack of a surface connection with the ocean to deposit thick evaporite sequences. Furthermore, if we look to analogies in the marine-fed saline giants subbasins of the Messinian, then sedimentation rates used by Strohmenger et al. for sealevel ties to evaporite packages, such as the A1 sulphates, are much too slow. Thick basin-centre evaporites require particular conditions of tectonic isolation to form, when this does occur the evaporites are laid down very rapidly (5th and 6th order cycles), as they were in the Mediterranean. Since 2005, studies of Zechstein sequence stratigraphy have come to the conclusion that the layering/geometries in the Zechstein Series largely reflects variation basin bottom topography and autocyclic/climatic changes. Accordingly, when building sequence stratigraphic interpretations, authors\tend to focus on the rock textures and assume basin isolation from any eustatic marine connection (Becker and Bechstadt 2006; Slowakiewicz and Mikolajewski 2009). Outcomes tend to underline the difficulty in applying a single interpretive model at the scale of the Zechstein Basin. To quote Becker and Bechstadt (2006, p. 1116)

"Sequence stratigraphic interpretation of isolated evaporite basins is challenging, given that physico-chemical conditions influence sedimentation rates and evaporite deposits geometries. Brine fluctuations, often independent from sealevel changes, create and destroy accommodation space. Sequence stratigraphic correlation with the Southern Zechstein Basin based on shallowing-upward parasequences reflects related water/brine level fluctuations in the two

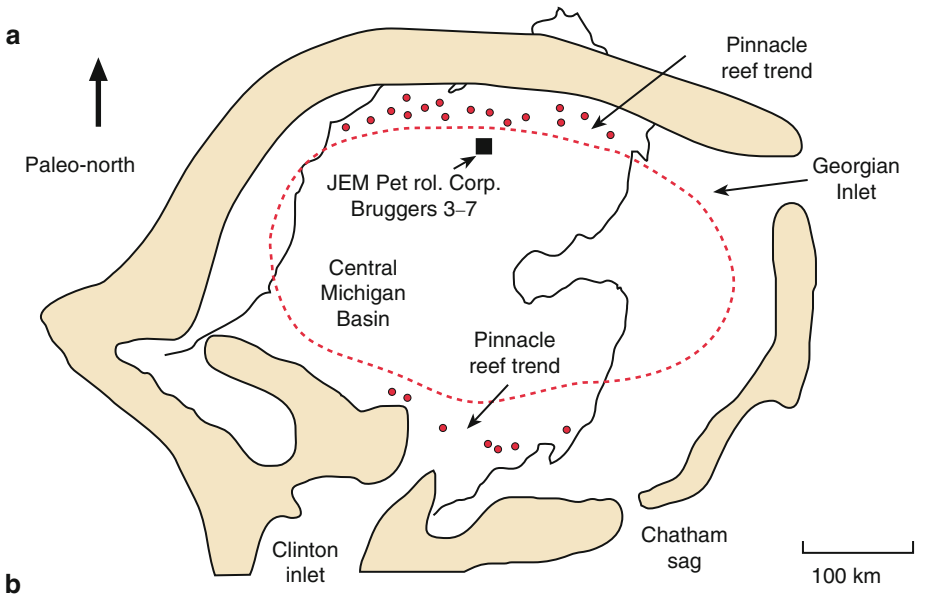

b

Silurian stages		Depositional setting			
North America	European	Group	Shelf platform and individual pinnacles	Interpinnacle and basinal areas	Group
Cayugan	Pridolian	Salina	Bass Islands Fm. Salina units B through F (see Fig. 5.50) A-2 Carbonate A-2 Evaporite		Salina
– –?– –	Ludlovian		Algal stroms (und.)	A-1 Carbonate	
	– – -?– –		Exposed	A-1 Evaporite	
Niagaran	Wenlockian	Niagara	Guelph Fm. (Brown Niagaran)	Cain Fm.	Niagara
			Lockport Fm.	(Gray Niagaran) (White Niagaran)	
	Llandoverian		Clinton Fm.	(Manistque Fm.)	

Fig. 5.67 Silurian evaporites in the Michigan Basin, USA. (**a**) Location of Salina Group, the evaporite-filled central Michigan Basin is identified by the dotted oval, and the evaporite-sealed northern and southern pinnacle reef trends are shown by the larger dots. Also shown is the position of the JEM Petroleum Corporation Bruggers well, Missaukee County, Michigan. (**b**) Stratigraphic chart of Silurian formations in the Michigan Basin (After Gill 1979)

regions. Correlation with the Southern Zechstein Basin results in a reinterpretation and redefinition of the cyclicity of this basin: in contrast to other cyclostratigraphic models assuming deepening-upward, the cycles in the Southern Zechstein and the Hessian Basins are both interpreted here as shallowing-upward successions."

Sequence Stratigraphy in the Silurian Salina Group of the Michigan Basin

The Michigan basin in the Late Silurian (greenhouse climate mode) was a roughly circular intracratonic sag basin, approximately 400 km in diameter and fringed by reef pinnacles passing updip into an extensive rimmed platform (Fig. 5.67a; Brennan and Lowenstein 2002). The reefs are encased in salts of the Salina Group. When Salina Group evaporite deposition commenced some 423 Ma the palaeolatitude was approximately 26°S, and approximately 20°S by 417 Ma, when Salina Group deposition ended (Brennan and Lowenstein 2002). Prior to its hydrographic isolation, marine waters entered from the southern Kokomo Sea, via the Clinton Inlet, and from the northern Moose River Basin via the Georgian Inlet (Briggs et al. 1980). A relative sea-level drop in the late Wenlockian produced restriction and isolated the Michigan Basin from the Silurian ocean;

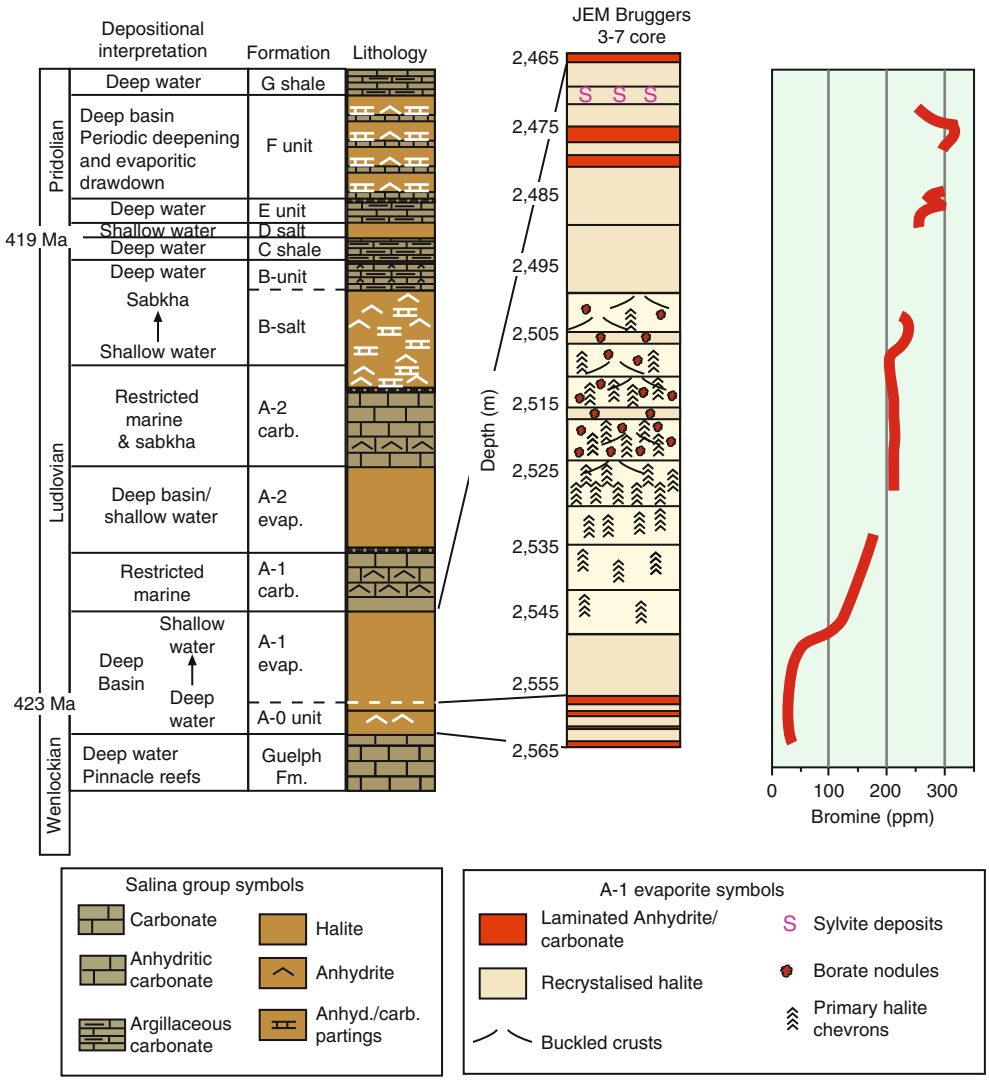

Fig. 5.68 Stratigraphy of the Salina Group (*left column*) and detailed facies of A-0 and A-1 Evaporites in Bruggers 3–7 core (*right column*), Michigan Basin (Upper Silurian). The thicknesses of the Salina Group Formations are not to scale. The depositional interpretations of the Salina Group are primarily from Leibold (1992) (After Brennan and Lowenstein 2002)

throughout, the earth was in greenhouse climate mode (Dellwig 1955; Dellwig and Evans 1969). The deep-water A-0 unit (calcite–anhydrite–halite), the first deposit associated with this sealevel drop, is conformably overlain by the A-1 Evaporite and defines the transition into mesohaline conditions as the surface connection to the open ocean was lost (Fig. 5.68; Dellwig 1955; Nurmi and Friedman 1977; Gill 1977; Briggs et al. 1980; Cercone 1988; Leibold and Howell 1991).

Middle Silurian pinnacle reef reservoirs in the Michigan Basin are isolated stromatoporoid/coral-crinoid buildups, which are encased and sealed by a combination of Upper Silurian halite, anhydrite and fine-grained carbonate (Figs. 5.66 and 5.67). Reef pinnacles form two hydrocarbon belts some 16–24 km (10–15 miles) wide that extend basinward from the steep inner face of an extensive, but nonproductive, barrier reef (Chap. 10). The basinal equivalent of the reefs is a thin carbonate some 18–24 m (60–80 ft) thick. The reef/bank rimmed platform is dolomitised, as are most of the pinnacles, although a few of the more basinal pinnacles are still limestone (Sears and Lucia 1979, 1980). Pinnacles are capped by an erosional unconformity and reef growth had ceased well before the basinwide drawdown events that deposited the encasing evaporite cycles (Fig. 5.67a; Gill 1985). Drawdown created the karst horizon that caps the marine reef sediments of the Guelph Formation and immediately underlies the stromatolitic capstones formed during deposition of the A-1 evaporitic carbonates (Mesolella et al. 1974). During drawdown the pinnacles formed topographic highs and were sites of marine groundwater escape (pisolitic/stromatolitic seepage facies) until they were enveloped in aggrading salts of the A-2 cycle.

The sealing evaporites of the Lower Salina Group were some of the first thick sequences of salt to be interpreted as containing textures of more than one depositional setting. The earliest depositional interpretations of these salts were as deepwater deposits (Dellwig 1955; Dellwig and Evans 1969). Nurmi and Friedman (1977) challenged many of Dellwig's conclusions. They interpreted much of the halite as having formed as stacked halite crusts precipitated beneath shallow brine sheets subject to periodic drying. The arguments of Nurmi and Friedman were rooted strongly in processes observed in Holocene salt crusts. A shallow to ephemeral water model came to dominate subsequent interpretations and have been reinforced by subsequent detailed geochemical studies (Fig. 5.52; Brennan and Lowenstein 2002).

Thus, the evaporites imply episodes of evaporative drawdown and that there was subaerial exposure of the reef crests prior to their encasement in salt, via a process of "fill and spill." The complex rapid rise and fall of the brine level over vertical distance of several tens of metres during the accumulation of the Salina Group drove ongoing alteration, dolomitisation and evaporite plugging, not just of the Salina Group but also in the Niagaran, especially in those pinnacles sitting below zones where thick sequences of evaporites were accumulating.

Detailed stratigraphic analysis of the evaporites and evaporitic carbonates in the vicinity of producing pinnacles clearly define the complexity of sequences accumulating under a system of basinwide evaporitic drawdown. Using more than 350 wells and numerous cores, Leibold (1992) and Howell and Leibold III (1992), defined four composite sequences: Niagaran, A-1 Unit, A-2 Unit, and the B Unit (Fig. 5.67). The Niagara Group carbonates comprise a dominantly intrabasinal highstand composite sequence that was deposited on a pre-existing carbonate ramp and was interrupted by at least one major drawdown event. Numerous Type 1 unconformities on the carbonate platform margin were recognised by Leibold (op. cit.) and related to evaporative drawdown events. Thus, the Niagaran is a composite sequence made up of two sequences separated by an unconformity. The lower sequence consists of three parasequence sets: aggradational ("White Niagaran" ramp), transgressive ("Gray Niagaran"), and progradational ("Brown Niagaran"). The Brown Niagaran includes a distinct stromatoporoid shelf-bank margin and a zone of pinnacle reef growth. Biostratigraphic, lithostratigraphic and isotopic evidence indicates Upper Niagaran water depths in the basin exceeded 250 m prior to drawdown. The Brown Niagaran parasequence set is interrupted by a drawdown unconformity, represented by the subaerial exposure surface mentioned earlier. It extends below the shelf margin into the inter-pinnacle reef areas and defines a type 1 boundary (Fig. 5.67).

A second drawdown event ended Niagaran deposition and initiated the A-1 Unit as a thick (140 m) lowstand evaporite wedge in the basin (Figs. 5.67 and 5.68). Deposition of the halitedominated A-1 Evaporite occurred in an initially somewhat deeper brine that progressively shallowed. The JEM Bruggers 3–7 core, Missaukee County, Michigan completely cored the A-1 evaporite (Fig. 5.68; Leibold 1992). The basal 10 m of the A-1 Evaporite is composed of alternating layers of coarse, clear halite (50–150 mm thick) and anhydrite (30–100 mm thick). It was interpreted as a possibly deeper water unit showing widespread halite recrystallisation, but models of meshwork halite (Dead Sea holomictic/meromictic analogue) were not available in the early 1990s. This unit is overlain by 25 m of chevron-rich halite, the upper 5 m contains bedding planes dipping up to 40°, which have been interpreted by Leibold (op cit.) as buckled pressure-ridged pan halite crusts, formed during subaerial exposure (Leibold 1992). This is overlain by the "mid-basin potash facies", which is up to 60 m thick and composed of halite and sylvite elsewhere in the Michigan Basin (Leibold 1992). The potash facies in the JEM Bruggers core does not contain bedded sylvite; however, primary fluid inclusions in the halite do contain daughter crystals of sylvite, carnallite, and tachyhydrite (Leibold 1992). These potash facies also contain borate nodules and buckled salt crust polygons indicating salinepan deposition with periodic basin desiccation. The mid-basin potash facies is overlain by halite that has been pervasively recrystallised (Leibold 1992) (Fig. 5.69).

Leibold (1992) and Raup and Hite (1993) analysed bromide from bulk halite samples in the JEM Bruggers 3–7 core and showed that coarse halite and chevron-rich facies at the bottom of the A-1 Evaporite display a systematic upsection increase in Br concentration, ranging from 25 to 200 ppm. This type of bromine profile, along with the upward increase in the density of chevrons, and buckled crust polygons towards the top of the chevron-rich facies indicate that this lowermost section of the A-1 halite formed by the progressive evaporation of a large shallow body of brine, which dried out at the top of the unit. In contrast, halite from the mid-basin potash facies does not exhibit any systematic increase in the Br concentrations. Instead, the Br is relatively high (210 ppm) throughout, which suggests these halites did not form strictly by the progressive evaporation of a large body of Silurian seawater (Fig. 5.68). The A-1 Evaporite is overlain by the A-1 Carbonate, which signifies a higher volume of marine brine in the Michigan Basin, this could indicate a more humid climate or a possible renewed surface connection to the Silurian ocean. The A-1 Carbonate is overlain by the A-2 Evaporite, which indicates a second period of increased aridity or the

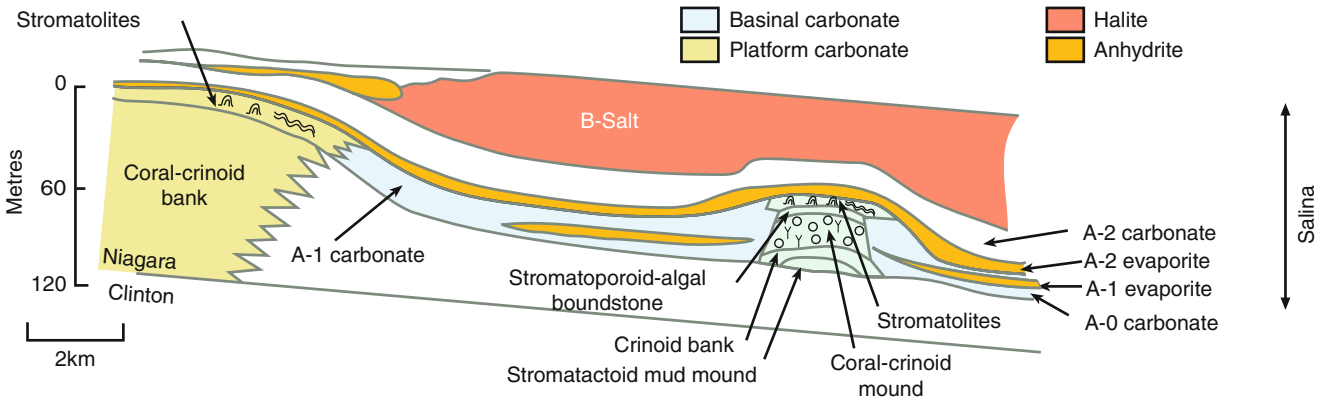

Fig. 5.69 Schematic showing facies relationships of a shelf to basin profile in the Silurian of the southern Michigan Basin (In part after Sarg 2001)

return to isolation of the Michigan Basin from the Silurian ocean. The A-2 carbonate, a gray, nonfossiliferous mudstone, conformably overlies the A-2 Evaporite. The B Evaporite conformably overlies the A-2 Carbonate and is composed of two units, the B-Salt and the overlying B Unit. The B-Salt deposits consist of halite interbedded with anhydrite and dolomite partings (Leibold 1992), which likely formed within a shallow isolated central basin. The B-Unit is interpreted by Leibold (op, cit.) as a deepwater, anhydrite-rich, argillaceous carbonate, which marks the beginning of a regional transgression. The C Shale, D-Salt, and the E-Unit possibly indicate alternating incursions of seawater and isolation and concentration of the basin waters (Droste and Shaver 1985) or more likely they are responses to climatically induced transitions from meromictic to holomictic basin waters.

The mid-Pridolian F-Unit is the uppermost evaporite formation of the Salina Group and comprises six separate halite units, F-1 to F-6, that are separated by shales, dolomites, and anhydrites (Sonnenfeld and Al-Asam 1991). The lowermost F-1-Salt is composed of continuous beds of chevron-rich halite separated by anhydrite partings (Dellwig and Evans 1969) and resembles similar facies in the A-1 Evaporite. Bromide concentrations increase systematically upsection in the halites of the F-1-Salt (Das et al. 1990), consistent with the profile expected for evaporation of a large body of seawater-fed brine. Sulphur and strontium isotopic analyses of the anhydrite in the F-1 salt are also consistent with Silurian seawater values (Das et al. 1990).

The thickness, orientation and mineralogical zonation of marginal evaporite wedges in the basal A-1 Evaporite overlying the Niagaran sequence required initial minimum brine depths of 20 m and so imply wind and water currents influenced evaporite deposition (Sarg 2001). Overlying lower A-1 Evaporite salts were deposited in shallower brines, less that a metre or two deep, as indicated by chevron-rich growth-aligned halite pan textures. Middle and upper A-1 evaporite lithofacies contain evidence of alternating very shallow brine and subaerial depositional conditions (Leibold 1992). The Middle A-1 lithofacies are sylvite- and borate-rich, with sylvite beds present only in the central Michigan Basin (Fig. 5.67a). Upper A-1 evaporite lithofacies, which Sarg (2001) calls transgressive (I prefer fill and spill), are dominated by stacked, saltpan morphologies. The brine level at this time was well below sealevel and the basin had no surface connection to the open ocean.

Periodic seawater flooding or climatically-induced freshening then renewed carbonate deposition as the A-1 carbonate was deposited across the basin and platform region (Leibold, op. cit.). The A-1 composite sequence was terminated by further drawdown, resulting in a second thick lowstand evaporite wedge (A-2 halite). Reflooding and/or climatically induced freshening initiated multiple stacked A-2 carbonate aggradational sequences, separated by several drawdown unconformities. The B Unit is a composite of carbonate/evaporite sequences, each consisting of an aggradational carbonate parasequence and a lowstand evaporite wedge. These sequences mark the final filling of the basinal depression created during Niagaran carbonate deposition. Thus the A-1 and A-2 units of the Salina Group each comprise a lowstand relative to external sealevel, with each evaporite sequence set overlain by a relative highstand carbonate sequence set. Both composite sequences are punctuated by several, widely-correlatable drawdown events. The B-Evaporite is dominantly a "lowstand" composite sequence consisting of stacked, shallowing-upward evaporite cycles.

Sequence stratigraphic interpretation in the Michigan Basin sequence underscores the difficulties in interpreting an isolated intracratonic basin using unconformity/bounding-surface terminology tied to a set of marine sealevel implications. It is very hard to do this reliably in a basin that lacked a marine connection for most of its evaporite history and in a hydrological situation where intrabasinal water level fluctua-

tions were not necessarily related to extrabasinal eustatic changes. Recognising regional unconformities in core and seismic is the key to any reliable sequence stratigraphic interpretations in this situation. Unfortunately unconformities are numerous in drawdown sequences and correlations of supposed regional unconformities from basin edge to basin centre are difficult. Often it is done based on marine eustatic assumptions and this of course leads to circular arguments in interpretations of eustasy based on a sequence stratigraphic interpretation.

Sarg (2001; his Table 1) lists the Michigan Basin as a type example of a third-order basin centre fill (10–100 m thick) with an onlap basin margin and he places it in the same classification category as the Z1–Z4 units in the Zechstein Basin. A fact to remember when attempting unconformity-based correlation and sequence stratigraphic interpretation is that evaporite aggradation rates are so rapid in a basinwide systems that the basin fill quickly aggrades to the intrabasin hydrological equilibrium (time frames of up to 1–2 km of fill in a few hundred thousand years). It means that in the 1–7 million year long history of any evaporite-filled basin there were long periods, post the attainment of hydrological equilibrium, when not much was happening depositionally. That is, based on the hydrologies detailed in Chaps. 2, 3 and 4 and the chronology of the Messinian in the Mediterranean, we know that evaporite basins fill rapidly with stacks of 5th and 6th order cycles. Using salt thickness to divide evaporite successions into second order (100–1,000 m) versus third order (10–100 m) cycles is an irrelevancy that comes from applying assumptions inherent in a marine eustatic terminology.

Thick-bedded marine-fed evaporites are intrabasinal responses to hydrological evolution and should not be tied to any marine eustatic implication. Marine-fed and the associated concept of hydrological equilibrium (drawdown) are not the same as assuming marine salts fill the basin to sealevel. When 1–2 km thick halite beds were accumulating in the Messinian in Mediterranean basin, the saltpan surface never came within a kilometre of sealevel in the adjacent Atlantic.

Sarg (2001) also argues that the coral-crinoid growth occurred in Michigan Basin pinnacles in a marine reconnection episode, following the A1 evaporite drawdown stage. He equates subsequent coral-crinoid growth to ongoing growth in the Niagaran Platform via a set of regional unconformities. Others have difficulty with this correlation and see stenohaline crinoidcoral deposition ceasing throughout the basin at the end of the Niagaran with subsequent mud mound growth occurring in mesohaline marine-seepage fed conditions. This group of workers choose a different set of unconformity correlations. They see the euryhaline stromatolite/stromatoporoid biomes as the major contributors to mound growth once the Michigan Basin lost its surface connection to the ocean.

This debate of a possible marine surface connection post-A1 carbonate and a definition of the A-0 carbonate, first detailed by Mesolella et al. (1974) in three models of pinnacle-evaporite inter-relationships, continues today. What we have learnt since the early 1970s is that all of the salts in the Michigan basin were deposited in shallow drawndown waters. At the time of evaporite deposition the basin's shelf margin and the crests of the pinnacle reefs were subaerially exposed, the tops of the inactive pinnacles acted as spring mound feeds to the surrounding lows characterised by a halo of anhydritic mudflats passing further out in to halite pans. Anhydrite is present both as a sabkha nodules and as widespread diagenetic cements within marine carbonate hosts. The possibility of widespread early burial anhydrite in Niagaran carbonate is something largely ignored by sequence stratigraphers working in pinnacles in the Michigan Basin, who tend to see anhydrite as a mostly marine mudflat facies not a seepage facies. With the possible exception of the pinnacle crests, no widespread open marine sediments accumulated in the Central Michigan Basin, even at times of freshened (but still evaporitic) carbonate accumulation, such as the A1 and A2 carbonates.

Jurassic Louann Salt, Gulf of Mexico'

Unlike the previous three examples, the Louann Salt has not been sampled or studied as a bedded unit. It has been mined, but only in the crest of diapirs in various onshore localities in the northern Gulf of Mexico. It has been extensively imaged seismically by the oil industry, and the intensity and density of this imaging is what makes the Louann unique in that it is the best documented examples for the study of the evolution of flowing salt features on a passive margin (Chaps. 6 and 10). In this section we shall look at the Louann as an example of the inherent complexity of a basinwide salt bed deposited in a subsealevel rift and consequently subject to the twin deformation mechanisms of gravity gliding and differential loading.

Because of pervasive halokinesis throughout its known extent, little is known of its original depositional layering and so its stratigraphy is typically given as a massive salt unit called the Louann Salt and further subdivisions are not attempted (Fig. 5.70). Anhydrite is present dispersed in the salt mass as are, locally, various potash and borate minerals. The distribution of these bitterns and whether they define particular isolated subbasins with the Louann Salt Province is not known. Seismic shows the current distribution of the Louann Salt is broken up into a series of basins and sub-basins separated by highs where salt is no longer present (Fig. 5.71).

Hudec et al. (2013a, b) use "Gulf of Mexico salt basin" to refer collectively to all Callovian salt basins and sub basins in the Gulf of Mexico (Fig. 5.71). As in many passive-margin salt basins, the main salt mass in the Gulf of Mexico currently lies in two pieces on the opposite sides of an ocean basin. The northern Gulf of Mexico salt basin is typically called the "Louann salt basin." The southern Gulf of Mexico salt basin has many different names, Hudec et al. (2013a) prefer "Isthmian salt basin" (*Cuenca Salina del Istmo*). The Louann salt basin consists of the central Louann salt basin

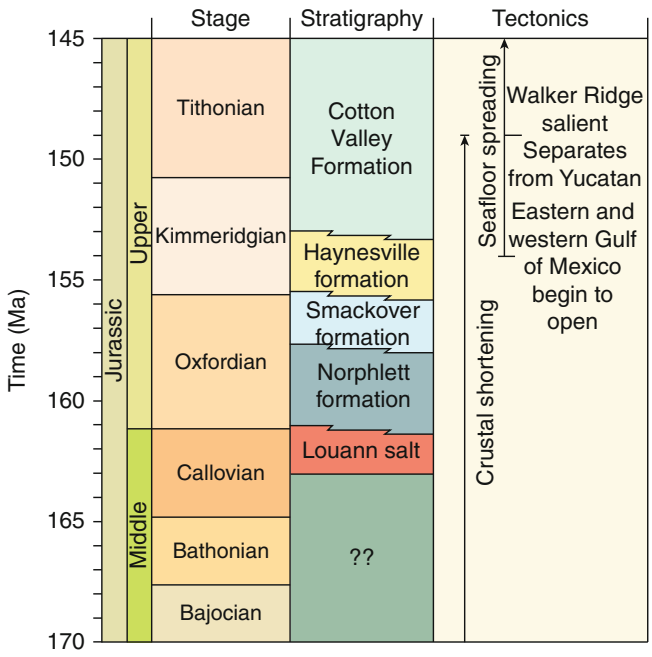

Fig. 5.70 Jurassic stratigraphy in the Gulf of Mexico

and two sets of interior basins around its periphery (Fig. 5.71). On the north, the Toledo Bend flexure separates the central Louann salt basin from the Mississippi, North Louisiana, and East Texas interior salt basins.

The paucity of salt domes and growth faults above the Toledo Bend flexure suggests that salt is thin or absent there, which, in turn, indicates a likely structural high during salt deposition. Anderson (1979) inferred that the flexure localized the Louisiana shelf edge throughout most of the Cretaceous. To the west, the Sabinas and La Popa interior salt basins and the Monterrey salt basin (part of the Monterrey trough) are separated from the central Louann salt basin by the Burro-Salado and Tamaulipas arches. The northwestern end of the Sabinas salt basin connects to the border rift system of Dickinson and Lawton (2001), but most of this rift does not contain significant Callovian salt.

Hudec et al. (2013a) divide the Isthmian salt basin into two subbasins, with thinner salt separating them across a basement ridge extending to the northwest from the northwestern corner of the Yucatan platform (Fig. 5.71). The Campeche salt basin lies southwest of this ridge, in the Bay of Campeche and adjacent onshore areas. The Yucatan salt basin is northeast of the ridge, in the offshore of Yucatan state.

The Proto Gulf of Mexico Basin began forming in Triassic rifting between the Yucatan microplate and the North American plate (Figs. 5.70 and 5.71). It was part of the disassembly of the Pangaean supercontinent. The advent of plate tectonic theory led to the theory, still popular today, that the main salt mass was deposited as a single thick body and was then split into two main bodies via the emplacement of oceanic crust. Until now, how these two main masses beneath the deep waters of the Gulf of Mexico relate to salt in the various peripheral basins was not well defined. Based on a new integration of seismic across the Gulf of Mexico Hudec et al. argue the system was akin to that of the Mediterranean and characterised by a main drawdown stage when the bulk of the Louann salt was deposited in a more central hydrographically isolated sump. In contrast, the timing of halite precipitation in the various marginal basins occurred in peripheral or marginal basins when water level in the central basin was higher. Also still somewhat contentious is the timing of salt deposition relative to the emplacement of ocean crust (sea floor spreading).

Utilising a synthesis of existing seismic across the Gulf of Mexico Hudec et al. (2013a, b), construct the following scenario for the Jurassic plate-tectonic evolution of the Gulf of Mexico basin and discuss how this evolution influenced Jurassic salt tectonics. Four interpretations, some based on new data, constrain their hypothesis. First, the limit of normal oceanic crust (LOC) coincides with a landward-dipping basement ramp near the seaward end of the salt basin, which has been mapped on seismic data. Second, the deep salt in the deep-water Gulf of Mexico can be separated into various salt provinces on the basis of position with respect to this ramp. Third, paleodepths in the postsalt sequence indicate that salt filled the Gulf of Mexico salt basin to near sea level. Fourth, seismic data show that postsalt sediments in the central Louann and the Yucatan salt basins exhibit large magnitudes of Late Jurassic salt-detached extension, which is not balanced by equivalent salt-detached shortening.

In their hypothesis, Callovian salt was deposited in preexisting crustal depressions on hyperextended continental and transitional crust. After salt deposition ended, rifting continued for another 7–12 m.y. before sea-floor spreading began (Fig. 5.72a–d). During this phase of postsalt crustal stretching, the salt and its overburden were extended by 100–250 km, depending on location. Sea-floor spreading divided the northern Gulf of Mexico into two segments, separated by the northwest-trending Brazos transform. The eastern segment opened from east to west, leaving the Walker Ridge salient in the centre of the basin as the final area to break apart. In some areas, salt flowed seaward onto new oceanic crust, first concordantly over the basement as a parautochthonous province, then climbing up over stratigraphically younger strata as an allochthonous province (Fig. 5.72e, f).

This scenario meshes well with the model of post rift basinwide deposition summarised in Figs. 5.72 and 5.73. The postrift subsealevel drawdown setting, where the salt mass is flowing basinward and is not broken up by rift-related faults in a set of fault-bound grabens facilitates a strong lateral or allochthonous component to the basin halokinesis (Warren 2010). As well as geometries in the Gulf of Mexico it also explains the allochthonous deep salt geometries of other larger circum-Atlantic Aptian salt basins such as the Santos and Angolan salt basins.

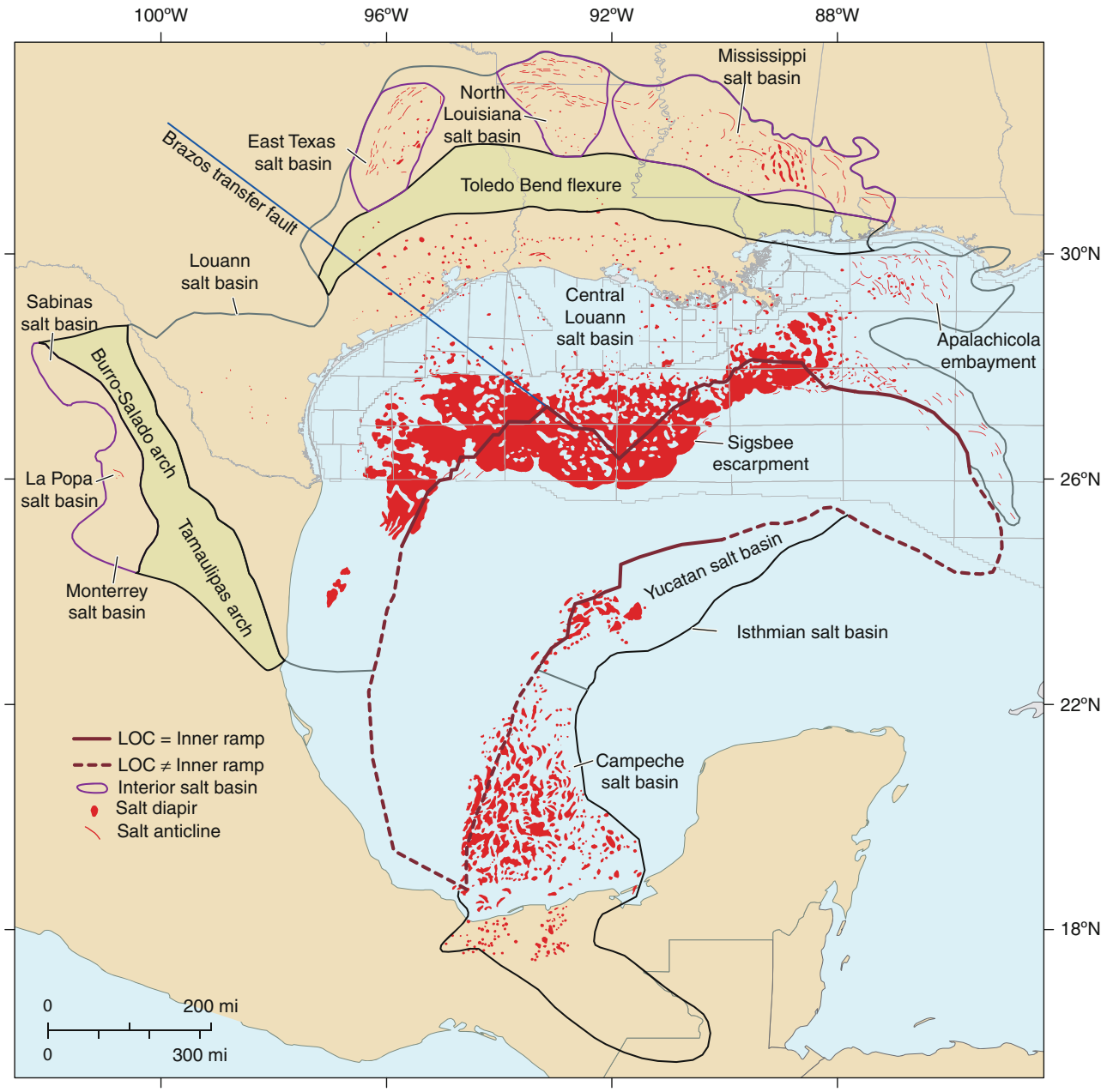

Fig. 5.71 Salt basins in the Gulf of Mexico region, showing locations of salt structures and interpreted limit of normal oceanic crust in the basin (*LOC* limit of oceanic crust; after Hudec et al. 2013a)

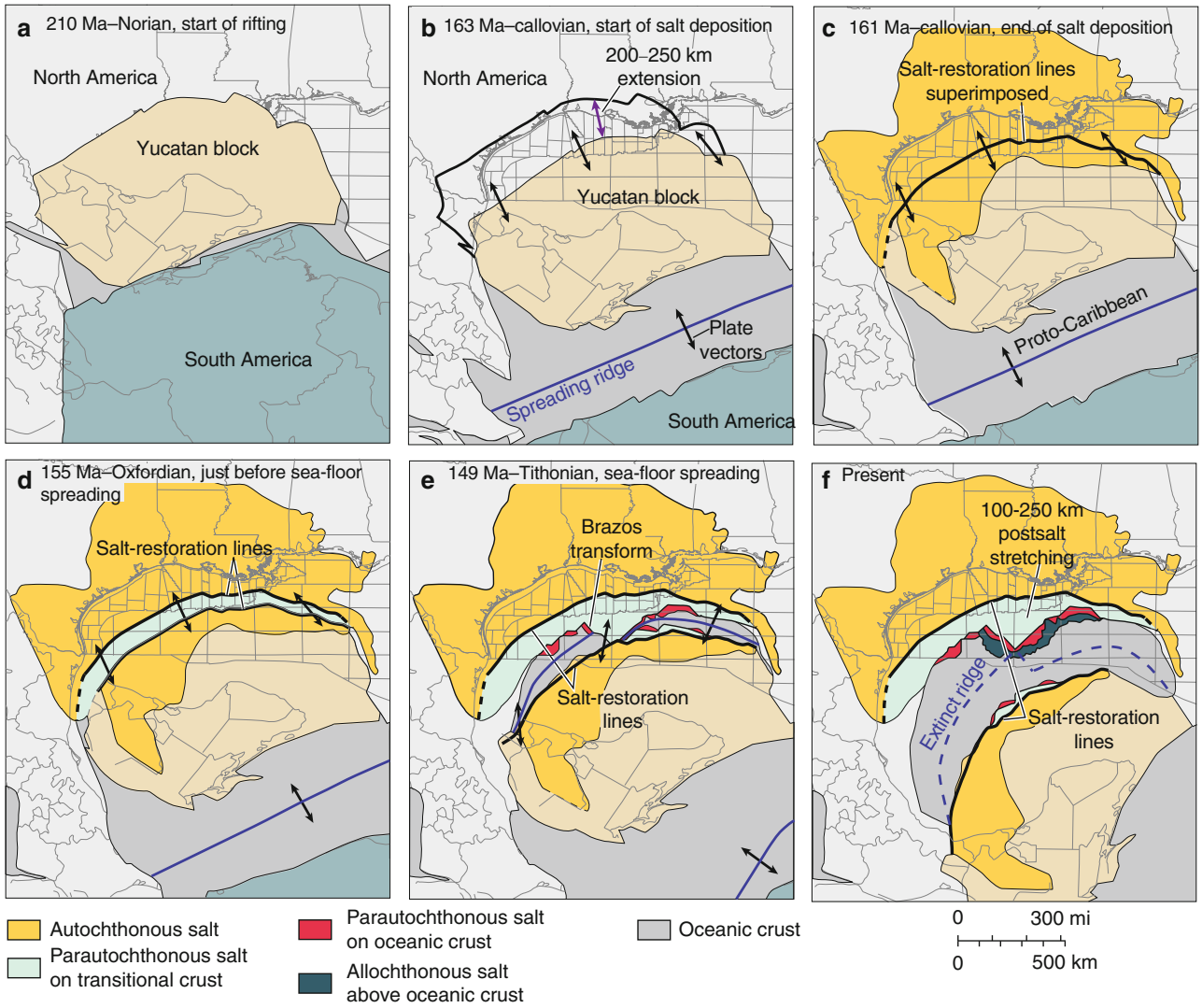

Fig. 5.72 Sequential plate restoration (After Hudec et al. 2013b)

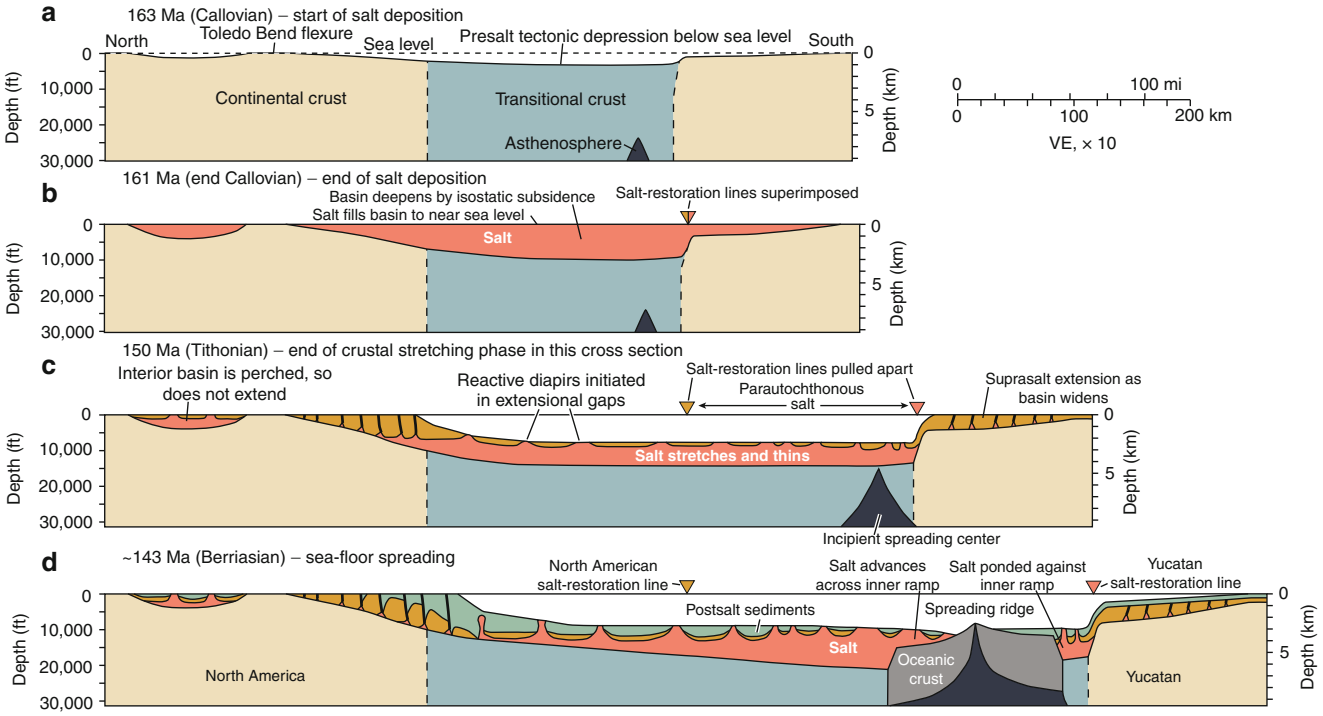

Fig. 5.73 Schematic section restoration of basin evolution, emphasizing salt and its overburden. Internal structures in the crust are not shown. Line of section passes through the Walker Ridge salient, where sea-floor spreading began relatively late (After Hudec et al. 2013b)

Summary

Modern and ancient evaporite basins can deposit kilometre-thick sequences in less than 300,000 years. Such infills only occur at times of complete basin isolation when there is no surface connection to the world's oceans. Once we realize that thick evaporite accumulations require subsealevel depressions to have a stable longterm brine curtain ($\approx 10^5$–10^6 years) in order to accumulate to substantial thicknesses and lateral extents, we reach an understanding of why the present is not a good time to study the scale and diversity of possible evaporite settings. High amplitude, high frequency 4th-order sealevel oscillations of our current "icehouse" climate do not allow the set up of stable brine curtains in present-day continental platforms. Nor are there suitable subsealevel marine-seepage rift or collision belts where conditions are suitable for the creation of marine-fed basinwide drawdown deposits. The last such basinwide event occurred in the Mediterranean some 5.5 Ma. Thick stable brine curtains are today only found in continental settings.

Sequence stratigraphic analysis must be tied to a subdivision of ancient evaporites into three depositional styles, continental lacustrine, marine platform and marine basinwide. All three are suitable for high-frequency seismic interpretation and the unique nature of salt mean it is easily recognised and traced in a seismic section. The hydrology needed to form a salt bed also makes it a close approximation to a time line in the basin architecture. But, of the three styles, a marine eustatic interpretation tied to sealevel is only possible in a marine platform evaporite succession. Once halokinesis occurs, the internal reflectors indicative of depositional layers and hence sequence boundaries are lost.

So, to return to the notion of strict uniformitarianism in the study of evaporites, with which we started this chapter, as Confucius once said: "Study the past, if you would define the future."

Flowing Salt: Halokinesis

6

Introduction

Many of the world's larger oil and gas fields occur in halokinetically-influenced structures across many of the world's salt basins (e.g. Campos Basin, Gulf of Mexico, North Sea, Lower Congo Basin, Santos Basin and Zagros). An understanding of the physics of salt and how salt flow influences tectonics and sedimentation is therefore critical to effective and efficient petroleum exploration (Chap. 10). And, I would argue, is also critical to a significant portion of the world's base and precious metal occurrences (see Chaps. 15 and 16). Halokinetic salt is also a resource[1] in salt, potash, gypsum and nitrate extraction (Chaps. 11 and 12). Salt dome salt has the potential to be employed as a repository for radioactive and other wastes, and can act as a highly efficient seal to sequestered CO_2 (Chap. 13).

Outcrops of flowing salt are rare because of halite's high solubility, but do occur in a number of arid settings and some are spectacular. In Iran, flowing glaciers of salt (namakiers are salt glaciers; *namak* is Farsi for salt) rise up to 400 m above the surrounding Zagros landscape. Diapiric salt also outcrops in the Andes, the Canadian Arctic, in Cardona in Spain, and subcrops near Hallestat/Dachstein in Austria and along the banks of the Nam Theun River in Laos. Flowing salt produces some of the most complex and visually impressive low-temperature geological deformation to be seen on the earth's surface. Work in numerous salt provinces over the past 50 years has now developed a series of saltflow models that are predictive and quantitative (Fig. 6.1a, b).

Salt tectonics (syn. halotectonics and halokinesis) is a general term that encompasses notions of lateral and vertical salt flow, trans-stratal salt movement, salt pillowing and diapirism. It refers to tectonic deformation involving halite or other evaporites as a substratum or source layer. Concepts of salt tectonics have undergone a major revision in the last 30 years to now encompass notions of strong lateral intra-stratal flow, as well as the long accepted vertical flow. This over-arching revision in our understanding is based mainly on advances in 3D seismic acquisition and processing, especially 3D prestack depth imaging, and the realisation that salt tectonics is best modelled by considering a salt bed as a pressurized fluid layer overlain by brittle sediment (Fig. 6.2; Hodgkins and O'Brien 1994; Ratcliff and Weber 1997).

Salt tectonics can be summarised in two simple geological principles. First, differential loading drives salt tectonics; this make halokinesis a much more passive process than had been believed. Second, salt is a very weak and incompetent layer in the subsurface; its lateral flow and sliding carries along its overburden in extension and acts as a décollement in compression. Salt sheets, tongues, and allochthonous nappes are major subhorizontal components of the salt tectonic realm (Fig. 6.1). Like any less competent layer in extension salt undergoes boudinage and drives fracturing in its more brittle overburden.

The word diapir originally comes from the Greek *diaperainen*, meaning "to pierce-through" and was coined by L. Mrazek in 1907 to describe salt features of the Romanian Alps. It was defined at a time when salt diapir emplacement was considered to be a forceful intrusive process, akin to igneous diapirism, and capable of pushing aside kilometres of overburden. Today, salt diapirs are defined as salt flow features showing discordant interactive contacts with the encasing sedimentary strata, with shapes and geometries that are a response to salt's inherent mechanical weakness. Salt

[1]That rising salt can maintain units of highly soluble nearpure halite near the earth's surface is why the richer sites of Neolithic salt exploitation in Europe were inland and centred on mines at Cardona and Hallestat, and in the fourth Century BC at Zanjan in Iran, as opposed to sites of seasonal evaporation along the coastal plain. Some diapiric salt masses have superstitious significance (Genesis 19:26); Lot's wife was noted in the journals of Fulcher of Chartres (Chaplain to King Baldwin) who accompanied the crusader Baldwin I across the Dead Sea valley in December 1100 AD. In reality, the apophenic feature described as Lot's wife is a 12 m-high column of salt lying at the foot of the much larger Mt Sedom (Usdum) on the edge of the Dead Sea. It is one of a number of dissolutional remnants along the gypsum-capped cavernous edge of an outcropping diapir composed of Miocene salt, which also makes up Mount Sedom (Frumkin 2009). But Sedom's description as a mountain is somewhat of a misnomer, it is certainly 8 km across, but only rises a 100 m or so above the floor of the Dead Sea Valley.

© Springer International Publishing Switzerland 2016

J.K. Warren, *Evaporites: A Geological Compendium*, DOI 10.1007/978-3-319-13512-0_6

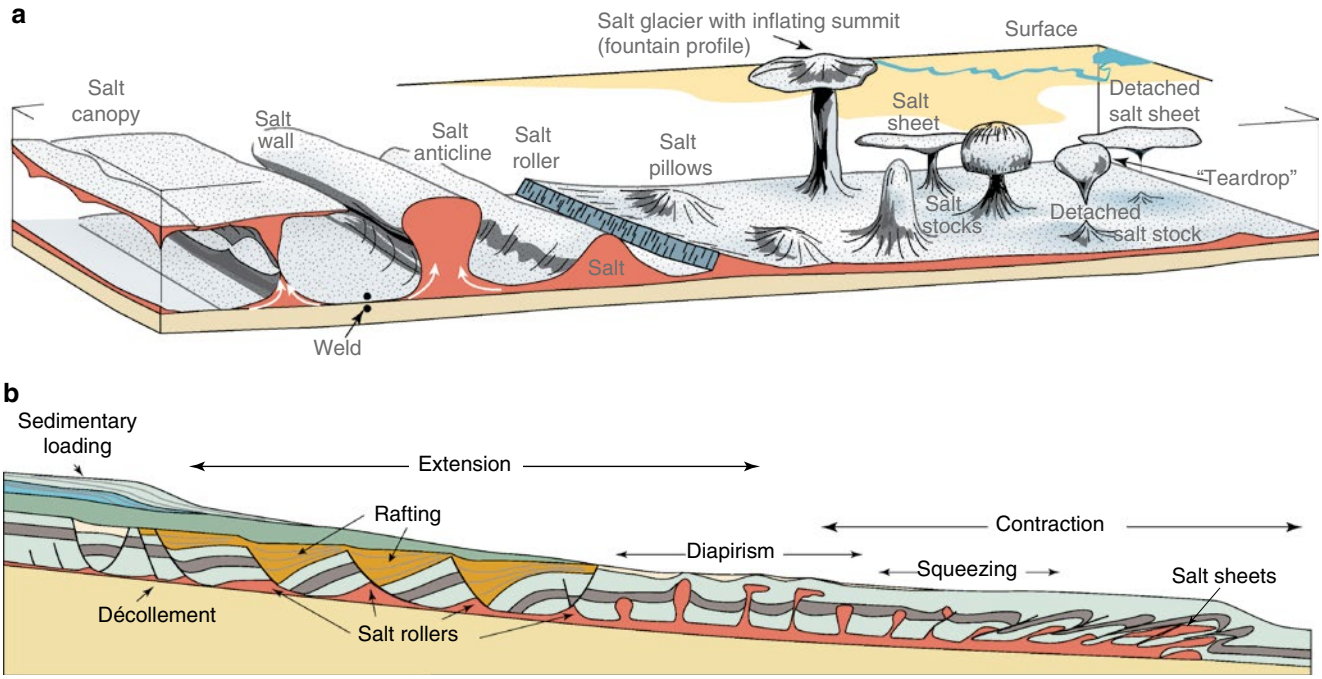

Fig. 6.1 Salt Structures. (**a**) Morphological classification of the different external shapes and deformation styles that define salt distribution in halokinetic basins. Structural maturity of the features increases left and right from the central part of the diagram, with linear structures on the left and vertical (plug) structures on the right. (**b**) Salt morphologies placed in the typical evolutionary framework of salt structures in a deforming passive-margin salt-floored succession, typified by up-dip extension and down-dip compression (After Jackson and Talbot 1986; Fossen 2010)

can push aside a thinned zone of weak overburden, but all current definitions of salt diapirism do not uncritically encompass notions of active piercement and the shouldering aside of kilometres-thick overburden successions. Where feasible, salt constituting a diapir should be further classified as either allochthonous or autochthonous.

Allochthonous salt structurally overlies parts of its (stratigraphically younger) overburden and is often no longer connected to the primary salt bed (mother-salt level). For example, spectacular allochthonous salt sheets in the northern Gulf of Mexico form a line of five or so huge asymmetric tongues of Jurassic salt that now overlie and seal Pliocene to Pleistocene sediments. They coalesce behind the Sigsbee Scarp to form a minibasin-covered salt tongue canopy, which can be considered analogous to gravitational nappes in salt-cored orogenic belts (Fig. 6.2a, b; Worrall and Snelson 1989; Wu 1993; Hudec and Jackson 2006). Allochthonous salt bodies climb the stratigraphy of the Gulf of Mexico via a series of tiers or canopies, leaving evidence of their passage as thin salt pods, dissolution residues and alteration aprons along salt welds or overburden touchdowns, much like a garden slug leaves behind a slime trail (Fig. 6.46). Autochthonous salt structures are those still firmly rooted in the stratigraphic level of the primary salt bed. Prior to the application of current seismic imaging and processing techniques most diapiric structures were interpreted as autochthonous thumb-like appendages connected at the level of the primary salt layer or its former position now marked by a salt weld. Sometimes the term parautochthonous is used to describe a salt geometry that is intermediate between allochthonous and autochthonous.

A whole new realm of salt/sediment configurations and oil exploration plays have opened up in the last few decades with the realization that; (a) salt sheets can be allochthonous and subhorizontal over large areas in a sedimentary basin, and (b) structures in the salt allochthon overburden are tied either to the trailing edge of the allochthon where salt is evacuating/ withdrawing, or the leading edge where salt is flowing at or near the surface. A range of potential subsalt hydrocarbon traps have now been successfully drilled in the Americas (Brazil, eastern Canada, Gulf of Mexico), where the move into deeper water revitalised what were considered mature exploration provinces (Montgomery and Moore 1997; Meisling et al. 2001; Mohriak et al. 2012).

This chapter will concentrate on salt structures, their geometries and the mechanisms that create them; the halokinetic breccias remaining once flowing salt has dissolved are discussed in Chap. 7. Diapirs do not just form in salt, they can occur in any geological material with markedly different pressure and strength compared to its overburden. Contrary to earlier notions of forceful diapirism, some of the principles and concepts developed in interpreting salt diapirism as Newtonian fluid responses can be successfully applied to overpressured shales, serpentinites and even molten granites

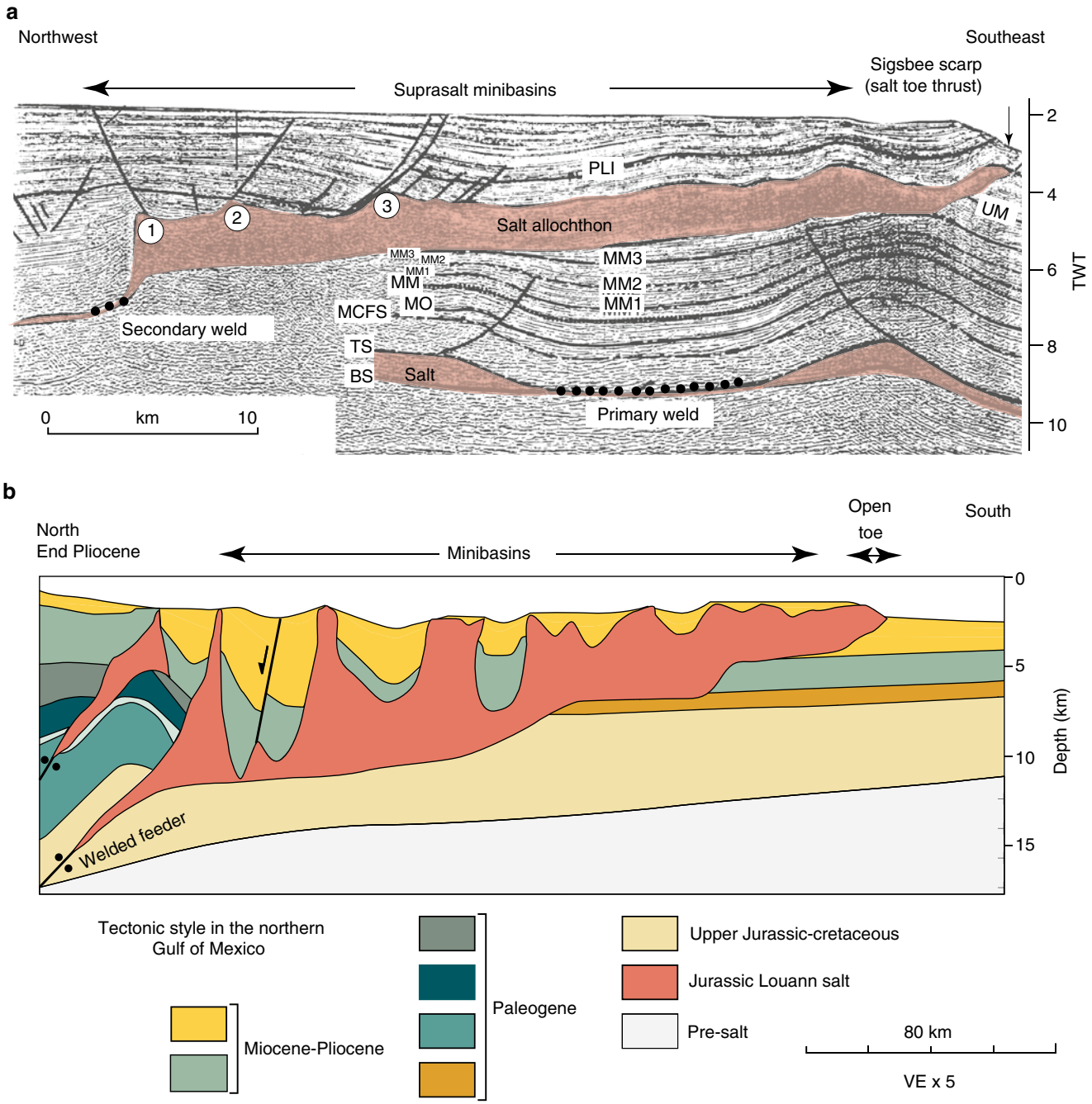

Fig. 6.2 Salt tectonic style in the Northern Gulf of Mexico. (**a**) Interpreted seismic profile through allochthonous salt sheets that build the Sigsbee Escarpment (to southeast), base of continental slope off Louisiana, Gulf of Mexico (After Wu 1993; Jackson and Vendeville 1994). Note how supra-allochthonous faults have initiated diapiric upwelling at 1, 2 and 3. The allochthon is underlain by shortened strata of the Mississippi Fan Foldbelt. *BS* base of Jurassic Louann Salt, *TS* Top of salt, *MCFS* Middle Cretaceous flooding surface equivalent, *MO* Middle Oligocene, *LM* Lower Miocene, *MM1* Lower Middle Miocene, *MM2* Middle Miocene, *MM3* Upper Middle Miocene, *UM* Upper Miocene, *PLI* Pliocene. Note how Jurassic salt has climbed the stratigraphy and now overlies and seals Neogene deepwater sediment. (**b**) Restoration of a salt-canopy geometry at the end of the Pliocene, East Cameron South, Garden Banks, and Keathley Canyon areas, northern Gulf of Mexico, based on seismic as shown in Fig. 6.2a where 10-km-wide open toe of emergent Louann Salt has been inferred at the Sigsbee paleoescarpment. Exposed salt massifs separate synclinal minibasins (After Peel et al. 1995; Hudec and Jackson 2006). Note the differences in horizontal and vertical scales between **a** and **b**

rising through the mantle (Talbot 1992a). Any rock will flow if it gets hot enough and deep enough, around 300 °C for a quartz-rich rock, closer to 550 °C for a feldspathic rock, and even more for olivine-rich rocks. What makes salt so interesting is that it is capable of flowing at surface and nearsurface temperatures and pressures.

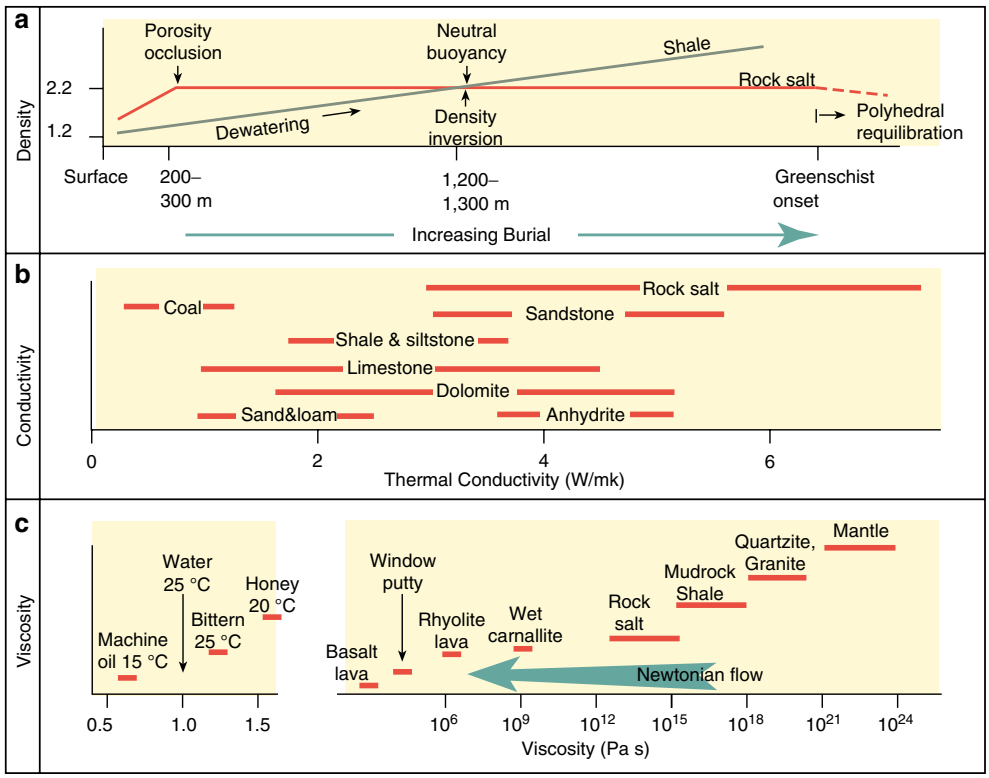

Fig. 6.3 Physical properties of rock salt compared to other lithologies. (**a**) Density changes with burial. (**b**) Thermal conductivity (see also Fig. 8.31a). (**c**) Viscosity

Physics of Salt Systems

Even with our greatly improved ability to seismically outline salt features, the comments made by Richter-Bernburg, more than two decades ago, still hold true today. In a 1980 review he noted that our geological understanding of the world's various salt structures is still very much like that of a sculptor to the human body; the whole figure can be perfectly described, especially using 3D seismic and forward modelling, but the anatomy, the inner organs and the complicated inner structures remain largely irresolvable, unless seen in a mine wall or a dissolving namakier (Strozyk et al. 2012). In a benchmark paper on the internal complexity of Zechstein salt structures in Europe Richter-Bernburg (1980) made a number of interesting observations:

- Salt deposits are not, or have not always been, in mechanical equilibrium with their ambient environment and deformations caused by salt flow have to be expected in all subsurface situations
- Isoclinal and overturned folds can occur in simple salt ridges so that stratigraphically older members of a formation can dip into the local area from above a particular horizon.
- By the diapir stage, possibilities are open for building folds of all imaginable – or even unimaginable – features and shapes (including migmatitic and boudinage styles). Axes of curtain folds in a diapir are not simply vertical, they may be inclined in all – mathematically! – possible directions.

He concludes that any prognosis about the interior structure of a halokinetic salt mass -even if it is scarcely diapiric- is not possible without seeing it from the inside. So before we look at the various external geometries sculpted by salt, which is the main concern for most of this chapter, let us look at the physical properties of salt that drive salt flow and at the internal textures indicative of this flow.

Density, Viscosity, Strength & Buoyancy

After it loses effective porosity, typically by 100–200 m burial, halite's density of 2.2 g/cc remains near constant throughout the diagenetic realm and it is near incompressible to depths of 6–8 km (Fig. 6.3a). With entry into greenschist depths, deeply buried halite can experience massive recrystallisation and dissolution, along with a slight decrease in density due to thermal expansion (Figs. 6.3a and 14.10; Lewis and Holness 1996). In contrast, burial compaction in shales and most other sediments is defined by a progressive loss of porosity, with an associated increase in density and strength until it exceeds that of the salt below. This means that salt has positive buoyancy when buried beneath nonevaporitic overburden to depths in excess of a kilometre. With a muddy overburden, the depth of density crossover, sometimes called the level of neutral buoyancy, is typically shallower than 1,300–1,500 m. It can be much shallower beneath reefs and other cemented carbonates, which can have densities equal to, or greater than,

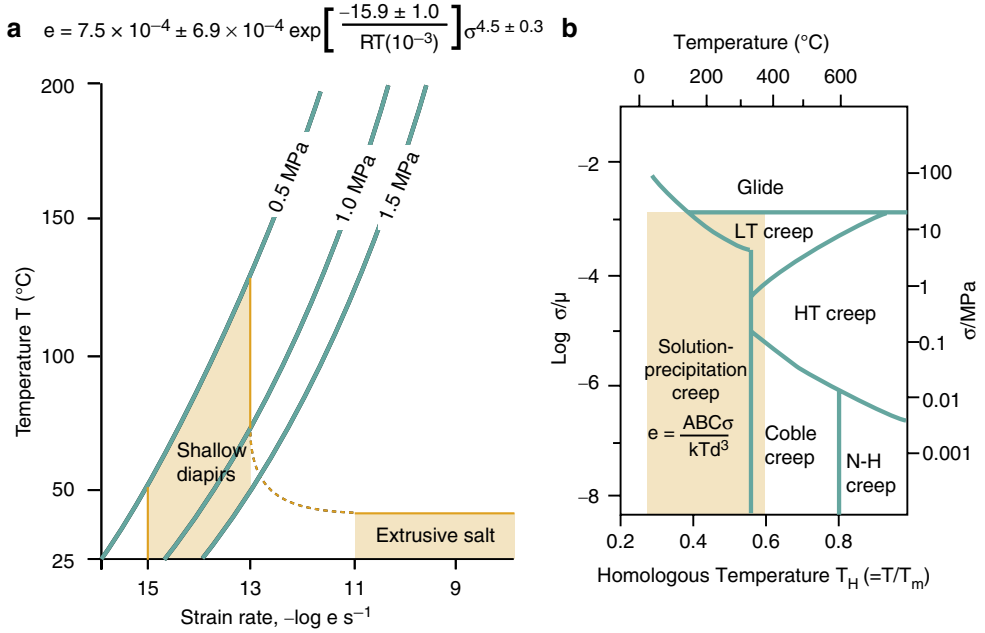

Fig. 6.4 Strain map showing conditions of temperature and strain where salt tends to flow rather than fracture (After Talbot and Jackson 1987a; Carter and Hansen 1983). (**a**) Power law behaviour of dry rock salt where the relation between steady-state strain rate (e) and differential stress (σ in MPa) is highly nonlinear (stress exponent, n = 4.5). This power law does explain deformation in salt diapirs but not the much higher strain rates of extruded salt/salt glaciers. There much of the flow is periodic and facilitated by the presence of water. R is universal gas constant and T the absolute temperature. (**b**) Diffusion mechanism map for damp rock salt showing dominant deformation mechanisms for different homologous temperatures and stresses. Shaded area shows the dominant field for most natural salt flow, which lies mainly in the solution-transfer field (solutant diffusivity terms; *C* grain boundary structure parameter, *k* Boltzmann constant, *d* grain size. *T m* melting point of halite, *LT* and *HT* is low and high temperature, *N-H* is Nabarro Herring (After Urai et al. 1986))

salt almost from the time of deposition. This can lead to rapid foundering and brecciation of reef materials, especially in areas of overburden extension and allochthon spreading.

Few other rocks are as thermally conductive or as close to truly viscous (Newtonian) as natural rock salt (Fig. 6.3b, c). Viscosity is a measure of a fluid's resistance to flow or its internal friction and is measured by the ratio of shear stress to the rate of shear strain. Laboratory measurements show wet carnallite can have a viscosity as low as 10^8 Pa.s, while dry halite has a viscosity around 10^{18} Pa.s (for comparison, honey at 14 °C has a viscosity ≈ 60 Pa.s; window putty ≈ 10^5 Pa.s; and road tar ≈ 10^7 Pa.s; 1 Pa.s = 10 poise). The viscosity of salt in the Gulf of Mexico is 10^{13}–10^{17} Pa.s, depending on moisture content, crystal size and temperature. An adjacent overburden of clay or sands is less viscous by four to five orders of magnitude. Davison et al. (1996a) estimates the ratio, sedimentary rock: evaporite rock viscosity, ranges from 50 to 10^4. As different parts of a diapir deform at different rates and by different mechanisms, the effective subsurface viscosity values for diapiric salt vary with position in the diapir, the water content of the salt and time. Due to its much higher moisture content (from meteoric water infiltration), diapiric salt is much less viscous when it reaches the surface as a tongue of extruded salt than at depth (Fig. 6.4a).

Across geological time frames, finer-grained wet salt approaches Newtonian[2] viscous behaviour, unless it is atypically coarse grained. And, like any fluid, it cannot support shear stress so a mound of wet salt emplaced on the earth's surface will spread under its own weight (gravity spreading). Using a viscous fluid model, salt diapirism and its relationship to its overburden can be likened to Rayleigh-Taylor instability with a viscous substratum (salt) and an overlying denser viscous fluid (overburden; e.g. discussions in Koyi 1991; Talbot 1992a, b). Under such a fluid-fluid model, diapirism is spontaneously initiated by small irregularities in the fluid-fluid interface that then amplify with time and buoyancy contrast. Diapirs rise continuously and inevitably until the less dense salt overlies its overburden. The only requirement for Rayleigh-Taylor instability in a fluid-fluid system is density inversion; diapirism modelled in such as way does not require any external trigger such as regional extension or differential loading. Under this fluid-fluid scenario, any regional extension thins the fluid overburden and the source layer, so reducing the overall thickness. The resulting diapirs are

[2]Newtonian (or viscous) flow occurs when the rate of shear stress is directly proportional to the shear strain (linear relation between stress and strain rate). Non-Newtonian flow is typified by a power law relationship between stress and strain.

Table 6.1 Representative strain and flow rates

Type of flow	Strain rate (s^{-1})	Speed (mm a^{-1})	Speed
Lava flow (faster when hotter)	10^{-5} to 10^{-4}	5×10^{11} to 3×10^{13}	1 to 60 km h^{-1}
Ice glacier (surges with increased temperature)	10^{-10} to 5×10^{-8}	3×10^{5} to 2×10^{7}	1 to 60 m day^{-1}
Salt glacier (surges when wet, after a rainstorm)	10^{-11} to 2×10^{-9}	2×10^{3} to 2×10^{6}	10 to 100 km Ma^{-1}
Mantle currents (temperature and pressure controlled)	10^{-15} to 10^{-14}	10 to 10^{3}	2 m a^{-1} to 5 m day^{-1}
Spreading salt tongue (<30 km wide extrusion)	8×10^{-15} to 10^{-11}	2 to 20	2 to 20 km Ma^{-1}
Spreading salt tongue (>30 km wide extrusion)	3×10^{-16} to 10^{-15}	0.5 to 3	0.5 to 3 km Ma^{-1}
Rising diapir in stem (increases with water content)	2×10^{-16} to 8×10^{-11}	1×10^{-2} to 2	10 m to 2 km Ma^{-1}

After Jackson and Vendeville (1994)

smaller, more closely spaced, and more slowly rising than those in unthinned counterparts (Koyi 1991).

Rather than model the salt's overburden as a viscous fluid, proponents of the "brittle school" tend to model salt as a pressurized pseudo-fluid at subsurface flow rates, and consider its sedimentary overburden liable to show brittle responses to stress (e.g. Jackson and Vendeville 1994). In most subsurface situations it means that relative density as a trigger and a subsequent control to halokinesis, is a less important consideration than relative strength of salt and its overburden. This style of modelling is better supported by the geological observations that; (1) diapirs rise episodically rather than continuously, (2) that salt flows when loaded (much like toothpaste is squeezed out it its tube) and (3) that faulting, rather than folding, characterises much of the early deformation in the overburden. In reality, the strength response of a buried salt bed and its overburden will depend on the strain rate and the rate of deformation in the overburden. Salt can fracture and fault at high strain rates (brittle response), but the required strain rate is much higher than experienced in many typical subsurface situations (Jackson and Talbot 1994; Davison 2009).

Subsurface nonevaporitic sediments, including indurated shales, show time-independent, pressure-dependent brittle behaviour under stress and deform most readily by frictional slip along faults. In contrast, bedded salt under stress typically flows and deforms via folding and recrystallisation rather than fracturing. Most adherents of the brittle school contend that varying combinations of regional extension, differential loading and gravity sliding, will localise, initiate and promote diapirism of salt and shale. The conclusions of the "brittle" school are supported by studies showing virtually all sediments at shallow crustal depths (<8–10 km) deform as faulted brittle masses, rather than by the creep and folding that typifies deforming evaporite salts. This depth range encompasses much of the realm of salt tectonics in sedimentary basins.

Evaporite salts are unique in their tendency to flow in the diagenetic realm. Representative strain rates and speeds of salt deformation are listed in Table 6.1. A strain value of $10^{-15}\,s^{-1}$ indicates that a rock stretches at a rate of 10^{-15} of its length per second and is representative of the slow strain rates encountered in rock deformation rates in active orogenic belts. A value of 10^{-9} is 1 million times faster and represents strain rates in active (wet) salt glaciers in Iran (1.6×10^{-13} to 1.8×10^{-8} per second; Wenkert 1979), which equates to an annual rate of rise of ≈2 m/year in the salt stem. But the rate of salt supply and surface flow is not constant. Salt glaciers (namakiers) in Iran always flow faster after a rain; the Dashti glacier at Kuh-e-Namak (28.26°N, 51.71°E) flows at up to 0.5 m/day during the few weeks of the annual wet season, but flows little if any during the dry season when the glacier expands and contracts diurnally in response to changes in surface temperature. The Kuh-e-Jahani salt glacier in Iran (28.60°N, 52.46°E) rises out of its orifice at 2–3 m/year, (Talbot et al. 2000), which is equivalent to a vertical strain rate of $1\times10^{-11}\,s^{-1}$. According to Davison (2009) this is close to the critical strain rate required for salt to fault.

But what do these observed rates of deformation mean in terms of driving mechanism and how does flow occur at the crystalline scale? First and foremost it means wet salt has little or no strength in most geological settings and so deforms by diffusion[3] creep in a fluid-like fashion. In contrast, cataclastic[4] or brittle responses to deformation, involving microfracturing and sliding of grains and grain fragments (grain crushing), are important deformation mechanisms in non-evaporite indurated sediments at low temperatures and confining pressures[5] (Talbot and Jackson 1987a, b; Kukla et al. 2011a).

[3]Diffusion creep changes the shape and size of crystals through the movement of vacancies and atoms within crystals and along grain boundaries. Indicative textures can include equant grain shapes, indented grains, overgrowths and a lack of crystallographic preferred orientation (although preferred crystallographic orientations can also form during diffusion creep)

[4]Brittle response encapsulate microfracturing, cataclasis, and frictional sliding involve the formation, lengthening, and interconnecting of microcracks; frictional sliding along microcracks and grain boundaries; and the formation and flow of pervasively fractured, brecciated, and pulverized rock and crystal fragments (micropemeability).

[5]Confining pressure describes an equal, all-sided pressure, such as lithostatic pressure produced by the weight of overlying rocks in the crust of the earth. It is considered equivalent to overburden pressure or geostatic pressure and is sometimes called vertical stress. It contrasts with the term formation pressure, which includes a pore pressure component.

Kinking of crystal lattices by various combinations of slip, glide or dislocations of grains in the halite lattice itself is known collectively as dislocation creep. Based on naturally and artificially deformed salt samples, Carter et al. (1993) concluded dislocation creep occurs at temperatures and pressures relevant to subsurface salt deformation. They found that short-term, high-stress flow properties of dry salt can be reasonably encapsulated in an empirical power-law equation (Fig. 6.4a). This power law explains the rates of creep and differential[6] stress fields interpreted in shallow (dry) diapiric salt. It does not explain the much higher strain rates of 10^{-8}–10^{-11} measured in salt allochthons and salt glaciers (extruded wet salt) at stress differentials estimated to be around 0.5 MPa and at ambient surface temperatures (Talbot and Jackson 1987a). Nor do their stress/strain triaxial experiments duplicate the elongate recrystallised textures of naturally deformed salt; such textures imply diffusional flow mechanisms (Urai et al. 1986).

Ductile flow occurs through three main mechanisms. (1) change of grain shape by crystal plasticity, which is referred to as dislocation creep; (2) change of grain shape by diffusion through or around grains, called diffusion creep; and (3) relative movement of grains, referred to as granular flow or grain-boundary sliding (Fig. 6.5a). Strain by diffusion of ions along grain boundaries is also known as Coble creep, while stain uptake through crystals via crystal lattice adjustment to imposed stress is known as Nabarro-Herring creep and is typical of most rocks at high temperatures (Fig. 6.4b). Diffusion creep textures may grade into ductile grain-boundary sliding and frictional grain-boundary sliding textures.

The high solubility of chloride salts means solution transfer creep (aka solution precipitation creep and pressure solution creep and stress-induced solution transfer) is the prevalent deformation mechanism in wet salt flowing in the diagenetic temperature realm (Figs. 6.4b and 6.5a; Urai et al. 1986, 2008). That is, diffusion mechanisms can operate at much lower temperatures and differential stresses in wet salt than in non-salt rock types, where temperatures measured in hundreds of degrees are more typical of diffusion. Hence, the use of the homologous[7] temperature scale (T_H) when discussing creep mechanisms. Triaxial deformation experiments by Urai et al. (1986) using carnallite, sylvite and rock salt showed that flow laws based on short-term high-stress experiments conducted on dry salt should not be extrapolated to salt deforming under lower strain rates and nondilatant conditions. They found that both dry salt (≈0.05 wt% inherent water) and wet (brine-saturated) salt both deformed by power law creep with $n > 5$ at strain rates faster than 10^{-7} s^{-1}, as found by Carter and Hansen (1983). However, the same rocks deformed by power law creep with $n \approx 2$ (dry) or $n \approx 1$ (wet) when samples were stained more slowly by suppressing the rate of dilatancy (either by increasing confining

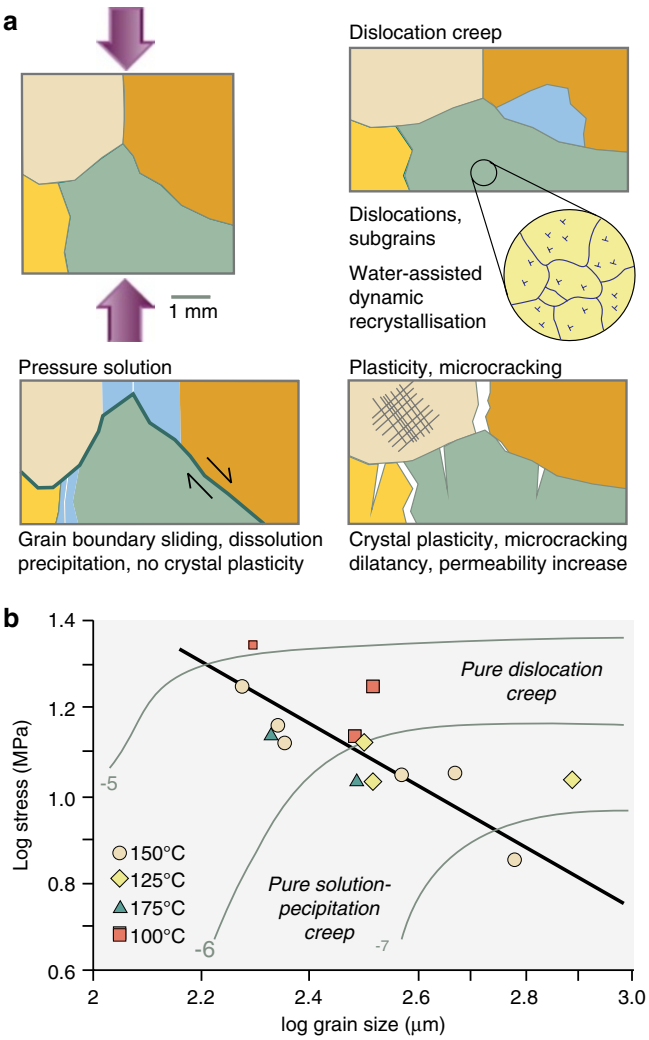

Fig. 6.5 Crystal-scale deformation. (**a**) Schematic showing the microstructural processes that can operated during the deformation of rock salt at temperatures in the range 20–200 °C. Different shades represent crystals with different orientation. The circular expanded inset illustrates subgrains (with same orientation) See text for further explanation. (**b**) Dynamically recrystallised grain size versus stress data for synthetic rock salt samples, superimposed on a deformation mechanism map, showing that halite deformed in the transition region between dislocation creep and solution- precipitation creep, both played a role in the deformation (After Ter Heege et al. 2005; Urai et al. 2008)

[6]Differential stress (sometimes called deviatoric stress) is any stress system where the forces acting on a unit cube are not the same in all directions, it is typically measured as σ_1–σ_3.

[7]Homologous temperature scales (T_H) make it possible to compare creep response for solids with different melting points. T_H is defined as T/T_m, which is the ratio of the material's temperature to its melting point (T_m). For water, with a T_m of 273 K, the homologous temperature at 0 K is 0/273 = 0, while at 0 °C the T_H = 1 (273/273), and 0.5 at −100 °C (137/273). Homologous temperatures involved in creep processes are typically greater than 0.5, with creep processes becoming more active as T_H approaches 1. This is why ice glaciers can flow like salt glaciers: that is, ice deforms by creep at the high homologous temperatures of natural glaciers, as does salt, as illustrated in Fig. 6.4b.

pressure to between 5 and 10 MPa, or adding brine under dilatant conditions).

Urai et al. (op cit.) also found that samples deformed under these more geologically realistic conditions had completely recrystallised into flattened fabrics very similar to those of naturally deformed salt, which is typically dominated by biaxially flattened geometries (Fig. 6.16a). The process of solution transfer creep in deforming salt produces new gneiss-like crystal textures made up of amoeboid-like strain-free flattened salt grains, showing flow parallel fabrics. Solution-transfer creep or pressure solution creep occurs in regimes of differential stress where halite grains dissolve in regions of high stress and reprecipitate in regions of low stress (Fig. 6.5a; aka strain shadows). The basic processes involved are the migration of existing grain boundaries and the formation of new high angle grain boundaries (Drury and Urai 1990). New crystals are less sub-structured and replace older more substructured grains as migrating crystal grain boundaries consume and sweep through the older milky inclusion-rich portions of the salt (Schenk and Urai 2004). Crystals in an area swept by grain boundary migration tend to be inclusion-free, with fluid inclusions now focused along the grain boundaries and so providing conditions suitable for pressure-solution induced creep of the salt mass (Urai et al. 1986; Spiers et al. 1990; Schenk and Urai 2004). Hence, much of this new salt is clear and sparry, rather than milky from intracrystalline inclusions.

Grain boundary migration in deforming wet salt typically leads to grain growth during recrystallization, but can also lead to grain size reduction if new grain boundaries are formed at grain boundary bulges or as a result of grain dissection by migrating boundaries (Fig. 6.5b; Ter Heege et al. 2005). New grain boundaries may also form from subgrain boundaries by progressive misorientation of subgrains or by migration of a sub-boundary through an area of cumulative lattice rotation. This is called rotation recrystallization. The relative importance of migration and rotation recrystallization is dependent on the deformation conditions (i.e. temperature, strain rate and stress). The mean grain size D of dynamically recrystallised materials has been found to be related to the steady state flow stress (σ) by a general theoretical relation of the type $D = K\sigma^{-p}$, a power law, where K and p are material and mechanism specific constants (see also Fig. 6.18 and discussion). Ter Heege et al. (2005) experimentally modelled the specifics deformation of wet salt and concluded that the equation is of the form:

$$\left(D/\beta\right) = 10^{-1.55\pm0.24}\left(\sigma/\mu\right)^{-1.85\pm0.23}\exp\left(14.2\pm2.8/RT\right)$$

with D denoting mean recrystallised grain size, Burgers vector $\beta = 3.99\times10^{-4}$ μm and the shear modulus $\mu = 1.5\times10^{4}$ MPa. Their experiment illustrates that there is a clear relationship between grain size, stress and deformation mechanism (Fig. 6.5b) with salt in a range of temperatures from 100 to 175 °C deforming by a combination dislocation creep and solution precipitation creep.

Figure 6.5 summarises the various microstructural processes that allow halite in the temperature range of 20–200 °C to adjust to imposed deviatoric stresses and so facilitate salt flow (Urai et al. 2008). At very low effective confining pressures (less than a few MPa) and high deviatoric stresses (>15–20 MPa), inter- and intragranular microcracking, grain rotation and intergranular slip are important strain accumulating processes, alongside crystal plasticity. Mechanical properties and dilatational behaviour within this scenario are dependent on the[8] effective mean stress or effective confining pressure. At sufficiently high deviatoric stress, the material fails in a (semi)brittle manner, with failure described by a pressure (or effective mean stress) dependent failure envelope. With increasing effective mean stress, microcracking and dilatancy are suppressed and plastic responses come to dominate.

Of the various plastic responses in the temperature range 100–200 °C, dislocation creep is important and, even at confining pressures as low as 10 MPa, polycrystalline halite can deform to large strains by this mechanism (Figs. 6.4 and 6.5b). During this process, subgrains are formed in the halite grains with the diameter of the subgrains showing a near-linear, inverse correlation with deviatoric stress. If the polycrystal precursor contains small but significant amounts of water in the form of saturated brine inclusions or grain boundary films, as is generally the case for both natural and synthetic samples, fluid assisted grain boundary migration typically operates. This is an efficient process for reducing dislocation density and hence removing the stored energy of dislocations, even at room temperature (Schenk and Urai 2004).

While dislocation creep processes take place in the crystal lattice of halite grains, fluid-assisted grain boundary migration involves solution-precipitation transfer across grain boundaries. Such solution-precipitation creep, or "pressure solution" plastic responses, involve mass transfer centred around grain boundaries (Fig. 6.5a). There, in the presence of a small amount of saturated grain boundary brine, grains dissolve at highly stressed boundaries and after diffusion of the material through the grain boundary fluid, the material crystallises at interfaces and strain shadow areas subject to low normal stress. This process is typically accompanied by intergranular sliding and rotation (grain rearrangement), and can lead to compaction of porous salt or to deviatoric strain (biaxial flattening of non-porous aggregates (Fig. 6.16a). Solution-reprecipitation creep is an important deformation mechanism in most wet rock systems in the Earth's crust, but is especially rapid in low-temperature extruded rock salt,

[8]Effective stress is equal to the total stress minus the pore pressure.

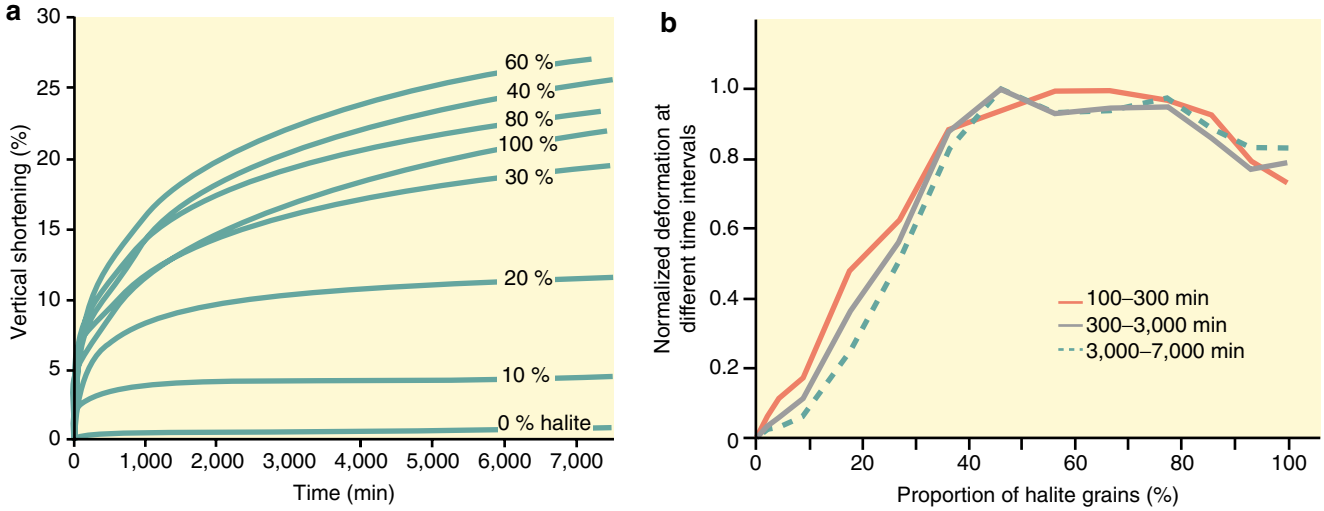

Fig. 6.6 Effect of impurities on salt compression, cementation and pressure solution. (**a**) Result of drained compaction experiments. Compaction curves $E(t) = (x_0\ x(t)/x_0)$ for different samples show that the total amount of compaction after 7,000 min (roughly 5 days) depends on the relative proportion of halite and calcite grains. The highest finite compaction (vertical shortening) does not occur in a sample composed of 100 % halite grains. (**b**) Effect of the mineralogical composition on the amount of vertical shortening on a halite-calcite aggregate. The three curves are normalized to the average maximum deformation of the tested samples at the given elapsed time and they show the same trend, within experimental errors. The mixtures with halite contents between 0 to about 40 % do not exhibit this behavior. The rate of deformation goes down during progressive deformation for halite proportions ranging between 10 and 40 % (After Zubtsov et al. 2004)

where it is the dominant low temperature stress-adjustment mechanism (Fig. 6.3).

The intensity of salt flow and recrystallisation (re-annealment) can in part depend on levels of impurities in deforming and compressing salt. Various lab-created mixtures of crushed halite aggregate and calcite crystals show an interesting set of responses under triaxial compression with free drainage of fluid products (Zubtsov et al. 2004). A 100 % halite sample, or an 80:20 halite-calcite mixture, are both less susceptible to compressional shortening than halite-calcite mixtures of between 40 and 60 % halite (Fig. 6.6a). This is true at all time ranges in the experiment, which ran for periods of up to 5 days (Fig. 6.6b). Mixtures with <30 % halite show less shortening than all samples with higher proportions of halite in the mix.

These responses indicates two mechanisms competing at the grain-to-grain scale: (1) intergranular pressure solution at grain contacts, which facilitates compression, especially across boundaries with different chemical potential, as typically occurs at contacts between grains with different mineralogies, and, (2) grain boundary healing (re-annealment), as occurs between halite-halite grains and studied in pure halites by Urai et al. (1986). This drives the ongoing annealment that then hinders further compaction. As the halite content in the mixture increases, more and more halite-halite grain contacts can heal and so act to resist compression. Volume loss by draining of pressure solution fluids becomes less efficient in such healed or partially healed contacts (Zubtsov et al. 2004). This is another illustration of pure salt's ability to act as an effective seal, it shows that even when faulted, salt will quickly anneal itself unless impurities can enter the fault plane.

When the creep and frictional strengths of wet and dry salt are compared with equivalent strengths of other sedimentary rocks, using a representative strain rate of 10^{-14} s^{-1}, it can be seen that even dry salt is much weaker than any overburden sediment, except perhaps for extremely shallowly-buried water-saturated muds, less than a few hundred metres deep, where water contents can be in excess 50 % (Fig. 6.7). Damp salt, which deforms by solution-transfer creep is hundreds of times weaker than dry salt, which deforms by dislocation creep, where stain uptake is dominated by slippage along lattice defects (Urai et al. 1986).

Because deforming salt has almost no shear strength at most geological time scales of applied stress, it is considered a pseudofluid (Fig. 6.7a; Weijermars et al. 1993). Damp salt does not even require external water to act as a Newtonian fluid (Urai et al. 1986). Rather, the minute quantities of brine caught up as inclusions and the intergranular films in confined natural salt are sufficient to effect salt strength. Water content in a deforming salt unit may be enhanced from an external source, as it does in Iranian namakiers, which tend to flow after rain. However, brine-filled inclusions, naturally present in the halite at the time of deposition can contain sufficient water (up to 4–5 % by volume) to allow salt to flow naturally at the earth surface conditions. In other words, wet salt can flow spontaneously by solution transfer creep, once

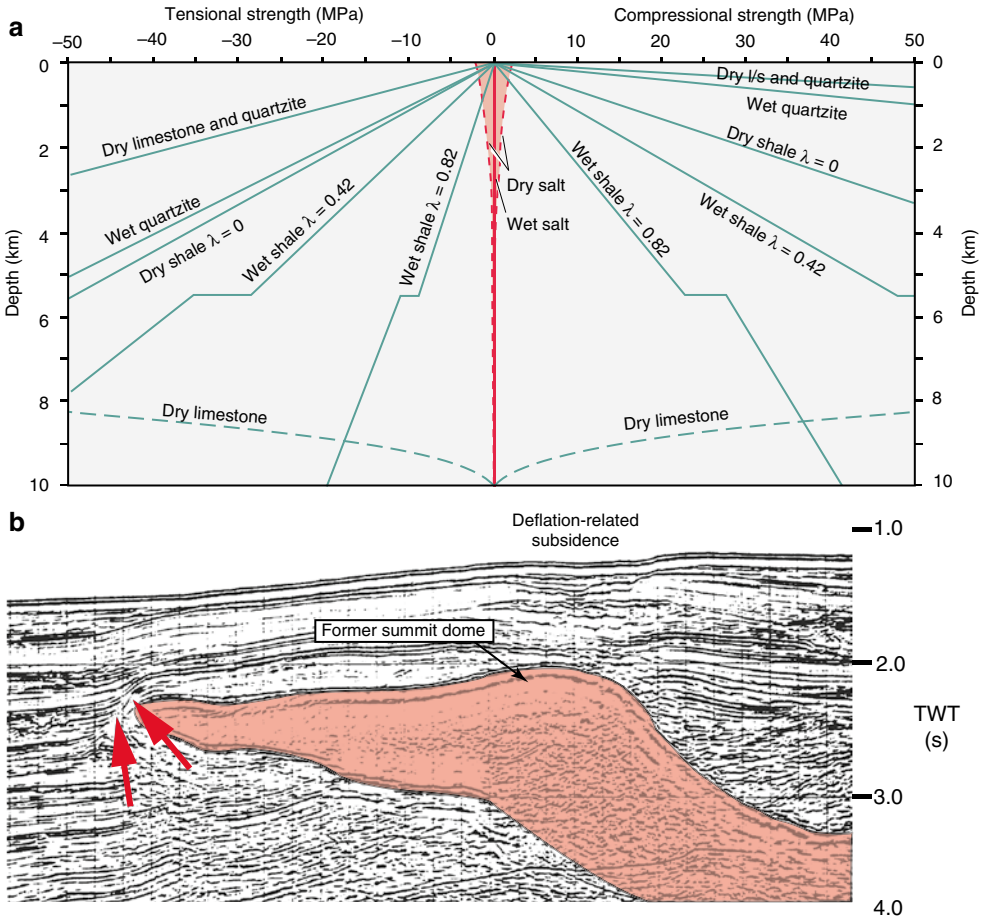

Fig. 6.7 Salt strength. (**a**) Comparison of creep and frictional strength of dry salt with equivalent strengths of dry and wet sedimentary rocks and sediments (After Jackson et al. 1994a, b). Creep strength is the deviatoric stress required to drive salt flow at a representative strain rate of 10^{-14} s^{-1}. Pore pressure coefficient (λ) is the ratio of pore pressure to lithostatic pressure: λ = 0 for dry rocks, λ = 0.46 for hydrostatically pressured rocks and λ = 0.86 for overpressured rocks. Note the extreme lack of strength of wet salt (*red line*) and the almost as weak field outline by dry salt (*shaded light red*). Wet salt is so weak (strength of 0.01 MPa at this strain rate) that its creep curves plot virtually on the central axis (hence modelled as Newtonian response). (**b**) Salt allochthon, northern Gulf of Mexico (After Nelson 1991). Onlap of frontal reflectors above a thin roof, averaging only 100 m thick (*red arrows* on left hand edge of salt tongue), indicates shallow emplacement of the allochthonous salt tongue

extruded at the surface it will collapse or spread under its own weight (gravity collapse or gravity spreading).

The extreme weakness of natural wet salt at the surface is seen in seismic onlap patterns of allochthonous salt sheets deforming by gravity gliding in the Gulf of Mexico. Salt sills are emplaced into low-density water-saturated shales at depths of less than 250–300 m beneath the sediment-water interface, with a mean depth of 150 m (Fig. 6.7b; Nelson and Fairchild 1989; Nelson 1991). Shales deeper than 300 m or so are too strong to be laterally intruded by a salt sheet. Were density contrast, rather than relative strength, the controlling factor then salt sheets would have spread out at depths ≈ 1,400 m, which is the level of neutral buoyancy beneath this part of the Gulf of Mexico (Nelson 1991). Salt weakness, or lack of strength, is thus more significant than buoyancy contrast in controlling the position of these allochthonous salt sheets.

In essence, the extremely weak nature of salt means that there can be essentially no shear stress acting on an interface between the salt and the adjacent formations. This means that there will be a tendency for principal stresses to re-orient themselves to be parallel and perpendicular to these weak planes. Ignoring how stress orientation and magnitude are affected by the presence of salt bodies can lead to costly well failures. In the Gulf of Mexico salt allochthons, Fredrich et al. (2003) found that stresses within the salt body may not be uniformly equal to lithostatic (as commonly assumed). Some of the drilling problems encountered when drilling through the bottom of a salt structure, that are usually attributed to very weak rock in a hypothesized rubble-zone (gumbo), may actually be associated with concentrated stresses at the bottom of the salt body.

The weakness of salt at geologic strain rates means the viscous forces in flowing salt cannot easily drag or stretch the overburden. Rather, thick flow-susceptible salt sheets act as a pressurized layer of lubricant that effectively decouples the overburden from the basement. A thick salt bed tends to act as a ductile "crack stopper" whereby it hinders faults and dykes propagating into higher or lower levels of the stratigraphy. A thick salt layer segments the basin sediments into suprasalt and infrasalt layers, which can deform independently or even by different processes. The impervious but fluid nature of salt focuses and entraps petroleum and mineralising fluids against a salt seal at the tops of subsalt faults, even if the faulting postdates deposition of the subsalt and suprasalt layers (Chap. 10). About the salt basin edge the degree of structural inheritance across a halokinetic salt layer depends on the distribution the mother salt in

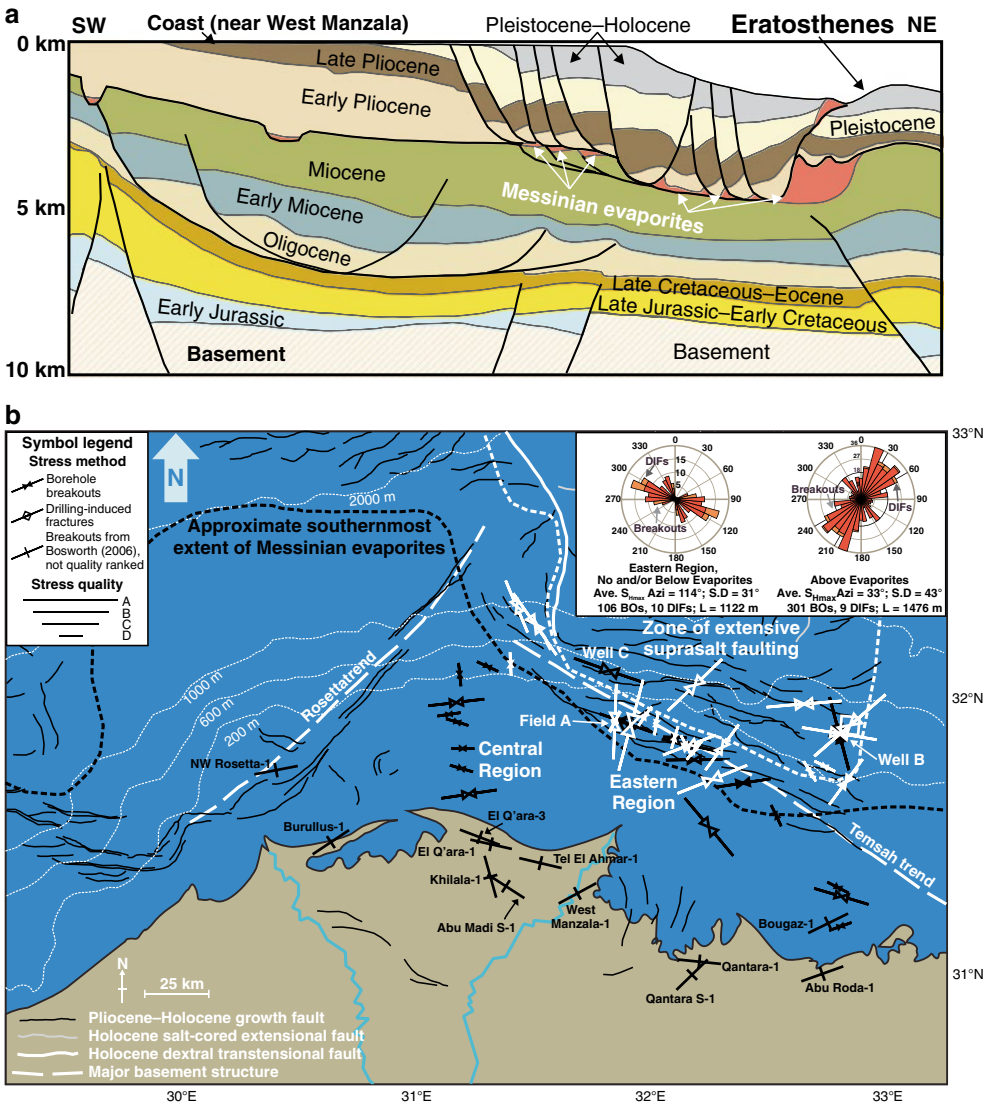

Fig. 6.8 Stress field in Nile Delta (**a**) Schematic cross section of the eastern Nile Delta illustrating major structural styles, in particular the suprasalt extensional faults that sole out on the withdrawal weld that is the Messinian evaporite level. (**b**) Present-day S_{Hmax} orientations interpreted from borehole breakouts and drilling-induced fractures (DIFs) in the Nile Delta. Stress orientations below or south of the Messinian evaporites (*black symbols*) indicate an approximately E-W S_{Hmax} orientation in the central region and an approximately ESE-WNW S_{Hmax} orientation in the eastern region of the Nile Delta. These orientations are broadly consistent with those observed in Bosworth (2006; black crosses). However, S_{Hmax} orientations are fairly scattered in sequences overlying Messinian evaporites (*white symbols*), although they show a predominately NE-SW S_{Hmax} orientation. Hence, the average S_{Hmax} orientation in sequences above the evaporites is approximately perpendicular to that observed below the evaporites (see inset rose diagrams), indicating that the subsalt and suprasalt sequences are mechanically detached. Furthermore, it is interesting to note that the S_{Hmax} orientations observed in suprasalt sequences are inconsistent with the predominately extensional faulting observed in this region. *Ave*. Average, *Azi* Azimuth, *BOs* Breakouts, *L* Total Breakout Length, *S.D* standard deviation (Adapted from Tingay et al. 2011)

relation to basin defining faults, prior to salt flow (Lewis et al. 2013).

Although widely assumed, actual quantified examples of differing stress tensors above and below a regional salt unit are rare. Recently, Tingay et al. (2011) examined present-day stress orientations, inferred from borehole breakout and drilling-induced fractures, in 44 boreholes in the offshore Nile Delta. There the presence of Messinian salt has influence stress fields. The salt extends part way beneath the Nile Delta and shows geometries indicative of loading and squeezing (Fig. 6.8a). A total of 446 breakouts and 19 drilling-induced fractures from 37 wells reveal sharply contrasting present-day maximum horizontal stress (S_{Hmax}) orientations in sequences above and below the extensive Messinian evaporites of the eastern Nile Delta (Fig. 6.8b). A typical deltaic margin-parallel S_{Hmax} (E-W in the central and ESE-WNW in

the eastern Nile Delta) occurs in parts of the Nile Delta that are below, or do not contain, evaporites. However, a scattered but largely margin-normal (NNE-SSW) S_{Hmax} is observed in sequences underlain by evaporites (inset in Fig. 6.8b). The ≈90° variation in present-day S_{Hmax} orientation above and below the Messinian salts provides convincing *in situ* quantified evidence that evaporite sequences act as major mechanical detachment horizons. In addition, the margin-normal S_{Hmax} orientation is subperpendicular to the strike of nearby active extensional faults, indicating the existence of non-Andersonian faulting in the suprasalt region. Furthermore, this evidence that the Messinian evaporites act as an effective mechanical detachment suggests that suprasalt faulting in the eastern Nile Delta is not the result of basement-related deformation and so raises doubts about the often-postulated extension of the Suez fault zone into the eastern Mediterranean.

Salt structure also alters the alignment of regional stress fields in compressional halokinetic regions in Germany (Brandes et al. 2013). The simple layer-cake geometry of the basin-fill in the Subhercynian Basin of northern Germany is dominated by several piercing and non-piercing salt structures sourced in Zechstein salt. Most Zechstein salt structures first formed in extension but underwent later compression (e.g. Fig. 6.77) On a regional scale, the Sub-Hercynian foreland basin-fill is characterized by a horizontal compressional paleostress vector that is mainly NNE-SSW-oriented, which reflects the Late Cretaceous inversion phase in Central Europe. However, the local paleostress field is distinctly perturbated due to the Zechstein salt structures. Along the edge of various salt pillows, the maximum horizontal paleostress vector is deflected by up to 90° from the regional trend. In the case of the Elm salt pillow, it forms a radial pattern. Brandes et al. (2013) derive four main controlling factors for the Subhercynian Basin and argue similar effects should typify salt-dominated contractional basins in a foreland setting. They are: (1) the wedge-shape basin-fill is the product of the dynamic load at the southern margin of the basin, (2) a basal salt layer fed the diapirs and acted as a detachment horizon during the later shortening, (3) detachment folding was the dominating deformation mechanism during contraction, and (4) the pre-existing diapirs controlled the position of the detachment folds.

Salt layers typically act as a lubricant in deforming sediment masses and in the extensional and compression examples just discussed. That is, the lubricious effects of salt layers are seen in the widths, taper angles, and internal structures of dynamic wedges at both converging and diverging plate boundaries. By lubricating regional décollements, even thin layers of salt influence how huge areas shorten or extend during gravity gliding. It leads to the complexities of raft tectonics, where rapidly opening ocean basins generate

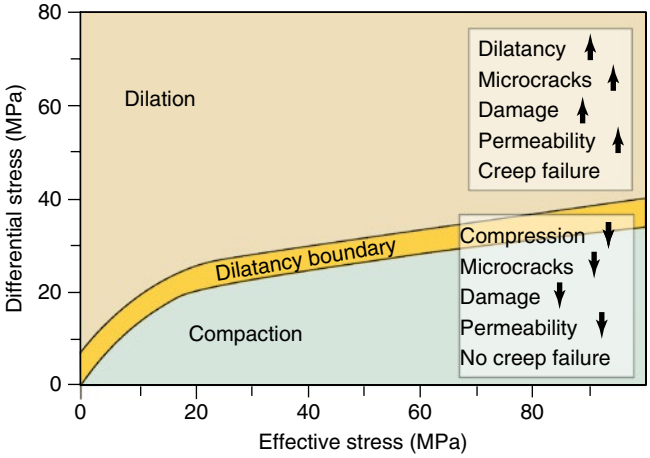

Fig. 6.9 Effective stress versus differential stress diagram for rock salt (After Schoenherr et al. 2007b). The dilatancy boundary separates domains where microcracking is suppressed (compaction domain) from those where rock salt dilates

floundering blocks of brittle sediments (tens of kilometres across and kilometres thick) that glide down into the widening basin atop a layer of lubricating salt. For the same reason fold thrust belts in converging plate margins that are deforming over salt layers are much wider, with critical taper angles <1–2°; while those deforming over more competent décollement layers are narrower, with taper angles nearing 8° (Davis and Engelder 1987).

Salt's fluidity and ability to reanneal make it a highly effective low permeability barrier to fluids escaping from the underlying sediments. As sediment is deposited atop an impervious but fluid salt layer, pressure beneath it builds as it acts as a pressure blanket. A layer of salt in a subsiding basin exaggerates overpressure in the section beneath the salt and mitigates transfer of overpressure to the section overlying the salt. If there are no breaches in the salt layer this can result in a tremendous increase of overpressure across the lower salt boundary (Fig. 8.22). Even thin salt sills can be highly efficient fluid seals. As a result, extremely overpressured sediments can be intersected immediately under a salt sill, creating a drilling hazard. When or where a salt sheet is breached by salt dissolution or salt evacuation, a highly pressured pulse of subsalt fluids may move up through the breach. In many situations the sole of a growth fault marks the breach and the extending fault becomes a conduit for the escape of hot basinal fluids, along with their elevated metal contents (Chap. 15).

In reality, a simple division into brittle versus viscous fluid response models is an oversimplification as salt and the adjacent sediments can, depending on the circumstances, exhibit either brittle or viscous responses to stress (Fig. 6.9; Davison et al. 1996a; Poliakov et al. 1996; Schoenherr et al. 2007b, c). Salt at the surface is brittle

enough to fault or shear, and such displacements are not uncommon in salt mines or in faults cutting across the surfaces of some dry salars of South America (Fig. 3.51). Likewise the overburden can show evidence of viscous behaviour. Sediments atop allochthonous salt sheets in the Mexican fold ridges in the Gulf of Mexico are mostly folded not faulted. Seismic also shows many diapirs have sedimentary margins with smooth drag profiles known as shale sheaths, rather than brittle faulted margins adjacent to fluid salt.

In some overpressured subsurface situations, halokinetic salt can become sufficiently dilatant as to allow entry or crossflow of pressurised fluids (Fig. 6.9). For example, salt cores recovered from the Cambrian Ara Salt in the South Oman Salt Basin are occasionally stained black with oil (Fig. 8.26; Schoenherr et al. 2007a, b; Kukla et al. 2011a, b). In some cases, up to 10 m of vertical section above the stringer contained mm-scale hydrocarbons lining polyhedral halite boundaries (Schoenherr et al. 2007a). In these stained zones cm-scale bands of millimetre-sized fluid inclusion-rich alternate with thinner fluid inclusion-free bands. In the same stained zones hydrocarbon-impregnated microcracks are frequently filled with solid bitumen, along with fluid inclusion trails with oil inclusions and gas bubbles. Subgrain-size piezometry on the Ara Salt indicates a maximum differential paleostress of <2 MPa (Schoenherr et al. 2007a) in rock salt adjacent to carbonate stringers. At a differential stress of <2 MPa, rock salt can dilate only at near-zero effective stresses (Fig. 6.7a). This is only possible at great depth when fluid pressure in the rock salt is very close to the minimum principal stress σ_3 (Fig. 8.25).

Thermal Effects

In addition to pressure/strength interactions, variations in burial temperature gradients can influence salt flow intensity. In terms of its thermal properties halite is an unusual mineral. It is one of the most thermally conductive sediments, at 43 °C the thermal conductivity of halite is 5.13 W/m-K, while a typical shale at the same temperature is 1.76 W/m-K (Figs. 6.10 and 8.25). Halite's volumetrics also respond differentially to heating. At a depth of 5 km, under a geothermal gradient of 30 °C/km, halite expands 2 % due to heat and contracts 0.5 % due to pressure (Jackson and Talbot 1994). Under such a scenario (assuming zero porosity at either depth) the base of a thick salt unit becomes slightly less dense with the increased temperatures associated with burial and so creates a temperature-induced density inversion. Thermally induced convective flow is theoretically possible in a salt layer thicker than 2.9 km under a geothermal gradient of 30 °C per km (assuming a viscosity of $<10^{16}$ Pa.s).

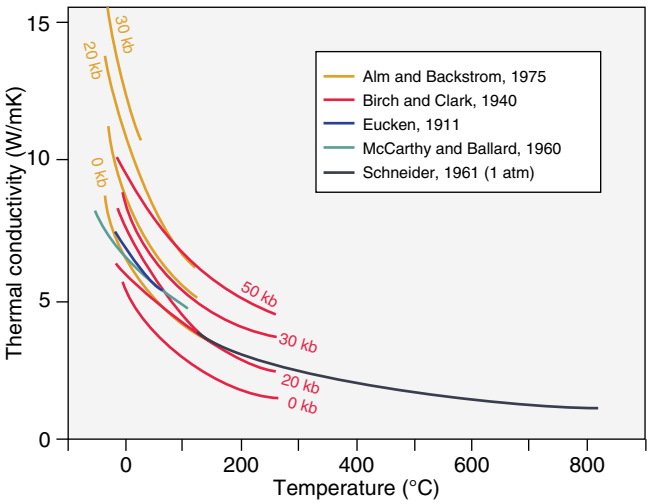

Fig. 6.10 Temperature and pressure effects on the measured thermal conductivity of halite (After Robertson 1988), see also Fig. 8.22

This mechanism may trigger diapirism in salt-filled rifts characterised by elevated nearsurface temperatures and high geothermal gradients (Talbot 1978). The volcano-shaped mounds associated with hot springs in Ethiopia's Danakil Depression, such as Da nakil Mound and its hornitos, may be located above the tops of thermally convecting plumes of salt (Fig. 11.16), as may the diapiric features on Europa, a moon of Jupiter (Pappalardo and Barr 2004) and the layered ice diapirs on Triton a moon of Neptune (Schenk and Jackson 1993; Talbot 2008).

Gussow (1968) argued that outcropping Iranian salt glaciers were catastrophic extrusives emplaced hot, in a similar way to a lava flow. He thought that heated salt was intrusive and that the salt glaciers have now cooled and so are no longer flowing. He was strongly influenced by early experimental work on dislocation creep using coarse-grained dry salt that had indicated salt could only flow at temperatures above 200 °C. We now know that most confined salt in the sedimentary realm is wet, extremely weak and capable of flow at earth surface temperatures. Later work in Iran by Kent (1979, 1987) and Talbot (1979) indicated that the salt in many namakiers is still flowing today. Temperature triggers, as first noted by Gussow (1968), do become an important consideration that can create intrusive sills and dykes once bedded salt enters greenschist facies conditions, as is perhaps seen in intrusive Neoproterozoic salt remnants in the thrust belt of the Damara Orogen in Namibia and in the Ugandan copper belt (Chap. 13 for discussion). Hot molten salt intrusion is not a major mechanism of salt emplacement in the diagenetic realm in this or in other sedimentary basins. Sodic carbonatites are another matter altogether and are discussed in Chap. 16, along with dolerite dykes cutting through salt masses,

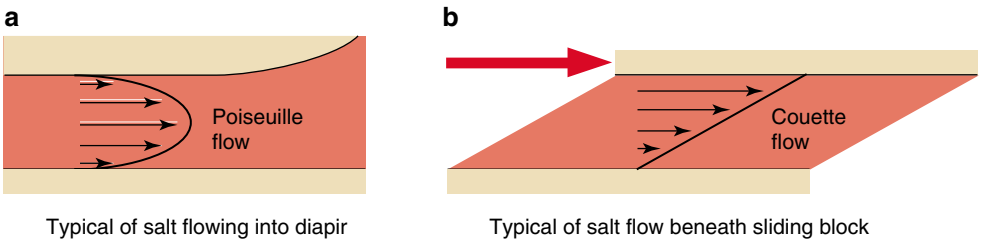

Fig. 6.11 Salt hydraulics illustrating the two main types of salt flow. *Arrows* indicate relative velocity of salt movement. Velocity profile is parabolic in (**a**) and linear in (**b**)

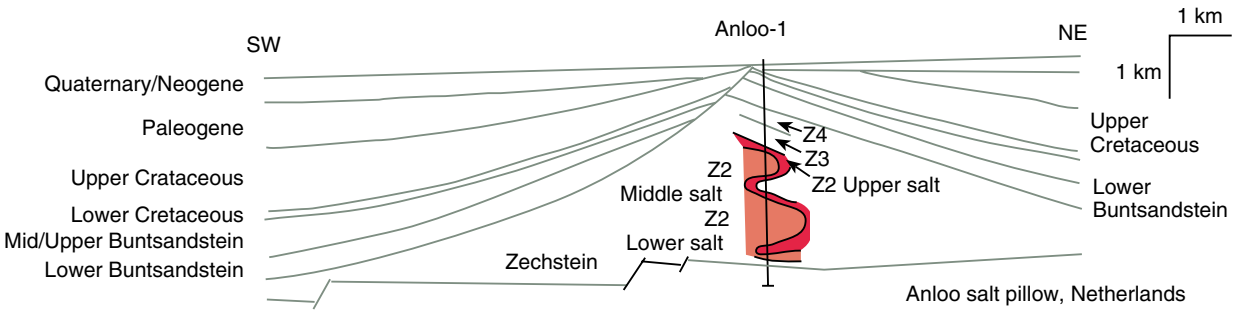

Fig. 6.12 Interpreted folded internal structure of the Anloo salt pillow (Permian Zechstein salt) based on regional seismic and fabrics observed in the Anloo-1 Well (After Geluk 1998)

Flow Textures and Rates

Meso and macroscale internal fold complexity reflects deformation textures that are occurring on the microscale and reflect the two main styles of hydraulics that describe salt flow; (a) Poiseulle versus (b) Couette flow (Fig. 6.11) Poiseuille flow, typifies flows into a rising salt structure whereby flow is restricted by the viscous shear forces (frictional) acting along the boundaries of the salt, creating boundary drag. This means the salt is flowing faster in the central part of the salt layer than along its top and bottom. It means thin salt layers flow slower than thick ones and flow in a thick salt layer (>tens of meters) is slowed down as salt withdrawal reduces the deflating salt layer to thicknesses of less than a few tens of meters. This helps explain why there are residual salt pockets in many salt welds. The other type of flow Couette flow, which involves simple shearing within the salt layer as the overburden is translated relative to the substrate (Fig. 6.11b). Couette flow typifies salt layers acting as décollements and gravity glide planes. Theoretically, in Couette flow there is no boundary effect, while in Poiseuille flow there is; but the two types of flow may well be superposed in many subsurface settings. For a detailed analysis of the variable stress regime in flowing salt and the drilling problems it can induce, the interested reader is referred to Weijermars and Jackson (2014).

Salt structures are zones where salt has thickened relative to its original stratigraphic thickness and, by definition, salt must have flowed into this thickened structure. In salt pillows the sense of flow thickening, based on the outline of the whole feature is mainly horizontal, while in diapirs there is a much greater component of vertical flow. In typical Zechstein "pillows" the predominantly horizontal flow of halite is indicated by a gross morphology with a gentle nonpiercement style of thickening, but coring shows thickening of the salt structure was driven by stacked large scale flow-folds with near horizontal axial planes, as seen in the Anloo pillow in the Netherlands (Fig. 6.12; Geluk 1998). In the late "pillow" stage, the flow direction changes from predominantly horizontal to an even less predictable system as the salt starts to pierce its overburden.

Internal Complexity

Richter-Bernburg (1980) argues for high levels of structural complexity in all salt deposits and that even our expectations of internally-consistent layering in a sequence of stratiform salt beds may not be true. He cites the Silurian Salina Salt in the Whiskey Mine near Cleveland in Michigan where apparent isoclinal folds, with horizontal axial planes, are exposed on a 3 m-tall mine face in an area of the Canadian Shield where typical formation dips are less than 5°. An underground visit in 1984 by Professor Bernberg and me to another nearby mine in the Salina Salt with similar features lead to a discussion of whether these features were actually isoclinal folds or stacked, slumped and backfilled syndepositional erosional channels. However, in other salt basins with structures showing external geometries of pillowing or diapirism, the complexity of the internal structures that form in halokinetic salt is indisputable (Balk 1953; Talbot and Jackson 1987a; Richter Bernberg 1980).

By the diapir stage the morphology of the salt structure exterior shows that the sense of salt movement is

predominantly vertical and that salt appears to break through its cover. Diapiric salt is often mined, so its internal structures have been be mapped. By this stage, vertical fold axes (Fig. 6.14c; curtain folds) have[9]) been superimposed on the horizontal fold axes. Frictional interactions between the edges of the diapiric salt and adjacent strata drives even more complex fold patterns as flow vortices are created by irregularities in the thickness of the diapir neck. An analogy for this curtain-style of flow folding is that created when a handkerchief is poked up and through a napkin ring. Once the salt is at the surface it spreads as a series of salt glaciers (namakiers) and allochthons rolling and advancing over the surrounding landscape, much in the same way as a military tank rolls forward on its track.

In many diapiric structures the central part of the salt neck contains salt from the older (lower) part of the salt stratigraphy and the margins are made up of younger units. This is true for the diapirs of Dasht-i-Kavir (Fig. 6.13) and many Zechstein diapirs such as Benthe, Reidel, Winschoten and Zuidwending diapirs (Fig. 6.14a). But, as noted by Geluk (1998), this is a generalisation for there are many Zechstein diapirs where the reverse is true (e.g. Gorleben, Hänigsen and Pieterburen diapirs). Internal complexity is especially obvious in Zechstein diapirs where potash layers have been mapped as part of the extraction and ore control process (Fig. 6.14a, b). Characteristic flow folding and shearing is outlined by halite beds swimming or floating in isoclinally-folded carnallitite beds, as in diapirs in Miocene potash of Sicily and Poland and Zechstein of Germany.

In all these examples, areas of high strain are largely accommodated by the least competent layer, typically potassium salt or purer finer-grained rock salt units (Figs. 6.14b and 6.15). Some halite layers between these high strain intervals can remain relatively undeformed and even retain remnants of primary fabrics, such as megapolygons and microkarst pits. As the structure continues to deform and fold into a series of constriction folds and if flow continues the more competent layers ultimately brecciate or stretch into boudins (Fig. 6.14c). Finally, the halite layers pervasively recrystallise via pressure solution creep and no primary texture remains. Similar boudins and folded claystone or dolostone masses are folded can be imaged as stringers at the seismic scale using 3D techniques (van Gent et al. 2011; Kukla et al. 2011a, b).

The internal complexity of salt structures is such that the near-surface portions of salt diapirs may be divided into a number of zones showing differential movement and separated by shear zones. This was first demonstrated by Balk (1953) in a classic paper mapping the internal

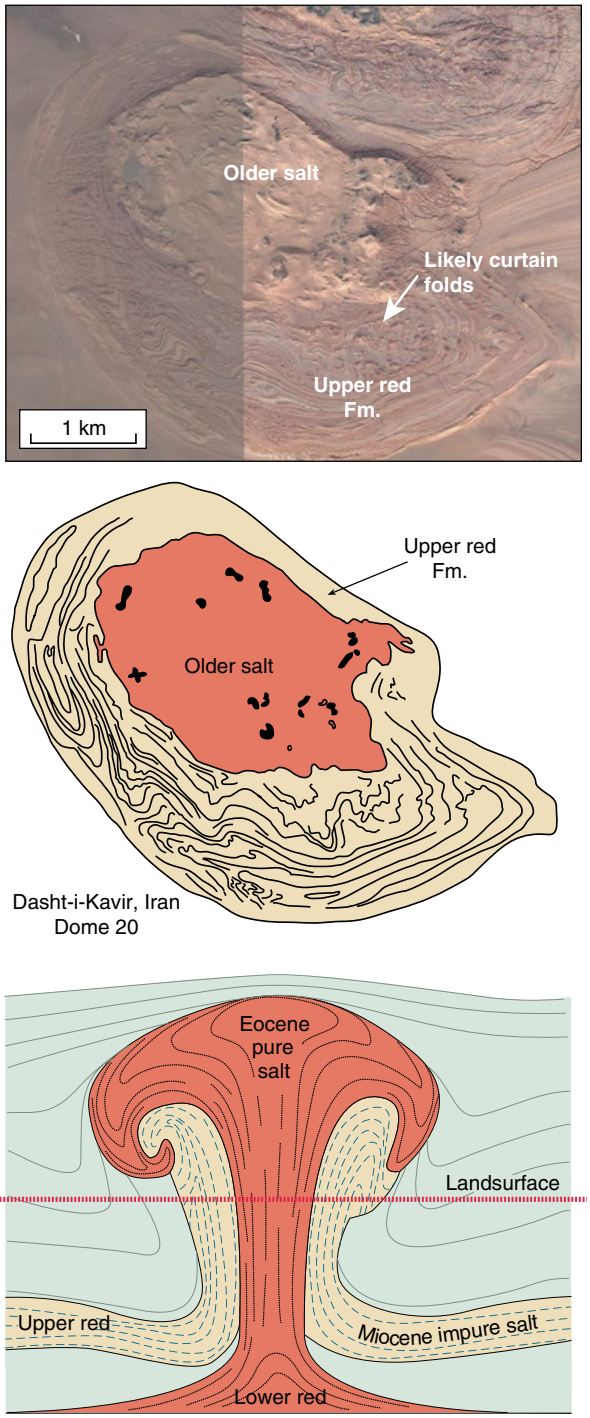

Fig. 6.13 Internal fabrics visible in salt structure outcrop (Dome 20 in the Dasht-i-Kavir, Iran). Its central portion is made up of Older Salt (Eocene), which is composed of relatively pure halite and is consider to be the halokinetic equivalent of the Lower Red Formation. Surrounding this, and making up the outer part of the dome, is the Miocene Upper Red Formation, which entrains alternations of clay, anhydrite and halite. These layers clearly outline the complex folding styles that characterises salt flow in the outer portion of the plug. The cross section illustrates the likely "curtain fold" style of this feature. *Red dashed line* indicates current landsurface level in the structure. Rafted blocks are also visible in the older salt mass (Bing® image mounted and scaled in MapInfo® software, (Schematic cross section is after Jackson 1990))

[9]Curtain folds are cylindrical fold having roughly radial axial trace and steeply plunging hinge within a diapir, possibly incorporating sheath folds originally formed in the source layer (Fig. 6.14c).

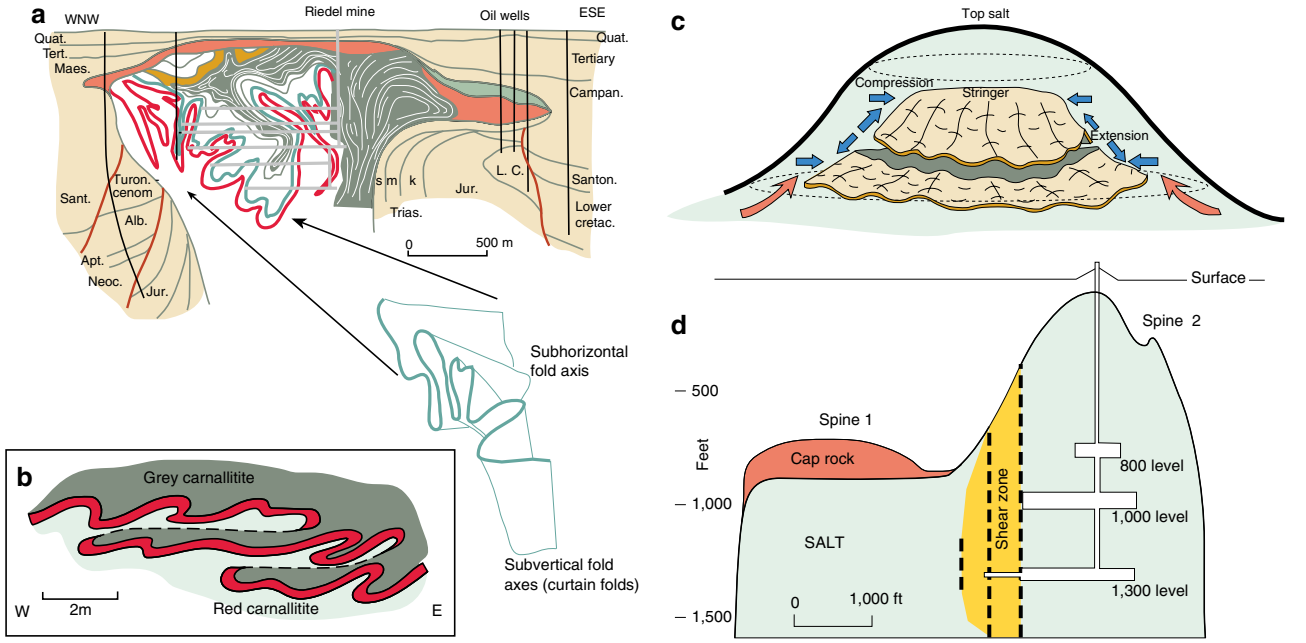

Fig. 6.14 Internal structures of salt diapirs, (**a**) Reidel diapir, Germany. The stratigraphically older part of the diapir (*grey*) of the structure sits atop the younger salt (*white*). Inset is a three dimensional diagram of the folds outlined by potash beds (ore horizon) in younger salt showing how axes of folds pass from a vertical orientation to a subhorizontal with depth. (**b**) Halite bed (*black*) defines sheath folds and shear planes floating in deformed carnallitic matrix in a potassic ore zone in the Krügershall Mine near Halle/Saale, Germany (After Richter-Bernburg 1980). (**c**) Formation of constriction folds (curtain folds) and concentric boudins due to flow into a salt dome. The combined effect of the tensile forces due to vertical extension and coeval horizontal compression due to the decrease in salt dome diameter results in the contemporary formation of contradicting structural styles (After van Gent et al. 2011). (**d**) Cross section through the Jefferson Island Salt dome, Louisiana, showing a wide boundary shear (black salt) separating an active salt spine from a less active caprock-capped part of the structural crest. North is to the left and the 800, 1,000 and 1,300 ft working levels of the mine are shown (After Kupfer 1976)

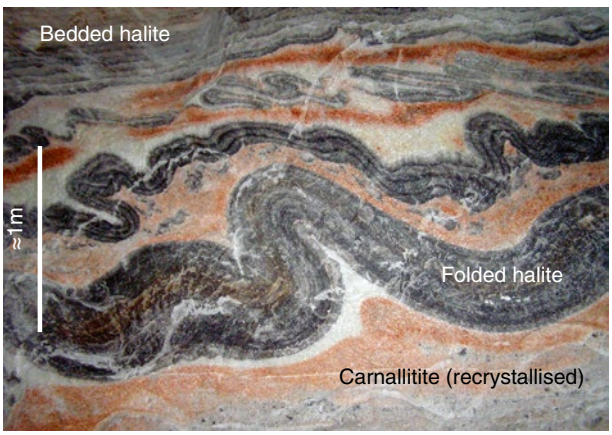

Fig. 6.15 Mine wall illustrating the varying response to differential stress in a number of halite and potash rich layers in a salt mine in Eastern Germany (Schofield et al. 2014)

complexities and shears in mined salt diapirs in the Gulf coast. Subsequent work by Kupfer (1976) on the same structures further refined notions of internal shear in diapirs. A shear forms where adjacent parts of a salt structure rise at different rates. This differential rise at the crest of a structure typically creates an active topographic high and a lack of thick caprock atop a rising spine, as is the case at Jefferson Island salt dome (Balk 1953; Kupfer 1976). The younger part of this salt stock is now 250 m (800 ft) higher than the adjacent flat-topped mass, which is also overlain by a cap rock (Fig. 6.14d). The boundary separating the spine from the less active portion of the crest is finer-grained and shale rich and it formed a limit to the former salt mining of the pure salt within the spine. Shale-rich shear zones at the edges of active spines and the clastic stain internal shears are sometimes called "black salt" by the miners and can show a greater propensity to leak water into a mine. The spine and its boundary shear are also seen in the Jefferson landscape, with a solution lake defining the zone of shallower salt created by the active spine. Shear zones within diapirs are potential problem zones if the crestal portions of domes are utilised for any type of fluid storage without an understanding of the significance of "black salt" (Fig. 13.48).

As a salt crystal moves in actively flowing salt, it recrystallises via various creep mechanisms. As it re-anneals, its outline stretches and deforms, leaving behind a strain memory of the stress regime in the various structures and crystal fabrics preserved in the diapir (Fig. 6.16a; Raymer and Kendall 1998; Talbot 1992a; Urai et al. 1986; Zak and Freund 1980). Studies

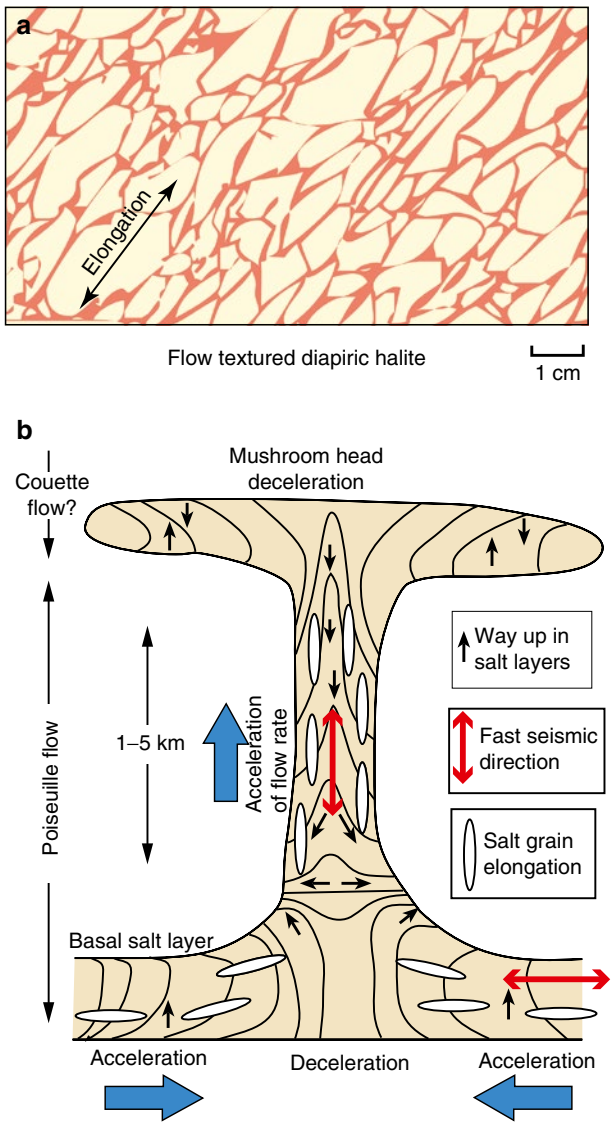

Fig. 6.16 Micro and macro scale flow texturing. (**a**) Digitised outline of flow textured halite crystals in a thin section of diapiric salt, no primary texture remains. (**b**) Schematic velocity fields in a flowing diapir derived from physical models. The deformed outlines of originally vertical markers are shown, as well as bed facing and salt elongation directions (After Davison 2013, Davison et al. 1996a, 2013)

of irradiated salt crystals show that the grains in flowing salt have such short strain memories that they rarely strain beyond length to width ratios of 4 or 5 before new flow aligned crystals are created and older sub-grain orientations are destroyed, like many other crystalline rocks in structurally complex lithologies, such as migmatites and mylonites (Figs. 6.5 and 6.7). A subgrain is a volume of crystalline material surrounded by subgrain walls composed of planar arrays of dislocations and are structures in halite best seen in irradiated samples (Fig. 6.17; Looff 2000). The subgrain walls separate crystalline material of the same composition with slightly misoriented crystal lattices (usually less than 1°).

Salt Crystal Size and Other Stress–Strain Indicators

Salt creep proceeds at stresses above a critical shear stress by glide and the multiplication of dislocations (Carter 1976). Dislocations are linear defects in the crystal lattice that divide slipped regions in the crystal from unslipped regions, allowing localized slip to occur and spread consecutively (Fig. 6.5a). With increasing deformation, dislocation density increases and work hardening occurs as the dislocations tangle and interfere with each other, limiting salt mobility. Recovery occurs by the diffusion of vacancies that allow dislocations to climb normal to their slip planes to avoid obstacles, and form stable subgrain walls (Fig. 6.17). Steady-state creep constitutes the bulk of the creep strain in naturally deformed deeper diapiric salt and occurs when the salt recovers at the same rate that it hardens, so that large creep strains can be achieved at constant stress and strain-rate (Carter 1976; Carter et al. 1993)

Hence, fine-scale grain-shape fabrics in confined flowing salt can record only the later stages of the strain history; its current and near current stress response. Total strains, resulting from superimposed deformations, are recorded by larger strain markers in the salt mass–primary anhydrite/dolomite layering or bedding, nodules, inclusions, and veins– all of which have much longer strain memories than individual halite crystals (Talbot and Jackson 1987a, b).

That is, constant readjustments and recrystallisation to the variable stress field experienced during flow does indicate the ambient stress field in a diapir (Fig. 6.5b). Most halokinetic salt crystals have long axes that are a few cm long and are steeply inclined to subvertical within a salt stem or wall (Fig. 6.16a). Between the elongate crystals are subgrain crystals with diameters that are a response to stress and can be approximated by an experimental power law equation noted by Carter et al. (1993) (see also Fig. 6.4a):

$$D(\mu m) = 214\sigma^{-1.15}$$

where D is the average subgrain size in microns and σ is differential stress in MPa.

This equation means crystal size in a diapir can be used to estimate differential stress in a salt mine or salt core. A detailed analysis of subgrain size immediately below the two-spined crest of the Weeks Island salt dome in Louisiana found differential stresses in the salt mass vary from 0.87 to 2.33 MPa at the 1,000 ft level (Fig. 6.18; Looff 2000). Higher stress levels and smaller subgrains indicate more actively moving salt. Finer-crystalline textures are generally associated with areas of salt spine beneath regions of higher surface topographic relief, while lows are tied to underlying zones of coarser-grained, recrystallised salt (Fig. 6.18).

Detailed mapping of internal mesoscale strain markers along with modelling experiments have clearly shown

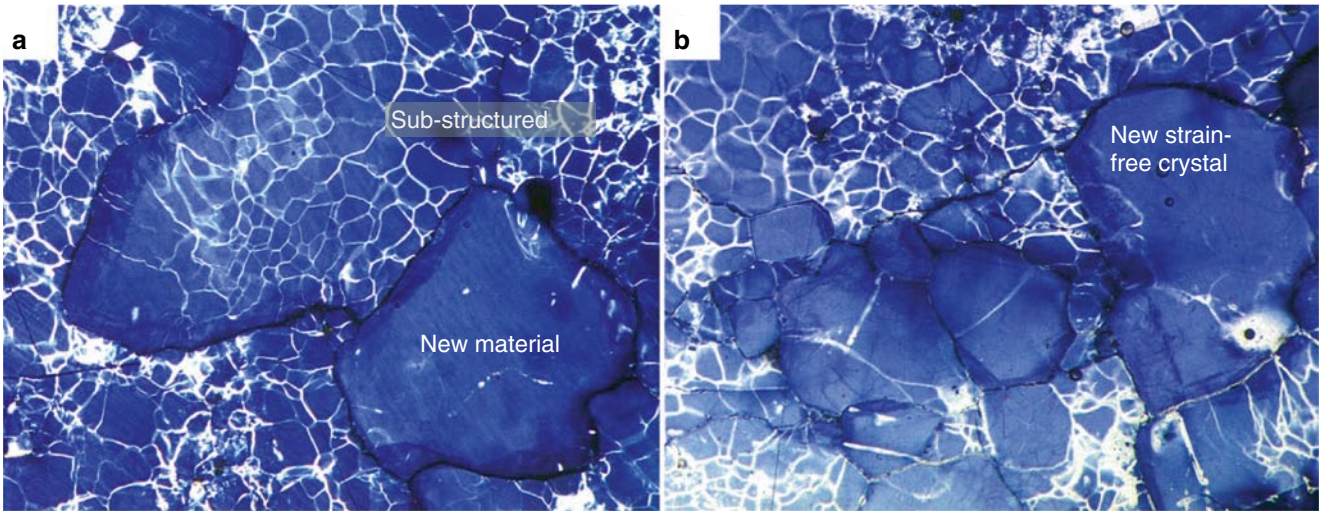

Fig. 6.17 Microstructures of sample from salt layer at a depth of 457.5 m in the Middle Triassic Rot Formation at Hengelo, Netherlands. Both are plane polarized transmitted light images of a salt sample from 475.5 m depth that was gamma-irradiated at 100 °C. (**a**) Migration of high angle grain boundaries as recorded by elongated subgrains, and strain-free new material, which grows at the expense of old, heavily substructured grains. Image width is 11 mm. (**b**) Strain-free grains that grew at the expense of deformed ones. The size of some of the new grains is comparable to that of subgrains. Image width is 7 mm (Both images courtesy of Zsolt Schléder; see Schleder and Urai 2005 for full details)

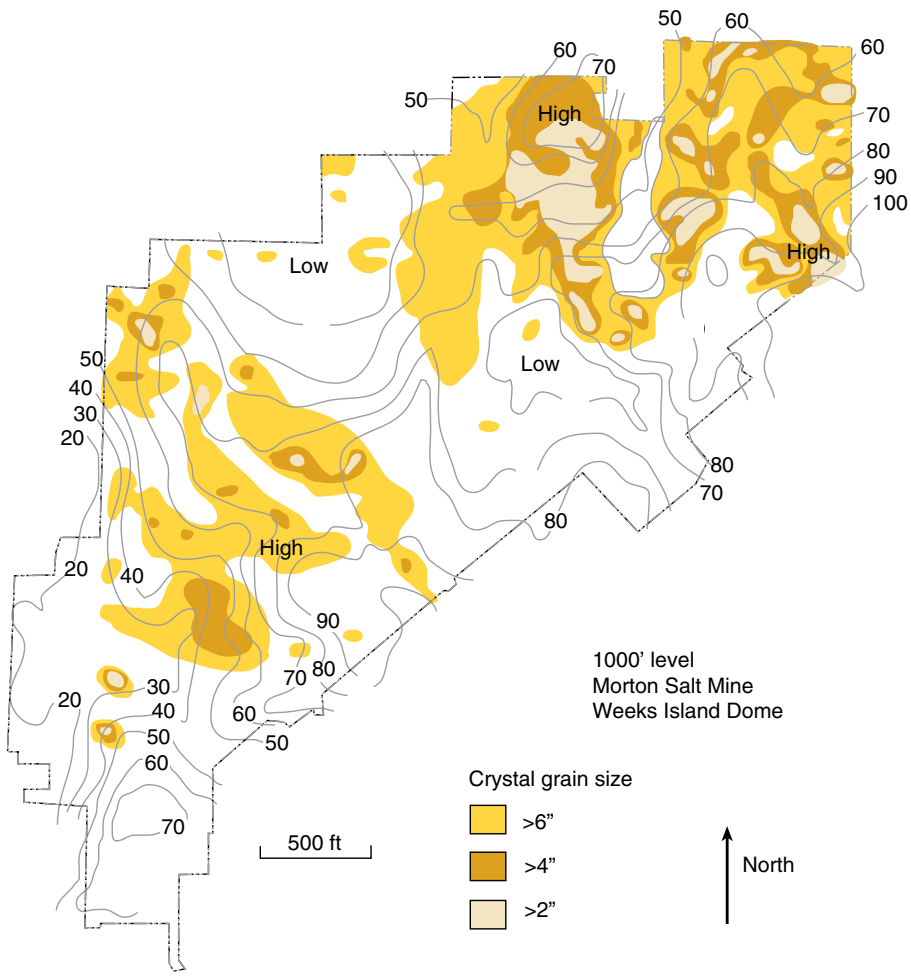

Fig. 6.18 Comparison of the salt grain size in the 1,000 ft level of the Morton Salt Mine, Weeks Island Louisiana, with surface topography over the mine. The finer-grained salt is generally associated with topographic high areas, while topographic depressions are associated with coarser-grained salt (After Looff 2000). See Fig. 13.48 for location of this the mine outline on Week Island

internal flow in deforming salt away from shear zone is not homogeneous (Kupfer 1976; Zak and Freund 1980; Burliga 1996; Davison et al. 1996a; Sans et al. 1996a, b; Smith 1996; Talbot and Alavi 1996; Geluk 1998; Schenk et al. 2006). Foliations in deformed salt in a diapir are often axial to folds that develop in the primary layering and to the flow folds that map local gradients in flow rates along internal stream lines and surfaces in the moving salt (Fig. 6.16b; Talbot 1979, 1992b). If these layers approach mechanical passivity then the flowing viscous salt "fluid" picks up internal flow folds wherever the salt slows and thickens to pass obstructions. Beyond the obstruction the flow accelerates and internal folds tighten and almost disappear in the narrowing flow before they refold at the next obstruction. If the internal markers are strain active, the slow (competent) layers fold, while fast (incompetent) layers mullion as they shorten within the slowing flow. Shears zones forming in a deforming salt body first grow in the least competent (usually potassic) horizons within the flowing salt mass. Between the shear zones, less deformed halite layers are carried laterally and upward into the diapir stem.

Davison et al. (1996a) show that fold wavelengths in Zechstein salt the North Sea (Fig. 6.76) are of the order of 20–30 km in layers with an original thickness of more than 1km and an overburden that is now more than 1km thick. The spacing of the folds controls the amount of salt that drains into any particular structure. With a circular drainage envelope of 10 km radius a 1.5 km-thick salt layer can supply of the order of 470 km^3 of salt to a single diapir. This is much greater than the volume of salt held in a typical North Sea diapir, which is around 25–75 km^3. It means there has been substantial salt loss by allochthon escape and crestal dissolution. The rate of salt supply is not constant throughout the drainage area as the rate of radial flow increases closer to the diapir. According to Davison et al. (1996a) the constriction associated with flow into the diapir neck creates strain within the neck up to 80 times greater than in the surrounding source layer. Thus, vertical flow in the centre of a diapiric neck produces extreme prolate strain textures that are in turn nullified at the top of the diapir where vertical flattening takes place via recrystallisation (Fig. 6.16b).

Various combinations of pressure solution creep and dislocation creep create the deformed, aligned and recrystallised halite textures seen in cores recovered from salt flows. Average halite grain size in cores from deformed recrystallised salt ranges between 5 and 10 mm in Zechstein salt in the North Sea and in Miocene salt in Mt Sedom in Israel and from 15 to 20 mm in Gulf Coast salt; all with L/S ratios typically greater than 1.5 (Davison et al. 1996a; Zak and Freund 1980; Talbot and Jackson 1987a).

Any interbedded sediment within the salt source layer strengthens a salt unit; it initially creates drag zones within the flowing salt, and so induces anisotropic strength and strain effects in the source layer as it moves toward the salt stem. This drag is often sufficient to generate small wavelength sheath folds. Once diapirism is more advanced, intrasalt beds (up to 40 m thick) in the mother salt are brecciated or boudinaged. Salt can then flow across former intervening layers, carrying along fragmented and fractured layer remnants, with the whole region then behaving like a pure salt mass. Thus, once the system attains diapiric status, the strength and resistance to flow created by more competent intrasalt beds is drastically reduced by boudinage and breakup. Once the intrasalt beds are broken, diapiric salt can develop internal vortices like a billowing cloud of smoke, which trap, encapsulate and lift the fractured blocks of intrasalt beds.

The captured fragments, usually dolomite, anhydrite or dolerite blocks, are referred to as "rafts" although they are not truly floating in the salt mass. Their density is typically higher than that of the salt. Rather, they are being swept upwards on a rising plume (Kukla et al. 2011a, b; Strozyk et al. 2012). Raft blocks can be porous and contain gas (including H_2S), oil or water and may create zones of unexpected overpressure when drilling salt. Once salt flow slows or ceases, blocks previously buoyed and caught up in the flowing salt mass of the diapir stem can sink back toward the base of the salt stem (Fig. 8.24a; Koyi 2001). The style of intrasalt boudinage depends on the degree of induration of the entrained sedimentary layers. Where the sediments are well indurated the breakup of intrasalt beds tends to create angular clasts, where less consolidated the beds tend to stream, streak and flow plastically, like the adjacent salt. Boudinaged and aligned angular clasts and blocks are a substantial component in any later halokinetic dissolution breccia (Figs. 7.29 and 7.30).

Microstructural Domains

There are predictable microstructural domains within this framework of flowing salt, as it migrates from the mother salt bed, through a diapir stem and into an extrusive structure, along with possible dissolutional reworking (Fig. 6.19; Urai et al. 2008). In undisturbed rock salt (position 1 in Fig. 6.19) the primary microstructures reflect the depositional conditions, with remnant fluid-inclusion-outlined chevron grains and microkarst textures. In regions of slightly deformed rock salt such as where the salt moves toward and first into the diapir stem (position 2), subgrains develop, together with incipient grain boundary migration zones. As migrating grain boundaries sweep through fluid-inclusion-rich primary crystals, the inclusion fluids collected at the grain boundary. Alternatively, salt solution-precipitation creep (pressure solution creep) is dominant in regions of finer grained flowing salt. Large contrasts in rheology are common in layered salt, even from the onset of tectonic deformation. As the salt

rises into the stem and deforms further (position 3), steady-state microstructures are produced after complete recrystallisation of the halite, although primary fluid-inclusions fluids are still preserved in intergranular positions. In the cooler portions of the diapir stem, high stress and small subgrains develop (position 4). On attaining the surface, weak mylonitic shear zones form and pressure solution mechanisms dominate (position 5), so allowing a namakier to flow downhill via gravity spreading, at unusually high strain rates compared to the stem and source levels (position 5). In the namakier, mesotextural indicators of Coutte flow are more common (Fig. 6.16b). Finally, at- and near-surface dissolution and ablation of the salt glacier edges occurs, typically driven by infiltrating rainwater, this facilitates halite recycling into ambient landscape sumps, which are often in rim synclines. In semi-arid to arid areas this leads to the formation of saline playas and chotts, where new salt crusts accumulate (Figs. 3.68 and 6.19). These are depositional sumps where the recycled salt can accumulate with primary bed (aligned-chevron) textures once more.

The change in salt crystal shape as it elongates in flow also produces seismic anisotropies within the flowing salt mass (Fig. 6.16b; Davison 2013). Pure halite has a seismic velocity of 4,500 ms^{-1}, which is often assumed to be a constant in velocity modelling of a salt mass. However, flowing salt bodies can contain varying amounts of anhydrite (velocity 6,500 ms^{-1}), or K-Mg-rich salts with velocities down to 3,500 ms^{-1}. A thick cap rock of anhydrite (up to 400 m) can occur due to salt dissolution along the top salt surface, so varying velocities are more realistic, even when used in initial velocity model testing in diapiric areas where the evaporite composition is unknown. All deformed salt bodies contain salt crystals that are preferentially elongated in the flow direction (Fig. 6.16a): they tend to be vertical in salt diapir stems and horizontal in source layers (Fig. 6.16b; Davison 2013). The P wave seismic velocity anisotropy has been measured at up to 7 % faster in the flow direction (Raymer et al. 2000). Individual interbeds of anhydrite and dolomite may also increase velocity anisotropy within the salt body if they maintain intact layers for long vertical distances. Currently, most seismic velocity models of diapiric salt do not encompass these known anisotropies.

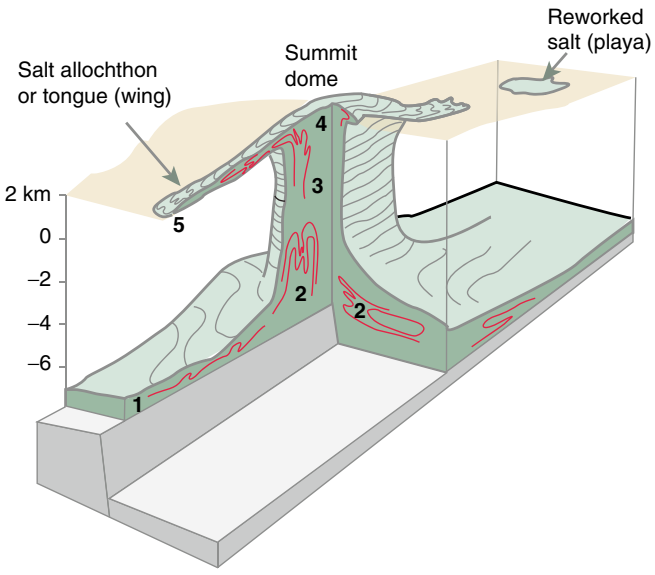

Fig. 6.19 Conceptual model of the rock salt cycle and associated rheological transitions and structures with respective microstructural domains (*1–5*). See text for detail (After Urai et al. 2008)

Triggers, Drivers and Outcomes of Salt Flow

We have seen that density inversion alone does not trigger salt flow; so what does? From our preceding discussion we know that pure salt is extremely weak compared to its surrounds (Fig. 6.7). Wet salt at or near the surface in a namakier or allochthon collapses under its own weight (gravity spreading) and so is capable of behaving like a Newtonian fluid across most geological time scales. In contrast any overlying or adjacent sediment responds brittlely in the same stress field. It seems salt structures in extensional basins that are accumulating sediment are triggered and driven by two main mechanisms; extension and differential loading. Both are derived from externally applied forces. Later in this chapter we shall look at salt flow in relation to external compressive forces, but for now we will focus on extensional systems.

Salt flow can be triggered syndepositionally by the accumulation and gravity-driven extension of overburden or by an externally imposed episode of regional extension and overburden foundering. Extension can be syndepositional with salt accumulation, or can occur long after bedded salt was first deposited and buried (Vendeville 2005; Hudec and Jackson 2006). Syndepositional movement was the case with the numerous early allochthons and minibasins in the Jurassic of the northern Gulf of Mexico and the Cretaceous of Santos Basin of Brazil. Initial halokinetic-sediment feedback began in the Mesozoic, yet further out in both basins flow continues today as allochthons of Mesozoic salt are emplaced atop Neogene deep-seafloor sediment. Over much of the current North Sea and NW Europe, salt flow was triggered by later regional extension. That is, flow of Zechstein salt (deposited in the Late Permian) began in the Triassic, some tens of millions of years after salt deposition had ceased. These Triassic extensional geometries were further complicated in the late Mesozoic to early Tertiary when there was a widespread episode of reactivated salt flow, triggered by compression tied to the Alpine orogeny (Mohr et al. 2007).

Studies of halokinesis conducted in the 1980s tended to place more significance on the triggering and driving effects of differential loading and gravity spreading (Trusheim 1960; Dailly 1976; Seni and Jackson 1983a, b; Jackson and Talbot 1986, 1991; Worrall and Snelson 1989; Nelson 1991). Studies in the early 1990s tended to emphasise the role of regional extension and gravity gliding (Duval et al. 1992; Vendeville and Jackson 1992a, b; Demercian et al. 1993; Jackson and Vendeville 1994). By the late 1990s, differential loading was physically modelled in the same way as extension had been and shown to be an equally valid mechanism for both triggering and driving salt flow in basins accumulating substantial volumes of sediment (Ge et al. 1997).

Now after more than three decades of detailed seismic mapping of salt structures in hydrocarbon-prone active halokinetic regions in the Gulf of Mexico, the Santos Basin, the North Sea and offshore West Africa, we know that both mechanisms can operate concurrently from the first onset of salt flow. Waltham (1997) argued that apparent differences in triggers (loading versus extension) are two end members of a response continuum, depending in large part on the thickness of the salt and the rate of deformation (Fig. 6.20).

Gravity gliding and gravity spreading are end-member modes of gravity tectonics, and both result in a decrease in gravitational potential energy. In gravity gliding, the driving energy causes motion parallel to the basal surface and is downdip along that surface (Fig. 6.21a). Gliding does not require internal deformation of the translating body, but a moving body with internal flow parallel to the basal slip surface is a variant of gliding. This means that sometimes a salt body that has experienced gravity gliding retains primary halite chevron textures away from the zone of translation or gliding (as is the case below salt-encased carbonate slivers in portions of the Ara Salt in Oman; *pers. obs*). The bottom surface must have a component of dip in the movement direction, whereas the dip of the top surface is not diagnostic of gliding: it may have no overall dip (or it may dip counter to movement. In gravity spreading, the driving energy causes motion of the material toward the basal surface (Fig. 6.21b), requiring deformation of the spreading body. Parts of the upper surface must have components of dip in the movement direction, but the dip of the basal surface may be opposite to this motion, or horizontal or in the same direction as the motion. That is, gliding is associated with a dip into the basin below the salt, spreading is often more tied to differential sediment loading.

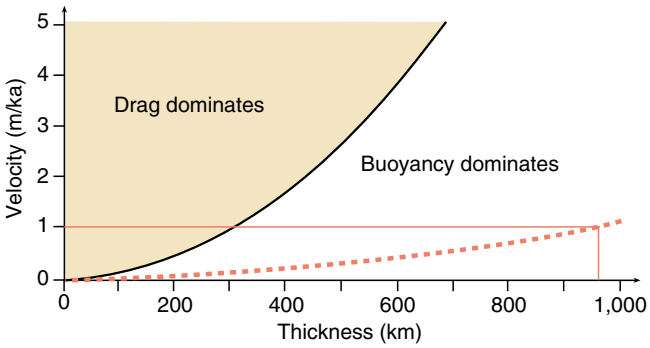

Fig. 6.20 Shaded interval shows the overburden velocity field where drag (largely a brittle response in the overburden) dominates over buoyancy contrast as a trigger of salt flow (viscosity is 1×10^{18} Pa.s). The dashed curve shows the overburden velocity field at which drag dominates over buoyancy if the viscosity is ten times higher (i.e. 1×10^{19} Pa.s). The crossline shows the salt thickness corresponding to an overburden velocity of 1 m/ka (After Waltham 1997)

Brun and Fort (2011) list the following sets of diagnostic structures useful in defining whether the dominant process sets were related to gliding or spreading. Good diagnostic structures for the dominance of gliding include sealed tilted blocks in the updip extensional domain and early folding and/or thrusting in the downdip contractional domain. Migration of the contraction is updip (landward) in settings dominated by gliding and seaward in pure spreading. Only if the seaward part of the salt basin is free of sediments, is early suprasalt rafting tied to ex tensional diapirism indicative of pure spreading. Otherwise, if rafting is synchronous with downdip contraction, then it indicates the dominance of gliding processes (Fig. 6.1b). Frontal salt nappes tend to form progressively in situations dominated by spreading processes, as a direct function of the amount of sediment deposited on top of the salt basin, but only if the seaward part of the salt basin is free of sediments. In situations dominated by gliding they form suddenly, after a long period of downdip contraction.

This paper by Brun and Fort (2011) and the reply by Rowan et al. (2012b) show there are still some fundamental

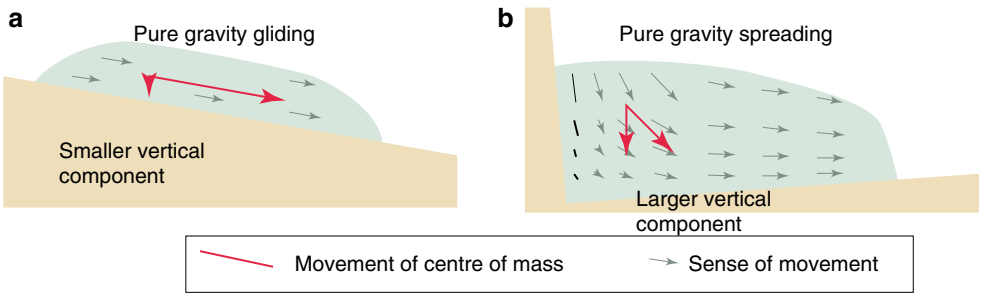

Fig. 6.21 (**a**) Gravity gliding versus (**b**) gravity spreading (See also Fig. 6.11)

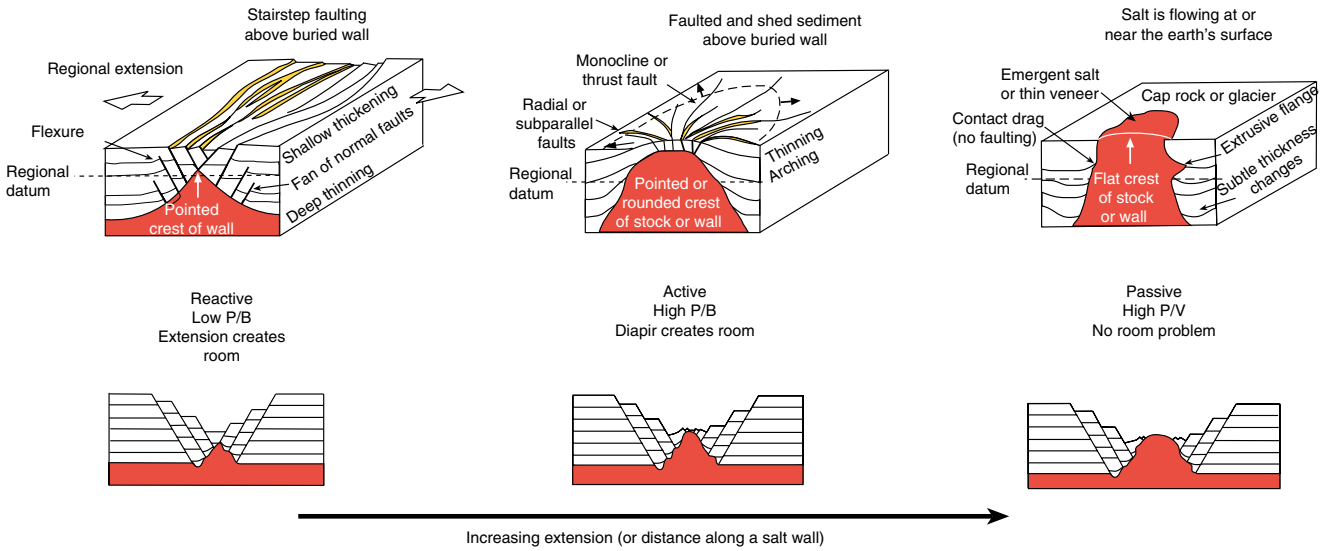

Fig. 6.22 Three piercement modes for diapirs (salt is red) and their characteristic structures. Regional datum is indicated by a *dashed line*). *P*, *V* and *B* refer to stresses due to salt pressure, salt viscosity and overburden brittle strength, respectively. Extension is accommodated by both graben-related faulting and diapir widening (In part after Vendeville and Jackson 1992a; Jackson et al. 1994a)

differences to be addressed in terms of dominant triggers and process sets driving salt tectonism. Brun and Fort (2011) argue that the dominant trigger for salt tectonics, at passive margins worldwide, is gliding down a margin dip. They go on to argue that salt tectonics triggered by differential sedimentary loading is a process that is difficult to reconcile with geological field evidence. Rowan et al. (2012b) argue the opposite.

Diapirs and Extension

During regional extension diapirs can "pierce" the overburden in three related ways: reactively, actively and passively (Fig. 6.22; Jackson et al. 1994a, b). A reactive diapir pierces by filling the space created by divergence of faulted overburden blocks. Reactive diapirism occurs during regional extension as salt approaches the surface beneath a subsiding graben in the thinned overburden. This surface graben is matched by development of an "inverse graben" at the underlying salt-sediment interface (isostatic balance). Salt fills the expanding space in the inverse graben and forms a reactive diapir that is triangular in cross section with flanking growth faults that become younger toward the diapir crest. If regional extension ceases before the onset of active diapirism, so does diapirism. Extension typically reflects a more regional set of tectonic processes such as gravity spreading or gliding of shelf and rise sediments in opening rifts. Diapiric salt at the reactive stage is not forcing aside overburden sediment, it merely reacts to regional stretching as it moves into space created by extension.

Extensional faulting is an effective mechanism for initiating diapirism in many situations, regardless of the prior overburden thickness, lithology or density (Fig. 6.22; Vendeville and Jackson 1992a, b). In such settings there is always a low ratio between salt pressure (Ψ) and brittle strength of the overburden. Reactive structures can be found either beneath newly-deposited thin overburden just starting to extend, or atop deeply buried salt beds in regions newly undergoing extension (Fig. 6.23).

An active diapir, by definition, lifts and shoves aside its overburden. Unlike reactive diapirism, this style of salt emplacement must deal with a "room" problem. It requires forceful intrusion to remove the roof of sediment atop the salt and is sometimes termed upbuilding. It is possible only if the overburden is relatively thin, whereby salt pressure exceeds the brittle strength of the overburden (Fig. 6.23). The roof must be thin enough for the pressure differential to lift it. For this to happen the roof is typically less than 20 % of the entire thickness of the overburden flanking the diapir (Jackson et al. 1994b). However, once initiated, a diapir can actively pierce each new increment of sediment that buries it. Repetition of active piercement events sheds successive episodes of thin cover sediment into a debris belt around the growing diapir.

Over time, an active diapir can pierce large cumulative thicknesses of sediment and create successive stacked unconformities about the diapir stem, which fade away with passage into areas above the withdrawal sink (rim syncline). Each unconformity defines an episode of active piercement. Fractures formed during shedding of crestal sediment in active diapirism are extensional, often filled

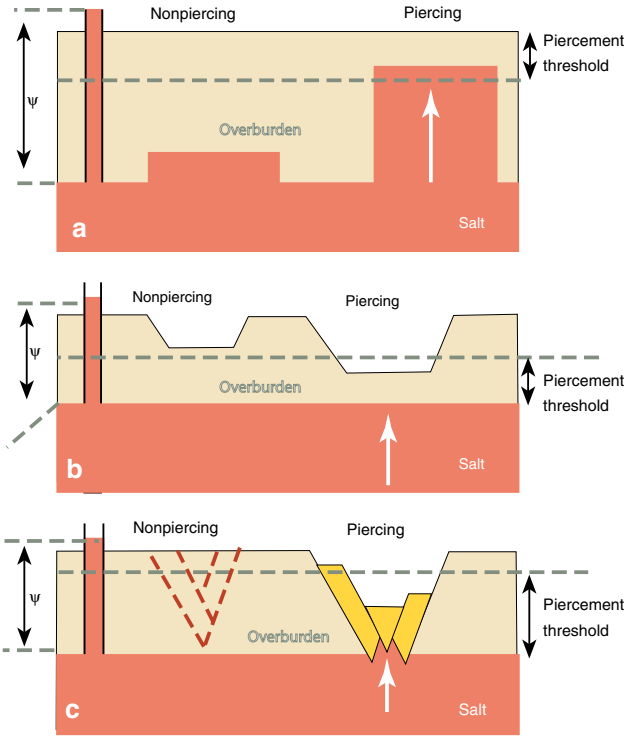

Fig. 6.23 Conditions for active piercement of salt (*red*) overlain by rigid brittle overburden (*brown*). Where the overburden is thinner than the piercement threshold, the salt can break through (*white arrows*) under non-extensional conditions above salt ridges (**a**) or below topographic troughs (**b**). In (**c**) the non-stretched salt roof is too thick to permit diapirism but where it is thinned by extension to below the critical thickness a diapir can break through. Ψ is the pressure head of salt (After Jackson and Vendeville 1994)

with infiltrated sediment and typically show little displacement of sedimentary layering on either side of the fracture (as is the case in fractured Lisan Fm. laminites atop actively flowing Sedom salt in the Dead Sea depression; Marco et al. 2002).

As well as active diapirism occurring by overthinning during extension (Fig. 6.22), there are numerous examples of compressional active diapirism driven by shortening or regional compression squeezing a salt structure and so forcing salt upward to uplift arch or intrude the roof, Regional tectonic forces typically are much greater the buoyancy forces active in extension, so compressional active diapirism can deform much thicker roofs than extensional active diapirism, as has occurred in numerous pierced anticlines in the Zagros belt, Iran (e.g., Fig. 6.32).

Once a diapir or salt wall emerges and flows onto the earth's surface it becomes a passive diapir, typically rimmed by salt allochthons; its edges spread and collapse under the weight of the extruded salt mass (Newtonian flow). A passive diapir crest maintains its position near the surface, while the adjacent sediment lows, along with the source salt layer they cover, subside. This is called downbuilding[10] with rim syncline maintenance and was first documented by Barton (1933). A passive diapir cannot continue to rise without ongoing sedimentation to load areas adjacent to the at-surface salt, but the area of the salt mound can widen and if extension continues will ultimately subside (falling diapir stage). A thin skin of sediment can form atop the salt high but it is continually breached, pierced, foundered and fragmented. Its remnants are erosively shed from the diapir crest, or carried away "conveyor belt style" by divergent lateral flow of the underlying salt allochthon. Thus little or no sediment accumulates atop the crest of a passive diapir. Most adjustments in the thickness of accumulating sediment in the adjacent subsiding basin is a response to the evacuation or withdrawal of salt at deeper levels below the accumulating sediment pile.

A lack of vertical constraint to the rising salt at the passive stage means there is no "room" problem; flanking strata need not be rotated, faulted or pushed aside as they must be during active diapirism. Faulting and folding are negligible in the sediments adjacent to passive diapirs, apart from a narrow drag zone along the salt-sediment contact (Fig. 6.22; Jackson et al. 1994a, b; Schultz-Ela 2003). Once the source layer is depleted, the diapir ceases to grow and is buried by further sedimentation. Shapes of passive diapirs are primarily a function of the ratio of salt flow rates to sedimentation rates. When balanced, the diapir stem grows vertically; when sedimentation rate is relatively slow, the salt leaks out over its surrounds to give flanges to the diapir and a more mushroom-like allochthonous aspect.

The sequence reactive -->active -->passive can be altered by changes in rates of extension, depletion of the source layer or changes in sedimentation rate, and so various evolutional paths are possible (Jackson et al. 1994a):

- Although a diapir may appear to be initiated passively, most likely it was reactive or active during its earliest stages. If the overburden was thin and unevenly deposited, the reactive and active stages are very brief, and the strata faulted during these very early stages can be too thin to be resolved seismically.
- A diapir that appears to have been passive may have passed through numerous cycles. Each cycle could have

[10]The process of downbuilding describes the situation where the rise of the salt relative to the source salt layer occurs coevally with further overburden deposition and loading, so the distance increases between the source layer and the surface of the basin, while the crest of the salt structure maintains the same position in earth space.

Its corollary is upbuilding, this describes the situation where salt rises after the overlying strata have already been deposited, thus the rising salt will warp and eventually break through overlying strata. The crest of the structure changes its position in earth-space as it grows.

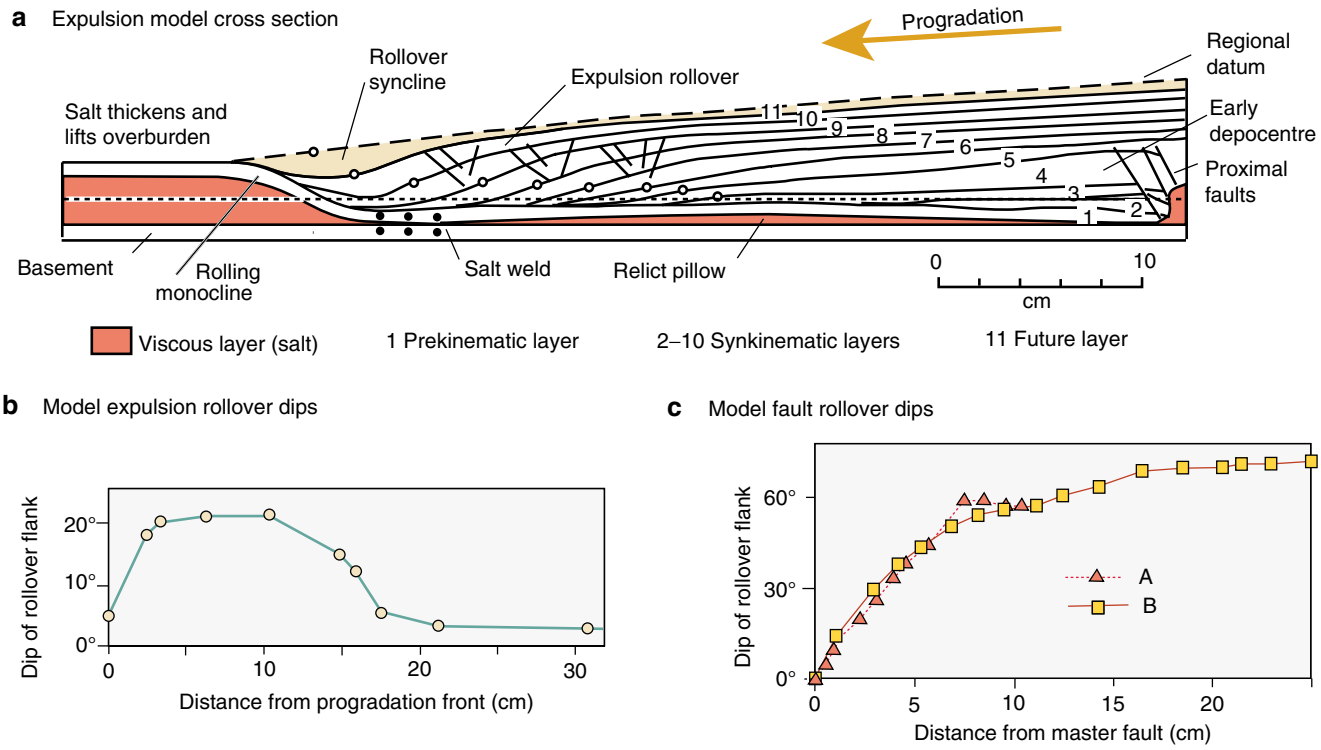

Fig. 6.24 Expulsion rollover characteristics. (**a**) Regional cross section with rolling monocline, rollover syncline, and expulsion rollover all migrating basinward with the basinward progression of the progradation front. *Dashed horizontal line* represents the top on an initially tabular salt body. *Open black circles* show positions of data points plotted in Fig. 6.24b. (**b**) Rollover plots of maximum dip associated with model illustrated in 6.24a. (**c**) Rollover plot of model experiments: result **a** is from experiment model 188 listed in Ge et al. (1997), result **b** is from experiment E30 in McClay (1990) (Modified from Ge et al. 1997)

comprised an episode of passive growth during slow sedimentation, followed by burial during a period of rapid sedimentation and be terminated by a brief active salt breakout. Each active stage removes the overburden roof by doming, local extension, entrainment, slumping, dissolution collapse and the creation of local unconformities.

- An active diapir can partially break through its roof, but never emerge, as: (1) the salt source layer may become depleted prior to breakout, (2) the salt source may be channelled off (pirated) by an emergent segment of an adjacent salt wall, or (3) without erosion or differential loading an active diapir only partially penetrates all but the thinnest roofs before reaching equilibrium (Schultz-Ela et al. 1993).

If a passive pluglike stock is later stretched during ongoing regional extension, the adjacent country rocks may also stretch, creating normal faults next to the diapir. But more typically the stretching is taken up in the much weaker salt body, so that passive elongated salt walls under extension are widened via ductile flow of salt. The much stronger flanking overburden may remain grossly intact and virtually devoid of normal faults at the scale of seismic resolution. An apparent absence of normal faults in sediments adjacent to a passive diapir wall means that even large amounts of regional extension may remain hidden within the expanding and deforming salt wall. This cryptic extension can be inferred by accurate reconstruction of cross sections backward in time. But this process is far from straightforward and requires additional constraints, such as independent data on the original length of the section or original thickness of salt (Schultz-Ela 1992).

Diapirism and Differential Loading

In a series of scaled physical models Ge et al. (1997) demonstrated the importance of progradation as a trigger for salt tectonics and formation of allochthonous sheets. They considered two end members in their modelling experiments. One group of experiments replicated salt with an underlying flat top to the basement (Fig. 6.24), while another group considered a basement with a stepped top, as would occur in a block faulted basement terrain (Fig. 6.25). Regional extension and contraction were excluded in their models.

The prograding wedges above a tabular, buoyant salt layer that was underlain by a flat basement top, expelled the salt basinward in a predictable sequence of structures. From proximal to distal they were: (a) sigmoidally distorted initially planar wedges, (b) relict salt pillows and salt welds, (c) basinward-dipping expulsion rollover and crestal graben, (d) rollover syncline, (e) landward-facing salt-cored monocline, and

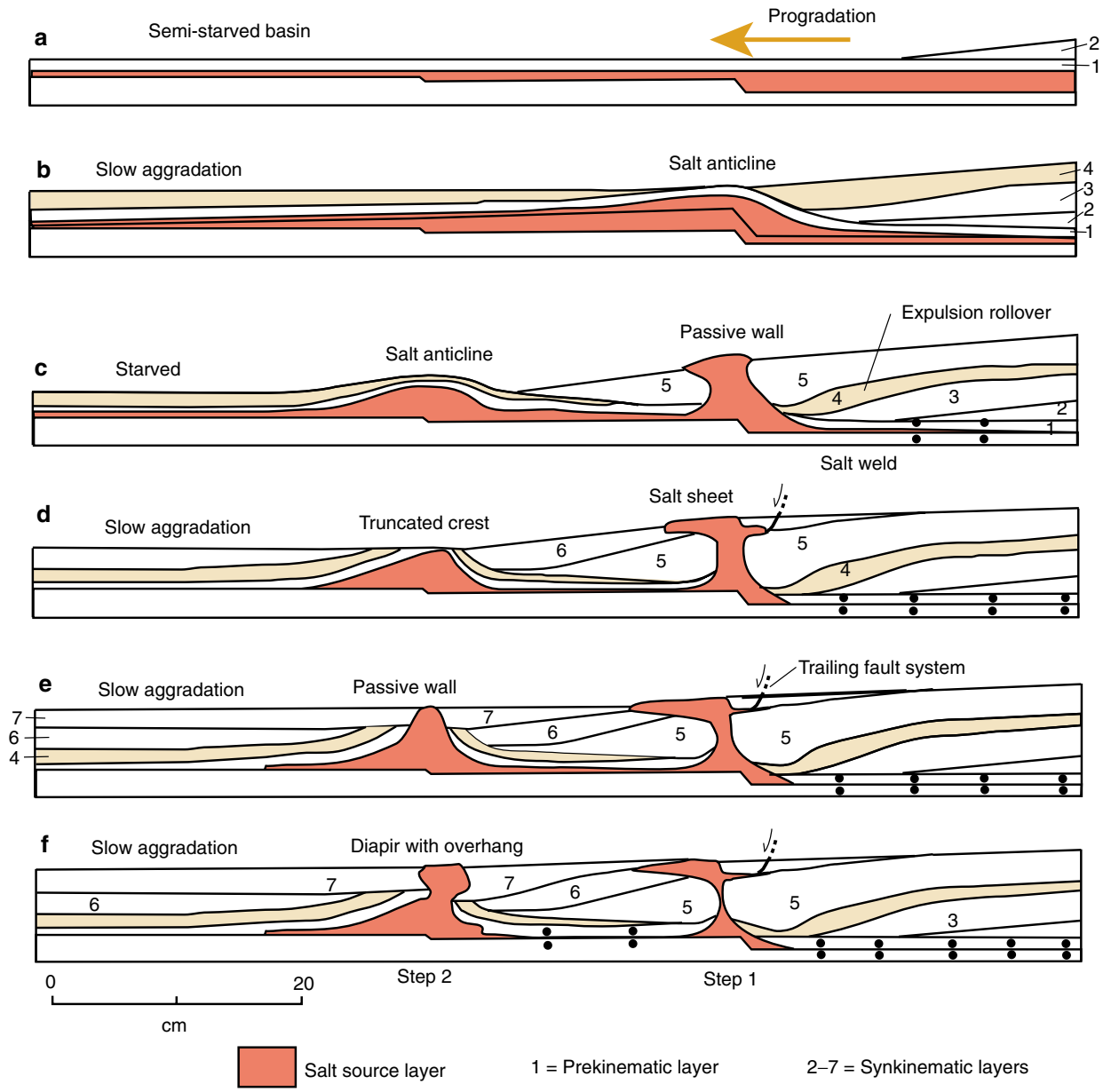

Fig. 6.25 Evolution of salt structures during progradation atop a salt basin that is underlain by a stepped basement. See text for detail on stages **a**–**f** (Modified from Ge et al. 1997)

(f) distal inflated salt layer (Fig. 6.24a). This deformation zone amplified and advanced basinward, together with the prograding sediment front. Complete evacuation of the salt left a basin-propagating salt weld below the prograding sediment wedge; incomplete evacuation left salt pillows as residual highs, but no diapiric salt structures were formed.

In contrast, modelling of progradation over a buoyant salt layer, which was underlain by landward-facing basement steps or fault escarpments (Fig. 6.25a), initially formed a broad anticline where the salt flow was focused across each basement step (Fig. 6.25b). Early on, differential loading by the prograding wedge expelled the salt basinward in an identical fashion to that which occurs in a basin with no basement steps. Then the lateral escape of the salt was altered as it was slowed across the friction point created by the basement step and salt backed up to form a broad asymmetric salt-cored anticline. Distal aggradation continued to pin the anticline and enhance differential loading. Next the anticline actively pierced its crest, which in the real world may have been thinned by faulting and erosion (Fig. 6.25c). Thereafter the diapir grew passively, locally sourcing allochthonous salt sheets. This deformation cycle repeated over each basement step so that the age, amplitude, complexity and maturity of salt-related structures decreased basinward (Fig. 6.25d–f).

As each allochthonous salt sheet was buried and evacuated by sediment loading, arcuate peripheral normal faults formed along the sheet's trailing edge, detached wrench faults formed along its lateral edges, and active piercement at

its leading edge allowed the sheet to break out and climb stratigraphic levels. This process formed a multi-tiered complex of salt sheets that migrated basinward with time. Ge et al.'s (1997) modelling clearly shows that immense landward-dipping (counter-regional) pseudofaults can arise entirely by salt expulsion rather than regional extension. Their physical model clearly shows that progradation alone can generate salt anticlines that mature into salt walls, stocks, glaciers or linked, multi-tiered complexes of evacuated sheets and salt welds. The prograding sediment wedge expels salt basinward regardless of density relationships. In such situations there is a relationship between underlying basement discontinuities and the location of salt diapirs and allochthons. A result that is not obvious in purely extensional regimes where the zones of diapirism tend to begin in zones of overburden thinning that can bear no relationship to subsalt discontinuities.

Salt can flow under both regional extension and progradation (loading). Both are typically present and interacting in a sedimentary basin where extension drives the subsidence that in turn creates accommodation space, which is then filled by sediment. Extension is perhaps the dominant mechanism triggering diapirism in deeply buried salt bodies, while progradation is a commonplace driving mechanism whenever salt is near the surface. Salt's propensity to flow means that diapirs, initially formed by early progradation of a wedge of continental shelf or platform sediment, can be later reactivated or overprinted during extensional or compressional regimes.

This leads to an obvious problem in distinguishing between expulsion rollover generated by progradation and a fault rollover in the hanging wall of a listric growth fault generated during extension. Ge et al. (1997) clearly show how dip analysis of the rollover plot can be used to help differentiate the two styles (Fig. 6.24b, c). They plot the maximum dip of each sediment wedge in the expulsion rollover (open circles in 6.24a, b) versus distance from the present progradation front. Maximum dip was measured on the basinward-dipping flank in the rollover syncline. The rollover plot is shaped like an asymmetric hill with dips increasing rapidly away from the front to a maximum and then decreasing less rapidly. The maximum dip corresponds to where the thickest salt was expelled. The oldest wedges preserved the initial depositional slope (5° in modelled system) and planar shapes, even though they were folded and then unfolded by the passage of the structural monocline that rolled through them as the salt evacuation front passed by.

The plot of a fault rollover in the hanging wall of a simple listric fault is quite different and shows no decrease in dip away from the present progradation front (Fig. 6.24c). Dips of the hanging wall cut off abruptly and then gradually increase to reach a maximum value away from the surface trace of the listric fault. The constant maximum dip away from the fault corresponds to flattening of the underlying fault. This type of analysis can only be carried out on syn-kinematic strata, which are distinguished from prekinematic strata as they show local lateral variations in thickness. If a listric fault has multiple flats and ramps, the prekinematic strata generate a tail of data points that are not diagnostic and should not be used. See Ge et al. (1997) for a full explanation of this methodology and its application. Some workers subdivide the effects of sediment loading on salt flow into (1) systems with linear progradation fronts moving out over a salt mass (Vendeville 2005) versus, (2) more lobate styles of sediment loading (Gaullier and Vendeville 2005). The former are appropriate to linearly-loaded continental margins, as along much of the Atlantic slope-and-rise of South America and the Gulf of Mexico, while the latter models are more appropriate to lobate loaded margins, such as the Gulf of Lions and the Nile Cone.

Sedimentation Rate Controls Diapir Shape

Observations in seismic lines collected in the late 1980s, which for the first time were showing the base of salt, indicated a stepped base to the flowing salt mass (ramps and flats), rather than the previous assumption of flat or planform salt bases. It helped change the notion of salt allochthon emplacement from that of a salt sill injected into marine muds a few hundred metres or more below the seafloor into one of salt glaciers marching out over the seafloor via a combination of ramps and flats tied to sedimentation rates on the seafloor.

Interaction of upwelling salt and sediment accumulating on the diapir's flanks controls the geometry of a passive or downbuilding diapir and its salt tongues or wings. If the rate of salt rise is less than the sediment accumulation rate, then a passive diapir narrows upward as onlapping sediments encroach onto the diapir ($R/A < 1$; Fig. 6.26a, b). When a large volume of salt is supplied to the growing structure, the diapir rises faster than the surrounding sediment can aggrade. The resulting laterally unsupported salt ridge repeatedly overflows its unsupported margins (gravity spreading), thus creating a salt tongue that widens upward over time ($R/A > 1$; Fig. 6.26a, b). Eventually, all diapirs are buried by the slowing and eventual cessation of salt supply. This typically happens once the mother salt (source layer) is thinned or depleted by salt withdrawal and overburden touchdown.

The gross flow rate of salt in passive diapirs reflects a balance between driving forces, retarding forces and salt supply (Jackson et al. 1994a). Any change in sedimentation rate versus rate of salt supply controls the overall planform (at-surface shape) of a passive diapir. If, during extension, the sedimentation rate is high compared to the rate of regional extension, a reactive diapir evolves into a squat deeply buried salt roller bounded by a listric (upward steepening) fault. Conversely, if the sedimentation rate is low compared to the

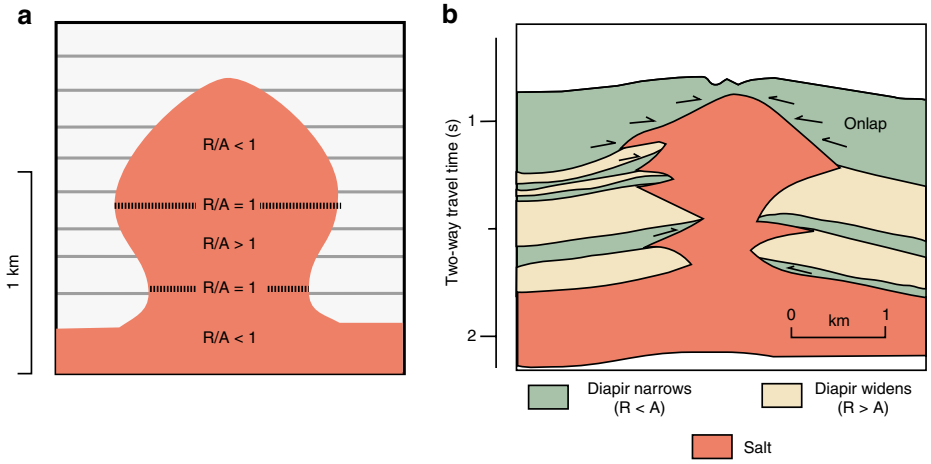

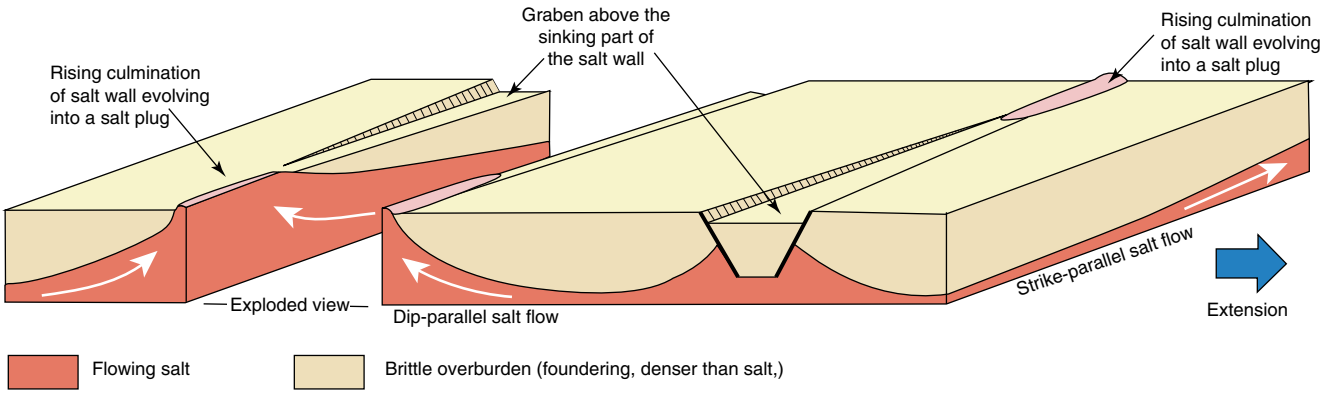

Fig. 6.26 Passive diapirs with extrusive flanges onlapped by overburden. (**a**) The shape of a diapir is controlled by the ratio of net diapiric rise R (incorporating the effects of dissolution), to aggradation rate (vertical accumulation of sediment). (**b**) A typical North Sea Diapir with allochthonous salt wings (After Jenyon 1986). (**c**) The stepped base of Mica (aka Mitchell dome) Garden Banks, offshore Louisiana, shows it was emplaced as an allochthon not a sill; high R/A causes salt flats (*SF*), low R/A causes salt ramps (*SR*) (After Vendeville and Jackson 1993)

Fig. 6.27 Once part of a salt wall begins to fall, subsidence can be enhanced by strike-parallel flow of salt from beneath the subsiding graben and toward parts of the wall that are still rising (After Vendeville and Jackson 1992b)

rate of regional extension, a reactive diapiric ridge evolves into a tall salt wall or a number of adjacent salt plugs that show steep or overhanging discordant contacts and shallowly buried crests (Vendeville and Jackson 1992a). Likewise, sedimentation rate also controls the form of advance of an allochthonous salt sheet (Fig. 6.26c). Salt flats indicate times of low sedimentation, while salt ramps indicate higher rates of sedimentation. Salt ramps are the remnants of an allochthon which was an active glacier moving across the seafloor. When the salt is completely evacuated the former ramp becomes a salt weld.

Within a single ovoid or elongate salt structure a diapir's rate of salt flux increases with increasing width. At the diapir's widest part, salt flow rates are high relative to sedimentation rates. Conversely, contact drag at the structure's extremities affects the narrower ends of an elliptical diapir more than at its wider parts. This slows the rate of rise at either end so creating relatively high aggradation rates. Thus salt spreads at the widest part of a diapir and retreats from its elliptical ends. Accordingly, an originally elongate salt wall evolves toward a string of pluglike passive stocks rising from the deeply buried reactive salt ridge (Fig. 6.27). The number of exposed plugs atop a salt wall declines as they exhaust their salt supply evolve into falling diapirs that are ultimately buried or evolve into mockturtle anticlines.

As a salt glacier is extruded onto the seafloor it can flow in any direction, depending on the local slope (gravity spreading); it can even flow landward into the depression atop an adjoining rollover syncline (rim syncline). Over time the breakout sites, where the salt climbs the section and

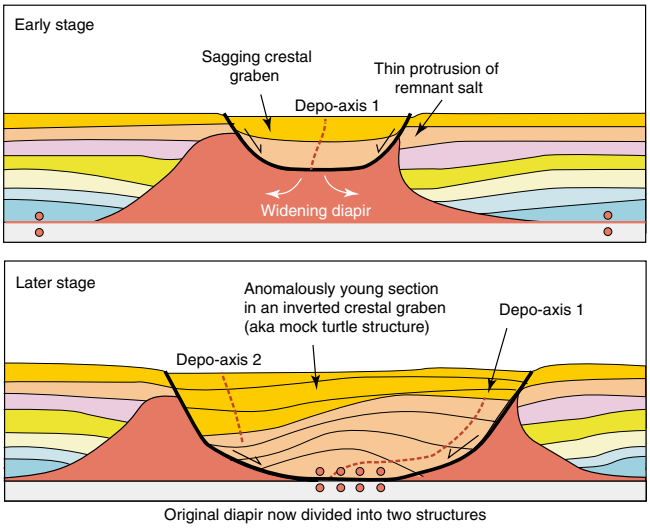

Fig. 6.28 Creation of an indented or falling diapir showing suprasalt depression that in its later stage develops into an inverted structure known as a mock turtle anticline

breaches to the surface, will ultimately shift basinward as salt is squeezed by the prograding basin fill (Fig. 6.25). Regionally, the depocentre of active diapirism in the Gulf of Mexico has been shifting basinward since the Jurassic when the mother salt bed, the Louann Salt, first breached the surface. As each newly-emplaced salt sheet is loaded by the prograding sediment pile, it carries its overburden basinward by gravity spreading. Thus, while a sheet evacuates into a new stratigraphic level it also generates halokinetic profiles atop it.

Extension, Falling Diapirs and Turtles

Salt-lubricated extension can initiate and maintain diapirism throughout the reactive, active and passive stages. When connected to an adequate salt supply, passive diapirs can widen between separating blocks of overburden, while still maintaining their crest at or near the surface (Vendeville and Jackson 1992b). That is, once it attains its maximum height, a reactive/passive diapir can continue to widen by viscous flow. Salt inflow fills an ever-widening gap between the extending fault blocks of overburden that are gliding apart on the salt source layer. Eventually the salt supply becomes restricted and ultimately depleted so that the passive diapir crest sags or falls as it evolves into a characteristic two-horned indented profile (Fig. 6.28 – early stage).

If the former diapir crest continues to sag, the crest inverts from a topographic bulge into a subsiding depotrough or graben, which is rapidly filled with sediment. This creates a sediment thick atop the diapir (Fig. 6.28 later stage). Slippage continues along the bounding faults of this deepening graben, but no new faults generally form within the graben. Such a crestal graben lacks the stair-step faults that characterise the smaller and shallower crestal graben of a reactive diapir. Adjoining the indentation are hornlike cusps of salt below each bounding fault of the graben.

That is, where extension continues after all salt supply to a passive-stage diapir is cutoff, overburden touchdown occurs in the position of the former passive diapir crest. The falling diapir overburden segments into two flanking triangular relics flanked by glide blocks composed of older overburden (Fig. 6.28 – later stage). The diapiric relics are now separated by deep, wide depocentres filled with younger sediments. If extension continues, the flanks of these diapiric relics subside until they too touchdown. Thus, ongoing extension and salt depletion causes even the young depocentre to subside until it too eventually inverts into a crestally-faulted arch, called a mock-turtle anticline. The creation of a mock turtle anticline can be accompanied by the creation of a number of crestal depocentres, rather than a single larger depocentre (see minibasins).

Turtle-structure anticlines, with crestal keystone grabens, form in the withdrawal sinks between falling diapirs and are a typical response to source-layer depletion under extension (Fig. 6.29a–e). Historically, turtle anticlines were attributed to the evolution of a salt pillow as it contracted into a upward-growing diapir (see Warren 1989 for dated discussion), but it is now known that they form during the falling diapir stage in an extending basin (Fig. 6.29c–e).

Once the salt supply to a diapir is restricted, more and more salt from the surrounds is withdrawn into the falling diapir (Fig. 6.29c). As this occurs the region of overburden touchdown forms creating an incipient turtle that then widens beneath the rim syncline sediments. Over time, the ongoing widening of this zone of salt withdrawal and touchdown causes the sediments of the rim syncline to invert into a turtle structure anticline, often with a keystone graben in the anticlinal crest (Fig. 6.29d).

The touchdown and inversion of the earlier rim syncline sediment pile can create a topographic high on the seafloor, which is a type of drape-induced anticline. Sediments deposited atop the anticlinal crest may be higher energy sands and carbonate buildups, as has occurred in the reefal carbonate reservoirs that characterise buildups in the James Limestone in the Gulf of Mexico (Fig. 10.55). Such depositionally enhanced potential reservoir intervals can be self-reservoiring, self-closing and self-draining petroleum systems.

In many diapiric settings, such as the North Sea and the Gulf of Mexico, salt walls can pass along strike from a section of the wall at the passive stage to a falling section of the wall marked by a thickening crestal graben. Once part of a salt wall begins to fall, subsidence can be enhanced by strike-parallel flow of salt from beneath the subsiding graben and toward parts of the wall that are still rising (Figs. 6.27 and

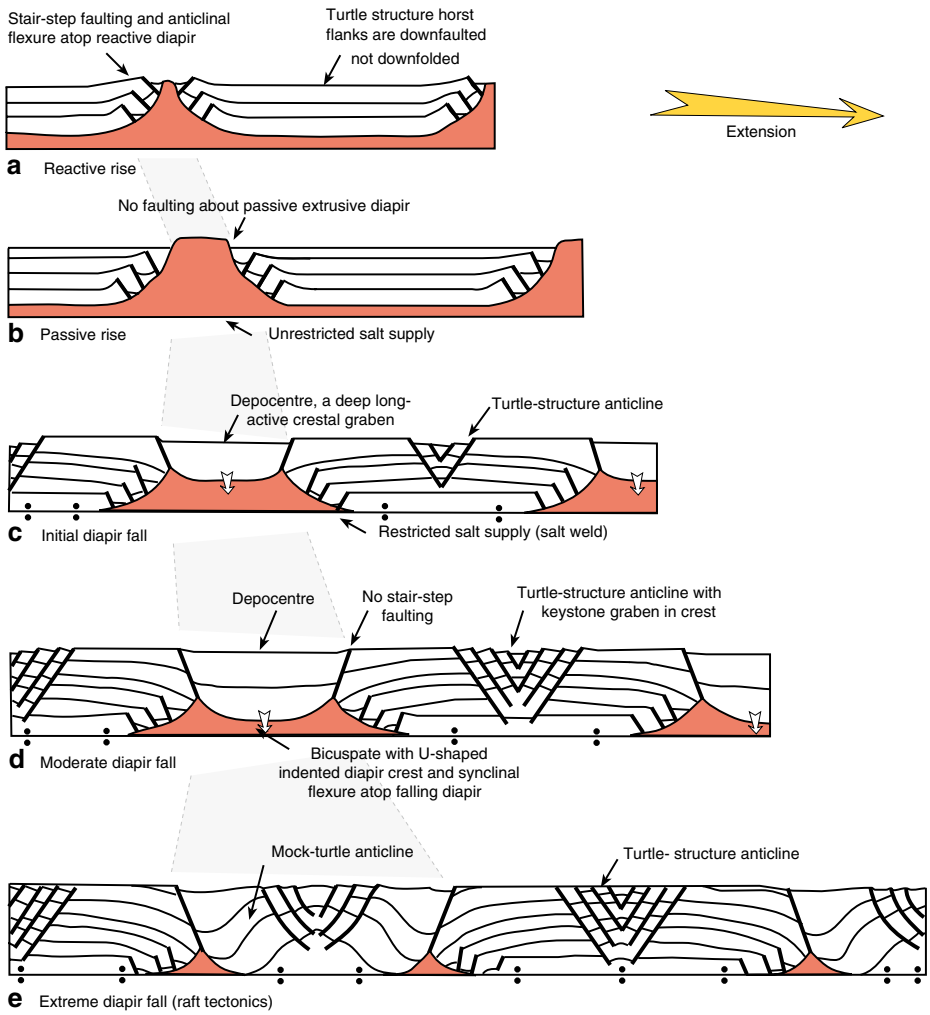

Fig. 6.29 Rise and fall of diapirs during synkinematic sedimentation and extension. The *dashed line* implies the various stages are not necessarily separate in time, but can be found along a single salt wall connected by strike -parallel salt flow (indicated by *grey shading* linking the profiles, see Fig. 6.27 for generalised 3D. See text for detail on stages **a**–**e** (after Vendeville and Jackson 1992b)

6.29). This effect is increased if the overburden filling the graben has an average density greater than that of the salt. Strike-parallel salt flow may keep parts of the wall emergent even after the salt source layer is exhausted.

In other words, stages a–e in Fig. 6.29 and time 1–4 in Fig. 6.30b, can occur along strike within a single salt wall. Where subsidence is accommodating regional extension, salt tends to move into the rising (reactive-passive) sections of the wall and away from subsiding depressions below the crestal grabens (Fig. 6.27). As salt flows into the intervening culminations along the wall they evolve from elongate walls into increasingly pluglike, rounded diapirs. If extension continues, these rising diapirs, which are commonly emergent, continue to widen and accommodate the regional extension without faulting. With sufficient extension, these diapirs ultimately exhaust their salt supply so that they too must subside and be buried.

Prior to the work of Vendeville and Jackson (1992b) on falling diapirs experiencing regional extension, many of the crestal indented structures produced by diapir fall were attributed to salt dissolution or forceful active intrusion at the crest; all three possibilities should be evaluated in any areas of crestal grabens or remnant salt cusps/rollers.

Falling Diapirs Drive Raft Tectonics

In some areas of falling diapirs the overburden becomes stretched to two or three times its original length by normal faulting, but the sub-salt basement is not involved. A weak intervening ductile layer or décollement of salt enables this prodigious extension of the overburden over a non-deforming basement. This style of overburden deformation is called raft tectonics and defines an extreme form of thin-skinned extension[11] or gravity sliding, whereby rigid sediment blocks slip downslope atop a décollement layer of evaporite or shale

[11] Thin-skin tectonics describes a situation where most of the deformation occurs in sediments above a regional décollement and structures in the basement below the décollement are different to those above. Sometimes called a "no basement" structural interpretation. Its corollary is "thick-skinned" tectonics, which involves related deformation of both basement and salt cover.

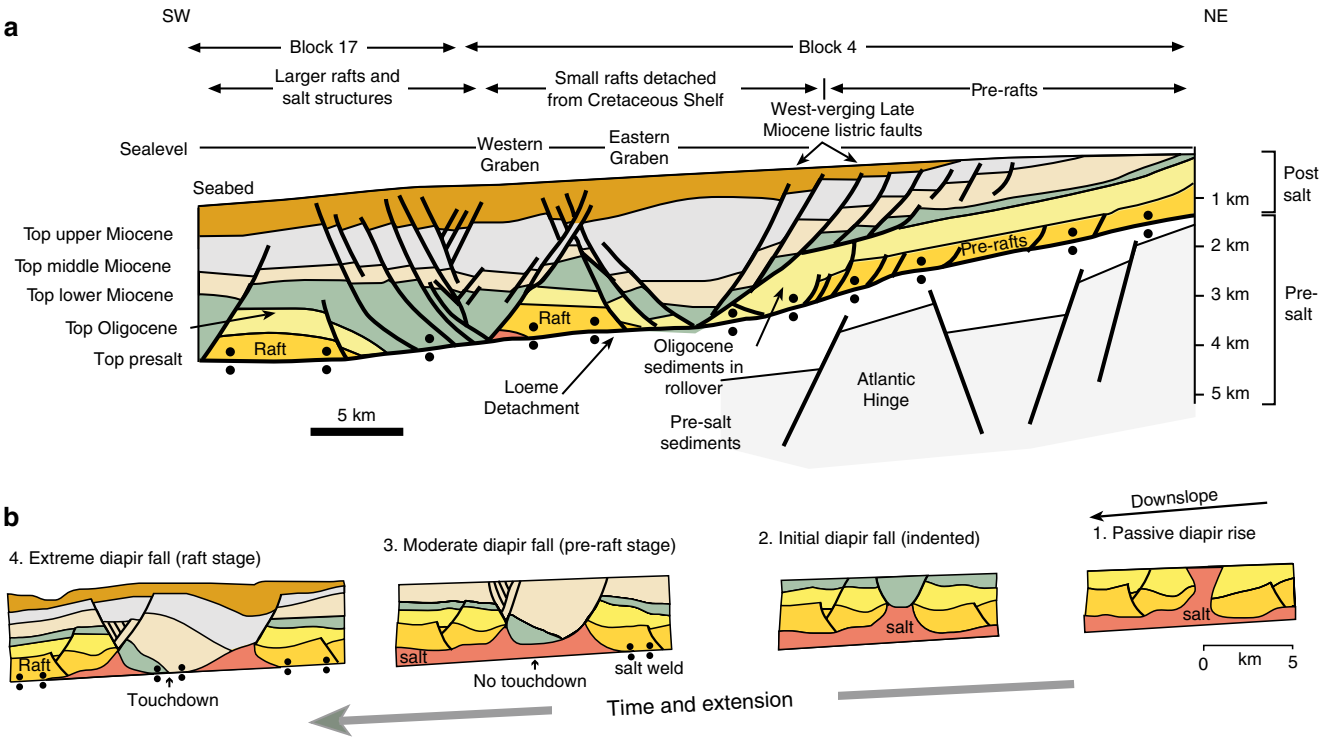

Fig. 6.30 Raft Tectonics, Angola. (**a**) NE-SW section through the Block 4 region of the Lower Congo Basin (Anderson et al. 2000). West-dipping listric faults affect the late Cretaceous sediments in the east of the block. Further west, Miocene extensional faults and associated grabens separate an isolated Cretaceous fault block (raft) from the equivalent Cretaceous sediments on the shelf. A similar structural style, characterised by thin-skinned faults, exists to the west but with relatively simple Cretaceous roll-over anticlines. Each of these isolated fault blocks is separated from neighbouring fault blocks by Miocene grabens (Eastern and Western grabens). The Miocene faults flatten downwards onto a salt detachment in the Loeme Formation. (**b**) Restoration model of a falling diapir in the zone of raft tectonics of the Kwanza Basin, Angola (After Schultz-Ela 1992 and based on a seismic line in Duval et al. 1992)

(Figs. 6.1b and 6.8a; Spathopoulos 1996; Cramez and Jackson 2000; Fort et al. 2004; Morley et al. 2011).

Raft tectonics characterises areas of large-scale extension where the hanging wall of an extensional salt-soled fault separates completely from the footwall, creating a fault weld via coherent slippage along the salt detachment surface (Fig. 6.30a; Duval et al. 1992). In other words these rafts are allochthonous fault-defined overburden blocks that have slipped downdip to become so far apart they are no longer in mutual contact across the growing fault that once separated them. Rafts characterise extensional geometries beneath the modern shelf and rise of Brazil in South America, Angola in central West Africa and the Gulf of Mexico (Fig. 6.1b; Anderson et al. 2000; Fiduk et al. 2004; Dutton and Trudgill 2009). Similar large rafts characterise blocks of Zechstein sediment in the NW Permian Basin of the North Sea (Clark et al. 1998). In this case, the blocks of sediment are composed of platform anhydrite, which slid into the basin atop a halite lubricated sole.

With less extension the fault blocks are called pre-rafts as they remain in mutual contact across the fault and parts of the hanging wall still rests on its original footwall. Rafting movement produces listric faults and sediment-filled grabens atop a deflating salt mass. Sediment-filled grabens separating raft blocks can be substantial structures; the Quenguela Graben in the Kwanza Basin is 20 km wide and 90 km long, the nearby Gaivota Graben is 15–20 km wide and 225 km long (Cramez and Jackson 2000).

With initial extension between two overburden blocks, a salt wall first rises passively to fill the increasing gap (Fig. 6.30b; time 1). Once the supply of salt can no longer keep up with demand, the diapir starts to fall. The crest of the sagging diapir becomes a subsiding trough that fills rapidly with sediment (Fig. 6.30b – time 3). While stretching and décollement are active the thickness of the evaporite layer is reduced both by downslope gravity drainage of the salt and ongoing dissolution. Once most of the salt is removed from under the sliding blocks, they ground or weld on the presalt layers and the downslope movement of the blocks stop (Fig. 6.30b – time 4). Stretching or extension that drives raft tectonics can usually be attributed to gravity gliding. Gravity gliding drives the translation of fault blocks down a gentle slope, driven by the downslope shear stress component of gravity on a tilted mass atop a mobile layer.

Regionally, salt basins characterised by raft tectonics can usually be divided into two different stress regimes (Fig. 6.1b;

Spathopoulos 1996; Cramez and Jackson 2000): an updip extensional regime located under the shelf and upper slope where salt décollement has facilitated the breakup of overlying sediments into raft blocks, and a downdip compressional or contractional regime typically under the lower continental slope where the up dip extension is taken up in a fold or thrust province (Fig. 6.1b). Raft tectonics requires the creation of substantial lateral space into which the overburden can expand during stretching. Downdip space is generated by: (1) formation of a downdip fold or thrust belt, (2) down dip displacement of autochthonous salt into allochthonous salt sheets that climb the stratigraphy, and (3) generation of new oceanic crust by a spreading ridge with allochthonous salt allowing overlying blocks to slide (Duval et al. 1992). Downdip compressional terrain is discussed in more detail later in the chapter.

Salt as Sheets, Allochthons and Breakouts

Allochthonous salt sheets are flowing salt masses that have been moved by low temperature tectonic processes, so that the front edge of the salt flow overlies younger strata and it is typically no longer connected with the mother salt bed. Allochthons have areas measured in hundreds of square kilometres and salt thicknesses ranging up to several kilometres. They typically indicate into-the-basin translation of the salt mass and its overburden. Salt allochthons typically lie at or very near the surface when actively inflating with salt (Fig. 6.31). Some authors draw a distinction between an allochthon and a namakier, using namakier to describe the structure created by the extrusion of allochthonous salt onto a continental landsurface, as exemplified by salt landforms in Iran. Others use the terms salt allochthon and namakier interchangeably.

In contrast to an allochthon, an autochthonous salt structure extends continuously down to the primary source layer and may not have experienced substantial lateral translation (Rowan et al. 1999). Allochthonous salt sheets characterise the present day continental margins of offshore Brazil, the Gulf of Mexico, West Africa, the North Sea and the Red Sea and outcrop as namakiers or their remnants in Iran, Algeria, Yemen, Mexico and Australia (Hudec and Jackson 2006). The recognition of allochthons as potential traps in deepwater petroleum provinces has opened up possibilities of prodigious subsalt hydrocarbon reservoirs, particularly in continental slope and rise sediments in the various circum-Atlantic salt basins (Chap. 10).

Over the past four decades, proposed mechanisms for salt allochthon emplacement include: recumbent folding, deep intrusion, shallow intrusion and surface extrusion (Fig. 6.31; Schultz-Ela and Jackson 1996). In all categories, a massive basinward flow of salt is a major part of the

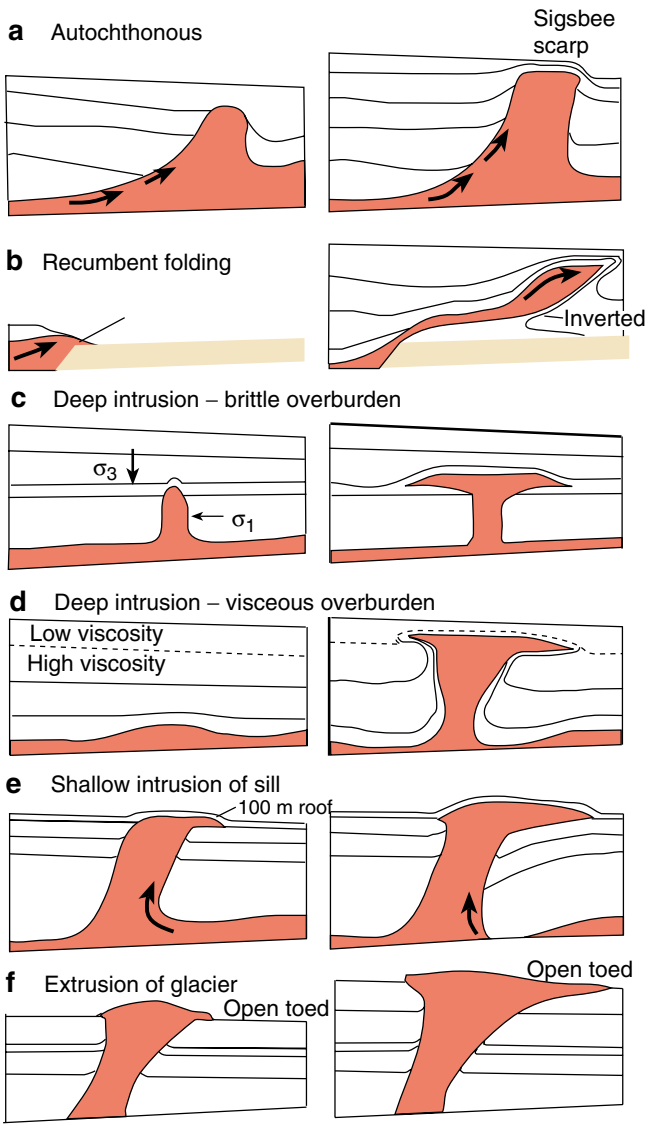

Fig. 6.31 Various hypotheses proposed for the emplacement of allochthonous salt sheets. See text for explanation of styles **a**–**f** (Modified from Schultz-Ela and Jackson 1996)

emplacement process in both subaerial and submarine settings (gravity gliding and gravity sliding). Ewing and Antoine (1966) envisaged the allochthonous Sigsbee Scarp was the basinward flowing edge of an autochthonous diapir (Fig. 6.31a). We now know their original interpretation, limited by the state of the seismic art at that time, was not correct in terms of its vertical connectivity to the mother salt bed. Amery (1969) discovered that the Sigsbee Scarp was the leading tip of a wedge of an allochthonous salt tier (Fig. 6.2).

Jackson and Cornelius (1987) modelled allochthonous salt sheets as flowing salt bodies ramping up to the nearsurface from a buried sub-salt step. On reaching the nearsurface the suprasalt wedge then spread rapidly under gravity

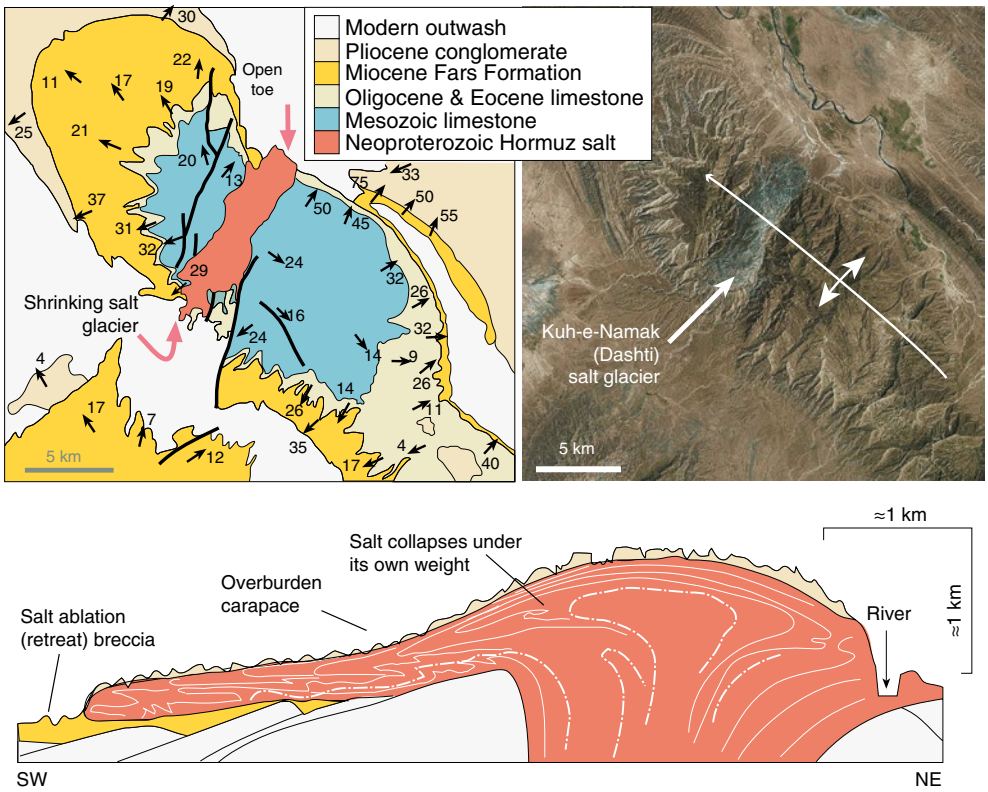

Fig. 6.32 (**a**, **b**) Surface geology (*left*) and Landsat image (*right*) of Kuk-e-Namak salt plug (Dashti Province), Iran, 28°16′N, 51°42′E. Faults, intersecting the plunging anticlinal dome, facilitated salt breakout and drove the formation of a surface salt glacier, or namakier, which is flowing away from the salt-core anticlinal ridge (see also Fig. 6.34). *Black arrows* indicate bedding dip and azimuth in the anticlinal beds. (**c**) Schematic cross section showing likely internal folds show how salt flows over the landscape like the rolling track of a military tank (After Kent 1958; Talbot 1979, 1998; Bing® image mounted in MapInfo® software)

as a recumbent fold anticline. Based on their modelling and analogs in the namakiers of Iran, they argued the allochthon edge advanced like a tank track rolling out over itself, creating a core of allochthonous salt and a laterally sliding carapace of deformed sedimentary overburden in a flow process know as tank-track advance or frontal rolling. This occurs when the advancing upper surface of a salt sheet moves faster than its base. Thus it advances and it rolls over and the lower portion adheres to the substratum below the salt. This advance lengthens the base of the salt, so forming a series of recumbent folds (Fig. 6.31b). As such an allochthon rolls out over the landscape it carries with it the veneer of accumulating and deforming sediment known as a carapace. When later buried and drilled, carapace sediments atop a salt sheet may be older than those below. This is case in the Vermilion #356 well drilled through a Gulf of Mexico salt sheet by Amoco in 1988. The highly overpressured section beneath the salt sheet is younger than the condensed suprasalt section in the same well (Harrison and Patton 1995).

D'Onfro (1988) modelled allochthonous salt sheets as dykes and sills that were intruded in areas of local compression, such as the toe regions of growth faults (Figs. 6.31c, d). Podladchikov et al. (1993) modelled asymmetric salt sheets as intruding laterally from a diapiric salt mass at depths of approximately 1 km depth. This level, according to the authors, lies just above an abrupt 1,000-fold downward increase in the viscosity in what otherwise are uniformly viscous sediments (Fig. 6.31d). Amery (1969, 1978) envisaged shallow allochthonous intrusion of the spreading salt layer as occurring beneath a thin sediment roof that was no more than 200–300 m thick. He visualised the salt as coming from an autochthonous diapir source. Nelson (1991) stated that most salt sheets in the Gulf of Mexico had been emplaced shallow at depths of around 100 m and never more than 300 m (Figs. 6.7b and 6.31e). Talbot (1993) pointed out the resemblance of salt sheet profiles to viscous fountains spreading laterally into unconsolidated surface muds (Figs. 6.31f). The stepped base to many salt allochthons attest to their emplacement as surface rather than shallow subsurface features (Fig. 6.26c). At-surface stepped allochthon emplacement mechanisms and associated salt flow textures were first supported by studies of salt features various Kuh-e-Namak outcrops in Dashti province and the Great Kavir regions of Iran (Fig. 6.32, Kent 1958; Talbot 1979; Jackson et al. 1990).

Periodic salt breakout is a consequence that is inherent to shallow or at-surface styles of allochthon emplacement. Breakout describes a process or place where a buried salt sheet is exposed by erosion or roof extension and where an exposed pressurised salt mass advances by extrusion and gravity spreading (Jackson et al. 1994a, b). The advancing sheet is termed open-toed when salt moves as an at-surface tongue or namakier with no more than a thin veneer of residual sediment, which is carried along by the expanding sheet as it flows toward topographic lows. This is illustrated by the

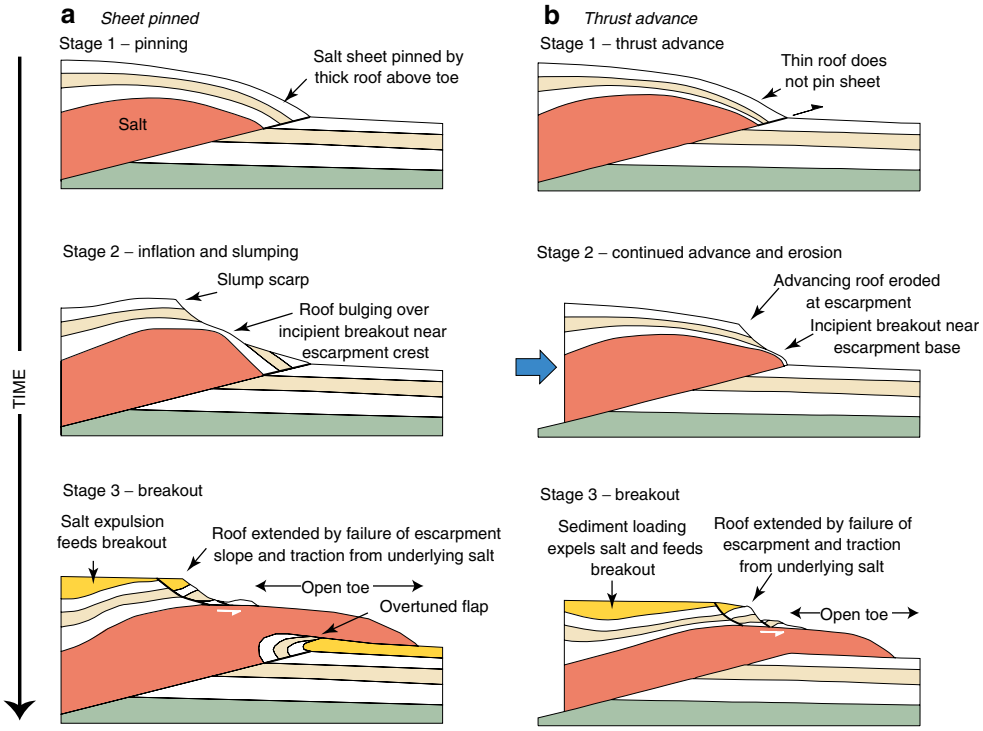

Fig. 6.33 Salt Breakout. The geometry of breakout at the toe of a salt sheet depends on whether the roof is thick and strong enough to pin the toe of the sheet (Hudec and Jackson 2006)

Kuh-e-Namak outcrop in Dashti Province, Iran (Fig. 6.32). This namakier is also interesting as in the same at-surface salt mass it exhibits simultaneous salt ablation retreat rims on the more extensive south-western margin and an open toe allochthon, maintained by river erosion and suffusion carapace removal, on the northeastern edge of the salt tongue (Fig. 6.32c).

There are two ways salt can breakout (sheet-pinned versus thrust advance) and they are dependent on whether or not the roof is thick and strong enough to pin the toe of the sheet (Fig. 6.33; Jackson et al. 1994b; Hudec and Jackson 2006). If the roof is thick and strong enough to pin the toe of the sheet, then the minibasins subsiding into the rear of the sheet and mostly off section in the illustration can laterally expel underlying salt, which then inflates (pressurises) the toe of the sheet (Fig. 6.33a- stage 1). This steepens the frontal escarpment, causing slope failure of its upper part (Fig. 6.33a-stage 2). Salt breaks through the thinned roof near the crest of the escarpment. Roof strata at the escarpment below the breakout are inverted to form an overturned flap (Fig. 6.33a-stage 3). If, however, the roof is not strong enough to contain the sheet, as illustrated in Fig. 6.33b, then the roof and salt sheet advance together as a thrust. If the leading edge of this thrust is sufficiently eroded, salt breaks out near the base of the escarpment, via a process known as thrust advance and open-toed advance begins.

During times of active extrusion a salt sheet forms a topographic or bathymetric high, with up to several hundred metres of relief above the surrounding seafloor. A feedback occurs between the rate at which salt is pumped to the surface and the rate at which meteoric or marine waters dissolves the salt. The rate of salt pumping is thought to be many times greater than the sedimentation rate during peak growth periods of the allochthon (Fig. 6.26). Expanding salt sheets are protected from dissolution by a combination of: (1) a sediment veneer or carapace, (2) an insoluble residue (caprock) of relatively impervious anhydrite/gypsum, and (3) an overlying layer of saturated pore brines where circulation of meteoric or marine pore water is locally restricted. If continuously deposited, a low-permeability sedimentary roof, alone, can protect underlying salt, even if the roof is continuously breached by deformation and erosion.

Historically, ancient equivalents of salt glaciers were not widely recognised in the rock record. Now, with our improving understanding of salt tectonics and the different styles of salt dissolution, ancient counterparts have been documented at increasing numbers of surface and subsurface locations, which include; Kazakhstan, Algeria, Tunisia, Yemen, Australia, Mexico and NW Europe (Volozh et al. 1994; Vila et al. 1994, 2002; Davison et al. 1996b; Dyson 1998; Giles and Lawton 1999; Mohr et al. 2007, respectively). Figure 6.34 illustrates an autochthonous salt tongue sourced in Permian Zechstein salt and emplaced onto an arid Triassic (Upper Keuper) landscape (Mohr et al. 2007). Through its partial dissolution at the time it was emplaced it supplied brine to adjacent playa sumps to form salt beds in the hyperarid Triassic desert (Warren 2008).

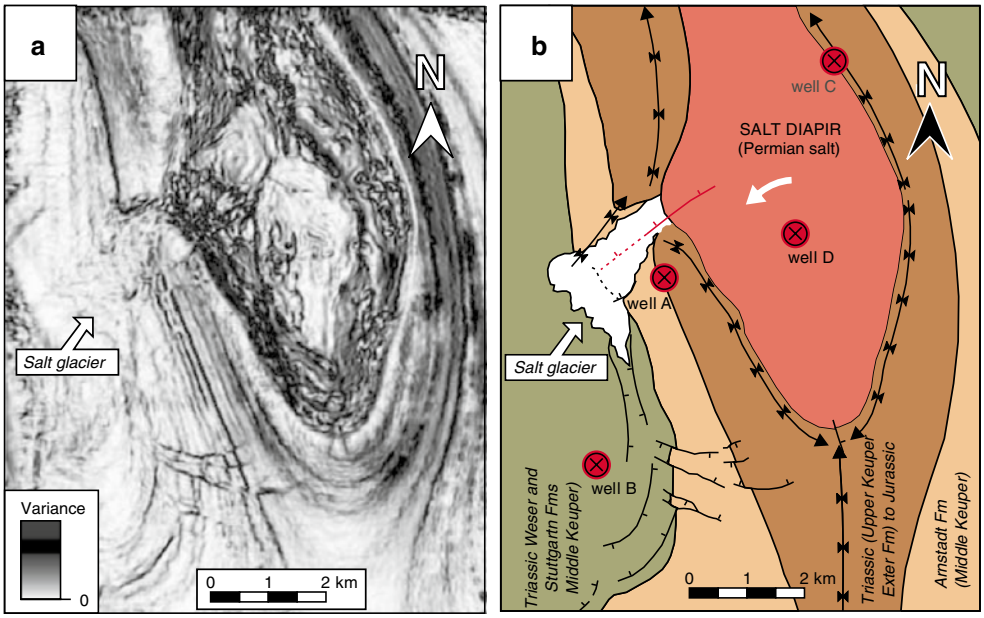

Fig. 6.34 Salt sheet emplacement in the Triassic (Keuper Sediments of Germany (After Mohr et al. 2007). (**a**) Variance map some 50 m below unconformity at base of the Cretaceous. It displays the uppermost salt extrusion as fan-like structure. There are three levels of salt tongue in this section of the salt wall. (**b**) Geological interpretation of **a** showing location geometry of Late Triassic salt glacier as well as the location of the wells used to verify the seismic interpretation and nature of the salt distribution

As any salt glacier or allochthon sheet spreads out over the surrounding landscape or seafloor, it also laterally transports and deforms its roof. Flow also induces drag folds and overturned flaps in subsalt sediments, to ultimately create transition zones known as basal shears. With the exception of the namakiers of Iran, most areas where allochthons outcrop are no longer characterised by salt actively flowing at the surface. Rather, the former presence of thick flowing sheets of salt are indicated by dissolution breccias and welds and associated deformation in the cap and the surrounds of the former sheet (Figs. 6.32, 7.29 and 7.30).

Inflation, Deflation, Welds and Basal (Subsalt) Shear Zones

There are two major stages in salt allochthon emplacement (Montgomery and Moore 1997): (1) Initial inflation and local loading of a salt mass, which then generates zones of salt withdrawal and diapir formation (Fig. 6.35a; times 1–3); and (2). Subsequent widespread suprasalt loading and salt deflation, which creates complex salt welds and suprasalt growth faults usually classified as regional or counterregional faults (Fig. 6.35a; times 3–5).This second stage creates salt tiers in levels of the stratigraphy that lie well above the primary salt level. Salt emplacement at all stages involves a combination of syndepositional dissolution and shearing at the allochthon contacts. Emplacement can be associated with gravity spreading and/or coalescence of a number of salt sheets to form a salt canopy, which is in turn evacuated by later sediment loading (Fig. 6.35b). Once emergent, an allochthonous salt sheet expands its area at the same time it is deflating, loading and segmenting into smaller second-generation structures via loading. The top and bottom contacts of the initial salt sheet come closer and closer together until touchdown occurs and the amalgamation surface becomes a salt weld.

Salt Inflation and Extrusion

There are four types of salt inflation or allochthon development possible in a sedimentary basin (Fig. 6.36; Hudec and Jackson 2006), they are; (a) Extrusive advance, (b) Open-toed advance, (c) Thrust advance, and, (d) Salt-wing intrusion. The style that dominates the allochthon at any time in its history depends on the source of the salt, the tectonic setting, and the sedimentary environment. Consequently, a wide range of evolutionary sequences or possible allochthon evolution lineages are possible Most common emplacement styles are plug-fed extrusions, plug-fed thrusts, and source-fed thrusts, which are defined by the geometry of the feeder structure and by their initial mode of advance (Fig. 6.37). Each lineage involves an evolution from extrusive advance, through open-toed advance, and then thrust advance. Allochthons can become pinned (forward advance slowed) via deposition of the wedge of thick overburden until salt breakout occurs and extrusive or open-toed advance takes over once more. Typically, the allochthon sheet stops moving into the basin when salt deflation cuts off the salt supply. It may then dissolve completely or be buried.

Plug-Fed Extrusion

A plug-fed extrusion or allochthon forms when a sheet extrudes from the top of a vertical or steeply dipping diapir (Figs. 6.36a and 6.37b). Plug-fed thrusts form when a diapir having a thick roof is shortened. The roof is too thick to be immediately disrupted, so the sheet initiates in the hanging wall of a diapir-roof thrust. If shortening continues, the sheet may breakout at the surface and evolve into an open-toed sheet. Given sufficient suprasalt sedimentation rates, this sheet is eventually buried. Compressional reactivation of

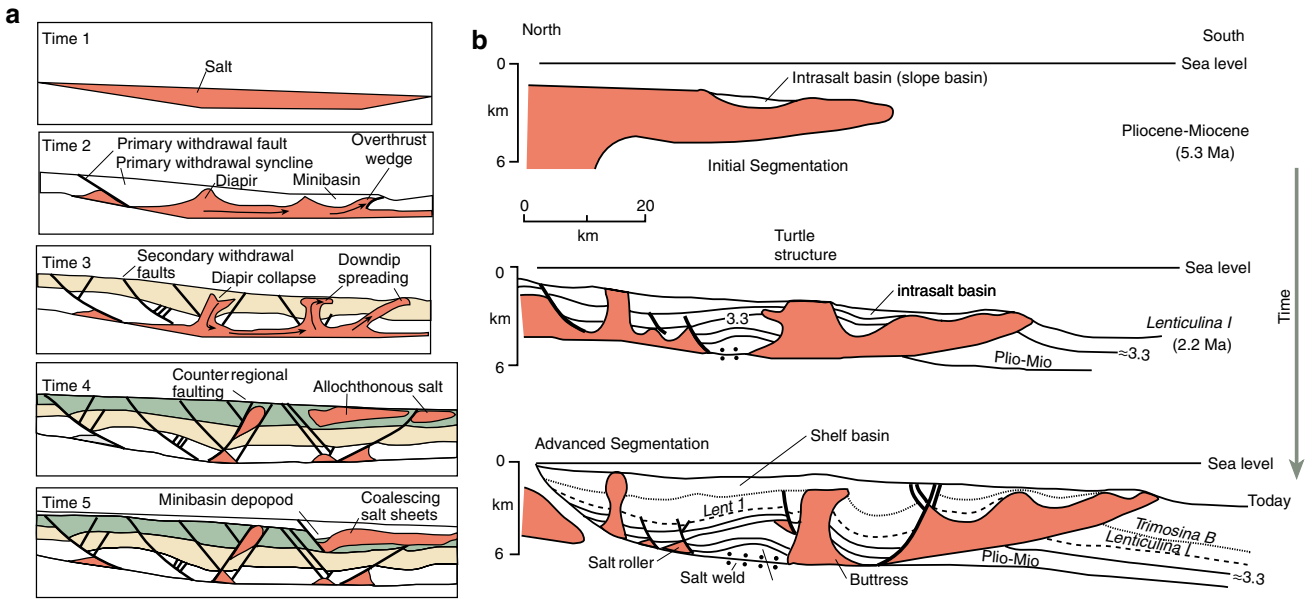

Fig. 6.35 Salt allochthon evolution. (**a**) Evolutionary model of the creation of allochthonous salt sheets in the Gulf of Mexico (After Montgomery and Moore 1997). (**b**) Schematic of evolution of eastern Green Canyon, Gulf of Mexico. At 5.3 Ma the salt sheet was extruded. From 6.3 to 3.3 Ma the ongoing basinward extension of the sheet promoted differential loading within half grabens. From 3.3 to 2.2 Ma the largest intrasalt basin displaced all the salt below it to create a salt weld and a structural inversion that was created by a turtle structure. Subsequently the sheet was further deformed as it continued to flow basinward and climb the stratigraphy (Modified from Seni and Jackson 1992a, b)

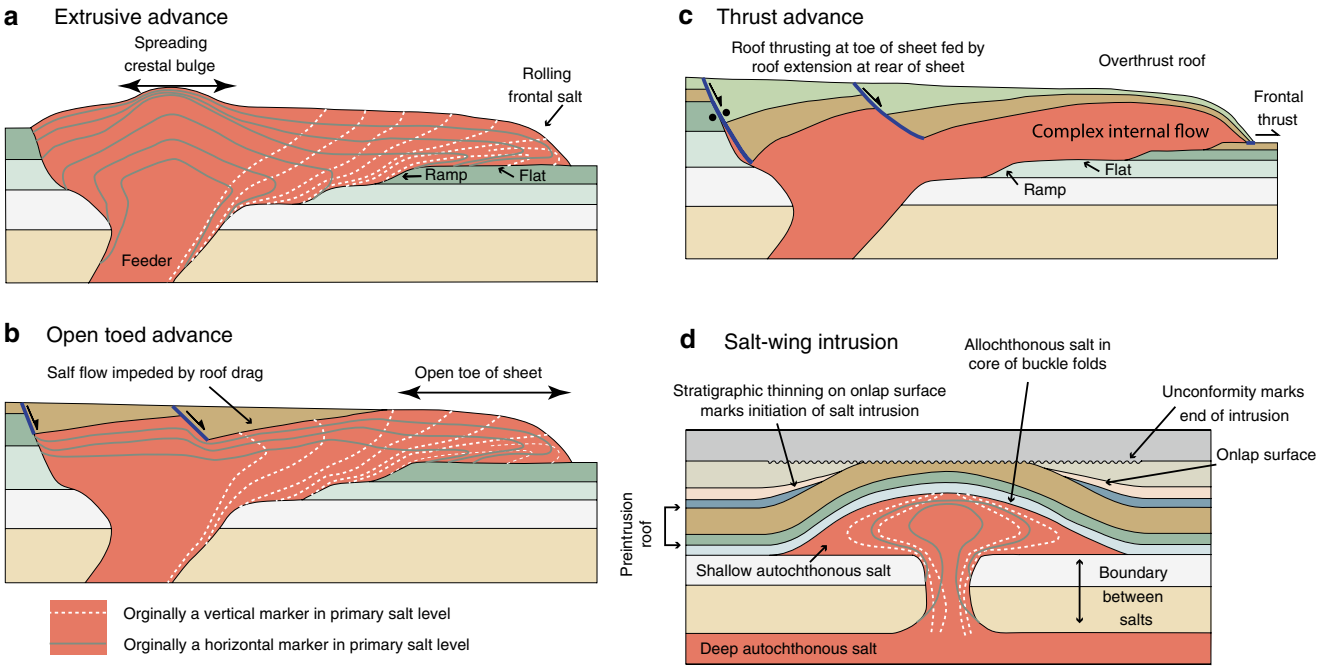

Fig. 6.36 Emplacement of salt sheets. Salt sheets can advance in four ways. In extrusive advance (**a**), an exposed salt sheet spreads at the surface without a roof. The salt flows outward by gravity, spreading from a summit formed by a dynamic bulge above the feeder. Deformation of passive marker lines here illustrates frontal rolling, which is common above lithified bedrock but less typical above unlithified subsalt strata. In open-toed advance (**b**), the sheet is extrusive at its toe but is partly buried by a roof strong enough to modify the underlying salt flow. The roof resists salt flow. Traction exerted on the roof by flow of the underlying salt may extend a sufficiently weak roof. In thrust advance (**c**), a buried sheet advances along with its roof in a thrust hanging wall. The roof is separated from peripheral sediments by a roof-edge thrust fault that projects from the tip of the salt to the surface. During salt-wing intrusion (**d**), a wedge of salt is emplaced along a thin delaminating stratigraphic layer in the flanking country rock. The roof is typically uplifted as a detachment anticline during regional shortening. This arching typically leads to onlap or erosion of the roof strata. These processes can occur sequentially during growth of a sheet to produce salt-sheet lineages as illustrated in Fig. 6.33 (After Hudec and Jackson 2006)

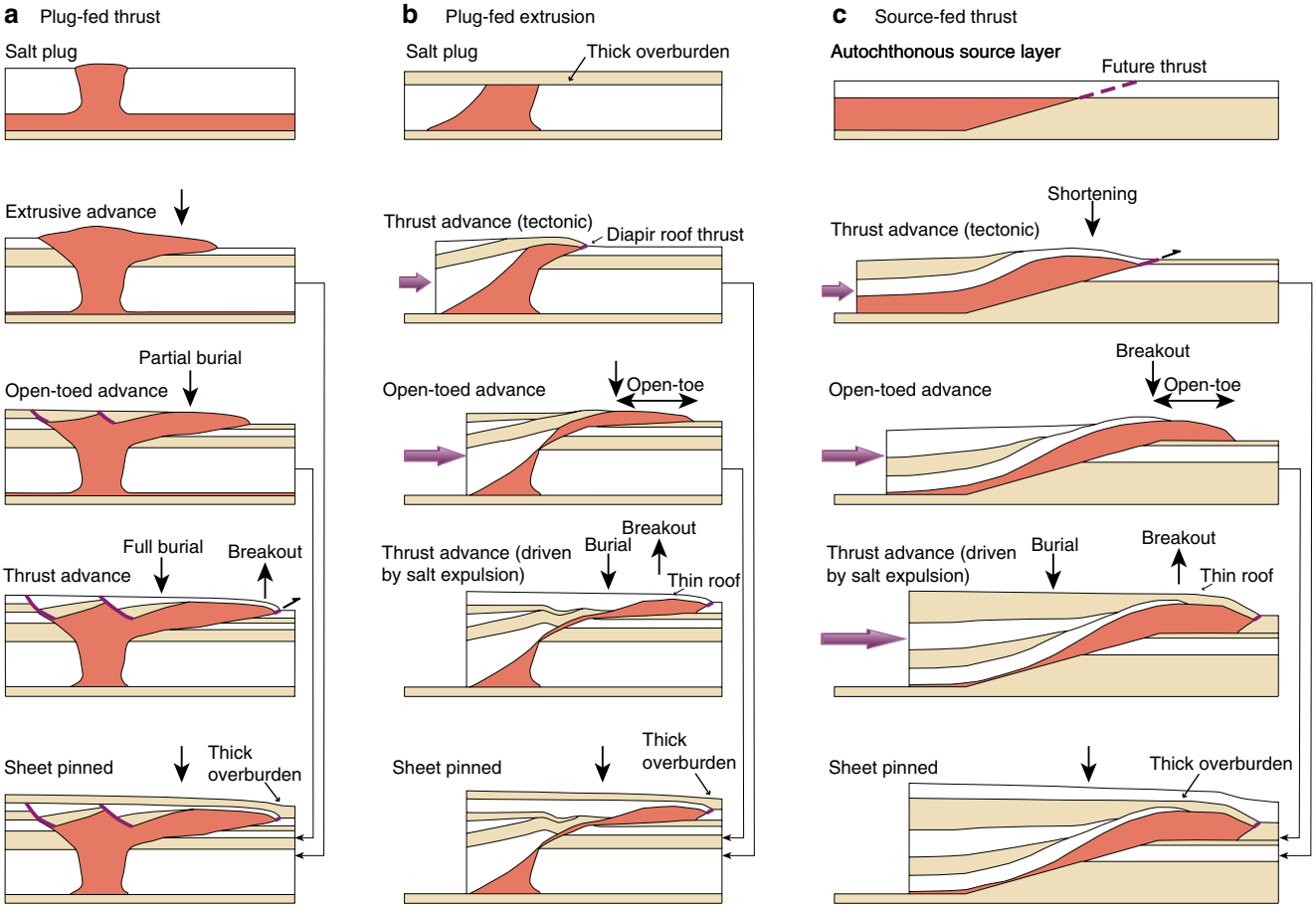

Fig. 6.37 Emplacement of salt sheets. Most salt sheets advance by a time related sequence of extrusion, open-toed advance, and thrusting. These modes may combine in many ways over the life span of a salt sheet, but three evolutionary sequences (or lineages) are particularly common. (**a**) Plug-fed extrusions. (**b**) Plug-fed thrusts, and (**c**) Source-fed thrusts. See Fig. 6.38 for 3D reconstruction of plug-fed versus source-fed styles (After Hudec and Jackson 2006)

buried diapirs is common in orogenic belts that involve salt basins and in some compressional provinces in deep-water passive margins (Mohr et al. 2007; Ventisette et al. 2005; Saintot et al. 2003). The term "salt plug", as used by Hudec and Jackson (2006) encompasses both salt stocks and salt walls (see Fig. 6.1a), although most plug-fed extrusions are sourced from stocks. Plug-fed extrusions are probably the most common type of salt sheet feeder, worldwide, and form in both passive margins and orogens.

Extrusive salt sheets spread whenever salt in a downbuilding diapir rises faster than dissolution, erosion, and sediment aggradation can remove or contain it (Fig. 6.26b). Plug-fed extrusion is typically initiated by decreases in dissolution, erosion, or sediment aggradation rates or an increase in salt-rise rate. Decreased aggradation can result from decreased sedimentation associated by changes in sea level, climate, source-area tectonics, or sediment-transport systems. Alternatively, slow aggradation may be caused by increased subsidence in local basins adjacent to the diapir. Slower sediment aggradation allows salt to spread more rapidly along a base-salt flat (Fig. 6.26c). Regional sediment starvation can therefore simultaneously initiate extrusive sheets from many domes. These sheets can eventually coalesce to form salt canopies, as in the continental rise of the Gulf of Mexico (Hudec and Jackson 2006).

Onshore, when salt is near to or at the surface, extreme aridity can retard salt dissolution and the extruded or open-toed allochthon's passage into thrust-advance or sheet-pinned styles. Limiting dissolution and allochthon passage into thrust-advanced and sheet-pinned styles is more difficult in subaqueous settings. Even an accumulation of a thin roof or carapace of caprock or sediment can retard dissolution in subaqueous settings. These sediment veneers tend to be ephemeral because vigorous, multidirectional spreading of a salt sheet tends to dismember any roof or cap rock. However, rapid sedimentation or cap-rock formation can create a new impermeable layer faster than the old one is disrupted. This can retard dissolution and the transition into deflation even in an actively spreading sheet. Mechanical erosion of evaporites is likely to be more important in spreading of the salt

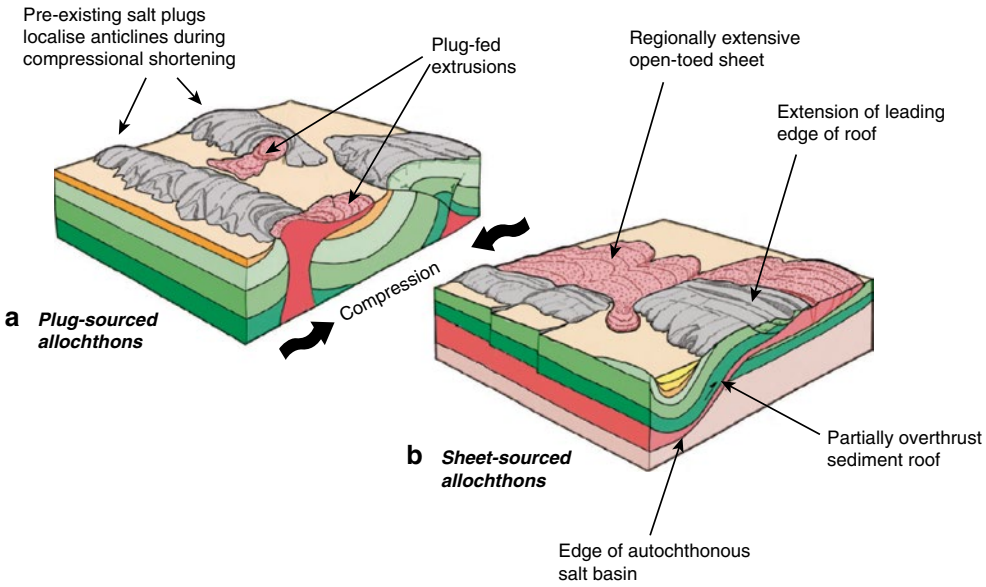

Fig. 6.38 Varying salt source geometries. (**a**) Plug sourced salt sheets. (**b**) Source-fed thrust décollement that broke out to form open-toed salt sheets (After Hudec and Jackson 2006)

sheet in arid or polar settings, where dissolution is less effective (Chap. 7). In humid or subaqueous environment the transition to deflation and gravity spreading is rapid if the load on the source layer is high (a viscous salt blowout). A sheet produced by a salt blowout, where salt escapes under elevated pressures, is more likely to have a flat base over a broad area because the sheet advances much faster than the sediments can aggrade. This effect is enhanced if the blowout occurs during a sedimentary hiatus.

Lateral shortening of a dome is especially effective in triggering a plug-fed extrusion (Fig. 6.37a). In addition to any salt blowout caused by the disruption of the plug's roof, inward convergence of the walls displaces salt from the diapir. As for sheets triggered by roof disruption, regional compression typically causes the rapid advance of sheets, which results in a flat base of salt.

Roof Deposition or Salt Burial

The flow of an unbuttressed extrusive sheet is typically radially outward, with a preferred direction down the local slope (Fig. 6.38a, b). This outward salt flow continually dismembers the roof sediment. Deposition of a permanent roof does not typically begin until either the sheet advance slows markedly, or the salt streamlines become parallel instead of radial (Fig. 6.36b). This transition can occur for three reasons (Hudec and Jackson 2006) and for each, a salt supply deceleration or change from radial spreading allows a continuous roof to accumulate.

First, sheet advance slows if salt supply from the feeder is reduced. This can occur if the source layer is depleted enough that increasing boundary drag (edge friction) slows salt flow, or if the feeder stops shortening under compression, or if the feeder pinches off. Diminishing salt supply marks the transition from a salt fountain to a salt droplet; a salt fountain comprises a summit dome that feeds one or more salt glaciers; a salt droplet continues to spread until the relief of the former summit dome dissipates, resulting in an extrusion having a flat-topped profile and steep margins (Figs. 6.1a and 6.36)

Second, sheet advance will slow even if the salt feeder and fountain remain active, simply because radially spreading sheets require a progressively greater volume of salt for each additional increment of advance. This requirement explains why the measured advance rate of salt glaciers tends to decline toward their terminus (Talbot et al. 2000).

Finally, a sheet will slow where it meets a buttress. Some buttresses are sedimentary and an extrusive sheet advances most slowly where aggradation is most rapid. Pre-existing topography, such as mountains, anticlines, or scarps, can create other buttresses, especially onshore. Sheets can also be buttressed against adjacent sheets during salt suturing as a canopy forms. Thus, a radially spreading sheet becomes constrained to flow more unidirectionally if it sutures on each flank to become part of a canopy.

In most sedimentary environments, but especially in prograding margins, a roof does not accumulate uniformly over the entire salt sheet. Thus, open-toed advance typically follows extrusive advance (Fig. 6.36a transition into to 6.36b). The style of deposition above the salt sheet (synclinal minibasin, roho, or counter-regional) varies with the depositional environment and geometry of the sheet. All three styles expel salt from beneath the sinking minibasins (see next section). Salt expulsion can drive sheet advance by recycling salt even if the feeder no longer supplies salt. Open-toed advance continues until the sheet toe is buried (Fig. 6.36c), which happens in two ways. First, sedimentation can bury the toe while the sheet is still advancing. If so, the sheet will most likely continue to advance by thrusting, as is true along nearly all of the modern Sigsbee Escarpment in the northern Gulf of Mexico (Fig. 6.49; Hudec and Jackson 2009).

Second, the sheet may continue to advance as an open-toed sheet for a long period before being buried by a permanent roof. Salt expelled from beneath subsiding basins flows into a variety of salt structures. Some salt flows into rising diapirs; some is trapped as relics along a basal weld; some is dissolved; and some may feed continued advance of the sheet. The amount of salt available for sheet advance ultimately diminishes to exhaustion. Once the toe is buried, there may not be enough salt to feed any further advance by thrusting. Counter-regional salt systems behave like this, as do the later stages of some roho systems.

Thrust Advance

Once completely buried, a salt sheet may advance as a thrust as long as forces driving sheet advance can overcome the strength of the roof (Fig. 6.36c). Bigger sheets tend to advance by thrusting for a longer time. For example, the giant Sigsbee Escarpment has, in places, advanced more than 5 km since the burial of its toe (Jackson and Hudec 2004). In contrast, small, isolated sheets like the Mica salt sheet (centred on Mississippi Canyon, Block 166, northern Gulf of Mexico) have advanced at most a few hundred meters since burial (Fletcher et al. 1995). Thrust advance becomes more difficult as the roof thickens and strengthens, and so even the largest sheet should eventually be pinned in place by its overburden.

During thrust advance, mass wasting may re-expose parts of a sheet's leading edge and allow salt breakout (Fig. 6.33, stage 2). In contrast to source-fed thrusts (see below), where salt breakout is important, the only known examples of present-day breakout from diapir-fed sheets along the Sigsbee Escarpment are small and insignificant. Because of their small size, the exposed parts of these toes are likely to be soon reburied and the salt sheets will then resume advance as thrusts.

Plug-Fed Thrusts

Plug-fed thrusts form when a diapir's overburden is shortened by thrusting, carrying a sheet of salt from the diapir in the base of the thrust hangingwall (Fig. 6.37a, b). The style of deformation occurs during regional shortening if a thick, strong overburden prevents a laterally shortened salt plug from piercing to the surface. Thrusting is facilitated if the plug is inclined because slip along the more gently dipping diapir flank may nucleate the fault. Sheets of this type occur in orogenic belts and in deep-water fold and thrust belts. Many sheets of this type never progress beyond their initial thrusting stage.

If the overburden is kilometres thick when shortening begins, salt is unlikely to pierce to the surface without substantial erosion (Fig. 6.23). Structural style typically changes abruptly along strike from a salt sheet near the plug to a salt-free thrust fault away from the plug. Where diapirs predate shortening, transpressional thrust networks can form oblique to the regional shortening direction (Jackson et al. 2004). Such thrusts tend to form parallel and adjacent to the flanks of salt walls even if this direction is strongly oblique to the regional maximum compressive stress.

Some plug-fed salt-cored thrusts, however, have overburden thin enough to be eroded off during shortening. Erosion of the overburden above the thrust allows the salt to break out. If vigorous salt flow overcomes dissolution and sedimentation, open-toed sheet advance can begin (Fig. 6.36b). Extrusion can be rapid because salt is pressurized by tectonic compression or by a location at the foot of a slope.

After breakout, an open-toed sheet extruding from a plug-fed thrust advances over the sediment surface until its feeder is completely pinched shut, or the source layer is depleted of salt. The sheet then evolves through stages typical of open-toed advance: progressive burial, possible thrust advance (driven by gravity spreading of the sheet instead of by regional shortening), and eventual pinning. This postbreakout history can obscure an origin as a plug-fed thrust, especially if most of the prekinematic roof has been eroded.

Source-Fed Thrusts

A source-fed thrust forms when a thrust imbricate detaches on autochthonous salt and carries a slice of salt in its hanging wall (Figs. 6.37c and 6.38b). In Hudec and Jackson's (2006) terminology, "source" refers to the autochthonous salt layer, the source level for all the salt structures in the basin. Source-fed thrusts range from thin slivers in the hanging walls of small thrusts to salt-cored nappes involving kilometre-thick salt sheets displaced by many kilometres (Fig. 6.38b). The largest thrust-fed breakouts form near the edges of salt basins, where the salt-lubricated detachment stiffens by facies changes, thins, or disappears. Here, translation, aided by a subhorizontal salt detachment, must be accommodated beyond the salt by thrusts or folds in the overburden. Thrust systems fringing salt basins can extend along strike for hundreds of kilometres. Examples include the Angola salt nappe (>900 km long), the Guadalquivir allochthon (350 km long), the Salt Range allochthon (230 km long), and the Mesozoic nappe on which the Atwater foldbelt is detached in the northern Gulf of Mexico (160–240 km long).

Small source-fed thrusts may be too small to expose salt sheets at the surface. These sheets are preserved in the thrust-advance stage. However, many basin-edge structures have tens of kilometres of slip. Examples with large slips include; the Guadalquivir allochthon (25 km roof overthrust), the Salt Range allochthon (as much as 35 km roof overthrust), the Angola salt nappe (>20 km roof overthrust), and the West Lufilian allochthon (65 km roof overthrust). Coupled with uplift and erosion of the roof, this displacement allows salt to break out at the sediment surface to form open-toed sheets that are partly covered by the overthrust sedimentary roof

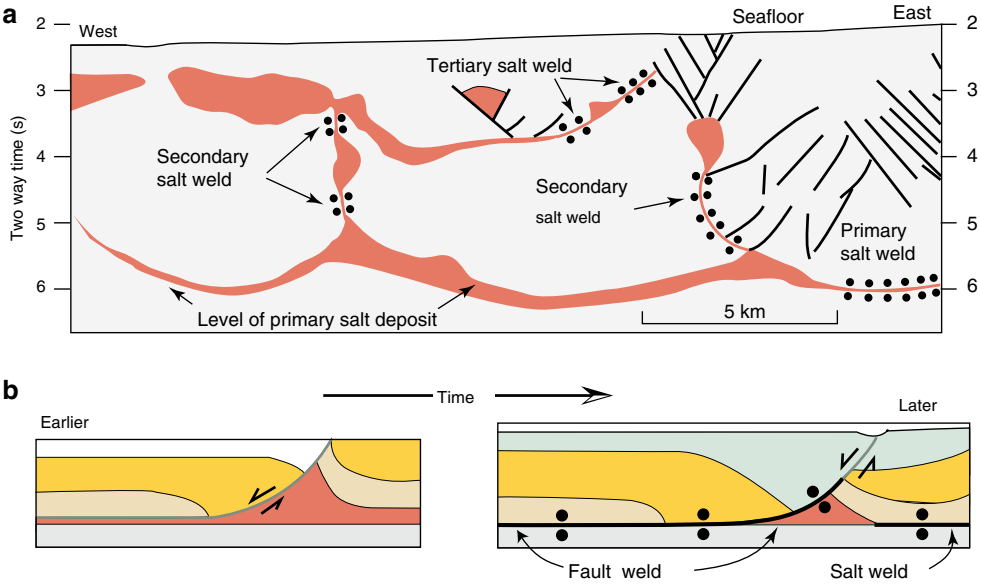

Fig. 6.39 Welds (**a**) Salt weld classification (see text for detail on weld types). This schematic cross section is based loosely on the geology of offshore Angola. (**b**) Salt weld versus fault weld (fault weld displacements can be normal or reverse-thrusted)

(Fig. 6.38b). Because shortening pressurizes salt, any breakout is likely to extrude rapidly as a salt blowout. An extrusive salt apron ahead of the thrust allochthon creates an excellent detachment for translation of the roof, which continues to advance. This detachment is so effective that the roof may extend while advancing over the lubricating sheet, as in the Scotian salt nappe, the Salt Range allochthon and the Rif allochthon in Morocco. Over time, the roof may advance completely across the salt, obscuring its origin as a salt breakout. Jackson et al. (2003) interpreted this style for the Neoproterozoic West Lufilian allochthon (Democratic Republic of Congo). There the evaporite sheet appears to have been extruded rapidly across a 65-km long flat, followed by more gradual overthrusting and buckling of the roof and burial by synorogenic sediments.

Large breakouts can obscure the origin of a sheet as a source-fed thrust. In orogenic belts, thrust ancestry is typically obvious from the regional setting (as in the Guadalquivir and Salt Range allochthons). However, on passive margins, some basin-edge nappes may have extruded out of the basin prior to deposition of a mechanically significant roof, driven by sediment loading farther updip and seaward tilting. If so, this would constitute another lineage: the source-fed extrusion. This origin has been proposed for the Mesozoic nappe below the Atwater foldbelt in the northern Gulf of Mexico.

Remembering that Hudec and Jackson's (2006) lineage classification, illustrated in Fig. 6.37, is based on the initial mode of sheet advance, the distinction between source-fed thrusts and source-fed extrusions must depend on roof thickness at the time of sheet initiation. This can be difficult to define as the evidence can be disturbed or obliterated by subsequent salt movements. A structure is a source-fed thrust if a mechanically significant roof was present at the onset of deformation, because the earliest phases of movement were by thrust advance. Breakout may have occurred very early during thrust advance if the roof was thin, but this does not change the classification of the sheet, as illustrated in Fig. 6.37c. Conversely, the structure is a source-fed extrusion if no mechanically significant roof was present when the sheet started to advance.

Given that most candidate structures for source-fed extrusion are deeply buried at the downdip ends of passive margins, little is known regarding the details of the preadvance roof. Hudec and Jackson (2006) recognize source-fed extrusions as a possible style, but think it is premature to recognize them as a common lineage until more details are available concerning their early history.

Salt Deflation and the Formation of a Weld

A salt weld forms when the salt sheet or primary bed is so thinned by withdrawal (deflation) that salt is no longer resolvable on seismic profiles (Fig. 6.39; Wagner III and Jackson 2011). Salt welds are also called evacuation surfaces, overburden touchdown scars, salt scars (literally *cicatrice salifére* in the French literature), or simply touchdowns. A salt weld is usually, but not always, marked by a structural discordance. Another distinctive feature is the common presence of a structural inversion above the salt weld, which often defines some sort of broad anticlinal structure (e.g. turtle and mock-turtle structures; Fig. 6.29). Subsurface welds are readily imaged in modern seismic surveys, but the temporal resolution of today's reflection seismic surveys is still too coarse to display the internal structure of welds (resolution is typically greater than ~30–50 m of halite for peak frequencies of ~10–30 Hz; Wagner III and Jackson 2011).

The term salt weld encompasses a zone that may or may not retain tens of metres of remnant evaporites and insoluble residues within the amalgamation interval that originally contained the halokinetic salt mass (Fig. 6.39). The position

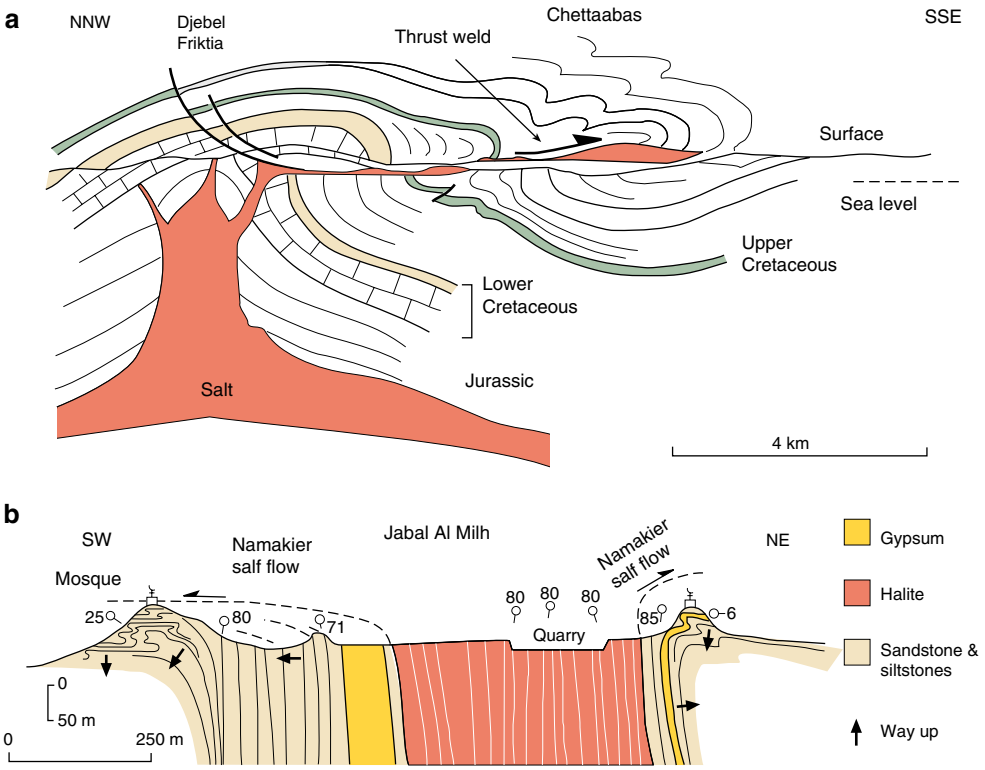

Fig. 6.40 Cross sections through outcropping salt allochthon terrains. (**a**) The Djebel Friktia allochthon, Algeria, shows how breakout of salt into the next allochthon tier typically evolves into a gravitational collapse 'thrust' off the original salt wall. This thrust is a gravitational adjustment to "down to the basin" extension in the overburden. Breakout occurs in areas where pressurized salt rises faster than extension and sedimentation can accommodate. (**b**) Recumbent folding and thrusting are the main deformation features observed in the siltstones and gypsum layers of the dissolution disturbed overburden at the margins of the Jabal Al Milh diapir, Yemen (After Davison et al. 1996b)

of a weld is usually, but not invariably, marked by structural discordance across the weld, as in the Friktia thrust weld (Fig. 6.40a).

A salt weld is a always surface joining strata originally separated by autochthonous or allochthonous salt (Fig. 6.39a. Lithologies on either side of the weld are in direct or near-direct contact, not separated by significant evaporite thicknesses or primary interlayered material. A primary weld joins strata originally separated by gently dipping autochthonous bedded salt at the level of primary salt deposition or mother salt bed (Fig. 6.39a). Secondary welds join minibasin or depopod strata originally separated by steep sided salt diapirs (walls or stocks). Tertiary welds join strata originally separated by gently dipping allochthonous salt sheets.

Each side of the weld can slip relative to the other, as it can in a more steeply inclined fault that is lubricated by salt. The latter structure is termed a fault weld, although all welds are tied to some sort of translation or shearing of strata above and below the salt sheet (Fig. 6.39a, b). A fault weld is a simply a recognisable fault surface or fault zone joining strata originally separated by autochthonous or allochthonous salt (Fig. 6.39b). Thus a fault weld can be a salt weld along which there has been obvious faulting or shearing. Faults styles and associated welds are discussed in detail later in this chapter.

As salt evacuates to form a weld, evidence of local salt loss is always recorded in overlying sediments via variable thicknesses, dispersal patterns, and facies distributions. An incomplete salt weld is a zone joining strata originally separated by autochthonous or allochthonous salt and still separated by up to 50 m of remnant evaporites and interlayered insolubles. A discontinuous weld is a salt body that is welded in places, but in other areas retains more than a 50 m thickness of evaporites and interbedded material. An apparent weld is a salt body that appears welded at the scale of observation, but which may actually contain more than 50 m of evaporites and interbedded material.

Better-documented geological examples of weld textures do not come from the subsurface but from outcrops of salt-cored structures in arid regions such as the Flinders Ranges Australia, Monterey region, Mexico and the Zagros and Qom foldbelts in the Middle East (Dyson and Rowan 2004; Rowan et al. 2012a; Morley et al. 2009). Figure 6.41 illustrates an outcropping example of a primary salt weld, left after dissolution/evacuation of Miocene salt, as studied by the author in central Iran. It outcrops in a succession of thrusted and overturned Miocene redbeds to the west of the Qom city and immediately south of the Indus thrust fault. The weld today is exposed as a near vertical (slightly overturned) outcrop pattern, marking the position of the former primary salt bed. Seismic across the outcrop into the adjacent Qom Basin to the south shows the outcrop is equivalent to a stratigraphic position once occupied by a 100 m plus-thick salt halokinetic mother salt bed (Morley et al. 2009). The outcrop consists of a central massive claystone residual

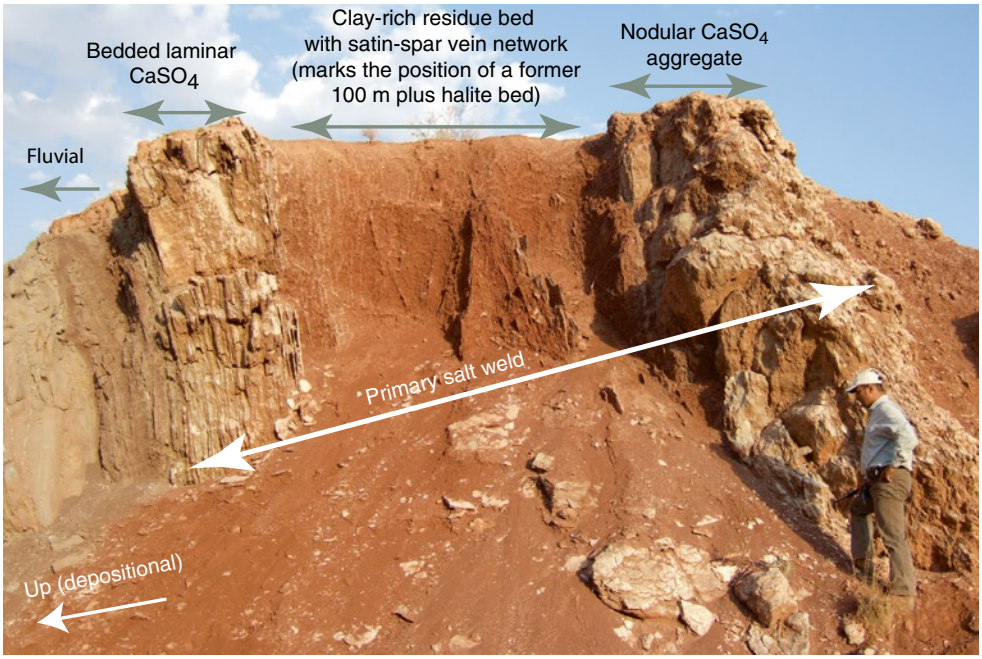

Fig. 6.41 Outcropping primary salt weld in thrust-upturned Miocene redbeds, located to the west of Qom City, Iran

bed, now crosscut by a network of cm-scale satin-spar veins. This unit is all that is left of the once 100+ m thick salt mass at the level of the primary mother salt. Either side of this residue claystone are stratabound beds of gypsum (anhydrite in the subsurface). Both these gypsum units are fractionated residuals formed as the salt flowed and dissolved in the subsurface. The lower gypsum bed is a nodular aggregate, with cm-scale textures indicative of a basal anhydrite, as exemplified by the diagenetic $CaSO_4$ bed (basal anhydrite) defining the underside of the Cretaceous Maha Sarakham salt, Thailand (Fig. 7.45). In contrast, the upper $CaSO_4$ bed is dominated by laminar textures similar in character to laminar $CaSO_4$ textures recovered in core from many Gulf of Mexico diapiric capstones.

Another example of a salt weld, visible in outcrop, comes from the La Popa basin, near Monterey, Mexico, there a subvertical salt weld is exposed for 25 km along its strike (see Fig. 6.106 and associated text for full geological detail; Rowan et al. 2003, 2012a). Traverses across the la Popa weld indicate significant strike-parallel variability in both weld structure and the geometry of adjacent strata. In some places the weld is a 2–4 m wide fault zone with brecciated and sheared siliciclastics, no remnant evaporites, and evidence of extensive fluid alteration adjacent to the weld. In other places, the weld contains up to 30 m of remnant gypsum, either massive or sheared, that locally contains inclusions of meta-igneous rocks or Jurassic dolostones that were carried up in the diapir. The La Popa weld ends in the west at an outcrop of gypsum several hundred metres in diameter that represents a remnant salt stock. In contrast, the weld trace is truncated in the southeast by an intra-Maastrichtian unconformity (see later in this chapter for geological detail).

Flow Edges, Basal Shearing and Salty Gumbos

Shearing associated with the margins of salt diapirs has long been recognised as creating shale sheaths and shear-defined cylinders of differential salt movement within downbuilding subvertical diapirs (Hanna 1953). This is especially obvious within subvertical salt structures that have been mined or crop out (Balk 1953; Kupfer 1976; Talbot and Jackson 1987a; Zak and Freund 1980). What differentiates classic subvertical diapir models from the lateral flow emphasis of more recent allochthon models is an understanding of the development of minibasins and listric faults in supra-allochthon sediments and the typical creation of a sheared interval at the basal sediment-salt contact (Fig. 6.42a).

Once an allochthonous salt sheet is detached from its source layer, pods of condensed sediment are deposited as a roof carapace (e.g. palaeontological equivalent of unit 5 in Fig. 6.42a). This suprasalt region loads and splits into a number of growth-fault defined suprasalt depopods (layers 1–4 in Fig. 6.42a). Sediment accommodation space is created at the up dip end of this expanding depopod system via growth faulting, while thrusting and erosion is occurring at the same time at the downdip end (Figs. 6.36b, c and 6.42b). The rotation of the suprasalt sediment prism as it accumulates is facilitated by the lateral migration of salt. Internal shear in the advancing salt sheet is greatest in the salt's basal shear zone.

Sediments beneath the base of subhorizontal allochthon sheets or the subsequent welds typically preserve shear features that encompass both external and internal shear zones. They include; evidence of sediment pressurization, entrainment of country rock within the salt body and structurally induced drag folds (Fig. 6.42a; Harrison and Patton 1995;

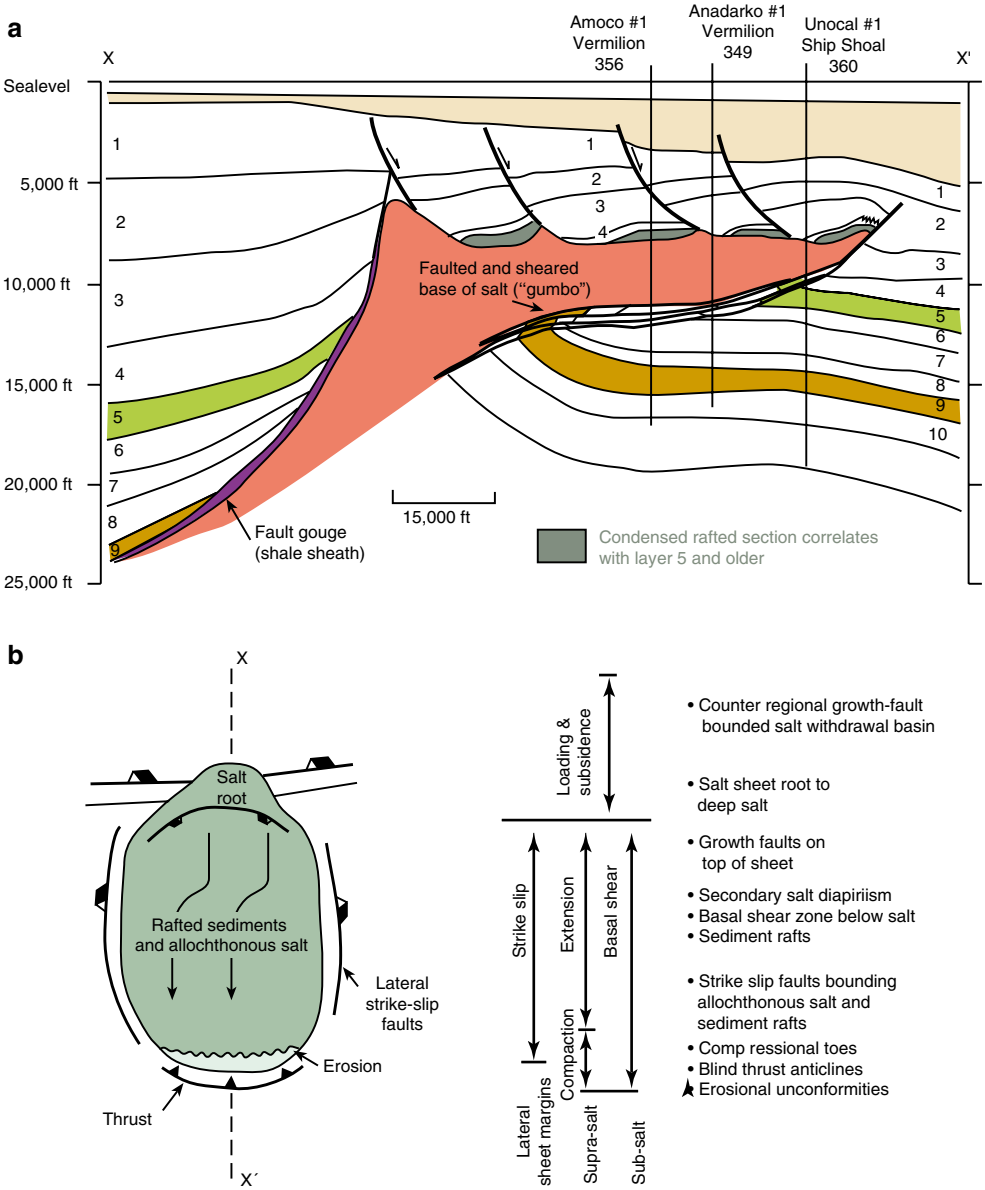

Fig. 6.42 Basal shear model (After Harrison and Patton 1995). (**a**) Cross section view with a thrust fault defining the rising compressional nose of the salt sheet. Relevant Gulf of Mexico wells are placed schematically on this section. (**b**). Map view. Down-to-the-basin translation of the composite salt/sediment glacier forms strike slip shears at the depopod margins. The compressional toe is a complex combination of normal fault and eroded blind-thrust anticlines (see later)

Alsop et al. 1996). Basal shear zones of allochthons are also called transition zones, gumbo zones[12], unconsolidated rubble zones, and can be considered as a subhorizontal type of shale sheath.

The basal shear zone is a response to thrusting along and within the base of the salt allochthon as it is emplaced at or near the sea floor (Harrison and Patton 1995). Consequent sediment loading atop the sheet drives further salt withdrawal and suprasalt sediment deformation (Fig. 6.42a). Salt flow within the salt sheet occurs via internal shear and pressure solution creep. The salt sheet remains impermeable as it experiences no brittle response to flow deformation as it rolls and extrudes out over its substrate.

As the sediment carapace thickens over the salt sheet, overpressures develop in the subsalt transition zone. The resulting anomalously high pore fluid pressures facilitate simple shear beneath the sheet by reducing the effective normal stress, thereby allowing lateral slippage of the sheet and its sediment carapace (gravity gliding; Baud and Haglund 1996). Whether shearing occurs within the salt sheet or in the immediately adjacent subsalt sediment is determined by which interval has the lower shear strength. Baud and Haglund (op. cit.) believe post first-emplacement shearing occurs within the salt sheet, at least until anomalously high pore pressures develop in sediments below the sheet.

[12]The term gumbo is used mostly by Gulf of Mexico drillers to describe the appearance of the large, pliable sticky and clumped cuttings that come up in the mud returns, whenever these basal salt transition zones are intersected. Gumbo is actually a thick seafood-based soup or stock that originated in the eighteenth century in the Creole region of southern Louisiana and is still a very popular dish in the southeast of the USA.

Measured pore pressures in the basal shear zone of Gulf of Mexico allochthons can be much higher than regional pore pressures and approach lithostatic fracture-inducing pressures in some subsalt shales. Measured gradients as high as 0.88 psi/ft or balanced mud weights of 17 ppg can characterise subsalt Gulf of Mexico drilling (Table 8.4; Harrison and Patton 1995). Field evidence cited in House and Pritchett (1995) indicates that the hyper-pressured interval below a salt sheet is typically 300–600 m (1,000–2,000 ft) thick and its upper part is likely to entrain the lithologically distinct "gumbo" or transition zone. In the Gulf of Mexico, "gumbo" zone are encountered beneath salt sheets emplaced into Pliocene, upper Miocene and middle Miocene age sections, but hyper-pressurised cells in the "gumbo" have been documented only below allochthons emplaced into Pliocene and upper Miocene sections (House and Pritchett 1995; Shaker 2008). This may indicate that hyperpressures are a geologically transient allochthon phenomenon and that, with sufficient time, a pressure equilibrium gradually re-establishes itself.

On passing through the salt allochthon the Amoco #1 well, Vermilion Block 356, immediately intersected such a pressured disturbed transition or "gumbo" zone (Fig. 6.42a). Cuttings from the gumbo zone documented a change with increasing depth below base of salt from a grey soft shale with pyrite traces into a firmer, medium to dark shale. Deep resistivities were less than 0.2 ohm.m in the shale in the first 120 m (400 ft) below the salt and increased to 0.4 ohm.m in the next 180 m (600 ft) possibly indicating decreasing pore water salinities or increasing organic content. The lowest resistivity zone corresponded to a wireline density $\approx$ 2.10 g/cc, which increased to 2.25 g/cc by 300 m below base of salt. RFT-measured pressures in thin sands in the disturbed (gumbo) zone were some 16.7 ppg equivalent, while in the same well, measured pressures were 16.1 ppg equivalent several thousand feet below the gumbo.

The South Marsh Island Block 169 Amoco #1 well in a transition zone immediately below its salt sheet intersected pressure gradients of 17.4 ppg equivalent. This pressure level is only 0.3 ppg less than the calculated fracture gradient for the matrix (House and Pritchett 1995). Below the "gumbo", pressure gradients decreased to more typical regional values of 16.5 ppg equivalent. Pressure data divide this well into a high-pressure zone (hyper-pressure cell) some 335 m (1,100 ft) thick immediately below the salt sheet and an underlying pressure transition zone some 245 m (800 ft) thick. Pressures below the transition zone were equivalent to regional overpressures.

Abnormally high pressures in transition zones (gumbo) typically indicate hydrologic isolation of this shale-rich section and a lack of hydraulic continuity (these shales do not readily dewater). Wireline image data show soft sediment deformation features, with higher levels of contortion in proximity to the allochthon contact. A similar style of disturbance is seen in outcrops in the former transition zone of Jabal Al Milh diapir, Yemen (Fig. 6.40b) and in subsalt thrust folds that define the Upper Cretaceous section of the Jebel Friktia allochthon (Fig. 6.40a). In situations where extruded salt is advancing across the seafloor, the initial soft-sediment disturbance textures in gumbo zones probably represent material slumped off the bathymetric scarp above the toe of salt and subsequently overridden as the salt extrudes basinward (McGuinness and Hossack 1993; Fletcher et al. 1995).

Jackson and Hudec (2004) have expanded on Harrison and Patton's notion of basal thrusting (Fig. 6.40a) by arguing that as salt allochthons continue to advance over the seafloor as a series of flats and ramps, they act much in the same way as a glacial ice sheet advances and ploughs over glacial till pushing a piling sediment at its nose. That is, as the allochthonous salt rides up over its underburden it pushes, deforms and thrusts portions of this water-saturated substrate. This in turn creates thrust ramps and duplexes in the subsalt "gumbo" sediments immediately beneath the salt sheet.

Once covered by extruded salt, a variably deformed subsalt transition (gumbo) zone typifies the lower contact of most active allochthon sheets. Before natural pressure bleed-off occurs it is outlined by abnormal pressure and temperature gradients. Differential translation is concentrated at and immediately below the base of the salt sheet. Salt-lubricated slivers line up as sub-parallel thrust planes along the pressurised base of the allochthon, as do repeat sections and recumbent subsalt folds (Fig. 6.42a; Harrison and Patton 1995). A lack of fluid movement in a disturbed zone due to low permeability can lead to anomalously low temperature gradients in this interval, with a low thermal gradient halo typically characterising the interval immediately below the thick, thermally conductive salt sheet. Thermal gradients in this halo gradually increase downward until a more normal regional gradient is achieved.

The laterally variable low temperature, high-pressure (gumbo) interval that occurs below most allochthon sheets is a potential problem zone for the drilling engineer (Chap. 8). Although not all intersected gumbo zones remain pressurised in the subsurface, prior to drilling, a basal shear zone in most active allochthon provinces is best considered as a potentially thick, highly pressured, faulted and folded interval, and planned for accordingly. Fluids in this deformed zone may migrate along fault planes, but typically not within the blocks of disturbed sediment matrix, which like the overlying salt, act as vertical barriers to fluid flow. Pressure build-ups within the gumbo shales probably lead to periodic matrix fracturing and bleed-off of elevated pressures (seismic pumping).

When pressurised, the base of salt or gumbo zone tends to act as a permeability barrier to rising basinal fluids, as does the overlying salt (House and Pritchett 1995). When rising fluids impinge on this zone they are forced to flow laterally, subparallel to the base of salt and through or beneath the gumbo until they encounter a breach point or the feather

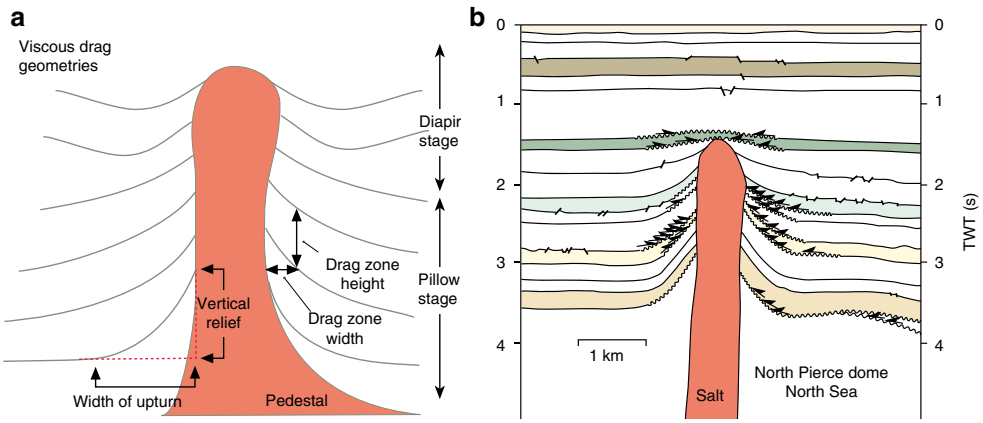

Fig. 6.43 Circum-diapir drag folds. (**a**) Dimensions and parameters of the diapir drag zone (After Davison et al. 2000b). (**b**) Interpreted onlap surfaces in the "drag-zone" or rotated drape-fold zone vicinity of North Pierce dome, North Sea (After Schultz-Ela 2003)

edge of the salt sheet (Chap. 8). But not all "gumbo" transitions are anomalously pressured and pressure character of the transition zone is not easily predicted ahead of drilling. For example, instead of being impervious, extra permeability can be created in a gumbo or transition zone via periodic salt evacuation from salt feeder stocks below an allochthon canopy.

Depending upon its local character, a gumbo zone can be a seal, or it can be a path for hydrocarbon migration, or even a potential reservoir. When pressurised a gumbo zone provides a potential trapping mechanism, much like a pressure-sealing fault. Hydrocarbons migrating laterally through a highly-pressured transition zone can be injected into low-pressured underlying sands and trapped due to the pressure differential. Or a transition zone can trap hydrocarbons migrating upward through subsalt sands as overpressures in the transition zone prohibit fluid invasion. If not overpressured, a fracture-susceptible gumbo zone can provide a permeability pathway for hydrocarbons migrating upward along base of a salt feeder as buoyant fluids move through the transition zone. Hydrocarbons can also migrate upward through suballochthon sands and then leak into the transition zone wherever the sand and transition zone contact one another. Lastly, subsalt transition zones could prove to be reservoirs themselves, as widespread leakage of hydrocarbons from below, or lateral migration of fluids through the gumbo, can saturate them. But most subsalt transition or "gumbo" zones are probably not of reservoir quality and observed log character shows most are disturbed and shale prone (LeBlanc 1994). Fluid modelling, based on allochthon-focused subsalt flow, has implications for the pulse-like fluid emplacement in suprasalt hydrocarbon traps (Fig. 8.28 and discussion) as well as mineralisation episodes and the development of footwall alteration haloes in many base metal deposits (Fig. 15.87 and discussion).

Developing pre-drill seismic techniques that can reliably define which welds seal and which leak, is still an expanding topic in salt basin research (Taylor et al. 2011). For example, below the salt canopy in Walker Ridge and Keathley Canyon in the Gulf of Mexico, variations in both pore pressures and elastic rock properties are highly correlated to age and lithology and so are seismically resolvable. Sub-salt geopressure increases there are typically associated with regional marls (high velocity, indurated lime-rich mudstones), which cap sequences of thick, low velocity, overpressured shale. As a result of their anomalous acoustic properties, these high-pressure indicator marls can readily be tied to seismic events and often mapped over extensive areas (seismic data quality permitting).

Near-Diapir Suprasalt Shear (Drag Zones)

Halokinetic deformation can create substantial faulted external or drag zones, not just in the gumbo and shale shear zones immediately adjacent to the deforming salt, but in broader intervals of nearby sediment. As it faults brittle strata, drag can also rotate neighbouring beds into steeply dipping attitudes that lie subparallel to the walls of the salt diapir (Schultz-Ela 2003; Alsop et al. 2000). Rotations can be as steep as 90° and can even overturn beds. Deformation in drag zones is driven by a variety of processes including downbuilding, differential compaction, grain boundary sliding, microfracturing, larger-scale faulting and pressure solution. The abutment of an inclined drag zone against a near-diapir fault can form intervals of stacked and compartmentalised oil and gas reservoir sands. Drag-induced stacking of inclined sand beds circumferential to the diapir stem explains why, in the early days of their production, reservoir sands adjacent to sub-vertical portions of onshore salt structures in the Gulf of Mexico constituted some of the most productive acreage (bbl equiv./km^2) in the world's oil fields (Fig. 10.54).

Drag zones develop sequentially; initial salt pillowing creates a broad gentle overburden flexure that increases in intensity as the structure evolves into a diapir (Fig. 6.43; Davison et al. 2000b). By the diapir stage the width of a drag zone is approximately equivalent to the width of the diapir at the diapiric base and decreases to 25 % of the diapir width toward the diapir crest. Vertical relief of the upturn in a bed

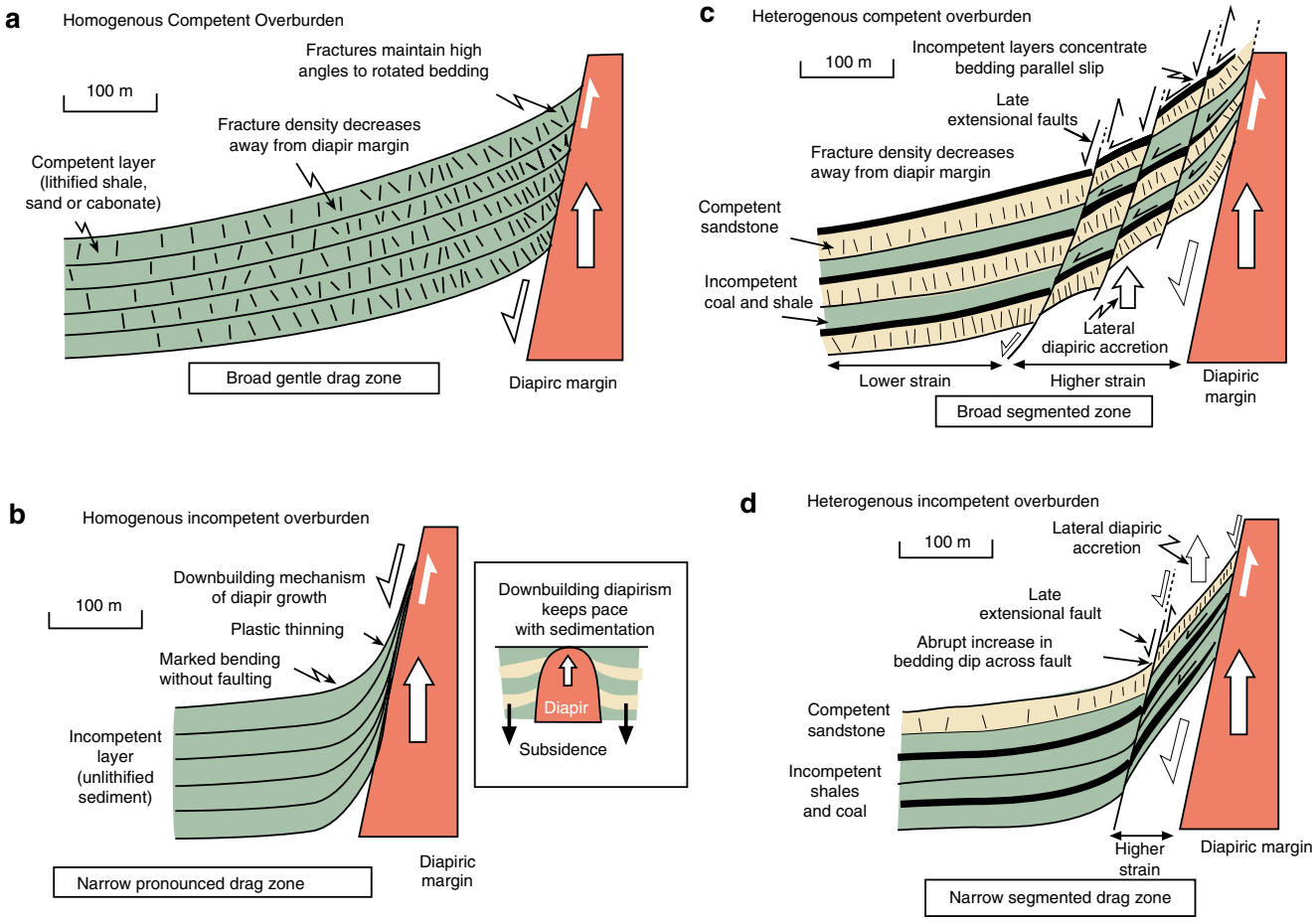

Fig. 6.44 Schematic profiles of diapir drag zones (After Alsop et al. 2000). (**a**) Broad drag zone within homogenous competent overburden. (**b**) narrow drag zone with incompetent inhomogeneous overburden. (**c**) Broad segmented drag zone within homogenous incompetent overburden. (**d**) narrow segmented drag zone within heterogenous incompetent overburden with marked internal competency contrasts. (**c**, **d**) also illustrate the process of lateral diapiric accretion where fault-bound material moves upward with the flanks of the diapir relative to sediments further out in the rim syncline

also decreases upward. Vertical relief is some 5 % of the diapir height near the crest and increases to 30 % near the diapir base, a consequence of the greater relative movement across the pre-movement and early syn-movement layers situated near the base of the diapir stem. The width of the drag zone increases proportionally with increasing diapir size and diapir height, while the total amount of bed upturn increases proportionally with the width of the drag zone.

In one of the few outcrop studies of the characteristics of diapir drag zones Alsop et al. (2000) relate variation across the drag zone to overburden competence (Fig. 6.44a–d). Their work focused on an outcropping diapiric province in Cape Breton Island, Nova Scotia, where five Visean-age salt diapirs penetrate Upper Carboniferous (Namurian-Stephanian) conglomerates, sandstones, shales and coal seams. The width of diapiric drag zones varies from 70 m up to 500 m. Narrow drag zones are a response to the low mean competence of shales and siltstones, which were probably shallowly buried and poorly lithified at the onset of diapirism (Fig. 6.44b). Broader drag zones are dissected by two sets of extensional fractures, together with major faults, suggesting that the overburden was semi-lithified and displayed greater flexural rigidity at the time of salt flow (the beam effect; Fig. 6.44a). Overburdens with high internal competency contrasts (e.g. interbedded sand-shale) generated strain localization and partitioning, with pervasive granulation seams and minor faults developed in the more competent sandstones and bedding-parallel shears in the coal and shale horizons. The various drag zones are segmented by steep outward-dipping faults associated with decametric, asymmetric drag profiles (Fig. 6.44c, d). These faults facilitate the upward movement of material and effectively enlarge the diapiric process into the adjacent overburden a process that Alsop et al. (2000) call lateral diapiric accretion.

In the subsurface, seismic of varying quality is usually all that is available to interpret drag zone geometries. Steep dips and irregularities in the distribution and density of adjacent salt means that the shape and extent of the diapiric drag zone is poorly defined in the inner shear zone area, especially when the diapir is bulbous. The width of the upturned zone

caused solely by frictional drag is difficult to estimate, as a large section of the upturned interval can be due to the salt pedestal effect (Vendeville and Nilsen 1995). The increased permeability around zones of fracture adjacent to diapirs means that drag zones can act as preferential conduits for fluids escaping from deeper levels. Pervasive fracturing in broader drag zones formed by more competent beds helps explain the pervasive entry of ferroan brines into adjacent carbonates and fracture defining haloes as is seen in the outcropping Proterozoic diapiric province of the McArthur Basin, Australia (Warren 1999). There the salt has long gone and only siderite/brunnerite diagenetic replacement haloes remain around fault welds and salt welds.

With prekinematic overburden, substantial drag-induced folds only form in exceedingly weak rock (Schultz-Ela 2003). Even then, most folding develops by nearsurface upward and outward rotation. Protrusions of overburden into a diapir, where the contact dips shallowly outward, are most susceptible to folding due to frictional drag created by the crossflow of salt. Based on modelling experiments, Schultz-Ela argues synkinematic sedimentation is much more likely to engender large and broad folds in the drag zone because onlapping wedges may be continually produced during downbuilding (Fig. 6.43b). These syndepositional folds can even form in strong layers. He argues folding of onlaps over rising salt is really drape[13] folding, so "drag" fold is actually a misnomer. Local gravity fold is perhaps a better descriptor of this style of deformation. Episodically deposited layers further enhance the potential for onlap folding.

For the same average aggradation rate, pulsed deposition of thick layers generates larger folds than do continuously deposited thin layers. Variation in thickness and timing of deposition increases the likelihood of multiple wide onlaps that evolve into substantial folds. Older layers tend to form the broadest and tallest folds because those layers prograded farthest across the diapir crest. As the salt contact steepens, the folded zone narrows as younger layers onlap onto older folds or the salt. Onlap folds can only form for a limited range of relative salt rise and deposition rates. Deposition much faster than the net rate of salt rise buries the diapir. Deposition that is too slow creates steep contacts or salt spilling onto the sediment surface, both of which result in little "drag" folding.

In three dimensions, outcrop and 3D seismic studies have shown that both radial and concentric faults occur in drag/drape zones around diapirs, and that the fault patterns are lithologically dependent and can rotate during the life of a diapir (Davison et al. 2000a, b). Ongoing drag or drape deformation can facilitate the creation of a hydrocarbon-bearing column adjacent to a diapir that is more than a km tall. Many fault patterns are approximately sub-radial due to the intersection of multiple fault trends and many faults curve to become roughly tangential to the diapir face to produce cuspate salt outlines in plan view (Chap. 10). In the context of rotated faults some types of Christmas-tree[14] diapirs are of interest. Christmas-tree diapirs are typically interpreted as indicators of stacked salt allochthon wings, however, Varela and Mohriak (2013) have suggested stacked salt wings may also be indicative of rotated salt-cored crestal faults which have rotated into a position lateral to the main salt mass via the ongoing rise of salt (Fig. 6.45).

Welds, Loading Detachments and Growth Faults

Many regional growth faults in salt allochthon provinces sole out onto residual fault welds, which can be many tens of kilometres in length. The link between growth faults and salt welds is an inherited relationship whereby sediment loading of a salt sheet or layer where one evolves or passes into the other (Jackson et al. 1994b; Fletcher et al. 1995; Wagner III and Jackson 2011). A thick salt sheet present before welding decouples faulted zones above and below it as it flows and deforms. This decoupling means most large suprasalt faults sole out into the level of the former sheet (Fig. 6.39b).

Burial of an evacuating salt allochthon beneath loading sediment typically occurs after pinch-off from the feeder diapir (Fletcher et al. 1995). This allows the former sea floor high created by the glacier to relax (deflate), especially at the updip end of the sheet. Sediment can then prograde across the sheet beginning at its updip end (Figs. 6.36 and 6.42). Even during burial of its updip end, an evacuating salt sheet typically retains several hundred metres of relief on the downdip end. Thus the downdip sheet continues to advance as a composite salt-sediment glacier. Sediments atop the allochthon are deformed, along with the flowing salt, as the gliding movement creates extensional breakaway zones at the updip end. In turn this initiates fault-bound minibasins at the updip end of actively flowing salt sheets (Figs. 6.36 and 6.39). Ongoing slippage creates a growth fault rollover anticline as salt continues to extrude at the downdip or compressional end.

The same salt mass can recycle multiple times as tiers ascending into ever-higher stratigraphic levels (Fig. 6.46). Each time salt activity is transferred to a higher level, a largely welded smear of salt (salt weld) with a vestigial salt

[13] In salt tectonics, a drape fold describes a zone of upturned strata adjacent to a diapir. Upturning results from arching of the diapir roof above flanking strata and is an important process in the formation of halokinetic sequences and is also known as a flap fold.

[14] Repeated extrusions can create stacked salt wings, so forming a serrated salt contact known as a Christmas-tree structure. Some can also form via fault rotation, not stacking of successive extrusive salt wings and tongues.

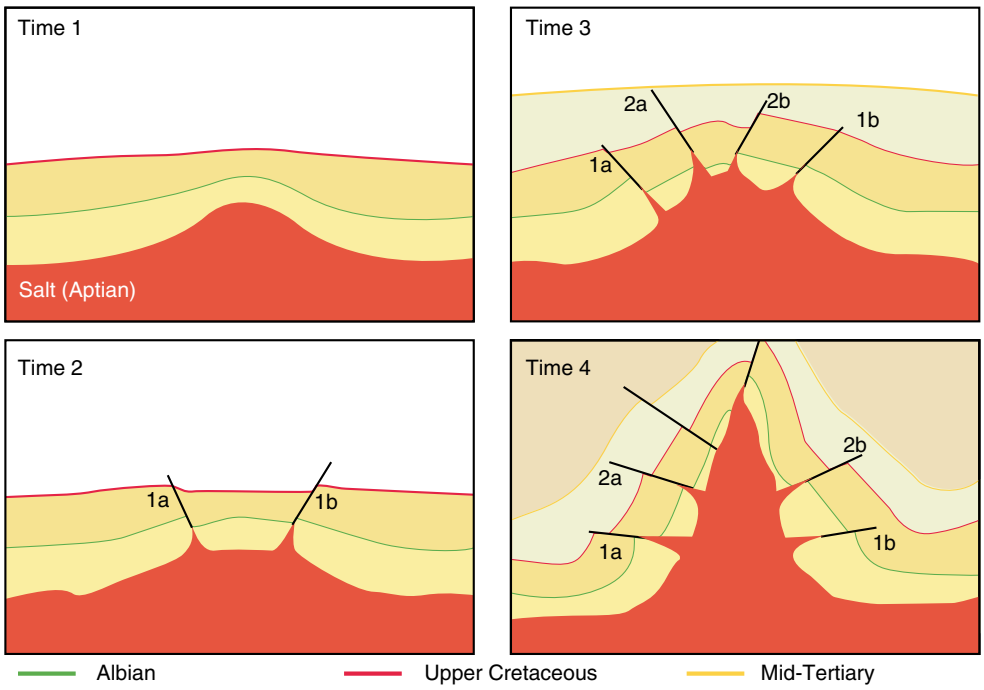

Fig. 6.45 Christmas-tree diapirs via fault rotation, not stacked extrusion (After Varela and Mohriak 2013). Time (*1*) Initial doming. Time (*2*) Crestal collapse graben with extensional faults; incipient salt intrusion along fault planes. Time (*3*) Crestal faults migrate to the diapir flank and have their dip angles reduced, whereas the bedding dips increase. New sets of crestal faults are formed toward the center of the structure. Time (*4*) Subhorizontal faults characterized by bedding with high dip angles; salt stringers forming an intrusive Christmas tree structure. Part of the salt in the apophyses may be squeezed back to the salt diapir because of the weight of the overburden or dissolved by formation waters

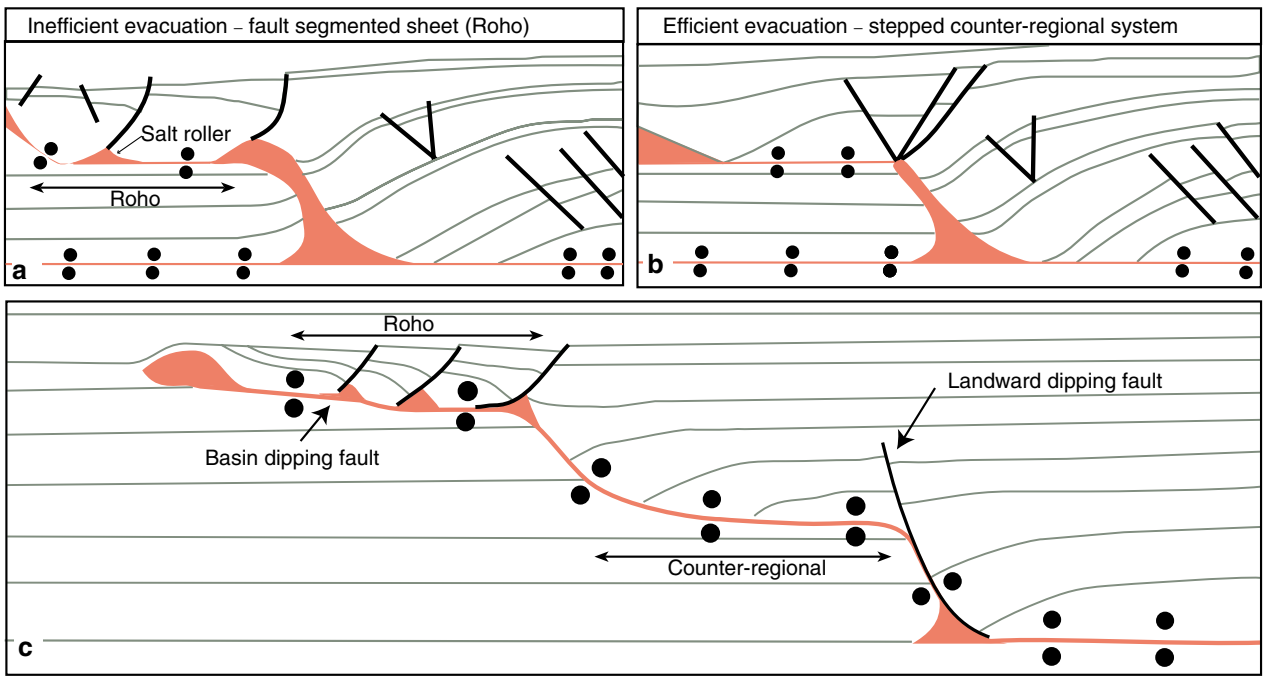

Fig. 6.46 Efficiency of evacuation is reflected in the suprasalt structuring. (**a**) With inefficient salt evacuation a fault segmented (Roho) system forms. (**b**) With efficient evacuation a counter-regional system is created. (**c**) Shows how the two systems can be created by the same salt body. See text for explanation, *black circles* define salt welds (In part after Jackson et al. 1994b; Rowan 1995)

structure (salt roller) is left behind at the lower levels. Substantial volumes of salt are lost via dissolution each time the salt approaches the seafloor or is bathed in less saline pore fluids. Thus, the ascending salt mass cannot recycle indefinitely and the driving mechanism is lost once a salt weld or overburden touchdown is created beneath the minibasins.

A salt sheet that is isolated from its feeder stock can advance further only by cannibalising its trailing edge (Fig. 6.42a; Fletcher et al. 1995; Schuster 1995; Jackson et al. 1994b). If the salt is inefficiently withdrawn from the trailing edge, the salt becomes progressively sequestered into residual smaller bodies and the overall structure is called

a fault-segmented sheet. In the Gulf of Mexico this is also called a "Roho"[15] or a listric weld system (Fig. 6.46a). Roho systems are characterised by major, listric, basinward dipping (down-to-the-basin) growth faults, that can sole out onto an allochthonous salt sheet, allochthonous salt canopy, or allochthonous weld. Sediment wedges in the fault blocks dip and thicken landward but become younger seaward. In the Gulf of Mexico systems that sole into allochthonous salt evacuation surfaces are also known as tertiary salt welds, as opposed to primary and secondary salt welds (Fig. 6.39a).

During shelf progradation over a salt sheet or a salt "wing" on a salt plug, the rear (landward) margin of the salt sheet gradually segments and deep withdrawal structures are enhanced. At shallower levels, vestigial salt forms a train of sequestered salt walls formed by the partitioning of a formerly continuous sheet of salt. Each residual salt structure is typically in the footwall of a normal fault or is separated from its neighbour by a syncline. Each residual wall is generally overlain by a splay of extensional faults, which are commonly listric.

If salt is more efficiently withdrawn from the deflating trailing margin shelf progradation then a stepped counter-regional system results (Fig. 6.46b). A counter-regional system is made up of landward-dipping, largely welded salt system whose upper part is a weld, remnant diapir, or normal fault. Sediment wedges dip and thicken seaward. The lower part of the system may ramp continuously down to the source layer or may include flat-lying segments. If the system has more than one ramp, it is a stepped counter-regional system. Strata above the deflating salt sheet gently subside to form a shallow flat step along the weld of vanished salt. The step resembles a landward dipping growth fault (Fig. 6.45c). However, the step can be merely a pseudo-fault, like the contiguous deeper step created by upward evacuation of the original diapir. In three dimensions the shallow step fault is the axis of a partly evacuated sheet that is shaped like a tongue with curled up lateral margins (Fig. 6.46b). Along the deepest axis of the tongue lies the deepest, most evacuated part of the salt sheet below the thickest overburden.

These two structures —the fault-segmented sheet (Roho) and the stepped counter-regional system— are end members of a load-induced evacuation series where the counter-regional systems define welds where salt has been completely evacuated and a Roho system defines less efficient evacuation. It is possible that as the salt climbs the stratigraphy the same salt body can create both Roho and counter-regional systems or welds depending on the efficiency of evacuation (Fig. 6.46c).

[15] The detachment surface for these into-the-basin "Roho" growth-faults is inefficiently evacuated salt. With 1960s and 1970s vintage seismic data, it was not possible to image below the salt evacuation surface (tertiary weld). An early seismic stratigrapher in Shell, Chuck Roripaugh, after being instructed to map to the Moho below areas of salt, jokingly labelled his map of the salt evacuation as "Roripaugh's Moho" which was later contracted to Roho. This in-house joke has since escaped into the public literature.

Minibasins, Canopies and Welds

Differential loading, created by the emplacement of a depositional lobe atop a salt allochthon, induces a differential fluid pressure in the salt below. Salt squeezes laterally into flanking areas and a bathymetric high, which dams the accumulating sediment, forms a rim adjacent to the sediment accumulating in the growing minibasin (Fig. 6.47a). A minibasin is an suprasalt depositional basin underlain and surrounded by allochthonous salt. The term intrasalt basin is sometimes also used to described salt-floored minibasins or depopods. In my opinion this is confusing as intra means within, these basins are never within, when depositionally active they are initially atop and laterally restrained by salt. Then in more mature extensional and compressional terrains, where most of the salt in a former salt wall has been largely squeezed from the system, the remaining adjacent depopods can be in lateral contact across a salt weld and floored by a salt weld (e.g. Fig. 6.40a). I use the term intrasalt to describe features completely encased in salt, as in the carbonate stringers of the South Oman Salt Basin.

A feedback process is created as the sediment-loaded minibasin floor subsides by pushing salt aside, so allowing the basin to receive additional sediment. The process continues until the minibasin floor touches down on the subsalt strata to form a salt weld (Fig. 6.47a). At that time, minibasin subsidence ceases. Once the minibasin touches down, subsidence shifts from the centre of the minibasin to its flanks, which are still underlain by salt. Both flanks subside, creating an anticlinal turtle structure. Subsequent depocentres form on both sides of the early depocentre (Fig. 6.29). At the same time, if there is sufficient salt supply then the level of the suprasalt minibasins may first fuse and then be covered by a salt canopy (Fig. 6.48 – Stage a). Ongoing loading by the expanding minibasins and their fills (or extensionally-driven minibasin foundering) drives a transition of the salt geometries from joined ridges and walls separating the basins, into isolated diapirs, encased and separated by a level made up of merged merging minibasins (Fig. 6.48 – Stage b). With enough salt supply a new salt canopy can form higher in the stratigraphy, while the former underlying salt tier is marked by welds (Fig. 6.48 – Stage c).

Intrasalt minibasins that form above tabular salt allochthons typically entrain a sediment fill that indicates an evolution from slope basins to shelf basins (Fig. 10.66). They are typically bound by arcuate growth faults formed largely by downslope salt withdrawal. Initially, the allochthon acts as a deflating cushion that accommodates sediment deposited in minibasins. After time, loading or extension, the original salt sheet transforms into thin but broad welds, which then act as major subhorizontal detachments for deep growth faults

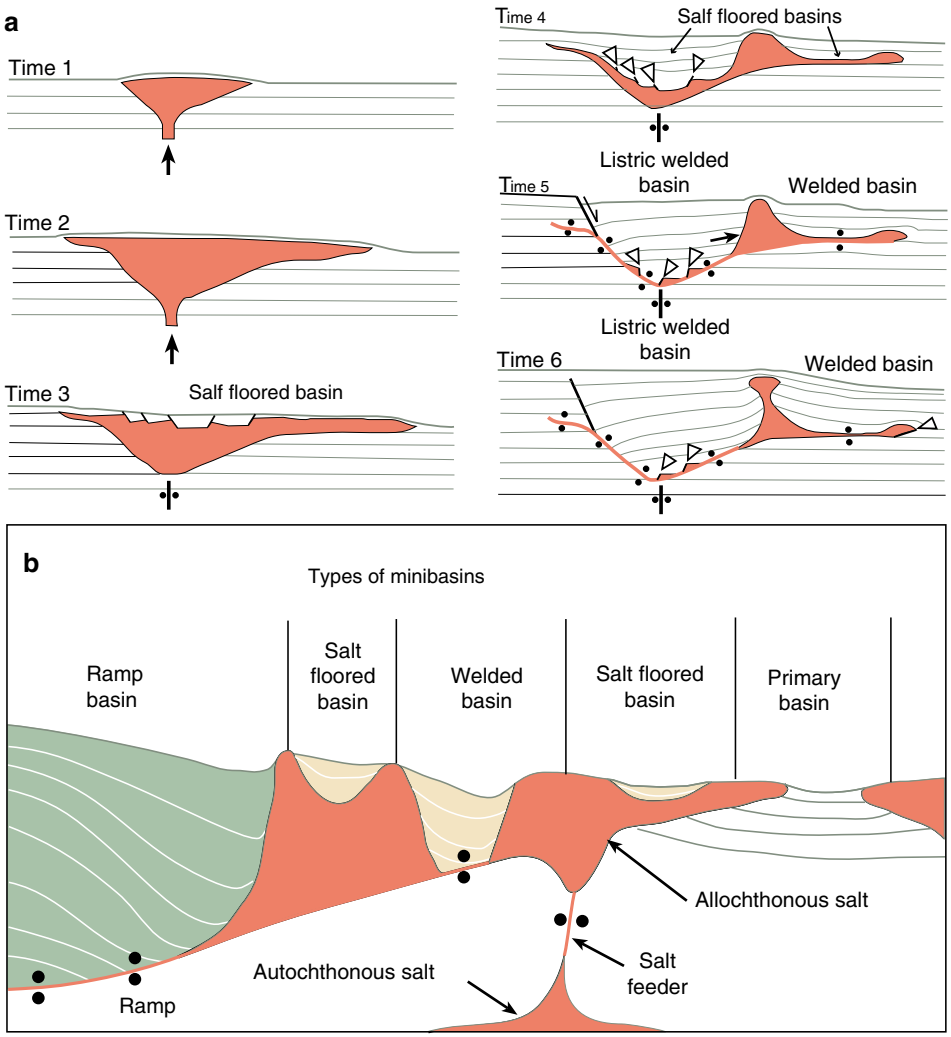

Fig. 6.47 Evolution of minibasins atop salt allochthons based on the northern Gulf of Mexico (as in Fig. 6.49). (**a**) Evolution of a minibasin as sediment loads a salt allochthon (After McBride et al. 1998a). (**b**) Types of minibasins (After Koch et al. 1998)

whose slip creates space for further sedimentation. Ultimately, the sheet itself is segmented into discrete salt structures separated by salt welds and fault welds. Second or third cycle tiers of salt structures can rise from these deformed sheets (Fig. 6.46).

Minibasins can contain upwards of 5 km of sediment fill, and in the northern Gulf of Mexico are divided into five types based on the relationship of the fill to the presence or absence of a underlying salt weld (Fig. 6.47b; Koch et al. 1998):

- Ramp (atop counter-regional)
- Salt-floored minibasin
- Welded minibasin
- Welded listric minibasin (Roho)
- Primary basin (seaward of the allochthon)

Ramp basins predominate on the slope in Garden Banks and Green Canyon of the Gulf of Mexico. They are characterized by a set of south-bounding, north-dipping salt welds (Fig. 6.35b). Most ramp basins have young thick depocentres adjacent to the counter regional ramp. Ramp basins tend to be asymmetric and larger in areal extent than the other types of minibasins. Welded basins were previously underlain by allochthonous salt that has been fully or partially evacuated. In the northern Gulf of Mexico they increase in frequency southward into the Walker Ridge and Keathley Canyon protraction areas where there is still a substantial volume of salt in the allochthon stratigraphy.

Welded listric (Roho) basins in the northern Gulf of Mexico have south-dipping arcuate faults that sole into the evacuating salt. Welded basins have a multitude of internal fault patterns and sediment fills, some are symmetrical with bowl-shaped fills, others have multiple depositional axes and bidirectional stratal fills. Primary basins in the Gulf of Mexico show no evidence of allochthonous salt and display continuous sedimentary fill from Cretaceous to Recent. Salt-floored basins are underlain by continuous allochthonous salt, which typically shields them from the underlying petroleum kitchens. Salt-floored basins occur along the down dip edge of allochthonous salt near the Sigsbee escarpment and above very young salt sheets in Garden Banks and Green Canyon (Figs. 6.1 and 6.49).

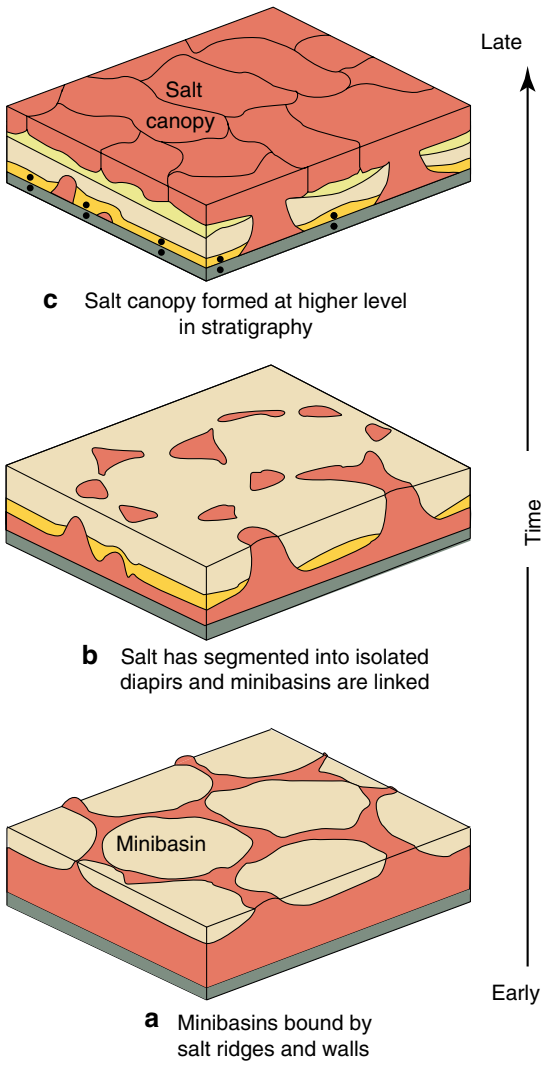

Fig. 6.48 Interrelated evolution of minibasins, welds and salt canopies across time. See text for explanation of stages **a**–**c**

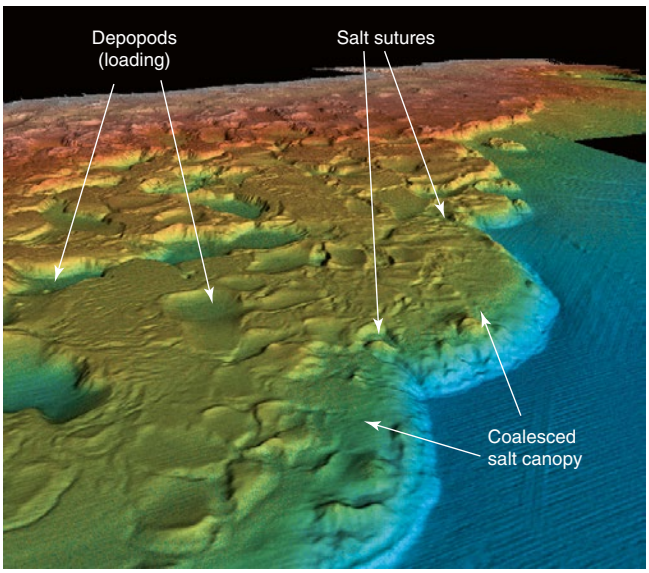

Fig. 6.49 Salt canopy including part of the Sigsbee Scarp located along the continental slope of rise of the Northern Gulf of Mexico. Image shows a series of salt-floored minibasin depressions atop a coalesced salt canopy with a thrusted front (Image courtesy of Martin Jackson). See Fig. 6.61 for location

As basin fill changes through geologic time, each of the five types of basin have differing capabilities for receiving and internally distributing the hydrocarbons supplied from mature more deeply buried source rocks. In general, hydrocarbon entry points to basin strata in the Gulf of Mexico salt basins are controlled through time by salt movement and carrier bed geometry. Koch et al. (op. cit.) argue ramp basins have attractive plumbing for hydrocarbons as well as an enhanced trapping focus (Chap. 10). Welded and welded-listric basins are dependent on the evacuation of the salt floor and leakage across the weld for any supra-weld hydrocarbon charge to occur in the minibasin sands; therefore, the age and areal extent of the weld are factors is assigning prospectivity. Primary basins appear to have access to underlying mature sources but may lack effective migration pathways and trapping geometries. Salt-floored basins are the lowest ranked basins due to separation from a mature subsalt source.

Within the four areas of minibasin development studied by Koch et al. (1998), most discoveries were in ramp and welded minibasins (about 1 BBOE in each basin type). Primary and salt-floored minibasins show minor discoveries and none of significant size. The feedback between allochthon style, deposition of potential reservoirs sands and hydrocarbon maturation is discussed in detail later in this chapter and in Chap. 10.

A widely used explanation for the subsidence that accommodates minibasin sediment is that salt is forced from beneath the sinking basin by the weight of its sedimentary fill and so the basin accumulates further sediment (i.e. depositional loading drives salt flow). At the broader scale the system is driven by into the basin gravity gliding. Loading as the explanation is valid if the average density of the minibasin fill exceeds that of salt, which in the Gulf of Mexico requires at least 2,300 m of siliciclastic fill to ensure enough compactional density (Fig. 6.50a). However, as noted by Hudec and Jackson (2009) most minibasins start sinking and accumulating sediments when overburden thicknesses are much thinner than this. They argue that our understanding of the driving mechanisms for minibasin creation and evolution is incomplete and identify five mechanisms, in addition to density-driven subsidence, that can create minibasins. They are: (1) Diapir shortening which occurs as squeezed diapirs inflate, leaving the intervening minibasins occupying bathymetric depressions (Fig. 6.50b); (2) Extensional diapir fall, when stretching of a diapir causes it to sag, producing a minibasin above its subsiding crest (Fig. 6.50c); (3) Decay of salt topography (deflation), occurs as the dynamic salt bulge subsides in response to the slowing of the upward flow of salt, this lowers the salt surface below the regional sediment surface and so permits sediment infill (Fig. 6.50d); (4) During

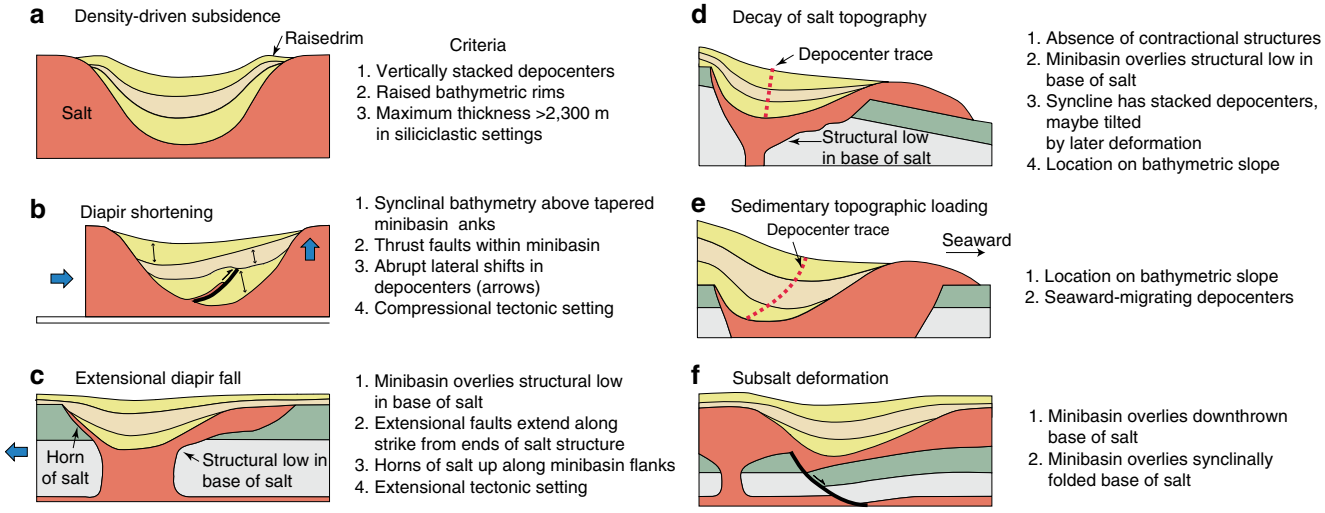

Fig. 6.50 Summary of minibasin-subsidence models and criteria used to distinguish them. See text for explanation of stages **a**–**f** (After Hudec and Jackson 2009)

sedimentary topographic loading, sediments accumulate as a bathymetric high above salt (Fig. 6.50e). (5) Lastly, subsalt deformation in the base of salt may produce relief at the top of salt (Fig. 6.50f).

All six mechanisms (including density-driven subsidence) produce different positions of the bathymetric lows, with respect to the flowing salt mass, which interacts with sediment transport to produce different facies patterns in each type of minibasin, each with characteristic recognition criteria (Fig. 6.50). The particular mechanism driving minibasin subsidence depends on the tectonic environment, regional bathymetry, and sedimentation rate, while their spatial variation on a continental margin creates provinces in which a given minibasin style is dominant.

At broader scales than individual minibasin sags, salt sheets can spread laterally as they deform until they eventually coalesce with neighbouring salt sheets. Collectively they create a salt canopy, a feature that dominates much of the foot of slope in the northeastern Gulf of Mexico (Figs. 6.48 and 6.49; Talbot 1993; Wu 1993). There individual lobate sheets coalesce westward into an extensive salt canopy whose leading edge is the Sigsbee Scarp. Adjoining salt sheets merge into canopies along salt sutures. The formation of a more or less continuous salt canopy must entail the upward and lateral movement of vast quantities of salt carrying with it an expanding overburden made up of minibasins actively accumulating sediments.

Canopies form as allochthonous salt sheets come together or coalesce with the position of merging defining canopy suture. Suture can occur beneath thin or thick roofs (Fig. 6.51a, b). Once formed a canopy can be loaded with sediment and then segments as the overlying minibasins merge (Figs. 6.51 and 6.48). When the canopy roof is thin, the adjoining sheets are salt glaciers, with a thicker roof confining the edges of adjacent sheets, the roof lies beneath

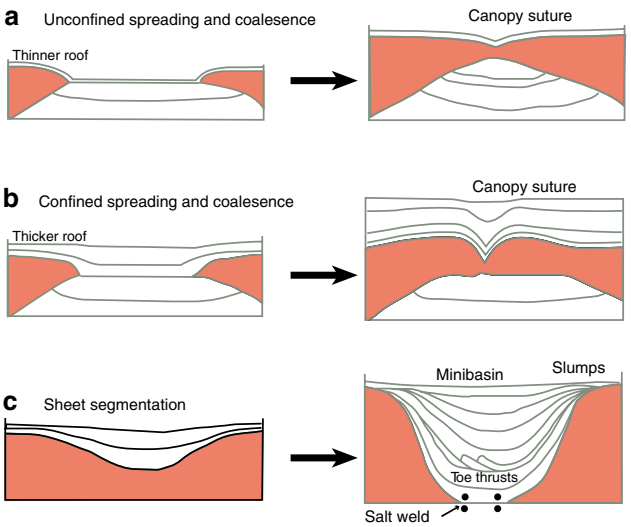

Fig. 6.51 Comparison of structures produced by (**a**) coalescence of unconfined salt glaciers, (**b**) coalescence of confined, buried salt sheets, and (**c**) segmentation of salt sheets by loading suprasalt minibasins (Jackson et al. 1994b)

cuspate sediment-filled synclines associated with small thrust faults and kinks (Jackson et al. 1994b).

Dooley et al. (2012) integrate and categorise notions of salt canopy evolution. At the broad scale of interactions within and between the canopy salt sheets where they touch they define autosutural and allosutural styles (Fig. 6.52a, b) An allosuture is formed by the two coalesced salt sheets fed by separate feeders, while an autosuture forms at the contact of two lobes fed from a single salt sheet, including any trapped sediments. Dooley et al. also refine the terminology that is applied to canopy sutures utilising, plan views and map views of an idealised sutural contact (Fig. 6.52c).

Autosutures can form in two ways. An overriding autosuture is produced when part of a salt sheet overrides its

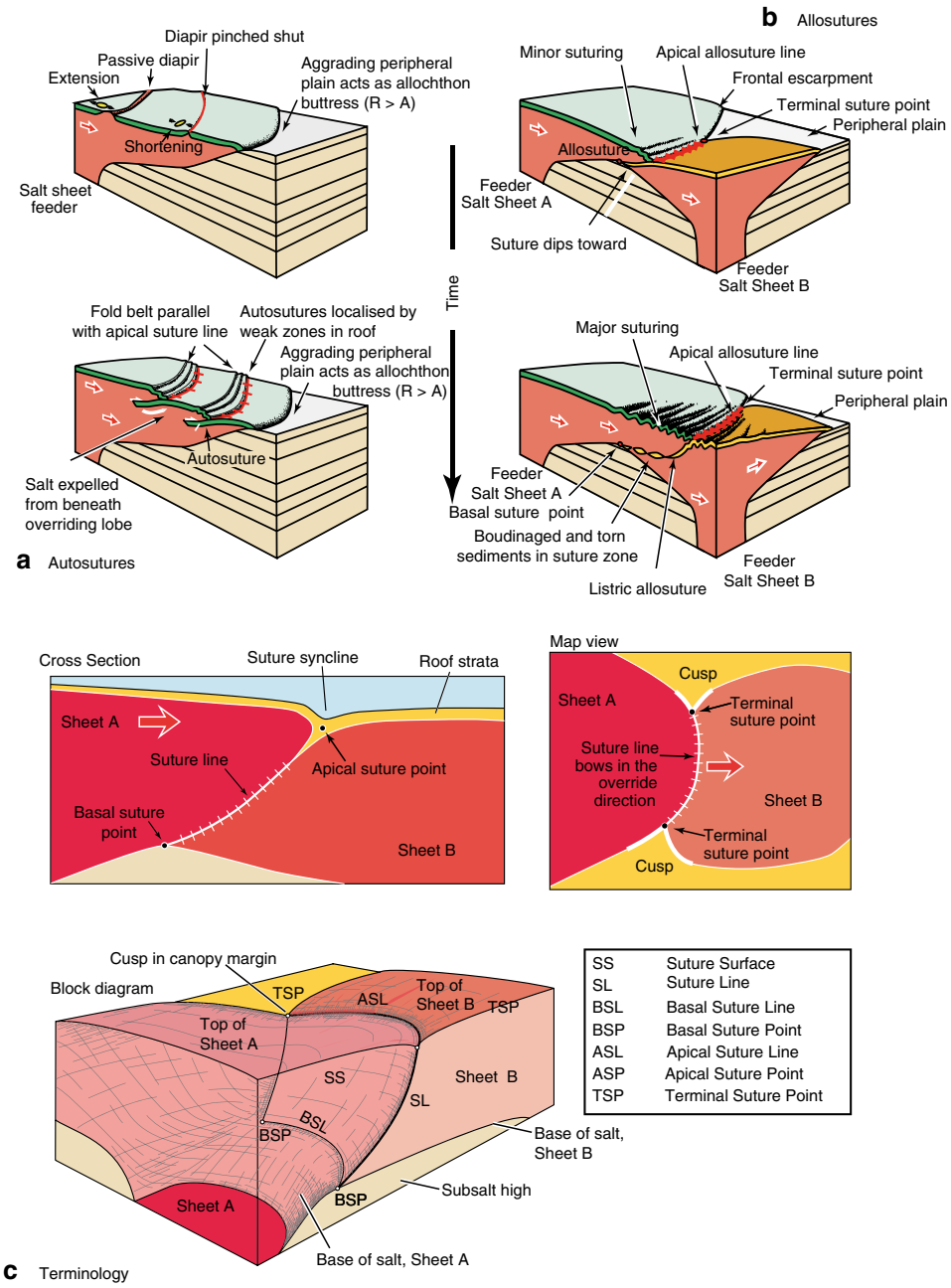

Fig. 6.52 Salt canopies and their sutured edges (After Dooley et al. 2012) (**a**) Autosutures. The roof of a salt sheet shortens where sheet advance is buttressed by peripheral plain or by another sheet. Overriding autosutures may initiate at any zone of weakness in the roof, especially pre-existing reactive diapirs formed by previous stretching as the salt sheet spreads. As it is overridden from the rear, the front of the roof is depressed into the salt. (**b**) Asymmetric allosutures. As one salt sheet overrides the other, sediments in the suture are depressed, stretched, and dismembered to form boudins in the salt. These sediments eventually tear off from the basal suture line. (**c**) Terminology for describing salt-sheet sutures in cross section, map view, and in three dimensions. Note that, in the block diagram, the sides around sheet A are transparent. The side showing sheet B is solid in order to illustrate a cross sectional view

neighbour in the direction of salt movement. The overridden roof subsides into the salt sheet, and these trapped sediments appear as intrasalt reflections on seismic data. An encircling autosuture forms when two lobes of a salt sheet separate to bypass an obstacle and then rejoin on the downstream side of the obstacle. Encircling autosutures tend to be short and parallel to the dominant salt-flow direction.

Allosutures separate sheets sourced from two different feeders. If neither salt sheet overrides the other, the resulting suture is symmetric, forming an upright zone of roof sediments trapped between the two sheets. More typically, one salt sheet is more vigorous (generally the larger sheet or the one whose feeder is farther updip) and overrides the other. Sediments trapped in an asymmetric allosuture are mostly from the roof of the overridden sheet. The overriding sheet shears and extends the roof of the overridden sheet, detaching it from the base of the canopy and obscuring its origin.

Based on their physical modelling and analysis of canopies in the Gulf of Mexico, Dooley et al. (2012) argue that if the type of canopy suture can be classified then it can be used to better understand geological evolution to its current state. Encircling autosutures have the clearest origin (Fig. 6.53a).

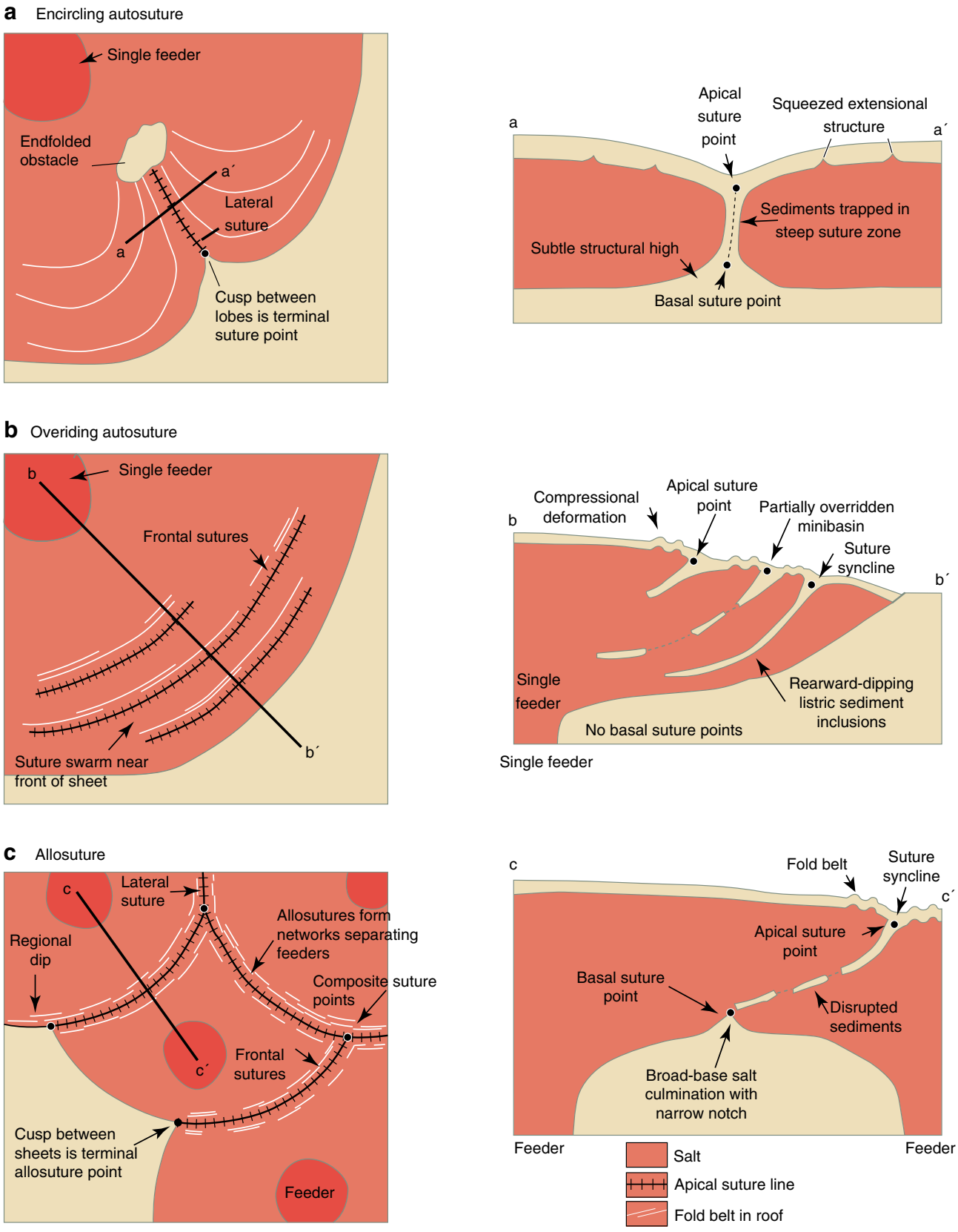

Fig. 6.53 Criteria for recognizing suture types (After Dooley et al. 2012)

Encircling flows typically meet as a short lateral suture just downdip of an enfolded obstacle, which is typically a grounded minibasin. Structural fabrics in the top of salt or roof reflect salt flow encircling this obstacle. The autosuture is merely an ornament on the periphery of a single sheet whose edge first divides into two small lobes and then sutures. Because encircling autosutures normally do not override much, sediments trapped in the suture typically remain connected to the basal suture line. Overriding typically forms one or more frontal autosutures near the toe of a salt sheet slowed by another sheet or by aggradation of the abyssal plain (Fig. 6.53b). Sediments trapped in the autosuture form a rearward-dipping, listric, intrasalt reflector that commonly terminates into a partly overridden minibasin along the apical suture line (Fig. 6.53b). Overriding autosutures may occur in swarms, resembling an imbricate thrust belt. Because an overriding autosuture forms by imbrication of the saltsheet roof, no basal suture line exists.

Allosutures are generally easy to identify, although they share aspects of both encircling and overriding autosutures (Fig. 6.53c). Because allosutures separate two independently sourced salt sheets, they are marked by a broad base-salt culmination below the basal suture line. These culminations, together with salt-sheet edges, form a regional network separating canopy feeders from one another. Most lobe boundaries in the canopy margin are terminal allosuture points (Fig. 6.48), although a few may instead be associated with encircling autosutures.

Finally, roof sediments trapped in allosutures may extend in a near-continuous band from basal to apical suture lines, if sheet override has been minor. However, these sediments may tear from the basal suture line after major override, which can be difficult to distinguish from an overriding autosuture.

Two factors can complicate suture interpretation. First, sutures are not the only sources of intrasalt reflections in canopies. Material originally interbedded with the salt, igneous intrusions, foundered roof material, and coherent seismic noise may also produce intrasalt reflections. In many cases, sutures can be distinguished from these by their association with lobe boundaries, apical and basal suture lines, or location with respect to feeders. However, this distinction may not be possible in cases where intrasalt reflections are highly dismembered as, for example, in the Zechstein and Ara salt masses. Second, subsalt structures may deform the base of a salt canopy, creating structural highs and lows in the base of salt that are unrelated to salt emplacement. According to Dooley et al. (2012) care must be taken to map subsalt structure as well as the base of salt so as to determine whether base salt highs and lows are related to canopy emplacement (ramps and flats) or to subsequent deformation.

As salt canopies spread, prior to merging and coalescing, they interact with adjacent and underlying sediments in four main ways, all of which drive compressive/ thrust deformation responses in the adjacent strata (Fig. 6.54; Hudec and Jackson 2009). In all situations, gravity spreading of a salt canopy produces thrust faults around the canopy rim. These thrusts may form by shear along the base of the salt (Fig. 6.54a), by frontal rolling of the canopy (Fig. 6.54b), by expulsion of underlying sediments (Fig. 6.54c), or by submarine landsliding off the canopy's frontal escarpment (Fig. 6.54d).

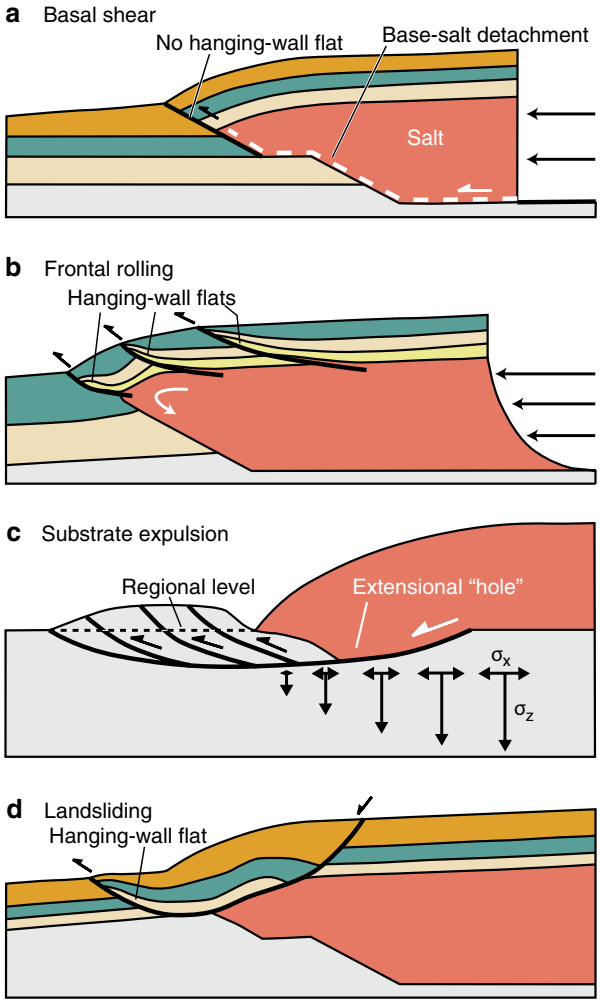

Fig. 6.54 Cross sections showing possible origins of canopy-margin thrust systems. See text for explanation of stages **a**–**d** (After Hudec and Jackson 2009)

Each mechanism has a characteristic structural style, providing clues to processes of shortening in canopy-margin thrust systems (Table 6.2). Canopy-margin thrust systems along the Sigsbee Escarpment in the deepwater Gulf of Mexico have three parts although all three may occur in any particular salt edge location (Fig. 6.55). First, nearly all canopy-margin systems include a roof-edge thrust, which cuts upsection from the tip of the salt canopy and separates condensed strata in the canopy roof from thicker sections on the adjoining peripheral plain. Second, roughly one-third of roof-edge thrusts overlie an imbricate wedge, which telescopes

Table 6.2 Salt advance mechanisms for salt canopies, as inferred from canopy margin thrusts

Thrust type	Key observations	Compatible advance mechanisms	Inferred advance mechanism[a]
Roof-edge thrust	Single thrust Thrust connects to salt tip Hanging-wall flats are rare Footwall cutoffs intersect base of salt	Basal shear, frontal rolling, landslide Basal shear, frontal rolling, substrate expulsion, landslide Basal shear, substrate expulsion Basal shear, frontal rolling	Basal shear
Imbricate wedge	Basal décollement of salt-floor wedges connect to base of salt Strike transitions between salt-tip and salt-floor wedges Imbricate wedges associated with roof-edge thrusts No significant structural lows in the base of salt updip of wedges	Basal shear, substrate expulsion Basal shear, substrate expulsion Basal shear Basal shear, frontal rolling, landslide	Basal shear
Salt-roof thrust	Thrusts are behind salt tip Significant hanging-wall flats	Frontal rolling Frontal rolling, landslide	Frontal rolling

After Hudec and Jackson (2009)
[a]Salt advance mechanism that is common to all key observations

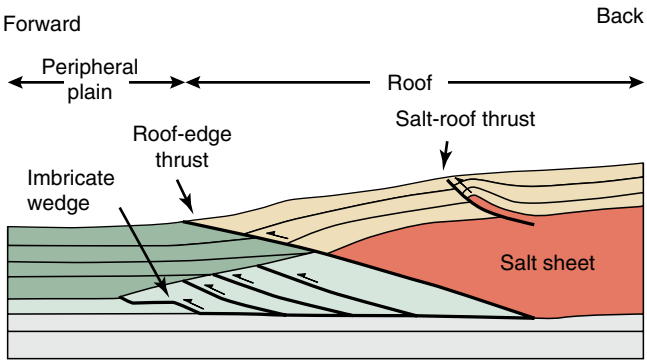

Fig. 6.55 Schematic cross section illustrating the three types of canopy-margin thrust. The diagram illustrates the proposed reference frame for salt-canopy margins: "forward" refers to the direction of canopy advance, and "back" is toward the interior of the canopy. Usage of forward and back in the literature is not yet consistent when describing the sense of salt flow with reference to the peripheral plain (After Hudec and Jackson 2009)

sediments on the peripheral plain above a bedding-plane décollement. Third, in a few areas, salt-roof thrusts shorten the roof of the salt sheet. Because roof-edge thrusts and imbricate wedges both form by shear along the base of the salt allochthon, their abundance along the Sigsbee Escarpment implies that basal shear is the primary mode of advance there. Despite the dominance of basal shear, however, the Sigsbee Escarpment exhibits a wide range of structural styles. Hudec and Jackson (2009) speculate that this range reflects variations in relief on the canopy margin, thickness of the roof above the canopy toe, strength of the base-salt zone, and strength of sediments on the peripheral plain.

Fault Families in Allochthons

In the past three decades our understanding of gravity gliding, gravity spreading and salt flow in the Gulf of Mexico, the Santos Basin of offshore Brazil, the Kwanza Basin of offshore Angola has improved to where linkages between faults, welds and salt-related anticlines in allochthon provinces can be predicted at the continental margin scale (Fig. 6.1b). Linkages between anticlines and extensional faults predominate, but links to contractional faults and strike-slip faults can also be predicted within a prograding sediment prism (Figs. 6.56, 6.57, and 6.58). The observed diversity of structuration reflects the linked nature of gravity-driven deformation in zones where sedimentary overburden spreads under its own weight and slides basinward atop salt detachments (Rowan et al. 1999; Hudec and Jackson 2006). These passive margin salt-floored systems are a subset of near-field[16] stress driven type 1 fold and thrust belts that includes shale detachments as well as salt-lubricated systems (Morley et al. 2011, 2014).

Linked gravitational systems, floored by salt, can range in scale from small, isolated, allochthonous salt sheets to the entire continental margin as it detaches and slides above autochthonous salt. Extension characterizes the landward and middle parts of salt-linked continental margin systems, while contraction usually occurs near the basinward limits of allochthonous salt (Figs. 6.1b). Strike-slip deformation typically connects these two domains. Where frontal contraction is not observed, downslope translation is usually accommodated by extrusion of allochthonous salt tongues.

Using a synthesis of existing seismic, Rowan et al. (1999) reclassified the salt-associated faulting and welding in the Gulf of Mexico into related families (Fig. 6.56). The classification is strictly geometric, without reference to kinematics, dynamics, or genesis but can be linked to the allochthon evolution outlined by Hudec and Jackson (2006); compare evolution streams

[16]Distinction between near-field and far-field is typically assumed, rather than defined. Far-field typically refers to continent-scale influences (e.g., continent-continent collision), while near-field refers to more local-scale stresses such as those involved in gravity gliding.

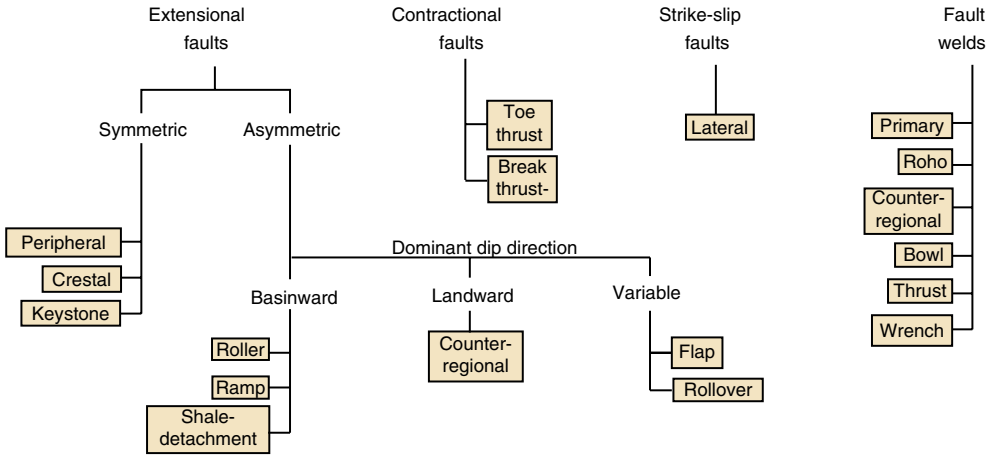

Fig. 6.56 Classification system based on fault families and fault welds observed in the northern Gulf of Mexico (After Rowan et al. 1999)

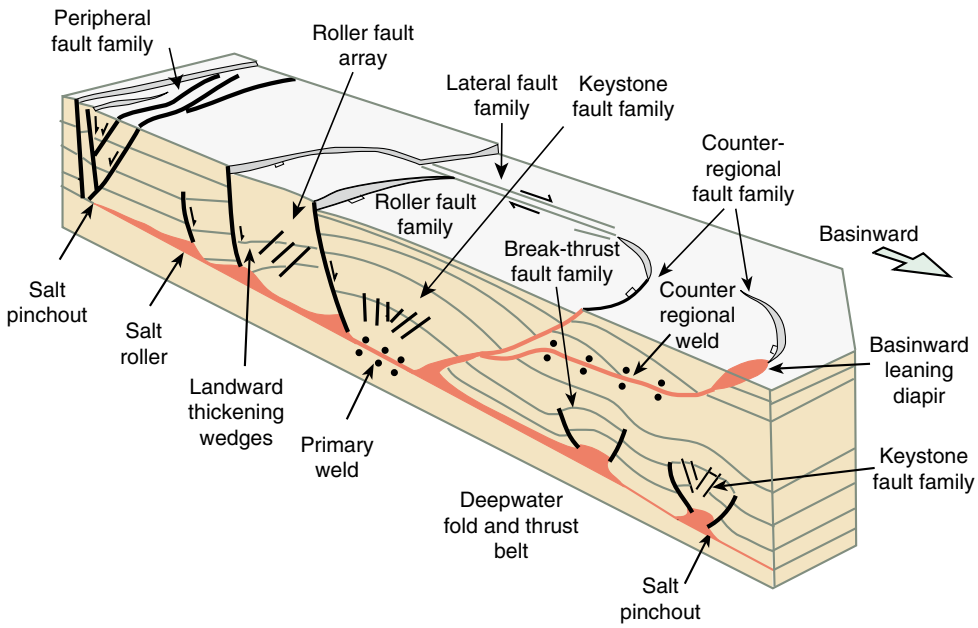

Fig. 6.57 Fault families in areas of salt flow centred on the primary salt level (autochthonous salt), which evacuates to leave behind the primary weld (After Rowan et al. 1999)

in Figs. 6.37 and 6.58. Like the evolution of the salt allochthons that drive them, the different fault families are connected by linked fault systems (inheritance), which, in turn, are associated with different types and stages in the gravity-driven evolution of flowing salt shelf systems. The transition from one fault family into another is related to position of the salt allochthon within the continental margin sediment prism (Fig. 6.56). Each fault family is an array of faults having similar three-dimensional form and geometric relationships with deformed strata and associated salt. A fault family can include not only a dominant style (e.g., a basinward-dipping, listric, growth geometry), but also smaller faults that accommodate the strains and displacements induced by the primary faults. These subsidiary elements include antithetic faults, whose dip is opposite to that of the primary faults, and faults at high angles to the dominant trend. The various fault families and fault welds are tied to five varieties of salt systems: autochthonous salt, salt-tongue systems (both stepped counter-regional and Roho evacuation styles), salt-stock canopies, and salt nappes.

Autochthonous salt tectonics: Autochthonous salt flow is centred on the level of the primary weld (Fig. 6.57). In the Gulf of Mexico the formation of the faulting is driven by two related mechanisms: gravity gliding and gravity spreading. Early salt flow is dominated by gravity gliding and association extension of the suprasalt strata. Oceanic spreading in the Gulf of Mexico began during the Callovian, around the same time the Louann Salt accumulated. The timing of oceanic spreading versus salt deposition in the proto Gulf of Mexico is contentious; some argue they were contemporaneous, others such as Hudec et al. (2013a) argue salt deposition preceded seafloor spreading by 7–12 million years and that oceanic spreading broke up the continuity of the original salt body.

Whatever the timing, subsequent cooling of the lithosphere during differential thermal subsidence probably tilted basinward the proto-Gulf of Mexico continental margin, so driving gravity gliding of the thin overburden above autochthonous salt. Increased clastic input along the continental

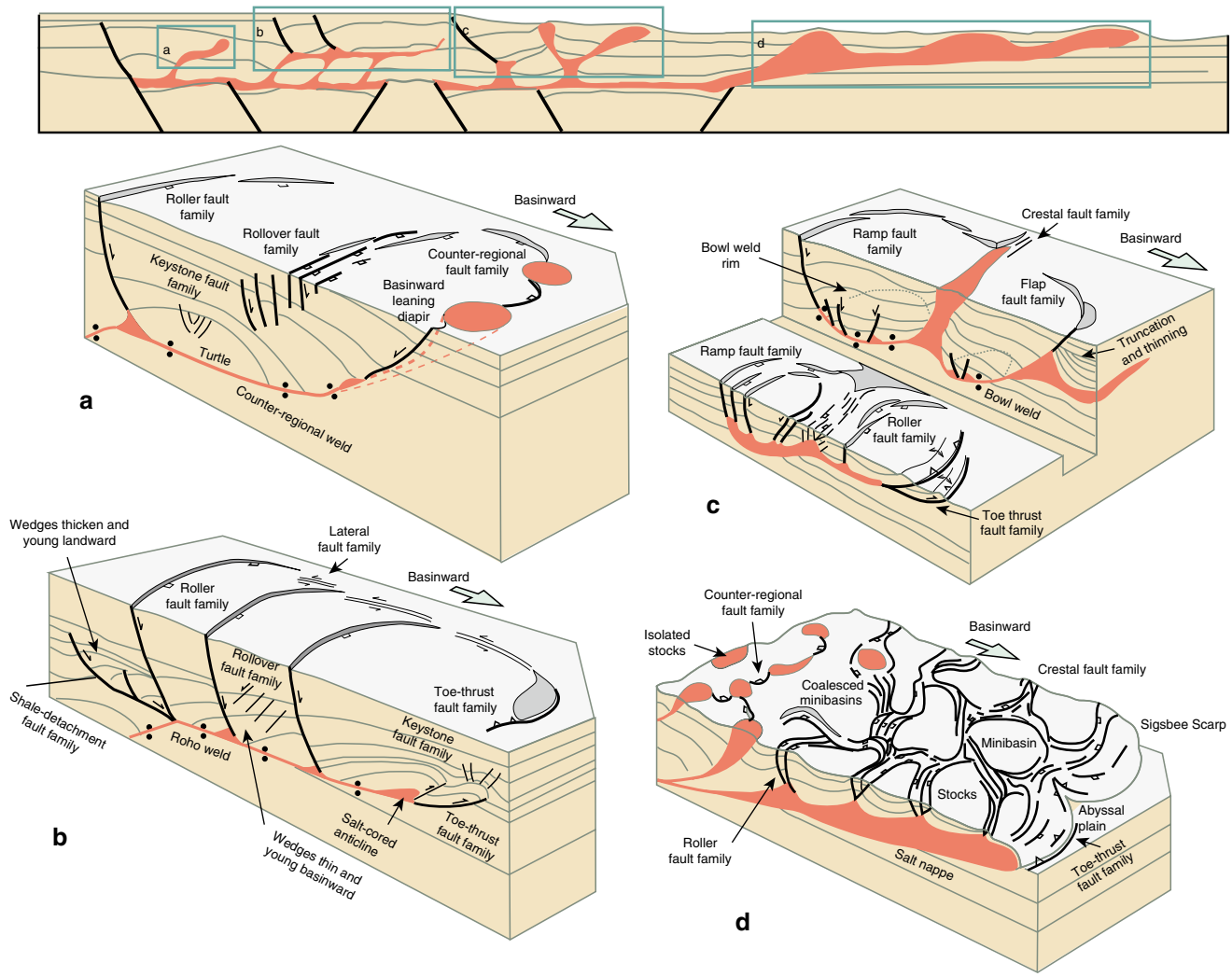

Fig. 6.58 Fault families in salt allochthon provinces, based on the Gulf of Mexico (After Rowan et al. 1999). (**a**) Typical assemblage of fault families and salt or fault welds in a stepped counter-regional allochthonous salt system. Roller faults are less common than the other types. (**b**) Typical assemblage of fault families and fault welds in a Roho allochthonous salt system. (**c**) Typical assemblage of fault families and salt or fault welds in an allochthonous salt-stock canopy. The frontal section shows a partially evacuated salt stock; the back cutout shows two coalesced stocks that have been completely evacuated. (**d**) Typical assemblage of fault families in a salt nappe advancing over the abyssal plain. The basinward area shows an immature stage of evolution; the more landward area shows more highly evolved structures

margin created a depocentre that flexed the underlying crust. This flexure probably reversed the basinward tilt of the autochthonous salt below the continental slope, thereby ending gravity gliding at this level in the stratigraphy; however, the continental margin remained gravitationally unstable and spread under its own weight, especially during Cenozoic clastic progradation. Thus, some of the structures established during early gravity gliding probably were reactivated during subsequent gravity spreading related to ongoing sediment loading and associated local inflation related to salt extrusion.

As a squeezed salt mass climbs the stratigraphy it separates from the primary salt level to become allochthonous salt. Ongoing allochthon loading and flowage forms the same spectrum of faults seen in autochthonous structures but now at levels above those of the mother salt bed (right side of Fig. 6.57). Peripheral and roller fault families accommodate basinward extension at the landward margin of the basin and throughout the salt basin, respectively. Early reactive diapirism can create crestal fault families in this extensional zone. The extension is balanced by a combination of distributed salt extrusion and contractional deformation at the basinward limit of salt. Salt extrudes mainly from basinward-leaning salt diapirs (overlain by counter-regional fault families), but also from more vertical salt stocks. Contraction at the toe of the system creates detachment folds and break-thrust fault families. Folding, whether due to slip on extensional roller faults, collapse of seaward-leaning feeder diapirs, or contraction, generates a combination of rollover and keystone faults. Lateral fault families segment extensional regimes, possibly

controlled by the geometry of faults in the rifted basement (e.g., Watkins et al. 1995; Rowan 1997). Remnant salt or primary welds provide the common link in autochthonous salt systems.

In a landward to basinward traverse, allochthonous fault associations break down into four interrelated fault families, which are shown in basinward order in Fig. 6.58a–d.

Stepped Counter-regional Salt System: Salt-tongue systems comprise subhorizontal salt sheets fed by one or more basinward-leaning feeder diapirs (Fig. 6.58a; Rowan et al. 1999). These systems can evolve as stepped counter-regional systems (Schuster 1995), consisting of a deep feeder weld, an intervening evacuated salt sheet, and higher level basinward-leaning diapirs and landward-dipping salt welds. The linked fault system associated with this counter-regional weld is relatively simple. It is dominated by a counter-regional fault family and associated rollover and keystone fault families. Additionally, a second counter-regional fault family may overlie the deep feeder (not shown). If there were any basinward translation during evacuation of the sheet, there may be a roller fault family detaching on the secondary weld,

Roho Salt System: Salt-tongue systems can also evolve as Roho systems (Fig. 6.58b; Schuster 1995). These are generally longer in the downdip direction than are stepped counter-regional systems. The extra length creates a greater elevation head for the salt and thus more gravity spreading. The result is a linked fault system dominated by a roller fault family. In places, shale-detachment fault families merge into the landward or lateral edges of the salt layer or weld. The extension on the combination of roller and shale-detachment faults is accommodated by salt extrusion or shortening along a toe-thrust fault family. Extension and contraction are linked by lateral fault families and a Roho weld. Minor structures include rollover fault families in the hanging walls of the roller faults and keystone fault families in the crests of contractional folds.

Salt-Stock Canopy System: Salt-stock canopies can be true or apparent depending on whether amalgamation occurred during stock growth or stock evacuation, respectively. In both, a complex linked fault system can develop with the link provided by remnant allochthonous salt and bowl welds (Fig. 6.58c; Rowan et al. 1999). Partly or fully evacuated stocks can have ramp fault families at the landward margins, flap fault families at the basinward margins, and older roller fault families in the central areas. Where the canopy feeds a subhorizontal salt tongue, reactive diapirs and crestal fault families can form at the stretched hinge between the stock and tongue. Translation above the tongue can create roller and toethrust fault families linked by lateral fault families.

Salt-Nappe System: Salt nappes are large allochthonous salt bodies that advance tens to hundreds of kilometres basinward over long periods of time (Worrall and Snelson 1989; Rowan 1997; Morley et al. 2011). The front of a salt nappe is an arcuate lobe of salt covered by a generally landward-thickening clastic skin. In its most immature, distal regions, the structure is dominated by circular to elliptical minibasins up to 40 km wide. They subside into the salt and are separated by reactive diapirs formed during radial gravity spreading of the salt nappe (Jackson and Vendeville 1994). Thus, the linked fault system is dominated by a polygonal pattern of crestal fault families (Figs. 6.58d). Toe thrusts can occur at the front of the nappe. Landward, the regular polygonal pattern degrades as minibasins coalesce. Interaction between salt deformation and sedimentary loading may result in various fault families (e.g., counter-regional, roller, flap, lateral) and welds; however, the three-dimensional geometry of fault families in mature salt nappes is unknown because mature examples have not yet been identified.

Linking Allochthons at the Basin Scale

Clearly, salt flow in a loading and extending halokinetic basin creates a number of predictable geometries, rollovers and fault patterns that are related by variations in rates of extension and loading as prograding suprasalt sediments evolve into ramps and welded basins (Fig. 6.59). In the Gulf of Mexico it is important to distinguish between the more landward intervals of salt flow, which are sourced in autochthonous salt and by definition are still linked to the primary salt level, and the more basinward flows sourced in allochthonous salt where the salt slug is no longer necessarily connected to the primary weld (Fig. 6.59a; Rowan et al. 2001). At this broad continental margin scale of flow, Karlo and Shoup (2000) argue that the thickness of the primary salt bed (Jurassic Louann Salt in the Gulf of Mexico) is what separates regions of autochthonous and allochthonous salt flow. Allochthonous salt tends to be sourced in the thickest portions of the primary salt, while autochthonous flow tends to be sourced in the thinner areas of the primary source bed (Fig. 6.59a). The resulting salt features and associated withdrawal basins make up an ordered but gradational sequence of structural styles across the shelf and slope (Karlo and Shoup 2000).

The sequence progresses from updip autochthonous basins with static diapirs that aborted and were buried, to the most downdip withdrawal basins that have been active at various levels in the stratigraphy since the Mesozoic and are related to an amalgamated and fully allochthonous salt canopy. They argue that differences in depositional thicknesses of the Louann Salt mean the thicker eastern half of the Gulf of Mexico basin has a full progression of salt-related structural styles, while the western half of the basin has a wide area lacking major salt structures that then abruptly juxtapose against tabular salt. The gravity slide detachments characteristic of the western half of the basin are superimposed over salt-related structures where original

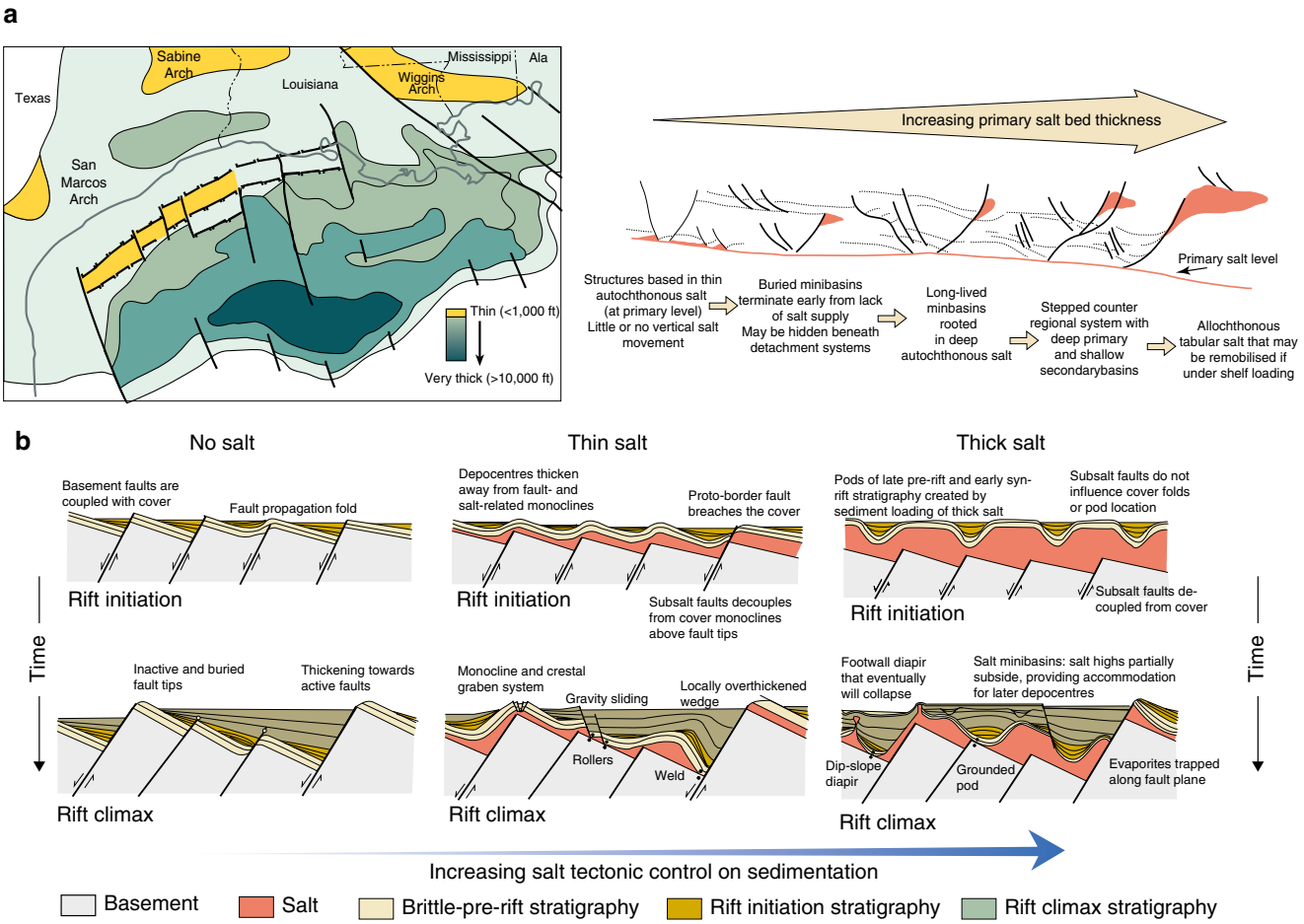

Fig. 6.59 Salt tectonic style is controlled by original thickness of the primary salt layer. (**a**) Approximate salt thickness at the time of deposition of the Jurassic Louann Salt whereby schematic cross section shows that autochthonous salt deformation tends to occur in zones of thinner primary salt. Allochthonous salt deformation is favoured by areas of thicker primary salt (After Karlo and Shoup 2000). (**b**) Tectonic evolution of salt geometries and minibasins in three situations seen in various North Sea grabens of; (i) no salt, (ii) thin salt, (iii) thick salt (After Duffy et al. 2013)

salt thickness was insufficient to maintain structural growth at higher levels.

The early work of Karlo and Shoup (op cit.) is supported by the results of Hall (2002) who found that most of the deep-water region of the northern Gulf of Mexico was underlain by an inflated mother salt layer during the Cretaceous to middle Miocene. The southern edge of this mega-pillow was either the depositional edge of the salt or a basement structure. Partial deflation of this mega-pillow during Late Miocene-Pleistocene sedimentation resulted in the formation of large structures overlying the mother salt level. The process of 'deep' structuring was synchronous with progressive emplacement of shallow (allochthonous) salt to form the Sigsbee canopy in the southern part of the present-day deepwater area.

A similar relationship between salt thickness and deformation style is seen in the Danish Central Graben (Fig. 6.59b; Duffy et al. 2013). Syn-rift basins lacking salt display classical half-graben geometries bounded by thick-skinned faults. In contrast, grabens that entrain increasing thickness of salt show a corresponding evolution in suprasalt depositional style with increasing degrees of structural decoupling between sub-Zechstein structure and cover fault and fold systems. The addition of mobile evaporites to the rift results in: (i) complex and spatially variable modes of tectono-stratigraphic evolution; (ii) syn-rift stratal geometries which are condensed above evaporite swells and over-thickened in areas of withdrawal; (iii) compartmentalized syn-rift depocentres; and (iv) masking of rift-related megasequence boundaries (Duffy et al. 2013). Evaporites clearly exert a significant influence upon rift structural style, the distribution and thicknesses of syn-rift units and the formation of allochthonous salt units higher in the stratigraphy.

Worldwide, detailed analysis of halokinetic basins, ranging from salt-floored passive margins to tectonically-induced contractional basins (with a concentration of detailed seismic coming from the hydrocarbon regions of the circum-Atlantic and Mediterranean), has shown there is a predictable timebased formative relationship in allochthon/minibasin associations. The common evolution to the various continental margins experiencing gravity-driven salt

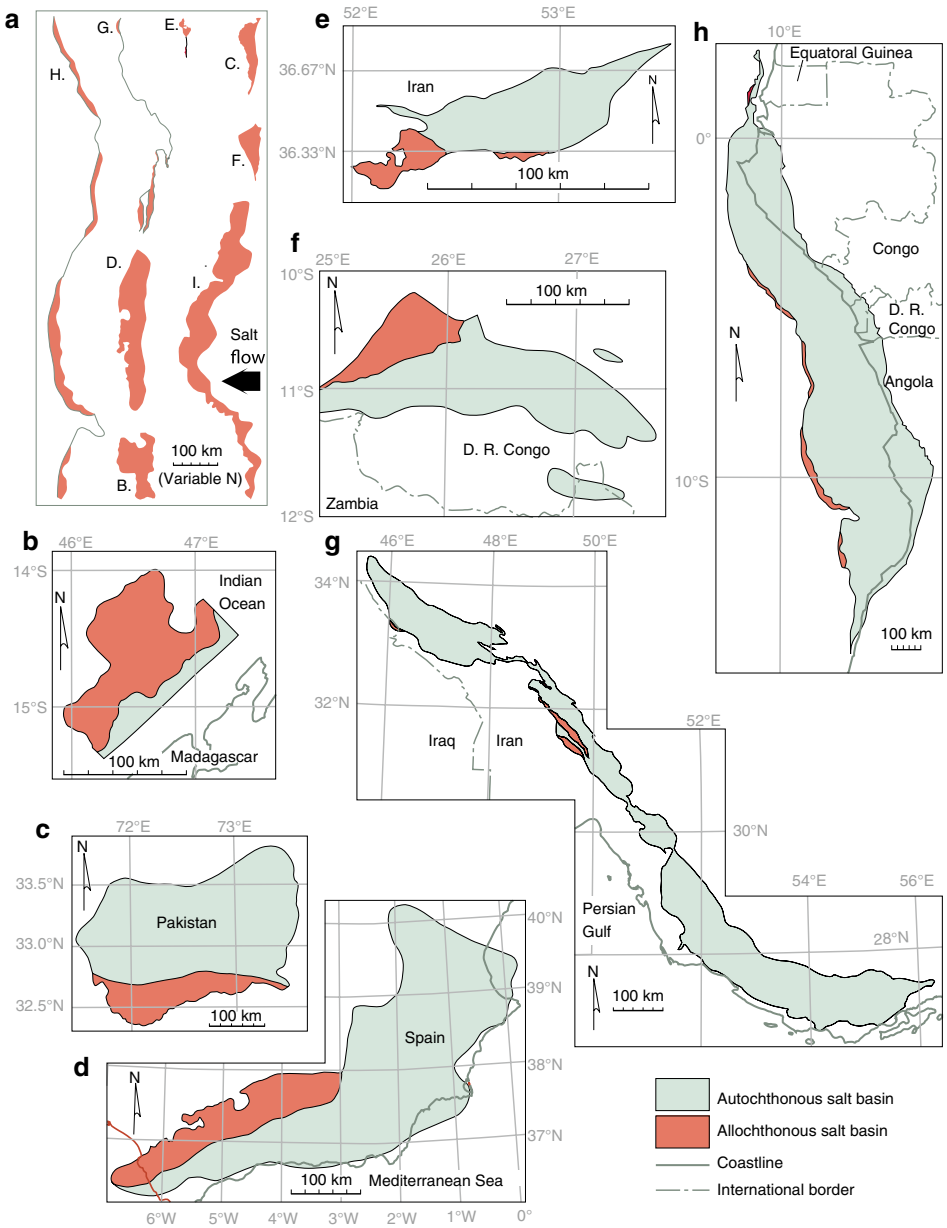

Fig. 6.60 Maps showing source-fed allochthonous fringes in evaporite basins across the world (After Hudec and Jackson 2006 and references therein). In each map, evaporite sheets have spread beyond the autochthonous salt basins (*shaded green*), which typically also contain additional allochthonous parts in them (not differentiated). (**a**) Compilation of selected allochthonous fringes (*A–I*) at a uniform scale but with variable North to show the wide range of allochthon sizes. Each allochthon fringe is oriented so that the dominant flow of the salt sheets is from left to right (indicated by *thick black arrow*) left. The deep-water allochthonous fringe of the Gulf of Mexico's passive margin (labeled I) is also shown in A but not shown in rest of diagram (see Fig. 6.61) for the detail of this allochthonous thrust fringe that is I. The autochthonous interior of the Gulf of Mexico fringe comprises mostly plug-fed sheets supplied by stocks. All other maps (B through H) are at different scales, indicated by 100 km scale bar, and have north to the top. (**b**) Majunga Basin, northwestern Madagascar passive margin; evaporites of probable Jurassic age. (**c**) Salt Range, Himalayan foreland, Pakistan; Punjab evaporites of Neoproterozoic–Cambrian age. (**d**) Guadalquivir Basin, Betic foreland, southern Spain; Keuper (Carnian-Triassic) evaporites. (**e**) Garmsar Basin, Alborz foreland, northern Iran; Eocene and Miocene Upper Red evaporites. (**f**) Katanga Basin, Lufilian foreland, Shaba Province, southern D. R. Congo; Neoproterozoic Roan evaporite residues (rauhwacke). (**g**) Gachsaran Formation, Zagros foreland, southwestern Iran; Miocene evaporites; many allochthonous salt sheets, derived from the Neoproterozoic–Cambrian Hormuz Formation are also present in much of this region. (**h**) Aptian salt basin, Angolan passive margin, offshore Equatorial Guinea to Angola

tectonics is characterised by; (1) an underlying initially thick 100–200 m + autochthonous salt bed (now with overlying plug and wall-fed allochthonous layers) and (2) a source-fed allochthonous margin or fringe to the autochthonous system, which is located along the downdip continental slope/edge (Fig. 6.60; Hudec and Jackson 2006).

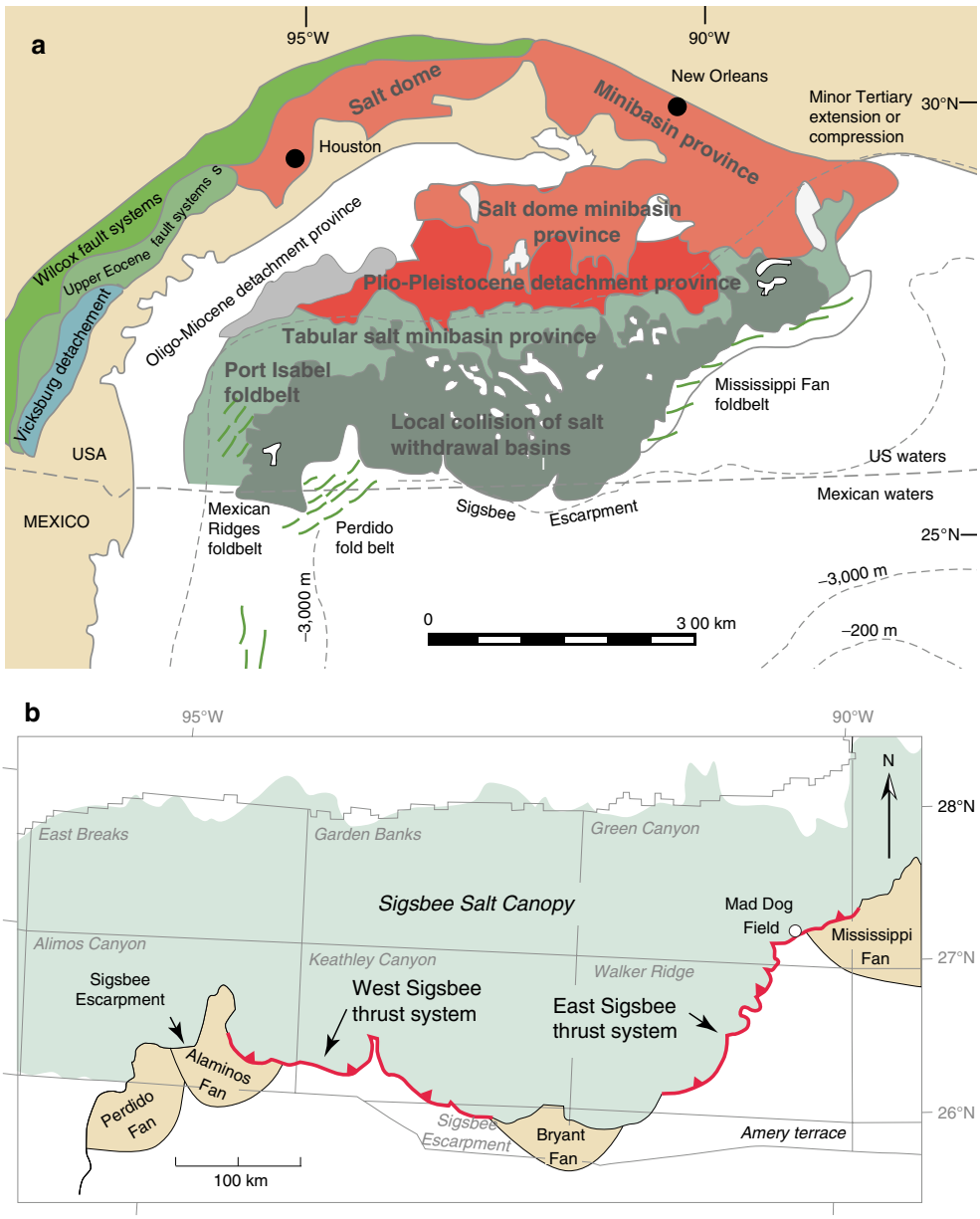

Fig. 6.61 Salt and allochthon distribution in the Gulf of Mexico. (**a**) Distribution of thrusts in the context autochthonous and allochthonous salt basins (After Hudec and Jackson 2006). (**b**) Map showing main structural units salt distribution and water depths, based on Morley et al. (2011)

Salt basins with this linked autochthon-allochthon style of salt tectonism range in scale from the supergiant 1,000 km-long salt canopy systems of the larger of the circum-Atlantic salt basins to the 100 km long systems of offshore Madagascar (Fig. 6.60). In the Gulf of Mexico, as in many salt floored continental margins, the allochthonous downdip basin margin links a deepwater fold and thrust belt to a deepwater thrusted edge to the allochthon and its latest canopy area (Fig. 6.61). Interestingly, the downdip canopy edge overlies oceanic, not transitional, crust and is a strong indication of how far downdip the Louann Salt has migrated (been thrust) as it climbed the basin stratigraphy (compare Fig. 5.56 and 5.57 with 6.61b)

Compressional Salt Tectonics

Contractional or tectonically shortened salt basins are numerous and can be loosely classified into three conceptually shingled compressional styles (Figs. 6.62 and 6.63; Letouzey et al. 1995):

- Zones of shortening at the toe of prograding and gravity-gliding systems (thin-skinned; Fig. 6.62a),
- Thin-skinned deformation in fold and thrust belts (Fig. 6.62b),
- Intracratonic inverted basins with or without wrench components – thick-skinned with basement involved in the compression (Fig. 6.62c).

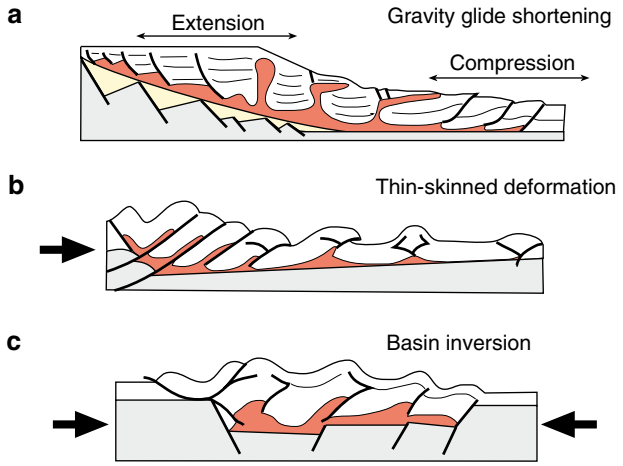

Fig. 6.62 Compression tectonics. (**a**) Gravity glide shortening at the toe of the continental slope. The basement is not involved in the deformation. (**b**) Thin skinned deformation in front of the fold and thrust belt where subduction is the driving mechanism in the inner foldbelt. (**c**) Intracratonic inverted basin. Driving mechanism is regional contraction, which is orthogonal or oblique to the pre-existing graben. Basement, salt and overburden are all shortened together (After Letouzey et al. 1995)

Contractional salt tectonism is produced either by convergent (including transpressive) plate tectonics, or is restricted to the seaward portions of divergent continental margins, where downslope gravity-sliding stacks and thrusts overburden blocks against each other as they slide basinward atop a salt décollement. Contractional salt tectonics require either the minimum principal stress (σ_3) to be vertical (so creating shortening) or the intermediate principal stress (σ_2) to be vertical (resulting in transpression; Jackson and Talbot 1994). Compression in a salt-entraining basin tends to thicken both salt and its overburden units. This increases overburden strength and laterally squeezes the feeding stem of any existing diapir, while the increased overburden strength tends to impede piercement. Shortening or squeezing of diapirs, that earlier formed in extension, is an under-recognized process in many gently-shortened salt basins.

Shortening with Gravity Gliding

Belts of upslope extension are paired or linked to downslope compression on rapidly prograding shelf-slope systems along salt-cored passive continental margins. Overburden sediment slides downslope atop a lubricating salt layer, with the translation largely driven by the increasing weight of sediment accumulating atop the salt (Fig. 6.62a). Shortening and gravity-driven compressional structures typify the toes of such systems, while extensional features and welds occur in the upslope position. Areas of extreme extension in the upslope regions evolve into regions of raft tectonics. In the zone between areas of extension and compression some large plates of sediment (up to tens of kilometres across and a kilometre or more thick) can shift or translate downslope with little intraplate evidence of migration until the downslope edge starts to experience compression and pop-up structures form, such as squeezed diapirs.

Salt-cored rising growth folds and active thrusts typify the compressional toes of such regions of into-the-basin salt translation. Compressional foot of slope examples, lubricated by salt décollement, include (Fig. 6.63): the Perdido and Mississippi Fan foldbelts in the Gulf of Mexico (Schuster 1995), the deep Campos and Santos Basins of offshore Brazil (Cobbold et al. 1995, 2001), offshore west Africa (Duval et al. 1992; Cramez and Jackson 2000; Brun and Fort 2004), the eastern Mediterranean adjacent to the Nile Deep Sea fan (Sage and Letouzey 1990), and offshore Yemen (Heaton et al. 1995). The salt in all the areas, with the exception of the Mediterranean, was precipitated in early post-rift time with consequent thermal subsidence generating a basinward tilt of the continental margin (typically > 1°–3°). The tilt was an early contributing factor to the décollement and gravity gliding, and is a likely triggering mechanism (Brun and Fort 2011). The other likely trigger is differential loading tied to the rapid progradation of the up-dip shelf margin sediments; (Rowan et al. 2012b). Compressional toe-thrust and diapiric systems are not the sole province of salt-floored systems, but also occur in fold and thrust belts along the deepwater edges of mud-rich evaporite-free continental margins, such as the Neogene fluvio-deltaic wedge of Brunei and the Niger Delta of Africa (Morley et al. 2011).

Because salt-floored extensional domains on active passive margins tend to lie in a more proximal shallower water positions they are, to date, better studied than the associated downdip compressional terrain. Contractional or compressional domains tend to lie in deeper water further out into the basin at the foot of a continental slope or a prograding delta front. Many of these offshore compressional areas are covered by waters that are still too deep to be exploited with current drilling technology.

Shortening in gravity-glide salt belts is usually accommodated in salt-cored compressional foldbelts with growth-folds near the toe of the salt layer or at the base of the continental slope. Contractional growth folds are the near-surface subseafloor expression of a ramping thrust fault at the downdip end of an inflating salt allochthon. If the crest of a salt-cored fold is eroded or weakened enough by crestal faulting, salt may burst through as an active diapir. Once it reaches the surface, it can continue to grow as a passive diapir instigating a new allochthon-floored stratigraphic level of into-the-basin gliding.

The Mississippi Fan or Atwater Foldbelt lies 200 km SSE of New Orleans and is defined by a such a series of ENE trending thrust-associated growth-anticlines down dip of the current allochthon salt sheet canopy and is sourced in the

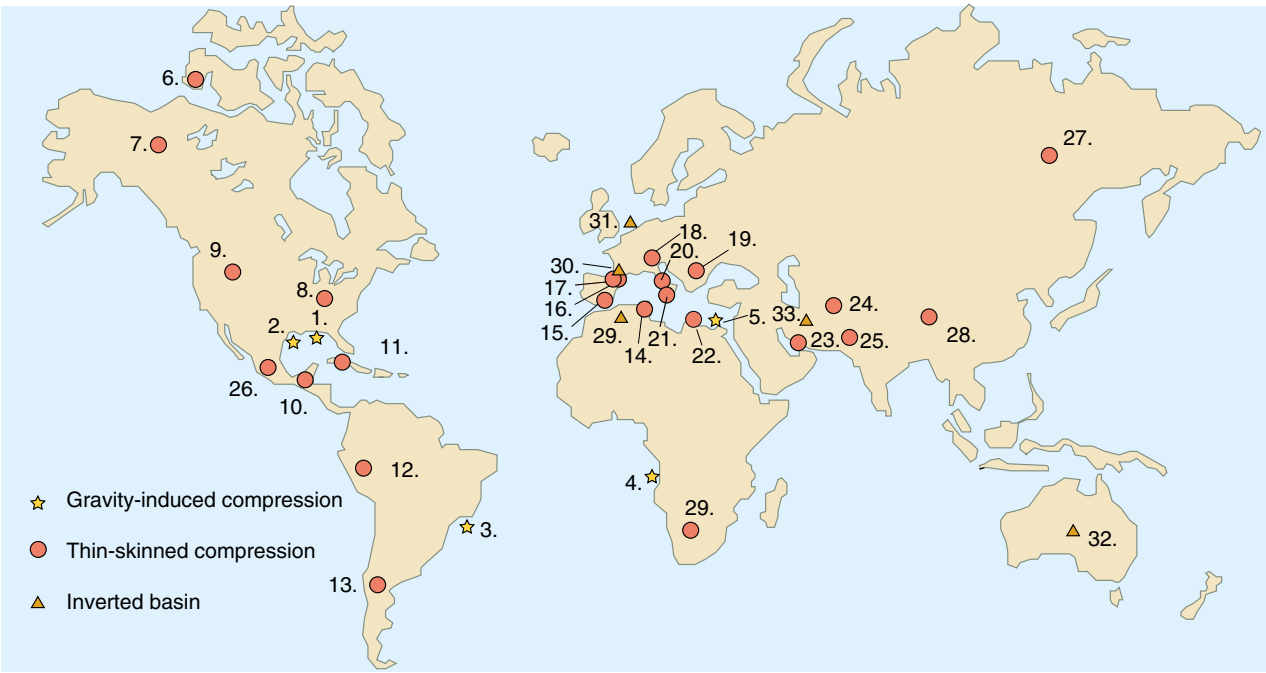

Shortening via gravity gliding at the toe of prograding shelf systems

1.	Mississippi Fan	Gulf of Mexico	Middle Jurassic
2.	Perdido	Gulf of Mexico	Middle Jurassic
3.	Campos, Santos	Brazil	Lower Cretaceous
4.	West Africa	Angola, Gabon	Lower Cretaceous
5.	Nile delta	Mediterranean	Upper Miocene

Thin skinned deformation in fold and thrust belts

6.	Parry Islands	Canada	Ordovician
7.	Franklins	Canada	Cambrian
8.	Appalachians	USA	Silurian
9.	Wyoming	USA	Upper Jurassic
10.	Guatemala	Central America	Middle Jurassic or Cret.?
11.	Cuba	Caribbean	Middle Jurassic
12.	Santiago	Peru	Permian
13.	Neuquen	Argentina	Jurassic or Cretaceous
14.	Rif-Tellian	North Africa	Triassic
15.	Betics	Spain	Triassic
16.	Iberics	Spain	Triassic
17.	Pyrenees	France and Spain	Triassic
18.	Southern Alps	France	Triassic
19.	Carpathians	Romania	Lower Miocene
20.	Apennines	Italy	Triassic
21.	Messinian	Eastern Mediterr.	Upper Miocene
22.	Mediterr. Ridge	Eastern Mediterr.	Upper Miocene
23.	Zagros	Iran	Infracambrian
24.	Tadjiks	CEI	Jurassic
25.	Salt Range	Pakistan	Infracambrian
26.	Sierra Madre Or.	Mexico	Jurassic
27.	Verkhoyansks	CEI	Cretaceous
28.	Kuqa foldbelt	Tarim, China	Tertiary
29.	Lufilian foldbelt	Central Africa	Neoproterozoic

Intracratonic inverted basins

29.	Atlas	North Africa	Triassic
30.	Aquitaine Basin	France	Triassic
31.	Southern Zechstein	North Sea	Permian
32.	Amadeus Basin	Australia	Neoproterozoic
33.	Central Iran	Middle East	Eocene-Miocene

Fig. 6.63 Worldwide occurrences of compressive deformation that involves salt sequences (In part after Letouzey et al. 1995; Davis and Engelder 1985, and SaltWork version 1.6)

Jurassic Louann Salt (Fig. 6.64; Rowan 1997). Today it is a zone of compressional response to updip loading and associated gravity spreading/sliding along a salt detachment, linked to updip normal faults. Faults and folds are dominantly south vergent, although symmetric box folds and backthrusts exist[17]. Updip, the shallow allochthonous salt sheets of the Sigsbee Nappe have over-ridden the landward portions of this same foldbelt to create a number of hydrocarbon targets. Thickness variations in sediments above the Top MMR and a lack of such variations in more recent sediments and the presence of an erosional unconformity atop the Mississippi Fan unit suggest structures actively grew near the seafloor prior to the current episode of Tertiary-age shortening.

Profile X-X′ shows a seismic interpretation of one such asymmetric faulted detachment fold cored by the Louann Salt (Fig. 6.64a; Rowan 1997). Data from the Shell 471–1 Atwater well constrain the interpretation in the upper part of the section. The frontlimb of the fold is cut through by a

[17] Backthrust describes a thrust fault that dips opposite to the general dip of thrust faults in a thrust belt and results in displacement toward the hinterland of the belt.

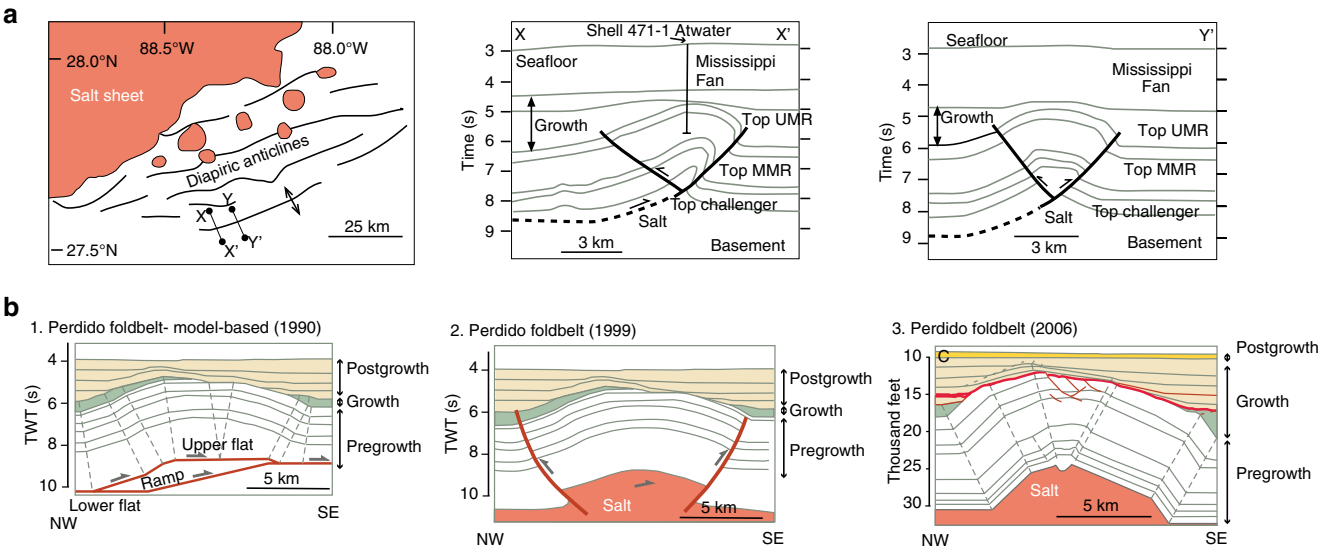

Fig. 6.64 Fold belt structures. (**a**) Thrust folding in downslope compressional belt, northern Gulf of Mexico (After Rowan 1997). Map shows the location of presumed salt-cored anticlinal structures in the Mississippi Fan foldbelt and locations of interpreted sections. X–X′, interpreted seismic section profile' through a salt-cored anticline showing an asymmetric faulted detachment fold. Y–Y′ Interpreted seismic section profile further along strike through the same structure, showing a symmetric faulted detachment fold. *UMR* Upper Mexican Ridges, *MMR* Middle Mexican Ridges. (**b**) Evolving interpretations of the Perdido foldbelt. (*1*) Duplex-cored fault-bend fold model (Mount et al. 1990), (*2*) Reverse-faulted salt-cored detachment fold model (Trudgill et al. 1999), and (*3*) Unfaulted kink-style detachment fold (After Camerlo et al. 2006) *TWT* two-way traveltime

major thrust fault, which is truncated up section by unconformable units of the Upper Mexican Ridges. A possible back thrust is interpreted as cutting through the backlimb and terminating against the main thrust fault. Both thrusts are characterized by fault to fold transfer, although the displacement of individual units can vary up-section. The overall geometry, fold-fault relationship, and the nature of the stratigraphic section, which consists primarily of alternating shales, chalk, marls, and turbidites, are all suggestive of an asymmetric faulted detachment fold (Mitra 2002). The upper part of the Upper Mexican Ridges (UMR) consists of growth units, which are strongly thinned and eroded on the crest of the structure, suggesting that the folds formed primarily during the deposition of these units (growth-fold deposition). The growth units thin onto the crest of the structure on both limbs and also are truncated on the backlimb.

The salt cored structure shown in profile Y–Y′ is located further east along the same ridge (Fig. 6.64a; Rowan 1997). It is interpreted as having a more symmetric pop-up geometry with a relatively flatter fold crest. Thrust faults on both limbs terminate upward within the Upper Mexican Ridges and downward within the Louann Salt. The thrust fault on the southern limb has a larger displacement; however, the difference in displacement on the two thrusts is smaller than in profile X–X′. Once again thickness changes in the upper part of the Upper Mexican Ridges (UMR) unit show it is also a growth fold, with fold-related seafloor topography controlling depositional patterns on the seafloor. The structural characteristics of this part of the fold ridge are suggestive of the symmetric faulted detachment fold model of Mitra (2002), with thrust faults propagating through rotated segments on both limbs.

However, a subsequent paper by Camerlo et al. 2006, dealing with the Perdido foldbelt, argues that an interpretation of a toe thrust and backthrust within the fold, much like the Mississippi foldbelt, may not be appropriate (Fig. 6.64b). The thrust interpretation with a thrust and backthrust, as made by Trudgill et al. 1999, Camerlo argues is not correct, rather the thrust interpretation is an artifact of the poor seismic imaging that occurs at depth with sloping beds. He asserts that the most likely interpretation, given the nature of the overburden, is not faulting but folding and that the folds are unfaulted kink-style detachments. That is, The Perdido foldbelt is composed of detachment folds flanked by megascopic-scale kink bands (Fig. 6.64b). The kink bands are seismically poorly imaged zones of low signal-to-noise ratio and low reflectivity. These seismic artefacts result from problems related to steep dip, primarily dip bias of amplitude and the sensitivity of positioning and coherence of dipping events to migration velocity. The kink-band interpretation is supported by the substantial width of the low-reflectivity zones on the flanks of the folds; the subparallel edges of the low-reflectivity zones; the formation of the low-reflectivity zones at a high angle to layering; the absence of backlimbs that would help to support blind reverse faults at depth; and

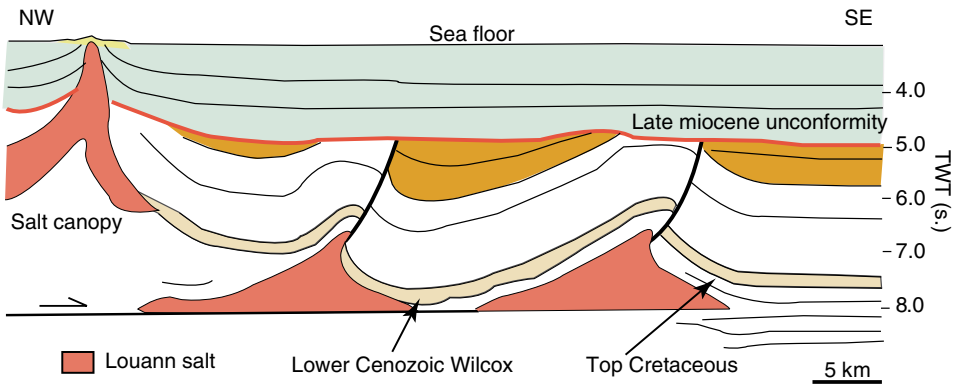

Fig. 6.65 Section across the Mississippi Fan Fold Belt, based on seismic line in Meyer et al. (2005). Indicates regional late Miocene salt inflation

the illumination of steeply dipping bedding in the low-reflectivity zones through improved seismic imaging efforts compares to the 1999 vintage data.

Both interpretations are quite distinct from the earlier interpretation of Mount et al. 1990 (Fig. 6.64b). It was made at a time when only the upper portion of the foldbelt could be seismically imaged. Their interpretation of a ramping thrust duplex was based on section balancing techniques, which largely ignore the influence of the salt cores, as they were too deep to be reliably imaged at that time The three models shown in Fig. 6.64b show substantial differences in the relative thickness of pregrowth, growth and postgrowth successions across the three interpretations. It underlines the difficulties in balancing sections when flowing salt is involved in the reconstruction.

At a somewhat broader scale, there are three main salt-formed compressional deepwater fold belts in the Northern Gulf of Mexico, the Perdido, Mississippi Fan and Port Isabel fold and thrust belts – DWFTB's (Fig. 6.61a). Meyer et al. (2005, 2007) and Morley et al. (2011) provide reviews of deepwater exploration in these trends, and their discussions are summarised in the following paragraphs. A cluster of deepwater hydrocarbon development projects (BAHA, 2002; Trident, 2001; Great White, 2002; Silvertip, Tobago) exist in the Perdido Fold Belt, but more numerous development projects are associated with the Mississippi Fan Fold Belt. Major discoveries in the Mississippi Fan Fold Belt include Neptune (1995), Mad Dog (1999), Tahiti (2002), Knotty Head (2005), Genghis Khan (2005) and Big Foot (2005). Thunder Horse (1999) is the largest of the DWFTB fields, with an estimated mean size of one billion barrels of oil equivalent (Chap. 10). It is the largest producing deepwater asset in the world. Conversely, the Port Isabel Fold Belt as has no discoveries (Cossey 2004).

The northwestern Gulf of Mexico contains the deepwater Perdido fold and thrust belt (Camerlo and Benson 2006). This belt is, however, just the external portion of a more extensive belt of contraction that includes the Port Isabel fold belt and the salt canopy area (Fig. 6.66; Morley et al. 2011). Up-dip extension of 60+km suggests the down-dip fold and thrust belts, and the salt canopy must accommodate a similar amount of contraction, of which the Perdido fold belt only accommodates 5–10 km. The Perdido fold belt mainly underwent deformation during the lower Oligocene, but minor deformation continued until the Middle Miocene. In map view, the folds range from linear, to more dome shaped, fold length appears to be limited in places by underlying NW-SE trending syn-rift basement structures (Trudgill et al. 1999).

A switch in depositional systems with time resulted in abandonment of the Perdido fan fold belt, and formation of the Mississippi Fan fold belt during the Miocene–Pliocene (Fig. 6.65 Wu et al. (1990a, b); Weimer and Buffler 1992). The two fold belts are separated by a wide region without demonstrable contractional deformation (Diegel et al. 1995). The Mississippi Fan Fold Belt is characterised by broad, upright folds to asymmetric, offshore and landward verging folds, cut by thrusts with wavelengths of about 8–12 km. They are salt-cored detachment anticlines, with welds at the base of the synclines (Rowan et al. 2004; Grando and McClay 2004; Figs. 6.64 and 6.65).

Precursor, small wavelength salt pillows formed in places during the Late Jurassic–Cretaceous in response to early contractional deformation, and later helped control the positions of Cenozoic age folding (Grando and McClay 2004). The Mississippi Fan fold belt is partially overlain by the Sigsbee Salt Nappe, whose emplacement is responsible for the withdrawal of salt along the basal detachment of the fold belt. This situation contrasts with the thick salt detachment of the Perdido Fold Belt (Trudgill et al. 1999).

Both fold belts underwent a late oceanwards tilting as a result of a wedge of salt being injected into, and inflating, the basal detachment (Fig. 6.66). In the context of the foldbelt it is important to note it inflates once the higher-level allochthon belt is welded (Stage 2 in Fig. 6.67). A complex system of extensional detachments exists up-dip, with detachments forming at different levels partly in response to large salt sheets migrating up through different stratigraphic levels over time (e.g., Diegel et al. 1995).

Regionally, the style and extent of the compression across a salt-lubricated toe of the slope system is largely controlled

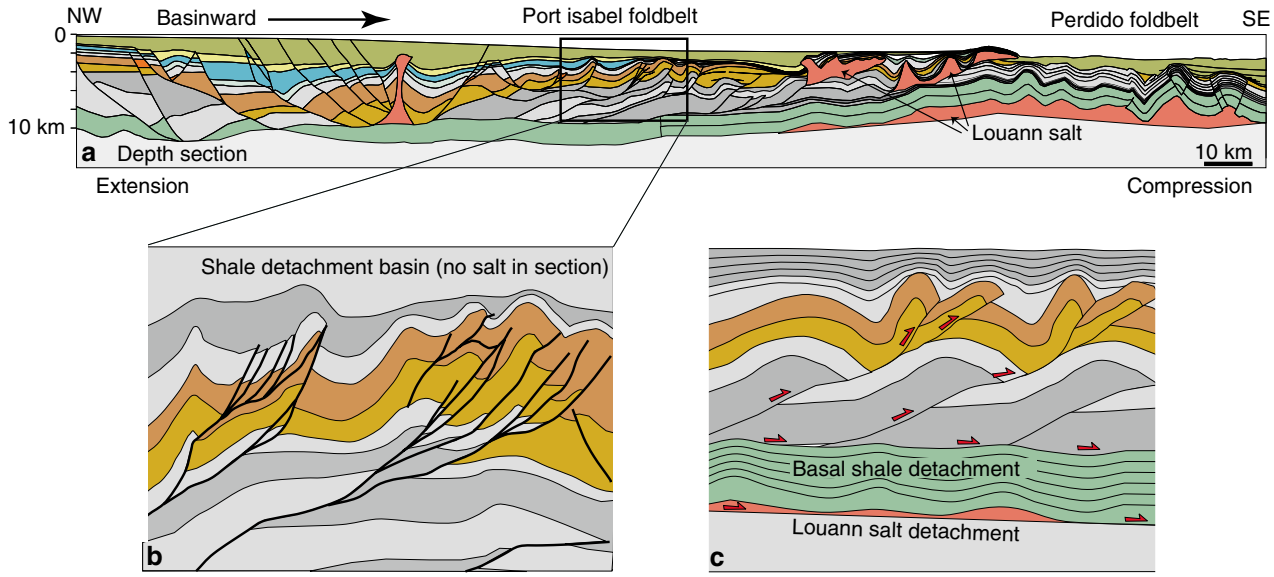

Fig. 6.66 Port Isabel Foldbelt, northwestern Gulf of Mexico. (**a**) Regional depth section showing linked proximal extension and distal contraction. Shortening (compression) is accommodated in: the Perdido Foldbelt above the Jurassic Louann Salt; extrusion of, and translation above, allochthonous salt; and the Port Isabel Foldbelt, detached on Eocene shales (2×1 vertical exaggeration). (**b**) Seismic interpretation of the Port Isabel Foldbelt, showing multiple shale detachment levels and associated fault-bend and fault-propagation folds. (**c**) Schematic cross section (not to scale) showing the relationship of the Port Isabel shale detachments (at the top of the green unit and higher) and the underlying, autochthonous Louann Salt detachment (After Rowan et al. 2004; Morley et al. 2011). See Fig. 6.61a for location

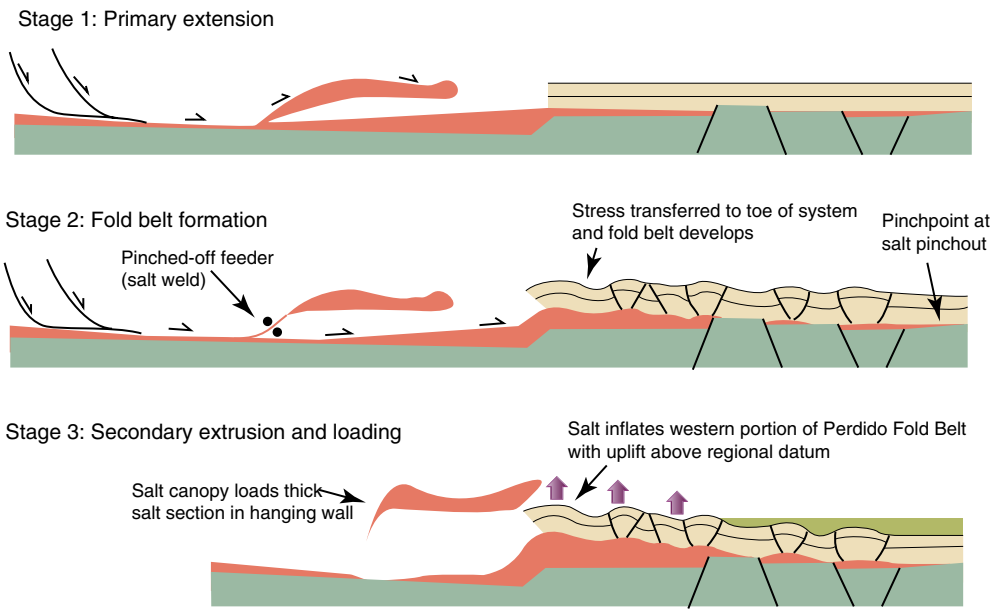

Fig. 6.67 Cross-sectional schematic illustrating the development of the Perdido fold belt via regional gravity spreading linked to up-dip extension. *Stage 1*: Paleogene initial loading and extension caused primary extrusion of salt and the development of a regional allochthonous salt canopy. *Stage 2*; Closure of the feeder salt diapirs transferred stress to the toe of the system, causing development of the Perdido fold belt. *Stage 3*: Further salt movement resulted in inflation of a salt wedge along the Perdido fold belt detachment (After Trudgill et al. 1999; Morley et al. 2011)

by the extent of the salt layer and the position of the salt edge or pinchout on the down dip side of the basin (Fig. 6.68; Letouzey et al. 1995). If the mother salt layer extends well out into the basin, with the salt pinchpoint beyond the zone of significant compression, the system tends to form a fold-belt dominated by salt-cored buckle folds with little or no evidence of thrusting. If, on the other hand, the salt layer pinches out near the toe of the slope, the friction coefficient at the base of the contracting sediment pile is greatly increased and forms a narrower thrust-faulted zone.

The degree of shortening in such compressional thrust terrains can be substantial. In the deep water Santos Basin, Brazil, the downdip section is shortened by up to 50 % of its original length as the seaward margin of the salt belt flows out over the backstop basalts of oceanic basement (Fig. 6.69). Many of these thrust blocks show typical contractional salt

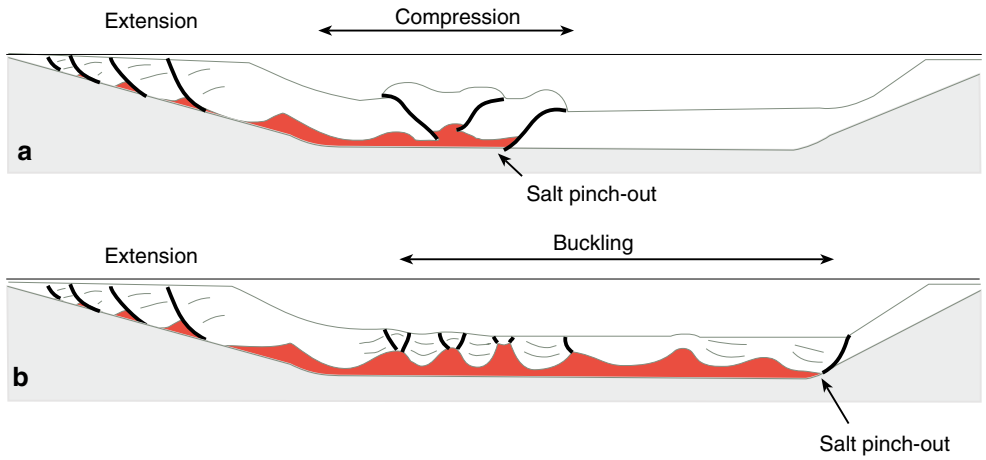

Fig. 6.68 Location of basinward pinchout of the salt layer controls the style of contractional/ compressional structures. (**a**) Where the salt layer does not extend out far past the foot of the continental slope, the frictional resistance increases at the base of the sedimentary pile and interferes with further basinward movement. This can create an imbricate thrust zone on the updip side of the salt pinchout. (**b**) Where the salt layer extends across the basin and well out from the foot of the continental slope, the contraction is taken up in a series of buckle folds with crests that tend to lack thrust zones (After Letouzey et al. 1995)

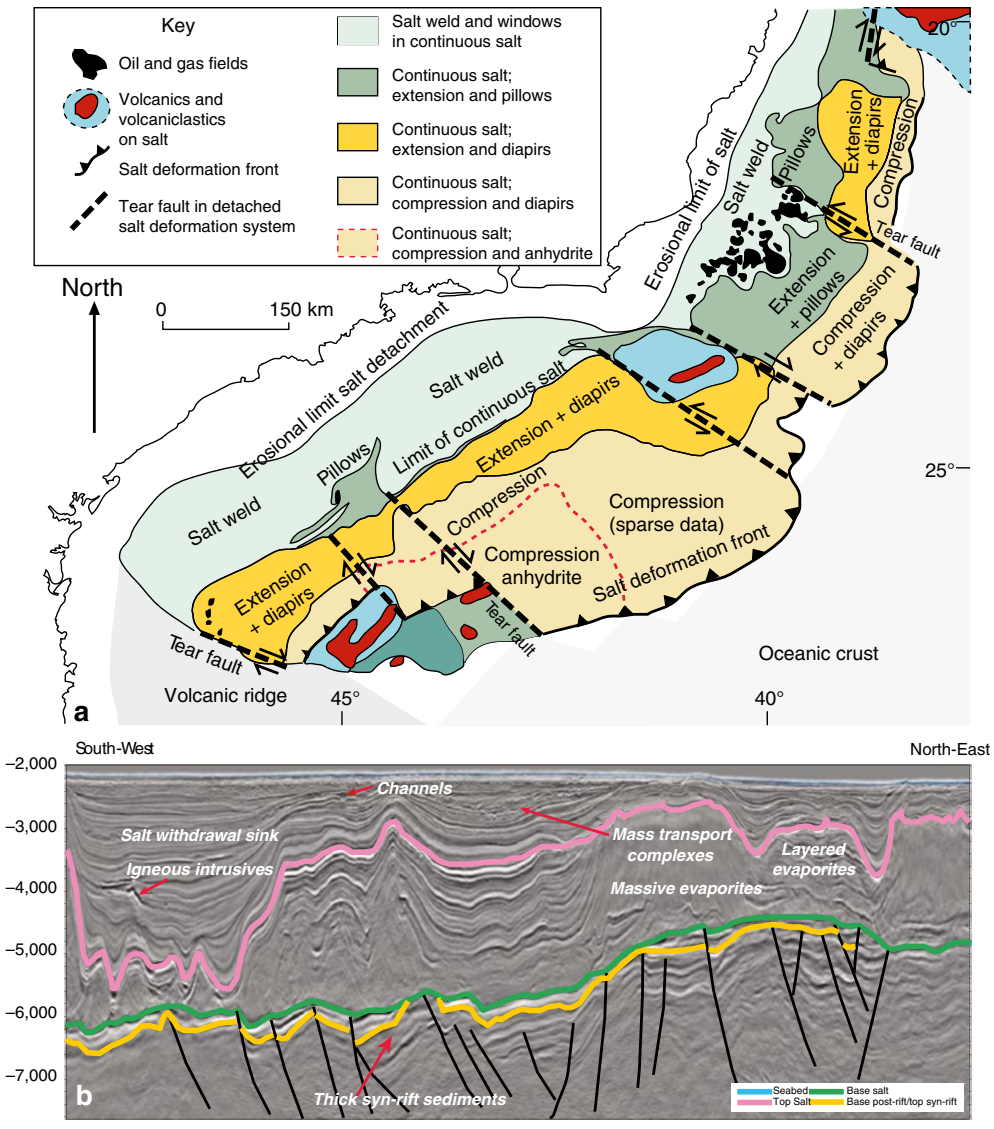

Fig. 6.69 (**a**) Map showing relationships between the various salt-detached basins in the Santos and Campos basins of offshore Brazil. Oil and gas fields in the northeast tend to occur updip of the limit of continuous salt in suprasalt turbidite reservoirs that are sourced from sub salt lacustrine sediments (After Meisling et al. 2001) In the southeast (Santos Basin) are subsalt, typically on basement highs capped by porous lacustrine carbonates as illustrated in (**b**) Typical subsalt relationships in the vicinity of Libra Field (Santos Basin) showing layered versus massive character of Aptian salt in this region (Seismic image courtesy of CCG)

thrust assemblages of sediment wedges in their footwall and chronologically older (Aptian) salt in their hanging walls. Interestingly, the giant oilfields of the Campos Basin and the fields of the Santos Basin only occur atop salt breakout windows on the inboard side of the belt of continuous salt or atop the zone of salt welds. This reflects the high seal integrity of continuous salt sheets, which prevent hydrocarbons generated in the mature subsalt salt source from reaching the suprasalt turbidite reservoirs (Fig. 6.69; Meisling et al. 2001). It is a very positive indicator of the possible presence of large subsalt traps some distance further offshore where halokinetic salt sheets constitute more continuous layers, including structures similar to Tupi.

At the scale of salt flow in passive margin sediments along the edge of a widening ocean basin there is also the process of increasing shelf edge to ridge distance to be considered. Over time this will create an increasingly broad compressional zone in the zone of transitional crust at the foot of the continental slope. This is clearly illustrated in the expanding compressional belt down dip of the zone of raft tectonic in the seaward margin of the Kwanza Basin, Angola (Fig. 6.70; Fort et al. 2004). A thick sequence of Cretaceous (Aptian) salt was laid down atop lacustrine sediments in the opening rift, followed by a transition into marine sediments the passive margin. Three groups of sediments make up this marine wedge; The Pinda Group (Albian to Late Cretaceous), consists of a carbonate platform followed by sedimentation increasingly dominated by marls and clays. The Iabe-Landana Group (Late Cretaceous to Eocene) consists of dominantly siliciclastic sediments, with locally significant carbonates. Most of these deposits are located on the current platform, pinching out seaward into condensed sections, indicating a long-term highstand during the Late Cretaceous. The Malembo Group (Oligocene to the present day) corresponds to a large, prograding clastic wedge. The salt has acted as a décollement allowing updip extension and downdip compression. The extensional domain is characterised by oceanward-sealed tectonic blocks, rollovers and diapirs, while the downdip compressional terrain is characterised by growth folds, squeezed diapirs and thrusts (Fig. 6.70).

The compressional zone is divisible into; (1) an inner more upslope subdomain characterised by formation of contractional diapirs by the compression of former extensional diapirs (squeezed diapirs) and (2) an outer more downdip subdomain characterised by growth folds and thrusts. The upper subdomain indicates the expansion of the compressional domain in a more upslope direction as formerly extensional suprasalt sediments slides and piles at the foot of slope (Figs. 6.69 and 6.70). The ductile diapir salt in the Kwanza salt style is trapped and pinched in anticlinal cores, leading to the formation of contractional diapirs that typically do not necessarily extrude at the surface but are stopped and sealed by further sedimentation. This type of updip extension and downdip compression indicates an initial salt geometry that wedged or thinned in both seaward and landward directions at the end of the margin-rifting stage (Aptian; Fig. 6.69a). Postrift cooling of the lithosphere then induced a seaward tilt in the margin and the development of gravitational instability, creating a seaward-gliding system with an extensional upper end and a compressional downdip end (Fig. 6.70b passing to 6.70c). The increasing into the basin tilt due to thermal subsidence drives an updip migration of the zone of compression or contraction (Fig. 6.70c). Over time diapirs that formed by extensional processes become squeezed and take on the structural and trap morphologies of diapiric structures indicative of this compression (see later).

Thin-Skinned Fold and Thrust Belts

Widening salt-floored rift basins are subject to later closure (Wilson Cycle; Fig. 5.32), so, independent of early glide-induced compressional stacking at foot of slope, compressional deformation is often later superimposed on originally extensional halokinetic margin by regional plate-driven collision (Fig. 6.62b) or its aulocogen counterpart in the continental interior (Fig. 6.62c). Salt acts as a lubricant to any consequent thrust sheet as it pushes landward. Thin-skinned fold and thrust belts form in orogenic chains where the basement is not involved in the deformation and evaporite layers are preferred detachment horizons (Letouzey et al. 1995). Resultant structures are predominantly oriented parallel to the intermediate stress direction and perpendicular to the maximum shortening. Examples of thin-skinned fold and thrust belts include (Fig. 6.63): the Parry Islands Foldbelt in Arctic Canada (Harrison 1995), the European Jura (Philippe 1994), the Spanish Alps (Flinch et al. 1996), the Lufilian foldbelt of Central Africa (Jackson et al. 2003), the Adelaidean foldbelt of southern Australia (Marshak and Flottmann 1996), the Kuqa foldbelt of Tarim Basin of NW China (Liang-Jie et al. 2004) and the Zagros Foldbelt of Iraq and Iran (Talbot and Alavi 1996).

The style of compressional deformation is dependent largely on the friction coefficient acting along the detachment level(s). The lower the basal friction level, the further the thrusts propagate out and so the wider the thrust belt, the thinner the cross section of deformation and the lower the critical taper angle (Fig. 6.71: Davis and Engelder 1985, 1987; De Celles and Mitra 1995). The critical taper angle in the thrust wedge (φ_c) is defined as the sum of the surface slope angle (α_n) and the detachment slope angle (β). The observed critical taper of a given fold thrust belt depends on the material strength of the thrust wedge, the resistance to sliding across the basal detachment, and the ratio of fluid pressure to overburden pressure, both in the wedge and across the detachment (van der Pluijm and Marshak 2004).

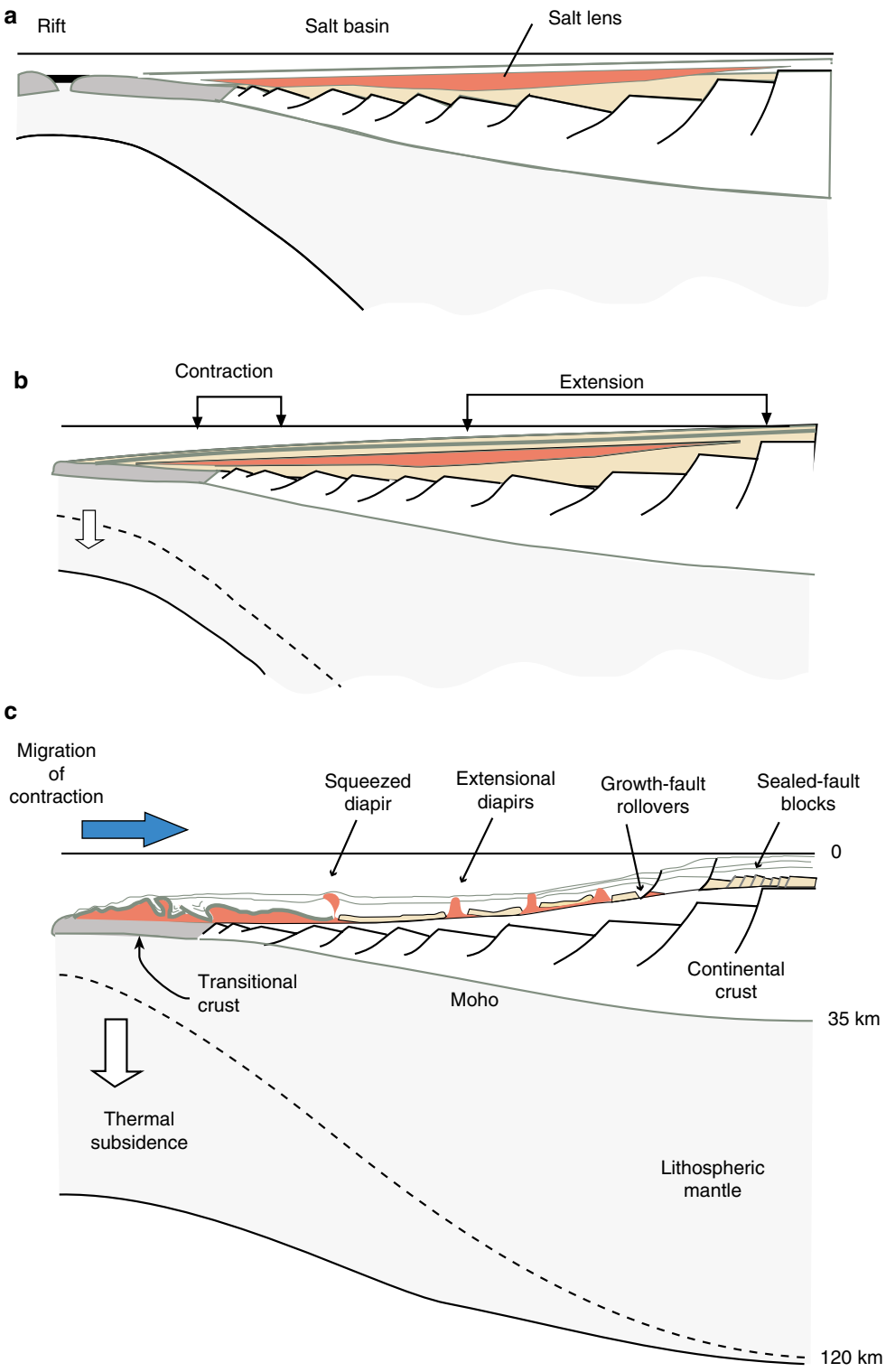

Fig. 6.70 Evolutionary model of gravity spreading above salt in a passive-margin tectonic setting, at lithospheric scale based on the offshore region of Angola, central Africa. (**a**) Initial stage following continental breakup. The salt basin is entirely covered by sediments that overlie oceanic crust. (**b**) Synchronous initiation of contraction downslope and extension upslope. The compressional domain initiates at some distance from the salt wedge toe. (**c**) Major displacement of extensional and compression domains during spreading. Compression migrates both downslope and upslope. Downslope migration reaches the salt toe. Upslope migration reaches the downslope part of the extensional domain, thus inducing diapir squeezing. Slope increases during spreading as a consequence of lithospheric cooling and subsequent subsidence (Fort et al. 2004)

If the effective strength of the wedge is increased (either by increasing rock strength or by decreasing fluid pressure), then the critical taper angle decreases. If the resistance to sliding on the basal detachment is increased (either by increasing the coefficient of sliding friction or by decreasing the fluid pressure), then the critical-taper angle increases. Fold-thrust belts basal detachments in salt are very weak and have a critical taper angle as low as 1–2°, whereas fold-thrust belts that have detachments in stronger rocks may have critical taper angles as high as 8–10° (Fig. 6.72).

Interestingly, regions of shale tectonics in offshore Brunei and offshore Barbados lie on this salty boundary, although

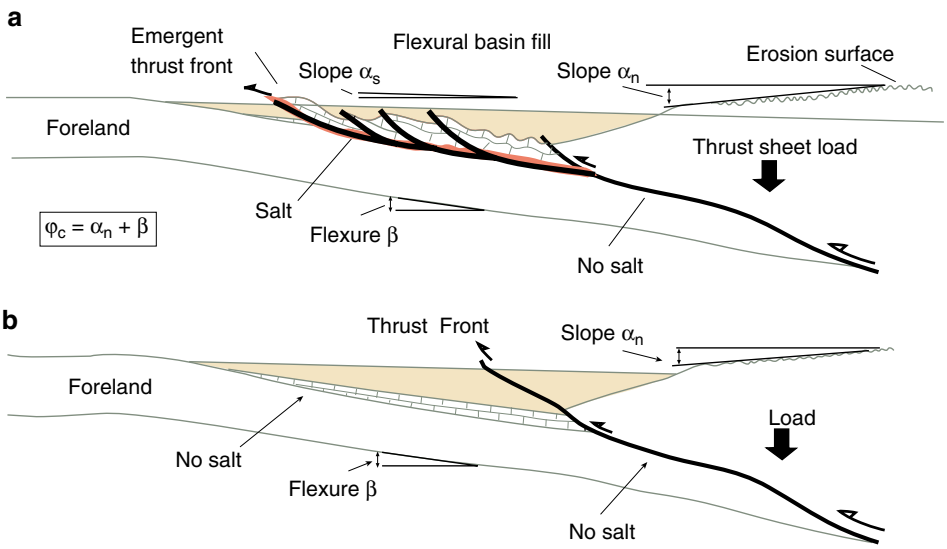

Fig. 6.71 Characteristics of thrust propagation and critical taper angle in a salt cored and nonsalt cored thrust (**a**) Salt lubricates thrust sheets. (**b**) No salt to lubricate thrust sheet. Salt cored thrusts are wider, show more extensive thrust propagation, thinner thrust cross section and critical taper angles ϕ_c <2°; while those deforming over other rock layers are narrower, with critical taper angles φ_c nearing 8–10° (After Davis and Engelder 1985, 1987; van der Pluijm and Marshak 2004)

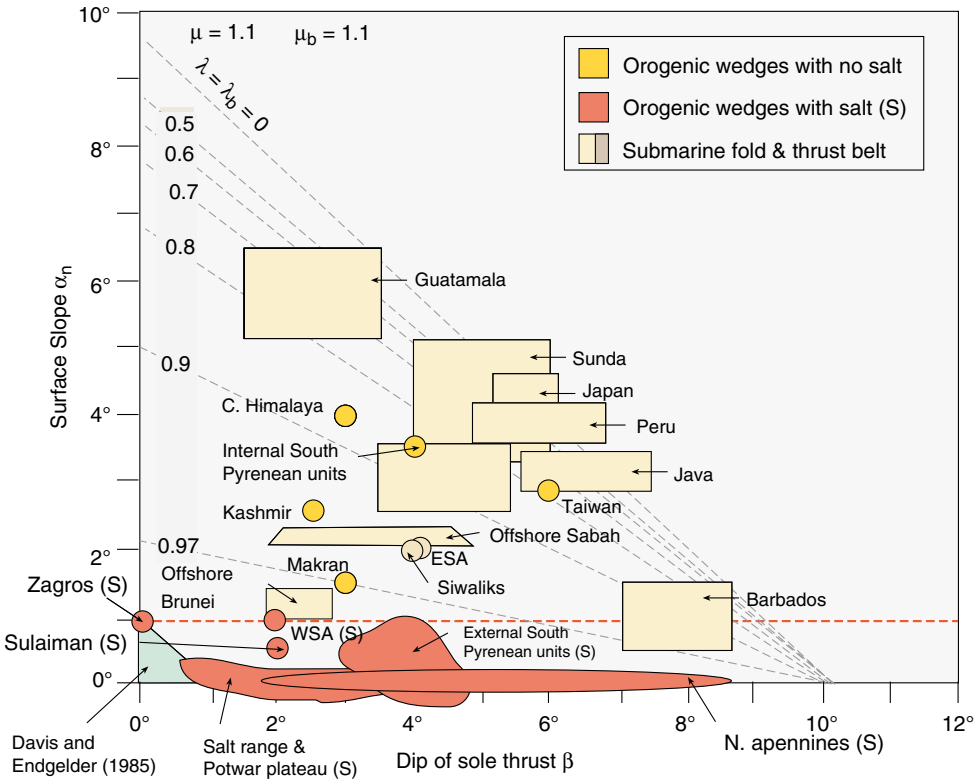

Fig. 6.72 Pressure and wedge character showing the relationship between surface slope (α), basal detachment dip (β), and pore-fluid ratio for orogenic wedges and submarine fold and thrust belts at critical taper, assuming a Coulomb material behavior (After Ford 2004; Morley 2007a, b; Warren et al. 2011). Orogenic belts with salt entrained in the décollement are indicated by (S). *μ* postulated coefficient of internal friction for the wedge, *μb* coefficient of internal friction at the base of the wedge, *λb* ratio of pore-fluid pressure to lithostatic pressure at the base of the wedge, *ESA* east Swiss Alps, *WSA* west Swiss Alps. The *green triangle plots* the region of the low basal friction wedge of Davis and Engelder (1985). As shown by Ford (2004), the region of low basal friction created by a salt décollement extends beyond the region indicated by Davis and Engelder (1985) and is indicated by the interval below the *dashed red line* (surface slopes <1°)

neither sediment wedge entrains salt. This is an indication of a muddy and highly pressured character in both prisms. Morley (2007b) argued that the very low surface slopes (1–2.5°) and basal detachment dips (2–5°) in the Brunei offshore wedge require basal pore-fluid pressures that must be near lithostatic for the wedge to propagate at such angles. That is, shale pressures approaching lithostatic in the mud-dominant wedge that is the continental margin of offshore Brunei is capable of near-Newtonian fluid-like behaviour. It is responding to gravity in a fashion similar to that of continental margins underlain by deforming and gliding salt (Warren et al. 2011).

A salt décollement in a compressional thrust terrain also enhances the development of major backthrusts and greater outward migration of the deformation front (Luján et al. 2003; Velaj et al. 1999). Pre-existing faults and salt welds in a halokinetic prism on a passive margin can be a major zone of weakness in the development of subsequent compressional structures. Hence the very close association between pre-existing faults and the current elongated salt structures of the southern North Sea (Fig. 6.76).

A fundamental consequence of salt weakness in many salt-detached thrust foldbelts is an absence of a preferred

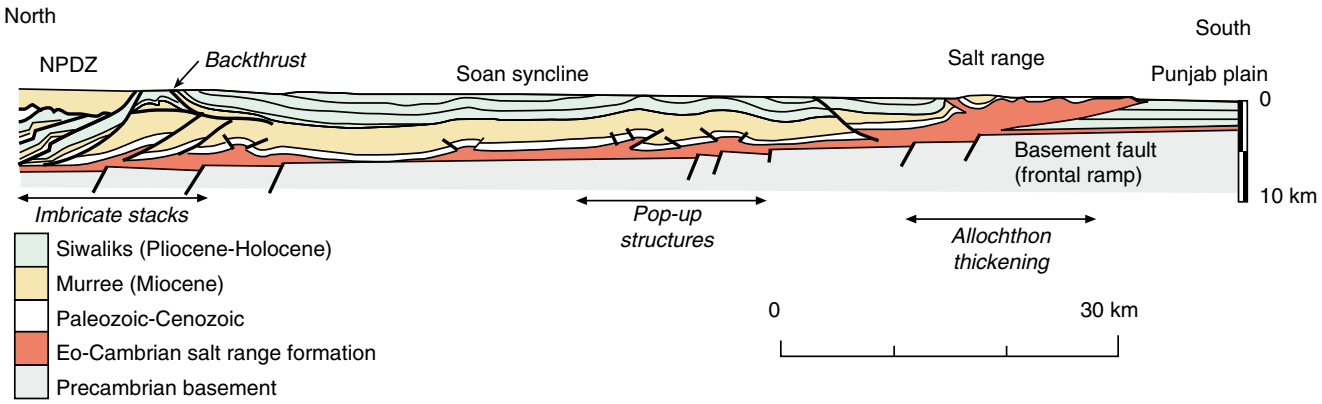

Fig. 6.73 North–south cross section in Pakistan across the Northern Potwar deformation zone (*NPDZ*), Soan syncline, and Salt Range (After Cotton and Koyi 2000). Three deformation zones can be seen: an imbricate stack (*NPDZ*) forming a wedge at the rear northern part; a zone of broad anticlines and synclines with pop-up and/or pop-down structures in the middle; and a zone of thickened allochthonous salt (Salt Range) in the south

direction of thrust transport (Davis and Engelder 1987; Harrison 1995; Bahroudi and Koyi 2003; Luján et al. 2003). The geometry of individual thrusts and anticlines reveals little or nothing about the location of the tectonic hinterland without some independent understanding of the regional geology. Angular folds (box folds, chevron folds and mitre folds) and backthrusts can predominate in a buckling thin-skinned salt-cored thrust belt, reflecting internal deformation of anisotropic multilayers above the thin, ductile salt substratum. If the deforming salt substratum is thicker, the multilayers tend to buckle as a single unit into large sinusoidal folds, with consequent loss of fold angularity. Mixtures of forethrusts and backthrusts are common even in individual salt-cored anticlines.

An active example of this style of thin-skinned thrust, lubricated by salt, is found in the Salt Range region of Pakistan (Fig. 6.73). The Salt Range and Potwar Plateau are the external and most recent expression of Himalayan shortening. This thin-skinned fold-and-thrust belt is detached upon thick Lower Cambrian evaporites of the Salt Range Formation. This basinwide evaporite unit underlies the Potwar Basin and is roughly equivalent in age to the Hormuz Formation in the Zagros Belt of the Arabian Gulf. The presence of thick salt facilitated rapid thrust propagation of the basal detachment before the main fault plane rose to form the Salt Range thrust above a basement frontal ramp at the southern termination of the basin.

A dextral wrench zone defines the western limit of the Salt Range and corresponds to the edge of the halokinetic Infracambrian evaporite (Cotton and Koyi 2000). There are three main zones of deformation across the Salt Range and Potwar Plateau: from north to south, these are the Northern Potwar deformation zone, the Soan syncline, and the Salt Range (Fig. 6.73). Deformation in the Northern Potwar deformation zone is characterized by the development of an imbricate duplex in the footwall of the Main Boundary thrust of the Himalayas. Deformation of the overlying Main Boundary thrust sequence constrains development of the Northern Potwar deformation zone to younger than 10 Ma. The northern limb of the Soan syncline marks the southernmost limit of uplift in the Northern Potwar deformation zone. The northern limb of the Soan syncline is steeply upturned, forming a monocline. A sequence of salt cored pop-up structures and broad anticlinal swells accommodated shortening formed to the south of the Soan syncline axis and have created a number of structural traps for hydrocarbons.[18] The contrast in deformation styles between the Northern Potwar deformation zone and the Soan syncline, seen in Fig. 6.73, is attributed to the lubricating effect of the Infracambrian evaporite sequence (Salt Range Formation).

The Salt Range today forms an approximate east–west hanging wall in a thrust that accommodates ~25–30 km of shortening (Baker et al. 1988; Aamir and Siddiqui 2006). The majority of deformation was accommodated within the hanging wall with some minor imbrication of the footwall. Deformation in the Salt Range area is considered to have occurred in two pulses, commencing ca. 5 Ma with a later pulse at 2 Ma. Lag time between pulses is attributed to breakback thrust development in the northern limb of the Soan syncline. The anomalous thickness of salt that has accumulated beneath the hanging wall of the Salt Range thrust is a result of differential loading by a prograding basin fill and

[18]The Potwar Basin is one of the world's oldest oil provinces. The first commercial discovery was made in 1914 at Khaur. Eastern Potwar region is an important oil- and gas-producing area. Discoveries in the eastern part of the Potwar Plateau, located southeast of the Soan syncline, are mostly from NE-SW elongated anticlines.

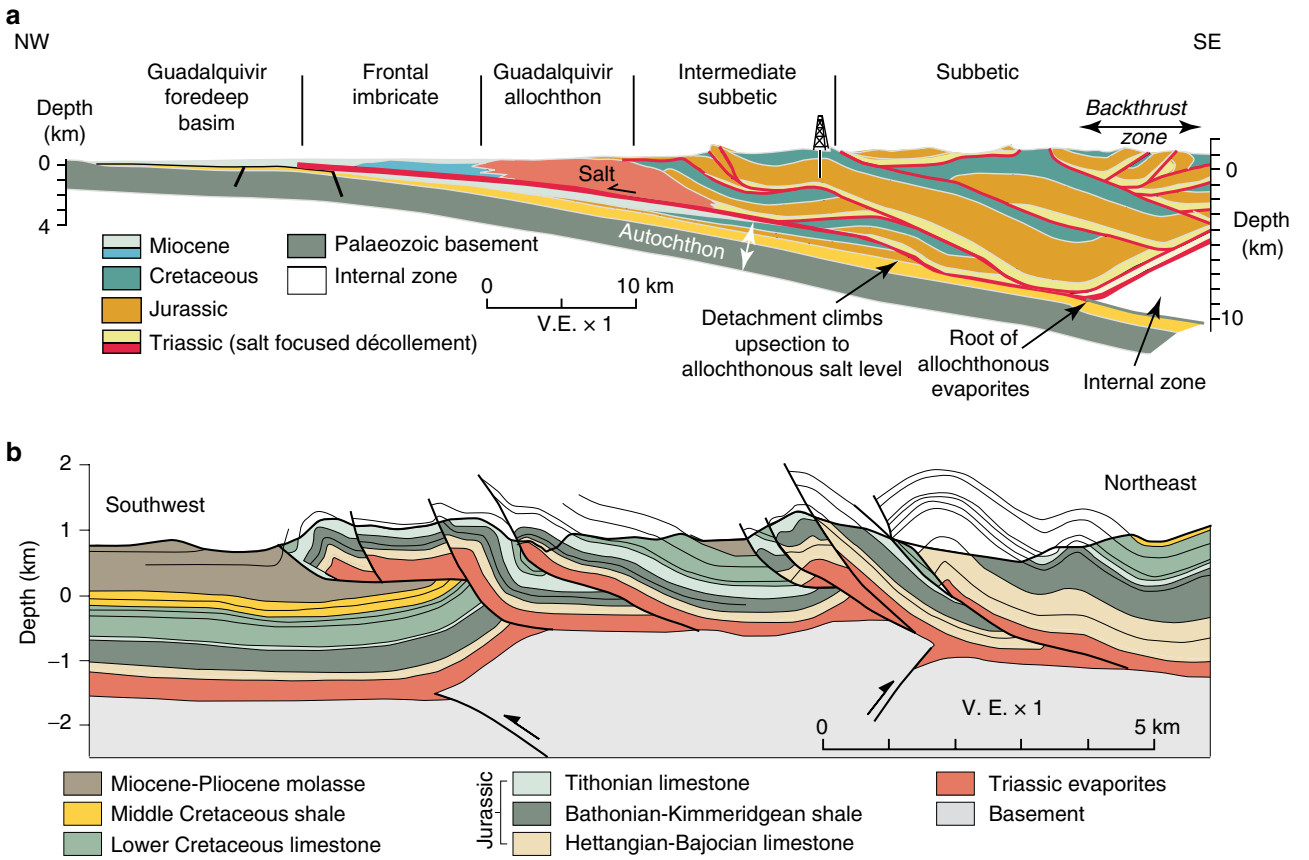

Fig. 6.74 Inversion focused by décollement in Keuper (Triassic) salt belts. (**a**) Exposed Keuper evaporites of the Guadalquivir allochthon at the leading edge of the Betic orogen southern Spain. Shortening expelled salt northwestward over lower to middle Miocene strata. The autochthonous Triassic evaporite basin sourcing the evaporite nappe is thought to be deep beneath the orogen, at least 30 km inboard of the exposed salt (After Berastegui et al. 1998). (**b**) Triassic salt sheets emplaced in thrust hanging walls by orogenic shortening, Digne, Barréme, Rhodanian Basins, southern Subalpine chains, southeast France (After Lickorish and Ford 1998)

deformation front moving south from the growing Himalayas. This combination of sedimentary and tectonic loading caused a southward migration of the Salt Range Formation (like squeezing toothpaste) to where the Neoproterozoic to Eocene sediments in the Salt Range are thrust over the Quaternary sediments of the Punjab Plain (Baker et al. 1988). Thickening has been assisted in the central Salt Range by the buttressing effect of a major basement fault in front of the southward-migrating salt (Fig. 6.73).

Another well-documented example with more than 200 km of salt-lubricated translation characterises the Triassic section of the external domain of the Betic Cordillera, near Gibraltar in the Mediterranean, where the thrust block is rootless and allochthonous (Fig. 6.74a; Berastegui et al. 1998; Luján et al. 2003). The frontal accretionary wedge of the Guadalquivir allochthon consists of Triassic evaporites and red beds that in outcrop form a gypsum-cemented melange/residual mixed with Upper Cretaceous-Palaeogene deepwater sedimentary rocks. Throughout the unit, Jurassic rocks are absent. The widespread Triassic evaporites of the Guadalquivir allochthon were originally emplaced as gravitational allochthonous masses or salt sheets at the foot of the Betic continental slope. This occurred originally in a passive-margin gravity glide setting, much like the present day emplacement of allochthonous sheets of Jurassic Louann Salt atop Neogene sediments in the Texas-Louisiana Gulf Coast or Aptian salt in the Santos Basin of Brazil. Later, during Neogene formation of the Gibraltar Arc, the Spanish evaporites were overthrust as an accretionary wedge to form the Guadalquivir allochthon. This explains the lack of Jurassic sediments within the melange of Guadalquivir allochthon. Triassic halokinetically pierced strata were thrust back up onto the former passive Betic margin, a lateral distance of some 200 km, from an area that lacked Jurassic deposits. Thus the Guadalquivir allochthon ended up atop sediment that was originally located well landward of the Guadalquivir prism (Fig. 6.74a).

The Tertiary foreland basin of the southern Subalpine chains preserves a stratigraphic record of late Alpine salt-associated deformation, both ahead of the thrust front in the Valensole basin, and in a series of thrust-sheet-top basin remnants. Stratigraphy and growth structures in these basin

remnants are used by Lickorish and Ford (1998) to identify the location and timing of deformation and hence to constrain the sequential restoration of a cross section through the region. They conclude the thrust belt developed as a single large thrust sheet riding on a weak Triassic evaporite layer (Fig. 6.74b). Minor breaching thrusts occur, in particular at inverted Mesozoic normal faults. The Digne thrust sheet show a dominantly SW direction of tectonic transport. Where some of the reactivated structures lie at a slightly oblique angle to the southwest transport direction there has been a partitioning of deformation into SW-directed thrusting and a component of dextral strike-slip taken up on minor faults. The total shortening across the fold and thrust belt is 21.5 km.

Deformation within the Digne sheet occurred in three stages. Firstly, during the late Eocene, Alpine collision in the hinterland caused flexure of the foreland plate to generate a simple broad marine foredeep. Slight detachment above the Triassic evaporites allowed gentle buckling of the floor of the foredeep. Secondly, in the Early to Mid-Oligocene overthrust shear associated with the SW emplacement of the internally derived Embrunais-Ubaye nappes into the foredeep caused substantial deformation in the underlying Digne sheet. A component of flattening strain was associated with overthrust shear beneath the nappes, but ahead of the nappe front gentle, upright folding and thrusting continued. Sedimentation stepped westward, became dominated by continental facies and confined to small thrust sheet top basins (e.g. Barréme). The Mio-Pliocene stage of deformation involved a change from thin-skinned to a thick-skinned out-of-sequence deformation when basement blocks were uplifted on deepseated structures across the region (e.g. Dôme de Chateauredon). Shortening associated with the uplift of the main Argentera basement massif at the internal boundary of the external fold and thrust belt was transferred onto the Triassic detachment from below, and transferred forward to reactivate the frontal edge of the Digne sheet, which was thrust out over the Valensole basin. A similar across-salt transfer from shallower thin-skinned thrusts to thick-skinned compressional thrusting below the Triassic salt (Ionian thrust) is seen in the offshore region between the mainland of western Greece and Zakynthos Island (Kokkalas et al. 2013)

Some of the Tertiary thrusting in the Digne region may have overprinted an earlier episode of Triassic salt flowing on the Jurassic seafloor. Graham et al. (2012) identified a completely overturned, highly condensed Jurassic section near Barles village that resembles the elevated roof of a Triassic salt body in a deep-marine basin. They argue this carapace became overturned as a flap in the Middle Jurassic when salt broke out at the seafloor and overran the inverted flap as an allochthonous extrusion, comparable to those seen in the deepwater Gulf of Mexico or Angola. Later, Alpine compression exploited the weakness of the salt sheet as the Digne Thrust moved over the inverted flap (Fig. 6.74b). Although the flap is in the footwall of the thrust, evidence of soft-sediment deformation and other anomalous structures within the flap suggest that it did not originate as an overturned footwall syncline.

Inverted Salt Basins

Varying degrees of inversion are common in many intracratonic basins, which tend to evolve into a compressional regime some time after subsidence of the initial extensional rift/sag has ceased (Figs. 6.62c). Salt-floored inverted basins typically pass laterally into a thin-skinned thrusted terrain. By the time inversion occurs much of the sediment atop the primary salt interval is indurated and the basin is laterally confined. Examples of salt-entraining inverted basins include (Fig. 6.63); the relatively mild effects of Tertiary shortening of Palaeozoic and Mesozoic sediments in the southern and central North Sea Basins (Hooper et al. 1995; Stewart and Coward 1995; Eggink et al. 1996; De Jager 2003; Rossland et al. 2013), through to more extreme basin overprints as seen in the Cretaceous shortening of Triassic basins in the Atlas foldbelt of north Africa and the offshore Spain (Vially et al. 1994; Zouaghi et al. 2005; Matias et al. 2011), the Palaeozoic shortening of Neoproterozoic basins in the Flinders Ranges and the Amadeus Basin in central Australia (Stewart et al. 1991), and the Eocene-Miocene shortening of Palaeozoic and Mesozoic basins in the Zagros of central Iran (Jackson et al. 1990; Callot et al. 2012).

Under a regional shortening event that is orthogonal or oblique to pre-existing structures, the inversion typically squeezes hanging wall blocks upward, as the original extensional normal faults become compressional (Fig. 6.75). Basement, salt and overlying sediments are all shortened with pre-existing salt structures (pillows, diapirs and walls) frequently taking up much of the initial compression.

Where the horizontal compressive stresses are near orthogonal to pre-existing extensional structures and where these are bound by high angle normal faults, much of the inversion above the salt layer is accommodated by forced folding rather than slip along the former faults (Letouzey et al. 1990). New low-angle reverse faults are firmly rooted in the décollement salt and typically originate at the crest of the upthrown basement block, and so passively transport the former high-angle normal fault planes (Fig. 6.75). This initiates short-cut[19] thrust geometries. If the horizontal

[19]Footwall shortcut thrusts: A low angle thrust fault developed in the footwall of a steep thrust fault. The resultant lower angle fault trajectory is kinematically and mechanically more feasible for large displacement than the high angle fault trajectory (McClay 1992)

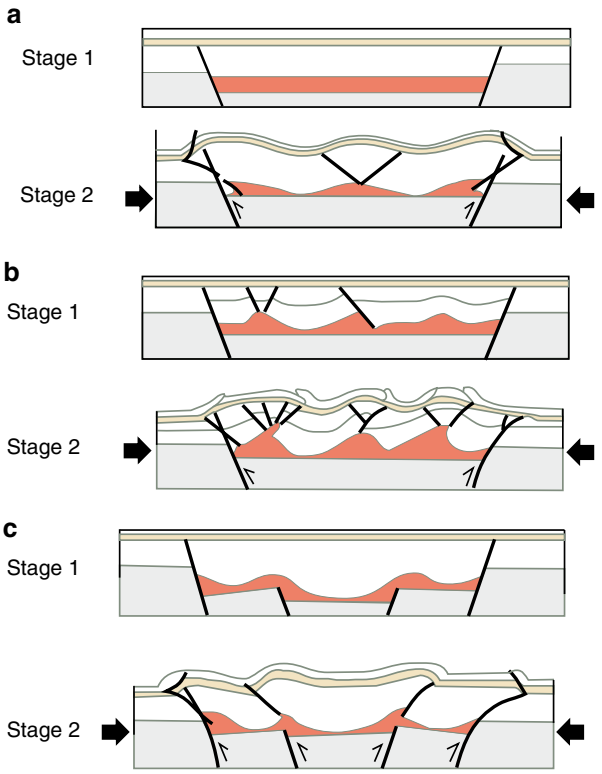

Fig. 6.75 Structural evolution of an inverted basement graben varies according to structures present in pre-existing graben (salt is *red*). (**a**) Folds and short-cut faults develop in homogeneous strata above inverted basement faults. Fold hinges in the graben are perpendicular to the regional compression. (**b**) Thrusts and folds are localised by pre-existing salt structures. (**c**) Thrusts and folds are localised by reactivation of basement faults (After Letouzey et al. 1995)

compression is oblique to the former normal fault, a strike-slip component is induced that can reactivate former high angle normal faults. In addition to conventional inversion features, such as forced folds (i.e. fault propagation folds over inverted basement blocks) and short cut faults over basement faults, strike slip will also form *en echelon* synthetic faults in the hanging walls of preexisting basement faults (Letouzey et al. 1995). Such *en echelon* systems define the basin edge of the Sahara flexure in Algeria (Vially et al. 1994).

Lateral pressures on a fluid salt décollement horizon undergoing compression promotes decoupling of the overburden and so create the following associations:

- Folding is more common than thrusting,
- Folds and thrusts lack consistent vergences, being commonly expressed as box folds and backthrusts;
- The cross sectional taper is typically low angle, which results in extremely broad fold and thrust belts;
- Complex three-dimensional edge effects form at the lateral boundary of the salt substratum.

Mild Shortening in Tectonically Confined Basins

Salt flow occurs within basins confined on either edge and subject to varying degrees of compression. Pre-existing basement structure is an obvious broad scale control on the development and location of the various salt features in these basins while formerly extensional diapirs experience compressional shortening. Salt walls and ridges of Permian salt in the southern North Sea Basin are type examples of extension followed by basin shortening and inversion. Many ridges tend to follow well-defined trends that parallel reactivated basement faults (Fig. 6.75c and 6.76: Remmelts 1995; Stewart et al. 1997; de Jager 2003). In other words, the present suprasalt patterns in much of the southern North Sea Basin are not decoupled from subsalt structure, unlike the current gravity glide systems of the Gulf of Mexico. Zechstein salt structures in NW Europe and the southern North Sea tend to first develop as extensional features atop the high of the upthrown basement block and are slightly offset but parallel to the controlling basement fault. At the same time salt was rising into these features, into-the-basin flow of salt was also creating downslope compressional buckles. Both these features typically first formed in the early Mesozoic, many millions of years after the Zechstein salt deposition had ceased (Mohr et al. 2004). Many such extensional diapirs were then further altered during subsequent late Mesozoic compression and inversion.

There are three salt domains (defined by parallel salt ridges) in the southern North Sea (Fig. 6.76; Remmelts 1995). The first, in the north, are elongate salt structures oriented north to northeast in a province that runs from the Central North Sea Graben to northern Germany. The second encompasses the region from English waters to onshore Netherlands where the salt structures are elongated northwest and made up of both pillows and walls. The third encompasses onshore southern Germany where an eastward trend is more obvious and encompasses both pillows and low salt walls. Small structures, with no preferred orientations, separate the three domains. The domains defined by the various salt ridges correspond to the structural grain in the basement.

Triassic extensional faults that strike north to north-northeast in the northern part of the basin form the boundary of the Central North Sea Graben, the Horn Graben and the Glückstadt Graben, while in onshore Germany this same orientation defines the Ems Low and the Weser Depression. Further south, extension was accommodated by transtensional slip in a northwest direction. Not only are the orientation of salt ridges and fault trends related across the domains, but so is the timing of salt movement and faulting. Salt piercement and basement fault movement is dominantly Triassic in the northern part of North Germany, while in the

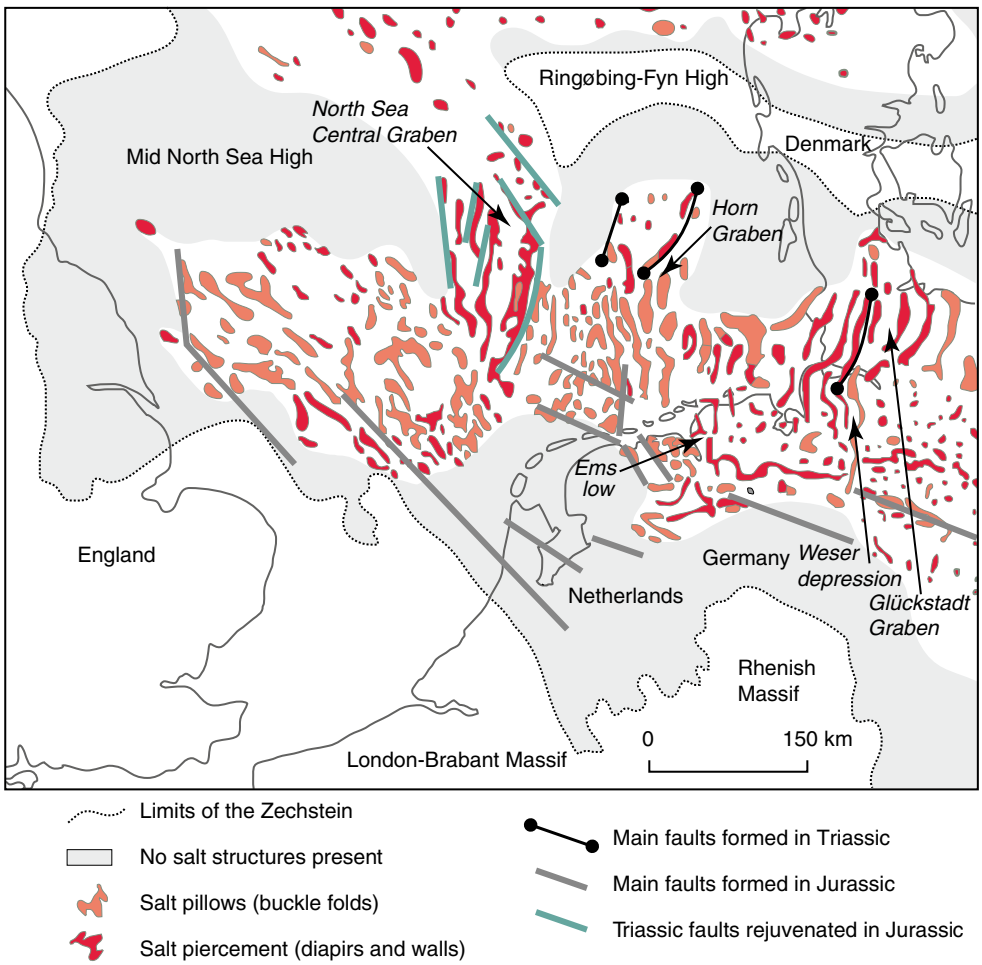

Fig. 6.76 Salt structures in the southern North Sea showing that salt flow tends to be restricted to the basin centre. The various structures show a regularity of ridge spacing and there is an association with the major fault directions in the basin (After Remmelts 1995)

south a Jurassic age prevails. Piercement is mostly Late Jurassic in the Central North Sea Graben, as is the main tectonic phase. Many Zechstein diapirs in onshore and offshore NW Europe were initiated along extensional faults that defined half-graben edges in Triassic to Jurassic times (Fig. 6.77a). The lack of primary rim synclines indicates that many of the structures became diapiric without going through a pillow phase immediately atop the primary Zechstein salt layer (Fig. 6.78). In extension, diapirs grew mainly by asymmetric downbuilding with salt rise focused on the upthrown block adjacent to the fault, probably with sporadic periods of bathymetric relief created at diapir crests (Fig. 6.78). The associated hanging wall tilt drove gravity gliding of the post-salt section, with resultant low-angle extensional faulting upslope and salt-cored buckling downslope with structural trends following basement grain (Fig. 6.77b; Thomas and Coward 1996).

The extensional half-grabens were subsequently tightened or compressed by a phase of thin-skinned inversion, associated with back-steepening of the margin fault system and a resulting reactivation of the extensional detachment system. The effects of this inversion have been noted in many parts of the northern North Sea, clearly post Early Cretaceous and Tertiary history of the southern North Sea Basin is compressional, not extensional. This is expressed as changes in basin tilt and in reverse slip on individual faults so that parts of the North Sea basin now tilt to the northeast, a reversal of the original Jurassic tilt direction in the UK section of the southern North Sea Basin (Fig. 6.79; Stewart and Coward 1995). This is especially obvious in thrust faults and structures that fringe the Broad Forties basin (Hayward and Graham 1989) but is seen across the North Sea Graben (Thomas and Coward 1996) and much of the southern North Sea Basin (Remmelts 1995; Stewart et al. 1997). Within the South Viking Graben, shortening estimates vary between 14 and 18 % and are expressed on seismic data by localized hanging wall folds and the back-steepening of faults along the fault complex of the western margin of the graben, together with out-of-graben thrusting up the hanging wall dip-slope.

In order to fully explain the elongate salt walls and pillows of the southern North Sea Basin the effects of both extension and inversion must be considered in the final analysis of the salt structure geometry. Recognition of significant

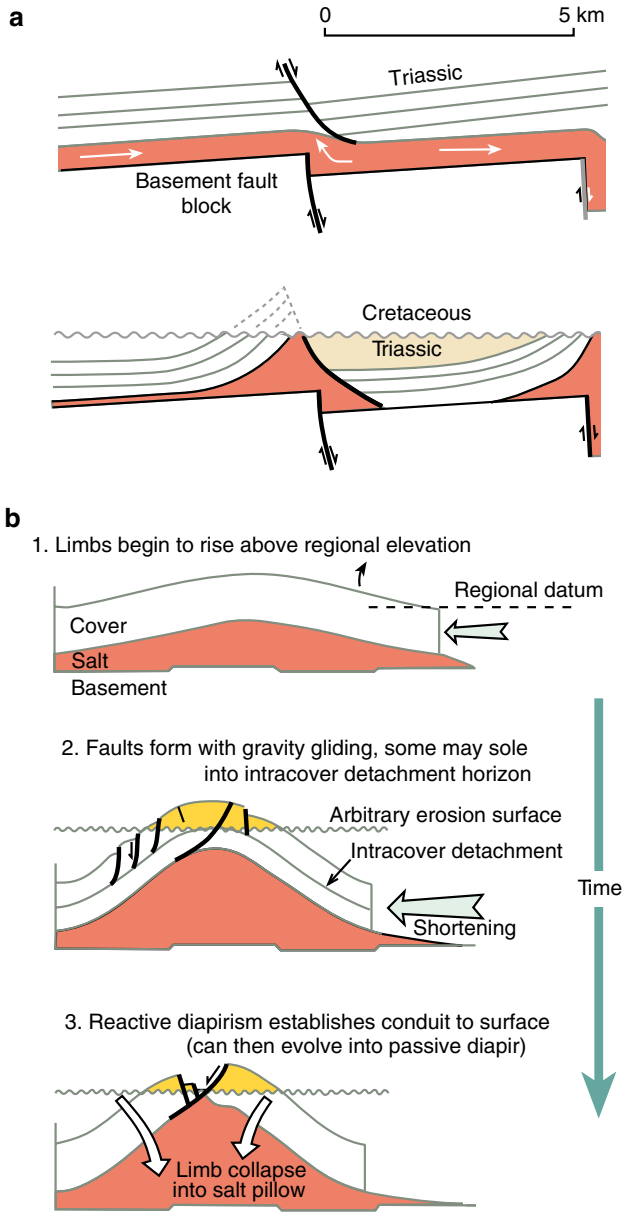

Fig. 6.77 Extension and conversion structures, North Sea. (**a**) Evolution of the Step Graben in the North Sea. Triassic extension focused the formation of salt structures atop normal faults in Sub-Zechstein basement. Early block faulting and accompanying rotation causes bedding plane parallel salt flow and pillowing atop the fault plane. This is followed by compression (shortening and inversion), tied to the Cretaceous unconformity and deposition of overlying sealing shales. Shortening drove oversteepening and flow reactivation during the Cretaceous Tertiary inversion (After Remmelts 1995). (**b**) Buckle fold evolution with crestal erosion culminating in diapirism (After Coward and Stewart 1995). See also Fig. 6.79

inversion can change the interpretation of some elongate salt-cored anticlines from salt pillows/swells to compressional buckle folds and squeezing of earlier extensional structures (Fig. 6.79). Clearly, any precontractional salt tectonics strongly influences the location of subsequent thrusts and folds (Letouzey et al. 1995).

During contraction and inversion, folds and thrusts are initiated where thickness variations in the salt were already present in the overburden (Fig. 6.77a; Vendeville and Jackson 1992a, b; Nalpas and Brun 1993). Erosional thinning of the overburden over salt ridges or salt walls also localises thrusts and folds, even when they are not related to basement normal faults (Fig. 6.77b). Décollement atop the compressed salt also induces normal-fault offsets on the top of salt that then localise thrusting and facilitate subsequent reactive diapirism (Fig. 6.77b).

Distinguishing Downbuilt and Reactivated (Mildly Squeezed) Diapirs

The preceding discussion of salt terrains where compression follows extension is both a response to gravity gliding in a passive margin and also occurs when continents collide (a corollary of the Wilson Cycle). It explains why many extensional diapirs suffer later horizontal shortening (squeezed diapirs). Examples are found in all three compressional terrains, namely; (a) thin-skinned fold and thrust belts at the toe of gravity-spreading systems on divergent margins, as in the South Atlantic, (b) thin-skinned fold and thrust belts driven by plate convergence, as in the foreland foldbelt of the Zagros Mountains, and (c) inverted, thick-skinned extensional basins, such as the North Sea. Styles range from salt structures that merely acted as foci of mild compression induced folding and faulting to diapirs that underwent considerable rise of salt or reactivation (Fig. 6.80).

Shortening squeezes salt in the diapir stem and so contributes to a short-term increase in salt supply. But this increase is temporary and decreases sharply, once shortening closes and empties the feeding stem of the diapir (Fig. 6.80). During shortening diapirs act as stress concentration zones where new folds/thrusts may form and propagate (Koyi 1998). Thrusts can propagate from the salt pedestal and so cut the feeding stem of the diapir. These diapirs sag with time, implying that some of the inactive diapirs in the Zagros mountain belt may have their feeder stems cut-off during the Zagros orogeny.

In the mildly compressed autochthonous salt region of the southern North Sea, the importance of Tertiary compression after Mesozoic extension was largely ignored until the early 1990s. Many diapirs cutting through the Tertiary section of the Central Graben, North Sea and the onshore basins of Germany, are now known to be rejuvenated diapirs with later episodes of salt flow driven by compression (Davison et al. 2000a, b; Scheck et al. 2003; Mohr et al. 2007; Dooley et al. 2009). Similar sets of rejuvenated diapirs can be also found nearby in the southwestern Nordkapp Basin (Henriksen and Vorren 1996). In all these basins diapirs first formed in Triassic extension and were rejuvenated during Late Cretaceous to Middle Tertiary shortening. It was an event that helped form the many Danian chalk reservoirs of the North Sea basin region offshore from Norway and Denmark.

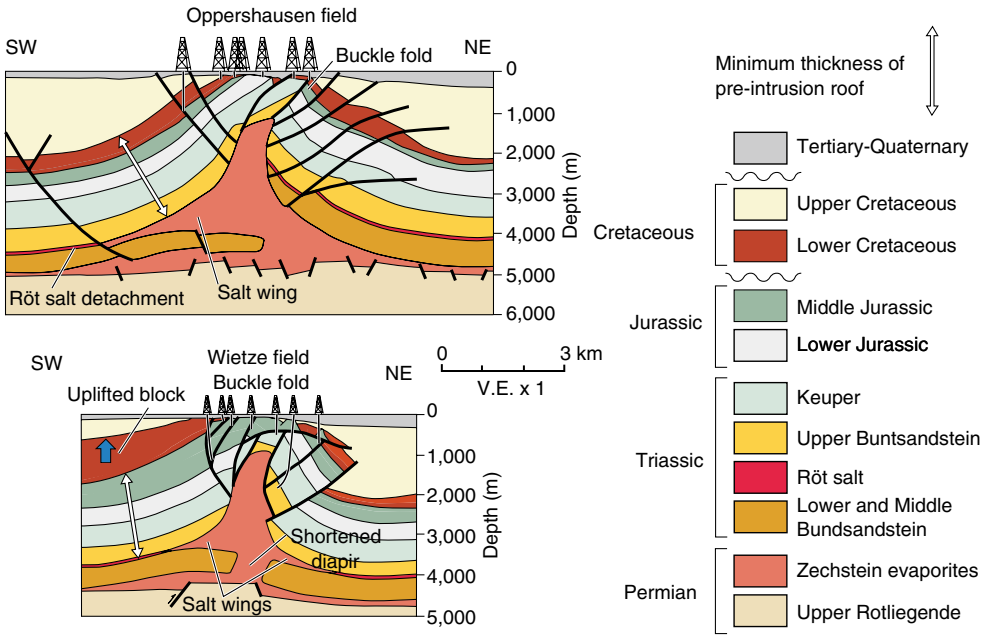

Fig. 6.78 Examples of compression-driven salt-wing intrusion from the Zechstein Basin, northwest Germany. Permian Zechstein salt wings were emplaced into the Triassic Röt salt layer during Late Cretaceous shortening. Shortening buckled strata above the Röt salt. Zechstein salt was emplaced passively into the cores of these detachment anticlines (After Baldschuhn et al. 2001)

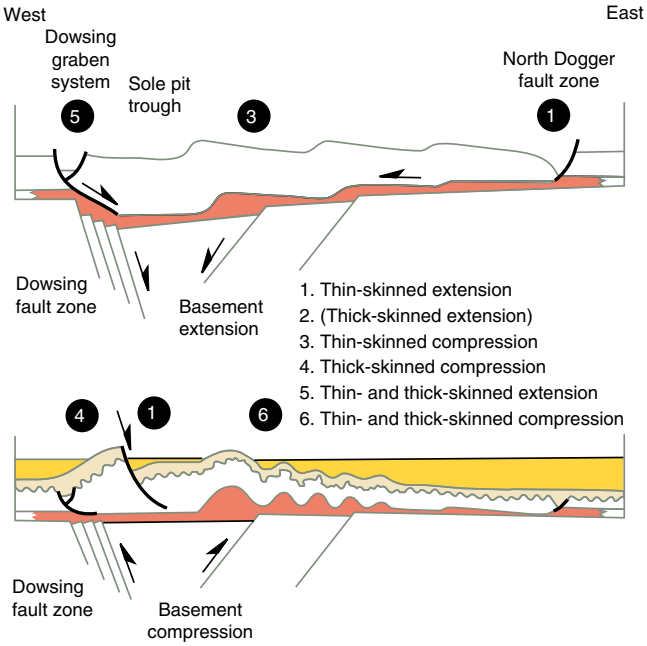

Fig. 6.79 Driving mechanisms for the evolution of suprasalt features atop the Zechstein salt in the western part of the southern North Sea Basin. All listed mechanisms, except thick-skinned extension, played a role. Salt structures evolved as the basin tectonics evolved from extension (*upper diagram*) to compression (*lower diagram*) and there is always an element of detachment tectonics, such as buckle folding, in the current distribution of the salt layer (After Coward and Stewart 1995)

Diapirs reactivated in compressional settings typically show common set of features (Table 6.3 and Fig. 6.81; Vendeville and Nilsen 1995; Davison et al. 2000b; Dooley et al. 2009); (1) Growth was episodic rather than continuous, allowing thick sets of strata to be deposited flat and horizontal as a thick roof atop the diapir crest during periods of diapiric quiescence, (2) Reactivated and compressed diapirs tend to have narrow or pinched-off stems, (3) Strata adjacent to the diapir are little deformed as most of the deformation is taken up in the diapir salt, (4) Many reactivated and squeezed diapirs show a triangular-shaped basal pedestal. A lack of primary rim synclines around these diapirs during times of tectonic quiescence indicates that the structures went diapiric without necessarily going through a pillow phase.

Most rejuvenated structures grew by localised downbuilding associated with crestal extension and near-crestal gravity sliding with sporadic periods of bathymetric relief at the active diapir crest. For example, salt-cored sea-bed relief controlled the deposition of Palaeocene and Eocene turbidite sandstones in the North Sea, which today thicken away from the compressionally re-activated diapir crests to form potential reservoir sands from 0 to 300 m thick (Fig. 6.100). The effects of compression on autochthonous salt structures in the North Sea tend to be most obvious in the vicinity of the diapirs and not in the interdiapir areas. Compression in the Central Graben of the North Sea was driven by downslope sliding of overburden above the Zechstein salt on the Eastern Platform area during late Palaeocene, and by regional Alpine shortening across the whole of the Central Graben during middle Miocene times. The various re-activated diapirs of the North Sea are much less deformed than those described in the Triassic-salt cored décollements of Spain and the French Maritime Alps (Fig. 6.78b; Roca et al. 1996; Dardeau and Graciansky 1990) or the Cegonha and similar compressional structures in offshore Angola (Fig. 6.70; Duval et al. 1992; Fort et al. 2004).

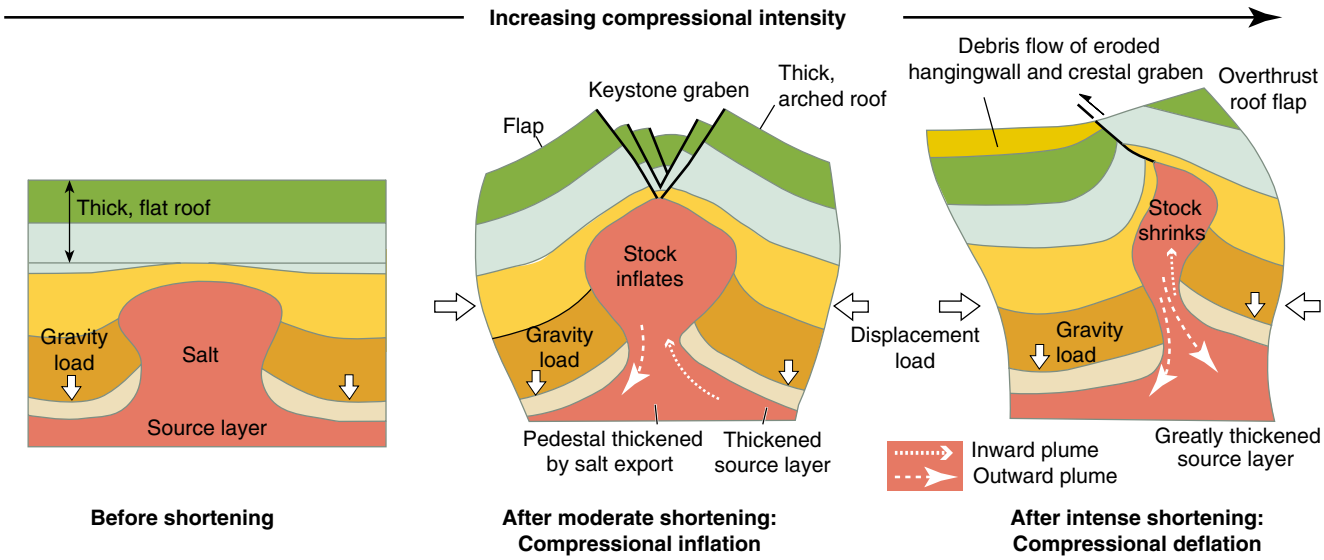

Fig. 6.80 Schematic showing gradual squeezing of a salt stock during regional shortening. After an early stage of salt inflation, diapiric salt is forced down into the source layer to thicken the pedestal, and the squeezed diapir shrinks (After Dooley et al. 2009)

Table 6.3 Criteria for separating downbuilt diapirs from diapirs which have been reactivated by regional compression

Criteria	Downbuilding	Rejuvenation driven by compression
Stratal thickness	Thick beds on the flanks thin over the salt, consistent with the syngrowth sedimentation patterns of Trusheim (1960) and Seni and Jackson (1983a, b).	Uniform bed thickness over crest when not tectonically thinned. Large thickness of overburden folded above crest. High angle onlap onto pre-inversion unconformity.
Lithological variation	Thick beds on the flanks thin over the salt, consistent with the syngrowth sedimentation patterns of Trusheim (1960) and Seni and Jackson (1983a, b).	Less concentric lithological variation produced when diapir inactive before inversion period.
Layer parallel shear	Normal sense of movement away from crest, caused by material sliding off crest.	Reverse sense of movement toward the crest.
Faulting	Small displacement normal faults on diapir shoulders, dipping away from the diapir. Crestal graben. Large listric growth faults along part of the salt contact.	Convex upward thrusts in the overburden on the shoulder of the diapir. Crestal horst as well as graben. Normal faults, strike-slip faults and thrust faults directly above the diapir e.g. Withjack and Scheiner (1982).
Drag zone geometry	Narrow and high relief.	Broad and lower relief.
Regional deformation	Regional extension faults.	Regional folds and thrusts and inverted extension structures in the cover.
Fold geometry of concordant overburden	Geometry moulds to the diapir.	Broad at top or, fold shapes unrelated to the underlying diapir shape.
Withdrawal basin	Primary and or secondary rim syncline sometimes present.	Absent when diapir is growing by compression. Diapir continues to grow even when source is severed by welding.

After Davison et al. (2000b), Vendeville and Nilsen (1995)

Specific features in the overburden atop a North Sea diapir, which may help in determining whether a diapir was rejuvenated by later compression after an earlier phase of extensional downbuilding, are illustrated in Fig. 6.81a (see also Letouzey et al. 1995; Vendeville and Nilsen 1995; Guglielmo et al. 2000; Dooley et al. 2009). Sediments atop rejuvenated North Sea diapirs exhibit some or all of the following characteristics: (a) localised unconformities with high angles of onlap above the unconformity; (b) thick lid of overburden strata (>300 m) updomed above the diapir; (c) reverse layer-parallel slip or concentric thrust faults localised at the diapir shoulders; (d) central horst block uplifted above diapir; (e) continued upward movement of the diapir even when pinched off from the source. The presence of layer-parallel reverse-slip and concentric reverse faults may not occur together. In experiments on active diapirs Schultz-Ela

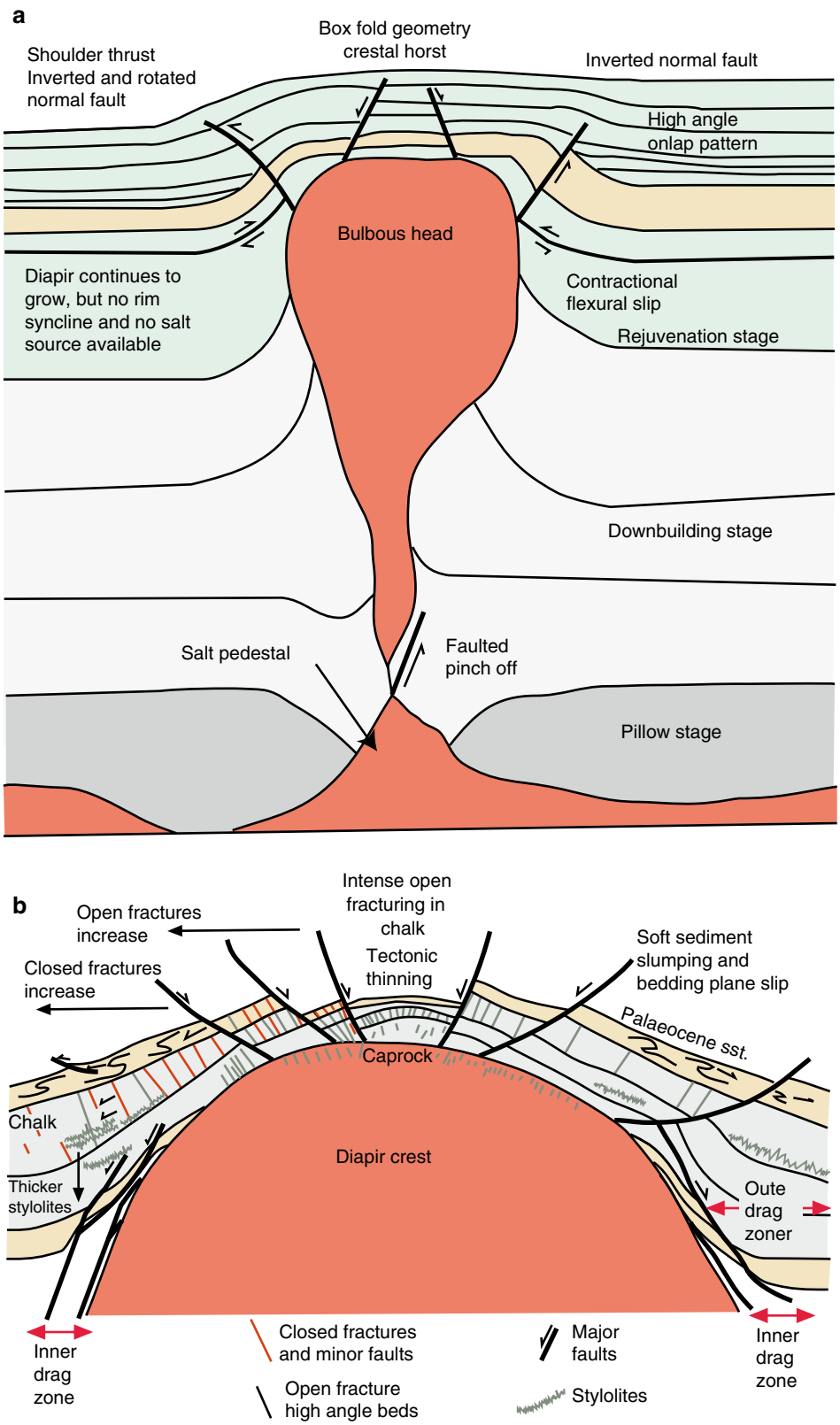

Fig. 6.81 Rejuvenated diapirs and suprasalt deformation. (**a**) Typical diapir crest showing deformation style in fractured chalks and Palaeocene sandstones (After Davison et al. 2000a). (**b**) Seismic scale geometry of diapirs affected by late compression with (a) compressional fold in overburden, (b) reverse layer-parallel slip, (c) wide drag zone, (d) thrust faults on shoulders, (e) lack of rim synclines (f) localised unconformities and high angle of onlap above unconformity restricted to immediate diapir vicinity, and (g) thick updomed strata above the diapir (After Davison et al. 2000b)

et al. (1993) showed that layer parallel slip occurs in overburden, which is anisotropic, and thrust faults at diapir shoulders occur in isotropic overburden. Crestal collapse grabens also occur above some rejuvenated diapirs, but crestal horst structures have only ever been produced in physical models of upbuilt diapirs (Davison et al. 1993). The

significance of the various fault patterns associated with the inversion of the diapir is discussed further in terms of hydrocarbon trapping in Chap. 10.

Suprasalt doming influenced the distribution of chalk and sandstone overburden in the North Sea via crestal thinning associated with intense extensional faulting, tensile fracturing, gravity sliding and pressure solution (Fig. 6.81b; Davison et al. 2000a). Salt buoyancy created topographic relief about the flanks of the thinned chalk layers, resulting in semi-indurated chalk sliding off the crests of the diapirs as shown by soft-sediment slump folding and bedding-parallel shear zones in the chalk in most producing offshore fields. For example, debris flows in the Kyle field carry clasts of caprock anhydrite indicating that the salt crest was exposed or was near the seafloor. Lithified angular clasts in the same debris flows indicate that chalk was already indurated and cemented at the time of extrusion, but nevertheless the diapir was able to actively break through and shed this lithified material. Topographic relief of several tens to hundreds of metres above the surrounding seafloor had developed atop reactivated diapir crests during the Late Cretaceous to Palaeocene period.

An associated flow of squeezed pore fluids through the chalk reservoirs in Banff, Machar, Kyle and North Pierce fields in the North Sea resulted in interconnected vuggy fractures filled with calcite. This calcite was probably derived from pressure solution, but much of the dissolved chalk atop the Machar diapir has since been removed from the system, with dissolution waters possibly escaping directly into the sea along major faults. A combination of all the rejuvenation effects produces what is an apparently intrusive single-event geometry. In reality, the overburden was tectonically thinned episodically and removed by gravity sliding, rather than actively pushed aside by rising salt in one event. Typical deformation patterns observed in chalks above a reactivated diapir are summarised in Fig. 6.81b.

Palaeocene sands overlie chalks in many diapiric fields in the Central Graben. Bedding-plane slip surfaces, with at least 10 m of displacement, are common in the Palaeocene siliciclastic rocks from South Pierce field in the North Sea (Fig. 6.81b; Davison et al. 2000a). Like the chalks, these overlying clastic sediments slid away from the diapir crest to accumulate on the diapir flanks as stacked and slumped deepwater sandstones. Sliding and shedding preferentially took place along mudstones, which preserve commonplace slump folds and polished faulted surfaces. Similar soft-sediment folds are not always present in the sandstones, which rode on the muddy slides and some coherent sandy blocks were translated large distances without any internal deformation. Thicknesses of the Tertiary sandstone packets increase from zero near the crest to 300 m on the flanks and indicate a combination off-crest channel stacking/ponding and crest-induced slumping. Davison et al. (2000a) argue that build-ups of tens of metres of supracrestal sediment were followed by up-doming of the salt diapir crest, which was accompanied by faulting and rotation of the strata until a critical angle was reached and then overburden slid off the diapir. Hence, as for their chalky precursors, these episodically active compressional diapirs were close to or at the seafloor during the Palaeocene to Eocene period, producing bathymetric highs that periodically shed their siliciclastic sediment cover (Fig. 6.100).

The notion that salt is susceptible to multiple episodes of deformation is not just seen in the North Sea. It also influences salt distribution in the Dniepr-Donets salt basins and large parts of the Zagros Belt. It is probably universal observation. Salt flow is driven by initial extension and then reactivated by later compression, which can be mild or intense. This set of compression driven structures may be subject further extension events. The various deformation events reactivating flow may be tens or even hundreds of millions of years apart. That is, salt structures in tectonically complex regions subject to ongoing externally applied stress will have responded by multiple episodes of deformation.

For example, the Ukrainian Dniepr-Donets Basin (DDB) is a Late Palaeozoic intracratonic rift basin, with sedimentary thicknesses up to 19 km, displaying the effects of salt tectonics during its entire history of formation, from Late Devonian rifting to the Tertiary (Stovba and Stephenson 2003). Hundreds of concordant and discordant salt structures formed during this time. Salt movement began during the Devonian synrift phase of basin development and exerted controls on the later distribution of salt structures although the geometry of basement faults is not solely responsible for the regular spacing of salt structures (Fig. 6.82). Postrift salt movements in the DDB occurred episodically. Episodes of salt movement were triggered by ongoing tectonic events, specifically two extensional events during the Carboniferous, an extensional reactivation at the end of Carboniferous-earliest Permian, and a compressional event at the end of the Cretaceous. Extensional events that induced salt movement were "thick-skinned," (i.e. basement involved in deformation) rather than "thin-skinned" (Fig. 6.82). Most overburden deformation related to salt movements was ductile regardless of sedimentary bulk lithology and degree of diagenesis, while the deformation of sedimentary cover in areas where salt is absent was mainly brittle. This implies that the presence of salt can change the predominant mode of deformation of overlying sedimentary rocks. Episodes of salt movement lasted longer than the periods of active tectonics that initiated them.

According to Stovba and Stephenson (2003), buoyancy, erosion, and differential loading all played a role in driving halokinesis once tectonic forces had pushed the salt-overburden system into disequilibrium; among these factors, erosion of overburden above growing salt structures acted as a key self-renewing force for development of salt diapirs.

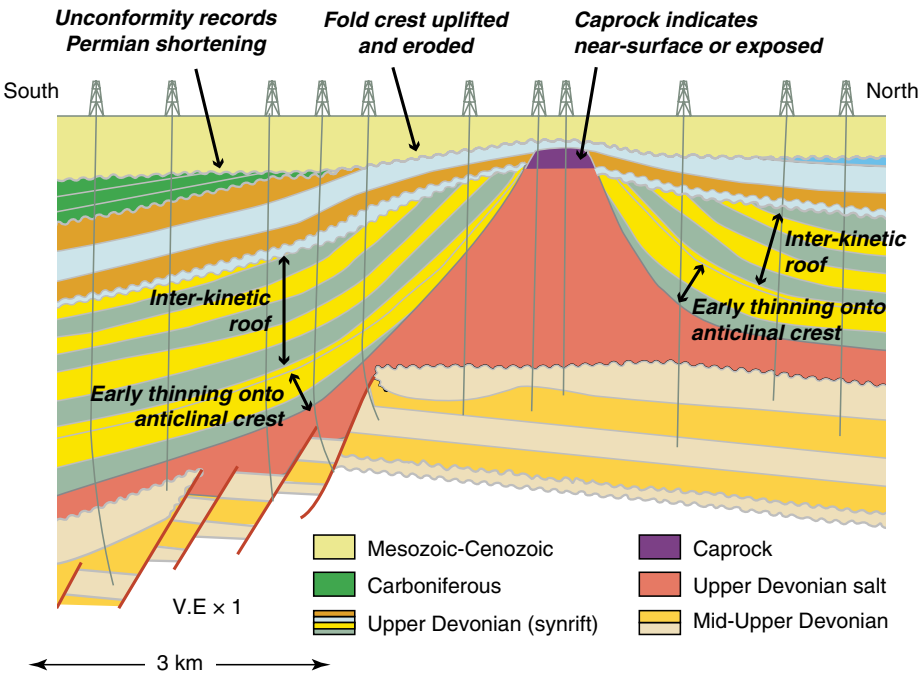

Fig. 6.82 Early thinning onto the crest of the structure suggests that the diapir originated as a low-relief salt anticline shortly after Late Devonian salt deposition. This anticline was then buried beneath a thick constant-thickness package (interkinematic section) before being reactivated and breaching its roof later in the Devonian. Signs that this reactivation was compressional are (a) the uplifted and eroded crest, (b) a thick interkinematic roof, and (c) a short-lived uplift. However, any shortening in the Late Devonian is counter to the consensus that the Late Devonian was a time of extension, volcanism, and basin formation (compare with section in the adjacent Dnieper-Donets Basin). This anticline suggests a previously unrecognized tectonic event in the Pripyat Trough. Alternatively the bedding geometries are inaccurate. A second episode of shortening in the Permian further amplified the structure and caused renewed crestal erosion (After Stovba and Stephenson 2003)

Very high sedimentation rates (related to high post-rift tectonic subsidence rates), particularly during the Carboniferous, were able to bury diapirs and to load salt bodies such that buoyancy, erosion, and differential loading forces eventually became insufficient to continue driving diapirism, until the system was perturbed by an ensuing tectonic event. In contrast, some salt anticlines and diapirs developed continuously during the entire Mesozoic because of much-reduced tectonic subsidence rates (and sedimentation supply) during this time. However, the Lower Permian salt series and overhangs of buried diapirs in the Dniepr-Donets played an important role in preventing overburden piercing (and fracturing) during the Mesozoic and, specifically, during the Late Cretaceous salt diapirism phase.

Before leaving the topic of basin inversion, it is instructive to return to the notion of how ambiguous some salt structures can be when trying to interpret their origin from shape alone (as needs be in most seismic interpretation). Figure 6.83 maps the distribution of some of the various salt valleys in the Canyonlands region of Utah. Did these salt structures, sourced in the Permian Paradox Formation, initiate and grow during contraction related to the Uncompahgre Uplift, or are they the result of subsequent Mesozoic sediment loading and extension? Elongated salt walls dominate, but more circular diapirs also occur. The salt walls seem to follow the NW–SE trend of long-lived basement faults (thick-skinned), while younger collapse-related faults occur in the overburden. Did these salt structures initiate and grow during contraction or extension? Simple questions are sometimes hard to answer. The valley system is further complicated by deep dissolution of the salt, which may obliterate the morphological evidence of contraction or extension (Chap. 7). Likewise, the Silver Pit structure in the North Sea is enigmatic and has been interpreted as both a squeezed diapir and as an impact crater (Underhill 2009) as has the Upheaval Dome in the Canyonlands of Utah (Jackson et al. 1998 vs Kriens et al. 1999).

Salt Extruding Today?

With enough time, halokinetic salt settings evolve from extensional to compressional and when tectonically active flowing salt can be near or at the landsurface in either setting. This can occur relatively early, a result of gravity gliding in the downdip portion of a passive continental margin, or it can occur later, the result of a transition from rift to drift to collision in continental margin sediments. Both are inherent transformations in continental edges that underline the Wilson Cycle (e.g., Zechstein diapirs of NW Europe). Halokinesis can be associated also with the set up of transpressional or transtensional zones along salt-floored strike-slip basins (portions of the Dead Sea transform, and parts of the Zagros collision belt).

Most examples of contemporary at-surface salt flow are in areas of active regional compression, in arid deserts, and especially in the Horse Latitudes of the Middle East. Regions where salt flows have been recently active are distributed more widely than the Middle East, but restricted to arid settings with limited liquid water, and so as well as deserts can include the frozen tundra of the Canadian Archipelago (Fig. 6.84a). Of the various examples, Iran is the premier region to study outcrops of active salt flows (Figs. 6.84b and

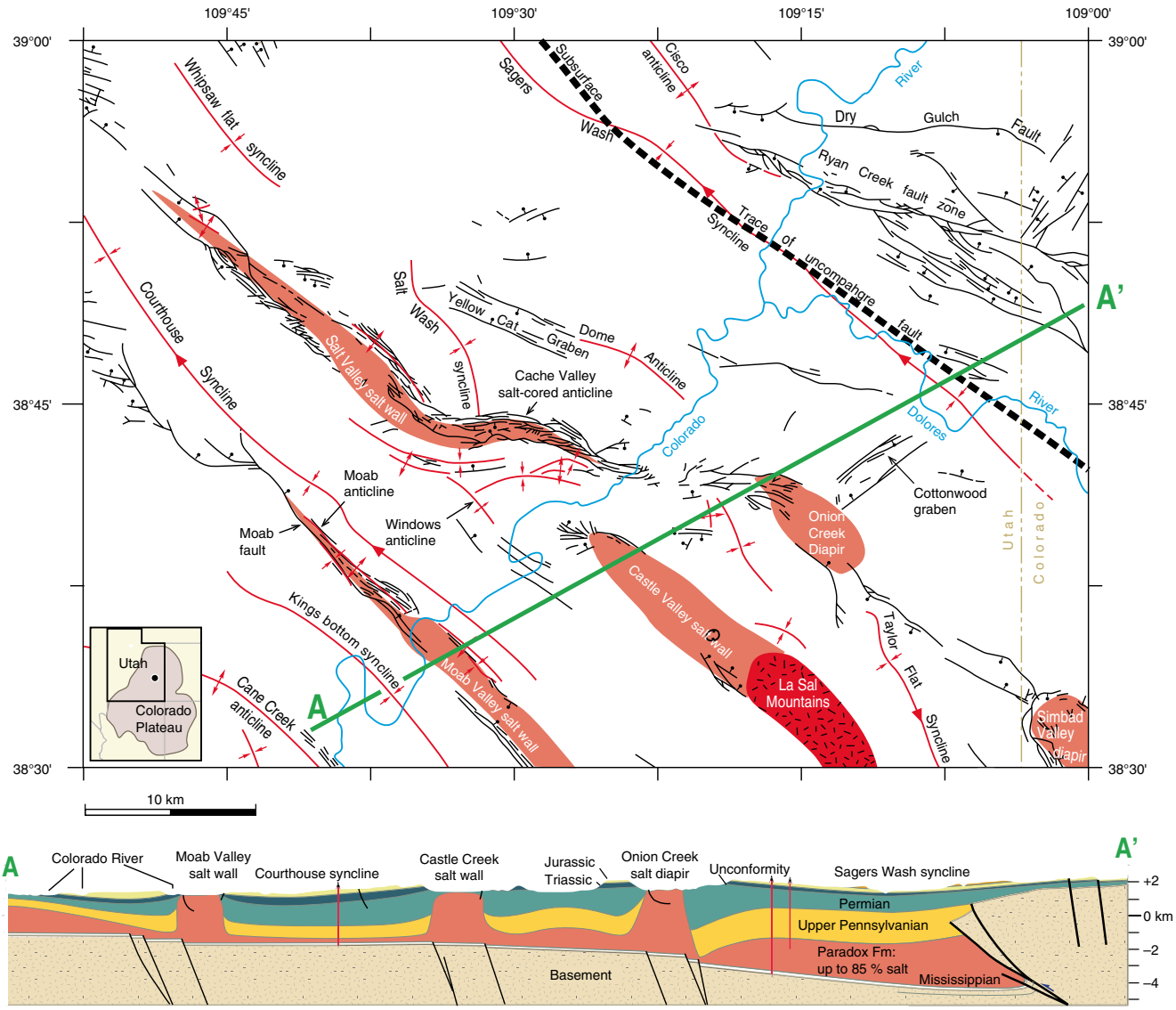

Fig. 6.83 Salt structures in the Moab area of southeast Utah in map view and cross-section. Elongated salt walls dominate, but more circular diapirs such as Onion Creek also occur. Figure based mainly on Doelling (2001) and Fossen (2010)

6.85). The common theme to all these examples is tectonic inversion and/or compression that is either active now, or was so in the recent past. Only in settings where the compression is ongoing, is salt flowing at the modern landsurface.

Free-flowing namakiers in Iran occur in two tectonic zones, the Alborz and the Zagros fold and thrust belts. The salt caught up in the tectonism of the Zagros is the Infracambrian/Cambrian Hormuz salt and its equivalents (Kent 1979), while that in the Alborz zone it is the salt of the Miocene Lower and Upper Red formations, first deposited in tectonically-induced collision basins and then caught up in the subsequent deformation (Morley et al. 2009). In both settings ongoing continent-continent compression drives lateral shortening, via buckling, which encourages thickening of salt in anticlinal cores. Some fold crests are erosionally thinned, others are cut by faults so that the anticline leaks salt to the surface along the fault intersection ("slicing the bladder"). With crestal erosion, this drives a loss of structural integrity allowing for buoyant (pressurised) salt emergence ("popping the pimple"), possibly aided by pinch-off from the mother salt layer. Similar buckled salt-cored anticlines, which are no longer active, constituted the source for ancient salt flows in the Nordkapp Basin in the southern Barents Sea (Dooley et al. 2009), the Dniepr-Donets Basin in Ukraine and in the Zechstein of NW Germany (Mohr et al. 2007). Once salt is extruded, the original salt-cored anticlinal source is subject to collapse and erosion, especially if the mother supply lessens or it is cut off by closure of the salt neck (Figs. 6.80).

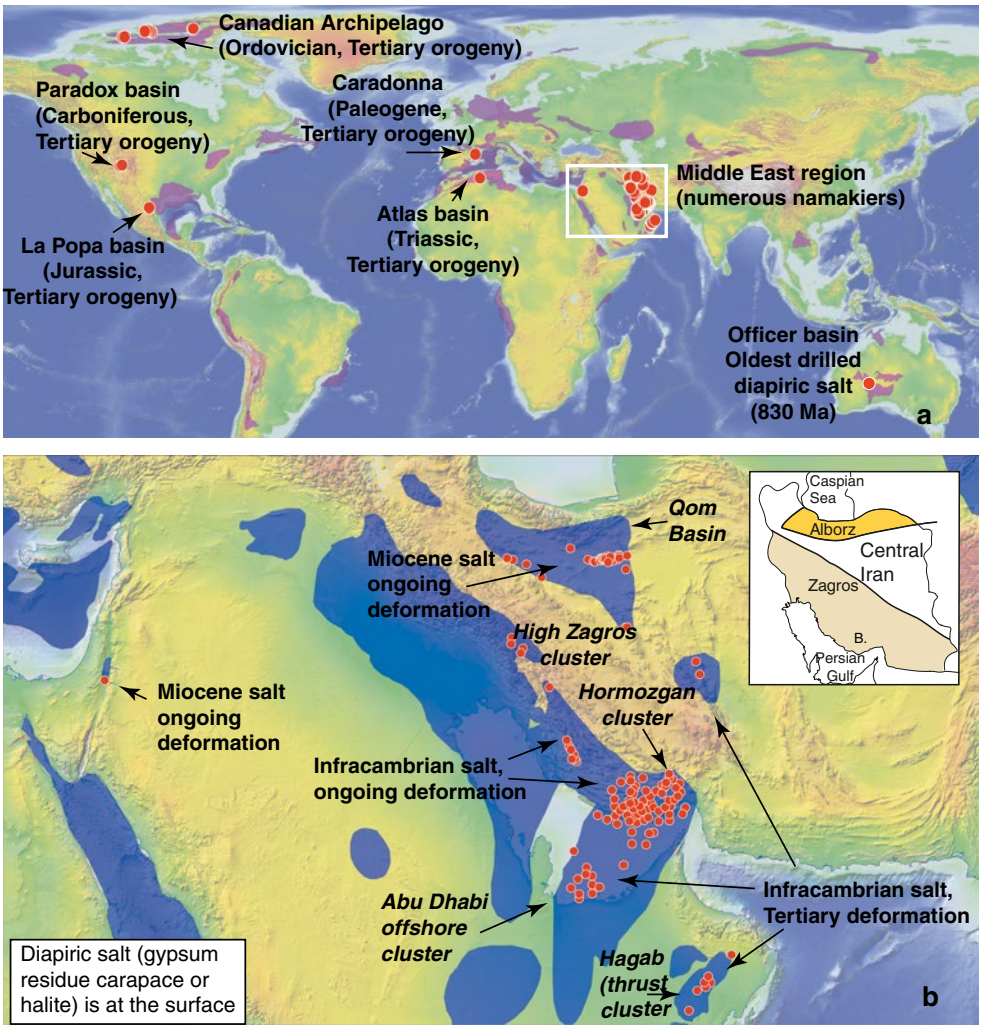

Fig. 6.84 Plot of selected documented examples where salt is at or very near the modern landsurface. Examples in Iran have salt flowing at the surface (namakiers). The remainder are recently active flows where salt is now in dissolutional retreat, marked by salt ablation breccias and brecciated dissolution carapaces typically with residual gypsum. (**a**) World; (**b**) Middle East. Plots also show the position of underlying halite basins with thick salt successions (Extracted with permission, from SaltWork database – Version 1.7)

As it has for interpreting triggers in salt under extension (Brun and Fort 2011), physical modelling of salt under compression creates a quandary as to whether buckling and thickening of salt in an anticline can build sufficient pressure to initiate active diapirism. This is especially so if the salt in the buckle-fold core is still connected to the mother salt layer. That is, physical models of a buckling compressional system using brittle overburden and a viscous salt-analogue silicone gel layer do not show breakout at the thickening anticlinal crests (Vendeville and Jackson 1992b; Letouzey et al. 1995; Koyi 1998). The silicone gel initially thickens in the rising anticlinal cores, then is squeezed out back down into the mother salt layer (the squeezed salt/gel takes the path of least resistance compared with breaking through the brittle overburden), or the gel is dragged along thrust planes. In all cases it does not emerge, but stays in normal stratigraphic contact with the overlying thrust sheet. Only when there is a preexisting diapir stem, or there is crestal erosion, or if the salt core is pinched off from the original mother salt level, is salt extruded and this episode is typically short lived ("popping the pimple").

And yet the scale of such flows can be impressive. In Iran, there are 300-m high glaciers of Miocene or Infracambrian salt flowing across today's landscape, both in the Qom Gamsar Basin region in the Alborz Tectonic zone and in the eastern foldbelt of the Zagros, respectively (Fig. 6.84b; Morley et al. 2009; Alsouki et al. 2011). The ubiquity of salt glaciers (namakiers) in both tectonic zones of Iran (Alborz and Zagros) clearly shows salt does breach salt-cored anticlines within regionally compressed and/or transtensional terrains. The question is; "When and how does it flow?"

The most impressive region for observing salt flowing at the surface is the Hormuzgan district, situated north and east of Bandar Abbas (Fig. 6.85a; Jahani et al. 2007) There, those Zagros folds with active namakiers tend to be located atop elongated symmetric whalebacks or box-shaped anticlines with crests generally aligned in a NW-SE direction and the main thrust detachment at the level of the Precambrian Hormuz salt (Alavi 2004).

The Zagros front is still advancing and every stage in the evolution of a namakier (from fountain to ruin) outcrops in this active mountain belt, which is still shortening at ca.

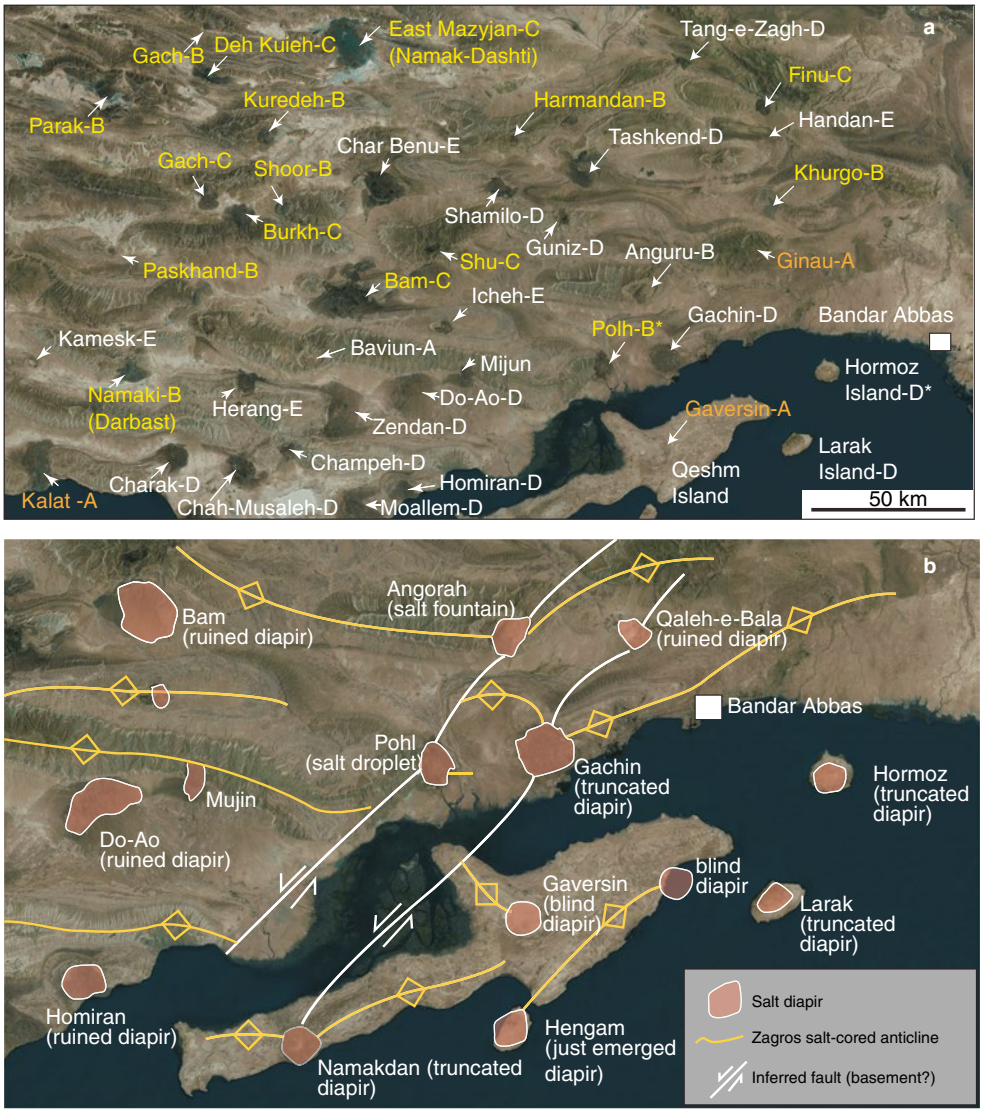

Fig. 6.85 Namakiers of Eastern Iran. (**a**) Salt glaciers (dark blebs) of Hormuz Salt flowing across the landscape of Iran north and east of the coastal town of Bandar Abbas, offshore islands are also cored by salt diapir and with now inactive glacier residues at surface. Classified A–E is indicative of stage of development; a = pre-piercement bulge, b = Exposed salt plug, c = salt namakier at surface, may be in retreat, d = namakier with near complete dissolution, e- degraded and dissolve core with little or no visible salt., That is, orange = pre breakout, yellow lettering = salt at surface, white = little or no salt remains only residues – see Chap. 7 for details on evolution Asterisk indicates a salt feature known to contain potash. Note that the name "Gach" appears more than once as it means gypsum in Farsi. (**b**) Diapirs in the vicinity of Bandar Abbas showing regional deformation structures (in part after Fürst 1976; Talbot et al. 2009a, b – Bing® images mounted and scaled in Mapinfo)

20–25 mm a^{-1} (Hessami et al. 2006). Regionally, the SW advance of the Zagros front, and the halokinesis associated with it, is extensively documented (Talbot and Alavi 1996; Talbot et al. 2009a, b). Diapirs, pressurized by their overburden and the stresses associated with the arrival of the Zagros front, burst out of their overburden to extrude as salt-cored islands in the Gulf or salt mountains onshore (Fig. 6.85). The southward migration of the Zagros front is still forming successive thrust anticlines and spawning reactive syn-Zagros diapirs that decrease in age southward along the N–S trending pre-Zagros pillows of Hormuz salt (Talbot and Alavi 1996). The regional stress field rotated slightly in late Neogene times at ca. 5 Ma (Lacombe et al. 2007; Jahani et al. 2007) and previously thin-skinned largely salt-floored deformation now involves a thick-skinned component with reactivation of faults in the basement (Molinaro et al. 2005). This is indicated by most modern active diapirs aligning along faults oblique to the Zagros fold axes (Fig. 6.85b and 6.86; Talbot and Alavi 1996). For example, the Zagros fold system in the Firuzabad region is overthrusted along, and cut off by, the Zandan Thrust, a branch of the Zagros Main Thrust, approximately 75 km east of Bandar Abbas. Salt breakout in the salt-cored anticlines there does not occur unless the crest of the anticline is faulted or eroded. Hundreds of kilometres to the northeast from the Hormuzgan district, in the hydrocarbon rich section of foreland foldbelt in the Fars district, the Miocene evaporites of the Fars/Gachsaran Formation can act as a secondary detachment level whereby pairs of shallow thrusts are rooted with opposite vergences toward the crest of the anticline (Figs. 10.79 and 10.80).

Bosak et al. (1999) and Fürst (1976) note that outcropping salt plugs and associated namakiers are mostly associated with sigmoidal bends in fold axes (these are the circular plugs noted by Fürst 1976) or occur near terminations of anticlines (plunge turnovers). Many active flows are sourced on anticlinal flanks and not in axial crests (Figs. 6.86 and

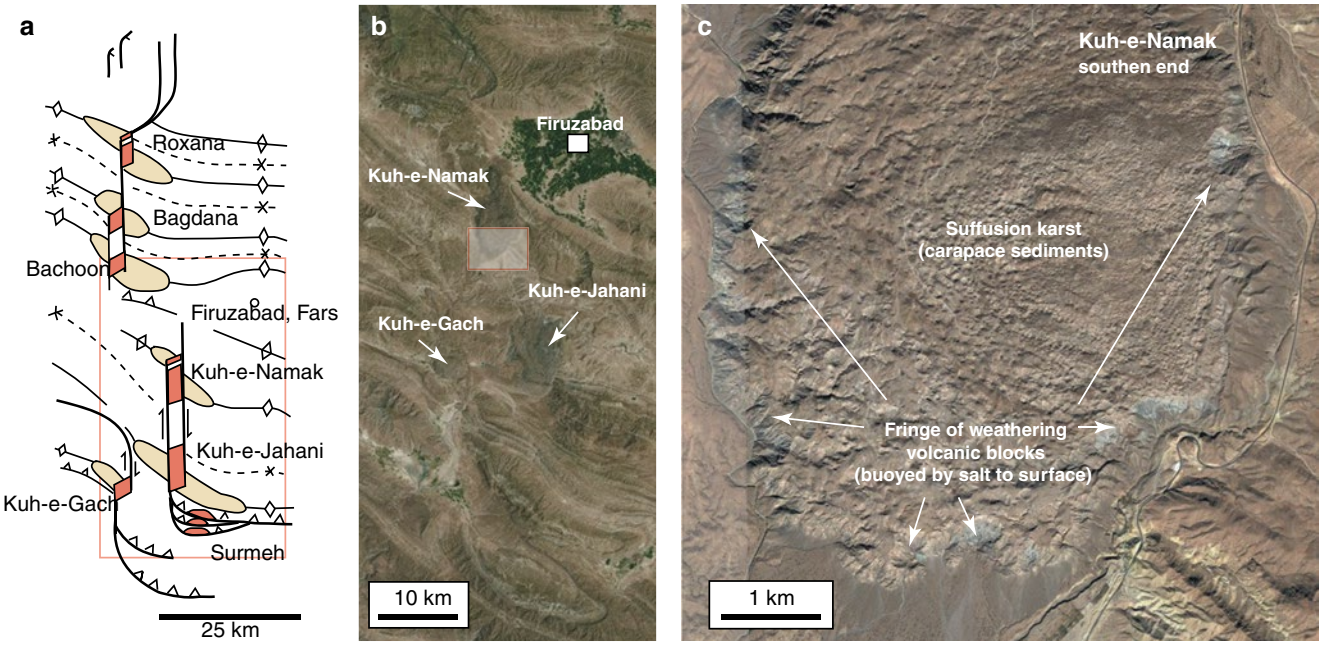

Fig. 6.86 Current kinematics of Mangarak fault zone, Firuzabad region, Zagros tectonic zone, Iran, showing the location of present and former salt extrusions (*red*). They occur in zones where a fault zone crosses salt-cored anticlinal culminations, shown as rhombic areas (After Talbot and Alavi 1996)

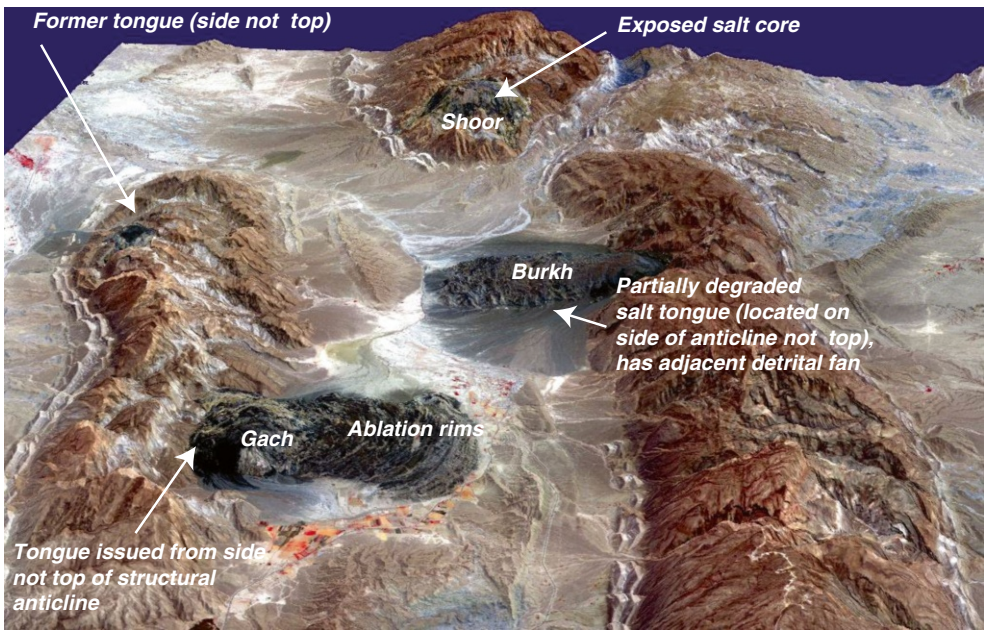

Fig. 6.87 Lateral view looking east across the Gach – Shoor namakier region, clearly shows the bladderlike nature of namakier flow – see text (Image courtesy of NASA, NASA/GSFC/ METI/ERSDAC/ JAROS, and the U.S./Japan ASTER Science Team; see http://asterweb.jpl.nasa.gov/gallery; accessed June 17, 2013)

6.87). Apparently, zones of fault-induced extensional shear are more important in controlling the site of salt emergence, rather than the zone of extension across the culmination of anticlinal crests (once the surface is breached via active diapirism salt drains out of the sides of sliced structures not the crests; in most Zagros namakiers we are slicing bladders, not popping pimples!). A few of the salt plugs on the anticlinal flanks lie closer to the synclinal axis than to the anticlinal axis. But in some of the less active namakiers the site of the original emergence can be difficult to define. Extruded salt always rolls downslope, so if it is cut off from its source, it will end up occupying flanks and synclinal axes, even if the source was the anticline crest.

Even so, the following generalizations can be made; (1) most salt plugs outcrop in bends or faulted displaced offsets of the anticlinal axes, (2) salt typically does not breakout in areas of straight (unfaulted) anticlinal axes. This led Talbot and Alavi (1996) to argue that Hormuz salt typically emerges

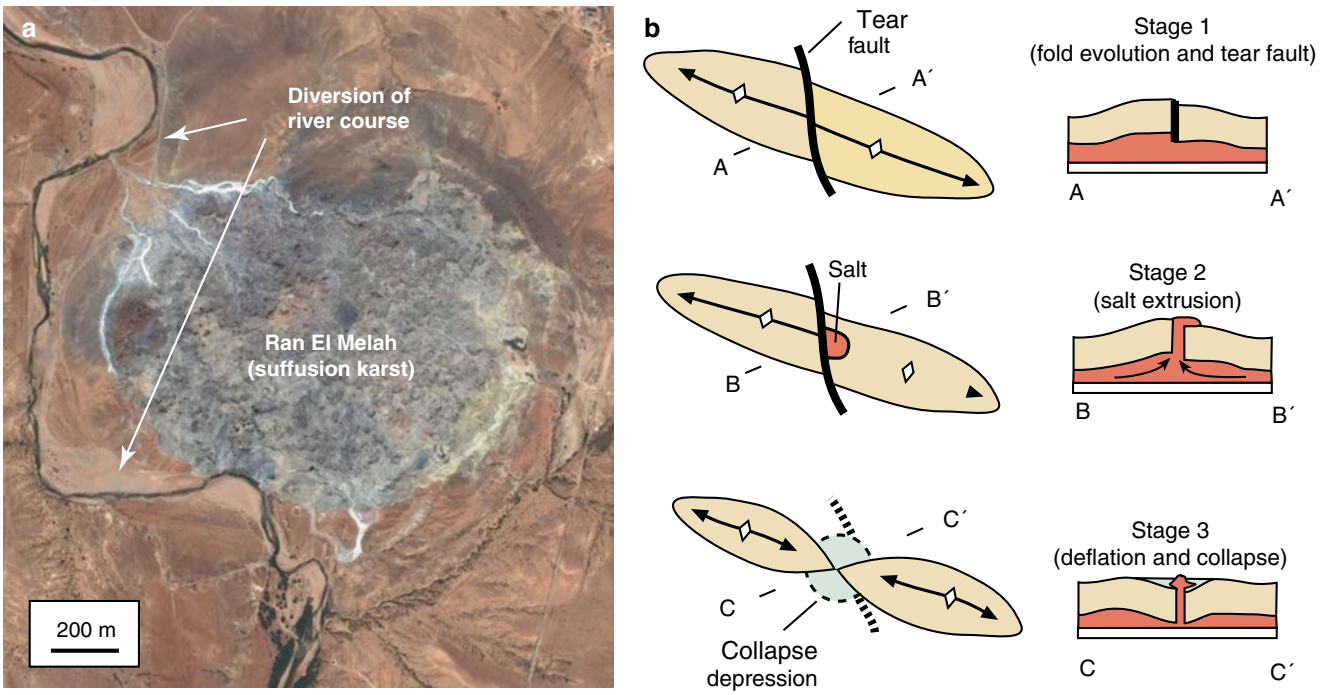

Fig. 6.88 Ran El Melah, Algeria. (**a**) Suffusion karst in a gypsum carapace, now outlining the namakier. Notice how the landscape high, created by the namakier has diverted the river course. (**b**) Schematic based on Ran El Melah and other Algerian examples showing how salt extrusions tend to occur where tear faults intersect salt-cored anticlinal culminations and the successive stage of dissolution and collapse the occur once supply to mother salt is cut off (After Letouzey et al. 1995)

as namakiers where the salt cored anticlinal crests are cut by faults, such as in the Kazerun and Mangarak fault zones (Figs. 6.85b and 6.86). A similar system of extensional tear faults across salt-cored compressional anticlines also explains emergent salt in Triassic salt now forming namakiers such as Ran Al Melah in the Atlas ranges of Algeria (Fig. 6.88; Talbot and Aftabi 2004; Vially et al. 1994). Ran Al Melah was the first active salt glacier documented in the geological literature (Ville 1856).

Other than faulted and eroded anticlinal buckle folds, additional salt or salt breccia-defined outcrops in compressional settings populate salt-lubricated thrust planes, some showing a strong strike-slip sense of movement. Examples include Miocene salts in the Carpathians of Romania, Triassic salts in Alpine thrust belts in southern France and Spain, the Neoproterozoic Roan breccias of the Lufilian foldbelt of Central Africa and the Callana Formation breccias of the Flinders Ranges of South Australia (Chap. 7).

Once again, this style is best seen in Iran, in the regional faults that define the margins of the Miocene section in the Qom Basin of central Iran (Fig. 6.89a). The Central Basin of the Iran Plateau lies between the geologically better-known regions of the Zagros and Alborz Mountains. Hydrocarbon exploration in the Central Basin has revealed the details of the late Eocene – Holocene evolution of the basin based on seismic reflection data, geological fieldwork, basin modelling, and satellite interpretation (Morley et al. 2009). The multistage basin history commenced with broad sag-type subsidence and isolated normal faults during Oligocene-early Miocene time. Short periods of hydrographic isolation allowed thick sequences of marine-fed salt to be deposited at this time. The basin evolved to an extensional or transtensional basin in the early-middle Miocene, with as much as 4–5 km of Upper Red Formation section (including continental evaporites) being deposited in some parts of the basin during this stage.

The upper part of the Upper Red Formation is associated with a change to transpressional deformation, with the development of thrusts and folds. This latest (probably middle and/or late Miocene-Holocene) deformation is transpressional, and includes a mixture of basement-involved strike-slip and thrust faults and thin-skinned folding and thrusting detached on the Oligocene halite dominant evaporites. Local detachment levels higher in the stratigraphy also exist some centred on the Upper Red Fm. continental evaporites (Fig. 6.88b). Subsidence in mini-foredeep basins and strike-slip fault bounded basins occurred during the transpressional stage, and several kilometres of Upper Red Formation were deposited in the main depocentres.

Northwest-southeast to north-northwest-south-southeast, striking dextral strike-slip to compressional faults dominate the area, with subordinate east–west and north–south fault orientations also present. These different fault sets combine in places to form major strike-slip duplex geometries. The

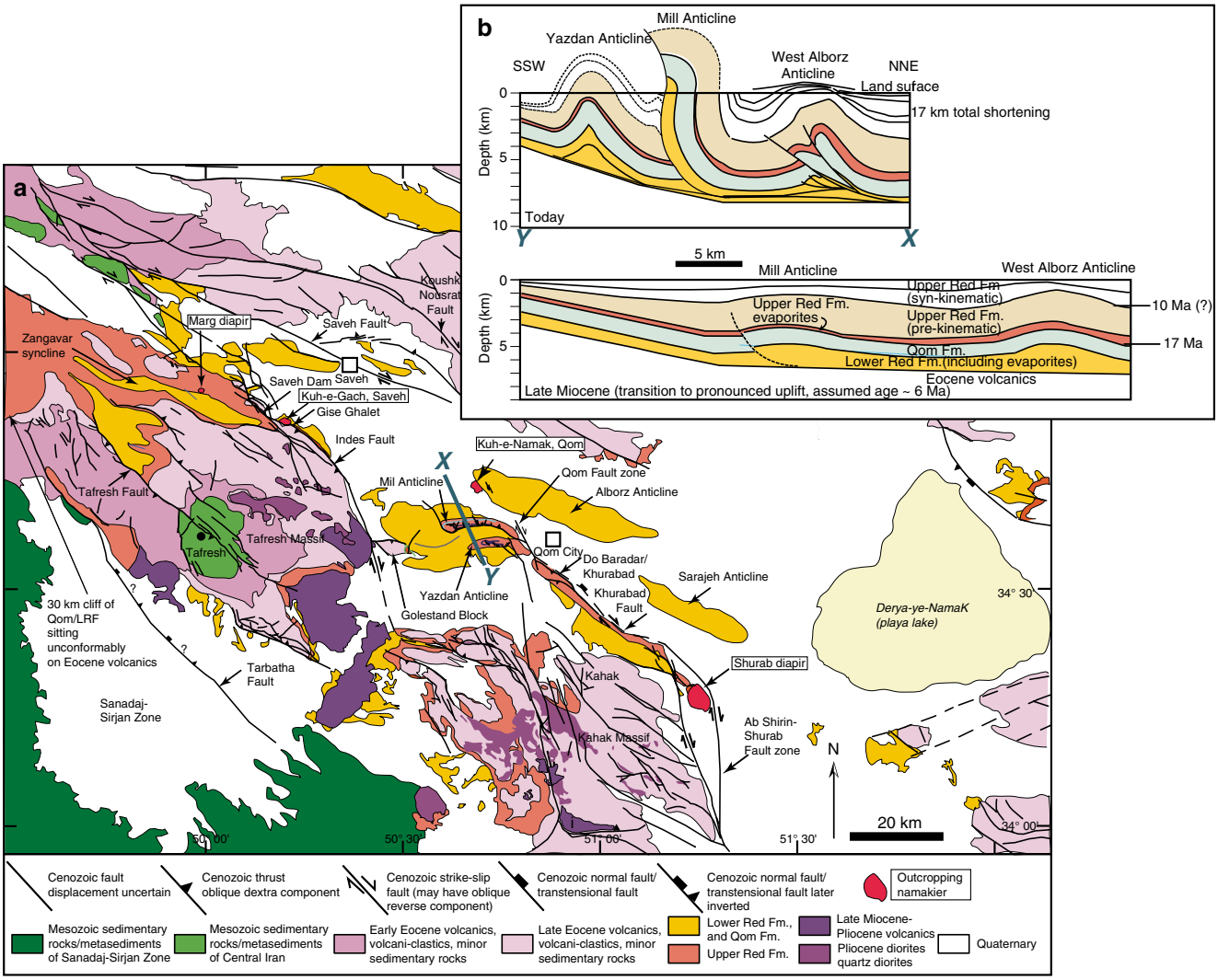

Fig. 6.89 Regional geology of central Iran, based on geological maps, satellite interpretation, and ground site checking. (**a**) Regional geological map. (**b**) Cross-section X–Y showing there has been at least 17 km of shortening/inversion since the Miocene in this saline basin with much of the compressional décollement focused into salt rich layers in the Miocene stratigraphy (After Morley et al. 2009)

Eocene volcanic belt (Urumieh-Dokhtar zone) along the southern margin of the basin forms a chain of massifs as much as 3 km high, the outcrops of which were exhumed by movement along major thrusts from 5 to 6 km depth between the middle Miocene and present day.

The Central Basin-Urumieh-Dokhtar zone forms a distinctive transpressional belt that underwent a minimum of 38 km shortening between the late Miocene and Holocene. The Central Basin and the Zagros and Alborz Mountains all indicate that the onset of widespread crustal shortening in Iran occurred late (latest early Miocene or later), relative to the initial collision of the Arabia Peninsula with Eurasia during the late Eocene or early Oligocene. Uplift of the Central Basin surface from approximately sea level to 900–1,000 m occurred during the middle or late Miocene, after deposition of the marine Qom Formation.

Within this complex milieu of deposition and interacting structure, local transtensional rhombs along the major faults have allowed pressured salt be pumped to the surface. One of the most impressive examples of salt emergence is the Kuh-e-Qom salt fountain (Figs. 6.89 and 6.90). Qom Kuh is one of four salt diapirs emergent along releasing bends pulled apart along major dextral transpressive faults crossing the Qom Basin in the central plateau of Iran. The others are Shurab, Kuh-e-Gach and Marg, indicated by rectangular boxes in Fig. 6.89a. Of the four, Kuh-Qom is the most active and is still actively flowing, while the other three are in varying stages of collapse and dissolution. Qom-Kuh is located on a releasing bend of an offset in the Qom Fault that cross-cuts the plunging nose of the Alborz Anticline (Fig. 6.90a). The Qom Fault intersects a number of normal faults in the vicinity of Kuh Qom which are exposed to the east of Qom

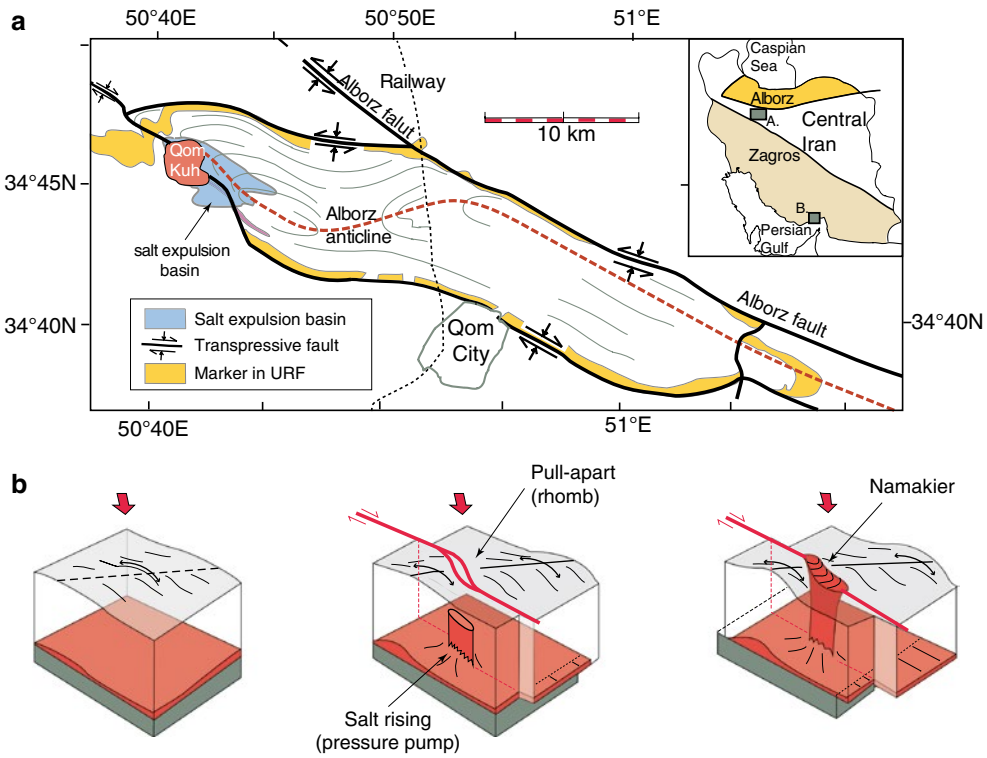

Fig. 6.90 Kuh-e-Namak, Qom. (**a**) Geological setting of Qom-Kuh with *inset* showing location in Iran in the framework of the Alborz and Zagros tectonic zones of Iran (After Emami and Hajian 1980; Talbot and Aftabi 2004). (**b**) Emplacement occurs as a transtensional lens escaping via a strike-slip rhomboid pull-apart. See Fig. 6.91 for regional geology of Kuh Qom

Kuh where it extends beneath alluvium to the northwest of the diapir (Fig. 6.91). Splays of oblique-reverse and oblique-normal faults offset the nearby asymmetric thrust anticline, known as the Alborz Anticline. These faults are well exposed in the 60 m-high river cliff that defines the eastern flank of Qom Kuh and in the adjacent river bench that has bevelled in Upper Red Formation marls at the 920 m above sea level (Fig. 6.91b). The faults are clearly seen in the zone separating the diapir from the hill created by the northern limb outcrop of the anticline. The largest of these faults has an irregular trace that was superimposed on a ductile dextral strike-slip shear zone before it offset the river bench some 1.5 m down to the east (Fig. 6.90d).

The salt fountain of Qom Kuh rises to 1,235 m asl and is 315 m above the surrounding plateau (Fig. 6.91d). The Qom Kuh namakier can be divided into two main components: (1) a smooth hemispheric dome or summit with a diameter of 2.5 km and surrounded by, (2) a slightly dissected apron of salt allochthonous atop Upper Red Formation and Recent gravels (Fig. 6.91b, d). Steps in the salt topography indicate that the extruded salt overflows a collar of Upper Red Formation up-tilted around the inferred diapiric vent. This raised collar is highest beneath the NE shoulder of Qom Kuh, where it is exposed in windows up to 1,100 m asl and lowest in its SW corner (Talbot and Aftabi 2004; Cosgrove et al. 2009). The river cliff truncates the eastern end of this bedrock collar (Fig. 6.91a, b). The apron of allochthonous salt is up to 200 m thick and about 0.75 km long to the west of the summit, and some 2 km to the south (Fig. 6.91d). The rhombic vent through which Qum Kuh extrudes was pulled apart between normal faults hard-linking a releasing offset along a regional transpressive strike-slip fault that trends west–east (Fig. 6.89b; Talbot and Aftabi 2004). In profiles though the summit, Qum Kuh can be considered as a pile of recumbent fold nappes of gneiss-like and mylonite-like Oligocene and Miocene salts that have extruded from depth and then gravity spread over recent alluvial gravels (Fig. 6.91c).

An ephemeral stream still flows anticlockwise around most of Qom Kuh, and is still eroding the cliff on the east side of Qom Kuh. Broken pottery lying on the river-bevelled bench to the east, and exposed by wind-deflation of the soils overridden by the southern namakier, suggest that the river eroded the salt of Qom Kuh in historical times (≈10,000 years according to Talbot and Aftabi 2004). Salt dissolved from the Qom Kuh namakier is now being re-precipitated as Holocene evaporite beds in the adjacent playa low, which is possibly situated atop an active salt withdrawal basin (Figs. 6.90b and 6.92b).

The rhombic transtensional nature of the salt neck to this graben structure that allows salt supply to Kuh-Qom salt fountain is seen more clearly in a rhomboid neck that now outcrops as Kuhe-Gach, Saveh, a highly dissolved namakier remnant (Figs. 6.89a and 6.92). Only the gypsum carapace and the reducing brine halo remain below the position of the former namakier (Fig. 6.92a–d). The leaching of the namakier creates reducing brines that colour the underlying redbeds grey, as it converts iron from its ferrous to ferric state

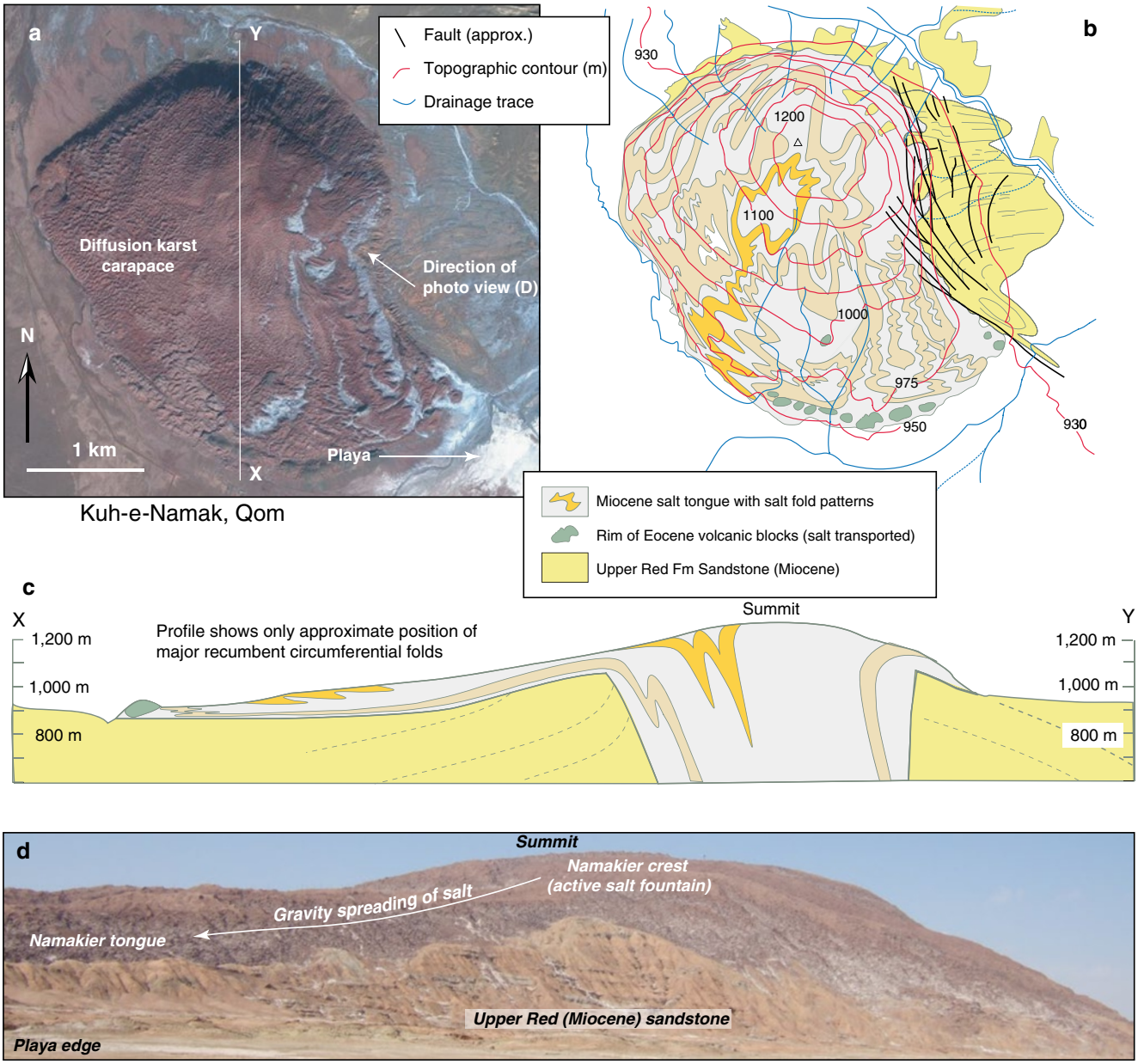

Fig. 6.91 Kuh-e-Namak Qom, Iran. (**a**) General plan view of namakier showing radial flow of salt away from the crest of the active salt fountain define by the summit of the kuh (Bing® image. **b**) geological interpretation of the namakier flows. (**c**) schematic section of the flow (X–Y). (**d**) Field photo showing the tongue lies atop salt inflated Upper Red Formation and how salt is flowing away from the summit (After Talbot and Aftabi (2004) and author's work in the region; see also Morley et al. 2009)

(Warren 2008). The topic of textures indicative of namakier weathering and retreat is discussed further in Chap. 7.

The regional work of Morley et al. (2009), based on a detailed field mapping program, assigns a mainly Oligocene age to the salt in this part of the Qom Basin. This is somewhat older than the dominantly Miocene age assigned by Talbot and Aftabi (2004). The nearby salt-thrust sealed Qom carbonate sediments of the Alborz anticline are famous, in 1956 they were the site of the of the world's largest uncontrolled oil well blow-out. The wildcat well (Alborz 5) blew out on August 26 1956 and leaked more than five million barrels of oil before it naturally bridged on November 18, 1956 (Mostofi and Gansser 1957; Gretener 1982). This drilling accident underlines the way in which a highly efficient salt seals can hold back substantial pressures, which in the case of the salt-sealed thrust fault to the Alborz anticline probably approached lithostatic (Fig. 6.89a; Chap. 8).

In summary, there is now widespread agreement that salt in compression plays a fundamental role in controlling the fold style and amount of shortening in thin-skinned

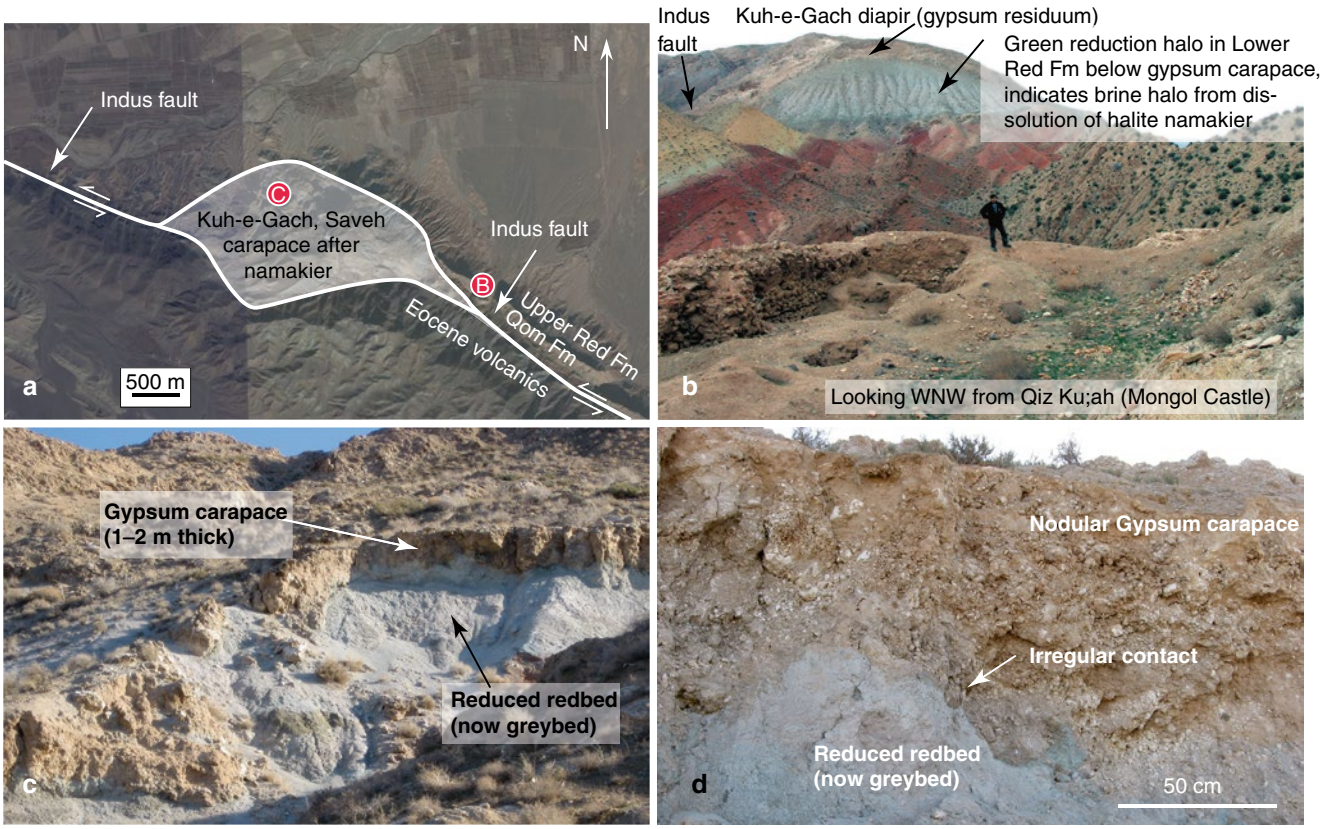

Fig. 6.92 Kuh-e-Gach, Saveh. (**a**) Interpreted Bing® image showing the releasing bend in the Indes Thrust Fault with a possible tear fault that allowed salt to escape to the surface from near the base of the Lower Red Formation. (**b**) View to north from Qiz Kaleh (Mongol Castle) showing diapir is a residuum after dissolution of former halite namakier and is now made up of a relatively thin carapace of gypsum (1–2 m) atop a green alteration zone in the Lower Red Formation red beds. (**c**) View of the carapace showing it is a veneer atop reduced (*grey*) shales that were once red. (**d**) Close-up of carapace-greybed contact

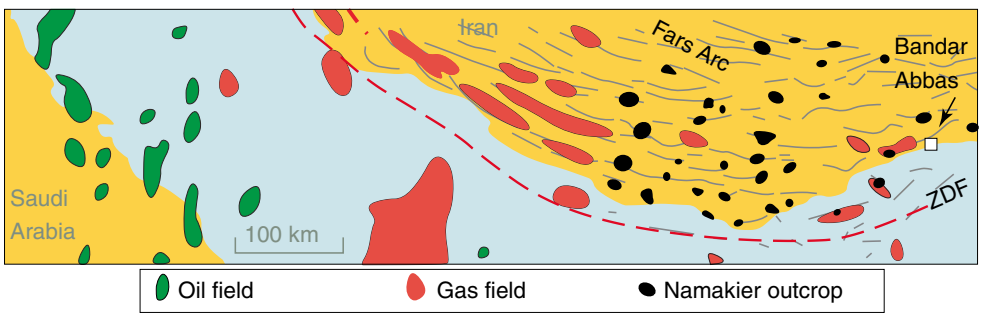

Fig. 6.93 Relationship between oil and Gas distribution and the Zagros deformation front (*ZDF*) which controls the WNW-ESE tend in Onshore Iranian gas field versus the N-S trends in Saudi Arabia. Notice the lack of gas fields in the zone where salt has breached the landsurface (to the west of Bandar Abbas)

salt-entraining thrust provinces. Outcomes range from mild inversion of an previously extensional system (such as modified pillow structures in the North Sea) to fully developed salt-cored, detached fold-and-thrust belts in the various alpine chains of Europe, North Africa, the Middle East, Southwest Asia and central Australia. It seems the presence of an at-surface namakier, as in the Hormuzagan region, indicates the likelihood of a loss of seal integrity via fault leakage; abundant active namakiers and significant gas filled anticlinal structures are for the most part mutually exclusive (Fig. 6.93; Chap. 10).

Browne Formation Oldest Known Salt

Neoproterozoic halokinetic sediments in the Officer Basin extend across in arid interiors of much of Western and South Australia, across some 320,000 km^2, and are largely concealed beneath sediments of the Gibson and Great Victoria Desert (Apak et al. 2002). Approximately 2/3 of the Officer Basin lies in Western Australia (Figs. 6.63 and 6.94a). Extensional faults have been recognised in Late Proterozoic and early Cambrian sequences of the northeastern part of the Officer basin (Southgate et al. 1989). Subsequent southward-

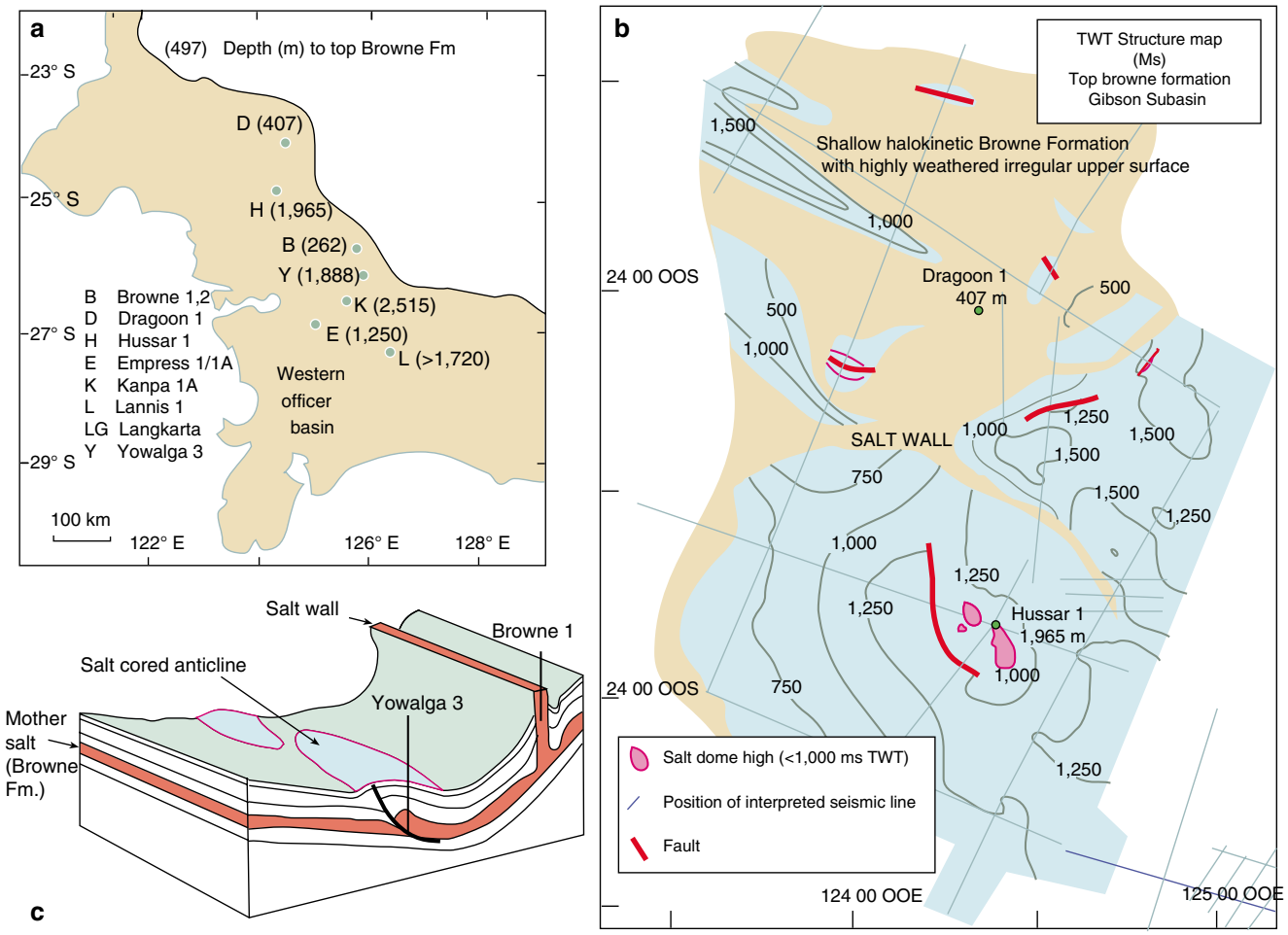

Fig. 6.94 Salt in the Browne Fm (830 Ma) Western Officer Basin, Australia. (**a**) Well positions and depth to top Browne Fm. intersection. (**b**) Interpreted Two Way Time (*TWT*) structure map of the top of the Browne Formation in the Western Officer Basin. Note the closed anticlinal feature cored by Hussar 1 and the poorly imaged northern region characterised by widespread relatively shallow and dissolved salt of the Browne Formation. This region is sampled by the Dragoon 1 well. (**c**) Interpreted styles of salt-induced deformation in the Browne Formation, Officer Basin. Note the penetrative salt walls, which approach the landsurface, and the deeper non-penetrative thrust-cored anticlines (After Apak et al. 2002; Simeonova and Iasky 2005)

directed thrusting of the Musgrave Block along the northern margin of the Officer Basin has long been recognised; for example, in the late 1980's seismic lines outlined several salt cored thrusts in the northern part of the Officer Basin that dip shallowly to the north. These thrusts have affected Cambrian sequences and may be equivalent in age and style to the Alice Springs Orogeny.

Shallow and subcropping halokinetic salt in the Officer Basin is centred on thick halite beds in the 830 Ma Browne Formation in the Western Officer and its as yet undrilled counterparts in the eastern Officer Basin (Fig. 6.94a). Highly leached outcrops of sulphate caprocks of the Browne Fm., equivalent to the Neoproterozoic Bitter Springs Formation in the Amadeus Basin, were first drilled in the 1960's in the Woolnough area during reconnaissance mapping of the region (Table 6.4). Outcrops near these wells (e.g., Browne 1 & 2 wells) are dominated by large blocks of Proterozoic dolomite and Permian sandstone up to hundreds of metres in diameter. They outline the various brecciated and weathered diapir tops, which drilling shows passes down into gypsiferous/anhydritic capstones that are hundreds of metres thick. The blocks indicate the brecciation of units emplaced as part of a series of salt flows, with blocks left as a residue on the ancient Australian landsurface, once the encasing more soluble evaporite minerals weathered away. The elongate orientation of many diapir crests in the western Officer Basin indicate emplacement as salt walls or salt-cored thrust anticlines, rather than isolated diapir stems (Fig. 6.94b). Equivalent salts have been recovered in the subsurface in various oil wells drilled through the top of the Neoproterozoic Browne Formation over much of the Western Officer Basin (Table 6.4; Simeonova and Iasky 2005).

Shallow drilling recovered a variety of actual evaporite salts, including halite, beneath outcropping diapir crests in

Table 6.4 Wells that intersect salt and/or its residues in the Neoproterozoic Browne Formation (830 Ma), Western Australia

Well	Location	Year drilled	Top Browne (m)	Thickness (m)	Logs through salt	Comments
Browne 1	25°51′15″S I25°48′58″E	1965	133	>180	ES, GR	Capped by Permo-Carboniferous glacials. Drilled through dissolution cap to recover gypsum below 180 m. No halite recovery.
Browne 2	25° 56′00″ S I25°57′45″E	1965	262	>40	ES, GR	Capped by Permo-Carb. glacials. Drilled through dissolution residues below 262 m. No halite recovery.
BMR Warri 20	24° 05′00″ S I24°33′00″E	1972	Surface (diapir crest)	>265	Limited resistivity, SP	0–200 m recovered gypsiferous dissolution residues. Halite recovered below 200 m.
BMR Madley 1	24° 13′40″S I24°20′50″E	1972	Surface (diapir crest)	>207	None	Drilled in interbedded gypsum dolomite breccia (dissolution zone) with trace halite toward base.
Dragoon 1	24° 04′49″ S I24°32′58″E	1982	407	>1,590	GR, SP, DDL.Sonic, FDC: CNL, HDT	407–650 interbedded $CaSO_4$ dolomite (dissolution residues). 650–2000 interbedded halite/mudstones with some halite beds more than 60 m thick
Empress 1 and 1A	27°03′13″S 125°09′24″E	1997	1,249	275	GR, Cali, Sonic, Shallow and deep LLm Density Neutron, Dipmeter	Interbedded claystone, dolomite, and halite. Most halite beds are around 5 m thick, dips on HDT up to 50° implying slumping or salt creep. Spear et al. 2014 sampled preserved chevrons in core (1,502 m) from this well for interpretation of palaeochemistry of seawater.
Kanpa 1	26° 31 ′42″ S I25°36′52″E	1983	2,515	1,156	GR, SP, DDL, MSFL, Sonic FDC, CNL, HDT/Velocity survey/ BHC, LSS, LL	HDT show consistent dips implying, stacked bedded salt. Halite beds are impure and up to 100 m thick. S
Hussar 1	24°49′14″S I24°22′34″E	1982	1,965	>85	GR, SP, DDL, MSFL, Sonic FDC, CNL, HDT, Velocity survey, BHC	From wireline log it appears that there is no weathered cap. Top halite is in sharp (erosional?) contact with overlying Hussar Fm.
Yowalga 3	26° 08′51″ S 125°55′09″E	1983	1,888	>2,308	BHC, DDL, MSFL, FDC CNL, HDT	Interbedded halite dolomite and muds, with some halite beds more than 200 m thick. HDT shows high dip variability in halite implying the unit is halokinetic

Data extracted from SaltWork database version 1.7

the Woolnough Hills and the Madley Hills. For example, a dissolution residue or cap zone passes into massive diapiric halite below 203 m to a TD of 265 m in the BMR Warrie No. 20 stratigraphic well on the Woolnough Hill diapir. The recovered halite is coarsely crystalline, colourless to pale orange and contains numerous fragments of anhydrite and

Table 6.5 Landscape relief around active salt structures

Offshore			
Abu Thama, Arabian Gulf	60 m	Neogene compressional reactivation	Purser (1973a)
Cabo St Tome, Brazil	97–144 m	Gravity gliding	Demercian et al. (1993)
Allochthons, Gulf of Mexico	130–260 m	Gravity gliding	Liro (1992), Wu et al. (1990a, b), Rezak (1985)
Offshore Mississippi Delta	100–240 m	Gravity gliding	Jackson et al. (1995)
Continental			
Al Salif, Yemen	45 m	Extensional with gravity gliding	Davison et al. (1996b)
Jabal al Milh, Red Sea	45 m	Extensional	Davison et al. (1996b)
Mt Sedom, Dead Sea	200 m	Transtensional	Frumkin (1994a, b)
Saharan Atlas, Algeria	300 m	Compression with likely salt source cut-off	Kulke (1978)
Kuh-e-Namak, Qom	305 m	Transtensional in compression belt	Morley et al. (2009)
Zagros Chain, Iran	300–1,500 m	Compression, some with salt source cut-off	Kent (1987), Talbot and Alavi (1996)

anhydrite-dolomite. Its texture suggests solution and recrystallisation processes have overprinted any original biaxially-stressed morphologies in the precursor halokinetic salt. Finely crystalline anhydrite and quartz are also scattered throughout the clear halite crystals.

Diapiric and pillow geometries, some of which have closed anticlinal crests in the outcropping Neoproterozoic section are seen in regional seismic lines, defining salt walls and salt-cored anticlinal thrust ridges in both the western Officer (Fig. 6.94b; Craig et al. 1984; Townson 1985), and in the Eastern Officer Basin (Sukanta 1993). Figure 6.94c illustrates the two dominant styles of salt geometry, based on seismic interpretation of salt-related structures in the western Officer Basin. The Empress 1A cored a 275 m thick section of interbedded halite dolomite and shale with individual halite beds up to 10 m thick. Thicker halokinetic salt sections of the Browne Formation were intersected in various wells to the north of this well (Table 6.4). The Browne Formation is 1,152 m thick in Kanpa 1A and more than 2,316 m thick in Yowalga 3, where the well bottomed while still in the salts Browne Formation (Fig. 6.94c). Wireline interpretation in Kanpa 1A shows much of the intersected halite is made up of stacked 10 m scale beds with one bed at a depth of 3,100 m being more than 100 m thick. Halite beds in Yowalga 3 are somewhat thicker but most are still no more than 30–40 m thick, although one bed at around 3,500 m depth is more than 150 m thick.

A Two Way Time (TWT) structure map to Top Browne is presented as Fig. 6.94b. The area can be subdivided into a northern zone of shallow Browne and a southern zone of deeper Browne Fm. Seismic quality is low in the northern area. The lack of identifiable reflectors is due to the relatively shallow position of the top of the Browne and its long term disturbance by deep meteoric flushing. In this region there are only a few resolvable zones showing interpretable sediment cover. Modelling using very approximate conversions for time to depth suggest some of these narrow sediment-filled troughs in the northern zone contain more than 1,000–2,000 m of post-Browne sediment. The steep sides to these zones clearly show the Browne to be halokinetic. In the southern zone the top of the Browne is seismically resolvable and it is covered by conformable layers of later sediments. There are also closed domes in this area, where the top Browne is deeper than 1,500–2,000 m. Two wells were drilled in the region covered by this seismic, Dragoon 1 and Hussar 1. Dragoon 1 is located on a closed structure in a halokinetic setting that appears to be a thrusted anticline, near identical in halokinetic setting to Yowalga 3. When drilling ceased Dragoon 1 was still in evaporites, after intersecting more than 80 m of salt in the Browne Fm. The upper contact of the Browne appears conformable with the overlying Hussar Fm. Dragoon 1 intersected the top of the Browne Formation at 407 m and passed through 200 m of dissolution residues before intersecting more than 1,400 m of interbedded halites and mudstone sequences until it TD'd at 2,000 m where it was still in the Browne Formation. Some of the halite interbeds in this well are more than 200 m thick.

Sediments and Flowing Salt

Wherever flowing salt approaches the land surface in both continental and offshore positions it creates topographic relief in the landscape and so influences the style and pattern of deposition (Table 6.5). Historically, sedimentological studies of this phenomena focused on predicting suprasalt deposition and its utility in predicting associated porosity trends (see summary in Warren 1989). Conclusions as to the position of sands, reefs and porosity belts in relation to salt structure highs in the landscape are still valid, but our understanding of mechanisms driving salt flow have substantially changed. With increasing recognition of the importance of lateral flow in allochthonous salt, the sedimentology of subsalt systems has become as important a topic to model and predict.

Reactive diapirism typically forms a graben or low atop the diapir crest. Active diapirism, passive diapirism and

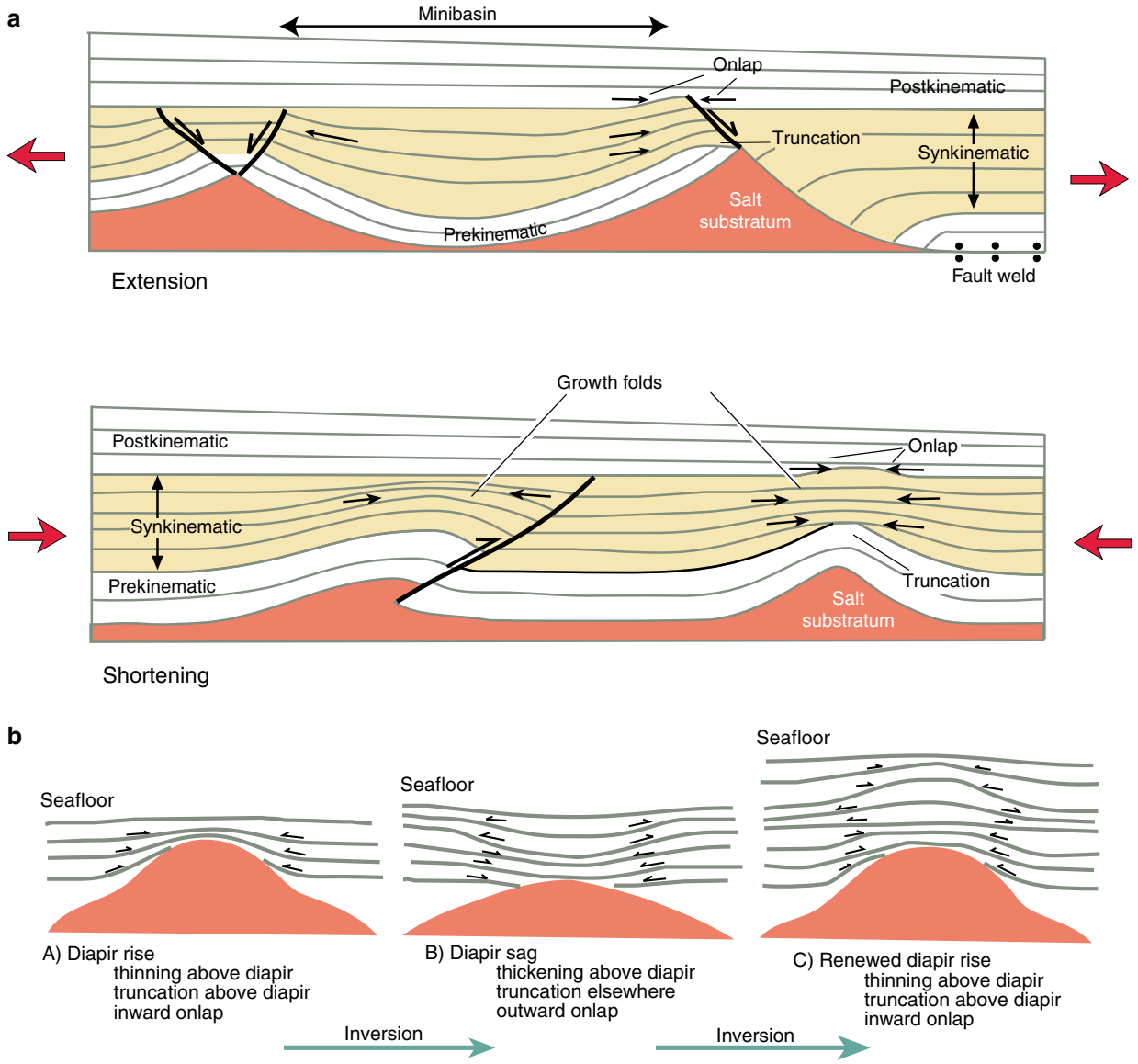

Fig. 6.95 Sedimentary record of salt flow. (**a**) Synkinematic during extension (*upper panel*) or shortening (*lower panel*). The prekinematic layer was deposited before salt movement began. The synkinematic layer was deposited during salt flow and includes many internal onlap or truncation surfaces. The postkinematic layer was deposited after salt flow ceased. Its base may onlap or truncate originally exposed surfaces in the synkinematic layer (After Jackson and Talbot 1994). (**b**) During two episodes of structural inversion caused by subsidence and renewed uplift of a diapir. The inversions are recorded by changes in bed thickness and onlap directions indicated by *barbed arrows* (After Jackson and Talbot 1994; Nelson 1991)

compressional growth folds are all marked by topographic highs about the crest of the salt body. Salt flow rates are in turn influenced by loading (sedimentation rates) and tectonics (rates of extension or compression). Interaction creates feedback whereby the geometry of a growing salt body is influenced by, and feeds back into, the depositional rate/water depth of the adjacent sedimentation setting. Once rising salt is sufficiently close to the surface to influence its topography, sedimentary feedback at the depositional surface typifies all styles of halokinesis. At the scale of seismic resolution this is recorded in changes in bed thickness (e.g. formation of suprasalt/intersalt basins or minibasins, thickness changes approaching active diapirs ridges and growth folds), as well as varying onlap and offlap relationships, and changes in bed attitude as the salt body is approached. At the lithofacies scale, it is recorded in changing styles of shallowing or deepening of the sequence (sanding or shaling upward parasequences), the development or the drowning of reefs and shoals, syndepositional bed disturbance, slumping and faulting, as well as the formation of local unconformities and karsting.

At the broad scale of seismically resolvable suprasalt sediment geometries, the style of sedimentation can be broken down into three groupings: prekinematic, synkinematic and postkinematic (Fig. 6.95a; Jackson and Talbot 1994). The

prekinematic layer records sedimentation before salt movement or any other deformation. A prekinematic sediment layer is an interval of strata where initial stratigraphic thickness is constant above a salt structure or its adjacent rim. That is, the prekinematic sediment layer is isopachous or its depositional thickness varies only as much as would be typical for the same sedimentation style in a region where no salt was present.

In contrast, the synkinematic layers record sediment thickness and facies changes related to salt-cored highs and crestal sloughing. Synkinematic layers thicken above withdrawal basins or locally thin against rapidly rising structures. For example, in the East Texas Basin in the Gulf Coast, the percentage of stratigraphic or seismic-stratigraphic thinning of synkinematic strata ranges from 10 to 100 % in units influenced by the flow of Jurassic Louann Salt (Seni and Jackson 1983a, b). Changes in bed thickness are frequently recorded by onlap or truncation at all levels of the synkinematic layer (Figs. 6.95a, b).

The postkinematic layer is the interval of strata deposited by sedimentation after salt flow, or any other deformation, has ceased. Basal postkinematic strata can onlap an underlying, uneven deformed surface but show no thickness changes that can be directly ascribed to deformation induced by local salt-flow. The postkinematic layer typically overlies the synkinematic layer.

Truncations (unconformities) are particularly useful in distinguishing the three suprasalt packages. Removal and termination of dipping deformed strata by subaerial or subaqueous erosion forms a truncation or sequence boundary. Truncations cutting across anticlines or fault blocks indicate that the structures had surface relief at the time of erosion (Fig. 6.95a). Undeformed truncations mark the base of the postkinematic layer. Where a truncation is itself folded or faulted, it marks an episode of deformation of the synkinematic layer.

Various terms have also been coined to describe synkinematic basins that fill with sediment as they load and subside adjacent to or atop relatively thick allochthonous or autochthonous salt, which ultimately evacuates to leave behind weld and ramp basins (Fig. 6.47). An older term for a sediment-filled basin atop a salt allochthon is a depotrough. In its strictest definition depotrough describes a basin filled with deepwater, mass flow or turbiditic deposits that uplap a diapir margin (Spindler 1977). The term depotrough is used by some as equivalent to depopod. But a depopod can also be a basin filled with shallow water deltaic deposits draping over or against a flanking salt diapir. In many prograding shelf situations a depotrough passes upward into a depopod. A better term to describe sedimentary basins created by the coming and going of flowing salt is minibasin. It has no genetic implications. Also, without drilling, there should be no assumption of predominant water depth or lithology accumulating during the fill of a minibasin. In much of the current literature there is a strong bias toward Gulf of Mexico models of sediment fill by deeper water siliciclastics passing up into fluviodeltaics. This bias reflects the excellent, but geographically localised, work that has been widely published on the slope and rise allochthons of offshore Gulf of Mexico. It has led some authors to discuss suprasalt reservoirs solely in terms of siliciclastic models. Outside of the Gulf of Mexico, modern and ancient minibasins are filled by other lithologies; such as chalks in the North Sea, or by shallow water lagoonal mudstones, grainstone shoals and reefs, as well as Mesozoic sabkhas and salterns in the Middle East.

Sedimentation and Evolving Salt Structures

The crestal positions of shallow salt structures in extensional regimes are intimately associated with faulting in the first two of the three evolutionary stages of diapirism (reactive and active versus passive). The reactive diapir is triggered by faulting in the extending brittle overburden whereby the hanging wall of an initial fault sinks into the source layer until resisted by increasing pressure forces in the salt source layer and the bending resistance of the overburden (Jackson et al. 1994a). Continuing expansion is accommodated by subsidence as new faults form repeatedly along the expanding axis of the graben. The central fault block or graben sinks and dwindles, while the diapir rises below it, regardless of overburden density. Progressively smaller fault blocks are supported by fluid pressure of the salt at progressively higher levels flanking the triangular diapir. Syndiapir sedimentation keeps diapirs in the reactive phase longer by continually filling the graben floor with new layers of sediment (Fig. 6.96). Reactive diapirism is controlled by the rate of regional extension; whenever regional extension ceases, a reactive diapir stops growing. In contrast both active and passive diapirs are strongly influenced by sedimentation rates and the deposition of sediment wedges (Ge et al. 1997).

At the time a reactive diapir is forming there is an active depression or graben atop the extending structure (Fig. 6.96). There are three depositional settings that can supply sediment to that depression: continental, marine shelf, and deepwater slope to basin. If the extensional graben or depression atop the reactive diapir is in a continental situation, then any surface waters, lakes or rivers, will tend to occupy that depression. In hydrologically-open settings, the deposits of a series of stacked fluvial channels may infill the lower parts of the depression. In more restricted to hydrographically closed scenarios the graben fills with deposits from a series of elongate saline lakes and mudflats. If the graben depression forms in a marine shelf setting it may fill with somewhat deeper water lagoonal muds while shoal water sediments and reefs occupy the very shallow waters atop the edges of the faulted graben margin. If the reactive stage creates a graben depression in deeper waters on the upper part of the

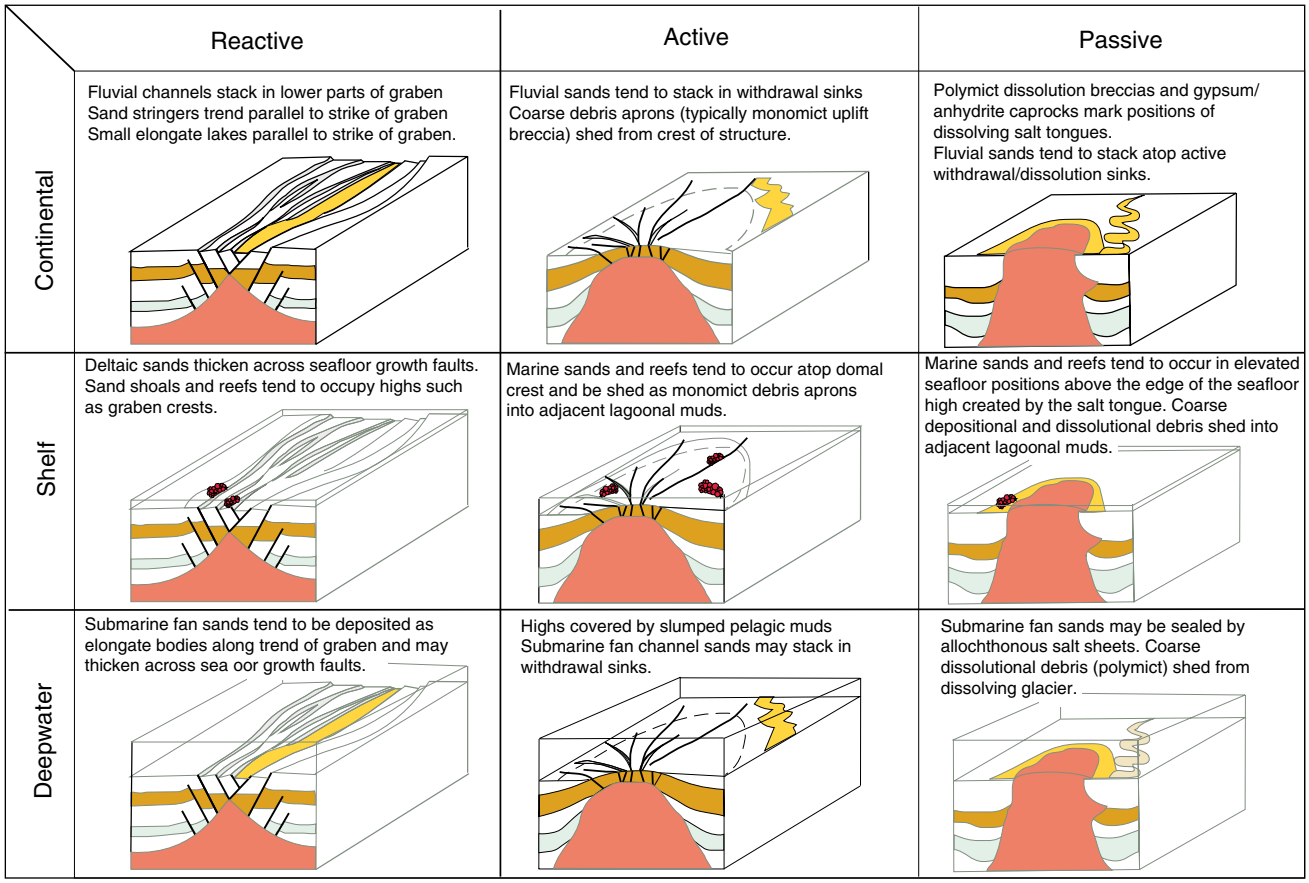

Fig. 6.96 Schematic cross sections showing the control exerted by shallow salt (topographic high) on the distribution of sands and reefs in synkinematic sediments. Sand distribution changes with the stage of salt structure and water depth in the depositional setting (Modified in part from Warren 1999). This sequence of schematics is drawn using a diapir outline, but similar depth-related sediment patterns also form about the seafloor highs created by nearsurface salt allochthons or atop turtle structure anticlines in interdiapir areas

continental slope, then a series of growth faults amid thickened deltaic sand traps may occur and help load the system. Conversely the graben may create a deep seafloor depression that stacks successive episodes of submarine channel and fan sands.

Once a reactive diapir becomes sufficiently tall and its roof sufficiently thin, then pressure at the diapir crest impels the system into the active stage. The diapir lifts its roof, as it rotates, breaks through and shoulders aside its overburden. Crestal erosion and near-crest sloughing then disperses the fragmented roof materials as a series of monomict debris aprons composed of sediments that formerly overlay the diapir crest. Throughout this time, and during the following passive stage, the area above and about the diapir or salt wall is a topographic high that does not accumulate sediment. In the continental realm, fluvial channel sands may stack into the depression created by any adjacent salt withdrawal sink. In the marine realm, the high often lifts the sea floor above wavebase and into shallow euphotic waters suitable for carbonate growth. The higher energy realm about a high on the open marine shelf means muds are winnowed to leave behind sands and gravels. In the transitional continental marine setting, the high-energy shorezone tends to lap up onto the edge of the high and wave-action reworks and winnows the debris apron of the active stage into well-sorted shorezone sands. Later in the passive stage the shorezone also picks up and redeposits exotic blocks derived by the dissolution of extruded salt to create polymict breccias and conglomerates.

Once salt is emergent at the land surface or on the seafloor the diapir has evolved into its passive stage (Fig. 6.96). At this stage the salt is extrusive and any thin sediment roof that may periodically develop atop the salt has little mechanical influence and is destroyed by ongoing active salt breakout. Dissolution of a salt sheet on or near the seafloor creates anhydrite/gypsum carapaces and may also supply a cap of exotic blocks that have been dragged up from greater depths. In some Neoproterozoic salt allochthons in Northern Australia, the transition from active to passive salt structure can be seen in a change of the debris apron constituents from monomict to polymict breccias. The increase in the variety of clasts is driven by dissolution of namakier salt, leaving behind a much broader range of clasts (pers. obs.). If the

breccias are not recognised as salt allochthon-generated, such units are easily misidentified as the outcome of long distance transport driven by tectonic uplift. In Proterozoic and Archaean salt allochthons the salt carrier has typically dissolved, even in the feeders to many of these breccias. All that remains are characteristic alteration haloes around salt and fault welds and indicators of the former presence of salt in the matrix of the breccia itself (Chap. 7). This has significance to many base metal deposits and exploration models (Warren 2000b). For example, in sedex exploration it is the difference between a predictive layered brine-pool model as the control on prepared ground for subsequent mineralisation, versus no discernable control other than a general notion of fault proximity (Chap. 15).

A salt-induced high on the seafloor can develop substantial relief over the surrounding region. A rich biota of bioherms and associated grainstone flats can form in shoalwater tropical seafloor settings. In the deeper water settings of the allochthons in the Gulf of Mexico the areas atop extrusive salt tongues have a relief measured in hundreds of metres above the surrounding seafloor (Table 6.5; Fletcher et al. 1995). Such deep seafloor highs tend to channel turbiditic sands into the relative lows along the allochthon edge. While the salt is replenished (salt fountain stage), the region about the salt remains a topographic high. The maintenance of the salt at or near the sedimentation surface by periodic overburden shedding means that both the active and the passive stages are characterised by many unconformities, debris aprons and thinning of strata in the vicinity of the diapir crest.

Three-thousand-year-old coral reefs that now lie some 18 m above sea level along the onshore portion of the active Al Salif diapir, Yemen (Davison et al. 1995, 1996b). This active stage diapir has lifted its roof and continues to do so today. The nearby Jabal al Milh diapir is the much-reduced remnant of a formerly active extrusive structure on a Pleistocene carbonate shelf (Fig. 6.40b). In both, the highs atop the structures strongly influence the facies distribution of nearby carbonate and evaporite sediments. Offshore from this region are a number of depositionally similar islands and grainstone shoals that likely indicate sea floor shoaling atop other diapirs and salt walls in the same Miocene salt.

Topographic lows form above peripheral sinks created atop areas of salt withdrawal. These are often areas of preferential sedimentation, that is, sediment thicks. Loading associated with accumulation of sediment in the sinks drives further salt flow. The lows persist until the salt is completely evacuated and a salt weld forms. Salt-flow induced highs and lows in the sedimentation surface persist until the diapiric ridge or crest is cut off from its supply by the formation of welds or touchdowns. Then the diapir and allochthon crests are buried by sediment that continues to aggrade until its thickness exceeds the piercement potential and the structure is no longer active.

Even though coal is not a sediment typically associated with evaporites, an ongoing low created during the formation of a suprasalt minibasin has preferentially accumulated a thick coal succession in the Pennsylvanian Joggins Formation, in the Cumberland Group of Nova Scotia (Waldron and Rygel 2005). This 1.5-km-thick coal-bearing unit is famous for upright fossil lycopsid trees, and is preferentially preserved in the Athol syncline in the western Cumberland basin. Seismic profiles show that the Athol syncline sits atop a salt weld and that the Joggins Formation thins on the flanks of adjacent evaporite-cored anticlines. During deposition of the Joggins Formation, at least 1 km of syndepositional subsidence was facilitated by flow of underlying salt into the adjacent anticlines.

Both subaerial and submarine glaciers are topographic highs at the time of salt emplacement so the syndepositional surface adjacent to a glacier is subject to slumping and mass wasting. Like a glacier of ice, a salt allochthon or namakier can spread out over its own moraine, so that the lower contact of a preserved allochthon is disturbed even while the salt rolls out over its own lower surface (Fig. 6.91). It seems that the preservation potential of salt wings and allochthons are higher if emplaced as a submarine glacier compared to a subaerial salt glacier (Peel et al. 1995). Submarine salt glaciers form in passive margin settings and are protected from pervasive dissolution by a thin membrane of supersaturated salt mud, which maintains its suprasalt position as the salt sheet is loaded and minibasins form in the relative quiescence of the sub-wavebase seafloor. Subaerial salt glaciers tend to form in compressive continental terrains where the salt source is more limited and their carapaces are exposed to the continuous rigours of subaerial weathering and rainfall dissolution. Caprocks atop salt glaciers in both settings can form either as biological precipitates or as accumulations of insoluble weathering products.

Siliciclastic Patterns

When a diapir crest is near the surface in a continental deltaic or fluvial setting it is a local topographic high focusing sand deposition into a series of stacked interdiapir channels. Even in a mature salt province, such as the modern siliciclastic Texas Gulf coast, salt structures are capable of maintaining a degree of topographic relief at the land surface and so act as a focus for off-structure fluvial sand accumulations (Fig. 6.97) and as a focus for sand distributions further out on the modern siliciclastic-dominated shelf (Morton and Suter 1996).

Through time, the salt crest's position in earth space is maintained by the withdrawal of salt from an adjacent rim syncline, with the creation of a topographic low in the landscape atop the sediment-accumulating rim syncline. The effect of this topographic differential explains the 10–100 % syndepositional thinning of lower Cretaceous Paluxy sands

over the Van and Hawkins salt pillows and the Hainesville diapir in east Texas and the associated stacking of fluvial sands in the interdiapir areas (Seni and Jackson 1983a). A net sandstone map shows that salt crestal areas contain between 5 and 20 % less sand as Cretaceous Paluxy sands were focused into withdrawal sinks between highs in the landscape created by the growing autochthonous salt structures (Fig. 6.98a). Sand pinchout and lateral passage into floodplain muds atop the various salt structures clearly shows that the thinning of the Paluxy sands onto the various salt structure crests is depositional, rather than a response to active piercement. Likewise, sand body distribution in the Paleocene-Eocene Wilcox Group around Bethel and Oakwood domes in the southern East Texas Basin indicate the effects of dome induced topography on coeval fluviodeltaic sedimentation in this Tertiary landscape (Fig. 6.98b; Seni and Jackson 1983a). To illustrate, there are four stacked channel-fill sands, each more than 15 m thick, in the rim syncline immediately east of the Bethel Dome. In contrast, there is only one sand body more than 15 m thick in the strata over the Bethel Dome, yet the percentage of sand in the thinned crestal succession is only slightly lower than in the stacked sands. Paluxy sands in the East Texas Basin were deposited around the basin margin as part of the Lower Cretaceous Trinity Group. At the same time, but further out in the basin, shelfal sediments were dominantly carbonates of the James Limestone and the Glen Rose Formation. There seafloor highs atop salt structures and turtle structures controlled local patterns of carbonate reef and shoal sedimentation (Fig. 10.55).

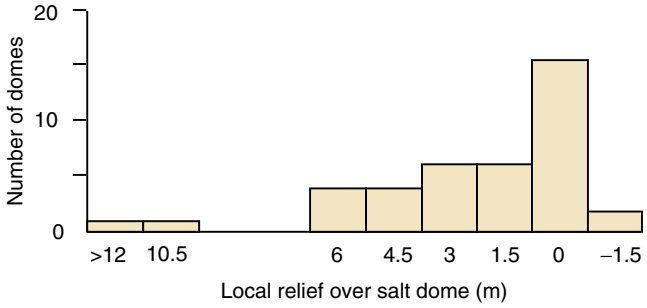

Fig. 6.97 Topographic relief developed over buried salt domes in the uppermost Texas coast (Beaumont-Port Arthur area; after Seni and Jackson 1983a)

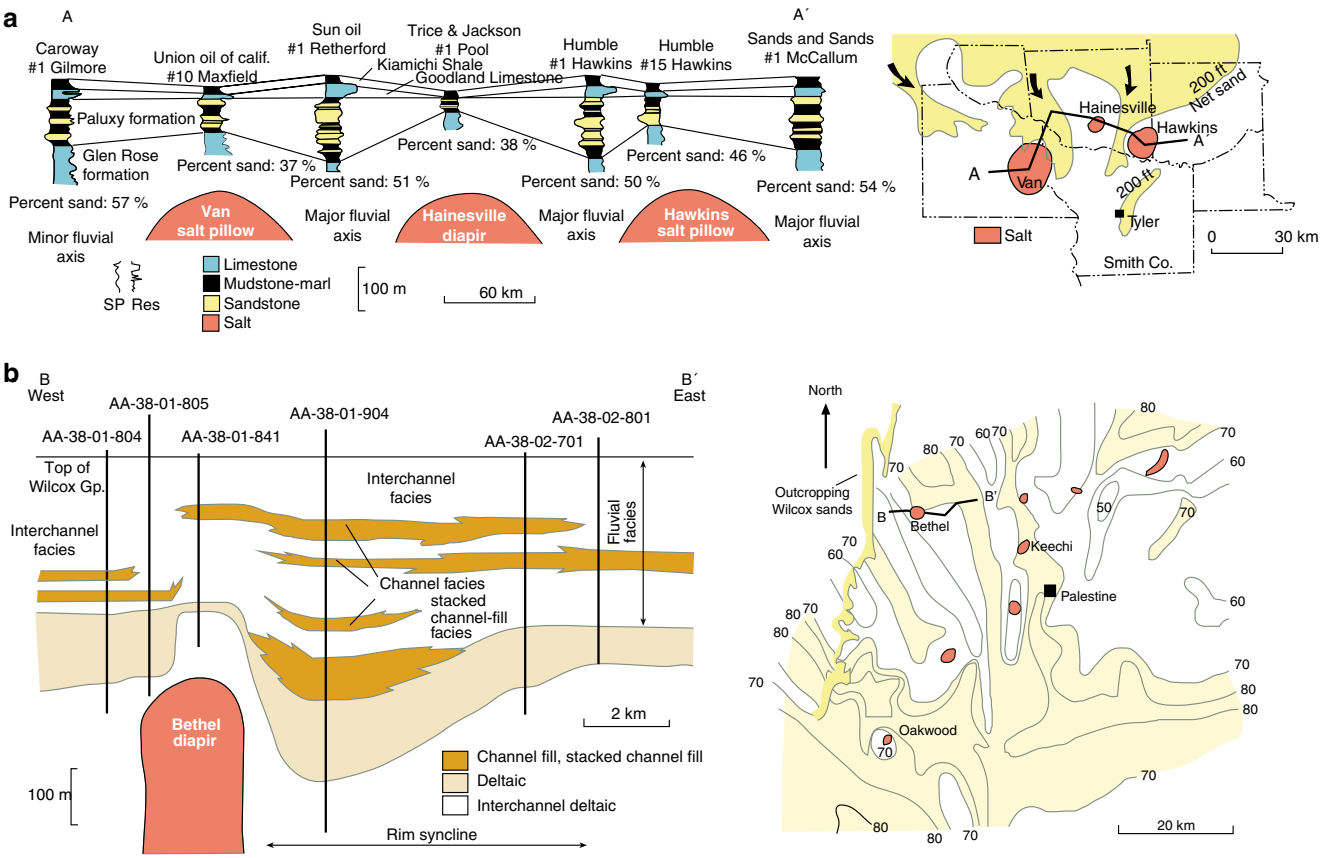

Fig. 6.98 Interaction of fluviodeltaic sedimentation and diapirism. (**a**) Decreased thickness and sand percentage over Van, Hainesville and Hawkins salt structures in East Texas Basin indicate that fluvial systems bypassed topographic swells over salt structures during Paluxy deposition. (**b**) Cross section across top of Bethel diapir and a percentage sandstone map showing how stacked fluviodeltaic sands of the Eocene Wilcox Group in the southern part of the East Texas Basin pinch out over the crest of the structure (After Seni and Jackson 1983a)

Salt squeezing at the basin scale created minibasins patterns that captured first cycle arkosic sediments in depositionally-loaded suprasalt "Haima pods" of the Thumrait region in the southern part of the South Oman Salt Basin (Fig. 6.99; Al-Barwani and McClay 2008). Palaeozoic fluvial depositional loading drove deformation of the thick sequence of underlying early Cambrian Ara. It created the various Haima "pods" or minibasins atop the loading and deflating salt mass. Syn-kinematic, predominantly clastic units of the Nimr and overlying Mahatta Humaid groups were deposited in these mini-basins. An interplay between depositional loading and salt withdrawal explains the marked lateral thickness variations of up to 1,000 m over 10 km laterally. Seismically, the underlying Ara Salt is typically opaque, with internal character obscured by multiples, generated by sub-horizontal reflectors higher in the section. Where internal salt geometries are imaged, complex internal structures are observed.

The main depositional stages and associated salt loading/deformation was driven mainly by pulses of sediment progradation sourced from the tectonically active upland to the west and northwest of the basin. Four main evolutionary phases for the mini-basins were defined by Al-Barwani and McClay (2008). Pre-existing basement topography and regional faults played a role in triggering and delineating the regional salt trends. That is, many of the salt ridges and salt walls parallel the main basement trends as seen in the regional aeromagnetics. This part of the South Oman Salt Basin has retained much the same facies distribution atop the salt since the Devonian, when clastic loading largely ceased. In contrast, in northern Oman, six salt domes have pierced the surface due to the reactivation of major basement faults and their caps still retain Ara salt as outcrop (Peters et al. 2003; Schoenherr et al. 2007a, b).

In a similar fashion, the fluviolacustrine sediments in the Triassic Chinle and Moenkopi formations, Paradox Basin, Utah responded to changes in the rate of accommodation space creation, driven by the interplay between climate, the rate of rise of salt walls and sediment loading (Fig. 6.99b; Matthews et al. 2007; Banham and Mountney 2014). Fluviolacustrine strata (mostly braidplain reservoirs) host significant hydrocarbon volumes in salt-confined minibasins, characterized by syndepositional growth of passive salt walls and diapirs. Two predictive models were identified

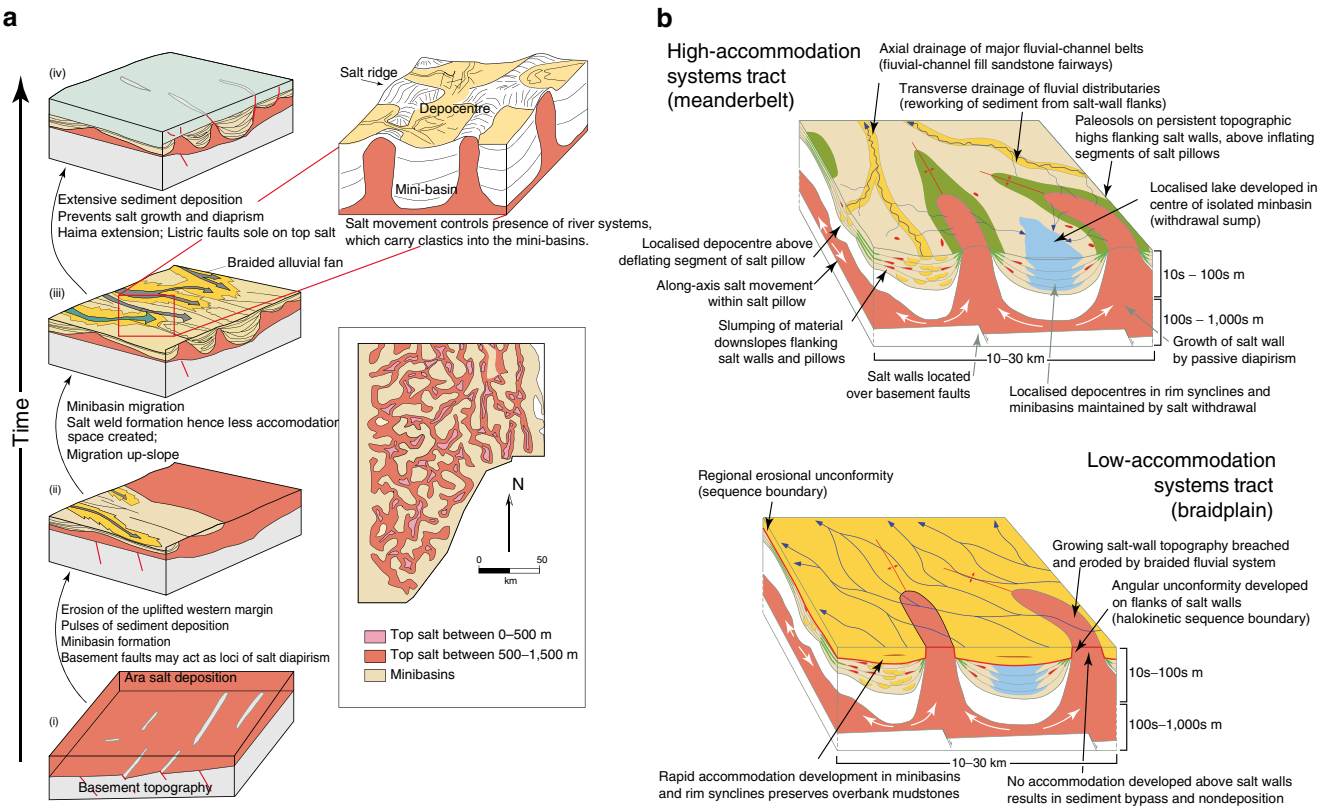

Fig. 6.99 Interactions between braid plain sediments and salt structures. (**a**) Basin scale schematic showing how pulsing sediment loading drove the formation of minibasins in the Thumrait area, Oman. Haima Group siliciclastics filling the various salt-floored minibasins show strong lateral thickness variations. The inset shows the actual scale and distribution of the numerous suprasalt minibasins in relation to top of the Ara salt (After Al-Barwani and McClay 2008). (**b**) Sequence stratigraphy in the Chinle Form, Utah and the differences in deposition style at times of high accommodation (meanderbelt) and low accommodation space creation (After Matthews et al. 2007; See text for detail)

(Fig. 6.99b; Matthews et al. 2007): (1) Low-energy fluvial systems and/or relatively high regional accommodation regimes (high-accommodation systems tracts) were controlled by localized, salt-induced topography. Fluvial sand fairways are confined to the axes of rim synclines, minibasins, and deflating salt-pillow segments (i.e., areas of salt withdrawal) that were occupied by regional fluvial-drainage systems; (2) High-energy fluvial systems and/or relatively low regional accommodation regimes (low-accommodation systems tracts) exhibit less local variability because rivers could breach and erode salt-induced topography. Such strata are characterized by widespread sheet sandstones, which thicken in areas of salt withdrawal.

A similar system of salt-related subsidence controls the stacking of fluvial channels in withdrawal sinks (minibasins) in Permian clastics of the southern Urals, Russia (Newell et al. 2012). There, calcrete carapaces tend to occupy intervalley highs atop buried saltwall crests.

Reactivation of pre-existing salt structures in parts of the North Sea, driven by the Alpine orogeny in the Cretaceous and early Tertiary, has squeezed diapir crests. In places along the continental slope they became topographic highs as deep seafloor sediment was accumulating. The syndepositional high then influenced deepwater sand distribution patterns (Figs. 6.80). The squeezed diapir's shape and its freeboard height above its surrounds influenced flow directions, current speeds, and thickness of turbidite sands accumulating as various fan lobes atop withdrawal sinks adjacent to the squeezed diapir high.

This was the case in the Eocene during the deposition of the deepwater Tay sand, which now constitutes the main reservoir in the various Gannet fields (Fig. 6.100a; Armstrong et al. 1987). Reservoir sands are broken down into three units; the lower, middle and upper sands, all deposited in a shoaling submarine fan complex. The area is underlain by various squeezed diapirs and some, like the Gannet North diapir, have exerted a major control on sand thickness and sand distribution. The seafloor highs, generated by areas of shallow reactivated Zechstein salt structures, created sand pinchouts as salt-cored highs deflected dense turbidity flows away from their edges (Fig. 6.100b). This minibasin system shows a classic vertical transition from stacked sheet to channel-levee geometries.

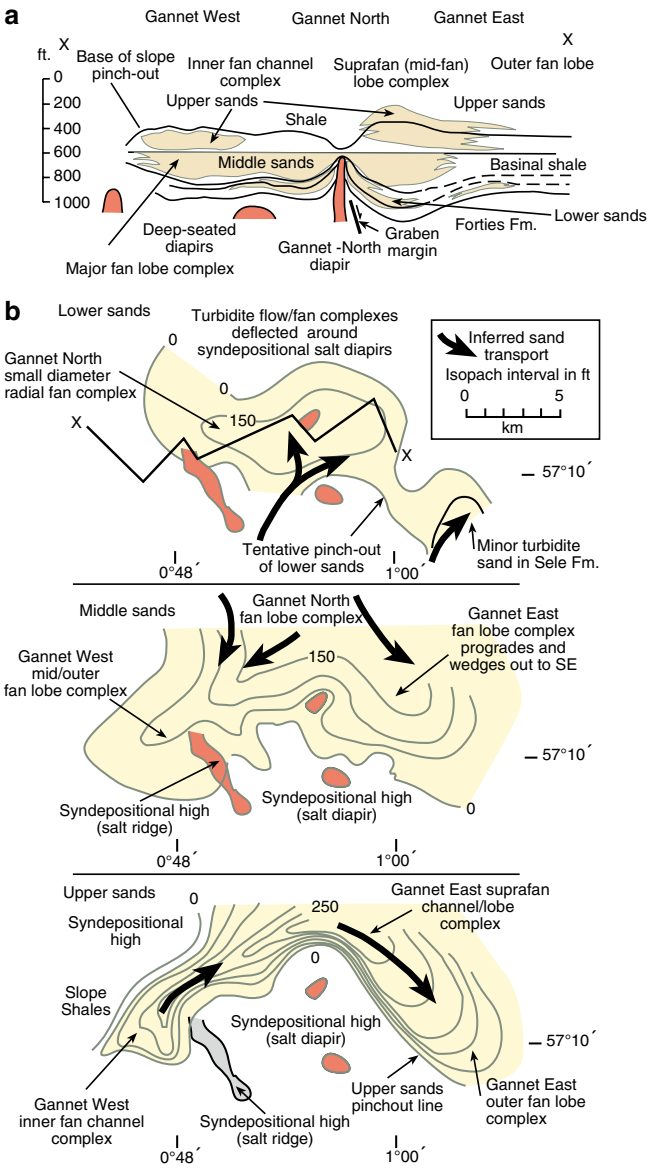

Fig. 6.100 Eocene Tay Sands of the Gannet area of the North Sea. (**a**) E-W cross section showing a strike section through the lower and middle sands and a proximal to distal section through the upper sand. Note the influence of reactivated diapirs on sand distribution. (**b**) Palaeogeographic reconstruction for lower, middle and upper sand intervals showing the effects on sand/fan distribution of diapir-induced syndepositional seafloor highs (After Armstrong et al. 1987)

Carbonate Patterns

The multiplicity of depositional settings above and around reactivated salt-cored highs in the Arabian Gulf gives an insight into the geometries of carbonate sands and porosity distribution in squeezed salt structures that are no longer extruding salt (Fig. 6.101; Warren 1989). Salt-cored seafloor highs surrounded by deeper gulf waters do not show the effects of widespread current reworking. These structures simply shed shallower water sediments centripetally into deep sub-wave base depths (Fig. 6.102). Facies patterns tend to form concentric rings, with the best-sorted sediments at or near the crest of the now buried structure. Sediment patterns tend to become more elongate and stream in the direction of current transport once the depositional surface lies above wave base. In the case of the various grainstone and rudstone shoals of the Great Pearl Bank this largely reflects waves driven by the Shamal. When exploring for porosity in an ancient counterpart one would drill on or near the crest of the structure, as identified in seismic.

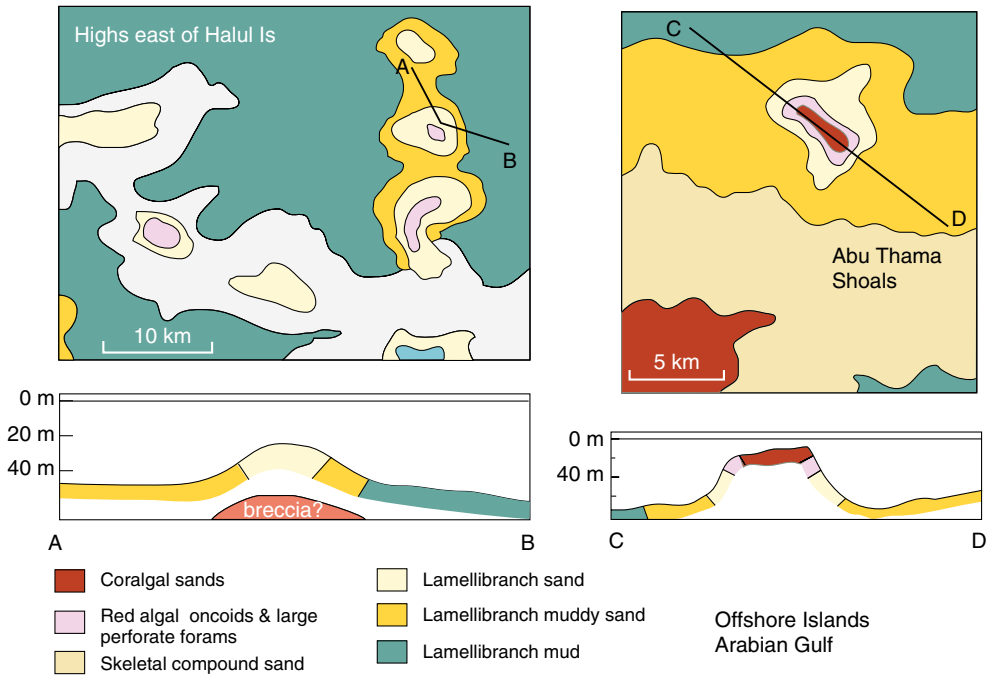

Fig. 6.101 Sediment distribution on sea floor shoals atop buried salt structures on the floor of the Arabian Gulf (After Purser 1973 a, b). See also Fig. 7.30

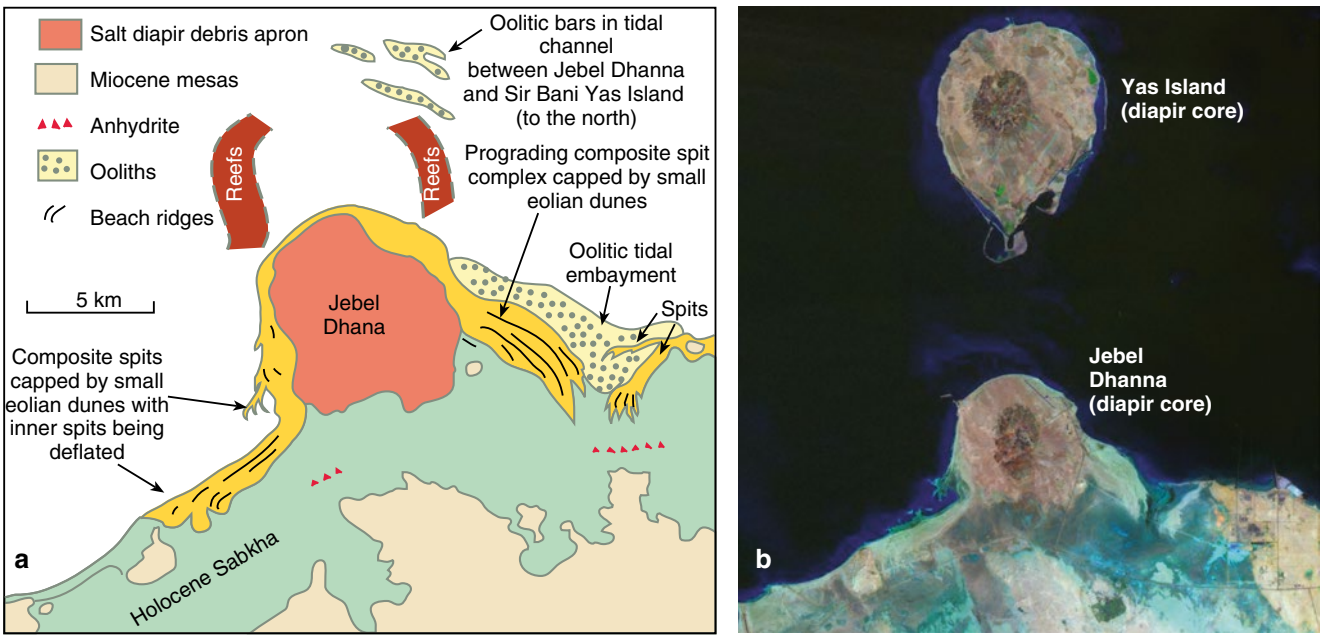

Fig. 6.102 Sediment distribution controlled by the near coastal and coastal shoals created by Jebel Dhanna and Yas Island diapirs, coastal Abu Dhabi, see Fig. 3.3a for location. (**a**) Holocene sediment coastal patterns and tails in the vicinity of Jebel Dhanna (In part after Kirkham 1997). Note that seaward extension of active reefs and offshore oolite bar thicks are both controlled by the position of the diapir. (**b**) Landsat 2000 image of coastal zone clearly shows diapir breccias forming cores to both diapiric outcrops (Image courtesy of NASA; the surface is now (2015) overprinted by refinery infrastructure)

Intermediate water depth highs in the Arabian Gulf are surrounded by waters of moderate to somewhat greater depths. Sediment shed from the carbonate high is reworked by tides and other currents, both across the high and into the shoal water areas surrounding the high. Often, this type of structure generates a down current sediment tail, creating a strong asymmetry to any reef or sand buildup on the structure itself. Sediment tails can be quite thick and extensive; off Dalma Island in the Arabian Gulf the modern downwind grainstone tail attains thicknesses of 20 m and is measured in kilometres. Exploring for relict primary porosity on the ancient equivalent of this type of marine platform structure

involves drilling both on or near the crest of the structure, as well as expecting and drilling sand trends that cut across the structural crest (Lomando et al. 1984; Lomando 1999).

The observation that sediment tails about Arabian Gulf salt structures tend to trend in the same direction as the prevailing winds of the region is a useful predictive tool. Once the position and trend of any ancient grainstone shoal is established about an individual salt structure, likely grainstone orientation and position of potential reservoirs about other time equivalent diapirs in the region can be predicted as likely to occur in the same quadrant. In the case of the Great Pearl Bank the region about the salt structure highs with the highest probability of sand occurrence lies south to southeast of the salt-cored seafloor high (Figs. 6.101 and 6.102).

In near coastal settings in the southern Arabian Gulf the windwave sediment trend is often modified by coastal parallel (longshore) transport processes. Leeward sediment tails often extend from the high to the shoreline, generating a progressive shallowing between the high and the mainland that ultimately create a tombolo. Studies of the peritidal sand tail that extends from Yas Island onto the mainland at Jebel Dhanna show that shallowing increases the velocity of tidal currents. This causes the sequence to shoal upward from bioclastic grainstones and wackestones into oolite shoals that trend at an oblique angle to the trend of the sediment tail (Fig. 6.102; Warren 1989). The Jebel Dhanna diapir-cored high also controls the seaward extension of Holocene sabkha in the coastal plain behind the headland. Such tombolo links between diapir-cored island shoals is not restricted to tropical shallow carbonate seaways. The modern siliciclastic sand shoals joining diapir-cored Magdalen Islands in the Gulf of St. Lawrence, Canada, are another such diapir-linked tombolo system. In this case they are located in a cool-temperature seaway at a latitude of 47°N.

In the modern Gulf of Mexico, a reef system is actively accumulating coarse biogenic sediment atop a salt cored high in the Flower Gardens Bank. Upper-slope siliciclastic deepwater muds completely surround the reef-capped high. Carbonate buildups top the Flower Garden Bank because of the shoaling effects of salt just below the seafloor. A brine lake occupies the central part of East Flower Garden Bank (Rezak and Bright 1981). Collapse foundering over the crest of the structure generated the graben that houses the lake, while ongoing salt dissolution and the focused escape of basinal brines maintain the dense waters of the lake. Healthy growing corals surround the lake, except where a canyon cuts a brine lip across the bank to the deep open seafloor. Halokinesis beneath the Flower Garden Banks has converted an otherwise muddy siliciclastic platform into a region suitable for carbonate reef growth. Shoaling lifted the seafloor into a clear, well-lit environment and has created a carbonate buildup in what is otherwise a muddy, siliciclastic province. Brine seeps atop salt allochthons, located in much deeper waters at the foot of the continental slope, have allowed chemosynthetic mussel communities (biostromes) to flourish at water depths that are a kilometre or more below the base of the euphotic zone (Chap. 9).

Ancient counterparts to the salt-cored islands in carbonate seaways, that is areas where carbonate sedimentation patterns are controlled by seafloor shoaling, occur in numerous diapir provinces ranging in age from Proterozoic to Neogene. Hydrocarbons and base metals have accumulated in brine lake laminites associated with some of these buildups (Warren 2000b; Chap. 15). For example, a series of Neoproterozoic stromatolite reefs fringe the western edge of the Enorama Diapir in the central Flinders Ranges (Fig. 6.103; Lemon 2000). The enclosing stratigraphic unit, the Enorama Shale, is the locally-named interglacial succession, lying between the Sturtian and Marinoan (Varanger equivalent) glacigenic units, thereby placing reef growth within the upper Cryogenian. A reef core facies of cumulate stromatolite domes first formed as mounds, which interfingered with the surrounding sediments, then as reefs, which stood well above the sea floor. Many mounds formed preferentially atop large debris blocks carried to the surface by diapiric salt.

The Enorama diapir breccia blocks are typical of many diapir remnants (stems and welds) in the Central Flinders Ranges (Lemon 2000). The breccias atop former salt stems and their surrounding debris aprons are made up of red and grey shales, sandstone blocks with halite casts, yellow dolomites with chert pseudomorphs of gypsum and anhydrite, and large blocks of amygdaloidal basalt and dolerite. All these blocks were carried up through the stratigraphy by allochthonous – autochthonous salt sources in the mother salt bed in the Callanna Group. Interaction with the surrounding sediments and inclusion of breccia fragments in the reefs and mounds shows continual movement and exposure of the diapir occurred throughout the deposition of the lower two thirds of the Enorama Shale. Lenses of diapir-derived polymict conglomerate are common along the flanks of the Enorama diapir and many of these show extensive evidence of shorezone reworking. Pebbles of conglomerate in cobbles of conglomerate within boulders indicate several phases of deposition followed uplift and erosion. The conglomerates commonly have a dolomicrite matrix, which cements very early to allow the reworking to be recorded. Thickening of the Enorama Shale towards the Enorama Diapir is particularly evident in the stacked halokinetic sequences at the northern end of the diapir. Associated stacked conglomerate lenses that thicken toward the diapir stem, show this was an area of ongoing aggradation and syndepositional growth of the diapir stem as it fed salt into various allochthon sheets, salt wings and Christmas-tree diapirs (Dyson 1998).

As the edge of the active diapir was unstable at times, not all mounds progressed to reefs. The maximum size of a mound plus reef at Enorama is $\approx$ 50 m high and 200 m across

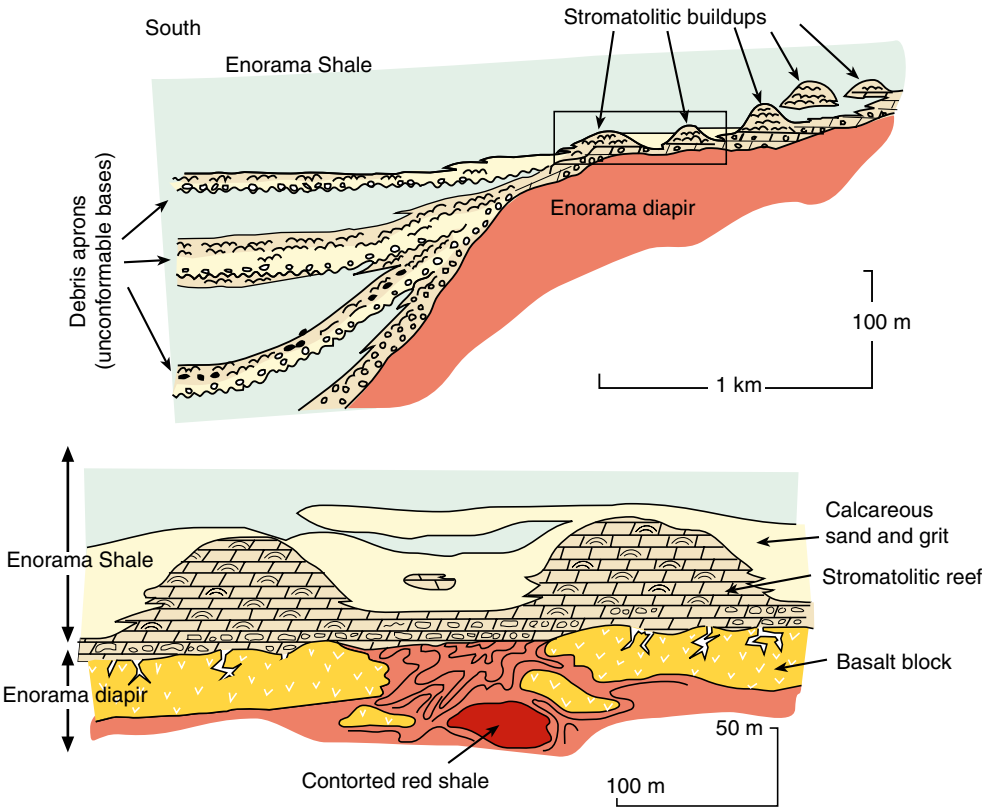

Fig. 6.103 Palinspastic reconstruction of part of the western Neoproterozoic margin of the Enorama diapir, Flinders Ranges, Australia Lower figure shows detail of contact of reef with diapiric breccia (After Lemon 2000)

the base. Syndepositional diapir activity is indicated by tilting of the surrounding sediments and by inclusion of insoluble debris shed from the diapiric island. Progressive movement is shown by cannibalisation and reworking of coarse shoreline conglomerates (Fig. 6.103). Diapir movement continued after deposition of the reefs ceased so that the entire succession in the drag zone close to the diapir is tilted up to near vertical in what would be called the shale-sheath position in a siliciclastic interval.

Enorama reefs interfinger with both shallow water limestones of the Etina Formation and deep water siltstones of the Enorama Shale. The base to the middle of the Enorama Shale is a transgressive systems tract, deposited during a steady rise in sea level. Onlap onto the diapiric island is marked by backstepping of each reef higher in the section (Fig. 6.103). Backstepping occurred as a number of pulses, each marked by channels of conglomerate shed from the diapir and by progressive convergence of local angular unconformity surfaces. Small pulses of salt uplift caused reefs to recolonise on higher ground, sometimes on previous reef growths, sometimes establishing a new mound. The reefs drowned as the sea floor next to the diapir subsided into the peripheral sink that flanked the diapir. On a mesoscale, the reefs are composed of a series of stromatolite mounds up to 6 m high and 15 m long. Lamination within the mounds is wrinkled and quite unlike nearby isopachous stromatolites that are characterised by smooth laminated micrites. The latter grew in shallow water as Etina limestones and are interbedded with the older parts of the widespread reef complex. The microscale wrinkly structure of the reef has a distinctive clotted texture with filamentous linkages, reminiscent of calcareous alga like *Epiphyton* or *Renalcis*. The entire reef complex has been completely dolomitised, probably by solutions emanating from the diapir. Early dolomite cement has allowed mimetic preservation of sedimentary textures and some minor porosity.

In summary, the reefs grew during a time of sea level rise and show a close relationship with rises in the Enorama Diapir, with each deepening upward reef succession being a response to a pulse of diapir growth. The diapir provided an area of shallow water around an island at a time when deeper water marine shale was being deposited in the rest of the basin. The mound to reef transition shows 'catch up' and 'keep up' growth habits, but the sudden demise of each individual reef appears related to a subsequent pulse of salt movement on the diapir, not to broader eustasy.

Sediments Tied to Salt Basin Evolution

There is an ongoing interaction between near-surface and at-surface flowing salt in sedimentary basins and consequent landscape elevations. This is seen in the resulting suprasalt or intersalt sedimentation patterns.

Suprasalt Clastic Sedimentation

Alexander and Flemings (1995) documented the spatial and temporal distribution of siliciclastic sand within an evolving Pliocene-Pleistocene salt-withdrawal shelf minibasin in the Gulf of Mexico; the Eugene Island Block 330 field. Part of it is a giant oil and gas field in offshore Louisiana and is located immediately landward of the deeper water Green Canyon area. The minibasin evolved through three phases: prodelta, proximal deltaic, and fluvial (Figs. 6.104). In the prodelta phase, bathyal and outer neritic shales and turbidites loaded and mobilised the underlying salt sheet (Fig. 6.104a). During the proximal deltaic phase, salt continued to withdraw from beneath the minibasin, and lowstand shelf margin deltas remained focused at a regional growth fault zone on the northern margin of the minibasin (Fig. 6.104b). Sediment accumulation and fault slip rates were high, as thick sequences of deltaic sands were deposited adjacent to the fault system. During the final fluvial phase, salt withdrawal waned; consequently, the creation of accommodation space within the minibasin ceased (Fig. 6.104c). The basin filled and, during lowstands, deltaic systems prograded southward. Unconformities developed in the minibasin during these lowstands. During transgressions, thick packages of shallow-water deltaic and fluvial sands (capped by shales) were deposited on top of the unconformities.

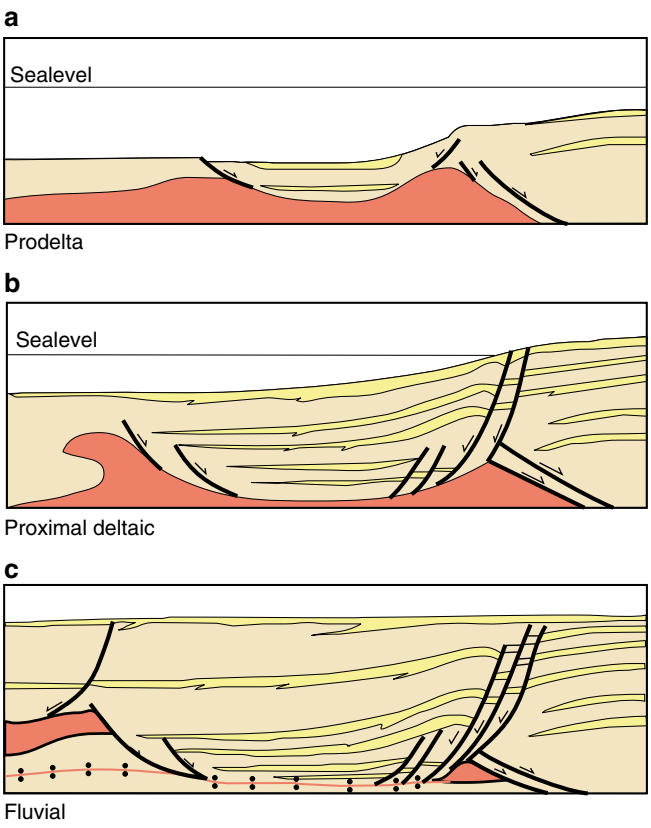

Fig. 6.104 Schematic of three-phase depositional evolution of intrasalt basin fill in the 330 Block, Gulf of Mexico (Alexander and Flemings 1995). Evolution began prior to 2.8 Ma and continues today

On a salt-floored continental margin that is being loaded by fluvio-deltaic wedges, the transition from deep water, when the floor of the minibasin first begins to subside as it is loaded, into a shelf and deltaic system is a natural evolution. The sedimentation model documented by Alexander and Flemings (1995) has a wider application to other salt-floored passive margins. Some authors in the Gulf of Mexico prefer to divide minibasin sedimentation into shelf-loaded and slope-load subcategories, but recognise it is all part of a feedback between basinward salt flow of the allochthon sheet and sediment loading (Figs. 6.42). Once the salt is evacuated from beneath a minibasin the basin can no longer subside and the depositional locus shifts basinward into the next minibasin atop the next tier of the allochthon. In the case of the Eugene Island minibasin this did not occur until the basin was filling with shelf sediments. In other basins this can happen while turbidites are still accumulating in the withdrawal sink. In this case the basin no longer accumulates turbidites, which now bypass the basin on their way downslope to the next active depopod.

Turbidite fill in Gulf of Mexico minibasins of the northern Green Canyon and Ewing Bank areas has been modelled by Rowan and Weimer (1998). They found that at the highest order of scale, external factors dictated the volume and type of systemwide clastic input. Regional factors, such as nearby salt structures and the position of deltas, then controlled the dispersal of the clastics to the continental slope. Local factors, such as the thickness of underlying salt, influenced minibasin-specific evolution. In the deepwater slope setting these factors interact at three scales: (1) a broad transition from sand-rich ponded settings to shale-dominated bypass settings during the Pliocene-Pleistocene, (2) fluctuations over periods encapsulating several sequences creating highly variable stratigraphic stacking patterns, and (3) a progression from ponded to bypass facies within individual sea level cycles. The most sand-rich gravity flows in an ideal sequence are deposited in the minibasin at the beginning of a sealevel cycle (i.e. during the lowstand) giving rise to sheetlike geometries. A transition to more mud-rich gravity flows leads to the formation of a channel levee system, where flows tend to be channelized and more organised. The gradual decrease of sediment volume within individual gravity flows during a sea level cycle increases the hemipelagic content (mixed pelagic and gravity flows) and eventually passes into a condensed section typified by pelagic mud-rich sediments or foraminiferal-rich oozes. The idealised fining upward succession is complicated by varying rates of salt withdrawal from the minibasin, which influences the volume of accommodation space within the minibasin. The distribution of accommodation space can be further complicated if the crest of a diapir undergoes dissolution to create a potential zone

for further sediment accumulation. Slides and slumps can occur anywhere within a sequence; they can originate from local slope failures or from oversteepened delta fronts and can be triggered by salt movement, dissolution or can be seismically induced.

Suprasalt Carbonate Sedimentation

La Popa Basin, Nuevo Leon, Mexico, is a salt influenced foreland basin near Monterey in Mexico, with excellent exposures of halokinetically influenced sedimentation around three salt stems (La Popa, El Papalote and El Gordo diapirs) and along the 25 km La Popa salt weld/wall (Fig. 6.105; Giles and Lawton 1999; Giles and Goldhammer 2002; Shelley and Lawton 2005; Buck et al. 2010). As in the Flinders Ranges, reef growth is a halokinetic response to pulses of diapir growth. A number of thick (<600 m) coral, sponge, red algal reefs, exposed as a series of carbonate lentils, are the most obvious sediments associated with halokinetic seafloor shoaling. These carbonate buildups, the La Popa, San Jose, El Toro and El Gordo lentils, developed as shoals atop significant seafloor highs created by the passive rise of salt diapirs during the Cretaceous and Lower Tertiary in what was a dominantly fine-grained siliciclastic shelfal environment.

The La Popa structure is interpreted as a 25 km long salt weld with parallel flanking synclines, previously it was

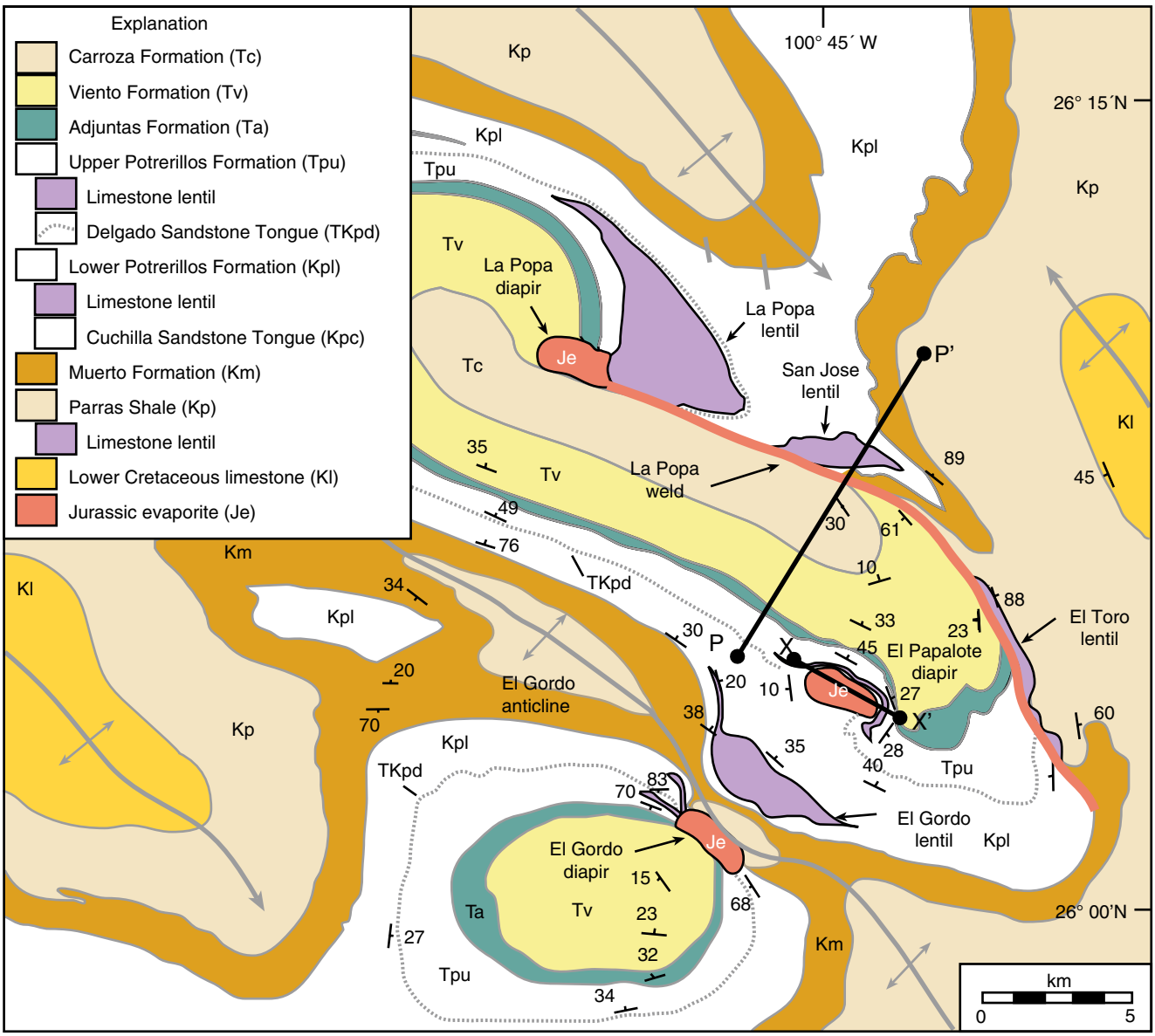

Fig. 6.105 Geologic map of the La Popa Basin, Mexico. Anticlinal fold axes indicate structures attributed to the Hildagoan (Laramide) shortening (After Giles and Lawton 2002). P–P′ and X–X′ are the locations of cross sections in Figs. 6.106 and 6.107

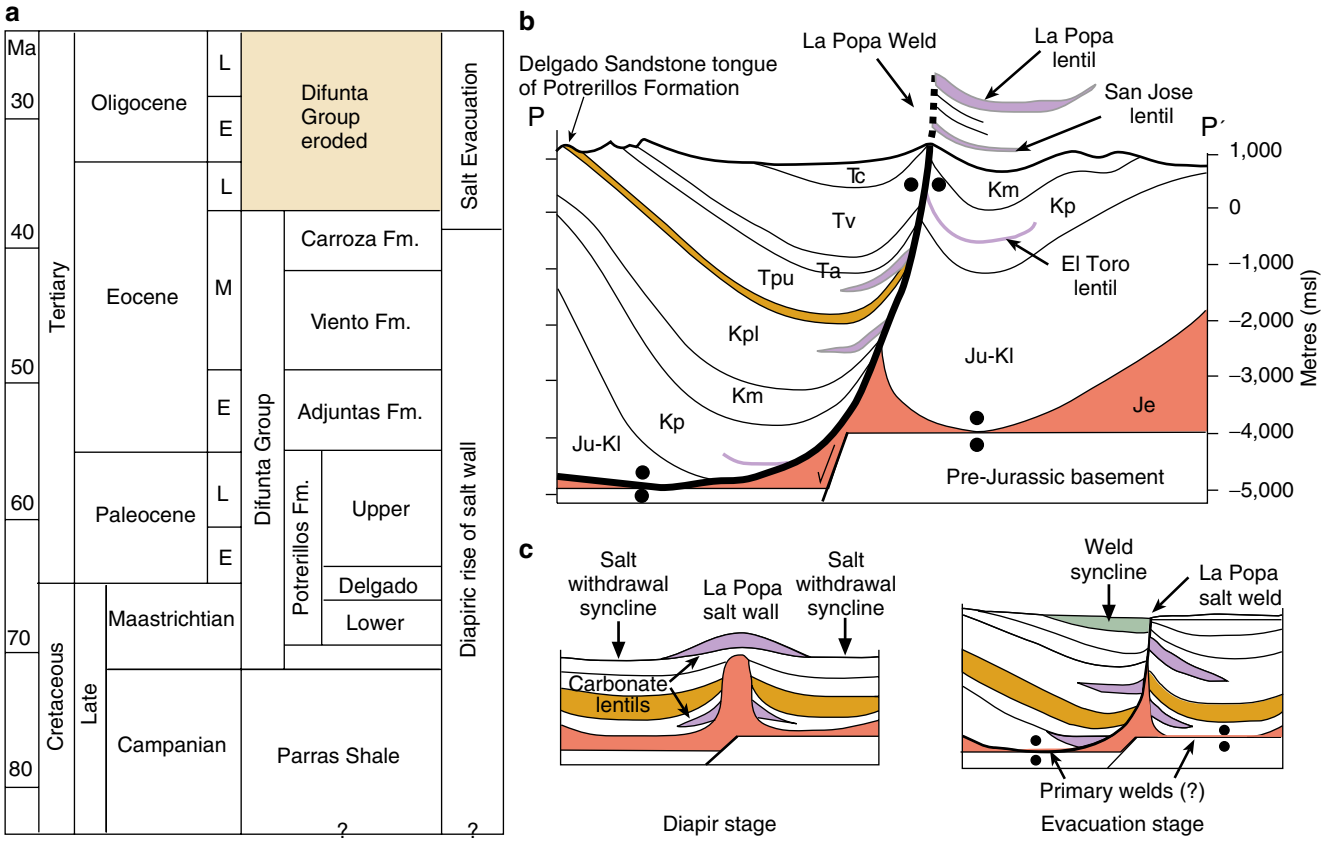

Fig. 6.106 The La Popa salt weld. (**a**) Stratigraphy of the La Popa Basin during the time when salt flow occurred (*L* Lower, *M* Middle, *U* Upper). (**b**) Cross section of the La Popa weld (see Fig. 6.105 for position). (**c**) Interpreted evolution of the La Popa structure (After Giles and Lawton 1999)

considered to be a reverse fault (Fig. 6.106a, b; Giles and Lawton 1999). The displacement surface is convex to the southwest and dips south to southwest. Stratigraphic displacement at the surface is zero at either end, and increases to ≈ 5 km halfway along the trace of the structure. The structure is the result of hangingwall subsidence during evacuation of Jurassic salt along a former diapiric salt wall. Sedimentation patterns on either side of the weld indicate the La Popa structure experienced a two-phase history in Late Cretaceous to Eocene time: (1) A diapiric phase marked by rise of an elongate, arcuate salt wall that was symmetrically flanked by withdrawal synclines; (2) a subsequent evacuation phase recorded by substantially increased subsidence of the hanging wall relative to the footwall and the stratigraphic "welding" of footwall and hanging wall along a steep planar discontinuity (salt weld) created as salt withdrew from the former diapir.

Superb exposures (over 10 km along strike) of the largest reef complexes along the northern side of the La Popa Weld show that during the diapir stage these Paleocene lentils initially accreted as coral, sponge, red algal reef and oyster biostrome complexes atop and immediately adjacent to the La Popa salt wall (Fig. 6.106c). Large, steep (200 m relief over 0.5 km) forereef clinoforms indicate northward (downwind) progradation of the La Popa lentil away from seafloor high created by the La Popa salt wall. With a probable lowering of the local rate of salt induced uplift near this part of the salt wall, this reefal system was subsequently truncated, onlapped and possibly overlapped by a southward prograding grainstone bar complex. This shoal was derived from a separate source to the north, perhaps from another salt-related bathymetric high tied to the La Popa Diapir. To the north and west of the La Popa diapir, the two carbonate complexes coalesced through time to generate a continuous carbonate sheet that now defines the La Popa lentil. It extended more than 5 km within what was at edge of a low created by a salt withdrawal/contractional syncline as salt was evacuated into the rising salt wall (Fig. 6.106c). Carbonate strata thin and become siliciclastic away from the La Popa salt wall and are intercalated with siliciclastics in the footwall syncline. The Delgado Sandstone Tongue of the Potrerillos Formation is a shelfal sandstone/siltstone that was deposited during salt wall growth as a complex, wave-dominated, eastward-prograding deltaic depositional system. Typical parasequences in the siliciclastic section comprise offshore shales overlain by lower to upper

shoreface sandstone. The Delgado Sandstone contains a lower, progradational parasequence set; it is part of a high-stand system tract that is in turn part of the underlying Middle Siltstone Member of the Potrerillos Formation. It also contains an upper retrogradational set, which is part of a transgressive system tract that persisted into the Upper Mudstone Member. The two system tracts are separated by an erosional sequence boundary that incises up to 10 m of underlying strata and locally preserves a lowstand system tract within the incised valleys.

During growth of the salt wall in the Early Tertiary, thick prodeltaic and tidally-influenced shoreface siliciclastics periodically accumulated in the adjacent withdrawal syncline (Buck et al. 2010). Flute marks on bases of turbidite beds and channel axis orientations indicate a dominant palaeoflow along synclinal axes, with a component of flow away from the salt wall. Siliciclastic units thin and fine toward the salt wall, near which they are upturned and contain numerous synkinematic angular unconformities. During evacuation the volume of the wall declined, causing the synclinal hinge of the hanging wall to migrate laterally toward the developing weld. Hangingwall strata deposited during the evacuation phase thicken, rather than thin, toward the weld. They define the weld syncline where sand-rich fluvial channels are concentrated directly adjacent to the weld.

To the south of the La Popa salt weld are the El Papalote and El Gordo diapirs, they have similar dimensions and are located 5 km apart (Fig. 6.105). The at-surface diapiric material in both diapirs and portions of the weld is today a complex mixture of gypsum, anhydrite and salt-transported exotic blocks of metamorphosed mafic intermediate igneous rocks and Jurassic carbonates (Garrison and McMillan 1999). The gypsum is created by rehydration of the anhydrite caprock atop the Jurassic salt of the diapir core. Petrology and geochemistry of the meta-igneous blocks indicate derivation from partial mantle melting during Jurassic rifting with greenschist facies metamorphism dated at 146 Ma ($^{40}Ar/^{39}Ar$ dating of biotite and potassium in meta-plutonic blocks). This date is younger than that of the hosting Minas Viejas evaporite beds suggesting high heat flow from the basement continued into the latest Jurassic. The various sedimentary and volcanic blocks were likely intercalated in bedded salt prior to halokinesis, while the plutonics were intruded into the syn-rift fill and all were fragmented by extensional tectonics and salt flow. Vitrinite values in the suprasalt sediment in the vicinity of the El Gordo diapir show a high degree of asymmetry, with the highest R_o values ($\approx$1.44 %) immediately northwest of the diapir, possibly indicating differentiated fluid histories in the diapir periphery.

El Papalote diapir is located on a major fold limb and has experienced approximately 100 m of net shortening, whereas El Gordo is located along the axis of the same fold and has accommodated over 2 km of shortening (Rowan et al. 2001). The corresponding halo of diapir-related drape folding, which is at most 800 m wide at El Papalote, is up to 2 km wide at El Gordo. Carbonate lentils, which formed over the bathymetric highs associated with both diapirs, are overall shallower, thicker, broader and record fewer halokinetic sequences at El Gordo than at El Papalote. Sandstone units start thinning within 300–800 m of the edge of El Papalote but within 1,000–1,500 m at El Gordo. Differences in style and distribution of halokinetic strata about the two diapirs imply that the uplift histories of the two features were different and that the buildup atop the El Gordo structure more closely approached sealevel (Rowan et al. 2003).

Sediments flanking the El Papalote diapir have been studied in more detail than the other two structures with a view to defining typical successions in an ancient withdrawal sink and to test if such successions are amenable to sequence stratigraphic analysis (Figs. 6.107 and 6.108; Giles and Lawton 2002). At the time sediments were accumulating, diapir-flanking strata thinned toward the diapir and were characterised by abrupt lateral facies changes and intense local deformation. Strata can be broken out into a series of "halokinetic sequences," which are defined as unconformity-bounded strata, genetically related to halokinetic processes.

Each halokinetic sequence contains a basal debris-flow bed overlying an unconformity, which is angular directly adjacent to the diapir and becomes disconformable to conformable with increasing distance from the diapir. Debris-flow or mass wasting beds contain polymict clasts derived from the diapir and material that mantled the diapir (Fig. 6.108). At the various times these beds were forming the diapir crest was exposed at the sediment-water interface and shedding carapace debris into the surrounding sediments. These mass wasting deposits are dominated by carbonate clasts. They are interlayered with autochthonous reefal and biostromal strata and together constitute the lentils mentioned earlier. Hence, debris and mass wasting beds grade upsection into oyster- and red algal-rich carbonate banks. This carbonate section is then onlapped by black basinal shales and capped by upward-shallowing and coarsening, lower shoreface siliciclastic strata, which lack diapir-derived detritus (Fig. 6.108). This lack of diapir detritus indicates that the diapir crest was no longer at the surface or had insufficient seafloor relief to act as a sediment source. Lower shoreface deposits are abruptly overlain by outer shelf shales, which in turn underlie the angular unconformity of the next halokinetic sequence.

Each halokinetic sequence was generated by the waxing and waning of an episode of salt fountaining and salt glacier flow (Figs. 6.106c and 6.108; Giles and Lawton 2002). Periods of salt rise and salt glacier advance followed by retreat create unconformities near the salt structure. They

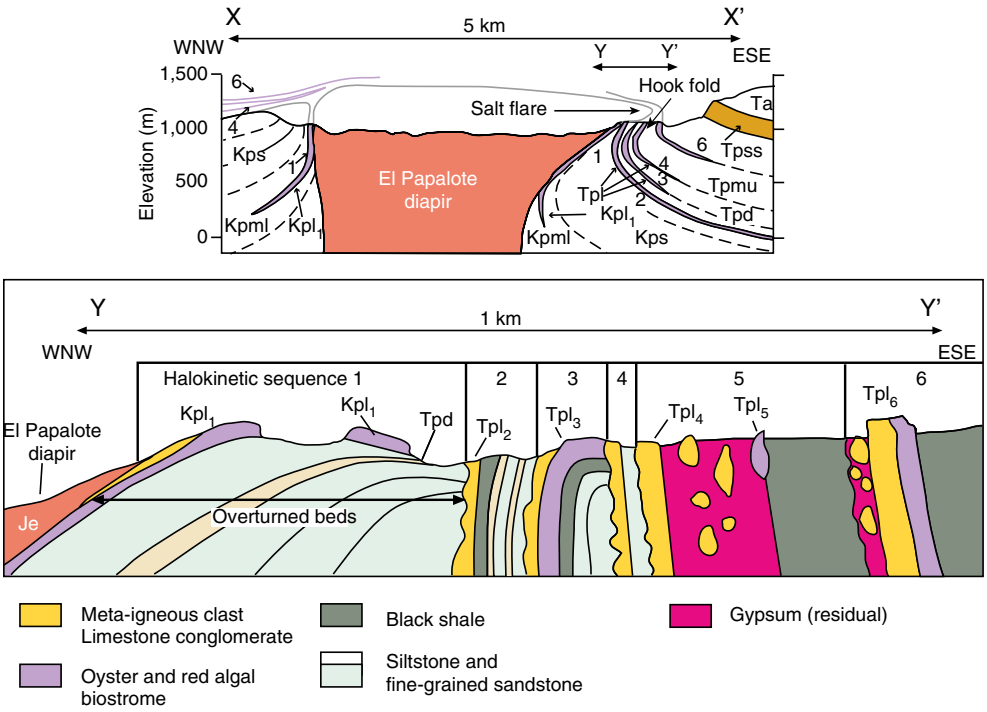

Fig. 6.107 Cross sections X-X′ and Y-Y′ through the El Papalote diapir (After Giles and Lawton 2002). Locality of cross section X-X′ is shown on Fig. 6.105

correspond to times of slow sedimentation and regional black shales in interdiapir withdrawal sinks. These black shales perhaps reflect basin deposition during deepening (maximum flooding events). Advances of glaciers over diapir-flanking beds provided a mechanism of deforming and overturning strata that underwent subsequent local truncation via subaqueous erosion processes during glacial retreat.

As in the modern Gulf of Mexico, glacial salt advance was also marked by development of a siliciclastic "shadow zone" on the downcurrent flank of the salt diapir high. Glacier advance at El Papalote is only displayed by strata on the east side of the diapir, indicating a down gradient flow of seafloor salt into the regionally extensive withdrawal syncline created by asymmetric salt supply to the adjacent and inflating La Popa salt wall. Quaternary counterparts to these carbonate debris aprons have been documented in weathering haloes about salt structures in the Arabian Gulf, while older counterparts occur in the Neoproterozoic salt structures in the Flinders Ranges of Australia. For example, Lemon (1985) documented and modelled similar asymmetric salt withdrawal controls on sedimentation about the Neoproterozoic Oratunga diapir in the Flinders Ranges, Australia.

Internally, the various halokinetic sequences show stratal onlap and thinning of beds toward the diapir. Adjacent to the diapir stem each halokinetic sequence is tightly folded and angular unconformities have truncation angle as high as 90° (Fig. 6.108b). The intensity of deformation and angle of truncation decrease rapidly away from the diapir and sequences are typically conformable by a distance of 250 m from the diapir and are known as hook[20] folds. The geometry resembles the hook of the letter 'J' (e.g. Sequence 3 in Fig. 6.107; Rowan et al. 2003). These 'J' hook folds and associated unconformities terminate directly against the diapir and outline salt cusps created by a combination of drape folding and fault reactivation during halokinesis. The amount of fault reactivation on these unconformities can be significant with the unconformity/fault preserving evidence of brittle shear and sense-of-shear indicators showing older beds were displaced away from the diapir.

Away from zones directly influenced by the diapirs and 'J' unconformities sediments tend to lack evidence of mass wasting and the interdiapir lows were filled by facies that shallow upward, from middle shelf lower shoreface shales to upper shoreface foreshore sandstones and tidal-lagoon sequences. These sequences do not terminate at the diapir but are spatially separated by a thick/wide package of older more tightly folded drag-zone strata (Figs. 6.107 and 6.108).

[20]Hook folds are defined by basal sequence boundaries that curve sharply upward within 50–200 m of the diapir contact and is truncated at up to 90° by an overlying unconformity marking the base of the next younger sequence (Fig. 6.107). Mass-wasting deposits are common at the base of the sequence, and facies change abruptly near the diapir. In contrast a wedge halokinetic sequence gradually taper toward the diapir and typically terminate against a truncating younger halokinetic sequence. The zone of drape folding is 300–1,000 m wide, angular truncation is typically less than 30°, mass-wasting deposits are less common than in hook halokinetic sequences.

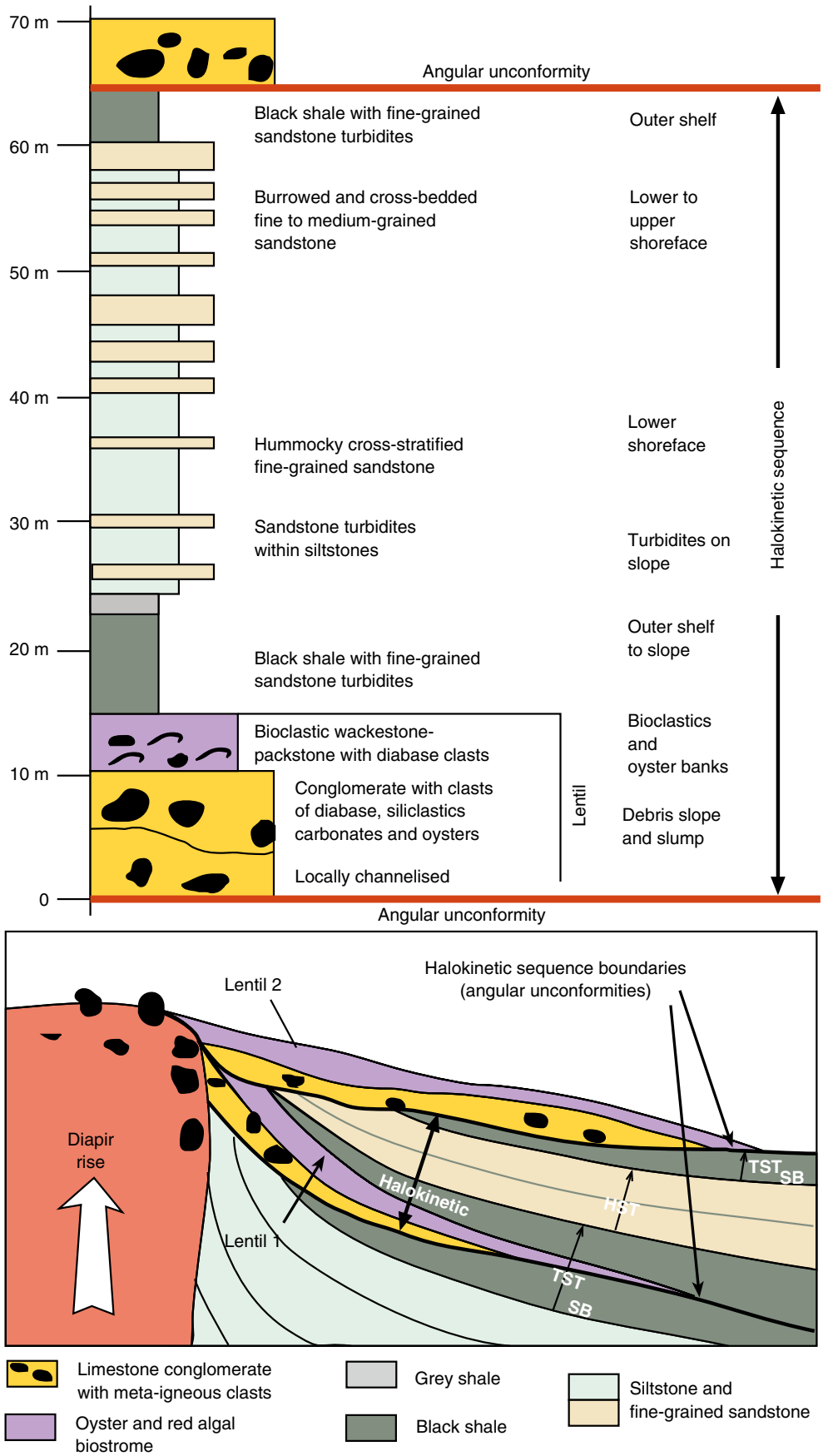

Fig. 6.108 Halokinetic sequence in a marine shelf setting, based on the stratigraphy of the lentil and associated sediments in the vicinity of the El Papalote diapir. Lower figure also shows the interpreted relationships between sediments and angular unconformities tied to diapir rise and to the sequence stratigraphic interpretation of the surrounding shelf and slope sediments. *SB* sequence boundary, *TST* transgressive system tract, *HST* highstand system tract (After Giles and Lawton 1999)

Subsalt Sections

Subsalt sediments, originally deposited adjacent to a seafloor allochthon and subsequently sealed beneath overflowing salt and its basal shear zone, have been studied extensively in the Gulf of Mexico, where numerous exploration wells have been drilled with subsalt targets (Chap. 10). Sub-allochthon sands in the Gulf of Mexico are mostly Miocene-Pleistocene deepwater-slope submarine fan channel and levee settings. The sandstones were deposited by turbidity currents associated with channel-levee systems carrying sediment from the outer shelf into bathyal water depths in the middle to lower continental slope (Snyder and Nugent 1995; Pilcher et al. 2011). Drilled facies vary from thick fining upward channelized deposits to thinly bedded levee sands and overbank splays. Sands range from friable to moderately consolidated, very fine to fine-grained, moderately to well sorted and slightly calcareous. Channel orientations can be strongly influenced by the seafloor topography generated by nearby salt allochthons. Once deposited the sands were then overridden and sealed by lateral flow of the allochthon sheets. The encroachment of the salt allochthon is associated with the creation of a salt-sealed gumbo or basal shear zone and defines one of four positions where subsalt sandy reservoirs are likely (Fig. 6.109). Economic and stratigraphic aspects of this very important subsalt-hydrocarbon association are discussed in detail in Chap. 10.

Caprock Formation (Diagenesis of Salt)

Caprock is a limestone/anhydrite carapace found atop many buried diapirs and allochthons (Fig. 6.110a; Halbouty 1979;

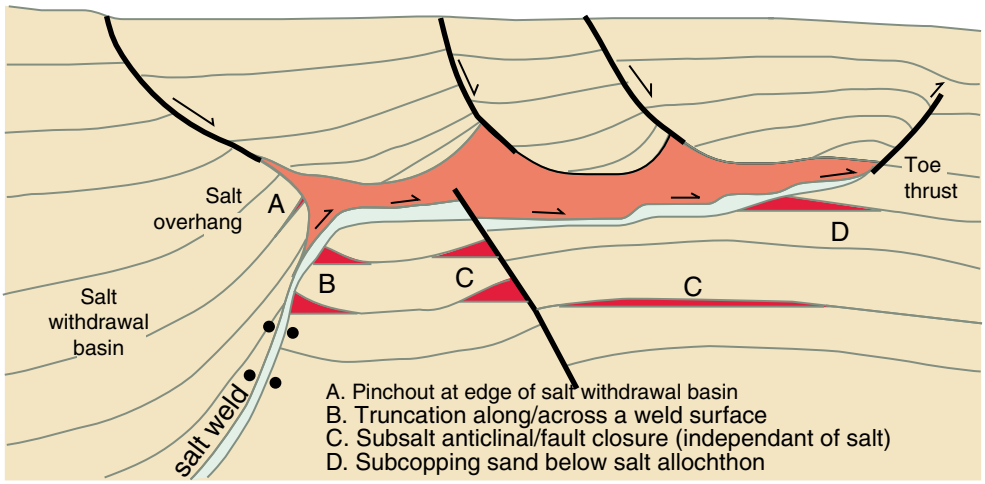

Fig. 6.109 Subsalt sediments buried beneath an encroaching allochthon is one (Style D) of four subsalt trap styles discussed in Snyder and Nugent (1995). See Chap. 10

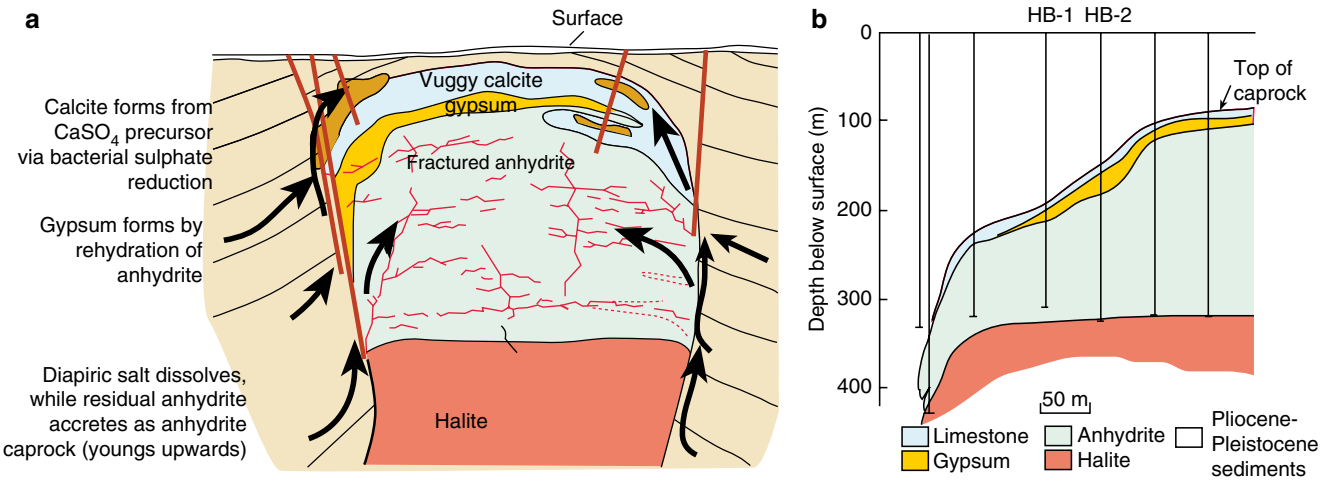

Fig. 6.110 Caprock zonation. (**a**) Caprock forms by the dissolution of the upper part of a salt structure once salt supply dwindles the rate of rise slows and it is flushed by undersaturated phreatic waters (*black arrows*). Dissolution of the halite leaves behind anhydrite that then accretes into an anhydrite caprock. The upper portion of the anhydrite unit rehydrates to gypsum that is then converted to limestone by bacterial sulphate reduction. (**b**) Section of Hockley dome caprock showing relative thickness of the caprock zones and depth below the landsurface based on drilling (After Hallager et al. 1990)

Prikryl et al. 1988; Kyle and Posey 1991; Light and Posey 1992; Jaworska 2010). It forms as a dissolution residue atop and on the flanks of diapirs, seafloor allochthons and even buried subaerial namakiers. Suprasalt caprocks thicken once salt supply starts to dwindle and the head of the salt plug or the top of any residual salt sheet is buried to depths where it can no longer actively pierce/breakout and shed sediment. The edge of any buried salt mass feels the increased effects of dissolution via the undersaturated crossflow of phreatic waters. Atop a buried, but still buoyant diapir, halite preferentially dissolves from the upper part of the salt mass/stem and a $CaSO_4$ unit accretes via underplating. The caprock underbelly has a continued supply of anhydrite residues as the top of the rising and dissolving salt stem is dissolved (Fig. 6.111; Hallager et al. 1990). In zones of longterm fluid crossflow and ongoing slow salt supply, this interface becomes a widespread laminar sulphate carapace, encasing a salt mass with caprocks some tens to hundreds of metres thick.

Caprock is most common and thickest on diapir crests that are currently close to the earth's surface but can be found atop and lateral to structures buried as deep as 3,000 m. Most diapir capstones are 100–150 m thick, but can be thicker than 300 m. Caprock is typically thicker over the crest of shallowly buried diapiric spines and thins along the flanks. Oil drilling over the Hockley dome, near Houston Texas, clearly defines a mineralogical layering of diagenetic products that is typical of caprocks worldwide (Fig. 6.110b). At its crest the Hockley Dome caprock is covered by only 30 m of Plio-Pleistocene sediments. The upper part of the caprock is a calcite unit up to 30 m thick. Over the crest the calcite is underlain by a gypsum zone up to 30 m thick. Further toward the flanks and somewhat deeper the gypsum unit is absent or patchy and the calcite is in direct contact with anhydrite. The calcite zone grades downward across a transition zone into a laminar anhydrite capstone up to 244 m thick. The Hockley caprock thins toward its edge and disappears, but in some

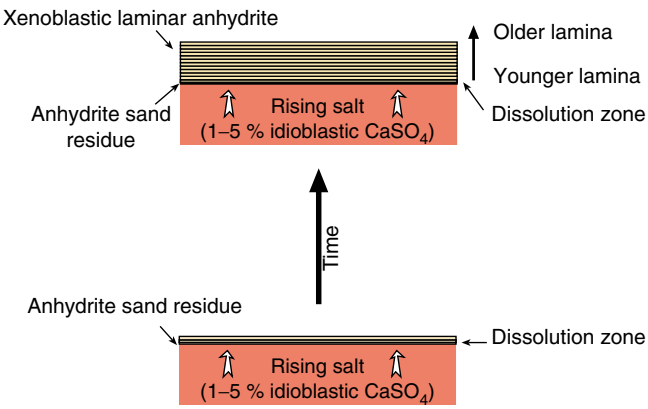

Fig. 6.111 Development of laminar anhydrite caprock via underplating across a zone of periodic dissolution at the halite-anhydrite contact

other nearby Gulf of Mexico diapirs the steep vertical walls of the diapir stem are also mantled with caprock.

Caprock extent reflects hydrodynamics about the upper part of the salt stem. The gypsum and limestone intervals in a caprock tend to be fractured and vuggy, typically containing accessory minerals such as baryte, celestite, strontianite, metal sulphides, rare tourmaline and fluorite derived from ascending basinal brines (Fig. 6.110a, b). Sulphur forms in vugs and fractures in the upper parts of caprocks where H_2S is oxidised by crossflowing waters (Figs. 12.68 and 12.69). Reactivated salt flow and associated carapace destruction means earlier allochthon and namakier residues can be carried to the margins and shed to become part of a polymict debris flow aprons that are perhaps parts of a unit that is termed a lateral caprock (in contrast to a "crestal" caprock).

The bulk of an actively accreting caprock is laminated and composed of unoriented, interlocking xenoblastic anhydrite crystal mosaics. Laminae are defined by thin intervals of dark sulphide/ bitumen accumulations or by intervals of more intense pressure-solution-sutured anhydrite. Deformed, banded anhydrite clasts are also contained locally within cm-spaced lamina (Ulrich et al. 1984, 1985). The laminar nature of a caprock reflects its formation via underplating, whereby the less soluble anhydrite and a few carbonate rhombs are left behind as undersaturated groundwaters dissolve halite from the upper part of the buoyant diapir stem (Fig. 6.111; Ulrich et al. 1985).

Anhydrite and carbonate typically comprise 1–5 % of the original undissolved salt massif in Gulf of Mexico diapirs. The salt/anhydrite contact tends to be subhorizontal to undulose, with local cm-thick metres-wide pockets of unconsolidated idioblastic anhydrite sand (euhedral grains freed from their encasing halite matrix). Above the halite contact and its sand pockets the anhydrite is laminated and consists of tightly interlocked xenoblastic crystals (Ulrich et al. 1985; Hallager et al. 1990). The transition from euhedral idioblastic anhydrite sand to xenoblastic anhydrite mosaics occurs in the first few centimetres above the salt stock. Outside of the sand pockets the porosity and permeability are consistently low to negligible.

Enclosed coarsely crystalline halite pockets, still with disseminated idioblastic anhydrite, can occur along some horizons in the caprock, especially in the lower portions of the anhydrite zone. Pocket shapes vary from tall and thin to broad and squat, maximum dimensions range from less than 0.5 m to about 2.0 m. These moundlike halite structures are mega-inclusion in the caprock anhydrite and are remnants of former zones of salt spine penetration along the salt-anhydrite contact. As the halite spine dissolves through several cycles of dissolution and accretion, a laminated anhydrite mound is preserved that sometimes contains minor amounts of base metals. Other clasts within the laminar anhydrite caprocks are remnants of anhydrite beds first deposited along with

mother salt, and then deformed and boudinaged into anhydrite "pencils" during salt flow (Hoy et al. 1962).

Gypsum forms sporadically along the upper side of the anhydrite portion of a caprock by hydration and is driven by the crossflushing of cooler less saline waters. Depending on permeabilities, this gypsum band is variably developed on and through the anhydrite, but deeper caprocks in the onshore Gulf of Mexico may lack a gypsum zone. Given the relatively high salinities and elevated temperatures that characterise the zone of onset of caprock formation, it may well be that gypsum formation postdates the formation of most calcite and sulphide minerals in the caprock and requires the pervasive entry of cooler meteoric water or seawater.

The calcite portion of the caprock occurs in hydrocarbon-bearing zones, mostly in the anhydrite zone where anaerobic SO_4-reducing bacteria break down the $CaSO_4$ phase into $CaCO_3$ and H_2S. Like the anhydrite zone, a calcite cap rock exhibits horizontal banding defined by alternating dark- and light-coloured layers of calcite that formed along the prevailing anhydrite/calcite contact during dissolution of anhydrite, coupled with SO_4 reduction (e.g. Prikryl et al. 1988). Dark calcite bands consist of fine-grained and typically pelletoidal calcite containing minor amounts of Fe, Zn, and Pb sulphides and bitumen. Light-coloured bands consist of coarse-grained euhedral calcite that apparently precipitated in open spaces and can also fill vugs.

In terms of porosity and permeability, it has long been assumed that most porosity and permeability occurs in the calcite layer in a caprock, and that the anhydrite and halite zones below this are tight. However, more detailed studies are showing that significant portions of the anhydrite zones in a caprock can be fractured and permeable. Lacazette et al. (2007) found that a caprock fracture system developed in the Sour Lake structure during caprock growth and was linked to salt-dome movement. The caprock was fractured both by faulting and extensional fracturing, resulting from dome emplacement and by mineral volume changes occurring during conversion of anhydrite to calcite. Isotopic data from the caprock limestones ($\delta^{18}O_{PDB}$: −4 to −8‰, and $\delta^{13}C_{PDB}$: −11 to −31‰) suggest that fluids evolved from deep bacterial to mixed meteoric during dome ascent.

Paleostress analysis based on fault-slip kinematics and extensional fracturing shows that caprock strain was due to dome inflation and that this expansion bears an overprint of the neotectonic (present-day) stress field. They document previously unrecognised pockets of fractured limestone occurring deep within the Sour Lake anhydrite layer and that these pockets constitute a significant part of the salt dome caprock volume. Some of these pockets were sampled by wells and imaged on the crosswell tomography. The fractured limestone pockets within the anhydrite likely resulted from bacterially-mediated diagenetic reactions which occurred when petroleum and brine flowed along faults created by dome inflation. The anhydrite portion of a caprock carapace should be considered potentially permeable intervals at geological time scales.

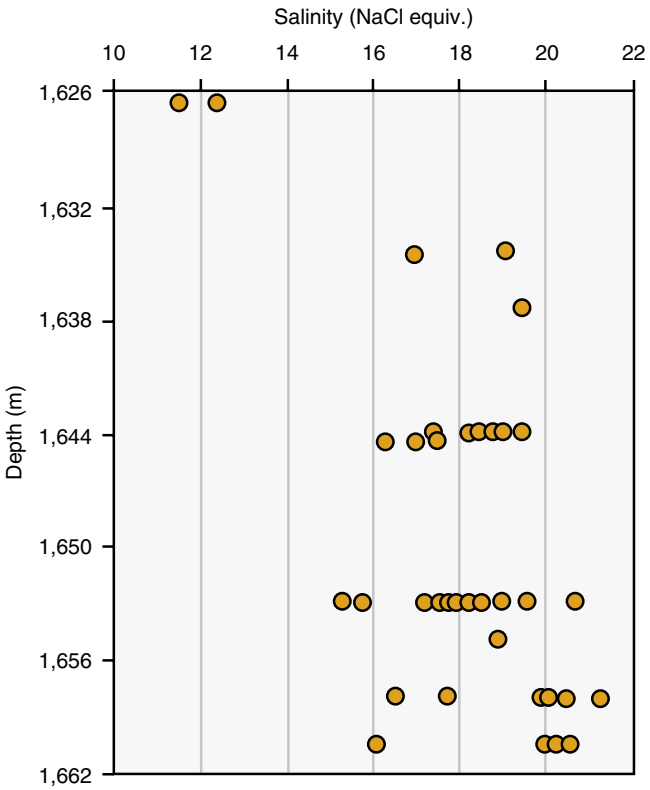

Fig. 6.112 Plot of fluid inclusions-based salinities in baryte and celestite in calcite cap rock versus depth (ft) in the Hockley Dome, Texas (After Saunders and Thomas 1996)

Massive amounts of the Sr minerals celestite ($SrSO_4$) and strontianite ($SrCO_3$) can occur in the lower portions of some calcite cap rocks, primarily in the light-coloured bands, along with minor amounts of baryte. Sulphide minerals can also be locally abundant in the lower portions of calcite cap rocks. The calcite cap rock at the Hazlehurst salt dome in Texas is approximately 30 m thick in the 2 drill holes that fully penetrated it (Saunders and Thomas 1996). The upper half of the cap rock consists of banded calcite similar to other Gulf Coast salt domes. Numerous near-vertical banded calcite-sulphide veins are also present in this part of the cap rock. The lower part of the calcite cap rock consists of horizontal sulphide + calcite bands that alternate with coarse-grained (white) calcite bands. Locally, sulphide-rich zones are more than a metre thick and consist principally of marcasite and pyrite, with minor amounts of sphalerite, galena, pyrrhotite, celestite, baryte and strontianite. Sulphate minerals are commonly intergrown with sulphides.

Fluid inclusion data in the calcite caprock of Hockley Dome, Texas, indicate that baryte and celestite precipitated at temperatures less than ~60 °C, from brines averaging around 200,000 mg/l total dissolved solids (Fig. 6.112; ~ 18 % NaCl

equiv.; Saunders and Thomas 1996). Fluid inclusion salinities in caprocks do not vary significantly with depth, suggesting that brine salinity did not change dramatically over time. Sulphur and carbon isotopic evidence also supports a biogenic origin for both carbonate and sulphide minerals in calcite cap rocks (Saunders and Swann 1994) or a combined basinal and biogenic origin (Hallager et al. 1990).

In the last two decades there have been a growing number of studies dealing with mineralised portions of caprock and the results are used to improve geological understanding of processes that create Mississippi Valley Type (MVT) base metal deposits (Chap. 15; Kyle and Price 1986a, b; Bechtel et al. 1999). In Tunisia, some of these mineralised caprocks the associated biolaminated muds and the iron-rich haloes adjacent to the salt stems contain sufficient lead, zinc or siderite to be mineable (Bechtel et al. 1998; Warren 2000b). Porosity in biogenic calcite caprocks can be as high as 40 %, with porosity types ranging from pinpoint to fracture to vuggy to cavernous. Caprock reservoirs[21] are shallow and so were attractive targets in the early heyday of drilling in Texas and many of the famous early discoveries were in caprocks; examples include Spindletop, Sour Lake, and Humble. Caprock reservoirs tend to be relatively small; the most difficult thing about working them in the early 1920s was their lack of predictability.[22]

The earliest-formed anhydrite lies at the top of the anhydrite zone, and the oldest calcite lies at the top of the calcite zone (Fig. 6.110). In other words the anhydrite and calcite caprock units grow from the bottom up and can be thought of as having a half life, like the basal anhydrites of the Maha Sarakham Fm. in Thailand (Fig. 7.45). That is, the thickness of any caprock zone is dependent on the rate of fluid flushing at the lower contact where it is forming and, at the upper contact, where it is being converted to another mineral phase or is dissolving. Ultimately, if crossflow continues, all that will be left of a caprock is a dissolution breccia or a weld.

Paleomagnetic age measurement of stratiform laminae of pyrrhotite and other sulphides in anhydrite cap rock, over a sampled section that represents about two thirds of the total anhydrite thickness in the Winnfield salt dome in northern Louisiana, indicate it formed between 157 and 145 Ma (latest Jurassic; Kyle and Gose 1991). Accumulation rates from these data indicate that the average rate for the oldest cap rock sampled is 5.7 m/m.y. and decreases to 2.8 m/m.y. for the younger lower parts of the caprock, indicating a waning rate of salt supply. The nearby 285 m-thick Hockley Dome cap rock is believed to have developed within the last 45 Ma giving same order of magnitude for the caprock accumulation rate (≈6 m/m.y.)

Caprocks are residuum responses to throughflushing waters atop and about largely inactive and buried salt structures. Historically they were interpreted as a diagenetic response to largely continental meteoric hydrologies imposed on dissolving diapir crests. Halbouty (1979), for example, noted that only 5 of 77 offshore wells drilled in diapiric crests intersected a caprock, but this analysis was done before any notions of allochthon shedding had been developed. Without doubt, actively forming caprock is found onshore wherever the active meteoric phreatic comes into contact with the upper part of a buoyant diapir crest (Schelkes et al. 2001). Yet, caprocks also form in offshore halotectonic slope-and-rise realms atop largely inactive salt structures that have not experienced substantial meteoric crossflow.

For example, a core through the Eureka dome, a structure located in the upper slope of the Gulf of Mexico, encountered 36 m (117 ft) of anhydrite caprock above the salt massif (Lehner 1969). Assuming an anhydrite content of around 5 % in the Louann Salt, this thickness of caprock requires the dissolution of more than 700 m of salt. Burk et al. (1969) reported caprock in core recovered from the Challenger Knoll in the Sigsbee abyssal plain. Authigenic tourmaline is anther mineral forming there (Chap. 13).

The allochthonous Sigsbee salt mass overrode the abyssal plain sediments and its upper surface was at or near the seafloor throughout the entire Cenozoic era and was probably never in contact with large volumes of meteoric waters. Apparently, circulating meteoric water is not necessary for salt dissolution and caprock formation. If such pore water is present, its relatively low salinity compared to phreatic seawater does accelerate the process of caprock creation. Substantial caprock can even form subaerially and active salt glaciers in Iran have a brownish laminated gypcrete capstone that can be 3–10 m thick over the actively flowing parts of the salt (Bosak et al. 1999).

The term "cap" may be somewhat of a misnomer as layered $CaSO_4$ dissolution residues also form offshore in the Gulf of Mexico, the North Sea and Thailand in zones of

[21] The early oil history of Gulf Coast, USA, has an interesting aside. Oldtime drillers found that drilling wells in graveyards led to a significant number of successes. High success rates associated with "graveyard-tology" meant that early last century the church elders and many still-living relatives developed a sudden if somewhat belated attachment to long-since-departed great aunt Maude. Bitter legal battles, fraught with claims along the lines of being the bastard child of aunt Maude, were fought over the percentage of royalties that one would receive for part of, or even a distant ownership of, a small piece of "Boot Hill." A reason exists for these early success rates. Many early east Texas fields were salt-structure associated, with the shallow reservoirs (vuggy and fractured caprock) lying directly over the crest of the structure. The surface expression of an underlying salt structure in the Texas Gulf coast is a small topographic high or hill, and since John Wayne was a whippersnapper, graveyards have been "up on Boot Hill." The first oil discovered in southern Louisiana in 1901 came from a similar salt-formed topographic feature known as Jennings Hill about 100 km west of Baton Rouge.

[22] The Spindletop discovery well blew out at a depth of 311 m (1,020 ft) and in 8 days it is estimated some 800,000 bbls of pressurized oil had escaped from the well.

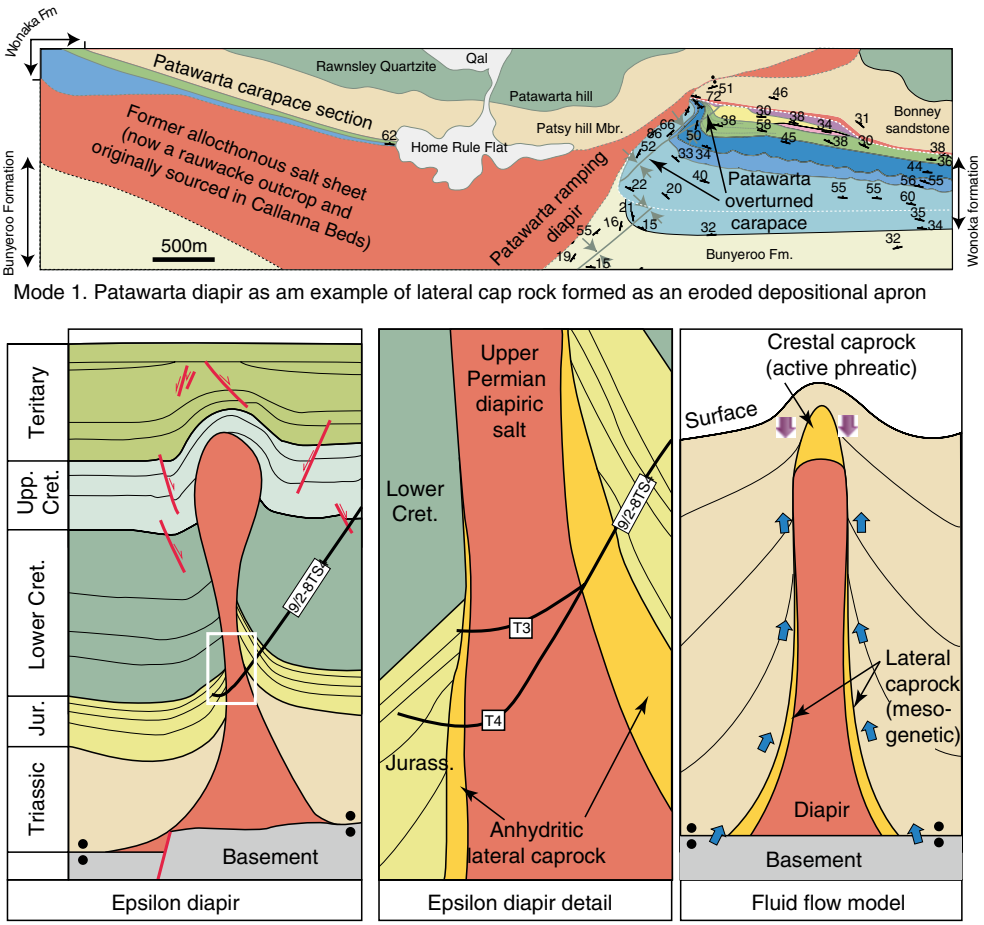

Fig. 6.113 Lateral caprock modes of formation. *Mode 1*: cross section based on Patawarta diapir, Flinders Ranges, South Australia, indicating formation via ongoing crestal erosion during downbuilding. *Mode 2*: cross section based on the Epsilon Diapir, illustrating formation via fractional dissolution of diapir salt in contact with undersaturated mesogenetic waters (*blue arrows*). Crestal caprock formed via active phreatic waters, eogenetic when sub seafloor, meteoric on land (*purple arrows*) (Adapted from Jackson et al. 2013; Kernen et al. 2012)

active fluid flushing on the margins and undersides of salt beds and allochthon sheets (see fractionated dissolution discussion in Chap. 7 and Jackson and Lewis 2012). For example, cores taken from the base salt contact in the Amoco #1 SL 12878 well in Plaquemines Parish, Louisiana, sampled a mineral assemblage of calcite, euhedral dolomite, ferroan dolomite, anhydrite, banded diagenetic calcite and trace sulphide minerals, the typical mineral association of a Gulf Coast caprock (House and Pritchett 1995). The notion of diagenetic anhydrite as residues from salt dissolution has led to a discussion of the major processes that form "lateral caprocks" about diapir edges that have experienced little or no exposure to meteoric waters and perhaps formed in settings that may not have approached the landsurface (Giles et al. 2012 vs Jackson et al. 2013).

The proponents of the drape-fold model of lateral caprock formation base their interruptions on mapping of field relationships in exposed salt structure margins in the La Popa, Mexico, Canyonlands, Utah and especially in the Flinders Ranges of South Australia (Giles et al. 2012; Kernen et al. 2012). There Neoproterozoic Patawarta salt sheet displays a laterally extensive (>10 km) dolomite caprock assemblage preserved in both subsalt and suprasalt positions along the sheet margins (Fig. 6.113; Mode 1). This caprock is 3–100 m thick and contains massive, laminated, and crackle breccia textures. The near-vertical to overturned subsalt caprock parallels steeply dipping strata of the Bunyeroo Fm in a tapered composite halokinetic sequence (CHS). The caprock terminates upward at an angular unconformity marking the upper boundary of the CHS. Basal strata of the overlying Wonoka Fm onlap the truncated caprock and contain conglomerates of caprock-derived detritus indicating that the caprock formed in a suprasalt position prior to deposition of the Wonoka, which forms another CHS but without caprock. The authors note similar, but not as well exposed, relationships in caprock and adjacent Permian and Mesozoic strata flanking the Castle Valley diapir in the Paradox Basin, Utah and the La Popa region of Mexico (Fig. 7.17).

They argue flanking and subsalt caprock forms via four steps: (1) caprock develops in a crestal position by crossflow waters; (2) continued diapiric rise and minibasin subsidence cause drape folding of roof strata and competent caprock, which detaches from the underlying halite-dominated diapir and rotates off the diapir top into a flanking position;

(3) topography generated by diapir inflation as diapir-rise rates exceed sediment-accumulation rates result in erosional thinning of the roof to create an angular unconformity that truncates the underlying CHS and flanking caprock; (4) increasing rates of sediment accumulation relative to diapir rise lead to onlap of the overlying CHS, which may or may not develop a new crestal caprock assemblage.

Contrasting with this dominantly sedimentary reworking mode of lateral caprock is the mesogenetic-diagenetic mode as outlined in Warren (2006) and Jackson et al. (2013). This mode of formation is created by the contact of a salt mass with an adjacent undersaturated water mass. This is the situation active on the basal edge of the Maha Sarakham evaporite mass, creating a diagenetic edge to the salt mass known as the "basal anhydrite" (El Tabakh et al. 1998a) and has formed the "lateral anhydritic caprock" to the Epsilon diapir and others in the North Sea (Mode 2 in Fig. 6.113). These diagenetic units are associated with a warm saline plume of pore fluids that typify the sediments adjacent to the salt edge.

Using a combination of seismic and wireline data from the Epsilon Diapir, Jackson et al. (2013) demonstrate that a weld is beginning to develop diagenetically via mesogenetic dissolution of halite along the squeezed diapir stem leaving bend an anhydritic residue. Borehole data indicate the structure today consists of an inner, ≈1,500 m thick, halite-dominated inner zone, and an outer, ≈250 m thick, anhydrite-dominated sheath or lateral caprock. This "lateral caprock" formed late in the basin history in response to the migration of NaCl-poor fluids up the margins of the diapir. Dissolution of large volumes of halite from the margins of steep-sided salt structures by the focused rise of deep, warm, basinal brines has implications for understanding the patterns and vigour of groundwater flow in sedimentary basins and the location of economically important metals (Chaps. 8 and 15, respectively).

Complications of Shale Diapirism

Both salt and shale form diapiric structures that, without drilling, can appear somewhat similar in seismic sections, especially in compressional settings (Fig. 6.114). Morley et al. (2014) and Warren et al. (2011) discuss the similarities and differences present in "diapiric" salt and shale provinces and outline ways of distinguishing the two styles (Table 6.6). Both salt and shale have sufficiently low permeabilities to allow units within folded and deformed compactional settings to create and hold back overpressured fluid columns ($k < 10^{-18}\ m^2$; Sibson 2003). In some situations, flowing shale ridges (argillokinesis) and flowing salt (halokinesis) can occur in the same basin stratigraphy, as in the Port Isabel and Mexican Ridges fold-belt provinces of the western Gulf of Mexico (Fig. 6.66; Rowan et al. 2004; Salomon Mora et al. 2011).

A key difference is where the overpressure resides and the effect of the structure's evolution on seal integrity. Salt's mobility is a inherent material property; so that structures in an active salt-cored fold and thrust belt continues to evolve until the salt is completely dissolved or ongoing salt withdrawal produces sufficient overburden touchdowns to stop further salt flow. While salt is flowing, it tends to maintain seal integrity whether or not there is an overpressured underbelly, which there typically is. Shale, on the other hand, only "flows" while it is overpressured. Whenever the main shale body depressurizes it freezes. While a shale is mobile (overpressured) it can generate a progression of kinematic geometries similar to those generated by the reactive and active phases of salt diapirism (Fig. 6.114a; Morley and Guerin 1996; Van Rensbergen et al. 2003). The presence of a mud diapir or volcano approaching the seafloor indicates a breach zone in an otherwise pressurized mud seal.

To illustrate the nature of a shale-cored fold and thrust belt let us look briefly at the highly visible set of thrust-cored ridges at the foot of slope of offshore Brunei (Fig. 6.115a). Modern growth faults are located near the present shelf-slope break of Brunei are prograding over older, inactive innermost deeper water folds (Plio-Pleistocene section in Fig. 6.115b). The average dip of the modern slope is between 1 and 1.5° toward the deepest region of the South China Sea, the northwest Borneo Trough. The slope is affected by an extensive train of folds, spaced between 5 and 15 km apart, that verge offshore (Fig. 6.115c). They are mostly fault-propagation folds that sole out into one or more detachments. These active thrust-cored growth anticlines outcrop or underlie much of the Brunei slope and rise and act as seafloor sediment baffles and catchment dams (Fig. 6.115c). Anticlines are cored by mud volcanoes (also called mud diapirs), while between the growing ridges are several northeastward-trending sediment-filled depressions that parallel the shelf margin and range from 2 to 10 km wide and 20 to 60 km long. These growth folds are the result of a downslope gravitational compression, which started in the upper Miocene and continues today (Morley et al. 2012). The remainder of the slope and rise area illustrated in Fig. 6.115c is a relatively flat terrain, mostly covered by a mass transport complex or landslide (Gee et al. 2007). This flow complex represents a catastrophic event that occurred in the relatively recent past and was perhaps emplaced as a single landslide, not as a series of time-separate debris flows. The collapsed headwall of this mass transport complex lies updip and immediately offshore from the Baram Delta (Fig. 6.115a).

Integrating the data (core sedimentology, organic character and isotope data) collected from a set of more than 100 piston cores over the area, shows the nature of the fluid system in and around mud volcanoes in the slope and rise of Brunei (Warren et al. 2011). Site 110 is one of a number of sites on the growth anticline crests where pressured fluids are

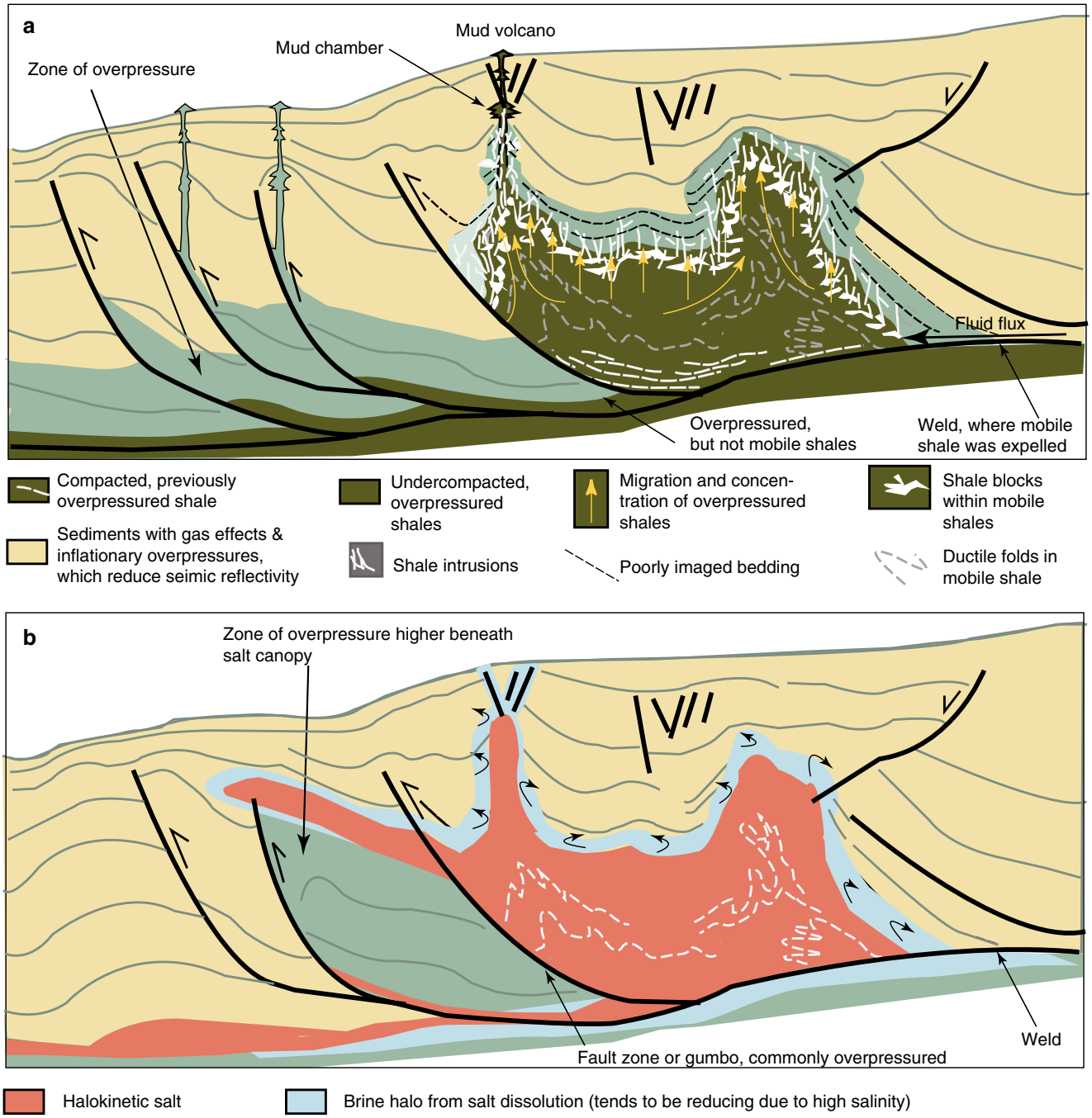

Fig. 6.114 Comparison of signatures of mud and salt diapirism. (**a**) Mud diapirism indicates a zone of fluid-charged overpressured fine-grained sediment (mostly mud). It can rise via stoping subvertical mud chimneys and periodically break out onto the sea floor. The seismic signature indicates zones of active or former fluid charge. The diapir as seen in the seismic signature is not a lithology but typically a gas effect. As such, the diapir zone can expand and encapsulate or cannibalize adjacent sediments without disturbing the bed orientation. (**b**) Salt diapirism indicates a zone of flowing impermeable salt (halokinesis). There is both a vertical and horizontal component to this flow and a strong response to sediment loading, and, on salt reaching the sea floor, it is tied to downslope gravity spreading. The seismic signature of a salt diapir or allochthon is a direct indicator of the salt mass, which is always impermeable. Flow sets up a mobile mass of impervious salt with edges subject to dissolution (like a block of ice). This mass and its brine halo focus fluid flow and overpressuring about its edges (After Morley et al. 2011, 2014)

on their way to the surface and forming mud chimneys and mud volcanoes (Fig. 6.116). It lies atop a thrust-cored growth anticline where rising overpressured fluids are causing the reflectors to rise and outline diapir-like convex-upward chimney geometries. These indicate fluid anomalies that are on their way to creating pressurised mounds on the sea floor. Seismic across other sites show collapse cones and pocks where the pressure has vented (Warren et al. 2011).

Table 6.6 Features typical of mud diapirism and salt diapirism

		Mud diapir (argillokinetic)	Salt diapir (halokinetic)
Tectonic setting where argillokinesis and/or halokinesis occurs	Rift to drift (passive margin (extensional) with depositional loading)	Yes, gravity-driven fold belt (especially in toe of slope) Examples: Mexican Ridges and Port Isabel foldbelts of western Gulf of Mexico; foldbelts in the Sergipe Alagoas and Pára-Maranhao basins of Brazil, Niger delta foldbelt; McKenzie delta foldbelt, Arctic Canada; Yangtze delta, East China Sea.	Yes, gravity-driven fold belt (especially in toe of slope) Examples: Slope and rise foldbelts of the circum-South Atlantic salt basins and the northern Gulf of Mexico; foldbelts in the Yemeni Red Sea; Nile deep sea fan; Rhone deep sea fan; Scotian Margin, eastern Canada.
	Collisional accretionary belts, transpressional belts, both can overprint a former passive margin	Yes (forearc and backarc basins) Examples: Barbados accretionary prism; Mediterranean Sea and Tethyan Belt, spanning from south of Greece over the Black and Caspian Seas into Azerbaijan, the Crimea and Taman Peninsulas, Iran, and Turkmenistan into the Makran coast; Borneo; South China Sea.	Yes (especially in zones of continent-continent collision, compression can reactivate former extensional salt diapirs). Examples: Qom Basin and Zagros foldbelt, Iran; Kuqa foldbelt, Tarim; Betics; Carpathians; Apennines; Sierra Madre; Neuquen, Argentina.
	Intracratonic sag	No.	No (unless basin inversion occurs – e.g. Amadeus).
Depositional Association	Marine	Typical of muddy continental slope and rise.	Typical of continental slope and rise, also shelf
	Lacustrine	Foreland basin.	Foreland basin.
Movement style and drivers		Requires overpressure. Shale can pass from ductile to fluidized, and back to ductile numerous times as the structure oscillates between inflation (gas explosions & diapir wings) and deflation (collapse after landsurface is breached). Overpressure is caused by combination of burial compaction, diagenesis of clay, organic maturation and compressive tectonics. Overpressure is lost when fluid-charged mass reaches the surface and there is typically only a relatively minor lateral sediment flow component when the fluid escapes onto the surface. Mud diapir provinces can form zones of extremely rapid subsidence atop salt withdrawal zones even if the mud source interval is not overpressured (Fort Isabel foldbelt).	Thick beds of wet salt undergoing loading or extension can be autokinetic, almost from the time of deposition. Salt continues to move in response to extension or loading and maintains its flow until overburden touchdown occurs. Salt in compression will fold but not pierce overburden, except under particular circumstances. When the salt reaches the surface there is a strong lateral component (downslope) to flow (allochthons and namakiers), salt flow can continue via gravity spreading for many kilometers way from vent. Overpressure is often focused beneath an allochthon as the salt mass is an excellent seal. Overpressure is also common in suprasalt minibasins where the feedback between loading and salt withdrawal facilitates rapid sedimentation until touchdown.
Causes of collapse of overburden or sediment immediately adjacent to structure		Structural collapse, typically occurs via venting/mud volcanism, which acts as a drain to overpressure and as breach zones to mud seals.	Dissolution or deflation of salt feature as it flows up and ultimately out of the subsurface to landsurface/seafloor. At surface flow slows then ceases as the allochthon is cut off from mother salt supply layer.

(continued)

Table 6.6 (continued)

	Mud diapir (argillokinetic)	Salt diapir (halokinetic)
Pockmarks	Indicate zones of pressure release often in zones of fluid escape through a zone of methane hydrate on basin floor.	Indicate zones of salt dissolution or of escaping fluids released to basin floor near the feather edge of salt sheet or above zones of overburden touchdown (welds).
Breccias in and around vent	Mud can carry blocks that assimilate into rising plume with diameters of several to hundreds of metres. Large blocks are also captured by crestal collapse.	Salt can carry blocks with diameters of kilometers. Blocks typically were originally intercalated with mother salt or source layer.
Fault association	Yes – shale diapirism initiated by faults that weaken the overburden. Pressurized mud then intrudes into the overlying sedimentary rock and may or may not reach the surface.	Yes – close association between fault welds and salt welds. Much synkinematic activity is driven by feedback between loading, salt withdrawal and creation of further accommodation space.
Fluid association	Warm subsurface fluids (typically gassy) escape along active faults or chimneys and carry mud with indicators of organic maturation. Thermal pools may or may not be present on seafloor. Overpressuring feeds hydrocarbons to the surface (seeps associated with volcanoes). The sense of fluid flow is dominantly vertical and there are no traps associated with lateral mud flow at the seafloor.	Warm subsalt fluids escape at feather edge of salt or atop active salt transecting faults or above zones of overburden touchdown. Fluids can carry mature hydrocarbons. Brine pools are present at zones of topographic closure on basin floor. Methane seeps are commonplace. Once salt is at seafloor it spreads under influence if gravity and there are a broad range of subsalt traps associated with lateral flow of salt.
Hydrocarbon traps	Detachment folds, diapir toplap, diapir top drape or rollover rims, radial faults, tilted fault blocks, erosional truncation and associated unconformity traps, lateral mini-anticlines, and downbuilt anticlinal flank traps. Mud volcano indicates a breach to a muddy seal interval	Detachment folds, diapir toplap, diapir top drape or rollover rims, radial faults, tilted fault blocks, erosional truncation and associated unconformity traps, lateral mini-anticlines, and downbuilt anticlinal flank traps, suballochthon traps, intra-salt traps. Salt acts as seal.

After Warren et al. (2011)

The convex-upward character of reflectors that pass into the rising fluid columns and the convex-upward sea floor atop the rising plumes (no collapse cones yet exist) imply that the pressured fluid column is yet to breach the sea floor from below site 110, but has reached the sea floor nearby (Fig. 6.116). For example, the plume that rises all the way to the sea floor in the mound downdip of site 110 and the lack of layering or a BSR in the plume position feeding this mound (indicated by purple arrow) imply that seepage of fluids onto the sea floor near site 110 occurs. The two intersecting section lines illustrate the precursor and the active phase of a rising fluid plume that will evolve into a mud volcano. What is so distinctive about the system is that, unlike a salt-cored system where the salt is flowing near or onto the seafloor (Fig. 6.116b), in a mud cored fold and thrust belt we are dealing mostly with gassy fluids leaking onto the seafloor not a flowing mass of shale (Fig. 6.116a).

Halokinetic flow in a salt province builds diachronous levels and tiers of allochthons all the way up through the basin stratigraphy to the seafloor. Salt flows and evolves into higher levels in the stratigraphy, long after the original salt level has become a primary weld. Movement of a shale diapir tends to be much more episodic and related to particular overpressuring events within the shale-dominated section of a prograding typically deltaic continental margin (e.g. load-driven compaction or thermobaric release of water or hydrocarbon generation). The "shale" freezes once the pressurised set of fluids in a shale, which defines the "shale diapir" mass,

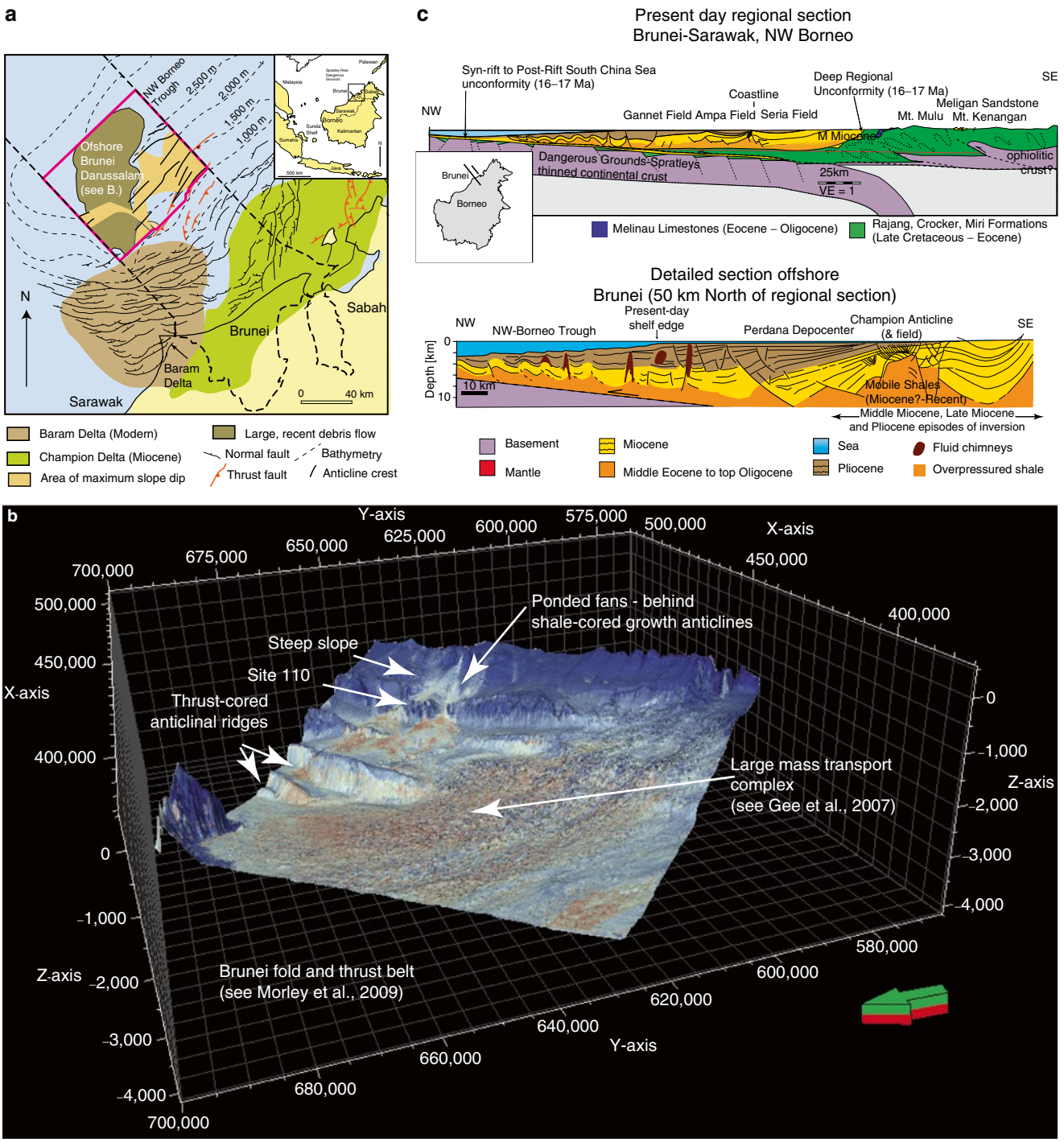

Fig. 6.115 Regional summary for offshore Brunei Darussalam (After Warren et al. 2011). (**a**) Regional sea-floor map showing Brunei-Malaysia borders (*dashed line*), the outline of study area (*pink rectangle*, centered on 5.718 N, 113.168E), and the dominant depositional styles (After Morley 2007a). (**b**) Sea-bottom map of the study area. Seismic amplitude extractions of the water bottom draped over the bathymetry of the deep-water slope and rise of Brunei showing the location of anticlinal ridges and the mass transport debris apron to the south (arbitrary z-axis scale; x and y scales UTM in m). The colour range represents a range of root mean square (RMS) amplitudes. Generally, the higher the RMS amplitude, the more consolidated the sediments. Areas in brighter orange are typically active sediment flow paths (channels, downslope of deep-sea fans, and fault scarps), lighter areas indicate a more compacted mud, whereas gray indicates a relatively stable ground. *Arrow* points north. (**c**) Regional and local cross sections of offshore Brunei Darussalam showing dominant down to basin style of gravity-driven sedimentation atop an inactive subduction zone (After Hall and Morley 2004). The pattern shows the overall progradation in a region of updip extension and growth faulting that passes downdip into compressional ridges and sediment dams and minibasins

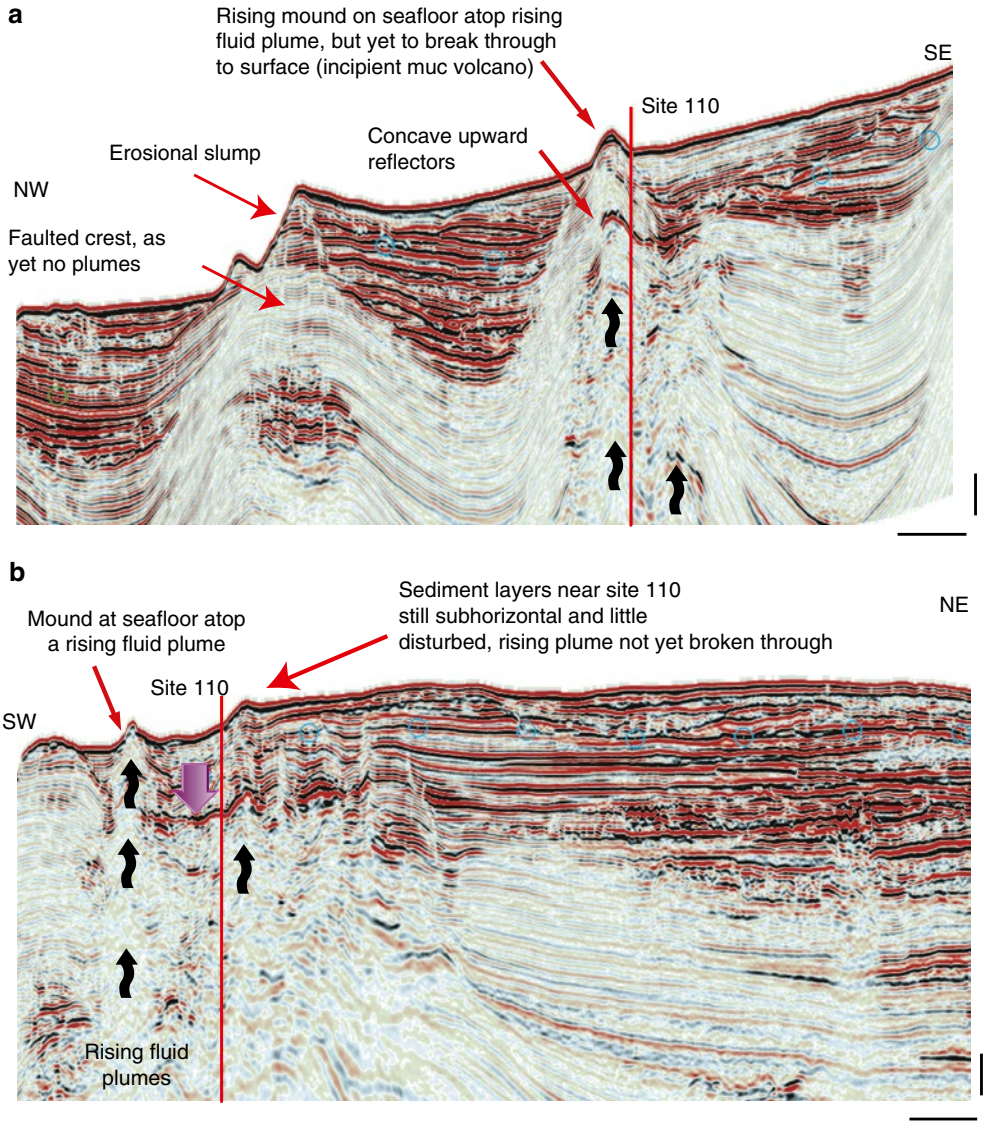

Fig. 6.116 Incipient mud volcano, in the slope and rise of the fold and thrust belt of offshore Brunei (After Warren et al. 2011). *Vertical red lines* indicate where inline and crossline seismic, illustrated in this figure, intersect one another (Horizontal bars = 1 km (0.6 mi); vertical bars = 1 ms. See Fig. 6.113= for the site location)

approaches the surface and the pressure buildup is released via mud volcanoes.

Mud "diapirs" are not created by the same digenetic mechanisms as salt diapirs, even if they occur in fold and thrust belts that show similar patterns of gravity-driven compressional folding. There is a basic distinction to be made between the actual volume of "sediment" flowing in a mud "diapir" or allochthon, versus the distribution of overpressured mud leaking pore fluids and imaged in seismic. What we resolve seismically as a "mud diapir" is not sediment that has experienced Newtonian flow. Rather, it is muddy and gassy sediment that is disturbed because it contains, or once contained, overpressured fluid. This is not the same as a body of flowing salt in a salt allochthon. This is why there are no equivalents to salt canopies and tongues in regions of mud diapirism. Rather there are local, often relatively narrow and cylindrical structures (mud volcanoes and chimneys) that define the vent and escape positions of overpressured fluids rising though the growth anticlines from below. Allochthons and diapirs in halokinetic systems act as a focus to fluid flow, in mud diapirs and walls they are the zones of fluid flow (Fig. 6.116 and Table 6.6).

For the same reason, shallow allochthons and widespread raft tectonics atop thin shallow décollement layers are much less common in mobile shale belts. Most shale diapirs show affinities to autochthonous rather than allochthonous salt systems. Laterally-limited shale allochthons do occur in the Niger Delta, where they form imbricate thrusts that pass down dip into gravity flows and slumped blocks of shale derived from the exposed mobile shale.

Where salt diapirs act as a focus to fluid flow in suprasalt sediments they can create seafloor effects similar to those in shale diapir provinces, as evidenced by (Cartwright et al. 2007; Camerlenghi et al. 2009): (1) localized development of

mud mounds above diapirs in the Gulf of Mexico (Roberts and Carney, 1997); (2) shallow gas anomalies clustered around and above salt diapirs in the North Sea (Heggland 2004), large pockmarks above diapir margins in west Africa and pockmarks on the deep sea floor in the Adriatic (Geletti et al. 2008) and (3) localized salinity anomalies around salt diapirs, as in offshore Louisiana (Esch and Hanor 1995). In the North Sea, gas chimneys in the Tertiary overburden are widely observed above salt diapirs; there and elsewhere salt-focused gas escape zones contribute to imaging problems at depth and to drilling hazards in the shallow subsurface (Heggland 2004).

A significant difference between salt and shale diapiric provinces lies in the permanence of the contact between the flowing unit and adjacent strata (Fig. 6.114). While flow in halokinetic terrains only takes place within the salt unit, shale "mobility" (the zone of pressured fluid) can spread out into adjacent beds as the overpressured interval spreads, this is why conformable layers are sometimes visible in a diapiric mud. That is, while overpressured, a stressed ("mobile") shale interval can facilitate fluid migration that cannibalises (overpressures) adjacent shale strata and so cut across time/bed boundaries giving an overpressured shale interval a chaotic indistinctly-layered appearance in seismic (Fig. 6.114a).

Morley and Guerin (1996) record how these differences in mechanical behaviour lead to differences in structural style. They note that prekinematic and synkinematic structures occur in both provinces, but much of the prekinematic deformation in mobile shale deltas, such as the Niger Delta of Africa and the Baram/Champion systems of Brunei, are destroyed by aggrading cannibalisation of the overpressured shale. Not recognising this cannibalising effect can lead to the inappropriate placement of the lower portions of growth faults during seismic interpretation of shale diapiric belts (Fig. 6.114a; Van Rensbergen and Morley 2000).

Fault-dominated minibasins occur above the flowing unit in both salt and shale mobile belts. Likewise, in the shale-dominant Niger Delta, the interval of overpressured shales beneath the actively accumulating delta prism varies from relatively thin intervals to massive chaotic zones some 4–6 km thick. The maximum minibasin thickness is the thickness of the mobile shale, plus the thickness of the overlying pregrowth fault strata (i.e. some 4–8 km). Such thicknesses are similar to those in salt-induced minibasins in the Gulf of Mexico.

Classic autochthon geometries are common to both salt and shale provinces, as are normal fault haloes that are created during reactive diapirism (Fig. 6.114). Early counter-regional faults and toe thrusts are early controls on the formation and position of subsequent minibasins in both settings. Salt has the potential to completely evacuate as it evolves into salt welds or overburden touchdowns. Mobile shale deformation may also create local touchdown areas (shale welds), but complete shale collapse is uncommon and large volumes of immobile dewatered shale are usually left after diapirism has ceased.

Van Rensbergen et al. (2003) go on to note that due to the requirement of overpressure for shale mobility and the need for hydrocarbon generation to instigate overpressuring, a gas-charged mobile shale can forcibly stope upward though its overburden via the process of shale cannibalisation. This tends to create narrow near vertical pipes, typically issuing pressurized fluids and some liquefied sediment onto the landscape as mud volcanoes. There are no equivalent narrow pipe-like cannibalistic stoping or diatreme-like features in the realm of salt flow, except where pressurised subsalt fluid breaches a salt layer and creates a similar set of mud diatremes.

Compressional growth anticlines cored by salt or overpressured mud can influence the distribution of deepwater sediments in the continental slope and rise in both settings. Such an anticlinal dam the shale diapiric zone of offshore Brunei is illustrated in Figs. 6.115 and 6.116. The geometry can be compared with similar fold and thrust anticlines, but with salt cores, in the Gulf of Mexico and Angola (Table 6.6).

Occasionally, mud diapirs can be underlain by active salt diapirs, as in the case in the Mercator mud volcano (MMV) in the Gulf of Cadiz (Haffert et al. 2013). As well as focusing upward fluid migration, this mud volcano is also an important zone for fluid and mineral diagenesis and the occurrence of authigenic gypsum and anhydrite crystals in the volcano muds. Modern near-surface muds in its vicinity show extremely high salinities (up to 5.2 M of NaCl) with pore brines sourced from underlying Triassic diapiric and evaporitic halite dissolution. The strong increase in salinity in the mud volcano pore fluids raises the gypsum-anhydrite transition zone from $\approx$1 km regionally to about 400 m sediment depth in the vicinity of the mud volcano. This transition is further shifted to immediately below the seafloor during intervals of active mud and fluid expulsion when the sediment surface temperature is heated up to at least 30 °C.

As a consequence, precipitation of authigenic gypsum near the sediment surface (1–2 m depth) is linked to the dissolution of evaporites below the MMV. Mechanisms generating supersaturation in the ascending gypsum-saturated MMV fluids are: (1) The slow and constant cooling of these fluids along the geothermal gradient during their ascent leading to formation of ubiquitous micro-crystals; and (2) The more rapid cooling after a heat pulse or transport from greater and warmer depths during an active mud volcano phase leading to the precipitation of cm-scale gypsum crystals or even fist-size concretions. The MMV fluids approaching the salt diapir from farther below have experienced a genesis similar to those of other mud volcanoes in the Gulf of Cadiz located above deep-rooted pressurised faults. These broader scale processes include clay mineral

dewatering, thermogenic degradation of organic matter and deep high-temperature leaching of terrigenous sediments or continental crust.

Summary

With the increasing use of 3D seismic for oil exploration in Phanerozoic basins, it has become obvious that models of predominantly vertical movement of salt from a mother salt bed into thumb-like autochthonous appendages are limiting. We now know that huge salt sheets (allochthons) can climb the stratigraphy as a series of predominantly subhorizontal sheets or tiers that are continually moving and squeezing as they are loaded by ongoing sedimentation. The end result is a feedback system where flowage creates withdrawal lows that fill with sediment, while at the same time the filling of the low with sediment triggers further salt flow. The upper side of the deforming salt sheet can also flow into more classic thumb-like styles of diapir geometries.

Prior to the advent of forward-modelling techniques in seismic processing and the gathering of 3D data networks we could not image beneath salt bodies and so tended to interpret the upper salt surface as the primary level of the salt body (Roho's moho). We now know this is not the case, many deforming salt beds flow into laterally extensive allochthons and canopies, which become rootless once the connection to the primary source or mother salt bed is converted to a salt weld or a fault weld. A salt weld forms as salt migrates or dissolves away to allow the former upper and lower contacts of the salt to come together or touchdown to form a salt weld. A fault weld forms where salt that was once within or lubricating a fault or shear plane is lost and the two sides of the fault come together. When a thrust plane is lubricated by salt that is subsequently lost by migration or dissolution, the plane may convert to a characteristic nearsurface dissolution breccia called rauhwacke (Chap. 7).

The end result of salt allochthons climbing through an aggrading and prograding shelf sequence is a layered and faulted stratigraphy with former sheets left as salt welds and fault welds, rather like a slug leaves a slime trail as it moves through a pile of leaf debris. The amount of salt left behind in the basin stratigraphy depends on the efficiency of salt evacuation. When the evacuation of the allochthonous salt sheet is efficient, all that is left behind is a series of stepped counter-regional fault welds and associated landward dipping faults. When the evacuation is less efficient the result is a series of salt rollers along the salt weld and an overlying fault-segmented sedimentary sheet cut by dominantly basin-dipping growth faults (a Roho system).

Wherever a salt allochthon is near the seafloor it can load, deform, coalesce or disaggregate as it continues its climb through the aggrading stratigraphy. Sediment loading atop a deforming allochthon creates fault-defined suprasalt basins or minibasins, often interacting with salt glaciers on the seafloor. Minibasins typically fill with a characteristic upward shoaling pattern of sediments passing from initial deeper-water laminated shales and mud to shallow water sands and carbonates. Processes of ongoing halokinesis and minibasin formation cease once the salt allochthon is sufficiently thinned, dissolved or buried. Thus, throughout the sedimentation history of a passive margin that is underlain by early thick salt beds there are many intervals where thick sheets of flowing allochthonous salt are present just beneath the deep sea floor and sandwiched into what are otherwise normal deeper marine bottom sediments.

Salt tectonics is also active in compressional terrains, which can occur at the foot of a gravity-glide sheets basinward of the continental slope. Flow is especially obvious in ancient foreland fold and thrust belts and inverted basins where weak subsurface salt acted a décollement layer and, if it makes it to the surface, the salt can create namakiers. The resulting growth anticlines are narrow and salt-cored, while the intervening synclines are broad. Most of the thrusts are blind and backthrusts typically occur in association with forward directed thrusts. Much of the salt in the cores of the anticlines is strongly folded and diapiric; although the notion that compressional diapirs can breach their overburden, without being erosionally thinned or disrupted by tear faults, has yet to be proven. There is now an appreciable body of evidence that many compressional diapirs feeding salt to the surface are actually reactivated extensional structures.

Salt Dissolution and Pointers to Vanished Evaporites: Karst, Breccia, Nodules and Cement

7

Introduction

Given enough time all subsurface evaporites eventually dissolve. Even in the subsurface sedimentary realm there are probably more intervals of dissolution residues than there are beds of salts. The rate of evaporite dissolution changes with temperature and rate and volume of crossflowing undersaturated pore waters (Fig. 7.1) Solubility of the chloride salts consistently increases with increasing temperature (prograde solubility), with the sulphates and the sodium carbonates it initially increases, but can then decrease at higher temperatures (retrograde solubility). Dissolution typically begins in the shallow subsurface as the edges of salt beds are flushed by meteoric or marine waters and continues deeper in the subsurface, wherever and whenever bed edges are flushed by undersaturated basinal brines. Partial dissolution, whereby crystals of more saline salts (typically halite and bitterns) are flushed, leaves behind residues of the less saline salts (typically gypsum-anhydrite, as in many caprocks).

Solubility varies from salt to salt (Table 7.1). For example, gypsum is moderately soluble in nearsurface meteoric waters with a saturation concentration of around 2,500 ppm at 40 °C. Halite is much more soluble, its saturation concentration is ≈350,000 ppm at 25 °C and, unlike the calcium sulphate salts, its solubility consistently increases with rising temperature (Fig. 7.1). Limestone dissolves more slowly than gypsum or halite, with a saturation concentration that varies according to ambient pH and CO_2 levels, but typically in the range 50–400 ppm.

When exposed to meteoric crossflows, gypsum is one to two orders of magnitude as soluble, while halite is more than three orders of magnitude as soluble as limestone. For example, in temperate-zone caves Klimchouk and Aksem (2000) used gypsum tablets of standard lithology and size (40–45 mm diameter, 7–8 mm thick), and placed them so they were exposed to surface precipitation (640 mm), cave air in zones of condensation, percolation, and static or semi-static

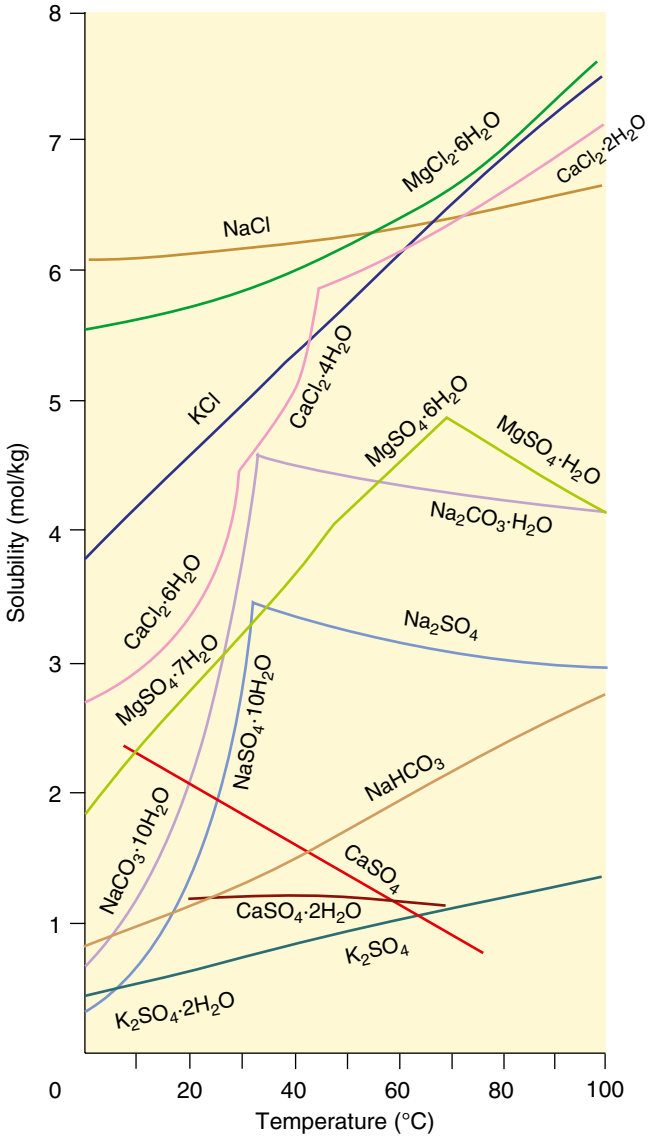

Fig. 7.1 Solubility of common salts in pure water as a function of temperature, expressed in mole anhydrous salt per kg H_2O, (After Braitsch 1964)

© Springer International Publishing Switzerland 2016
J.K. Warren, *Evaporites: A Geological Compendium*, DOI 10.1007/978-3-319-13512-0_7

Table 7.1 Solubilities in freshwater of various evaporite salts in comparison to limestone at 25 °C (relative solubility calculated from molar concentrations)

Mineral name	Composition	Solubility in freshwater (moles/l)	Solubility with respect to limestone
Limestone	$CaCO_3$	0.00014	1
Magnesite	$MgCO_3$	0.001	7.1
Gypsum	$CaSO_4{\cdot}2H_2O$	0.014	100
Nahcolite	$NaHCO_3$	1.22	8.7×10^3
Mirabilite	$Na_2\ SO_4{\cdot}10H_2O$	1.96	14.0×10^3
Natron	$Na_2\ CO_3{\cdot}10H_2O$	2.77	19.8×10^3
Epsomite	$MgSO_4{\cdot}7H_2\ O$	3.07	21.9×10^3
Thenardite	$NaSO_4$	3.45	24.6×10^3
Hexahydrite	$MgSO_4{\cdot}6H_2O$	4.15	29.6×10^3
Sylvite	KCl	4.78	34.1×10^3
Bischofite	$MgCl_2{\cdot}6H_2O$	5.84	41.7×10^3
Halite	NaCl	6.15	43.9×10^3
Kieserite	$MgSO_4{\cdot}H_2O$	6.25	44.6×10^3
Antarcticite	$CaCl_2{\cdot}6H_2O$	7.38	52.7×10^3

water in caves and boreholes. Aggressive groundwaters were able to dissolve gypsum tablets at rates up to 26 mm/year; the solution rate under active unconfined circulation averaged about 11 mm/year; whereas in the bulk aquifer the solution rate was about 0.1 mm/year. At Ripon in Yorkshire, a 3 m cube of undercut gypsum that fell into the River Ure was completely dissolved in 18 months and the nearby gypsum face was undercut another 6 m in the next 10 years (Cooper 1998).

Rates of gypsum dissolution can increase where there are significant amounts of halite dissolving nearby, this is attributed to the ionic strength effect (Fig. 2.18b; Ford and Williams 2007; Waltham et al. 2005). This can be an important booster to gypsum karstification where halite is intercalated with anhydrite or gypsum. Dissolution of exhumed anhydrite is often associated with a transformation to gypsum, its "in situ" measured dissolution rate is approximately 20 times slower than that of gypsum, essentially because the latter is precipitating onto the anhydrite surface as molecules dissociate there (Ford and Williams 2007, p. 71).

Rates of halite karst can only be measured where halite is at or near the landsurface. This tends to be in zones of halokinesis in arid areas, otherwise halite is long dissolved before it can approach the surface. In the 14 km^2 area of the active salt diapir of Mount Sedom in Israel, in a region with an annual rainfall around 50 mm, Frumkin (1994a) estimated the regional karst denudation rate to be about 0.50–0.75 mm/year, with most of this occurring within the subsurface rocksalt mass rather than near the surface.

Whatever the mineralogy, an evaporite mass will rapidly dissolve when in contact with a crossflow of meteoric or undersaturated basinal water. So, unlike carbonate karst, the effects of nearsurface evaporite solution on cavern formation and land surface subsidence are obvious in time frames measured in years, not millennia and the associated visible effects of this rapid collapse can be impressive[1] at the human perception scale.

This chapter deals with subsurface and near surface regions where hypersaline depositional and burial hydrologies are replaced by pore waters undersaturated with respect to the various evaporite salts. This situation is ubiquitous, it occurs wherever ancient evaporites are exhumed and once again enter the active phreatic (telogenetic) zone. Dissolution is also typical of evaporites in the deeper subsurface (mesogenetic realm) wherever undersaturated basinal waters are flushing the edges of impervious evaporite beds (Chap. 8). Dissolution leaves behind solution breccias and other indicators of the former presence of now-leached evaporites (vanished evaporites or "the salt that was").

Even as an evaporite bed accumulates, or soon after its deposition ceases, pore waters in the depositional environs can be periodically freshened, either by climatic excursions or by progradation of sheetwash/fluvial/marine flood sediment. In this scenario karstification is part of the ongoing

[1]The cluster of water-filled sinkholes atop dissolving evaporites and locally known as "Hell's Kettles" (Lat 54.492655, Long −1.567459) located to the south of Darlington, UK, formed in 1179 AD via a catastrophic collapse of the landsurface. A twelfth century annalist describes their formation as follows:

"In the reign of Henry II, the earth rose high at Oxendale, in the District of Darlington, (Oxendale is now Oxney flat) in the likeness of a lofty tower, and so remained from nine in the morning until evening, when it sank don with a terrible noise, to the terror of all that heard it, and being swallowed up it left behind a deep pit."

After the collapse the local clergy had a field-day; the "Hell's Kettles" dolines have long been reputed to be bottomless pits, said to harbor the tortured souls of the sinful dead.

depositional story and explains many microkarst textures described in Chap. 1. In one of the first uses of the term "the salt that was," Schreiber and Schreiber (1977) described Miocene gypsum beds in Sicily where early halite layers were seasonally dissolved, even as the gypsum bed was accreting. This is an example of the syndepositional end of a salt dissolution spectrum that extends into much longer time frames that encapsulate the burial and metamorphic realms.

At a millennial time scale, periodic evolution of a syndepositional hypersaline hydrology into a less saline groundwater system creates karst effects and textures at the contact between the evaporite bed and its overburden. This can drive freshened pore water ingress and karstification of the upper few metres of an accumulating evaporite bed. This scenario is typical of many continental playas where fluvial and bajada sediments periodically build out over a saline pan, or where marine transgressions pass over saltern beds. Its effects are discussed later in this chapter in the section dealing with syndepositional karst. But most of the chapter deals with the various outcomes and indicators of longer time frames where overburden is indurated and the dissolution process effects deeper subsurface (meso-genetic) and uplifted (telogenetic) bedded and diapiric salts.

Because of their high solubility, exhumed ancient evaporites outcrop best in arid or frozen regions of the world. These are areas with lower crossflow volumes of liquid groundwater and so are zones where even halite can make it back to the shallow subsurface, before complete disintegration (Fig. 6.84). Exhumed anhydrite typically converts to gypsum some tens to hundreds of metres below the landscape over those areas of the world featuring subcropping and outcropping evaporites. This telogenetic gypsum has a fresh set of textures that make it difficult to interpret its original depositional fabric. Subcropping halite, with its much higher solubility, tends to dissolve completely before reaching the surface. In all but the most arid environments, gypsum, not halite or anhydrite, is the commonplace outcrop expression of an underlying evaporite mass, be it bedded or halokinetic.

Outcropping gypsum caprock, with well-developed karst, encases salt diapirs in the Middle East, north Africa and central Australia and defines halite subcrop in the Qinghai (Tibetan) plateau, the Pecos Valley of West Texas, the Magdalen Islands in the Gulf of St. Lawrence, Canada, and in the Sierra del Fraile, in northeastern Mexico (Fig. 7.2). Gypsum capstones can occasionally outcrop in humid tropical regions. For example, a gypsum caprock sporadically outcrops along the erosional banks of the Nam Theun River in Laos. This site lies within the axis of an evaporite-floored synclinal trough, it is surrounded by tropical pine forest, and caps an actively dissolving residual mass of stratiform Cretaceous halite (*pers. obs.*). Halite can reach the surface in arid zones where salt is actively flowing into diapirs and allochthons, as at Mt Sedom in the Dead Sea Valley and in the salt glaciers (namakiers) of Iran (Fig. 6.84).

Individual exposures of outcropping salts are usually no more than a few square kilometres, whereas dissolution breccias, insoluble residues and their characteristic subsidence terrains such as blind-valleys and suffusion karst, subcrop more widely, as do many other indictors of evaporites (Fig. 7.2). The mining of rock salt, or the drilling of boreholes into or through rock salt, have accidentally intersected or created caverns leading to a number of large, anthropogenically-enhanced collapse sinks, subsidence cones and subrosion[2] features, which are discussed further in Chap. 13. Natural karst hazards are discussed later in this chapter.

Complete evaporite dissolution means no salt remains, while partial or preferential dissolution means the vertical or lateral extent of the remaining salt sequence is reduced and the more soluble salts have gone. Salt bed dissolution can be syndepositional, as can nodule and crystal replacement, or can occur later during shallow burial with vadose or shallow phreatic groundwater flow driving cavern formation and overburden collapse. Bed alteration and solution can occur much later under deeper phreatic basin hydrologies, where circulation is driven by compactional and thermobaric flushing. It can occur later still, when uplifted salts beds are once again flushed by deeply circulating meteoric waters during collision, inversion and overthrusting (Table 7.2; Fig. 1.9).

Dissolution also occurs in the more enigmatic meta-evaporitic and igneous realms, where it is accompanied by deep burial mineral transformations such as scapolitisation, albitisation and tourmalinisation (see Chap. 14 for details). Evidence for vanished evaporites can remain in the rock record long after the actual salts have gone. This is why many indicators of ancient evaporites plot outside known salt basins (Fig. 7.2).

Brines generated at an evaporite dissolution front can seep into adjacent sediments where new authigenic evaporite cements and nodules precipitate. Dissolution brines can rise along brine escape conduits, such as faults and fractures, into the higher portions of the sediment pile, where they cool or mix with waters of differing chemistries and so precipitate authigenic cements. Although dissolutional hydrology is transitory, the evidence of former evaporite beds –the evaporite that was– is permanent and ranges from dissolution breccias and residues, to replaced evaporite crystals and nodules, to authigenic evaporite cements near flow conduits such as unconformities, faults and fractures.

[2]The term subrosion refers to the burial-related dissolution of salt.

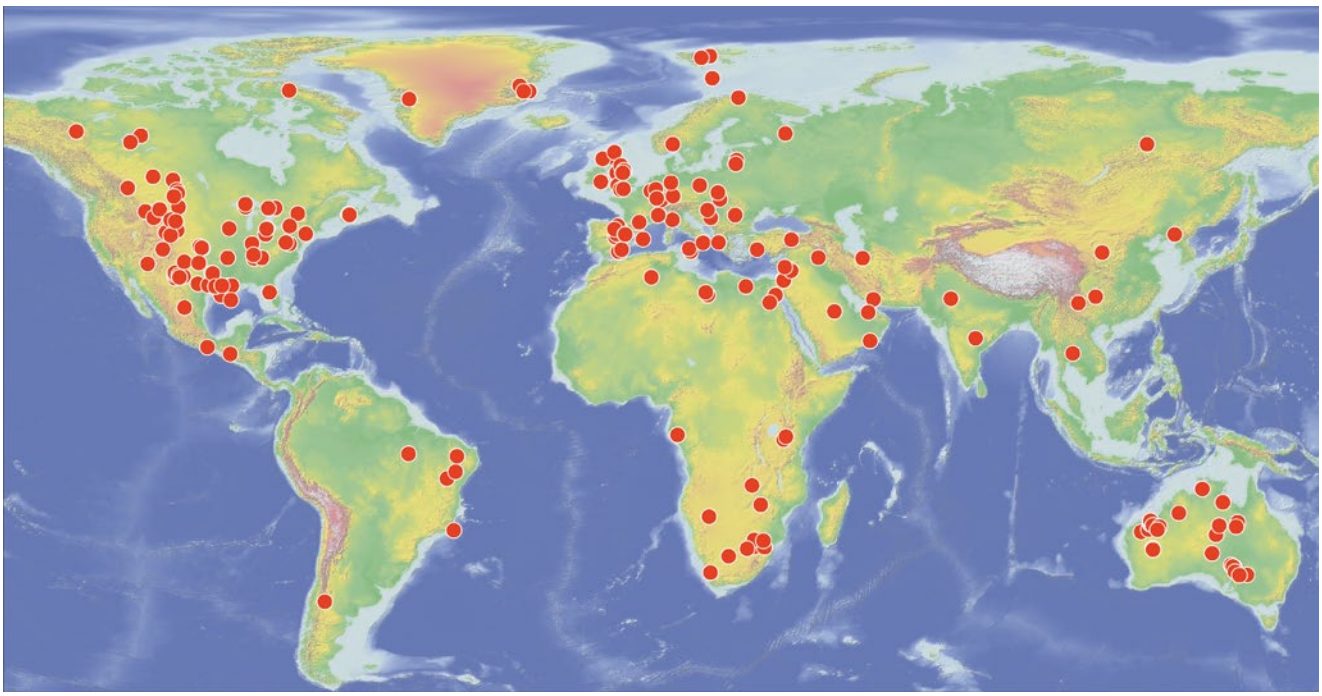

Fig. 7.2 Selected locations of indicators of former "vanished" evaporites (positions extracted with permission from Saltwork® Pte Ltd GIS database, version 1.7)

Table 7.2 Selected examples of indicators of evaporite dissolution ("vanished evaporites")

Indicator	Examples	Reference
Modern gypsum karst	Miocene gypsum host, Sivas, Turkey	Dogan and Ozel (2005)
	Late Miocene gypsum host, Sicily and Calabria	Ferrasse et al. (2002), Iovine et al. (2010)
	Tertiary gypsum hosts, Ebro and Madrid basins, Spain	Rodriguez-Aranda et al. (2002), Gutiérrez et al. (2008)
	Permian gypsum host, Ripon, UK	Cooper and Waltham (1999), Jones and Cooper (2005)
	Pennsylvanian – Permian gypsum, Sth Dakota, USA	Epstein (2001)
	Devonian gypsum host, Northern Lithuania	Paukstys et al. (1999)
Modern halite karst	Bedded Quaternary halite, Dead Sea Margin	Closson et al. (2007), Frumkin et al. (2011)
	Miocene halite host (diapiric), Mt Sedom, Dead Sea	Frumkin (1994a, b)
	Neoproterozoic halite host (diapiric), Zagros Chain	Bosak et al. (1999), Zarei et al. 2012
Solution collapse breccia	Cretaceous Kirschberg breccia, Texas	Warren et al. (1990), Zahm and Loucks (2011)
	Cretaceous Carib Halite residues, Columbia, Venezuela, Trinidad	Higgs (2009)
	Paleotopography below giant Lower Cretaceous Athabasca oil sands	Broughton (2013)
	Triassic breccia beds, Ionian Zone, NW Greece	Pomoni-Papaioannou and Karakitsios (2002)
	Gypsum/anhydrite cavity cements, Permian Werra Anhydrite, Poland	Hryniv and Peryt (2003)
	Permo-Carboniferous, Central Spitsbergen, Svalbard	Eliassen and Talbot (2005)
	Lower Carboniferous, Vesder, Belgium and Wexford, Ireland	Swennen et al. (1990), Nagy et al. (2005)
	Pennsylvanian Amsden Formation, Montana	Luebking et al. (2001)
	Devonian Carbonates, western Canada	Stanton (1966)
	Devonian, Cadjebut area, Lennard Shelf	Warren and Kempton (1997)

Table 7.2 (continued)

Indicator	Examples	Reference
Preferential dissolution residues	Miocene gypsum breccias in halite, Poland	Babel (1991)
	Miocene gypsum residues atop diapirs, Cratone Basin, Italy	Lugli et al. (2007)
	Basal Anhydrite, Khorat Plateau, Thailand	El Tabakh et al. (1998a), Warren (1997)
	Anhydrite residues via solution of Maha Sarakham Salts, Khorat Plateau, Thailand	Sessler (1990) Utha-aroon et al. (1995)
	Permian salt beds, Texas Panhandle	Hovorka (2000)
Rauhwacke	Quaternary-weathered brecciated detachment horizons in nappes of European Alps and Spain	Warrak (1974), Schaad (1995), Orozco et al. (1999), Alberto et al. (2007)
Silicified evaporites and nodules	Miocene lacustrine evaporites, Calatayud Basin, Spain	Orti and Rosell (2000)
	Miocene gypsum nodules, Mogrha Fm., Western Desert, Egypt	Khoriby (2005)
	Eocene chert/anhydrite nodules in Kef Eddour Member, Tunisia	Henchini and Slim-S'Himi (2006)
	Late Palaeozoic carbonates, Bear Island, Svalbard	Folk and Siedlecka (1974)
	Permian Park City Fm., Wyoming	Ulmer-Scholle and Scholle (1994)
	Mississippian strata, Kentucky and Tennessee	Milliken (1979)
	Silicified halite casts, Archaean, South Africa	Eriksson et al. (2005)
Calcitised evaporites	Anhydrite nodules, Lower Triassic red mudstones, Central Spain	Bustillo et al. (1999), Caja et al. (2003)
	Calcitized gypsum, Münder Formation, Upper Jurassic, Germany	Arp et al. (2008)
	Anhydrite nodule and cements, Permian Khuff Formation, Abu Dhabi	Worden et al. (2000)
	Anhydrite, Permian Zechstein EZ-1 Carbonates, Europe	Harwood (1980)
	Laminar anhydrite/gypsum, Permian Castile Fm., Texas & New Mexico	Stafford et al. 2008a, b
	Mississippian nodular anhydrites, Saskatchewan	Kendall (2001)
	Calcitized swallowtail gypsum, Palaeoproterozoic Tulomozero Fm, Africa	Brasier et al. 2011
	NeoArchaean gypsum and anhydrite, South Africa	Gandin and Wright (2007)
Calcitised dolomites (dedolomite)	Permian Blaine Formation, SW Oklahoma, USA	Raines and Dewers (1997)
	Permian Raisby Fm. (Zechstein), NE England	Lee and Harwood (1989), Lee (1994)
	Permian Tansill Fm, New Mexico	Lucia (1961)
	Mesozoic limestones, French Jura	Shearman et al. (1961)
	Late Palaeozoic flushing Devonian anhydrite, Winnipegosis Fm, Canada	Fu et al. 2008
Celestite nodules	Miocene lacustrine gypsum (bacteriogenic dolomite)	Sanz-Montero et al. (2009)
	Purbeckian of Dorset, UK	Salter and West (1966)
	Salina Dolostones, Silurian, Ohio	Carlson (1987)
Fluorite cements	Eocene mudstones, Florida	Cook et al. (1985)
	Mesozoic evaporites replaced by fluorite, celestite, baryte, Mexico	González-Sánchez et al. (2009)
	Deeply circulating evaporite-associated Mesozoic brines, Spain	Piqué et al. (2008)
	Visean evaporites, France	Rouchy (1986)
Baryte nodules and cements	Arid soils, central Australia	Sullivan and Koppi (1993)
	Carbonate-baryte-uranium mineral association at deepsea brine vents, salt allochthon province, Gulf of Mexico	Sassen et al. (2004)
	Magnet Cove baryte, Nova Scotia	Mossman and Brown (1986)
Authigenic anhydrite/halite cements	Satin-spar filled hydrofractures during Tertiary inversion of Mercian (Triassic) mudstones, SW England	Philipp (2008)
	Cretaceous Pearsall and Glen Rose Fm., Texas	Woronick and Land (1985)
	Keuper, Rhaetian sands, Germany	Pape et al. (2005)
	Permian Rotliegende Sands, North Sea, Europe	Sullivan et al. (1994), McNeil et al. (1998)
	Jurassic Smackover Fm., USA	Heydari and Moore (1989), Heydari and Baria (2006)

Evaporite Landforms

As salt dissolves in the shallow subsurface it creates void space into which overlying strata can drape or brecciate to create characteristic landforms at both local (m to km) and regional (km to tens of km) scales (Fig. 7.3). We can divide solution-related landforms into two styles: active karst and palaeokarst. Paleokarst refers to ancient karstic features that are no longer active and were tied to basinal flushing hydrologies or landsurfaces no longer present. Active karst is responding to the ambient hydrology and typifies the landscapes discussed in the following section.

Local Scale Karst

Regions underlain by an evaporite subcrop exhibit dissolution landforms similar to carbonate karst and so include many varieties of karren, sinkholes (dolines), blind valleys and poljes (Ford and Williams 1989). Bedrock exposures of gypsum or salt at a finer scale are sculpted into irregular surfaces called rillenkarren and other solution flutes (Macaluso and Sauro 1996; Stenson and Ford 1993). Local-scale karst features that define subsidence basins range in lateral extent from the metre-scale cones of suffusion karst to kilometre-scale doline depressions (Fig. 7.3).

Dolines or Sinkholes

Dolines (aka sinkholes) are closed circular to elliptical hollows or depressions, often funnel shaped, with diameters ranging from a few metres to a few kilometres and depths from a metre or so to hundreds of metres (Fig. 7.3; Ford and Williams 2007). They indicate subsidence and collapse of underlying salt or carbonates. Valley sides may be steep and can expose karstified gypsum, or be gentle and covered by desert soils. Active sinkholes atop shallow bedded evaporites typify terminations of dry arroyos in many deserts. Larger sinkholes may enclose one or more smaller sinkholes and can be further subdivided into collapse, suffosion and solution dolines (Fig. 7.3). A collapse sinkhole forms by the collapse of a roof span into an underlying solution cavity. Suffosion dolines are smaller features (1–5 m diameter) covered and filled with soils and debris washed into its fissures by rainfall or sheetflood. They indicate that the dissolving salt mass is close to the landsurface. Solution (subsidence) dolines tend to be larger downwarped doline craters or bowl-like subsidence depressions. Compared to collapse and suffusion dolines they have lower slopes into the deeper parts of the doline, the doline walls are usually hosted in nonevaporites and the dissolving salt bed can lie some distance below the landsurface. At the larger end of the scale of doline development a subsidence doline merges into a subsidence basin. This is a large solution hollow that creates enough accommodation space to be considered a small sedimentary basin, which is filling with varying combinations of fluvial and lacustrine sediments.

Dissolution, collapse and suffosion are more active, more rapid, more frequent and more obvious in evaporite compared to carbonate terranes. In the Perm and Bashkir regions of Russia, Gorbunova (1979) reported doline densities atop weathering evaporites and carbonates of 32 and 10/km^2 respectively, although densities up to 1,000/km^2 can occur in many evaporite-cored fold axes or at contacts of evaporites with other lithologies. Densities of 1,100–1,500/km^2 have

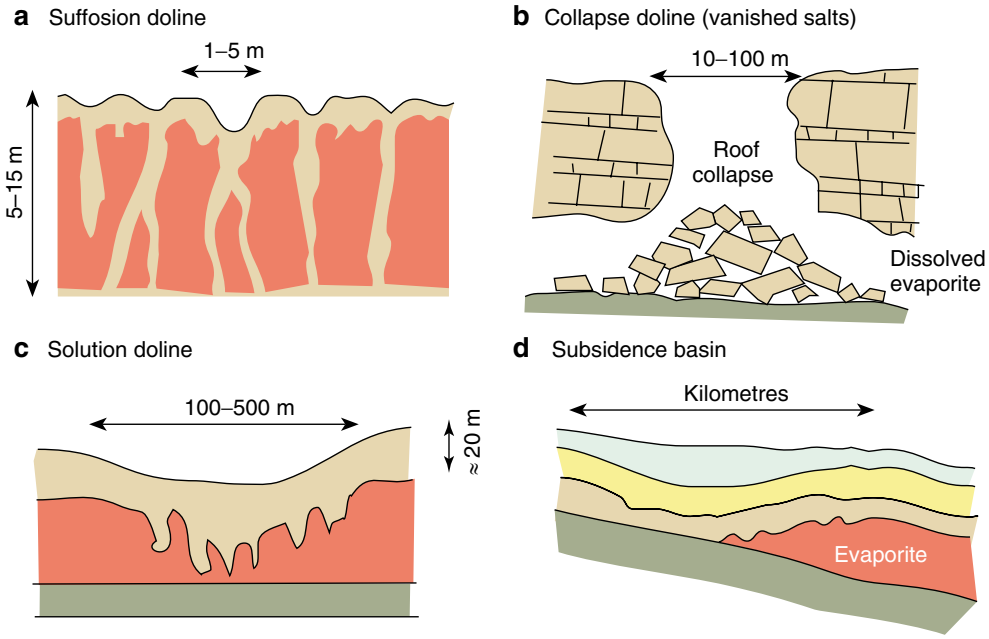

Fig. 7.3 Typical scales and origins of evaporite karst features formed at the land surface, atop a dissolving evaporite unit (*red*). See text for details of **a**–**d**

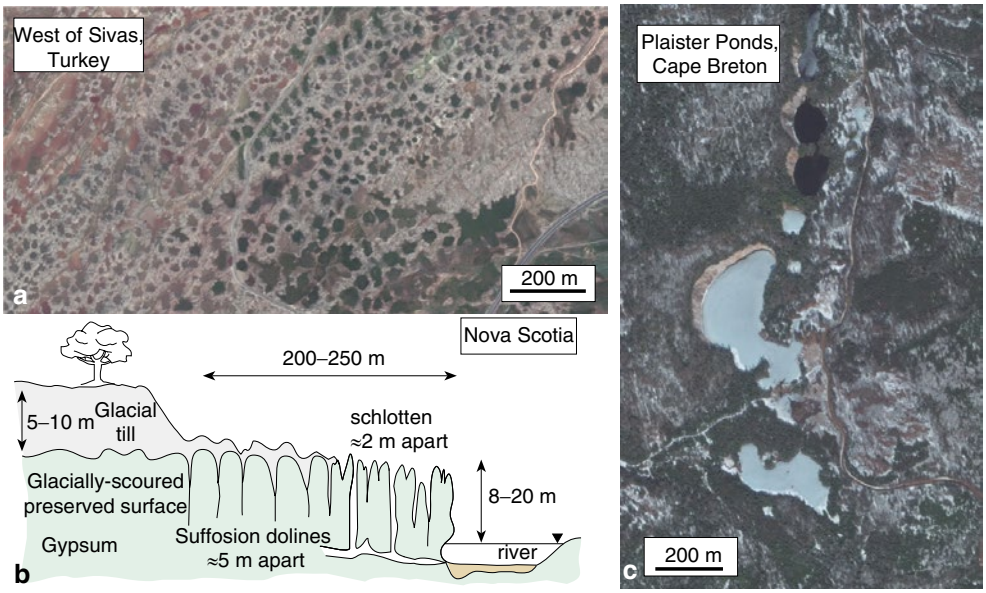

Fig. 7.4 High densities of dissolution depressions on evaporites. (**a**) Karst polygon terrane atop a Miocene gypsum outcrop (Hafik Fm.), some 20 km west of Sivas, Turkey. (**b**) model of suffosion karst development on subcropping till-covered gypsum (Carboniferous) in Nova Scotia, Canada. (**c**) Natural water-filled steep sided collapse dolines known as Plaister Ponds, near Baddeck on Cape Breton Island (Scaled Bing® images mounted and scaled in MapInfo)

been documented in evaporite karst in the Italian Alps and in regions to west of Sivas, Turkey (Fig. 7.4a). Such high densities occur in regions of high hydraulic gradients and mean the dolines have diameters around 5 m or less (Belloni et al. 1972). The inherently high solubility of evaporite salts also explains densely-packed schlotten depressions and large karren shafts seen in gypsum karst of the Sivas region of Turkey and Antigonish County, Nova Scotia, where extrapolated doline densities in the latter case range up to 10,000/km^2 (Fig. 7.4a, b; Kacaroglu et al. 1997; Martinez and Boehner 1997). Extrapolated, because such dense networks do not extend over any more than a square kilometre or two and are typically found near retreating escarpment edges underlain by shallow subcropping salts.

Suffosion Dolines

High levels of dispersed impurities (mostly clays and muds, often dolomitic) in a rapidly dissolving evaporite mass, means a soil or carapace of insoluble residues quickly covers the subcropping top and edges of a dissolving salt mass (Figs. 7.3a and 7.4a). This carapace is continually undermined by ongoing rapid solution so that residual debris is washed into the doline crevices. This creates characteristic soil-covered dimpled landscapes that typify high-density doline terrains. Suffusion is a form of mantle karst where the dissolving salt bed is never more than a few metres below the landsurface.

Collapse Dolines

Collapse dolines are steep-sided sinkholes, often defined by cave entrances (Fig. 7.3b). They form when solution of an underlying evaporite bed creates a roof span in the regolith that can no longer be supported by the overlying lithology. Doline walls are frequently asymmetrical; one wall is steep and the other one is gentle. Steep-sided collapse dolines are typical of regions with unconsolidated overburden, such as glacial till (Fig. 7.4c). Doline floors, when not water covered, tend to display either concave-up or flat geometries. Apart from blocks of the collapsed roof span, active doline floors can be veneered by thin collapse breccias. The high density of dolines in areas of evaporite subcrop and the ubiquity of the associated breccias indicates the inherently higher solubility of the evaporite salts compared with interbedded and overlying carbonates.

Solution Dolines

Larger sinkholes (subsidence dolines) with characteristic low angle widespread edge flexures and slopes indicate deeper, more widespread salt dissolution compared to collapse dolines and are linked to the creation of a bowl of subsidence (Fig. 7.3c). They occur in most regions of deeper evaporite karst including; Italy (Belloni et al. 1972; Burri 1986; Ferrarase et al. 2002), Spain (Gutiérrez 1996) and the Pecos Valley of West Texas and New Mexico (Gustavson et al. 1982; Davies 1984a, b; Quinlan et al. 1986). In contrast to the numerous small steep-sided suffosion and collapse dolines formed atop shallow subcropping shallow evaporites, these larger, bowl-like dolines can have diameters of 100–500 m and depths of 10–20 m. Most have a soil cover and a thick sediment fill, with dissolving salt units at depths measured in tens to hundreds of metres below the land surface. They are mature dissolution forms and are transitional to subsidence basins where even thicker more widespread sediment fills are to be found (Fig. 7.3d).

Following the definitions of Waltham et al. (2005), Gutiérrez (2010), constructed a nongenetic evaporite-related

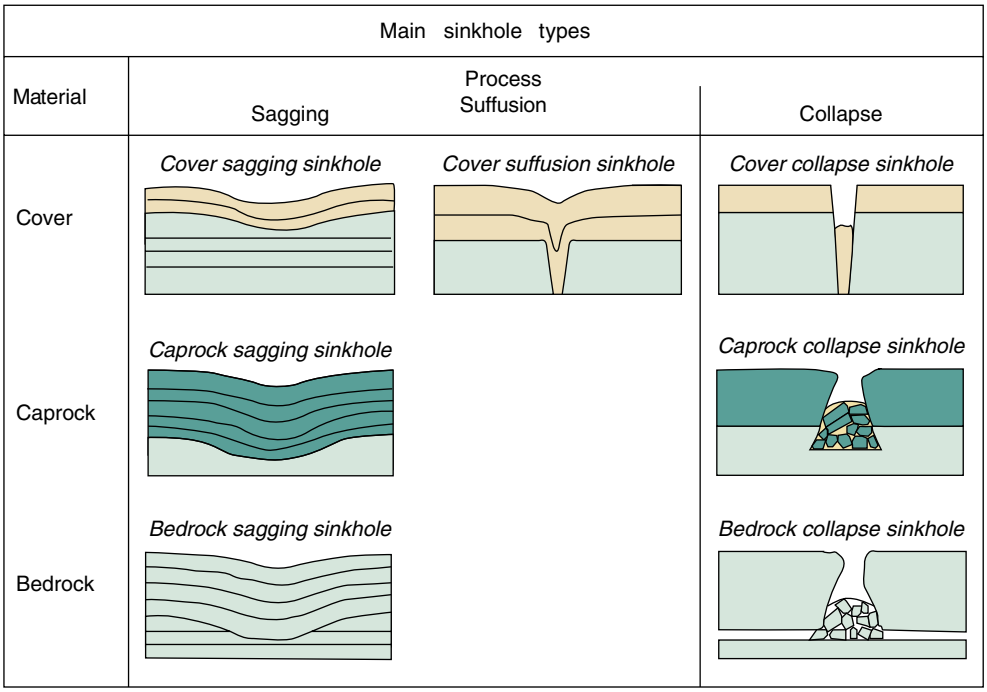

Fig. 7.5 Doline (sinkhole) classification for features found in a landscape underlain by dissolving evaporites, indicated by *light green* (After Gutierrez 2010; Waltham et al. 2005)

subsidence dolines or sinkholes classification based on terms that refer to the material affected by downward gravitational movements (cover, bedrock or caprock) and the main type of process involved (collapse, suffosion or sagging; Fig. 7.5). The classification also applies to carbonate karst. The term "cover" refers to allogenic unconsolidated deposits or residual soil material, bedrock to karst rocks and caprock to non-karst rocks. Collapse indicates the brittle deformation of soil or rock material either by brecciation or the downward migration deposits through conduits and its progressive settling, while sagging is the ductile flexure (bending) of sediments caused by the lack of basal support. In practice, more than one material type and several processes can be involved in the generation of sinkholes. These more complex sinkholes can be described using combinations of the proposed terms with the dominant material and/or process followed by the secondary one (e.g. cover and bedrock collapse sinkhole, bedrock sagging and collapse sinkhole),

The cover material may be affected by any of three subsidence mechanisms. The progressive corrosional lowering of the rockhead may[3] cause the gradual settling of the overlying deposits by sagging, producing cover sagging sinkholes. An important applied aspect is that the generation of these sinkholes does not require the formation of cavities. These depressions arc commonly shallow, have poorly defined edges and may reach several hundred metres across.

Cover deposits may migrate downward into fissures and conduits developed in the rockhead by action of a wide range of processes collectively designated us suffusion: downwashing of particles by percolating waters, cohesion-less granular flows, viscous gravity flows (non-Newtonian), fall of particles, and sediment-laden water flows. The downward transport of the cover material through pipes and fissures may produce two main types of sinkholes depending on the rheological behaviour of the mantling deposits. Where the cover behaves as a ductile or loose granular material, it may settle gradually as undermining by suffosion progresses. This creates sags and slumps in the overburden materials. Where cover behaves in a more brittle manner, collapse breccias form.

Sinkholes that result from the combination of several subsidence processes and affect more than one type of material are described by combinations of the different terms with the dominant material or process followed by the secondary one (e.g. bedrock sagging and collapse sinkhole). The mechanism of collapse includes any brittle gravitational deformation of cover and bedrock material, such as upward stoping of cavities by roof failure, development of well-defined failure planes and rock brecciation. They define suffosion as the downward migration of cover deposits through dissolutional conduits accompanied by ductile settling. Sagging is the ductile flexure of sediments caused by differential corrosional lowering of the rockhead or interstratal karstification of the soluble bedrock. Sag plays an important role in the generation of sinkholes in evaporites (not included in previous genetic classifications mostly based on carbonate karst). They conclude collapse processes are more significant in extent and rate in areas underlain by evaporites than in carbonate karst, primarily due to the greater solubility of the evaporites and the lower mechanical strength and ductile rheology of gypsum and salt rocks.

[3]Rockhead is the buried interface between the underlying bedrock and its soil cover.

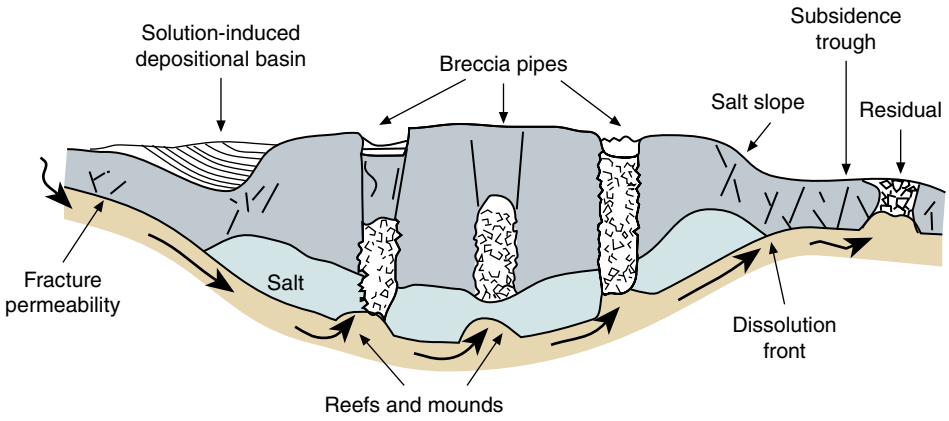

Fig. 7.6 Interrelationships between larger scale dissolution features, artesian flow and various types of upward stoping breccia pipes (not to scale; in part after Ford and Williams 1989)

Breccia Chimneys and Pipes

Breccia pipes develop as steep-sided chimney-like features on the same scale as collapse dolines or sinkholes and show typically circular outlines at the surface. Some consider them a subset of caprock collapse dolines and tie them to a specific process set namely formation by progressive upward stoping from the base of the salt bed, not its upper portions. This contrasts with the subsidence/sag-dominated set of process set that creates most meteoric suprasalt dolines. In regions of thick evaporites the stoping process is driven by the focused upward escape of undersaturated basinal or deeply circulating meteoric waters leaking from levels below the sealing evaporite bed. Waters creating a stoping pipe can be focused into point or line sources via underlying biogenic buildups or fracture networks (Fig. 7.6). Quinlan (1978) reviewed the nature and distribution of more than 5,000 breccia pipes within or atop salt or gypsum in the United States. Pipes ranged from 1 to 1,000 m in diameter and up to 500 m in depth. Similar crosscutting pipes in halite of the Devonian Prairie evaporite interrupt workings of potash mines in Saskatchewan, where they may propagate from depths as great as 1,200 m, and may lie beneath a thousand or more metres of cover strata (Figs. 7.7). Unexpected intersection with a breccia pipe in an exploited bed can lead to catastrophic flooding and ultimate loss of a mine (Figs. 11.69 and 11.75).

One of the most impressive regions of widespread and well-documented breccia piping is seen in the coal mine regions of northern China. There, more than 2,800 breccia pipes have been recorded in the mines of Shanxi and Hebei regions (Lu and Cooper 1997). The pipes originate in Ordovician gypsum, interbedded with limestones, and passing upwards through the Permo-Carboniferous coal measures. Vertical transmissivity in the pipes creates a major mining hazard due to large volumes of entrained water, which are more than sufficient to flood a mine. Pipes vary in diameter from tens of metres to hundreds of metres, with the larger pipes transecting more than 500 m of overburden. Some have reached the modern landsurface, others are blind chimneys. Pipe densities reach 70 per km^2 in the Shanxi coal basin, where more than 1,300 pipes occur. Interestingly, most of the pipes are located about the margin of the coal basin and none are known in the deeper parts of the Shanxi basin centre.

Breccia pipes in an evaporite mass may exhibit one of four possible states (Fig. 7.6): (a) Active, and propagating upwards towards the surface, but not yet expressed there – a blind chimney; (b) Active or inactive, expressed at the surface as a closed depression or a depression with a surface outflow channel; (c) Inactive, and buried by later strata – paleokarst chimney; (d) Inactive and standing up as a positive relief feature on the landsurface because the breccia (probably cemented) is more resistant to weathering than the upper cover strata – a residual pipe. Downward flexure in the uppermost strata atop a growing pipe forms a bowl of subsidence and sinkhole.

In some intrasalt pipes the halite or gypsum is entirely removed, leaving only an accumulation of insolubles and collapsed breccia blocks. In others, portions of the less soluble salts remain in the pipe. Mature pipes are typically filled by a jumble of intrasalt and suprasalt breccia blocks. In some, a lower brecciated zone is succeeded by an upper zone in which the overlying strata failed as a coherent block, settling downwards via a cylindrical pattern of steep to vertical faults with downthrows of up to 200 m.

Landscape Residuals; Karst Domes and Castiles

Karst domes remain as features of positive relief once the surrounding evaporite mass has completely dissolved. Unlike chimneys, the cores of evaporitic karst domes can expose blocks from below, as well as above the original salt level. Some evaporitic karst domes are related to the stratigraphic level of former bedded salt, others are the remains of now dissolved salt thrusts, diapirs and allochthons (see diapiric breccias and rauhwacke). Domes and residuals are dramatic landscape features in the gypsum terrain of northern Alberta, Canada (Wigley et al. 1973; Tsui and Cruden 1984) and the Arkhangelsk gypsum karst region inland of the Barents Sea coast of Russia (Korotkov 1974). Canadian karst domes range from 10 to 1,000 m or more in length or diameter, and can rise up to 25 m above the surrounding land surface.

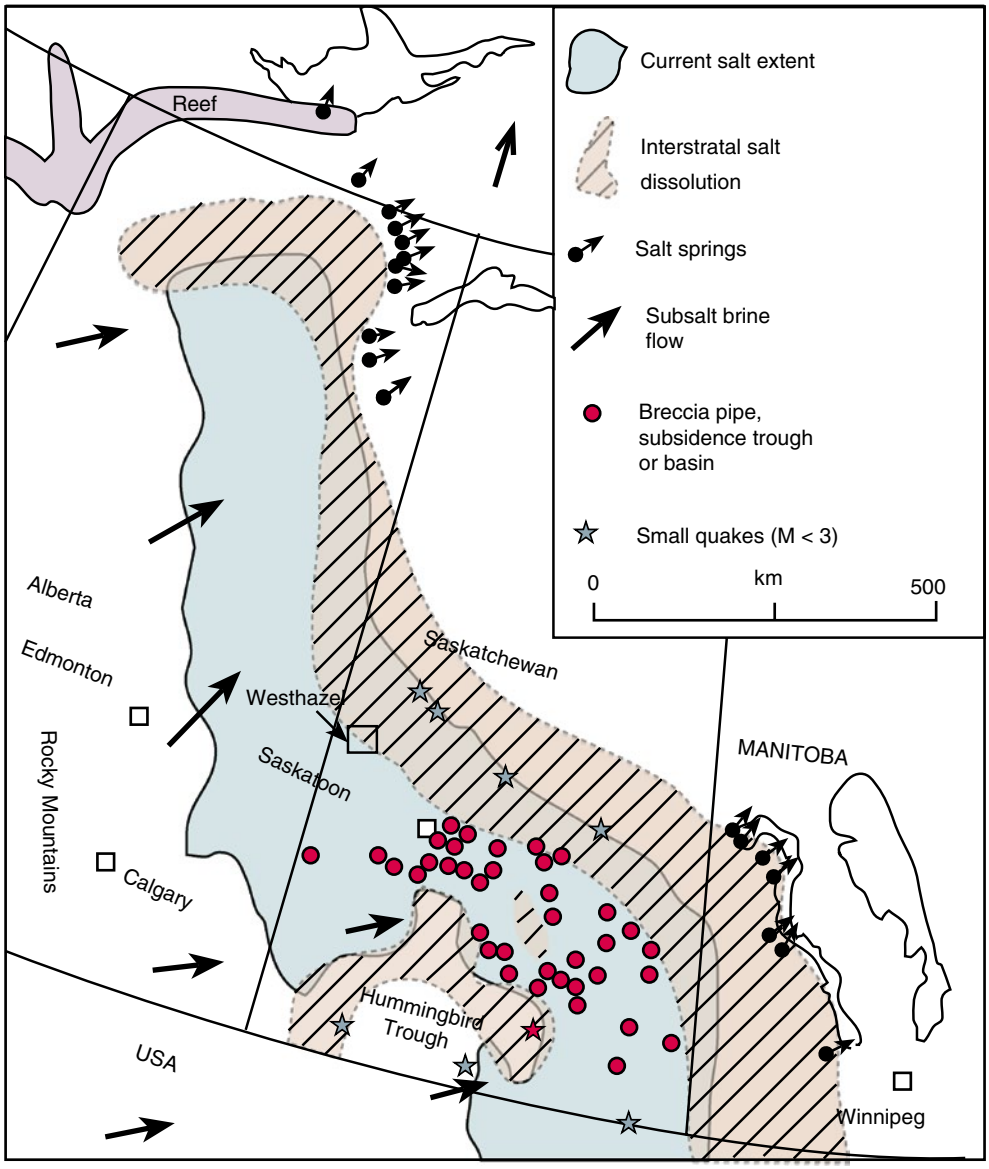

Fig. 7.7 Regional distribution of evaporite karst features in the Prairie Provinces of Canada, including a large subsidence basin known as the Hummingbird Trough. These features were created by the dissolution of thick widespread Prairie Evaporite at various times from the Devonian to the present (In part after Ford and Williams 1989)

Many domes are highly fractured, with individual overburden blocks displaced by heaving and sliding, with the residual gypsum showing well-developed flow foliation.

At the extreme end of disturbance and dissolution the domes are megabreccias; positive relief features made up of upthrust jumbles of large blocks the size of houses. The largest reported Canadian example is in a steep-limbed anticline that extends along the shore of Slave Lake for a distance of 30 km, it is up to 175 m in height with a crest that is marked by a 'chaotic structure and trench-like lineaments' (Aitken and Cook 1969). These spectacular karst domes occur in regions of widespread permafrost so that accumulation of ground ice in initial fractures in the evaporite layer probably contributes to the heaving, folding and other displacement of breccia fragments in the dome. Tsui and Cruden (1984) attributed the examples that they studied in the salt plains of Wood Buffalo National Park Canada (Lat. 59–60°N) to hydration processes operating on subcropping bedded gypsum during the postglacial period. Ford and Williams (1989) argued such features indicate local injection of gypsum residuals during times of rapidly changing glacial ice loading. Whether they are created by glacial unloading/reworking or are a type of gravitationally-displaced dissolution breccia in a permafrost region is debatable; that they are a type of evaporite residue is not. They characterise parts of the region defined by dissolution of shallow subcropping Devonian salt in Northern Alberta.

Residuals composed of cemented sinkhole or breccia pipe fillings can create hills surrounded by lower relief remnants of the former host bed (Fig. 7.6). More than a thousand such hills occur on the gypsum plains of western Oklahoma (Fay and Hart 1978). Those karst mounds or hills with a doughnut

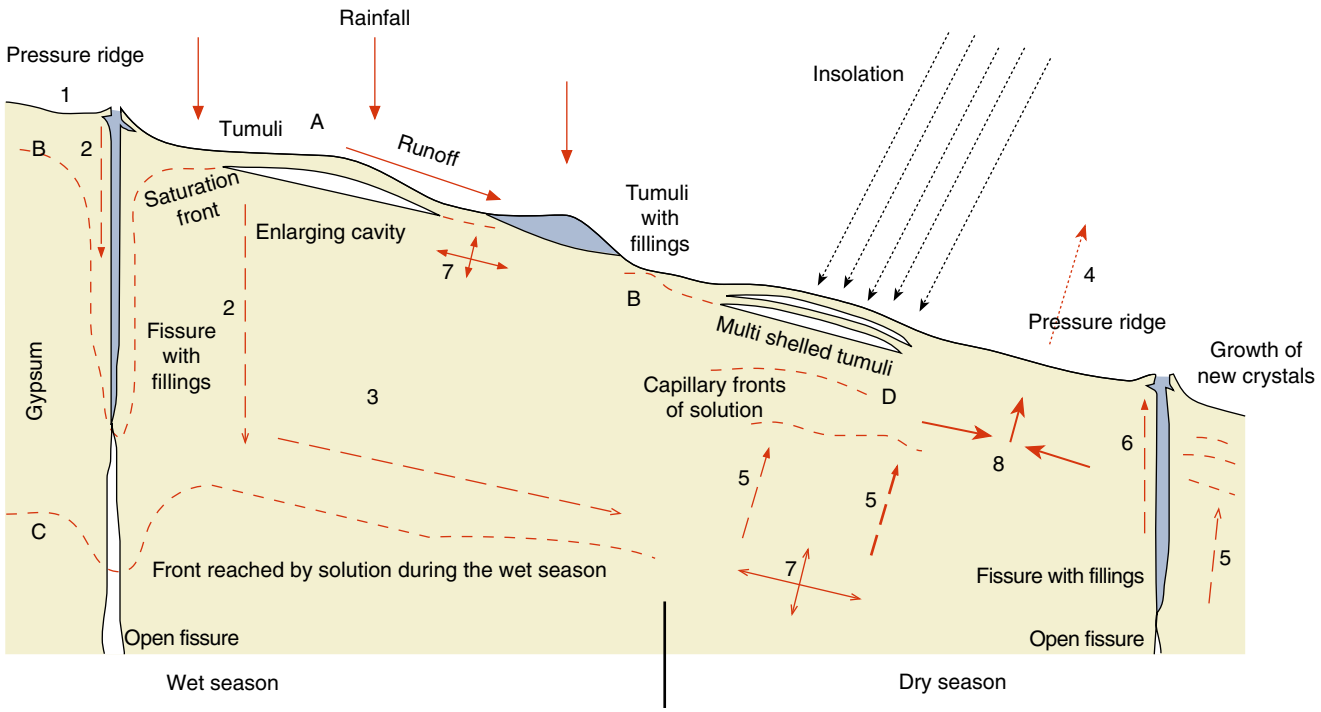

Fig. 7.8 Main processes occurring inside an outer gypsum layer directly exposed to the atmosphere in a typical Mediterranean climatic regime. During wet winters, rainfall drives an overland flow and the water dissolves the gypsum at the surface (*A*) while a portion of the runoff manages to penetrate inside the intercrystalline pores of the rock. The water reaches saturation (with $CaSO_4$) at the surface and a few decimetres into the rock (the *B* line (dashed) may be considered a saturation front). The solution continues to penetrate both inside the pores and along fissures and joints (*2*), creating a downward reaching front of newly arrived meteoric water (*C*). Nearsurface water in this front can also flow laterally (*3*). During the dry season, the pores lose water by evaporation (*4*). The inner solution becomes oversaturated and moves by capillary action towards the surface (*5*). In the *D zone*, there is precipitation of gypsum both by evaporative loss and by brine heating as it approaches the landsurface (gypsum has retrograde solubility). In the fissures and cavities, the pore fluids now migrate upwards (*6*) and new gypsum crystals may develop. The mass transfer from the inner towards the outmost zone results in pressure relaxation (*7*) in the *C zone*, where open fissures may exist, and in pressure increase (*8*) in the *D zone*. In soil-covered gypsum settings, runoff inside the sediment cover causes solution of the underlying gypsum both at the interface and in the fissures and other discontinuities of the rock. In this way, covered solution pavements and expansion tumuli can develop below the landsurface, and only become obvious after erosion of the soil cover (After Ferrarase et al. 2002)

form (a central depression), rather than a rounded form, are believed to be cemented expressions of former sinkhole fills within bedded evaporites, rather than residual breccia pipes (Myers 1962). Hills made up of cemented breccia pipe residuals are typically a few tens to hundreds of metres in diameter and can rise 5–40 m above their surrounds.

Castiles are another exhumed feature in a gypsum karst terrain. In their type area of the Delaware Basin, south of Carlsbad Caverns, NewMexico, they make up steep-sided hills and mesas rising 3–30 m above the Gypsum Plain (Kirkland and Evans 1976, 1980). They are composed of calcite, now exposed by the preferential dissolution of the surrounding bedded gypsum, in an area near the solution edge of the sulphate facies of the Castile Formation (Fig. 7.12). Similar features occur in areas of exhumed Miocene evaporites along the margin of the Red Sea (Aref 1998b). Castiles first form in the subsurface as a byproduct of the metabolic activities of sulphate-reducing bacteria, which locally replace gypsum with biogenic calcite (Figs. 7.63 and 9.65).

Evaporite Expansion Morphotypes at Outcrop

As well as the classic karst features, which are a response to dissolution and volume loss, some outcropping gypsum beds, especially in regions of anthropogenically induced rapid soil erosion, indicate local volume changes; as in parts of Sicily and Spain where weathered late Miocene gypsum is now exposed at the landsurface (Fig. 7.8). Such regions are characterised by extensive alteration and recrystallisation of the gypsum regolith and soil textures that indicate repetitive cycles of expansion and contraction of the nearsurface gypsum. The gypsum has evolved into pedogenic mounds and polygons related to exhumation into an active hydrology some millions of years after its deposition (telogenesis). The resulting medium-sized dome-like hills are covered by a mosaic of smaller landforms, related to different types of karren and of "expansion" forms such as tumuli and polygons. According to Ferrarase et al. (2002), the various gypsum morphotypes can be classified into two main categories: those that originated by solution and those that originated through recrystallisation.

Fig. 7.9 Gypsum tumuli, 1–3 m in diameter (colloquially known as "igloos"), growing in a capillary fringe on the margin of Salar de Agua Amarga, in the high altitude desert belt of the Andes. The host gypsum bed is Late Quaternary and predates the current halite system. (**a**) Field of Tumuli. (**b**) Close up of one the tumuli mounds shown in **a** (Photos courtesy of Tom Carpenter)

Outcrops of gypsum lacking soil cover and influenced by alternating seasonal water conditions of surplus and deficit are affected by both solution and recrystallisation processes. During the wet season, the water soaks into the rocky subcropping gypsum mass, filling all the fissures and pores of the outer layer from a few centimetres to some metres below the surface. During the dry season, there is a capillary-driven upward motion of the water solution. Near the surface, gypsum precipitates from the oversaturated solution, increasing the crystal size or forming new crystals. In this way, during the dry season, there is a pressure increase in the outer gypsum layers, which is responsible for the development of a "gypsum weathering crust." It is characterised by many different expansion forms such as gypsum tumuli, pressure ridges and pressure humps.

Tumuli (aka bubbles, tents or "igloos") are hollow subcircular domes, developed in pre-existing coarsely crystalline gypsum crusts in the uppermost stratum of the gypsum regolith. They vary from a few centimetres to several metres in diameter and reach maximum heights of a little over a metre (Fig. 7.9a, b; Ferrarase et al. 2002; Pulido-Bosch et al. 2004). Thicker crusts (≈1 m thick) support the development of mega-tumuli and dome-like hills 10 m or more across. Earlier studies in the Mediterranean and Canada interpreted tumuli doming as an indication of volume expansion related anhydrite rehydration. This is clearly not the case in the modern active examples illustrated in Fig. 7.9b where the host crusts retain its bottom-nucleated texture. Today, tumuli are interpreted as indicative of volume addition via capillary rise and not anhydrite alteration.

Stenson (1990) studied fresh development of tumuli in the floor of a gypsum quarry in Nova Scotia that was abandoned some 35 years earlier. In an area of a few hectares there were 69 new tents (inverted-v) or tumuli (rounded), ranging 0.8–8.2 m in diameter. Crustal hydration was apparent, but here the process may have been aided by mechanical 'pop-up' due to lithostatic pressure release in an artificial excavation. Development of dome-like tumuli-overprinted hills does not seem to be controlled by variations in strike, dip, or fissuring of the gypsum beds. Their evolution seems to be linked to the fact that on most of the tumuli surfaces the weathering crust is evolving through a nearly isotropic field of stresses, which is a result of capillary-driven volume increase in the outer gypsum layer giving an "igloo-like" appearance to some tumuli fields (Fig. 7.9; Ferrarase et al. 2002).

Regional-Scale Karst

The distribution of landscape features above an actively dissolving salt mass depends on the extent and depth of the underlying salt. That is, at the regional scale is the dissolving salt bedded or diapiric? Elongate depressions, known as subsidence troughs, tend to define the subcropping edges of shallow gently-dipping salt beds. In contrast, smaller zones of circular sinkholes, solution lakes and cenotes tend to form atop the crests of shallow diapiric salt. In regions where the crest of the halokinetic salt is still rising, there is ongoing retention of positive relief atop the structure, even though sinkholes and capstones are continually forming within this zone of positive relief. Salt dissolution and loss of volume facilitates gravitational extension in the overburden and can be expressed as active normal faults intersecting the land surface. In some cases these faults can be misinterpreted as tectonically, not sedimentologically, driven features (Gutierrez et al. 2012).

Subsidence Basins or Troughs

Subsidence troughs are large-scale elongate depositional depressions created by interstratal solution along the dissolving edge of shallow salt bodies. The largest solution-induced depositional basins tend to occur along the margins of the great interstratal halite deposits, creating a solution form that may be represented by a shallow salt slope at the surface (Fig. 7.6) They can be filled or partly filled by clastic sediments (Figs. 7.10a–c and 7.11; Olive 1957; Quinlan 1978; Simpson 1988). Salt-edge leaching of the shallow dipping

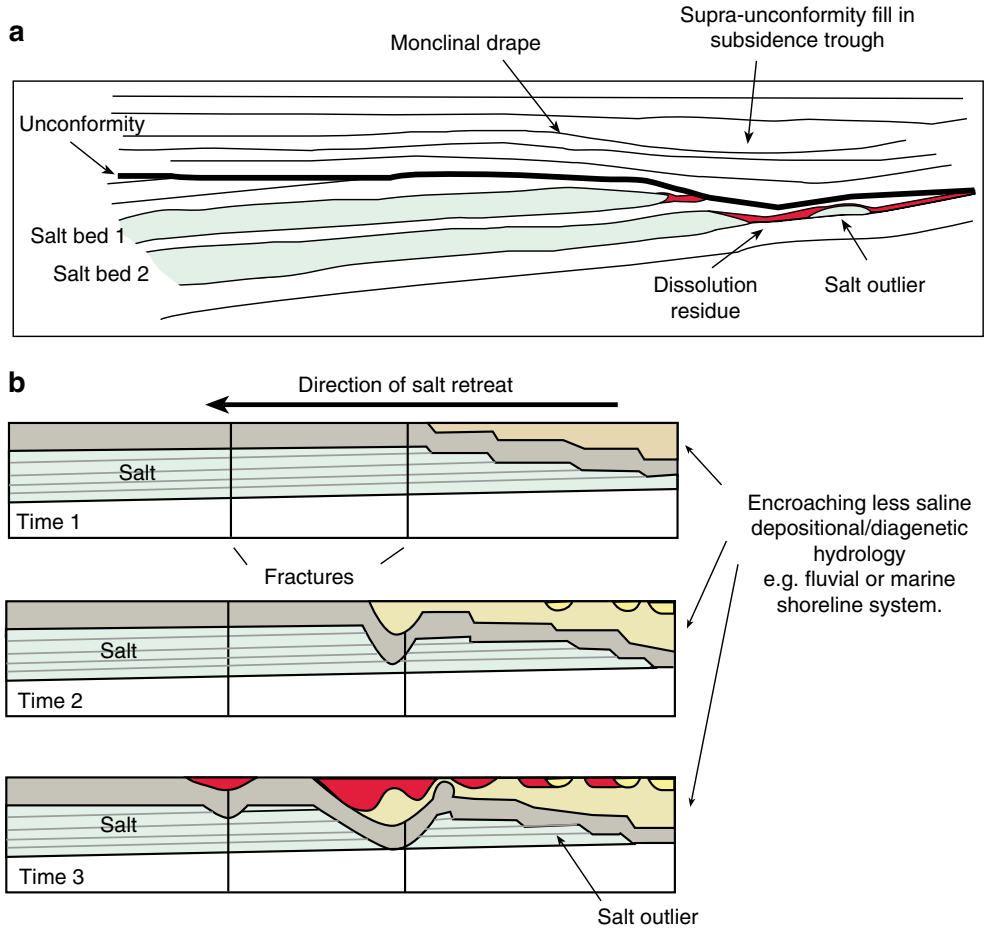

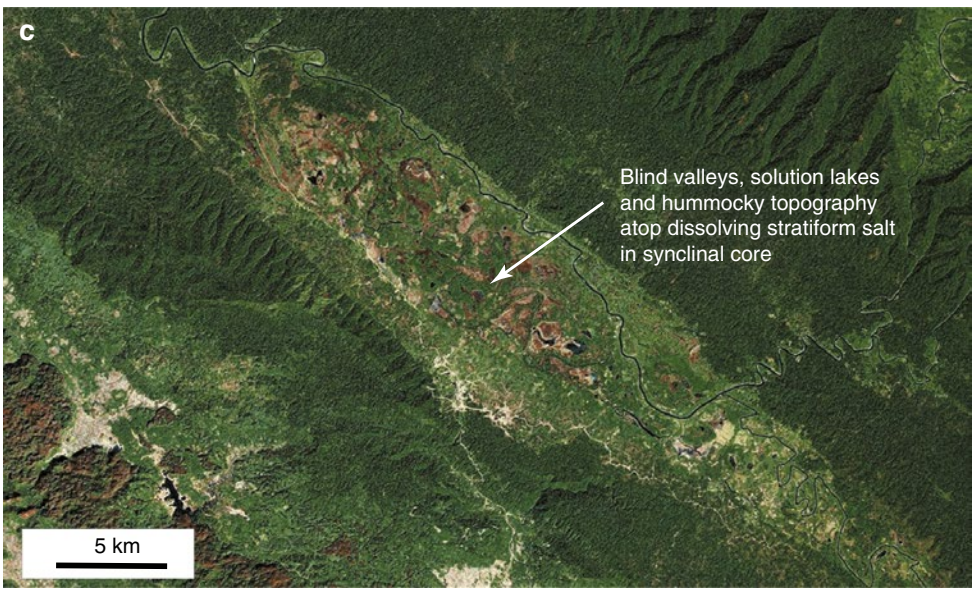

Fig. 7.10 (**a**) Subcrop salt dissolution creates characteristic sag geometries visible in seismic reflectors. (**b**) Schematic dip section showing the sequential development of a regional subsidence trough, based on studies of the Hutchison Salt Member, Kansas (Modified in part from Anderson et al. 1994a). (**c**) Nam Theun syncline, Laos, with Nam Theun River running along the northeastern edge of a dissolving stratiform salt mass that is equivalent to the Cretaceous Maha Sarakham salt of Thailand (17.709056 N, 105.22245 E; Landsat image courtesy of NASA)

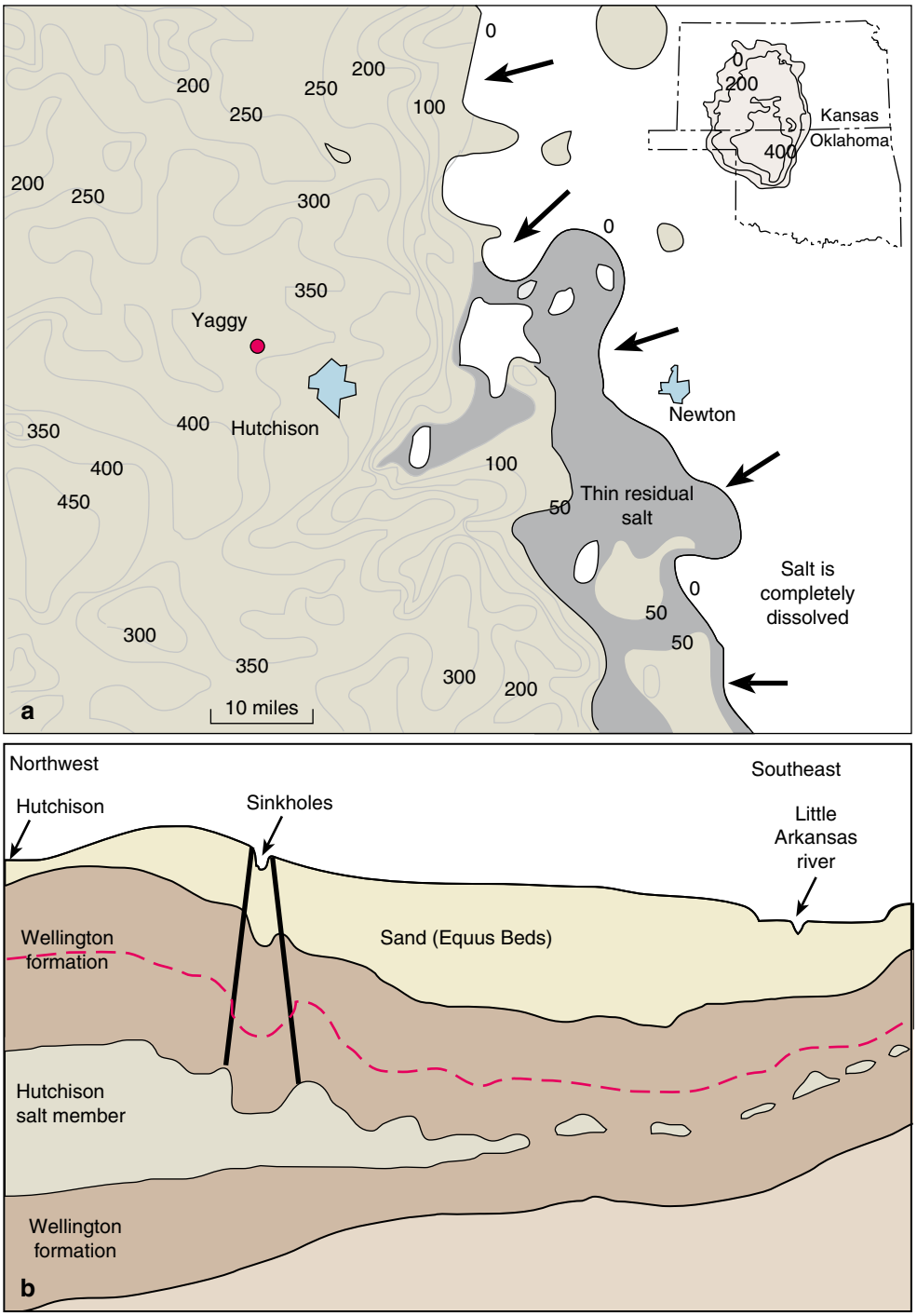

Fig. 7.11 Karstified edge of Hutchison Salt Member. (**a**) Thickness of the Permian Hutchison Salt, Kansas. *Arrows* indicate the direction of retreat of the dissolution feather edge of the salt body, Thickness is in feet and *grey shading* indicates salt thicker than 50 ft. Note the remnant outliers to the east of the dissolution edge (In part after Walters 1978). (**b**) Schematic east-west section in the vicinity of the town of Hutchison (After Watney et al. 2003)

salt underscores a set of self-perpetuating processes. Fractures created by the collapse of overburden and intrasalt beds into accommodation space (generated by salt cavities) provide new fissures and sinks that act as additional conduits for further percolation of meteoric or upwelling of undersaturated basinal waters into the salt. This in turn instigates yet more salt solution in the vicinity of the collapse and typically creates an elongate corridor of subsidence at the surface.

Large solution-induced depositional basins and monoclines outline the edges of the great interstratal salt deposits of the world. Depression corridors some 5–500 km long, 5–250 km wide, with up to 100–500 m of subsidence induced relief and sediment fill define saline karst plains along the edges of bedded and dissolving saline giants in the Devonian subcrop of Canada (Tsui and Cruden 1984), the Permian Basin of New Mexico, Oklahoma and Texas (Bachman

1984), the Perm region of Russia (Gorbunova 1979) and the Jurassic Hith region of Saudi Arabia (Amin and Bankher 1997a, b). Associated sediment infill typically reduces the regional solution edge landscape to a few tens of metres of relief. For example, the Rosetown Low and the Regina Hummingbird Trough accumulated more than 100 m of depression trough sediment during interstratal dissolution of the underlying Prairie salt (Devonian) in southern Saskatchewan (Fig. 7.10b; DeMille et al. 1964). The concurrence of a supra-unconformity thick, adjacent to the sub-unconformity feather-edge of a bedded salt sequence, is at a scale that is easily recognised in seismic and constitutes one of the classic signatures of a salt collapse-induced hydrocarbon trap (Figs. 7.10a and 10.91).

A solution depression tends to capture rivers that, via seepage loss, tend to be losing streams in the vicinity of the solution front, so encouraging further salt solution and collapse. Examples of modern fluvial capture by subsidence troughs include the nearsurface edges of the Hutchison Salt Member in Kansas, the Maha Sarakham Formation in NE Thailand and along the Nam Theun valley in Laos (Fig. 7.10c; Anderson et al. 1994a; Supajanya and Friederich 1992) and rivers in the Ebro Basin, NE Spain (Benito et al. 2000; Guerrero et al. 2013). The associated accumulation of fluvial and other sediments rapidly fill most modern solution troughs, so that surface relief is usually no more than metres to tens of metres across the subsidence corridor. Pleistocene and Holocene sedimentation rates in active US and Canadian subsidence corridors are ≈5–10 cm/1,000 years. The Uralian troughs of the former Soviet Union are no longer active and so show somewhat lower rates of 0.3–3 cm/1,000 years.

Interestingly, the foci of many small recent Saskatchewan earthquakes (magnitude <3–4 on the Richter scale) are located near the dissolving edge of the Prairie Evaporite salt (Fig. 7.7; Gendzwill and Unrau 1996). As bedded salt dissolves, support is removed from the overburden, which then slumps. If the overburden is weak or extensively fractured, it settles quietly. However, if the overlying rock is an indurated carbonate, it may resist movement, forming a bridge over the growing cavern. The roof span can fail violently when the undermined area gets large enough, so causing a small earthquake. Dissolution of the salt is possibly localized by faults and fractures, which provide seepage paths for the entry of undersaturated ground waters. Landscapes above many of the small Saskatchewan earthquakes lack extensive solution lakes, implying they may be sites upward stoping breccia pipes that have not yet breached (blind chimneys). Similar scale earthquakes can also define times of catastrophic failure in some salt mines and brine fields. On March 12, 1994 a 3.5 M quake documented the collapse of a mine panel in the Retsof Mine near Cyberville, New York state. Ensuing flooding caused the loss of the mine, which was until then the largest salt mine in the United States (Fig. 13.31).

Hutchison Salt, Kansas

As well as their vertical expression being maintained by dissolution, subsidence troughs also migrate laterally, mirroring the retreat of the dissolving salt front (Figs. 7.10b and 7.11a). The westward-dipping Hutchinson Salt Member of the Permian Wellington Formation is 50–90 m thick and underlies much of central and south-central Kansas. Ongoing edge dissolution since the late Tertiary has created a subsidence corridor with contemporaneous valley-fill of Quaternary alluvium. In places, the alluvial fill extends more than 25 km to the east of the present-day edge of the main body of contiguous rock salt. The salt margin has receded this distance over the past several million years. Subsidence and collapse atop the active dissolution front creates numerous sinks, blind valleys and other salt karst features in the land surface and a pockmarked irregular thickness in the shallower parts of the salt bed (Fig. 7.10b).

Oil well drillers call this region of dissolution cavities and fractures the "Wellington Lost Circulation Zone" and it extends for more than 100 miles N-S parallel to the dissolution edge of the salt bed (Fig. 7.11a). Hutchison Salt is leaching vertically from the top down, and horizontally inward along the outer edge of the salt shallow dipping salt bed. Dissolution is driven by sustained contact with a crossflow of unconfined and undersaturated groundwater. As a result, over distances of 5–15 km westward, the eastern margin of the dipping and dissolving salt bed thickens by up to 90 m (from east to west). Locally, the salt member is preferentially leached along NNE-trending palaeoshear/fracture zones to leave behind thick stepped outliers (Fig. 7.11b). Walters (1978) calculated an average lateral retreat of 3.2 km per million years since the late Pleistocene. He also pointed out that this rate is not constant. Dissolution was more rapid in the Early Pleistocene as the salt front was shallower. Now, when the front affecting the shallow dipping beds is deeper, groundwater crossflow and associated dissolution is slowing.

Natural subsidence and the rapid appearance of collapse dolines atop the dissolving Hutchison Salt Member has resulted in periodic ponding of surface waters in numerous dolines, abandonment of at least one oil well, and ongoing damage to numerous county roads (Figs. 13.42 and 13.53). Because this damage can be in the vicinity of an oilfield, much of the surface subsidence has been popularly attributed to poorly controlled drilling and development by unscrupulous oil companies. Any subsidence that occurs significant distances from any known well site is popularly attributed to unrecorded abandoned wells or complex asymmetric patterns of salt dissolution that originates at a drillhole. To test the validity of this widely accepted anthropogenic salt-dissolution model, so popular with the environmental movement, a 4 km seismic reflection profile was acquired along an east-west-oriented county road adjacent to an abandoned oil

well (Anderson et al. 1998). The expectation was that the residual Hutchinson Salt Member would be anomalously thin near an area of historical subsidence such as near the Burton oilfield. It should be thicker away from intensely drilled areas. Contrary to expectations, the residual Hutchinson Salt Member is relatively thick (20–30 m) below areas of significant recent surface subsidence.

Nor is there any evidence of recent surface subsidence at locations along the seismic profile where the rock salt edge has been totally leached. Dissolution and subsidence at these sites largely predates European settlement of Kansas. Sinkhole development via catastrophic collapse is a natural phenomenon and should be expected along this irregular salt dissolution front that forms atop and beneath a salt unit. Anderson et al. (1998) concluded that no modern catastrophic sinkhole development in the area has a clear-cut anthropogenic cause. As in the Prairie Evaporite, it seems focused collapse is largely a natural process influenced strongly by pre-existing geologic conditions. But, the rate and extent of collapse can be anthropogenically enhanced, typically in the vicinity of a few poorly completed wells, abandoned prior to the 1950s when the industry and society in general had a very different attitude to the landscape. These anthropogenic hazards combined with pressurized gas storage in shallow bedded salt in the presence of old poorly-documented brine solution wells has had some tragic outcomes (see Hutchison gas explosion; Chap. 13).

Natural salt karst collapse occurs quickly, well within a human lifetime. We cannot greatly influence the process of salt karst collapse, so we should plan geographic placement of infrastructure so that as much as possible it avoids it.

Delaware Basin, West Texas

The Delaware Basin of West Texas and southeast New Mexico, in the southwest portion of the Permian Basin, contains bedded evaporites of the Late Permian Castile, Salado and Rustler Formations. Outcrops and subcrops of these three formations constitute an area of widespread subsidence troughs, collapse sinks, dolines and breccia chimneys, all created by ongoing removal of underlying bedded Permian salts. The Delaware is an eastward-dipping basin, largely surrounded by the Capitan Reef and its equivalents (Fig. 7.12). The area called the "Gypsum Plain" of Texas lies to the west of the Pecos River and comprises about 2,600 km^2 of subcropping gypsum of the Castile Formation (Olive 1957; Quinlan 1978; Kirkland and Evans 1980; Anderson 1981; Stafford et al. 2008a, b; Holt and Powers 2010). South of Carlsbad and Carlsbad Caverns, the plain exhibits many small examples of solution subsidence troughs, typically 0.7–15 km in length, 100–1,500 m wide, but no more than 5–10 m deep (Fig. 7.12: Stafford et al. 2008a). The plain is also where the "Castile" landforms, mentioned earlier, are to be found. Additional gypsum outcrops are present to the east in the Rustler Hills and to the north in Reeves County, Texas.

In the centre of the Delaware Basin the thick evaporites of the Castile and Salado Formations and the thinner evaporites of the Rustler Formation are underlain by relatively permeable carbonates and siliciclastics, including some prolific hydrocarbon reservoirs in Permian backreef of the Central Basin Platform (Fig. 7.13). Reef mounds, fractures and faults in these underlying sediments have provided focused conduits for upward stoping chimneys through the buried evaporites as well as the subsurface formation of now-exhumed Castiles to the west. An eastward-flowing deeply-circulating regional artesian hydrology, in combination with centripetal escape of buoyant hydrocarbon-rich basinal waters, drives the formation of these features, with their surface expressions occurring in areas such as the Wink Sink (chain of breached chimneys) and the Gypsum Plain (Castiles). The ongoing flushing of the basin fill evaporites by this confined hydrology means only 30–40 % of the original halite volume remains in the basin (Anderson 1981).

The upper sides of the shallow dipping salt beds are also affected by the hydrologies of the zone of active phreatic circulation. The Pecos River has migrated back and forth across the top of subcropping evaporites for much of the Tertiary. Its ancestral positions drove substantial salt dissolution, now evidenced by large sediment-filled subsidence basins and troughs in the centre of the Delaware basin (Figs. 7.12 and 7.13). The regional eastward dip of the Delaware basin sediments means first halite and then gypsum has disappeared along the updip eastern edge of the basin. Relatively undisturbed salt remains along the more deeply buried western side of the basin that abuts and covers the Central Basin Platform. Bachman and Johnson (1973) estimate the horizontal migration rate of the dissolution front across the basin as high as 10–12 km per million years, while Anderson (1981) concluded more than 40 % of the original halite is gone. Multiple smaller examples of sediment-filled subsidence troughs occur at the edge of the gypsum plain of the Delaware Basin south of Carlsbad Caverns, where depositional troughs, 0.7–15 km in length, 100–1,500 m wide and no more than 5–10 m deep, are well documented, as are subsidence sinks within the subsidence swales, such as Bottomless Lake and region where the watertable intersects a subsidence chimney (Fig. 7.13a, b; Quinlan et al. 1986).

The San Simon swale is a 25 km^2 depression defining a residual karst feature atop the Capitan Reef on the northeastern margin of the Basin (Figs. 7.12 and 7.13a). San Simon Sink, atop a subsidence chimney within the swale, is the lowest point in the depression and is some 30 m deep and 1 km^2 in area. It in turn encloses a secondary collapse sink some a few hundred metres across and 10 m deep (Fig. 7.13b). During a storm in 1918 a sinkhole formed a gaping hole about 25 m

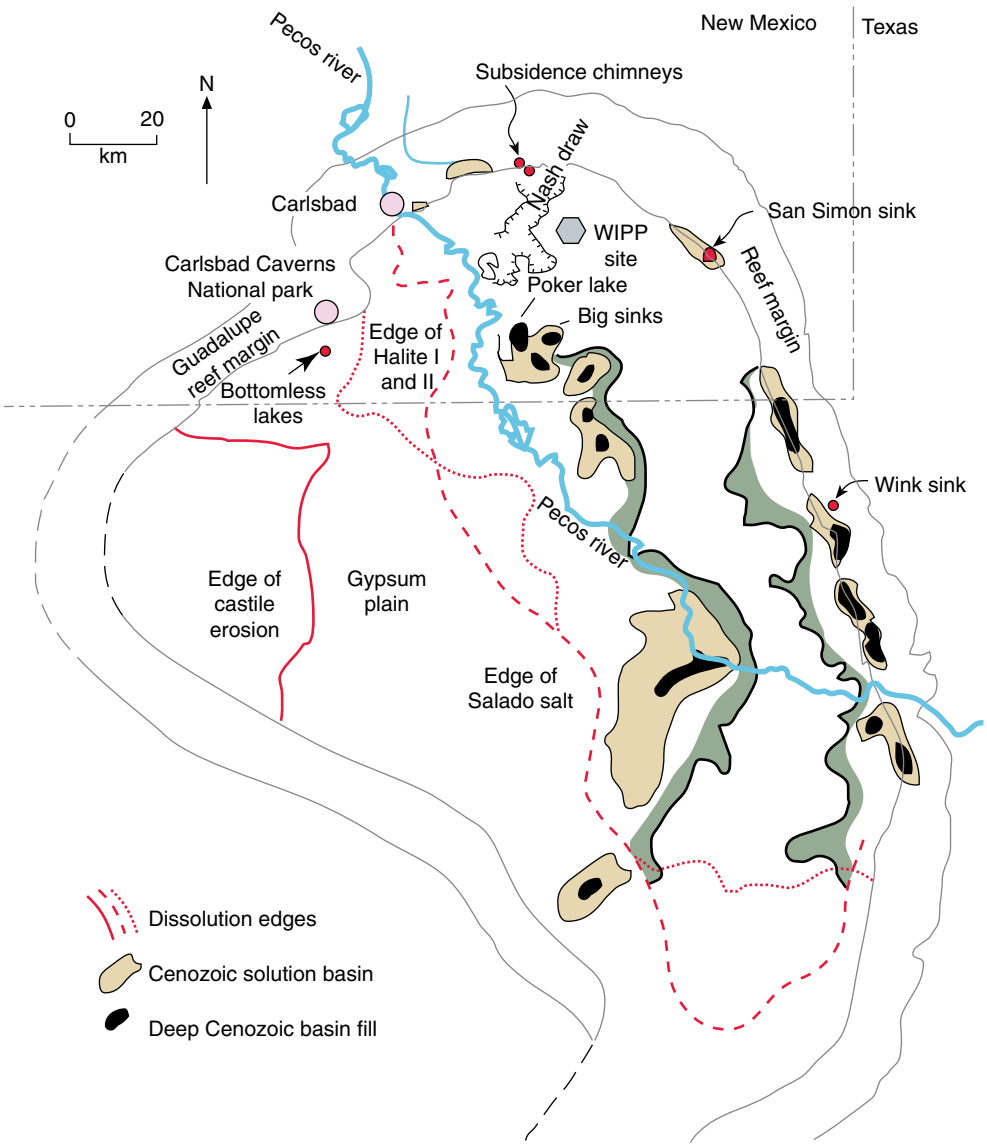

Fig. 7.12 Karst features in the Delaware Basin and the positions of dissolution edges of various salt units, USA (After Anderson 1981; Davies 1984a, b)

across and 20 m deep in the sink. In one night, nearly 23,000 cubic metres of soil and bedrock disappeared into the cavern. Annular rings that cut the surface around the San Simon sinkhole today suggest ongoing subsidence and readjustment of the sinkhole is still occurring in response to earlier collapses. The position of the San Simon sink over the Permian reef crest led Lambert (1983) and many others to suggest that the sinkhole originated as a groundwater cavity breakthrough, atop a series of stoping reef-focused breccia pipes. Sinkhole breakouts, which can emerge in a matter of hours, continue to form across this dissolution basin, in some case aided by poorly-monitored brine extraction operations and improperly-cased water wells. But the majority of the sinkholes are natural, not anthropogenically enhanced (Land 2013).

Nash Draw is a southwesterly trending depression or swale, some 25 km long and 5–15 km wide, at the northern end of the Delaware Basin with its sump in a salt lake (Poker Lake) at the southern end of the draw (Fig. 7.12). The underlying evaporitic Rustler Formation and parts of the Salado Formation has largely dissolved so that more than 100 caves, sinks, fractures, swallow-holes, and tunnels make up a complex local karst topography, which is still active today (Bachman 1981). An extensive drilling program conducted for the nearby WIPP site (now a low level radioactive waste repository) showed that natural dissolution of halite in the Rustler and upper Salado formations is responsible for the subsidence and overall formation of Nash Draw (Lambert 1983; Holt and Powers 2010).

To the west of Nash Draw the WIPP/DOE drilling program clearly defines the formation of a solution trough in the Dewey Lake Redbeds, created by preferential leaching of halite beds in the Rustler Formation, with interstratal

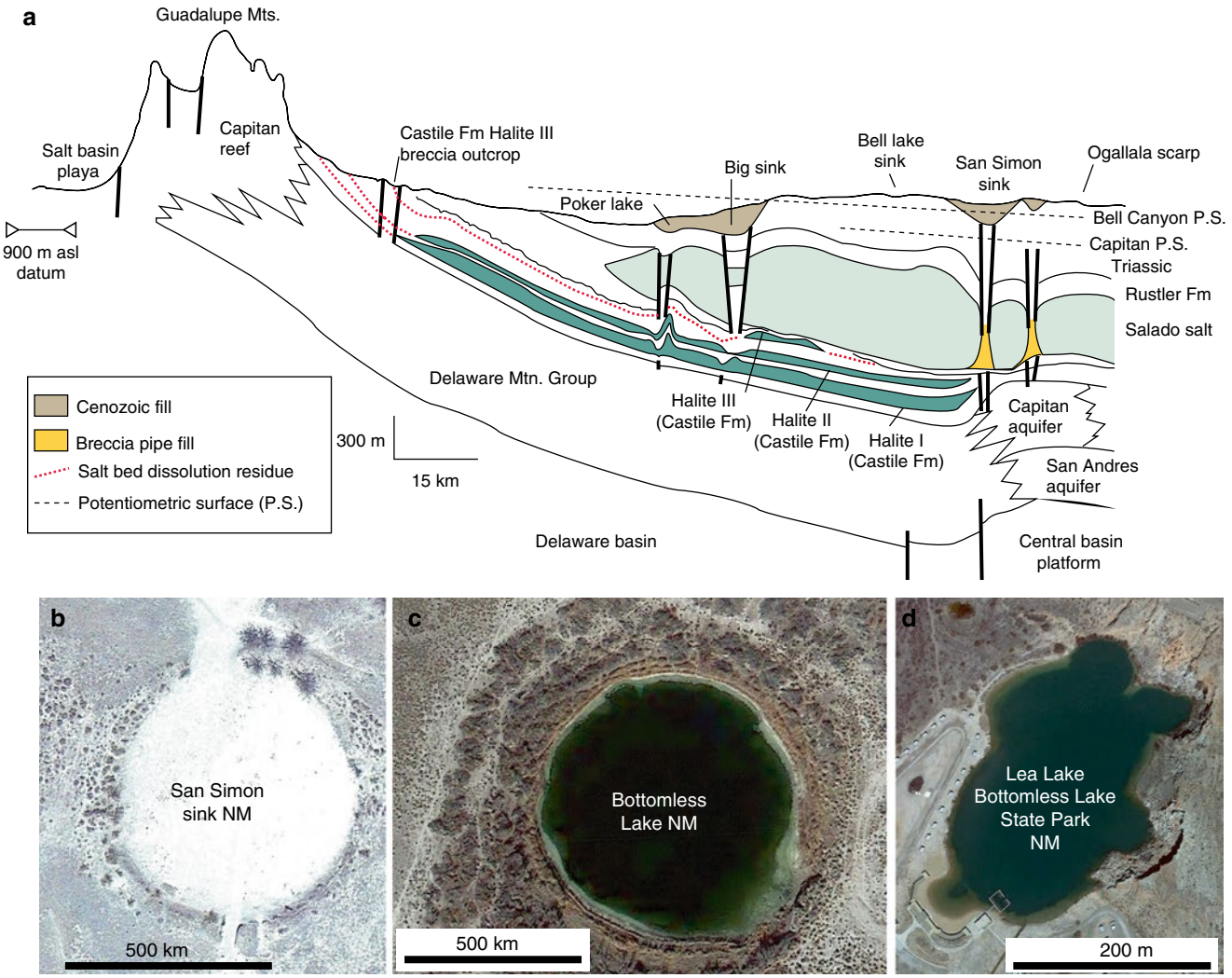

Fig. 7.13 Salt dissolution features, New Mexico. (**a**) Diagrammatic cross section from Salt Flat playa to Ogallala Escarpment showing the extent of salt dissolution in the Castile and Salado halites and the expressions of that dissolution on the landscape (After Anderson 1981). (**b**) San Simon Sink, New Mexico. (**c**) "Bottomless" Lake, south of Carlsbad, New Mexico. (**d**) Lea Lake, Bottomless Lakes State Park, near Roswell, New Mexico. Refer to Fig. 7.12 for geographic locations

anhydrite and breccia residuals (Fig. 7.14). This dissolution occurred at a level some 400 m above the salt-encased storage level of the WIPP waste isolation facility is not considered a significant risk factor in terms of longterm site stability (Holt and Powers 2010). A heated scientific (and at times not so scientific!) debate of just how deep surface karst penetrates into the bedded halite of the Salado Formation in the vicinity of the WIPP site continues today (see Chap. 12 for detail of waste isolation in bedded and diapiric salt).

Further north, near the subcropping western edge of the North-west Permian Shelf is Bottomless Lakes State Park, located some 20 km southeast of Roswell. Encircling the lakes are the gypsum, halite and dolomitic redbeds of the Artesia Group and San Andres Formation. Away from the lakes are numerous other sinkholes and collapse dolines, most of which are circular, steep walled or vertical holes, 50–100 m across and 30–60 m deep, with the greatest density of features aligned along the eastern side of the Pecos River floodplain. Water in the various sinks that make up the Bottomless Lakes is crystal clear and generally brackish to saline (6,000–23,000 ppm), attesting to its passage through subsurface layers of gypsum and salt. Although the lakes are around 30 m deep, dark-green moss and algae coat the bottoms giving the impression of great depth and hence the name of the park (Lea Lake; Fig. 7.13c.) To the west, many of the playas in depressions near Amarillo in the High Plains of Texas have a similar genesis as solution depressions atop dissolving Permian salt, but most do not intersect the regional watertable and so do not hold permanent surface water (Paine 1994). Further south, near Carlsbad Caverns, there are other subsidence chimneys that form lakes

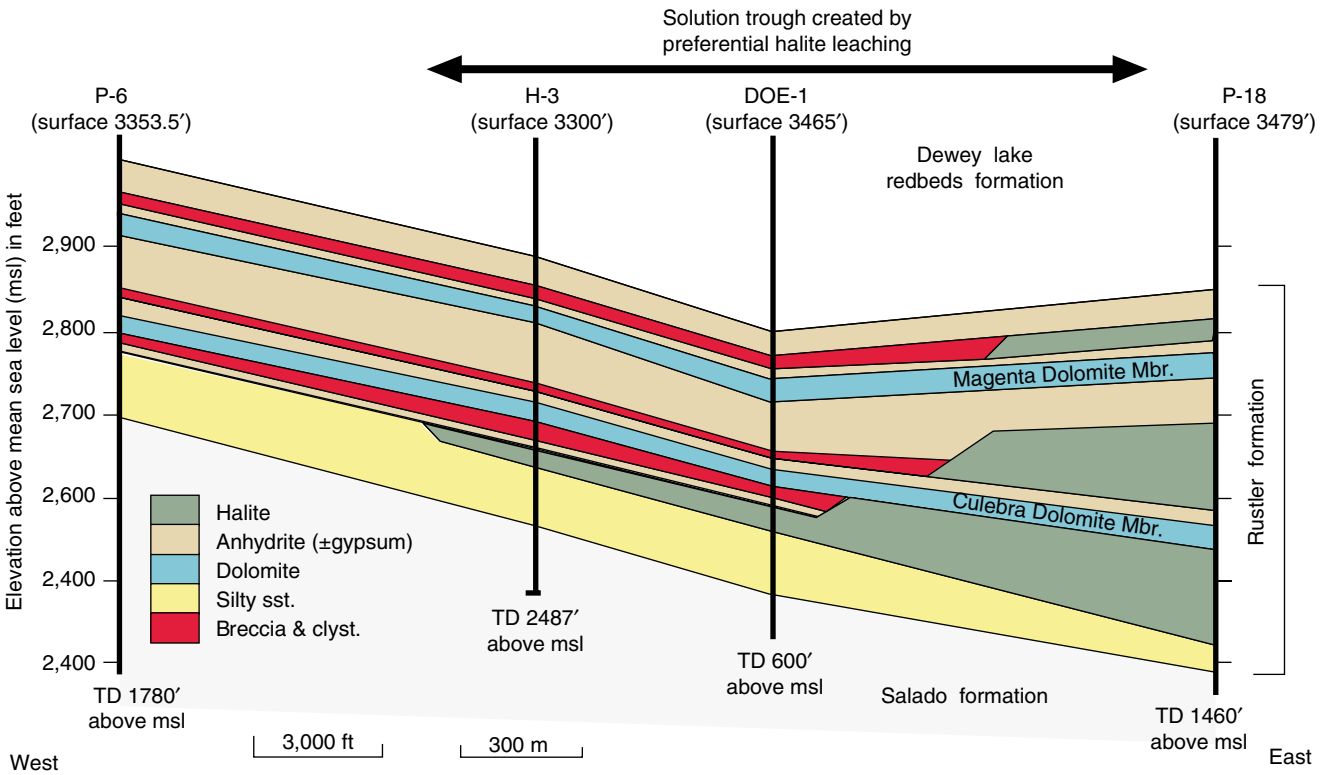

Fig. 7.14 Differential dissolution of halite in Rustler Formation in the vicinity of the WIPP site (see Fig. 7.12 for location). Note the anhydrite-gypsum and breccia residuals (as distinct from the bedded anhydrite). The solution trough lies some 400 m above the level of the salt-encased WIPP (waste isolation pilot plant) subsurface waste storage facility in the Salado Formation

where they intersect the watertable and are locally known as "Bottomless" (Fig. 7.13d).

Although much of the preceding discussion focused on salt dissolution influencing Tertiary to recent sediment pattern in West Texas, this is merely part of a longer acting set of dissolution-sedimentation interactions that have influenced sedimentation motifs as far back as the Triassic. For example, in the Texas Panhandle the extent and thickness of the late Triassic Dockum Group strata are best preserved in the central portions of a local syndepositional basin that was produced by dissolution of underlying Permian salt (Dickerson et al. 2014). This longterm influence of retreating salt mass edges over tens to hundreds of millions years is obvious in the sediments of various ages that surround many salt basins, worldwide.

Holbrook Anticline, Arizona

Subsidence driven by natural salt solution at depth generates regional-scale drape or monoclinal folding in strata atop the retreating salt edge. This is the corollary of the formation of a subsidence trough (Fig. 7.15a). The 70-km long dissolution front in the Permian Supai Salt of Arizona is defined by more than 500 sinkholes, fissures and subsiding depressions some 40–50 m across and 20–30 m deep (Neal 1995; Johnson 2005). Away from the main dissolution zone the northeasterly-dipping Schnebly Hill Formation (aka Supai Salt) is composed of up to 150 m of bedded halite, with local areas of sylvite along its northern extent (Fig. 7.15a). Atop the solution front there are a number of topographic depressions with playa lakes that in total cover some 300 km^2. Salt-dissolution induced features include areas known as; The Sinks, Dry Lake Valley, and the McCauley Sinks (Neal et al. 2001; Martinez et al. 1998). The Sinks region includes more than 20 steep-sided caprock sinkholes, with some that are more than 100 m across and up to 30 m deep (Fig. 7.15b). Regional expanses of Supai Salt removal produce a regional gravity depression, largely coincident with a surface topographic depression, where there is as much as 100 m of collapse and topographic displacement. The solution front is essentially coincident with the updip end of the Holbrook Anticline, a flexure defined by dip reversal in an otherwise northeasterly dipping succession (Fig. 7.15a).

Rather than orogenically driven, the Holbrook Anticline is a subsidence-induced monoclinal flexure created by the northeasterly migrating dissolution front (Fig. 7.15a, b). It may be the largest single solution-collapse fold structure in the world (Neal 1995). The reverse dip of the flexure directly overlies the salt-dissolution front and marks the location of

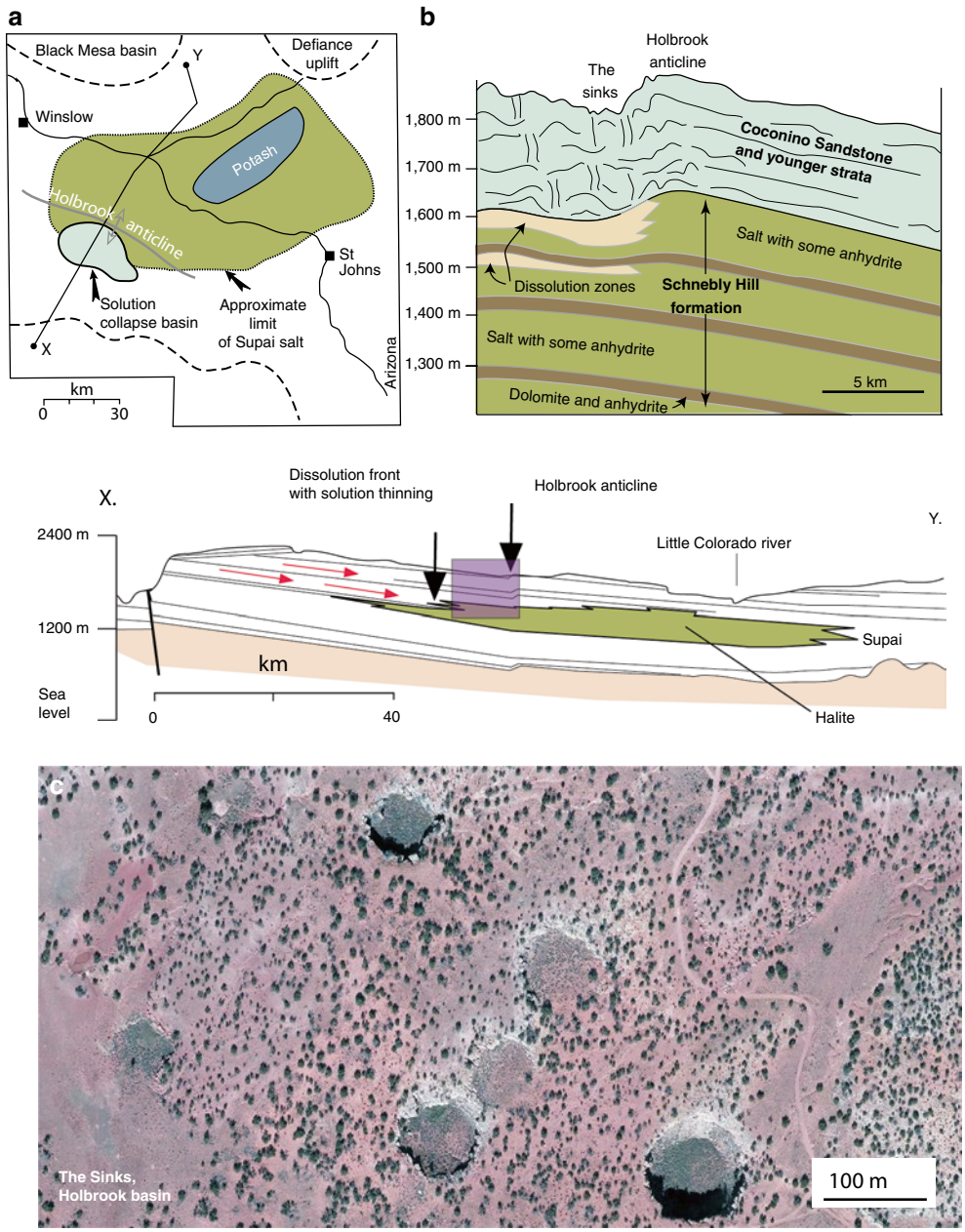

Fig. 7.15 Holbrook Anticline, Arizona. Shows distribution of dissolution features seen at the surface at various scales and their relationship to the underlying Permian Schnebly Hill (Supai) salt. (**a**) Map view (**b**) Cross sections show the Holbrook Anticline is a monocline flexure created by dissolution of the underlying Schnebly Hill Formation. (**c**) aerial view of the Sinks region (In part after Neal 1995; Johnson 2008a) McCauley Sinks region, Arizona (Bing® image mounted and scaled in MapInfo)

two major collapse depressions known as The Sinks and Dry Lake Valley, both occur where salt is within 300 m of the surface (Peirce 1981). Although it has periodically held surface water, reports of several hundred acre-feet of flood water in the Dry Lake Valley playa draining overnight supports the notion of active fissure and cavern formation related to salt removal at depth. Major surface drainage events took place in 1963, 1979, 1984 and 1995, with more than 50 new sinkholes forming in the valley during that period. The continuing rapid appearance of new sinkholes testifies to the ongoing nature of dissolution in the underlying evaporites. According to Neal (1995), dissolution front features began forming in the landscape in the Pliocene and continue to form today.

The caprock collapse sinkholes centre in the Coconino Sandstone bed that overlie the salt, which is located 200–300 m below the at-surface features. These caprock sinkholes define regions of focused breccia pipe development and discreet upward cavity migration (chimney stopping). The underlying salt is bedded and there are no indications of halokinesis anywhere in the basin. Sinkhole regions lie just ahead of a dissolution front that is migrating downdip, driven by the widespread dissolution of halite.

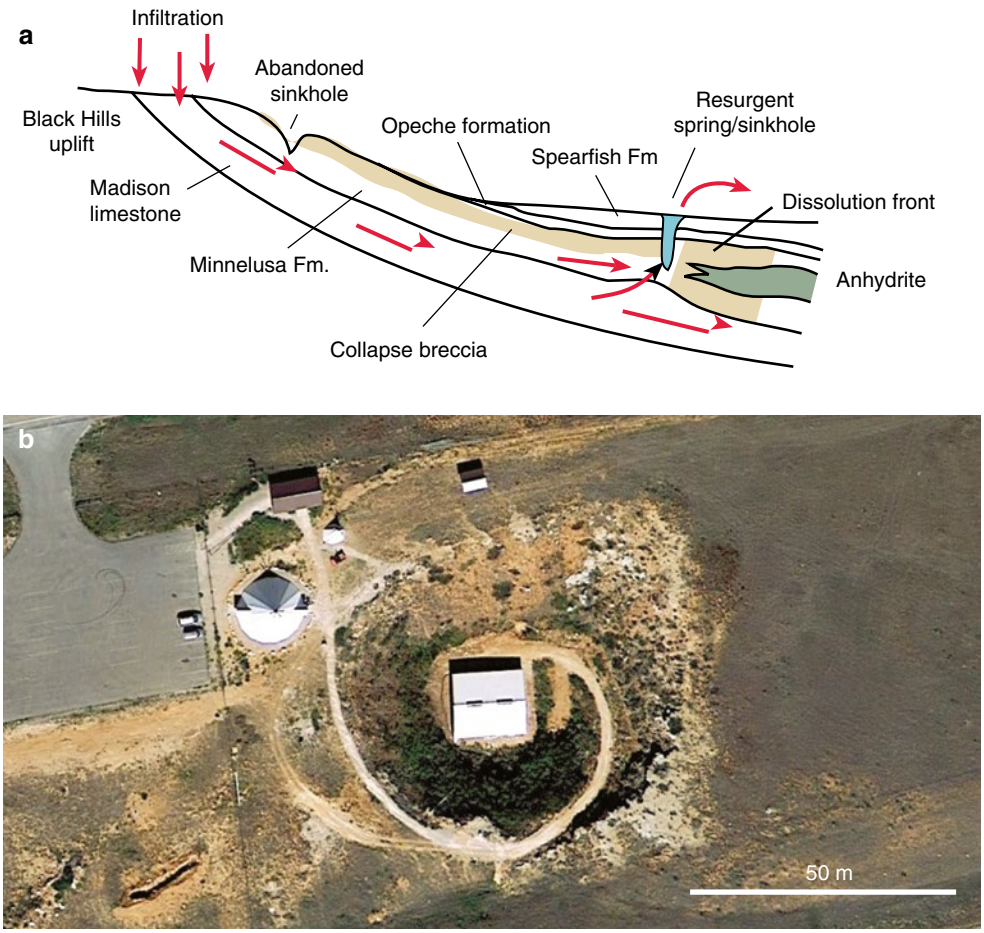

Fig. 7.16 Evaporite karst, South Dakota. (**a**) Minnelusa dissolution; as the Black Hills are slowly lowered by erosion, the anhydrite dissolution front in the subsurface Minnelusa moves downdip and radially away from the centre of the uplift. As the front expands the resurgent springs defining the outflow pipes dry up and new ones form down dip (After Epstein 2001). (**b**) Vore Buffalo Jump sinkhole, near Sundance, Wyoming (Image courtesy of Google Earth)

Other karst features attributed to evaporite dissolution in the Holbrook basin are; pull-apart fissures, graben sinks (downward dropped blocks), breccia pipes and plugs, and numerous small depressions with and without sinkholes (Neal et al. 1998, 2001). Interestingly, many of the "karst" features occur in sandstones, not limestones, such caprock collapse sinkholes can form wherever pervasive dissolution has removed the underlying salt, independent of caprock lithology (Fig. 7.5). The presence of the more than 500 karst features in the Holbrook basin, some of which formed in days, evokes practical karst hazard and infrastructure concerns, even in such a sparsely populated region (Martinez et al. 1998).

Black Hills, South Dakota

Another area of ongoing evaporite karstification is the Black Hills region of South Dakota (Fig. 7.16a; Epstein 2001; Rahn and Davis 1996). Substratal salt bed dissolution, centred on anhydrites in 4 beds, mostly in the Minnelusa Formation (Pennsylvanian – Permian), has produced breccia pipes and pinnacles, regional collapse breccias, sinkholes, and extensive disruption in the overburden of otherwise stratiform beds. Anhydrite removal in the Minnelusa probably dates back to the early Tertiary when the Black Hills were first uplifted and it continues today[4]. In the 1990s, houses in Rapid City, South Dakota, were damaged by the sudden development of collapse sinkholes, up to 10 m across, which formed in the brecciated outcrop zones of gypsum relic beds up to 9 m thick (Rahn and Davis 1996).

Evidence for recent natural collapse includes fresh scarps surrounding shallow depressions, steep-sided sinkholes more than 20 m deep, and sediment disruption and contamination in water wells and springs. Several sinkholes in the Spearfish Formation west of Spearfish, South Dakota, which today support fish hatcheries and are used for local agricultural water

[4]The Plains Indians that inhabited the area 300 years ago trapped and slaughtered thousands of buffalo as their primary food by stampeding the animals over the rim of a large steep-sided sinkhole near Sundance, Wyoming (the Vore Buffalo Jump; Fig. 7.16b).

The Mammoth Site in Hot Springs, South Dakota, is a salt dissolution sinkhole in the Spearfish Formation. There some 26,000 years ago, well before humans had migrated to north America, mammoths and other megafauna died after falling into what was then a steep sided water-filled sinkhole.

supply, probably originated as the surface expressions of stoping chimneys initiated some 150 m below in the salts of the Minnelusa Formation (Fig. 7.16a; Epstein 2001).

As the anhydrite dissolution front migrates further down dip and radially away from the centre of the Black Hills uplift, resurgent springs that once defined the active edge of the subsidence trough are overstepped. They dry up and new ones form further downdip. Abandoned sinkholes and breccia pipes, preserved in cross section on downcut canyon walls, attest to the former positions of the outward migrating artesian dissolution front (see also Fig. 7.72). The Spearfish Formation, mostly comprising redbed shale and siltstone, is regionally considered to be a confining layer to the active aquifer system. However, secondary fracture porosity develops locally via collapse/subsidence within the lower Spearfish Fm. as a consequence of cavity creation, via salt dissolution, in the Minnelusa Fm. (volume contraction fractures) or the hydration of anhydrite to gypsum (volume expansion fractures). Thus, updip of the anhydrite solution front, localised fracturing in the overlying lower Spearfish Formation makes a respectable aquifer, especially for a regional shale, and it yields potable water through both pumped wells and springs.

As well as the active karst centred on the Minnelusa Formation there is abundant evidence of multiple-cycle paleokarst in the same strata. Many active modern caves transect and expose these older paleokarst features in the cave walls (Palmer and Palmer 1995). The Kaskaskia paleokarst zone for example, is part of the Mississippian-Pennsylvanian unconformity in North America, is typified by ancient sinkholes, fissures, and dissolution caves at and near the top of the Kaskaskia Sequence (Madison Limestone and equivalents) and is covered by basal Absaroka siliciclastics (Chesterian to Morrowan). In the Black Hills, the Kaskaskia unconform-ity/paleokarst postdates earlier paleokarst features produced by sulphate-carbonate interactions. These include ancient cemented evaporite breccias, dissolution voids, saline bedrock alteration zones, and uranium mineralization in chimney stopes. Both the Kaskaskia paleokarst and earlier evaporite dissolution features are intersected by post-Laramide caves, which are part of the uplift hydrology that is still actively altering and dissolving shallow Minnelusa sulphates and limestone. Uranium deposits, aquifers, and petroleum reservoirs in the region are concentrated along both the paleokarst Kaskaskia horizon and earlier sulphate-related Minnelusa features. Each phase of karst modified and preferentially followed the zones of porosity and structural weakness left by earlier dissolution phases, producing an interrelated complex of modern and now-relict karst features.

Subsidence and Landscape in Diapiric Regions

When diapiric salt is actively flowing near the surface it typically elevates the landscape (Table 6.5). In continental settings this places highly soluble halite, and somewhat less soluble gypsum/ anhydrite caprocks, in the zone of active phreatic and vadose groundwater flow. This in turn creates dissolution caverns, cavern collapse fractures, slumping and landscape/gully retreat, typically focused in to the vicinity of subcropping salt dome crests. Sinkholes in such settings tend to form atop landscape highs, rather than in the intervening lows between the diapirs. Such diapir karst landforms dominate the Texas coast of the Gulf of Mexico, the Zagros/Hormuz region of the Middle East and parts of the drainage feeding the Ebro Basin of Spain.

Salt Valleys, Moab region. Utah

The salt valleys over the axis of the salt-cored anticlines in the Paradox fold and fault belt (Canyonlands, Utah and Colorado) are in large part created by subsidence of the anticline crests (See Fig. 6.83 for location). The resulting depressions that occupy the crestal positions of salt-cored anticlines may be 50 or more kilometres long, kilometres wide and several hundreds of metres deep. Traditionally, the collapse of the anticlinal salt crests was attributed to crestal dissolution of the salt walls (diapirs) that form the anticline cores (Fig. 7.17; Doelling 2001). Other workers, calling on scaled physical models and their own field observations, have proposed that the salt valleys are more the result of regional extension and that salt dissolution had only a minor

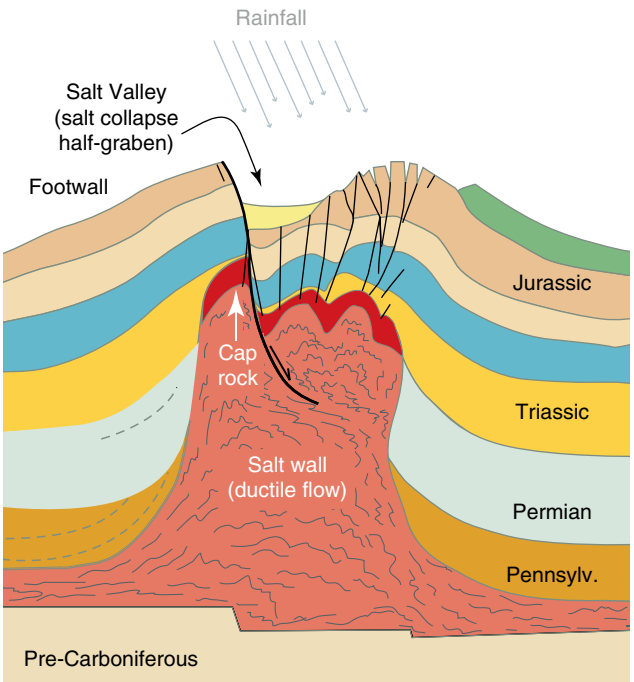

Fig. 7.17 Schematic illustrating typical crestal collapse structures and the formation of sediment-filled salt collapse grabens, as seen on the crest of many elongate salt walls in the Paradox Basin in southeast Utah. The collapse structure at the top of the salt wall is in part generated during salt dissolution by reactivation of a regional system of Tertiary joints, although most of the faulting is likely related to cataclastic deformation bands formed earlier and at greater depths (After Fossen 2010)

influence in the development of the axial depressions (Walsh and Schultz-Ela 2003). The problem as to the relative importance of karstic collapse versus diapir fall in extension is still not fully resolved. Neither school denies the existence of widespread salt karst across the region, only its relative import in forming the valley depressions.

Gutiérrez (2004) presents several arguments and lines of evidence that refute the tectonic extension model for the collapsed salt valleys and supports a salt-dissolution-driven subsidence interpretation. Field evidence against regional-extension diapir fall driving valley formation includes: (1) A thick cap rock is consistently present at the top of the salt walls; (2) The concentration of subsidence deformation structures is along the crest of the anticlines (salt walls), while extension would drain the base of the structure first; (3) Mapped deformational structures not consistent with the proposed NNE extension, especially the crestal synforms and NE–SW grabens; (4) Dissolution-induced subsidence structures controlled by ring faulting, reveal deep-seated dissolution penetrating the walls; (5) Large blocks of wall material have foundered several hundred meters into the salt wall; (6) Abundant evidence of recent and active dissolution subsidence; (7) The documented aseismic nature of the recently-active collapse faults. He concludes that, although underground salt dissolution seems to be the main cause for the generation of the salt valleys, this phenomenon may have been favoured by regional extension tectonics, which further enhanced the circulation of groundwater and salt dissolution.

Similar salt-dissolution geomorphic expressions to the Utah canyonlands typify outcrops in parts of the western Ogaden Basin, Ethiopia (Mége et al. 2013). There the uplift and incision of the Ogaden plateau is cut down to the base of the Gorrahei Formation, an upper Cretaceous evaporite formation. Debuttressing of this and the overlying sedimentary formations resulted in widespread and spectacular gravitational-spreading landforms across a minimum surface area of 15,000 km^2.

Five Islands, Gulf of Mexico

Five salt-dome crests, locally known as "the Five Islands," are located near the western boundary of the Mississippi River delta plain in coastal south Louisiana. The present landscape of the islands reflects a combination of salt-dome induced uplift and salt dissolution (Lock and Kupfer 2003; Autin 2002; Autin and McCulloh 1995). The islands, align in an approximately NW-SE trend, are named Jefferson Island (JI), Avery Island (AI), Weeks Island (WI), Cote Blanche Island (CBI) and Belle Isle (BI) (Fig. 7.18a). The five salt domes coring the islands have pierced, uplifted and shed sediment, while their surrounding flanks subsided and accumulated sediment. Each dome is nearly circular in plan, with maximum elevation ranging from approximately 52 m asl on Weeks Island to 23 m asl on Jefferson Island. Avery, Weeks, and Cote Blanche Islands are large mounds with small sinkhole ponds, whereas the crests of Jefferson Island and Belle Isle are marked by larger lacustrine collapse structures (Figs. 13.46 and 13.48). Each "island" landform is, surrounded by lowland Pleistocene terraces and/or Holocene delta plain marshes (Fig. 7.18a, b). Sediment cover on the mound is made up of the Late Wisconsin Peoria Loess covering alluvial deposits of the Prairie Complex. The Prairie Complex crops out parallel to the coast and consists of alluvial deposits of the Late Pleistocene Mississippi and Red Rivers.

On Weeks Island the high salt island landform has a base that is marked by a pronounced increase in topographic slope between 15 and 23 m MSL. A generally north-south trending ridge is mostly underlain by loess-covered sandy deposits of the Prairie Complex and so forms the "Devil's Backbone," which defines the highest part of the island (Fig. 7.18b). The middle (level) salt island landform occupies elevations of 8–23 m, and the low salt island landform occupies lower elevations down to sea level. Both landforms are underlain by mostly sandy, but locally loam-covered deposits of the Prairie Complex. The lowermost landscapes are tributary gully fills and perimeter colluvial aprons, still maintained by slow uplift of the salt core. Geomorphic evidence of ongoing salt-induced uplift on Weeks and the other islands includes; surface lineations, linear gullies, and excessively-steep land surface topography coincident with steep topography on spines that define the top of the underlying salt (Autin and McCulloh 1995).

Thus topographic features on all of the Five Islands were formed by a combination of; (i) rising diapiric salt spines, (ii) sediment reworking and development of a drainage network moving sediment away from uplifted areas, and (iii) subsidence creating sediment sinks (Autin 2002). Uplands are drained by small gullies that dissect the dome landscape and cut into the Peoria Loess. The gullies contain a graded wash fill that passes laterally and downdip into the aggrading colluvial aprons. Where the low salt island landform approaches sea level, the apron's fill in turn interfingers with finer grained aggrading sediment of the adjacent Holocene coastal marsh. Active dissolution of the salt crest creates sinkholes and water-filled ponds atop the salt and typify degradational dissolution zones on both the high and low salt island landscapes.

The boundary between aggradational and dissolutional components of the landscape may in part coincide with underlying anomalous zones of differential shear within the underlying salt indicated by shear zones, locally known as black salt (Fig. 6.14d; Kupfer 1976; Lock 2000). The problematic development of an active sinkhole on Weeks Island, first noticed in 1992, occurs in a position of sharp change in landform slope (transition from high island to gully fill). It lies atop the projected alignment of what is known as Shear Zone E in the underlying salt (Autin and McCulloh 1995) and its development along with karst dolines focused in black salt is discussed in detail in Chap. 13).

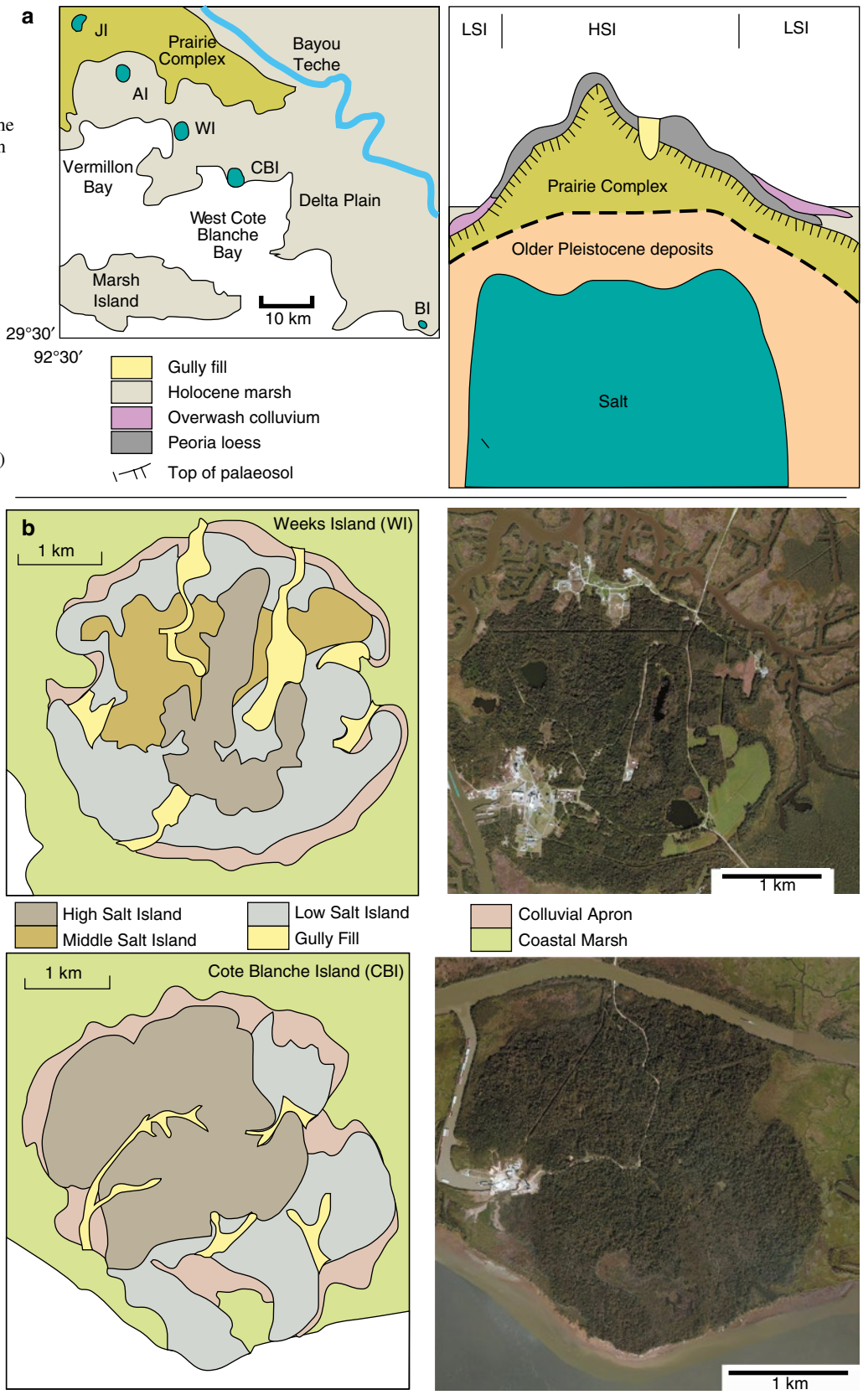

Fig. 7.18 Five Islands Domes, Gulf of Mexico. (**a**) The Five Islands of south Louisiana are aligned in a NW-SE direction along the western margin of the Mississippi River delta plain. The idealised salt dome cross section illustrates the relationship between salt island landform components and surficial stratigraphy. A palaeosol marks the top of the uplifted Prairie Complex across the islands. Beneath the high salt island landsurface (HSI) the Peoria Loess and local gully fill sediment veneer the Prairie Complex. Holocene marsh and overwash colluvium occur as veneer deposits beneath the low salt island (LSI) landsurface. (**b**) Geomorphic features of Weeks Island and Cote Blanche Island, the surface features of Weeks Island largely reflect the dissolution topography of the underlying salt, which includes the various solution ponds

Zagros/Hormuz Region, Arabian (Persian) Gulf

Active salt glaciers (namakiers) typify the foreland fold region of the Zagros-Hormuz province (Infracambrian-Cambrian salt), in a region made up of a number of E-W trending anticlinal mountain ridges and synclinal valleys and in the Qom region of central Iran (Miocene salt). Many islands and ridges further to the south also have squeezed Hormuz salt cores, but salt is no longer flowing at the surface (Fig. 6.85). More than 200 degraded namakiers and salt plugs (diapirs, domes) occur throughout the Arabian Gulf region, many are associated with hydrocarbon and metal sulphide shows (Kent 1979; Talbot and Jarvis 1984).

Salt flow at the surface in the region of Zagros namakiers of southeast Iran, such as the Konasariah extrusion, began in the Pliocene and continues today with average uplift rates ≈ 2 mm/year with the velocity of the salt flow decreasing away from the salt vent (Fig. 7.19a, b). Similar geomorphology also typifies actively extruding Miocene salt fountains in Central Iran, as in namakiers the vicinity of the holy city of Qom (Fig. 7.20; Warren 2008). In both regions, the upper portions of actively flowing namakiers retain few deeply penetrating caves beneath their sediment carapace due to ongoing salt replenishment.

Karst and karren features are most obvious away from the active vent, nearer the dissolving edges of active glaciers, especially in areas where the salt supply has slowed and the namakier edge is retreating to form steep slopes with little or no soil cover (Zone 4 in Figs. 7.19 and 7.20; Zarei et al. 2012). As a general rule, the upper portions of an actively flowing salt mound are covered by residual soils of the insoluble components (suffusion karst) that , which remained in place as the flowing salt is dissolved. Dolines below the surface of these soils enlarge and the soils thicken as the moving salt dissolves in its passage away from the vent. Ultimately, once the supply of mother salt is depleted the at-surface namakier dissolves to leave behind no more than a gypsum-encrusted surface (e.g. Kuh-e-Gach described in Warren 2008).

Iranian namakiers possess different diameters (1–15 km) and range in outline from conical to cigar shaped, with varying intensities of surface karst and rilling (Fig. 6.87). Salt plug landscapes can be divided in four types based on the intensity of supply versus dissolution (Bosak et al. 1999); active, passive, ruins of plugs and unbreached plug domes (Fig. 7.21). Active plugs are positive relief features with centrifugal drainage networks and the plug surface dominated by flowing halite with relatively minor development of karst. Small ephemeral features, including shallow caves, are

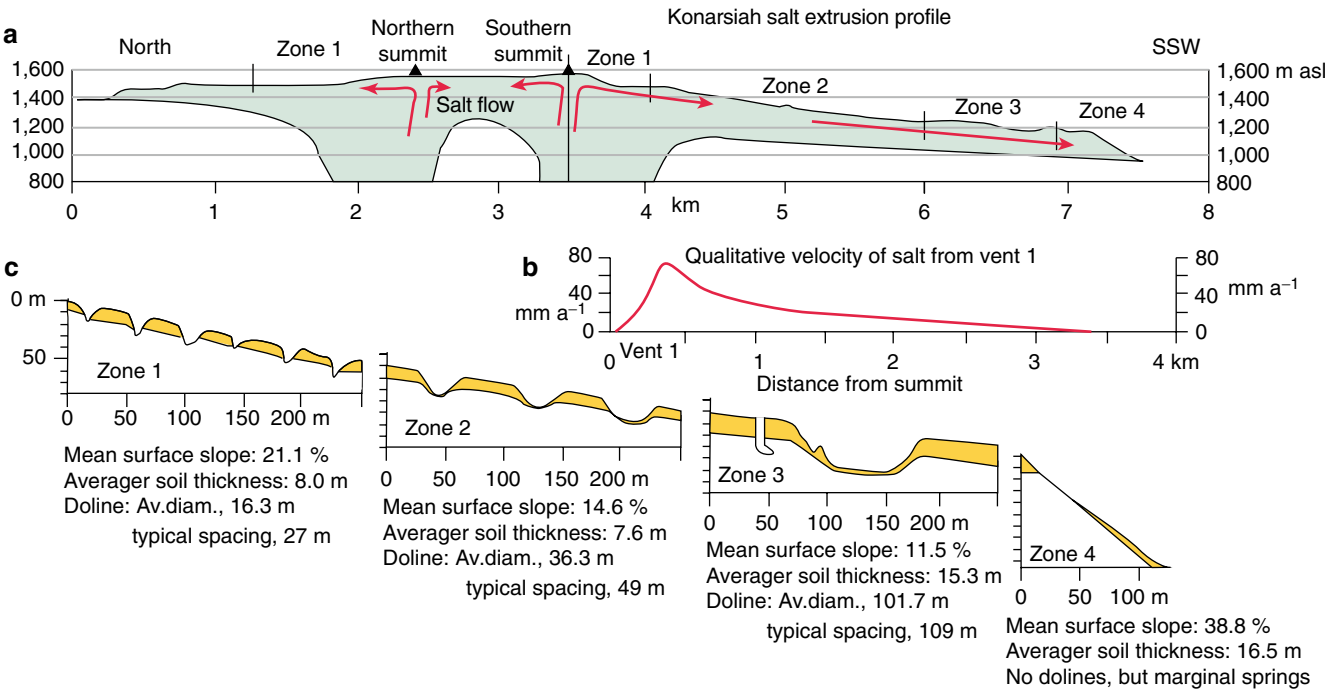

Fig. 7.19 True scale profiles of Konarsiah salt extrusion, Iran and its four zones. (**a**) Elevation profile along a dogleg path. (**b**) Qualitative graph of horizontal velocity of salt flow from southern summit toward the SSW. (**c**) Diagrammatic scaled representations of karst features, soils and salt surface from zones 1–4 (After Zarei et al. 2012)

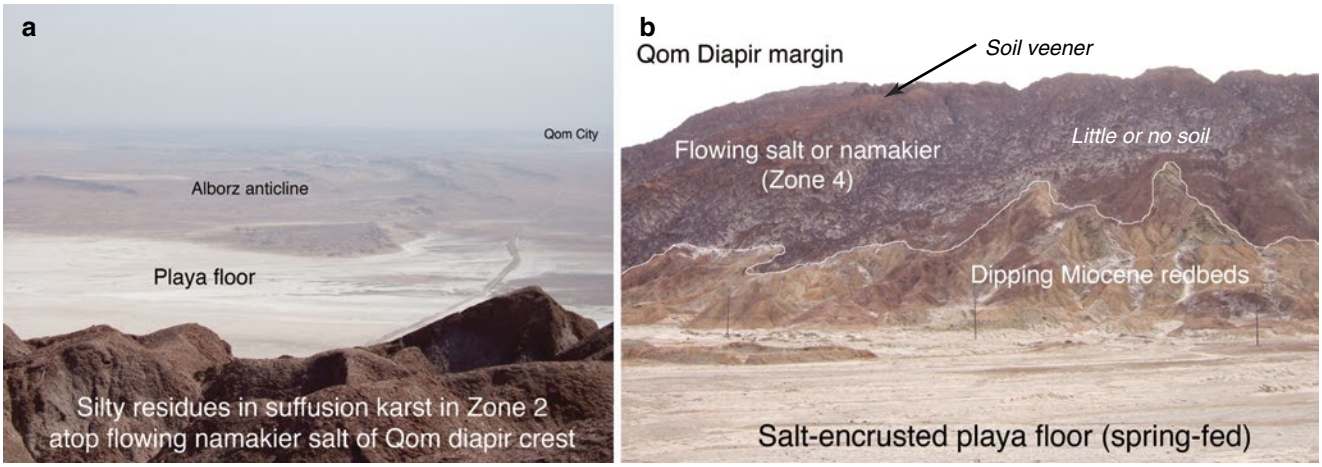

Fig. 7.20 Surface features on the Qom diapir, Iran (After Warren 2008). (**a**) View to northeast from midway up diapir tongue showing Zone 2 Suffusion karst features in the foreground. (**b**) Zone 4 features on the edge of the salt tongue showing relative loss of soil on steep dissolution edge of tongue, while the edge of the playa is supplied saline waters via dissolution of the salt tongue

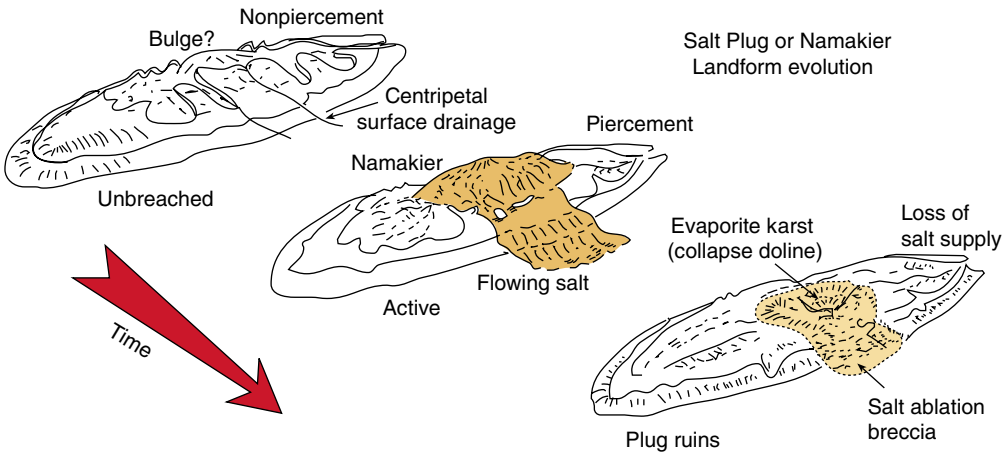

Fig. 7.21 Landform evolution in an area where salt is flowing at the surface in a salt glacier (namakier). Based on various salt plugs in the Zagros foreland belt near the Straits of Hormuz (e.g. Fig. 6.85)

typical of the salt glacier surface, but in an active namakier the salt is flowing too fast to preserve them for more than a few hundred to a few thousand years depending on the lateral extent and rate of extrusion of the diapir. Even so, these features are of interest as they illustrate karst forming on a mobile substrate (Bruthans et al. 2009; Filippi et al. 2011; Zarei et al. 2012). The karstic carapace atop the moving and dissolving namakier is dominated by soils, typically composed of a combination of dissolution residues, fluvial deposits and wind transported dust (loess). As the moving salt dissolves, dolines develop in the surface of these soils, they enlarge with time as the soils thicken.

Once a supply from the mother salt layer ceases, the namakier stops its outward expansion and begins to shrink to ultimately subside and disappear. This occurs over time scales of hundreds to thousands of years post flow, to leave behind a salt-ablation carapace. As the salt dissolves, soils that previously had accumulated about to namakier edge, now touch down over the whole extent of the former salt glacier. Ultimately, karstification and salt core collapse becomes so pervasive across the former namakier extent so that only the edges of the relict plug still show any positive relief (Fig. 7.21). Salt plug ruins are even more disturbed and indicate complete cessation of any surface salt flow. Overall, in the local Iranian landscape underlain by salt, inactive plugs tend to be negative landscape features (depressions). Exotic "Hormuz" blocks of various sizes are scattered as dissolution residues about the edges of the "ruined" depressions, but no salt outcrops (Fig. 6.86). Internally draining dendritic stream networks feed into the collapsed core of the ruined plug, creating a reversed drainage direction compared to that of an active plug.

To the south of the active onshore Zagros namakier province are numerous salt-cored islands in various stages of namakier dissolution, such as Hormuz, Das and Yas islands (Fig. 6.85). These once extrusive salt masses are now largely inactive with only minor at-surface evaporite residues present, mostly as gypcretes and caprock remnants. Highest parts

of the islands are typically covered by dissolution breccias that cap the salt core below. Salt beneath the breccia carapace is pervasively karstified and where relatively shallow, as at Hormuz Island, it is covered by suffusion karst and cross-cut by tube caves (Fig. 7.30). Active flow of the squeezed salt in the various island cores seems to have ceased sometime in the Miocene so that terrains of exotic blocks now outline much of the surface expression of former outcropping salt masses.

Salt Dissolution: Solution Breccias and Residues

Evaporite solution breccias (syn. evaporite collapse breccias) form whenever the removal of evaporite salts allows the intercalated or overlying rock to settle and become fragmented. Breccia horizons and a pile of finer-grained insolubles are the typical end result of complete subsurface dissolution of an evaporite. Frequently, especially in outcrop or about the buried edges of an evaporite bed, they are the only evidence of a former evaporite unit (McWhae 1953; Middleton 1961; Stanton 1966; Elliott and Warren 1989; Swennen et al. 1990). In evaporite paleokarst such breccias are one of the most reliable indictors of the former evaporites, even in situations where all soluble salts have been flushed.

The impervious internal make-up of a buried salt mass means it dissolves like a melting block of ice. That is, it shrinks via a series of retreating fronts, all moving from the edges inward and all defined by an expanding rind of insoluble residues. Retreat is most rapid along solution fronts in contact with large volumes of undersaturated pore water crossflow, as occurs along the upper side of shallow salt layers, atop shallow diapir crests, in zones near active faults that intersect bedded or halokinetic salt, or about the feather edge of subcropping inclined beds and allochthons. Pervasive and rapid dissolution creates cavities filling with collapse clasts derived from adjacent lithologies (collapse solution breccia). Slower dissolution rates create higher salinity pores forming residual rinds made up of less soluble salts (typically anhydrite or gypsum). As dissolution eats inward it can also create free-flowing residues of sand- to mud-sized insolubles, which in their turn infiltrate and sometimes fill spaces between breccia clasts. These fines, known as dissolution flour, are varying combinations of quartzo-feldspathic mud, microcrystalline dolomite and calcite rhombs, all previously dispersed through a now-dissolved salt mass.

Defining Evaporite Dissolution Breccia

Breccia is a nongenetic rock type that ranges across sedimentary, igneous and structural regimes. As a rock descriptor

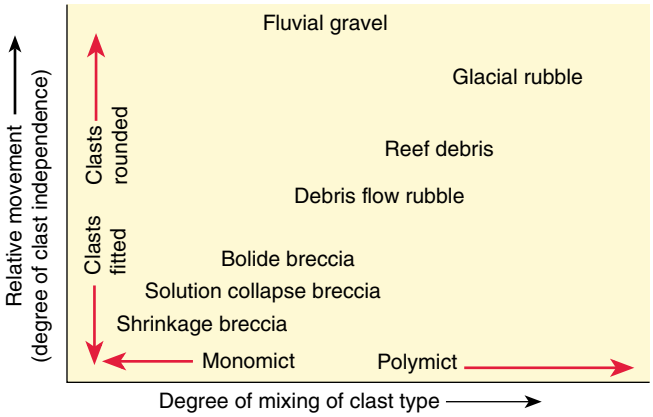

Fig. 7.22 Evaporite solution breccias classification (based on the degree of clast movement and mixing after von Engelhardt et al. 1977)

it needs a prefix to define its origin. Depositional breccias can be thought of as "proto-conglomerates" that is, deposits composed of clasts or eroded fragments not transported sufficient distances to become rounded and so become a conglomerate (Fig. 7.22). Nonevaporitic sedimentary breccias of this kind are commonplace. They form in glacial or alluvial outwash, can be an outcome of waves impacting reefs or sea cliffs, or can form in response to slope failure As a group, depositional breccias tends to indicate lateral rapid change in energy levels.

Some evaporite breccias are also depositional or "proto-conglomerates" composed of gypsum, anhydrite or halite clasts in an evaporite matrix, they are common in many large-scale ancient evaporite basins, perhaps even on Mars (Wezel and Baioni 2010). For example, evaporite depositional breccias laid down is slope settings typify portions of the Appenine and Sicilian Messinian (Manzi et al. 2005), and the Zechstein of Germany (Schlager and Bolz 1977). Reworking, gravity displaced downslope transport, and redeposition in relatively deep-water basin interior settings typify both cases, via a variety of gravity-flow processes, including slumping, massflowage, and turbidity current. Large volumes of reworked bottom-nucleated evaporite crystals, mostly gypsum clasts, accumulated in foot of slope positions due to intense erosional denudation of primary gypsum deposits, first precipitated in shallow, restricted platform basins (Fig. 5.60).

In contrast, evaporite-dissolution collapse breccias are diagenetic horizons, usually dominated by cm-metre angular collapse clasts in a mud-sand matrix of dissolution flour. Internally, they can appear similar to some depositional breccias. Commonly used sandstone and carbonate breccia classifications do not adequately address the variable character of solution collapse breccias as they emphasise depositional energy levels and the style and rate of surface sediment supply, not overburden and intrasalt collapse. Hence, we need to define a relevant breccia classification (Fig. 7.23), then we

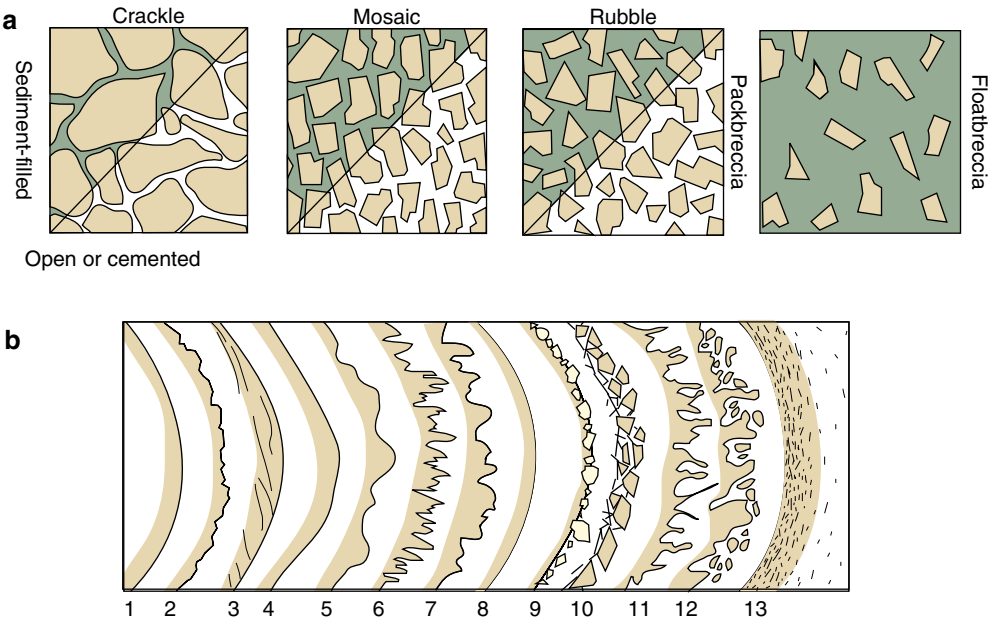

Fig. 7.23 Breccia description. (**a**) Nongenetic classification of breccias (After Stanton 1966; Morrow 1982). (**b**) Nature of clast contacts; *1* smooth, *2* slightly pitted, *3* striated, polished, *4* faceted, *5* solution rounded and pitted, *6* stylolitic, *7* ragged, *8* weathering rim or alteration rind, *9* microfragment armouring, *10* fragments in process of breaking out, *11* jagged, *12* crumbled, *13* diffuse, gradational (After Laznicka 1988)

can reliably discuss how evaporite solution breccias relate to sedimentary breccias.

Breccias are by definition composed of angular clasts, typically rock fragments of granule or pebble size and larger. Whenever classifying a breccia one should ask the following (Morrow 1982):

- Are clasts of a single lithic type (monomict/oligomict) or of widely variable types (polymict); are lithic types in clasts similar or different from the rocks bounding the breccia body; are clasts composed of durable rock fragments or of a mixture of hard and soft clasts?
- Are clasts closely fitted, loosely fitted, or spatially independent, i.e., crackle or mosaic- packbreccia or floatbreccia (Fig. 7.23a)?
- Do clast shapes and clast-to-clast contacts indicate either plasticity of clasts or brittle behaviour at the time of sedimentation? What is the nature of the clast edge (Fig. 7.23b)?
- Are spaces between clasts filled with cement or with detrital matrix; i.e. clast-support or matrix-support?
- Does a weathering rind or coat extend all around a clast, or is it developed only on one side, or is there no indication of weathering?
- What is the nature and style of clast size and size grading; evidence for bedding; imbrication or other spacial alignment of clasts?
- What is the overall size and shape of the breccia deposit; is there a sharp lower contact and/or sharp upper contact; is the breccia body discordant (trans-stratal) or concordant (interstratal) in relation to bounding rocks?

Packbreccias are clast supported, while floatbreccia clasts float in a finer matrix of granules, sand or mud. Distinction between crackle, mosaic and rubble breccia depends on whether the clasts are fitted, mildly disoriented or totally independent (Fig. 7.23a). Crackle denotes a fabric in which there is little relative displacement of fragments. Mosaic implies fragments are largely but not wholly displaced. Rubble breccias are completely disordered and no fragment boundaries match. Some packbreccias have particulate matrices, others are cemented by spar or silica, indicating clast support at the time of formation. Elements other than fabric, such as the size and shape of the breccia body, its stratigraphic setting, the depositional setting of adjacent sediments and lateral equivalents to the breccia provide evidence of origin. Intrastratal breccias indicate former bedded salts, while trans-stratal breccias characterise breccia chimneys and halokinetic dissolution breccias.

Evaporite solution or collapse breccias tend to form diagenetically as undersaturated pore waters flush a buried evaporite bed. Clasts in the resulting breccia can be derived from a lithology that once overlay the dissolving salt bed, or can come from thin stringers and beds that were once entrained in the now dissolved salt. Distance travelled by the clasts before being redeposited is negligible in many dissolution breccias, often only centimetres to a few metres. Timing of clast movement may be episodic or a single widespread instantaneous event. That is, clasts in an evaporite solution breccia may have moved into a cavity in concert, like a school of fish, or they may have gently sloughed and foundered a few at a time, with little breakage or change in orientation. The distance of movement is dependent on the size

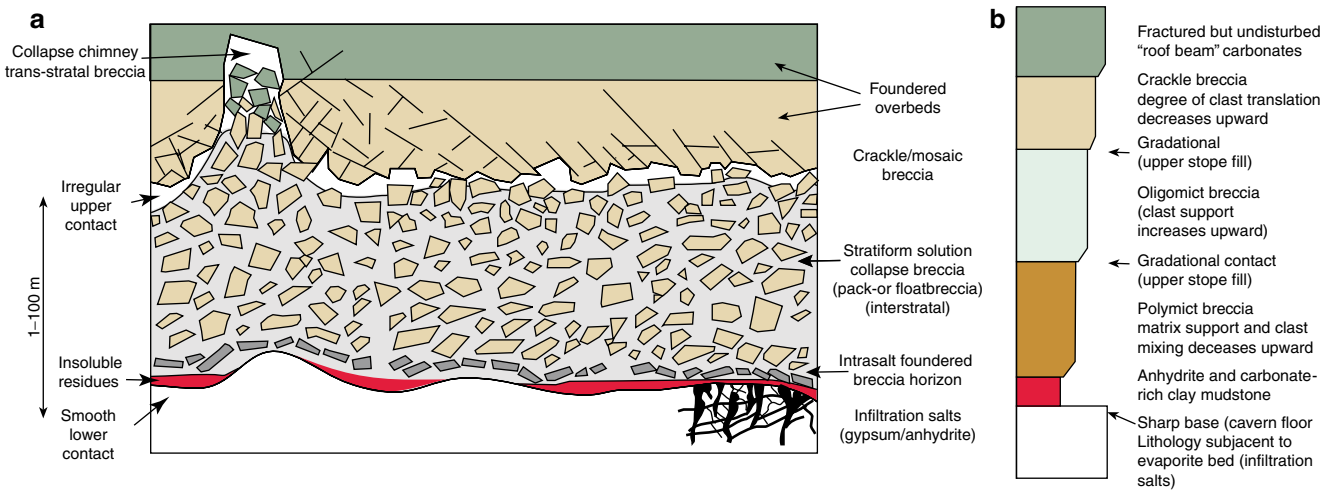

Fig. 7.24 Lithological distribution in an evaporite dissolution triggered collapse breccia. (**a**) lateral facies distribution. Left half of figure illustrates relationships in a trans-stratal chimney, right half in a stratiform solution collapse breccia. (**b**) Ideal vertical sequence of breccia cumulates in an evaporite solution breccia

and lateral extent of the solution cavity into which the clasts move and whether the clasts originally resided in thin interbeds within the dissolving evaporite or if they were part of a thick strong roof-spanning lithology that once overlay the dissolving salt bed. If the cavity is only a few millimetres to centimetres high, the overburden founders gradually and gently and so clast orientation and fitting is little disturbed by the process of dissolution, then crackle and mosaic breccias will be commonplace. If large local cavities develop, the collapse of the roof span is more likely to be catastrophic and the result to be dominated by disturbed rubble or packbreccias (Fig. 7.23a).

Bedded Solution-Collapse Breccias

Stanton (1966) in a benchmark paper on formation of evaporite dissolution breccias demonstrated solution, subsidence, and evaporite flowage act simultaneously during subsurface brecciation. The resulting evaporite solution breccia in the Upper Devonian Leduc Formation, Alberta Basin, Canada, is made up of cm-dm angular dolomite clasts in a matrix of dolomite mud or anhydrite. He concluded that, in the dissolution of interbedded halite-anhydrite-dolomite succession, an anhydrite-supported floatbreccia is a transitional stage to a dolomite clast-supported packbreccia. Angular fragments of the dolomite overburden and interburden in an anhydrite-supported breccia (floatbreccia) are loosely supported by solution-thinned, but still abundant, nodular anhydrite with folded and stretched textures indicating viscous flowage during dissolution. As breccia forms and flows, dolomite fragments are continuously broken and rebroken, while the supporting anhydrite matrix carries a high proportion of loose, whole or broken dolomite rhombs (silt-sand size crystals). Ultimately, a dolomite packbreccia forms by the complete solution of the anhydrite. It then consists of tightly packed dolomite fragments and clasts, within a matrix of sand-sized detrital rhombs and dolomite microspar cement.

At the bed scale, evaporite solution breccias typically have planar to slightly irregular, continuous lower contacts, often coated with insoluble residues (Fig. 7.24a). The footwall edge to a breccia is usually covered by a few centimetres of mud- to sand-sized insoluble residues. The thickness of a pure evaporite that dissolves to produce a thin layer of insoluble residues may be substantial. For example, the Hartlepool Anhydrite contains only 0.5–0.8 % insolubles (Smith 1972). Complete solution of a 100 m thick bed produces a layer of insolubles a mere 50–80 cm thick. In many breccia beds the insoluble residues now make up the matrix between clasts that were derived by the breakup of thin beds of carbonates or clastics. These are the fragmented remains of thin intrasalt beds that were once supported and interlayered by the now dissolved salt. This interval tends to be more polymictic than the upper, roof-derived, part of the breccia unit.

Insoluble residues typically consist of fragmented chert, detrital quartz, silt, clay and dolomite rhombs, which are later cemented by authigenic phases (typically calcite, dolomite or silica cements). Many evaporite beds originally entrain dispersed syndepositional silt-sized dolomite rhombs. When the encasing salts dissolve, a dissolution residue or matrix is left behind; it is dominated by solution-disaggregated dolomite crystal silts and sands and is sometimes called "chalky dolomite." A high degree of initial

intercrystalline porosity in the residue makes it an excellent potential aquifer for later mineralising solutions or hydrocarbons, especially when it forms at burial depths where much of the adjacent nonevaporite sediment is tight, having lost its porosity via mechanical and chemical compaction.

Siliciclastic and carbonate sand, bound by early evaporite cements (e.g. halite cements in aeolian, wadi, or oolite sands), can also be leached during burial diagenesis to create permeability in an otherwise tightly cemented sand. In extreme cases the result is disaggregated freeflowing subsurface sand, with depositional levels of permeability that remain until it is recemented by subsurface processes.

Sometimes, rocks in the footwall beneath the breccia bed are locally veined and cemented by infiltrations of satin spar and poikilotopic gypsum or anhydrite. Smith (1972) argues the fractures hosting such footwall stockworks were first created by the pressure of crystallisation of the evaporite itself; others envisage a more passive process of cement fill within pre-existing joints or fractures. In my own work I have found the joints are often the result of passive fill in joints and fractures created by the extensional stress in units above or below a dissolving salt unit. Because pure halite has often completely dissolved, its former presence is difficult to determine, especially in core or image logs, but these tell-tale fracture-fills remain in the log signature (especially in image logs) and indicate a much thicker former salt bed.

The basal zone of insoluble residues passes up into the main breccia body, an interval dominated by packbreccia or floatbreccia. Breccia fragments and clasts in the main breccia can be angular or solution-rounded (Fig. 7.24a). Almost all rubble texture in a breccia is generated by the collapse of overlying or interbedded lithologies into cavities created by dissolving salt beds. Where the original sequence was made up of interbedded salts and other lithologies, the resulting clast rubble typically collapses in sequential order, so that the rubble pile retains the crude stratigraphic order of the former intrasalt beds.

Clasts are composed of varying amounts of sandstone, dolomite, limestone, mudstone and chert fragments. The main breccia may be polymict or monomict, depending on the nature of the intrasalt beds and the overburden. Breccias can be clast- or matrix-supported (packbreccia versus floatbreccia) depending on the amount of residue entrained in the evaporitic interval prior to dissolution. Pure evaporites, interbedded with indurated dolomites and other nonevaporite strata, tend to produce clast-supported packbreccia fabrics. Evaporite sequences interbedded with, or underlying, nonconsolidated sediments, or evaporites with a high content of dispersed impurities, tend to produce matrix-supported floatbreccia fabrics.

Unlike its lower contact, the upper contact of the main breccia interval is typically gradational, progressing from rubble-breccia in the main body into mosaic, crackle then ultimately into unaltered overburden (Fig. 7.24b). A breccia begins to accumulate on the bottom of a growing cavern marking the contact of undersaturated pore waters and the salt. As the salt begins to dissolve, the insoluble clay-sized material that was present as impurities in the salt accumulates in thin layers on the floor of the cavern. Later in the dissolution process, and higher in the breccia sequence, angular to etched clasts of mixed intrasalt and roof rock form a polymictic breccia. Polymictic breccia passes upward into a monomict breccia made up of angular clasts of roof rock. Gradually, the overlying rock is not broken into clasts but is merely fractured and expanded to form crackle breccia. Crackle fractures, if they are not filled with cement, can provide excellent pathways for subsurface mineralising fluids and can act as reservoirs for oil and gas.

The contrast between a sharp lower contact and a gradational upper contact is one of the most reliable characteristics of a solution breccia, especially if coupled with pseudomorphs and satin-spars. It can be used both in outcrop and subsurface studies (core and image logs) to separate an evaporite solution breccia from a depositional breccia (protoconglomerate), which has evidence of syndepositional infiltration and depositional drape along its upper contact, and a tectonic breccia, which has cataclastic and typically symmetrical contacts related to fault or shear zones.

Where complete removal of less soluble evaporites has not yet occurred, evaporite salts, such as flow-textured laminar to nodular anhydrite, remain as part of the matrix within the main breccia interval. In cores through thick-bedded evaporites the upper bed contact is often defined by a zone of disturbance in the anhydrite textures. The typical fabric is very similar to soft sediment disturbance textures associated with rapid water escape in sands. The anhydrite just below the contact is typically made up of angular but contorted anhydrite blocks in a finer anhydrite matrix. Often, there are also highly distorted and folded blocks or fragments of dolomite and other disturbed intrasalt beds. I have seen these zones at the contacts of many thick anhydrite beds with the adjacent nonevaporite strata including; the San Andres and Seven Rivers formations of West Texas, the Khuff Formation in Abu Dhabi and Saudi Arabia, caprocks to Gulf of Mexico diapirs and Zechstein Formation anhydrites in NW Europe. These disturbed contacts define intervals of subsurface dissolution where the process of dissolution and brecciation is not complete. In many cases dissolution processes may no longer be active, as the adjacent nonevaporite beds no longer have sufficient permeability to transmit undersaturated fluids. They are a form of frozen dissolution breccia that define the early fluidisation stage, where the bed is dissolving from its edges inward like a melting block of ice.

Local reprecipitation of evaporites into the breccia matrix may also generate large poikilotopic crystals, which encase the dissolutional residues. Such cements are typically

coarse-grained anhydrites with a somewhat anhedral form and isotopic signatures indicative of elevated temperatures typical of the mesogenetic realm. Pseudomorphs of now-dissolved evaporite minerals and nodules, composed of calcite, silica or celestite, may also remain either in the matrix or within clasts. Cement may be a fine-grained crystalline precipitate of equidimen-sional calcite crystals, as described by Swennen et al. (1990) in the Belle Roche breccias in Belgium, or a sparry coarsely crystalline dolomite or calcite (burial spar). Coarse sparry or saddle dolomite is often associated with mesogenetic evaporite solution breccias in Mississippi-Valley-type deposits (Olson 1984; Warren and Kempton 1997). Isotopic and petrographic character in dolomite burial cements in evaporite solution breccias are often complex and multistage. For example, there are six burial-related stages of dolomite formation and two episodes of breccia formation preserved in the evaporite solution breccias of the Tripolis Unit, Mainalon Mountain, Greece (Papioanou and Carotsieris 1993; Karakitsios and Pomonipapaioannou 1998).

The lower Visean Belle Roche breccia (east Belgium) is a classic multistage evaporite dissolution collapse breccia (Fig. 7.25; Swennen et al. 1990). Its origin as a dissolution breccia is indicated by: (a) the sharp lower contact of the breccia and a gradual transition into the overlying strata,

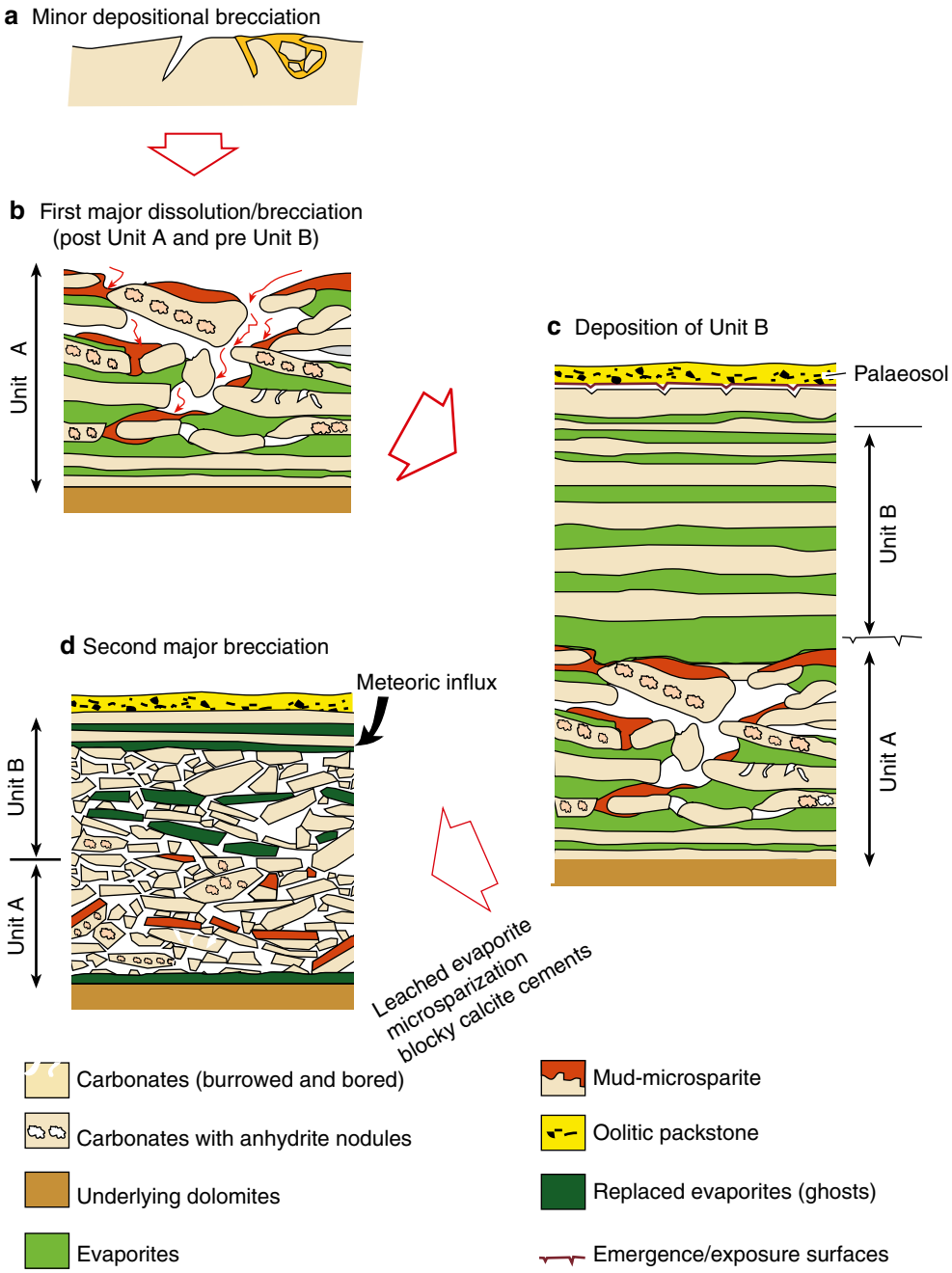

Fig. 7.25 Sequential brecciation episodes in the lower Visean Belle Roche breccia (After Swennen et al. 1990). (**a**) Minor syndepositional dissolution and fracture brecciation mainly related to shrinkage. (**b**) This occurred shortly after deposition of bedded evaporites of unit A and involved incompletely lithified clasts, infiltration of freeflowing mud with ooids. (**c**) Resumption of evaporitic sedimentation to deposit unit B with palaeosol cap. (**d**) Second major brecciation event driven by meteoric influx. It overprinted both unit B and unit A. The brecciation process was mostly foundering rather than cavern collapse, and so stratigraphic order was retained in the breccia stack. Foundering means the overlying beds parallel the general stratification

(b) the presence of semicontinuous clast layers within the breccia giving it a crude 'stratification', and (c) the existence of several types of evaporite pseudomorphs that are now composed of calcite, dolomite and silica. The majority of the sedimentary carbonates making up the breccia fragments show primary features indicating they were originally deposited under hypersaline subaqueous conditions and were interbedded with the now-dissolved evaporite beds. Similar evaporite solution breccias, with similar textures are found in similar age rocks in the Wexford basin, Ireland (Nagy et al. 2005).

Belle Roche breccia has a typical interlocking packbreccia fabric showing a subparallel clast alignment and crude internal layering that indicates foundering by gradual subsidence, rather than catastrophic collapse into a large cavity (Fig. 7.25b, c; Swennen et al. 1990). Multiple brecciation episodes are obvious in the lower breccia (Unit A), where brecciated and veined fragments occur within a microsparite (neomorphosed mud) matrix. There were at least two major brecciation episodes (Units A and B) driven by the successive dissolution of interlayered evaporite units. The second brecciation event related to infiltration of meteoric water and to the complete dissolution of any remaining evaporites (Fig. 7.25d). Meteoric infiltration was probably triggered by uplift related to an orogenic event at the end of the Visean (Sudetic orogenic phase).

Isotopically, three periods of brecciation are seen, the first of which took place early in the diagenetic history. The early breccia matrix consists of infiltrated marine sediments. The fragments and the sedimentary matrix subsequently neomorphosed and lithified in meteoric waters in the shallow burial environment. Multiple water-rock interactions in an open system caused an oxygen isotopic composition of the limestones in equilibrium with meteoric water. This $\delta^{18}O_{PDB}$ composition varies between 8.9 and 5.5‰ depending on the palaeogeographical position (Fig. 7.26). The early diagenetic interaction led also to a spread in the carbon isotopic composition, which ranges between an Early Visean marine ($\delta^{13}C_{PDB} \approx +1$‰) and a palaeosol ($\delta^{13}C_{PDB} \approx -3$‰) isotopic composition. Due to the localised migration of fluids along fractures in the subsurface, a second evaporite dissolution, collapse brecciation and cementation period occurred.

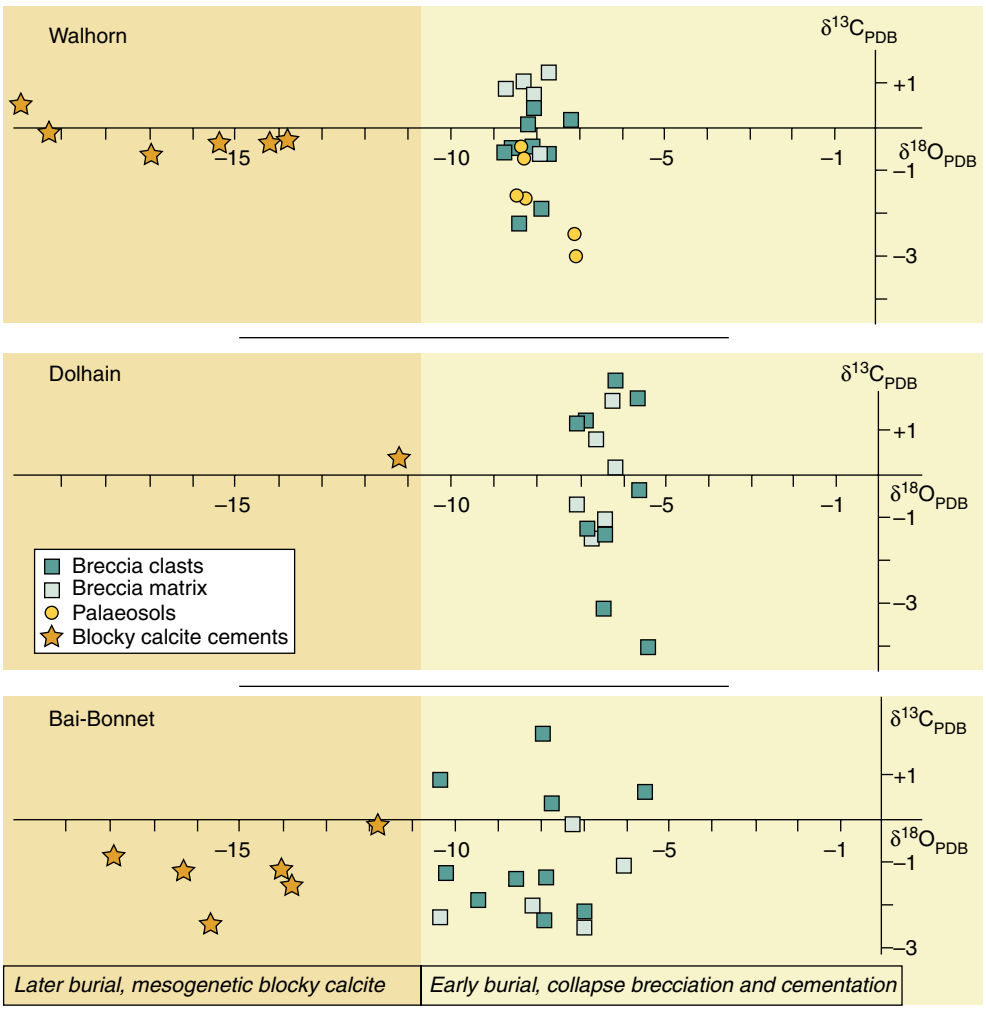

Fig. 7.26 Carbon and oxygen isotope values in Lower Visean limestone breccia components and paleosols at three different localities in Belgium: Walhorn, Dolhain, and Bai Bonnet. Plot shows there are two periods of cementation, (1) An earlier burial period tied to clast, matrix cement and paleosol signatures and, (2) A later warmer mesogenetic period when the blocky calcite cements formed (After Muchez et al. 1992)

During this period, breccia fragments and the early diagenetic matrix locally neomorphosed a second time. The oxygen isotopic composition of the limestone constituents became more negative due to ongoing interaction with increasingly warmer mesogenetic burial fluids. In time, and with further burial re-equilibration, the $\delta^{18}O$ composition of the breccia fragments and matrix moved toward the plot field of the dull orange-brown luminescent blocky calcite cements ($\delta^{18}O_{PDB} \approx -15$ to 20‰), filling the secondary cavities. A third period of brecciation and neomorphism caused the pervasive development of orange-yellow zoned and bright luminescent microsparites to sparites and of granular to blocky calcites with the most negative $\delta^{18}O$ values (Fig. 7.26).

Some of the breccias in this region were dolomitised relatively shallow in active-phreatic mixing zones, via processes facilitated by bacteria (Nielsen et al. 1997). Locally, high degrees of dolomite supersaturation were produced in anaerobic to dysaerobic zones during bacterial sulphate reduction. The sulphate came from the dissolving evaporites and organics from adjacent interbeds. The resulting dolomite precipitates show characteristic bacterial morphologies, such as spheroidal and dumb-bell shaped inclusion patterns, overgrown by dolomite cements with rhombohedral outlines. The dumbbell-shaped portions of the crystals are interpreted as bacterially-related precipitates based on; (1) textural similarities with documented bacteriogenic precipitates, (2) the presence of 'bacterial' microspheres and framboidal pyrite embedded within the dolomite, and (3) their general geological setting. Geochemical characteristics of the dolomites and associated minerals also support a bacterial origin. The bacteriogenic intervals show a ubiquity of framboidal pyrite, depleted in ^{34}S ($\delta^{34}S_{CDT} = -22.4$ to -25.5‰), testifying to a period of bacterial sulphate reduction. The isotopic composition of the spheroidal dolomites ($\delta^{13}C_{PDB} = -2.4$ to -3.2‰ and $\delta^{18}O_{PDB} = -3.8$ to -3.4‰) suggest a contribution from oxidized organic carbon produced during bacterial sulphate reduction. The ^{18}O depletion of the spheroidal dolomite crystals and their occurrence adjacent to, and within evaporite karst cavities suggests a possible mixing zone origin, with a contribution from meteoric waters. The rhombohedral cement-overgrowths have $\delta^{18}O_{PDB}$ values in the range 0 to +5.3‰, indicating precipitation from normal to slightly evaporated contemporaneous seawater. This dolomitisation event predates the onset of blocky calcite cementation in all localities.

In general, as a thick widespread evaporite bed dissolves, it does so more rapidly and pervasively in zones of greatest fluid access. This can be along a fault-bound edge, along a thinned feather edge, along an upper or lower contact, or along joints and fracture planes that cut the bed. As the salts dissolve, carbonate cements may precipitate as cement rinds within stratiform cavities, or along cross-cutting fracture planes. Alternating episodes of dissolving, fracturing and cementing will form veined fracture infills and fragments with clasts of cement within the disappearing bed. With further collapse, these cements may be rebrecciated and cemented numerous times into internally complex clasts and fragments. Ongoing repetition of this process can create clasts made up of nothing but multiple episodes of vein and cavity-fill cements. Some fracture and block-defining cements can remain, and, with the disappearance of the supporting evaporite, evolve to form an open lacework or cellular grid of cemented materials and residues called a boxwork[5] limestone. Such boxworks are especially obvious in nearsurface dissolution settings, as in rauhwacke terrains or phreatic zones of growing tepee structure crusts. Once a rock is more deeply buried and compressed, the boxwork either collapses or is only preserved as delicate laceworks encased within massive cements. For example, even after burial, local relics of boxwork texture can still be seen beneath the V's of the Permian tepees of West Texas and the Triassic tepees of Italy (Kendall and Warren 1987).

Flow of water through cavities during breccia collapse in the active phreatic zone can rework fine-grained matrix material. Localised cm-dm cavities can fill with waterlain laminae that are typically overprinted by water escape features, slumps and, less commonly, with ripples and cross-beds. If the cavity lies in the vadose zone, or if a deeper phreatic cavity contains biogenic or thermochemical gases, such as methane or H_2S, then the cavity may be ornamented with microstalactites, "snottites" and other speleothems. Calcitic vadose speleothems ornament cavities in dissolution breccias in the Kirschberg Evaporite breccia of central Texas (Warren et al. 1990), while pendulous sphalerite stalactites, precipitated in thermochemically-derived H_2S/methane-filled bathyphreatic[6] cavities, typify the evaporite-replacing breccia ores in the Cadjebut Pb-Zn mine, Australia (Warren and Kempton 1997). Cavities and flow paths associated with deeper evaporite dissolution events and the formation of MVT style mineralisation can also be associated with the formation of mesogenetic hydrothermal zebra dolomites (Diehl et al. 2010).

Breccia Extent

Evaporite solution breccia beds can be syndepositional, or form much later after millions of years and hundreds to thousands of metres of burial, halokinesis, and uplift. Breccia beds

[5]The term boxwork is nongenetic, it describes an aggregate with plates or septa which intersect at various angles leaving open boxlike spaces, which may be subsequently infilled or cemented.

[6]Bathyphreatic is used to describe the hydrologic zone typified by deep, near-stagnant waters, situated at depths well below the zone of active phreatic circulation.

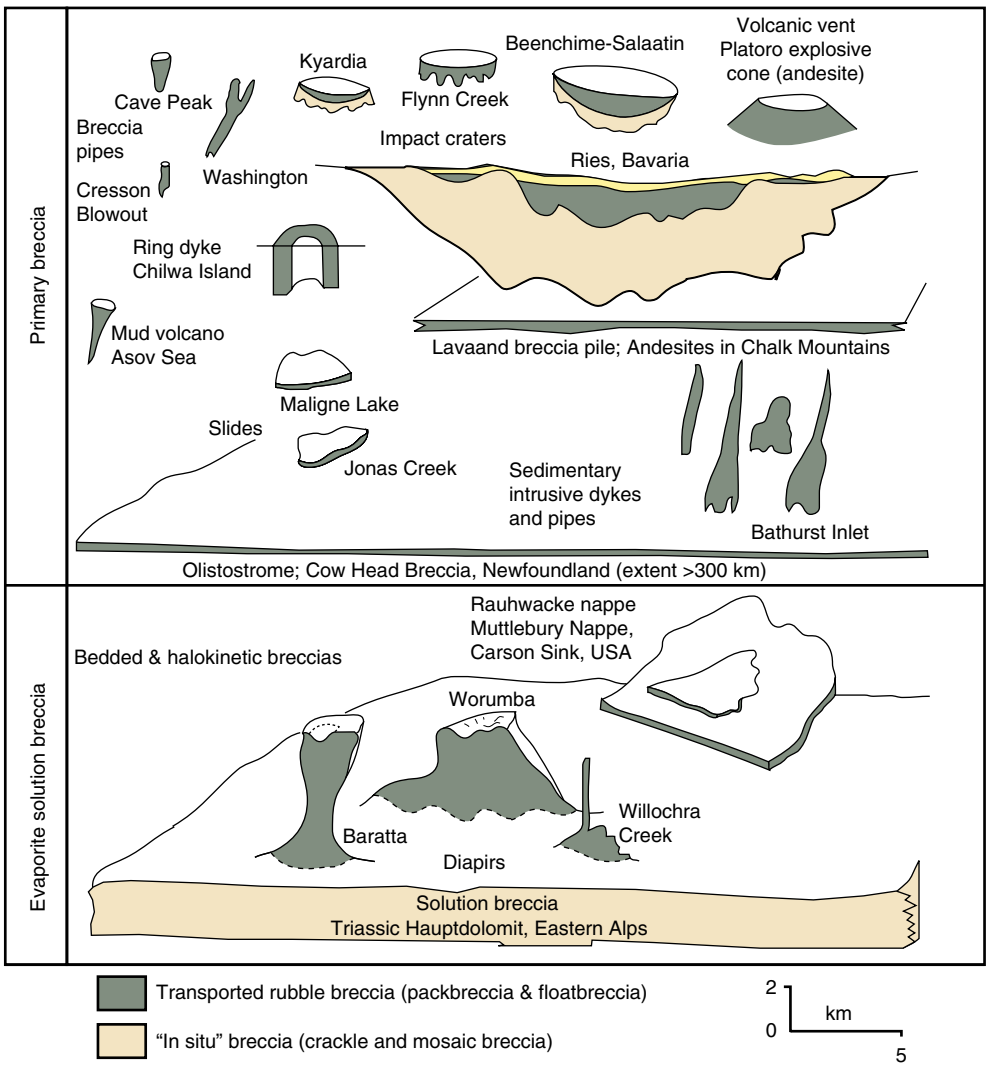

Fig. 7.27 Size and shape of various breccia bodies that occur in sedimentary successions (Modified in part after Laznicka 1988). Evaporite-related ("evaporites that were") geometries are illustrated in the lower part of the figure

tend to be widespread and stratabound, with geometries that indicate the distribution of the precursor evaporite (Fig. 7.27). If the precursor layer was part of a stacked cyclic sequence of platform evaporites interlayered with carbonates or siliciclastics, the breccias tend to stack into interstratal cyclic horizons. This is the most easily recognised style of evaporite solution breccia. If the precursor evaporite was part of a halokinetic or remobilised sequence then the solution breccia is trans-stratal and follows the distribution of former salt stems, salt welds, or thrust planes. Recognising this second type of collapse breccia is more difficult, especially in core.

Intensity of brecciation and the general geometry of the foundered strata in the breccia bed can vary widely from place to place, even within a single unit (e.g. Smith 1972). The geometry of collapse indicators is related to variations in:

(a) Inflow geometry of the solution front: water may enter along a fracture, fault, blanket aquifer, reef, diapir margin, etc. The timing of development of the solution front may in turn be related to episodes of seismic or tectonic instability (e.g. seismic pumping driving episodic basin dewatering, or periodic uplift or sea level lowering creating a gravity head to drive meteoric flow).
(b) Rate of evaporite solution: this is dependent on the rate of formation water crossflow and the saturation state of the cross-flow. This is in turn controlled by climate, tectonics, regional uplift, development of major unconformities, etc.
(c) Confining pressure: related to thickness of overburden at the time of collapse. This is in turn related to the age of collapse (burial/uplift timing).

Stratiform Breccias

The simplest and most general styles of interstratal collapse are typified by blanket aquifers and broad areas of gentle sagging and floundering, where diffuse undersaturated water flow over large areas has slowly removed bedded evaporites

Table 7.3 Features of an interstratal breccia created by foundering, which is the most common mechanism creating an evaporite solution breccia

Characteristic features of an interstratal dissolution breccia	Commonplace textures and features of the adjacent crackled matrix. Equivalents also occur in some recemented breccia fragments, details on their genesis given later.
Sharp lower contact and irregular upper contact to breccia bed. Oligomict clasts derived from overlying and intrasalt lithologies. Breccia body shows a crude stratification, with clasts of differing lithologies often stacked in original stratigraphic order. Depositional textures in some breccia fragments indicate hypersalinity during deposition. Zone of insoluble residues (silt, chalky dolomite, etc.) lies atop lower contact, and sometimes has infiltrated into fractures beneath. Evaporite cements in fractures beneath lower contact. Several types of evaporite pseudomorphs (nodules, radial textures, length slow chalcedony, etc.) are present in clasts or matrix and interclast cements.	Pseudomorphs of former crystals retaining shapes after bird-beak gypsum, axe-head anhydrite or halite hoppers, now filled or partially filled (moulds and casts) with calcite, chalcedony or quartz, baryte, celestite, strontianite. Thumbnail to fist-sized rounded moulds or vugs, in limestone or dolomite host, with irregular edges defining positions of former chicken-wire, nodular or spherical evaporite (cauliflower vugs). Vugs may be filled or partially filled with calcite, chalcedony or quartz, baryte, celestite, strontianite. Silica fill in vugs (geodes) is a varying combination of length-slow chalcedony (quartzine) and spherulites composed of lutecite. Euhedral crystals of authigenic limpid dolomite or quartz (some are double-terminated) in dolomites adjacent to breccia horizon. Minute rectangular relics of anhydrite in quartz or other minerals such as calcite (obvious in quartz because of contrasting moderate birefringence and the rectangular cleavage – but are very small). Coarsely recrystallized (sparry) limestone and dolomite, often porous, and without skeletal debris. Internally the sparry interval may be massive, laminated or contorted. Form by calcitisation or dedolomitisation when evaporite dissolved (especially common in association with telogenetic alteration). Net-textures, a small-scale relic of original bedded gypsum/anhydrite, typically with displaced impurities that outline edges of structures, typically relict patches in secondary, sparry limestone. Small contortions typically related to flow of insoluble residues and characterised by sedimentary structures that are slumped or fractured during subsurface movement in response to evaporite dissolution.

In part after West (1979)

(Table 7.3; Fig. 7.27; Hauptdolomit). The blanket aquifer can lie above, below, or even within the dissolving evaporite bed. Overburden brecciation in such gently foundering regions is minor, so fossils and sedimentary structures are mostly preserved in blocks with near-original orientations. Larger interbed and overburden clasts tend to be tabular, and only slightly separated or disorientated, i.e., dominated by mosaic to crackle breccias.

In areas of more focused dissolution where large caverns and solution planes have formed within the dissolving evaporite beds, the whole of an overlying sequence can be reduced by chimney stoping and doline collapse to a rubble breccia — a mass made up of completely disarticulated and rotated (commonly rectangular) blocks and fragments ranging from silt-size to blocks many metres across. In still other areas, foundered strata can be bound by sharp folds or dislocations that are in effect normal faults. Such areas of intense brecciation are often the end product of localised collapse and can grade laterally and vertically into almost unbrecciated equivalents. These dislocations can be sharp and clean, or associated with areas of intense diagenetic alteration, including calcitisation, silicification, dolomitisation and precipitation of ferroan carbonates. This latter group of intensely altered and replaced breccia intervals within a carbonate or sandstone host can be part of a larger group of fault-focused, often metalliferous, deposits with hydrologies driven by evaporite solution (Warren 2000b).

Hydrology and Texture

Salt beds that dissolve during early burial tend to create characteristic ductile breccia textures and soft sediment slumps in the overburden. These are features that can be used to distinguish syndepositional from later more brittle modes of mesogenetic collapse breccia formation related to subsurface or basinal waters or to even later uplift and re-entry into the active phreatic (telogenetic) zone (Fig. 1.9). Evaporites dissolving early in their burial cycle, even while subjacent strata are accumulating, tend to evolve into ridge and furrow dissolution geometries that influence thickness and depositional style in the lower parts of the overlying sediments. Overlying clastic beds are typically no more than partially lithified when the underlying evaporite dissolves and so are highly disturbed by ongoing soft-sediment textures, which are driven by collapse of their substrate. Such syndepositional collapse and accommodation creates widespread intrabed slumps, water escape textures and other soft sediment deformation features in the beds immediately above the dissolution horizon. Breccia clasts in such scenarios are typically contorted (early plastic deformation) and typically show rounded to crumbly edges.

In contrast, bed collapse after induration tends to create angular clasts and caprock collapse breccias dominated by structures indicative of more brittle collapse failure and sharp-edged angular clasts. This group includes trans-stratal joint and chimney stopes that may have tens to hundreds of metres of relief, as well as pervasive interstratal angular

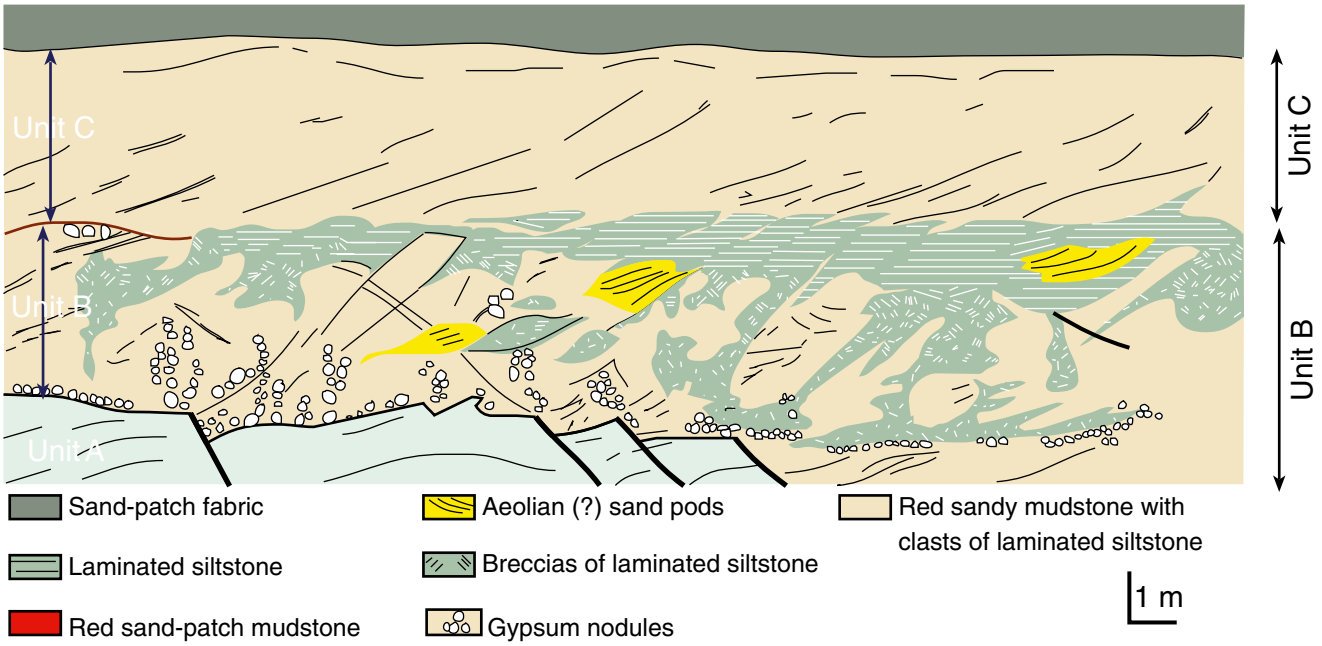

Fig. 7.28 Syndepositional collapse features related to dissolution of an underlying evaporite bed in the Lower Blomiden Formation (Late Triassic) near Blomiden, Nova Scotia. See text for discussion of units A–C (After Ackermann et al. 1995)

breccias derived from overlying strata, where the clasts show little or no evidence of internal deformation (Fig. 7.5). Stopes form in the rock above the growing salt cavities, as the roof collapses and accumulates in an aggrading cavern, maintained by ongoing dissolution of the salt. Fractures and faults form in the rock layers for some distance above and around stoped perimeters. Porosity and permeability created by this fracturing and faulting can provide pathways for late stage cements and can trap or transmit hydrocarbons and metalliferous fluids (Chaps. 10 and 15).

Early dissolution of a nearsurface evaporite tends to be a response to facies-controlled permeability corridors in the blanketing unconfined aquifers. Areas of preferential ingress into the evaporite bed are controlled by depositional permeabilities within the overburden (e.g. ingress beneath porous and permeable sand-rich fluvial channels versus less ingress beneath relatively impervious mud-rich floodplain sediments). In contrast, the hydrologies of later dissolutional systems tend to be more directional and focused by secondary permeability features. By then, the overlying and underlying beds are indurated and relatively impervious so that major zones of undersaturated infiltration or crossflow with the evaporite edges are controlled by joints, faults, fractures or reef crests, as well as regional tilting or sag. Undersaturated pore water arriving at the site of dissolution can be either from meteoric or basinal sources and enter from above or below the evaporite bed.

The feedback between early shallow salt dissolution and partially consolidated overlying sediment styles can be traced for over 35 km of the outcrop length in the Blomiden Formation (Late Triassic) of the Mesozoic Fundy rift basin of Nova Scotia (Ackermann et al. 1995). This unit exemplifies syn-dissolutional salt loss, which was induced by shallow groundwater freshening tied to fluvial sedimentation. Fluvial sands of variable thickness (unit C) lie atop a highly chaotic and slumped mudstone with evaporite nodules still visible in its lower parts (unit B; Fig. 7.28). The primary lamination in clasts in the chaotic mudstone unit preserves much of the evidence of syndepositional collapse of the evaporite substrate. It is characterized by highly disrupted bedding that is commonly cut by small (<0.5 m) domino-style synsedimentary normal faults. It also preserves evidence of downward movement of fines, of geopetal structures, of variable thicknesses related to local hollows after evaporite solution, and of irregular, partially faulted contacts with the overlying unit. Unit B is underlain by a normally faulted massive mudstone (unit A).

Although the thickness of the fluvial sandstone (unit C) is highly variable, the overlying flat-bedded mudstone exhibits only gentle regional dip, hence the bulk of the evaporite layer must have dissolved prior to the deposition of the flat bedded floodplain mudstones. Like unit B, the sands of unit C exhibit numerous soft sediment deformation features including; dewatering structures, convoluted bedding, kink bands, and convergent small-scale fault fans. The frequency and intensity of these features increases dramatically above low points in its base, showing unit C sands were laid down within local solution depressions or furrows that were still expanding as sediment was deposited. Unit B (the chaotic unit) is characterised by blocks of laminated claystone, which become increasingly disrupted and brecciated downward toward its base where locally abundant gypsum nodules are still preserved. Lenses and fissure fills of mudstone to coarse sandstone within the

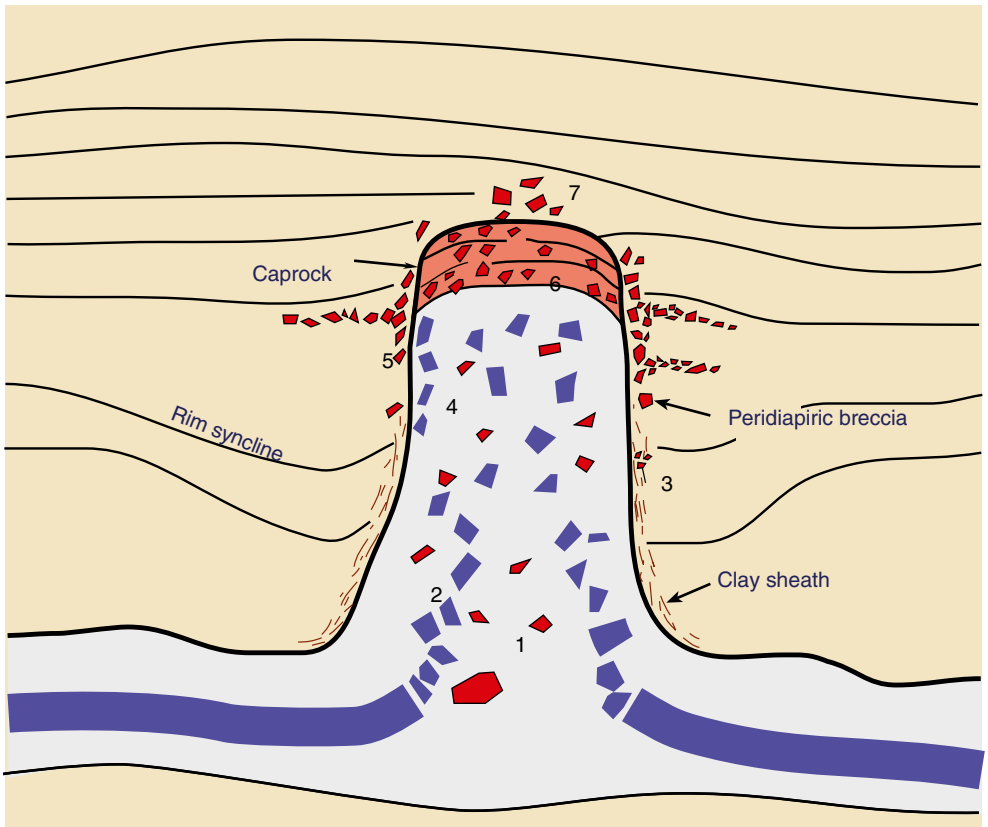

Fig. 7.29 Distribution of diapir associated breccias. (*1*) Slabs of anhydrite in granular halite; (*2*) Internal flowage breccia formed by dismemberment of competent internal beds; (3) Breccia pockets in "clay sheath"; (*4*) Transported flowage breccia of wallrock fragments incorporated into outer zones of stock; (*5*) Peridiapiric ablation breccia, extent is greater in zones of former salt glaciers; (*6*) Caprock breccia; (*7*) False caprock breccia, a dissolution breccia generated by salt collapse (After Laznicka 1988)

chaotic unit often entrain clasts of laminated mudstone originally derived from immediately overlying beds.

Both the chaotic unit and the overlying fluvial sands were deposited as an underlying evaporite layer underwent syndepositional subsidence and karst collapse. Groundwaters driving the dissolution were probably tied to the same river system that was depositing units B and C. The former presence of underlying evaporites is now solely indicated by residual gypsum nodules within the lower part of unit B (Fig. 7.28).

In contrast, breccias that form after induration of overlying strata tend to be combinations of interstratal and trans-stratal geometries with collapse breccia clasts that are made up of well-indurated angular blocks. Post-induration interstratal breccias tend to follow the lateral distribution of the evaporite bed from which they formed, while trans-stratal (transformational) breccias tend to cross cut the strata and form by a combination of chimney growth and overburden stoping (Fig. 7.29). Soft sediment deformation features are less pervasive in post-induration breccias and are typically restricted to intervals where insoluble residues accumulated in joint and fracture-defined fluid-filled cavities.

Post-induration interstratal breccia beds tend to have sharp flat bases and uneven, wavy to transitional blocky upper surfaces, as described earlier. If the dissolved evaporite was pure, with few intrasalt beds, the resulting rubble breccia unit is thin, but widespread. For example, a clean 100 m thick bed of salt may, when dissolved, leave behind a residue bed and rubble breccia that is no more than 0.5–2 m thick, but that residue may form a continuous marker horizon with a lateral extent of hundreds of kilometres. Core recovery from such intervals is often difficult. Even with good core recovery, recognising beds composed of little more than solution residues is difficult, they are easily mis- interpreted as unconformities, tectonites, or syndepositional intraclast breccias. Preserved evaporite indicators, such as "cauliflower" chert or calcite concretions, are one way to define the evaporite association of such breccias.

Spectacular breccia-filled trans-stratal solution chimneys focused on former positions of the Salina Group salts and influencing the overlying Detroit River Group distribution dominate Silurian outcrops in the Mackinac Straits area of Michigan and western Lake Erie (Carlson 1992; Black 1997). They are paleokarst features created by evaporite dissolution and joint-controlled stoping. There are three styles of breccia in the region: (1) megabreccia beds in which blocks up to several 100 m in size moved intact except for some minor tilting; (2) relatively thin intraformational or intrastratal breccia developed along the bedding planes both regionally and within layers in the megabreccia blocks; (3) thicker trans-stratal breccias extending vertically from a few feet to several 10s m and abutted by undisturbed bedded strata. The thickest trans-stratal breccias stope vertically up to 460 m and at one site the individual blocks have fallen 290 m.

Some solution caverns have recently been reactivated on a much smaller scale (Carlson 1992). But most of the intense evaporite karstification, chimney stoping and celestite replacement took place in the Late Silurian. Not all breccia chimneys reach the surface, and areas of this "blind" salt karst can only be located using geophysical techniques.

The evaporite dissolution features in the Mackinac Straits area of Michigan illustrate the multicyclic karstic signatures with multiple times of formation that typify the periphery of many evaporite dissolution zones of saline giants. At least three major evaporite dissolution events have created deep karst overprints in two zones along the northern Michigan Basin (Black 2012). Dissolution of outer margin Silurian evaporites resulted in the Mackinac Breccia during the early Devonian. Then rebound and exposure or a later, delayed brief basin rebound drove the development of surficial evaporate epikarst[7] in the middle Detroit River Group. This occurred before the next subsidence phase and renewed deposition of intracratonic sediments, which continued into Mesozoic. Hundreds of millions of years later, Pleistocene glaciation pumped fresh water into shallow Silurian and Devonian carbonate aquifers in the Michigan Basin and this in turn stressed various intracratonic beds via repeated glacial-induced loading and unloading. Buried early-Devonian paleokarst in the Detroit River Group focused the effects of hydrostatic pressure buildups along hydraulically open faults and fractures which first developed the ancient karst.

The current karsted zone in the Michigan Basin varies from totally removed evaporites and collapsed formations along the northern margin of the Detroit River Group subcrop, to an irregular still active evaporite dissolution front along the current salt edge, some 29–39 km further basinward. The last glacial retreat from the Lake Huron basin, approximately 10,000 years before present, opened and flooded the basin. The lake level dropped approximately 150 m in the Lake Huron basin to Lake Stanley stage at 10,000–7,500 ybp to approximately 58 m asl compared to the 177 m above sea level of present-day Lake Huron. This is likely the time when most of the visible collapse sinkholes in Northern Michigan formed. Some of these sink-holes have been identified beneath the waters of Lake Huron recently by subbottom profiling. Water venting from them, into the lake, has conductivity values ranging from 123 to 1,821 μS/cm, attributed to high levels of chloride and sulphate (Black 2012). A benthic ecosystem of anoxic chemosynthetic bacteria composed of biolaminites and filamentous bacteria grows in the vicinity of the vents. There are no known land springs from this system, which has an active swallow area of hundreds of square kilometres.

Diapiric Solution Breccias

Salt diapir (halokinetic) breccias are transtratal features that ultimately contain no salt, but outline a former diapir geometry. Diapiric solution breccias and their reworked debris aprons (salt ablation breccias) are forming today in and around at-surface salt diapirs in a number of areas worldwide, including the Arabian/Persian Gulf (Fig. 6.84; Table 7.4). Once the stem salt or its allochthon has dissolved, the only evidence of former flowing salt may be a few pseudomorphs after halite or calcium sulphate, either in the breccia clasts or in the interclast matrix. The breccia itself is typically an allochthonous assortment of angular clasts in a matrix made up of insoluble residues (sometimes called "rock flour"), which is typically dominated by finely crystalline carbonate, clay, sericite and chlorite. Classic examples, where little or no salt remains, outcrop extensively in the Mesozoic and Tertiary sediments of the La Popa Basin in Mexico, in the Neoproterozoic strata of the Flinders Ranges of South Australia, the Macdonnell Ranges of the Amadeus Basin of Central Australia, and in sediments caught up in the Damara Orogen and the Lufilian foldbelt of southern and central Africa (Table 7.4; Giles and Lawton 2002; Mount 1975; Lemon 1985; Kennedy 1993; Behr et al. 1983; Jackson et al. 2003). Some of the breccia blocks carried up from depth by flowing salt can be large (a kilometre or more across); they typically line up parallel to the salt stem edge or weld, or form a chaotic carapace at the exposed top of the former salt stem.

Diapiric breccias are always trans-stratal and clasts tend to be polymict associations of allochthonous fragments. Clasts of varying diameters are combinations of; (a) material that was once an intrasalt bed, (b) buoyed material that was plucked or was enclosed by flowing salt, and (c) material that was derived from the collapse of overburden as the active diapir deflated and dissolved (Fig. 7.29). The complex folding that accompanies salt flow means breccia bodies defining a former diapir are much less likely than bedded solution breccias to preserve original stratigraphic layering of any intrasalt beds.

Breakage and rotation of intrasalt beds begins once the encasing salt begins to move. Flowing salt can also pluck large blocks from strata adjacent to a salt wall or in contact with the flowing bed of the mother salt layer. Once caught up in flowing salt, the clasts are carried toward the surface to accumulate as breccia masses in stratigraphically higher regions of former salt, either in stems and feeders or spread out laterally across areas of former allochthons. Clasts often include metamorphic-grade minerals, such as magnesian-talc,

[7] Epikarst: pertains to the upper/outer layer of karstified rock in the unsaturated zone, immediately below the soil layer.

Exokarst: pertains to features found on a surface karst landscape, ranging in size from karren to dolines and subsidence bowls.

Endokarst: pertains to all features beneath the surface and hosted by a vertically layered karst system. It includes the full spectrum of underground voids and the dissolutional features present on the rock surfaces surrounding them. Klimchouk (2012) argues usage of the term endokarst should be expanded to include much hotter and deeper process sets that includes igneous and metamorphic fluids acting to create porosity at great depth.

Table 7.4 Areas of modern outcropping and subcropping diapiric salt karst

Modern at-surface diapiric salt karst	Age of mother salt	Reference
Cordillera de la Sal, Atacama Desert, Chile	Miocene salt	Fryer (2005)
Cardona diapir, Spain	Triassic salt	Lucha et al. (2008)
Vrancea Subcarpathian Hills, Romania	Miocene salt	Giurgiu (2005)
Mt. Sedom, Israel	Late Miocene-Pliocene, Sedom Fm	Frumkin (1998)
Zagros Mt. Diapirs, southern Iran	Infracambrian Hormuz Salt	Bruthans et al. (2010)
Qom diapirs, central Iran	Miocene, Lower Red Formation	Warren (2008)
Arabian/Persian Gulf, diapirs	Infracambrian Hormuz Salt	Kent (1970)

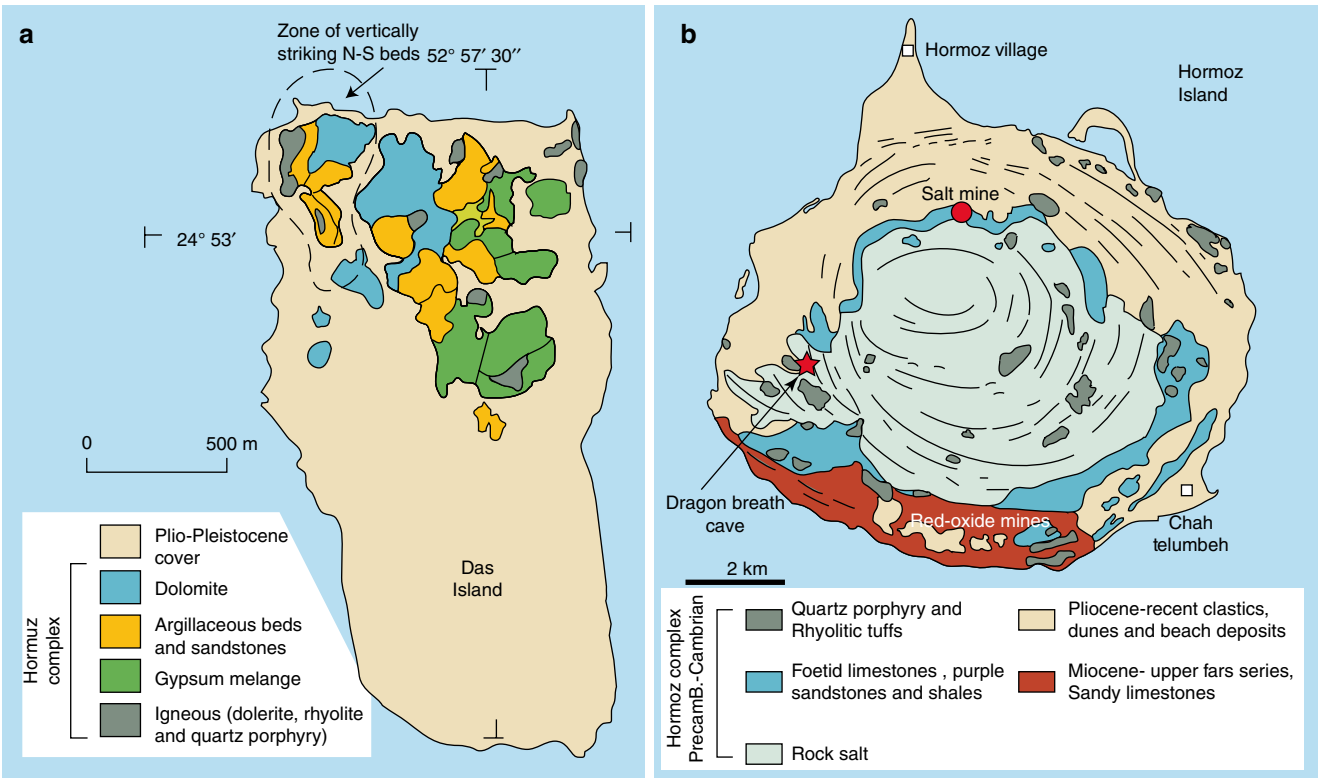

Fig. 7.30 Evaporite dissolution breccias on Gulf Islands cored by Hormuz Salt Series diapirs. (**a**) Das Island, showing chaotic nature of the Hormuz Complex that includes blocks of ferruginised and rafted material that are hundreds of metres across (After Kent 1987). Surficial geology is no longer visible in current satellite imagery due to construction of a refinery on the island. (**b**) Hormuz Island; still shows salt ridge cored curvilinear outcrop patterns due to shallow halokinetic salt subcrop and numerous blocks of Precambrian volcanics hundreds of metres across and carried to the surface by salt flow as is seen today in Qom salt fountain (After Hurford et al. 1984)

sodian-scapolite and dravite-uvite tourmaline, which likely indicate clasts were carried from depths where the metamorphic/diagenetic grade was higher than the current stratigraphic level of the breccia. Solution breccia emplacement in the Damara Orogen also encompasses processes of fluidisation and cataclasis within mobile evaporite units in thrust belts and welds. These breccias were actively forming at greenschist and higher metamorphic grades and so lie outside the sedimentary focus of this chapter (see Fig. 14.2).

Recognising the occurrence of higher temperature and metamorphic grade indicators is useful when a core or cuttings are recovered from a well that has intersected a breccia body and an attempt is made to distinguish interstratal breccias and transtratal chimneys from diapiric breccias and welds, as well as from associated allochthon debris aprons. Halokinetic breccias can also outline former thrust or glide planes after the dissolution of the original halite or calcium sulphate horizons that lubricated the thrust. Such thrust-weld breccias are termed rauhwacke and are discussed later in this chapter.

Diapiric dissolution breccias define areas above subcropping salt plugs in numerous islands in the Arabian Gulf, in what is one of the world's largest salt provinces and also one of its largest hydrocarbon provinces. Most of these diapir-cored Gulf Islands are plug ruins that have experienced little salt movement since being squeezed by the mid Miocene collision of the Arabian and Iranian plates. Today these regions of outcropping Hormuz Complex are heavily eroded and largely covered by Neogene shoal water carbonates and marine-cut platforms, as in Das and Hormuz islands (Fig. 7.30a, b).

These diapiric breccias are the outcrop expressions of what is locally called the Hormuz Complex or the Hormuz Salt Series, from the type section on Hormuz Island where the breccia is still actively forming (Fig. 7.30b). The breccia complex is a polygenetic assemblage of lithologies that includes both nonevaporite blocks carried along by salt flow and remnants of the supporting salt and gypsum/anhydrite matrix. The Hormuz Formation at the mother salt level was originally deposited as a basinwide evaporite near the Precambrian/Cambrian boundary and has since been mobilised numerous times into salt structures that intersect various levels of the overlying stratigraphy (Kent 1987; Talbot 1998). The range of clasts in the Hormuz Complex is diverse, but uniform over most of the Gulf islands. In none of the outcropping breccias are there any clasts derived from the cubic kilometres of indurated Palaeozoic and later sediment, through which the salt passed on its passage to the surface (Fig. 7.29; Kent 1970, 1987). One of the most characteristic raft lithologies is a black foetid finely laminated and bedded dolomite that is often coarsely recrystallised and shows evidence of deep burial diagenesis. It was deposited in the same hypersaline setting that was also responsible for the deposition of the thick salt beds that became the Hormuz Complex. Similar foetid dolomite blocks characterise megabreccias in regions of outcropping diapiric breccias of the Neoproterozoic Ara Formation in Oman (Peters et al. 2003). In the South Oman Salt basin these dolomites are still encased in salt and act as self-reservoired and self-sourced carbonate slivers sealed in salt (Fig. 10.67). Siliciclastic blocks composed of sandstones and siltstones are also widespread in the Arabian Gulf breccias, they are mostly reddish, grey or greenish grey and variably indurated. Throughout the region, both dolomites and siliciclastics can outcrop as spectacular rafted blocks up to several 100 m across (Fig. 7.30).

Igneous rocks are another important component of rafted megabreccia blocks in many diapiric breccias worldwide (Wilson 1975). In Gulf island breccias the igneous rafts tend to be dominated by acid tuffs (trachytes and rhyolites) along with acid intrusives and dolerites (Fig. 7.30; Kent 1970). On the Iranian mainland the igneous rafts in namakier residues are referred to as "greenstone" blocks, as they are dominated more by basalts and dolerites. Throughout the salt-cored Gulf islands and on the Iranian mainland, large volumes of red specular haematite characterise outcrops of the Hormuz Complex. Some rafts of silicified shale are crosscut by malachite-stained joints. On Hormuz Island the outermost ring of the salt plug itself is made up of haematitic tuffs, locally so rich in iron oxide that it is mined as a source of pigment (Fig. 7.30b; Kent 1987). The significance of Fe-rich phases in terms of ferroan chloride brine haloes and metal transport in halokinetic provinces is discussed further in Chap. 15 and in Warren (2000b, 2008). Salt-buoyed and salt-encased xenoliths exposed in salt mines in Five Islands region of Louisiana have been used in the salt-covered region of the Gulf of Mexico to determine the transitional nature of the subsalt igneous basement (Stern et al. 2011). Other than these xenoliths there are no other samples to study of the deep Jurassic basement.

Texturally near-identical Neoproterozoic diapiric megabreccias, breccias and breccia trains crop out in the Flinders Ranges of South Australia (Figs. 7.31 and 7.95b; Dalgarno and Johnson 1968). Many breccias in anticlinal cores of the Flinders ranges halokinetic terrane are still located at or near the level of the mother salt bed (Callanna Beds) with current outcrop patterns largely indicative of the positions of deeper basement faults (Backé et al. 2010). Today, they define the polytectonic remnants of former autochthonous salt pillows or glide planes and inversion structures, rather then true salt-cored diapirs. Some structures, such as the Oratunga and Wirrealpa diapirs, still preserve evidence of their earlier formative extension phase and show subcircular patterns of outcrop and breccia wings at allochthonous stratigraphic positions well above the level of the original mother salt bed. Almost all the transtratal breccias line up along major regional shears and faults (welds) surrounded by jostling depopods or minibasins, indicating that the mother salt bed was flowing as the basin was under extension. The salt was then remobilised during the inversion phase and the transition from haselgebirge to rauhwacke textures (Fig. 7.31a). Lemon (1985, 1988, 2000), Dyson (2004) and Rowan and Vendeville (2006) clearly illustrate synkinematic controls on sedimentary facies and thicknesses adjacent to many of these breccia masses in the Flinders Ranges (Fig. 7.31b, c).

Diapiric breccias in Flinders Ranges are heterogenous, with polymict clasts set in a strongly folded and disrupted matrix, dominated by weathered pale-grey siltstones and fine sandstones. Clasts are mixtures of dolomites with gypsum and anhydrite pseudomorphs, dolomitic sandstones, siltstones and sandstones with displacive halite casts along bedding planes, and angular igneous fragments of diabase and basic volcanics, including amygdaloidal basalts (Lemon 1985). The margins of many former diapirs in the Flinders Ranges are also characterised by numerous sub-economic copper shows in a haematitic matrix, much like the copper shows in the Gulf Islands.

Banded and aligned fabrics of clasts in the breccia masses of the Flinders Ranges diapirs indicate that shaping, disruption, mixing, and alignment of clasts occurred during salt-buoyed flow. Rafts showing coherent flow alignment can be blocks of megabreccia up to 500 m across (Fig. 7.31b, c). Long axis alignments of large raft blocks near the edge of a breccia mass are frequently near vertical and aligned subparallel to the diapir margin. Rafts nearer the centre of the breccia mass are more randomly distributed, a feature that indicates frictional alignment of large clasts near the diapir edge at the time salt was flowing or flow was collapsing.

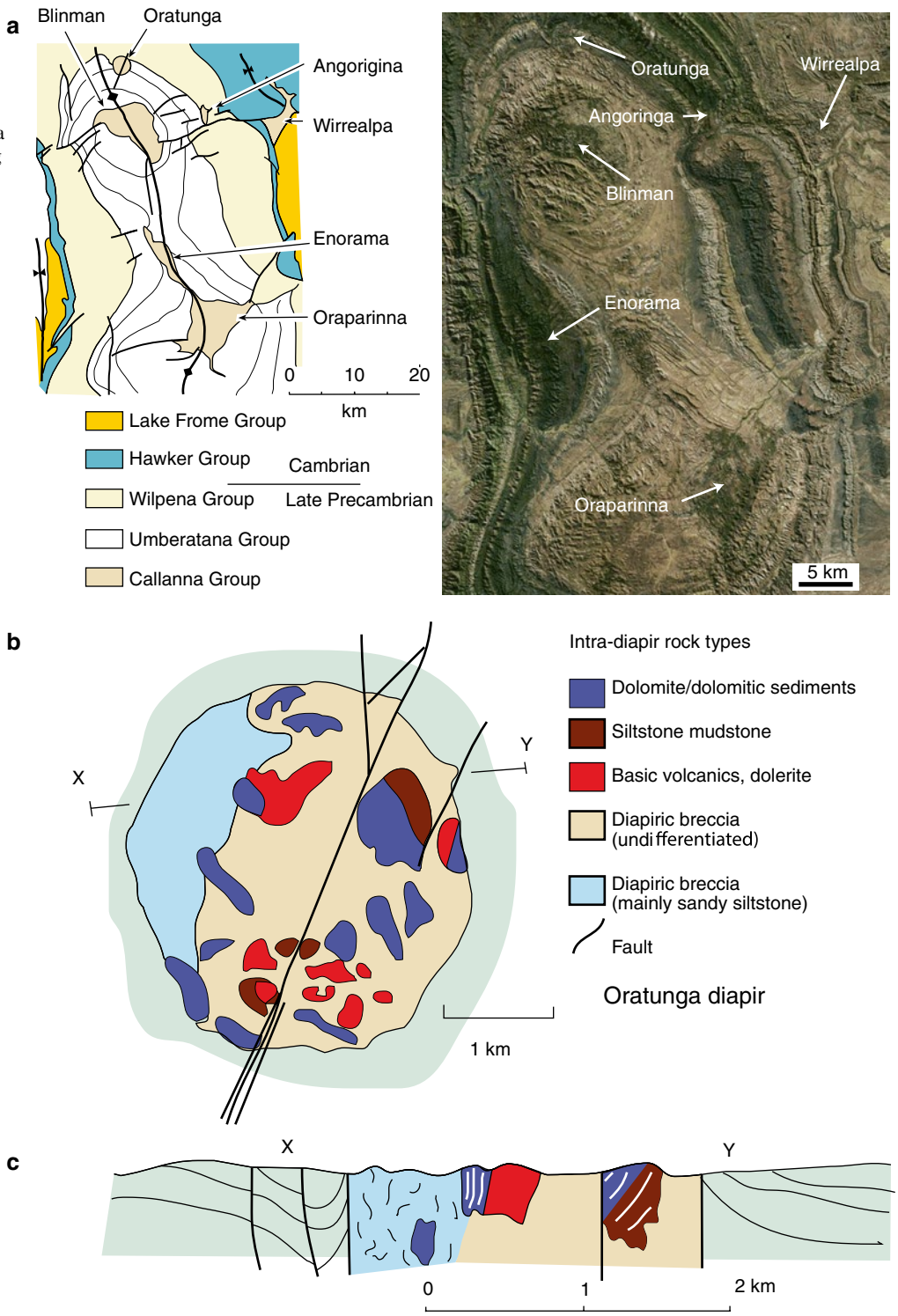

Fig. 7.31 Halokinetic breccias, Flinders Ranges, Australia. (**a**) Regional distribution of halokinetic breccia in the Callanna Formation. (**b**) Distribution of large megabreccia lithoclasts or rafts in outcropping breccia matrix that define the Oratunga Diapir. (**c**) East-west cross section of Oratunga Diapir (Modified from Lemon 1985)

There is similarity between the size and lithology of rafts found in Neogene diapir crests in the Arabian Gulf and those in breccia masses in the Flinders Ranges. Steeply dipping bedding in rafts located near the diapir edge is also a feature of both areas and suggests flow alignment (Fig. 7.30 and Fig. 7.31b).

Matrix minerals in the Flinders Range's breccias include: carbonate, chlorite, feldspars (both detrital and authigenic), haematite, magnesio-riebeckite, quartz, stilpnomelane, and talc. Mount (1975) interpreted them as zeolite facies minerals formed during breccia emplacement via reactions involving hypersaline fluids. Although all the at-surface breccias

lack preserved salts he argued conditions during breccia formation were aqueous, low pressure, and hypersaline. Mineral-forming reactions occurred in an oxidative low-grade metamorphic environment replete with CO_2 , with open system fluid throughput and low temperatures (150–300 °C). He concluded this palaeohydro-chemical system had strong affinities to natural hydrothermal and geothermal systems. It indicated a later deeper burial stage comparable to the current salt-filled diagenetic systems of the Iranian namakiers. The matrix minerals formed as solution flour at a time when most of the salt had already dissolved from the system and only the breccia bodies remained to outline the former salt geometry.

The late extension-stage geometries shown by the halokinetic breccias of the Flinders Ranges also means that where the crestal rather than the stem or feeder portions of the diapir breccia crop out they tend to show classic "falling diapir" geometries with suprasalt depopods, along with oversteepening related to subsequent compression and diapir squeezing (Fig. 6.80). Examples include the Wirrealpa and Oraparinna diapirs (Dyson 1998, 1999). The falling diapir stage is characterised by crestal collapse and the formation of fault-defined graben thicks in the overlying sediments (Fig. 6.93b). As the diapir was collapsing, the underlying salt was thinning and dissolving. This facilitated the growth-fault focused escape of formerly confined basinal fluids on to the seafloor. This mechanism explains the formation of large fault-fed baryte masses atop many former diapir crests, along with the various small copper shows found in association with the diapir breccia margins (Chap. 13; Warren 2000b).

Mount (1975) noted breccia/host rock contacts were invariably abrupt and coincided with planes of weakness in the host strata. The breccia edge – country rock contacts match across some diapir stems, despite synformational sculpting and quarrying by invading diapir material. Adjacent host strata were rarely brecciated against a diapir, illustrating again the passive nature of the intrusion. His observations help explain why material from overburden strata located adjacent to a rising salt stem is not broken into rafts and transported to the surface. Salt emplacement is predominantly a passive process driven by the flow of pressurised salt into pre-existing planes of entry. Where contact deformation has occurred, it usually predates diapirism and was due to glide plane faulting that then controlled subsequent breccia geometry. Mount (op. cit.) termed this style of contact 'permitted intrusion.' He argued it occurred under extension of the cover or overburden, perhaps induced by regional extension. Alteration of the host rock adjacent to contacts was absent but for minor dolomitisation and sideritisation in certain areas.

Instead of using models of forcible injection for diapir emplacement that prevailed in the 1960s and 1970s in the Flinders Ranges, Mount (op. cit.) used the outcrop geometries to stress the passive nature of salt flow into tensional structures. He concluded that "diapir" in terms of the then popular notion of active piercement, was not the most appropriate term to explain breccia emplacement in the Flinders Ranges. His understanding of the dominantly passive nature of the diapiric process preceded by almost two decades our current models of brittle overburden atop weak flowing salt. In 1975 he stated, "… The overburden was relatively brittle, its weight the prime driving force to the intrusions. Mobility of source material, rather than factors such as density, was paramount to diapirism. The mobility is explained by the former presence of saline evaporites in the interstices of the breccias."

Diapiric Versus Salt Ablation (Retreat) Breccias

Diapiric collapse breccias are classified as a type of evaporite solution breccias in the preceding discussion and are typically considered the result of subsurface dissolution of a diapiric feature that retains the outline of the original subsurface salt stem or allochthon. But this definition does not encompass the notion of breccias created by the leaching of an at-surface salt allochthon or namakier, nor does it include breccia created by the dissolution of salt-lubricated thrust sheets (rauhwacke; Table 7.5). When a namakier shrinks it does so via at-surface dissolution of the salt mass, much in the same way a glacier retreats as it melts (Fig. 7.21). Likewise, the outer edge of a salt glacier expands and contracts like the outer edge of an ice glacier. When the salt mass retreats it leaves behind a jumbled mass of material it once buoyed, which can include megabreccia blocks tens of metres across, as well as the insolubles of its carapace and insoluble intrasalt layers. These chaotic breccias are similar to a diapiric collapse breccia, but contain a much more polymict assemblage of clasts than an evaporite collapse breccia (after bedded salt) and often show evidence of mechanical reworking of portions of the breccia material by waves or currents. A separate term is probably needed to distinguish them from the more general term diapiric breccia; I call them salt ablation or salt-retreat breccias (Table 7.5).

Salt ablation breccias are forming today atop and peripheral to the dissolving edges of retreating namakiers in the Zagros of southwestern Iran (Fig. 7.32; Talbot and Jarvis 1984; Bosak et al. 1999). Wherever an active but shrinking salt tongue subcrops or lies beneath a dissolution-derived gypcrete carapace, the clasts accumulate by breakup of the soft overburden and by stacking of fragments and rafts formerly held within the now dissolved salt matrix. The resulting namakier breccia is composed of a coarse, unsorted, heterolithic (polymict) rubble supported by a fine-grained calcareous matrix dominated by solution flour. This material can be mixed with fluvial and alluvial material (note the fans

Table 7.5 Comparison of salient features for separating the main types of breccias created by dissolving evaporites

Feature of interest	Evaporite collapse breccia (stratiform after bedded salt)	Evaporite collapse breccia (transtratal after diapiric salt)	Salt ablation (retreat) breccia (stratiform after an at-surface allochthon)	Rauhwacke breccia (transtratal dissolution residues) from a salt-lubricated compressional thrust sheet(s)
Timing of brecciation	Subsurface	Subsurface	Can be at-surface or nearsurface	Subsurface and telogenetic
Overall shape of unit	Stratiform (sometimes with local chimneys) with passive base	Transtratal (includes salt and fault welds), shale sheath drag zone	Stratiform with disturbed lower contact (former gumbo)	Transtratal (regional extent) defines salt-influenced thrust wedge geometries
Diversity of breccia clasts	Upward transition from low-polymict to monomict (crackle)	Polymict from intrasalt layers and plucked subsurface material	Polymict intermixed with surface sediments (e.g. fluvial, alluvial, reef)	Polymict from intrasalt layers and plucked subsurface material
Metamorphic grade of clasts in breccia	Matches adjacent sediments	Higher than adjacent sediments	Higher than adjacent sediments	Higher than adjacent sediments (fluid focus and squeezing can create alteration halo)
Vertical stacking in the breccia mass	Broadly matches the original stratigraphic order, even in any stoped transtratal chimneys	Chaotic (salt flow churns clasts along diapir stem then via dissolution and welding)	Chaotic for salt-carried clasts, but more cover sediment toward its top (e.g. reef carapace on blocks)	Flow aligned in thrust sheet can become less ordered due to telogenetic collapse
Image logs and seismic	Discernible in image log but ambiguous, can be confused with stratiform conglomerate bed, etc. Typically mapped as an unconformity in seismic.	Discernible in image logs, but ambiguous, can be confused with tectonic breccia. Seismic geometries are characteristically transtratal.	Discernible in image logs, but ambiguous, can be confused with stratiform conglomerate. Seismic geometries (wings and tongues) are characteristic but difficult to resolve. Features are transitional or subcomponent of diapiric breccias.	Discernible in image log especially by consistent dips shown in parallel flow textures in structurally controlled laminar anhydrites preserved in subsurface thrust sheets
Examples	Cretaceous Kirschberg breccia (Zahm and Loucks 2011)	Flinders Ranges diapirs (Backé et al. 2010)	Zechstein of onshore Germany (Mohr et al. 2007)	Western margin of South Oman Salt Basin (pers. obs.)

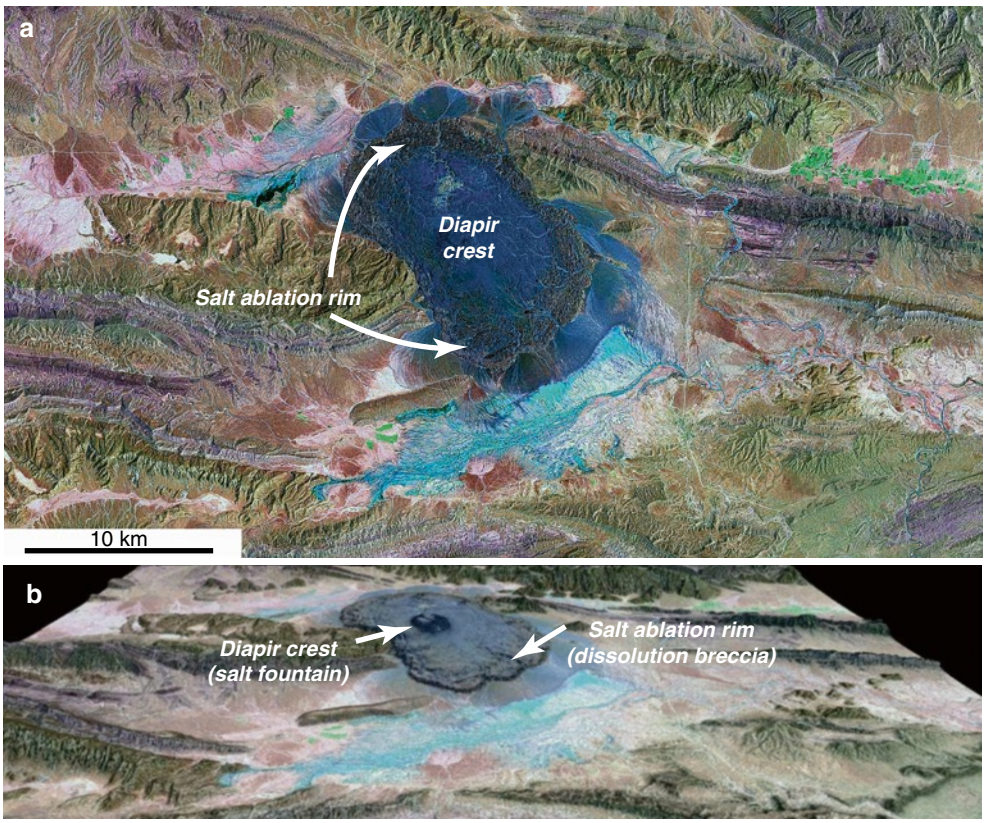

Fig. 7.32 East Mazyjan diapir, (Iran; 27.98 N, 54.91 E). showing the active salt fountain crestal region passing centripetally out to salt ablation rim with associated salt ablation breccias. (**a**) Plan view. (**b**) Lateral view using DEM overlay on Landsat image (After Warren 2008)

fed by alluvial streams that cross the ablation zone in Fig. 7.32a) or marine carbonate debris from times when the sea encroached on the salt tongue.

Ongoing dissolution of the namakier leaves behind a rubble moraine at the level of the former salt allochthon (Fig. 7.21). Thus, salt ablation breccias associated with salt cores of the various island diapirs of Arabian Gulf are jumbles of exotic material carried to the surface by upwelling salt, which is then combined with the disrupted remnants of the Neogene marine carbonate shoals and buildups that once covered earlier now-dissolved salt tongues (Hormuz Complex). The mixing of contemporary sediment (alluvial or marine) with salt-buoyed megabreccia blocks and insolubles in the salt, and the stratiform circum-stem or circum-weld nature of its occurrence, is what distinguishes a salt ablation breccia from a diapiric breccia formed by subsurface salt dissolution (Table 7.5).

Breaking out the age of the former cover sediments within buried salt ablation breccias is useful in attempting to time episodes of at-surface salt in Phanerozoic successions adjacent to former salt stems. Such a combination of marine, fluvial and cave sediments, along with karst phenomena including dissolution breccias was studied and dated in the Namakdan diapir on Qushm Island, using a combination of ^{14}C, U-series, and OSL methods (Bruthans et al. 2010) The Namakdan diapir hosts the world's longest salt cave (3 N Cave; 26.612 N, 55.508 E). The main factors influencing the diapir morphology are; sea-level oscillations, uplift rate of the diapir and its surroundings, and erosion. Although the diapir uplift rate has been constant for the last 50 kyr (≈4 mm/year at a distance 600 m from the diapir edge), the uplift rate decreases with the distance from the diapir centre. Drag-induced host rock deformation extends for ≈ 300 m from the outside edge of the diapir, and host rocks in this zone have an uplift rate of 0.4–0.6 mm/year, which is two to three times greater than the regional uplift rate. Based on known sea-level oscillations, radiometric dating, and geological evidence, the Namakdan diapir was repeatedly flooded by seawater between 130 and 80 kyr BP. At that time a submarine residuum, composed mainly of gypsum and dolomite, formed cap rock and its breccia on the water-covered parts of the diapir. After 80 kyr BP, surficial drainage network and karst development started. Blind valleys and their corresponding cave systems evolved continuously for 20–30 kyr (see later). Between 9 and 6 cal kyr BP the rate of sea-level rise exceeded the Namakdan diapir uplift rate by the factor of 3. As a consequence there was upward incision of cave streams and gravels filling blind valleys near the former seashore. Cave passages, accessible today on the Namakdan and Hormuz diapirs, started to form 3–6 cal kyr BP when sea level stabilized and downward stream incision began. Older cave levels are still preserved, but are mostly filled with sediments and salt precipitates (see later).

Belous et al. (1984) described reworked breccia trains (salt ablation breccias) composed of fragments of Devonian basalt and limestone at several stratigraphic levels in sediments surrounding the Late Palaeozoic Adamovsk salt stock in the southern Ukraine. They attributed breccia trains to lateral redeposition of salt-lifted blocks during periods of stock unroofing, possibly via a salt glacier mechanism. Similarly, drilling in 1991 in the Tapley Hill Formation on the flank of the Blinman Diapir (Flinders Ranges, South Australia) intersected an anhydrite-cemented breccia, with most clasts not derived from the enclosing shale (Cooper 1991). The intra-Tapley breccia is interpreted as a salt ablation breccia, it is a residue of a salt glacier once flowing across the Neoproterozoic seafloor under a relatively deep water mass. Recognition of numerous salt ablation breccia levels in circum-stem positions about the Pinda and Wirrealpa structures in the Flinders Ranges, South Australia, led Dyson (1998, 2004) to describe the precursors to the current breccia- defined outlines as "Christmas-tree" diapirs, a sedimentary origin that is somewhat different interpretation to that illustrated in Fig. 6.45.

Salt-Cored Thrust and Fold Breccias, Rauhwacke and Orogeny

Rauhwacke horizons are the weathered and leached remnants of what were once 'weak' salt-entraining tectonised layers (Jeanbourquin 1988, 1994; Warren 1999). Under stress, their evaporitic precursors acted as rheologic inhomogeneities providing surfaces of décollement during orogeny. Halite, or sometimes anhydrite/gypsum, are the main lubricants during the formation of stratiform tectonite or décollement layers. The inherent lack of strength of halite or anhydrite/gypsum under stress, when compared to other lithologies, focuses the greater part of the detachment, fold or thrust plane movement into the salt-entraining interval, which can also move salt into higher levels in the thrust sheet (Chap. 6).

Rauhwacke are evaporite solution breccias (Table 7.5) that define outcrops and subcrops of evaporite-lubricated thrust-planes and have been described from the Appalachians, Jura Mountains of Switzerland, the Atlas Mountains of Morocco, the Zagros and the Salt Range of Pakistan (Davis and Engelder 1985; Som-maruga 1999; Jadoon and Frisch 1997; Alavi 2007; Fudral et al. 2010). Jordan and Nuesch (1989) and Jordan et al. (1990) describe deformed flow-aligned anhydrite textures in décollement horizons preserved in tunnels intersecting the main Alpine thrust planes. Similar features occur in laminar anhydrites in thrust sheets along the western margin of the South Oman Salt Basin (pers. obs.). In both cases these features are typified in wells by consistent flow-annealed dips in the anhydrite (as seen in image logs) that contrast strongly with the highly fractured

patterns in the nonevaporite lithologies making up the footwall and hanging-wall lithologies.

These laminar anhydrites are deeper less-leached equivalents of near-surface zones where meteoric waters create rauhwacke from their evaporitic tectonite precursor. That is, rauhwacke units are the weathered outcrop expressions of evaporite-lubricated thrust planes, glide planes and detachment terranes within orogenic belts. In some older studies, the rauhwacke itself was considered to have facilitated thrusting. In other, seemingly conflicting studies, rauhwacke was considered to be obviously nontectonic as it could contain channel fill sediments, parallel lamination, cross-lamination, graded bedding, clastic dykes and other sedimentary structures. Now we know that much of this confusion was created by a lack of understanding of its evaporite genesis and poor definition of the term itself. An evaporite-lubricated thrust horizon or décollement is where the rauhwacke protolith forms. Subsequent weathering and mechanical reworking of the thrust horizon, first in subcrop and then outcrop, created rauhwacke layers with sedimentary structures. That is, rauhwacke is herein defined as an exhumation-driven post-thrusting evaporite dissolution/alteration overprint on a former salt-lubricated thrust or tectonic melange. Erosional unroofing to the level of the evaporite-facilitated thrust creates rauhwacke, which can then be reworked by fluvial and other surface processes. Rauhwacke is an evaporite dissolution overprint, it is not the cause of the thrust event.

Conceptually, rauhwacke as a process overlaps with those that create both salt fold and fault welds and in some situations may have once fed salt into what are now salt ablation breccias in other cases its precursor was a halite tectonite or salt lubricated thrust associated with halite mylonites and "haselgebirge" (Leitner et al. 2011). Rauhwacke typically forms a dissolution residue in the nearsurface and at outcrop as the more soluble evaporite components are leached from an unroofed thrust breccia, or deeper in the subsurface as the sheared evaporite and its surrounds are metasomatically converted to less soluble salts, such as calcite spar or dolomite. Halite is typically a major component at depths where translatent thrusting occurred, but was subsequently dissolved to leave behind deformed anhydrite at shallower depths. Rauhwacke breccias in outcrop are dominated by carbonate and clastic fragments in a cataclastic matrix. Boxwork and cellular honeycomb textures, so common in rauhwacke horizons, are the outcrop expressions of pervasive weathering of an evaporite precursor.

As well as the tectonite specific usage of rauhwacke, the term is sometimes still used interchangeably with the French terms cornieule or cargneule. In this broader sense of usage the term rauhwacke describes a porous or cavernous carbonate sedimentary rock (especially a cellular dolomite), with angular cavities filled with soft, friable, evaporitic residues that easily dissolves or falls out to leave a rough, corroded and fretted angular surface (e.g. Schreiber 1988; Fudral et al. 2010). This less specific usage is associated with widespread textures indicating preferred dissolution of dolomite or evaporite clasts leaving behind the surrounding calcite cement. Evaporite boxwork or cellular or honeycomb fabric, all nongenetic terms, and not rauhwacke should be the preferred descriptors when angular salt solution textures cannot be tied to décollement.

Surface-related karsting of different tectonised protoliths forms structurally and geometrically distinct types of rauhwacke in the Swiss Alps. Schaad (1995) identified two end members in rauhwacke outcrop in the region (Fig. 7.33a, b): (a) dolomite-bearing gypsum, and (b) gypsum-bearing dolomite. Dolomite-bearing-gypsum rauhwacke develops as karst-fill sediment within the thrust plane, and is typified by unstructured, often polymictic units, with geometries that reflect the shape of the precursor karst cavity. In contrast, gypsum-bearing dolomite rauhwacke makes up stratiform geometries that are dominated by dolomite breccias with crackle to mosaic textures. This form of rauhwacke is a solution-collapse breccia developed after the solution of widespread tectonised once halite-rich evaporite beds and salt masses. Sometimes, karstification of thrust plane evaporites is aided by synformational fluvial or fluvioglacial processes that are focused into valley depressions created by salt edge retreat, much in the same way as gently-dipping evaporite beds dissolve in the near subsurface. Pomoni-Papaioannou and Karakitsios (2002) recognise similar features to Schaad (*op. cit.*) in the rauhwacke horizons that define major evaporite (Carnian) lubricated thrusts in central western Crete and the Ionian zone of the Greek mainland (Fig. 7.33c). They go on to note that rauhwacke can be observed for more than 700 km along the outcropping base of the external nappes of the Hellenides.

Most of the deformation/lubrication in the precursor horizon to a rauhwacke breccia comes from the unique Newtonian flow properties of halite. But there is an under appreciated aspect of gypsum flow in a dissolution zone that may also contribute to the deformation in a rauhwacke horizon. Gypsum tends to deform more rapidly when bathed in increasingly saline solutions (de Meer and Spiers 1999). This means that where an exhumed anhydrite unit has converted to telogenetic gypsum, those parts of the gypsum subject to crossflow by increasingly saline brines are more susceptible to ongoing deformation.

As with all evaporite solution breccias, much information relevant to the rauhwacke protolith must be inferred rather than directly observed at outcrop. But in some relatively unleached thrust windows in the European Alps there are transitions between salt-cored tectonite protolith and rauhwacke that are still preserved as subcrop and even occasional outcrop. In the Austrian Alps, Spötl (1989a, b) describes

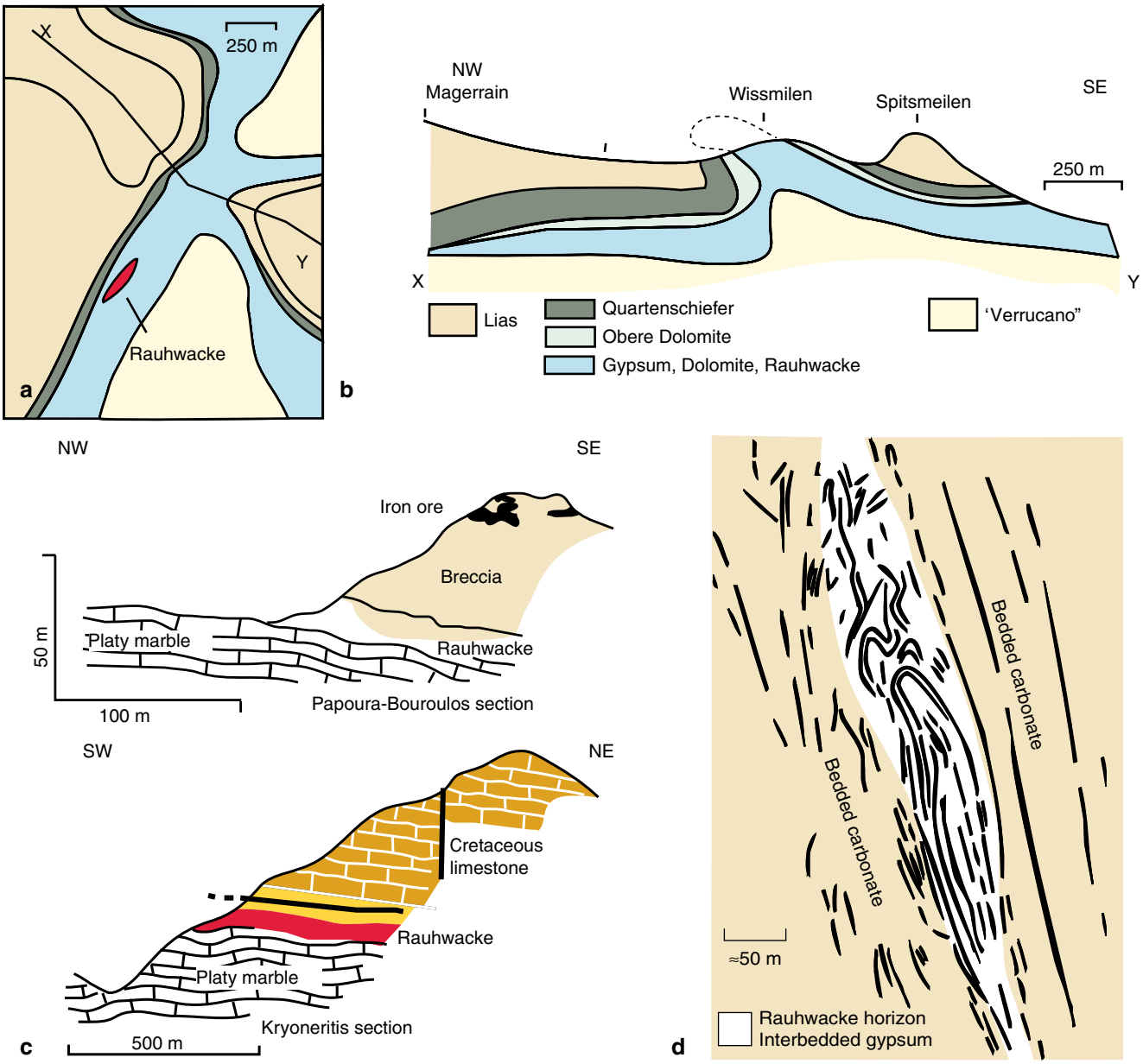

Fig. 7.33 Rauhwacke. (**a**) Plan view of rauhwacke developed atop subcropping gypsum (After anhydrite) in thrust décollement of the European Alps (From Schaad 1995). (**b**) Cross section X-Y, with position shown in 7.33a. (**c**) Geological sections in the Rodakino region, Crete showing development of rauhwacke along décollement, which was lubricated by Triassic evaporites (After Pomoni-Papaioannou and Karakitsios 2002). (**d**) Outcrop trace showing increase flow deformation in a rauhwacke layer (formerly halite-rich) in the Gillen Member of the Neoproterozoic Bitter Springs Formation, Amadeus Basin, central Australia (After Lindsay 1987)

tectonised evaporitic breccias that were created, and are still preserved, in the faults and thrusts of the Upper Permian-Lower Triassic Haselgebirge Formation. All these salty tectonic breccias, with 30–65 % halite, once flowed and fragmented during the Alpine Orogeny (Middle Cretaceous – Late Eocene) and are part of a giant regional tectonic melange created when Mesozoic salt was caught up in a continent-continent collision belt (Fig. 7.34; Schorn et al. 2013a, b). The Haselgebirge Fm. was also involved in tectonism well before the Alpine thrust event. The subduction or tectonism driving this salt-cored thrust melange was tied to the closure of the Meliata-Hallstatt ocean to the south of the Northern Calcareous Alps and may have preceded the main Alpine Orogeny by 50 million years (Spötl et al. 1998). Many of the Haselgebirge outcrops are sheared compressional remnants of earlier formed rift-stage salt walls and diapirs (Schorn and Neubauer 2014).

Haselgebirge Fm. breccias contain polymict clasts (from cm to several tens of metres in diameter) that in the subsurface are embedded in a halite matrix (Spötl et al. 1998;

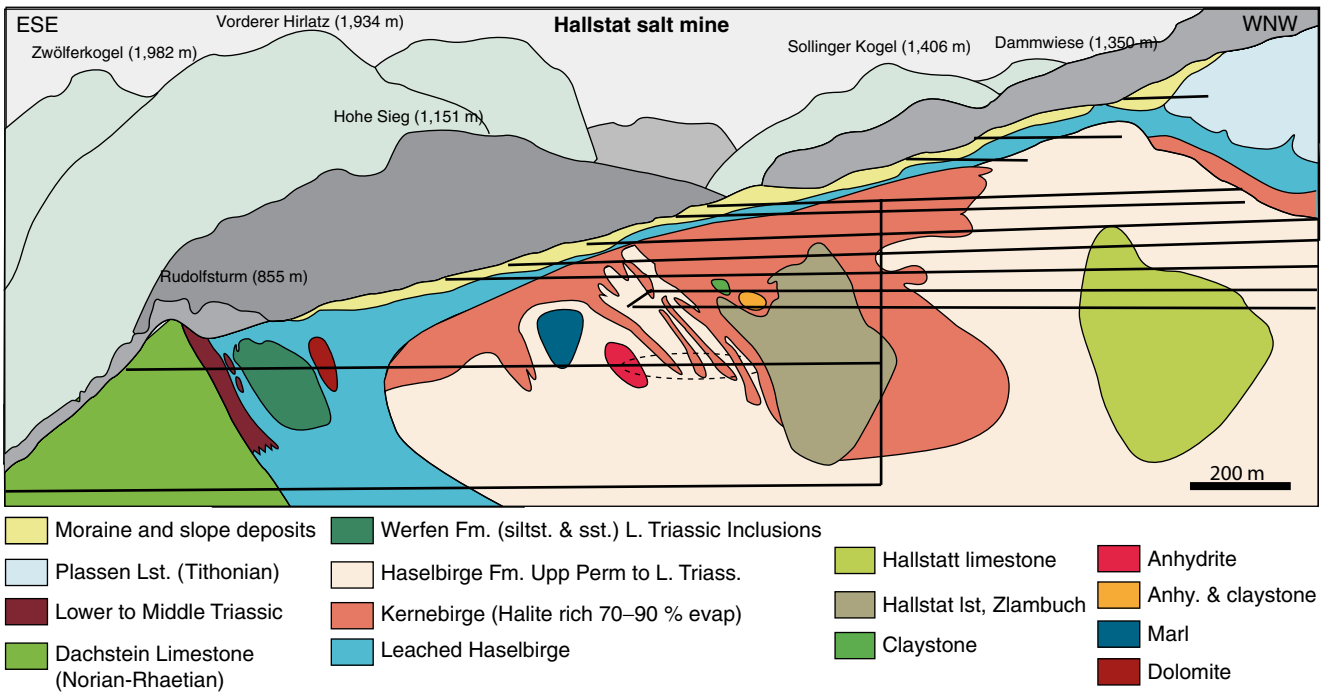

Fig. 7.34 Simplified ESE-WNW-trending profile through the Hallstatt salt mine area (After Schorn et al. 2013b)

Leitner et al. 2011). The breccia matrix contains varying amounts of clay and silt impurities[8] (normally in the range of 15–55 %) plus minor quantities of anhydrite. In addition to clasts form by the tectonic breakup of the initial intrasalt beds (shales, silts, sandstones, anhydrites, scarce pyroclastic rocks), while nappe transport drove huge blocks of faulted Mesozoic carbonates, marls and shales into the underlying visco-plastic (halokinetic) Haselgebirge Fm. Like their brecciated surrounds, these partially or completely isolated overburden blocks show evidence of severe strain that includes; internal fragmentation, stretching, translation and rotation. Overburden pressure seems to have controlled the degree of brecciation and slickensides within these detachments.

In the subsurface the tectonised "Haselgebirge" breccias sit within intervals of recrystallised halites and anhydrites, still preserving what at first sight appears to be mm-cm scale depositional lamination. Closer inspection of the layered halites and anhydrites defines preserved isoclinal noses and overfolds, along with flow aligned, pervasively recrystallised halite, clearly illustrating the tectonite origin of the laminae (Spötl 1989a; Leitner et al. 2011). Pervasive salt flow and recrystallisation means most relics of primary structures in the halite beds are destroyed or strongly deformed. Recognisable remnants of primary sedimentary features in the Haselgebirge Formation are preserved only within blocks and fragments composed of carbonate and anhydrite. For example, Leitner et al. (2013) describe partially-deformed syndepositional skeletal halites in a mudstone matrix in a clast that is now pseudomorphed by anhydrite and polyhalite. $^{40}Ar/^{39}Ar$ analyses date the polyhalite from within a number of deformed halite hoppers at 235–232 Ma (Middle Triassic), some 20–25 Ma after sedimentation. That is, the polyhalite replacement took place pre-deformation, fed by crossflowing brines at relatively shallow burial depths.

All the clast fragments and blocks were once more competent intrasalt beds, which have been progressively fragmented by tectonism and flowage to now constitute the majority of clasts in the Haselgebirge Fm. breccias. According to Leitner er al. (2011) the Haselgebirge in the Alps is a proto-cataclasite that originated by the interaction of recrystallisation of halite and the (hydro)fracturing of mudrock under tectonic deformation experiencing paleo-differential stresses ranging up to 2.5–4.5 MPa. The various breccias preserve evidence of their progressive tectonic evolution from limited ductile halite-encased deformation → brittle fracturing → boudinage → individual rotation of newly developed clasts → development of localised matrix-supported breccias (not laterally persistent) → laterally persistent matrix breccias with increasingly homogenous grain sizes (Spötl 1989a, Spötl et al. 1998; Leitner et al. 2011).

In the early stages of intrasalt bed breakup the clasts were angular. With ongoing clast deformation and rotation, the

[8]High levels of impurities meant Haselgebirge salt could not be exploited using conventional mining techniques. Instead the sinkwerk method was used. A sinkwerk is a chamber or sump in a salt mine filled with water to dissolve salt. The resulting brine is then pumped via pipelines to a saltworks for processing at the surface.

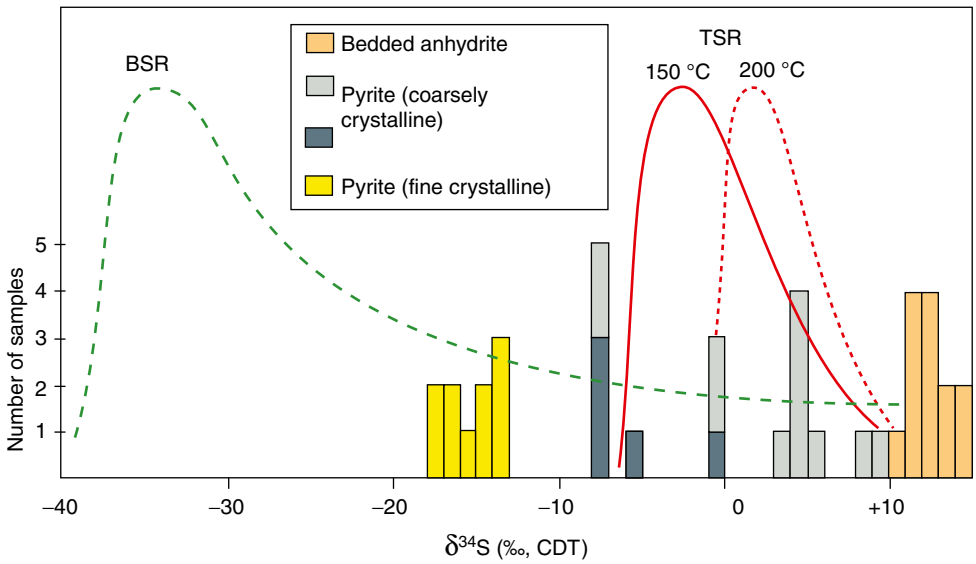

Fig. 7.35 Frequency distribution of sulphur isotope values for sulphates, sulphides and native sulphur from the Haselgebirge Fm. melange, Austria (After Spötl et al. 1998). Theoretical $\delta^{34}S$ distribution curves for pyrite produced during bacterial (BSR) and abiogenic thermal sulphate reduction (TSR) processes are shown. Note that pyrite $\delta^{34}S$ values are close to and within compositions expected for TSR

clasts become rounded and develop slickensided boundaries. The brecciation of the intrasalt beds reflects the different responses of anhydrite or carbonate to strain, when compared with halite. In response to shear stresses of much less than 1 MPa at geologically significant stain rates, halite typically flows and recrystallises via pressure solution (Fig. 6.4a). Due to their higher strength, shale, carbonate or anhydrite intrabeds respond in a brittle fashion and tend to brecciate, not flow, at the same strain rates.

The higher temperature origin of most of the diagenetic products in the Haselgebirge unit is clearly seen in the sulphur isotopic evolution of sulphate reduction products (Spötl et al. 1998) and the high temperatures indicated by recrystallised halite fabrics (Leitner et al. 2011). Sulphates in the Haselgebirge matrix largely preserve their Permian-early Triassic marine signatures and range in $\delta^{34}S$ from +9.8 to +13.8‰ (Fig. 7.35). Matrix dolomite alteration was driven by thermochemical sulphate reduction (TSR) and is indicated by the replacement of anhydrite by calcite + pyrite ± native sulphur and would have required temperatures in excess of 150 °C (see Chap. 9 for detail on TSR and BSR). Pyrite associated with TSR is coarsely crystalline and characterized by a small sulphur isotope fractionation relative to the precursor Permo-Triassic anhydrite.

Interestingly, the carbonates associated with TSR show low Fe/ Mn ratios reflecting rapid reaction of ferrous iron during sulphide precipitation. As a result, TSR-related dolomite and calcite typically show bright Mn(II)-activated cathodoluminescence. This is in marked contrast to the dull cathodoluminescence of many (ferroan) carbonate cements in many nonevaporitic deep-burial settings. In addition to carbonates and sulphides, authigenic silicate formation in the Haselgebirge was closely related to TSR (T > 150 °C), and included authigenic quartz, K-feldspar, albite and K-mica. Increasing illite crystallinity in the Haselgebirge also defines the sequence's entry into the anchizone (see Chap. 14 and Fig. 14.7 for further discussion of meta-evaporites and related clay transformations). Likewise, halite recrystallization temperatures of 110–150 °C are indicated by grain-size piezometry (Leitner et al. 2011).

Similarly, the rauhwacke that characterises outcrops of the Triassic Burano Evaporite Formation from the Secchia River Valley of Italy is intensely modified and tectonised as its evaporitic precursor was the main décollement horizon during the formation of the Northern Apennines chain (Lugli 2001). Inclusion temperatures of the various burial products clearly show a high temperature (greenschist) genesis (Fig. 7.36). Regionally, the Burano Formation is up to 2,200 m-thick and composed of metre-to decametre-scale interbeds of gypsum-anhydrite and dolostones with minor halite. The deposit has been affected by a complex array of postdepositional modifications, thermal events and large-scale evaporite dissolution, all acting to destroy an evidence of the environment of deposition. Carbonate clasts are composed of; massive and-or laminated dolomitic mudstones, wackestones, oolitic packstones and oolitic, peloidal, bioclastic grainstones. All can appear as mega-boudins within a calcium sulphate groundmass. The dolostones, (with a $\delta^{18}O = -5.7$ to -3.7‰; $\delta^{13}C = +1.3$ to $+3.0$‰; PDB) have been overprinted by sparry magnesite during Mg-metasomatic replacement ($\delta^{18}O = -14.0$ to -2.6 ‰; $\delta^{13}C = -2.6$ to $+1.4$ ‰; PDB) via orogenically-driven hydrothermal circulation (Lugli 2001; Lugli et al. 2002). Homogenization temperatures of fluid inclusions in hydrothermal magnesite range from 275 to 310 °C (Fig. 7.36a).

Anhydrites in the Burano are characterized by flow structures such as centimetre-scale pseudo-lamination composed of aligned prismatic crystals with transposed isoclinal folds

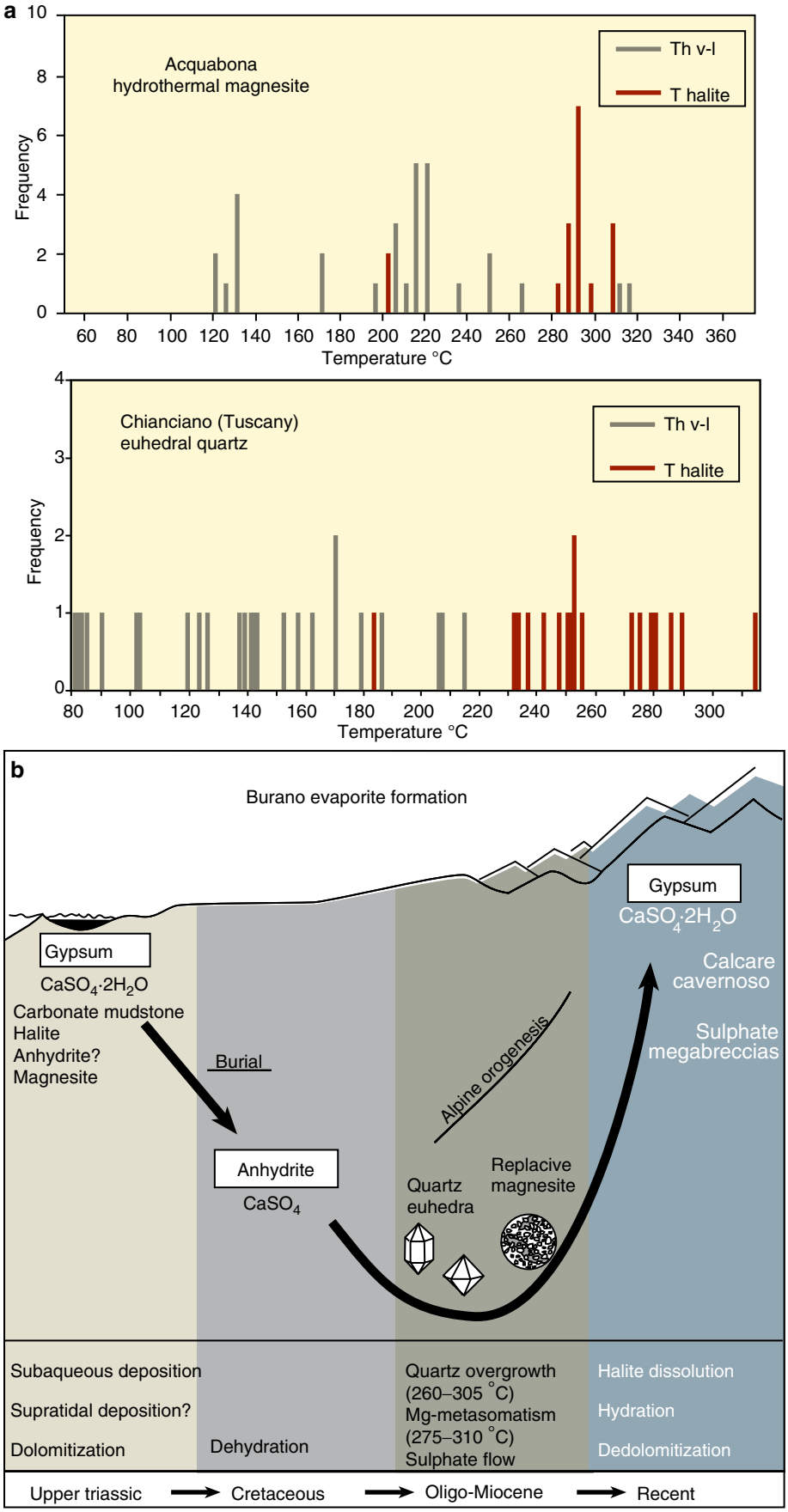

Fig. 7.36 Burano Evaporite Formation (After Lugli 2001), (**a**) Frequency histogram of fluid inclusion results from vapour to liquid homogenization temperatures (v-l) and halite melting temperatures (halite) in fracture-filling sparry magnesite from the Acquabona region and authigenic quartz euhedra from Chianociano region in Tuscany. (**b**) Reconstruction of the geologic history. Not to scale and adapted from the original gypsum-anhydrite-gypsum burial cycle of Murray (1964)

outlined by dolostones fragments. No primary textures remain. Homogenization temperatures of fluid inclusions in authigenic quartz incorporated into sulphate rocks range from 260 to 305 °C (in the Emilia area) and from 230 to 315 °C (in the Tuscany area; Fig. 7.36a). Outcropping and nearsurface gypsum is composed of xenotopic irregular cloudy crystals and, more rarely, by centimetre-scale idiotopic crystals showing the same structures as the anhydrite rocks. The gypsum is a late alteration product from anhydrite, formed during migration of sharp hydration fronts and meteoric flushing. Hydration is a two step process as indicated by the presence in the gypsum encasing corroded anhydrite micro-relics and by authigenic quartz crystals that still include anhydrite (Fig. 7.36b).

Evolution of Burano Evaporites during the Apennines tectogenesis was ongoing and tectonically driven by the processes of burial compression and exhumation (Fig. 7.36b; Lugli 2001). It can be divided into: (a) prevalent deposition of gypsum in the Upper Triassic; (b) gypsum dehydration at burial conditions to form anhydrite (Cretaceous?); (c) syntectonic flow of anhydrite rocks, brecciation of dolostones; syn-growth stage of quartz euhedra at deep burial conditions possibly related to the development of the Oligocene-Miocene greenschist facies of the Apuane metamorphic complex; (d) hydrothermal deposition of sparry magnesite and partial Mg-metasomatic replacement of dolostones by magnesite; (e) sub-surface dissolution of halite to form thick matrix-supported residual caprock-like anhydrite megabreccias; (f) complete regypsification of anhydrite at subsurface conditions; and (g) evaporite dissolution at surface exposure producing dolostone breccias with partial calcitisation and removal of most evaporite clasts ("calcare cavernoso" or rauhwacke).

Rauhwacke sheets (carbonate thrust breccias) also define outcrop of tectonic slices in nappe piles now dominated by pelitic rocks of Early Mesozoic age in the Carson Sink region of Nevada (Muttlebury and Lovelock Formations; Speed 1975; Speed and Clayton 1975). There the most extensive carbonate breccia nappe, the Muttlebury Nappe, extends over an area of 100 km^2 (Fig. 7.27). The outcropping rauhwacke sheets are interlayered and interlensed with non-brecciated marble slabs. The coarse grain size and granoblastic texture of the "marble" suggests an origin via metamorphic overprint of at least moderate grade. But the degree of apparent recrystallisation in the Muttlebury marble contrasts with a lack of recrystallisation and metamorphic alteration in the intercalated limestones and rauhwacke breccias. That is, the apparent metamorphic grade of these marbles is seemingly incompatible with that of the adjacent unmetamorphosed sedimentary carbonates and is best explained by emplacement along an evaporite-lubricated thrust. A nearby 30 m -thick gypsum klippe shows internal isoclinal folding due to strong translatent movement. Speed and Clayton (op. cit.) correlate it as a lateral equivalent to rauhwacke of the Muttlebury Nappe. Remnants of the same folding style are preserved in the matrix of some breccia beds in the rauhwacke of the Muttlebury Nappe.

Chert caught up in the granuloblastic calcite marbles, and interlayered with rauhwacke sheets of the Muttlebury Nappe, contains ubiquitous length-slow chalcedony, implying a possible evaporite precursor for the marbles. But the genesis of the marble is best resolved using their stable isotopic signatures (Fig. 7.37; Speed and Clayton 1975). Carbon and oxygen isotope ratios of calcites from various carbonate rocks in the Carson Sink, including the marbles, fall into two distinct trends. One has nearly constant $\delta^{13}C$ and variable $\delta^{18}O$

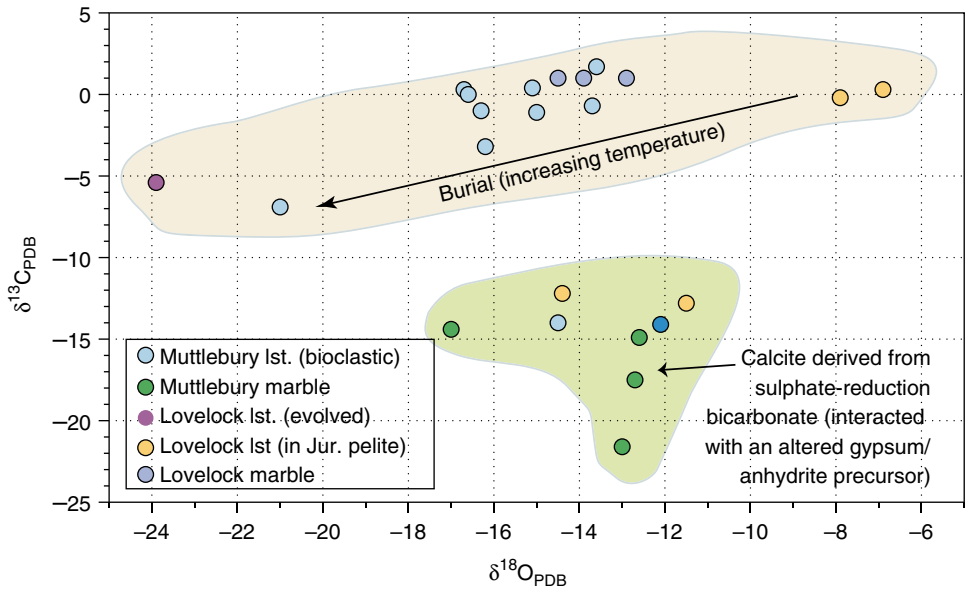

Fig. 7.37 Plot of $\delta\ ^{13}C_{PDB}$ versus $\delta\ ^{18}O_{PDB}$ for specimens from the Muttlebury and Lovelock Formations and from limestones in pelitic rocks below the Muttlebury Formation. C-O co-variance fields define two trends, burial and sulphate reduction – see text (Replotted from Speed and Clayton 1975)

related to rock-fluid re-equilibration under increasing burial temperatures; the other has nearly constant $\delta^{18}O$, and a $\delta^{13}C$ signature that varies between −7 and −25 ‰ (PDB). The first trend encompasses all the fine-grained carbonate rocks and calcarenites of the region, whereas the second encompasses all analyses of the problematic granuloblastic calcitic marbles. Speed and Clayton's (1975) interpretation of the isotopic trend of the Muttlebury Marble is that the marble's precursor was a coarse-grained gypsum or anhydrite-lubricated décollement caught up in active thrust and glide planes. When active it had acted much like the anhydrite-lubricated Alpine thrusts (Fig. 8.12).

These calcium sulphate-cored décollement sheets were subsequently calcitised bioepigenetically (perhaps during early telogenesis), with the sulphate-reducing bacteria utilising sulphate from the décollement plane and organic carbon from sources outside of the sulphate beds, perhaps the nearby euxinic limestones, or perhaps hydrocarbons percolating and focused by the now inactive thrust sheet (hence its $\delta^{13}C$ signature). Thus, Speed and Clayton argue the process of marble formation in the thrust nappe was similar to that now forming the calcitised sulphurous cap rocks of diapirs in the Gulf of Mexico.

In my opinion the rauhwacke breccias in the Muttlebury Formation, now interlayered with somewhat enigmatic bioepigenetic marbles, are altered intraformational tectonic breccias. The marbles, with their more negative carbon values, were created by meteoric/telogenetic dissolution of calcium sulphate remnants in previously salt-lubricated thrusts. Crossbedded calcarenites and quartz sands are water-reworked matrix components in the rauhwacke breccia, much like in the type area of rauhwacke in the Alps; they are mechanically reworked accumu-lations of insoluble residues and stringers that were originally disseminated through the antecedent sulphate beds.

Older but impressive examples of salt-lubricated thrust sheets and evaporite-hosted rauhwacke melange outcrop in Neoproterozoic sediments caught up in orogenic belts in the Katangan copper belt of Central Africa, and in outcrops in the Flinders Ranges of South Australia and the Amadeus Basin of Central Australia (Figs. 7.31 and 7.33d, respectively). The original evaporite matrix to the breccias has long since dissolved in these outcrops of former salt lubricated thrusts leaving behind a complex highly brecciated melange, sometimes entraining large megabreccia blocks that can be kilometres across. In subcrop of such sequences there can be numerous pseudomorphs after anhydrite preserved, as in the Mine Series associated with Cu mineralisation in the Katangan belt and its equivalents (Muchez et al. 2008; Kamona and Friedrich 2007).

Rauhwacke in many Proterozoic basins that have experienced regional compression occurs in close association with diapiric breccias that indicate an extensional halokinetic stage that preceded compression and thrusting. Even after the halite and anhydrite have dissolved, both the breccia blocks and the finer-grained matrix still retain a number of indicators of the former presence of widespread evaporites and include; (a) pseudomorphs of gypsum, anhydrite and halite crystals, (b) dolomite textures in breccia fragments that mimic anhydrite nodules, enterolithic folds, and chicken-wire textures, (c) doubly terminated euhedral quartz and length-slow quartz, (d) minor volumes of actual calcium sulphate (mostly regypsified at outcrop) as a pore filling cement, (e) hypersaline fluid inclusions in authigenic phases and (f) meta-evaporitic alteration haloes about the breccias bodies that indicate an evaporite source. Rauhwacke horizons are the structured remnants of much thicker salt masses (Fig. 7.38).

Melanges of dissolution residues in both Australia and Africa outline a combination of diapiric structures and subsequent thrust welds. The original salt in both areas was first precipitated in rifts, which evolved into passive margins, with both autochthonous diapirs and allochthonous salt tiers, and then into salt-lubricated thrust belts during subsequent orogenesis. The salt was sourced in the Callanna Group in the Flinders Ranges and the Roan Supergroup in the Katangan Copper belt (Lemon 1985; Jackson et al. 2003). The details of the diapiric breccias in the Flinders Ranges were discussed earlier (Fig. 7.31). Many workers in the Flinders Ranges focused on the diapiric nature of the breccias, although salt-lubricated thrust plane (inversion) rauhwacke breccias are widely visible in outcrop. Work by Jackson et al. (2003) and Backé et al. (2010) has clearly defined the intimate interrelationship between halokinesis, thrust plane development, inversion and salt in the Katangan and Adelaidean foldbelts. Classic diapiric geometries are outlined by the brecciated residuals of the Roan Supergroup, as in the Mukondo Diapir (Fig. 7.38b). Former salt-lubricated thrust planes are now outlined by rauhwacke breccia sheets in both the Katangan Copperbelt of Shaba (Democratic Republic of the Congo) and Zambia. These regions also contain the world's largest concentration of stratiform copper-cobalt ores, with their genesis largely focused by the interactions between metalliferous basinal brines and salt sheets (Warren 2000b; El Desouky et al. 2009).

During the Lufilian orogeny, the Katangan basin structure was radically transformed first by extrusion of allochthonous evaporites, then by orogenic shortening (Fig. 7.38c; Jackson et al. 2003; El Desouky et al. 2009). Salt tectonics began during deposition and gravity gliding of the Roan Supergroup between 1050 and 950 Ma. In mid-Roan time, salt walls and extrusions of evaporites began to be emplaced (former salt now outlined by breccias and gigabreccias – as in Flinders Ranges). In early Kundelungu time (940–850 Ma) the evaporitic diapirs enlarged. Lufilian deformation began by laterally squeezing diapirs to form salt welds between 850

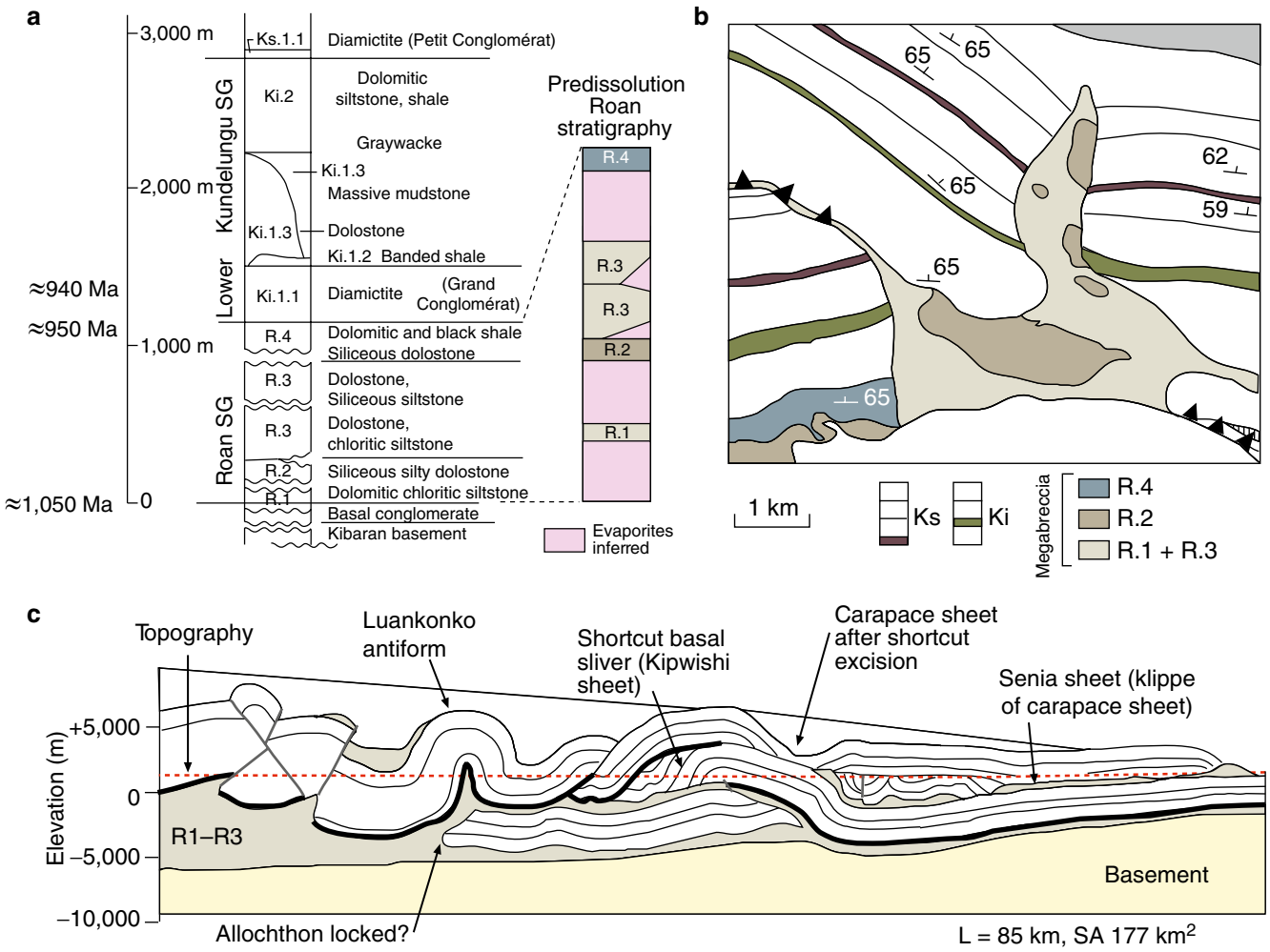

Fig. 7.38 Lufilian halokinetic breccia or rauhwacke (After Jackson et al. 2003). (**a**) Katangan stratigraphic column with a side column showing qualitatively restored evaporite thicknesses. Basal units below R.1 are based on the Zambian Copperbelt not the Katanga region. (**b**) Map of Mukondo Diapir, representing a down-plunge oblique section. In the diapir's northern apophysis, the Roan evaporite-gigabreccia passively pierced 2 km upward through accumulating Ki and Ks overburden in the southern limb of Mutaka Synform. This diapir appears to be rooted in autochthonous Roan. The separate Roan diapir in the extreme northeast is allochthonous. (**c**) Regional reconstruction of Katangan thrust section at the end of Lufilian time with no vertical exaggeration. The level of the modern topography indicated by dashed red line

and 650 Ma. Then, a large sheet of commingled Roan evaporite and carbonate-dominated sediments and ores was extruded northward by ≈65 km. Extrusion was fast enough to blanket a uniform pre-orogenic footwall unit without overriding any synorogenic deposits, much like the Salt Range in Pakistan today (Fig. 6.73). Continued shortening then emplaced large thrust sheets, lubricated by the pre-existing salt-sediment extrusive sheet. Restorations by Jackson et al. (2003) suggest that the Lufilian foreland in the Katangan area shortened from 193 to 85 km and that the depositional northern edge of the evaporite basin controlled the shape of the Outer Lufilian Arc.

Bed geometries in both the Flinders Ranges and the African copper belt show that a post salt-solution distinction between rauhwacke and diapiric breccias is difficult in core and, without sufficient outcrop analogs or seismic, can be near impossible. Lithologically, at the lower temperature end of the burial spectrum, the components of rauhwacke and diapiric breccia residuals are near identical. Our increased understanding of tiered allochthon emplacement of salt masses, and the time equivalence of early updip extension and downdip compression, makes such a distinction increasingly irrelevant at the lower temperature end of burial. When formed, updip extensional diapirs pass downdip into compressional toe-of-slope regions and both areas will become compressional (inverted) later in the Wilson Cycle (Fig. 5.32).

Rauhwacke and its precursor salt-lubricated thrust planes and alteration haloes tend to be dominantly interstratal stratiform surfaces defined by focused slippage, adjacent fault

plane brecciation and subsequent solution collapse. Such thrust planes often separate a brittle-faulted hanging wall from a less altered footwall succession (thin-skinned tectonics discussed in Chap. 6 and illustrated in Fig. 7.38c). Occasionally a rauhwacke breccia cuts up-section as a thrust ramp or riser. In contrast, diapiric solution breccias tend to be identified by largely trans-stratal geometries that outline the shape of the precursor salt diapir. But salt-lubricated allochthon sheets evolve into thrust planes, while former salt welds and diapirs can be reactivated to become the inverted base of salt-lubricated thrust sheets (see Fig. 6.75a). When diapirs, allochthons, depopods and detachment surfaces are part of the same salt-lubricated system, the two breccia styles merge and become near impossible to separate. Older 1950s vintage notions that salt diapirs indicated active halite intrusion and so were a separate tectonic style to thrusting, led to heated but possibly unnecessary argument in the 1960s and 70s on ways to separate diapirs from décollement in the Flinders Ranges outcrops (e.g. Burns et al. 1977). We now know they are part of the same salt-lubricated association with diapiric intervals and salt tiers often acting as a plane of weakness for subsequent thrusting as the basin passes from extension into compression (Wilson Cycle; Backé et al. 2010).

The presence of halite in the thrust melange that precedes the leaching of salt that creates rauhwacke is inherent to the definition. However, in some tectonised situations, the evaporite unit that is caught up in folded and tectonised intervals can be a buried unit made up of a combination of anhydrite and carbonate beds, with the anhydrite converting to gypsum at shallower depths. This is the situation that created folded tectonised carbonate breccias in the Lower Cretaceous Oncala Group of the Cameros Basin in Northern Spain (Quijada et al. 2014). These stratiform fold breccias were previously interpreted and sedimentary slump or collapse breccias. The breccias consist of angular carbonate mudstone fragments floating in a matrix of calcite and quartz crystals. The breccias are made up of variably folded and collapsed interbeds that are laterally associated to, and made up of, alternating layers of carbonate mudstone and calcite with numerous quartz pseudomorphs after gypsum, showing strong similarities to the breccia fragments and matrix. This suggests the now brecciated beds were originally composed of alternating carbonate mudstone and $CaSO_4$ layers.

Oncala breccias are associated with frequently polyharmonic deformation structures, with axial trends that are consistent with respect to the regional tectonic structure, indicating that they are related with the Alpine contractional deformation of this area of the Cameros Basin. In combination these features suggest that the carbonate breccias were formed by tectonic deformation of alternating layers of carbonate mudstone and calcium sulphate, which have very different rheological behaviours. As a result, during tectonic deformation, sulphate flowed and carbonate layers were broken and displaced, producing a breccia of carbonate fragments within a sulphate groundmass. Later, the sulphate groundmass was replaced by quartz and calcite, and the breccia acquired the composition we now see in outcrop.

Worldwide, where a concept of salt allochthon breccia versus rauhwacke, and former flowing salt beds, needs to be better defined is in the higher-temperature higher-pressure realm of metamorphism. Rauhwacke when used to define a type of breccia has inherent notions of a thrust sheet, inversion and an alteration halo about the salt-cored thrust plane. Fluids focused along the salt-cored thrust can penetrate, alter and even mineralise adjacent strata. Salts can survive as halite to burial temperatures in excess of 450 °C and as anhydrite to temperatures >900 °C (Chap. 14). Rauhwacke as a concept explaining near-fault alteration has been applied to salt-lubricated thrust residues and alteration/mineralisation haloes within this temperature range (greenschist to amphibolite facies). But notions of diapirs and salt welds are largely restricted to the sedimentological literature, yet diapirs and welds too must pass into the metamorphic realm. Published salt allochthon and weld models, based largely on seismic interpretations of sedimentary basins, have no such notion of alteration haloes, yet extensive contemporary ferroan carbonate haloes are seen in outcrop in Algeria, the Flinders Ranges and the McArthur Basin. Combining the two notions into a single model of structural evolution and mineralised fluid focusing will give increased exploration success in copper and base metal metamorphic/halokinetic terrains such as the Mt Isa-Cloncurry belt of Queensland, Australia and the Yunnan province of China (Chap. 15).

Partial Salt Dissolution: Residues of Less-Soluble Salts

Whenever a thick evaporite bed comes into contact with undersaturated waters it dissolves to leave behind a bed of insoluble residues. So far we have concentrated on characteristics of evaporite solution breccias with insoluble residues that no longer retain preserved salts. But there are intermediate stages in many subcropping and subsurface beds and diapirs in sedimentary basins, where less soluble salts remain after the more soluble salts have dissolved. The result is a cumulate laminar layer or breccia dominated by less soluble salts, typically anhydrite, that were originally dispersed through a now largely dissolved halite bed. At the same time as the beds dissolve, pore fluid salinity increases at the dissolution contact. As this water mixes with throughflowing waters in adjacent beds it can precipitate anhydrite or gypsum cements in nonevaporitic strata (burial and telogenetic salts).

If the dissolution is rapid and focused, overburden and intrasalt beds brecciate and fail via incremental crack-seal

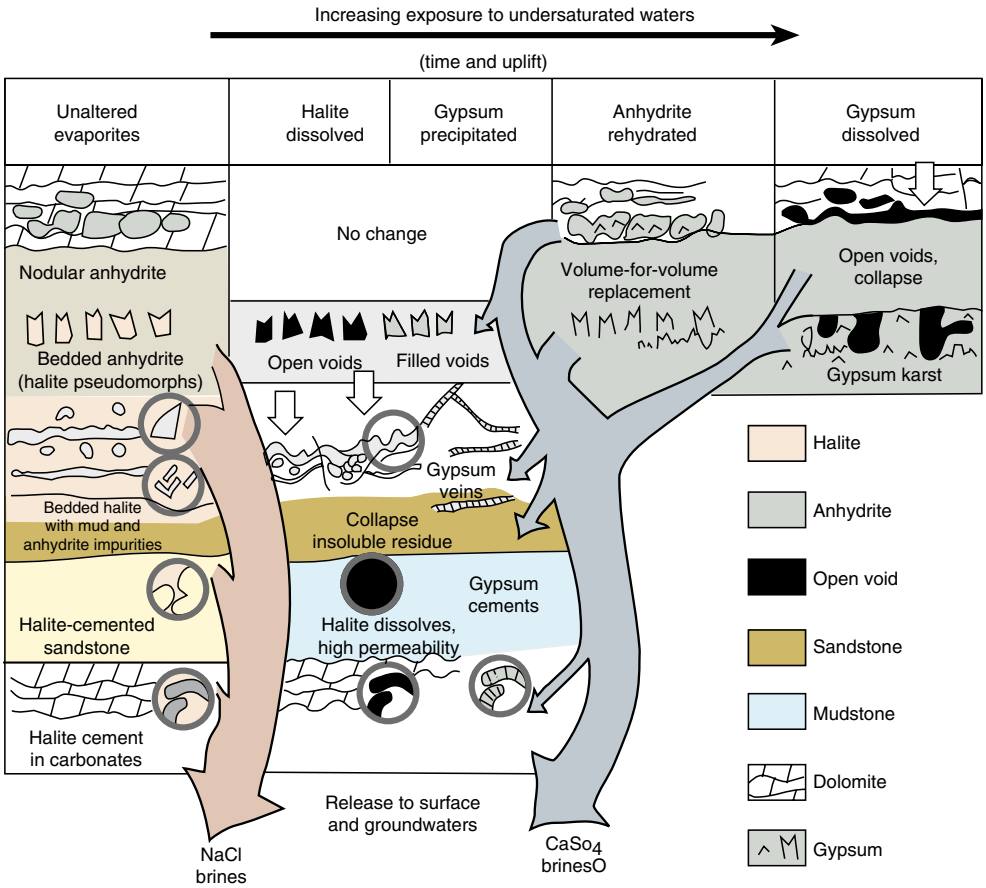

Fig. 7.39 Salt-dissolution processes related to ongoing exposure to undersaturated waters. Unaltered evaporite is shown on the left, initial alteration in contact with somewhat undersaturated water in the middle, and intense alteration after prolonged contact with undersaturated water is shown on the right. Degree of exposure to undersaturated water is largely related to uplift and time (After Hovorka 2000)

processes, with residual anhydrite or alabaster matrices surrounding the former intrasalt breccia blocks. If the dissolution is slower and subsidence or "let down" of the overburden gentler, then a residue bed of layered sulphates forms (Fig. 7.39). In this case the overburden span or roof tends to subside in parallel, with no more than minor crackle fracturing at the contact with the accreting laminar sulphate bed. If the subsiding overburden is a clay, then satin spar veins fed by high salinity brines coming off the dissolution front can infill any gravitational and hydraulic fractures forming brittle structures in response to collapse-induced extensional stress.

Less soluble salts tend to accrete at the boundary of the salt bed in contact with the undersaturated crossflow. If dissolution occurs at the top of a salt bed then accretion occurs along the base of the residue bed (youngs downward – as in anhydrite caprock atop a diapir). If it occurs along the underside of a thick salt unit, the less soluble salts accrete to the top of the bed (youngs upward – an "upside-down" caprock known as a basal anhydrite). It occurs at the margins of a salt structure then it is called a "lateral" caprock (Fig. 6.113). In all cases, the accretion of less soluble salts generally leads to a distinctive wavy-laminated fabric, either in anhydrite or in mud-sized residual material (that includes carbonates as well as clays). The wavy structure forms as small and disaggregated layers of insolubles are wrapped around larger clasts or nodules of anhydrite.

The mineralogy and thickness of the residue layer depends on the proportion of insolubles in the original evaporite bed and the salinity and chemical composition of the undersaturated waters. Relatively pure halite or potash units tend to produce thin layers of residual impurities. Anhydrite or mudstone insolubles hosted in the original intrasalt beds are typically first incorporated as bedding-parallel elongate clasts in the bed, often with minimal modification to their pre-collapse textures. Ultimately, with enough time, freshening and flushing, all the residual anhydrite dissolves and only nonevaporite clasts and fine-grained insolubles remain (typically muds and loose silt-sized dolomite rhombs).

Focused Rapid Dissolution – Evaporite Clasts

Differing solubilities between bittern, halite and $CaSO_4$ salts mean that breccias can be created by the rapid preferential dissolution of more soluble salts driving collapse that leaves behind less soluble salts in the matrix. Brecciated beds of

less soluble strata are typically composed of angular blocks of bedded gypsum/anhydrite, which fragment and settle as the supporting halite or bittern beds dissolve. These fractionated breccia beds are sometimes encased or underlain by halite, showing evidence of flow or slippage into chambers created by differential dissolution. Other times the breccias have characteristic smooth bases and more irregular tops. Sulphate-matrix collapse breccias typify parts of the subcropping margin of the Permian Castile Formation of the Delaware Basin in West Texas and New Mexico (Hovorka 2000), and the Middle Miocene (Badenian) gypsum of southern Poland and the Ukraine (Babel 1991) and the Permian Khuff Formation of Abu Dhabi and Saudi Arabia (pers. obs.).

Babel (op. cit.) describes preferential intra-evaporite dissolution processes in gypsum of the Middle Miocene (Badenian), southern Poland. Gypsum-clast breccias can form by the early diagenetic dissolution of halite beds within a thick laminated gypsum section. Sometimes the transformed interval is a single cm-thick bed and halite dissolution is interpreted to have occurred during a short freshening interval that only affected sediments just below the sediment-brine interface. Other times, the dissolution front was thicker, altering substantial thicknesses of halite to form crackle/rubble zones in bedded calcium sulphates that are tens of metres thick. Dissolution in some areas took place while parts of the gypsum beds were still water-saturated and soft, leading to complex soft-sediment deformation textures. Dissolution in other areas occurred after the gypsum was indurated and created classic collapse breccia intervals, with smooth bases and irregular crackled upper surfaces. Residual intervals within gypsum karst are typically defined by very fine-grained gypsum and clay horizons that routinely also define the base of a collapse interval. The brecciated intervals pass up or later-ally into faint or unlaminated gypsum alabaster (aka compact gypsum), often precipitated from telogenetic fluids tied to the rehydration of exhumed anhydrite.

Because partially-dissolved evaporite breccias define the edges of many buried evaporite units, and are typically associated with syn-dissolutional flowage of some of the remaining salt layers, they are easily confused with primary debris flows in the evaporite bed. This is especially so when the dissolving salt beds are adjacent to pinnacle reefs, which have acted as artesian aquifers during evaporite drawdown, as is the case with many of the inter-reef salt beds adjacent to the pinnacle reefs in the Silurian of the Michigan Basin (pers. obs.). Separating primary emplacement from a secondary dissolution origin can be difficult in brecciated and clast-rich beds and residues. Genesis is best resolved using oriented core, image logs and ties to detailed seismic mapping of salt collapse haloes above and around pinnacles.

Diffuse Dissolution -Markers and Residue Beds

Gypsum-anhydrite caprocks atop diapirs are widely recognised products of preferential salt dissolution. Less widely recognised stratiform equivalents to caprocks occur where undersaturated groundwaters flush the upper and lower contacts of stratiform or bedded halite. Such a set of processes affects halite beds in Maha Sarakham evaporites beneath the Khorat Plateau of NE Thailand (Fig. 7.40; Sessler 1990; Utha-aroon et al. 1995; Warren 1997) and the San Andres salts of the Palo Duro Basin of West Texas (Hovorka 2000; Gustavson et al. 1994). As any thick salt mass dissolves the mineralogy of the various residues typically depends on how long the evaporites were in contact with invading undersaturated waters and on the chemical make-up of the crossflowing waters; invading waters can be meteoric or basinal.

Gypsum has been reported as deep as 4,000 m in the oilfields of west Texas (Amadi et al. 2012), but most telogenetic rehydration probably occurs within a few hundred metres of the surface and much within the topmost few tens of metres (Ford and Williams 2007). Rehydration of buried anhydrite advances along reopening joints or new fractures, with the consequence that the hydration front can be highly irregular. It is common to find small patches of anhydrite surviving in gypsum cliffs where there has been rapid exposure. Quinlan (1978) argued that hydration involves dissolution with immediate reprecipitation.

In a relatively impervious rock, the slow hydration of anhydrite to gypsum and the related volume increase creates a swelling pressure of 295 kPa or 2.92 Atm (Azam 2007). Beyond a 200 m depth (≈bathyphreatic), hydration products are probably slowly dispersed in fluid crossflow with little expansion of rock volume (Gorbunova 1977) or via satin-spar precipitation in veins created by hydrofracturing or halite dissolution (Philipp 2008). Above that depth, mineral volume expansion of 30–67 % may occur, causing flow, folding and gypsum intrusion at depth, brittle fracture towards the surface, and recreation of some bulk porosity in the $CaSO_4$ unit. At the surface tightly folded or small-scale block-faulted topography may appear along with blisters, tents and tumuli (see earlier). Little or no groundwater flow occurs within the deeper telogenetic zones where anhydrite begins to rehydrate. As exhumation proceeds, overburden lessens, and the amount of halite that is preferentially dissolving increases. A thick exhuming evaporite mass tend to dissolve most along its upper surface where porosity and permeability is enhanced by ongoing undersaturated crossflows.

Gentle Dissolution at the Top

Uplift, or simply the cessation of evaporite deposition, allows undersaturated waters to come into contact with a salt bed. Undersaturated meteoric pore waters tend to pond atop the

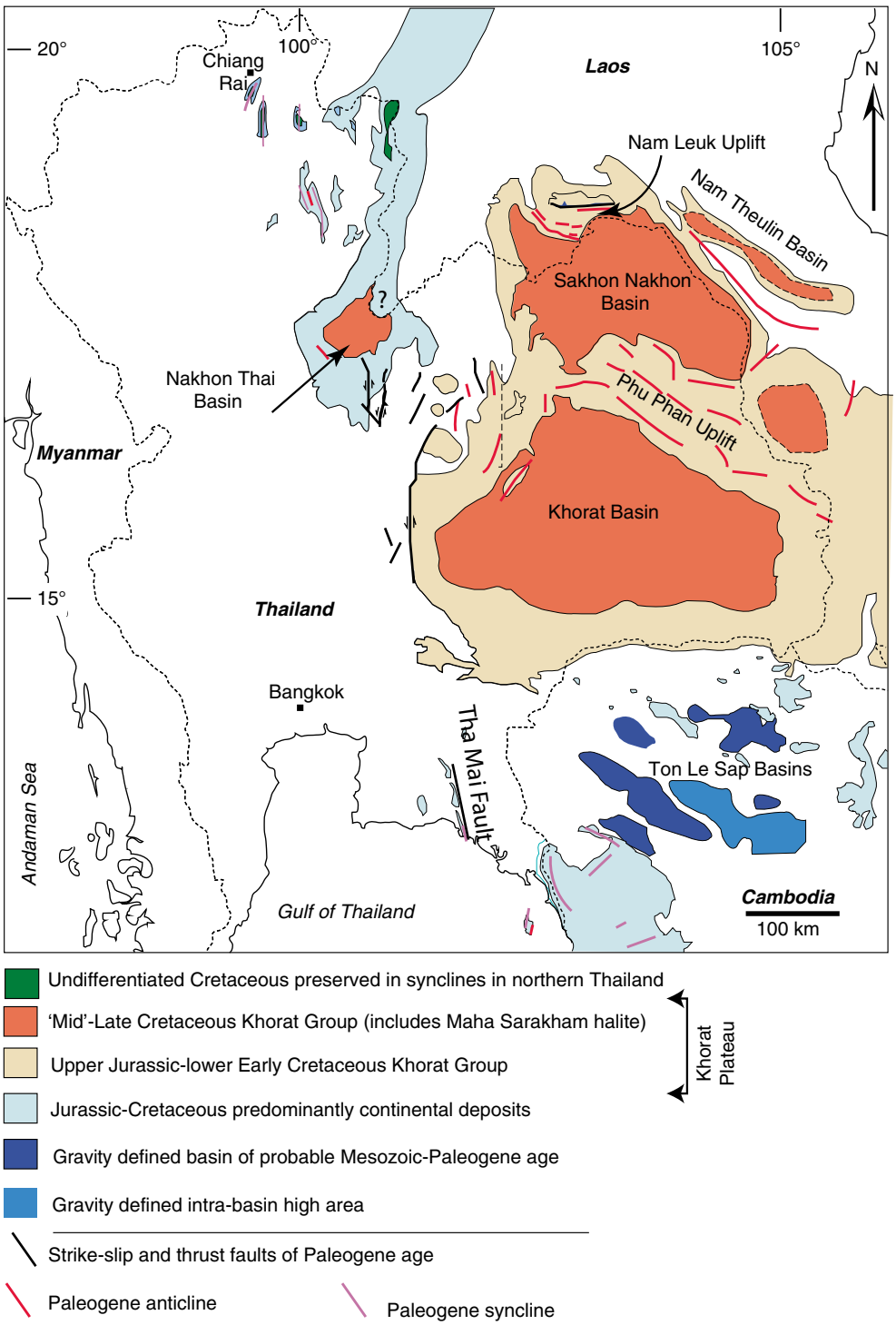

Fig. 7.40 General Geology of the Khorat Basin in Thailand and surrounds (After Morley 2012)

relatively impervious buried salt and so a shallowly-buried, or an exhuming, salt mass dissolves most from the upper salt mass contact down.

Maha Sarakham Salt, Thailand

Cretaceous Maha Sarakham sediments of NE Thailand are Albian-Cenomanian age and unconformably overlie continental deposits of the upper Jurassic to Aptian Khorat Group (Racey 2009; Morley 2012). Maha Sarakham sediments were deposited as a thick sequence (up to 1,000 m) of basin-wide evaporite interlayered with clays (Fig. 7.40). Beds tend to be stratiform about the basin edge and halokinetic in the thicker, deeply buried beds of the present centre (Fig. 7.41a). Three thick evaporite units (informally called

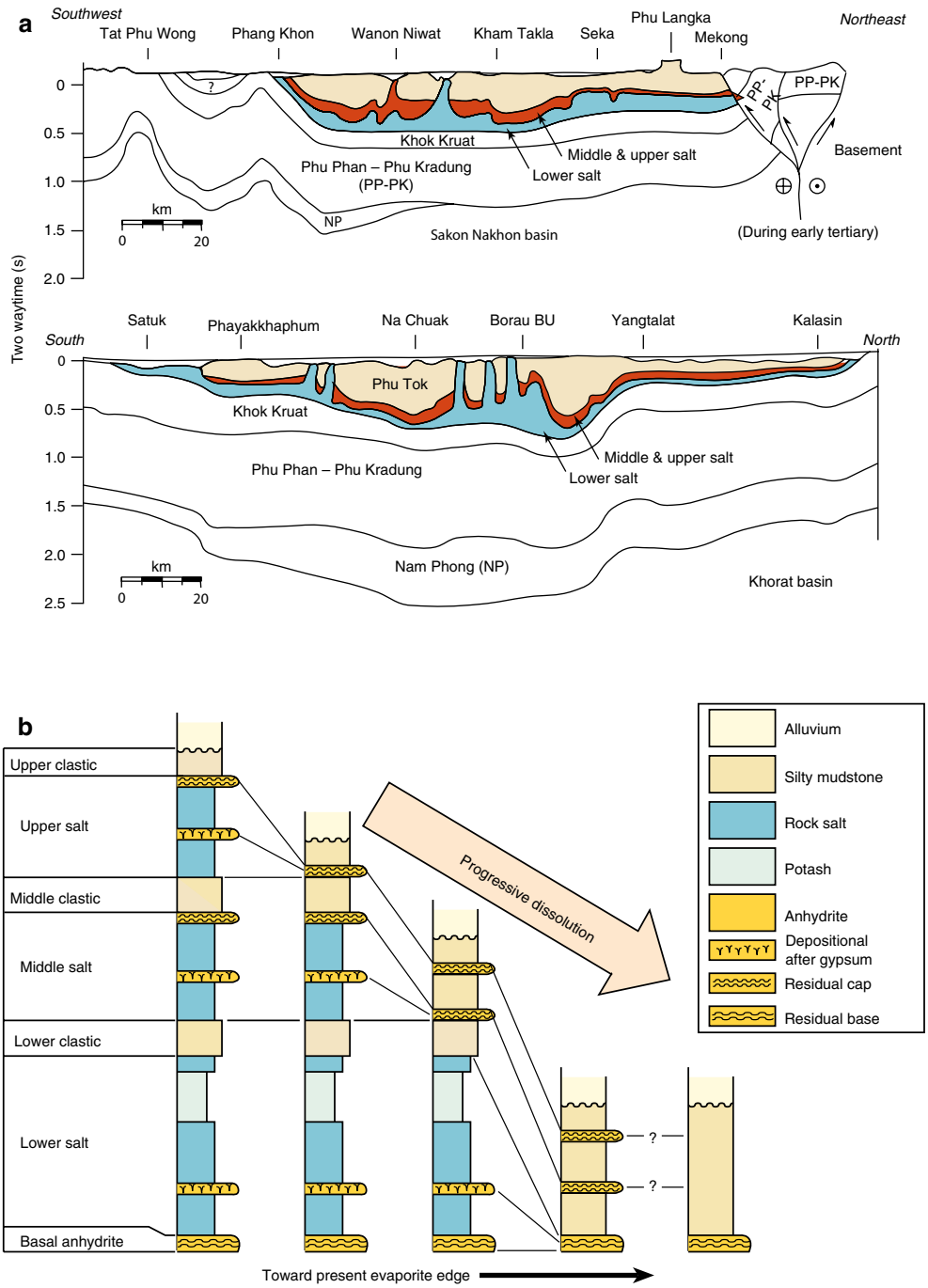

Fig. 7.41 (**a**) Regional subsurface structure of Maha Sarakham Formation showing preferential development of diapirs in lower salt toward the basin centre and dissolution toward structural edges of basin. (**b**) Progressive dissolution of halite and accretion of residual anhydrite beds toward the present basin edge (After Utha-aroon et al. 1995). See Fig. 11.37 for detailed stratigraphy related to potash occurrence

the Lower, Middle and Upper Salt), or their residual equivalents, are present throughout the basin (Fig. 7.41b). Evaporite minerals in the various beds include: sulphates, rock salt and potash minerals. Potash is found mostly in the upper part of the Lower Salt unit, but saltern halite is by far the most common salt and many beds preserve pristine chevron textures (Chap. 11). The salterns occasionally freshened so cm-scale gypsum nodules and beds with subaqueous textures (<1 m thick) were deposited in an otherwise dominantly halite succession, typical of Cretaceous marine evaporites (Fig. 7.42a). All the gypsum was converted to anhydrite during shallow burial and only returns to gypsum during exhumation and halite dissolution. The three main halite units that make up the Maha Sarakham Formation are laterally continuous and are traceable basin-wide. Nevertheless, ongoing interplays between salt dissolution and flowage have been active from the Cretaceous until today. Associated bed "sandwiching" means lithostratigraphic correlation from one place to another is not a straightforward exercise.

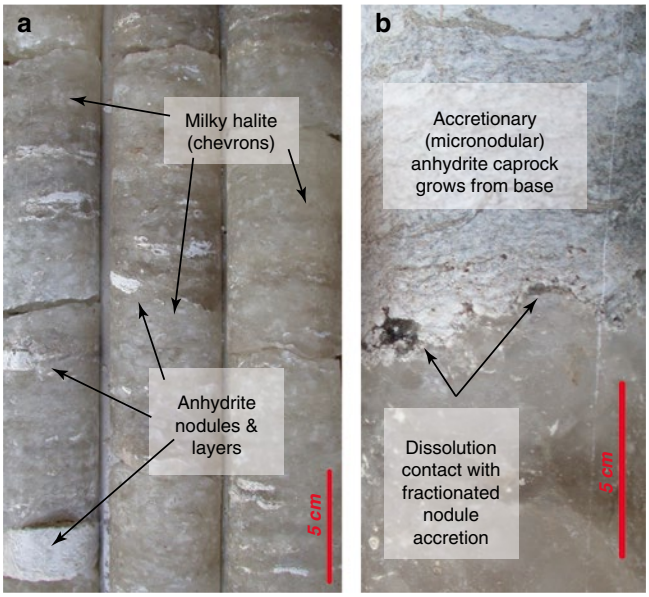

Fig. 7.42 Formation of the laminar bed of nodular anhydrite residues at the upper contact of the lower halite member of the Cretaceous Maha Sarakham Formation, NE Thailand. (**a**) General distribution of white-grey anhydrite nodules and layers dispersed in chevron halite in core. (**b**) Contact between dissolving halite and upper white-grey unit of dispersed anhydrite nodules and blebs. This laminar accretionary anhydrite bed defines the upper dissolution contact of the lower halite member. Some 2 m above this contact are the redbeds of the lower clastic member. The anhydrite unit preserves the shapes and sizes of the anhydrite blebs that were dispersed through the halite prior to its dissolution (as in Fig. 7.42a). These nodules and blebs are left behind to form a layered and accreting sulphate unit as halite is dissolved at the halite anhydrite contact (Scale bar is 5 cm long)

Thick clastic redbeds of mudstone separate each of the three main salt beds and are informally called the Upper, Middle and Lower Clastics (Fig. 7.41b). In core the clastic units are largely homogeneous clay beds, with locally laminated and stromatolitic horizons, infrequent nodular caliche horizons, occasional anhydrite nodules, root structures and mudcracks. Near their contact with adjacent salt beds there are beds of anhydrite residues overlain with clays hosting fractures and fissures filled with satinspar anhydrite and halite, indicating dissolution of a portion of the adjacent salt bed.

Depositionally, the lower halite in the Maha Sarakham is composed of chevron halite with dispersed cm-scale anhydrite nodules and stringers after gypsum (Fig. 7.42a). The earliest evidence for salt dissolution is cm-dm karst-pits filled by coarse recrystallised halite cement forming a syndepositional dissolution texture identical to that in the modern Qaidam Basin. Salt dissolution next occurred in shallow burial along bed boundaries where clastic units were in contact with bedded salts. Waters undersaturated with respect to halite, moved through adjacent redbed aquifers, initially as the clastics underwent deep weathering then as the buried clastics acted as conduits for compactional and basinal waters. This style of clastic-groundwater-driven dissolution left behind accreting residue textures at each major salt/clastic contact. Where the dissolving salt bed was composed mostly of clean halite all that now remains is a thin laminar residue of accreted insoluble clay residues. Due to the highly saline and anoxic nature of the brine leachate, the iron in these zones is reduced and where the salt bed is still actively dissolving the colour of the adjacent clastic has been altered from red to green.

In other regions of the basin, where the dissolving halite contained numerous anhydrite nodules, micronodules and stringers, the resulting dissolution residue is composed of stacked micronodular anhydrites that can be partially rehydrated to gypsum (Fig. 7.42b). These residual beds can occur along both the upper and lower dissolving bed contacts of all three salt units. At the contacts of the Upper and Middle Salt members the $CaSO_4$ residuals tend to be dm-m thick on the upper bed contact, but somewhat thinner on the under-side (cm-dm). On the underside of the Lower Salt member, the $CaSO_4$ residual is much thicker (≈1–2 m) and probably evidences a much greater volume of focused throughflushing driven by dewatering of the underlying Khorat Group sediments (see later basal anhydrite section).

Each $CaSO_4$ residual bed is made up of undulose thinly-layered to laminated light grey to off-white anhydrite/gypsum nodules and micronodules. Individual layers may be as thick as 2 cm (Fig. 7.42b). Lamina/layer orientation ranges from horizontal to vertical, with clays and organic matter defining the laminae and the nodule edges. Where a halite residual undergoes more localised dissolution the anhydrite beds are broken and brecciated, with interclast matrix infiltrating from the adjacent clastic member. Brecciated textures are most common in residues of the Upper Salt member as this unit is more effected by modern nearsurface meteoric leaching. If the Upper Salt member is still present in the stratigraphy it protects the Middle Salt member from surface driven dissolution.

Within the Middle Salt member is a basinwide dm-m-thick anhydrite marker bed. Complete dissolution of the halite encasing the marker bed of the Middle Salt member, and associated gentle foundering of the overlying middle clastic member, stacks the marker bed along with other anhydrite nodules and stringers in their original stratigraphic order (Utha-aroon et al. 1995). This gentle style of oriented solution-stacking of the intrasalt sulphate beds even preserves the subaqueous gypsum pseudomorphs of the anhydrite marker bed in their original growth position. Recognition of preferential dissolution occurring in a basin's stratigraphy allows a correlation across areas where halite beds have disappeared and only the anhydrite residuals remain (Fig. 7.42b). The final stage of salt dissolution occurs when the anhydrite residuals completely dissolve and brecciate to leave the three clastic members stacked one atop the other.

Where the Upper and Middle Salt members of subcropping Maha Sarakham Fm have completely dissolved, the present-day landsurface is defined by topographic depressions adjacent to a blind valley karst system atop a suprasalt high. Fluvial systems flow into this depression and feed subsurface waters to the dissolution front, which in turn focuses and stacks Quaternary fluvial channel sands. Outcropping and subcropping examples of this style of sequential halite dissolution define caprock outliers of the Maha Sarakham Formation in the Nam Theun syncline in central Lao (Fig. 7.10c). As about the edges of the much larger Khorat Plateau, Cretaceous halite along the syncline axis is retreating from the meteoric-flushed edges and top of the salt bed, leaving behind distorted and slumped remnants now patchily exposed in erosional banks along the river (pers. obs).

Some geomorphologists working in the salt solution terrains of NE Thailand have not recognised the effects of salt solution on the stacking pattern of fluvial systems. Instead, they have interpreted the thickened sections of Quaternary fluvial sediments as indicating a deepening of the river thalweg and have related it to Quaternary uplift and not dissolution downcutting. Effects of preferential dissolution along the edges of a bedded halite unit further emphasize the pitfalls of using simplistic notions of lateral correlation between thin marginward anhydrite and thick basin-centre halite (Fig. 5.38c).

Palo Duro Basin, West Texas

Hovorka (2000) has described the textures and effects of salt solution on the widespread Permian salt beds of West Texas (Fig. 7.43). She focused on the solution processes occurring beneath the High Plains of the Texas Panhandle, an area typified by landscape stability and the slow, longterm deposition of overburden. There the upper surface of the salt approximately parallels the hydrologic flow lines and so lies at a low angle to the land surface. In the Palo Duro Basin the top-of-salt lies at a depth of 250–300 m, approximately paralleling the low relief Southern High Plains. This salt dissolution surface regionally crosscuts Permian stratigraphy, so that in the northwest, the Seven Rivers Formation is the uppermost salt-bearing unit and overlying salts have been dissolved; while down hydrologic gradient to the southeast, the younger Salado halite is partly preserved.

Hovorka's examination of the residues left after regional low-angle salt dissolution in the Palo Duro Basin showed that salt dissolved and residues formed via incremental dissolution of the uppermost salt unit over a wide area. It was accompanied by passive stratiform subsidence of overlying strata (Fig. 7.43). Horizontal fractures in overlying strata indicate vertical extension, while syntaxial satin spar gypsum fillings show that the fracture opening occurred incrementally as underlying salt was dissolved (Gustavson et al. 1994). Typically, the creation of overburden voids atop most salt beds in West Texas does not lead to catastrophic collapse. Rather, stratiform beds of insoluble residues, perhaps associated with satin-spar veining in associated mudstones, are the best evidence that impure salt beds have been dissolved.

Diagnostic features of the regional low-angle crosscutting dissolution surface atop salt units in the Palo Duro Basin are: (1) Mixtures of insoluble components from the previously underlying halite with a wavy lamination in anhydritic intervals. This reflects the accretion of newly released insoluble components against existing insoluble residues. (2) Residual beds in positions that are laterally equivalent to preserved salt, (3) Anhydrite residual beds that stack one atop the other with little or no internal deformation, providing there were depositional sulphate beds in the original salt. (4) Syntaxial, horizontal, gypsum-filled fractures in overlying units. These are the same sets of features that define regional dissolution

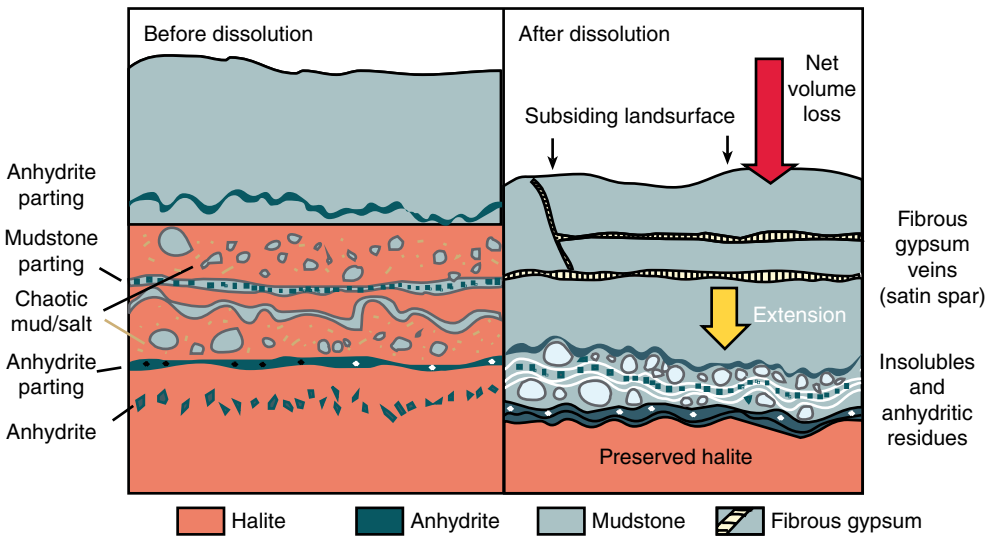

Fig. 7.43 Crossflow of undersaturated groundwater at the top of an impure halite bed creates an insoluble residue of anhydrite and mud under conditions of regional, low-angle salt dissolution and passive letdown of overlying strata, which fracture and are cemented by satin spar gypsum (After Hovorka 2000)

atop Cretaceous halite in the Maha Sarakham of Thailand (Utha-Aroon et al. 1995) and probably characterise all shallow low angle salt beds undergoing exhumation.

Dissolution from the Bottom

Undersaturated escaping basinal waters, or deeply circulating meteoric waters, can drive dissolution on the underside of a thick salt bed. In this situation the salt dissolves from the bottom up, and the residual wavy-layered anhydrite bed has a finite thickness controlled by its inherent crossflushing hydrology. To date this mode of preferential salt solution has only been documented in Maha Sarakham, probably because it is one of the few, if not the only, saline giant where both the upper side and the underside of the thick salt unit has been extensively cored and studied. However, similar near-constant thickness layers of anhydrite typify the base of many other saline giant basins, worldwide (Table 7.6).

Table 7.6 Various basins with possible dissolution-derived basal anhydrites

Basin	Age	Reference
South Pyrenean foredeep	Eocene	Rosell and Orti (1980)
Zechstein Basin	Permian	Peryt et al. (1993)
Delaware Basin	Permian	Presley (1987)
Maritimes Basin	Carboniferous	Lynch and Giles (1996)
Elk Point Basin	Devonian	Williams (1984)
Canning Basin	Devonian	Cathro et al. (1992)
Precaspian Basin	Silurian	Okere and Toothill (2012)
East Siberian Basin	Cambrian	Aitken (1981)
Mackenzie Basin	Early Palaeozoic	Aitken (1981)

In part after El Tabakh et al. (2003)

Basal Anhydrite, Thailand

Preferential dissolution of the underside of the Maha Sarakham Formation of NE Thailand is occurring where it is bathed in a crossflow of compactional and thermobaric waters (Warren 1997; El Tabakh et al. 1998a). The resulting basal anhydrite passes downward, via a thin cm-thick organic-rich residue layer, into underlying nonevaporite sediment made up of calcite-cemented fluvial sands and shales of the Khok Kruat Group. The basal anhydrite bed is characterised by a near constant basinwide thickness and consistent stratigraphic textures across the underside of large portions of the salt (Fig. 7.44). In many evaporite basins of the world, similar constant thickness beds are described as basal anhydrites, but are assigned a primary depositional origin.

To explain the subsurface processes that effect the underside of thick evaporite beds, the salts of the Khorat Plateau of Thailand are ideal. The region is unique in that the various salt layers of the Maha Sarakham Formation have been extensively and continuously cored from top to bottom and a simple gamma log suite run in the boreholes. This was done in the 1970s and 1980s in a World Bank funded exploration project for potash salts. The cores were double-sealed in plastic wrap and archived at a DMR core store in Udon Thani, where they are still available for study. Everywhere it was cored the underside of the thick Lower Salt of the Maha Sarakham Formation is typified by a thin, distinctive basal anhydrite bed composed of flattened mosaic nodules, with a bed thickness that is surprisingly consistent (Fig. 7.44). Work to date has clearly shown the basal anhydrite is a diagenetic unit created by ongoing salt dissolution. It is a pressure-welded nodular anhydrite unit that accreted in the subsurface as a buildup of insoluble residues on the underside of a basinwide dissolving halite sequence (Fig. 7.45a). The process was driven by the escape of undersaturated compactional and thermobaric waters. It is, in effect, an upside-down caprock (Fig. 7.45b).

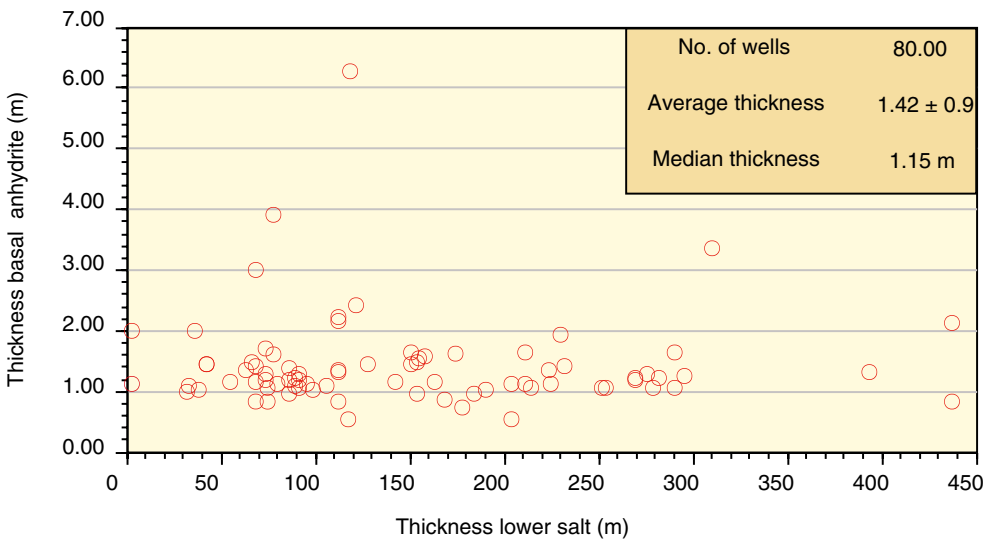

Fig. 7.44 Crossplot of thickness of the basal anhydrite unit versus thickness of the overlying "Lower Salt" in the Maha Sarakham Formation, Thailand

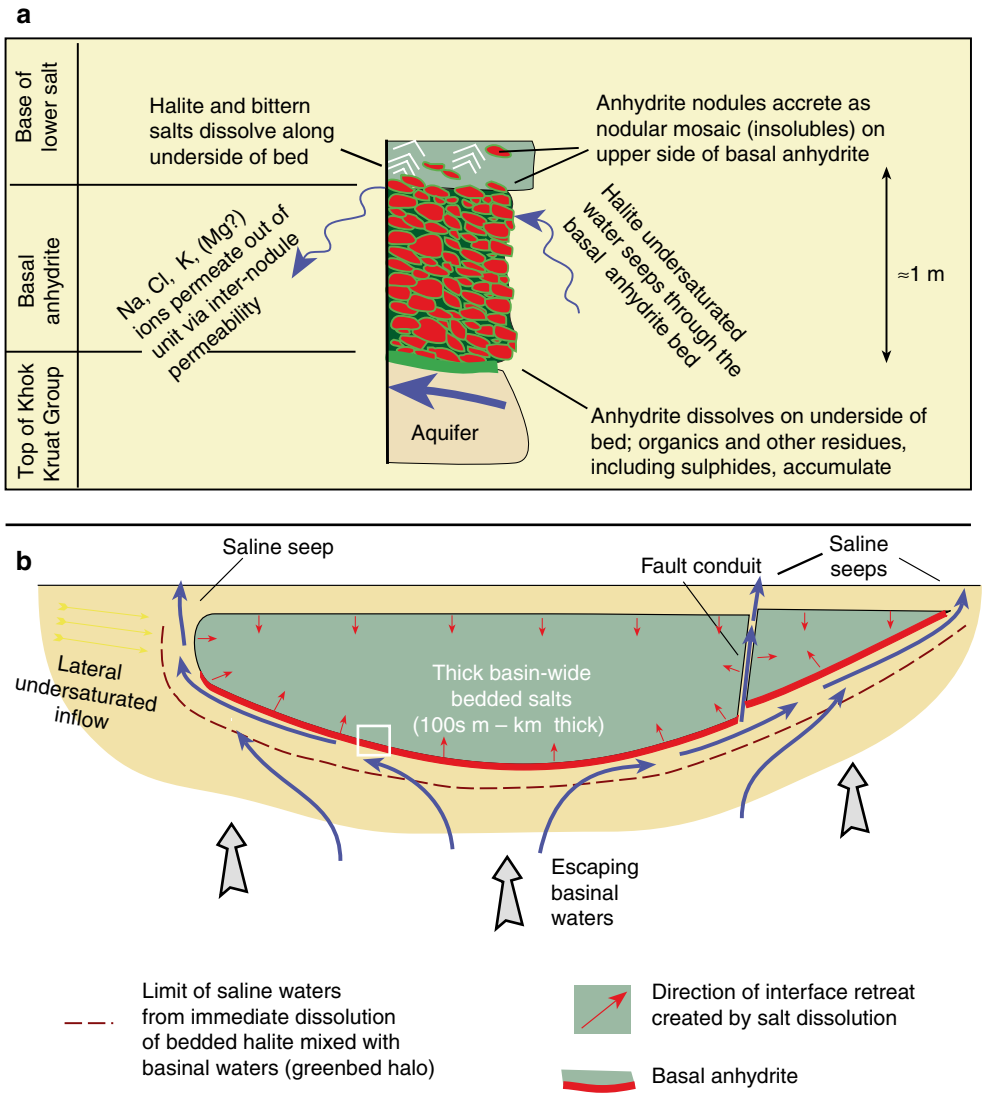

Fig. 7.45 Mode of formation of a diagenetic basal anhydrite. (**a**) Vertical profile through a dissolution-generated basal anhydrite. (**b**) Schematic *cross section with white box* showing relative position of vertical profile (Modified from Warren 1997)

Unlike depositional anhydrites within saline giant fills, which typically thicken into the lowstand platform wedge, the basal anhydrite of the Maha Sarakham has a near constant thickness across the entire basin that is independent of the thickness of the overlying Lower Salt (Fig. 7.44). There are a few wells where the anhydrite is thicker than 1–2 m, but there the anhydrite shows evidence of flow thickening and the wells are typically located at or near the dissolution edge of the Lower Salt where larger karst cavities can form and suprasalt and sub-salt sulphate residues can fold, fault and stack (Fig. 7.41b). The near constant thickness of the basal anhydrite across the Khorat and Sakon Nakhon basins reflects the intrinsic self-limiting permeability of a nodular anhydrite unit accreting beneath a salt overburden. Wherever upwelling basinal waters contact the underside of the Lower Salt unit it dissolves, leaving behind a nodular anhydrite residue. The nodular residue continues to accrete along its top by gathering anhydrite nodules via preferential solution of the salt host. These nodules were originally suspended within the now dissolving bedded halite. At the same time as new nodules are accreting along the upper side of the basal anhydrite, the anhydrite may be dissolving along its underside.

The overall dissolution process is driven by escaping compactional waters flushing the underbelly of the salt (Fig. 7.45b). If the basal anhydrite accretes to where it is more than a metre or two thick it starts to act as an aquitard for waters seeping through its internodular porosity. This slows water access to the halite contact. Thickness can increase until it reaches a point where undersaturated compactional waters can no longer flow through internodule permeability, to reach the halite-anhydrite dissolution front. Once undersaturated waters no longer access the halite dissolution front, anhydrite accretion slows and even shuts down along the upper side of the basal anhydrite unit. Even so, compacting undersaturated waters continue to flow along the underside of the basal anhydrite, where anhydrite dissolution occurs. Once sufficient anhydrite dissolves from its

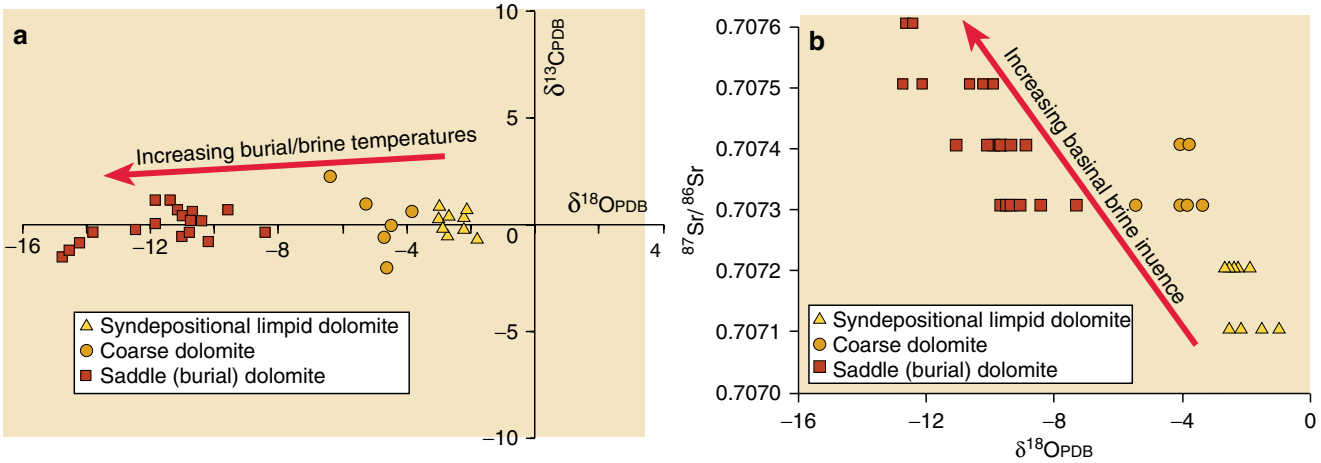

Fig. 7.46 Isotopic signatures in the three types of dolomite occurring in the basal anhydrite of the Maha Sarakham Fm. Thailand. (**a**) Crossplots of dolomite $\delta^{18}O$ and $\delta^{13}C$ isotopic values showing influence of increasing temperature related to ongoing burial. (**b**) Crossplot of $\delta^{18}O$ versus $^{87}Sr/^{86}$ Sr showing influence of ongoing basin brine evolution from limpid dolomite through coarse and saddle dolomite precipitates (After El Tabakh et al. 2003)

underside, undersaturated waters can again reach the halite and dissolve it anew. Basinwide near-constant thickness of the basal anhydrite reflects a buffering interaction between the rate of anhydrite nodule accretion or docking on its upper surface and the rate of anhydrite loss on its lower surface. In effect a basal anhydrite has a "half-life." The actual thickness is determined by the inherent transmissivity of the material between the nodules.

Coarse and saddle burial-stage calcian dolomite precipitates from brines flushing internodular zones in the basal anhydrite. Crystals continue to grow and re-equilbrate into higher temperature forms in response to ongoing burial. This is shown by the evolving carbon and oxygen isotope signatures, as well as $^{87}Sr/^{86}Sr$ ratios, which all define a burial trend from early limpid dolomite through coarsely crystalline dolomite through to saddle dolomite with precipitation signatures indicating increasingly higher temperature basinal fluids (Fig. 7.46a, b; El Tabakh et al. 2003; Warren 2000a).

The laminar underside of the basal anhydrite is made up of what remains once the anhydrite is dissolved, namely, an undulose cm-thick microlaminar organic-rich insoluble residue layer. It contains micronodules and fissure fills of metal sulphides (mostly pyrite and bornite) created by metal fixing and driven by thermochemical sulphate reduction (Warren 2000b). Overall this "upside-down" cap rock is very similar to a pressure solution mega-seam and its diagenetic mode of formation is not all that dissimilar except that the fluid flow is more one sided. This model, explaining laterally extensive, constant thickness basal anhydrites on the undersides of thick halites as a form of dissolution residue, has implications for other evaporite basins that possess basal anhydrite units with near constant thickness.

Caves in Evaporite Karst

At first sight, medium to large scale evaporite karst surface landforms, such as dolines, polje-like depressions, subsidence bowls and collapse dolines, appear near-identical to those found in and on carbonate karst. Likewise, all the smaller-scale intracavern features, both dissolutional (pipes and cavities) and constructive (speleothems), can be preserved as karst zones in and above an evaporite host, even when the formative hydrology becomes inactive and the system is buried (palaeokarst). But, as we shall see, the much higher rates of dissolution of halite and gypsum compared to limestone or dolomite means there are significant differences in rates of formation and cave geometries compared to carbonate caves in nonevaporitic hosts. One cannot simply take models of caves developed by studies of carbonate karst and use them to unreservedly interpret evaporite caves. Differences reflect the inherently higher solubility and flowability of the host salts at earth surface conditions and means most evaporite-hosted caves show peculiarities compared to carbonate karst.

The high solubility of evaporite beds atop deeply-circulating pressurised and jointed aquifers (confined hydrologies) means deep-phreatic chimneying is a common cave-forming mechanism in and atop buried salt beds (Fig. 7.6). When a stoping chimney cave breaches the watertable, it can lead to the rapid creation of numerous steep-sided water-filled collapse dolines. This in turn means high volumes of sediment can swallowed quickly, especially in suprasalt regions with strong roof spans covered by loose sediment. In such settings, large at-surface natural sinkholes can form in days or even hours[9].

[9]The Catholic Church in the early Middle Ages of Europe explained such rapidly formed sinkholes as being "Gateways to Hell," the result of the parishioners sinning a little to much, and/or not paying sufficient tithes to ameliorate the work of the Devil.

Most of the action in uplifting salt beds and masses begins well below the watertable. It takes place hundreds of metres below the surface at bathyphreatic depths where anhydrite is reconverting to gypsum and where caprocks and other dissolution residues are forming. Early dissolution is greatest at contacts between the salt bed and joints or fractures in adjacent aquifers. Thus patterns of jointing or fracturing control the extent and style of caves in a salt host and typically creates high-density maze caves. With halite, the only type of NaCl mass that makes it to the surface is in active or recently active diapirs and namakiers, and so becomes a host to accessible vadose caverns. Prior to its dissolution this cave-hosting diapiric halite is impervious, flowing and re-annealing. Hence, most of the karst action accessible for study in halite caves is vadose and tied to perched watertables, which is most obvious near the margins of namakier salt sheets, well away from locations of active salt fountains.

If phreatic caves ever do form nearer salt fountain domes, these early cavities are quickly closed by the pressurized salt flow needed to bring salt to surface and make it accessible to speleologists. Rather than being telogenetic features, many of the metre-scale blebs of finely-layered gravitationally-aligned laminar halite seen within diapirs intersected in deep salt mines, and floating in a matrix of flow foliated coarse-crystalline halite, are the result of mesogenetic salt precipitating in gas-filled open cavities within the diapir mass. These laminar cavity filling growth-aligned halite textures are not telogenetic. Neither are they salt clasts preserving primary (relict) depositional texture of the mother salt. They indicate the existence of former or present-day gas-filled (often CO_2) cavities, which are a hazard occasionally encountered during potash mining, for example in the diapirs of NE Germany (Hedlund 2012). Their presence and their ability to blow out mine walls clearly show that pressurized gas pockets and associated cavern fill textures are not uncommon mesogenetic features in flowing salt. But most of the shallow cavities and fill textures studied by speleologists in salt are telogenetic.

Cave-forming processes are either vadose or phreatic and many caves show textural evidence indicating transit from one realm to the other. At any one time the transition from vadose to phreatic landforms is tied to depth to watertable. This is seen in the gypsiferous cap karst to diapirs and allochthons of Triassic salt in the Betic Cordillera of Spain (Calaforra and Pulido-Bosch 1999). The crests of the salt structures are dominated by collapse dolines (vadose), this passes radially out into the belt of solution dolines occupied by seasonal saline lagoons and further out into rim of saline springs that form wherever the watertable intersects the landsurface (phreatic). Some caves pass from phreatic to vadose a number of times in response to watertable fluctuations tied to varying climate and tectonics.

Vadose processes characterise the uppermost part of a karst aquifer and have air in pores above any water surface or perched watertable. Water drainage is free-flowing under gravity; cave passages drain downslope and show strong gravitational orientations (numerous sub-vertical features). Because they form above the watertable, vadose cave walls are subject to surface seepage, evaporation and drying. Speleothems decorating the cave walls indicate varying combinations of gravity and airflow and include; stalactites, stalagmites, cave popcorn, helicites and flowstones.

Caves can form in a salt bed on its way down (syndepositional to early burial phreatic), on its way up (evaporite telogenesis begins at bathyphreatic depths) and at the bottom of the bed's burial history (mesogenetic gas-driven karst).

Gypsum Caves

Active caves beneath gypsum karst landforms first formed as deep phreatic maze caves and are characterised by dense passage networks with numerous contemporaneously closed loops, typically in bedded evaporites. Vadose cross sections of the same system can be quite large due to the high solubility and relative homogeneity of the host, especially if formed in a thick capstone. Heimkehle cave in the Zechstein anhydrites in the Harz Mountains of Germany has a overall passage length of more than 2 km, with large rooms up to 22 m high and 65 m wide. It was large enough to be used in World War II to house a factory manufacturing parts for JU88 aeroplanes. Other gypsum caves, some more than 150–200 km long, are well documented in Miocene gypsum hosts in west Ukraine (Table 7.7; Klimchouk 2000; Klimchouk and Andrejchuk 2003; Andrejchuk and Klimchouk 2004; Klimchouk 2007) and much of our current understanding of the gypsum karst process comes from this region.

Gypsum cave walls in the vadose realm are relatively undecorated compared to carbonate caves. But calcitic speleothems can form and are well documented, as are alabastrine flowstones and selenite rinds on cave walls, in northwest Texas (McGregor et al. 1963), in Alabaster Cave and others in the Blaine Gypsum in western Oklahoma (Johnson 1996; Bozeman and Bozeman 2002), and in quarries intersecting the gypsum karst system in the Kirschberg Evaporite member near Fredericksburg, Texas (Warren et al. 1990).

Phreatic Gypsum Caves

Phreatic caves in bedded evaporites atop artesian aquifers typically grow as upward stoping and branching blind flow loops caverns (phreatic cupolas) and chimneys, which can begin to grow deep below the watertable as bathyphreatic or hypogenic[10] karst. For example, deep artesian systems drive

[10]Cave origin can be epigenic (by shallow circulation of meteoric groundwater) or hypogenic (by rising groundwater or production of deep-seated solutional aggressiveness). Epigenic mazes form by diffuse infiltration through a permeable insoluble caprock or by floodwater supplied by sinking streams. Most hypogenic caves involve deep sources of aggressive waters and are instigated at bathyphreatic depths (Palmer 2011).

Table 7.7 Representative morphometry of gypsum maze caves that formed as confined aquifer phreatic systems, compared to Mammoth Cave (unconfined aquifer system) and Carlsbad and Lechuguilla caves (now both unconfined aquifer systems but first formed as sulphuric acid caves with gypsum precipitates)

Cave location and host lithology	Length (km)	Area of cave ($m^2 \times 10^6$)	Volume of cave ($m^3 \times 10^6$)	Area of cave field (km^2)	Volume of rock ($m^3 \times 10^6$)	Specific volume (m^3/m)	Passage density (km/km^2)	Cave porosity (%)	Areal coverage (%)
Optymistychna Cave, W. Ukraine, Neogene gypsum	214	0.260	0.52	1.48	26.03	2.8	127.03	2.00	17.57
Ozernaja Cave, W. Ukraine, Neogene gypsum	111	0.330	0.665	0.74	13.20	6.0	150.00	5.04	44.59
Zoloushka Cave, W. Ukraine, Neogene gypsum	89.5	0.305	0.712	0.63	18.93	8.0	142.06	3.76	48.41
Mlynki Cave, W. Ukraine, Neogene gypsum	24	0.047	0.080	0.17	2.38	3.3	141.18	3.36	27.65
Kristalna Cave, W. Ukraine, Neogene gypsum	22	0.038	0.110	0.13	1.82	5.0	169.23	6.04	29.23
Estremera Cave, Madrid, Spain, Neogene gypsum	3.5	0.008	0.064	0.06	0.71	18.3	59.32	9.04	13.56
Mammoth Cave, KY, USA, Carboniferous limestones	550	1.386	8	36.78	3,310.2	14.5	14.95	0.24	3.77
Lechuguilla Cave, NM, USA, Permian limestone	193.4	–	–	–	–	–	–	–	–
Carlsbad Cavern, NM, USA, Permian limestone	49.6	–	–	–	–	–	–	–	

After Klimchouk (2003, 2007), Palmer and Palmer (2000); and listed references

cupola karst and blind chimney stopes in the Black Hills of Dakota (Fig. 7.16), the Elk Point Basin of Canada (Fig. 7.16) and the Optymistychna Cave, western Ukraine (Fig. 7.47). Deeper in a basin, where bathyphreatic caves are bathed by centripetal mesogenetic crossflows, water flow is slow and phreatic karst is influenced by the escape of H_2S- and CO_2 -rich basinal waters, not necessarily by confined meteoric head. Fluid flow at these greater depths is driven by pore water gradients that reflect potentiometric variations in temperature, organic maturation, pressure and salinity of basinal waters.

Passages in mesogenetic and telogenetic evaporite-hosted caves tend to first develop near fractures and joints in adjacent aquifers and then expand into maze cave networks. Once growing in the main evaporite mass, some phreatic maze passages can show internal upward-directed switchback gradients independent of jointing in adjacent aquifers. Cave orientations within the evaporite bed and away from the aquifer inflow level are tied to internal inhomogeneities in the host bed such as less soluble or more soluble intrasalt beds and changes in mineral proportions.

Phreatic tubes are the most common passage shape in smooth-walled blind-dissolution pockets and cupolas in bathyphreatic gypsum caves. Tube or channelway shapes range in cross section from near-circular (isotopic dissolution of soluble host) to elliptical tubes to canyon-shaped keyholes (Fig. 7.48; Klimchouk 1992, 1996). Ornamentation is minimal where undersaturated crossflow drives the rapid dissolutional breakdown of the cave wall and the resulting passages are smooth, with local scalloped dissolution irregularities. Dense intersecting maze cave networks first form in the early stages of exhumation at the contact between a tight but soluble gypsum/anhydrite unit and a less soluble carbonate or siliciclastic aquifer (Figs. 7.47 and 7.48). This less soluble bed is the supply conduit for groundwater crossflows that dissolve the edges of the initially impervious anhydrite/gypsum bed. The greatest rate of water supply to the dissolving gypsum contact is along joints and fractures in the adjacent aquifer bed (especially with limestone aquifers). Accordingly, the meshwork of caves penetrates the gypsum bed and tends to follow joint and fracture patterns of the adjacent aquifer.

More stagnant phreatic portions of telogenetic $CaSO_4$ cave systems can be saturated and so precipitate isopachous crusts and crystal rinds. Gypsum is the commonplace isopachous precipitate in voids in this setting, while anhydrite tends to dominate in cavities in the deeper mesogenetic realm (Garcia-Guinea et al. 2002). By the time phreatic maze caves are exhumed and enter a vadose setting, where they are accessible for speleological study, much of the earlier phreatic ornamentation has already been dissolved by the increasing undersaturated throughflow and cavern interconnection. This is associated with uplift into the more hydrologically-active phreatic realm, which always precedes entry into the vadose realm (Warren et al. 1990).

Some of the longest and most complex phreatic maze cave systems in the world are found in Miocene gypsum in west Ukraine. Optymistychna Cave, with more than 214 km of surveyed passages, is the world's longest gypsum cave and the second or third longest cave of any type (Table 7.7; Fig. 7.47; Klimchouk 2007). The world's longest cave, at

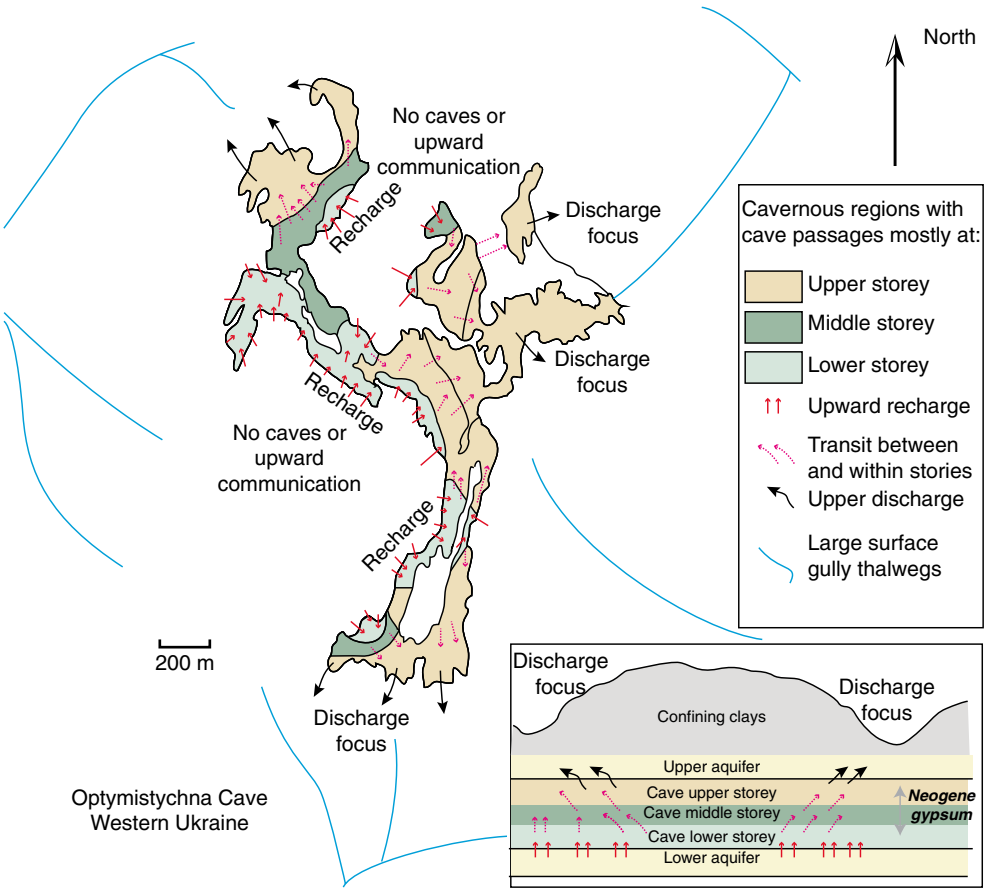

Fig. 7.47 Optymistychna Cave, western Ukraine, is part of a 214+ km long maze in a confined Neogene gypsum host, showing multi-story cave levels and the reconstruction of its recharge-discharge arrangement during the time of its formation. Inset diagrammatically shows the hydrostratigraphy and the stair-case effect of the recharge-discharge offsets. The relative thickness of the 18 m-thick gypsum bed (18 m) is exaggerated in the cross section (After Klimchouk 2007)

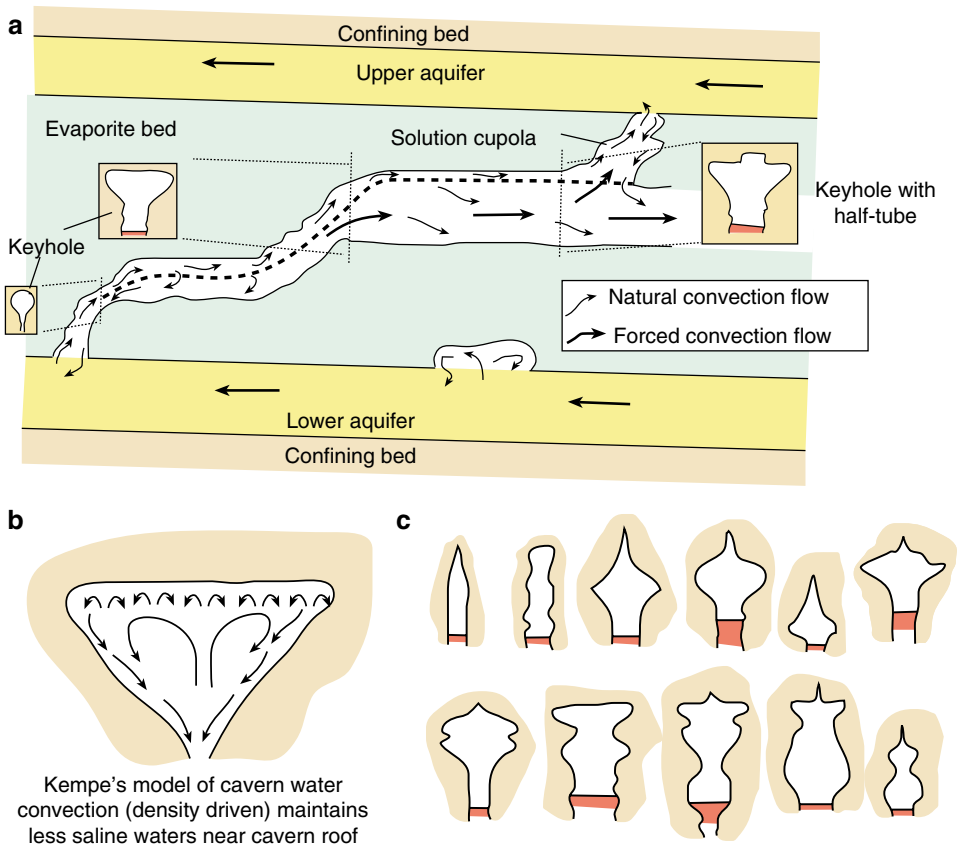

Fig. 7.48 Maze caves. (**a**) Formation of upward expanding dissolution cupolas by pressurized buoyant currents, such a system drives the formation of gypsum caves in the western Ukraine. The diagram shows the schematic relationship between lines of natural and forced convection flow on the mature stage of artesian speleogenesis, when conduit connection has already been established through the gypsum, but forced flow is slow due to the major constraint of the upper confining bed, see also Fig. 7.47. (**b**) Cross section of Kempe's (1972) model for phreatic tube cavern development via dissolution due to natural density convection, (**c**) examples of typical cross-sections from the gypsum caves of the western Ukraine showing varieties of notching or faceting effects from differing rates of lateral expansion (dissolution) (After Klimchouk 1992, 1996; Kempe 1972)

550 km, is the carbonate-hosted Mammoth Cave of Kentucky. The West Ukraine region contains the five longest known gypsum caves in the world, accounting for well over half of the total known length of known gypsum caves on Earth. By area and volume the world's largest gypsum caves are: Ozernaja (330,000 m^2 and 665,000 m^3; with 122 km of documented passages it is also the world's 10th longest), Zoloushka (305,000 m^2 and 712,000 m^3), followed by Optimisticheskaja Cave (260,000 m^2 and 520,000 m^3). They are all complex joint-controlled maze caves, formed under confined aquifer conditions that existed from the Pliocene to the Early Pleistocene (that is karstification on the way up – telogenesis or gypsum exhumation, initially focused on the underside of the bed). Their growth patterns indicate upward-transverse phreatic groundwater circulation, with ultimate cavern fusion across the gypsum bed. All these west Ukrainian caves were fed by artesian crossflow in sub-gypsum and supra-gypsum aquifers that were sourced in the Carpathian Mountains.

High rates of dissolution in phreatic gypsum caves, relative to rates of water crossflow, are indicated by bevelled, faceted and "keyhole" cross sections in the Ukrainian caves (Fig. 7.48a; Klimchouk 1996; Pfeiffer and Hahn 1976). Keyholes indicate density stratification and convectional circulation in cave-forming waters, with shapes sometimes complicated by lithological discontinuities in the gypsum bed (Fig. 7.48b; Kempe 1972). Convection in caves is most pronounced where sluggish artesian flow and low flow velocities dominate.

This was the case in the Pliocene to early Pleistocene history of the maze caves of the western Ukraine (Klimchouk and Andrejchuk 2003). At that time the deeply buried gypsum dissolved via upward growing but blind, phreatic cavities, with a reflux of somewhat denser "spent" waters sinking toward the base of the cave. Spent water was replaced by less dense inflow waters supplied from the lower aquifer. This set up a natural density-stratified convection, which maintained fresher (less dense) waters near the phreatic cave roof. Upward growing blind caves tend to expand more at their tops driving the transition from subcircular to keyhole caverns along the cave conduit. After dissolving gypsum and increasing in density, a portion of the "spent" cave water sank all the way back into the underlying aquifer where it once again joined the regional throughflow in the lower aquifer. Once a stoping cave breached the top aquifer water flow direction in the cave was controlled by temperature, pressure and density contrasts between aquifers on either side of the gypsum bed. It seems that post-breach most of the cave water continued to rise through the cave system into the overlying aquifer (Figs. 7.48a and 7.49) Similar keyhole and cupola morphologies are developed in low flow rate bathyphreatic sulphuric acid caves in carbonate hosts (e.g., early stages in the formation of the Carlsbad and Lechuguilla caverns; Fig. 7.62).

Formation of keyhole passages is not an exclusively phreatic phenomenon in density-stratified gypsum caves. Keyholes in the vadose portions of many telogenetic carbonate caves indicate the transition of the cave passage from phreatic, with circular cross sections, to vadose with

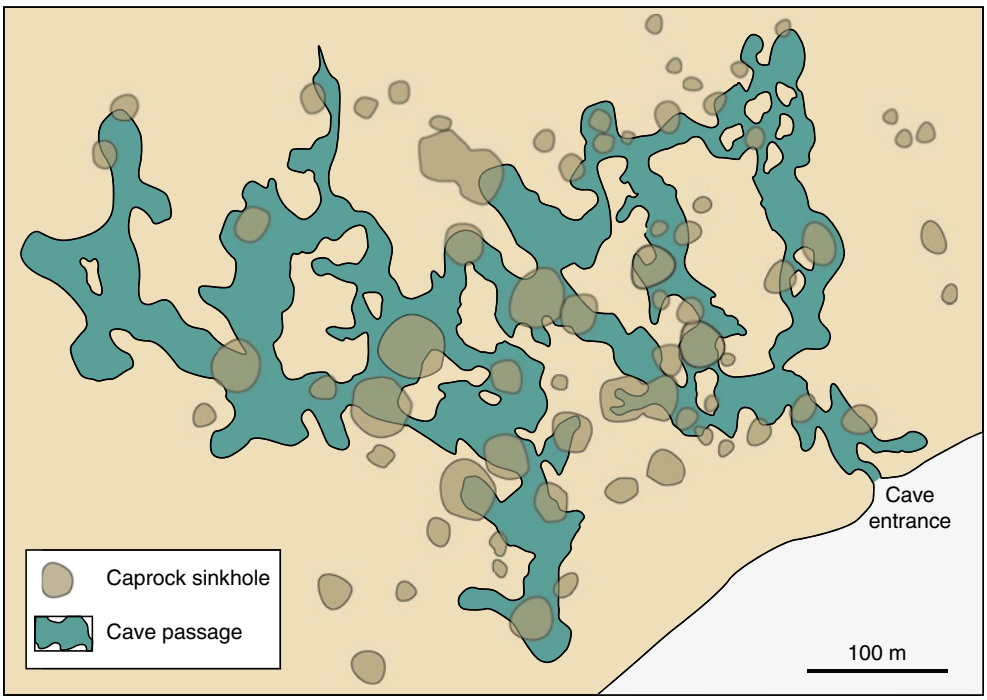

Fig. 7.49 Map illustrating the correlation between caprock sinkholes and vadose passages in Permian gypsum subcrop in the region of Kungur Caves in Russia (Waltham et al. 2005)

deepening drainage slots at the base of the passages (e.g. Calaforra and Pulido-Bosch 2003). Phreatic stoping, followed by vadose cavern enlargement, probably explains the close correlation between caprock sinkhole distribution and position of underlying vadose passages in Permian gypsum subcrop in the Kungur Cave region in the Russian Urals, where the caprock thickness is a little as 25 m (Fig. 7.49).

Vadose Gypsum Caves

A lowering of the watertable, either by uplift or climatic change tied to increasing local aridity, converts a former phreatic cave into a vadose cave. This is the recent history of the accessible portions of the gypsum maze caves worldwide, including documented examples in New Mexico, the western Ukraine and Saudi Arabia where the passage into the middle-upper Pleistocene marks the transition from phreatic to vadose in most of the accessible caves. It is characteristic also of the very recent history of some natural phreatic caves where watertables were artificially lowered to allow quarrying of gypsum (Klimchouk 2012).

Climate shifts or watertable fluctuations at the early end of the burial cycle can create alternating vadose-phreatic conditions in evaporite beds in the early stages of burial and so create an early watertable-associated karst level in the accumulating evaporites. That is, a gypsum bed hosting a vadose hydrology on its way down into burial, may pass through the watertable a number of times before its ultimate burial and passage into the mesogenetic realm. This is the case today in the captured recharge playas in central Australia (Fig. 2.63) and about the edges of some halite-filled salars in the Andes (Fig. 3.43) and many Canadian salt lakes (Last 1993a), where fluctuating hydrologic conditions alternate between vadose and phreatic. Similarly, Quaternary climate shifts have variably karstified the gypsiferous sediments of many Sinic playas. For example, Yauro and Cooper (1997) document Pleistocene lake basins in north-west China, such as in the Chaidamu Basin, where exposed gypsum beds evidence karst overprints that include: corroded flutes, fissures, small caves and associated collapse breccias and roof falls, followed by phreatic evaporite cement overprints. Watertable fluctuation is a hydrological overprint that is preserved as alternating ornamented surfaces in gypsum caves, disconformities and cave fills in many ancient lacustrine gypsum units.

Miocene Epikarst in the Madrid Basin, Spain

The Miocene sedimentary record of the Madrid Basin displays several examples of palaeokarstic surfaces sculpted within the gypsum bed at the same time that the overlying strata were deposited (Rodríguez-Aranda et al. 2002; Cañaveras et al. 1996; Sanz-Montero et al. 2006). The karst indicates a time of freshening (early burial karst) in the same lacustrine setting that was also depositing further gypsum atop the karst. One of the better documented of these palaeokarstic surfaces separates the Lower and Intermediate units at the boundary between what are two main lithostratigraphic units in the basin (Fig. 7.50). There epikarst formed in Aragonian lacustrine gypsum as it was covered by terrigenous deposits of the overlying Intermediate unit. Karst features include infiltrations of the overlying Aragonian marls into the gypsum of Lower unit for up to 5.5 m below the epikarst surface. The presence of a shallow, but fluctuating, watertable at the time of karstification, along with low hydraulic gradients in the evaporite basin, were the main factors controlling karst style.

Karstification was extensive and rapid, it took place in a relatively short time frame of several thousands of years (Fig. 7.50; Rodríguez-Aranda et al. 2002). Stage 1 of the karstification was the accumulation and bioturbation of a bed of lenticular gypsum in a moderately saline lake (Fig. 1.39). During periods when the lake dried out, plants colonised the poorly indurated and exposed gypsum ground (Stage 2). These halophytic plants contributed to the local transformation of primary gypsum to anhydrite through a dissolution–reprecipitation process, similar to that reported from vadose zones in supratidal sabkhas, salinas and losing playas. Stage 3 corresponds to the death and decay of plants, with the root holes behaving as preferential conduits for entry of meteoric water. Anhydrite, which had formed in the soil via respiring plant roots, was unstable and transformed to secondary gypsum. Continued vadose flushing of the initial conduits resulted in the formation of cylindrical and funnel-shaped pits that mimic, but do not strictly represent, root casts or rhizoconcretions (Stage 4). Both the vertical vadose conduits and gypsum caves only penetrated a few metres below the palaeokarst surface, suggesting the ongoing presence of a shallow, still saline watertable. The position of the watertable played a critical role throughout (stages 1–6) and limited the depth reached by both exokarst and endokarst features (Fig. 7.50). In addition, the formation of roughly planar, horizontal cavities was probably related to the top of the watertable, which also represented the maximum depth for root penetration (stage 4).

Formation of horizontal caves was constrained by stratification planes in the gypsum host rock. Conduits and caves were coeval with larger gypsum dolines, and all were partially to completely filled by varying combinations of clayey mudstone, carbonate and detrital gypsum (stage 5). Clays in the karst fill are mostly coarsely laminated, green mudstone beds, possibly reworked from mudflat and alluvial fan deposits that are laterally associated with the lacustrine gypsum (Rodríguez-Aranda 1995). Clay infiltration was probably tied to periodic floods of the karstified surface, with the caves and doline floors making depressions where waters ponded with a relatively high concentration of suspended fine-grained siliciclastic material and organic detritus.

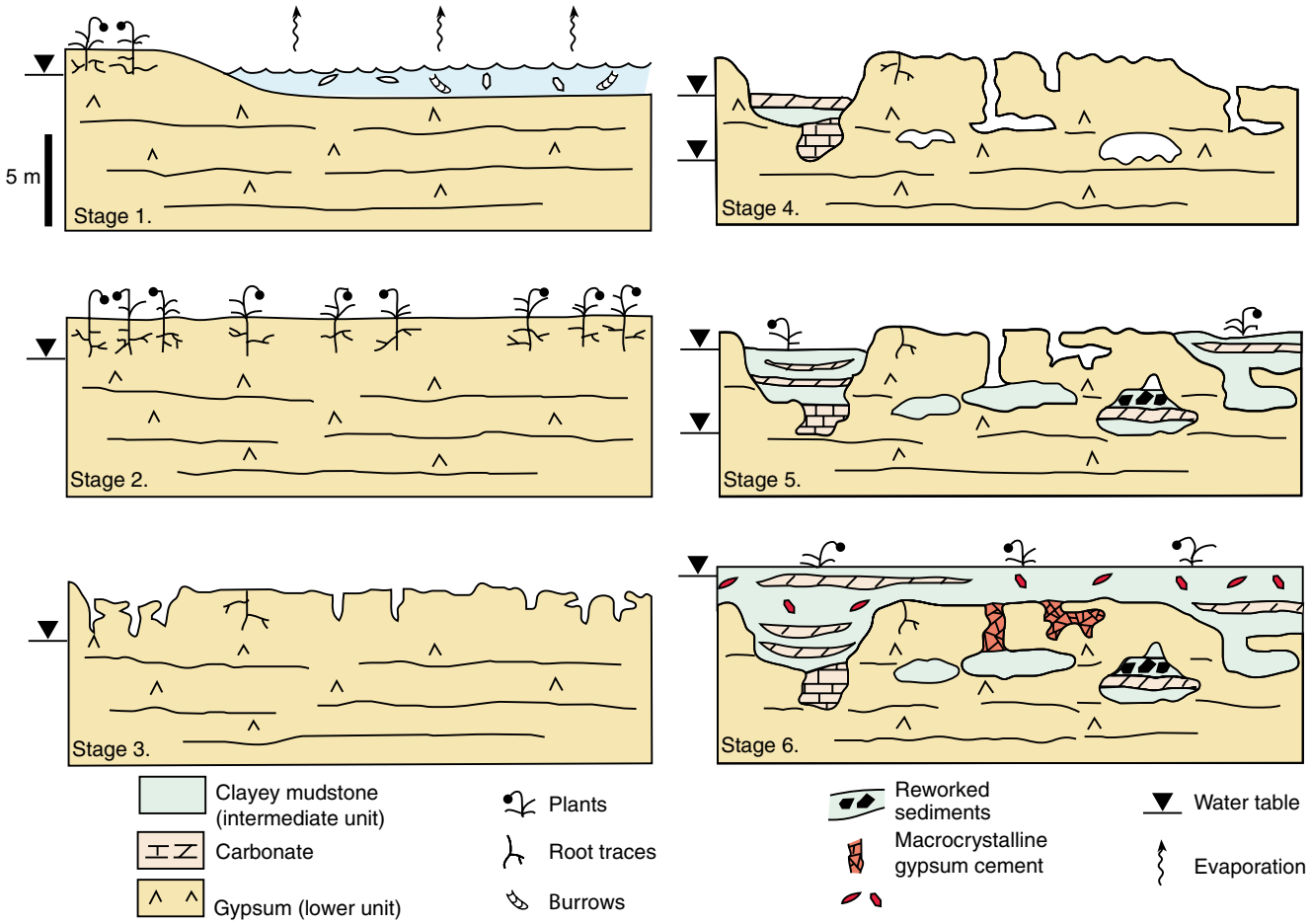

Fig. 7.50 Development of epikarstic surfaces and associated endokarst in the Miocene Gypsum of the Madrid Basin. See text for detail of the evolutionary stages (After Rodríguez-Aranda et al. 2002)

These mudstone fills in the gypsum caves are similar to the mud-filled cavities observed by Last (1993a) in modern saline lakes of the northern Great Plains of western Canada, and are consistent with the episodic clastic input patterns recognized in similar gypsum karst in the Sorbas Basin, SE Spain (Calaforra and Pulido-Bosch 1999, 2003).

Carbonate is present in the sedimentary fill of both dolines and gypsum caves. Carbonate in the dolines consists of massive to peloidal dolomicrite or nodules developed in laminated claystone, whereas carbonate in caves typically consists of calcite rafts and patches of reworked calcitised gypsum. The doline carbonates were probably deposited in shallow water that was episodically ponded in the karstic depressions. The carbonate nodules are probably pedogenic, arguing for punctuated deposition with times of subaerial exposure during the sedimentary fill of the dolines. Calcite rafts in clayey cave deposits suggest inputs of clastic sediment alternated with periods of standing water when calcite rafts precipitated at the air–water interface of pools in the caves (Taylor and Chafetz 2004). Sanz-Montero et al. (2006) argues that much of the dolomite replacing and mantling corroded gypsum crystals in the Madrid Basin is microbially facilitated.

Alluvial fine-grained sediments of the Intermediate unit then accumulated and filled any remaining irregularities in the epikarst surface, which was pocked by numerous doline depressions and unfilled cavities (pits and conduits) (Stage 6). Once dolines were entirely filled by fine-grained sediment and the adjacent epikarst surface was also covered, a sedimentary discontinuity was preserved between the top of the bedded gypsum and the overlying clay. Clay had by then accumulated in the various pits and conduits that were not filled in earlier stages of karstification.

Infill of the remaining cavities includes macrocrystalline gypsum cement meshworks or mosaics that are especially obvious in cavities with little or no earlier detrital fill (Stage 6). They indicate saline phreatic conditions where a rise in the watertable accompanied the deposition of the terrigenous sediments that now sealed the palaeokarstic surface. The same saline pore waters, perhaps derived by ongoing subsurface gypsum dissolution, also drove the precipitation of displacive gypsum crystals in some nearsurface clays.

Subsequent to this early paleokarst, somewhat younger paleokarst features overprint the same gypsum beds. They are driven by later uplift and telogenesis and typified by sagging and suffosion overprints at the lower boundaries of various Plio-Pleistocene terrace deposits in the Madrid Basin (Gutiérrez et al. 2008).

Modern Karst in Cretaceous Gypsum, Texas

At the other end of burial cycle are telogenetic vadose gypsum caves responding to recent uplift of buried anhydrite beds and the transition from phreatic maze caves to vadose caves with gypsum and calcite speleothems. Ornamented vadose gypsum caves, a late stage of this conversion, are today exposed within the workings of the Fredericksburg Gypsum Quarry in a 10-m (30 ft) thick gypsum bed. The gypsum is the nearsurface remnant of the Cretaceous Kirschberg Evaporite Member, which was exposed during the late Tertiary exhumation of the Edwards Plateau (Warren et al. 1990). Early stages of the uplift were typified by the rehydration of anhydrite back to gypsum and the formation of fibrous vein fills.

Complete telogenetic dissolution of the evaporite level is indicated by a widespread evaporite solution breccia, which constitutes one of the most permeable and most important aquifer intervals in the Edwards Plateau (Barker et al. 1994).

Relatively impervious nodular gypsum hosts most of the caves, with nodules showing varying overprint by coarser crystalline gypsum daisy textures. Much of the cave fill and ornamentation is made up of a more permeable alabastrine gypsum precipitate (Fig. 7.51a). Where a gypsum bed is completely dissolved by cave expansion all that remains of the former gypsum karst is a jumble of speleothem clasts beneath and within a dolomitic crackle breccia. Most of the larger blocks in the breccia were derived from the overlying Edwards Formation and are now encased in a residuum or matrix of silt- to sand-sized dolomite rhombs ("chalky"

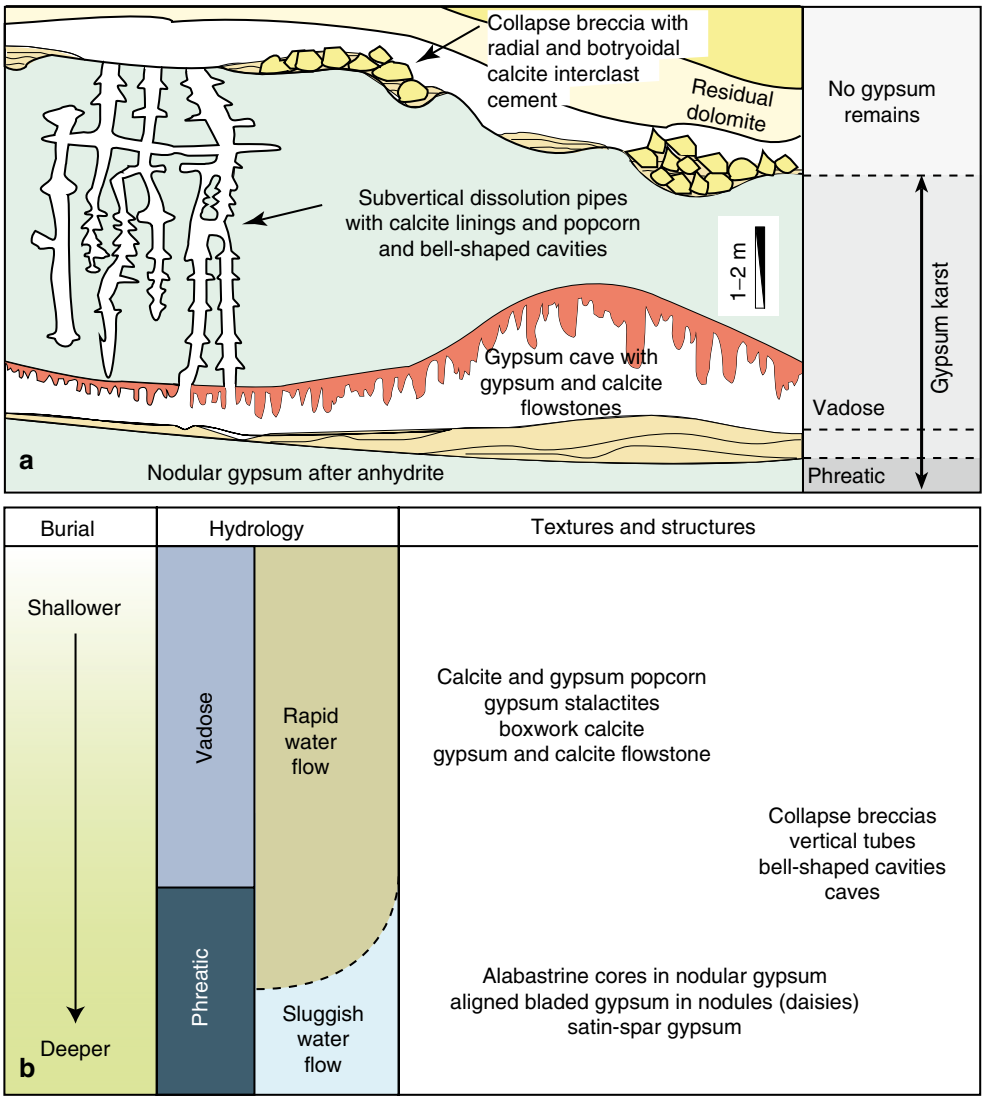

Fig. 7.51 Model karst and related calcite textures developed though sequential complete dissolution and retexturing of an uplifted gypsum bed – based on textures in the subcrop of the Fredericksburg Gypsum in central Texas. (**a**) Schematic cross section through the dissolving now vadose gypsum bed. (**b**) Textural evolution related to groundwater regime (Modified from Warren et al. 1990)

dolomite). The rhombs were originally floating in a matrix of gypsum/anhydrite and their equivalents can still be found as dispersed rhombs and layers in nearby, as yet undissolved, gypsum beds.

Friable alabastrine gypsum up to 10–20 cm thick, coats cave walls in zones of sluggish and perched groundwater crossflow. It is made up of silt-sand sized euhedral prisms with a delicate open "pack-of-cards" texture that could only be preserved in caverns experiencing very low rates of fluid cross flow. Gypsum is also locally reprecipitating as small stalactites and stalagmites in vadose cavities. Walls tend to be smooth and unornamented in other nearby caves with more active throughflow.

The following sequence of exhumation and karsting was listed by Warren et al. (1990) as indicative of a transition from deep phreatic to vadose hydrologies (Fig. 7.51b):

- *Formation of nodular "daisy-head" gypsum* As uplift raised this bed of nodular anhydrite into the zone of rehydration, replacement by gypsum was at first slow but pervasive, with near-stagnant phreatic fluids oozing into the calcium sulphate bed. At the microscale, stagnant deeper phreatic waters seeped into the nodular anhydrite bed. Flow was focused along inter-crystalline porosity films within the dolomite rims surrounding the calcium sulphate nodules or it was focused along thin-bedded dolomite stringers within the anhydrite bed. Millimetre to cm-sized, aligned gypsum crystals nucleated off these flow paths and grew inward toward the nodule core via dissolution and replacement of the anhydrite to form daisy-textured gypsum. The main mesoscale permeability entries into the gypsum bed were provided by fractures in the adjacent aquifers, which began to render a maze cave network.
- With further uplift there was a change to more active hydrologic conditions, which modified the rate of gypsum growth and fine gypsum crystallites that characterise alabaster came to be the dominant precipitate. Replacive gypsum grew more rapidly through the unit as a microcrystalline alabaster texture overprinted some of the nodules. The adjustment in gypsum texture as the unit was exhumed probably reflects more pronounced fluctuations in temperature and saturation tied to increased groundwater crossflow (Fig. 7.51b). This was probably related to greater access of undersaturated phreatic water to the unit as the dense network of joint-controlled maze caves permeated the gypsum and were fed from joints and fractures in the adjacent aquifer and possible increasing influence of unconfined waters atop the exhuming evaporite.
- *Karst structures and calcite/gypsum speleothems* As the gypsum bed passed into the zone of active phreatic flow and then vadose infiltration, the process of gravity-driven karstification began in earnest. Nodular and alabastrine gypsum now was subject to widespread dissolution. Phreatic groundwater entry was first along joint mazes, while vadose infiltration in the exhumed parts of the unit tended to expand former phreatic caves and to create new vertical pipes with scalloped edges indicating the downcutting process. Gypsum and calcite speleothems formed in caves and pipes within regions of less active vadose crossflow, mainly as cave popcorn, flowstone and alabastrine laceworks (Fig. 7.51a).
- *Brecciation and complete loss of gypsum* Complete dissolution of the gypsum bed produced zones of collapse breccia, with circumclast radial and botryoidal calcite cement (speleothems). Collapse occurred gradually over wide areas of contact between the bedded gypsum and adjacent strata so that the overlying beds tend to be lowered gently into broad folds. Regionally, the overburden stratification was little disrupted by widespread foundering associated with the complete flushing of gypsum. Regionally a residual zone of pulverulent dolomite rhombs ("chalky" dolomite) overlain by packbreccia now defines the cap to the dissolved gypsum bed. Where gypsum remains, some of this unconsolidated dolomite residuum is washed from the upper surface of the dissolving gypsum into karstholes and pipes that cut down into the gypsum to accumulate on the conduit floors with classic "vadose silt" textures.

There is abundant calcite precipitating as void fill in rubble breccia cavities and pipe linings, but there is no discernable conversion of the chalky dolomite to calcite (dedolomitisation) in this system. XRD shows chalky dolomite remains well ordered and near stoichiometric. The lack of dedolomitisation raises the question: Is dedolomitisation commonplace in evaporite beds on the way down in the burial cycle, when newly formed dolomite is more likely to be a less -ordered highly-metastable form of dolomite? The corollary is that it is less common in evaporite beds on the way up (see calcitisation of evaporites discussion later in this chapter)?

The end result of unroofing an ancient evaporite bed in this humid region of central Texas, where the karsted gypsum beds never outcrops, is a stratiform chalky calcitic/dolomitic residuum layer that underlies a gently folded and collapsed packbreccia bed (Warren et al. 1990). The former position of a regional decametre-thick $CaSO_4$ bed is now defined by cm-metre thick interstratal packbreccia characterised by brecciated and rebrecciated fragments of calcite popcorn, boxwork and botryoidal calcite, all intermixed with fragments of the overlying strata and the dolomite residuum. None of the original evaporite salt remains in the final breccia.

Zahm and Loucks (2011) have mapped this dissolution breccia and associated fracture patterns in outcrop, for more

than 100 km across the Comanche Shelf of central Texas (along Interstate Highway 10). They defined three consistent intervals across the outcrop and subcrop belt: (1) a characteristic substratal fracture/alteration interval beneath the evaporite zone; (2) an intrastratal interval containing the evaporites or fractured breccia residuals; and (3) a suprastratal interval overlying the evaporite level that typically shows deformation and fractures generated by collapse into the caverns created by evaporite dissolution. Deformation within the substratal interval is characterized by low-intensity opening-mode fractures with orientations that parallel pre-existing Palaeozoic structures, which unconformably subcrop below the zone of interest. Intrastratal deformation, which is characterized by both extensional and compressional structures and fractures, including normal and reverse faults and folding. Faults and fold axes within this zone also tend to parallel pre-existing structural trends. In addition, zones of extensive chaotic brecciation occur in localized areas. Finally, suprastratal deformation includes extensional and compressional faulting and zones of high intensity opening-mode and shear fracture zones. Clearly evaporite dissolution, independent of any external tectonic stress can create fractures. This and the associated creation of open fractures in overburden has important environmental implications wherever a fractured aquifer so created is proposed as a possible subsurface brine disposal level, as in fractured Devonian carbonates beneath the Cretaceous tar sand areas of Alberta (Chap. 10). Such systems must be shown to be sealed, with no collapse fracture-related connections to shallower aquifers.

Modern Gypsum Karst in Saudi Arabia

Similar telogenetic gypsum transformations, associated with gypsite/alabaster replacement, brecciation and karstification, are seen at Dahl Hit (*dahl* = *cave*) at Ain Hit in eastern Saudi Arabia (Fig. 7.52a, b). There the 72 m-thick type section of the Hith Formation outcrops in the roof and sides of a large collapse-prone doline mouth to a phreatic tube cave. In the subsurface the Hith Anhydrite is a major regional seal to the prolific reservoirs of the Arab Formation of Saudi Arabia and the western Emirates and it is typically more than 120 m thick in these oilfields (Chap. 10). The tubular cave mouth defines the lower part of the breached doline floor and leads down into a phreatic tube cave that has yet to be completely surveyed. The cave entrance is located at the Hith Anhydrite's contact with the limestones of the overlying Sulaiy Formation. The cave is steeply inclined (≈30°) and floored by a scree slope composed of packbreccia created by gypsum layer breakdown. Blocks in the packbreccia are jumbled combinations of collapsed carbonate overburden and transforming blocks of Hith Formation anhydrite. Larger blocks range up to 3–5 m across. Like most phreatic tube caves, the cave walls are smooth and unornamented with the floor covered by angular blocks of fallen roof. Much of the fine bottom sediment that covers the packbreccia on floor of the water-filled parts of the tube cave is composed of insolubles from dissolution of the Hith Anhydrite.

For centuries Hit Dahl at Ain Dit was a source of fresh water for the local population (*Ain* = *water spring*). But overpumping in the last few decades has led to a drastic drawdown of a potable water layer that once floated atop more saline phreatic water in the cave proper. The rapid lowering of the watertable destabilised the cave roof. Dahl Hith is now a dangerous cave to visit. On my last visit in 2005 a large section of the roof had just collapsed in the preceding days. Much of the interior of the cave fissure is now packed with freshly collapsed blocks making cave access much more difficult than in the past. Recently (2011), the watertable has risen by more than 25 m, unfortunately it seems this may be due to an influx of polluted water (possibly excessive agricultural runoff or sewage entering the groundwater) and the former clear waters are now at times clouded by bacterial blooms and scums, metabolising the high levels of phosphates and nitrates now in the system (<http://www.saudi-caves.com/sewage/index.html> last accessed June 10, 2014).

At outcrop scale (Fig. 7.52c) the retreating dissolution edge of the gently dipping Hith Fm. creates an obvious zone of bedding disturbance, megabrecciation, slumping and folding in the Sulaiy Formation. The current contact with the dissolved and monoclinally dipping Hith Formation (≈30–40°) at Hit Dahl is defined by large collapse features and rotated mega-blocks of overburden in the flexure zone atop the shallow subcrop edge of the anhydritic Hith. A megabrecciated zone defines overburden collapse along the subcropping monoclinal edge of the Hith in Saudi Arabia and it can be traced as an elongate at-surface expression of the Hith for more than 550 km along strike. Similar, also spectacular, collapse dolines and rotated mega-blocks characterise gypsum karst features in the subcrop belt of the Eocene Gachsaran Formation in the foreland foldbelt of Iran (Cucchi and Zini 2003).

Active collapse fractures, visible in plan view of the cave entrance and in the Hit cave wall, show the effects of solution-related extensional collapse on the meteoric conversion of grey anhydrite to white-buff alabastrine gypsum (Fig. 7.52a, d). Bedding parallel layering in the Hith is largely preserved on conversion to the fine alabaster crystals, which create an almost mimetic preservation of precursor texture. Thin extension fractures parallel to the main fracture/collapse allow the formation of thin alabaster streaks, which are clearly visible in the left third of the photo (Fig. 7.52d).

The nature of the anhydrite-to-gypsum conversion front at Dahl Hit varies from fracture parallel, as seen in Fig. 7.52d to bedding parallel, as seen in Fig. 7.52e. In the latter case the upper boundary of the residual anhydrite block shows a nodular replacement contact with the newly precipitated alabaster. In contrast, its lower contact shows a more feathered

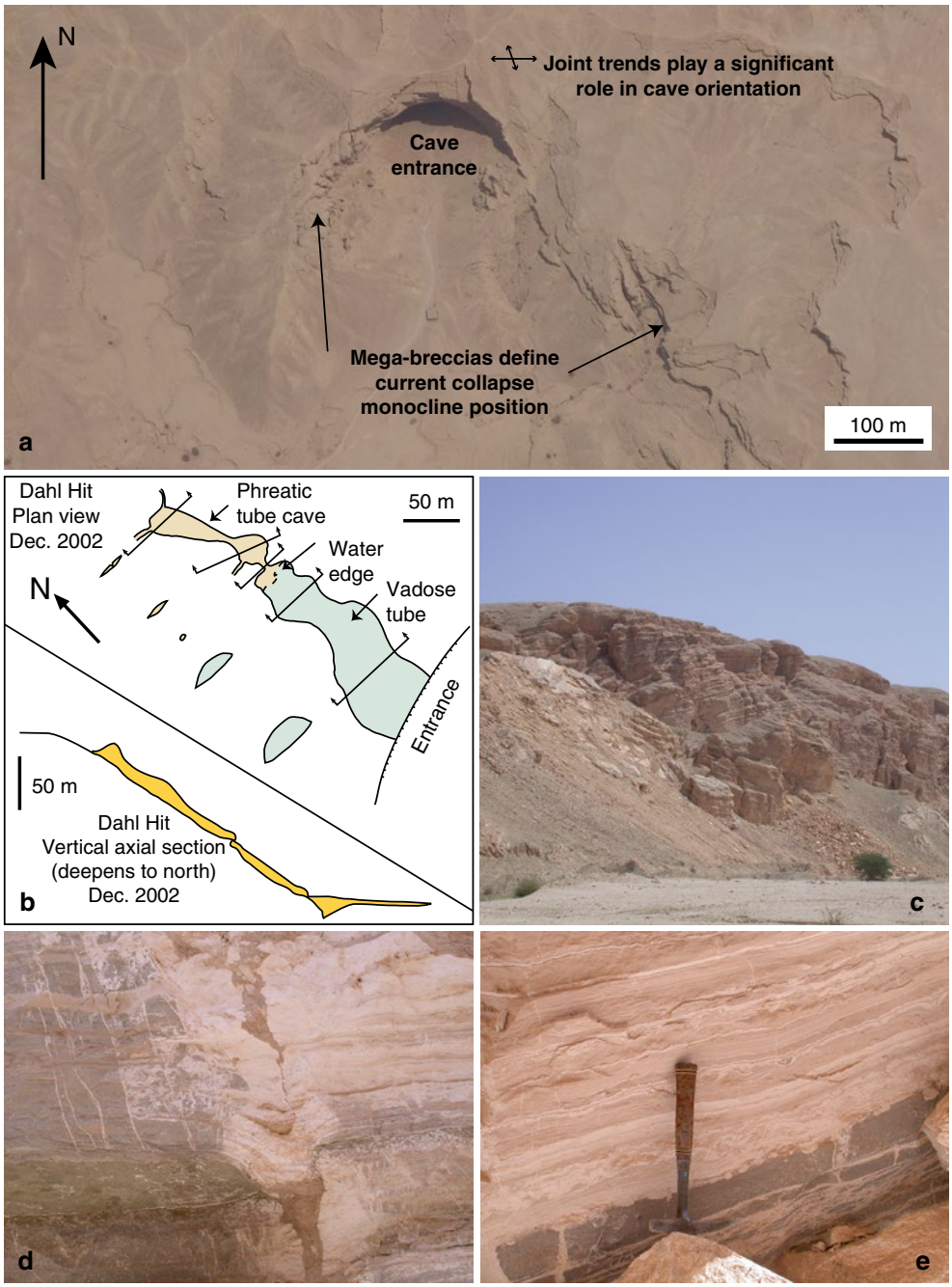

Fig. 7.52 Dahl Hit at Ain Hit in Saudi Arabia. (**a**) Plan view showing joint-set control on cave mouth. (**b**) Surveyed geometry of Dahl Hit (Replotted from Gregory et al. 2002). (**c**) Mega breccia along collapse monocline is an overburden disturbance created by the nearsurface conversion and dissolution of the underlying Hith anhydrite. Cliff ≈ 100 m. (**d**) Contact between alabastrine gypsum and anhydrite in the area of the cave entrance showing a v-shaped breccia- and clay filled cavity some 50 cm across. (**e**) Detail of the conversion front with buff alabastrine gypsum at top, grey remnant anhydrite below, upper conversion contact is nodular, lower transition is feathered, Bedding parallel white veins in the alabastrine gypsum are satin spar gypsum. Images **c** through **e** illustrate the effects of anhydrite conversion at the outcrop edge of the Jurassic Hith Fm. anhydrite at Hith Dahl

relationship. White bedding-parallel satin-spar has formed in small fractures in the anhydrite and parallels the main entry fractures creating the alabaster zone. Satinspar is the last gypsum phase to form and has also grown in bedding-parallel fractures as well steeper veins that crosscut some anhydrite-alabaster contacts. Veins were created by extension in response to the growth of void space. Most of the grey anhydrite is being replaced from the edges inward, but the alabaster, which is less consolidated and somewhat more permeable, can accommodate a much higher density of bedding parallel fractures. It is a largely inhomogeneous response to tension created by dissolution and contrasts with the more isotopic response seen in the satinspar growing in the Permian clays where the Khuff anhydrite subcrops.

The replacement sequence at Hit Dahl is laminated anhydrite passing directly into laminated alabaster. It may reflect the much lower rates of fluid rock interaction experienced by the Hith Fm. during uplift as compared to the more humid conversions occurring deeper and earlier in the uplift history at Fredericksburg, Texas. The greater disturbance in the overburden at Hit Dahl compared to Fredericksburg reflects the greater thickness and resulting locally steeper dip of the monoclinal defining the edge of the dissolving $CaSO_4$ bed and perhaps a greater strength in the roof span in Saudi.

Halite Caves

Because of its high solubility, halite does not make it into outcrop or shallow subcrop as easily as gypsum/anhydrite. Where halite is at the surface it tends to be in regions of Pleistocene halite deposition (salt on its way down) or in zones of active diapirism (salt coming up very quickly). Chabert and Courbon (1997) noted caves in ancient rock salt in several regions: Algeria (in diapirs, mostly as shafts and short caves up to 280 m long), Chile (diapirs, with caves 250–500 m long), Israel (in a diapir as tube caves several hundred metres in length), Romania (in diapirs, with caves up to several hundred metres long), Spain (in diapirs, with caves up to 650 m long), Tajikistan (several caves 300 to 2,500 m long and up to 120 m deep), and in the namakiers of Iran and the offshore island relicts where cavern lengths range from several hundred metres to kilometres (Table 7.7).

Halite in an active namakier rises and spreads rapidly, so any karst in an active salt diapir tends to be a feature associated with the immediate underside of a caprock. Karst processes cannot deeply penetrate while salt is flowing, even when the plug rises more than 300 m above the surrounds. So, more extensive halite hosted caves are best developed about the margins of a namakier where halite's susceptibility to rapid dissolution means the length of a cave developed below the caprock can be substantial. There is a report of a single salt halite cave (Cave 3 N) on Qeshm Island, Iran, with a passage length of more than 9 km (Bruthans et al. 2002). Once the rate of diapir rise has slowed or ceased the positive topography of the now inactive diapir controls the depth of development of doline collapse on the diapir itself. That is, deeper collapse dolines can now form in the more central topographically higher portions of a salt structure, once the rate of rise has slowed (e.g. Calaforra and Pulido-Bosch 1999).

The high solubility of halite means a halite cave system can form in a few hundred years rather than the thousands to tens of thousands of years needed to form carbonate karst (Bruthans et al. 2010). Not only is rate of cavern formation very fast (dissolution/downcutting of 20 mm/year), these rapidly forming karst features are hosted in and atop a flowing rock mass. This means some of our notions of karst process and cave stability, related to the rate and density of cavern expansion, need to be modified when dealing with halite karst. For example, unlike gypsum and carbonate karst, jointing is not significant in controlling cavern orientation in namakier karst.

Modern Halite Karst in the Dead Sea Depression

Halite caves occur in the Mt. Sedom diapir, where halokinetic Miocene salt is sporadically exposed beneath a weathering and fractured gypsiferous caprock (Fig. 7.53; Frumkin and Raz 2001; Frumkin and Ford 1995). Water enters the various caves in Sedom diapir through breaches in the caprock. Most of the caves in the higher parts of Mt. Sedom salt are vadose inlet caves; these are meandering steeply inclined tubes and canyon slots located within or immediately below the caprock. They form where salt solution quickly carves out near vertical slots and shafts (typically < 2 m wide and much deeper) that lead down from the surface, sometimes along pre-existing fractures and shears in the salt. Inlet caves in the central portions of the mountain can only be accessed through their sinks and appear to have no distinct outlet. All

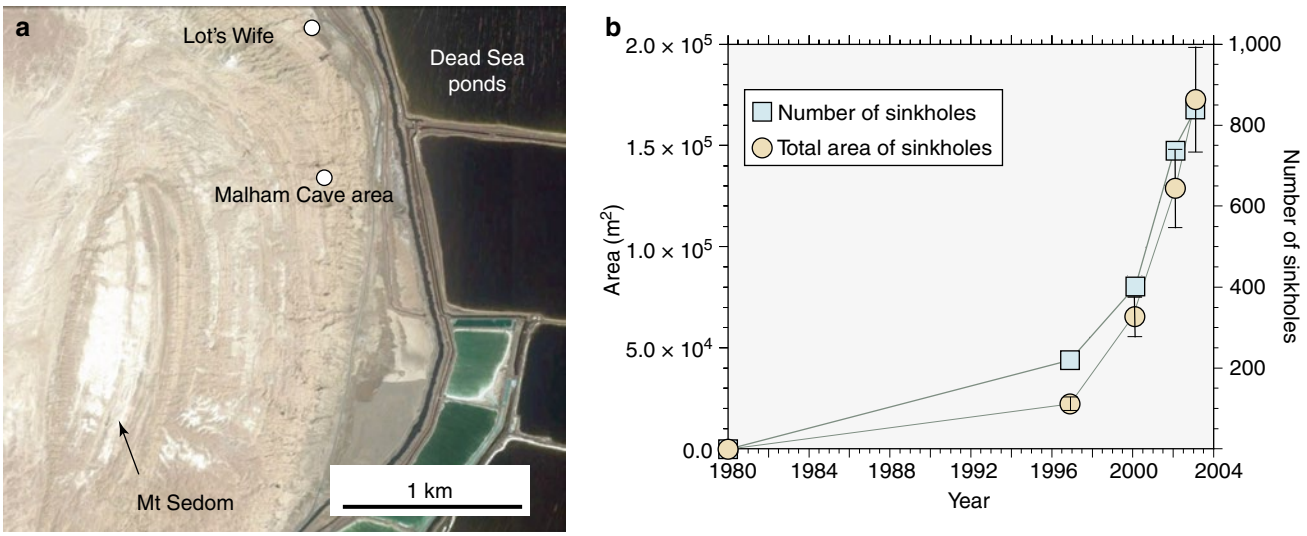

Fig. 7.53 Dead Sea karst. (**a**) Mount Sedom, Israel, showing typical anticlinal core and low elevation (Google Earth image). (**b**) Growth rate of sinkholes along the west coast of the Dead Sea, both in numbers and area coverage. The sinkhole development significantly accelerated since 1997; currently there are more than 1,000 sinkholes, and their numbers are increasing at a rate of 150–200 per year (After Yechieli et al. 2006)

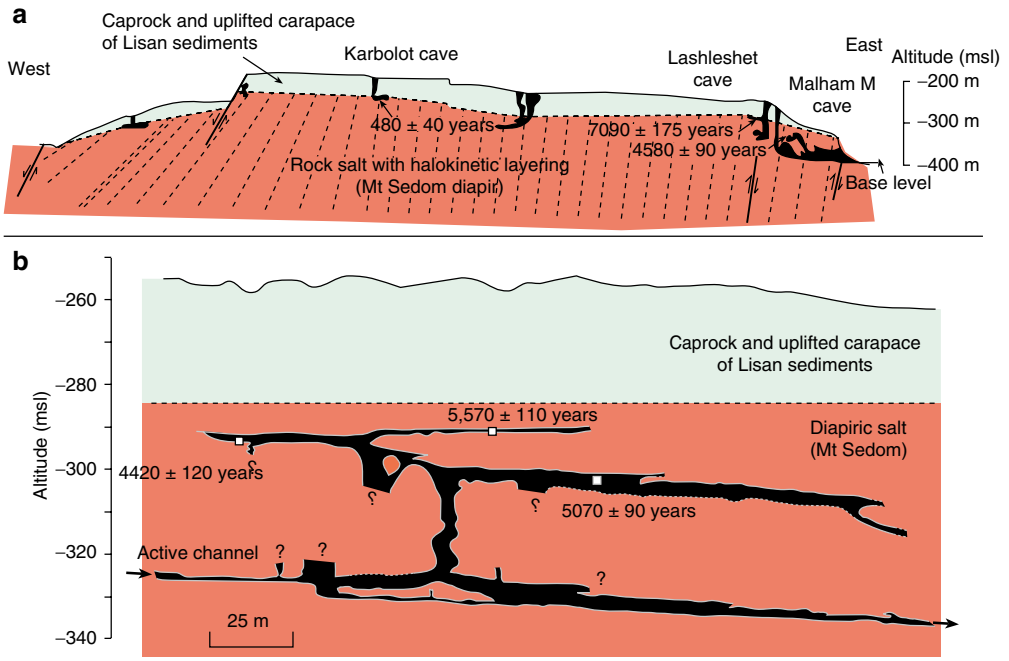

Fig. 7.54 Halite caves beneath the caprock carapace of Mt Sedom, Israel (After Frumkin 1996). (**a**) East-West cross section through the southern part of Mount Sedom, showing ages of upper levels of caves in ^{14}C yr B.P. Dashed lines indicate dip of salt layers within the diapir. Caves are coloured black. The oldest cave date comes from Lashleshet Cave, which lies at the top of the eastern escarpment, implying this was the earliest region on the Sedom uplift to experience vadose flushing. (**b**) Vertical section along part of Malham South Cave, showing several dated levels. The age of the uppermost level (5,570 ± 110 year B.P.) indicate the minimum exposure age of this site created by the halokinetic uplift of the landsurface (See Fig. 4.53 for location of Mt Sedom)

terminate several tens of metres above the regional watertable (e.g. Karbolot Cave; Frumkin 1994a, b, 1996).

The lower parts of inlet caves often contain steep silt and clay banks with surge marks that indicate occurrence of low energy water ponding, with variable residence times. Silt and clay sediments settling at the bottoms of inlet caves impede infiltration, extending the residence time of pond water (Frumkin 1994a, 1996). Three of the studied caves in northern Mount Sedom had perennial ponds throughout the period 1984–1995. The ponds are perched, without any lithologic control, tens of metres above the nearest potential outlet at the foot of the mountain (Fig. 7.55a). Water level in each pond differs from the others by tens of metres. All pond waters are highly concentrated, up to 324 g/l, with solutes consisting mainly of sodium and chlorine. Fresh inflow waters reach halite saturation within a few hours of reaching the pond. Both dissolution and precipitation features form the pond edges, and their equivalents can be seen on cave walls wherever ponds have dried out. Dissolution is indicated by horizontal notches, which connote density stratification in the ponds when aggressive fresh flood waters temporarily diluting the upper parts of the pond. Subsequent saturation of holomictic pond waters is indicated by the growth of cm-scale halite crystals on the bottom and sides of the ponds.

Towards the periphery of Mt Sedom, the inlet caves lead down to laterally expanding vadose cave levels that drain onto the Dead Sea plain. Sedom Cave, is the longest laterally expanding diapir cave, with an aggregate length between two subparallel conduits of 1.8 km. Malham Cave, another large perched and laterally expanding cave, lies a few hundred metres south of Sedom Cave (Fig. 7.54b; Frumkin 1996). It has an aggregate passage length of more than 5.5 km and reaches to some 194 m below the landsurface. There is an upper tier of largely inactive passages and a lower active channel level. ^{14}C dates on fossil wood in the upper cave level shows meteoric waters began to sculpt the upper cave more than 5,500 years ago. Ongoing uplift of Mt Sedom salt means the active channel level in Malham Cave is now downcut some 10–12 m lower than when it began. Malham Cave passages quickly developed an open outlet through which floodwater escaped directly to the Dead Sea floor, proving that during this period some 4,000 years ago rock salt had already risen above region hydrological base level at the Malham outlet point within the eastern escarpment (Fig. 7.54a). Lashelshet Cave, an inlet cave on the highest point on the diapir cross section, has an even older age of more than 7,000 years since cave initiation. Caves in the northern part of Mt Sedom did not begin to form until some 3,000 years later (Frumkin 1996).

Based on their study of the caves of Mt Sedom, Frumkin and Ford (1995) concluded cave passages develop in two main stages: (1) an early stage characterized by inlet caves with high downcutting rates into the rock salt bed, and steep passage gradients; (2) a mature laterally expanding stage characterized by lower downcutting rates and the establishment of a wider subhorizontal perched stream bed armoured with alluvial detritus. This style of cave tends to develop toward the periphery of the diapir mound. In the mature expanding stage downcutting rates are controlled by the uplift rate of the diapir and changes of the level of the Dead Sea.

Passages may aggrade to create wide flat bevelled passages and slots with thick sediment armoured bases (Frumkin 1998). A lack of a consistent phreatic level in the blind bottoms of perched water levels and the presence of the horizontal slots in the lower levels of Sedom Cave means dissolution in both types of caves is largely restricted to times of flooding and perched or backed up freshwater in the vadose zone. This explains the tapering passages of inlet caves and the widespread alternation of armouring and bevelling as well as formation of narrow horizontal meandering slots toward parts of the top of the meandering channel that is now Sedom Cave.

Mass balance calculations in the halite caves of Mt Sedom yield downcutting rates of 0.2 mm s^{-1} during peak flood conditions, this is about eight orders of magnitude higher than reported rates in any limestone cave stream (Frumkin and Ford 1995). However, floods have a low recurrence interval in the arid climate of Mount Sedom so that longterm mean downcutting rates are lower: an average rate of 8.8 mm/year was measured for the period 1986–1991, while Frumkin (2000) estimate the average regional vadose downcutting rate in the Mt Sedom karst region to be 20 mm/year. This is still at least three orders of magnitude higher than rates established for limestone caves and more than able to cope with the rate of supply of the diapiric salt.

The highly impervious nature of halite and its resupply in actively growing diapirs means that, unlike carbonate and gypsum caves, there is no real watertable level to define maximum cave development in a rising salt stem. Rather, the inlet caves are simple dissolution tubes where rainwater has accessed halite and sank until it was saturated and then dissolution stopped until the next flood. Toward the edge of the rising stem these inlet caves breached the edge of the salt mound and vented their perched groundwaters to the surrounding plain (Fig. 7.54; Sedom and Malham caves). This creates a downcutting and laterally expanding cave system, which is still some metres to tens of metres above the base level of the regional watertable in the surrounding plain. The expanding cave level is dominated by mostly horizontal growth, often with a sediment-armoured floor. It has numerous benches in the walls that probably reflect changes in the hydrological base level.

Dense anastomose cave networks that characterise gypsum caves are not found in the halite caves of Mt Sedom. This reflects the ability of diapiric halite to re-anneal and the fact that all exhumed halite that makes it to the surface is diapiric, not bedded. At-surface halite is not sandwiched between jointed aquifers above and below the dissolving layer. Rather it is a growing mound subject to dissolution at its top and sides.

Away from Mt Sedom, there are active collapse sinkholes and caverns forming in the alluvial fans and clastic aprons that overlie the bedded Quaternary lacustrine halite of the Dead Sea (salt on its way down in the burial cycle). In the sediments around the lakeshore the pace of collapse has accelerated in the last 60 years due to a drastic lowering of the circum-lake watertable and the associated lakeward migration of the saline-fresh water interface (Fig. 2.64). For example, a series of collapse dolines 2–15 m diameter and up to 7 m deep, appeared in 1990 in the New Zohar area. In January 2001 a large sinkhole, some 20 m deep and 30 m wide, cut though the asphalt surface of the main road along the western shore of the Dead Sea. It was opened by the passage of a busload of tourists on their way from Ein Gedi to the solarium. Existing tourist facilities, such as the Ein Gedi beachside parking, were shut down after the road was damaged and several buildings have since collapsed into sinkholes. Sinkholes have since developed in other areas about the Dead Sea Margin including Qalia, Ein Samar, Ein Gedi and Mineral Beach. The process began in the southern part of the Dead Sea coast and slowly spread northward along the Israeli coast and is more localized in the northern and southern parts on the Jordanian side and has increased as the sea level fell (Ezersky and Frumkin 2013; Arkin and Gilat 2000).

Three main types of sinkhole or doline fill have been recognized atop the dissolving Holocene salt beds of Sedom; (1) gravel holes in alluvial fans, (2) mud holes in the intervening bays of laminated clay deposits between fans, and (3) a combination of both types at the front of young alluvial fans where they overlap mud flats. Fossil, relict sinkholes have been observed in the wadi channels cutting into some old alluvial fans, showing this is a natural and ongoing process. While lake levels continue to fall (Fig. 4.45), the potential for subsidence hazards related to karst collapse is ongoing.

Sinkholes and related subsidence has been the focus of much geological study, but Closson et al. (2010) pointed out that an even more significant and ultimately damaging environmental effect of the ongoing water level lowering are hectametre and larger scale landslides along the retreating shorezone. In the 1990s, international builders created major tourist resorts and industrial plants along the Jordanian and Israeli shore while, during the same period, geological hazards triggered by the level lowering spread out. From the beginning of the year 2000, sinkholes, subsidence, landslides,

and river erosion damaged infrastructures more and more frequently: dykes, bridges, roads, houses, factories, pipes, crops, etc all suffered as a result. There is evidence of an older set of widespread ground collapses, sinkholes and caves that are tied to an earlier substantial fall in the Dead Sea water level some 4 ka. It may even be that the events described in Genesis 14 in the Christian Bible took place at the time of a substantially lowered sea level. The described battle, which occurred prior to the fall of Sodom and Gomorah, perhaps took place on the subaerially exposed flats of the Southern Basin of the Dead Sea. The "pits of slime" described in the fall perhaps were solution collapse sinkholes activated by the 4,000 ka fall in the Dead Sea water level (Frumkin and Elitzur 2002).

Modern Halite Karst in Crests of Diapiric Hormuz Salt (Precambrian) in the Arabian Gulf

Namakier outcrops in and about the Arabian Gulf range from structures actively extruding salt to those in ruins where salt has not flowed for tens of thousands of years (Fig. 7.21). Likewise the halite caves developed in the namakiers of Iran, or their offshore island counterparts, show a broad range of ages and styles of salt cave development tied to the time since cessation of salt flow (Filippi et al. 2011; Bruthans et al. 2010; Talbot et al. 2009).

Surfaces of actively flowing namakiers on the Iranian mainland are characterised by karren flutes and pinnacles, with numerous small-medium dolines, collapse structures, swallow holes and small caves at their base. Caves tend to be sediment-armoured meandering tube caves or subvertical canyon slots that are centred on joints in the salt beneath a thin suffusion mantle. In contrast, the halite caves in the diapiric cores of the many islands in the Arabian Gulf have a more mature bevelled meandering style with thicker sediment armouring on the cavern floor. Many of these caves breach the retreating edges of former namakiers and salt fountains.

Salt movement in the various diapiric cores of these islands is inactive or is greatly reduced compared to the Miocene when these structures were active namakiers. For example, Dragon Breath Cave on Hormuz Island is a linear meander tube cave fed by an ephemeral stream in a shallow valley filling with alluvium (Figs. 7.55 and 7.56; Bosak et al. 1999; Filippi et al. 2011). The surrounding landscape is classic salt karst with numerous depressions, blind valleys, ponors and subrosion sinks. Together they form a highly pockmarked centripetally-ringed topography, which outlines those central parts of the island underlain by shallow subcropping Hormuz salt. The cave itself is one of a number of tube caves exiting about the edge of the zone of diapiric salt. Hosted in steeply dipping diapiric salt, it is around 100 m long with its main passage created by a minor ephemeral stream. Its near flat roof, with an average inclination of 5.4 %, is a notable feature and reflects either joint-related dissolutional spalling of the roof or an earlier watertable slot related to backup of a freshened water body.

The current cave passage has cut down a metre or more into earlier cave floor sediments (sediment armour), which contain clasts up to 50 cm in diameter. The cave formed by initial ingress along a linear joint, which was then widened by salt dissolution, so allowing meandering of the stream trace within the salt. It is a cave system very similar to the mature stages of laterally expanding caves in Mt Sedom. The base level of the cave correlates with the surface of a widespread marine terrace, which is now uplifted some 20 m above sealevel and defines much of the periphery of Hormuz Island. The raising of the marine terrace is related to the ongoing raising of the island via salt flow.

Bruthans et al. (2000, 2010) show that the style of karst landform developed in dissolving diapiric salt in the Arabian Gulf Islands reflects the thickness of the carapace that caps the dissolving salt core. They distinguished four classes of diapir cap, each with a specific association of superficial and underground karst forms, namely: (1) outcropping salt, (2) thin capping (0.5–2 m), (3) capping with moderate thickness (5–30 m), (4) capping with greater thickness (more than 30 m). Cap thickness controls or reflects: (1) the density of recharge points, with high densities of recharge points in the thinner caps; (2) the amount of concentrated recharge which occurs at each recharge point, with suffusion karst characterising thinner caps; (3) the rate of lowering the ground surface atop the salt, with the faster rates of lowering occurring beneath thinner caps, and (4) the amount of load transported by underground flood-streams into cave systems. The volume of sediment load tends to be locally higher and focused beneath the thicker caps, especially where inflow streams abut the edges of a dissolving salt dome. The thickness of caps atop expanding halite caves does not appear to influence the shape or style of the cave developed within the salt mass; more important seems to be the thickness of cap in the recharge area of the cave and the type of recharge into the salt environment. That is, how much water is passing into the salt and is its flow ongoing or ephemeral?

Halite caves in the relatively mature salt stems of the various islands of the Arabian Gulf, unlike carbonate systems, can swallow and store huge volumes of clastic sediment, volumes that would clog the entrance to a carbonate system. The extreme solubility of halite enables the pace of dissolution/corrosion enlargement in a salt cave to keep pace with large amounts of sediment carried into the cave by external inflows. Stream sediments arriving at the cave entrance, including boulders, move inside and are trapped within the salt itself. Sediment is not dumped outside the cave entrance, which is the typical situation in blind valley river mouths at carbonate caves (Bruthans et al. 2000). For example, coarse-grained sediment fractions are carried hundreds of metres

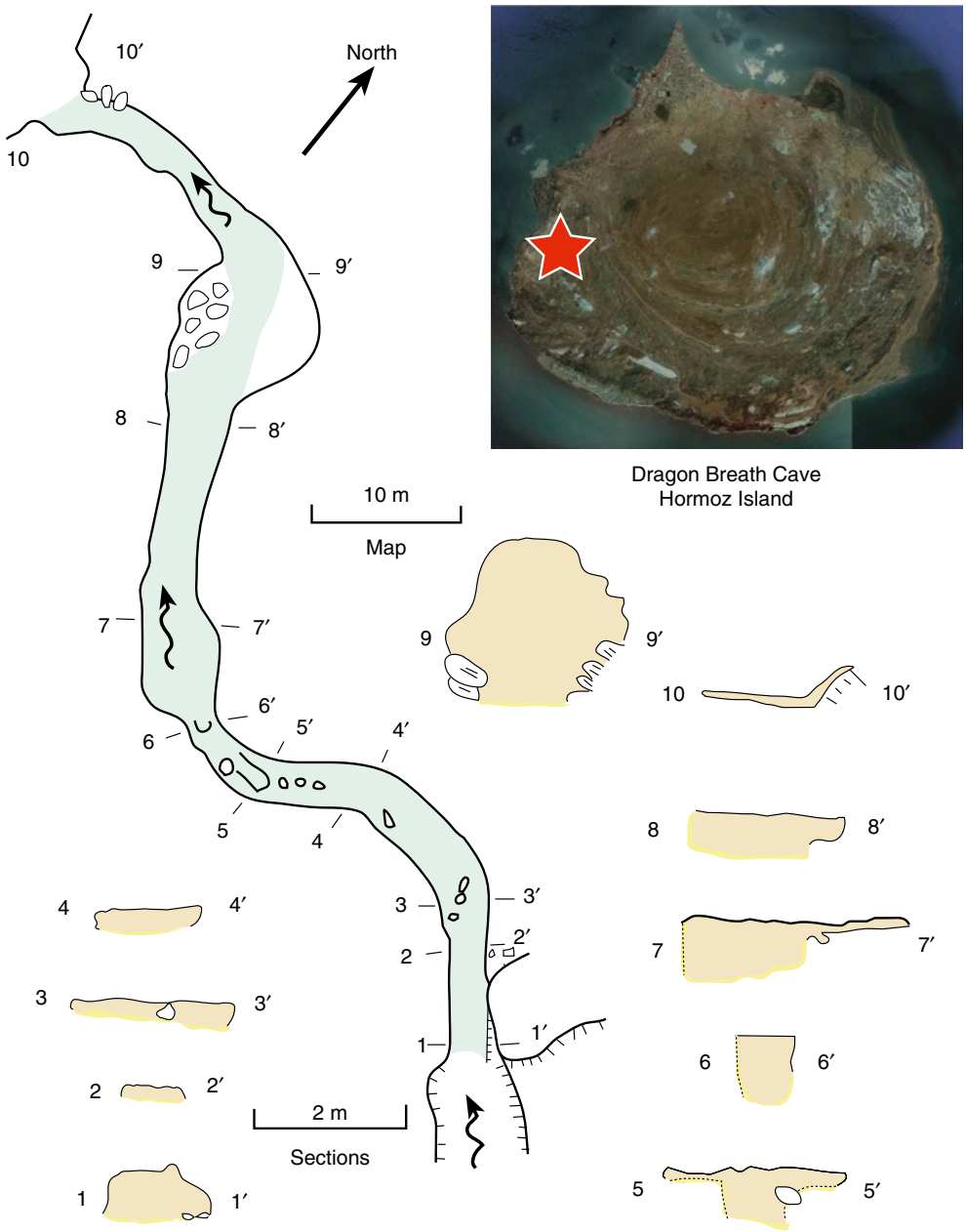

Fig. 7.55 Map of Dragon Breath Cave, a meandering karst cavity draining the edge of the inactive diapiric core of Hormuz Island, Arabian Gulf (After Bosak et al. 1999). Star marks cave position on insert, see Fig. 7.30b for location of cave in the island geology (Landsat image of island courtesy of NASA)

into the cave by two large intermittent streams entering the upper part of the Ponor Cave (Hormuz Island). The clasts in the resulting intra-cave alluvial fan conglomerates range from cobble of several centimetres up to 1 m diameter boulders, only sand-sized particles make it to the lower part of the same cave.

Caves capable of storing such coarse alluvium within the cavern itself are halite-specific with no equivalent in a carbonate karst terrain. There the boulder-size fraction in the cave itself is the result of roof fall and almost all stream-borne coarse alluvium is deposited outside the cave.

Cave walls in zones of less intense dissolution and stream crossflow are decorated with halite, gypsum and anhydrite speleothems. Anhydrite forms speleothems in preference to gypsum in those parts of the cave with very high salinity waters. Some of these speleothems can be quite large, up to a few metres long. Compared to the growth rates of calcite speleothems in carbonate caves the growth rates of evaporite speleothems are phenomenal. Halite stalactites, several metres long and curving into the direction of airflow, formed in the mouth of Dragon Breath cave in a few years rather than millennia needed for carbonate counterparts (Bosak et al. 1999). In August 1997, a network of numerous halite stalagmites and stalactites blocked the entrance to Dragon Breath Cave. In March 1998 there were no remains of the speleothem meshwork, while in

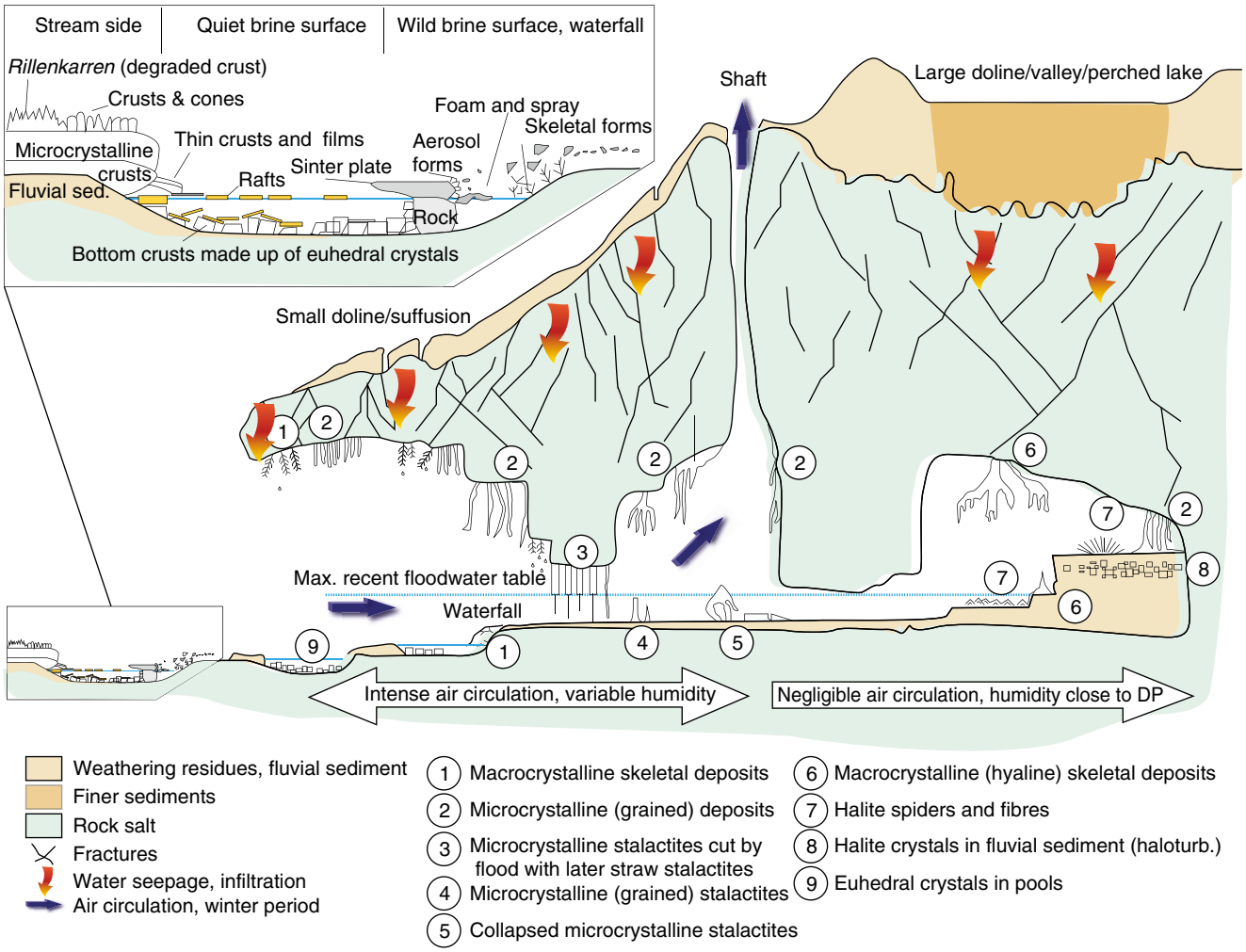

Fig. 7.56 Halokinetic salt cave ornamentation (inspired by the 3 N Cave, Namakdan) with various secondary halite deposits and the dependence of their occurrences on the environmental conditions (After Filippi et al. 2011)

February 1999, the stalagmites had reappeared (Bosak et al. 1999). Similar halite structures occur in the caverns of Mt Sedom and on the wet roofs of some salt mines.

In summary, karst deposits forming in namakiers encompass a range of mechanisms and textures (Fig. 7.56; Filippi et al. 2011): (i) via crystallization in/on streams and pools, (ii) from dripping, splashing and aerosol water, (iii) from evaporation of seepage and capillary water, and (iv) other types of evaporative deposits. The following examples of halite textures are distinguished in each of the above-mentioned groups: (i) euhedral crystals, floating rafts (raft cones), thin brine surface crusts and films; (ii) straw stalactites, macrocrystalline skeletal and hyaline deposits, aerosol deposits; (iii) microcrystalline forms (crusts, stalactites and stalagmites, helictites); (iv) macrocrystalline helictites, halite bottom fibres and spiders, crystals in fluvial sediments, euhedral halite crystals in rock salt, combined or transient forms and biologically induced deposits. The occurrence of particular forms depends strongly on the environment, especially on the type of brine occurrence (pool, drip, splashing brine, microscopic capillary brine, etc.), flow rate and its variation, atmospheric humidity, evaporation rate and, in some cases, on the air flow direction. Combined or transitional secondary deposits can be observed if the conditions changed during the deposition. Euhedral halite crystals originate solely below the brine surface of supersaturated streams and lakes. Macrocrystalline skeletal deposits occur at places with rich irregular dripping and splashing (i.e., waterfalls, places with strong dripping from the cave ceilings, etc.). Microcrystalline (fine grained) deposits are generated by evaporation of capillary brine at places where brine is not present in a macroscopically visible form. Straw stalactites form at places where dripping is concentrated in small spots and is sufficient to assure that the tip of the stalactite will not be overgrown by halite precipitates. If the tip is blocked by halite precipitates, the brine remaining in the straw will seep through the straw walls and helictites start to grow.

Macrocrystalline skeletal deposits and straw stalactites usually grow after a major rain event when dripping is strong, while microcrystalline speleothems are formed continuously during much longer periods and ultimately (usually) overgrow the other types of speleothems during dry periods. The rate of secondary halite deposition is much faster compared to carbonate karst. Some forms lengthen more than 0.5 m during the first year after a strong rain event; however, the age of speleothems is difficult to estimate, as they are often combinations of segments of various ages and growth periods alternate with long intervals of inactivity.

Evaporite Speleothems in Non-evaporite Karstified Host

Evaporite minerals can form speleothems in the drier parts of carbonate caves where airflow dries cave capillary waters to salinities appropriate for precipitation (Table 7.8). Gypsum, epsomite, and mirabilite are the usual sulphate minerals found in caves. By far the most representative of this group and perhaps the second most common cave mineral is gypsum (Onac 2005). It forms a huge variety of speleothem types ranging from the less spectacular white, soft moonmilk deposits composed of microcrystals, to curving clusters, to prismatic crystals up to 2 m long. It also forms the enormous and spectacular stalactites (the so-called chandeliers) exposed in Lechuguilla (New Mexico) and Cupp-Coutunn (Turkmenistan) caves. Two other common cave sulphates that usually occur as colourless white fibrous efflorescences on cave walls and sediments are mirabilite and epsomite. Both minerals are highly sensitive to variations in relative humidity and temperature.

Gypsum and epsomite speleothems are especially common in vadose caves in areas receiving less than 250 mm of rainfall per year. Even in the ever-wet climate of New Guinea, powdery gypsum crusts can coat carbonate substrates in caves like Selminum Tem and Atea Kanada in a region where the annual rainfall is more than 4,000 mm. But these are relatively minor portions of the total volume of cave decoration with the sulphate sourced in the weathering of pyritic impurities and are only found in parts of the cavern system subject to vigorous air circulation.

Table 7.8 Evaporite minerals and their mode of occurrence in cave speleothems

Mineral	Composition	Type of occurrence
Gypsum	$CaSO_4 \cdot 2H_2O$	Dripstone, wall crusts, flowers, bladed crystals, pore cement in cave soils
Halite	NaCl	Dripstone, wall crusts, flowers, pore cement in cave soils
Epsomite	$MgSO_4 \cdot 7H_2O$	Dripstone, flowers, pore cement in cave soils
Hexahydrite	$MgSO_4 \cdot 6H_2O$	Loose crusts on cave walls and floors
Mirabilite	$Na_2SO_4 \cdot 10H_2O$	Dripstone, flowers, loose tufts of crystals
Bloedite	$Na_2SO_4 \cdot MgSO_4 \cdot 4H_2O$	Loose crusts on cave walls and floors
Celestite	$SrSO_4$	Loose crusts on cave walls and floors
Baryte	$BaSO_4$	Loose crusts on cave walls and floors

The most common vadose evaporite speleothem is gypsum, which forms as relatively fine-grained granular crusts on the limestone wall of most arid-zone carbonate caves. It grows and accretes via uniform seepage and evaporation of brines escaping from the porous cave wall. This is an ongoing process whereby older crusts become detached, fall off and, if not dissolved by throughflowing waters, accumulate on the cave floor as new crusts continue to form on the walls. It is really a form of salt weathering that just happens to occur inside a cave. Gypsum also accumulates as granular layered rinds in many phreatic and bathyphreatic carbonate caves that were moulded by sulphuric acid speleogenesis in their early stages of formation (see later).

But the most noticed evaporite speleothems in carbonate karst are not various crusts and small prisms but the spectacularly curved gypsum and halite flowers (rarer epsomite and mirabilite) that protrude as lacy intertwined ribbons hanging from cavern ceilings and walls (Fig. 7.56; Filippi et al. 2011). These cave flowers (oulopholites) typically grow as curved radiating masses of very long (up to 50 cm), narrow crystals. New growth originates at the base of the crystal strings as saturated brines emerge from the cave wall, driven by capillary evaporation. Faster growth in the centre of a bundle of crystals creates the radiating or flower-like pattern. Often they grow from waters issuing from crevices and fractures in the cave wall and their growth contributes to parts of the cave wall breaking away or spalling (salt weathering). Changes in cave atmosphere and rates of capillary supply drive varying growth rates and hence the curvature of the crystals, much like the controls on helicites (twisted stalactites). Oulopholites are especially sensitive to seasonal changes in cave airflow. The growth of gypsum anemolites (wind-controlled oulopholites) in a cave in the Ukraine was found to vary with changes in cave humidity (Maltsev and Ford 1991). When air moves into this cave each summer, and cave humidity is 70–90 %, accretions of up to 7 mm form. In winter, the airflow reverses, the humidity rises and the same structures tend to dissolve.

Baryte and celestite (Table 7.8) are relatively insoluble in comparison to other cavern sulphates (Onac 2005). Celestite typically forms crystalline crusts on cave walls or as distinct blue needles atop gypsum crusts, while baryte has been documented as a cement in numerous cave soils. Only under special conditions does direct precipitation of these less soluble sulphates from meteoric waters take place in caves, rather both minerals occur in caves invaded by thermal

waters or hydrothermal solutions. Occurrences of celestite are known from Crystal Cave (Ohio), Lechuguilla Cave (New Mexico), Cango Cave (South Africa), and Valea Rea Cave (Romania). Baryte is known from caves in England, Italy, Hungary, France and Russia.

Sulphate speleothems are not restricted to evaporative crusts in caves in warmer climates, Harmon et al. (1983) reported at least three sulphate minerals (gypsum, epsomite, and mirabilite, the latter possibly cryogenic) in speleothems in Castleguard Cave in the Canadian Rockies, with the most spectacular forming large ice-clear stalactites of epsomite and mirabilite. Some 60 other sulphate salts have been described from caves (e.g., alunite, chalcanthite, halotrichite, jarosite, melanterite, etc.), these minerals are much less common than those listed in Table 7.8. Hill and Forti (1997) list ten sulphate salts as derived from normal vadose karst processes; many others come from the interaction of karst waters with ore bodies. White (1988) lists four possible sources of cave sulphate, divided into two distinct source groups;

- Carbonate bedrock source:
  (a) Dissolution in sulphate-bearing beds
  (b) Oxidation of pyrite in the bedrock
  (c) Weathering of anhydrite nodules
- Deep groundwater source:
  (a) Movement of deep H_2S waters into contact with phreatic karst waters to form sulphuric acid, which may dissolve calcite and deposit gypsum.
- To this list Hill and Forti (1997) add guano and weathering basalts.

As well as salt flowers in carbonate caves, halite is a rapidly growing vadose speleothem in its own right. Halite speleothems in carbonate caves form best in arid regions, where parent materials are leached from the regolith by circulating brackish groundwaters and redeposited under evaporative conditions in the cave environment. Lowry (1967) discussed halite speleothems from the carbonate caves beneath the Nullarbor, while Goede et al. (1992) notes the region has what may be the world's largest halite speleothems in a carbonate cave. Nullarbor's saline speleothems in Mullamullang Cave include the distinctive "coffee and cream" textures made up of a mixture of fine powdery and more coarsely crystalline magnesian calcite crusts, and varying levels of iron and manganese oxide, intermixed with fragments of halite and gypsum flowers.

Huge single evaporite crystals with geode-like textures can form in zones where saturated brine pools covers the cave floor or can rim a deep phreatic cavern. Where fluid chemistry fluctuations are minimal in these gypsum saturated phreatic waters, clear impurity-free gypsum blades can grow as single crystals up to a metre or more in length and decimetres in width (e.g. phreatic crystals in sulphuric acid caves in Lechuguilla caverns of New Mexico, the lmeria caverns in Spain and the Dnestrovsko-Pricernomorskij karst caves of the western Ukraine).

More unusual cave precipitates tied to gypsum include; alunite ($KAl_3(SO_4)\cdot 2(OH)_6$), and rare phosphate–sulphate sanjuanite $Al_2(PO_4)(SO_4)(OH)\cdot 9(H_2O)$ and rossiantonite ($Al_3(PO_4)(SO_4)\ 2(OH)_2(H_2O)_{14}$). All are secondary mineral deposits hosted in different quartz-sandstone caves in the Gran Sabana region, Venezuela (Sauro et al. 2014). The cavernous hosts to these gypsum and other sulphate speleothems encompass the 'tepuis' (table mountains) along the topographic edge of the Guyana Shield (Venezuela and Brazil) and formed in the Precambrian quartz-sandstones of the Roraima Supergroup. Due to the extended time scale required for speleogenesis in such hard and barely soluble quartz-sandstone lithologies, some of these caves are considered to be as old as 20–30 My. Deposition of sulphates in these caves is not linked to the quartz-sandstone host rock (Sauro et al. 2014). Rather, these mineral deposits originate from a long term external atmospheric sulphate source, with potential contributions of marine non-sea salt sulphates, terrestrial dimethyl sulphide and microbially reduced H_2S from the forests or peatbogs within the watershed. Air currents within the caves are the most plausible means of transport for aerosols, driving the evaporative accumulation of sulphates and other secondary minerals in specific locations. Moreover, the studied sulphate minerals often co-occur with silica speleothems of biological origin. Although this association would suggest a possible biogenic origin for the sulphates as well, direct evidence proving that microbes are involved in their formation is absent.

Hazards Tied to Evaporite Karst

Surface constructions and other anthropogenic activities atop or within evaporite karst is even more problematic than in carbonate terranes due to inherently higher rates of dissolution and stoping (Yilmaz et al. 2011; Cooper and Gutiérrez 2013). Unlike the relatively slow formation of limestone karst, gypsum/ halite karst develops on a human/engineering time-scale and can be enhanced by human activities. In 2006, the Nanjing Gypsum mine in China broke into a phreatic cavity in a region of gypsum karst, driving complete flooding of the mine in some 3 days. Associated groundwater drainage caused a sharp drop in the local piezometric level of up to 90 m in a well in nearby Huashu village. Resultant ground subsidence severely damaged nearby roads and buildings (Wang et al. 2008). In Ukraine, dewatering of gypsum karst to facilitate sulphur mining substantially increased the rate of gypsum dissolution and favoured the expansion of sinkholes within an area affected by the associated cones of depression (Sprynskyy et al. 2009). Overburden collapse into nearsur-

Table 7.9 Processes and mechanisms driving the creation of gypsum karst hazards, with examples

Action	Subsidence mechanisms	Examples
Removal of ground fluid	Loss of buoyant support for soil particles; compaction of sediment; possible failure of material bridging a void, thus, causing catastrophic collapse	Sinkholes overlying gypsum karst in Lithuania (Paukstys et al. 1999). Earthquakes beneath Hamburg, Germany (Dahm et al. 2011)
Shrinkage of organic or clay-rich materials	Consolidation of sediment; net loss of organic material	Shallow depressions from desiccated swelling clays (Biddle 1983; Driscoll 1983); subsidence of peat in subsidence hollows (Cooper 1998)
Hydrocompaction of sediments	Softening and yield of metastable interparticle bonds by the introduction of water	Building subsidence caused by compaction of gypsiferous silt in alluvial fan, e.g., Calatayud Spain (Gutiérrez and Cooper 2002) This effect is aggravated by broken water pipes in Calatayud and leaking septic tanks in Mosul, Iraq (Jassim et al. 1997)
Fluvial karstification of gypsum bedrock	Loss of mechanical support; syn- and post-sedimentary subsidence of alluvial deposits into depressions forming at the alluvium/gypsum contact	Subsidence depressions on alluvial flood plains, Calatayud Graben, Spain (Gutiérrez 1996), river valley 'subrosion' (Ford 1997)
Downwashing of unconsolidated sediments	Downward movement of sediments into existing voids or breccia pipes resulting in gradual growth of shallow depressions	Sinkholes in Lithuania (Paukstys et al. 1999); sinkholes in Ripon (Cooper 1986)
Gradual collapse of unconsolidated materials overlying gypsum karst	Sagging of materials overlying a void leading to concomitant lowering of the cover/gypsum interface, and growth of a surface depression	Sinkholes in West Ripon (Cooper 1998).; minor earthquakes beneath Hamburg, Germany (Dahm et al. 2011)
Catastrophic collapse of unconsolidated sediments into existing voids (may be preceded by a period of gradual subsidence)	Collapse that probably requires a triggering mechanism; travelling of a void upwards through unconsolidated sediment possibly accompanied by removal of sediment by rapid water flow through the void	Sinkholes in Ripon (Cooper 1986, 1998); sinkholes in China (Yaoru and Cooper 1997); sinkholes in glacial drift overlying gypsum karst, Nova Scotia (Martinez and Boehner 1997)
Catastrophic collapse of competent strata into voids (breccia pipe propagation)	Failure of material bridging void; development of sinkhole generally requires a triggering mechanism	Sinkholes in Ripon (Cooper 1986), New Mexico (Martinez et al. 1998), NW territories, Canada

After Lamont-Black et al. (2002)

face gypsum caves can create stoping chimneys, which break out at the surface as steep-sided dolines, often surrounded by broader subsidence hollows. Such swallow-holes, up to 20 m deep and 40 m wide, continue to appear suddenly in gypsum areas throughout the world.

Although halite is even more susceptible to dissolution, it typically is not an urban engineering problem; large numbers of people simply do not like to live in a climate that allows halite to make it to the surface. However, in the Dead Sea region the lowering of the water level encouraged karstic collapse in newly exposed mudflats and has damaged roads and other man-made structures (Frumkin et al. 2011). Catastrophic doline collapse atop poorly managed halite/potash mines and solution brinefields is an anthropogenically-induced or enhanced geohazard in developed regions and will be discussed in more detail in Chap. 13.

Gypsum karst is a documented natural hazard in many parts of Europe (Fig. 7.59) and similar areas of shallow subcropping gypsum are common in much of the rest of the world (Table 7.9). For example, areas surrounding the city of Zaragoza in northern Spain are affected, as is the town of Calatayud (Gutiérrez and Cooper 2002; Gutiérrez et al. 2008). Gypsum dissolution is responsible for subsidence and collapse in many urban areas around northern Paris, France (Toulemont 1984), in urban areas in and around Stuttgart and other towns peripheral to the Harz Mountains in Germany (Garleff et al. 1997), in Pasvalys and Birzai in Lithuania (Paukstys et al. 1999), in the Muttenz-Pratteln area in northwestern Switzerland (Zechner et al. 2011), in the Perm area of Russia (Trzhtsinsky 2002), in the Sivaz region of Turkey (Karacan and Yilmez, 1997), in the region centred on the city of Mosul in northern Iraq (Jassim et al. 1997) and in a number of areas of rapid urban development in eastern Saudi Arabia (Amin and Bankher 1997a, b). Large subsidence depressions caused by gypsum dissolution in China have opened up in the Taiyuan and Yangquan regions of Shanxi Coalfield and in the adjacent Hebei Coalfield.

Variation in the watertable level, induced by groundwater pumping, is another anthropogenic trigger for dolines surfacing. As the watertable declines it causes a loss of buoyant support to the ground, it also increases the flow gradient and water velocity, which facilitates higher rates of crossflow and deeper aquifer recharge in subsequent floods and so reduces the geomechanical strength of the cover and washes away roof span support. Dolines can also be associated with groundwater quality issues. Collapse dolines or sinkholes are frequently used as areas or sumps for uncontrolled dumping industrial and domestic waste. Because of the

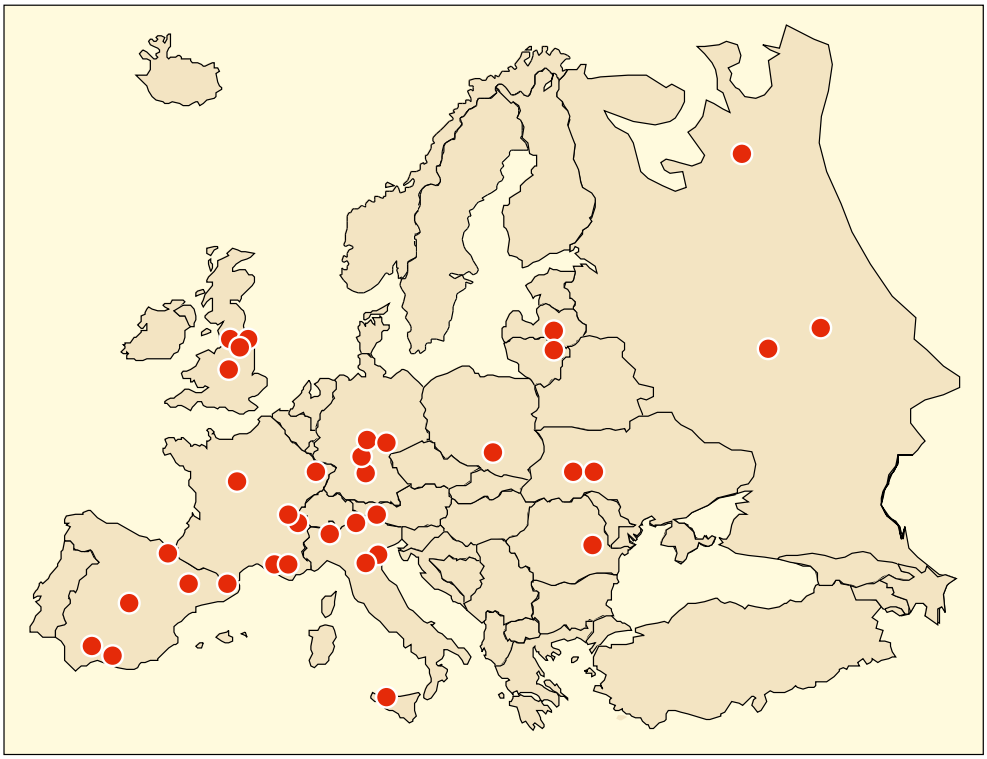

Fig. 7.57 Areas in Europe associated with the development of intervals subsidence and collapse tied to with gypsum karst

direct connection between them and the regional aquifer, uncontrolled dumping can cause rapid dispersion of chemical and bacterial pollutants in the groundwater. In the case of Riyadh region Saudi Arabia, a lake of near raw sewage has appeared in Hit Dahl (cave) and is likely related to the increased utilisation of desalinated water for sanitation and agriculture. In the Birzai region of Lithuania numerous sinkholes developed in Devonian gypsum subcrop are in direct connection across the regional hydrology. Accordingly, the amount of agricultural fertilizer use is limited in order to help protect groundwater quality.

One of the problems associated with rapid surfacing of evaporite collapse features is that any assignment of sinkhole cause will typically lead to an assignment of blame, especially where anthropogenic infrastructure has been damaged or destroyed by the collapse, or lives may have been lost. Areas of natural evaporite karst are typically areas of relatively shallow evaporites. Shallow evaporites makes such regions suitable for extraction via conventional or solution mining. When a collapse does occur in a mined area, one group (typically the miners) has a vested interest in arguing for natural collapse, the others, typically the lawyers and their litigants, will argue for an anthropogenic cause. The reality is typically a combination of natural process enhanced to varying degrees by human endeavours. In the examples in this section much of the driving process for the collapse is natural, while the cause of any unexpected karst-related disaster is typically geological ignorance combined with political/community intransigence. See Chap. 13 for a further discussion of karst and stope examples that include collapses and explosions where the anthropogenic drivers can dominate (Fig. 7.57).

Problems in the Ripon Area, UK

The town of Ripon, North Yorkshire, and town's surrounds experiences the worst ongoing gypsum-karst related subsidence in England (Cooper and Waltham 1999). Some 43 events of subsidence or collapse in the caprock over the Ripon gypsum have occurred over the last 160 years, within an area of 7 km^2 (Figs. 7.58 and 7.59). This gives a mean rate of one new sinkhole every 26 years in each square kilometre. Worldwide, the highest documented event rate occurs in Ukraine, in an area of thin and weak clay caprocks above interstratal gypsum karst, where new sinkholes appear at a rate of 0.01–3.0 per year per km^2. (Waltham et al. 2005). In the Ripon area, numerous sags and small collapses also typify surrounding farmlands. Subsidence features are typically 10–30 m in diameter, reach up to 20 m in depth and can appear at the surface in a matter of hours to days. To the east of the town, one collapse sinkhole in the Sherwood Sandstone is 80 m in diameter and 30 m deep, perhaps reflecting the stronger roof beam capacity of the Sherwood Sandstone.

Shallow subcropping Zechstein gypsum occurs in two subcropping bedded units in this area, one is in the Permian Edlington and the other is in the Roxby Formation

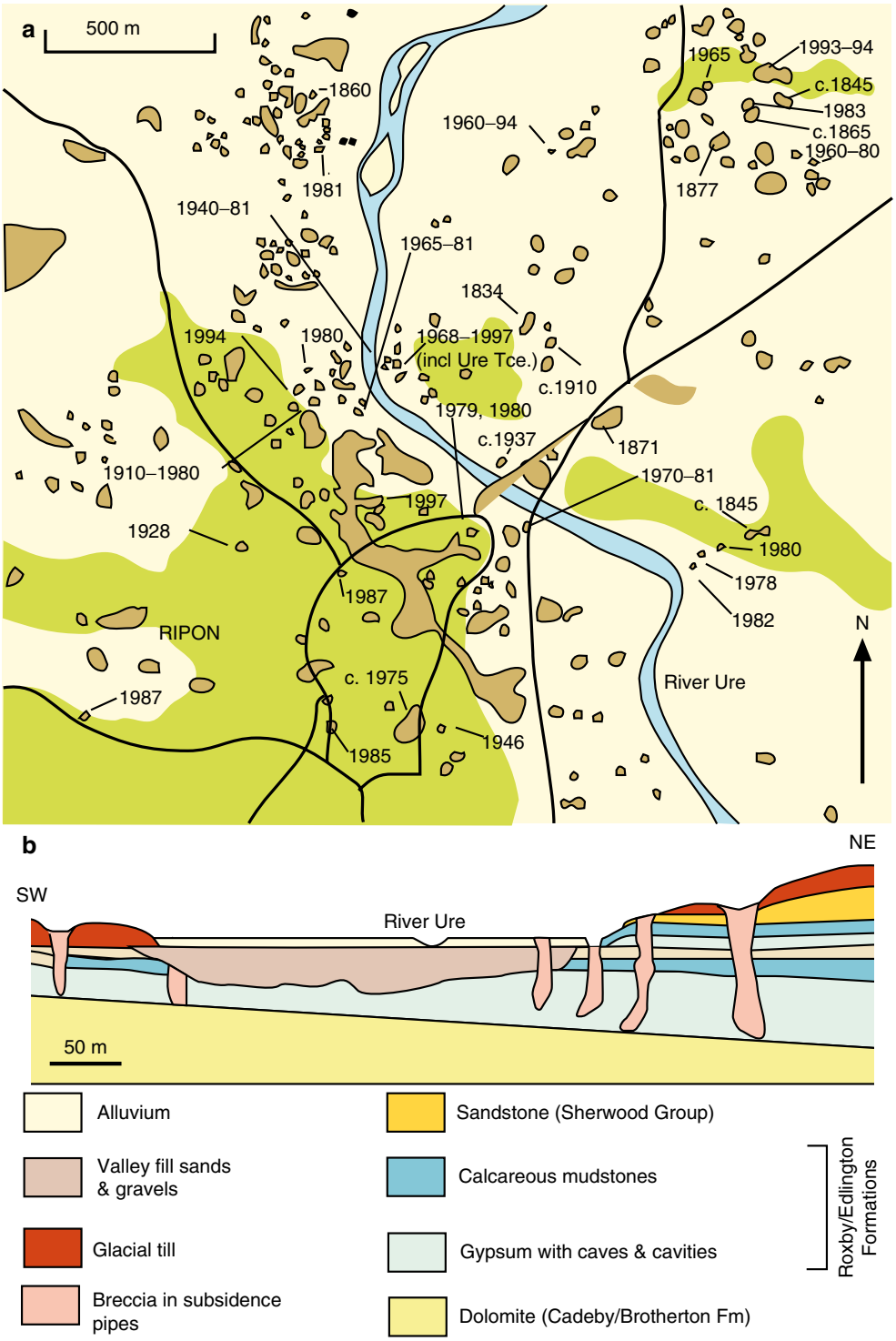

Fig. 7.58 Ripon karst (**a**) Surface distribution of karst features (*shaded brown*) and time of formation, where known, of subsidence features surfacing in and around the town of Ripon, United Kingdom. Urban areas are shaded green. (**b**) Idealised geological cross section (After Cooper and Waltham 1999; Jones and Cooper 2005)

(Fig. 7.58b). Together they form a subcrop belt about a kilometre wide, bound to the west by the base of the lowest gypsum unit (at the bottom of the Edlington Formation) and to the east by a downdip transition from gypsum to anhydrite in the upper gypsum-bearing unit of the Roxby Formation. The spatial distribution of subsidence features within this belt relates to joint azimuths in the Permian bedrock, with gypsum maze caves and subsidence patterns following the joint trends (Cooper, 986). Most of the subcropping gypsum is alabastrine in the area around Ripon, while farther to the east, where the unit is thicker and deeper, the calcium sulphate phase is still anhydrite.

Fluctuations in the watertable level tied to heavy rain or long drought are thought to be the most common triggering

Fig. 7.59 Catastrophic collapse in areas of Ripon gypsum subcrop, UK. (**a**) Subsidence crater caused by the dissolution of Permian gypsum in area known as Corkscrew Pits at Hutton Conyers, near Ripon. Looking N. These subsidence hollows formed after the dissolution of Permian gypsum. The water-filled hollow in the foreground is about 3 m in diameter and some 1.5 m deep. The farmer has been tipping waste in it for about 15 years, but it keeps subsiding. Behind it is another much larger hollow and to the right, part of three intersecting hollows called Corkscrew Pits are visible. (**b**) Collapse at the rear of a house in Ure Terrace in the village of Ripon, April 1997 (Photographs courtesy of British Geological Survey)

mechanism for subsidence. Many of the more catastrophic collapses occur after river flooding and periods of prolonged rain, which tend to wash away cavern roof span support. Subsidence is also aggravated by groundwater pumping; first, it lowers the watertable and second, it induces considerable crossflow of water in enlarged joints in the gypsum. When recharged by a later flood, the replacement water is undersaturated with respect to gypsum.

Thomson et al. (1996) recognised four hydrogeological flow units driving karst collapse in the Ripon area:

1. Quaternary gravels in the buried valley of the proto-River Ure
2. Sherwood Sandstone Group
3. Magnesian Limestone of the Brotherton Fm. and the overlying/adjacent gypsum of the Roxby Fm.
4. Magnesian limestone of the Cadeby Fm. plus the overlying/adjacent gypsum of the Edlington Fm.

Local hydrological base level within this stratigraphy is controlled by the River Ure, especially where the buried Pleistocene valley (proto-Ure) is filled by permeable sands and gravels, as these unconsolidated sediments, when located atop a breached roof beam, are suscepible to catastrophic stoping to base level (Fig. 7.58). In the area around Ripon the palaeovalley cuts down more than 30 m, reaching levels well into the Cadeby Formation, so providing the seepage connections or pathways between waters in all four units wherever they intersect the palaeovalley. There is considerable groundwater outflow along this route with artesian sulphate-rich springs issuing from Permian strata in contact with Quaternary gravels of the buried valley (Cooper 1986, 1995, 1998).

The potentiometric head comes from precipitation falling on the high ground of the Cadeby formation to the west and the Sherwood Sandstone to the east. Groundwater becomes largely confined beneath glacial till as it seeps toward the Ure Valley depression, but ultimately finds an exit into the modern river via the deeply incised sand and gravel-filled palaeovalley of the proto-Ure. Waters recharging the Ure depression pass through and enlarge joints and caverns in the gypsum units of the Edlington and Roxby Formations, so the highest density of subsidence features are found atop the sides of the palaeovalley. This region has the greatest volume of artesian discharge from aquifers immediately beneath the dissolving gypsum bed. Although created as an active karst valley, the apparent density of subsidence hollows is lower on the present Ure River flood-plain than the surrounding lands as floodplain depressions are constantly filled by overbank sediments (Figs. 7.58 and 7.59a).

Cooper (1998) defined 16 sinkhole variations in the gypsum subsidence belt at Ripon, all are types of entrenched[11],

[11] *Entrenched karst* occurs where the entire thickness of the soluble rock is entrenched along the sides of valleys but the insoluble cap spans most interfluves.

Subjacent karst occurs where the soluble rock is locally breached by erosion over a minor part of its thickness, karst features may be expressed at the surface as combinations of springs and collapse features. *Mantled karst* is wholly or partly covered by a relatively thin veneer of post-karst rock or sediment and is part of the contemporary landscape.

subjacent and mantled karst. Changes in karst style are caused by; the type of gypsum, the nature and thickness of the overlying deposits, presence or absence of consolidated layers overlying the gypsum and the size of voids/caverns within the gypsum.

To the west of Ripon, the gypsum of the Edlington Formation lies directly beneath glacial drift. These unconsolidated drift deposits and the loose residual marl atop the dissolving gypsum gradually subside into a pinnacle or suffusion (mantled) karst. But between Ripon town and the River Ure, the limestone of the Brotherton Formation overlies the Edlington Formation. There the karst develops as large open caverns beneath strong roof spans (entrenched karst). Ultimate collapse of the roof span creates rapid upward-stoping caverns in loosely consolidated sediment. Stopes break though to the surface as steep-sided collapse dolines or chimneys with sometimes catastrophic results. A similar entrenched situation is found east of the Ure River but there karstified gypsum units of both the Edlington and the Roxby formations are involved.

When a chimney breaks through, the associated surface collapse is very rapid[12]. A recently documented example of one such subsidence crater, which opened up in front of a house on Ure Bank terrace on 23rd and 24th April, 1997, is documented by Cooper (op. cit.) as follows (Fig. 7.59b).

> "…The hole grew in size and migrated towards the house, to measure 10 m in diameter and 5.5 m deep by the end of Thursday. Four garages have been destroyed by the subsidence. This collapse was the largest of one of a series that have affected this site for more than 30 years; and earlier collapse had demolished two garages on the same site and an 1856 Ordnance Survey map shows a pond on the same site. The hole is cylindrical but will ultimately fail to become a larger, but conical, depression. As it does so, it may cause collapse of the house, which is already damaged, and the adjacent road. The house and several nearby properties have been evacuated and the nearby road has been closed. The gas and other services, which run close to the hole, have also been disconnected in case of further collapse..."

Cooper (1998) found the sites of most severe subsidence in the Ripon area (including the house of Ure terrace; Fig. 7.59b) are located at the sides of the buried Ure Valley, an area where the water seeps from the gypsum into the river gravels. In 1999 the Ure Terrace sinkhole was filled using a long conveyor belt that was cantilevered over the hole so that no truck needed to back up close to the sinkhole opening. The hole was surcharged to a height of 0.5 m. The hole remains unstable, but the collapse of the fill is monitored to document fill performance and the fill is periodically topped up. After the sinkhole was filled, the road adjacent to the sinkhole was re-opened and the site of the sinkhole fenced. The severely damaged Field View house remains standing next to the sinkhole. The nearby Victorian Ure lodge was not directly damaged by the 1997 sinkhole, but its western corner fell within the council-designated damage zone, and was left unoccupied. It fell into disrepair and was subsequently demolished,

Problems with Miocene gypsum, Spain

Karstification has led to problems in areas of subcropping Miocene gypsum in the Ebro and Calatayud basins, northern Spain. Cliff sections and road cuts indicate the widespread nature of karstification in the gypsum outcrops and subcrops in Spain (Fig. 7.60a, b) Areas affected are defined by subsidence or collapse in Quaternary alluvial overburden and include; urban areas, communication routes, roads, railways, irrigation channels and agricultural fields (Soriano and Simon 1995; Elorza and Santolalla 1998; Guerrero et al. 2013). In the region there can be a reciprocal interaction between anthropic activities and sinkhole generation, whereby the ground disturbance engendered by human activity accelerates, enlarges and triggers the creation of new sinkholes. Subsidence is particularly harmful to linear constructions and buildings and numerous roads, motorways and railways have been damaged. Catastrophic collapse and rapid karst chimneying into roads and buildings can have potentially fatal consequences. For example, several buildings have been damaged around the towns of Casetas and Utebo. In the Portazgo industrial estate some factories had to be pulled down due to collapse-induced instability (Castañeda et al. 2009). A nearby gas explosion was attributed to the breakage of a gas pipe caused by subsidence. The local water supply is also disrupted by subsidence and pipe breakage so that 20,000 inhabitants periodically lose their water supply. The most striking example of subsidence affecting development comes from the recently built village of Puilatos, in the

[12] A. H. Cooper in a lecture to the general public argued that collapse dolines breaching the landscape between Ripon and Darlington were the inspiration for thn Alice in Wonderland (see also <http://www.bgs.ac.uk/caves/alice_in_wonderland.html> last accessed Jan 5, 2015).

In Chap. 1, Lewis Carroll wrote:

"...The rabbit-hole went straight on like a tunnel for some way, and then dipped suddenly down, so suddenly, that Alice had not a moment to think about stopping herself, before she found herself falling down what seemed a deep well. Either the well was very deep, or she fell very slowly, for she had plenty of time as she went down to look about her, and to wonder what would happen next..."

Charles Lutwidge Dodgson, who later adopted the Lewis Carroll pseudonym, was born in Cheshire and spent his early days at Croft, near Darlington. There, a trio of ponds called Hell's Kettles were believed by locals in the Dark Ages to be bottomless links to hell. The pits are now known to be gypsum collapse features only 22 ft deep but they may have inspired this passage from the Carroll's first chapter. In 1852 Carroll moved with his parents to Yorkshire when his father became Canon Dodgson of Ripon. Here, he first met Mary Badcock. Carroll, a keen mathematician, scientist and photographer, took pictures of Mary that were later adapted by Sir John Tenniel into illustrations in the first edition of Alice in Wonderland.

Fig. 7.60 Gypsum karst, Calatayud region, Spain. (**a**) View from the town of Cataluyud toward the retreating front of Miocene gypsum and the contact with the encroaching flood-plain of the Rio Jalón. (**b**) Mantled steep edge of a collapse doline exposed in a highway cut on the approach to Cataluyud. Bedded gypsum makes up the right half of the exposure, doline-fill alluvium the left, indicating why strong lateral contrasts in mechanical strength exist in the region

Gallego Valley. This was severely damaged by subsidence and abandoned before it could be occupied.

Collapse affects irrigation channels in the countryside with substantial economic losses (Elorza and Santolalla 1998). In 1996 a doline collapse surfaced and cut the important Canal Imperial at Gallur village. New dolines often form in close proximity to unlined irrigation canals. The ongoing supply of fresh irrigation waters to field crops can also encourage sinkhole generation in the fields. Though not directly visible, natural sinkholes also form in the submerged beds of river channels cutting regions of subcropping gypsum (Benito et al. 1998). On December 19th, 1971, a bus fell from a bridge into the Ebro River at Zaragoza, near where the so-called ‘San Lazaro well’ (a submerged gypsum sinkhole) is located. Ten people lost their lives in this accident, nine of them where never found. Locals suggested that bod-

ies were carried into the sinkhole and sank into the caverns fed by this losing stream. Karstification in the Zaragoza region is characterised by the preferential intrastatal dissolution of glauberite beds, which are more soluble than the gypsum interbeds, this leads to collapse and rotation of gypsum blocks and river capture (Guerrero et al. 2013).

Sometimes even well-intentioned attempts to remediate culturally significant buildings under threat of karst collapse can exacerbate collapse problems. Gutiérrez and Cooper (2002) cite examples from the city of Calatayud, Spain. Subsidence-induced differential loading across doline edges drives the tilting of the 25 m high tower of the San Pedro de los Francos church, which leans towards and overhangs the street by about 1.5 m. In places, the brickwork of the church indents the pre-existing tower fabric, which probably dates from the eleventh Century or the beginning of the twelfth Century. This indentation and the non-alignment of the church and the tower walls indicates that most of the tower tilting occurred prior to the construction of the church. In 1840, the upper 5 m of the tower was removed and the lower part buttressed for the safety of the Royal family, who visited the town and stayed in the palace opposite. On 3rd June 1931, San Pedro de los Francos church was declared a "Monument of Historical and Artistic value." Due to its ruinous condition, the church was closed to worship in 1979. Micropiling to improve the foundation was started in 1994, but this corrective measure was interrupted when only half of the building was underpinned. Very rapid differential settlement of the building took place in the following year, causing extensive damage and aggravating the subsidence problem. Colegiata de Santa María la Mayor was constructed between the thirteenth and eighteenth centuries, it has an outstanding Mudéjar (a 72 m high tower) and numerous Renaissance features; it is considered the foremost monument in the city of Cataluyud. As with the San Pedro de los Francos Church, recent micropiling work, applied to only one part of the cloister, has been followed by alarming differential movements that have drastically accelerated the deterioration of the building. Large blocks have fallen from the vault of the "Capitular Hall" and cracks up to 150 mm wide have opened in the brickwork of the back (NW) elevation, which has now been shored up for safety. The dated plaster telltales placed in these cracks to monitor the displacement demonstrate the high speed of the deformation produced by subsidence in recent years. On the afternoon of 10 September 1996, the fracture of a water supply pipe flooded the cloisters and the church with 100 mm of muddy water. Ten years earlier a similar breakage and flood had occurred. These breaks in the water pipes are most likely related to karst-induced subsidence. Once they occur, the massive input of water to the subsurface may trigger further destruction via enhanced dissolution, piping and hydrocollapse (Gutiérrez and Cooper 2002).

Gypsum Karst in Mosul, Iraq

A similar quandary of multiple areas of structural damage from gypsum-induced subsidence affects large parts or the historic section of the city of Mosul in northern Iraq (Jassim et al. 1997). The main part of its old quarter is over a century old and some buildings are a few hundred years old. Mosul lies on the northeastern flank of the Abu Saif anticline and near to its northern plunge (Fig. 7.61). It was built on the western bank of the Tigris River on a dip slope of Middle Miocene Fatha limestone that is directly underlain by bedded gypsum and green marl (equivalent to Lower Fars Formation). Houses in the old city were built on what seemed to be at the time a very sound rock foundation.

Water distribution in the city was done on mule back in the early part of last century and the estimated water consumption did not exceed 10 l per person per day (Jassim et al. 1997). Discharge from households was partly to surface drainage and partly to shallow and small septic tanks. The modern piped system of water distribution did not start until the 1940s, resulting in a sudden increase in water consumption (presently around 200 l per person per day) and it was not associated with a complementary sewer system. Increased water consumption meant larger and deeper septic tanks were dug at the perimeter of buildings (which never seemed to fill) resulting in a dramatic increase in water percolating downwards, water that was also more corrosive than previously due to the increased use of detergents and chlorination. This water passes through the permeable and fractured limestone to the underlying gypsum. On its way through the limestone it enlarges and creates new dissolution cavities, but eventually finds its way into the older gypsum karst maze, which is then further widened as water drains back into the Tigris. Caverns in the gypsum enlarge until the roof span collapses. Since the 1970s more and more buildings in the old city have fractured and many are subject to sudden collapse. The problem is further intensified due to the expansion of the city in the up-dip direction (west and south-west) including the construction of industrial, water-dependent centres with integrated drainage. Water seeping/draining from these newly developed up-dip areas eventually passes under the old city before discharging in the Tigris river. The process was slightly arrested in the 1980s by the completion of a drainage system for the city, but the degradation of the old city continues.

Coping: Man-made Structures Atop Salts

The towns of Ripon in the UK and Pasvales and Birzai in Lithuania house some 45,000 people, who currently live under the ongoing threat of catastrophic subsidence, caused by natural gypsum dissolution (Paukstys et al. 1999). Special measures for construction of houses, roads, bridges and railways are needed in these areas and should include:

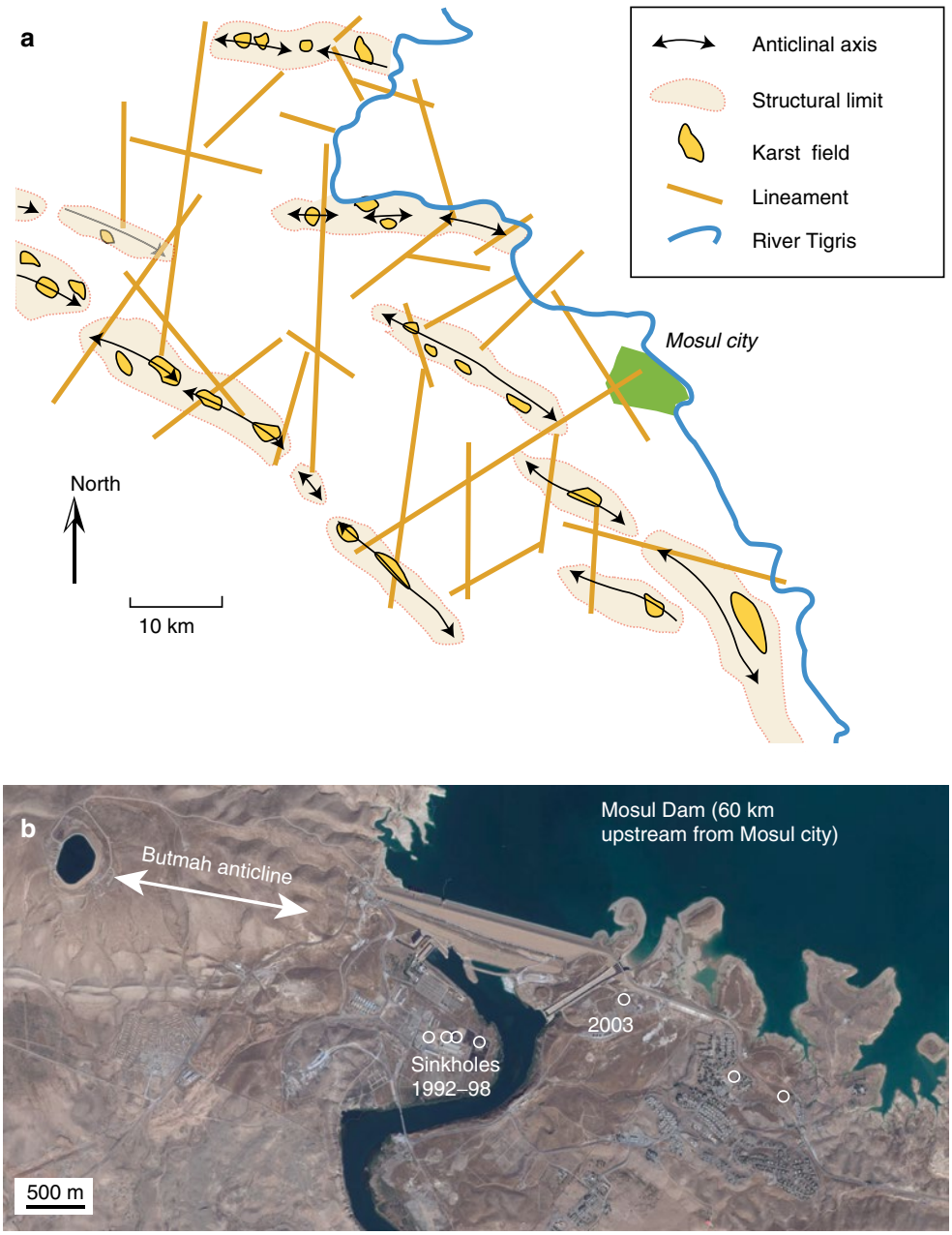

Fig. 7.61 Karst problems in Iraq. (**a**) Evaporite karst zones developed in anticlinal crests exposing a gypsiferous zone in Miocene lower Fars (Fat'ha) Formation (after Jassim et al. 1997). (**b**) Karst development in the foundation region of the Mosul Dam, Iraq. The white circles indicate at-surface karst features (Scaled and annotated Bing® Image)

incorporating several layers of high tensile heavy duty reinforced plastic mesh geotextile into road embankments and car parks; using sacrificial supports on bridges so that the loss of support of any one upright will not cause the deck to collapse; extending the foundations of bridge piers laterally to an amount that could span the normal size of collapses; and using ground monitoring systems to predict areas of imminent collapse (Cooper 1995, 1998).

Dams to store urban water supplies are costly structures and failure can lead to disaster, large scale mortality and financial liability (Cooper and Gutiérrez 2013). For example, at two and a half minutes before midnight on March 12, 1928 the St. Francis Dam (California) failed catastrophically and the resulting flood killed more than 400 people. The collapse of the St. Francis Dam is considered to be one of the worst American civil engineering disasters of the twenteenth century and remains the second-greatest loss of life in California's history, after the 1906 San Francisco earthquake and fire. The collapse was partly attributed to dissolution of gypsum veins beneath the dam foundations. The Quail Creek Dam, Utah, constructed in 1984 failed in 1989, the underlying cause being an unappreciated existence of, and consequent enlargement of, cavities in the gypsum strata beneath its foundations.

Unexpected water leakage from reservoirs, via ponors, sinkholes and karst conduits leads to costly inefficiency, or

even project abandonment. Unnaturally high hydraulic gradients, induced by newly impounded water, may flush out sediment that previously blocked karst conduits. It can also produce rapid dissolutional enlargement of discontinuities, which can quickly reach break-through dimensions with turbulent flow. These processes may significantly increase the hydraulic permeability in the region of the dam foundation, on an engineering time scale. Accordingly, numerous dams in regions of the USA underlain by shallow evaporites either have gypsum karst problems, or have encountered gypsum-related difficulties during construction (Johnson 2008b). Examples include; the San Fernando, Dry Canyon, Buena Vista, Olive Hills and Castaic dams in California; the Hondo, Macmillan and Avalon dams in New Mexico; Sandford Dam in Texas; Red Rock Dam in Iowa; Fontanelle Dam in Oklahoma; Horsetooth Dam and Carter Dam in Colorado and the Moses Saunders Tower Dam in New York State. Up to 13,000 tonnes of mainly gypsum and anhydrite were dissolved from beneath a dam in Iraq in only 6 months causing concerns about the dam stability (Fig. 7.61b). In China, leaking dams and reservoirs on gypsum include the Huoshipo Dam and others in the same area. The Bratsk Dam in eastern Siberia is leaking, and in Tajikistan the dam for the Nizhne-Kafirnigansk hydroelectric scheme was designed to cope with active gypsum dissolution occurring below the grout curtain. Gypsum karst in the foundation trenches of the Casa de Piedra Dam, Argentina and El Isiro Dam in Venezuela, caused difficult construction conditions and required design modifications.

Another illustration of the problems associated with water retaining structures and the ineptitude, or lack of oversight, by some city planners comes from the town of Spearfish, South Dakota (Davis and Rahn 1997). As discussed earlier in this chapter, the Triassic Spearfish Formation contains numerous gypsum beds in which evaporite-focused karst landforms are widely documented across its extent in the Black Hills of South Dakota (Fig. 7.16). The evaporite karst in the Spearfish Fm. has caused severe engineering problems for foundations and water retention facilities, including wastewater stabilization sites. One dramatic example of problems in water retention atop gypsum karst comes from the construction in the 1970s of now-abandoned sewage lagoons for the City of Spearfish.

Despite warnings from local ranchers, the Spearfish sewage lagoons were built in 1972 by city authorities on alluvium atop thick gypsum layers of Spearfish Formation. Ironically, at one point during lagoon construction, a scraper became stuck in a sinkhole and required four bulldozers to pull it out. Once filled with sewage, within a year the lagoons started leaking badly; the southern lagoon was abandoned after four years because of ongoing uncontrollable leaks, and the northern lagoon did not completely drain, but could not provide adequate retention time for effective sewage treatment. Attempts at repairs, including a bentonite liner, were ineffective, and poorly treated sewage discharged beneath the lagoon's berm into a nearby surface drainage. The lagoons were abandoned completely in 1980. This was after a US $27-million lawsuit was filed in 1979 by ranchers whose land and homes were affected by leaking wastewater. A mechanical wastewater treatment plant was constructed nearby on an outcrop of the non-evaporitic Sundance Formation. The engineering firm that designed the facility without completing a knowledgeable geological site survey was reorganised following the lawsuit.

Likewise, the development of Chamshir Dam atop Gascharan Formation outcrop and subcrop in Iran is likely to create ongoing infrastructure cost and water storage problems (Torabi-Kaveh et al. 2012). The site is located in southwest of Iran, on Zuhreh River, 20 km southeast of Gachsaran city. The area is partially covered by evaporite formations of the Fars Group, especially the Gachsaran Formation. The dam axis is located on limestone beds of Mishan Formation, but nearly two-thirds of the dam reservoir is in direct contact with the evaporitic Gachsaran Formation. Strata in the vicinity of the reservoir and dam site have been brecciated and intersected by several faults, such as the Dezh Soleyman thrust and the Chamshir fault zone, which all act in concert to create karst entryways, including local zones of suffusion karst. A wide variety of karstic features typify the region surrounding the dam site and include; karrens, dissolution dolines, karstic springs and cavities. These karst features will compromise the ability of Chamshir Dam to store water, and possibly even cause breaching of the dam, via solution channels and cavities which could allow significant water flow downstream of the dam reservoir. As possible and likely partial short term solutions, Torabi-Kaveh et al. (2012) recommend the construction of a cutoff wall and/or a clay blanket floor to the reservoir.

Clearly, difficulties in building hydraulic structures on soluble rocks are many, and dealing with them greatly increases project and maintenance costs. Gypsum dissolution at the Hessigheim Dam on the River Neckar in Germany has caused settlement problems in sinkholes nearby. Site investigation showed cavities up to several meters high and remedial grouting from 1986 to 1994 used 10,600 tonnes of cement. The expected life of the dam is only 30–40 years, with continuing grouting required to keep it serviceable.

Grouting costs in zones of evaporite karst can be very high and may approach 15 or 20 % of the dam cost, currently reaching US$ 100 million in some cases. In karstified limestones grouting is difficult, yet in gypsum it is even more difficult due to the rapid dissolution rate of the gypsum. Karst expansion in limestone occurs on the scale of hundreds of years, in gypsum it can be on the order of a decade or less. Grouting may also alter the underground flow routes, so translating and focusing the problems to other nearby areas.

In the Perm area of Russia, gypsum karst beneath the Karm hydroelectric power station dam has perhaps been successfully grouted, a least in the short term, using an oxaloaluminosilicate gel that hardens the grout, but also coats the gypsum, so slowing its dissolution. The Mont Cenis Dam, in the French Alps, is not itself affected by the dissolution of gypsum. However, the reservoir storage zone is leaking and photogrammetric study of the reservoir slopes showed ongoing doline activity over gypsum and subsidence in the adjacent land.

Probably the worst example tied to an evaporite karst hazard is the significant dam disaster waiting to happen that is the Mosul Dam in Iraq (Fig. 6.71b; Kelley et al. 2007; Sissakian et al. 2014). It is ranked as the fourth largest dam in the Middle East, as measured by reserve capacity, capturing snowmelt from Turkey, some 70 miles (110 km) north. Built under the despotic regime of Saddam Hussein, completed in 1984 the Mosul Dam (formerly known as Saddam Dam) is located on the Tigris river, some 50 km NW of Mosul.

The design of the dam was done by a consortium of European consultants (Sissakian et al. 2014), namely, Swiss Consultants group, comprising: Motor Columbus; Electrowatt; Suiselectra; Societe Generale pour l'Industrie. The construction was carried out by a German-Italian consortium of international contractors, GIMOD joint venture, comprising: Hochtief; Impregilo; Zublin; Tropp; Italstrade; Cogefar. The consultants for project design and construction supervision comprised a joint venture of the above listed Swiss Consultants Group and Energo-Projekt of Yugoslavia, known as MODACON.

As originally constructed the dam is 113 m in height, 3.4 km in length, 10 m wide in its crest and has a storage capacity of 11.1 billion cubic meters. It is an earth fill dam, constructed on evaporitic bedrock atop a karstified high created by an evaporite cored anticline in the Fat'ha Formation, which consists of gypsum beds alternating with marl and limestone (Fig. 7.61b). To the south this is same formation, with the same evaporite cored anticlinal association that created all the stability problems in the city of Mosul (Fig. 7.61a). The inappropriate nature of the Fat'ha Formation as a foundation for any significant engineering structure had been known for more than a half a century. Then again, absolute rulers do not need to heed scientific advice or knowledge. Or perhaps he didn't get it from a well-paid group of Swiss-based engineering consultants. As Kelley et al. (2007) put it so succinctly.... "The site was chosen for reasons other than geologic or engineering merit."

The likely catastrophic failure of Mosul Dam will drive the following scenario (Sissakian et al. 2014); "… (dam) failure would produce a flood wave crest about 20 m deep in the City of Mosul. It is estimated that the leading edge of the failure flood wave would arrive in Mosul about 3 h after failure of the dam, and the crest of the flood wave would arrive in Mosul about 9 h after failure of the dam. The total population of the City of Mosul is about three million, and it is estimated that about two million people are in locations within the city that would be inundated by a 20 m deep flood wave. The City of Baghdad is located about 350 km downstream of Mosul Dam, and the dam failure flood wave will arrive after 72 h in Baghdad and (by then) would be about 4 m deep."

The heavily karsted Fat'ha Formation is up to 352 m thick at the dam and has an upper and lower member. The lower member is dominated by carbonate in its lower part (locally called "chalky series") and is in turn underlain by an anhydrite bed known as the GBo. Gypsum beds typify its upper part, and the evaporite interval is capped by a limestone marker bed. The upper member, crops out as green and red claystone with gypsum relicts, around the Butmah Anticline. Thickness of individual gypsum beds below the dam foundations can attain 18 m; these upper member units are intensely karstified, even in foundation rocks, with cavities meters across documented during construction of the dam. Gypsum breccia layers are widespread within the Fatha Formation and have proven to be the most problematic rocks in the dam's foundation zone. The main breccia body contains fragments or clasts of limestone, dolomite, or larger pieces of insoluble rocks of collapsed material. The upper portion of the accumulation grades upward from rubble to crackle mosaic breccia and then a virtually unaffected competent overburden. Breccia also may form without the intermediate step of an open cavity, by partial dissolution and direct formation of rubble. As groundwater moves through the rubble, soluble minerals are carried away, leaving insoluble residues of chert fragments, quartz grains, silt, and clay in a mineral matrix. These processes result in geologic layers with lateral and vertical heterogeneity on scales of micro-meters to meters.

High permeability zones in actively karsting gypsum regions can form rapidly, days to weeks, and quickly become transtratal. So predicting or controlling breakout zones via grouting and infill can be problematic (Kelley et al. 2007; Sissakian et al. 2014). For example, four sinkholes formed between 1992 and 1998 approximately 800 m downstream in the maintenance area of the dam (Fig. 7.61b). The sinkholes appeared in a linear arrangement, approximately parallel to the dam axis. Another large sinkhole developed in February 2003, east of the emergency spillway when the pool elevation was at 325 m. The Mosul Dam staff filled the sinkhole the next day, with 1,200 m^3 of soil. Another sinkhole developed in July 2005 to the east of the saddle dam. Six borings were completed around the sinkhole and indicated that the sinkhole developed beneath overburden deposits and within layers of the Upper Marl Series. Another cause for concern at Mosul Dam in recent years is a potential slide area reported

upstream of the dam on the west bank. The slide is most likely related to the movement of beds of the Chalky Series over the underlying GBo (anhydritic) layer.

To "cope" with ongoing active karst growth beneath and around the Mosul Dam, a continuous grouting programme was planned, even during dam construction, and continues today, on a six days per week basis. It pumps tens of thousands of tons of concrete into expanding karst features each year (Sissakian et al. 2014). The dam was completed in June 1984, with a postulated operational life of 80 years. Due to insufficient grouting and sealing in and below the dam foundation, numerous karst features, as noted above, continue to enlarge in size and quantity, so causing serious problems for the ongoing stability of the dam. The increase in hydraulic gradient created by a wall of water behind the dam has accelerated the rate of karstification in the past 40 years. Since late 1980s, the status of the dam and its projected collapse sometime within the next few decades has created ongoing nervousness for the people of Mosul city and near surroundings. All reports on the dam since the mid 1980s have underlined the need for ongoing grouting and monitoring and effective planning of the broadcasting of a situation where collapse is imminent. For "Saddam's dam" the question is not if, but when, the dam will collapse. To alleviate the effects of the dam collapse, Iraqi authorities have started to build another "Badush Dam" south of Mosul Dam so that it can stop or reduce the effects of the first flood wave. However this new dam has a projected cost in excess of US$ ten billion and so lies beyond the financial reach of the current Iraqi government. Recently, problems related to the dam increased with the takeover of the region by the forces of ISIL[13].

Given the existing geologic knowledge base in the 1980s, in my opinion, one must question the seeming lack of understanding in a group of well paid consultant engineers as to the outcome of building such a major structure, atop what was known to be an active karstifying gypsum succession, sited in a location where failure will threaten multimillion populations in the downstream cities. The same formation that constituted the base to the Mosul dam was known at the time to be associated with ground stability problems atop similar gypsum-cored anticlines in the city of Mosul to the south. Even more concerning to the project rationale should have been the large karst cavities in highly soluble gypsum that were encountered a number of times during feasibility and construction of the dam foundations (Fig. 7.61a). Or, perhaps, as Lao Tzu observed many centuries ago, " …So the unwanting soul sees what's hidden, and the ever-wanting soul sees only what it wants."

Canals, like dams, that leak in gypsum karst areas can trigger subsidence, which can be severe enough to cause retainment failure. In Spain, the Imperial Canal in the Ebro valley, and several canals in the Cinca and Noguera Ribagorzana valleys, which irrigate parts of the Ebro basin, have on numerous occasions failed in this way. Similarly, canals in Syria have suffered from gypsum dissolution and collapse of soils into karstic cavities. Canals excavated in such ground may also alter the local groundwater flow (equivalent to losing streams) and so accelerate internal erosion, or the dissolution processes and associated collapse of cover materials. In the Lesina Lagoon, Italy, a canal was excavated to improve the water exchange between the sea and the lagoon. It was cut through loose sandy deposits and highly cavernous gypsum bedrock, but this created a new base level, so distorting the local groundwater flow. The canal has caused the rapid downward migration of the cover material into pre-existing groundwater conduits, producing a large number of sinkholes that now threaten an adjacent residential area. Pipelines constructed across karst areas are potential pollution sources and some may pose possible explosion hazards. The utilization of geomorphological maps depicting the karst and subsidence features allied with GIS and karst databases help with the grouting and management of these structures. In some circumstances below-ground leakage from water supply pipelines can trigger severe karstic collapse events. Where such hazards are identified, such as where a major oil and gas pipeline crosses the Sivas gypsum karst in Turkey, the maximum size of an anticipated collapse can be determined and the pipeline strength increased to cope with the possible problems.

Solving the Problem?

Throughout the world, be it in the UK, Spain, eastern Europe, or the Middle East, it is a fact that weathering of shallow gypsum forms rapidly expanding and stoping caverns, especially in areas of high water crossflow, roof beams and unconsolidated overburden and in areas of artificially confined fresh water. Rapid karst formative processes and mechanism will always be commonplace and widespread

[13] On August 7, 2014, the Islamic State of Iraq and the Levant (ISIL) movement captured the Mosul Dam complex from the Peshmerga. ISIL control of the dam created fears that its power supply could be restricted, or the water flows to downstream areas greatly inhibited. In a less likely scenario, there were worries the dam could be breached, causing widespread flooding and destruction downstream. On August 17, 2014, Peshmerga and the Iraqi Army launched a successful operation to retake control of the dam from ISIL militants. United States air strikes assisted the Kurdish and Iraqi military, damaging or destroying 19 vehicles belonging to ISIL, as well as a checkpoint near the dam.

Some estimates suggest that the dam would begin to crumble within weeks if grouting stopped, which explains why ISIL brought in their own engineers to keep the grouting process going. Any group trying to establish a new state needs control of water supplies and power-generation, so it was in the interests of ISIL to keep the dam intact. (It was not known at the time of recapture if they had planted explosive charges throughout the structure, just in case they needed a Doomsday option).

Table 7.10 Summary of possible changes in the karst system (natural or anthropogenic) that can accelerate of trigger karst development in evaporitic terrains

Type of change	Effects	(1) Natural processes. (2) Human activity
Increased water input to the ground (cover and bedrock).	Increasing percolation accelerates suffosion. Enhances rate of dissolution. Increases weight of sediment. May reduce mechanical strength of sediment.	(1) Rainfall, floods, snow melt, permafrost thaws. (2) Irrigation, leakages from utilities (pipes, canals ditches), water impoundment, runoff concentration (urbanisation, soakaways) or diversion, vegetation removal, poorly monitored drilling, unsealed wells, fluid injection, solution mining.
Watertable decline.	Increases effective weight of sediment (loss of buoyant support). Slow phreatic flow replaced by more rapid downward percolation favoring suffosion, especially when water-table is lowered below the rockhead. Suction effect	(1) Climate change, sea; level decline, entrenchment of drainage network, tectonic uplift. (2) Water abstraction, dewatering for mining operations, decline of lake water levels.
Impoundment of water.	May create very high hydraulic gradients favoring dissolution and internal erosion processes. Imposes a load.	(1) Natural lakes. (2) Reservoirs, lagoons.
Permafrost thawing.	Favors dissolution Significant reduction in strength of sediments	(1) Climate change. (2) Development, deforestation, water storage.
Static loads	Favors compaction and the failure of cavity roofs.	(1) Aggradation processes. (2) Engineered structures, dumping, heavy vehicles.
Dynamic loads.	Favors the failure of cavity roofs and may cause liquefaction-fluidisation processes involving a sharp drop in the mechanical strength of soils.	(1) Earthquakes, volcanic explosions. (2) Artificial vibration (blasting, explosions)
Thinning of sediments over voids	Reduces the mechanical strength of cavity roofs. May concentrate runoff and create a local base level for groundwater flows.	(1) Erosion processes. (2) Excavations.
Underground excavations.	Disturb groundwater flows. May intercept phreatic conduits. May weaken sediment over voids.	(1) Biogenic pipes. (2) Mining and tunnelling
Waterproofing of reservoir bottoms.	Trapped pressurised air in the vadose zone during rapid rises of watertable.	(2) Waterproofing blankets in reservoirs

After Gutierrez (2010)

(Table 7.10). Resultant karst-associated problems can be both natural and anthropogenically induced or enhanced. It is fact that natural solution in regions of subcropping evaporites is always rapid, and even more so in areas where it is encouraged by human activities, especially increased cycling of water via damming, groundwater pumping, burst pipes, septic systems, agricultural enhancement and uncontrolled storm and waste water runoffs to aquifers.

Typically, the best way to deal with a region of an evaporite karst hazard is to map the regional extent of the shallow evaporite solution front and avoid it (Table 7.11). In established areas with a karst problem the engineering solutions will need to be designed around hazards that will typically be characterised by short-term onsets and often tied to rapid ground stoping/subsidence events, followed by ground collapse. If man-made buildings of historical significance are to be restored and stabilized in such settings, perhaps it is better to wait until funds are sufficient to complete the job rather than attempt partial stabilization of the worst-affected portions of the feature. Significant infrastructure (including roads, canals and dams) should be designed to avoid such areas when possible or engineered to cope with and/or survive episodes of ground collapse. A piecemeal approach to dealing with evaporite karst can intensify and focus water crossflows rather than alleviate them. In the words of Nobel prizewinner, Shimon Peres; "If a problem has no solution, it may not be a problem, but a fact – not to be solved, but to be coped with over time."

Sulphuric Acid Speleogenesis

Historically, most carbonate karst networks have been interpreted as epigenic (surface-driven) responses to vadose/shallow-phreatic leaching of carbonate bedrock, in a hydrology driven by throughflowing fresh to brackish meteoric waters. Leaching and cavern/joint enlargement is seen as a response to waters enriched in carbonic acid. Carbonic acid is derived from CO_2 in the atmospheric and soil zones. Most vadose cave ornamentation is a response to CO_2 degassing at or above the watertable and precipitates are dominantly calcite, with lesser volumes of other carbonate minerals (aragonite, magnesite) and rare sulphates.

Yet, we have seen how gypsum maze caves do not fit neatly into this epigenetic meteoric/watertable dominated template for karst formation. Telogenetic gypsum karst in an evaporite basin starts deeper (hypogenic), typically in water crossflows driven by deep artesian circulation or escaping

Table 7.11 Problems and outcomes in some regions of gypsum subcrop

Problem	Effected regions/area	Outcomes/responses	Responses	Relevant references
Cities and towns in regions underlain by shallow evaporate (subcrop)	Paris (France), Dzerzhinksk (Russia), Zaragoza, Calatayud and the outskirts of Madrid (Spain), Birzai and Pasvalys (Lithuania), Ripon and Darlington (UK).	Building instability, problematic restorations	Documentation, probing, mapping, avoidance where possible	Cooper and Gutiérrez (2013), Tolmachev et al. (2003), Tolmachev and Leonenko (2011), Galve et al. (2009), Thierry et al. (2009), Gutiérrez et al. (2008), Waltham et al. (2005)
Dams, ponds, pipelines, canals and water wells in regions underlain by shallow evaporate (subcrop)	Various dams in USA and Middle East Sewage ponds, Spearfish (USA) Oil pipeline across Sivas region (Turkey)	Dam storage leakage and possible dam collapse (e.g. Mosul Dam, Iraq) Pipeline leakage and associated pollution – Poor quality water supply (e.g. Birzai Lithuania) Subsidence associated with water abstraction	Karst characterization and mapping in regions of intersection. Forward planning of infrastructure character and limitations, avoidance on placing infrastructure atop active evaporite karst. Monitoring is required and increased pipeline strength planned so as to allow drape without breakage. Avoidance where possible	Cooper and Gutiérrez (2013), Sissakian et al. (2014), Kelley et al. (2007), Torabi- Kaveh et al. (2012), Yilmaz et al. (2011), Johnson (2008b),
Roads and rail networks underlain by shallow evaporate (subcrop)	Highways in US, Europe, the Middle East and elsewhere	Road subsidence, collapse, loss of line of site below bridges and overpasses	Appropriate planning and highway construction techniques including strengthening road bases, grouting, as well as bridge pylons capable of integrity in situation of ground collapse. Avoidance where possible	Alberto et al. (2008), Cooper and Saunders (2002), Frumkin et al. (2011), Tolmachev et al. (1999)
Unexpected problems in salt related conventional mining, solution wells, salt storage caverns	Common to all is a combination of short-term profit, poor understanding of the geology, no monitoring of possible subsidence and ground collapse, poor contingency planning.	Rapid formation of at-surface collapse dolines, loss of infrastructure, and sometimes loss of life (minimal compare to above ground storage problems and explosions)	Monitoring, technical understanding and forward planning. Better training and appropriate qualifications of all involved personnel	See Chap. 13 for full discussion, documentation and recommendations (Tables 13.6, 13.7, 13.8, and 13.9)

In part after Cooper and Gutiérrez (2013)

Table 7.12 Active and inactive sulphuric cavern systems, not all are related to evaporite dissolution, but all accumulate gypsum

Active sulphidic caves and hypogenic karst	Australia: Odyssey Cave Brazil: Toca da Boa Vista and Toca da Barriguda caves Canada: "Sulphur" Cave, Banff National Park Italy: Frasassi Caves (Grotta Grande del Vento Grotta de Fiume); Submarine caves as in Grotta Azzurra region Mexico: Cueva de Villa Luz; Sistema Zacatón Romania: Movile Cave Turkey: Hypogene karst features (Obruks) Turkmenistan: Cupp-Coutum Cave USA: Cesspool Cave, Virginia; Crystal Beach Cave, Florida; Lower Kane Cave, Wyoming; Parker Cave, Kentucky; Deep portions of the Edwards Aquifer, Texas	Jennings (1985) Klimchouk (2007) Ford (1997) Vlasceanu et al. (2000), Galdenzi and Menichetti (1995), Forti et al. (2002) Hose et al. (2000), Klimchouk (2007) Forti et al. (2002) Bayari et al. (2009) Maltsev and Malishevsky (1990) Andrejchuk and Klimchouk (2001) Engel et al. (2001), Egemeier (1981)
Inactive sulphidic caves and hypogenic karst	China: Yangcheng gas field South Africa: Mbobo Mkulu Cave Thailand: Nang Nuan oilfield USA: Carlsbad Cavern and Lechuguilla Cave, New Mexico	Hao et al. (1998a) Martini et al. (1997) Heward et al. (2000) Hill (1990)

basinal fluids. In the last two decades the importance of similar hypogene leaching of carbonates has been recognised in systems driven by the ascent, mixing and cooling of H_2S- and CO_2 -rich basinal brines. Examples are now documented in what were once considered classic regions of meteoric leaching (Table 7.12; Davis 1980; Egemeier 1981). Caverns can form in carbonate hosts well below the watertable where there is frequently a calcium sulphate association in the

deeper parts of the hydrology, both in basinal generation of H_2S and in the typical early byproducts of cavern creation.

Bathyphreatic caves are still classified by some carbonate sedimentologists as a form of hydrothermal karst with an implication of hot hydrothermal waters. There certainly are some bathyphreatic caves developed as carbonate karst that do have an association with hot circulating waters, especially those caves forming host cavities to some MVT deposits (Warren and Kempton 1997). But many sulphuric acid groundwaters that form caves and cavern gypsum, such as those of the Carlsbad system, were probably not all that hot. The term hypogene (formed at depth) is more appropriate than hydrothermal (waters with elevated temperature) in classifying caves formed by cooling and mixing of hydrocarbon-rich basinal waters, which have encountered deeply buried beds of sulphate evaporites on their way to the surface. Significant hypogenic karst collapse features typify the Konya Closed Basin of central Turkey, where they are known as obruks[14].

Hypogene caves in carbonate hosts can contain substantial volumes of gypsum precipitated as cavern fills and limestone replacements at scales ranging from microcrystalline crusts on the cave wall to cavern-filling accumulations of phreatic gypsum crystals deposited either as pelagic laminites or as spectacular crystal-clear prisms that can be metres long and wide (Buck et al. 1994). The accumulation of large volumes of cave-fill gypsum, independent of the climate at the landsurface, does not fit well with older notions of surface-driven meteoric circulation and arid cave atmospheres for gypsum speleothems. Hypogene caverns and their gypsum fills can develop wherever oxygenation of rising H_2S-laden hypogene waters occurs, this typically first occurs at bathyphreatic depths, and can be hundreds of metres below the meteoric watertable.

Early stages of hypogenic caves display no relationship to meteoric recharge conduits in their overburden as this is typically an epigenic overprint formed during later uplift. Hypogenic cave passages typically follow ramiform, network, or spongiform patterns (Palmer 2011; Klimchouk 2012a). Time and ongoing exhumation brings a hypogene cave closer to the land surface and moves it out of its formative bathyphreatic hydrology. By the time hypogene caves are accessible to speleologists the evidence of the formative hydrology is largely overprinted by classic meteoric-driven karst textures and precipitates.

H_2S needed to drive hypogene cavern formation is carried by escaping basinal waters that have experienced biochemical or thermochemical reduction of sulphate evaporites and petroleum. Less commonly, they are derived by groundwater oxidation of pyrite, or they entrain volcanogenic thermal waters. As anoxic, H_2S-enriched basinal waters rise along fractures in a limestone host, it cools and mixes with the underside of a layer of meteoric pore water, which typically is oxygenated. As sulphide-rich waters mix and become oxidized, the most aggressive byproduct of their oxidation is sulphuric acid, which can be biologically-mediated by sulphur-oxidising bacteria (Chap. 9). This aggressive water leaches and dissolves the surrounding carbonate aquifer, so that hypogene caverns tend to have large chambers with narrow connections and deep shafts along fracture or joint avenues where the sulphide-rich waters rose (inverted tear-drops). As the acid is spent the concentrations of calcium and sulphate in the cave waters can build to gypsum saturation and the resulting gypsum ornamentation can be spectacular.

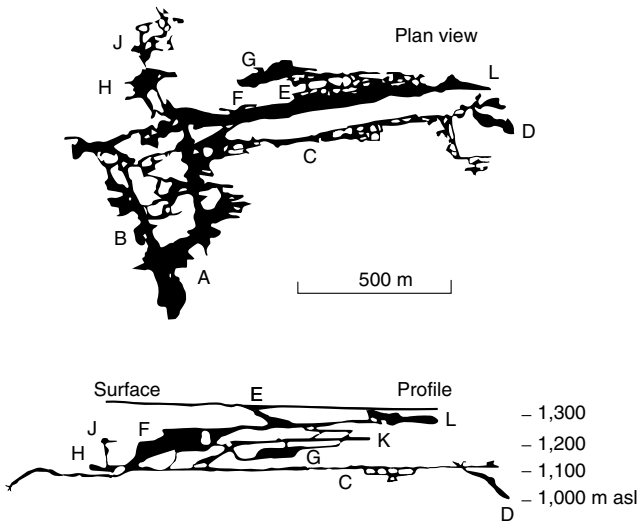

Fig. 7.62 Carlsbad caverns, New Mexico. Map and profile view showing multi-tiered extent across 300 m depth (After Klimchouk 2007)

The best-documented example of sulphuric acid speleogenesis in the western literature is the Carlsbad-Lechuguilla cavern system in Permian reefal limestones of the Guadalupe Mountains, USA (Figs. 7.62 and 7.63a; Hill 1990, 1995; Palmer and Palmer 2000; Klimchouk 2007; Stafford et al. 2008a, b). Although meteoric processes now form calcitic speleothems in these caves, the early host caverns were etched bathyphreatically by sulphuric acid and walls were free of calcite speleothems. Sulphuric acid caverns created by mixing of H_2S waters with oxygenated phreatic waters began to form in the Carlsbad system some 10–12 Ma and as much as 200 m below the watertable. Remnant blocks of laminar pelagic gypsum, a widespread byproduct of sulphuric acid leaching, still cover the floor of the now largely inactive and exhumed Carlsbad Cavern (*pers. obs.*).

[14]Obruk is an internationally recognized Turkish geomorphic term, describing hypogenic collapse dolines, which crop out in the currently semiarid and almost flat land of Konya Closed Basin in central Turkey. These megadolines, with surface diameters and depths reaching several hundreds of meters, are still surfacing with an estimated temporal frequency of once per 5–10 years (Bayari et al. 2009).

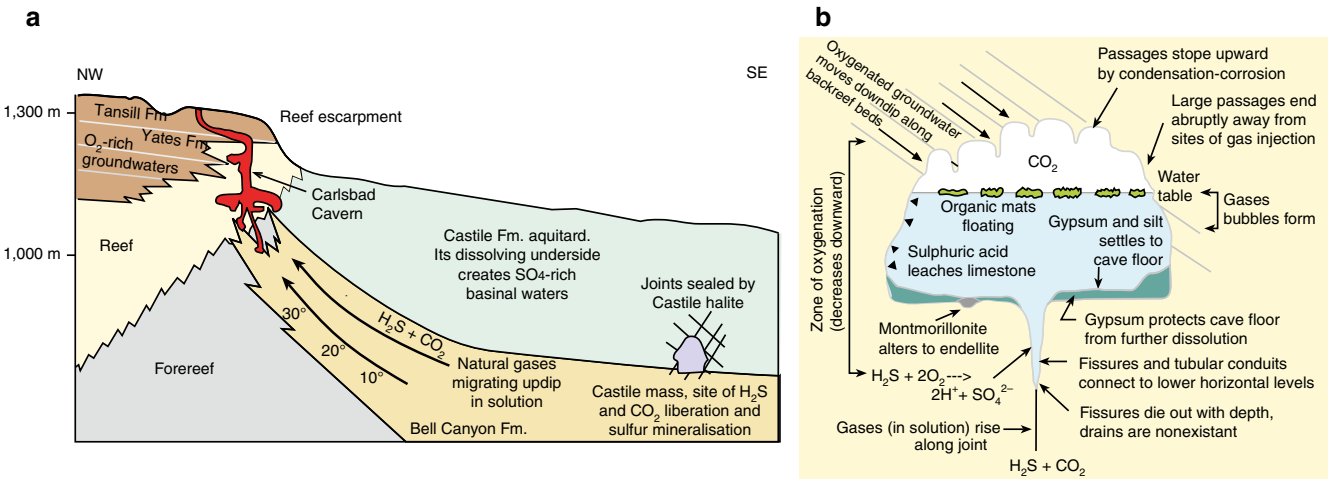

Fig. 7.63 Sulphuric acid speleogenesis. (**a**) Schematic section of Delaware Basin. Escape of natural gas from hydrocarbon kitchen in the basin centre is focused along the dissolving underside of the laminated anhydrite of the Castile Formation. It reacts thermochemically with the sulphate ions to produce H_2S, CO_2 and calcite replacement of the anhydrite (this forms the characteristic Castiles when later exhumed). H_2S and CO_2 continue their focused escape through the Bell Canyon Formation toward the basin margin where they enter limestones of the Capitan and Goat Seep Reefs. There the gases mix with oxygenated groundwater, hydrogen sulphide in solution and dissolved oxygen combine to form sulphuric acid, which then leaches the host limestone, especially along the more permeable joints and fissures. (**b**) Hydrogen sulphide reacts with dissolved oxygen to form sulphuric acid which leaches a cavern. The sulphuric acid is neutralised by the limestone so that caverns tend to terminate abruptly away from zones of gas injection. Oxygenation and hence the acidic reaction die out with depth so that large rooms do not extend far below the horizontal extent of the cavern. With successive lowering of base level, driven by uplift and climatic change, new horizontal levels became connected with older horizontal levels by spring shafts and joint chimneys (After Hill 1990; Forti et al. 2002). The gas-filled cavern top and an associated watertable is only present during the more mature stages of exhumation. The process of mixing of H_2S-rich and meteoric waters that creates the hypogene cavern is a totally phreatic system and is largely unrelated to the presence or absence of a watertable

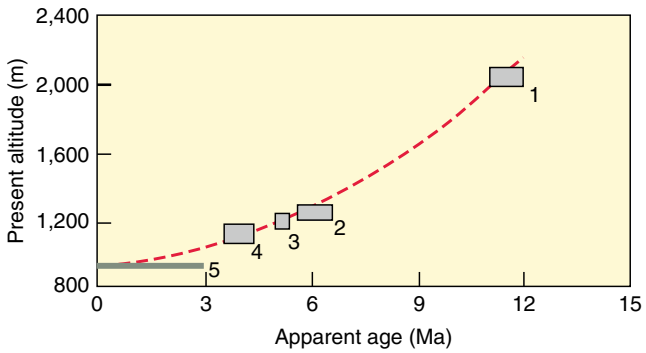

Fig. 7.64 Age versus elevation for several cave levels in the Guadalupe Mountains (After Polyak et al. 1998). *1* Cottonwood Cave and Virgin Cave; *2* Endless Cave and Glacier Bay (Lechuguilla Cave); *3* Lake Lebarge (Lechuguilla Cave); *4* New Mexico Room, Big Room, and Green Clay Room (Carlsbad Cavern); *5* present watertable

$^{40}Ar/^{39}Ar$ dating of fine-grained alunites that were formed during hypogene leaching, and still present in residual clays, show that the "Big Room" level of Carlsbad Cavern formed 3.9–4.0 Ma, while the upper level of Lechuguilla Cave formed 5.7–6.0 Ma (Fig. 7.64). Other older and now more elevated hypogene caves in the Guadalupe Mountains formed at various times from 6.0 to 11.3 Ma (Polyak et al. 1998). Alunite ages increase with, and are strongly correlative to, cave elevation, indicating an 1,100-m decline in the watertable tied to ongoing Neogene uplift and tilting (Fig. 7.64).

The cavern forming process is driven by chemical changes in oil- and gas- rich basinal waters moving up dip from the evaporite-sealed Delaware Basin (Fig. 7.63a). Rising waters derive much of their sulphate content by dissolution of the underside of Castile anhydrite and this also drives karst/pipe formation within the Castile Formation (Stafford et al. 2008a). Some of the sulphate undergoes thermogenic and biogenic sulphate reduction to form H_2S and CO_2, with bacteriogenic "Castile" calcite precipitated as a sulphate-reduction byproduct along the contact between the underlying aquifer and the Castile Fm. Sulphate-H_2S enriched basinal waters then enters the Capitan and Goat Seep strata via crosscutting joints, typically along local aquifers created by the steeply dipping forereef beds, or via lenses of the sandy equivalents to Bell Canyon siliciclastics.

Rising basinal waters carry large volumes of H_2S, CO_2 and methane in solution. As it rises the waters depressurize and release the various dissolved phases as gas bubbles (degasses). By the time the water comes to within a few metres of the watertable it has released almost all of its gas as bubbles (Fig. 7.65; Palmer and Palmer 2000). We shall focus on the H_2S because of its role in precipitating hypogene gypsum fills, but released CO_2 and methane released as gas bubbles from ascending brines also play a role in hypogene caves. Like H_2S, they can create chemosynthetic ecosystems in the deep phreatic, systems which function independent of energy input from the surface (Chap. 9).

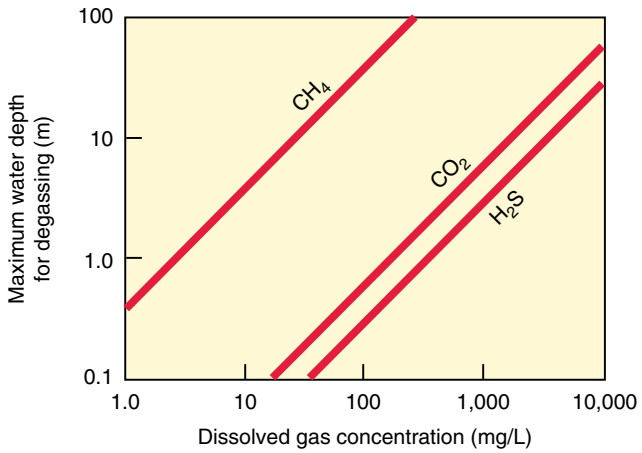

Fig. 7.65 Maximum depth at which degassing of H_2S, CO_2, and CH_4 can take place below the unconfined watertable. Partial degassing occurs at depths well below the respective lines, but no degassing will occur above the line (After Palmer and Palmer 2000)

On arrival in the shallower phreatic levels of the basin, the H_2S reacts with oxygenated groundwater to form sulphuric acid:

$$H_2S + 2O_2 \rightarrow HSO_4^- + H^+$$

Once formed, the sulphuric acid immediately attacked the limestone host and etched out the early outlines of the various Carlsbad caverns via the reaction:

$$HSO_4^- + H^+ + CaCO_3 + 2H_2O \rightarrow Ca^{2+} + SO_4^{2-} + 3H_2O + CO_2$$

This adds further sulphate to the already sulphate-enriched cave waters. If the dissolving carbonate host is dolomitic, then significant magnesium is also added to the cave water. Expanding horizontal benches in such hypogene phreatic caverns indicate intervals of most intense phreatic mixing between H_2S and SO_4 saturated basinal waters. They are located in the lower portion of the oxygenated active phreatic system and may not necessarily be tied the presence of a watertable.

Sulphuric acid caves have sponge-like(spongiform) edges and no calcitic speleothems ornament the growing cavity. Cave walls tend to end abruptly in the horizontal plane as the acidity of the cave waters is quickly quenched away from fissures supplying H_2S. Likewise, since the level of dissolved oxygen in cavern waters decreases with depth, the fissure passages and pits tend to terminate vertically via a rapid narrowing downward channelway This forms an inverted "tear drop" cavern, a shape less seen in epigenic carbonate karst (Fig. 7.63b).

Ongoing leaching means calcium and sulphate levels continue to build in cavern waters, which are already near or at gypsum saturation from earlier leaching of the Castile Formation. Gypsum starts to precipitate in the cave water column and on the cave walls. Fine laminated and layered pelagic gypsum builds up beneath the water-covered parts of the cave floor, typically atop endellitic silts. Huge centripetal splays (metres long and decimetres wide) of ice-clear prismatic gypsum precipitate in stable phreatic portions of the cavern system. Alabaster crusts can coat vadose areas of the cave walls, often in association with the growth of acidophilic archaea and sulphur-oxidising bacteria.

Smectitic clays, released by the leaching of the carbonate bedrock settle through the quiescent cave waters, along with the gypsum crystallites forming in the supersaturated cave waters, to form a pelagic ("rain-from-heaven") unit of laminated gypsum and silt on the cave floor (Fig. 7.63b). Acidic cave waters convert some of the accumulating smectite to endellite ($Al_2Si_2O_5$ $(OH)_4 \cdot 2H_2O$), a brightly coloured clay indicative of acidic conditions in hypogene caves. Two other low-pH, sulphuric-acid indicator minerals, alunite and natroalunite, also occur in association with the endellite (Cunningham and Takahashi 1992; Hill 1995). The same sulphuric acid environment facilitates the formation of secondary late-stage, uranium-vanadium minerals tyuyamunite and metatyuyamunite at redox boundaries in the caves and their presence helps explain elevated levels of radon that typify the modern cave air in the various Carlsbad caverns (Hill 1995).

Even though further uplift has drained the waters from today's caverns, relicts of the gypsum spar and blocks of layered granular pelagic gypsum remain. Such blocks are sporadically scattered over the deeper parts of the floor of the "Big Room" in Carlsbad Cavern as remnants of a former gypsum layer that was up to 10 m thick. Internally, the blocks and rinds of the pelagic units show a laminated or microfolded fabric indicative of it subaqueous origin (pers. obs). In Lechuguilla Cave, phreatic spar gypsum ornamentation forms "chandeliers" or "ferro di lancia" accumulations of ice-clear gypsum crystals, which now, with subsequent watertable lowering, protrude from the exposed and accessible areas of the cave.

Even more widespread and spectacular examples of gypsum chandeliers line the Cupp-Coutum and other now inactive hypogene sulphuric acid caves of Kugitangtau Ridge, Turkmenistan (Maltsev and Malishevsky 1990). The phreatic calcium sulphate textures record a phase of hypogene activity within a pre-existing karstic groundwater conduit system (Bottrell et al. 2001). Hypogene fluids entered the caves through fault zones and deposited sulphate, sulphide and carbonate minerals under phreatic conditions. Locally, intense alteration of limestone wall rocks also occurred at this stage. Elsewhere in the region, similar faults contain economic quantities of galena and elemental sulphur mineralization. Comparisons between the Pb and S isotope compositions of minerals found in cave and ore deposits confirm the link between economic mineralization and hydrothermal activity at Cupp-Coutunn. The predominance of sulphate mineralization in Cupp-Coutunn implies that the fluids were

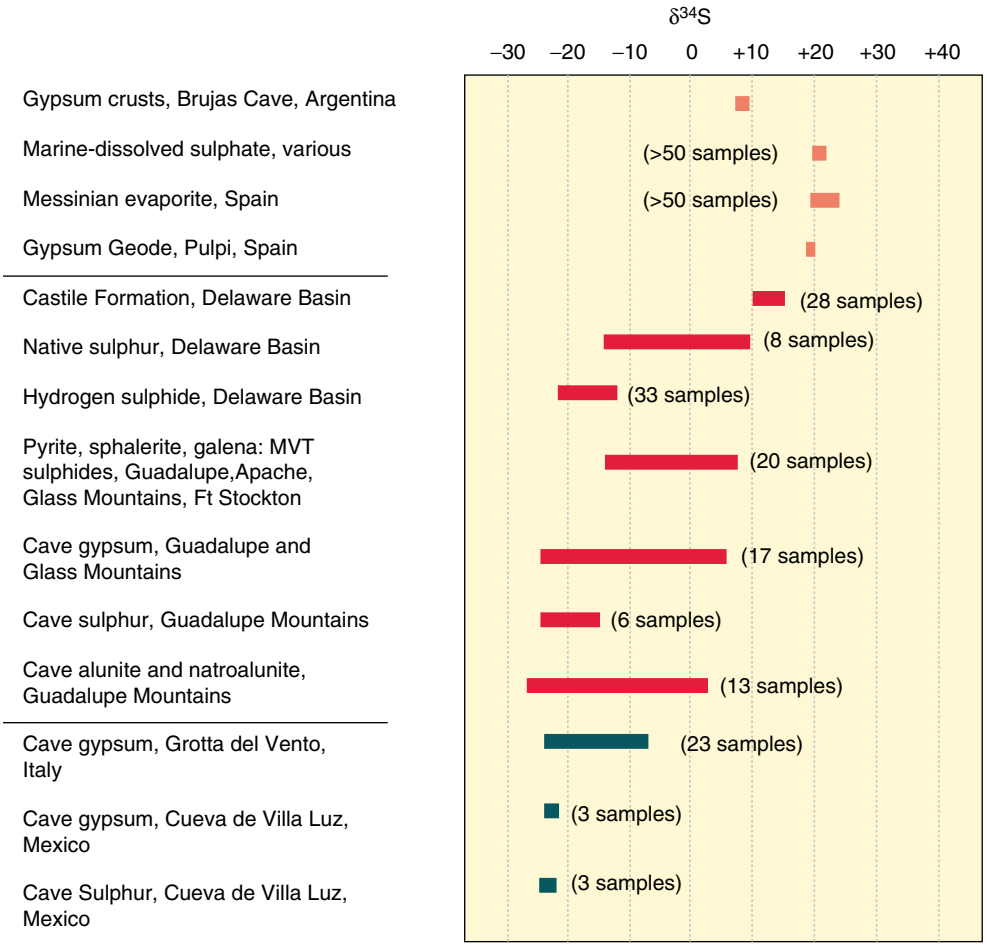

Fig. 7.66 Range of sulphur isotope values for various H_2S associated cave deposits in the USA, Italy and Mexico (After Hill 2000; Hose et al. 2000; Polyak and Guven 1996; Galdenzi and Maruoka 2003; Garcia-Guinea et al. 2002; Sancho et al. 2004). Cave gypsum and sulphur in the Delaware Basin are significantly enriched in the light isotopes compared to the Castile Formation. Their isotopically light composition within the basin (H_2S gas, native sulphur) and in the reef (sulphides and sulphur/gypsum cave deposits) reflect bacterial sulphate reduction where sulphate solutions mixed with hydrocarbons to produce isotopically light hydrogen sulphide. Similar products from sulphuric acid caves in Italy and Mexico also plot in the negative sulphur range and are clearly not indicative of a meteoric or marine source

more oxidized in the higher permeability zone associated with the karst aquifer.

Following the hypogene phase, speleothemic minerals were precipitated under vadose conditions (Bottrell et al. 2001). Speleothemic sulphates show a bimodal sulphur isotope distribution. One group has compositions similar to the hydrothermal sulphates, whilst the second group is characterized by higher $\delta^{34}S$ values (Fig. 7.66). This latter group may either record the effects of microbial sulphate reduction, or reflect the introduction of sulphate-rich groundwater generated by the dissolution of overlying evaporites. Oxygen isotope compositions show that calcite speleothems were precipitated from nonthermal groundwater of meteoric origin. Carbonate speleothems are relatively enriched in ^{13}C compared to most cave deposits, but can be explained by normal speleothem-forming processes under thin, arid-zone soils dominated by C_4 vegetation. However, the presence of sulphate speleothems, with isotopic compositions indicative of the oxidation of hydrothermal/hypogene sulphide, implies that CO_2 derived by reaction of limestone with sulphuric acid ('condensation corrosion') contributed to the formation of ^{13}C-enriched speleothem deposits.

Blocks composed of white, fine-grained, pelagic (phreatic) gypsum cover large floor areas (over 1,000 m^3) of the upper cave level of the Grotta Grande del Vento, Italy (Galdenzi 1990; Galdenzi and Maruoka 2003). In this case the gypsum does not form the spectacular "ferro di lancia" found in New Mexico and Turkmenistan, although there are some coarsely crystalline aligned prisms that are interpreted to have grown in the cave mud. Today's gypsum textures on the walls of the Frasassi caves are much less diverse and more localised than when sulphate precipitation was at its peak in the hypogene phreatic caverns of the early Pleistocene (Galdenzi and Maruoka 2003; Tisato et al. 2012). What makes Grotto Grande so interesting is that the process of gypsum formation is still active in some accessible parts of the cave where H_2S-rich waters mix with oxygenated ground waters. Hollow vaterite spherules have been precipitated in the laboratory from bacterial cultures collected from such caves in Italy and Spain (Sanchez-Moral et al. 2003).

Native sulphur can be found in sulphidic caverns of New Mexico either admixed with gypsum in the remnant pelagic blocks or as canary-yellow sulphur crystal coats on the undersides of dipping beds of the forereef or the siliciclastic

Bell Canyon Formation. $\delta^{34}S$ values are as low as −25.8‰ (CDT) in this cave sulphur. Similar values in the cave gypsum (−25.6‰) and the endellite, indicate that they too are end products of microbial reduction reactions metabolising escaping hydrocarbons. Their isotopic signatures are not products of meteoric diagenesis (Fig. 7.66; Hill 1990).

Throughout the various caves of the Guadalupe Mountains, sulphur isotope results have been crucial in defining its hypogenic speleogenesis (Fig. 7.66; Hill 1990, 2000). Cave gypsum with such negative values could not have been derived directly from Castile anhydrite beds, without bacterial mediation (mostly by anoxic sulphate reducers at depth, then sulphate oxidisers near the watertable). Thus, inorganic models based on local brine pooling and saturation (Bretz 1952) or the inorganic cooling of basinal water (Queen et al. 1979) are not directly applicable to Carlsbad precipitates. Such inorganic models are more relevant to the ice-clear 8 m long, 1 m wide, gypsum crystals filling giant geodes in a Triassic limestone host at Pulpí in SE Spain (Garcia-Guinea et al. 2002) and to gypsum crusts in Brujas Cave, Argentina (Sancho et al. 2004).

The average isotopic composition of marine-fed Castile gypsum/anhydrite is +10.3‰. If the cave gypsum had precipitated directly from cooling Castile brines, then gypsum in the cave fill should have a similar signature to the Castile Formation; clearly, it does not (Fig. 7.66). Sulphur isotope data also discount sulphate derivation from a pyrite precursor, as proposed by Jagnow et al. (2000). Metal sulphide values in the Guadalupe Mountain samples (mostly pyrites) range from $\delta\ ^{34}S = -9.3$ to +12.6‰ (mean = −2.2‰ for 20 samples; Fig. 7.66). As there is no significant isotopic fractionation involved in the subsurface leaching of sulphides (less than 1‰), it must be concluded that the isotopically lighter signatures of cave floor gypsum and sulphur (mean $\delta^{34}S = -16.8$‰ for 22 samples) are not derived from a pyrite source. Instead, the consistent isotopically light signature in the cave precipitates support a model of bacterial sulphate reduction acting on Castile Formation sulphate (and hydrocarbons) and ultimately creating sulphuric acid leading to caves with gypsum as a widespread precipitate.

Sulphuric acid speleogenesis is no longer active in the accessible portions of the New Mexico or Turkmenistan caves. But sulphuric acid driven cave expansion is occurring today in the Cueva de Villa Luz in Mexico (Hose and Pisarowicz 1999; Hose et al. 2000), Grotta Grande del Vento in Italy (Galdenzi 1990) and the Movile Cave in Romania (Sarbu et al. 1994). In all three examples, the cave water and cave atmosphere is enriched in hydrogen sulphide and the biochemical action is centred around the watertable (Table 7.13).

Oxidation of sulphide-rich waters seeping from the cave walls and the associated precipitation of fine-grained gypsum is largely microbially driven (Fig. 7.67). It is localised to seepages at or near the watertable and the precipitation

Table 7.13 Levels in waters from some H_2S enriched settings

Location	H_2S (mg/l)	Reference
Henderson oil field, Delaware Basin, 120 km east of Guadalupe escarpment	600	Wiggins et al. (1993)
Sulphur Springs Tabasco, Mexico	394	Palmer and Palmer (1998)
Sharon Springs Sulphur Spa, New York	103	Palmer and Palmer (1998)
Lower Kane Cave, Wyoming	6	Egemeier (1981)
Hellespont Cave, Wyoming	15	Egemeier (1981)
Movile Cave, Romania	10	Sarbu et al. (1996)

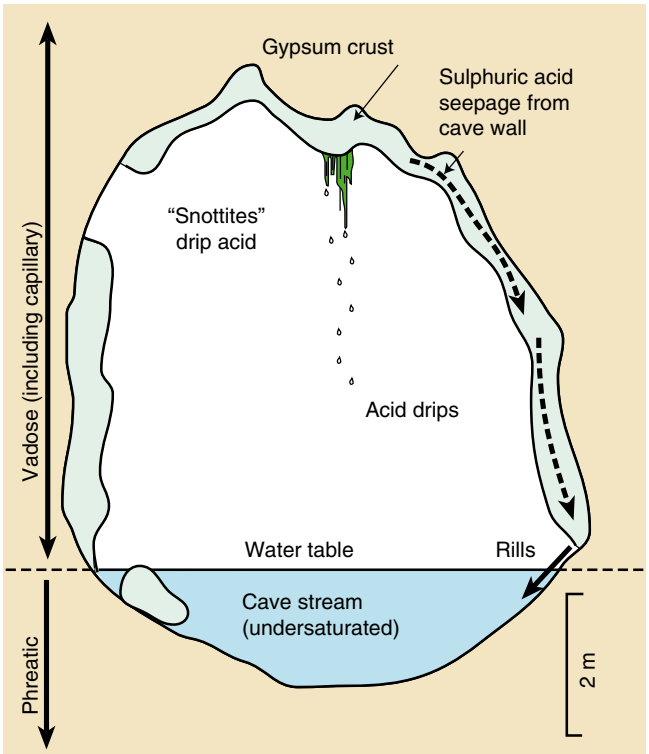

Fig. 7.67 Mechanisms for cave enlargement. *1*. Conversion of limestone to gypsum crust by sulphuric acid, dissolved by the cave stream and by infiltrating freshwater. *2*. Drips of sulphuric acid from the gypsum wall crust and snottites corrode limestone below. Microbial activity enhances the oxidation reactions that produce the acid. *3*. Sulphuric acid seeps through the gypsum crust and dissolves the limestone at the base. Solutional rills are common (after Hose et al. 2000)

chemistry is facilitated by sulphur-oxidising bacteria. Near identical microbial mat communities float at the air/water interface in the active sulphuric waters of Movile Cave, Romania, and coat the cave walls (forming snottites) in Cueva de Villa Luz, Mexico. In all, the process set today is mostly vadose and tied to the changing chemical conditions across the watertable interface. Textures in vadose wall gyp-

sum are not the same, nor as widespread as the relict phreatic pelagics and gypsum spars we see in palaeohypogene caves in New Mexico and Turkmenistan.

Measured H_2S levels in the cave atmosphere of Cueva[15] de Villa Luz reach 210 ppm, while SO_2 typically exceeds 35 ppm, conditions which require researchers to use masks and breathers. These gases, plus oxygen from the cave air, are absorbed by water films that gather on the cave walls, via infiltration and condensation. Sulphur-oxidizing bacterial colonies in water films on cave walls and floating on cave waters facilitate the conversion of the abundant hydrogen sulphide to sulphuric acid. Microbes probably also facilitate the conversion of carbon dioxide to carbonic acid. Low pH waters (0.0–3.0, with a mean of 1.4) drip from microbial veils on the cave walls onto the limestone floor. Such wall growths look like delicate stalactites made of phlegm, locally dubbed "snottites" (Fig. 7.67). As the acid drips, it forms rillen and incised channels in wet limestone walls adjacent to the main cave stream. On the cavern slopes, above main stream level, the sulphuric acid reacts with the surrounding limestone to produce a pasty plastering composed of microcrystalline (alabastrine) gypsum and microbes, with surface pH values between 0.5–3.0.

Cueva de Villa Luz is fed by more than 25 groundwater springs, with a combined flow of 200–300 l/s. Inlet water chemistry defines two categories: (a) those with high H_2S content (300–500 mg/l), mean $P_{CO2} = 0.03–0.1$ atm, and no measurable O_2; and (b) those with less than 0.1 mg/l H_2S, mean $P_{CO2} = 0.02$ atm, and modest O_2 contents up to 4.3 mg/l. Both water types have a similar source, as shown by their dissolved solid content. However the oxygenated water has been exposed to aerated conditions upstream from the cave inlets so that much of the original H_2S has been largely lost via outgassing and oxidation to sulphate, increasing the sulphate concentration in the waters by about 4 %. Modelling of the cave water chemistry shows that it can be produced by dissolution of sulphate, carbonate, and chloride minerals, which are present deeper in the basin (Hose et al. 2000).

Two cave-enlarging mechanisms were identified in the Cueva de Villa Luz (Fig. 7.67; Hose et al. 2000): (1) Sulphuric acid from oxidation of hydrogen sulphide prior to its exit into the cave, which converts subaerial limestone surfaces to gypsum and is aided by the activities of sulphur-oxidising bacteria. Most of this gypsum ends up falling into the cave stream where it is redissolved and lost via the stream exiting the system. (2) Strongly acidic droplets, formed on microbial filaments, which dissolves limestone as it drips onto the cave floor. Possible sources of H_2S in the Cueva de Villa Luz system are the evaporites of the Villahermosa petroleum basin, which is less than 50 km downdip and to the northwest, or the hydrothermal system of the El Chichon volcano located some 50 km to the west. Depletion of ^{34}S values for sulphur stabilized from H_2S in the cave atmosphere (−11.7‰), along with the hydrochemistry of the spring waters, favour an evaporite – sulphate reduction origin over a volcanogenic source.

In part, so much more gypsum occurs in the caverns at Carlsbad, compared to the amount of gypsum accumulating on cave walls in other active sulphuric acid caves of today, simply because there was so much more dissolved gypsum entering the cave system along the edges of a dissolving evaporite bed. When it was active, the Carlsbad system was located in the outflow zone of a large regionally draining basin, with escaping waters focused into the growing cave system by the dissolving under-side of the bedded basinwide anhydrite of the Permian Castile Fm. Likewise the gypsum-rich Turkmenistan caverns are tied to nearby dissolving Miocene evaporites.

But there is another key difference when comparing gypsum precipitation processes at Carlsbad to modern sulphuric acid caves, such as Cueva de Villa Luz. Gypsum textures in now inactive hypogene karst fills of Carlsbad and similar systems elsewhere indicate significant volumes of phreatic gypsum accumulated within expanding caves, situated as much as 100–200 m below the meteoric watertable. In contrast in all the accessible parts of the active sulphuric acid caves of Mexico, Italy and Romania, the documented gypsum precipitation is a microbially-mediated vadose seepage process, where H_2S rich waters condense and seep down vadose cave walls. It leads to unique lithoautotrophic systems centred on the sulphate oxidisers in the vadose zone at or immediately above the watertable.

So, how relevant are these modern biogenic gypsum products compared to the much more spectacular and voluminous gypsum precipitates forming in inaccessible blind and deep hypogene caverns, some tens to hundreds of metres below the watertable? We can access the results of this bathyphreatic hydrology only as relicts that have survived exhumation into the vadose realm, as in the deeper levels of Carlsbad Caverns. In terms of models of gypsum precipitation and the relative contribution of sulphur-oxidising microbes to gypsum formation in hypogene karst systems, we have the same scale and process-comparison problems that plague all studies of ancient evaporite deposition. What we have available to develop analogues in modern sulphuric caves, such as Cueva de Villa Luz, is from vadose cave regions that are accessible and measurable, but how reliably can we generalise our conclusions on what forms hypogene gypsum using only these models of vadose cave wall products.

Studies of process in active sulphuric acid caves is restricted to parts of a cave system where people can crawl, sweat, swim and sample. These accessible parts are probably not the parts of a brine-flushed carbonate cavern system where most gypsum precipitates and accumulates. To interpret processes for hypogene gypsum we must use the textures

[15] Translates as "Cave of the Lighted House." The cave has at least 24 natural skylights, mostly vertical shafts and is lined with dissolution features such as natural bridges, boneyards, and rillenkarren walls.

and extent of the bathyphreatic gypsum itself. Even if such places were accessible in some yet to be discovered part of an active hypogene cave system, the elevated levels of H_2S would make it extremely toxic to generalist lifeforms like us. Some carbonate workers would argue that H_2S-related karstification of marine carbonates, with significant hypogene gypsum as a byproduct is not a widespread diagenetic process. They argue that the bulk of published karstification studies in the literature support this contention.

To this I would argue that the literature on carbonate karst reflects a sampling bias. That is, most studies of modern karst process are done in caves that are accessible for study. By definition, these caves are near to and connected to the landsurface and so are in locations where meteoric karst predominates. Most H_2S-related karstification takes place at greater depths in basins where buried $CaSO_4$ is dissolving and so supplying H_2S via TSR or BSR. In Chap. 9 we shall see that H_2S (sour gas) is a significant fluid component in most carbonate-evaporite basins and that much of this H_2S is produced by thermochemical sulphate reduction. Evaporite-associated examples from the Gulf of Mexico, the eastern US and Canadian shelf, the Mediterranean and the Middle East will be discussed.

H_2S can also be a significant component in fluids hosted in normal marine shelf sediments flushed by altered marine brines. For example, fluids collected during the drilling of the southern Australian continental margin (Leg 182 of the Ocean Drilling Program), show unusually high salinities (to 106‰) in nonevaporitic Miocene to Pleistocene carbonate and siliciclastic sediments (Swart et al. 2000). High contents of H_2S (to 15 %), CH_4 (to 50 %), and CO_2 (to 70 %) were encountered at three drill sites and are associated with H_2S dominated clathrates. Outside of deep seafloor brine lakes, these levels of H_2S are some of the highest yet reported during the history of either the Deep Sea Drilling Project or the Ocean Drilling Program. The high concentrations of H_2S, necessary for the formation of hydrates under these conditions, were provided by the abundant SO_4 tied to the high salinities of the pore fluids, and the associated high concentrations of organic material. One hypothesis for the origin of these fluids is that they were formed by evaporation of brines on the adjacent continental shelf during previous lowstands of sea level. They then sank into the underlying sediments (brine reflux) where their residuals remain today.

High solubility of evaporites underlines the importance of hypogenic rather than epigenic processes during the onset of evaporite karst. Recognition of solubility at depths measured in hundreds of metres has significance implications for storage of hazardous wastes in evaporite beds accessible from the surface. Historically, most karst-specific studies of the WIPP area in west Texas addressed the karst hazard issue utilizing epigenic karst concepts (Bachman 1990; Hill 2003; Lorentz 2006; Powers et al. 2006). This can confuse interpretations of observed permeability features when dealing with hypogenic karst.

Identification of a hypogenic origin for many caves in the Rustler and Seven River Formations (Stafford et al. 2008a, b) and interpretation of regional karst development in the context of hypogenic speleogenesis calls underlines a hazard for the WIPP site in terms of the longterm stability of intrasalt permeabilities. Another historical example of possible concern in the framework of epigene versus hypogene effects would the Neckar nuclear power plant in Germany. It is situated in the Neckar River valley above a multi-aquifer system containing a sulphate bed undergoing dissolution. Ground deformations recorded in the immediate vicinity of the plant and a major 60 m-deep collapse occurred in 1964 a few kilometres away (Klimchouk 2007). Also of possible concern is the Rovensky nuclear power plant in Ukraine, where old and recent collapse and subsidence features were recorded in the immediate vicinity of the plant and induced by hypogenic karst in the confined Cretaceous chalk aquifer, a part of the Volyno-Podol'sky artesian basin.

Mineralised Hypogene Breccias

As they form, or after they form, hypogenic and mesogenetic evaporite solution breccias can act as permeable foci for base metal, sulphur, and hydrocarbon accumulations. Where the dissolving bed contains sulphate evaporites, it can act also as a source of sulphur to base metal sulphide precipitates and so become a locus for ore deposition (Warren 2000b). This is clearly seen in the ores of the now depleted Cadjebut Mine on the Devonian Lennard Shelf, West Australia (Warren and Kempton 1997). Other evaporite associated Pb-Zn deposits, tied to evaporite precursors, are discussed in Chap. 15.

The Cadjebut zinc mine (now abandoned) is situated at the southern margin of the Emanuel Range and is hosted by platform carbonates of probable Givetian age near the base of the Pillara Limestone (Fig. 7.68). The orebody lies approximately 500 m to the north of the Cadjebut Fault and trends subparallel to it over a strike length of 3 km. Surface expression of the orebody is the "No Way Gossan," which crops out 100 m to the west of the mine portal. The orebody is roughly linear in shape, trending toward the northwest and dipping with the host dolomite at 5–10° to the northeast.

Cadjebut Mine had pre-mining reserves of 3.8 million tonnes of 17 % combined zinc and lead. Ore grade mineralization (Zn-Pb) occurs as two stratabound lenses, referred to as "lens 1" and "lens 2" (Fig. 7.69), ranging in thickness from 4 to 6 m. The width of the orebody varies from 50 to 150 m, as defined by a cut off grade of 7 % lead-zinc, and is flanked to the north and south by hypogene alteration haloes of marcasite, calcite and baryte (Tompkins et al. 1994a, b). The contact between ore grade mineralization (>7 % Zn + Pb) and the alteration halo is usually abrupt over a distance of a few metres. In section, the ore-bearing lenses are stacked vertically above one another and separated by about 5–6 m of barren or weakly mineralized dolostone (Fig. 7.69). In

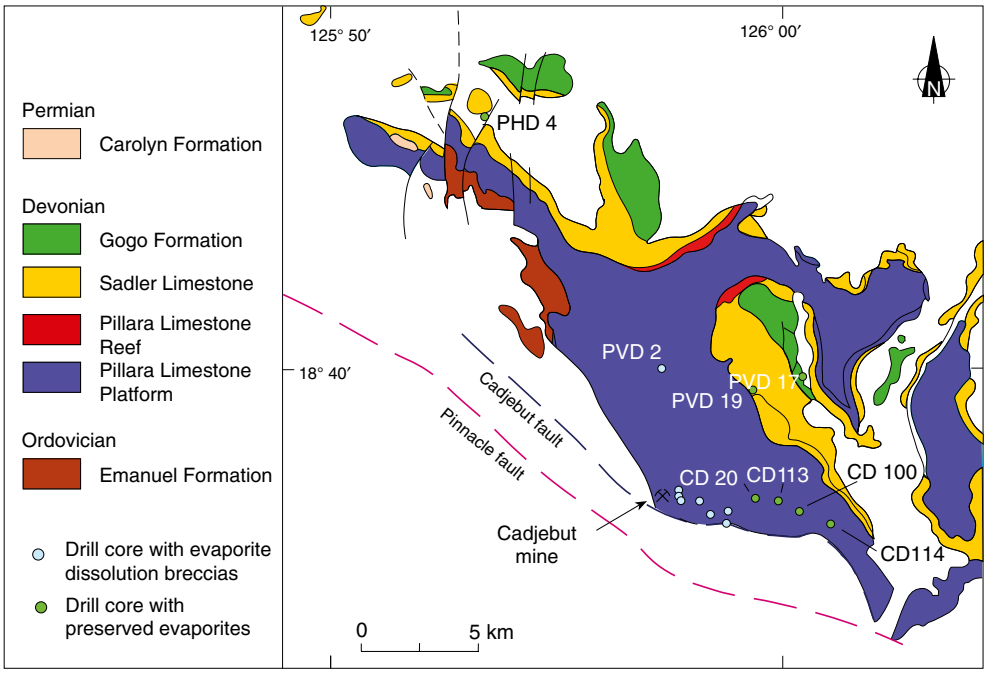

Fig. 7.68 Regional mine geology showing Cadjebut evaporites and mineralisation, also shows selected cored wells with and without evaporites (After Warren and Kempton 1997)

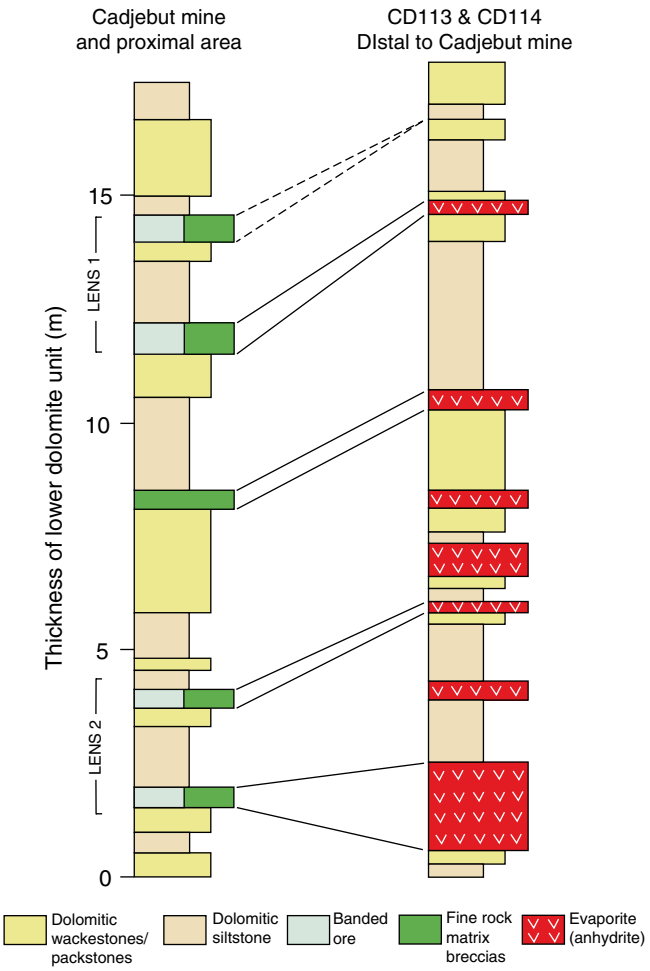

Fig. 7.69 Cadjebut mine area geology, showing lateral correlation passage from ore lense to solution breccia to equivalent evaporite bed in more distal positions from mine. See Fig. 7.68 for locations (After Warren and Kempton 1997)

plan view, both ore lenses have a broad sinusoidal shape and display the same geometrical congruence.

Two dominant ore types are present (Fig. 7.70): (a) stratiform, rhythmically banded zinc-rich ore; and (b) stratiform to stratabound, lead-rich breccia-hosted cavity-fill ore. The rhythmically banded ore occurs as four stratiform horizons, two throughout lens 2 and two in the northern part of lens 1. Rhythmically banded baryte and/or rhythmically banded marcasite form a halo around the orebody and are associated with the rhythmically banded zinc-rich ore.

There is a one-to-one correlation of sulphide-mineralised horizons in the Cadjebut Mine with evaporite dissolution breccia horizons in the immediate area around the mine, and with remnant bedded anhydrite units away from the mine (Fig. 7.69). Calcium sulphate beds were the precursor lithology to the sulphide ore lenses at Cadjebut. The stratabound linear nature of the Cadjebut deposit reflects a time when upwelling metalliferous basinal fluids interacted with bedded stratiform nodular anhydrite beds and trapped hydrocarbons to precipitate lead and zinc sulphides. Current structure in the mine region still preserves a gentle drape anticline, which Warren and Kempton (1997) interpret as a partial artifact of the mineralisation structure, enhanced by the sequential loss of the surrounding evaporites, after ore had locally replaced a bedded anhydrite precursor. The linear nature of the anticlinal structure indicates some form focusing of ore fluids and hydrocarbons, either atop an active underlying fault, or within a pre-existing anticlinal trap, perhaps created as a rollover drape on the edge of a evaporite-dissolving front (e.g. Fig. 7.71a). Hydrocarbon residues (bitumens) are still present in the ore zones.

The rate of evaporite dissolution versus the rate of supply of mineralising fluid controlled the large scale textures

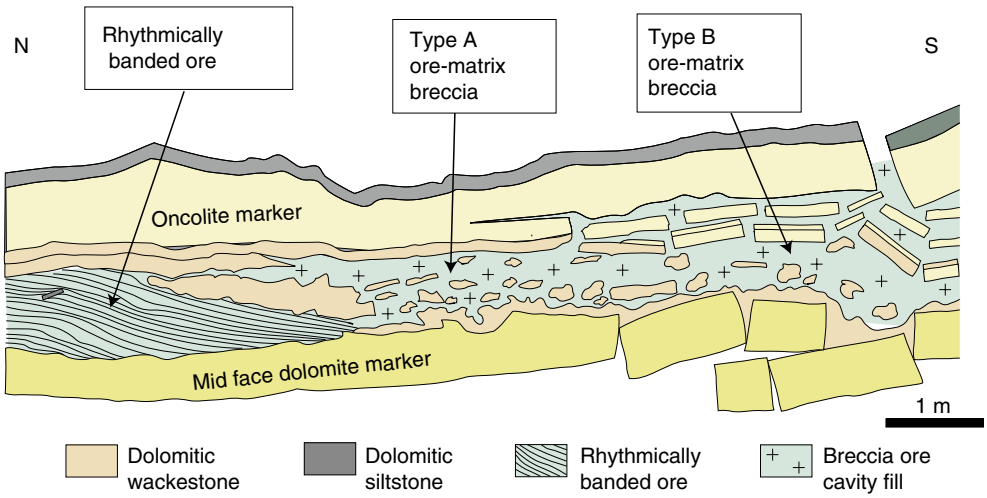

Fig. 7.70 Ore types in the Cadjebut Mine based on mapped mine panels (After Warren and Kempton 1997)

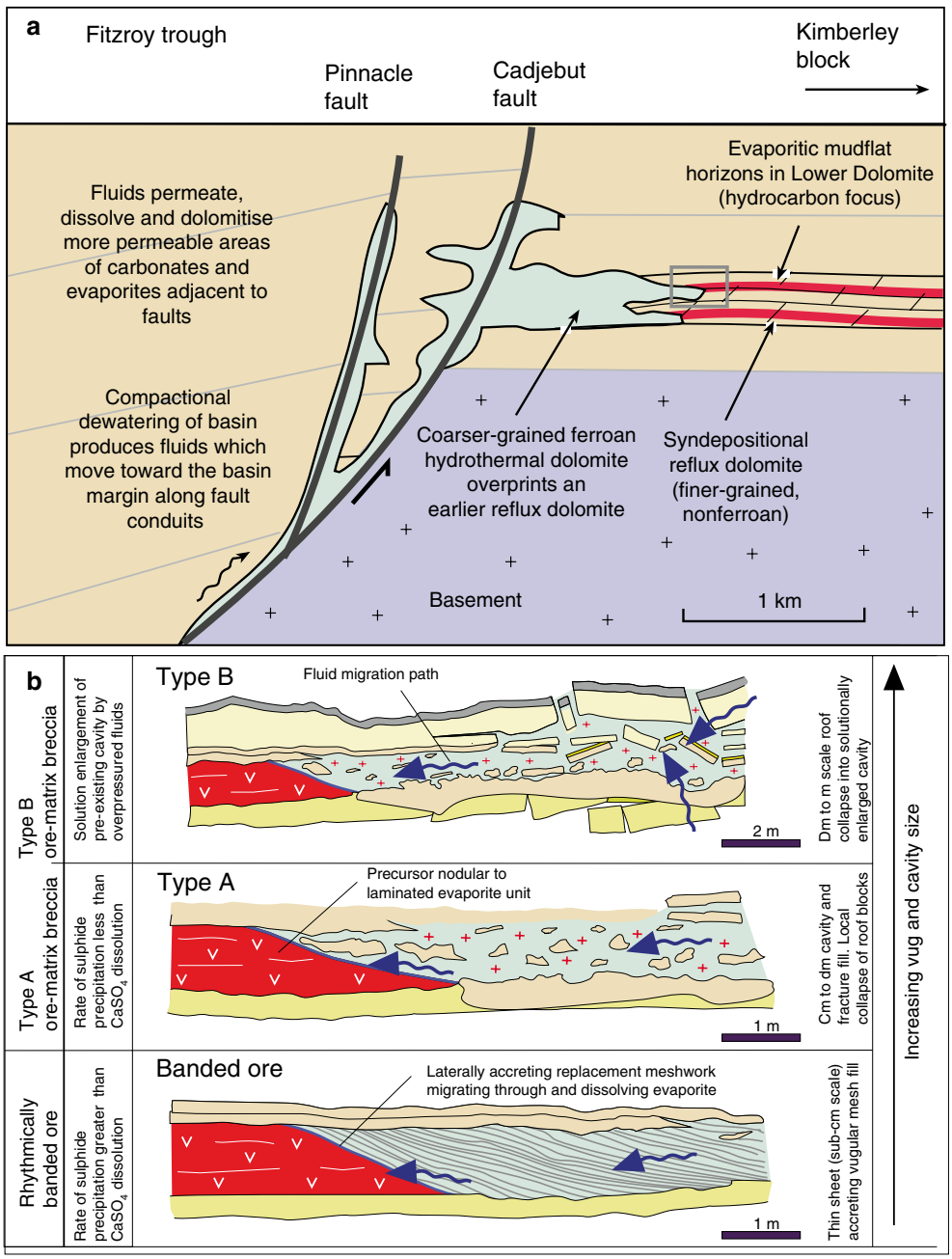

Fig. 7.71 Cadjebut MVT ore, NW Australia. (**a**) Schematic cross section showing the relationship between basinal fluids moving up along regional extensional faults to act as sources for burial dolomite in the platform carbonates, and the focusing/replacement effect of sulphate beds in the evaporitic mudflat sediments of the Lower Dolomite (rectangle indicates zone of sulphide mineralisation. (**b**) Schematic showing controls on ore texture reflect an interplay between rate of supply of metalliferous fluid and the rate of evaporite dissolution (After Warren and Kempton 1997)

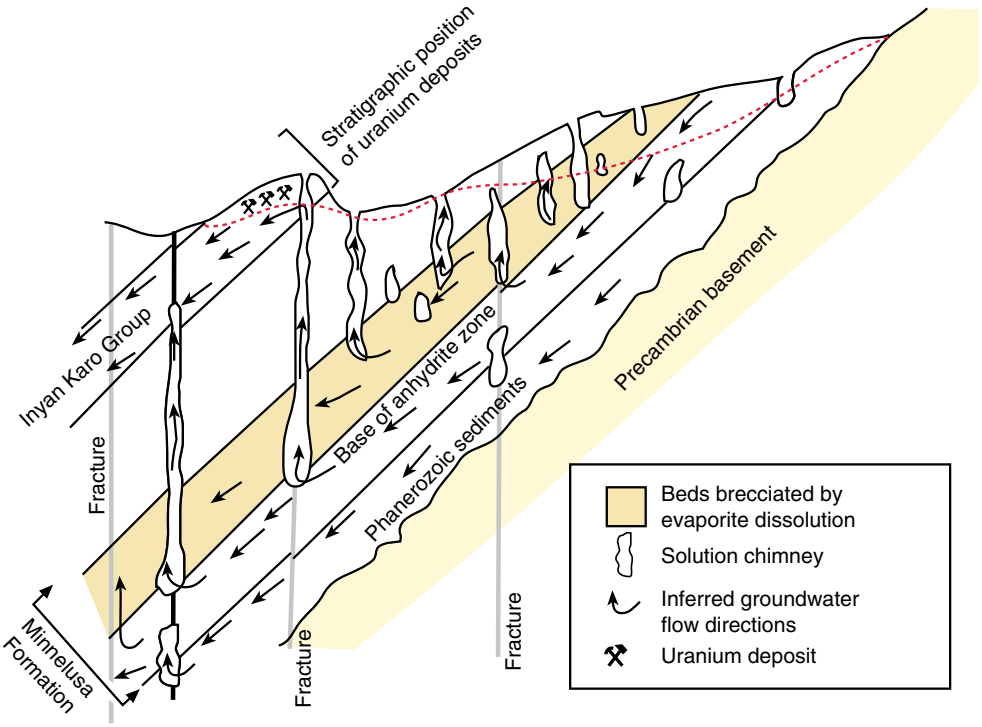

Fig. 7.72 Infiltrated uranium mineralisation in the Cretaceous Inyan Kara Group sand-stones, southern Black Hills (South Dakota). Solution collapse chimneys and breccias in the Late Palaeozoic Minnelusa Formation transport uraniferous groundwaters to precipitation sites (Modified from Gott et al. 1974)

within the Pb-Zn ores (Warren and Kempton 1997). Lead-zinc mineralisation in the Cadjebut Mine occurs as three distinct ore types (Fig. 7.71b):

- Stratiform rhythmically-banded zinc-rich ore,
- Stratiform Type A ore-matrix breccia ore, and
- Crosscutting Type B ore matrix breccia ore.

The rhythmically-banded ore formed under conditions where the potential for sulphide precipitation exceeded the rate of evaporite dissolution. This occurred in cm-sized laminar dissolution meshworks that ate their way into the anhydrite beds (Fig. 7.71b). Millimetre-laminated colloform to pendulous microstalactitic sphalerites were the dominant precipitates. Type A ore matrix breccia formed in irregular cm-dm stratabound cavities. These formed at times when the rate of sulphide precipitation was slower than the rate of sulphate dissolution. Such hypogene cavities were not sufficiently large to instigate catastrophic roof collapse. Type B ore-matrix breccia ores formed in dm-metre sized crosscutting cavities, fractures and veins. Cavern space was sufficiently large to allow the single-event roof span collapse and rotation of metre-sized roof blocks into the caverns. Type B ore-matrix breccias are lead-rich compared to the banded ore and are interpreted by Tompkins et al. (1994a, b) to postdate the formation of banded ore. All the Cadjebut ore textures were created from sulphate supplied by the dissolving evaporites across mm-dm-sized replacement fronts or meshworks under deep bathyphreatic and likely overpressured gassy conditions (Warren and Kempton 1997).

Evaporite solution breccias can also focus the deep-meteoric confined flow of radiogenic hypogene groundwaters and so control the distribution of economic uranium deposits. For example, in the uranium district of southern Black Hills, South Dakota, Gott et al. (1974) showed how an extensive blanket of collapse breccia and trans-stratal breccia chimney fills were produced by the dissolution of gypsum and anhydrite beds in the upper part of the Late Palaeozoic Minnelusa Formation (Fig. 7.72). Up to 83 m of evaporites were removed and numerous breccia chimneys were created that extend up to 430 m vertically into Cretaceous continental sandstones of the Inyan Kara Group (Fig. 7.72). The chimney fill consists of downward displaced sandstone blocks that were later cemented by calcite.

As breccia pipes stoped toward the surface, Gott et al. (1974) argue that this phreatic chimneys created a plumbing system through which artesian oxidised waters leached and transported uranium from deeply buried uraniferous sands and granites up into the Cretaceous section (Fig. 7.16a). There they encountered organic-entraining Cretaceous sands and so precipitated carnotite-dominated infiltrations along redox mixing interfaces in water-filled cavities.

Filled Vugs and Nodules

Replaced nodules and characteristic vug shapes are some of the most used indicators for the former presence of evaporites in both the core and outcrop (Table 7.2). They typically define former crystal clusters and nodules of gypsum,

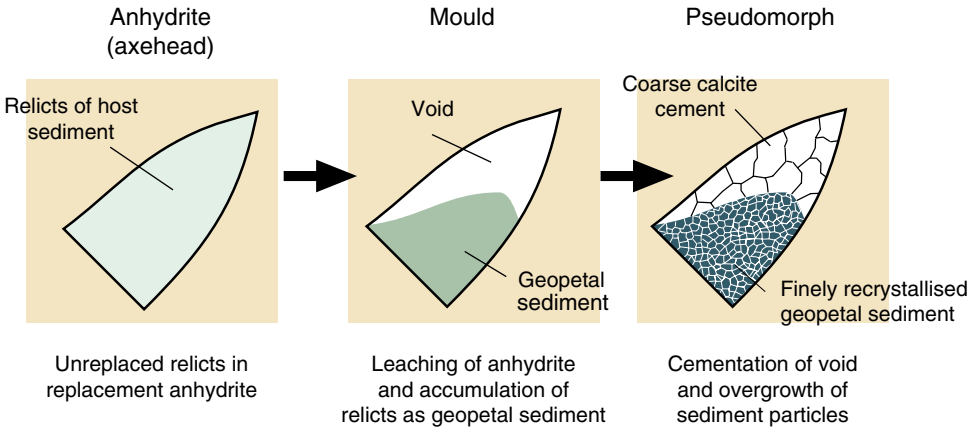

Fig. 7.73 Replacement of axe-head anhydrite by carbonate spar showing how void shape needs to be preserved for reliable genetic interpretation. The fill is also a geopetal

anhydrite or halite in a matrix composed of mud or silt. Unlike the interiors of halite or anhydrite beds, buried evaporite nodules in a non-evaporite matrix are not isolated from the ongoing effects of crossflowing nearsurface and basinal waters. Whenever an undersaturated pore fluid flushes the matrix, it also dissolves or replaces the salts. So, the burial evolution of an evaporite crystal cluster on its way down is typified by leaching of the soluble salt and its replacement by the pseudomorphing mineral phase, typically a carbonate spar or silica, with internal layering that preserves the thermal and chemical history of the cross-flowing pore waters.

Resultant replaced crystals and vug fills are composed of varying combinations of silica, calcite, dolomite, celestite, baryte and strontianite. Internal textures and nodule fabrics can be spectacular and include; linings and splays of silicified and calcitised evaporite crystallites, evaporite moulds and residues, calcitised evaporitic dolomites (dedolomites), cross-cutting drusy dissolution veins and solution enlargement fabrics, with late stage hydrothermal precipitates often infilling the last porosity. Despite the diagenetic complexity, most nodules and vugs mimic the shape of the evaporite parent and this typically leads to recognition of the evaporite connection. When mineralised and exhumed, the vug-fill can weather out of the softer matrix to create dispersed surfaces of nodules or clustered piles, leading to colourful descriptions of such outcrops as "Mendip potato stones" and "Bristol diamonds."

An open vug in a rock indicates that something has dissolved, while a nodule composed of chert or calcite indicates that something has been replaced or filled. Deciding whether or not that something had an evaporite forebear is frequently dependent on shape and texture. Smooth walled nodules, especially ones now composed of chert or baryte, are a commonplace diagenetic replacement in normal marine sediment and need not indicate an evaporite precursor. A reliable evaporite indication of a syndepositional $CaSO_4$ nodule only comes if the rugose irregular surface texture and the shape of the precursor anhydrite nodule or layer remains. In other words, nodules with surfaces of irregular ridges and vugs, textured like the flowerets of a cauliflower, likely indicate an evaporite antecedent. Such nodules are usually described as "cauliflower" textured (e.g. cauliflower chert or cauliflower vug). If Magadi-style silicate gels were the nodule's parents, then nodule surface should show remnant crocodile-skin texture. Without this, or if only smooth walled nodules shaped like cucumbers and melons are present then a thin section of the nodule, especially of its outer portion is needed as this is where small relict crystallites or replaced lath outlines indicative of former salts may still be visible.

Similarly, if single coarse-grained crystals or crystal clusters (desert roses) were either dissolved or replaced and now constitute open or filled moulds, then the original crystal shape should be clearly discernable in order to reliably proclaim its parenthood (Fig. 7.73). If lenticular gypsum was replaced, it should have the bird-beak shape of its precursor, while lenticular anhydrite replacements may be axe-head or barrel shaped (Figs. 1.29 and 1.45). If displacive halite clusters were replaced there should be evidence of cubes and hoppers on the outside of the vug or nodule.

Preservation of the shapes of evaporite crystals with similar outlines creates difficulties when trying to separate silicified replacements of beds of growth-aligned gypsum from beds of nahcolite/trona. Yet it is the separation of these pseudomorphs that is the fulcrum to arguments such as the nature of early Archaean seawater. Both gypsum and trona have a monoclinic bladed form and both can form nodules or grasslike beds of growth-aligned prisms. Once the actual salt has gone, defining original salt mineralogy and separating crystals with similar shapes using partly altered pseudomorphs can be very difficult.

Silicified Evaporites

Silicified anhydrite nodules and $CaSO_4$ crystals are widely reported and reliably documented in sediments as old as Early Archaean and as young as Holocene (Table 7.14).[16]

[16]Quartzine is a form of chalcedony composed of fibres having a positive crystallographic elongation parallel to the c axis.

Table 7.14 Selected examples of silicified evaporites

Occurrence and age of host	Comments	Reference
Silica precipitates in Holocene alkaline lakes along the Coorong coastal plain, South Australia. Type area for "Coorong style" chert.	Direct precipitation (?bacterially mediated) of opal-cristobalite in small mm-scale vugs in and on the surface of tepee-overprinted strandzone magnesite/dolomite crusts around the edge of Milne Lake and probably in crusts in other lakes accumulating evaporitic lacustrine dolomite, magnesite, hydromagnesite, aragonite and gypsum.	Peterson and Von der Borch (1965)
Nodules and polygons of chert in diatomaceous beds of the late Pleistocene High Magadi beds, Lake Magadi, Africa. Type area for "Magadi-style" chert.	Chert in nodules and polygons is a weathering product of sodium silicate gels. Conversion involves shrinkage and induration. It creates a characteristic "crocodile-skin" texture on the surface of newly formed chert. This texture is associated with soft sediment deformation in the surrounds and sodium carbonate salts in adjacent sediments.	Eugster (1967), Jones et al. (1967), Hay (1968)
Pleistocene nodules in saline mudflats, Lake Olduvai, Africa.	Magadi-style chert nodules (crocodile-skin) formed by replacement of a sodium silicate (magadiite) precursor.	Hay and Kayser (2001)
Double-terminated euhedral quartz in Pleistocene sabkha dolomite, offshore Al Jabyl, Saudi Arabia (Pleistocene "Herikimer diamonds").	Megaquartz as individual crystals and clusters of crystals and overgrowths on detrital quartz. Individual crystals up to 1 mm long, many with shallow dolomite mould impressions on their crystal faces, some partly, or completely, engulf dolomite rhombohedra.	Chafetz and Zhang (1998)
Gypsum-rich silica nodules, Moghra Formation, Miocene, Northwest Qattara depression, Western Desert, Egypt	Nodules occur in two shale horizons, consist mainly of quartz and are composed of gypsum-free matrix and gypsum-rich megacrystalline quartz. The matrix consists of microflamboyant quartz (less than 36 μm in diameter) and chalcedony. The megacrystalline quartz occurs as lenticular and prismatic forms (length: 90–250 μm; width: 30–90 μm). Structure of the silica nodules begins with quartzine in its outer rim, then gypsum-free microcrystalline quartz in the middle part and ends with gypsum-rich lenticular to prismatic megaquartz in the nodule center.	Khoriby (2005)
Chert nodules in gypsiferous limestones of the Kef Eddour Member (Ypressian-Priabonian- Eocene) near Metlaoui and Sehib (Tunisia)	Silica with $\delta^{18}O$ values from +25 to +28.6 ‰ (SMOW)]replaced the outer parts of anhydrite nodules at pH < 9. In contrast, pore-fluid pH values > 9 in the innermost parts of the anhydrite nodules prevented silica precipitation. This chemical barrier is preserved in the microquartz rims left after dissolution of the remaining anhydrite.	Henchiri and Slim-S'Himi (2006)
Quartz geodes and nodular chert in Campanian (Cret.) marly clays and calcarenites, Basque-Cantabrian Basin, Northern Spain.	Silica replacement of cauliflower geodes and chert as spherulitic fibrous quartz (quartzine-lutecite). There are small anhydrite laths included in some of the megaquartz crystal fills.	Gomez-Allday et al. (2002)
Quartz geodes and chert hosted in Triassic red mudstones, Bristol district of the UK.	Silica replacement in open voids after cauliflower textured anhydrite. Loose euhedral double-terminated quarts crystals aggregating on bottom of some geodes after the $CaSO_4$ is dissolved and are called "Bristol Diamonds."	Tucker (1976a)
Nodules developed in a single layer in Bundsandstein (Triassic) redbeds, Iberian Range, Central Spain.	Cauliflower shaped chert nodules and geodes, some are filled with concentric layers of quartz and carbonate, others are still open and partially filled and fractured. Relict anhydrite textures and rare laths, bacteria played a role in dolomitisation of some nodules.	Alonso-Zarza et al. (2002)
Chert nodules in Triassic of North Carolina, USA.	Cauliflower chert with relict anhydrite.	Wheeler and Textoris (1978)
Nodules and crystals in Lower Purbeck Beds, (Jurassic) Dorset, UK.	Silica replacement of individual and clustered gypsum bird-beaks and enterolithic anhydrite nodules (with small relics of anhydrite preserved).	West (1964, 1973)
Discrete horizons, scattered nodules in layers and individual replaced crystals in Seven Rivers, Yates and Tansill formations, Guadalupe Mountains, (Permian) Delaware Basin, USA.	Cauliflower nodule and geodes. Nodules, bird-beak gypsum, axehead anhydrite were all replaced by silica and calcite spar. Initial replacement by black megaquartz (with anhydrite, dolomite, water and hydrocarbon inclusions). This was followed by blocky calcite spar fill of voids created by late-stage dissolution of remaining anhydrite (telogenetic).	Ulmer-Scholle et al. (1993)
Thin layers of chert nodules in fluvio-lacustrine muds sandwiched in acidic volcanics of the Lower Permian Bolzano Volcanic Complex, Northern Italy.	Magadi-style chert showing soft-sediment deformation and shrinkage cracks (crocodile-skin), imply a sodium silicate parentage. Transformation to quartz and concomitant (re)crystallization created a variety of silica textures, dominated by microflamboyant quartz.	Krainer and Spötl (1998)
Fist-sized nodules and geodes in layers and dispersed zones in Fort Payne Fm., Warsaw Limestone, St Louis Limestone (Mississippian) of south-central Kentucky and Tennessee, USA.	Concludes that megaquartz characterized by strong undulose, radial extinction, the existence of anhydrite laths included in megaquartz crystals with 'cubic' appearance terminations, the growth of spherulitic, fibrous-radial quartz aggregates (quartzine-lutecite), and crusts of zebraic chalcedony are all evidence of silica replacing anhydrite nodules.	Milliken (1979)

(continued)

Table 7.14 (continued)

Occurrence and age of host	Comments	Reference
Fist-sized nodules and layers in Fort Payne Fm. and Warsaw Limestone, (Mississippian) near Woodbury, Tennessee, USA.	Silica replacement of anhydrite to form cauliflower cherts with outlines reminiscent of the nodules in the Abu Dhabi sabkha. Soft sediment deformation in the surrounding matrix argues silicification took place prior to complete induration of matrix. Silica was derived from sponge spicules.	Chowns and Elkins (1974)
Silicified nodules and clasts representing anhydrite pseudomorphs in Mississippian Wexford Fm., Ireland.	Evaporites indicators mostly as chert nodules and clasts representing pseudomorphs of former now silicified gypsum within the breccia unit and also as distinct anhydrite/gypsum beds, over 2 m thick, within the breccia and as rare gypsum veins.	Nagy et al. (2005)
Silicified anhydrite nodules, Pimenta Bueno Formation, Siluro-Devonian in the Parecis Basin, central Brazil.	The playa-lake deposits show early diagenetic dolomitisation of lime mud, precipitation of anhydrite nodules and extensive silicification. Theses anhydrite nodules were replaced by gypsum and chalcedony during telodiagenesis.	Goldberg et al. (2011)
Pseudomorphs after anhydrite in the Mines Subgroup (Neoproterozoic), in the Katangan Copperbelt, Democratic Republic of Congo.	Silicified anhydrite defines oval, round and cauliflower-shaped nodules, or in lenses that may be wedge-shaped, or as laths. There are two main types of siliceous replacement and cementation. Type 1: dolomite precipitated first and was replaced by Cu–Co sulphides and authigenic quartz. Relicts of anhydrite and halite are still present. Type 2, authigenic quartz and sulphides precipitated prior to dolomite and the crystals are free growing	Muchez et al. (2008)
Palaeoproterozoic chert nodules in the Bartle Member (2.2 Ga) of the Killara Formation, Yerrida Group, Yerrida Basin of Western Australia	Association indicates an evaporitic-pyroclastic-thermal-spring environment associated with rifting at about 2.2 Ga. The chert member contains silica pseudomorphs after evaporite minerals that in places enclose relict isolated crystals and aggregates of crystals of gypsum and anhydrite. The evaporite minerals are associated with minerals such as baryte and analcime	Pirajno and Grey (2002)

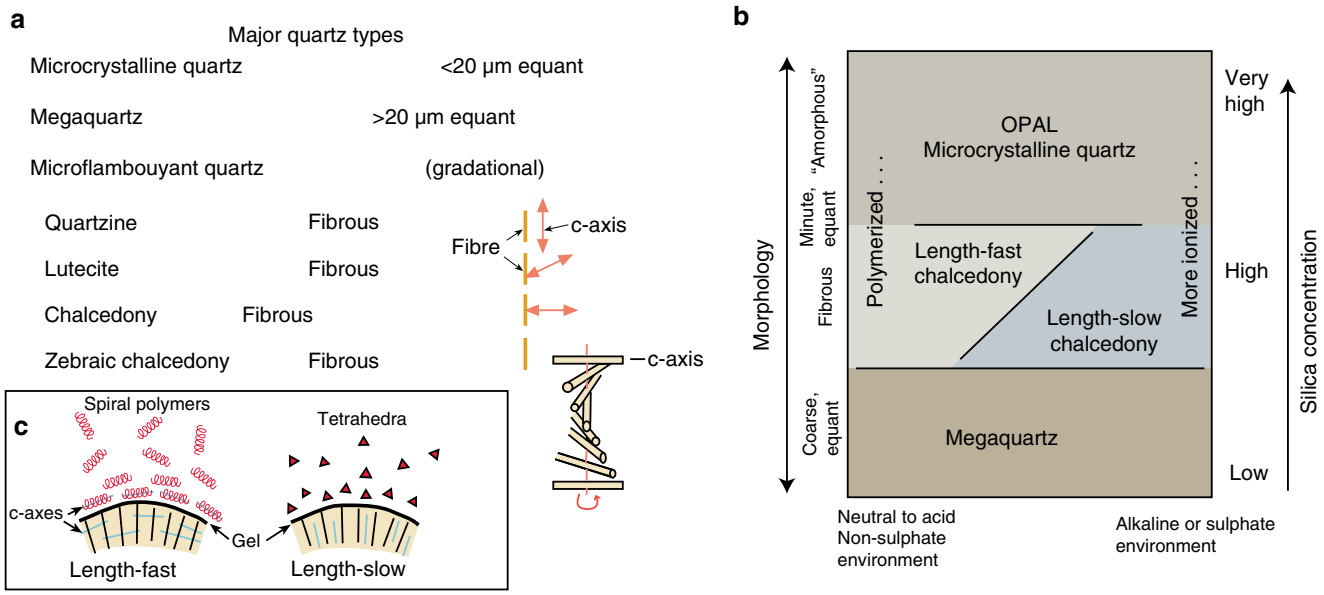

Fig. 7.74 Chalcedony as an indicator of vanished evaporites. (**a**) Major quartz types based on crystal size and orientation of chalcedony fibres with respect to c-axis (After Milliken 1979). (**b**) Style of chalcedony precipitate is controlled by the degree of polymerization, which in term reflects environment of precipitation. (**c**) Crystallite orientation (single tetrahedra versus spiral polymers) with respect to growth surface controls formation of length slow versus length fast crystals – see text (**b** and **c** after Folk and Pittman 1971)

Quartzine and lutecite[17] (aka length-slow chalcedony) typically infill or replace nodules that preserve characteristic cauliflower shapes of the antecedent anhydrite/gypsum nodule (Fig. 7.74a; Arbey 1980; Hesse 1989). According to Folk and Pittman (1971), rates of nucleation and crystallization are the main controls on crystal size and variety of silica precipitating in a void in a dissolving nodule. Rates in turn depend on the level of silica saturation or its concentration in the mother brine (Fig. 7.74b, c). According to Keene (1983), precipitation of length-slow quartz is favoured in waters with high SO_4 and Mg levels.

[17]Lutecite is a form of chalcedony characterised by fibres that are seemingly elongated about 30 °C to the c axis.

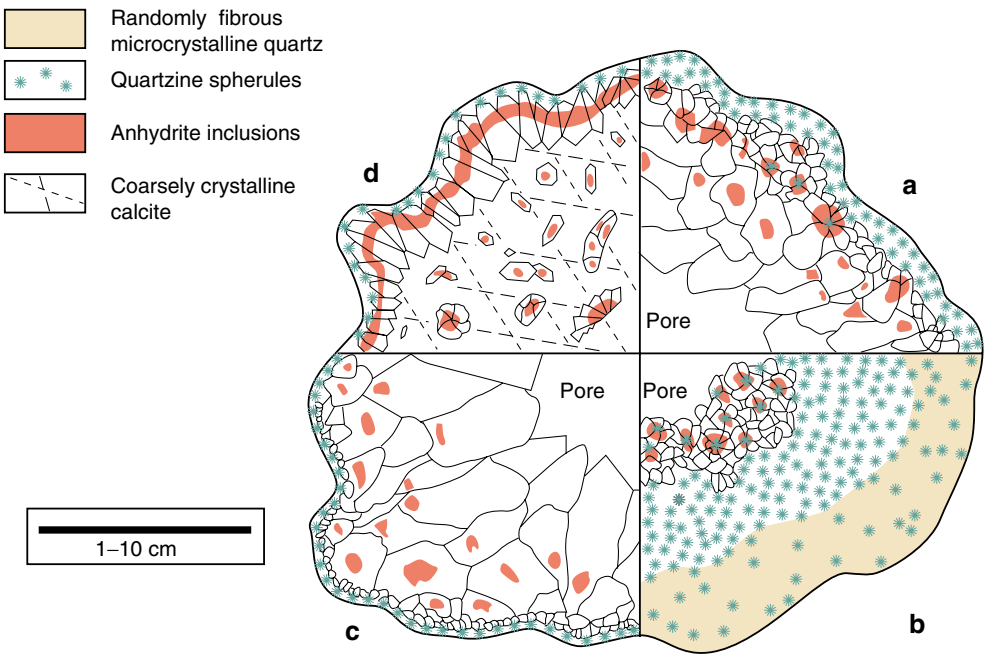

Fig. 7.75 Texture in silicified-calcitized anhydrite nodules. (**a**) Most common style of nodule with thin rim of spherulitic quartzine followed inward by megaquartz characterised by increasing crystal size and with frequent anhydrite inclusions. (**b**) Nodule with a large proportion of fibrous quartz. Thick rim of spherulitic quartz passes inward to strongly undulose megaquartz. Some of the megaquartz has anhydritic nuclei. (**c**) Nodule with a thin rim of spherulitic quartzine passing inward to a large proportion of megaquartz. (**d**) Nodule with megaquartz rim and an interior filled with calcite. Calcite may have filled a cavity or replaced earlier silica. Late stage cavity-fill calcite is often defined by a thin rim of authigenic baryte or sulphide, prior to precipitation (Modified from Milliken 1979)

High (alkaline) pH levels in the mother solution tend to ionize dissolved silica. Neutral or low pH levels favour silica crystallites made up of combined $Si(OH)_4$ groups. These tend to polymerise into spiral chains at lower pH and higher concentrations. At high concentrations and high pH the silica precipitates possess a fibrous chalcedonic form reflecting their rapid rates of precipitation. High pH at the precipitation site means silica crystallites also tends to be present in solution as single ionized tetrahedra that attach themselves one by one to the growing surface, so creating fibres of quartz with the c axes oriented parallel to the long axis of the growing fibres (length-slow). Under low pH or in non-sulphate settings the silica is polymerized into spiral silica chains that attach tangentially to the growth surface of the silica gel, with their c-axes parallel to the growing crystal surface and perpendicular to the eventual direction of the fibres (Fig. 7.74c; length-fast; Folk and Pittman 1971).

Milliken (1979) summarised the typical petrographic and hand specimen scale features of silica that replaced $CaSO_4$ nodules in Mississippian sediments of southern Kentucky and northern Tennessee (Fig. 7.75). Such nodules typically have knobbly irregular cauliflower-like surfaces, while diagnostic internal textures include: (1) length-slow chalcedony after lathlike evaporites, especially anhydrite; (2) quartzine; and (3) small amounts of lutecite associated either with megaquartz that shows strong undulose extinction, or with euhedral megaquartz (Chowns and Elkins 1974). The megaquartz often encloses small blebs of residual anhydrite.

Many buried calcium sulphate nodules are silicified in a multistage process that involves both replacement and void filling (West 1964; Chowns and Elkins 1974). The process commences about the margins of a nodule (stage 1) with a volume for volume replacement of anhydrite by microcrystalline quartz. It normally ends with the growth of euhedral drusy quartz crystals into a central vug (stage 2 and 3). This mode of replacement exemplifies textural changes as seen from the edge toward the centre of the geode in texture style A in Fig. 7.75. However, as noted by Milliken (1979) this edge inward evolution of the geode or nodule fill is typified by a variety of textural styles, which she denoted a styles A through D.

Stage 1 chalcedony or quartzine mimics or pseudomorphs the felted lath textures of the precursor anhydrite in the outer portion of the nodules in all styles. Anhydite pseudomorphs occur as radiating or decussate aggregates with a distinctive flow-like pattern indicating a felted anhydrite precursor. Identical decussate and flow textures occur in laths that make up sabkha anhydrite nodules and define their explosive mode of growth (Fig. 1.45). As well as silicified lath microtextures, outlines of larger crystals that predated anhydritisation and silicification may be preserved by the nodule margin, these crystal outlines vary from prismatic to bladed. Many silicified nodules still retain the knobbly cauliflower outline of its

precursor anhydrite, other nodule edges preserve the interfacial outlines of gypsum or trona or borate precursors.

Stage 2 microquartz and quartz fill can assume euhedral faces as they grow into voids created by the dissolution of the nodule. At the same time the quartz may continue to engulf and pseudomorph small areas of residual anhydrite or other less common evaporite salts (e.g. styles A, C, D). Quartz crystals precipitated at this stage are commonly zoned, with more anhydrite inclusions found within the inner zone of the pseudomorph. Some quartz crystals are doubly terminated and probably grew via the support of a dissolving meshwork of anhydrite (Friedman and Shukla, 1980). With the final dissolution of the supporting mesh these quartz crystals sometimes dropped to the floor of the void to create a geopetal indicator. For example, such highly birefringent anhydrite spots define cauliflower nodules in 2.2 Ga sediments in the Yerrida Basin, Australia (El Tabakh et al. 1999a).

Stage 3, the final stage of the void fill is typified by the precipitation of coarse drusy euhedral quartz with no included anhydrite. This coarse quartz resembles coarse vein quartz.

Sometimes the processes of void fill may be arrested to leave a hollow core in the silica-lined geode (styles A, B, C). The void may be filled by a different burial stage cement such as baryte, sparry carbonate (e.g. ferroan dolomite or calcite), or even metal sulphides. This is the case with the large (up to 1 m diameter) silicified cauliflower-shaped anhydrite nodules of Proterozoic Malapunyah Formation of the McArthur Basin in Northern Australia where baryte, then metal sulphides and then sparry calcite typify the latter stages of void fill (pers. obs.). Similar fracture-filling baryte characterises the later diagenetic stages of silicified and calcitised anhydrite nodules in the Triassic Bundsandstein redbeds of the Iberian Range of central Spain (Fig. 7.84; Alonso-Zarza et al. 2002). Such geodes are typically excellent indicators of burial cement stratigraphy in a mudstone matrix that otherwise preserves few indicators of the evolving pore fluid chemistry.

Cauliflower chert may retain no evidence of former anhydrite lathes mimicked in chalcedony, but can be completely filled by various styles of coarser-grained megaquartz. The resulting nodules still retain the outline of the precursor evaporite nodule (Fig. 7.75). Work on diagenetic timing of numerous silicified $CaSO_4$ nodules (e.g. Milliken 1979; Geeslin and Chafetz 1982; Gao and Land 1991; Ulmer-Scholle and Scholle 1994) shows that most silica replacement begins with shallow burial, either in the zone of active phreatic flow or in the upper portion of the zone of compactional flow (probably at depths of less than 500–1,000 m). Early silica replacement in the zone of active phreatic flow is indicated by a lack of compressional flattening of the nodule, by the preservation of delicate surface ornamentation and the preservation of compactional drapes around replaced nodules. If replacement of an anhydrite nodule occurs later in the burial cycle, many anhydrite nodules have by then become flattened or sluggy and no longer retain a rugose surface. The result can be a series of "cucumbers" rather than "cauliflowers."

Milliken's (1979) isotopic evidence implies much silica replacement in the nodules she studied was relatively early in the burial cycle at temperatures that were <40 °C. Silica was supplied by throughflushing pore fluids with compositions ranging from seawater to mixed meteoric-seawater. Of course, nodule replacement by silica or calcite does not have to happen on the way down in the burial cycle, it may also happen during uplift back into the telogenetic realm, where the strata have once again entered the zone of active phreatic flow.

Historically, there were no documented examples of the process of evaporite replacement by quartz in Quaternary sediments. Now, autochthonous, doubly-terminated, euhedral megaquartz crystals have been observed infilling voids in a gypsum- and anhydrite-bearing Pleistocene sabkha dolomite sequence in the Arabian Gulf, as well as forming overgrowths on detrital quartz grains (Chafetz and Zhang 1998). These siliceous sabkha precipitates are forming within metres of the present sediment surface with a silica source that is probably recycled biogenic material. Individual quartz crystals attain lengths of 1 mm. Many quartz crystals faces preserve impressions of dolomite rhombs or they partly, or completely, engulf dolomite rhombohedra. This process of replacement is early burial, to see the full suite of silica replacement textures and the variations in timing of the replacement means one must study ancient evaporite sequences.

Overall, the texture of silica infill or replacement in a nodule is dependent on the rate of sulphate dissolution, timing of silica precipitation and rate of silica supply. Some nodules are dominated by the early *lit par lit* replacement textures (styles A and C in Fig. 7.75), others have textures indicating silica cements growing into an open phreatic void left after the complete dissolution of the $CaSO_4$. Such nodules may still retain a hollow centre where the anhydrite once resided (Fig. 7.76). When a silica-filled geode did not start to accumulate silica until after all the $CaSO_4$ dissolved, the main evidence for an evaporite precursor comes from the shape of the replaced nodule and its stratigraphic position within the evaporitic depositional sequence, e.g. beneath an erosional surface that defines the top of the capillary zone.

Not all the anhydrite nodules, now replaced by silica, were syndepositional. Maliva (1987) showed that nodular anhydrite parent, now indicated by quartz geodes in the Sanders Group of Indiana, first precipitated in the subsurface, while its surrounding matrix of normal marine Sanders Group sediment was still unlithified (Fig. 7.77). Anhydrite nodules formed in the subsurface during early burial as hypersaline reflux brines sank into the normal marine

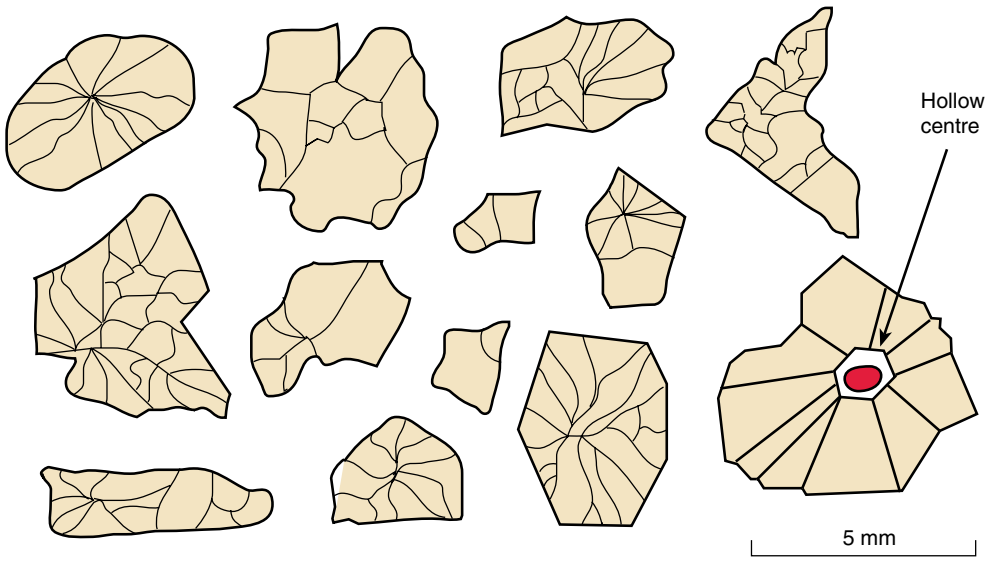

Fig. 7.76 Sketches showing various shapes of the quartz nodules and internal arrangements of megaquartz crystals from replaced anhydrite nodules in the Mesoproterozoic Wollogorang Formation of northern Australia and the Neoproterozoic Gaissa Sandstone/Porsanger Dolomite of Finnmark, Arctic Norway (In part modified from Tucker 1976b)

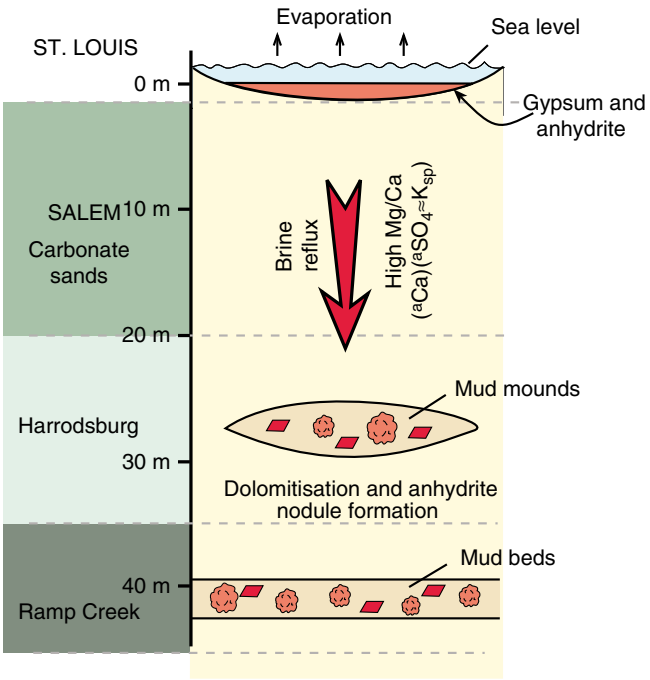

Fig. 7.77 Precipitation of anhydrite and gypsum during St. Louis Limestone deposition formed a dense magnesium- and sulphate-rich brine that percolated downward and seaward through the then unlithified sands of the Salem Limestone. Dolomitisation of carbonate mud mounds and beds in the Harrodsburg and Ramp Creek Formations released calcium causing pore waters to become supersaturated with respect to anhydrite, resulting in the precipitation of anhydrite nodules that were later silicified (After Maliva 1987)

limestones of the Ramp Creek and Harrodsburg Formations. Silica subsequently replaced the anhydrite. These geodes are almost invariably associated with the development of reflux dolomite.

Similarly, not all silica-replacing anhydrite in a particular region need come from the same source or be emplaced by the same set of processes. Silicified nodules within middle-upper Campanian (Cretaceous) carbonate sediments from the Lafio and Tubilla del Agua sections of the Basque-Cantabrian Basin, northern Spain preserve cauliflower morphologies, together with anhydrite laths enclosed in megaquartz crystals and spherulitic fibrous quartz (quartzine-lutecite). All this shows that they formed by ongoing silica replacement of nodular anhydrite (Fig. 7.78; Gómez-Alday et al. 2002). Anhydrite nodules at Lafio were produced by the percolation of saline marine brines, during a period corresponding to a depositional hiatus. They have $\delta^{34}S$ and $\delta^{18}0$ mean values of +18.8 and +13.6‰ respectively, consistent with Upper Cretaceous seawater sulphate values. Higher $\delta^{34}S$ and $\delta^{18}0$ (mean values of +21.2 and 21.8‰ characterise nodules in the Tubilla del Agua section and are interpreted as indicating a partial bacterial sulphate reduction process in a more restricted marine environment (Fig. 7.78a). Later calcite replacement and precipitation of geode-filling calcite in the siliceous nodules occurred in both sections, with $\delta^{13}C$ and $\delta^{18}0$ values indicating the participation of meteoric waters in both regions (Fig. 7.78b). Synsedimentary activity of the Penacerrada diapir (Kueper salt – Triassic), which lies close to the Lafio section, played a significant role in driving the local shallowing of the basin and in the formation of the silica in the nodules. In contrast, eustatic shallowing of the inner marine series in the Tubilla del Agua section led to the generation of morphologically similar quartz geodes, but from waters not influenced by brines derived from the groundwater halo of a diapir.

The chemistry that controls the precipitation of silica as it replaces calcium sulphate in early diagenesis is not well understood. Is it a response to biogenic or abiogenic changes in pH and alkalinity? When opal cristobalite was observed filling mm-scale fenestral vugs in strandzone crusts in a Holocene dolomite/magnesite lake in the Coorong it was

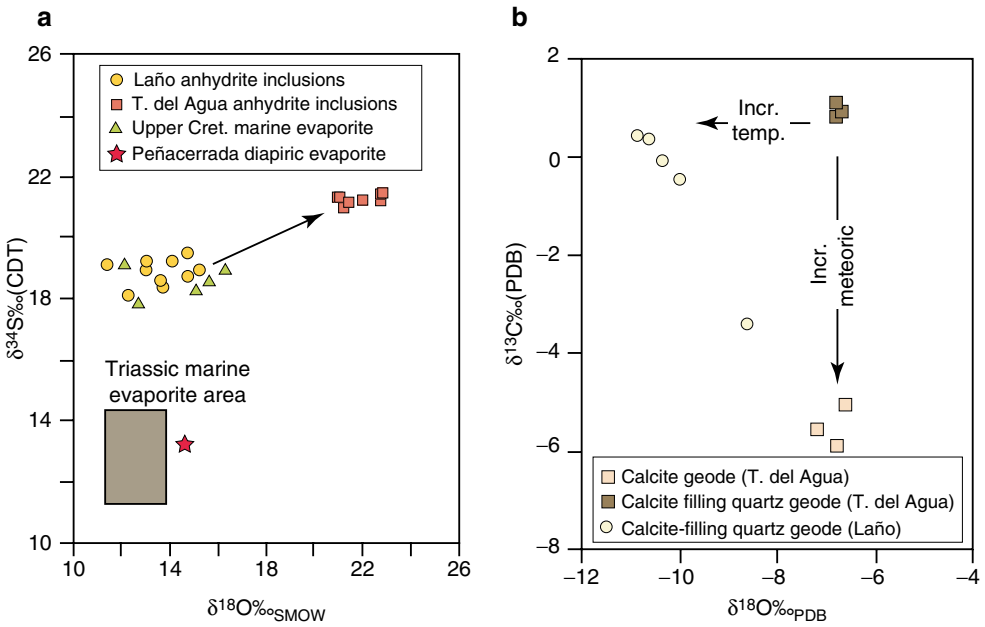

Fig. 7.78 (**a**) Plot of oxygen versus sulphur isotope composition of the Laño and Tubilla del Agua anhydrite inclusions together with other Triassic and Upper Cretaceous evaporite values from Spain. (**b**) Oxygen versus carbon isotope composition of the Laño and Tubilla del Agua calcites. The Tubilla del Agua values define a vertical meteoric calcite line where the lighter ^{13}C values indicate the vadose zone while the higher values denote a phreatic zone. More negative ^{18}O values from the Laño section indicate an increase in temperature of the pore-waters

considered an inorganic precipitate (Peterson and Von der Borch 1965). It formed where the pH of surface waters fluctuated between 10.2 and 8.5, and the seasonal fall in pH was considered to drive inorganic precipitation of silica dissolved in the schizohaline lake waters. The Coorong region came to be considered the type area for inorganic evaporitic precipitation of chert and a style of chert formation known as "Coorong-style." In the last decade sulphate-reducing bacteria have been shown to form dolomite in hypersaline coastal salinas in Brazil (Chap. 4) and some have applied similar notions to interpret the Coorong lake carbonates, that is, both regions are typified by bacterially mediated precipitates (Rosen et al. 1988; Wright 1999). The notion that silica precipitation in "Coorong-style" cherts is also microbially mediated is a distinct possibility.

Birnbaum and Wireman (1985) argued that bacterial degradation of organic matter must be important in forming silica precipitates in most evaporites. They demonstrated, through experiment, the strong influence of bacterial sulphate reduction on silica solubility. The ability of sulphate-reducing bacteria to remove silica from solution is related to local changes in pH and to hydrogen bonding within amorphous silica, followed by polymerization to higher weight molecules. During silica replacement of sulphate evaporites at relatively shallow burial depths, the pore fluid becomes depleted in dissolved sulphate as it is reduced to H_2S by the action of anaerobic sulphate-reducing bacteria, which metabolise sulphate from an anhydrite or gypsum substrate. Where this selective dissolution of the sulphate occurs in the presence of amorphous silica the reaction is accompanied by the precipitation of silica. Hence the microscale mimicry of the lath outlines in the outer parts of many replaced nodules. According to Birnbaum and Wireman it reflects bacterially-mediated silica replacement of nodules in relatively shallow burial settings where bacteria flourish.

Abiological processes, including thermochemical sulphate reduction are more important at greater burial depths where bacteria no longer survive. Providing matrix permeability is retained, silica replacement can continue into the thermobaric stage and can even persist into exhumation. Replacement under a thermobaric regime is frequently indicated by the preservation of hydrocarbon inclusions in the infilling silica cement.

Not all silicified nodules in evaporitic lacustrine sequences are replacements of $CaSO_4$ nodules, some form by transformation of sodium silicate gels. In the saline alkali lakes of the African rift valley, magadiite ($NaSi_7O_{13}(OH)_3{\cdot}3H_2O$) is a common sodium silicate associated with volcanogenic sediments (Eugster 1969). It forms beds and nodules in sediments outcropping about the margins of many of the trona-containing lakes in the East African Rift, including Lake Magadi and Lake Natron. Other sodium silicates such as kenyaite and Na-Al silicate gels and zeolites are also present locally in the African rift lakes.

Magadiite nodules in Lake Magadi weather into cherts called Magadi-style cherts with a characteristic reticulate or "crocodile-skin" surface created by shrinkage during the transformation from sodium silicate gel to chert nodule. When buried, Magadiite rich layers in the diatomaceous host sediment pass along strike into outcrop and into beds of crocodile skin chert (Fig. 4.42). Conversion of magadiite to bedded and nodular chert is thought to take place close to the sediment surface and be related either to the mobilisation and flushing of sodium by dilute waters in these shallow

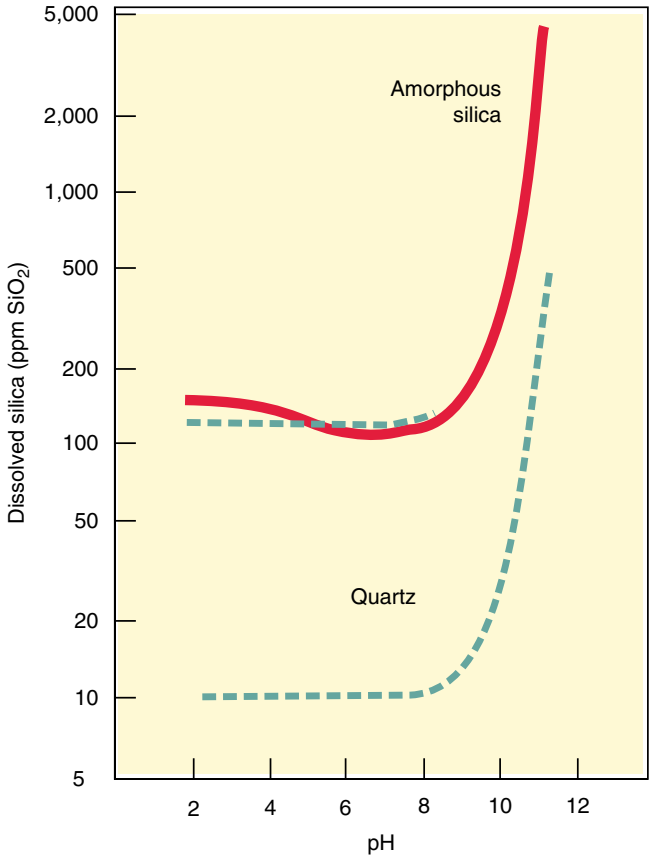

Fig. 7.79 Silica solubility curves at 25 °C. *Solid line* shows experimentally determined variation in solubility of amorphous silica with respect to pH. *Dashed lines* bracket the quartz solubility field (After Krauskopf 1967 – see also Fig. 4.41b)

environments or to spontaneous conversion to chert in deeper brine-saturated zones. Eugster et al. (1967) proposed that magadiite is precipitated by diluting silica-rich, sodium carbonate brines with fresher waters. Mixing lowers the pH, and although the pH change may have been as little as 0.5, a decrease in pH from 10.3 to 9.8 lowers amorphous silica saturation by more than 500 ppm (Fig. 7.79). Silica solubility changes very little when pH varies below a maximum of 8. Highly alkaline sodium carbonate waters containing abundant SiO_2 readily form in the Magadi rift valley via weathering and rapid subsurface hydrolysis of labile volcanic materials. Given the hydrogeochemistry needed for highly alkaline brines, evaporite minerals likely to be found in association with Magadi-style cherts are the sodium carbonates (trona, gaylussite or pirssonite; searlesite); gypsum is not present (Fig. 2.19; Hardie and Eugster 1970).

Surdam et al. (1972) listed the following textures as indicators of Magadi-style cherts that have evolved from a sodium silicate gel: (1) Preservation of the soft-sediment deformation features of the putty-like magadiite, such as enterolithic folding, lobate nodular protrusions, casts of mudcracks and trona crystals, and extrusion forms; (2) Contraction features, such as reticulate cracks and polygonal ridges on the surface of the chert, reflect the loss of volume in the transition (crocodile-skin chert; Fig. 4.42). In Phanerozoic strata an ability to separate cauliflower cherts (after gypsum/anhydrite nodules) from crocodile-skin cherts (associated with silicate gels in trona/natron soda lakes) is considered important in defining marine-fed versus continental hydrologies. However, it has yet to be shown that any of these textures are unique to magadiite-chert transitions.

Ancient Magadi-style chert nodules crop out in lacustrine rocks of the Middle Devonian (Middle Old Red Sandstone) Orcadian Basin, Scotland (Parnell 1986) and the fluviolacustrine sediments of the Permian Balzano volcanic complex in Italy (Krainer and Spötl 1998). The Scottish cherts are replacive nodules within organic-rich laminates and are the deposits of a stratified alkaline lake. Nodules exhibit soft sediment deformation features including sediment injection along shrinkage fractures within the nodules and preserved stellate quartz pseudomorphs after an evaporite mineral, possibly trona. Nodules were nucleated about vertical cracks in the host sediment and show polygonal or parallel aligned patterns. Thus the precipitation of the magadiite precursor must have occurred from nearsurface alkaline groundwaters flushing through partially consolidated sediments.

The Italian cherts form thin layers within a fluviolacustrine succession sandwiched between acidic volcanic rocks of the Lower Permian Balzano Volcanic Complex in northern Italy. These cherts are interpreted as analogs to Magadi-style abiogenic chert (Krainer and Spötl 1998). They show soft-sediment deformation features, shrinkage cracks, and well-preserved palynomorphs that document early diagenetic silica precipitation, volume loss by dehydration, and consolidation prior to mechanical compaction of the enclosing sediment. Similar chert layers were also noted in Triassic playa deposits of North Carolina replacing evaporite siliceous gels in 60 cm-thick siliceous beds intercalated with 20 cm-thick limestone tufa beds (Wheeler and Textoris 1978).

But evaporite-associated chert can probably accumulate in any number of highly alkaline settings, with or without trona extend all the way back to the Archaean (Pirajno and Grey 2002). White magadiite veins constitute rectilinear polygons (1–3 m across) in modern playa sediments in Alkali Lake, Oregon, and in adjacent muds associated with alkali salts and brines (Rooney et al. 1969). The same beds do not host substantial volumes of sodium bicarbonate salts. Jones et al. (1967) noted up to 2,700 ppm of dissolved silica in the present-day brines from Alkali Lake playa. Such values represent a substantial supersaturation with respect to amorphous silica, even at the playa's current pH levels, which are near 10.5 (Fig. 7.79). This level of supersaturation, in the absence of extensive trona suggests that these lacustrine sodium silicates precipitated directly from a hypersaline

silica-saturated solution without the need for a sodium silicate precursor. The debate as to how, where and when crocodile-skin chert can precipitate continues, as yet unresolved.

In thin section, Schubel and Simonson (1990) showed that chert with a magadiite precursor has a characteristic rectilinear or grid-work orientation of quartz crystals, visible in thin section. The texture seems to be inherited, a pseudomorph after the original spherulitic magadiite structure, which shows similar extinction patterns due to presence of 10–20 μm spherical aggregates of plate-like crystals. This microscale pseudomorphing implies a direct volume-for-volume replacement of magadiite by chert. Unfortunately the level of detailed preservation needed to make such distinctions is not usually preserved in older cherts where megaquartz dominates the fill. It is useful in separating cherts from magadiite precursors versus chert from other hypersaline associations in Neogene strata, and perhaps in a few examples it can be utilised in rocks from as far back as the Mesozoic.

As mentioned earlier, Folk and Pittman (1971) and Folk and Siedlecka (1974) concluded that length-slow chalcedony (lutecite) in chert nodules is a useful indicator of the former presence of evaporites (both anhydrite or magadiite precursors). But the occasional presence of length-slow chalcedony in nonevaporitic regimes, such as in turbidites and basalts, has shed suspicion on its absolute reliability. Heaney (1995) further refined the significance of lutecite by showing that in the early stages of its diagenetic evolution it is largely composed of a form of silica called moganite. Moganite is a polymorph of SiO_2 that is microcrystalline, fibrous and optically length-slow. Water content is ≈2 %, slightly higher than chalcedony and lower than opal (6–10 %). It is abundant in, but not restricted to, cherts formed in evaporitic environments. Nonevaporitic silica precipitates typically contain between 5 and 15 wt% moganite, whereas undeniably evaporitic specimens contain between 20 and 75 wt% moganite. No chert from nonevaporitic settings has been found to contain more than 25 wt% moganite. Consequently, enhanced moganite concentration (>20 wt%) in microcrystalline silica is a valuable indicator for vanished evaporites. Heaney noted a frequent association of moganite with "Magadi-style" crocodile-skin chert and suggested that moganite is a diagenetic alteration product of the hydrous Na-silicate magadiite. Unfortunately moganite is a metastable phase and all samples analysed by Heaney that are older than Cretaceous contain little or no moganite.

The transformation of magadiite to moganite must occur over hundreds to thousands of years in alkaline lake systems, whereas the inversion of metastable moganite to quartz probably requires tens of millions of years. But the moganite-evaporite association is broader than magadiite in soda lake cherts as moganite is forming as an authigenic phase in inland playas of central Australia and these Na-Cl brine systems never contained trona, magadiite or volcaniclastics (English 2001). The source of silica is a deeply weathered granitic terrain soaked in stagnant brines.

When dealing with chert nodules, lutecite is only a reliable evaporite indicator when it occurs in suitable host lithologies, is stacked into appropriate vertical sequences and occurs in association with other indicators of "the evaporite that was." The only undeniable single indicator that a chert has an evaporitic parentage is when relicts of the precursor salt still remain within the nodule.

Calcitisation and Dedolomitisation

Calcitisation and dedolomitisation are two often-associated diagenetic processes affecting both evaporite salts (anhydrite/gypsum) and evaporitic dolomites. Calcitisation of evaporites refers to the replacement of an evaporite bed by calcite or limestone. Dedolomitisation refers to the conversion of a dolomite to a limestone. Calcium sulphate evaporites are calcitised in two settings; the meteoric, via groundwater flushing and spar fill of the resulting voids, and in the deeper subsurface, via sulphate reduction (both bacterial and thermochemical). Waters in deeper burial settings situated below the active phreatic tend toward anoxia and in addition to H_2S can carry organics as suspended or dissolved hydrocarbons.

As well as replacement, the flushing of bedded evaporites by surface-derived, low-sulphate meteoric waters also brings on evaporite rehydration, dissolution. Calcite cements typify the nearsurface, while anhydrite conversion, via slow hydration, characterises the deeper near stagnant portions of the same meteoric flow system. Replacement is often bioepigenetic in shallower settings and thermochemical in even deeper and hotter settings. Thus the products of calcitisation tend to have diagnostic isotopic signatures.

Calcitisation of Evaporites

Like silicification, replacement of evaporite crystals and nodules typically by calcite, can occur at any time in the burial cycle from eogenesis through mesogenesis and into telogenesis; whenever the throughflushing waters are undersaturated with respect to the evaporite salts and supersaturated with respect to $CaCO_3$ (Table 7.15). The process is generally known as "evaporite calcitisation' and mainly involves substitution of calcite for gypsum or anhydrite and, to a lesser degree, of glauberite or thenardite. Evaporite calcitisation is most common during the meteoric/eogenetic alteration of evaporite units.

In South Australia, hollow aragonite (micrite rind) pseudomorphs after Holocene gypsum grow in the shallow subsurface about edges of coastal salinas in areas of active marine phreatic flushing (von der Borch et al. 1977; Warren 1982a). Similar early pseudomorphs after bottom-nucleated gypsum have been recognised in the Lower Carboniferous of the Vesder region, Belgium (Fig. 7.25; Swennen et al. 1981). There the process was under the influence of sulphate-reducing

Table 7.15 Selected examples of calcitisation and dedolomitisation in evaporitic settings

Occurrence and age	Comments	Reference
Gypsum replacement in sub-tepee limestones in Holocene carbonate, Marion Lake, Australia.	Aragonite skins formed on dissolving gypsum prisms in the boxwork limestone forming where a prism of less saline marine seepage water interacts with the outer edge of the Holocene gypsum fill. This an excellent example of a gypsum-shaped crystal void in the midst of its creation.	Warren (1982a)
Calcitised gypsum beds in Miocene-Pliocene sediments, Calatayud Basin, northern Spain.	Early calcitisation of lacustrine evaporite (gypsum, anhydrite) and/or magnesium carbonate (dolomite, magnesite) deposits driven by the encroachment of meteoric waters either at the contact of these deposits with overlying freshwater or where percolating freshwater enters at very shallow burial depth. Calcitisation occurs during the interaction between magnesite and Ca-enriched waters derived from the dissolution of gypsum or glauberite.	Sanz-Rubio et al. (2001), Cañaveras et al. (1998)
Calcitised beds in Tertiary lacustrine dolomites, Madrid basin, central Spain.	Mineralogy of bedded carbonates is now dominated by calcite and the limestones contain moulds of gypsum. Occurrences of calcitised dolomite textures in these facies suggests the influence of fresher water during expanding lacustrine cycles or further subsurface interactions with less saline groundwater.	Calvo et al. (1995)
"Gypsum-ghost" limestones adjacent to selenite lithofacies in the Miocene of northern Carpathian Foredeep, Poland.	Mass-balance chemistry shows a deficit of calcium and sulphur contents in the limestones compared to the composition of the selenitic gypsum and implies that the gypsum-ghost limestones system was open to mass transfer and cannot be related to simple and regionally extended replacement of solid sulphate rocks by limestones plus native sulphur; it is a transitional facies.	Gasiewicz (2000)
Calcitised Danian dolocretes in lacustrine beds, Provence Basin, France.	Dolocretes deposited around the palaeolake or playa margin subsequently leached and calcitised. Dolomite rhombs can be hollow. Fabric-destructive calcitisation attributed to drop in the lake level, when the upper part of the dolocrete was subjected to vadose flushing, whereas the fabric-preserving calcitisation (poikiliotopic) resulted from rise in lake level.	Colson and Cojan (1996)
Marbles in the Muttlebury Nappe, Jurassic Lovelock Formation, West Humboldt Range, Nevada.	Outcropping rauhwacke sheets are interlayered and interlensed with non-breccia marble slabs. The marble slabs are calcitised anhydrites from the original décollement of the thrust. They were produced bioepigenetically by the action of sulphate-reducing bacteria on the $CaSO_4$ antecedent.	Speed (1974, 1975)
Calcitisation of the Permian Raisby/ Cadeby Formation, UK.	Groundwater flushing converts nodular calcium sulphate into spar-filled cauliflower-shaped geodes. Fill is multistage telogenetic and with a consistent unroofing history outlined in zoned calcite linings of the geode fills.	Lee and Harwood 1989; Lee, 1990
"Castiles" or calcitised evaporites within the Ochoan (Lopingian) Permian rocks of the western Delaware Basin	Bacterial calcitisation of sulphate evaporites if the Castile Fm to form the characteristic "limestone buttes" via bacterial sulphate reduction and near-surface, methane seeps driven by hypogene waters escaping from the basin. Additional calcitized evaporites occur in the carbonate facies on the margins of the Delaware Basin where anhydrite nodules have been replaced by calcite spar as gravity-driven meteoric waters passed downdip flowing eastward through the Capitan backreef sediments.	Kirkland and Evans (1976), Scholle et al. (1992), Stafford et al. (2008a, b)
Calcitisation of Permian Karstryggen Formation, Central East Greenland.	Groundwater driven karstification on "the way down" created spar filled vugs after nodular anhydrite and was often associated with the precipitation of celestite.	Scholle et al. (1990, 1993)
Calcitised anhydrite in Poplar and Ratcliffe beds in association with Watrous Formation, Mississippian, Williston Basin, USA.	Anhydrite calcitisation occurred only after the Watrous unconformity was shallowly buried by redbeds, and replacement probably involved sulphate-reducing bacteria. Replacement calcite contains pseudomorphs and relicts of anhydrite, and pseudomorphs of secondary gypsum, indicating calcitisation occurred only after original Mississippian gypsum was altered to anhydrite.	Kendall (2001)
Dedolomites in the Mississippian Madison Group of Wyoming and Utah.	Two types of fracture-related dedolomites, one precedes and one postdates regional dolomitisation. The early dedolomite occurred as active groundwaters flushed anhydritic sequences during shallow burial. The later post-stylolitisation fracture-associated dedolomite records chemistries and isotopic signatures of deep tectonic-vein mineralisation.	Budai et al. (1984)
Calcitised anhydrite, Winnipegosis Formation, Middle Devonian, Saskatchewan.	Calcitisation of organic layers and anhydrite section occurred before compaction and was driven by the activities of sulphate reducing bacteria. It preserves characteristic structures of antecedent (lamination, nodular outlines).	Shearman and Fuller (1969), Fu et al. (2008)
Calcite-filled pseudomorphs in the Cambrian Parakeelya Alkali member of the Observatory Hill Formation, Australia.	Calcite pseudomorphs after trona and shortite occur in the perennial lake and saline mudflat facies of this alkaline playa. Cauliflower-shaped vugs are more commonplace in overlying marine section. Fills are composed of poikilotopic calcite with dull luminescent cores and alternating dull and semiluminescent rims. Replacement occurred deep and in association with thermochemical sulphate reduction.	Southgate et al. (1989), White and Youngs (1980)

(continued)

Table 7.15 (continued)

Occurrence and age	Comments	Reference
Calcitised sulphate evaporites in the Palaeoproterozoic Tulomozero Formation carbonates of the Onega basin	(a) Calcite pseudomorphs of inclusion-containing nodules, swallow-tail twinned crystals and evaporite dissolution breccias. Euhedral crystals with swallowtail twinning indicate gypsum was an initial early diagenetic phase, and not solely the result of anhydrite hydration following burial. (b) Displacive crystalline carbonates, interpreted as calcitised (and in places dolomitised?) calcium sulphates which had entirely displaced and/or encapsulated their host silts. (c) Quartz nodules with minor residual components of anhydrite, dolomite and hematite	Brasier et al. (2011)

bacteria and the precipitates in zones of dissolved crystals are now composed of sparry calcite. Later in the burial history, compaction- or thermobaric-derived mesogenetic waters can leach $CaSO_4$ or other salts from the system to create characteristic voids that are then filled by burial-stage calcite. Examples of this deeper end in the burial spectrum include spectacular Au-enriched silica-rimmed dolomitic nodules after anhydrite in the Triassic redbeds of Spain (Bustillo et al. 1999; Alonso-Zarza et al. 2002). Even further along the burial cycle calcitisation can occur during exhumation and uplift during gypsum speleogenesis driven by hypogene waters, as occurred during formation of the castiles of west Texas (Stafford et al. 2008a).

Thus calcite replacement of calcium sulphate salts is not depth specific and can be driven by various hydrological processes (Pierre and Rouchy 1988):

1. Sulphate dissolution during flushing by bicarbonate-rich waters derived from:
   - dissolved atmospheric CO_2,
   - oxidation of organic compounds (marine or terrestrial),
   - thermal decarboxylation of organic matter.
2. Bacterial sulphate reduction in organic-rich or hydrocarbon-flushed sediments. Sulphate reduction may also be later and deeper where it is abiotic and thermochemically induced (Chap. 9).

Calcitisation of evaporite nodules is most widely documented where meteoric waters react with an evaporite bed in the active phreatic zone and not in the deep subsurface (Table 7.15). Meteoric flushing can occur soon after an evaporite unit is deposited (early mesogenetic replacement "on the way down") or it can occur after deeply buried evaporite units are uplifted move back toward the zone of active meteoric throughflow (telogenetic/hypogene or "on the way back up"). And, as we have already seen, the replacement process can continue "while at the bottom" in the mesogenetic setting and wherever epithermal fluids flush calcium sulphate nodules. This can be as part of an active volcanogenic system (Bustillo et al. 1999) or even in association with the cycling of seawater through hydrothermal anhydrite in mid ocean ridges (Chap. 16). In hydrologically-mature sedimentary basins, uplift-related meteoric flow is typically forced by head-driven circulation from high-elevation recharge areas (Fig. 8.17), which can drive calcitisation and replacement to depths of more than a thousand metres.

Late-stage calcite replacement of evaporite nodules postdates silicification in the Tosi Chert, Wyoming (Ulmer-Scholle and Scholle 1994). It was thermochemically driven and was associated with hydrocarbon migration. Similar pseudomorphic replacement by calcite or dolomite of euhedral trona and shortite crystals occurs in the saline facies of the Cambrian Lake Parakeelya Member, South Australia. It was mesogenetic and took place during burial diagenesis as basinal brines flushed the system at temperatures of up to 110 °C. The catabaric dissolution and removal of the sodium carbonate salts took place either coincident with or following the generation of hydrocarbons (Southgate et al. 1989).

One of the best documented examples of calcitised evaporites forming long after deposition and burial of the primary salt beds ("on the way back up") comes from the onshore Permian Raisby Formation of the UK. There, alteration processes related to relatively recent re-entry from the hypogene into the zone of active meteoric flushing, can be studied both in outcrop and in core. The Raisby Formation (formerly the Lower Magnesian Limestone) is the first major carbonate unit deposited in the English Zechstein series and outcrops as escarpments and coastal cliffs along the NW coast of the UK (Fig. 7.80). It is overlain by the Ford Formation (formerly Middle Magnesian Limestone), a classic wedge-shaped carbonate shelf succession, which today crops out in a north-south belt up to 5 km wide. It is interpreted as a barrier reef/shoal sequence with backreef and lagoonal facies composed of white to buff, soft, bedded oolitic and fine grained dolomite. The reef faces is buff to brown hard massive to rubbly reef dolomite and associated talus, passing up into algal-laminated dolomite with oncoliths. Bryozoa, crinoids, brachiopods, bivalves and gastropods are abundant, except near the top of the buildups where stromatolitic and encrusting algae dominate and define the transition into more hypersaline conditions. Its slope and

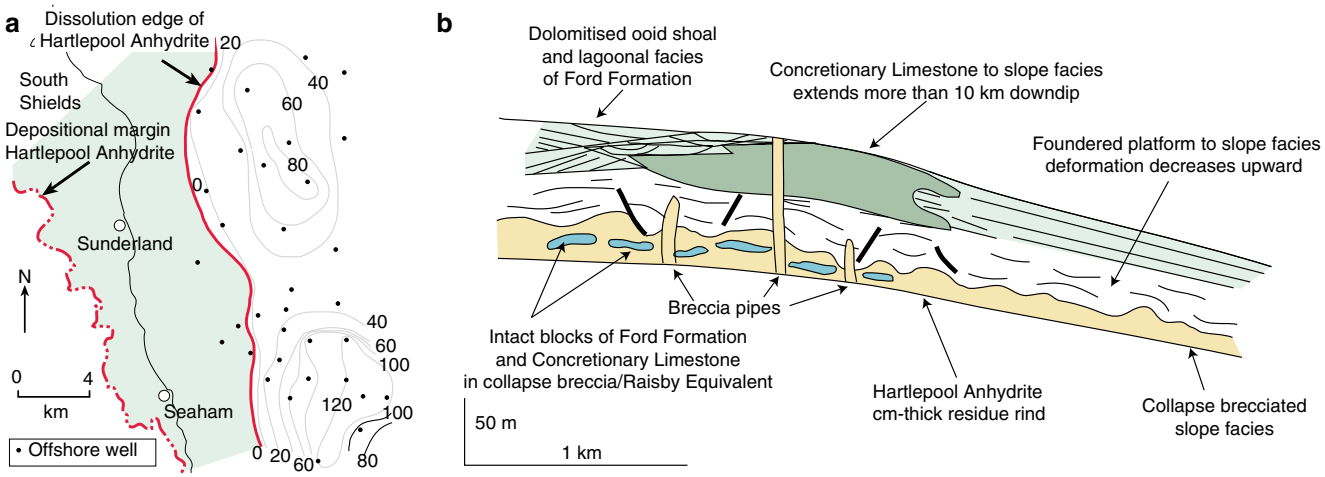

Fig. 7.80 Evaporite dissolution in the Permian Zechstein on the NW coast of England. (**a**) Extent of the dissolution zone of the Hartlepool Anhydrite from offshore anhydrite to onshore dissolution residue. Hartlepool isopachs in metres. (**b**) Facies patterns in the Raisby and related formations that make up the Zechstein unit formerly known as Magnesian Limestone. The cross section shows the relationship to dissolution residues of the Hartlepool Anhydrite seen in coastal outcrops where the anhydrite has dissolved

basin facies today consist of seaward dipping buff fine-grained dolomite. Offshore to the Raisby Formation lies the Hartlepool Anhydrite (Fig. 7.80a). Onshore the former position of the Hartlepool Anhydrite is defined by a regionally extensive dissolution residue at the base of the Raisby (Fig. 7.80b).

Outcropping Raisby dolomites contain nodular cavities, pores and pseudomorphic voids, which are lined or filled by calcite spar. Deep borehole cores sampling the Raisby Formation may still retain nodules and euhedral crystals of gypsum and anhydrite that are near-identical in size and shape to the cavities and pseudomorphs now seen in outcrop. This indicates that calcium sulphate nodules were once abundant in the subcropping Raisby Formation, but almost all the original salts have since been removed by crossflows of meteoric groundwaters.

Thus calcitisation of evaporite nodules is still active in appropriate zones of groundwater flushing along much of the coastal zone of NW England (Figs. 7.80 and 7.81; Lee and Harwood 1989; Lee 1994, 1995). Much earlier in the burial history of the Raisby Formation, primary Permian gypsum was replaced by anhydrite nodules. Later, coarser replacive burial anhydrite formed, postdating both pressure-solution and any further dehydration of any residual primary gypsum. During further mesogenetic burial, some of the anhydrite in the nodules was replaced by catabaric baryte, dolomite and sphalerite. Upon uplift of the Raisby Formation during the Tertiary, any remaining nodular anhydrite was telogenetically rehydrated to porphyroblastic gypsum. With further exhumation the gypsum was then dissolved by meteoric groundwaters and multiple stages of meteoric calcite cement

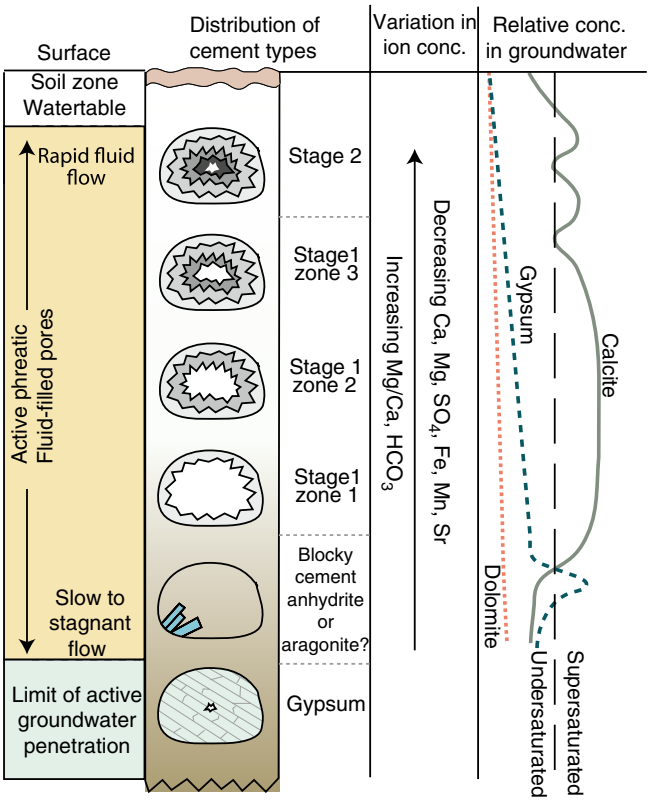

Fig. 7.81 Nodule evolution in the Raisby Formation, UK. *Vertical axis* indicates distance from the land surface, but may also indicate evolution through time of any one cavity. The lowermost cavity is filled with gypsum derived by rehydration of buried anhydrite. Contact with meteoric water causes dissolution of gypsum followed by local anhydrite pore cement that is then replaced by calcite. Succeeding calcite fill of cavities indicates increasing oxygenation and activity of groundwater system (After Lee and Harwood 1989)

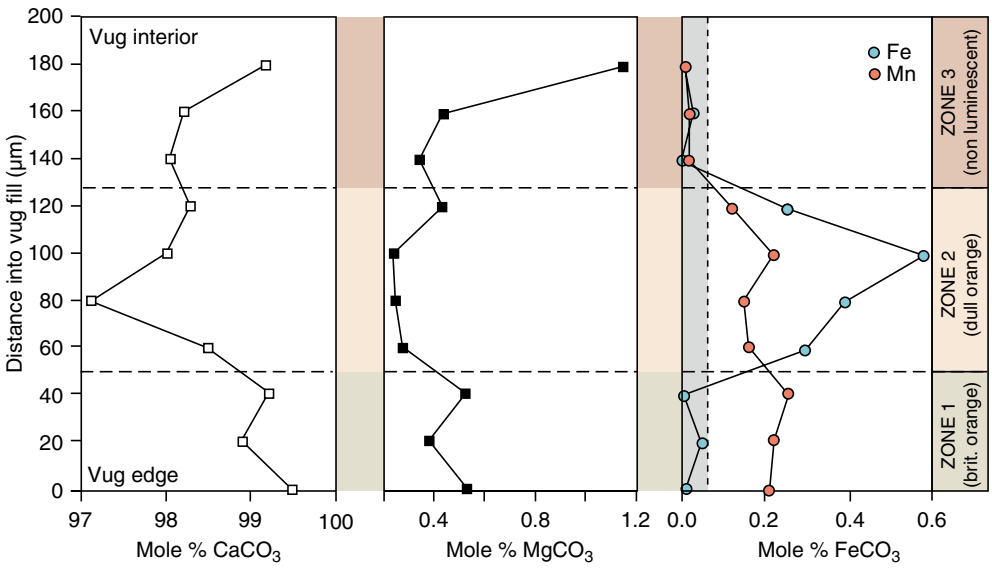

Fig. 7.82 Microprobe traverse through a Stage 1 cement crystal growing inward from the nodule wall showing distinct geochemical differences between Zone 1 (*bright orange*), Zone 2 (*dull orange*) and zone 3 (*nonluminescent*). *Shaded areas* indicate values are below reliable detection limits (After Lee and Harwood 1989)

precipitated within the voids (Fig. 7.81). All meteoric phreatic waters in this part of the UK are currently undersaturated with respect to dolomite and saturated with respect to calcite. Thus the calcite void fills in the Raisby Formation are made up of clear, inclusion-free, non-ferroan, low-magnesian telogenetic calcite.

There is an enigmatic episode of what was interpreted by Lee and Harwood (1989) as a widespread, but minor nearsurface anhydrite cement. It precipitated after regional exhumation had rehydrated all the buried anhydrite to gypsum and the gypsum had dissolved to form voids (Fig. 7.81). This early blocky crystal phase predated calcite void fills. It is encased in zone 1 calcite and is now replaced by calcite. Its blocky rectilinear prism termination precludes either a gypsum or a baryte precursor. The process and the mechanism which could have created an anhydrite-saturated pore water in the voids after gypsum leaching, in what must have been a shallow unroofing setting, is not well understood. Lee and Harwood (op. cit.) argue that if it is a calcite pseudomorph of anhydrite it perhaps indicates a short-term increase in salinity of nearsurface pore waters brought on by widespread meteoric dissolution of large volumes of subjacent halite (see also Handford and Moore, 1976).

The succeeding calcite infill of the leached gypsum nodules occurred in two phreatic (isopachous) stages; Stage 1 crystals are circumvoid equant, while stage 2 crystals are coarser, circumvoid and columnar (Fig. 7.81). Under cathodoluminescence the stage 2 columnar crystals are nonluminescent and alternate with internal sediment layers. Stage 1 crystals show three geochemically distinct cathodoluminescence zones probably related to increasing oxygenation of the crossflowing pore waters (Fig. 7.82). The successive zonation reflects increasing groundwater flow in the phreatic zone as the exhumed rocks approach the landsurface. Stage 1 – zone 1 (bright orange) cement has high Mn and low Fe and Mg values. Stage 1 – zone 2 (dull orange-luminescent) has relatively high Fe and Mn and low Mg values. Stage 1 – zone 3 (nonluminescent) has negligible Mn and little Fe in the calcite. Stage 2 cements have much higher Mg levels than stage 1, while the orange luminescing cements (zones 1 and 2) contain much higher levels of Sr than zone 3 or stage 2 cements (Fig. 7.82). This geochemical and cathodoluminescent zonation in calcitised nodule in the Raisby Formation is typical of increasing oxygenation in the pore fluids. It tracks the telogenetic passage of the uplifted strata from stagnant hypogene into an increasingly oxygenated and active groundwater system. But what of the early blocky calcite that Lee and Harwood (op. cit.) interpreted as post-gypsification anhydrite?

The process of meteoric calcitisation of $CaSO_4$ nodules is complicated in some parts of the Zechstein subcrop in central Germany by the presence of neoformed aragonite growing in anhydrite/gypsum vugs (Peckmann et al. 1999). It may be this calcite replacement of aragonite prisms that gives the unusual blocky crystal outlines that were interpreted as an unusual post-gypsification anhydrite in the preceding discussion of the Raisby Formation. Similar misinterpretations of blocky elongate calcite prisms as pseudomorphs after gypsum, not as aragonite cementstone replacements, have complicated the evaporite history of the Proterozoic McArthur Basin in northern Australia (Warren 1999; Chap. 8). Low $\delta^{13}C$ values (−10‰ PDB) of the aragonite inclusions growing in the Zechstein gypsum nodules indicate that some of its carbon is derived from organic matter that has been oxidized by bacterial sulphate reduction. The residual aragonite inclusions bear rhomb-shaped crystals of calcite that replace former dolomite. Elevated Mg/Ca ratios due to this dedolomitisation may have promoted the precipitation of aragonite instead of calcite during gypsification. This aragonite

has precipitated in the near-surface meteoric–vadose zone in recent times, it is a telogenetic precipitate. Aragonite crystals display a platy habit, while SEM analyses show that two types of micro-rods are associated with these plates (Peckmann et al. 1999). The mineralized micro-rods are interpreted to be fossilized bacteria. Aragonite inclusions, most of which contain organic-rich aggregations, yield a distinctive biomarker pattern. High concentrations of specific unsaturated fatty acids are clearly indicative of newly produced organic matter and reflect the presence of a discrete microbial community being associated with the formation of the aragonite. At one locality the aragonite is accompanied by native sulphur and the formation of sulphur was mediated by H_2S-oxidizing bacteria. This is corroborated by the presence of densely packed curved aragonite rods representing permineralized bacterial cells on and within the sulphur.

So far, most of our discussion has emphasised the importance of bicarbonate-rich deep meteoric circulation in calcitising exhumed calcium sulphate beds. But is this always so? The work of Peckmann et al. (1999) shows that aragonite can be a local product of bacterial sulphate reduction acting on gypsum nodules during exhumation of diapir crests. Kendall (2001) argues that biogenic sulphate reduction can be a more widespread process in shallow burial and that bacterial metabolism can calcitise widespread evaporite beds beneath unconformities, independent of active meteoric circulation. He cites beds of anhydrite nodules that are locally replaced by calcite, pyrite and celestite beneath an unconformity atop Mississippian anhydrites of Saskatchewan (Fig. 7.83a). Triassic clastics (Watrous Formation) immediately above the unconformity are green (reducing), rather than red (oxidising), and there is a regionally developed subunconformity alteration zone, where carbonates are dolomitised, and porosity is filled with anhydrite.

The unconformity lacks karstic features (unlike equivalent age surfaces in the USA), and probably formed in a hyperarid climate. Mississippian anhydrites near the unconformity are not preferentially dissolved, nor were they extensively hydrated. Anhydrite calcitisation probably involved sulphate-reducing bacteria and occurred only after the unconformity was shallowly buried by redbeds. Hydrogen sulphide, generated by bacteria in saline brines reduced redbed pigments to form the green halo. Replacement calcite contains pseudomorphs and relicts of anhydrite, and pseudomorphs of secondary gypsum. These indicate calcitisation occurred only after original Mississippian gypsum was altered to anhydrite and this, in turn, was partially converted back to secondary gypsum beneath the unconformity.

Replacement occurred concurrently with the formation elsewhere of a dolomitised zone beneath the unconformity. Sulphur isotopic ratios of replacement pyrite are depleted relative to Mississippian sulphate values, consistent with the activities of sulphate-reducing bacteria. $\delta^{34}S$ values for Mississippian Tilston and overlying Frobisher Evaporite anhydrites cluster around +18 to +19 ‰, comparable with Mississippian sulphate evaporite values worldwide. Values from the much younger replacement anhydrite porphyroblasts, and one value from anhydrite in the dolomitised zone are similar. Sulphides, associated with replacement calcite from the Filmore area, have $\delta^{34}S$ values that are depleted (by up to 19 ‰) relative to the Mississippian sulphates. Whole-rock analyses of Mississippian (Alida and Tilston Beds) limestones exhibit a narrow range of $\delta^{13}C$ ratios of +1.5 to +2.2 ‰, averaging +1.8 ‰, but have a wider range in $\delta^{18}O$ −1.2 to −6.4 ‰, averaging −3.86‰ (Fig. 7.83b). Carbon and oxygen are both depleted compared with estimated Mississippian marine carbonate values; almost certainly due to the addition of later diagenetic cements (Kendall 2001).

Mississippian dolomites have heavier $\delta^{13}C$ values (+2.6 to +3.6 ‰) and appear to be less altered. Their $\delta^{18}O$ ratios, however, are more varied. Two populations are present: one has preserved Mississippian compositions or is slightly depleted (−2 to −3‰ $\delta^{18}O$), but most are heavier – clustering around values of +0.9‰ $\delta^{18}O$, possibly reflecting precipitation from evaporated Mississippian seawater (Fig. 7.83b). A single analysis of dolomite from the dolomitised zone has a markedly different composition from the early diagenetic Mississippian dolomites. Replacement calcites have a narrower range of isotopic compositions, averaging −3.9 $\delta^{18}O$ and +1.5 $\delta^{13}C$. These averages are almost the same as those calculated for whole-rock analyses of the Mississippian limestones (−3.9 $\delta^{18}O$ and +1.8 $\delta^{13}C$). But the carbon isotopic ratios of replacive calcites, do not support this interpretation, rather they are identical to those of Mississippian limestones (Fig. 7.83b).

Kendall (2001) argues simple replacement of sulphate by pore-water bicarbonate (in equilibrium with host limestones) is unlikely because protons generated during the reaction should have created acidic conditions in which calcite would have dissolved. He notes a full explanation of the calcitisation remains elusive, but may involve replacement occurring in an active arid-zone groundwater system and/or bacterial sulphate reduction occurring upstream of the site of calcitisation.

Bustillo et al. (1999) describes some unusual mineralized and silicified carbonate-rich nodules hosted in Lower Triassic red mudstones in Central Spain (Fig. 7.84). From their borders to their centres, the nodules (geodes) display a characteristic zonation of; (a) a millimetric carbonate crust, (b) a quartz rim, (c) massive dolomite centres, (d) gold-bearing iron-rich infills (haematite laths and goethite with up to 7,000 ppm of gold) and (e) uplift related calcite cements that

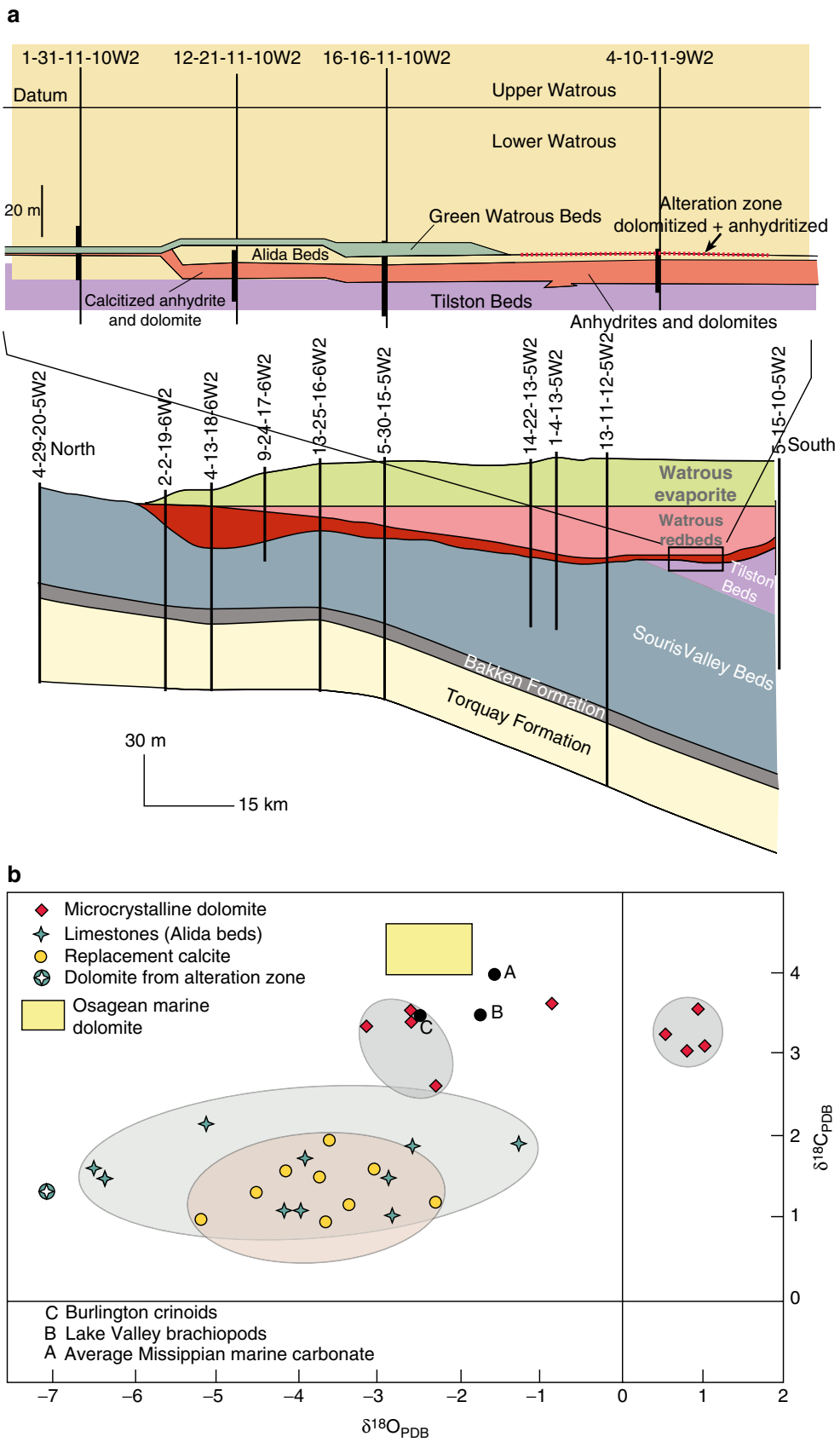

Fig. 7.83 Bacterial calcitisation, Saskatchewan (After Kendall 2001). (**a**) Diagrammatic section showing the regional unconformity, the northwards disappearance of older Triassic, Permian, Pennsylvanian and late Mississippian strata, and the northwards overstep of the Watrous by Jurassic deposits. Inset shows anhydrite (or calcitised anhydrite) and dolomite constitute the Tilston Evaporite. Most of Tilston Beds and overlying Alida Beds are limestones. Note the very thin calcitised anhydrite zone at the base of the Tilston Anhydrite (*arrowed*), and a dolomitised zone beneath the unconformity in the 4-10-11-9 W2 well. (**b**) Carbon-oxygen isotopic ratio cross-plot of calcites that have replaced anhydrite, host rock dolomites, and limestones of overlying Alida Beds. Note overlap of limestone and replacement calcites, and their clear distinction from dolomite values

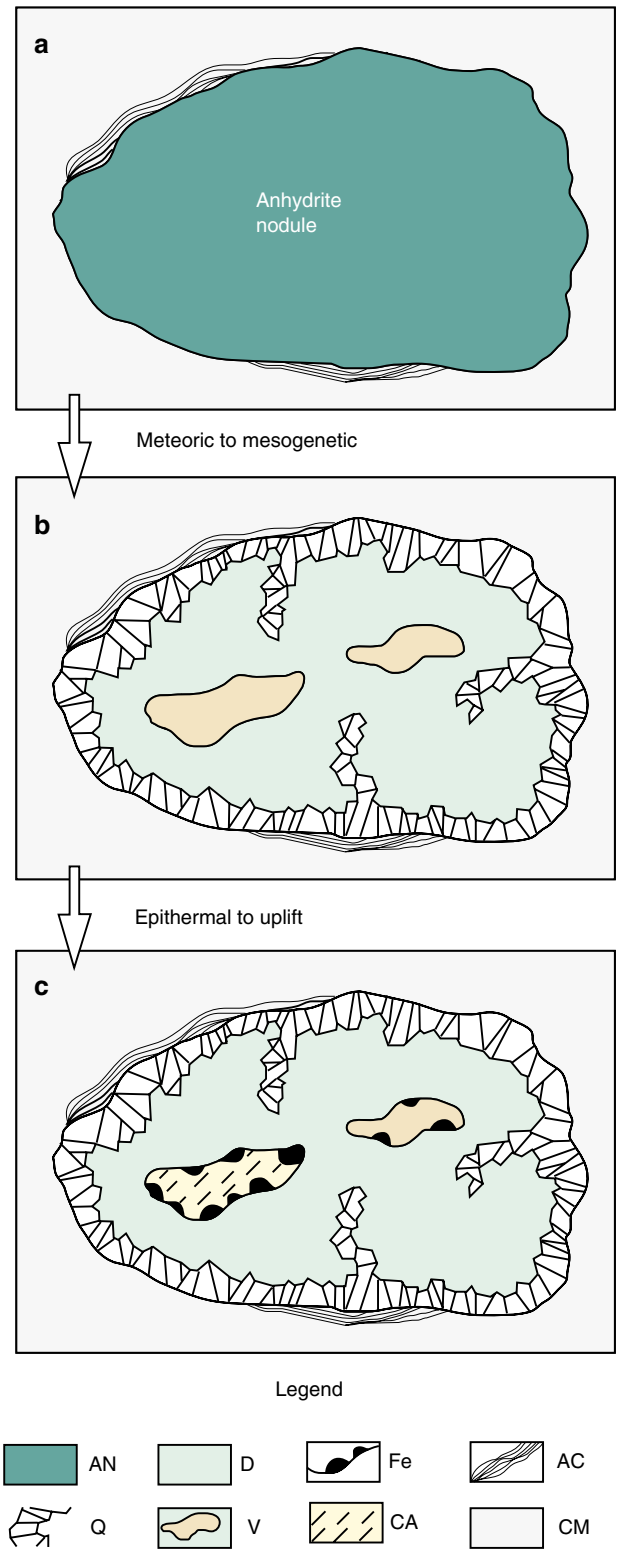

Fig. 7.84 Model of the Tordelrabano geodes, Spain (After Bustillo et al. 1999). Abbreviations: *AN* anhydrite, *D* dolomite, *Fe* oxides and hydroxides of iron, *AC* carbonate crust, *Q* quartz, *V* voids, *CA* calcite, *CM* mudstones. (**a**) Anhydrite nodules form in mudstones from early hypersaline fluids. Later, a crust (probably edaphic) forms around the anhydrite nodule. (**b**) Replacement of the anhydrite by dolomite and quartz from continental groundwaters. Voids form by dissolution of anhydrite or dolomite. (**c**) Filling of the voids by hydrothermal minerals (gold-bearing hematite–goethite). Subsequent precipitation of telogenetic calcite sometimes seal the central hollow. Textural evidence indicates that the geodes were originally nodular anhydrite, subsequently replaced by quartz and dolomite. The resultant porosity from this replacement ("on the way down"), or porosity created by later dissolution, has been filled by epithermal gold-bearing iron-oxide hydroxides, romanechite and calcite.

$\delta^{13}C$ values indicate the participation of meteoric waters in an early burial environment, which was characterized by both a sub-desert climate and a temperate-tropical climate. Oxygen signatures reflect very variable temperatures for all minerals, with the exception of late stage calcite, which was precipitated at <38 °C ("on the way up"). Iron-oxide temperature values in the gold rich cores can reach 85 °C (epithermal). The mineralogical assemblages denote a multistage history to the nodules characterised by early silica, then dolomite infill of a dissolving nodule (early diagenetic replacement "on the way down") followed by the epithermal[18] activity. This mineralization is linked to the Late Hercynian, calc-alkaline volcanism of Central Spain (the Hiendelaencina mining district). Once again, the evaporite replacement process is ongoing, not early versus late, but occurred throughout the burial cycle.

Dedolomitisation (Calcitisation) of Dolomite Matrix

One of the first reports of the alteration of dolomite to calcite was by the Swiss geologist on Morlot (1847) based on solution experiments and field studies in Styria. He coined the term dedolomite and suggested that groundwater leaching of pre-existing evaporite deposits, containing gypsum or anhydrite, would be enriched with calcium and sulphate, creating fluids driving calcitisation of former dolomites. Dedolomitisation of dolomite matrix is frequently associated with calcitisation of entrained evaporite nodules. Dedolomitisation describes the conversion of a dolomite back to a limestone by the growth of calcite rhombs within the dolomite matrix.

$$MgCa(CO_3)_2 + CaSO_4 \cdot 2H_2O \rightarrow 2CaCO_3 + Mg^{2+} + SO_4^{2-} + 2H_2O$$

This process can continue until the dolomite is completely converted to a limestone, or it may be arrested when the calcitisation of the matrix is no more than partial. Dedolomitisation has long been interpreted as a product of evaporite diagenesis and is typically ascribed to telogenetic calcium-rich groundwaters derived from a nearby dissolving gypsum/anhydrite or glauberite unit (Lucia 1961; Warrak 1974; Lee 1994). An evaporite association is the emphasis of the dedolomitisation discussion in this section; but dedolomitisation can also occur under the influence of calcium-rich basinal waters (mesogenetic), where the elevated levels of calcium are independent of evaporite dissolution. For

[18] Epithermal, said of a hydrothermal mineral deposit located within 1 km of the Earth's surface and precipitated in a temperature range of 50–200 °C, mainly occurs in veins.

example, Land and Prezbindowski (1981) documented dedolomitisation from hot, calcium-rich brines moving up into a dolomite reservoir in the Cretaceous Edwards Group of the Gulf Coast. They attributed the high calcium content of these brines to the authigenic albitisation of plagioclase in down-dip sandstones.

Texturally, calcitised dolomites (dedolomites) are identifiable if one or more of the following features are present in the limestone (Armenteros 2010 and references therein): (1) large rhombs, isolated or contiguous, comprising an equicrystalline mosaic of anhedral calcite; (2) preservation of the outlines of primary rhombic crystal dolomites that are either filled with sparite or are empty; (3) preservation of limpid rims and internal remains of the original dolomite rhomb outlines within a pervasive calcite cement; (4) preservation of the cloudy cores and clear rims of an earlier dolomite mosaic, later replaced by calcite (typically visible using CL microscopy); (5) rhombs with calcitised cores and/or calcitised zones; and (6) dedolomitised/calcitised rhombs with obliteration of the original crystalline structure. The presence of dolomite crystals with leached centres in a dedolomite indicates that the original dolomite nucleus probably contained inclusions of low-Mg calcite precipitated rapidly or fluid-filled microcavities. The preservation of cloudy cores and clear rims indicates most likely the replacement by a thin-film solution front without creation of substantial void space.

The textural variability of the dedolomitization/calcitization process is mainly controlled by the texture of the precursor rock. Where the micrite matrix is pervasively dolomitised, the reaction took place primarily through dissolution/precipitation; conversely, where significant amounts of micritic matrix remain, the reaction proceeded through mole per mole (mimic) replacement. In that case the transformation of dolomite to calcite took place across a submicron- thick solution film between the original dolomite host and the authigenic calcite, just as it does during neomorphism of aragonite and-or high-Mg calcite. In other cases, there is little textural preservation of the finer details of the precursor, calcite simply seems to fill the voids generated by earlier dissolution of dolomite (Armenteros 2010).

Thus, replacement can be either pseudomorphic or non-pseudomorphic. In the dolomites of the upper Muschelkalk of Prades (Catalonia, Spain), dedolomitisation took place through both processes simultaneously: non-pesudomorphosic calcite after dolomite is associated with wall fractures, and pseudomorphic replacement typifies the bulk rock (Ayora 1999). A non-pseudomorphic dedolomitisation reaction may produce a change in porosity because the molar volume of dolomite (65.365 $cm^3\ mol^{-1}$) is less than two times the molar volume of calcite (36.934 $cm^3\ mol^{-1}$) (Ayora 1999).

Evaporite-derived dedolomites are often associated with evaporite dissolution breccias, which indicate the now dissolved bed that supplied the excess calcium needed to dedolomitise (Lee 1994; Fu et al. 2008). Dedolomite under this scenario forms via the reaction of calcium sulphate-rich solutions with a pre-existing dolomite to produce calcite with magnesium sulphate as a possible byproduct. The latter is rarely preserved, as it is highly soluble, and either remains as dissolved ions in the escaping waters or is quickly redissolved and flushed by through-flowing groundwaters (Shearman et al. 1961). The $CaSO_4$ dissolution process is often driven by meteoric flushing of nearsurface oxidising waters and former ferroan dolomites are preferentially replaced. The resulting calcitised dolomites are outlined by intervals stained red with iron oxides and hydroxides.

With uplift-related (telogenetic) dedolomites the distribution of dedolomite can reflect variations in the regional hydrology. This can be seen in the dedolomites of the Lower Cretaceous Edwards Group in the Balcones fault zone area of south-central Texas (Ellis 1985, 1986). The Edwards Group consists of 120–180 m of porous limestone and dolomite that accumulated on the Comanche shelf in shallow-water subtidal, intertidal, and supratidal marine environments. During early burial diagenesis, carbonate mud neomorphosed to calcitic micrite, aragonite and Mg-calcitic allochems were altered to calcite or were leached, and evaporites formed in tidal-flat sediments. Each of these phases had a characteristic stable isotope signature (Fig. 7.85) Dolomite is widespread and formed in environments ranging from hypersaline to fresh-water as shown by the two isotope clusters in the Edwards dolomite.

Late Tertiary faulting along the Balcones fault zone, tied to Jurassic salt withdrawal, initiated a circulating, fresh-water aquifer system to the west and north of a fairly distinct "bad-water line," which roughly parallels the Balcones fault zone. To the south of the bad-water line, interstitial fluids remained relatively stagnant and contain over 1,000 mg/l dissolved solids. Because of the differences in the chemistry of the interstitial fluids, post-faulting diagenesis in the two zones has been very different. Water in the bad-water zone can be saturated with respect to calcite, dolomite, gypsum, celestite, strontianite, and fluorite, whereas water in the fresh-water zone is saturated only with respect to calcite. Due to the change in water chemistry, rocks in the fresh-water zone have been extensively recrystallised to coarse microspar and pseudospar, extensive dedolomitization has occurred, and late sparry calcite cements have precipitated. This created a suite of covariant isotope trends and clusters with the dedolomite showing a distinctive set of carbon and oxygen values relate to soil water influences (Fig. 7.85). In contrast, rocks in the bad-water zone retain fabrics associated with pre-Miocene diagenesis and there is little or no evidence of widespread dedolomite. The importance of meteoric diagenesis in the formation of dedolomite in shallow, subsurface telogenetic environments is illustrated by the

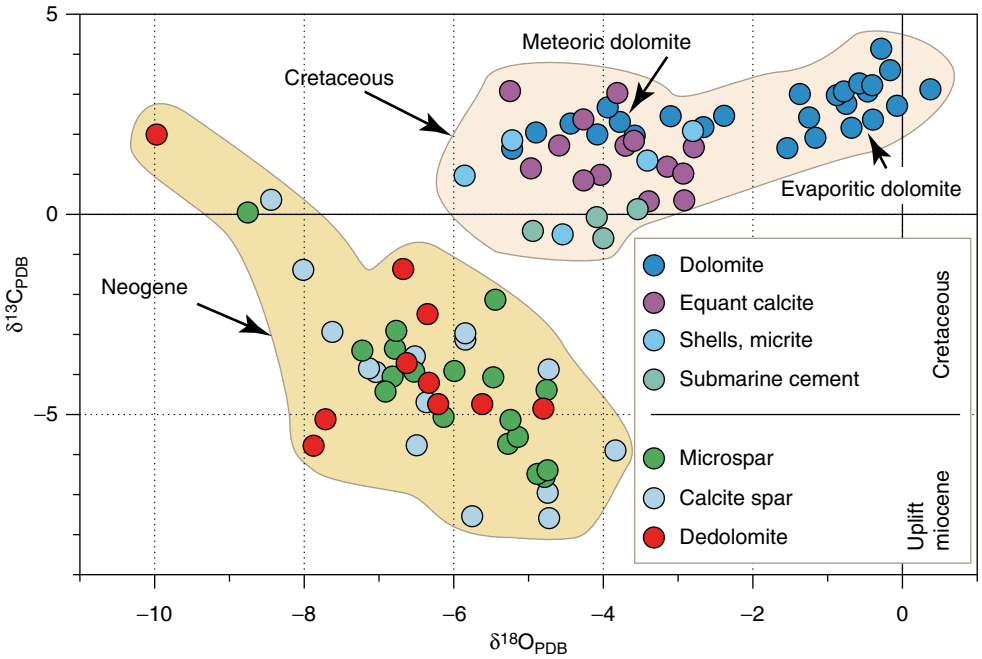

Fig. 7.85 Crossplot of $\delta\ ^{18}O_{PDB}$ and $\delta\ ^{13}C_{PDB}$ of selected samples taken from the Edwards Group, Balcones fault zone, central Texas, showing two clusters related to Cretaceous diagenetic overprints and Neogene telogenesis including dedolomite formed by $CaSO_4$ dissolution tied to uplift of the Edwards Plateau (Replotted from data in Ellis 1985)

fact that the Edwards Group had a stable mineralogy of calcite and dolomite before the circulation of fresh water began and drove the precipitation of meteoric spar, microspar and dedolomite. Isotopic values for the dedolomites follow a similar trend to those of the microspars and pseudospars. As with the microspars and pseudospars formed by entry of telogenetic water, it can be shown that dedolomites are in isotopic equilibrium with Edwards water on a regional scale, which supports the contention that the dedolomites are forming from present-day formation-water (Ellis 1985).

Also, carbonates in both the fresh-water and bad-water zones were deposited in similar environments and underwent the same diagenetic history until the establishment of the fresh-water zone in the Miocene. If dedolomite was related to subaerial exposure prior to the Miocene, it would have formed in both zones since erosion surfaces are found in both zones. Furthermore, dedolomite occurs throughout the entire 100- to 200-m thickness of the fresh-water zone in the cores studied. It is not concentrated in a few zones as would be expected if it formed during subaerial exposure (Ellis 1985). Clearly, in spite of the "stable" mineralogy related to mesogenetic stabilisation of the Edwards dolomites, considerable additional diagenesis occurred in the superimposed Neogene fresh-water zone, and dedolomitisation probably continues to occur today.

Dedolomites such as those of the Edwards Plateau, created by meteoric flushing of calcium-sulphate evaporite salts, typically occur beneath exposure surfaces, dissolution breccias or unconformities. Well-exposed and studied examples of dedolomites, associated with meteoric karstification of a shallowly buried sulphate system, typify Miocene lacustrine sequences of the Madrid Basin in central Spain and the Calatayud Basin of NE Spain (Cañaveras et al. 1996; Arenas et al. 1999; Sanz-Rubio et al. 2001). A variety of calcite spar mosaic fabrics, initiated by dedolomitisation and calcitisation of magnesites, formed in association with well-defined solution collapse breccias (Fig. 7.86). Dominant dedolomite textures are made up of sutured calcites and radial-fibrous calcites, the latter consisting of pseudospherulite mosaics and fibrous crusts. Other subordinate dedolomite fabrics consist of micro- to mesocrystalline mosaics of rhombic, occasionally zoned calcites, as well as reworked pseudospherulite crystals.

The diagenetic carbonate zone (DCZ) that hosts these textures in the Madrid basin overlies and grades laterally into lacustrine dolomite (lower dolomite unit – LDU) and evaporites (evaporitic unit – EU), and in turn is capped by a palaeokarst or exposure surface (Figs. 7.86a; Cañaveras et al. 1996). The boundary between the DCZ and the LDU is transitional and is defined by grading in the $\%MgCO_3$ profile (Fig. 7.86b). Mg values range from 0.1 to 1.2 % in the dedolomites of the DCZ and micrites of upper limestone unit (ULU) and from 8 to 14 % in the underlying dolomites of the LDU.

Geochemical evidence indicates dedolomitisation occurred in the shallow subsurface in early burial (<40 m depth) via the throughflushing of oxidizing meteoric-derived ground waters (Cañaveras et al. 1996). $\delta^{18}O$ values of the dedolomites in the DCZ average −6.7‰ and range from −6.1 to −7‰, while $\delta^{13}C$ averages −8.2‰ and ranges from −7.4 to −9.2‰. The $\delta^{18}O$ values in the LDU average −0.3‰ while $\delta^{13}C$ averages −6.1‰. Isotope values in the ULU

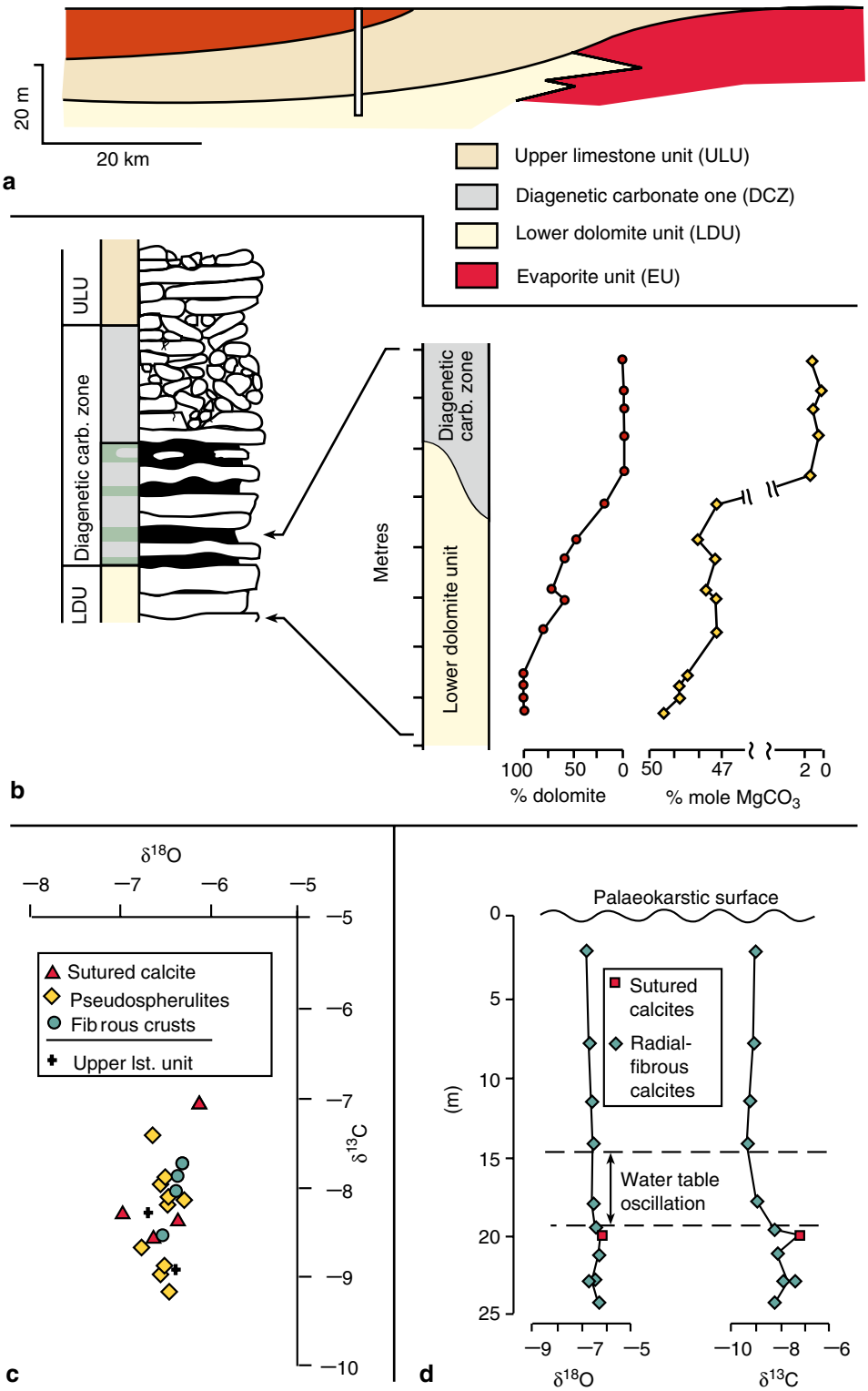

Fig. 7.86 Dedolomite in the Madrid Basin, Spain. (**a**) Distribution of the main subunits in Middle to Upper Miocene lacustrine units of the Madrid Basin, central Spain. (**b**) Shows the position of the solution collapse breccia in controlling the dedolomites and the nature of the contact between the lower dolomite unit (*LDU*) and the dedolomites of the diagenetic carbonate zone. (**c**) Oxygen-carbon crossplot of different types of calcite that make up the dedolomite. (**d**) Vertical trends in $\delta^{18}O$ and $\delta^{13}C$ in section of the Diagenetic Carbonate Zone (*DCZ*). The zone of carbon depletion between 15 and 20 m below the palaeokarst surface corresponds to a trend of more constant $\delta^{18}O$ values above this interval and more variable values below. These observations are consistent with the preservation of a palaeowatertable within the DCZ (After Cañaveras et al. 1996)

range from −6.4 to −6.8‰ in $\delta^{18}O$ and from −8.2 to −8.9‰ in $\delta^{13}C$ (Fig. 7.86c). The values of the dedolomites are consistent with precipitation from meteoric waters and give precipitation temperatures of 8–12 °C. Vertical trends in $\delta^{18}O$ and $\delta^{13}C$ can be used to define the average position of the watertable in the DCZ at the time the dedolomites were forming (Fig. 7.86d). This too supports a palaeokarst model characterized by an irregular shallow watertable and a narrow vadose zone (Cañaveras et al. 1996). The diagenetic system behaved as an open system for nearly all trace elements

analysed; but in the shallower zone (vadose zone) the system was partially closed with respect to strontium. The dedolomitisation was driven by two combined hydrographical patterns: authigenic recharge through limestone aquifers and allogenic recharge from adjacent mountains (Fig. 8.17).

Meteoric water influx at the margins of some shallow carbonate/evaporite lakes may be responsible for calcitization of the dolocrete and dolomitic muds fringing the lakes. Moreover, the calcitization, which occurs during early diagenesis due to drops in lake level, may either preserve or destroy the original dolomite fabric.

Dedolomites can also be formed via evaporite dissolution in the deeper subsurface mesogenetic realm where dissolution-derived basinal brines are escaping into the basin margin. Budai et al. (1984) suggested a subsurface setting for burial dedolomites of the Mississippian Madison Group of Wyoming and Utah. Two stages of fracture-related dedolomite are present, one that precedes and one that postdates regional dolomitisation. The early dedolomite occurred as active groundwaters flushed evaporitic sequences during shallow burial (on the way down in the burial cycle). The later post-stylolitisation fracture-associated dedolomite records chemistries and isotopic signatures of deep burial and tectonic-vein mineralisation. Associated with this late dedolomite are calcitised anhydrite nodules and stylolite-bitumen-related dedolomites that also indicate burial-related episodes of dedolomitisation. This episode of dedolomitisation took place during hydrocarbon maturation as basinal brines were moving through the Madison reservoir. Then hot Ca-enriched brines were able to dissolve anhydrite and dolomite, while at the same time precipitating calcite along stylolitised seams and within anhydrite nodules.

Celestite as an Evaporite Indicator?

Celestite ($SrSO_4$) occurs as crystals, nodules and cements in many bedded carbonates, particularly karstified limestones, but also in dolomitic and marly hosts (Hanor, 2000). Evaporite-associated celestite may replace or pseudomorph individual evaporite crystals, or it may be isopachous and passively fill fissures, vugs and nodular cavities created by the dissolution of an evaporite precursor, or it may form interclast cements within dissolution breccias. Internal textures preserved within a celestite nodule replacing an evaporite or an intergranular aggregate depend on the ratio of rock to fluid interaction and the timing of flushing.

Celestite, in association with baryte and strontianite can form massive intervals in diapir caprocks and haloes about the dissolving edges of salt allochthons. Caprock occurrences were discussed in the previous chapter and will not be discussed here. $SrSO_4$ in a bedded evaporitic carbonate host forms either as a primary precipitate from brines (Wood and Shaw 1976) or, more usually, by the diagenetic interaction of gypsum or anhydrite with groundwater-borne Sr-rich waters (Table 7.16). In this case the dissolution of a calcium-sulphate-containing bed supplies the SO_4, which then combines with Sr to precipitate as celestite, typically in zones of mixing between hypersaline and meteoric waters. West (1964, 1965, 1973, 1979) discusses the evaporite-celestite association in detail and the interested reader is referred to these benchmarks. Scholle et al. (1990) is recommended for a more general summary of celestite occurrence in sediments worldwide.

The Coahuila and the Burrros-Picachos platform sediments in Mexico is one of the largest exploited celestite regions in the world (Table 7.16; Dill et al. 2009 and references therein). Other significant evaporite/hydrothermal celestite deposits are located in Cretaceous evaporitic hosts in the Neuquen basin, Argentina, and in Northern Tunisia. In Europe, Spain is the leading strontium producer with its main output coming from the Montevives and Escuzar deposits, Granada. Both these celestite deposits are hosted in lower Miocene evaporitic sections of the Granada basin, which is an intermontane depocentre lying on the boundary between the internal and external zones of the Betic Cordillera. The primary mineralization is located in what is interpreted as a lower marine evaporitic unit, some 90 m thick. In Montevives the celestite replaces calcite in two stromatolitic limestone layers with ore thickness varying between 0.2 and 1 m an average grade of 86 %. The replacement of stromatolitic calcite and the infilling of fissures and cavities by celestite seem to be synsedimentary in the Montevives deposit, induced by salinity changes due to the mixture of sulphate salt waters and fresh waters during late Miocene times. In contrast, the Escuzar deposit is somewhat later and obviously karst related. Boulders of mineralized limestone with strontium, celestite and dolomite fill karst caverns in a gypsum host within the lower evaporite unit.

Similar, but not exploited, celestite-bearing beds of Lower Messinian age, and intercalated with clay and gypsum, also typify other basins of the Betic Cordillera. To the east, there are numerous celestite shows tied to $CaSO_4$ occurrences near Copaceni, Romania of Badenian age and near Cifteagil, Turkey. Various types of celestite occurrences hosted by Tertiary evaporite deposits and molasse-type volcanogenic sediments are found in the Sivas Basin, in east-central Anatolia, Turkey. Celestite deposits occur also as a fringe to Messinian gypsum beds at the southeastern edge of the Troodos ophiolite complex, near Maroni, Cyprus. They are part of a Neogene celestite occurrence (mostly Miocene hosts) that constitute a belt of calcareous-evaporitic sediment, that extends from the Iberian Peninsula, through the Mediterranean area, into the Arabian Gulf (Dill et al. 2005). Further eastward, and stratigraphically equivalent to Neogene Mediterranean sequences, are gypsum–strontium deposits

Table 7.16 Worldwide occurrences of celestite and associated properties

Country	Host rock age	Reference	Strandzone/ evaporite	Subaerial exposure	Hydrothermal	Assoc. clastics	Assoc. baryte	Celestite $^{87}Sr/^{86}Sr$	Oceanic $^{87}Sr/^{86}Sr$	Interpreted Sr Source
Algeria-Tunisia	Eocene	Chabou-Mostafai et al. (1978)	Yes	Yes	–	Yes (updip)	No	–	–	Groundwater influx from granitic source
Argentina	Cretaceous (Neocomian)	de Brodtkorb et al. (1982)	Yes	Minor	Yes	Yes (above)	Some	0.7072	0.7072	Seawater
Canada	Carboniferous Mississippian	Kendall (2001)	Yes	Yes	No	Yes (above)	No	–	–	Shallow brine drives bact. sulphate reduct.
Germany	Jurassic (Malm)	Müller (1962)	Yes	Some local	Some local	Some (above)	No	–	–	Seawater
Great Britain	Triassic (Rhaet)	Wood and Shaw (1976)	Yes + inland basins	Minor	No	Some	Minor	0.7105	0.7076	Groundwater alteration of older limestones
Greenland	Permian (Kazanian)	Scholle et al. (1990)	Yes	Yes (exten-sive)	Minor locally	Yes (below)	No	0.71344	0.7068	Groundwater from redbeds
Iran	Oligo-Miocene	Bazargani-Guilani and Tak (2008)	Yes	Yes	Yes	Yes	Yes	–	–	Groundwater flushing of volcaniclastic redbeds
Italy	Pliocene	Babieri and Masi (1984)	–	–	–	–	Yes	–	–	Evaporites
Mexico	Cretaceous (Albian)	Kesler and Jones (1981)	Yes	Minor to none	Minor	Yes (below)	Yes	0.70765	0.7072	Limestone diagenesis; groundwater
Norway	Silurian (Wenlock)	Olaussen (1981)	Yes	Yes (exten-sive)	No	Yes (above)	No	–	–	Groundwater alteration of aragonitic limestone
Poland	Miocene (Badenian)	Kasprzyk (1994)	Yes	Yes	No	No	Yes			Groundwater alteration of Ca sulphate beds
Poland	Permian (Zechstein)	Hryniv and Peryt (2003, 2010)	Yes	Yes	No	Yes (below)		–	–	Groundwater alteration of Ca sulphate beds
Spain	Eocene	Taberner et al. (2002)	Yes	Yes	No	Yes (above)	Some	0.70776–0.70784	0.7071	Groundwater leaching Sr in overlying redbeds
Spain	Miocene	Martin et al. (1984)	Yes	Yes (exten-sive)	No	(abov + below)	No	–	–	Marine Sr: mixing zone precipitation
Turkey	Miocene	Tekin et al. (2001)	Yes	Yes	–	(above + below)	No	0.70782	0.7083–0.7087	Alteration of volcanics
United States	Silurian	Carlson (1987)	Yes	Yes	Some	No	No	–	–	Dolomite or evaporite dissolution
United States	Carboniferous Mississippian	Frazier (1975)	Yes	Some	Yes	Yes	No	–	–	Seawater brines
USSR (former)	Permian (Lower)	Zaritsky (1961)	Yes	Possible	–	Yes	Yes	–	–	Seawater; groundwater redistribution

In part after Scholle et al. (1990), Hanor (2004)

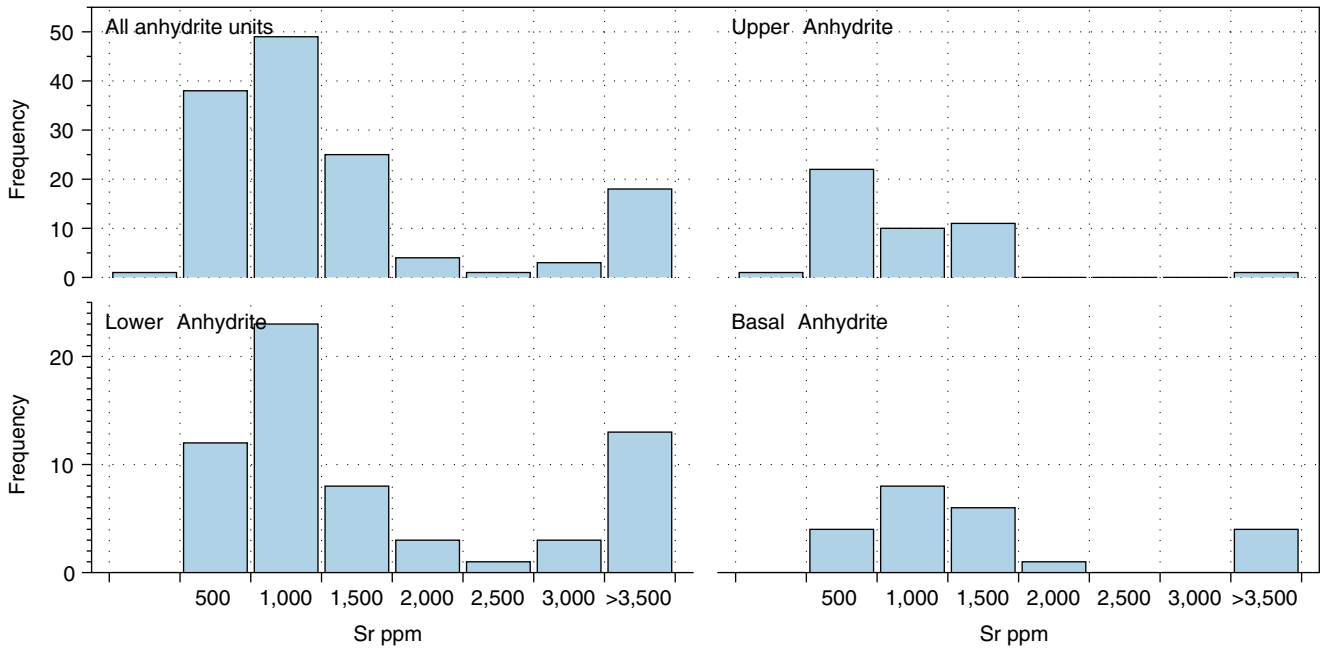

Fig. 7.87 Histograms showing strontium content of the main anhydrite units (*upper, lower and basal*) and a total frequency plot for the Polish Zechstein (Replotted from Hryniv and Peryt 2010)

that occur parallel to the Trucial Coast of the Arabian Gulf in Qatar and, to a lesser extent, the United Arab Emirates (Dill et al. 2005, 2009).

A number of papers over the past two decades have tied minor celestite occurrences with microbial microenvironments, often in saline settings with abundant gypsum (Sanz-Montero et al. 2009; Ziegenbalg et al. 2010). Experiments carried out by Schultze-Lam and Beveridge (1994) documented the epicellular precipitation of celestite on unicellular cyanobacteria. Douglas (2002) also found that celestite formed in the exopolymers surrounding purple sulphur bacteria in microbial mats from a Bahamian hypersaline pond. Gypsum-hosted endoliths in Death Valley, California (Douglas and Yang 2002) showed that organisms were able to precipitate Sr-rich minerals, such as celestite and carbonates, within a layered plexi. Each mineral type was segregated into a restricted chemical zone together with a specific microbe that helped to create the chemical conditions present at that particular depth in the community (Douglas 2005). In addition, Taberner et al. (2002) interpreted celestite as a byproduct of sulphate reducing bacteria in Eocene reefs and basinal sediments of NE Spain.

Strontium occupies calcium sites in the gypsum or anhydrite lattice, where it can be enriched ten times over the Sr content in enclosing dolostones (Carlson 1983). Strontium levels are around 2,000 ppm in marine gypsum and up to 5,000 ppm in anhydrite of marine origin (Stewart 1968). A study of strontium levels in the various anhydrites of the Zechstein series in northern Poland shows variations between units and a marked bimodal occurrence set (Fig. 7.87; Hryniv and Peryt 2010). Particular anhydrite levels differ, especially in the frequency of samples showing elevated Sr content. The greatest variation is seen in the Lower Anhydrite. This agrees with sedimentological observations indicating that the greatest differentiation of depositional environments occurred during the deposition of the Lower Anhydrite unit in Poland. It seems Sr content is a good indicator of brine concentration during primary gypsum precipitation and it seems that subsequent gypsum–anhydrite transformation does not affect the parent strontium distribution. The histograms of Sr content in the Basal Anhydrite indicate a slightly higher brine concentration than during Lower Anhydrite deposition, and the latter in turn was higher than brine concentration during the Upper Anhydrite sedimentation. The consistent elevated grouping seen across all three units and also clearly seen in the total frequency plot is indicative of samples and textures altered by diagenetic solutions with much of the Sr possibly coming from a source external to the host anhydrite. In general it seems that primary gypsum has somewhat elevated Sr contents compared to anhydrite (Table 7.17)

In this context it is notable that anomalously high concentrations of Sr occur within secondary gypsum samples in the Miocene (Badenian) gypsum of southern Poland, not in primary-textured gypsum (Kasprzyk 2003). This suggests localised primary gypsum leaching as the source or, alternatively, a supply of Sr form circulating pore fluids sourced by an anhydrite to gypsum phase change. Either interpretation

Table 7.17 Strontium levels (ppm), averages in parentheses in various $CaSO_4$ settings

Location, age	Brine source	Primary Gypsum			Secondary Gypsum			Diagenetic gypsum		Anhydrite	Reference
		Selenitic	Clastic, "balatino"	Undifferentiated	Alabastrine	Lam-nodular	Undifferentiated	Vein	Interstitial	Laminar-nodular	
Upper Miocene, Spain	Mainly marine	734–17,95 (15)						243–311 (4)			Lu and Meyers (2003)
Messinian, Nijar, Spain	Mainly marine	560–17,95 (>40)	1,209–4,872 (6)					228–368 (7)			Lu et al. (1997, 2001), 2002)
Fortuna gypsum, Miocene, Spain	Marine to continental	217–1,817 (230)	485–4,986 (43)			106–1,873 (45)					Playa et al. (2000)
Gypsum, Messinian Spain, Badenian, Poland	Marine	217–2,500 (520)	182–279 (10)		208–464 (21)						Rosell et al. (1998)
Castile Fm, Permian, USA	Marine									1,500–7,700 (>30)	Leslie et al. (1997)
Lake Lisan and Dead Sea Gypsum, Israel	Marine			265–560 (4)							Stein et al. (1997)
Triassic, Spain	Marine									190–2,951 (98)	Orti et al. (1996)
Permo-Triassic,, North Calcareous Alps	Marine				607–1,192 (3)	806^336° (3)					Spoil and Pak (1996)
Messinian, SE Spain	Marine	620–1,280									Michalzik (1996)
Messinian, de San Miguel de Salinas (Alicante).	Continental	450 (1)	829–1,457 (4)				257–622 (13)		60–159 (9)		Rosell and Orti (1992)
Madrid Basin, Spain	Continental		3,100–3,744 (>10)				576–1,890 (>20)				Ordonez et al. (1989)
Ebro Basin, Spain	Marine				95–1,825 (77)	95–2,855 (46)				634–1,922 (10)	Salvany (1989)
Madrid Basin, Spain	Continental		1,460–4,774				390–905				Fort and Bustillo (1986)
Messinian, Mediterranean	Marine	300–5,000"	1,000–2,250"								Dronkert (1985)
General data evaporites	Marine	700	600–3,000				100–838			540–1,220	Geisler-Cussey (1987)
de la Trinitat (Delta de l'Ebre), Spain	Marine (saltworks)	922–1,808 (7)	419–1,456 (22)								Utrilla (1985)
Coastal salinas of Santa Pola (Alicante, Spain).	Marine (saltworks)	1,000–2,600	400–1,600								Orti et al. (1984)
Secondary gypsum crystals, Brown Hills Transantarctic Mountains.	Continental								151–253 (2)		Faure and Felder (1981)
General data evaporites	Non specified									500–5,220 (314)	Dean (1978)
Modern, Persian Gulf	Marine and continental	210–570 (6)		410–2,080 (30)	10–3,000 (151)						Butler (1973)

After Playa and Rosell (2005)

is supported by the petrography, which shows that replacive celestite is common in the secondary gypsum, whereas no discrete Sr mineral phase is seen within the anhydrite.

Such leaching of gypsum/anhydrite can create Sr-rich waters, as can the early dissolution of aragonite, which has enriched levels on Sr in the lattice when compared to calcite (Rodríguez-Aranda et al. 2005). Worldwide, most evaporite-associated regions of elevated strontium occur about basin margins rather than in the basin centre. This underline the importance of exposure/karstification in locally increasing Sr levels. Celestite volumes tend to build to ore grade levels in evaporite areas with a volcanic/volcaniclastic or magmatic association, such as the Coahuila and the Burrros-Picachos platform sediments (Dill et al. 2009). Such regions offer the possibility of brine leaching and enhancement Sr levels in hydrothermal-epithermal waters.

Documented sources of strontium-rich waters capable of precipitating celestite include:

1. Marine-derived brines (Frazier 1975; Baker and Bloomer 1988)
2. Waters formed during the conversion of aragonite to calcite (Nickless et al. 1975)
3. Waters formed during the dolomitisation of limestones (Wood and Shaw 1976)
4. Waters formed during the conversion of gypsum to anhydrite (Kushnir 1982; Orti et al. 1998)
5. Waters formed during the dissolution of subaerially exposed gypsum (Taberner et al. 2002)
6. Resurgent basinal waters that have leached Sr from feldspars and clays in arkosic redbeds (Scholle et al. 1990)
7. Red bed successions prograding atop a carbonate evaporite system and carrying a progradational meteoric hydrology that leaches Sr from the redbeds (Taberner et al. 2002) or from volcaniclastics
8. Shallow subunconformity waters with elevated Sr from bacterially-mediated calcitisation of anhydrites (Kendall 2001).

West (op. cit.) notes that sedimentary celestite has, in most cases, formed by direct replacement of gypsum or anhydrite; it tends to remain, even when exposed at the surface as it is much less soluble than either of those minerals. West's papers on celestite occurrences and controls in the Jurassic Purbeck evaporites of the United Kingdom remain as highlights in competent scientific documentation of field relationships and observation-based interpretation of process. He concludes that celestite formed by the selective removal of strontium from groundwater by reacting with dissolving beds and nodules of calcium sulphate.

Groundwaters containing a large proportion of calcium ions and a small proportion of strontium ions most commonly exist where limestones occur in proximity to the site of precipitation, likely facilitated by microbes. Celestite is less common where sandstones are the aquifers adjacent to a gypsum bed. The groundwater may be ascending or descending as it reaches the $CaSO_4$. Celestite beds of appreciable thickness are thus formed in Purbeck strata at the upper and lower boundaries of gypsum or anhydrite beds in contact with these groundwaters. Purbeck celestite replaced both nodular anhydrite and bird-beak gypsum roses (West 1964). Ongoing flushing by bicarbonate-rich groundwaters locally converted celestite to calciostrontianite (Salter and West 1966).

Carlson (1987) documented groundwater-driven replacement of calcium sulphate salts by celestite in Silurian carbonates of northwestern Ohio. Associated textures indicate evaporite dissolution and karstification. Celestites occur along the western margin of the Ohio (Cayugan) basin within the Greenfield Dolomite and undifferentiated Salina dolostones. The celestite replacements are more durable than the original evaporite salts, which have long since vanished from the outcropping carbonate. Replacement styles include: lenticular and prismatic crystals, replaced cauliflower nodules of anhydrite and laminar celestite beds replacing laminated evaporites. Remnants of the replaced material can be preserved as euhedral, deeply embayed outlines or within internally zoned growth bands that entrain inclusions of dolostone and anhydrite. Poikilo-topically enclosed remnants of anhydrite in celestite prisms with lenticular outlines show simultaneous extinction in thin section, possibly indicating that at the time of celestite replacement the gypsum was a single crystal and not a felted anhydrite mat. Alternatively, these lenticular crystals may be after axe-head anhydrite, implying a possibly later origin for at least some of the $CaSO_4$ than argued by Carlson. Other nodular and laminar celestite pseudomorphs display relict chickenwire and enterolithic structures indicating a primary anhydrite parentage.

Early, almost syndepositional, replacement of $CaSO_4$ nodules by celestite occurred in both the vadose and the active phreatic zone of the evaporitic Silurian Steinsfjord Formation of the Oslo Region, Norway (Fig. 7.88; Olaussen 1981). Marl and carbonate host sediments were deposited in supratidal, intertidal, and restricted subtidal environments. Celestite occurs in two distinct textural associations within these peritidal sediments: (1) as aggregates of tiny celestite crystals in nodular dolomicrites of the high intertidal facies, or (2) as anhedral or euhedral prismatic crystals infilling intrapores and interpores in the low intertidal to subtidal facies. Celestite is thought to have precipitated from SO_4 -enriched porewaters via the solution of calcium sulphate. Solution occurred early during evaporitic mudflat progradation as it was flushed by land derived meteoric waters (Fig. 7.88). Released sulphate then reacted with strontium generated by an aragonite to dolomicrite transformation within the high intertidal and an aragonite to calcite transformation in the low intertidal-subtidal.

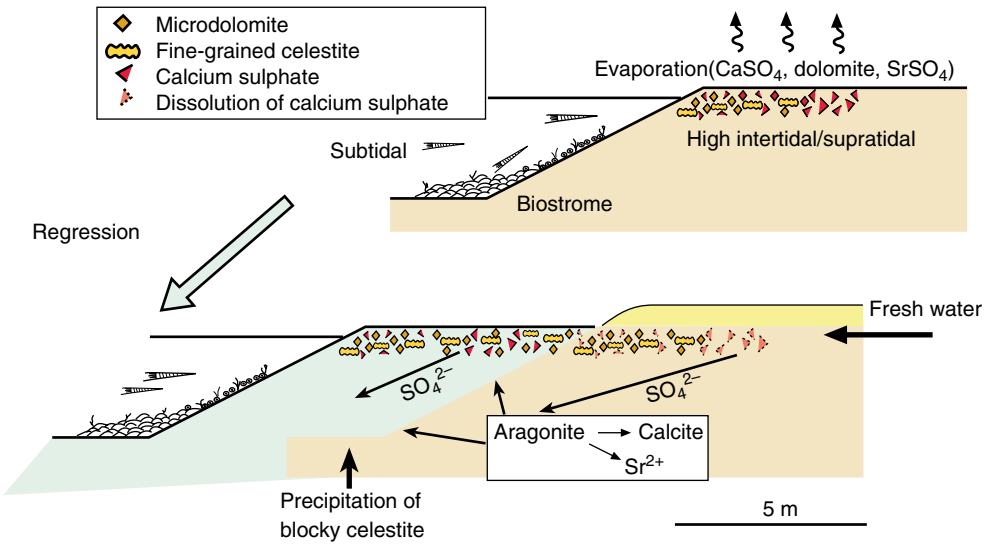

Fig. 7.88 Formation of early celestite replacement in the Brattstad Member of the Steinsfjord Formation, Norway. Strontium is derived from freshwater leaching of anhydrite and aragonite (After Olaussen 1981)

A similar progradational hydrology is documented in fracture-filling cements at La Tossa reef near Igualada, NE Spain, but in this case it was driven by a meteoric hydrology that continued to focus Sr flow well after the time of gypsum accumulation (Taberner et al. 2002). Fissure cements in other Eocene reefs along the same basin margin, such as Calders reef, tend to be dominated by baryte with only minor celestite. All reefs in the basin grew atop delta-lobe sandstones and prodelta marls, which at La Tossa, but not Calders reef, are overlain by Upper Eocene evaporites and hypersaline carbonates (Fig. 7.89a). Stable isotopic analyses of all reef carbonates indicate meteoric recharge was responsible for aragonite stabilization and calcite cementation.

Celestite precipitation at La Tossa began as reef stabilization occurred in early burial. Strontium needed for celestite precipitation was partly derived in situ from dissolution of aragonite corals in the reef and more basinal counterparts. However, $^{87}Sr/^{86}Sr$ data also suggest that Sr at La Tossa was also derived from dissolution of the overlying nearby calcium sulphate evaporites (Fig. 7.89b; Taberner et al. 2002). As the reef became lithified and stabilized, early burial fluid flow was increasingly focused in fractures and the cavities that linked them. The amount of residual strontium released from aragonite dissolution and recrystallization, along with gypsum dissolution, would have built up to supersaturated levels in the remaining interstitial fluids in the fractures.

^{18}O isotopic data suggest that local meteoric waters at La Tossa (a celestite-rich area) were enriched in Sr compared with those responsible for stabilization in other reefs in the area where fracture-filling cements are richer in baryte, with lesser celestite (Fig. 7.89b). At Calders, as in the La Tossa reef, meteoric cementation was completed before sulphate (baryte and minor celestite) cements precipitated in fractures and dissolution cavities. Calders reef is directly overlain by fluviodeltaic facies, related to the progradation of the St Llorenc del Munt fan-delta and so were susceptible to groundwater invasion immediately after deposition (Fig. 7.89a). Baryte may have formed in preference to celestite as a result of more efficient flushing of Sr from Calders reef before sulphate authigenesis.

Relatively low $\delta^{34}S$ and $\delta^{34}S$ enrichment ratios show that celestite at La Tossa reef formed from residual sulphate in pore waters after bacterial sulphate reduction. Taken together they also imply that there was a prior episode of sulphate recycling at La Tossa. Meteoric water reaching the La Tossa reef and nearby basinal areas was most probably charged with SO_4 from the dissolution of nearby younger Upper Eocene marine evaporites. This sulphate-rich groundwater, combined with organic matter present in the sediments, fuelled bacterial sulphate reduction in the meteoric palaeoaquifer. Strontium isotopes show a clear separation between the reef celestites and the subsequent evaporite phase (Fig. 7.89c). A progressive build-up of SO_4 and Sr concentrations occurred, it became relatively more important in time and drove ongoing celestite precipitation as more and more evaporites were dissolved.

In the other reefs (Calders Reef) a similar ongoing post stabilization source for Sr from dissolving gypsum was not present and so the volumes of celestite cement in their fractures are less. Furthermore, meteoric recharge at La Tossa post-dated the 34 Ma (Upper Eocene) time of evaporite deposition. Reef complexes in other parts of the same basin (e.g. Calders Reef) were stabilized by direct contact with waters from the deltaic wedge well before the time of any evaporite formation.

One of the most impressive examples of celestite precipitated in an active phreatic hydrology at a gypsum-limestone boundary is the evaporite-solution breccia-associated celestite mineralization in the Upper Permian successions in the Karstryggen Formation, central East Greenland (Fig. 7.90; Scholle et al. 1990). With an area of 80 km^2 and a potential resource of 25–50 tonnes at a grade of 50–60 % and local

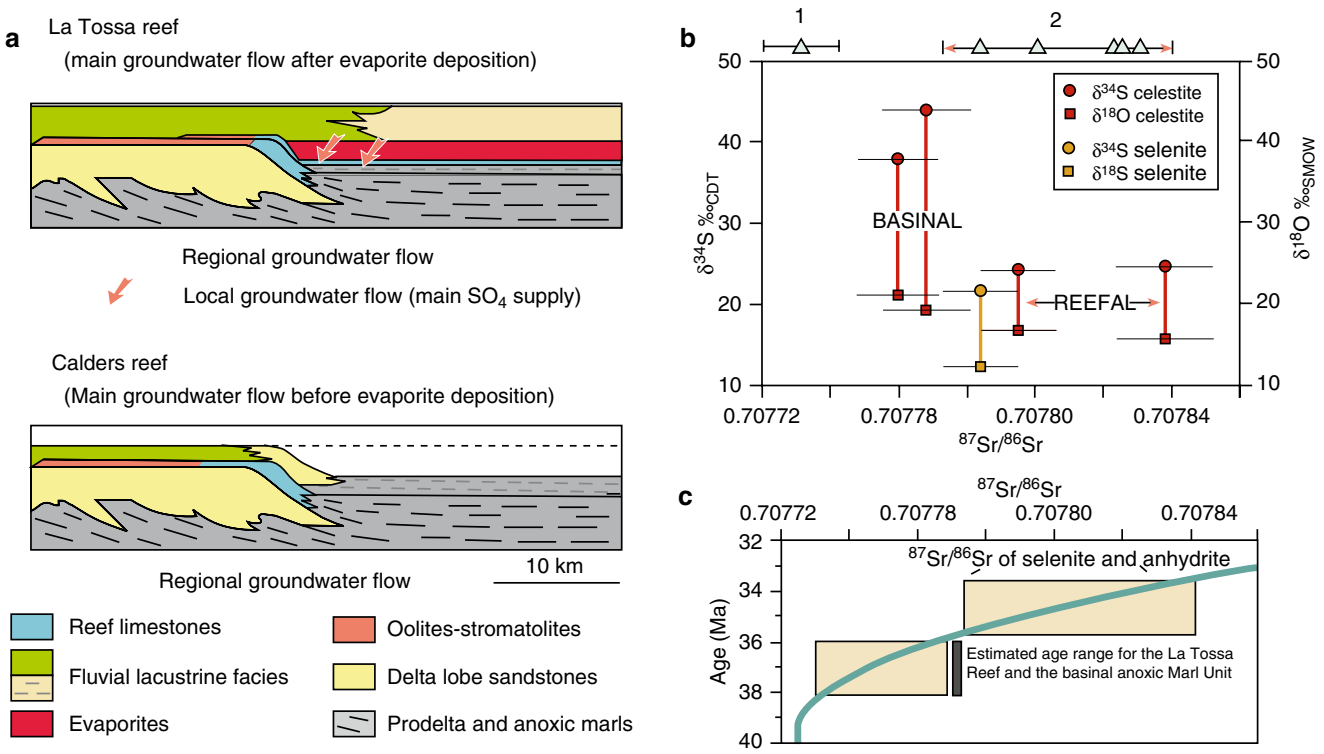

Fig. 7.89 Celestite in the Eocene La Tossa and Calders reefs, Spain (After Taberner et al. 2002). (**a**) Early diagenetic palaeohydrology determined for the basin margin La Tossa reef at Igualada, compared with the interpreted flow system at Calders reef. Arrows indicate the direction of fluid flow. The reef at Calders was flushed by lateral groundwater flow before evaporite deposition, whereas the major meteoric influence at La Tossa, Igualada, occurred after evaporite deposition and featured a local ongoing meteoric flow system that leached SO_4 and Sr from basinal evaporites. (**b**) Combined $\delta^{34}S$ and $^{87}Sr/^{86}Sr$ and δ^{18} O — $^{87}Sr/^{86}$ Sr cross-plot for celestite samples filling cavities in La Tossa reef and basinal sections. Isotopic ratios for the marginal selenitic gypsum are also plotted. The strontium isotopic composition are plotted as open triangles for stage 2 (meteoric-stabilisation) calcite cement from the reef (*1*) and the range of $^{87}Sr/^{86}Sr$ values for the Upper Eocene Lower Anhydrite Unit and selenitic gypsum (*2*). Celestite cements in reef fractures show $\delta^{34}S$, $\delta^{18}O$ and $^{87}Sr/^{86}$ Sr ranges that are closer to those of the Upper Eocene evaporites, whereas those celestites that depart from these values are from the basinal samples and later stage calcite cements in the reef. (**c**) Temporal variation in marine $^{87}Sr/^{86}Sr$ values. Except for near the inflection point, the errors in age estimates are incorporated in the thickness of the line. The measured $^{87}Sr/^{86}$ Sr values from the evaporites give an age of 34 ± 0.9 Ma for their formation. The age of the reef is constrained by the stratigraphic relationships with the evaporites and by comparison with outcropping reefs from the eastern margin of the basin

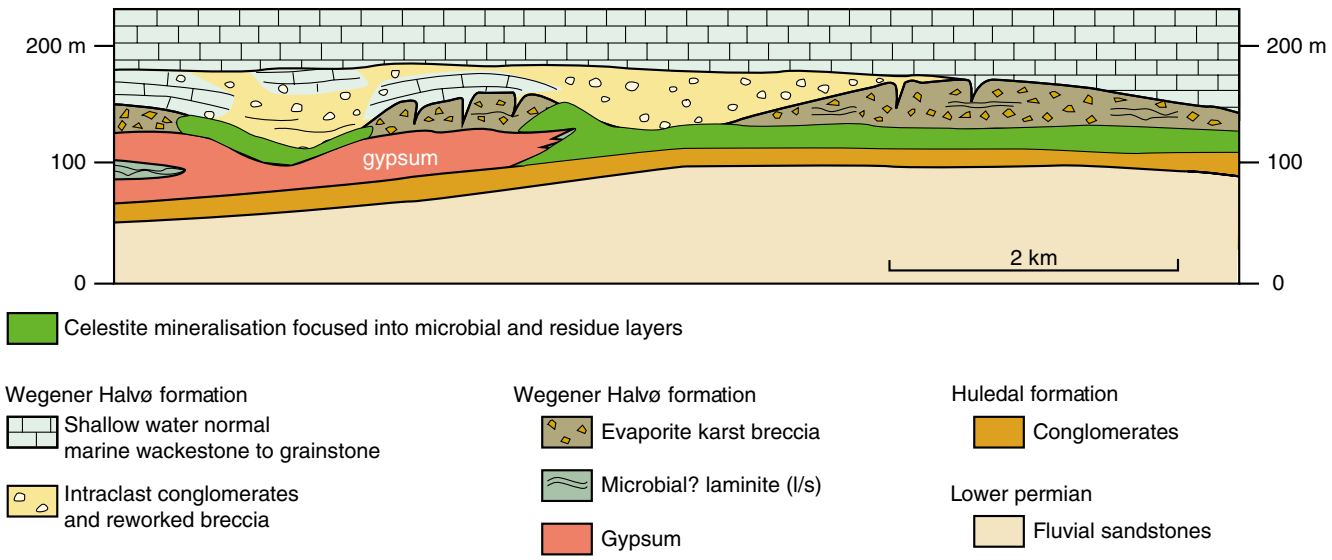

Fig. 7.90 Simplified east-west cross section in the Redval area Greenland showing the close lateral association between the calcium sulphate unit and the celestite mineralisation (After Scholle et al. 1990)

high-grade zones of more than 90 % celestite it constitutes one of the world's largest strontium deposits. It formed during replacement of the margins of a pre-existing gypsum (anhydrite) bed that had precipitated in one of several small structurally-controlled evaporite basins along the edge of a larger marine embayment. Celestite replaces both carbonate and evaporite minerals, as well as forming a passive void infill in pre-existing karst. There is a strong lateral association between the dissolutional edge of the saltern gypsum layer and the zone of celestite replacement. The timing of celestite emplacement at the boundary of the gypsum is not well constrained. The sulphate came from the dissolution of calcium sulphate, while the isotopic values indicate the strontium-rich waters came from the deep meteoric or compactional flushing of underlying red beds.

Not all evaporite-hosted celestite requires flushing of the edge of a sulphate bed by meteoric hydrologies. Celestite precipitating waters can also come from mixing of waters sourced in the burial dewatering of hydrated salts. Paleokarst cavities in the Lower Werra Anhydrite (Zechstein) of northern Poland are usually filled by bluish semitransparent anhydrite and more rarely by celestite, polyhalite, halite, and carbonate (Hryniv and Peryt 2003). In small karst cavities (a few centimetres across), rims of rod-like anhydrite crystals arranged in narrow bundles line the fissures, with the inner part of the cavity filled by a mosaic aggregate of short prismatic crystals of anhydrite and celestite, as well as coarse irregular anhydrite. Celestite crystals and fan-shaped aggregates, as well as spherulites of anhydrite, are rare in the smaller cavities and fissures. In bigger cavities (some ten centimetres across), multiple zones of fibrous anhydrite are arranged in different directions in the middle part of the cavity fill. The innermost parts of the larger karst cavities still remain as hollow in some cases, with the cavity walls encrusted by coarse, well-developed crystals of anhydrite and celestite.

Karst cavities in the Lower Werra Anhydrite developed in the subsurface by dissolution of $CaSO_4$ strata in halite-rich intervals flushed by gypsum dehydration waters. During gypsum dehydration, dissolution of halite increased the sodium chloride content of the solution and thus the solubility of calcium sulphate (Fig. 2.18b). Dissolved calcium sulphate was leached by diffusion and/or downward flow in the interstitial spaces, and the minerals in karst cavities precipitated from the same solutions as solutions became oversaturated. The work of Hryniv and Peryt (2003) shows that karst in sulphate deposits can develop non-telogenetically during ongoing burial and dewatering in a system without uplift and/or near-surface meteoric flushing.

So far, we have considered celestite as tied to direct dissolution of former bedded and nodular calcium sulphates, typically with nodular and enterolithic textures that indicate the evaporite association. But there are also laterally extensive stratiform and layered celestine deposits that are sufficiently rich in strontium to be mineable and hosted in epeiric carbonates. De Brodtkorb et al. (1982, 1997) described such an economic celestite-baryte deposit in Early Cretaceous strata from the extra-Andean region of Neuquen, west central Argentina. The ores are located in the sub-Andean Mesozoic belt and show a conspicuous stratabound character with an aerial extent that closely relates to the presence of regionally extensive platform sulphates. Isotopic $^{87}Sr/^{86}Sr$ data confirm an evaporitic origin for this celestite (Table 7.16). Host sediments were deposited during the transition to an epicontinental marine shelf environment from an earlier saltern. The celestite is always hosted in saline and hypersaline facies, as these beds were the source of the sulphate. Celestite forms as either syngenetic nodular beds with texture similar to those described earlier, or as more epigenetic stratabound ores composed of "in situ" celestite with texture showing stalactite growth and cavity infilling in its carbonate host, possibly as replacements of bedded saltern sulphates. There are also epigenetic vein-type ores. Open fill textures are interpreted as burial phreatic, precipitated by mesogenetic Sr-enriched solutions dripping into gas filled dissolution cavities in a previously karstified (?bathyphreatic) sulphate evaporite and carbonate host. Some have argued these enigmatic stratiform ores are primary seawater-derived precipitates, others see there origin as mesogenetic replacements of bedded calcium sulphate salterns.

Many stratiform celestites, including the Argentinian ores, have crystals encasing inclusions of solid hydrocarbons and textures showing they precipitated in association with saddle dolomite, burial anhydrite and metal sulphides. Hanor (2004) documents the worldwide association of such stratiform sediment-hosted celestite with epeiric carbonate platforms (Table 7.17). He notes their association with bedded platform sulphates and also points out that the largest known sedimentary celestine occurrences, each with several million metric tons of $SrSO_4$, cannot be readily explained as primary precipitates or nearsurface meteoric replacements of nodular sulphate evaporites. The largest deposits, as in South America and Greenland, tend to occur as epigenetic replacements in carbonate and evaporite hosts within epeiric platforms that range in age from Silurian to early Pliocene. There is variable evidence of associated hydrothermal activity in these deposits, and Sr isotopes typically have a more radiogenic signature than the prevailing seawater of the time (Table 7.17). Hanor argues the key to explaining the origin of these massive sediment-hosted celestites lies in determining why celestite is the replacement phase in these deposits and not baryte ($BaSO_4$), which is orders of magnitude less soluble.

Hanor (op. cit.) concludes that stratiform celestite hosted in epicontinental platforms did not form syndepositionally from Sr-enriched brines created by the evaporation of seawater. Sr is removed from concentrating marine brine during

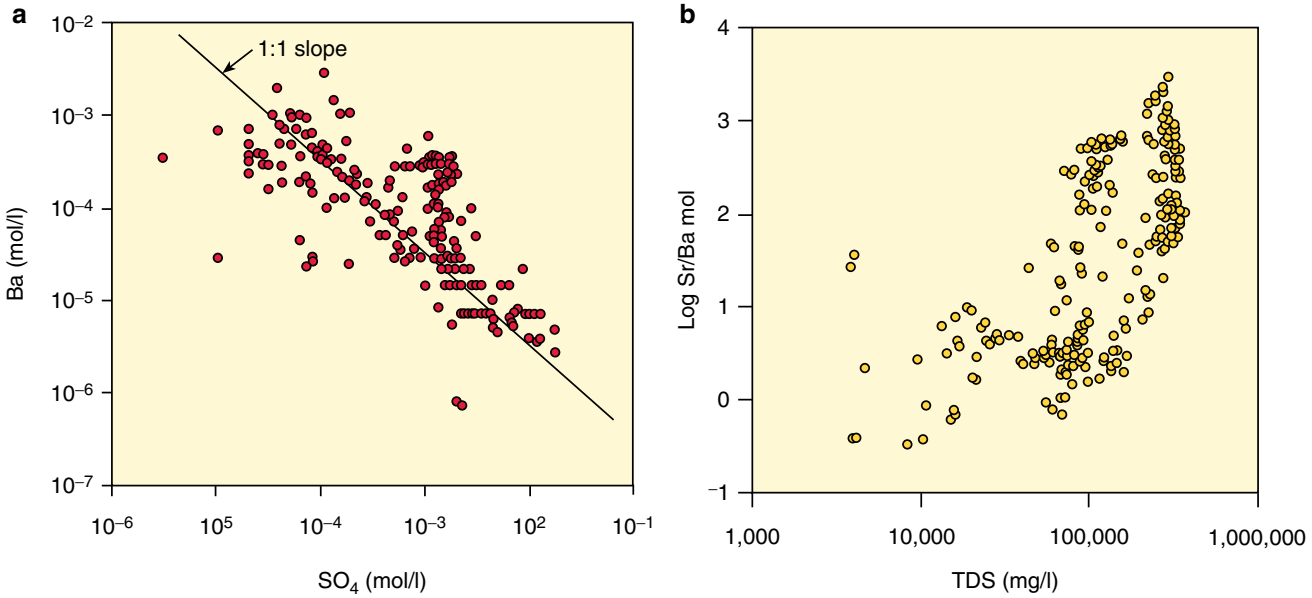

Fig. 7.91 Ba in subsurface basinal brines (After Hanor 2004). (**a**) Variation in dissolved Ba versus dissolved sulphate in basinal brines. (**b**) Variation in Sr/Ba ratio versus the salinity of basinal brines (See Fig. 8.40 for Sr trend)

the halite stage of evaporation as a dispersed sulphate phase and not as precipitated as bedded celestite. The association of large stratiform celestine deposits with marine platform carbonate–evaporite sequences most likely reflects, at least in part, the significant difference in the geochemical behaviour of Sr and Ba during mesogenetic diagenesis.

Concentrations of Sr in subsurface sedimentary fluids are buffered by silicate–carbonate mineral assemblages. Concentration of Sr in solution in modern subsurface waters increases significantly with increasing salinity (Fig. 8.40). The concentration of Ba, in contrast, is controlled by equilibrium with the baryte solid phase and is inversely related to the concentration of dissolved sulphate in subsurface fluids (Fig. 7.91a; Hanor 2004). Basinal fluids having the highest Sr/Ba ratios are also the most saline and have moderately high levels of sulphate (Fig. 7.91b). Thus hypersaline mesogenetic brines flushing through a carbonate platform will be more likely to be saturated with celestine than baryte. The precursors to such waters were produced in hypersaline pans and salterns by the evaporation of seawater. As these brines reflux into underlying or laterally adjacent sediments, they leach substantial amounts of Sr as they attempt to achieve chemical equilibrium with their host sediments. In contrast barium concentrations in subsurface reflux brines are kept relatively low by the presence of dissolved sulphate. Precipitation of widespread mesogenetic celestine occurs where these diagenetically altered reflux fluids come into contact with beds containing calcium sulphate minerals and/or sulphate-rich waters. Thus Hanor argues, the stratiform celestite ores of the world are not recrystallised primary precipitates or derived in meteoric mixing zones. They are the result of deeply circulating (hypogene) hypersaline brines moving through an anhydritic epeiric platform under a hydrological drive that is tied to platform restriction and creation of dense reflux brine. The elevated Sr does not come from the parent connate water, but from rock-fluid (brine) interactions with buried platform carbonates and sulphates. Hydrocarbons are often mobile in the same sediments at the same time.

Not all celestite – calcium sulphate associations are hosted in sediments. An unusual late-stage celestite is intimately associated with hydrothermal $CaSO_4$ (now gypsum) in the Asaka gypsum mine (Koriyama City, Japan). Celestite occurs on the sides of fibrous (satinspar) gypsum crystals and veins in the mine area. The satinspar indicates telogenetic alteration. The celestite is interpreted by Matsubara et al. (1992) as a hydration product of strontian anhydrite (SrO up to 0.94 wt %), which occurs in the same area. The hydration is very late, associated with uplift and meteorically-driven conversion of strontian anhydrite to gypsum, where the $SrSO_4$ molecule remains intact during the conversion and eventually crystallises as celestite. Chapter 16 discusses the worldwide occurrence of hydrothermal anhydrites and their association with high-temperature sulphide mineralisation.

Fluorite as an Indicator?

Fluorite (CaF_2) and baryte ($BaSO_4$) are not uncommon as hydrothermal phases in mineralised sedimentary carbonates especially in MVT (Mississippi Valley Type) settings. Compared to sediment-hosted celestite, the range of mesogenetic associations

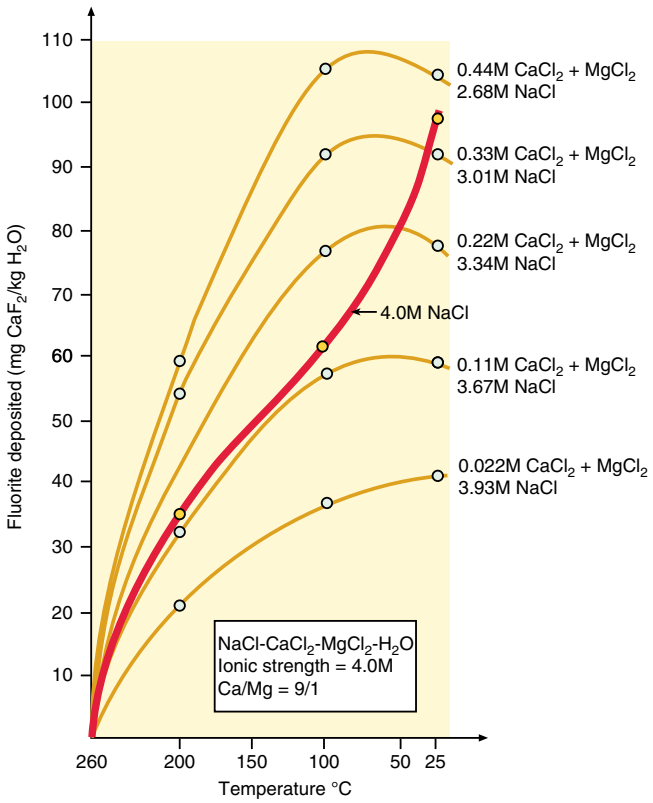

Fig. 7.92 Quantity of fluorite precipitated by cooling of $NaCl \pm CaCl_2 \pm MgCl_2 \pm H_2O$ solutions with Ca/Mg ratio of 9:1 and an ionic strength of 4 M from 260° to 25 °C (After Richardson and Holland 1979)

is more cosmopolitan and their appearance in a carbonate platform host typically reflects the carbonate's high susceptibility to replacement, especially when flushed by somewhat acidic, cooling hydrothermal and basinal fluids.

According to Richardson and Holland (1979), the solubility of fluorite in NaCl solutions increases with increasing temperature at all ionic strengths up to about 100 °C (Fig. 7.92). At NaCl concentrations above 1.0 M, the solubility of fluorite increases continuously above 100 °C, and it increases also with increasing $CaCl_2$ and $MgCl_2$ concentrations in the NaCl-dominant solutions. According to Munoz et al. 1999, this means that most nonmagmatic fluorite-carrying basinal waters in a sedimentary basin are derived in part from interactions with dissolving evaporites. The interaction allows such hydrothermally circulated waters (high salinity and $CaCl_2$ -bearing) to attain the elevated levels of dissolved fluorine required to precipitate significant volumes of fluorite during subsequent brine cooling. Elevated salinities in the subsurface can come from evaporite dissolution or from brine reflux. Much of the nonmagmatic fluorite dissolved in these saline brines is sourced by subsurface flushing of organic-rich black shales.

For example, fluorite is a minor late stage mesogenetic cement in Devonian carbonates in the Keg River Formation, Canada (Aulstead and Spencer 1985). The fluorite was carried to the site of precipitation by rising and cooling basinal brines that had flushed deeply buried bedded evaporites and organic laminites. Similar late-stage fluorite cements in voids and fractures have precipitated from structurally-focused basinal brine flows in the Jurassic reefal carbonates in Zaghouan Province in north-eastern Tunisia, in the Smackover Formation of the Gulf of Mexico, in the Upper Permian Karstryggen Formation of Greenland and in many other buried and faulted carbonate platforms subject to metal sulphide and saddle dolomite emplacement (Souissi et al. 1997). All these fluorites precipitated from highly saline brines sourced in deep halokinetic settings where mesogenetic salt dissolution dominates.

Likewise, the isotopic signatures of authigenic fluorites in a number of European fluorspar deposits show the supplying hydrothermal waters were sourced in, or carried by, brines from dissolving or tectonically juxtaposed evaporites. Examples include vein fluorites (Pb-Zn-F) associated with the Permian Haselgebirge evaporites in the Austrian Alps (Götzinger and Grum 1992), massive fluorites in veins that crosscut Cambro-Ordovician clastics in the southwestern Massif of Albigeois, France (Munoz et al. 1999) and in Toarcian shales atop the main unconformity atop the French Massif Central (Fig. 7.93a; Boiron et al. 2010). The latter is the most important fluorite district in France is thought to have formed during Mesozoic times (150 Ma, Bonhomme et al. 1987) during a third stage of extensional tectonics occurring much after the main rifting of the Atlantic ocean, and before the Gascogne gulf rifting, considered as Aptian-Albian.

Munoz et al. (1999) proposed a model of continental brine circulation (salinity: 20–26 wt% eq. NaCl, Ca–(Mg)–Na brines and T_h between 85 and 170 °C), penetrating deeply into the basement, with the formation of ores along faults where the fluorite deposited as a consequence of temperature drop.

Although, the main ores precipitate from saline waters with $\delta^{18}O$ around 0–3.2‰ and δD in the range of −15 to +63‰, Munoz et al. considered that isotopic features were indicative of meteoric waters that underwent an isotopic shift by interaction with host rocks. This was the main argument in favour of the continental origin of the saline brines the precipitated the fluorite. Boiron et al. (2010) noted that more recent paleogeographic reconstructions and fission track data tend to indicate that the French Massif Central was in great part covered by the sea during Lias and Dogger times making a continental/meteoric brine source less likely and argue for a more likely marine/evaporitic basinal brine source (Fig. 7.93a).

Likewise the largest fluorite and celestite province in the world is derived from hypersaline basinal waters and occurs with the borders of the Cretaceous carbonate-evaporite

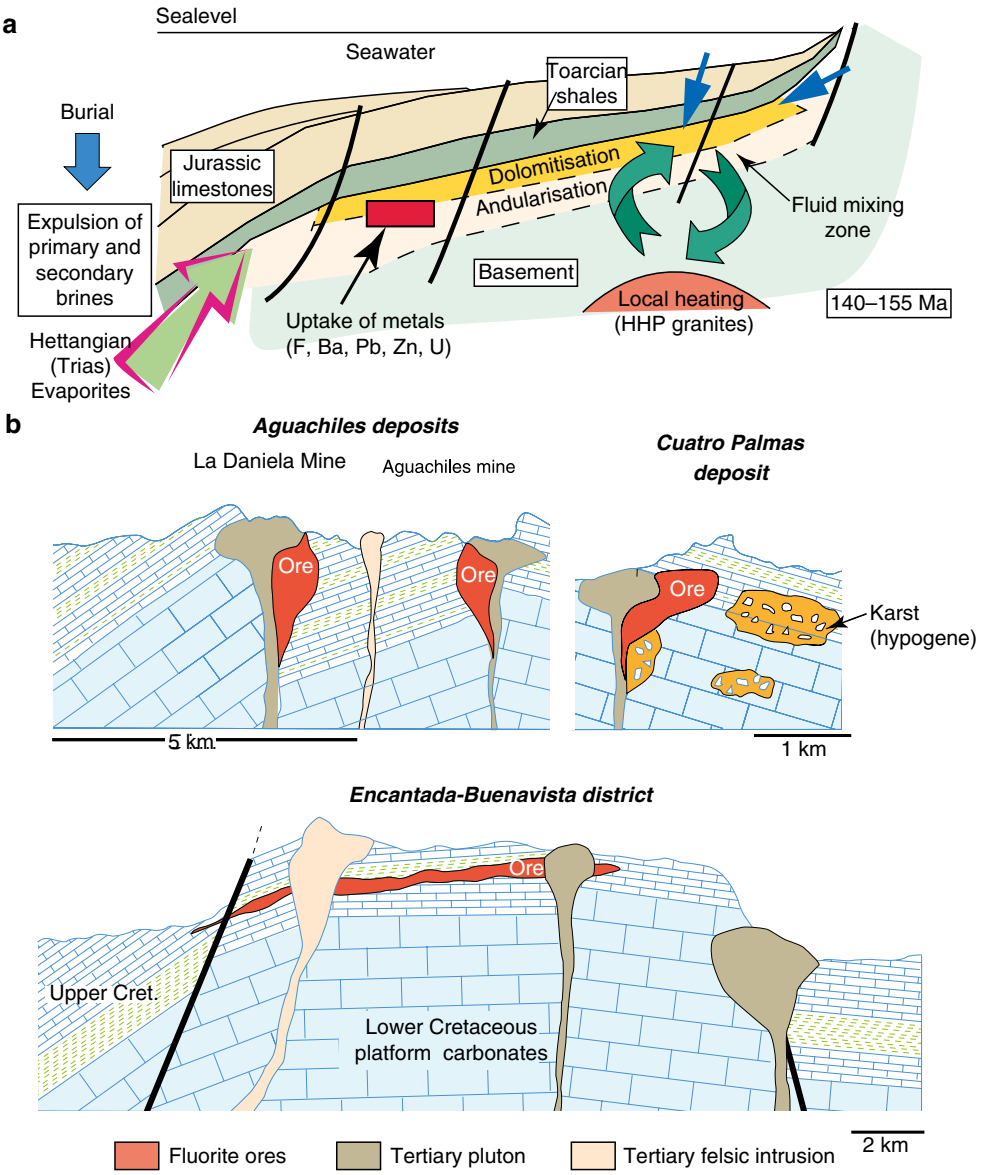

Fig. 7.93 Fluorite at the scale of basinal fluid escape. (**a**) Schematic of fluid circulation in the north-western part of the French Massif Central at the unconformity between the basement and sedimentary cover, showing the upward evaporitic brine migration below the Toarcian shales and associated mixing in fault zones (After Boiron et al. 2010). (**b**) Schematic cross sections of three different types of fluorite mineralization and emplacement; Aguachiles = unconformable fluorite lenses; Cuatro Palmas = Cave-filling fluorite; Encantada-Buenavista = fluorite mantos (After González-Partida et al. 2003)

platforms of Mexico (González-Partida et al. 2003). The various deposits define the border of the Morelos platform (La Azul deposit), the border of San Luis Valles platform (El Refugio deposit, El Realito deposit and Las Cuevas deposit), the border of Tamaulipas platform (numerous prospects, minor celestite and baryte deposits), along with that Zaragoza deposit, El Tule deposit, Sto. Domingo deposit, El Triangulo deposit, Aguachiles deposit, Cuatro Palmas deposit, Boquillas deposit, Pico Etereo deposit, and La Encantada–Buenavista deposit (Fig. 7.93b). Brines related to the various fluorite orebodies had a genetic relationship to the hypersaline basinal brines moving up dip from the Jurassic petroleum basins located west of the fluorite bodies. These brines have strong similarities to reported fluids from Mississippi Valley type deposits and the fluorite province is less than 80 km from the San Vicente MVT Pb-Zn district (Chap. 15). The fluorine-rich fluids were created in part by mesogenetic evaporite dissolution and migrated toward the platform margins during the mid-Tertiary (30–32 Ma) collision event along extensional faulted zones created during basin-and-range style tectonism. Mixing of two different salinity brines was responsible for precipitation and mineralization. Heat from magmas, related to the tectonic extension, caused decrepitation and changes in the shape of fluid inclusions near the fluorite contact zones but were not necessarily integral to the ore precipitation (González-Partida et al. 2003).

There is also a halokinetic/hydrocarbon/thrust fluid link to crosscutting fluorite veins in Jurassic carbonates of the Koh-i-Maran, Baluchistan in the North Kirthar Range, Pakistan (Guilhaumou et al. 2000) and the halokinetic Triassic evaporites of Tunisia (Dill et al. 2014). Clearly, the dissolution of deeply buried halite (both bedded and diapiric)

can supply the saline chloride brine needed to act as a fluoride and metal carrier in nonmagmatic sedimentary systems (see Chap. 15 and Warren 2000b).

As well as these broad-scale metallogenic basin-margin associations, fluorite also forms a widespread, but volumetrically minor, early diagenetic and even syndepositional authigenic mineral phase in some evaporitic matrices, where its precipitation may even be related to solar concentration of a surface brine. For example, fluorite has precipitated as ooids and pellets in a 40 cm thick tuff bed in the Gila Conglomerate of New Mexico (Sheppard and Mumpton 1984). It also forms microscopic near-spherical grains in lacustrine tuffaceous zeolitised Pliocene mudstones in Oregon. There overall fluorite content is around 5 % but is <16 % in the zeolitic tuff and is attributed to diagenesis of sediments in an alkaline lake independent of hydrothermal activity (Sheppard and Gude 1968). Fluorite also occurs as sparse isotropic euhedral cubes (50–200 μm diameter) within primary gypsum nodules at depths of 235–240 m below the present land surface in Eocene carbonate mudstones of Florida. Celestite also occurs in the same sediment. Cook et al. (1985) argued that the Florida fluorite was syndepositional with the precipitation of gypsum in the capillary zone of an Eocene sabkha mudflat. If so, it was ultimately derived by the evaporative concentration of normal seawater. Additional fluoride in the parent pore waters may have been derived by fluvial transport of salts weathered from Appalachian volcanics.

Cook et al.'s conclusion is perhaps supported by the work of Kazakov and Sokolova (1950) who documented sedimentary fluorite in various marine carbonates/evaporites in Russia in hosts that range in age from Cambrian to Cretaceous. In related laboratory experiments they observed that fluorite can precipitate from seawater brines concentrated three to four times by volume, especially if an additional (fluvial of volcanogenic) source of dissolved fluoride was available in the depositional setting.

In a similar fashion, Sheppard and Mumpton (1984) explain the primary precipitation of early diagenetic fluorite using the analogy of high fluoride alkaline lakes in the East African Rift, such as Lake Magadi, Lake Natron and Lake Manyara (Table 4.4). Subsequent to Surdam and Eugster's (1976) documentation of fluorite as a common authigenic phase in Pleistocene sediments of the Magadi Basin, Icole et al. (1990) documented stromatolitic layers that are mainly composed of fluorite rather than calcium carbonate in lower Pleistocene lacustrine beds along the western edge of Lake Natron, Tanzania. Without doubt these are early rather than later burial diagenetic precipitates. Moreover, Pleistocene fluorite is replaced by dolomite in the uppermost parts of some of the stromatolite layers, but this replacement still preserves the original sedimentary texture. Fluorite is also reported in sediments of Lake Bogoria, Kenya, in an interval that also contains sodium silicate gels (magadiite; Renaut et al. 2002). There is even a palaeobiological response to the high levels of fluorine in saline lake waters in the rift valley. Many fossil fish, preserved in the Plio-Pleistocene phosphoritic lacustrine sediments of Lake Manyara, are hyperostitic (enlarged and fused bone structures), a biological response to elevated fluorine levels in the lake waters (Schlüter and Kohring 2002).

The elevated fluoride concentrations in saline waters of the East African rift are linked to a number of sources and processes. Regionally these high values are in large part related to the development of saline (concentrated) groundwaters that have earlier flushed and leached hyper-alkaline volcanic rocks of the rift zone, including nepheline and carbonatite magmas and associated ash deposits (Chap. 16). These igneous sources can accumulate large concentrations of fluoride from melts and their epithermal volatile fractions. Hence, saline water sumps in the rift zone can accumulate fluoride directly as a result of weathering of these rocks, as well as further concentrating contributions from high-fluoride geothermal/hydrothermal solutions. The fine-grained and friable ashes surrounding most of the saline lakes are likely to be particularly reactive. Weathering of the silicate minerals in the lavas and ashes by silicate hydrolysis reactions produces Na-HCO_3 -rich groundwaters, which are relatively depleted in Ca and Mg. Hence, high concentrations of fluoride can occur as the solubility of fluorite (CaF_2) is not a limiting factor in the saline lakes (Edmunds and Smedley 2013; Ayenew 2008). Jones et al. (1977) reported extremely high fluoride concentrations (up to 2,170 mg/l) in saline groundwaters from boreholes in Magadi lake sediments.

Crocker (1979) proposed that granular blockspar (fluorite) ore in the Proterozoic Transvaal Supergroup of South Africa indicates primary synsedimentary endogenic fluorite mineralisation and is a time-specific precipitative stage tied to Precambrian dolomite evaporite facies. Rouchy et al. (1987) documented an association between fluorite, native sulphur and Visean (Carboniferous) evaporites. In an earlier paper, Amieux (1980) showed fluorite was a characteristic diagenetic stage in the black shale to evaporite transitional facies within the Ludian (Lower Oligocene) sediments of the Mormoiron Basin, Vaucluse, southeastern France. There the major fluorite precipitation phase postdates major dolomitisation and gypsification but precedes celestite and silicification. Likewise strontianite, celestite and fluorite formed lenses during the Middle Muschelkalk and layers in the Central European basin, when it was sealed off and subject to extensive evaporation (Dill et al. 2009). There, fluorine is considered an indicator for an intermediate levels of evaporation and is intimately bound to the dolomite–sulphate facies.

But, fluorite is not solely sourced or carried in evaporite brines, nor deposited only in a saline sedimentary host. That

is just the focus of fluorite discussion in this chapter. Fluorite can be found in fissure veins and stockworks in granitic rocks, greisens, pegmatitic carbonatites, metamorphics, and igneous rocks that include volcanic sublimates (Hodge 1986). These are not necessarily tied to an evaporite source nor an interaction with an evaporite-derived brine. Nor are some of the vein and stratified (manto) fluorite deposits that are associated worldwide with areas of rifting and faulting, where fluoride-rich hydrothermal fluids may migrate up from the lower crust or mantle to replace carbonate hosts (Van Alstine 1976).

Baryte as an Indicator?

Baryte is typically a diagenetic or secondary phase (replacement or pore fill cement) formed by the mixing of fluids; one containing barium (Ba^{2+}) and another containing sulphate (SO_4^{2-}), such that supersaturation is achieved upon mixing. Thus baryte in the sedimentary realm occurs in a wide variety of settings ranging from lakes and soils to cold seeps and vents on the deep open ocean floor to restricted epicontinental seaways (Johnson et al. 2009; Griffith and Paytan 2012). Baryte, like fluorite, is also a widespread hydrothermal precipitate or replacement. Increasingly, microbes are seen as playing a significant role in the precipitation of near-surface baryte, often with gypsum and dolomite as a co-precipitates (García-del-Cura et al. 2014; Sanz-Montero et al. 2009; Bonny and Jones 2008).

Because its geochemistry is similar to the major rock-forming cation, K+, the primary source for sedimentary baryte is via leaching of K-minerals, such as K-feldspars and K-micas. Baryte's occurrence is not specific to evaporitic sequences, but it is a commonplace replacement/cement in evaporitic hosts. This is especially true in those parts of a basin where evaporite-focused fluid flow brings together hot Ba-rich basinal brines (Cl-rich waters flushing and leaching arkoses (alkali feldspars and micas), redbeds, volcanics and volcaniclastics) and sulphate-rich waters from dissolving sulphate evaporites (anhydrite beds and nodules, halokinetic basal anhydrites, allochthon décollements, dissolution residues and diapir caprocks).

Economically, baryte's occurrence is mostly as gangue in various hydrothermal beds and veins entraining metalliferous ores, especially in halokinetic settings (Chap. 15). Baryte also forms stratiform layers, veins, nodules and cavity fills in sulphate-rich sediments, especially in the early Archaean, and is also a commonplace precipitate in black smokers and volcanic-hosted massive sulphide (VHMS) deposits (Chap. 16). In such cases, much of the sulphate is nonevaporitic, it comes to the precipitation site either as sulphide in solution which is oxidised to sulphate at the site of deposition or as sulphate ions carried by hydrothermally circulated seawater (Shikazono et al. 2012). Baryte is also a widespread modern precipitate in deepwater cold seeps, mud volcanoes, springs and brine lakes on the supra-allochthon floor of the Gulf of Mexico (Fu et al. 1994) and their Neogene caprock counterparts (Saunders and Thomas 1996). In the following section we focus on baryte with an obvious evaporite association.

Baryte can directly replace sedimentary gypsum or anhydrite throughout a rock layers diagenetic history. At 25 °C and 1 bar, the value of the equilibrium constant, K, for the replacement reaction:

$$CaSO_4 + Ba^{2+} \Leftrightarrow BaSO_4 + Ca^{2+}$$

as calculated from Gibb's Free Energy values, and assuming pure solids is:

$$K = 10^{5.5} = a_{Ca^{2+}} / a_{Ba^{2+}}$$

Thus, it is thermodynamically feasible for baryte to replace calcium sulphate at earth surface temperatures whenever the activity ratio of ($a_{Ca^{2+}}/a_{Ba^{2+}}$) is less than $10^{5.5}$, a condition met in many subsurface waters (Mossman and Brown 1986). At more elevated temperatures the limiting activity ratio is even less due to the retrograde solubility of anhydrite.

Loosely arranged platy crystals of baryte form pseudomorphs after lenticular gypsum in Quaternary arid soils from central Australia (Sullivan and Koppi 1993). In older sedimentary deposits, evaporitic baryte typically replaces nodular forms with irregular and coalesced outlines reminiscent of anhydrite or gypsum, or forms stratiform layers. In several such cases, isotopic analysis indicates the sulphate in the nodules and layers was remobilised from a calcium sulphate precursor such as; caprock sulphate (von Gehlen et al. 1962), sedimentary gypsum (Kesler et al. 1988; Parafiniuk 1989), or anhydrite-rich evaporites (Mossman and Brown 1986; Frimmel and Papesch 1990).

Stratiform baryte is often found as a late stage precipitate in association with pervasive ferroan carbonate haloes in the alteration zones around growth faults and salt welds in halokinetic provinces. These haloes tend to define zones where escaping Ba-rich hypersaline basinal waters are flowing out of the basin via halokinetically-focused fault conduits, often feeding stromatolitic baryte seeps on the seafloor (Warren 1999, 2000b). In ancient counterparts where the seepage conduits can outcrop (as in the Neoproterozoic sediments in the Adelaide fold belt) it is clear that the ascending iron- and barium-rich fluids interacted with sulphate present in anhydrite or gypsum nodules/beds, other times with sulphate beds or dissolution residues or with seawater sulphate. Modern examples of salt focused brine outflow in halokinetic provinces tend to occur in relatively deepwater muddy hosts. This is where the most active salt allochthon flow occurs, as on the continental slope and rise of the Gulf of Mexico or the tectonic high of the Mediterranean ridges (Castellini et al.

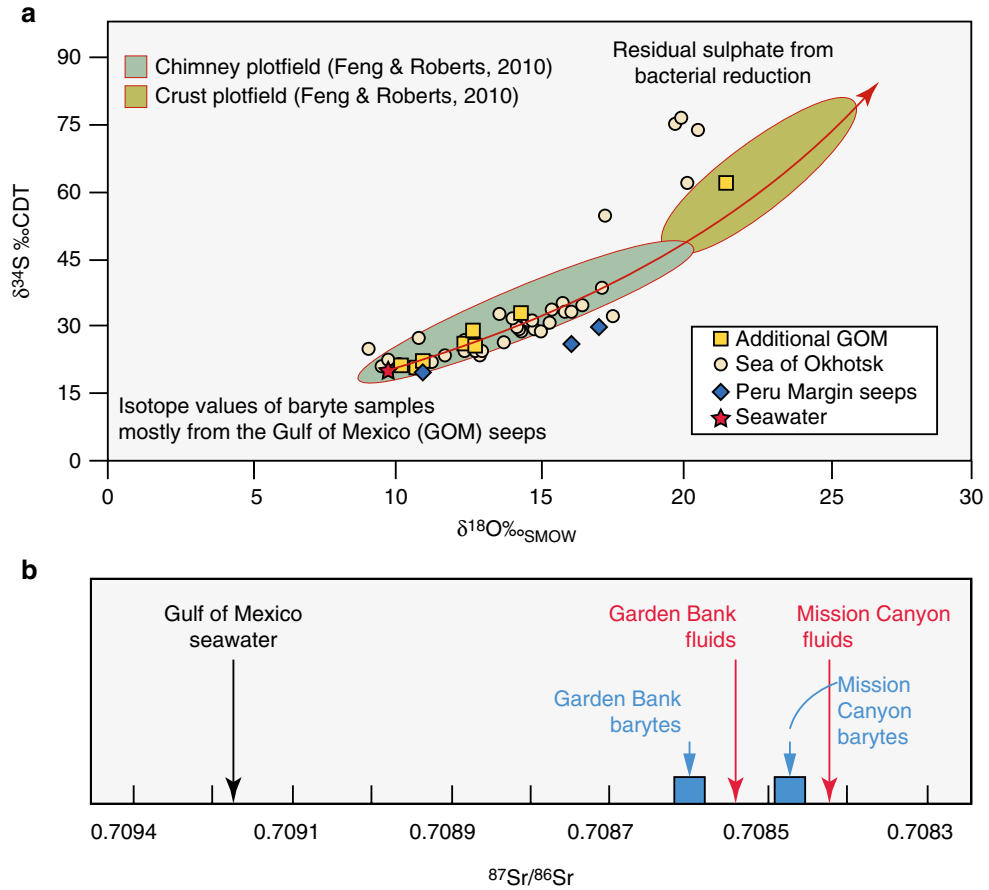

Fig. 7.94 Gulf of Mexico, cold seep baryte chemistry. (**a**) Plot-fields from sulphur and oxygen isotopic compositions of baryte samples from hydrocarbon seeps of the Gulf of Mexico (*green ellipses*, after Feng and Roberts 2010). Aquilina et al. (1997) interpreted their data (*blue diamond*) from the non-salt-allochthon Peruvian seep margin as having equilibrated at temperatures higher than 100 °C. Cooler temperatures are suggested from more recent investigations at hydrocarbon seeps in the Gulf of Mexico (*orange squares*, Fu, 1998 and *green plotfields*, Feng and Roberts 2014) and Derugin Basin, Sea of Okhotsk (*brown circles*; Greinert et al. (2004)). The data from the Gulf of Mexico baryte data show two trending covariant lines with slopes between 2.5 (chimneys) and 4.0 (crusts), The elevated sulphate values can be assumed to be residual sulphate which was isotopically changed during microbial sulphate reduction. (**b**) $^{87}Sr/^{86}Sr$ values for Gulf of Mexico seawater, seep fluids, and barytes (After Feng and Roberts 2010)

2006). Because brine lakes are commonplace in such settings, it can precipitates baryte layers in association with organic- and pyrite-rich laminites under the influence of sulphate reducing bacteria (Chap. 9).

The volume of cold-seep baryte in halokinetic salt basins in particular, and beneath continental margins in general, was under appreciated prior to the increase in deep seafloor surveying over the last few decades. Much of this new information in terms of the 3-dimensional aspects of seep position came from seismic data cubes collected as petroleum exploration moved into the increasingly deeper water offshore drilling realm. The northern Gulf of Mexico continental slope is now known for an extensive number of salt-edge focused hydrocarbon seeps, along with co-associated authigenic carbonate and baryte seeps. Baryte occurrences and volumes in the Gulf of Mexico region are now known to be more substantial than once thought (Feng and Roberts 2010). Seafloor observations and samples acquired at numerous sites atop various autochthonous and allochthonous salt sheets in the Gulf of Mexico indicate that baryte occurs on the seafloor as widespread chimneys, cones, crusts, irregular mound-like buildups up to meters high and as a material disseminated in seafloor sediment hosts (Fig. 9.58). Many of these features are focused atop faults and Jurassic salt edges.

Barytes exposed at the GOM seafloor usually have a porous fabric and are typically covered by dark-brown manganese rich coatings. Samples of baryte may also contain minor amounts of magnesium-calcite, pyrite, and detrital silicates. On a $\delta^{34}S_{Baryte}$ versus $\delta^{18}O_{Baryte}$ diagram, samples show linear or concave-upward trends that project down toward the isotopic composition of seawater sulphate (red arrow in Fig. 7.94a). Covariant isotope trend suggests that baryte is formed from seawater sulphate that has been isotopically modified to varying degrees by microbial sulphate reduction processes. Variations in sulphur and oxygen isotopes occur within individual study sites but there are

common trends across multiple sites(Feng and Roberts 2010). The variations primarily reflect local controls on the flux of barium rich seep fluids, e.g., rate changes in bacterial sulphate reduction and different possible electron donors in a closed or semi-closed pore-fluid system.

Historically, the origin of the fluid precipitating cold seep baryte has been the subject of some debate. Some argue for a local seawater source, others for a more distal subsurface fluid origin. Strontium isotope data in the Gulf of Mexico suggest a brine source that is likely deeper, rather than derivation from ambient or shallowly circulating seawater (Fig. 7.94b; Feng and Roberts 2010). Clearly, less ^{87}Sr is seen the GOM pore fluids than in contemporaneous GOM seawater, suggesting these saline pore fluids have been modified by inputs from less radiogenic sources, such as more deeply buried marine sediments or oceanic crust. A deep-seated source for the barium is further indicated by the $^{87}Sr/^{86}Sr$ ratios of barytes precipitating from the escaping pore fluids. It seems Sr isotopes vary over a narrow range regardless of location within the Gulf of Mexico. The $^{87}Sr/^{86}Sr$ ratios of seafloor barytes collected from the Garden Banks and Mission Canyon areas are consistently slightly lower than their respective ambient saline pore fluids (Fig. 7.94b). Based on this slight, but consistent, difference across both areas, Feng and Roberts (2010) concluded that the Sr in GOM baryte seeps mainly originated from hypersaline fluids that had flushed and leached more deeply buried sediments, with a small portion of Sr coming from ambient seawater ($^{87}Sr/^{86}Sr = 0.70917$).

Baryte in cores from the Walton-Magnet Cove baryte mine region, Nova Scotia, show a wide variety of massive stratiform to nodular textures frequently intermixed with siderite. Siderite forms a prebaryte, presulphide envelope to the deposit (Fig. 7.95a; Savard et al. 1998). Isolated light coloured baryte nodules, typically hosted in a Carboniferous matrix of ferroan dolomite, show complete gradations from chickenwire to enterolithic and are interpreted as a direct replacement of precursor nodular anhydrite hosted in intertidal and supratidal platform carbonates (Mossman and Brown 1986). The mine itself exploited a lenticular to stratiform mass of baryte, not nodules, and preserved liquid hydrocarbons in the ore zone (Fig. 7.95a; Boyle 1962). Unfortunately the Magnet Cove Baryte Mine ceased operations some 40 years ago and the mine pit and shaft workings are now flooded. Boyle described the structure of the deposit as "exceedingly complex." The region is marked by two major sets of faults oriented east-west and northwest-southeast. At the now abandoned Walton deposit the dominant feature is an east-west fault zone in the footwall of the baryte mass that joins a northwest fault that lies close to the hanging wall of the baryte mass.

Much of the baryte ore in the Magnet Cove deposit is associated with the Pembroke Formation (Fig. 7.95a). Regionally the Pembroke Formation is a complex multi-origin breccia intimately associated with halokinesis and base metal mineralisation and regionally it is tied to former salt and thrust welds (Waldron et al. 2010; Lavoie et al. 1998). Faults in the Magnet[19] Cove Mine are pre-ore and constitute brecciated intervals over several metres wide. Post-ore movement also brecciated the baryte and metal sulphides. The age of the faulting is probably post-Triassic. The ore-hosting sequence is the outcropping remnant of a halokinetic and allochthonous evaporite zone at the top of the Horton Group and it lies along the regional salt weld of the Ainslie Detachment. The likelihood of halokinetically focused extensional faults carrying Ba-rich basinal fluids into sulphate-rich horizons was not considered in the published literature on the Magnet Cove mine. But all the work on the mine geology, and its mineralogy, was published before notions of salt allochthons, rauhwacke and burial anhydrite existed.

Halokinetic fault-focused salt welds define the position of the massive baryte deposit in the Neoproterozoic Oraparinna diapir and other baryte occurrences associated with halokinetic structures in the Flinders Ranges of South Australia (pers.obs.). The similarities between Magnet Cove and Oraparinna in both structural style and position atop a halokinetic breccia are obvious (Fig. 7.95b). Unlike Magnet Cove, the baryte occurrence in the Oraparinna diapir was recognised as a halokinetic association (Dalgarno and Johnson 1968). The ore at Oraparinna occurs in 1–2 m wide extensional fracture fills. Like Magnet Cove, the detailed evolution of the Oraparinna diapir is yet to be fully documented in the light of modern ideas of salt allochthons and salt-cored thrusts. Suprasalt minibasins can be seen to separate the various diapir outcrops throughout the Flinders Ranges and clearly illustrate the evolution of an active extensional diapiric province into a subsequent compressional regime. As in Magnet Cove, a geological map of the structure shows a distribution of facies that reflect the strong influence of diapiric and subsequent thrust breccia (rauhwacke) on the adjacent facies and faults (Fig. 7.95b). Salt flow and passive diapirism controlled both the position of a collapse graben atop the Oraparinna diapir during its "falling diapir" stage and focused the subsequent compression of the same succession. What is yet to be studied in the Oraparinna Baryte Mine is the timing of baryte emplacement relative to salt dissolution and faulting in this succession.

[19] In 1955 Magnet Cove Barium Corporation, a subsidiary of Dresser Industries Inc., Dallas, Texas, purchased the property from Canadian Industrial Minerals Limited. Diamond drilling in 1956–57 discovered a lead-zinc-copper-silver ore body below the baryte deposit and sulphide production began in 1961. In 1967 Magnet Cove Barium Corporation became Dresser Minerals, which operated the mine until it closed in 1978. The Walton Mine produced baryte for 38 years. Most of the baryte was shipped to United States and Caribbean destinations where it was used as a weighting agent in drilling fluids with smaller amounts shipped to the Middle East for the same purpose.

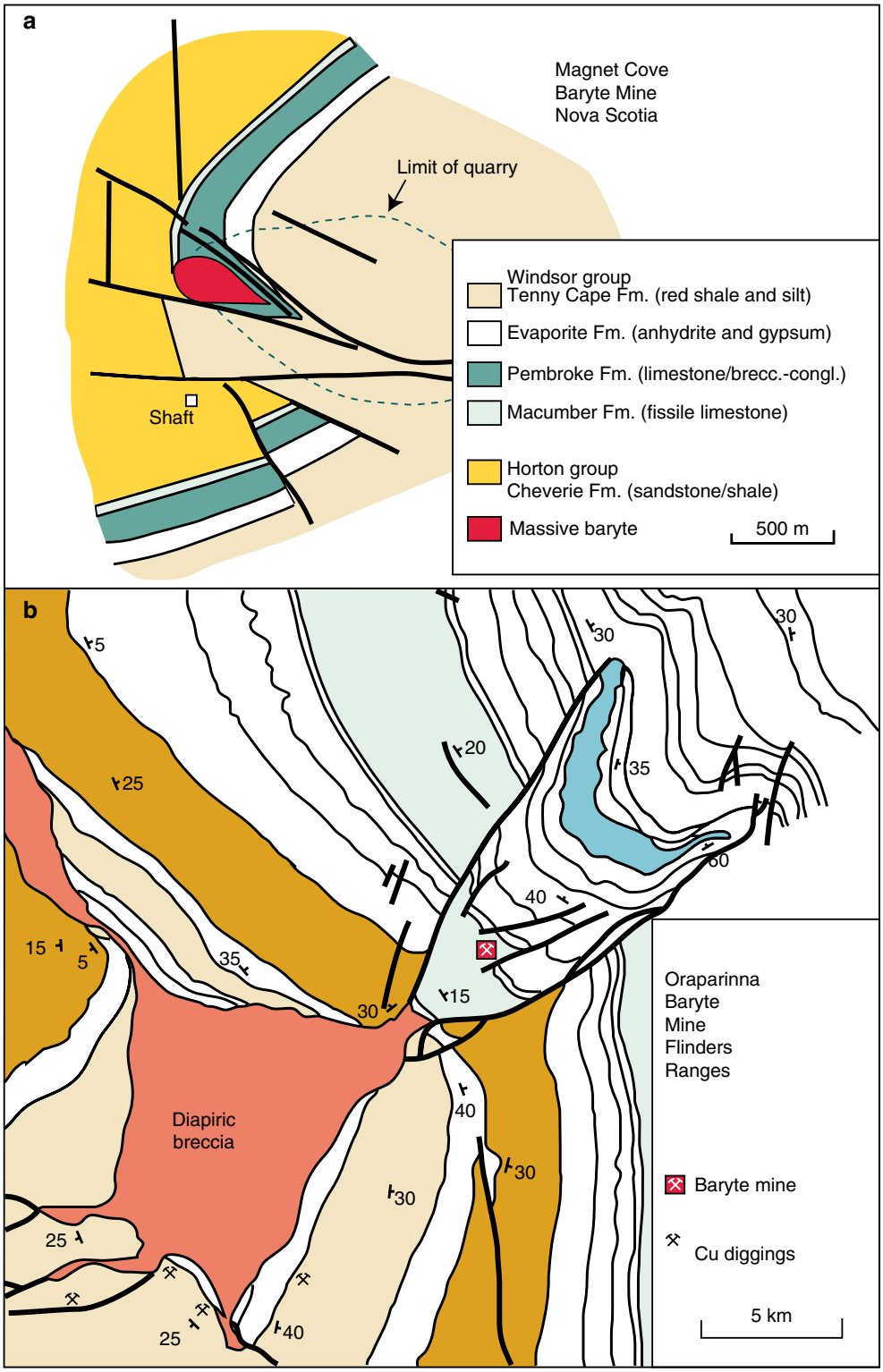

Fig. 7.95 Massive and vein-fill baryte deposited via halokinetic focusing. (**a**) Geology of the Carboniferous halokinetic section in the vicinity of the Walton-Magnet Cove Baryte Mine (aka Walton Mine), Nova Scotia (After Boyle 1962). A baryte mine and lead-zinc-silver-copper deposit. During its operation it was Canada's largest baryte mine and one of the largest baryte deposits in the world. See Fig. 15.46a for location. (**b**) Oraparinna Baryte Mine located in the compressed zone of an original falling diapir (Neoproterozoic Oraparinna Diapir) Flinders Ranges, South Australia (Redrafted from regional geological map of Dalgarno and Johnson 1966; see Fig. 7.31 for regional setting of the Oraparinna Diapir)

A well-documented younger analogue for baryte emplacement about salt structures is the fracture fill atop the Machar diapir in the North Sea (Fig. 10.56). Many individual fractures host multiple generations of carbonate, baryte and fluorite growth (Doran et al. 2004). Fluid-inclusions in the fracture-fills show maximum salinities (22 wt% NaCl eq.), suggesting that fluids had dissolved salt from the diapir during their ascent. Maximum fluid-inclusion temperatures (150 °C) from wells spanning the crest and flank of the Machar structure, are much hotter than expected for present

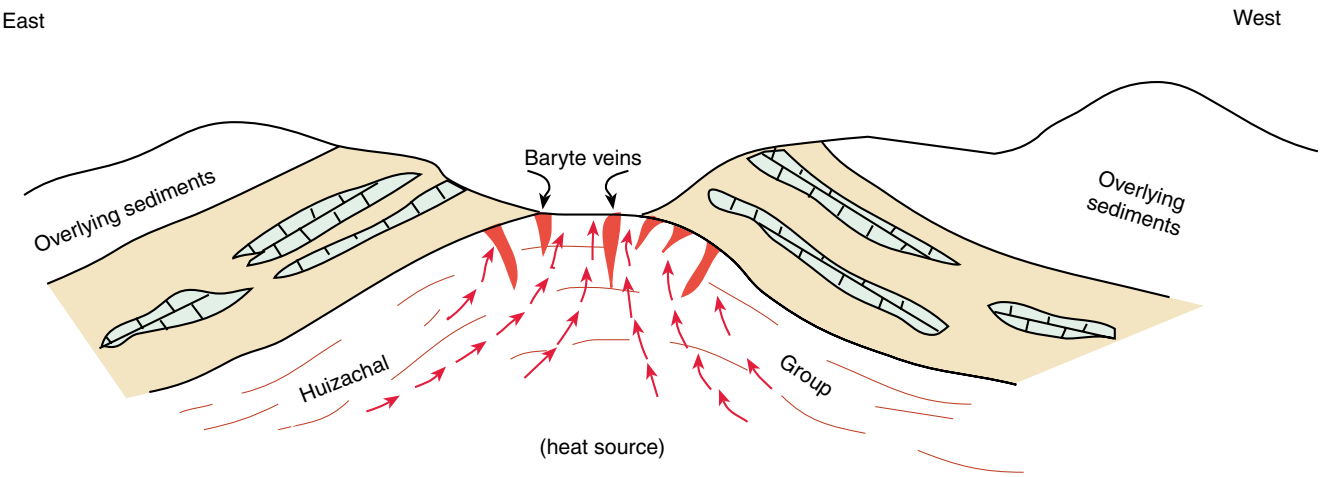

Fig. 7.96 Highly schematic E-W cross section through the Galeana district showing localisation of baryte veins at the contact with the Huizachal red beds, directly beneath the Olvido gypsum (*brown*). Baryte formed as ascending Ba-rich waters ponded beneath the gypsiferous residues (caprocks to allochthonous salt) of the Olvido Fm. (Modified from Kesler et al. 1988)

depths of 1,900–2,800 m. Carbon isotope signatures of the fracture-filling calcites range from +2 to +7 $^{13}C_{PDB}$ ‰ and exceed those of tightly constrained chalk matrix 0 to +3 $^{13}C_{PDB}$ ‰. Thus at least some of the carbon was derived externally to the chalk. Oxygen isotopes from fracture filling calcites (16–25 $^{18}O_{smow}$ ‰) are depleted relative to chalk matrix values (24 to 29 $^{18}O_{smow}$ ‰). The combined data sets indicate that fracture-filling material could not have formed from local chalk matrix pore-fluids. The likely explanation is pulsed expulsion of hot saline and hydrocarbon-bearing fluids from geopressured sandstones in the adjacent rim syncline that are then cemented on cooling into fractures at shallow depths.

A similar set of hypogene chloride-rich waters flowing along faults probably controlled the formation of mined willemite (Zn-oxide ore) in Cambrian ooid grainstones and archeocyathid mounds in the vicinity of the Beltana diapir in the Flinders Ranges, situated some 80 km northwest of the Oraparinna diapir (Groves et al. 2003). There the ore was first emplaced during a series of Cambro-Ordovician compressional events that reactivated salt diapirs and salt flows, which were first emplaced during Neoproterozoic extension and loading.

Yet another halokinetically focused baryte association is documented in the Galeana Baryte District of Mexico. Gypsum residues of the evaporitic Olvido[20] Formation (Upper Jurassic) form an anticlinal trap, seal and sulphate source to barium carried by basinal waters which had flushed the underlying redbeds of the Huizachal Group. Baryte occurs mostly as monomineralic veins and lenses in a limestone matrix along this contact (Fig. 7.96; Kesler et al. 1988; Conklin 1974). Halites and anhydrites of the halokinetic Olvido Formation created the seal and the faulted structures that focused ore precipitates. Regionally, the Olvido Formation defines the salt-cored Sabinas foldbelt, which is made up of a number of salt allochthon tiers and salt-cored detachments. This foldbelt is now in compression and thrust welds are common, in part in response to the Laramide orogeny. But when Ba-rich fluids were migrating it may well have been in its earlier stage of halokinetic extension (as was likely the case in the Oraparinna diapir). The spectacular salt allochthons of the La Popa basin, detailed in Chap. 6, are part of the same Sabinas foldbelt and were also created by the flowing salt of the Olvido Formation. There is an ongoing debate as to the ultimate origin of the barium now precipitated in the various vein fills. Kesler et al. (1988) argue it was sourced by Tertiary volcanism and that baryte mineralization occurred during the early Oligocene when magmatic activity in the Altiplano mobilized barium from the La Boca Formation, and barium-rich fluids reacted with gypsum of the Minas Viejas (Olvido) Formation. In contrast, Kroeger and Stinnesbeck (2003) conclude it was sourced in Jurassic volcanism and tied precipitation in extension veins synchronous with to Oxfordian carbonatite emplacement. In my opinion, a basinal brine, migrating toward the basin margins is an additional possibility. In terms of ore distribution, the differentiation of barium origins is largely academic. Ore control is clearly structural and related to mechanical strength contrasts, which were controlled by evaporite distribution and halokinetic style at the time of emplacement.

[20] Kroeger and Stinnesbeck (2003), established that the terms Minas Viejas and Olvido Fms. are synonyms for the same stratigraphic unit. Its outcrop distribution is now broken up by the effects of dissolution, tectonism and halokinesis, but originally it was deposited as single basinwide succession.

The Galeana barium district now lies at the western margin of the Sierra Madre Oriental in southern Nuevo Leon, Mexico, and it has been one of the leading $BaSO_4$ producers for the country. Ore-grade baryte fills reactivated steeply dipping (50–88° NW) fractures striking N40–50°E and, to a lesser extent, steeply dipping (60–85° SW) fractures striking N60–80°W, all formed at the crest of the San Marcos anticline (Fig. 7.96). Massive baryte veins also carry up to 10 wt% $SrSO_4$. Baryte likely formed when ascending barium-rich basinal brines ponded beneath, and partially dissolved, the relatively impervious halites of the Olvido Formation to create the anhydrite precursors to the gypsiferous residues that now define the outcrop of the Olvido Formation in the Galeana district. After baryte precipitated subsalt, the anticlinal crest was erosionally breached and so exposed mineable baryte at the surface.

Baryte is a widespread authigenic phase in bedded sandstones of the Salt Wash Member in the Late Jurassic Morrison Formation on the Colorado Plateau (Breit et al. 1990). There it forms as intergranular cements, poikilotopic cements, euhedral crystals and replacements of detrital grains. Areas that contain abundant baryte in the sandstone host coincide with the extent of evaporites in the underlying halokinetic Pennsylvanian Hermosa Formation. A genetic link between the baryte and the dissolving evaporite is reinforced by similar ranges in sulphur isotope data in both the gypsum and the baryte (Fig. 7.97a showing strong overlap in the $\delta^{34}S$ range from +8‰ to +14‰). Sulphate, derived from the dissolving evaporites, is thought to have risen along faults into the Morrison Formation; a process perhaps aided by halokinetic focusing (Fig. 10.87).

Evidence of a fault conduit for the Ba-rich waters is further supported by $^{87}Sr/^{86}Sr$ ratios in the baryte cements, which tend to decrease with increasing distance from the supplying fault from 0.7103 to 0.7084 (Fig. 7.97b; Breit et al. 1990). This trend reflects the mixing of radiogenic strontium from waters ascending the faults ($^{87}Sr/^{86}Sr = 0.7100$), with strontium in waters derived by dissolution of early diagenetic carbonate cements in the sands ($^{87}Sr/^{86}Sr = 0.7080$). As the $^{87}Sr/^{86}Sr$ values along the faults exceed those in the underlying Hermosa anhydrite (0.7085) it is thought that radiogenic strontium was also added to the ascending waters by reactions between the rising brine and the arkosic horizons that intersect the fault conduit. These same arkosic sands are also a source of the copper in ores in similar structural settings in the nearby Lisbon Valley (Chap. 15). A similar isotopic argument is used to show an evaporitic sulphate association for mesogenetic baryte mineralisation in the orefields of the northern Pennines (Crowley et al. 1997) and the Ain Allega and El Guiba halokinetic deposits in Tunisia (Abidi et al. 2012).

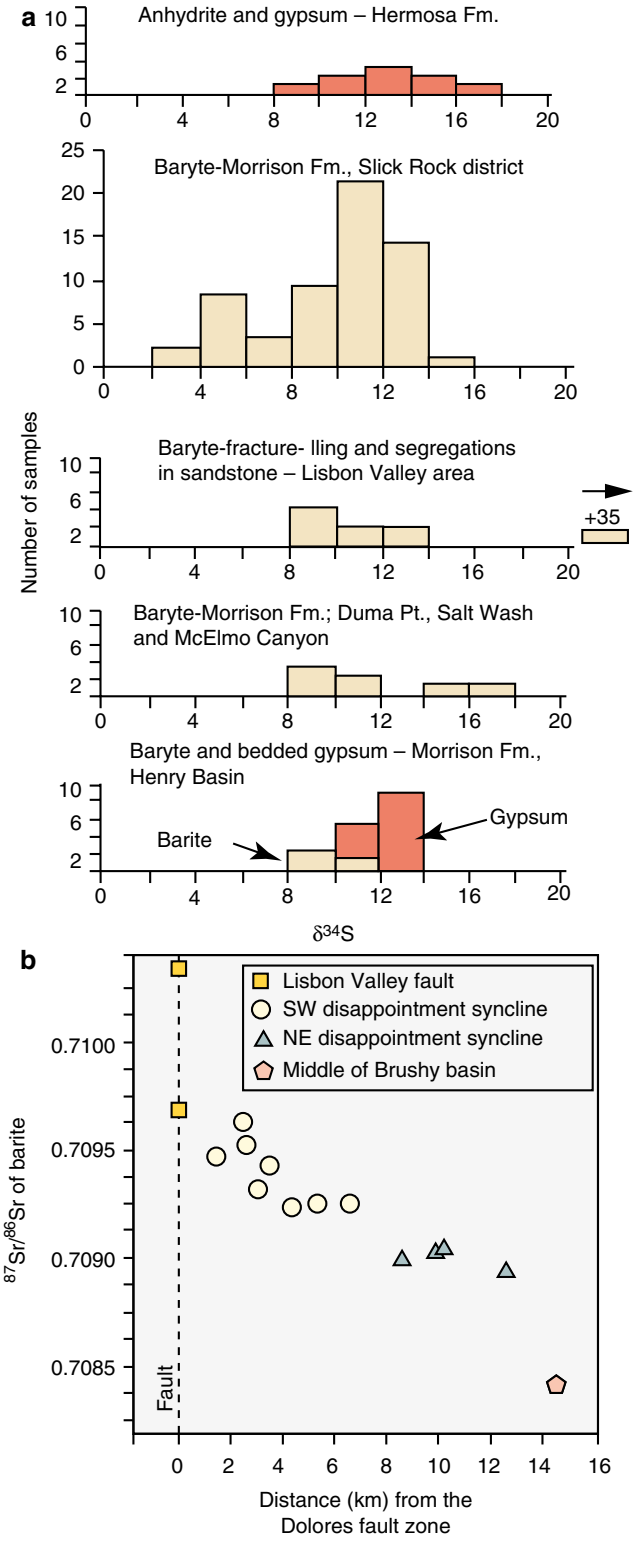

Fig. 7.97 Baryte in the Morrison Fm., Colorado Plateau. (**a**) $\delta^{34}S$ values (CDT) of baryte and gypsum in various regions in the Colorado Plateau. (**b**) $^{87}S/^{86}Sr$ of baryte versus distance from the Dolores fault zone in the Slide Rock district (After Breit et al. 1990)

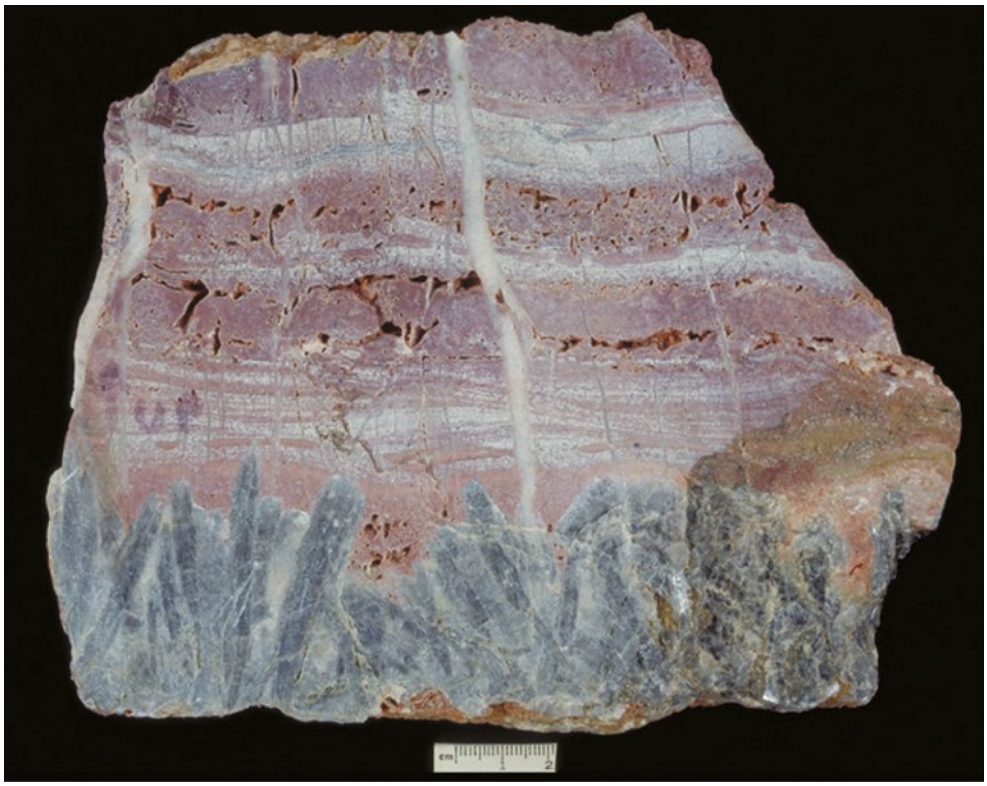

Fig. 7.98 Lower third of this slabbed specimen is composed of growth-aligned baryte (is it a possible replacement of bottom-nucleated evaporite; or, is it a primary baryte precipitate, associated in some areas with silicified marine-derived nahcolite evaporites?). The growth-aligned layer is overlain by current-rippled and silicified volcaniclastic sands. Sample collected from the early Archaean 3.45 Ga Warrawoona Fm. near North Pole, Western Australia

Local concretions of baryte precipitates in sandstones can create rosettes known as "sand rosettes" or "desert roses," where the baryte acts as a poikilitic cement that encases sand grains. Such baryte is thought to have been precipitated by reactions between soluble sulphate (usually from nearby dissolved gypsum or anhydrite) and basinal waters carrying $BaCl_2$. Baryte spar is a commonplace burial cement in reservoir sandstones where two basinal brines mix. The hydrodynamics of such deep mixing is often driven by tectonics, for example, the inversion tectonics of the North Sea (later in this chapter). Oxidised pyrite can also act as a source of sulphate in subsurface waters, especially in the vicinity of dewatering organic-rich shales.

A more enigmatic but significant baryte-evaporite associations is found in early Archaean metasediments. Some of these beds constitute the oldest sediments in the world, namely the ≈3.46 Ga Warrawoona Megasequence at North Pole, Western Australia, with equivalents in South Africa. Both areas are characterised by baryte beds with obvious growth-aligned textures (Fig. 7.98). Interpretations are that the baryte either pseudomorphs bottom nucleated subaqueous evaporite or that it represents a primary seafloor precipitate. The proponents of both interpretation can be involved in ongoing heated discussion that has significant implications for models of the earth's early atmosphere (e.g. Bose et al. 2012; Shen et al. 2009 and Runnegar et al. 2001). The various arguments as they relate to evaporite evidence of atmospheric evolution, were discussed in Chap. 2. Baryte, tied to evaporitic precursors, can also be preserved within meta-evaporite sequences (Chap. 14).

Authigenic Anhydrite as a Burial Salt

As we have seen, some forms of silica, calcite, dolomite, celestite, fluorite and baryte can be precipitates that mimic the outline of their evaporite precursor. They form in the positions of former evaporites either syndepositionally, mesogenetically and telogenetically, wherever waters of appropriate chemistry can cool, heat, mix or change redox state. We shall now see that some evaporite salts, especially anhydrite spar, can also precipitate mesogenetically via fluid mixing over wide areas. This can create substantial quantities of cements in the subsurface that are not directly related to the former position of a primary evaporite mass. Such precipitation takes slowly in relatively stable mixing zones, so crystals tend to be coarse and poikilotopic or replacive, often co-associated with late diagenetic calcite, saddle dolomite,

hydrocarbons and metal sulphides. Precipitative conditions are typically anoxic and thermochemical sulphate reduction is likely in these sulphate-rich settings (Table 7.18). Calcium and sulphate are typically carried to the precipitation site in chlorine-rich saline basinal brines, generated by the dissolution of evaporites, and capable of precipitating their dissolved load at chemical interfaces. This may be in strata adjacent to the dissolving evaporite bed or some distance away in fluid mixing zones related to fluid trapping and sometimes as mixing haloes along fluid escape conduits such as faults and fractures (Table 7.18).

Morphologically near-identical coarse poikilotopic anhydrite cements can also form during early syndepositional brine reflux within brine-saturated pores beneath an accumulating evaporite (Purvis 1989; Luczaj and Goldstein 2000). These syndepositional reflux salts are true evaporites in that they formed in a hydrology driven by solar evaporation. In contrast, burial salts that form in brines generated by the subsurface dissolution of salt beds are not "true" evaporites as they are not directly precipitated by processes driven by solar evaporation, nor do they replace the volume occupied by primary and secondary evaporite salts (Fig. 1.9). They are, in reality, evaporite transformation salts or burial salts. Distinguishing early reflux evaporite cement spar from later burial anhydrite spar can require detailed petrographic and isotopic study, especially in the absence of saddle dolomite or metal sulphides.

Anhydrite is a late stage burial salt in quartzose Rotliegende reservoir sands in Leman Field, North Sea and throughout regions of deeply buried Rotliegende Formation

Table 7.18 Selected examples of sparry burial anhydrite

Occurrence and age of host	Burial anhydrite fabric and subsurface temperature at time of precipitation	Reference
Yacoraite Fm. (Upper Cretaceous), Argentina.	Sparry anhydrite cement, containing hydrocarbon inclusions and brine, fills intergranular, mouldic and vuggy porosity in a carbonate host. Indicates anhydrite precipitated at 121–137 °C from 17 % equiv. wt. NaCl brine ($NaCl–MgCl_2$ –Na_2 SO_4 –$NaHCO_3$ –$NaCO_3$ basinal brine).	Cesaretti et al. (2000)
Maha Sarakham Fm. (Upper Cretaceous), NE Thailand.	Coarsely crystalline saddle dolomite rhombs float within a matrix of coarse, recrystallized anhydrite spar in the Basal Anhydrite. Isotopes indicate dolomite precipitated at temperatures ≈ 72–123 °C.	El Tabakh et al. (2003)
Smackover Fm. sandstones, (Upper Jurassic), Gulf of Mexico.	Anhydrite both as poikilotopic spar masses in which detrital grains are replaced and as smaller patches that have replaced single detrital grains. Precipitation temperatures >100 °C. Anhydrite is a relatively late cement and postdates all other volumetrically significant authigenic phases in the sandstones, including K-feldspar, dolomite, quartz, and most calcite cements.	Dworkin and Land (1994)
Smackover Fm. dolomites, (Upper Jurassic), Gulf of Mexico.	Anhydrite spar partially replaced allochems and prebitumen calcite cements in mesogenetic pores. Solid bitumen precipitated where hydrocarbons were present. Emplaced in temperature range 100–150 °C.	Heydari (1997, 2000)
Khuff Fm. (Upper Permian-Lower Triassic), Abu Dhabi, UAE and Saudi Arabia.	Burial stage poikilotopic crystals fill pore spaces between the detrital carbonate components. Crystals are typically 500 mm in length but locally may reach up to 3 mm.	Worden et al. (1995, 2000), Ehrenberg et al. (2007), Al Eid and Al Tawil (2009)
Kurrachine Dolomite, Trias-sic, Syria	Following fracturing and mesogenetic leaching by sulphate-bearing warm fluids, significant vuggy porosity was created, but was subsequently occluded by anhydrite burial cements made up of coarse mosaic anhydrite spar and occasional poikilotopic spar.	Hips and Árgyelán (2007)
Prider Fm. (Lower Permian) Kansas, USA.	Burial stage poikilotopic anhydrite cement replaces echinoderm fragments, parts of oncolites, some dolomite spar, and some stylolite seams. Precipitation occurred in the range 65–90 °C, with a few samples possibly up to 150 °C.	Luczaj and Goldstein (2000)
Rotliegende Fm. (Lower Permian), onshore and offshore NW Europe.	Poikilotopic sparry anhydrite enclosing sand grains. Distribution shows a strong fault/ fracture control. Precipitation temperatures in the range 120–140 °C.	Duguid and Underhill, (2010), Gauthier et al. (2000), Sullivan et al. (1994)
Swan Hills Fm. (Middle to Upper Devonian), Canada.	Coarse bladed crystals of sparry anhydrite enclosing dolomite clasts and possibly related to faults. Fluid inclusions in the anhydrite show crystals formed from basinal fluids at temperatures in excess of 90 °C. Machel (2013) documents the wider occurrence of burial anhydrite in Devonian carbonates in the Alberta Basin, than previously noted.	Duggan et al. (2001), Machel (2013)
Dirk Hartog Group, (Silurian) Gascoyne Basin, Australia.	Sparry anhydrite includes blocky poikilotopic cement filling interparticle and mouldic pore spaces in oolitic horizons, and as a bladed cement in larger, often vuggy pore spaces. Formed at elevated subsurface temperatures.	El Tabakh, et al. (2004)
St Peter Sandstone (Ordovician) Michigan Basin, USA.	Late stage sparry anhydrite cements that precipitated in crosscutting fractures and postdates with late stage dolomite that had precipitated at higher temperatures.	Winter et al. (1995)

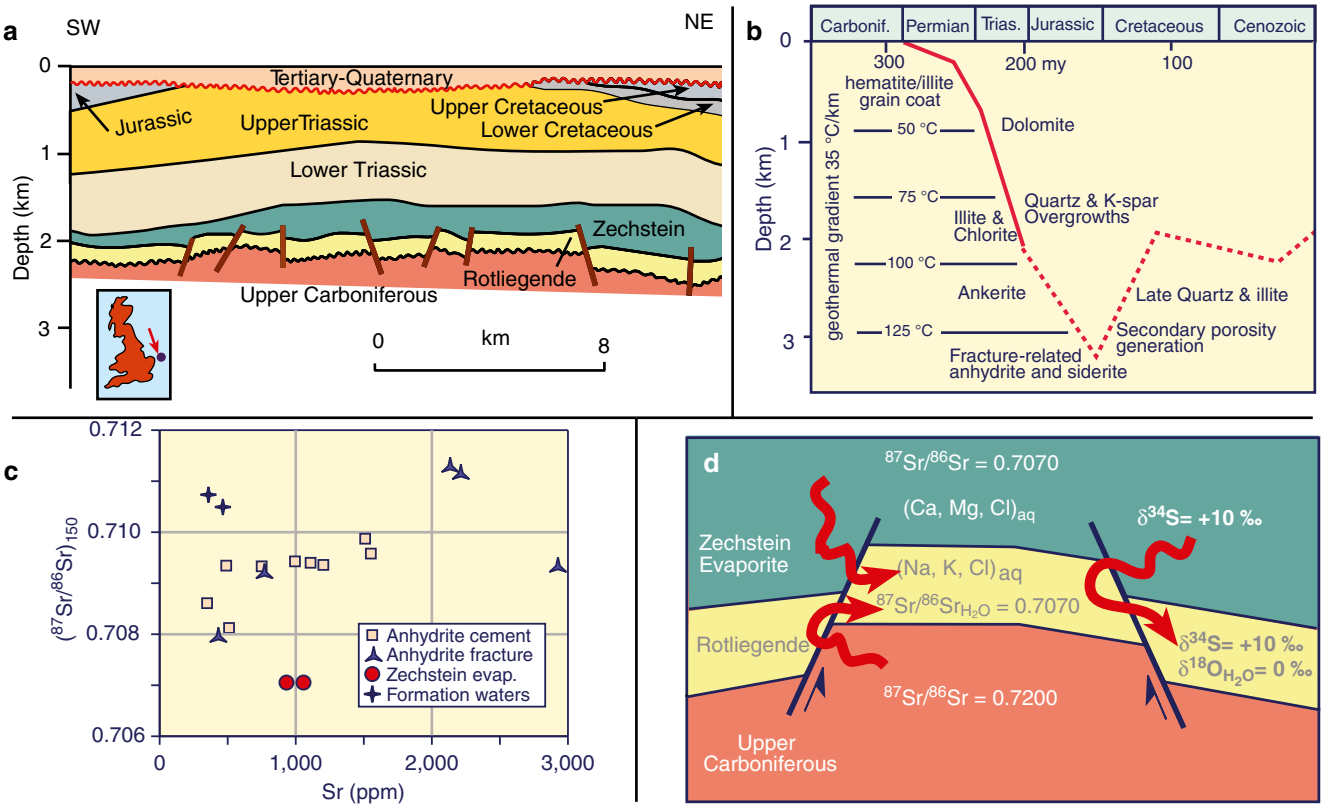

Fig. 7.99 Late stage anhydrite in Leman Field, North Sea. (**a**) Location of the Leman gas field and regional geological cross section. (**b**) Subsidence history of Rotliegende reservoir sandstone showing time and temperature of anhydrite precipitation postdates other diagenetic events and precedes secondary porosity formation. (**c**) Strontium isotopic ratios and composition of various anhydrite burial salts compared with formation waters and Zechstein salts. There is a general trend of increasing isotopic ratio with increasing Sr content. (**d**) Schematic section showing major sources of sulphur, strontium and carbon along with their migration from above and below the Rotliegende and subsequent mixing that precipitated anhydrite cements and fracture fill (Modified form Sullivan et al. 1994)

(Fig. 7.99a; Sullivan et al. 1994; Gauthier et al. 2000). Poikilotopic anhydrite spar in Leman field is best developed along coarser-grained sand laminae, suggesting their inherent higher permeabilities influenced sites of precipitation. The same sparry anhydrite cement also encloses late authigenic ankerite, ferroan dolomite and pressure-solved cemented grains, showing its deep burial origin. Anhydrite tends to be best developed in and near fractures forming cements zones up to 0.5 cm wide and 0.5 m long in Leman core. Crystals in fractures are bladed, coarsely crystalline and tend to grow subparallel to the fracture walls. Cemented coarse-grained laminae and anhydrite-filled fractures frequently intersect suggesting both styles represent the same generation of anhydrite cement.

Timing is best resolved using Sr and O isotopic analysis of the anhydrite cements. Oxygen isotope compositions indicate precipitation temperatures between 120 and 140 °C in waters with a $\delta^{18}O$ composition similar to the present day formation waters (≈0‰ SMOW; standard mean ocean water). These are the maximum inferred burial temperatures for the Rotliegende sandstone in Leman Field. Such temperatures occurred during the Late Jurassic-Early Cretaceous, at the start of basin inversion with maximum burial depths of 3.5–4 km (Fig. 7.99b). When corrected for their 150 Ma precipitation age, the Sr isotope ratios in the various anhydrite burial cements, and their Sr contents, are highly variable. ($^{87}Sr/^{86}Sr$) ratios range from 0.70797 to 0.71129 and Sr contents from 351 to 2,952 ppm (Fig. 7.99c). Fracture-filling anhydrite spar also traverses this entire strontium range, implying an origin from the same fluid. There is also a general trend of increasing Sr ratio with increasing Sr content of the anhydrite burial salts.

According to Sullivan et al. (1994) the late stage anhydrite indicates an unusual, short-lived event that juxtaposed the Zechstein evaporites and sandstones. The resulting geometry facilitated cross-formational fluid flow via fractures that were tectonically induced by inversion. At that time pore fluids were squeezed from the overlying Zechstein evaporites and underlying Carboniferous mudstones into the lower pressures of the Rotliegende regional aquifer (Fig. 7.99d). Mixing of the two waters precipitated dolomite and anhydrite cement, which in turn produced a Na-K-Cl

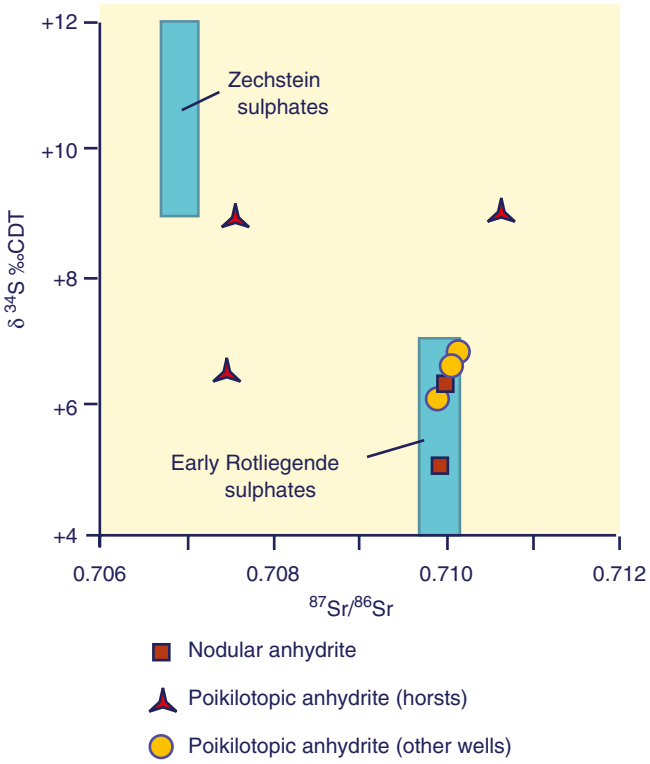

Fig. 7.100 Plot of sulphur versus strontium isotopic ratios for coarse anhydrite cements from the German Rotliegende. It clearly shows the affinity of anhydrite cements in horst blocks for Zechstein sources rather than an early Rotliegende signature (After Gaupp et al. 1993)

formation water. This pore water was lower in Ca + Mg than the overlying Zechstein, which in turn supplied most of the sulphate and some of the Sr to the anhydrite cements. Like the isotopic evidence, the chemical evidence shows the burial anhydrite precipitated from extremely saline formation waters derived by deep subsurface mixing of Zechstein evaporite brines and deeply circulating meteoric waters. Even today, the Zechstein brines in the Leman Field are extremely saline (165,530–238,531 mg/l), with cation/ chloride ratios indicating ongoing mixing of Zechstein marine evaporite brines with fossil meteoric water.

Onshore in northern Germany the Rotliegende gas reservoirs also contain coarse authigenic poikilotopic anhydrite cements, particularly in the vicinity of faults. Cross-formational flow of Zechstein fluids and fault-related fluid flow was responsible for this anhydrite, especially during times of mixing tied to fault activity (Gaupp et al. 1993; Gauthier et al. 2000). This is clearly seen in the isotopically distinct values of burial anhydrite within horst blocks compared to samples with similar authigenic and nodular anhydrite styles, but from wells outside of the horsts (Fig. 7.100). Anhydrite cements in sands atop horst blocks show affinities to Zechstein sulphates. In contrast, anhydrites in the other wells, where uplift has not juxtaposed Rotliegende sands to Zechstein fluids, retain an isotopic signature typical of early Rotliegende time. Once again, this observation underlines the importance of active faulting in facilitating brine mixing, which then precipitates authigenic minerals in the deep burial setting.

Late stage anhydrite and halite cements also characterise deeper burial cements in the aeolian and fluvial feldspathic sandstones of the Upper Jurassic Norphlet Formation and other Smackover sandstones of the Gulf Coast (McBride et al. 1987; Dworkin and Land 1994). Coarsely crystalline anhydrite, along with quartz and ferroan dolomite, precipitated as intergranular cements. Anhydrite averages 3 % by volume (maximum 21 %) in Norphlet wells in Mississippi and 1.3 % in Alabama. It occurs as scattered sparry crystals, in spherical and poikilotopic patches up to several centimetres across and can completely cement some sand laminae. All the anhydrite cements are patchily distributed in the Norphlet reservoirs and, as in the Rotliegende, tend to be better developed in the coarser sand laminae.

Oxygen isotopic values from the anhydrite averages 15.6 ‰ (SMOW). According to Dworkin and Land (1994) this burial anhydrite precipitated in near oxygen (and strontium) isotopic equilibrium with ambient burial fluids at temperatures of between 90 °C and 100 °C at depths ≈ 2.3 km (Fig. 7.101a). Authigenic halite cements, along with late stage carbonates, followed at temperatures up to 120 °C (<3 km burial). Subsequent dissolution of the cements, along with some labile detrital grains, created secondary porosity that makes up at least half of the economic porosity in the Norphlet tight gas sand reservoirs in this region. Potassium-rich brines, generated by dissolution of nearby bitterns, tended to stabilise K feldspar in the Norphlet so that authigenic K-spar can even coat quartz grains, as well as its more commonplace occurrence as overgrowths on detrital K-spar grain substrata.

Dworkin and Land (1994) argue that the expected isotopic composition and trace-element concentration of a marine brine-reflux-derived anhydrite cement in Smackover Formation quartzose sands should be: $\delta^{34}S_{CDT} = +16‰$, $\delta^{18}O_{SMOW} = +14‰$, $^{87}Sr/^{86}Sr = 0.7069$, Sr = 1,500–2,500 ppm, Ba < 20 ppm, and Mg > 200 ppm (indicated by the brown box in Fig. 7.101b). When geochemical analyses of Smackover anhydrite cements are compared with the predicted composition, it is apparent that most of the coarsely crystalline anhydrite is not a marine reflux cement. Rather, two groupings or generations of anhydrite cement can be distinguished using a strontium isotope to strontium content crossplot (Fig. 7.101b). An early cement, that may have been derived from slightly modified Late Jurassic seawater (possibly via reflux), is characterised by its Jurassic isotopic signature and high strontium content (>3,200 ppm). A second group of cements, that represent the bulk of coarsely crystalline cements in the Smackover sandstones, has a depleted strontium content (<3,000 ppm) and an elevated isotopic ratio. It may have

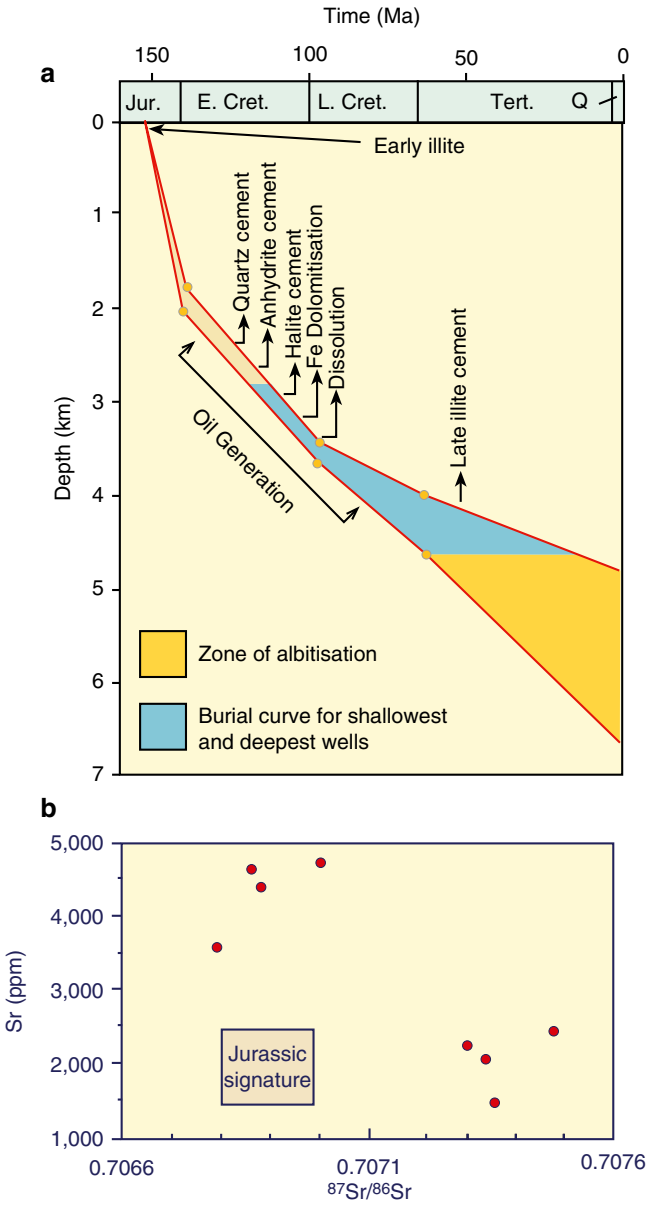

Fig. 7.101 Norphlet Formation (After Dworkin and Land 1994, 1996). (**a**) Burial evolution and diagenetic history. (**b**) Sr isotope signatures

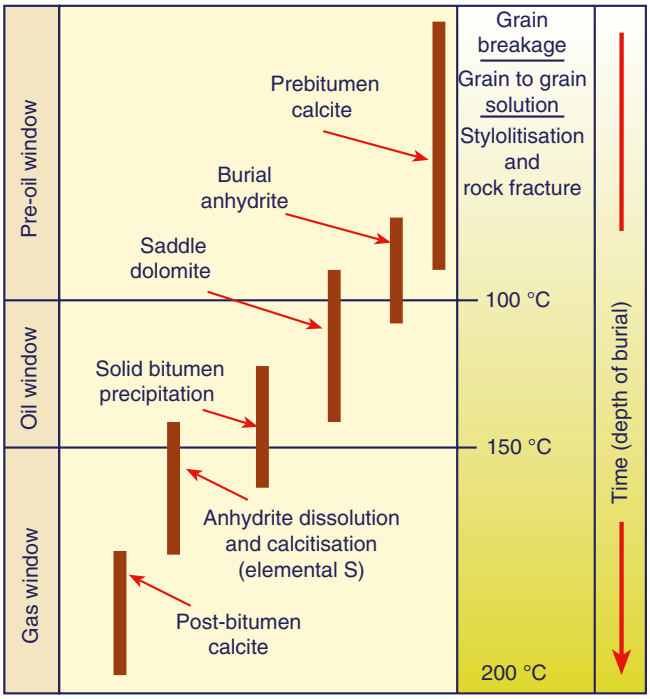

Fig. 7.102 General paragenetic sequence for the Smackover Formation in the northern Gulf of Mexico showing approximate temperature range of various events (After Heydari and Moore 1989; Heydari 1997)

precipitated later in the burial history or may represent burial recrystallisation of the first cement. It probably formed at slightly higher temperatures, which would have maintained relatively low strontium concentrations, and in the presence of pore fluids that had radiogenic Sr isotopic compositions. Such radiogenic pore fluids were probably derived from waters that were involved in the burial dissolution of feldspars.

As well as in Smackover sandstones, dissolution-derived sulphate-rich basinal brines also precipitate anhydrite burial salts in Smackover carbonates of the Gulf of Mexico (Fig. 7.102; Heydari and Moore 1989; Heydari 1997). Precipitates are made up of orthorhombic laths and blades that form spars replacing both allochem grains and calcite cements. The anhydrite spar and the calcite spar formed prior to reaching the oil window and are post stylolitisation. The arrival of liquid hydrocarbons and the precipitation of solid bitumens temporarily retarded further precipitation of calcite, anhydrite and dolomite burial cements. Later, the anhydrite was dissolved and replaced by a more finely crystalline calcite spar and elemental sulphur via thermochemical sulphate reduction processes. This occurred at the higher temperatures that typify the gas window.

Dissolution-derived late burial anhydrite is also widespread in the Lower Cretaceous carbonates of the Pearsall and Lower Glen Rose Formations, South Texas (Woronick and Land 1985). As in the Smackover, the anhydrite spar formed late, after the development of saddle dolomite cements. It crystallised mostly as bladed to fibrous anhydrite laths some 0.1–6.0 mm in length. Much of this anhydrite fills pre-existing intergranular pore space in the carbonates, but it can also replace fossils, matrix material and earlier calcite cements. Once formed, it was subject to corrosion and replacement by calcite. $\delta^{18}O_{SMOW}$ values for the anhydrite range from 19.5 to 22.9‰, values that are much more enriched than the Cretaceous seawater sulphate (+15‰). Woronick and Land (1985) interpret these enriched values as proof that none of the subsurface anhydrite in the Pearsall and the Glen Rose (including some associated nodular anhydrite) was precipitated directly from Cretaceous seawater.

They argue that even the nodular anhydrite (previously used as a sabkha indicator) was not primary but had recrystallised in the subsurface. This is supported by $\delta^{34}S_{CDT}$ values of the anhydrite and the modern Edwards Formation brines, which lie between 20 and 26‰. Directly precipitated Cretaceous marine evaporites should have $\delta^{34}S_{CDT}$ values of less than +16‰ (Fig. 2.35a).

They envision a basinward flowing deep meteoric aquifer, driven by hydrostatic flow, that was essentially saturated with respect to calcite, dolomite and $CaSO_4$. Periodically the meteoric waters mixed with upwelling hotter basinal fluids that were derived from more deeply buried and dissolving Jurassic salts. These basinal fluids contained abundant carbon dioxide, calcium, strontium (radiogenic) and barium, together with small amounts of lead, zinc and hydrocarbons. Mixing of the two waters caused the precipitation of burial anhydrite, as well as other burial cements, including saddle dolomite and metal sulphides.

Other carbonate platform sequences that entrain burial anhydrite cements derived from evaporite dissolution and upflow of sulphate-enriched basinal waters include (Table 7.18); the Devonian Keg River and Swan Hill formations of Alberta (Aulstead and Spencer 1985; Duggan et al. 2001) and carbon-ate reservoirs in the Middle Ordovician Trenton Group, SW Ontario (Middleton et al. 1993; Haeri-Ardakani et al. 2013).

All these examples of sparry burial anhydrite demonstrate an obvious association between advanced dolomitisation of platform carbonates and the precipitation of later diagenetic poikiloptopic and replacive anhydrite spar. This process, also called anhydritization by Kendall and Walters (1978), is widely observed, and has significantly reduced porosity in potential reservoir dolomites in the Devonian of Canada, the Permian Khuff of the Saudi Arabia and the Emirates, the Zechstein of NW Europe, the Jurassic of the Gulf of Mexico and the Arab cycles of the Middle East (see Chap. 10). As yet, it has attracted the interest of relatively few researchers and documentation is sparse. As a process it should characterise burial diagenesis in most deeply buried sulphate evaporite systems.

However, not all burial or sparry anhydrite or subsurface gypsum is associated with alteration of "true" evaporites. Anhydrite is a retrograde salt, so intergranular and replacive anhydrite cement precipitates in ocean crust or other volcanogenic settings when unmodified connate seawater is heated above 150 °C (Blount and Dickson 1969, 1973; Chap. 16). This is a widespread process in hydrothermal circulation cells in midoceanic ridges and is probably also active in the deeper portions of many sedimentary basins.

In shallower burial settings, aqueous sulphides can also be oxidised to sulphates, which then precipitate as an authigenic $CaSO_4$ phase. This often happens in surface regions of pyrite oxidation and mixing such as in mine wastes, lake bottoms and in seep positions on the seafloor, especially when microbially facilitated. Pyrite oxidation has formed 1.5–4 mm-sized euhedral tabular to lenticular gypsum crystals in sediments atop Mound Perseverance, a modern giant cold-water coral mound in the Porcupine Basin, located some 50 km west of the Irish coast (Pirlet et al. 2010) Non-evaporitic gypsum is also found as a gossan precipitate worldwide and in glacio-lacustrine deltaic sequences in tributary valleys of the Cuyahoga River, Ohio (Bain 1990). Crystals in the various tributary valley deltas display two styles of diagenetic gypsum related to the host sediment: (a) euhedral, translucent tabular crystals up to 4 cm across in pliable prodelta mud, or (b) bladed, dovetail poikilotopic gypsum sand crystals and rosettes up to 8 cm across growing within grain-supported delta-front sand. All these gypsums formed diagenetically as a result of oxidation of sulphides by calcium-rich, oxidizing porewaters mixing with more reduced waters where pyrite (the sulphur source) is present. In the Ohio examples, oxidizing, calcium bicarbonate rich water moves through delta-front and delta-top sands and migrates into and out of pyritic prodelta muds. As a result of this migration, pyrite is oxidized to form iron oxides and iron hydroxides, colouring the sediment yellow to red. At the same time, sulphides are converted to sulphates, which react with the calcium-rich water, resulting in the precipitation of gypsum. But such oxidative sulphate sources for $CaSO_4$ are relatively uncommon in the deep subsurface where pore waters are typically anoxic and reducing and interfaces with oxidising waters are not common.

Enigmatic Outlines in Pseudomorphs

This chapter discusses how evaporites can be replaced by various minerals at any time in their burial and uplift history. So far, I have focused on the more commonplace evaporites — namely, gypsum, anhydrite and halite morphologies — that are pseudo-morphed by silica, calcite, dolomite, baryte and celestite. These three evaporite salts constitute more than 90–95 % of modern and ancient precipitates, but there are also carbonate or silica pseudomorphs preserving the outlines of other evaporite salts, such as trona, gaylussite, pirssonite, glauberite, thenardite and other less common precipitates. Figure 7.103 illustrates some of the idealised and a few of the more typical shapes of these somewhat less common salts. If their euhedral forms are well preserved by their carbonate or siliceous replacements, they can be recognised still.

But all evaporites are soluble, so the preservation of a crystal form is often accompanied by enlargement or partial collapse of the void during the replacement process. This complicates the process of recognition and is, for example, the main reason why Archaean baryte at North Pole is still variably interpreted as a gypsum or nahcolite association.

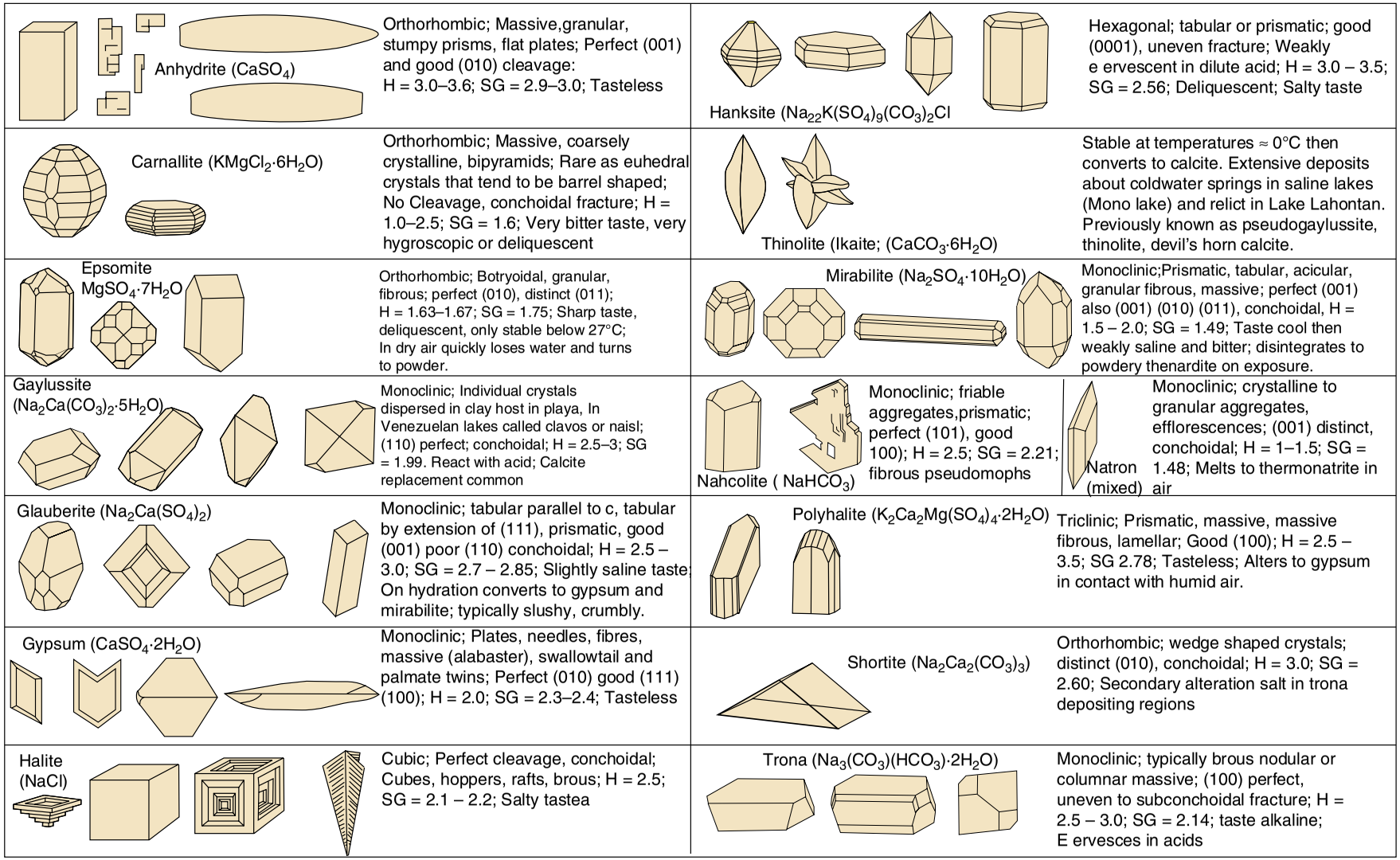

Fig. 7.103 Characteristic shapes of some of the various depositional evaporate salts and their physical properties

Table 7.19 Evaporite minerals susceptible to replacement by calcite and likely to show lozenge or discoidal outlines

Mineral	Formula	Crystal habit	Brine type
Gaylussite[a]	$Na_2\ Ca(CO_3)_2{\cdot}5H_2\ O$	Often elongated; also flattened wedged-shaped.	Na—CO_3 —Cl
Glauberite[a,b]	$Na_2\ Ca(SO_4)_2$	Tabular, prismatic, dipyramidal, and may be rounded or step-like.	(Mg) Na—SO_4 —Cl
Gypsum[b]	$CaSO_4{\cdot}2H_2\ O$	Thin to thick tabular; elongate; step-wise depressions or rough; acicular; prismatic with nearly equant cross section. Lenticular crystals with rounded or irregular terminations. Warped or curved irregular surfaces, long prismatic crystals occur bent into irregular or hoop-shaped forms.	(Mg) Na—SO_4 —Cl
Ikaite	$CaCO_3{\cdot}6H_2\ O$	Distinct asymmetry with a tendency toward a sigmoidal shape when viewed from the side and square-prismatic in overall shape that taper to the ends; strongly ribbed normal to the length.	Na—CO_3 —SO_4 —Cl
Mirabilite[b]	$Na_2\ SO_4{\cdot}6H_2\ O$	Short prismatic to acicular crystals.	Na—CO_3 —SO_4 —Cl and (Mg) Na—SO_4 —Cl
Pirssonite[a]	$Na_2\ Ca(CO_3)_2{\cdot}2H_2\ O$	Short prismatic; also tabular or pyramidal.	(Mg) Na—CO_3 —Cl
Thenardite[b]	$Na_2\ SO_4$	Dipyramid; tabular; rarely prismatic.	Na—CO_3 —SO_4 —Cl and (Mg) Na—SO_4 —Cl

After Finkelstein et al. (1999)
[a]Indicates likely diagenetic mineral
[b]Indicates a depositional association

Sodium carbonate salts are more likely to alter to calcite with burial as they already contain elevated levels of bicarbonate ions when they are deposited (Table 7.19; Southgate et al. 1989; Finkelstein et al. 1999). When preserved as isolated replacement crystals in a mudstone matrix, their calcitic pseudomorphs have easily confused or misinterpreted as gypsum, baryte of other lenticular forms.

Misidentifying a pseudomorph can lead to significant differences in the interpretation of depositional setting. In the case of the Upper Oligocene Creede Formation, southwestern Colorado, the interpretation of lenticular calcite in lacustrine laminites, as either ikaite or gypsum, is one of the pivotal pieces of evidence in defining the lacustrine depositional setting as deep, cold, fresh, and profundal versus shallower, periodically meromictic and hypersaline (Larsen and Crossey 1996 vs Finkelstein et al. 1999).

Because ikaite is only stable at near freezing temperatures, it is typically converted to thinolitic calcite (syn. jarrowites, devil's horn calcites, glendonites). Internally, ikaite pseudomorphs may preserve a characteristic granular structure made up of sand-sized, rounded to rhombic, calcite grains set in a matrix of sparry and spherulitic cements (Shearman et al. 1989; Shearman and Smith 1985). But the shape of a thinolitic calcite is easily confused with the outlines of other evaporite salts that have no implication of degassing in CO_2-saturated coldwater spring seeps.

Likewise, the recognition of ikaite in Neoproterozoic glacial sediments interlayered with pisolites and ooids can be used to imply that the high supersaturation of Precambrian seawater meant that coated grains were possible cold water precipitates. They were not exclusively tropical precipitates, unlike pisolites and ooids in today's oceans and inferred for similar coated grain textures throughout the Phanerozoic (James et al. 2005). Alternatively the interlayering of glendonites and coated grains can be used to support a "freeze or fry" climate model tied to "Snowball Earth."

For years, before ikaite was shown to be a cold water precipitate, not an evaporite, many crystals described as ikaite were considered named in a way that could be used interchangeably with the mineral gaylussite, or ikaite was described as pseudo-gaylussite. In terms of depositional setting, ikaite and gaylussite are not coprecipitates, but from older literature associations one could easily think they were.

Separating ikaite/gypsum/gaylussite is not the only difficult choice when attempting to identify the precursor to a fuzzy-edged angular outline, now filled by a later mineral phase. Other problem pseudomorph associations include baryte/ siderite/gypsum; acicular aragonite/gypsum; pyrite/ halite and even anhydrite/gypsum. The difficulty in deciding on the likely precursor of a possible pseudomorph, when the replacement process can destroy to varying degrees the original outline, emphasises the need to look at all sources of evidence when interpreting any ancient succession now leached of the original salts or the daughter products.

Summary

Evaporites are soluble in most subsurface situations. Even preserved evaporite beds show varying degrees of dissolution about their edges. The longer an evaporite bed remains in the subsurface the more likely it is to dissolve. Preservation or loss it is not a question of whether an evaporite will

dissolve in the subsurface, but when. This is why there are few preserved beds of evaporite salts older than Neoproterozoic. As thick evaporite units dissolve they leave behind characteristic breccias and other textures and replacements that allow the recognition of former extensive salt beds. The breccias can be interstratal beds or trans-stratal chimneys, distinguishing the two forms differentiates between blanket or more focused inflows. Dissolution can be driven by basinal fluids escaping from below or by fluids infiltrating from above. Salt units may not dissolve until they have flowed into diapirs and welds (halokinetic breccias) or have acted as décollement surfaces in fold and thrust belts (rauhwacke). All evaporite salt units will ultimately dissolve, many disappear in the diagenetic realm while others may be preserved until they attain metamorphic grades or interact with a magmatic body.

Hypersaline Fluid Evolution During Burial and Uplift

8

Basin-Scale Burial Hydrology

In Chap. 2 we discussed the hydrology of evaporite depositional and early diagenetic (eogenetic) settings, in this chapter we consider diagenetic evolution in subsequent hydrological stages in a sedimentary system containing thick salt, that is, rock-fluid interactions in an evaporite-entraining sequence experiencing ongoing burial, followed by possible uplift (mesogenesis followed by telogenesis. Thick, buried and dissolving evaporites influence subsurface hydrology and formation water chemistries throughout the burial cycle, as they interact with regional and local thermal and pressure regimes. Remobilization of salt and introduction of brine-carried carried components, notably dolomite and anhydrite, can have a significant impacts on reservoir quality, e.g. the Simonette oil field, Swan-Hills Formation (Devonian) Alberta, where late anhydrite and burial dolomite represent up to 50 % of the rock volume (Duggan et al. 2001). Evaporites that enter the metamorphic realm can have an extensive influence consequent rock type and distribution, well after the primary sedimentary and diagenetic salts are long gone (Chap. 14).

Flushing by basinal pore waters drives diagenetic alteration, recrystallisation and dissolution of evaporites within four hydrotectonic realms, namely (Fig. 8.1; Table 8.1):

1. Passive-margin burial,
2. Pull-apart burial,
3. Collision margin burial, and
4. Post-orogenic burial.

All four can be inter-related by the Wilson Cycle. Throughout their burial history, salt beds and allochthons act as foci for escaping basinal and tectonic fluids. Subsurface breaching of a stratiform salt aquitard, either in response to dissolution or to halokinesis, typically focuses crossflows of basinal fluid. Fluid may rise or sink through a breach, depending on the local temperature and pressure regime. Fluids flowing through a breach will mix with extrinsic basinal or meteoric fluids with differing chemistries and physical properties, so facilitating precipitation of authigenic phases at or near a salt breach (burial salts and metal sulphides).

The salt-floored passive margin burial realm is characterized by updip extensional tectonics, differential loading, growth faulting, relatively slow and steady subsidence and, in most salt-floored passive margins, by salt flow (Fig. 8.1a). Compressional tectonics is commonplace in downdip positions in the same salt-floored continental margins. The Mesozoic and Tertiary evolution of the Gulf of Mexico and Atlantic-margin basins are typical examples of this salt-lubricated hydrologic style (Fig. 6.1). Down to a depth of a kilometre or so, the shallower parts of this realm are typified by active to stagnant phreatic circulation. Below is the zone of compactional flow, which entrains both horizontal (average rates of 6 cm/year) and vertical flow regimes (average rates of 0.15 cm/year). Deeper still, or in zones of thermal anomalies around growing salt structures and shale diapirs, is the zone of thermohaline flow.[1]

Away from local thermal anomalies, temperatures increase steadily with depth according to regional geothermal gradients, which range from 15 to 30 °C/km in most passive margins. Nonevaporitic sediments shallower than 2–3 km depth are typically hydrostatically pressured, while deeper strata, especially thick impervious shales in rapidly accumulating depocentres such as suprasalt minibasins, tend to be geopressured. A transition to overpressuring can occur at much shallower depths (≈1 km or less) where evaporites, not shales, are the predominant basin aquitard (e.g. Jowett et al. 1993). This reflects very rapid rates of basinwide evaporite sedimentation and a complete loss of intrasalt porosity at shallow depths within these basinwide units.

Pull-apart or transform burial is characterised by extensional tectonics and rapid subsidence, along with high

[1]Thermohaline flow involves, or is dependent upon, density contrasts, which are related to the conjoint effects of temperature and salinity variations.

© Springer International Publishing Switzerland 2016

J.K. Warren, *Evaporites: A Geological Compendium*, DOI 10.1007/978-3-319-13512-0_8

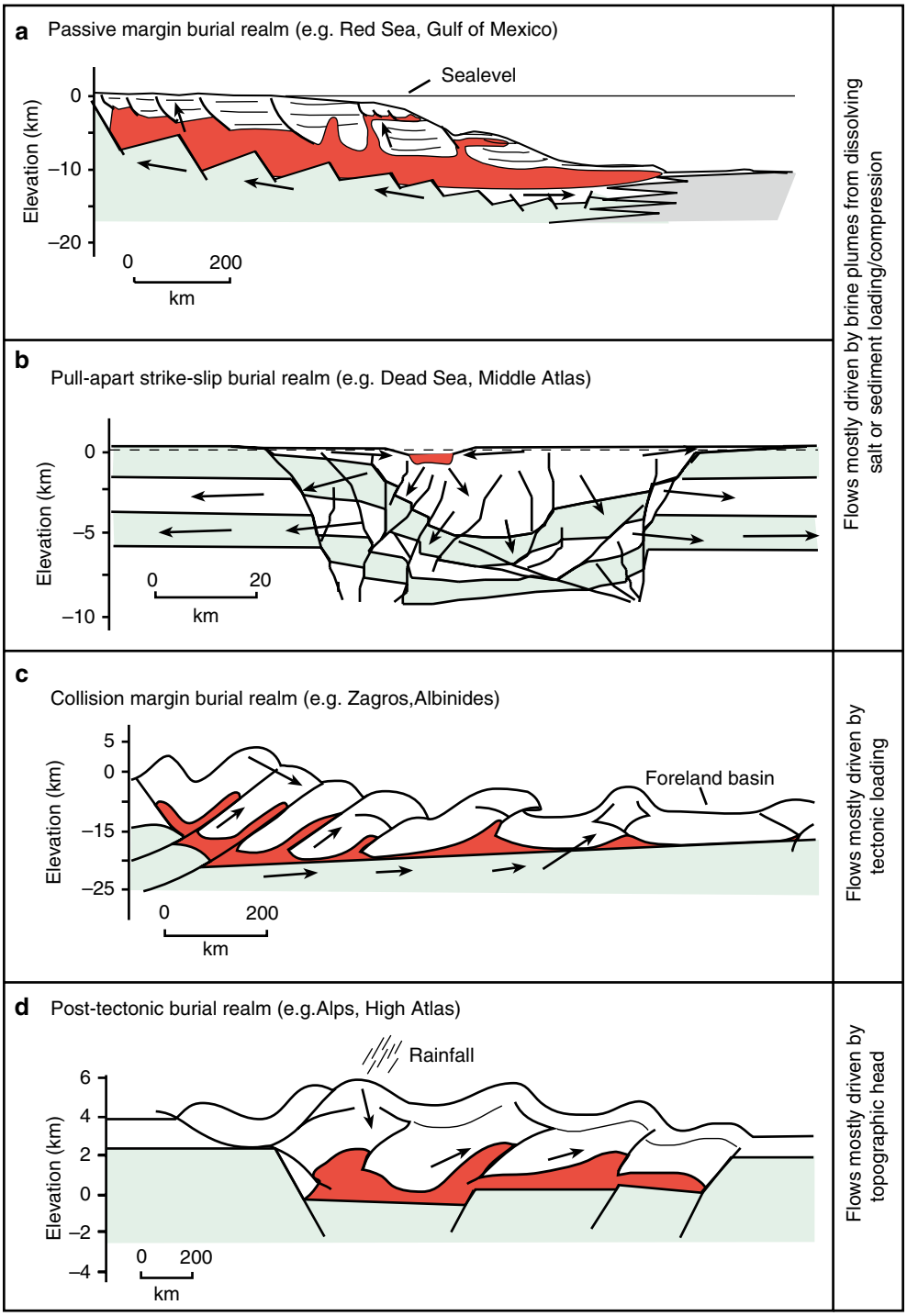

Fig. 8.1 Hydrotectonic flow patterns. (**a**) Passive margin circulation with water flow driven by sediment compaction and catabaric/thermohaline flow. Gravity drives nearsurface flow. (**b**) Pull-apart circulation where dissolution-derived brine plumes from rapidly-buried thick evaporites drive deep lateral circulation into basement aquifers. (**c**) Collision margin circulation where thrust sheet emplacement and loading drives burial water from sediments caught up in the orogenic belt into the craton interior. (**d**) Post-tectonic circulation where deep burial flow in the basin sediments is driven by gravity head supplied by the adjacent weathering mountain belt. Note the varying vertical and horizontal scales

Table 8.1 Selected examples of brines derived from buried evaporites, in many cases the associated density and temperature contrast in the brine also aid basinal fluid circulation

	Location and age of brine source	Role of salt	Reference
Passive Margin/ intracratonic sag burial	Gulf of Mexico, Jurassic	Fluid flow in overpressured Mio-Pliocene sediment (especially) near salt diapir crest is driven by brines derived from dissolution of salt mass. Facilitates suprasalt gravity gliding. Sub-allochthon brine flow is focused by sheet geometry and basin evolutionary stage.	Gradmann et al. (2012), McCammon and Hanor (2013)
	Gulf of Lions, France, Miocene	Stratiform Late Miocene evaporite layer forms a widespread blanket that focuses fluid circulation and heat flow in units below salt with thrust subcrops	Burrus and Audebert (1990), Camerlenghi et al. (2009)
	Canning Basin margin carbonates, Australia, Devonian	Chloride-rich metal carrying brines, created by dissolution of Silurian salt dissolving in basin centre, escaped along extensional faults into basin margin to form saddle dolomites and MVT deposits.	Warren and Kempton (1997), Middleton and Wallace (2003), Wilde et al. (2005a)
	Carbonates from southwestern Ontario, Canada, Ordovician to Devonian host with Silurian evaporite	Petrography, geochemistry (stable and radiogenic isotopes), and fluid inclusion microthermometry of matrix dolomite, fracture-filling calcite, and saddle dolomite indicate thermal buoyancy resulting from thermal anomaly and migration of hydrothermal fluids through regional aquifers with brines from dissolved Silurian salt moving from the centre of the Michigan Basin toward its margin	Haeri-Ardakani et al. (2013)
Pull-apart	Dead Sea Rift, Middle East, Miocene	Dissolution of Dead Sea halite (Pliocene marine-fed drawdown system) acts as brine source in many deep water wells as far as 100 km away from the rift. Brine supplied for last 3–6 Ma with its layering and flow direction dominantly controlled by structural evolution.	Stanislavsky and Gvirtzman (1999), Gvirtzman and Stanislavsky (2000), Stiller et al. (2009), Katz and Starinsky (2009)
Collision margin burial	Timor Gap, Northwest Australia, Silurian	Mio-Pliocene inversion event reactivated fault-focused brine flow to surface breaches supplied from Mesozoic reservoirs with the brine originally derived from Silurian salt and showing episodic rejuvenation of long-lived structures.	O'Brien et al. (1999), Lisk et al. (2000), Harrowfield and Keep (2005)
	Pyrenees, Southern France and Northern Spain, Triassic	Evaporitic basinal fluids became syntectonic fluids in igneous basement. Brine direction was an evolving system with flow intensity and style of injection controlled by the structural stage of overthrust.	Bitzer et al. (1998), Travé et al. (2000), McCaig et al. (2000), Abalos et al. (2008)
	Slave Point Formation, Canada, Devonian	Post Cambrian to pre-Cretaceous compression, associated with orogeny, squeezes basinal brine through carbonates of southern Rockies and drives formation of saddle dolomites of Presqu'ile and MVT deposits.	Nesbitt and Muehlenbachs (1994), Morrow et al. (2002); Lonnee and Machel (2006)

(continued)

Table 8.1 (continued)

	Location and age of brine source	Role of salt	Reference
Post Orogenic burial	Ebro Basin, Spain, Triassic	Dissolution of buried evaporites caught up in the hydrology of compressional belt supplied much of the ionic content (& meganodules) to active evaporite systems in the Miocene outflow zones in adjacent foreland depressions	Salvany et al. (1994), Sánchez et al. (1999), Ortí et al. (2012)
	San Andres Formation, West Texas, Permian	Modern, deeply circulating Na–Cl brines in arkosic sandstone aquifers acquired their high salinity through the dissolution of halite and so displaced Permian age reflux brines and drove local gypsification of anhydrite (1,829 m)	Bein and Dutton (1993), Stueber et al. (1998), Amadi et al. (2012)
	Alberta Basin, Canada, Devonian	Two brine system; a 'heavy brine' that is a residual Middle Devonian evaporitic brine and a 'light brine' that probably originated from dilution of 'heavy brine' by deeply-circulating meteoric fluids in post-Laramide time.	Michael et al. (2003), Gupta et al. (2012)

sedimentation rates in the basin depocentre (Fig. 8.1b; Table 8.1). Pull-apart basins are an integral part of intraplate and interplate strikeslip fault zones in both rift and collision settings and tend to form at bends or sidesteps in the main strike-slip fault system (Fig. 5.32). Hence, in many salt tectonic provinces, such as the Zagros fold and thrust belt, there is a kinetic and mechanical relationship between releasing bends of strike-slip faults and the positions of salt diapirs (Fig. 6.90; Koyi et al. 2008).

When located in arid zones, sediment fill in a rapidly subsiding pull-apart basin can entrain thick salt beds, which subsequently become halokinetic. Such salt masses typify modern pull-aparts, such as the Dead Sea basin in the Middle East and Salar de Antofalla in NW Argentina (Stanislavsky and Gvirtzman 1999; Kraemer et al. 1999). Rapid burial, so typical of this setting, quickly moves thick salt sequences into the subsurface, while contemporaneous salt dissolution can move large volumes of dense hypersaline brines into adjacent aquifers. High rates of subsidence and sediment fill, along with consequent overpressuring, means porosity in associated nonevaporitic sediments can be maintained to much greater depths compared to similar lithologies in a typical passive margin deposit.

The collision margin burial realm is characterized by compressional tectonics, thrust faulting, extensive fracturing of strata and episodic movements of basinal fluids, typically in response to tectonic loading (Fig. 8.1c). Hot (100° to >250 °C), saline and highly pressured fluids are driven laterally out of the collision zone, via porous and permeable horizons, typically toward the craton or continental interior and vertically along faults and fractures (Oliver 1986). Such systems tend to characterise foreland basins, which in arid regions can become areas of interior drainage that quickly fill with various salts, as in seen in the widespread Miocene marine evaporites of the Zagros/Arabian Gulf region or the lacustrine trona deposits of the Eocene Green River Formation in the USA.

Buried evaporite beds caught up in a compressional suture are likely to be pressurized and remobilised, while cross-flows of less saline basinal fluids, as they are squeezed out of the non-evaporite sediments in the collision zone, can drive evaporite dissolution further toward the basin edge. The resulting chloride-rich brines may in turn become metal carriers. Compression-driven hydrologies can precipitate widespread burial dolomites and PbZn deposits, both within the orogenic belts and in the adjacent continental interior. The similarity between geochemistry of fluid inclusions in sphalerite in strata-bound sulphide deposits and that of oil field brines in the U. S. Gulf Coast sedimentary basin led Sverjensky (1986) to conclude that oil field brines can readily evolve into ore-forming solutions (Chap. 15).

The post-orogenic burial setting is characterized by a lack of intense tectonic activity, the dominance of topographically driven flow, telogenesis, and by relatively high fluid flow rates, which in zones of deep artesian circulation range from 1 m/year to 30 m/year (Fig. 8.1d). Flow is driven by elevation gradients created during uplift in the preceding orogenic phase. Postorogenic fluid flow takes over once the main phase of tectonic collision ends. This hydrologic style drives the dissolution of many buried salt units in continental interiors, encompasses the generation of Na-Cl brines, and gypsification of anhydrite (at depths that exceed 1,800 m), as is occurring today in the Permian and Michigan basins of the USA, the European Alps and the High Atlas.

Steep topographic gradients about basin edges of all three basin stages can create topographically-driven nearsurface fluid flow rates as high as 20 m/year in aquifers in the high relief portions of the basin (rift rim, transform edge, and

orogenic uplift zones). These are much higher rates compared to flow in low relief topographic settings such as passive margins and intracratonic sags, where nearsurface regional flow rates are typically ≈ 1 m/year, with local thermal- and density-driven flow rates up to 10 m/year. Fracturing and karstification in any aquifer system creates higher local flow rates that can be orders of magnitude greater than that measured in the matrix.

Gradients within shallow aquifers beneath the more central parts of a basin's depocentre are less than in the steep-sided tectonically active margins, but can still be of the order of metres per year. Deeper aquifers in all basins have much slower flow rates (compared to nearsurface rates) and are typically measured in metres per year or less. Free convection cells driven by the buoyancy forces associated with temperature and salinity fields about salt allochthons have flow rates in typical temperature and density drive convection cells ≈ 1 m/year, depending on thickness of the aquifer, fluid-density gradient, and regional permeability (Hanor 1987). Flow rates in deep aquifers within the cores of orogenic belts are typically ≈ cm/year and dissipate quickly when stress is alleviated (Garven 1995). Regional flow rates generated by compaction in a mud-rich sedimentary basin are typically much less than a cm/year, with locally or temporally higher rates during fault or microfracture venting of overpressured zones.

The presence of a subsurface evaporite unit, as it flows and dissolves, creates brine and density inhomogeneities that facilitate active and long term brine mixing interfaces and much higher local rates of subsurface fluid flow. For example, flow rates within descending brine plumes beneath thick buried and dissolving Miocene salt masses in the Dead Sea region are as high as 10 m/year (Stanislavsky and Gvirtzman 1999). These rates approach those in aquifers in the margins of a high relief basin. Flow gradients tend to be highly variable throughout all sedimentary basins containing flowing and dissolving salt.

The various tectonic process and the associated flow-drivers can co-exist in any salt floored basin, long after the original tectonic setting that deposited and buried the salt has passed (Fig. 8.2). In the salt floored Sverdrup Basin of the Canadian Archipelago the source of high salinity subsurface waters is clearly dissolving salt structures (Fig. 8.2) but the pore fluid movements are also influenced by the generation of biogenic and thermogenic gas, independent of salt dissolution and its Mesozoic sediment hydrology (Grasby et al. 2012). The Sverdrup Basin shows a general increase in average salinity values with depth, but at any given depth in the Sverdrup Basin there tends to be a much higher degree of variability at a particular depth than in other less tectonically mature salt-floored basins such as the Gulf of Mexico (Fig. 8.3a). Fresh to brackish to saline waters are observed in each Sverdrup sequence down to the 4 km limit of data availability (as studied by Grasby et al. 2012 and references therein). The Mesozoic section of the Sverdrup Basin was deposited in an open marine to freshwater siliciclastic system. Sedimentary basins of this nature that lack evaporite deposits typically do not have brines present (e.g. Mahakam basin, Indonesia; San Joaquin basin, California; Pattani basin, Thailand; Beaufort Basin, Alaska). In such basins where seawater evaporation wasn't significant, or secondary dissolution of evaporite beds was not prevalent, formation water salinities seldom exceed that of seawater itself (Fig. 15.3).

While the average salinity range for some formations in the Sverdrup Basin are near that of seawater, others greatly exceed seawater salinity (over 200 g/L) (Fig. 8.3a).

While evaporite units were not deposited in the Mesozoic section studied here, thick deposits of halite and gypsum are present in the underlying Late Carboniferous (Bashkirian) Otto Fiord Formation (Fig. 8.2b). These evaporite units form salt diapirs, which penetrate the Mesozoic sequence, and are exposed at the surface in many parts of the basin, as well as forming salt-cored anticlines (Fig. 8.2a). High salinity Na–Cl dominated spring systems, found on both Axel Heiberg and northern Ellesmere islands are also shown to derive salinity from sub-surface halite dissolution, whereby active modern hydrogeological systems are bringing freshwater into the subsurface and dissolving buried salt deposits.

Brines in the Sverdrup Basin are Na–Cl dominated and show a 1:1 NaCl ratio, consistent with halite dissolution driving brine generation. The spatial variation of TDS shows that the highest salinity brines in the basin are found in the region where there is a high occurrence of salt cored uplift and surface expression of diapirs (Fig. 8.2a), similar to diapirs that locally generate brines in other basins such as the Gulf of Mexico and Zechstein basins. As a result, while waters of the Sverdrup Basin are in general similar to the salinity of seawater, high salinity brines are formed locally due to halite dissolution in areas where salt diapirs have pierced major aquifer units and thermohaline mixing dominates.

Large regional aquifers (e.g. Heiberg and Isachsen formations) show the widest range of salinities and have averages much higher than seawater, whereas less regional, or shaly, systems (e.g. Roche Point, Bjorne formations) have a lower range of salinity and averages close to seawater (Fig. 8.3b). But in the vicinity of salt piercement these otherwise lower salinity range aquifers host hypersaline pore fluids. According to Grasby et al. (2012) this is similar to other basins where there appears to be a lithologic control on salt dissolution, such as the Gulf of Mexico and Tarim basins (see later). The high permeability of regional sand aquifers allows for faster generation of brines through density-driven circulation as well as being more prone to topographically and compaction-driven fresh water influx, especially about the basin margins.

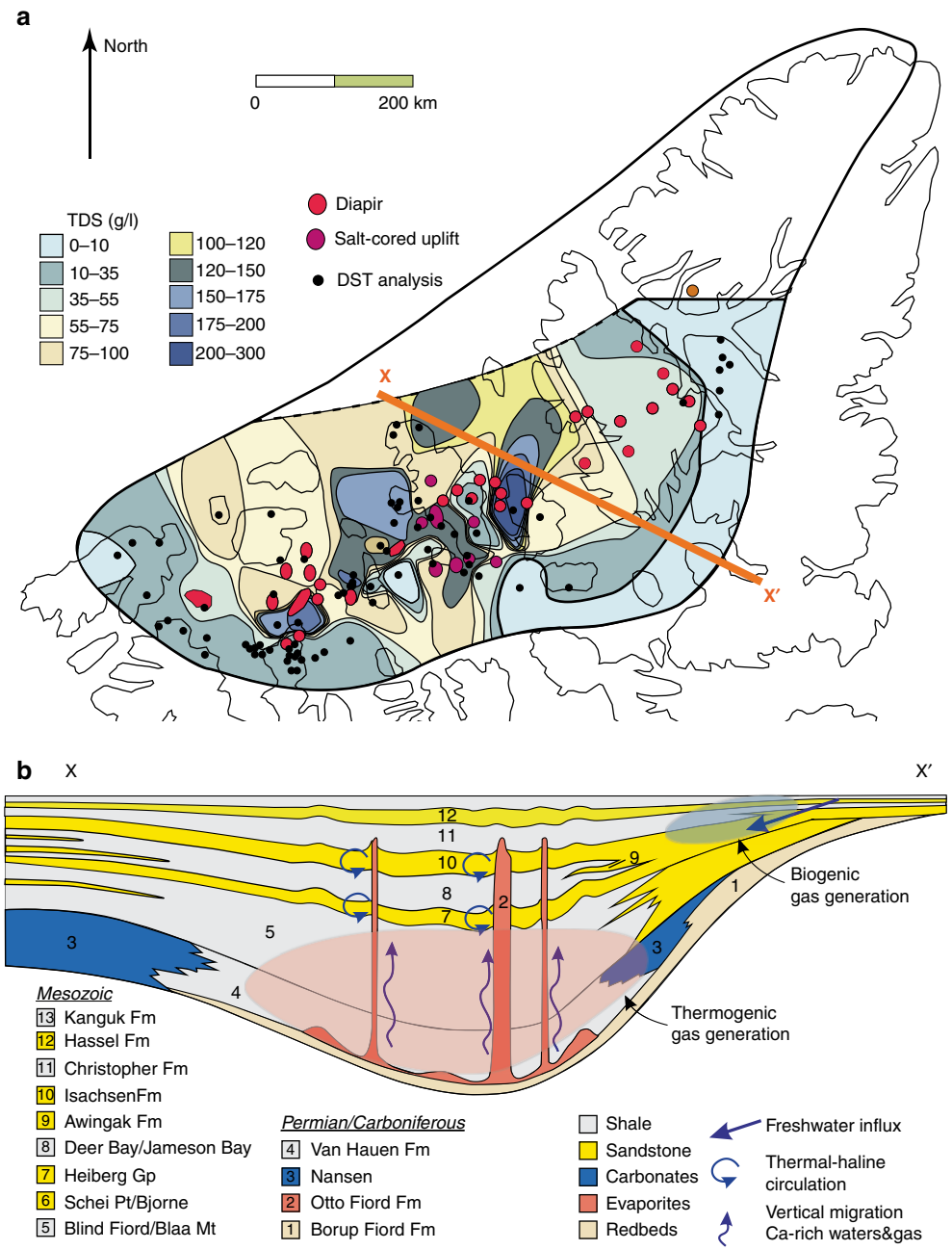

Fig. 8.2 Salt and salinity in the Sverdrup basin. (**a**) Spatial variability of TDS in the Sverdrup Basin along with locations of salt-cored anticlines and surface exposed diapirs. (**b**) Cross section in the Sverdrup Basin (see (**a**) for location) showing simplified stratigraphy and sandstone aquifers, along with major salt related and catagenic fluid flow processes thought to affect formation waters in the basin (After Grasby et al. 2012)

Thus, while formation waters in the Sverdrup Basin are in general consistent with a seawater origin, there is high variability in formation water geochemistry. Local anomalies of very high salinity waters are associated with salt piercement structures and salt dissolution driving thermohaline circulation (Fig. 8.2a). Dissolution of halite from the diapir edges formed localised brines with over an order of magnitude higher TDS concentration than average for the basin (Fig. 8.3b). In contrast, fresh water influx lowered salinities along the basin margins. This fresh water influx also appears to have initiated generation of biogenic gas by lowering TDS and concentrations of SO_4 below inhibitory levels and depressing the local temperature field that would normally inhibit methanogenesis. At the same time catagenesis is associated with the vertical migration of Ca-Na-HCO_3 enriched basinal brines. Mixing interfaces between these various waters drives more intense diagenetic alteration in these zones.

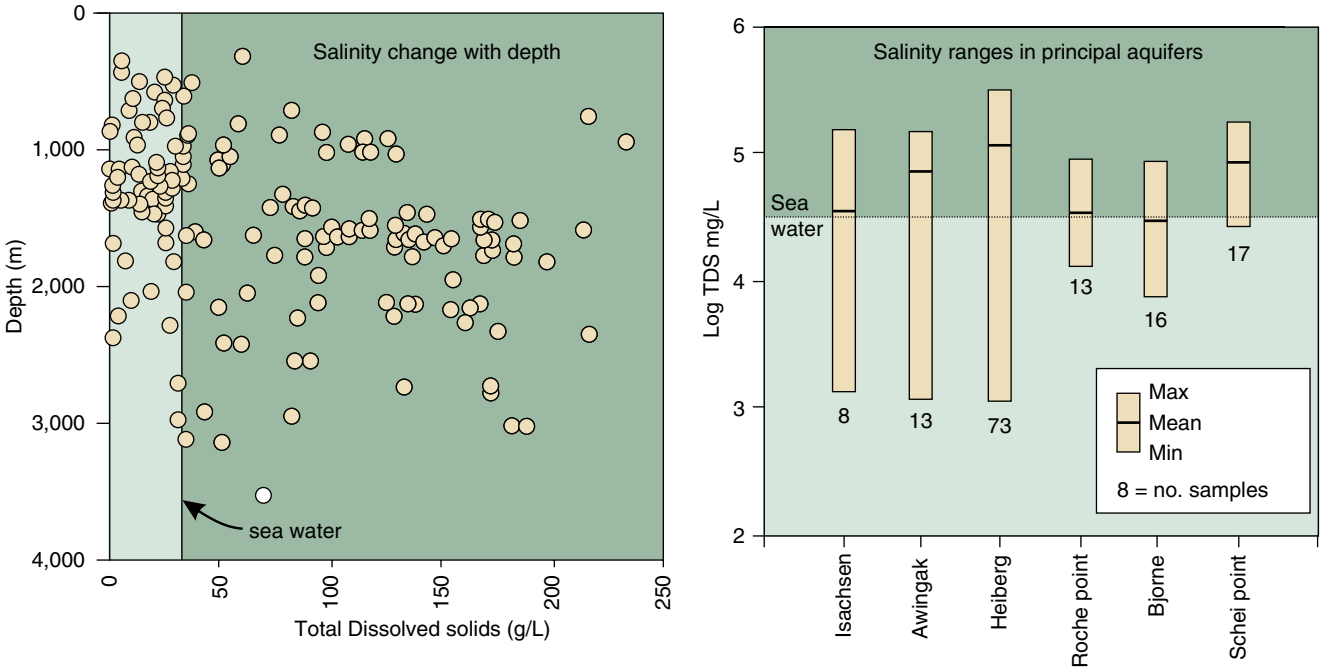

Fig. 8.3 Pore fluid salinity in various wells in the Sverdrup Basin, Canada. (**a**) Plot of total dissolved solids vs. sample depth for all formations, (**b**) plot showing mean average and range of total dissolved solids (TDS) for key sandstone aquifer units Seawater salinity is defined by the contact between light (fresh-brackish) and dark (hypersaline) *green* shading (After Grasby et al. 2012)

Fluids in Subsiding Basins

The zones of compactional and thermobaric/thermohaline flow lie beneath the zone of active phreatic circulation. The zone of active phreatic flow is typically tied to topography, surface-related processes, such as brine reflux and the position of the shoreline (see Chap. 2). The compactional and thermohaline zones, rather than the active phreatic zone, dominate the greater part of any sediment pile accumulating within an extensional zone in a passive margin, or in the subsiding foreland depression fill of a compressional regime or in the rapidly subsiding parts of pull-apart basins. As well local cementation, these same fluids can drive the formation of exotic or "out of sequence" cements (Neilson and Oxtoby 2008).

Compactional Fluids

The compactional regime is characterised by the upward and outward expulsion of pore waters formerly trapped within the compacting sediment pile. If fluid cannot freely escape, the compacting sediment may become overpressured. Compactional waters include connate[2] waters, waters modified by brine-rock interactions, and meteoric waters originally buried within shale, sand or carbonate aquifers. Compactional or consolidation-related flow is a typical response to basin subsidence and ongoing sedimentary loading, which drives out interstitial fluids from compressible and hydraulically conductive buried strata. As it needs overburden loading to drive it, compactional fluid flow is characteristic of the mechanical dewatering stages of the basin's burial history and it dominates the early subsiding and filling stages of a sedimentary basin. Compactional loading of more mature sediment piles can be reactivated in regions of thrust sheet stacking, which can renew brine expulsion from the buried matrix (Fig. 8.1c; Garven 1995). In this case it is the loading of the thrust sheets and the lateral compression of the basin that drives further fluid expulsion. It is a process that is quickly alleviated once thrust stacking ceases (Bitzer et al. 1998).

Compactional flow as an early-burial fluid migration mechanism is typical of young rapidly subsiding nonevaporitic

[2]Connate waters are subsurface waters with chemistries near-identical to those of waters, which were present in the pores at the time of deposition (Hanor 1994a). The term connate comes from the Latin (*connatus* = born with). Connate properties of subsurface brines include connate isotopic properties, connate Br/Cl ratios and other ionic proportions. Very few subsurface waters are truly connate because ongoing subsurface chemical alteration and diagenesis (water-rock interaction) influences the chemical make-up of most entombed waters. Some authors use the term connate interchangeably with the more general term subsurface water, but to avoid confusion its use should be preserved for those waters and brines that are truly connate (Hanor 1994a). Hence, most basinal brines are not connate, this is especially obvious in subsurface regions where thick evaporites are dissolving creating high salinity Na-Cl dominated brines.

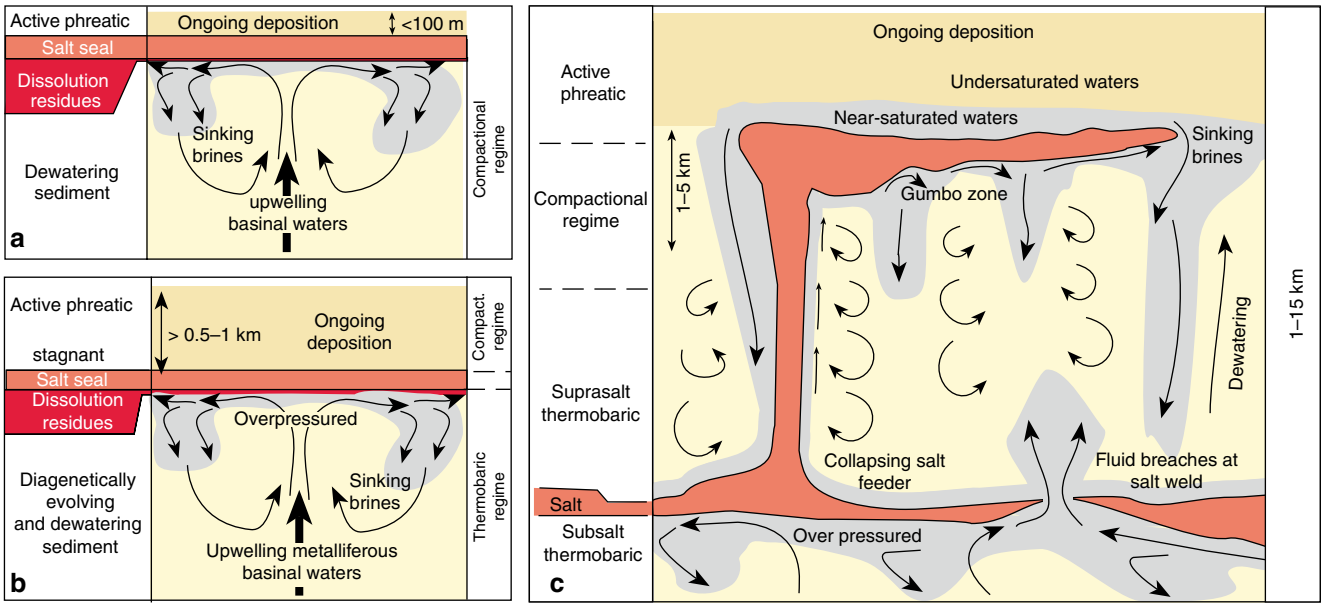

Fig. 8.4 Brine flow regimes. (**a**) Compactional regime. (**b**) Thermobaric regime. (**c**) Flow regimes in diapiric province, also shows potential region for escape of hydrocarbon bearing or possibly metalliferous fluids at breach zones in flowing salt bed (salt welds, growth faults, fault welds, etc.)

basins, where it dominates mud-rich sections deeper than 1,000–2,000 m (e.g. many Tertiary basins in SE Asia). Sediment ages in these basins typically range up to a few tens of millions of years. Differences in pressure heads between adjacent areas are the main driving force to fluid flow and the systems are often compartmentalised by growth faults and mud diapirs. Most expelled fluid tends to move upward through still porous overlying strata during the earliest stages of compaction (Magara 1986). Then, in the later stages of compaction, as interbedded clays become relatively impermeable, the principal direction of fluid migration becomes stratigraphic and is controlled by interbedded permeable beds of less compacted and variably cemented sandstones and carbonates.

In contrast, a subsiding basin succession entraining a widespread evaporite bed always contains a highly effective aquitard/aquiclude, almost as soon the salt is deposited. If water-saturated sediments are compacting beneath a thick rapidly accumulating unit of basinwide evaporites, its underside deflects the otherwise upward flow of escaping compactional waters (Fig. 8.4a). Rising compactional water is initially undersaturated with respect to the evaporite salt but the salt's edges quickly becomes a zone of salt dissolution and accreting insoluble residues (Chap. 7). Water flows obliquely along the underbelly of the dissolving evaporite bed until it reaches a breach in the salt or the edge of the bed. There fluid flow may once again become strongly vertical. As a general rule of thumb, thick evaporite units in a subsiding basin will focus and pond upward-escaping compactional waters and restrict regions of brine escape to areas atop fractures, growth faults, dissolution-induced breaches, or dissolution edges of the evaporite unit. Halokinesis, through its inherent thickening and thinning of bedded salt, may help focus fluid escape via welds into breached salt withdrawal basins, typically situated between growing salt anticlines, allochthon sheets and diapirs (Fig. 8.4c).

Thermobaric-Thermohaline Fluids

Thermobaric fluid[3] flow occurs in the deeper parts of a sedimentary basin where the temperatures and pressures are greater and is intimately related to compactional flow in its uppermost parts (Fig. 8.4b, c). By definition, it is a zone of widespread diagenetic alteration where significant volumes of "new" pore waters are released by dehydration of clay minerals and catagenesis or the dehydration of hydrated evaporite minerals, such as gypsum to anhydrite or carnallite to sylvite. Fluids in the thermobaric/thermohaline regime move in response to pressure/density gradients generated by the related phase changes, such as the generation of hydrocarbons, or the release of mineral-bound water, or ongoing lithostatic loading (Fig. 8.5). Density contrasts created by salinity or temperature gradients beneath or adjacent to a

[3]Thermobaric is typically considered to indicate a higher-pressure, higher-temperature pore fluid and is contrasted by some authors with thermohaline waters indicating higher-temperature higher-salinity fluids. Sometimes the terms are considered interchangeable and some authors use them in place of the term hydrothermal, others consider them separate definitions. Usage of all three terms in the literature can be poorly constrained. Using a general term such as "subsurface waters" with an appropriate discriminator as a prefix, such as; hypersaline, pressured, heated, etc., may be more apt.

dissolving salt bed can drive laterally extensive subsalt convective flow cells made up of thermobaric/thermohaline pore waters. Chemical changes in the sediment matrix mean thermobaric/thermohaline waters frequently contain methane, carbon dioxide and hydrogen sulphide derived from the thermal alteration of organic matter, as well as metals leached from basinal shales and volcaniclastics (Aquilina et al. 2011). Interfaces associated with mixing of varying thermobaric and thermohaline water masses are regularly focused into fault damage zones where permeabilities are periodically elevated (Table 8.2).

Low permeabilities of deeply buried sediment between or below impervious evaporite beds mean typical regional rates of fluid flow in intra or subsalt beds are slow (mm-dm/year) except in zones of seismic pumping and faulting (Table 8.2; Shaker 2008). As in compactional zone hydrologies, it is in the interval adjacent to a salt bed where overpressure tends to develop best and long-term flow rates are elevated, regularly aided by processes such as natural hydrofracturing. Rates of fluid flow and the rate of creation of mixing zone interfaces can be enhanced by the formation of temperature anomalies in the buried sediment, which are tied to the higher conductivity of salt.

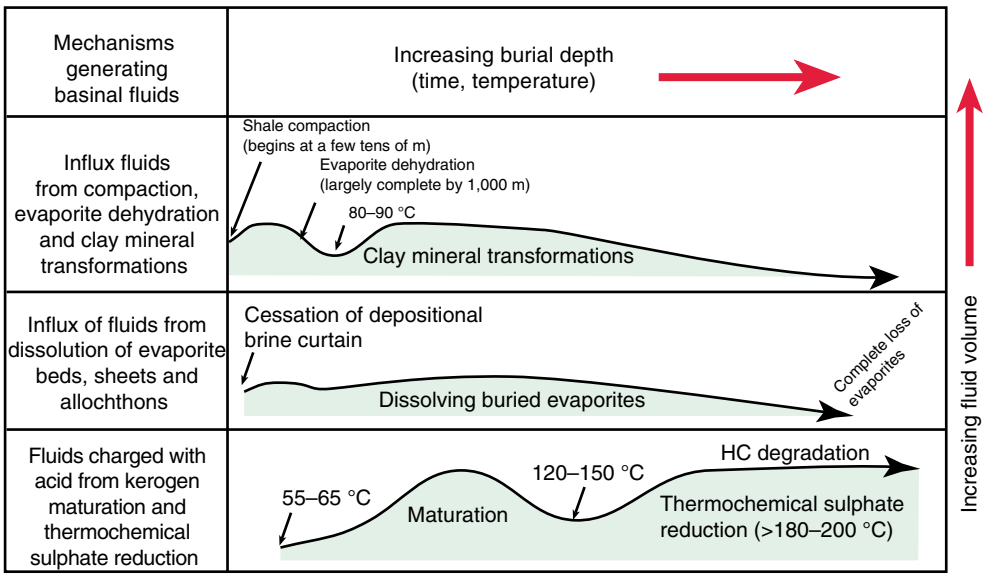

Fig. 8.5 Mechanisms that release thermobaric waters into a basin with thick buried evaporites. Increasing burial releases fluids (brines, acids or gases) as indicated by the shaded portions of each row. The fluids would interact and when undersaturated with respect to the salt mass may have increased the rate of salt dissolution. (No vertical scale is implied)

Table 8.2 Selected examples of mesogenetic hypersaline subsurface flow-focused diagenetic alteration.

Occurrence, host age and reference	Hydrothermal aspect	Comment
Pb-Zn-Ba ore, Jebel Hamra, Central Tunisia; Cretaceous – Upper Aptian; (Bejaoui et al. 2013)	Pb-Z-Ba mineralization is spatially and possibly genetically related to E-W trending fractures, which acted as conduits and/or depositional sites for circulating hydrothermal fluids. Fluid inclusion and sulphur isotope data suggest the contribution of evaporite-derived basinal brines in ore formation.	Mineralization occurs as stratiform lenses, and breccia- and paleokarst-fillings. Ore reserves are around 0.5 Mt and grades are 7 % Zn and 3 % Pb. Sulphide mineralization occurs as local replacement of dolomitised and silicified carbonate strata. Combined field, sedimentological, mineralogical, isotopic and geochemical data of the Lower Cretaceous mineralization in Jebel Hamra is compatible with Mississippi-Valley-type mineralization.
Dolomites in Albenza Formation, Alps, Northern Italy Jurassic (Ronchi et al. 2011)	An increase in the precipitation temperature (up to 130 °C) and a decrease in diagenetic fluid salinity (from marine to brackish) are observed from the first pervasive replacement dolomite to the dolomite cement phases. Dolomitization was limited to palaeohighs or faulted platform margins in the Early Jurassic carbonates. The pervasive replacement phase is interpreted based on a 'compaction model'; the formation fluids expelled from compacting basinal carbonates were funnelled along faults into permeable palaeohighs.	Petrographic analyses showed a first, pervasive, replacement dolomitisation phase (D1) followed by volumetrically less important dolomite cement precipitation phases (D2, D3 and D4). The $\delta^{18}O_{PDB}$ values fall between −8.2 and 0.1‰, with the more depleted samples belonging to dolomite cement-rich dolostones; the $\delta^{13}C_{PDB}$ ranges from 2.6 to 3.7 %. Analysis of trace elements showed different Fe and Mn contents in the sub-surface and outcropping dolostones, and a higher Fe in the younger dolomite cements. Dolomite cements precipitated according to the 'tectonic squeegee' dolomitisation model

(continued)

Table 8.2 (continued)

Occurrence, host age and reference	Hydrothermal aspect	Comment
Hydrothermal dolomite, Reinecke field, West Texas; Upper Pennsylvanian Lower Permian; (Saller and Dickson 2011)	Fine to coarsely crystalline dolomite with undulose extinction that formed diagenetically late and constitutes ≈25 % reservoir matrix. These dolomites overgrow stylolites, indicating precipitation during deep burial. Low $\delta^{18}O$ values, consistent with primary fluid inclusions, indicate dolomite precipitation or recrystallization at 92–118 °C.	Two types of dolomite; (a) stratiform, replaced micrite-rich facies, and is interpreted as early dolomite that recrystallized in hydrothermal brines. (b) crosscuts stratigraphy and depositional facies with vertically continuous morphologies that trend NW-SE. This dolomite forming in hydrothermal brines derived from latest Permian-aged highly evaporated seawater brines that descended deep into the basin because of their greater density and then ascended because of heating and thermal convection.
Jean Marie Member (Redknife Fm.) July Lake Area, NE British Columbia, Canada Devonian (Upper) (Wendte et al. 2009)	Pure dolostones occur as metre-thick bodies, at the very top of the Jean Marie in only a few wells. Dolomite also occurs as a selective replacement of internal sediment infilling fractures. This mode of occurrence, as well as the patchy distribution of pure dolostones at the very top of the Jean Marie, suggests that matrix replacement dolomites formed from fluids that were delivered from flow through a vertical, or near-vertical, fault-conduit system, rather than from fluids that were delivered from flow laterally through matrix pores in a stratal-controlled system	Later mineral phases, including (in paragenetic order) saddle dolomite cement, sphalerite, dickite and baryte, are also interpreted as part of the fault/fracture controlled system of diagenesis. The homogenization temperatures of saddle dolomite range from 80 °C to 163 °C and those of sphalerite and baryte, collectively, from 55 °C to 126 °C, with a broad range of calculated salinities for all these phases ranging from approximately 9.0–27.0 wt% $NaCl + CaCl_2$ equivalent. The wide range of salinities for these phases is interpreted to be from the mixing of evaporative brines with less saline formation waters away from the fault/fracture conduits. Hydrothermal diagenesis possibly starting as early as latest Devonian and continuing into the early Mississippian, at burial depths no deeper than approximately 900 m
Trenton-Black River dolomites, Mohawk Valley, New York State, USA; Silurian; (Slater and Smith 2012)	Linear dolomite bodies occur in outcrop suggest that host carbonates have undergone significant fault-related hydrothermal alteration. Dolomite occurs in the Lower Ordovician Tribes Hill Formation, which is regionally a Lower Ordovician shaly limestone with patchy dolomitisation	The outcrop has an en echelon fault, fracture, and fold pattern. Most of the dolomitisation occurs in fault-bounded synclines or sags flanked by anticlines. The dolomite structures are highly localized, occurring around faults, and are absent away from the faults and fractures. Area serves as a scaled analog for the Trenton–Black River hydrothermal dolomite reservoirs of eastern United States
Bitumens in Ara Group salts, South Oman Salt Basin Cambrian-Precambrian Boundary (545 Ma (Schoenherr et al. 2007a, b, c)	Vitrinite reflectance shows highly heterogeneous maximum paleo-temperatures. Paleo-temperatures of 380 °C were obtained from coke-like solid reservoir bitumen, which most likely formed from thermal cracking of oil. This process is related to hydrothermal fluids, deriving from deeper pre-salt strata, which entered the intra-salt carbonate stringers during times of basement tectonic activity via hydrofractures	Solid reservoir bitumens from the Ara Group indicate a polyphase hydrothermal evolution. Salt diapirs encase isolated, partly highly overpressured carbonate bodies (intra-salt "stringers") which represent a predominantly self-charging hydrocarbon system. A large number of stringer cores show that reservoir quality is decreased by the presence of solid reservoir bitumen. High maturities ("pyrobitumens") occur in close vicinity to the fractures and precipitation of "migrabitumens" with increasing distance to the hydrothermal source
Sparry magnesites and dolostones of the Ibor Group, Western Spain; Ediacarian 635–542 Ma); (Herrero et al. 2011)	D_1 is a relatively early dolomite replacement of fine grained peritidal limestones. Coarser crystal size of D_2, which shows similar geochemical features as D_1, formed by dolomitisation of coarser grained limestones. The replacement of D_1 and D_2 by M_1 and M_2 advanced along stylolites, fractures and bedding planes fed by hydrothermal fluids, co-associated presence of talc and forsterite. D_3, a coarse dolomite, completely destroyed any previous texture and D_4 (dolomite cement) post-dates magnesite formation.	Dolostones (D_1–D_4) and magnesites (M_1–M_2) formed by hydrothermal replacement of primary peritidal limestones. Oxygen and carbon isotopes of D_1–D_4 overlap with $\delta^{18}O_{SMOW}$ values ranging from −15.12 to −13.12 ‰ and $\delta^{13}C_{PDB}$ from −0.13 to +3.21 ‰. Sr isotope values for D_1 and D_2 range from 0.7028 to 0.7091. Magnesites (M_1 and M_2) show oxygen values higher than −12.77 ‰, and $\delta^{13}C_{PDB}$ values show the same variability as for the dolomites. D_3 and D_4 oxygen isotope values are between −11.76 and −11.09 ‰, and the carbon isotope values range are similar to the other diagenetic phases. Sr isotope values for the magnesites and late dolomites (D_3 and D_4) are 0.7095–0.7104, being higher than those of the D_1 and D_2 dolomites

Fluid density tends to increase in thermobaric/thermohaline waters in contact with the dissolving edges of salt units and the direction of regional brine flow is typically focused by the salt edge (Fig. 8.4). These brines have locally anomalous chemistries and can drive diagenetic alteration when mixed with cooler less-dense brines derived from adjacent sediments. For example, the Slave Point, Sulphur Point and Keg River formations of Northeast British Columbia contain numerous gas fields, particularly along the preferentially dolomitised reefal shelf edge margin (Morrow et al. 2002). The typical reservoir facies is a coarse-crystalline white dolomite known as the Presqu'ile Dolomite. It follows the shelf edge within the Slave Point Group, but coarse-crystalline dolomite is also regionally extensive within underlying strata. The dolomite is made up of two geochemically distinct but related phases, both precipitated from thermobaric waters, along with exotic cements such as anhydrite and celestite (Fig. 8.6a; Neilson and Oxtoby 2008).

The organic-rich Klua Shale, the Otter Park Shale, and marlstones equivalent to the Sulphur Point and Slave Point formations are aquicludes that blocked the upward and lateral flow of warm dolomitising brines derived from dissolution of buried evaporites (Fig. 8.6b). Presqu'ile dolomitisation along the Slave Point shelf edge is interrupted in places where the Klua Shale extends shelfward underneath the Slave Point Formation. The Watt Mountain shale was also a regional aquiclude that prevented upward circulation of dolomitising fluids in areas behind the Slave Point shelf edge. The flow of dolomitising NaCl-$CaCl_2$-$MgCl_2$-H_2O brine solutions began early in the shallow subsurface perhaps even as their brine source (Slave Point evaporite) was still being deposited. This precipitated dolomite cements (type 1) at temperatures >50 °C, during northwestward-directed shallow subsurface brine reflux from the Elk Point evaporite basin. This was followed by later upward-directed subsurface convective flow of NaCl-$CaCl_2$-$MgCl_2$-H_2O and NaCl-$MgCl_2$-H_2O brines, generated by the ongoing burial dissolution of evaporites, mixing with less saline thermobaric waters escaping from nearby shale and so precipitating later dolomite cements (type 2). These type 2 dolomites are much less voluminous than type 1 and precipitated at temperatures ≈ 130 °C during the Late Devonian-Carboniferous. Later lower salinity brines that precipitated late calcite cements and some latest type 2 dolomite may have interacted with connate fluids of marine origin or, less likely, with meteoric fluids (Morrow et al. 2002; Wendte et al. 2009).

The importance of a buried, slowly dissolving, salt mass in focusing thermobaric fluid flow throughout much of a basin's burial history was also illustrated by Wolfgramm and Mumm (2000). They used fluid inclusion analyses to reconstruct the spatial and temporal variation of fluid composition and thermal properties within sediments beneath the Zechstein salt in northeast Germany. Precipitates from early thermobaric fluids, migrating in the deeper parts of the basin, were characterised by complex salinities, with sulphur contents that increased toward the contact with the Zechstein. This suggests a partial exchange with the overlying evaporites. Inclusions of coexisting fluids dominated by NaCl,

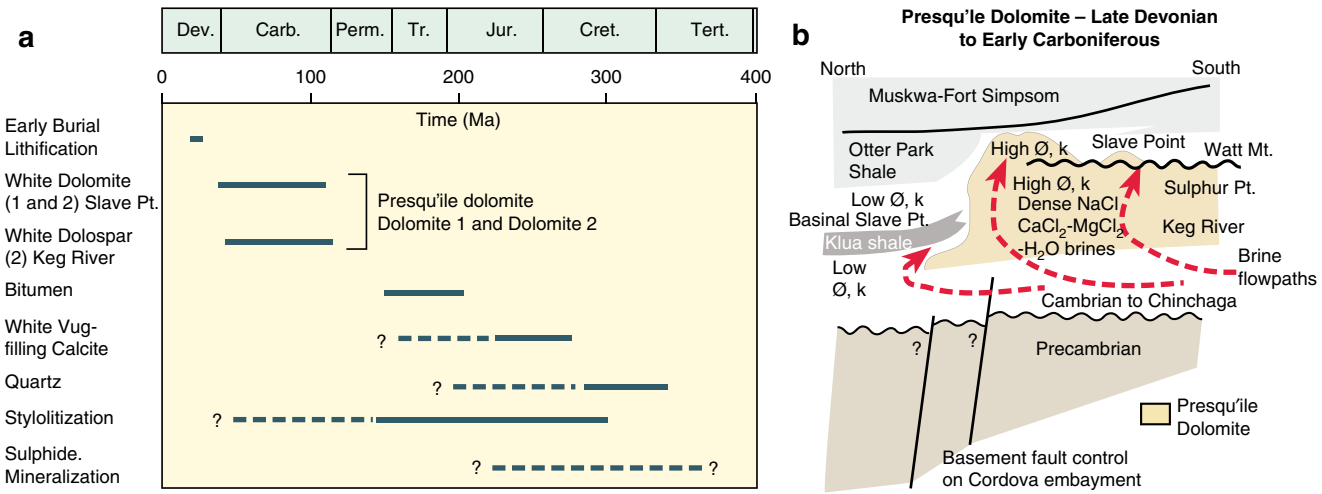

Fig. 8.6 (**a**) Chart of diagenetic events for the Keg River to Slave Point strata. Presqu'ile dolomitisation (dolomite 1 and dolomite 2) precedes the thermal maturation of organic material and the emplacement of reservoir bitumen. Calcite cementation coincides approximately with the onset of gas generation followed by minor quartz and sulphide (sphalerite and galena) cementation. (**b**) Schematic reconstruction of time of dominant Presqu'ile dolomitisation around the Cordova embayment. Dense residual Elk Point brines flowed downdip and northwestward by gravity displacement of less dense subsurface fluids. This flow was confined beneath the Watt Mountain Formation shale. The absence of this confining layer allowed upward flow of brines into the overlying porous Slave Point Formation, where downdip brine flow may have been deflected upward against the low permeability basin fill of shaly units of the Cordova embayment. Initially, dolomitisation occurred at temperatures below 50 °C, but an increase in basal heat flow and ongoing burial caused dolomite precipitation to continue at 130 °C (After Morrow et al. 2002)

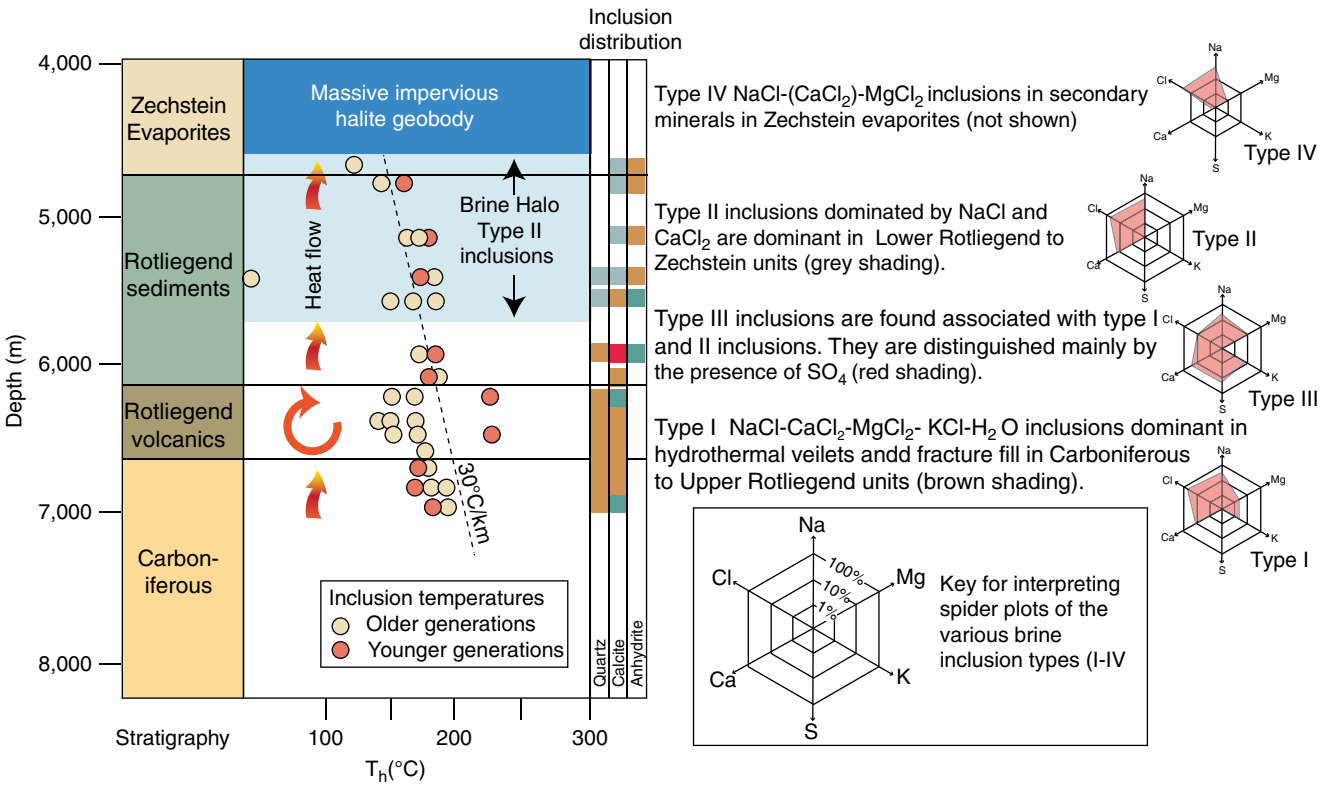

Fig. 8.7 Inclusion homogenisation temperature (T_h) versus depth in the Parchim 1/68 well, NE German Zechstein Basin. Plot is based on measurements of inclusions with varying chemistries (Type I–IV) collected from authigenic cement phases (quartz, calcite, anhydrite) Plot distribution shows the strong influence of salt dissolution brines on authigenic/pore water chemistry across a zone several hundreds of metres thick below the dissolving Zechstein salt mass (Adapted from Wolfgramm and Mumm 2000)

$CaCl_2$ and KCl are largely restricted to authigenic minerals in the Upper Carboniferous sediments and Rotliegend volcanics located in juxtaposition to the overlying evaporites. Younger, secondary fluid inclusions, sometimes containing gas phases, show increasing temperatures related to further burial. Thermal properties of all fluid inclusions indicate steep thermal gradients below the base of the Zechstein and Rotliegend sediments with type II fluids indicating an ongoing plume of brine sourced in the dissolution of Zechstein salts (Fig. 8.7). This documents convective or advective heat and associated focused subsalt fluid flow in the deeper thermobaric parts of the basin. Throughout its burial history the Zechstein salt mass acts as the seal and upper focus to a widespread convective brine system until its continuity is broken by salt withdrawal and thinning.

Deep Flow in Pull-Apart Basins

Another variation on this compaction/thermobaric theme is the evolving hydrology created by rapid subsidence and fluctuating tectonics that typify transtensional basins or pull-apart basins. The best-documented example of hydrological evolution associated with a salt mass in such a setting is the Dead Sea (Stanislavsky and Gvirtzman 1999; Katz and Starinsky 2009). Deep saline pores brine in the Dead Sea region are in part a residual product of intensively evaporated seawater that seeped into the depression back in the Miocene to accumulate as a widespread marine-fed basinwide halite. In places in the Dead Sea depression (e.g. Mt Sedom and surrounds), this halite is still near the surface, kept there by ongoing salt flow (Fig. 8.8a). Dissolution of buried Miocene salt and the associated migration of residual brine today drives zones of dolomitisation within the adjacent Cretaceous carbonate aquifers. This dissolutional brine occurs in deep wells located more than a 100 km from the Dead Sea depression. The feasibility of such longterm lateral migration of brine from Dead Sea evaporites over the past 3-6 Ma, was verified by palaeohydrologic modelling (Stanislavsky and Gvirtzman (1999).

Their results show that two basin-scale ground-water systems coexist in the present Dead Sea rift valley, one atop the other but with opposite flow directions (Fig. 8.7b, c). The upper system is a topography-driven flow of meteoric water fed from the surrounding highlands, which flows eastward into the rift via shallow aquifers (<1 km deep). The second system is a density-driven migration of the Dead Sea brine moving in the opposite direction (westward) through deep

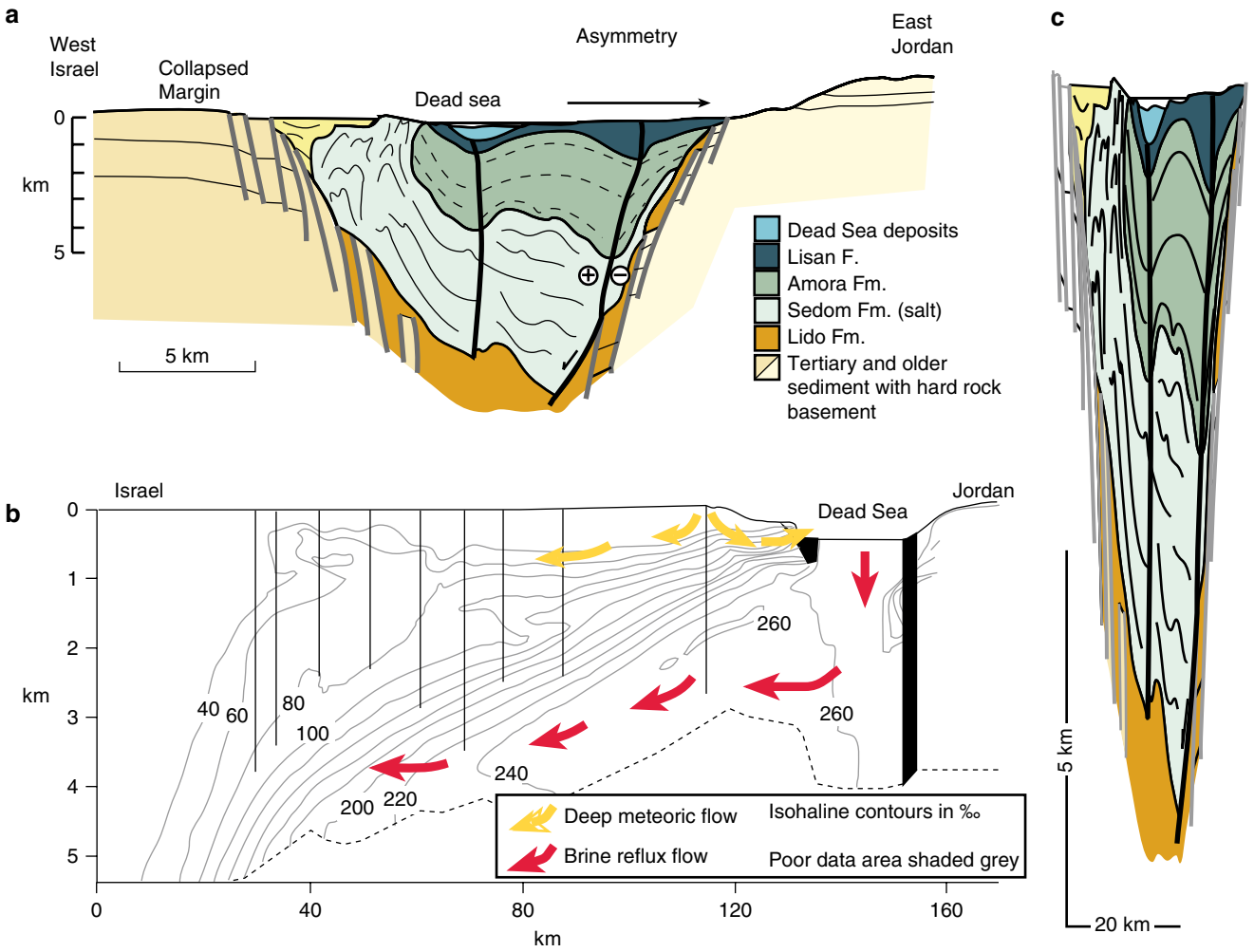

Fig. 8.8 (**a**) Dead Sea cross section showing asymmetric nature of fill. Shallow hard rock basement (aquiclude) occurs to the west of the basin fill (After Zak and Freund 1980). (**b**) Present deep westerly brine flow driven by dissolution of deeply buried Miocene salt (brine curtain: After Stanislavsky and Gvirtzman 1999). (**c**) Schematic geology based on 8.8a (which is a same scale section) stretched to match the same proportions as the vertically exaggerated scale of Fig. 8.5b so as to better demonstrate the importance of dissolving Miocene salt in driving deep brine flow

Jurassic and Triassic aquifers (up to 4–5 km deep). This deep flow is maintained by ongoing dissolution of the thick halokinetic Miocene evaporites.

The longterm configuration of these flow systems has been modified by the hydrological evolution of the Dead Sea depression (Katz and Starinsky 2009). There was an earlier (1.5–2.0 Ma) pervasive westward intrusion of brine into adjacent somewhat shallower (1–2 km) aquifers. The total mass of salt that entered the Cretaceous Judea and Kurnub aquifers at that time was 1.9×10^{11} and 3.9×10^{10} kg of salt per 1 m width slice of cross section (Stanislavsky and Gvirtzman 1999). Subsequent subsidence meant more than 80 % of that earlier shallow outward-directed brine pulse seeped back into the Dead Sea depression. In contrast, for more than 2 Ma, deep highly-saline dissolution-derived density-driven brines have been flowing westward toward the Mediterranean from the Dead Sea Basin. They have displaced older pore waters in deeply buried (2–4 km) Jurassic and Triassic aquifers across a lateral distance of more than 150 km. Clearly, this is a region where ongoing brine flushing of adjacent deep aquifers is driven by ongoing salt dissolution.

Flow in and Adjacent to Collision Belts

Compactional and thermobaric flow regimes are active as long as sediments are accumulating within areas of subsidence. With the cessation of sedimentation/subsidence, or with tectonic uplift, compaction driven flow decreases and ultimately ceases and most overpressure dissipates. When a mature basin, which is characterised by hydrological equilibrium in its sediment pile, then undergoes collision, overthrusting and basin inversion, a whole new set of

disequilibrium processes are set up and can drive renewed deep-fluid migration (Fig. 8.1c). Reverse faults and thrust welds in stacked thrust sheets in growing overthrust belts can focus fluid escape, while the thrust sheet loading acts as a huge press. Compression drives thermobaric waters out of the deeper parts of the compressing basin into the shallower basin margins, with periodic fault release sucking fluid into the fault ("squeegee" mode).

Some authors have explained MVT sulphides as forming in the basin margin zones of compressional terranes where these escaping chloride-rich metalliferous "squeegee" waters mix with topographically driven meteoric waters (Oliver 1986). This process was thought capable of precipitating sulphides in passive margin carbonate platforms located hundreds of kilometres in front of the active thrust belt. Subsequent modelling of fluid flow and heat transport in compacting and dewatering thrust belt by Deming et al. (1990) showed flow velocities created by the "squeegee" effect are in the order of centimetres per year and thermal anomalies of the order of 5 °C, neither are sufficient to make significant contributions to mass and energy transfer. Likewise, Bethke and Marshak (1990) argued that rates of fluid expulsion in convergent margins are far too low to produce efficient advective heat transport. Most models assume thrust systems that are hosted in otherwise laterally homogenous aquifers. Actual measurements, based on texture and time-aware samples for isotope determinations in fold and thrust belts, rather than generalised assumptions in computer modelling, shows orogenic thrust-focused flow is a reality, in both evaporitic and non evaporitic compressive belts (Warren et al. 2014).

The inherent assumption in this modelling of chemical equilibrium between porewater and the enclosing rock in a sedimentary basin is perhaps justified by the inherently low flow rates associated with long term widely dispersed leakage (homogenous drainage) of compactional fluids in nonevaporitic mineralogically stable sediments. But assumptions of homogeneity of fluid flow are weaker in areas when episodic and focused dewatering (seismic pumping) is occurring in association with a mass of compressed impermeable sediment, especially if it contains a salt mass. Flow velocities about the edges of any compressed but impervious salt mass can be locally high in relation to reaction rates. Drilling in compressional terranes in the Middle East and the Gulf of Mexico shows overpressure beneath sealing salt sheets periodically approach lithostatic (Shaker 2008). Vein textures and inclusion studies show hydrofracturing tends to occur preferentially and numerous times in zones of sediment adjacent to salt lubricated décollement. As fluid is sucked into these near-salt zones during fault release (typically along the base of the décollement) it doesn't come from the salt (it is impervious) but from the adjacent sediment. Then as compression takes over once more we have a system where the pore fluids drawn into the region of contact with the salt are renewed in an undersaturated state with respect to the salt mass and so are capable of dissolving salt as they are squeezed out ("squeegee" mode) along the underside of the salt mass. This gives a mechanism that drives the ongoing creation of chloride-rich waters capable of constant renewal and of carrying hydrocarbons and metals. The redox front across this interface and breach points in the salt are both capable of focusing base and precious metal precipitation (Warren 2000b).

Hence, inversion-related thrust faulting, which juxtaposes potential aquifers against pressured and dissolving evaporite beds, can mobilise focused thermobaric brine escape from deep aquifer systems. It can move hydrocarbons and metals, while at the same time precipitate late-stage authigenic evaporite cements. This is clearly seen in the authigenic sulphate cements in the Rotliegend Formation in Leman Field in the Southern Permian Basin of the North Sea (Fig. 7.99; Gaupp et al. 1993; Sullivan et al. 1994). Coarse-grained burial-stage poikilotopic anhydrite cements increase in abundance in the vicinity of faults cutting the Rotliegend sands. Isotopic data show this late stage anhydrite precipitated at maximum burial of 3.5–4 km during the Late Jurassic- Early Cretaceous, that is, at the start of basin inversion. The data indicate an unusual, short-lived catastrophic event of cross-formational fluid flow along fractures and reactivated faults induced by basin inversion. Late stage magnesite and dolomite cements may also be related to influx of the same subsurface brines.

Remobilization of basinal brine during inversion typically occurs during a compressional event many millions of years after first burial (Wilson Cycle) and may revitalise the formation and migration of hydrocarbons. For example, rising saline chloride-rich formation waters in Mesozoic hydrocarbon traps in the Timor Sea, Northern Australia are sourced in more deeply buried Palaeozoic evaporites (Figs. 8.9 and 8.10; O'Brien et al. 1999; Lisk et al. 2000; Rollet et al. 2006). Some 5.5 Ma there was a transient fluid flow event, driven by Mio-Pliocene inversion, and associated far-field fault reactivation, ultimately driven by the collision of the Australian plate with SE Asia. It had a major impact on the seal integrity of numerous fault dependent hydrocarbon traps in the Timor Sea and allowed hot (90–130 °C), highly saline (>200,000 ppm) brines from deep Palaeozoic evaporite-derived brines to migrate up the reactivated faults to chemically and thermally overprint the reservoir and other shallower intervals Fig. 8.9). Apatite fission track data suggest that this regional episode of fluid migration was short and lasted for between 10,000 and 100,000 years. It resulted in the development of a prominent, localised Late Tertiary heating 'spike', that if ignored can significantly affect the accuracy of modelled thermal histories in the region.

Upon entering a shallow clastic aquifer system (centred on the Eocene Grebe Formation), microbial oxidation of

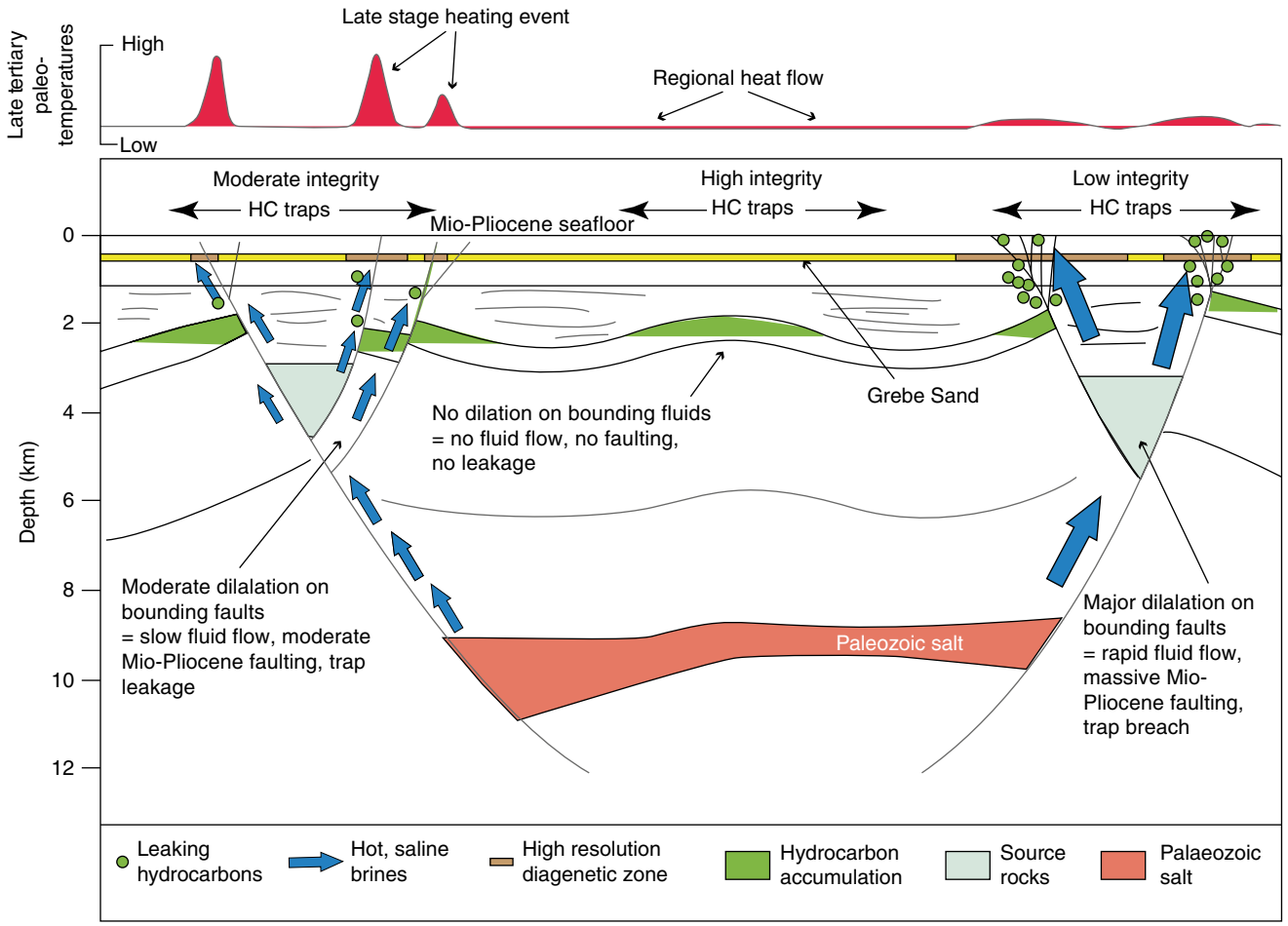

Fig. 8.9 Schematic representation of the latest Miocene/Early Pliocene fluid flow event in the Timor Sea (After O'Brien et al. 1999)

the hydrocarbons liberated CO_2 which, in turn, resulted in significant and very isotopically light carbonate cementation that creates a negative displacement in the $\delta^{13}C$ signature in intervals where it is pervasive as in the East Swan 2 well (Fig. 8.10). This cementation event produces sufficient acoustic impedance with the surrounding uncemented sands that it allows these hydrocarbon-related diagenetic zones (HRDZs) to be mapped seismically. Since both the size and acoustic response of the HRDZs are directly proportional to the amount of hydrocarbons that have leaked from the fault traps, their presence or absence provides a powerful indicator, predrill, of both trap integrity and the likely thermal regime that the traps have experienced.

There are three categories of traps: (1) high, (2) moderate, and (3) low integrity traps (Fig. 8.9). These have characteristic hydrocarbon fill-spill, fluid flow and thermal histories. In moderate and light intensity traps, dilatation was moderate to intense respectively, and allowed hot, highly saline brines from dissolving Palaeozoic evaporites to migrate up the reactivated faults and so chemically and thermally overprint the reservoir and shallower intervals with "thermal spike" cements. Leaky fault segments over partially breached traps typically only extended for 200–1,000 m, whereas over the breached traps, leaky segments extended for 3,000–5,000 m. Regions of high integrity traps are largely unreactivated and hence the conduits for brine migration from depth were absent. Consequently, these trap regions are the most representative of the thermal histories of the source rock depocentres.

Another example of fault -evaporite fluid/matrix cement interaction in a collisional setting and its influence on fractures and related fluid flow is seen in the fractured Oligocene carbonate lacustrine reservoirs of the western Qaidam Basin, China (Fig. 8.11; Zeng et al. 2012). Most fractures in the various carbonate reservoirs are small and related to steeply dipping faults, bedding-plane slip faults, terranes and so probably not directly related to crossflows of warmer salt dissolution and subvertical opening-mode fractures. Other fractures are diagenetic in origin. Fracture occurrence and abundance patterns are controlled largely by lithology, bed thickness, and proximity to larger faults.

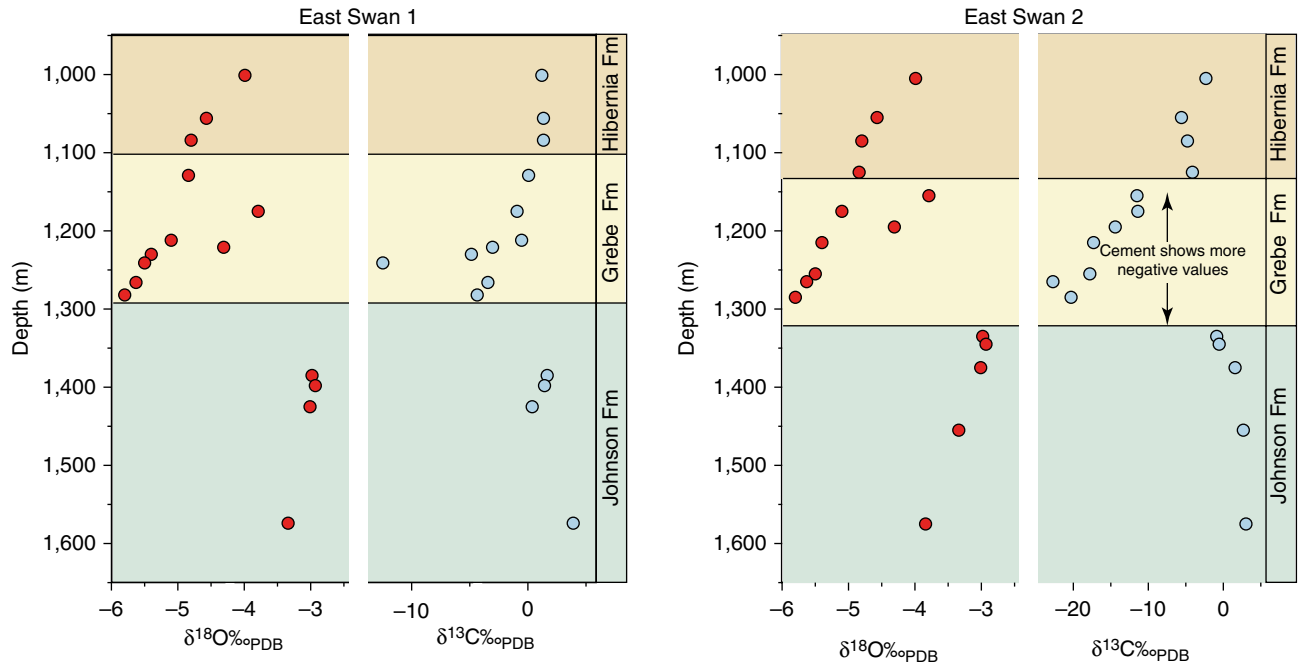

Fig. 8.10 Stable isotope measurements for authigenic calcite cements in the East Swan-1 and -2 wells in the Timor Sea, offshore NW Australia (Replotted from Table 2 in O'Brien et al. 1999)

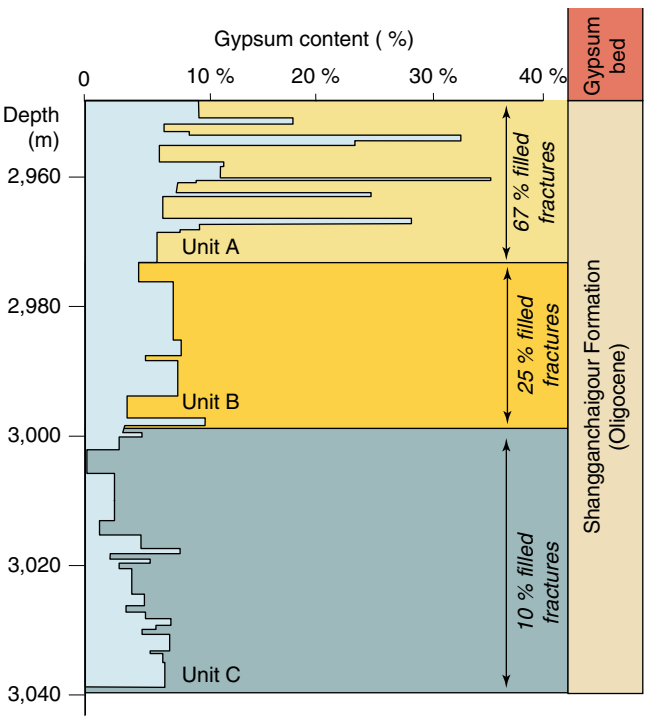

Fig. 8.11 Relationship between the gypsum content and the proportion of all-filled fractures in core in a well in the Oligocene Shangganchaigou Nanyishan field, NW Qaidam (After Zeng et al. 2012). The gypsum beds lie above *unit A*. In unit A, 67 % of the fractures are filled; in *unit B*, 25 %; in *unit C*, < 10 %. N = 150

Non-economic fractures are generally filled with calcite, gypsum, or glauberite ($Na_2\,Ca[SO_4]_2$). The amount of fracture-filling determines the effectiveness of fractures as fluid conduits and hence the distribution of high-quality reservoirs. Open fractures provide the main pathways for fluid flow; open fractures are parallel to and occur near faults, and many do not coincide with the present-day direction of the maximum horizontal compressive stress. The main control on those cements that degrade the fracture flow properties is proximity to evaporite beds in the lacustrine stratigraphy (Fig. 8.11). Once again this is an example of how highly saline evaporite precipitating fluids occur in a cementation halo, in this case adjacent to a rotated and deformed $CaSO_4$ bed.

As well as upward directed fluid flow and elevated pressures associated with collision, effects of thrusting can drive salt-derived fluids downward into lithologies where they would not otherwise be present, such as when evaporitic basinal fluids become syntectonic fluids in igneous basement caught up in a fold and thrust belt. For example, deep basinal brines, derived from dissolving Triassic evaporites, were driven, via fractures and shears, into hard rock basement (phyllites and gneisses) of the Pyrenees during the Alpine orogeny (Fig. 8.12; Travé et al. 2007; McCaig et al. 2000).

Detailed inclusion work by McCaig et al. (2000) suggest that the fluid history of the Pyrenees evolved through stages: (1) Upper Triassic evaporite formation with sinking of reflux

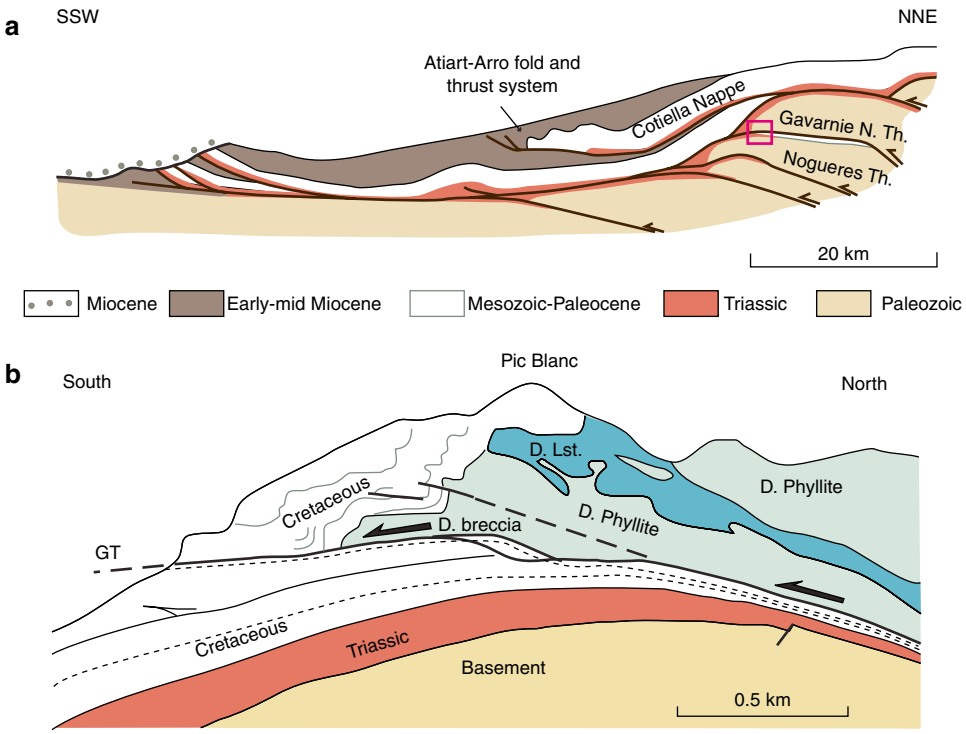

Fig. 8.12 Pyrenees thrust belt, Spain. (**a**) Regional schematic showing relation of various thrusts to evaporite décollement, *red rectangle* indicates approximate position of (**b**) (After Travé et al. 2007). (**b**) Detailed cross-section through the Plan de Larri in the central-western Pyrenees centred on the Gavarnie Thrust (*GT*; After McCaig et al. 2000). D. phyll. is mostly low grade Devonian phyllite; D. lst is mostly low grade Devonian carbonate; the Triassic section is Upper Triassic shales, carbonates and evaporites; D. breccia is a Late Cretaceous breccia weld (rauhwacke) that in outcrop is composed mostly of Devonian clasts; Cretaceous is mostly Upper Cretaceous carbonates

brines into underlying redbeds and fractured basement rocks; (2) Circulation of brines with formation of Pb-Zn deposits along faults at some time between the Triassic and the Upper Cretaceous; (3) Renewed extension with erosion of Triassic rocks in many areas and further drawing down of Triassic brines into the basement; (4) Deposition of Upper Cretaceous and Palaeocene carbonates containing connate waters of marine origin: (5) Formation of the Pyrenean thrust belt with overpressuring and expulsion of the brines along shear zones and faults including fractured basement, and; (6) Creation of topography with a high-level circulation system in the Mesozoic thrust sheets driven largely by topography. At the southern margin of the Axial Zone there was limited mixing of the deeper, overpressured brines with these more dilute, hydrostatically pressured fluids. An important point noted by McCaig et al. is that because of their density, hypersaline brines are difficult to expel from the upper crust, and may be involved in a succession of alteration and mineralisation events in the same general area over hundreds of millions of years.

Although the décollement to the Pyrenean thrust is in a Triassic salt layer, isotopically much of the cement signature in outcrop studies of the various thrusts indicate a thermal separation in oxygen values in early and later cements. This is also seen in backthrust thrust terranes and so probably not directly related to crossflows of warmer salt dissolution waters. For example, in the El Guix and L'Escala features, the thrust-related vein and fracture C-O plotfields consistently have more negative oxygen values compared to matrix limestones indicative of warmer fluids or greater burial the thrusts (Fig. 8.13). In the Atiart feature a separation is much less clear, perhaps arguing for a more pervasive meteoric overprint and less tectonic cement maturity there (for more detailed discussion see Warren et al. (2014) on the use of C-O isotopes in interpreting burial stages and permeability evolution in thrust terranes). Travé et al. (2007), conclude the fluid precipitating the calcite veins in the upper mineralised backthrust (as sampled in Atiart Arro outcrops) was consistent with a meteoric origin for the source waters. In contrast, the fluids precipitating calcite veins in the other thrust -related fractures such as the salt core-El Guix thrust, was consistent with a warmer formation water origin. However, presence of Na in all the fractures of the backthrust Ariart array, including the upper mineralised backthrust (meteoric dominated) indicates that these fractures also served as a pathway for a hypogene fluid in contact with underlying evaporites.

Worldwide, it is likely that dense salt-dissolution-derived brines, sourced deep in the basin by ongoing salt solution, are involved in a number of alteration and mineralisation events in the same general area of the basin. But they probably move in short-lived diagenetic pulses or events

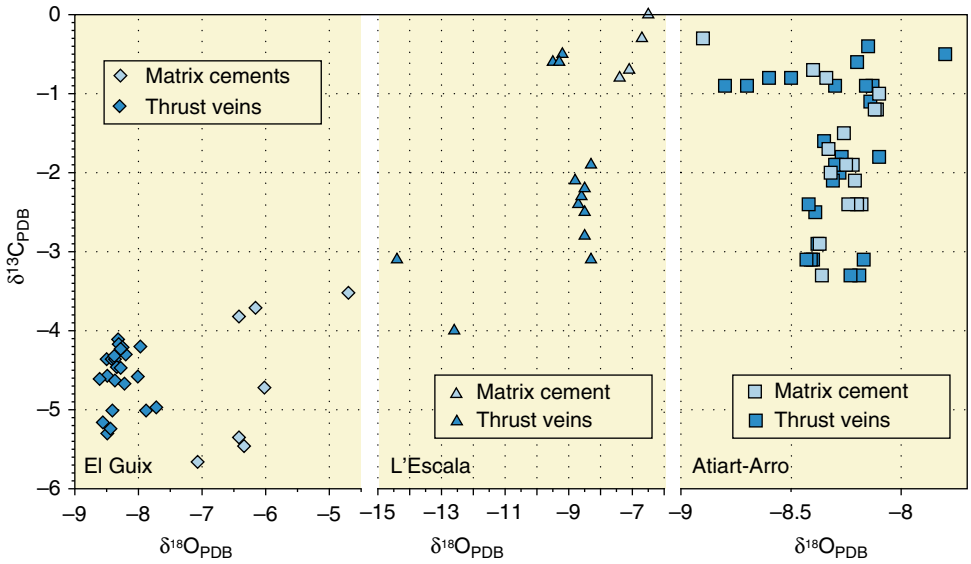

Fig. 8.13 $\delta^{18}O$ versus $\delta^{13}C$ of calcite cements in the veins and host rocks from three different thrusts in the Pyrenees (Travé et al. 2007)

(≈10^5–10^6 years), which are likely spread over hundreds of millions of years. Such fluid movements occur as flow events in reactivated parts of the basin as it experiences the various stages of the Wilson tectonic cycle (i.e. rift, collision and post-collision; Fig. 5.32). Even after a salt bed passes into the metamorphic realm it, and its brine halo, can continue to act as a source of Na and Cl. In that case the participating sodium and chlorine ions come not from halite (gone by 450–500 °C) but from compressed scapolite cages and other meta-evaporitic daughter phases, e.g., the Mt Isa-Cloncurry region of Australia (Chap. 14).

Flow in Post-orogenic Hydrologically-Mature Basins

After inversion or uplift, evaporite beds re-enter the zone of deep meteoric (artesian) circulation and active phreatic flow (telogenesis). Meteoric fluids enter via infiltrating rainfall and groundwater as strata are increasingly flushed by meteoric waters (Fig. 8.1d). Gravitational pore-brine sinking, driven by topographic gradients and recharge along the uplifted margin of the basin, is the most important mechanism driving fluid migration. This gravity-driven circulation is sometimes termed centripetal flow, as it encompasses flow into the basin centre from the surrounding highland areas. It is antithetic to centrifugal flow, which characterises the compactional, thermobaric and compressional regimes that tend to move water in the opposite direction, from the basin centre toward the basin edges.

Three conditions must be met to allow topography driven flow: (1) the basin needs to be partially elevated above sea-level/brine level, (2) the flow system requires ongoing water replenishment via infiltrating rainfall and groundwater in the uplands regions, and (3) aquifers must have sufficient permeability at depth to allow the entry of waters into the deep subsurface. An exception to the general requirement of a meteoric feed and suprasealevel hydrologies is a subsealevel foreland basin or saline giant undergoing evaporative drawdown, such as the Mediterranean in the Late Miocene (Messinian), where seawater was the major gravitationally driven groundwater feed.

Another exception to the general assumption that centripetal flow is driven by a potentiometric head that is always supplied by the uplift, may occur in glacial times. Today the Williston Basin in Manitoba has a hydrology controlled by recharge in the Rocky Mountains, but in Pleistocene glacial meltwater periods this may have not been true. The km-scale thickness of the continental ice sheet and consequent loading over subglacial lakes may have provided sufficient hydrologic head to reverse the regional-scale flow system of evaporite-dissolution derived basinal brines in the Williston Basin (Grasby and Betcher 2000). Similarly, in the Michigan basin, the meltwaters of the retreating icesheet moved dilute waters (<20 g/1 TDS) some 110 km laterally into the Devonian carbonate aquifers, significantly depressing freshwater-saline water mixing zones (McIntosh et al. 2011).

More typically, salt dissolution in the post-orogenic continental realm feeds brine into adjacent deeply-circulating confined aquifers beneath and atop thick well-preserved evaporite intervals. For example, over the last 5–10 Ma, subsurface Na–Cl brines in various subsalt sandstone aquifers along the edges of the Anadarko, Midland and Palo Duro Basins have acquired their high salinity through the dissolution of Permian halite by deep meteoric circulation of groundwaters. These basins make up the northern portion of the Permian Basin of West Texas and Oklahoma (Fig. 8.14; Bein and Dutton 1993).

System	Series	Group/ formation	General lithology	Hydrogeological unit
Tertiary		Ogallala	Fluvial and lacustrine clastics	Upper Aquifer System
Cretaceous		Fredericksburg	Limestone sandstone	
		Paluxy		
Triassic		Dockum	Fluvio-deltaic and lacustrine clastics	
Permian	Ochoan	Dewey Lake	Sandstone salt, anhydrite salt	Evaporite Confining System (ECS)
		Rustler		
		Salado		
	Guadalupian	Tansill	Anhydrite	
		Yates	Sandstone	
		Seven Rivers	Anhydrite	
		Queen	Sandstone	
		San Andres-Grayburg	Dolomite-sandstone	
	Leonardian	Clear Fork	Limestone-dolomite	Deep-basin Brine Aquifer System
		Wichita		
	Wolfcampian	Wolfcamp	Shelf limestones, minor shale	
Pennsylvanian		Cisco		
		Canyon		
		Strawn		
		Atokan	Shale	
		Chester		
Mississippian		Mississippian Lime	Limestone	
Devonian		Woodford	Shale limestone	
		Devonian		
Silurian		Silurian	Shale, limestone	
Ordovician		Montoya	Limestone shale, limestone dolomite	
		Simpson		
		Ellenberger		
Precambrian			Igneous, metamorphic	Basement aquiclude

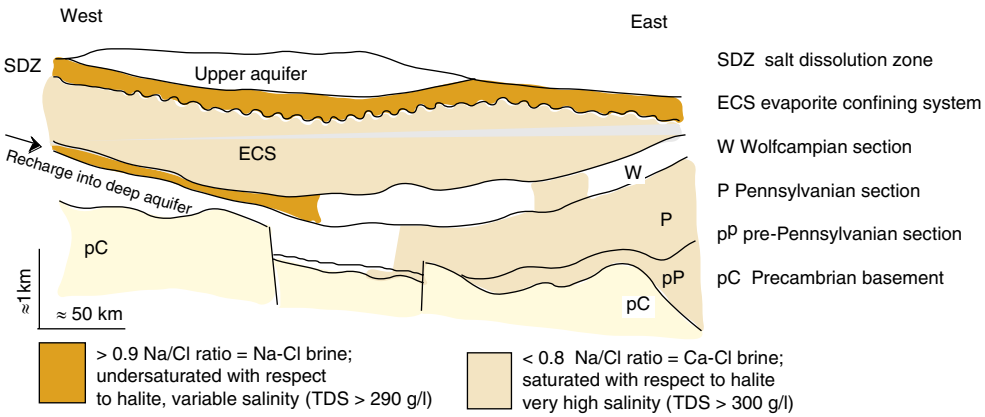

Fig. 8.14 Na/Cl molal ratios define subsurface hydrology in Permian Basin, West Texas and Oklahoma. The relict Ca-Cl brines are held in place by the low permeabilities of the evaporite confining zone, while Na-Cl brines derived by halite dissolution are to be found in the salt dissolution zone (*SDZ*) and the Wolfcampian section (*W*) of the deep basin aquifer (After Bein and Dutton 1993). The *upper part of the figure* shows the relevant stratigraphy of the region, *centred* on the Central Basin Platform and the occurrence of the major hydrogeologic units within this stratigraphic framework (After Stueber et al. 1998)

Topographically driven, initially fresh, meteoric water moved into the western half of the deep-basin brine aquifer through nearsurface salt dissolution zones and then downward as Na–Cl brines seeped along the various deep aquifers to depths of thousands of metres (SDZ = salt dissolution zone in Fig. 8.14). Above the deep aquifer are Ca–Cl basinal brines that are relict Permian mixtures of descending evaporitic brines and connate Permian and Pennsylvanian seawaters. Little or no Neogene meteoric Na–Cl brine has penetrated this Ca–Cl brine zone, which is hosted by the evaporite confining system (ECS). The lack of ingress reflects the extremely low permeability of deeply buried halite and intrasalt shale, anhydrite- or halitecemented strata that dominate the ECS ("block of ice" analogue). Ages of the Ca–Cl brine in the ECS, based on ^{4}He and ^{40}Ar analyses of carbonates in the central part of the deep aquifer, range from 100 to 300 Ma (Zaikowski et al. 1987), making it a true "fossil" groundwater. This is the same salt where viable halobacteria have been cultured from brine inclusions preserved in its chevron halite (Vreeland et al. 2000).

To the south of the Palo Duro Basin, in the carbonate platform of the eastern Central Basin platform in West Texas, halite beds occur only in Upper Permian (upper Guadalupian and Ochoan) strata in the Permian Basin. As in the Palo Duro Basin, late stage uplift has influenced pore water composition of some of the original reflux brines in the more permeable subsalt beds. Extremely saline evaporated seawater apparently descended into adjacent Palaeozoic carbonates during halite deposition in the Late Permian, mixing with and displacing marine formation waters by buoyancy-driven convective flow (brine reflux; Stueber et al. 1998). These modified evaporitic brines were the dominant fluids in the Palaeozoic carbonates until the late Tertiary, when topographically-driven meteoric water began to flow into deeper Palaeozoic strata from outcrops and nearsurface aquifers in southeastern New Mexico in association with tectonic uplift that began at 5–10 Ma.

Meteoric water dissolved halite and anhydrite from Permian evaporites near the basin margin and seeped eastward along the regional hydraulic gradient, while mixing with and displacing modified evaporitic brine in the deeper parts. These meteoric waters, driven topographically, have now migrated large distances to displace saline waters deep and drive biodegradation in a basin characterised by numerous oil reservoirs with solution-gas drives.

The original dense brine that sank from Salado and Rustler evaporites into the underlying carbonates of the Central Basin Platform during the Late Permian may not have been of uniform composition, making it more difficult to separate it chemically from brines influenced by connate water or any subsequent deeply circulating meteoric waters (Fig. 8.15) That is, initial brine composition was not solely of a composition that resulted from 23-fold concentration of seawater (Stueber et al. 1998). Multiple depositional cycles in Salado evaporites, as described by Lowenstein (1987a), represent periodic invasions of seawater into the Salado basin, followed by progressive drawdown and concentration of brine. Therefore, the degree of seawater concentration reached during each cycle probably varied, and the projection of the data trend plotted to a 23-fold concentration in the upper panel of Fig. 8.15 is an oversimplification (Stueber et al. 1998).

The dense reflux brines that began to sink into underlying carbonates during the Late Permian probably had a range of initial compositions along the seawater evaporation trajectory and lay somewhere to the right of the halite precipitation point (Fig. 8.15a). The range of Br concentrations above 450 mg/l observed in formation waters from the 365 m (1,200 ft) thick Pennsylvanian–Wolfcampian carbonate section in the Central Basin Platform below the Salado and Rustler evaporites is largely a relic of this inhomogeneity.

The present locations of the most saline formation-water compositions below the seawater evaporation trajectory in the Permian of West Texas probably indicate relict evaporitic brines mixed with seawater when they entered the carbonate strata, much like the mixing that has been documented for the Messinian drawdown and is occurring today in the Dead Sea depression. As the brine mixed with phreatic seawater, each evaporitic brine composition along the seawater evaporation trajectory to the right of halite saturation would have been displaced along a line essentially parallel to the portion of the seawater evaporation trajectory prior to halite precipitation (Fig. 8.15a, b). When the range of data points representing formation waters with present Br levels greater than 450 mg/l is projected along such lines back to the seawater evaporation trajectory to the right of halite saturation, a range of seawater evaporitic concentration between 11 and 16.5-fold is indicated for the more saline waters. The concentration dissolution trends are also clearly seen in the Cl/Br and Na/Br crossplot, while the $\delta^{18}O$ – Br crossplot clearly shows the effect of meteoric mixing (dilution) on both these values (Fig. 8.15b, c, respectively).

Thus, modified evaporitic connate brines were the dominant precipitative fluids for cements and replacement in the Palaeozoic carbonates of the Central Basin Platform and the Palo Duro Basin until the late Tertiary, when meteoric water began to flow into deeper Palaeozoic strata from outcrops and nearsurface aquifers in southeastern New Mexico, in association with tectonic uplift that began at 5–10 Ma. Neogene meteoric water dissolved halite and anhydrite from Permian evaporites near the basin margin and sank eastward along the regional hydraulic gradient, mixing with and displacing the modified evaporitic brine in deeper hydrogeologic systems of the Devonian and San Andres aquifers. The mixing curve is indicated by the dashed line, lowered Br values and the negative $\delta^{18}O$ signatures (Fig. 8.15a, c). These

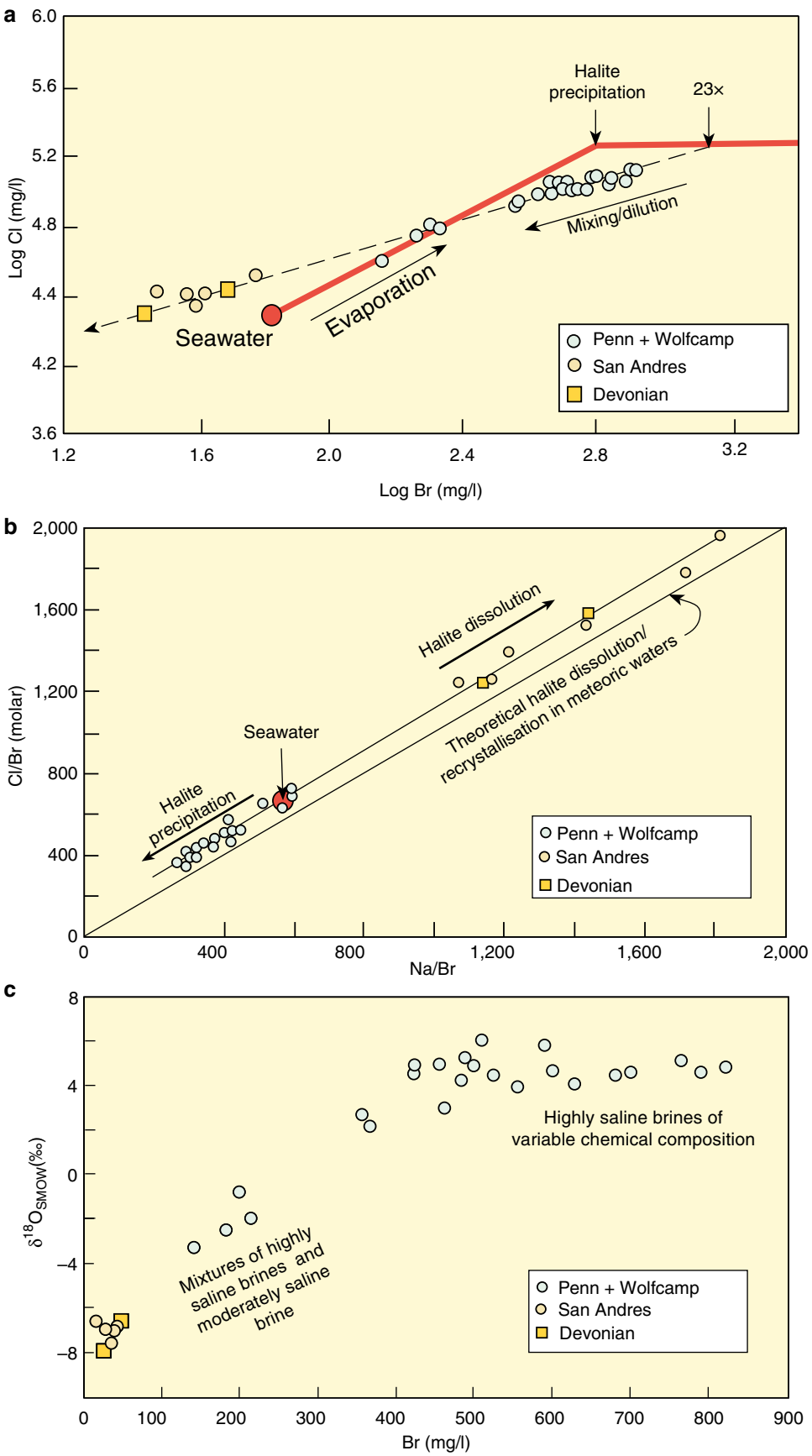

Fig. 8.15 Chemical character of 32 formation-water samples from carbonate reservoirs in the Southwest Andrews area (After Stueber et al. 1998). (**a**) Log Cl versus log Br. Seawater evaporation trajectory is from Carpenter (1978). *SW* seawater composition. Halite precipitation = 450 mg/l = 2.65 Log Br (mg/l). *Dashed line* marks the likely mixing trend among the brines. (**b**) Cl/Br vs. Na/Br molar ratios in formation waters relative to the compositional trend formed by seawater evaporated past halite precipitation and seawater that has dissolved halite. Regression line drawn through data points has $r^2 = 0.99$. The range of theoretical compositions that result from dissolution and recrystallisation of halite in fresh water is also shown. (**c**) Oxygen isotope composition plotted against Br concentration

late Cainozoic meteoric fluids probably are responsible for widespread biodegradation of oil in the San Andres/Grayburg interval in the Andrews oilfield area. More regionally such deep meteorically driven dissolution of gypsum/anhydrite beds supplied sulphate-ions for the bacterial production of reduced sulphur with the organics supplied by trapped and upwelling hydrocarbons. This reduced sulphur was then oxidised to form economic accumulations of natural sulphur in West Texas (Chap. 12; Hentz and Henry 1989; Lee and Williams 2000).

The Alberta Basin, Canada, is another area of post orogenic fluid circulation where evaporite-derived subsurface waters currently interact with less saline deeply circulated meteoric waters within artesian aquifers (Fig. 8.16a;

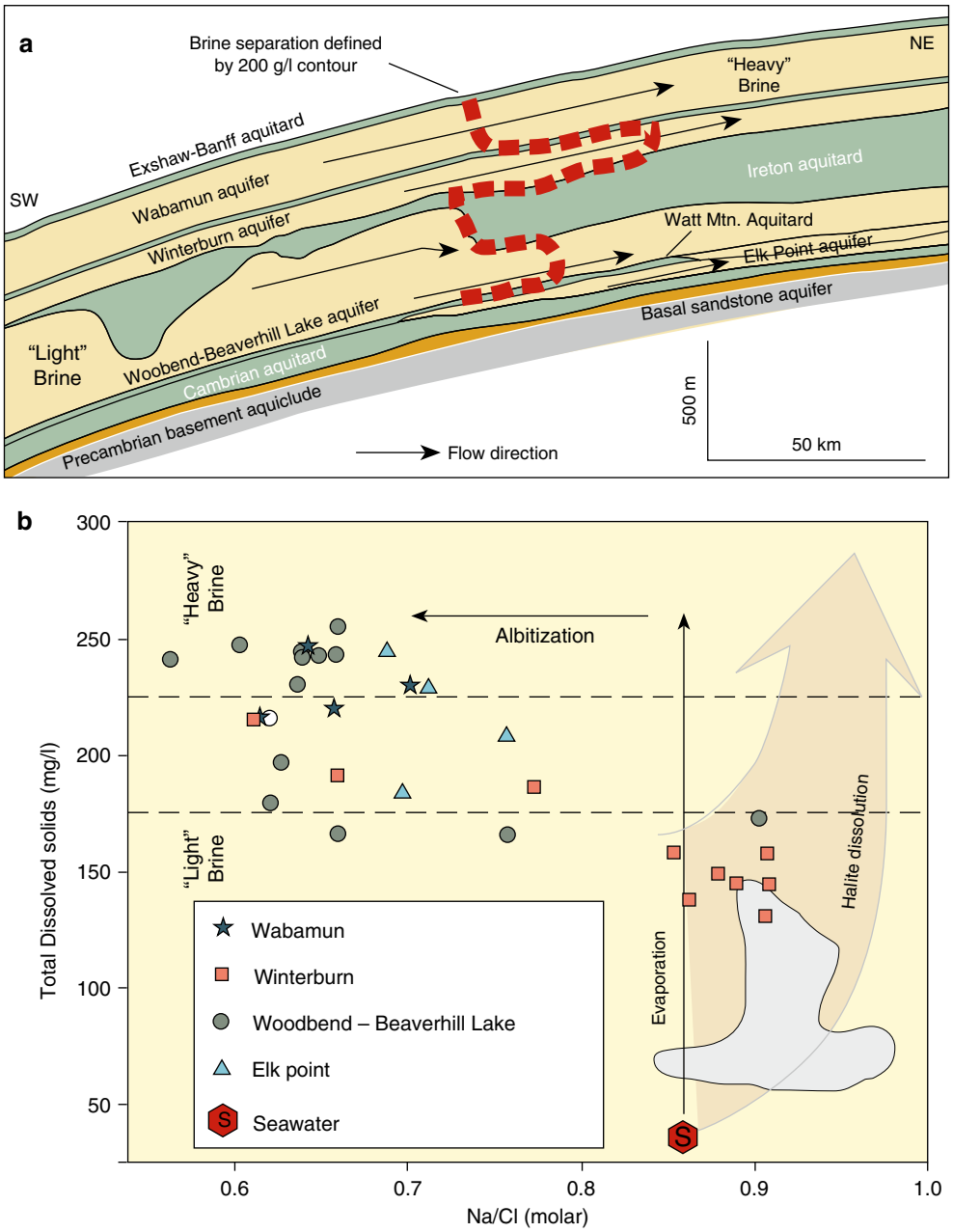

Fig. 8.16 Basinal fluids in Devonian of Alberta Basin (After Michael et al. 2003). (**a**) Hydrogeological cross-section perpendicular to the deformation front to the west showing conceptually the differential advancement of the less saline formation water displacement front against a high-saline connate brine reservoired in the Cambrian–Devonian hydrostratigraphic group. (**b**) Distribution of Na/Cl ratios versus salinity in Devonian formation waters showing some processes that may have influenced the brines. The grey plot field shows the distribution of hydrochemical measurements for Mississippian strata where halite dissolution driven by deep meteoric circulation controls much of the hydrochemistry of the deep aquifer

Michael et al. 2003; Gupta et al. 2012). Regionally, the Devonian succession contains two brines types (a 'light brine' with TDS <200 g/l and a 'heavy brine' with TDS >200 g/l), and both brines are pressurized by the potentiometric head supplied by the Rocky Mountains to the west, with the dominant artesian flow indicated by arrows in Fig. 8.16a.

The subsurface interface between the two brine types is typically lobate and controlled by permeability variations in the host aquifer, as evidenced by concurrent, steep changes in hydraulic head, and salinities (Fig. 8.16a). Hydraulic heads in the lower two aquifers (Elk Point and Woodbend–Beaverhill Lake), range from 625 to 750 m, whereas heads in the upper two aquifers (Winterburn and Wabamun) range from 500 to 800 m. This implies that the Ireton is an effective aquitard between the lower two and the upper two aquifers. According to Michael et al. (2003) the geological and hydrogeochemical data suggest the following processes determined the present composition of the 'light' and 'heavy' brines: original seawater, evaporation of brines beyond gypsum onset but below halite saturation, dolomitisation, clay dehydration, gypsum dewatering, thermochemical sulphate reduction, and halite dissolution. As in the San Andres Fm., the two brines can be separated by Na/Cl proportions; lighter brines show values >0.9 indicative of derivation from halite dissolution, while heavy brines tend to show values <0.7 reflecting a more relict marine-derived signature (Fig. 8.16b).

An influx of meteoric (from the south) and metamorphic (from the west) waters is recognized only in the 'light brine.' Albitisation (sodic replacement) is unequivocally identified only in aquifers hosting the "heavy brine." The "heavy brine" is likely a residual Middle Devonian evaporitic brine from the Williston Basin of the Elk Point Basin, or it may have originated by partial dissolution of thick, laterally extensive Middle Devonian evaporite deposits to the east. The "light brine" probably originated from dilution of 'heavy brine' by deeply circulating meteoric fluids in post-Laramide times, similar to the dilution seen in the San Andres aquifer.

This notion of a early pore brine remaining in place for extensive periods of time and preserving its connate character for hundreds of millions of years is testament to the long term low permeability of evaporite beds. Utilising present-day profiles of isotopes, solutes, and helium in porewaters recovered from 860 m of Cambrian to Devonian strata on the eastern flank of the Michigan Basin, Clark et al. (2013) argue for such long term pore brine immobility. Their focus was on a 240-m-thick, halite-mineralized, Ordovician shale and carbonate aquiclude sampled some 400–800 m below the modern landsurface. It sits unconformably on Precambrian basement and hosts Br-enriched, post-dolomitic brines (5.8 molal Cl), which they interpret as originating via reflux from Silurian seawater-derived brines that were precipitating the overlying Salina salts. Authigenic helium has been accumulating in this salt-sealed aquiclude for more than 260 Ma and is isolated from underlying allochthonous, ^{3}He-enriched helium that originated from the rifted Precambrian base of the Michigan Basin and the Canadian Shield. This Palaeozoic age and consequent immobility of the pore fluids in this Ordovician aquiclude strengthen the safety case for a deep longterm waste repository in the region.

So far, we have discussed brine styles and long term stability in the deeply buried stable portions of post-orogenic aquifers. But, when buried evaporites are caught up in the hydrology and stress fields of compressional tectonic belts they can be subject to syn- and post-orogenic deep meteoric flow. Their dissolution can supply much of the ionic content to actively accumulating evaporite systems in hydrologic outflow zones in an adjacent foreland depression. This was the case in the Miocene saline lakes of the Ebro Basin of NE Spain (Sánchez et al. 1999; Salvany et al. 1994). The current saline lakes in the same area (such as Lake Banyoles and Salada Mediania) are considered to be karstic relics of a more active saline hydrology that was set up during the Early and Middle Miocene, via intense compressional deformation and associated high relief in the basin margin.

Evaporite sedimentation at that time took place under a gravity-fed continental brine hydrology not connected to the sea (Sánchez et al. 1999). The sedimentation around the margins of the Ebro Basin was detrital, originating from alluvial systems that surrounded large saline mudstone plains (Fig. 8.17). These plains were linked to extensive saline and carbonate lakes in lacustrine systems that in their central depressions were dominated by playa depressions up to 100 km long and 30–50 km wide.

Three concentric hydrologically controlled and segregated subenvironments characterised the lacustrine depression: (1) central lake areas dominated by gypsum and halite pans; (2) intermediate lake areas with pervasive laminated gypsum and anhydrite as well as diagenetic glauberite, and (3) marginal lake areas with nodular diagenetic anhydrite, which gradually passed into distal alluvial plains (Fig. 12.27). In some marginal lake areas that were isolated from the central lacustrine systems there were small evaporitic lakes up to a few kilometres across. There local deposits of carbonate, gypsum and anhydrite precipitated from moderately concentrated brines, along with abundant diagenetic chert (Salvany et al. 1994).

Evaporitic successions in the central gypsum-halite lake area attain thicknesses of more than 200 m and almost all of it was derived from evaporation of deeply circulated meteoric waters that had dissolved Mesozoic evaporites and carbonates in folded basement in the adjacent Iberian Highlands (Fig. 8.17). Most of the carbonate-rich marginal lakes corresponded to zones of the first diffuse emergence of this deeply-circulated groundwater. Waters then fractionated as they moved toward the lowest parts of the lake depression. Since the Miocene the groundwater hydrology has evolved

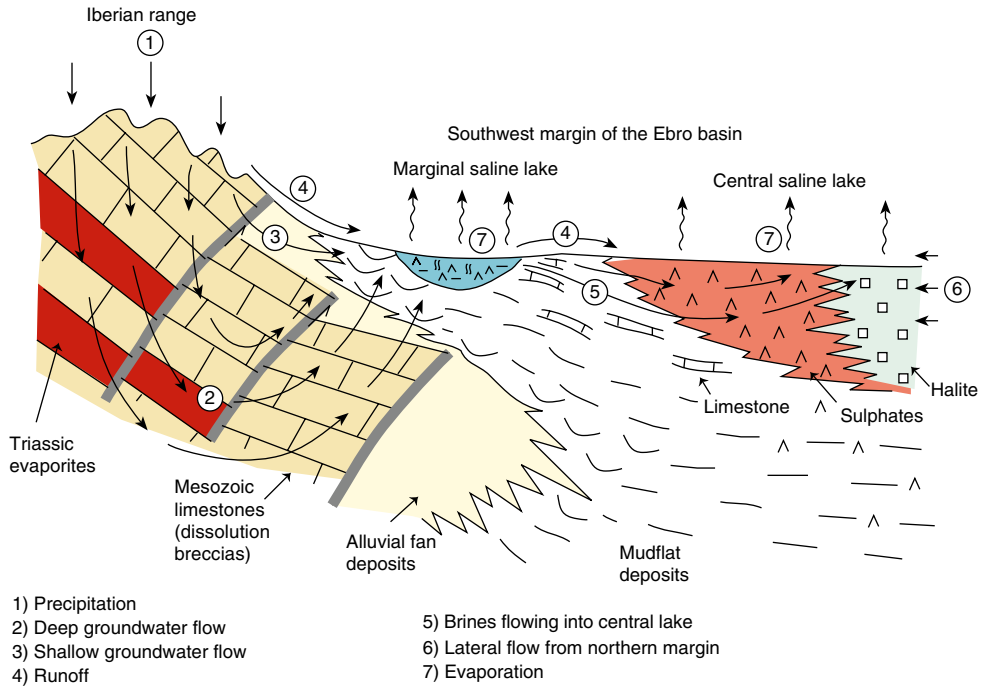

Fig. 8.17 Palaeohydrologic pattern of the compressional (thrust) margin of the Miocene Ebro Basin, Spain (After Salvany et al. 1994). The Miocene lacustrine evaporites in the Ebro Basin are ultimately derived from the deep meteoric leaching of Triassic evaporites in the Iberian Range along the southern margin of the basin. Ongoing surface and nearsurface evaporative fractionation of shallow brines divided the Miocene chemical sediments into a series of bioturbated carbonate-rich gypsum lakes and a more central gypsum-halite-rich lake system

and matured to that of today where focused springs, rather than diffuse resurgence zones, define zones of initial groundwater outflow (Sánchez et al. 1999). Anhydrite meganodules, forming diagenetically in zones of hypogene crossflow into Miocene gypsum, are another consequence of this saline crossflow of brines from dissolving Triassic evaporites (Fig. 1.56; Ortí et al. 2012)

In summary, dissolving subsurface evaporites contribute to basinal pore salinities, chemistries and can drive fluid flow and mineral alteration at all stages of burial and uplift, and continue to do so as long as salt and permeability live on in the sediment pile.

Alteration, Pressure Cells and Salinity-Driven Convection

All water-bearing sediments compact and alter within the zones of compaction and thermobaric waters, as various connate or subsurface waters escape from the sediment pile. Pore waters issuing from compacting sands, shales and limestones are typically not halite-saturated, so salt masses tend to dissolve wherever fluids from dewatering sediment piles come into contact with salt beds or allochthons.

Evans and Nunn (1989) and Ranganathan and Hanor (1988) analysed salinity-driven convection in permeable sands near salt structures in the Gulf Coast. Sarkar et al. (1995) modelled salinity-driven free convection in less permeable shale-dominated media beneath a dissolving salt sheet or allochthon. Morton and Land (1987), Land (1991), and McKenna and Sharp (1997) noted salinity inversions in the south Texas portion of the Gulf of Mexico basin, where more saline pore waters (including brines >100,000 ppm total dissolved solids) overlie less saline waters (≈20,000 ppm). Strong buoyancy gradients exist where such inversions occur, as the shallower pore waters are both cooler and more saline than deeper pore waters. Most of these hydrologies are maintained by the rise of brine along fractures and faults from basinal depths where deeply buried salt is actively flowing and dissolving. Convective return of brine occurs in areas away from the supplying structure (Sharp et al. 2001).

Haloes, Convection and Saltout

Over time, the ongoing dissolution of the edges of a salt bed, allochthon or salt wall sets up a dense subsurface brine halo. As it builds, the halo becomes so saline and dense that it starts to drive free convection. Saline pore waters slowly sink beneath the underbelly of the dissolving salt bed or allochthon, or spread laterally atop the upper side of a salt bed or edge of a diapir. Pore water from the salt underbelly sinks to depths where it reheats, flows laterally and then rises to

return once more to the underside of the evaporite bed to complete the convection cell (Figs. 8.4b and 8.18). Such density-driven convective circulation is an important mechanism of depositing and remobilising pervasive secondary salts (burial salts) in subsalt beds that were originally nonevaporitic. It also creates basal "caprock" residues along the underside of the bed or allochthon and lateral caprocks on the margins of a salt structure (Fig. 6.113).

Buried evaporite beds in contact with adjacent aquifers become sites of phreatic salt flushing as soon as the solar-driven active phreatic brine reflux hydrology starts to dissipate. Hence, burial dissolution of salt from its edges inward begins as soon as the bed enters the zone of compactional water flow (Chap. 7). This explains why the upper and lower contacts of many thick ancient evaporite beds are not depositional contacts. Rather they are zones characterised by dissolution residues, recrystallisation and pressure solution textures. For the same reason, well preserved primary and syndepositional textures in bedded evaporites are rarely found at the contacts with adjacent non-evaporite lithologies. Depositional fabrics are best preserved internally within an evaporite bed, away from the edges where basinal fluids are eating into and altering the original evaporite textures. Diagenetic waters continue to dissolve or "melt" evaporite contacts until the evaporite dissolves or all effective permeability is lost in the adjacent beds.

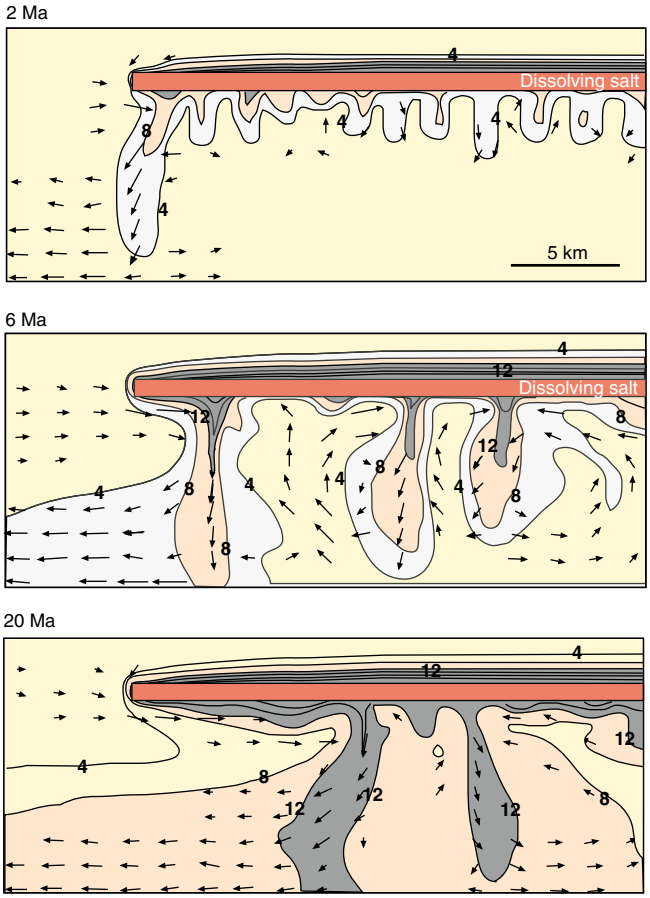

Fig. 8.18 Modelled temporal evolution of brine plumes associated with ongoing dissolution of a salt sheet in a shale matrix at times of 2, 6 and 20 Ma (After Sarkar et al. 1995). Contours of plumes are given in terms of salinity difference: calculated as pore water salinity minus seawater salinity (3.5 %). Numbers are in wt%. The leftmost plume, best developed in earlier stages, is mostly fed by a brine cascade focused by ongoing dissolution of the salt edge. Without halokinesis this would be a retreating bed feather-edge. Vertical exaggeration is 2×

The modelling of plumes beneath salt beds and subhorizontal allochthonous salt sheets, such as occur in the Gulf of Mexico, shows free convection has the potential to be a significant mechanism in both salt dissolution and mass transport, even if the sediments beneath the salt have permeabilities as low as 0.01 md (Fig. 8.18; Sarkar et al. 1995). In such low permeability sediment it will take some 10 Ma for the subsalt convection to develop to full strength. Once active, an average of 3–5 m of salt is dissolved off the underbelly every million years, with a maximum darcy flux of 3 mm year^{-1}. Measured matrix permeabilities of overpressured shales immediately beneath allochthonous salt (the gumbo zone) are much higher than 0.01 md and so the actual flow and dissolution rates are much higher.

Chloride-rich density-derived convective flow cells are an inherent part of the hydrology beneath all dissolving evaporite seals. They continue to repeatedly cycle subsalt pore water through the underlying sediment column until subsalt permeability is shut down by compaction and thermobaric cementation. It can move volatile-entraining chloride-rich brines through base metal and organic-containing shales and cupriferous redbeds beneath buried salt beds and sheets. Wherever such waters break out from beneath the salt seal into suitably prepared ground, the associated cooling and brine mixing can precipitate metal sulphides or facilitate the focused escape of liquid and gaseous hydrocarbons (Warren 2000b). Breaches typically occur via growth faults, salt welds or via seismic pumping along thrusts and thrust welds; all these features centrifugally drain basinal pore waters from beneath a salt bed or allochthon sheet. Simultaneously, the escape can drive other diagenetic reactions such as secondary porosity formation (via brine mixing and changes in pCO_2) or the precipitation of authigenic burial cements.

Where halite dissolution is occurring along the flank of a salt stock or diapir (shale sheath), the resulting dense pore fluids move into adjacent upturned permeable beds (Fig. 8.4c). Any cavity created by local dissolution of the salt stem is quickly filled, either by salt flow from the stem, or, if dissolution is rapid enough, by the collapse of sedimentary beds against the stem to form "downthrown" slivers and blocks (Chap. 6). As dissolution of the salt stem proceeds, the resulting high salinity (high density) pore brines can spall off a sinking brine halo that is maintained by ongoing dissolution. Such high salinity pore waters tend to sink away from

the stem down the more porous extensional portions of adjacent steeply dipping beds. Unlike the self-limiting rate of salt loss associated with the undersides of subhorizontal salt geometries, steeply dipping beds about a salt stem create a plumbing system with a tendency to self drain and so facilitate further dissolution of the stem and the set up of conditions suitable for the "salt-out" of rising hydrocarbons.

The evolution of such a suprasaltself draining, self-convecting fluid system has been modelled by Wilson and Ruppel (2007). They conclude that thermohaline suprasalt convection associated with salt domes can drive significant fluid flow, mass and heat transport in suprasalt positions in halokinetic continental margins, especially if halite dissolution is considered part of the suprasalt modelling. Likewise, they found suprasalt faults cause significant, but highly localized, increases in flow rates, typically tied to seafloor seeps and discharge zones. Transient models that include halite dissolution show an evolution of flow during brine formation from early salt-driven convection to later geothermal convection, with characteristics of the latter controlled by and interplay between seafloor relief and evolving salt geometry (Fig. 8.19). Their modelling shows suprasalt dissolution atop a salt structure creates hypersaline haloes more than a few hundred metres to a kilometre thick in time frames of 100,000–250,000 years after creation of the structure (Fig. 8.19).

Predicted fluid flow rates are around a few millimetres per year or less for homogeneous sediments with a permeability of a millidarcy, comparable to compaction-driven flow rates. Sediment permeabilities likely fall below 1 md at depth in the Gulf of Mexico salt province basin, but such thermohaline convection can still drive pervasive mass transport across the seafloor, affecting sediment diagenesis in shallow sediments (Fig. 8.19). They conclude that in more permeable settings, such flow drives water circulation of fluid cells with differing temperatures and so can influence methane hydrate stability, the positions of seafloor chemosynthetic communities, and the longevity of fluid seeps. Across a time frame of a million years, one of the most significant effects of the dissolution of the upper portion of the salt is the increasingly thicker halo of hypersaline brines in the overlying sediment mass (note there is no significant additional sedimentation that would drive ongoing salt flow via differential loading in their simple model.

However, it does show that active suprasalt fluid circulation in convective cells is driven by thermohaline processes,

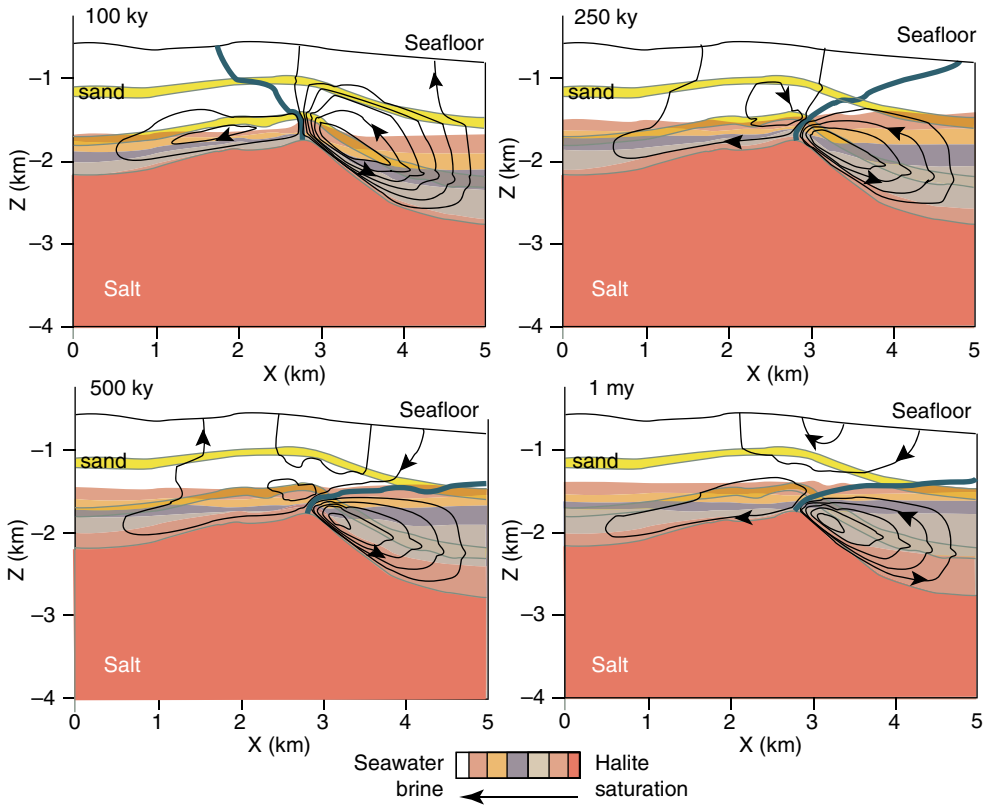

Fig. 8.19 Stream function and salinity distribution for the fully-coupled transient case, with two permeable suprasalt sand layers (*yellow*) included in the modelled muddy sediments. *Black lines* indicate convective flow direction, shading denotes normalized salinity, with white corresponding to salinity close to that of seawater and *pink* representing salt saturation. *Thick dark green line* indicates flow divide between clockwise and counterclockwise convective flow cells. (*A*) 100 kyr. (*B*) 250 kyr. (*C*) 500 kyr. (*D*) 1 Ma (After Wilson and Ruppel 2007)

tied to salt dissolution in the sediment mass atop the salt. It also illustrates that pore salinities increase in the lower part of the sediment column atop a dissolving salt structure. This set of inherent and related fluid flow processes can enhance hydrocarbon foci so define hydrodynamic suprasalt trap configurations and saltouts.

Hydrocarbons rising through suprasalt and subsalt brine haloes are less soluble than if in fresher pore waters. Price (1976, 1981) noted that at standard temperature and pressure (STP) the solubilities of n-pentane and methyl-cyclohexane decreased from 40 ppm in fresh water to 3 ppm in water with a salinity of 300,000 ppm. This means hydrocarbons dissolved in less saline basinal waters tend to "salt out," or exsolve, in the vicinity of brine plumes adjacent to a salt stock or along the underside of a salt bed or allochthon. "Salting out" is a direct result of the increase in the salinity of the carrier fluid as the salt body halo is approached (Fig. 8.20).

The accumulation of oil and gas along the underside of a salt seal, or adjacent to a salt stock, drastically slows the rate of salt dissolution. Halite is near insoluble when in direct contact with exsolved hydrocarbons rather than pore waters. Such conditions help explain why hydrocarbon legs adjacent to a salt stem have a propensity to stack one atop the other, with the hypersaline halo hydrology of the stem acting as highly efficient top and lateral seals. Of all the various evaporite traps, stacked salt-stem focused and sealed, steeply-inclined reservoir beds are among the most highly productive regions in the world in terms of barrels of oil equivalent (BOE) per unit area (Halbouty 1979).

Large-scale vertical migration of subsurface waters and crude oils, via shears and fractures against salt structures, was noted in the Louisiana Gulf Coast by Hanor and Sassen (1990). They concluded that the vertical upward flux of brine and hydrocarbons in this system followed extensional fault and fracture permeability in sediments adjacent to the salt and did not otherwise move vertically through shales sandwiched between the various sand reservoirs. In the immediate region about the salt stem they found that higher salinities were localised in the same areas where hydrocarbon production occurred over and around the salt domes. This implies dissolution of salt is driven by the same warm fluids rising from geopressured intervals and carrying with them buoyant hydrocarbons into shallower depths. Thus, most of the vertical fluid transport out of the deeper levels in a halokinetic basin is focused into the zone of structural disturbance adjacent to diapir stems.

Put simply, salt stems, beds and allochthons create temperature, salinity and fracture discontinuities that induce local thermohaline fluid flow. As long as sediments adjacent to a subsiding/ flowing stratiform salt bed or allochthon can maintain some degree of permeability, much of the more interesting subsurface hydrology occurs in and around brine haloes, centred about intervals or masses of slowly dissolving salt. Ongoing thermohaline-driven dissolution, alteration and flow near the edge of the bed or stem, and extending into adjacent beds, creates chemical and pressure gradients that exert significant influence of the style and patterns of subsurface fluid flow. This in turn exerts a strong influence on the location and style of various hydrocarbon and metal accumulations (see Chaps. 10 and 15).

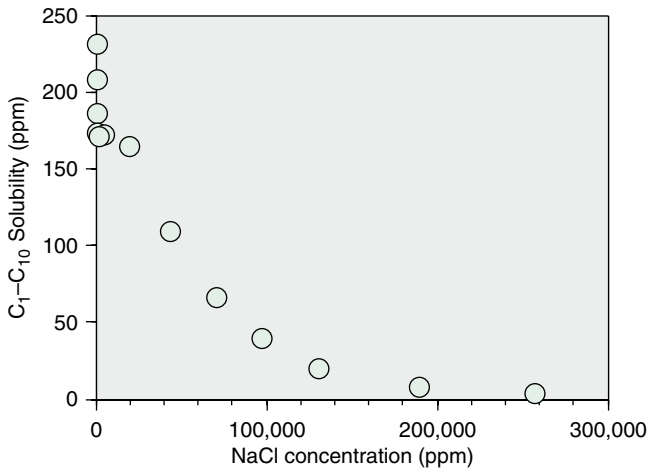

Fig. 8.20 Aqueous solubility of a C_4–C_{10} petroleum distillation fraction as a function of NaCl concentration at a near constant temperature (≈ 195 °C) and pressure (765 bars) (Replotted from data in Table 4 of Price (1981))

Evaporites as Pressure Seals

Abnormal formation pressure is any pressure that exceeds or falls below the normal pressure to be expected at a given depth, it is sometimes described as disequilibrium compaction. A formation can only be abnormally pressured if the following conditions are met; (1) there must be porosity, as the formation must have the means of storing a pressurized fluid, (2) there must be a horizontal and vertical seal. An abnormally pressured zone will be unable to retain its pressure differential if it is adjacent to a permeable boundary.

The various terms and parameters use to describe a subsurface pressure regime are illustrated in Fig. 8.21a (After Shaker 2008). Normal or hydrostatic pressure is the pressure exerted by a column of fluid extending down to the depth of interest, for a typical porewater column it increases at a rate around 0.465 psi per foot of depth (≈10.5 kPa/m). Hence, the normal pressure expected at 10,000 ft is 4,650 psi; abnormal pressure at this depth would be higher or lower than 4,650 psi (32 MPa). In reality, a hydrostatic pressure gradient will vary slightly, depending on the salinity of the pore fluid and the presence or absence of a salt seal (Table 8.3). For fresh water the gradient is 0.43 psi/ft (9.8 kPa/m) and for a salt-saturated solution it is 0.53 psi/ft

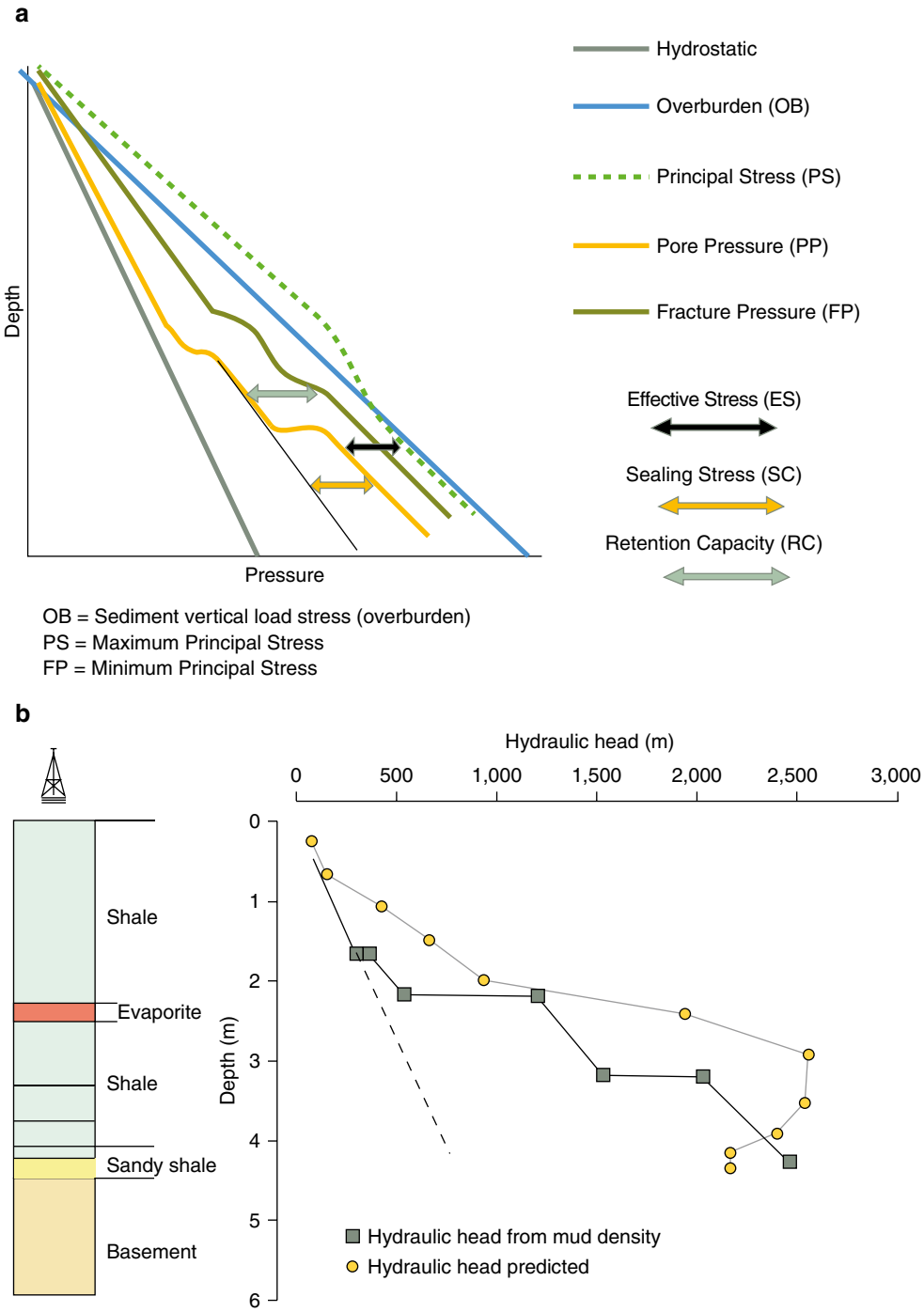

Fig. 8.21 Overpressure. (**a**) Illustration of pressure related terms (After Shaker 2008). (**b**) beneath Messinian evaporites in the Gulf of Lions in the Mediterranean, as indicated by mud densities in the offshore well drilled at kilometre 155 and by predictive modelling (After Burrus and Audebert 1990)

(11.9 kPa/m). Overburden pressure, also called lithostatic pressure, confining pressure or vertical stress, is the pressure or stress imposed on a layer of rock at a particular depth by the weight of overlying material. It is transferred via point-to-point grain contacts and so is related to the density of the overlying rock column. Effective stress is the difference between external stresses acting on the rock matrix (overburden pressure) and pore pressure. Fracture pressure in drilling is the magnitude of the pore pressure at which mud circulation is lost. The retention capacity is defined as the least principal stress minus the pore pressure.

Stress fields, in particular the maximum (PS) and minimum (FP) principal stresses, determine the actual pressure envelopes in a subsurface sediment column (Shaker 2008). Principal stress dictates the progress (transgression and regression) of the pore pressure (PP), with fracture pressure (FP) representing the breaching limit (Fig. 8.21a). These

Table 8.3 Pressure gradients of various fluid columns, including brines of different salinities

Fluid type	Density (g/cc)	API (degrees)	Salinity (g/l)	Gradient (kPa/m)
Brine	1.250	−18	374	12.25
	1.20	−14	398	11.76
	1.115	−8	222	11.27
	1.125	−6	182	11.02
	1.100	−3	147	10.78
	1.075	0	108	10.54
	1.050	3	71	10.29
Seawater	1.025	7	35	9.99
Freshwater	1.000	10	0	9.80
Heavy oil	0.950	18		9.31
Light oil	0.850	35		8.33
Distillates	0.650	88		6.37
Deep gas	0.500			4.90
Shallow gas	0.300			2.94

relationships can be stated in a simple equation, as defined by Terzaghi (1943):

$$PP = PS - ES \text{ or } PP = PS - \left(PS - PP\right)$$

Therefore, principal stress is the driving mechanism of a pore pressure build up. Sealing capacity (SC) is expressed by the transgression of the excess pressure in a specific subsurface pressure compartment, whereas retention capacity (RC) represents the maximum capability of trapping in a specific hydrocarbon column, When hydrocarbons are present then buoyancy pressure is part of the pressure regime. In a confined reservoir it is created by the density difference between hydrocarbons present and water, it is equal to the water gradient minus the hydrocarbon gradient, multiplied by the height of the hydrocarbon column.

About 80 % of the abnormally pressured basins of the world appear to be controlled by low permeability seals (Hunt 1990). Most intervals of abnormal pressure can be related to faults, thick shales, extensive salt seals, or various combinations. Typically pressure gradients are classified as:

- Underpressured (subnormal): <0.465 psi/ft
- Normally pressured: 0.465–0.65 psi/ft
- Moderately overpressured: 0.65–0.8 psi/ft
- Highly overpressured: 0.8–0.9 psi/ft
- Extremely highly overpressured: >0.9 psi/ft

Overpressured cells are the most common type of abnormal pressure and are characterised by fluid-supported pressures (typically geopressured[4] rather than hydropressured). Underpressured cells are matrix-supported pressure seals and are not as common as overpressured cells. Underpressure may be the result of the depletion of a reservoir of some or all of its producible fluids, or can form by surface exposure of the permeable bed at a topographic depth greater than interval where the pressure is being measured or where it is penetrated by the drill bit, or forms by the uplift of a fully enclosed and compacted formation. Both underpressured and overpressured cells are sealed or isolated from their surrounds, otherwise pressure gradients would quickly return to normal. Evaporites play important roles in such isolations due to their inherent low permeabilities. A salt unit does not generate overpressure as it lacks porosity, but due to its exceptional seal capacity can hold back substantially pressurized fluid columns.

Possible causes of abnormal pressuring in sediment pore waters held back by the evaporite seal are numerous and can overlap in the same sequence. They include:

1. *Epeirogenic Movements:*
   (a) Compactional disequilibrium during subsidence associated with rapid deposition (geopressured). Porosity reduction beneath a rapidly accumulating mass of sediment is inhibited by the difficulty in expelling pore fluids from relatively impervious sediment. As water is not very compressible, most of the overlying sediment's weight is then borne by the pore water, rather than the matrix so creating high fluid pressures in the undercompacted unit. Thus the creation of overpressures by compaction disequilib-

[4]Geopressures (a form of overpressure [pore fluid pressure exceeds hydrostatic]) are found in units of rock in which the free flow of fluids has been effectively prevented by either the in-situ formation of an impermeable barrier bed, or the appropriate placement of such a barrier through tectonic activities such as: folding, faulting, or diapiric action of shale or salt. A hydro-pressured zone is an overpressured sequence where hydraulic communication to the surface is maintained and the excessive pressure is due to the weight of the overlying fluids (measured as topographic head in confined artesian waters).

1 psi/ft = 22.5 kPa/m = 0.0225 MPa/m = 22.5 MPa/km.

1 MPa = 145.038 psi.

rium typically requires high sedimentation rates (or erosion rates for underpressure) and a permeability seal or aquitard.

(b) Uplift and topographic recharge (artesian) means that in areas of recharge (high elevation and descending flow) the fluid pressures are below hydrostatic. In areas of discharge (low elevation and ascending flow) the fluid pressures are above hydrostatic (hydropressured). If a seal is present adjacent to the artesian aquifer, then overpressure or underpressure can develop.

2. *Hydrocarbon Generation:*
Maturation of trapped organic matter generating fluids that cannot easily escape to the surface. Thermal maturation of kerogen in hydrocarbon source rocks is associated with marked increases in the volume of pore fluid and thus can also lead to overpressure generation. That is higher density kerogen is replaced by lower-density oil and gas, which requires more volume for the same mass. This is true of the generation of both oil and gas from kerogen, although the latter process is more important in terms of changes in the volume of pore fluids. The driving maturation process can be biogenic as well as the more typical thermogenic.
3. *Mineral conversion:*
Volume changes in reactions involving clay mineral transformation with the associated release of fluid. For example, under high pressure and temperature, structural water is expelled from smectite (montmorillonite) as it converts to illite. Transformation of gypsum to anhydrite (or carnallite to sylvite) can occur fairly early on in the burial process and in the case of gypsum creates up to 38 % free water in pore spaces. If the transforming unit is encased in salt then drainage is restricted and an increase in pore pressure can result especially if the pressurised unit is carried along by halokinesis. But in nonencased beds, the transformation tends to occur at shallow depths where it is usually possible for most of the expelled water to escape.
4. *Aquathermal Pressuring:*
Water expands with temperature more than mineral grains do. Thus, as sediments are heated with burial, the expansion of water generates fluid pressure. This effect is much smaller than compaction disequilibrium and requires a near perfect pressure seal to be effective.
5. *Buoyancy Forces:*
Created by density differences between reservoir fluids. Hydrocarbon column heights can result in substantial overpressure at the top of reservoir compartments, especially when appreciable amounts of buoyant gas are present.
6. *Tectonic Stresses:*
Compressive and dilational regional stresses create pressure cells. For example, if large-scale tectonic stresses change over geologically short periods of time, the driving tectonic compression can generate pore pressure in a fashion analogous to compaction disequilibrium. Deglaciation in regions of former thick ice sheets can also drive pore pressure changes
7. *Osmotic Pressures:*
Created by salinity contrasts across semipermeable membranes (shales and clays) with associated water flow to equalize brine concentrations as long as salinity contrast is maintained by ongoing saline recharge.

Other than this list of possible general causes for abnormal pressures, our discussion will now consider only intervals of abnormal pressure where evaporites have played a role in the creation or retention of anomalous geopressure or hydropressure. The evaporite unit typically does this by acting as a highly effective permeability barrier. For a more general discussion on overpressuring, its causes and effects, the reader is referred to Hunt's excellent paper or subsequent review papers by Yu and Lerche (1996); Converse et al. (2000); Swarbrick et al. 2002 and Gutierrez et al. 2006.

Salt-Maintained Overpressure

Salts (especially halite) are second only to clathrates in ability to form an effective seal to circulating pore waters and hydrocarbons, including methane. Like clathrates, evaporite layers can generate overpressures at very shallow burial depths, unlike clathrates they do not dissolve in response to rising temperature. Evaporites create the highest and sharpest depth-related pressure differentials known in sedimentary basins in both overpressured and underpressured settings (Fertl 1976). Salt-sealed overpressured intervals can be as shallow as a few hundred metres below the surface or deeper than 6,000 m.

Unlike thick shales, evaporites better fit Hunt's (1990) definition of a true pressure seal, which he defined as an impermeable rock with zero transmissivity maintained over long periods of geologic time. Very little subsalt fluid can escape through a salt mass, which until breached tends to hold back all the compactional and thermohaline waters, gases or liquid hydrocarbons rising from below. In contrast, shale seals consistently leak all these fluids to varying degrees. In consequence, fluid pressures can rise rapidly in porous sediments encased within or beneath a rapidly aggrading salt seal, even at relatively shallow depths. Likewise, pore pressures tend to rise in geopressured, finedgrained, poorly-drained muddy sediments accumulating in a rapidly-subsiding salt withdrawal basin (minibasin). Hence, both subsalt and suprasalt associations can quickly become overpressured (Fig. 8.21b; Burrus and Audebert 1990; Yassir and Bell 1994; Lerche and Petersen 1995).

Early onset of subsalt overpressure, and consequent slowing of subsalt fluid escape means that brine-saturated shales and silts below the contact with the salt can remain unconsolidated or semiconsolidated (hence porous and overpressured) to much greater depths and ages than would compacting shales without an evaporite cover. This is the case in many Permian shale beds beneath Zechstein evaporite pressure seals in northern Germany. Despite their Permian age, subsalt Zechstein shales tend to retain fresh, highly porous and plastic physical properties, so that when intersected by the drill bit they are prone to severe heaving, especially below depths of 1-2 km (Thomeer and Bottema 1961; Williamson et al. 1997). Drilling through sharp pressure boundaries into these shales in order to test underlying Rotliegend sands can be a problem, as can drilling on the way through porous rafts of Permian anhydrite or overpressured dolomite "floaters" suspended in halokinetic Zechstein salt (Finnie 2001; Strozyk et al. 2012).

Similar heaving shales beneath thick salt beds and allochthons are encountered regularly in the Gulf of Mexico, Russia, the Middle East, Asia and North Africa (Fertl 1976). Overpressured rafts ("stringers") of porous Neoproterozoic platform carbonate and basinal silicilyte, suspended in halokinetic halite, are widespread in the South Oman Salt basin (Kukla et al. 2011b). Internally, when drilled a salt seal appears normally pressured, but its lack of permeability means it can be holding back a substantial fluid column and the well can transition into lithostatic pressures, even though the drill bit has only breached the lower salt contact by a few centimetres. Casing set in halokinetic salt can be subject to longterm intrasalt creep and this too can create longterm well stability problems (Chap. 13).

Some of the highest measured bottom-hole pressures (formation pressures) in the world, and some of the highest wellhead flow pressures (measured while wells are in production), are found in subsalt reservoirs. These high pore pressures can occur not just in compressed subsalt muds of Tertiary age, but also in evaporite-sealed fractured and vuggy carbonates that are not particularly young. For example, in the gas and condensate fields of the Central Mississippi salt basin, highly overpressured intervals occur in deeply buried dolomitic Jurassic Smackover Formation reservoirs. Down to depths of 3,600 m the fluid pressure gradients approximate hydrostatic (0.465 psi/ft or 10.5 kPa m^{-1}). By 6,000 m a powerfully overpressured zone subsalt zone is entered and the gradient increases to 1.0 psi/ft or 20.35 kPa m^{-1}. This approximates the lithostatic (overburden) stress for that depth. There salt rollers in Jurassic Louann Salt are associated with deeply buried growth faults, which cut the overlying Smackover carbonate reservoirs. Faults sole above the Smackover within an anhydrite seal (typically Haynesville Fm. and equivalents) and so fail to leak fluids from the intervals below the anhydrite seal, allowing pressures to build (North 1985).

Another example of an overpressured basin in older strata lies beneath the Permian salt seal of the Tengiz oilfield in the Precaspian basin of western Kazakhstan. The structure traps some 25×10^9 bbl of oil in an upper Palaeozoic carbonate platform (Fig. 8.22a; Anissimov et al. 2000; Collins et al. 2006). The field is part of the giant Palaeozoic carbonate platform in the Primorsky Bend on the northeast Caspian Coast. The reservoir is made up of Upper Devonian to middle Carboniferous carbonates that are variably overlain by a 150–200 m thick shale and then sealed by thick Permian halite. This halite enables overpressuring with pressure gradients beneath the seal of $\approx$20 kPa m^{-1}, values similar to those in the Smackover and once again approaching lithostatic. Gradients in the nearby water-filled Karaton structure are slightly less due to pressure loss through a breach in the evaporite seal (Fig. 8.22b).

Likewise, the Permian salts of the Zechstein Group form seals to overpressured gas reservoirs in eolian Rotliegend sands of the southern North Sea (Fertl 1976). In the Groningen gas field in the Netherlands, one of the world's largest gas fields ($\approx$100 tcf), the gas reservoir is only slightly overpressured (0.5 psi/ft or 11.3 kPa m^{-1}). But formation pressures in Rotliegend sands below Zechstein salt in northern Germany are much higher ($\approx$0.9 psi/ft or 20.5 kPa m^{-1}), and in some areas in the Main Zechstein dolomite (Hauptdolomit) once again approach lithostatic (1.0 psi/ft or 22.6 kPa m^{-1}).

The Buntsandstein in the Lower Saxony basin, Germany, is another interesting overpressured and hydrofractured example related to Permian Zechstein salt. But in this case the overpressure developed in a Triassic redbed sandstone situated above the halokinetic Zechstein salt, but below the bedded Triassic Röt halite (Nollet et al. 2005). Two generations of vein cements occur in the sandstone. The first generation formed as carbonate cements in fractures developed in weakly consolidated rocks, without any significant increase in fracture permeability. Veins were filled syntectonically by fibrous calcite and blocky to elongate-blocky quartz. The stable isotopic signatures ($\delta^{18}O$ and $\delta^{13}C$) of this vein fill indicates that the calcite veins precipitated from saline connate waters at temperatures of 55–122 °C (Fig. 8.23a).

The second vein generation, composed of blocky anhydrite spar, crosscuts these earlier calcite veins and was syntectonically (halokinetically) precipitated in open fractures. Fluid inclusions indicate that these anhydrite veins precipitated from hypersaline brines at a minimum temperature of 150 °C (Fig. 8.23b, c). Based on $\delta^{34}S$ measurements, the source of the sulphate is seen to be hypersaline fluids migrating from underlying halokinetic Zechstein evaporites. Macro- and microstructures indicate all veins were formed during subsidence (not later diapir squeezing) and that the anhydrite veins formed under conditions of overpressure,

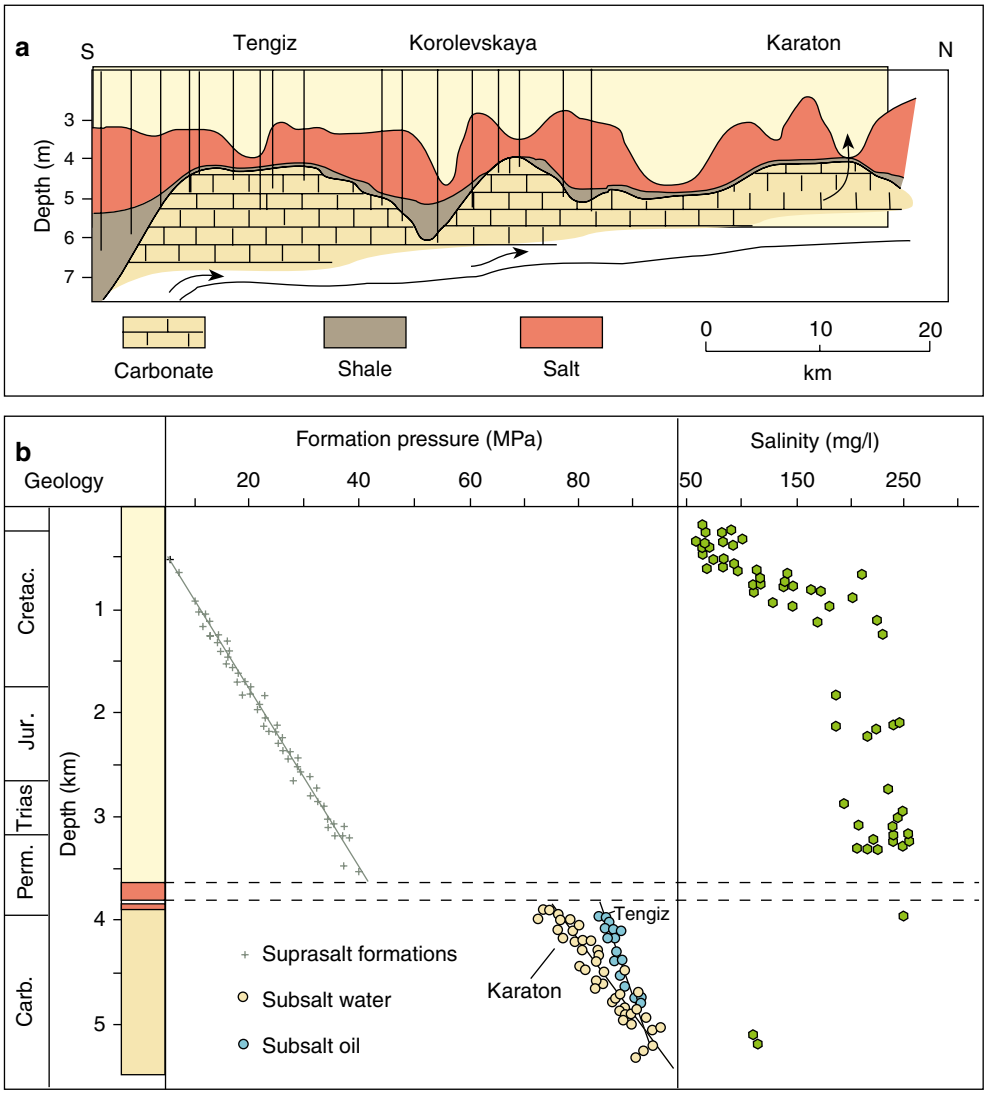

Fig. 8.22 Tengiz oil field, Kazakhstan. (**a**) East west cross section showing how the evaporite seals the oil in a number of carbonate buildup traps. When the salt is breached at the Karaton structure the oil has escaped and the structure is water filled. (**b**) Measured pressure plotted against depth, clearly shows the base of the evaporite is the top of the overpressure (After Anissimov et al. 2000)

generated by hydraulic inflation, rather than non-equilibrium compaction beneath seals. The latter is more typical of salt sealed overpressure or geopressure. Large volumes of $CaSO_4$ -enriched fluids formed as gypsum dehydrated (under significant pressure) in the underlying Zechstein unit and was released into the Buntsandstein during progressive burial and hydrofracturing.

One of the most impressive examples of the ability of an evaporite seal to generate and maintain an overpressured subsalt cell comes from the Alborz discovery in Central Iran (Gretener 1982; Mostofi and Gansser 1957). Five other earlier wells had failed to reach target due to drilling difficulties due to "an extremely troublesome evaporite section that continually menaced drilling and caused numerous sidetrack operations." The discovery well (Alborz 5) had drilled through some 2,296 m of middle to late Tertiary clastics and some 381 m of Oligo-Miocene salt. On its way to the blowout point it had penetrated normally to slightly overpressured salt (halokinetic) and then penetrated some 5 cm into the fractured subsalt Qom Limestone (Oligo-Miocene). On August 26, 1956, the entire drill string and mud column were blown back out the hole. At that time the mud pressure was 55 MPa (8,000 psi) at a reservoir depth of 2,700 m (8,800 ft), a pressure depth ratio of 20.5 kPa/m or 0.91 psi/ft (a lithostatic value!). In 82 days, the well released five million barrels of oil and a large but unknown quantity of gas before it self-bridged and the flow died on November 18, 1956. The temperature of the oil at the surface was measured at 115 °C and at the time of the blowout the mud column density was 2.07×10^3 kg/m^3 (129 lb/ft^3).

Some of the oldest documented occurrences of preserved overpressure, associated with producible hydrocarbons, come from blocks of Neoproterozoic silicilyte (Al Shamou or Athel), encased within the halokinetic Ara Salt of Oman. Initial fluid pressures within fractured slivers of the Athel Silicilyte in the South Oman Salt Basin can be as high as 19.8 kPa m^{-1} (Amthor et al. 1998). This, and other older (preTertiary) examples of salt-sealed overpressure clearly

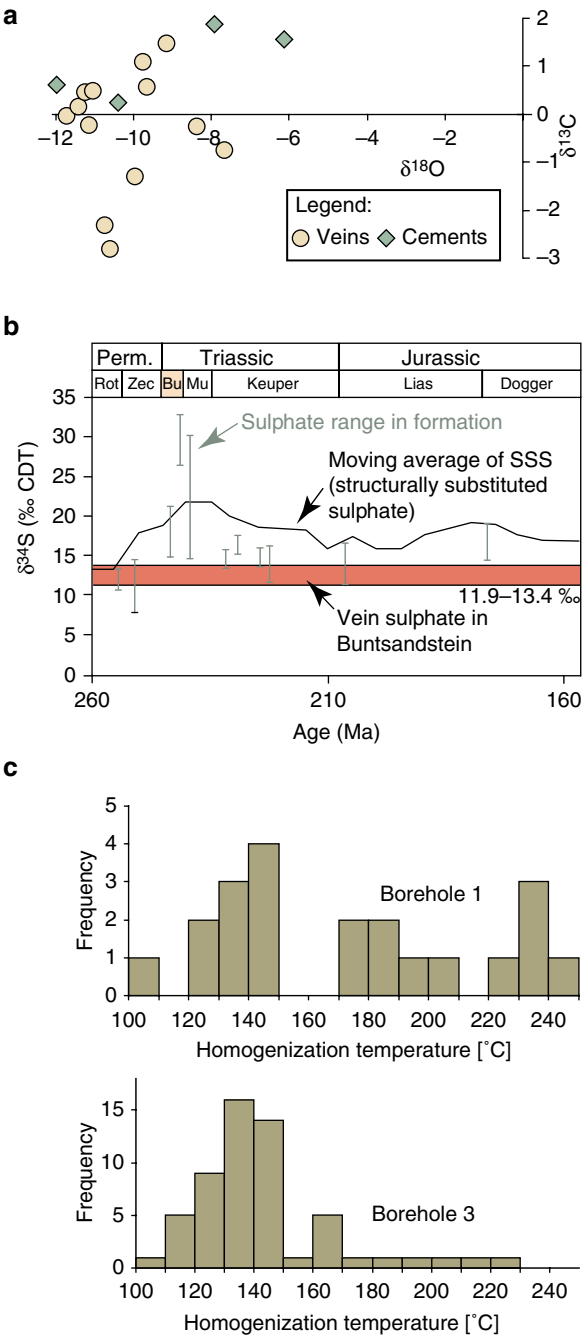

Fig. 8.23 Anhydrite in the Buntsandstein (After Nollet et al. 2005). (**a**) Carbon isotopic signature ($\delta^{13}C$) plotted against oxygen isotopic signature ($\delta^{18}O$) for the calcite veins and cements in borehole 1–4. Veins and cement values show strong overlap indicating that they precipitated from the same or related fluids. (**b**) Sulphur isotopic signature during Permian to Jurassic time compared with results of veins in the Buntsandstein. The data correlate with Zechstein sulphur isotopes, which suggests that the anhydrite layers in the Zechstein are the source rock for the anhydrite veins in the Buntsandstein (*Rot* Rotliegend, *Zec* Zechstein, *Bu* Buntsandstein, *Mu* Muschelkalk). (**c**) Homogenization temperatures of fluid inclusions in anhydrite veins represented in a histogram for samples from the two analysed boreholes. The wide range in homogenization temperature (from inclusions in the same sample) suggests that the primary inclusions in the vein crystals are re-equilibrated during further basin evolution. This means that only the lower values of T_h represent the minimum temperature of vein formation

illustrate the ability of evaporites to maintain seal integrity over time frames of 250–500 Ma and atop pressure fields approaching those that induce hydrofracturing. In contrast, most compacting and subsiding shaly sediments, with permeabilities ranging from 10^{-4} to 10^{-8} darcies, are thought to be too permeable, by several orders of magnitude, to preserve overpressures for time frames longer than 200–250 Ma (Lee and Williams 2000).

If hydrofracturing occurs, with associated pressure release, growth-pulsed fibrous cements of halite, gypsum and carbonate may precipitate in new fracture nets immediately beneath the evaporite seal. But in systems where the evaporites are subsequently dissolved only carbonate vein fills and their fracture nets will remain as brittle sediment indicators beneath a layer of dissolution breccia or insoluble residues.

Salt's impervious nature and its ability to flow, while intrasalt beds fracture, leads to additional interesting pressure scenarios wherever stringers[5] and rafts are caught up in masses of halokinetic salt. Fracturing of intrasalt beds and their encasement in flowing salt is an inherent mechanism in almost all autochthonous and allochthonous salt masses. It creates un-expected pressure rises when drilling through thick sequences of salt. Porous blocks or stringers intersected while drilling halokinetic salt can be isolated or clustered (Fig. 8.24a). Common practice is to bleed them down, since they typically have limited extent within the salt mass. At the well site the observed rate of depletion should give some idea of how long the process may take. In the worst case scenario one raft will "blow-out" into another in a cluster leaving the rig operator to wait until equilibrium is re-established. Generally, no pressure transitions are observed prior to drilling into a stringer, reflecting their isolated nature and sharp boundaries with the salt. The isolated stringer typically occurs in boudinaged or folded clusters remnants of what were once intrasalt beds. Beds were broken into folded or boudined clusters in zones of extension and compression within the flowing salt mass (Fig. 8.24b).

In the Zechstein, for example, the Z3 bioclastic layer of dolomite, Plattendolomit, is deposited on top of the Z2 Stassfurt halite (Fig. 5.64). A $CaSO_4$ layer was precipitated as gypsum, followed by the Z3 evaporites and the Leine halite (Finnie 2001). Water from the gypsum was expelled as the sulphate dewatered and transformed into anhydrite. The overlying halite did not permit the upward movement of this water and so it was forced into the adjacent porous platy

[5]The terms raft and floater are sometimes used to specify layered, competent blocks of non-salt lithologies of varying sizes now encased in halokinetic salt. The terms raft and floater imply buoyancy, but carbonate, dolomite dolerite and anhydrite have a higher density than halite and are expected to sink under the influence of gravity over geological timescales (Van Gent et al. 2011). The term stringer may be more appropriate than raft or floater.

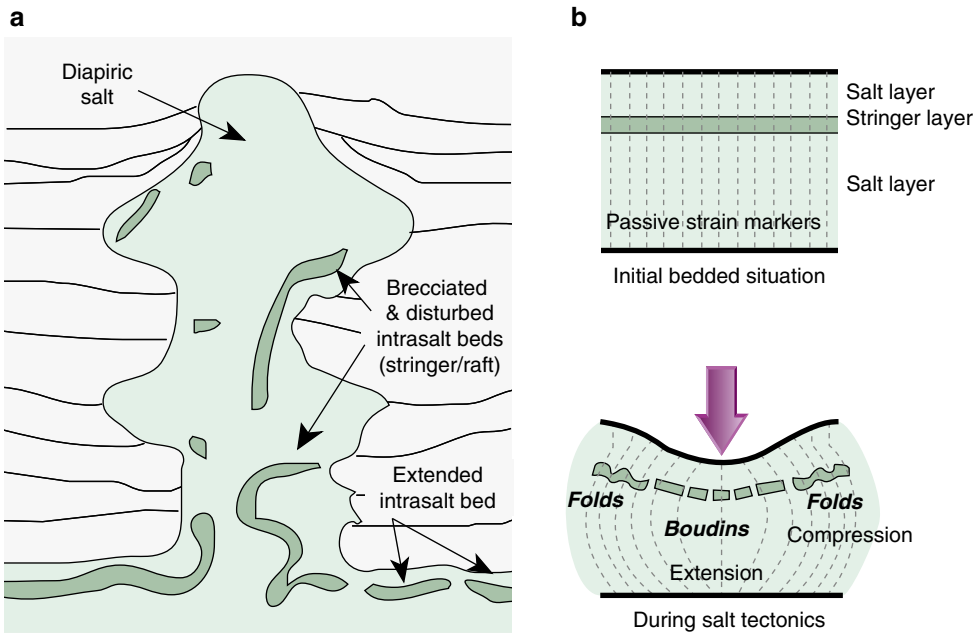

Fig. 8.24 Pressurised stringers and rafts. (**a**) Likely distribution style of isolated overpressured blocks of deformed and fractured intrasalt beds (*shaded green*) in a diapir or salt wall (Based in part on modeling of Koyi 2001). (**b**) Model explaining origin of folded and boudin style stringers in deforming salt (After van Gent et al. 2011)

dolomites. The Plattendolomit already contained fluid and so excess fluid was accommodated in part by pressure-driven leaching. When the Zechstein's most mobile salt layer, the Z2 Stassfurt halite, began to move, it carried with it the overlying Platten/Hauptanhydrite, which buckled and deformed much more brittlely than the surrounding halite. Eventually these intrasalt beds fractured into discrete stringers and were carried along encased by the flowing Stassfurt salt as it pierced the base of the Z3 (Fig. 8.24). Stringers floating in the salt become overpressured by either; (i) being uplifted to shallower depths where they continue to hold their deeper pressures because of the surrounding impermeable salt, or (ii) overpressures are generated in the raft by the folding and squeezing nature of almost all subsurface salt creep in the inverted structures of the North Sea (van Gent et al. 2011).

Source rock maturation within the stringer carbonate can also contribute to the overpressure. Intrasalt stringers or floaters tend to de-pressurise when these overpressured porous rock masses come into contact with minibasin sediments at the edge of the salt mass, or with any other permeable units at the upper or lower edges of the encasing and flowing/dissolving salt mass.

This is most clearly seen in the black-salt encased Late Neoproterozoic to early Cambrian intra-salt Ara (stringer) reservoirs of the South Oman Salt Basin (Fig. 8.25; Kukla et al. 2011b). These carbonate bodies are isolated in salt and frequently contain low-permeability dolomites and are characterized by high initial hydrocarbon production rates due to hard overpressures.[6] But not all stringers are overpressured and a temporal relationship defined by increasingly overpressured reservoirs within stratigraphically younger units is observed. There are two distinctly independent pressure trends in the stringers; one is hydrostatic to slightly-above hydrostatic, and the other is overpressured from 17 to 22 kPa m^{-1}, almost at lithostatic pressures (Fig. 8.25a).

The black staining of the halite is caused by intragranular microcracks and grain boundaries filled with solid bitumen formed by the alteration of oil (Fig. 8.26a–c). The same samples show evidence for crystal plastic deformation and dynamic recrystallization. Subgrain-size piezometry indicates a maximum differential paleostress of less than 2 MPa. Under such low shear stress, laboratory-calibrated dilatancy criteria indicate that oil can only enter the rock salt at near-zero effective stresses, where fluid pressures are very close to lithostatic. In Schoenherr et al's (2007b) model, the oil pressure in the carbonate stringer reservoirs reservoir increases until it is equal to the fluid pressure in the low but interconnected porosity of the Ara Salt, plus the capillary entry pressure (Fig. 8.27). When this condition is met, oil is expelled into the rock salt, which dilates and increases its permeability by many orders of magnitude. Sealing capacity is lost, and

[6]The term hard overpressure is an often misunderstood term, dating back to Loucks et al. (1979), who recognized three pressure regimes that they defined in terms of pressure-depth gradients:

(a) Normal pressure (0.465 psi/ft, 8.9 PPG equivalent mud weight, 1.07 kg/l),

(b) Soft overpressure (0.465 to 0.700 psi/ft, 13.5 PPG equivalent mud weight, 1.62 kg/l), and

(c) Hard overpressure (> 0.700 psi/ft, 13.5 PPG equivalent mud weight, 1.62 kg/l)

The term hard overpressure is also mis-used without reference to pressure gradient to describe narrow transition zones (as often typifies overpressure transitions in the immediate vicinity of a salt seal).

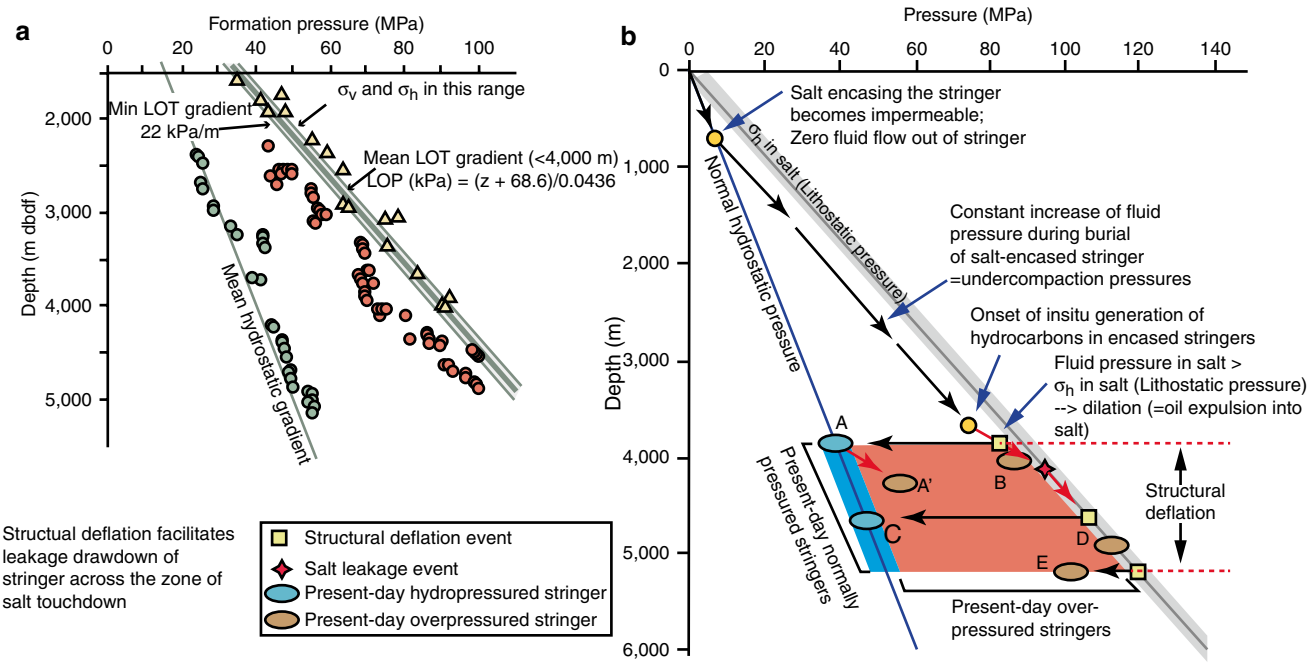

Fig. 8.25 Overpressure in the carbonate stringers of the South Oman Salt Basin (After Kukla et al. 2011a, b). (**a**) Measured formation pressures in the Ara carbonates (*circles*) versus depth. The plot shows two different pressure populations: one at near-hydrostatic pressures, with a mean pore-pressure coefficient $\lambda = 0.49$ (*green circles*), and one at near-lithostatic pressures, with a mean pore-pressure coefficient $\lambda = 0.87$ (*red circles*). *Brown triangles* are leakoff test (LOT) data, and z is depth in metres. The *thick grey band* represents the range of differential stress difference ($\sigma_1 - \sigma_3$ [maximum principal stress – minimum]) in rock salt as derived from integrated density logs and subgrain size piezometry. tvdbdf = true vertical depth below derrick floor. (**b**) Schematic illustrating mechanisms of overpressure generation and pressure deflation in the Ara Stringers through the burial process (see text for detail)

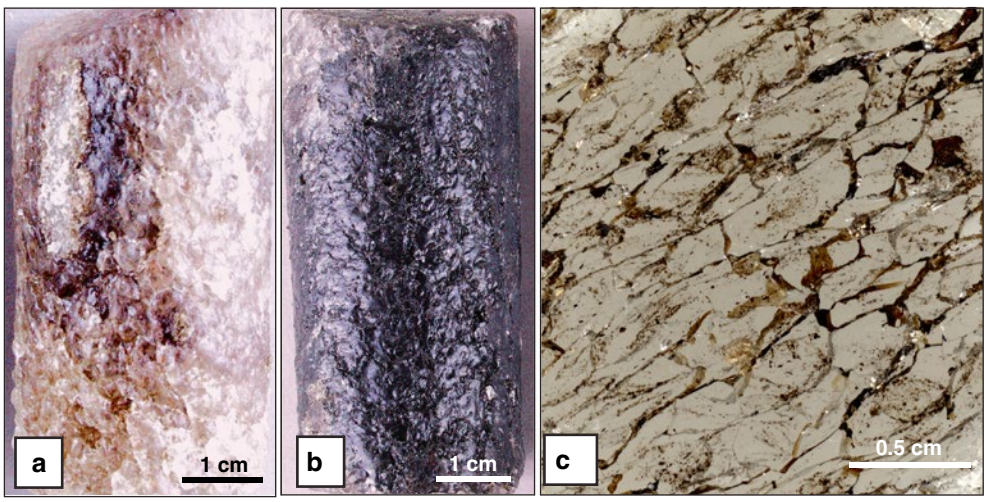

Fig. 8.26 Hydrocarbon-impregnated halite ("black halite") from the Ara Salt, South Oman Salt basin. (**a**) Lightly impregnated salt core, (**b**) Heavily impregnated zone in salt core, this is classic Omani "black salt". (**c**) Photomicrograph of naturally-impregnated salt showing interconnected polyhedral porosity outlined by the darker hydrocarbons (All images courtesy of Janos Urai; see Schoenherr et al. (2007b) for full detail on creation of black salt polyhedral porosity)

fluid flow will continue until the fluid pressure drops below the minimal principal stress, at which point rock salt will reseal to maintain the fluid pressure at lithostatic values.

Inclusion studies in the halite indicate ambient temperatures at the time of entry were in excess of 90 °C, implying hydrocarbons could move into polyhedral interconnected tubes in the halite. These conduits were created in response to changes in the polyhedral angle in the halite in response to elevated temperatures (Lewis and Holness 1996).

Hydrocarbon-stained "black salt" can extend up to 100 m from the pressurised supplying stringer into the Ara salt (Fig. 8.26). It indicates a burial-mesogenetic pressure regime and is not the same process set as seen in the telogenetic "black salt" regions of the onshore Gulf of Mexico. The latter are created by dissolution, meteoric water entry, and clastic contamination, as in the crests of nearsurface diapirs such as Weeks Island (Fig. 13.48). An Ara stringer enclosed by oil-stained salt but now below the lithostatic gradient likely indicates a later deflation event that caused either complete

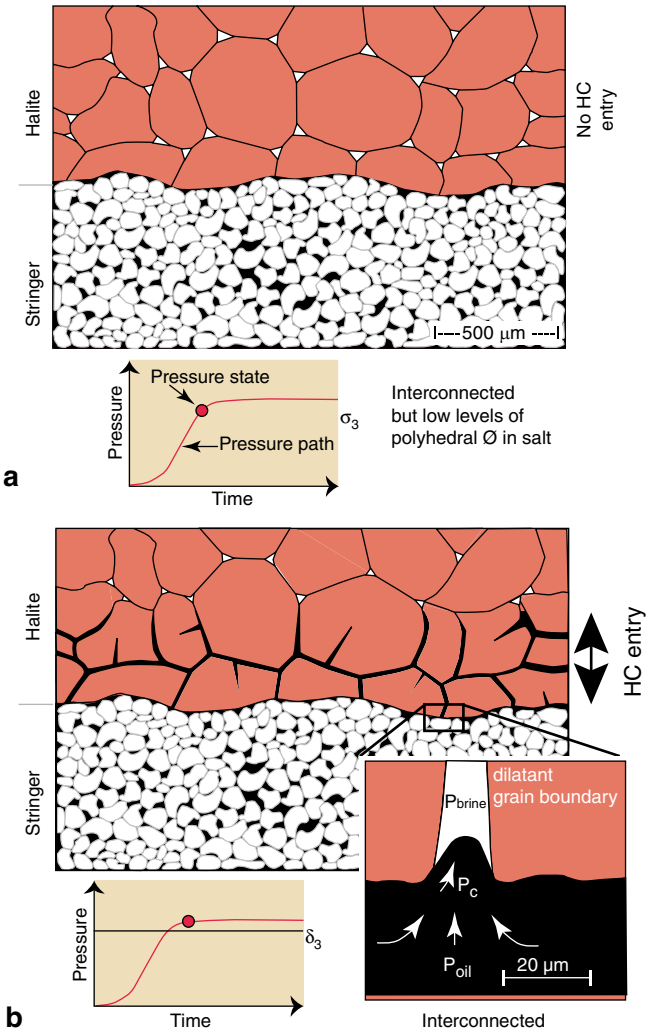

Fig. 8.27 Entry of pressurised hydrocarbons (*HC*) into polyhedral salt pores. (**a**) Schematic cross section in (a) shows the interface of stringer reservoir and Ara Salt. Halite has an interconnected but low porosity represented by the triangular white spaces between the salt crystals (cut perpendicular to the triple junction tubes – thermal response in salt). The *red dot* in the schematic pressure-versus-time diagram indicates that the oil pressure (P_{oil}) is equal to σ_3 in the Ara Salt. (**b**) Because of overpressure buildup, P_{oil} in the stringer exceeds the minimum principal stress (σ_3) of the salt by the capillary entry pressure (P_c), allowing the entry of oil into the triple junction tubes of the salt, leading to a diffuse dilation of the Ara Salt by grain boundary opening and intracrystalline microcracking (After Schoenherr et al. 2007b)

(C) or partial (E) loss of overpressures. Alternatively, stringers showing overpressure, but below the lithostatic gradient (E), might be explained by regional cooling or some other hitherto unexplained mechanism (Fig. 8.25b; Kukla et al. 2011a, b).

Structural, petrophysical and seismic data analysis suggests that overpressure generation in the Ara is driven initially by fast burial of the stringers in salt, with a subsequent significant contribution to the overpressure from thermal fluid effects and kerogen conversion of organic-rich laminites within the stringer bodies. If the overpressured stringers come in contact with a siliciclastic minibasin, they will deflate and return to hydrostatic pressures (A) in Fig. 8.25b. When the connection between the minibasin and the stringers is lost, they can regain overpressures because of further oil generation and burial (A'). If hydrocarbon generation in undeflated stringers stops relatively early, the fluid pressures do not reach lithostatic pressures (B). If hydrocarbon generation continues, the fluid pressures exceed the lithostatic pressure (red star), leading to dilation and oil expulsion into the rock salt to what is locally known as "black salt" (D and E).

As well as these examples of overpressure associated with older evaporites, overpressure readily develops in salt-sculpted Tertiary basins. For example, overpressure occurs in salt shear (gumbo) transitions beneath some, but not all, shallow salt allochthons in Green and Mahogany canyon regions in the Gulf of Mexico (Fig. 5.71; Beckman 1999: Shaker 2008). Where salt allochthons are climbing the stratigraphy, subsalt sealing and associated overpressure can occur beneath the salt mass at shallower levels than is observed in overpressured shale basins.

In terms of extension and compression regimes within a single allochthon tongue, Shaker (2008) noted that in extensional regions in halokinetic basins the magnitude and direction of the principal stresses are controlled by sediment load, salt thickness, and salt emplacement-displacement history. Therefore, the maximum principal stress is not necessarily represented by the vertical weight of the overburden, as is usually assumed in quiescent terranes. Salt buoyancy usually acts upward and has the tendency to accelerate and decelerate the principal stress above and below the salt, respectively. A distinctive shift of the pore pressure envelopes and normal compaction trends takes place across the salt body in several wells drilled trough salt below minibasins in the Mississippi Canyon, Green Canyon, and Garden Banks areas of the Gulf of Mexico. A lower pore pressure gradient has been observed below the salt and a higher gradient above the salt barrier. On the salt-rooted minibasin scale, a high-gradient was also observed in areas where the salt was emplaced and a lower gradient where the salt withdrew (Shaker and Smith 2002). On the other hand, in the compressional portion of a salt allochthon system, lateral stress generated by the salt movement piling up salt at the foot of the slope acts as the maximum principal stress, whereas the load of sediment represents the minimum stress.

Extreme overpressuring is commonplace in subsalt settings in the Gulf of Mexico at depths of 3,000–4,000 m and it variability creates drilling problems, as evidenced in the BP Horizon spill and explosion on April 20, 2010. Gas generated at greater depths in these regions can be trapped under the salt seal at pressures approaching lithostatic. It means drilling under the allochthonous salt on the Gulf Coast slope can intersect undercompacted sediments that are moderately

Table 8.4 Typical mud weights used to drill overpressured sub-allochthon intervals in the Gulf of Mexico

Well	Top salt (m)	Base salt (m)	Total salt thickness (m)	Total well depth (m)	Mud weight above salt (ppg)	Mud weight below salt (ppg)	Density profile (g/cc) (above/in salt/ below)	Sonic log below salt (μs/ft)
West Cameron, Block 505, No. 2	4,300	4,780	480	5,640	12	18	2.45/2.05/2.25	140
Garden Banks, Block 171, No. 1	2,590	2,925	335	3,230	12	14	2.15/2.05/2.25	140
Vermillion, Block 356, No. 1 South	2,592	3,231	639	5,180	13	18	No data	140
South Marsh Island, Block 200, No.1	2,685	2,987	302	n/a	15.6	17.2	2.15–2.25/2.05/2.152.	130

After O'Brien and Lerche (1994)

to extremely overpressured and friable (Hunt et al. 1998). The influence of highly effective Jurassic salt seals on pressure gradients in the Neogene stratigraphy of the Gulf of Mexico is seen in the increased mud weights typically required for safe drilling, once an evaporite allochthon is breached by the drill (Table 8.4). Most wells intersecting salt allochthons in the deepwater realm of the Gulf of Mexico are overpressured at some depth below the base of salt with mud weights controlling pressures ranging from 14 to 17.5 ppg.

For example, in the offshore Mahogany area, salts sheets are encountered below 2,300 m (7,500 ft) subseafloor with an average thickness of 1,150 m (3,800 ft; Walton and Urband 1997). The interval of disturbed sediments (gumbo), first sealed below the salt as the allochthon sheet rolled into place across the seafloor, now extends 300–500 m (1,000–1,500 ft) below the salt base. Formation temperature at the salt base is around 75 °C (170 °F). Rotary sidewall cores collected from the salt show it is very dense and competent. Fracture gradient checks performed in and below the salt mass by pump-in leak-off tests, approach 0.988 psi/ft (19 ppg). The fracture pressure is only 0.5 ppg higher than the pore pressure in those wells. Yet in other subsalt wells the underlying disturbed sediments cannot support a mud column of 16.9 ppg (0.879 psi/ft gradient). Pore pressure gradient decreases as drilling progresses below the salt, until the sediments became more competent and less affected by the influence of early sealing beneath the salt allochthon trap.

But subsalt pressures in allochthon basins are very unpredictable, as it is not the salt itself that generates abnormal pressure (it lacks porosity). The overpressure comes from the inability of basinal fluid to move through the salt mass or to drain freely from thick underlying shales. For adjacent sediment to be abnormally pressured, fluid must be generated by compactional or thermobaric/catabaric processes in the sediments beneath the salt. The salt mass itself is only the barrier to this escaping fluid. So, where sediments immediately below a salt mass are not carrying overpressured fluids, the contact with the salt is not overpressured. In fact, lower than regional pressure gradients are found below some salt allochthons, as well as the more typical higher pressures. For example, a few subsalt wells in the Mississippi Canyon region have mud[7] weights indicating much lower subsalt pressures (11–12.5 ppg mud weights).

Such lowered pressures may indicate zones of rapid salt solution and creation of pore space via dissolutional collapse. Nor can overpressure be correlated to the thickness of the overburden atop a salt allochthon. The only generalisation is that, if abnormal pressures are present immediately beneath or adjacent to a salt mass, the pressure boundary will typically be sharp and correspond to the contact with the salt mass.

Thick shale-rich suprasalt successions in the withdrawal sinks (minibasins) of some more deeply buried salt units are also overpressured (Fig. 6.47). Shale-sealed sands sometimes show evidence of permeability connections through shale gouge zones about salt masses. Shaker (2004) argues that at the scale of salt-rooted minibasins, higher pressure gradients tend to occur in areas where the salt was present, while lower gradients tend to occur in areas where the salt has been withdrawn into adjacent allochthons. But this is a dynamic situation in which seal rupture (often along growth faults in the edges of minibasins and atop a zone of thinned salt) is followed by a cycle of fluid movement, a pressure drop, resealing, and renewed pressure buildup from the continuous generation of thermogenic gas. It creates dynamic pressure regimes where overpressuring beneath salt allochthons can occur a number of times in the minibasin history and is sometimes called seismic valving or pumping (McBride et al. 1998a, b).

Seismic valving defines a fluid system where the build-up of fluid overpressure within an aquifer, juxtaposed against a fault, temporarily attains lithostatic pressure and so drives the periodic release of fluids that move out depressurise the aquifer. It contrasts with the seismic pumping mechanism in

[7]Drilling mud weights (pounds per gallon or ppg) are sometimes used to estimate pore pressure in permeable formations as they tend to take in drilling mud if the mud pressure is significantly in excess of the pore pressure and produce fluids into the well if the converse is true.

which faulting, driven by externally imposed stresses, controls periodic fluid movements along the fault (Sibson 1981, 2003). The two processes can be closely interrelated in time and space

Conceptually, the close interrelationship between the terms seismic pumping and seismic valving is best explained using the analogy of a hand-driven water pump that is being used to raise water from a water well. As the handle of the pump lifts the piston it creates a low-pressure region that draws in water across a one-way valve into the pump cavity (seismic pumping). Then as the action of the handle is reversed it compresses the water beneath the piston forcing water out of the pump faucet (seismic valving). Likewise, fluid flow in an extensional regime is related to cycles of dilatancy and fault release in the region of the fault. Extensional dilatancy in the fault and its vicinity draws in pore waters (and hydrocarbons) from its surrounds. This is followed by an episode of fault release, whereby overburden loading now compresses and drives water up along the fault into higher levels. Hence, with salt-induced seismicity active in a normal fault or growth fault, the episode of fault release drives fluid up along the steeply dipping fault.

Seismic pumping and valving of fluid flow is also possible in a reverse fault or thrust scenario. Once again the time of fault release is the time when fluid is sucked into the fault plane ("squeegee mode" mentioned earlier). But the low angle of the thrust means it does not easily drain up the fault to the surface but remains under subsequent compression to act as a fracture propagator, as evidenced in multistage fracture filling mineralisation associated with the thrust. This is especially so in sediment beneath salt-lubricated (and sealed) thrusts.

Active growth fault zones at the edge of a salt-cored minibasin and typically soling into salt welds have created fluid conduits supplying the numerous shallower reservoirs in Eugene Island and Ship Shoal areas (Farley 2005). One such fault was intersected in South Addition Block 330, offshore Louisiana and was sampled at a depth of 2,460 m by the extended "Pathfinder" well (Fig. 8.28; Anderson et al. 1994b). Oil and gas in this region is being produced from Neogene reservoirs as young as 400,000 years old and the field is located beneath numerous active seafloor seeps. Eugene Island is one of the largest Pleistocene oil fields in the world and is surrounded mostly by gas-dominated fields in the south additions of offshore Louisiana. More than 600 million BBL of oil equivalent has been produced from this field since its discovery in 1971 (Fig. 8.28a, b). Sediments filling the minibasin consist of alternating sequences of sands and shales that are likely floored by deepwater turbidites from the ancestral Mississippi River delta. The studied fault sits atop a breached salt allochthon and defines the edge of a classic salt-floored Gulf Coast minibasin.

In spite of the removal of what was once an underlying salt allochthon via earlier salt evacuation, deeper sediments are still geopressured. The pressure buildup reflects ongoing rapid deposition of thick deepwater shale above the evacuating salt allochthon. Rapid mud deposition produced permeabilities in the lower part of the minibasin fill that were too low for the compacting pore fluids to escape. Oil and gas still seeps from silty shales, adjacent to the fault zone, which has been naturally fractured. Coring revealed that fracturing extends at least 100 m from the growth fault into the shales of the upthrown block. Hydrocarbons in the fault zone are geochemically identical to those sampled from producing reservoirs located within sands that abut shallower splays of the same fault zone system (Fig. 8.28b, c). Hydrocarbons did not flow from the growth fault at economically viable rates during drillstem tests. Analysis of fluid pressures shows that the main 'A' fault is currently a profound lateral permeability barrier, with an 1,800 psi water pressure differential across it. Even so, Anderson et al. (op cit.) noted that the larger the drawdown pressures applied across perforated intervals, the lower the permeabilities of the fault zone. Flowable hydrocarbons are present and must be partially supporting the matrix. The balance between tectonic stresses and pore pressures, within the relatively tight zone defined by the growth fault, was found to be such that with an increase in pressure of 500 psi or so, large volumes of fluid could be transmitted from depth, suggesting a method that may allow production from such deep zones in the future.

Pressure data in Block 330 supports the notion of periodic fluid flow in the fault being driven by a combination of "seismic valving" and "seismic pumping" within salt-floored extensional basins. Based on their studies of the Eugene Island growth fault, Anderson et al. (1994a, b) and Losh et al. (1999, 2002) concluded that hydrocarbon migration associated with the fault was episodic. It was driven by pressure increases deep within the geopressured turbidites of the subsalt play, which rose until stresses reopened fractures in the various fault zones that connected with the upper reservoir chambers (seismic valving). At that time, large volumes of hydrocarbons were released rapidly as transient bursts towards the surface. With each pressure release, the faults closed back up. Losh et al. (1999) modelled coupled heat and mass flux in the A6ST well and concluded that the palaeothermal anomaly in the fault zone was short-lived, having a duration of less than 150 years. The anomaly could have been produced by a 2×10^6 m^3 pulse of fluid ascending the fault at an actual velocity of over 1 km/year (darcy flux of 330 m/year) from 3 km deeper in the basin. Simple Darcy law computation indicates transient fault permeability on the order of 110 md during this flow.

Pulsing of fluid up weld-floored growth faults is probably the norm in this style of trap. Put another way, with added pressure, fluid (including oil and gas) is expelled up the fault

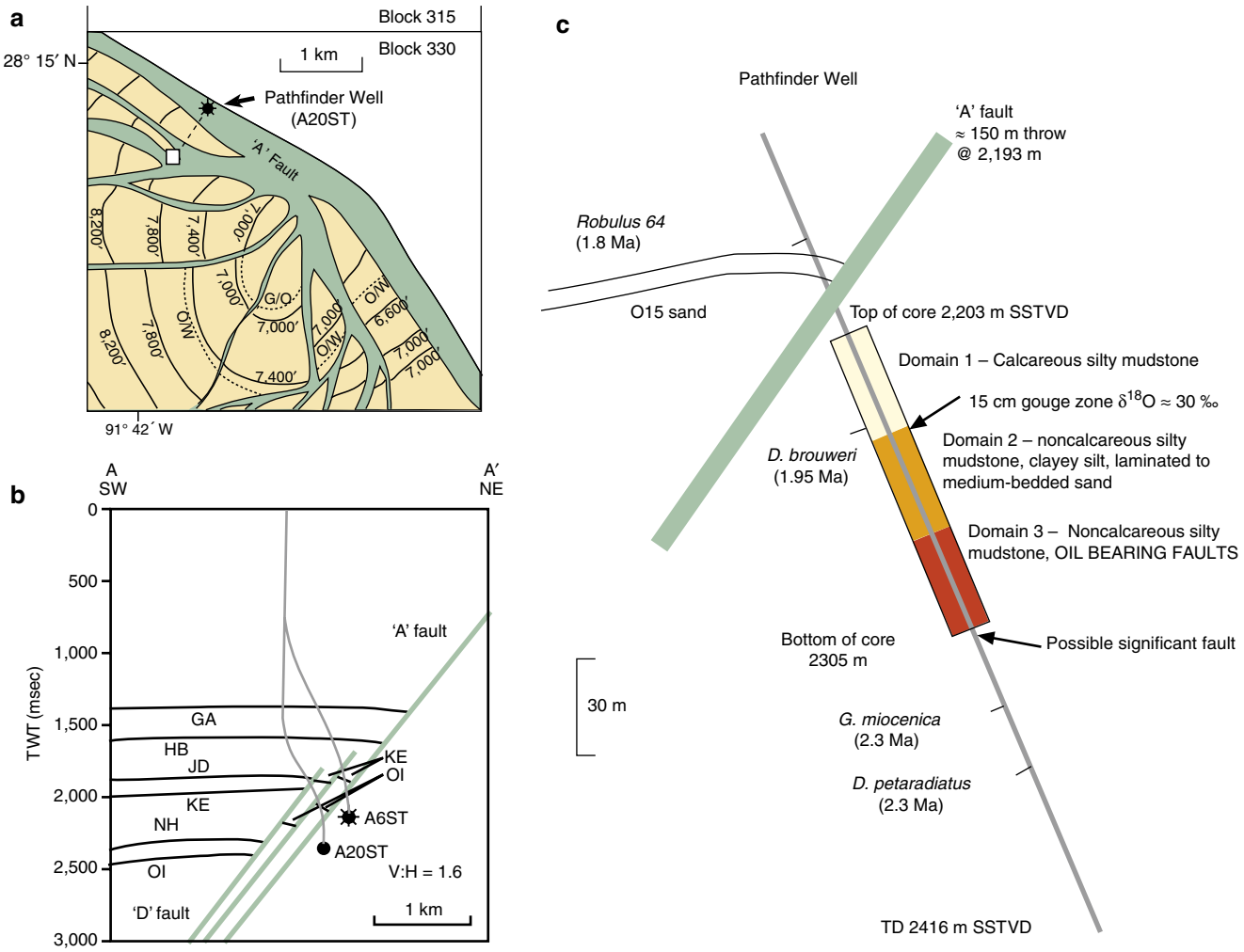

Fig. 8.28 Growth fault characteristics, Block 330 Eugene Island, Louisiana. (**a**) Structure contour map of O1 sand, showing position of the Pathfinder well. (**b**) Southwest-northeast cross section AA' showing Pathfinder (A20ST) and A6ST well trajectories, the 'A' fault, subsidiary structures and selected sand tops. Depth in milliseconds two-way travel time (TWTT); 1 ms approximately corresponds to 1 m depth in this section. (**c**) Summary cross section of core from Pathfinder well showing core location relative to 'A' Fault zone and biostratigraphic markers. *SSTVD* subsea true vertical depth (After Anderson et al. 1994b)

zone, but then the very act of releasing the fluids drops the pressure and the fault becomes tight once more. Over and over, the cycle repeats. A pulse of high-pressure fluid ascending the fault lowers effective stress in the fault zone sufficiently to produce a significant transient increase in fault permeability. If the fluid is in an area of the fault adjacent to downthrown, relatively low pressure reservoir sands, so the fluid will discharge into them. Permeability in and adjacent to the fault then decreases, such that fluid cannot re-enter the fault zone and escape from the reservoir.

On the broader scale, salt's ability to deform with its accumulating overburden into growth fault-defined minibasins means pressure cells in suprasalt sediments not only show episodic changes in a high-gradient vertical pressure transition, they can also be subject to rapid lateral changes in pressure. Many lateral seals in this situation are subvertical and tend to follow fault trends with their geopressured tops sometimes defined by high temperature carbonate cements. Using a 3D model of fluid flow history in the Eugene Island area, Anderson et al. (1991) concluded that many convective heat flow anomalies at the surface indicated the upward movement of hot subsurface fluids along various salt-floored growth faults. Many of the larger fluid compartments in this laterally restricted system consist of a series of smaller compartments, each with a single top seal and several side seals, which are active growth faults (Gordon and Flemings 1998). Similar episodic salt movement of various fault-defined pressure cells within the Jurassic Smackover Formation, atop the Louann Salt of the Mississippi Salt Basin, US Gulf Coast, has created a meshwork of large fluid compartments. Adjacent internal pressures range from normal (hydrostatic) in one compartment to 70 MPa (10,000 psi) above normal on the other side of the fault.

Controlling Unpredicted Pressure Changes

Drilling through salt can be rapid and predictable if there are few interlayered nonsalt beds. Typical rates of penetration (ROP) in salt masses are 15–40 m/h, meaning that a km section can usually be drilled in 2 or 3 days with a PDC (polycrystalline diamond cutter) bit. ROP is important because speed minimizes hole closure from creep. Salt is essentially impermeable, so the effect of drilling fluid density (mud weight-MW) on ROP is small. MW management and increased weights can be used to control closure rate, while sustaining reasonable penetration rates. However, high MW carries risks of lost circulation in unexpected non-salt zones (Dusseault et al. 2004).

Massive salt does not present as many drilling problems as fractured shales within and adjacent to the salt, but there are other challenges in drilling salt such as washout, rapid borehole closure, mud weight control issues, and casing placement decisions. Of these, the most problematic are subsalt overpressured or pressured reversion regions and the prediction of pressure regimes encountered during the penetration of extensive rubble or sheared zones (gumbo), which are common underneath salt tongues and sometimes within and lateral to diapirs. In such zones it may be difficult to decide where salt ends and nonsalt sediments start. Not knowing where these contacts are can be problematic as principal stresses are perpendicular and parallel to any plane without shear stress. Thus the orientation of principal stresses is likely to be affected by the presence of weak salt bodies or nearby severely overpressured formations (Fredrich et al. 2003).

Overpressures beneath evaporites are more of a problem to predict than pressures encountered when drilling thick variably pressured shales (e.g. Zilberman et al. 2001; Merrell et al. 2014). Most current overpressure control methods, which use slightly overbalance methods of mudweight to minimise formation damage, were first developed in shale sequences, where there is typically a well-defined transition over tens to hundreds of metres into the zone of overpressure. Transitions are often identifiable by changes in resistivity, density and sonic signatures in MWD (measurement while drilling) logs. Close monitoring of bottom hole pressure and the recognition of this transition zone allows the drilling engineer to set casing, if needed, and to increase mud weight before entering the zone of overpressure. Evaporite seals can be much thinner (down to 3 m), with sharp pressure transitions at their lower boundaries across a few cm. A sharp dissolutional contact along the underside of almost all thick evaporites and the inherent ability of a salt mass to support high fluid overpressure beneath intervals as little as 3–4 m thick means there may be little, if any, development of a pressure transition zone. Highly pressured sediments can be entered immediately below the base of the evaporite, whereas pressures appear normal as the evaporite is drilled (e.g. Alborz 5 blowout).

If a basal anhydrite (upside-down caprock; see Chap. 7) has developed on the underside of a halite mass, there may be a slowing of the drill penetration rate immediately prior to entry into the overpressured interval. However floating anhydrite or dolomite rafts in diapiric halite also slow drill penetration rates. In one situation pressure tends to bleed off with time; in the other the well may be susceptible to a major high fluid volume blowout.

Low strength casing set in a thick halokinetic salt mass, which tends to heave over time, will deform and can even shear during the active life of the well (Merrell et al. 2014). Likewise, "drilling on" through heaving and often geopressured shales beneath a salt allochthon (gumbo) is a challenge for the drilling engineer, further compounded by the possibility of encountering heaving intrasalt "shales" or overpressured intrasalt anhydrite and dolomite rafts on the way to the lower contact (e.g. Seymour et al. 1993; Zilberman et al. 2001). A lack of consolidation/induration in muddy Neogene sediments about a salt allochthon means it can be quite difficult to attain a tight cement seal behind casing in such weak and friable overpressurred lithologies. It is highly possible that a lack of consolidation behind cemented casing was a contributing factor to the blowout and spill that was the BP Horizon.[8] Macondo disaster, which occurred in the Gulf of Mexico on April 20, 2010. It was also a contributing factor in the subsequent technical difficulties experience when trying to re-establish control (kill the well) once the blowout had occurred.

Important factors controlling subsalt pressure distribution below both primary beds and allochthons are:

- Lateral extent and thickness of the salt body (Fig. 8.29a; diameter of drainage collection)
- Presence of areas of halokinetically thinned, or faulted or discontinuous salt (Fig. 8.29b; leakage)
- Depth of salt burial, salt buried at shallower depths (>1–2 km) may not have developed widespread overpressured intervals in the underlying sediments (with allochthons this is typically due to a lack of lateral or updip seal)

[8]Deepwater Horizon oil spill is also referred to as the BP oil spill, the BP oil disaster, the Gulf of Mexico oil spill, and the Macondo blowout. At approximately 9:45 pm CDT, on 20 April 2010, highpressure methane gas from the well expanded into the drilling riser and rose into the drilling rig, where it ignited and exploded, engulfing the platform. At the time, 126 crew members were on board The disaster claimed the lives of 11 rig personnel whose bodies were never found. The explosion and fire was followed by the sinking of the Deepwater Horizon oil rig and consequent loss of well control. Oil flowed onto the deep seafloor for 87 days, until the well was capped and flow greatly reduced on 15 July 2010. After several failed efforts to contain the flow, the well was declared sealed on 19 September 2010. The total discharge from the Macondo spill is estimated at 4.9 million barrels (210 million US gal; 780,000 m^3). The U.S. government's September 2011 report pointed to defective cement in the well as the main cause of the blowout (Graham et al. 2011).

- Rate of burial, slow burial may have allowed overpressure to dissipate in the subsalt beds
- Presence of a widespread sand-rich section underlying the salt may facilitate drainage and loss of pressure. More laterally restricted sand-rich sections under the salt can form both an excellent trap and reservoir for hydrocarbons (Fig. 8.29c)
- Presence of a shale sheath or gouge about a salt structure. Suprasalt sands that connect to this gouge may be overpressured but tend to be in pressure connection. Intervening sands that are unconnected to the gouge can be independently overpressured (Fig. 8.29c).

Likely variations in formation pressure on entering and exiting an evaporite unit mean mud weights are often designed specific to the geology being drilled. For example when seeking a target in the Najmah Formation, which lies below the Gotnia Salt and its Hith Anhydrite cap, the following procedure is followed (Al-Saeedi et al. 2013; Fig. 8.29d). Hith formation in a 12¼" well section is opened with

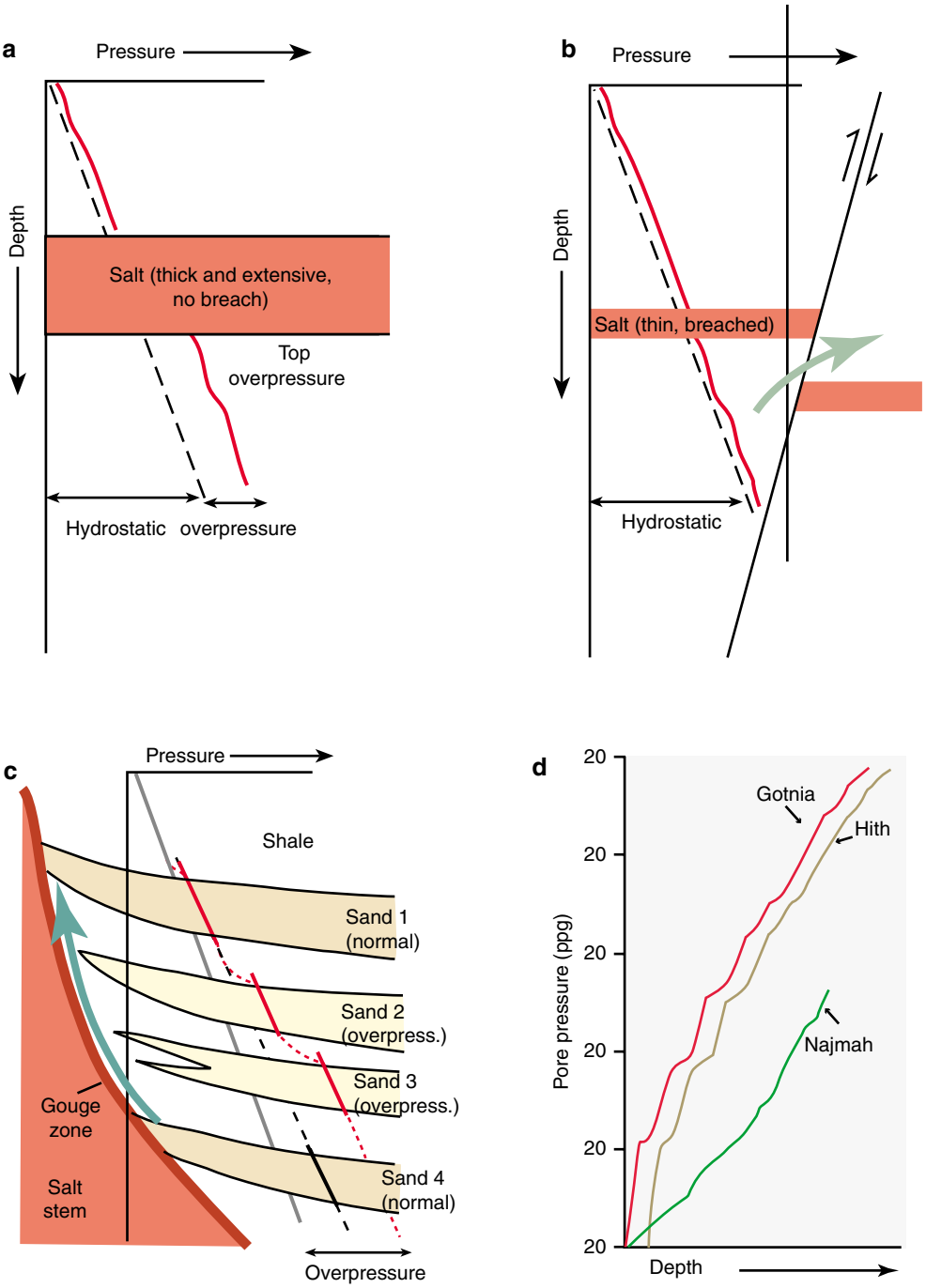

Fig. 8.29 Pressure profiles of various evaporite profiles. (**a**) Overpressure beneath a thick laterally extensive salt bed or allochthon. (**b**) Normally pressured beneath a thin discontinuous (faulted) salt layer. (**c**) Overpressure in suprasalt sands encased in shale. Sands which are in contact with the shale gouge tend to be in pressure connection, while those which are not are independently pressured (in part After Shaker 2004). (**d**) Mudweights utilised to drill Gotnia salts and underlying Najmah reservoir in northern Kuwait (After Al-Saeedi et al. 2013)

18.5 ppg mud. Formation integrity tests are carried out, up to 21 ppg, prior to opening the Gotnia formation. This ensures supra-Hith wellbore integrity if increased mudweights are required later. Then, prior to entering Gotnia first salt, mud weight is increased to 19.3 ppg. In the Raudhatain wells of North Kuwait the Gotnia salt is opened with 19.5 ppg mud weights. Significant offset well data from the previous wells in the area is taken into consideration in setting mud weights. Currently, the applied overbalance pressure over the Gotnia formation is limited to 0.7 ppg. Salt drilling is done with a controlled rate of penetration of 25–30 ft/h, even though salt can be drilled much more rapidly. Flow checks are done at every drilling break and bottoms up are circulated at the top of every salt-anhydrite layer in the Gotnia to confirm the thickness. This also ensures that the connection gases from the previous connection have been circulated out of the well prior to making the next connection. This is done in order to minimize the impact of head reduction (H_2S is a possible hazard in this geology). If the gas units are ±50, then the mud weight is increased prior to drilling further.

To minimise the possibility of blowouts, contingency plans are in place prior to drilling each Gotnia well. Two large volume mud plants have been established in North Kuwait specifically tied to drilling Gotnia penetrating wells. Prior to any well entering Gotnia Formation salts, it is standard practice that 2,000 bbls of 20-ppg kill mud are stored on the rig and, while drilling the Gotnia section, 400 MT of baryte is maintained on location 1,500 bbls of kill mud is kept ready in the mud plant with proper logistics support to transport this mud to the rig site in any emergency. Any kick taken on well bore with the mud weights above 19.8 ppg is controlled by bull[9] heading the gain back into the formation. This is done on the basis of experience gained from the previous wells to control the large volume of kick, protect the casing and to avoid the risk of taking H_2S gas in the well bore.

To counter the mud losses, 200 bbls of an 80 ppb LCM pill is prepared and kept ready prior to entering the Gotnia layers. Only in rare cases are MWD tools used in this Gotnia section (Al-Saeedi et al. 2013). When they are, the concentration of LCM pills does not exceed 45 ppb, due to the limitation of the downhole tools. At the first sign of losses, this pill is pumped into the well bore and it is allowed to soak for 2 h. In case of complete losses, pills are tried up to two times to control the losses. If there is no sign of healing with maximum of two pills, drillable plugs are set and cement plugs pumped to cure the losses. According to Al Saeedi et al., these practices have greatly helped in avoiding more days spent on mud-loss control situations.

Drilling Mud Chemistry in Salt Systems

Although drilling salt may appear to be simple, salt behaviour can be complex especially if the mud chemistry allows substantial amount of salt to pass into solution. Drilling fluids saturated with drill cuttings from mixed mineralogy salt formations can have a particularly complex chemistry, which can be difficult to understand and control. It means there can be drilling mud related problems, typically related to varying combinations in and around the well bore of saline precipitates, salt flows and salt dissolution, namely:

- Dissolution of salt resulting in hole enlargement (subsaturation).
- Temperature fluctuations driving unwanted combinations and precipitates.
- Deformation of salt, reducing the hole diameter and leading to stuck pipe.
- Degradation of well control – resulting from unexpected inflows of hydrocarbons, CO_2, H_2S or brine liquids and lost circulation.
- Recrystallization of salt and other intramud and intrafiltrate precipitates, stripping the emulsifiers and wetting agents from standard oil- and synthetic- base muds, resulting in water wet solids in the mud stream and a degradation of mud properties.

Halite-anhydrite lithologies, even when bedded as across much of the Arabian Peninsula, are complicated systems to drill, especially if the target subsalt reservoir is a fractured carbonate with matrix storage. In this case there is the possibility of exiting the salt into a system that maybe normally pressured or highly overpressured. If the mud weight is weighted to deal with overpressure but the reservoir is normally or even underpressured the chances of mud-induced formation damage are high.

One of two approaches is used with water-based fluids if they are chosen for drilling evaporites: (1) Use of a saturated salt system or, (2) Use of a slightly undersaturated system to encourage hole enlargement, which keeps salt deformation from engendering stuck pipe. The undersaturated option is sometimes difficult to manage, depending on the actual conditions, can easily lead to excessive hole enlargement, which may cause further complications in obtaining a collapse – resistant, tightly bonded and cemented casing. Water-based drilling fluids should be designed to be compatible with the

[9]Bull heading is the most common method of a contingency well kill. If there is a sudden need to kill a well quickly, without the time for rigging up for circulation, the more blunt instrument of bullheading may be used. This involves simply pumping the kill fluid directly down the well bore, forcing the well bore fluids back into the reservoir. However, it can be limited by the burst-pressure capabilities of the tubing or casing, and can risk damaging the reservoir by forcing undesired materials into it. The principal advantage is that it can be done with little advanced planning.

salt to be drilled. This can be difficult for mixed solutions, like halite-carnallite, where non-standard oilfield salt additives, like magnesium chloride, would be required, and may not be readily available. It is important to have the mud system completely saturated when the salt is first penetrated to prevent excessive hole enlargement in the top of the salt. Once the salt is being drilled, the system will stay mostly saturated due to some level of formation dissolution.

In some areas, the use of undersaturated salt systems has been perfected so that the rate of salt dissolution is matched to the rate of salt creep. One difficulty with this approach is that for long salt sections, the rate of intrasalt creep can vary internally, and the mud in the annulus can saturate at the bit (from salt cuttings), then it can not dissolve more salt as it circulates up the annulus. This method is best used in areas where the salt section is short and where it is a common practice on existing offset wells.

Al Saeedi et al. (2013) concluded that, when using water-based mud to drill salt-anhydrite in environmentally sensitive areas, saturated salt systems should be utilized in order to avoid excessive hole enlargement. Although the drilling fluid is saturated at surface temperatures, in down hole conditions, due to high temperatures, the solubility of salt increases slightly, providing conditions promoting salt dissolution, resulting in hole washouts. The selection of the type of salt additive for a salt saturated mud system is another important aspect of bore hole conditioning, depending on the type of salt in the formation. In case of soluble bitterns in the formation, like potassium and magnesium salts, magnesium chloride may be needed in the mud system to saturate the system, but it is not a commonly available oil field chemical. Using regular mud additives, like sodium chloride or calcium chloride, still tends to dissolve some magnesium salts, resulting in unwanted hole enlargement, adding an additional mix of Na, Ca and Cl into the drill mud can create unwanted precipitates

The presence of anhydrite in a formation also influences the type of mud selected for drilling calcium sulphate units (Al-Saeedi et al. 2013). When $CaSO_4$ is dissolved in water, it forms Ca^{2+} and SO_4^{2-} ions, of which calcium creates more harm in a water base mud. Anhydrite drilling with a water-base mud causes aggregation and flocculation due to calcium sulphate passing into solution, resulting in thickening of the mud. Calcium sulphate also increases apparent viscosity, gel strengths and yield point in the mud. Partially-soluble calcium also increases hardness in the filtrate and the likelihood of scale. Also, evaporite minerals like anhydrite tend to percolate readily into water base muds. Though these problems can be overcome by using effective thinners and soda ash, there is a limited space for error in these sensitive formations and these factors have determinable effects. In contrast, using and oil-base mud to drill salt-anhydrite interfaces, gives a lower water content in the mud system. This reduces the amount of salt dissolution and hole enlargement to a greater extent. From the early days, the Gotnia Formation in Kuwait was drilled with a high oil/water ratio oil-based mud to better preserve the hole gauge.

Oil- or synthetic base muds can also be used to drill salt sections. The oil-wetting ability and lower water contents reduce salt dissolution and control hole enlargement, but salts will still dissolve into the water phase, keeping it saturated. There are several reactions that can occur due to the excess lime concentration and high chlorides. The reactions can be unpredictable and vary depending on salt composition and temperature. These systems can be formulated with a variety of salts in the water phase as an alternative of calcium chloride. Sodium-chloride and magnesium chloride internal phase systems have been used successfully.

Although oil-based systems are preferred for drilling salt, so that a gauge hole can be preserved, salt dissolution products can be more detrimental to inverted emulsion muds than to water base muds. The most damaging aspects are recrystallization of salt and magnesium hydroxide precipitation. Both reactions produce extremely fine particles with a tremendous surface area. This can lead to a rapid depletion of emulsifiers and oil-wetting agents. Consumption of the emulsifiers and wetting agents can result in water-wetting of solids.

Salt-Generated Underpressure

Most naturally underpressured cells are created by a combination of uplift and erosion or by glacial rebound. Abnormal pressures in an underpressured interval are less than would be expected if a normal hydrostatic gradient was present. Underpressure occurs when the confining pressure on a subsurface sediment compartment is reduced and, providing the matrix is flexible, this allows the compartment to relax and expand. If little or no fluid can enter the compartment, then existing pore fluids in the expanded compartment must fill a somewhat larger space and so the pressure drops. An analogy is often made to what happens when a water-soaked sponge is held in a bucket of water. Overpressure is the situation in the water-filled pores of the sponge when the sponge is squeezed, while underpressure is analogous to when the squeezed sponge is released and water is drawn back into the pores of the sponge.

Reduction of lithostatic load in natural situations is most often related to uplift and erosion of a low permeability sediment pile (like shales and claystones). This typically instigates an elastic dilation of rock-pore volumes and so induces underpressuring drawing in fluids from adjacent strata (e.g. lenticular sands). Rather than tectonic uplift, in regions of former ice sheets, fluid underpressuring is often tied to a rapid load reduction via melting of the former glacier and

associated isostatic rebound. Anthropogenically-induced underpressure is regularly associated with hydrocarbon extraction. In all underpressured situation where an evaporite is present it acts as an aquitard or aquiclude preventing easy entry of water as load is released.

A not uncommon effect of underpressuring in some depleting oil fields is the creation of a cone of subsidence, as has happened on the seafloor atop Ekofisk field in the North Sea. Ekofisk is a supra diapir field that was discovered in 1969. Four wells were placed on production within 18 months of the discovery and consistently produced at rates of up to 40,000 bbl/day (Van den Bark and Thomas 1980). Full production began in 1971, by 1984, the seabed atop the salt-cored structure had subsided some 3 m, prompting a major project to jack up the offshore platforms. It was decided that water-injection pressure maintenance should be used to arrest the reservoir pressure decline and so minimize future seabed subsidence. Void fluid replacement equivalent to extracted volume was achieved in 1993, but subsidence continued. Additional laboratory studies found that water injection had induced shear in the chalk. Shear failure and water-weakening of the rock matrix was driving additional deformation of the chalk, even under conditions of near-constant or decreasing stress levels. Despite ongoing void-replacement waterflooding, seabed subsidence continued until 1998, when the subsidence rates slowed dramatically. It seemed the water-weakening effect was expended and the reservoir pressure had once again increased (Agarwal et al. 2000).

One of the most striking examples of salt-associated underpressuring comes from the Keyes Field in the Oklahoma Panhandle. It produced gas from a depth of 1,460 m (4,790 ft) for more than 50 years with a pressure-depth gradient shown in Fig. 8.30 (Hunt 1990; Powley 1980). Keyes Field is located in an area of the Amarillo Uplift that rose by around 1,500 m (4,920 ft) during the Laramide orogeny and later cooled. Fluid pressures above the Keyes gas sand and down to the Blaine Anhydrite show a normal gradient of 44.5 psi/100 ft. Below the Blaine there are two anomalous pressure cells. The upper anomalous cell extends from the base of the Blaine Anhydrite to the top of the Wellington Salt seal (at a depth of 853 m or 2,800 ft). Fluid pressure at its top (≈1,000 ft or 305 m depth) starts at zero and increases down to the top of the Wellington Salt. The gradient in this upper cell is 44 psi/100 ft. The lower cell extends from the base of the Wellington Salt to the top of the Precambrian basement. Beneath the Wellington Salt pressures once again start around zero, then increase along a gradient of 0.465 psi/ ft (10.5 kPa/m). Overall the Keyes Field is underpressured by some 9 Mpa (1,300 psi) for its current depth. Lithologies at the base of each of the pressure cells support the full weight of the overburden. That both evaporite beds are acting as highly effective seals to their respective pressure regimes is indicated by the fact that fluid pressures start again at zero in the zone immediately beneath each evaporite. In terms of hydrocarbon components, underpressured compartments are important in that they indicate isolation of rocks in the underpressured cell, prior to extraction this isolation has prevented water washing and biodegradation of accumulated oils at depths where these processes would otherwise be important influences on oil quality.

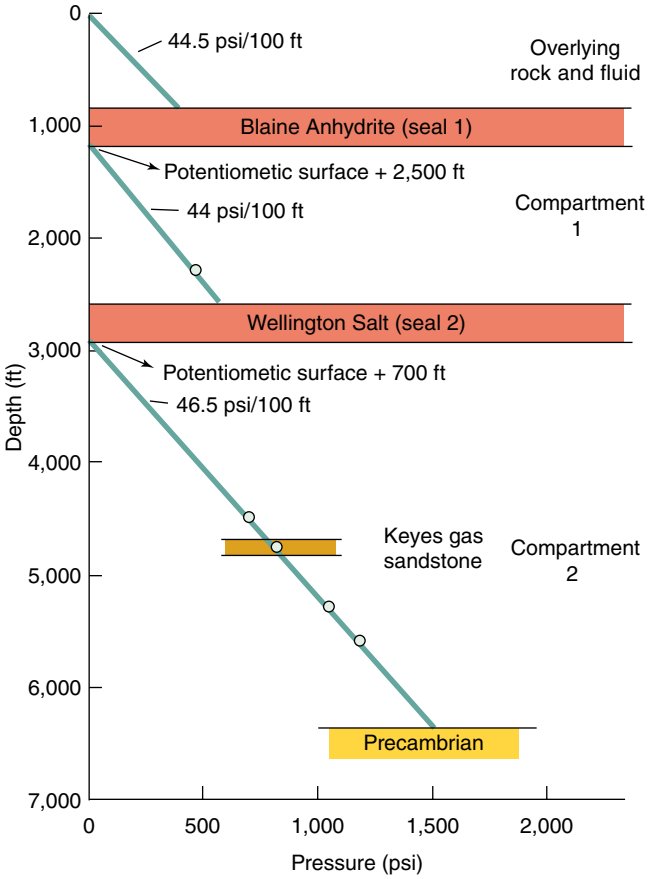

Fig. 8.30 Pressure-depth gradient for the Keyes gas field, Cimarron and Texas counties, Oklahoma. Underpressured intervals are due to uplift and the maintenance of isolated pressure cells across evaporite aquicludes (After Hunt 1990; Powley 1980)

Temperature Anomalies and Brine Flow

Thermal anomalies associated with buried salt have been known since the 1930s (Hawtof 1930) and can have significant influence on the maturation state of source rocks for hydrocarbons. Such anomalies relate to halite's higher thermal conductivity compared to most rock types (Fig. 8.31a). Thermal differentials drive basin fluid circulation, especially thermohaline circulation in sediments adjacent to an interval of halokinetic salt. At room temperature the thermal conductivity of salt is typically three times that of adjacent

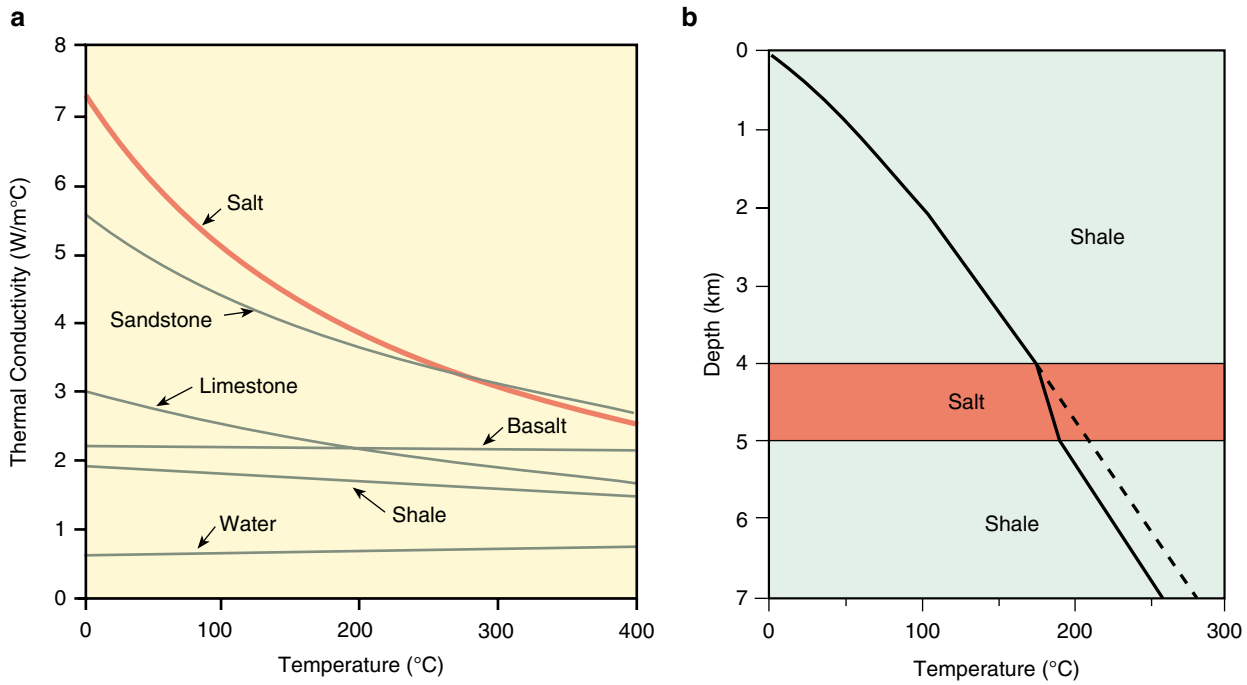

Fig. 8.31 Thermal properties of salt. (**a**) Thermal conductivity of various rock grain types (zero-porosity lithologies) and water as a function of temperature. (**b**) Vertical steady-state temperature gradient for a shale section with salt (*solid line*) and without salt (*dashed line*). The temperature plot (**a**) was used to construct the steady state profiles of Figs. 8.32 and 8.33 (After Mello et al. 1995)

shales. At 150 °C its thermal conductivity is about two thirds of its 25 °C value and still more than twice that of an adjacent now-compacted shale. Thus a salt bed or salt structure, with its much higher conductivity, exerts a strong influence on the thermal depth profile in an evaporite-entraining basin (Fig. 8.31b; Yu et al. 1992; Petersen and Lerche 1995; Mello et al. 1995).

When conductive salt remains as a bed, it raises the temperature gradient in sediments atop the salt bed, lowers the temperature gradient in the salt layer and makes beds below the salt layer cooler than they would be if the salt was not present. For example, with a 1 km-thick salt bed encased in shale, sediments below the salt are 20 °C cooler than they would be if salt were not present (Fig. 8.32a). According to Mello et al. (1995) the cooling effect is proportional to the thickness of the salt layer. All subsalt sediments are subject to non-transient cooling effects that last as long as the salt remains. Such temperature differences obviously affect organic maturation in sediments above and below the salt layer.

If the salt bed has flowed and a salt diapir is present, but with its crest buried well below the sediment surface, the conductive spine of salt sets up a thermal dipole with a positive anomaly atop the spine and a negative anomaly at its base (Fig. 8.32b). Sediments atop the spine are hotter than they would be without the salt, while sediments below the structure are cooler. Elevated vitrinite reflectance values above buried salt structures have been recognised in the oil industry for many years. However, the cooling effects on beds below a salt bed, diapir or sheet were largely ignored until the work of Mello et al. (1995).

If the diapir crest is at the sedimentation surface, as it is during the passive salt diapir stage, the structure acts as a thermal monopole. The salt spine acts as a sink that channels or drains heat to the surface (Fig. 8.32c). In this situation, temperatures around and beneath the salt spine and its source layer are less than would exist in a basin without salt. The amplitude of the negative anomaly locally reaches −85 °C and its cooling effect extends out for more than three times the diameter of the salt spine (Mello et al. 1995).

The contrast in thermal regimes where a thermal dipole is created when the salt crest is deeply buried versus a monopole where the crest is at the surface raises the question, how close to the surface need a diapir crest be before it starts to act as a heat sink rather than a heat source? Modelling by Mello et al. (1995) suggests the following rule of thumb; the maximum negative anomaly amplitude is reduced 10–15 °C for every 250 m of increase in the depth to the top of the salt spine (assuming a shale-rich host). The amount of heat drained from a basin is thus sensitive to the depth to the top of a salt structure and the length of time for which the salt remains at or near the surface before the structure is buried. Basins characterised by syndepositional salt flow and the maintenance of salt spines near the surface will produce the coldest situation with respect to subsalt sediments. This mechanism may help explain why many oil-prolific salt basins still produce large amounts of hydrocarbons today,

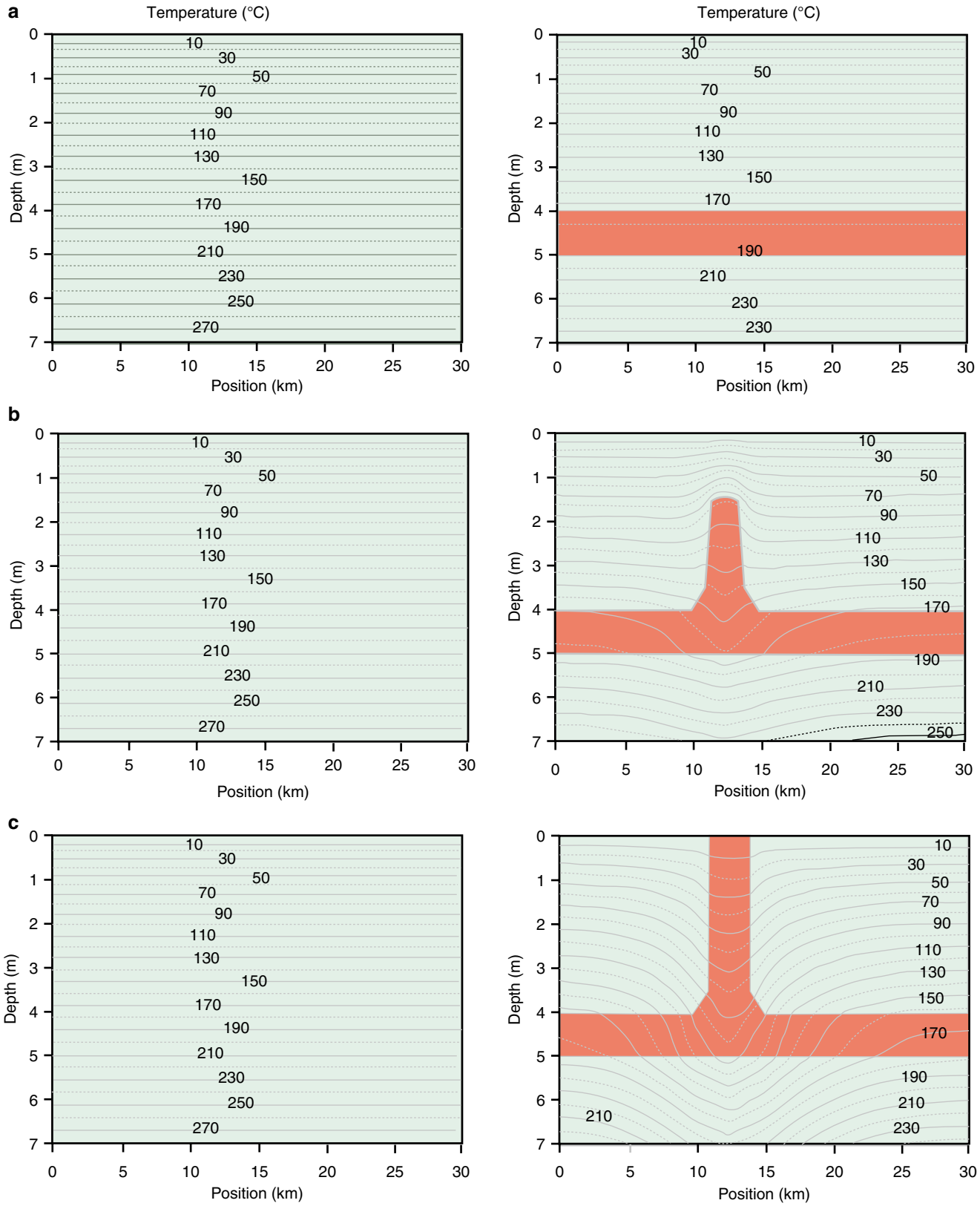

Fig. 8.32 Model of steady-state temperature distribution for a shale section containing salt with varying geometries (shown on *right hand side*) versus the same shale section with no salt (*left hand side*). All calculations use shale and salt thermal properties and gradients given in Fig. 8.31. (**a**) Salt layer, note that sediments below the salt layer are 20 °C cooler than in a shale section with no salt. (**b**) Salt diapir that is connected to its source layer and is not in contact with the surface. Notice the elevated temperatures atop the salt spine and the reduced temperatures beneath the spine – a thermal dipole. (**c**) Salt diapir that is connected to its source layer and is also at the sediment surface. The salt spine acts as a highly efficient heat drain that collects and channels heat from around and beneath the spine and delivers it to the surface. In this situation there is no heating associated with the spine, only cooling – a thermal monopole (After Mello et al. 1995)

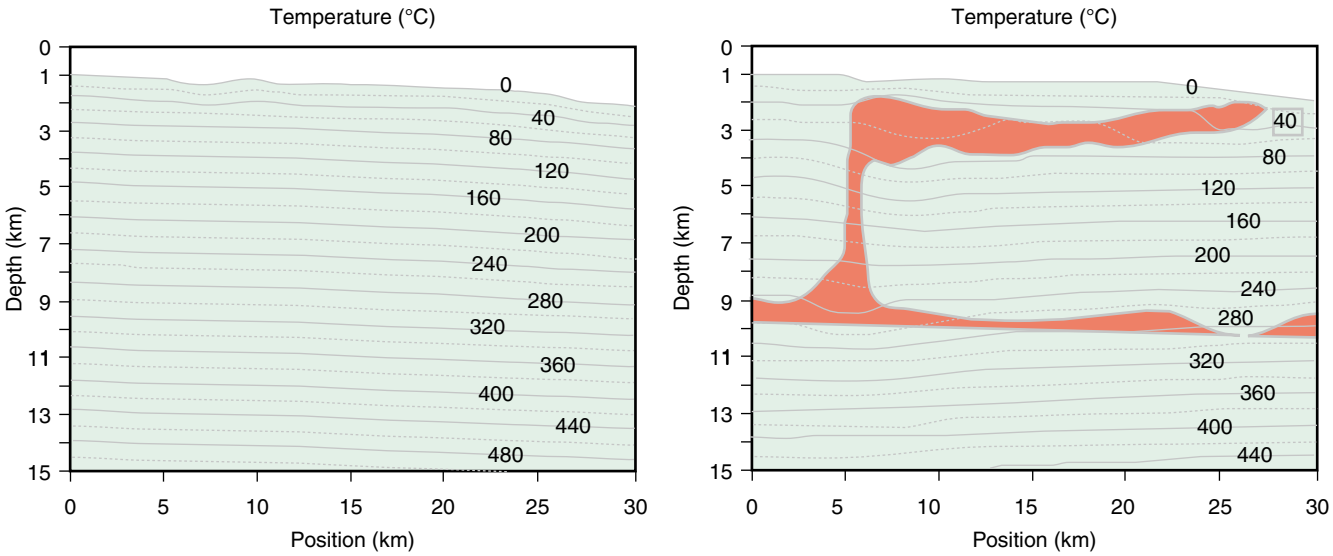

Fig. 8.33 Model of steady state temperature distribution created by the emplacement of an allochthonous salt sheet (*right hand side*) versus profile in a shale section with no salt (*left side*). Three major negative anomalies are associated with this geometry: a zone of cooling beneath the sheet; a negative or cooling anomaly associated with the dome, which feeds the sheet; and a zone of cooling beneath the lower sheet (After Mello et al. 1995)

when some thermal calculations, which do not account for salt effects, suggest that most of the known source rocks in the basin should be overmature (Mello et al. 1995).

Of course, simple salt spines, as modelled in Fig. 8.32b, c, are regularly part of a much more voluminous allochthonous salt complex, where salt sheets form layers or tiered canopies at a number of different stratigraphic levels. Figure 8.33 presents a thermal model for such a system based on structures in the Gulf of Mexico. The salt sheet is modelled as a steady-state regime in a shale host; it lies within 500 m of the sediment-water interface and still connected with the mother salt bed. It should generate three negative thermal anomalies (Mello et al. 1995):

- a negative thermal anomaly beneath the salt source layer (mother bed);
- a thermal anomaly associated with the salt stem that feeds the allochthonous salt sheet;
- a thermal anomaly below the salt tongue itself.

There are also some positive anomalies above the salt dome and its tongues, but these are small (<15 °C) compared with the magnitude of the negative thermal anomalies. The minimum anomaly with the greatest magnitude is ≈−82 °C located directly beneath the salt dome (Fig. 8.33; position 5 km, depth 10 km). The salt source layer or mother bed contributes only −10 °C of the thermal anomaly in the deepest parts of the section. Constructive interference between the salt sheet and the feeding salt spine creates a local thermal anomaly of −55 °C at the inside inflection point of the two structures (Fig. 8.33; position 7.5 km and depth 4.5 km).

Application of salt related thermal anomalies to lateral variations in source rock maturation and fluid flow in NW Europe is discussed in Magri et al. (2008), in the Triassic of the Jeanne d'Arc basin, offshore Newfoundland, Canada by Baur et al. (2010), and the effects of evaporites in the Paradox Basin, Utah by Rasmussen and Rasmussen (2009). But understanding and predicting thermal anomalies tied to salt distribution is useful in more than source rock maturation studies. Subsurface changes in temperature drive a variety of subsurface physical phenomena, which include oil viscosity, thermal expansion properties of lithologies and the magnitude of chemical and mineral solubilities, which also tied to salt mineralogy and the distribution of top and lateral caprocks. In combination, they drive lateral variations in thermohaline flow patterns in salt basins.

Fluid Flow in Halokinetic Basins

Most subsurface heat transfer in a sedimentary basin is via fluid flow. So, the distribution of thermal anomalies around salt structures by definition also indicates brine flow patterns. Accordingly, flow is enhanced by density plumes created during salt dissolution.

Suprasalt Fluid Flow and Alteration

Like dissolution from the underbelly of a salt layer, dissolution atop and adjacent to a salt spines creates free convecting density plumes in adjacent minibasin sediments.

Thermal drive created by thermal anomalies interacts with density plume drive to speed up flow rates in fluids convecting adjacent to the salt spine. If the crest of a diapir has risen to where it lies once again in the active phreatic flow regime, intense dissolution-and caprock formation generates brine plumes. Both top and lateral caprock scenarios generate plumes of dense chloride-rich brine, carried most readily by adjacent sand aquifers (Hanor and Mercer 2010; Steen et al. 2011; McCammon and Hanor 2012).

Using a dense network of well log data collected in the vicinity of the Bay St. Elaine salt dome in SE Louisiana, Cassidy and Ranganathan (1992) calculated salinity profiles in various strata surrounding the now buried dome crest (Fig. 8.34). Salinities range from approximately 4–12 wt%, with most isosalinity lines sloping away from the salt dome. On the southwestern side of the dome (cross sections OA and OC), salinities are 2–4 wt% higher at a given depth than on opposite sides of the dome, possibly reflecting a greater rate of salt dissolution and enhanced

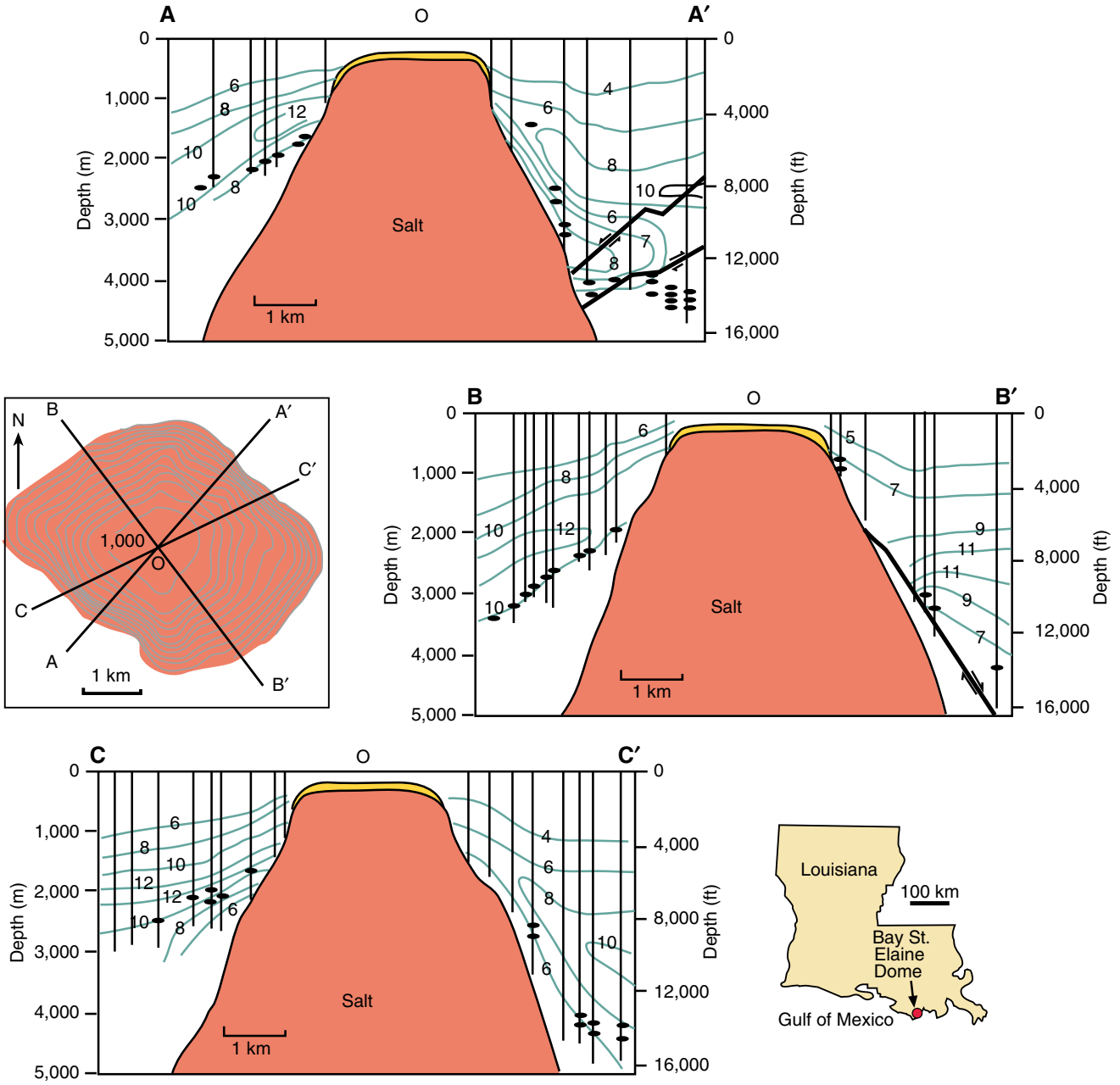

Fig. 8.34 Cross sections of pore water salinity (wt%) about the Bay St. Elaine salt dome, Louisiana (depth contours on plan view are 1,000 ft). Sections OA' and OC' show lobes or plumes of relatively fresh subsurface waters (<6 wt%) adjacent to the NE flank of the dome. *Black ellipses* on wells show intersected hydrocarbon zones (After Cassidy and Ranganathan 1992)

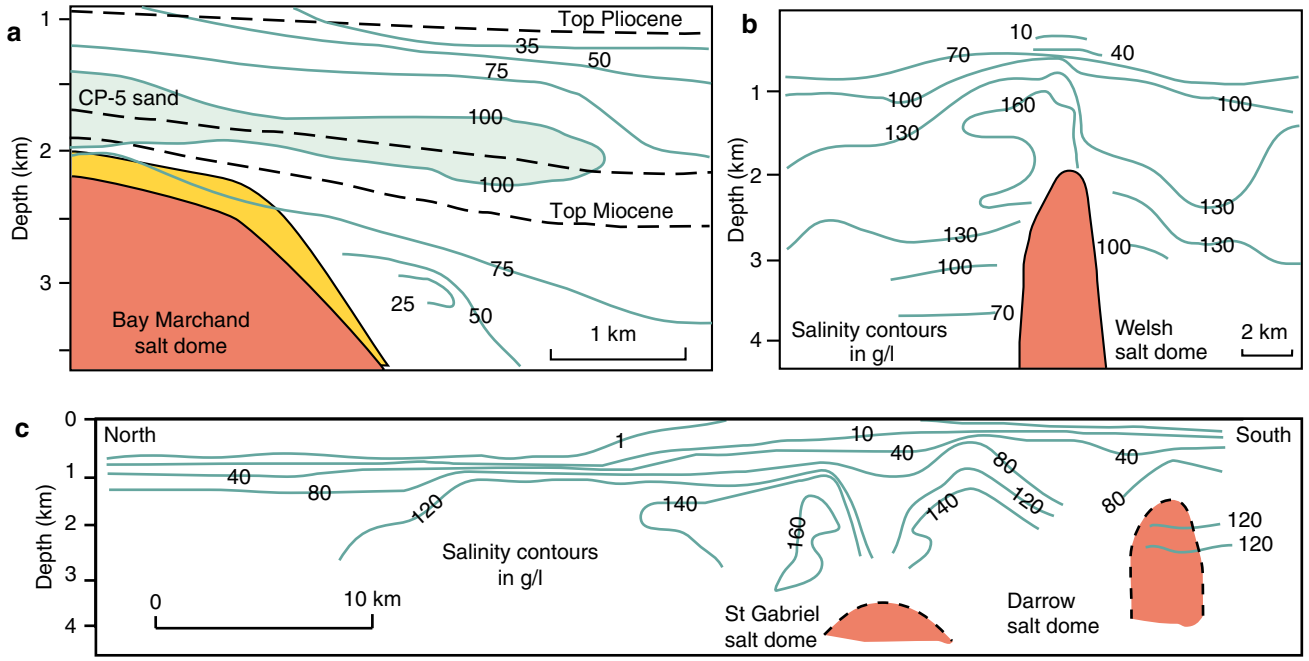

Fig. 8.35 Cross section of salinities in the vicinity of several diapirs in the of the Louisiana Gulf Coast showing the various shallow salinity plumes (g/l) generated by subsurface brine dispersion away from the dissolving crests of the salt domes. (**a**) East west section on the southwest flank of the Bay Marchand Dome. The cross hatched axis of the high salinity plume corresponds to the CP-5 Sand (After Bruno and Hanor 2003). (**b**) Welsh dome section where a regional high salinity layer (<130 g/l) sits atop a zone of overpressure, with higher salinity in the vicinity of the dissolving salt crest (After Bruno and Hanor 2003). (**c**) Salinity fields mapped around the St. Gabriel dome where saline waters occur near to, but not atop, the dome crest. Darrow dome data are limited but appear to follow the regional pattern of high salinity water near dome crest (After Bennett and Hanor 1987)

fluid transfer of heat. Lowest salinities occur on the northeastern side (cross sections OA' and OC', Fig. 8.34). On all sides of the dome, salinities increase with depth from the shallowest sands to a surface that roughly coincides with the top of overpressured sediments. Within the overpressured section, salinities decrease as depth increases, to levels on some flanks that are one-half the maximum value found in the hydrostatically pressured zones. For example, the saltiest waters in cross section OC have a salinity of 12 wt% and occur just above the shale sheath. Within the shale sheath, salinities of interstitial waters are as low as 6 wt%. Similarly, in section OC', the saltiest waters have a salinity of more than 10 wt% at a depth of 3 km. In hydrostatically pressured sections on the southwestern flank (cross sections OA and OC) and the northwestern flank (cross section OB), salinities are greatest near the dome and decrease away from the dome. In the overpressured section as well as in the shallower parts of sections OA' and OC', salinities are lowest adjacent to the dome, and increase away from the dome, perhaps reflecting a salt-stem-focused resupply of freshened compactional waters from below. Salinity contours are deflected downward near the fault on the southeastern side of the dome (cross section OB'), but seem unaffected by the faults on the northeastern side (cross section OA').

In a hydrostatically pressured section, one would expect elevated salinities near the salt dome, assuming that the dome is the major source of dissolved salt (Hanor et al. 1986). However, the observed salinity distribution (Fig. 8.34) in the vicinity of the Bay St. Elaine dome cannot be explained merely by radial diffusion of salt as it is dissolved from the dome into a static downwelling fluid column. With radial diffusion,[10] the salt concentration should be highest near the dome and decrease away from the dome. A common observation in the subsurface waters of the Gulf Coast is that salinities of interstitial waters in the overpressured suprasalt section are actually lower than salinities of waters at the base of the hydrostatically pressured section (Fig. 8.35; Hanor et al. 1986). However, the lobe of relatively fresh water (salinity of less than 6 wt%) next to the dome in cross sections OA' and OC' (Fig. 8.34) dips too steeply to be explained merely by the slope of the overpressured section near the dome.

[10]Diffusion is the movement of ions from areas of high concentration to low concentration and follows Fick's first and second laws. Diffusion is a slow process even in liquids and even slower in a porous medium in muddy sediments because ions can migrate only through the pores and the rate depends on pore throat size.

Cassidy and Ranganathan (1992), argue that the observed salinity pattern at Bay St. Elaine indicates fresher overpressured pore waters are now escaping upward in a halo around the diapir, especially on the northeastern flank of the dome (cross sections OA' and OC'), where the areas of highest salinity are separated from the dome by relatively fresh (salinity of less than 6 wt%) pore waters. The low salinity of waters immediately adjacent to the northeastern flank of the dome also may reflect a greater degree of insulation of the salt dome from dissolution on this flank. They note an alternate explanation is that the compactional pore waters may be upwelling at a slight distance away from the salt-sediment contact, thereby retaining their low salinities as they ascend. The presence of faults on the northeastern side (cross section OA') does not appear to affect the salinity contours. There are not enough control points under the fault in section OB' to evaluate the sealing versus nonsealing nature of the fault.

The salinity field documented about the Bay St. Elaine dome is in striking contrast to the salinity fields mapped around the Bay Marchand and Welsh domes (Fig. 8.35a, b). There, much saltier waters occur next to the domes in sands feeding an adjacent brine plume. The plume extends as a brine layer sourced in regions near the dome tops down to the zone of freshened and geopressured waters at some depth below (Bennett and Hanor 1987; Hanor 1994a, b). Bay Marchand dome is part of a deep-seated allochthonous salt ridge that also includes the Caillou Island and Timbalier salt domes (Figs. 8.35a, 10.53). Something like 7.2×10^{11} kg of solid NaCl must have been dissolved to account for the elevated salinities around the Bay Marchand dome (Bruno and Hanor 2003). This mass is equivalent to something 0.3 km^3 or a 300 m reduction in the height of the current dome. This is a lower limit to the total volume of salt dissolved from the dome as it is based on dissolved ions creating the pore content only of the current system. Most likely, there were earlier pore volumes from dissolved salt that are now flushed from the system. In Welsh dome, the zone of highest salinities occurs atop the crest of the dome and not in a sinking plume off to the side of the dome (Fig. 8.35b). Bennett and Hanor (1987) calculated that in this system the volume of brine in the current porosity corresponds to dissolution of at least 2 km of salt from the structure. A lack of a crestal collapse graben over this structure implies salt is still being replenished in the diapir stem. The salinity pattern above Welsh Dome cannot be explained by downwelling of salt dissolution-derived brines. Rather, the upward transport of dense high-salinity brines to levels well above the salt crest is perhaps indicative of episodic expulsion of saline fluids rising along the dome edge.

The salinity halo about St Gabriel dome is characterised by a crestal zone that is fresher than the more saline brine layers/plumes on either side of the dome crest (Fig. 8.35c). It is yet another brine distribution pattern in this region of the Gulf Coast and may reflect a situation of fresher upwelling geopressured waters, which are locally displacing a more saline brine layer created by dome crest dissolution.

Clearly, salt is still dissolving from the crests of shallowly buried salt structures in the Gulf Coast, this is especially so where there is a well-developed brine plume indicating solute transport directed away from the salt (Bay Marchand and Darrow domes). Clearly also, there are nearby domes in the same region where this brine is locally displaced by salt stem-focused upwellings of subsurface waters. These waters may be more saline (Welsh Dome) or less saline (Bay Marchand and St Gabriel). The interactions are complex and there is no simple single model to explain the variety of pore salinity fields. They vary according to differences in the rates of crestal salt dissolution versus rates of stem-focused upwelling and are tied to the laterally varying mechanics of compaction flow and salt withdrawal, fluid buoyancy effects, and different suprasalt permeability fields (Cassidy and Ranganathan 1992).

Density inversion created by the nearsurface dissolution of a diapir crest, in conjunction with a thermal drive and overpressured shales, is sufficient to drive large-scale suprasalt convective cells in the Gulf of Mexico with flow rates of metres per year (Hanor 1994a). This is two to three orders of magnitude faster than the mm/year rates that are typical of the thermobaric zone in nonevaporitic basins. Similar elevated flow rates typify the dissolving crests of many structures in the North Sea diapir fields (Williams and Ranganathan 1994).

Circumsalt fluid flow drives diagenetic alteration in sediments adjacent to a salt stem. This is demonstrated by zones of calcitic alteration on the west flank of the West Hackberry Dome, Louisiana Gulf Coast (Fig. 8.36a; McManus and Hanor 1993). Drilling has defined some 5×10^{10} kg of authigenic calcite-pyrite cement in Miocene sands adjacent to the salt spine at depths of 1.4–2.1 km, across a 1.5×1.5 km area. The Sr, C and S isotopic compositions of the cements show Ca and S were derived from dissolution of the salt-dome anhydrite cap and that carbonate was derived both by thermochemical oxidation of methane and by sulphate reduction, possibly at temperatures as low as 70 °C. Constraints on the maximum aqueous concentrations of Ca, which can be released by dissolving diapiric salt, require that more than 5×10^9 m^3 of aqueous fluid, equivalent to a fluid volume/pore volume ratio of >250:1, were involved in destroying salt, transporting Ca and SO_4, and precipitating these cements. Thus, the presence of such cements about a salt structure requires a dynamic subsurface mass-transport regime involving either large volumes of throughflushing fluid or fluids that are extensively recirculated.

An equivalent to this subsurface calcite/pyrite cement halo outcrops in a quarry in the Eocene Carrizo Sandstone adjacent to the Butler salt dome, east Texas (Fig. 8.36b;

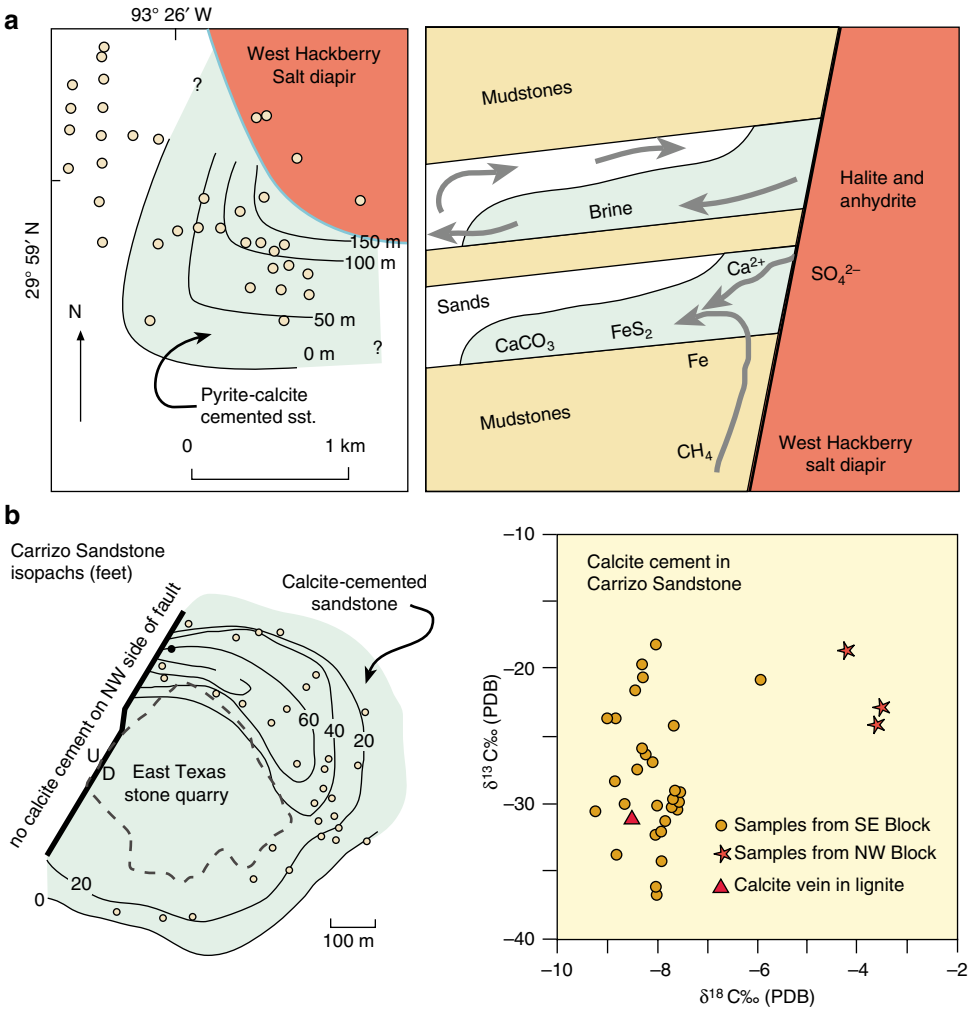

Fig. 8.36 Pyrite and calcite cements in diapir edge sands. (**a**) West Hackberry Dome, Louisiana showing cumulative thickness in metres of cemented sands, *brown dots* show borehole control. Model schematic shows hydrological circulation at the time of cementation. Dense brines with Ca and SO_4 derived from dissolution of salt stock flow down basal parts of sand beds. Upward flow of less dense fluid above brine plume. Thermogenic methane migrates up side of dome. Thermal reduction of S and oxidation of C results in precipitation of calcite and iron sulphides (After McManus and Hanor 1993). (**b**) Isopach map of the cemented zone in the subcropping Carrizo Sandstone based on drill information (*small brown dots*). The NE-trending fault forms the northwestern boundary of the cemented zone. The detailed thickness of the cemented zone within the quarry is unknown but probably was 40 ± 20 ft. Also shown are the carbon and oxygen isotope compositions of calcite cements in the Carrizo Sandstone cores (Enos and Kyle 2002)

Enos and Kyle 2002). The Carrizo is a fine- to medium-grained quartzarenite to sublitharenite with up to 42–50 % cement, principally poikilotopic calcite with local pyrite. Shallow drill holes in the surrounds of the quarry shows cemented zone is delimited by a steeply dipping normal fault, which is radial to the northeast part of dome crest. Cements extend southeast of the fault as a lenticular body some 750 m across and thickest near the fault where it is more than 25 m thick. Pyrite concretions are found on both northwest and southeast sides of the fault, as well as along the fault plane, whereas the calcite cement is present only to the southeast of the fault. $\delta^{13}C$ values for the calcite (–19 to –37 %) suggest bicarbonate was supplied mainly by bacterial oxidation of methane, whereas $\delta^{18}O$ data for calcite (–6 to –9 %) indicate meteoric water was involved in supplying diagenetic fluid. $^{87}Sr/^{86}Sr$ values for calcite (~0.7073) are within the range for Middle Jurassic seawater, suggesting that dissolution of anhydrite from the Louann Salt provided the Ca. Pyrite is more ^{34}S-rich ($\delta^{34}S$ range of 10–16 %) than typical sulphides in Gulf Coast salt dome cap rocks and is interpreted to represent H_2S supplied from deep sour gas reservoirs.

Early H_2S supply from deep sour gas reservoirs was channelled upward along the flank of the nearby Butler Dome and outward along the radial fault, resulting in early pyrite precipitation along the fault zone and in adjacent sediments. Early pyrite cements along the fault may have formed a barrier to subsequent fluid circulation, blocking the northwestward movement of both Ca-rich waters from the dome and

deep natural gas moving along the fault, thus confining calcite precipitation to the southeast of the fault. Bacterial oxidation of this thermogenic gas resulted in calcite precipitation, although mixing with shallow ground water bicarbonate may account for the broader range in $\delta^{13}C$ values in the calcite cement. Enos and Kyle (2002) propose that this type of cementation occurs in similar settings associated with circumsalt hydrocarbon leakage to shallow levels and may represent a previously unrecognized self-sealing type of hydrocarbon trap.

Rapid upward advection[11] of hot brines along the flanks salt domes in the Northern Gulf of Mexico Basin and in the Danish Central Trough seems to require an adjacent and deeper overpressured shale or mudstone succession to focus flow up the sides of the salt structure (Williams and Ranganathan 1994). The upward passage influences pore fluid chemistry interfaces, especially redox fronts, near the stem. This creates higher temperature gassy fluid haloes with interfaces that can precipitate metal sulphides and other diagenetic minerals. Inclusions in some of these diagenetic precipitates indicate temperatures were some 40–80 °C above the ambient temperature of the laterally adjacent sediment. Williams and Ranganathan (1994) conclude that thermal perturbations in excess of 60 °C can be repeatedly produced near the margins and crests of salt domes via focused dewatering of thick strongly overpressured minibasin intervals around the dome.

Dewatering can be triggered and stopped by cyclically pulsing the permeability at the salt stem sediment interface (analogous to seismic valving). Modelling shows the upwelling thermal plumes about the dome crest will dissipate within 100,000 years from the cessation of dewatering (Williams and Ranganathan 1994). Stratigraphically shallow and gravitationally unstable brine plumes from salt dissolution, once formed, will also dissipate once the salt has dissolved, but fade more slowly by sinking and mixing on a 1 Ma. time frame.

Burial Dewatering of Hydrated Salts

So far we have focused on subsurface hydrologies in halite-rich shale-dominated basins undergoing various styles of salt flow and dissolution. Halite is the dominant mineral in most thick basinwide evaporite successions, but in some basins anhydrite, not halite, is the dominant salt. In such settings there can be interesting subsurface hydrological effects tied to dewatering of the gypsum precursor to the anhydrite. Conversion occurs whenever a thick gypsum bed is buried and passes into the thermobaric zone. As the burial temperature rises above 60 °C, bedded gypsum alters and dewaters to nodular or laminar anhydrite, with an accompanying 39 % decrease in rock volume. Potentially, at around a kilometre of burial, this can generate a pressure kick that is significantly in excess of hydrostatic. The conversion of gypsum to anhydrite also defines the depth below which calcium sulphate stylolites cannot form and anhydrites may flow (Fig. 1.57).

Conversion depth influences early organic maturation and rock strength (Jowett et al. 1993). Because gypsum dehydration occurs during shallow burial, it is unlikely to be responsible for overpressures that occur at greater depths, where the primary role of the evaporite in the pressure system is as a pressure seal to underlying compacting fine-grained sediments or as a facilitator, via its evacuation, to the rapid accumulation of thick piles of geopressured sediment.

Conversion to anhydrite is accompanied by a four- to sixfold increase in thermal conductivity (gypsum ≈ 0.8 W/m·K; anhydrite ≈ 5.6 W/m·K) and the consumption of heat. At 25 °C the transformation of gypsum to anhydrite releases 4 kcal/mol. In a hydrologically-open compacting sediment pile, gypsum conversion is typically complete by 800–1,000 m of burial, corresponding to a total pressure of ≈250–300 atm (25–30 MPa). Transformation may occur at much shallower depths if the pore fluids are saline, or may not be complete until greater depths if the overlying unit is overpressured (Fig. 8.37; Jowett et al. 1993; Testa and Lugli 2000). When modelling organic maturation in an ancient calcium sulphate basin, via thermal modelling and backstripping techniques, it is important to know the depth at which the gypsum to anhydrite conversion occurred.

In a simple sensitivity test, using a basal heat flow of 2×10^{-6} cal/cm^2/s or 2 HFU's, Jowett et al. (1993) calculated the thermal gradient through bedded anhydrite is 18 °C/km, while through gypsum it is 63 °C/km. With such large differences in thermal gradient, using the wrong lithology over a particular burial depth range can create large errors in organic maturation modelling. For example, assuming 500 m of anhydrite instead of 800 m of decomposing gypsum will produce a 42 °C discrepancy at the base of the evaporite unit (Fig. 8.37a versus b). Such an error significantly effects thermal maturation, so that a source beneath the anhydrite would not reach the oil window, while that beneath the gypsum would.

[11] Advection is a general term used to describe transport of fluids, solids and heat through porous media. It requires permeability to move pore fluids so that ion transport is related to the average linear velocity of water in the pores, which is equal to Darcy velocity divided by effective porosity. In the vicinity of a dissolving salt bed it is associated with dispersion, which describes movement within groundwater as ions or contaminants spread out by mechanical mixing and diffusion. For example, a slug of brine into fresh porewaters mixes with the fresh as it moves away from the dissolution front. The brine covers a larger area as its concentration declines.

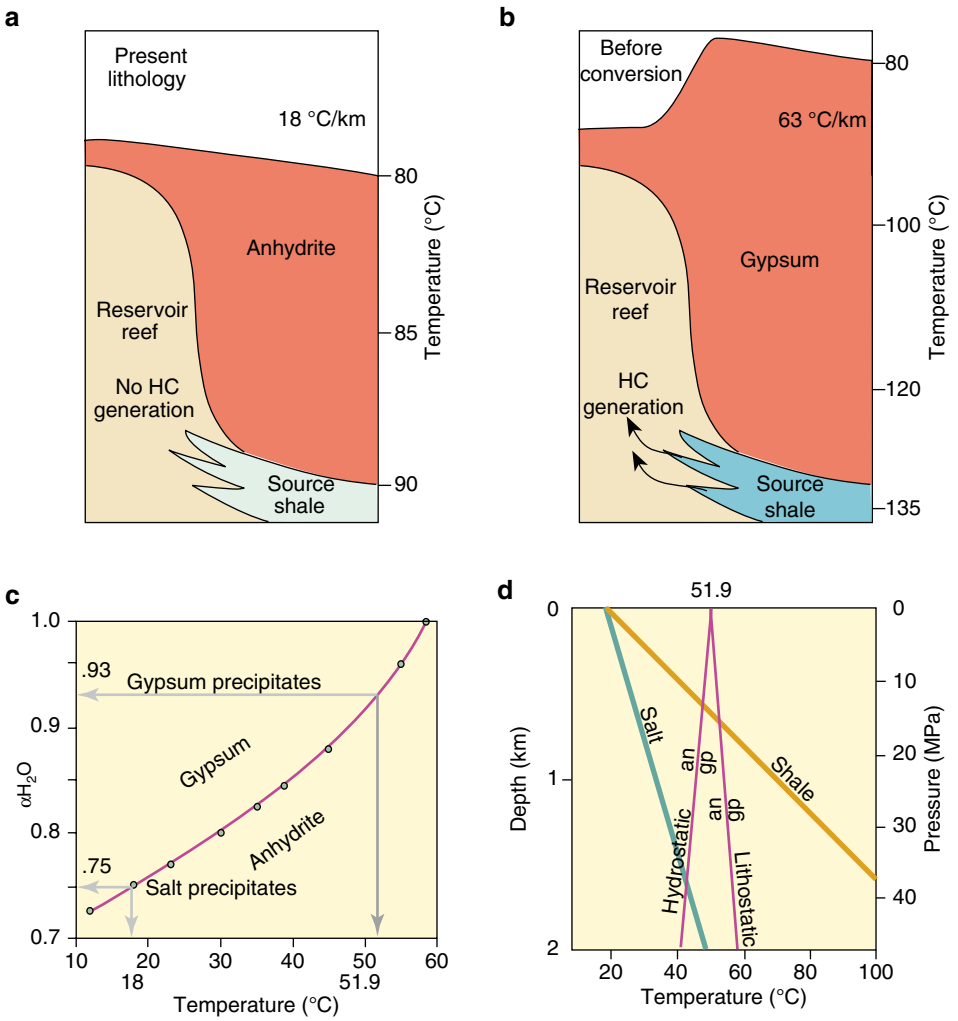

Fig. 8.37 Gypsum to anhydrite conversion (After Jowett et al. 1993). (**a**) In an evaporite basin containing 500 m of anhydrite, the calculated palaeothermal temperature implies the underlying source would not reach the "oil window." (**b**) If the conversion to anhydrite is later, so that the basin can be decompacted prior to gypsum converting to anhydrite, then the low thermal conductivity of the gypsum increases the geothermal gradient and the source rocks do reach the "oil window." (**c**) The laboratory relationship between the activity of water and the temperature of the gypsum to anhydrite conversion (After Hardie 1967). (**d**) Depth relationship for the temperature of the gypsum-anhydrite conversion below a shale insulator and a shale conductor. Conversion of gypsum to anhydrite occurs where the temperature line intersects the geothermal gradient in the overlying rock. Hence the conversion depth is much greater beneath halite (conductor) than beneath shale (insulator) (After MacDonald 1953; Hardie 1967; Hanshaw and Bredehoeft 1968)

The temperature, and hence the depth at which the transformation occurs depends on the activity (salinity) of the pore waters where the transformation is taking place. Transformation to anhydrite occurs at progressively higher temperatures as the activity of water (α_{H2O}) increases. When pore fluids have a α_{H2O} of 0.93 (equivalent to precipitation of gypsum from seawater) the transformation takes place at 52 °C (Fig. 8.28c; Hardie 1967). When the water is at halite saturation with a α_{H2O} of 0.75 the transformation occurs at 18 °C. The α_{H2O} in pore waters in ancient evaporites is indicated by the associated lithologies. If a thick anhydrite bed (deposited as gypsum) is associated with normal siliciclastics (shales and sandstones), the α_{H2O} of the burial fluids at the time of transformation was ≈0.93 and occurred at a temperature ≈50 °C. If the anhydrite retains evidence of coeval halite, or early diagenetic halite cement, then the temperature was around 20 °C at the time of transformation and so occurred at much shallow depths, perhaps within metres of the surface (Hovorka 1992).

When gypsum converts to anhydrite, the molar volume of the solid phase decreases by $\Delta V_s = -28.37$ cm^3/mol of anhydrite formed, corresponding to a volume decrease of some 39 % (Zen 1965; Hanshaw and Bredehoeft 1968). But the released fluid means there is a corresponding increase in molar volume of pore fluid of ΔV_f –36 cm^3 for the 2 mol of water created by the conversion. Because pressures on the fluid (P_f) and pressures on the solid (P_s)

are different, the molar entropy change (S) and the molar volume change (ΔV) are related by the equation (Hanshaw and Bredehoeft 1968):

$$dP_s / dT = S / \left(\Delta V_s + V_f dP_f / dP_s\right)$$

The measured entropy change is $\Delta S = -135.84 + 65.17 \log_{10} T - 0.043\ T$ (Hardie 1967), where T is the temperature in degrees Kelvin.

In a hydrostatically pressured system with free drainage allowing escape of the conversion water (e.g. gypsum with intercalated sand beds or porous carbonates) the overburden pressure is taken up only in the solid phases, so favouring the denser solid phase (anhydrite). In this situation, $dP_f/dP_s = \rho_f/\rho_s \approx 0.4$, and the slope on a dP_s/dT on a P–T plot is negative. That is, the conversion temperature decreases with depth and gypsum converts at shallower depths (Fig. 8.37d). If, on the other hand, the water from the conversion cannot freely escape from the decomposing gypsum, pore fluids may become geopressured (e.g. escaping pore fluids from a buried gypsum bed sealed beneath a thick widespread salt unit and intercalated with tight shales or lime mudstones). Overburden pressure is then taken up in both the solid and fluid phases. In this case P_f can approach P_s, dP_f/dP_s approaches unity, and the slope of dP/dT becomes positive (Hanshaw and Bredehoeft 1968). Then the conversion temperature increases with depth and for a given geothermal gradient the conversion of gypsum to anhydrite occurs at progressively greater depths. Hanshaw and Bredehoeft (1968) calculated the lithostatic conditions created by the conversion can only be maintained for a "geologic instant," even when the confining beds have hydraulic conductivities as low as 10^{-10} cm/s ($\approx 10^{-3}$ md as in a tight shale).

Most natural systems lay somewhere between the hydrostatic and the lithostatic curves, the dominance of one over the other is difficult to quantify, it can only be estimated by looking at the nature and thickness of the overburden and the intercalated lithologies within the converting calcium sulphate bed. If the water of hydration cannot drain freely from the dewatering gypsum, the bed converts to a quicksand-like consistency, typically indicated by thick nodular sequences of enterolithic folds with crestal fold vergences that may be oriented in the direction of minimum stress (Warren 1991). Escaping conversion water ultimately seeps into adjacent strata and escapes the unit. This escaping water of crystallisation can help lubricate nearby growth faults and other relatively shallow slippage features, including nappes.

Based on the ubiquitous presence of flow-aligned anhydrite textures in décollement sutures in the European Alps and elsewhere (e.g. Jordan and Nuesch 1989; Jordan et al. 1990) it seems that a common effect of sulphate dehydration is an initial decrease in the intrinsic strength of the $CaSO_4$ unit and an enhanced ability to act as a lubricant. Laboratory testing of mechanical strength during the dehydration of gypsum to bassanite ($CaSO_4.1/2H_2O$) under closed drainage supports these observations (Fig. 8.38). There is a large decrease in differential stress under undrained conditions at temperatures ≈ 110 °C, indicating high pore pressures induced by gypsum dehydration (Heard and Rubey 1966; Murrell and Ismail 1976). Thus a non-draining dehydrating gypsum bed can act as a zone of weakness or décollement at the base of a thick salt or shale succession. However, in the low temperatures of the laboratory the reaction product is bassanite not anhydrite; a mineral that, like dolomite, is very difficult to manufacture under the kinetic restraints of the laboratory, but is abundant in the real world.

Building on earlier work, but now using varying degrees of pore fluid drainage, the experiments of Olgaard et al. (1995) and Ko et al. (1995) clearly show that under well drained conditions the weakening of the gypsum tends to occur in the early stages of the dehydration reaction (Fig. 8.38). Their experiments were run at varying temperatures (23–150 °C), at confining pressures that mimic free to limited drainage (0.1–200 MPa), and at strain rates $0\ 7 \times 10^{-7}$ to $6 \times 10^{-5}\ s^{-1}$. As more porosity was created by ongoing dehydration there followed a rapid decrease in pore pressure. The experimental peak in pore pressure corresponded to an observed weakening and embrittlement in the gypsum. Under drained conditions this weakening occurred in the first 1 % of the reaction.

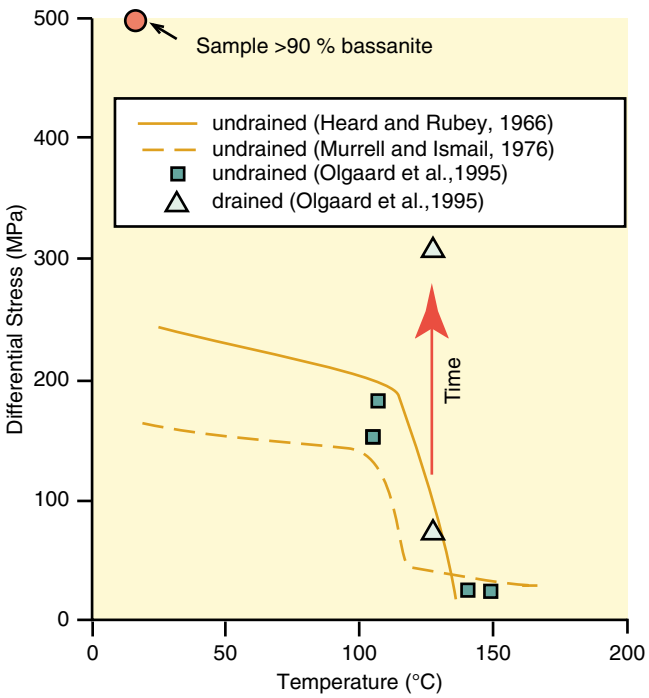

Fig. 8.38 Plot showing differential strength of dehydrating gypsum decreases above 110 °C in undrained conditions where the water of crystallisation cannot freely escape. Under drained conditions there is an initial decrease in differential strength followed by an increase. This is shown by samples at either end of time *arrow* (After Ko et al. 1995)

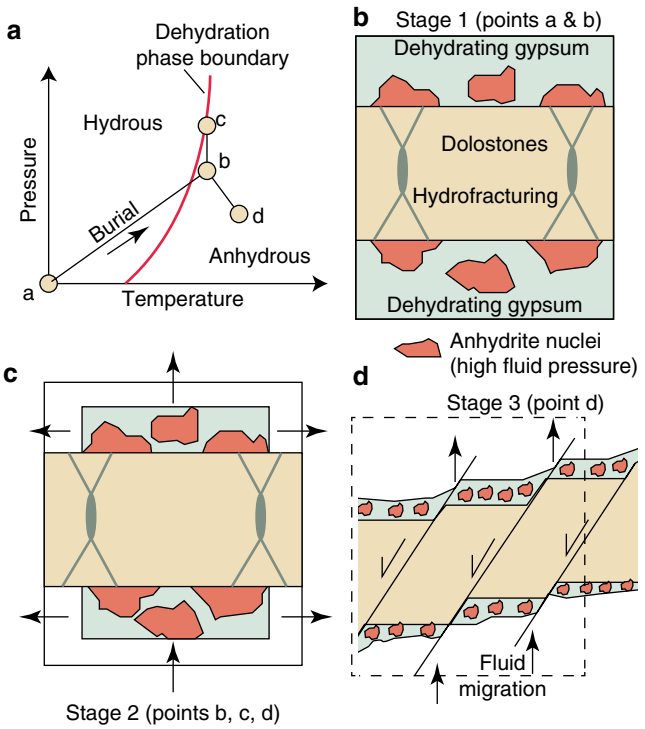

Fig. 8.39 Gypsum dewatering and faulting (After de Paola et al. (2007). (**a**) During burial (increasing pressure and temperature), gypsum dehydration reactivation begins beyond the dehydration phase boundary (indicated by *point b*). At this stage a pressure increase (*point c*) can stop the reaction until further thermal energy is input into the system (further burial) or a pressure decrease (*point d*) can drive the state of the rock further into the anhydrous phase stability field. (**b**) Gypsum dehydration reaction increases fluid pressures, trapped at the gypsum-dolostones interface, promoting hydrofracturing and faulting within the brittle dolostone layers. The permeability increases within the dolostone layers and causes fluid discharge. (**c**) Negative volume change, following fluid expulsion within the dehydrated rocks, which causes vertical thinning and isotropic horizontal extension. (**d**) The superposition of brittle cyclic fracture openings and slip along faults within the dolostones as well as ductile deformation (flowage and boudinage within the gypsum-anhydrite rocks) favour fault-linkage and upward propagation of the fault system within the Triassic Evaporite unit

Ultimate strength was recovered within 3 % of the reaction and ultimately exceeds that of pure gypsum. They concluded that, unless the surrounding rocks had very low permeabilities, the pore pressures during real world dehydration could only equal or exceed lithostatic pressures during the earliest stage of the gypsum dehydration reaction.

Microstructural observations of Ko et al. (1995, 1997) showed that the initial stage of loss of water of crystallisation creates isolated areas of dehydrated gypsum surrounded by new fluid-filled porosity. Excess pore pressures develop as long as this porosity is not interconnected or fluid is produced faster than it can escape through any newly forming interconnected porosity. Under slow fluid leakage conditions an excess pore pressure first develops, which leads to weakening; but this is followed by strengthening (shown by time arrow in Fig. 8.38). The drainage evolution of the various mosaics or networks of dehydrated gypsum within the converting gypsum unit control the timing of the development of minimum strength and maximum pore pressure. While the dewatered regions are isolated, a pore pressure can build up, which, as it becomes more pervasive, weakens the gypsum. But, as the locally dehydrated intervals start to fuse with each other, pore fluids can now flow from one area to another and ultimately escape into the adjacent non-calcium sulphate surrounds. This strengthening of the dewatering gypsum over time marks an internal transition from undrained to drained behaviour.

One of the limitations to this experimental work is that it was conducted using a gypsum sample held in a confining pressure sleeve, such that, once the pore meshwork was connected, the dewatering fluid could "flow away." This relatively easy egress may not reflect the subsurface reality of an anhydrite bed sandwiched between or within an impervious possibly halokinetic halite mass. Such was the case with $CaSO_4$ -filled fractures in the Buntsandstein, where the gypsum-anhydrite conversion was likely later and deeper in the burial cycle (Fig. 8.23; Nollet et al. 2005).

Dewatering gypsum will create characteristic faulting patterns in the various intrasalt and suprasalt beds. These dewatering (burial) related faults exhibit a diverse range of strikes, and can develop under conditions where the regional tectonic stress field is weak or absent (e.g. polygonal faults). De Paola et al. (2007) document a complex system of synsedimentary faults in the Umbria-Marche Apennines (Italy), they are geometrically similar to polygonal fault systems and developed during an early Jurassic extensional episode. This particular fault pattern was created during relatively early burial via gypsum dewatering. It differs from many extensional fault systems in that it lacks the aligned structures that are developed within a classical bimodal conjugate. "Andersonian"[12] set of faults. Rather, faulting is primarily controlled by the development of volumetric instability in Triassic evaporites due to burial dehydration (anhydritisation). Once again, these less predictable structural alignments reinforce a general notion that even shallow-buried evaporites (not just halites but also dewatering gypsums) tend to be "squishy" or fluid-like in their responses to stress (as emphasised in Chap. 6). Adjacent non-evaporite beds tend to behave more competently-brittlely when subject to gravitationally derived stress

The lithological architecture of the Triassic Evaporites (Burano Fm.), comprising interbedded Ca-sulphate layers and dolostones, played a fundamental role in controlling the

[12] Andersonian theory of faulting relates the principal stress axes to faulting and assumes no shearing stress can act at the Earth's surface (air-rock interface). Thus, in terms of the principal stress axes, σ_1 bisects the acute angle between the conjugate shear fractures. σ_2 is defined by the intersection of a pair of conjugate shear fractures, while σ_3 bisects the obtuse angle between the conjugate shear fractures.

deformation processes. Cyclic fluid overpressure build-up/release and the coexistence of brittle and brittle-ductile flow processes led to horizontal isotropic and non-planar extensional strain fields within the dehydrating rock mass, which favoured the development of complex deformation patterns.

During burial (increasing pressure and temperature) and weak gravitationally driven extension, gypsum dehydration reactivation begins beyond the dehydration phase boundary (point B to the right of red line in Fig. 8.30a; De Paola et al. 2007). At this stage, increased pressure (Fig. 8.30a, point C) can stop the reaction until further thermal energy is input into the system (further burial) or there is a decrease in pressure (Fig. 8.30a, point D), which can drive the state of the calcium sulphate bed further into the anhydrous phase stable field. In the initial phases of gypsum dehydration (Fig. 8.30a, point B), increasing fluid pressures, especially in areas adjacent to gypsum-dolostones interfaces, causes patchy mechanical weakening (strength reduction and embrittlement tied to fluid loss in conversion to anhydrite) and so promotes hydrofracturing and faulting within the dolostone layers tied to zones or patches of anhydrite formation in the gypsum (Fig. 8.30b; Stage 1). Brittle deformation within the dolostone units causes an increase in crack porosity and permeability, favouring local fluid pressure reductions, thus driving the state of the gypsum-bearing rocks further into the stability field of the anhydrous assemblage (toward point D in Fig. 8.30a).

Fracture opening and slip along extending faults within the brittle dolostones allow large volumes of fluids to be drained from the dehydrating gypsum layers, via interconnected fracture networks running along pathways of cataclastic fault planes (Fig. 8.30b). Fluid drainage into the fracturing dolomites results in volume contraction of the dehydrating calcium sulphate rocks that is accommodated by vertical thinning and horizontal isotropic extension (Fig. 8.30c, stage 2). Horizontal isotropic extension, counteracting the horizontal shortening, prevents the space compatibility problems arising via volume reduction during dehydration (Fig. 8.30c; as explained in Cartwright and Dewhurst 1998). This state of non-plane strain is accommodated within the composite gypsum-dolostones sequence by mixed deformation processes: flow and boudinage within the ductile gypsum-bearing rocks, and brittle hydrofracturing and faulting within the dolomitic rocks (Fig. 8.30d). Repeated fault reactivation, under transiently increasing fluid pressure conditions, favours fault-linkage and upward propagation of the fault system within the Triassic Evaporites and into the overlying carbonates of the Calcare Massiccio formation (Fig. 8.30d, stage 3). With further reaction, the increase in porosity and permeability makes drainage more efficient and the pulse of excess pore pressure decreases rapidly (Fig. 8.38; Olgaard et al. 1995; Ko et al. 1997).

Thus De Paola et al. (2007) have developed a mechanical model showing that the studied fault patterns developed under a stress field consistent with almost homogeneous stress intensities within the horizontal plane, tending to create polygonal failure patterns. Local relatively-early gypsum dehydration induced strain fields and transient fluid pressure conditions that were dominant over weak regional extensional tectonics. Their findings are relevant to many other areas where complex faulting patterns—including polygonal faults—occur in association with dewatering (pressurised) evaporite or clay-rich sedimentary sequences (Morley et al. 2014).

As well as acting as a lubricant, escaping water of crystallisation can act as a catalyst in dissolution-reprecipitation reactions within saline units subjacent to the dewatering salts such as gypsum, carnallite and polyhalite. So, as buried gypsum dewaters to anhydrite the escaping water is saturated with respect to $CaSO_4$ but undersaturated with respect to other evaporite minerals, possibly including any nearby carbonates (Sass and Ben-Yaakov 1977) and any halite or bittern salts. As such water seeps through the surrounding rocks it can leach minerals to create secondary porosity or bring about mineralogical transformations. Throughflow of such waters has dissolved marine carbonate grains to form anhydrite-filled moulds during Permian brine reflux in the shallow subsurface of the Palo Duro Basin, Texas (Bein and Land 1982).

With complete dewatering, a gypsum bed that is 100 m thick will convert to a 62 m anhydrite bed (Borchert and Muir 1964; p. 133). This releases a total of 48.6 m^3 of water per square metre of cross-sectional area. At 30 °C this volume of $CaSO_4$ -saturated water can dissolve 8.1 m^3 of halite or 54 m^3 of carnallite or convert 81 m^3 of carnallite to sylvite:

$$KMgCl_3 \cdot 6H_2O + 4H_2O \rightarrow KCl + Mg^{2+} + 2Cl^- + 10H_2O$$

Similar fluid rock interactions in the subsurface obviously influence many of the minerals and burial cements we now see in evaporites and adjacent beds. As well as basinal fluids evolved from dissolving evaporites, fluids from dewatering evaporites (especially gypsum and the hydrated bittern salts, such as carnallite) may also exert a substantial influence on the diagenetic and metallogenic evolution of the sediment pile (Chaps. 15 and 16).

Brine-Rock Burial Evolution

Approximately 20 % by volume of most sedimentary basins is made up of pore water of varying salinity, temperature, pressure and ionic proportions. Most fluids stored in the deeper parts of these basins are highly-saline brines and

mostly calcium chloride waters with major cations present in the proportion Na > Ca > Mg (Collins 1975). More than 70 % of oil field waters are either saline (10,000–50,000 mg/l) or brines (>50,000 mg/l). More than 50 % of the world's basinal waters are more saline than seawater (>35,000 mg/l). All formation waters (aka subsurface or basinal waters) in a sedimentary basin originate from meteoric, marine, or hydrothermal sources, or a combination (Moldovanyi and Walter 1992). Mechanisms proposed to account for elevated salinities of subsurface waters compared to most nonevaporitic surface waters include; membrane filtration or reverse chemical osmosis (reviewed by Graf 1982), expulsion of evaporatively concentrated (connate) seawater (Rittenhouse 1967; Carpenter 1978; Stoessell and Moore 1983), halite and potash salt dissolution (e.g., Land and Prezbindowski 1981; Hanor 1988), and meteoric water-rock interactions in sediments over thermal anomalies or in tectonically active areas (Hardie 1990). Most of these alternatives can be rejected as significant factors in hypersaline brine formation (Land et al. 1988; Hanor 1994a, b). It is now generally accepted that subsurface brines more saline than 100,000–120,000 mg/l are mostly related to evaporites via their depositional brine aprons or their subsequent dissolution haloes. Significant modifications to the connate fluid chemistry must occur during burial diagenesis in response to changing solution-mineral equilibria with increasing temperatures.

Several workers have suggested that ionic compositions in all basinal pore water indicate mixtures in varying proportions of (a) brines associated with evaporite residues, (b) head-driven deeply circulating meteoric inflows and (c) compaction waters (Kharaka et al. 1985; Egeberg and Aagaard 1989; Moldowan et al. 1994; Land 1995a, b). For much of the ensuing discussion we concentrate on subsurface brine chemistries associated with connate brines or evaporite dissolution.

Brine Chemistry at Depth

Hanor (1994a, b) studied the chemistry of basinal waters worldwide and divided them into three groups; (a) Na-HCO_3 and Na-acetate waters, typically with TDS <10,000 mg/l, (b) Cl-dominated halite undersaturated waters with salinities between 10,000 and 250,000–300,000 mg/l, these waters include Na-Cl waters and Na-Ca-Cl at higher salinities and, (c) Cl-dominated halite-saturated waters, with salinities typically in excess of 300,000 mg/l. Major cation concentrations show a systematic trend with increasing concentration. Ca and K become increasingly dominant, while Na and pH decrease with increasing brine concentration, especially above 300,000 mg/l (Fig. 8.40). In moderately saline waters, the monovalent cations Na and K have 1:1 slopes when plotted against TDS, while the divalent cations Mg, Ca and Sr show 2:1 slopes. The pH of moderately saline waters lies in the range 7–9, while high salinity brines are in the range 3–4. Most highly concentrated basinal brines are acidic; this has important implications for the leaching and transport of

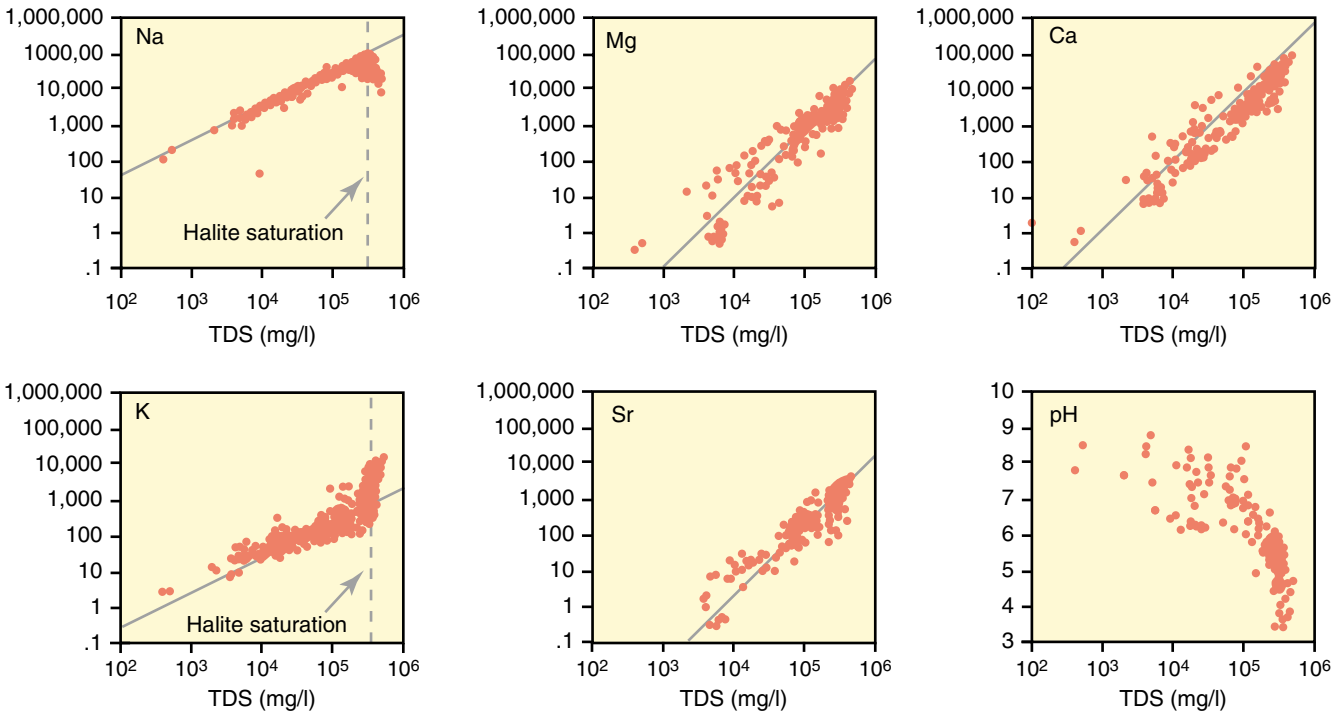

Fig. 8.40 Scatter plots of the covariance of log Na, Mg, Ca, K, Sr and pH with log TDS (total dissolved solids) for typical saline basinal waters worldwide (After Hanor 1994a). Note the 1:1 slopes for Na and K and the 2:1 slopes for the divalent cations. All values, except for pH, are in mg/l

metals in the relatively low temperature range (<200 °C) that typifies sedimentary basins (Warren 2000b).

Well-defined ionic trends with increasing salinity seen in Fig. 8.40 led Hanor (1988, 1994a, b) to suggest that the chemistry of most deep subsurface brine in salt-entraining basins is controlled by the subsurface dissolution of halite and the subsequent buffering of pore water compositions via interactions with multiphase silicate-carbonate mineral assemblages. Dissolution of halite produces a progressively more NaCl-dominated fluid without any systematic increase in K, Ca, Mg and Sr ions, which are supplied by fluid interactions with the adjacent silicate-carbonate assemblages. Such water-rock interactions explain the Na–Ca–Cl brines so common in subsurface brines. These proportions cannot be explained by a simple evaporitic concentration of seawater beyond gypsum saturation and the retention of connate reflux waters. Marine brines precipitating halite contain little or no Ca^{2+} as it has been depleted by $CaCO_3$ and gypsum/anhydrite precipitation (Fig. 2.12). Volumetrically important subsurface reactions capable of modifying connate brines towards higher Ca/(Na + Ca) values include dissolution of anhydrite, albitisation of plagioclase feldspars, and dolomitisation of limestones (Land 1987). Potassium (as well as Ba and perhaps Sr) can come from albitisation or illitisation of K-feldspar, especially in redbed and volcaniclastic sequences.

In terms of anions, the inherently high solubility of dissolving evaporites means they typically supply unbuffered components into pore waters, the most obvious being chlorine and bromine (Ranganathan 1991). Other than halite cement, there is no source of chlorine in nonevaporitic lithologies (except minor hydroxl-bearing minerals such as mica or apatite). Hence, average chlorine content in nonevaporite basins worldwide is only 48,640 mg/l (Br = 155 mg/l), while the average for basins entraining buried salt or their dissolution breccias is 118,392 mg/l (Br = 1,583 mg/l; Worden 1996). Palaeozoic basin brines also show higher average chlorine contents than Mesozoic basins, which are in turn higher than Tertiary basins (Worden 1996). The difference probably reflects the longer time for more pervasive evaporite solution and circulation in the older basins. Worden (1996), like Hanor, concluded that in an evaporite-entraining basin the dissolution of halite is the major control on the chlorine content of subsurface waters.

If dissolution of thick buried salt explains the elevated salinity of deeply buried highly saline basinal brines, then any sediment undergoing burial will ultimately come into contact with these brines. It will experience water-rock diagenetic interactions tied to basinal fluids derived from this dissolving evaporite and these interactions will continue into the later deeper stages of the rock's burial history. The tie of basinal brine chemistry to buried dissolving salt is clearly seen in the pore water chemistry of the deeply buried Permian Gharif Formation in the Ghaba Salt Basin of Oman (Hartmann et al. 2000). The degree of diagenetic overprint varies, depending on burial history. Sandstone at shallow depth (>2,600 m) shows intense dissolution of aluminosilicate and carbonate minerals, combined with minor kaolinite precipitation and compaction, whereas deeply buried sandstone (>2,600 m) is highly compacted and tightly cemented by quartz, carbonate, and sulphate minerals.

The Lower Gharif in the Ghaba Basin consists of coastal-plain siliciclastic rocks passing upward into the marine bioclastic– oolitic Haushi limestone. The Middle Gharif is characterized by fluvial cross-bedded sandstone interbedded with red–brown, mottled siltstones and mudstones containing calcrete and root traces. The top part consists of alluvial-plain mudstone with less calcrete. None of the three formations entrain evaporites. The cementation history in these Gharif sands illustrates what is a typical depth-related set of burial cement stratigraphies for many sedimentary basins.

Eight carbonate cement phases were differentiated in the sands of the Gharif Fm. by Hartmann et al. (2000). In general, the sequence is: calcrete/dolocrete, calcite I/dolomite I and calcite II as consecutive eogenetic phases all predating early quartz I, this is followed by burial diagenetic dolomite II and calcite III/Fe-dolomite/ankerite. Calcrete and dolocrete are present in fluvial sandstone of the Middle and Upper Gharif. Trace amounts of calcite I and dolomite I overgrow reworked caliche nodules. Pore-occluding, poikilitic, brightly luminescent calcite II is present in shallow wells and in the Huqf–Haushi outcrops. Later-formed, patchy poikilitic, brightly luminescent calcite III is restricted to samples from depths of <2,600 m. Dolomite II is present in some wells as small, red-luminescent rhombohedra. Fe-dolomite/ankerite occurs in various amounts (0–27 ‰) as intergranular rhombohedra that fill pores and corrode earlier quartz I and feldspar overgrowths.

Caliche carbonates have $\delta^{18}O$ and $\delta^{13}C$ values from −0.3 to −0.7 and −1.8 to −2.2 ‰, respectively (Fig. 8.41a). Pristine shell material and "whole-rock" shallow-marine Haushi limestone (Lower Gharif) show $\delta^{13}C$ values between 0.5 and 5 ‰ and $\delta^{18}O$ values ranging from −1.6 to −2.6 ‰. The stable-isotope composition of early calcite II ranges from −7 to −10 ‰ and from −19 to −23 ‰ for $\delta^{18}O$ and $\delta^{13}C$, respectively. Calcite III, which formed after calcite II, has $\delta^{18}O$ values of −4 to −9 ‰ and $\delta^{13}C$ values of −2 to −14 ‰. Fe-dolomite/ankerite has $\delta^{18}O$ values ranging from −4 to −9.5 ‰ and $\delta^{13}C$ values of −3 to −11 ‰ (Fig. 8.41a). All these isotopic values of the various cements in these sandstones are consistent with ongoing burial diagenesis in an environment characterised by increasing temperature in the presence of hydrocarbons. The calcite II cements formed from meteoric waters that infiltrated the Gharif sands during the late Triassic Early Jurassic. This was followed by burial and the entry of high salinity pore water from dissolution of

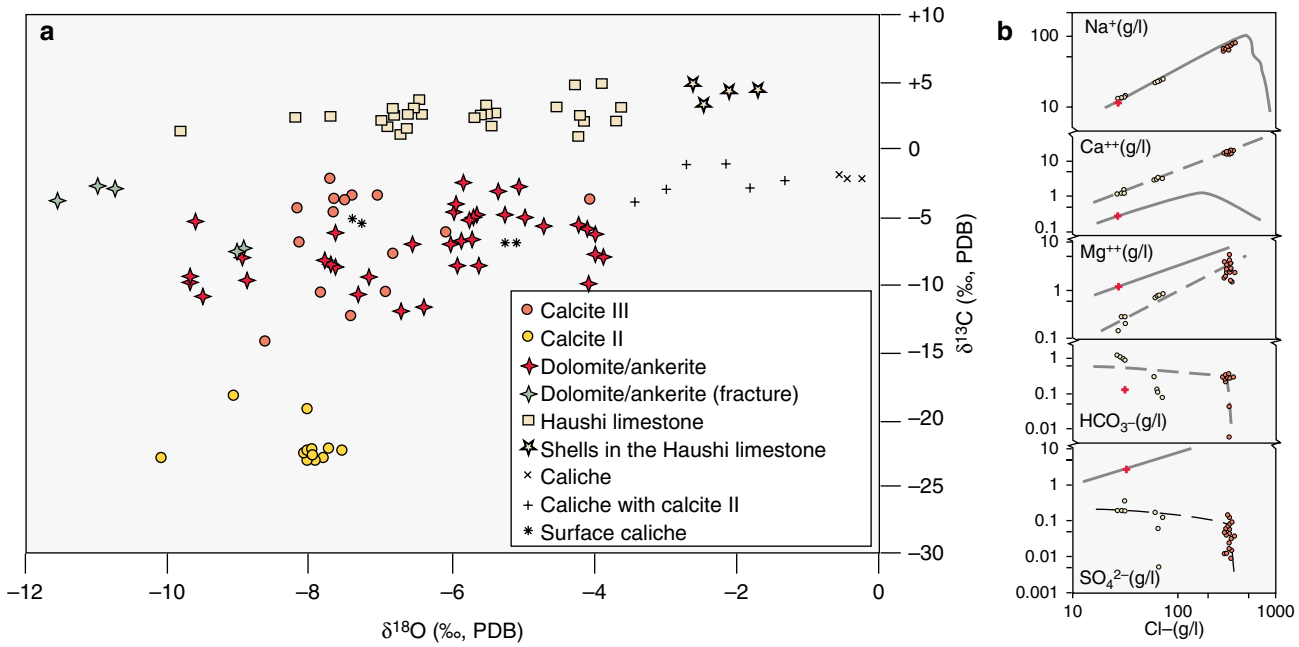

Fig. 8.41 Hydrological signature of the Permian Gharif Formation, Oman. (**a**) Stable isotope signatures of Gharif Formation minerals – see text for explanation of trends. (**b**) Variation in dissolved cations and anions as a function of dissolved chloride in Gharif Formation pore waters. *Light brown circles* represent low-salinity brines influenced by meteoric waters. *Light red circles* indicate highly saline brine samples derived from subsurface dissolution of the Ara Fm. salt. *Dashed lines* represent the present trends between dissolved ions and chloride. *Solid lines* are the seawater evaporation dilution lines from Carpenter (1978). *Crosses* represent the seawater concentration for each dissolved ion (After Hartmann et al. 2000)

the Ara salt. During this time of deeper burial and more saline pore waters the Fe-dolomite and ankerite cements precipitated.

The current pore waters in the Gharif are Na–Cl brines with various amounts of Ca, Mg, SO_4, and HCO_3 (Fig. 8.41b; Hartmann et al. 2000). Dissolved Na increases with increasing Cl along the seawater evaporation–dilution curve (Carpenter 1978), confirming dissolving halite as the main ion source to the present saline brines. Values for Mg and Ca also increase, but values for Mg are depleted and those of Ca are enriched relative to the seawater evaporation–dilution curves, imply ongoing rock-fluid interactions. In addition, all brines are depleted in sulphate, but mostly enriched in bicarbonate compared to seawater, perhaps reflecting sulphate reduction processes (Fig. 8.41b).

With time and burial the carbonate minerals precipitating from the evolving pore waters of the Gharif Fm. in the Ghaba Salt Basin evolved from depositional pore waters of low salinity (<50 g/l) with $\delta^{18}O_{SMOW}$ values of −0.5 to −1.5 ‰ in the more marine Lower Gharif to 2 ‰ in the arid fluvial Middle and Upper Gharif (Fig. 8.41b). During subsequent shallow burial (Late Triassic to Early Jurassic), the pore water in the Gharif members changed to high-salinity brines (≈180 g/l) with $\delta^{18}O_{SMOW}$ values of −4 to −7 ‰. The current highly saline, deep-burial pore water with a heavy $\delta^{18}O$ signature (0.5–5 ‰) is the result of rockwater interactions in what is a rock-dominated system. Thus present porewater compositions in the deeper parts of the basin, as indicated by both isotopic and ionic compositions, mainly reflect interaction with pore fluids derived by deeper subsurface dissolution of underlying Neoproterozoic Ara Group evaporites. This process is coupled to the precipitation of late diagenetic carbonates and sulphates. Subsequent recharge of isotopically light surface water was driven by inversion along the uplifted southeastern basin margin and was driven by obduction of the Oman Mountains in the Late Cretaceous and the creation of the Huqf-Haushi Arch (Figs. 10.8b and 10.67a).

Ceriani et al. (2002) documented a similar post-rift burial infiltration of saline brines in non-evaporitic sediments deposited in an evaporite-floored aborted rift. They studied the evolution of quartz overgrowths and burial dolomite cements in the Upper Sarir Sandstone (Lower Cretaceous) in Abu Attifel oilfield in the Sirt Basin, Libya. Fluid inclusions along the grain-overgrowth boundary of early quartz overgrowths yield homogenization temperatures from 130 to 141 °C and salinities between seawater and freshwater. Aqueous fluid inclusions in later quartz overgrowths have homogenization temperatures from 114° to 129 °C and salinities between 18 and 21 wt% NaCl equivalent. Fluid inclusions in adjacent dolomite burial cements have variable homogenization temperatures (120–141 °C) and high salinities (20–22 wt% NaCl equivalent).

This cooling trend in homogenization temperatures of fluid inclusions, tied to increasingly saline pore waters, is the result of quartz cements first forming in a bath of hot, low-salinity, connate fluids at a burial depth around 2.5 km. These hot fluids were flowing through the Sarir sands, driven by the increased heat flow related to regional rifting of the Sirt Basin. Later quartz overgrowths and burial dolomite cements precipitated during a time of regional cooling tied to the end of the rifting. Authigenesis occurred at a depth of around 3.8 km and was driven by the cooling of pore fluids concurrent with the invasion of dense saline fluids from subadjacent areas of salt deposition and brine reflux. The most likely brine source was a reflux plume from a thick section of Eocene evaporites, although dissolution of subadjacent Cretaceous salts cannot be entirely ruled out (Ceriani et al. 2002). A similar evaporite-associated reflux model was used to explain cool pore brines associated with U-rich dolomitisation and subsequent anhydrite precipitation and replacement in the lower Krider Member of the Nolans Limestone in the Hugoton Embayment in Kansas (Luczaj and Goldstein 2000).

Worldwide, the ionic proportions in a subsurface saline brine can reflect either the original make-up of the waters in the pores at the time of deposition (such as connate waters in inclusions in chevron halite in the Permian Nippewalla Group; Fig. 2.42), or the effects on ongoing subsurface fluid flow and rock reactions changing the original depositional proportions (as in the salt-dissolution-derived Na-Cl waters of the Gharif Formation).

With evaporite-associated subsurface waters there is still considerable debate about the role of residual evaporated seawater (=connate brine) in the chemistry of basinal brine versus dissolving buried evaporites (Moldovanyi and Walter 1992). In part, the debate centres on the ability of thick evaporite sections to store connate brine from the time of deposition due to the early creation of evaporite seals by early porosity loss. Most halite-dominated sequences are tight by 100–500 m burial. A "connate" versus "water-rock interaction" argument is made more difficult by requisite hydrology needed to precipitate and preserve a thick, near monomineralic, evaporite sequence. Significant volumes of salts can only accumulate where ongoing brine reflux drives the associated flux of considerable volumes of brine into the adjacent underlying sediments where it disperses into the regional flow system (as in the Sarir Sandstone).

This is the concept of brine disposal, brine leakage, brine reflux or the brine curtain as enumerated by Holser (1979), Sanford and Wood (1991), Rosen (1994) and Warren (1999), respectively. It is summarised in Chaps. 2 and 5. The drawdown hydrology that typified the depositional hydrology of most ancient evaporite settings means that substantial volumes of relatively unmodified but dense pulses of concentrated seawater (=connate) or continental brines can be drawn into and stored in sediments about and beneath the evaporite bed and its brine curtain (Fig. 2.75). This refluxed connate brine could be stored in subadjacent continental strata (e.g. fluvial or eolian sediments) as well as in a marine host and can be released later during burial diagenesis and compactional flushing. The question becomes not whether connate pore waters were present beneath and within a thick evaporite bed, but when were these waters flushed from the system and how much water rock interaction took place during and after that flushing.

One reason for confusion between connate and dissolution derived subsurface waters is that some older studies did not distinguish between brine samples collected from porous beds encased within an evaporite sequence and those pore waters collected in adjacent more permeable sediments located above and below an evaporite bed. When this distinction is made, those brines collected within sediments with relict pore fluids encased by a bedded salt unit (with chevrons) are typically found to be connate brines, while those outside the evaporite succession are more likely to reflect chemistries related to salt dissolution and ongoing water rock interaction. For example brines within an evaporite aquitard and a nearby deep brine aquifer in the Palo Duro Basin of West Texas have $\delta^{37}Cl$ values of −0.4 to 0.0 ‰ (Fig. 2.41b; Eastoe et al. 1999). They were not generated by dissolution of halite.

Another possible confusion in terms of a meteoric versus dissolution origin of diagenetic cements in carbonates in evaporite-entraining basins lies in the possible misinterpretation of oxygen isotope signatures of some burial cements precipitated from hypersaline pore waters. The work of Dickson et al. (2001) on carbonates of the Central Basin Platform West Texas underlines this dilemma. Pennsylvanian to Lower Permian cyclic platform carbonates from the Southwest Andrews area of West Texas are now 3 km below the landsurface. Isolated samples of brachiopod shell, zones of calcite cement, and saddle dolomite from limestone cores of the Southwest Andrews oilfields were analysed isotopically in order to determine if: (1) diagenesis was dominated by early, meteoric processes, as suggested by earlier bulk rock isotope studies, (2) whether significant burial diagenesis occurred in hypersaline waters, and (3) whether most burial cements are allochthonous or internally derived.

Bulk isotopic analyses of the limestones show systematic variation in $\delta^{13}C$ and $\delta^{18}O$ that historically have been interpreted according to a geochemical model tied to length of subaerial exposure and stratigraphic position (Fig. 8.42; Dickson et al. 2001). Chemically zoned calcite cements show four growth stages. Stage 1 and 2 cements have average $\delta^{13}C$ values of −4.6 ‰ and average $\delta^{18}O$ of −5.0 ‰, and most are thought to have precipitated early during subaerial exposure, while bathed in meteoric waters. A few stage 1 cements with average $\delta^{13}C$ values of −4.7 ‰ and $\delta^{18}O$ of −1.4 ‰ apparently precipitated below the sediment surface from modified seawater in a sulphate reduction zone.

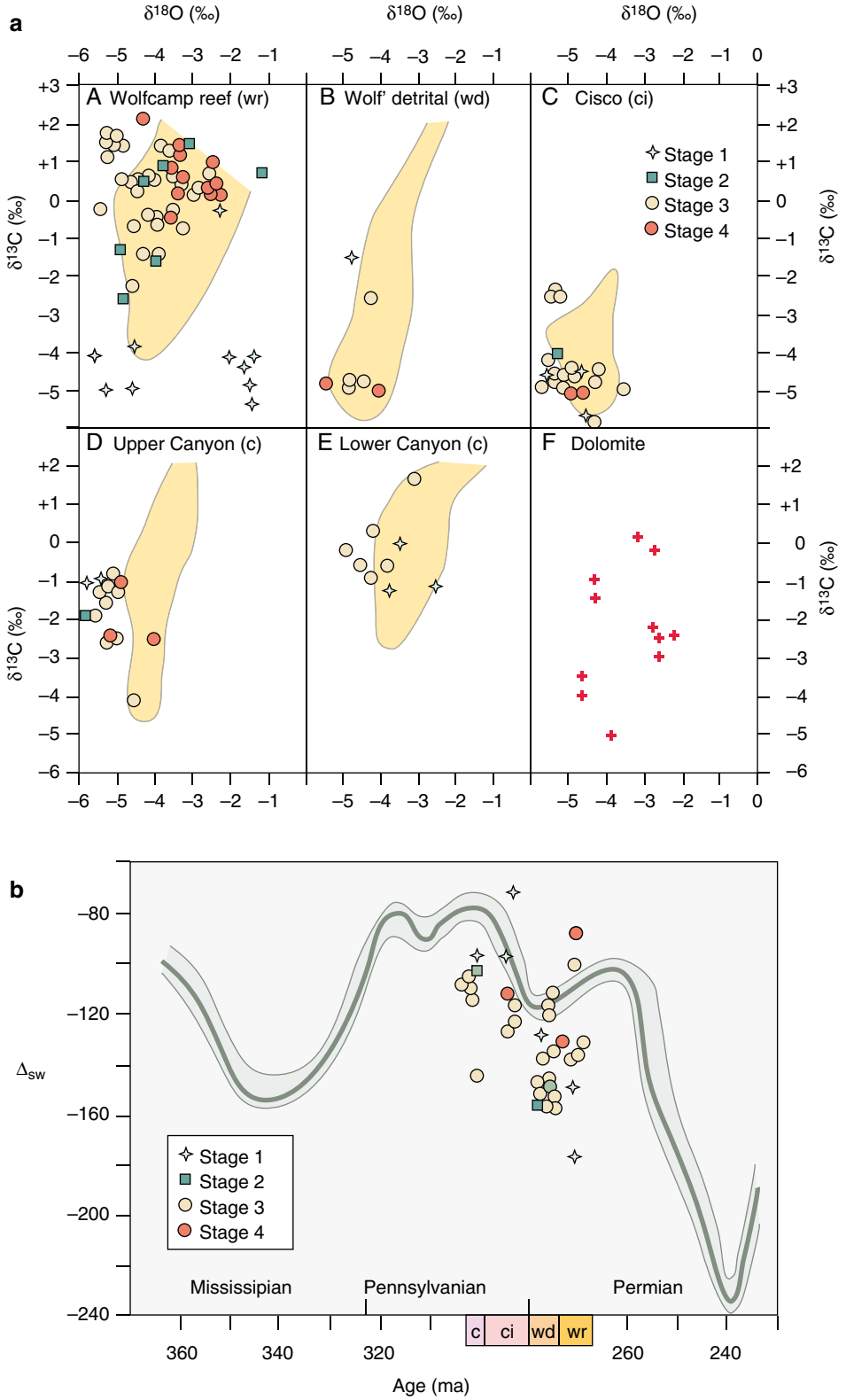

Fig. 8.42 Isotopes from the Palaeozoic carbonate platform of the southwest Andrews area, West Texas (After Dickson et al. 2001). (**a**) Carbon–oxygen isotope scatter-plots (A–E) of calcite cement crystals from Wells V7, X1, and Parker "B" 12. The cements are zoned and are grouped into four stages, stage 1 being the oldest and stage 4 being the youngest. Plots are listed by stratigraphic occurrence (*a*) Wolfcampian reef, (*b*) Wolfcampian detrital, (*c*) Cisco, (*d*) Upper Canyon, and (*e*) Lower Canyon intervals, while (F) is a carbon–oxygen isotope scatter plot of data from individual crystals of saddle dolomite in all stratigraphic intervals, except the Wolfcampian detrital. (**b**) $^{87}Sr/^{86}Sr$ data from selected separated cement stages (1–4) of the same calcite crystals as in (**a**) plotted on the late Palaeozoic seawater strontium isotope curve and its 76 % confidence band (*grey*; curve from Denison et al. 1998). Δ_{SW} is defined as:

$$\Delta_{SW} = \left({}^{87}Sr/{}^{86}Sr_{unknown} - {}^{87}Sr/{}^{86}Sr_{modern\,seawater} \right) \times 10^5$$

But stage 3 and 4 calcite cements precipitated later, thin sections show they are postcompaction and now make up to 25 % of the total rock volume. They have $\delta^{13}C$ values (−0.2 to −4.4 ‰) that vary according to stratigraphic position, and are similar to bulk rock samples of the host limestone. Their $\delta^{13}C$ values indicate these later cements are locally derived via dissolution of adjacent strata. $\delta^{18}O$ values of stage 3 and 4 cements (−5.5 to −3.5 ‰) are isotopically indistinguishable from the stage 1 and 2 cements precipitated from meteoric water (Fig. 8.42a). The expected decrease in $\delta^{18}O$ expected from elevated temperatures during burial (the present formation temperature is ≈55 °C) has been negated by their precipitation from late Permian hypersaline brine with $\delta^{18}O$ values of +5 ‰. These stage 3 and 4 cements are composed of sparry calcites and saddle dolomites with $^{87}Sr/^{86}Sr$ values that are lower than $^{87}Sr/^{86}Sr$ values for contemporaneous Permian marine carbonate (≈0.70830; (Fig. 8.42b). This indicates incorporation of Sr with low $^{87}Sr/^{86}Sr$ values (0.70672–0.70682), which were derived from the same late Permian hypersaline brines. Entry into normal marine carbonates was driven by ongoing brine reflux during the deposition of the overlying Permian evaporites.

Dickson et al. (2001) went on to conclude that the buried platform carbonates of Southwest Andrews area have several diagenetic features, all driven by the creation of a reflux curtain, which are probably more common as diagenetic overprints in ancient evaporite-associated limestones than previously recognized. They note: (1) Burial cements have $\delta^{18}O$ values similar to meteoric cements yet they were precipitated from later hypersaline pore waters with $\delta^{18}O$ values some 5 ‰ greater than contemporary seawater. (2) Deep-burial cements have $\delta^{13}C$ values similar to the bulk rock because carbon was derived from pressure dissolution of nearby carbonate. (3) Bulk-rock isotope values are characteristic of marine limestones subjected to meteoric diagenesis, yet they have suffered substantial deep burial diagenesis under the influence of hypersaline waters.

The chemical and isotopic compositions of highly saline water in evaporite-entraining basins complicate simple notions of meteoric versus normal-marine burial diagenesis, especially in intervals close to the dissolving evaporites. Most pore waters are not simply derived during the congruent dissolution of halite beds, nor are they only connate brines (Land 1995a; Levet et al. 2002). Na and Cl dominate the ionic composition of most sedimentary brines, even in basins that lack preserved evaporites, with the next most abundant cation being Ca and the next most abundant anion Br. This is not the ionic hierarchy of seawater, where the next most abundant cation is Mg and the next most abundant anion is SO_4, hence most subsurface waters in a sedimentary basin are no longer connate outside of sediments/ brine inclusions encased in salt that preserve primary chevrons.

Today, the three mostly commonly offered explanations for the formation of Na-Ca-Cl basinal brines are (Land 1995b): (1) preservation of seawater-derived brines that have precipitated halite (raises the Br/Cl ratio) as well as participated in dolomitisation and $CaSO_4$ precipitation (exchanges Mg for Ca and removes calcium sulphate from the brine), (2) subsurface halite dissolution accompanied by salt recrystallisation (partitions bromide into the brine) in association with the dissolution of detrital anorthite (component of detrital plagioclase) - this mechanism may include the deep circulation of meteoric water or escaping compactional waters from thick shale sequences, and (3) reverse osmosis (shale membrane filtration) driven by pressure resulting from compaction, whereby water molecules, uncharged species and small and univalent cations preferentially pass through the shale, so creating calcium, chloride and bromine rich residual brines.

Some or all of the mechanisms may be acting concurrently in most sedimentary basins either as time sequential overprints on the same strata or in different areas and depths in the same basin (Demir and Seyler 1999). It means that when compared with water stored in the same strata, but from other areas of the basin, subsurface formation waters may show differences in salinity, element content and/or isotopic composition on a local scale of hundreds of meters or across kilometres. Therefore, using geochemical information obtained from one regional part of the basin for the reconstruction or modelling of the fluid evolution in the entire sedimentary basin can be highly problematic (Lüders et al. 2010).

Effects and Indications of Water-Salt Interactions

This chapter has shown that dense subsurface waters derived from dissolving evaporites, tend to move through permeable sediments or along permeable conduits such as faults and fractures. They drive various diagenetic processes and flow is typically maintained by density gradients (indicated by thermal or salinity changes). Ongoing diagenesis (or rock-fluid interaction) in nonevaporitic strata also means ionic concentrations of most basin waters are buffered and controlled by the solubility of minerals in the sediment. The low solubility of the common cement minerals such as calcite and quartz means large fluxes of pore waters through nonevaporite lithologies are required to move and precipitate significant volumes of such cements (Bjørlykke and Gran 1994). In contrast, in the temperature range of sedimentary basins, little water flows through the interior of a salt bed or allochthon. But inherently high solubility means that when the edges of a dissolving evaporite unit are flushed by basinal water crossflows, the dissolving salt contributes large

volumes of ions to adjacent more permeable sediments. Even so, most basin brines, even in intervals adjacent to the dissolving evaporite, have salinities well below halite saturation (350–400 g/l). A possible exception is the Michigan Basin where some of the higher salinity basinal brines are clearly halite-buffered (Wilson and Long 1993).

Solution of buried evaporites explains why: (a) salinities increase in a systematic almost linear fashion with depth in sedimentary basins with bedded evaporites near the base of the sequence (Dickey 1979); (b) salinity around active salt stems/domes indicates the advective flow of waters up along the stem and then horizontally into overlying beds (Hanor 1988; Bray and Hanor 1990); (c) pore waters in sediments adjacent to a dissolving halite-dominated section lack sulphate, while evaporite sections with a greater proportion of gypsum/anhydrite can generate sulphate waters (Pluta and Zuber 1995); (d) in halokinetic provinces such as the central graben of the North Sea the salinity of the pore waters correlates better with the inverse distance to the nearest evaporite mass than it does to burial depth (Gran et al. 1992); and (e) why there is no significant increases in salinity with depth in the northern North Sea (59–62°N), which is an area with no known evaporites (Bjørlykke and Gran 1994).

The total volume of salts in the world's oceans is about 2.2×10^7 km^3 and there is about the same amount of Cl in the world's sedimentary basins (salts and porewaters) as there is Cl in the modern ocean (Borchert and Muir 1964). This means that of all the major sediment types, evaporites have the shortest mass half ages estimated to be $\approx2\times10^8$ years (Garrels and Mackenzie 1981). Hence, there are no significant potash or thick halite deposits preserved that are older than Neoproterozoic (Warren 2000c, 2010). Evaporite dissolution throughout burial and metamorphism and the associated discharge of Na-Cl rich brines into the basin's subsurface waters, and ultimately to the ocean, explains much of the short mass residence time for chloride. For the same reasons, the residence time for Cl in the world's oceans is the longest of any element and is of the same order ($\approx2.2\times10^8$ years) as halite's mass half-life (Land 1995a).

Hence, the chlorinity of the Precambrian oceans could not be more than around 50 % different from today. It also means that when large ancient basinwide salt basins rapidly accumulated their salts via drawdown, they could have substantially altered oceanic salinity. For example, the Permian Zechstein evaporites of northwest Europe, with a volume of 2.4×10^6 km^3, is equivalent to some 10 % of the volume of the current oceanic reservoir.

High concentrations of the ions from dissolution of buried salts typically indicate effective diffusive or advective transport of the ions from the salt-sediment contact and concentrations usually decrease further away from salt beds or domes. Steep gradients or abrupt changes in subsurface salinity, rather than gradual changes, typically indicate limited advective mixing of pore water across a permeability barrier (Bjørlykke and Gran 1994). Near a subsurface evaporite unit the chemical composition of the pore water concentrations are high and can approach equilibrium with the major evaporite minerals (typically halite or anhydrite). Burial cements can precipitate in pores in this zone when saturation is reached. The precipitation of evaporitic burial cements is even more likely when subsurface waters of differing salinities and compositions are mixed (Chap. 2; Sullivan et al. 1994).

Subsurface halite-dominated sequences dissolve in two ways; by incongruent[13] or congruent dissolution. Incongruent dissolution occurs typically at low water rock ratios, whereby the halite recrystallises as more soluble components are lost to adjacent pore fluids. For example, when halite recrystallises in the presence of waters with a bromine content less than that of the original salt-precipitating (connate) water, it will become bromine depleted. At the same time the pore waters become relatively enriched in bromine, supplied by the rupture and dispersion of bromine-enriched connate fluid inclusions during the recrystallisation process. Congruent dissolution is the total or bulk dissolution of salt via through-flushing basinal brines. It forms subsurface Na-Cl brines with high chlorine contents and higher Br/Cl ratios compared to nonevaporitic subsurface waters (Worden 1996).

Congruent dissolution of potassium-rich bittern salts is an even more effective means of creating-Br enriched hypersaline waters as minerals like sylvite entrain order-of-magnitude higher levels of bromine compared to sedimentary halite. Congruent or incongruent dissolution of K-salts leads to waters that are bromine-enriched relative to evaporated seawater (e.g. Fig. 2.33). Hanor (1994a) proposed that K-salt dissolution explained the bromine enrichment seen in many basinal brines in sedimentary basins with buried evaporites.

Incongruent dissolution is used to explain the bromine depletion of recrystallised Jurassic halite remaining in diapir crests in the Gulf of Mexico (Stoessell and Carpenter 1986) and is thought to be an important process in regions of salt flow and deformation worldwide (Land et al. 1995, 1988). In the Champion-Klepac #1 well in the Gulf of Mexico, sylvite occurs atop a thick halokinetic halite succession at the top of the diapiric Jurassic Louann Salt (Fig. 8.43; Land et al. 1995; Land 1995a, b). The well recovered some 150 m of salt, which is underlain by more than another kilometre of salt. The bittern sequence lacks $MgSO_4$ salts, giving a mineralogy that, according to Hardie (1990), is a prime candidate for a

[13] Incongruent dissolution of a mineral occurs via decomposition or reaction in the presence of a liquid, converting one solid phase into another solid, e.g. the conversion of orthoclase to kaolinite or carnallite to sylvite. It may not involve porosity creation.

Congruent dissolution describes the transition from a solid substance to a liquid of the same composition. By definition it involves a stage of porosity creation.

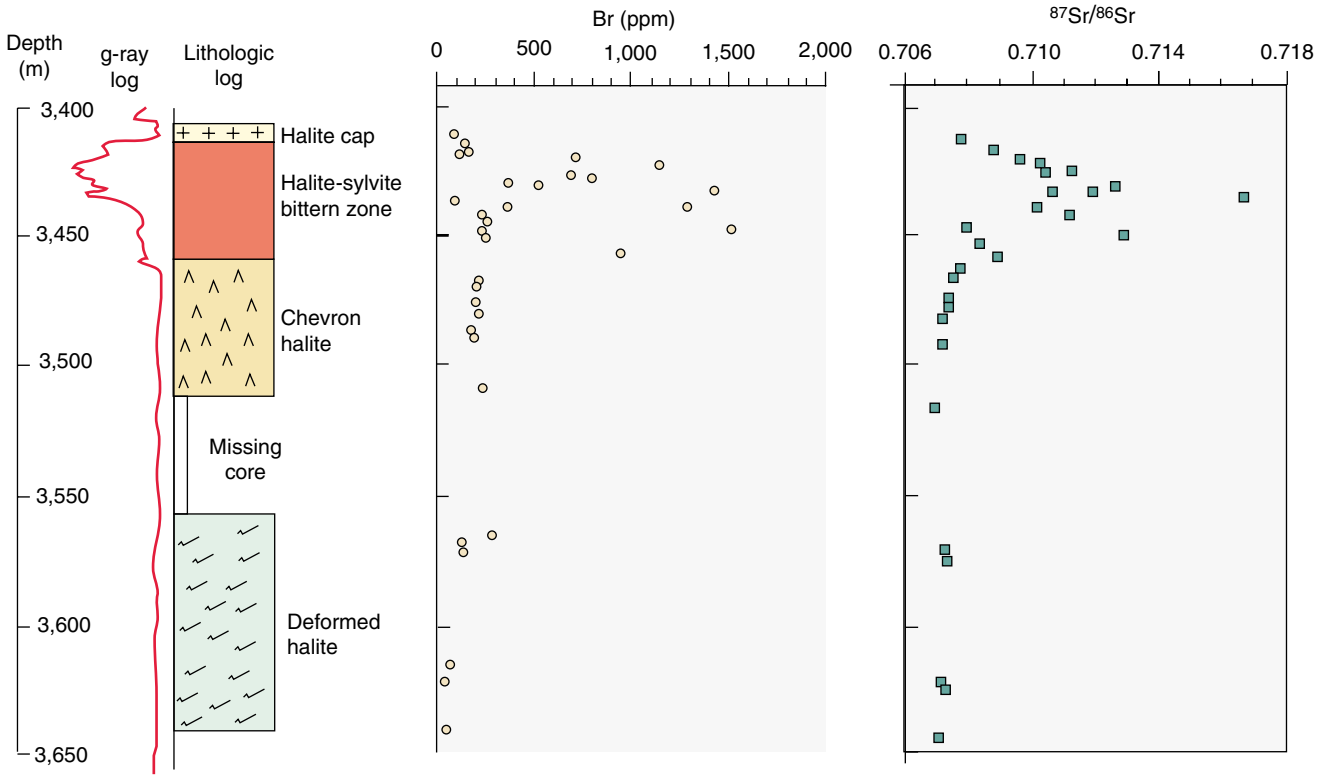

Fig. 8.43 Gamma-ray log, lithologic log, Br concentration and $^{87}Sr/^{86}Sr$ ratio in whole rock samples from the cored interval through the Louann Salt in the Champion-Klepac #1 well (After Land et al. 1995). The well was drilled to a total depth of 4,800 m. Based on the monotonous gamma log, pure halite, at least 1,050 m thick, underlies the cored interval

nonmarine, possibly hydrothermal, brine source, or perhaps indicates evaporation of a Jurassic seawater with ionic proportions different from today (Fig. 2.45).

Alternatively, Land et al. (op. cit.) argue the sylvite is the result of incongruent halite -bittern solution. The present bittern zone, encased in recrystallised halite, is interpreted to be a diagenetically modified "fractionated residue" created during the dissolution of more soluble marine bittern phases, such as carnallite, that were once present along with the sylvite. Sylvite is less soluble in halite-saturated subsurface waters than other bittern salts, which were primary coprecipitates (kieserite, epsomite, carnallite, etc; see Figs. 2.15 and 2.16). Incongruent formation of recrystallised halite and the associated accumulation of the sylvite residue supplied Mg, Br and SO_4 to the escaping pore brines.

Bromine values from deformed halite lower in the Klepac core can be used to argue that incongruent halite dissolution and recrystallisation during halokinesis can supply bromine to escaping pore fluids. Br values in the primary halite chevron-dominated succession beneath the bittern succession are uniform and centred around 200 ppm (range 170–234 ppm). This fits into the range of typical marine values (Holser 1979). Values in the deformed salt are much lower, averaging 110 ppm and decreasing to values of 29–60 ppm in the lower portions of the core. Did the bromine escape during incongruent recrystallisation of the flowing salt, or was the halite reworked and recrystallised at the time of deposition? Resolution hinges on an improved understanding of how flowing salt recrystallises (Fig. 6.5). Over a time frame of millions of years can the outer portions of a thick flowing salt periodically pressurise and leak fluid, or is the flow mechanism purely one of localised halite recrystallisation, pressure solution and edge dissolution within a relatively closed hydrology? At the present time we simply do not have the answer.

Crustal Cycling of Brines?

Cratonic or shield brines, which are ubiquitous hypersaline waters in open faults and fractures at depths >1 km in Precambrian rocks around the world, are among the most enigmatic of all crustal fluids with respect to their age and origin (Bottomley et al. 2002). Not only do shield brines have very high salinities (up to 300 g/l), which are comparable to sedimentary formation brines in evaporite-floored basins, their chemical compositions are of the Ca-Cl type and their O and H isotopic compositions plot well above the global meteoric water line in $\delta^{18}O$ versus $\delta^{2}H$ plot space (i.e., they are depleted in ^{18}O or enriched in ^{2}H relative to meteoric water). Arguments for both in situ water-rock interactions (Frape et al. 1984), and ancient, concentrated marine sources have been presented to explain their compositions and

widespread occurrences (Bottomley et al. 1994, 1999) and to model per descendum flow paths for some types of shield-hosted ore deposits (e.g. Mernagh et al. 1994).

Bromine elevation in a pore water in a sedimentary host is readily explained by the subsurface dissolution of the more saline evaporite salts, but saline Na-Ca-Cl type groundwaters and brines also occur in deep mines over extensive areas of the Canadian Precambrian Shield. These waters have elevated Br/Cl ratios which imply the chlorinity of these waters was derived from the deep infiltration of residual evaporitic brines, perhaps as remnants of the great marine/hypersaline apron that typify strata of the Palaeozoic era in this region (Bottomley et al. 1994, 1999). Boron concentrations in these waters are generally low ($<\approx 2$ mg/l) relative to seawater or to Alberta Basin Devonian formation waters. However, the $^{11}B/^{10}B$ ratios of these waters are significantly greater than the average value for continental crustal rocks. Moreover, Bottomley et al. argue that the boron isotopic ratios generally trend to higher values with increasing chlorinity, which supports the conclusion from the Br-Cl relationship that most of the chloride in these shield brines is of marine origin, rather than a product of water/basement rock interactions. In a subsequent paper Bottomley et al. (2002) used ^{129}I measurement to determine the minimum age of brines in basement fractures in the Con gold mine in Yellowknife (Northwest Territories), and found the brines are at least Cretaceous and probably Devonian. He concludes a Pleistocene age and cryogenic origin is impossible.

Seawater freezing was proposed by Herut et al. (1990) and Starinsky and Katz (2003) as an alternative explanation for the saline chemistry of Canadian Shield brines (Fig. 8.44). Based on minerals present in salt lakes in Antarctica such as Lake Bonney and Vanda Lake, we know that seawater freezing can form various sodium and magnesium salts and high salinity brines. Thick beds of mirabilite occur on the McMurdo Ice Shelf. From experiment, we know that when seawater freezes at −1.9 °C, a small amount of calcium carbonate is the first salt to drop out, usually as aragonite. Next, sodium sulphate

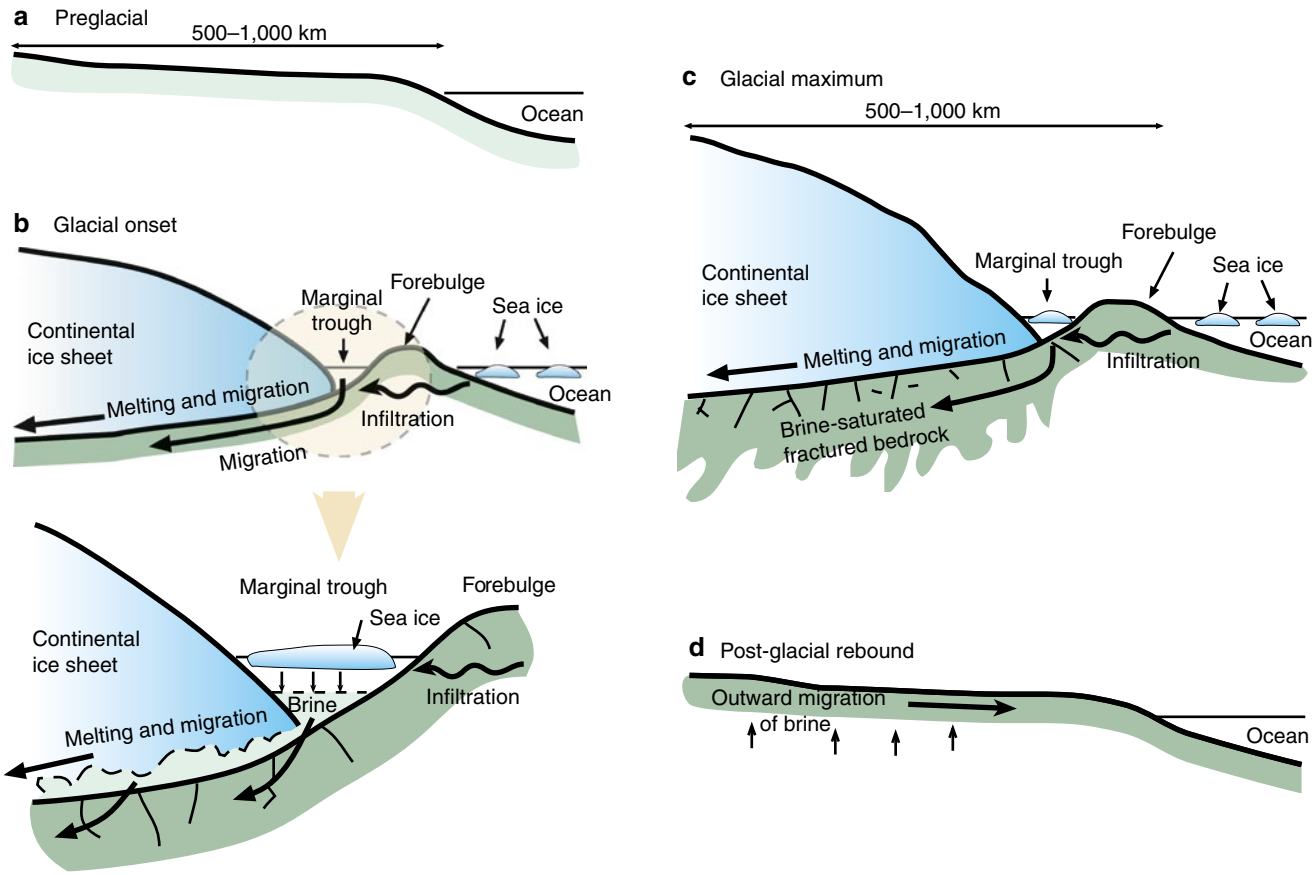

Fig. 8.44 Isostatic and hydrological evolution of a marine-cryogenic basin: (**a**) Continent-ocean boundary before the onset of a glacial cycle. (**b**) An ice sheet develops on the continent, depressing the crust underneath and forming a forebulge along the coast. Seawater infiltrates into the marginal trough between the ice edge and the forebulge and sea ice crystallizes on its surface. The resultant brine sinks to the bottom and infiltrates the underlying sediments and rocks via cracks and shear zones and by non-equilibrium melting of the ice sheet base. Then, it migrates inland, along the inclined ice-rock contact, towards the centre of the depression. Loss of brine from the trench is compensated by fresh seawater flow through the forebulge. (**c**) During the glacial maximum the basement rocks below the ice sheet become saturated with brine. (**d**) Increased melt water head developing during glacial decline, accompanied by postglacial lithospheric rebound, drive the brines outwards from the centre of the glaciostatic depression to their present sites (After Starinsky and Katz 2003)

precipitates as mirabilite at −8.2 °C, sodium chloride as hydrohalite ($NaCl{\cdot}2H_2O$) at −22.9 °C, and then sylvite + $MgCl_2{\cdot}12H_2O$ at −36° (Nelson and Thompson 1954). At −54 °C this cryogenic sequence of salts ultimately produces a calcium chloride brine slurry that precipitates antarcticite ($CaCl_2{\cdot}6H_2O$). One of the few places in the world where this mineral occurs naturally is in a brine lake known as the Don Juan Pond in the Dry Valleys (Wright Valley) of Antarctica, where the TDS of the bottom brine can exceed 500 kg/m^3 (Torii and Ossaka 1965).

Up to the point of halite precipitation, seawater freezing has the same effect on chlorine-bromine relationships in residual brines as solar-driven evaporation. So, seawater freezing beneath thick ice sheets may be an important process controlling the composition of formation waters seeping into fractures and cracks in sub-glacial hard rock sequences. However, recent work on the origin of the various salts in Antarctic salt lakes has shown that, while the mirabilite in Lake Bonney and Vanda Lake are derived by seawater freezing, the antarcticite in Don Juan Pond may not be. Rather, it formed by freezing of a resurgent brine that was created by water-rock interactions in a deeply circulated groundwater moving through fractures within a granite host (Takamatsu et al. 1998).

The influence of glaciation in driving cryogenic brines into fractures below the icesheet is now well documented in polar shield regions. In temperate regions that were covered by glacial ice in the Late Pleistocene periodic ice sheet loading can also influence the direction and volume of deep meteoric or hypogene waters in a sedimentary basin. In a study of brine springs discharging from Devonian carbonates of the Western Canada Sedimentary Basin, Grasby and Chen (2005) concluded that spring waters possessed a distinct water chemistry, compared to subsurface brines in laterally equivalent units deeper in the basin (Fig. 8.45).

Deep-basin brines on the Devonian strata in the Western Canadian Sedimentary Basin have Na/Cl molar ratios typically <0.8, which is related to water-rock interaction buffering Na. In contrast, brine springs have Na/Cl molar ratios close to one, which is again indicative of halite dissolution, as are their Br/ Cl ratios but they are different proportions to the deep subsurface brines, with the southern Saskatchewan brines occupying an intermediate position (Fig. 8.45a). Grasby and Chen (2005) documented a progressive shift in Na/Cl molar ratios and Br/Cl ratios from deep-basin (connate) brines with an altered seawater signature, to waters near the edge of the basin with a signature of dissolved evaporites (Fig. 8.45b). This trend indicates that the model for cryogenic ice-forced formation of shield brines, as documented by Starinsky and Katz (2003), does not directly apply to the pore waters of the WCSB.

But, stable isotope data suggest that the waters discharging in the brine springs originated as Pleistocene meltwater. These waters are interpreted to originate as an influx of sub-glacial meltwater driven by ice-load as it induced a reversal of the basin-scale artesian flow system (Fig. 8.46). Esker distribution shows a notable relationship between shield and

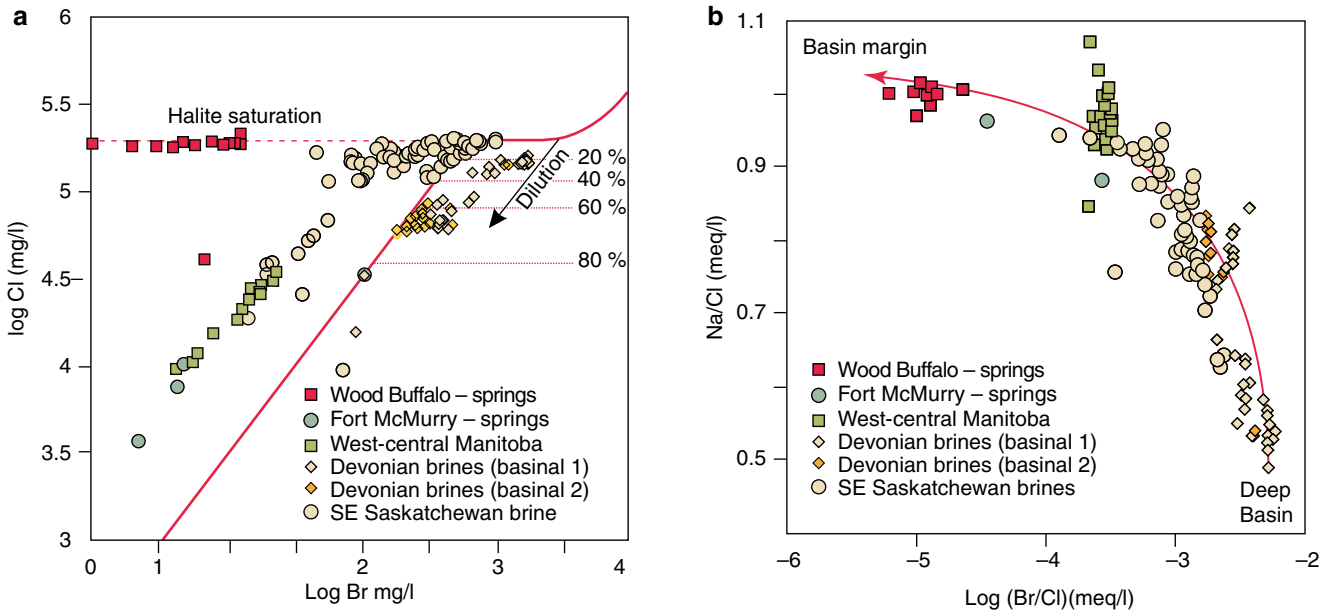

Fig. 8.45 Brine chemistry in West Canadian Sedimentary Basin. (**a**) Plot of Br versus Cl for deep-basin Devonian brines, brine springs discharging from Devonian outcrop belts in west-central Manitoba and NE Alberta, and intermediate basin waters in southern Saskatchewan. Also shown as *red line* is evaporation/dilution trend for seawater). (**b**) Plot of Na/Cl vs Br/Cl showing progressive shift in conservative ion ratios going from deep-basin waters to brine discharge along the basin margin – mixing curve?). Units are in milliequivalent per liter (meq/l) (After Grasby and Chen 2005 and sources therein)

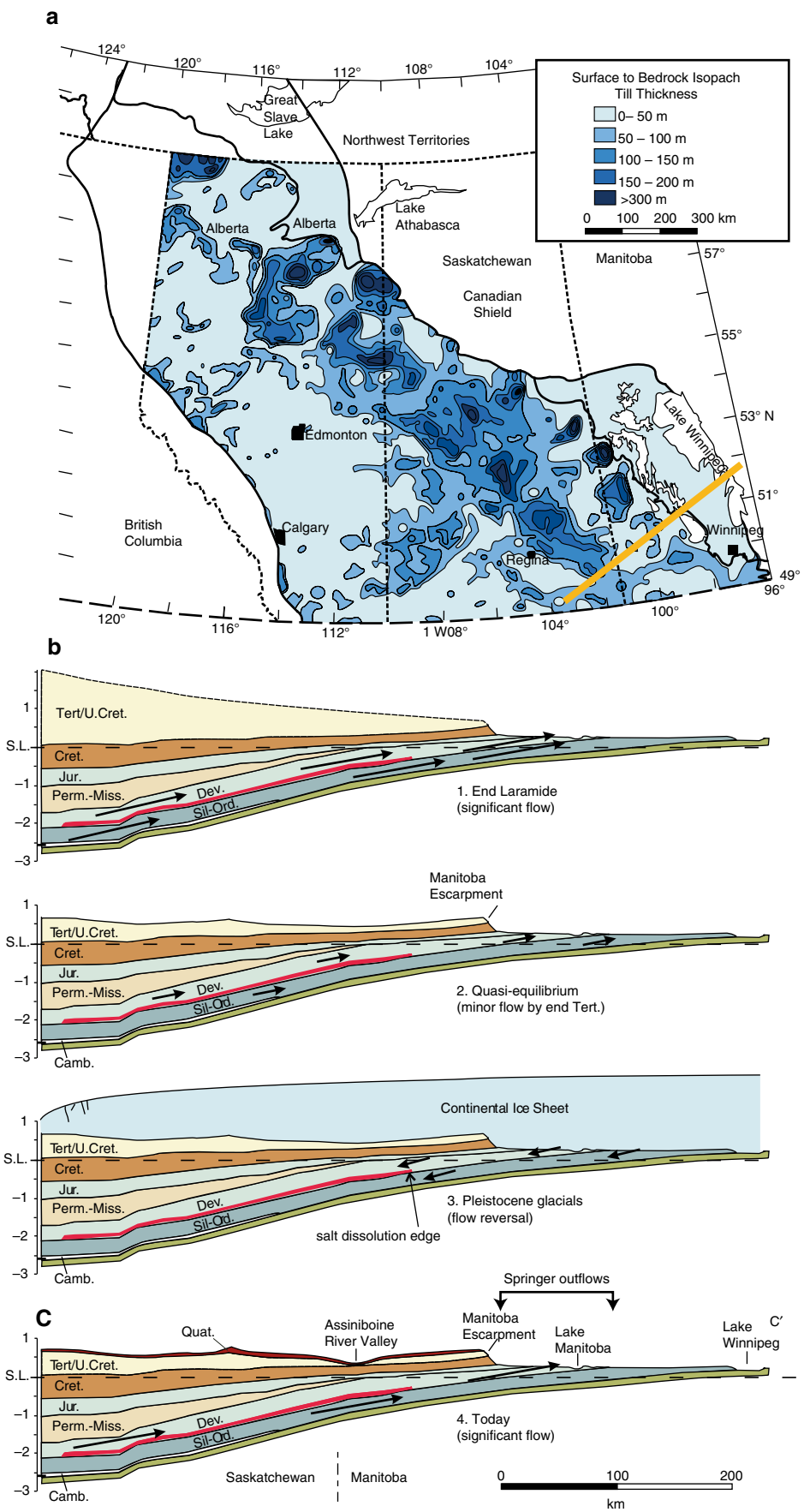

Fig. 8.46 Glacial-induced flow reversal in the West Canada Sedimentary Basin. (**a**) Regional map of till thickness – *orange line* indicates cross section position illustrated in **b**. (**b**) Schematic sections showing evolution of basin hydrodynamics for the past 50 Ma. with Devonian evaporite extent shown in *red*. (*1*) Initial onset of topography-driven basin-scale fluid flux in response to tectonic rebound of the western margin of the basin at end Laramide time, (*2*) Diminished flow due to Tertiary erosion lowering the topographic gradient across the basin leading to quasi-stationary hydrologic equilibrium, (*3*) Loading tied to Pleistocene continental glaciation reverses the topographic gradient across the basin and thus the direction of fluid flow, leading to significant subglacial meltwater recharge along the carbonate outcrop belts in NE Alberta and central Manitoba and increased salt dissolution in the relatively shallow (hypogene) subsurface, (*4*) In response to off-loading of the melting ice sheet, the hydrodynamic system of the basin shows a transient response trying to re-establish a new hydrologic equilibrium. This reversal drives a discharge of glacial meltwaters that have now obtained a high salinity from dissolution of salt beds, this still drives the observed modern-day spring outflow system on the basin margin (After Grasby and Chen 2005)

sedimentary rocks and the dissolution front of the Prairie evaporites (Fig. 8.46a). An integrated sedimentary basin/ice sheet model supports the interpretation that high permeability carbonate units acted as preferential subglacial drains that in turn affected esker development. The fluid flow history of the Western Canada Sedimentary Basin is characterized by back-and-forth pore-fluid movement through geological time, in response to changing boundary conditions (Fig. 8.46b). Grasby and Chen (2005) conclude that the brines discharging from the northern and eastern edge of the WCSB are not related to deep-basin brines, rather they were once fresh glacial waters that came in contact with, and dissolved, subcropping evaporite units on the northeastern margin of the basin and subsequently mixed with deeper basin brines. If so, then the modern-day flow systems and brine chemistries, driven by glacial loading and unloading, may not be indicative of historic (pre-glaciation) movements of economic fluids through the basin.

In warm pore fluids at the other end of the temperature and sedimentary-burial spectrum, there is the possible creation of hot hypersaline brines in a fractured hard-rock basement host beneath the evaporite basin, via infiltration of connate waters. This leads to an interesting quandary; have hypersaline basinal brines entered and influenced the chemistry of the hard rock basement that lies beneath most evaporite-floored sedimentary basins (such as the Gulf of Mexico), or are these waters juvenile residuals from magmatic or metamorphic fractionations (Markl and Bucher 1998)? Land (1995b) argues for the former. Using quantified mass volume and element residence times he concludes that as the porosity of rocks is reduced during burial, discharge of saline formation waters contributes to crustal chloride cycling. During deep burial, corrosive saline formation waters dissolve metastable detrital minerals derived from crustal/basement rocks and transfer incompatible elements such as Li and B from the igneous crust to the sedimentary crust. Likewise, albitisation transfers Ca from the crustal silicate (igneous) mineral reservoir to the crustal carbonate and aqueous (sedimentary) reservoirs. Metamorphism, and then melting of albite-enriched rocks, accounts for the elevated sodium contents of igneous rocks relative to sedimentary rocks. In this way average sediments have become enriched through time in Ca, Cl, Br, S, Li, and B, and depleted in Na relative to average igneous crust.

In support of the ability of evaporite brines to enter and so influence basement chemistry during metamorphism and overpressuring, McCaig et al. (2000) documented evaporite-derived Na-Cl brines in inclusions in the northern end of the Alpine shear zone, Europe (Figs. 8.12 and 8.47a, b). The brines occur where the regional shear cuts the Neouvielle granodiorite in the Hercynian Axial Zone and also to the south in several localities in the footwall and hangingwall of the Gavarnie Thrust on the southern margin of the Axial Zone. Inclusion fluids generally decrease in salinity from 27 to 35 % at the northern end of the transect to 7–22 % on the southern margin of the Axial Zone. The evaporitic origin is seen in the Cl-Br-Na systematics of the fluid inclusions, which show chemistries consistent with a change from halite to halite + sylvite precipitation with progressive evaporation. The fluids in the basement shear zones are interpreted to have essentially the same evaporitic origin as those still contained in nearby Triassic sediments. Brine inclusions in the sediments have Cl/Br ratios lower than seawater indicating relict signatures derived by marine evaporation and halite precipitation in the upper Triassic. It is possible that final concentration of brines in the Neouvielle Massif also involved retrograde hydration reactions via removal of water by precipitation of hydrous minerals.

The somewhat lower salinities seen at the southern margin of the Axial Zone are interpreted by McCaig et al. to reflect mixing of evaporite-derived brines with a higher level fluid (connate or meteoric water) circulating within the Mesozoic carbonates of the higher thrust sheets. At one locality where Triassic evaporites are still present, high Cl/Br ratios at relatively low salinities are present in inclusions within the underlying Triassic redbeds, but low Cl/Br ratios at higher salinities are seen lower in the sequence. This is consistent with dissolution of halite by a dilute fluid, but with limited penetration downwards.

In a related paper, Travé et al. (2000) demonstrate the involvement of evaporite-related fluids in sediments atop the evaporite-lubricated thrust of the Al Guix anticline in the Pyrenees of NE Spain (Fig. 8.47). The El Guix anticline is the southernmost structure of the south-Pyrenean fold-and-thrust belt. Compressional activity in the area represents the latest stages of Alpine compressional tectonics and overprints the Upper Eocene-Oligocene fluvio-lacustrine deposits that overlie halokinetic Triassic evaporites. Based on a detailed structure of the timing and chemistry of various microfracture cements Travé et al. (2000, 2007), conclude that the Pyrenean fold-and-thrust belt and its deformed southern foreland basin were hydrologically compartmentalised, both in time and space (Fig. 8.13). During the early Eocene, when the thrust front affected soft-sediment in the Ainsa basin, medium-scale fluid flow cells dominated the thrust faults. Fluids in the basin were largely formation fluids derived from Eocene marine waters with a minor meteoric influence. During the middle Eocene; coeval with the Gavarnie thrust emplacement, the thrust fault was dominated by medium scale fluid flow system and a fluid that was basically a hypersaline Sr-rich brine stored within Triassic redbeds. No evidence was found of any significant input of either surface or metamorphic fluids during this time. During the same period, the thrust faults in the crystalline basement of the central Pyrenees were dominated by a large scale fluid flow mainly derived from the underlying silicate rocks as a

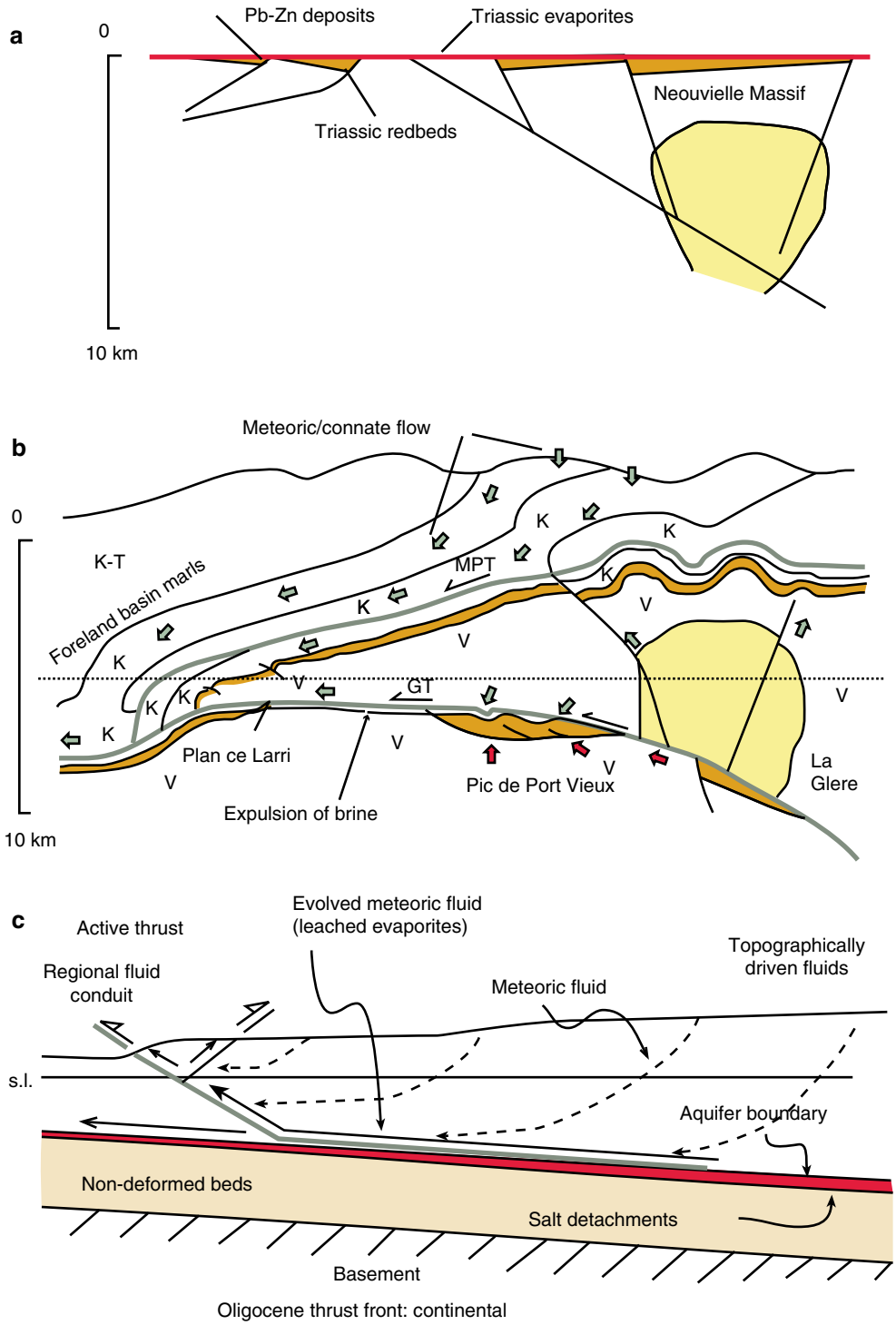

Fig. 8.47 Model for fluid evolution and mixing in the Pyrenees. (**a**) Situation at the end of the Triassic: Brines from marine-fed Triassic evaporites sink and displace older formation waters in the underlying redbeds and fractured basement rocks. Pb-Zn deposits formed along normal faults sometime between the Triassic and the middle Cretaceous, due to circulation of metalliferous basinal brines, probably due to density convection. (**b**) Situation during Eocene thrusting. Section above the present exposure level is conjectural (above *dashed line*). Detail of part of section below thrust line is given in Fig. 8.7. *Arrows* show inferred directions of fluid flow. Note local movement of fluid into the Pic de Port Vieux culmination driven by dilatancy. *V* Variscan basement (Silurian and Devonian phyllites, Cambro-Ordovician schists and late granitoids). *K* Cretaceous to Palaeocene carbonates, *K-T* Tertiary marls and flysch of the foreland basin, locally interthrusted with Cretaceous carbonates, *GT* Gavarnie Thrust, *MPT* Mont Perdu Thrust (**a**, **b** After McCaig et al. 2000; Horizontal and vertical scales are equal, but there is no precise correspondence between the two diagrams). (**c**) Fluid flow in the El Guix anticline during the Oligocene when deeply circulating and evolved meteoric waters mixed with evaporitic waters from Triassic evaporites that also created the décollement for the thrust plane (After Travé et al. 2000)

result of metamorphic devolatilisation reactions. During the Oligocene, the most external part of the fold-and-thrust belt developed on top of a salt detachment horizon (Fig. 8.47c). Then the thrust front affected mostly cemented continental materials of late Eocene-Oligocene age and the thrusts were conduits for meteoric fluids and also for evolved meteoric fluids migrating a short distance upwards after being in contact with the underlying evaporitic beds focused by the décollement.

Thus, the fluid history in the Pyrenean collision zone evolved through a series of stages in time and space, linked also to economic accumulations of base metals Travé et al. (2007): (1) Upper Triassic evaporite formation with sinking of brines into underlying redbeds and fractured basement rocks; (2) Circulation of brines with formation of Pb-Zn deposits along faults at some time between the Triassic and the Upper Cretaceous; (3) Renewed extension with erosion of Triassic rocks in many areas and further draw down of Triassic brines into the basement; (4) Deposition of Upper Cretaceous and Palaeocene-Eocene carbonates containing connate waters of marine origin: (5) Formation of the Pyrenean thrust belt with overpressuring and expulsion of the brines along shear zones and faults; (6) Creation of topography with a high-level circulation system in the Mesozoic thrust sheets driven largely by topography (McCaig et al. 2000). At the southern margin of the Axial Zone there was limited mixing of the deeper, overpressured brines from evaporitic sediments with more dilute, hydrostatically pressured fluids (Travé et al. 2000).

A similar interaction between hydrothermal ($\approx$200 °C) fluid circulation, associated with the cooling of a granite mass, and hypersaline fluid circulation driven by sinking of dense hypersaline brines, derived in Triassic evaporitic rifts of the Western Approaches, is important in controlling the fracture-related low temperature base metal and uranium accumulations of South Cornwall (Gleeson et al. 2001).

It seems that the role of evaporite basin brines extends well beyond the limit of sediments within a sedimentary basin. We shall pursue this topic further in a discussion of meta-evaporites in Chap. 14 and in various metal accumulations in Chaps. 15 and 16. For now, to complete this section, let us consider the observations of Yardley (2013) in a recent review paper on the role of basinal brines in crustal processes.

He noted the following;.... “In recent times, the role of basinal brines in giving rise to mineralisation and metasomatism in underlying basement has been recognised in a number of areas. Dolomite veins in Caledonian metamorphic rocks of SW Scotland have been linked to penetration of post-orogenic basinal brines by Parnell et al. (2000a), while Holness (2003) has found widespread evidence of fluid penetration into crystalline rocks during exhumation. In the Cloncurry district of Queensland, widespread growth of actinolite and albite (i.e. sodic-calcic metasomatism) has affected basement crystalline rocks as they cooled through greenschist facies conditions under an extensional regime (De Jong and Williams 1995). Subsequent isotope studies implicate a major contribution from the infiltration of basinal fluids (Kendrick et al. 2008). Infiltration of both formation brines and associated hydrocarbons into Precambrian basement rocks has been recognised on the western flanks of the Oslo Graben by Munz et al. (1995, 2002) and Gleeson et al. (2003), and is associated with quartz veins and albitisation. Boiron et al. (2010) have documented a range of examples of ore deposits linked to brines moving between basin and basement, and cite Precambrian unconformity-type U deposits as an important example. Basement rocks beneath sedimentary basins fracture and extend during basinal development, and since the cooled basement rocks are essentially fluid absent at this stage (Yardley 2009), fluid from the overlying basement is readily drawn down. This will be particularly effective if the basal formations in the basin are overpressured.”

Clearly the influence of evaporite-derived subsurface waters extends beyond the sedimentary realm into the metamorphic and igneous realms (Chaps. 14 and 16, respectively).

Halotolerant Life in Feast or Famine: Organic Sources of Hydrocarbons and Fixers of Metals

9

Introduction

A hydrocarbon source rock is generally considered to be a fine-grained rock that, during its burial and heating, generates and releases enough fluids to form commercial accumulations of oil or gas (Fig. 9.1a). Back in 1981, Kirkland and Evans made the observation that some 50 % of the world's oil sequestered in carbonate reservoirs may be associated with mesohaline micritic source rocks. Heresy or not, the notion that much of the oil in carbonate reservoirs, sealed by evaporite salts, may have been sourced in earlier less saline, but still related, evaporitic (mesohaline) conditions, is worthy of consideration. The association between mesohaline waters, the accumulation of organic-rich sediments and the evolution of the resulting evaporitic carbonates into source rocks has been noted by many, including: Woolnough (1937), Sloss (1953), Moody (1959), Dembicki et al. (1976), Oehler et al. (1979), Malek-Aslani (1980), Kirkland and Evans (1981), Jones (1984), Hite et al. (1984), Eugster (1985), Sonnenfeld (1985), Ten Haven et al. (1985), Warren (1986), Evans and Kirkland (1988), Busson (1991), Edgell (1991), Beydoun (1993), Benali et al. (1995), Billo (1996), Aizenshtat et al. (1998), Carroll (1998), Schreiber et al. (2001), Love et al. (2007), Schnyder et al. (2009), Warren (2011), Comer (2012).

As long ago as the middle of last century, Weeks (1958, 1961) emphasised the importance of evaporites as caprocks to major hydrocarbon accumulations. He also pointed out that many of the cycles of deposition that involve organic-rich carbonate marls or muds also end with evaporites. Many of these authors noted an association with Type I-II hydrogen-prone kerogens in evaporitic source rocks and related this to the ability of halotolerant photosynthetic algae and cyanobacteria to flourish in mesohaline waters. Such kerogens tend to be oil-prone rather than gas prone and typified by long-chain hydrocarbons (Fig. 9.1b).

Much of the organic matter preserved in evaporitic carbonates, and the resulting source rocks, originated as planktonic blooms (pelagic "rain from heaven") or from the benthic biomass ("in situ" accumulations). Such organics typically settled out as seriate pulses of organic matter (often pelleted) that sank to the bottom of a layered brine column. Each pulse was tied to a short period when surface brines were diluted and halotolerant producers (mostly cyanobacteria and algae) flourished in the freshened lit zone. That is to say, the laminated mesohaline mudstones that constitute evaporitic source rocks reflect biological responses to conditions of "feast or famine" in variably layered bodies of brine. Warren (1986, 2011) referred to the schizohaline salinity cycles of saline settings as repetitive episodes of "life or death."

Organic matter buried in organic-rich sediment undergoes numerous compositional changes before it becomes a source rock, at first dictated by microbial agencies and then by thermal stress (Horsfield and Rullkotter 1994). This continuum of processes is called thermal maturation. Based on vitrinite reflectance (R_o) measurements of macerals, a maturing source rock can be divided into three consecutive stages: eogenesis (diagenesis)[1] ($R_o < 0.5$ %); catagenesis (0.5 % $< R_o <$ 2.0 %); and metagenesis (2.0 % $< R_o <$ 4.0 %), with the oil generation window typically in the R_o range 0.5–1.3 % (≈65–150 °C: Table 9.1). Reflectivity is measured by shining a beam of monochromatic light (with a wavelength of 546 nm) on to a polished surface of the vitrinite macerals and measuring the percentage of the light reflected with a photometer. Put simply, it measures the degree of darkening (roasting?) of the organics associated with heating of the rock during burial and is not really a direct indication of oil maturation.

[1]The term *diagenesis*, as used by petroleum geochemists, describes processes of organic modification or alteration in the presence of pore waters where circulation is driven by surface processes. This usage is much more restrictive than the sedimentological use of the term which encompasses all alteration or modification from the time of sediment deposition until the onset of metamorphism. In order to minimise any possible confusion, the term *eogenesis* is preferred by some workers, but this is a different meaning to eogenetic as used by Choquette and Pray (1970).

© Springer International Publishing Switzerland 2016

J.K. Warren, *Evaporites: A Geological Compendium*, DOI 10.1007/978-3-319-13512-0_9

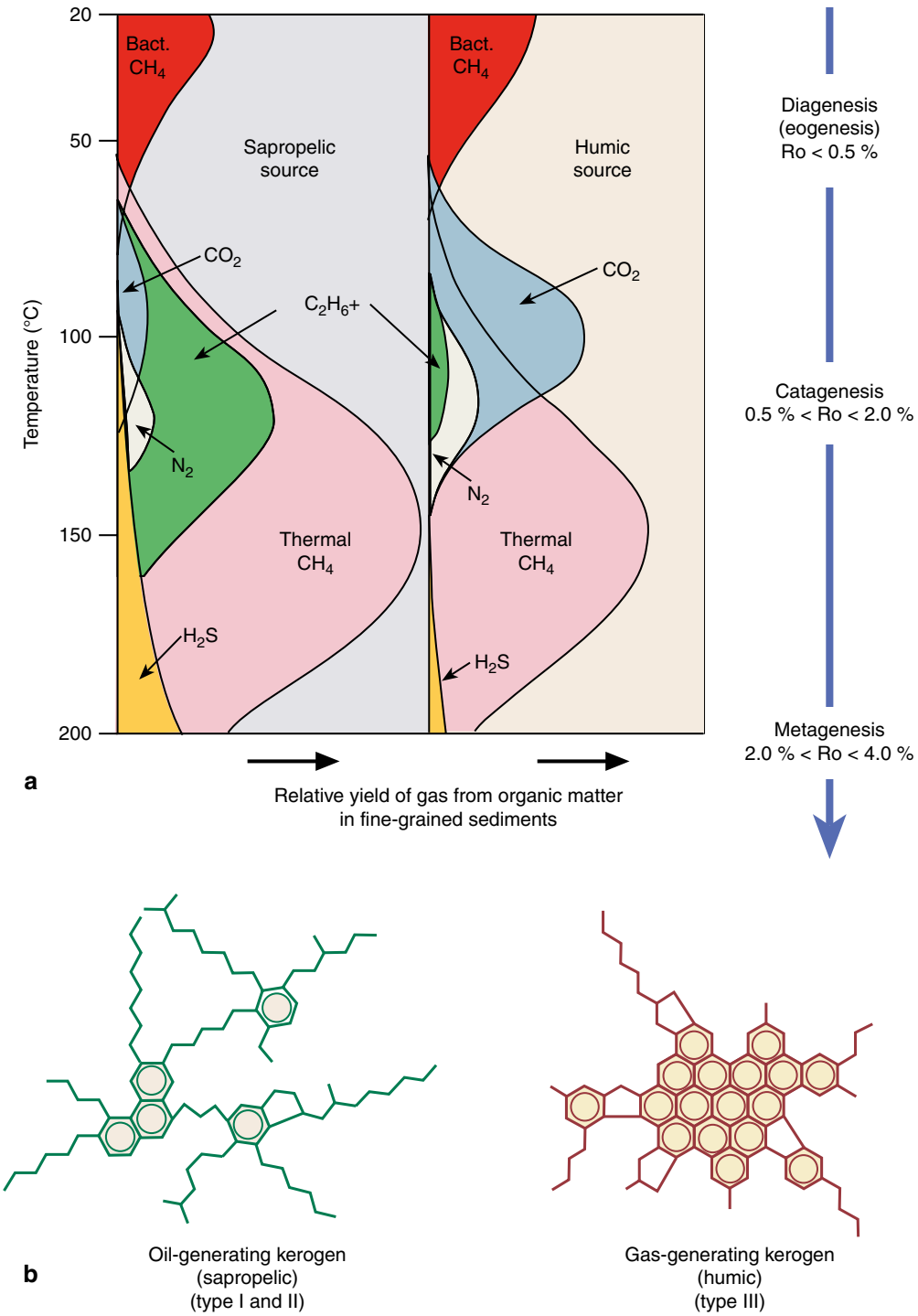

Fig. 9.1 Organics and source rocks. (**a**) Relative volumes of gases and liquids derived from a sapropelic and a humic source rock (After Hunt 1996). Evaporitic source rocks tend to be sapropelic and contain less iron as a reductant so they are also likely to generate more H_2S. (**b**) Molecular structure of typical oil-generating (sapropelic) and gas-generating (humic) organic matter showing the greater preponderance of long-chain hydrocarbons in the sapropelic material (After Hunt 1996)

Macerals are recognizable remains of different types of organic matter that can be differentiated under the microscope by their morphologies. As originally defined, macerals are the microscopic organic components of coal and consist of an irregular mixture of different chemical compounds, which are analogous to minerals in inorganic rocks, but differ from minerals in that they have no fixed chemical composition and lack a definite crystalline structure (Fig. 9.2). Macerals change progressively both chemically and physically during ongoing burial and heating; as the rank of macerals (coaly material) advances or the maturity of the organics increases. Macerals in any sediment can be classified into four major groups: vitrinite, inertinite, alginite and exinite (Fig. 9.2a). Liptinites broadly encompass the alginites

Table 9.1 The generation defined oil and gas window approximately related to some common maturity parameters

Parameters (oil and gas)	Temperature (°C)	Vitrinite reflectance (R_0%)	Transformation ratio[a] (0–1)	Spore colour index (1–10)	Rock Eval (T_{max} – °C)
Oil maturation					
Early mature	80–115	0.5–0.7	0.05–0.15	4.0–5.0	432–442
Mid mature	115–145	0.7–1.0	0.15–0.65	5.0–7.0	442–455
Late mature	145–165	1.0 to >1.3	0.65–0.95	7.0–9.0	455–465
Post mature	>165	>1.3	>0.95	>9.0	>465
Gas maturation					
Early mature	115–145	0.7–1.0	0.05–0.45	5.0–7.0	455–465
Mid mature	145–220	1.0–2.2	0.45–0.85	7.0–9.0	465–525
Late mature	>220	2.2 to >3.0	0.85–0.95	10	525–575
Post mature	??	>3.0	>0.95	10	>575

After Cornford 2005
Figure 9.1 also shows relationship between maturation, R_o and temperature
[a]Transformation ratio (LLNL) of Type II kerogen for oil maturation, and Type III kerogen for gas maturation

and exinites. Vitrinite is derived mostly from woody plant tissue and includes the macerals collinite and telinite, most coals have a high percentages of vitrinite macerals (Fig. 9.2b). The inertinite group comprises fusinite, micrinite, sclerotinite, and semi-fusinite, which are all rich in carbon but poor sources of volatiles. The exinite/alginite (liptinite) macerals, characterized by high hydrogen content (and hence excellent liquid hydrocarbon-generating potential), include alginite, cutinite, resinite, and sporinite (Fig. 9.2b). Alginites are commonplace macerals in evaporitic settings, while vitrinites are rare, reflecting a lack of higher plants in most hypersaline settings. A lack of vitrinite and poor calibrations to alginite maturation indices can lead to poor correlations between actual source rock maturity and that indicated by vitrinite-based estimates in evaporitic source rocks.

This is the case for the Type II source rocks in the Hanifa-Hadriya interval in Saudi Arabia (Ayres et al. 1982), which contains little or no vitrinite. Reflectance measurements determined from a few phytoclasts in such mesohaline source rocks may be unreliable and other geochemical evidence, such as thermal alteration indices (TAI) or biomarker maturity parameters, should always support R_o measurements of maturity in such sediments (Table 9.1). Significant proportions of oil-prone macerals or bitumens, as are common in many mesohaline source rocks, tend to retard the normal progression of vitrinite reflectance with maturity (Price and Barker 1985).

Transformation of organic matter to liquid and gaseous hydrocarbons is the result of thermal cracking of kerogen[2]. Kerogen is the major global precursor of petroleum and its formation, mostly via biologically-induced alteration of plant and animal detritus, its formation is complete by the end of eogenesis. Around 90 % of the organic material in a source rock at the onset of catagenesis is dispersed kerogen, consisting of a range of residual materials with basic molecular structures that are dominated by stacked sheets of aromatic hydrocarbon rings, in which atoms of sulphur, oxygen, and nitrogen also occur. Attached to the ends of the rings are various hydrocarbon compounds, including normal paraffin chains (Fig. 9.1b). Mild heating of kerogen over long periods of time results in the cracking of the kerogen molecules and the release of the attached paraffin chains.

Further heating, perhaps assisted by the catalytic effect of clay mineral transformation and evaporite dewatering in the source rock matrix, may then produce soluble bitumen compounds, followed by the various saturated and unsaturated hydrocarbons, asphaltenes, and others of the thousands of hydrocarbon compounds that make up crude oil mixtures. Thus kerogen cracking is induced by burial and heating and it releases micropetroleum (a mixture of liquid and gaseous hydrocarbon products that are soluble in organic solvents) into the pore system of the source rock. The maturity and evolution of the kerogen is paralleled and indicated by increasing maceral (vitrinite) maturity (Table 9.1). Once released into the pores of the source rock, micropetroleum migrates toward the surface via secondary migration pathways and along the way a portion of this material can be trapped in a variety of reservoirs of varying quality.

The nature of the organic precursors to kerogen exerts a strong influence on kerogen structure and bulk composition, and hence on subsequent oil- and gas-generating characteristics. Source rock kerogens enriched in long chain hydrogens (aliphatics or parafins) tend to be oil-prone type I sapropelic source rocks and are associated with algal, bacterial and archaeal precursors (indicated by C_2H_6+ in Fig. 9.1a). Kerogens that are strongly depleted in long-chain hydrogens are typically type III humic (vitrinitic) source rocks, associated with organics sourced

[2]Kerogen is the solid organic assemblage in a rock that is insoluble in organic solvents and encompasses numerous macerals.

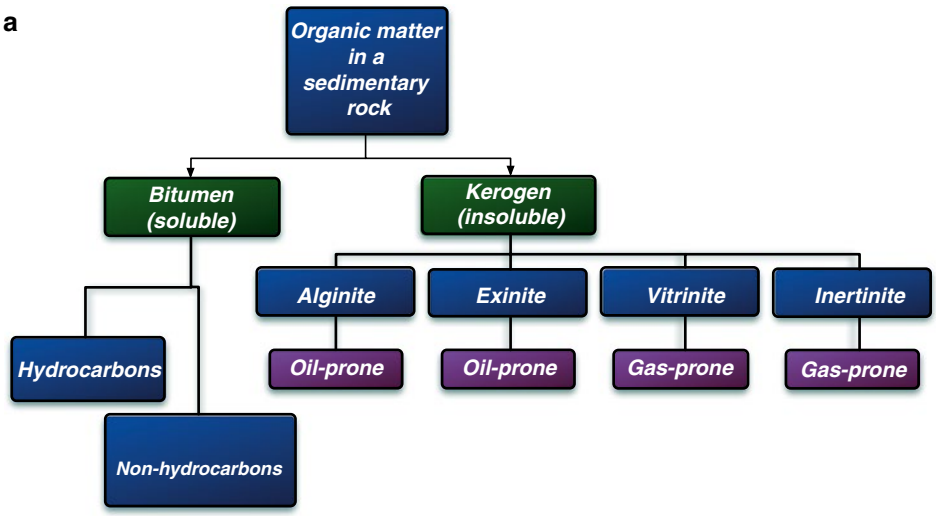

b Equivalent kerogen nomenclatures

Hydrocarbon potential	Coal petrography	Palynology	Chemistry	Rock-eval	Comments
Oil-Prone (cracking to condensate and gas)	*Liptinite*	*Algal amorphous*	*Sapropel*	*Type I (Type (IS)*	Pure algal Includes bacterial biomass.
Light oil condensate-prone	*Exinite*	*Herbaceous*		*Type II (Type (IIS)*	Cuticle gives waxy oil.
Gas-prone	*Vitrinite*	*"Woody"*	*Humic*	*Type III*	Type II can be a mix of I, III and IV. Amorphous vitrinite & oil-impregnated fluorescent vitrinite exist.
Dead carbon	*Inertinite*	*"Coaly"*	*Not recognised*	*Type IV or IIIB*	Minor gas potential from semi-fusinite.

Fig. 9.2 Kerogen (After Cornford 2005) (**a**) Simplified classification of organic matter in sedimentary rock. Bitumen is extracted from ground rock using organic solvents and consists of hydrocarbons and non-hydrocarbons. Treatment of the extracted residue with hydrochloric (HCl) and hydrofluoric (HF) acids removes most carbonate and silicate minerals, respectively and leaves behind the kerogen. This kerogen residue consists of various macerals that can be identified by organic petrography. (**b**) Approximate equivalence of terms used to describe kerogen using different techniques for its study

from higher plants (Figs. 9.1a and 9.2b). They are gas prone and the gaseous products are dominated by methane (dry gas), sometimes with associated hydrogen sulphide or nitrogen. Like hydrocarbons, hydrogen sulphide is generated both biochemically and thermochemically.

Obviously, not all source rocks are evaporitic. Organic matter accumulating in mesohaline sediment is derived from the activities of the halotolerant[3] and halophilic biomass, mostly algae, bacteria and archaea. Kerogen derived from burial of this organic matter will be composed of their somewhat altered remains, as will the expelled hydrocarbons. Sapropelic organic matter is created by decomposition and polymerization of high-lipid organic materials (with aliphatic long-chain hydrocarbons), which are commonplace in algal and bacterial sediments deposited under anaerobic conditions. Hence, sapropelic organic matter tends to be associated with oil-prone Type I or Type II proto-kerogens (Figs. 9.1b and 9.2b). Humic organic matter tends to contain less long chain hydrocarbons and so constitutes a large proportion of the more gas-prone source rocks found in coaly sediments and in dispersed terrestrial organics deposited in prodelta settings. It is mostly associated with Type III protokerogens.

Unoxidised evaporitic organic matter tend to be hydrogen-rich and oil-prone; its sapropelic kerogens (Type I or Type I-II) contain higher proportions of long chain hydrocarbons from cyanobacterial, archaeal and bacterial precursors.

[3]Halotolerant organisms can tolerate high salt concentrations but grow better at somewhat lower salinities. Halophilic organisms grow best at very high salt concentrations and can be killed by lower salinities. *Haloxene* organisms cannot tolerate high concentrations of salts.

Higher plant material, which is the source of much of the humic component in nonevaporitic kerogen simply does not accumulate in large volumes in an evaporitic source rock; higher plants need fresh water and do not flourish in hypersaline waters.

The remainder of this chapter summarises and classifies evaporitic source rocks, looks at controls on organic enrichment in saline environments, and at the styles of hydrocarbon generation and metal-fixing associated with organic-prone mesohaline evaporites in the diagenetic realm. The following chapter looks at how evaporites form the seals and traps to reservoirs that store the generated hydrocarbons.

Evaporitic Source Rocks

Mass balance calculation of oil in the global petroleum system shows that 40 % of the world's generated oil is lost to the surface, 58 % is dispersed in the subsurface as oil, gas and pyrobitumens located somewhere between source and reservoir, while 2 % is to be found in pooled accumulations suitable for exploitation (Hunt 1996). Estimated reserve volumes, plus ultimate undiscovered resources, for conventional oil and gas are about the same, each is about 2×10^{12} BOE (barrels of oil equivalent) or 3.2×10^{11} m^3.

A plot of Phanerozoic source rocks shows that more than 90 % of the world's discovered original reserves of oil and gas comes from six intervals of geological history, covering only 35 % of Phanerozoic time (Fig. 9.3a; Klemme and Ulmishek 1991). The six intervals are (Fig. 9.3b): (1) Silurian, which generated 9 % of the world's recoverable reserves, (2) the Upper Devonian (Tournisian), 8 %; (3) Pennsylvanian-Lower Permian 8 %; (4) the Upper Jurassic, 25 %; (5) the Middle Cretaceous, 29 %; and (6) the Oligo-Miocene, 12.5 %. More than 78 % of the world's oil and gas is sourced in sediments deposited in restricted or silled anoxic systems located in intrashelf basins on platforms, or in restricted areas formed by circular and linear sags. Four of the six stratigraphic intervals occurred in worldwide first-order sealevel highs (transgressions) associated with greenhouse climatic conditions and the deposition of mostly sapropelic organic matter. The other two, Pennsylvanian-Lower Permian and the Oligo-Miocene, which source 20.5 %

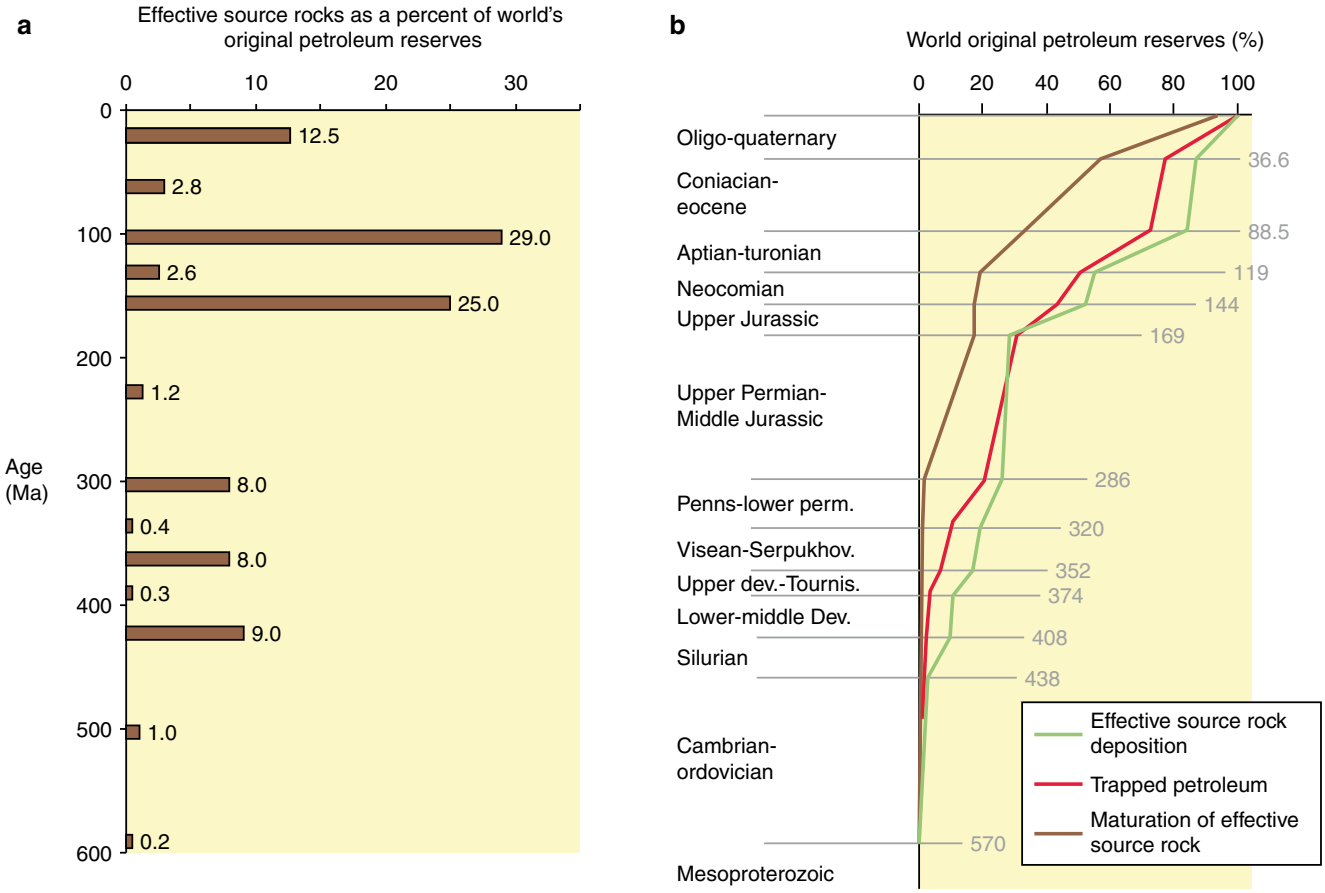

Fig. 9.3 Source rocks across time. (**a**) Time distribution of effective source rocks as a percentage of the world's original petroleum reserve generated by these rocks. (**b**) Cumulative plot of effective source rock deposition, maturation and trapped petroleum as a percentage of the world's original petroleum reserves (After Klemme and Ulmishek 1991)

of the world's oil and gas, occurred during times of lowered sea level (regressions) and deposited mostly type III kerogens (Hunt 1996). These were times of polar glaciation (icehouse climate mode). Something like two-thirds of the world's oil was generated in Tethyan basins in a system that covers less than a fifth of the world's land area and continental shelves. The efficiency of the Tethyan petroleum system, centred on the countries of the Middle East was facilitated by the deposition of widespread seals, such as the saltern anhydrites of the highly-effective Hith and Khuff formations and the basinwide halites of the Fars/Gachsaran (Chap. 10). As well, these strata experienced gentle structuration of reservoir beneath the evaporite seal via draping, sometimes in association with flow and dissolution of Infracambrian Hormuz salt, or folding of a Gachsaran Formation seal caught up in the foreland fold and thrust belt along the Zagros collision zone.

A common theme to most source rocks, both evaporitic and nonevaporitic, is that they require anoxic conditions to accumulate and preserve their organics. This in turn requires some way of restricting the influx of oxygenated waters to the depositional site and is usually accomplished by thermal or density stratification of a water body, typically in a setting where plankton flourish periodically in the upper water mass. This is why so many subaqueous evaporitic settings are also settings where organics tend to accumulate. By definition, evaporites require restricted inflow conditions to accumulate, they are also typically areas of density-stratified waters with high salinities in the lower denser more saline water mass. Levels of dissolved gases are negligible to non-existent in the lower brine body as it does not easily exchange with the atmosphere, so encouraging long-term bottom anoxia.

This does not mean all of the world's source rocks were deposited in evaporitic settings, only that the restricted conditions that favour the accumulation of evaporites are similar to conditions that favour the accumulation of some types of organic-rich bottom sediments, especially in the interval that precedes deposition of actual salts. In arid climates any minor changes in inflow conditions, such as hydrographic isolation from the ocean, can easily force a transition from one into the other. Hence the common association of source rocks with layered basin waters typical of the early mesohaline phase and the onset of evaporitic sedimentation in many lacustrine/epeiric settings (Table 9.2). In the marine realm, the same need for tectonic or eustatic restriction to create a basin suitable for source rock accumulation (intrashelf, circular or linear sag) also explains why, if further restriction and hydrographic isolation from the ocean ensues, the same region is easily covered by a sequence of salts (Fig. 5.32).

Worldwide, studies of ancient evaporitic basins have shown that organic-rich mesohaline sediments can accumulate beneath ephemeral surface brines, in salterns, or in basin and slope settings in both marine and continental settings (Kirkland and Evans 1981; Oehler 1984; Warren 1986; Evans and Kirkland 1988; Rouchy 1988; Busson 1992). The most prolific accumulations of organics in ancient evaporitic sediments tend to have been deposited as laminated micritic carbonates beneath density-stratified moderately-saline (mesohaline) anoxic water columns of varying brine depth.

There are three, possibly four, major mesohaline density-stratified settings where organic-rich laminites (source rocks) accumulate in saline settings that are also associated with, or evolve into, evaporite deposits (Fig. 9.4; Table 9.2):

1. Basin-centre lows in marine-fed evaporitic drawdown basins (basinwide salts).
2. Mesohaline intrashelf lows atop epeiric evaporitic platforms.
3. Saline-bottomed lows in perennial underfilled saline lacustrine basins.
4. Closed seafloor depressions in halokinetic deepwater marine slope and rise terrains.

Basin Setting 1: There are two depositional styles for basin-centre or basinwide mesohaline source rocks; (a) Basin-centre drawdown laminites intercalated and often sealed by basinwide salts, (b) Basin-centre laminites where the basin margin is a shallow, restricted, at times evaporitic, platform surrounding a slightly mesohaline deepwater starved-basin centre with bottom waters that were never drawndown or concentrated to where basinwide salts precipitated. Matrices in setting 1b basin-centre laminites range from fine-grained limestones through marls to siliciclastic muds.

In source setting 1a the basin is largely isolated from a surface marine connection and high levels of organics accumulate as radiogenic "black shales" (typically carbonate laminites), which are intercalated with, and overlain by, thick basinwide evaporite salts (typically halite-dominated). These laminites accumulate on the bottom of mesohaline density-stratified stagnant brine pools in topographically closed parts of the basin floor during the early stages of hydrographic isolation and drawdown. Inactive, typically subaerial, shelf margin reefs and pinnacles typically lie updip or encircle the basin-centre lows (Chap. 5). Subsequent encasement of these platform buildups and other potential reservoirs by "fill and spill" evaporites means these basins easily become highly focused hydrocarbon flow systems. Hydrocarbons accumulate in the reefs or shelf margin shoal reservoirs beneath basinwide evaporite seals. Such systems typify the marine-fed Silurian reef/Salina Salt association in the Michigan Basin, USA (Gardner and Bray 1984), the Devonian Rainbow Reef reservoirs of the Black Creek/Muskeg Basin of Alberta (Clark and Philp 1989) and Messinian marls of the Lorca Basin, Spain (Russell et al. 1997).

Table 9.2 Selected evaporitic source rocks

Formation/group, locality and age	Basin style	Characteristics and depositional setting	Reference
Messinian carbonates Lorca Basin, Spain, Late Miocene	1a Basinwide evaporite, marginal basin	Organic-rich laminated mudstones deposited in pre-evaporitic mesohaline marginal basins with density- and salinity-stratified brine columns. The basin underwent sporadic phases of circulatory restriction with marked production and preservation of organic matter, culminating in evaporative sedimentation (latest Miocene). As the water in this basin evolved toward evaporative conditions, a number of organic-rich depositional phases (>25 wt% TOC) occurred. During the early parts of these phases, the upper water was nutrient rich and comparatively normal marine, and the bottom water was anoxic and more saline. This was followed by rising salinities in the surface waters, holomixis and short phases of evaporite formation. Biomarkers in authigenic carbonates were synthesized by extremophilic (thermophilic and/or halophilic) bacteria.	Benali et al. (1995), Russell et al. (1997), Rouchy et al. (1998), Baudrand et al. (2010), Dela Pierre et al. (2012)
Gessoso-Solfifera Formation, Sicily, Late Miocene (Messinian)	1a Basinwide evaporite, marginal basin	Biomarker compositions from immature organic sulphur-rich marl samples from 10 of the 14 evaporite cycles in an Italian Messinian evaporitic basin (Vena del Gesso) indicate large variations in the composition of species in the water column (e.g., dinoflagellates, diatoms and other algae, cyanobacteria, methanogens, green sulphur bacteria and bacterivorous ciliates) and in contributions from the continent (i.e., land plants) within each marl bed and between marl beds. The marl beds were deposited within a stratified lagoon where anoxic conditions extended into the photic zone for much of the time	Damste et al. (1995), Keely et al. (1995)
Organic-rich marls, Gulf of Suez, Middle to Late Miocene	3 Rift basin, Continental to transitional marine	Inclusion studies show evaporitic environment of deposition (reducing conditions and high salinities), favoured oil generating kerogen. The oil produced from syn-rift (Miocene) reservoir rocks is a naphthenic, non-waxy crude with API gravity ranging from 27.9 to 34.9° and sulphur content between 0.88 and 0.98 wt%. These type B oils are distinguished from clastic sourced oils by a predominance of gammacerane and relatively low oleanane concentrations, suggesting that they were generated from mature marine carbonate source rocks, inferred to occur within the Upper Cretaceous Brown Limestone and Middle Eocene Thebes Formation. High sulphur oils are typically indicative of carbonate-evaporite source rocks	Kholief and Barakat (1986), Katz (1995a, b), Rouchy et al. (1995a, b), Cole et al. (1995), Dolson et al. (2001), Bakr and Wilkes (2002), Younes and Philp (2005)
Alcanar Formation (Casablanca Beds), Tarragona Basin, Middle Miocene, Offshore Spain	3 Rift, transitional	Hypersaline organic-rich carbonate marl/mudstone source rock, (gammeracene in Amposta oil). All source rocks subject to rapid maturation during rapid Pliocene burial.	Barbé et al. (1988, 1990)
Bresse and Valence salt basins, France, Paleogene	3 Rift basin, Continental to transitional marine	Organic matter is mostly immature and occurs in intercalated non-halite beds. Type III kerogen is tied to terrigenous deposition. Type I kerogen is abundant in mesohaline evaporitic laminites of Valence basin. Type II is more abundant in Bresse basin. Organics accumulated beneath a perennially stratified brine column of up to tens of metres. Syndepositional dissolution of halite may have aided the accumulation of significant amounts of oil-prone organic matter in non-soluble brecciated residues.	Curial et al. (1990)
Bituminous Limestone, Carmague Basin, France, Oligocene	3 Continent-continent collision sag	Continuous Neogene subsidence so saline lacustrine source-rocks are within oil or gas window. Sulphur- rich crude geochemistry in Gallician and Ste Cecile wells suggest confined lagoonal-saline lacustrine bituminous limestone source.	Connan and Dessort (1987), Mascle and Vially (1999)
Salt IV Formation, Mulhouse Salt Basin, Europe, Lower Oligocene	3 Rift basin, Continental to transitional marine	Biomarker assemblages are dominated by acyclic isoprenoids, especially phytane ($0.13 < Pr/Ph < 0.52$), n -alkanes with specific distribution patterns, and steranes. Large differences in distributions indicate changes in palaeoenvironment. The largest changes are in desmethyl- and methylsterane distributions and are probably linked to occasional reconnection of the stratified evaporite basin to the sea, leading to a dinoflagellate bloom in the upper waters of a density-stratified brine column.	Damste et al. (1993), Hofmann et al. (1993a, b), Hollander et al. (1993), Keely et al. (1993)

(continued)

Table 9.2 (continued)

Formation/group, locality and age	Basin style	Characteristics and depositional setting	Reference
Qom Fm., Qom Basin, Iran, Oligo?-Miocene	Rift or foreland (poorly constrained)	Laminated micritic carbonates below salt of Upper Red Formation, in a compressional basin, related to Zagros collision belt.	Shakeri et al. (2007), Morley et al. (2009)
Eocene Qianjiang and Lower Eocene-Paleocene Xingouzhui Formation of Jiangling-Dangyang area, Jianghan Basin of northwest China, Eocene-Paleocene	3 Foreland flexure basins, mountain-front fault depressions	Anoxic evaporitic lacustrine source rocks generated most of the crude oils. High salinity and low Eh enhanced preservation of oil-prone organic matter and facilitated incorporation of sulphur. Anoxia and the unusual presence of abundant sulphate as gypsum resulted in microbial reduction of sulphate to sulphide and incorporation of this sulphur into the kerogen. Biomarkers show that source rock in the Sha 13 well (1,322 m) was deposited under more saline, lower Eh conditions than the Ling 80 well (1,808 m), although both are from the Qianjiang Formation. Sha 13 sample is more organic-rich (6.62 vs. 1.27 wt% TOC), has a higher hydrogen index (794 vs. 501 mg HC/g TOC) and faster reaction kinetics. Kerogen from the Sha 13 sample is Type I because it has a high hydrogen index and an atomic S/C ratio (0.074).	Jiang and Fowler (1986), Huang and Shao (1993), Peters et al. (1996), Grice et al. (1998), Ritts et al. (1999), Hanson et al. (2001)
Green River Formation, Uinta Basin, Wyoming and Utah, Eocene	3 Foreland flexure basin from Laramide orogeny	Laminated organic mudstones and oil shales deposited in deeper anoxic bottom waters of a perennial saline and density-stratified alkaline lake. Gilsonite and tabbyite bitumens are associated with Parachute Creek Member, deposited during a major expansion and freshening of ancient Lake Uinta. Compound specific isotopic analyses of b-carotene and phytane ($\delta^{13}C = -32.6$ to $-32.1‰$) from these bitumens reflect input from primary photosynthetic producers such as cyanobacteria. Sterane $\delta^{13}C$ values (− 34.5 to −29.2‰) reflect contributions from lacustrine algae, while extremely depleted $\delta^{13}C$ values for methylhopanes (−58.1 to −61.5‰) suggest input from methanotrophic bacteria. Variations in the $\delta^{13}C$ values of the a-b-hopanes (−51.4 to 37.7‰) imply additional input from other bacterial sources. The wurtzilite bitumen generated from the saline facies of the Green River Formation was deposited during a later regression of Lake Uinta. Compound specific isotopic analyses of phytane ($\delta^{13}C = -30.1‰$) and steranes ($\delta^{13}C = -29.6$ to −26.7‰) from this bitumen indicate continued input from primary producers and eukaryotes. The higher relative concentrations of gammacerane ($\delta^{13}C = -26.9‰$) indicate increasing input from aerobic species. Slight enrichment in $\delta^{13}C$ in the wurtzilite extract (and several biomarkers) suggests sulphate-reducing bacteria outcompeted methanogens, thereby, eliminating the influence of methanotrophs in this later saline stage of deposition.	Ruble et al. (1994), Katz (1995)
Shahejie Formation, Shengli Oil Province, Bohai Bay Basin, East China, Eocene	3 Continental half-graben, Palaeogene rift with Neogene subsidence	Source rock is mainly the lower part of the Third Member (Es 3) of Eocene Shahejie Formation and is a lacustrine organic-rich dark mudstone/oil shale with good quality Type I-II kerogen at the oil-generative stage at Ro = 0.4–0.8 %. First Member (Es 1) of Oligocene portion of Shahejie Formation has excellent oil potential in the nearby Gunan Basin but is immature in the Fulin Basin. Oil and rock samples from both basins can be grouped into three major biomarker families. First family shows low Pr/Ph (<1), a high gammacerane index (>0.3) and notable beta-carotene, typical of carbonate-evaporite environments. It exists in Es 1 rocks and the related oils and is early mature [β β/(β β + α α) = 0.2–0.3], and [S/(R + S) = 0.10–0.20]. Second family shows high Pr/Ph (>1), a low gammacerane index (<0.2) and abundant 4-methyl steranes, indicative of freshwater lacustrine conditions like those in Es 3. It shows higher maturation [β β/(β β + α α) = 0.30–0.50] and [S/(R + S) = 0.35–0.55] and notable diasteranes. Third family is transitional, has source and maturity ratios between the above families, and occurs in the Es3 unit samples from the basin interior.	Chen et al. (1996), Jin et al. (2010), Wang et al. (2010)

Organic shales, Interior Basin and N'Komi rift, Cretaceous	3 Continental rift	Kissenda and Melania Shale members deposited as mesohaline lacustrine muds beneath stratified brine column, pre Aptian Salt	Kuo (1994)
Bucomazi Formation, Cabinda, offshore Angola, Cretaceous	3 Rift basin, continental to transitional marine	The Lower Congo hydrocarbon habitat is dominated by the Pre-Salt Bucomazi petroleum system. These lacustrine, often super-rich, laminated evaporitic sediments reveal considerable organofacies variations between their early lacustrine basin fill and later sheet drape development with three major depositional regimes reflecting salinity and water depth control. ^{13}C depleted basal sediments, showing strong gammacerane/4-methyl sterane signatures, were segregated by a major isotopic excursion. This event represents the transition from an early saline playa lake to a deeper water salinity-stratified mesohaline lake supporting a high level of bottom anoxia. For the intermediate sediments, sterane and tricyclic diterpane abundances, plus sterane/hopane ratios, had marine connotations and can be interpreted as the result of intermittent marine incursions. Foreshadowing irreversible oceanic ingression, a resurgence of gammacerane abundance in the uppermost sediments typified littoral-shallow marine depositional conditions.	McHague (1990), Burwood (1999), Burwood et al. (1992, 1995), Burwood and Mycke (1996), Schoellkopf and Patterson (2000), Farrimond et al. (2004), Hartwig et al. (2012)
Lagoa Feia Formation, Campos Basin, Brazil, Early Cretaceous	3 Rift basin, continental to transitional marine	Rift-stage lacustrine sediments are the source rock of all petroleum so far discovered in the Campos Basin, the most prolific oil province in Brazil. These organic-rich shales were deposited in anoxic brackish to saline lakes. Petroleum migration pathways involve direct contact between source and reservoir rocks within the rift sequence. Later migration to the marine sequence reservoirs is related to windows in the halokinetic salt layer connected to growth faults and unconformities.	Trindade et al. (1995), Mello and Maxwell (1991), Beglinger et al. (2012)
Organic rich evaporitic mudstones, Durlston and Lulworth Fms, (Purbeck LS. Group), Dorset Coast UK, Earliest Cretaceous	3 Coastal synrift lagoons and lakes at edge of carbonate platform	Total organic carbon (TOC) of up to 8.5 wt% and high hydrogen index (HI) values (up to 956 mgHC/gTOC) and biomarkers point to a Type I OM, generally considered as derived from algal-bacterial biomass. Similarities to coastal lagoons of southern Australia (Marion Lake and Coorong regions). Interpreted as responses to a period of enhanced primary productivity within salinity -stratified coastal lagoonal/lacustrine settings at times of low sea level. Biomarkers support upward freshening and presence of *Botrycoccus*	Riboulleau et al. (2007), Schnyder et al. (2009)
Neuquen Basin, Argentina Jurassic-Cretaceous (Upper Valanginian-Lower Barremian)	2 Backarc-Foreland Basins	Agrio Fm., La Manga Fm. deposited in epeiric intrashelf basin sags, transgression typically atop evaporitic/eolian continental cycles. Throughout the Jurassic and Cretaceous periods, depositional patterns were related to waxing and waning of a narrow seaway that was connected to the Pacific realm through gaps in the magmatic arc. Widespread anoxia (temp/salinity) and Type II organic matter preservation occurred in the context of peak transgressions during the Toarcian, Oxfordian, Tithonian, late Valanginian and Hauterivian. A protracted history of regular subsidence and moderate heat flow at a back-arc position, together with the presence of widespread evaporite seals, has resulted in regional zonation of the stacked hydrocarbon occurrences. Halokinesis in Huitrin Fm (Permian)	Uliana and Legarreta (1993), Carozzi et al. (1993), Urien and Zambrano (1994), Lazo et al. (2005), Tyson et al. (2005)
Kimmeridgian Shale, North Sea, Jurassic	1b Evap-carb platform surrounding sediment-starved deep marine basin centre generated by ongoing Permian-Mesozoic rifting	Seawater flowed southwards from Boreal Ocean into Tethyan Ocean but evaporation in the shallow waters of the archipelago of islands and shoals created waters of increased salinity and in some cases local strong brines and evaporites, which sank and flowed as saline bottom currents (from 34 to 42‰) into deeper water. Areas of ponded deeper mesohaline water were commonplace in the more rapidly subsiding grabens, separated by sills, denser waters accumulated until they were able to spill over the sills. In this way more saline waters migrated along the sea bottom depressions, their paths being determined by local tectonic features, but mostly in a north to south direction. A stable water stratification ensued, the halocline being at about 50 m water depth and periods of widespread increased salinity are marked by "hot" shales.	Cooper et al. (1995), Miller (1990)

(continued)

Table 9.2 (continued)

Formation/group, locality and age	Basin style	Characteristics and depositional setting	Reference
Malm Zeta, East Bavarian carbonate platform (Solnhofen), Germany (Malm)	1b Marine platform (sub wave-base)	Evaporitic platforms in an arid zone carbonate archipelago with anoxic mesohaline base to water column with density and thermally stratified bottoms in inter-reef depressions (Lagerstatten assemblages)	Schwark et al. (1998)
Shelf margin laminites in salinity-stratified intrashelf lows across the Arabian Gulf region from Syria, NW Iraq, Iran through the Arabian Gulf to central Oman (e.g., Diyab, Tuwaiq and Hanifa Formations), Upper Jurassic (Oxfordian-Kimmeridgean), also Middle Triassic Kurra Chine Dolomite in Syria and Cretaceous (Valanginian) Garau Formation in Iran	2 Density- stratified intrashelf basins surrounded by evaporitic platform. Some lows are possibly tied to salt withdrawal	Organic-rich laminated mudstones and wackestones deposited in pre-salt intrashelf, mesohaline basins on a gently downwarped epeiric platform. Intrashelf basins that retain organics all have a density and salinity stratified water column with mesohaline bottom carbonates. These basins source more than 90 % of the hydrocarbons in the Middle East. They are argillaceous dolomitic limestones that feed the most prolific petroleum system in the world and underlie the world's richest reservoir: the Arab D in the Arab Formation. One of the most prolific source units is the Hanifa Fm. in the Arabian Basin of Saudi Arabia. In the deeper parts of the intrashelf Arabian Basin (waters ≈ 30 m deep) the Hanifa is composed of laminite muds and marls, while in the surrounding shelf it is dominated by grainstones and packstones. Within the Hanifa laminites there are discrete but minor primary laminae of anhydrite (originally gypsum), as well as early diagenetic anhydrite nodules, both indicators of occasional hypersalinity. There are also laminae of fibrous calcite, which some authors have interpreted as another indicator of hypersalinity. The Hanifa is a widespread and prolific source, it can entrain more than 30 m of laminites; total organic carbon exceeds 1 %, with some sections having more than 5 %. The kerogen is predominantly hydrogen rich, the generated oils have a high sulphur content, a Pr/Py <1, and a predominance of even-numbered normal alkanes.	Ayres et al. (1982), Palacas (1984), Kirkland and Evans (1981), Evans and Kirkland (1988), Droste (1990), Beydoun (1993), Carrigan et al. (1995), Whittle and Alsharhan (1996), Fox and Ahlbrandt (2001), Ibrahim et al. (2002), Goff (2005), Abboud et al. (2005), Rabbani and Kamali (2005)
Upper Hamanlei (Antalo) Limestone Fm. Blue Nile (Abay) Basin, Ethiopia, Jurassic (Oxfordian-Kimmeridgean)	3 Intracratonic postrift? flexure sag basin	Lacustrine, schizohaline black shales/mudstones of the Upper Hamanlei (Antalo) Limestone Fm deposited in a continental intracratonic rift sag basin. These lacustrine source rocks sit atop sulphate-rich mudflat sediments of Middle Hamanlei (Gohatsion) sediments which created density stratified bottom waters via their dissolution.	Wolela (2007)
Smackover trend of Mississippi, Alabama and Sunniland of Florida, northeastern Gulf of Mexico, Upper Jurassic	2 Shallow restricted-circulation salinity stratified intrashelf basin on a broad carbonate platform	Oil and gas in this trend are generated from algal-rich light-brown to black laminated lime mudstones (argillaceous content <6 %) of the Lower Smackover Formation. Deposition occurred in intraplatform depressions surrounded by a broad carbonate platform. Bottom waters were stratified with slightly saline waters supplied from the broad platform surrounds and the shoaling carbonate system was sealed by the sulphate evaporites of the Buckner Anhydrite.	Oehler (1984)
Cifuentes Fm., Cuban Basin, offshore Cuba, Upper Jurassic (Tithonian)	2 Marine-fed rift graben, rift to drift transition	Transition to incipient ocean/passive margin carbonate platform. Marine hypersaline elevated sulphur source, similar to Sunniland oil source in Florida	Grimalt et al. (1991), Campos et al. (1996), Magnier et al. (2004)
Ionian/Adriatic basins, Offshore western Greece and onshore Albania, Upper Jurassic (Toarcian to Tithonian)	1a Synrift to postrift sag	A mesohaline stratified column in shallow restricted sub-basins in Triassic Ionian evaporitic basins. Lack of detailed stratigraphy in subsurface evaporites of Ionian zone means precise position of the shale source horizons is poorly defined but this evaporitic succession is more than 200 m thick with local mesohaline carbonate mudstones with TOC of 0.6–11.2 wt% (average 2.2 wt%).	Zappaterra (1994), Cota and Baric (1998), Rigakis and Karakitsios (1998), Karakitsios and Rigakis (2007)
Tithonian marls, Sureste Basin, Middle Jurassic	2 Platform	Massive calcareous black shales and dark grey, clayey laminated mudstones, averaging 220 m thickness, deposited under anoxic density-stratified conditions on a marine carbonate shelf	SantamarÌa-Orozco et al. (1998)

Todilto Formation, Toldilto Basin, USA, Middle Jurassic	3 Foreland flexural basin (lacustrine?)	The Limestone Member of the Todilto Fm. is a widespread carbonate laminite up to 3 m thick, overlain in the subsurface by up to 30 m of $CaSO_4$ known as the Gypsum Member, although it is mostly anhydrite. The Limestone Member is the source rock for 6 known hydrocarbon accumulations in the sands of the underlying Entrada Fm, while it and the overlying $CaSO_4$ are the seal. The quantity of TOC is low (≈1 %) for such a thin source rock and it has some unusual characteristics compared to most evaporitic source rocks. Laminite couplets are 0.15 mm thick yet are laterally continuous for up to 3.7 km and form widespread cohesive "sheets", which invariably contain remnants of vascular plants. The Todilto is probably lacustrine with a marine seep hydrology, similar in hydrology to the coastal salinas of southern Australia. The organics reflect the growth of a healthy conifer cover in its surrounds and its waters were density-stratified lacustrine, probably fed via a marine seepage inflow and periodic seasonal runoff. This maintained a density-stratified brine column, first at carbonate saturation during deposition of the Limestone Member, then at gypsum saturation during the deposition of the Gypsum Member.	Vincelette and Chittum (1981), Evans and Kirkland (1988)
Offshore east coast of USA, Middle to Lower Jurassic	2 Rift	Epeiric carbonate platform margin with local deeper-water anoxia in part related to anoxic slightly saline marine bottom	Sassen and Post (2008)
Dagorda Fm, Coimba Fm, Benha Fm., Lusitanian Basin, Offshore Portugal, Lower Jurassic	1b Rift to post rift sag	Laminated organic-rich mudstones, deposited in density-stratified waters in a post-rift thermal subsidence sag depression. Setting similar to Kimmeridgian shale in North Sea?	Kassler (1979), Uphoff (2005)
Posidonia Shale Beds, Mittelplate Oil field, Germany, Central European Basin, Lower Jurassic	2 or 4 Euxinic rim syncline depressions	Epeiric shelf seaway (Taorcian), with evaporitic platform highs possibly underlain by Zechstein salt structures, that is, restricted anoxic sea floor depressions in topography created by halokinetic Zechstein Salt	Littke (1993)
Manari Fm, Pirara Fm, Takutu Basin, Guyana, Early Jurassic (Taorcian?)	3 Rift, Lacustrine	Laminated grey brown micritic shale with Type I/II kerogen. Deposited at 2 degrees N palaeolatitude in an intracratonic Jurassic rift valley	Webster (2004)
Carnian "Kueper" Basin, NW Jordan	2a Intracratonic (postrift sag basin)	Organic-rich shales are common, especially as part of evaporite–carbonate cycles. Black shales from RH-1 well (850–1,380 m) are slightly carbonaceous, non to slightly calcareous with amorphous organic matter and some miospores and plant tissue. (rapidly subsiding intraplate epeiric basin, possibly depositionally analogous to Purbeck Group on Dorset coast)	Dill et al. (2012), Makhlouf and El-Haddad (2006)
Organic mudstones intercalated with evaporites, Mandawa Basin, Tanzania, Triassic	3 Rift basin, continental to transitional marine	Total organic carbon (TOC) values range from 1.23 to 7.41 % (wt) of kerogen Type II/III. The evaporite (hypersaline) influence is indicated by the presence of C-24-tetracyclic terpanes, gammacerane and C-35- homohopanes. The relative abundance of tricyclic terpanes (C-19-C-28 +) with respect to pentacyclic terpanes (C-27-C-35,) seem to change with depth, whereby the tricyclic/hopanes ratio apparently increases with depth. The mixed organic input from marine and terrestrial precursors are indicated by mixed abundances of C-27-, C-28-, C-29- steranes.	Kagya (1996)
Morondava Basin, Madagascar, Liassic	3 Rift to drift	Andafia Fm (Jurassic) and more local Sakamena Fm (Permo Triassic) Fm. Towards the end of the rift period, restricted marine conditions resulted in the deposition of Liassic evaporites in Madagascar, Tanzania, Kenya, Ethiopia and Somalia. Geochemical work by the EARHS identified an outstanding regional source-rock in association with these evaporites in Madagascar and Tanzania	Rayer and Slind (1999)
Irati Formation, Parana Basin, Brazil, Upper Permian (Artinskian)	3 Intracratonic sag	Irati Formation (upper Assistencia member) deposited in an intracratonic, schizohaline lacustrine depression as a bituminous shale (made up of black laminated mudstones with TOC up to 16.3 %)	De Araújo et al. (2005), Santos et al. (2009)

(continued)

Table 9.2 (continued)

Formation/group, locality and age	Basin style	Characteristics and depositional setting	Reference
Oil Shales, Junggar Basin, NW China, Upper Permian	3 Controversial, with tectonic interpretations ranging from foreland flexure to regional transtensional basin	Junggar Basin is one of the largest oil-producing basins in China, its Upper Permian oil shales are among the thickest and richest lacustrine source rocks in the world. Together the Jingjingzigou, Lucaogou, and Hongyanchi Formations of the southern Junggar Basin comprise over 1,000 m of organic-rich lacustrine facies. They record an evolution from relatively shallow, evaporative lakes to freshwater lakes with fluvial systems. Jingjingzigou Formation was deposited in a perennial saline lake characterized by low TOC and HI, and biomarker features (such as abundant β-carotene) consistent with a specialized saline or hypersaline biota. Biomarker distributions in Jingjingzigou Formation extracts most closely resemble oils from the giant Karamay oilfield. Overlying Lucaogou Formation represents one of the richest and thickest lacustrine source rock intervals in the world, yet it contradicts conventional lacustrine source rock models in at least two important aspects. First, deposition occurred at middle palaeolatitudes (39–43° N) rather than in the tropics. Second, limited nutrient supply in a drainage basin dominated by intermediate volcanic rocks appears to have caused low to moderate primary productivities. Stable salinity stratification and low inorganic sedimentation rates in a deep lake nonetheless resulted in deposits with up to 20 % TOC and HI near 800. Overlying Hongyanchi Formation has 1–5 % TOC but low HI, and was deposited in freshwater oxic to sub-oxic lakes.	Carroll (1998), Carroll et al. (1992), Tang et al. (1997)
Ravnefjeld Formation, East Greenland, Upper Permian	3 Rift basin, continental to transitional marine	The Ravnefjeld Formation is subdivided into five units that can be traced throughout the Upper Permian depositional basin. Two of the units are laminated and organic rich, and were deposited under anoxic conditions. They are considered good to excellent source rocks for liquid hydrocarbons with initial average TOC (total organic carbon) values between 4 and 5 % and HI (hydrogen index) between 300 and 400. The cumulative source rock thickness is between 15 and 20 m. The source rocks are separated and enclosed by three units of bioturbated siltstone with a TOC of less than 0.5 % and an HI of less than 100. These siltstones were deposited under relatively oxic conditions. The organic geochemistry of the source rocks is typical for marine source rocks with some features normally associated with carbonate/evaporite rift environments [low Pr/Ph (pristane/phytane), low CPI (carbon preference index), distribution of tricyclic and pentacyclic terpanes]. The establishment of anoxic conditions and subsequent source rock deposition was controlled by eustatic sea level changes.	Christiansen et al. (1993)
Ucayali Basin, Middle-Late Permian	3 Foreland basin	Ene Fm., passing from marine carbonate (Copacabana Fm) up into evaporitic continental/volcanics	Mathalone and Montoya (1995)
Fish River Subgroup, Nama Group, Nama Basin, Namibia, Early Permian, (Artinskian)	3 Rift	Organics form Permian saline Lake hosted in calcite vein fill in sub-unconformity Cambrian host. Saline lacustrine indicated by abundant gammacerane, β-carotene and 3b-methylhopanes while 24-isopropyl cholestanes and dinosteroids not detectable. Saline lacustrine equivalent to Irati Fm (Perm.) in Brazil	Gierlowski-Kordesch and Kelts (1994), Summons et al. (2008)
Phosphoria Formation, Little Sheep Creek, Montana, Permian	1b Foreland flexure basin	Correlations between biomarker indicators of anoxia and salinity suggest that anoxia was in part the result of a chemocline separating normal marine waters above from more saline bottom waters. Anoxia and salinity in the bottom waters increased with time making conditions in the basin progressively more hostile to benthic organisms.	Dahl et al. (1993)
Kupferschiefer Formation, NW Europe, Permian	1a Rift basin, restricted marine	Thin, widespread organic-rich laminated mudstone deposited in shallow mesohaline marginal sea-lakes with waters which were <100 m deep and mostly 10–30 m deep. Surface exchange with Zechstein ocean was restricted by palaeohighs.	Bechtel and Puttmann (1997), Slowakiewicz and Mikolajewski (2009)

Sub salt-allochthon oil seeps, Windsor Group, Nova Scotia, Canada, Carboniferous	3 Rift basin, continental to transitional marine	The oil seeps are either associated with upper Horton Group (Ainslie Formation) or basal Windsor Group (Macumber Formation) sediments. The biomarker distributions of the samples are similar to Stoney Creek oils and their lacustrine carbonate source rock (Albert Shale) of the Moncton Sub-basin, New Brunswick, as are oils from seeps in the Pugwash Salt mine.	Fowler et al. (1993)
Black shales in the Paradox Member of the Hermosa Formation, Paradox Basin, USA, Carboniferous (Pennsylvanian)	1a Foreland flexural basin	Organic-rich black shales (informally known as the Cane Creek, Chimney Rock, Gothic shales) form a carbonate laminite basal sequence to a number of salting-upward evaporite cycles in the Paradox Member. Mineralogically the shales are between 30 and 50 % calcite or dolomite with clays and quartz sand forming the remainder of the matrix. TOC values of 5 % of hydrogen-prone organics in the black shales are usual, with values of 10 % not uncommon and the highest values more than 20 %. The organics are mixtures of halotolerant debris and marine-style organics formed when surface waters were at marine salinities, as well as occasional terrestrial organics washed into the basin from the surrounding hinterland.	Evans and Kirkland (1988), Hite et al. (1984)
Anhydritic lacustrine beds, East Shetland Platform, North Sea, Middle Devonian	3 Rift basin, restricted marine	The UKCS well 9/16–3 drilled on the western flank of the Beryl Embayment indicates local development of hypersaline environments equivalent to the Achanarras/Sandwick fish bed. Shows close affinity with contemporaneous Middle Devonian source rocks of the Inner Moray Firth and crude oil in Beatrice oil field.	Duncan and Buxton (1995)
Muskeg Formation and Lower Keg River Member, Alberta, Devonian Canada	1a Rift basin, restricted marine	Laminated organic-rich bituminous mudstones deposited in pre-evaporitic density stratified water columns. Vertical migration from the Muskeg formation to the Muskeg Reservoirs may have occurred through local fracturing of anhydrites driven by the dissolution of Black Creek halite.	Clark and Philp (1989), Stasiuk (1994)
Pricaspian Basin, Kazakhstan, Devonian and Permian evaporites	1a Rift to foreland at onset continent-continent collision	Izembet (Zilair) Formation and equivalents, as well as Carboniferous black shales. Deposited as hypersaline carbonate source rock (black shales) contemporaneous with Devonian depositional shelf reservoirs and Kungurian (foreland) base salt in Karachaganak, Zhanazhol oils and Astrakhansk condensate (Precaspian basin)	Chakhmakhchev and Suzuki (1995), Ulmishek (2001a), Gürgey (2002)
Devonian oils, Appalachian Basin	1a Epeiric intracratonic margin passing into foreland basin	Hydrocarbon coats on mesogenetic quartz cements in Ohio portion of Appalachian basins (foreland basin) show some hypersaline source affinities, similar to Michigan Basin.	Obermajer et al. (1998), Dix and Robinson (2003)
Laminated evaporitic, A-1 mudstones, Michigan Basin, Silurian	1a Rift basin, restricted marine	Biomarker characteristics indicate a carbonate/evaporite source rock deposited under hypersaline conditions in a strongly reducing environment. The source rocks occur in the basin centre in organic-rich laminites of the inter-reef A-1 Salina Formation, a mesohaline carbonate deposited beneath a density stratified brine column.	Gardner and Bray (1984), Obermajer et al. (1998), Obermajer et al. (2000)
Oils, Tarim Basin, Tabei Uplift, NE China, Cambro-Ordovician	1b Platform, intracratonic sag	Evaporitic source rock (limestone and dolomite interbedded with mudstone and sulphates) in central and northern parts of basin (also Ordovician). Biomarkers indicate some source rocks (Tabei) come from diaromatic carotenoids of photosynthetic sulphur bacteria	Liu et al. (2003), Sun et al. (2003)
Chandler Formation, Amadeus Basin, Australia, Lower Cambrian	1a Foreland flexure	Thin bituminous pre-evaporitic carbonate mudstone deposited subaqueously in a restricted basin immediately prior to the deposition of the thick halites of the Chandler Formation.	Bradshaw (1988)

(continued)

Table 9.2 (continued)

Formation/group, locality and age	Basin style	Characteristics and depositional setting	Reference
"Q" oil associated with Ara Salt, south Oman Salt Basin, Oman Neoproterozoic-Early Cambrian	1 Rift then collision	The Q oil family is highly unusual and distinct from the more prevalent Huqf oil family by having an extraordinarily high C27/C29 sterane ratio and $\delta^{13}C$ values near −30‰. Tends in the patterns of norsteranes in south Oman carbonate stringer oils suggest the Q oil source originates from one of the upper units of the Ara carbonate and evaporite sequence likely a siliciclastic source rock lying stratigraphically above the A6 carbonates The high relative abundances of 24-isopropylcholestanes in Q oils likely originate from demosponges and the 17-methylpentatriacontane, which is so abundant in Q oils, is a biomarker for early arthropods that inhabited the salt basins of Oman at the very beginning of the Cambrian Period.	Grosjean et al. (2012)
Hormuz Series, Arabian Gulf and counterparts in India and Pakistan, Neoproterozoic to Early Cambrian	1 Rift basins, restricted marine	Almost all the Persian Gulf and large areas of southern Iran and northeastern Arabia are underlain by a thick sequence of sediments, known as the Hormuz Series. It is made up of interbedded salt, anhydrite, dolomite, shale and sandstone. It is not only the cause of many salt-dome-related oil and gas fields but is also considered to have been a major source rock for hydrocarbons in Ordovician, Devonian, Carboniferous, Permian and perhaps younger reservoirs. These oils have characteristic biomarkers and highly depleted carbon isotopes signatures indicative of their prokaryotic precursor.	Alam and Ahmed (2008), Amthor (2000), Edgell (1991), Grantham et al. (1988); Peters et al. (1995), Quadri and Quadri (2003), Schoenherr et al. (2007a, b, c, 2009)
Browne Fm, B1, B2 and B4 members, Officer Basin, Neoproterozoic (780–800 Ma)	1a Postrift sag	Organic rich, laminated dolomites interlayered with evaporites, kerogens are now mostly overmature	Apak et al. (2002), Ghori (2002), Craig et al. (2013)

See Fig. 9.7 for location

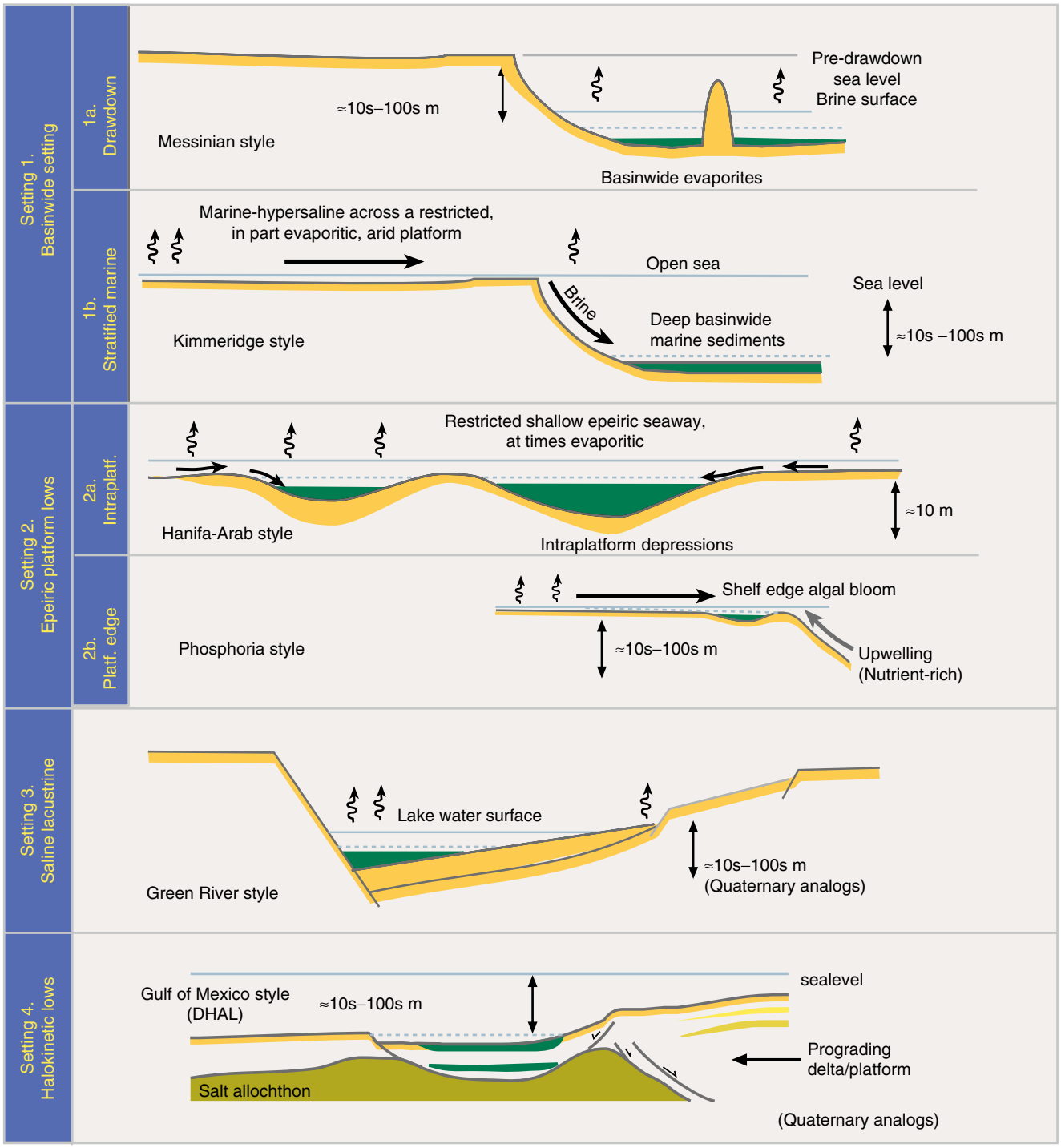

Fig. 9.4 Dominant depositional styles for evaporitic source rocks (*shaded green*). All the water bodies show evidence of salinity-related density stratification (indicated by *dashed line*), this is also reflected in an associated heliothermic stratification. (*DHAL* Deepsea hypersaline anoxic lake)

Expulsion efficiencies suffer from encasement and widespread salt plugging of the potential source rocks in many evaporite-rich setting 1a basins. This tends to retain volatiles in the source beds until the whole system becomes overmature. For example, in the Gibson Dome No, 1 well, in the Paradox Basin almost all of the black shales intercalated in the halite cycles in the Paradox Member are mature enough to have generated oil (Hite et al. 1984). But the hydrocarbons have been largely retained in this mature source rock, reflecting the highly efficient sealing effects of the intercalated evaporite beds and salt cements (mostly halite). Only where the black shales are intercalated or in contact with porous

carbonates have the hydrocarbons escaped. The source potential of these shales is very high; the "Gothic shale" is capable of generating almost 5,000 barrels per acre. But that potential is never more than partially realised. Paradox "shales" are responsible for an accumulative production of a little more than 400 million barrels of oil and about 1 TCF of gas in the Paradox Basin in fields such as Ismay and Aneth (Peterson and Hite 1969).

This problem of evaporite plugging plagues many basinal source rocks where the basin centre evolved to accumulate basinwide evaporites and is one of the main reasons for the dearth of large onshore oilfields beneath bedded salt or within intrasalt carbonates in the Zechstein basin of NW Europe. Organic-rich source intervals such as the Stinkdolomit, Stinkkalk, and Stinkscheifer are widespread, but the associated oil accumulations are never more than localised and small scale. Setting 1a sediments can be characterised by very rich organic source beds but the intercalated seals prevent most of the volatiles from ever escaping into a reservoir. In the South Oman Salt basin this source-seal association characterises earliest Cambrian intrasalt source rocks that supply hydrocarbons to intrasalt carbonate stringer reservoirs (Grosjean et al. 2009). In even older examples, where formerly thick salt has been leached and basin temperatures extended beyond the oil window into the greenschist metamorphic realm, such episodes of later burial dissolution of salt facilitates contact of formerly encased organics with basinal waters carrying Cu, Pb and Zn. The newly released volatiles and kerogens in these systems can play an important role as reductants and metal fixers, as in the Mesoproterozoic Pb-Zn laminates in McArthur Basin, NW Australia, that, (Warren 2000b).

Basin Setting 1b: Basin-centre mesohaline accumulations in this setting are much more efficient petroleum producers than style 1a as they lack intercalated beds of basinwide halite or anhydrite, which otherwise plug and cement source intervals. Style 1b source rocks develop where dense mesohaline bottom waters pond in the deeper parts of deep density-stratified restricted-marine basins. Slightly elevated bottom brine salinities are maintained by a series of dense brine underflows, fed from nearby shoalwater evaporitic platforms (Fig. 9.4). A deepwater "marine" centre typifies such basins, along with widespread evaporitic and shoal water carbonate sediments in the surrounding platforms and shelves. Setting 1b basins are best thought of as stunted or underdeveloped basinwide evaporite systems. Development of the basinwide evaporite hydrology was suspended prior to the basin centre drawdown reaching the state of complete hydrographic isolation, which is needed for widespread salt precipitation. Evaporitic conditions (mostly bedded anhydrites) dominated on isolated platform depressions about the basin margin. Typical examples of this style of association are Kimmeridge shales of the North Sea (Miller 1990; Cooper et al. 1995), organic-rich laminites of the Cherry Canyon Formation in the Permian Delaware Basin of West Texas (Jones 1984), the Devonian Woodford Shale in the US midcontinent (Comer 2012) and possibly some of the Devonian laminites of the Alberta Basin (Clark and Philp 1989).

In this setting, waters in the deepwater basin centre remain starved of sediment and density-stratified, with the upper less saline part of the water column typified by normal marine water maintained through surface connections to the open ocean. The little sediment matrix that does accumulate in the basin centre settles into an anoxic thermally/density stratified bottom so that the sediment matrix of the source laminites is dominated by a planktonic or nektonic biota and a more or less constant elevated organic content. Carbonate banks or reefs in the surrounding platform grade landward through lagoonal and evaporitic platform facies in to terrestrial clastics. At times of slightly lowered sea level these epeiric platforms can go evaporitic and so deposit widespread platform salts (Chap. 5). Such basins show a centrifugal salinity gradient where the highest salinity areas are in the surrounding shallow evaporite platforms, which supply dense saline waters that trickle and seep basinward to pond in seafloor lows at the anoxic base of a density stratified water column.

With setting 1b, the formation of evaporites and saline waters about the basin edge is not typically followed by the deposition of basin-centre evaporites. At the time the deepwater organic laminites are accumulating, the deep basin centre waters lie at the bottom of the thick density-stratified water column in a semi-enclosed seaway. Bottom brines may be no more than 3–5‰ more saline than the normal marine waters. For example, at the time the Purbeck evaporites were accumulating on the adjacent platform, the anoxic bottom waters in the marine basin centre, atop the accumulating Kimmeridge shales, had salinities around 42‰, temperatures ≈30 °C and densities ≈1.0270. The overlying near normal marine waters had salinities of 34–39‰, surface temperatures of 26 °C in the south and as low as 6 °C further north in the region of the Boreal Ocean inflow and densities around 1.0267 (Miller 1990).

Basin Setting 2: Upper Jurassic source rocks of the Middle East are well studied examples of the epeiric shelf or marine evaporitic platform settings and typify style 2 source rocks, which are deposited within local somewhat deeper, density-stratified mesohaline intrashelf lows (Fig. 9.5; Table 9.2; Ayres et al. 1982; Evans and Kirkland 1988; Droste 1990; *pers obs*.). In the Tethyan of the Middle East this style of source rock feeds a petroleum system that is probably the most efficient in the world. It evolved from Upper Jurassic source rock accumulators (typically with TOC's ≈1 % and occasionally up to 6–10 %) into evaporitic mudflats sealing the mostly bioclastic reservoirs of the

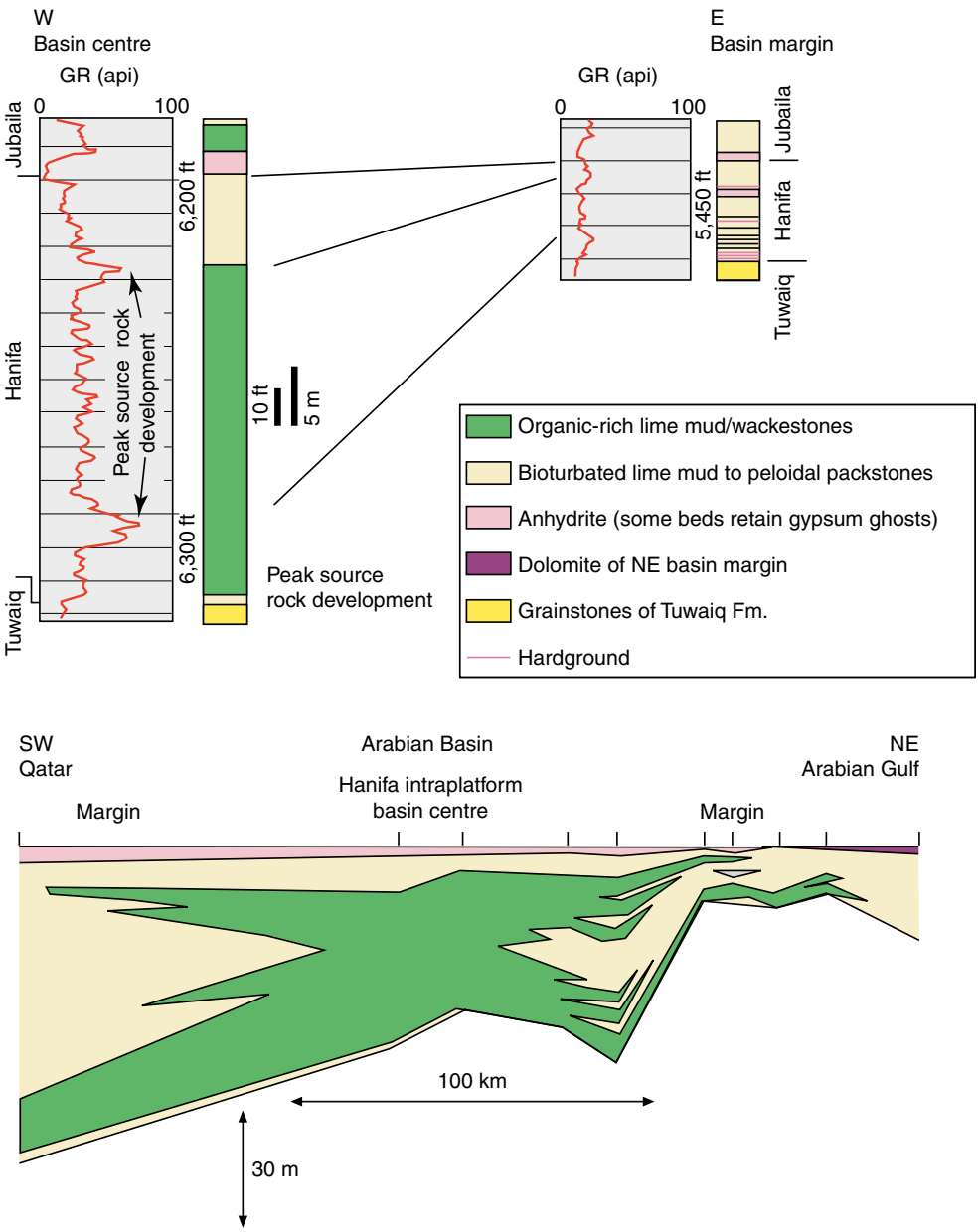

Fig. 9.5 Characteristics of the Hanifa Formation, Saudi Arabia, a setting 2 intraplatform basin source rock that was deposited beneath relatively shallow and anoxic mesohaline bottom waters in a slight depression on the shelf and was surrounded by epeiric evaporitic sedimentation, as indicated by the presence of anhydrite in the Hanifa Fm (After Droste 1990). Peaks in the organic content of these carbonate mudstones are indicated by peaks in the gamma curve. Cross section is redrafted from Carrigan et al. 1995

carbonate platform of the Arab cycles, beneath the regional Hith Anhydrite seal, which was deposited on a saltern-covered platform (Fig. 10.8). The laminite source rocks in the various intrashelf depressions were deposited at times of widespread epeiric carbonate deposition and stagnant oceanic circulation.

It was a time when much of the Arabian platform was covered by a warm shallow greenhouse sea precipitating varying combinations of carbonates and evaporites. Denser warmer waters, generated by evaporation of epeiric waters and water of the surrounding evaporitic mudflats, were concentrated to where they were somewhat more saline than normal seawater. Dense brines then trickled and seeped over the shallow seafloor into the lower parts of restricted intrashelf basins, to create density-stratified water bottoms that were not more than tens of metres deep and no more than 10–30‰ more saline than seawater (Ayres et al. 1982). Ongoing mixing and dilution of the bottom-hugging brines during their passage to the lows meant the basal water mass in the intrashelf lows, although saline, rarely attained gypsum saturation (mostly mesohaline anoxic brines). The overlying column was usually near normal marine salinity. Salt withdrawal and dissolution of salt diapirs and allochthons, sourced in the Precambrian Hormuz salt, perhaps helped create the intrashelf depressions and may also have played a role in generating a portion of the bottom brines. As for the source rocks of the style 1b Kimmeridge Clays where

halokinesis and salt solution of Zechstein mother salt played a role in generating local briny anoxic bottoms, so too in the Jurassic of the Middle Eas (Clark et al. 1999).

Thus, one of the most prolific intrashelf source rocks in the Middle East, the Hanifa Formation, was deposited in the intrashelf Arabian Basin of Saudi Arabia (Figs. 9.5 and 10.14; Droste 1990). It sources most of the hydrocarbons reservoired in the Arab cycles of Saudi Arabia and is regionally sealed by the Hith Anhydrite. The organic-rich portion of the Hanifa, deposited in the "deeper" parts of the intrashelf basin (waters ≈ 30 m deep), is composed of laminite muds and marls, while in the surrounding Arabian shelf it is dominated by grainstones and packstones. All Hanifa facies can be locally overprinted with later anhydritic burial and reflux cements and later diagenetic dolomites. As the various depressions filled with laminites they shallowed to where the stratification was lost and the sediment became an open marine packstone-wackestone, equivalent to sediments deposited over the rest of the Arabian Platform.

Later episodes of hydrographic isolation of the platform, via buildup of a transgressive platform rim and a slight fall in sea level, then drove deposition of anhydritic saltern or mudflat caps of the various Arab cycles A-D and ultimately the deposition of the regional Hith Anhydrite seal (Fig. 10.14). Within parts of the Hanifa laminites there are discrete laminae and thin beds of primary anhydrite, as well as early diagenetic anhydrite nodules, both indicators of periodic hypersalinity. Likewise, the restricted evaporitic caps to some of the source cycles in basin margins to the Hanifa Formation in the Arabian Basin can locally preserve aligned gypsum ghosts, indicating a subaqueous gypsum precursor in the shallower parts of the epeiric seaway (Fig. 9.5). Similar, but volumetrically less prolific, intrashelf source rocks characterise parts of the Lower Smackover Formation (Upper Jurassic) of the northeastern Gulf of Mexico, as in the Mississippi Interior Salt Basin (Oehler 1984), and parts of the Cretaceous Sunniland Formation of Florida (Palacas et al. 1984).

A variation on this density-stratified mesohaline epeiric platform-depression style of source rock accumulation is the phosphate and organic-rich sediment of the Phosphoria Formation in the USA (Stephens and Carroll 1998). This laminated unit sources much of the oil in Wyoming and was deposited in shelf edge depressions of the Phosphoria Sea adjacent to an area of marine upwelling. The nutrient- rich waters facilitated algal blooms near and atop the shelf edge, while bottom-hugging brines, seeping seaward from the evaporitic hinterland, ponded in stagnant shelf edge depressions. Overlap of the two systems created local anoxic shelf-edge mesohaline depressions with anoxic bottom waters that preserved a rain of organics detritus from the overlying algal blooms (Fig. 9.4). This system requires an epeiric evaporitic hinterland to supply bottom-hugging brines and, like the saltern-sealed Jurassic intrashelf depressions of the Middle East, has no modern counterpart.

Basin setting 3: These source rocks accumulated in sediment-starved or underfilled saline lakes in arid climates. The laminites typically accumulated in the early continental stage of infill in an opening rift, prior to its opening into a marine-fed marginal evaporite basin, or in the restricted lacustrine stage of a foreland flexure in a collision belt (Figs. 5.32 and 9.5). Modern underfilled saline rift lakes have some of the highest rates of organic productivity known and can accumulate high levels of organics within carbonate laminites. Some of these lacustrine laminites accumulate beneath deep density-stratified water columns, while others accumulate as "moat facies" or microbial mudflats about lake margins (Fig. 9.6; Table 9.2). The likelihood of numerous water level changes during the life of a saline lake especially effect laminites deposited in shoal water moats and margin mudflats and so can lower their preservation potential (Bohacs et al. 2000). Most oil-prone style 3 lacustrine source rocks were deposited at the bottom of perennial salinity-stratified hydrologies, with water column depths measured in metres to tens of metres, not as subaerially exposed algal mudflats. Examples include the Wilkins Peak Member of the Eocene Green River Formation, USA, the Lagoa Feia Formation of the Alagoas portion of the Campos Basin in Brazil, the Bucomazi Formation in offshore West Africa and the Jingjingzigou Formation in the Junggar Basin, China (Table 9.2).

The desiccation needed to form underfilled lacustrine succession typically means that saline lacustrine phases have lesser aerial extents compared to times of freshwater deposition. But this does not necessarily mean the evaporitic lacustrine source rocks are less prolific than their freshwater counterparts. Within the Green River Formation there are two associations (fresh and saline) of lacustrine organic laminites exemplified by the Luman Tongue and the Laney Member (Fig. 9.6a; Horsfield et al. 1994). The Luman Tongue consists of organic-rich mudstones deposited as profundal sediments at a time when lake waters were relatively fresh. Proximal organic-poor sediments, as well as coals and thin sandstones, were deposited in the lake plain. The highest levels of TOC in the Luman Tongue are found in lake margin deposits, which contain a mixture of alginite and vitrinite, but they have a low hydrogen index and a low petroleum generation potential (Fig. 9.6b, c). In fact, the petroleum generation potential of these freshwater deposits is no more than moderate.

In contrast, the organic percentages of the carbonate laminites of the Laney Shale are much higher (6–22 %) and they are hydrogen prone. The most organic-rich samples were deposited in the lowest parts of the lake and are composed mostly of alginite with relatively minor contributions from higher plants. The much higher petroleum potential of the

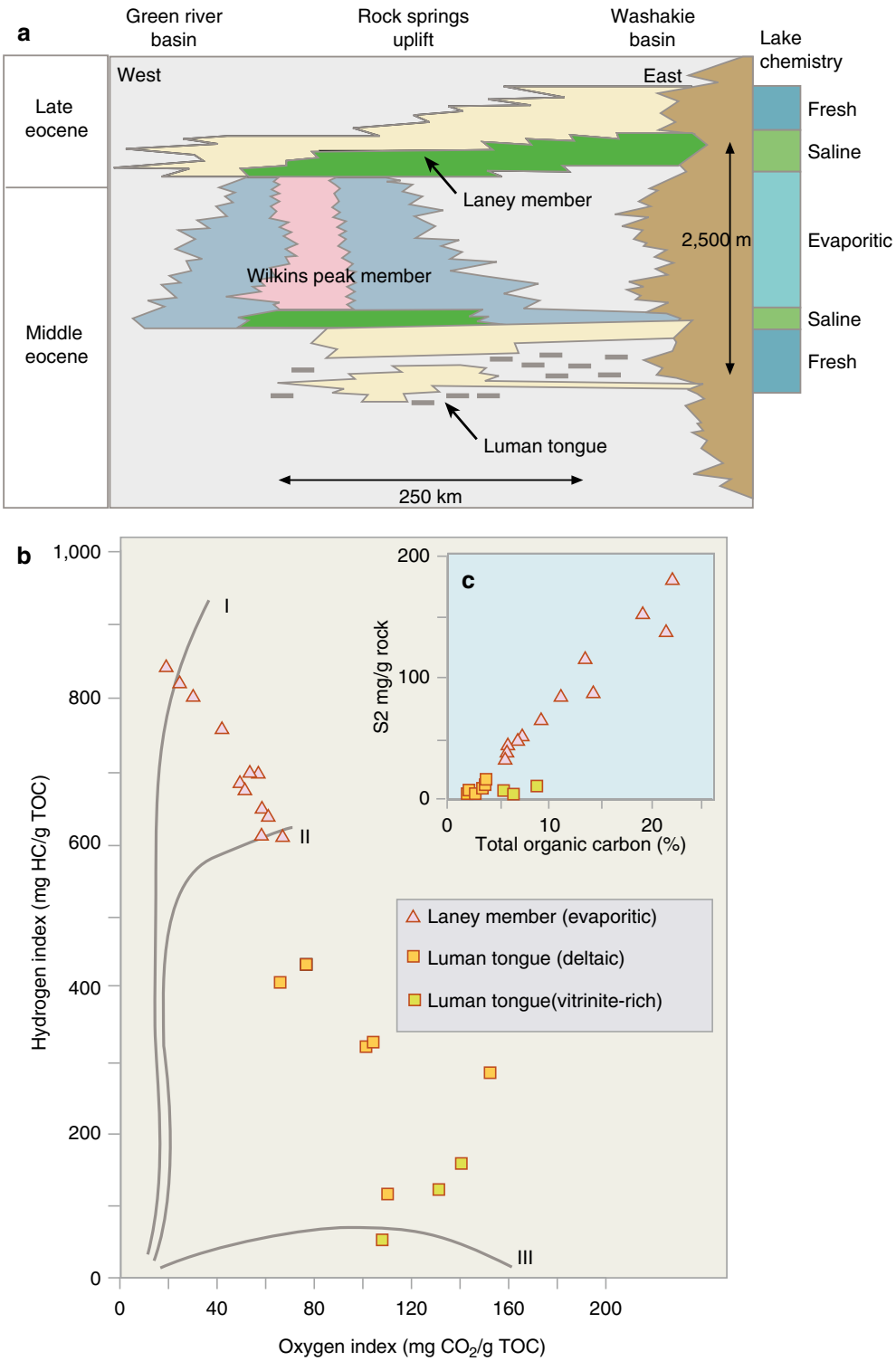

Fig. 9.6 Kerogen character of Laney Member and Luman Tongue of the Eocene Green River Formation, USA. (**a**) Schematic E-W cross section showing lateral extents and thicknesses of various lacustrine units (After Bohacs et al. 2000). (**b**) Hydrogen and oxygen indices. (**c**) Pyrolysis yields of hydrocarbon-equivalents (mg/g rock) plotted against organic carbon percentages (**b**, **c**: After Horsfield et al. 1994)

Laney shale reflects the marked density stratification of Lake Gosiute waters at the time the Laney was accumulating. At that time bottom anoxia was stabilised by the perennial highly saline bottom waters (Fischer and Roberts 1991). The vertical transition from saline lacustrine Jingjingzigou Formation to the highly prolific brackish oil shales of the lacustrine Lucaogou Formation in the Permian Junggar Basin of NW China may represent a similar dissolution-induced transition in the lake water column and help explain the lakes unusual latitude (Table 9.2; Carroll 1998).

Fig. 9.7 Worldwide distribution of evaporite-related source rocks named with respect to hosting basins (Replotted from Salt-Work GIS database version 1.7 see Table 9.2 for bibliographic details)

Basin Setting 4: is an increasingly documented open-ocean evaporite-associated source rock setting where density-stratified saline bottom brines and organic-enriched laminites accumulate in brine-bottomed depressions atop and adjacent to shallow and dissolving salt allochthons (Fig. 9.4). With burial these laminites may act as source rocks, but unlike the restricted settings of the preceding three styles, deposition typically occurs beneath open marine water atop continental slope and rise sediments. The laminites accumulate on the floor of deep brine pools that form on or near the margins of actively flowing and dissolving shallow salt allochthons. This association is discussed in detail later in this chapter and it is also a significant setting for the formation of base metal-hosting laminites as in Tunisia and the Red Sea (Warren 2000b). As yet it is not a widely documented environment for hydrocarbon source rocks, but it may in part explain the higher than expected source potential of many prodelta and slope muds in the passive margin fill of evaporite-floored halokinetic rifts.

Source rocks of settings 1a, 2 and 3 are typified by the accumulation of mm-scale layers of oil-prone organics typically in a matrix of fine carbonates. Setting 1b typically contains higher levels of siliciclastic fines and in many cases is a basinal marl or occasionally a laminated siliciclastic carbonate shale. The matrix of setting 4 laminites tends to be composed of whatever detrital sediment is accumulating atop the salt allochthon. In many situations, such as the Gulf of Mexico and the Mediterranean allochthon terranes, this matrix is a siliciclastic mud/clay laid down at the distal ends of prodelta wedges. In others, such as the Jurassic and Cretaceous of the Arabian Gulf and the Triassic of Tunisia, the matrix was carbonate mud.

The presence of mesohaline and marine carbonate muds, rather than aluminosilicate clays, in the matrix of many organic-rich evaporitic source rocks can change maturity and migration parameters. Mesohaline carbonate source rocks are susceptible to early generation of bitumens and volatiles compared with terrigenous shales. The proportion of bitumens (extractables) in the organics of carbonate source rock is high compared to that of shales as most mesohaline carbonates are largely isolated from high levels of terrigenous influx and the associated load of "spent" or oxidised organic matter (Warren 1986). For the same reason much of the early asphaltic product in a mesohaline carbonate laminite begins to migrate early in the burial history, whereas similar materials are held longer in the lattice of aluminosilicate clays (Warren 1986; Cordell 1992). Espitalie et al. (1980) showed that carbonate source rocks are likely to provide larger volumes of hydrocarbons for pooling than analogous terrigenous shales for the same levels of TOC. Geochemical analyses show that heavy oils from carbonate source rocks can form at marginally mature stages and at lower temperatures than required for oil generation from terrigenous shales, although much of the key data is ambiguous (Jones 1984).

Evaporitic source rocks deposited from mesohaline waters are a reality (Fig. 9.7; Table 9.2). No matter what the evaporitic depositional setting (Fig. 9.4), like non-evaporitic source rocks, they are typified by the common overriding

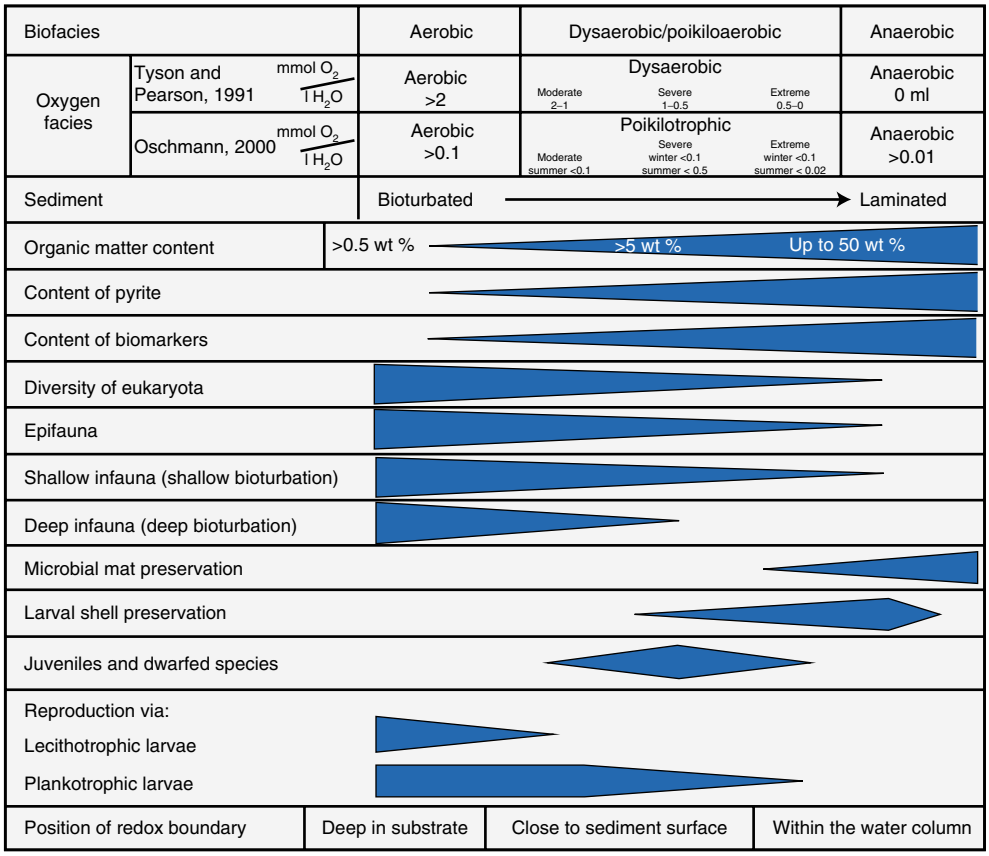

Fig. 9.8 Comparison of typical features of anaerobic, dysaerobic and aerobic sediments in evaporitic and nonevaporitic settings (After Oschmann 2011)

characteristics of anoxia and lamination. Preserved lamina in most source rocks indicates microbial binding coupled with a lack of effective grazers and burrowers (Fig. 9.8). So let us now look to the modern, and at relevant processes in biomarkers to see why this is so and how saline source rocks differ from non-saline source rocks.

Halobiota: Adaptations and Bio Markers

As long ago as 1826 during his voyage on the Beagle, Charles Darwin described biological aspects of the production of solar salt from an inland lake some 23 km from El Carmen, Patagonia. Although unfamiliar with bacteria (after all, Louis Pasteur was only a 4 year-old child at the time), he recognised that there was a "putrefying life-form" in the mud; that algae caused a green colour on the lake; that flamingoes fed on the brine shrimp and worms; and that other "infusorial animalcula" were part of the salt producing system. Yet in 1957, in his classic book on evaporites, Lotze made the statement: "Nicht das Leben, sondern der Tod beherrscht die Salzbildungsstätten" (Not life, but death rules the locales of salt deposition). Likewise, the name of the Dead Sea in the Middle East comes from the time of the Roman occupation when it was given the Latin name *Mortuum Mare* for its perceived lifelessness[4].

For many geologists, saline environments are seen as biotal deserts, largely devoid of biological activity and hence little source rock potential. Like Sir Charles Darwin, we now know that this is not the case. Rather, many modern saline water bodies are sites of periodic but intense organic activity, where numerous highly specialized algal, bacterial and archaeal species infrequently flourish and die back (cycles of feast or famine). Occasionally, they can leave behind substantial volumes of oil-prone organic residues in laminated bottom sediments, especially in mesohaline carbonates, which on burial can evolve into prolific source rocks. Even in modern saline settings, where evaporite depositional settings are not as diverse or widespread, conditions are such that mesohaline carbonates can preserve high levels of total organic carbon (TOC; Fig. 9.9).

[4]The Dead Sea described in Pliny the Elder's *Natural History* as being free of life.

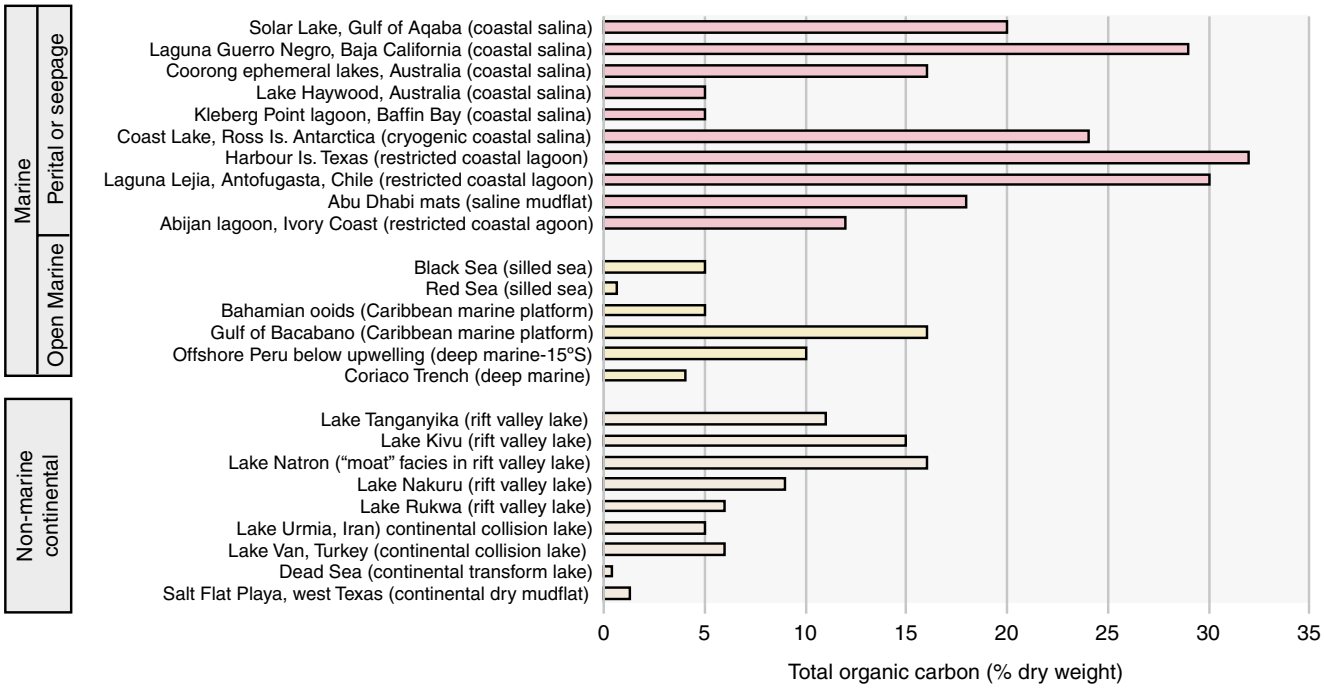

Fig. 9.9 Total organic carbon (TOC as dry wt. percent) in various modern saline settings (Compiled from various sources listed in this chapter and Warren 1986)

Metabolic Pathways in Producers and Consumers

Before we discuss how halotolerant and halophilic biomass accumulates in saline environments, we need to review some basic biology and biochemistry. Our understanding of the taxonomy and biogeochemistry of the prokaryota, the cyanobacteria, bacteria and archaea, which dominate the biota of many hypersaline waters, has undergone quantum change in the past few decades. In the late 1970s, Professor Carl Woese proposed, on the basis of ribosomal RNA affiliations (gene mapping), that life be divided into three domains instead of two, namely: Eukarya, Eubacteria, and Archaebacteria (Woese and Fox 1977; Woese 1993). He later decided that the domain Archaebacteria was a misnomer, and shortened it to Archaea while assigning Archaebacteria as a life kingdom name (Table 9.3). He did the same for domain Eubacteria, shortening it to Bacteria and designated the other prokaryote kingdom as Eubacteria (Woese et al. 1990). This reclassification recognises 3 domains and 6 kingdoms making up the entirety of life on Planet Earth (Table 9.3; Fig. 9.10a).

DNA base -pair studies (16S rRNA gene sequencing) show that species of the domain Archaea are as different from species of Bacteria as from *Homo sapiens* (Fig. 9.10a, b). But Woese's notion of three domains of life, proposed more than 40 years ago, did not take the biological world by storm. Before the advent and take-up of hybridization and genome mapping techniques as a basis for classifying all life, the inferred evolutionary relationships among microbes were contradictory and very messy. Microbial species and interspecies relationships were not easily established on the basis of intricacies of differences in cellular structure, which are often minimal, or by staining, or by the fossil record. None of these approaches when applied to microbes are species-, or even phyla-, specific. For example, based on their morphology, the archaeal *Halobacteriaceae* can be grouped with the bacterial gram-negative rods (a gram positive or gram negative description indicates whether or not the microbial cell wall reacts with Gram's stain). The advent of gene-based classifications threw classic morphological and stain-based microbial groupings into disarray. All the dust has yet to settle from this cladistic confrontation between morphology and gene-mapped subdivisions between and within the microbial and eukaryotal realms (Roger and Simpson 2009). For example, the term halobacteria is now mostly used colloquially to describe the halophilic archaea, while commonly used metabolic terms, like sulphate-reducer and sulphur-oxidizer, are polyphyletic (Table 9.3).

The initial chagrin of those botanists and zoologists versed in classic ecological and cladistic techniques to Woese's laboratory-based tripartite domains is understandable; after all, in his nonanthropocentric regime large

Table 9.3 Life chart showing its domains and kingdoms and some of the relevant parameters and phyla/families

Domain	Bacteria	Archaea	Eukarya			
Kingdom	Eu-bacteria	Archaea-bacteria	Protista	Fungi	Plantae	Animalia
Cell type	Prokaryote	Prokaryote	Eukaryote	Eukaryote	Eukaryote	Eukaryote
Cellular style	Unicellular (with no cell nucleus)	Unicellular (with no cell nucleus)	Unicellular and multicellular	Unicellular and multicellular	Multicellular	Multicellular
Metabolic style	Autotroph and heterotroph	Autotroph and heterotroph	Autotroph and heterotroph	Heterotroph	Autotroph	Heterotroph
Typical environmental conditions	Moist	Extreme (typically anoxic = anaerobic)	Moist	Moist	Moist	Moist to dry
Examples (mostly at phyla level)	Cyanobacteria, Proteobacteria, Chlorobiaccae, Flexibacteria, Spirochaetes, Bacteriacea	Euryarchaeota (halophiles and methanogens), Crenarchaeota (sulpho-archaea), Nanoarchaeota, Korarchaeota	Red, green and brown algae, amoebas, dinoflagellates, sporozoa, ciliates, zoo-flagellates, slime moulds, water moulds	Sac fungi, club fungi, black moulds	Angiosperms, gymnosperms, horsetails, ferns, mosses, bryophytes	Sponges, Cnidarians, flatworms, roundworms, rotifers, mollusks, annelids, echinoderms, arthropods, vertebrates

See also Table 9.4 and Fig. 9.9

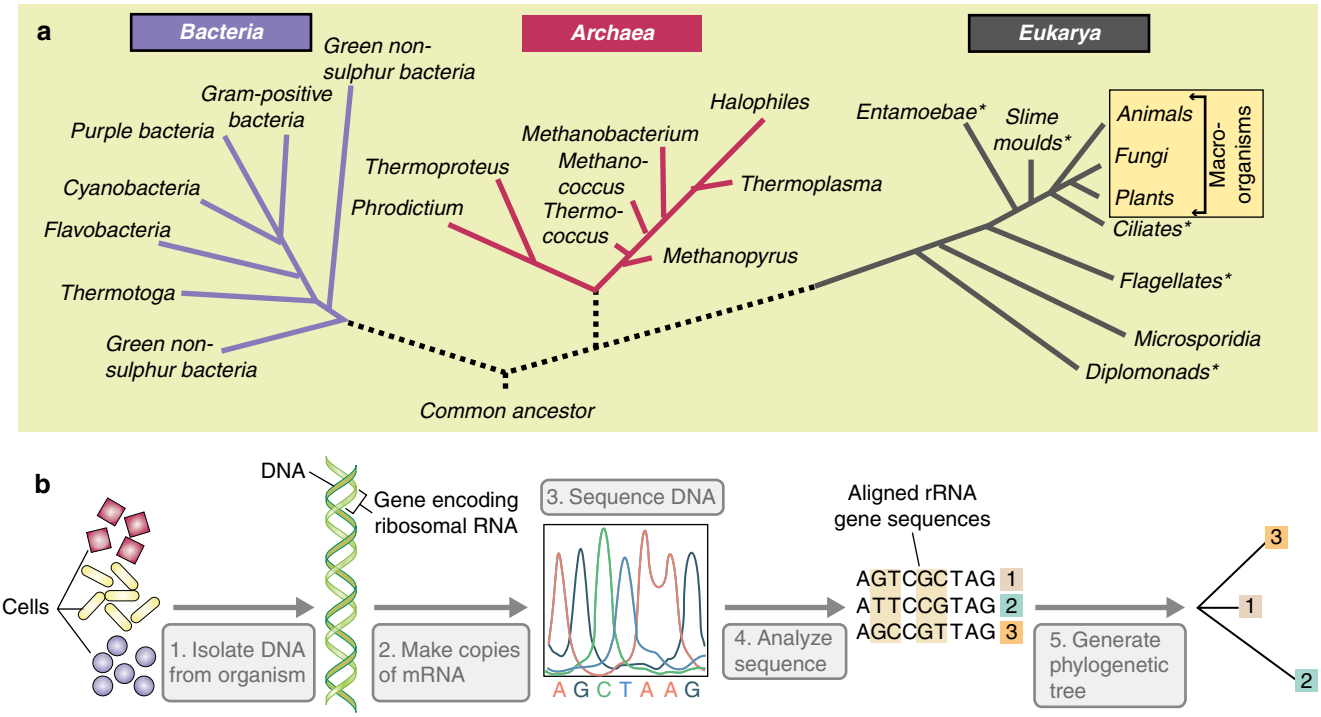

Fig. 9.10 Life domains mapped by gene splicing. (**a**) Tripartite classification of the domain of life based on genetic differences (as proposed by Woese et al. 1990). The *asterisk* (*) in the Eukarya domain indicates the denoted group belongs to the Protista. (**b**) The technique used in defining ribosomal RNA gene phylogenies. *1*. DNA is extracted from cells. *2*. Copies of the gene encoding rRNA are made by the polymerase chain reaction. *3*, *4*. The gene is sequenced and the sequence aligned with sequences from other organisms. A computer algorithm makes pair-wise comparisons at each base and generates a phylogenetic tree, *5*, that can be used to depict evolutionary relationships and affinities (See Madigan et al. 2015 for details of technique)

portions of the classic realms of botany and zoology are relegated to a few twigs on the outermost branches of the Eukaryan limb (Fig. 9.10). Even today some books and articles today still refer to archaea as types of bacteria and illustrations of the domains of life are focused on the Eukarya. Many macrobiologists still feel Woese's system

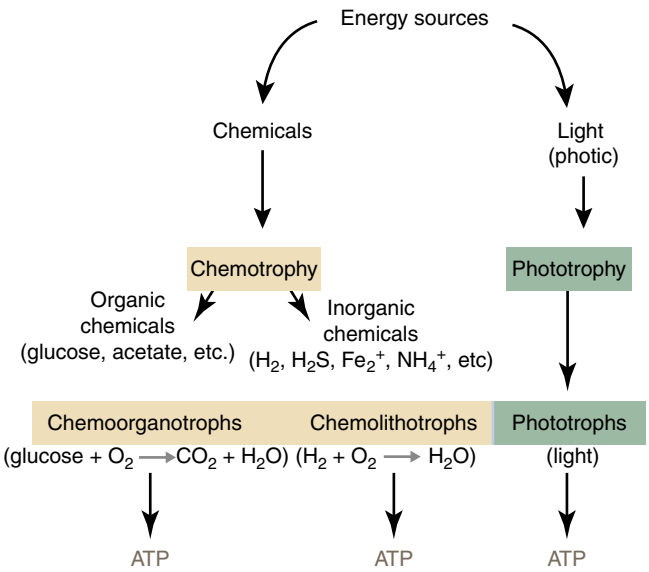

Fig. 9.11 Energy and carbon flows in a framework of metabolic energy conservation in the microbial realm

gives too much prominence to the microbial in terms of the world's biomass. In this Woese's detractors may be wrong. Estimates of the subsurface intraterrestial prokaryotic biomass, aka subsurface lithoautotrophic microbial ecosystem (SLiME), place it as high as 100 trillion tonnes (1×10^{14} to 1×10^{18} g of carbon; Pedersen 2000; Fredrickson and Onstott 1996). As such, if it could be stacked above ground, this amount of "gray goo" would cover the earth with a biological layer some 15 m thick. Since the surface biosphere mass is approximately 4.6×10^{17} g of carbon, the biomass of the rock-bound subsurface microbial biosphere may well exceed that of the surface biosphere. Woese's tripartite conclusions, with various modifications, are slowly moving into the general biological literature (Roger and Simpson 2009).

Cyanobacteria, formerly known as blue-green algae, are now placed in the bacterial kingdom as cells lack a membrane -bound nucleus. And yet, like many other prokaryotes, but they are not totally comfortable in their new cladistic home. Unlike any other bacteria, cyanobacteria photosynthesise aerobically. Instead of the bacteriochlorophyll pigments found in purple and green bacteria, cyanobacteria contain chlorophyll-a, as do all eukaryotic phototrophs, and produce free oxygen as a photosynthetic byproduct, as do all plants (Fig. 9.11). Yet cyanobacteria lack the organized chloroplasts of eukaryotes and have their photosynthetic apparatus distributed peripherally in thylakoids within the cellular cytoplasm. Cyanobacteria are a significant component to modern laminated mat communities in many saline settings. These biolaminites are still called "algal mats" by some geologists, who are not aware of the cladistic rehousing of the former "blue green algae, and they still refer to ancient counterparts as "cryptalgalaminites" – a more appropriate designation is microbialite or for finely layered forms as laminar microbialite or stromatolites (Chap. 1).

Light Dwellers and Pigmentation

Where light penetrates a water mass, photosynthesizers can live. Photosynthesizing autotrophic[5] cyanobacteria (prokaryotes) and algae (eukaryotes) are the dominant primary producers in modern mesohaline waters, along with lower and varying inputs from the higher plants and photosynthesizing bacteria. When nutrients are available, halotolerant alga and cyanobacteria constitute the bulk of the planktonic biomass in the upper layer of a stratified brine column and construct the upper parts of microbial mats in oxygenated settings wherever light penetrates to the sediment surface. And so, all three domains of photosynthetic life are represented in saline environments, although most higher plants only survive at the lower end of the mesohaline range.

The loss of various colour spectra as white light penetrates deeper into a brine column or sediment has led to the evolution of colour-adapted layered photosynthetic communities utilising a ranges of colour-specific pigments. In a clear well-lit brine body, reds and yellows are lost within a few metres of the brine surface, wavelengths in the blue colour spectra can penetrate up to 100 m, depending on water turbidity (Fig. 9.12).

[5] *Autotrophs* (literally "self feeders") are organisms capable of producing organic compounds from simple inorganic compounds (producers not consumers). Autotrophs use carbon dioxide (CO_2) as a sole source of carbon for growth and obtain their energy from light (photosynthetic autotrophs or photoautotrophs) or from the oxidation of inorganic compounds (chemosynthetic autotrophs or chemoautotrophs) (Fig. 9.11).

Photoautotrophs use light as a source of energy and CO_2 as a source of carbon (oxygenic photosynthesis).

Chemoautotrophs use endogenous light-independent reactions to obtain energy, these reactions involve inorganic molecules and an electron donor other than water and do not release oxygen.

Lithoautotrophs depend upon inorganic compounds as electron donors for energy production.

Heterotrophs (literally "feeders on others") use organic molecules synthesized outside their body as a source of energy and carbon (consumers, detritovores, decomposers). They are *saprophytes*, obtaining their nutrients from dead organic matter. Most *chemotroph*s are autotrophic, but some are heterotrophs (*chemoheterotrophs*), which use inorganic oxidation for energy but use organic matter for carbon as well as supplemental energy. Photosynthetic bacteria have the biochemistry for either anoxygenic photosynthesis (non O_2-producing) or oxygenic photosynthesis (O_2-producing). Most photosynthetic bacteria are autotrophs that fix CO_2 (photoautotrophs), but some rely on organic matter for their carbon (photoheterotrophs). Adaptive prokaryotes switch their modes of metabolism depending on environmental conditions (Peters et al. 2005).

Although the cyanobacteria are prokaryotal, like eukaryotic algae and higher plants, they are photoautotrophs that produce oxygen and so they live in oxic settings where light, nutrients and CO_2 are available. The typical aerobic photosynthetic reaction is

$$CO_2 + 2H_2O = CH_2O + H_2O + O_2$$

That is, carbon dioxide and water react in the presence of chlorophyll and sunlight to form carbohydrate plus water plus oxygen (Fig. 9.12a).

All aerobic photosynthesising organisms that split water molecules and generate oxygen, contain varying proportions of the pigments chlorophyll- α, phycobilin and β-carotenes. Chlorophyll-α is a green pigment that absorbs red and blue-violet light (680 nm), hence the green colour of photosynthesising cyanobacteria and plants. It is made up of molecules that contain a porphyrin 'head' and a phytol 'tail' (Fig. 9.13a, b). The polar (water-soluble) head is made up of a tetrapyrrole ring and a magnesium ion complexed to the nitrogen atoms of the ring, its phytol tail typically extends into the lipid layer of the thylakoid membrane. Chlorophyll-β is a closely related molecule and occurs only in green algae and plants, while chlorophyll-c is found only in the photosynthetic members of the Chromista supergroup. This is a polyphyletic grouping within the Protist Kingdom – it includes diatoms, kelp and coccoliths, as well as dinoflagellates, which are alveolates along with the foraminifera (Table 9.3).

Phycobilisome[6] pigments are water-soluble proteins that occur only in the cyanobacteria and red alga (rhodophytes). Phycobilin absorbs light in the blue-green, yellow, and orange regions of the spectrum compared to chlorophyll, which absorbs light in the blue and red regions (Fig. 9.13b). Its presence allows communities to photosynthesise into deeper waters and sediment depths, where only the longer wavelengths penetrate (blue-green spectrum). Phycobilin molecules are linear tetrapyrroles and are structurally related to chlorophyll-α, but lack the phytol side chain and the magnesium ion (see biomarker discussion later in this chapter). They must pass their absorbed photic energy to chlorophyll and so occur in chlorophyll-rich oxygen-evolving photic reaction centres called chloroplasts. Cyanobacterial chloroplasts make up an extensive, intracellular system of flattened, membranous sacs, called thylakoids, the outer surfaces of which are studded with regular arrays of phycobilisome granules.

Carotenes are accessory water-insoluble pigments in most oxygenic photosynthesizers and are directly attached to cellular membranes. They are orange-red or yellow in colour and absorb the blue-violet and blue-green wavelengths missed by chlorophyll (Fig. 9.13b). Structurally they are isoprenoids (terpenes) and are what give autumn leaves their colour when deciduous plants re-absorb chlorophyll in preparation for winter. In the hypersaline realm, carotene pigments from algae like *Dunaliella sp*. and some archaea are what give the characteristic red or pink colours to brines whenever they are blooming (Oren 2009).

In contrast to the cyanobacteria, all other photosynthetic bacteria in saline waters are [5]chemoautotrophs and flourish in anoxic conditions (Fig. 9.12b). Anoxygenic photosynthesis, which can be found in purple bacteria, green sulphur bacteria, green non-sulphur bacteria, and heliobacteria, differs from oxygenic photosynthesis in that it requires only one photosystem and, since no splitting of water occurs, no oxygen is produced (Fig. 9.12b). The green and purple sulphur bacteria take their hydrogen atoms from biologically or volcanogenically produced H_2S and generate sulphur as a waste product (hence their names; Table 9.4). In contrast, the purple and green nonsulphur bacteria use electrons from organic substrates or hydrogen gas, not a sulphur source (Table 9.4).

[6]Pink to purple colours that typify many hypersaline water bodies comes from concentrations of mostly carotenoid pigments present in the cytoplasm of various halophilic microorganisms. Most haloarchaea are red due to a high content of C-50 carotenoids of the bacterioruberin series in the cell membrane (Fig. 9.13). Photosynthetic cyanobacteria and eukaryotes (e.g., unicellular green algae of the genus *Dunaliella*) contribute to the pigmentation of the hypersaline waters thanks to the presence of chlorophylls and C-40 carotenoids (mostly all-*trans*- and *9-cis*- β-carotene). Chloroplasts in *D. salina* and *D. parva* accumulate large quantities of this β-carotene at their peripheries in the form of droplets (plastoglobuli) and so blooms appear brown-red, not green like most other alga and cyanobacteria. The carotene seems to act as photoprotective 'sun-screen' to protect chlorophyll integrity and shield cellular DNA from the high levels of irradiance that characterizes the normal habitat of halophilic *Dunaliella*. It may also act as a 'carbon sink' to store excess carbon produced during photosynthesis under conditions where growth is nutrient-limited but photosynthetic carbon fixation must continue.

Chlorophylls absorb red and blue wavelengths much more strongly than they absorb green wavelengths, so chlorophyll-bearing cyanobacteria and most photosynthesizing plants appear green. In contrast, the carotenoids and phycobiliproteins strongly absorb green wavelength, so microbes and algae with large amounts of carotenoid pigments appear yellow to brown, those with large amounts of phycocyanin appear blue, and those with large amounts of phycoerythrin appear red.

Pigment levels can indicate the stratification of the microbial community in any photoresponsive biomass in a brine column. Red wavelengths (long wavelengths) in white light are absorbed in the first few metres of a brine column or the uppermost millimetre or two of a microbial mat (chlorophyll utilizers flourish). The blue and green wavelengths (shorter) reach deeper into the brine column.

Halophilic archaea were first investigated microbiologically as a common cause for spoilage of salted fish, with their carotene imparting a characteristic red colour. None of the halophilic archaea have been proved to cause disease, so their effects on salted foodstuffs are largely aesthetic. Haloarchaeal spoilage explains the red colour and the foul smell in "red herring." The phrase "throw in a red herring" means to mislead. Spoiled salted fish were once used by poachers to distract hunting hounds. Poachers would interpose themselves between the prey and the hunting party and drag a sack of red herring across the trail to mislead the dog pack, which would follow the scent trail left by the red herring and not the prey. This would give the poachers the opportunity to bag the prey.

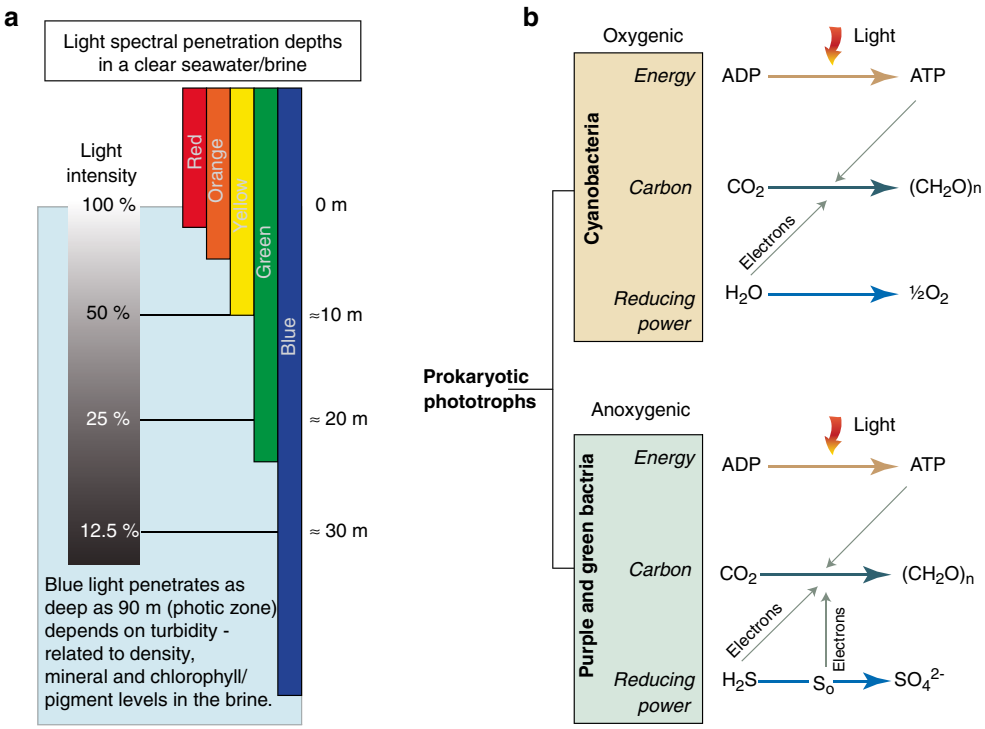

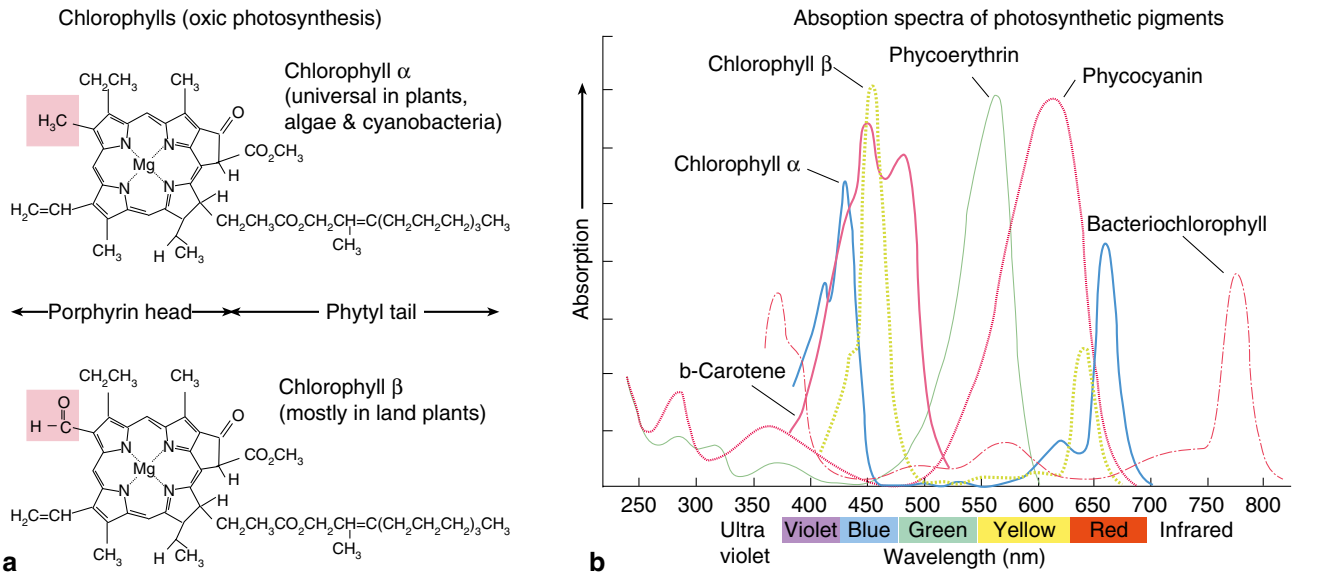

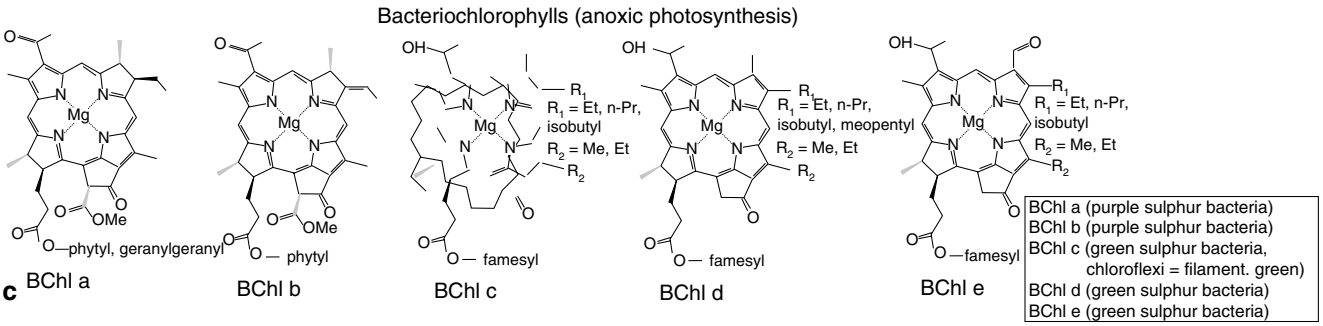

Fig. 9.12 Light penetration and photosynthesis. (**a**) Spectral attenuation of the spectra in sunlight penetrating a brine varies with depth showing different wavelengths penetrate to different depths. (**b**) Prokaryotic photosynthetic pathways and products – cyanobacterial pathway is oxic, bacterial pathway is anoxic

Fig. 9.13 Structures and features of the main photosynthetic pigments. (**a**) Chlorophyll α & β showing porphyrin head and phytyl tail. *Coloured box* shows difference in structure that defines the two forms. (**b**) Absorption spectra of the Chlorophylls, β-carotene and phycobilisomes (phycoerythrin) is dominant in *blue-green* coloured cyanobacteria and phycocyanin in red coloured cyanobacteria. (**c**) Bacteriochlorophyll structures

Table 9.4 Summary of metabolic styles of prokaryotes focusing on Archaea and Bacteria

Phylum or family			Informal Group	Dominant metabolic pathways and lifestyles
Prokaryotes	Halo-adapted Bacteria	Cyanobacteria	Cyanobacteria (T, L)	Aerobic oxygenic photolithotrophs with chlorophyll-a plus phycobiliproteins for light gathering; they use hydrogen by splitting water as electron source and generate oxygen; use the Calvin cycle to generate carbohydrates; some heterocystous cyanobacteria (*Anabena*, *Nostoc*) form heterocysts, which facilitate nitrogen-fixation.
		Proteobacteria	Purple sulphur bacteria (T, L)	Anaerobic obligate photoautotroph (use H_2S, not water) and may form sulphur granules. Contain bacteriochlorophyll a or b. Divided into two families, the *Chromatiaceae* and *Ectothiorhodospiraceae*, which respectively produce internal and external sulphur granules Group includes many sulphur-reducers (e.g., *Pseudomonas*) and some sulphate-reducers (e.g., *Desulphovibrio*). Many species are halophilic or alkaliphilic and are common in saline settings with abundant sulphate reducers (produce the H_2S they require), eg. in meromictic saline lakes..
			Purple non-sulphur bacteria (T, L)	Oxygen-tolerant anaerobic facultative photoautotroph. Most can grow as photoheterotrophs, photoautotrophs or chemoheterotrophs – switching pathways depending on: intensity of anaerobiosis, availability of carbon source (CO_2 for autotrophic growth, organic compounds for heterotrophic growth), and availability of light (needed for phototrophic growth). Originally thought that these bacteria could not utilise H_2S as an electron donor, hence "non-sulphur" in their group name. Sulphide can be used if present at low levels. Higher concentrations of H_2S (in which the purple and green sulphur bacteria thrive) are toxic.
	Archaea	Chlorobiaccae	Green sulphur bacteria (T, L)	Anaerobic obligate photoautotroph (use H_2S sulphide ions, sulphur, hydrogen or ferrous iron as an electron donor, not water). Sulphur deposited extracellularly can be further utilised. Contain chlorophyll a and bacteriochlorophyll c, d or e. Some species can survive in extreme low-light conditions.
		Flexibacteria	Green non-sulphur bacteria (L)	Anaerobic thermophilic photoheterotroph in sulphide-rich zones, but are capable of autotrophy. Remove hydrogen in simple organic molecules (such as ethanol, lactic acid of pyruvic acid) or hydrogen gas substrate. Can grow lithotrophically or organotrophically under appropriate conditions, or as thermophilic aerobic organotrophs.
		Spirochaetes	Spirochaetes (L)	Free-living (flagellate) mostly obligate anaerobic chemoheterotrophs, some species can live in saline waters, like Mono Lake. Constitutes a broad association other species are symbiotic, parasitic. Also aerobic, microaerophilic, facultatively aerobic, or anaerobic organotrophic species. Can catabolize carbohydrates, amino acids or lipids.
		Bacteriacea	Flavobacteria (L)	Anaerobic organotrophs, e.g., halocline dwellers in Urania Basin. *Bacteroides* ferments sugars to acetate and succinate, whereas *Flavobacteria* ferments glucose (almost exclusively). Chemoautotroph, parasite. *Psychroflexus tropicus* is an obligate halophilic species growing in a hypersaline lake in Hawaii.
		Euryarchaeota	Halophile (L)	Aerobic photoautotroph, chemoautotrophs that require very high salinities (1.5–5.5 M, prefer 3–4 M) and complex nutrients for growth. CO_2 fixed via Calvin cycle. Anaerobic respiration used by some *Halobacterium* species with nitrate, sulphur, thiosulphate as terminal electron acceptors. Includes *Halobacterium*; *Halobaculum*; *Natrosobacterium*; *Natrialba*; *Natrosomonas*; *Natrarococcus*; *Haloarcula*; *Halococcus*; *Haloferax*; *Halorubrum.*
			Methanogen (T)	Strictly anaerobic chemoautotrophs; *Methanopyrus* is an extreme thermophile; some can fix nitrogen. Lithotrophs generate methane using hydrogen and carbon dioxide (*Methanobacterium*, *Methanothermus*, *Methanococcus*, *Methanogenium*, *Methanoplanus*). Organotrophs – generate methane from methyl groups of formate, methanol (*Methanosphaera*, *Methanosarcina*, *Methanococcoides*) or acetate.
		Crenarchaeota (sulpho-archaea)	Thermophile (T)	Range of obligate anaerobic chemotrophs, some aerobes that require temperatures above 50 °C for growth (sometimes higher than 70 °C, highest temperature 115 °C) and use sulphur as electron acceptor (except *Sulpholobales*, which uses oxygen or ferric iron, grows in Italian sulphur springs at 80 °C and in a pH of 2–4, dies if pH >7). Organotrophs oxidize organic compounds for energy (oxygen or sulphur serves as final electron acceptor). Lithotrophs – can also grow organotrophically using sulphur as an electron acceptor.
			Acidophile (T)	Acidophilic thermophilic aerobic chemoautotroph, organotroph. For example, *Sulpholobales* (*see above*)
		Nanoarchaeota	Symbiont on *Ignoccus* (T)	Phylum currently has only one representative, *Nanoarchaeum equitans* hosted on hot vent archaeal community in Iceland. Its cell is only 400 μm long.,
		Korarchaeota	New group of extreme thermophile (T)	Only described from 16S rRNA gene sequence which show it does not belong to the main archaea groups of Euryarchaeota and Crenarchaeota (if it is a real phylum then it is the closest to life's universal ancestor in the earliest Archaean ≈3.7 Ga).

T thermophilic, *L* can construct laminated microbial communities

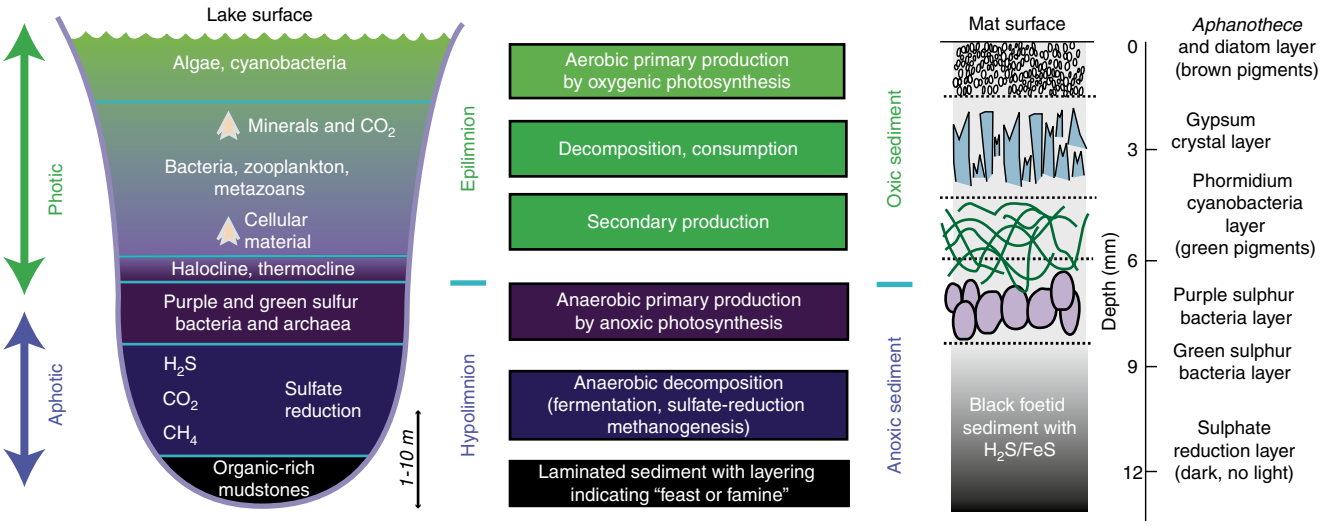

Fig. 9.14 Salinity (temperature) layering in a brine lake water column and a microbial mat show similar metabolic stacking of the halobiota (not to same scale) with anoxic waters below the halocline and oxic waters above in the water column. The same oxic to anoxic transition with depth occurs in a halotolerant microbial mat. This oxic/anoxic salinity/density related layering in the brine column of the lake, and the pore fluids of the mat, controls the distribution of the microbial communities and so stacks their metabolic requirements, pathways and products (including biomarkers)

They utilize a single type of photosynthetic reaction centre with a different photosynthetic pigment (bacteriochlorophyll) to the cyanobacteria and higher plants. Phycobilins and chlorophylls, characteristic of the cyanobacteria, are not found in these chemoautotrophs. Various forms of bacteriochlorophyll absorb light of longer, less energy-rich wavelengths compared to chlorophyll and phycobilins of the cyanobacteria (Fig. 9.13b, c). Green bacteria pigments are dominated by bacteriochlorophyll c (740 nm); d (725 nm), or e (714 nm), while purple bacteria pigments utilise longer wavelength light, via bacteriochlorophyll a (800–890 nm) or bacteriochlorophyll b (1,015 nm). Hence, purple bacteria typically live deeper in the photic zone[7] or in a microbial mat than green bacteria or cyanobacteria.

Green sulphur bacteria (Chlorobiaceae) and purple sulphur bacteria (Chromatiaceae) typically oxidise H_2S via anoxic photosynthesis and produce native sulphur or sulphate byproducts, some species can also use inorganic elemental sulphur, sulphide, or thiosulphate as the electron donor during anaerobic photosyntheis. Their metabolism means Chlorobiaceae and Chromatiaceae inhabit a zone in the chemocline of stratified water masses where sulphidic conditions occur in a light-penetrated zone (photic zone euxinia; Fig. 9.14).

The following simplified equation typifies anoxygenic photosynthesis in purple or green sulphur bacteria:

$$CO_2 + 2H_2S = CH_2O + H_2O + 2S$$

That is, carbon dioxide and hydrogen sulphide react in the presence of bacteriochlorophyll and sunlight to form a carbohydrate (such as glucose) as well as water and sulphur. Many purple and green sulphur bacteria store elemental sulphur as a reserve material that can be further oxidized to SO_4 by using it as a photosynthetic electron donor. Some of the green sulphur bacteria are probably the most energetically efficient of all phototrophic organisms; they can live photosynthetically in environments where light intensities that are less than 0.01 % of typical daylight. Green sulphur bacteria have been found living near a black smoker off the coast of Mexico at a depth of 2,500 m. At this depth, the bacterium, designated GSB1, lives off the dim glow of the nearby thermal vent. Other purple sulphur bacteria live at a depth of 100 m in the Black Sea.

Non-photosynthesizers and Layering

All the groups we have discussed to date are primary producers that are light-dependent and, along with halotolerant photosynthetic eukaryotes, make up the base of the food chain in most modern hypersaline ecosystems. But there are other classes of green and purple sulphur microbes that are [5]lithotrophs and chemotrophs, they can metabolise sulphur independent of a light source (they are chemoautotrophs not photoautotrophs). In many saline microbial communities these non-sulphur bacteria regularly inhabit unlit layers beneath the lit-community layers above, where the aerobic cyanobacteria and anaerobic purple and green sulphur bacteria (photosynthesizers) thrive, while a community of sulphate

[7]The *euphotic* (photic) zone describes the upper part of a water mass exposed to sufficient sunlight for photosynthesis to occur. Below is the aphotic zone. The lit zone can extend down to a few cm in a turbid water body, or as much as 200 m in clear waters (Fig. 9.12).

reducers and fermenters live below. This metabolic layering is seen in both microbial mats and stratified brine columns (Fig. 9.14). In addition, these lithotrophic microbes can be a significant biomass component in deep seafloor seep communities and in cavern waters formed by the action of sulphuric acid where gypsum is a byproduct.

Lithotrophic sulphur-oxidisers in saline waters do not require light to metabolise and include both bacteria (e.g., *Thiobacillus sp*.) and archaea (e.g., *Sulpholobus sp*.). Other lithotrophs in saline waters use substances such as nitrate and reduce it to nitrite (e.g., strains of *Nitrobacter sp*.). *Sulpholobus* is an archaeal hot spring dweller and transforms H_2S to elemental sulphur, it flourishes at temperatures in excess of 90 °C and can live in environments where pH hovers around 1, such as the gypsum wall coats and "snottites" in sulphuric acid caves (Fig. 7.67). *Thiobacillus sp*. are widespread in marine and hypersaline settings, where they oxidize thiosulphate and elemental sulphur to sulphate. For example, a unicellular halophilic, chemoautotrophic sulphur oxidizing bacterium, *Thiobacillus halophilus*, was described in a hypersaline salt lake in western Australian where it grows in waters with salinities of up to 240‰ (Wood and Kelly 1991). In the last few years, as a result of genetic typing, many of the sulphur-oxidizing bacteria originally classified under the genera *Thiobacillus* have been reclassified into the α, ß, and γ subclasses of the Proteobacteria. It probably means there is a broader range of sulphur-oxidising forms in hypersaline environments than current species listings suggest. It also means and that the current informal separation of sulphur-oxidisers into the purple and green bacterial groups is likely polyphyletic and certainly still confused (Table 9.4). Much of the sulphide this group metabolises is biogenic, a byproduct of nearby sulphate reducers, except perhaps around brine springs, cold seeps and hot hydrothermal vents, where it can be thermogenic.

Archaea, which make up life's third domain, are mostly extremophiles thriving in highly stressed conditions, including the extremely saline (Kates et al. 1993; Turich and Freeman 2011). Archaea are further subdivided into two kingdoms: (1) the Crenarchaeota; of which all members presently isolated are either thermophiles that metabolise sulphur (via sulphur oxidation, respiration and reduction) or are pscyhrophiles (cold-dwelling), and (2) the Euryarchaeota; a diverse group, which includes the halophilic Halobacteriaceae, some thermophiles and all methanogens (Table 9.4). Some sulphur-oxidizing archaea are also acidophiles that can grow at a pH approaching zero, others are hyperthermophiles growing at temperatures of up to 115 °C about vents on the deep seafloor.

Archaea and bacteria that require extreme salinities to metabolise are called halophiles, those that can tolerate salinities in excess of 25 % are termed hyperhalophiles, most modern hyperhalophiles are archaea. Many aerobic halophilic archaea (order Halobacteriales) are moderate thermophiles with growth optima at temperatures between 35 and 50 °C and sometimes even higher. This may be an adaption to the high temperatures that typify stratified waters in heliothermic salt lakes worldwide. One of the most impressive extremophiles is *Halobacterium lacusprofundi*, it is both a halophile and a psychrophile and thrives in microbial mats in the supersaline (≈350‰) cold bottom waters (<0 to 11.7 °C) of meromictic Deep Lake in Antarctica (Franzmann et al. 1988). The lake lies in a small isolated depression in the Vestfold Hills, with a brine surface that is some 50 m below sea level. Its perennial waters are thermally and chemically stratified, while its bottom water mass is too saline to freeze. Bottom water temperatures fluctuate between +10 and −15 °C, remaining below 0 °C for 8 months of the year. The microbial diversity in Deep Lake is extremely low and is dominated by haloarchaea, with apparently low numbers of *Dunaliella sp*. and bacteria (of the beta- and gamma-proteobacteria) also present in the bottom sediment (Cavicchioli 2006).

Halophilic archaea in hypersaline depositional settings typically function as heterotrophs (decomposers), with the ability to facultatively photosynthesise whenever conditions are suitable. Other archaea are anaerobic chemoautotrophs that are sulphur dependent and can flourish in the dark (Table 9.4). They thrive in the vicinity of hydrothermal/volcanogenic vents in saline lacustrine rifts or in marine hydrothermal brine springs atop salt allochthons or in the basal waters of density-stratified brine lakes and seaways. They also inhabit subsurface hypersaline brines that characterize bathyphreatic/hypogene hydrologies atop dissolving sulphate caps of salt allochthons. Sulphur-dependent archaea resemble ancestral prokaryotes, as do modern methanogenic archaea, and in the early Archaean their ancestors were the dominant life forms (Fig. 9.15).

All methanogens are obligate anaerobic archaea and today thrive in three habitats; (a) bodies of anaerobic mesohaline to fresh water (e.g., the warm anoxic bottom brines of Solar Lake), (b) haloes about anoxic brine springs and, (c) the anaerobic digestive tracts of ruminants and some molluscs. So, all biogenic methane passed into the atmosphere comes from symbionts in the guts of animals, as well as from decomposers in salterns, swamps, marshes, paddy fields, dumps and sewage works. The world's biogenic methane is due to the work of a few dozen species of methanogenic archaea. They are a little modified cosmopolitan group of strict anaerobes, with a clear ancestral line extending back to the early Archaean (Margulis and Dolan 2002). Methanogens are able to grow at temperatures between 4 and 100 °C, at pH values from 3 to 9, and at salinities ranging from hypersaline to freshwater. Despite this huge taxonomic diversity, the substrates that can be used by methanogens are rather limited – hydrogen, acetate, formate,

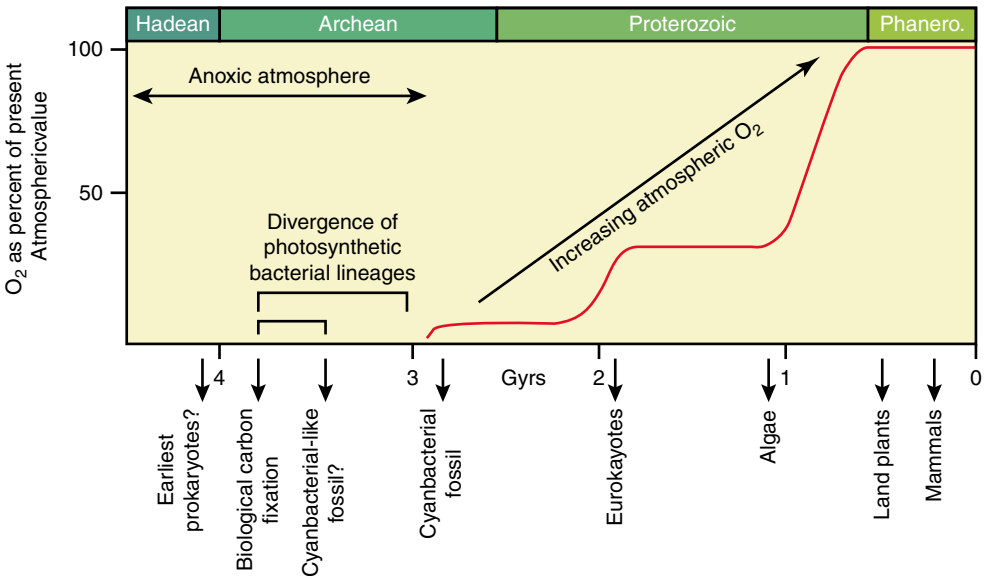

Fig. 9.15 Evolution of photosynthetic metabolism across geological time (In part after Xiong and Bauer 2002)

some alcohols, and methylated compounds (Schubert 2011). The most important of these are hydrogen and acetate, which give rise to two different kinds of methanogenesis: (1) the fermentation of acetate to CO_2 and CH_4 and (2) the reduction of CO_2 with H_2. More than 70 % of today's methanogens use the latter pathway.

Halophilic bacteria as a group is more biochemically divergent than the halophilic archaea and capable of using a range of aerobic and anaerobic metabolic styles (Table 9.4). Some halophilic purple and green nonsulphur bacteria are chemoautotrophic halophiles that can function independent of a light source, while other halotolerant and halophilic bacteria (including cyanobacteria) are oxygenic photoautotrophs (oxidisers). Within the anaerobic halophilic bacteria of the order Haloanaerobiales there are several moderately thermophilic representatives. *Halothermothrix orenii*, the first truly thermophilic halophile discovered, was isolated from Chott El Guettar, a warm saline lake in Tunisia. It grows optimally at 60 °C and up to 68 °C at salt concentrations as high as 200‰ (Cayol et al. 1994). The halophilic *Acetohalobium arabaticum* strain Z-7492 has a temperature optimum of 55 °C (Kevbrin et al. 1997). Under suitably stressed conditions many halophilic bacteria become heterotrophic, utilising either anaerobic or aerobic respiration pathways.

By evolving the ability to symbiogenetically split water as a hydrogen source some 2.5 billion years ago, and so excrete oxygen, the prokaryotic cyanobacteria ultimately enabled the eukaryotic lineages to flourish and displace anaerobic bacteria and archaea as the middle to late Precambrian world's primary producers (Fig. 9.15; Margulis and Dolan 2002). By the Mesoproterozoic this had allowed eukaryotic photosynthesis to develop and ultimately led to the evolution of the higher plants. As oxygen became more plentiful in the ocean and the atmosphere, it was increasingly difficult for anaerobes to flourish in most surface waters. Some retreated to the inhospitable and typically anaerobic environments where they still flourish today, others acquired aerobic bacteria as endosymbionts and today thrive in the aerobic/dysaerobic conditions that typify the hypersaline bottom waters of many density-stratified brine bodies.

Many halotolerant and halophilic bacteria and archaea living in hypersaline surface waters are heterotrophs and usually feed on the remains of other organisms. Heterotrophic metabolism shows variation in the terminal electron acceptor. In aerobic respiration it is oxygen and the breakdown product is CO_2, in anaerobic respiration it may be sulphate or nitrate and the breakdown product is H_2S or nitrite (Table 9.4). In all life forms, including [5]heterotrophs, energy is obtained from high-energy electrons using cyclic or non-cyclic electron transport schemes during which the energy is transferred into and stored as adenosine triphosphate (ATP), while low energy electrons are released by the end reaction. Adenosine triphosphate (ATP) is the basis of all life as it is the energy-carrying molecule found in the cells of all living things. ATP captures chemical energy obtained from the breakdown of food molecules and releases it to fuel other cellular processes.

Exceptions to this general metabolic scheme are the fermenters, like the methanogens, are groups where energy is stored in the form of proton-motive force (PMF), as well as in ATP. Fermentation may be the only metabolic mechanism in halotolerant and halophilic species that inhabit the lowermost living parts of a microbial mat or flourish in the vicinity of the halocline in layered brine column communities, while it may be an emergency system in others (Table 9.4). Fermentation always occurs under anaerobic conditions when there is no electron acceptor. It breaks down an organic compound, such as a sugar or amino acid, into smaller

organic molecules that then accept the electrons released during the breakdown of the energy source. As glucose is broken down to lactic acid, each molecule of glucose yields only two molecules of ATP, and considerable quantities of glucose must be degraded to provide sufficient energy for microbial growth. Only a relatively small output of energy is obtained per glucose molecule consumed, as the organic molecule is only partially oxidized. Hence, the presence of fermentative halotolerant bacteria and archaea and their less efficient metabolisms, rather than oxic decomposers, facilitates preservation of larger quantities of organic end products (proto-kerogens).

Methanogenesis and sulphate reduction are two terminal anaerobic biomineralization pathways in hypersaline systems that convert low molecular-weight products of other bacterial processes (degradation of polymers, fermentation) into CO_2 and methane (Teske et al. 2003). Sulphate-reducing bacteria are physiologically and phylogenetically highly diverse compared to the methanogens and range across a number of bacterial groups. Sulphate-reduction is also found in some archaea such as the genus *Archaeoglobus* of the archaeal phylum *Euryarchaeota*. These various sulphate-reducers constitute a phenotypic group, extending across the Bacteria and Archea, and capable of oxidizing a wide variety of low-molecular weight compounds (short-chain fatty acids, alcohols, alkanes, aromatic compounds, acetate) to CO_2. When biochemical conditions are anoxic and suitable for growth, the environmental range of sulphate-reducers is limited only by sulphate availability. When sulphate is depleted, methanogenic archaea become the dominant anaerobic microbial population. Autotrophic methanogens (all archaea) utilize hydrogen as an energy source for the reduction of CO_2 to methane; specialized genera of methanogens are also capable of inter- and intramolecular disproportionation of C_1 and C_2 carbon compounds (methanol, methylamines, acetate) to methane and CO_2.

Where methane and sulphate coexist in any anoxic environment (for example, at the interface of sulphate-reducing and methanogenic sediment layers, or at methane seeps and vents beneath marine or hypersaline waters), sulphate-dependent anaerobic methane oxidation takes place, whereby methane of biogenic origin is oxidized to CO_2 with sulphate as the terminal electron acceptor (Teske et al. 2003).

The varying metabolic pathways of the microbial communities inhabiting a layered brine column create an interdependent layered microbial ecosystem that reflects the varying degrees of light penetration, oxygenation and anoxia within a variably layered brine body (Fig. 9.14). A similar layered pore fluid community (greater anoxia with depth) also characterises microbial mats. In a brine column, oxygenic photosynthesizers (mostly alga and cyanobacteria) characterize the upper well-lit oxic portions of the brine column (Fig. 9.14). Below this community of producers, the remainder of the photic zone is characterised by downward decreasing light levels and the increasing dominance of oxygenic decomposers (bacteria, zooplankton and metazoans) over producers, with secondary production occurring in the microbial community (green and purple sulphur bacteria) that floats atop the halocline. If light penetrates to anoxic waters below the halocline, anoxic photosynthesizers flourish there (sulphur-oxidising phototropic bacteria and archaea). As light levels fall away in the anoxic waters below, the biota is increasingly dominated by the anaerobic decomposers (sulphate-reducers, methanogens and fermenters). If light does not reach the halocline, specialised forms of chemosynthetic green and purple sulphur oxidizers (not photoautotrophs – e.g., some flavobacteria) occupy the narrow interface at the halocline created by the contact between oxic and anoxic waters. In schizohaline settings subject to periodic freshening of the surface waters, the associated bloom of halotolerant producers (alga and cyanobacteria) in the upper water column can swamp the ability of the various decomposers to degrade all the organic matter before it reaches the bottom and so laminated organic-rich and hydrogen-prone mesohaline carbonates can then accumulate on the bottom.

In the same way, a microbially layered gypsum crust or a carbonate mud shows prominent coloured bands due to the presence of different types of brightly pigmented photosynthetic prokaryotes. This vertical colour zonation seen in all growing microbial communities in saline sediments is related to the same vertical zonation in light wavelengths that is seen in a brine column (Fig. 9.14). Typically, the upper layer of the microbially bound sediment pile is orange-brown, due to the presence of unicellular cyanobacteria (*Halothece*-type). This layer may be a few millimetres to a few centimetres thick depending on the intensity of light penetration. Below, is a brightly green layer is with mainly filamentous (*Phormidium*-type) cyanobacteria. Below is a purple-red layer of photosynthetic purple sulphur bacteria, and below that is a black, sulphide-containing layer (Ionescu et al. 2007).

As the potency of sunlight is only slightly attenuated by any overlying shallow brine sheets, the upper layer of a microbially-bound sediment (microbialite) experiences high light intensities. Accordingly, unicellular cyanobacteria in the uppermost brown layer are characterized by low chlorophyll contents and high carotenoid pigment content, as well as large quantities of mycosporine-like amino acids that provide protection against harmful ultraviolet radiation (Ionescu et al. 2007). The underlying layer of green-coloured cyanobacteria experiences light intensities approximately two orders of magnitude lower than at the microbialite surface. This green layer contains high concentrations of chlorophyll -α and phycocyanin, and lower concentrations of carotenoid pigments (Fig. 9.13b). The underlying red-purple layer, is

situated below the oxic/anoxic boundary, typically contains both *Chromatium* or *Halochro-matium* and *Ectothiorhodospira–Halorhodospira*-like purple bacteria. These anaerobic genera utilise the remaining infrared light, which was not absorbed by the communities above, as an energy source. Sulphide, produced by bacterial sulphate reduction in the lowermost black layer, seeps up into this zone where it serves as the electron donor for their photosynthesis. Also below this layer along with the sulphate reducers are the anaerobic fermenters and methanogens.

Salinity Tolerance

Photosynthesis is the only significant means by which new organic matter is synthesized on Earth. It is the ultimate source of biomass in almost all ecosystems, including hypersaline settings, and accounts for most organic matter buried in sediments and rocks, including biomarkers (Fig. 9.16; Peters et al. 2005a, b). Since the Archaean, almost all organic matter has been produced by photosynthetic fixation of carbon from CO_2 in a process set known as primary productivity (Fig. 9.15).

Photosynthesis can occur with (aerobic), or without (anaerobic) oxygen as a by-product. Respiration and other processes (such as sulphate reduction, methanogenesis and fermentation) result in the near complete oxidation of organic matter and its recycling back to the atmosphere as CO_2. Across Earth history, around 0.1 % of the carbon biomass (via primary productivity) was preserved in sediments and so was then available for petroleum generation (Tissot and Welte 1984). In the following discussion the various biological components of the carbon cycle will now be used to discuss adaptations and niche extent in the halobiota living under hypersaline conditions.

Progressive brine concentration leads to sequential blooms of diverse macro and microbial species adapted to different ranges of salinity (Figs. 9.17 and 9.18). As modern surface brine is concentrated from 60‰ to around 200‰, dense eukaryotic algal and cyanobacterial populations appear, grazed by ostracodes, brine shrimp and brine fly larvae (Fig. 9.17a, b). Halotolerant protists are also found feeding in this salinity range, along with yeasts and other fungi. Halotolerant microbial mats cover the bottom of many hypersaline ponds and shallow lakes at this stage. In anoxic waters in this salinity range there are a variety of sulphur-oxidizing, sulphate-reducing, homoacetogenic, methanogenic and heterotrophic bacteria and archaea flourishing at the base of stratified brine columns or in the lower parts of meso-haline microbial mats. Increasing osmotic stress and loss of appropriate habitat as a water body shrinks with ongoing desiccation means much of the macroscopic stenohaline[8] benthic fauna dies off or dies back to refugia about springs and seeps (Fig. 9.17c).

From about 240‰ to more than 320‰, halophilic archaea and bacteria come to dominate (Ghai et al. 2011). As ever more elevated salinities are attained, most other biological activity first slows and then ceases. At the elevated salinities where halophiles and hyperhalophiles flourish, a few eukaryotes, such as brine shrimp, and a handful of algae, including various *Dunaliella sp*. (a naked unicellular biflagellate green alga), are the only other living forms that the halophilic microbes encounter (Fig. 9.18a, b).

Primary Producers (Photosynthesizers)

Primary production is the synthesis of new organic material from inorganic molecules such as H_2O and CO_2 under aerobic or anaerobic conditions. It is dominated by the process of photosynthesis, which uses sunlight to synthesise organic molecules such as sugars, although chemosynthesis, which can occur in the dark, represents a small fraction of primary production. In reverse order of importance, organisms responsible for primary production in hypersaline conditions, include higher plants, algae and some bacteria (including cyanobacteria).

Higher Plants

A variety of obligate and facultative halophytic higher plants (angiosperms) can survive in moderate-to-high salinity conditions that surround saline pans and lakes. Many such terrestrial halophytes must survive long periods of drought and live where vadose soils completely desiccate, such plants are called xero-halophytes. Xero-halophyte adaptations include, deep and extensive roots, high levels of water storage (cacti), highly reduced leaf areas sometimes reduced to spines and scales, fine hairs on the leaf surface, sunken stoma and stoma that only open at night and permanently rolled leaves or leaves with a propensity to roll in drought and so reduce their surface area. They can have leaves with salt bladders that can excrete salt with the evaporation water (e.g., saltbush genera such as *Atriplex*, *Halimione*, *Rhagodia* and *Chenopodium*), so that over time the leaf can be covered by extruded salt crystals. Most xero-halophytes cannot survive in water-logged saline conditions where roots are subject to long term low oxygen conditions. There the halophytic succulents tend to dominate and constitute a group generally known as the samphires, they include genera such as *Salicornia Arthrocnemum*, *Halocnemum and Halosarcia*. These succulents are capable of surviving on the landward edges of saline mudflats and pans where they can be continually immersed in saline waters for weeks to months.

Then there are the hydro-halophytes that grow in settings subject year-round to partial or complete submersion in brine. Modern hydro-halophytes are most common along the lower salinity edges of mesohaline waters (e.g., mangroves

[8] Stenohaline describes the salinity tolerance of an organism that cannot cope with a wide range of salinity.

Euryhaline is the opposite of stenohaline and describes organisms able to adapt to a wide range of salinities.

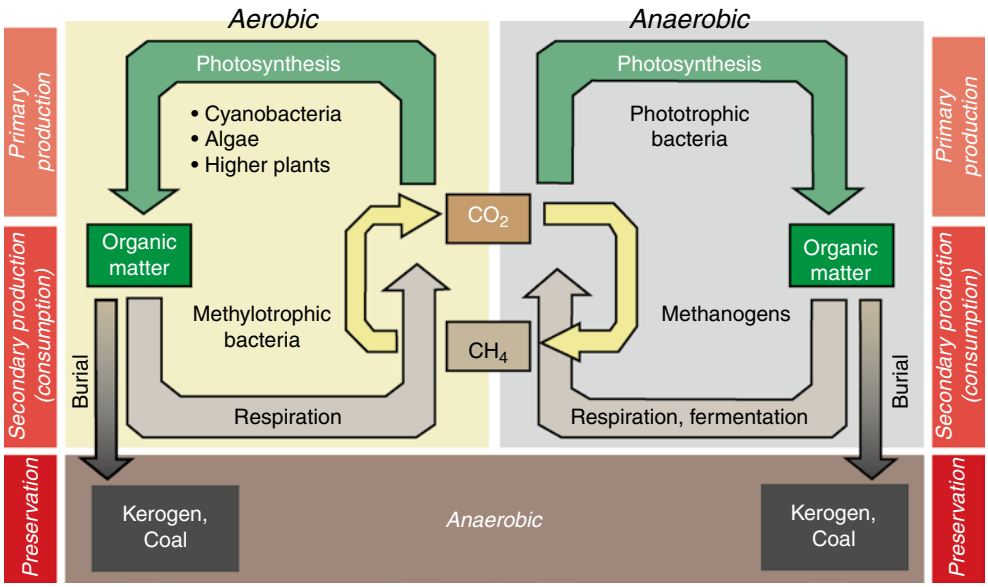

Fig. 9.16 Carbon fixation and cycling. New organic matter is produced by photosynthetic fixation of carbon from CO_2 (primary productivity). This can occur with (aerobic), or without (anaerobic) oxygen as a by-product of photosynthesis. Respiration and other processes (such as sulphate reduction, methanogenesis and fermentation) result in the near complete oxidation of this organic matter back to CO_2

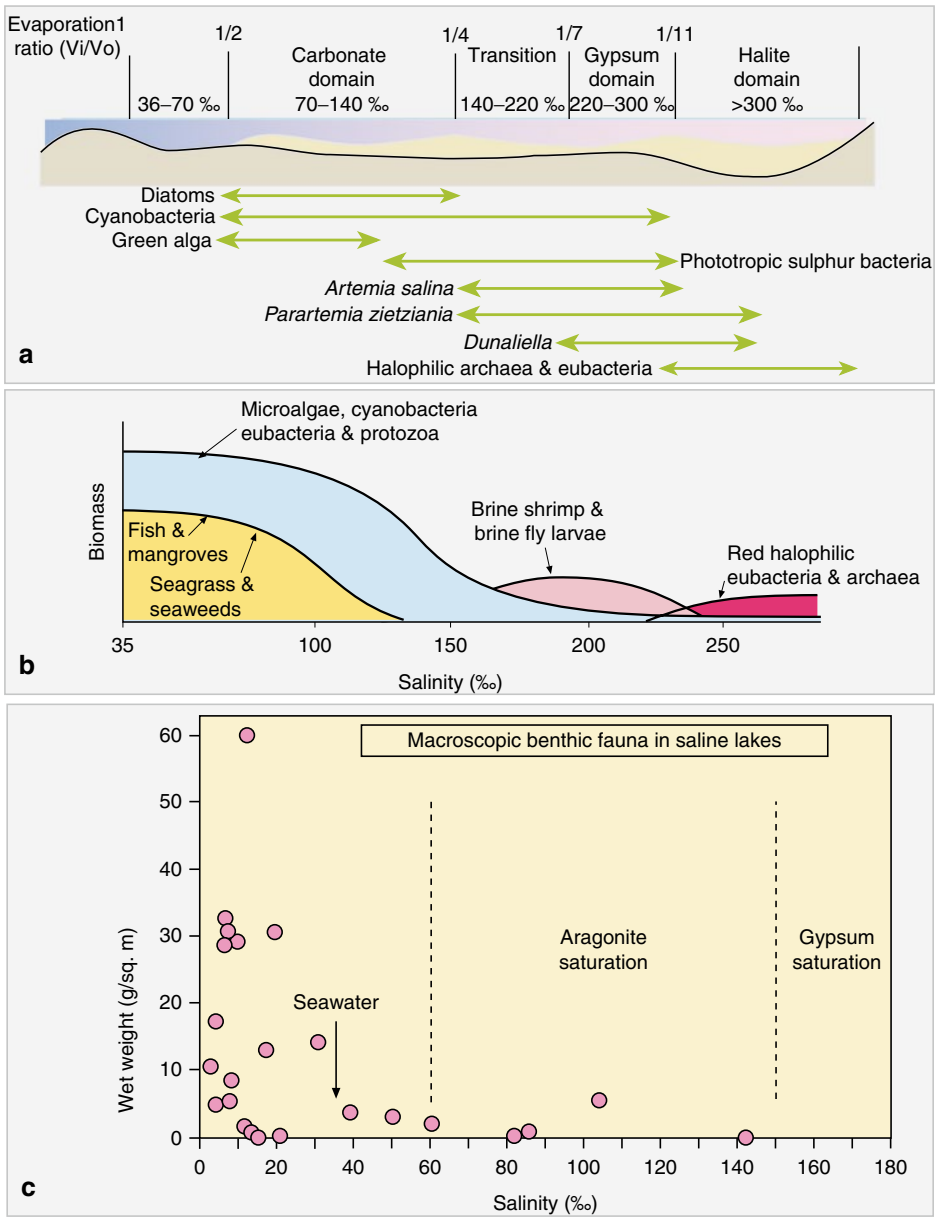

Fig. 9.17 Salinity tolerances. (**a**) Typical salinity ranges of the halotolerant biota where V_i is the volume of inflow to the basin and V_o is the volume of outflow (includes evaporation and reflux; after Barbé et al. 1990). (**b**) Typical salinity ranges and biomass proportions of the biota in modern marine saltwork ponds. (**c**) Standing crop (g/m^2) of the macroscopic benthic fauna in selected athalassic (nonmarine) saline lakes of the world (After Hammer 1986)

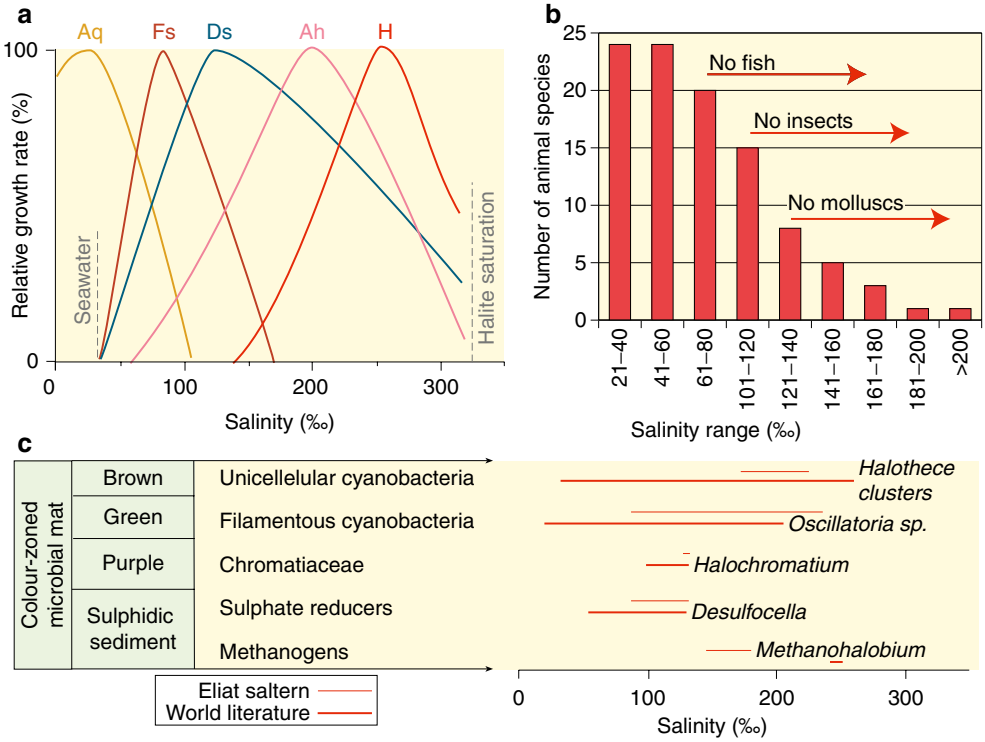

Fig. 9.18 Salinity tolerances. (**a**) Optimal ranges of selected halotolerant and halophilic micro-organisms. *Agmenellum quadraplicatum* (*Aq*) is a slightly halotolerant cyanobacterium, *Fabrea salina* (*Fs*) is a moderately halophilic protist, *Dunaliella salina* (*Ds*) is a halophilic green alga, *Aphanothece halophytica* (*Ah*) is an extremely halophilic filamentous cyanobacterium, and *Halobacterium sp*. (*H*) is an extremely halophilic archaea (After DasSarma and Arora 2001). (**b**) Decrease in variety of animal species in saline lakes of southeastern Australia (After Bayly and Williams 1973). (**c**) Range of observed optimum salinities for phototrophs in various microbial layers and for the sulphate-reducing bacteria and methanogenic bacteria in microbial crusts. It plots the ranges for a mat from a gypsum saltern in Eliat, Israel and compares values to those in the worldwide literature (Plotted from data listed in Table 2 in Sørensen et al. (2004))

on the landward side of Khor al Bazam in Abu Dhabi) but cannot flourish in environments where longterm salinity is greater than 5–10‰ above seawater. For example, mangrove seedlings cannot survive immersion for more than 48 h in mesohaline salinities of 60‰. Salt in adult mangroves is preferentially stored in the bark and in old leaves and is dispersed back into the environment when the leaves or bark are shed.

One of the more interesting mangrove occurrences in a saline setting is the healthy mangrove population (*Avicennia marina*) lining the seawater spring ponds in the hydrographically isolated Lake Macleod, Australia. The mangrove stands occupy an area around 22.5 ha and survive in and about perennial seawater seeps, regions where the escaping seawater has travelled more than 18 km underground via a calcarenite dune aquifer. The trees can reach 5 m height but many are stunted by the inherent elevated salinities (Ellison and Simmonds 2003).

Continually submersed halophytic angiosperms are largely restricted to saline-tolerant varieties of seagrass. All marine seagrasses die back once bottom salinities exceed 60–70‰. For example, four species of *Halophila sp*. collected in Redfish Bay, Texas, were able to grow in tanks with salinities of up to 74‰, without chlorophyll levels being affected, but only for a relatively short period of time (McMillan and Moseley 1967). In more continental settings the subaqueous angiosperm with the highest salinity tolerance is *Ruppia sp*. (aka duckweed or widgeon-grass), with an occurrence range of 0.6–390 g/l TDS (seawater salinity ≈31–34 g/l TDS = total dissolved solids). It thrives in normal marine waters, but also in the schizohaline coastal lakes in the Coorong region of southern Australia and near marine spring outflow zones in Lake Macleod, Western Australia. Perennial *Ruppia sp*. communities in the Coorong Lakes occupy deeper (up to metres deep), well lit permanent water bottoms with salinities of 12–50 g/l. Annual or seasonal communities inhabit shallow lake bottoms, characterised by less permanent waters with seasonal surface water salinities up to 230 g/l prior to complete lake desiccation (Brock 1982a, b). In ephemeral lakes in Western Australia, Geddes et al. (1981) found healthy *Ruppia sp*. growing in waters of 4–78 g/l TDS, but at 82–142 g/l, only drupelets (fruits) were present. *Ruppia* taxa are opportunist plants that die back to root mats when salinities rise or the saline lake dries out.

They quickly return to a growth phase once surface waters return to suitable salinities. An ability to quickly revitalise is why *Ruppia* species fluorish in shallow waters ponds in front of delta sediment prisms in Cuenca de Pozuelos, a high altitude saline playa in North-west Argentina (McGlue et al. 2012).

Preservation potential of organics from continental xerohalophytes is low, as organic matter in desert soils is typically oxidised and degraded. Organic remains of halophytes growing in submersed or brine saturated soils are more likely to be preserved. Kenig et al. (1990) found that, along with intertidal microbial mats, the other major contributors to organic matter preserved in the modern supratidal sediments of the Abu Dhabi sabkha were derived from mangroves (especially cuticle from *Avicennia sp*.) and lagoonal seagrasses (especially *Halodule sp*.).

Charophytes (stonewarts) are another group of opportunistic submersed mostly freshwater plants that includes halotolerant species, which can flourish in lower salinity regions of a saline lake or lakewide at times of brine freshening (Fig. 9.17a; Soulié-Marsche 2008; Burne et al. 1980). They are not known to occur in marine waters. The general outline of the complete plant, somewhat resembles an aquatic horsetail due to the whorls of branchlets arising from a "stem." They are photosynthesizers, thought to show strong affinities to green alga, although some taxonomists link them more closely to bryophytes and are thought to be ancestral associates of some of the first land plants. Their fossil record extends back to the Silurian, but the whole living plant is rarely fossilised, what is typically preserved are calcified female fructifications, termed gyrogonites, which display a characteristic and unique spiralled structure. These "oogonia" are a major contributor to the numerous calcispheres found in ancient saline mudstones and lunettes.

Lamprothamnium papulosum is the most common charophyte in the saline lakes of Australia. Studies of this species in saline lakes in the Coorong region, Australia, show it can be part of a healthy bottom community at 70‰, although it does not generally successfully germinate or grow above 53‰ (Burne et al. 1980). This is two to three times the typical salinity association documented for modern charophyte occurrences in brackish lakes in the northern Hemisphere.

Charophyte remains are not uncommon fossils in ephemeral saline lakes and sabkhas worldwide as they regenerate readily in freshened waters, even after considerable periods of desiccation. However, germination and growth require a transient period of suitably freshened water cover. Charophytes in saline lakes are opportunist species that dieback or retreat to "seep" refugia in harsh times. Widespread oogonia horizons in evaporitic sediments indicate episodes of freshening, as in the carbonate lakes of the Coorong and the coastal gypsum salinas in the "Chain of Lakes" at the southern end of Yorke Peninsula, South Australia and the sabkhas of North Africa (Soulié-Marsche 2008; Burne et al. 1980). *Lamprothamnium williamsii* is abundant in 65 ka coxiellid beds in Lake Eyre where it presence indicates a more humid period in the lake's hydrology (García and Chivas 2004). Likewise, sediment layers with the remains of *Lamprothamnium papulosum* in Fuente de Piedra, southern Spain, indicate times of freshening in a saline lake with a flora typically dominated by *Dunaliella sp*. (Garcia and Niell 1993).

Alga and Cyanobacteria

Rather than higher plants, halotolerant green algae and cyanobacteria, are the dominant primary organic producers in moderately hypersaline (mesohaline to penesaline; 60–200‰) settings. With elevated salinities restricting the grazers, green algal densities in a surface brine layer can be more than 10^5 ml^{-1}. Mesohaline algae are mostly obligately aerobic, photosynthetic, unicellular microorganisms. Green algae of the genus *Dunaliella*, e.g., *Dunaliella salina*, *D. parva*, and *D. viridis*, are ubiquitous in modern brine lakes, such as Great Salt Lake, Hutt Lagoon and the Dead Sea, where they constitute the base of the food chain for the halotolerant fauna (Fig. 9.18a; DasSarma and Arora 2001). Most species of green algae are moderate halophiles, with only a few extreme halophiles, e.g., *Dunaliella salina*, *Dunaliella viridis* and *Asteromonas gracilis*. For example, salinity contrasts in Great Salt Lake, Utah, seem to control cyanobacterial distributions and their associated pigmentation controls red-green brine colouration (Roney et al. 2009). Cyanobacterial distributions and pigments influence brine colour and the distribution of water colours in Great Salt Lake can be used to map salinity. *Aphanothece halophytica* proliferates in the highly saline pink waters of the northern arm (27 % salinity), while *Nodularia spumigena* fluorishes in the green waters of the less saline south (6–10 %) (Fig. 9.18a). Anthropogenic ponds at Hutt lagoon show a similar set of seasonal biogenic brine colours (Fig. 9.19).

The halophilic *Dunaliella parva* (a flagellate alga of the Chlorophyceae) is the sole primary producer in Dead Sea brines, with several species of hetrotrophic haloarchaea dependent on its periodic blooms. *Dunaliella sp*. can survive in marginward refugia, even when the upper and low water layers in the Dead Sea are NaCl-saturated. *Dunaliella salina* is one of the most environmentally tolerant eukaryotic organisms known and can cope with a salinity range from seawater to NaCl saturation, and a temperature range from <0 °C to >38 °C (Oren 2005). *Dunaliella* in the Dead Sea is capable of growing rapidly under hypersaline conditions, and this may be responsible for producing isotopically heavy $\delta^{13}C$. The consumption of this isotopically heavy glycerol by *Halobacteriales*, which feed on the *Dunaliella* blooms would in turn lead to a ^{13}C enrichment of the total biomass (Grice et al. 1998).

Fig. 9.19 β-Carotene manufacturing plant on the saltflats of Hutt Lagoon, Western Australia (Image mounted and scaled in MapInfo®, using a Bing® image base)

Halophilic *Dunaliella sp*. can contain high levels of β-carotene and pigment levels tend to increase with increasing salinity. It means that blooms in hypersaline pans can be harvested and processed to manufacture β-carotene. *Dunaliella salina* contains more than ten times the levels of β-carotene compared to other halophilic Dunaliella species and at higher salinities cells can contain as much as 10–14 % β-carotene dry weight, so it is the preferred commercial species (Moulton and Burford 1990). Two of the largest β-carotene producers in the world are Western Biotechnology Ltd. (Perth, Western Australia) and Betatene Ltd. (now Cognis Nutrition and Health, Melbourne, Victoria), both began operations in 1986 in Australia and now supply more than 90 % of the world's needs. Both operators grow the algae in large and shallow (approx. 20 cm deep) wind-stirred ponds constructed either on the bed of the hypersaline coastal salina known as Hutt Lagoon, or formed by artificially expanding and isolating a lagoon flat (Fig. 9.19).

Each of the artificial production ponds atop the surface of Hutt Lagoon is 5 ha in area and was constructed using earthen berms. The Hutt Lagoon production plant has a total current pond area of 50 ha and there are also smaller ponds for research purposes. Ponds used by Betatene Ltd. at Whyalla in coastal South Australia are even larger. High salinity is maintained in the shallow pond waters using a combination of wind-driven mixing, solar evaporation and seawater pumped into the ponds. Uncontrolled episodes of freshening (rainfall) can lower pond salinities. This can favour the growth of the less carotenogenic species (*D. viridis*, *D. minuta and D. parva*) as well as allowing grazing protozoa such as the ciliate *Fabrea salina* and the amoeba *Heteroamoeba sp*. to invade the pond. Such invasions can rapidly decimate algal production.

Along with *Dunaliella sp*., numerous species of cyanobacteria flourish at the elevated salinities where the activities of metazoan grazers are severely limited. Typically they construct laminated microbial mats and stromatolites in water-covered mesohaline areas and peripheral strandzone mudflats (Fig. 1.10). Various cyanobacterial species constitute the upper parts of these microbial "high rises" with species dominance in the layer changing according to their tolerances to salinity and light (Figs. 9.14). *Microcoleus chthonoplastes* is a cosmopolitan mat former and is the dominant filamentous blue-green in flat laminated mats in Guerrero Negro in Baja California Sur, Mexico, in Solar Lake in the Sinai and in Deep Lake in South Australia. In Guerrero Negro it grows best in brine-covered pans with a salinity range of 60–95‰. *M. chthonoplastes* tends not to do as well beneath pan waters with longterm salinities above 100‰. In Solar Lake it flourishes beneath waters with an annual salinity range of 45–180‰ and it still manages to photosynthesise, although not all that well, at salinities approaching 300‰. *Arthrospira subsalsa*, another filamentous cyanobacterial form, flourishes in mats worldwide at salinities of up to 150–180‰. At higher salinities and higher light intensities the nonfilamentous unicellular and coccoid cyanobacterial species come to dominate. The halophylic unicellular *Aphanothece halophytica* dominates mat surfaces in Guerrero Negro in pans with surface salinities up to 200‰. In Sabkha Gavish in the Sinai it occurs across an even broader salinity range of 250–330‰. Why the same cyanobacterial species seems to have different salinity ranges in different parts of the world is not clear. It may reflect a response to differing temperature regimes or to different rates of change in salinity of the waters atop the growing mats.

Recently, Davila et al. (2013) have documented a halophilic cyanobacterial community that lives as endoliths in

subaerially exposed halite nodules in the hyperarid Atacama Desert. They photosynthesise occasionally and utilise hypersaline pore brines created by deliquescence of halite at times of slightly increased atmospheric humidity, independent of rainfall events.

Diatoms (halotolerant bacillariophytal algae with siliceous tests) are another commonplace primary producer in mesohaline and lower penesaline environments (Fig. 9.17a). Their buoyant cells, often augmented by chitin threads or colonial adaptions, enable them to keep within the photic zone better than many other algae. They flourish at times of freshened lake waters or in perennial seepage and dissolution ponds (posas) about the edges of some salars, where they become a major component in some lacustrine stromatolites (Fig. 1.11b, c). Several benthic diatom species are conspicuous in building stromatolites, for example, *Mastogloia sp*., *Nitzschia sp*., *Amphora sp*., *Diploneis sp*. They function in a manner analogous to that of cyanobacteria in that they produce extracellular gel, are motile, phototropic, can trap and bind sediment, and produce surface irregularities of the mat (Winsborough et al. 1994).

Some varieties of benthic diatoms can live in lake brines with longterm salinities around 120‰, while the upper limit for diatom growth is around 180‰ (Clavero et al. 2000; Cook and Coleman 2007). The most halotolerant diatom taxa in the saltern ponds of Guerrero Negro are *Amphora subacutiuscula*, *Nitzschia fusiformis* (both *Amphora* taxa), and *Entomoneis sp*.; all grow well in salinities ranging from 5 to 150‰. Three strains of the diatom *Pleurosigma strigosum* were unable to grow in salinities of less than 50‰ and so are true halophilic alga. A similar assemblage of *Amphora sp*., along with *Cocconeis sp*. and *Nitzschia sp. d*ominate the high salinity (150‰) saltern ponds near Dry Creek, Adelaide, Australia (Cook and Coleman 2007).

Anoxic Sulphur-Oxidising Bacterial Photosynthesizers

Sulphur oxidation as a general biogenic process involves the oxidation of various reduced sulphur compounds, such as H_2S, inorganic sulphur (S^0), and thiosulphate ($S_2O_3^{2-}$), to form sulphate (SO_4). It occurs within the sulphur cycle in both oxygenic and anoxic environments (Fig. 9.20a). In this section we shall concentrate on photosynthetic sulphur oxidisers (anoxic primary producers), not the chemolithic sulphur oxidisers, which inhabit oxic settings. These anoxic photosynthesizers are colloquially known as the purple sulphur bacteria and green sulphur bacteria. In a microbial community, both groups occupy the anaerobic photosynthetic niche between the chemolithotophic aerobic sulphur-oxidising bacteria above and aerobic heterotrophs below. Purple sulphur bacteria tend to be metabolically more versatile than green sulphur bacteria, but both predominantly utilize the sulphide and sulphur in waters rising from below, as their electron source (Fig. 9.20a). In both microbial mats and stratified water bodies, the purple sulphur bacteria typically inhabit the lit brine layer immediately above green sulphur bacteria, both groups occupy a light-penetrated zone that is located directly beneath the oxic-anoxic interface.

Anoxygenic halotolerant to halophilic sulphur-oxidising photobacteria are a prolific group of primary producers and can create dense biolaminae in a variety of a sulphide-rich lit environments. Halophilic phototrophic sulphur-oxidising bacteria are typically filamentous CO_2 -fixers (both green and purple sulphur bacteria) utilising sulphide or H_2S, not water, as an electron donor for their photosynthesis (Table 9.4; Fig. 9.12b). They grow in hypersaline niches where light reaches into anoxic, sulphide-H_2S containing water columns or in microbially-bound anoxic pore waters a few millimetres below the surface of a mat. These anaerobes obtain their energy from light, especially from near-infrared radiation (800–900 nm), a part of the light spectrum that is not absorbed by the chlorophyll pigments in the cyanobacterial layers above.

Sulphide, produced by sulphate reduction in the layers below, serves as electron donor in the oxidation process. Different sulphur oxidising bacterial species thrive in different salinities, ranging from seawater to halite precipitating (Fig. 9.20b). As they use H_2S as the electron donor and produce various oxidised sulphur metabolites, the final product of this metabolic pathway is sulphate or sulphur and yellow sulphur nodules in modern mats can indicate their presence (Fig. 9.20a).

Typical sulphur-oxidising primary producers in mesohaline waters and microbial mats include; *Chromatium salexigens*, *Thiocapsa halophila*, and *Rhodospirillum salinarum*, with optimal growth in these species between 60 and 110‰ (Fig. 9.20b; Caumette 1993; Ollivier et al. 1994). Phylogenetic studies in the last two decades have moved fully halophilic sulphur oxidising species, once classified as *Ectothiorhodospira sp*., into a new genera the *Halorhodospira*; that is, *Ectothiorhodospira* is now considered the basonym for the halophilic bacterial grouping *Halorhodospira*. In highly alkaline soda lakes where Dunaliella is absent, anoxygenic phototrophic purple bacteria of the genera *Ectothiorhodospira* and *Halorhodospira* predominate and, instead of *Dunaliella sp*., form the base of the food chain utilised by haloarchea.

For example, shallow brines of the small soda lakes in the Wadi Natrun can be coloured an intense purple-red, due to the development of the purple sulphur oxidising bacteria *Halorhodospira halophila*. In contrast, *Halorhodospira abdelmalekii*, and *Halorhodospira halochloris* show green pigmentation in pure cultures, while pigmentation in *Halorhodospira halophila* is always purple-red. Small natural brine puddles in hypersaline locations may show separate development of green- and red-coloured species of

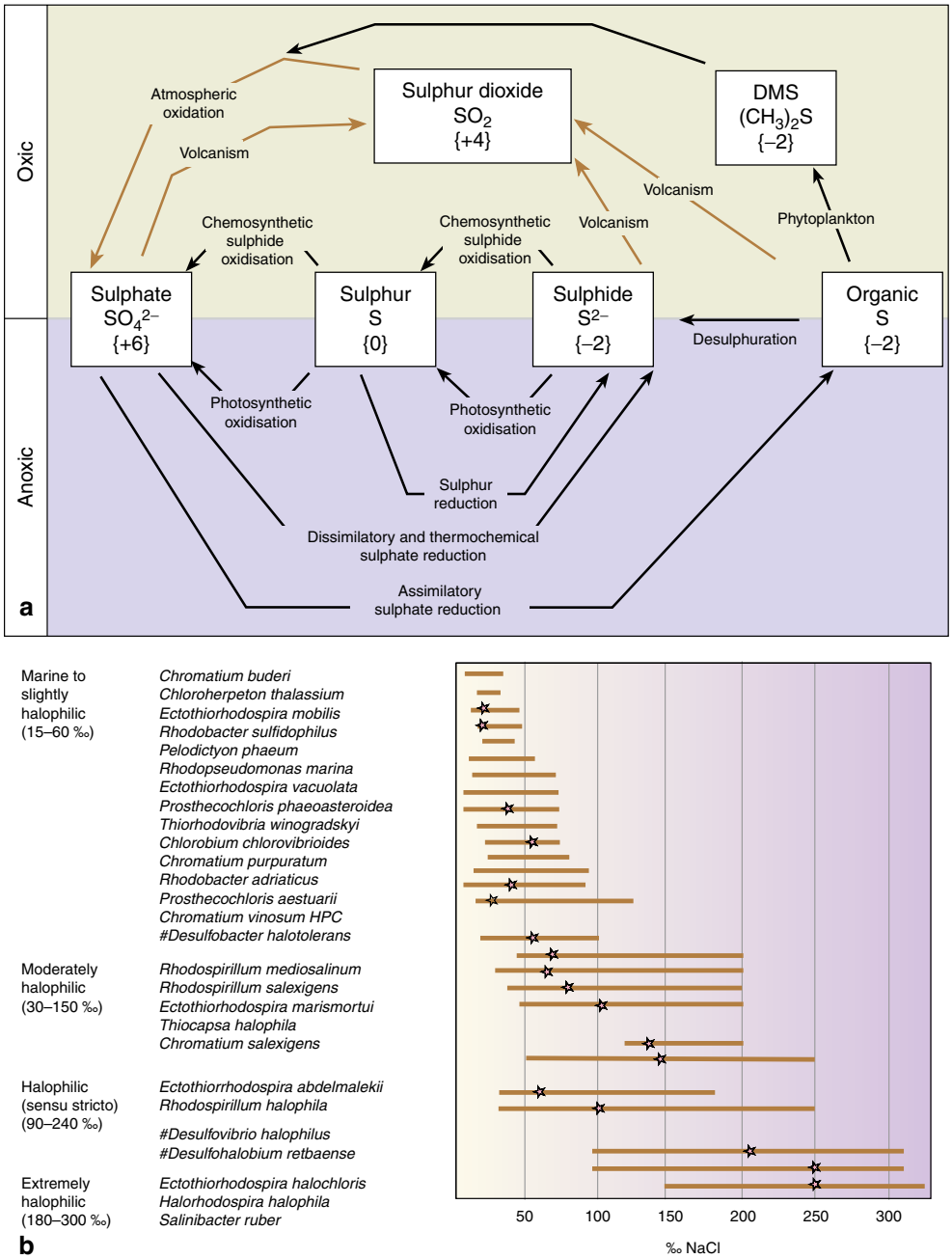

Fig. 9.20 Sulphur cycle and salinity tolerance. (**a**) Summary of the sulphur cycle showing the two types of microbially-mediated sulphur oxidation photosynthetic versus chemosynthetic (oxidation states of sulphur are shown in parentheses). Microbial pathways shown by solid lines; brown lines show geological processes involving sedimentary organic-sulphur, calcium sulphate (gypsum/anhydrite) and Fe-sulphide (pyrite). (**b**) Salinity tolerances in phototrophic halophilic bacteria including the sulphur oxidisers and the sulphate-reducers (#). *Star* on bar indicates the salinity for optimal growth (In part after Caumette 1993; Ollivier et al. 1994)

Halorhodospira, while top layers of the sediments of Wadi Natrun lakes (Egypt) show separate layers of the green-coloured and the red-coloured *Halorhodospira sp*. (Imhoff 1988); Imhoff et al. 1979).

Halorhodospira abdelmalekii, *Halorhodospira halochloris*, and in particular *Halorhodospira halophila* are among the most halophilic phototrophic bacteria known and confirm the observation that bacteria are capable of inhabiting the same highly saline environment as halophilic archea. Isolates of *Halorhodospira halophila* from soda lakes in the Wadi Natrun have salt optima of 250‰ total salts and can survive in halite-saturated solutions (Fig. 9.20b). The moderate halophile *Ectothiorhodospira marismortui* is a strict anaerobe found in the hypersaline growths about sulphur springs in the Dead Sea. Seep waters at the time of this purple sulphur oxidising bacteria was collected had a pH around 5.2, a salinity ≈170‰ and a temperature of 40 °C. Isolates of this species grew poorly at a pH of 5.5 but thrived in the neutral pH range between 7 and 8 (Oren 2005, 2009).

Bacterial Chemosynthesizers

The habitat range of the halobiota described so far exists in, or near, an environment that is lit and the community layering is controlled by whether the setting is oxic or anoxic. But

there is also a range of halotolerant and halophilic bacterial chemotrophs (mostly thiotrophic[9]) that can flourish in environments where light no longer penetrates. They fix CO_2 as cellular material using chemical compounds without the need for light and often occupy trophic levels also occupied by the decomposers and fermenters. There are separate phyla of sulphur-oxidizing and sulphur- reducing chemotrophic bacteria but as in much of the field of microbial cladistics, an agreed classification is still a matter of intense debate.

Bacterial Sulphur-Oxidizers

Sulphur-oxidizing chemosynthesizers (non-photosynthesizers) include halotolerant variants, such as the filamentous *Beggiatoa* (*qv*), *Thiothrix*, *and Thioploca*. They are anaerobes, they use sulphur as an electron donor and oxidize it by adding oxygen in seawater and lower-end hypersaline brine settings. The final product of the reaction is sulphate. This group does not require light, only sulphide, and is often found at the interface between oxic and sulphidic environments in microbial mats in saline lagoons and on the deep seafloor near brine lake edges or in the vicinity of hydrothermal and sulphidic seeps.

Beggiatoa sp. dominate the white mats and bacterial meadows typical of the chemosynthetic communities covering the deep sea floor near brine seeps and hydrothermal vents. These sites are typically on water bottoms well below the depth of light penetration. Unlike most bacteria, *Beggiatoa* and its mats in these settings can be recognized by eye, by recognising its typical stringy morphology. It is a filamentous bacterium, which is motile via gliding and stores elemental sulphur inside the filaments, giving filaments and mats a shinning white appearance. Filaments can be several millimeters to centimetres long and are formed by long rows of cells with diameters between 1 and 200 μm. Such white *Beggiatoa* mats typically occupy the zone between the oxygenated water column and underlying anoxic sediment, they inhabit the narrow chemical interface where the O_2 and sulphide diffusion gradients meet (Gilhooly et al. 2007).

In saline lakes, such as Guerrero Negro, Mexico, the *Beggiatoa* community of the hypersaline microbial mats of occupies the sulphide-oxic interface, typically located a few millimetres below the mat surface in daylight hours. At night its biosignature disappears from the mat community, suggesting it may have exited into the overlying water column as it tracks a rising sulphide-oxygen boundary (Jesse et al. 2009).

In addition to oxygen, the larger-diameter *Beggiatoa* species (>4–10 μm diam. filaments) can also use internally-stored nitrate in the oxidation of sulphides. The nitrate can act as an alternative electron acceptor for sulphide oxidation. Nitrogen utilisation increases the rate of sulphide oxidation in oxygenated waters and also allows these nitrate storers to survive periods of anoxia. Other chemotrophic sulphur bacteria live as symbiotic sulphur-oxidising bacteria in animal tissues of invertebrates in the same un-lit brine pool communities as *Beggiatoa* (Levin 2005). These brine-controlled chemosynthetic cold-seep communities, situated atop salt allochthons, are discussed later.

Bacterial Sulphate-Reducers

Dissimilatory[10] sulphate reduction induces large ^{34}S isotope fractionations and can produce sulphide depleted in ^{34}S by 4–49‰ compared to the sulphate precursor. When iron is present pyrite is typically precipitated, when no iron is present, as in a limestone host, then biogenic calcite is the precititate as in many salt allochthon caprocks. In general, the rate-limiting step in sulphate reduction is the breaking of the first S-O bond, namely the reduction of sulphate to sulphite (Fig. 9.20a). Dissimilatory sulphate reduction can occur up to quite high salt concentrations and black, foetid sulphide-containing sediments form the bottom to modern coastal salinas and salt works, well into the penesaline salinity range (Oren 2001).

There are more than 120 species of sulphate-reducing prokaryotes, belonging to four bacterial and two archaeal phyla. Amongst the sulphate reducing bacteria, the most salt-tolerant is the halophilic *Desulphohalobium retbaense*. Isolated from Lake Retba in Senegal, it is capable of growing at NaCl concentrations of up to 250‰ (Ollivier et al. 1994). Two other sulphate-reducing halophilic isolates are *Desulphovibrio halophilus* and *Desulphovibrio oxyclinae*, which can tolerate NaCl concentrations of up to 180–225‰ (Fig. 9.17b; Caumette 1993; Krekeler et al. 1998). Another isolate, similar to *Desulphovibrio halophilus* has been collected in brine pool samples from the allochthon-associated deep-water brine lakes on the floor of the Red Sea. There it grows at salinities up to 240‰, but only slowly. *Archaeoglobus* and *Sulphobus* are two known archaeal sulphate reducers, both are thermophiles and live in active hydrothermal regions.

[9]Thiotrophic describes an organism that oxidizes sulphur compounds as a major part of its metabolism. Purple and green sulphur bacteria are generally not called thiotrophic because they gain energy by photosynthesis and are thus classified as phototrophic, even though sulphide is required for this process.

[10]Dissimilatory sulphate reducers release large amounts of hydrogen sulphide (H_2S and HS) to the ambient environment, as products of their energy metabolism and so cause the characteristic smell of rotten eggs in the host sediment. The process is carried out by a heterogeneous group of bacteria and archaea that occur in anoxic environments with temperatures up to 105 °C.

Assimilatory sulphate reduction is conducted by some bacteria in order to synthesize sulphur-containing cell components. It is another form of intracellular sulphate reduction, it is a metabolic process set that reduces sulphate to typically produce sulphide groups attached to amino acids, which are assimilated as useful components into the cell.

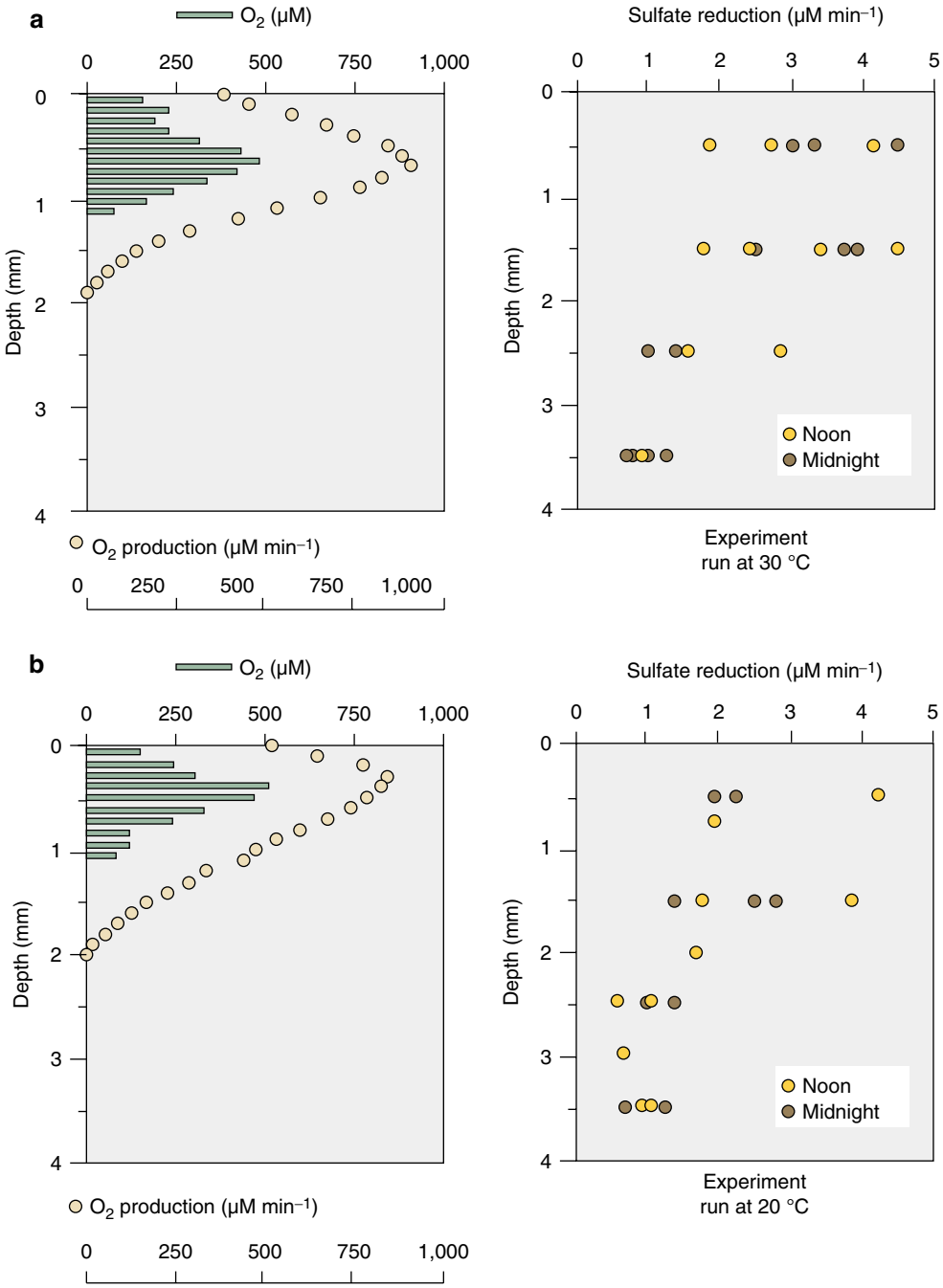

Fig. 9.21 Depth related distribution of dissolved oxygen and oxygen production rate measured at noon (*left hand figures*) plotted against sulphate reduction rate (*right hand figures*) sulphate reduction measurements were made at noon and midnight. Experiment in (**a**) was run at 30 °C and (**b**) at 20 °C. In both cases the sulphate reducers extend well into the oxic portions of the microbial mats (After Canfield and Des Marais 1991)

As we saw in the previous section in any microbial mat the zone of photosynthetic oxygen synthesis overlaps with a zone of sulphide production by sulphate reduction and the two can be separated by a zone of oxygen-dependent microbial sulphide oxidation (inhabited by the purple and green sulphur oxidising bacteria). These metabolic activities create steep, opposing gradients of oxygen and sulphide, which fluctuate with the rhythm of day and night (Canfield and Des Marais 1991). Historically it was assumed sulphate-reducing bacteria were obligate anaerobes, but in cyanobacterial mats from the saline evaporation ponds in Baja California, Mexico, this may not be so. *Desulphobacter* and *Desulphobacterium* are always restricted to the greater depths in the mats, which are anoxic. However, the *Desulphococcus* and *Desulphovibrio* groups are predominant in the upper part of the layered microbial community and thriving in the lower part of the photo-oxic zone (Fig. 9.21; Risatti et al. 1994), where they are able to deal with temporal exposures to oxygen concentrations as high as 1.5 mM (Sigalevich and Cohen 2000).

Most halophilic and halotolerant sulphate-reducing bacteria are incomplete oxidisers that grow on lactate and produce acetate. Dissimilatory sulphate reduction provides relatively little energy, and therefore the need for sulphate reducers to spend a substantial part of their available energy budget for the production of organic osmotic solutes may set the upper limit to the salt concentration at which these bacteria can grow (Oren 2001 and later discussion in this chapter). Oxidation of lactate to acetate and CO_2 yields much more energy. Recently, the first halophilic acetate-oxidizing sulphate-reducing bacterium was isolated: *Desulphobacter halotolerans* was collected from the hypersaline bottom sediments of Great Salt Lake, Utah. It has a rather restricted salinity range, being unable to grow above 13 % NaCl (Brandt and Ingvorsen 1997). Even so, it possesses the highest NaCl tolerance reported for any member of the genus *Desulphobacter*.

No viable bacterial sulphate-reducing communities have been collected at the more extreme salinities, where halite precipitates, although when radioactive tracers are used to define rates of sulphate reduction it is obvious that sulphate reduction does occur at elevated salinities approaching halite saturation. In modern coastal salt pans northeast of Capetown, South Africa, the rate of dissimilatory sulphate reduction increased up to salinities of 272–311‰, beyond that, toward halite saturated salinities, the rate of isotope uptake decreased (Porter et al. 2007). Some sulphate reducers may also be alkalophiles; for example, *Desulphonatronovibrio hydrogenovorans* is a H_2 -utilising sulphate-reducing bacterium isolated from the trona beds of Lake Magadi, it functions optimally at pH 9.5 and 3 % w/v NaCl.

Halobiotal Heterotrophs (Consumers)

Secondary production describes the generation of biomass by heterotrophic (consumer) organisms in an ecosystem. It is associated with the transfer of organic material between various trophic levels, and represents the quantity of new tissue created through the use of assimilated food (Fig. 9.16). Secondary production is typically defined as including all biomass generated by heterotrophs. Organisms responsible for secondary production in hypersaline sediments include a few animals (vertebrates and invertebrates), protists, fungi and many species of bacteria and archaea (Figs. 9.17 and 9.18).

Vertebrates

Marine fish species can survive and even flourish in perennial seawater spring pools and seeps that line the edges of coastal salinas. For example, Timms (2009) found healthy populations of the Port Lincoln Hardyhead (*Leptatherina presbyteroides*) in a number of marine spring pools about the edges of coastal salinas of South Australia. Likewise Logan (1987) noted the estuarine Yellowtail Trumpeter (*Amniataba caudavittata*) and the Few-ray Hardyhead (*Craterocephalus pauciradiata*) living in seawater seep pools about the edges of Lake Macleod. At times of salina-wide freshening these fish species, along with marine forams and diatom in the refugia, as well as other halotolerant species spread out into other parts of the salina, dying back to the spring-seep refugia when the lakes dry out once more. But none of these species have evolved to survive at elevated salinities much beyond that of seawater (>35–40‰).

The highest natural brine salinities at which viable fish populations have been observed, living in a permanent brine lake, are around 60–90‰. For example, the white-lipped or alkaline tilapid fish (*Oreochromis alcalica*) lives in such mesohaline waters in African rift lakes and even flourishes at 36–40 °C and in pH ≈ 10.5 within thermal spring and moat brines about the edges of Lake Natron and Lake Magadi. Desert pupfish in the Sonoran Desert can survive for short periods in waters of drying pans that are as saline as 100–140‰ (Helfman et al. 1997, p.313). Unlike desert pupfish, tilapids are one of the few higher organisms that can tolerate perennial hypersalinity (DasSarma and Arora 2001). Rates of survival among the tilapia are dependent on the rate of salinity rise, with maximum hypersalinity tolerance occurring when elevated salinities are attained gradually (Gonzalez 2012). In the lab, black-chinned tilapia (*Sarotherodon melanotheron*) populations survived well, up to around 120‰ when the salinity was raised 2–8‰/day.

All fish living in saline settings tend to inhabit perennial waters centred on spring refugia and expand into broader niches at times when an upper fresher oxygenated layer typifies the upper portion of the brine column. But this can be a hazardous environment in a saline setting, especially if the upper oxygenated water mass has an anoxic underbelly. Stratified water masses are subject to instability either via dessication and salinisation, or equally destructive wind-induced holomixis. In the modern Salton Sea there is a strong correlation between winds that overturn the stratified lake waters and significant fish and barnacle kills due to inimical waters (low oxygen, high H_2S and ammonia) rising into the upper water column (Marti-Cardona et al. 2008). Following death, fish carcasses float to the lake surface and deposit and accumulate along the Salton shore, which retains wave washed sediments that are rich in disarticulated fish and single bone and scale elements, along with a significant component of barnacle shells.

Malenda et al. (2012) argue similar mass kills of Triassic fish species took place during deposition of the saline lacustrine Lockatong Formation in the northeast USA. High wind events caused overturning of the lake waters, either depleting oxygen levels or toxically poisoning the fish with upwelling H_2S and ammonia-rich brines. After death, bacterial

decomposition bloated the fish by generated gas in tissues causing the fish carcasses to float. The decomposing fish carcasses were driven shoreward by wind and wave action and deposited on the shoreline and were possibly scavenged by phytosaur populations the Mesozoic equivalent to today's flocks of gulls in the Salton Sea.

As well as leaving traces or their avian presence as tracks and nest mounds preserved in the rock record (Scott et al. 2009, 2012), many modern birds in saline lakes also feed on organic-rich detrital lake rims. Others feed on the periodic planktonic blooms that occur at times of lake water freshening. One of the most spectacular examples of avian exploitation of the halotolerant plankton is the pink flamingo (lesser flamingo) population of African rift lakes. Stilts, gulls and pelicans are other opportunist avians that feed on halobiotal blooms that occur in periodically freshened salinelakes and their remains and trace.

The influence of flamingo grazing on organic matter and type is documented in Laguna de Pozuelos (Fig. 9.22; McGlue et al. 2012; Ferrero et al. 2004). The climate of the basin is cold and semiarid (Köppen BSk adjacent to ET) showing an annual temperatures average below 9 °C near lake and it is markedly seasonal, with a rainy season in summer (between December and March) and a dry season throughout the rest of the year. Average annual rainfall is about 350 mm making it one of the most humid intermontane depressions in the region.

The lake supports a rich diatom flora (estimated density of the diatoms suspended in the water is 4×10^3 cell l^{-1} and 2×10^3 cells g^{-1} of those in the sediment) consisting mainly

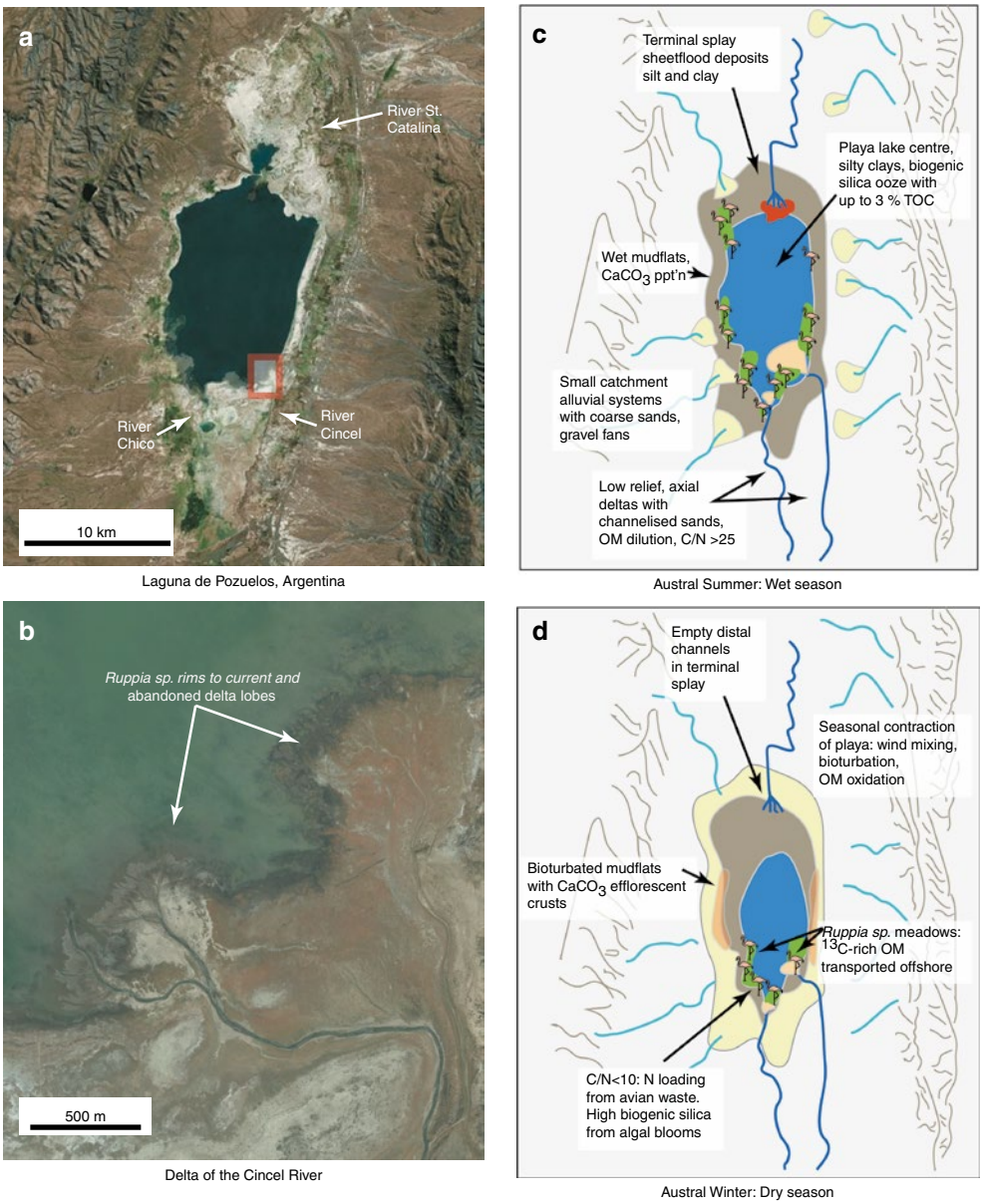

Fig. 9.22 Laguna de Pozuelos, Argentina. (**a**) The laguna is an intermontane location and is seasonally fed from snowmelt mostly by three rivers (Chico, Cincel and St Catalina) and a series of bajada inflows. (**b**) Detailed view of the delta lobes at the mouth of the Cincel River. Ruppia sp. meadows rim the strandzones of both the active and inactive delta lobes. (**c**) Wet season (austral summer) when river inflow is active (*dark blue* for main inflows) and flamingo population is spread across the lake edge feeding on duckweed. (**d**) Dry season (austral winter) when lake levels are low, flamingoes an their duck weed food-source are confined to southern margins of seasonal changes in flamingo distribution indicated by pink flamingo symbol (In part after McGlue et al. 2012)

of *Cocconeis placentula*, *Nitzschia perspicua*, *Nitzschia hungarica*, *Navicula minuta* and *Navicula perminuta*, which are indicators of moderate alkaline (pH = 8.0–8.5) waters. The abundance of *Nitzschia sp*. Indicates waters masses with elevated mesohaline salinity, at least in dry periods. Zooplankton shows an average annual density of 220 individuals l^{-1}, the predominant invertebrate fauna consists of copepods (*Beckella sp*., *Attheyella sp*.), Cladocera (*Daphnia sp.*) and rotifers (*Hexarthra sp.*). This planktonic microfauna supports an extraordinarily numerous colony of flamingos that graze by filtering the waters. In summer the flamingo colony increases extraordinarily in size with as many as 25,000 flamingoes (made up of 4 species) in the shallows of the lake feeding on the halotolerant plankton (mostly diatoms) that flourishes in the lower salinity upper water mass that has spread over much of lake (Fig. 9.22c). The extent of the perennial lake waters varies from less than a few square kilometres when dry, and the basin is experiencing a few drought years, to more than 150 km^2 when water full.

Silty clays and diatom ooze are the dominant playa-lake centre facies, with concentrations of total organic carbon commonly exceeding 3 wt% in this sub-environment (Fig. 9.22c). Elemental and stable isotopic analyses point to a mixed organic matter composition in the playa-lake centre, with substantial contributions from algae and transported aquatic macrophytes. Bulk sediment and organic mass accumulation rates in the southern playa-lake centre approach 0.22 g cm^{-2} $year^{-1}$ and 2.89 mg cm^{-2} $year^{-1}$, respectively, indicating moderately rapid deposition with negligible deflation over historic time. Playa margin facies contain higher percentages of fragmented biogenic carbonate (ostracods and charophytes) and inorganically precipitated aragonite crusts due to seasonal pumping and evaporation of ground water with much of the precipitation occurring in the dry season (Fig. 9.22d). Organic matter accumulation is limited along these heavily bioturbated wet and dry mud flats. Fluvial–lacustrine transitional environments, which are key waterbird habitats (Fig. 9.22b), are either silty terminal splay (northern axis) or sandy deltas (southern axis) containing highly oxidized and partially allochthonous organic matter. Organic matter accumulation is limited along heavily bioturbated wet and dry mud flats. Fluvial–lacustrine transitional environments, which are the key flamingo habitats (Fig. 9.22b), they are either silty terminal splay (northern axis) or sandy delta (southern axis) deposits that contain highly oxidized and partially allochthonous organic matter.

TOC values tend to be elevated in the perennially subaqueous laguna centre and are consistently more than 3 wt%, whereas samples from the southern deltas and playa margins typically exhibit TOC values < 1.5 wt% (Fig. 9.22). Laguna bottom samples typically contain low total nitrogen levels with C:N (carbon:nitrogen) values ranging from 2 to 79, with a mean of ≈ 22 (McGlue et al. 2012). Samples collected from mud flats north-west of the main Río Santa Catalina channel and within the mouth of the Río Cincel delta exhibit low total nitrogen, leading to C:N values >30. Most of the laguna sediments have C:N values <20, which is typical for lakes with mixtures of algal and higher plant matter. An exception to this pattern is observed near the Río Chico delta, where values of total nitrogen substantially increases and C:N values fall to <5.

Flamingo activity is high year round in this locale, probably due to the availability of nutrients for the phytoplankton and favourable shallow water depths allowing the birds to filter feed across large parts of the delta. Seasonal foraging probably impacts both the carbon and nitrogen cycles across other similar microhabitats in the laguna and leads to period input of organics with elevated $\delta^{13}C$ values. Avian waste products, especially urea, are rich in organic nitrogen and ammonia, which likely explains the higher nitrogen levels in the sediments in regions of year round flamingo filter-feeding. Local eutrophication from these waste products probably drives phytoplankton blooms, as evidenced by elevated concentrations of biogenic silica in the distal Río Chico environment (from diatoms, especially *Cocconeis placentula*, *Nitzschia hungarica* and *Navicula sp*.). A similar set of avian-induced eutrophication processes is seen in many of the east African rift lakes where flamingo populations build to phenomenal numbers as they feed on halotolerant plankton blooms in mesohaline lake waters. Likewise the mesohaline waters of Great Salt Lake, Utah, act a food stop for over million migrating birds made up of some 250 different bird species (Aldrich and Paul 2002). These birds feed mostly on large populations of brine shrimp, *Artemia salina*, and the brine flies, *Ephydra ripara*, which flourish in both arms of the lake.

Throughout the Neogene in African rift lakes, hippopotami (*Hippopotamus amphibius*) are probably the largest vertebrates capable of leaving traces of its presence in semi-arid to arid alkaline lake-margin sediments. This is especially so in regions of muddy organic-rich sediments near brackish lake margin springs, as in the saline-alkaline mudflats rimming the crater lake of the Ngorongoro Crater, Tanzania (Deocampo 2002). There the organic content of muds that infill hippopotami trackways or furrows leading to the spring is as high as 17 % TOC versus organic contents around 6–7 % in mudflat sediments adjacent to the trackways. A population of some 15–20 hippopotami are known to inhabit Lake Nakuru, feeding on grassy meadows along the lake shore at night and spending their days defecating, while immersed in the mesohaline lake waters (Matagi 2004).

Invertebrates (Ingesters, Grazers and Pelletizers)

Large numbers of a relatively few species of halotolerant invertebrates can survive, graze and produce pellets in low to moderately mesohaline environments. This can be seen in the broad range of salinities tolerated by a number of

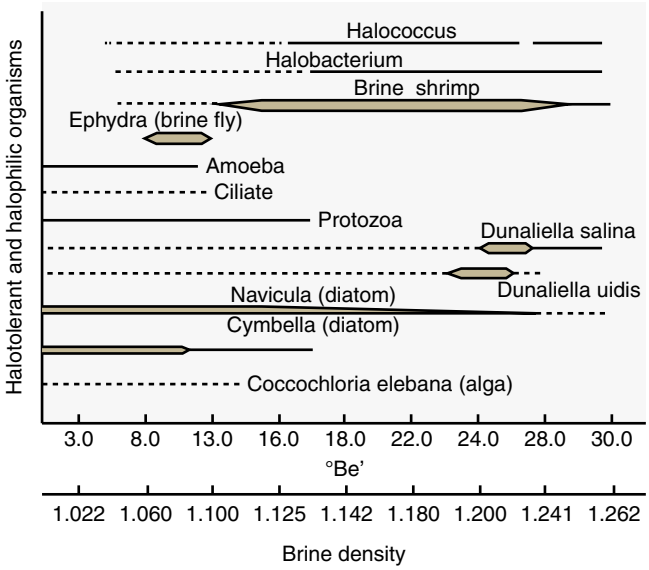

Fig. 9.23 Salinity ranges of halotolerant and halophilic organisms in the mirabilite-accumulating Barkol Lake, China (After Dongyan et al. 1998)

well-adapted species in marine and continental saline settings (Fig. 9.17a). The salinity ranges in the mirabilite-precipitating waters of Lake Barkol, China, are a good example of such biological adaptation (Fig. 9.23) The lake has a salt content of 215–338 g/l, a pH of 7.2–7.81, a δD and $\delta^{18}O$ range of −23.7 to +2.4‰ and −11.13 to +4.53 %, respectively. Brine shrimp (*Artemia salina*), an invertebrate heterotroph, in the lake can ingest, graze and defecate across a broad salinity range and this is typical of brine shrimp in saline settings worldwide.

As in the oceans, faecal pellets of the zooplankton (invertebrates) in stratified brine lakes and salterns (e.g., brine shrimp in Fig. 9.23) are very important in rapidly moving planktonic organic matter to the water bottom. That is, pelletisation is a biogenic mechanism that quickly moves suspended planktonic algal and bacterial debris from it original site, where it is floating in an oxygenated freshened upper water layer, into a sediment layer beneath hypersaline anoxic bottom brines. There, the anaerobic decomposers are far less efficient destroyers of long chain hydrocarbons than their aerobic counterparts. Cosmopolitan examples of pellet producers that feed on alga and bacteria during times of freshening and feast in saline settings include; copepods, brine shrimp, ostracodes and halotolerant molluscs such as *Fragum erugatum*.

Fragum erugatum thrives beneath the mesohaline bottom waters of Shark Bay, Australia where it can survive salinities in Hamelin Pool of up to 70‰, but flourishes at salinities around 50–55‰. In the well-lit low nutrient mesohaline bottoms where it filter feeds and defecates, its metabolic efficiency is greatly enhanced by the rich xooanthellate flora that symbiotically populate its mantle (Berry and Playford 2002). During intense storms (hurricanes or cyclones) the remains of this almost monospecific benthic community have been washed into laterally accreting beach ridges that now define the edge of Hamelin Pool.

A more unusual saline symbiosis in a marine invertebrate association is found in mollusc biostromes adjacent to hypersaline waters of brine lakes that occurs on the deep dark sea bottom, atop salt allochthons in the Gulf of Mexico. There, even though these molluscs cannot tolerate elevated salinities, biostromes of chemosynthetic molluscs rim the halocline-defined edge of methane-and H_2S saturated brine lakes, situated atop salt allochthons. Biostromes are dominated by *Calyptogena* clams, along with serpulid worms, sea anemones, galatheid crabs (stone crabs like *Paralomis sp.*), swimming holothurians and amphipods (Macdonald et al. 1990). The worms and molluscs are chemotrophs with symbiotic chemosynthetic microbes (including purple-oxidising bacteria and methanogenic archea) that inhabiting their flesh/gills and thrive on the H_2S and methane escaping across the halocline.

On land, insects flourishing about the edges of hypersaline lakes include halotolerant brine flies, such as *Ephydra hians* and *E. gracillis*. Their eggs hatch, and their larvae feed and pupate in microbial mats and berms of organic scum about the strandlines of most modern saline lakes (Fig. 9.17b). Both the larvae and the adult flies are scraper-gatherers feeding on the cyanobacteria and diatoms in benthic mats. Brine-fly larva of various species are well adapted to saline conditions as they burrow and ingest microbial mat materials. Adults are grazers and form thick flying and feeding "carpets" around the edges of salt lakes. *Ephydrella marshalli* larvae collected from subaqueous benthic mats about the edges of commercial salt works/lagoons on Port Phillip Bay, Victoria, have survived several days immersed in hypersaline sodium chloride media at ≈200‰ (up to 5850 mOsm/l; Marshall et al. 1995). Likewise larvae of dolichopodid brine fly *Hydrophorus plumbeus* collected in Mono Lake[11] survived immersion for a week in NaCl brine with a salinity as high as ≈190‰ (5,600 mOsm/l; Herbst and Bradley 1988). Adult flies have extra long body hairs that enable them to encase themselves in an air bubble and so walk about on the underside of the water surface of a brine lake. They do this to

[11] The term mono, used in the name Mono Lake, California, is likely a Yokut Indian word for naturally salted brine-fly pupae, a local delicacy before European settlement. However the Yokut people lived 200 miles north of Mono Lake, they harvested brine flu in Owens Lake, not Mono Lake. Prior to European settlement a small group of people (≈200 persons) calling themselves Kutzadika'a inhabited the Mono Lake region. The name Kutzadika'a, roughly translated, means "fly eaters" and Kutsavi was the Kutzadika'a term for brine fly, not Mono. Numbering around 200 individuals, the Kutzadika'a spent most of the year in the Mono Basin following an annual cycle of food gathering that seasonally focused on brine fly.

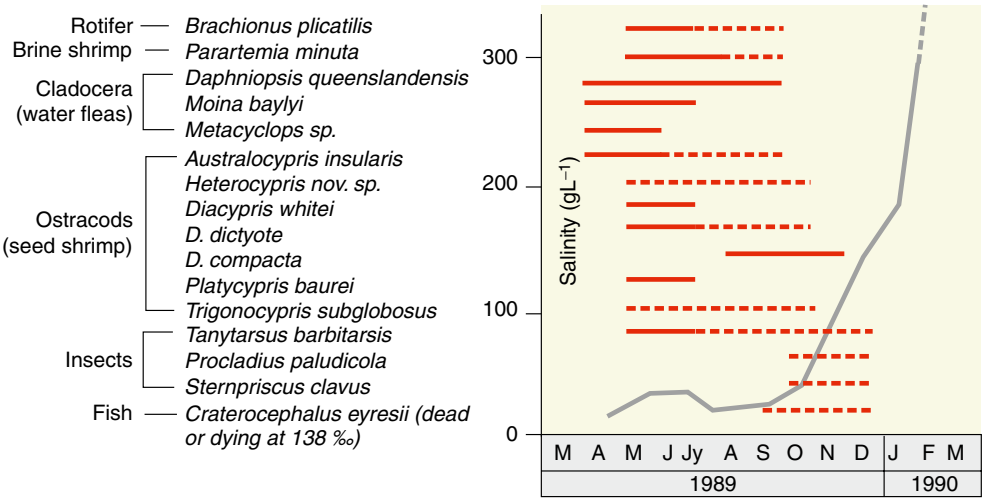

Fig. 9.24 Salinity related occurrences of major macrofauna during the 1989 flooding of Lake Torrens, Australia (After Williams et al. 1998)

gain access to richer food sources and to lay eggs. Brine flies evolved at the start of the Cenozoic and since then, through larval burrowing have restricted the preservation of lacustrine microbiolites, while also creating a diagnostic trace fossil assemblage in saline lacustrine settings (Eggermont and Verschuren, 2006).

Adults and larvae of staphilinid salt beetles also inhabit saline settings. In the Sinai and Tunisian sabkhat as well the Solar Lake cyanobacterial margins, adults of the salt beetle *Bledius carpa* excavate chambered burrows to depths of 10–12 cm in which they store and feed on lumps of cyanobacterial mat (Gerdes et al. 2008). When the mat surface is flooded the beetles can survive for weeks in their submerged burrows.

The contribution of insects to the surface biomass can be high in evaporitic settings, mostly as chitin. But, in terms of their preservation potential as fossils, the remains of most flies and insects, and their carapaces, rank low unless encased in saline concretions (Park and Downing 2001). Then the three dimensional preservation of insect soft tissues is possible via replacement with silica-based minerals as well as calcite, celestite, apatite, and gypsum. But the more usual evidence of arthropods and other invertebrates living in saline settings is via mineralization of faecal pellets and the preservation of burrow traces.

Halotolerant pellet-producing planktonic crustaceans include; ostracodes such as *Cypridistorosa*, *Paracyprideinae sp.*, *Dia-cypris compacta*, and *Reticypris herbsti*, copepods such as *Nitocra lacustris* and *Robertsonia salsa*, and brine shrimp such as *Artemia salina*, *Parartemia zietzianis* and other related species. Halotolerant ostracode remains are a common component of mesohaline sediments, dense populations spread out from refugia and flourish at times of freshened surface water layers (Fig. 9.24). For example, *Platycypris baueri* has the broadest salinity range of any ostracode found in Australia, it is able to survive at salinities ranging from 5 to 195‰, but is much more abundant in the middle of this salinity range and does best in waters with salinities above 70‰ (De Deckker 1981). Yet, it was not present in this upper salinity range during the 1989 flood of Lake Torrens, Australia, when it occurred only at much lower salinities (Fig. 9.24; Williams et al. 1998). The species diversity plot in Lake Torrens shows a typical saline pan biotal response to strandline retreat. This allows the halotolerant terrestrial insect population to follow the retreating strandline to scavenge and feed on the decomposing victims of the increasing salinity in the retreating brine sheet. Thus they are found scurrying about the edges of highly saline water sheets but do not actually inhabit the water.

Brine shrimp (*Artemia sp.*), another cosmopolitan pellet producer in saline settings, survive across a wide range of salinities from 25 to 340‰, with their optimal range around 60–100‰ (Post and Youssef 1977; Torrentera and Dodson 2004). *Artemia salin*a inhabits various mesohaline coastal salinas, atop calcarenite aquifers in the Yucatan, Mexico. These marine-fed North Coast hypersaline pools and salterns show a range of extreme alkalinity, salinity and temperature conditions, as well as hypoxia and in some instances, total desiccation (Fig. 9.25). Weather is characterized by three seasons: rain from the end of June to October, cold storms from October–November to March, and the dry season from March to June. The four locations, Celestun, Chuburna, Xtampu and Las Coloradas salinas, exhibit a similar range in water temperature, nitrites, and phosphates, but at a single time can differ in salinity, oxygen content, water depth, nitrates, ammonia, silicates, carbonates, sulphates, and pH, much like the coastal salinas of the Coorong and Brazil (Fig. 9.25).

The dominant multicellular organism and pelletiser in all these hypersaline ecosystems is *Artemia*. Brine shrimp abundance and population dynamics were significantly correlated

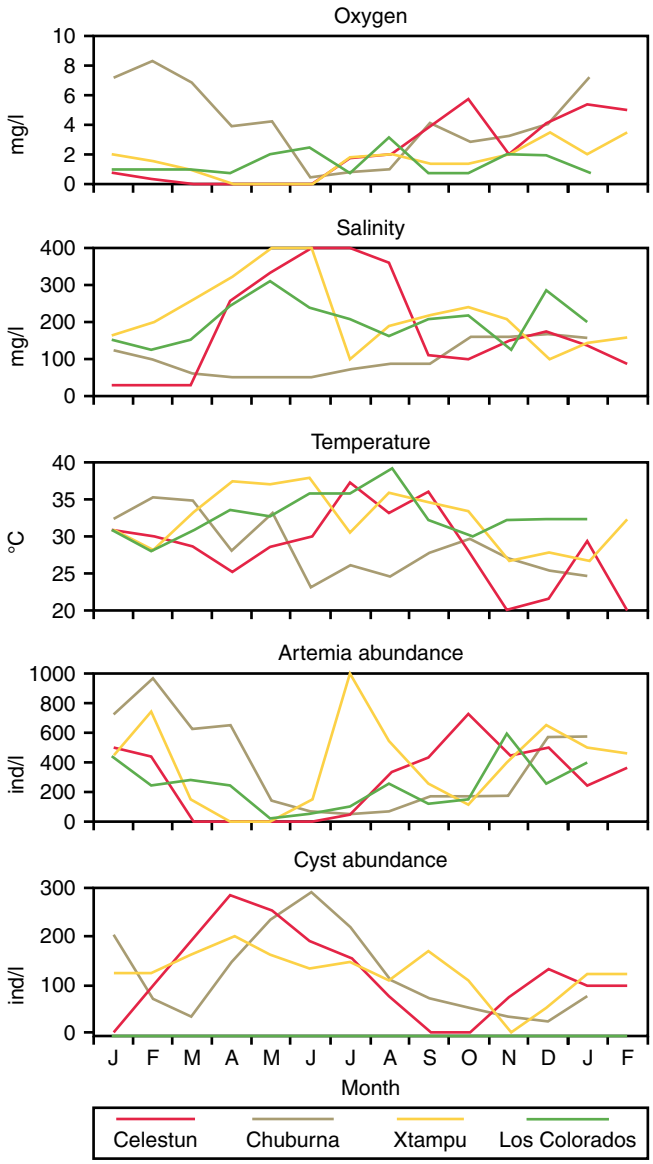

Fig. 9.25 Monthly variations in dissolved oxygen, salinity, temperature, and relative abundance of Artemia individuals and cysts in the Yucatan hypersaline habitats for Celestun, Chuburna, Xtampu and Las Coloradas mesosaline waters (After Torrentera et al. 2004)

with specific environmental conditions, most often water temperature, salinity, and oxygen concentration. Elevated temperature, salinity and low oxygen levels were consistently detrimental to levels of brine shrimp across all settings and encouraged cyst formation. The different schedules of *Artemia* numbers and cyst production at each location suggests hydrological and hence habitat partitioning among the brine shrimp populations (Torrentera and Dodson 2004). Interestingly, large flocks of flamingoes, along with other costal birds including herons and pelicans, inhabit all these saline waters and, along with *Artemia spp*., feed on the planktonic blooms.

Parthenogenetic variants of various *Artemia* species as well as bisexual forms, flourish in marine and continental saline waters worldwide (Triantaphyllidis et al. 1998). Brine shrimp are well adapted to the fluctuating oxygen and salinity levels that characterize mesohaline ecosystems. When conditions become too harsh then the adults respond by producing encysted eggs, which are often found in amongst the pellets in modern evaporitic sediments. Encysted *Artemia* eggs, with their natural cyst coat of glycerol and trehalose can hatch after 4 years of anoxic storage in a laboratory, something that the eggs of most arthropod species cannot achieve (Wharton 2002). Geddes (1975a, b, c) argued increased osmotic stress is the dominant limit on the upper salinity tolerance of adult Australian brine shrimp (*Parartemia zietzianis*) and this is probably also true for most, if not all, *Artemia sp*. in hypersaline waters (Geddes 1981). Halotolerant ostracodes and brine shrimp feed on plankton living in the upper water mass of density-stratified brine columns but can also ingest benthic mats wherever a less saline water mass intersects the lake margin or when bottom waters salinities are suitably lowered (De Deckker 1981; De Deckker and Geddes 1980).

Historically, based on studies in the Northern Hemisphere, centred on Great Salt Lake, brine shrimp have long been considered to be obligate planktonic filter feeders. Any grazing of benthic mats was assumed to take place by accident when the organisms' constant random swimming knocked pieces from the mats into the brine column where it was ingested. But observation of the feeding habits of austral brine shrimp, feeding on microbial scum in the subaqueous gypsum domes of Lake Inneston, South Australia (pers obs.) and on the benthic mats of Lake Haywood in Western Australia (Savage and Knott 1998), show brine shrimp are capable bottom feeders that choose to feed on benthic mats in shallow hypersaline lakes. They will alter their normal planktonic feeding pattern to do so. The animals roll over so their ventral surface faces the benthic mat and their phyllopods continue to beat although all forward motion has ceased. The phyllopods brush the mat, releasing diatoms and cyanobacterial cells, along with crystallites, which are then ingested by the shrimp (Savage and Knott 1998). Both ostracodes and brine shrimp can produce large amounts of pelleted carbonate detritus, which can be a common component of many ancient evaporitic laminites and source rocks (Finkelstein et al. 1999).

Halotolerant gastropods, another pellet producer, follow a benthic lifestyle that allows them to graze on halotolerant algae and plants. Modern examples, such as *Coxiellada sp*., flourish during short periods of freshening in saline environments and are quite common in saline lakes in central Australia and the schizohaline lakes of the Coorong region and the maar lakes in Victoria, Australia. These coxiellids withstand lake desiccation and high salinities (up to 124 ‰) by sealing its aperture with mucous along the edge of its

operculum (De Deckker 1982). Nevertheless, it cannot survive in lakes that remain dry for several years and requires a relatively high frequency of flooding to survive. Low beach ridges, composed almost exclusively of dead coxiellid tests, define the strandzones and berms of many Australian salt lakes. Isolated tests of immature coxiellid gastropods can be found in penesaline sediments well away from the freshened lake margin (e.g., in the somewhat deeper water lacustrine clays of Lake Eyre and some Coorong Lakes). They may have been deposited there as a result of juveniles of the species travelling and grazing upside down along the underside of water-air interface, held there by surface tension forces. As the feeding gastropods grow they become too heavy and lose contact with the air-brine interface. They sink through the salinity-layered water column, only to osmotically desiccate and die in the anoxic hypersaline bottom waters. Complete shells are incorporated in the bottom laminites to give some characteristic biometrics in a biocoenosis of these lacustrine sediments (mostly diminutive adults and very few juveniles).

Marine cerithid gastropods are also halotolerant and can survive in salinites of 80–90‰. The cerithid *Pirenella conica* is typical of these euryhaline snails and is found grazing biolaminites and sandy beaches in the intertidal zones of saline lagoons and sabkhas of the Middle East from Israel to the Emirates and the Red Sea (Taraschewski and Paperna 1981; Jones et al. 1978). These pelletising cerithids are what restricts the seaward extent of the cynaobacterial mats in the lagoons of the Abu Dhabi and Saudi sabkhat.

Some marine foraminifera are commonplace epibionts on marine seagrasses and so where seagrasses can live and survive, so can some species of foram. This is evidenced by the rich benthic foraminiferal biota living on seagrass banks in Shark Bay, Western Australia where mesohaline salinities ranging from 40 to 56‰ and occasionally up to 70‰, yet even at this level of salinity stress a few porcelaneous taxa still grow and survive (Davies 1970). The large benthic foram *Marginopera vertebralis* is one of the Shark Bay inhabitants; Pleistocene tests of this species, with elevated carbon and oxygen isotope values, have been interpreted as indictors of hypersaline waters along the semiarid southern Australian shelf during Pleistocene sea level lows (Rivers et al. 2009). One of the most impressive modern halotolerant forams is *Peneroplis planatus*. In Khor al Bazam, Abu Dhabi, it is epiphytic on seagrass in lagoon waters with a salinity of 42‰ and on seaweed growing in the same mesohaline lagoon in salinities ranging up to 70‰ (Murray 1970).

The ability of some marine foram species to survive across a range of salinities has led to some interesting death assemblages in continental lacustrine sediments of inland Australia. Viable marine foraminifera were documented in waters in a number of Australian salt lakes by Cann and De Deckker (1981). Some species can encyst and survive fluctuating salinities and periods of desiccation in both coastal and inland salt lakes, whereas others can only be found in permanent waters. Forams in continental settings generally prefer salinities and/or chemistries of lakes that approach that of seawater, optimum growth and the appearance of new generations typically occur at these thalassohaline values.

Two such species that flourish during short periods of flooding in the inland Australian salt lakes, such as Lake Eyre, are *Ammonia beccarii* and *Elphidium crispum. A. beccarii* requires water chemistries and salinities similar to seawater, i.e., with sodium and chloride as dominant ions. Although this species can survive a broad range of salinities (from 7 to 67‰), it grows and reproduces most successfully at salinities between 20 and 40‰ (Cann and De Deckker 1981; De Deckker 1982). Encysted forms of *A. beccarii* cannot survive summer droughts in modern coastal salinas and require permanent surface waters in order to persist. *E. crispum* is a marine foram species that thrives in ephemeral saline lakes of the Coorong without needing avian replenishment after a drought. It can survive summer evaporative episodes by encysting in numbers necessary for widespread re-establishment in the following winter freshening. The salinity range of this species is as yet unknown, although it is thought to survive at relatively high salinities (De Deckker 1982).

Encysted forms of both species are carried hundreds of kilometres inland on the feet and feathers of coastal sea birds, which flock every few years to newly flooded inland salt lakes, such as Lake Eyre, in order to nest and feed (a time of "feast" in mesohaline lake waters). If surface water salinities are suitable the forams bloom. Later, as salinities in these inland lakes increase once more, the foram population dies back and tests are deposited in a lacustrine sediment matrix (Ludbrook 1965). In the Dead Sea Rift, similar avian-transported A*mmonia beccarii tepida* fossils typify marl and sandstone beds in lacustrine evaporitic sediments, which have accumulated at times of freshening of upper lake waters across the past 2 million years (Almogi-Labin et al. 1995). Occurrences of *Ammonia beccarii* in mesohaline lacustrine sediments of the Pliocene Bouse Formation, southwest USA, are assigned a similar avian transport genesis (Spencer et al. 2013). Even more ancient counterparts, preserving evidence of this opportunistic lifestyle, could create a palaeontological dilemma.

Halotolerant protists, like the forams just discussed, lack a cell wall, can be planktonic or benthic and typically ingest algae and bacteria. Protists are unicellular eukaryotes that were once classified as single-celled animals under the general term protozoa, but as some are not animals this term is now obsolete. Protists are phylogenetically grouped in the Eukaryota at the same level (Kingdom) as animals, plants and fungi. Protists encompass groups such as the rotifers, forams, radiolaria and alga, the term is sometimes described as the

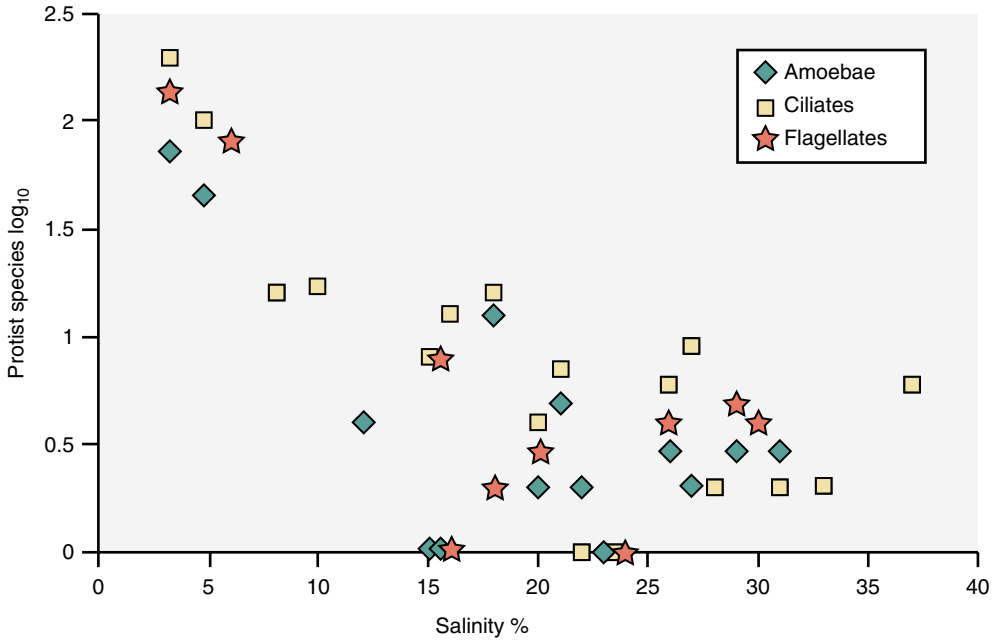

Fig. 9.26 Number of documented protist species in various saline settings across a range of salinities (After Hauer and Rogerson 2005)

polyphyletic "grab-bag for all eukaryotes that are not animals, plants or fungi" (Simpson and Roger 2004). Identified protist species living in hypersaline waters include the moderate halophile ciliate *Fabrea salina*, it has been collected from Hutt Lagoon in coastal West Australia, where it feeds on populations of *Dunaliella salina* (Fig. 9.19). In the coastal salinas of Sfax, Tunisia *Fabrea salina* is the main competitor heterotroph to the brine shrimp, *Artemia salina* (Elloumi et al. 2006). Another well-adapted protist is the extreme halophile *Porodon utahensis* from the Great Salt Lake, Utah (DasSarma and Arora 2001). Salt-tolerant rotifers (aka wheel animalcules) include species such as *Brachionus angularis* and *Keratella quadrata*. There is also a highly adapted set of protists inhabiting the halocline in the various deepsea brine lakes on the seafloor of the eastern Mediterranean (Edgcomb et al. 2009). Like the invertebrates and vertebrates, the number of viable generalist protist species decreases with increasing salinity and only more specialised species flourish at elevated salinities (Fig. 9.26; Hauer and Rogerson 2005).

Fungi, mostly yeasts (unicellular fungi), are another significant component of a saline salt lake biomass, like *Hortaea werneckii*, a black yeast that occurs in its highest numbers in waters at salinities indicating the onset of halite saturation and yet it can also live in fresh water and on us. In the latter case it causes a rare superficial and non-invasive skin infection *Tinea niger* with typical symptoms being non-scaly, smooth, black-brown painless spots, usually on the palm of the hands and the soles of the feet. It is a truly halotolerant species (Gunde-Cimerman et al. 2000; Gostincar et al. 2011).

Such fungi are chemoheterotrophic eukaryotes that grow best in aerobic saline conditions on carbohydrate substrates at moderate temperatures and in acidic to neutral pH brines. For example, a saprophytic hyphomycete (a minute fungi), *Cladosporium glycolicum*, was found in the Great Salt Lake Utah, growing on submerged wood panels at a salinity exceeding 260‰ it has also been isolated from brines in the Dead Sea. *Debaromyces hansenii* is another halotolerant yeast that when isolated from seawater can grow aerobically in salinities up to 250‰ and is capable of assimilating hydrocarbons, it has commercial significance as a biocontrol in the wine and chees industries, as do other salt-adapted fungi (Gunde-Cimerman et al. 2005, 2009; Gostincar et al. 2011). *H. werneckii* is polymorphic and is heavily melanised (black) with thick cell walls and it adapts its shape and lifestyle according to ambient salinity. At the highest salinities it exhibits an isodiametric type of thallus expansion, resulting in highly resistant meristematic cell clumps with endogenous conidiation (asexual spores). At lower salinities it grows as yeast cell clumps or as hyphae (filaments), depending on the substrate.

Extremophiles (Mostly Archaea)

The term extremophile is used to describe a group of organisms that from an anthropocentric viewpoint, "live in the borderlands of physiological possibilities" and utilises a number of specialised biochemical pathways (Table 9.5). This life group has evolved to flourish in extremes that can be defined in terms of temperature, salinity, acidity/alkalinity aridity, oxygen levels, pressure, radiation and various combination (Table 9.6; Seckbach 2005). We shall focus our attention on extremophiles that are well adapted to evaporitic environments (Fig. 9.27).

Table 9.5 Examples of the biochemical metabolic pathways utilised by archaea

Biochemical pathway reaction	Biochemical pathway reaction
Hydrogen oxidation	$2H_2 + O_2 \rightarrow 2H_2O$
Sulphur reduction	$H_2 + S^0 \rightarrow H_2S$
Sulphide oxidation	$4H_2S + 2O_2 \rightarrow 4H_2SO_4$
Sulphur oxidation	$2S^0 + 3O_2 + 2H_2O \rightarrow 2H_2SO_4$
Nitrate reduction	$H_2 + NO_3 \rightarrow NO_2 + H_2O$
Iron reduction	$H_2 + 2Fe^{3+} \rightarrow 2Fe^{2+} + 2H^+$
Methanogenesis (autotrophic)	$CO_2 + 4H_2 \rightarrow CH_4 + 2H_2O$
Methanogenesis (heterotrophic)	$4CH_3OH \rightarrow 3CH_4 + CO_2 + H_2O$
Methanogenesis ("acetoclastic," heterotrophic)	$4CH_2COO^- + H_2O \rightarrow 3CH_4 + HCO_3^-$
Aerobic respiration	Organic compound $+ O_2 \rightarrow 2H_2O + CO_2$

Table 9.6 Extremophile characteristics

Environmental parameter	Type	Location and conditions	Examples
Salinity	Halophiles	Salt lakes, sabkhas and salterns (neutral and alkaline pH) up to and including halite saturation. Adaptation to cope with extreme osmotic pressure (salt in/out and glycerol)	Cyanobacteria, brine shrimp, diatoms, flagellates, *Dunaliella*, *Halobacteriaceae* (see text for detailed discussion)
pH	Acidophile	pH >5 and as low as 0–1 in some hydrothermal springs	*Acidithiobacillus sp*., *Picrophilus oshimae*, *Cyanidium caldarium*, *Dunaliella acidophila*, some fungi – *Trichosporon cerebriae*
	Alkaliphile	pH >9 in some African rift lakes	*Natronobacterium*, *Natrialba sp*., *Bacillus alcalophilus*, *Halomonas sp*., *Chromohalobacter sp*., *Arthrospira sp*.,
Temperature	Psychrophiles	−20 °C to >15 °C	*Psychrobacter*, *Polaromonas*, cyanobacteria, sea-ice diatoms and icy green algae, some insects.
	Thermophiles	45–80 °C	*Alicyclobacillus sp*.
	Hyperthermophiles	80–114 °C	*Aquifex*, *Thermotoga Cyanidium caldarium*, *Sulpholobus*, *Methanothermus*, *Pyrolobus fumarii* (alive at 114 °C) *Methanopyrus kandleri* (alive at 122 °C), prokaryotes such as *Mastigocladus*,
Hydrostatic pressure	Barophiles Piezophiles	Weight lovers Pressure lovers	Prokaryotic strain MT41 can tolerate pressures of more than 100 MPa
Radiation	Ultraviolet and ionizing	High level of radiation	Cyanobacteria, desert plants, archaeon *Thermococcus gammatolerans* and bacterium *Deinococcus radiodurans*
Thriving in organic solvents and under various atmospheres	CO_2 gas	Thriving in pure gas	*Cyanodiaceae* (grown in pure CO_2)
	Organic toxic solutions	Solutions with damaging agents	
Gravity	Hypergravity	>1 earth gravity	Such microorganisms not known on Earth (may be a significant factor in extraterrestrial environments)
	Hypogravity	<1 earth gravity	
Desiccation	Xerophiles	Anhydrobiotic conditions, low water activity	Prokaryotes, extreme halophiles on endoliths, fungi and lichens. Anhydrobiotic states in bacteria, yeast, fungi, plants, and animals such as nematodes and brine shrimp

After Seckbach 2005

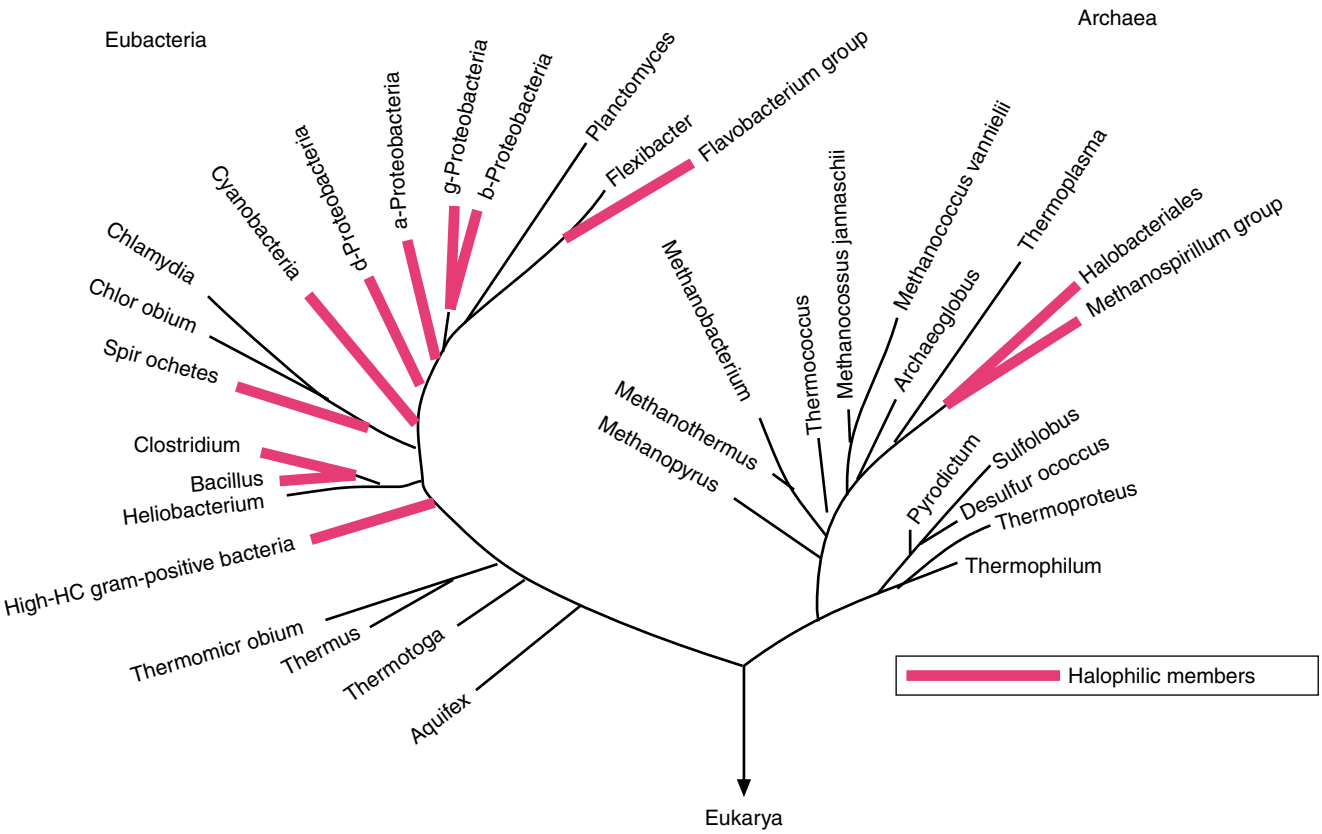

Fig. 9.27 Phylogenetic tree of the Bacteria and the Archaea, based on 16S rRNA sequencing comparisons, Bold lines indicate branches containing representatives able to grow at or near optimal rates at NaCl concentrations exceeding 15 % (After Ventosa et al. 1998)

As surface water salinities rise above 200–240‰, rates of oxygenic photosynthesis in algae and cyanobacteria slow and ultimately cease. Halophilic bacteria and archaea come to dominate, many as decomposers and fermenters (Fig. 9.17). Of the halophilic bacteria, two groups are well represented in elevated salinity ranges; the fermentative bacteria belonging to the family Haloanaerobiaceae and the halophilic members of the autotrophic sulphur-oxidizing bacteria of the family Ectothiorodhospiraceae. Both families were discussed earlier in this chapter. As the name suggests, the group loosely called halobacteria[12] flourish in supersaline waters, most halobacteria are not bacteria but archaea, which constitute the family Halobacteriacea. In taxonomy, the Halobacteriaceae are a family of the Halobacteriales in the domain Archaea.

One species of halophilic bacteria is worthy of special mention is *Salinibacter ruber* as, unlike most other Bacteria, it can flourish in the range of extreme salinities that until recently were considered to be the exclusive province of the Archaea. It constitutes a new genus and species, first isolated from brines found in saltern crystallizer ponds in Alicante and Mallorca, Spain (Oren 2002). *Salinibacter* is a motile rod, pigmented red (probably by a carotenoid) with an absorption maximum at 482 nm and a shoulder at 506–510 nm. Because of the red pigmentation, colonies of this bacteria in superhaline waters have probably been overlooked in the past. Historically, red colonies growing at salinities in excess of 250 g/1 have been widely considered to be archaeal. But this bacterial organism is no less halophilic than the archaeal halophiles: no growth was obtained below 100 g/1 NaCl, and for optimal growth concentrations between 150 and 230 g/1 are required. The physiological properties of *Salinibacter* are unusual for most bacteria: the organism apparently uses KCl to provide osmotic balance, while lacking high concentrations of organic osmotic solutes. Thus, its physiology resembles that of the halophilic Archaea more than that of other aerobes within the domain

[12]The term halobacteria (as opposed to the family *Halobacteriacea*, which exclusively encompasses the halophilic archaea) is a terminological carry-over from the old two-part morphology-based classification of life (see earlier discussion of Woese and his influence on microbial nomenclature and classification). When trying to make sense of the taxomic complexities that typify the microbial realms one should always remember that in contrast to eukaryotic nomenclature, there is no such thing as an official classification of prokaryotes. It remains a matter of scientific judgment and general agreement. The closest approximation to an "official" classification of prokaryotes would be one that is widely accepted by the community of microbiologists. The debate continues.

Table 9.7 Metabolic associations of some of the main halophilic archaeal genera

Metabolic process	Energy source	Carbon source	e- donor	e- acceptor	Conditions	Occurrence	Cultured representatives
Aerobic respiration	Organic matter (sugars, amino acids, glycerol…)	Organic matter	Organic matter	O_2	Moderate to extreme salinities (from 7 to 370 ‰)	Salt lakes	Haloarcula, Haloferax, Halorubrum, Natrinema
Anaerobic respiration		Organic matter		Nitrate, DMSO, organic acids	High pH	Soda lakes	Halobacterium, Haloarcula, Haloferax
Fermentation	Sugars, amino acids	Organic matter		Organic matter	Oxic, anoxic	Hypersaline Antarctic lakes	Halobacterium
Nonphotosynthetic photo heterorophy	Light	Organic matter	Organic matter	–		Solar salterns	Halobacterium

After Likens 2010

Bacteria. It tends to fluorish in lakes with elevated salinities and is a co-inhabitant with halophilic archea in many modern salt lakes (Boutaiba et al. 2011).

We shall now concentrate on salinity ranges of halophilic archaea known as haloarchaea. Haloarchaea require salinities in excess of 100‰ to live, and most achieve optimal growth at higher salinities, typically in the range 200–250‰. Haloarchea can survive in salinities approaching halite saturation (350–370‰). All known extremely halophilic archaea stain gram negative, do not form resting stages or spores and reproduce by binary fission or budding (Table 9.7). Cell diameters range from 0.1 to 15 μm and the length of a filament can be up to 200 μm (Oren 2002) They are morphologically diverse and cell shapes include spheres, spiral, rods, lobed, plate-shaped, irregular-shaped or pleomorphic variations. One of the more unusually-shaped Haloarchaea is the "Square Haloarchaeon of Walsby" or *Haloquadratum walsbyi*, which is square and thin in shape, giving it a morphology much like a postage stamp. Haloarchea may exist as single cells, as aggregates, or form filaments. Most Haloarchaea are considered pleomorphic, able to take on a range of shapes-even within a single species, they can extrude biofilms and can exchange their DNA at the genera level. This set of characteristics makes identification by any microscopic means difficult, so gene-sequencing techniques are used for species identification.

As of 2014, the family Halobacteriaceae currently possesses about 40 recognised genera and 144 species, with new genera and species being added every year (http://www.bacterio.net). Main taxonomic criteria for the identification and recognition are the sequence of the 16S rRNA genes and the composition of their characteristic membrane polar lipids, which are unique to the group and are composed of ether-linked phosphoglycerides (Fendrihan et al. 2006; Stan-Lotter 2011). Some of the more currently accepted haloarchaeal genera are as follows: *Haloarcula* (10 species); *Halobacterium* (*16 species*); *Halobaculum* (2 species); *Halococcus* (8 species); *Haloferax* (11 species); *Halorubrum* (25 species), *Haloterrigena* (9 species); *Natrialba* (6 species); *Natronobacterium* (6 species); *Natronococcus* (4 species); *Natronomonas* (2 species).

Cosmopolitan haloarchaea genera are *Halobacterium*, *Haloferax*, and *Halococcus* (Table 9.7). Haloarchaeans tend to prefer somewhat acidic to near neutral pH brines and so are commonplace in marine-fed brines, seeps, sea-bottom brine lakes and continental salt lakes. Some Archaea flourish in caprock brines, along with the sulphate-reducing bacteria and are also resident in sulphuric acid caves. *Halococcus sp*. are strict aerobes, their name reflects their coccoid cell shapes; they form pairs, tetrads, sarcinae or irregular clusters. Cells produce several orange or red carotenoid and retinal pigments needed to better cope with high levels of ultraviolet light that characterise supersaline brine sheets in arid settings. *Haloferax* prefers high Mg waters and is a major constituent in the halophilic biota of the Dead Sea. The pleomorphic *Haloarcula* typically grows with square and triangular shapes, with straight edges, sharp corners, and is very flat. In its square form it has a shape that is very similar in appearance to the interstices and brine vacuoles in a mass of halite crystallites.

Interestingly, highly saline microbial communities are dominated by extremely halophilic archaeal cells with square-shaped morphologies, they are likely pleomorphic genera and account for up to 75 % of total prokaryotes beyond 350 g/l (Likens 2010). Densities in these brines can be as high as 10^8 haloarchaeal cells per ml. These highly angular shapes are unusual for a lifeform and only possible because internal salt concentrations are as high as they are outside the cell (see cellular adaptations). It mean there is little or no net osmotic pressure on the cell wall, allowing it to adapt such high surface-area shapes. Similar shapes are not possible for organisms with 'normal' ionic strengths in the cell interior. Their cell shapes show surfaces and outlines that are indicative of "minimization of surface energy," whereby curved edges and spheroid outlines dominate.

Of the recognized genera of haloarchaea, two have representatives that live only in high pH soda lakes, such as Wadi Natrun and Lake Magadi, they are; *Natronobacterium* and *Natronococcu*s. They grow in highly alkaline trona-rich brines (pH 9–11) with very low levels of Mg (<0.024 g/l) and show optimal growth around 200‰. This group of Archaea is not found in marine-fed salterns or less alkaline continental systems (Grant et al. 1999). How *Natronobacterium* and *Natronococcu*s, and also the alkaliphile bacterium *Bacillus alcalophilus*, survive in soda lakes with these extreme chemistries is a problem not yet well understood (or at least it is a problem for us, trying to understand how they get can away with it). At such elevated pH levels any protons (H^+) pumped to the outside of a cell by electron transport or rhodopsin membranes, are sucked up by the hydroxyl ions and gone forever. Even though the resulting electric potential is still there, it can't be harvested by an ATPase-based metabolism, unless it can recycle protons from outside the cell (see next section).

How alkaliphiles get around this problem is not known, and it is probably the issue that limits the upper pH range of life. Proposed and partially documented high-pH coping mechanisms in alkaliphiles include; (i) buffering cell cytoplasm using polyamines rich in amino acids with positively charged side groups (lysine, arginine, and histidine), (ii) introducing acidic compounds to protect the cell from the alkaline environment (e.g., teichoic acid, acidic amino acids, and uronic acids), (iii) Na^+-ion channels actively driving the transfer of protons into the cell, (iv) synthesis of specific enzymes resistant to high pH.

Methanogenic archaea, as the name implies, produce methane as a byproduct of their autotrophic metabolism. Methanogens are all Archaea and constitute the strictest anaerobic grouping known. In saline settings, most methanogens do best in anoxic waters with salinities less than 150‰. No other group of living things breathe methane and so their metabolic enzymes are unique (as are the related biomarkers). Several, mostly moderate halophilic, methanogens have been identified in saline ecosystems and include *Methanohalophilus halophilus* from a microbial mat in Shark Bay, *M. mahii* fromsediments of the Great Salt Lake, and *M. portucalensis* from a coastal saltwork sediments in Portugal (Horikoshi et al. 2011). The slight halophile *Methanosalsus zhilinac* is also an alkaliphile and a slight thermophile. The extremely halophilic methanogen, *Methanohalobium evestigatum* comes from a salt lake in the Crimea; it has an NaCl optimum of 260‰ and is also a thermophile with a temperature optimum of 50 °C. Worldwide these and other methanogens form the base level in chemosynthetic foodchains in salt lakes and are common contributors to the chemosynthetic biota of deep-sea brine pools atop salt allochthons in the Gulf of Mexico (Fig. 9.58).

Methanogenesis oxidizes hydrogen using metabolic mechanisms that are not sufficiently efficient to rip out all the hydrogen from the carbon chains. As a biochemical process it occupies a terminal position in the degradation of carbohydrates in the reaction cycle of hypersaline ecosystems. Methanogenic Archaea in hypersaline environments utilise noncompetitive organic substrates such as methanol, methylated amines, and dimethyl sulphide, which originated largely from the breakdown of osmoregulator amines (osmolytes). Methanogens do not utilise carbon dioxide, acetate and hydrogen, which are the substrate for the sulphate-reducing bacteria living nearby. The reason for this metabolic restraint is the greater effectiveness of sulphate-reducing bacteria, which are out-competing methanogens for hydrogen and acetate (i.e., methanogens eat the leftovers).

Cellular Adaptations to Hypersalinity

Halotolerant and halophilic species have developed special biochemical mechanisms to cope with the tendency for cells to desiccate in the high osmotic pressures of mesohaline and hypersaline waters namely; slime, osmolytes, halo-adapted membranes and specialized proteins. Halotolerant cyanobacteria constitute a significant component of the upper layers in microbial (algal) mats in modern sabkhas and shallow brine lakes where they are subject to both periodic desiccation and hypersalinity. Such microbial mats show a worldwide recurrence of a few well-adapted cosmopolitan cyanobacterial species in the upper stories of a microbial mat; *Microcoleus chthonoplastes*, *Lyngbya sp*., *Entophysalis sp*., and *Synecococcus sp*. All are slimy; they are embedded in matrices of extracellular polymeric mucous that stores large amounts of water. It protects the cell from osmotic stress and acts as a buffer against extreme temperatures and ultraviolet rays (Gerdes et al. 2000a).

Other halotolerants and all halophiles adapt to osmotic stress at the intracellular level. *Dunaliella parva*, a halotolerant unicellular green alga that flourishes in mesohaline waters (optimum = 120‰, survival 20–340‰), distributes glycerol throughout its cytoplasm to increase the total solute concentration in the cell and so better cope with the high osmotic pressure induced by its high salinity surrounds. Glycerol is an osmotically active substance (osmolyte) that takes up space in the cellular fluids. It lowers the relative water content of the cell and so raises the internal osmotic pressure. Cytoplasmic concentration of glycerol in *Dunaliella parva* can reach 7 mol/l and can constitute over 50 % of the dry weight of cells growing in salinities ≈280‰. *Dunaliella* is the main primary producer in the Dead Sea brines and produces isotopically heavy ^{13}C products. The consumption of this isotopically heavy glycerol by Halobacteriales (main heterotroph in Dead Sea) in turn leads to ^{13}C enrichment of

their biomass (Grice et al. 1998). Glycerol is used as an osmolyte in other halotolerant and halophilic algae, as well as by yeasts, fungi and brine shrimp. Halotolerant and halophilic prokaryotes also use a variety of other sugars, sugar alcohols, amino acids and compounds derived from them (such as glycine betaine and ectoine) as osmolytes, leading to characteristic biomarker assemblages in ancient saline sediments (Turich and Freeman 2011).

Halophilic archaea have two main intracellular defence mechanisms to cope with the extreme osmotic gradients induced by hypersaline to supersaline conditions. One is a modification of the plasma (cell) membrane; the other is an adaptation of the protein structure itself. Unlike most life, the plasma membrane of halophilic archaea is dominated by rhodopsins and the cell membrane does not actively exclude salts, so the overall internal salt concentration in haloarchaeal cytoplasm is high. But the cell membrane is selective, it tends to exclude sodium, while actively pumping potassium into the cell against a thousand-fold concentration gradient. The total ionic strength remains the same on both sides of the plasma membrane, but the ratios of specific ions differ inside and outside the cell wall. Potassium is the dominant cation within the cell. Many cell functions require potassium, but would be disrupted by high levels of sodium. Cells of halophilic archaea can contain up to 4 mol/l of potassium chloride, which is eight times its concentration in seawater. Anaerobic fermentative halophilic bacteria of the order Haloanaerobiales use a similar "high potassium in the cell" strategy.

Rhodopsins (bacteriorhodopsins) constitute much of the protein in the purple patches in the cell membranes of photo-active haloarchaea. Patches contain 25 % lipids and 75 % protein, all of which is bacteriorhodopsin (Fig. 9.28a). Bacteriorhodopsin structure is arranged in groups of 3 protein molecules surrounded by a lipid with a few more lipids in the centre of the molecular cluster. These light-sensitive purple pigments convert light energy into chemical energy (proton pump) and so power the cell's ion pump (Fig. 9.28b). Thus, the purple membrane is a site of photosynthesis, but not the chlorophyll-based photosynthesis of cyanobacteria and eukaryotes. Purple membranes obtain energy from light but, unlike chlorophyll, do not use light to generate reducing power and cannot fix CO_2. Haloarchaea with purple membranes are still mostly heterotrophic but can function as facultative autotrophs in low oxygen conditions where they supplement their metabolic power with photosynthesis via the purple membrane patches. Almost all of this extra energy is used to pump potassium across the cell membrane and so maintain the cellular ionic balance (Fig. 9.28b).

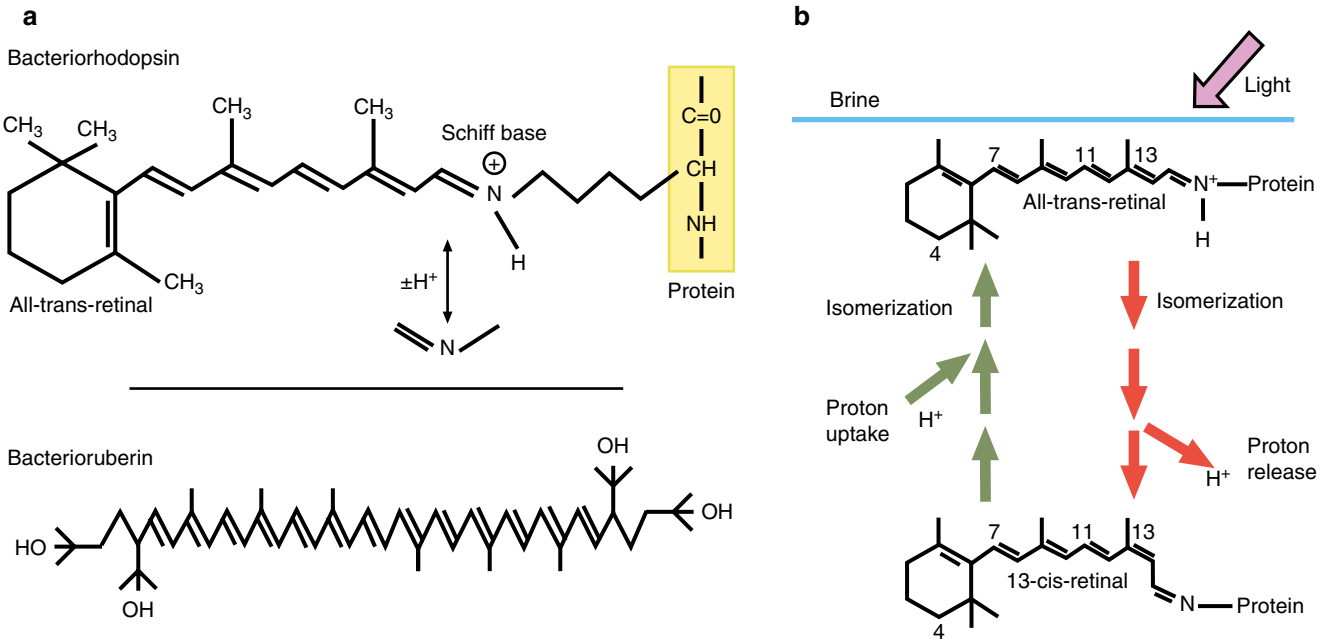

Fig. 9.28 Fischer projections of bacteriorhodopsin, bacterioruberin and the proton pump (MW = approximately 25,000), (**a**) Molecular structure emphasising retinal. Overall, bacteriorhodopsin is a protein that has 7 alpha-helical segments each spanning the halobacterial cell membrane. It contains one molecule of retinal per protein molecule which is bound via a Schiff base to the side chain -NH_2 group of a lysine residue. The Schiff base lysine is located 40 amino acids from the N-terminus and is near the outside of the membrane in the second helical segment. Interaction of retinal with the protein causes a large red shift, and hence light absorption is at 560–570 nm. The pigment looks purple when bound to the protein. Also shown is the structure of bacterioruberin. (**b**) Photon pumping; light rapidly changes the "straight" all-trans form of retinal in bacteriorhodopsin into the "bent" 13-cis form of retinal, with a concomitant release of a proton outside the cell membrane. The 13-cis form spontaneously returns to the all-trans form in a light-independent reaction, with the concomitant uptake of a proton from within the cell

As an example of the adaptive chemistry of this halophilic lifestyle, consider the archaea *Halobacterium halobium*. Its cell carries a combination of orange-red carotenoids: mostly β-carotene (C-40) and bacterioruberins (C-50). It is an aerobe facultative anaerobe. When oxygen levels fall, as often happens in hypersaline water bodies, but light still penetrates the brine, anaerobic photophosphorylation takes place in the cell membrane in the absence of chlorophylls and redox carriers. Waters and sediments where *H. halobium* flourishes then take on a blue or purple tint, as in the Dead Sea. In the past, prior to gene sequencing studies, bacteriorhodopsin's characteristic purple colour led to many haloarchaea in their photoactive stage being described as a separate species of purple bacteria. In the same brines but with higher oxygen levels, the main cellular metabolism of *H. halobium* is heterotrophic, not photoautotrophic. Cells in the heterotrophic mode are mostly coloured by carotenoids and now waters where it is thriving appear red, not blue-purple. This is its more normal respiratory metabolic mode in hypersaline waters, where it depends on b and c cytochromes as well as cytochrome oxidase to create ATP via the breakdown of glycerol and the other cellular contents from the now dead algae (especially *Dunaliella*) and cyanobacteria. This cytochrome-mediated pathway is not a particularly effective metabolic pathway for decomposers living at lower salinities. But in hypersaline waters these more efficient metabolic pathways cannot function. So, these highly salt-adapted halophilic cells can respire and produce ATP using their red membranes (carotenoids), under little or no stress from any other competing life forms, even if brines maintain relatively high levels of oxygen. The adaptive chemistry of *H. halobium* means it acts as a decomposer in oxygenated water, and as an anaerobic phototroph in dysaerobic to anoxic, but lit, hypersaline waters. There it can survive, although at lower metabolic rates, by using its purple membrane patches (bacteriorhodopsin) to pump protons across the cell membrane (Oesterhelt and Marwan 1993; Kates et al. 1993). Interestingly, the same species can colour the waters it inhabits either red or purple in response to changing oxygen levels.

Bacteriorhodopsin in the purple membrane of haloarchaea is best described as a two-dimensional oriented crystal containing the pigment molecule retinal. When bacteriorhodopsin captures a photon with its retinal "antenna" this induces isomerization of the retinal, which then becomes detached from the protein, triggering conformational changes in the protein itself (Fig. 9.23b). This eventually leads to a bleaching and the pumping of a photon across the cell membrane. Bacteriorhodopsin has an orderly orientation or "sidedness" in the plasma membrane, such that when it releases hydrogen/Na^+ ions in an illumination and bleaching cycle, the hydrogen ions are expelled only at the outer side of the membrane (ion pump). Conversely when bacteriorhodopsin regains its colour the necessary hydrogen can only approach from the inside of the membrane. Thus a cycle of bleaching and recovery sets up a hydrogen ion pump, which in turns sets up an energy gradient that drives ATP synthesis.

What is so impressive about bacteriorhodopsin is its extreme durability and stability. It survives intact at temperatures up to 140 °C and can reliably run through a photocycle more than 10 million times. There are a large number of intermediates in the bacteriorhodopsin reaction cycle, each of which can be addressed by light of a specific wavelength. This has led many to proclaim its potential in the development of biomolecular computers and biological solar cells. Synthetic bacteriorhodopsin is a working biostable optical switch, it can be fabricated in a monolayer by self-assembly and reliably store data with 10,000 molecules per bit. In the early 1970s it was extensively studied in the former Soviet Union as a way to counteract the West's dominance in semiconductors, some of this research is still classified as a state secret in Russia today.

Some halophilic archaeal strains, including *Halobacterium salinarium*, contain another rhodopsin pigment in their purple membrane called halorhodopsin. It acts as a Cl- pump, once again generating energy in highly saline conditions. It is usually present in the cell membrane in much smaller amounts than bacteriorhodopsin, but contains the same retinal pigment. It too absorbs light, which it converts to an ion gradient. However instead of pumping protons out, like bacteriorhodopsin, it pumps chloride ions inwards, which helps maintain osmotic balance in highly saline conditions. Since chloride ions have a negative charge, moving chloride inwards is equivalent in terms of energy to moving a proton outwards. Thus halorhodopsin generates a chloride ion gradient, which also supplies energy to the cell.

All this membrane adaptation merely shifts the osmotic balance problem from the cellular to the molecular level. Ions within the cell's cytoplasm still compete with proteins and other biomolecules for that universal solvent, water. In order to cope with high osmotic stress at the molecular level, halophilic archaeal proteins have evolved to maintain a high negative charge on the protein surface. This attracts water molecules and envelops the protein in a protective shroud of bound water.

For example, in the Dead Sea halophilic archaea (*Haloarcula marismortui*) the proteins of its metabolic enzyme (malate dehydrogenase) and its electron transfer protein (ferredoxin) are both wrapped in coats of acidic amino-acid sidechains, both of which carry a negative charge in neutral media. This predominance of charged amino acids on the surface of enzymes and ribosomes stabilizes the hydration shell of various cytoplasm molecules in high salinity intracellular surroundings, even when the extracellular brines are well into the halite saturation field. High-density surface charge binds water molecules to the

protein surface much more effectively than any mesophile protein. Hence, *Haloarcula* proteins do not dehydrate or unfold (denature) even when exposed to extremely high salinities. But, high levels of shielding cations (mostly potassium) are lost via osmosis in low salinity environments and an excess of negatively charged ions then destabilizes the molecular structure by ionic repulsion and the proteins lyse or disintergrate. Any species using a "salt in cytoplasm" strategy has an innate restriction to highly saline environments (obligate halophiles). Ironically, the intracellular acids that unfold normal proteins, counteract this tendency in the halophiles.

In summary, bioadaptations at the cellular level to highly saline conditions can be divided into two groups of responses (Oren 2001):

(a) **The "high-salt-in" option**. Accumulation of salts in the cytoplasm at concentrations equal to or higher than those of the outside medium. Generally, KCl is used as the main intracellular salt. Aerobic halophilic archaea (family *Halobacteriaceae*) utilise this strategy, as do fermenting bacteria, bacterial acetogenic anaerobes (*Haloanaerobium*, *Halobacteroides*, *Sporohalobacter*, *Acetohalobium*), and some sulphate reducers. This strategy is relatively inexpensive energetically, but requires far-reaching adaptations by the intracellular enzymatic machinery to the presence of high salt concentrations. Cells utilising this strategy show limited adaptability to changing salt concentrations (obligate halophiles) and have achieved success only after a long and complex evolutionary history.

(b) **The "low-salt-in" option**. Exclusion of salts from the cytoplasm and the accumulation of organic osmotic 'compatible' solutes (osmolytes) to provide osmotic balance. This strategy is used by halophilic and halotolerant eukaryal microorganisms, by most salt-requiring and salt tolerant bacteria, and also by halophilic methanogenic archaea. This strategy is energetically expensive; the energetic cost depends on the type of organic solute synthesized. No major modification of the intracellular machinery is needed in comparison to non-halophiles, and in most cases cells can rapidly adapt to changes in salinity, as exemplified by *Dunaliella salina*.

As Oren (2001) clearly illustrates, organisms living in increasingly high salinity environments have to devote increasing large proportions of their bioenergetic budgets to osmoregulation, either to synthesize organic solutes or to activate and maintain ionic pumps. This creates a natural salinity-related control over various metabolic pathways, their energy efficiencies and hence their biomarker distributions in the resulting sediments. The following metabolic styles function best at high salinities (Fig. 9.29):

1. Those processes that use light as an energy source (and are generally not energy-limited).
2. Heterotrophs (bacteria as well as archaea) that perform aerobic respiration, denitrification, and other dissimilatory processes that yield large amounts of ATP.
3. All types of metabolism performed by organisms that use the 'high-salt-in' strategy, even if the efficiency and amount of ATP obtained in their dissimilatory metabolism is low.

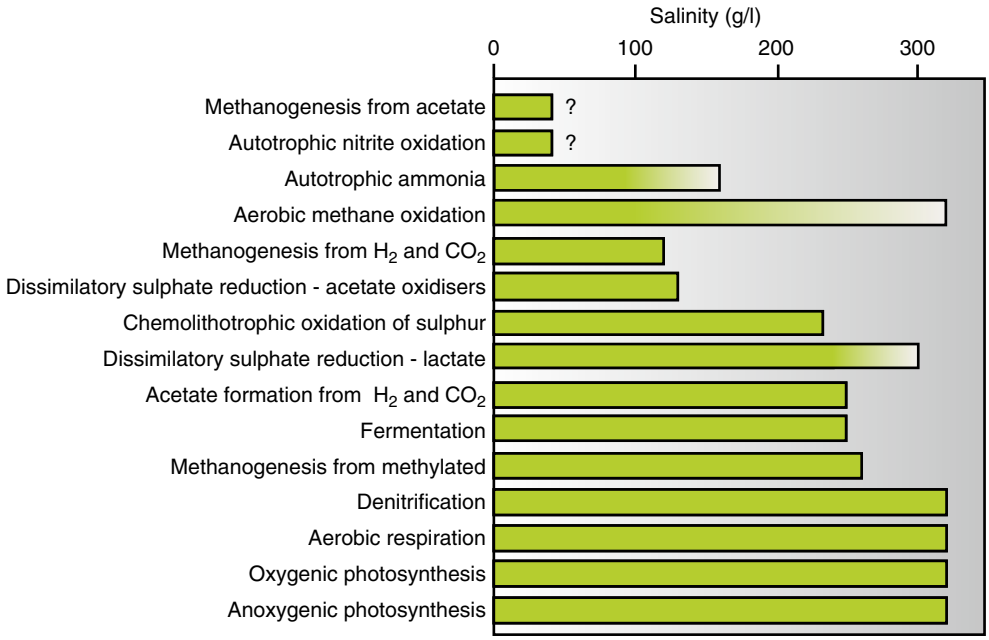

Fig. 9.29 Approximate upper salinity limits of selected microbial metabolic pathways (After Oren 2001 and references therein). Values presented are based on laboratory studies of pure cultures (*green bars*) and on activity measurements of natural communities in hypersaline environments (*white bar ends*)

Growth of phototrophic microorganisms in hypersaline surface waters is generally limited by the availability of inorganic nutrients and not by lack of light energy (Oren 2001). Accordingly, both oxygenic (*Dunaliella sp*., cyanobacteria) and anoxygenic phototrophs (*Halorhodospira*, *Thiohalocapsa*, *Halochromatium*), all produce organic solutes for osmotic stabilization. They may be found up to very high salt concentrations and in several cases can survive well into the halite saturation field. However, in the case of chemolithotrophs and anaerobic heterotrophs the amount of energy generated in the course of their dissimilatory metabolism is often insufficient to supply the demands of cell growth, osmotic adaptation, and life maintenance. Longterm growth and survival in hypersaline environments is not possible in such species. The 'high-salt-in' strategy is preferable for strongly energy-limited organisms (haloarchaea and fermentative halophilic bacteria) as it is energetically much less costly than the production of organic osmotic solutes. Clearly, salinity controls the various metabolic styles at the cellular level (Fig. 9.29; Oren 2001). Biomarker distributions indicative of the various metabolic pathways will likewise become salinity-related indicators in the rock record.

Life in a Layered Microbial Mat?

The laminated sediments (biolaminites or microbiolites) that typify many evaporitic carbonates and described by sedimentologists using the general, and perhaps somewhat dated, terms algal mats and cryptalgalaminites are in effect microbial "high rises," as are many living stromatolites (Chap. 1). They, and their entrained biomarkers, indicate the activities of an ecologically and phototopically layered microbial community (Ionescu et al. 2007). As a mat surface accretes, its organic constituents are buried. The biochemical make-up of the initial halobiota, which flourished in the hypersaline conditions at or above the mat surface, is altered by the metabolic activities of various decomposers flourishing below.

In order to investigate early or syndepositional changes in the dominant organic constituents and the main diagenetic processes, Grimalt et al. (1992) studied organic profiles in cross sections through two different cyanobacterial mats in a modern marine-fed salina in southern Europe. Changes in lipid composition were compared to the vertical distributions of the various microbial populations. Vertical distributions in the lipid patterns were defined using enrichment cultures from typical species of cyanobacteria, diatoms, purple bacteria, sulphatereducers and methanogens obtained from the layered mats.

Cyanobacteria *Phormidium valderianum* and *Microcoleus chthonoplastes* were the dominant primary producers in the sampled mats, they occurred almost as monocultures in the upper 6 mm of the mats (Fig. 9.30a). Worldwide, these and other cosmopolitan filamentous cyanobacterial photosynthesizers are the most obvious organisms in most mesohaline algal mats and surficial gypsum crusts (Canfield et al. 2004). Their chlorophyll creates a green layer a few mm thick beneath a sticky or slimy mucosal surface. As layers of these mucilaginous sheathed cyanobacteria aggrade via periodic growth spurts, it creates biolamination and the mineralised counterparts constitutes the layered and clotted textures seen in modern and ancient microbial structures, such as stromatolotites and bacteriogenic mud mounds (Chap. 1).

Below the cyanobacteria is a layer of aerobic to dysaerobic heterotorphs (bacteria and archaea), which in the presence of oxygen break down the organic materials produced by the living cyanobacteria (mostly abandoned algal sheaths and slime; Figs. 9.30 and 9.31). But because oxygen is only produced by photosynthesis, these organisms can only perform this process during daylight. The next layer below is dominated by chemolithotrophic sulphur bacteria, these are lifeforms that use the redox energy contained in the biochemical gradient between reduced sulphur compounds produced by sulphate reducers (below) and oxygen produced by the cyanobacteria (above). Utilising this redox gradient these purple sulphur bacteria synthesize organic matter and create the characteristic purple-orange layer seen below the green layer in an aggrading microbial mat. As they can only metabolise in a suitable redox gradient, they need to locate themselves exactly within this gradient, so they are typically the most motile forms in a microbial mat. The redox gradient lies deeper in the mat community during the day due to oxygen production by the cyanobacteria, but it rises and can even reach the mat surface in the dark of night (Fig. 9.30b). Below the chemolithotrophs are the phototrophic green sulphur bacteria. They are anaerobic photosynthesizers that fix sugars by utilising the infrared portion of the light spectrum as they convert sulphide to sulphate. Infrared radiation penetrates deeper into microbial sediment than the visible light used by the cyanobacteria, with depth of penetration aided by transparent gypsum crystals.

Below are the sulphate reducers, fermenters, and methanogens (Fig. 9.30b). Fermenters are relatively inefficient decomposers and do not completely break down the organics but break them into alcohols, lactates and other compounds exploited by other decomposers. During the day the sulphate reducers metabolise organics deep in the microbial mat via anaerobic respiration utilising a variety of chemicals including manganese, nitrate, sulphate and even CO_2. At night they rise somewhat with redox gradient and at times of prolonged bottom brine anoxia and brine column turbidity can even reach the mat surface or enter the lower parts of a density stratified brine column (Fig. 9.31; Des Marais 2003). They are very important decomposers in most mesohaline microbial mats and give the lower parts of a mat its characteristic "rotten egg" smell. Generally sulphate reducers consume up to a third of the organic carbon present at this depth in a typical mesohaline microbial mat.

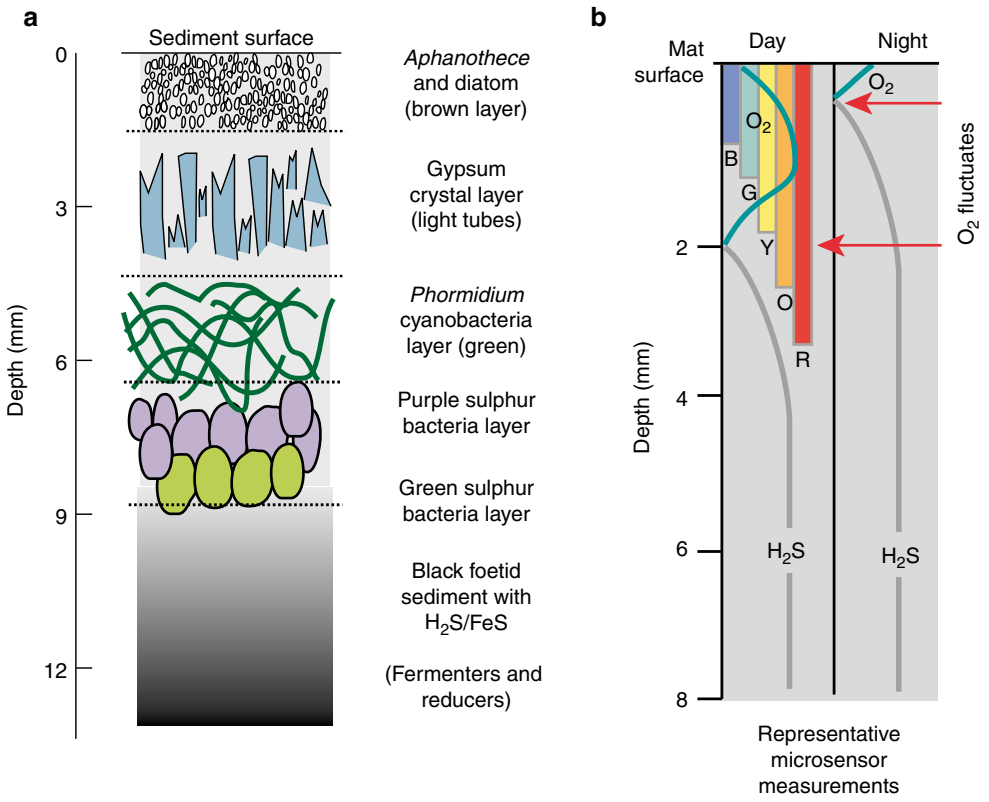

Fig. 9.30 Community and light layering in a microbial mat. (**a**) Typical microbial community in an evaporitic laminite in a modern coastal salina with salinity in the range 130–200‰ (After Caumette 1993). (**b**) Schematic of vertical gradients of O_2 and H_2S during the day and at night. The vertical bars at upper left represent the relative depths of penetration of blue (*B*), green (*G*), yellow (*Y*), orange (*O*), and red (*R*) light. Profile is for a filamentous micritic mat. Profiles in filamentous and unicellular mats are qualitatively similar, although the depth scale (mm) of such profiles tends to be greater for unicellular mats. It will also be deeper in mats growing in an around clear crystals such as gypsum or halite, which act as light tubes (After Des Marais 2003)

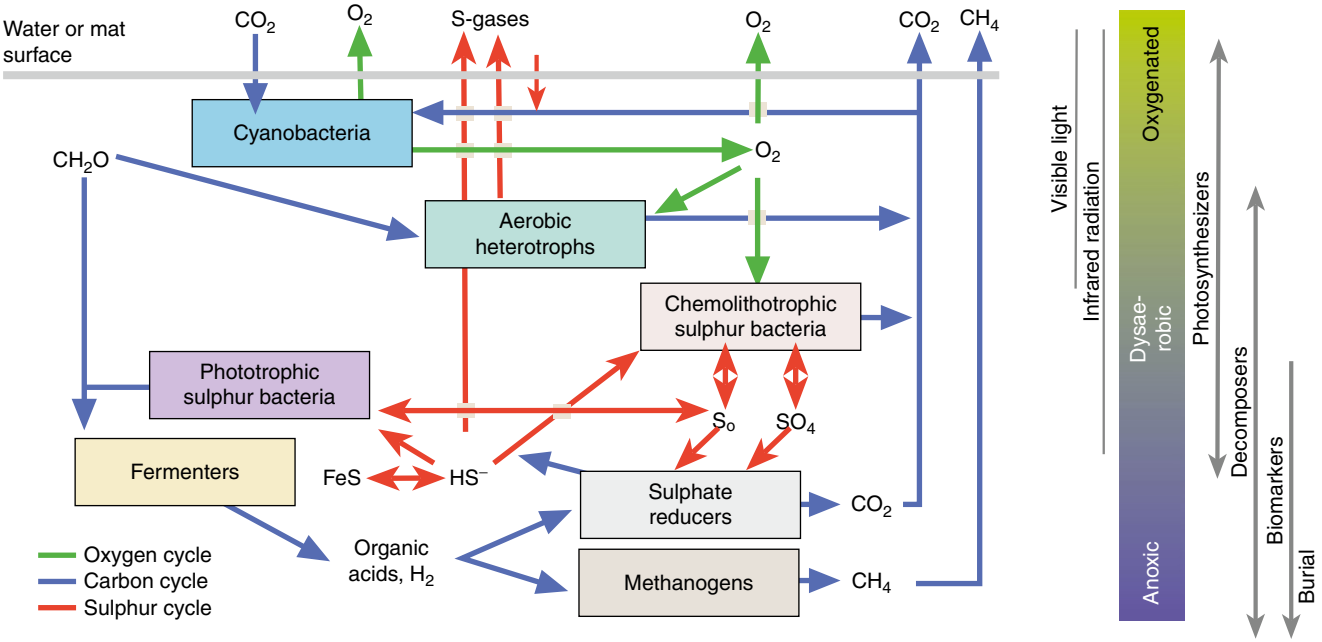

Fig. 9.31 Inter-relationships between microbes and the oxygen, carbon and sulphur cycles in the uppermost 5–10 mm of a microbial mat. The oxic-anoxic transition shifts lower in the mat in the daytime and higher in the mat at night (photosynthesis has stopped)

Deeper still in the mat are the methanogens (Fig. 9.31). All are anaerobes and utilise simple compounds created by the fermenters, such as CO_2 and hydrogen, along with organic components such as methanol, acetic acid, formic acid and methylamines to produce methane (Table 9.6). The methanogenetic metabolic pathway produces little biochemical energy and is usually the "last resort" community and makes up the lowermost living layer in the microbial high-rise.

Grimalt et al. (1992) found that the uppermost layers, dominated by cyanobacteria, typically leave no more than minor traces in the solvent-extractable lipids (biomarkers) in buried mat sediments.

Rather, the predominant fatty acid distributions in the lower parts of a mesohaline mat sediment parallel the compositions observed in the enrichment cultures of purple bacteria and appear to be mixed with acids characteristic of heterotrophic bacteria, including purple bacteria and sulphate-reducers. In other words, the organic signatures, even as the mats are accumulating a few millimetres above, are those of the decomposers not the primary producers. This implies that many biomarkers used to typify organic production in hypersaline settings typically do not come from organics of the primary producers but from the products of the decomposer community.

Anaerobic decomposers flourish within the sediment at the base of benthic mat communities or within the brine column at the halocline of a density stratified brine body. Defining where halotolerant and halophilic decomposers lived in ancient microbialites is not possible from their organic signatures alone; it requires a sedimentological interpretation of the sediment matrix, which is usually a laminite. But, as discussed in Chap. 1, evaporitic laminites and biolaminites are subaqueous sediments with near identical textures beneath stratified and unstratified brines across water depths ranging from less than a metre deep to hundreds of metres.

Biomarkers and Microbial Responses to Changing Salinities

Salinity-controlled transitions between a halotolerant and halophilic biota can been seen, indirectly in their organic residues and subsequent biomarkers. Biomarkers can be thought of as molecular or chemical fossils with a basic carbon skeleton derived from once-living organisms. Biomarkers are found in all modern sediments, as well as in petroleum and rock extracts and can provide information about species diversity, depositional environment, thermal maturity, migration pathways and hydrocarbon alteration (Table 9.8; Brocks and Summons 2003; Peters et al. 2005).

Commonly accepted environmental generalisations based on biomarker distributions include the notion that variation in the ratio between the isoprenoids[13] pristane and phytane indicates oxidising versus reducing conditions (this assumes pristane and phytane are both breakdown products of chlorophyll). In an oxidising environment the cleavage of the phytol side chain of chlorophyll is followed by decarboxylation to produce phytane (Fig. 9.32a). In a reducing environment the sidechain cleavage of chlorophyll is followed by its reduction to ultimately produce pristane. Low pristane/phytane ratios are thought to indicate reducing conditions, while higher values (>1) indicate oxidising conditions (Table 9.8). But Philp and Lewis (1987) have shown that the chemistry of chlorophyll breakdown is much more complicated in many natural systems and that variations in the ratio may also indicate varying inputs from the archaea, which contain much higher levels of phytane chains than bacteria. Values of pristane/phytane less than 0.5 may indicate hypersaline conditions where archaea dominated and ^{13}C values can be elevated (Grice et al. 1998).

Differences in the distribution of n-alkanes are also thought to indicate depositional differences in the organic contributors. Waxes in higher plants have significant concentrations of the long chain $C_{22–36}$ alkanes[14] with a pronounced odd/even distribution, such organics tend to be relatively rare in evaporitic source rocks, unless surface waters were freshened by periodic runoff from the land. Much of this terrestrial

[13] 9.6 Isoprenoids are a major class of nonsaponifiable lipids that occur in plants, animals, and bacteria and are characterized by chains of modular groups of five carbon atoms in which the typical pattern has four of the carbon atoms in a linear chain and a single carbon attached at the carbon one position removed from the end of the chain. The term isoprenoid is derived from the name of the five-carbon, doubly unsaturated branched hydrocarbon isoprene, which could in principle be the simplest monomeric chemical precursor for this class of compounds.

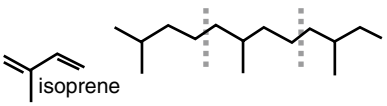

Isoprenoids are also known as terpenes. Terpenes are usually grouped according to the number of isoprene (C_5H_8) units in the molecule: monoterpenes ($C_{10}H_{16}$) contain two such units; sesquiterpenes ($C_{15}H_{24}$), three; diterpenes ($C_{20}H_{32}$), four; triterpenes ($C_{30}H_{48}$), six; and tetraterpenes ($C_{40}H_{64}$), eight. The carotenoid pigments are the best known tetraterpenes in the geological realm.

[14] Aliphatic hydrocarbons are any chemical compound belonging to the organic class in which the atoms are not linked together to form a ring. They are divided into three main groups according to the types of bonds they contain: alkanes, alkenes, and alkynes. Alkanes (n-alkanes) have only single bonds and a continuous chain structure, alkenes contain a carbon-carbon double bond, and alkynes contain a carbon-carbon triple bond. Aromatic hydrocarbons are classified as either arenes, which contain a benzene ring as a structural unit, or non-benzenoid aromatic hydrocarbons, which are characterized by special stability but which lack a benzene ring as a structural unit.

Table 9.8 Depositional significance of selected biomarkers

Setting	Biomarker/indicator	Detail
Hypersaline	Gammacerane	High relative to C31 hopanes in oils derived from sources deposited under hypersaline depositional conditions. High values indicate stratified water column during source deposition (Sinninghe Damste et al. 1995).
	Pristane/phytane	Very low values (<0.5) in oils derived from source rocks deposited under hypersaline conditions, indicates contribution of phytane from halophilic bacteria/archaea (ten Haven et al. 1987, 1988).
	Acyclic isoprenoids	Acyclic isoprenoid hydrocarbons are the predominant components in the organic matter extracted from sedimentary cores and oils of various hypersaline settings (Wang 1998). For example, the dominant hydrocarbons in Miocene/Pliocene sediments from the Dead Sea Basin, Israel, are regular isoprenoids with 19–25 carbon atoms (Grice et al. 1998)
	Low diasteranes	Oils from the hypersaline sources typically have very low amounts of diasteranes, which commonly suggests a source rock that has low content of catalytic clays, consistent with carbonate or evaporite source rocks (Mello and Maxwell 1991; Peters and Moldowan 1993). The amount of diasteranes in oils also decreases in highly reducing noncarbonate environments with increasing salinity (Philp and Lewis 1987).
	Elevated acidic amino acid content in fossil DNA	Strong linear correlation ($R^2 = 0.97$) between the salinity of an environment and the ratio of acidic to basic amino acids encoded by inhabitants of modern Dead Sea suggest it might be preservable in fossil DNA or fossil amino acids, serving as a proxy for the salinity of an ancient environment. (Rhodes et al. 2010)
	Other biomarkers	Predominance of even n-alkanes within C20–C30 range (especially mid-chain alkanes), presence of β-carotene and γ-carotene, dominance of the C27 steranes (Malinski et al. 2009).
	Organic sulphur compounds	There is a high abundance of organic sulphur compounds (thiolanes, thianes, thiophenes and benzothiophenes) in many anoxic hypersaline settings (Wang 1998). The distributions of the C-20 isoprenoid thiophenes in combination with those of the methylated 2-methyl-2-(4,8,12-trimethyltridecyl) chromans can be used to discriminate non-hypersaline from hypersaline paleoenvironments (Sinninghe Damste et al. 1989)
	Carbon isotopes	Depleted ^{13}C values (−20 to −30‰) are consistent with typical saline lake environments and reflect depletion of CO_2 by photosynthetic organisms (Peters et al. 1996).
	n-heneicosadiene	There is a predominance of n-heneicosadiene in the top layer of the gelatinous mat, which grows in the most extreme salinities of the various Abu Dhabi microbial mat communities. Its source is not yet known, but is considered to be an aerobe favoring the extreme conditions where it is found (Scherf and Rullkötter 2009)
	Novel McDGs	Novel non-isoprenoid macrocyclic glycerol diethers (McDGs) that contain a C32 diabolic acid-derived alkyl moiety (i.e., 15,16-dimethyltriacontane), with some components bearing additional methyl branching at C-7 and/or C-24. These McGDs are suggested to have been synthesized by some extremophilic (thermophilic and/or halophilic) bacteria (Baudrand et al. 2010)
	Archaeol/(Archaeol + Caldarchaeol) *100	Relative amounts of acyclic diether and tetraether membrane lipids synthesized by Archaea correlate with salinity from 0 to 250 practical salinity units (psu) in modern and ancient hypersaline settings. Reflects fact that because Archaea survive and thrive over a broad salinity range, well beyond that of haptophyte algae and other halotolerant plankton (Turich and Freeman 2011).
Anoxic	C35 homohopanes	High relative to total hopanes in oils derived from source rocks deposited under anoxic conditions (Peters and Moldowan 1993). Abundance of C35 homohopanes in oils (relative to C31–C34 homopanes) is correlated with source rock hydrogen index (Dahl et al. 1994).
	Pristane/phytane	>1.0 can indicate anoxic conditions, but the ratio is affected by many other factors.
	Isorenieratane and derivatives	Presence in oil indicates anoxic photic zone during source rock deposition, these compounds are biomarkers for green sulphur bacteria (Summons and Powell 1987).
	V/(V + Ni) Porphyrins	High = reducing conditions (Lewan 1984).
	Fossil okenane	Interpreted as a biomarker for planktonic purple sulphur bacteria of the family Chromatiaceae in the 1.64 Ga Barney Creek Fm. As such okenane is strictly a biomarker for anoxic and sulphidic conditions in the presence of light (photic zone euxinia) and indicates an anoxic/oxic transition in the photic zone (typically 12–25 m below water surface (Brocks and Schaeffer 2008). Also common in Lake Mahoney bottom sediments.
	28,30-bisnorhopane	High in a number of reducing environments (Schoell et al. 1992; Moldowan et al. 1994).
Lacustrine	Botryococcane	Presence = lacustrine source. Absence = meaningless (e.g., Moldowan et al. 1985).
	β-Carotene	Presence = lacustrine source. Absence = meaningless (Jiang and Fowler 1986).
	Sterane/Hopanes	Low in oils derived from lacustrine source rocks. (Moldowan et al. 1985)
	C26/C25 tricyclic terpanes	>1 in many lacustrine-shale-sourced oils (Zumberge 1987; Sajnovic et al. 2008)
	Tetracyclic polyprenoids	High in oils from freshwater lacustrine sources (Holba et al. 2000).

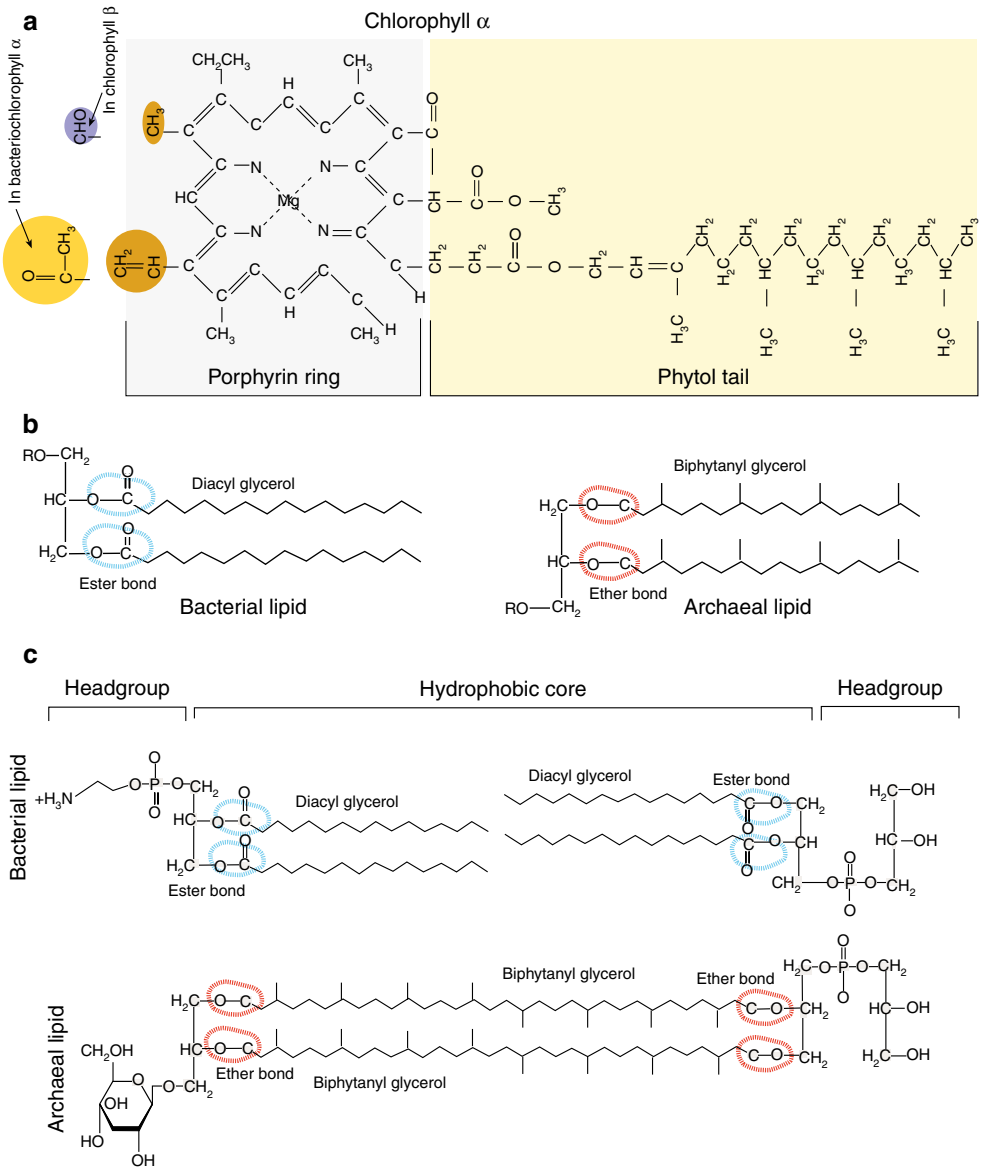

Fig. 9.32 Various molecular structures. (**a**) Chlorophyll a structure showing porphyrin ring and phytol tail. Alternate structures from bacteriochlorophyll a and chlorophyll *b*. (**b**) Phosphatidylanolamine forms a bi-layer lipid in bacterial cells. The acyl chain is usually, but not always straight. Some bacterial lipids have a methyl branch of a cyclohexal group at the end of the acyl chain, other lipids have one or more unsaturated bonds and the connection of glycerol to the acyl chain is via an ester linkage. (**c**) Lipids are monolayers in Archaea and the phytanyl chain contains isoprenoid-like branches. An ether linkage connects the phytanyl chain. Archaeal membranes also contain bilayer-forming diether lipids

organic material is oxidized and biodegraded before it makes it to the final site of deposition on the brine pool floor. In contrast a high algal input is characterised by n-alkanes in the $C_{16–18}$ region.

At its simplest, much of the utility of biomarkers in saline environments comes from salinity-related differences in contribution to organic matter of the general categories of primary producers (autotrophs), namely prokaryotes (cyanobacteria and bacteria) and eukaryotes (higher plants, algae) and archaea. Most triterpanes are associated with prokaryotic sources, whereas steranes tend to be produced by eukaryotes. Thus, the triterpane/sterane ratio can be a rough measure of the prokaryote/eukaryote contribution to the organic material. As salinity increases, the less salinity-tolerant eukaryotic organisms (mostly green algae) give way to more halotolerant bacteria and cyanobacteria (tricyclic and hopane producers) with a corresponding increase in the triterpane/sterane ratio (e.g., Summons et al. 1999). Thus high alkalinity/salinity settings are characterised by tricyclics (C_{20}-C_{24}; m/z 191), β-carotene ($C_{40}H_{56}$ compound; m/z 125) and gammacerane (C_{30} triterpane; m/z 191), all with prokaryote sources. Hence, high levels of gammacerane and β-carotene in ancient organic signatures are typically associated with nonmarine highly saline environments (Peters and Moldowan 1993; Peters et al. 2005).

Lipids, entrained as organic residues in modern evaporitic carbonates and gypsums from modern saline pans (mesohaline and lower penesaline waters), are mostly derived from heterotrophic bacteria acting on cyanobacteria and green algae (Figs. 9.17 and 9.18). The resulting n-alkane distributions show a high predominance of n-docosane. In the modern evaporitic carbonate domain (mesohaline), the C_{20}

highly-branched isoprenoid olephines, tetrahymanol (from bactiverous ciliates) and large amounts of phytol are precursors to most lipids found in buried evaporitic sediments. In contrast, the main lipid contributors to organics preserved in modern halites and bittern beds are the extremely halophilic archaea and their organic signatures are enriched in the isoprenoids, especially phytane (Table 9.8; Barbé et al. 1990; Wang 1998).

Likewise, Waples et al. (1974) and ten Haven et al. (1986), noted that Tertiary sediments deposited in many saline evaporitic lagoons retain high concentrations of regular C_{25} isoprenoids. They related it to the activities of the photolithotrophic *Chlo-robiaceae sp*., an anaerobic green sulphur bacteria, known to flourish at the halocline of modern saline lakes. It is thought to have flourished in similar stratified settings in ancient mesohaline to hypersaline seaways. Its biochemistry leads to the preservation of a series of 1-alkyl-2,3,6-trimethyl benzenes, thought to be derived from the breakdown of its aromatic carotenoids in sulphate- and sulphide-rich brines (Summons and Powell 1987). Ten Haven et al. (1988) went on to propose that there are a number of biomarkers indicating likely hypersalinity at the time of deposition including; short sidechain steranes, 5α(H), 14β(H), 17β(H) pregnanes and homopregnanes, as well as high gammacerane indices (gammacerane/C_{30} hopane). Gammacerane is a pentacyclic C_{30} triterpane thought to be a diagenetic alteration product of tetrahymenol (Table 9.8). The principal source of tetrahymenol is bactiverous ciliates, such as protists like *Tetrahymena*. Thus the presence of tetrahymenol is not restricted to any particular environment but the presence of tetrahymenol (and its daughter gammacerane) in large amounts suggests the presence of a stratified water column and possibly hypersalinity in the depositional setting (Table 9.8; Sinninghe Damste et al. 1995; Peters et al. 2005, p.576).

For Archaea, the cell membrane itself, due to its high thermal stability, is a good candidate for a biomarker. Archaeal cytoplasmic membranes do not contain the same lipids that prokaryotes and eukaryotes do. Instead, their membranes are formed from isoprene chains (ether lipids) made up from C_5 isoprenoid units (as for the side chains of ubiquinone) rather than C_2 units (ester lipids) in the normal fatty acids of the non-archaea (Fig. 9.32b). Halophilic Archaea do not have fatty acids, rather the cell wall is constructed of lipids, mainly of glycerol, connected to phytanyl chains some twenty carbons in length by ether bonds to form phytanylic diether. Typically these are organized in bilayers that make up the cell wall. In the case of archaea living in extreme conditions, two glycerol molecules can be connected to a double chain of phytanol to create a tetraether structure of forty carbons (Fig. 9.32c). Phytane-rich isoprene derivatives indicative of ancient archaea have been found in Mesozoic and Palaeozoic evaporitic sediments, and more generally in older Precambrian sediments (Hahn and Haug 1986). Interestingly, their chemical traces have even been tentatively identified in sediments from the Isua district of west Greenland, the oldest known sediments on Earth, some 3.8 billion years old. Biomarker evidence for green and purple sulphur bacteria is found in Palaeoproterozoic marine sediments from northern Australia in the form of a new carotenoid biomarker – okenane (Brocks et al. 2005).

Bacterioruberin constitutes the purple patches in the archaeal cell wall and we have already discussed its stability with respect to high temperatures in the living environment. It may well constitute an excellent as yet unrecognised biomarker for haloarchaea in ancient evaporitic sediments that were precipitated in moderate to extreme salinities (Brocks and Summons 2003). The likely fossil equivalent of bacterioruberin is perhydro-bacterioruberin, but it has yet to be discovered in geological samples. However, it is worth bearing in mind that some high-molecular weight biomarkers may have escaped detection because they are difficult to analyse using conventional GC-MS methods.

Do Biomarkers Indicate Hypersalinity?

Work in modern hypersaline systems clearly shows that archaea and bacteria can both flourish as heterotrophs in upper penesaline and supersaline waters at salinities higher than 200–250‰ and that cyanobacteria and some green algae can still survive and grow at these salinities (Caumette 1993; Ollivier et al. 1994). Hence, respective biomarker signatures in ancient counterparts will not be mutually exclusive and none of the biomarker indicators listed in Table 9.8 are exclusive indications of hypersalinity.

Also, some of the widely used biomarker-derived maturity indicators for low maturity oils, such as low levels of diasteranes, T_s/T_m ratios <1, somewhat low homohopane and sterane isomerization values, all historically derived from studies in ancient marine settings, are not as reliable when applied to relatively young saline-lacustrine oils, such as those sourced from hypersaline Oligocene laminites in the northern Qaidam Basin, China (Hanson et al. 2001). These sediments and their outcrop equivalents have vitrinite reflectance values in the range 0.68–1.0, all within the oil window (Fig. 9.1). The discrepancy between mature indications coming from vitrinite studies and the immature indications derived from various sterane isomerization ratios in these young hypersaline-sourced oils are perhaps explained by a lack of time for various sterane equilibria to develop. Some of these hypersaline oils come from hydrogen-rich type I lacustrine source sediments in the Qaidam Basin fill that may be as little as 3 million years old. But some other so-called maturity indicators, such as the low levels of diasterane probably are better tied to deposition of the source organics in

noncarbonate shales accumulating in hypersaline waters (Philp et al. 1991).

The fluctuating salinities that controls life in the depositional setting of all modern and ancient evaporites means that there is no simple single biomarker indicator for hypersalinity in any ancient sediment. For example, the 2-methyl hopanoids[15] are thought to indicate a cyanobacterial association (Table 9.8) and cyanobacteria are commonplace in mesohaline waters. But the presence of cyanobacteria and hence 2-methyl hopanoids are not limited to this setting. Likewise, the pentacyclic triterpenoid gammacerane is present in trace amounts in almost all bitumens and oils, but tend to be more abundant in sediments that were deposited under a stratified water column. This is a hydrological condition that is typical of, but not exclusive to, hypersaline lacustrine settings (Sinninghe Damste et al. 1995). A similar argument can be made for low pristane/phytane ratios that are used as indictors of both reducing conditions (assumes a chlorophyll precursor) and halophilia (assumes an archaeal precursor).

All biomarker signatures are indirect and somewhat ambiguous indicators of hypersalinity via assumptions of the relative make-up the original primary producers. In addition, all traces of biomarkers from the primary producers preserved in ancient strata have been overprinted by the effects of syndepositional decomposers, as well as subsequent mixing from various sources during catagenesis. The overprinting effects of the decomposers in microbial laminites are clearly seen when molecular characteristics of modern hypersaline sediment from the Ejinur salt lake (northern China) are compared to Tertiary (Eocene) core samples from Qianjiang Formation (hypersaline lacustrine) of Jianghan Basin, central eastern China (Fig. 9.33a; Wang et al. 1998b). N-alkanoic acids in saline sediments from both areas (Ejinur and Jianghan) show a pronounced even-over-odd predominance (EOP) and a bimodal distribution. In the lower molecular weight range, the C_{16} and C_{18} components are prominent, with the former dominant. For higher homologues (greater than or equal to C_{20}), docosanoic (C_{22}) and tetracosanoic (C_{24}) acids dominate the n-alkanoic acid homologues in the Jianghan and Ejinur samples, respectively. Alkanoic acids with an isoprenoid skeleton are more abundant in Jianghan samples, including C_{20}, C_{21}, C_{24}, C_{25} and C_{30} homologues, with a C_{25} component (3,7,11,15,19-pentamethyleicosanoic acid) most pronounced in the lower part of the Qianjiang Fm. The carbon skeletons of these isoprenoid acids in both units are attributed to archaeal decomposers.

Iso and *anteiso* branched carboxylic acids are prevalent in both the Ejinur samples and in the upper portion of the Qiangiang Formation. They derive from bacteria, probably sulphate-reducing bacteria, and their abundance clearly shows once again the importance of bacterial decomposers, along with haloarchaea, to the biochemical signature of organic matter in modern and ancient saline lake sediments. The presence of hopanoid acids and a 3-carboxy steroidal acid further attest to contributions from bacterial and eukaryotic sources, respectively. The occurrence of particular carboxylic acids in the Jianghan samples illustrate these compounds, indicators of halotolerant and halophilic decomposers, can survive as biomarkers in hypersaline source rocks.

Across a broader time and geographic scale, acyclic isoprenoid hydrocarbons are the dominant components in organic matter extracted from sedimentary cores and oils sampling various hypersaline settings in China; the results encompass the Tertiary Janghan salt lake basin, the Cretaceous Taian salt lake basin, and the Triassic, Permian and Cambrian Yangtze evaporitic marine platforms (Wang 1998). Inland saline lake basins in China such as Jianghan and Songpu are characterized by a tremendous predominance of phytane (C_{20}), which ranges up to 15 % of the total extract. The evaporitic marine sediments are also unique in retaining a complete series of super-long-chain acyclic isoprenoids, up to C_{40} (Fig. 9.33a). These isoprenoids in the marine evaporites possess head-to-head, tail-to-tail or regular linkages that indicate significant contribution from various archaea to the biomarker signature, i.e., a mixed archaeal contribution from halophiles, methanogens and acidothermophiles. Based on the split in distribution and composition of isoprenoids between the inland salt lakes and the evaporitic marine platform settings, Wang (1998) concluded that the archaeal biota in modern and Cenozoic inland salt lake sediments of China are likely dominated by halophilic archaea, while the halobiotal signatures of Mesozoic and Palaeozoic evaporitic marine sediments were predominantly those of methanogens and acido-thermophiles. He also found that the concentration of the various chlorine salts in the sediments is more directly proportional to the abundance of phytane than to sulphate, once again indicating the dominance of halophilic archaea in waters at the halite precipitation stage. He also noted that reduced species of sulphur, sulphide and organic sulphur compounds in the anoxic brines played a key role in the preservation and formation of the abundant phytane in these inland salt lake basins.

A predominance of degraded green algal and cyanobacterial biomarkers in mesohaline settings can be recognised in biomarkers preserved in even older, but organically

[15] Hopanoids are a group of compounds (triterpenoids) produced by prokaryotic organisms, and the diagenetic alteration products of these compounds (found in oils, rock extracts and sediment extracts). Just as steroids (steranes) are a useful group of biomarkers for identifying input from various eukaryotic organisms (e.g., plants and animals), an analogous group of compounds, hopanoids, are a useful group of biomarkers for identifying input from various bacteria. Hopanoids serve the same function in bacteria as sterols do in eukaryotes: they act as cell wall rigidifiers. In petroleum and its source rocks, hopanoid biomarkers exist as a subset of a group of compounds called triterpanes (isoprenoids).

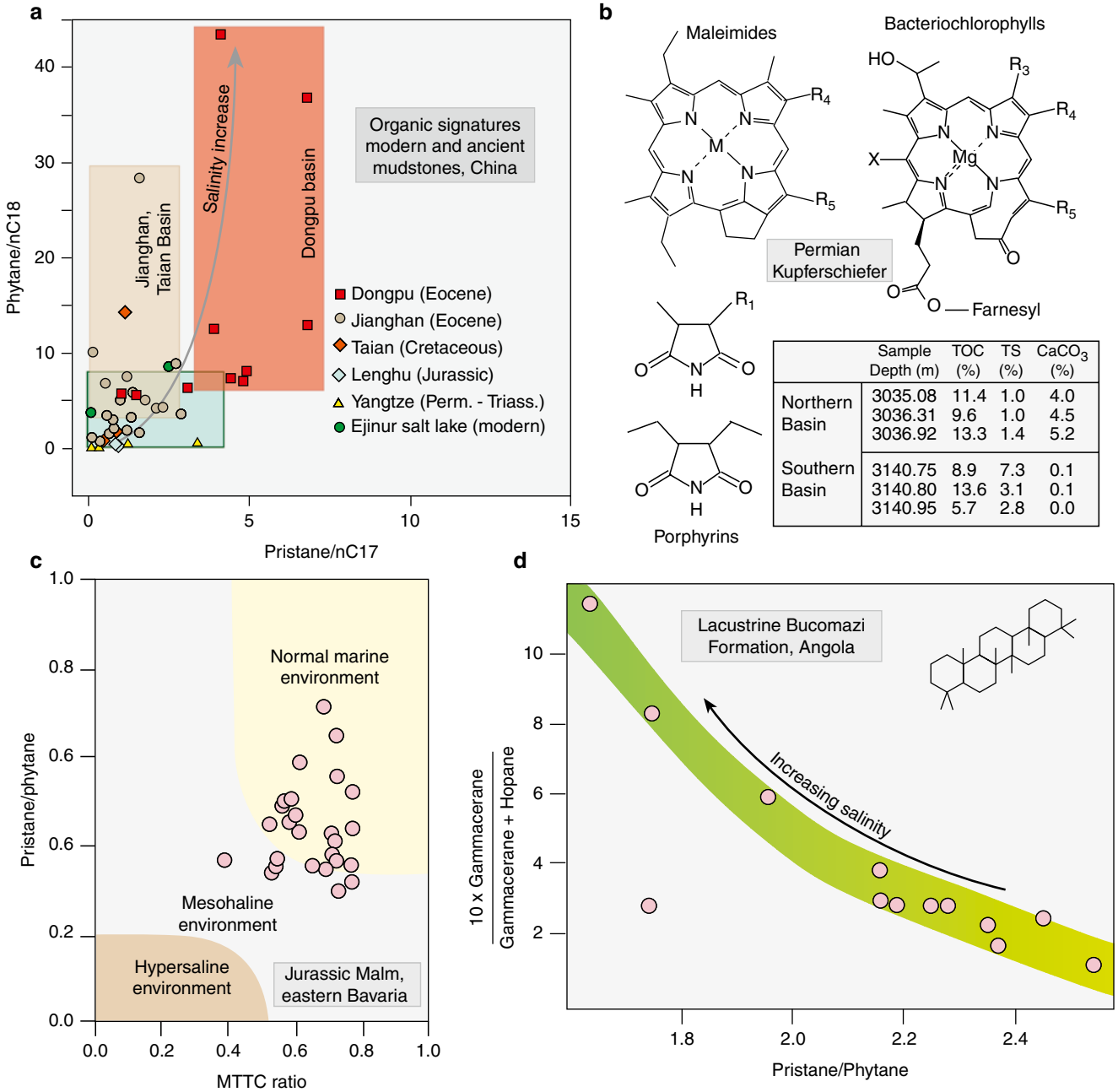

Fig. 9.33 Biomarkers. (**a**) Cross plot of Pristane/nC_{17} versus Phytane/nC_{18} ratios for various saline/hypersaline settings in China (After Wang 1998). (**b**) Structure and properties of representative bacteriochlorophylls, maleimides and porphyrins from source rocks in the northern and southern Zechstein basins, offshore NW Europe (After Pancost et al. 2002). Compare with primary structures shown in Fig. 9.28. (**c**) Relationship between pristane/phytane and the methyltrimethyltridecylchhroman (MTTC) ratio in Jurassic Malm carbonates of eastern Bavaria (After Schwark et al. 1998). The MTTC ratio is defined as 5,7,8-trimethylchroman/total MTTCs. (**d**) Variations in pristane/phytane ratio and the gammacerane index for oils from lacustrine source rocks in Angola (*Inset* shows gammacerane structure). Independent biomarker evidence suggests a marine source for the point that lies off the shaded trend (After Peters et al. 2005)

immature, evaporitic source rocks. The degree of methylation of 2-methyl-2-trimethyl-tridecylchromans (MTTCs) and the abundance of maleimides and bacteriochlorophylls implies a euhaline to mesohaline (≥30–40‰) marine-fed setting for the accumulation and preservation of organics during Kupferschiefer sedimentation in the Permian of NW Europe (Fig. 9.33b; Bechtel and Puttmann 1997; Pancost et al. 2002). These biomarkers are thought to be derived from green/purple sulphur bacteria (decomposers) within organic-rich laminites and suggest that the bottom waters were saturated with H_2S at the time of deposition. Maximum water depths were probably less than 100 m (it was a stratified

mesohaline drawdown basin at the onset of Zechstein salinity; see Chap. 5). Decomposers probably lived near the brine boundary between the photic zone and the anoxic (euxinic) bottom water at typical water depths of 10–30 m below the water surface, as in modern marine-fed density-stratified systems, much like in Lake Mahoney today (Fig. 9.45). Primary production in the upper water mesohaline column was dominated by photosynthetic cyanobacteria or green algae, while sulphate reduction in the bottom sediment was tied to the availability of abundant sulphate and organic detritus from the overlying water column.

Methanogenesis was also active during Kupferschiefer deposition. This is reflected in the light carbon isotopic composition of organic matter that had originated via recycling of CO_2 generated by methane-oxidizing bacteria in the water column (Bechtel and Puttmann 1997). Saccate pollen is the only morphologically preserved body fossil in organic matter within this laminated Kupferschiefer sediment, all other traces of cellular/microbial morphologies/fossils are gone. Euxinic conditions were confirmed by Pancost et al. (2002) over a much larger area of Kupferschiefer deposition than studied by Bechtel and Puttmann. They concluded that almost all of the Kupferschiefer seaway was subject to periods of photic zone euxinia and stratification during the early mesohaline history of the Zechstein Sea.

By themselves, high pristane/phytane ratios, high amounts of gammacerane, and MTTC ratios are not totally reliable indicators of hypersalinity. More reliable determinations can be made when two or more of these biomarkers are crossplotted and the resulting output shows a consistent trend. Figure 9.33c plots pristane/phytane ratio against the MTTC ratio in the Jurassic Malm Zeta laminites of eastern Bavaria in SW Germany (Schwark et al. 1998). The output shows a covariant decrease in the two measures, lipids from phototropic organisms and show ^{13}C values consistent with the heterotrophic metabolism of which is interpreted as indicating a trend from normal marine to mesohaline deposition.

A similar covariant trend can be seen in saline lacustrine source rocks when the pristane/phytane ratio is crossplotted against the gammacerane index in Mesozoic source rocks from the offshore of west Africa (Peters et al. 2005). Figure 9.33d plots variations in pristane/phytane (a redox and archaeal indicator) and gammacerane index (an indicator of salinity stratification in saline waters) for oils from a set of lacustrine source rocks. Increasing salinity in the depositional setting explains the covariant trend in the plot, whereby higher salinity was accompanied by density stratification and associated reduced oxygen levels in bottom waters. Independent biomarker evidence suggests a marine source for the point that plots off the shaded salinity trend in this figure (after Peters et al. 2005).

Although the levels of entrained organics are very low, similar covariant trends in pristane/phytane and gammacerane occur in $C_{21–25}$ isoprenoids, along with relatively heavy $\delta^{13}C$ signatures, in biomarkers extracted from the Miocene halites of the halokinetic Sedom Formation in Israel. They are enriched by 7‰ compared to lipids from photropic organisms and show ^{13}C values consistent with the heterotrophic metabolism of Halobacteriales. It indicates a predominance of halophilic archaea possibly consuming the remnants of *Dunaliella*-like bloom, when the salt was deposited in a CO_2 -limited system (Grice et al. 1998; Schouten et al. 2001).

A recent development in biological indicators during salinity progression comes from the work of Turich and Freeman (2011). In a wide-ranging study of archaeal biomarkers they found a distinct evolution in archaeol molecules related to increasing salinities in hypersaline waters. They found the relative amounts of acyclic diether and tetraether membrane lipids synthesized by Archaea correlate with salinity from 0 to 250 practical salinity units (psu) in modern settings (Fig. 9.34) They then examined the preservation of the lipid biomarker-salinity relationship in ancient sedimentary organic matter mostly using samples from two sequences of marls and diatomites deposited just prior to the Messinian Salinity Crisis in the Mediterranean. The archaeol ratio-based salinity estimates were consistent with expected absolute salinity, as well as the amplitude of isotope variations leading up to the Messinian Salinity Crisis. Their lipid biomarker approach to salinity reconstruction complements existing paleosalinity proxies, as listed in Table 9.8, because: (i) Archaea survive and thrive over a broad salinity range from 7 to 340‰, which is well beyond that of haptophyte algae and other plankton, which define much of the microfossil record in mesohaline settings, and (ii) it provides finer salinity resolution for the wide range of salinities broadly defined as hypersaline using existing biomarkers. Using their proxy, there is the potential to provide novel insights into salinity variation within desiccating basins in climatically sensitive seas (e.g., Dead Sea, Permian Delaware Basin), evolution of brines, timing of onset of hypersaline conditions and evaporite deposition, as they have done for the Messinian (Fig. 9.35).

In addition to the signature from their particulate organics, modern brines can also contain large amounts of dissolved organic matter (DOM), with levels that increase with increasing salinity (Hite and Anders 1991). This liquified organic is often entrained within brine inclusions in halite and other salt crystals and is not picked up in standard TOC determinations. Levels of volatile fatty acid (VFA), especially acetic acid, are also high in these saline brines and possibly reflect a higher bacterial contribution (Jørgensen et al. 2008). The relative contribution of DOM to the source potential is poorly understood in subsurface evaporitic systems where crossflowing basinal brines are dissolving buried halite and may also have significance in the survival of Archaean "proto-life" (Pasteris et al. 2006).

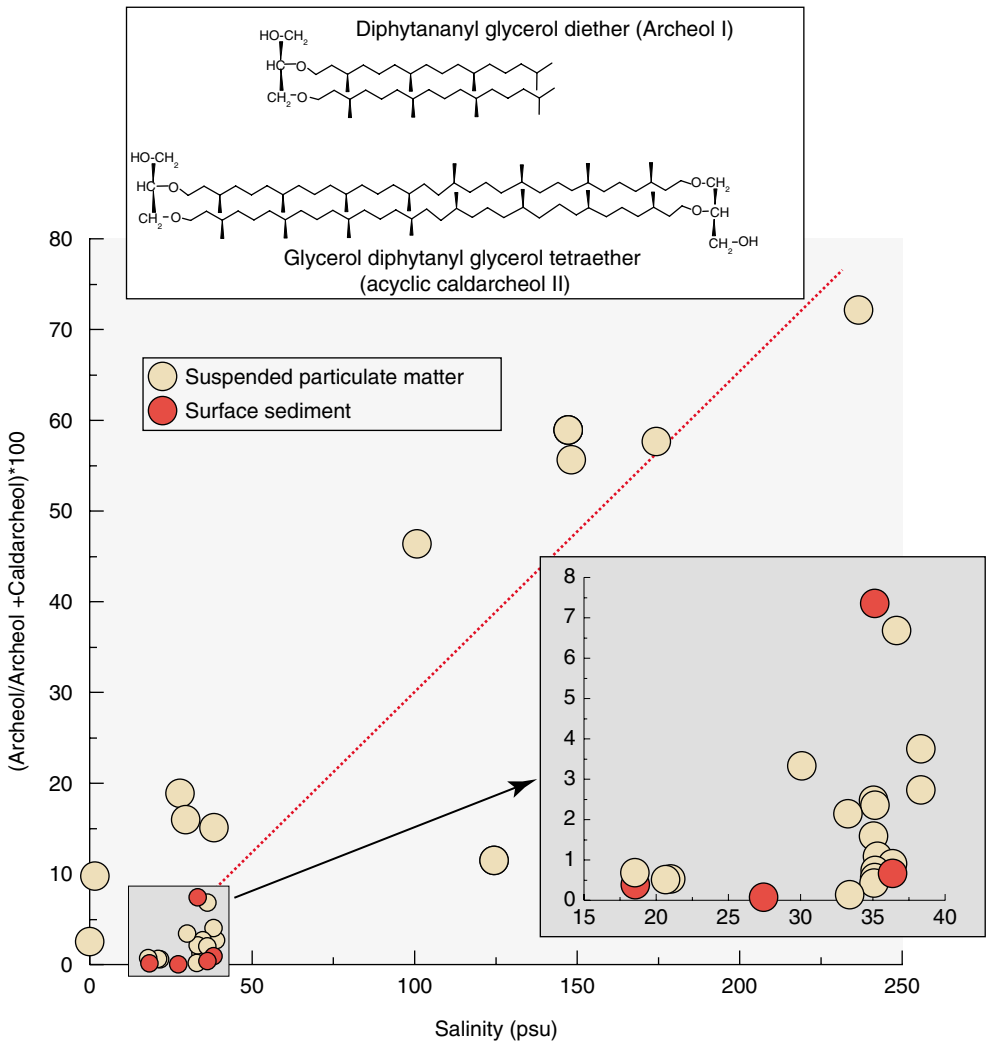

Fig. 9.34 Salinity and relative abundance of archaeol to caldarchaeol from modern suspended particulate matter in marine and marine derived waters plotted against salinity. *Brown circles* in the plot indicate suspended particles, while *red circles* indicating samples with some terrestrial influence. *Upper inset* shows Fischer projections of the utilised biomarkers; diphytanyl glycerol diether (archaeol, I) and glycerol dibiphytanyl glycerol tetraethers (acyclic caldarchaeol, II) as synthesized by Archaea (After Turich and Freeman 2011)

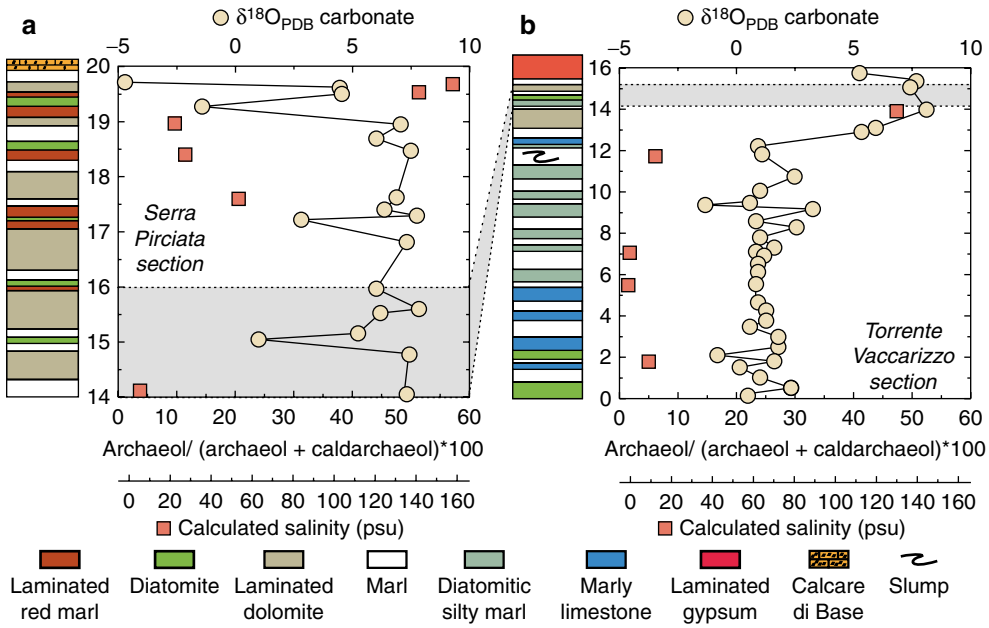

Fig. 9.35 Stratigraphy plotted against the archaeol/caldarchaeol * 100 (ACE index) also with calculated salinity outputs based on the modern calibration of the ACE (illustrated in Fig. 9.34). For two detailed hypersaline Messinian sections in Italy. (**a**) Serra Pirciata and (**b**) Torrente Vaccarizzo (After Turich and Freeman 2011)

Organic Enrichment

The amount of organic matter preserved in an evaporitic sediment with the potential to become a source rock is a function of three factors, as expressed in the equation (Bohacs et al. 2000; Katz 2005):

$$Organic\ Enrichment = (P - De)/(Di)$$

where P is production, De is destruction and Di is dilution.

Maximum enrichment occurs when production is maximised and destruction and dilution are minimised. Production at mesohaline salinities is mostly via photosynthetic fixation of CO_2. It includes autochthonous organic matter, formed at or near the site of accumulation and derived from algae, bacteria and aquatic plants, as well as allochthonous organic matter carried in during floods (Bohacs et al. 2000). Katz (1990) showed that varying levels of solar input and water chemistry/stratification exert the largest effects on overall primary production in mesohaline settings. Initial destruction of organic matter is mostly a function of the efficiency of the various scavengers and grazers, which is generally a function of the availability of oxygen (Demaison and Moore 1980). In increasingly saline settings, bacteria then archaea dominate the scavenger/decomposer population, while the health of the metazoan grazers is largely inhibited by higher salinities. Dilution by an influx of minerals to a possible area of organic enrichment can limit levels of organic enrichment by decreasing the proportion of organic matter relative to inorganic matrix. The source of dilution can be detrital or evaporite precipitates.

Dissolved gas levels and temperature changes associated with heliothermal bottoms can create extreme levels of environmental stress in communities also attempting to cope with hypersalinity. For example, oxygen is supplied to any water body via exchange with the atmosphere and as a byproduct of photosynthesis of the biota living in the waters. In well-oxygenated water columns most of the organics produced by primary production are destroyed by microbial respiration and the conversion of organic matter back to CO_2. Much of the improved preservation potential, associated with "higher than marine" bottom salinities in mesohaline to hypersaline settings on biotal diversity, reflects the effect of increasingly low levels of dissolved oxygen in the bottom and pore waters. Oxygen levels in natural brines tend to decrease with increasing salinity (Fig. 9.36a). If not enhanced by the activities of bottom -living aerobic photosynthesizers, natural bottom brines will be dysaerobic to anaerobic by the time salinities reach halite saturation (Kinsman 1973; Warren 1986).

Dissolved CO_2 shows a similar depletion in nutrient-poor waters characterised by little no biological activity (Fig. 9.36b). Dissolved CO_2 levels in marine-fed modern salt

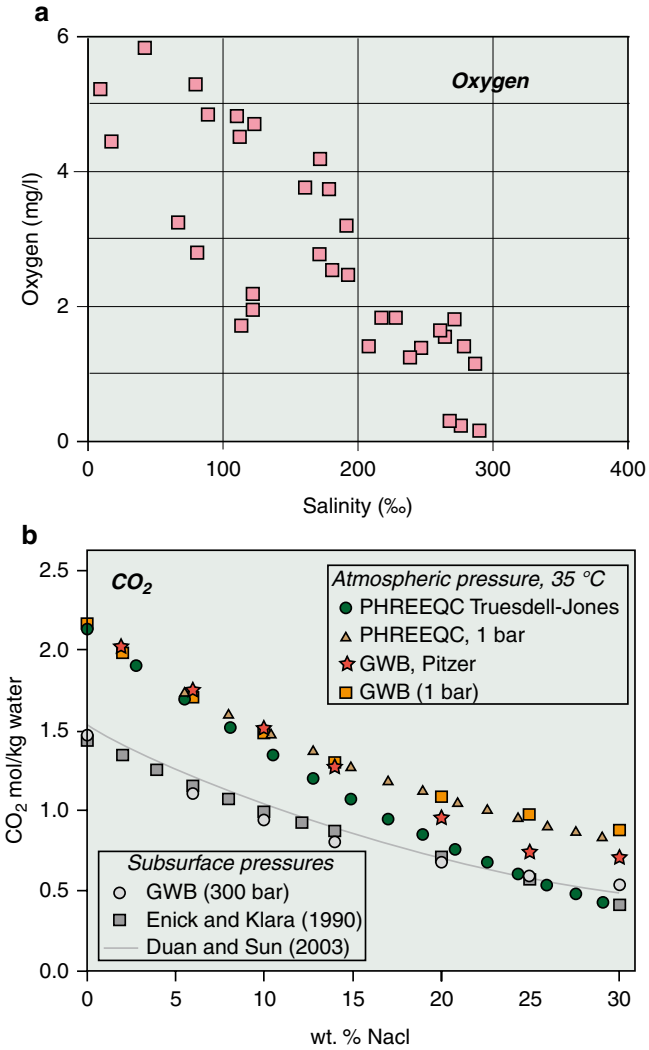

Fig. 9.36 Solubility of oxygen and CO_2 in brine. (**a**) Oxygen in natural brines (Replotted from Warren 1986), (**b**) CO_2 from various modelled brines (After Allen et al. 2005)

pans decrease to around 50 % of the original value as the brine concentration increases from 1.5 to 4 times that of seawater (Lazar and Erez 1992). CO_2 concentration in brine is also pH dependent; CO_2 content approaches zero in a marine brine at a pH of 8.5–9.0, which is the alkalinity of a brine with a salinity around 70‰ (Moberg et al. 1932). Likewise, measurements of CO_2 in the Dead Sea in 1992 showed its solubility was about 20 % of seawater (Barkan et al. 2001). Primary producers, such as algae and cyanobacteria, which are dependent on CO_2 for photosynthesis will suffer shortages at higher salinities.

The bottom-dwelling halobiota can also suffer increased thermal stress in increasingly hypersaline stratified water bodies, due to the tendency for the water mass to become heliothermal. This is because specific heat of any brine decreases as the salinity increases (Kaufmann 1960). For

example, when the salinity of the surface waters of the Dead Sea increased from 210‰ in the 1940s to 275‰ in the early 1980s, the specific heat decreased from 3,085 J/kgK to 2,985 J/kgK (Niemi et al. 1997; p. 127). Specific heat is the amount of heat needed to raise one gram of a substance by 1 °C. For a given amount of heat input, a unit volume of hypersaline water will show a greater increase in temperature than a less saline water. Given the same degree of insolation, it means density-stratified water columns generally are heliothermic, with bottom brines tending to be warmer than fresher surface waters. The resulting greater increase in temperature in a hypersaline bottom water compared to a less saline water can detrimentally effect thermally-intolerant benthic species. The temperature differences can be substantial, with surface waters at ambient atmospheric (≈30 °C) while bottom waters approach temperatures of 60 °C in some density-stratified perennial desert lakes such as Solar Lake[16] in the Sinai (Fig. 2.48).

An interesting association of halophilic microbes can be found in the heliothermal lakes of the Vestfold Hills in Antarctica (Gibson 1999; Cavicchioli 2006). The region is largely snow and ice-free and is thus classified as an Antarctic oasis. It contains a great variety of mesohaline lake systems with over 300 lakes and ponds including what is possibly the largest concentration of meromictic (stratified-heliothermal) lakes in the world. There are 37 permanently stratified water bodies, including six marine basins and seven seasonally isolated marine basins. The stratified basins also have great variety of hydrological styles, ranging in salinity from 4 to 235 g l^{-1}, in temperature from −14 to 24 °C, in depth from 5 to 110 m, in area from 3.6 to 146 ha and surface level from 30 m below to 29 m above sea level.

Three of hypersaline lakes, Organic Lake, Ekho Lake and Deep Lake, have been studied in some detail (Bowman et al. 2000). Like many of the other brine-filled depressions, these lakes are subsealevel relics of an earlier marine embayment, isolated from the ocean by isostatic uplift some 6 ka, but still receiving salt input via marine aerosols (Gibson 1999). Organic Lake is a shallow meromictic brine lake with waters as much as 7.5 m deep and an oxycline at 4–5 m. Its surface waters are moderately saline (8 g/l) and their temperature fluctuates between −14 and +15 °C. Bottom waters are perennially saline with a TDS of 210 g/l and a near constant temperature of −7 °C. Nearby Ekho Lake is 42 m deep, meromictic and heliothermally heated with bottom waters maintaining a year-round temperature of 15–16 °C. Salinities range from 14 g/l at the surface down to 160–180 g/l on the lake bottom, which is permanently anoxic below an oxycline at 12–20 m.

[16]Israelis living in desert kibbutz communities construct artificial black plastic line pans in the desert, fill them with stratified waters and plumb household water pipes through the bottom brine in the pans to create a domestic water heater.

The most hypersaline lake is Deep Lake. Its waters are up to 36 m deep, but unlike the other two lakes it is holomictic and aerobic all the way down to the sediment-water interface. Although salinities are around 320 g/l, its water temperatures can be as low as −18 °C due to a lack of brine stratification and associated heliothermy. The biota in holomictic Deep Lake is almost 100 % haloarchaeal and it is home to that very robust microbe *Halobacterium lacusprofundi*, (Franzmann et al. 1988; see earlier). The biotal make up of the two meromictic lakes (Organic and Ekho lakes) is more complex with varying combinations of the Proteobacteria and Cytophagales. Ekho Lake also contains a number of the Haloanaerobiales, perhaps reflecting its warmer year-round bottom temperatures, a biotal result of heliothermic heating in this frigid region's cryogenic hydrology.

But the dominant biomass control in most mesohaline to hypersaline environments, at least for most multicellular life, is not dissolved gas or even temperature in the ambient environment, but the increase in osmotic pressure that comes with increasing salinity. At a concentration of 300‰, sodium chloride brine exerts an osmotic pressure on a cell of more than 100 atm (Bass-Becking 1928; Reed et al. 1984). Cells of species that typically inhabit marine or brackish waters quickly desiccate in such brines, leading to rapid death (e.g., Geddes 1975b), hence the adaptations at the cellular level that typify halotolerant and halophilic organisms.

The tendency of bottom waters in many deeper hypersaline water masses to become anoxic, hotter, and osmotically pressured, has helped create many ancient lagerstaette associations (fossil "death communities"), with inherent excellent preservation of fine details in the entrained fossil forms. For example, the widely known Cretaceous Solnhofen micritic plattenkalk of Bavaria preserves the feathers of the bird-like dinosaur *Archaeopteryx* and many "death-dance" trackways of finely preserved marine crustaceans that once wandered into the hypersaline and anoxic bottom water layers of the Solnhofen lagoon. Similarly, the communities of chemosynthetic mussels, which inhabit nutrient-rich deep dark bottoms about the edges of modern anoxic brine lakes atop dissolving salt allochthons, can suffer mass extermination when sediment slumps occur and mollusc biostromes, carried along by the slump, end up in the anoxic H_2S-rich, death-dealing hypersaline waters of the brine lake (MacDonald 1992).

High pore water salinities, extreme osmotic stress, a propensity for anoxia in the stratified bottom waters, anoxic pore brines and high bottom temperatures all tend to exclude aerobic burrowing and grazing animals from evaporitic bottom sediments. This minimises a biota that would otherwise oxidise and destroy microbial debris in similar sediments deposited beneath less saline waters.

Biological Responses to Variably Layered Brines: Cycles of "Feast or Famine"

Brines in modern evaporitic depressions are typically layered, with denser more saline waters supporting an ephemeral mass of less dense inflow water. The bottom layer in a perennial brine system tends to be more stable compared to the upper and its physical condition changes little until stratification is lost via mixing of the two water masses. Once mixing occurs the waters in the lake can completely evaporate. Conditions in the floating less dense upper layer are both ephemeral and variable, with wide fluctuations in salinity before desiccation or mixing. When salinities are lowered, this upper layer periodically supports a widespread planktonic bloom (feast). Then, as ongoing evaporation concentrates the upper layer, conditions become increasing less suitable for life (famine) and a mass die-off occurs, first of the haloxene species, then the halotolerants, then the halophiles. The bloom and the following dieback creates a pulse of organic matter that can swamp the abilities of the anaerobic decomposers in the lower water column to strip it of its hydrogen. Organics can then reach the sediment interface with their long-chain alkanes still largely intact. In conditions where light penetrates to the bottom of the brine column, even when the waters atop the sediment surface are oxygenated, the halotolerant primary producers can be sufficiently productive and the underlying anoxic decomposers sufficiently inefficient that substantial volumes of hydrogen-rich microbial matter can be retained into burial.

When surface water salinities are suitable, evaporite basins have some of the highest measured rates of organic productivity in the world (Fig. 9.37; Warren 1986). When biodiversity is low and salinity is high, a proliferation of well-adapted species can generate productivity levels that are much higher than those observed in most nonevaporitic settings. These saline systems are indicative of general principles seen in all stressed ecosystems, namely, as the harshness or abiotic stress in a system increases the biotic stress decreases on a few well-adapted species (less predators and grazers). The total biodiversity (number of species) decreases, while at the same time the biomass (total mass of organisms in the system) initially increases (Garcia and Niell 1993). Ultimately, it too declines as conditions become unsuitable for any life (inset in Figs. 9.37).

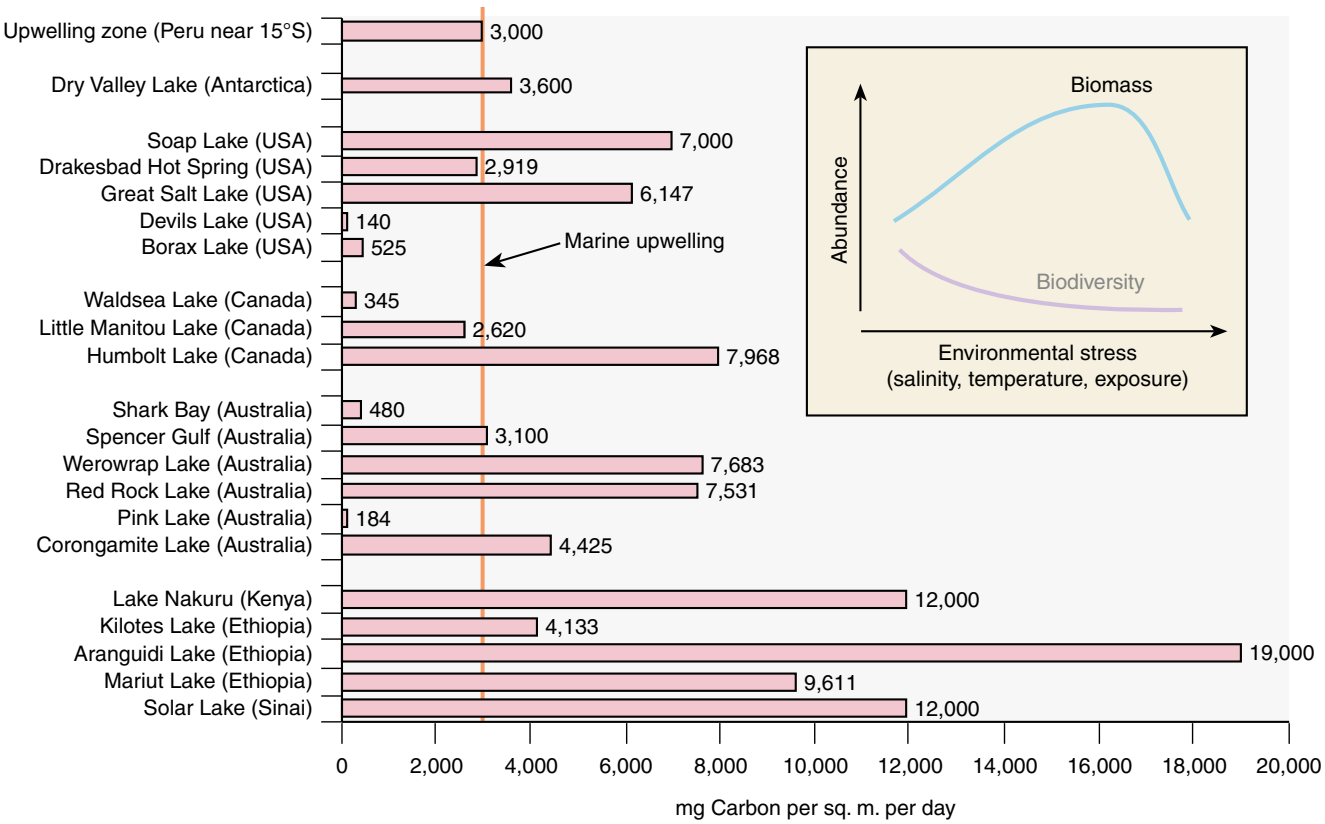

Fig. 9.37 Organic productivity (maxima) in various saline ecosystems. Typical marine upwelling zone ≈250–500 mg C/m²day (the solid line is world marine maxima based on an upwelling zone, offshore Peru); tropical shoal water seagrass banks ≈500–1,200 mg C/m²day; open marine waters are less than 100 mg C/m²day and average 20 mg C/m²day and coastal waters 40–50 mg C/m²day. But, preservation is more important than production rate in terms of source potential (Compiled from sources listed in Warren (1986) and this chapter)

Salinity Change Influences Organic Productivity: A Flamingo Connection in East African Saline Lakes

One of the most visually impressive indications of periodic but very high levels of organic productivity in a well adapted biota in a salinity-stressed layered water body resides in the "flamingo connection." Flamingos (*Aves*, *Phoenicopteridae*) represent an ancient lineage of long-legged, microphagous, colonial wading birds. Although often misperceived as tropical species, flamingo distribution is more closely tied to the great deserts of the world and to hypersaline lake sites, than it is to equatorial regions (Bildstein et al. 1993). Flamingoes are filter feeders that thrive on the dense halotolerant cyanobacterial blooms in the mesohaline shallows of saline lakes around the world. This creates a connection between flamingoes, mesohaline planktonic blooms and saline lakes, first noted in the geological literature for the east African rift lakes by Kirkland and Evans (1981) and well documented in Lake Nakuru by Vareschi (1982). Sedimentary textures and structures associated with flamingoes, where they dominate the macrofauna in some modern saline lakes, are described by Scott et al. (2009, 2012). Ancient avian counterparts can leave a characteristic set of trackways and trace fossils that can be used to refine mid-late Tertiary lacustrine depositional models (Melchor et al. 2012).

Two species of flamingo flock in huge numbers in the East African rift lakes, namely, the greater and the lesser flamingo (*Phoenicoptus ruber roseus* and *P. minor* respectively), the lesser flamingo has spectacular pink-red[17] colouration in their feathers. These bright pink waders feed and breed in mesohaline rift lakes where cyanobacterial blooms can be so dense that a secchi disc disappears within a few centimetres of the lake's water surface (Warren 1986). Lake Natron, where trona is the dominant evaporite, is a major breeding ground for flamingoes in East Africa and is the only regular breeding site for the lesser flamingo in Africa (Simmons 1995). Lesser flamingoes build nesting platforms on the trona pavement in the more central parts of the lake. These spectacular birds not only feed in saline waters, they can choose to nest on evaporite pavements!

Worldwide, only six sites are used for breeding by the lesser flamingos: Lake Natron (Tanzania), Etosha Pan (Namibia), Makgadikgadi-Pan (Botswana), Kamfers Dam (South Africa), as well as two pans in the "Little Rann of Kachchh" (India). Recent estimates of lesser flamingos at the main distribution areas are as follows: 1.5–2.5 million in eastern Africa; 390,000 in northwestern India; 55,000–65,000 in southwestern Africa; and 15,000–25,000 in western Africa. The highest population densities occur in Kenya (1.5 million) and Tanzania (600,000) (Childress et al. 2008). Lesser flamingoes are well adapted to the harsh conditions associated with living and breeding in hypersaline alkaline conditions. Worldwide, they follow an itinerant lifestyle, ranging across their distribution areas in search of saline water bodies with appropriate cyanobacterial blooms. In the east African rift the flocks can travel up to 200 km a day between feeding and breeding sites, which are generally at geographically separate locations (Fig. 9.38a).

Lake Natron has the highest concentration of breeding flamingoes in any lake in East Africa. Both the greater and the lesser flamingo are found there, with the lesser flamingo outnumbering the greater by a hundred to one. Lesser flamingoes bred at Lake Natron in 9 out of 14 years from 1954 to 1967. But while Lake Natron is an essential breeding site, it is not a focal feeding site for flamingoes.

Major feeding sites in the Africa rift valley are Lakes Nakuru and Bogoria (formerly Lake Hannington) in Kenya and entrain waters that are mesohaline with an abundance of halotolerant cyanobacteria, dominated by *Arthrospira* (Figs. 9.39 and 9.40). Lake Nakuru is a mesohaline soda lake with a pH ≈ 10.5 and a typical annual salinity range of 15–45 ‰, nearby lake Bogoria is somewhat larger, also an alkaline soda lake, with somewhat higher salinities. The Lake Nakuru depression measures some 6.5 km by 10 km, with a water covered area of some 5–45 km^2 experiencing an annual pan evaporation rate of 1,500 mm beneath a Cfb Köppen climate (Fig. 9.38b; Vareschi 1982; Krienitz and Kotut 2010). It contains a eutrophic bottom water mass in the lake centre, with thermally stratified water column that can be up to 4.5 m deep. The Lake Bogoria' water mass is up to 4 km wide, some 17 km long with thermally stratified eutrophic waters up to 10 m deep. It lies beneath a Cfb climate with a pan evaporation of 2,600 mm. It is fed by a combination of rainfall (≈760 mm/year) and numerous (>200) hydrothermal springs about the lake edge (Fig. 9.38c).

Water depths in both lakes vary from year to year, in large part depending on the vagaries of annual runoff/inflow. The higher level of hydrothermal inflow in Bogoria's hydrology, along with its somewhat steeper hydrographic profile, means the lake area and water depth varies less from year to year compared to Nakuru (Fig. 9.38d). Lakes Nakuru and Bogoria, which at peak breeding times can support lesser flamingo populations in excess of 1.5 million birds, have surface areas that are less than half those of lakes Natron and Magadi, which in turn have small areas compared to most ancient lacustrine evaporites and yet Nakuru and Bogoria are two of the most productive ecosystems in the world. What makes both lakes so productive are dense populations of halotolerant cyanobacteria, especially *Arthrospira sp*., which flourish and periodically reach peak growth in their waters.

To utilise dense cyanobacterial populations, which flourish in mesohaline lakes worldwide, flamingo beaks have

[17] An aviator once described Lake Nakuru as "a crucible of pink and crimson fire," with a million flamingos painting an astonishing band of colour that burst into pieces as the birds took flight.

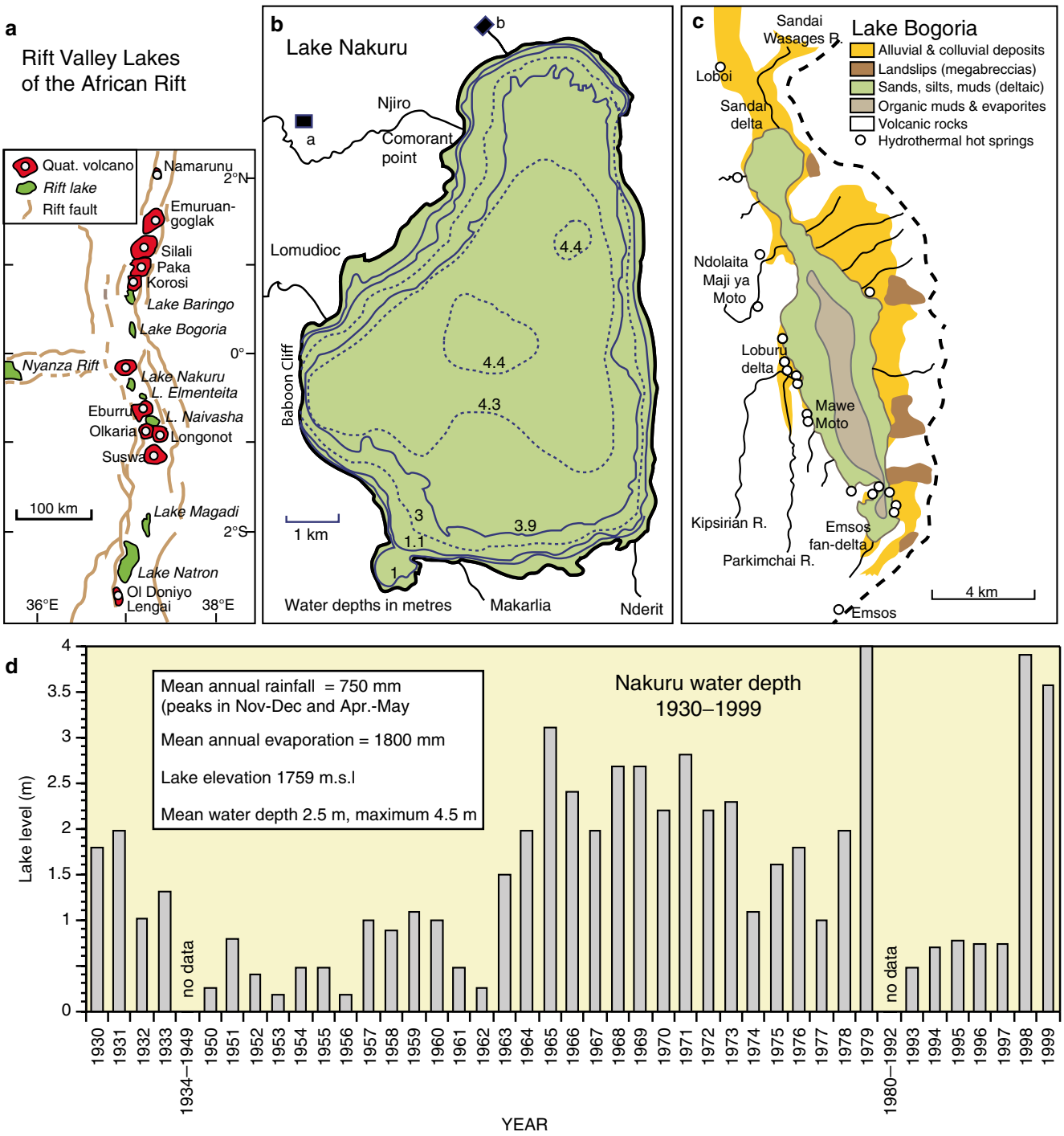

Fig. 9.38 African rift valley (**a**) Location of lakes and Quaternary volcanoes in the African rift valley centred on Lake Nakuru and Lake Bogoria. (**b**) Lake Nakuru bathymetry (Dec 1979) and subsequent strandzone changes. Solid isopleths are actual shorelines at different lake levels over a 20 year period; from outer to inner are December 1979, January 1969, January 1967 and January 1961. Dashed isopleths are based on soundings taken in December, 1971. Two sewage plants are located at *a* and *b* (After Vareschi 1978) (**c**) Surface geology of Lake Bogoria (After McCall 2010). (**d**) Lake levels in Lake Nakuru from 1930 to 1999. Data are not sufficiently detailed to record times of complete lake drying or drought and there are also substantial times when no data were collected/published (1934–1949 and 1978–1992)

evolved into highly efficient plankton-extraction apparati unlike that possessed by any other bird group on earth; the affinity is more to the baleen of whales (Bildstein et al. 1993). A flamingo beak houses a high volume water-filtering system made up of a piston-like tongue and hair-like structures called lamellae made up of rows of fringed platelets that line the inside of the mandible. In the lesser flamingo, the lamellae fibres have the appropriated spacing for capturing coiled filaments of *Arthrospira*. Lamellar spacings are wider in the beaks of the greater flamingo than those in

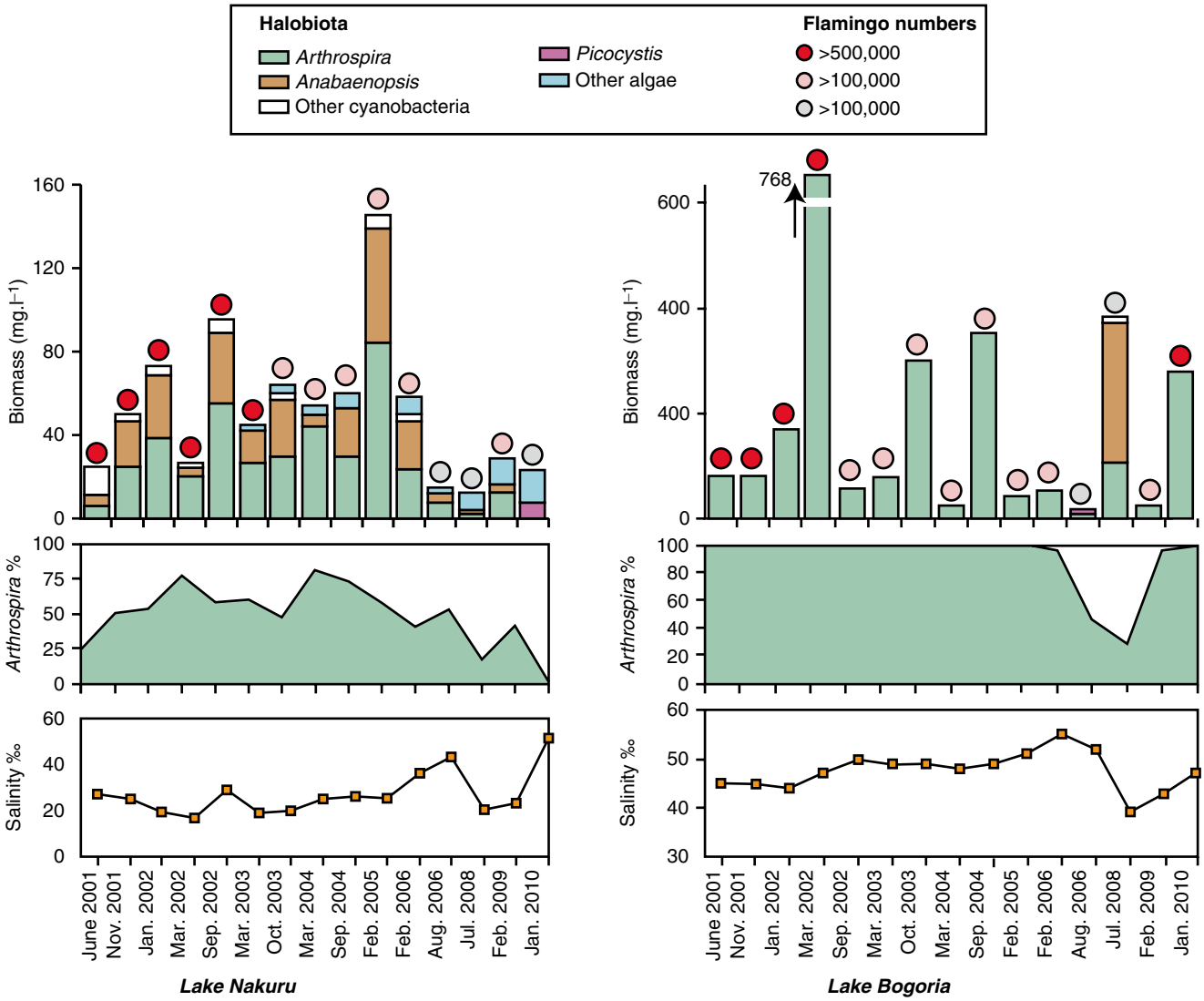

Fig. 9.39 Changes in total phytoplankton biomass, biomass contribution of the dominant phytoplankton species, number of flamingos, percentage contribution of *Arthrospira* to total phytoplankton biomass, and salinity in Lake Nakuru and Lake Bogoria in the African rift valley for the period 2001–2010. Note that the time scales are irregular but the same for the two lake while vertical scales differ in magnitude for some of the measured parameters (After Krienitz and Kotut 2010)

the beaks of the lesser flamingo so these larger-sized birds are more generalist feeders of lake zooplankton. Thus, in any mesohaline lake where the two bird species feed and coexist, they do not compete for the same food source.

By swinging their upside-down heads from side to side just below the water surface and using the piston-like tongue to swish water through their lamella-lined beaks, flamingoes siphon the lake plankton into their gullets at phenomenal rates. Lesser flamingoes can filter as many as 20 beakfulls of plankton-rich water a second. This means some individuals filter upwards of 20,000 l of water per day. How the birds manage to do so in brackish to mesohaline waters, while maintaining their osmotic integrity, remains a mystery. When the rift lakes are typified by dense cyanobacterial blooms, each adult bird ingests around 72 g dry weight of *Arthrospira* per day (Vareschi 1978). This means the Nakuru flock is able to ingest 50–94 % of the daily primary production in the lake (about 60–80 t). Rates of planktonic renewal in these rift lakes is obviously extremely high. Rates of biomass production by *Arthrospira* can be spectacular. Vonshak (1997) reported doubling times of 11–20 h of *Arthrospira* in a culture growing under mesohaline conditions at 35 °C.

Flamingoes are mostly nocturnal feeders and will feed for up to 12–13 h in a 24 h period. As mentioned, the preferred planktonic food of the lesser flamingo is the cyanobacterium *Arthrospira platensis* (formerly *Spirulina platensis*), which is typically the main phytoplankton component in Lake Nakuru and Lake Bogoria waters (Fig. 9.39). Unfortunately,

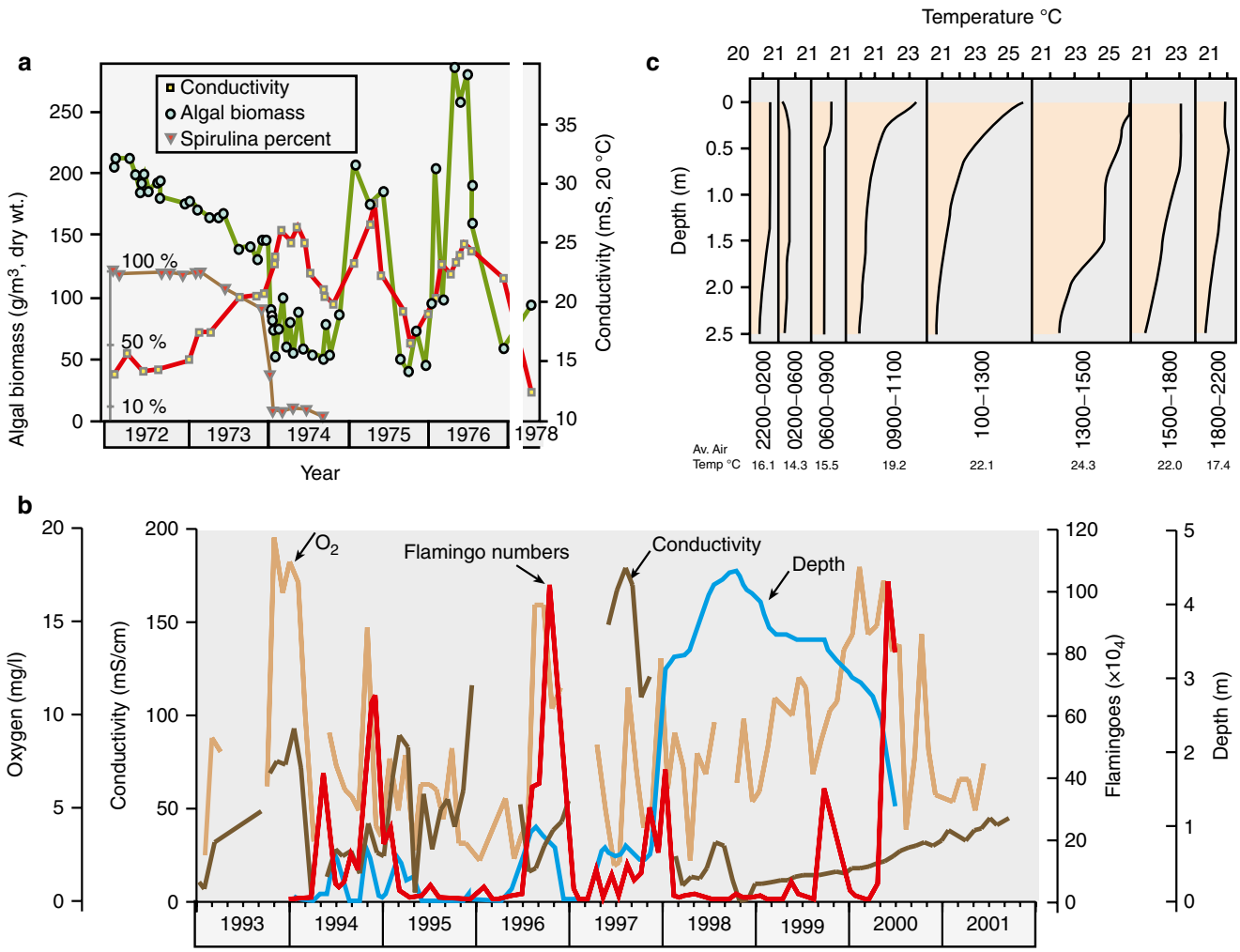

Fig. 9.40 Lake Nakuru. (**a**) Trends of algal biomass and conductivity of lake water during 1972–1978. The percent contribution of *Arthrospira platensis* to the total algal biomass is also shown. (**b**) Monitored water depths, conductivities, oxygen levels and flamingo numbers at Lake Nakuru for the period 1993 to mid 2001. Water depth and flamingo data only available from 1994 to mid 2000. Data is digitised and replotted to a common time scale from data in an online progress report by Odada et al. 2006 discussing conditions in the Lake Nakuru area (http://www.worldlakes.org last accessed Sept 24, 2012) (**c**) Mean water temperature profiles at different times of day from 1972 to 1973 (**a**, **c**: After Vareschi 1982)

the dense populations of *Arthrospira* function best at a preferred range of temperature and salinity, meaning acme populations tend to collapse irregularly and unpredictably in both Lake Nakuru and Bogoria, leading to highly-stressed malnourished flocks of flamingoes subject to mass dieback (Fig. 9.39; Vareschi 1978; Krienitz and Kotut 2010).

Arthrospira has high levels of the red pigment phycoerythrin and so when ingested in large volumes it accumulates in flamingo feathers to give the birds their world famous colouration, hence the "flamingo connection." Once digested, the carotenoid pigment dissolves in fats, which are then deposited in the growing feathers. The same effect is seen when shrimp change colour during cooking due to carotenoid alteration. The amount of pigment laid down in the feathers depends on the quantity of pigment in the flamingo's diet. Lesser flamingoes, with beak design maximised to feed on *Arthrospira* have a more intense pink colour in their feathers than greater flamingoes. The latter species sits higher in the Lake Nakuru food chain and so gets the slight pink tinge in its feather colour, mostly second-hand from the lake zooplankton, which also feed on *Arthrospira*.

As well as possessing very high levels of phycoerythrin in its cytoplasm, *Arthrospira* is also unusual among the cyanobacteria in its unusually high protein content (some ten times that of soya). This, and the high growth rate of this species, explains why Nakuru and Bogoria acme populations can support such spectacular population levels of flamingoes. A lack of cellulose in the *Arthrospira* cell wall means it is a source of plant protein readily absorbed by the gut, making it a potentially harvestable human food source in saline water

bodies in regions of desertification. In Lake Chad, and in some saline lakes in Mexico, *Arthrospira* accumulates as a lake edge scum that has been harvested for millennia by the local people (including the ancient Aztecs) and used to make nutritious biscuits.

When *Arthrospira* stocks are low in the rift lakes, the lesser flamingo can consume benthic diatoms. However, net primary productivity of benthic diatoms in East African soda lakes is one to two orders of magnitude less than that of *Arthrospira*, and the carrying capacity of the habitat with diatoms is lower by the same order (Tuite 2000). This lower productivity is seen in the peak 25,000 bird population, which are diatom feeders, in Laguna de Pozuelos in Argentina (Fig. 9.22; area ≈100–130 km^2, more than three times that of Nakuru, yet the peak flamingo numbers are two orders of magnitude lower).

In Lake Nakuru, *Arthrospira* and other lake plankton are also consumed by one species of introduced tilapid fish and one species of copepod and a crustacean. Rotifers, waterboatmen, and midge larvae also flourish in the mesohaline waters of Lake Nakuru. The mouth-breeding tilapid *Sarotherodon alcalicum grahami* was introduced to the lake in the 1950s to control the mosquito problem and fish-feeding birds (such as pelicans) have flourished ever since (Vareschi 1978). During times of nonoptimum water conditions, when either freshening or somewhat elevated hypersalinity lessens the number of *Arthrospira*, the tilapids can displace the flamingoes as the primary consumers of planktonic algae.

In 1972 Lake Nakuru waters held a surface biomass of 270 g/m^3 and an average biomass of 194 g/m^3 but, as in most hypersaline ecosystems, Nakuru's organic production rate varies drastically from year to year as water conditions fluctuate (Fig. 9.40a; Vareschi 1978, 1979). *Arthrospira* was in a long-lasting bloom in 1971–1973, and accounted for 80–100 % of the copious phytoplankton biomass in those years. In 1974, however, *Arthrospira* almost disappeared from the lake and was replaced by much smaller-diameter planktonic species, such as coccoid cyanobacteria that dealt better with elevated salinities. This transfer in primary producer make-up in the lake waters made the flamingoes less efficient feeders. When the relatively large filaments of *Arthrospira* dominate the lake plankton, a flamingo's beak filters between 64 and 86 % of the plankton held in each mouthful of lake water (Vareschi 1978). When the much smaller coccoids come to dominate the filters are much less efficient feeding mechanism. The change in plankton species was also tied to a serious reduction in algal biomass (and protein availability), which in 1974 was down to 71 g/m^3 in surface waters and averaged 137 g/m^3 in the total water mass. As a result the flamingo numbers feeding in the lake declined from 1 million to several thousands and the flamingoes moved to other lakes, like Bogoria, where *Arthrospira* were flourishing (Vareschi 1978).

The lower salinity limit for an *Arthrospira* bloom is ≈5‰ and it does better when salinity is more than 20‰. The species dominance of *Arthrospira* and its higher biomass in somewhat more saline lake waters is clearly seen in the near unispecific year-round biomass of nearby Lake Bogoria (salinity 40–50‰). Its surface salinity is higher year round than Lake Nakuru (salinity ≈ 30‰) and the somewhat fresher waters of Lake Elmenteita (salinity ≈ 20‰; Fig. 9.38a). Because of this, Lake Bogoria is a more reliable food source for feeding flamingoes compared to either Nakuru or Elmenteita. Birds tend to migrate there to feed when conditions for *Arthrospira* growth are not ideal in other nearby alkaline lakes (too fresh or too saline). This was the case in 1999 when high rainfall and dilution of lake waters caused the *Arthrospira* levels to fall in both Nakuru and Elmenteita. It was also true in late 2012 when Nakuru water levels were at near historic highs and the waters too fresh to support a healthy *Arthrospira* population.

The driving mechanism for the abrupt change in biomass in Lake Nakuru in the period 1972–1974 was not clearly defined. It was thought to be related to increased salinity and lowering of lake levels, driving the growth of coccoid species other than *Arthrospira sp*. that were better adapted to higher salinity, but offering less protein to the feeding birds (Fig. 9.40a; Vareschi 1978). There is also the simple fact that, in a lake with no surface outflow, ever more saline waters cover ever-smaller areas on the lake floor. There have been times in the last 70 years when most of Lake Nakuru has dried up and pools of saline water only a few tens of centimetres deep remained. This was the case in 1962 and most recently the case in 2008 (Fig. 9.38d).

After the lake level lows of the 1960s, during the mid to late 1970s and in the 1980s the Nakuru hydrology returned to more typical inherent oscillations in water level and salinity (schizohalinity). The flamingo populations in Nakuru returned to impressive numbers but followed the vagaries of *Arthrospira* blooms. Since the early 1990s more reliable long-term data sets on physical lake condition and flamingo numbers have been compiled (Figs. 9.39 and 9.40b). In that time frame, in 1993, 1995 1998, 2008 and 2012, the flamingo populations feeding in Lake Nakuru were once again at very low levels and the remaining bird populations were stressed and subject to mass dieback.

In 1998, unlike 1974, the stress on the flamingo population was related to lake freshening driving the decrease in *Arthrospira* biomass, not increased salinity and desiccation. In the preceding bountiful year (1996), the *Arthrospira*-dominated biomass had bloomed at times when salinities were favourable and died back at times of elevated salinities and lake desiccation, as in 1974. By 2000 formerly low salinities had once again increased making surface waters suitable for another widespread *Arthrospira* bloom and the associated return of high numbers of feeding flamingoes, which continued until 2007 (Fig. 9.40c).

Freshening favours a cyanobacterial assemblage dominated by picoplanktic chlorophytes (*Picocyctis salinarum*) and the nostocalean *Anabaenopsis*, the latter creates slimy masses that clog the flamingo's feeding apparatus. The combination drives much of the flamingo population to starvation (Krienitz and Kotut 2010). With freshening, comes also the possibility of the growth of strains that produce toxins (such as *Anabaenopsis* or *Microcystis*), possibly not in the feeding areas, which tend to remain too saline for *Microcyctis*, but in the spring waters where the flamingoes fly in order to bathe and cleanse their feathers (Kotut and Krienitz 2011).

It seems that breeding flamingoes come to Lake Nakuru to feed in large numbers when there is water in the lake with appropriate salinity and nutrient levels to facilitate an *Arthrospira* bloom. In some years when heavy rains occur, lake levels rise significantly and the lake waters, although perennial, stay in the lower salinity tolerance range for *Arthrospira platensis*, keeping cyanobacterial numbers and protein levels at the lower end of the spectrum, as in the El Niño period between October 1997 to April 1998. Once lake levels start to fall, salinities and rates of salinity change return to higher levels, then water conditions once again become appropriate for an *Arthrospira* bloom. But environmental stress on the flamingoes also comes with further elevated salinities and desiccation moving lake hydrochemistry into salinities at the upper end of *Arthrospira* tolerance.

One of the reasons Lake Nakuru is suitable for phenomenal cyanobacterial and algal growth at times of *Arthospira* bloom is the maintenance of suitable temperatures and oxygenation in the upper water mass, where the photosynthetic *Arthrospira* thrive. Nakuru develops a daily thermocline in the upper 1.5 m of the water column that dissipates each day in the late afternoon via wind mixing. Overturn recycles nutrients (derived from decomposition of bird and other droppings, including those of resident hippopotami) back to the oxygenated lit surface waters to facilitate an ongoing bloom the next day (Fig. 9.40c).

Numbers of flamingoes feeding in Lake Nakuru and Lake Bogoria are used in popular press as indicators of the environmental health of the lakes. Thousands of birds died in Lake Nakuru in 1995 and more than 30,000 birds may have died in Lake Bogoria in the first half of 1999. The most dramatic die-offs in the last decade were at Lake Nakuru in August 2006, when some 30,000 died, and Lake Bogoria in July 2008, when 30,000 birds died Some environmentalists have argued in the popular press that mass die-offs and their perception of lowered numbers of flamingoes in Lake Nakuru and Lake Bogoria in the 1990s were indicators of uncontrolled forest clearance, an uncontrolled increase in sewerage encouraging eutrophication, and increase in heavy metals from increasing industrial pollutants in the lake, along with general stress on the bird population from tourists and the drastic increase in local human population centred on the town of Nakuru (third largest in Kenya). Numbers of people in the town, which is the main city in the rift valley, have grown by an average of 10 % every decade for the past 30 years.

But like much environmental doomsday argument, it is more based on opinionated[18] prediction than on scientific fact. When numbers of feeding flamingoes in Lake Nakuru are compiled across last two decades it is obvious that flamingo numbers oscillate widely, but it is also obvious that the peak numbers in 2000s are equivalent to the peak numbers in 1990s. A notion of longterm fall in numbers of feeding flamingoes in the lake is not based on scientific reality.

Likewise, when studies were done on the cause of the mass dieoff in Lake Bogoria in 1999, it was found to have a natural not an anthropogenic cause (Krienitz et al. 2003; Ballot 2004). The flamingoes had ingested the remains of toxic cyanobacteria that constitute part of the population of the microbial mats that had bloomed to form a floor to the fresh water thermal spring areas about the lake edge. There the mats are dominated by thermally tolerant species; *Phormidium tere-briformis, Oscillatoria willei, Arthrospira subsalsa* and *Synechococcus bigranulatus*. The influence of cyanotoxins in the deaths of the birds is reflected in autopsies which revealed: (a), the presence of hot spring cyanobacterial cells and cell fragments (especially Oscillatoria willei), and high concentrations of the cyanobacterial hepato- and neurotoxins in flamingo stomach contents and faecal pellets; (b), observations of neurological signs of bird poisoning – birds died with classic indications of neurotoxin poisoning – the ophistotonus behaviour (neck snapped back like a snake) of the flamingoes in the dying phase, and the convulsed position of the extremities and neck at the time of death. Cyanobacterial toxins in stomach contents, intestine and faecal pellets were 0.196 g g^{-1} fresh weight (FW) for the microcystins and 4.34 g g^{-1} FW for anatoxin-a. Intoxication with cyanobacterial toxins probably occurred via uptake of detached cyanobacterial cells when birds come daily to the springs to drink and wash their feathers after an overnight feeding session in the saline waters of the lake proper.

When heavy metal studies were undertaken in Nakuru lake sediments, the amount of heavy metals (Cd, Cr, Cu, Hg, Ni, Pb, Zn) were found to be in the typical range of metals in

[18] Aka a "Chicken Little" or "the sky is falling" attitude to the world: such reportage, so popular in much of the world's newsprint and in the religious extremes, be it reporting environmental Armageddon, the "end of peak oil," or the coming of the next prophet, sells more newspapers and gets more zealous believers than any "good news" stories or fact-based analysis and discussion. In the prevailing zeitgeist, being a skeptic and advocating testing of all hypotheses (the basis for scientific endeavour) is considered a negative position; The questions; Leading questions, so common with the popular press, like; "When did you last beat you wife?" and "Are you a climate skeptic?" and your ability to reply without prejudicing popular perceptions is key. Otherwise when you answer either question with statement like "I don't beat my wife" or "The proposition that climate change since the start of the Industrial Age ties mostly to anthropogenic causes, is still equivocal," typically puts you in the same place in the minds of the true believers Prejudice be it green, left wing, right wing, religious or otherwise will always color the perceptions of such a listener.

sediments in lakes worldwide. The exception is Cd, which is elevated and can perhaps be ascribed to anthropogenic activity (Svengren 2002). All other metals are present at low levels, especially if one considers that Lake Nakuru lies within a labile catchment where the bedrock is an active volcanogenic-magmatic terrane.

Rise and fall of lake levels, drastic changes in salinity, a periodically stressed biota, and a lack of predictability in water character are endemic to life in saline ecosystems (cycles of "feast or famine"). Natural variations controls the number of feeding flamingoes in Nakuru and Bogoria. Oscillations in one or more of these factors are not necessarily anthropogenically induced. In general, sufficient base-line scientific data in these schizohaline ecosystems is not yet available and so accurate determinations of the relative import of increased human activity versus natural environmental stresses on longterm bird numbers are not possible.

Nearby Lake Magadi is also characterised by seasonal freshening, high productivity levels and bright red waters. In this case the colour comes from haloalkaliphilic archaea, not cyanobacteria. Archaeal species belonging to the genera *Natronococcus*, *Natronobacterium*, *Natrialba*, *Halorubrum*, *Natronorubrum and Natronomonas*, all occur in soda brines of Lake Magadi. Lake centre brines where this biota flourishes is at trona/halite saturation with a pH up to 12. Stratified moat waters around the trona platform edge are less chemically extreme and moat bottom sediments preserve elevated levels of organics (≈6–8 %). Lake Magadi also harbours a varied anaerobic bacterial community in the moat waters, including cellulolytic, proteolytic, saccharolytic, and homoacetogenic bacteria (Shiba and Horikoshi 1988; Zhilina and Zavarzin 1994; Zhilina et al. 1996). When the homoacetogen *Natroniella acetigena* was isolated from this environment its pH growth optimum was found to be 9.8–10.0, and it continued to grow in waters with pH up to 10.7 (Zhilina et al. 1996).

Regionally, salinities in the east African rift valley lakes range from around 30–50‰ total salts (w/v) in the more northerly lakes in the rift (Fig. 9.32a; Bogoria, Nakuru, Elmenteita, and Sonachi) to trona and halite saturation (>200‰) in lakes to the south (Lakes Magadi and Natron). Yet across this salinity range a combination of high ambient temperature, high light intensity and a continuous resupply of CO_2, makes some of these soda lakes amongst the highest in the world in terms of their seasonal planktonic biomass (Grant et al. 1999) and also places them among the world's most productive ecosystems (Fig. 9.37; Melack and Kilham 1974). Organic production is periodic, and pulses of organic product periodically swamp the ability of the decomposers and so accumulate as laminites in the lake centres.

As we have seen, the less alkaline lakes are dominated by periodic blooms of cyanobacteria, while the hypersaline lakes, such as Magadi, can on occasion support blooms of cyanobacteria, archaea and alkaphilic phototrophic bacteria (Jones et al. 1998). Halotolerant and halophilic biota living in the variably saline and layered water columns constitute small-scale "feast or famine" ecosystems, which at times of "feast" are far more productive than either tropical seagrass meadows or zones of marine upwelling (Fig. 9.37).

The "flamingo connection" supports a general observation that short periods of enhanced organic productivity are followed by episodes of lessened productivity in various schizohaline lake waters worldwide. It reflects the general principle that increased environmental stress favours the survival of a few well-adapted and specialised halotolerant species adapted to the feast and famine life-cycle that exists in most saline depressions. This same general principal of schizohaline ecosystems can be clearly seen in the decrease in invertebrate species (grazers and predators) with increasing salinity in the carbonate lakes of the Coorong of Southern Australia, where only brine shrimp remain alive in waters with salinities in excess of 200‰ (Fig. 9.41).

"Feast or Famine" in the Dead Sea

Effects of occasional freshening on biomass in stratified brine columns that are supersaline, not mesohaline, is clearly seen in the present "feast or famine" productivity cycle of the Dead Sea (Figs. 9.42 and 9.43; Oren and Gurevich 1995; Oren et al. 1995; Oren 2005). *Dunaliella sp*., a unicellular green alga variously described in the past as *Dunaliella parva* or *Dunaliella viridis*, is the sole primary producer in the Dead Sea waters. Then there are several types of halophilic archaea of the family Halobacteriaceae (prokaryotes) which consume organic compounds produced by the algae.

Two distinct periods of organic productivity (feast) have been documented since the Dead Sea became holomictic in 1979 (Oren 1993, 1999). The first mass developments of *Dunaliella sp*. (up to 8,800 cells/ml) began in the summer of 1980 following a dilution of the saline upper water layers by the heavy winter rains of 1979–1980 (Fig. 9.42a, b). The rains drove a rapid rise of 1.5 m in lake level and an increase in the level of phosphates in the lake's surface waters (Fig. 9.42c). This bloom was quickly followed by a blossoming in the numbers of red halophilic archaea (2×10^7 cells/ml), *Dunaliella* numbers then declined rapidly following the complete remixing of the water column and the associated increase in salinity of the upper water mass. By the end of 1982 *Dunaliella* had disappeared from the main surface water mass. Archaeal numbers underwent a slower decline.

During the period 1983–1991 the lake was holomictic, halite-saturated and no *Dunaliella* blooms were observed. Viable halophilic and halotolerant archaea were probably present in refugia about the lake edge during this period, but in very low numbers. Then heavy rains and floods of the winter of 1991–1992 raised the lake level by 2 m and drove a new episode of meromictic stratification as the upper five metres of the water column was diluted to 70 % of its normal

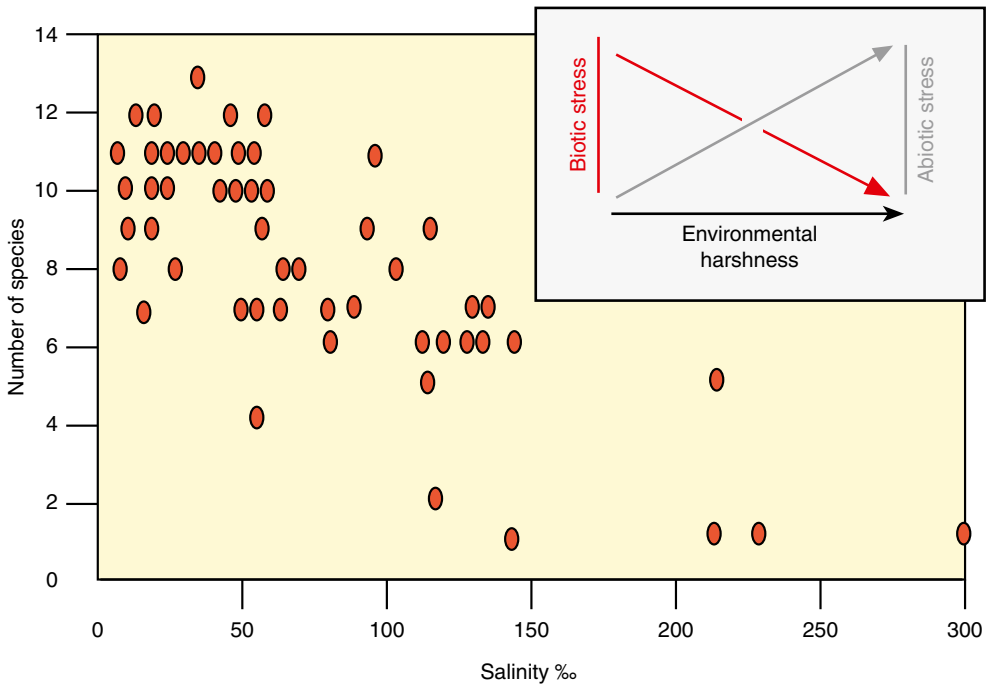

Fig. 9.41 Effect of increasing salinity on metazoan species diversity in the saline lakes of the Coorong region, South Australia (After De Deckker and Geddes 1980)

surface salinity (Fig. 9.42). High densities of *Dunaliella* reappeared in this upper less saline water layer (up to 3×10^4 cells/ml) at the beginning of May 1992, rapidly declining to less than 40 cells/ml at the end of July 1992 (Fig. 9.43). An associated bloom of heterotrophic haloarchaea (3×10^7 cells/ml) continued past July and continued to impart a reddish colour to the surface and nearsurface waters.

Much of the archaeal community was still present at the end of 1993 but the amount of carotenoid pigment per cell had decreased two- to three-fold between June 1992 and August 1993 (Oren and Gurevich 1995). A remnant of the 1992 *Dunaliella* bloom maintained itself at the lower end of the pycnocline at depths between 7 and 13 m (September 1992—August 1993), perhaps chasing nutrients rather than light. Its photosynthetic activity was low, and very little stimulation of archaeal growth and activity was associated with this algal community (Fig. 9.43). It seems that once stratification ends and the new holomictic period begins, the remaining Archaeal community, which was largely restricted to the upper water layers above the halocline, spreads out more evenly over the entire upper water column until it too dies out. No substantial algal and archaeal blooms have developed in the Dead Sea since the winter floods of 1992–1993 until mid 2015.

Colouration of the Dead Sea waters from the initial algal bloom allowed Oren and Ben Yosef (1997) to use Landsat images, collected in May 1991 and in April and June 1992, to plot the development of the *Dunaliella sp*. bloom. In contrast, the carotenoids of the subsequent archaeal bloom did not produce a recognizable spectral signal in the images. The April 1992 image obtained at the time of the onset of the algal bloom, prior to its lakewide spread, suggests it originated in shallow areas near the shore of the lake, where light penetrated to the bottom of the brine column. It was probably instigated by resting cells that had survived in near surface sediment of the shallow lake margin and were reinvigorated by the combination of lowered salinities and light.

The ultimate decline of the lakewide bloom of halophilic archaea in the Dead Sea appears to be related to viral infection (Oren et al. 1997). For example, in October 1994, during the decline of the halophilic archaeal population in the upper 20 m of the Dead Sea water column, there were between 0.9 and 7.3×10^7 virus-like particles per ml of brine. Virus-like particles outnumbered archaea by a factor of 0.9–9.5 (averaging 4.4). Water samples collected during 1995 contained low numbers of both archaea and virus-like particles (1.9–2.6×10^6 and 0.8–4.6×10^7 ml^{-1}, respectively in April 1995), with viral numbers sharply declining afterwards (less than 10^4 ml^{-1} in November 1995 January 1996). Oren et al. (*op cit*.) suggest that viruses play a major role in the decline of halophilic archaeal communities in many other hypersaline environments where protists and metazoa are absent.

Enhancement in organic productivity levels (feast) by well adapted, highly productive halotolerants during times of freshening in hypersaline settings is also seen in marine-margin mudflats For example, a study of benthic mats in Storr's Lake

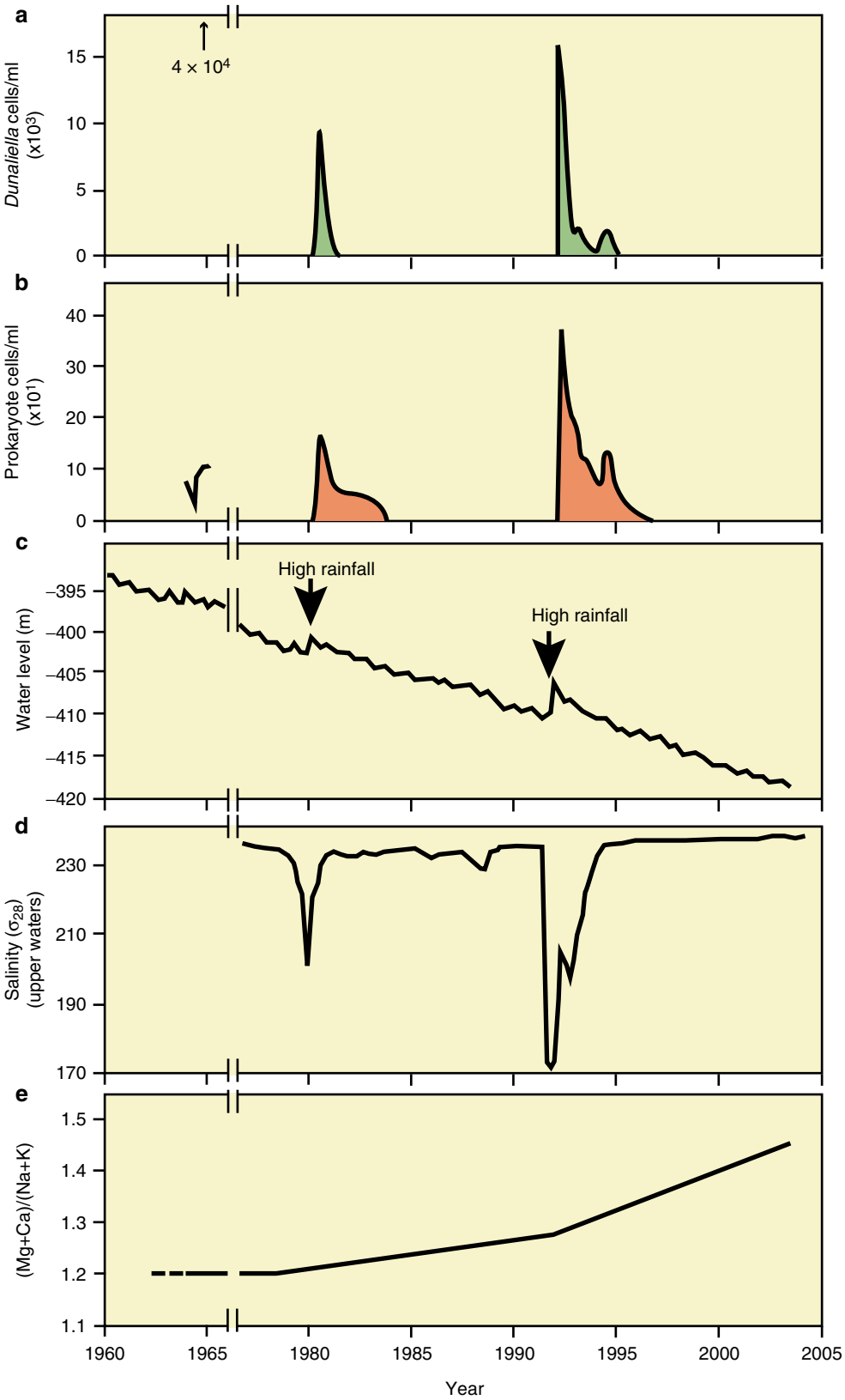

Fig. 9.42 Blooms and salinity in the upper meters of water column, 1963–2004, Northern Basin of the Dead Sea (After Oren 2005). (**a**) Population density of the unicellular green alga Dunaliella. (**b**) Community density of prokaryotes. (**c**) Water level of the Dead Sea. (**d**) Salinity of the upper water layer (expressed as σ_{25} – the density excess in kg m^3 to the standard reference density of 1,000 kg m^3). (**e**) Molar ratio of divalent and monovalent cations ($[Mg^{2+} + Ca^{2+}]/[Na^+ + K^+]$) of Dead Sea water

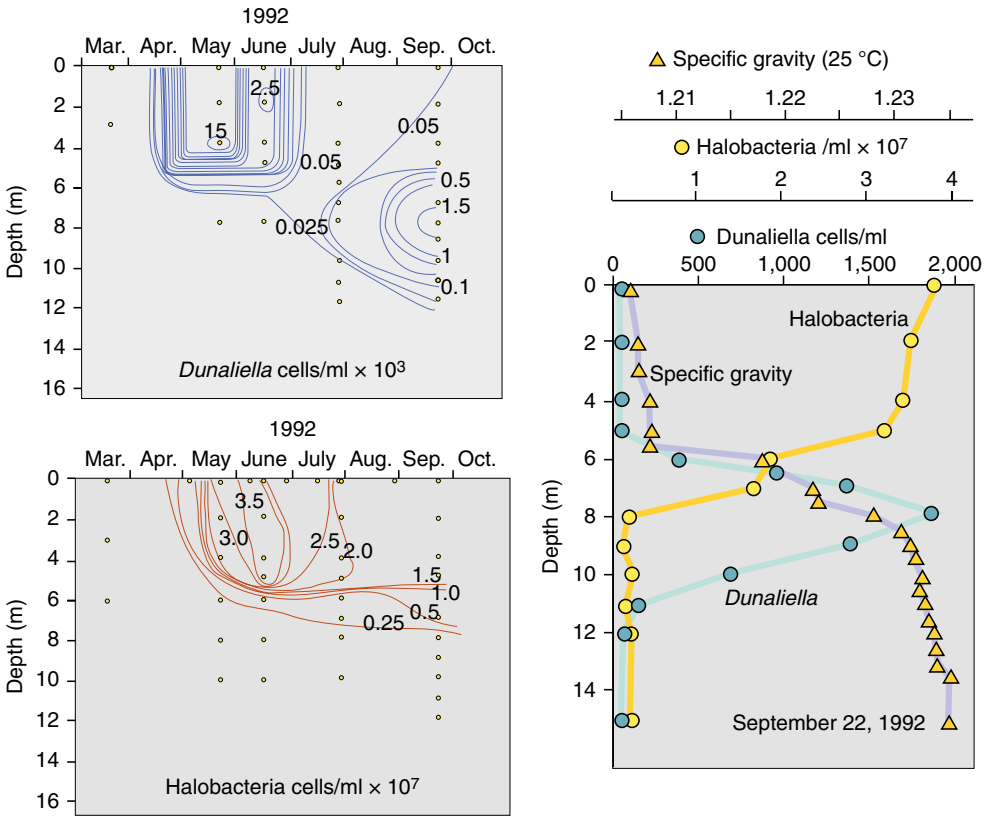

Fig. 9.43 Biodynamics in the Dead Sea, Middle East showing changes in the vertical distribution of *Dunaliella* and halobacteria during the rain flood-induced density stratification of the Dead Sea in 1992 (After Oren 1993). Note the vertical distribution of *Dunaliella* and halobacteria relative to the halocline on 22 September 1992

in the Bahamas showed that a reduction in brine salinity from 90 to 45‰ significantly enhanced CO_2 and N_2 fixation rates, but additions of inorganic nutrients and dissolved organic carbons (DOC) did not show any significantly enhanced rates compared with the salinity controls (Pinckney et al. 1995). That is, dissolved organic carbon/dissolved organic nitrogen uptake in the mats was not influenced over the entire range of salinities (45–90‰) seen in this study of mesohaline growth. Rather, abiotic (osmotic) stress, induced by hypersaline conditions in these Bahamian lagoons, created lower productivity in the saline-tolerant (haloxene) microbial mats, even when nutrient levels were high. When the osmotic stress on the biota was relieved by a lowering of salinity, mats underwent enhanced primary production and nitrogen fixation. Changing nutrient levels were far less significant than changing salinity levels as controls on mat productivity. Salinity-induced stress in these halotolerant microbial mats outweighs nutrient levels, which are the typical limiting factor regulating phototrophic growth in normal marine and brackish waters.

Feast or Famine in the Messinian Lorca Basin, Mediterranean

"Feast or famine" cycles, as just noted in the African rift lakes and the Dead Sea, suggest that periodic freshening of surface waters in stratified brine bodies (usually by meteoric water or seawater influx) tend to facilitate the accumulation on an anoxic stratified bottom of organic-rich pulses of organic matter, dominated by halotolerant remnants. The notion that subsequent accumulation of a thick salt seal atop mesohaline source rocks, once the basin was cut off from a surface marine connection, helps explain the intimate association between evaporites and underlying or interbedded hydrocarbon seen in the many occurrences listed in Table 9.2.

For example, organic-rich evaporitic marls were deposited beneath stratified brines in the Lorca Basin, located within the tectonically evolving Betic Cordillera of southeastern Spain. It was a rapidly subsiding basin in an open-marine setting during much of the Miocene (Benali et al. 1995). By the Upper Miocene (Messinian) the basin was becoming more restricted and accumulating thick diatomite-bearing sediments (Tripoli Unit), which are overlain by the Main Messinian Evaporite series. This evolution from marls to gypsum/halite beds records the onset of the "salinity crisis" throughout the Mediterranean region (Fig. 5.50a). Restriction by the time of the deposition of the Tripoli Unit in the Lorca Basin led to intercalations of thin precursor evaporitic layers, mostly subaqueous and sabkha Ca-sulphates, with diatomites (Fig. 9.44; Rouchy et al. 1998). Prior to the main salinity crisis, the alternation of evaporites and diatomite cycles indicates periodic restriction and the development of mesohaline conditions, followed each time by an episode of marine reflooding.

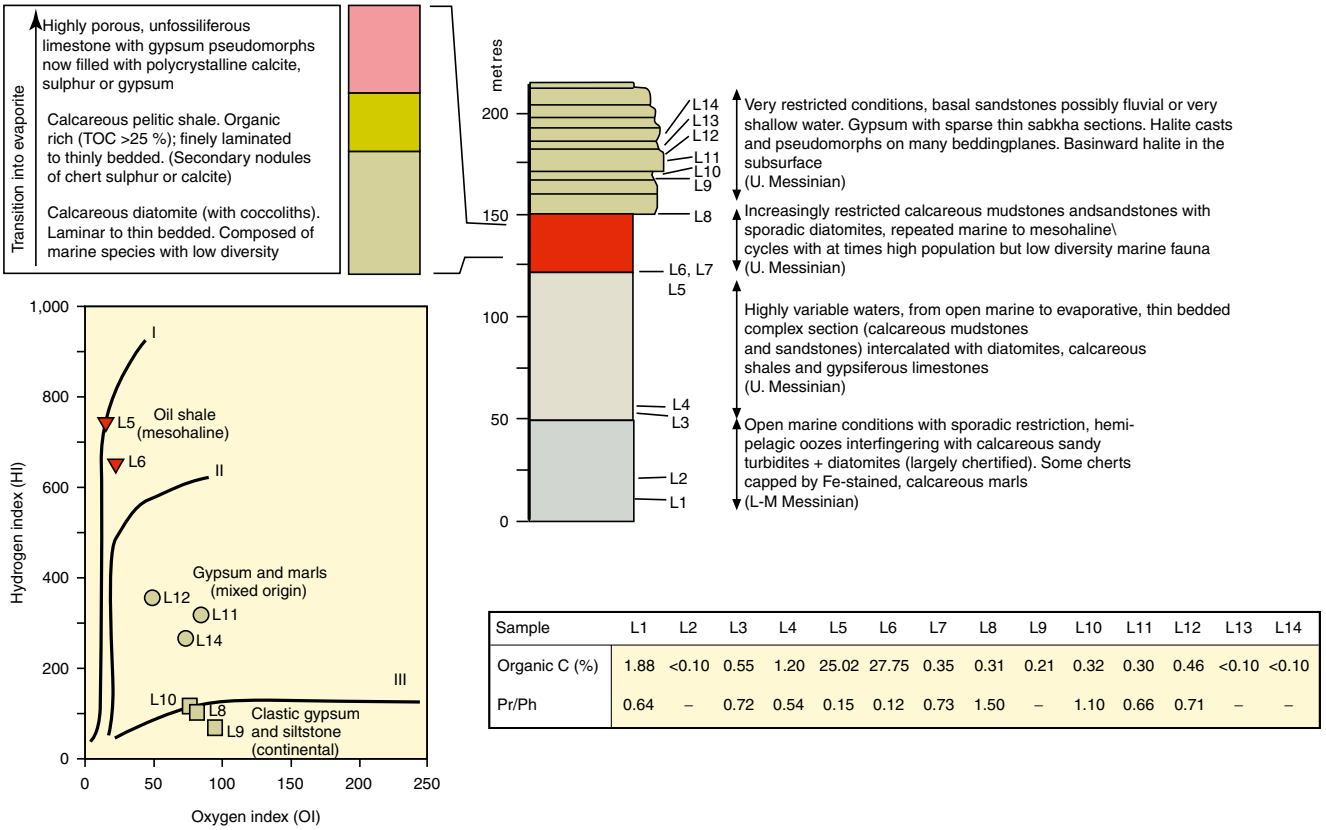

Sample	L1	L2	L3	L4	L5	L6	L7	L8	L9	L10	L11	L12	L13	L14
Organic C (%)	1.88	<0.10	0.55	1.20	25.02	27.75	0.35	0.31	0.21	0.32	0.30	0.46	<0.10	<0.10
Pr/Ph	0.64	–	0.72	0.54	0.15	0.12	0.73	1.50	–	1.10	0.66	0.71	–	–

Fig. 9.44 Lorca Basin, Spain, showing organic character of normal marine, mesohaline and evaporitic Messinian sediments with the richest organic contents in the mesohaline transition into evaporite deposits (After Benali et al. 1995)

Schizohalinity drove both the varying levels of primary production in surface waters and the preservation of organic matter in the hypersaline bottom sediments, finally culminating in widespread evaporative sedimentation in the latest Miocene. As basin waters evolved toward perennial hydrographic isolation and holomixis there were unusual evaporative conditions that heralded the main salinity crisis. These were a number of salinity stratified mesohaline surface floods when the resulting anoxic bottoms accumulated oil shales with up to 25 % TOC (Fig. 9.44; expanded section). When oil shales were accumulating, the system was meromictic; upper water mass was nutrient-rich and mesohaline with near normal marine salinities, while the bottom waters were anoxic and somewhat more saline than surface waters (Benali et al. 1995). Later in the basin history, when mixed gypsum marls and clastic gypsum sequences were accumulating, the oil-prone quality of any potential kerogen in the basin was diluted by rapid deposition of gypsum precipitates and an influx of oxidised organic detritus.

The formation of organo-sulphur compounds, replacement of sulphates by carbonates and the high levels of elemental sulphur are other byproducts of early diagenetic/microbial processes occurring in the Lorca oil shale. The high abundance of phytane, 2,3-dimethyl-5-(2,6,10-trimethylundecyl)-thiophene, mid-chain C_{20} isoprenoid thiophenes and bithiophenes and bis-O-phytanyl and O-phytanyl-O-sesterterpanyl glycerol ethers indicates that the organic matter in these sediments was deposited under anoxic hypersaline conditions (Table 9.8; Russell et al. 1997). Isopranyl glycerol ethers occur in sulphur-bound macromolecular matter, which contrasts with the low concentrations of these compounds as free lipids. However, the distribution of these isopranyl glycerols is paralleled by the occurrence of free phytanic acid in both the oil shales and intercalated laminated carbonates and by 3,7,11,15,19-pentamethyleicosanoic acid in the laminated carbonates. A high level of input from bacterial decomposers is indicated by 2-hydroxytetracosanoic acid, noctadec-11-enoic acid, hopanoic acids and the distributions of iso- and anteiso-C_{15} and C_{17} homologues and minor amounts of iso-C_{16} and anteiso-C14. These branched fatty acids are characteristic of sulphate-reducing bacteria, which would have inhabited the anoxic bottom brine. The relative proportions of the iso- and anteiso-compounds in the total fatty acid distributions are tied to the proportion of reduced sulphur in the sediments.

As in Lake Nakuru and the Dead Sea, cyanobacterial and halotolerant algal blooms in freshened surface waters created these organic-rich Messinian carbonates. Blooms of halotolerant species, followed by die back, drove cycles of "feast or famine" in the Lorca oil shales.

The Where and When of Productivity

Most biological studies in freshwater lakes and in the oceans have found that the highest levels of organic productivity (primary productivity) occur annually within the zone of maximum light penetration in the upper few metres of the water column. long-term salinity stratification or meromixis in the perennial waters of an evaporite basin, can change the locus of maximum organic productivity, especially in situations where the required nutrients lie at or below the halocline. Haloarchaea in the Dead Sea can survive by facultative photosynthesis long after their primary food source has died back (Fig. 9.43). But is there a more general layering of the halobiota in stratified brines where the chemical interface created by the coming and going of the halocline allows life to flourish via chemosynthesis, not photosynthesis? If so, then bacterial productivity in upper fresher waters of a layered brine column may come to rely on nutrients supplied from permanently saline and anoxic bottom waters.

Mahoney Lake is a small (19.8 ha), up to 15 m-deep meromictic oligotrophic mesohaline lake in British Columbia, Canada. The lake originated as a glacial kettle after the retreat of the Wisconsin ice sheet some 13,000 years ago. A halocline separates a variably oxygenated mixolimnion[19] from a permanently anoxic sulphidic monimolimnion at a depth of around 6 m in the lake brine column (Fig. 9.45a). Total dissolved solids vary from 10,000 mg/l near surface to 85,000 mg/l near bottom, with rapid changes across the halocline. It has been a saline meromictic/holomictic system for the last 9,000 years, with some meromictic episodes lasting as long as 1,100 years. The oldest sediment layers that contain okenone (a purple sulphur bacteria biomarker) are 11,000 years old, okenone likely also indicates times of brine stratification in the lake waters (Fig. 9.45b; Overmann et al. 1993, 1996). The high salt content of the bottom waters in this small endorheic basin is thought to be derived by weathering of alkali-rich Tertiary-age rocks of the Marron Formation. Heterotrophic bacterial production in the lower mixolimnion at times exceeds concomitant primary production in the upper waters of the same mixolimnion by a factor of 7 (Fig. 9.45c). In this highly productive sulphidic interval lives an extremely dense population of the phototrophic purple sulphur bacteria *Lamprocystis purpurea* (aka *Amoebobacter purpureus*, which is present year round as a layer or "bacterial plate" centred on the lake halocline (Klepac-Ceraj et al. 2012). The Mahoney Lake halocline harbours the densest population of phototrophic sulphur bacteria ever reported in a natural body of water. It is sufficiently abundant to form the base of a food chain, where it constitutes 70 % of the diet of planktonic copepods living in the upper water mass.

Each year, following ice melt, a layer of freshened water enters the lake, renewing a well-defined uppermost oxygenated layer (mixolimnion), which disappears within a few months. For example, the stability of the mixolimnion declined sharply between May and July 1993, in parallel with the disappearance of the low-salinity uppermost surface water layer, the warming of the lower waters of the mixolimnion, and the resulting loss in density stratification (Fig. 9.45c; Overmann et al. 1996). This allowed mixing across the perennial halocline and the release of nutrients into the lower parts of the mixolimnion. For most of an annual cycle any bacterial growth in the lower mixolimnion is limited by the supply of inorganic phosphorus or nitrogen, which can come from above or below. In Mahoney Lake, liberation of phosphorus from upwelling of the remains of purple sulphur bacteria in the lower waters, and degradation of allochthonous dissolved organic carbon floating at the halocline, act as a carbon source for the bacteria and so render heterotrophic bacterial production largely independent of photosynthetic phytoplankton cycle in the overlying waters of the uppermost mixolimnion.

That is, the *L. purpurea* layer acts as a 'nutrient cap,' limiting the upwelling of nutrients, it also acts as a shading sheet, so beneath it there is little light penetration (Overmann et al. 1996). Enrichment cultures from the bacterial plate suggests it contains very few *Chlorobiaceae* (green sulphur bacteria). Lake sediments are correspondingly rich in the pigment okenone, a biomarker for *Chromatiaceae*, and they lack isorenieratene, a biomarker for *Chlorobiaceae* (purple sulphur bacteria – Table 9.8). Analogously, okenone diagenetic products in sediments and sedimentary rocks are diagnostic of ancient, highly euxinic systems with penetration of sulphide only to

[19] Jargon of lacustrine stratification

Mixolimnion: the upper, low density, freely circulating water layer of a meromictic lake.

Monimolimnion: the deep, usually salty, layer of a meromictic lake typically it is a perennially stagnant or noncirculating water mass.

Meromixis: a condition in a lake (meromictic lake) where the bottom noncirculating water mass is adiabatically isolated from the upper water mass.

Holomixis: a condition in a lake describing complete overturn and mixing of the lake water mass.

Hypoliminion: is the lowermost water mass in a lake, characterised by a generally uniform temperature (or density) profile.

Eutrophic lake: a lake characterised by an abundance of nutrients and a seasonal deficiency of oxygen in the hypolimnion. Waters are usually shallow and sediments are organic-rich laminites.

Oligotrophic lake: a lake characterised by a deficiency in nutrients. The bottom sediments typically contain low levels of organics and the water column is deep.

Monomictic Lake: A lake which undergoes one period of complete mixing during the year separated by one period of thermal stratification.

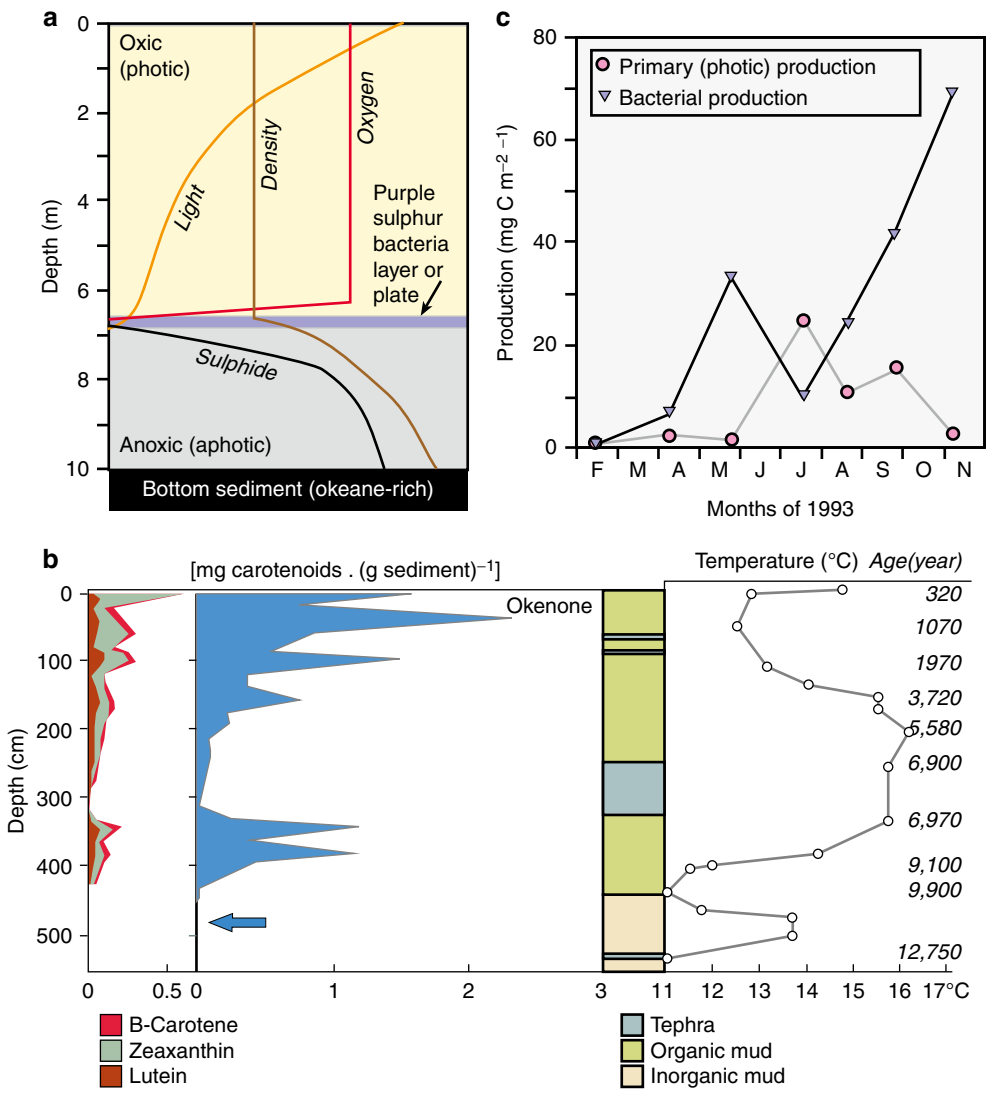

Fig. 9.45 Lake Mahoney, British Columbia, Canada. (**a**) Stratification in the brine column showing the position of the purple sulphur-oxidising bacterial community at the halocline. (**b**) Sediment core showing vertical distribution of okenone, zeaxanthin, lutein and b-Carotene. Concentration in pre dry mass of sediment Dated by tephras and ^{14}C dates of sediments. Blue arrow indicates oldest sediment layer containing detectable concentrations of okenone and β-carotene. (**c**) Integrated primary production and bacterial production in the mixolimnion during 1993. Both were measured simultaneously during incubation around solar noon (After Overmann et al. 1993, 1996)

shallow depths within the photic zone (see Table 9.2; the 1.7 Ga Barney Shale in Northern Australia).

The nature of the sulphidic microbial community that resides in the aphotic hypolimnion and/or in the lake sediments is poorly known, and it is unclear whether the sulphate reducers that supply sulphide for phototrophy live only within, or also below, the plate of purple sulphur bacteria centred on the halocline. Klepac-Ceraj et al. (2012), profiled distributions of 16S rRNA genes and suggest that microbial diversity is greatest in the hypolimnion (down to 8 m) and in the bottom sediments. They found biotal diversity is lowest in the photosynthetic plate (>7 m). Shallower depths (5–7 m) are rich in Actinobacteria, Alphaproteobacteria, and Gammaproteobacteria, while deeper depths (up to 8 m, bottom sediments) are rich in Crenarchaeota, Natronoanaerobium, and Verrucomicrobia. The heterogeneous distribution of Deltaproteobacteria and Epsilonproteobacteria between 7 and 8 m is consistent with metabolisms involving sulphur intermediates in the halocline, with sulphate reduction in the hypolimnion (Fig. 9.45a).

Similar purple bacterial layers cap the haloclines of brine lakes on the deep seafloor of the Urania Basin in the Mediterranean Sea. The bacterial community utilises sulphur compounds crossing the brine interface from anoxic waters below and thrives many thousands of metres below the photic zone (Sass et al. 2001). Sulphur-oxidising bacterial communities, independent of light penetration, probably occur atop marine suprasalt brine-lake haloclines worldwide.

The effect of salinity stratification on productivity in many saline lakes does not follow the predictable annual cycle seen in saline Lake Mahoney and in most freshwater temperate dimictic lakes (dimictic = seasonally mixed). This lack of annual cyclicity in the organic production is clearly seen in the timing of meromictic stages of the Dead Sea (Fig. 9.43).

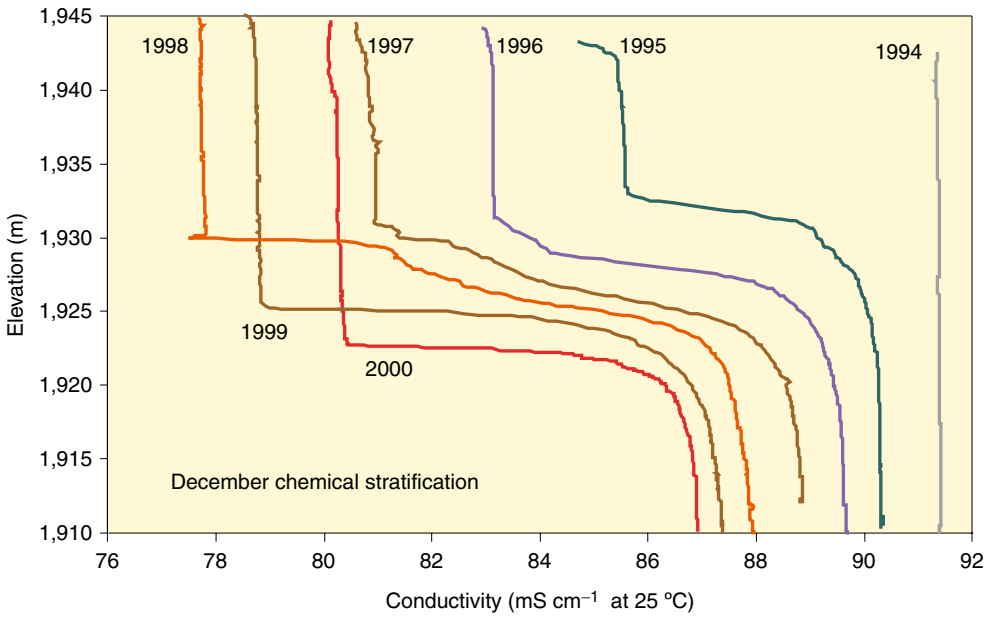

Fig. 9.46 Mono Lake, California, conductivity profiles in December for the years 1994–2000 (Figure was redrafted from a database downloaded from http://www.monobasinresearch.org/data/, last accessed Jan. 15, 2013)

Multiple years of stratification without breakdown (meromixis) is also characteristic of Mono Lake, California where photosynthetic activity was measured in its hypersaline and stratified waters during an 8-year period from 1982 to 1990 (Jellison and Melack 1993). Exceptionally large volumes of freshwater runoff in 1982 and 1983 led to a 2.6-m rise in surface elevation of Mono Lake and the onset of a new period of meromixis in the lake (Fig. 4.23). In 1984 chemical stratification accounted for a density difference of $1.2–1.5 \times 10^{-2}$ g/cc between the 2 and 28 m water depths. At the same time the midsummer density difference between 2 and 28 m depths that was due to temperature was approximately 0.5×10^{-2} g/cc. Salinities ranged from 77 to 98 g/l across the interface and sodium, chloride, sulphate, and carbonate were the major ions in both the upper and lower water mass.

This 8-year time frame in Mono Lake spans the onset (1983), persistence (1984–1987), and breakdown of meromixis (1988). Following the onset of meromixis, the algal biomass in the lake each spring and autumn decreased from 1984 to 1986: annual primary photosynthetic production was reduced from 269 to 462 gC m^{-2} $years^{-1}$ (1984–1986) compared to nonmeromictic conditions of 499–641 gCm^{-2} $years^{-1}$ (1989 and 1990). A gradual increase in photosynthetic production then occurred, even before meromixis ended, because of increased vertical flux of ammonium from the anoxic saline bottom, due to deeper mixing and the buildup of ammonium in the monimolimnion. Annual primary production in the lake was greatest in 1988 (1,064 gCm^{-2} $years^{-1}$) when the weakening of chemical stratification and eventual breakdown of meromixis in November of that year allowed a large upward influx of ammonium (source of nitrogen) into the photic zone.

Another transition from monomixis to meromixis occurred in Mono Lake from 1994 to 1995 (Fig. 9.46; Melack and Jellison 1998). During the preceding monomictic conditions in 1993 and 1994, the lake had thermally stratified in March and had mixed to the bottom by each December. During meromictic conditions in 1995, 1996 and 1997, the absence of holomixis during winter once again resulted in persistent anoxic conditions beneath the chemocline, the accumulation of ammonium in the monimolimnion, its depletion in the mixolimnion, and low mixolimnetic chlorophyll concentrations in the spring and autumn. The meromictic state continued until mixing in 2003 and was preceded by a trend of year-to-year deepening of the chemocline, which indicates increasing liability to mixing in a meromictic lake. The same deepening of the halocline marks the transition to holomixis in the Dead Sea (Fig. 4.43).

The TOC content of a core through the laminites of Mono Lake, sampling the last 300 years, shows an overall tendency toward increasing TOC content in the period 1700–1800, then a consistent trend hovering around 6 % but with wider variations in TOC in the last 60 years, since the diversion of the inflow to the Los Angeles water supply in 1941 (Fig. 9.47; Benson et al. 2003). The highest values of TOC in the core occur in this time frame, 14 % around 1970, as do some of the lowest, e.g., around 4 % in 1943 and 1980. Clearly, the perennially anoxic saline bottom waters of the lake, with a pulse of productivity (a time of feast) in those years when the lake transitions from meromictic to holomictic, have facilitated the preservation of organics at levels that in ancient counterparts would characterise a source rock. Whether the fluctuations in TOC levels in the bottom sediments reflect varying intensities in algal blooms or some other factor related to the volume of organics reaching the bottom is not yet defined.

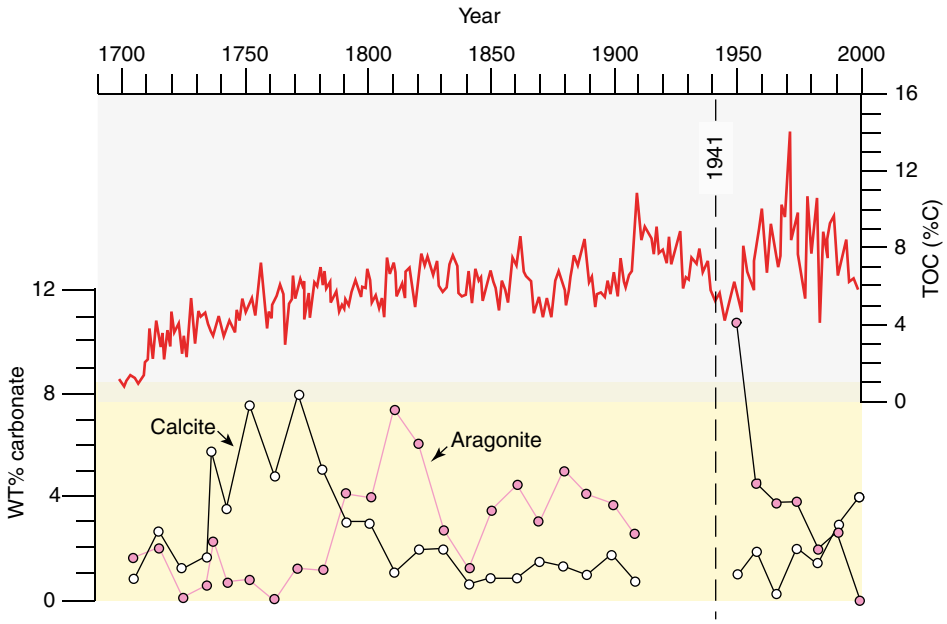

Fig. 9.47 TOC and carbonate proportions in a core through Mono Lake laminites deposited in the last 300 years (After Benson et al. 2003)

Predicting Preservation of Benthic Organics

Predicting how organic productivity in surface waters relates to organic preservation under a variable layered brine column is difficult. It is commonly assumed in source rock modelling that saline waters at the base of a stratified saline water column are anoxic and will always favour the preservation of organic matter product by plankton (Demaison and Moore 1980). The effectiveness of stratified brines in the preservation of pelagic organic matter originally produced in photic and oxygenated water is especially obvious when comparing open marine and density-stratified hypersaline environments. Estimates for the preservation efficiency of primary organic matter in the modern shallow open-marine oxygenated bottoms centre around 0.1 % (Menzel and Ryther 1970), while on the floor of the anoxic Black Sea it is about 4 % (Deuser 1971). In contrast, preservation efficiency beneath density-stratified hypersaline lakes and epeiric seaways subject to times of feast or famine can be as high as 85 % (Hite and Anders 1991). This vast improvement in preservation in part reflects the "salting effect" of a perennial dysaerobic to anoxic saline bottom brine layer and the periodic proliferation of a photosynthetic biomass in a freshened upper brine body. Plankton that is blooming in a stratified brine column is liable to mass mortality as ongoing evaporation increases nearsurface salinities to intolerable levels ("feast or famine"). Schizohaline surface waters means most organic-rich evaporitic mesohaline sediments are deposited as laminites, facilitated by repetitive "life and death cycles" in the halobiota (Warren 1986).

Yet mesohaline to moderately penesaline bottom waters of some density-stratified shallow modern brine lakes are oxygenated, not anoxic. Bottom microbial mat communities below such waters are dominated by halotolerant oxygen-producing photosynthesising benthic cyanobacteria. These benthic primary producers create and maintain elevated oxygen levels in the well-lit bottom waters immediately above the mat and are the hypersaline equivalents of marine seagrasses. But, benthic microbial mats tend to be anoxic no more than a few millimetres below such photosynthesising surface layers of microbes (Fig. 9.30). Burial via mat aggradation tends to quickly move newly created cyanobacterial organics into an anoxic regime, where organic preservation is much more likely. An association of permanent bottom hypersalinity and anoxia a few mm below the sediment brine interface, tends to prevent burrowers from entering the bottom sediment in a mesohaline bottom covered by microbial mats. Burrowing is a major mechanism for maintaining oxygenation in normal marine sediment, where it tends to prevent substantial accumulations of organic matter in marine water covered bottom sediments.

Lake Hayward, Australia is meromictic and a good case in point; it is a shallow perennial hypersaline coastal salina filled by brines less than 2 m deep. Photosynthesis via its benthic microbial mat community, is normally sufficient to supersaturate the bottom with dissolved oxygen, even during periods of brine column stratification, yet bottom sediments contain 5–7 % TOC (Burke and Knott 1997). Laminated microbial mats in the permanently submersed mesohaline centre of the lake are dominated by photosynthesising cyanobacteria *Cyanothece sp*., while *Microcoleus sp*. are dominant in the biolaminites of the lake's seasonally desiccated strandzone. In daylight the oxygen saturation can be as high as 270 % in the uppermost photosynthesising mat and the immediately overlying bottom waters (Burke 1995).

Year	Salinity g/l)	Temp (°C)	Dissol.O_2 (%Sat.)	H_2S (mg/l)
Site1				
1985	162–187	30.0–35.0	200–330	0
1986	176–210	22.0–39.5	41–250	0
1987	178–184	33.0–34.6	140–250	0
30 Nov, 1988	222	42.4	0	35.4
1989	180–234	24.5–43.0	0–46	0–1.7
23 Sep, 1993	160	28	378	0
Site 2				
30 Nov, 1988	216	43.2	0	23.8
1989	180–192	24–36	50–137	0–trace

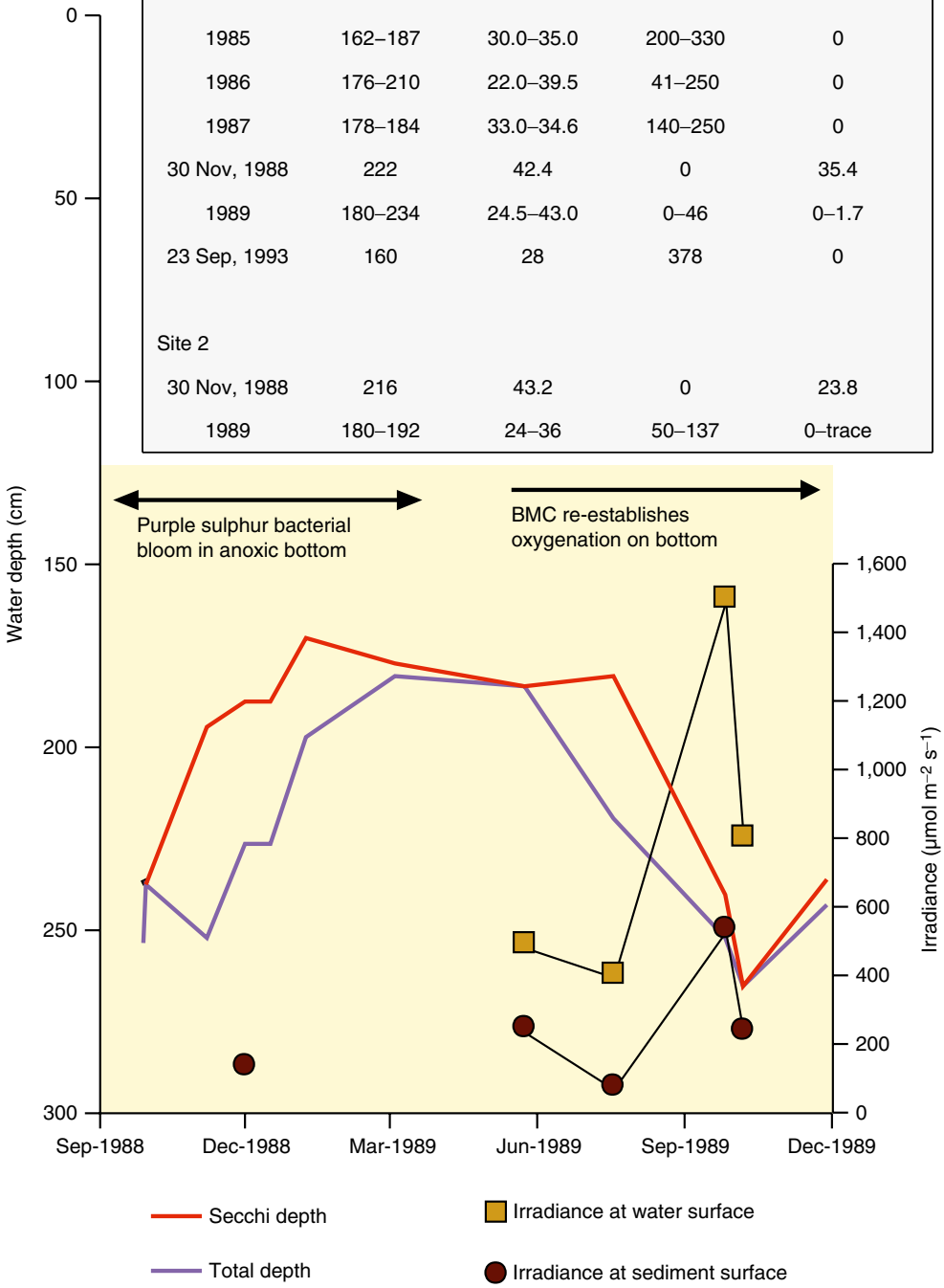

Fig. 9.48 Effect of gypsum precipitation on benthic microbial communities and oxygenation in Lake Hayward, West Australia (Compiled from data in Burke and Knott 1997)

However, after an unusually dry year in 1987, the lake salinity in the upper waters increased to 260 g/l and gypsum precipitated in upper portions of the lake water column (Fig. 9.48; Burke and Knott 1997). Turbidity generated by gypsum crystallisation in the brine mass was sufficient to obscure the benthos completely, despite the shallowness of the lake (secchi curve in Fig. 9.48). As a result, the amount of benthic oxygenic photosynthesis was greatly reduced and benthic mats began to decay. During brine stratification in the following winter (1988), bottom waters became anoxic and supported a healthy population of purple sulphur-oxidising bacteria.

However, during the next few years, after each subsequent brine column overturn, healthy cyanobacterial mats were

reestablished and they were able to again supersaturate the bottom waters with oxygen year round. It seems that the development of a healthy microbial benthic mat community in Lake Hayward prevents periodic bottom anoxia, whereas nearby meromictic lakes, that do not contain a healthy halotolerant microbial benthos, tend to annual anoxia during stratification. The lake illustrates a general principle that healthy halotolerant microbial mat functions as a strong homeostatic mechanism in allowing longterm stability of elevated oxygen levels in bottom waters of the shallow brine lake, but an increase in salinity can make the bottom anoxic.

Gypsum precipitation in the brine column is not the only cause of brine column turbidity and bottom anoxia in shallow waters. Planktonic blooms (a time of feast) can also substantially reduce light penetration to the bottom of a shallow brine lake (Horsfield et al. 1994). If the bloom is intense it can prevent benthic cyanobacteria from photosynthesising. The shaded part of system eutrophies as decomposing planktonic remains rain down through the now dark brine column. Decomposition in the upper portions of the column uses up all the oxygen in the water column. The oxic-anoxic interface rises from the sediment into the brine column, killing off any oxygen-requiring benthic species. Such hypertrophication overwhelms the delivery of oxygen to the bottom by the photosynthetic benthos and facilitates higher levels of organic delivery to bottom sediments than occurs with the benthic mats. This eutrophic and slimy bottom style of deposition naturally characterises the central portions of Solar Lake, Egypt (Fig. 4.12). It may explain why the TOC of its bottom sediments, accumulating beneath pore waters that are perennially anoxic, are elevated compared with microbially-bound bottom sediments of Lake Hayward (15–20 % versus 5–6 %).

In a study of eutrophication in modern saltfields Javor (2000) found that in shallow gypsum and the pre-gypsum ponds there was an interesting inverse relationship between the level of nutrients (nitrates and phosphates) in the brine column and the development of microbial mats on the water covered pan floor. In a high nutrient brine system (eutrophic or well-nourished) the algae and bacteria flourished as planktonic forms and the biomass buildup in the upper parts of the brine column tended to shade the sediment surface so that there was little or no development of a microbial mat and bottom waters were dysaerobic to anoxic. In a low nutrient (oligotrophic) system there was little or no planktonic development of algae or bacteria and microbial mats tended to flourish on the perennial pond floor. She found benthic mats in low nutrient systems formed from salinities of 50,000 ppm to gypsum saturation. At lower salinities benthic mats were destroyed by the feeding activities of invertebrates and fish.

Most benthic microbial mats beneath hypersaline waters depend, in large part, on nutrients recycled by the bacterial decomposers that make up the underside of the living part of the mat. Even if nitrogen and phosphorus levels in the overlying brines are low, there may be sufficient nutrient recycling within the mats to allow the bottom mats to continue to grow. Javor (*op. cit.*) found that once a gypsum crust becomes well established over the floor of a crystalliser pond there was little recycling of nutrients from beneath the crust. From this point downstream in the crystalliser pans, nitrate and phosphate nutrients concentrated by evaporation were recycled into the biomass living in the brine column and not within the benthic mat. In oligotrophic gypsum ponds the gypsum crust is stable and the bottom waters are oxygenated. In eutrophic gypsum ponds at the same salinities the bottom waters become anoxic and sulphate-reducing bacteria flourish. In these systems the gypsum dissolves and the bottom is typically covered by a black slimy organic-rich mud, containing no more than a few embayed and dissolved gypsum remnants, much like the central facies in Solar Lake. If portions of this slimy bottom become suspended and are flushed into the next stage of the crystalliser brine stream they create a problem in the final product known as "black spot." Brine shrimp are often added to the mesohaline ponds of a saltworks to control planktic blooms and so minimise "black spot."

That organic enrichment occurs naturally in the mesohaline carbonate stage and not in subsequent gypsum or halite layers is clearly seen in the evaporitic marls and salts of the Oligocene Mulhouse Basin (Fig. 9.49; Hofmann et al. 1993b). This deposit is one of a few ancient evaporitic settings where organic chemistry has been studied in a detailed fashion, rather than as generalisations from spot samples. Organic matter occurs mostly in finely laminated carbonate marls (varves), which can contain up to 7 % TOC, anhydrite beds contain 0.08–0.78 % TOC, halite beds 0.01–0.25 % TOC and the potash beds <0.1 % TOC. The marls are characterized by thin, continuous bedding-parallel laminae that are not disturbed by any bioturbation.

Layering is interpreted as seasonal varves with the clay and carbonate forming alternate sheets in the couplet (see inset in Fig. 9.49). In spring and summer the increased temperature in surface waters favoured precipitation of micritic carbonate, in autumn and winter the phytoplankton died back and rainfall/runoff transported clastic debris into the basin. On the basis that the laminar couplets in these mesohaline carbonates are varves, Hofmann et al. (1993b) were able to plot the relationship between sedimentation rate and TOC content in the marls (Fig. 9.49). Marls deposited during times of low sedimentation rate tend to be organic-rich, while marls deposited at times of higher sedimentation tend to contain lower amounts of organics. They concluded that the even-lower levels of organics typifying the more saline salt beds (anhydrite and halite) indicate even more dilution, due to inherently higher sedimentation rates.

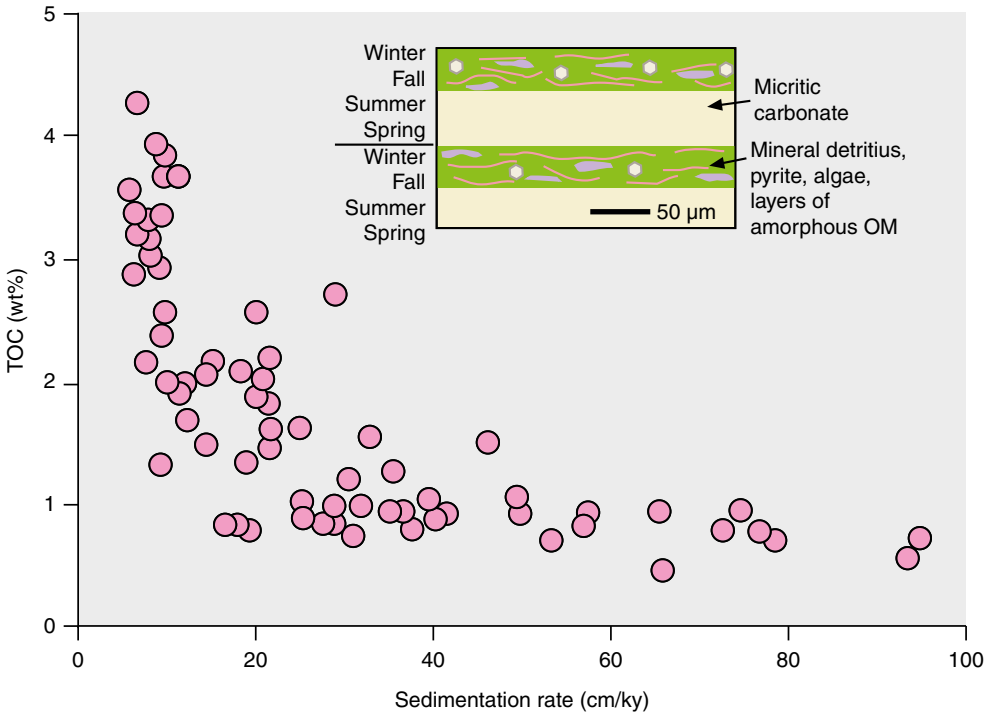

Fig. 9.49 Sedimentation rate versus percent of total organic carbon content (*TOC*) in laminite marls from the Oligocene evaporites of the Mulhouse Basin, Europe. *Inset* shows the scale and mineral/organic distribution in the laminae (varve couplets) of the sampled intervals (After Hofmann et al. 1993b)

Proximity of organic-rich mesohaline laminites to ancient bedded evaporites has lead some geologists to postulate that bedded salts are potentially also organic-rich sediments with the same level of source potential as mesohaline carbonates. This is not borne out by TOC analysis of evaporitic salts in the Mulhouse Basin. Likewise, worldwide measurements of total organic matter levels in ancient $CaSO_4$ and NaCl lithologies tend to be normal or depleted (Katz et al. 1987). Mesohaline carbonates, not higher salinity salts, are the source rocks to many ancient evaporite-associated reservoirs (Fig. 9.4). But, levels of dissolved organic matter and volatile fatty acids rise in increasingly saline brines and may be considered potential mobile or liquid sources if caught up in intercrystalline interstices and inclusions (Hite and Anders 1991). Levels of DOM and VFA may be high in such penesaline salts and could be released in the subsurface when halite beds are dissolved by crossflows of surface brines. But in general the typically low levels of solid organic matter in bedded halite reflects the higher depositional rates of evaporitic salts when compared with evaporitic carbonates (dilution effect). Under the same rate of supply of detrital organics, the higher rate of halite accumulation dilutes the associated organic content compared to carbonate sequences.

Whatever the finer controls on accumulation levels, observations of organic accumulations in modern and ancient mesohaline saline systems show that peaks or pulses in primary production ("feasts") in density-stratified brine lakes are controlled by two factors; (1) the occasional presence of an ephemeral less saline surface water mass, and (2) a periodic supply of nutrients (nitrate/ammonia and phosphate), possibly from a combination of inflow/runoff and leakage from the lower hypersaline water mass. The biota contributing the organic pulse, which ultimately reach the bottom sediments to form organic-rich laminae, are largely dependent on the timing of photosynthetic activity. Modern saline lakes with a well defined annual freshening of surface waters will deposit varved evaporitic carbonates (e.g., Lake Tanganyika with up to 7–11 % TOC in deep bottom laminites; Cohen 1989), while other brine lakes and seaways, with less predictable stratification, may form similar carbonate laminites, but the organic layering may not be annual (Dead Sea, Mono Lake analogs).

Populations of purple-sulphur oxidising bacteria define the position of the oxic-anoxic interface in hypersaline settings. They reside a few millimetres below the mat surface beneath shallow brines with healthy cyanobacterial mats on the bottom. In deeper brines they reside at the halocline. Shading of a healthy cyanobacterial mat, either by planktonic blooms or mineral saturation in the brine column, allows the oxic-anoxic interface to rise from within the mat into the brine column and bring with it its healthy population of purple bacteria. If organic debris from a planktonic bloom settles to the sediment surface at this time there is less likelihood it will be broken down by fermenters and decomposers before it is buried. Hence, elevated TOC levels from times of planktonic feasting are more likely to be preserved.

Life, Brine Seeps and Dissolving Salts

There is an association between chemosynthetic communities, saline anoxic bottom brines, biogenic limestone crusts organic-enriched laminites, metal sulphides and salt allochthons in some modern marine slope and rise settings (Warren 2000b). Historically, a relatively deep open marine setting was not considered an area where hypersaline bottom brines facilitated the accumulation of organic and metal sulphide-rich mesohaline sediments. Yet it is in seafloor settings where shallow salt allochthons are actively flowing and dissolving and, as such, is a zone of potential mesohaline source rocks (Fig. 9.4). So far, most of the scientific work on this topic is focused on the biogenic process sets visible in the brine seeps and mud volcanoes that typify parts of the seafloor underlain by flowing and dissolving salt.

As a rising allochthonous salt sheet reaches a position just beneath the seafloor it is dissolving from its edges inward, while at the same time it is releasing and focusing chloride-rich brines into its surrounds (Fig. 9.50a; Sassen et al. 2004). The brines are generally carrying varying combinations of liquid hydrocarbons and thermogenic methane from mature source rocks, as well biogenic methane and thermogenic liquids and gases from sediments caught up in rapidly subsiding sediments atop salt floored minibasins, and H_2S from thermochemical and biochemical reactions in lateral and crestal caprocks. Gassy and hydrocarbon-liquid bearing brines move along the salt edge, and associated faults, to feed seeps and vents to the seafloor.

Such brine-issuing vents are well documented in the 200–1000 m depths of the Gulf of Mexico and even deeper such as the 1,920 m-deep seafloor on top of Green Knoll, an isolated salt diapir rising seaward of the Sigsbee Escarpment in the northern Gulf of Mexico (Fig. 9.50a). There methane- and chloride-rich vent brines are supplied in part by congruent seawater dissolution of the underlying Louann salt, and in part by hydrocarbon-rich basinal waters escaping from deeper within the salt sealed sediment column (Table 9.9; Aharon et al. 1992). In the Gulf of Mexico, typically the venting Na-Cl brines are up to seven times saltier than ambient seawater and the geometry of their subsurface passage to the seafloor largely reflects breaks in the continuity of allochthonous salt sheets that underlie much of the continental slope (Thrasher et al. 1996; Sassen et al. 2004).

Venting of hydrocarbon-rich (methane) hypersaline anoxic brines onto the seafloor, both by lateral flow and by diffusion upward through the underlying clastic sediments, gives rise to characteristic seafloor seeps, with methane hydrates and methane-saturated anoxic brine lakes, ranging in diameter from 1 m to 20 km, and surrounded by a rim of bacterially-formed calcite-cemented crusts (Collett et al. 2009). The seeps are inhabited by methane-oxidising archaea. Their metabolic processes, in combination with bacterial sulphate reduction give rise to the characteristic set of seep carbonates that precipitate as nodules and sheets in the vicinity of the vent sites (Fu Chen et al. 2007). Likewise, only specialised microbes (extremophiles) inhabit the bottom waters and sediments of the brine lakes and mud volcanoes, while spectacular chemosynthetic mollusc-tube worm biostromes grow in normal marine waters about the brine lake and mud chimney edges. Venting hypersaline brines can either seep and dissipate via mixing with oxygenated marine bottom waters on the open ocean floor to form spectacularly red braided channel-ways or can seep into closed depressions on the seafloor to form lakes of density-stratified anoxic bottom brine. It is here on the floor of these brine pools, especially in Precambrian counterparts to modern examples of the brine deeps of the Red Sea that organic- and sulphide-enriched laminites accumulate (Chap. 15).

Geological and Hydrological Features

Venting anoxic Fe-carrying chloride brines create seafloor redbeds at sites were brines move onto the ocean floor but do not pond in seafloor depressions (brine lakes). Brine redbeds are loosely consolidated red-orange iron-oxide deposits, with surfaces characterised by anastomose and braided patterns created by brines trickling as thin brine sheets disperse as sheets over the seafloor (Aharon et al. 1992; Sassen et al. 2004). Redbed clays are coated by red iron-oxides, and can also contain sand-sized crystals of authigenic euhedral dolomite and botryoidal hematite. Similar iron-oxide deposits (redbeds) define the oxygenic edges of the Red Sea brine pools including the Atlantis II deep. The ferrous iron of the redbeds was originally extracted in its ferric form during the flushing of buried sediment by dissolution derived anoxic pore waters in the peridiapiric and salt sheet surrounds (Hanor 1994a). Once vented onto the oxygenated seafloor, the dissolved iron precipitates as hematite and other ferrous hydroxides. In this dispersed seepage setting scenario the seafloor surface itself constitutes a redox front between the escaping reduced basin brines and oxygenated marine waters.

Figure 9.51a, b shows clearly that red iron oxides are stable in the oxygenated conditions that typify the open seafloor (see also Sheu and Presley 1986a, b). In contrast, in the more reduced conditions in highly saline subsurface waters and bottom waters of brine pools, precipitated iron phases are dominated by pyrite, siderite and other ferroan carbonates. The pH does not vary widely in such reduced saline settings (Fig. 9.51b), and the relationship between pyrite and siderite becomes clearer when activities of dissolved sulphur or dissolved bicarbonate are plotted against Eh. Pyrite is the stable

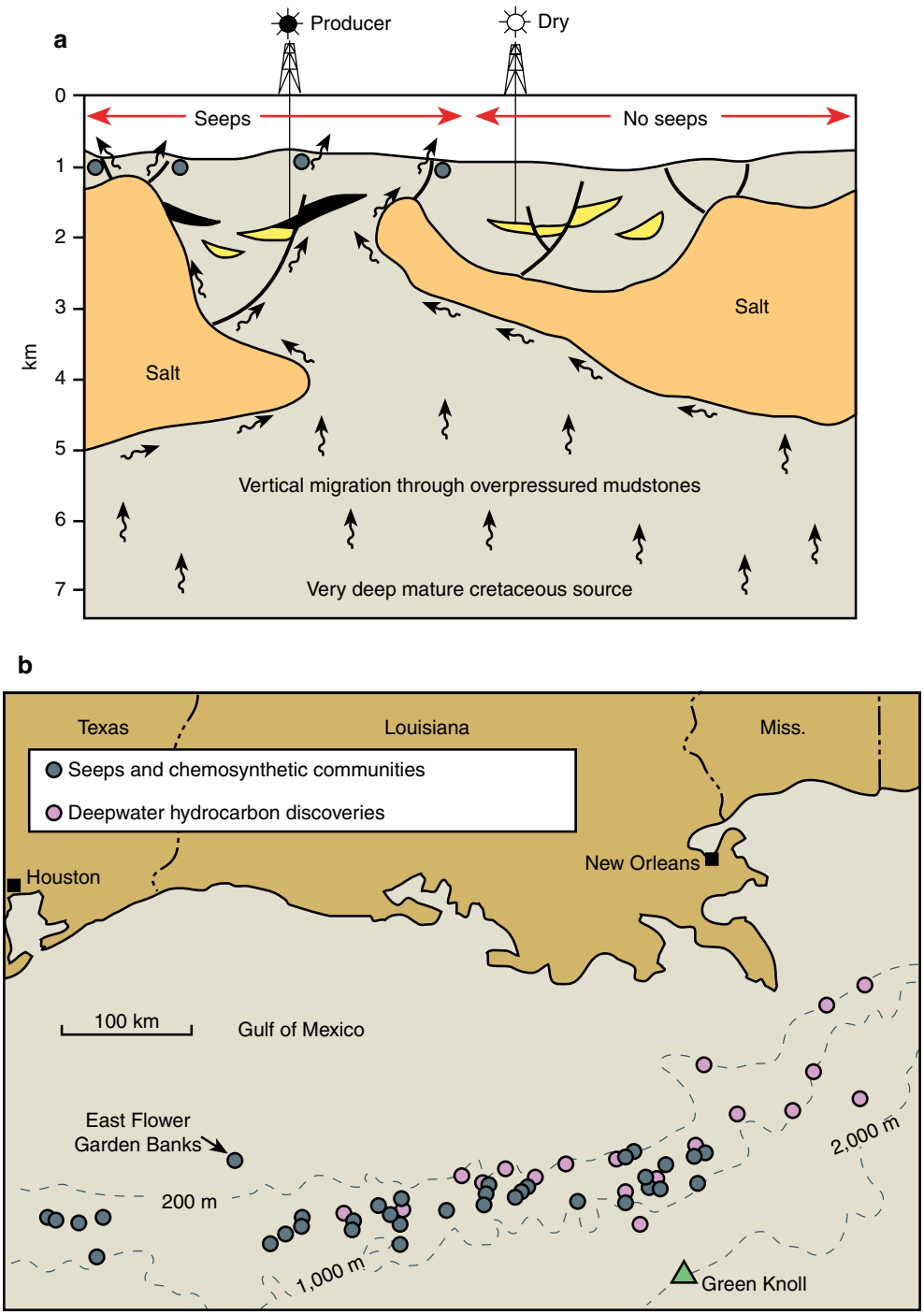

Fig. 9.50 Brine seeps. (**a**) Model of hydrocarbon migration and seepage in the deepwater Gulf of Mexico. Seepage indicates a change in the salt continuity in an intrasalt basin, but it does not indicate the presence of an effective migration pathway to a specific hydrocarbon trap. (**b**) General association of seeps, chemosynthetic communities and hydrocarbon discoveries in the deepwater Gulf of Mexico (After Thrasher et al. 1996)

phase in anoxic conditions where levels of dissolved sulphide are high (Fig. 9.51c), while siderite and other ferroan carbonates are the stable phases under anoxic conditions where the activities of dissolved sulphide are very low and bicarbonate activities are high (Fig. 9.51d).

On its way to the surface the same brine chemistry precipitates the pyrite and ferroan carbonate cements in peridiapiric sands as around the Hackberry dome and in the Carrizo sand outcrop (Fig. 8.36). It also explains the formation of iron silicates, such as chamosite and berthierine (the Fe_3O_4 silicates in Fig. 9.51c, d), in anoxic environments where the activities of both sulphide and bicarbonate are very low. This siliceous Fe-phase chemistry has important implications in terms of the reduction state of Archaean and Proterozoic seawater chemistry and the precipitation of banded iron ores (Chap. 2).

Dense anoxic brines pond in stratified hypersaline lakes on the modern deep seafloor wherever vented brines can seep into closed depressions. Such seafloor lakes typify deep seafloors atop shallowly-buried salt masses around the world and are now called deepsea hypersaline anoxic lakes (DHALS). The venting and ponded bottom brines create water column brine interfaces with the overlying seawater

Table 9.9 Chemistry (mmol/kg) of two venting Green Knoll brines versus surface and deep seawater from the Gulf of Mexico – GOM

	World-mean	Vent GK2	Vent GK11	GOM surface	GOM-deep
Na	469	3,810	1,625	500	486
K	10.2	30.1	171.7	10.3	11.1
Ca	10.3	29.3	17.7	8.8	9.7
Mg	52.8	33.1	46.9	53	50.6
Cl	545	3,903	1,898	589	553
Br	0.84	1.3	2.1	0.86	0.85
SO_4	28.2	43.6	40.5	30.5	29.7
HCO_3	1.8	1.8	3.6	2.0	2.0
Sr	0.09	.0617	90.2	.0684	.0845
Li	0.024	.0357	46.3	.0297	.0293
Mn	0.007	.0985	.0723	–	.0017
Fe ($\times 10^3$)	0.06	>1.7	<0.6	–	<0.2
$\delta^{18}O_{SMOW}$	0	0.1	−0.1	1.7	−0.15
$\delta^{13}C_{PDB}$	0	−2.4	−3.7	0.6	0.6
Cl (‰)	19.37	138.4	67.3	20.9	19.6
T (°C)	25	4.2	4.2	29.3	4.2
pH	8.1	7.35	7.25	8.0	7.6
Depth (m)	0	1,922	1,918	0	1,958

After Aharon et al. 1992

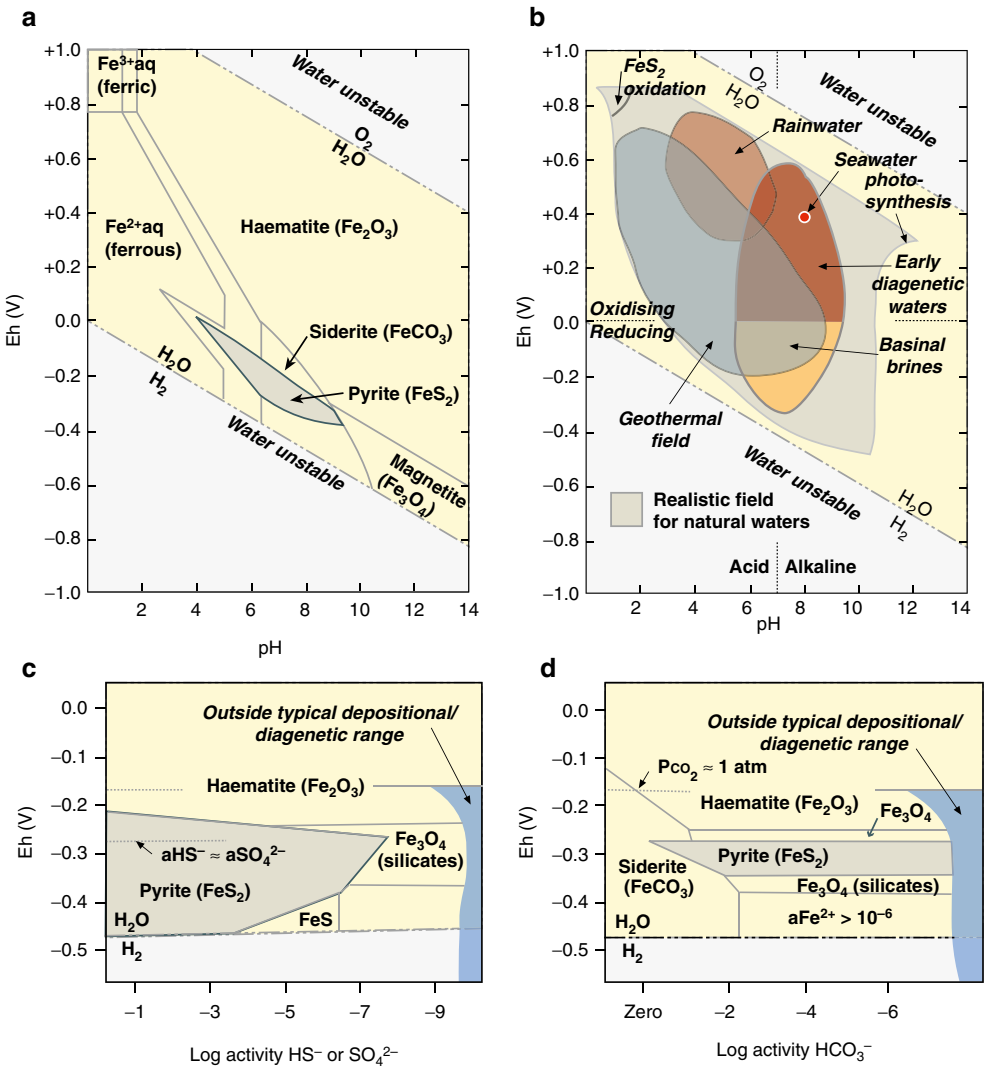

Fig. 9.51 Iron stability: phase diagrams showing the stability of iron mineral phases with respect to (**a**, **b**) Eh and pH, (**c**) Eh and sulphide/sulphate activity and (**d**) Eh and bicarbonate activity (After Garrels and Christ 1965; Hesse 1986; Taylor and Curtis 1995)

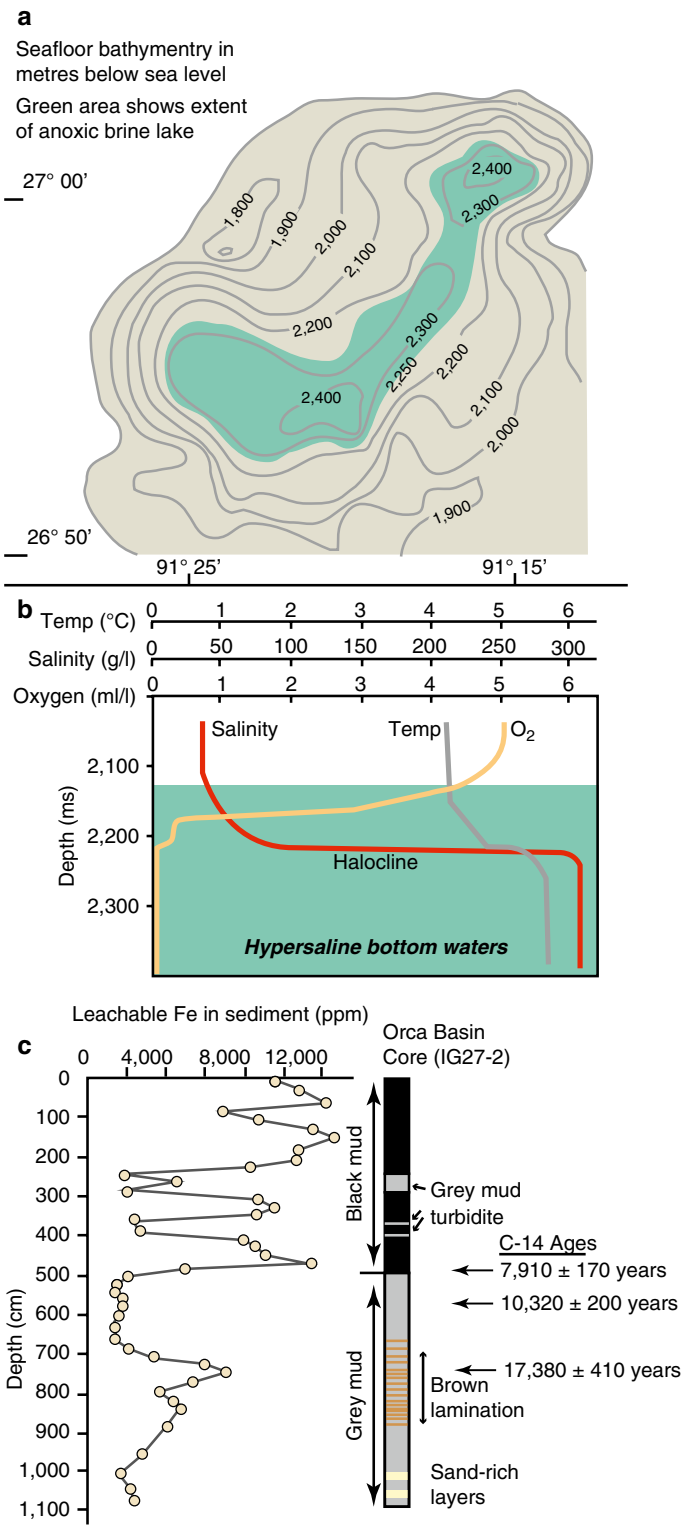

Fig. 9.52 Orca Basin, northern Gulf of Mexico. (**a**) Location and bathymetric profile (in metres below sealevel). *Grey area* outlines the extent of deep highly saline anoxic bottom waters (DHAL) created by the dissolution of nearby allochthonous salt. (**b**) Temperature, salinity and dissolved oxygen profile in the basin (After Williams and Lerche 1987). (**c**) Various sedimentary units as recovered in core IG 27–2. Plotted in depth against the leachable iron (Fe) fraction in the sediments Measured ^{14}C ages are also shown (After Addy and Behrens 1980)

and host well-adapted chemosynthetic communities. These brine-filled lows tend to form via local subsidence atop dissolving shallow allochthonous salt sheets or atop areas of salt withdrawal as underlying salt is withdrawn into adjacent growing salt structures (growth-fault and rim syncline depressions). The redox interface in such seafloor pools is located at the halocline and so is some metres to tens of metres above the seafloor.

For example, the Orca Basin in the Gulf of Mexico is a brinefilled minibasin at a depth of 2,400 m, some 600 m below the surrounding seafloor with an area more than 120 km^2 (Fig. 9.52a). Its bottom is covered by a 200 m

column of highly saline (259‰) anoxic brine, which is more than a degree warmer than the overlying seawater column (Fig. 9.52b). The pool is stable and has undergone no discernable change since it was first discovered in the 1970s. It is a closed dissolution depression fed by brines seeping from a nearby subsurface salt allochthon (Addy and Behrens 1980). A large portion of the particulate matter settling into the basin is trapped at the salinity interface between the two water bodies. Trefry et al. (1984) noted that the particulate content was 20–60 µg/l above 2,100 m and 200–400 µg/l in the brine column below 2,250 m. In the transition zone, the particulate content was up to 880 µg/l and contained up to 60 % organic matter.

A core from the bottom of the Orca brine pool captured laminated black organic-enriched pyritic mud from the seafloor to 485 cm depth and entrains three intralaminite turbidite beds of grey mud with a total thickness of 70 cm (Fig. 9.52c; Addy and Behrens 1980). This is underlain by grey mud from 485 cm to the bottom of the core at 1,079 cm. The laminated black mud was deposited in a highly anoxic saline environment, while grey mud deposition took place in a more oxic setting. The major black-grey boundary at 485 cm depth has been radiocarbon dated at 7,900 ± 170 years and represents the time when escaping brine began to pond in the Orca Basin depression. Within the dark anoxic laminates of the Orca Basin there are occasional mm- to cm-thick red layers where the iron minerals are dominated by hematite and other iron hydroxides and not by pyrite. These layers represent episodes of enhanced mixing across the normally stable oxic-anoxic halocline and indicate the short-term destruction of bottom brine stratification. When the plot of leachable iron is plotted it is obvious that the pore brines in the black mud intervals can store iron in its soluble ferric (3+) form, a reflection of the anoxia typifying these black mud pore brines.

Similar suprasalt brine pools, with microbial distributions tied to density layering in the brine column, typify the salt-floored compressive deep seafloor atop the accretionary complex of the Mediterranean Ridge. There, sheets of Miocene evaporites have been folded and thrust to shallow depths below the deep seafloor. The consequent dissolution of Messinian evaporites created saline brine pools, such as the Bannock, Tyro, Discovery, L'Atalante, and Urania brine lakes and basins (Westbrook and Reston 2002; Cita 2006). The Discovery, L'Atalante, and Urania brine lakes constitute what is sometimes referred to as the "anoxic lake region" of the Mediterranean Ridge. The "anoxic lake region" and the brine lakes of the Tyro Basin lie on the growing front of the Hellenic side of the accretionary wedge, while Bannock Basin is located atop the toe of the accretionary complex. Brine lakes on the Hellenic side of the ridge are a response to sediment deformation with a strong diapiric component. Fluids are driven out of the compacting pre-Messinian sediments, as it is overridden by the growing Messinian salt wedges (Figs. 5.49 and 5.53). Rising fluids dissolve and breach the evaporite cover wherever it is thin, leading to the escape of hypersaline fluids both ahead of the deformation front and through the pre-Messinian wedge. In contrast, the brine lakes of the Bannock Basin are a result of a seamount as it was dragged into the accretionary complex by the subducting African plate. The disturbance created a reinvigorated hydrology as it ploughed through evaporites of the accretionary complex and allowed hypersaline fluids to escape to the seafloor (Fig. 9.53).

Life, Fe and Sulphur in Seafloor Brine Lakes

The various brine lakes on the deep-sea floor of the Mediterranean, occur thousands of metres below the photic zone, within depressions that entrain bottom waters up to ten times as saline as Mediterranean seawater. In the Bannock Basin the various brine-filled depressions or sub-basins create a closed outer moat around a central seafloor mound that is 10 km across (Fig. 9.53a). The chemical composition of the Tyro Basin bottom brine is related to the dissolution of the underlying halite-dominated evaporites, while the chemical composition of the Bannock Basin (Libeccio Basin in the Bannock area) implies derivation from dissolving bittern salts (de Lange et al. 1990). In the "anoxic lakes region", sodium chloride is predominantly sourced in the L'Atalante and Urania lakes, but L'Atalante is much richer in potassium chloride than the other lakes. The Discovery basin brine is almost exclusively the product of dissolution of magnesium chloride (bischofite) salts. It has a density of 1,330 kg/m^3, which makes it the densest naturally occurring brine yet discovered in the marine environment (Wallmann et al. 2002). Its concentration profile in sediment beneath the brine lake shows the age of this lake is between 700 and 2,000 years. The high concentration of magnesium chloride drives dissolution of biogenic calcium carbonate, but facilitates excellent preservation of siliceous microfossils and organic matter. In basin bottom muds there are large euhedral crystals of gypsum, up to 10 cm across, precipitating from these brines (Cita 2006).

Biomarker associations of the organics accumulating in these brine lakes define two depositional styles: typical marine and hypersaline (Burkova et al. 2000). Algal and bacterial biomarkers typical of saline environments were found in layers 0.60–0.75 m below the sediment surface in the Tyro Lake Basin, as well as normal marine indicators derived from pelagic fallout ("rain from heaven"). Saline indicators include; regular C-25 isoprenoids, squalane, lycopane, isolycopane, tetraterpenoid and tetrapyrrolic pigments, monoalkylcyclohexanes, tricyclic diterpanes, steranes, hopanes, bio- and geohopanes. According to Burkova et al. (2000), the saline organic signatures come from microbial mat layers, redeposited from a Messinian source into the sapropels of

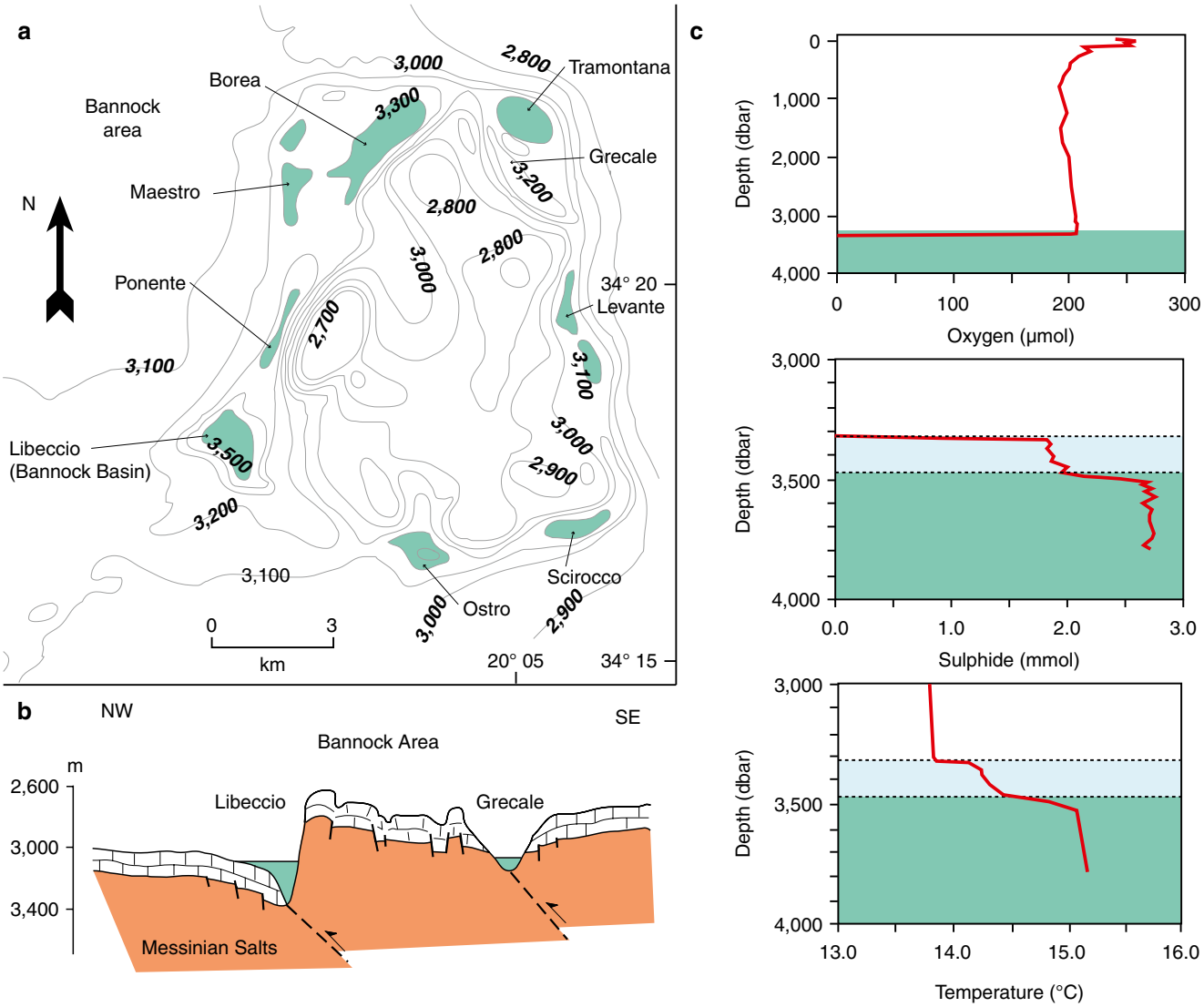

Fig. 9.53 Brine pools (DHALS) in the Bannock Basin, Mediterranean Ridge. (**a**) Bathymetry of Bannock area, seafloor contours in metres (After Camerlenghi 1990). (**b**) Interpreted cross section based on seismic profiles (After Camerlenghi 1990). (**c**) Water column and brine column characteristics (oxygen, sulphide and temperature profiles; replotted from data tables in Bregant et al. 1990)

the modern depression. Alternatively, they may indicate the activities of a chemoautotrophic community, which flourishes at the halocline or around active brine vents. As in the Orca Basin, the organic content of the bottom sediments of the Mediterranean brine pools is much higher than is found in typical deep seafloor sediment (Fig. 9.54a).

Anoxic hypersaline brines in Mediterranean brine lakes are highly sulphidic and among the most sulphidic bodies of water in the marine realm, with H_2S concentrations consistently greater than 2–3 mmol (Fig. 9.53c; Table 9.10; Henneke et al. 1997). The brine body below the Urania chemocline is more than 100 m thick and contains up to 11 mM hydrogen sulphide, making it the most sulphidic water body in the known marine realm. In combination with the sulphide are very high levels of methane both in and below the halocline (≈5.56 mM; Borin et al. 2009). In contrast, there is little to no H_2S in the anoxic bottom brine of the Orca Basin (Table 9.10). There the iron concentration is 2 ppm, a value more than 1,000 times higher than in the overlying Gulf of Mexico seawater. Such high levels of reducible iron in the Orca Basin are thought to explain the lack of H_2S in the bottom brine and a preponderance of framboidal pyrite and extractable iron in the bottom sediments (Sheu 1987). Both the Orca Basin, and the brine pools on the floor of the Mediterranean, show sulphate levels that can be more than twice that of the overlying seawater.

Pyritic sulphur is the main phase of inorganic reduced sulphur in the Tyro and Bannock basins, where it makes up

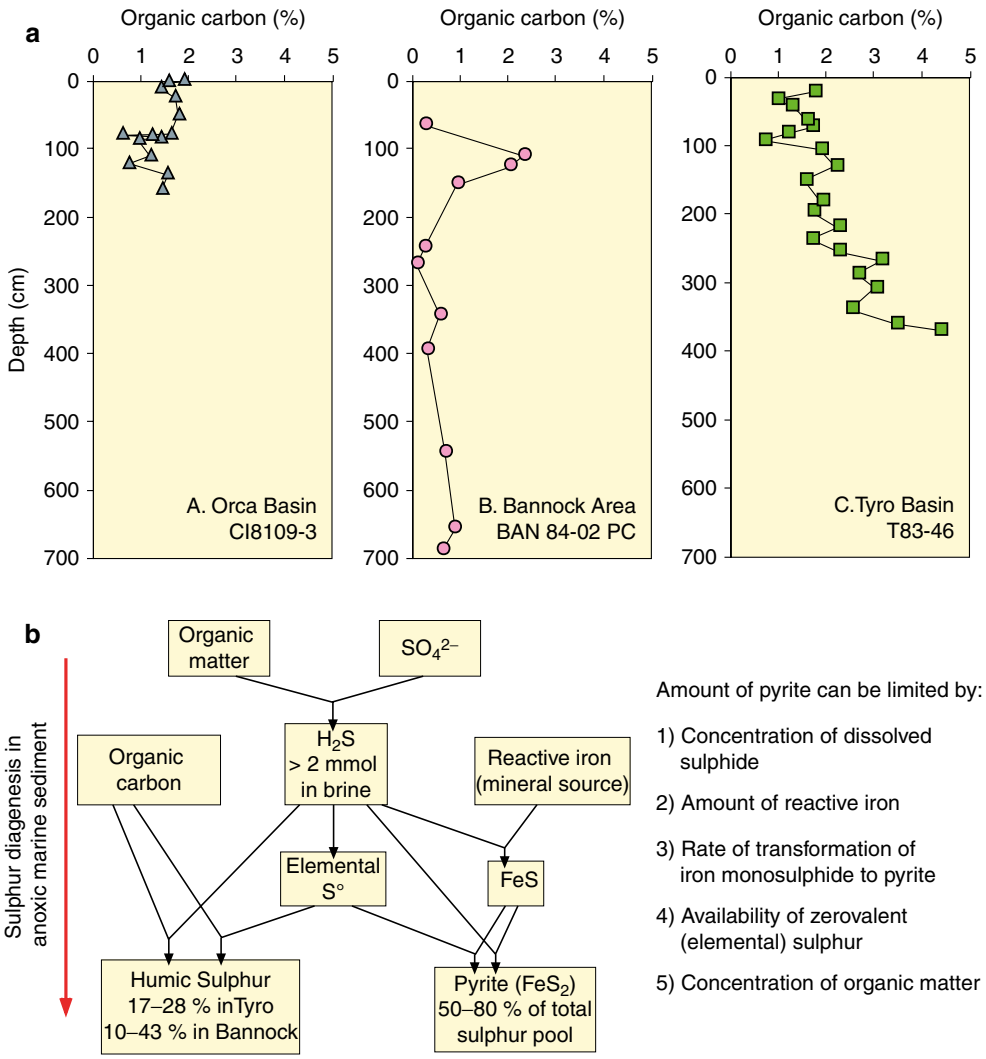

Fig. 9.54 Organic characteristics of brine pool bottom sediment. (**a**) Total organic carbon as % dry weight versus depth (Plotted from Tyro and Orca data in Table 1 of Sheu 1987, and Bannock data from Henneke et al. 1997). (**b**) Modes of occurrence of sulphur in brine pool bottom sediments (After Henneke et al. 1997)

Table 9.10 Chemical make-up of various salt allochthon-associated brine pools compared to oxygenated seawater from the Mediterranean

Region of brine occurrence	Salinity (‰)	pH	O_2 (µM)	H_2S (mM)	SO_4 (mM)	Ca (mM)	Cl (mM)	PO_4 (µM)	NH_4 (µM)
Urania Basin (Mediterranean)	200	6.8	0	8.6–11	85	34	2,830	41.2	ND
Libeccio Basin (Bannock area – Mediterranean)	321	6.5	0	1.67	99	21	5,333	12	3,080
Tyro Basin (Mediterranean)	ND	6.75	0	2.15	49	34	5,350	10	1,260
Orca Basin (Gulf of Mexico)	258	5.5	0	0.60	47	32	5,000	82	500
Seawater (Mediterranean)	39	8.2	200	0	31	11	660	0.2	0.2

After Sass et al. 2001

50–80 % of the total sulphur pool. It is also present at the same levels in cores from the two basins, that is, around 250 µmol per gram dry weight (Henneke et al. 1997). Humic sulphur accounts for 17–28 % of the total sulphur pool in the Tyro Basin and for 10–43 % in the Bannock Basin (Fig. 9.54b). Sulphur isotope data show negative $\delta^{34}S$ values for both pyritic sulphur, with $\delta^{34}S = -19$ to $-39‰$; and for humic sulphur, with $\delta^{34}S = -15$ to $-30‰$; indicating that both pyritic and humic sulphur originated from microbially produced H_2S within the brine column.

Marine sediment fills in all the active brine lakes of the Mediterranean Ridge range in age from Holocene to Late Pleistocene and are typically made up of turbidites interlayered with laminated intervals composed of alternating green gelatinous muds and grey reduced oozes. Usually, the density of the bottom brine layer in the Bannock region is high enough to support a layer of finely dispersed organic debris, allowing substantial bacterial mats to float at the seawater-brine interface (halocline) and so form suspended deep mid-water bacterial mats (Erba 1991). While the organics

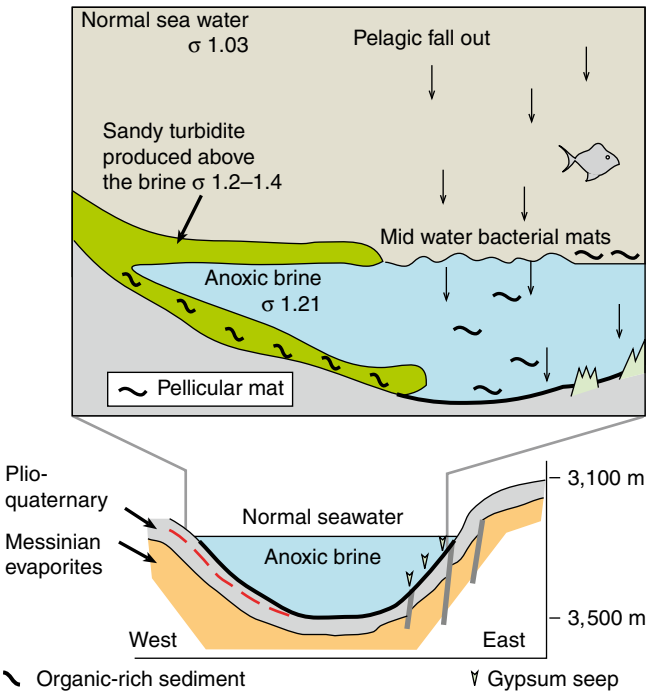

Fig. 9.55 Formation and sedimentation model for pellicles in Mediterranean seafloor brine lakes. Bacterial (pellicular) mats grow mid-water at the interface between normal seawater and anoxic brine and trap biogenic and inorganic particles. When pelagic sedimentation prevails, pellicles sink to the basin floor after load increases to breach levels at the halocline interface (*right side*). Occasional turbidity currents and sediment slumping disrupts the interface and transports fragments of pellicles to the basin bottom in coarser sandier layers (After Erba 1991)

float on the oxic side of the halocline they are subject to oxidation and biodegradation (Fig. 9.55). Owing to the high density of the bottom brines, moving this floating organic material to the floor of density-stratified brine pools appears at first to be a difficult proposition. Bottom sediments in the Urania Basin for example contain very little particulate organic matter (>1 % TOC). Yet, organic contents in the anoxic bottom muds beneath Tyro and Orca basins can be as high as 4–5 % organic carbon (Fig. 9.54a). The propensity for organics to remain suspended at the halocline can be overcome when mineral crystals, such as pyrite, precipitate at the interface via diffusive brine mixing in combination with bacterial sulphate reduction. Newly formed crystals attach to organic matter floating at the halocline to create a combined density that carries the suspended pellicular organics to the pool floor. In such a brine pool scenario, the redox front that fixes pyritic sulphur occurs at the halocline, and not at its more typical marine position located at or below the sediment-seawater interface. The metal sulphide crystals then sink, carrying organic matter coats to form characteristic metal and organic rich laminites on the floor of the anoxic brine lake.

So, organic debris first formed at the halocline can then accumulated as pellicle layers within the pyritic bottom muds (laminites). Pellicular debris is also carried to the bottom during the emplacement of turbidites when the halocline is disturbed by turbid overflow (Fig. 9.55; Erba 1991). Hence, pellicular layers are typically aligned parallel to lamination, or are folded parallel to the sandy bases of the turbidite flows, or line up parallel to deformed layers within slumped sediment layers. Individual pellicle layers are 0.5–3 mm thick and dark greenish-grey in colour. Similar pellicular layers cover the surface of, or are locked within, recent gypsum crystals recovered from bottom sediments of the Bannock area. This gypsum is growing today on the bottom of the Bannock Basin, atop areas about the brine pool margin that are directly underlain by dissolving Miocene evaporites (Corselli and Aghib 1987; Cita 2006). Other than the Dead Sea, it is one of the few modern examples of a deepwater evaporite, but its seepage-fed genesis means it is a poor analogue for deepwater basinwide salt units.

The community of bacteria and archaea flourishing at the halocline in sulphidic marine brine pools on the deep Mediterrannean floor is quite diverse, largely independent of primary production in the euphotic zone, with the number of identified unique halobacteria and haloarchea species expanding every year (Albuquerque et al. 2012). Bottom brine in the Urania brine lake has a salinity of 162‰ and the chemocline of the brine lake is some 3,490 m below the ocean surface, so only a very small amount of phytoplanktonic organic carbon ever reaches the 20 m thick chemocline. Yet the oxic waters of the upper part of the chemocline support a rich bacterial and archaeal assemblage in and below the interface between the hypersaline brine and the overlying seawater, much like the chemosynthetic bacterial community associated with the halocline in Lake Mahoney (Sass et al. 2001; Borin et al. 2009).

Sulphide concentration in Urania Basin increases from 0 to 10 mM within a vertical interval of 5 m across the interface (Fig. 9.56a). Within the halocline, the total bacterial cell counts and the exoenzyme activities are elevated and biogenic activity continues below the halocline. Bacterial sulphate reduction rates measured in this layer are ≈14 nmol SO_4 cm^{-3} day^{-1} and are among the highest in the marine realm. They correspond to the zone of maximum bacterial activity in the chemocline (Fig. 9.56b). Particulate organic content is 15 times greater than that in the overlying normal marine waters. A similar focus of microbial occurrence (bacterial and archaeal) is seen at the halocline in l'Atalante Basin and is probably typical of all chemocline layers in the various Bannock brine lakes (Yakimov et al. 2007).

Employing 11 cultivation methods, Sass et al. (2001) isolated a total of 70 bacterial strains from the chemocline in the Urania Basin (Fig. 9.56a). These strains were identified as the flavobacteria, *Alteromonas macleodii*, and *Halomonas aquamarina*. All 70 strains could grow chemo-organoheterotrophically under oxic conditions. Twenty-one of the isolates could grow both chemo-organotrophically and chemo-lithotrophically (decomposers and fermenters). While the most probable numbers in most cases ranged

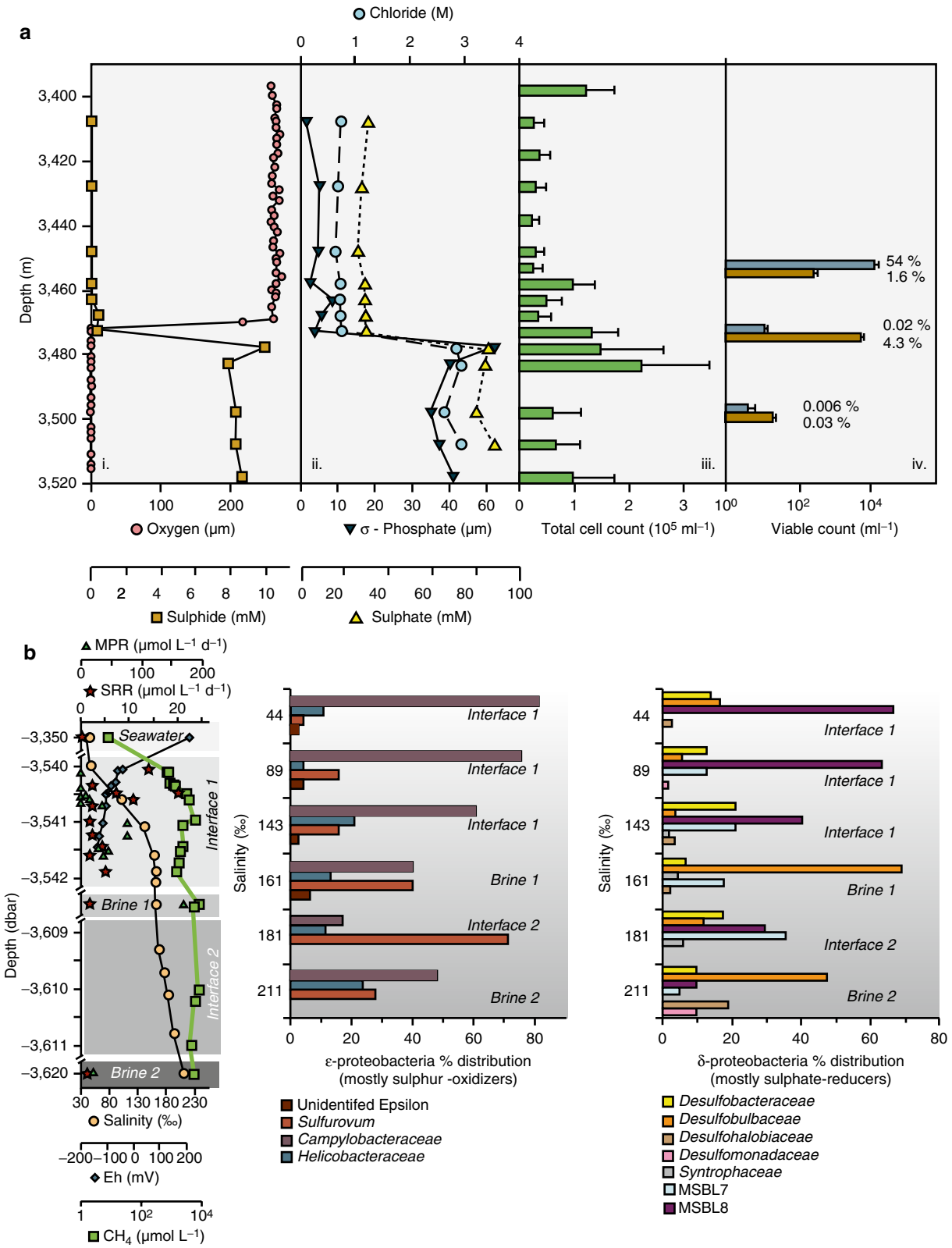

Fig. 9.56 Urania Basin, Mediterranean Ridge. (**a**) Physicochemical parameters, total cell counts, and MPN across the oxicanoxic boundary of the Urania Basin, Mediterranean Ridge (After Sass et al. 2001). (*i*) Oxygen and sulphide concentrations; (*ii*) Sulphate, orthophosphate and chloride concentrations; (*iii*) Total cell counts; (*iv*) Viable cell counts in anoxic media containing the amino acid mixture (*solid bars*) and in oxic media containing thiosulphate (*cross-hatched bars*). The percentages are relative to the total cell count and the error bars indicate standard deviation. (**b**) Relative distribution of sequences belonging to the ε-and δ-Proteobacteria (mostly sulphate reducers) are stratified across the halocline and below in the water column of the Urania basin (After Borin et al. 2009). The methane production (MPR) rate is an order of magnitude higher than the rate of sulphate production rate (SPR) over much of the halocline, as are relative levels of methane versus H_2S. Note that the depth scale on the salinity-Eh profile is not continuous but focused into salinity-controlled zones that tie to the microbial samples

between 0.006 and 4.3 % of the total cell counts, an unusually high value of 54 % was determined above the chemocline with media containing amino acids as the carbon and energy source.

Subsequent detailed work focused on the various layers that make up the Urania halocline showed the high sulphide levels in and below the halocline, make it a mecca for bacterial sulphate reducers, as do high levels of methane for the methanogens (Fig. 9.56b; Borin et al. 2009). Microbial abundance showed a rapid increase by 2 orders of magnitude from 3.9×10^4 cells mL^{-1} in the deep oxic seawater immediately above the basin, up to 4.3×10^6 cells mL^{-1} in the first half of interface 1. Although less pronounced than in the first chemocline, a second increase in microbial counts occurred in interface 2. Deceleration of falling particulate organic matter from the highly productive interface 1, is probably responsible for stimulating microbial growth and hence cell numbers in interface 2. That is, compared to the overlying seawater column, bacterial cell numbers increased up to a hundred-fold in interface 1 and up to ten-fold in interface 2. This is a consequence of elevated nutrient availability, with higher numbers in the upper interface where redox gradient was steeper. Bacterial and archaeal communities, analysed by DNA fingerprinting, 16S rRNA gene libraries, activity measurements, and cultivation, were highly stratified within the various layers of the chemocline and metabolically more active along the various chemocline layers, compared with normal seawater above, or the uniformly hypersaline brines below.

Detailed analysis of 16S rRNA gene sequences revealed that in both chemocline interfaces the ε- and δ-Proteobacteria were abundant, predominantly as sulphate reducers and sulphur oxidizers, respectively (Fig. 9.56b). The only archaea in the first 50 cm of interface 1 were Crenarchaeota, which consist of organisms having sulphur-based metabolism, and hence could play a role in sulphur cycling in the upper interface. In the deepest layers of the basin below the halocline, MSBL1, putatively responsible for methanogenesis, dominated among archaea (Fig. 9.57). The work of Borin et al. (2009) illustrate that a well adapted and complex microbial community is thriving in the Urania basin's extreme chemistry, The elevated biomass centred on the halocline is driven largely by sulphur cycling and methanogenesis.

Similar detailed studies of interface-controlled chemosynthetic communities in other Mediterranean DHALs have been documented in Lake Thetis (Ferrer et al. 2012; Oliveri et al. 2013) and Lake Medee (Yakimov et al. 2013). Medee Lake is the largest known DHAL on the Mediterranean seafloor and has two unique features: a complex geobiochemical stratification and an absence of chemolithoautotrophic Epsilon-proteobacteria, which usually play the primary role in dark bicarbonate assimilation in DHALs interfaces worldwide. Presumably, because of these features, Medee is less productive and exhibits reduced diversity of autochthonous prokaryotes in its interior brine layers. Indeed, the brine community almost exclusively consists of the members of euryarchaeal and bacterial KB1 candidate divisions which are ubiquitous in the DHAL biota worldwide. In Medee, as elsewhere, they are thriving on small organic molecules produced by a combination of degraded marine plankton and moderate halophiles living in the overlying stratified brine column.

In another DHAL, the Kebrit Deep on the deep floor of the Red Sea, a similar assemblage of halophilic archaea and bacteria flourish in hypersaline waters below the chemocline (Fig. 9.57). Kebrit Deep (24°44'N, 36°17'E) measures 1 by 2.5 km, with a maximum depth of 1,549 m and is one of the smallest salt allochthon-associated brinepools of the Red Sea. It is located near the site of the well-known metalliferous Atlantis II deep (Fig. 15.14). The Kebrit Deep is filled by an 84 m thick, anaerobic, slightly acidic brine lake (pH approximately 5.5) with a salinity of 260‰ and a temperature of 23.3 °C (Antunes et al. 2011). The brine has a high gas content that is made up largely of CO_2, H_2S, small amounts of N_2, methane and ethane, with remarkably high quantities of H_2S (12–14 mg S l^{-1}; Hartmann et al. 1998). The presence of sulphur is self-evident by the strong, characteristic odour present in brine samples, and hence the name of basin (Kebrit is the Arabic word for sulphur). Like the Atlantis II deep there are impregnated massive sulphides accumulations on the floor of Kebrit Deep. Kebrit samples are porous and fragile, and consist mainly of pyrite and sphalerite. Prior to gene sequencing studies, sulphur isotope values provided strong evidence for biogenic sulphate reduction being involved in sulphide-forming processes in Kebrit Deep. They are linked to bacterial methane oxidation and sulphate reduction centred on the brine-seawater interface (see Chap. 15 for metallogenic details).

Most of the archaeal sequences in Kebrit Deep cluster within the *Thermoplasmatales* (Marine group II, Marine Benthic group D, and the KTK-4A cluster) among the *Euryarchaeota*, while the remaining sequences do not show high similarity to any of the known phylogenetic groups (Fig. 9.57). One of these sequences was shown to cluster with the later described SA2 group, while another (accession number AJ133624) clusters together with two gene sequences from L'Atalante Basin waters, defining a novel deeply-branching phylogenetic lineage within the Crenarchaeota.

Gene sequencing studies on water samples from the brine–seawater interface in the Kebrit deep retrieved sequences from the KB1 group, as well as *Clostridiales* (mostly *Halanaerobium*), *Spirochetes* (ST12-K34/MSBL2 cluster), *Epsilonproteobacteria* and *Actinobacteria*, but no archaeal sequences were detected in these interface samples (Antunes et al. 2011). Under strictly anaerobic culture conditions, novel halophiles were isolated from samples of these

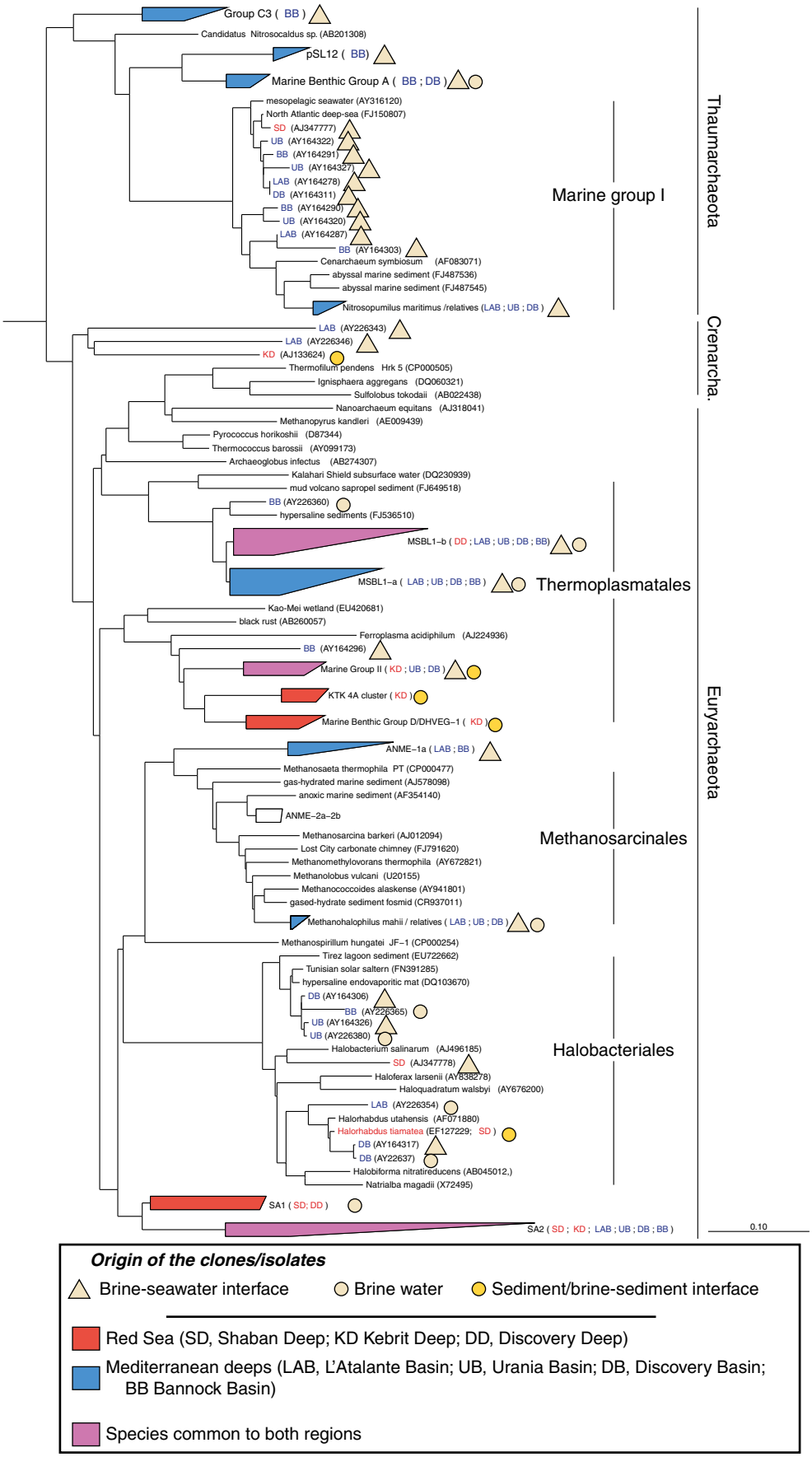

Fig. 9.57 Major lineages of Archaea as identified via gene splicing techniques in samples of deep-sea brines from the Red Sea, in *red*, the Mediterranean Sea, in *blue* and those that occur in both brines, in *purple* (After Antunes et al. 2011)

waters and belong to the halophilic genus *Halanaerobium*. They are the first representatives of the genus obtained from deep-sea, anaerobic brine pools (Eder et al. 2001). Within the genus *Halanaerobium*, they represent new species that grow chemo-organotrophically at NaCl concentrations ranging from 5 to 34 %. They contribute significantly to the anaerobic degradation of organic matter, which formed at the brine-seawater interface and is slowly settling into the bottom brine. Similarities in the make up of the Archaeal population, tied to similar metabolic process sets at the brine interface across various deep seafloor brine lakes in the Gulf of Mexico, the Mediterranean and the Red Sea is illustrated in Fig. 9.57.

Neither Tyro nor Bannock Basin bottom sediments show a significant correlation between pyritic sulphur and the organic carbon in the bottom sediments, suggesting predominantly syngenetic pyrite evolution in bottom sediments of these brine lakes (Henneke et al. 1997). That is, both pyritic and humic sulphur preserved in the bottom sediments formed either in the lower water column or at the sediment-brine interface, not in the sediment itself. Ongoing diagenetic processes within the bottom sediments only form an additional 5 % of the total pyrite. Van der Sloot et al. (1990) clearly showed that metal sulphides, as well as organics and other minerals, precipitate at the brine-seawater interface in the Tyro Basin, as they do in the Orca Basin. They found extremely high concentrations of Co (0.015 %), Cu (1.35 %) and Zn (0.28 %) in suspended matter at the halocline. These high particulate Co, Cu and Zn concentrations correspond to sharp increases in dissolved sulphide across the interface (a redox front), and indicate precipitation of metal sulphides at the interface. Humic sulphur in the bottom sediments correlates with the pyritic sulphur distribution and is related to the amount of gelatinous pellicle derived from bacterial mats growing at the halocline between oxic seawater and bottom brine (Erba 1991; Henneke et al. 1997).

Additionally, the degree of pyritisation in the sediments (DOP ≈ 0.62) indicates that present-day pyrite formation is limited by the reactivity of Fe in the Bannock and Tyro basins and not by the availability of organic matter, the latter being the process that limits pyrite formation in most normal marine settings (Fig. 9.54b). The degree of pyritisation (DOP) is defined as [(pyritic iron)/(pyritic iron + reactive iron)]. Raiswell et al. (1988) showed that DOP in ancient sediments can distinguish anoxic from normal marine sediments. Anoxic sediments show DOP values between 0.55 and 0.93, while normal marine sediments have DOP values less than 0.42. The DOP levels in the Bannock and Tyro basins confirm observations made in ancient anoxic sediments. Thus, although the Tyro and Bannock basin brines differ in their major element chemistry, reflecting a different salt source, their reduced sulphur species chemistry appears to be similar, but is significantly different from normal marine systems and capable of precipitating metal sulphides above the sediment surface.

Pools of hypersaline, anoxic brines, underlain by laminated pyritic organic-rich sediments, are far more widespread in halokinetic terrains than just in the Orca, and Mediterranean Ridge basins. For example, similar brine seeps and pools have now been documented atop and adjacent to numerous salt allochthons along much of the continental slope of the Gulf of Mexico. In the Green Canyon area, wherever shallow allochthonous salt sheets are dissolving just beneath the seafloor, organic-enriched pyritic sediments are also commonplace (Fig. 9.54a, b; Reilly et al. 1996). Similar cool-seep systems are active today along the foot of the Florida Escarpment and the Blake Ridge, where they are focused and in part fed by subadjacent dissolving salt allochthons (Paull et al. 1992).

Rim Life, CH_4 and H_2S in Seafloor Brine Lakes

On the deep dark seafloor, a light-independent chemosynthetic seep biota grows and flourishes in salt sheet focused regions of both hydrocarbon (methane) and H_2S outflow (Fig. 9.58a). Escape of nutritive methane and H_2S into brine-filled pockmark pools and minibasin salt lakes supports symbiont-containing mussel, clam and tubeworm communities, which can construct dense biostromes around the pool rims, especially in regions of the rim edge stabilised by the precipitation of biogenic carbonate cements. They are common atop salt-allochthon floored basins, where edges of salt allochthons focus the upward escape of gaseous and liquid hydrocarbons.

Where sea bottom temperatures are suitably low, methane hydrates (clathrates) form atop focused outflow zones and oil seeps are common at the sea surface above vent clathrates (Dalthorp and Naehr 2011). Gas hydrate or clathrate is an ice-like crystalline mineral in which hydrocarbon and non-hydrocarbon gases are frozen within rigid molecular cages of water. They can be thought of gaseous permafrost. Their occurrence is not just tied to the cold temperature portion of the deep seafloor; clathrates are the dominant seals to large gas reservoirs in the permafrost regions of Siberia. Methane hydrates are commonplace associations where methane, which can be thermogenically or biogenically sourced, occurs just below the deep cold seafloor. In much of world it accumulates in many seafloor regions independent of any underlying evaporite occurrence (Thakur and Rajput 2011). Evaporite edges just tend to focus the outflow zones (Fig. 9.58).

Clathrate formation on the seafloor requires bottom temperatures not encountered until the seafloor bottom lies beneath a water column 450–500 m deep. Beneath the clathrate-covered seafloor, temperature increases with depth

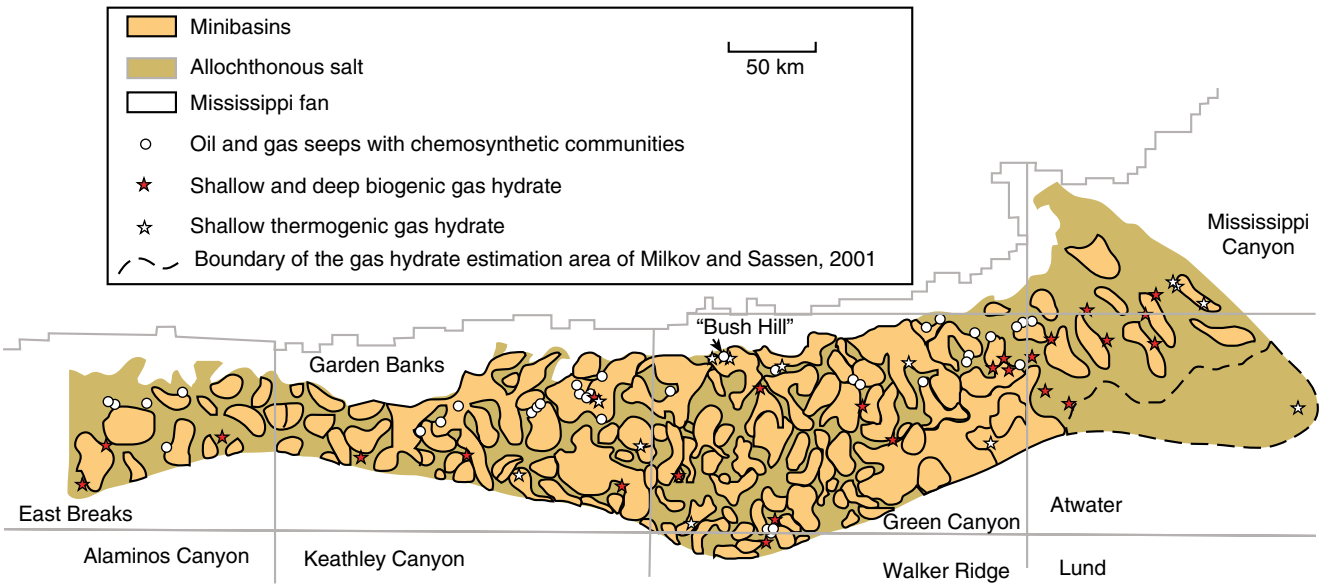

Fig. 9.58 Seeps in the northern Gulf of Mexico showing selected occurrences of seeps and methane hydrates, some with well developed chemosynthetic communities (After Milkov and Sassen 2001)

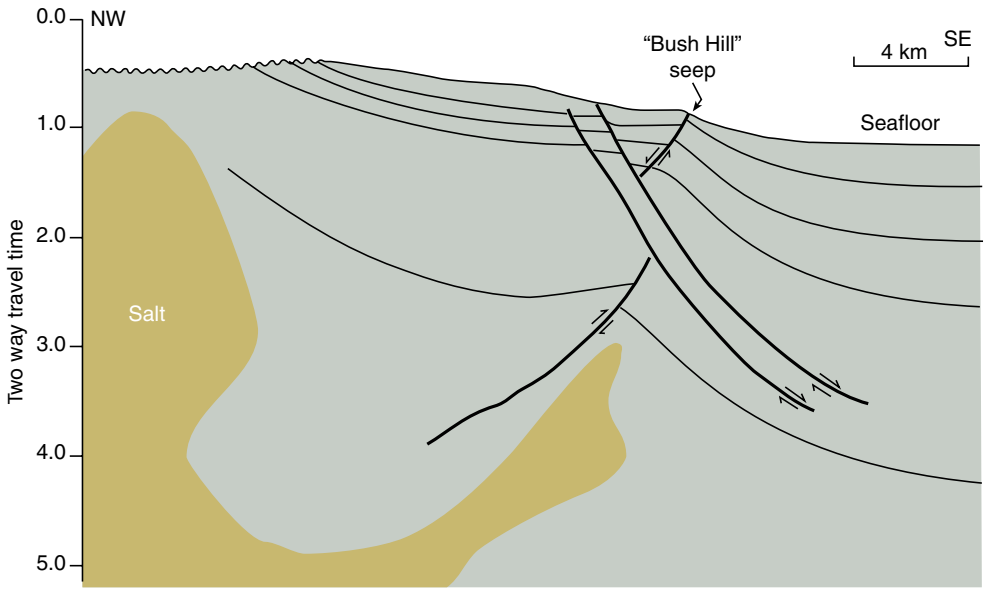

Fig. 9.59 Interpretation of seismic line showing strong structural control on location of the chemosynthetic seep at "Bush Hill" (After Reilly et al. 1996)

and this limits the depth at which gas hydrates will occur, so below most clathrate layers an accumulation of free gas is likely. Clathrates, seeps and brine pools are not unique to, but are often very obvious about, salt allochthon edges where salt flow induces extensional faulting and funnels a focused rise of methane, degraded oil and H_2S to the cold seafloor (Chap. 6). Hence, breaks in the lateral extent of the various salt sheets act as a focusing mechanism for escaping thermogenic and biogenic methane and other gases and fluids (Fig. 9.58; MacDonald et al. 2000, 2003). Rapid burial of organic-entraining sediments in supra-allochthon minibasins encourages the creation of biogenic methane that sources much of the gas escaping to the seafloor away from salt-edge focused seeps. Hence, in the salt allochthon province of the northern Gulf of Mexico there is a definite association between brine pool chemosynthetic communities, thicker gas hydrates and the edges of minibasins (Fig. 9.59; Reilly et al. 1996; Milkov and Sassen 2001).

In all these setting clathrates are a food source for various methanogenic microbes and so there are various multicellular lifeforms dependent on these microbes. One obvious dependency is seen in the eco-niche occupied by a small 2–4 cm-long highly specialised polychaete called *Hesiocaeca methanicola*. It was recently discovered (in 1997) flourishing

in regions of methane hydrate atop the deep seafloor in the Gulf of Mexico (Fisher et al. 2000). These "ice worms" inhabit indentations ("burrows") in blocks and layers of methane clathrate and glean or harvest biofilms of the methanotropic bacteria that are metabolising methane on the block surface. In turn, the ice worm supplies oxygen to the methanotropes and via its movement appears to contribute to the dissolution of hydrates. Mature ice worms can survive in an anoxic environment for up to 96 h.

The mussel-tubeworm dominated seep biota in the Gulf of Mexico is dependent on chemosynthesising microbes as a food source. This community is the coldwater equivalent to chemosynthetic hydrothermal communities flourishing in the vicinity of black smoker vents (MacDonald 1992; MacDonald et al. 2003). In both settings it is methane and sulphide, not light, that provides the energy source for the bacteria and archaea that make up the base of the food chain. Methanotropic bacteria live symbiotically on a seep mussel's gills, taking in methane and convert it to nutrients that nourish the mussels. Seep mussels and clams (*Bathymodiolus childressi*, *Calyptogena ponderosa and Vesicomya cordata*) continually waft methane-rich water through their gills to help their chemo-autotrophic bacterial symbionts grow and periodically harvest some of the excess growth. Their lifestyle means that seep mussels need to live near a supply of dissolved gas, they can inhabit isolated seep outflows on the deep seafloor where gas is bubbling out, including the edges of mud volcano pools, but do best about the more stable and quiescent edges of methane-saturated brine pools and lakes. There they grow as a fringe to the brine pool, and exist about the pool rim wherever they can keep their siphons above the halocline. They construct a biogenic edge (biostrome) to the brine pool atop and within sediments generally cemented by methanogenic calcite. Such rims typically extends some 5–10 m behind the pool edge (Smith et al. 2000). The inner edge of the mussel biostrome is elevated only a few centimetres from the surface of the pool and is distinguishable by an abundance of smaller individuals, present in high densities. At the outer edge of the mussel biostrome, there is a high frequency of disarticulated shells and low densities of still living larger individuals.

Also living atop seafloor seeps and about some brine pools are knots and clusters of chemosynthetic polychaete tubeworms (*Lamellibrachia luymesi* and *Seepiophila jonesi*). These tubeworms (aka seep beard-worms) can be up to 2.5 m log and possess a microbe-dependent metabolism evolved to exploit the abundant H_2S and methane associated with the hydrocarbon-rich brine seeps (Fig. 9.59). They grow as rims and clumps atop H_2S seeps, as at Bush Hill on the floor of the Gulf of Mexico (Fig. 9.59; Reilly et al. 1996; McMullin et al. 2010). Tubeworm "bushes" in cold seep regions of the Gulf of Mexico are typically rooted in the H_2S-rich muds. Growing individual tubes actively extend down into the H_2S-rich mud as well as up into the O_2-rich water column giving the cluster a morphology similar to a tree or shrub. Their "roots" extend into the earth, while "branches" extend above. Continuing the plant analogy, it seems that tubeworm shrubs absorb H_2S through their "roots" and O_2 through their "branches" (Freytag et al. 2001; Bergquist et al. 2003). As a group, seep tubeworms are related to the giant rift tubeworm (*Riftia pachptila*), which inhabits active hydrothermal seeps in active seafloor rifts.

Via a specialised haemoglobin molecule, vestimentiferan tubeworms in the Gulf of Mexico provide H_2S and O_2 as nutrients to sulphur-oxidising bacteria living symbiotically in trophosome structures, which extend for up to 75 % of the length of each tubeworm. Unlike hydrothermal tubeworms such as *Riftia pachptila* that grow to lengths of more than 2 m in less than 2 years, *Lamellibrachia luymesi* grow very slowly for most of their lives. It takes from 170 to 250 years to grow to 2 m in length, making them perhaps the longest living known invertebrate species (Bergquist et al. 2000). With five or six species currently known to flourish there, the brine-fed cold seeps of the Gulf of Mexico host the highest biodiversity of vestimentiferan siboglinid tubeworms worldwide.

Interestingly, when the fast growing giant hydrothermal tubeworms (*Riftia pachptila*) were first collected from the vicinity of black smokers in the 1977, figuring out what they lived on in deep dark waters was mystifying: especially as adults had no mouths, guts, or anuses! They were first thought to be absorbing tiny food particles through their skin. The function of the trophosome was unknown but thought to be related to dealing with toxicity not feeding, after all these structures were lined with sulphur crystals. It is now known that the sulphur-oxidising bacteria, which inhabit the trophosome cells of these specialised siboglinids, use H_2S to produce nutrients in the form of organic carbon for the tubeworms to metabolise. Elemental sulphur is the common metabolic intermediate or food source of the sulphur-oxidising bacteria that live symbiotically in rift and cold seep tubeworms.

There is a time-based evolution in the biotal make-up of chemosynthetic communities in the Gulf of Mexico (Glover et al. 2010 and references therein). The earliest stage of a cold seep is characterised by a high seepage rate and the release of large amounts of biogenic and thermogenic methane, H_2S and oil (Sassen et al. 1994). As authigenic carbonates with characteristic negative $\delta^{13}C$ values precipitate as a metabolic byproduct of microbial methanogenesis, they provide a necessary stable substrate for the settlement of larval vestimentiferans and seep mussels. These seep communities begin with mussel (*Bathymodiolus childressi*) beds containing high biomass communities of low diversity and high endemicity. Individual mussels live for 100–150 years, whereas mussel beds may persist for even longer periods,

with growth rates of mussels largely controlled by methane concentrations (Nix et al. 1995).

The next successional stage consists of vestimentiferan tubeworm aggregations dominated by *Lamellibrachia luymesi* and *Seepiophila jonesi*. Young tubeworm aggregations often overlap in time with, and normally persist past the stage of mussel beds. These tubeworm aggregations and their associated faunas go through a series of successional stages over a period of hundreds of years. Declines in seepage rates result from ongoing carbonate precipitation occluding pores and so forming aquitards, as well as the influence of *L. luymesi* on the local biogeochemistry as it extracts ever larger volumes of H_2S. In older tubeworm aggregations, biomass, density, and number of species per square meter, decline in response to reduced sulphide concentrations.

Once seep habitat space becomes available, more of the nonendemic background species, such as amphipods, chitons, and limpets, can colonise the mussel and tubeworm aggregations. Due to the lowering concentrations of sulphide and methane, the free-living microbial primary productivity is reduced. The number of associated taxa is positively correlated with the size of the tubeworm-generated habitat, so diversity in this stage remains fairly high although the proportion of endemic species is smaller in the older aggregations. This final stage may last for centuries, as vestimentiferan tubeworms can live for over 400 years (Cordes et al. 2009).

Even as seepage of hydrocarbons declines in a particular seep site, the authigenic carbonate layers of relict seeps can still provide a stable seafloor substrate for marine filter feeders, such as cold-water corals. The scleractinians *Lophelia pertusa* and *Madrepora oculata*, several gorgonian, anthipatharian, and bamboo coral species form extensive reef structures atop now inactive seeps on the upper slope of the Gulf of Mexico (Schroeder et al. 2005). The corals obtain their food supply from the water column and are not dependent on chemosynthetic microbes. The coral communities also harbour distinct associated assemblages, consisting mainly of the general background fauna, but also contain a few species exclusively associated with the corals and a few species that are common to both coral and seep habitats.

Although individual tubeworms and molluscs in chemosynthetic brine pool communities may live for more than 300–400 years, vagaries in the rate of brine and nutrient supply to the seafloor mean many mussel and tubeworm colonies are overwhelmed by a rising halocline and so die in a shorter space of time. Their partially decomposed remains can spread out as part of the organic-rich debris atop the halocline, along with bacterial, algal and faecal residues, where it is acted upon by a rich community of aerobic and anaerobic decomposers. If the organic matter is mineralised or attaches to other interface precipitates such as pyrite, it sinks to the anoxic brine pool bottom, where it is largely preserved and protected from further biodegradation.

The inherently unstable nature of the seafloor in the vicinity of active salt allochthons and brine lakes means it is subject to slumping, especially in the vicinity of brine fed mud volcanoes. In such settings, parts of the carbonate-rich biostrome rim are periodically killed "en masse" as sediment about a brine pool edge collapses, slumps and slides into anoxic pool waters, carrying with it the chemosynthetic community. As well as further elevating levels of preserved organics in the brine pool bottom sediments, this process also creates potential fossil lagerstaette (see later discussion of Burgess Shale). Death of seep communities, even if it survives such catastrophic events, ultimately comes when the supply of seep gases and liquid hydrocarbons is cut off to any single seep.

Hardgrounds, Settings and Stable Isotopes

Associated with the brine-pool communities, and helping form an initial stable seafloor substrate for the colonising seep invertebrates, are calcite-cemented biogenic crusts. These cemented hardgrounds precipitate as a microbial byproduct wherever methane and H_2S are bubbling up in and around brine pool edges and gases are being metabolised by chemosynthetic archea and bacteria (Canet et al. 2006; Fu Chen et al. 2007; Feng et al. 2009). The resulting biogenic calcite crusts have $\delta^{13}C_{PDB}$ values ranging to as low as −53‰, which is characteristic of methanogenic carbon (Fig. 9.60a). Seep sediments retain a group of unsaturated 2,6,10,15,19-pentamethylicosane (PMI_{Δ}) compounds, also produced by methane-oxidizing archaea, with $\delta^{13}C_{PDB}$ values ranging from −107.2 to −115.5‰. In combination the isotope values, textures and biomarkers indicate a combination of bacterially catalysed methane oxidation and sulphate reduction plexi in the crusts.

Fabrics of the two flat sides of methanogenic calcite crusts crust are texturally distinct. The "top" side is composed entirely of microcrystalline calcite, while the bottom is composed entirely of "wormy" carbonate cement that is interpreted as a random, low fidelity replacement of bacteria. Microcrystalline calcite is coated by "wormy" carbonate cement in the interior of the thick crust, and dispersed pyrite framboids appear to be indicators of collaborating colonies of methane-oxidizing archaea and sulphate-reducing bacteria. Fu Chen et al. (2007) propose that the "wormy" carbonate texture, particularly with microcrystalline calcite and pyrite framboids present, is a likely indicator of biologically controlled fabrics produced during methane oxidation and sulphate reduction.

Hypersaline brines and entrained gases escaping and pooling on the Gulf of Mexico seafloor do so either into quiescent brine lakes and pools or as mud chimneys and volcanoes (Fig. 9.61; Joye et al. 2009). Both environments are

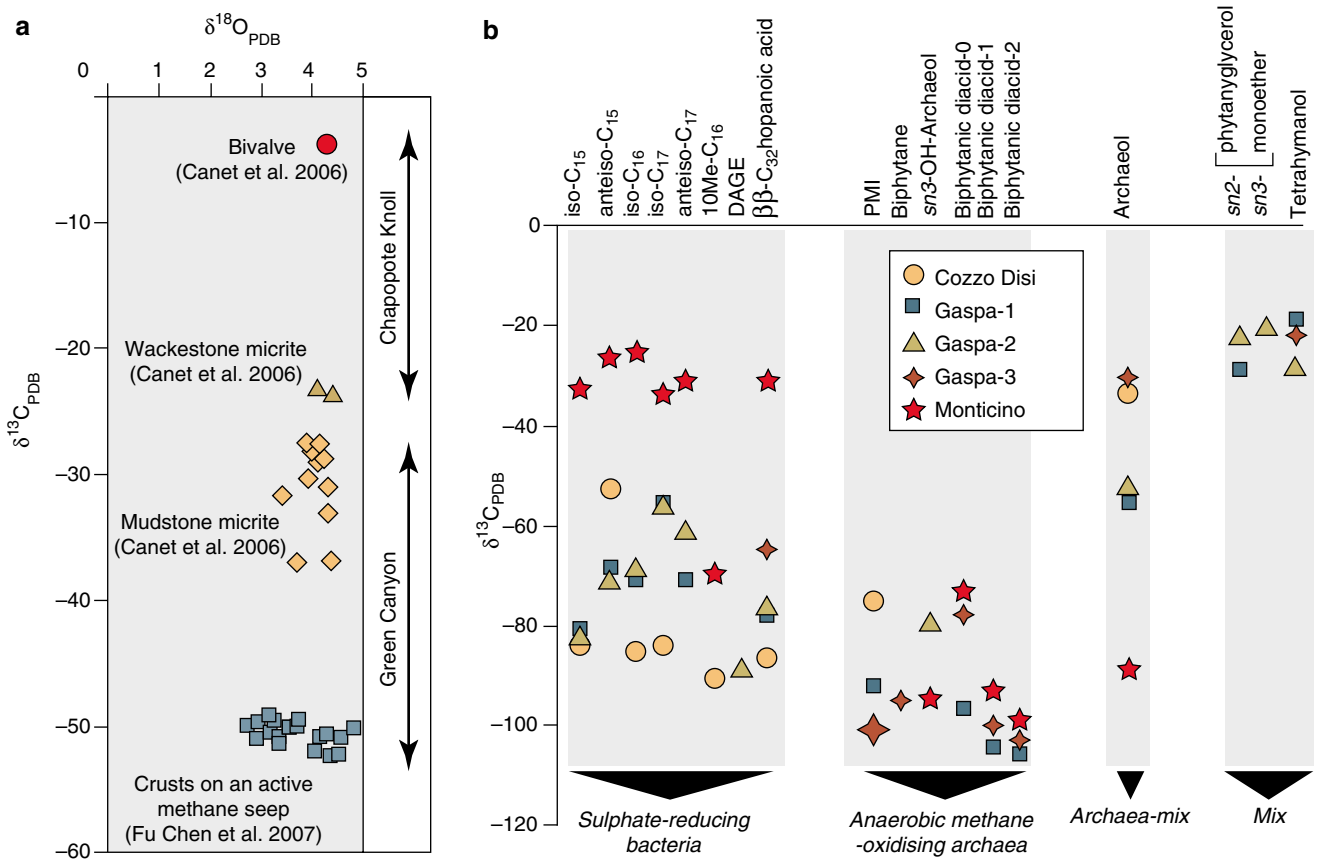

Fig. 9.60 Isotope characteristics of cemented crusts and Messinian carbonates. (**a**) Carbonate-cemented seep crusts at methanogenic brine seep sites in the Gulf of Mexico (Data replotted from Canet et al. 2006; Fu Chen et al. 2007). (**b**) Carbon isotopic composition of selected molecular fossils in authigenic seep carbonates in Messinian sediments from locations in Sicily and the Northern Apennines (After Ziegenbalg et al. 2012). The plot illustrates a shift toward less negative $\delta^{13}C$ values of biomarkers from anaerobic methanotrophic archaea (ANME) to markers from sulphate-reducing bacteria (SRB), archaeol (archaea-mix), and other water column-derived compounds (others). The wide span of $\delta^{13}C$ -archaeol values reflects a mixture from ANME-sourced archaeol and archaeol derived from other, non-methanotrophic archaea. Note that SRB lipids from Monticino cluster at less negative $\delta^{13}C$ values (*red stars*)

anoxic and hypersaline, brine pools are typified by low fluid-flow rates and waters free of suspended sediment, while flow rates in mud volcano chimneys are more vigorous and the waters tend to be more turbulent and carry more suspended load. The sharp salinity transition between hypersaline brine and seawater typifies the water column in both settings, and a higher suspended particle load underscores the more rapid fluid-flow regime of the mud volcano (Fig. 9.61a, f). Brines in both are mildly sulphidic; concentrations of dissolved inorganic carbon are elevated relative to seawater. Microbial abundance is 100 times higher in brines than in the overlying seawater (Fig. 9.61a, f), showing that brine-derived substrates produce high microbial biomass. The brines are gas charged; the dominant dissolved alkane is methane (94–99.9 %) with a stable carbon isotopic composition, ^{13}C, of −62‰.

The brines form via halite dissolution and contain no sulphate. Seawater sulphate diffuses into the brine, and concentrations decrease with depth, reflecting a combination of microbial consumption through sulphate reduction (both sites) and upward advection of sulphate-free brine in a mud volcano (Fig. 9.61b, g). The hydrogen profile in the mud volcano brine is fairly uniform (hundreds of nanomolar), reflecting the potential importance of autotrophic acetogenesis and/or hydrogeno-trophic methanogenesis. In the brine pool, however, hydrogen concentration increases to micromolar levels between ≈25 and 100 cm depth and remains high (≈μ6 M) to 180 cm, promoting acetogenesis. Such high hydrogen concentrations indicate active fermentation and substantial inputs of labile organic matter. Concentrations of dissolved organic carbon (DOC) increases with depth (Fig. 9.61b, g), suggesting a deep-subsurface DOC source (thermogenic?). In the brine pool, extra labile DOC, probably coming from the surrounding chemosynthetic community can further stimulate fermentation (Joye et al. 2009).

Rates of acetate production and levels of sulphate reduction are much higher in brine pools, whereas the mud volcano supports much higher rates of methane production

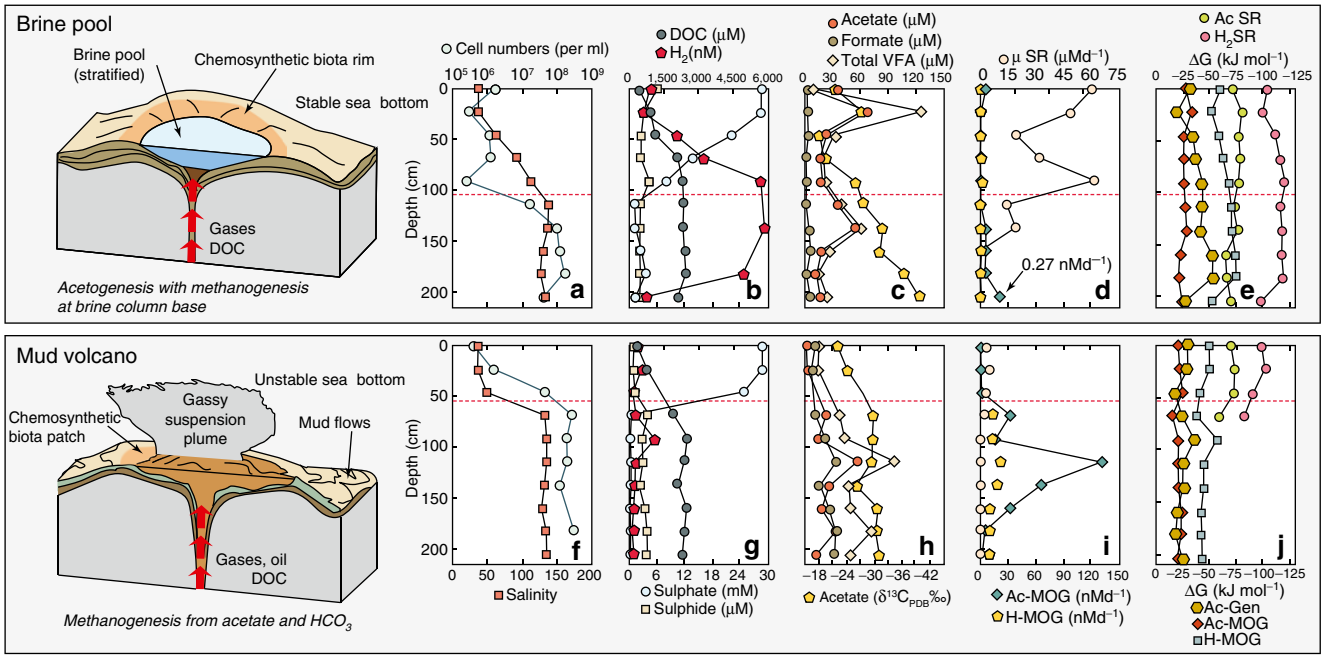

Fig. 9.61 Depth profiles of microbial abundance, geochemistry, activity and energetics in the brine pool halocline. Charting of the profiles as (**a**–**j**) as vertical comparison for brine pool (as **a**–**e**) and mud volcano (**f**–**j**). *Red dashed line* indicates position of the halocline. Microbial abundance (cell count and salinity as **a**, **f**); Hydrogen (H_2), Sulphate (SO_4), Hydrogen sulphide (H_2S) and DOC concentration as (**b**, **g**); VFA concentration and the acetate carbon ^{13}C as (**c**, **h**); Rates of microbial processes for methanogenesis as (**d**, **i**), the rate scale for profile D is 100 times lower than the scale for (**i**); and the Gibbs free energy ΔG yield as (**e**, **j**). Abbreviations; *SR* sulphate reduction, *Ac-MOG* acetate-based methanogenesis, *H-MOG* hydrogen-based methanogenesis, *Ac-SR* acetate-based sulphate reduction, *H-SR* hydrogen-based sulphate reduction, *Ac-Gen* acetatogenesis (After Joye et al. 2009)

(Fig. 9.61d, i). Joye et al. (2009) found no evidence of anaerobic oxidation of methane (AOM), despite high methane fluxes in both settings. It suggests both these systems are leaking methane into the overlying water column. Joye et al. conclude that the contrasting halo-adapted microbial community compositions and metabolisms are linked to differences in dissolved-organic-matter input from the deep subsurface and different fluid advection rates between the two settings.

Ancient Saline Seeps

Isotope character of ancient methanogenic seep carbonates and cements in the Messinian 'Gessoso Solfifera' Formation in Sicily, at Cozzo Disi and Contrada Gaspa, as well as in the northern Apennines from the Monticino locality, were studied by Ziegenbalg et al. 2012 (Fig. 9.60b). Historically, these authigenic carbonates (that include the native sulphur deposits of the Cosi Disi mine) were thought to be a result of microbial degradation of organic compounds in a sulphide-rich evaporitic setting and probably related to bacterial sulphate reduction. But, prior to the Ziegenbalg et al. study, organic indicators of actual mechanisms were not well documented (Fig. 9.60b). $\delta^{13}C_{PDB}$ values are as low as −49‰ and reflect incorporation of carbon derived from the oxidation of methane, which was suggested in earlier isotopic studies to have been linked to bacterial sulphate reduction.

Molecular fossils extracted from the limestones reveal that methane was indeed oxidized in an anaerobic process by archaea and sulphate-reducing bacteria. The observed biomarker patterns resemble those of methane-seep carbonates, such as those in the brine pools on the deep sea floor of the modern Gulf of Mexico. The latter form as a consequence of the anaerobic oxidation of methane (AOM). Supporting this interpretation, AOM-specific, ^{13}C-depleted archaeal biomarkers were identified in the Messinian carbonates, such as tail-to-tail linked pentamethylicosane (PMI; $\delta^{13}C$ −101 to −75‰), as well as compounds derived from sulphate-reducing bacteria (iso- and anteiso-fatty acids; $\delta^{13}C$ as low as −85‰).

Although the biomarker results clearly point to anaerobic oxidation of methane in the formation of the Italian crusts, the compound inventory also reveals distinct differences to patterns found at marine methane-seeps in modern settings (Fig. 9.60b). For example, sn3-hydroxyarchaeol is in some samples the only hydroxyarchaeol present, something usually not found at seeps. Archaeol is less depleted in ^{13}C than PMI at most sites (^{13}C; −55 to −30‰), pointing to the co-occurrence of methanogenic or halophilic archaea with

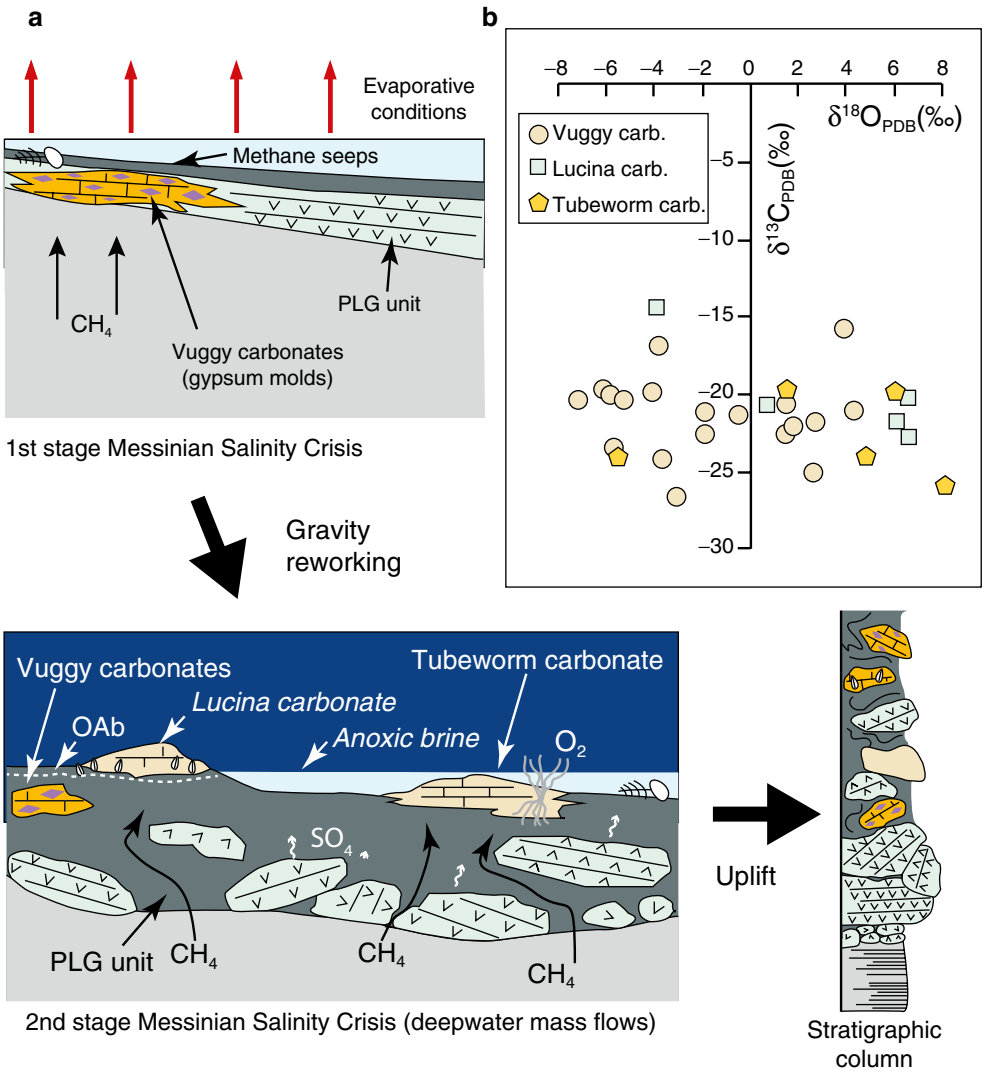

Fig. 9.62 Miocene seep carbonate, Piedmont Basin Italy, (**a**) Evolution of hydrocarbon seeps during the Messinian salinity crisis (MSC). Stage 1: Formation of the vuggy carbonates during the first MSC stage with seeps synchronous with evaporites. Note that the stratigraphic relationship between vuggy carbonates and gypsum are not longer preserved in Stage 2) Formation of tubeworm and Lucina carbonates occurred in the second MSC stage; *OAb* oxic-anoxic boundary. *Vertical column* on *right* shows the final stratigraphic column after the various seep carbonates have been involved in gravitationally driven tectonic reworking. (**b**) Stable isotope plot showing distinctive plotfield of each of the 3 seep carbonates (After Natalicchio et al. 2013)

archaea involved in AOM. In addition; (1) The presence of calcite pseudomorphs after lenticular gypsum, (2) ^{18}O-enrichment in carbonates, and (3) the biomarkers O-phytanyl-O-sesterterpanyl glycerolether (extended archaeol), tetrahymanol, and possibly phytanylglycerol monoethers as well as non-isoprenoidal macrocyclic glycerol diethers, confirm that carbonate formation took place under evaporitic conditions in the overlying brine columns (Fig. 9.62a). AOM has previously been shown to be inhibited in some brine pools on the modern seafloor, but the work of Ziegenbalg et al. 2012 demonstrate that AOM functions in solar-driven hypersaline environments as well as on the deep sea floor.

The formation of seep carbonates at first beneath a hypersaline sea, during precipitation of the Messinian evaporites of Italy, was confirmed in a geological study of rock textures and stable isotope signatures in transported limestone blocks in Messinian mass transport complexes in the Tertiary Piedmont Basin, NW Italy (Fig. 9.62; Natalicchio et al. 2013). Seep carbonates are preserved as blocks within a chaotic unit emplaced during drawdown tied to the Messinian salinity crisis (Fig. 9.62a, b). All these carbonates show characteristic negative $\delta^{13}C_{PDB}$ values (from −27 to −15‰), defining a stable isotope plot field that overlaps seep micrites in the modern Gulf of Mexico. It indicates the involvement of hydrocarbon-rich fluids in the genesis of the Italian seep carbonates (Fig. 9.62c compared with 9.60a). Three types of carbonates are recognised: (i) vuggy carbonates; (ii) *Lucina* carbonates; and (iii) tubeworm carbonates (Fig. 9.62a, b).

Vuggy carbonates blocks are characterised by carbonate pseudomorphs after gypsum and probably formed during the first stage of the salinity crisis. They are the product of a complex diagenesis, influenced by both hypersalinity and cross seepage of hydrocarbon-rich fluids. These rocks lack chemosymbiotic biotal assemblages, reflecting their

formation under extreme environmental conditions of the Messinan salinity crisis, inhospitable for most metazoans. In contrast, *Lucina* and tubeworm carbonates are characterised by chemosymbiotic macrofauna, represented respectively by *Lucina* bivalves and putative vestimentiferan tubeworms. These carbonates indicate the escape of brines into lower salinity likely-normal marine waters in the overlying deep-water column.

The latter biotal assemblage has not been widely documented in ancient seep carbonates and prior to the work of Natalicchio et al. (2013) had not been reported from the Messinian sediments of the Piedmont Basin. Both *Lucina* and tubeworm carbonates are interpreted as the product of hydrocarbon seepage during the second stage of the salinity crisis related to the gravity-induced collapse and mass transport of olistostrome blocks from earlier formed gypsum saltern (Fig. 9.62b; see Chap. 5, especially Fig. 5.53 associated text for discussion of relevant literature). These two types of seep carbonates formed under less severe conditions than the vuggy carbonates, allowing the survival of seep-dwelling metazoans. During this second stage of the Messinian Salinity Crisis, the seafloor was probably characterised by an irregular topography and a thin bottom layer of dense anoxic brines, produced by the dissolution of evaporites, dominantly gypsum.

It seems that the Miocene vestimentiferan worms were able to thrive on carbonate cemented seep that were morphologic highs, with the posterior part of worm tubes located just below the oxic–anoxic interface, but the anterior part projecting into oxic water, as in the Gulf of Mexico today. On the adjacent *Lucina* seeps, not only were *Lucina* bivalves oxygen-dependent, but many specimens reveal boreholes in their shells, reflecting drilling predation by an oxygen-dependent set of marine borers (Taylor and Glover 2009). Unlike the tubeworms, the infaunal *Lucina* bivalves were only able to live at seeps positions with an overlying oxic water column, much like *Bathymodiolus childressi* in modern Gulf of Mexico brine lakes and seeps. Subsequent and ongoing gravity-driven transport brecciated the various seep-limestone blocks, so that currently they outcrop at various stratigraphic levels in the Messinian transport complex (lower right of Fig. 9.62a).

Outcropping in the Canadian Northwest Territories are Cretaceous counterparts to Gulf of Mexico methanogenic brine-seeps (Savard et al. 1996). Ancient methane-rich mud mounds grew atop growth faults activated by salt diapirism in the Sverdrup Basin. Crusts still preserve relic splays and isopachous layers of fine, acicular aragonite, and large botryoids of low-magnesium calcite, showing spectacular entanglement of former fibrous calcite and aragonite cements, as occurs in seep crusts today in parts of the Gulf of Mexico. These ancient hardgrounds also show the characteristic ^{13}C depleted values of methanogenic cements.

A similar set of brine-pool seafloor-seep deposits typify even older, locally-cemented and fossil-rich lenses of Cambrian carbonates hosted in the basinal Burgess Shale, near the Cathedral escarpment in British Columbia (Fig. 6.93; Johnston et al. 2009). The Middle Cambrian Burgess Shale Formation, is remarkable for its preservation of non-biomineralized fossils. It is exposed in an outcrop belt that extends some 60 km from the type area around Field, British Columbia, to a mountain known as The Monarch on the eastern edge of Kootenay National Park. World famous Cambrian soft-body fossils assemblages (including forms such as *Hallucigenia* a precursor to the velvet worms) are known from several localities in the Burgess Shale. For more than three decades, the Burgess Shale fossil assemblages have been interpreted as a "normal fore-reef faunal complex." This unusual soft tissue biotal assemblage is used to illustrate the Cambrian explosion and the associated plethora of soft-bodied Cambrian life forms, that are long since extinct (Collins et al. 1983).

These sites invariably occur in close proximity (≈50 m according to Johnston et al. 2009) to the Cathedral Escarpment, a steeply dipping surface marking the headwall of the gravity-collapsed margin of the platformal carbonates of the Cathedral Formation, against which the Burgess Shale accumulated. The trend of the Cathedral Escarpment coincides with a fault-controlled, linear, palaeotopographic feature known as the Kicking Horse Rim. Faults along this structure were probably important conduits for dolomitizing and mineralizing brines rising from deeper saline strata along the platform margin during the Middle Cambrian, even as the Burgess Shales were accumulating (Powell et al. 2006). The altered strata that precipitated from the fault-focused magnesian brines have now been metamorphosed to lower greenschist facies and currently host clinochlore and minor double-terminated quartz euhedra. Based upon the bulk-rock composition, the protolith of these seep-related magnesian-rich strata is inferred to have been composed of Mg smectite, with lesser kaolinite, and minor brucite.

Epiphyton-rich carbonate megablocks occur within the basinal strata adjacent to the Cathedral escarpment. Previously these blocks were interpreted as olistoliths and were thought to have spalled off the Cathedral Escarpment. However, the biota and texture in these "blocks" are unlike the peritidal strata that comprising the adjacent Cathedral platform margin. More likely they are part of local deep-water carbonate mud mound chemosynthetic seep association that grew in the basin near the faulted Escarpment face (Johnston et al. 2009). Evidence for early brines crossflows and surface brine lakes on the deep seafloor includes the aforementioned lenses of dark, magnesium-rich clinochlore (>30 wt% MgO vs ≈2 % in background shales) within the Burgess Shale. The clinochlore distribution defines an alteration halo best developed in proximity to the escarpment wall.

These clinochlores are interpreted as precipitates from seafloor brine seeps, analogous to those currently forming at the foot of the Florida Escarpment and on the distal shelf and slope of the northern Gulf of Mexico. Similar magnesian brucite/brunnerite alteration haloes about brine-fed faults occur along faults that sole out in rauhwacke levels in Neoproterozoic outcrops in the Flinders Ranges and the Mesoproterozoic carbonates of the Mcarthur Basin, Australia (Chaps. 7 and 15).

Like modern brine seeps focused along the base of the Florida escarpment, fault-fed brines likely formed standing pools on the Cambrian deep seafloor along the foot of the Cathedral fault escarpment. There Cambrian brine lakes hosted abundant chemosynthetic organisms in a narrow biotal fringe around brine pool peripheries, but not within the highly saline and anoxic waters of the brine pools (Fig. 9.63). Sponges, priapulid worms, hyoliths, linguliform brachiopods and trilobites predominate in this fringe facies. Shales only a few metres basinward from the pools are interpreted as hemipelagic muds, nearly barren of animal fossils. Increased biologic productivity localized at the seeps would account for the patchy distribution of fossils in the Burgess Shale in a narrow zone close to the Escarpment. The discovery of brine seep deposits and associated fringing communities at this well known Burgess Shale locality shows that at least some assemblages in the Burgess Shale were preserved within their habitat and were part of a deep seafloor community supported by chemosynthesis. Instability on the brine pool margins, as we see in the Gulf of Mexico seafloor today, probably aided rapid pickling in waters of the brine lake and facilitated the preservation of soft tissue in a Cambrian lagerstaette.

If the evaporite and saline chemosynthetic indicators that made up of various brine pool/seep systems are not recognised in ancient counterparts, then, once the underlying or adjacent allochthonous salt sheets have dissolved or moved on, the evaporite hydrology that focused the accumulation of organic-rich pyritic brine pool sediments will become an enigma (Warren 2000b). In the Phanerozoic, any remaining organic constituents will be made up primarily of marine plankton, a benthic marine biota and bacteria from a normal marine setting. Sediments above and below the pyritic pellicular laminites and possible lagerstaette are also made up of normal marine deepwater deposits. There will be little geochemical evidence to show that these organic-rich pyritic sediments were preserved in a hypersaline deep marine environment.

Evidence of the significance of flowing evaporites in creating such a sequence will only come from sedimentological and structural analysis of core or outcrop from below and adjacent to the laminites, and the recognition of halokinetic breccias, salt welds, chemosynthetic biostromes and marine-cemented hardgrounds within a deeper water marine sediment matrix.

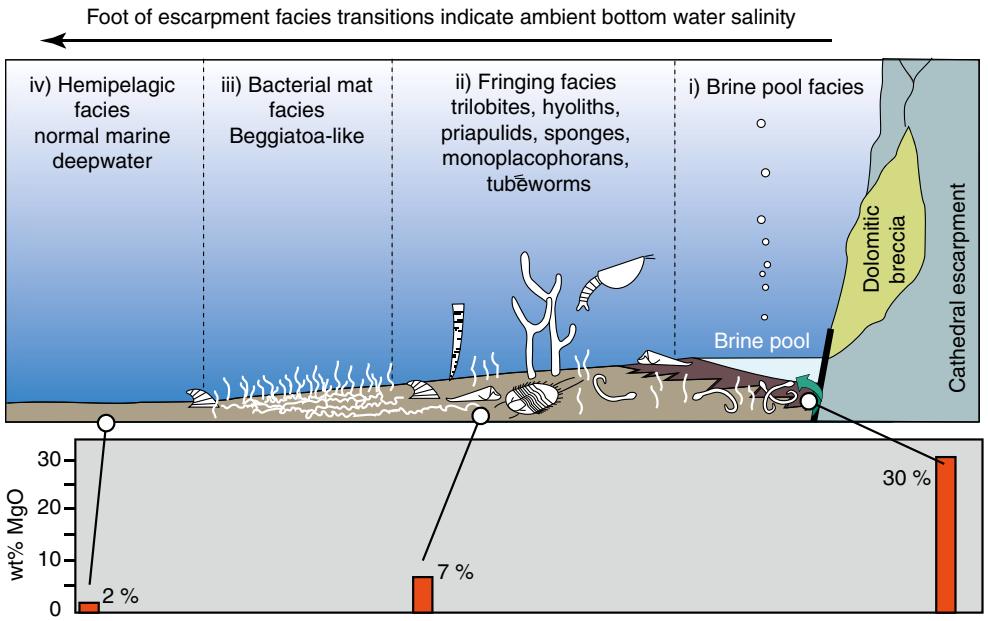

Fig. 9.63 Salinity-related facies transitions in the Burgess Shale brine pools at Monarch Assiniboine and located at the foot of the Cathedral Escarpment, British Columbia: (*i*) brine pool facies; (*ii*) fringing fauna facies: examples of fauna shown include trilobites, hyoliths, priapulids, monoplacophorans, sponges, and pogonophoran (?) worm tube Byronia. White filaments mark inferred presence of sulphur-oxidizing bacteria like modern *Beggiatoa*; (*iii*) bacterial mat facies with rare fauna; (*iv*) hemipelagic facies. To right is Cathedral Escarpment with it characteristic dolomitized breccia; brines rising along the fault scarp indicated by green arrow. Lower part of figure plots typical MgO values for facies (*i*), (*ii*) and (*iv*) of 30, 7 and 2 wt%, respectively (After Johnston et al. 2009)

Life in the Saline Subsurface

It is becoming increasingly obvious that chemolithotrophic microbial communities influence diagenesis to depths well below the eogenetic realm (Fry et al. 2008; Reith 2011; Parkes et al. 2011). Some microbial members of the seep communities have chemolithotrophic metabolisms that can continue to be active in H_2S and methane-rich pore waters into biozones possibly extending a kilometre or two below the surface. Some predict the extent of viable chemolithotropes, possibly utilising hydrogen, could be deep as 15 km (Hazen and Schiffries 2013). But such extreme biozone depths are not yet sampled and beyond 500 m depth no reliable cultures have been recovered (due to possible sample contamination problems, related to nonsterile drilling fluids or access to samples by contaminated mine waters).

As any organic matter in evaporitic sediments is buried it becomes hotter and this, along with increasing pressure, will ultimately kill off most of the chemosynthetic biota. Pore water can also be anomalously heated locally by intrusions and crossflows of fault-focused hydrothermal fluids. Organics, both conventional source rock precursors and chemolithotrophic debris, are altered in a number of ways in the subsurface burial environment, mostly tied to rates of temperature increase and the presence or absence of oxygen and other gases in the pore fluids (Fig. 9.64).

Subsurface interfaces (mixing zones) between hypersaline water, typically with reducing dysaerobic to anaerobic chemistries, and less saline waters, typically with more oxidised and oxygenated chemistries, create redox fronts in aquifers adjacent to subsurface evaporites. In hypogene and outcropping aquifers the interface is often defined by a colour transition from green (reduced) to red (oxidising) forms of iron in the sediment matrix. Less saline waters tend to dissolve evaporites and create secondary porosity (mostly vuggy and collapse fracture), while at the same time chloride or sulphate rich ions pass into solution.

Sulphur occurs in variety of oxidation states in the subsurface with the three oxidation states of −2 (sulphide and reduced organic sulphur), 0 (elemental sulphur) and +6 (sulphate) being the most significant. Where the sulphate in solution interacts with the organics in the vicinity of the redox interface, H_2S is generated via sulphate reduction, either biogenic or thermochemical. H_2S in solution creates acids that can dissolve adjacent carbonate matrix, and then reprecipitate the bicarbonate as deep phreatic blocky calcite cements, along with pyrite and other metals on the reducing side of the redox interface (Fig. 9.64). Much of the H_2S that is found in elevated amounts in an evaporitic basin is bacterially or thermochemically generated via sulphate reduction from sulphate carried by brine and derived from dissolving sulphate beds. Additional H_2S in an evaporite basin can be generated from local magmatic and biogenic sources.

Any association of dissolved sulphate and hydrocarbons (or organic matter) is thermodynamically unstable in all diagenetic settings and the chemical response is sulphate reduction (Machel 2001). Sulphate reduction

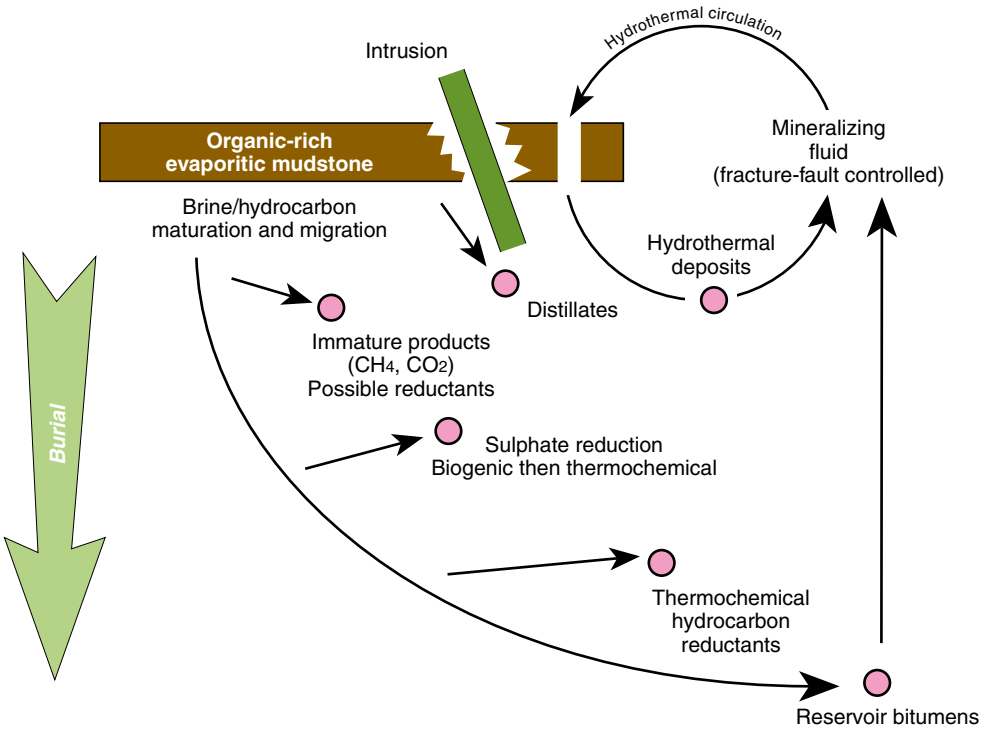

Fig. 9.64 The role of organic-rich evaporitic mudstones in burial diagenesis. The mudstones can act as a source of hydrocarbons and as a reductant for metals

reactions can be bacterially mediated through the activities of sulphate-reducing bacteria (bacterial sulphate reduction-BSR) or inorganically mediated under conditions of increased temperature and pressure (thermochemical sulphate reduction – TSR). Both scenarios require the presence of organic matter, or its more evolved subsurface equivalent in the form of hydrocarbons (oil or gas), and result in similar but not identical carbonate cements, mostly blocky calcite or occasional mesogenetic dolomite. The bacterially-mediated sulphate reduction system operates at lower burial temperatures <110 °C, mostly <60–80 °C, in a temperature range equivalent to vitrinite reflectances R_o of 0.2–0.3. Thermochemical sulphate reduction processes require temperatures of more 120 °C and R_o values ranging from 1.0 to 4.0 (Fig. 9.65). Both these processes, BSR and TSR are very important in the realms of economic geology as the H_2S produced can react with metal-bearing fluids to precipitate metalliferous sulphides (Fig. 9.64; and ore deposits as discussed in Chaps. 15 and 16).

Bacterial Sulphate Reduction (BSR)

BSR takes place in surface and nearsurface environments where sulphate-reducing bacteria utilise dissolved sulphate and organics/hydrocarbons to produce H_2S (Fig. 9.65a, c; Trudinger et al. 1985; Machel 1987, 2001; Hill 1995; Riciputi et al. 1996; Aref 1998b). So far we have discussed bacterial sulphate reducers in the context of stratified brine columns, where they flourish in anoxic cool waters beneath the halocline, or in benthic cyanobacterial mats where they occupy the low anoxic portions of the mat. In this section we will look at the nature of BSR in the extended subsurface, where bacteria inhabit warmer fluids in pores and fractures, either in sediments entering the burial environment or in sediments undergoing telogenesis as they are uplifted and re-enter cooler nearsurface settings. When the term bacterial sulphate reducer is used it now known to be used phylogenetically as there are both bacterial and archaeal members of the grouping (220 species of 60 genera), some of whom inhabit bottom brines and oilfield waters with salinities in excess of 200 ‰.

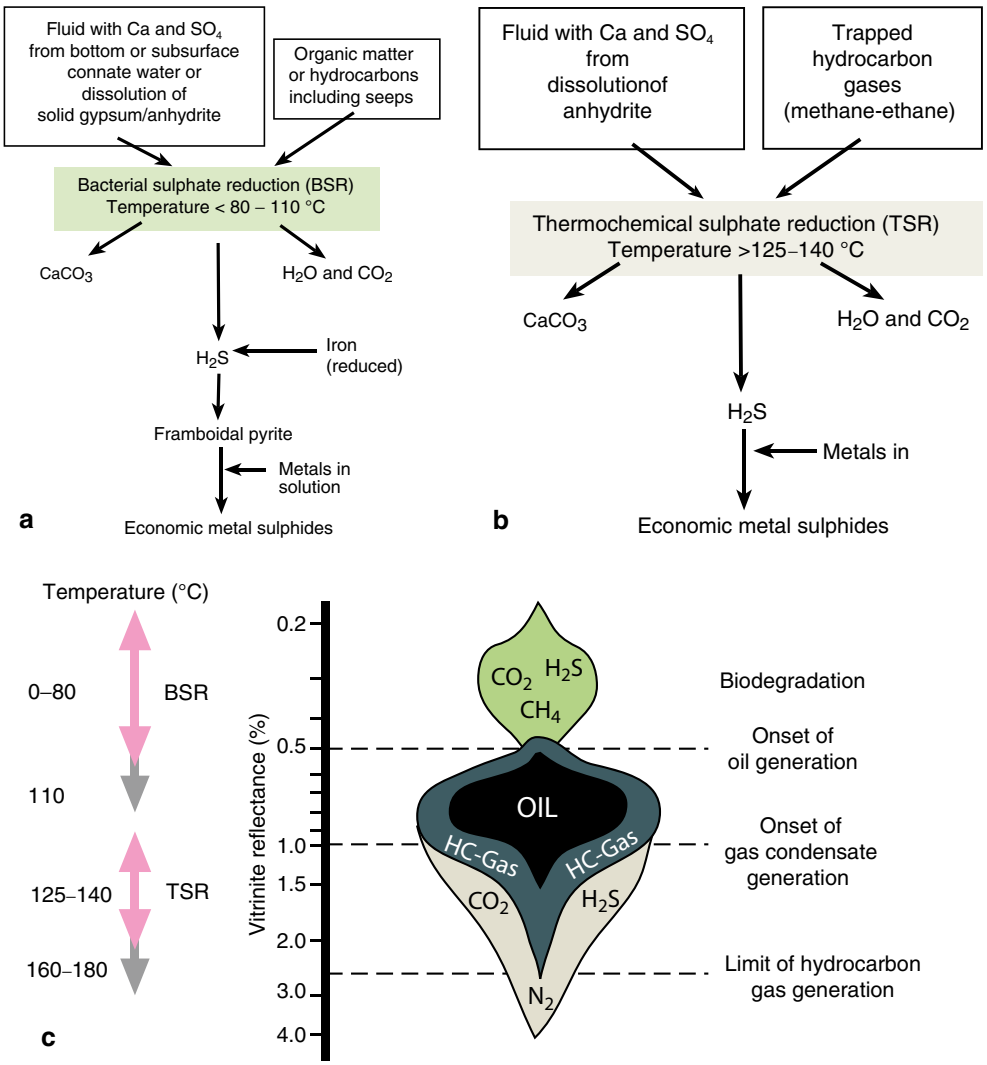

Fig. 9.65 Chemical pathways and thermal regimes associated with sulphate reduction. (**a**) Bacterial sulphate reduction – BSR. (**b**) Thermochemical sulphate reduction – TSR. (**c**) Thermal regime and hydrocarbon generation stages tied to characteristic values of vitrinite reflectance (In part after Machel 2001; Warren 2000b) Note that there is a lack of biogenically produced pyrite framboids during thermochemical sulphate reduction

Bacterial sulphate reduction occurs at temperatures typically <80 °C, although hyperthermophilic archaeal sulphate-reducers (*Archaeoglobus* sp.) can grow around hydrothermal vents on the deep ocean floor at temperatures up to 114 °C. In regions with normal geothermal gradients the temperature range <60–80 °C corresponds to burial depths from the surface down to 2,000–2,500 m. Tentative identifications of sulphate reducers, active in formation waters of sandstone reservoirs in the Samotlor high-temperature oil reservoir (Western Siberia, Russia) and collected from depths of 2,500 m, were documented by Bonch-Osmolovskaya et al. (2003). BSR processes and bacterial sulphate reducers are widespread in many anoxic saline subsurface sediments and not directly related to evaporite beds. But the discussion in this section concentrates on those types of sulphate reduction that are commonplace in regions of dissolving evaporites and associated saline pore waters. Such systems tend to form bioepigenetic limestones and cements with textures and isotopic signatures typically indicating an evaporite precursor or association.

Bacterial sulphate reduction is usually expressed by the equation;

$$Ca^{2+} + 2SO_4^{\ 2} + 2CH_4 + 2H^+ \rightarrow 2H_2S + CaCO_3 + 3H_2O + CO_2$$

It is the metabolic process set used by a group of prokaryotes to obtain energy by oxidizing organic compounds or molecular hydrogen (H_2) while reducing sulphate (SO_4^{2-}) to hydrogen sulphide (H_2S). In a sense, these organisms "breathe" sulphate rather than oxygen, in a form of anaerobic respiration used for the last 3.5 billion years. At pH < 6–7 the produced H_2S is undissociated; at pH > 6–7, H_2S dissociates so that H_2S —> $H^+ + HS^-$ (Hill 1995). In this equation, SO_4 indicates dissolved sulphate, which is derived either from shallow phreatic refluxing brine/seawater or from dissolving sulphate evaporites such as gypsum, glauberite, or anhydrite. $CaCO_3$ represents bioepigenetic limestone products, which typically precipitate as cements or replacements of precursor evaporite sulphates. CH_4 represents a host of possible organic compounds or hydrocarbons, mostly organic acids and other products of aerobic or fermentative biodegradation.

The initial S–O bond rupture during the BSR commonly involves a kinetic fractionation of about −15 to −30‰ in the $\delta^{34}S$ values depending on the specific types of bacteria involved and their growth rates (Table 9.11). Subsequent sulphur isotope fractionation can be even larger, if intermediate compounds, such as thiosulphate or polysulphides, are produced. Bacterial reduction of these compounds involves additional negative fractionations, and disproportioning of enrichment of the resulting sulphide in ^{32}S. In this way, composite negative sulphur fractionations of up to −65‰ can be obtained during BSR (Machel et al. 1995).

Table 9.11 Summary of sulphur isotope fractionations of inorganic compounds

Isotope fractionation	Process	$\delta^{34}S_{CDT}$ (‰)
SO_4^{2-} --> S^{2-}	Bacterial sulphate reduction (BSR)	−15 to −65‰
	Thermochemical sulphate reduction (TSR)	−20‰ at 100 °C
		−15‰ at 150 °C
		−10‰ at 200 °C
Maturation		< −2‰
S^2 --> S^o	Oxygen	−5 to −7.5‰
	Sulphate	±0 to −3‰
	Hydrocarbons	?
	Anaerobic bacteria	±0 to +2‰
	Aerobic bacteria	±0 to −18‰
S^o --> SO_4^{2-}		±0‰

After Machel et al. 1995

There are two well established genera of sulphate-reducing bacteria, *Desulphovibrio* and *Desulphotomaculum*, they seem to be quite unrelated to each other and their relation to other bacterial groups is also obscure. Members of the better known genus, *Desulphovibrio*, are mesophilic (prefer a moderate temperature range) and can be moderately halophilic (Fig. 9.19b); at the present time the genus is thought to contain seven species. *Desulphotomaculum* species are somewhat more difficult to isolate and purify. They are characterised by spore formation and are sometimes thermophilic; only one moderately halophilic strain has been reported in the five recognised *Desulphotomaculum* species (Postgate 1984).

Mesophilic isolates of the genus *Desulphovibrio* will typically not grow above 45 °C. Thermophilic isolates of the *Desulphotomaculum* genus have been grown at temperatures as high as 70 °C – the most common species of thermophile being *Desulphotomaculum nigrificans*. However, Rozanova and Khudyakova (1974) isolated an apparent *Desulphovibrio sp*. having a maximum growth temperature of 85 °C, while Zobell (1957) claimed that he had isolated viable sulphate-reducing bacteria from an oil-bearing reservoir where growth was occurring at 104 °C under a pressure of 1,000 atm. Both these higher temperature reports were not biologically documented under absolutely sterile collection conditions. The upper temperature limit for subsurface biogenic sulphate reduction is usually considered to be 80–85 °C (Trudinger et al. 1985), a reasonable estimate for documented sulphate reducers in most evaporitic and shallow subsurface settings. It means the most vigorous bacteriogenic reduction (>50 °C) typically extends from any nutrient-rich brine column oxic-anoxic interface down to redox fronts at burial depths of a kilometre or so.

Under suitably pressurized deep-sea seep conditions, and perhaps some subsurface conditions, biogenic sulphate

reduction can extend into higher temperature regions. Work in the anhydritic deep-sea hydrothermal vent sediments of the Guaymas Basin in the Gulf of California has revealed biologically mediated sulphate reduction by hyperthermophilic Archaea at temperatures up to 110 °C, with an optimal rate at 103–106 °C (Huber et al. 1989; Jørgensen et al. 1992). But such hyperthermophilic sulphate reducers are not recovered from formation brines of most subsurface hydrocarbon-rich settings, otherwise sweet (non H_2S) oils would be a rare style of oil occurrence at temperatures less than 110 °C (Machel 2001).

Bacterial sulphate reduction in evaporitic settings typically occurs near an aerobic/anaerobic interface. It may be a density interface in a layered brine column, it may be at the aerobic-anaerobic interface just below the sediment surface, it may be at an oil/water contact at greater depths, or it may be a subsurface diffusion or mixing zone, focused by faults, fractures and bedding boundaries. Although most geologists think of the BSR communities as anaerobes, work on microbial mats has shown some members of the phylogenetic SRB can, in fact, tolerate and even respire oxygen (Baumgartner et al. 2006). Investigations of modern microbial mat systems have demonstrated that some members of the SRB are both abundant and active in the oxic zones of microbial mats (Fig. 9.20).

Additionally, SRB have been found to be highly active in the lithified zones of microbial mats, suggesting a connection between sulphate reduction and mat lithification. For example, much of the micrite precipitated as syndepositional cement in marine stromatolite laminae in metre-high structures in tidal channels of Lee Stocking Island in the Bahamas, are a byproduct of bacterial sulphate reduction. This BSR-induced precipitation occurs within millimetres of normally oxygenated seawater (Visscher et al. 2000). Likewise BSR controls the precipitation of microbial carbonate in mm-layered mats in a modern hypersaline lake on Eleuthera Island in the Bahamas and primary dolomites in Brazilian coastal salinas (Dupraz et al. 2004, 2009).

At broader subsurface scales, anoxic interfaces suitable for BSR tend to form near the dissolving margins (top or bottom) of shallow salt beds and allochthons, or within diapir caps, or near fractures and other breaches in dissolving calcium sulphate beds. These are all sulphate-rich environments where focused crossflow and mixing occurs between reduced basinal waters and more oxic waters. Wherever hydrocarbons are involved, most sulphate-reducers cannot directly digest long chain n-alkanes (paraffins) as nutrients. Instead, they depend on metabolic residues of hydrocarbon biodegradation, such as the various organic acids produced by aerobic biodegradation of oil (Davis and Kirkland 1970; Machel 1987, 1995; Lock et al. 2004). Thus, sulphate reducers in the deeper subsurface have been historically thought of anaerobes, which depend on aerobic bacteria to create suitably biodegraded hydrocarbon substrates. Sulphate-reducing bacteria then oxidize the biodegraded hydrocarbons to HCO_3 and bitumen residues, while simultaneously reducing the dissolved sulphate to H_2S. Where methane is the main carbon source, all the methane is oxidized into HCO_3, and no bitumen residue forms (Machel 1989). Production of H_2S favours the precipitation of carbonate cement or the replacement of dissolving sulphates by calcite. H_2S may escape into the atmosphere or come into contact with dissolved oxygen in an aquifer or a diffusion zone, where it is oxidized into elemental sulphur, as in most shallow sulphur deposits (Chap. 11; Berner 1980).

Sulphate-reducing bacteria are responsible for the laminar vuggy bioepigenetic limestones that make up the caprocks of the Gulf Coast and Zechstein diapirs, the Castile Formation mounds in the Gypsum Plain, Culberson County, West Texas, the Messinian Gessoso Solfifera of Sicily, as well as numerous other calcitic limestones that replace sulphate evaporites worldwide (Kyle and Posey 1991; Peckmann et al. 1999). Subsequent weathering of the encasing gypsum means indurated and less soluble calcitic buttes tend form irregular steep-sided hillocks, as in the Castiles rising 3–30 m above the Gypsum Plain of West Texas (Kirkland and Evans 1980; Stafford et al. 2008a, b). Castile calcite masses did not precipitate at the surface, they originally formed hypogenically, some hundreds of metres below the surface (Fig. 7.63a).

The bacterial/hydrocarbon association of these bioepigenetic limestones is evidenced by their negative $\delta^{13}C$ and $\delta^{34}S$ signatures (Fig. 9.66a, b). Carbon in calcite making up a Castile is sourced by the breakdown of organic matter or hydrocarbons and does not come from dissolution of marine limestone (Fig. 9.66c lists typical $\delta^{13}C$ values from various organic sources). Sulphate-replacing calcites formed by BSR are typically ^{13}C depleted, and this isotopic signature, along with their more negative sulphur isotope signature (compared to marine sulphates), is used to characterise BSR-induced calcites worldwide (Figs. 9.66 and 9.70).

Widespread bioepigenetic limestone buttes or castiles today outcrop in areas of exhumed Miocene evaporites along the margin of the Red Sea (Aref 1998b; Pierre and Rouchy 1988). There, carbonate masses are vuggy and form irregularly stratiform limestones within or adjacent to capping beds of sulphate evaporites. As in the Castiles of West Texas and the diapir caprocks of the Gulf Coast, the vuggy Red Sea buttes are stained by hydrocarbon residues and smell of hydrocarbons when broken with a hammer. Associated natural sulphur (S_2) is usually yellow, but may be brown to black due to bitumen staining. The carbonate masses replacing the gypsum or anhydrite are made up of varying amounts of aragonite, calcite, or dolomite. $\delta^{13}C_{PDB}$ mean values for carbonate minerals typical of organic-derived signatures and

ranging from −3.3 to −31.3‰ (Fig. 9.66a). There is some overlap, but most are heavier than the $\delta^{13}C$ values of nearby crude oils (−28.1 to −29.3‰). Oxygen values from the Red Sea castiles define two groups. One is clustered around 0‰ and is dominated by aragonitic mineralogies with lesser calcite and is thought to indicate BSR replacement of gypsum that occurred soon after deposition. The other group is mostly calcite and dolomite, its $\delta^{18}O_{PDB}$ values range from −6 to −11‰ and is interpreted as a later meteoric-influenced BSR, occurring during halokinetic uplift and telogenetic flushing of rising diaper caps by fresher groundwaters. This stage is likely akin to that forming the patchy BSR limestones in meteoric-overprinted caprocks atop coastal plain diapirs in the Gulf of Mexico.

The activities of the BSR biota metabolising hydrocarbons and gypsum in the Red Sea buttes is characterised by a presence of a community of sulphate-reducing bacteria thriving on carbon substrates contained in petroleum. Specifically, a set of nonisoprenoidal macrocyclic glycerol diethers (McGDs), tentatively ascribe to sulphate-reducing bacteria, have a stable carbon isotope composition close to that of petroleum n-alkanes associated with the resulting carbonates (Aloisi et al. 2013). The presence of archaeol that is ^{13}C-enriched, relative to bacterial lipids, suggests that Archaea are present but either indirectly involved or not involved in the transformation of petroleum-derived carbon. The lipid biomarker pattern is distinct from those observed in settings where sulphate reduction is coupled to the

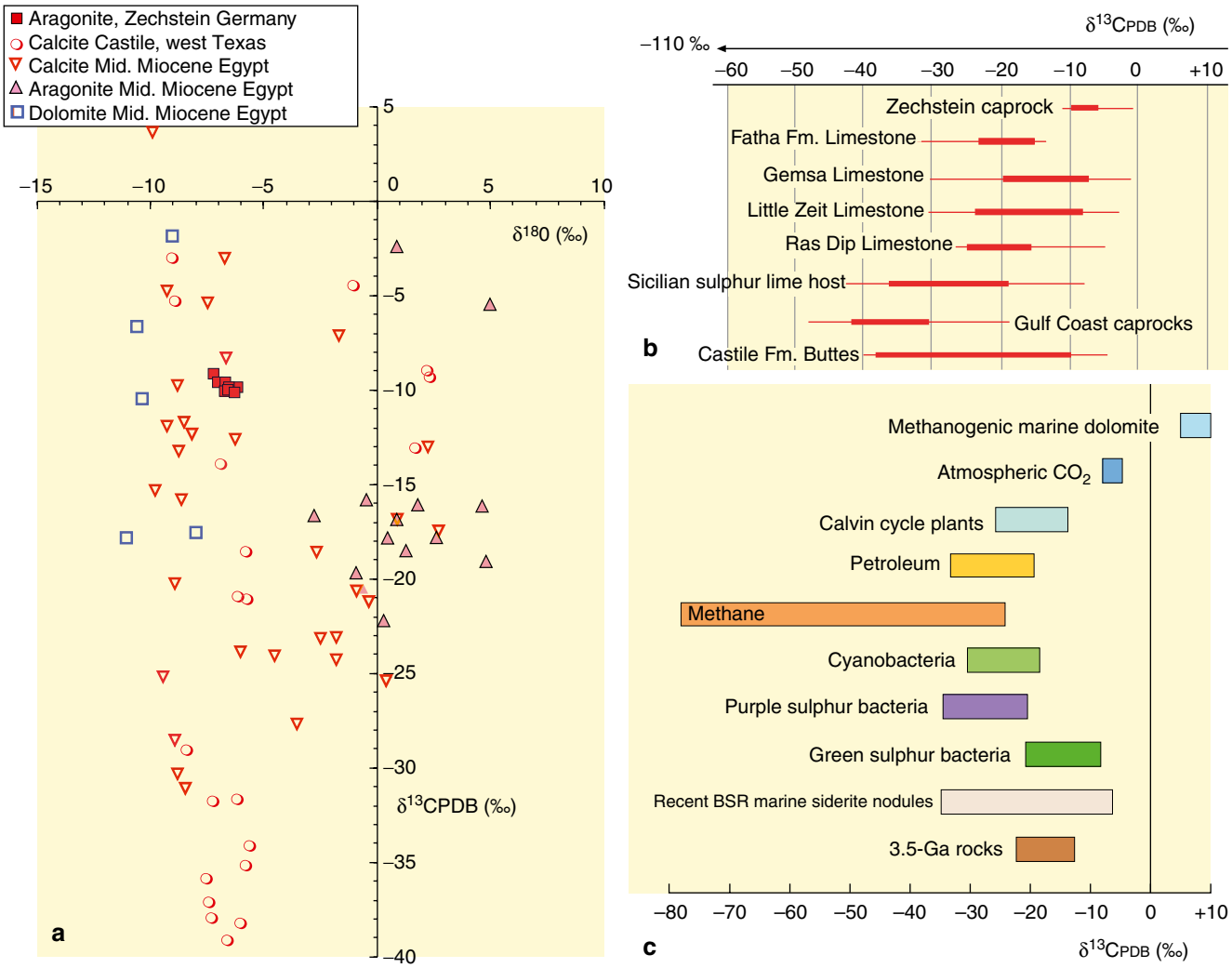

Fig. 9.66 Stable isotope signatures of bacterial calcite. (**a**) Outcropping samples from calcite buttes of the Castile Formation, Delaware Basin, West Texas, various Middle Miocene outcrops along the Red Sea coast and aragonite inclusions in gypsum of Zechstein, Germany. (**b**) Bioepigenetic carbonates from Miocene of Gulf of Suez, caprocks in the Gulf of Mexico, sulphur deposits of Sicily and Castile Fm. buttes in West Texas. Thin line indicates range, thick line plots standard deviation about mean (Both figures replotted from data in Aref 1998b; Jassim et al. 1999; Kirkland and Evans 1976; Peckmann et al. 1999; Pierre and Rouchy 1988 and references therein). (**c**) Typical $\delta^{13}C$ ranges of various microbial and higher plant materials and products

anaerobic oxidation of methane. The results suggest that petroleum migration has triggered the microbial transformation of gypsum into carbonates in the Gulf of Suez, independent of archaeal metabolism.

In the 1st Eocene reservoir interval of the giant Wafra field, Partitioned Zone, Saudi Arabia and Kuwait, is replete with bacterial sulphate reduction calcite cements and associated oil biodegradation (Wani and Al-Kabli 2007). The bacteriogenic cements occur mostly in vugs left by anhydrite dissolution and have covariant plot fields that overlap those of similar BSR cements in the Castiles of West Texas (Fig. 9.67a, b compare with Fig. 9.66a; Saller et al. 2014). Such calcites in Wafra field formed late in the diagenetic evolution, in a zone of mixing between rising oilfield brines and sluggish descending meteoric waters (Fig. 9.67b, c). Brine flows in both directions and is focused by the under-

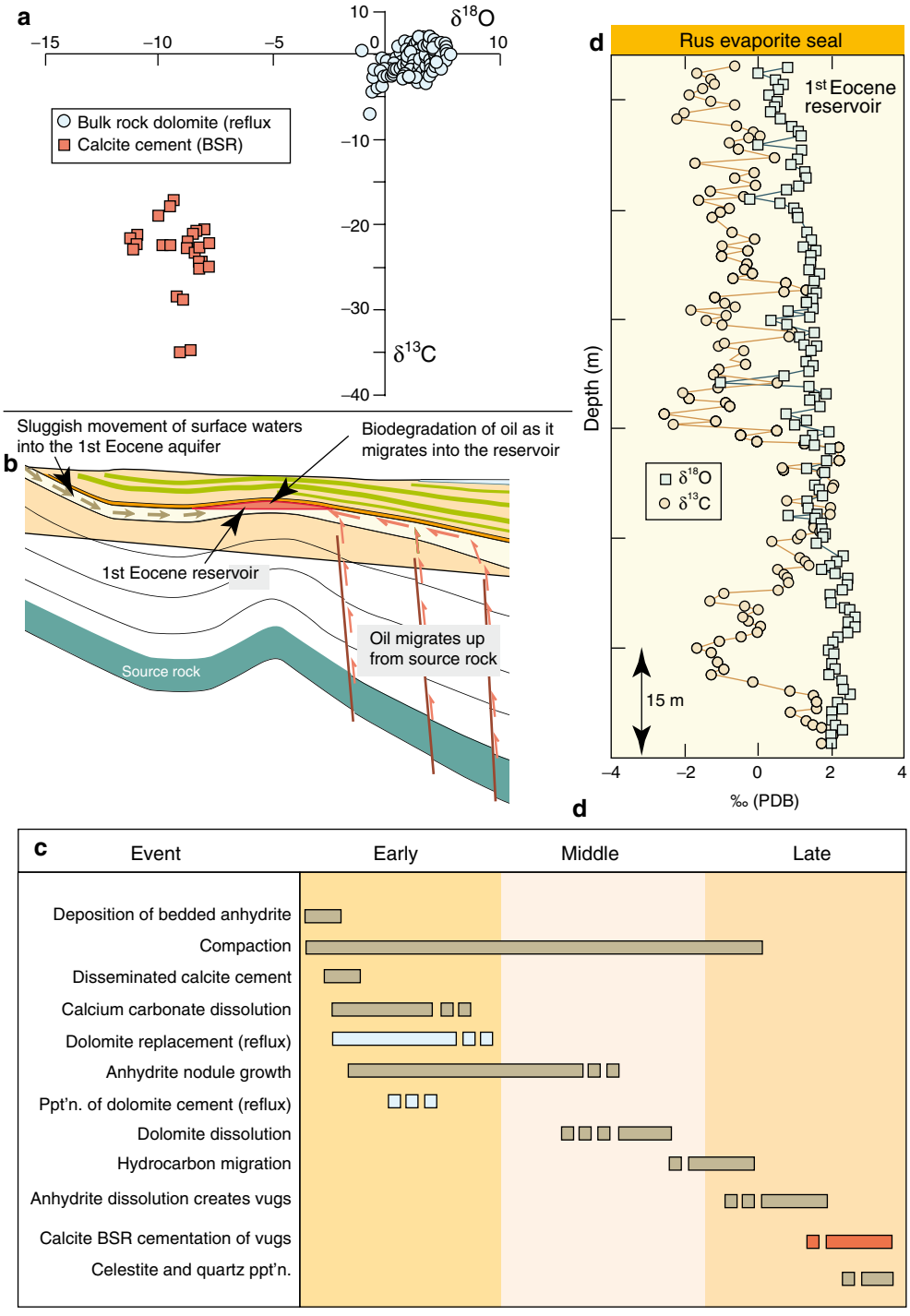

Fig. 9.67 BSR cements and oil biodegradation in the giant Wafra Field, Partitioned Zone, Saudi Arabia and Kuwait. (**a**) Stable isotopic analyses of bulk dolomite samples (dominantly co-variant reflux dolomite signatures) and calcite cements lining vugs showing dominantly BSR signatures. (**b**) Schematic model for biodegradation of oil as it migrates into the First Eocene reservoir. (**c**) Relative timing of various diagenetic events in the First Eocene reservoir, with *red-blue shading* as in (**a**). (**d**) Plot of stable isotopic compositions versus depth for bulk dolomite samples in a representative well. The general vertical trends are interpreted as secular changes in seawater during the late Paleocene and early Eocene. Some covariant spikes of $\delta^{13}C$ and $\delta^{18}O$ could be related to contamination by small amounts of calcite with very low $\delta^{13}C$ and $\delta^{18}O$ values (After Saller et al. 2014)

side of the regional Rus evaporite seal. As a consequence of the biodegradation, which is tied to an episode of leaching of anhydrite nodules and cements, heavy oil is currently extracted from very porous vuggy dolomites at depths of ≈300–400 m within the Paleocene-Eocene Umm Er Radhuma Formation.

Porosity in the dolomites in the vuggy intervals is typically 30–50 %, associated permeability ranges from 100 to 2,000 md, with the reservoir characteristics determined largely by diagenesis (Fig. 9.67c). Early diagenesis was dominated by reflux dolomitization, dissolution associated with dolomitization, and precipitation of sulphates. The highest permeabilities now occur in subtidal facies. Low-permeability typifies tidal flat facies and the combination or the two depositional associations now layers the reservoir response. Heavy oil preferentially fills high-permeability dolomites of the subtidal facies; whereas, low-permeability, tidal-flat facies are typically filled with water because their pore throats were too small to allow entry of viscous oil.

Late-stage diagenesis is dominated by bacterial sulphate reduction (BSR), which drove dissolution of prior sulphate nodules, calcite cementation, sulphur precipitation, and biodegradation of oil. BSR is indicated by very low $\delta^{13}C_{PDB}$ compositions of calcite cements (−17.1 to −34.9 ‰), which require an organic carbon source, probably oil (Fig. 9.67a). The oxygen isotopic compositions of the calcites support precipitation from formation waters similar to those in the current reservoir (Fig. 9.67d). BSR probably started during initial oil emplacement and continues to the present. BSR intensity is heterogenous, resulting in produced oils with gravities of 14–21° API. Even heavier oils remain in the reservoir, they did not flow during primary production. Secondary and tertiary recovery approaches are planned for the field. Primary production was likely greatest in areas and intervals with lighter, less viscous oil and perhaps less intense BSR.

Microbial creation of stratiform bioepigenetic limestone is a widespread but under-recognised process at the dissolving edges of many gypsum/anhydrite masses interacting with escaping hydrocarbons. It typifies near surface seeps in the Fergana and Amudarya depressions of central Asia and the Mesopotamian depression in Iraq (Jassim et al. 1999). Bedded examples of coarsely crystalline gypsum replaced by texturally similar bioepigenetic calcite characterise contacts of some Upper Miocene gypsum outcrops in the Lorca Basin (Rouchy et al. 1998). Likewise the Ratynsky Limestone, with its characteristic light carbon signature and sulphur association, is a bioepigenetic limestone bed that defines the top of outcropping and subcropping artesian gypsum karst in the western Ukraine (Andrejchuk and Klimchouk 2001).

Thermochemical Sulphate Reduction (TSR)

During thermochemical sulphate reduction, H_2S is produced as sulphate is inorganically reduced, via inorganic reactions with hydrocarbons, at temperatures typically in excess of 140 °C, which is too hot for any known life (Fig. 9.65b, c; Worden et al. 1995; Heydari 1997; Machel 2001). Reactive hydrocarbons caught up in the TSR reaction are mostly branched and n-alkanes, with lesser cyclic and mono-aromatic species in the gasoline range. Historically, the efficiency of thermochemical sulphate reduction in producing H_2S was inferred from experimental evidence or from levels of sour gas (H_2S-entrained) in deep oil and gas wells, rather than direct observation of subsurface processes (Trudinger et al. 1985; North 1990). In the past three decades this has now changed with the direct documentation of TSR-produced H_2S (sour gas) in natural gas reservoirs in the Permian Khuff Formation of Abu Dhabi (Worden et al. 1995, 1996; Worden and Smalley 1996) and identification of oil markers that, in association with sulphur isotopes ($\delta^{34}S$), can identify oils that have experienced TSR (Amrani et al. 2012).

In sour Khuff reservoirs hotter than 140 °C, anhydrite has been partially replaced by TSR calcite, and hydrocarbon gases have been partially or fully replaced by H_2S. That is, anhydrite and hydrocarbons have reacted to produce calcite and H_2S.

Worldwide, the lowest temperature at which TSR occurs may be lower than the 140 °C seen in the Khuff Fm. Machel (1998) suggests that the onset of TSR occurs in a range from 100 to 145 °C depending on variations in chemical kinetics, which will differ from basin to basin. If so, then one can expect TSR-derived H_2S to form at shallower depths than the 4,000 m suggested by the work of Worden et al. (1995) or Heydari (1997).

Carbon and elemental sulphur isotope data from the gases and minerals in the Khuff Fm. show that the dominant general reaction is (Worden et al. 1995, 1996; Worden and Smalley 1996; Heydari 1997):

$$CaSO_4 + CH_4 \rightarrow CaCO_3 + H_2S + H_2O$$

Gas chemistry and isotope data also show that C_2+ gases react preferentially with anhydrite via reactions like:

$$2CaSO_4 + C_2H_6 \rightarrow 2CaCO_3 + H_2S + S^o + 2H_2O$$

Sulphur is generated by this reaction and is locally present, but is also consumed by the reaction:

$$4S^o + CH_4 + 2H_2O \rightarrow CO_2 + 4H_2S$$

The frequently quoted and experimentally observed reaction between anhydrite and H_2S with CO_2 to produce calcite and sulphur:

$$CaSO_4 + 3H_2S + CO_2 \rightarrow CaCO_3 + 4S + 3H_2O$$

has been shown, by gas chemistry, calcite $\delta^{13}C$ and sulphur $\delta^{34}S$ data, to be insignificant in the Khuff Formation.

Rather, a direct reaction between hydrocarbons and anhydrite occurs in solution. It takes place within residual pore waters that are initially dominated by carbonate dissolved out of the marine carbonate matrix. The first-formed replacive calcite thus contains carbon that was derived principally from a marine dolomite matrix with a $\delta^{13}C$ signature of 0 to +4‰. Continuing reaction leads to the progressive domination of pores water derived by TSR carbonate, with a minimum $\delta^{13}C$ of about –30‰ (Fig. 9.68a). The spread of carbon isotope values in the replacive TSR calcite shows that in the earliest stages of TSR the ambient formation water was dominated by bicarbonate derived from dissolution of the matrix dolomite. As TSR commenced, the first-formed aqueous carbonate species plus the newly dissolved calcium from the dissolving anhydrite led to supersaturation with respect to calcite. However, this calcite was initially dominated by the dolomite-derived carbonate and thus inherited the dolomite's heavier carbon isotope signature. As TSR proceeded, the methane-derived carbonate came to dominate, leading to ever more negative $\delta^{13}C$ and $\delta^{18}O$ values in the resulting calcite (Fig. 9.68a).

When petrographically determined amounts of replacive calcite in the Khuff Formation are plotted as a function of depth (Fig. 9.68b) it shows that TSR starts around 4,300 m depth (corresponding to a present-day temperature of 140 °C) for all of the anhydrite types apart from the coarsest (poikilotopic variety), which shows signs of reaction only below 4,500 m. This implies that availability of sulphate from anhydrite is the rate-limiting step during the earlier stages of reaction when anhydrite is replaced *in situ* by calcite on the very edges of anhydrite nodules and crystals (Worden et al. 2000). Later, as TSR proceeds, and the thickening calcite rind begins to isolate the anhydrite from the dissolved methane, the reaction becomes transport controlled. TSR ceases once calcite has effectively armour-plated (totally isolated) the remaining anhydrite. Finely crystalline anhydrite underwent more extensive and more rapid TSR than coarser anhydrite crystals because these had a greater ratio of surface area to volume, allowing more and faster dissolution and requiring more calcite to isolate them from methane. Localized loss of H_2S occurs in the Khuff reservoir by reaction with indigenous Fe-bearing clays. Consequently, Khuff reservoirs with a relatively high siliciclastic content have less H_2S than would be expected from the advanced state of anhydrite replacement with calcite in these units.

Thermochemical sulphate reduction produces substantial volumes of very low salinity subsurface water in the vicinity of the reaction zone. Locally, the salinity of formation water in evaporite lithologies undergoing TSR is, therefore, not necessarily high. In the Khuff reservoir the water salinity and isotope data show that the original formation water was locally diluted between four and five times by water from TSR (Worden et al. 1996). A typical Khuff gas reservoir rock volume calculation suggests that initial formation water volumes can only be increased by

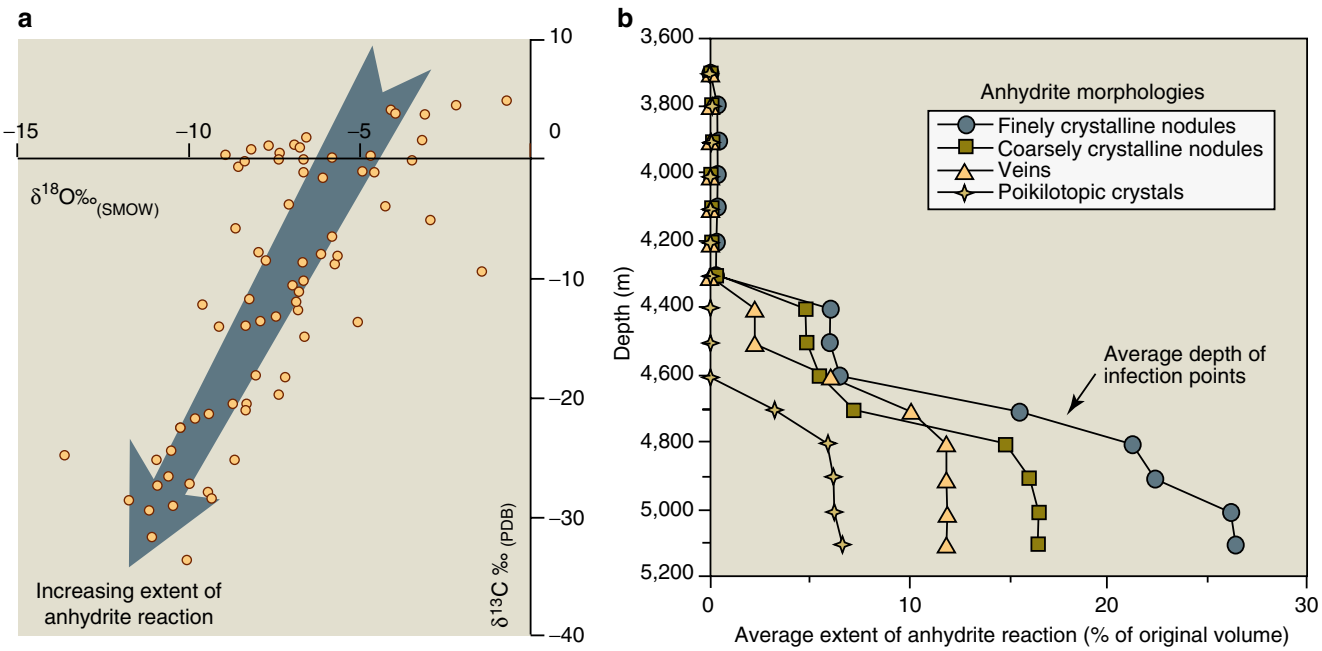

Fig. 9.68 Thermochemical sulphate reduction in the Permian Khuff Fm., UAE. (**a**) Stable isotopes of thermochemical calcite. *Arrow* shows trend of increasing calcite reaction. (**b**) Depth versus the average extent of anhydrite replacement by calcite for the different types of anhydrite. Anhydrites with smaller crystal sizes are more reactive at any given burial depth (After Worden et al. 2000)

about three times as a result of TSR. The extreme local dilution shown by the water salinity and $\delta^{18}O$ data in the Khuff must, therefore, reflect transiently imperfect mixing between TSR water and original formation water. Dissipation of this water into surrounding lithologies may aid further dissolution of adjacent evaporites. TSR is believed to cause the dilution of formation waters by up to 50 % locally and up to 30 % on a reservoir scale (Worden et al. 1996; Yang et al. 2001). On the other hand, there might be other reactions involved in TSR, some of them consuming water, so that the amount of water produced is probably highly variable and, according to Machel (2001), negligible at a regional scale.

Anhydrite dissolution and calcitisation in the Jurassic Smackover Formation in Mississippi, USA, does not occur below temperatures of 140–150 °C, suggesting that, as in the Khuff, it is a thermochemical process (Fig. 9.69a). Thus, gas window diagenesis in deeply buried dolomitised Smackover reservoirs is largely driven by thermochemical sulphate reduction. Reaction of sulphate with H_2S generates S° that, in turn, reacts with CH_4 to form more H_2S in a self-reinforcing cycle (Heydari 1997, 2000). Closed-system diagenesis prevents the escape of H_2S and, with sulphate abundantly available (Buckner Anhydrite), but without Fe^{2+} to remove H_2S by pyrite precipitation, the reaction tends to continue until all hydrocarbons are consumed. TSR-generated CO_2 results in precipitation of post-bitumen calcite with negative $\delta^{13}C$ compositions.

Concentration of H_2S in Mississippi Smackover reservoirs varies consistently with temperature (Fig. 9.69b; Heydari 1997). Reservoirs studied are of the same age (150 Ma), similar lithology (clean oolitic limestone), and bounded by impermeable layers (Buckner anhydrite above and lime mudstones below). Heydari (1997) found that concentration of H_2S is very low in reservoirs that have experienced temperatures of 120 °C or less for more than 50 m.y. This suggests TSR has not yet occurred, and therefore it is not a time-dependent process and not necessarily kinetically or rate driven. High H_2S concentrations occur in reservoirs with temperatures in excess of 140 °C and levels tend to increase with temperature, so suggesting TSR is occurring and is ongoing. If so, it is a temperature-dependent process (thermodynamically-driven).

Amrani et al. (2012) defined a set of organo-geochemical criteria for produced oils, which can be used to define the degree of TSR alteration of Smackover oils. Oils that experience TSR exhibit significant ^{34}S enrichment in the benzothiophenes (BTs) compared to dibenzothiophenes (DBTs), while in unaltered oils both compounds have similar isotopic compositions. The $\delta^{34}S$ values of BTs are close to those of sulphate-bearing evaporites of the Smackover Fm., whereas the $\delta^{34}S$ values of DBTs are spread over a wider range and gradually approach those of the BTs (Table 9.12; Fig. 9.70). They propose that BTs can be a sensitive tracer for the intensity of TSR alteration of an oil or condensate as they form readily under TSR conditions, with large ^{34}S enrichments

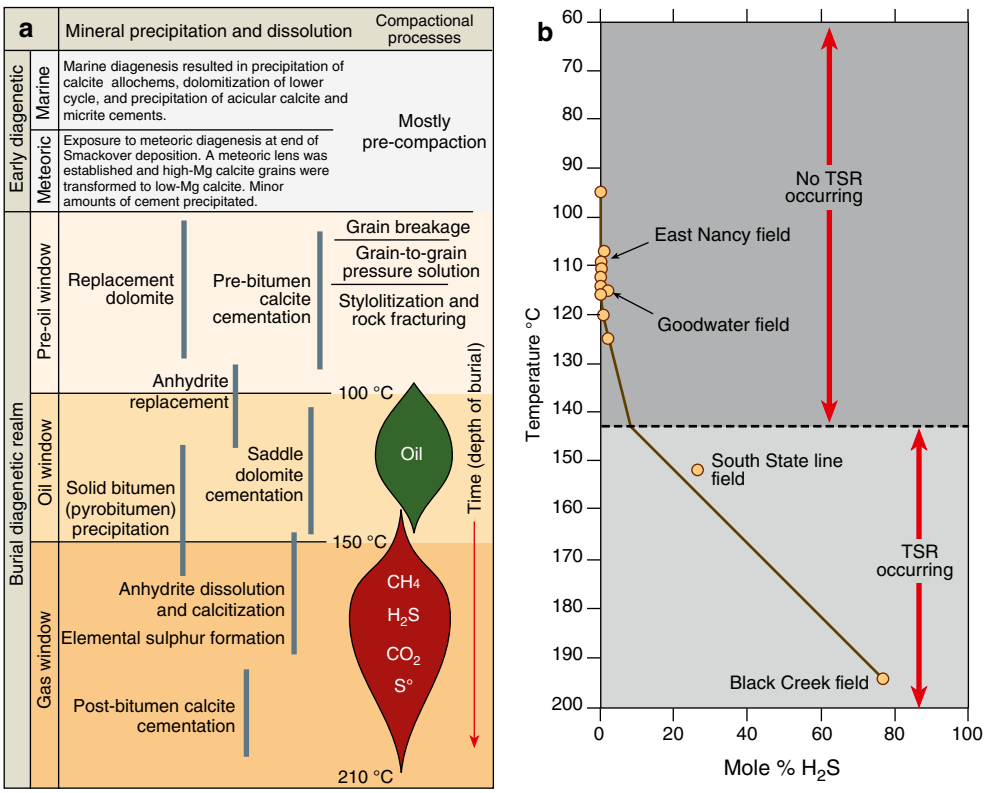

Fig. 9.69 Thermochemical sulphate reduction in the Smackover Formation, Gulf of Mexico. (**a**) Paragenetic sequence of the Smackover Formation at Black Creek Field summarizing major products of marine, meteoric, pre–oil window, oil window, and gas window diagenetic stages. (**b**) Concentrations of H_2S in Mississippi Smackover reservoirs vary consistently with temperature (After Heydari 1997)

Table 9.12 Bulk geochemical data for oil and condensate samples from oils in the Smackover Formation (After Amrani et al. 2012 and references therein) with the degree of TSR alteration based on the isotope and DBT thiadiam characteristics, as determined by Amrani et al. 2012

Field	Depth (m)	Temp (°C)	ρ° (API‰)	H_2S Mole %	S wt%	$\delta^{34}S_{(oil)}$ ‰	$\delta^{13}C_{(oil)}$%	DBT[a] ppm	Thiadiam[b] ppm
TSR unaltered									
Turkey Creek	4,056–4,062	93	0.757 (55.5)	0.0	0.8	–0.9	–23.93	431	21
Wallers Creek	4,758–4,762	126	0.835 (38.0)	0.0	0.1	–12.5	–23.94	192	2
Blacksher	5,142–5,146	138	0.828 (39.4)	0.0	0.1	5.6	–23.90	270	2
Slightly TSR altered									
Hatters Pond	6,005–6,011	160	0.756 (55.6)	0.6	0.1	5.1	–23.00	81	20
Cold Creek	6,049–6,058	160	0.757 (55.5)	0.0	0.1	–0.6	–23.70	118	17
TSR altered									
Appleton	4,230–4,242	137	0.781 (49.7)	2.0	0.35	10.7	–24.30	691	60
Vocation	4,588–4,591	127	0.775 (51.1)	5.7	0.3	6.4	–22.50	803	58
Huxford	4,835–4,841	132	0.774 (51.2)	6.1	0.2	5.7	–22.80	983	43
Chatom	5,303–5,340	138	0.787 (48.3)	16.7	1.0	12.2	–21.7	1,564	149
Big Escambia Creek	5,043–5,067	143	0.828 (39.4)	30.0	1.4	24.0	–20.85	2,345	296
South State Line	5,683–5,719	151	0.863 (32.4)	31.4	0.8	21.0	–20.13	6,313	685

[a]DBT content refer to dibenzothiophene and its alkylated groups including methyl-, dimethyl- and trimethyl-dibenzothiophenes
[b]Thiadiam content stands for thiadiamondoids including thiaadamantanes (trimethyl- and tetramethyl-thiaadamantanes), thiadiamantanes (thiadiamantane, methyl-, dimethyl- and trimethyl-thiadiamantanes) and thiatriamantanes (thiatriamantane, methyl-, dimethyl- and trimethyl-thiatriamantanes)

relative to the bulk oil. In contrast, DBTs exhibit relatively small changes in $\delta^{34}S$, preserving their original $\delta^{34}S$ values longer than do BTs because of their greater thermal stability and slow rate of formation. If this relationship holds in other oil basins then a comparison of the $\delta^{34}S$ values of BT and DBT can be used to detect TSR alteration from the very early stages up to highly altered oils (Table 9.12; Fig. 9.70).

Sour (H_2S-entrained) natural gas, associated with thermochemical sulphate reduction, typifies dolomite reservoirs in the Lower Triassic Feixianguan Formation, Northeast Sichuan Basin, China (Jiang et al. 2014). The sulphate comes from dissolution of the abundant Triassic saltern anhydrites, which also act as seals across oilfields of the region. Reservoirs were initially filled with oil, later replaced by gas during burial to 7,000 m followed by uplift to about 4,000 m. A plot of carbon and oxygen stable isotope clearly breaks out the host matrix limestones and dolomites from the various burial cements. Isotope plots, broken out by timing and texture, defines three separate C-O plot fields, related to pre-TSR, TSR and post TSR calcite cements (Fig. 9.71a). The TSR plot field, with its negative carbon isotope values, overlaps with the TSR plot fields seen in other already discussed examples (e.g., Fig. 9.68).

Pre-TSR diagenesis (in time order), included host neomorphism and recrytallisation of the host dominated by eodiagenetic dolomitization via brine reflux, fracture-related calcite cementation, baryte, quartz, celestite, and fluorite mineralization and a dolomite recrystallization stage at burial temperatures up to 130 °C (Fig. 9.71b). TSR followed, and resulted in anhydrite replacement by TSR-calcite, petroleum destruction, formation of sulphur-rich pyrobitumen and elemental sulphur and generation of large volumes of H_2S, CO_2. Diagenesis during TSR can be subdivided into oil-stage TSR and gas-stage TSR with oil-stage TSR defined by the presence of primary oil and bitumen inclusions in the TSR-calcite.

Based on aqueous inclusion homogenization temperatures, oilstage-TSR commenced at a temperature of 116 °C with a mode between 130 and 140 °C (Fig. 9.71b). Gas-stage TSR started at a temperature of 135 °C and continued to maximum burial temperatures of about 220 °C. Trace amounts of pyrite, baryte, quartz and celestite grew during

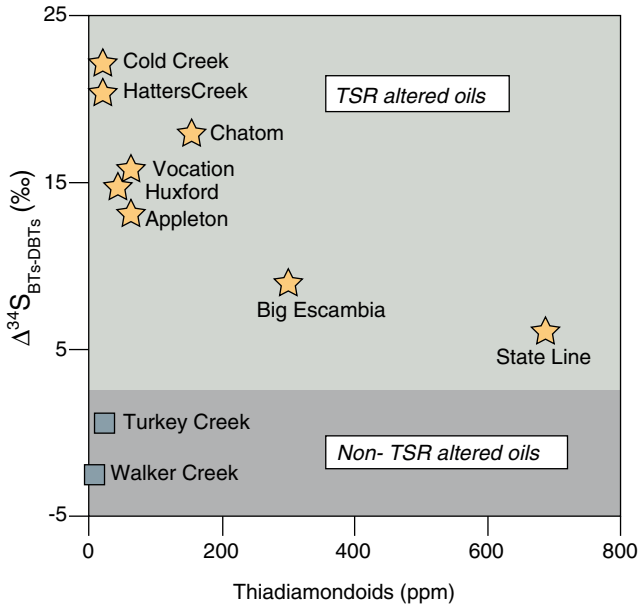

Fig. 9.70 ^{34}S fractionation between BTs and DBTs isomers (Δ^{34}SBTs-ΔBTs) as a function of total thiadiamondoid concentration (Table 9.11), which includes thiaadamantanes (trimethyl- and tetramethyl-thiaadamantanes), thiadiamantanes (thiadiamantane, methyl-, dimethyl- and trimethyl-thiadiamantanes) and thiatri-amantanes (thiatriamantane, methyl-, dimethyl- and trimethyl-thiatriamantanes). The plotted $\delta^{34}S$ values for alkylated BTs and DBTs are the numerical averages of all measured isomers (After Amrani et al. 2012)

TSR. Post-TSR diagenesis was dominated by fracture-related calcite precipitation as well as celestite and sparry anhydrite crystallization. Formation water salinity increased from depositional values (3.5 wt%) up to 24 wt% during pre-TSR dolomite recrystallization, probably due to an influx of evaporite-dissolution associated water from the overlying Jialingjiang Formation. Later pre-TSR baryte, quartz, celestite, and fluorite mineralization was associated with a transient decrease in water salinity (Fig. 9.71c) During TSR, formation water salinity decreased from 26 wt% to as low as 4 wt%, as a result of fresh water being produced by TSR reactions (Jiang et al. 2014).

The Sichuan example illustrates that, if anhydrite and methane remain in reservoirs reaching 140 °C and above, thermochemical sulphate reduction can continue into the low temperature end of the metamorphic realm (>200 °C). Alonso-Azcarate et al. (2001) documented vein deposits containing native sulphur, gypsum, quartz and rare sphalerite in the very low-grade greenschist metasediments in Cervera del Rio Alhama of the Mesozoic Cameros Basin, NE Spain. In outcrop the veins are hosted by lacustrine evaporites, which now comprise alternations of dolomite and recrystallised gypsum layers, the latter was anhydrite during metamorphism and converted to gypsum during telogenesis. Fluid inclusion homogenization temperatures and quartz-sulphate oxygen isotope geothermometry indicate formation of the veins around 225 °C. Fluid inclusions contain sulphur along with a gas phase comprising H_2S, N_2, CO_2 and minor CH_4. These are all reactants and products of sulphur generation via thermochemical sulphate reduction (TSR) in the anchizone. The conversion utilised organic matter, followed by a partial re-oxidation of some H_2S via SO_4 to then produce sulphur. These TSR reactions differ from those observed in most petroleum-related sour gas settings in that there is no evidence for secondary carbonate precipitation during TSR and in that significant S isotopic fractionation exists between sulphate (around +20‰) and reduced products (sulphur is around – 11‰).

H_2S, Natural Gas and Metallogeny

Clearly, at lower temperatures H_2S (sour gas) is bacterially produced from organic matter by BSR, and nonbiogenically by TSR at higher temperatures (Fig. 9.65a, b). In deep evaporite sealed oil and gas provinces, the proportion of bacteriogenic H_2S that becomes one of the many constituents of the trapped natural gas in a reservoir is negligible compared to H_2S produced by TSR (Hunt 1996). However, further updip, the proportion of bacteriogenically-produced H_2S can be much higher and in the near surface caprocks, hypogene caves and sea bottom brine lakes can exert major control on the precipitation of metal sulphides (Chaps. 15 and 16). Isotopically, there is significant overlap in the sulphur signal between BSR and TSR as there tends to be only minor fractionation of the precursor S-isotope signature during TSR, although, in general, bacterially formed H_2S tends to show more negative sulphur isotope values (Fig. 9.72).

H_2S is one of the deadliest[20] gases produced naturally in large amounts. At nearsurface conditions it is almost three times as soluble as CO_2 and more than 70 times as soluble as methane. Its critical temperature of 100.4 °C is also much higher than that of CO_2. Above this temperature all

[20] Small amounts of hydrogen sulphide occur in crude petroleum, but natural gas can contain up to 90 %. At very low concentrations of less than 10–100 ppm it smells like rotten eggs and there is a common misapprehension that its foul odour is a warning. At 100 ppm the gas kills the sense of smell in 3–15 min and will cause you to cough or your eyes to water. Over 100 ppm your eyes and throat may begin to sting. At 200 ppm, your eyes and throat will begin to burn and you will get headaches. Only 600 ppm, or 0.06 of 1 % will cause death, if you are not treated very quickly. Over 1,000 ppm causes respiratory paralysis and a sudden agonizing death from asphyxiation.

H_2S is heavier than air, invisible, highly explosive and can destroy steel and rubber seals very quickly. Modern drill rig floors are all fitted with gas sniffer warning systems.

Hydrogen sulphide is considered a broad-spectrum poison, meaning that it can poison several different systems in the body, although the nervous system is most affected. The toxicity of H_2S is comparable with that of hydrogen cyanide or carbon monoxide. It forms a complex bond with iron in the mitochondrial cytochrome enzymes, thus preventing cellular respiration.

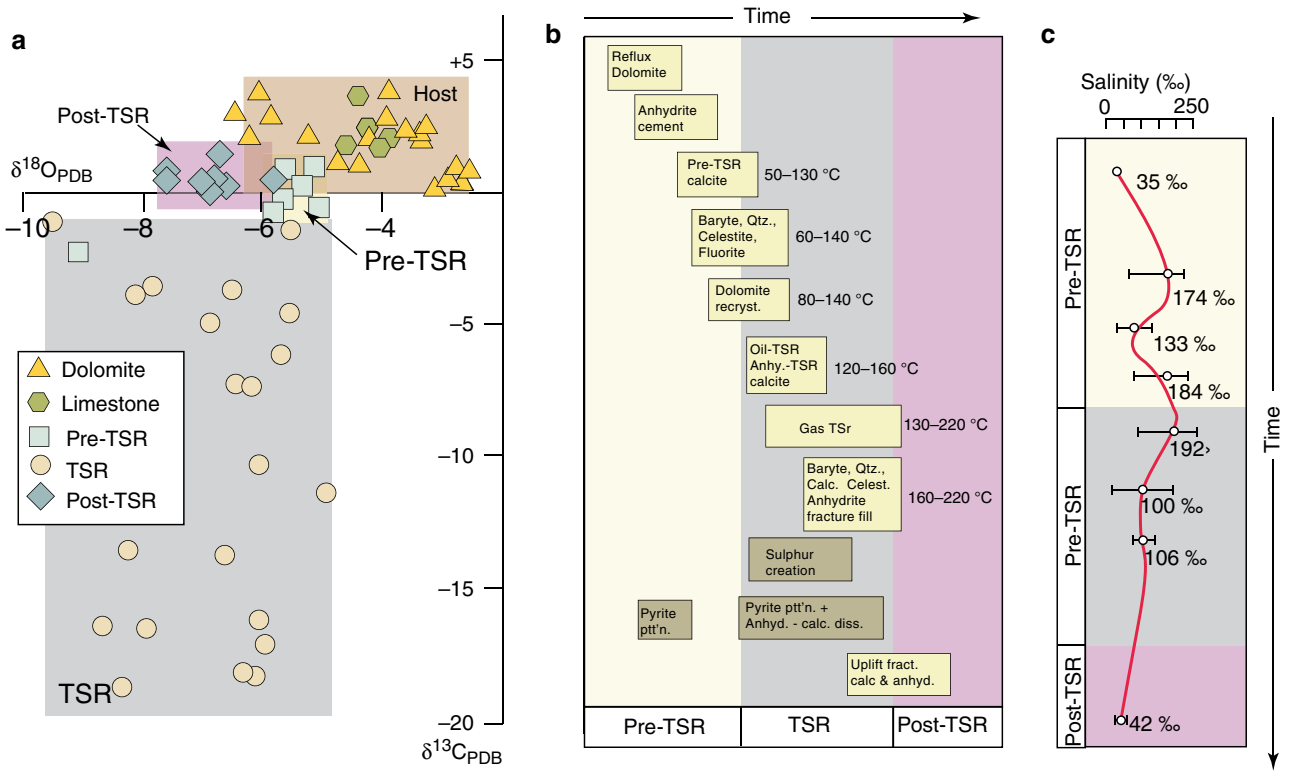

Fig. 9.71 Thermochemical sulphate reduction (TSR) in Jialingjiang Formation, NE Sichuan Basin, China. (**a**) The carbon and oxygen isotopic compositions of Feixianguan Formation host carbonates and the pre, syn and post-TSR isotope fields of the various calcite cements. (**b**) Paragenetic sequence with inclusion-determined temperature ranges, (**c**) Inclusion-determined salinities of the three cementation phases in the calcite cements (After Jiang et al. 2013, 2014, and references therein)

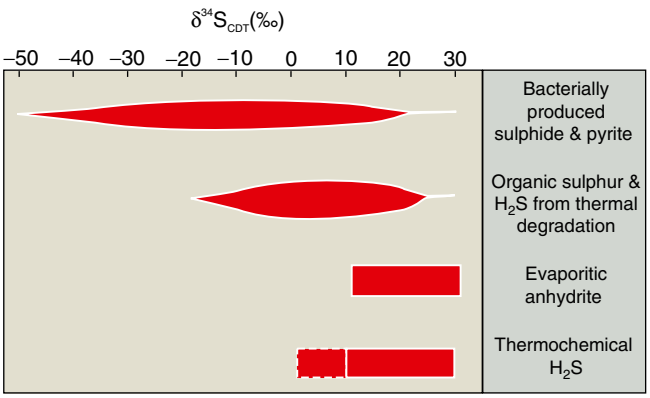

Fig. 9.72 Typical ranges of naturally occurring sulphur isotopes under thermochemical and bacterial sulphate reduction (After Emery and Robinson 1993)

undissolved H_2S is in the gas phase. Large quantities of both CO_2 and H_2S gas are thermochemically generated at temperatures greater than 120–140 °C in mature to overmature source rocks. Peak generation for methane is around 140 °C, while H_2S has not yet reached its peak generation at temperatures of 170 °C (Figs. 9.65c). H_2S forms best at temperatures beyond where petroleum geochemists have already lost interest, but its genesis is of great importance in the formation of base and precious metal deposits (Warren 2000b).

Because of its high reactivity, it is difficult for H_2S to migrate from its source to a distant reservoir (Hunt 1996). Away from direct contact with deeply buried reactive and dissolving anhydrites, H_2S in most oil and gas reservoirs is largely the product of sulphate reduction from sulphate ions in solution or the thermal decomposition of sulphur-containing oil. Interestingly, all the natural gas reservoirs with high thermochemical H_2S contents, listed in Table 9.13, are interbedded with anhydrites, or have anhydrite above or below the reservoir horizon. At its critical temperature of 104 °C and a pressure of 14 MPa (2,000 psi), H_2S is forty times more soluble in water than at surface conditions.

Wherever H_2S in solution comes into contact with metalliferous chloride brine it is likely to be involved in a number of metal sulphide forming reactions (Chap. 15). Sulphide products range from the cool shallow biogenic precipitation of syngenetic framboidal pyrite at seafloor brine-lake interfaces to the formation of hot, subsurface hydrothermal

Table 9.13 Regions of natural gas deposits with high H_2S contents. In all these, the deposit is stored in a carbonate reservoir that is interbedded with anhydrite, or there is an anhydrite unit above or below the deposit

Region	Reservoir age	Lithology	Depth (m)	% H_2S in total gas
South Texas, USA	Upper Jurassic (Smackover)	Limestone	5,793–6,098	98
Alberta, Canada	Devonian	Limestone	3,800	87
Mississippi, USA	Upper Jurassic (Smackover)	Limestone	5,793–6,098	78
Irkutsk, Russia	Late Cambrian	Dolomite	2,540	42
Wyoming, USA	Permian (Embar)	Limestone	3,049	42
Asmari-Bandar Shapur, Iran	Jurassic	Limestone	3,600–4,800	26
Lacq, France	U. Jurassic and L. Cretaceous	Dolomite and limestone	3,100–4,500	15
East Texas. USA	Upper Jurassic (Smackover)	Limestone	3,683–3,757	14
Alberta, Canada	Mississippian	Limestone	3,506	13
Weser-Ems, Germany	Permian (Zechstein)	Dolomite	3,800	10
South Texas, USA	Late Cretaceous (Edwards)	Limestone	3,354	8
Pont d'As-Meilllon, France	Upper Jurassic	Dolomite	4,300–5,000	6
Urals-Volga, Russia	Late Carboniferous	Limestone	1,500–2,000	6

After Hunt 1996

sulphides, which often also involve dissolution and alteration of the adjacent carbonate rock matrix. For example, in a Mississippi Valley type (MVT) scenario, a metal sulphide phase typically coprecipitates with hydrothermal or saddle dolomite in bathyphreatic or vuggy porosity at temperatures in the range of 60–180 °C (Hill 1995):

$$H_2S + CO_2 + MeCl^+ + Mg^{2+} + 2CaCO^3 + H_2O = MeS + Ca^{2+} + CaMg(CO_3)^2 + HCO_3^- + Cl^- + 3H^+$$

The formation of metal sulphide from hydrogen sulphide generated by TSR can be expressed in the general reaction;

$$H_2S + Me^{2+} = MeS + 2H^+$$

Such reactions create acid, which in turn is capable of forming secondary porosity in a deeply buried limestone host. It is why bathyphreatic vuggy porosity with sphalerite stalactites are found in many MVT ore deposits, such as Cadjebut in Western Australia where these metalliferous dripstones formed in methane-rich bathyphreatic vugs and pores (Warren and Kempton 1997).

When considering the association of sulphate evaporites with mineralization and developing exploration paradigms it is important to realise that it is not the sulphate evaporites that are directly responsible for the precipitation of metal sulphides during bacterial and thermochemical sulphate reduction (Warren 2000b). Rather, evaporite dissolution or reaction places sulphate/sulphide in a fluid medium so that it can then react with liquid or gaseous hydrocarbons. It is this sulphate-entraining solution that is reduced in the presence of organic matter or hydrocarbons to form H_2S. And it is the H_2S in solution that then precipitates the metal sulphides at or near a redox interface, which is a zone where slightly more oxidised metalliferous chloride brines can interact with a H_2S buildup on the reduced side of the interface.

Thus, ore textures in areas where sulphate evaporites are dissolving and metal sulphides are precipitating are most likely to be open space or porosity-fill textures. Ore textures and the degree of layering will depend on a number of factors including: the size of the dissolution front (interpore versus laminar versus vug versus solution-collapse cavern), the rate of fluid crossflow at the interface, the degree of stability of the redox interface, and the distance the sulphate ion travels before it is reduced (Warren and Kempton 1997). Precipitation of the metal sulphides may occur directly across from a dissolving sulphate bed or nodule, where it is producing H_2S on the other side of a fluid-filled reaction interface. Or it may occur after H_2S, derived from TSR, has seeped and migrated into a closed structure (aka prepared ground) located elsewhere in the sedimentary succession.

When H_2S accumulates at an interface where oxygen is also present and large volumes of metalliferous brines are absent, it can form accumulations of native sulphur, rather than metal sulphides, via the reactions:

$$2H_2S + O_2 = 2S° + 2H_2O\,(pH < 6-7)$$
$$HS^- + O_2 + H^+ = S° + H_2O\,(pH > 6-7\text{ to }9)$$

Elemental sulphur can form and persist near a redox interface where Eh ≈ –0.2 to +0.2. This is thought to be the mechanism that generated the economic evaporite-associated sulphur deposits in hydrocarbon leakage haloes within the Gulf of Mexico diapir caprocks and the stratiform sulphur deposits of Culberson Co. West Texas (Fig. 12.69). The presence of abundant free sulphur (S°) in peridiapiric Pb-Zn deposits such as Bou Grine is used by some workers to argue that in such situations the supply of metals to a sulphate/sulphide reduced environment was the reaction-limiting step (Bechtel et al. 1996).

Sulphur sourced from TSR in the deep subsurface may not all be consumed by the reaction of methane and water, especially where metalliferous fluids are not present in sufficient quantities to form metal sulphides. However, as sulphur melts at temperatures between 113 and 120 °C, any such sulphur formed during TSR (requires temperature >140 °C) will be molten. Such sulphur occurrences typically occur in deep stratigraphic zones dominated by carbonate and calcium sulphate lithologies (Hunt 1996). For example, molten sulphur was recovered from a depth of 6,098 m (20,000 ft) in the Jurassic Smackover carbonate-evaporite sequence in southern Mississippi on the US Gulf Coast. It was also recovered from the Cambro-Ordovician Arbuckle limestone-dolomite at a depth of 9,586 m (31,441 ft) in the Bertha-Rogers well in the Anadarko Basin, Oklahoma. Wells in the Permian Zechstein dolomites in western Germany have recovered molten sulphur from depths between 3,000 and 4,300 m (10,000–14,000 ft).

Elemental sulphur reacts with H_2S to form polysulphides, which are powerful oxidants that quickly convert any saturated hydrocarbons to thiopenes, thiols and sulphides (Hunt 1996). This reactivity means that all the hydrocarbons from pentane, through butane, propane, ethane and finally methane are oxidised to CO_2 at elevated temperatures in the presence of H_2S. Hence, it is no surprise that whenever molten sulphur is recovered, no appreciable amounts of methane or the higher hydrocarbons are present.

Criteria used to distinguish BSR from TSR metal sulphide outcomes include textural features and sulphur isotopic compositions (Pirajno 2009). With BSR, pyrite framboids (the equidimensional, raspberry-shaped spheroids found in many diverse environments, both modern ancient; Rickard 1970) are typical. For TSR, pyrite tends to be euhedral or a replacement of other minerals and is often associated with coarse calcite spar. Finely disseminated stratabound pyrite associated with kerogen is likely to have formed by BSR. The most reliable indicator for biogenic (BSR) sulphide is the sulphur isotopic composition of resulting minerals (Fig. 9.72). Fractionation of sulphur isotopes during dissimilatory sulphate reduction produces sulphides that are depleted in ^{34}S. Thus, strongly negative fractionations, ranging from −15 to −65 ‰ characterise BSR, whereas for TSR negative fractionations are smaller and temperature dependent with values around −20‰ at 100 °C, −15‰ at 150 °C and 10‰ at 200 °C and tending to decrease further with increasing temperature (Table 9.11; Machel et al. 1995). TSR sulphur isotope values show a much stronger overlap with typical marine sulphide values, especially at temperatures above 150 °C.

Hydrothermal Cracking in Saline Rift Lakes

Not all the hydrocarbons found in evaporitic sediments have necessarily evolved from millions of years of gentle kerogen burial into basin depths where temperatures exceed 60 °C in the sediment layers. In some evaporitic situations the heating and evolution of entrained organics is much more rapid, driven by the near surface circulation of hydrothermal waters typically tied to magmatic injections in igneous sills and dykes. Such magmatic heating of organic matter can be commonplace in evaporite accumulating areas where the evaporite depression was tectonically induced, as in many rift settings. Hence, hydrothermal hydrocarbons may be an integral part of source rock evolution of the early brackish to mesohaline lacustrine fill of evaporite-sealed rift successions, with organics typically first accumulating on the bottom of density/salinity stratified lakes (Tiercelin et al. 1993).

One such example is the oil now seeping onto the lake floor off Cape Kalamba in Lake Tanganyika at the south end of the Ubwari Peninsula (Tiercelin et al. 1989; Simoneit et al. 2000). The area lies at the intersection of faults controlling the morphology of the northern basin of the Tanganyika Rift. Oil samples collected at the surface of the lake 3–4 km offshore from Cape Kalamba lack typical suites of polynuclear aromatic hydrocarbons. This indicates an origin via hydrothermal alteration of immature biomass in the organicrich mesohaline sediments of the lake bottom. Based on the constituents of the modern bottom sediments, the prime producers were diatoms and cyanobacteria, which constitute most of the 6 % TOC that is found in sediments on the modern deep lake floor. Compositions of the oils and nearby tar balls demonstrate a <200 °C temperature during formation/generation, similar to the fluid temperatures identified at the Pemba hydrothermal site some 150 km north of Cape Kalamba (Table 9.14). Hydrothermal petroleum

Table 9.14 Hydrocarbon gas composition in the North Tanganyika and Lake Kivu geothermal fields, East African rift

North Tanganyika (Pemba)	CH_4 (µl/l)	C_2H_6 (µl/l)	C_2H_4 (µl/l)	$C_3H_8+C_3H_6$ (µl/l)	C_1/C_2+C_3 (µl/l)	$\delta^{13}C_{PDB}$ ‰
Hot spring fluid	1.32	0.0145	0.0136	0.138	9.5	–
Hot spring fluid	0.62	–	_ 0	0.122	5	–
Water above bubble vent	3.81	0.253	–	0.184	8.8	
Cape Banza						
Surface water atop vent field	8.14	–	0.47	0.120	13.7	–
Chimney vent fluid	614	–	58	–	8	–
"Big Chimney" vent fluid	842	–	51.9	–	12.9	–
Lake Kivu		–				
50 m	<10	–	–	–	–	–
480 m	400	–	–	–	>300	−58

After Tiercelin et al. (1989)

generation seems to have occurred in the lake depression slightly before 25 Ka, during a drier climatic environment when the lake level was lower than today. Hydrothermal smokers or chimneys also occur on the subaqueous floor of the Lake Tanganyika (Barrat et al. 2000). It may well be that the deposition of any future overlying evaporite seal in this underfilled lacustrine situation may focus the flow of micro-petroleum into more appropriate landward sands, but ancient economic lacustrine counterparts of this style of hydrothermal oil have yet to be documented.

Not all hydrothermally-cracked oil is found in lacustrine rift-valley fills. Equally impressive in terms of hydrocarbon volumes and origins are the oils forming in the hydrothermally-flushed deepwater sediments on floor of the Guaymas Basin in the Gulf of California (Fig. 9.73a). The area, known to be actively producing hydrothermal hydrocarbons, measures some 3×9 km, with a thickness greater than 120 m, given a 2 % TOC and a 50 % expulsion efficiency, at least 30 MMbbl of oil could be generated from this region (Simoneit 1991). Radiocarbon dates show this oil forms in association with thermochemical sulphate reduction in less than 5,000 years (Didyk and Simoneit 1989; Peter and Scott 1991a, b). But unlike the rift association of east Africa, the anhydrite in this hydrocarbon system is largely hydrothermal and is created by the convective heating of seawater (retrograde solubility).

Leg 64 of the DSDP intersected sills and hydrothermal alteration at depth in all holes drilled in the basin. Thermogenic hydrocarbon gases, H_2S and CO_2 were seen at all sites, as were thermally altered lipids (bitumens) in positions close to, or below the sills (Simoneit et al. 1984). A number of hydrothermal mounds rise 20–30 m above the southern Guaymas Trough floor, below waters some 2,000 m deep. Most are actively discharging vent fluids at temperatures up to 315 °C and bottom pressures of 200 bars. Samples collected from the mounds are strained and cemented with petroleum bitumens and smell strongly of "diesel."

Muddy sediments and hydrothermal fluids of the Guaymas Basin are enriched in organics derived from diatomaceous oozes and microbial detritus. The basin hinterland is desert, so levels of terrigenous detrital organics are low. Buried diatom-rich sediments contain up to 3–4 % oil-prone TOC and average around 2 % TOC, which is cracked by the circulating hydrothermal fluids to generate thermally derived hydrocarbons. In general the n-alkanes range from C_{12} to C_{35} with a maxima at C_{19}, C_{22}, and a strong odd-to-even carbon-number predominance $>C_{24}$ (CPI in range 1–2), while pristane and phytane are about equal (Pr/Ph = 1.06; Fig. 9.73b, Simoneit 1991). Petroleum is carried as droplets entrained in the venting hydrothermal fluid or as a bulk phase. It also occurs in pore spaces and cavities in the chimneys and mounds and in hydrocarbon-bearing inclusions within amorphous silica and anhydrite. Thermal stress causes rapid maturation and petroleum expulsion in sediments exposed to temperatures of more than 50 °C. The "oil window" migrates upwards in the sediment column as the magmatic heat front rises (Simoneit 1991).

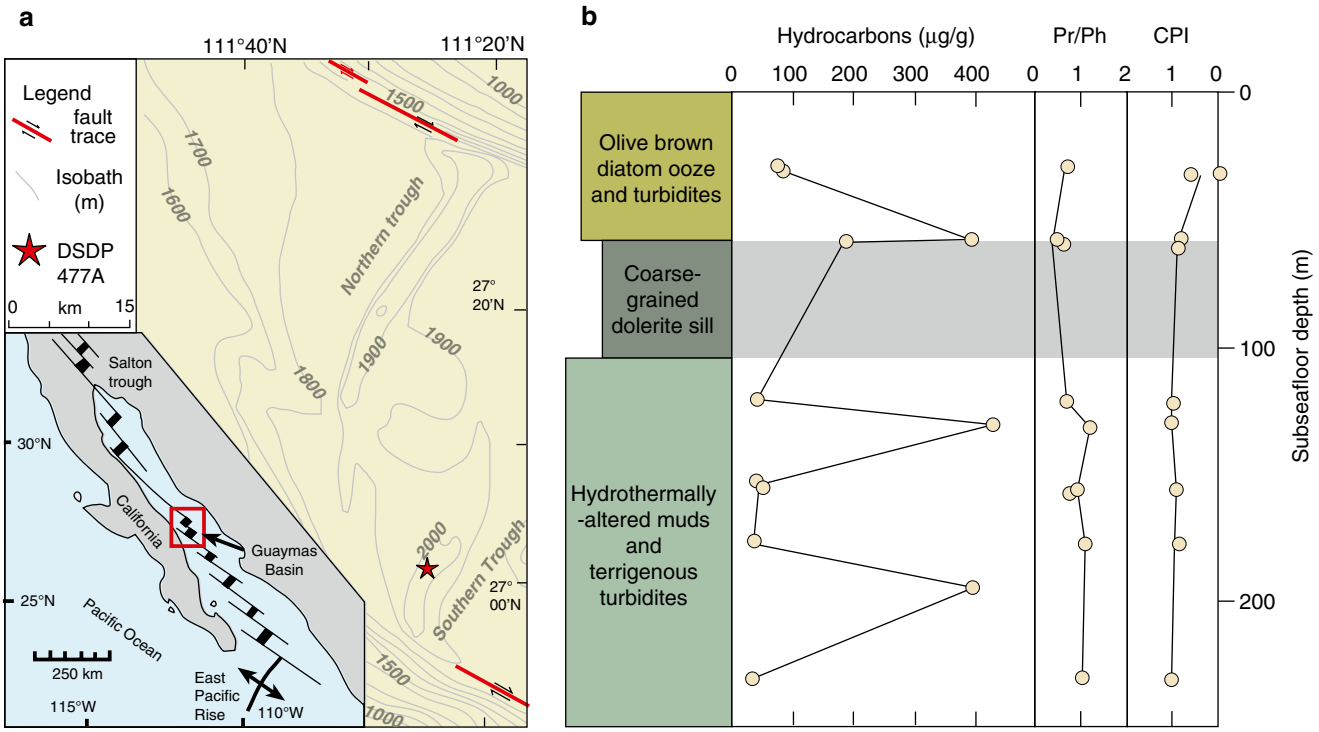

Fig. 9.73 Guaymas Basin. (**a**) Location of DSDP drill hole 477A. (**b**) Lithologic column, hydrogen concentration, pristane to phytane ratio (*Pr/Ph*) and carbon preference index (*CPI*) in DSDP hole 477A (After Simoneit 1991)

Hydrothermal oil generation processes in the Guaymas sediment column differ significantly from the conventionally accepted scenario for petroleum formation in sedimentary basins, where organic matter input, subsidence, geothermal maturation, oil generation, and oil migration are discrete and successive steps that occur over a long period of geological time and a thermal history related to regional sediment burial (Simoneit 1994). Rather, in hydrothermal petroleum formation several of the steps of oil generation occur simultaneously and can complete the organic matter maturation to oil-generating processes in geological time measured in thousands, not millions or tens of millions, of years (Table 9.14).

Another area of hydrothermal petroleum is the Davis-Schrimpf seep field in the onshore Salton Sea, Southern California (Fig. 9.74a; Svensen et al. 2007; Mazzini et al. 2011). This is the onshore extension of the same ridge system that defines the Guaymas Basin more than 500 km to the south. As in the Guaymas Basin, saline water-, mud-, gas-, and petroleum bearing seeps are part of the geothermal system in the Salton Sea. Seeps in the Davis-Schrimpf seep field (≈14,000 m^2) show considerable variations in water temperature, pH, density, and solute content. Water-rich springs tend to be hypersaline, have low densities compared to gryphon outflows (<1.4 g/cm^3), while Cl contents areas high as 45,000 ppm, and temperatures range between 15 and 34 °C. In contrast nearby gryphons expel denser water-mud mixtures (to 1.7 g/cm^3), have lower salinities (3,600–5,200 ppm Cl), and temperatures range between 23 and 63 °C. The main driver for this seep system is CO_2 (>98 vol% of expelled gas). Halogen geochemistry of the waters shows 2 trends indicates that mixing of slightly deeper and shallow pore waters occurs and it seems that near-surface dissolution of halite may overprint the original fluid compositions, so creating the trend dichotomy (Fig. 9.74b).

δD and $\delta^{18}O$ increase proportionally, with salinity and isotopic composition of the waters indicate a dominantly meteoric origin, modified by surface evaporation, with little or no evidence of deep fossil or magmatic components (Mazzini et al. 2011). Very high Cl/Br (>3,000) measured at many seep water pools suggests that increased salinities result from dissolution/recycling of halite crusts near the seep sites. Carbon isotopic analyses conducted by Svensen et al. (2007) suggest that hydrocarbon seep gases have a thermogenic origin. Their

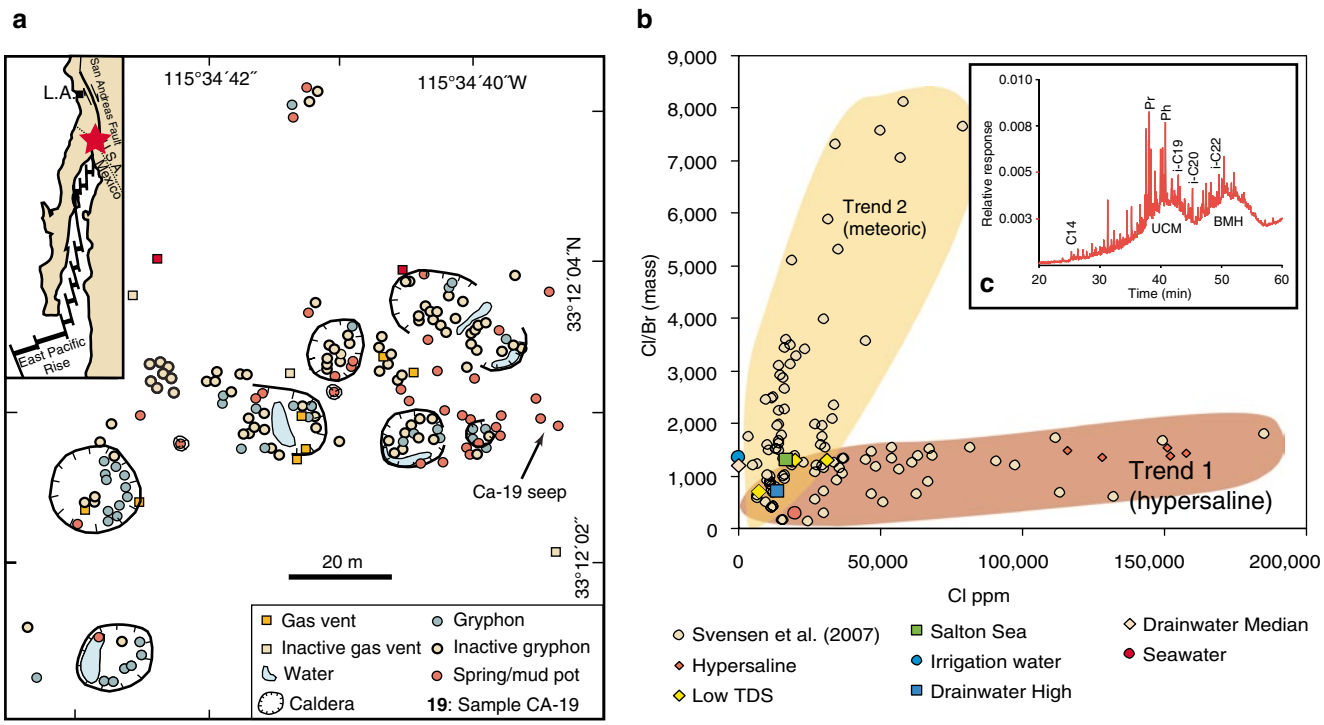

Fig. 9.74 Brines and hydrothermal oil in the Salton Sea, Southern California (After Svensen et al. 2007 and references therein). (**a**) Davis-Schrimpf seep field is characterized by clusters of gryphons, local subsidence structures, and calderas. Generally, gryphon mud towers are as high as 3 m with a central conduit, where mud and water chambers are located below ground level. Mud pots and springs are open circular depressions as much as 30–50 cm below ground level, but may occasionally form positive structures to a few tens of centimeters high. (**b**) Analyses of gryphon and spring water collected from Davis-Schrimpf field show a wide range in Cl and Br contents as do other seep an subsurface waters collected in the region. Compositions of waters define two trends in Cl–Br space related to salinity and origin of the waters. (**c**) Organic geochemistry of CA-19 seep fluid. Gas chromatography shows occurrence of homologous series of normal alkanes (n-Cxx) and isoalkanes (i-Cxx). Presence of unresolved complex mixture (UCM) and high concentrations of Pr and Ph suggests influence of biodegradation. Biomarker hump (BMH) is typical for source rocks with low to moderate maturity

hypothesis of hydrocarbon generation via hydrothermal cracking is supported by the presence of petroleum in a water-dominated spring, composed of 53 % saturated compounds, 35 % aromatics, and 12 % polar compounds (Fig. 9.74c).

At various seafloor and onshore spreading axes, hydrothermal systems, active under a cooler sedimentary cover, generate petroleum from the generally immature organic matter in the sediments (e.g., Guaymas Basin, Escanaba Trough, Salton Sea, etc.). The alteration reactions are primarily reductive and to a lesser extent oxidative, and are generally associated with the emplacement of hydrothermal anhydrite and baryte (Table 9.15). The process occurs in heated systems with high water to rock ratios, where the interplay of high temperature water, carbon dioxide and methane under pressure represents the effective and efficient thermal driving force for reactions and solvent for product extraction and migration. Migration of hydrothermal petroleum can occur as a bulk phase, or in emulsion and solution.

Table 9.15 Overview of hydrothermal processes affecting organic matter alteration

Hydrothermal petroleum generation		
Alteration reactions (importance)	Compound type	
(a) Reduction (primary)	Aliphatic hydrocarbons	
(b) Oxidation (minor)	PAH, alkones	
(c) Synthesis (trace)	Thioheterocyclic compounds	
Hydrothermal petroleum migration		
Source of organic matter	Products	Relative concentration
(a) Marine (Guaymas Basin)	Gas (CH_4-C_{10})	High
	Oil (C_8--C_{40+})	Intermediate
	Asphalt (>C_{40})	Minor
(b) Terrigenous (Middle Valley)	Gas (CH_4-C_{10})	Trace
	Oil (C_8--C_{40+})	High
	Asphalt (>C_{40})	Intermediate
Hydrothermal fluids as solvents		
Fluid	Relative importance state:	Effect:
(a) Water	Dominant/ near-critical	Enhanced oil solubility
(b) Methane	Minor/supercritical	Complete oil solubility
(c) Carbon dioxide	Minor/supercritical	Complete oil solubility
Hydrothermal petroleum migration		
(a) Effective in systems with high water to rock ratios (unlike conventional sedimentary basins)		
(b) Migration styles		
Bulk phase (trapped in filled veins and voids)		
Emulsion (trapped in fluid inclusions)		
Solution (precipitated as wax crystals in chimneys and fluid conduits)		

After Simoneit 1994

Hydrothermal oils and the associated deep seafloor circulation in the Guaymas basin have been used as a modern analogue to explain the hydrocarbon-entraining Proterozoic ore systems in the McArthur Basin, Australia (Chen et al. 2003) and Besshi-type ore deposits (Chap. 16). Polycyclic aromatic hydrocarbons in ore and mudstones within the McArthur River ore deposit show compound distribution patterns similar to those of hydrothermally generated petroleum in the Guaymas Basin, both are significantly different from those found in conventional oil accumulations. The polycyclic aromatic hydrocarbon abundances and their isomer distributions result from a temperature gradient between the source of mineralizing fluids and the sediments, indicating an active hydrothermal system fringed the McArthur ore system during ore precipitation within partially-lithified seafloor sediments.

Although the evidence is clear for hydrothermally-cracked hydrocarbons migrating through sediments at active spreading centres, the inherent association with active faulting and tectonism in modern ocean spreading centres means most hydrocarbon product is lost to the overlying seawater column through a lack of appropriate longterm traps and seals (Kvenvolden and Simoneit 1990). Perhaps such systems are more likely to trap oils in areas where there is a fortuitous association between hydrothermal circulation and downdip end of salt allochthons flowing basinward across a deep seafloor in a salt floored rift, as in some parts of the Red Sea troughs and in the Proterozoic McArthur succession (Chap. 15).

There is an even older example in this hydrothermally-cracked oil spectrum. It is indicated by oil remnants in a 3.2 Ga Early Archaean deep-sea volcanogenic massive sulphide deposit in northwest Australia (Rasmussen and Buick 2000). Archaean seawater lacked sufficient sulphate or Ca to form anhydrite, so oil was preserved in fluid inclusions within hydrothermal baryte, and as pyrobitumens intergrown with polymetallic sulphides. Petrographic textures show that the oil was emplaced and thermally altered (cooked) before latestage sulphide mineralization. Its presence implies subseafloor hydrothermal petroleum generation was active during the Early Archaean, possibly providing an energy and carbon source for a subsurface microbiota that was metabolizing hydrothermal sulphur species.

Summary

Evaporites and associated brines play a significant role in the deposition, accumulation and subsurface evolution of both the organic matter and its hydrocarbon products as well as related metal sulphide accumulation, throughout eogenesis, mesogenesis, telogenesis and metamorphism.

Organic matter in modern hypersaline systems tends to accumulate in bottom sediments beneath density-stratified saline water and sediment columns in evaporitic settings where upper portions of layered hydrologies are subject to oscillations in salinity and brine level. Organic matter is not produced at a constant rate in such systems, rather, it is produced as pulses by a halotolerant community in response to relatively short times when less stressful conditions occur in the upper part of the layered hydrology (Fig. 9.75). This happens when an upper less-saline water mass forms on top of nutrient-rich brines or within wet mudflats when waters in and on top of the uppermost few millimetres of any microbial mat freshen.

The resulting bloom (a time of "feasting") by halotolerant algae and cyanobacteria is a time characterized by very high levels of organic productivity (Fig. 9.75a). In mesohaline waters where light penetrates to the bottom, the organic-producing layer is generally the upper algal and bacterial

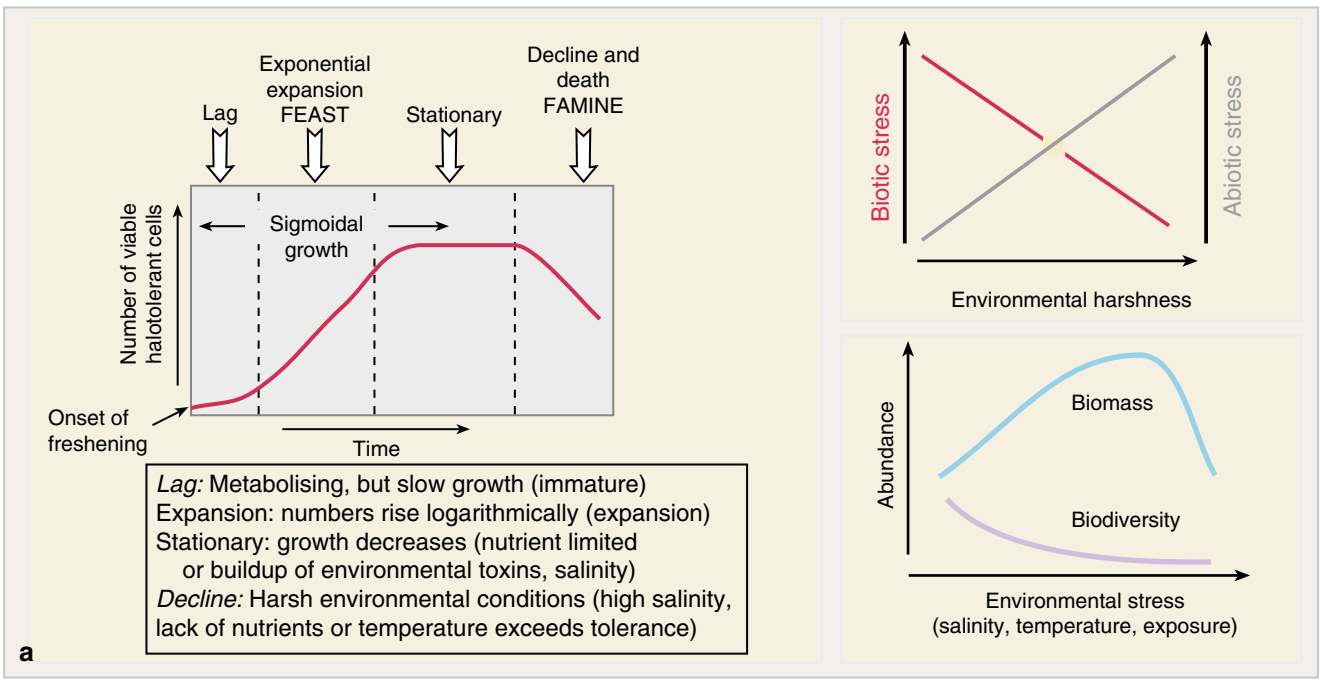

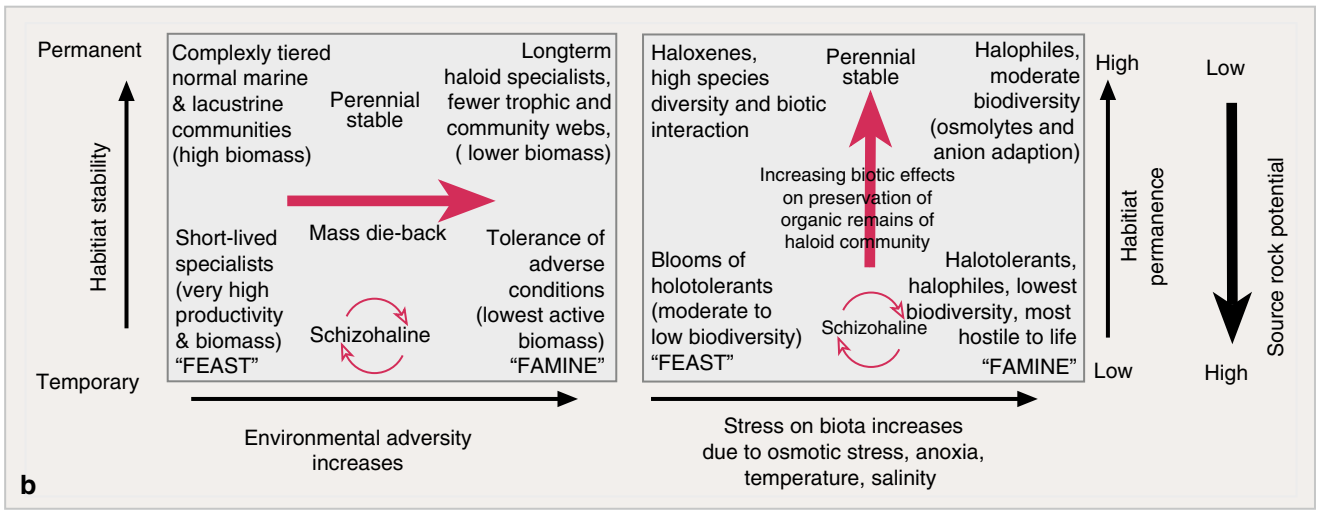

Fig. 9.75 Life in saline systems. (**a**) General ecological principles in stressed saline ecosystems. Sigmoidal growth curve of life moving into a newly created niche (as is created by a freshening event setting up a layered brine). As environmental harshness increases due to abiogenic stress factors (such as increasing salinity, osmotic stress and temperature) the level of biogenic stress (predation or grazing) decreases allowing a few well adapted species to flourish leading to a decrease in biodiversity and a short-term increase in biomass. (**b**) Schematic summary ("halomancy") of the interrelationships between habitat stability, environmental stress or adversity, biodegradation, anoxia and source rock potential in an evaporite basin, showing why schizohaline environmentally stressed mesohaline systems tend favour the accumulation of organic matter in bottom sediments

portion of benthic laminated microbialites (typically characterized by elevated numbers of cyanobacteria). In stratified brine columns, the typical producers are the planktonic algal or cyanobacterial community inhabiting the upper freshened water mass. Halotolerant autotrophic microbial communities, living off the remains of this plankton, float mid-water at the halocline of the density stratified brine columns. Similar aerobic decomposers can also constitute bottom-layer communities in zones of oxygenated oligotrophic waters.

Short pulses of extremely high organic productivity during times of freshened mesohaline surface waters in-turn create a high volume of organic detritus settling through the water column and/or construction of benthic microbial mats. Then, with the end of the freshening event, the ongoing intensely arid climate that characterizes evaporitic depressions means that salinities, temperatures and osmotic stresses increase rapidly in the previously freshened water mass. This leads to a time of mass die-off, in the once flourishing mesohaline community ("famine;" Fig. 9.75). First, these increasingly salty waters can no longer support haloxene forms. Then halotolerant life dies back and finally, by the halite precipitation stage, only a few halophilic archaea and bacteria remain in the brine column (typically acting as heterotrophs and fermenters). Repeated pulses of organic matter created during a freshening event in a stratified brine column thus create laminated bottom sediment.

Hydrogen-rich algal and eubacterial debris is best preserved within sediments where pore waters are anoxic and remain so until the resulting kerogen is sufficiently buried for it to generate liquid and gaseous hydrocarbons (Demaison and Moore 1980). Thus the preservation of organics with long-chain hydrocarbons intact is most likely in settings characterized by long-term anoxia (typically inhabited by less efficient decomposers). This tends to occur beneath stratified eutrophic saline brine columns with a permanent anoxic mesohaline bottom water mass and a transiently freshened upper water mass. Preservation is also possible in benthic mats in shallow oligotrophic systems with permanently hypersaline pore waters, but the propensity for periodic bottom oxygenation means preservation potential of oil-prone mats is less likely in this setting, as is also the case in mats of the strandzone.

Increasing rates of mineral precipitation at higher salinities means levels of hydrogen-prone organics are highest in sediments deposited in schizohaline waters that remain in the mesohaline field. Once ambient salinities pass into the penesaline and supersaline, the proportion of organics in the sediment becomes insignificant as it is rapidly diluted by large volumes of gypsum and halite (or trona and glauberite in some continental penesaline/supersaline waters).

Feast and famine cycles are a biotal response to environmental salinity conditions that at first are eminently suitable and then increasingly adverse to life. It reflects the typical biological response to rapid niche creation and expansion as the freshened water layer sets up in the evaporitic depression, and is known as the sigmoidal growth response (Fig. 9.75a). Freshening of surface waters creates a vacant ecological niche into which microbial life rapidly expands, flourishes and then once more dies back as drying or brine concentration shrinks suitable niche space.

Long-term stability in any ecosystem leads to domination by "specialist" species that are well adapted, diverse and efficient in terms of energy flow-nutrient utilisation (Fig. 9.75b). This biodiverse community takes up and recycles carbon very efficiently through the system and the potential for large volumes of carbon passing into the burial realm is low and hence source potential is also low (a good analogy in the marine realm is the ecosystem that typifies a stable tropical coralgal reef).

In contrast, a schizohaline system is one defined by high habitat instability, its lack of habitat permanence encourages opportunistic lifestyles (cycles of "famine or feast"). Opportunist species expand rapidly into any suitable niche space, but then just as quickly die back or encyst as conditions become adverse. Such systems are characterised by high biomass pulses and relatively low species diversity, leading to pulses of organics accumulating in the evaporitic depression, with the remains likely to be buried and "pickled" beneath anoxic bottom brines and pore waters, giving such systems a higher source rock potential (Fig. 9.75b).

Some hypersaline settings are intermediates in that their waters are constantly hypersaline, stressful to most life, but suitable to a few well-adapted species. These regions are usually populated by a few very specialized species (e.g., "high-salt-in" halophiles) that can survive and flourish in conditions where most life dies. They photosynthesise and metabolize successfully in these hypersaline conditions (for example, by living near haloclines), but do so at rates that are much slower than the growth rates attained by halotolerant "opportunists" at times of "feast." The long-term cycling of organic materials means bottom sediment layers tend to have lower levels of entrained organics preserved compared to the schizohaline-mesohaline.

There are four main geological association where feast and famine conditions during deposition encourage the preservation of elevated levels of hydrogen-prone organic matter, namely; mesohaline platforms and basinwide settings, especially in the early mesohaline stages of salt precipitation. These evaporites source rock association have no modern day counterparts, whereas the mesohaline lacustrine and deep seafloor stratified brine lake associations for source rocks.

Once the enhanced levels of organics stored in an evaporitic host enter the burial realm, other aspects of the evaporite association can further aid in preservation of evaporitic protokerogens. Shallowly buried sediments and their pores

beneath hypersaline depositional settings are generally filled by anoxic high-salinity pore fluids. This is especially so in a reflux curtain, which tends to slow or prevent the entry of less dense fresher waters. The latter tend to carry communities of the more efficient oxygenic decomposers. Dense, highly-saline reflux curtains below salt beds can persist for tens of millions of years and last to depths that are well into the catagenic realm. This prevents or slows entry of oxidising waters from above or below, other than in local fault or salt wedge edge-focused regions in the basin hydrology. However if the organics are encased in salt, this can slow or prevent the release of catagenic fluids and the evolving organics can remain until the temperatures of thermochemical sulphate reduction and then metamorphosis are reached. If the kerogens remain encased in salt, the lack of any effective permeability can be a negative in terms of hydrocarbon transfer and storage, but a positive in the creation of chloride-rich metal sulphide carriers as fluids are released when halite ultimately dissolves at uppermost diagenetic or lower end metamorphic realm and beyond.

Hydrocarbons and Evaporites

10

Introduction

Even though evaporites constitute less than 2 % of the world's sedimentary rocks, one-half of the world's largest oilfields are sealed by evaporites, the other half are sealed by shales (Fig. 10.1; Grunau 1987). Kirkland and Evans (1981) argued that evaporites overlie or seal carbonates containing an estimated 50 % of the world's known total petroleum reserve. Of the world's 25 largest gas fields, 9 are sealed by evaporites and 16 by shales and hydrates. Sixteen are capped by Mesozoic seals, 7 by Palaeozoic seals, and only two by Tertiary seals. Fourteen are in the 1,000–2,000 m seal-depth interval, nine in the 2,000–3,000 m interval; and two in the 0–1,000 m interval. As one would expect, more gas fields than oilfields are sealed by Palaeozoic caprocks, and more oilfields than gas fields are sealed by Tertiary caprocks. Surprisingly, the seal depth intervals for the 25 largest oil and gas fields do not differ significantly. However, Grunau argues many "supergiant"[1] gas accumulations below depths of 3,000 m and have either not yet been discovered, or have not yet been put in production (e.g. much of the Khuff-hosted gas in North Dome in the Middle East).

The exemplary ability of evaporites to act as seals holding back large hydrocarbon columns is clearly seen in the Middle East, where Ghawar, the world's largest oil field, is sealed by bedded evaporites of the Arab Formation and the overlying Hith Anhydrite seal Fig. 10.1a). This seal holds back an estimated remaining reserve of more than 100–200 billion barrels. Evaporites also seal Safaniya the world's largest offshore field, also in Saudi Arabia, with estimated reserves of more than 25–30 billion barrels of oil and 5 billion cubic feet of natural gas. Likewise evaporites are the seal to North Field in offshore Qatar, the world's largest single gas field (non-associated gas) with more than 500 tcf of reserves (Fig. 10.1b; Alsharhan and Nairn 1997). This gas is reservoired and sealed in the evaporitic dolomites of the Permian Khuff Formation and recent announcements by the Qatari Government have documented more than 900 tcf of certified non-associated gas in the structure.

According to Klemme (1983) all the supergiant gas fields in the world are overlain directly, or somewhat directly, by laterally extensive evaporite beds or by permafrost carapaces with their attendant gas hydrates. Most of the giant Russian gas fields (largely in Siberia) have hydrate seals, while those of the Middle East are mostly sealed by evaporites. In 53 % of the gas fields that have a net recovery of 3.5 tcf or more, evaporites are either associated with the reservoirs or form the trap (Billo 1996). Evaporite seals play a significant role in facilitating Suadi Arabia's position as the world's dominant producer of crude oil (Fig. 10.2).

All of the giant gas fields in thrust belts have an evaporite seal (Downey 1984) reflecting salt's ability to maintain seal integrity as it deforms, while underlying sediments fracture into salt-sealed reservoirs. Chengzao and Qiming (2008) conclude that high-quality regional salt cap rocks are essential for the formation of the super-rich, abnormally pressured, giant gas fields, such as Kela-2 in the Tarim basin, while buried anticlines under the overthrust décollement zone are favourable gas habitats. Deforming shallow salt allochthons in the Gulf of Mexico and elsewhere, not only control the seafloor topography focusing deposition of nearby sand and carbonate buildups, but later can flow over these deposits to create the seal (Fig. 6.66). Halokinesis creates both suprasalt and subsalt traps. The presence of an impervious salt bed or allochthon also helps maintain higher than expected porosities and pressures in underlying reservoirs (Fig. 8.22).

In the gently-folded belt in front of the main Zagros deformed zone in Iran and Iraq an intimate association exists between sediment deposition, salt flow and the creation of salt-sealed reservoirs. This foreland basin is an area

[1] A giant oil field contains more than 0.5×10^9 barrels of expected ultimate recoverable oil, while a supergiant contains more than 5×10^9 barrels (Fitzgerald 1980). The equivalent separation between giant and supergiant gas fields is 0.5×10^9 and 5×10^9 BOE, respectively.

BOE is barrels of oil equivalent on a BTU basis; 1 barrel of oil = 5.61 ft^3, so the respective cutoffs for giant and super giant gas fields are 3 and 30 tcf (trillion cubic feet).

© Springer International Publishing Switzerland 2016

J.K. Warren, *Evaporites: A Geological Compendium*, DOI 10.1007/978-3-319-13512-0_10

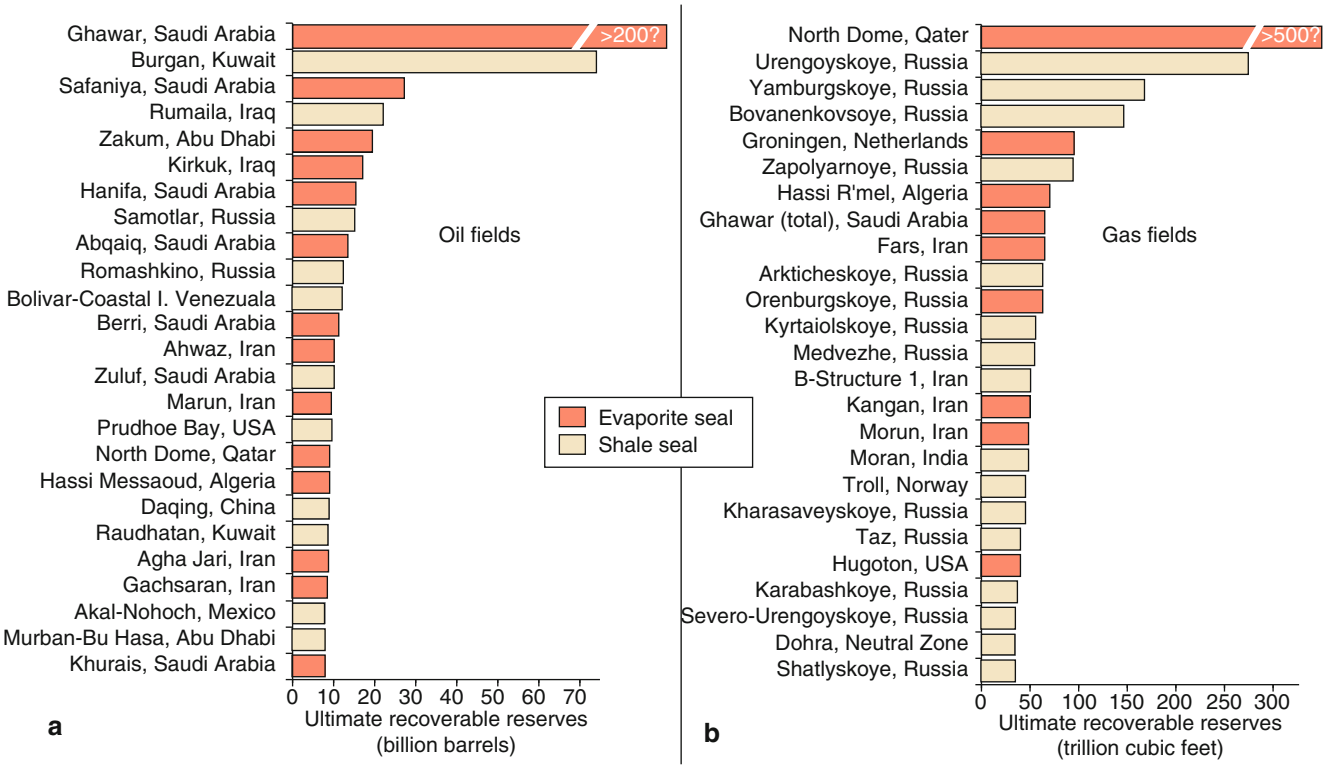

Fig. 10.1 Seal type and ultimate recoverable reserves in 25 of the world's largest oil (**a**) and gas (**b**) fields (In part after Grunau 1987)

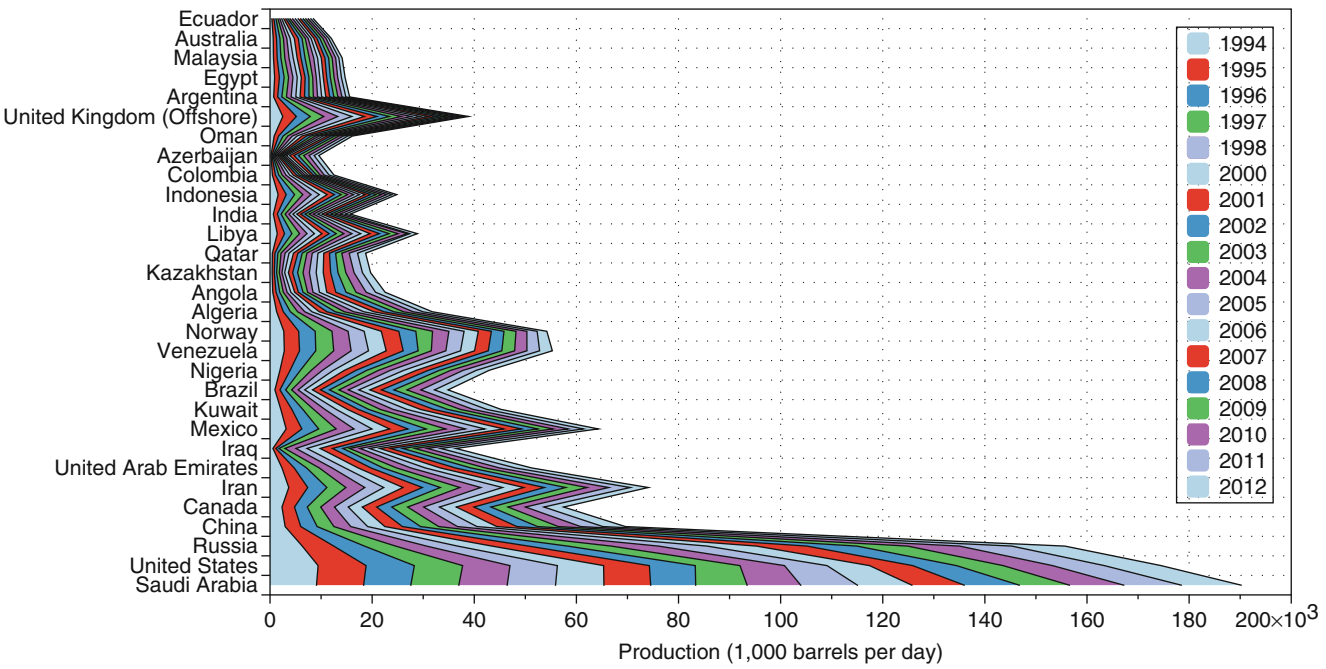

Fig. 10.2 Annual crude oil production from top 20 producing countries, cumulative area plot, ranked by 2012 production (Data downloaded and replotted from U.S. Energy Administration website <http://www.eia.gov> last accessed September 10, 2013)

undergoing compression and syndepositional folding, where crests are still growing at the surface (growth folds) and so controlling the distribution and structuration of both reservoir and seal. The same collision system also created the restriction that allowed the Fars-Gasharan seal to precipitate. It is an area with a great deal of potential for future evaporite-associated discoveries, as evidenced by the 1999 discovery of the Azadegan oil field, near Ahwaz in the Zagros Foldbelt of southern Iran. As announcedby NIOC (National Iranian Oil Company) in September 1999, the structure holds a possible 24–26 billion barrels of oil in place over an area of more than 520 km^2, with something like 5–6 billion barrels of recoverable oil. If the size of the projected field is confirmed by ongoing drilling, it will become one of the world's supergiant fields. To put this level of reserves into some perspective, 26 billion barrels of oil in place is more than the total known reserves in China.

The International Energy Agency (IEA) has predicted that unconventional oil, which includes bitumen, heavy oil, and tight oil, will contribute only 13 % of the global supply and unconventional gas consisting of tight gas, shale gas, and coalbed methane, 26 % of the global gas supply by 2035. Conventional petroleum supply will come largely from the remaining reserves and reserve growth from both discovered and undiscovered giant fields. Today, most of the larger simpler more readily and predictably exploited siliciclastic reservoirs have been found (Fig. 10.3). There is the exception of deepwater realm settings, targeting turbidite and other deepwater sands sealed by muds. But, in many frontier regions for such deepwater sands, such as the Gulf of Mexico, offshore Brazil, Angola and Namibia, salt plays a role either as seals or the creation of suprasalt trap configurations. Oil and gas exploration in circum-Atlantic Aptian basins is increasingly focused on carbonate and lacustrine reservoir systems, these too are settings where evaporite seals and brine-derived diagenetic fluids are more common.

The importance of the evaporite-hydrocarbon association is clearly seen in a compilation of giant oil and gas discoveries across the period 2000–2012 (Fig. 10.3; Bai and Xu 2014). Of the 120 giant oil and gas fields discovered in that period some 54.6 % were hosted in marine carbonates and 12 % in lacustrine carbonates, meaning less than a third of new giant discoveries were in siliciclastic reservoirs (Fig. 10.3a). Some 56 % of these oil and gas giants had an evaporite seal, with 82 % of the marine carbonates having an evaporite seal and 91 % of the lacustrine carbonates having an evaporite seal (Fig. 10.3b, c). Clearly, carbonate reservoirs with evaporite seals constitute the majority of the giant oil and gas discoveries in the period 2000–2012, and the proportions of this association are likely to increase in conventional discoveries across the next decades.

Of the 120 oil and gas giants discovered in the period 2000–2012, one is a megagiant field with a recoverable reserve of 50 Bboe or more and 6 are supergiant fields with recoverable reserves of 5 Bboe or more. The seven largest fields are: Galkynysh (aka Yolotan or Osman) gas field in the Ama-Darya basin of Turkmenistan with an original[2] 2P reserve of 67.1 Bboe, making it likely the second largest known gas field in the world; Kashagan oil field (18.1 Bboe) in the North Caspian basin; Kish 2 gas field in the Arabian basin (Iran): Lula (previously known as[3] Tupi), Franco and Libra oil fields in the Santos basin of offshore Brazil; and Sulige gas field (5.7 Bboe) in the Ordos basin, China. In this listing, the geology of Galynysh is not yet reliably published, of the remaining 6, only Sulige does not have an evaporite association (Saltworks® data base, version 1.6). In this scenario, evaporites studies can only become more important in both exploration and development in the years to come.

Predicting the position and quality of potential reservoirs in evaporite terranes is difficult without integrating notions of feedback between deposition, diagenesis and structural evolution. Therein lies the difficulty in placing evaporite-associated reservoirs and traps in classic terms of structural, stratigraphic and diagenetic traps. When classifying a field with an evaporite trap, the fact that salt is so mobile, so soluble, and so diagenetically active, separates it from other trap styles in a petroleum system. It means that a salt unit, by its comings and goings, plays ongoing and multiple roles in generating reservoirs and traps from the time of deposition through diagenesis to structuring. Tying the resulting oil and gas field to a static and categoric breakdown is near impossible as salt-induced structuring, diagenesis and deposition are often penecontemporaneous and in a state of intimate feedback with adjustments contuing throughout the mesogenetic and telogenetic realms.

Over the years, I have come to regard conventional pigeonholes for salt-associated traps (such as depositional, diagenetic, structural) as next to useless in predicting likely positions of hydrocarbons in evaporitic provinces. Rather, as a salt unit is typically the most obvious feature on a seismic section, especially in carbonate terrains, I use a much simpler classification of; "Where's the salt?" At their simplest, evaporite-associated reservoirs all occur adjacent to either bedded or halokinetic salt, or their solution residues (Table 10.1; Fig. 10.4). With bedded or halokinetic salt or solution breccias, there are three possible positions of potential reservoir, namely; subsalt, intrasalt and suprasalt. Within

[2] 1P reserves = proven reserves (both proved developed reserves + proved undeveloped reserves).

2P reserves = 1P (proven reserves) + probable reserves; hence proved AND probable.

3P reserves = the sum of 2P (proven reserves + probable reserves) + possible reserves; hence, all 3Ps are proven AND probable AND possible.

[3] Name changed to honour former Brazilian President, Luiz Inacio Lula da Silva.

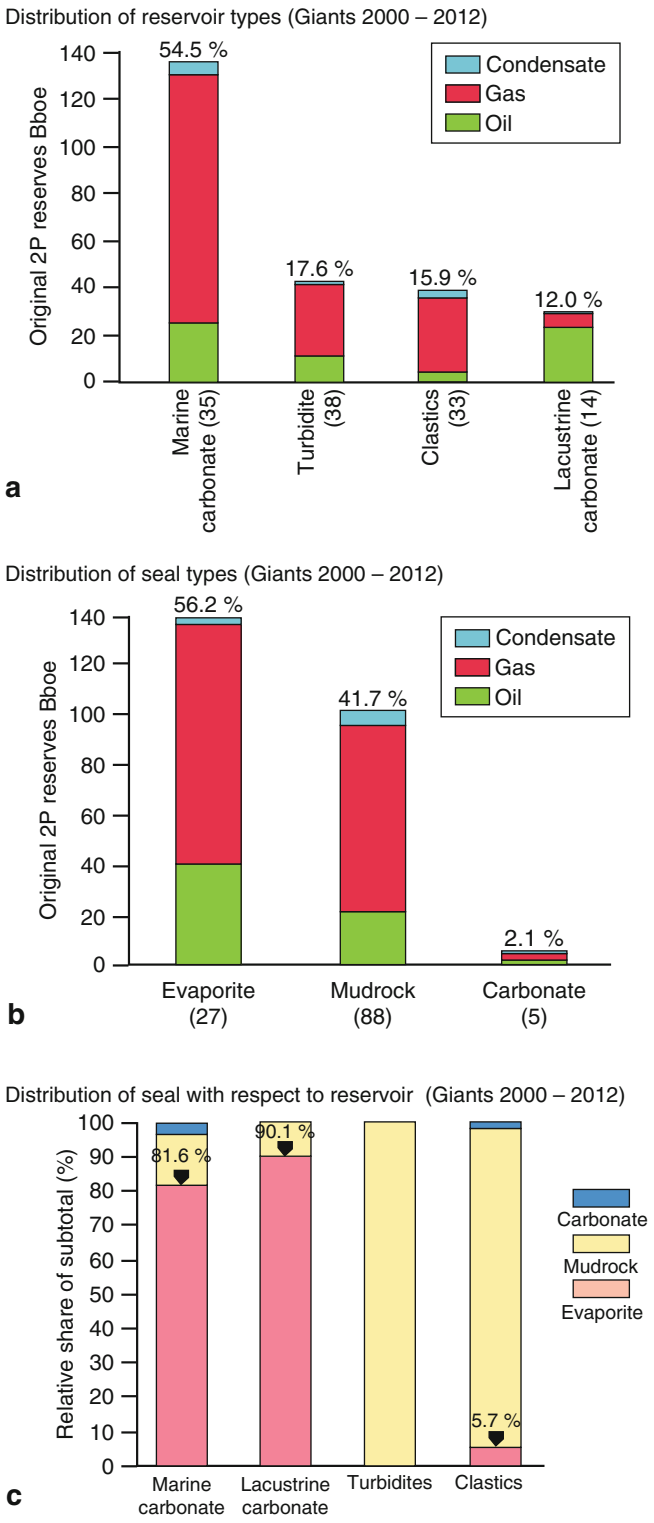

Fig. 10.3 Evaporite seals to giant fields discovered in the period 2000–2012. (**a**) Dominant reservoirs for oil and hydrocarbon type. (**b**) Seal mineralogy. (**c**) Relations of reservoir to seal mineralogy (After Bai and Xu 2014)

Table 10.1 Role of evaporites in creating hydrocarbon reservoirs and traps

		Effect of evaporite on nearby reservoir		Effect of seal itself	
		Depositional	Subsurface/diagenetic	Depositional	Subsurface/diagenetic
Bedded salt	Suprasalt	Presence of brine, either from salt dissolution or deposition of nearby salt can prevent accumulation of carbonates or siliciclastics containing a normal marine biota.	Solution of bedded salt creates collapse sinks and fronts that can enhance deposition of porous sediments or encourage collapse fracturing in overlying beds	Not applicable	Dissolution of salt creates a dense brine plume that aids in the formation of hydrodynamic traps
	Intrasalt		Solution of surrounding salt creates fractured and brecciated intrasalt beds that can stack into porous solution breccias	Not applicable	Permeable intervals are encased in bedded salt
Halokinetic	Subsalt	Evaporite bed acts as a source of Mg-rich brine that improves permeability of underlying or adjacent bed (creation of mouldic porosity and brine reflux dolomite)		Evaporite bed acts as top seal and/or lateral seal to reservoir (well documented)	Evaporite bed acts as a source of saturated brine for cement plugging of underlying or adjacent unit
	Suprasalt	Shallow halokinetic salt focuses the deposition of porous sediment around areas of uplifted seafloor or land surface. Can also influence the formation of slumps and CCD-related sedimentation	Dissolution of the upper salt surface creates a caprock reservoir	Salt flows carries blocks of anhydrite/dolomite and allochthon dissolution creates salt ablation (retreat) breccias	Passage of salt allochthon creates adjacent zones of alteration/cementation that may continue to act as a barrier to fluid flow even when the salt is no longer present (weld)
	Intrasalt	Not applicable	Salt flow can break up, fracture and rotate organic-rich intrasalt beds, allowing them to become self-sourcing reservoirs encased in a halokinetic salt seal	Brecciation of intrasalt bed leads to overpressured blocks within the salt mass	Salt flow allows salt unit to maintain seal integrity
	Subsalt	Not applicable	Brine plume created on the underside of a dissolving salt allochthon can alter underlying beds, which in some situations (e.g. fluid breakthrough) can enhance permeability of underlying beds via dolomitisation/fracturing	Salt allochthon acts as top seal or lateral seal to reservoir sands (well documented). The ability of salt to maintain seal integrity under both extension and compression is significant	Passage of salt allochthon creates adjacent zones of alteration/cementation that may continue to act as a barrier to fluid flow even when the salt is no longer present (weld)

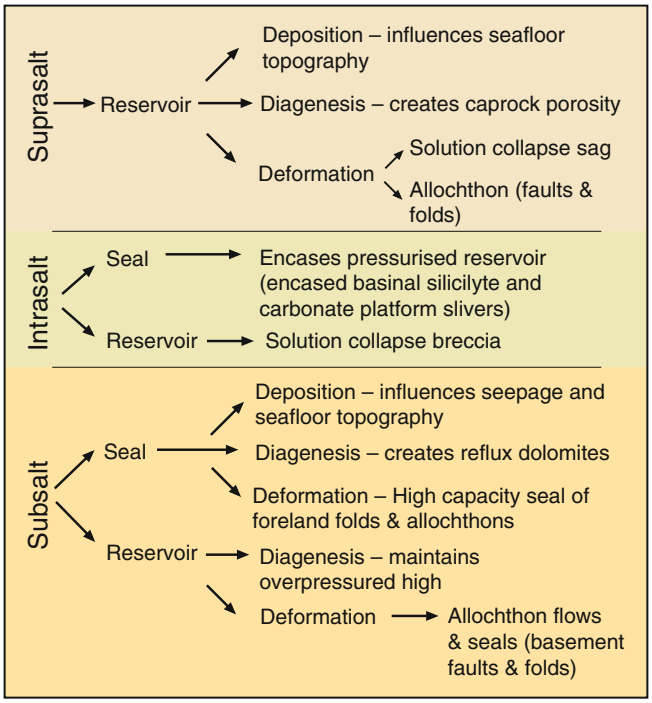

Fig. 10.4 Classification of evaporite seals and associated reservoirs relative to the salt body position and the dominant mechanisms

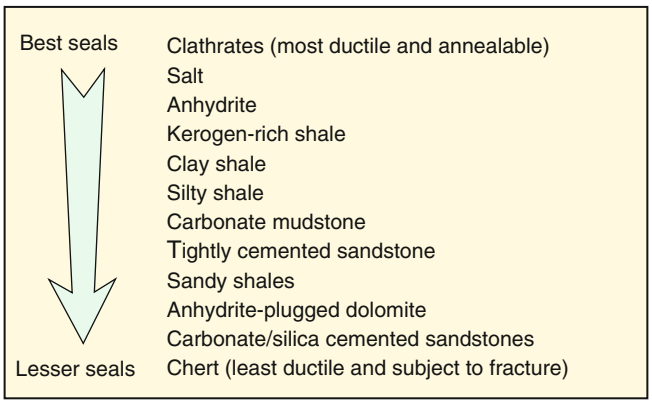

Fig. 10.5 Differing ability to form a seal is related to a rock's inherent ductility in the subsurface (In part after Downey 1984)

a single hydrocarbon fairway there may be reservoirs sitting in more than one position. Where I can, I further classify each reservoir in terms of the relative roles of deposition, diagenesis and structure as controls on the position of the targeted hydrocarbon accumulations.

Understanding and predicting lateral continuity of both bedded and halokinetic salt seals is an important exploration and development tool. Think about this, when a seal bed with a vertical permeability of 10^{-8} darcies is a mile long on each side and is cut by a single fracture 6 μm wide, then the drainage through that single fracture is equivalent to the total fluid flux through the square mile of seal. Downey (1984) calculated that a single fracture 25 μm wide atop a 150 m oil column would leak oil at rate of more than 150 million barrels per million years. Halite is such an excellent seal as it tends to flow rather than fracture. When is does fracture in the subsurface the crack quickly reanneals and sutures via pressure-solution recrystallisation (Chap. 6).

Continuity of ancient saltern and mudflat seals and their ability to resist fracturing via reannealing means salt beds can gather and constrain subsalt hydrocarbons over large drainage areas. In suprasalt traps, the role of salt in creating reservoirs and traps ranges from stratigraphic seal, through diagenetic trap, to a creator of structural traps (anticlinal

[halokinetic], fault and drape traps). The key factor in assessing the capacity of any seal, including salt, is timing of any microfracturing or fracturing relative to hydrocarbon emplacement in an underlying or adjacent potential reservoir. In other words, does any loss of seal capacity precede or postdate possible storage of hydrocarbons in the reservoir? We shall soon examine a number of examples from various bedded and halokinetic reservoir associations. First, we need to consider why salt units are excellent longterm seals; it's a discussion where salt's inability to maintain ongoing penetrative fractures cannot be overestimated.

Seal Capacity of Evaporites

In Chap. 9 we saw that there is a depositional association between evaporites and some types of organic-rich oil-prone source rocks. In Chap. 6 we saw how flowing salt created structures capable of trapping substantial volumes of hydrocarbons. But, of the various reasons for the evaporite-hydrocarbon association (source, trap and seal), the most commonly cited is the efficiency of evaporite layers in holding back substantial hydrocarbon columns for lengthy periods of time, even as adjacent nonevaporite strata fracture and leak. Using a worldwide database of 350 giant oilfields, MacGregor (1996) showed oil pools are dynamic short-lived phenomena, with a median age of 35 Ma. A third of them show evidence for post-entrapment destructive processes, particularly erosion, fault leakage, gas flushing and biodegradation. Biodegradation began in many cases prior to complete filling of the trap. Re-entrapment of oil released from spilling or breached traps was common to all regions. He found the main controls on oilfield preservation to be post-entrapment tectonism and seal type, with temperature and hydrodynamic regimes being secondary factors. He concluded the potential for giant oilfields is greatest in tectonically quiescent basins with evaporite seals. As areas with the best development of this association he cites as the Middle East centred on Saudi Arabia/UAE and the Permian Basin of the southwest USA. Billo (1996) noted a similar association when discussing the same areas.

So Why Do Evaporites Seal?

In terms of seal capacity and resistance to fracturing, the most effective sedimentary seals are gas hydrates, followed by evaporites, then shales (Fig. 10.5; Downey 1984). To seal an economic accumulation of hydrocarbons, any sealing surface or lithology needs to be laterally continuous, maintain a constancy of properties over large areas, be relatively ductile, and be widespread over a sedimentary basin. A fundamental requirement for any effective seal is that the minimum[4] displacement pressure of the lithologic unit comprising the sealing surface be greater than the buoyancy pressure of the hydrocarbon column in the subjacent accumulation. Hence, the size of the pore throats and the density of entrained hydrocarbons and water are of great importance in determining whether or not a particular lithology can act as a seal. Density/buoyancy differences between oil and gas means there are fields, such as some evaporite-cemented San Andres Formation mudstones in the Permian Basin of Texas, where dolomitic mudstones act as a seal to liquid hydrocarbons, yet flow gas.

Any lithology can be a seal, but other than[5] clathrates, evaporites are the most effective regardless of hydrocarbon type and structural setting (Fig. 10.5). Unlike the low temperatures requirements for a clathrate seal, evaporite seals, with their extremely high[6] entry pressures, ductility, very low permeabilities and large lateral extents, can maintain seal integrity over wide areas, even when exposed to a wide range of subsurface temperature and pressure conditions. A typical shale seal has a permeability $\approx 10^{-1}$ to 10^{-5} md, with rare values as low as 10^{-8} md (Fig. 10.6a). Quantitative measurement of evaporite permeability is beyond the capacity of standard instruments used in the oil industry and is mostly a topic of study for engineers working with waste storage caverns (see Chap. 13). Their work shows the permeability of halite is a nanodarcy or less, that is, undamaged subsurface salt has measured[7] permeabilities that are less than 10^{-21} m^2 (10^{-6} md) with some of the tighter halite permeabilities $\approx 10^{-7}$ to 10^{-9} md and typical massive anhydrites $\approx 10^{-5}$ md (Beauheim and Roberts 2002). Pore pressures in such halites typically approach lithostatic (Ehgartner et al. 1998).

Measures of salt permeability or brine permeation are typically described through Darcy's law (Bérest et al. 2011).

[4]Entry pressure is the minimum capillary pressure required to force oil or gas from one water-filled pore to the next.

[5]Gas or methane hydrates (more precisely called clathrates) are the solid form of mostly methane trapped in a crystalline framework of ice and are only found in low temperature seafloor or permafrost conditions. They seal onshore supergiant fields of west Siberia and Timan-Pechora basins of Russia and occur also as solid bacterial-associated products in the deep seafloor, where temperatures are low and water depths exceed 500 m. Seafloor clathrates are thought to contain more than 20 quadrillion cubic metres of methane. In oil equivalents this is around 15 trillion m^3 (116 trillion barrels), more than 30 times the likely volume of oil and gas reserves (Hunt 1996).

[6]Synonymous with minimum displacement pressure.

[7]In most oilfield applications the millidarcy (md), which is 0.001 darcies, is used as a measure of permeability. Permeability is fundamentally a L^2 unit. In SI it is expressed in μm^2, which is 10^{-12} m^2. In conventional metric use it is expressed in m^2 (metres squared) or cm^2. The conversion between oilfield and SI units is 1 darcy = 9.869×10^{-13} m^2. In practical terms, 1 md and 1 μm^2 are essentially equivalent, while in terms of hydraulic conductivity, 1 darcy = 10^{-5} m/s.

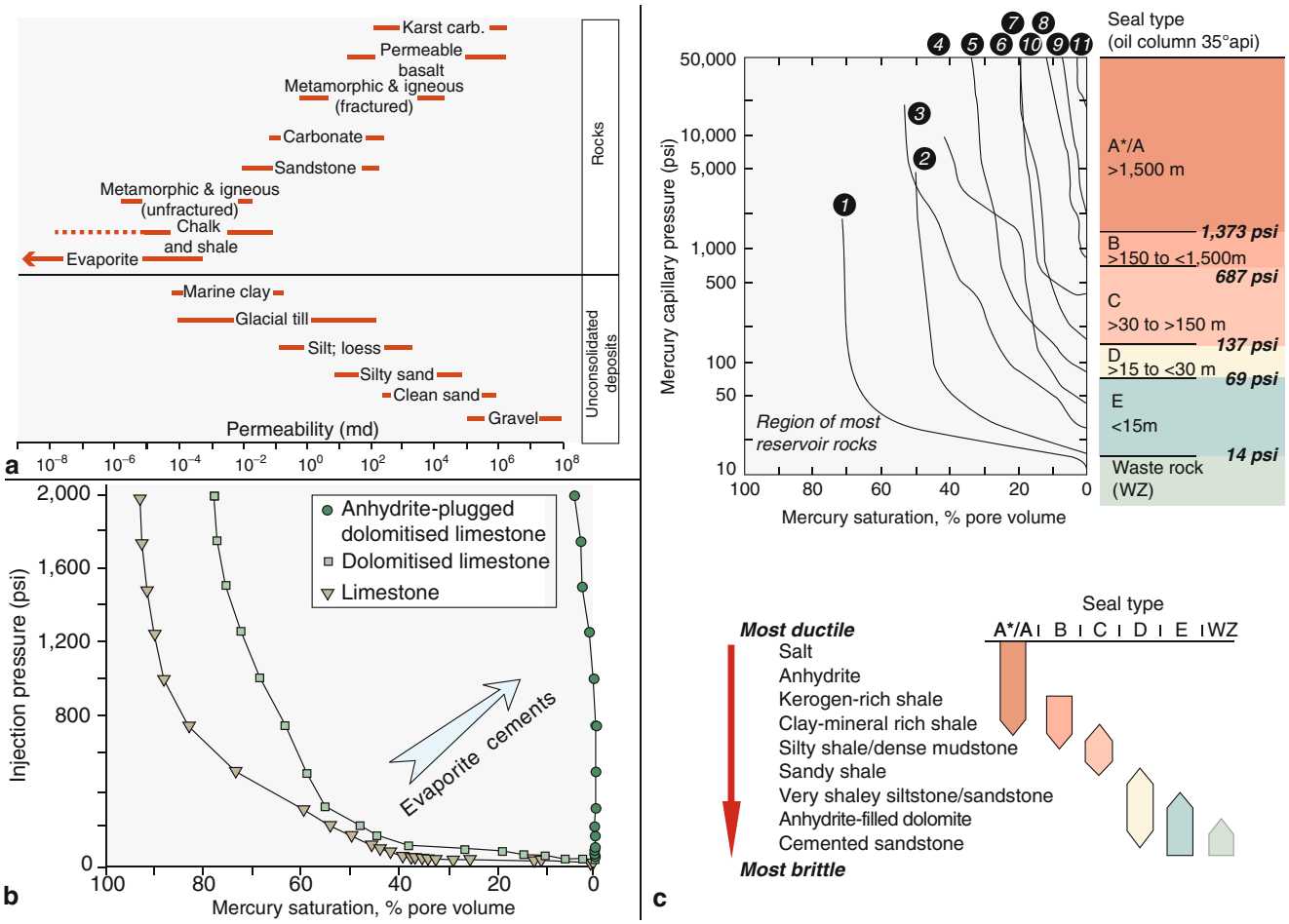

Fig. 10.6 Seals. (**a**) Relative ranking of permeability of various lithologies (In part after Beauheim and Roberts 2002) (**b**) Hg-injection curves from representative lithologies in a sequence undergoing reflux dolomitisation and overdolomitisation (From Warren 1992). (**c**) Seal classification (A-E) based on air-mercury pressure curves for typical seal lithologies, denoted 1–9 (After Sneider et al. 1997 and Sneider 1995)

However, some authors believe that undisturbed rock salt is both liquid-tight and gas-tight in its primary state, and that the origin of the non-zero permeability measured during laboratory tests is likely due to damage that occurred during test sampling and preparation, or to undetected tiny leaks from the testing equipment. For these authors, the permeability observed in the vicinity of a well bore or a salt storage cavern (Chap. 13) is a secondary permeability, i.e., induced by the stress changes generated via drilling and cavern creation. According to Bérest et al. (2011) these differing views may also be explained, in part, by differences in salt compositions and crystal character. Bedded salt formations can contain a significant amount of insolubles (clay, anhydrite), which might be more permeable than the salt itself.

In terms of oil and gas seals, little or no leakage will take place through a laterally continuous evaporite seal when the reservoired hydrocarbon is oil. Even when the reservoired hydrocarbon is methane, little or no loss occurs, even by diffusion (Ehgartner et al. 1998). The much greater efficiency of evaporite seals is clearly seen in the total hydrocarbon volumes held back by the two lithologies. Total worldwide shale sediment volume in the crust is more that an order of magnitude greater than that of evaporites, yet the split between reservoired hydrocarbons below a shale or an evaporite seal is roughly 50:50 (Grunau 1987). Likewise, typical volumes of salt-sealed giant fields discovered in the last decade are much larger than that in mudrock-sealed systems (Fig. 10.3b).

Typical bedded evaporites, especially beds composed of monomineralic assemblages such as massive nodular anhydrite or massive halite, have measured entry pressures in excess of 3,000 psi. Most impure evaporite beds have entry pressures greater than 1,000 psi, as do many evaporite-plugged reflux dolomites (Figs. 10.6b and 10.7). Contrast this with most shales, which tend to be water-bearing (mostly bound and structural water) and have typical entry pressures between 900 and 1,500 psi (Fig. 10.6c; Sneider 1995, Sneider et al. 1997). Although such shales are respectable seals, over time shale allows substantial diffusive leakage of methane and even liquid hydrocarbons via inherent microporosity, less so if the shales are organic-rich. Even ignoring salts abil-

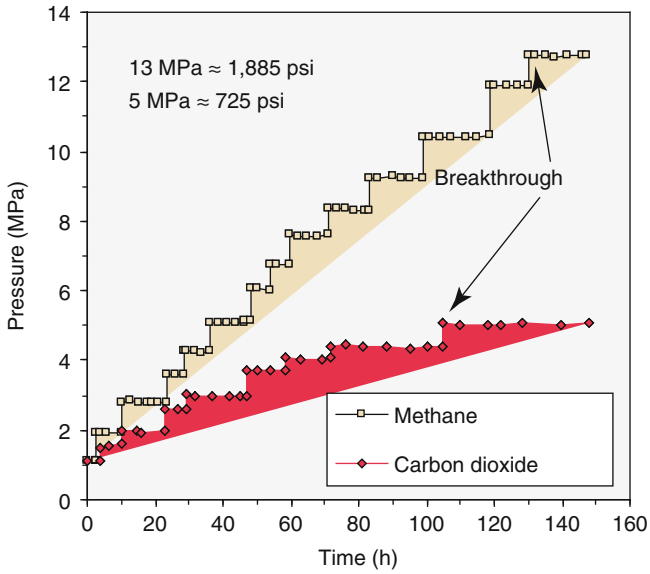

Fig. 10.7 Comparison of laboratory-measured breakthrough pressures between CH_4/brine system and CO_2/brine system for Midale anhydrite seal-rock (After Li et al. 2005)

ity to reanneal under stress, an evaporite seal has much lower intrinsic permeability that helps maintains its integrity. With permeabilities of 10^{-7} md, a hydraulic gradient of 0.01, and a porosity of 0.01, a brine would take somewhere between 3 and 30 million years to flow 1 m into an unfractured halite seal, while anhydrite, which has permeability some 100 times higher, a brine would take between 30,000 and 300,000 years to flow 1 m into the seal (Beauheim and Roberts 2002). Evaporites are excellent longterm seals to substantial hydrocarbon columns.

With the exception of clathrates, thick halites and some anhydrites, almost all fine-grained subsurface rocks will at some time in their burial history be subject to microfracturing and leakage. Otherwise, organic-rich mudstones and shales could not act as source rocks and there would be no primary migration of hydrocarbons. In contrast, rather than fracturing, most salt seals tend to lose their seal integrity either through dissolution windows or through salt-flow-induced breaches, which are defined by areas of overburden touchdown and focused subsalt leakage. Thick salt beds experience brittle fracture only at very shallow nearsurface and typically vadose conditions, such as Salar Grande in South America (Fig. 3.51).

Halite's very high ductility and its ability to flow, reanneal and re-establish lattice bonding by solution creep when subject to stress give it a low susceptibility to fracturing (Fig. 6.5b). The ability of a halite unit to maintain seal integrity, and so prevent the escape of hydrocarbons, reflects a combination of an ability to flow and reanneal under stress, and the small size of molecular interspace in its ionically-bonded NaCl lattice. Massive bedded halite units contain few, if any, interconnected pore throats. The distance between NaCl lattice units is 2.8×10^{-10} m, while the smallest molecular diameter of a hydrocarbon molecule (methane) is 3.8×10^{-10} m. The most common way that hydrocarbons migrate through an unfractured undissolved halite bed is if the halite contains impurities that render it locally porous and make it brittle during deformation.

Whether buried halite beds that enclose organic intrabeds can release volatiles during catagenesis is still a matter of some discussion among organic geochemists. The longterm lack of fracture or pore throats in buried salt beds is why organic-rich intrasalt carbonate or shale laminites tend to be inefficient source rocks in style 1a source rocks (Fig. 9.4). Likewise, possible flushing and maturation effects are poorly understood in subsurface situations where encased organic-rich beds are in contact with hydrated salts converting to their anhydrous equivalents (such as gypsum to anhydrite or carnallite to sylvite, mirabilite to thenardite). Loss of water of crystallisation has the potential to allow organic-rich fluids to escape as the hydrated salts transform to their anhydrous forms. Typically, such burial transformations occur in the first kilometre of burial and may only allow immature hydrocarbons to escape into adjacent more porous sediments (Hite and Anders 1991). There they must be stored, mature and remigrate in later burial if they are to act as source rocks (Warren 1986). Many intrasalt organic-rich beds survive well into the metamorphic realm and evolve into graphitic quartzites and marbles encased in meta-evaporitic albitites and scapolites.

As a general rule, even as a halite bed fractures, its inherent lack of strength and the consequent ability to flow means any microscale intercrystalline fractures quickly reanneal by a combination of flow and pressure-solution induced recrystallisation. Current consensus is that some thin impurity-rich salt beds, interlayered with carrier beds, do leak small amounts of volatiles, but much less efficiently than thicker organic-rich mudstones and shales; whereas organics encased in thicker salt beds probably cannot leak from the unit until the enclosing salt dissolves or natural hyrofracturing occurs (as in the Ara Salt of Oman, Fig. 8.27). Evaporite beds and allochthons constitute some of the strongest longterm subsurface barriers to the vertical migration of hydrocarbons in a sedimentary basin both as a seal to hydrocarbons and in CO_2 sequestration.

Of possible concern in the latter situation is where measured seal capacity values and breakthrough pressures, obtained in the hydrocarbon field development stage, are then applied without re-evaluation in a CO_2 sequestration evaluation/study. This is especially so when potential CO^2 sequestration barriers are anhydritic carbonate seals, especially with elevated impurity levels (Li et al. 2005). In Midale evaporite seals (Mississippian-age anhydrites and dolomitic anhydrites) in Weyburn Field, southeastern Saskatchewan,

the gas breakthrough pressure was found to be nearly proportional to the interfacial tension of the gas/brine system. Hence, the breakthrough pressure in this CO_2/brine system (sequestered CO_2) is significantly reduced compared with that of the original CH_4/brine system (original gas field), due to the much lower interfacial tension of the former fluid (Fig. 10.7). That being the case, if the pressure during or after CO_2 injection is the same or higher than the original hydrocarbon reservoir pressure (pre-hydrocarbon depletion), then a seal rock that held back the original gas in a gas reservoir or an oil reservoir with a gas cap, may not be tight enough to seal injected/sequestered CO_2. Breakthrough pressure of seal rocks for a given reservoir should be re-evaluated whenever a depleted hydrocarbon field is chosen as a possible CO_2 storage site.

Environments Favouring Seal Continuity

When assessing any hydrocarbon accumulation the top, lateral and bottom seals must be identified and evaluated. Theoretically, the thickness of a seal does not contribute to seal capacity: a clay shale (4–10 μm particle size) with an entry pressure of 600 psi is theoretically capable of sealing a 900 m oil column. In reality, it is unlikely a shale bed only a few cm thick is a laterally continuous, unbroken, unbreached unit, capable of maintaining stable lithic character over a sizeable area. A thin evaporite perhaps could be, but a thicker seal provides many layers of contingent sealing beds and so gives a larger probability of a sealing surface being continuous over an entire prospect. Evaporite seals more than 30 m thick are considered excellent, while shale seals more than 50 m thick and evaporite seals more than 10 m thick are typically considered adequate.

Seal continuity rather than measured seal capacity is likely the most important factor in assessing seal quality. In the laboratory, one can measure the displacement or entry pressure necessary to force a given hydrocarbon mixture through a rock sample under given conditions of temperature and pressure. However, there are many difficulties in extrapolating quantitative data from a capillary pressure test on a 4–8 inch (10–20 cm) diameter core into a reliable prediction of the seal character across the entire sealing surface. A simple domal closure of 2,950 ha (6,400 acres) provides a ratio between a typical seal sample (4 inch diameter whole core) and the area of top seal of 1 to 3.5 billion. Average values of seal properties measured from core without a reliable geological model for the reservoir are next to useless in quantifying seal integrity. What is needed is knowledge of the likeliest weakest points in the seal across the structure of interest. It's the difference between guarantees that you will on average survive if you swim in these shark- and stinger-infested waters, versus you are advised not to swim in this lagoon. Most of us prefer the second option, it's the same when investing tens to hundreds of millions of dollars in developing an oil or gas field.

Saltern and deepwater evaporite beds make excellent seals because the density-stratified hydrology of their depositional setting guarantees there was little lateral variation in depositional rock properties over large areas of the salt-covered basin floor (Chaps. 2 and 5). Evaporite-plugged mudflat units also make effective seals, as do platform carbonates plugged by evaporite cements precipitated from dense reflux brines. But high levels of entrained impurities, less predictable depositional topography and lateral variations in early diagenetic fluid flux rates mean that, compared to saltern and basinwide-style seals, these dirtier seal types are more subject to problems with lateral continuity, as well as showing a higher propensity for stress fracture and failure.

Deposition of saltern anhydrite atop the various Arab cycle carbonate reservoir sands of Saudi Arabia and the Emirates not only formed the highly effective Hith seal (Fig. 10.8a), but aided in the preservation of underlying reservoir porosity and permeability by preventing later entry from above of meteoric waters capable of precipitating eogenetic intra-reservoir carbonate cements.

Once dissolution starts to thin a previously effective seal, it begins to leak. Even the Hith Anhydrite can leak once it is less than 10 m thick, as can be seen by the migration of Jurassic-sourced oil in Cretaceous reservoirs along the edge of the Hith Anhydrite (Fig. 10.8a; Hawas and Takezaki 1995). In my opinion, this leakage in the thinned Hith can be tied to increasing proportions of dolomite residues near the dissolutional feather edge of the Hith and a consequent propensity for brittle responses near this edge, with local faulting tied to collapse fracturing. There would be little loss of seal capacity in an anhydrite bed as thin as 10 m if it remained as relatively pure nodular anhydrite.

Leakage is obvious in Al Rayyan Field, Qatar, where the upper Arab anhydrite, the intra "C" anhydrite, and the intra "D" anhydrite of the Arab Formation do not form effective

Fig. 10.8 Evaporites as seal and a control of charge distribution. (**a**) Hith Anhydrite isopach showing thickening from the UAE west into Saudi Arabia and some of the main fields producing from Jurassic reservoirs in this region (In part after Alsharhan and Kendall 1994). Note the lack of Jurassic reservoirs to the east of the Hith erosional edge showing the effectiveness of the saltern evaporite in holding back substantial oil and gas columns sourced in Hanifa mudstones (see Fig. 9.4). (**b**) Distribution and timing of charge in the oil and gas fields along the highly productive eastern margin of the South Oman Salt Basin is controlled by the retreating dissolution edge of the Neoproterozoic Ara Salt and the underlying Huqf Fm. source rock, which became mature in the Cretaceous. Oil fields *shaded red, stars* indicate gas fields (After Terken et al. 2001)

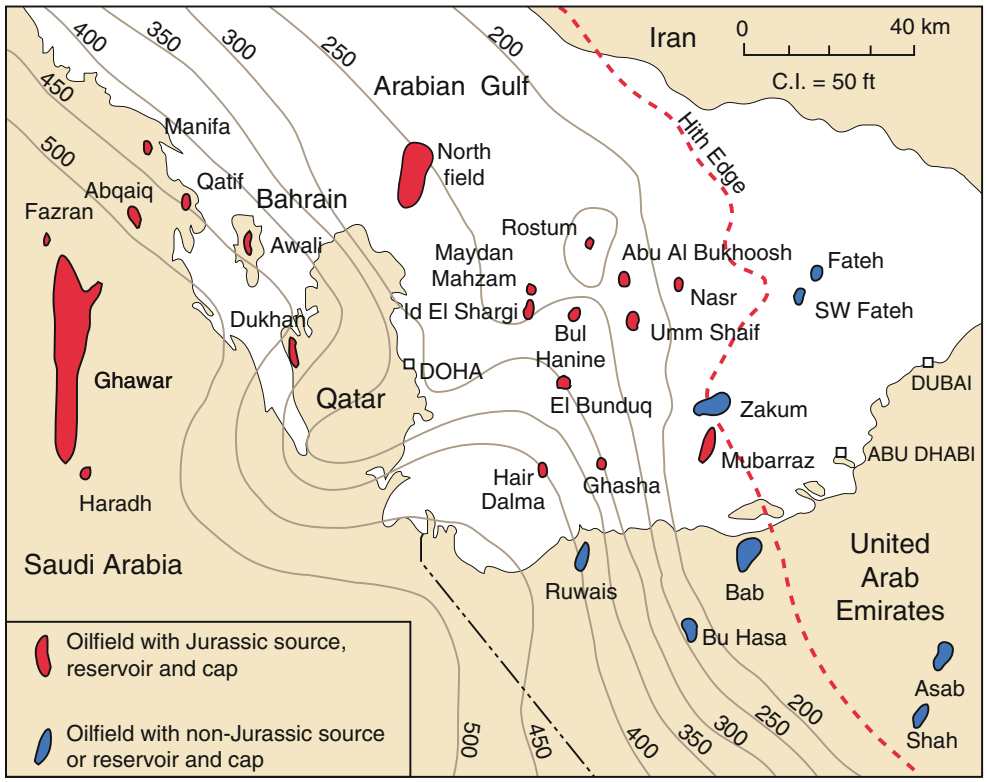
Iran
0
40 km
C.I. = 50 ft
Arabian Gulf
Hith Edge
Manifa
North field
Qatif
Bahrain
Abqaiq
Fazran
Awali
Rostum
Maydan Mahzam
Abu Al Bukhoosh
Fateh
Nasr
SW Fateh
Id El Shargi
Bul Hanine
Umm Shaif
Dukhan
DOHA
Ghawar
Qatar
El Bunduq
Zakum
DUBAI
Mubarraz
ABU DHABI
Hair Dalma
Ghasha
Haradh
Saudi Arabia
United Arab Emirates
Ruwais
Bab
Bu Hasa
Asab
Shah
Oilfield with Jurassic source, reservoir and cap
Oilfield with non-Jurassic source or reservoir and cap
400
350
300
250
200
450
500

a

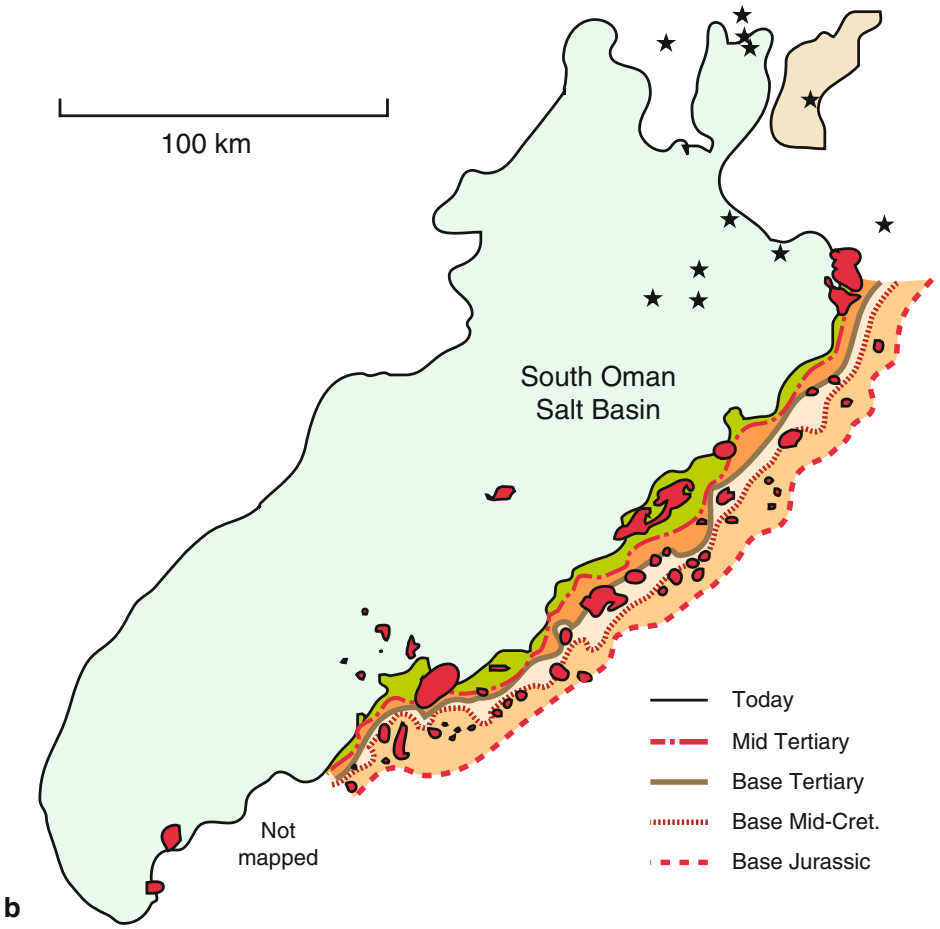
100 km
South Oman Salt Basin
Not mapped
Today
Mid Tertiary
Base Tertiary
Base Mid-Cret.
Base Jurassic

b

seals; only the Hith acts as a regional seal for the field (Brown and Loucks 2001; Clark et al. 2003). The intra "C" and intra "D" beds are interpreted as depositionally discontinuous with relatively high dolomite contents. This reflects original shoalwater carbonate deposition in the cycle capstones, which were deposited as thinned, and perhaps pinched-out, evaporitic mudflats onlapping the carbonate shoal reservoir. Likewise, the intra "C" sabkha unit, with its higher fraction of intercalated porous dolomite intrabeds, promotes seal failure via fracturing and faulting. The discontinuous salina deposits in the intra "D" anhydrite also lack sufficient lateral continuity to form an effective seal over the structure. Brown and Loucks (op. cit.) found that the major cause of seal failure in the thin, upper anhydrite is fault offset, whereby fault throw exceeds seal thickness. The high fraction of brittle dolomite in these anhydrite intrabeds results in wider seal damage zones, allowing greater potential for along-fault leakage. In contrast, where fault throw in the field does not exceed the thickness of the Hith, nor the thickness of the middle, and lower anhydrites in the Arab cycles in the field, the evaporites capping the various intra-Arab cycles remain as intact seals. Faults intersecting these beds also cause less structural (brittle fracture) damage due to the higher anhydrite fractions of the beds, so that along-fault leakage from connected intrasalt beds is minimal.

Hydrocarbon migration and trapping in the south Oman salt basin, with its subsalt Neoproterozoic Huqf source rock, is strongly controlled by the continuity of the Neoproterozoic Ara Salt. In the centre of the basin, where thick Ara salt is still present, there is an additional substantial volume of bituminous oil still trapped in intrasalt organic-rich Ara carbonate and siliceous stringers of the salt-sealed Athel silicilyte (Schoenherr et al. 2007b; Ramseyer et al. 2013). In the updip peripheral syncline along the east flank, salt dissolution controls structural style and trap formation (Heward 1990), with retreat of the salt edge the main factor in charge timing (Fig. 10.8b; Terken et al. 2001). Traps in Palaeozoic clastics in the eastern basin margin were initially formed by halokinetic structuring in the Paleozoic, and subsequently filled by salt dissolution breaches driving dissolution drape and oil emplacement. The subsalt Neoproterozoic Hufq source rock began to generate oil in the middle of the Cretaceous and the retreat of the salt's dissolution edge can be mapped in the successive fillings of the various fields that define the productive eastern margin of the basin. As the result of the westward retreat of the dissolving salt edge through time, traps get progressively younger toward the basin centre (Fig. 10.8b).

Salt dissolution has today removed most of the salt along the east flank of the south Oman salt basin, and its timely removal is largely responsible for the present-day hydrocarbon-filled structures. Oil accumulations mimic a negative image of the salt structures first formed during the earlier halokinetic stage as early salt withdrawal basins then became inverted into oil bearing turtle structures. Anticlines resulted from drape of strata over Haima and Al Khalata turtle structures and drape over deeper laterally discontinuous siliceous and carbonate stringers floating in the Ara Salt. Where salt dissolution occurred, formerly salt-encased stringers leaked and became the grounded remnants that now form chaotic solution residue horizons both in outcrop and in the subsurface (Terken et al. 2001; Peters et al. 2003).

Wherever marine carbonate reservoir sands are sealed by salterns or basinwide salt beds, the width of the subeconomic transition zone from economic reservoir into an overlying depositional seal is typically narrow and sharp. Such seals are created as basin isolation drives rapid platform or basinwide drawdown (e.g. anhydrites capping the Arab cycles in Ghawar or Salina Fm. salt seals of the Michigan Basin). The narrow transition reflects a rapid onset of hydrographic isolation, which typifies many marine-fed saltern and basinwide evaporite settings (Chap. 5: a corollary of Walther's Law). However, reflux brines associated with evaporite deposition can complicate the poroperm transition across the depositional contact as they drive formation of salt cements, which can plug porous carbonates in the zone below the evaporites. Likewise, a continuous depositional transition from reservoir to seal generates an uneconomic hydrocarbon-filled gradational depositional passage into a seal. Such gradational transitions from reservoir to seal characterise many nonevaporite sealed stratigraphic traps, such as reef-grainstone shoals drowned beneath onlapping lagoonal shales, or point bar sands buried beneath floodplain muds.

Gradational contacts tend to show subeconomic transitions from reservoir to seal both vertically and laterally. Much of the hydrocarbon can lie in partially salt-plugged porous dolomites that are "not quite reservoir, hardly seal" (Fig. 10.6b). Compared to pure-evaporite seals beneath many allochthonous salt bodies, both salt-plugged and shale-sealed intervals are much more prone to longterm leakage and the creation of thicker transition zones from reservoir to seal. Understanding and predicting the distribution of salt plugging is a significant problem in reliably modelling reserves and production estimates in evaporite-sealed reservoirs worldwide.

The transition from a potential dipping reservoir sand into a near vertical diapir stem or a subhorizontal salt allochthon tends to create sharp effective lateral and top seals. This is due to the passive mode of salt emplacement, which creates a sharp rather than a transitional boundary. Syndepositional stacking of reservoir sands against a passive diapir stem seal in the Gulf of Mexico has created some of the most productive acreage anywhere in the world (in terms of recovered bbl/acre; Halbouty 1979). Sharp contacts also create potentially hazardous sharp transitions into zones of high overpressure (see Chap. 8).

Reservoirs and Traps

At its simplest, evaporite-associated reservoirs occur adjacent to either bedded or halokinetic seals (or their solution residues) in subsalt, intrasalt or suprasalt positions (Table 10.1). Bedded salt seals are further subdivided into lacustrine, platform or basinwide settings, while halokinetic salt seals are either autochthonous or allochthonous.

Bedded Salt Seals

The main function of bedded evaporites in the evaporite hydrocarbon association is as a seal to subsalt accumulations of oil and gas (Table 10.2). In some cases, high levels of primary intergranular porosity in grain-dominated limestones are preserved beneath a salt seal (e.g. Jurassic Arab cycles on the Arabian Peninsula) or intercrystalline porosity fashions a variably dolomitised subsalt limestone reservoir (e.g. San Andres reservoirs on the Central Basin Platform fields of West Texas). Impermeable evaporite beds and salt-plugged dolomites capping various upward-shoaling platform cycles, effectively seal off underlying porous carbonates from later surface-driven influxes of freshwater or other suprasalt diagenetic fluids. Evaporite horizons, or any pervasively-plugged adjacent diagenetic haloes, are not potential reservoirs, unless a bed dissolves into a solution breccia, or intergranular salt cements are leached from previously salt-plugged sands or dolomites.

During evaporite deposition there is usually an associated hydrological system of basinward flushing dense brines (reflux). This occurs in the early stages of salt deposition and shallow burial (<100–200 m burial) prior to the loss of intrasalt and subsalt permeability, especially where a gypsum saltern is accumulating atop a marine platform carbonate. Circulation is driven by gravitational instability, set up by an updip dense brine plume or brine curtain below accumulating evaporites (Fig. 2.81).

At its periphery this refluxing plume mixes with and displaces less dense subsurface and connate waters to create or enhance the reservoir properties of adjacent subsalt limestones via reflux dolomitisation. As dense Mg-rich brines seep downdip from the platform saltern or mudflat they create intervals of porous dolomites in more distal zones, located seaward of overdolomitised evaporite-plugged areas. In some cases the most extensively dolomitised carbonates in these more distal zones are high-energy, shallow water grainstones and packstones. These were the sediments with the higher permeabilities at the time of dolomitisation. However, in areas of pervasive syndepositional marine cementation, some originally porous carbonates may have already lost much of their intergranular permeability via overgrowths of isopachous rim cements. In this situation the less cemented platform mudstones act as aquifers to the refluxing brines and so are preferentially dolomitised. Likewise, in more restricted portions of an epeiric carbonate platform where the only sediment beneath a salt seal is lagoonal mud, it is dolomitised and sometimes converted into a reservoir with intercrystalline permeability (e.g. the Levelland-Slaughter trend in the San Andres Fm, West Texas and New Mexico). In some muddy platform carbonates, only the pelletal and sandy burrow fills retain sufficient permeability to be dolomitised, while their muddier surrounds are not (e.g. Red River Dolomite of North Dakota). Whatever the setting, the rule of thumb is that refluxing brines will preferentially dolomitise whatever carbonate facies is capable of acting as an aquifer at the time of reflux.

The economic significance of reflux dolomite was first noted in the 1960s in the various evaporite-associated Permian dolomite reservoirs of West Texas (Adams and Rhodes 1960). Reflux dolomitisation also controls porosity/permeability distribution in the finer-grained parts of some Jurassic Arab Formation reservoirs in Saudi Arabia, as well as the Permian Khuff Formation in the Arabian Gulf, the Smackover Formation carbonates of the Gulf of Mexico, the Upper Permian Changxing Formation and the Lower Triassic Feixianguan Formation, NE Sichuan Basin, China, and many other oil and gas fields across the globe where dolomites occur beneath an evaporite seal (Sun 1995; Warren 2000a; Jiang et al. 2013). Yet, in other depositionally similar evaporitic settings, some of the mesohaline laminites that underlie bedded salts are not dolomitised, typically because they were evaporite-cemented in the strandzone prior to the onset of reflux flushing. They were too tight to transmit the volumes of Mg-rich brine needed for dolomitisation. Likewise, dolomites immediately below a saltern or mudflat brine source tend to be overdolomitised and/or evaporite-plugged, there the aquifer limestones were located in the zone of most intense flushing by salt-supersaturated brines (Fig. 10.9). Syndepositional permeability in units deposited immediately after a transition into widespread evaporite deposition and the condition of subsalt aquifers, controls the type and extent of the brine reflux alteration halo. So, porosity evolution in subsalt sediments can vary widely, according to the ambient hydrology.

Worldwide, Phanerozoic dolomite reservoirs are defined by four syndepositional associations (Sun 1995; Warren 2000a): (1) evaporitic mudflats in a carbonate platform, most often a ramp profile (roughly equivalent to peritidal-dominated carbonate of Sun 1995), (2) saltern-sealed platform carbonates with mudflat development over palaeotopographic highs – this system typically develops across an epeiric platform behind a rimmed shoal profile (roughly equivalent to subtidal carbonate associated with evaporitic tidal flat/lagoon of Sun 1995), (3) basinwide evaporite seal (subtidal carbonate associated with basinal

Table 10.2 Some of the many Palaeozoic platform reservoirs and fields sealed by bedded evaporites

Field or area	Reservoir and age	Reservoir	Trap type	Seal	Reference
Gulf of Suez	Rudeis and Belayim Middle Miocene	Cyclic shallow ramp lagoonal carbonates deposited within a restricted embayment	Dolomites created by brine reflux	Massive basinwide evaporites	Orszag-Sperber et al. (1998), Sun and Esteban (1994)
Mesopotamian Platform	Euphrates-Jeribe Early Miocene	Locally dolomitised and packstones, with red algae, mollusks and benthic foraminifers	Reflux dolomites, skeletal buildups and biostromes	Saltern and mudflat evaporite cap	Buchbinder (1996), Sun and Esteban (1994)
Oolitic to siliciclastic ramp reservoirs, offshore Angola	Pinda Group (Albian)	Littoral sandstones with interparticle porosity to various types of dolomitised marine shelf to shoreline carbonates with mouldic, vuggy, and intercrystalline porosity	Late Cretaceous segmentation of the reservoir series by salt tectonic gravitational gliding into halokinetic "turtleback" and rafts	Evaporitic mudflats/shales	Eichenseer et al. (1999)
Sunniland Field, Southern Florida	Sunniland limestone, Early Cretaceous	Dolomitised bank margin grainstones and mudstones	Low relief anticlinal trap, possibly halokinetic	Massive saltern anhydrite	Halley (1985), Loucks and Crump (1985)
Walker Creek Field, Chatom Field, and Mt Vernon Field, Gulf of Mexico Basin, Arkansas, USA	Smackover Formation, Jurassic (Oxfordian)	Oolitic-pisolitic dolomitised limestone retaining varying levels of primary intergranular porosity and calcite cement	Up-dip and down-dip depositional pinchout of oolitic grainstone bars, modified by halokinetic faulting (underlying Louann Salt)	Saltern and mudflat (Buckner Anhydrite)	Chimene (1991), Feazel (1985), Druckman and Moore (1985)
Appleton Field, Gulf of Mexico Basin, Alabama, USA	Smackover Formation, Jurassic (Oxfordian)	Dolomitised algal peloid ooid grainstone with intercrystalline and vuggy porosity	Combination structuralstratigraphic trap Up-dip and down-dip depositional pinchout of oolitic grainstone bars on high of crystalline basement	Saltern and mudflat (Buckner Anhydrite)	Haywick et al. (2000), Petta and Rapp (1990)
Ghawar, Qatif, Uthmaniya and other Arab Fm. fields in Saudi Arabia	Arab Formation, Late Jurassic (Tithonian and Kimmeridgian)	Partially dolomitised skeletal, peloidal and oolitic grainstone (Arab D), peloidal/oolitic/skeletal grainstone (Arab C)	Low amplitude anticlines related to basement faulting and possible halokinesis of Hormuz Salt	Nodular anhydrites and tight mudstones of Arab cycles and the overlying Hith Anhydrite	Cantrell et al. (2001), Saner and Sahin (1999, 2000), Meyer et al. (1996), Wilson (1985)
Feixianguan sour gas fields in the Sichuan Basin, China	Lower Triassic Feixianguan Formation and lesser production from Upper Permian reefalcarbonates	Dolomitised oolitic shoals and reef carbonates	Low angle drape structure and bedded $CaSO_4$ intralayers	Anhydrite cements and nodules are present in the ooidreplaced dolomites	Jiang et al. (2013, 2014)
McElroy Field, Central Basin Platform, Texas, USA	Grayburg Formation, Permian (Lower Guadalupian)	Dolomitised shelf carbonates ranging from mudstones to fusulinid wackestones	N-S trending asymmetrical anticline with steeper eastern limb. Permeability pinches out to west due to increasing evaporite plugging (anhydrite and gypsum)	Evaporites and siltstones of the Queen Formation; Anhydrite plugged porosity is heterogeneous.	Harris and Walker (1990)
Ghawar, Qatif, Uthmaniya and other Khuff Fm. fields in Saudi Arabia	Khuff Formation (Members A-C), Permian	Dolomitised and leached peloidal grainstones, wackestones and mudstones, variable anhydrite cements	Low amplitude anticlines related to basement faulting and possible halokinesis of Hormuz Salt	Saltern cap and varying development of evaporitic mudflats	Al-Jallal (1995), Dasgupta et al. (2002)
Reeves Field, Midland Basin and Levelland-Slaughter trend, Northern Platform, Permian Basin, Texas USA	San Andres Formation, Permian	Dolomitised skeletal wackestones and mudstones	Stratigraphic with structural assist via draping over former shelf edge	Strandline anhydrites of the San Andres Formation	Chuber and Pusey (1985)

Pecos Slope Field, Permian Basin, New Mexico, USA	Abo Formation, Permian (Leonardian)	Fluvial sandstone	Tectonically fractured stratigraphic wedge-out of fluvial clastics	Anhydrite of the Yeso Formation	Bentz (1992)
Tarchaly, Rybaki, Sulecin' Barnowko--Buszewo fields, west Poland and Thuringian basin fields, East Germany	Zechstein main dolomite; Early Permian	Dolomitised oolitic/pisolitic grainstones and mudstones	Shelf margin buildup beneath evaporite seal, structurally assisted	Zechstein anhydrite cap (basinwide)	Depowski and Peryt (1985), Peryt and Dyjaczynski (1991), Gorski et al. (1999), Karnin et al. (1996)
Aneth Field, Paradox Basin, Utah	Hermosa Formation (one main reservoir, several semi-isolated intervals), Pennsylvanian	Leached and recrystallized oolitic limestone and dolomitised mudstone	Dolomitised carbonate mound	Evaporitic organic-rich dolomitic shale	Peterson (1992)
Lisbon Field, Utah, USA	Leadville Formation; Mississippian	Dolomitised (sucrosic) and karstified platform carbonates (wackstone-packstone)	Faulted anticline beneath supra-unconformity halokinetic evaporites of the Paradox Basin	Paradox Salt (basinwide)	Miller (1985)
Stanley Field, Williston Basin, North Dakota, USA	Mission Canyon Formation; Mississippian	Pisolitic-oolitic limestone with local skeletal marine grainstone. Fenestral porosity with primary interparticle and intraparticle	Updip facies change to fractured evaporitic mudflats and porous grainstones from downdip wackestone and mudstone	Massive platform anhydrite of the Rival Member top seal	Beach and Giffin (1992)
Elkhorn Ranch Field, Williston Basin, North Dakota, USA	Mission Canyon Formation; Mississippian	Dolomitised skeletal mudstones and wackestones	Hydrodynamic trap where structure assists in localising accumulation, but trap stratigraphic passage is into an anhydrite seal	Massive platform anhydrite top seal of the Mission Canyon Formation	DeMis (1992)
Glenburn Field, Williston Basin, North Dakota, USA	Mission Canyon Formation; Mississippian	Pisolitic limestone exhibiting subaerial exposure and vadose diagenesis with porosity pinchouts via evaporite plugs	Solution collapse anticline in underlying Devonian Salt	Massive saltern anhydrite and ferruginous shale caps, structurally assisted (anticlinal)	Borchert et al. (1990), Gerhard (1985)
Little Knife Field, Williston Basin, North Dakota, USA	Red River, Duperow, Mission Canyon; Ordovician, Devonian, Mississippian	Dolomitised shallow shelf to evaporitic mudflat carbonates	Combination anticlinal nose and porosity pinchout	Massive Mission Canyon platform anhydrite top seal, lateral change to nonporous carbonates	Wittstrom (1990), Lindsay and Kendall (1985)
A and E pools, Rainbow Field, Canada	Keg River Formation, Rainbow Member, Middle Devonian (Givetian)	Dolomitised limestone and limestone	Pinnacle reef enclosed in evaporites and bituminous carbonates	Muskeg Member evaporites	Schmidt et al. (1985)
Pinnacle reef fields, Michigan Basin, SE Michigan USA	Guelph Formation and equivalents; Middle Silurian	Dolomitised and karstified pinnacle reefs	Pinnacle reef enclosed in evaporites and bituminous carbonates	Salina Group evaporites	Gill (1985), Obermajer et al. (2000)
Medicine Pole Hills Field, Killdeer Field, Pennel Field, Williston Basin, North Dakota, USA	Guelph Formation and equivalents; Middle Silurian	Sucrosic dolomites of evaporitic mudflats (intercrystalline and vugular porosity)	Combinations of anticlinal noses and porosity pinchout, preferential dolomitisation at top of anticline and evaporite karst	Red River Anhydrite	Fischer et al. (1990), Clement (1985), Montgomery (1997)

evaporites of Sun 1995), and (4) nonevaporitic carbonate sequences associated with topographic highs/unconformities: platform-margin buildups or burial related fault/fracture controls. Three of the four worldwide dolomite-hydrocarbon associations show an intimate association with evaporites. Brine reflux is the dominant process in dolomite creation in all three, although it can be overprinted by later burial dolomites. The process of mixing-zone dolomitization typically considered part of process set (4) has received enough criticism in recent years to suggest that it no longer be considered viable for making large amounts of dolomite. In its place Li et al. (2013) propose a somewhat more specific model, which still requires fluid mixing whereby an ascending flow of freshwater mixes with evaporated seawater about the edge of a saline basin, leading to extensive dolomitization (e.g. Fig. 5.39).

Dolomite reservoirs created by brine reflux can be subdivided using the dominant depositional style of the evaporite capstone, namely, platform and basinwide (Fig. 5.9). In platform evaporite-sealed dolomite associations, the evaporite seal is typically ≈5–10 m thick (although it can be 20–30 m thick) and is usually dominated by saltern or mudflat anhydrite interlayered with shoaling platform carbonates. This evaporite cap can be further subdivided into evaporitic mudflat or saltern-dominated. Basinwide seals to carbonate reservoirs tend to be thick (>100 m), halite-prone in the basin centre and to cap carbonate buildups about the basin edge. Such buildups typically grew prior to the saline giant stage. Ongoing or longterm regional reflux beneath accumulating evaporites in both platform and basin settings can "overdolomitise" the reservoir and encourage evaporite plugging leading to occlusion of effective porosity (Warren 2000a for summary). In platform settings such porosity-depleted overdolomitised zones tend to be most common in regions of restricted carbonate deposition beneath leaky evaporitic mudflats (these are the typical caps to Sun's peritidal association). These sediments tend to accumulate in the more updip evaporite-dominated portions of a carbonate platform, where underlying carbonates have been flushed for extended periods by hypersaline brines. With basinwide-sealed associations, a later burial overprint and pervasive intra-reservoir karst/fracturing events seem to be needed to create and maintain economic porosity levels.

"Peritidal" Muddy Carbonates with Evaporitic Mudflat Seals

Evaporitic mudflats dominate the ephemeral water portions of an evaporite basin. As discussed in Chap. 5, the use of a tidal nomenclature is not appropriate in a highly restricted to hydrographically isolated epeiric setting where saltern evaporites are accumulating. Strandzone rather than the intertidal and supratidal in the peritidal is more appropriate, but peritidal terms are used in the following discussion to conform to historic subdivisions. Strandzones can create dolomite-forming hydrologies within stacking muddy epeiric platform carbonates whereby highly saline Mg-rich brines, sourced in the mudflats, seep into adjacent restricted lagoonal marine carbonates (Fig. 10.9). Without subsequent fracturing, leaching and other diagenetic enhancements to their permeability, such fine-grained mimetic syndepositional dolomites constitute no more than a few economic reservoirs. Those intervals that do constitute reservoir tend to be low permeability systems, which are patchily distributed in a host formation that is extensively plugged with variable levels of evaporite cement. Enhancements to this generally low and patchy permeability can occur if karst, fracturing or burial leaching subsequently modify the host lithology. Early diagenetic permeability tends to increase where the dolomitised marine mudflat was located further out on the platform and away from areas of most intense dolomitisation and evaporite plugging.

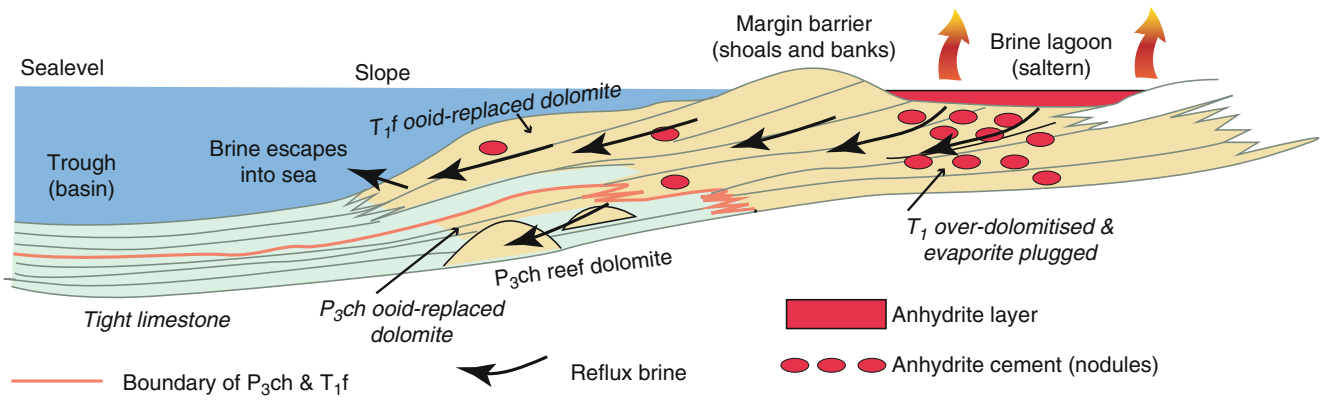

Fig. 10.9 Model of reservoir creation via saltern brine reflux, based on dolomite distribution in the Upper Permian Changxing Formation (P_3ch) and the Lower Triassic Feixianguan Formation (T_1f), NE Sichuan Basin, China (After Jiang et al. 2013)

Ordovician Red River Fm., Williston Basin, USA and Canada

The Red River Formation was deposited in an epeiric seaway that occupied the Williston Basin in the Middle to late Ordovician. The Williston Basin is located on the southern edge of the Canadian Shield, straddling the US-Canadian border and centred on Saskatchewan and North Dakota (Fig. 10.10). The Williston Basin was an intracratonic sag basin in the middle of the Laurentian craton. The Late Ordovician succession comprising Red River strata (Fig. 10.10a) exhibits a series of large-scale cycles of limestone, dolomite and anhydrite units deposited across a broad, shallow, low-relief epeiric sea (El Taki and Pratt 2010). The Lake Alma anhydrite unit (Unit "A") is present over the entire study area, whereas the Coronach anhydrite (Unit "B") occurs only in the southern and southwestern portion of Saskatchewan and adjacent USA, and the youngest anhydrite (Unit "C") is only present in North Dakota (Fig. 10.10c).

The basin itself is circular, about 800 km across, and is filled with up to 4,600 m of Phanerozoic sediments. The Palaeozoic

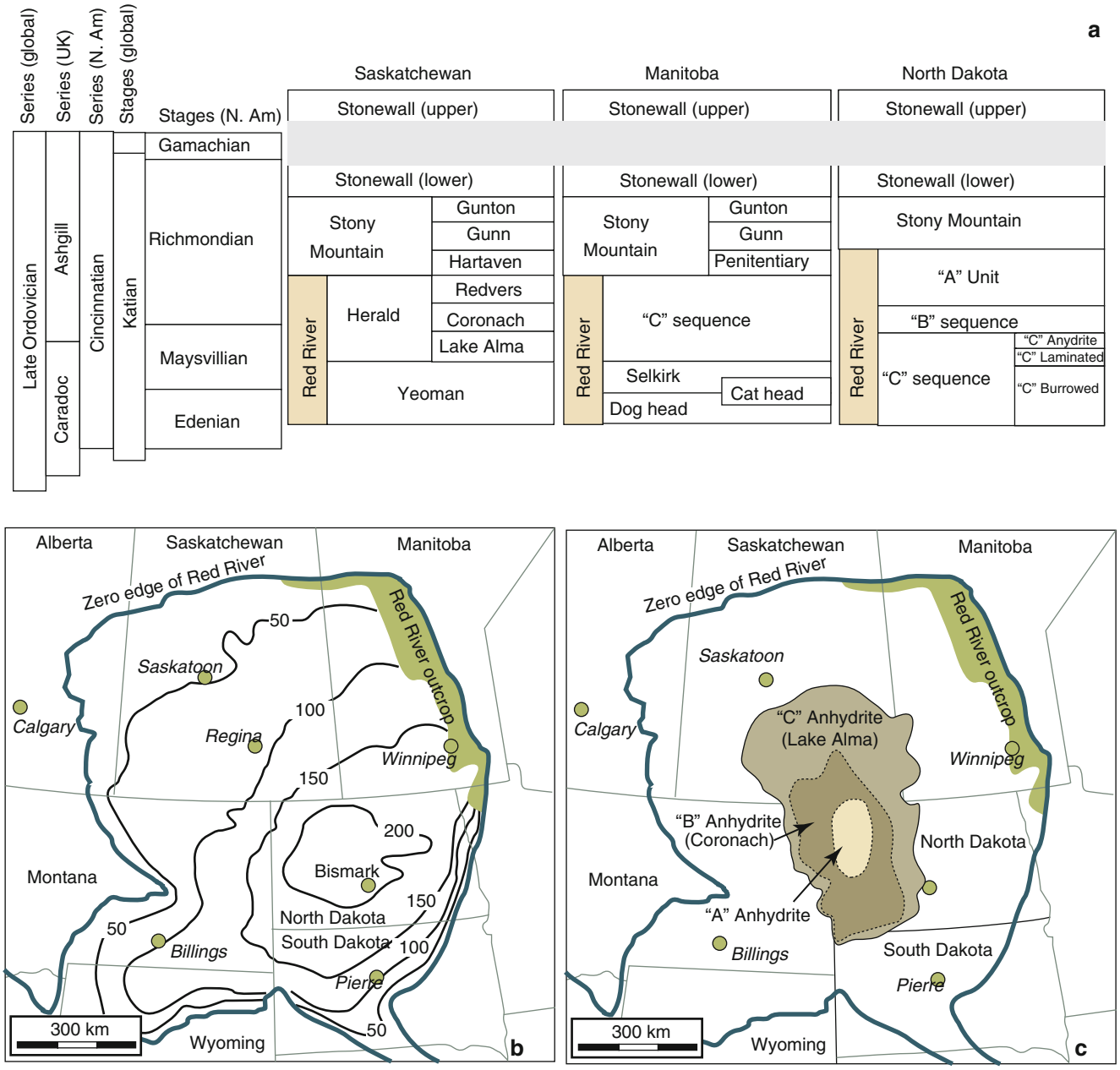

Fig. 10.10 Red River Formation in the Williston Basin. (**a**) Lithostratigraphic nomenclature of the Red River, Stony Mountain and Stonewall strata in Saskatchewan, Manitoba and North Dakota. (**b**) Isopach map of Red River strata showing the depocentre near Bismarck, North Dakota. (**c**) Distribution of the three successive anhydrite units (A-C) in Red River strata (After El Taki and Pratt 2010)

succession is predominantly carbonate and up to 2 km thick. It is overlain by a Mesozoic succession of mainly fine terrigenous clastic rocks up to 1.5 km thick and a Tertiary succession of mostly coarse terrigenous clastics that is less than a kilometre thick. The maximum thickness of the Red River Fm. occurs in the basin centre close to Bismarck, North Dakota, and where it is slightly more than 200 m thick (Figs. 10.10b and 10.11; Pu and Qing 2003). Like most intracratonic sag basins, the Williston Basin preserves sediments deposited across substantial stretches of geological time.

During the Cambrian and Ordovician there was first a phase of tension in the basin, likely related to rifting along the margins of Laurentia, as Rodinia continued its rifting trajectory, which was followed by far-field compression driven by the Taconic Orogeny (Allen et al. 2010; Middle Ordovician to early Silurian). Sedimentation was broadly affected by local as well as regional fault systems, which were later reactivated at various times. Accordingly, dolomudstones and anhydrites of the Lake Alma and Coronach members host a variety of synsedimentary deformation features —seismites— induced by earthquakes generated by movements of these faults, while the low-energy, subaqueous environmental setting was conducive to their preservation (El Taki and Pratt 2010). Within the basin are several major epeirogenic structures of which, in terms of controlling hydrocarbon distribution, the Cedar Creek anticline and Nesson anticline are the most prominent. Both anticlines have long episodic histories of responding to farfield tectonic movement. Elsewhere in the basin, the subsurface dissolution of Palaeozoic evaporites resulted in collapse and inversion structures in post-Middle Devonian strata, such as the Birdbear structure in Canada (McTavish and Vigrass 1987).

Red River strata in North and South Dakota consist of three carbonate-evaporite depositional sequences known as the A, B and C cycles (Fig. 10.10a, b; Pu and Qing 2003). Each sequence starts with a burrowed, normal-marine mudstone to wackestone and packstone at the base, followed by a laminated mudstone representing more restricted mesohaline deposition, which in turn is overlain by a bedded to enterolithic evaporative mudflat anhydrite which can be traced over much of the basin. Similar evaporite capped cycles typify the Lake Alma and Conanach formations in Canada.

Industry terminology in the oil fields of the USA informally defines these evaporites as capstones to the "A," "B," and "C" cycles. Some workers also distinguish a lower "D" zone that lacks an anhydrite cap (Fig. 10.11b). In ascending order, a typical Red River cycle consists of: (1) locally dolomitised burrowed carbonate mudstones and skeletal wackestones that define a "Burrowed Member," which is around 9 m thick in the B zone and up to 90 m thick in the C zone; (2) irregularly laminated carbonate mudstones that constitute a 3–12 m-thick "Laminated Member;" and (3) an impure 3–6 m capping anhydrite showing nodular-mosaic, nodular, or enterolithic textures (Fig. 10.11c). All members thin toward the edge of the basin where the anhydrites disappear completely.

Subtidal lithologies in each cycle are classic Zone X sediments composed of partially dolomitised burrowed biomicrite wackestones with fragments of echinoids, brachiopods, bryozoans, trilobites, molluscs, ostracods, and gastropods, and lesser amounts of solitary corals and stromatoporoids (Fig. 5.19). These subtidal dolomitic units are poorly bedded and heavily bioturbated and were laid down in a quiet-water epeiric platform setting.

The Red River Formation is 90–180 m thick in Cabin Creek Field on the Cedar Creek anticline in Montana, on the southwest side of the Williston Basin. Its lower part is a tight bioturbated marine limestone (Ruzyla and Friedman 1985). The average depth to pay across Cabin Creek Field is 2,750 m, with a 15.2 m net pay thickness, a productive area of 30.5 km^2 (7,620 acres), and an estimated 224 million barrels of oil in place. Here, and throughout much of the Williston Basin, economic porosity is largely restricted to bioturbated and partially dolomitized platform limestones and in many subsurface situations the burrows have controlled the intensity and style of dolomite (Gingras et al. 2004).

The overlying strandline (intertidal?) portions of a cycle are dolomitic biomicrite wackestones, deposited under somewhat more energetic bottom conditions (Zone Y). These deposits are still muddy but contain graded beds, crossbeds, ripple marks, imbricate shell lags and conglomerates. They also contain allochems characteristic of strandlines, such as oncolites, ooids, intraclasts, and peloids. The overlying anhydritic sediments in each cycle (Zone Z) include wavy-laminated micritic dolomites and organic-rich mudstones, along with evidence of completely restricted and at times subaerial conditions in the form of desiccation cracks, erosion surfaces, intraclast breccias, solution collapse breccias, and nodular anhydrites. This capstone in the vicinity of the Cabin Creek anticline was deposited on the platform in a mudflat mosaic of sabkhas and salinas. Offstructure, wireline signature shows the thickness and purity of nodular anhydrite in the seal bed increases, indicating a greater propensity for subaqueous deposition.

Evaporitic strandzone sediments in the reservoir interval in Cabin Creek Field show evidence of subsequent leaching; they contain empty gypsum and anhydrite moulds, corroded anhydrite crystals and solution collapse breccias. Early micritic dolomites of the supratidal are mimetic, typically laminated, but these units tend to be overdolomitised and salt plugged, so are relatively poor quality reservoirs. Upper contacts of the evaporite-cemented dolomite intervals are typically sharp, often erosional and pass abruptly up into the limestones of the next cycle suggesting exposure prior to the passage into the next cycle. This style of transition also

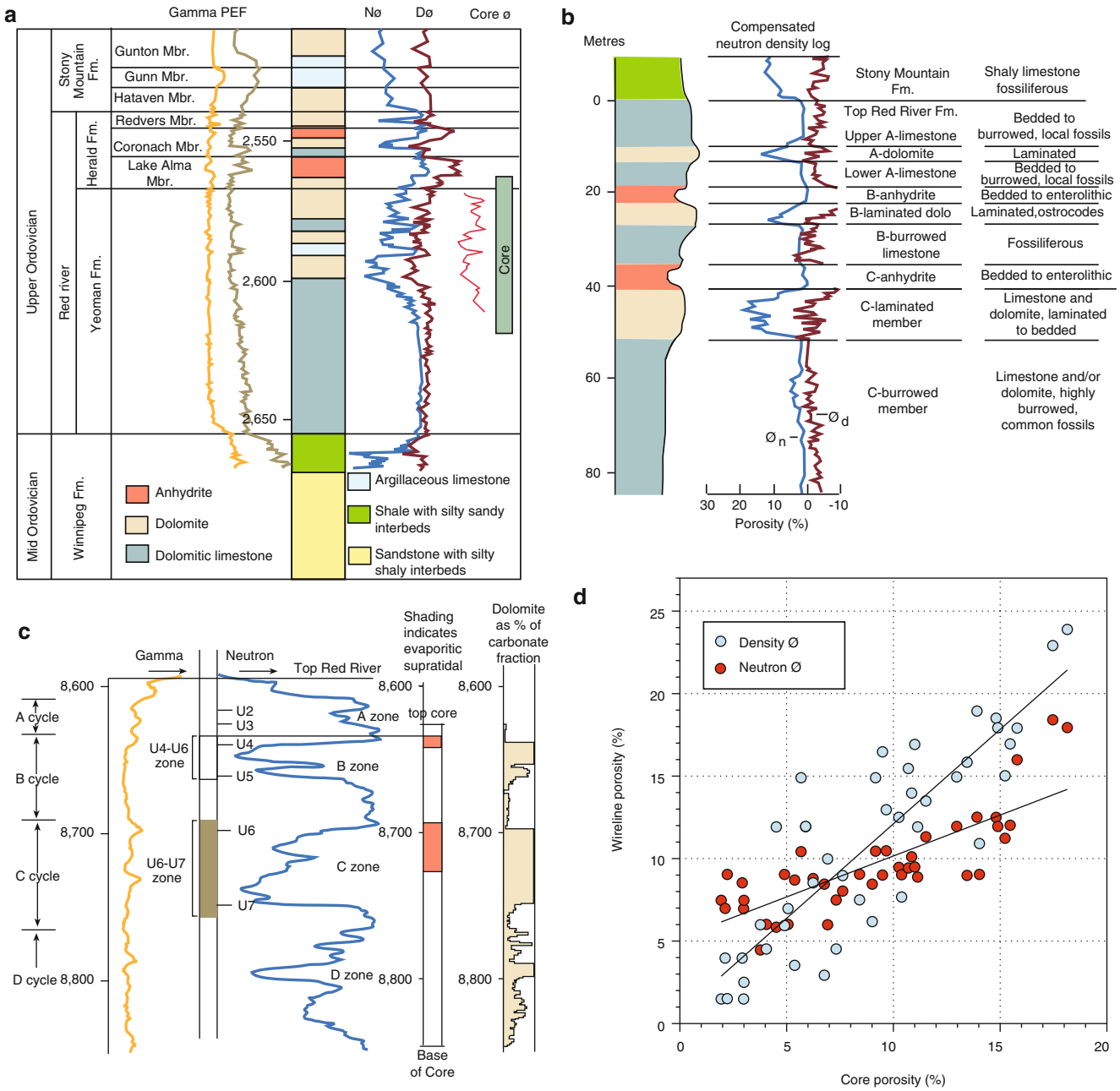

Fig. 10.11 Evaporitic mudflat (peritidal) style of deposition in the Ordovician Red River Dolomite, North Americas. (**a**) Red River stratigraphy with wireline data from well 7-3-7-11 W2 in Midale area, Saskatchewan (After Pu and Qing 2003). (**b**) Typical section showing detailed sedimentary character of the main cycles (After Longman et al. 1983). (**c**) Core section in the Cabin Creek Field, shows the close relationship between dolomite occurrence and evaporite beds (After Clement 1985) (**d**) Relationship between core porosity, neutron log and density log porosity in well 14-16-7-11 W2 in Midale area Saskatchewan (After Pu and Qing 2003)

characterises sediments inmodern evaporite mudflats and sabkhas. In contrast, the bases of the various dolomite intervals are transitional and conformable with the underlying marine limestone interval, this pattern is typical of a brine transition driven by an early reflux hydrology.

As in Cabin Creek Field, Red River dolomite throughout the rest of the Williston Basin is mostly of two types; (a) a mimetic evaporitic-mudflat reflux mesohaline dolomite, which is primary and precipitated penecontemporaneously as wavy-laminated or peloidal mudstones intercalated with the strandline (supratidal) carbonates; and (b) an associated, perhaps slightly later, somewhat coarser-grained brine-reflux dolomite, which dolomitised underlying portions of the intertidal and subtidal sediments immediately below and downdip of the micritic mudflat dolomite (Pu and Qing 2003; Clement 1985; Longman et al. 1983).

The proportion of dolomite decreases downward from the base of each evaporitic mudflat (supratidal) unit due to the sinking and mixing of dense hypersaline waters, which originated in the strandzone (supratidal?). Brine reflux dolomites selectively replace skeletal fragments and burrows of the marine carbonate platform. Within productive areas, dolomitised limestones consistently show improved porosity and permeability compared to nearby undolomitised limestones (Fig. 10.11c).

Red River reservoirs throughout much of the Williston Basin are not hosted in mesohaline mudflats, but in porous dolomitised marine lenses, typically some 27–43 m below the "C" Anhydrite Member and its equivalents. Permeable lenses vary in thickness from less than 3 m up to 60 m thick and are up to 1.5 km across (Fig. 10.12). The lateral extent of these porous lenses and the possible interconnections between them is poorly understood because most producing fields are small and consist of only a few wells. Most cored reservoir intervals are dominated by *Thalassinoides-like* burrow networks, with individual dolomitised burrows 1–2 mm to >1 cm across within a less dolomitised matrix. Reservoir porosities are typically less than 15 % and permeabilities less than 30 md, with most wells showing a poor to moderate relationship between porosity and permeability (Fig. 10.13). Porosity development seems to be related to the degree of dolomitisation, with some porosity enhancement of partially dolomitised intervals occurring during later burial by partial dissolution of residual calcite matrix. The initial formation of dolomite may well have been bacterially mediated and focused along organic-rich linings of the burrows (Gingras et al. 2004). The mechanism was perhaps similar to that of the sulphate-reducing bacteria forming modern dolomites in the mesohaline salinas of Brazil (Fig. 4.17). Dolomite-lined burrow meshworks then acted as a focus for subsequent dolomitisation.

There is general agreement that dolomites of the mottled Red River C member are genetically related to Mg-rich brines seeping through restricted marine muddy carbonates. These dense hypersaline basin waters were depleted of their calcium and sulphate, either through attendant deposition of aragonite and gypsum, or perhaps by ongoing bacterial sulphate reduction. What is not agreed is whether the dolomitising brines were descending or ascending at the time of widespread dolomitisation. Longman et al. (1983) argued that brine migration was localised by "holes" in the anhydrite mudflat seal (Fig. 10.12a). Fracturing, minor faulting, or early expulsion of subsurface waters from the carbonate host probably formed the "holes." When the descending Mg-rich hypersaline brines first entered the underlying carbonate sediments beneath the "holes" they were oversaturated and precipitated cryptocrystalline dolomite (overdolomitisation), but as they migrated away from the holes they lost their potency and produced rhombs floating in a dissolving calcitic matrix. This calcite may have been precipitated as an early diagenetic phase or left as unreplaced vestiges of original calcite (or aragonite subsequently altered to calcite) during dolomitisation.

Perkins (1991) agreed with the brine reflux model for the widespread mimetic dolomite fabric but went on to argue that following further burial, limestones tended to chemically compact through pressure solution, whereas late stage fractures were localized in the more brittle dolomitised portions of the Red River Formation. These fractures served as conduits for late stage leaching fluids, possibly associated with hydrocarbon generation, which locally enhanced porosity in dolomite intervals adjacent to active fractures through the removal of associated calcite. On the scale of individual burrows, late-stage leaching is reflected in "overly porous" dolomite haloes around cemented burrow centres and highly porous dolomite seams along stylolitic contacts.

Kendall (1983) also agrees with a brine reflux model but argues that once the gypsum cap was deposited (prior to its burial conversion to anhydrite) it was an aquifer not an aquitard and that the brine flux could just as easily been upward and focused via brine resurgence through more permeable intervals in the gypsum bed. He goes on to suggest that the control on the dolomite intensity was a series of megapolygonal sutures, much like the resurgence of saline groundwaters seen atop giant polygonal cracks in Pleistocene playas (Fig. 2.59).

The complexity of dolomite-reservoir to seal interrelationships in the Red River Dolomite is symptomatic of similar relationships in many other mudflat-associated dolomite reservoirs (Warren 2000a). The dolomitisation process is ongoing from deposition through burial and uplift. Likewise, the burial evolution of the adjacent evaporite seal is also ongoing from first deposition until complete subsurface dissolution. The evaporitic interval can act as both as a source of fluids, as in reflux dolomites and dissolving salt beds, or as a focus to fluid access as when rising basinal fluids pool and spread beneath a laterally extensive evaporite seal, or where a breached salt bed or allochthon facilitates the ingress of fluids either from below or above the breach. Generally, dolomite reservoirs contain multiple styles of dolomite created at different times in the hydrological evolution of the adjacent evaporite seal (Warren 2000a).

Platform Carbonates with Bedded Saltern Seals

Porosity in saltern-sealed carbonates typically occurs as multiple zones within stacked shallowing-upward evaporitic cycles that pass into mudflats near the basin edge or intrabasin highs (Warren 2000a). The saltern evaporite platform reservoir grouping in part corresponds to the "subtidal carbonate associated with evaporitic tidal flat/lagoon" grouping of Sun (1995). Each economic zone is formed by porous, partially to completely dolomitised subtidal limestones. Reservoirs

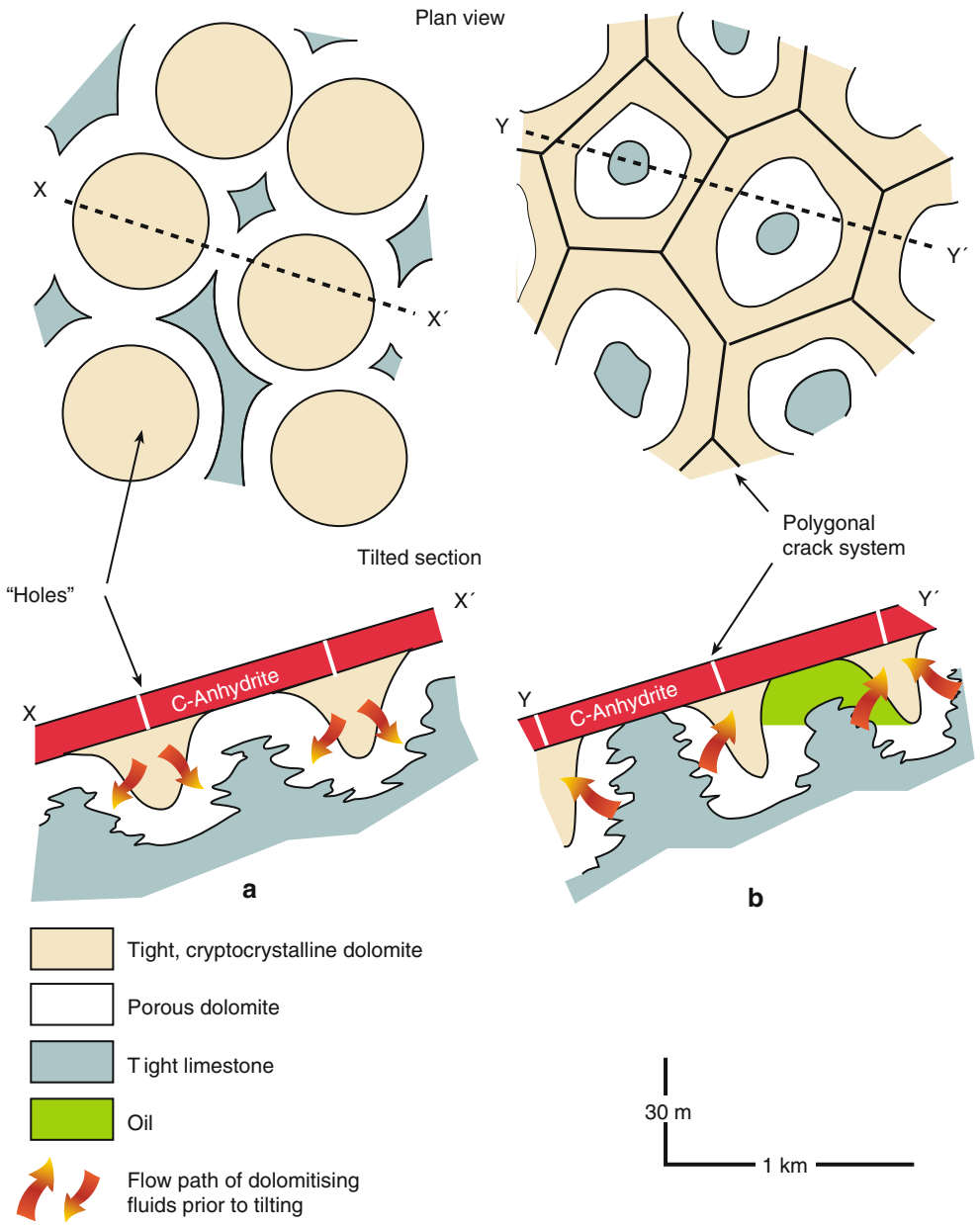

Fig. 10.12 Models explaining the occurrence of patchy diagenetic dolomite that characterises much of the reservoir in the various fields in the Red River Formation. (**a**) The descending hole model of Longman et al. 1983. (**b**) The ascending megapolygon model of Kendall (1983). See text for discussion

are typically capped by tight, dominantly saltern evaporites, with local highs indicated by seal transitions from saltern into evaporitic mudflat. Reservoir quality in the subtidal carbonate is related to depositional facies and varying intensities of diagenetic overprint.

Reflux dolomitisation is a common permeability enhancing mechanism beneath many leaky pans and saltern seas (as in the reef-rimmed Permian Basin of West Texas). But retention of relict primary porosity in epeiric limestones beneath tight sub-saltern units, rather then intensity of reflux dolomitisation near the platform edge, is a significant control on reservoir quality in the Middle East (as evidenced by the many saltern-sealed interior mounds and shoals making up the main Arab D reservoirs across the Arabian Peninsula; Fig. 10.14). In both settings, better quality reservoirs tend to occur in higher energy, grain-dominated limestones (oolitic/peloidal/pisolitic packstones) or dolostones, but quality reservoirs can also form in lower-energy lagoonal dolo-mudstone/wackestone with an overprint of coarsely crystalline dolomite.

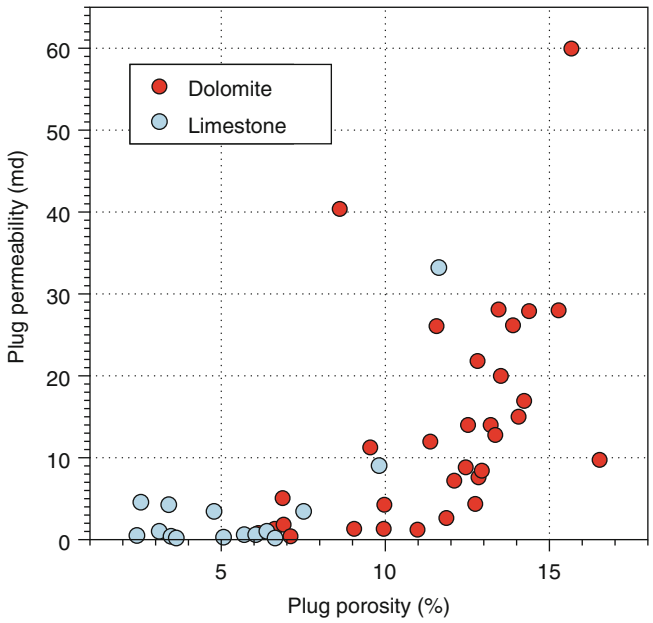

Fig. 10.13 Cross plot of core porosity and permeability in the Red River Formation in well 3-8-1-11 W2, Midale Field, Saskatchewan. Clearly shows the improvement in porosity and permeability associated with dolomitisation (Replotted from Pu and Qing 2003)

Finely crystalline, mud-dominated mimetic dolomites typically form a thin cap beneath a saltern seal or stacks in updip evaporitic mudflat positions, where they lie nearer the brine source. Such mudflat dolomites are typically low permeability sediments that require further diagenetic enhancement to attain reservoir quality (see previous section).

Jurassic Arab Formation, Arabian Gulf

The Late Jurassic (late Kimmeridgian) Arab Formation within and around the Arabian Gulf hosts some of the most prolific oil fields in the world, including Ghawar and Safaniya fields (Ehrenberg et al. 2007; Lindsay et al. 2006; Pollastro 2003; Lucia et al. 2001; Sahin and Saner 2001; Meyer et al. 2000; Cantrell et al. 2001; Beydoun 1998; Alsharhan and Kendall 1994; Wilson 1985). This prolific petroleum system includes several regional organic-rich source rocks, stacked reservoirs and multiple seals (Al-Husseini 1997). Jurassic strata were deposited across a broad platform (Murris 1980) that is sometimes characterized as "layer cake." Chronostratigraphic correlation from outcrops to wells, well to well, and from country to country, defines a late Jurassic regional anhydritic sealed carbonate platform encompassing

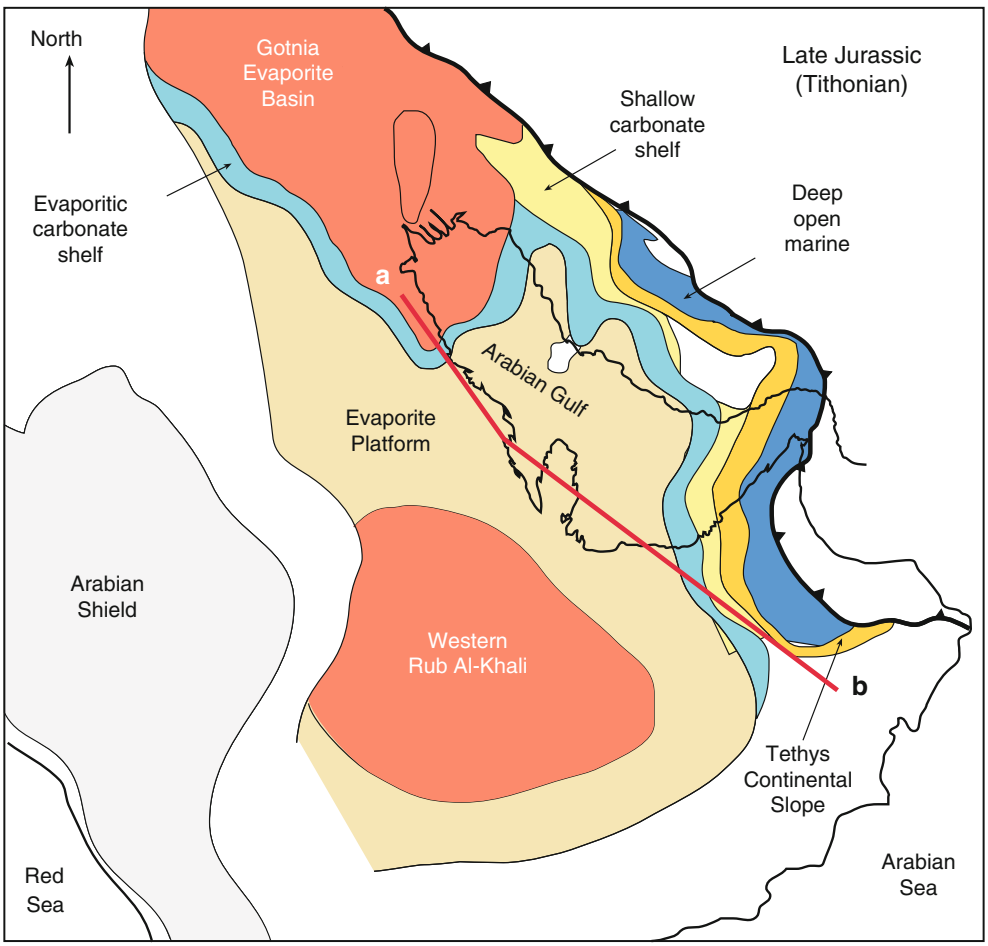

Fig. 10.14 Late Jurassic Tithonian palaeogeography of the Arabian Gulf (After Al-Husseini 1997). Deposition of the four carbonate-anhydrite cycles of the Arab Formation and the overlying Hith Anhydrite constitute the dominant regional reservoirs and caprocks. The western Rub' Al-Khali and Gotnia basins were inland salterns characterised by halite rather than platform-wide anhydrite, which is the dominant evaporite salt in the Arab and Hith formations

large intrashelf basins with grainier rims. At times of hydrographic isolation, the platform evolved into a widespread saltern that with further isolation was characterized by halite-filled depressions known as the Gotnia and Rub Al-Khali salt basins (Fig. 10.14; Al-Husseini 1997).

The proposed regional stratigraphic framework for the Jurassic, as defined by Al-Husseini (1997), is as follows; (1) Upper Triassic-? Lower Jurassic continental clastics (Minjur Formation and equivalents) and the subsequent pre-Toarcian unconformity indicating regional erosion and non-deposition over the Arabian platform. (2) A Toarcian sequence (Marrat Formation and equivalents) providing a basal Jurassic regional datum, except in Oman. (3) Late Toarcian and Aalenian corresponding to a substantial sea-level lowstand and a regional depositional hiatus. (4) The Middle Jurassic Dhruma Formation corresponding to four different sequences with a major intervening hiatus. The Upper Dhruma Member, together with the Tuwaiq Mountain Member, forms the topmost sequence (Fig. 10.15). The correlation between the Dhruma, Tuwaiq Mountain, Hanifa and Jubaila formations, to their equivalents in other Arabian Gulf countries, still requires clearer definition. (5) The Arab and Hith Anhydrite formations are Tithonian, based on their sequence assignment, while the Sulaiy Formation is mostly Berriasian and straddles the Jurassic Cretaceous boundary.

The four Tithonian Arab Formation carbonates (A-D members) were deposited as transgressive to early highstand deposits, while the Tithonian Arab, Gotnia and Hith anhydrites are perhaps late highstand deposits which overstep inland salterns (Gotnia and western Rub' Al-Khali basins). Each carbonate and overlying anhydrite cap in the four Arab cycles (Arab A-D) are interpreted as complete third-order cycles by Al-Husseini (1997). The equivalents to the Kimmeridgian Jubaila Formation and Tithonian Arab carbonates are absent because of non-deposition in Kuwait. The Tithonian Hith Anhydrite provides a regional stratigraphic datum in the Arabian Peninsula, except in Oman and the eastern United Arab Emirates (UAE). There the Arab and Hith Anhydrite formations are absent as they have been eroded or were never deposited, so the former eastern and southeastern extent of the Hith is not well understood.

The main reservoirs within this prolific petroleum system are oolitic-peloidal grainstones and dolomitised limestones, within a regionally extensive, mostly muddy, carbonate platform that is now called the Arab Formation. The Arab Formation is typically divided into four cycles (A through D from base to top); all cycles can produce, but the Arab D is the most productive over much of the Gulf. Each cycle shoals up from a more marine base to restricted-marine, variably dolomitised, limestone to mudflat dolomites and evaporites. The lower portion of the Arab D is typically a bioclastic lime mudstone or wackestone with normal marine fossils. Away from topographic highs, local organic-rich mudstones were deposited in intrashelf basins and are lithologically identical to similar intrabasinal successions in the underlying Diyab Formation. The lower Arab D is overlain by a middle unit of clean washed calcarenite, largely composed of sorted and rounded skeletal particles and ooids (grainstone-packstone), and an upper variably developed thin dolomitic mudflat sequence, which grades across a metre or two of anhydrite-plugged carbonate into massive to nodular anhydrites of the Arab D capstone. This anhydrite was deposited within a regional sulphate saltern/pan with local, but still widespread, evaporite mudflats atop local highs. Evaporitic mudflats also encircled the depositional edges of the basin. Microfossil and macrofossil content in the marine portion of the Arab D is a useful discriminant of water depth and restriction (Fig. 10.16; Wyn Hughes 1996; Lindsay et al. 2006).

For example, Al-Awwad and Collins (2013) show that locally the reservoir lithofacies in Khurais Field, Saudi Arabia, are made up of: couplets of (1) lime mud and (2) intraclastic lithofacies representing basinal turbidites; (3) pelletal lithofacies representing lower shoreface sands and silts; (4) stromatoporoid lithofacies representing a reef; (5) *Cladocoropsis* and (6) dasyclad lithofacies representing a lagoon; (7) peloidal and (8) oolitic lithofacies representing shore-attached sand sheets; (9) cryptomicrobial lithofacies representing supratidal flats; (10) anhydrites representing sabkha followed by salina deposits; and (11) stratigraphically reoccurring dolomite (Fig. 10.16). These are arranged in two, partially preserved, third-order sequences, the upper of which represents the Arab-D Member and the lower of which represents the upper Jubaila Formation. Within these sequences lie six fourth-order high frequency sequences, composed of fifth-order parasequences and parasequence-scale cycles. The preserved upward shallowing trend of the Arab-D reservoir is manifested laterally by a regional eastward thickening interpreted to be the result of an eastward progradation across the shallow Late Jurassic epeiric shelf and into the relatively deep Arabian intrashelf basin.

Regionally, atop the anhydrite-capped marine-dominated limestone and dolomite of the Arab D are the more restricted cyclic carbonates-anhydrites of the Arab A-C. These sediments in the United Arab Emirates show depositional relationships that correspond to the outline of the current and possibly the late Jurassic edge of the evaporite basin, although exact detail has been obscured by edge dissolution and erosion (Fig. 10.17). Wireline signatures in the anhydrite caps to the various A-C cycles in oil fields in both Saudi Arabia and eastern Abu Dhabi indicate evaporite mudflats made up of mosaics of sabkhas, ephemeral brine pans and salinas (personal observation) and are very similar to signatures in shoal water portions of the Arab D capstone. As in the Arab D cap, the proportion of subaqueous anhydrite increases in the capstone away from the crests of many fields, showing that many current highs were also highs in the Jurassic. Unbreached anhydrite caps in all Arab D cycles are highly effective seals, for example, the anhydritic cap to the Arab D holds back a 400 m-oil column in Ghawar Field,

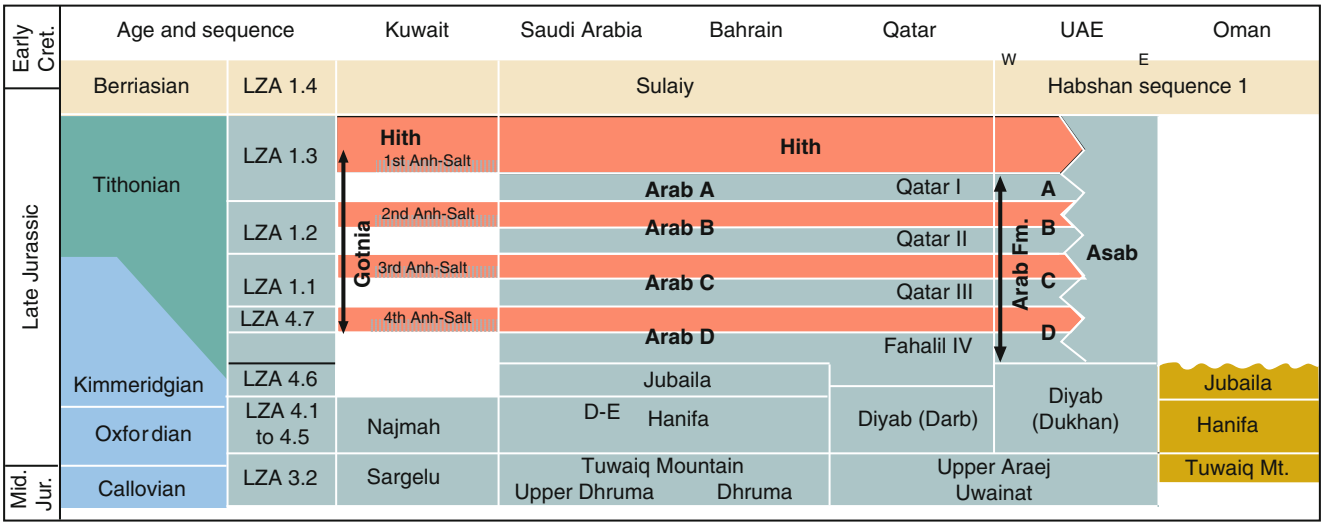

Fig. 10.15 Stratigraphy of the Late Jurassic sediments of the southern Arabian Gulf (After Al-Husseini 1997)

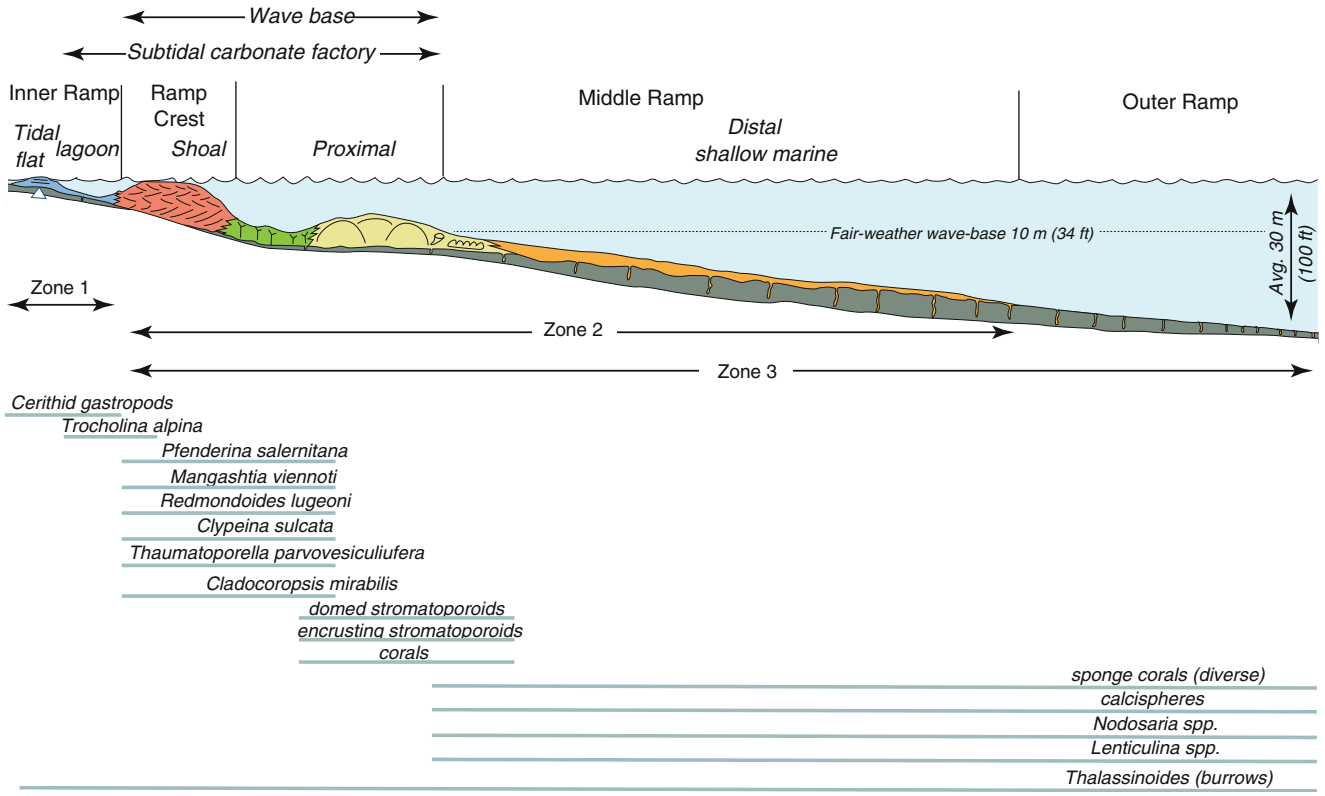

Fig. 10.16 Palaeoenvironmental distribution across zones 1–3 of various biotic elements within the carbonate stage of the Arab-D reservoir, based on Ghawar but applicable to other Jurassic reservoirs in Saudi Arabia (After Lindsay et al. 2006). The schematic reconstruction does not include the evaporitic saltern stage. This model depicts deposition of one ideal carbonate cycle from the inner ramp, ramp-crest shoal, proximal, and distal middle ramp to outer ramp. *Grey coloured* unit is a transgressive mud-rich deposit that forms the base of a cycle capped by a firmground that developed during maximum flooding and was extensively burrowed by *Thalassinoides*. Subsequent units tend to shoal upward and are progradational or regressive. *Orange coloured* unit is distal middle-ramp debris-flow deposits of rudstone and floatstone. *Brown fill* indicates proximal middle-ramp biostromes and mounds of stromatoporoids and corals. *Green* with fork shapes is proximal middle-ramp *Cladocoropsis* banks deposited in sheltered areas between and upslope of biostromes and mounds. *Red* is the cross-bedded ramp-crest grainstone shoal. *Blue* is inner-ramp lagoon intertidal islands. Those facies and rock types that are abundant in each reservoir zone are *underlined* by the titles and associated *arrows* showing depositional extents of zone 1, zone 2, and zone 3. Distribution of common to abundant faunal and floral elements (both laterally at any one time and stratigraphically through the reservoir zones) is shown by *grey bars*

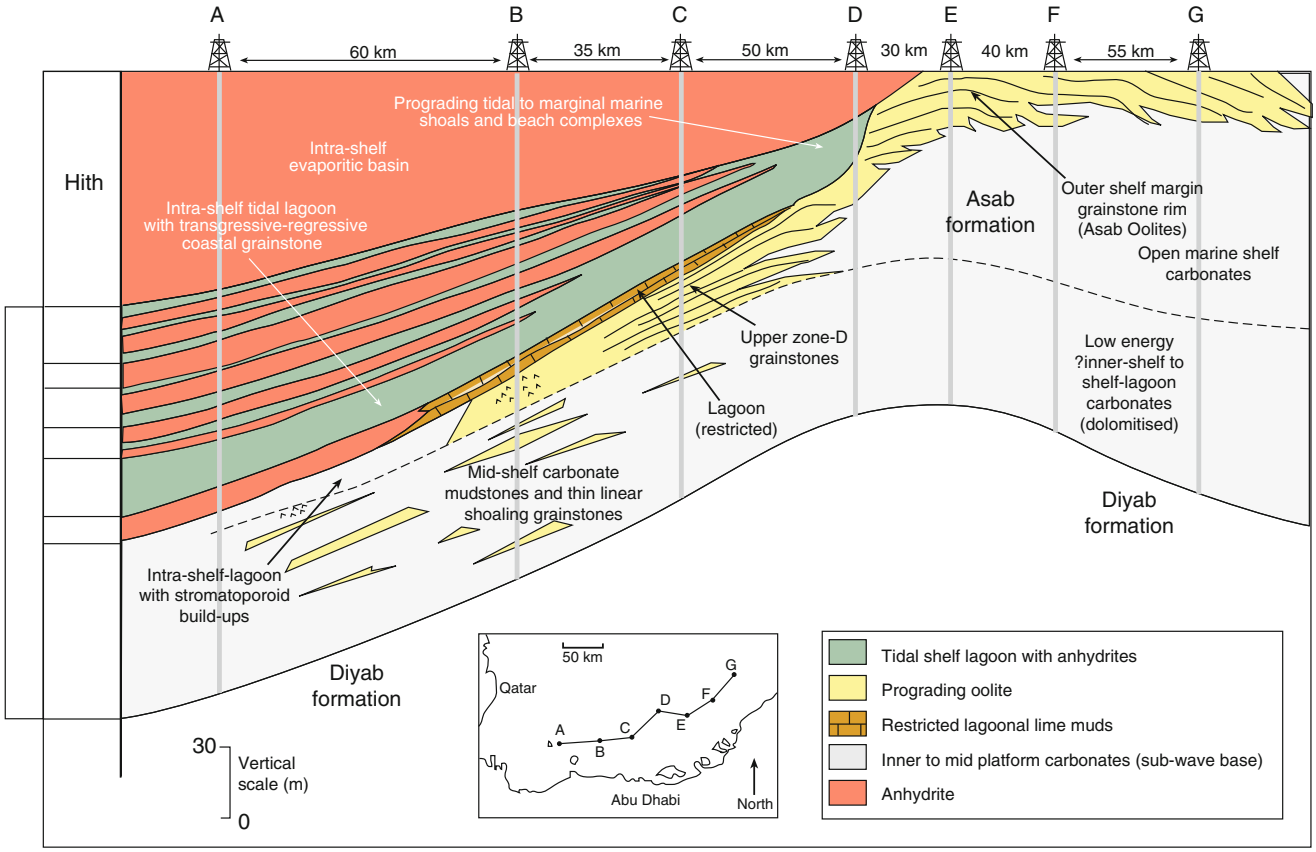

Fig. 10.17 Schematic east-west cross-section of the Arab and Hith formations, offshore Abu Dhabi. Note: Datum is possibly affected by erosion and evaporite dissolution with the amount of truncation increasing to the east. Facies relationships between wells are schematic (After Al Silwadi et al. 1996)

Saudi Arabia. Wireline signatures in the crest of the field indicate a mosaic of salinas and sabkhas.

The Asab Formation in the eastern United Arab Emirates is laterally equivalent (although not necessarily time equivalent) to the Arab Formation (Fig. 10.17). Definitions of Arab-A,-B, and -C vary from field to field across the Gulf and do not necessarily represent the same chronostratigraphic unit. The combined Arab-ABC is defined by Grötsch et al. (2003) as a lithostratigraphic unit composed of high-frequency dolomite-anhydrite shallowing-upward cycles capped by the massive Lower and Upper Hith Anhydrite. The top of the underlying Arab-D reservoir in the eastern UAE is typically picked at the top of a clean gamma-ray trend, which is usually an oolitic and bioclastic grainstone section. Its top typically coincides with the first occurrence of a gamma kick, indicative of a black marker limestone that commonly contains pyrite. However, in my opinion, this marker is not always a depositional unit and may be a dissolution residue created by fluid crossflow along the underside of the anhydrite sealing the Arab D. Although a useful correlative marker of the reservoir top, it probably does not represent a time-line.

If we assume the Arab D is the base of the section throughout the Arabian Peninsula, then the difficulty in breaking out three separate cycles (Arab A-C cycles) atop the Arab D reflects the high degree of textural similarity of all restricted and dolomitised evaporite-capped shoaling cycles. The inherent lack of an entrained time-significant fossil assemblage and the vagaries of syndepositional evaporite dissolution in all evaporitic mudflats makes detailed well-to-well correlation at the level of the Arab A-C very difficult. There are more than three anhydrite beds in the A-C interval (Fig. 10.17). Short but significant episodes of subaerial exposure and freshening characterised the brine sheets depositing these marine-fed mudflat cycles. Intraformational evaporite dissolution residues, sometimes show high gamma kicks and without reference to core can be easily misinterpreted as maximum flooding surfaces.

Capping the cycles of the Arab Formation is a thick regional unit of subaqueous saltern anhydrite, the Hith Anhydrite, which extends over much of the Arabian Gulf region. In Saudi Arabia and the eastern UAE, it holds back almost all of the oil and gas sourced in Jurassic mudstones. It is only at the edge of the Hith in the central and western UAE

that Jurassic sourced oil is found as widespread accumulations in the overlying Cretaceous succession (Fig. 10.8a).

Deposition of the various widespread anhydrite caps in the Arab Formation across the Arabian Plate indicate higher order sealevel falls, within what was a second order sequence accumulating during the late Kimmeridgian. For much of this time, when evaporites were not accumulating, open-marine to restricted-marine epeiric carbonates were the dominant sediments (Fig. 10.17; Sharland et al. 2001; Al-Saad and Sadooni 2001). During the preceding Hanifa and Jubaila time (middle Oxfordian and early Kimmeridgian, respectively), local organic-rich intrashelf basins deposited starved-basin sequences of laminated organic-rich dark-coloured marls and mudstones (Fig. 9.5; Ayres et al. 1982).

Prior to hydrographic isolation that marked the end of the Arab D, oolite/peloidal shoals and patchy coral-algal stromatoporoid banks were deposited as local higher energy shoals across the muddy epeiric platform that typified marine stages of Arab Formation deposition across the Arabian Peninsula (Fig. 10.16). Regionally, similar but more laterally continuous Kimmeridgian equivalents to these higher energy marine carbonates lined the epeiric platform margin. This band of shelf-edge shoals was a hydrodynamic barrier that periodically restricted free surface exchange between Arabian Platform waters and deeper open-marine (Tethyan) waters to the east and facilitated deposition of the various anhydrite capstones (Fig. 10.14). This shoal-rimmed margin thus separated a muddy interior epeiric platform, with its intrashelf depressions, from the deeper open-water marine slope carbonates. Edges of the various intrashelf basins of the epeiric shelf behind the main shelf margin shoal were ramp-style progressions around somewhat deep (≈30 m) intrashelf basins (Sharland et al. 2001). Much of the regional platform-margin shoal rim was destroyed during later continental collision.

Regionally, much of the reservoir quality in the undolomitised or poorly dolomitised limestone reservoirs in the Arab D can be directly tied to partially-preserved primary porosity in grainstone (ooid, skeletal and peloid) shoals and local reefal (stromatoporoid) debris aprons in the epeiric interior seaway. In many parts of the platform interior (e.g. the offshore UAE) the shoaling of the Jurassic seafloor and the formation of seafloor shoals in the Arab Formation was facilitated by salt structures sourced in the Precambrian Hormuz salt.

After deposition of the Arab D, ongoing higher order eustatic changes formed the numerous parasequences that make up the widespread A-C cycles of the Arab Formation in the epeiric shelf interior. Eustatic fluctuations drove periodic marine flooding episodes on the platform, followed by filling of accommodation space, hydrographic isolation and capping by evaporites and exposure surfaces. With each transgression another more open marine platform unit defined the base of a cycle and was deposited as marine to mesohaline, skeletal-poor peloid wackestones/mudstones. Local shoaling on the epeiric platform led to progressively higher bottom energies culminating in thin local buildups of ooid and peloid grainstones that are now producing intervals in the Arab ABC.

Progressive platform restriction followed, via a combination of active carbonate aggradation and high order falls in relative sealevel (3rd to 5th order), which periodically exposed the shelf margin within an environment of net evaporation across the arid platform. This drove numerous brining-upward depositional cycles in the Arab ABC, with most, but not all culminating in the deposition of mudflat gypsum. Gypsum beds were porous at the time the various Arab ABC sulphates were deposited and brine reflux drove the formation of mimetic dolomites in the immediately underlying limestones. Dolomitisation is less pervasive, but still significant, in terms of reservoir quality in the underlying Arab D (Fig. 10.19). Thus syndepositional reflux dolomitisation occurred many times during the accumulation of evaporite caps to the various muddier units of the Arab Fm. and each probably indicates platform restriction related to higher order sealevel falls or local halokinetically- or basement fault-induced seafloor uplift. Some evaporite beds associated with these higher-order relative sealevel falls were leached by a subsequent rise in sealevel, so that all that remains of some of these higher order evaporite deposits are nodules cementing carbonate remnants in thin dolomites, along with widespread cm-scale dissolution surfaces and residues, often associated with gamma peaks in the wireline log (pers. obs.).

Any model explaining reflux dolomitisation on the Arabian Shelf as only occurring during the deposition of the four major cycle caps in the Arab Formation is too simplistic, as is the notion that the reservoir sediments of the Arab D cycle are the same as those of the subsequent A-C cycles. Given that the Arab D is the dominant producer throughout the Arabian Peninsula, we shall now focus on the detail of its reservoir characteristics and any relationship to diagenesis, perhaps tied to reflux and vertical crossflows that were focused by its evaporite seal.

The best-documented and regionally largest accumulation of hydrocarbons in the Arabian Peninsula occurs in Ghawar Field in Saudi Arabia (Fig. 10.18). It not only stores hydrocarbons in the Jurassic section, but also entrains rich gas reserves in the underlying Permian Khuff Formation and with more than 150–200 billion barrels of ultimate recoverable oil is the world's largest single oil-filled structure. Even so, it is approaching the 50 % recovered mark.

Production began in Ghawar field in 1951 and reached a peak of 5.7 million barrels per day in 1981. This is the highest sustained oil production rate achieved by any single oil field in world history. At the time that this record was achieved, the southern areas of Hawiyah and Haradh had not

yet been fully developed. Production was restrained after 1981 for market reasons, but Ghawar remains the world's most important oil field. Its daily production of 30–31° API oil exceeds 5 million barrels per day, which is more than half of Saudi Arabia's cumulative oil production. Ultimate recoverable resource estimates for Ghawar range from 66 to 150 Gb, with some estimates exceeding 200 Gb. By 2005, Ghawar's cumulative production was some 61 Gb, if an assumption of around 150 Gb is used and assuming that the production was near constant at around 5 Mbpd for 2006 and 2007, then produced share of ultimate recoverable resource by end of 2007 was 43 % (Höök et al. 2009). This is in line with the 48 % of Ghawar reserves produced as stated by Saudi-Aramco.

The following discussion will only deal with the geology of the Jurassic section in Ghawar. Detailed studies of various aspects of Ghawar and its outcrop equivalents in Saudi Arabia have been published by Lindsay et al. (2006), Cantrell et al. (2001), Cantrell and Hagerty (1999, 2003), Stenger et al. (2003), Lucia et al. (2001), Meyer et al. (1996, 2000), Saner and Sahin (1999), Douglas et al. (1996), Wyn Hughes (1996), Powers (1962). The following section is a summary of aspects of this work, along with some comments of my own.

Ghawar Field, Saudi Arabia

The Arab-D carbonate reservoir of the Upper Jurassic Arab Formation in the onshore Ghawar Field was discovered in 1948. Following further separate discoveries in culminations along the structure's main axis, five production areas were quickly identified as parts of a single giant Ghawar oil field (Stenger et al. 2003). From north to south Ghawar is made up of Ain Dar, Shedgum, Uthmaniyah, Hawiyah and Haradh (Fig. 10.18a). At the Arab-D level, the field is a NNE-trending composite anticline, 230 km long and about 30 km wide, with a productive area of more than 693,000 acres in a single, pressure-continuous reservoir.

Within the Jurassic section, the Ghawar produces from the evaporite-sealed Arab D, with the reservoir section extending down into mudstones of the uppermost Jubaila Formation. Production layering is typically broken out into 4 zones with the main production intervals broken into further finer subdivisions (Fig. 10.19). Limestones of Zone 1 and 2 typically constitute the best quality Arab D reservoirs (Fig. 10.18b). Arab-C, Hanifa and Fadhili oil reservoirs are also present in parts of the field, but the Arab-D reservoir accounts for nearly all of the oil reserves and production.

Across the field the Arab-D reservoir is comprised of a series of stacked shallow water, platformal carbonate sediments deposited as a cleaning-up and a shallowing-up carbonate succession stacked into metre-scale cycles or parasequences. The bulk of the reservoir is comprised of limestone, though some dolomite is present. Anhydrite is present in the reservoir as cement, but typically in minor amounts (Table 10.3). The cleanest and most porous rocks – hence the most favourable in terms of production – are situated in the grainier upper portion of the reservoir (Zone 2) Interparticle porosity predominates in the various reservoirs,

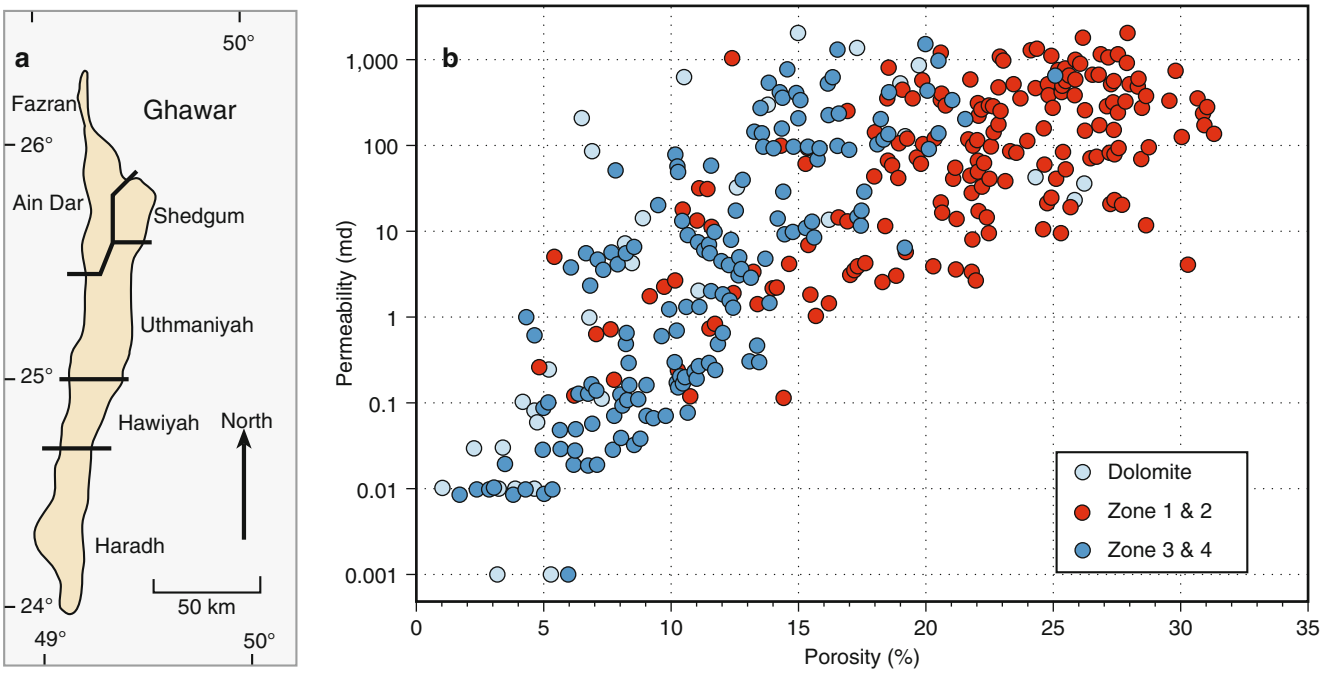

Fig. 10.18 Ghawar field, Saudi Arabia. (**a**) Subdivisions of field. (**b**) Poroperm crossplot of typical Zone 1 and 2, Zone 3 and 4, as well as dolomites, from cores in the Arab D reservoir of Ghawar Field, Saudi Arabia (After Cantrell and Hagerty 2003)

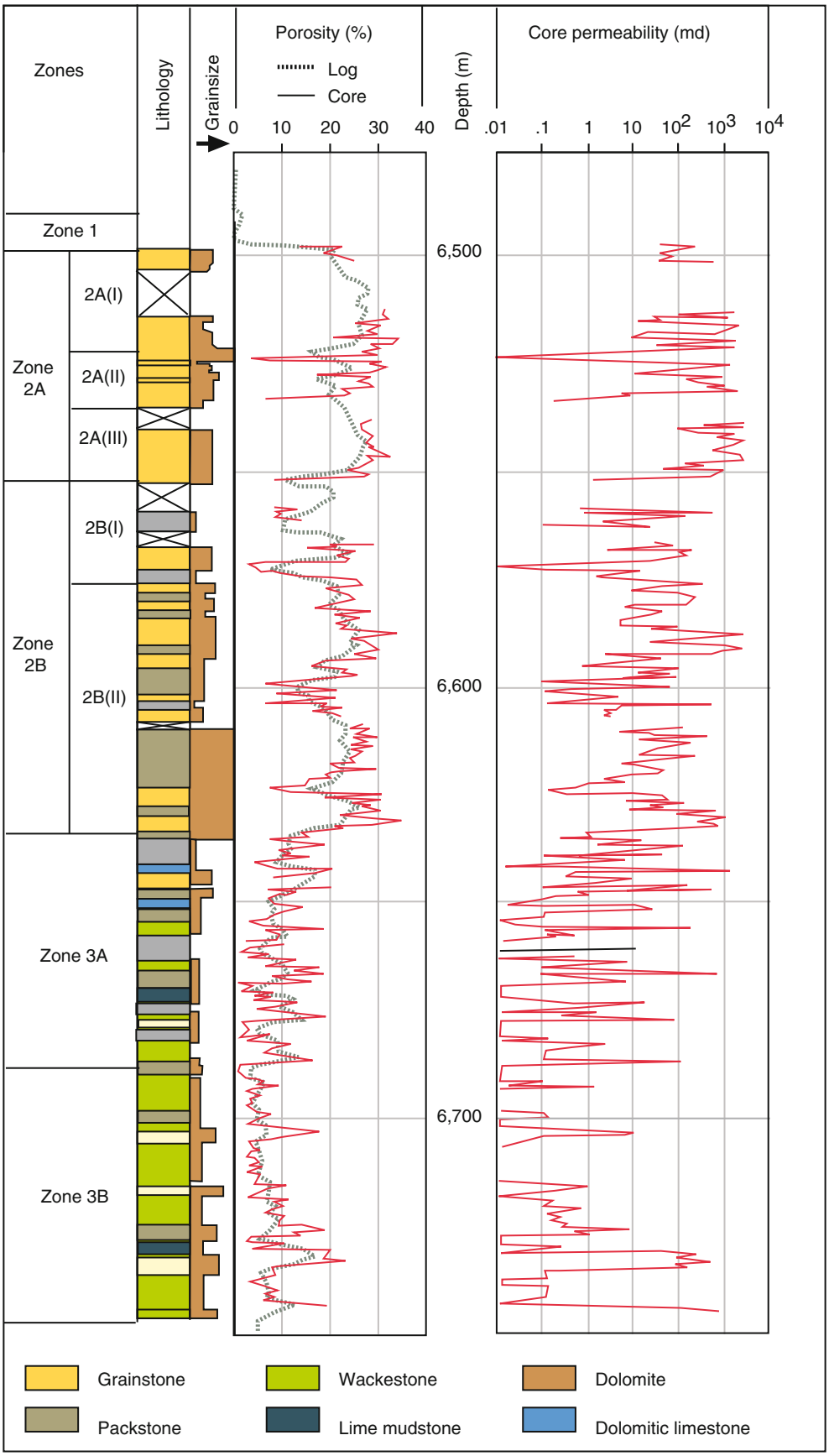

Fig. 10.19 Reservoir zonation, porosity and permeability in the Arab D Formation in Uthmaniyah Field, which is an operational area within the much larger Ghawar Field, Saudi Arabia (After Saner and Sahin 1999)

Table 10.3 Characteristics and distribution of carbonates lithofacies, Arab-D reservoir, Ghawar Field

	Skeletal-Oolitic (SO)	*Cladocoropsis* (CLADO)	Stromatoporoid Red Algae-Coral (SRAC)	Bivalve-Coated Grain-Intraclast (BCGI)	Micritic (MIC)	Dolomite (DOLO)
Depositional types	Grainstone, mud-lean packstone, packstone	Mud-lean packstone, grainstone, packstone	Mud-lean packstone, grainstone, packstone, boundstone	Packstone, mud-lean packstone, grainstone, wackestone	Wackestone, mudstone, packstone	Indeterminate
Major grain types	Micritized grains, Foraminifers (including Miliolids), Dasycladacean algae, ooids, bivalves	Micritized grains, *Cladocoropsis*, Dasycladacean algae, foraminifers (including Miliolids)	Micritized grains, stromatoporoids, corals, foraminifers (including Miliolids)	Micritized grains, bivalves, coated grains, intraclasts, foraminifers	Micritized grains, bivalves, foraminifers (including *Kurnubia*), intraclasts	Anhedral to euhedral dolomite rhombs
Minor grain types	Echinoderms, stromatoporoids, corals, *Cladocoropsis*, gastropods, composite grains, intraclasts, ostracods, red algae, brachiopods	Stromatoporoids, echinoderms, bivalves, corals, ooids, gastropods, brachiopods, composite grains, red algae	*Cladocoropsis*, bivalves, echinoderms, Dasycladacean algae, intraclasts, coated grains, composite grains, gastropods	Miliolid foraminifers, corals, stromatoporoids, Dasycladacean algae, echinoderms, gastropods, *Cladocoropsis*	Coated grains, Miliolid foraminifers, Dasycladacean algae, intraclasts, ostracods, echinoderms, gastropods, stromatoporoids, corals	Relict and leached bivalves, *Cladocoropsis*, stromatoporoids, Intraclasts, echinoderms, ind. grains
Sedimentary structures	Cross bedding, burrows, hardgrounds, fining upward graded beds, borings, horizontal laminae	Burrows, hardgrounds, cross bedding, horizontal laminae	Burrows, borings, hardgrounds, fining upward graded beds, crossbedding	Burrows, hardgrounds, borings, fining upward graded beds, cross bedding	Burrows, hardgrounds, wavy laminae, horizontal laminae, borings, fining upward graded beds	Relict burrows?, hardgrounds?, carbonanceous? laminae
Pore types	Interparticle, mouldic, intraparticle, intercrystalline, fracture	Interparticle, intraparticle, mouldic, intercrystalline	Interparticle, mouldic, intraparticle, intercrystalline, fracture	Interparticle, mouldic, intraparticle, intercrystalline, fracture	Interparticle (within burrow fills), intraparticle, mouldic, intercrystalline, fracture, vug?	Intercrystalline, mouldic, fracture
Diagenetic modification	Leaching and recrystallization, isopachous bladed calcite cement, dolomitisation, physical compaction, stylolitisation, equant calcite cement, kaolinite emplacement, anhydrite emplacement/replacement, silicification	Leaching and recrystallization, dolomitisation, equant calcite cement, stylolitisation, anhydrite emplacement, silicification	Leaching and recrystallization, dolomitisation, anhydrite emplacement, stylolitisation, isopachous bladed calcite cement, equant calcite cement, pyrite, dedolomitisation	Leaching and recrystallization, dolomitisation, stylolitisation, equant calcite cement, anhydrite emplacement, isopachous bladed calcite cement, pyrite	Leaching and recrystallization, dolomitisation, stylolitisation, anhydrite emplacement, pyrite, silicification, equant calcite cement, kaolinite	Dolomitization, leaching, anhydrite emplacement, equant calcite cement, stylolitisation, kaolinite, dedolomitisation
Distribution (Ghawar Zone/Formation)	1, 2A, 2B, 3A, 3B	2A, 2B	2A, 2B, 3A, 3B, Jubaila	2B, 3A, 3B, Jubaila	1, 2A, 2B, 3A, 3B, Jubaila	1, 2A, 2B, 3A

After Cantrell and Hagerty (2003). See also Fig. 10.16

though locally, other porosity types are important; for example, mouldic and intercrystalline porosity in dolomitised portions of the reservoir. Each of the major upward-shoaling cycles that make up the Arab D was initiated in deeper subtidal water that shoaled to near sea-level. The proportion of skeletal grainstones and packstones, along with ooid grainstones, increase within each cycle and within the Arab D overall. The top of the Arab-D carbonate is characterized by a thinner unit of dolomitised carbonate mudstone (Zone 1), capped by an evaporite seal.

By far the most abundant reservoir rock texture in the Arab-D is packstone; likewise, the most abundant reservoir lithofacies is skeletal-oolitic (SO; Tables 10.3 and 10.4; Cantrell and Hagerty 2003). The other significant lithofacies in the Ghawar reservoir are; *Cladocoropsis* (a characteristic finger-shaped and sized stromatoporoid) lithofacies (CLADO), stromatoporoid-red algae-coral lithofacies (SRAC), bivalve-coated grain-intraclast lithofacies (BCGI), micritic lithofacies (MIC) and dolomite lithofacies (DOLO), all of which are described in detail by Mitchell et al. (1988). Similar, if not identical, lithofacies make up Arab D reservoirs in other fields in Saudi Arabia and the western United Arab Emirates (e.g., Al-Awwad and Collins 2013). In a detailed petrographic and petrophysical characterisation of the Ghawar Arab D reservoir Cantrell and Hagerty (2003) defined seven related limestone reservoir rock types based on the values of: (1) the amount of cement, (2) the amount of matrix (lime mud), (3) the grain sorting/grain packing, (4) the dominant pore type, and (5) the size of the largest moulds (Tables 10.4 and 10.5; Fig. 10.20).

At the broadest scale of reservoir classification the Arab D reservoirs are either limestone or dolomite (Table 10.5) In terms of porosity and permeability in the limestones, the amount of matrix is the most important of these five parameters and breaks down into three reservoir types (1-III). Cantrell and Hagerty (op cit.) break our two broad families, A and B in each of the three reservoir types (Table 10.5). Family, A, is relatively coarse-grained and poorly sorted rock with relatively large moulds. Family, B, is a generally fine to medium-grained, well-sorted rock with few or small moulds. Together this constitute 6 families of reservoir rock in the Arab D. Reservoir rock type IV is a seventh limestone family in Ghawar. Type IV limestones contains more than 10 % cement, this modifies pore size distribution enough to warrant a separate limestone reservoir family (Fig. 10.20). Each of the seven limestone types is characterized by distinctive porosity-permeability relationships (Fig. 10.20). Similar matrix-lean limestone reservoir characterise better quality reservoirs in Abqiq Field in Saudi Arabia and the Jurassic Arab Formation reservoirs of Qatar (Figs. 10.21 and 10.22, respectively).

Dolomites in Ghawar constitute reservoir rock type V and are further subdivided according to their dolomite crystal texture, although stratigraphic position and porosity can also

Table 10.4 Interrelationships between texture, lithofacies and modes of occurrence in Arab D reservoir in Ghawar Field, Saudi Arabia

	Lithofacies						
Texture	SO	CLADO	SRAC	BCGI	MIC	DOLO	Total
Grainstone	24	–	8	6	6	5	44
M. I. Packstone	30	4	15	19	–	–	68
Packstone	61	9	34	65	14	–	183
Wackestone	2	–	2	2	26	–	32
Mudstone	–	–	–	–	22	1	23
Boundstone	–	–	2	–	–	–	2
Indeterminate	–	–	–	–	–	26	26
Total (samples)	117	14	61	92	62	32	378

After Cantrell and Hagerty (2003). See Table 10.3 for a description of the various lithofacies units

Table 10.5 Classification of reservoir rocks, Arab-D reservoir, Ghawar Field

Limestone								Dolomite			
Cement	<10						>10	Texture			
Matrix	0–15		16–40		>40			Fabric preserved (Reservoir zone 1)	Sucrosic (Ø > 12 %)	Intermediate (Ø 5–12 %) I	Mosaic (Ø >5 %)
Sorting	>0.5 (poor)	>0.5 (good)									
Pore Type			BP < MO + WP		BP > MO + BP						
Largest Mould (mm)			>0.3	>0.3		>0.3	>0.3				
Reservoir Rock type	IA	IB	IIA		IIB	IIIA	IIIB	IV	Vfp	Vs	Vi	Vm

After Cantrell and Hagerty (2003)

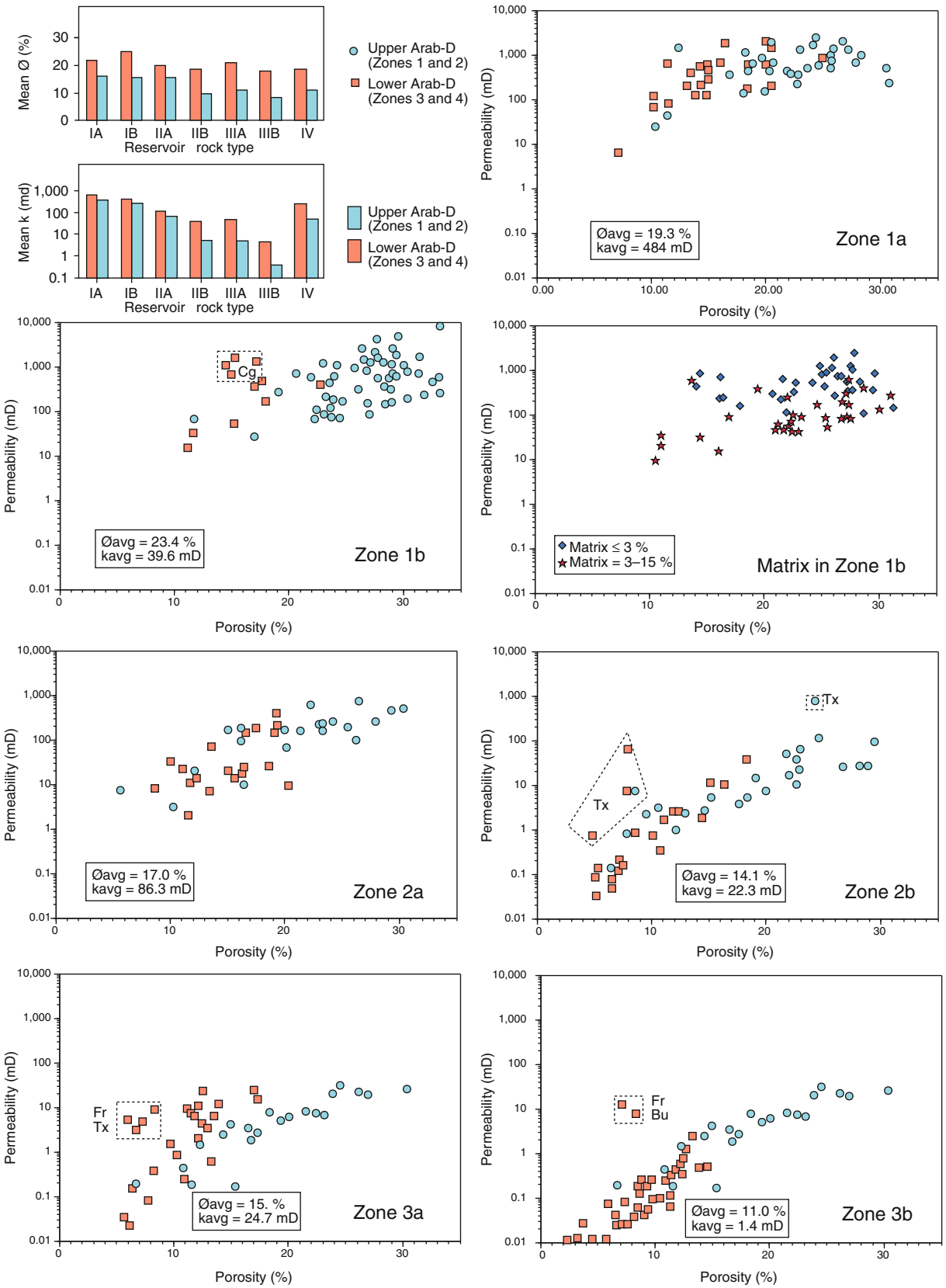

Fig. 10.20 Porosity-permeability cross plots of individual limestone reservoir rock types as defined in Table 10.5 (After Cantrell and Hagerty 2003). Outliers from the main poroperm trends are labeled according to their non-uniformity or textural characteristics (*Bu* burrows, *Cg* coarse grained, *Fr* microfractures, *Tx* textural variations, *kavg* average permeability, in millidarcies, *Øavg* porosity, in percent bulk volume). See also Fig. 10.16

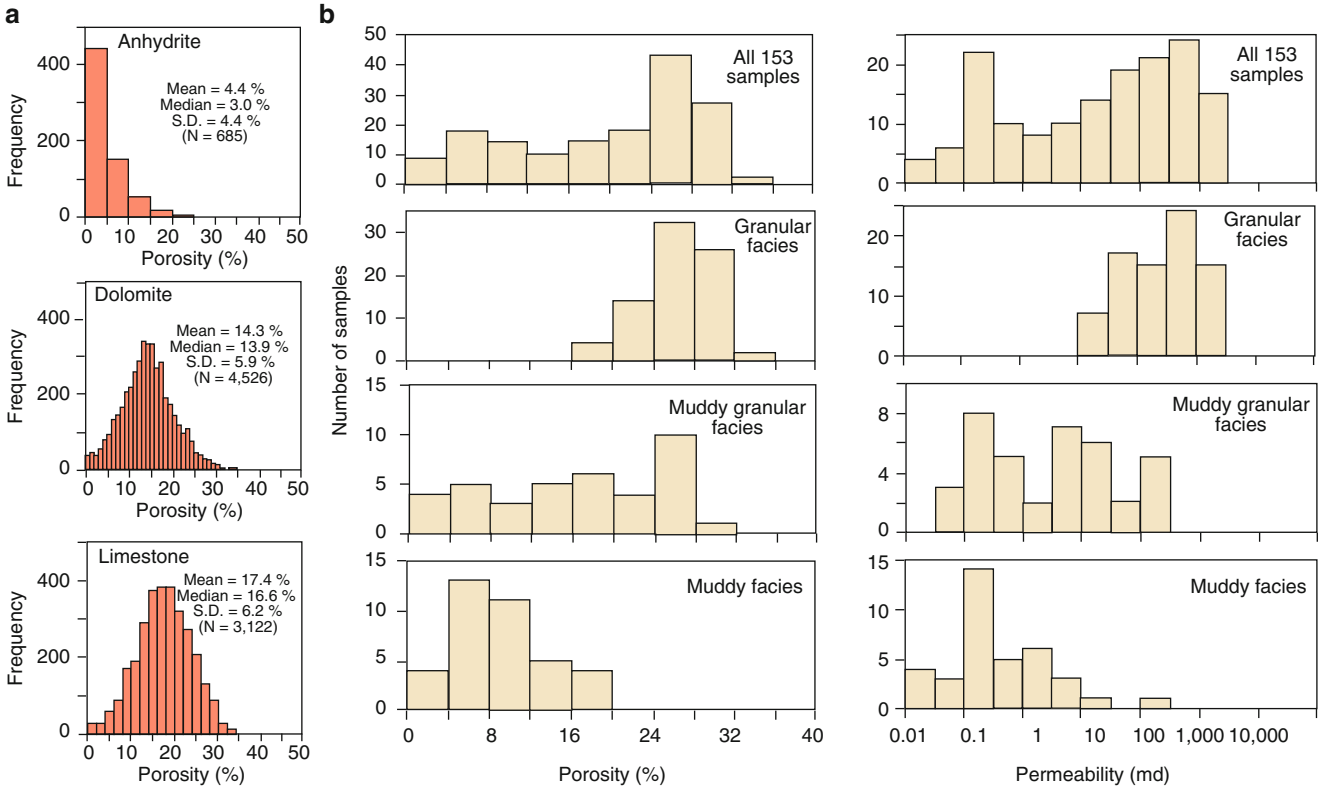

Fig. 10.21 Petrophysical character of the Arab D, Abqaiq Field, eastern Saudi Arabia (After Sahin and Saner 2001). (**a**) Well log porosity for each of the three wireline defined lithologies in Zone 1 of the Arab D. (**b**) Core plug-defined distribution of porosity and permeability in the various limestone dominated lithofacies of the Arab D

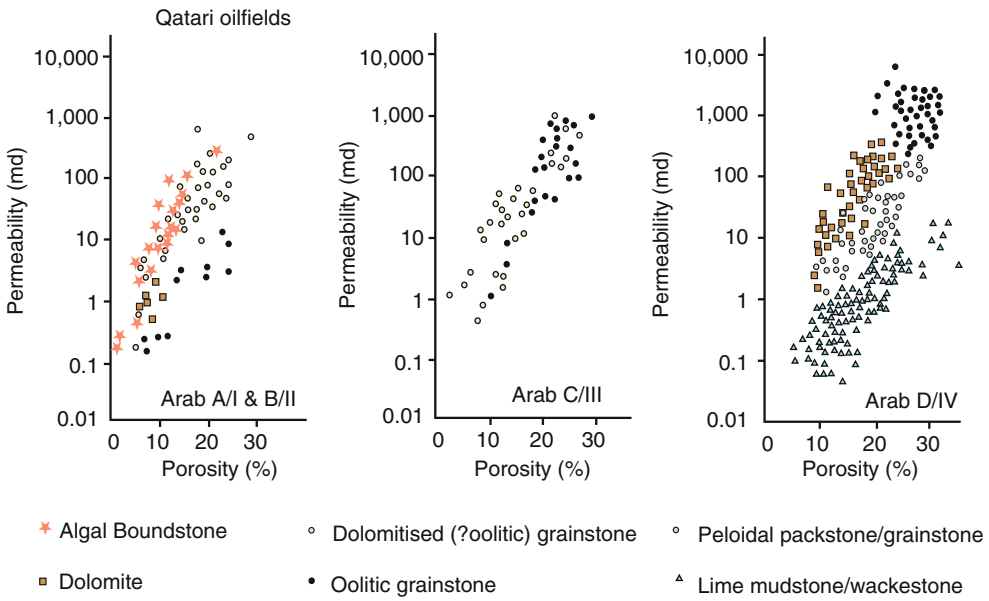

Fig. 10.22 Porosity and permeability in the Arab A through D in Qatari oilfields showing the importance to reservoir quality of graininess in the limestones and dolomitisation in the Arab D (Alsharhan and Nairn 1993)

be effective pointers in their classification (Table 10.5; Fig. 10.23a; Cantrell and Hagerty 2003). The four dolomite textures are: fabric preserving (Vfp), sucrosic (Vs), intermediate (Vi) and mosaic (Vm). The mimetic Vfp dolomite is only found in Zone 1 of the Arab-D (immediately below the anhydrite cap) where it is the major dolomite type. Sucrosic (Vs) dolomite occurs in dolomites with more than 12 % porosity, Vm less than 5 % and Vi between 5 and 12 %. Vfp dolomites have pore systems similar to their precursor limestone, but the pore systems of the other dolomite types are unique.

Powers (1962) and Lucia et al. (2001) concluded that once an interval in the Ghawar Field of Saudi Arabia is dolomitised, its reservoir quality is tied to the proportion of dolomite and dolomite crystal size (Fig. 10.23b, c). In general, when dolomites are compared to limestones in the Arab D they show lower porosities (Fig. 10.22). This is clearly seen in wireline-based porosity histograms of Zone 1 in the Arab D from Abqaiq Field, a supergiant field with 17 billion barrels of proven reserves, in eastern Saudi Arabia (Fig. 10.19; Sahin and Saner 2001). In part, this decrease in porosity with dolomitisation is a reflection of the originally lower precursor porosity in muddier transitional sediments that typically underlie a mudflat or saltern seal (mimetically dolomitised Zone 1 carbonates – Vfp).

Anhydrite-derived, corrected porosity in wireline-defined anhydrites in Zone 1 is greater than zero in Abqaiq Field, eastern Saudi Arabia (Fig. 10.21a; Sahin and Saner 2001). This value comes not from the actual anhydrite beds, which are tight, but from the thin dolomite stringers that are intercalated within the anhydrite; they sit at the limits of vertical resolution of the wireline tool in such finely layered sequences. Controls on the Arab D reservoir are similar to those in Ghawar, with limestone matrix type rather than dolomitisation as the prime control (Fig. 10.21b). Once the proportion of dolomite in a muddy succession attains 80–90 %, the reservoir character substantially improves compared to its muddy limestone precursor (Fig. 10.23b).

In many fields the dolomitisation process is most pervasive in lime mudstones below an evaporite unit or its former solution residues (e.g. Zone 1 in Ghawar). The reason why dolomites can form excellent reservoirs in tight mud-rich lime precursors in many mudstone of the Arab cycles (and the Permian Khuff of Saudi Arabia, Permian and Triassic dolomites in the Sichuan Basin of China and San Andres of West Texas) is the development of intercrystalline porosity. Hence, within the muddier facies of Ghawar there is a significant tie of reservoir quality to dolomite percent and crystal size, as in the coarsely crystalline sucrosic intervals in the dolomitised interval of Ghawar. Crystal size in the dolomites is related to reservoir quality with coarser crystals defining the higher porosity/permeability intervals, probably reflecting a propensity for larger pore throats and remnant dissolution voids in the more coarsely crystalline dolomites (Fig. 10.23c). Locally such coarsely crystalline dolomite can create high permeability "super-k" layers (Meyer et al. 2000).

But dolomites in the Arab Formation in Saudi Arabia are not from a single generation of reflux dolomite, nor are the dolomitised units laterally homogenous. When dolomite is subdivided by texture and stratigraphy (not porosity as was done in Table 10.5; Fig. 10.24; Cantrell et al. 2001) then five types of dolomite occur in the Arab D reservoir in Ghawar Field, namely:

1. Finely crystalline, non fabric preserving (NFP) dolomite in Zone 3 (lower Arab D) with considerable preserved calcite, low oxygen isotope values and generally poor reservoir quality. Dolomite is typically associated with hiatal surfaces.
2. Medium crystalline NFP dolomite with elevated oxygen isotope values and very poor reservoir quality in Zone 2 (upper Arab D). Occurs essentially as dolomite beds with little or no reservoir quality.
3. Medium to coarsely crystalline (NFP) dolomite with low oxygen isotope values and very good reservoir quality in Zone 2. Petrographically it is similar to medium-crystalline NFP dolomite but shows a lighter isotopic signature. It is an important reservoir component as it occurs in 'super k' intervals (Meyer et al. 2000).

   It is characterised by a high degree of intercrystalline porosity and locally retains leached mouldic porosity (typically after *Cladocoropsis*).
4. Finely crystalline fabric preserving (FP) dolomite in Zone 1 (uppermost Arab D) with elevated oxygen isotope values and generally fair to poor reservoir properties. It is minor in terms of overall reservoir volume in the Arab D and also occurs in association within and below the overlying C-D anhydrite transition. Typically it forms layers or thin sheetlike beds in Zone 1. Reservoir quality typically reflects the characteristics of the overprinted limestone facies, most of which were relatively mud free and partially cemented mudlean packstones.
5. Rare locally occurring saddle dolomite (not sampled in the Cantrell et al. 2001 study).

Overall, dolomite comprises around 14 % of the Arab D in Ghawar, with the highest proportion in Zone 1 below the anhydrite cap (Figs. 10.25 and 10.26; Cantrell et al. 2001). Zones 2B and 3A have less dolomite, but it is still a significant fraction of the reservoir matrix. Dolomite is a relatively insignificant contributor to reservoir matrix in Zones 3B and 2A. Within each reservoir zone much of the total dolomite percentage in a well comes from individual layers, which are intercalated with limestones. Laterally many of these dolomite layers can vary greatly in the proportion of dolomite (e.g. Zone 2B). On a Ghawar-wide basis dolomite increases

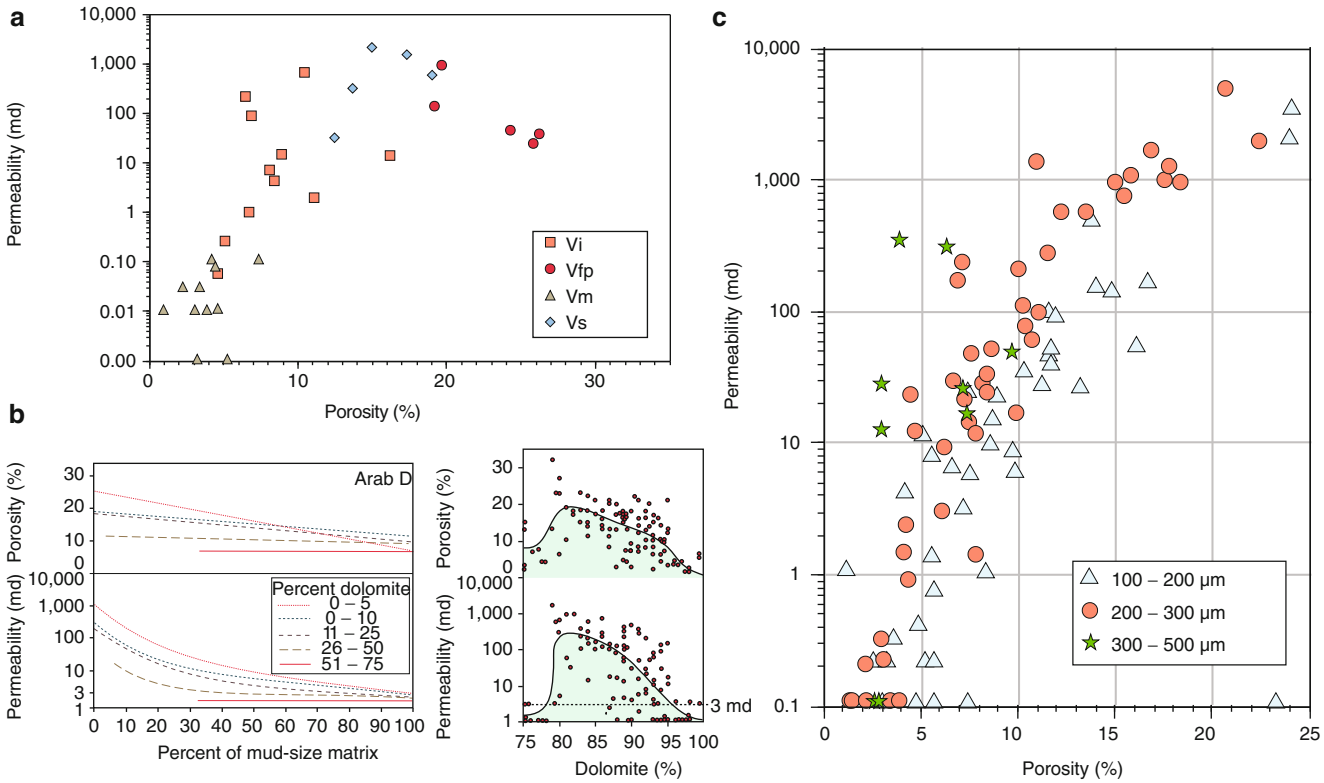

Fig. 10.23 Reservoir properties of dolomites in the Arab D, Ghawar Field, Saudi Arabia. (**a**) Textural-petrophysical classification of dolomite reservoirs (After Cantrell and Hagerty 2003). (**b**) Effect of mud size and dolomite percentage on porosity and permeability in the Arab D in Ghawar Field. There is a drastic increase in permeability when the dolomite proportion is between 80 and 90 % (After Powers 1962). (**c**) Interparticle porosity permeability crossplot for dolomites of various crystal sizes (After Lucia et al. 2001)

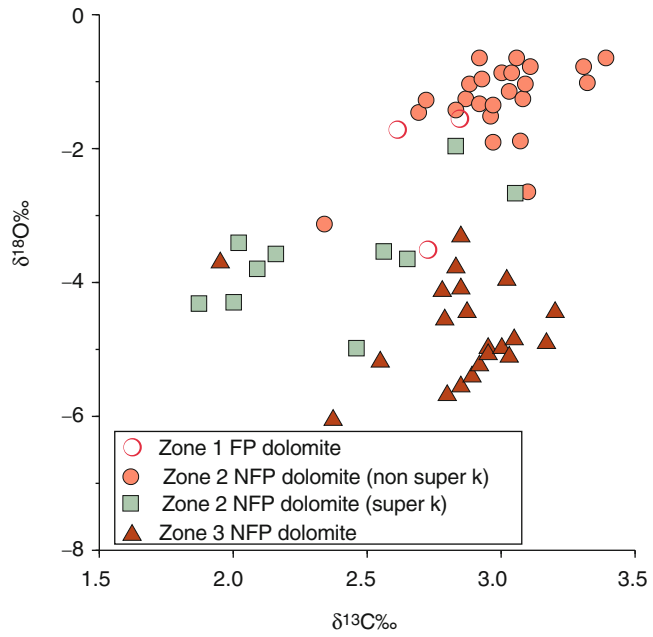

Fig. 10.24 Isotopic compositions of dolomites in Arab D, Ghawar Field, Saudi Arabia, based on textures (After Cantrell et al. 2001)

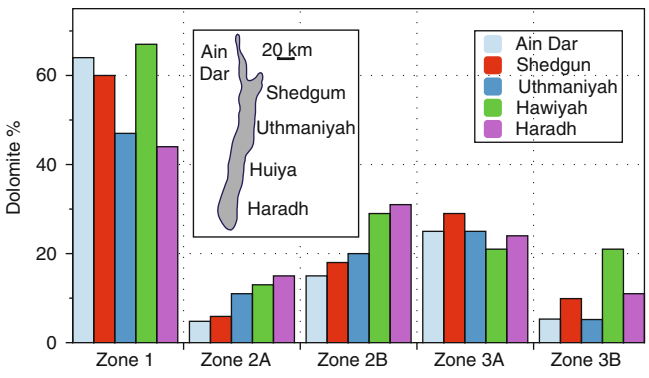

ZONE	Dolomite (%)	Dolomite thickness (m)	Zone thickness (m)
1	55.3	1.4	2.5
2A	10.1	1.5	14.5
2B	24.8	5.2	21.0
3A	21.8	4.1	18.8
3B	10.5	1.7	16.0
Total Arab D	13.9	9.9	71.3

Fig. 10.25 Block diagram shows average percent dolomite in different Arab D reservoir zones for each field area of Ghawar Field, Saudi Arabia. The table summarises dolomite percent for all Arab D in Ghawar Field (Data re-charted from Cantrell et al. 2001)

systematically from north to south in Zones 2A and 2B, but zone 3A displays an inverse trend by generally decreasing from north to south (Cantrell et al. 2001).

When Cantrell et al. (2001) mapped dolomite distribution over Ghawar Field they identified a series of parallel linear trends of high dolomite content that extended for tens of kilometres along northeasterly trends (Fig. 10.26). These trends are especially obvious in Zone 2B but are also discernable in Zones 2A and 3A. Locally the trends connect areas of pervasive dolomitisation, where much of the section (virtually 100 % of Zones 1, 2A, 2B and 3A) is replaced by dolomite. There may also be some saddle dolomite in these same areas, but it is rare. Northeast trends are present, but less obvious, in southern Ghawar. The trends suggest some structural control to the dolomite distribution and, according to Cantrell et al. (2001), indicate diagenetic patterns that are responses to a series of underlying fractures or faults. These structural features facilitated movement of dolomitising fluids into the reservoir.

As for the dolomites in the Red River Formation discussed previously, what is not clear in Ghawar is whether the dolomitising fluids (other than zone 1 dolomites) were ascending or descending when they drove the dolomitising process. Similar fault- and fracture-controlled distributions of dolomite have been documented by Warren and Kempton (1997) in metalliferous evaporite-sealed Devonian carbonates of the platform margin of Canning Basin, Australia and by Hurley and Budros (1990) in the Silurian Scipio Albion Trend in Michigan. Dolomite's propensity for ongoing alteration and replacement in Ghawar, and its proximity to a fluid-focusing evaporite layer (first as a fluid source and then as a seal) throughout its burial history, means the origin of the Ghawar dolomites is probably not a simple unidirectional fluid flow story (Warren 2000a). Fractures in the host carbonates may have been conduits for descending reflux fluids early in the burial history, but may have then acted as conduits for upwelling fluids later in the field's burial history. During this upwelling stage, various unbreached evaporite seals acted to pond and store escaping basinal fluids. Such flow reversals would overprint early-formed dolomites with later burial signatures.

Partially preserved primary pore spaces in the Arab D limestones throughout the region typically remain as well-defined relicts in evaporite-sealed banks of weakly dolomitised coral-stromatoporoid reefs and skel-ooid grainstones and grain dominant packstones. These build-ups and shoals are also characterised by leached moulds of stromatoporoid and coral branches and other aragonite allochems. Yet, once the overlying evaporite cap was deposited, there is little evidence of subsequent meteoric diagenesis or karst, and little or no evidence of later pervasive diagenesis and calcite cementation. Much of the leaching in the reservoir seems to have been early and perhaps was an integral part of the same reflux hydrology that was dolomitising portions of the Arab Formation adjacent to evaporite beds. Considering their age (≈150 Ma) and relatively deep current burial (1,200–3,000 m), this preservation of widespread primary void skeletal moulds in any limestone is unusual. Wilson (1985) argued the early emplacement of the evaporite capstones atop limestone buildups and the subsequent deposition of the Hith Anhydrite was what preserved economic porosity levels into the burial realm. Burial beneath saltern and mudflat sediment in an environment that was consistently arid and hot meant that once all the gypsum had converted to tight nodular anhydrite beds within the first few hundreds of metres of burial, the resulting seals slowed fluid flow and largely prevented further influx of suprasalt subsurface waters, which would otherwise drive pervasive shallow subsurface cementation in most of the carbonate.

The relatively pristine relict porosity in the reservoir limestones, with solution-mouldic and variably-dolomitised overprints that characterises the Arab D in Ghawar, is a reservoir style that is part of a wider association seen in many evaporite-sealed limestone and dolomite reservoirs worldwide. Such reservoirs tend to show widespread leaching of aragonite allochems without associated karst surfaces or meteoric calcite cements. High Mg-calcite allochems (red algae, echinoids, crinoids) in the same sequence are relatively unaltered or mimetically replaced by dolomite. The process driving this precompaction leaching was not entry of meteoric waters, but flushing and brine mixing driven by early burial through flushing of hypersaline marine brines (Sun 1992). As well as the enhancing porosity in the Arab cycles, such evaporite-associated reflux waters have enhanced porosity levels in formerly aragonitic sediments of the Permian San Andres Fm. of West Texas, and the Miocene carbonates of the Middle East and SE Spain.

Slaughter-Levelland Trend, West Texas and New Mexic

Another region of variably dolomitised limestone forming high volume evaporite-sealed reservoirs within an epeiric carbonate platform is the Slaughter-Levelland trend of New Mexico and Texas (Fig. 10.27a). There the main play is in the Permian San Andres Formation with the occurrence of better quality reservoir defined by the transition from platform carbonates in the south into updip massive anhydrites and halites in the north. The lower member of the San Andres contains two evaporite-sealed intervals (P_1 and P_2) that form the main reservoirs (Fig. 10.27b). The producing style is a stratigraphic-diagenetic trap defined by updip pinchout (to the north) from a porous dolomite into nonporous evaporite-plugged dolomite beneath regionally extensive evaporite seals. Production from most dolomite reservoirs in the trend is slow but constant.

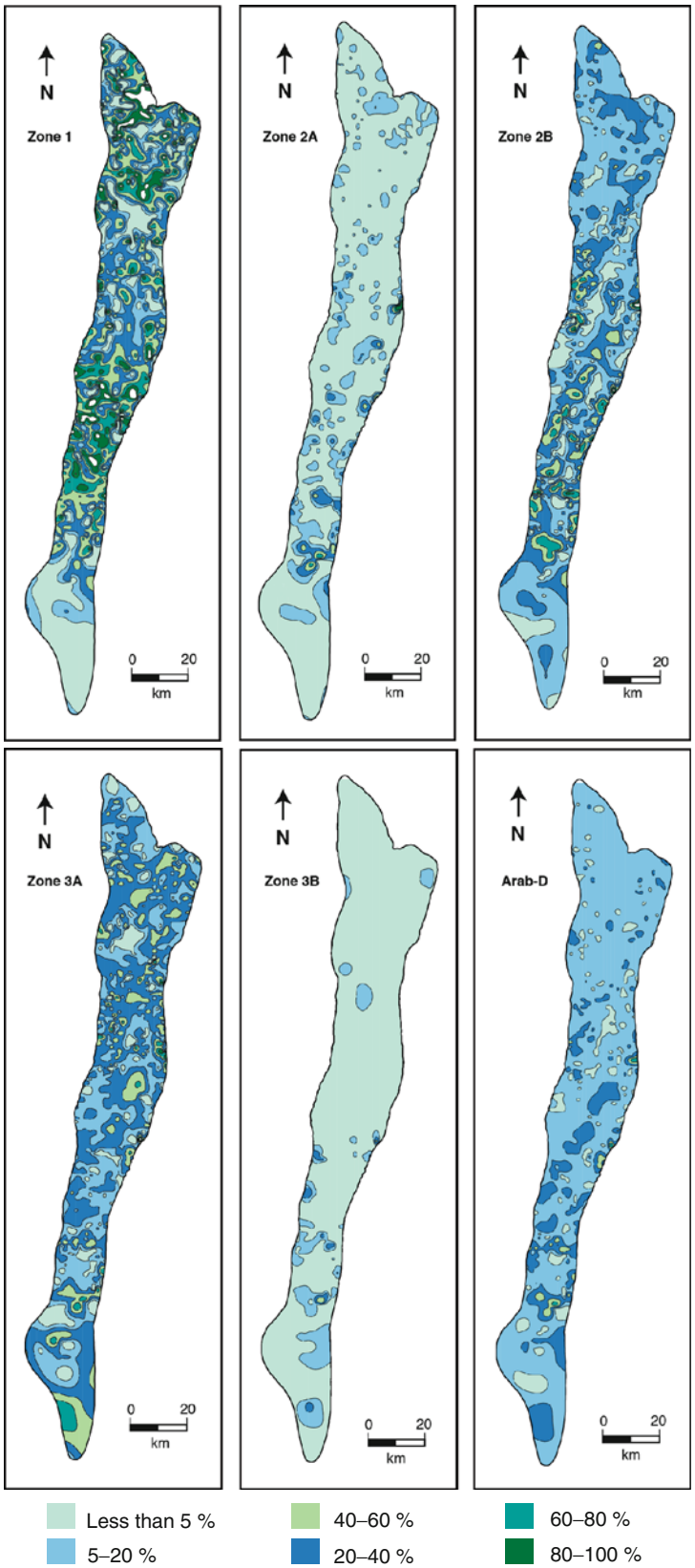

Fig. 10.26 Map of the percent dolomite in the various reservoir zones of the Arab D in Ghawar Field, Saudi Arabia (After Cantrell et al. 2001). Clearly shows a linear fracture-related distribution Zone 2 and in the total plot for the Arab D (*right hand side* of figure)

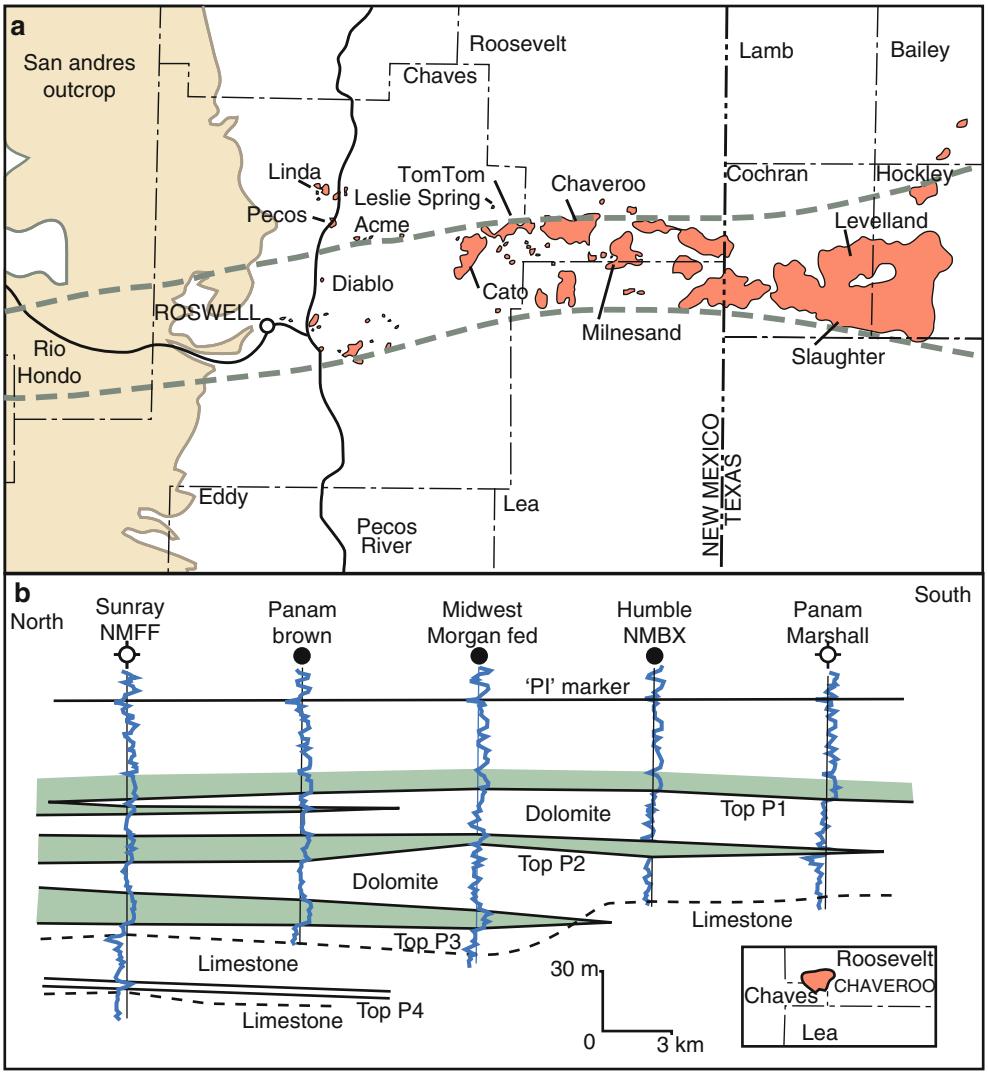

Fig. 10.27 San Andres Formation in the Levelland-Slaughter trend near Roswell, New Mexico (After Elliott and Warren 1989; Warren 1991). (**a**) North-south section through Chaves and Roosevelt counties in the vicinity of Chaveroo Field. (**b**) Map of the Levelland-Slaughter trend and its equivalents in the San Andres outcrop belt west of Roswell

Cleaning-upward cycles in the lower member can be divided into 5 lithofacies groupings (P_1 to P_5) stacked into shoaling upward successions, with each cycle being 15–50 m thick (Elliott and Warren 1989). Shaly carbonate mudstones define the base of each cycle; they are the initial low-energy deeper water deposits formed atop a flooding surface. These laminar mudstones are overlain by more massive biomicritic packstones and wackestones (≈10 m thick) containing brachiopods, bryozoa, crinoids, molluscs, and cephalopods, sometimes forming what may be local low relief bioherms with phylloid algal debris. These various mudstones were deposited on an open marine shelf, initially below wave base and under low-energy conditions.

Next come the dolomitised intervals (typical matrix porosities 10–12 %; permeabilities 20–30 md), which constitute the main reservoir in the trend (Fig. 10.28a). It is by far the most variable carbonate unit and in places retains remnants of primary texture, giving three variably dolomitised subtypes:

1. Wispy laminated to microstylolitised biomicrites, intramicrites, and peloidal micrites and packstones that entrain poorly preserved open marine faunas. Skeletal material is typically preserved as moulds, which near to the anhydrite cap are filled or partially filled with anhydrite cement. This is the most common reservoir unit in the Slaughter-Levelland trend.

2. Oolitic peloid-foram grainstones, which were deposited as localized shoals (uncommon unit in the Slaughter-Levelland trend).
3. Inter- to supratidal mudstones with fenestra, pisolites, biolaminites, and possible desiccation cracks (uncommon unit in the Slaughter-Levelland trend).

Next comes a massive to laminar anhydrite unit that historically was interpreted as a sabkha deposit (Ward et al. 1986). It is metres-thick in the Slaughter-Levelland trend and is made up of a dm-scale interbedded nodular anhydrite and laminated anhydrite. Some cores immediately to the north of the field preserve vertically aligned anhydrite nodules (gypsum "ghosts"), which pass downward into laminated and bedded nodular mosaic anhydrite (Fig. 10.28b). The alignment, the lamination, the purity, the thickness of the units, and the fact that it is laterally equivalent to subaqueous platform gypsum to the north implies that in the Levelland–Slaughter area this unit was laid down near the depositional edge of a saltern (Elliott and Warren 1989). In the Palo Duro Basin, situated further to the north of the Slaughter-Levelland trend, the equivalent to the various saltern anhydrite caps are overlain by saline-pan halites.

To the west of Roswell the outcrop, equivalents to the anhydrite seals are dissolution breccias, which can be used as a regional mapping datum in the vicinity of the Rio Hondo outcrops (Elliott and Warren 1989). Lateral facies changes can be seen in each outcropping cycle, showing the carbonate intervals were deposited as facies mosaics on an extensive relatively low energy muddy carbonate marine platform, with each cycle separated by evaporites.

The mosaic distribution of the reservoir carbonates and a lack of grainstone and shoreline/strandline shoals, either in outcrop or the subsurface, led Elliott and Warren (1989) and Warren (1991) to revise the reservoir model for San Andres deposition the Levelland-Slaughter Trend. In contrast to previous models that saw the reservoirs in the Slaughter Levelland trend as sabkha-sealed depositional pinchouts, they argued sabkhas are a relatively minor component in the widespread subaqueous saltern seal. Rather than a stratigraphic control the reservoir dolomites were created by brine reflux through relatively muddy epeiric platform carbonates via brines fed from updip salterns (Fig. 10.29; Warren 1991).

This saltern edge model of San Andres deposition offers a different exploration strategy for the San Andres reservoirs on the Northwestern Shelf of the Permian Basin and elsewhere (Warren 1991). Generally, saltern-associated reservoirs do not form by updip pinchout of marine grainstones and mudstones into stacked sabkhas. Rather, the reservoir trend marks the transition from an updip, evaporite-plugged, partially-dolomitised subtidal–intertidal section into a dolomitised, subtidal–intertidal sequence characterized by intercrystalline and relict interparticle porosity. Unlike areas closer to the source of the reflux brines and beneath the saltern proper, these regions are not pervasively plugged with evaporite cements. This dolomitised zone passes down-dip into more tightly-cemented open marine subtidal limestones. Updip plugging was driven by episodes of widespread evaporite deposition and the associated sluggish reflux of supersaturated brine into the underlying newly forming dolomites. The downdip subtidal–intertidal section saw some evaporitic plugging, but it did not suffer the longterm massive influx of evaporite cements experienced further updip. Its more marine-marginal position allowed the porosity to remain open and magnesium-rich solutions associated with brine reflux to enter the carbonates to evolve into more coarsely crystalline dolomites. The Levelland-Slaughter reservoir trend is not a palaeoshoreline, nor is it a stratigraphic pinchout trap. It is a diagenetic front and trap with the best reservoir quality defined by the zone immediately downdip of the thinning edge of the San Andres saltern (Warren 1991).

Dolomitised Limestones, Central Basin Platform, West Texas

The same diagenetic control to reflux dolomite intensity seen at the regional scale in the Levelland Slaughter trend is also true at the oil field scale on the Central Basin Platform to the south. Saller and Henderson (1998) noted similar variations in reflux-related "dolomite intensity" controlling reservoir properties in the evaporite-sealed North Riley Field at the northern margin of the Central Basin platform and in South Cowden Field on the east-central margin of the Central Basin platform, Texas (Fig. 10.30a). The main reservoir units in North Riley Field are permeable dolomites of the Leonardian (Permian) Clear Fork Formation, while dolomites of the Grayburg Formation (Guadalupian, Permian) are the main reservoir in South Cowden Field. Replacive dolomitisation and the creation of intercrystalline porosity in both fields was driven largely by the reflux of evaporatively concentrated seawater circulating shortly after deposition of the original limestone matrix.

Ongoing reflux-driven evaporite plugging means porosities and permeabilities are lower in platform-interior dolomites and higher in dolomites near the platform margins in both fields (Fig. 10.30b). Reservoir porosity and permeability are not strictly facies dependent in either field. As in the Slaughter-Levelland trend, Saller and Henderson (*op cit.*) found the distribution of porosity and permeability is largely the result of location within the diagenetic dolomitising system and to a lesser extent reflects the original depositional permeability of the limestones.

Due to inherently higher brine densities beneath an evaporite-depositing lagoon or saltern, the dense saline dolomitising brines, generated by evaporative concentration of seawater in restricted evaporitic mudflats and salterns, percolated downward and seeped basinward

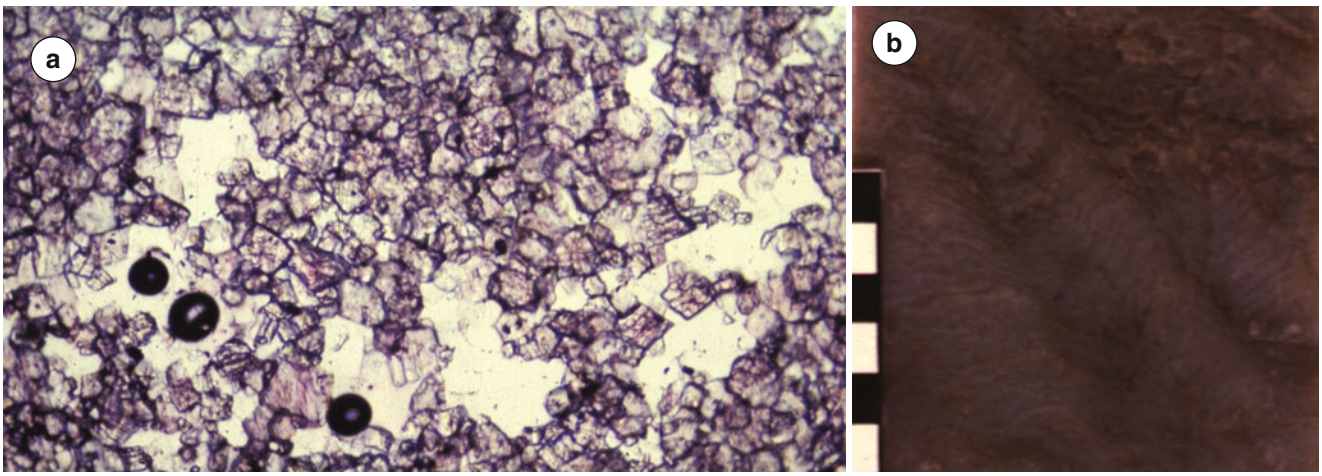

Fig. 10.28 Lithofacies of the San Andres Formation. (**a**) Dolomitised pel-mouldic wackestone/packstone showing angular highly altered pelloidal outlines, moulds can be plugged by anhydrite (image is about 2 mm wide). (**b**) Elongate nodules of anhydrite typical of the seal facies showing remnant subaqueous gypsum ghosts with internal swallowtail-V's still visible (scale bar in cm)

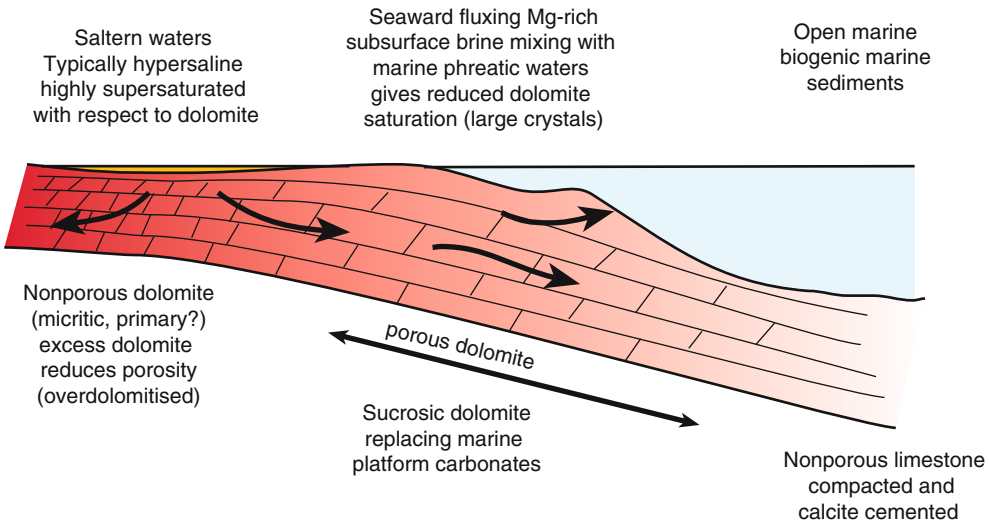

Fig. 10.29 Reflux brines drive dolomitisation in marine carbonates some distance downdip from intervals of more restricted shoreward carbonate that tend to be overdolomitised and evaporite plugged (After Saller and Henderson 1998 and Elliott and Warren 1989, see also Fig. 10.9)

(refluxed) through the sediments. Refluxing brines, supersaturated with respect to dolomite and calcium sulphate, precipitated large quantities of dolomite and anhydrite cement in the proximal parts of the reflux system. This lowered dolomite saturation in waters flowing into distal portions of the reflux system. Lower dolomite saturations resulted in less dolomite, fewer nuclei and larger crystals (not overdolomitised) along with more intercrystalline porosity and permeability retention in distal parts of the system (Fig. 10.29). Many platform-interior wells in both fields are structurally higher than wells near the platform margin, yet structurally lower wells near the platform margin are more porous and permeable, and have produced three to ten times more oil than the platform-interior wells (Saller and Henderson 1998).

Reservoirs in the Jurassic Smackover Fm., Gulf of Mexico

More than 1 billion barrels-equivalent of oil and gas has been discovered in the Smackover of the northeastern Gulf Coast Basin (Prather 1992a, b). The majority of these hydrocarbons are found in a few large fields such as Jay, Big Escambia Creek, Blackjack Creek, Chunchula, and Hatter's Pond, and the fields in the Mobile Bay complex. Except for the fields in the Mobile Bay complex, which have Norphlet Sand reservoirs, the Smackover Formation is the primary hydrocarbon reservoir in the large fields and many smaller fields, such as Vocation, Barnett, Uriah, and Appleton. Like the Arab D in the Middle East, the richness of Smackover hydrocarbon system in the region is a result of the co-occurrence of microlaminated lime mudstone source rocks, dolostone reservoir

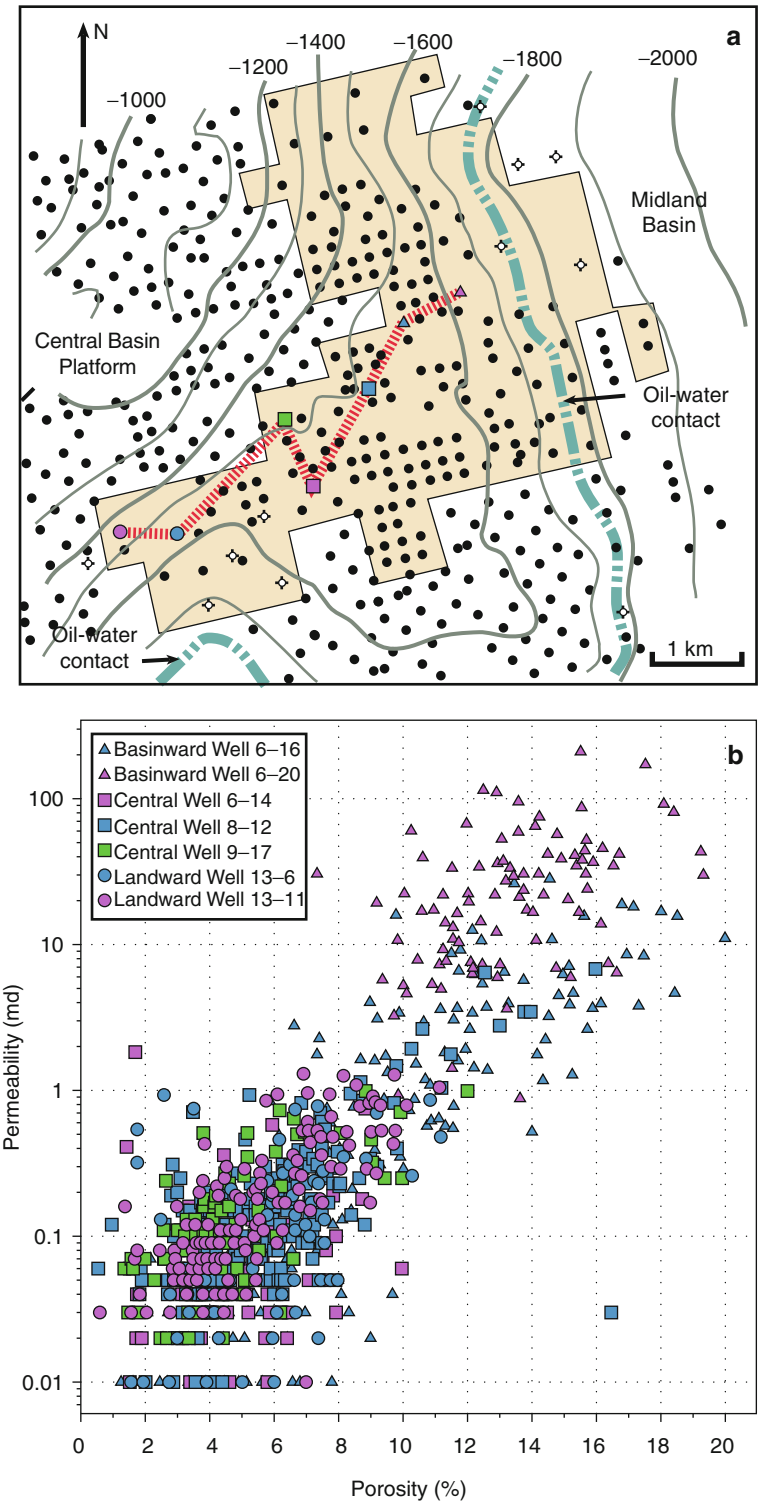

Fig. 10.30 South Cowden Field, West Texas (After Saller and Henderson 1998). (**a**) Well transect runs from the overdolomitised evaporite-plugged platform (○) to a dolomitised transitional zone (□) to the more basinward partially dolomitised platform wells with minor evaporite plugging (△) (**b**) porosity permeability from all measured plugs in wells along the transect. Increase in reservoir quality corresponds to a decrease in evaporite plugging and an increase in dolomite crystal size along the downdip reflux pathway (as shown in Fig. 10.29)

rocks, and an evaporite cap, all within an overall shoaling depositional package (Moore 1984; Heydari 1997).

The Smackover Formation forms a subsurface arc about the Gulf of Mexico and was deposited in a transgressive-regressive event during Upper Jurassic (Oxfordian) time (Fig. 10.31a). It is underlain by the siliciclastic eolian-wadi Norphlet Formation in more marginward areas and by the Louann Salt Formation further out in the Basin. The Smackover, and the overlying Buckner Anhydrite Member of the Haynesville Formation, were deposited in three depositional stages that correspond to periods dominated by marine transgression, aggradation,

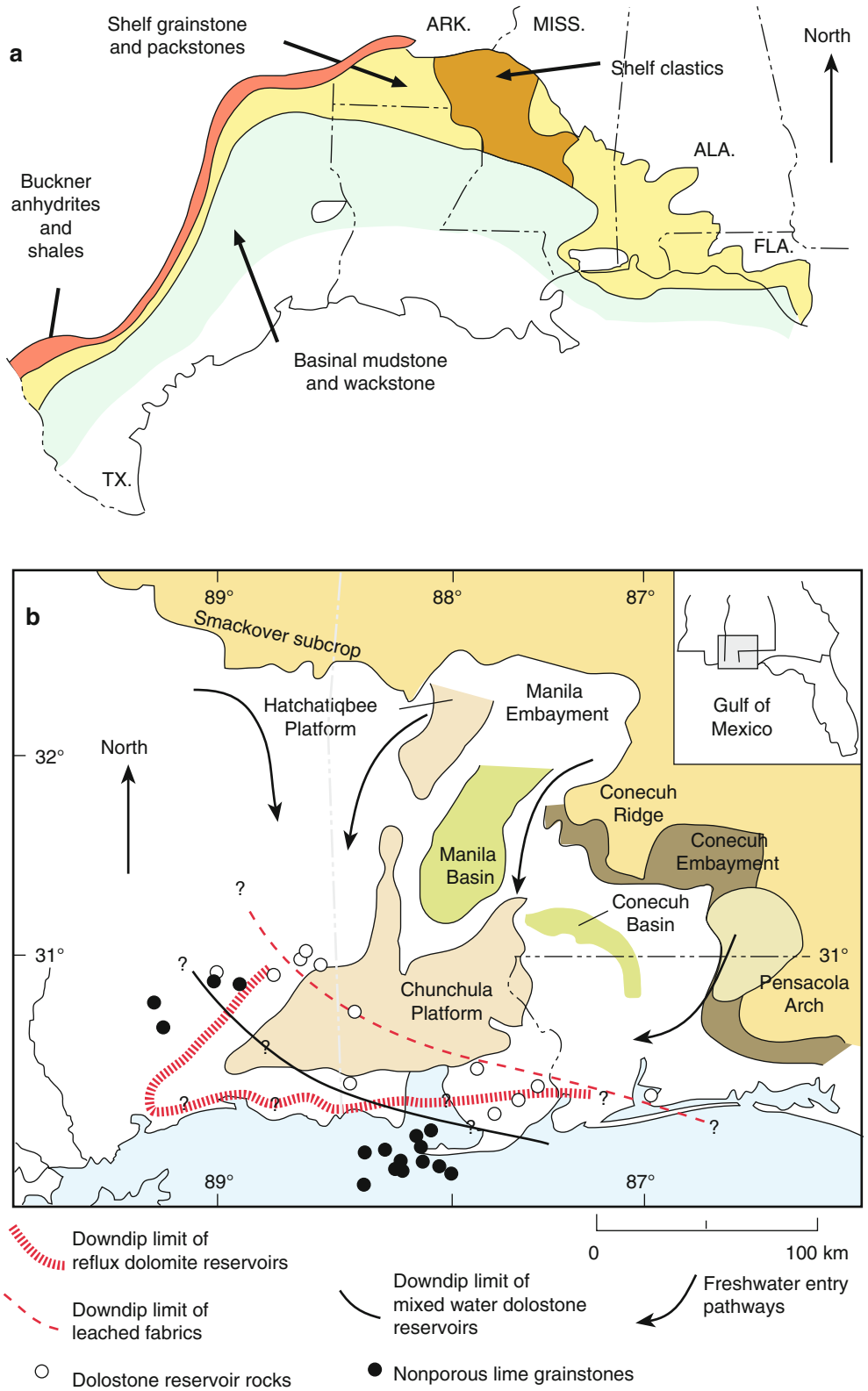

Fig. 10.31 Smackover Formation, Northern Gulf of Mexico. (**a**) Generalised map of Smackover distribution along the coast of the United States (After Melas and Friedman 1992). (**b**) The downdip limit of reflux and shallow burial mixed water zones occurs between dolostone reservoir rocks and nonporous lime grainstones (After Prather 1992a)

and ultimately progradation. The Buckner Evaporite and its equivalents, which form the seal to the various upper Smackover fields was interpreted as sabkha until the mid 80s (Lowenstein 1987a). But in the 90s its interpretation changed to an evaporitic mudflat, a mosaic of sabkhas and salinas passing up and laterally into a saltern (Mann 1988, 1990; Mann and Kopaska 1992; Prather 1992a, b; Benson et al. 1996).

The Smackover is a combination of platform dolomites, shelf-margin oolitic and peloidal grainstones, and slope and basin limestones. It can be subdivided into three informal units, the lower, middle, and upper Smackover (also known as Smackover C, B and A, respectively). Each unit was deposited in a different depositional setting on a gently shoaling carbonate ramp. Lower Smackover deposition accompanied a rapid sea level rise that inundated most palaeohighs in the basin to produce a depositional system that was first transgressive and then aggradational in nature (Benson et al. 1996; Prather 1992a, b). Most sediment in the lower Smackover is basinal and consists of laminated dark brown to black mudstone, alternating with laminae of pyritic siliciclastic silt or sand. Locally it is organic rich and has acted as a source rock for the hydrocarbons accumulated in the overlying Smackover sands (Heydari 2000). Lamina style in the lower Smackover changes upward from very thin parallel laminae near the base to thicker irregular laminae higher in the section. Algal patch reefs grew in lower Smackover time around the periphery of some palaeohighs, driven by the rising sea.

The middle Smackover is composed of sediments deposited on a low-energy, open-marine platform, laid down as sedimentation caught up with relative subsidence. Short-term sea level fluctuations produced numerous shallowing-upward packages (parasequences) in the middle Smackover. Two lithofacies are typical of the middle Smackover: a wispy-laminated, crustacean-pellet carbonate mudstone containing a sparse pelagic fauna and a densely burrowed skeletal-pellet wackestone containing a benthic fauna. Tidal flat, lagoon, and shoal complexes formed in topographically higher parts of the northern Gulf, while sub-wavebase sediments were deposited in deeper waters and away from salt structure-induced seafloor shoals.

The upper Smackover consists of several grain-supported lithofacies deposited in shoal settings ranging from strandzone (tidal) bars and channels to beaches, islands, and algal-stromatoporoid reefs. Burrowed pellet and oncolite packstones and algal-stromatoporoid boundstones formed as moderate-energy outer shoals, and sequences of crossbedded mixed allochem, oolite, and oolitic grainstones comprised the current-reworked inner shoals. During upper Smackover deposition, sea level was relatively stable allowing the Smackover to aggrade and prograde. Upper Smackover deposits are peritidal or strandzone dominated. Short-term sea level fluctuations produced shallowing upward packages capped by exposure surfaces in crestal locations and deposited widespread syndepositional isopachous marine cements of aragonite (now calcite).

During lower Buckner deposition, evaporitic mudflats form over the crests of the palaeohighs and pass off-structure and landward into salterns. Short-term sea level fluctuations produced a series of higher-order shallowing-upward evaporitic mudflat cycles behind the main oolite shoal. Development of subaqueous gypsum increased during ongoing restriction of the northern Conecuh Embayment and ultimately led to widespread deposition of the subaqueous saltern evaporite seal that defines the upper Buckner Anhydrite. This unit seals most Smackover reservoirs.

Dolomitised upper Smackover facies constitute the most productive reservoirs. In fact, dolomitisation and leaching are critical to the preservation of economic levels of porosity throughout the Smackover in the northern Gulf of Mexico (Fig. 10.32). Historically, a minimum of 4 % porosity and 0.1 md permeability in Smackover carbonates is considered to be reservoir grade (Becher and Moore 1976). Economic Smackover porosity is of three main types:

1. Partially preserved primary interparticle porosity
2. Leached mouldic porosity
3. Intercrystalline porosity within coarsely crystalline dolomites

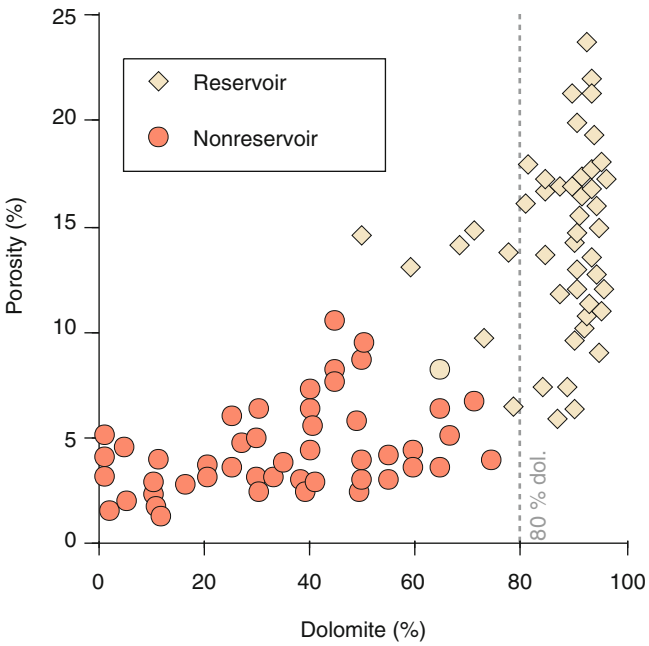

Fig. 10.32 Relationship between porosity and the degree of dolomitisation in Jay Field, Conecuh Embayment. The lower Smackover facies in the field shows low porosity and are relatively less dolomitised compared to the upper Smackover grainstones, which have high porosity and are extensively dolomitised (Data from point count data and are replotted from Melas and Friedman 1992)

Most reservoirs are found in: (a) grainstone shoals, (b) fractured and dolomitised sediments of the inner-shelf and, (c) algal stromatoporoid buildups (Mancini et al. 2000). The best reservoirs in Arkansas, Louisiana and eastern Mississippi are in dolomitised intervals that preserve incompletely cemented interparticle and mouldic porosity (Fig. 10.31a). The updip Smackover close to the palaeoshoreline in this region often contains leached mouldic porosity due to mixed-water flushing. In east Texas, Alabama, and Florida, the precipitation of dolomite with intercrystalline porosity has enhanced the reservoir potential of the Smackover grainstones.

Dolomitization is usually required to form a reservoir in innershelf Smackover sediments and enhances the reservoir character in the grainier shoal sediments. A rule of thumb in the region is that a minimum of 80 % dolomite is necessary for consistently good reservoir quality (Fig. 10.32), but rocks that are 100 % dolomite, or dolomites with pervasive evaporite cements, are not good reservoirs. Individual reservoirs can be as thick as 10 m, with porosities as high as 26 %, and matrix permeabilities as great as 6.5 md. Although enhanced reservoir quality is often related to reflux dolomitisation, the distribution of dolomite, like that of the interparticle porosity and the mouldic porosity, is in large part inherited from porosity trends in the original depositional setting.

Geochemical and petrographic data suggest that calcite/aragonite alteration and dolomitisation took place in: (1) phreatic seawater-seepage, (2) brine reflux, (3) nearsurface mixed-water, (4) shallow-burial mixed-water, and (5) deeper burial environments. These settings overlapped in time and space to form a "platform-scale" dolostone composed of a complex mixture of dolomites and authigenic cements (Prather 1992a). Of the five, the brine reflux and the deeper burial settings can be thought of as end members of a diagenetic spectrum creating dolomites. They are also the most easily separable of the five using isotopic signatures (Fig. 10.33a). The other three form a related but overlapping group of subsurface alteration features. Texturally, without isotopic data and with the exception of early isopachous rim cements, it is very difficult to assign origins to the various replacements and cements that typify the Smackover reservoirs.

Brine reflux dolomitisation of the upper Smackover was largely driven by movement of hypersaline brines created by deposition of the overlying Buckner Anhydrite member of the Haynesville Formation. Flushing by dense brine explains the distribution of early dolomite in southeastern Alabama and western Florida (Barrett 1986; Saller and Moore 1986; Worrall and Warren 1986). Such beds constitute thin zones within the upper 5–7 m of the Smackover throughout the Conecuh Embayment and show enrichment in $\delta^{18}O$, which is indicative of precipitation from evaporated brines. Replacement of precursor marine cements by dolomites rich in ^{18}O places this phase of dolomitisation early in the paragenetic sequence, consistent with a reflux origin parallel to the basin strandline or palaeoshoreline. Thicker zones (5–15 m) of isotopically-enriched reflux dolomite occur locally around the Conecuh Ridge, Pensacola Arch, and over the Chunchula Platform (Fig. 10.31b). Time-slice lithofacies maps show that these thicker dolomite zones correspond to the locations of coastal evaporitic mudflats, which were first established on palaeotopographic highs within a pericontinental setting (Prather 1992a). These zones show aggradational geometries produced during an early regressive phase of Smackover/Haynesville deposition. Thicker zones of enriched dolostone probably formed in these areas because of the ongoing aggradation of the reflux dolostone host through time.

Thin zones of enriched dolostones similar to those over most of the Conecuh embayment also occur sporadically around the flanks of the Chunchula Platform, Manila Basin rim, and the flanks of the Hatchatiqbee Platform (Fig. 10.31b). The downdip limit of thin reflux dolostones tentatively, inferred from very limited well control, appears to parallel depositional strike. Thinness or absence of enriched dolomite zones updip of this line may be associated with rapid progradation of the shoreface/coastal-sabkha couplet resulting in rapid lateral shifting of reflux zones, which prevented aggradation of reflux zones and allowed little time for refluxing brines to circulate deeper into the upper Smackover grainstones.

Brine reflux was driven by Buckner deposition and was tied to regional drawdown hydrology in the region behind the oolite shoals. Drawdown driving the reflux also influenced porosity evolution in the adjacent Smackover shoals that formed the isolating sill. For example, the drop in relative sea level in the Conecuh Embayment during the Oxfordian (Prather 1992b) exposed thick submarine oolite sand bars of the upper Smackover on the southern flank of the Conecuh Basin. It created a subaerial sill, which separated the Conecuh Basin from the Gulf, as more than 100 m of Buckner salts were laid down as a saltern within the isolated intraplatform sag. The sill today consists of a thick (18–55 m) lower unit of medium to finely crystalline sucrosic dolostone and oolite dolograinstone overlain by a thinner upper unit of finely crystalline oolite dolograinstone. $\delta^{18}O$ analysis indicated that the dolostone in the sill is composed of three populations of dolomite. Two populations of dolomite depleted in ^{18}O occur in the lower sill (Fig. 10.33b, groups II and III). A third population found in the upper part of the sill is relatively enriched in ^{18}O (Fig. 10.33b, group I). The contact between the upper and lower units is gradational over about 1 m and has no apparent relationship to stratal boundaries. This contact was first noted by Vinet (1982) in wells from Jay, Blackjack Creek, and Big Escambia Creek fields, and was subsequently located in more wells by Prather (1986).

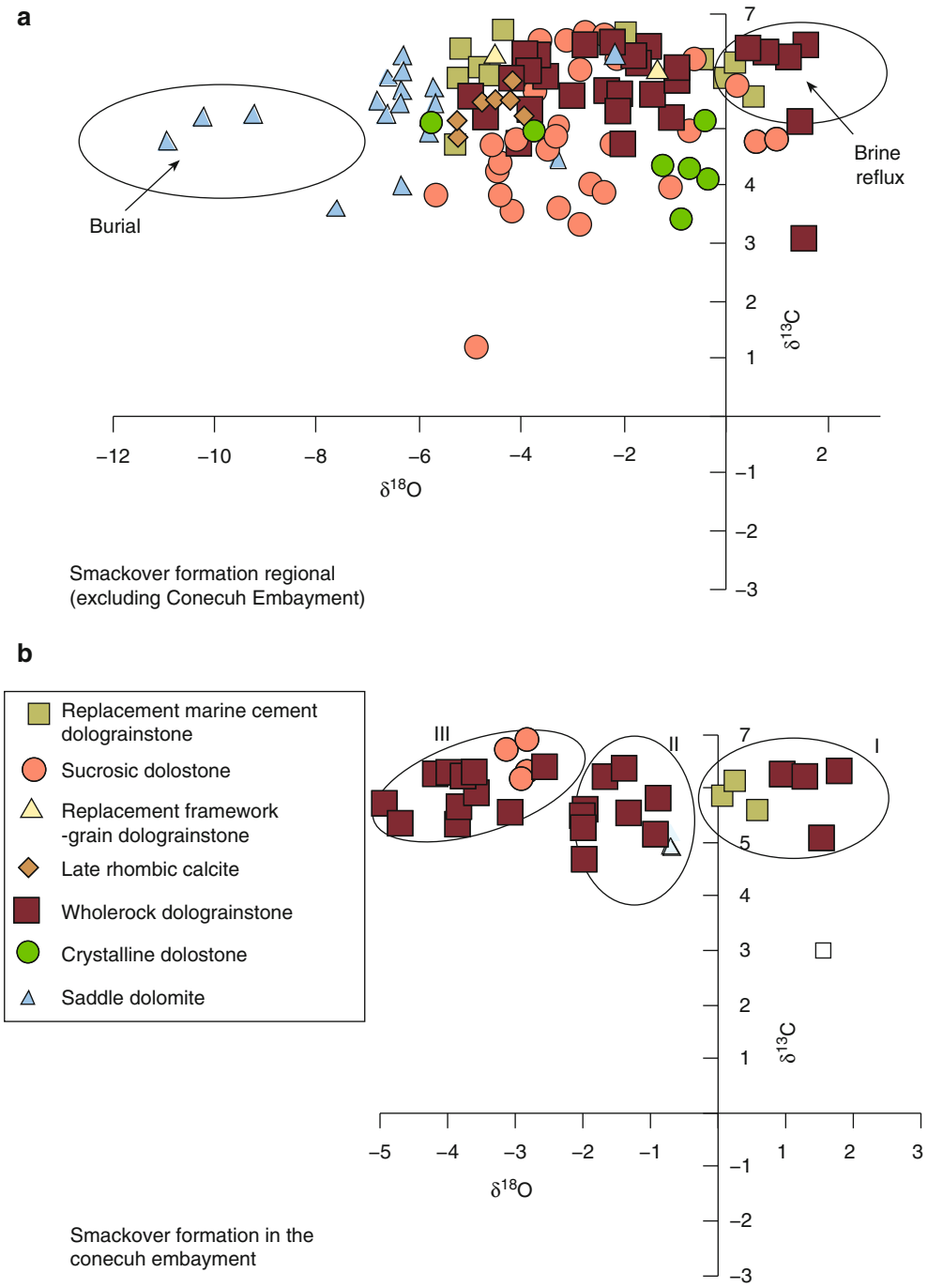

Fig. 10.33 Stable isotopic signatures of the Smackover Formation, Northern Gulf of Mexico (After Prather 1992a). (**a**) Plot of $\delta^{18}O$ and $\delta^{13}C$ of dolomites from the Northern Gulf of Mexico, excluding the Conecuh Embayment and deeper burial dolomites. (**b**) Plot of $\delta^{18}O$ and $\delta^{13}C$ of dolomites from Conecuh Embayment

The association of a relatively abrupt localized geochemical and lithologic discontinuity within rocks beneath a sill that was subaerial during a sea level lowstand suggests the discontinuity may represent a fossil watertable (Prather 1992a). If this is the case, the following events must have taken place: (1) partial dolomitisation of the lower unit as seawater seeped through the sill to recharge the saltern brines in the Conecuh Basin, (2) complete dolomitisation of the upper unit by reflux processes as the upper sill was buried during aggradation and progradation of Buckner evaporites (fill and spill sedimentation of the basin), and (3) continued burial dolomitisation of the lower unit by ^{18}O-depleted dolomitising fluids. Each of these events gave rise to each of the three isotopic groups of dolomite from

the sill: (1) seawater seepage dolomite with $\delta^{18}O$ values of −0.6 to −1.9‰, (2) reflux dolomite with $\delta^{18}O$ values of 2.0–1.0‰, and (3) later burial dolomites with $\delta^{18}O$ values of −2.6 to −4.6 ‰ (Fig. 10.33b).

In the vicinity of local freshwater entry points, an earlier nearsurface mixed-water environment locally affected sediments from the landsurface down to depths of several tens of metres thick. Freshwater entered the Smackover either through groundwater sinks (exposed palaeohighs or islands) or via the updip part of the regional groundwater flow system. Under these conditions, freshwater supply to coastal areas of the Northern Gulf, such as the Conecuh embayment, probably was limited to what was supplied by the updip drainage system between the Conecuh ridge and Pensacola arch. These waters leached aragonite allochems, leaving behind hollow grains preserved only by their micrite envelops. According to Prather (1992a) the $\delta^{18}O$ contents of these replacement dolomites are slightly depleted relative to seawater-seepage dolomites, slightly enriched relative to later rhombic dolomite cements, and closely associated with freshwater-phreatic calcite cements, suggesting a nearsurface mixed-water origin. Dolomite-replaced precursor marine cements, with only slightly depleted $\delta^{18}O$ compositions relative to seawater-seepage dolomites, have been encountered only in the Conecuh embayment. This is consistent with the notion that they are connected to isolated mixing zones. Their localized distribution probably reflects the limited extent of freshwater environments in such an arid climate.

Rhombic dolomite crystals of the shallow-burial mixed-water environment typically have cloudy cores and clear rims. These rhombic dolomite cements overgrow neomorphic fabrics, which formed after a period of leaching and sparry calcite precipitation. Paragenetic relationships show that vuggy and oomoldic pores within the Conecuh embayment and throughout the Northern Gulf region are virtually contemporaneous (Prather 1992a). Extensive leaching of this kind suggests considerable local artesian influxes of fresh to brackish water after evaporite deposition had ceased. The wide band of leached fabrics that parallels the updip limit of the Smackover suggests freshwater entry probably occurred along the Smackover outcrop in western Alabama and where Haynesville alluvial-fan sandstones interfinger with upper Smackover grainstones around the Conecuh Ridge and Conecuh embayment (Fig. 10.31a). Leaching trends similar to this are described by Moore and Druckman (1981) from the updip Smackover of Arkansas and Louisiana.

Their marginward position suggests that the downdip limit of leached fabrics is controlled by a change from less stable aragonite oolites updip to more stable calcite oolites downdip. In eastern Mississippi, Alabama, and Florida, however, the trend of leached fabrics is perpendicular to depositional strike. Therefore, the distribution of leached fabrics in the east is possibly more related to the downdip position of a zone of undersaturated groundwater (Fig. 10.31b). Sparry calcites that line the large vugs in the Smackover of the Conecuh embayment have somewhat depleted $\delta^{18}O$ signatures and low Fe^{++}/Mn^{++} ratios, which suggest precipitation in warm, slightly reduced, fresher subsurface waters. Abrupt changes of formation-water redox conditions or trace-element concentrations outlined by cathodoluminescent zonation patterns indicate these spars probably precipitated at sufficiently shallow burial depths to receive some recharge of oxidized fresher water from the surface after evaporite deposition had ceased.

These isotopically depleted dolostones of the deeply circulating regional fluid mixing stage constitute the signature of the most widespread reservoir rocks in the Smackover. They perhaps define areas where deeply circulating meteoric fluids (artesian waters) mixed with marine-phreatic or basinal brines and overprinted sediments from a few metres to hundreds of metres below the Buckner seal. They are confined to grain-supported and boundstone rock types below the Haynesville Formation, suggesting that the fresher water inflows, which mixed with formation brines, were confined to an aquifer lying below the evaporites and fine-grained siliciclastic rocks of the Haynesville Formation. By the time such brines were circulating, they were excluded from the now-tight carbonate mudstones and wackestones of the lower Smackover Formation. Recharge of the regional aquifer probably occurred as phreatic head rose along the Smackover/Haynesville subcrop during basinward tilting. Associated progradation of the overlying Cotton Valley strandline drove basinward migration of a thick continental freshwater lens atop the saltern evaporites.

In a tectonically stable area such as the Gulf Coast, large variations in recharge of regional confined aquifers, like the Smackover, are likely to occur only in response to substantial fluctuations of sea level (Harrison and Summa 1991). Maximum downdip limit of the regional mixed-water zone and associated dolostone reservoirs is likely, therefore, to have occurred during prominent sea level lowstands, such as those proposed for the Valanginian (Haq et al. 1987). The distribution of dolomite depleted in ^{18}O suggests that the interpreted regional mixedwater zone must have migrated downdip a minimum of 193 km from points of recharge along the Smackover subcrop and the Conecuh embayment (Prather 1992a).

Later precipitation of saddle dolomite in the deeper burial environment has been linked to chemical compaction of dolostones, thermochemical sulphate reduction, hydrocarbon migration, and epigenetic sulphide emplacement (Heydari 1997). Their depleted $\delta^{18}O$ values suggest formation temperatures higher than the other Smackover dolomites (Figs. 9.69a and 10.33a). Hydrocarbon inclusions suggest that the saddle dolomites are late burial cements that were at

least contemporaneous with hydrocarbon migration, which began in the middle Early Cretaceous. In the Smackover, as in the Arab D, evaporites played an early role in the formation of reflux dolomite and then a subsequent role as a focus (aquiclude) for regional flows of deeply circulating groundwaters and basinal waters.

Prather's analysis did not consider the possible influence of salt tectonism on isotopic evolution. In contrast, Heydari (2010) placed the isotopic signatures of Smackover dolomites in the Mississippi Salt Basin (situated east of the area in Alabama studied by Prather) in a halotectonic context and interpreted, what are isotope fields that overlap with Prather's C-O plotfields, in a somewhat different diagenetic context (Fig. 10.34). He defines two dolomite types with distinct geochemical compositions occurring near the inferred palaeoshoreline. One type of dolomite is fine crystalline (10–30 μm) and has positive $\delta^{18}O$ and positive $\delta^{13}C$ compositions (averaging +4.1‰ PDB and +5.0‰ PDB, respectively). It forms a relatively poor quality reservoir. The second Smackover Formation dolomite occurs on salt diapirs in the basin centre. This dolomite is coarsely crystalline (50–150 μm) and has negative $\delta^{18}O$ and positive $\delta^{13}C$ compositions, which is significantly lower than the palaeoshoreline (reflux) dolomite (averaging −2.2‰ PDB and +4.1‰ PDB, respectively). It forms excellent reservoir and is likely derived from more diagenetically evolved set of subsurface solutions tied to suprasalt convective flow.

Dolomite also occurs in the overlying Buckner Formation seal. This Buckner Formation dolomite occurs in nodular anhydrite layers, and formed by replacement of lime mudstone layers adjacent to anhydrite beds. The Buckner dolomite is finely crystalline (30–40 μm) and its $\delta^{18}O$ and $\delta^{13}C$ values are intermediate between the two Smackover Formation dolomites (−0.3‰ PDB and +4.4‰ PDB, respectively).

According to Heydari (2010), lithofacies association, geographical distribution, and isotopic compositions of dolomites of the Smackover and Buckner formations indicate three different processes of dolomitization (Fig. 10.34). The Buckner Formation dolomite formed as "primary" precipitates when saltern anhydrite was being deposited, and as a replacement of lime mudstones from a brine that had reached anhydrite saturation. Therefore, its isotopic composition is indicative of a Late Jurassic anhydrite-saturated seawater. The Smackover Formation dolomite that occurs along the presumed palaeoshoreline has $\delta^{18}O$ and $\delta^{13}C$ values, which are more positive than those of the Buckner Formation dolomite, suggesting it formed from more evaporated (possibly halite saturated) seawater, very likely within salt ponds. Dolomitization of the Smackover Formation on salt diapirs was accomplished by the seepage of evaporated, Mg-rich Buckner brine into Smackover grainstones through subaerial exposure surfaces on crests of salt diapirs. However, its $\delta^{18}O$ and $\delta^{13}C$ values are lower than those of the Buckner Formation dolomite suggesting that either the brine was diluted by meteoric water due to the exposed nature of the crestal structures or dolomite was recrystallised in meteoric water during burial.

Reservoirs Sealed by Bedded Basinwide Evaporites

As well as saltern evaporites sealing and driving alteration processes in intercalated platform carbonates, there a number

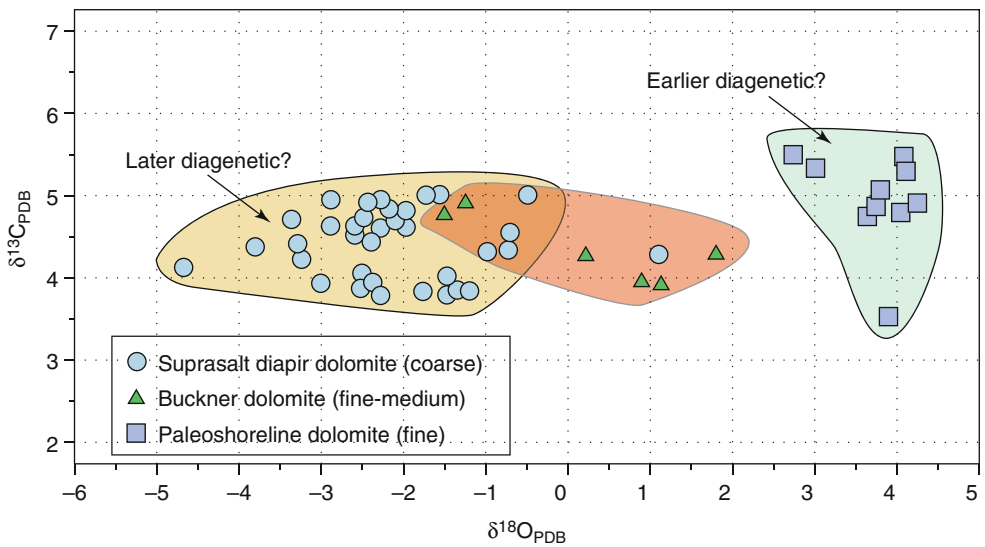

Fig. 10.34 Cross plot of $\delta^{18}O$ and $\delta^{13}C$ compositions of the three dolomites in Mississippi Salt Basin. The $\delta^{18}O$ and $\delta^{13}C$ values are the highest in the palaeoshoreline dolomite of the Smackover Formation, the lowest in the high-rise salt structure dolomite of the Smackover Formation, and intermediate in the dolomite of the Buckner Formation (Replotted from Heydari 2010). Note the values overlap with those of Prather 1992a – Fig. 10.33

of reservoirs sealed by thick caps of basinwide salts. Where the traps are stratigraphic, permeability tends to be developed in dolomitised carbonates beneath bedded seals. Such reservoirs tend to be patchy and of lesser quality compared to reservoirs hosted in the downdip areas of the saltern-sealed traps discussed in the previous section. But where the subsalt traps are structural, broadly-drained anticlinal culminations, as in the Miocene successions of the foreland foldbelt of the Zagros in Iraq and Iran, the fields are large and many are supergiants. This structural association reflects ability of evaporites to maintain seal integrity under deformation, while the underlying and intercalated dolomites and limestone fracture. This structural association is discussed in more detail later in the chapter, for now our discussion will focus on the effects of syndepositional reflux dolomitisation on reservoir quality below basinwide evaporites.

Eocene and Miocene Associations, Middle East

Carbonate platform and sandstone reservoirs beneath Tertiary-age basinwide seals in the Arabian Gulf and the Gulf of Suez have been overprinted to varying degrees by reflux dolomite. The evaporites define two main age-related saline associations:

Lower Eocene and Middle Miocene (Fig. 10.35). The Eocene evaporites are saltern evaporites precipitated in an intracratonic sag on the continental side of a foreland bulge in front of the rising Zagros chain. Across the Gulf they constitute widespread 10–20 m thick anhydrite/gypsum units within the Rus Formation and its equivalents. Salts in the Rus can perhaps also be considered the youngest example of widespread platform evaporites and accumulated immediately prior to the onset of icehouse eustasy (Chap. 5).

Miocene basinwide seals in the region are better known and perhaps more significant economically as they form caps to giant and supergiant fields in the Asmari limestone reservoirs of the Zagros fold belt. These salts accumulated in an isolated foreland deep in front of the Zagros suture and make up the Fars/Gachsaran formations in the Northern Arabian Gulf (Fig. 10.35 Alavi 2004; Gerdes et al. 2010). Today, the dissolution residues typify outcrops in the Dam Formation, the Fars equivalent in of Qatar and Saudi Arabia (Dill et al. 2005). Similar Middle Miocene basinwide evaporites are also highly effective seals to producing intervals in the rift-infilling Ras Maalab Group in the Gulf of Suez (Alsharhan 2003).

Eocene evaporites (bedded anhydrites) of the Rus Formation seal platform carbonate reservoirs in the northern Arabian Gulf (Iraq and Iran) and extend south over much of Saudi Arabia and the UAE (Steinhauff et al. 2007). Rus anhydrite is an important seismic reflector on the Arabian Plate where it is present above the Mesozoic and lower Cenozoic carbonate platforms. It provides reservoir top seal locally (e.g., Neutral Zone, Kuwait). In the subsurface the Rus typically comprises stacked meter-thick anhydrite parasequences interbedded with thinner limestone, dolomite, and marly beds with gross thickness in the shallowbasin centers of more than 200 m. Sub-meter scale, anhydrite bed sets can be traced on wireline logs for 100s of kilometers. Typically, the Rus has distinctive physical properties, including strong impedance contrasts with over- and-underlying strata. Less common are seismic zones lacking coherent reflectors and distinctive physical properties. Well penetrations show that many incoherent seismic reflectors at the level of the Rus typically include rubble and pass upsection into outcrop zones showing widespread evidence of evaporite dissolution.

Reservoir quality associated with the Rus seal in Iran, Iraq and Kuwait tends to be patchy and constitute the upper portions of thicker stacked Mesozoic pay horizons in giant and supergiant fields of the Northern Gulf. For example, in the 45 by 25 km anticline that is the Nahr Uhm supergiant field in Iraq the structural closure for the various pay zones varies with depth and ranges from 200 m for the Dammam (Eocene) down through the Rus Formation to about 800 m for the Lower Cretaceous Yamama reservoir. The Cretaceous is the main production focus for many of the huge fields of Iraq and Kuwait, but the Rus level can be host to significant volumes of heavy oil and bitumens. Such zones are typically overprinted by degradation products related to bacterial sulphate reduction, as in in the first Eocene reservoir level at the Giant Wafra Field, partitioned zone (PZ), Saudi Arabia and Kuwait (Fig. 9.67; Saller et al. 2014).

In the western and southern Gulf (Kuwait, Saudi Arabia, Qatar and the Emirates) the Rus anhydrite thins and is not present above many structural highs including much of the Qatar Arch, the Ghawar field, the Dammam Dome, and other large anticlines. Features attributed to karst are noted in many areas in this part of the Gulf. A lack of Rus anhydrite over these features can be explained by (1) non deposition because the structures were moving; (2) deposition followed by erosion, or (3) extensive subsurface dissolution of carbonate and sulphate-evaporite units under Middle Pleistocene wetter climatic conditions. Where the Rus and overlying Dammam outcrop or subcrop the succession is typically leached of its bedded and nodular evaporites (Dill et al. 2003; Holail et al. 2005). Once leached of its salts, the Rus section constitutes an important aquifer capable of producing potable groundwater. Only dissolution residues and collapse horizons remain in outcrop as indicators of the former presence of widespread bedded evaporites in the Rus Formation, along with associated slumps, digitate stromatolites, hollow cauliflower cherts and calcite nodules (pers. obs).

But the most productive Tertiary reservoirs in the northern Arabian Gulf are Miocene and are platform or deeper water carbonates (Asmari, Euphrates, Jeribe formations) that are sealed by Middle Miocene bedded salts of the Lower Fars/Gachsaran and equivalents (Fig. 10.36a). Core analysis of lower Miocene platform carbonates below these seals in

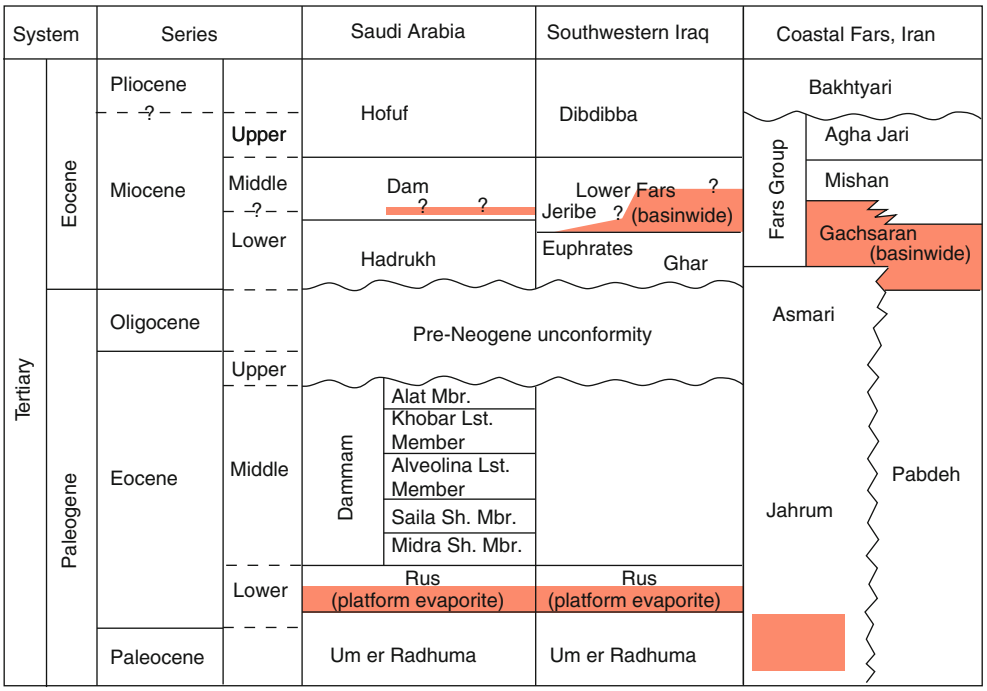

Fig. 10.35 Schematic Tertiary Stratigraphy of the Arabian Gulf, with evaporite-entraining successions shaded red (In part after Tleel 1973; Sharland et al. 2001; Alavi 2004)

Iraq show that openmarine subtidal carbonates have moderate to good porosity (10–35 %), but have highly variable permeabilities ranging from less than 1 md to several hundred millidarcies. Restricted tidal flat (evaporitic mudflat) carbonates intercalated in the same sections are tight (Figs. 10.36b and 10.37; Sun and Esteban 1994). In general, the best reservoir quality in the lower Miocene carbonates of the Middle East occurs in: (1) mud-lean skeletal packstones in which leached mouldic and vuggy porosity is well connected (e.g., Euphrates and Jeribe formations of Iraq and Syria), (2) oolitic packstones-grainstones with well-preserved primary intergranular porosity (e.g., local occurrence in the Jeribe Formation of Iraq), (3) coarsely crystalline dolomite (e.g., Euphrates and Jeribe formations of Iraq and Asmari Formation of southwestern Iran); and (4) highly fractured carbonates (e.g., Asmari Formation of southwestern Iran). Dolomitisation in many reservoirs substantially improves reservoir quality, especially in intervals hosting coarsely crystalline dolomites (Fig. 10.37). Asmari reservoirs and their seals are discussed later in this chapter.

In the Middle Miocene carbonates of the Gulf of Suez and the Red Sea, the spatial tie of the dolomites to basinwide rift evaporites, and their preferential distribution along the former platform margins, together with their relatively heavy oxygen isotopic values (averaging +4.65‰; Sun and Esteban 1994), all suggest that the bulk of the dolomite was formed by the lateral migration of evaporitic basinal brines into the shallow platform (a type of density-driven brine reflux). The formative hydrology was driven by the rise of brine levels associated with the evaporite filling the basin centre (Sun 1992; see also "spill and fill" discussion in Chap. 5 and later in this chapter). In contrast, downdip reflux of descending hypersaline brines, generated within platform salterns, were the main cause of extensive dolomitisation in the lower Miocene (Rus level) carbonate reservoirs of the Middle East. Differences in the two styles of hydrology can be recognised by mapping isotopic signatures of cements in cores from well to well and documenting the close stratigraphic relationship of reservoir quality to the transition zones between open marine platform carbonates (now dolomitised) and mapping (in seismic) the positions of restricted saltern evaporites or their residues.

Reservoir porosities in many of the evaporite-sealed Tertiary carbonate successions bear little relationship to depositional facies, rather they are strongly influenced by the distribution of anhydrite cements, burial corrosion, dolomite crystal size and fracture intensity. Undolomitised carbonates in the reservoir-hosting formations typically occur only in local areas: (1) encased units in marls, (2) platform interiors, and (3) areas with active freshwater drainage. This association of undolomitised intervals with basin margins or marine-cemented and exposed shoals is similar to that in the Smackover and San Andres formations.

Dolomite preferentially replaces magnesium-calcite skeletal grains (red algae, benthic foraminifera, and echinoderms) and micritised nonskeletal grains (ooids and peloids)

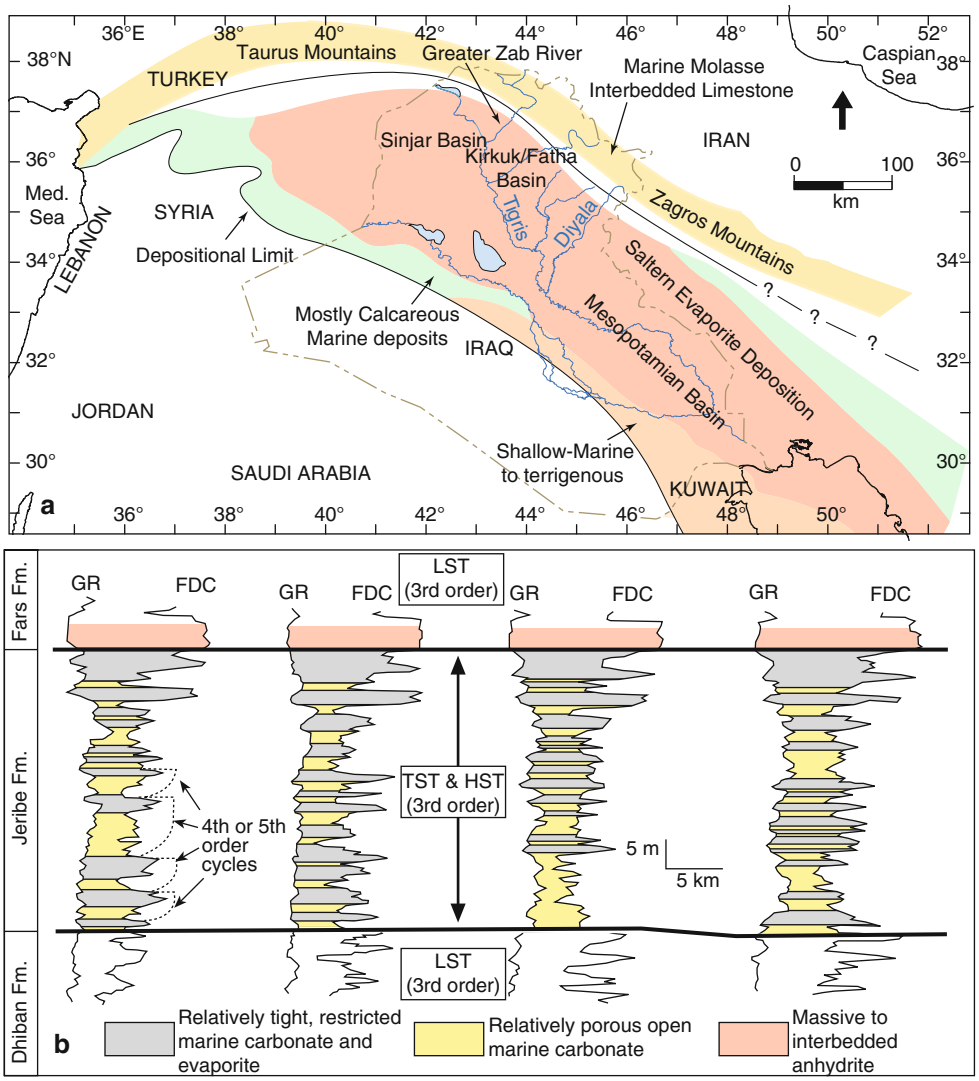

Fig. 10.36 Middle Miocene Fars evaporite seal in northern Gulf. (**a**) Distribution map showing the extent of Fars Evaporite and its equivalents in the Mesopotamian Basin and the locations of the Fatha/Kirkuk and Sinjar sub-basins (After Al-Juboury and McCann 2008). (**b**) Stratigraphic cross section of the Lower Miocene succession in the Middle East, centred on Iraq, showing higher order (4th or 5th) platform evaporite cyclicity within a 3rd order depositional sequence, which is made up of the lowstand Dhiban Formation, followed by transgressive and highstand platform carbonates of the Jeribe Formation, followed by lowstand evaporites of the Lower Fars (After Al-Murani 1986; Sun and Esteban 1994). Note the high porosity in the open marine carbonate intervals in the Jeribe Formationa and its equivalents, while the intercalated restricted marine carbonates and evaporites are tight (see Fig. 10.35a for Gulf nomenclature of the various Formations)

throughout most of the dolomitised Miocene carbonate section of the Arabian Gulf and the Gulf of Suez (Sun and Esteban 1994). Micrite matrix, internal muddy sediments, and micritised outer margins of aragonitic skeletons are also extensively replaced by dolomite. The replacement dolomites are subhedral to anhedral, finely crystalline (<10 μm) and show excellent preservation of original depositional fabric (mimetic dolomitisation), indicating that the dolomitisation was either syndepositional or relatively early in burial (Warren 2000a). Less common are coarsely crystalline dolomite cements lining secondary mouldic pores, often after dissolved evaporites. Sucrosic dolomites (40–80 μm, euhedral-subhedral) occur locally in some mixed carbonate-siliciclastic facies.

A particular diagenetic feature of evaporite-associated Miocene dolomite reservoirs of the Middle East is extensive leaching of skeletal aragonite without prominent karst surfaces or predolomite calcite cements (Fig. 10.37; Oswald 1992; Sun 1992). Mouldic and even vuggy porosity is well developed in carbonate hosts that contained abundant skeletal aragonite, whereas precursors dominated by high-Mg calcite bioclasts, such as red algae, echinoderms, and benthic foraminifera, are commonly mimetically replaced by reflux dolomite, with only minor moulds and other dissolution voids. As such, these nonvuggy units tend to show better-behaved poroperm relationships and more predictable wireline to core responses. Sun (1992) proposes that invading

hypersaline brines rather than fresh waters were the cause of large-scale leaching of skeletal aragonite.

With progressive burial and compressional folding, these evaporite-sealed Miocene dolomites have experienced repeated episodes of anhydrite cementation, fracturing, and late stage corrosion of pore walls (Sun and Esteban 1994). Anhydrite cementation is the most widespread porosity-occluding process. In many cases, both primary and mouldic porosities are almost entirely filled by anhydrite cements. Laterally, the distribution of anhydrite cements is highly variable in these Miocene reservoirs, but as a general rule, they are more abundant in relatively coarse, grain-supported carbonates, or those carbonates containing abundant skeletal aragonite, suggesting that original porosity and permeability played a major role in controlling access by later sulphate-bearing fluids. Brine-driven dolomitisation and skeletal aragonite dissolution during the early diagenetic stage produces excellent permeability networks. It enabled ongoing active circulation of anhydrite precipitating fluids and, if some permeability remains, even controlled the subsequent ingress of later burial fluids (including oil and gas).

Tectonically-induced fractures are common in the Lower Miocene carbonates of the Middle East, particularly along the Taurus-Zagros belt where these carbonates are intensively folded and fractured (Fig. 10.36a). There appear to have been several stages of fracturing. Most of the early-formed fractures were occluded by anhydrite cements, whereas relatively late-formed fractures, which postdate anhydrite cementation, remain open and effective. In places where the carbonate hosts have a relatively low matrix porosity and permeability, such as the Asmari Limestone in southwestern Iran, fracturing plays a vital role in enhancing the reservoir quality (McQuillan 1985). The mechanism of production in most Asmari reservoirs of southwestern Iranian oil fields is related mainly to open fractures beneath the Fars/Gachsaran seal (see later discussion), although variations in matrix porosity (e g., mouldic or intercrystalline) locally influence production.

According to Sun and Esteban (1994) the last diagenetic event before hydrocarbon emplacement in subsalt Miocene carbonates of the Middle East was burial corrosion through which reservoir quality was typically improved, particularly in the hydrocarbon-producing reservoirs in tectonically active zones in the Gulf of Suez and Iraq/Iran. These late stage corrosive events can bear little or no relationship to depositional facies or stratigraphic position in the reservoir. Corrosion preferentially affects anhydrite cements, relatively fine-grained sediments, and matrix materials. Typically, the current reservoir quality of many Miocene carbonates in the Middle East reflects the intensity of such corrosive events. The combination of vugs and chalky microporosity, which dominates effective porosity in the matrix of most producing Miocene reservoirs, was largely produced by late stage corrosion. Other important porosity types, including moulds,

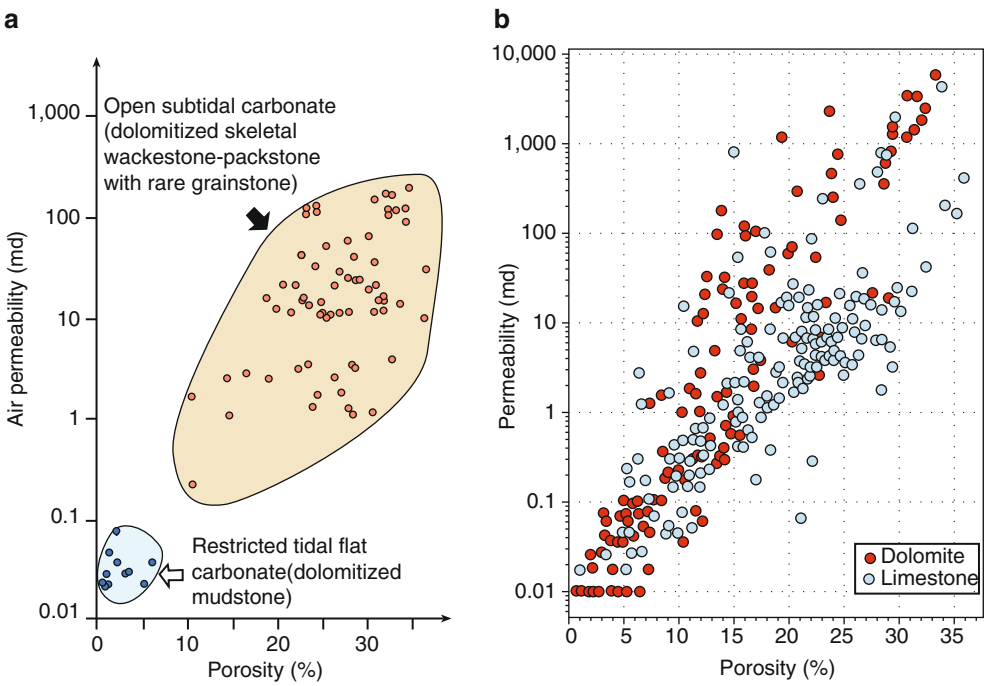

Fig. 10.37 Poroperm in the Tertiary of the Middle East. (**a**) Permeability versus porosity in Lower Miocene carbonates (Replotted from Sun and Esteban 1994). (**b**) Permeability versus porosity in Kirkuk Field, Iraq, showing the improvement in reservoir quality typical of dolomitised limestone successions (Cretaceous-Miocene)

intergranular pores, and fractures, were enlarged by corrosive processes. The distribution of such burial pore types is characterized by a lack of linear or branching permeability passages related genetically to identifiable recharge and discharge points, making these reservoirs difficult, but locally prolific producers.

Intensity of late stage corrosion is perhaps tied to levels of sulphuric acid created by the mixing of waters with different H_2S contents, or by oxidization of H_2S in an evaporite-rich hydrocarbon environment (Sun and Esteban op. cit.). In places, organic acids released through source rock maturation may have also contributed to the late stage corrosion and related to sulphate-reduction overprints. The development of the permeability network and the availability of migration pathways (faults and fractures) regionally connecting acidic subsurface fluids were two key factors controlling the degree to which fine-grained dolomites or anhydrite cements were corroded.

Silurian Pinnacle Reef Fields, Michigan Basin

Since the late 1960s, production from the numerous evaporite-encased Niagaran reefs of the Michigan Basin has been the main local source of oil and gas production for the state of Michigan (Figs. 10.38 and 10.39; Wylie and Wood 2005; Gill 1977, 1985, 1994; see Fig. 5.68 for detail on seal geology). Productive reef-substrate areas range from around 40 acres (0.16 km^2) to 840 acres (3.4 km^2). Recoverable reserves in individual pinnacles range from 30,000 to 22 MM BBL of oil equivalent (BOE). The ten largest fields in the Niagaran pinnacle play were found by drilling of the first 25 % of the exploration wells. The discovery per wildcat peaked at 1.55 MM BOE after 500 wildcats, and declined steadily thereafter to a level of 0.02 MM BOE per well after 1,900 wildcats, indicating that the play reached a state of maturity, as did the move to horizontal drilling to improve recovery efficiency. About 25 % of the discovered reserves were found in 5 % of the fields, indicating a more even reserve distribution pattern

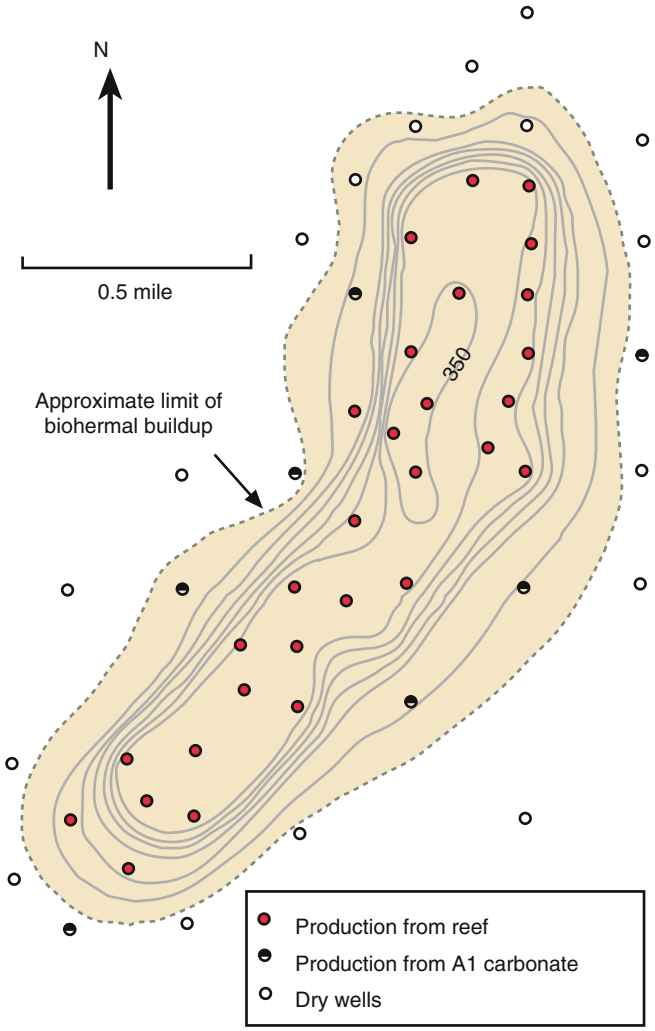

Fig. 10.38 Belle River Mills gasfield. Cumulative thickness or isopach of biohermal and organic reef stages, configuration at termination of organic reef stage (After Gill 1985)

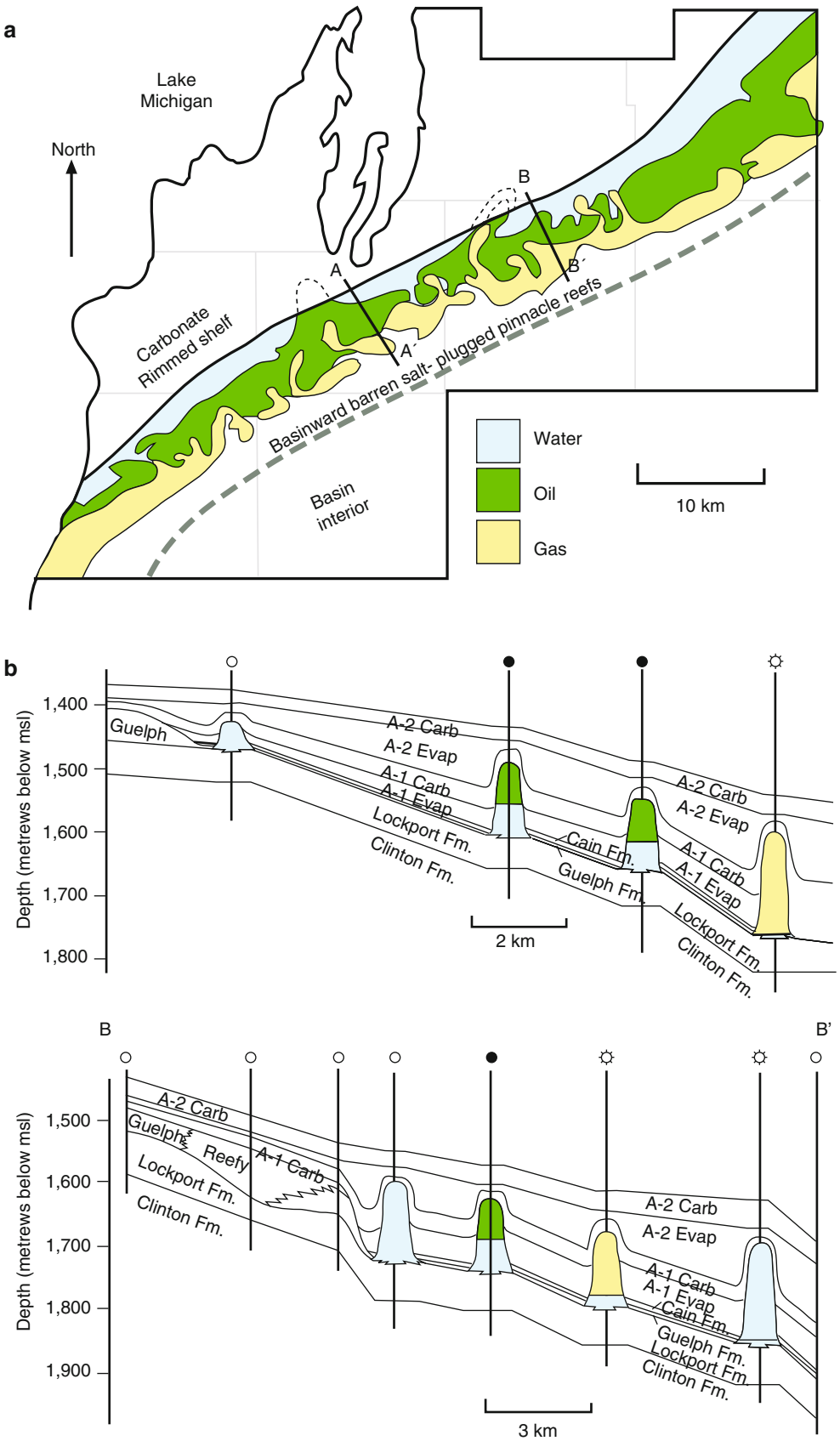

Fig. 10.39 Evaporite-sealed Silurian pinnacle reefs in the Northern Michigan Basin. (**a**) Distribution of salt plugged, gas-, oil- and water-bearing reefs. AA′ and BB′ show the positions of cross sections in Fig. 10.39b. (**b**) Cross sections through the pinnacle reef belt showing classical Gussow-migration controlled separation of oil and gas in the reefs. Pinnacles in positions more basinward than shown are not economic due to widespread salt plugging (After Gill 1985)

than in many other reefal plays, perhaps a reflection of the high efficiency of basinwide evaporites as seals to pinnacle reefs. Consequently, the relative rate of growth of discovered reserves was slower than in other reef plays.

Downdip pinnacle reefs in the Michigan Basin illustrate a major negative to any relatively un-fractured reef play that is sealed by thick basinwide evaporites. That is, the deposition of a thick sequence of salt atop and adjacent to the reef buildup typically leads to high volume flow of dense saturated brines through the underlying porous strata at the culmination of the reef (potential reservoirs). This tends to overdolomitise and extensively plug most of the uppermost porosity in downdip carbonates located in brine saturated lows. Such a poroperm distribution is clearly seen in the Niagaran trend (Fig. 10.39a), which shows a band of evaporite-plugged pinnacle reefs down-dip of the main pinnacle reef play. Within the pinnacle reef play the occurrence of oil updip of the gas accumulations is an indication of classic Gussow style migration and segregation (Fig. 10.33b).

Why updip reefs remain as reservoirs and the downdip reefs are salt plugged is an interesting quandary. In my opinion it reflects the likely recharge hydrology that influenced the basin when it was hydrographically isolated and the A1 and A2 halites were being deposited. As we saw in Chap. 5, the potentiometric surface created by hydrographic isolation created a marine-fed seepage margin to a drawndown saline giant (Fig. 5.69). Toward the basin edge, this head was sufficient to displace any dense reflux brines from the surrounding basinwide brine plume and so allow deeply circulated seawater to rise through the pinnacle reefs and from part of the marine-feed outflow zone. Crests of pinnacle reefs allowing groundwater egress have characteristic seepage carbonate caps (pisolite, tufa, stromatolite and anhydrite haloes) that differentiate them from the surrounding halite plain. Pinnacles further out in the basin did not have sufficient head to prevent the ingress of sulphate-saturated waters and so their porosity was plugged. Reef caps to these salt-plugged reefs lack or have attenuated indictors of seepage outflows. This palaeohydrology also explains why oilfields in pinnacle reefs that acted as marine seeps, such as the Bell River Mills gasfields, not only produce from the reef facies but also produce from the A1 carbonate fringe. Back in the Silurian these units were part of a single flow unit supplying pressurized phreatic seawater to the basin (Fig. 10.38). The hydrology that established the active seep reefs can be used as an exploration and development tool in such drawdown basins.

Once again, the presence of a thick sequence of bedded impermeable evaporites exerts a strong influence on reservoir distribution and quality from the time of first deposition well into burial. The Salina salts today acts as highly effective seals to oil and gas accumulations in the pinnacle reefs. During the early drawdown stage the formative hydrology perhaps allowed some pinnacle reefs to remain open, while others further out in the basin were plugged by evaporite cements from brine reflux. Then during later burial the salt bed focused the flow of upwelling basinal waters and the precipitation of later authigenic cements both along its underside and within the salt-sealed pinnacle reefs. Another interesting feature of the Niagaran pinnacle reef play is that many fractures and adjacent pinnacle matrices are overprinted by late stage saddle dolomite and calcite, with ponding of the precipitating fluids driven by circulation of late stage basinal fluids beneath the highly effective evaporite seal (Cercone and Lohmann 1986). The source of these basinal fluids is not well understood, but is thought to be from the leaching of underlying Ordovician shales by hypersaline brines.

This argument is supported by the occurrence of fault and fracture-controlled hydrothermal (thermobaric) dolomite reservoirs in Ordovician (sub-Niagaran) marine carbonates in a syncline that defines the oilfields of the nearby Scipio Albion trend (Fig. 10.40). Oil and gas have been produced in this region from what are interpreted to be fault-controlled hydrothermal dolomite reservoirs in the Ordovician Trenton and Black River carbonates since the late nineteenth century (Harding 1974; Hurley and Budros 1990; Smith 2006).

Whereas the play has been active for more than 130 years, new fields are still being discovered because of their unconventional structural style. At least 30 new gas fields were discovered in the Black River Group in New York over the last 15 years (Slater and Smith 2012). The fields are detectable on seismic profiles as elongate, faultbound structural lows or sags associated with transtensional wrench faulting (Smith 2006). Dolomite and porosity form around the faults but are absent away from the faults where the formations are composed primarily of impermeable limestone that forms a lateral seal (Smith 2006). Cores collected from these fields and others like them typically contain matrix dolomite as well as fractures, breccias, and vugs lined with white saddle dolomite (Davies and Smith 2006). Fluid inclusions and geochemical analyses suggest that the dolomites formed in a burial environment from high-temperature saline brines that passed through the basement or immature siliciclastics overlying the basement before precipitating the dolomite. These structures have been interpreted to form when oblique strike-slip faulting allows pressurized fluids to travel upward along fault planes to shallower units (Harding 1974). Metal sulphides, baryte and coarse sparry anhydrite are coprecipitates from the basinal fluids that formed this set of late-stage coarsely crystalline saddle dolomite. Yoo et al. (2000) argued for an evaporite source to these fluids. Later in this chapter we shall return to this association in a discussion of structurally-focused hydrothermal dolomite overprints and density-driven deep convective circulation cells below the dissolving undersides of highly effective evaporite seals.

Evaporite-Sealed Platform and Reefs, Devonian, Canada

The Keg River Formation forms the lower portion of the Upper Elk Point Subgroup in the western Canada Sedimentary Basin (Fig. 10.41a). Carbonate, evaporite and minor siliciclastic rocks of the subgroup were deposited in the widespread Elk Point Embayment which extended from northeastern British Columbia and the District of Mackenzie southeastward into the Williston Basin of southern Saskatchewan, Manitoba, North Dakota and Montana (Meijer Drees 1994). Early Devonian (pre-Keg River time) in the Alberta Basin of Canada was dominated by multiple-cycle platform evaporitic deposits ending with deposition of planar anhydrite sheets of the Chinchaga Formation and shales of the Ashern Formation (Tinker and Kirby 1991).

The lower Keg River/Winnipegosis was deposited as a marine carbonate ramp in shallow waters <75 m deep. Contemporaneous faulting and uplift during Middle Devonian time initiated development of a platform margin composed of stacked, porous (15–25 %) packstone and grainstone shoals (Fig. 10.41a).

Pinnacle and bank growth in on or near the platform edge was contemporaneous with epeiric shelf deposition. Keg River/Winnipegosis deposition ended with hydrographic isolation of the basin and subsequent deposition of the basinwide (intracratonic) evaporites of the Middle Devonian Muskeg/Prairie Formation. Figure 10.41b shows the geological nomenclature used in various parts of the Elk Point Basin (aka Western Canadian Sedimentary Basin)

Since the initial discoveries in the mid-1960s, the subsalt Keg River/Winnipegosis interval has produced hydrocarbons from a variety of dolomitic trap types, with the largest volumes coming from evaporite-sealed pinnacle reefs such as Leduc, Judy Creek and Swan Hills. In 1991, Tinker and Kirby listed the following produced volumes; Rainbow/Zama sub-basin (>650 MMBO cum.) and in equivalents in southern Saskatchewan (>2 MMBO cum.); shelf-margin carbonates at Temple Field (>3 MMBO cum.); middle shelf carbonates at Senex (>2 MMBO cum.); inner shelf carbonates in northeastern Montana, southern Saskatchewan, and southern Alberta (>10 MMBO cum.); and inner shelf siliciclastics at Utikima Lake (>75 MMBO cum.) (Fig. 10.41a).

Historically, regions of high production in Middle Devonian carbonates lay to the north and north-northwest of Calgary, where evaporites acted as the seal for most of the higher volume fields with Keg River/Winnipegosis production (Fig. 10.41a). Production in the Swan Hills an Rainbow-Zama sub-basin has been declining since the mid 1980s. More recent discoveries are smaller and lie along the basin edge, mostly in a region some hundreds of kilometres to the north of the areas of classic production and extending into British Columbia. There the evaporite seal is missing (whether from dissolution or lack of deposition is still contested) and much of the economic porosity is in patchy zones of late stage hydrothermal dolomites, now beneath shale seals.

Today, through enhanced recovery and directional drilling, the Middle Devonian Keg River/Rainbow pools in the mature production area of the Rainbow/Zama sub-basin have produced more than 1.1 billion-barrels of oil, mostly from evaporite-sealed pinnacle reefs and platform dolomites. Historically, the most productive reservoirs were pinnacle buildups encased by basinwide evaporites of the Muskeg/Prairie formations (Figs. 10.41b and 10.42; Schmidt et al. 1985; Majid 1987). Reservoirs in buildups in the upper member of the Keg River Formation consist of floatstone, rudstone and boundstone, with wackestone, packstone, and grainstone matrix. The principal faunal constituents are crinoids, brachiopods, stromatoporoids, corals, and *Stachyodes sp*. All are indicators of open marine sedimentation prior to the onset of evaporite precipitation. Reservoir porosity is a combination of primary intergranular and intragranular and secondary vuggy textures in partially dolomitised intervals. The primary role of the evaporite is as a seal to accumulations in the more permeable carbonates, but evaporite precipitation also drove earlier reflux dolomitisation and anhydrite plugging of the reef and platform strata during its precipitation as a saltern seal facies in the basinwide succession.

Prior to the basin's hydrographic isolation the buildups in the upper Keg River member in Alberta were patch reefs or banks, which grew in an open marine epeiric interior seaway fronted by Presqu'ile barrier to the westnorthwest (Fig. 10.41). Water depth was the main factor controlling the distribution of the more porous intervals of the bank and patch reef facies (Fig. 10.42). The back reef of the main platform became more restricted and anhydrite was precipitated as platform evaporites at times of hydrographic isolation on the shelf, prior to the main basinwide event. At times of open marine connection patch reefs were developed in areas of deeper water, whereas banks were formed in shallower areas of an open lagoon on the shelf. A direct relationship between the thickness of overlying anhydrite seal (Muskeg Formation) and hydrocarbon occurrences in the platform carbonates of the Keg River Formation was defined by Majid (1987). He concluded that trends beneath the evaporite seal can be reliably modelled using depositional fabric and seal thickness. Where the thickness of the anhydrite is more than 10 m atop areas of patch reefs, it constitutes an adequate seal. In contrast, buildups covered by less than 10 m of anhydrite constitute regions of higher risk (Fig. 10.42).

Areas of more recent exploration focus in the Keg River and its equivalents are located mostly in British Columbia to the north of the classic areas of Rainbow reef and platform production just described. There, late stage dolomitisation exerts a more significant control over reservoir quality and

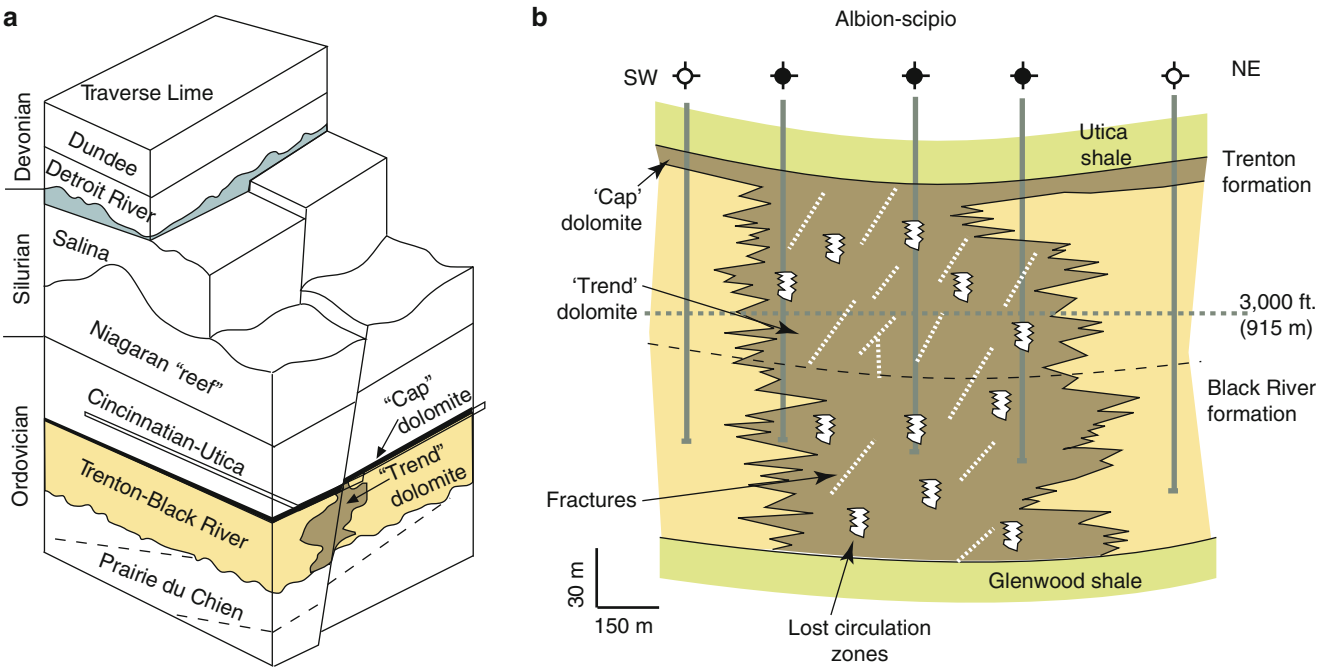

Fig. 10.40 Fault-focused late dolomitisation in the Scipio-Albion trend, Michigan (After Hurley and Budros 1990). (**a**) Structural stratigraphic interpretation of the Albion-Scipio trend. The fault/fracture set that controls dolomitisation is pre Devonian. (**b**) Structural cross section of the Scipio-Albion Field. Note that the field is located in a synclinal trend (not usual for a hydrocarbon trap) and there is a rapid lateral transition from a regional nonreservoir limestone into a permeable reservoir dolomite that also hosts late stage anhydrite and other authigenic burial salts. Lost circulation and fracture zones in such fields are common indicators of secondary dolomite-hosted porosity. Note that the seal is a shale not evaporite in this system, but the chloride-rich basinal brine responsible for the hydrothermal dolomite has a chemistry strongly influenced by evaporite dissolution deeper in the basin

porosity development does not always follow the depositional plumbing predicted by depositional facies. Much of the evaporite is missing and shale is the seal. But effective porosity development at the reservoir level still requires what Morrow et al. (2001) termed a "hydrostratigraphic template," first created by a combination of depositional fabric and early reflux dolomitisation. The high-salinity chloride-rich late stage brines driving this burial dolomitisation were largely sourced in regions of dissolving salts (Fig. 8.6).

Such a hydrostratigraphic template defines hydrocarbon occurrences in the July Lake gas pool of the Keg River Platform and the Helmet and Peggo gas fields in the Slave Point Formation, all located along the shelf-to-basin transition of the Cordova Embayment in northeast British Columbia (Wendte et al. 2009; Qing and Mountjoy 1994). There, burial-stage, coarsely crystalline replacement dolomites and associated saddle dolomite cements and zebra dolomites form a widespread diagenetic facies in the Middle Devonian Presqu'ile barrier that extends southwestward from outcrop near Pine Point to the subsurface of the Foothills in northeastern British Columbia. Dissolution and subsequent precipitation of coarsely crystalline burial and saddle dolomites creates hydrocarbon reservoirs with intercrystalline porosity in otherwise tight limestone hosts. The same system hosts sub-salt breccia Mississippi Valley–type Pb-Zn deposits at nearby Pine Point (Chap. 15). Porous burial dolomites replacing blocky sparry calcite cements, occur continuously across the sub–Watt Mountain unconformity. They postdate stylolites and earlier replacement dolomites, overlap sulphide mineralization and show regional oxygen isotope signatures that are indicative of deep hot saline basinal fluids escaping via fault and fracture feeds into the adjacent carbonate platform sediments (Fig. 10.43).

Recognition of late stage dolomite as a reservoir-former led to a re-examination of core from some of the producing intervals in platform-interior dolomites in the more mature Rainbow subbasin to the south. Previously, platform carbonate production away from the main pinnacle reef plays had been related to what were considered in the 1970s to be thin pinnacle reefs, biostromes and low relief shoals, all with a depositional control to the reservoir plumbing. But the mechanism and chemistry of porosity retention was never well documented by the explorationists. Subsequent core and thin section studies in the same dolomitised platform intervals established that production was actually tied to later secondary porosity, not relict primary porosity. It was mostly associated with dolomitised subtidal facies at the bases of stacked metre-scale evaporitic depositional cycles (Muir and Dravis 1995). For example, the Keg River and Muskeg pools on Comet Platform are combination

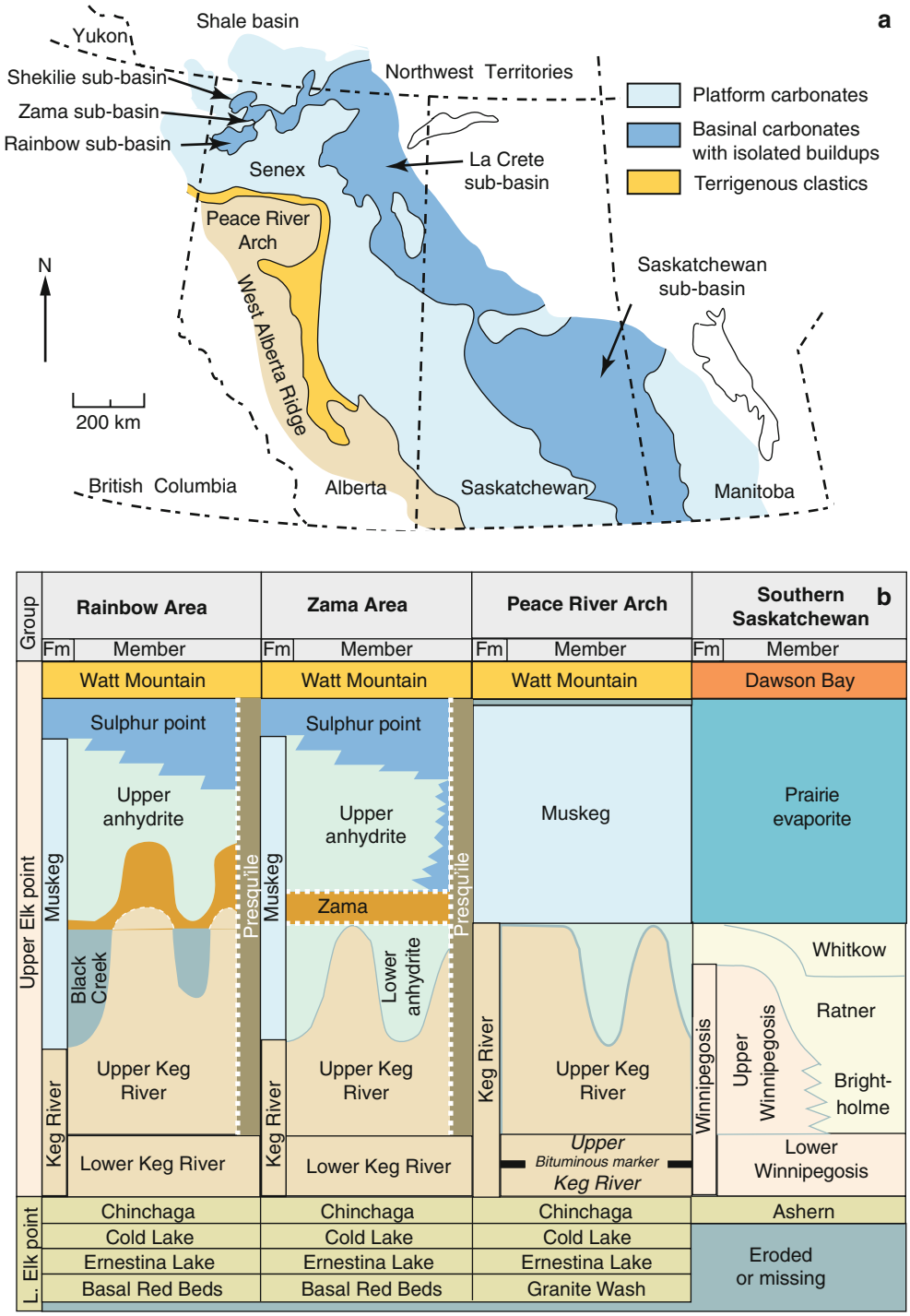

Fig. 10.41 Keg River Formation and its seal. (**a**) Paleogeographic map showing the major palaeoenvironmental facies of the Middle Devonian Keg River Formation deposited in the Elk Point Basin, Western Canada. (**b**) Stratigraphic nomenclature of the Elk Point Group in the Rainbow and Zama areas, Peace River Arch and northeastern Alberta, and southern Saskatchewan (After Wiebe et al. 2013)

structural-stratigraphic-diagenetic traps with reservoir quality strongly influenced by fracture intensity. Reservoir facies are confined principally to fractured platform-interior beds of restricted subtidal *Amphipora*-peloidal dolopackstones and dolowackestones. They constitute the base of anhydritic 7–12 m thick depositional cycles, which are correlatable across the Comet Platform. It is likely that the underside ot these dolomites focused the flow of the burial-stage porosity-creating and dolomitising fluids.

Better quality reservoirs in the platform interior occur at or near the base of each major cycle and result from dissolution of the platform carbonate, tied to the precipitation of burial dolomite cements. For example, the Keg River pool on the western edge of the Rainbow-Zama sub-basin is locally

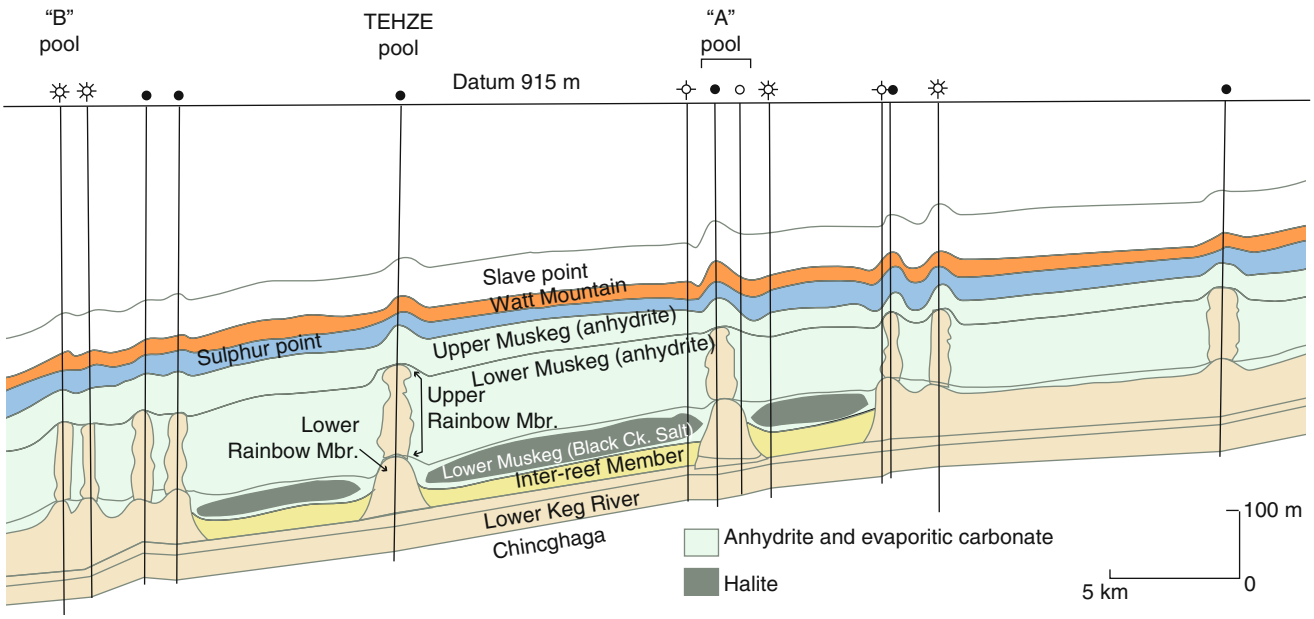

Fig. 10.42 Rainbow Basin, Alberta. NE-SW cross section through the mature Rainbow area showing development of carbonate platform in the Upper Keg River and the platform evaporite seal created by the basinwide anhydrite salts of the Muskeg Formation (After Schmidt et al. 1985)

dominated by spectacular zebra dolomites with vuggy porosity tied to anhydrite dissolution, while Muskeg pool dolomites all exhibit mouldic and vuggy porosities (Muir and Dravis 1992; Morrow 2014). Termination of stylolites and fractures into these secondary pore types confirm their burial origin.

Regional tectonic influences on oil pool development in the Comet Platform are indicated by horizontal fractures, vertically-oriented stylolites, and spectacular burial-stage evaporite solution-collapse breccias. Pools are localized over regional fault and fracture trends that affected the carbonates, but did not fracture the evaporite seal, and are related to reactivation of the Great Slave Lake shear zone. Faults and fractures aided burial diagenesis and the creation of late secondary porosity development by focusing the ascent of hot, dolomite-dissolving basement-derived and calcium-rich basinal fluids. Seismic data indicate these faults were largely collapse structures generated by salt loss and subsalt breaching in the underlying Cold Lake Salt Formation. Further, some of these faults localized precipitation of massive diagenetic anhydrites (retrograde precipitates) that now provide updip side closure to some pools. This current understanding of reservoir control is a long way from the simple early notions in the 1970s of relict primary porosity in a carbonate biostrome.

Much of the hydrocarbon-hosting porosity is enhanced or sometimes induced by the cross flow of calcite undersaturated dolomite-precipitating evaporite derived hot brines (Morrow 2014). The passage of these aggressive waters is indicated by ubiquitous zebra and boxwork fabrics in cross-stratal Manetoe and Presqu'ile hydrothermal dolomites in Devonian strata in Northern Canada (Fig. 10.43). Early indications of the presence of this characteristic texture is indicated by sets of weakly imbricated, decimetre-sized curvilinear lenticles of white dolospar, developed within sub-metre sized tongues of greyish-white dolomitised crinoidal packstone and grainstone. This nascent zebra fabric has developed along wavy to nodular intra-bed sedimentary partings. Primary bedding can be traced through dolomitised masses containing these fabrics, into the surrounding undolomitised limestone. Similar textures occur in the Pb-Zn ore peripheries hosted in the Devonian Cadjebut Fm of the Canning Basin, Australia (Wallace et al. 1994; Warren and Kempton 1997 – see Chap. 15 for further discussion of the MVT- Zebra texture association).

All zebra and boxwork fabrics are confined within single beds in the Elk Point Basin, consistent with an early burial time of origin. No change in bed thickness occurs across zebra or boxwork fabrics within beds; this indicates a dissolutional, rather than a dilational, origin for the creation of pore space partly cemented with white dolospar. The dolomitised groundmass displays an abruptly gradational or sharp transition to centripetal saddle dolomite cement, which partially to nearly completely, occludes vugs. Circulation of geothermally heated hypersaline Devonian Elk Point basinal seawater-influenced brines led to dissolution and replacive dolomitization of limestone adjacent to vugs, and near-contemporaneous precipitation of white dolospar within dissolutional vugs, consistent with geochemical simulations (Fig. 10.43b). The presence of downward-extending galleries of white dolospar-cemented solution-collapse breccia provides further support for an interpretation of regional thermally driven convection of hydrothermal evaporative seawater-influenced brines across a broad area of northern Canada.

The absence of gases under pressure in vacuoles within fluid inclusions from Manetoe and Presqu'ile dolospars is also more consistent with a dissolutional and contemporaneous dolomitization origin for these fabrics, rather than an origin involving dilational fracturing for space creation and dolospar precipitation. The ubiquitous presence of zebra and boxwork fabrics in hydrothermal dolomite reservoirs indicates that they are not confined to fault zones and instead occur wherever precursor limestones had relatively greater porosity and permeability prior to dolomitization. Dissolution by hot, basement-derived fluids throughout most of the region is supported by the presence of diagenetic fluorites, megaquartz and polysulphide minerals, helium gas, fluid inclusions, and high carbon dioxide and hydrogen sulphide gases in these hydrocarbon pools (Davies and Smith 2006).

Thus, these platform-interior pools in the Devonian carbonates of the Elk Point Basin are combination structural-stratigraphic-diagenetic traps with reservoir quality tied to reactivated basement faults and are not directly to depositional porosity in pinnacle reef occurrences. Once reservoir quality in platform cycles was tied to salt solution-brine induced fractures, rather than to inferred low relief pinnacles, it permitted correlation of larger 7–12 m-thick composite cycles over distances of several kilometres. This meant reservoirs could be more effectively zoned (Muir and Dravis 1995). By 1989, daily cumulative oil production rates in platform dolomites were increased from 500 m^3/day (1988) to 1,400 m^3/day as a direct result of this revised understanding of reservoir layering. It also led to improved conformance, sweep, and minimization of oil sandwich loss in these miscibly- and gas-flooded pools and to more effective horizontal well design.

Clearly, reservoir quality in the Rainbow-Zama sub-basin, and equivalents to the north, is in large part tied to the ongoing diagenetic evolution of the dolomitised host and its strong interaction with evaporite aquicludes that controlled subsequent brine passageways. As well, later salt-dissolution brines were derived by early brine reflux and later tectonically driven induced fracturing, basinal fluid flow and brine escape to form a characterised suite of dolospar and coarse burial anhydrite cements tied to this dolospar. As Warren (2000a) observed, ancient dolomite is never a single-phase mineral. In all areas of Keg River associated production there are at least two styles of dolomite present, an earlier brine reflux dolomite, created when the overlying evaporite was porous and a supplier of dense Mg-rich brines and a later dolomite formed when the evaporite bed was a seal that focused and facilitated convective circulation in sediments beneath and adjacent to the slowly dissolving salt mass.

Reservoir Quality Tied to Bedded Evaporite Seal Type

Depositional facies preserved in a sealing salt bed atop an oil or gas field can be useful indicators of palaeotopography, energy levels and volumes of syndepositional authigenic cements in the underlying reservoir. Lowermost facies in a bedded evaporite seal can typically be related to the topography of the reservoir's upper contact at the time the seal was precipitated. This means wireline signatures of the seal can be used to differentiate stratigraphic traps from simple drape traps. Drape traps are created by compactional or structural draping sometime after the reservoir and seal were deposited. Other than possible erosional thinning, wireline signatures through seal facies in this scenario typically show no depositionally-controlled thickness changes or internal depositional differentiation between top seal and lateral seal.

In contrast, repeated evaporitic transgressions over an underfilled carbonate or siliciclastic platform can deposit alternating cyclic carbonates/siliciclastics and evaporites in broad, shallow to ephemeral brine environments. Depositional textures in the sealing evaporites are then controlled by zones of marine-fed brine springs and the permanence and depth of the saltern and evaporitic mudflat brines. Top seals to pre-existing highs such as shelf margin reefs or shoals, dune crests or slope carbonate buildups show internal fabrics related to palaeorelief. Such topography-related facies mosaics typify the wireline and core textures in the lower levels of the basinwide evaporites sealing the Silurian pinnacles of the Michigan Basin. Nodular mosaic anhydrites of supratidal sabkhas dominate evaporitic mudflat seal facies atop and adjacent to the crests of underlying pinnacle reefs, while subaqueous saltern facies, made up of bedded massive/mosaic anhydrite and allochthonous dolomite-anhydrite breccias, typify the lateral seals (Figs. 5.67 and 5.69). Pisolitic textures and sometimes tepees tend to form in regions of brine-spring outflow on a now exposed drawndown basin floor.

Mapping of Permian anhydrites textures (salinas versus sabkhas) in the Khuff C in the Hawiyah area in Ghawar field, Saudi Arabia, showed the sabkha successions on the highs sourced much of the anhydrite-plugging cements in the underlying Khuff carbonate reservoir (Al Eid and Al Tawil 2009). Similar textural transitions occur between sabkha and salina seals that make up the top seal to karstified shelf margin reservoirs of the Permian San Andres reservoir of Yates Field, West Texas, as well as other Guadalupian sequences in the Permian Basin of West Texas. Around two thirds of the reservoirs in Permian rocks of West Texas and New Mexico are sealed by bedded platform evaporites (Fig. 10.44; Table 10.6), most show an intimate relationship between evaporite facies in the seal and reservoir quality beneath (Ward et al. 1986; Warren 1991; Sarg 2001).

Yates Field, West Texas

Yates Field, discovered in 1926, is located in the southernmost Central Basin Platform of West Texas and is one of the most prolific reservoirs ever discovered in the United States (4 billion barrels original oil in place). It is shallow

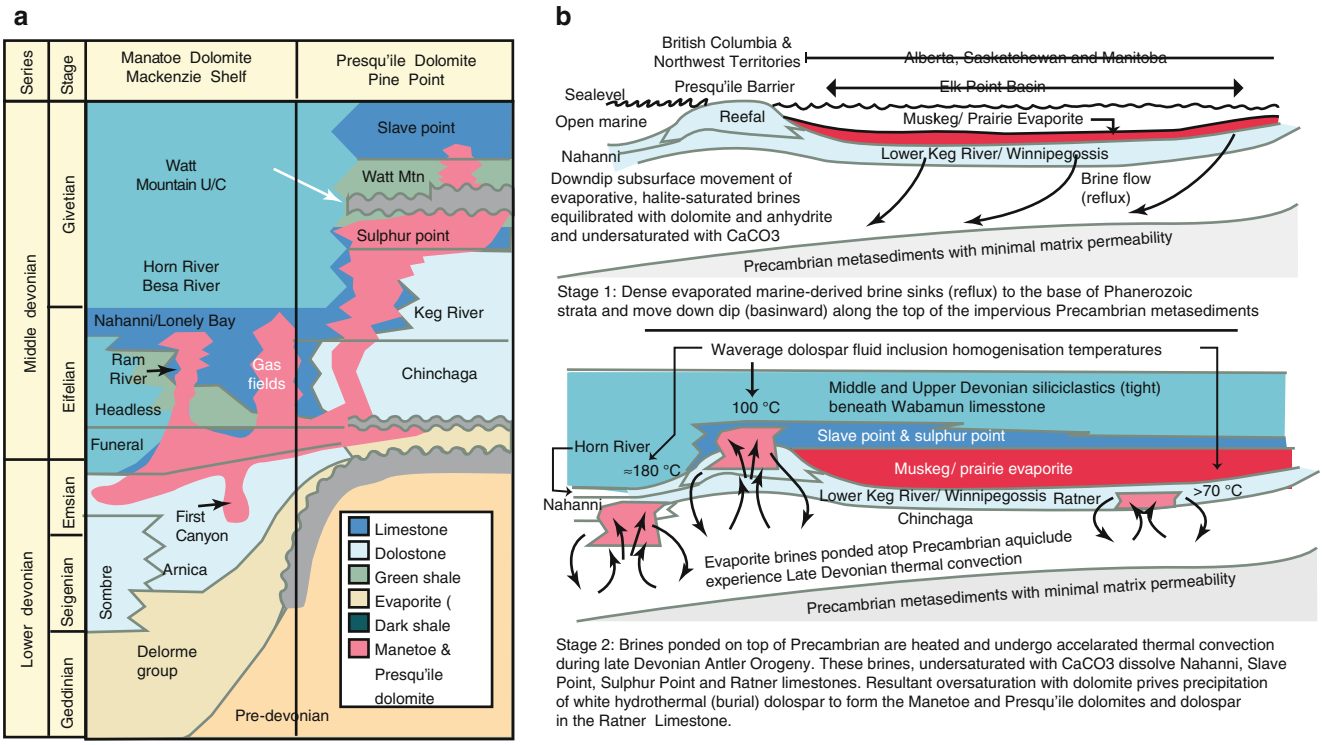

Fig. 10.43 Late porosity evolution in Devonian Elk Point Basin, Canada. (**a**) schematic chart of Devonian stratigraphic relations across the southern Northwest Territories of Canada. The Manetoe Dolomite has partly replaced Lower and Middle Devonian limestone and shaly limestone units (Landry, Headless and Nahanni formations) in and around Ram River. The Presqu'ile Dolomite analogously has replaced Middle and Upper Devonian limestone and shaly limestone units (Sulphur Point, Watt Mountain and Slave Point formations) in the Pine Point area. (**b**) Schematic representation of the origin of Elk Point evaporative hypersaline seawater brines and their role as hydrothermal fluids during Late Devonian geothermally driven diagenesis. Buoyant circulation of geothermally heated, dolomite-saturated, but calcite undersaturated, subsurface Elk Point brines is hypothesized to have caused some dissolution of Middle and Upper Devonian limestones (Landry, Nahanni and Sulphur Point) in the shallow subsurface in Late Devonian time. This dissolution resulted in equilibration with respect to calcite, but oversaturation with respect to dolomite so that these limestones were partially dolomitized to form the Manetoe and Presqu'ile dolomites, as well as dolomitization within the Ratner Limestone of Saskatchewan (After Morrow 2014)

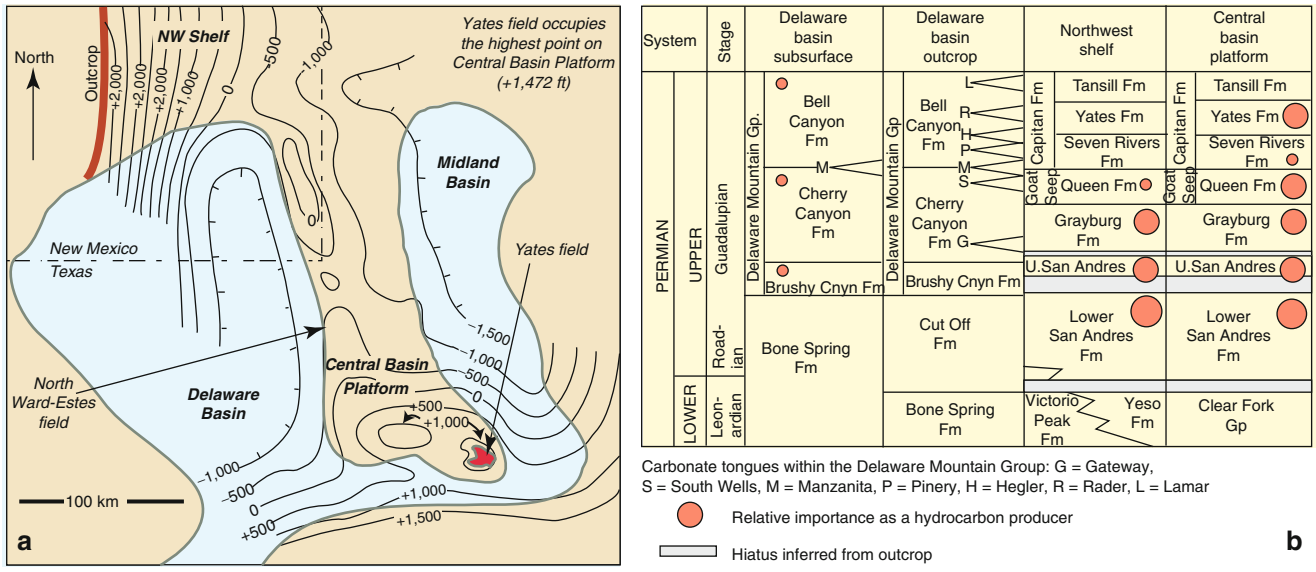

Fig. 10.44 Geographic and stratigraphic setting of Yates Field, west Texas. (**a**) Regional structure on top of San Andres -Grayberg shelf and shelf margin carbonates and coeval basin carbonates and clastics. (**b**) Stratigraphy of the latest Leonardian-Guadalupian units of the Permian Basin, West Texas (After Kerans et al. 1994). Almost all of the fields on the Northwest Shelf and the Central Basin Platform are sealed by bedded mudflats or saltern evaporites (In part after Craig 1988; Tinker et al. 1995)

Table 10.6 Characteristics of fields in the San Andres Formation of West Texas, which are sealed by bedded salts composed of anhydrite and halite

Field	Discovery (year)	Depth (m)	Temp (°C)	Oil gravity (API)	CumulativeOil (MMBO)	Original oilcolumn (m)
Wasson	1936	1,520	41	31	1,712	137
Slaughter-Levelland	1936–1945	1,490	–	30	1,514	–
Yates	1926	460	28	31	1,172	137
Goldsmith	1936	1,310	35	36	756	91
Seminole	1935	1,580	42	37	525	80
S. Cowden-Foster	1932	1,650	48	35	501	244
N. Cowden	1930	1,340	46	35	488	244
McElroy	1926	880	30	32	466	122
Vacuum	1929	1,400	38	38	432	–
Hobbs	1928	1,230	–	34	297	76
Sand Hills	1944	980	30	33	248	152
Midland Farms	1944	1,460	39	46	242	–
Means	1934	1,340	38	29	229	70
Dune	1938	1,010	31	34	183	244
Eunice-Monument	1929	1,100	–	32	175	–
Maljamar	1926	1,100	–	37	145	–
Jordan	1937	1,130	31	35	129	91
Waddell	1927	1,070	31	34	101	91

(305–460 m; 1,000–1,500 ft) and produces mostly from the Upper Permian San Andres Formation, with additional secondary production from stringers in the overlying Grayburg, Queen and Seven Rivers Formations. The field covers approximately 100 km^2 with more than 1,600 wells in the field. The field is now largely depleted of easily recoverable hydrocarbons, but continues to produce utilising enhanced recovery techniques. Estimated recovery after 84 years of production since 1927 is about 35 % after primary depletion, water and gas injections (Cheng and Kwan 2012).

At the level of the Permian section, it sits on the structurally highest point of the Central Basin platform (Fig. 10.44a). Structural closure is dominated by a broad asymmetric domal or anticlinal feature, which appears to be formed by the intersection of two separate tectonic structures that combine to create the horseshoe-shaped high that defines the outline of the field. Yates Field was discovered in 1926, high pressures, supplied by the combined gravity segregation, bottom water and gas cap drives, resulted in unusually high initial production rates and it produced by depletion drive until 1976. As pressure depleted throughout that half century, free gas evolved and migrated rapidly through the natural fracture system to the structural top of the field to form a slowly expanding gas cap drive beneath its evaporite seal. The efficiency of the evaporite seal atop the fractured reservoir system can be seen in an official proration test on the Mid-Kansas Oil and Gas Co. and Transcontinental Oil Co. #30 I. G. Yates "A" well, which in 1929 lists a daily potential production of 204,681 barrels (Hennen and Metcalf 1929) in a system that is less than 500 m below the land surface.

Yates Field is one of a number of fractured dolomitic reservoirs in San Andres Formation of West Texas with an evaporite topseal centred on the Seven Rivers Formation (Guadalupian; Fig. 10.44b). Systems tracts in the seal facies are characterized by stacked successions of metre-scale, brining upward parasequences deposited across an epeiric platform interior. Depositional facies in the seal in all these fields can be used to infer palaeotopography in the underlying San Andres reservoir and to separate the relative importance of deposition, drape and tilt in controlling the hydrocarbon distribution in carbonates below the seal.

Evaporite deposition during Seven Rivers time in Yates Field occurred in two major settings, sabkha (subaerial mudflat) and salina (subaqueous) in an evaporitic mudflat seal, with their areal separation controlled by the positions of underlying carbonate shoals. Wireline character through areas of subaqueous anhydrite is blocky, indicating 10–30 m thick sequences of relatively pure subaqueous evaporite (Fig. 10.45a). Wireline signatures in areas of sabkha in the seal facies are richer in dolomite matrix and individual cycles are thinner (≈1 m) giving a stacked spikier wireline signature to both the gamma and the neutron-density logs (Fig. 10.45b; Warren 1991). Subaqueous signatures dominate in what were the topographic lows, while subaerial evaporites are more common above what were the topographically higher parts of the seaway floor. When seal facies are defined in this way, mapped and related to production statistics across the field, it shows that for cumulative production in the Yates Field unit, as of October 1986, only 85 million barrels of oil had been produced from under the thick

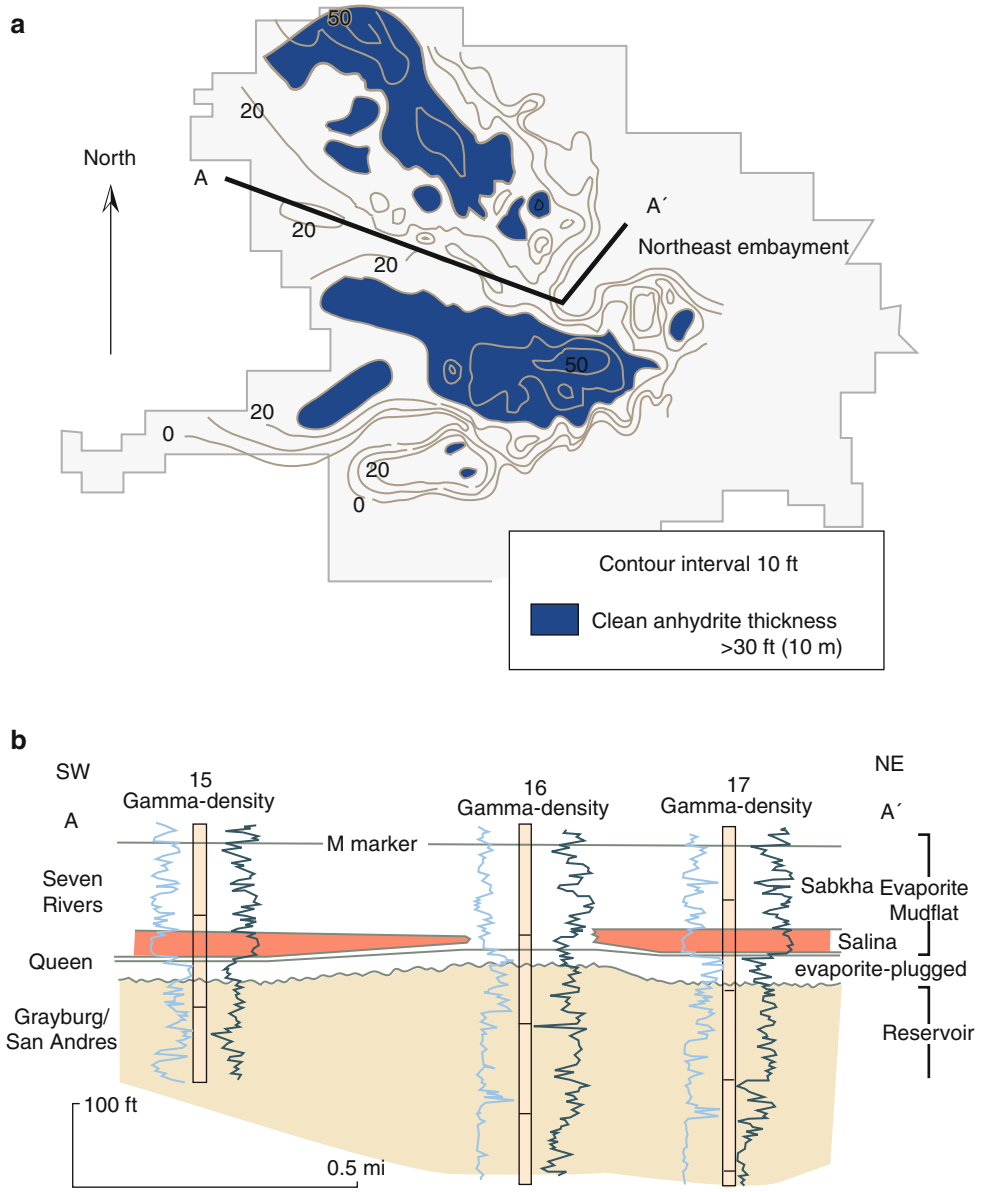

Fig. 10.45 Yates Field, West Texas. (**a**) Isopach of the massive anhydrite that typifies much of the base of the Seven Rivers seal to the field, thicknesses were mapped based on core and log signature. Clearly shows the subaqueous evaporites formed in lows that define the palaeotopography and hence quality of the underlying reservoir (see text). (**b**) Section using wireline lsignature to define depositional setting of the seal facies in the Seven River Fm. atop the San Andres Reservoir. Shows how the position of the salinas in the evaporitic mudflat defines the off structure positions (After Warren 1991)

salina accumulations, whereas almost 985 million barrels had been produced from the area under the sabkhas. Yet the two styles of anhydrite deposition cover roughly equivalent areas of seal over the field (Fig. 10.45a; Warren 1991).

Assuming that the M datum in the Seven Rivers approximates a level depositional surface, then the thick anhydrite in the lower Seven Rivers indicate palaeo-lows, while thin areas define ancient highs (Figs. 10.45b and 10.46). Massive anhydrite is found only over the central and western parts of the field. The anhydrite thins to zero roughly parallel to the platform margin, and shelfward of the San Andres shelf edge. The isopach map of the massive clean anhydrite (Fig. 10.45a) shows closed contours surrounding pod-shaped areas of salina anhydrite (originally gypsum) up to 15 m (50 ft) thick. Two salina areas were generally present in Yates Field during early Seven Rivers time, one on the northern and the other on the southern side of the field. The north and south salina ponds are flanked by smaller pod-shaped thicks and are separated by a line of zero evaporite trending north-northwest through the central part of the field. This linear feature is referred to as the northwest trend. Massive anhydrite is also absent in cores and logs in the northeast

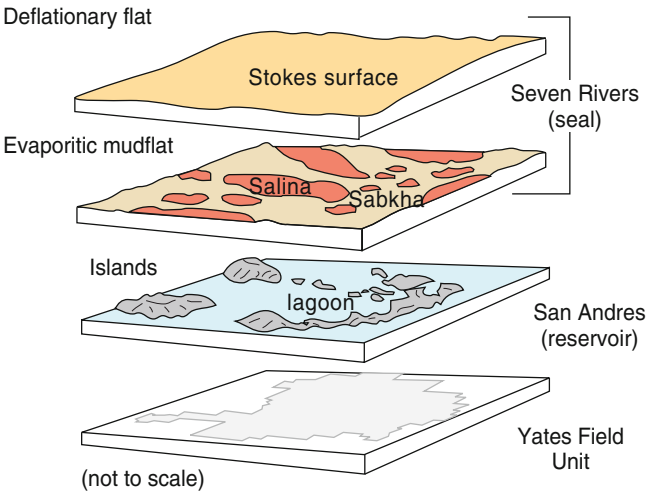

Fig. 10.46 Geological evolution of Yates Field region. During San Andres time the reservoir (fusulinid grainstone) was a set of karstified carbonate islands. By Seven Rivers time the reservoir was buried but the underlying palaeotopography (and the associated differential compaction) was still sufficiently developed to control the position of the depositional lows (salinas) and highs (sabkhas) (After Warren 1991)

corner of the field and forms what appears to be an embayment largely devoid of evaporite at the basal level of the Seven River and so defines the area of production called the "northeast embayment."

Evaporite facies distribution in the basal part of the Seven Rivers Formation was controlled by palaeotopography, which was in turn controlled by the depositional facies relationships in the underlying San Andres Formation (Fig. 10.46). The San Andres lagoon was an area that was depositionally low and one that remained low throughout Queen and Seven Rivers deposition, because of dewatering and mudstone compaction. When sufficiently karstified and fractured the lagoon muds hold producible fluids, are poorer quality reservoirs compared to adjacent karstified fusulinid shoals (Craig 1988). The lagoonal low was covered by a thick section of massive salina anhydrite that today provides a lateral seal to the adjacent sabkha-capped reservoirs. Sabkha-crested topographic highs sit atop the more permeable reservoir intervals, which are made up of karstified and fractured San Andres mounds and shoals (Craig 1988). The platform-edge fusulinid grainstones to packstones that are the main reservoir in Yates Field were cemented, fractured and karstified early. The lack of early burial compaction, compared to adjacent lagoonal mudstones, meant areas atop mounds and shoals remained as highs during early burial and into the time when the sealing evaporites were deposited.

That is, during lower Seven Rivers time, the then-buried San Andres depositional segregation still controlled the facies mosaic in the evaporite seal. Once this marine-fed evaporite system filled the available accommodation space, subsequent depositional style was controlled by a series of aggrading Stokes surfaces within an aggrading eolian sandflat/mudflat. At times of higher eolian sand flux the mudflat became a deflationary sand flat (Fig. 10.47b). Such deflationary sandflats can constitute reservoirs in other parts of the Central Basin Platform, as in North Ward-Estes Field.

North Ward-Estes Field, Texas

North Ward-Estes Field, Ward County Texas, is the largest and most prolific of a chain of producing fields in the Guadalupian Yates Formation, which extends along the western margin of the Central Basin platform for approximately 150 km, with a width of 1.5–6.5 km (Fig. 10.47a; Andreason 1992). Cumulative oil production within the North Ward-Estes Field from 1929 through 1989 was more than 365 million BBL, with oil-in-place estimated at more than 1 billion BBL. Siliciclastic reservoirs in the middle shelf provide most of the hydrocarbon production within the trend, whereas associated interbedded dolomites contributed patchy minor amounts of economic porosity to this play. Porosity distribution in the various Ward-Estes reservoir layers is best modelled using a depositional model based on a continent-coupled eolian to evaporitic mudflat to shelf setting, with superimposed early evaporite dissolution along the strandzone. Hydrocarbon traps form on gentle structural culminations sealed by updip evaporites. Hydrocarbon maturation and migration from the Delaware basin to the shelf reservoirs occurred during the Cretaceous and early Tertiary (Hills 1984).

In his comprehensive analysis of the late Guadalupian (Permian) Yates Formation reservoir sands, Andreason (1992) showed that the siliciclastic facies were part of a broad, evaporative mudflat that extended across a wide area of platform behind the Capitan reef. Cyclic sea level fluctuations produced a succession of dolomites, evaporites, and siliciclastics as the evaporative coastal plain oscillated across the Yates shelf. Moving landward, the environments were; (1) lagoon, (2) intertidal algal flat, (3) beach ridge, (4) siliciclastic sabkha, and (5) sand sheet/playa mud flat/salina/saltern (Fig. 10.47a). Evaporitic cycles, which formed on the inner shelf and landward, grade upward from massive subaqueous-dominant anhydrites into nodular mudflat anhydrites with increasing volumes of siliciclastic mudstone interbeds (playa mudflats). Carbonate-based depositional cycles consist of basal lagoonal peloid and skeletal dolostones, which grade upward into tidal-flat dolostones, beach-ridge sandstones, and finally into siliciclastic sabkhat.

The characteristic disrupted (haloturbated) textures of the Yates siliciclastics were created by surficial and interstratal halite growth during seasonal flooding and subsequent desiccation in a sabkha environment (Andreason 1992). A siliciclastic accretionary complex, composed of stacked beach ridges and detrital sabkhas, formed behind a pisolitic strandzone. Local siliciclastic accumulations also occurred over

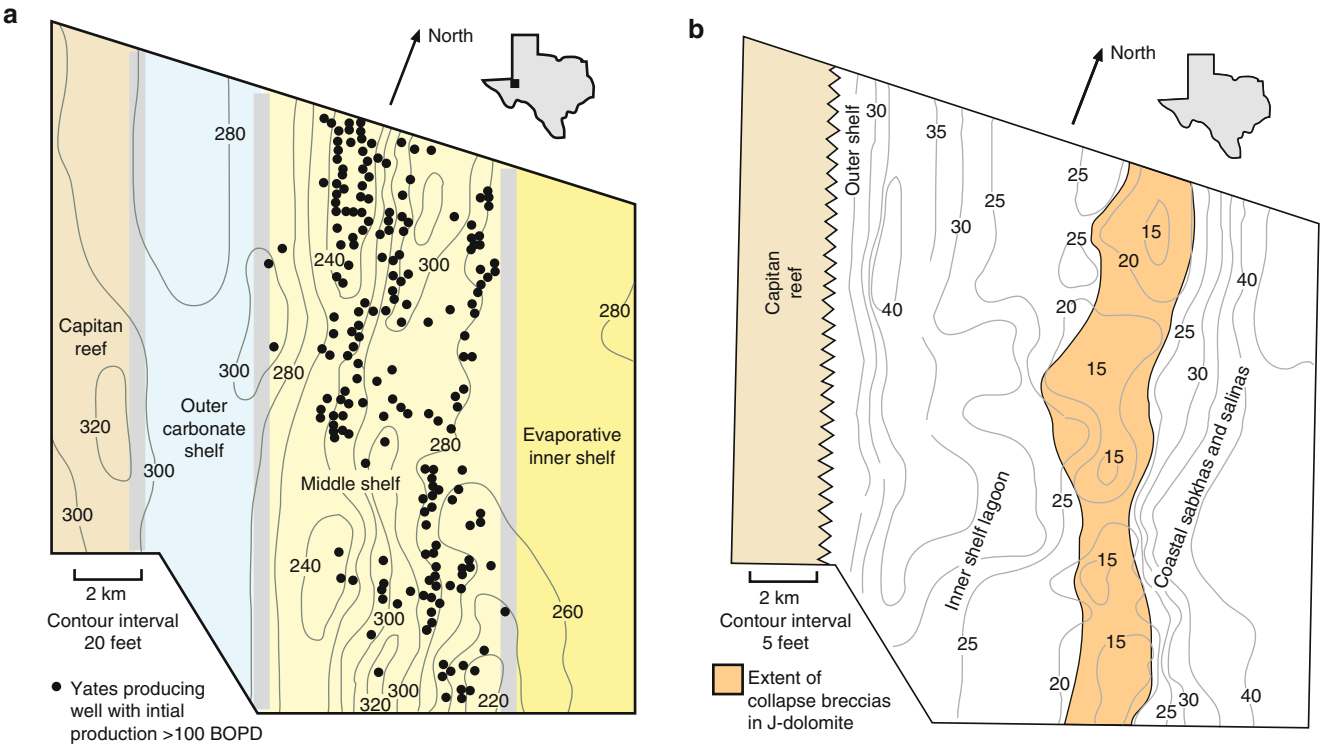

Fig. 10.47 Characterisation of Yates Fm., Ward-Estes Field (After Andreason 1992). (**a**) Total Yates interval isopach showing Yates shelf is divisible into; (1) an outer shelf that includes the Capitan Reef, the backreef flats and the pisolite shelf crest, (2) a middle shelf composed of stacked beach ridges and siliciclastic sabkhas, and (3) evaporitic mudflats made up of extensive flats, salinas and stabilised sand sheets. Hydrocarbons are concentrated in the middle shelf. (**b**) Isopach of the intra-Yates J-Dolomite unit. Shaded unit defines the extent of the evaporite collapse breccias that separates inner shelf lagoon from evaporitic mudflat. Depression defined by collapse was filled with greater thicknesses of overlying siliciclastic sand. See Fig. 10.44a for location

sinks or depressions produced by the dissolution of underlying bedded sulphates. Such dissolution breccias are defined by stacked horizons, made up of sharp clast-to-clast angular rudstones to floatstones with sharp basal contacts with the underlying cryptalgalaminated dolostones and sharp to gradational crackle upper contacts with the overlying subtidal carbonates (peloidal and fossiliferous dolostones). Because of pervasive soft-sediment deformation atop the dissolving mudflat evaporites, these intervals are easily misidentified in core as storm beds or erosive marine transgressive surfaces. Breccia beds correlate with anhydrite beds (mostly subaqueous) in the inner shelf and with dolomitic mudstones to the west (middle to outer shelf). That dissolution was early is indicated by the excellent correlations between the zone of collapse and a region of differential thickening within the overlying siliciclastics (Fig. 10.47b). What is unclear is whether dissolution was driven by a relative sea level rise or fall.

As we saw in Chap. 2, preservation of evaporites into the early burial realm depends on the maintenance of a narrow range of saline conditions. Dissolution occurs if undersaturated fluids contact the bed at any time during the evaporite's deposition or shallow burial, either from an influx of fresh, meteoric water or from "freshened" seawater. Solution breccias of the lower Yates occur only in the middle shelf and develop preferentially along the seaward extent of the region of massive epeiric saltern sulphates, suggesting dissolution was driven by influxes of normal marine water during relative sealevel rises (Andreason 1992).

The boundary between the collapse breccias and the massive sulphates marks the position of a concentration boundary on the submerged shelf where evaporative outflow exceeds marine free inflow and gypsum saturation was reached. Andreason argues this concentration boundary was shifted laterally relative to the magnitude of the sea level rise. When located seaward of this concentration boundary, and given sufficient time, evaporites originally present within the now-disturbed siliciclastic facies and the massive sulphate deposits underwent dissolution. Although the shelf position of the collapse breccias strongly suggests dissolution during a relative sea level rise, the possibly of dissolution by meteoric waters during periods of subaerial exposure and sealevel falls cannot be totally excluded.

The Yates Formation is part of the Seven Rivers, Yates, and Tansill trilogy, which in ascending order comprise the shelf-equivalent formations of the upper Guadalupian Capitan reef and represent a complex of lagoonal, coastal and evaporitic platform environments (Figs. 10.44b and 10.48). The Yates

Formation is unique among upper Guadalupian shelf formations in the Permian Basin in that it marks a period of major siliciclastic shelf deposition, as compared with predominantly carbonate and evaporite deposition of the Seven Rivers and Tansill formations (Fig. 10.48; Andreason 1992). The increased siliciclastic influx onto the shelf, particularly along the western margin of the Central Basin Platform and the northern margin of the Delaware Basin, probably indicates filling of the Midland Basin, which was located to the east (Fig. 10.44a). Eolian and wadi-driven siliciclastics, having filled the available accommodation space, now moved westward, fed from the distant hinterlands to the east and northeast and previously trapped by the shallow Midland pontic sea. The erg migrated across the vast deflationary region of the filled Midland Basin and Central Basin Platform to prograde into the Delaware Basin. Siliciclastics and evaporites had reached the southern portions of the Central Basin platform from the northeast (Midland Basin) by the beginning of the late Guadalupian, as evidenced by the prevalence of these deposits within the upper Queen Formation (Tucker and Chalcraft 1991).

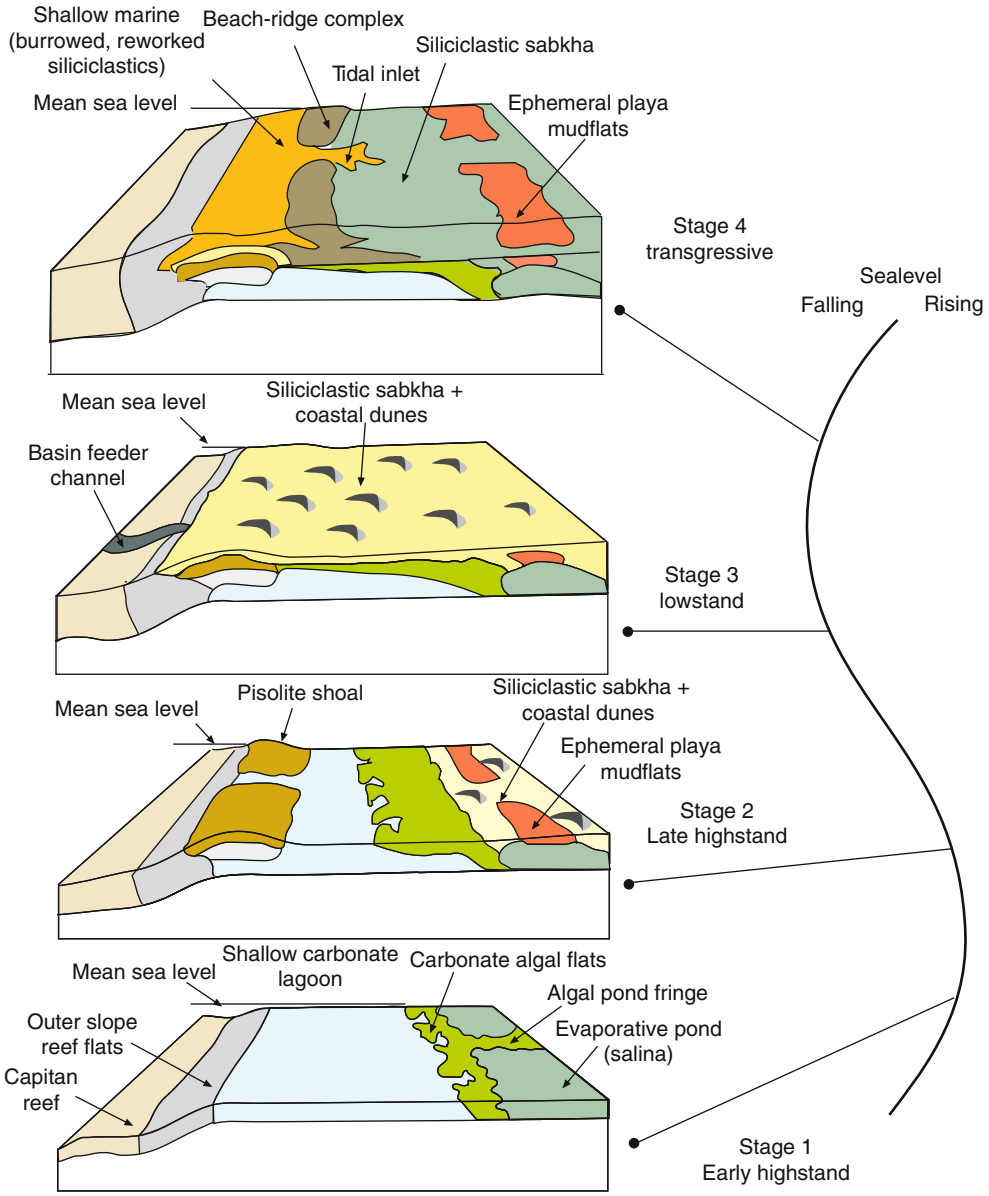

Fig. 10.48 Evolution of Yates Shelf (After Andreason 1992). Early highstand (Stage 1) is characterised by shelf submergence, lagoonal carbonate deposition across the middle shelf and massive evaporites precipitating in embayments and isolated ponds on the inner shelf. As the shelf becomes more emergent during late highstand (stage 2), broad tidal flats extend across the middle shelf and the pisolitic shelf crest becomes re-established. Eolian driven siliciclastics bypass the shelf during lowstand (Stage 3) and deposit within the Delaware Basin, As sealevel rises during the transgressive phase (Stage 4), beach-ridge complexes and siliciclastic sabkhas accrete and prograde in response to a rising watertable. This is the phase when most of the siliciclastic Yates reservoirs were deposited

It was a depositional setting much like the modern coastal zone for southeast Qatar and eastern Saudi Arabia (Figs. 2.59 and 3.64), but in a coastal strandzone under greenhouse, not icehouse, eustatic control. Throughout the late Guadalupian, the Midland Basin was a site of siliciclastic, anhydrite, and halite deposition within eolian, evaporative mudflat, and playa environments (Ward et al. 1986). In addition, the advancement of a siliciclastic wedge within the upper Seven Rivers Formation from the northeast onto the Central Basin Platform supports the possibility of siliciclastics migrating across the Midland Basin by the close of Seven Rivers deposition. Palaeogeographic reconstructions by Handford (1981b) place prevailing winds from the northeast, off the Central Basin Platform. These eolian systems prograded across the Yates Shelf during periods of relative sea level fall and subaerial exposure of the shelf (Fig. 10.48).

What is most important in terms of exploration and development models based on this evaporite-sealed siliciclastic setting is that the thickening and stacking of the better quality reservoir sandstones was controlled by an aggrading marine fed saline watertable at the edge of an aggrading pisolitic shoal. Accommodation space for the sands was created by the syndepositional dissolution of a saltern edge along the seaward side of what is now a zone of stacked thick anhydrite beds. The generation of accommodation space for thicker better quality quartzose sands was diagenetically not depositionally controlled. The resulting thickened intervals of higher quality quartzose reservoir sands were then sealed by bedded saltern anhydrites of the Tansill Formation.

Rotliegende Sands of Northern Netherlands and North Sea

Rotliegende Formation sandstones in the southern North Sea are important Lower Permian gas reservoirs, with recoverable reserves of 4.25×10^{12} m^3 (150 tcf; Fig. 10.49a; Glennie 1990; Sweet 1999), they also host much of the onshore gas of the Netherlands and NE Germany including the giant Groningen gas field in the Netherlands. Rotliegende reservoirs in the Netherlands are mostly sandstones and conglomerates deposited in an arid alluvial to marginal desert sand/mudflat and fluvial environments. They are intercalated with shales and evaporites deposited in saline lake/playa settings (Legler et al. 2011; Figs. 10.49b and 10.50a). The northward transport of metamorphic, volcanic, and sedimentary rocks shed from Variscan highlands supplied most of the siliciclastics. In the Netherlands, reservoir quality was significantly affected by early diagenetic processes in a marginal desert/playa lake environment (Figs. 10.49b and 10.50a, b; Amthor and Okkerman 1998).

Further offshore in the southern Zechstein Basin, burial-related products and processes are perhaps more significant and have received more attention than early diagenetic processes as controls on reservoir quality (Figs. 7.99 and 7.100). According to Amthor and Okkerman (op. cit.) previous studies of burial anhydrite cements have largely neglected the effects that early diagenesis can have on reservoir quality and well productivity of Rotliegende sandstones. They argue that much of the precipitation of the main porosity-occluding cements (dolomite, anhydrite, and quartz) occurred early, not late, in the diagenetic history of the Rotliegende reservoirs of the Northern Netherlands and was tied to variations in the syndepositional hydrology. Oxygen isotope values of dolomite cements ($\delta^{18}O_{SMOW} = 18.4–23.4‰$) suggest that meteoric water played a major role throughout the diagenetic history (Fig. 10.50c), and that precipitation of the cements occurred at low temperatures (<80 °C) characteristic of a desert and shallow burial. The strontium isotopes of dolomite cements ($^{87}Sr/^{86}Sr = 0.70935–0.71387$) and the sulphur isotopes of anhydrite cements ($\delta^{34}S_{CDT} = 6.7–9.7‰$) are consistent with formation from continental water within a

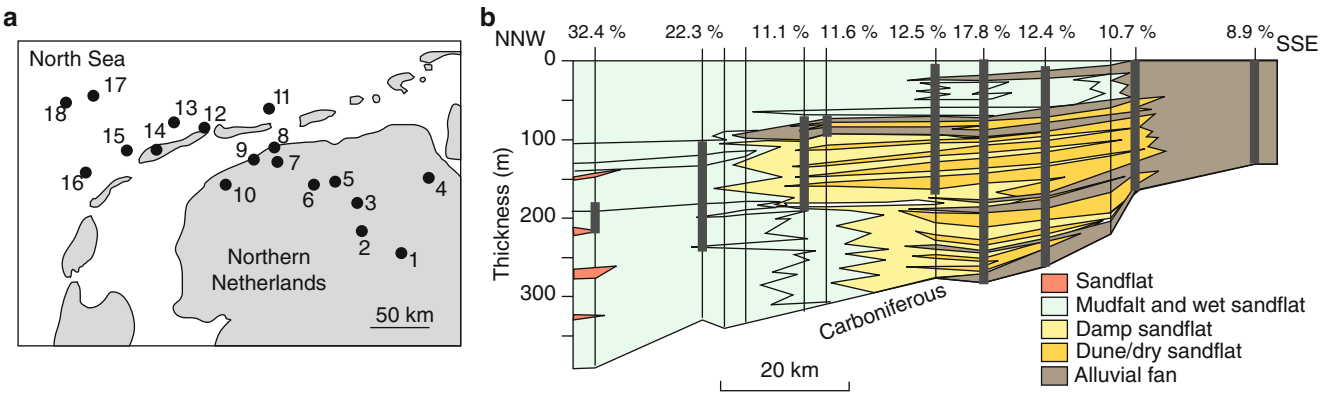

Fig. 10.49 Characterisation of Rotliegende Sand reservoirs (After Amthor and Okkerman 1998). (**a**) Well locations in Northern Nederlands and North Sea. (**b**) Cross section (perpendicular to depositional strike) of the Rotliegende Sand (Slochteren Sandstone) showing the major depositional environments. The average abundance of dolomite and anhydrite (total indicated in percent) increases in a NNE direction from the proximal alluvial fan and dunes/dry sand flat to the distal desert lake (saline pan and mudflat) environments

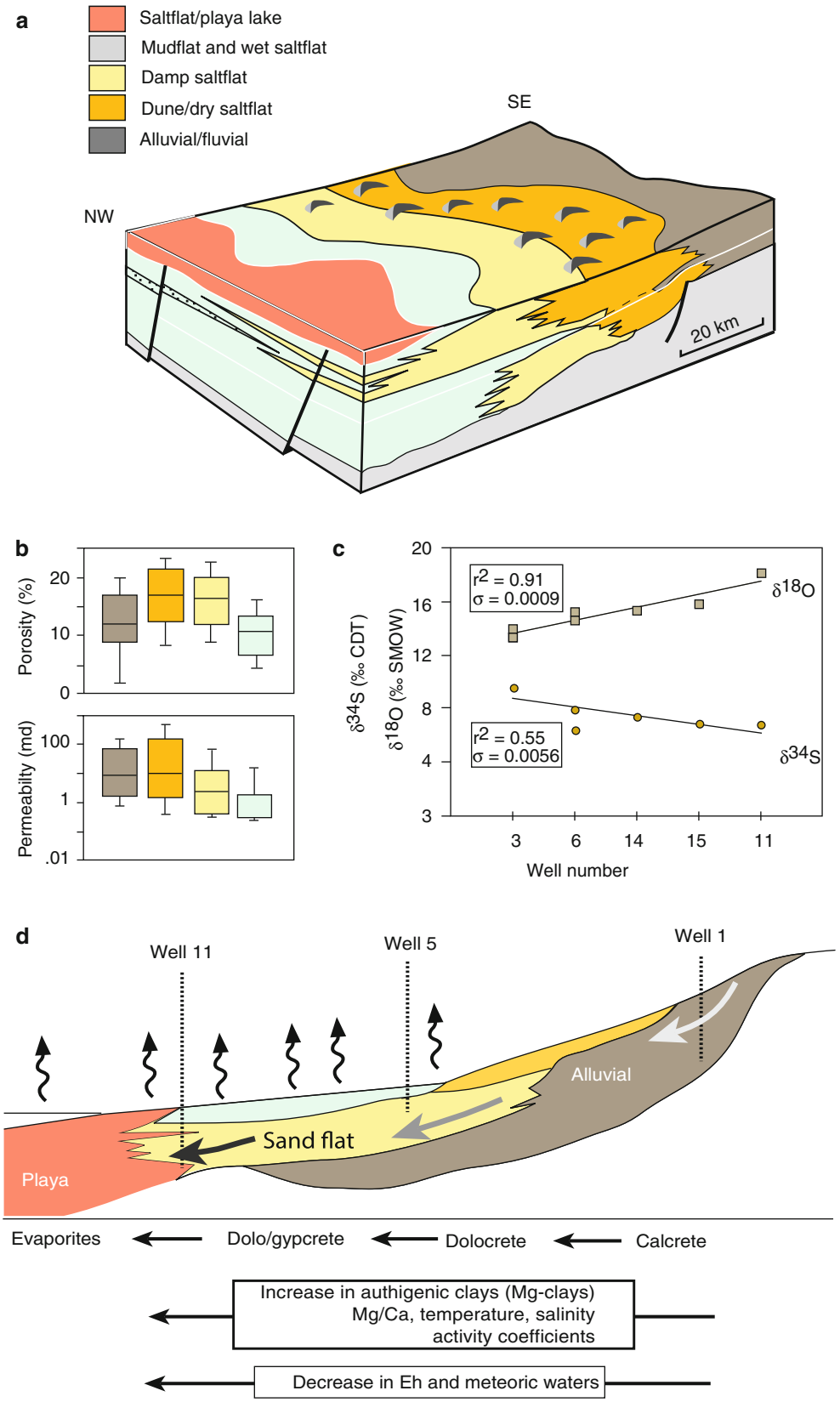

Fig. 10.50 Rotliegende of Northern Netherlands (After Amthor and Okkerman 1998). (**a**) Depositional setting. (**b**) Distribution of porosity and permeability, indicating a relationship between depositional environment, early diagenesis, and reservoir quality. (**c**) $\delta^{34}S$ and $\delta^{18}O$ of anhydrite cements relative to geographic well position; oxygen isotopic compositions increase progressively from proximal to distal wells, whereas the sulphur isotopic compositions decrease. Such depletion in $\delta^{34}S$ and concomitant enrichment in $\delta^{18}O$ is the result of progressive evaporation in an arid alluvial to marginal desert-sabkha Rotliegende depositional setting. (**d**) Conceptual model of groundwater evolution and its precipitates across an alluvial to sand flat/playa profile with the likely positions of three Rotliegende wells from Fig. 10.49a indicated

restricted basin and rule out Permian or younger seawater seeps as a source for these cements.

The early diagenetic origin of the cements is also suggested by the fact that the majority of sandstone samples have lost more porosity via cementation than through compaction. Most samples with high amounts of porosity loss via cementation (20 %) were affected by early dolomite and anhydrite cements (Fig. 10.49b). The relative abundance of dolomite and anhydrite cements can be correlated with depositional environment. Wet depositional environments with watertables close to the surface (interdune and fluvial sandstones) show the highest amount of dolomite and anhydrite cements, whereas dry environments with relatively deep watertables (e.g., dune sandstones) are characterized by low amounts of cements (Fig. 10.50d). The precipitation of early diagenetic cements has strongly influenced the present day porosity patterns in the reservoir, with depositional environments interpreted as depositionally "drier" showing less cements. Early capillary and vadose precipitation of cements significantly altered the porosity patterns in the sandstones and playa mudstones. In effect, the intensity of subsequent cementation in this system largely tracks the palaeohydrology of the depositional setting.

A similar set of syndepositional palaeohydrological factors controls subsequent reservoir quality in the Carboniferous eolian sabkha reservoir sands in the anhydritic Juruá Formation in the Solimões Basin (Elias et al. 2004). This is the largest gas sand reservoir in Brazil.

Exploration Paradigms in the Bedded Evaporite Hydrocarbon Association

Bedded evaporite seals encompass both platform and basinwide settings (Fig. 10.51). Within both subsalt setting dolomitisation and other diagenetic alteration features are important controls on reservoir creation and retention in most scenarios, even in the largest accumulations such as the Arab cycles in Ghawar, Saudi Arabia. Understanding the timing and relative importance of seal focused brine reflux and later hydrothermal circulation or recirculation is important. In subsalt and salt-adjacent settings, the resulting intercrystalline poroperm geometries are superimposed on pre-existing depositional facies. Tying the dolomite distribution back to the salt/brine source means the poroperm distribution is understandable at both the exploration and reservoir scale (Fig. 10.51). The effects of evaporite brine derived fluids can be early, as in brine reflux settings, or much later, as in hydrothermal- burial dolomite settings, as in the various Devonian carbonate hosted gas field of British Columbia. Reflux dolomitisation can convert low permeability mudstones into reservoir quality intervals, as in the Levelland Slaughter trend, or alter reservoir properties in the original depositional system to enhance, alter or destroy reservoir poroperm. Multiple dolomite-related poroperm changes can occur even in a single field, related to superposition of different episodes and styles of dolomitisation (Warren 2000a), as in Ghawar, Saudi Arabia.

Another typical result of intense reflux is salt plugging (usually anhydrite cements) immediately below or adjacent to the brine source. In this case the poroperm is enhanced not in the immediate vicinity of the salt bed but at some distance further out along the brineflow pathway (Levelland-Slaughter and Feixianguan fields). In other cases, formerly porous reef fringe sediments can have porosity completely plugged by the entry of salt saturated brines. This is the case with downdip pinnacles in the Michigan basin. There, a reservoir fairway was created in up dip pinnacles by ongoing marine-seep flushing. In such a scenario, the presence of seepage indicators in a pinnacle fringe facies can be a useful indication of which pinnacles remain open hydrological conduits during evaporative drawdown episodes (Fig. 10.51).

Regionally, preservation and prediction of both primary and secondary porosity in bedded evaporite-sealed reservoirs is controlled in large part by varying combinations of the following factors. (1) A relatively arid climate, which means a relatively limited recharge of fresh groundwater during the evaporite drawdown stage, thus minimizing meteoric leaching and calcite cementation. (2) The presence of an extensive cap or lateral facies made up of impermeable saltern and mudflat dolomite and anhydrite. This bedded evaporite and associated cement plugging effectively seals off large parts of the underlying permeable carbonate from ongoing early phreatic cementation as it slows or stops surface-groundwater driven flushing by large volumes of meteoric or sulphate-bearing fluids. (3) Early marine cementation and hypersaline reflux dolomitisation, which strengthens the reservoir rock framework below the evaporite seal, thus retarding physical compaction and making it more likely to fracture. (4) The presence of thick evaporites atop carbonates tends to form pressurised buffer zones below the salt seal. Hence, a thick evaporite retards mechanical compaction in sediments beneath it via the early onset of overpressure, it also prevents an influx of surface-derived cementing waters into the carbonate reservoir.

This generalised listing of controls has been in the literature for two decades (e.g. Sun and Esteban 1994; Warren 1989) and helps explain the evaporite-hydrocarbon association mentioned at the start of this chapter. Yet, the bedded evaporite-hydrocarbon association has been poorly understood by exploration and development teams designing exploration or development programs in bedded evaporite-sealed systems, and has led to some expensive errors and remediation programs. To create a predictive understanding of reservoir quality beneath bedded evaporite seals is more difficult as it requires knowledge of evaporite texture, likely fluid migration pathways, and the ability to understand and construct models of seal-related diagenesis in the potential

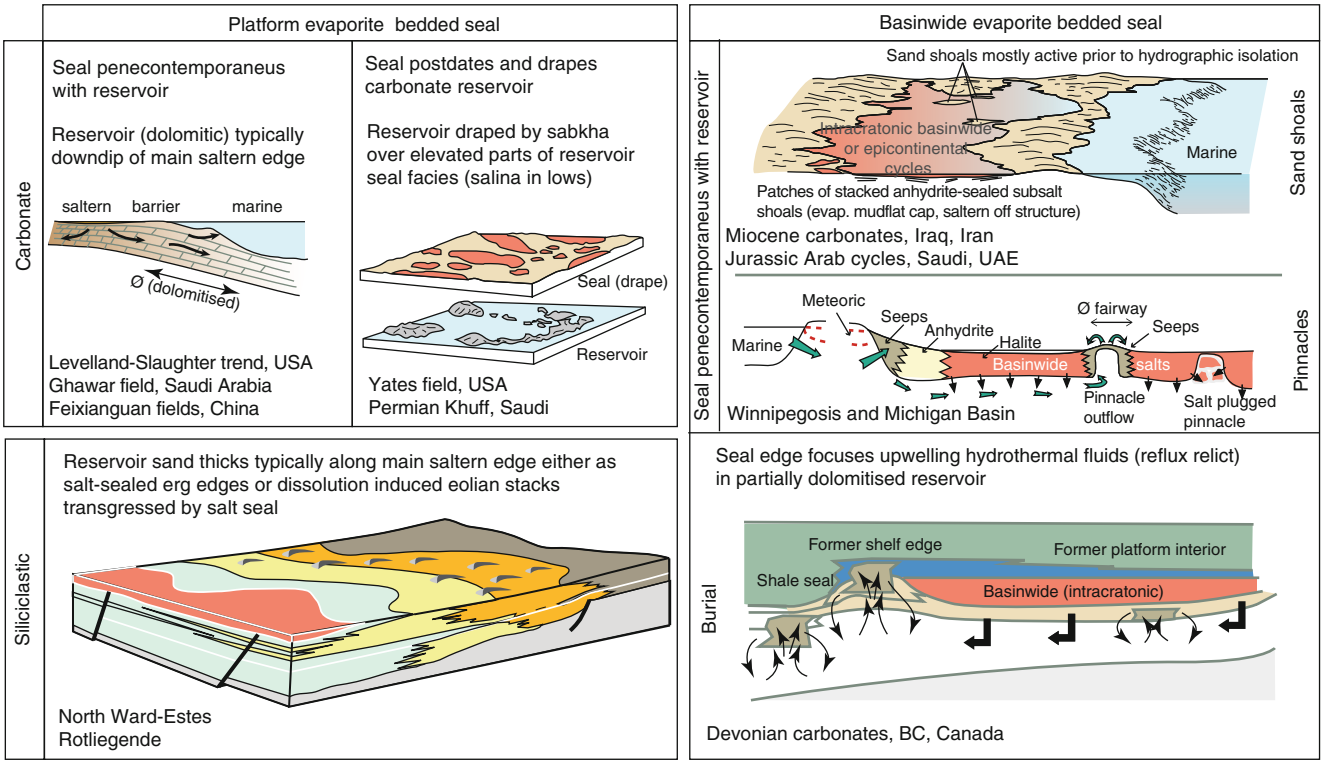

Fig. 10.51 Summary of the various ancient platform and basinwide bedded evaporite settings where a combination of evaporite sealing, dolomitisation (both early and lake) and focused evaporite related fluid flow create a variety of hydrocarbon traps. See also Table 10.7

reservoir carbonates below the bedded evaporite seal. What follows is a listing of some of the pertinent observations I use to understand poroperm distribution in subsalt and salt-adjacent bedded evaporite association (Table 10.7).

Importance of Recognising Depositional Differences

Our discussion so far has demonstrated how bedded evaporites constitute the seal to many of the world's largest oil and gas accumulations (Fig. 10.1). Without exception, the largest of the various oil and gas fields sealed by bedded evaporites are subsalt and mostly hosted in partially dolomitised marine platform carbonates. In most giant and supergiant fields the evaporites not only hold back the hydrocarbon column, but also help create and maintain reservoir quality. The most impressive examples are the various Arab D reservoirs in the Middle East, with slightly smaller but still very significant accumulations in oil pools in San Andres Formation of West Texas and reservoirs in the Sichuan Basin of China. In all these examples the depositional porosity of the reservoir has been altered and variably enhanced by brine-related allochem leaching and early reflux-driven dolomitisation. The degree of meteoric overprint at this early burial stage of diagenesis is minor to nonexistent. Syndepositional edge-of-evaporite dissolution from seawater freshening can occur and it leads to substantial thickening of high quality groundwater-controlled eolian depopods, as in the billion barrel North Ward-Estes Field (Table 10.7). Deeply circulating regional meteoric influx driven by a lateral groundwater head, mixing with brines of the reflux plume, can also occur create or alter poroperm distributions below evaporite seals and so influence reservoir quality, as in the Smackover Formation reservoirs of the Gulf of Mexico.

In my experience, most variation in subevaporite reservoir quality is the end product of a combination of depositional facies and varying intensities of evaporite plugging, dissolution, reflux dolomitisation and burial stage cementation. Lateral and vertical variations in all but the latter are typically indicated by facies variations in the seal itself. Yet, for much of the oil industry, evaporite plugging and reflux dolomitisation are associations that geological and geophysical staff do not quantitatively integrate into a reservoir model (other than via loosely controlled geostatistical formulations). The relevance of a bedded evaporite at any scale, beyond the consideration of its seal integrity in exploration or field development, is not part of most reservoir evaluation studies (The typical question to be asked and answered of the evaporite seal in a petroleum system is; Is it thick enough? Typical magic numbers worldwide for answering yes are; greater that 10 m thick for a clean anhydrite seal, and greater than 5–10 m thick for halite). Once the integrity of an evaporite seal or cap to a potential reservoir is considered established, further study of the seal properties or intra-seal textures is not considered relevant, other than hoping

Table 10.7 Identification and prediction of features associated with bedded evaporites that are useful in helping define distribution of subsalt or salt adjacent reservoirs Refer also to Fig. 10.51

	Feature	Outcome	Recognising in the subsurface
Platform evaporite	Anhydrite is the dominant seal mineralogy	Immediate subsalt region is typically evaporite plugged Depositional facies variations in subseal facies may be indicated by textures in the seal itself	Require understanding of variations of intrasalt wireline signatures (gamma-neutron-density FMI or acoustic image logs) sabkha versus salina in seal?
	Reflux dolomitisation in subsalt and salt-adjacent positions	Best reservoir is typically located downdip and basinward of thickest saltern interval Hydrodynamics define stepout distance from saltern edge to likely economic reservoir poroperm	Resolve whether the current salt edge indicates the primary position, or is the result of salt dissolution. Reliably recognise signatures of marine flooding, subaerial exposure and salt dissolution horizons (core tied to gamma-neutron-density, FMI and acoustic image logs)
Basinwide evaporite	Halite is the dominant seal mineralogy	Anhydrite proportions typically higher in intracratonic settings and/or atop former subsalt highs	Require understanding of variations of intrasalt wireline signatures (gamma-neutron-density FMI or acoustic image logs)
	Diagenetic overprints can control poroperm distribution (stable isotope and trace element values are useful discriminants of fluid source)	Non-intracratonic salt systems tend toward halokinesis	Halokinetic reservoir associations are discussed later in chapter
		Shelf edge with buildups: Shelf edge is typically exposed during episodes of evaporative drawdown, and may be karstified	Definable patterns of drawdown-induced seepage fringe outflow and associated alteration in basinal sediments
		Downdip pinnacle reefs: Crests acting as seep outflows during drawdown	Indicated by reef fringe cap facies made up of seep indicators, such as pisolites and tepees
		Problems related to salt plugging of reef further out in basin	Circum-basin poroperm fairway can be defined by combination of wireline and seismic mapping of basin architecture
Common features of note in both platform and basinwide settings			
Intrabasin deposition	Thick evaporite beds require stable long term aridity	Typically meteoric effects are minor in most parts of drawndown part of basin during time the evaporite seal is precipitated	Meteoric waters can be derived updip via deep meteoric circulation and outflow occurs in particular circum salt or salt-adjacent positions (stable isotope and trace element values are useful discriminants)
Dissolution is ongoing	Exposure surfaces	Penecontemporaneous local intrabed dissolution can occur during short term freshening via increased marine or meteoric seepage (recognition of intra salt leachate styles)	Stable isotope and trace element values are useful discriminants using core or cuttings. If regional, can be inferred by anomalies in wireline or seismic
	Early burial	Brine reflux	Identified by subsalt dolomite intensity map – wireline derived tied to basin architecture
	Later burial	Hydrothermal brine crossflow alters poroperm distribution	Occurs in particular positions in basin architecture (fault, fracture and folding controls), typically salt adjacent, but can be subsalt
	Edge effects (Mesogenetic focus)	Presalt can create karst overprint in subsalt reservoir facies	Defined by combination of core study, wireline and seismic mapping of basin architecture
		Synsalt, can created zones of non salt sediment thicks (e.g. increased thickness in fluvial sediments or eolian sandflats)	
		Post salt, act as escape conduits for subsalt basinal fluids can be carrying hydrocarbons and/or metals	
	Uplift (Telogenetic focus)	Dissolution reservoir associations are discussed later in chapter	
Confusion between dissolution residue layers and marine flooding surfaces (different diagenetic associations)		Ambiguity can lead to errors in basin history, diagenetic history, maturation timing, etc	Distinction requires core, or wireline tied to seismic, or core-calibrated FMI interpretation.

for, or establishing, its lateral persistence. Rather, subsequent study and measurement focuses on the properties of the reservoir itself, the seal is rarely cored and, if it is, this is usually the result of an error in picking depth to top reservoir.

Attempting to better understand diagenetic intensity in the reservoir using signatures from wireline tool measurements taken across the seal intersection is typically considered too difficult, or the possibility is not even understood. Yet, as any carbonate geologist will testify, diagenesis is what distinguishes properties in any carbonate reservoir from those in a sandstone (Ahr 2008). Pervasive, but variable, diagenetic intensity is what controls carbonate reservoir quality in every bedded evaporite-sealed petroleum system worldwide. Almost all of the matrix quality in the world's giant and supergiant bedded evaporite-sealed carbonate fields was established during deposition and early burial. This is when surface topography controls intensity of circulation in the diagenetic hydrology (Table 10.7). Resultant poroperm plumbing can be locally enhanced by later fracture development and perhaps the formation of coarsely crystalline saddle dolomites (typically fed by fractures and faults). In petroleum systems exemplified by the examples of Yates and North Ward-Estes fields, reservoir quality is predictably tied to the style and position of the early evaporite hydrology and is indicated by evaporite textures in the seal. The same approach is also useful in other reflux-dominated carbonate reservoirs, as in the Arab and Khuff formations in the Middle East.

Much more reliable seal prediction and modelling (both seismic and reservoir scale study) is done by the oil industry in sandstone-shale associations than in carbonate-evaporite systems. Our understanding of reservoir problems in a carbonate reservoir is more often post-mortem than predictive. More reliable maps of anhydrite plugging at the reservoir level and flow unit correlations for waterfloods in carbonates are sorely needed. In bedded evaporite-sealed systems this requires the integration of field-scale maps of seal facies with maps of reservoir properties in intervals below the seal. This is not currently done by most oil companies. Worldwide the focus of the map of lateral and vertical rock property variation is in the reservoir itself and it is almost never related to variation in seal facies. Yet wireline property variation in the evaporite seal is easily done. There is no complication of the wireline signature by porosity or fluid variation. That is, evaporite seals are tight, they lack porosity and fluid content, so what is seen in a wireline signature in an evaporite seal intersection is directly related to style and purity of the evaporite and these properties are directly relatable to deposition style (Chap. 5).

The first step is the construction of a map of the facies mosaic preserved in the seal, using wireline-based core-calibrated image and conventional logs. At the local scale such a map uses separation of sabkha from salina signatures, at the broader scale it uses wireline-based separations of evaporitic mudflat from saltern. Next a field-wide map of reservoir quality is constructed or existing maps of quality can be checked by recalibration to existing core and wireline/image data (in a producing field this data is available at varying degrees of reliability). The fieldwide facies mosaic map derived from the seal is then overlain on the fieldwide map of reservoir quality and production data. A match or mismatch of the two outputs tests whether the early burial hydrology and associated palaeotopography has controlled much of the reservoir leaching/dolomitisation and anhydrite plugging.

These maps can then be used to better define untested reservoir zones. With a depositional seal, rather than a drape seal, the better quality reservoir sweetspots are typically below mudflat seals (Fig. 10.51). If the evaporite seals across stacked platform cycles are sufficiently thick and possess sufficient impedance contrast, then a seismic facies map can be constructed over the area of interest and be used to better identify potential sweetspots and other directional drilling targets in the field. This approach of integrating evaporite signatures into maps of reservoir properties is especially useful in carbonates beneath epeiric platform anhydrite beds in systems that have not been substantially overprinted by later stage burial alteration or halokinesis.

But, porosity/permeability in any evaporite-sealed system continues to evolve to varying degrees, long after the reservoir has subsided into the mesogenetic realm and early evaporite plugging (via brine reflux) of the subsalt interval has ceased. In some fields the burial overprints are significant and can control reservoir quality, in others they do not. Porosity evolution in the mesogenetic realm is typically driven by focused vertical and lateral flow of ascending basinal brines. Close to their feeders, these waters pervade permeable intervals below the evaporite seal and so overprint the platform carbonate/dolomite to varying degrees, especially atop zones where active faults and fractures cut the reservoir but do not penetrate the evaporite seal. In more diagenetically mature fields, such as the Keg River pools in the western Rainbow-Zama sub-basin, much of the lateral variation in reservoir quality is tied to burial stage leaching of anhydrite cements, the precipitation of saddle and zebra dolomite, and the formation of coarse, patchy but connected, intercrystalline burial-stage porosity (Fig. 10.51; Table 10.7). Now the reservoir-altering fluids are fed by ascending brines rising along faults and fractures, these structures are sometimes visible in seismic and this association can be used as an exploration tool. Zones of most intense alteration tend to occur in haloes around the fault or in zones immediately below the evaporite seal and sometimes the drilling target is a narrow zone at the base of a synclinal trough (as in Scipio Albion trend, Michigan Basin). Convincing management to drill a syncline is not an easy task!

In more diagenetically mature portions of a basin, these fault-focused ascending basinal waters can carry high levels of metals and can form MVT deposits via thermochemical sulphate reduction (as in the growth fault-fed accumulations of lead and zinc in the Devonian Platform of the northern edge of the Canning Basin, Australia). In such stratiform MVT deposits the evaporites are typically long gone and all that indicates their former presence are laminar beds of metal sulphides with their coarsely crystalline dolomite gangue (Chap. 15). Even in less diagenetically mature supergiant oil and gas fields, where relict depositional porosity is the dominant control over reservoir quality and reservoir topography can be defined in the wireline signature of the seal, the early stages of overprint from ascending basin fluids will have locally altered reservoir quality, especially in the vicinity of active faults and fractures (as in the Arab D reservoir in the 150 billion barrel-plus Ghawar Field of Saudi Arabia).

Importance of Recognising Bed Dissolution

Listings of controls of permeability in evaporite-sealed systems, such as that by Sun and Esteban (1994), also underline another problem with many current field-scale geological studies of reservoir quality controls in evaporitic successions. Such studies, even where core is available, have typically not considered the likely presence in many evaporitic platform reservoirs of thin horizons that once were much thicker sequences of bedded evaporite. Yet bedded evaporites are highly soluble both at the surface and in the subsurface (Chaps. 1 and 7), their residues are widespread and they can create regional markers easily misidentified in wireline as a correlatable well-to-well flooding surface (Table 10.7).

Carbonate reservoirs worldwide are made up of stacks of platform cycles or parasequences, some with and some without evaporitic capstones. When they were deposited, evaporite capstones in both ramp and shelf settings typically mark the tops of zones of shoaling and perhaps cleaning-upward carbonate parasequences situated in a zone of hydrographic isolation behind some sort of grain shoal. Associated reflux brines were often responsible for formation of stratiform reflux dolomites in the carbonates below, along with variable levels of intergranular anhydrite cement that plug the upper portions of the carbonate cycle. Sometimes the evaporite capstones are absent because they were never deposited, other times the evaporitic capstones to these parasequences have been leached, along with the evaporite plugging cements in the underlying reservoir intervals.

Post-dissolution, all that may be left of a former bedded saltern evaporite is 5–50 cm thick stratiform layer of fines, made up of insoluble residues that once were dispersed in the evaporite bed (eolian silts, clays and dolomite rhombs). The overlying succession often shows a characteristic vertical transition of mosaic to crackle breccia or into a zone of syn-depositional solution collapse. Leaching of former anhydrite cements from intergranular positions in the carbonates below the residuum layer can create a high permeability interval below the residuum layer, while suprasalt fractures can poroperm in this zone (see later in this chapter). Sometimes beds on either side of the dissolution residue layer may retain nodules of chert, baryte with minor relict anhydrite. The nodules, when present tend to be dispersed as a band on either side of the residuum layer. Using cores and FMI imagery, the associated breccias, sharp bases, crackled and fractured tops, along with slumps into karstic accommodation space created by salt dissolution can be used to define the former positions of these now dissolved parasequence tops.

Unfortunately, many practising geologists in the oil industry are well versed in sequence stratigraphic principles, but not accustomed to thinking and interpreting stratiform surfaces from well to well, other than as a depositional interface or perhaps as a marine or subaerial exposure surface. When they see residual horizons in core and an associated clast-to clast breccia they tend to interpret it as either a storm bed or as zones of seafloor disturbance and starved sedimentation "formed at a time immediately prior to the creation of a maximum flooding surface." These layers of dissolution residuals are often clay rich and radiogenic and so show up as spikes on the gamma log through the carbonate platform. If the now dissolved bed was previously associated with an underlying zone of anhydrite cement, then dissolution of this anhydrite can create a zone of high permeability in the interval below the gamma kick (Table 10.7).

Without core or core calibrated image-log control, intervals with such high gamma signatures can be easily misidentified as thin shales or mudstones that define flooding surfaces along the muddy base of the next parasequence cycle. Widespread gamma kicks in a carbonate reservoir can then be miscorrelated well-to-well as depositional surfaces beneath low permeability muddy carbonates at the base of the next shoaling cycle. They are then tied from well to well and used to define regional flooding surfaces. These are in turn used as intra-reservoir well-to-well markers to zone up the reservoir into flow units across a field. This misidentification is especially common in correlation studies done in thick carbonate sequences, largely lacking any other markers, and where the team conducting a reservoir zoning study uses a sequence stratigraphic framework for correlation and quality prediction between wells. This leads to poorly understood zones of fluid leakage or influx across flooding surfaces within in the reservoir model. Diagenetic alteration features tied to former salt levels are not mapped by a evaporite residuum unaware reservoir model. As discussed in Chap. 5 most sequence stratigraphic and seismic studies currently conducted in carbonate terrains do not deal well with the "comings and goings" of subsurface evaporite beds.

Such inappropriate interpretations are not too much of a problem when the reservoir is in the early stages of primary

production, or if the field is a single-phase gas field. But they become problematic when the same layer-cake reservoir model is utilised in developing notions of linked flow units via what are considered viable well to well correlations. In the more mature stages of planning of field development it is very important to reconsider any laterally continuous zone in the field, especially if defined by a gamma kick atop or within what is often a dolomitised or high porosity level. It should be redefined for what it is based on its signature in core or a core-calibrated image log and not assumed that it is always indicative of some sort of correlative well-to-well maximum flooding surface.

Gamma kicks in wirelines taken through anhydritic evaporite platform carbonates do not necessarily indicate depositional shale/micrite. Rather, if it is indicating a solution residuum layer, then depending on how and when it formed and how the overlying section was let down during dissolution, some of these stratiform residuum horizons may indicate a set of formative processes that have created widespread crosscutting extensional fractures and microfractures in the overburden. In other words, the question should be asked; did undersaturated water access the dissolving evaporite from the side, top or base of the former evaporite bed? – as discussed in Chap. 7. Thus gamma kicks associated with an evaporite residuum can be associated with laterally extensive zones of higher fracture permeability above or below the marker. If the creation of the residuum layer was tied to the dissolution of former anhydrite cements in the underlying carbonates then high permeability occurs below the marker. If the formation of the residuum was created by lateral solution loss, then solution induced fracturing can occur across a retreating front in the layer above. In either case there is the distinct possibility that adjacent high flow units are joined by dissolution induced vertical fractures.

Such a misidentified system becomes more problematic once production induces an oil–water interface rise. Water then penetrates unexpectedly into what were projected to be longterm productive intervals separated by "shales" based on depositional assumptions of well-to-well marker or flooding surface correlations. Unrecognised high-permeability vertically-linked zones will drastically reduce sweep efficiencies when production planning of a waterflood continues to evolve based on inappropriate correlations of intra-reservoir permeability. There will be early and unexpected water breakthroughs during the waterflood. Depositional marker-based models do not account for likely vertical fluid transfer via cross fractures that developed at the time of evaporite dissolution. Nor does a sequence-stratigraphic-focused team tend to consider the possibility that likely zones of highly interconnected permeability can be formed by the leaching of former anhydrite or even halite cements in the grainy interval below the now dissolved evaporite unit (e.g. some very high permeability intervals that cut across depositional facies in the carbonate host).

But the reality is that most reservoir models for waterfloods and longterm production must be constructed over large areas of a producing field where closely spaced core to wireline calibrations are not available. The two end-member modes of marker occurrence (dissolution residue versus marine shale) can sometimes be separated using a high-resolution conventional wireline tool, such as the MFSL, or better yet an image log. Many residue horizons are systematically associated with a halo of anhydrite or chert nodules on either side of the gamma kick, flooding surfaces typically are not, and marine chert nodules, if present, tend to occur within the marker and not above. Clearly, any wireline-based definition of a dissolution surface can be complicated by the development of patchy high density, high resistivity carbonate cements. In this situation wireline separation of the two styles of picks is best done by an interpreter with an detailed understanding of the significance of evaporite cements in the reservoir and who is using a core-calibrated set of wireline and image log signatures, rather than just conventional log shapes for correlation (Table 10.7).

Changing Directions of Brine Flux in an Evaporite Sealed System

At the regional scale, brine reflux flushing is most active in the early stages of evaporite deposition, when the evaporite beds retain porosity and permeability and concentrated Mg-rich brines sink from the overlying free brine pool, through the still permeable bedded evaporite (usually gypsum), and into the underlying sedimentary succession. Elliott and Warren (1989), Saller and Henderson (1998) and Lucia (1999) all point out that the downward cyclic transition from a relatively impervious overdolomitised and salt-plugged platform dolomite (typically with thick intercalated saltern and mudflat seals) into partially dolomitised subtidal platform carbonate reservoirs (with thinner seals) corresponds to a downward decrease in the flux of saturated reflux brines and an increase in dolomite crystal size. This corresponds to a downward decrease in dolomite saturation as the refluxing brines sink deeper and further from the brine source. Thus, better-quality reflux-enhanced platform reservoirs occur in structures not directly beneath the thicker accumulations of saltern salts, where salt plugging, overdolomitisation and mimetic dolomites tend to dominate. Better potential reservoirs tend to occur more toward the seaward margin of the thickest saltern accumulation where coarser dolomite, partial dolomitisation and thinner evaporites are found.

Long term salt plugging, tied to large crossflow volumes of saturated brine reflux waters, means that many hydrocarbon accumulations in reef pinnacles sealed by basinwide evaporites are typically smaller and less productive fields compared to their platform counterparts (e.g. the relatively

small volumes of hydrocarbons in salt-encased Silurian pinnacles of the Michigan Basin and the pinnacles of platform edge of the Rainbow-Zama sub-basin). A lack of widespread potential reservoir in the muddy deepwater setting that immediately predates most basinwide evaporite beds adds to the likelihood of smaller accumulations beneath basinwide salt seals, compared to platform settings. Even so, thick massive basinwide evaporites trap and preserve some of the geologically oldest oil and gas fields in the world (e.g. fields producing from platform carbonate slivers suspended in the Neoproterozoic Ara Salt of Oman). The situation is different when draping of epeirogenic regional highs are fed hydrocarbons beneath a salt seal. This is the case with some giant Miocene- Cretaceous hosted fields in Iraq and western Iran. There the continuity of intracratonic bedded salt seals constitute zones of lateral seal integrity and subsalt drainage feeds into what are low-quality reservoirs but capable of holding significant volumes of extractable oil and gas.

This is why Sun (1995) found porosity distribution in such variably dolomitised reservoirs associated with basinwide evaporites typically show no direct relationship to stratigraphic position or depositional trend. His conclusions emphasise the problems of reliable porosity prediction in a syndepositional hydrological system characterized by large autocyclic fluctuations in hydrologic base level (≈1 km) over time frames of thousands of years (Chap. 5). It also indicates the lack of differentiation of strandzone versus basin-centre reflux dolomites by most workers, yet both dolomite styles typify basinwide evaporite settings (Warren 2000b). Unlike the dolomites associated with platform evaporites, this group of basinwide reservoir seals cuts across both icehouse and greenhouse periods as basinwide evaporites require tectonics that are independent of sealevel character (Chap. 5).

An evaporite bed can only act as a seal once it has lost its intrinsic permeability. For a gypsum bed converting to anhydrite this happens somewhere in the first 500–1,000 m of burial, while for halite it can happen as shallow as a hundred metres below the landsurface. Until then, the permeable evaporite bed facilitates brine reflux, but once tight it only supplies brines to its surrounds via dissolution of its edges and focuses fluid flow along its underside. This transition in rock properties has an interesting effect on diagenesis and explains much of the later stage dolomitisation overprint on early reflux dolomites that are seen in many evaporite-sealed reservoirs (e.g. Canadian pinnacle reef traps and the dolomites of the Arab cycles in Saudi Arabia). As the evaporites were accumulating they flushed the underlying carbonates with dense sinking Mg-rich brines. Once buried and tight, the evaporite seal then prevents the free vertical escape of hot rising brines, which ponded in carbonates immediately below the slowly dissolving underside of the evaporite seal. The resulting chemical interface drives salting out of hydrocarbons, creates predictable zones of burial porosity, and drives the precipitation of authigenic or burial cements, including coarse sparry dolomite. It means most dolomitic reservoirs below an evaporite seal retain evidence of diagenesis first driven by descending reflux brines, which were created as the evaporite seal precipitated. Then later the same subsalt carbonate gathers a new diagenetic signature (of varying intensity) via the seal-focused flushing of hot ascending basinal brines moving along active subseal fractures.

Halokinetic Salt Traps

In many parts of the world, such as offshore Brazil, offshore west Africa, the North Sea and the Gulf of Mexico, a significant part of the association of evaporites with hydrocarbons can be tied to salt's ability to flow, and by its flow generate large and numerous structural and stratigraphic traps. As in bedded evaporites, emplacement of broad sheets of salt against more porous sediment greatly improves the efficiency of hydrocarbon drainage, both in terms of area drained and in tightness of the reservoir seal (Demaison and Huizinga 1991; Hindle 1997).

We saw in Chap. 6 how advances in 3D depth migration and computing power, still occurring today, have revolutionized subsalt and suprasalt hydrocarbon exploration. Only a decade or so ago, most seismic reflection information in halokinetic provinces was acquired as 2D data; today, most seismic data is acquired as 3D data volumes. A 3D cube provides a dense grid of subsurface information, which can be used to more accurately map salt body contacts and shapes. Older vintage seismic used mathematical models for conventional migration and processing, which assumed that the acoustic properties of subsurface sediments did not make abrupt lateral variations. This assumption obviously breaks down near salt flows; a solution required cheap computing power, more sophisticated depth migration techniques and denser data grids. Positioning of contacts in older vintage data can sometimes be improved using more recent processing algorithms and greater computing power, offering a cheaper but less accurate alternative to reshooting a grid.

By the late 1980s, the notion that salt flow could be a horizontal as well as a vertical emplacement process was increasingly accepted by the geological community. This new paradigm, along with increased computer processing speed, power and storage, opened up a whole new set of subsalt or more correctly suballochthon or salt tiered plays in the deep waters of the slope and rise in the circum-Atlantic salt basins and similar terranes elsewhere in the world. At the same time drilling technology was improving rapidly, along with geosteering capabilities and broader MWD logging tool suites. Each year wells are being spudded in progressively deeper water. For example, ultradeepwater exploration in Gulf of Mexico, in the decade through to the early millennium, has

found more than 3–4 billion BOE in nine major discoveries, in a hydrocarbon exploration province previously considered mature (Table 10.7; Enger and Logan 2001). But, before we discuss these increasingly exploited sub-allochthon traps we will look at the suprasalt trap, which was the classic exploration association in halokinetic regions prior to the 1980s.

Historic limitations in seismic resolution meant that, until the 1980s, exploration for suprasalt-related oil and gas traps was undertaken using salt models dominated by notions of subvertical thumb-like intrusives, fed salt by a direct connection to a mother salt bed below. Interpretations of the many producing salt structure peripheries in the onshore and shelf waters were biased toward this older notion of strongly vertical salt flows with salt pillows as the precursor to subvertical diapir stems. We now know that many nonpiercing pillow structures can be compressional features created during inversion or foot of slope gravity gliding (Fig. 6.67). Other pillows do form in response to depositional loading as a flow stage preceding the diapiric stage (Fig. 6.1). This is the classic model of Trusheim (1960) and based on his extensive work in the Zechstein salt structures of northern Germany. More recent work, even in this classic area, shows thumb-like geometries and associated assumptions of a connection to a more deeply buried mother salt bed are not necessarily correct (Mohr et al. 2004). Isolated rising blebs cut off from the source layer are more likely in the mature portions of many salt basins undergoing compression and inversion. This offers possibilities for future sub-salt flange sealing plays even in very mature regions of onshore and shelf exploration in the Gulf of Mexico and onshore Europe. But, such traps are likely to be small and discontinuous. Currently the possibility of drilling giant structures in the deep waters of the Gulf of Mexico and other circum-Atlantic salt basins are more appealing to exploration economics within large and mid-sized oil companies.

Supradiapiric Traps

Oil and gas reservoirs atop salt structures are as varied as the shapes and timings of the salt structures that caused them. Salt buoyancy means areas above shallow actively flowing salt structures are topographic highs, while the areas between are topographic lows Fluvio-deltaic, coastal, and submarine slope deposits are usually sand poor over the salt crest (Fig. 6.96). Most of the coarser-grained sediments in either setting is deposited in troughs as various types of channel fill and shoreface deposit, especially in landscape depressions atop zones of active salt withdrawal. In continental settings the pinchout of the high-porosity sand occurs along the flanks of a salt structure, usually well down-dip from the crest. Occasionally, reservoirs can form in the muddy crestal sediments in a continental setting due to diagenesis associated with subaerial exposure and/or unconformities. In arid coastal areas the crest could have been covered by evaporitic mudflats as environments tied to the development of early dolomite in pelleted mudstones with the associated formation of good intercrystalline porosity.

High-porosity sediments tend to form atop or immediately adjacent to a suprasalt crestal shoal in nonpiercement structures in shelf settings (Fig. 6.96). Boundstones, skeletal and oolitic grainstones, and well-winnowed siliciclastics are found on such highs. For example, studies by Mancini and Benson (1980) and Ahr and Palko (1981) of the Jurassic Smackover Formation reservoirs in southwest Alabama and Louisiana show that reservoirs often occur in oolitic-pisolitic grainstones located over salt pillow crests, while Montgomery et al. (1999a, b) describe hydrocarbon accumulations in numerous inboard Jurassic (Cotton Valley – Bossier) reefs atop salt pillows and diapirs in the East Texas Basin (Fig. 10.52). Similar Jurassic stromatolite and coral stromatoporoid reefs are found in the Smackover atop other salt pillows, such as the Walker Creek Field, Arkansas, in the Hico Knowles Field, Louisiana (Baria et al. 1982), and Hatters Pond in southwest Alabama. There the Smackover buildups are typically 3–40 m (10–130 ft) thick, commonly elongate, and several square kilometres in plan.

Reef rubble zones throughout the Smackover trend tend to have reservoir-quality porosity, but reef boundstones are economic only when extensively leached, dolomitised, and fractured. Such alteration can create commercial production from reef crests with mean porosities of 15 % and permeabilities of 20 md. Hatters Pond Field is typical of a field where the reef crest is tight and depositional facies crosscut the reservoir trend. The distribution of the reef was controlled by the position of the Jurassic high above a growing autochthonous salt pillow, while the trap was created during Cretaceous faulting associated with the structure's diapiric stage (Worrall and Warren 1986). The level of the reservoir dolomite lies well below the reef crest and above a dolomite unit characterised by post-hydrocarbon saddle dolomite. As in bedded evaporites, the initial porosity controls in carbonate reservoirs atop salt pillows and diapirs are often depositional, but are usually complicated by closures and diagenetic alteration haloes related to fault welds and subsequent fluid flow.

Siliciclastic examples of closure forming high capacity suprasalt reservoirs by sand-shale juxtaposition across clay-smeared extensional faults can be seen atop salt structure crests in the West Bay Field in Louisiana and the Heidelberg Field in Mississippi (Halbouty 1979). Bay Marchand – Caillou Island Field is a classic example of this style of fault-controlled suprasalt sand reservoir above the crest of salt structure (Figs. 8.35 and 10.53). The three diapirs that constitute the field structure are passive diapirs atop a salt wall feed. Under the new paradigms of flow that have been

developed since this structure was documented by Frey and Grimes (1970), it can now be seen to be the remnant of what was an active salt feeder system, with the current fault weld once acting as a salt wall feeding diapiric allochthons higher in the section. Most of the extension driving the faulting was a response to gravity gliding and salt deflation and not the active intrusion visualised in the original interpretation. The faults show radial, peripheral, or tangential patterns relative to the salt stock. Elsewhere in the Gulf of Mexico similar faults have downfaulted, uplifted, or overthrusted sands against impervious shales and multiple stacked reservoirs are stacked up against the fault (e.g. Bryan Salt Mound, Brazoria County, Texas).

Many of the numerous radial faults drawn in older interpretations of suprasalt traps (pre-1990), were published prior to the industry's recognition of salt's intrinsic lack of strength under tension. These interpretations tended to visualise faulting (mostly inferred rather than intersected) as a response to buoyancy and active salt intrusion. This is understandable as in most cases much of the salt that fed into an allochthon has long since dissolved or moved on to higher levels in the stratigraphy, via what are now deflated salt welds. In more recent interpretations of the same structures the faults are seen to be a response to salt withdrawal and to downbuilding in the adjacent sediments. High resolution seismic has shown that many of the inferred radial faults of older interpretations do

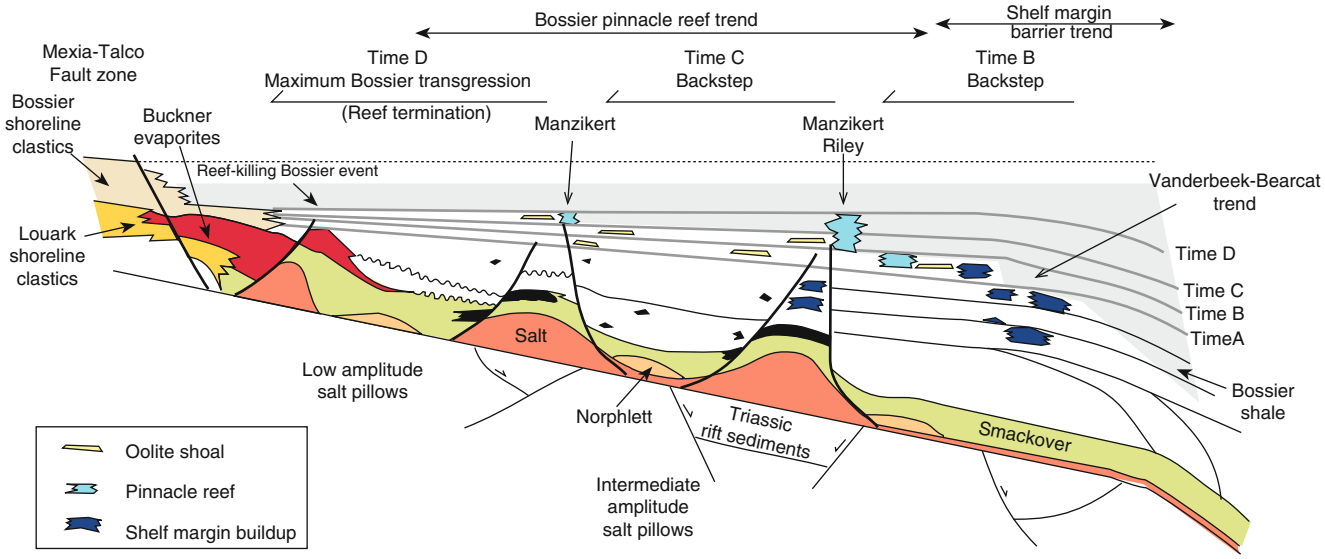

Fig. 10.52 Regional model of the development of outboard shelf/ramp margin buildups (structural control to shelf margin) and the "inboard" pinnacle reefs growing in seafloor shoals created by salt pillows in the Marquez Platform, East Texas Basin in Upper Cotton Valley to Lower Bossier time (After Montgomery et al. 1999a)

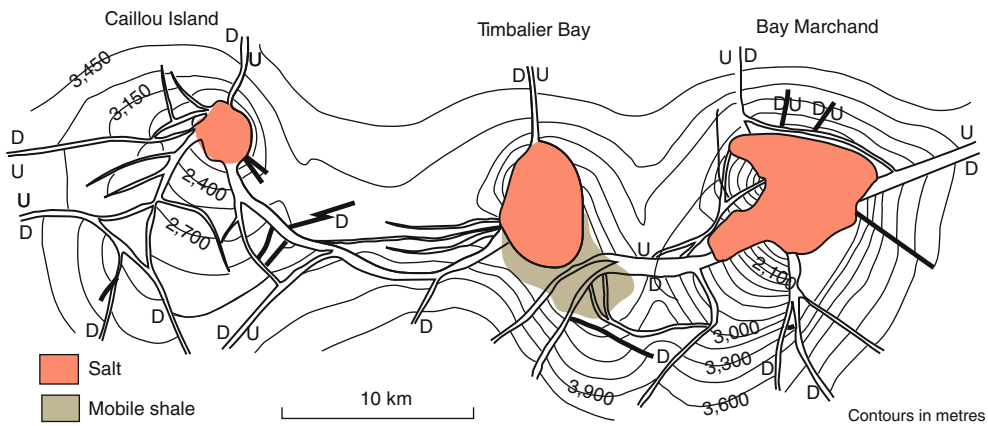

Fig. 10.53 Structure contours (in metres) on the productive Upper Miocene sand in the vicinity of the Bay Marchand – Timbalier Bay – Caillou Island diapirs, coastal Louisiana. Diapirs merge at depth into a salt wall and occur along a main extensional fault linking all three domes, each with its own association of radial faults (After Frey and Grimes 1970)

not exist. Such faults were inferred in order to explain discontinuities between sands in adjacent areas. In reality, many of these discontinuities, are more often a response to unconformities and depositional pinchouts rather than fault-outs, especially in flank traps.

For example, a reinterpretation of the Cote Blanche Field in Louisiana in the mid 1990s, based on newly acquired 3D seismic reduced the number of radial faults in the crest of the field to nine, compared to more than thirty in mid 1970s vintage 2D interpretations. However, radial faults do occur about salt structures and are largely a response to salt deflation during the passive stage of diapirism or are a response to later basin inversion and diapir squeezing. In halokinetic extensional terranes that have been subject to later compression, such as in parts of the North Sea, offshore UK and Norway, there many of the earlier radial faults are reactivated and have evolved into inversion structures (Fig. 6.81).

Syndepositional suprasalt traps occur in the sand-rich edges to withdrawal synclines, along with associated pinchouts onto the diapir crest (Fig. 10.54a). An example of this type of reservoir is the West Saratoga Field, Hardin County, Texas. There, multiple Yegua sand reservoirs shale out as they pass into the Saratoga Salt Dome (Galloway et al. 1983). The secondary peripheral sink continued to subside as the diapir grew (downbuilding), resulting in steep dips in the sand units as they shale out into the diapir stem (Fig. 10.54a) Subsequent loss of salt supply and cap rock formation may cause loss of salt volume and local collapse around the salt stem (Fig. 10.54b). Steeply dipping suprasalt reservoirs are characterized by stacked thick oil columns, which may approach 300 m (1,000 ft) where they pile one atop the other alongside the salt or a clay-smeared fault weld. Efficient gravity segregation aided by water influx results in high recovery efficiencies.

Grainstone shoals and reefs may rim the diapir or allochthon crest in carbonate shelf settings. With ongoing subsidence, these units tend to aggrade into a porous rim around the salt stem. A good example of this style of grainstone trap is the West Purt Field in the East Texas Basin, where the reservoir (Rodessa Limestone, Lower Cretaceous), is a fractured mollusc peloid grainstone and rudstone unit abutting the northwest side of the Brushy Creek Diapir (Lomando et al. 1984). The same style of carbonate facies, growing around diapirs and salt welds, now outcrops as the various carbonate lentils associated with the La Popa weld in Mexico (Fig. 6.105).

Pulsing salt emplacement, with numerous switches from active to passive, means that any sediment deposited above a passive allochthon or diapir crest is temporary. Whatever the depositional setting atop the crest, it is shed periodically into the structure's flanks. The resulting salt ablation unconformities can cut into flanking coarser grained deposits, which may then be sealed by subsequent finer-grained deposition or by the encroachment of allochthonous salt (Figs. 6.106 and 6.108). The resulting unconformities and truncational traps can be located some distance from the diapir stem. The dip of such unconformity traps is as steep as the dip of the adjacent shaled-out sands. Unconformity traps have thick oil columns and can stack, but show a limited lateral extent away from the

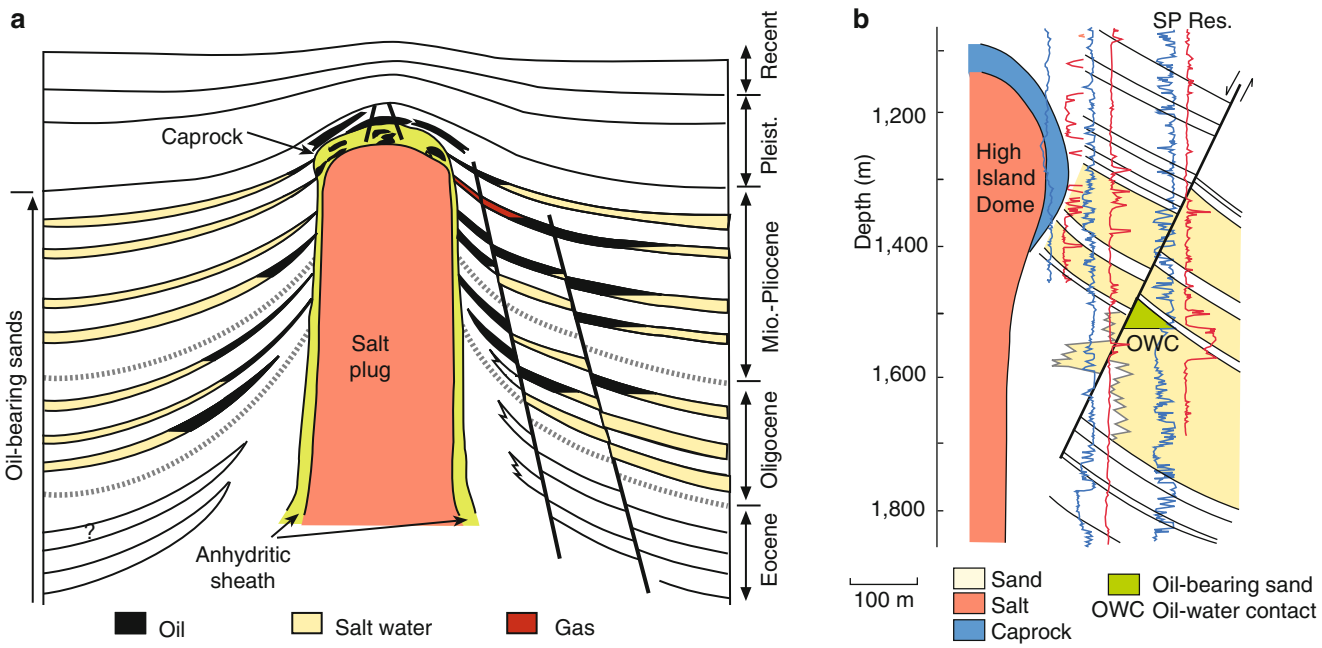

Fig. 10.54 Reservoir sands in the Gulf of Mexico (**a**) Stacking of Tertiary-age peripheral reservoir sands creates some of the most productive acreage in the world (After Halbouty 1979). (**b**) Cross section of the south flank of the High Island Dome, Chambers County, Texas, where the trap is interpreted as due to peripheral faulting juxtaposing a reservoir sand to a shale seal across the fault (After Galloway et al. 1983)

salt stem. A good example occurs along the north side of Nash Dome in Texas, where steeply dipping Frio sands (Oligocene) are truncated by multiple dome-flank unconformities.

Stacked flank traps dominate below the crestal level of many producing salt structures in the onshore Gulf of Mexico, reflecting sedimentation about a salt system during the passive stage of its growth. The crest of the structure maintained its position in earth space while the flanks subsided so that most flank traps are of two interrelated types (Fig. 10.54a; Halbouty 1979): (a) Traps created by sedimentation and erosion contemporaneous with salt movement; (b) Traps created by the relative upward movement of the salt (downbuilding). Stacked flank and unconformity traps have yielded greater volumes of hydrocarbons per acre than any other type of trap in the Gulf of Mexico (Halbouty 1979).

The diapir stage is also the time when turtle structure anticlines form in the salt-withdrawal basins between diapirs. The region above a turtle is often a topographic high where high-energy shelf sands and reefs accumulate atop an anticlinal drape, creating an excellent trap for the subsequent accumulation of hydrocarbons. A good example is the giant Fairway Field in Lower Cretaceous James Reef Limestones in Henderson and Anderson counties, east Texas (Terriere 1976; Achauer 1985). The reservoir is a rudist-reef complex above a shoaling turtle structure and is situated on a saddle between the salt-withdrawal areas of Boggy Creek, Brushy Creek, and La Rue Domes (Fig. 10.55).

The growth of a turtle structure between the La Rue, Brooks and Boggy Creek diapirs converted what was a muddy area of open shelf limestones into a shoal area of rudist reefs and grainstone shoals. Postdepositional faulting truncated the northwestern and northeastern margins of the trap, which is now a southeast-plunging nose (Fig. 10.55a). Reservoir porosity is largely secondary and is better quality in the meteorically leached portions of mechanically deposited suprasalt rudist grainstone belts rather than in the reef proper (Fig. 10.55b). Secondary porosity development tied to halokinetic activity after the reef growth stopped is also the case in many other rudist grainstone buildups atop or adjacent to salt structures in the Gulf of Mexico and the Middle East (e.g. Mishrif Formation in Umm al Dalk Field, UAE). The main control on reservoir quality in these

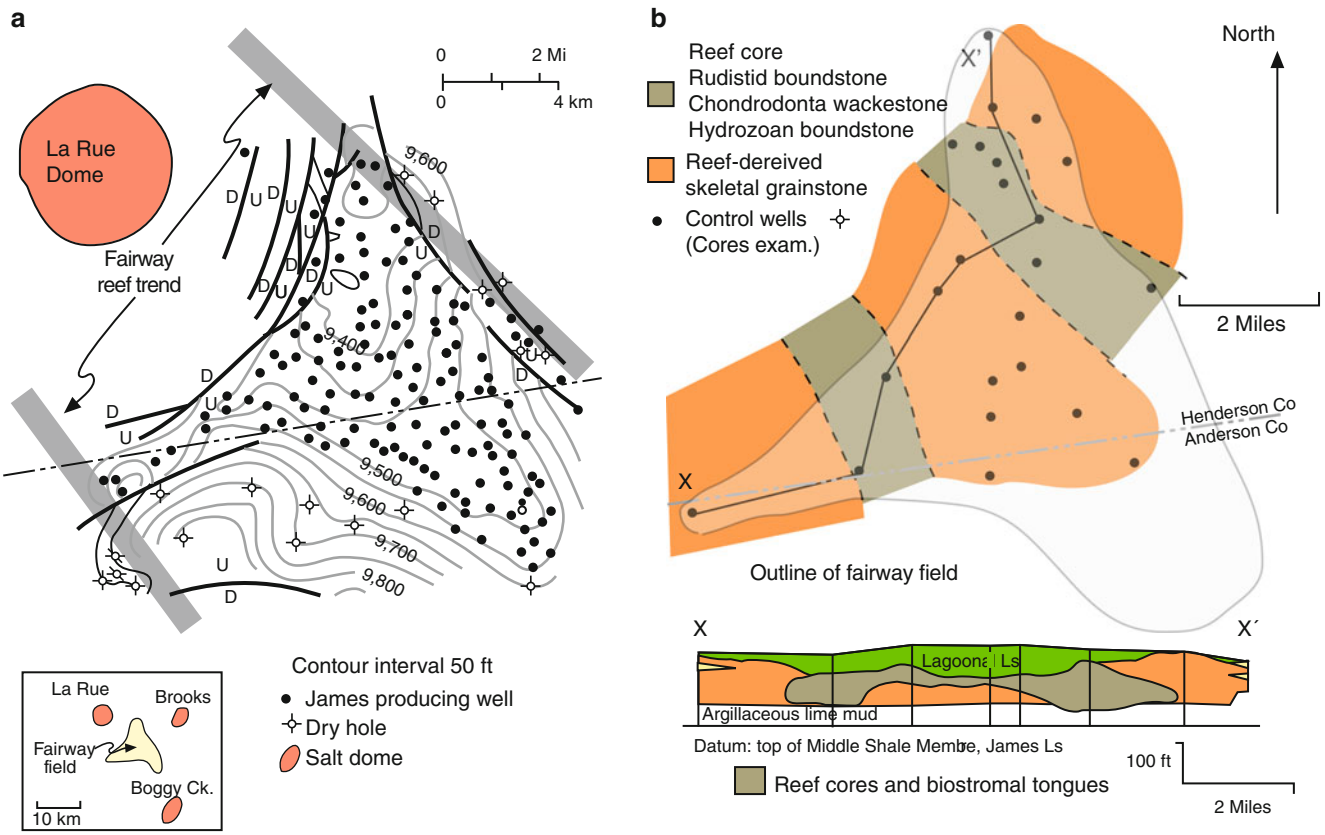

Fig. 10.55 Fairway Field, East Texas Basin (After Achauer 1985). (**a**) Structure map on top of Cretaceous James Limestone Fairway Field, Henderson and Anderson Counties, Texas. The trap is a fault bounded southeast-plunging nose crossed by the northwest trending James Reef Complex. Inset shows Fairway Field formed atop a turtle structure between three salt domes. (**b**) Facies map and interpreted depositional setting of the James Limestone. The main reef core lies in the northwestern part of the field, while satellite reefs to the southeast and southwest are composed of corals, stromatoporoids, algae, and rudists. Carbonates sands and gravels were deposited in the southern part of the field; while elsewhere, muddy lagoonal sands are the dominant lithology

Cretaceous oil and gas fields is karstification and exposure, driven by periodic seafloor shoaling near or atop the underlying salt structure. Pervasively dolomitised Albian oolite pisolite sands also form extensive reservoirs atop turtle structures in the offshore of Angola (Eichenseer et al. 1999).

Chalk reservoirs above salt structures, such as Danian chalks in Ekofisk, Machar and Medan fields in the North Sea, often had the crestal reservoir properties enhanced by the movement of subadjacent salt during basin inversion (Fig. 10.56). Tension was created in the chalk unit above the growing salt structure and this lead to gravitationally-induced microfracturing (D'Heur 1990a). Oil migrated up these fractures in the chalk and, when the oil column in the fracture system was 50–100 m tall, the buoyancy force was sufficient to overcome the high entry pressures inherent in narrow pore throats. Oil was then stored in the matrix as well as in the various fractures. Hardman and Kennedy (1980) postulated that this process explains why high-relief features in the North Sea chalk/salt structures have better oil saturations and why low-relief traps can have waterwet matrix porosity. Early entry of oil into matrix pores and the associated overpressures then retarded the normal sequence of chalk lithification with burial by inhibiting chemical diagenesis and reducing overburden pressure on the matrix grains (D'Heur 1990a, b). These processes were most effective in reservoirs above the centre of the salt structure and with time migrated out into the flank reservoir; hence the reduction of porosity and increase in water saturation radially and the concave-upward oil water contact at West Ekofisk.

In a study of fracture distribution in chalks reservoirs from a number of rejuvenated diapir fields in the North Sea, including Machar, Davison et al. 2000b found that almost all (>99 %) faults and fractures observed are extensional, and form at high angles (>70°) to bedding. Fracturing in the chalks is a response to the rejuvenation of salt flow as the North Basin underwent mild inversion in response to the Alpine

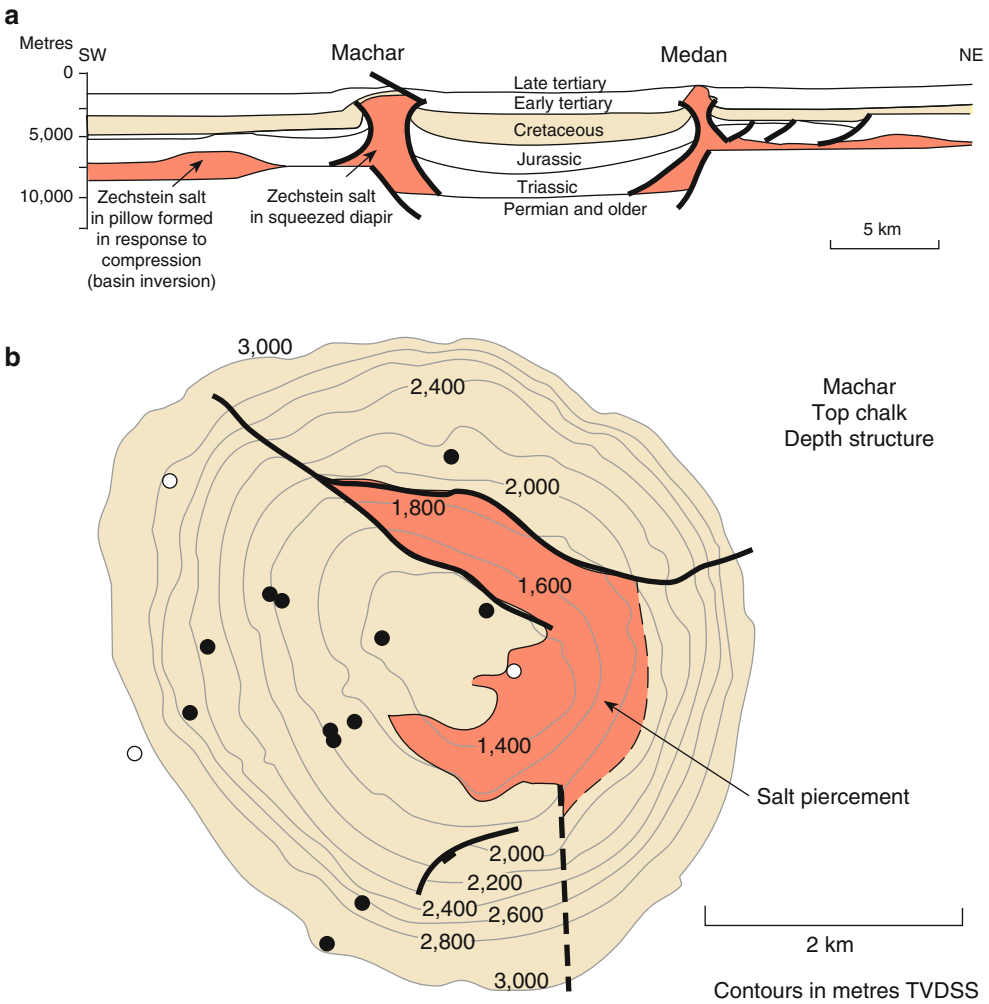

Fig. 10.56 Machar Field, UK sector North Sea. (**a**) Interpretive cross section showing position of field and a geometry that is a response to compression of a formerly extensional salt structure. (**b**) Contoured top of chalk in metres TVDSS showing zone of piercement of Zechstein salt (After Foster and Rattey 1993)

Orogeny. The greatest amount of interconnected fracturing and brecciation (natural rubble zones) in the chalk unit is in wells at or near the crests of this and other North Sea suprasalt chalks such as Ekofisk (Casabianca et al. 2007). The fractures are commonly open, indicating that deformation has continued until the present day, and/or cementation has been inhibited owing to the presence of hydrocarbons, which began to accumulate in the fractures after chalk deposition. Close to the diapir contact (<50 m), the fractures in the chalk are cemented with calcite or anhydrite, which is interpreted to be due to increased fluid flow concentrated along the diapir contact.

This plume of rising saline fluids rising along the dissolving diapir has created a celestite halo in the cap of Machar Field. The fracture intensity within the chalk does not vary consistently from base to top at any one position on the diapir. Reservoir productivity in the chalk is significantly enhanced by fracture permeability over the crest of the diapir structure, where intrinsic permeability in the chalk is insufficient to sustain economic flow rates. However, the chalk is absent on parts of the crest due to non-deposition or downslope sliding (Fig. 6.81b; Davison et al. 2000a; Casabianca et al. 2007). These are areas where salt sometimes made it to the Cretaceous seafloor as small allochthon wings off the main salt trend stem. Stylolite and dissolution residue seams, which are parallel to bedding, can slow vertical flow rates in the chalk (Davison et al. 2000b). They are made of clays and other insolubles and show very low permeabilities on the order of nannodarcies.

The main controls on intrinsic chalk poroperm in the Cretaceous Tor and Palaeogene Ekofisk chalk reservoir units are; (1) Sorting as expressed by Dunham texture, so that mudstones tend to have highest porosity and packstones the lowest; (2) Sorting of the carbonate mud, where a mixture of clay-size chalk particles and silicates tend to reduce porosity; and (3) Intensity of porefilling cementation. The presence of chalk clasts as an indicator of re-deposited chalk seems to have no relationship to porosity (Fig. 10.57; Fabricius et al. 2007). The relative significance of these parameters varies from field to field, while the most significant production qualities are related also to fracture intensity, which varies with proximity to faults and crestal position. What is also interesting is that chalk porosity varies by more than 20 % within a reservoir in a single field but appears to be depth insensitive across the fields, perhaps related to compression induced fracturing and associated early emplacement of hydrocarbons in the reservoir matrix.

Understanding the fault and fracture network in Machar chalk as a response to diapir squeezing and the rise of the diapir crest created a new fracture and fault model for the field. Using this knowledge in the field development plan, along with greatly improved seismic imaging, controlled acidising of the chalk, and steered MWD drilling technology, converted Machar from a field that appeared subeconomic in the early appraisals of the late 1980s with test wells returning at best 8,000 bopd to the current producing field with acidised intervals in fractured zones capable of reliably producing at rates of up to 30,000 bopd.

Even as a diapir crest becomes buried and caprock formation comes to dominate, potential reservoirs can still be created. Caprocks host hydrocarbons in many Gulf of Mexico domes show porosities as high as 40 %, with porosity types ranging from pinpoint to vuggy to cavernous. Caprock reservoirs in the Gulf of Mexico onshore are shallow and so were attractive targets in the early heyday of drilling in Texas. Many of the famous early Texas reservoirs were in caprocks; examples include Spindletop (the most famous), Sour Lake, and Humble. Caprock reservoirs tend to be made up of relatively small, but numerous, pools. Today, most onshore diapir crests have been drilled and offshore the small size of possible caprock pools means they are not primary targets in most exploration programmes.

Traps can occur below a salt wing (remnant allochthon) or an overhang in a squeezed salt structure with a shape like an inverted teardrop. Prolific production comes from beneath the overhang of Barber Hill Dome in Chambers County, Texas; High Island Dome in Galveston County, Texas; Batson Dome in Hardin County, Texas; and the Weinhausen-Eicklingen and other salt domes in the Zechstein Basin of northwest Germany (Figs. 10.58 and 10.59). Sands below the Barber Hill overhang in east Texas have produced more than 100 million barrels of oil (Halbouty 1979). All these traps are onshore and were interpreted under the classic styles of Trusheim's pillow to diapir model using the notion that salt was capable of sill-like intrusion at depth. Today they would be interpreted as remnant allochthons created by passive diapirism or allochthons created by reactivated flow due to salt squeezing.

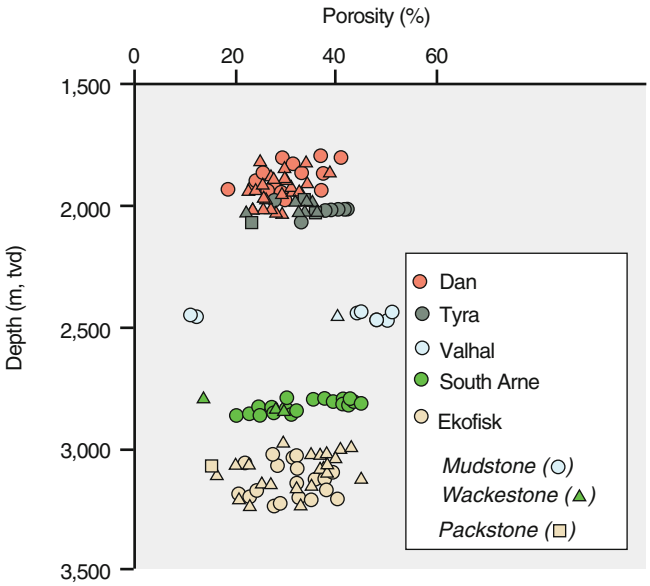

Fig. 10.57 Plug porosity versus depth in chalk reservoir units from 5 suprasalt fields in the North Sea (After Fabricius et al. 2007)

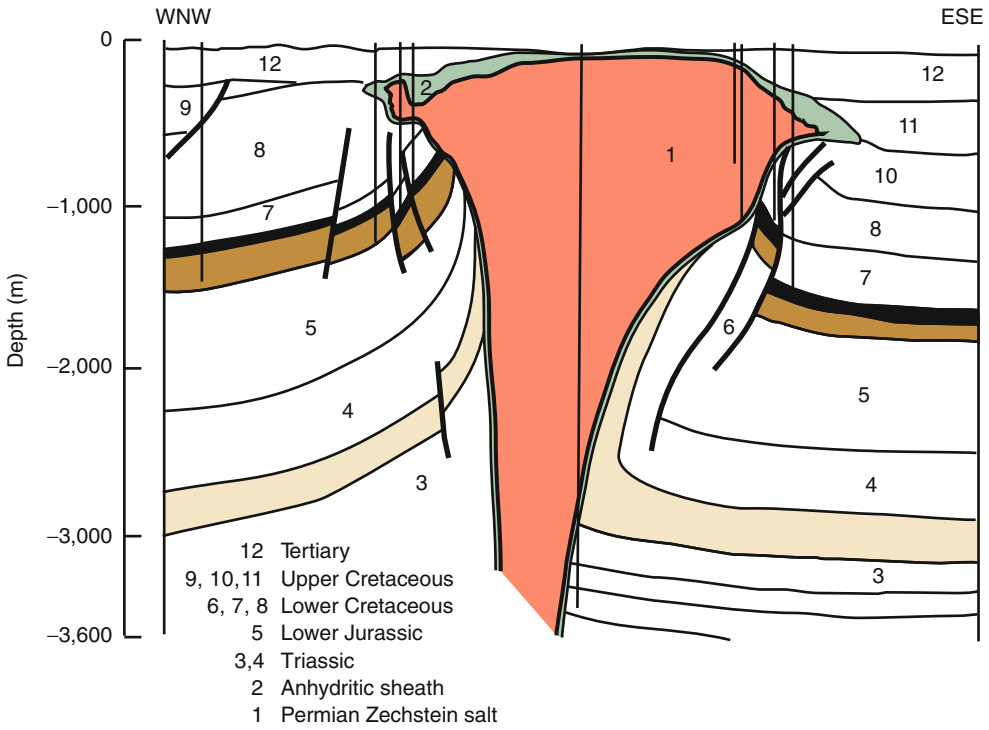

Fig. 10.58 Cross section through traps below flank overhangs of the Weinhausen-Eicklingen salt dome, Hanover Basin, northern Germany (After Lotze 1957). The current geometry also suggests that the structure also underwent compression in the Alpine orogeny

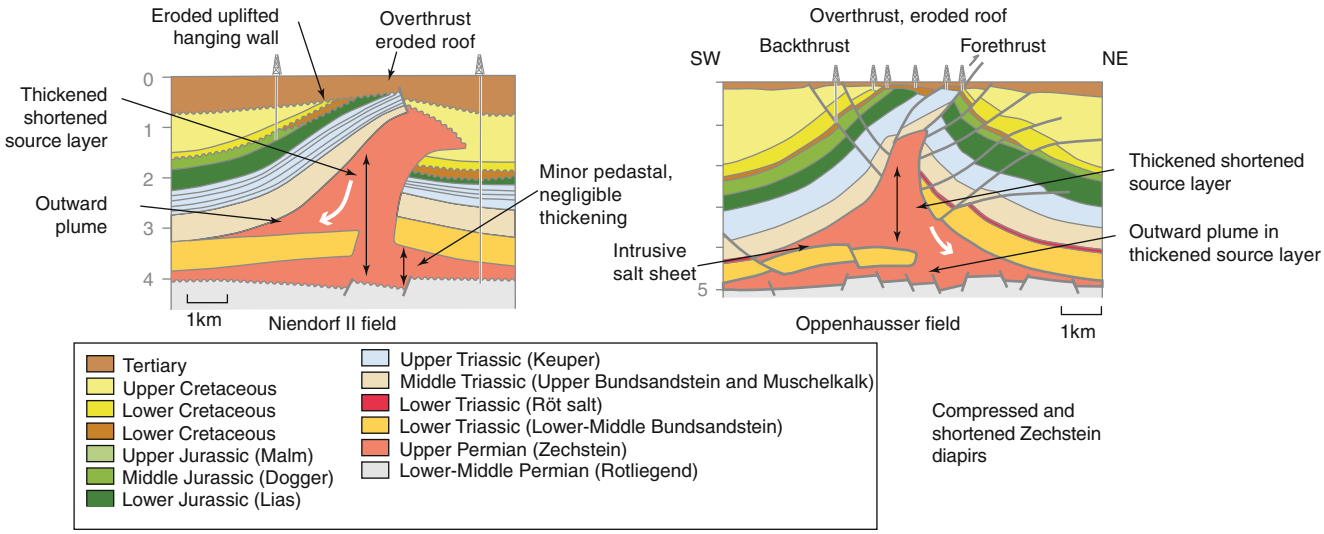

Fig. 10.59 Compressed and shortened Zechstein diapirs with salt sealed overhangs. (**a**) Niendorf II diapir, northwest Germany (**b**) Opperhausen diapir, northwest Germany (After Dooley et al. 2009)

Tiered Allochthon Plays in the Deepwater Realm

Across the last three decades, offshore exploration in the offshore Atalintic has expanded into a deepwater realm where much of the trap structuration in the continental slope and rise is a response to salt flow, often creating multiple salt tiers in the stratigraphy. In this region the deeper water offshore province of Gulf of Mexico and more recently offshore Brazil, have been a focus for the development of improved deepwater drilling and seismic technology (Fig. 10.60a). Much of the currently published exploration paradigm for deepwater tiered-salt allochthon plays comes from the Gulf of Mexico. However, similar paradigms for allochthon development are being used to drive exploration in other circum Atlantic basins located in offshore Brazil and west Africa.

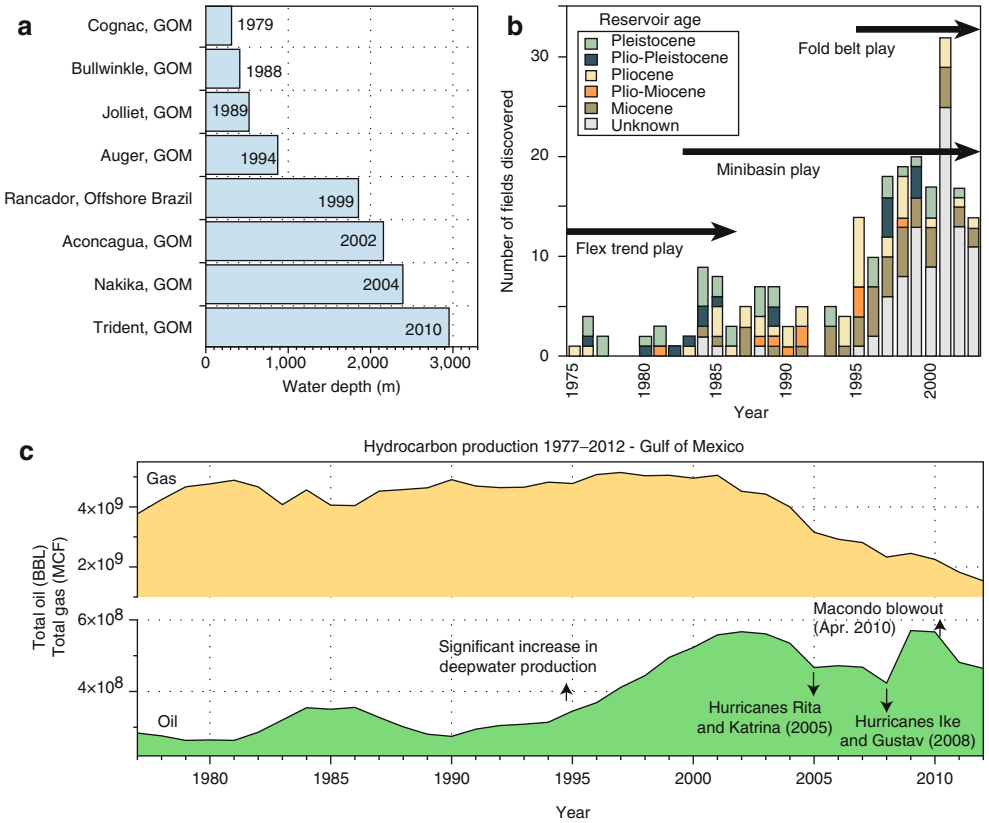

Fig. 10.60 Deep water exploration. (**a**) Water depth to seafloor for deepwater developed fields across the period 1979–2010, with much of the technology expansion driven by Gulf of Mexico (*GOM*) developments. This figure shows a technology-driven expansion of offshore drilling by the oil industry into ever greater water depths in salt allochthon provinces -see also Table 10.8. (**b**) The number of GOM discoveries for the years 1975–2003, showing reservoir age and dominant play type. It also shows the large increase in discoveries from 1995 onward after the passing of the Royalty Relief Act removed some government tax restrictions to deepwater exploration. There were no discoveries in 1978, 1979 or 1992 (After Richardson et al. 2004; Cossey 2004). (**c**) Hydrocarbon production from Gulf of Mexico replotted from BOEM data (<http://www.data.boem.gov> last accessed Dec. 20, 2013)

As yet this work is not as extensively documented as the Gulf of Mexico, but it constitutes a rapidly expanding dataset (Beglinger et al. 2012).

Since 1975 more than 23 billion barrels of oil equivalent have been discovered in the deepwater Gulf of Mexico, while some 9.2 tcf of gas and 2,200 mmbl were produced between 1979 and the end of 2002. Deepening water depths of the various discoveries reflect this time-related technological development (Fig. 10.60a; Table 10.8). There were 232 commercial fields discovered in the Gulf of Mexico during the period from 1975 to the end of 2003 (Cossey 2004). The mean size of these discoveries is 94.3 mmbl oil equivalent. The two largest deepwater fields found to date in the Gulf of Mexico (GOM) are Mars (750 mmbl oil equivalent) and Thunder Horse (1,000 mmbl oil equivalent and possibly as high as 2,000–3,000 mmbl). Thunder Horse was not discovered until 1999, a quarter century after the 1975 discovery of Cognac, the first deepwater field (Table 10.8). Initial well flow rates in wells in the GOM deepwater province did not exceed 10,000 bbl/day until 1995, some 20 years after the discovery of Cognac. Three years later, individual well rates at Ram-Powell and Troika had exceeded 20,000 bbl/day.

Likewise, the salt-cored fold and toe-thrust play has been a successful one in the Gulf of Mexico (Fig. 10.60b, c; Table 10.8). Major discoveries in the Mississippi Fan (Atwater-Valley) Fold Belt include Neptune (discovered 1995), Mad Dog (1999), Tahiti (2002), Knotty Head (2005), Genghis Khan (2005) and Big Foot (2005). Thunder Horse (1999) is the largest of the known fields, with an estimated mean size of 1 billion barrels of oil equivalent (Cossey 2004). "First oil" from Thunder Horse came on line on June 14, 2008. Since then, Thunder Horse has steadily ramped up its production by bringing on new wells. In March 2009, Thunder Horse produced close to 250,000 barrels per day (40,000 m^3/day) oil equivalent in oil and natural gas from seven wells. Plans were in place to add two additional wells in 2009 to further develop the north end of the field. By January 2010 total daily production during 2009 had declined from near 250,000–175,000 barrels per day (40,000–27,800 m^3/day). A similar lower than expected rate

Table 10.8 Some of the salt allochthon related discoveries in the deepwater Gulf of Mexico in the past 3 decades

Project/field name	Area/blok	Water depth (m)	Total depth (m)	Discovered/ drilled	First production	Est. equiv. reserves MMbbl	Comments
Atlantis	GC 699	2,133	5,951	1998	2007	575	Deepest moored floating oil and gas production facility in the world and also one of the largest oil fields in the Gulf of Mexico. Structure is an elongated faulted anticline with overall 4-way dip closure from the top of the Miocene down to the top of the autochthonous salt. Approximately 60 % of the geological structure lies beneath salt and the Sigsbee Escarpment
Auger	GB 426	872	5,000	1989	1994	220	Salt withdrawal minibasin -turbidite play. Initial development costs exceeded US$ 1 billion. Auger's tension leg platform (TLP) has 17 wells connected to system and is also processing hub for nearby fields (Now, Cardamom, Habanero, Serrano, Llano, Oregano and Macaroni). Oil from Auger is sour. Initial wells flow at more than 10,000 bbl/day. Prodigous production rates made sub sea completions economic in the Gulf of Mexico.
Baha	AC 600	2,323	–	1996	–		First ultradeepwater well in Gulf of Mexico, well did not reach target but proved sands were present in ultradeep plays. This discovery initiated the Perdido Foldbelt play in water depths greater than t 8,000 ft (2,400 m).
Bullwinkle	GC 65	412	4,800	1983	1989	190	Pinchout trap in Upper Pliocene, lower Pleistocene sands in salt withdrawal basin (first minibasin play). Has produced more than 120 million barrels of oil and 185 billion cubic feet of natural gas. Deepest fixed-leg platform in the Gulf. Field is now in decline, initial high production rates
Champlain	AT 63	1,359	7,300	2000	–	50	Draped deepwater sands over salt-cored detachment fold. The trap style is a crestal four-way with a larger three-way dip closure with updip salt truncation
Chimichanga	GB 127	192	4,490	1995	–	400 Gcf	Second commercial subsalt discovery, drilled 396 m of salt, tested 2,100 bbl of oil/day, and 20 MMcf of gas/day. Hydrocarbons in Pliocene age, upper slope channelized turbidite sands are located adjacent to and below a major tabular salt mass. (Flex trend)
Cognac	MC 195	312	2,805	1975	1979	150	Historically, deepwater oil production began in 1979 with Shell's Cognac Field First proof of Flex trend and first GOM drilling success in 1,000 ft (300 m) of water. It won the American Society of Civil Engineers 1980 award for "Outstanding Civil Engineering Achievement"
Diana	EB 945	1,372	3,350	1990	2000	100	Deepwater discovery in turbidite sands located on east flank of a north-south–trending salt-cored ridge in the western GOM
Enchilada	GB 128	215	5,625	1994	–		Salt weld discovery. Hydrocarbons in Pliocene age, upper slope channelized turbidite sands are located adjacent to and below a major tabular salt mass (Flex trend)
Europa	MC 935	1,180	5,700	1994	2000	160	Multiple Miocene sands
Gemini	MC 292	1,038	5,479	1995	1999		Third commercial discovery in subsalt play (Pliocene-Miocene sands) Gemini salt body currently overhangs the apparent sediment entry point of deepwater reservoir sands into the Gemini basin. Projected recoverable reserves for the project are estimated at 250–300 billion cubic feet of gas and 3–4 million barrels of condensate
Genesis	GC 205	792	3,700	1988	1999	98	Turbidite sands located on the eastern flank of a buried salt ridge. SPAR platform

Table 10.8 (continued)

Project/field name	Area/blok	Water depth (m)	Total depth (m)	Discovered/ drilled	First production	Est. equiv. reserves MMbbl	Comments
Hickory	GI 116	98	6,584	1998	–		Penetrated 2,438 m (8,000 ft) of salt. atop local minibasin play with subsalt basin open to the northeast, toward potential sand sources.
Jack 2	WR 759	2,088	8,598	2006	–		Willcox test, deepest extended drillstem test in deepwater Gulf of Mexico history proved the viability of the Lower Tertiary deepwater play (Wilcox-equivalent Eocene/Paleocene). Drilled in 7,000 ft (2,130 m) of water and penetrated 20,000 ft (6,100 m) beloe the seafloor.
Kaskida	KC 292	1,786	9,906	2006	–	3,000?	First Willcox subsalt test situated significantly inboard of Sigsbee escarpment, northern frontier of Willcox prospect, intersected 2,444 m (800 ft) of net pay. Edge of a primary basin is juxtaposed against a secondary minibasin across a high-angle weld. One of the largest Paleogene discoveries.
K2	GC 562	1,221	3,979	1999	2005	100	Drilled through 3,050 m (10,000 ft) of salt canopy in Miocene fold belt trend.
Lena	MC 280	305		1976	1984		Lena, the third field in Gulf of Mexico, started production in 1984. The field is situated in lowstand fan on the western flank of a salt diapir within a faultbounded intraslope basin
Mad Dog	GC 782	1,372	6,957	1998	2005	450	91 m (300 ft) of net subsalt pay discovered in Mississippi Fan fold belt. Field extends across the Sigsbee Escarpment. Truss spar platform. Infrastructure (spar platform) damaged by Hurricane Ike in 2008
Mahogeny	SS 349	113	5,048	1993		100	Put on line before Mica, became the first commercial development in the Gulf of Mexico subsalt play. Wells did not produce at projected rates.
Magnolia	GB 783	1,432	5,141	1999	2006	150	Tension leg platform (TLP) installed in record water depth for TLP. Located on southern edge of Titan mini-basin where multiple deep water reservoir sands are positioned across a series of down-to-the-basin and antithetic faults adjacent to salt bodies
Mars	MC 807	896		1989	1996	400–500	TLP located due south of Mississippi mouth in some 3,000 ft of water. Stacked Miocene sand reservoir interval several hundred meters thick, confirmed the Mini-Basin trend in the Gulf as a bona fide play. First well came in at 15,000 barrels per day. Initial flow rates some early wells were as high as 50,000 bbl/day Platform was damaged during installation Hurricane Katrina.
Mensa	MC 731	1,621	4,815	1986	1997		Upper Miocene; proximal lobate turbidite sheet sand associated with a faulted four-way closure
Mica	MC 211	1,328	3,890	1980			First significant intersection of hydrocarbons in 5 thin pays below salt
Neptune	At 573	588		1996	2008	150	First discovery in the Western Atwater Foldbelt. oil in Lower to Middle Miocene turbidite sands. Developed by a standalone Tension Leg Platform (TLP). First spar production facility in GOM
Pompano	VK 990	393		1981	1994	75	Upper Miocene reservoir in a turbidite channel system draped over a salt cored plunging anticline
Popeye	GC 116	610	3,505	1985	1996		Turbidite in minibasin between a salt-stock system to the west and an extensional salt tongue to the east
Ram-Powell	VK 956	980		1985	1997		Miocene sand reservoir. Field went onstream in 3,200 ft of water. TLP was considered a “Mars” clone.

(continued)

Table 10.8 (continued)

Project/field name	Area/blok	Water depth (m)	Total depth (m)	Discovered/ drilled	First production	Est. equiv. reserves MMbbl	Comments
Redhawk	GB 877	1,615	7,163	2001	–		Produced from the world's first truss spar facility
St. Malo	WR 678	2,145	8,859	2003	–		First subsalt well of Wilcox Trend, drilled through 3,048 m (10,000 ft) of Sigsbee salt canopy, intersected 137 m (450 ft) net pay. Wilcox-equivalent Eocene/Paleocene deepwater play
Tahiti	GC 640	1,224	8,170	2002			Middle Miocene trap beneath 3,353 m (11,000 ft) of salt canopy
Tanzanite	EI 346	96	3,607	1998			First well tested 1,917 bbl/day of oil and 29.7 MMcf/day of gas, one of the highest in the shallow Gulf of Mexico
Thunder Horse	MC 778	1,844		1999	2007	640	Largest field in the Gulf of Mexico, but wells not producing at projected rates (initial estimates of 1 billion bbl of oil equivalent). Thunder Horse sands were unusually high pressure/high temperature reservoirs. Reserves were estimated at 757 Mb in 2002, 653 Mb in 2004 and 643 Mb in 2006. Thunder Horse complex was brought on production with the largest semi-submersible platform ever built (130,000 t) at a cost in excess of US$ 6 billion. Drilled in 6,000 ft of water. Platform required repair and re-righting after Hurricane Dennis in 2005. By March 2009, production had ramped up to 250,000 barrels per day, 4.5 % of total U.S. daily production.
Troika	GC 244	829		1994	1997	200	S10 turbidite reservoir has outperformed the original reservoir model. Initial flow rates were as high as 31,000 bbl/day
Ursa	MC 809	1,225		1989	1999	400	Deepwater sands located within an intraslope, salt-bounded minibasin. Ursa TLP was designed to accommodate initial well-production rates of 30,000 barrels per day; in September 1999, a well at Ursa broke all records with a production rate of nearly 50,000 barrels of oil equivalent per day
West Toga	GC 726	1,433	7,827	2007			Discovered 107 m (350 ft) of net oil in 3 Miocene sands
Zinc	MC 354	451		1977″	1993		Flex trend discovery.

Compiled in part from Graham et al. (2011), Richardson et al. (2004), Dribus et al. (2008)

of production is also seen in wells in Mad Dog field. Reasons for this decline are still being investigated.

Several early subsalt wells were accidental subsalt penetrations where operators were drilling to test anomalous seismic reflectors and found salt where they expected hydrocarbons. The first subsalt well drilled in the Gulf of Mexico Outer Continental Shelf was Placid Oil Company's Ship Shoal 366 well in 1983. This well encountered three separate salt intervals, but only 90 m of subsalt sediment were penetrated. Over the next several years, sporadic subsalt drilling continued. One of the more interesting early subsalt wells was Diamond Shamrock's 1986 well, South Marsh Island 200, which encountered a reservoir-quality sand with a massive 245 m net thickness. The potential for worldclass reservoir sands beneath salt allochthons became apparent with this well, but the absence of reliable subsalt targeting from existing seismic technology limited drilling activity (Farmer et al. 1996).

Porosity and permeability in what are producing deepwater sands in these subsalt fields can be impressive, even though deposition has occurred on deepwater bottoms, situated well out on the continental slope and rise, sometimes in regions that were more than 100 km from their contemporary shorelines. Sands in the Auger Field (Garden Banks 426) retain porosities of 26 % and permeabilities up to 350 md. Pliocene and Pleistocene turbidite sands in Green Canyon 205 Field have reported porosities ranging from 28 to 32 % with permeabilities between 400 md and 3 darcies. Connectivity in these deepwater sheet sands and amalgamated sheet and channel sands is high for deepwater turbidite reservoirs worldwide and recovery efficiencies are in the 40–60 % range (Table 10.8; Cossey 2004).

High production potential of ultra-deepwater reservoirs in the Gulf of Mexico deepwater was documented in Troika and Mars discovery wells, where initial flow rates from turbidite sands were as high as 31,000 and 50,000 barrels of oil per day per well, respectively, far surpassing the previous Gulf of Mexico single well record of 12,000 barrels of oil per day at Auger. This compared nicely to 500–1,000 b/d from a good well on the shelf in the Gulf of Mexico. Although these GOM fields do not compare in size (storage) to the Middle East, they can generate Middle Eastern rates of production, at least in the early stages. The surprising discovery in 1994 of how productive these reservoirs were in tests at Shell Oil's Auger platform entirely changed the company's cost structure for this deepwater play. However, as mentioned earlier, a number of later deepwater projects (including Thunder Horse and Mad Dog in the Gulf of Mexico) have not produced at the peak rates anticipated, and production has declined much more rapidly than predicted, both as a consequence of the reservoir complexity, strength of the water drive, and technology problems arising from remote, high pressure, high temperature subsurface conditions (Cohen 2007; http://www.theoildrum.com/node/6415). Accordingly estimates of ultimate recoverables have been reduced across these fields (Table 10.8).

Regionally-Tiered Salt Plays in the Gulf of Mexico

Regionally, there are three subsalt-associated allochthon trends in the deepwater Gulf of Mexico (Figs. 10.60b and 10.61a): (i) Flex trend, (ii) Minibasin, and (iii) Foldbelt (Cossey 2004). The term subsalt is used by GOM explorers to describe plays obscured by a salt canopy. The flex trend describes the shallowest region of the three plays (in terms of water depth) and it covers a geographic area encompassing the outermost shelf and uppermost slope. Geologically it constitutes the halokinetic zone in front of the Plio-Pleistocene Roho, and is an area where there is no widespread salt canopy. It can be further divided into a "toe thrust" or flex belt and a "primary basin" belt (Fig. 10.62a). Large volumes of salt have been lost in this region via allochthon evacuation, dissolution and weld creation. In terms of salt allochthon evolution much of the Flex trend and the Primary Basin region has evolved well past the canopy stage and the area is now a relict thrust foldbelt (Fig. 10.62b; toe thrust zone). The minibasin play, as the name implies, encompasses sand deposition associated with the development suprasalt depopods and minibasins (Fig. 6.47). It is typically located in somewhat deeper water in the Gulf of Mexico than the toe thrust belt, and its exploration began in 1983 with the discovery of Bullwinkle. The foldbelt trend is located beneath and downdip of the canopy belt and encompasses reservoirs developed by compressional folding at the downslope end of a developing allochthon belt. It constitutes the deepest water region of current areas of exploration activity in the Gulf of Mexico (Figs. 10.62b and 10.63).

Flex trend exploration began in the early 1970s with the discovery of Cognac Field located just beyond the present-day shelf edge where there is a "flex" in the sea floor profile (Cossey 2004). Some of the larger flex discoveries were Lena, Zinc, Pompano and Green Canyon 18 (Table 10.8). Most discoveries in the Flex Trend are fields with small reserves, characterised by discontinuous sands with producing wells showing relatively low flow rates. Exploration wells in this trend generally targeted "bright spots" on 2-D seismic. Gemini, for example, showed up as a very strong event on the seismic. Texaco was so confident of its Gemini prospect that based on a very strong event on the seismic they stopped drilling and set casing just before entering the pay zones. In fact, this hydrocarbon-indicating anomaly could be seen on non-reprocessed, mid-1980s vintage 2D seismic.

Exploration for minibasin plays typically targets the flanks of intraslope basins where reservoir sands pinch out and form combination structural/stratigraphic traps, or it targets zones of drape over turtle structures. Many minibasins plays are sealed and obscured by allochthonous salt sheets, which can fuse into a salt canopy (Chap. 6). Some of the larger mini-basin fields discovered to date are Auger, Mars, Diana, Genesis, Troika and Europa. Ram-Powell field was discovered in 1985 and is a very large, stratigraphic trap, developed in a more unrestricted mini-basin. Larger minibasins typically have turtle structures developed in their centres. The first mini-basin fields brought on-line (Bullwinkle in 1989, Auger in 1994) produced at much higher than expected rates, had better than expected aquifer support and needed fewer wells to develop them. Much of the early production from these minibasin fields ended up facility constrained.

Suballochthon exploration for minibasin traps in the deepwater offshore Gulf of Mexico was first successful south of New Orleans in the region known as the "Isolated Salt Tablets" province or Florida slope. It is located in the easternmost Mississippi Canyon area in waters 1,000–2,000 m deep (Fig. 10.62a; Shirley 2000; Hall 2002). Productive reservoirs there are Pliocene to Miocene unconfined turbidites occurring some 3,000–4,500 m subseafloor. These are usually sealed beneath allochthonous salt and are considered combination structural/stratigraphic traps. Exxon made the first deepwater subsalt discovery of oil and gas in this region with its Mississippi Canyon 211 well. This prospect, nicknamed "Mickey" because of the resemblance of three allochthon sheets in plan view to the head and ears of "Mickey Mouse" has hydrocarbons below salt canopy and lies beneath 1,310 m (4,300 ft) of water. Reserve estimates for "Mickey" range between 50 and 150 million barrels of oil equivalent, but the discovery was deemed subeconomic and has yet to be put on production. The "Mickey" discovery indicated the prospectivity of subsalt plays in this region and focused

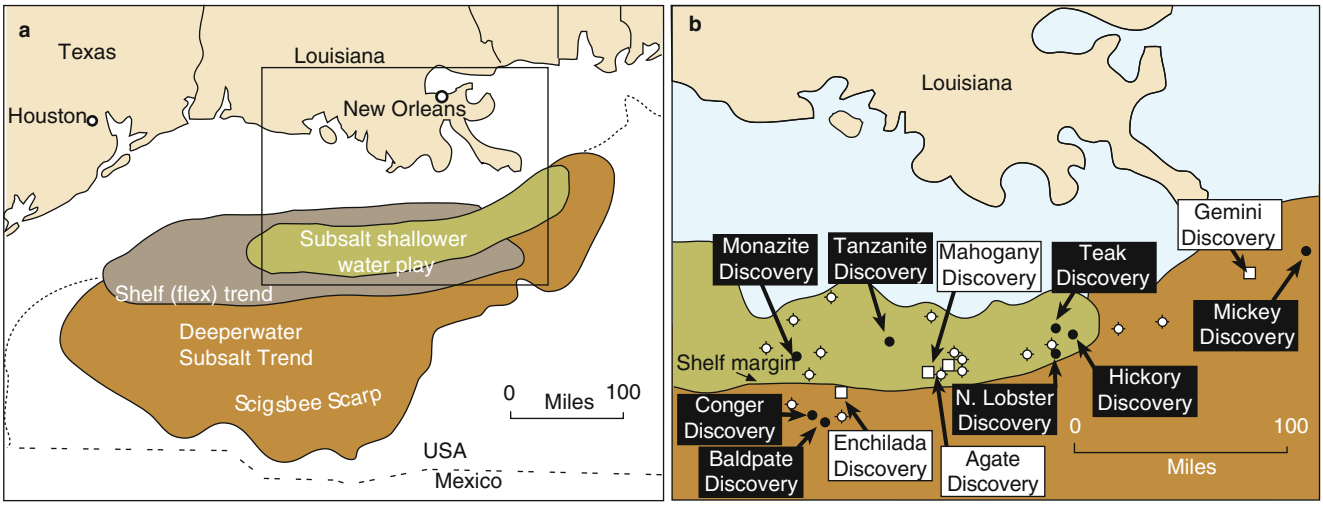

Fig. 10.61 Allochthon-related discoveries in the Gulf of Mexico. (**a**) Distribution of shelf and deep water salt plays in the Northern Gulf of Mexico. *Rectangle* indicates position of Fig. 10.61b (In part after Cossey 2004). (**b**) Selected early discoveries, until the mid 1990s, in the updip slope and rise minibasin province in the eastern Gulf of Mexico (drilling in relatively shallow water, near shelf break – see Table 10.8)

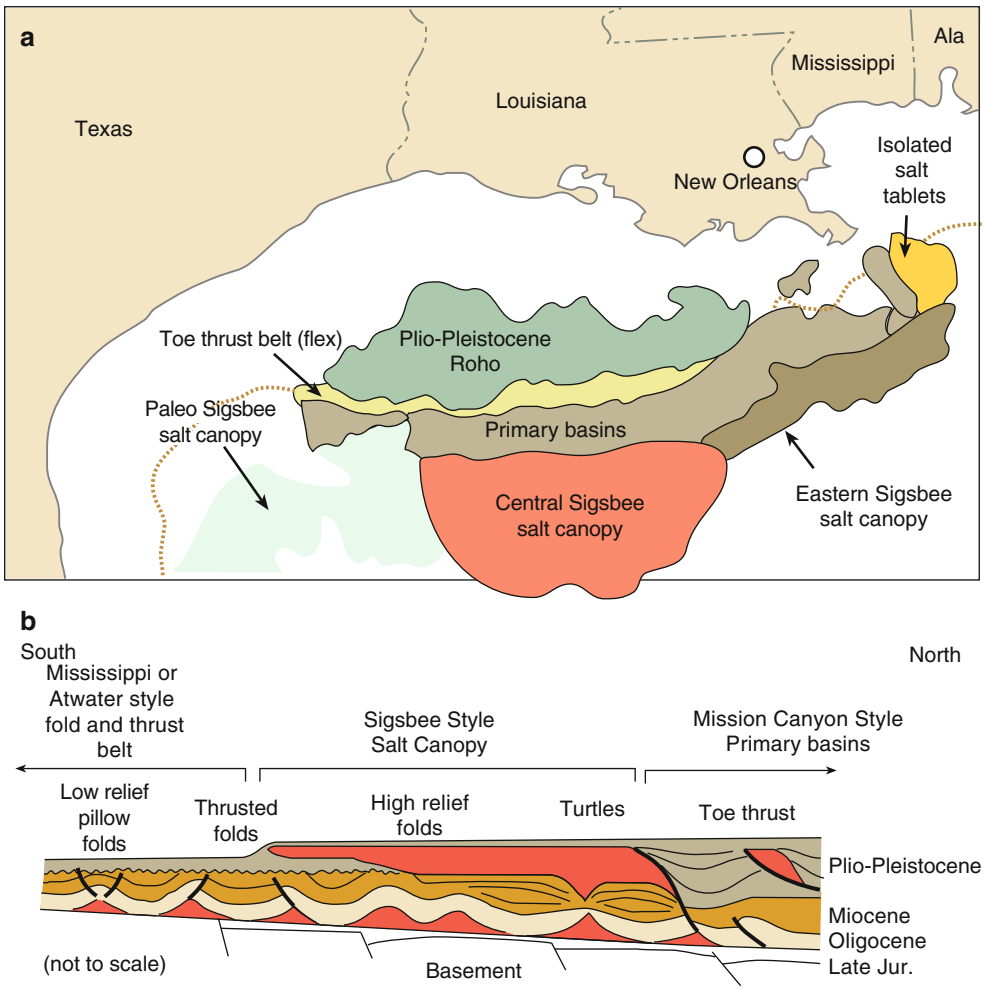

Fig. 10.62 Distribution of the various salt fairways in the Northern Gulf of Mexico. Also shows an idealised south to north cross section illustrating typical subsalt and suprasalt structures where the position of the salt defines major play types. Note that the low relief pillow folds in the south are autochthonous and probably define the original southern extent of thick Jurassic salt in the basin

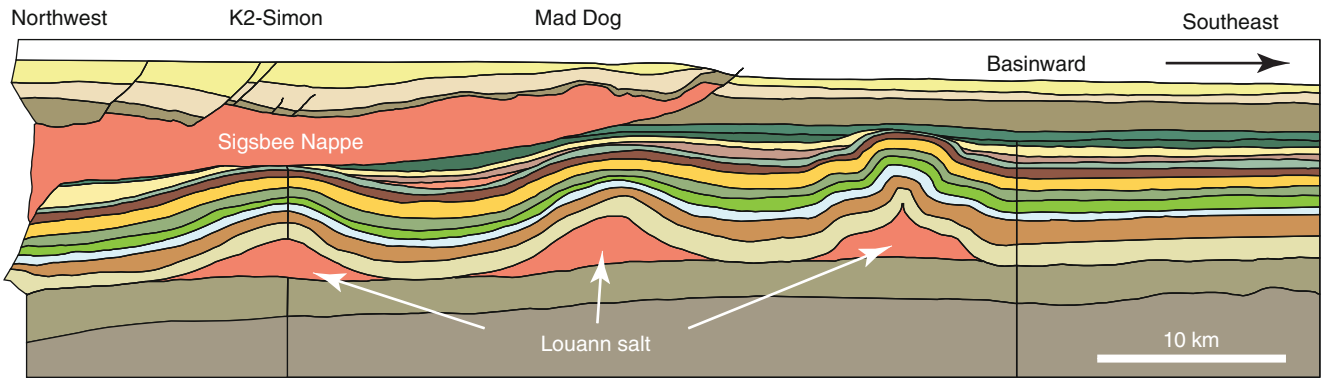

Fig. 10.63 Depth section through the western part of the Mississippi Fan Foldbelt showing a series of symmetrical, salt-cored detachment folds between welded synclines and the resulting closure that formed the Mad Dog and K2-Timon fields (After Rowan et al. 2004). See Fig. 6.61 for location

exploration efforts into sub-allochthons, both on the shelf and in deeper water.

As drilling technology and subsalt imaging improved throughout the later 80s and into the 90s, subsalt exploration moved into progressively deeper water. Drilling now reliably reaches larger potential suballochthon minibasin structures, including turtles located further out in the Gulf and targets requiring the drilling of more than 3,000 m of salt (Table 10.8; Richardson et al. 2004). Minibasin fields currently contain the largest economic resource base in the deepwater Gulf. The subsalt "Mahogany" Field, operated by Phillips Petroleum, is a minibasin play that was discovered in 1993 by the Ship Shoal 349 well in the Mission Canyon region. This field, which began production in December 1996, was the first commercial subsalt oil development in the Gulf of Mexico. In 1994, Shell Offshore, Pennzoil, and Amerada Hess announced another significant minibasin discovery in Garden Banks 128 well, nicknamed "Enchilada" (as in the idiomatic "it's the big enchilada"). Enchilada has combined reserves estimated at 400 bcf of gas and 25 million bbl of oil/condensate (DeLuca 1999), and was brought online in July of 1998. In 1996, nine subsalt wells were drilled and three were discoveries. The largest discovery (Anadarko and Chevron) was "Gemini" in Mississippi Canyon Block 292 with estimated reserves of 250–300 Bcf of gas and 3–4 million bbl of condensate (DeLuca 1999). It currently produces from a single reservoir using a subsea system. Gemini was the first deepwater subsalt production in the Gulf of Mexico – and showed explorers the potential for prolific production from the deeper water portion of the subsalt play.

In June 1999 one of the Gemini wells tested around 76 million cubic feet of gas and 1,370 barrels of condensate a day. Agate Field in Ship Shoal 361 was discovered in 1996 by Anadarko and Phillips and is produced through a tieback into the neighbouring Mahogany platform. Anadarko, along with partner BHP, also announced a second subsalt discovery in 1996 in Vermilion 375, called Monazite. The discovery well revealed multiple pay zones, but because of problems during testing, the hole was plugged and abandoned. Amerada Hess and Oryx made a major discovery in late 1997 in their Penn State prospect in Garden Banks 216, the field came on stream in 1999 through a tieback to the Baldpate production facilities. In July of 1998, Anadarko announced a subsalt discovery at the Tanzanite prospect in 95 m (314 ft) of water in Eugene Island 346 with reserves estimated at 140 million BOE. Later in 1998, Anadarko also announced the discovery of their Hickory prospect in Grand Isle 116 in 97 m (320 ft) of water. The discovery well, drilled to a total depth of 6,580 m (21,600 ft), penetrated approximately 2,400 m (8,000 ft) of salt before passing into the reservoir. Reserves are estimated at 40 million BOE (DeLuca 1999).

Thunder Horse Field (formerly known as Crazy Horse Field) in Mississippi Canyon Blocks 776, 777 and 778 is a substantial minibasin field with a turtle style of reservoir development. It is located in the Boarshead Basin, 200 km south-east of New Orleans and is the largest deep water discovery made to date in the Gulf of Mexico (Enger and Logan 2001). It had initial estimated reserves of greater than a billion barrels of oil equivalent in early and middle Miocene sands at about 7,000–8,500 m (23,000–28,000 ft) depth. BP-Amoco has said reservoir characteristics are excellent and compared Thunder Horse favourably to Magnus Field in the UK North Sea, where wells flowed at rates exceeding 20,000 bbl/day at peak. Thunder Horse showed that deepwater subsalt sands can be productive, even at depths well below 7,500 m. It is one-and-one-half to twice the size of the next biggest structures in the region (Enger and Logan 2001) and is one of three large discoveries on a turtle structures worldwide. Other turtle-associated discoveries are Pluto (aka BS and T; Mississippi Canyon 718) and Mensa (Mississippi Canyon 731). Both the Thunder Horse field and Pluto discoveries are partially covered by shallow salt canopies.

Methods of most effectively exploring for minibasin plays are still emerging, especially if a turtle is obscured by a salt

canopy (Shirley 2000). Deeper turtle structures are still difficult to reliably image on 3D seismic data, especially beneath thick salt canopies and there are no diagnostic hydrocarbon-indicating amplitudes (bright spots) related to this play, so structures rather than accumulations are targeted. Geologically, turtle structures can be complicated as these structures were synclines at the time they were receiving sediments (Fig. 6.29). Then the structure inverted due to ongoing salt withdrawal. That in itself implies there is a complex relationship between timing of trap formation, hydrocarbon charge and migration. The key uncertainty with turtle structures in this style of play is whether a trap was in place during the hydrocarbon migration phase. Also, there can be crestal faulting on these structures that can degrade the top seal of the traps, but the size of the potential discoveries makes the risk worthwhile.

Petroleum systems in the foldbelt give prominence to underlying high-relief salt-cored folds (mostly to the west) and thrusted folds to the east in what is called the Atwater Valley style structural province (Hall 2002). Lower and middle Miocene turbidite reservoirs extend across the crests of folds, which typically formed during foot of slope compression in the mid-Miocene to Early Pliocene. Three major foldbelt trends are considered prospective: the Mississippi Fan, the Perdido and the Port Isabel foldbelt, all are located in deeper water downdip of the salt canopy/minibasin trend (Figs. 6.65 and 6.66) The Foldbelt play began to be exploited in 1995 with BP-Amoco's discovery of Neptune in Atwater Valley 575 in the Mississippi Fan foldbelt. Soon thereafter BP discovered Atlantis and Mad Dog (Fig. 10.63; Hall 2002). K2/Timon was found just north of the earlier discoveries, and more recently Texaco discovered the Champlain Field in the middle of Atwater Valley, extending the play further east (Table 10.8; Rowan et al. 2004).

To date, in the Mississippi Fan belt, a significant portion of the discoveries are centred in the foldbelt of the western part in a small area of the southeast Green Canyon area. All are near the edge of the Sigsbee Escarpment and within 50 km of each other in water depths ranging from 1,200 to 3,000 m (4,000–6,500 ft). Target reservoirs are found in the 5,000–8,000 m (17,000–26,000 ft) depth range, and the structures can be prolific with greater than 300 million barrels of oil equivalent. Mad Dog is currently one of the more prolific of the foldbelt discoveries, with reserve estimates ranging from 400 to 800 million barrels of oil equivalent from about 100 m of net hydrocarbon pay in a large, high relief fold under the edge of the Sigsbee Escarpment (Fig. 10.63). Atlantis, vies with Mad Dog in terms of field size. Current seismic quality in this part of the fold-belt province is good to fair, but companies are exploring very high relief features, which are difficult to miss. For example, Mad Dog is a 3,000 m relief feature below the Sigsbee Nappe. Even though imaging is not the best quality, it's hard to overlook a 3,000-m-tall closed structure. Plays in the area known as the Eastern Sigsbee Escarpment do not involve the search for the subtle trap! The province's western portion is relatively well drilled now, so the play's future lies in taking the charge risk and moving east to determine how far the play will extend. In contrast, the Perdido Foldbelt Play is under explored. The play is similar to the Mississippi Fan Foldbelt Play in that it consists of very large compressional foldbelt structures. Like the Mississippi Fan Foldbelt Play, the compressional folds extend a considerable distance landward beneath the Sigsbee Salt Canopy. However, the plays differ in the age of the structures and the targeted reservoir.

Early exploration drilling in the deepwater Gulf of Mexico in the early 2000s found over 2 billion BOE (Richardson et al. 2004). Today the traditional deepwater mini-basin plays are still providing many successful exploration opportunities (e.g. the Thunder Horse and North Thunder Horse discoveries in southern Mississippi Canyon), but recent discoveries in new foldbelt deepwater plays continue to expand the exploration potential of the deepwater Gulf of Mexico (e.g. Perdido). Currently, some 99 % of total production in the deepwater Gulf of Mexico is from Neogene reservoirs (Pleistocene, Pliocene, and Miocene; Fig. 10.60).

Several recently announced deepwater discoveries encountered large potential reservoirs in sands of Paleogene age (Oligocene, Eocene, and Paleocene); for example, the Tiber discovery in 2009 and the Coronado Discovery in March 2013. Transocean's Deepwater Horizon semisubmersible made the historic discovery for BP at the company's Tiber[8] prospect in the Keathley Canyon in September 2009. Drilling in 1,220 m of water and to a world-record total depth of 10,685 m, Deepwater Horizon tapped in a pool of crude estimated to contain 4–6 billion barrels of oil equivalent, one of the largest U.S. discoveries. Six months later, in March 2010, Shell (with partners Chevron and BP) started production at its Perdido spar in 2,438 m of water in the Alaminos Canyon. A hub for the development of three fields, Perdido was the world's deepest offshore platform, and the first project to pump oil and gas from the Lower Tertiary in the Gulf of Mexico. In 2010, Petrobras began to develop the Gulf's first floating production, offloading, and storage facility to produce from Lower Tertiary reservoirs at its Cascade and Chinook prospects. By end 2010, the industry had announced 19 discoveries in the Lower Tertiary trend, 14 of them containing more 100 million barrels of oil equivalent. However the aftermath of the BP Horizon spill in April 2010 was a decline in exploration, from which the Gulf is still recovering (Fig. 10.60c).

[8]The Tiber oilfield was drilled in 2009 by the semi-submersible oil rig Deepwater Horizon. The same rig was destroyed as the result of an explosion 7 months after the discovery at Tiber, while drilling its next well at Macondo in April 2010.

Minibasin Plays

Salt-withdrawal minibasins are characterized by Karlo and Shoup (2000) as either; (1) shelf-loaded, or (2) slope-loaded (Figs. 10.64 and 10.65). Salt withdrawal minibasins on the shelf, which mostly host fluvio-deltaic reservoirs of the shelf trend in northern Gulf of Mexico, are rooted in autochthonous salt at depths of 12,000–14,000 m (40–45,000 ft). They typically show continuous subsidence in a seaward-migrating belt of sediment loading from the Cretaceous onward, with some basins beginning to fill with sediment even earlier in the Jurassic. The basins are aligned in sub parallel linear trends with salt domes intermittently dispersed along the bounding faults. Updip they tend to be simple minibasins while their downdip extent is defined by stepped counter-regional fault basins, often with a secondary turtle structure on the 'step,' along with some local Roho development (Fig. 10.66; Karlo and Shoup 2000). Associated salt masses grade from simple diapirs updip into larger volume, overhung salt domes and successively into salt wings and allochthons downdip. Block 330 is one such system (Figs. 6.104 and 8.28).

Plio-Pleistocene Roho systems are shelf-loaded features (Fig. 10.65) with updip zones of extension marked by a series of nested highly listric faults, which display a characteristic horseshoe geometry in map view (Fig. 10.65b; Karlo and Shoup 2000). Deltaic sands and shales tend to be stacked in lower parts of the seafloor in a feedback between depositional loading of the rotated wedges associated with these growth faults. The central portion of the same depositional system is typically manifest as a complicated zone of remnant salt, perched diapirs, salt-floored faults, and strike-slip faults. Basinward of this region is the compressional toe, which consists of a melange of salt and deformed sediment. All faults sole into the evacuated remnant of the original salt tablet, which typically overlies a salt-withdrawal minibasin. In map view, the overall geometry of the salt-based detachment system is constrained by the geometry of the salt tablet upon which it is forming.

Slope-loaded minibasins (turbidite reservoirs) are similar to shelf minibasins in terms of sand distributions, but involve much more salt than the shelf systems (Fig. 10.64). These slope withdrawal basins are typically flanked by salt walls, with little fault rim development. Formation began with ponding of turbidites triggering loading and the creation of diapirs. Because of the great thicknesses of autochthonous salt involved, turbidite ponding is more or less continuous, so long as there is salt withdrawing from the basin. Should the depocentre shift during the diapiric phase, a salt wing forms during the hiatus and overflows the basin resulting in the formation of a salt canopy. Once the allochthonous salt has been evacuated, subsequent turbidite deposition bypasses the basin.

Regionally, within the Gulf of Mexico, these minibasin systems and associated trap types can be placed in a tiered system of primary and secondary minibasins, with much of the trapping occur-ring at the primary basin level (shaded

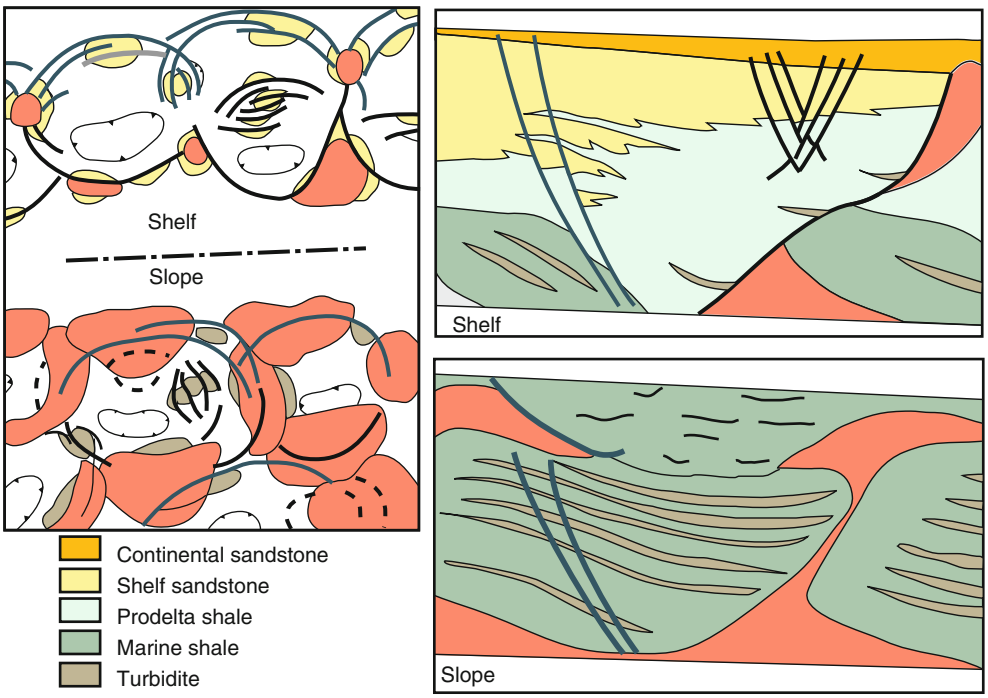

Fig. 10.64 Model of reservoir styles showing distribution of subsalt traps in both shelf and deepwater minibasin (primary basin) settings (After Karlo and Shoup 2000)

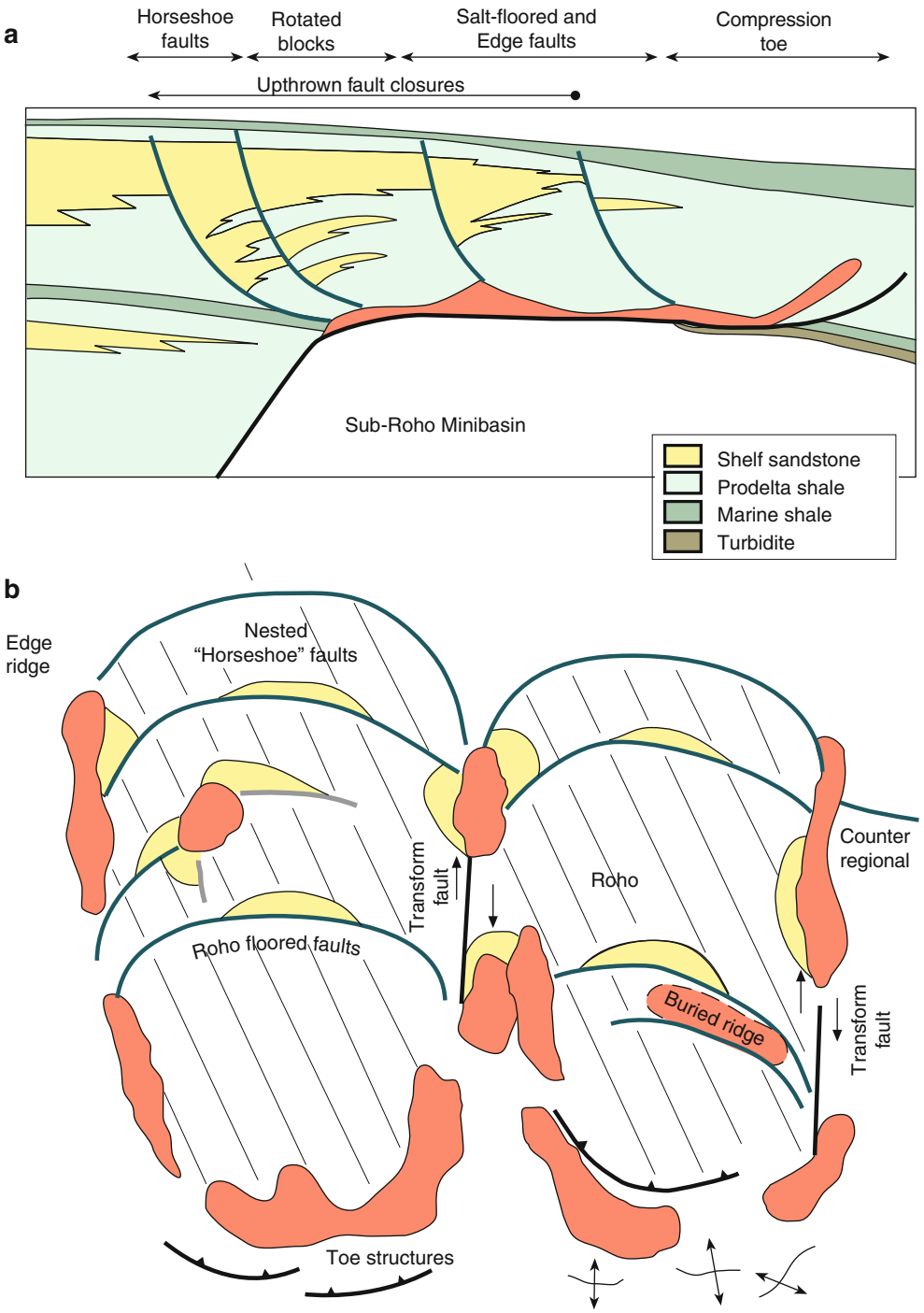

Fig. 10.65 Model of reservoir styles showing distribution of Roho (suprasalt) traps in both shelf and deepwater minibasin (primary basin) settings (After Karlo and Shoup 2000)

grey in Fig. 10.66; Pilcher et al. 2011). Most primary basins that trap hydrocarbons are encased entirely in salt or in some combination of salt and welds (Fig. 10.66c). Pilcher et al. (2011) notes most petroleum exploration in the deep-water Gulf of Mexico is currently focused on primary basin targets and increasingly those at their lateral boundaries. However, as these boundaries are usually poorly imaged, robust structural models are critical to interpretation of their evolution and relative petroleum system risk.

Using three-dimensional seismic data, Pilcher et al. (2011) define three tectonostratigraphic provinces that characterize primary basin depocenters: (1) a disconnected salt-stock-canopy province in Mississippi Canyon; (2) an amalgamated salt-stock-canopy province in northern Atwater Valley,

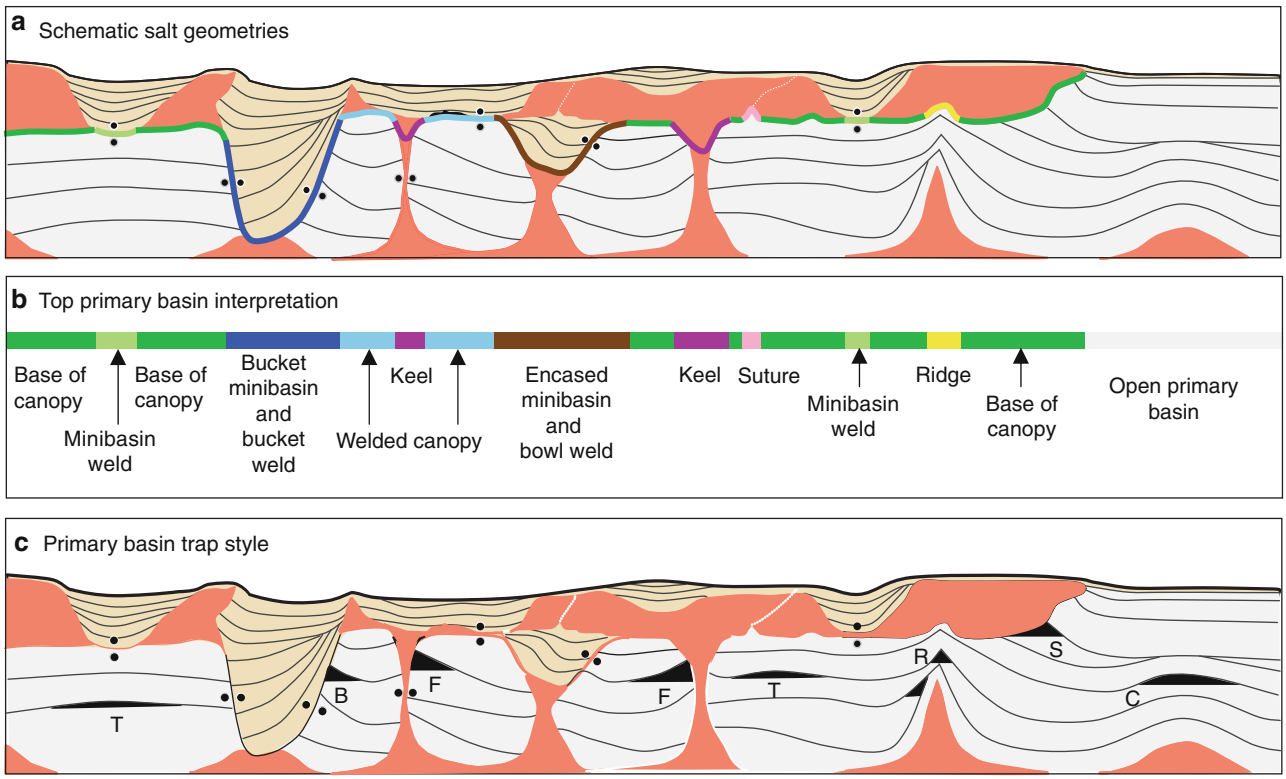

Fig. 10.66 Schematic representation of salt-related geometries in the deep-water Gulf of Mexico (After Pilcher et al. 2011). (**a**) Interpretation of top primary basin surface and distinction between primary and secondary basins. Salt is red, primary basins are gray, secondary basins are brown, and welds are indicated by paired *black dots*. (**b**) Classification of the top primary basin surface according to the nature of the surface. This classification allows primary basin bounding features such as feeders, ridges, and bucket welds to be mapped. (**c**) Schematic salt geometry highlighting primary basin trap types: turtle structure (*T*), bucket weld (*B*), salt feeder (*F*), salt ridge (*R*), base-of-salt truncation (*S*), and salt cored fold (*C*)

southeastern Green Canyon, Walker Ridge, and southern Keathley Canyon; and (3) a bucket-weld province in western Green Canyon, Garden Banks, and northern Keathley Canyon. They recognize six trap types in the primary basins (Fig. 10.66c): (1) autochthonous salt-cored folds, (2) turtle structures, (3) base-of-salt truncations, (4) salt feeders, (5) salt ridges, and (6) bucket welds. Most primary basin explorations to date have targeted traps in one of the first four styles. Future primary basin exploration will increasingly focus on the traps formed by bucket welds and salt-cored ridges. The contrasting evolution of these features has implications for reservoir continuity, charge access, and trap configuration. Of primary basin boundary trap types, salt feeders have the lowest petroleum system risk followed by bucket welds, with salt-cored ridges having the highest risk.

Intrasalt Halokinetic Plays

Known salt-associated reservoir distribution in the Gulf of Mexico is external to the salt mass, typically in subsalt or suprasalt positions in what is a tiered salt stratigraphy (Fig. 10.66) but there are a few situations worldwide where economic accumulations of hydrocarbons are trapped as intrasalt or salt-encased reservoirs. Usually the permeability of such accumulations is low and volumes of producible hydrocarbons are sub-economic. But, bedded masses of carbonate and porcellanite (silicilyte) in Infracambrian salt in the South Oman Salt Basin Oman are currently in production, extracting hydrocarbons from stringers (aka slivers) suspended in Infracambrian Ara Salt of the Huqf Supergroup (Fig. 10.67). The chronostratigraphic nomenclature of Oman is summarized in (Fig. 10.68).

Across the various Oman salt basins, wherever the Ara salt seal is breached, the Neoproterozoic organic-rich evaporitic sediments of the Huqf Supergroup have sourced most of the oil and gas stored in halokinetically structured suprasalt Phanerozoic reservoir sands in the Ghaba and Fahud salt basins (Fig. 10.67a; Terken et al. 2001) Likewise there is a concentration of large fields in Permian-age clastics along the dissolution edge (Eastern Flank) of the South Oman Salt Basin (Fig. 10.8b). Diapirs crop out across the Ghaba Salt Basin, while there are no such suprasalt diapir outcrops in the South Oman Salt Basin (Peters et al. 2003; Reuning et al. 2009). This distribution is a reflection of the migration pathways that

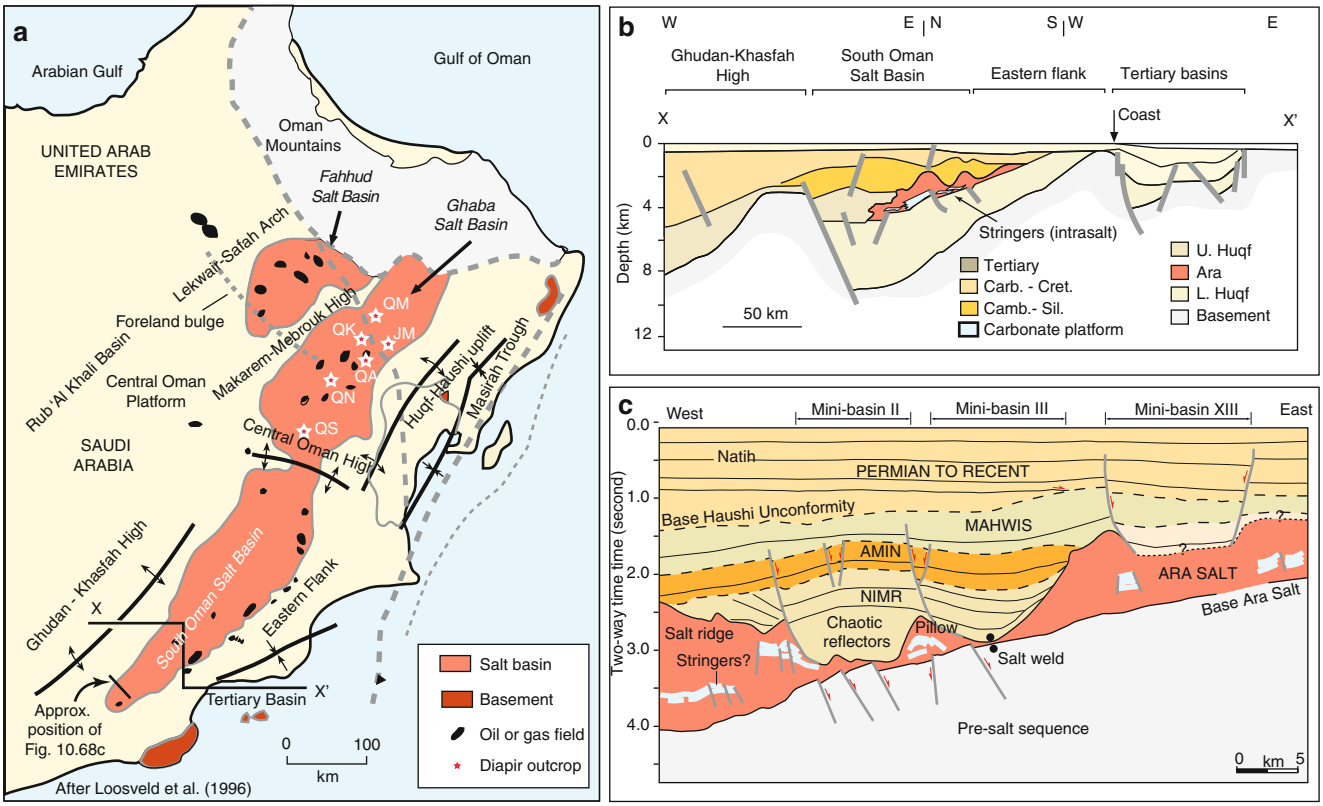

Fig. 10.67 Salt Basins of Oman. (**a**) Map view of three main salt basins. Palaeozoic strata capping the Ghaba Salt Basin and along the eastern flank of the South Oman Salt Basin are the main oil and gas producers, not Neoproterozoic platform carbonates or Athel Fm. silicilyte slivers, which host stringer reservoirs more toward the centre of the South Oman Salt Basin. Location of the six surface-piercing salt domes in the Ghaba Salt Basin (indicated by *star*) are: Qarn Sahmah (*QS*), Qarat Kibrit (*QK*), Qarat Al Milh (*QM*), Qarn Nihayda (*QN*), Qarn Alam (*QA*) and Jebel Majayiz (*JM*). (**b**) Cross section (X – X′) through the South Oman Salt Basin, schematically showing position of carbonate platform and stringers in the Ara Salt (After Loosveld et al. 1996 and Schröder et al. 2000a, b). (**c**) Section (seismic overlay) showing interrelationship between overburden loading (minibasins II, III and XIII) and distribution of carbonate reservoir stringers within the halokinetic Ara salt (After Al-Barwani and McClay 2008)

defines the two separate distribution styles of Phanerozoic age reservoirs in the two salt basins, Hydrocarbons in both basins were sourced in the Infracambrian Huqf Supergroup with generation from this ancient source rock beginning in the middle of the Cretaceous period (Fig. 10.8b; Terken et al. 2001).

Ara Group Intrasalt Reservoirs, Oman

The Neoproterozoic/Early Palaeozoic Ara-Group that hosts the various stringer reservoirs (carbonate and silicilyte) is the terminal subdivision of the Huqf-Supergroup of Oman (Fig. 10.68). Deposition of the Huqf spanned several tens of millions of years during the Vendian (Neoproterozoic) and early Cambrian and included deposition of the Ara Group salts. The Ara Group evaporites are a part of a broader penecontemporaneous Hormuz-Ara halite-hydrocarbon association that extended across the Middle East as a series of Neoproterozoic-Cambrian salt basins. Thick, variably halokinetic salt successions of this age occur in Oman (Ara salt in the South Oman, Ghudun, Ghaba and Fahud salt basins), in eastern Arabia and southern Iran (as the Hormuz salt in the Gulf Basins), in the Kerman region of Iran (Ravar Fm.) and across into NW India and Pakistan (Salt Range Fm.). Most of the salt bodies about the margins of these various salt basins show evidence of dissolution and salt flow-related withdrawal, suggesting that salt extent at the time the basins were actively accumulating halite was more widespread than it is today. All these basins constitute a series of basinwide evaporites precipitated in marine-fed seepage depressions or foreland sags created by the docking of continental masses at major subduction sutures. These systems were actively accumulating evaporites in regions of continental margin subduction that were tied to zones of active volcanism (Much like the Mediterranean in the Messinian and the Red Sea in the Middle Miocene). That there was an active volcanic influence at the time that Ara and Hormuz salt was accumulating is further evidenced by blocks of intrasalt rhyolitic volcanics and stringers in diapir outcrops in the Ghaba Salt basin (Fig. 10.67a; Reuning et al. 2009).

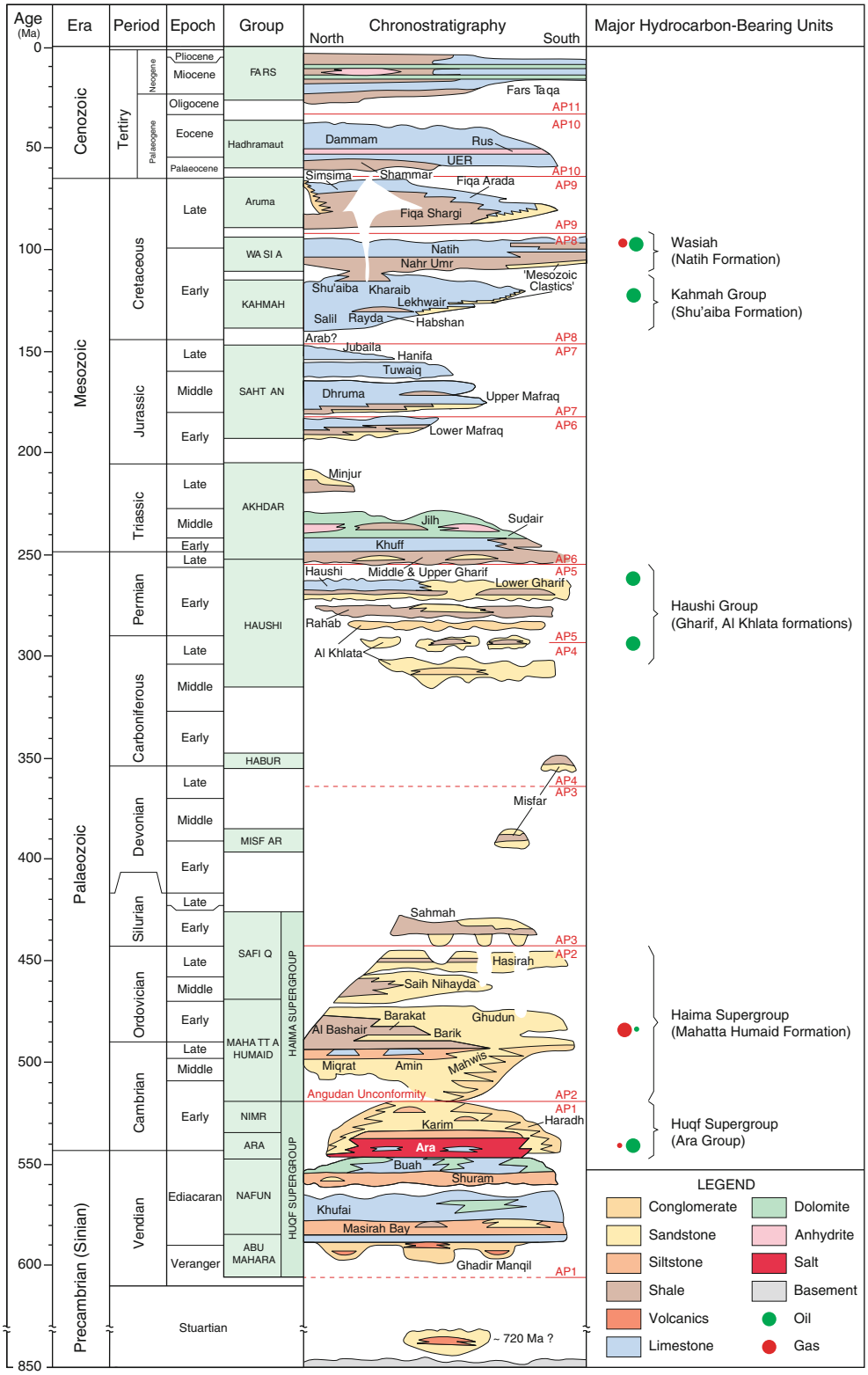

Fig. 10.68 Stratigraphy of Oman (After Sharland et al. 2001)

Carbonate Stringer Reservoirs in the South Oman Salt Basin

Depositional cycles within the Ara Group tend to be lithologically symmetric, with thick dolomitised carbonate platforms sandwiched between anhydrite, halite, and some thin intervals of potash salts. The Ara Group platform successions in the South Oman Salt Basin are conventionally broken down into five to six 3rd-order carbonate-evaporite cycles (Fig. 10.70; Schoenherr et al. 2007a, b, c; Schröder et al. 2000a, b, 2003, 2005; Gorin et al. 1982). Each depositional cycle starts with an erosion base often atop a dissolution breccia atop the salts of the previous cycle follow by variably dolomitised shelf carbonates (now somewhat disaggregated by halokinesis into salt-encased stringers with variable porosity) passing laterally and vertically in saltern anhydrites and up into halite at the top of the cycles. In parts of the Ara basin fill, the halite layers in cores collected between carbonate layers preserve aligned chevron depositional textures, while elsewhere thicker halite layers show widespread evidence of saltflow textures typified by pervasive biaxial flattened crystals and local stress-free mosaic (pers. obs.).

The regional subdivision of the South Oman Salt basin at a time of relative highstand in the various depositional cycles when carbonate deposition dominated is illustrated in Fig. 10.69. At that time the basin consisted of thrombolite-rimmed north and south carbonate platforms separated by a zone of deeper water carbonates or porcellanites (Fig. 10.69b). Better quality reservoirs tend be associated with the platform edges, but much of the original poroperm distribution has been strongly altered by a combination of dolomitisation, over-dolomitisation and variable intensities of pore fill by halite cement (Schoenherr et al. 2009). The stratigraphy of the stacked cycles defines what is a typical marine-fed intracontinental sag basinwide evaporite. In each cycle the carbonate is interpreted as representing the less saline highstand stage flood of the basin sump, with the subsequent progradation of a carbonate ramp prior to a basinwide episode of sulphate then halite-dominant evaporite fill. Today all the cored sulphate in the South Oman Salt Basin is platform anhydrite that is tied to the platform interior cycle, but it retains pseudomorphs after selenitic gypsum, showing it was originally deposited as a gypsum saltern atop thrombolite-rimmed platforms (Schröder et al. 2003).

Internally, the various carbonate and sulphate facies of the undeformed platform blocks are simple to interpret depositionally. Energy related facies developed in different water depths in an into-the-basin deepening ramp system, within what was an intracratonic rift or sag (Fig. 10.69b). Salt layers in the Ara Group are roughly time equivalent to cycles in the Hormuz Formation to the north (Schröder et al. 2003; Sharland et al. 2001). Finely laminated organic-rich dolomites and some thrombolite buildups of the carbonate platform facies occupied an outer to middle ramp setting, typified by lower energies and outcrop at the margins of the basin. Further out in the current basin they are overlain by shallow water platform mudstones, packstones, and evaporites (Fig. 10.69b).

I do not consider the Ara carbonate platforms, with thrombolites and stromatolites interlayered with salts, as indicators of an open-marine surface hydrographic connection to the ocean. Rather the thrombolites and stromatolites in the Ara stringers of the SOSB indicate times when an intrabasin drawndown water body possessed salinities suitable for the growth of marine-seepage-fed halotolerant biota (stromatolites and thrombolites). Thrombolites and stromatolites were widespread in marine waters of the early Cambrian marine waters of Namibia (Grotzinger et al. 2005), and this is the analog typically used for the Ara thrombolites. But, as we know from modern and Messinian and Silurian evaporite analogs the thrombolite/stromatolite association is not specific to open marine conditions (Chaps. 1, 4, and 5). Rather, throughout the Phanerozoic, the thrombolite-stromatolite association in evaporite basins (especially when interlayered with basinwide salts) is specific to episodes of microbial growth in the upper euphotic portions of salinity-stratified water masses. In this setting thrombolite capstones indicate times and places where basin salinity hovered around marine-like levels. The distinction is significant as it explains a lack of marine time equivalents to the Ara Group strata that would otherwise indicate a linkage and tie to succession to a worldwide eustatic curve. Ara Group thrombolite build-ups show more depositional affinity with subsalt lacustrine reservoir facies the typify the south Atlantic Aptian salt basins rather than any open-marine facies.

In evaporite basins the occurrence of salt-encased thrombolites and stromatolites does not indicate a time of a surface connection to the ocean, but relative intrabasin highstands with thrombolite mounds growing on water covered topographic highs (with positions controlled by the draping of underlying topographic highs). In the Silurian and Messinian the thrombolite stage indicates the onset of drawdown and the loss of a surface or hydrographic connection to the ocean. Today, in evaporitic waters, conditions where thrombolites flourish and come to dominate the halotolerant biota are typically in saline schizohaline lacustrine settings (e. g. Lake Clifton and Sleaford Mere in Australia) and not open marine settings. At times of restriction onset, healthy thrombolites and stromatolite populations flourished in the Messinian (Late Miocene) intrabasin highstands has seen during marine to evaporitic marine-seepage carbonate transitions into the various halite/gypsum-filled basins of Spain and Sicily. Likewise, stromatolites and thrombolites are growing today in a number of hydrographically isolated Holocene marine-seepage basin in southern and western Australia.

Conceptually, it is important to recognise that within the drawndown evaporite basin stage that defines Ara Group sedimentation, the Ara platform carbonates grew during episodes of higher relative water levels in the drawndown basin, when the waters atop the basinwide halocline were less saline. In contrast, thick Ara halites beds typify times of the lowest water

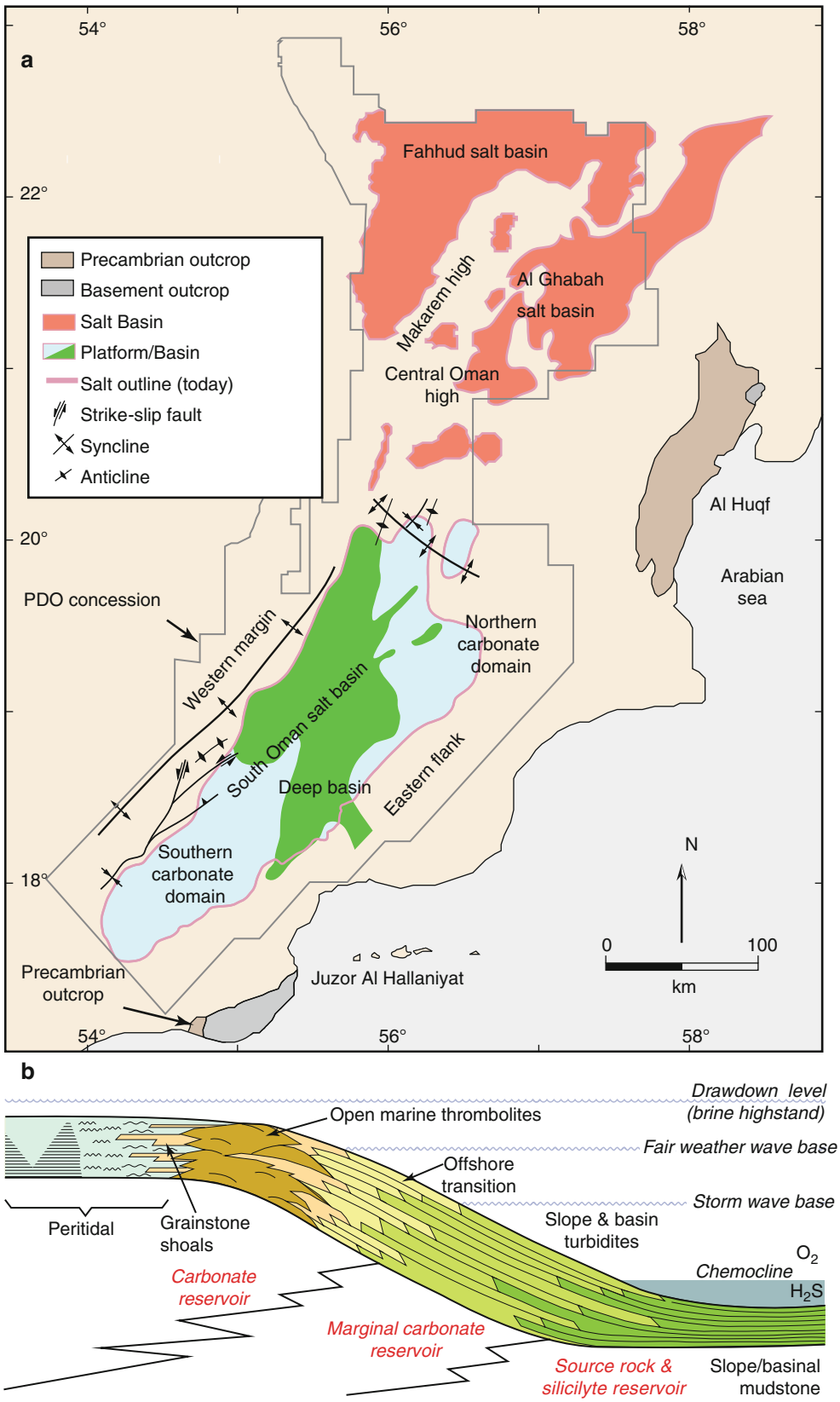

Fig. 10.69 Geology of the South Oman Salt Basin. (**a**) Distribution of the main depositional and tectonic elements. At the times of relative highstand in the deposition of the lower parts of the sequence cycles (illustration for cycle A3/4) the basin can be subdivided into two main carbonate platforms and a central deeper basinal section, where bacterial porcellanites (silicilytes) accumulated (After Al-Siyabi 2005). (**b**) Schematic showing facies distribution of an Ara carbonate platform and basin with interpreted reservoir and source rock occurrences during a relative highstand (fresher) in the drawndown South Oman Salt Basin at a time when thrombolite buildups were flourishing (After Al-Siyabi 2005). Later encased by "fill and spill" halite

levels in the basin, when basin sump water columns were holomictic and saturated, while anhydritic platforms define intermediary brine levels with basinwide anhydrite deposition requiring holomictic waters at $CaSO_4$ saturations (Chap. 5). This oscillating drawdown (fill and spill) hydrology has significant implications in terms of salt plugging of the carbonate stringer reservoirs and the timing of the synprecipitational dissolution breccias, which occur in the various cored Ara carbonate sequences and their outcrop equivalents (pers. obs.).

Even as each cycle was forming, earlier Ara halite-rich evaporite sections, laid down across this large drawdown basin, were exposed about the same basin edges by ongoing drawdown and lowering of the brine level. In these exposed areas intra-stringer halite was being recycled into the brine sumps to form a thicker purer cleaner halite that typifies the mostly halokinetic Al Noor Formation halites (Fig. 10.70). This purer cleaner halite unit is was loaded and deformed by the deposition of the Nimr-Mahwis succession (Fig. 10.67c) Prior to its deformation and edge dissolution the halite once extended all the way across the South Oman Salt Basin and probably beyond. It was thickest in the regions of the Waad and Waghald Basins, which were minibasin lows at the time the halite was accumulating (see silicilyte discussion). They were longterm brine sumps with positions controlled by an earlier basin topography inherited from Buah time. Widespread halite deposition slowed at the top of Birba Formation and so the background volcanism, which had periodically supplied epiclastic fine-grained sediments and tuffaceous ash layers throughout the precipitation of the Birba Formation came to dominate the depositional signature atop this salt. This was the time when the U shale and the Theleilat Formations were deposited in what were still saline, perhaps stratified, basinal successions within the intracratonic sump. Previously, this background volcanogenic sedimentation across the region had been swamped by the high rates of sedimentation associated with evaporite deposition. Much of the halite texture and geometry in the overlying Al Noor Formation halite is dominated by halokinetic textures induced by a combination of salt flow, sediment loading and salt dissolution.

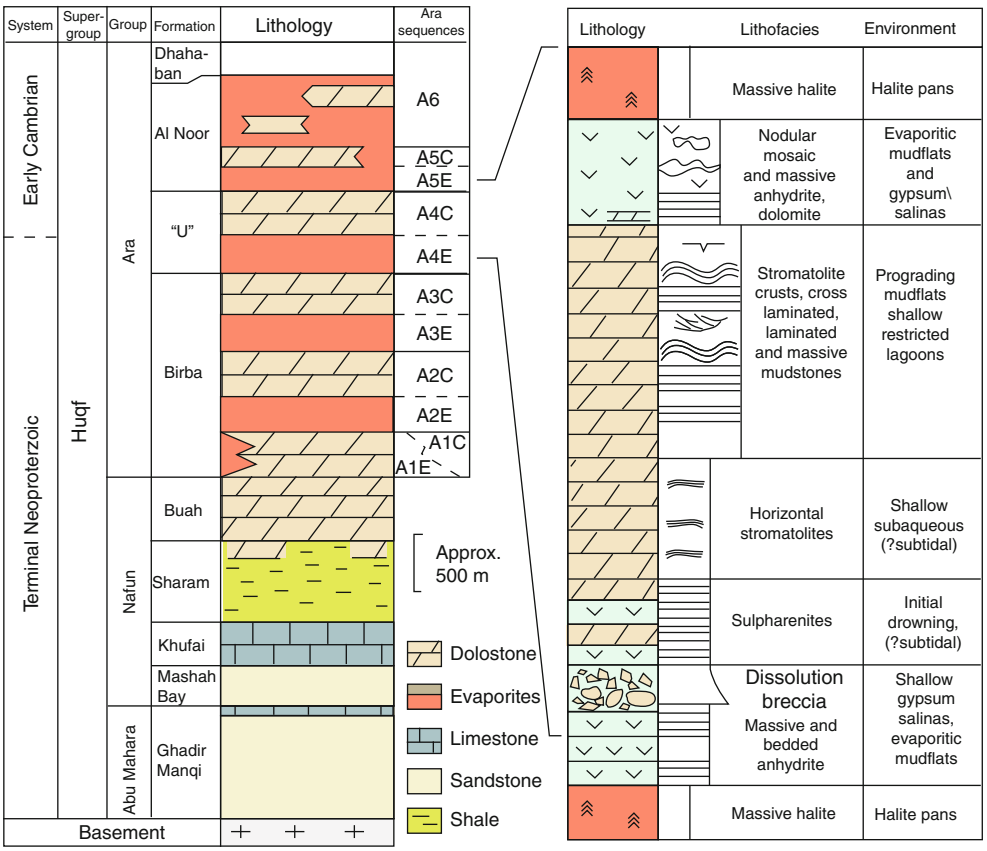

Fig. 10.70 Typical Ara carbonate platform cycle (A4) in the Neoproterozoic Ara Formation of the South Oman Salt Basin. Further out in the now chaotic central parts of the basin, some consider the Athel Silicilyte was originally deposited as a time-equivalent to the A4 carbonate, others argue that prior to halokinesis the silicilyte once lay immediately atop the unconformity capping the A3 carbonate (more likely). It can even be argued that in the original basin centre stratigraphy, prior to halokinesis, there was more than one level of mesohaline silicilyte deposition. This quandary could perhaps be resolved by more detailed determinations of basinwide versus platform evaporite signatures using wirelines and cores from across the basin (After Schröder et al. 2003, 2005) See also Fig. 10.69

In concert with the chevron textures preserved in the halite interlayers of the Birba formations (where salt has not flowed) there are well-preserved sedimentary structures (e.g. palmate gypsum morphologies and desiccation cracks) in the anhydrite layers of the Birba Formation cycles that suggest a shallow (<5 m deep) subaqueous environment for the various carbonate-sulphate platform cycles (Schröder et al. 2005). Sabkha deposits represent only a minor fraction of the total salt sulphate in each Birba cycle. Following times of basinwide saltern sulphate accumulation, brine depths shallowed further and thick beds of basin centre halite precipitated, along with rare thin beds containing rare potash salt cements. These beds rapidly aggraded to cover and seal the carbonate/sulphate platform. Bromine geochemistry in the halite beds show a consistent range of values between 40 and 150 ppm (Fig. 10.71; Schoenherr et al. 2009). The Br values likely indicate a first-cycle marine source to seepage brines precipitating the various Ara halite cycles, with some minor contributions from continental and/or hydrothermal waters. Interestingly the associated halite cements in the intervening carbonate layers are higher. This is indicative of the fact reservoir quality is not typically tied to depositional facies in the various Ara carbonate cycles. Rather reservoir quality is typically tied to varying intensities of dolomitisation and halite cementation (Fig. 10.72).

When porosity and permeability is tied back to position in the various carbonate layers it is immediately obvious that pore occluding halite cement is a major control on porosity and permeability, the other is dolomitisation (Fig. 10.72) The well permeability profile illustrated in Fig. 10.73 is typical of many of the low permeability wells that typify the Birba cycle carbonate layers and clearly shows the detrimental influence halite plugging on reservoir quality. In such low permeability wells the thrombolite and grainstone units tend to retain little or no permeability across zones of halite plugging. Locally there are zones of corrasion and this enhances porosity as seen in the high permeability spikes. Earlier work in the early 2000s tended to ignore the influence of halite cements and focused more on dolomitisation intensity and style. Dolomitisation is certainly another influence on reservoir quality and is vital in wells that lack halite cements However, when both these diagenetic factors are present, dolomitisation style is secondary to the degree of salt plugging. In almost all wells depositional porosity is lacking (Figs. 10.72 and 10.73)

There are two stages of dolomitisation in most carbonate layers and a later stage of post-dolomite corrasion (Fig. 10.72). The earlier episode of dolomite formation is related to brine reflux and the second to subsequent burial. Brine reflux dolomites tend to finely crystalline and mimetic. Later dolomites tend to be more coarsely crystalline. The separation of the two dolomite styles into earlier (somewhat

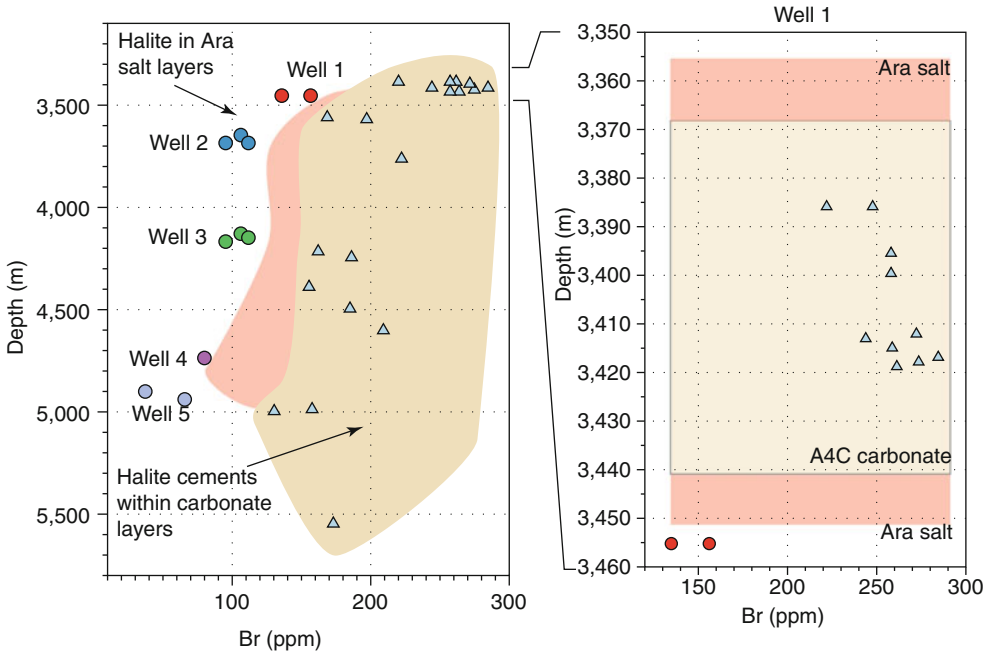

Fig. 10.71 Bromine values in the Ara Group. (**a**) Distribution of Br contents in pure Ara salt intervals and halite cements in various Ara carbonate stringers with depth showing most Br contents of the pure Ara salt (*red field*) are markedly below the Br values of the halite cements in associated carbonate stringers (*brown field*). (**b**) Detail of Well 1 values clearly showing that Br content of halite cements in the carbonate stringer A4C are some 150 ppm higher than Br contents of the underlying Ara salt. The two stratigraphically uppermost cement data points are from one halite vein. The remaining data points cluster around 260 ppm and are from early pore-cementing halites that degrade porosity in the carbonate bed (Replotted from values in Schoenherr et al. 2009)

lower temperatures) and later (warmer) diagenetic events is clearly seen in stable isotope C-O crossplots (Fig. 10.74). Finely crystalline dolomites dominate the matrix fraction while coarse dolomites tend to replace or encase the earlier finer crystals. The increasingly negative oxygen isotopes value seen in the dolomites indicates ongoing dolomite growth and replacement during increasingly warmer burial conditions (indicated by arrow in Fig. 10.73)

There is an interesting variation in the carbon isotope value plot field in a well that cored the A4C carbonate (Fig. 10.74-shaded region). Dating of associated ashfalls implies the A4C carbonate in this well straddles the Cambrian-Precambrian boundary (Al-Husseini et al. 2003; Amthor et al. 2003). A short-lived negative excursion in the carbon isotope composition of seawater is globally coincident with the Precambrian-Cambrian boundary. It is thought to indicate a mass extinction event within Terminal Proterozoic ecosystems at or very near the Precambrian boundary. This A4C carbonate interval is one of the few worldwide that preserves sediments across the Precambrian-Phanerozoic boundary. In A4C sediments below the isotope-defined boundary, the characteristic Proterozoic zone fossils *Cloudinia* and *Namacalathus* make their last appearance in the rock record.

Across much of the South Oman Salt Basin the Ara carbonate layers underwent a complex diagenetic evolution, typically with one stage of halite cementation occurring in a shallow (early) and another in a deeper (later) burial environment (Fig. 10.75). Early and late halite cements are defined by their microstructural relationship with a widespread pore-occluding solid bitumen phase. This bitumen phase includes locally abundant occurrences of the rare mineral whewellite ($CaC_2O_4.H_2O$). It is a known crystalline organic mineral, which can form as a low-temperature primary hydrothermal mineral in carbonate-sulphide veins, via oxidation of organic material in the surrounding rock. Whewellite typically shows an association with baryte, sphalerite, pyrite, bitumen and siderite in crosscutting veins (Fig. 10.75c).

The early phase of halite cementation is post-dated by this solid reservoir bitumen (with brecciated whewellite). This halite cement phase is most pervasive towards the top of carbonate stringers, where it plugs nearly all available porosity in facies with initially favourable poroperm characteristics (Figs. 10.73 and 10.75a, b). Bromine geochemistry reveals significantly higher bromine contents (up to 280 ppm) in the early halite compared with the late halite cement (173 ppm). Both intracarbonate halite cements show bromine values that

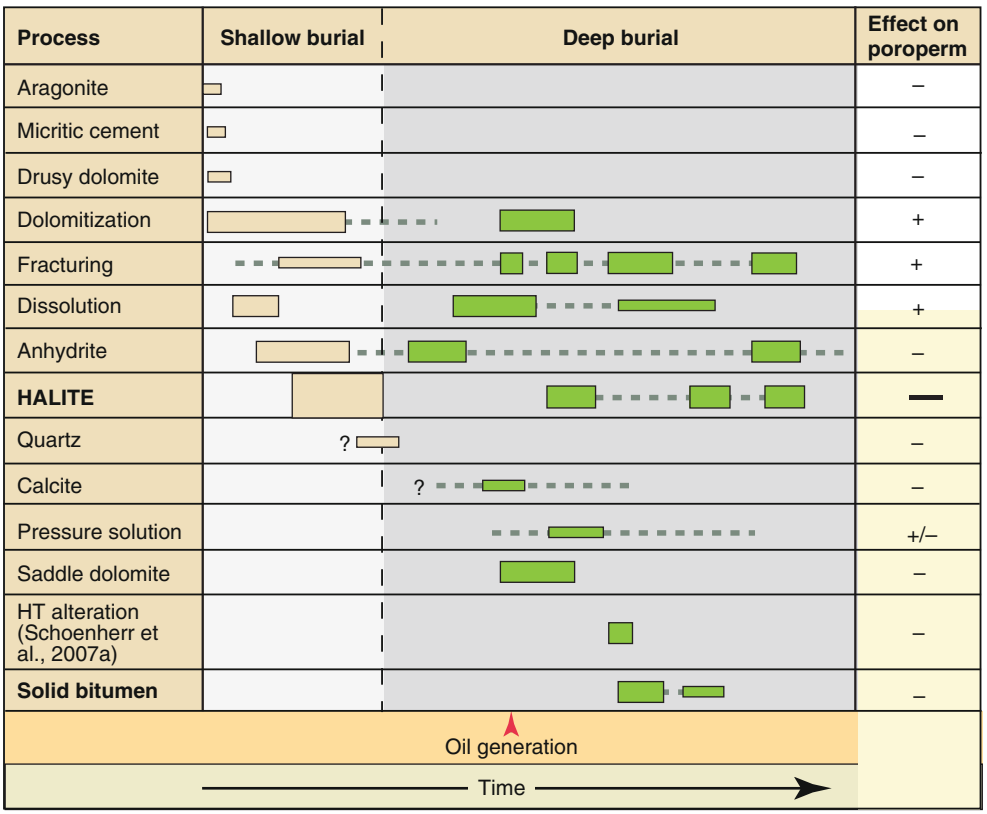

Fig. 10.72 Regional paragenetic sequence of reservoir quality controls in Ara stringer carbonates deduced from 190 samples from the A1C to A4C carbonate levels in 24 wells in the Greater Harweel and the Greater Birba Area (After Schoenherr et al. 2009). HT refers to hydrothermal alteration as described by Schoenherr et al. 2007a). *Thick coloured bars* indicate major diagenetic processes, *thin bars* indicate minor diagenetic processes; *dashed grey lines* indicate uncertainty of process duration. '+' denotes enhancement and '–' denotes degradation of the poroperm quality. Size of the symbol indicates relative importance in reservoir quality evolution

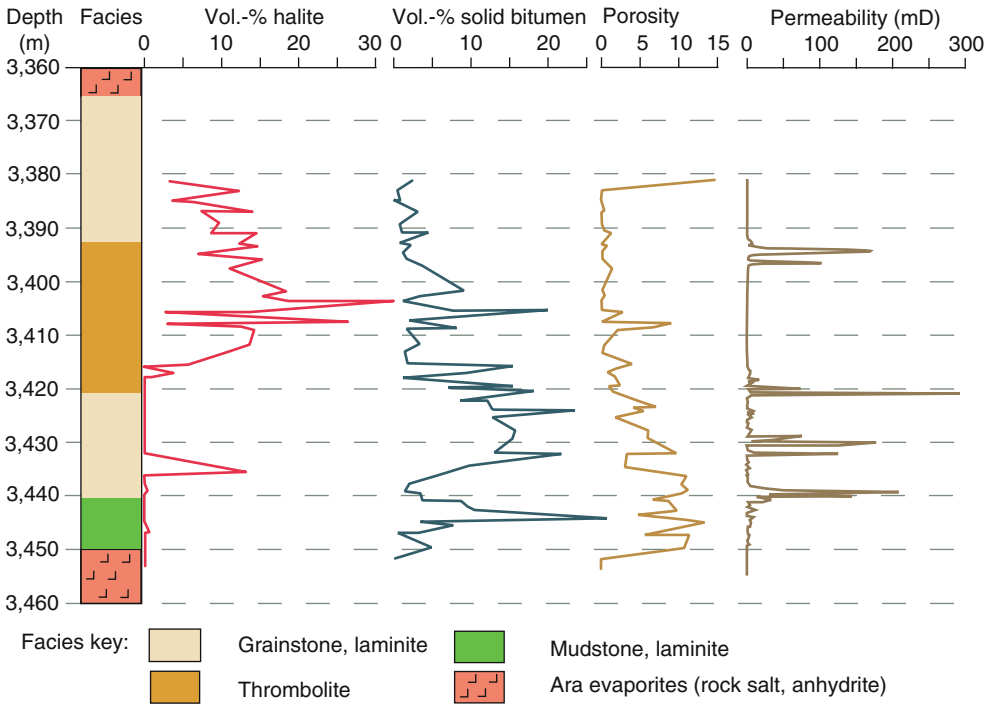

Fig. 10.73 Poroperm data and vertical distribution of halite and solid bitumen in the A1C cycle thrombolitic carbonate of a representative well. Core from 3,385 m is pervasively halite-cemented and also cross-cut by whewellite-cemented veins. Core from 3,399 m is a bitumen-cemented and halite-cemented thrombolite. Clearly, diagenesis related to the evaporite sealed and derived brines, play a significant role in the current reservoir quality. Depositional facies are secondary controls (After Schoenherr et al. 2009)

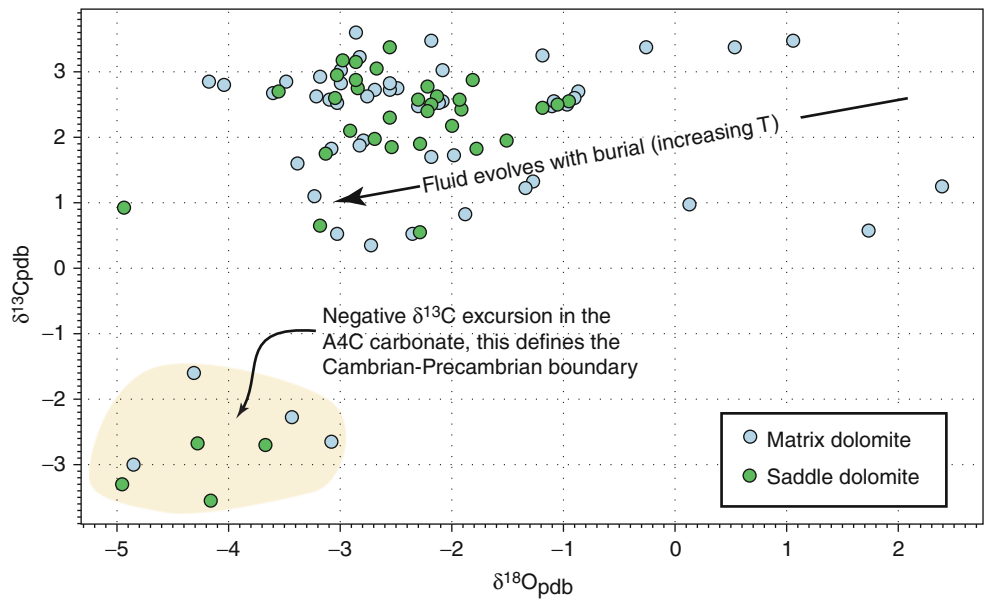

Fig. 10.74 Stable isotope data (covariant plot of $\delta^{18}O$ vs. $\delta\ ^{13}C$) in saddle and matrix dolomites from intra-salt Ara carbonate cycles. Shaded data within frame shows a shortlived negative $\delta^{13}C$ excursion in the A4C stringers at the Precambrian–Cambrian boundary (Replotted from Schoenherr et al. 2009)

are higher than the chevron halites preserves in the Ara Salt layers (Fig. 10.71).

The distribution patterns and the (high) bromine contents of early halite are consistent with precipitation caused by seepage reflux of highly saturated brines during deposition of the overlying rock salt interval (Fig. 10.75a). Later in burial history, relatively small quantities of early halite were dissolved locally and re-precipitated as indicated by inclusions of streaky solid bitumen within the late halite cements. Late halite cement also seals fractures, which show evidence for repeated reopening. Initially, these fractures formed during a period of hydrothermal activity and were later reopened

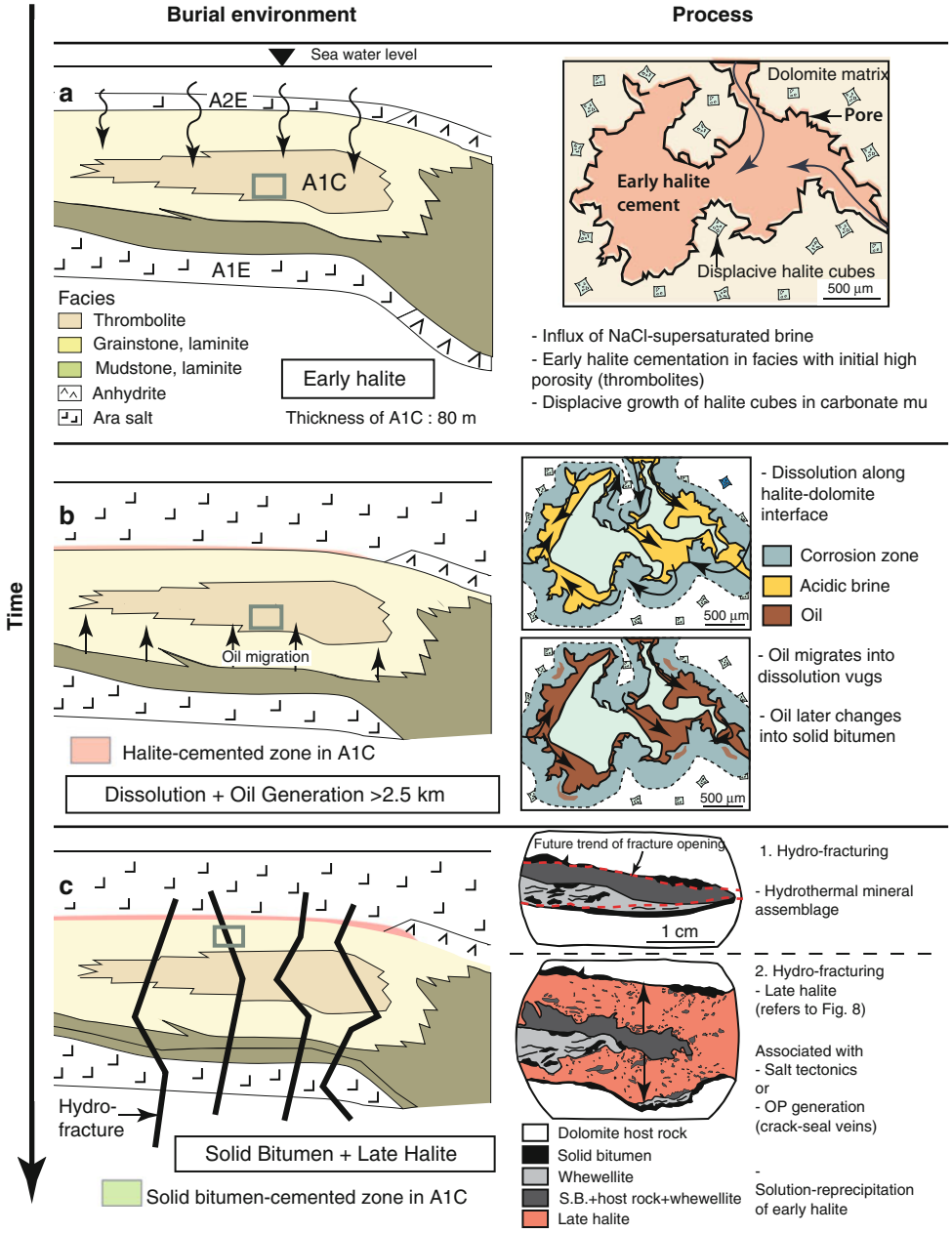

Fig. 10.75 Schematic illustrating the evolution of early and late halite cementation in the A1C stringer with time. Facies distribution of the A1C is adapted from Al-Siyabi (2005). Grey frames in burial environment of A to C represent corresponding micro-scale processes. (**a**) Early halite cementation in the A1C interval is due to infiltration of hypersaline brines, seeping from above during deposition of the overlying evaporite interval A2E. (**b**) This stage is marked by oil generation from the organic-rich mudstones and laminites. Because the upper part of the A1C was cemented by halite (*dashed zone*), oil migration is restricted to the lower portion. Oil migration was preceded by a 'roll front' of acidic brines which caused slight dissolution of the dolomite and the halite cements at their immediate contact. (**c**) The formation of fractures in the Ara Group was accompanied by strong overpressuring and the presence of hydrothermal fluids, causing solid bitumen formation. A second phase of overpressure (OP) build-up led to the formation of halite-cemented (crack-seal) veins

by a crack-seal mechanism caused by high fluid overpressures (Fig. 10.75b, c). Porosity plugging by early halite cements affects the poroperm characteristics of the Ara carbonates much more than the volumetrically less important late halite cement (Fig. 10.73). Schoenherr et al. (2009) argue that the formative processes and hydrologically controlled distribution patterns of halite cements in the South Oman Salt Basin can be generalized to other petroliferous evaporite drawdown basins.

In addition to the diagenetic complexity of carbonate reservoir pores, mostly occluded by early reflux halite cement spar, much of the halite in the Ara salt layers was variably recrystallised during halokinesis, especially in the halites of the Al Noor Formation in the Ara Group. Most of the deformation evident in the Ara Group has been taken up in intervals of flowing salt, rather than by internal deformation and folding of the platform carbonates and sulphate layers, which owing to greater mechanical strength tends to retain their integrity in the various stringers and blocks. Halokinetic salt also encases the silicilyte slivers or blocks in the more central portions of the South Oman Salt Basin and is why it is difficult to place the various slivers suspended in Ara salt into a depositional reconstruction of the basin (Fig. 10.67c). For example are the laminated organic-rich cherty slivers (Al Shomou Fm silicilytes that we discuss in the next section) still near their original somewhat deeper water depositional position in the basin palaeogeography, or have they slide tens of kilometres or more across the basin via salt-lubricated gravity gliding and raft tectonics? The latter scenario, which is likely, would create a more complex jumble of slithers with porosity distributions largely unrelated to current block orientations.

Athel (Al Shamou) Silicilyte Stringer Reservoirs

Intrasalt targets in the Athel Formation (Al Shomou silicilyte) represent one of the more complex deep oil exploration plays in onshore Oman and constitute a significant part of Petroleum Development Oman's undrilled prospect portfolio (Reinhardt et al. 1999; Peters et al. 2003). During the late 1970s to early 80s Petroleum Development Oman (PDO) drilled several significant oil and gas shows as intrasalt objectives within the more basinal parts of the Ara Salt of the South Oman Salt Basin, such as Marmul No. 7 (Fig. 10.76). These potential reservoirs were in porous (15–25 %), overpressured siliceous microlaminated sediments that were stratigraphically trapped and fully encased in halokinetic salt at depths of 3–4 km. Based on these intersections, the size of potential intrasalt pools was thought to be large, with individual slabs or slivers of possibly oil-saturated silicilyte seen in seismic to be up to 2×6 km across and more than 300 m thick (Amthor et al. 2005).

In 1989 and 1995, respectively, Al Noor and Al Shomou were drilled as two sliver prospects in the Athel Formation silicilyte (Figs. 10.76a and 10.77). The first two wells in the Al Noor Field encountered over 300 m of pay within low permeability fractured intervals that well tests showed had levels of 8–9 md/m. Reserves of 15.0×10^6 m^3 oil were calculated from these early intersections with an expectation of oil-in-place in the fields of up to 2 billion barrels (Wong et al. 2000). Oil recovered from the wells was attractive, although it was largely hosted in an unusual reservoir of microlaminated organic-rich chert or silicilyte, which contains up to 90 % microcrystalline silica and have a likely microbial source (Fig. 10.76b) Silicilyte is a general term for a fine-grained silica rock; porcellanite might be a more appropriate term as these cherts retain producible levels of microporosity. The chert was deposited at or near the Cambrian-Precambrian boundary (Ramseyer et al. 2013)

The produced oil is light (48° API) with a viscosity of 0.3–0.36 mPas^{-1} and a bubble point of 277 bar. The initial solution gas-oil-ratio was 400–550 m^3/m^3, with H_2S levels of 1.5 mol% and CO_2 levels of 3 mol%. It was recovered from wells with early flow rates of up to 8,800 bbls/day. Average well flow rates varied between 40 and 110 m^3/day prior to reservoir stimulation, post-stimulation figures have not been released. The silicilyte slivers define a play type worth pursuing, but a number of dry holes drilled after the initial successful wells defined inherent complexities with respect to reservoir quality prediction, hydrocarbon charge, production behaviour, and seismic imaging. Inherently high variability in the silicilyte permeability both vertically and laterally means successful future exploitation must involve targeted directional drilling and reservoir stimulation (Ramseyer et al. 2013).

The silicilyte play is an unusual basinal evaporite association, characterized by light and sour oil, hard overpressures and a high-porosity, low-permeability silica matrix (0.2–0.3 md) constituting a fine-grained microlaminated chert that is consistently rich in organic matter (Wong et al. 2000; Amthor et al. 1998; Amthor and Frewin 1999). Encasing halite has prevented hydrocarbon expulsion from the silicilyte, explaining inherently high formation pressures ≈19.8 kPa/m and high present-day oil saturations ≈65–90 %. The absence of oil expulsion is evident from Rock Eval data, which are characterized by high production indices. A good correlation between S_1 and the generative potential $S_1 + S_2$ suggests that hydrocarbons were indeed generated in situ and did not result from migration of hydrocarbons generated at deeper horizons. This also fits with the typical tight character of source rocks in style 1a basinwide evaporite settings (Chap. 9). As a source rock the Athel Formation silicilyte is also unique (Terken et al. 2001). Finely disseminated kerogen occupies up to 10 % of the rock volume, with a third of the organic matter concentrated in stylolites. Source rock extracts reflect the Infracambrian age of the formation, namely; light $\delta^{13}C_{PDB}$ of −37 to −35‰, a strong predominance of C29 over C28 steranes, and high 24-isopropyl/n-propyl

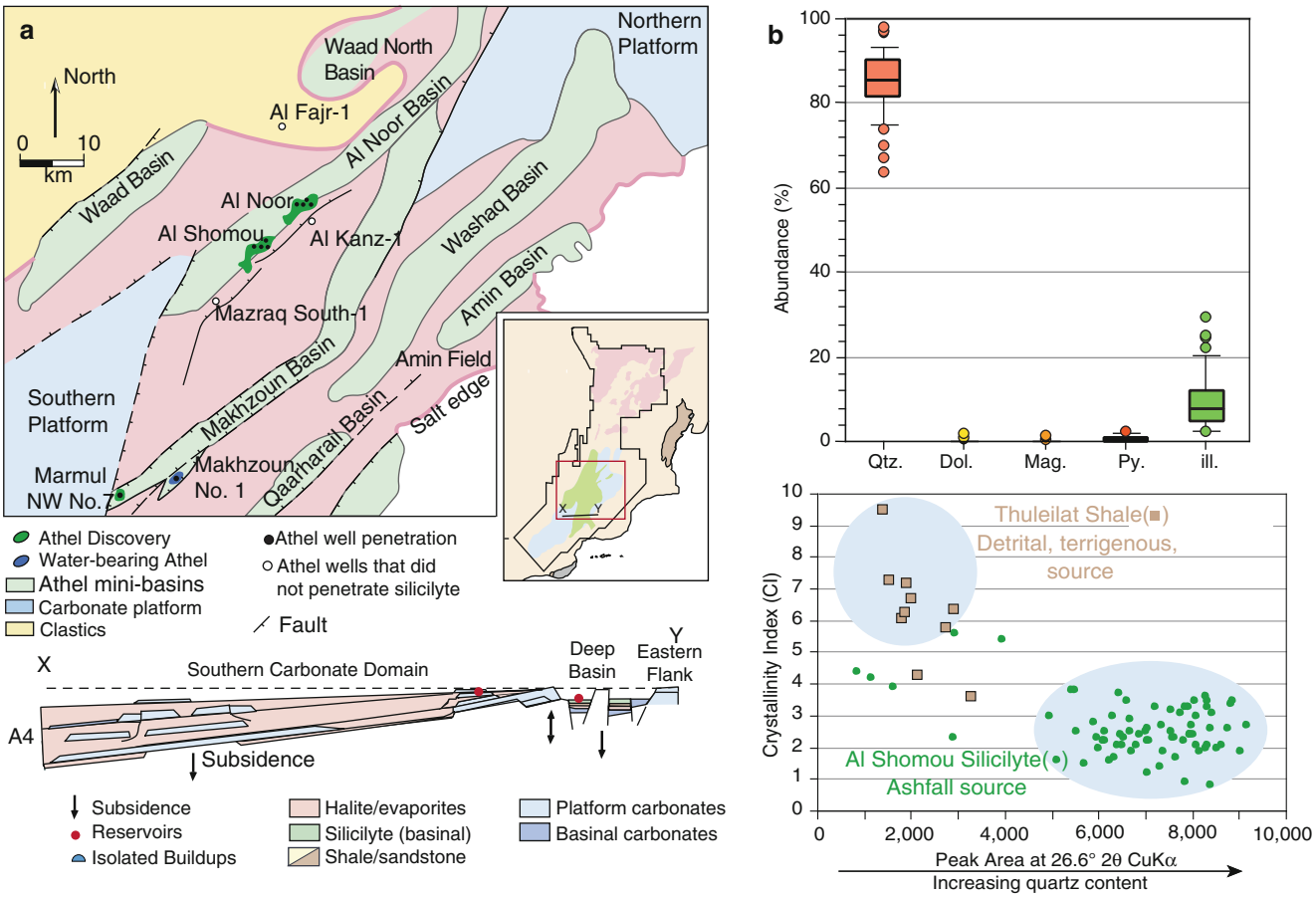

Fig. 10.76 Al Shomou (Athel) silicilyte. (**a**) Athel play map generated after drilling a number of unsuccessful penetrations illustrating the control of structural elements on the distribution of the Athel silicilyte in the SOSB. The occurrence of silicilyte in this model is restricted to lows between underlying Buah topographic highs which influence subsequent salt-cored seafloor topography. (**b**) Geochemistry of silicilyte showing X-ray determined mineralogical abundance and a crossplot of crystallinity index versus quartz content for samples from the Al Shomou Silicilyte and the Thuleilat Shale. Samples from the Thuleilat Shale have a higher crystallinity index and a lower concentration of quartz which is interpreted to reflect a higher detrital/authigenic ratio in the Thuleilat Shale (After Amthor et al. 2005)

cholestane ratios. The kinetic behaviour of the Athel is similar to that of the Miocene Monterey Formation, which, like the Athel, generates oil at low temperatures. Thin microfractures control production and much of the oil in fractures in this silicilyte reservoir is probably self-sourced from the adjacent matrix.

Varying thicknesses created by deep salt structures atop potential reservoir slivers, and the occurrence of reservoir slivers near the base of the thick halokinetic salt unit, has hampered reliable seismic positioning of these deep (>3,000 m) intrasalt reservoir objectives. Likewise, pressure transient tests in the intersected reservoir indicate an effective reservoir permeability that is one-tenth of that measured using cleaned core plugs (O'Dell 1998). The difference in well and plug determinations is likely caused by a combination of pressure-sealed fractures and the pervasive plugging effect of bitumen in the reservoir (bitumens are removed in standard plug preparation) Uncertainty in these and many other aspects of silicilyte understanding meant that until very recently the Athel Silicilyte or Al Shomou play was not pursued as a high value target within the PDO exploration portfolio. Improvements in seismic processing, targeted hydrofracturing, and geosteering technology, means it is possible to now pursue salt-encased permeable slivers as difficult but viable exploration targets.

Since the mid 2000s, wells in the two known silicilyte fields have been the successful subject of what was perhaps one of the largest fracture jobs in the region. PDO also instigated a number of detailed sedimentological and engineering studies to better understand what characterises reservoir versus nonreservoir associations in the silicilyte slivers (Ramseyer et al. 2013). Several factors are listed by Schröder et al. (2000b, 2003) as explaining the porosity dichotomy between Neoproterozoic platform carbonates and basin centre silicilytes:

- Downward circulation of saline brines caused mimetic dolomitisation and deterioration of reservoir characteristics in underlying platform carbonates. Any lithofacies close to overlying evaporites also suffered from evaporite

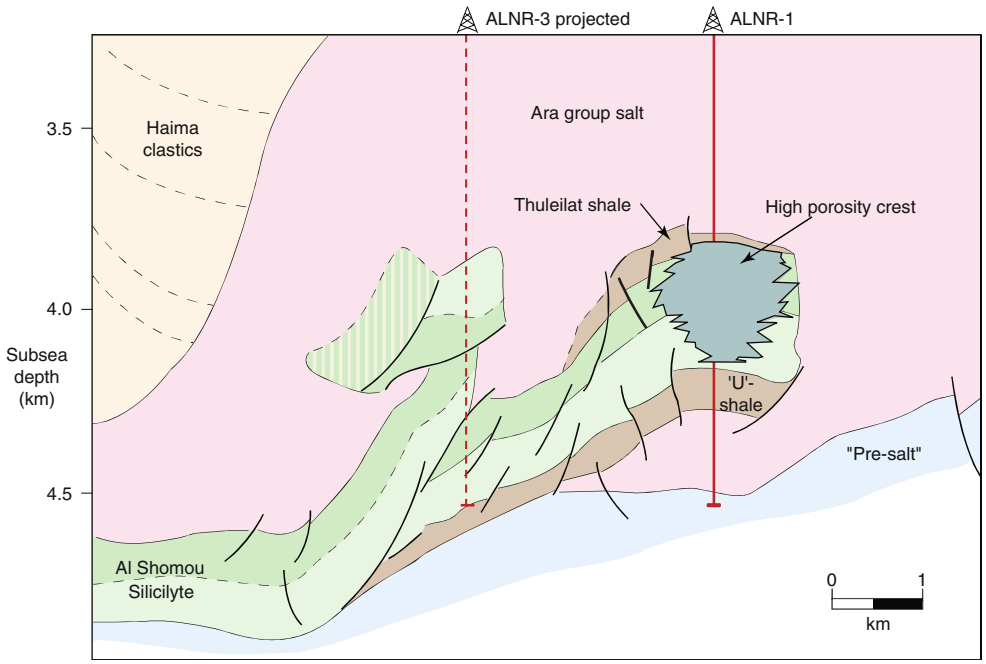

Fig. 10.77 Interpreted trace of seismic section across the Al Noor structure illustrating the positions of wells Al Noor-1 (ALNR-1) and Al Noor-3 (ALNR-3). Well Al Noor-1 (ALNR--1) targeted a thick intra-salt reflectivity package as part of the intra-salt carbonate stringer campaign. The well encountered a 400-m-thick, overpressured sequence of oil-bearing siliceous rocks. Well Al Noor-3 (ALNR-3) was drilled to appraise the down-dip extension of the proven oil column and to test a separate compartment of the Al Noor structure. The well did penetrate two Al Shomou Silicilyte slabs but encountered a significant deterioration in reservoir quality down-dip from the high-porosity crest (After Amthor et al. 2005)

cementation – i.e. shallow water carbonates at the top of stringers, as well as thin stringers.

- Early maturation of organic matter flushed the pore networks in the deeper water siliceous organic-rich laminites (silicilytes) with hydrocarbons that then prevented subsequent cementation by later carbonate and evaporite cements.
- Early reflux brines tended to flush the larger connected pores of the shallower and higher energy grainier carbonate units (e.g. thrombolite shoals) and so they were more easily filled with evaporite cements than the smaller hydrocarbon-rich pore networks of the basin centre silicilyte laminites.

Porosity evolution in the silicilyte laminites contrasts with that of thrombolite buildups and shallow water packstones where high porosities have been almost completely plugged by dolomite and halite cements, so typical of a depositional association with a basinwide evaporite unit. Thus production in Al Noor and Al Shomou fields comes from salt-encased organic rich blocks of chert of the Athel Silicilyte, not from platform dolomite sulphate successions (Peters et al. 2003).

Depositionally, the Al Shomou silicilyte is unusual compared to typical Phanerozoic marine cherts. It formed by primary silica precipitation of a marine-derived brine (as opposed to replacement of a carbonate or other mineral precursor) in an anoxic, sulphur-rich, stagnant and highly saline basin (Ramseyer et al. 2013). It is a primary hypersaline chert precipitated at the Neoproterozoic/Cambrian boundary. In core, the Al Shomou silicilyte is typically made up of metre-scale interlayers of finely microlaminated, porous silicilyte alternating with non-porous silica-cemented silicilyte. The latter act as vertical baffles to flow within the reservoir. In the absence of outcrop analogs, borehole-imaging logs are extensively used to delineate and to correlate reservoir units. FMI shows that more than 70 % of the lithofacies in the Athel Fm. are constituted of beds thinner than 1 m, along with cm-diameter dolomite nodules (possibly the result of bacterial sulphate reduction). Cemented fractures (some with fibrous halite fills) are locally common, typically reducing the horizontal connectivity. The rock matrix consists up to 80 % of microcrystalline quartz with high amounts of intercrystalline microporosity (up to 30 %). The very small modal crystal size of 2–3 μm and widespread bitumens in the silicilyte pore throats result in microdarcy levels of reservoir permeability (Ramseyer et al. 2013; Amthor et al. 1998; Peters et al. 2003). The present-day thicker (distal) silicilyte sections in the basin tend to have a higher average porosity than thinner (proximal) sections toward the platform.

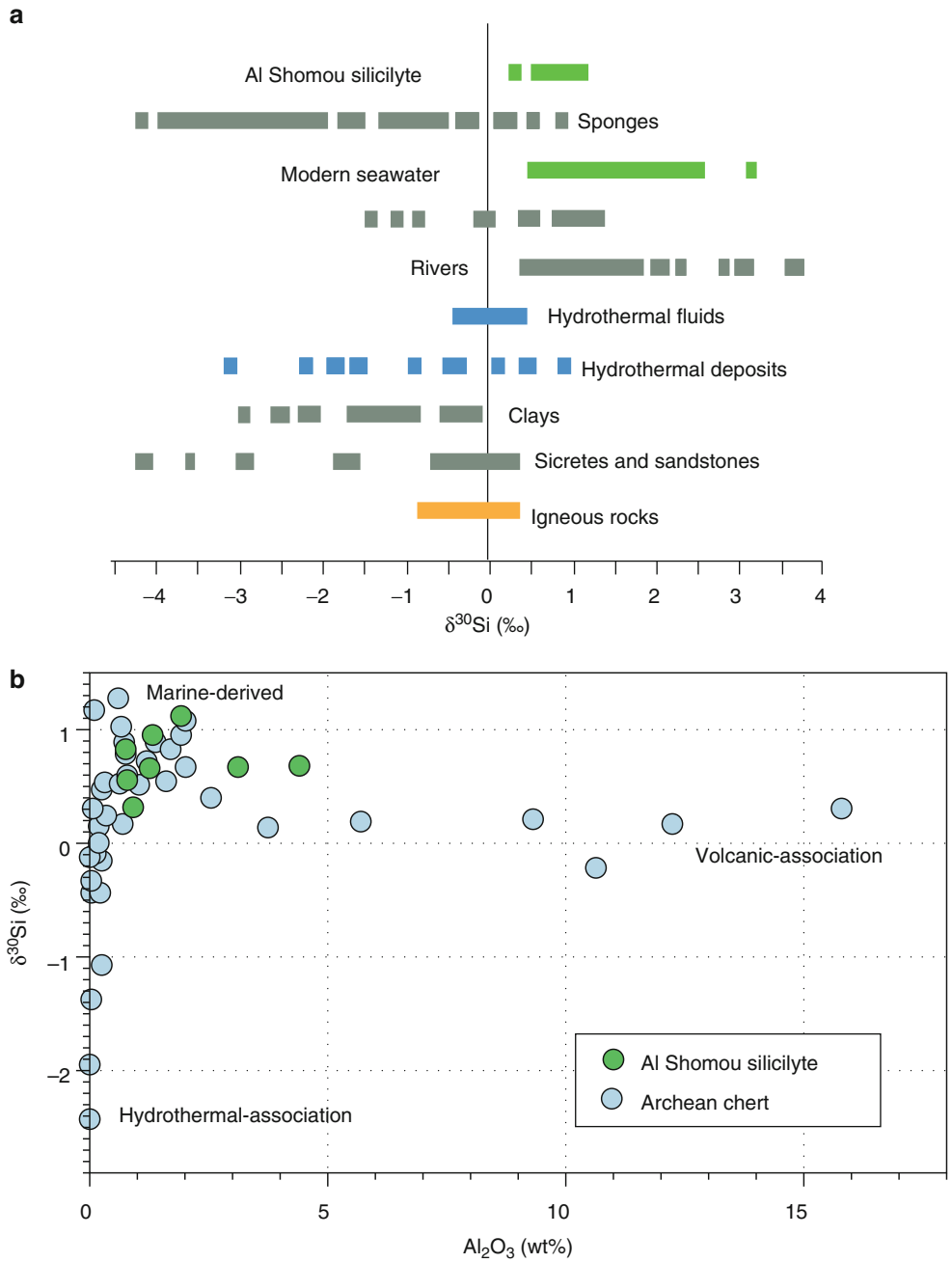

Fig. 10.78 Silica isotopes. (**a**) δ ^{30}Si composition of main modern Si reservoirs (**b**): δ^{30}Si composition of Early Cambrian silicilyte samples in comparison with Archaean chert samples (Data for both plots derived from Ramseyer et al. (2013) and references therein)

The homogeneous distribution and high values of stable Si isotope composition (avg. $\delta^{30}Si = +0.83 \pm 0.28$) coupled with a low molar Ge/Si ratio ($<0.25 \times 10^{-6}$) of the microcrystalline matrix quartz clearly reveal dissolved silica in seawater as the Si source, accordingly hydrothermal or biogenic (e.g. sponge-derived) silica can be excluded (Fig. 10.78a, b; Ramseyer et al. 2013). Silica precipitation from seawater was likely the result of a dramatic increase in salinity in response to salt dissolution atop and adjacent to the edges of transtensional depressions on the deep basin floor, thus markedly reducing the solubility of amorphous silica in these brine-filled seawater depressions (DHALs). This saturation triggered the formation of silica-gel, which accumulated at the basin floor forming a soft silica-rich layer on bacterial mats giving rise to a laminated sediment. The mean number of laminae is ≈32 per year suggesting that layering is non-annual and controlled

by processes such as fluctuations in nutrient supply, lunar driven re-mixing or diagenetic segregation. The transformation of the silica-gel to microcrystalline quartz occurred below 45 °C indicating a less than −4.5‰ $\delta^{18}O$ composition of the pore-water during microcrystalline quartz formation.

Based on the hydrology of all Phanerozoic evaporite basin drawdown settings, I would argue that the time of Athel Silicilyte deposition probably corresponded to a hiatus in the accumulation of the platform carbonates. The palaeogeographic setting at the time of silicilyte deposition was that of a relatively-shallow restricted marine-fed sag basin. Silicilyte probably accumulated in the somewhat deeper density stratified (meromictic) portions of this rift or intracratonic sag basin immediately prior to the onset of an episode of halokinetic halite emplacement across the central parts of the basin. At that time the basin was bound by exposed and hydrographically isolated carbonate-sulphate platforms along the basin edge. Silica levels in Neoproterozoic seawater were much higher than the biologically-limited silica chemistries of Phanerozoic seawater. Bottom stratification resulted in the preservation of substantial amounts of organic matter in the silicilyte and the formation of hydrocarbon source rocks of exceptional quality and thickness (SPI = 28–65 ton HC/m^2; Amthor et al. op. cits.).

Thick organic-rich basinal laminites are not uncommon in many marine-fed Proterozoic basins without an evaporite fill (e.g. oil and gas shales of the Velkerri Fm. of Central Australia; Warren et al. 1998; Craig et al. 2013). What makes the slivers in the Ara salt so economically interesting is that their organic maturation took place while encased in halite (Schoenherr et al. 2007c). The liquid fraction could not leak away, so the matrix permeability did not degrade to levels where it was subeconomic, unlike the Mesoproterozoic oil shales of northern Australia and many other Proterozoic oil shales.

Subsalt Reservoirs in Compressional Evaporite Provinces

There are more than twenty world-scale fold and thrust belts that have at some time slipped atop a layer of evaporites (Fig. 6.33; Davis and Engelder 1987). Such movement in a zone of horizontal compression often results in "thinskinned" or gravity-driven tectonics and the deposition of sediments atop salt-cored growth folds. Deformation in the overlying rocks produces seafloor or landscape topography and syndepositional inhomogeneity in overburden porosity and thickness, as well as stress instability in the salt bed. Both processes can initiate diapirism and allochthon breakout in a compressional terrain. Even when there is no development of piercement from salt-cored anticlines, folds show considerable anticlinal thickening in the salt layer, and associated synclinal thinning, as in the Jura and the SE Zagros. Any diapirism typically follows fault planes or tensional shears in the overburden (Figs. 6.86 and 6.88). Overburden deformation styles tend to have geometries that are controlled by the regional state of stress, and that geometry is frequently inherited by the salt structures. The close correspondence between the elongate salt structures of the North Sea and northern Germany to regional tectonic fabric clearly demonstrate this relationship (Fig. 6.76). Perhaps the best-studied hydrocarbon province controlled by salt-influenced folding and thrusting is in the Zagros Mountain region of the Arabian Gulf. In terms of hydrocarbon volumes, it is certainly the most prolific foldbelt in the world and holds as much as a third of the total reserves of the Middle East. Beydoun et al. (1992) estimated that there are more than 200 billion barrels of recoverable hydrocarbons in the Zagros foreland basin.

Zagros Foldbelt, Iran

Oil accumulations in anticlines of the Zagros Basin are the result of a Late Tertiary foreland basin foldbelt growing at the outer edge of the vast hydrocarbon-rich Palaeozoic-Mesozoic passive margin shelf of the Arabian plate (Fig. 10.79; Verges et al. 2011; Versfelt 2001; Beydoun et al. 1992). This foreland succession shares many of the same source rocks and salt seals as the relatively undeformed petroleum system of the Arabian Plate to the south. The two regions are separated across the Zagros deformation front. Compressionally driven folding and thrusting of the Zagros alpine belt began in the Eocene and continues today, still driven by the collision of the Arabian and Iranian plates. Miocene uplift of the growing alpine belt and subsidence of the adjacent foreland created a hydrographically isolated subsealevel depression in an arid climate (Fig. 5.32). The Fars/Gachsaran basinwide evaporite precipitated and today seals many of the giant and supergiant fields in the region. Compressional tectonics in this foreland foldbelt, especially in the Dezful Embayment, has formed some of the largest structurally-trapped oil fields in the world (Figs. 10.79 and 10.80). In Iran, mostly in the Dezful embayment, ongoing Late Tertiary folding, concurrent with deposition, means that the lower members of the basinwide evaporites of the Gachsaran Formation (seal) typically thin as they overlap or wedge out onto growth folds in the Asmari Limestone reservoir (Fig. 10.80b; Alavi 2004; Ala 1982 and references therein). Syndepositional compression led to the deposition of sandier units above the crests of growing thrust folds, and the sealing of these porous units by evaporites deposited within hypersaline seaways generated by the collision. In Iraq, mostly in the Kirkuk embayment, many of the reservoirs are in folded Mesozoic carbonates.

Late Tertiary collision of Africa and Eurasia did three things to create conditions that trapped enormous volumes of

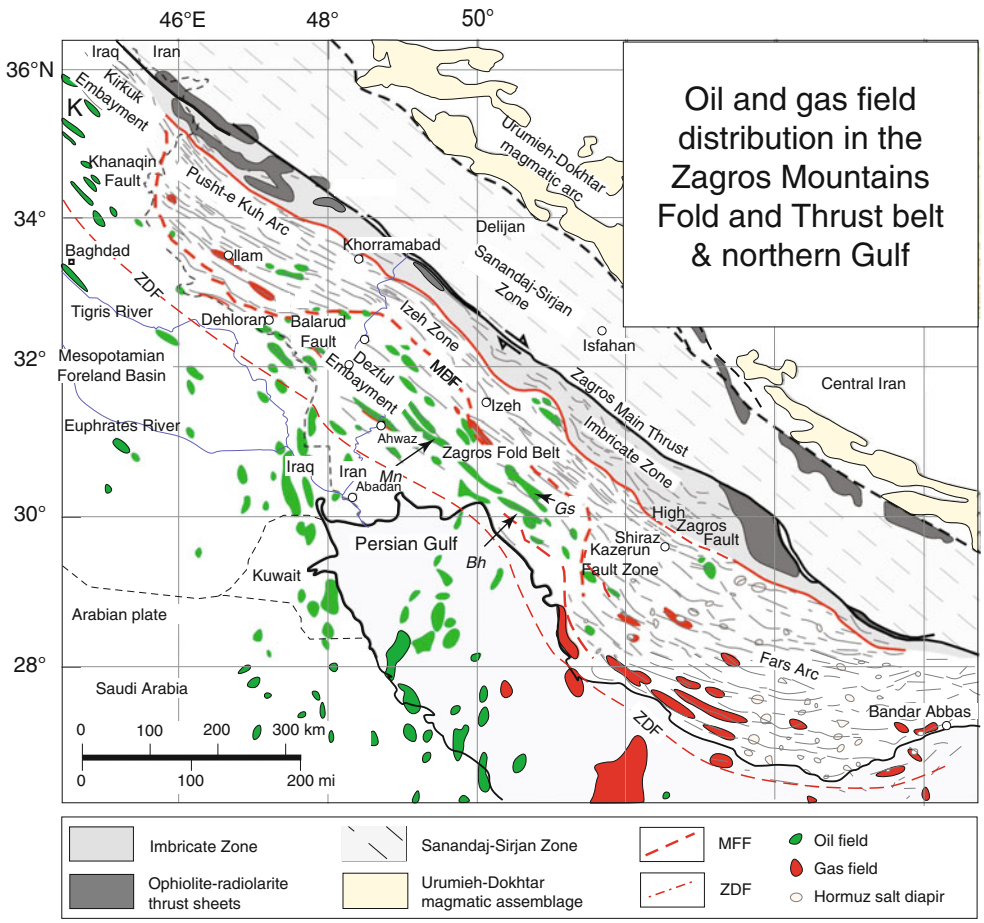

Fig. 10.79 Oil and gas fields in the Zagros and northern Gulf region plotted on a tectonic base of the Zagros Mountains (After Verges et al. 2011) showing the traces of anticlines in the Zagros fold belt, Mesopotamian foreland basin, and Persian (Arabian) Gulf. The imbricate zone, including ophiolites and volcanic arc outcrops, the Sanandaj-Sirjan zone, and the continental Iran block are also shown. Oil and gas fields display the northwest–southeast Zagros trend, and the roughly north–south Arabian trend, in the Abadan plains and Persian Gulf. The two domains are separated by the Zagros deformational front (ZDF) (*MFF* mountain front flexure, *Bh* Bibi Hakimeh, *Gs* Gachsaran field, *Mn* Marun field)

hydrocarbons in Iran and Iraq. First, it deformed a number of fracture-susceptible carbonate reservoirs into whaleback folds, which are world renowned for their huge amplitude and areas of closure; along-strike fold dimensions often exceed 160 km. These dimensions together with brittle fracture in the Asmari limestone reservoir have created fields such as Gach Saran and Bibi Hakimeh, which have estimated ultimate recoveries of oil of 12 and 8 billion barrels, respectively (Fig. 10.80a, b). They occur in a gently folded evaporite-sealed province that has recoverable reserves estimated at more than 87 billion barrels of oil and 514 trillion cubic feet of gas, and has produced more than 6 million barrels of oil per day (Burwood 1984; Beydoun et al. 1992).

Evaporite-sealed muddy limestones of the Asmari Formation and it equivalents (Fig. 10.79; Oligocene-Miocene), are the prime reservoir in this foreland foldbelt and provide the reservoir to something like 90 % of the oil in the oil fields of southwestern Iran (Dezful Embayment). There are lesser but still considerable volumes in Tertiary carbonate reservoirs in oilfields in the folded foothill belt of Iraq where it is known as the "Main Limestone" of the Kirkuk Group (Beydoun et al. 1992). Fractured Cretaceous carbonates of the Bangestan Group, along with minor eolian sand layers in some fields near the Kuwait-Iraq border, are primary reservoirs in Iraq and secondary reservoirs in Iran where they are often situated below Asmari production levels in the same wells in the same fold structures (multiple or stacked columns).

In its main producing area, the Asmari Fm. is predominantly a shallow-water non-reefal micritic platform limestone containing variable levels of dolomite and anhydrite plugging (Honarmand and Amini 2012; van Buchem et al. 2010; Mossadegh et al. 2009; Aqrawi et al. 2006). Matrix porosity and permeability are low in limestone matrices with typical porosities of up to 15 % and matrix permeabilities of up to a few millidarcies. Matrix porosities are significantly

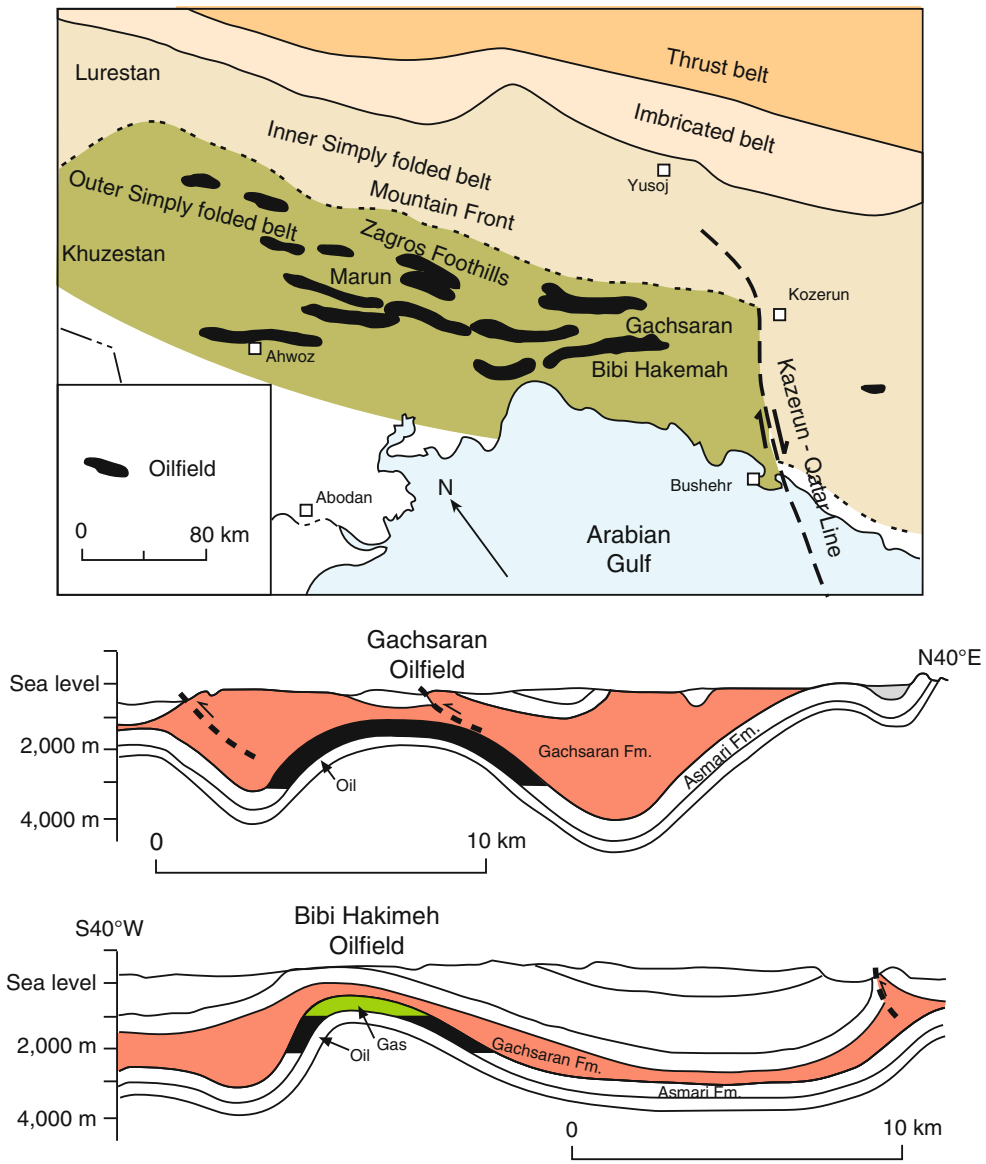

Fig. 10.80 (**a**) Oilfields in the foreland foldbelt of the Dezful Embayment in front of the thrust belt that is the Zagros Mountains, Iran. (**b**) Cross section through the Gachsaran and Bibi Hakimeh fields showing hydrocarbon storage in fractured muddy carbonates sealed by unfractured evaporites of the Gachsaran Formation (After McQuillan 1985)

higher when dolomitised, mostly as the result of brine reflux (Fig. 10.81a). Clearly dolomitisation, and the creation of intercrystalline permeability, improves storage capacity in Asmari reservoirs. Later burial dolomite spar tends to occlude porosity, and even in reflux settings some intervals can be overdolomitised (pers. obs.) Dissolution, first of aragonite allochems, and then mesogenetic corrosion of calcite also improves reservoir quality (Fig. 10.81b). Detritmental diagenetic processes related to $CaSO_4$ precipitation include reflux anhydrite and later burial anhydrite cement spars.

At the trap scale, the Asmari and its equivalents typically owes its excellent reservoir qualities to extensive brittle fracturing induced by Neogene compression beneath a ductile Fars/Gachsaran seal (Fig. 10.80). Wells intersecting fractured intervals of Asmari Limestone in the classic Gachsaran and Bib Hakimeh fields have tested at rates of up to 19,080 m^3/day (120,000 bbl/day) and have sustained production rates of 12,700 m^3/day (80,000 bbl/day), with estimated averages for wells producing from the fractured Asmari in various fields ranging from 3,180 to 3,975 m^3/day (20,000–25,000 bbl/day). Where wells fail to penetrate fracture intervals in the Asmari in the same fields they are essentially nonproductive (Fig. 10.82; McQuillan 1985; Beydoun et al. 1992).

Also, the continent-to-continent approach prior to final collision and suturing created a subsealevel soft suture belt that in the Miocene hydrographically isolated the foreland

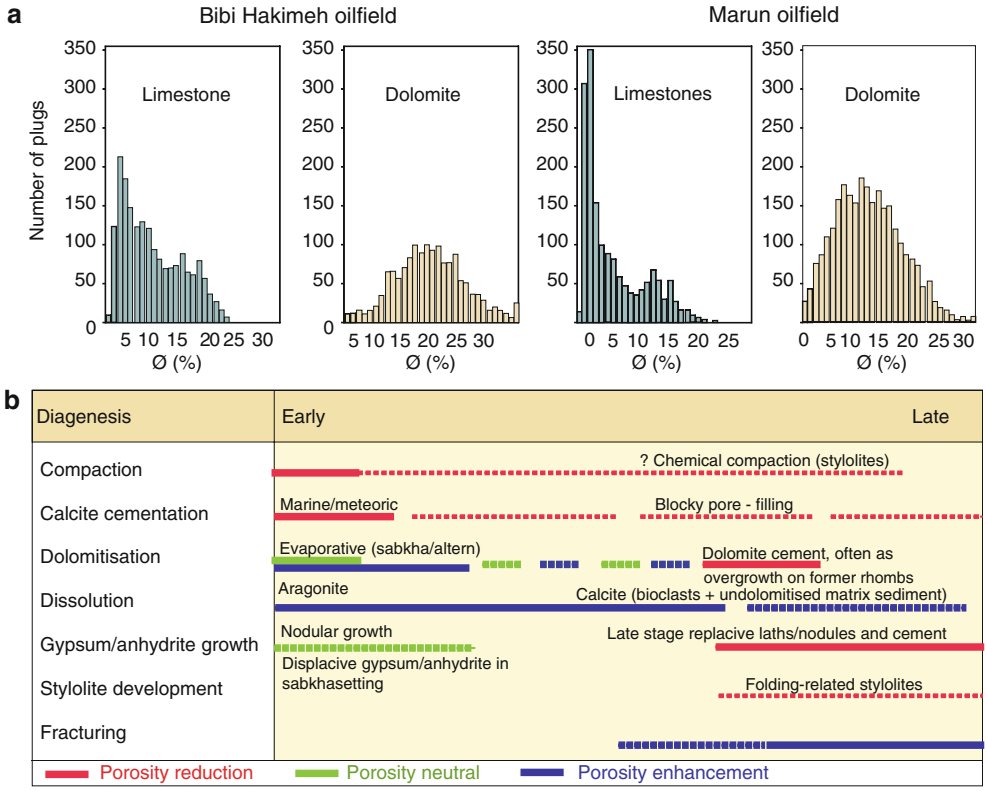

Fig. 10.81 Poroperm controls in the Asmari reservoirs of Iran. (**a**) Frequency histogram of core plug porosity (Ø) of limestones and dolomites in the Asmari Formation in the Bibi Hakimeh field (*left*), 1,660–2,130 m, and the Marun field (*right*), 3,000–3,700 m. The average porosity of dolostones is higher than that of limestones in both fields, see Fig. 10.80 for location. (**b**) Paragenetic summary of the main diagenetic processes which have influenced the reservoir quality (porosity) in the carbonates of the Asmari Formation (After Aqrawi et al. 2006)

basin sump from the open ocean and so deposited the Lower Fars or Gachsaran Formation as a marine-fed basinwide evaporite which subsequently acted as a longterm ductile seal to the growing folds (Kashfi 1983,1985). The presence of this impermeable unit, with its anhydrite base and halite top, is critical in sealing reservoirs in the Asmari Limestone and its equivalents and in maintaining seal integrity atop growing whaleback anticlines as underlying carbonates fractured and faulted. Erosion or nondeposition of the Lower Fars seal on growing folds to the northwest and southeast of the main producing Asmari folds in Iran and in parts of Iraq has destroyed the trapping potential of many otherwise suitable whaleback growth folds. In the SE portion of the Zagros Belt, continent-to-continent collision acted as a huge bellows to the underlying Hormuz salt which by flowing up toward the surface further exaggerated the structural closure of many existing nearsurface folds and also reactivated older Jurassic structures further out in the Gulf.

Although the presence of an evaporitic seal overlying a reservoir is always good news for sealing hydrocarbons, a thick underlying salt unit deformed into salt covered structures that breakout onto the surface is not always so useful in terms of accumulating large quantities of hydrocarbons in large broadly draining structures. Along-strike changes in the tectonic style of the Zagros Mountains demonstrate this point. The NW part of the Zagros foldbelt is the most prolific hydrocarbon area and is characterized by a thick and relatively deep section of fractured Asmari. It has been gently folded into whaleback anticlines and sealed beneath laterally continuous Gachsaran/Fars evaporites (Ala 1982; McQuillan 1985). There is no halokinetic surfacing of Hormuz Salt in the Dezful area to break up the continuity of these broad anticlines. Oil fields in this part of the outer Zagros foldbelt were relatively easy to define back in the 1920s by a combination of seeps and surface mapping and with development wells stepping out along anticlinal axes.

But salt-cored folds in the region of the Zagros foldbelt in southeast Iran in the region of Bandar Abbas are characterized by namakiers sourced in the underlying Hormuz Salt (Fig. 6.85). Most of the fields in this region are relatively small and gas prone (Fig. 10.79; Ala 1982; Versfelt 2001). There the Asmari is thinner and often outcrops as erosionally-breached salt-cored anticlines. In addition the Fars Gachsaran is less evaporitic and more carbonate rich in that area (Gill and Ala 1972). The style of deformation in this area is uplift with salt-cored transtensional shear faults and greater verti-

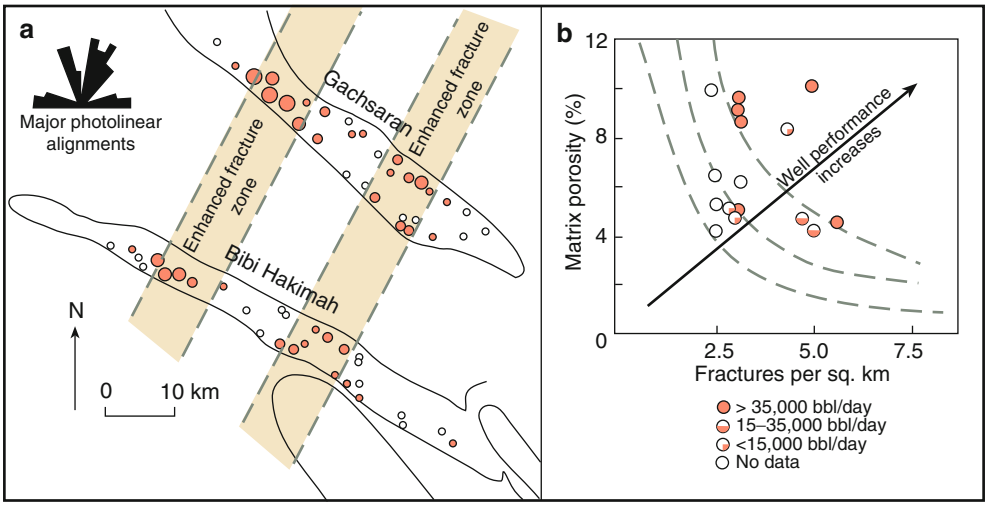

Fig. 10.82 Gachsaran and Bibi Hakimeh fields, Iran. (**a**) Formline map; areas of solid circles are proportional to maximum allowed production rates. *Open circles* are non-commercial or nonproducing wells. High production wells lie in zones of enhanced fracturing induced by deformation controlled by basement features. (**b**) Well production rates in Bibi Hakimeh Field as a function of matrix porosity and fracture density. See Fig. 10.80 for location (After McQuillan 1985)

cal components to the fault breaches compared to areas to the west. This greater intensity and verticality perhaps relates to withdrawal of thick successions of Hormuz salt into adjacent salt diapirs and glaciers. During ongoing periods of vertical uplift and diapir induced breaching many hydrocarbons either escaped through fractures in the exposed Asmari and its less evaporite-rich cap or underwent secondary migration, possibly becoming trapped on the western side of the Oman Mountains (Kashfi 1983). Gravity-driven shear faults developed in association with salt intrusions and a poor development of an evaporite seal, probably facilitated the migration and escape of hydrocarbons. The presence of a thicker Hormuz section in this part of the Arabian Gulf may well have prevented the transferral of the fracture system from the basement into the Asmari, the same fracture system that McQuillan (1985) uses in explaining the prolific production of the giant fields in the thrust belts further to the Northwest. Offshore from the Southern Zagros some large structural accumulations in the Tertiary strata may still remain to be discovered, but future onshore exploration will probably be for smaller stratigraphic or combination traps situated about and sealed by halokinetic structures.

The stacking of salt tiers in this region creates an interesting contrast in structures and related responses at potential reservoir levels compared to reservoir distribution in the extensional tiers in the Gulf of Mexico. Thick salt creates two mobile groups in the stratigraphy as well as thinner depositional salt beds occurring within the Competent Group (Fig. 10.83; Verges et al. 2011; Fard et al. 2011). These thin beds tend to focus zones of structural release and transfer in the Competent Group of units. Folds in the Pusht-e Kuh arc are exposed along the upper part of the 7-km (4.34-mi)-thick Competent Group level, which is folded between the main detachment at or near the base of the cover sequence (lower Mobile Group) and the Gachsaran evaporites (upper Mobile Group). Intermediate detachment levels, sometimes evaporitic (Triassic Dashtak, middle Cretaceous Garau and Kazhdumi, Paleocene Amiran, and middle Miocene Kalhur formations) within the Competent Group control the geometry of anticlines at surface as well as their variations with depth.

The Kabir Kuh anticline is the largest and highest anticline exposed in the Pusht-e Kuh arc (Fig. 10.83). Mapping of the anticline in its central part displays box fold geometry, characterized by a wide and rounded crestal domain, which is slightly tilted to the southwest. This geometry developed above an intermediate detachment at the level of 1.3-km (0.81-mi)-thick Triassic Dashtak evaporites within the Competent Group. Below this detachment, the geometry of the fold changes to more acute with a narrower crestal region. Although conjectural, Verges et al. (2011) propose low-angle thrusting forming a tectonic wedge to accommodate shortening at the deepest part of the anticline (Palaeozoic sequence). Subsidiary thrusts, related to fold tightening, likely reactivate axial surfaces, as well as local detachment levels, that propagate displacements of the crest of the anticline above its forelimb, as inferred along the southeastern segment of the Kabir Kuh anticline.

In terms of reservoir and structural understanding during exploration in a compressional salt-tiered region is notable that anticlines in the Passive Group may be displaced, sometimes by a few kilometers, from beneath anticlines in the Competent Group (potential deeper reservoirs). In the same way, the internal mechanically weak layers of the Competent

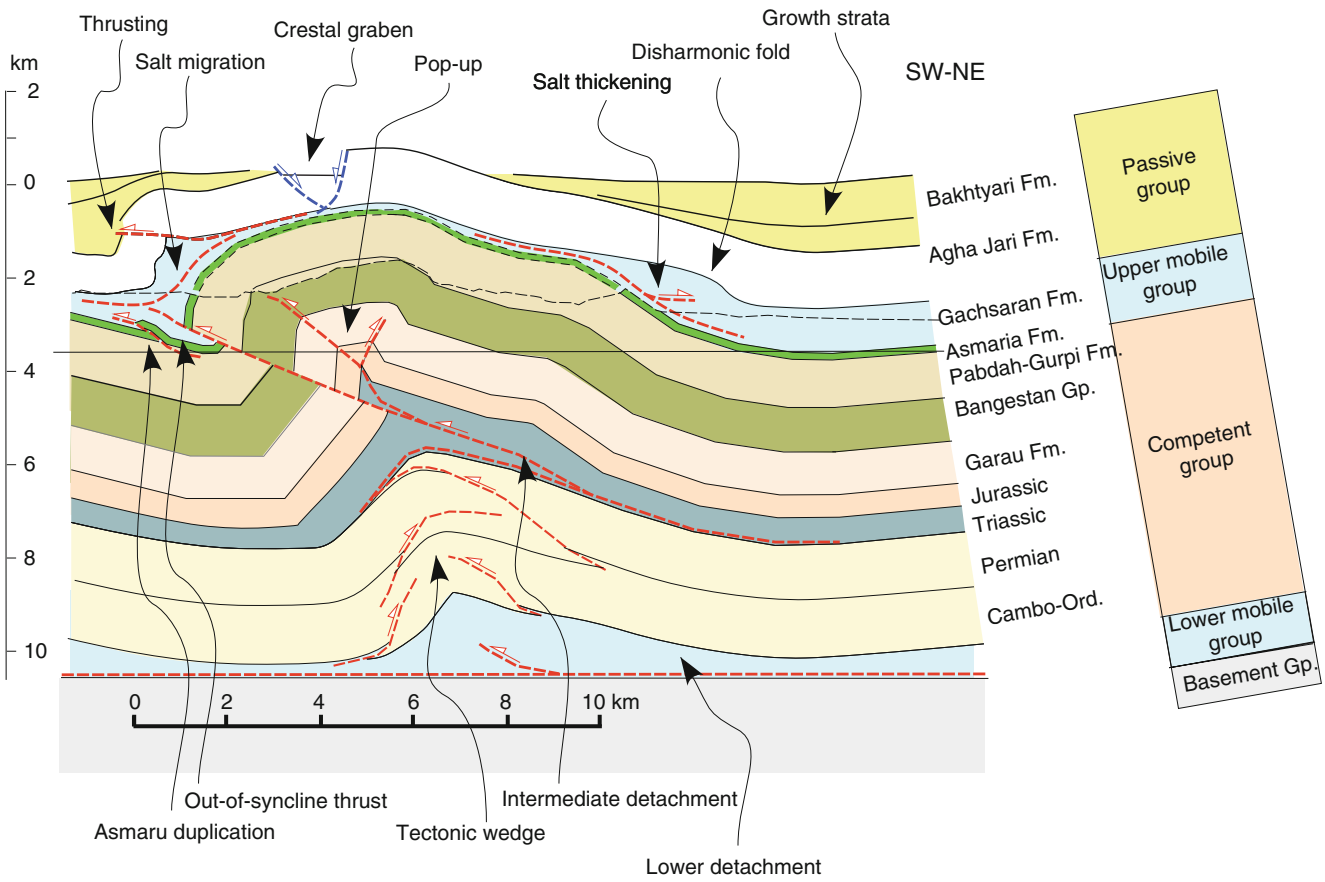

Fig. 10.83 Conceptual model of folding integrating observations from the Pusht-e Kuh arc (Competent Group) and Dezful embayment (Passive Group) tectonic domains (After Verges et al. 2011)

Group may form intermediate detachments that can produce a significant change in fold style with depth and displace the upper part of the structure, shifting again the position of the anticline crests.

Alpine Foldbelt in Albania and Romania

Giant salt-sealed highly deformed structures characterise onshore oil fields in the compressional Alpine fold and thrust belt (Albanides) of the Ionian basin in Albania. The Triassic evaporites form a regional detachment layer, but are also cut by thrust ramps that carry evaporites to the surface in their hanging walls (Fig. 10.84; Velaj et al. 1999; Graham Wall et al. 2006). Contraction of the Ionian zone reached a peak in the late Oligocene–Miocene Alpine Orogeny during an intense episode of overthrusting and major folding. The oil and gas fields in the region produce mainly from fractured Cretaceous–Eocene carbonates (e.g., Balshi-Hekal, Visoka, Gorisht-Koculi, Cakrani, Amonica, Finiq-Krane, and Delvina fields). Where a detachment is located at the top of the evaporite section, salts are dragged up in the footwall along thrusts. Faults develop both at the base and the top of the evaporite. Simple shear deformation along the thrusts causes greater than 80 % thinning of the evaporite, so that thinned salt sheets of only 40–200 m thickness are now preserved in regions where the original evaporite thickness was in excess of 2,000 m. Where thrust ramps cut through the evaporite and cause repetition of the complete evaporite layer, salt is remobilised into salt-filled compressional anticlines or it escapes at the surface to produce smeared-out allochthonous extrusions capable of sealing large volumes of hydrocarbons.

The most spectacular example of this is the Dumrea structure, where the mobilised evaporites have a complex shape that evolved from an overthrusted allochthonous sheet, which today subcrops at the modern landsurface (Fig. 10.84a). The Dumrea salt allochthon is up to 5.6 km thick, as proved by drilling, and has been displaced laterally by up to 25 km. It has the effective geometry of a giant sheath fold (Fig. 10.84b). Untested traps still exist below the allochthonous evaporites and good quality non-biodegraded hydrocarbons are possible at depth, as was the case in the Delvina Field in southern Albania (Fig. 10.84c). Shallower oil fields in the Albanides, not sealed by evaporites, typically contain very heavy oil due to ongoing bacterial degradation (e.g., Balshi-Hekali and Patos-Marinza fields).

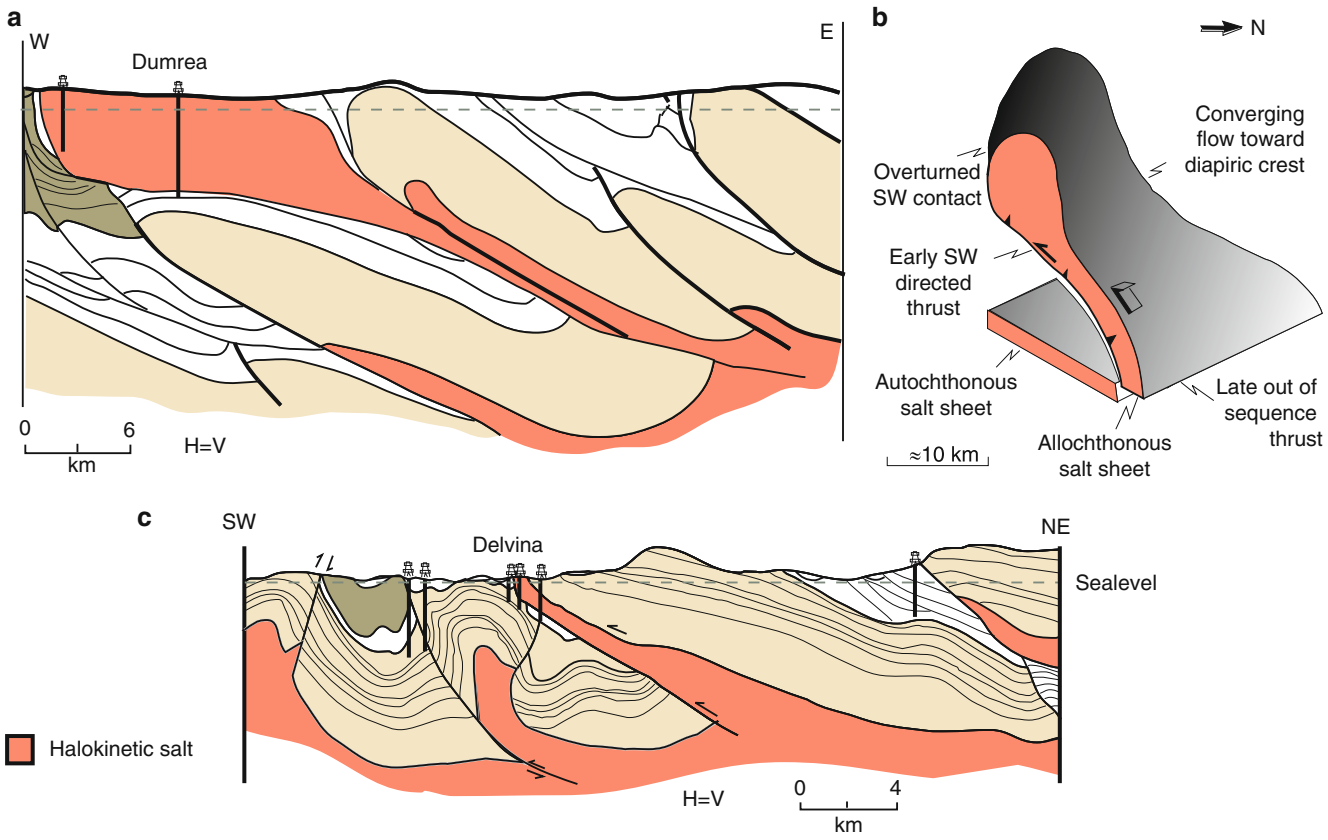

Fig. 10.84 Giant fields in the Albanides, Ionian Basin. (**a**) West-east–trending cross section through the Dumrea evaporite body showing the structure of Dumrea Field. (**b**) Three-dimensional block diagram of the Dumrea diapir. (**c**) Cross section of the Delvina gas condensate field trapped below a thrusted Triassic evaporite sheet (After Velaj et al. 1999; Velaj 2002)

The process of fracture and fault formation in carbonates of the Albanides fold-thrust belt was systematically documented by Graham Wall et al. (2006) using scaled studies of structural elements from hand sample, outcrop, and geologic-map scales. Calcite cement and bitumen distribution in these structures can be used as a paleoflow indicator of the various fluid migration stages in the evolving fracture and fault systems. Two prefolding pressure-solution and vein assemblages were identified: an overburden assemblage and a remote tectonic stress assemblage (Fig. 10.85a, b). Sheared layer-parallel pressure-solution surfaces of the overburden assemblage define mechanical layers. Shearing of mechanical layers associated with folding resulted in the formation of a series of folding assemblage fractures at different orientations, depending on the slip direction of individual mechanical layers.

Prefolding- and folding-related fracture assemblages together formed fragmentation zones in mechanical layers and are the sites of incipient fault localization (Fig. 10.85d–f). Further deformation along these sites was accommodated by rotation and translation of fragmented rock, which formed breccia and facilitated fault offset across multiple mechanical layers. Strike-slip faults formed by this process are organized in two sets in an apparent conjugate pattern. Calcite cement and bitumen that accumulated along fractures and faults are evidence of localized fluid flow along fault zones. By systematic identification of fractures and faults, their evolution, and their fluid and bitumen contents, along with subsurface core and well-log data, Graham-Wall et al. (2006) identified northeast-southwest-trending strike-slip faults and the associated structures as the dominant fluid (hydrocarbon) pathways at the reservoir and petroleum system scale in the compressional Albanides fold-thrust belt (Fig. 10.85f).

The nearby Romanian section of the Carpathians Mountains of eastern Europe is another collisional thrust-fold Alpine belt where hydrocarbon accumulation is intimately related to the presence of structurally-smeared basinwide evaporite seals, in this case of Lower Miocene age (Fig. 10.86; Paraschiv and Olteanu 1970). Most of the reservoirs are Pliocene lacustrine sands, interbedded with fine-grained marls. The latter may well have been both source and seal. Suitable Pliocene sands with sufficient thicknesses and favourable reservoir facies only occur in the Ploiesti area at the convexity of the Carpathian Bend. Like the Zagros Mountains and the Albanides this hydrocarbon

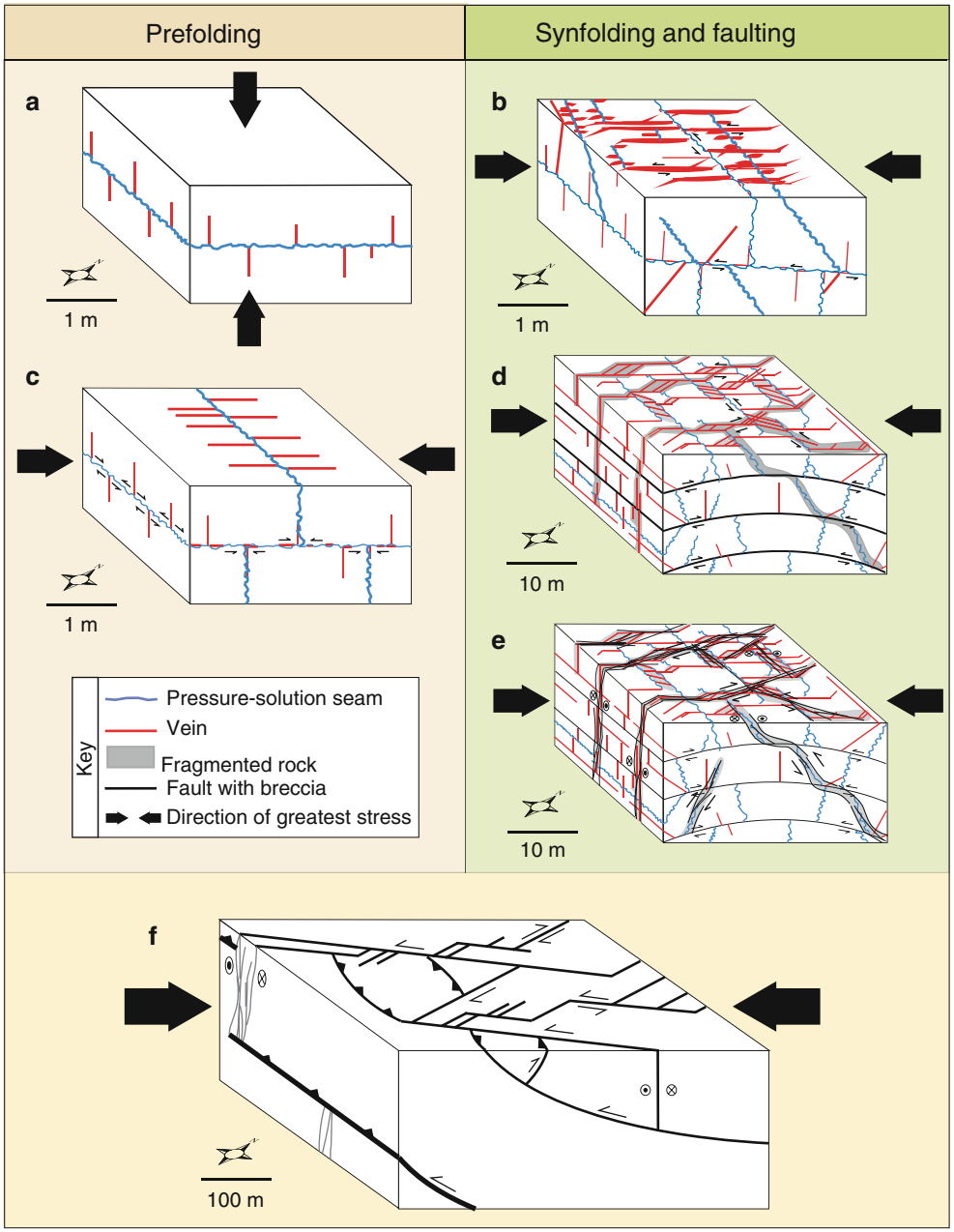

Fig. 10.85 Conceptual model of fault evolution in brittle carbonates of the Albanides involving prefolding and synfolding structural element development in response to mobile halokinetic deformation: (**a**) Overburden assemblage (prekinematic), (**b**) Remote tectonic stress assemblage, (**c**) folding assemblage, (**d**) the linkage of fracture assemblages to form localized fragmentation zones, (**e**) the linkage of fragmentation zones to form through-going faults, and (**f**) northeast-southwest–trending strike-slip faults formed through processes (**d**) and (**e**) with linkages visualized at the reservoir scale (After Graham-Wall et al. 2006)

province is another halokinetic province where the original basinwide evaporites have been squeezed into a compressive layer during large scale thrust movement. Where a thrust ramps toward the present surface the Miocene salt defines stocks, sills, dyke-like masses and other irregular shapes, whose original injection pathways were perhaps controlled by pre-existing diapirs, faults, folds and fault/fold intersections.

Rocky Mountain Foldbelt, USA

Deformed basinwide salt also plays a role in sealing the Nugget Sandstone reservoir in the Painter and East Painter fields of the Rocky Mountain thrust belt in the USA and the much more gently deformed sequence of Leadville Formation carbonates in the Lisbon Field, Utah. The Mississippian Leadville Lime-stone reservoir in Lisbon Field in the northern Paradox Basin, Utah, lies below a thick

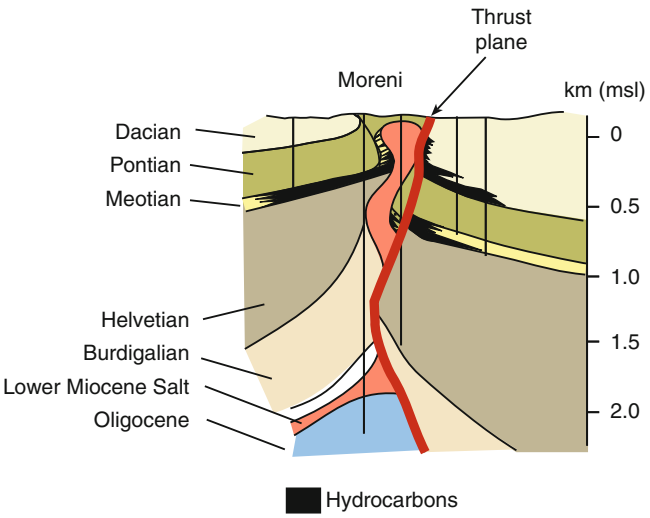

Fig. 10.86 Cross section through the Moreni-Gura Ocnitei oilfield, the largest field in the Carpathian foredeep. Productive sandstones are Pliocene in age. Structure is a sheared anticline where lower Miocene salt (*red*) has lubricated the thrust and now forms a lateral seal to multiple reservoir sands. Also note the greater concentration of oil on the right side of the thrust, which is the downthrown side of the principal fault (After Paraschiv and Olteanu 1970)

section of halokinetic Paradox salt and has produced some 50 Mmbl and 760 Bcfg since its discovery in 1959 (Fig. 10.87a). The trap is an elongate, asymmetrical, northwest-trending salt-cored anticline with nearly 600 m of structural closure (Fig. 10.87b; Miller 1985). The field is bound on its northeast flank by a major, basement-involved normal fault with nearly 760 m of displacement. A number of smaller northeast-trending normal faults dissect the reservoir into segments with fractured sweetspots located close to these secondary faults (Miller 1985).

The Leadville Limestone was deposited as an open-marine, carbonate-shelf system with local crinoid banks, mud mounds and peloid/oolitic shoals. Two dolomite types characterise the Leadville reservoir, a tight stratiform micritic mimetic dolomite and a later coarser saddle dolomite. Solution-enlarged fractures and breccias are also common in the reservoir interval. The dichotomy in dolomite type and the association of the saddle dolomite with faults and fractures is similar to the evaporite-focused occurrences seen in earlier in the various examples from the Middle East. But in the case of Lisbon Field the evaporite seal maintained its seal integrity even when the salt first underwent extension in the Palaeozoic and then compression during the Laramide orogeny. The oil in the structure is thought to be sourced from the overlying and now fractured Gothic Shale member in the Paradox Salt. Interestingly, such a subsalt trapping scenario may be a useful analog in exploration for sub-Ara Salt traps in the Proterozoic Buah Formation in the South Oman Salt Basin petroleum system.

More highly deformed salt levels in the Painter and East Painter fields maintain seal integrity atop the deformed and fractured reservoir intervals in the giant Painter and East Painter fields. Triassic salt also acts as the isolating décollement surface to the overlying overthrust plane (Fig. 10.88a; Dischinger and Mitra 2006). The Painter reservoir structure consists of a rounded asymmetric fold in the Jurassic Nugget Sandstone reservoir (eolian) sealed by the Gypsum Spring Member of the Twin Creek Limestone and the overlying salt. Significant thickening was accommodated in the underlying ductile Ankareh shales and the Thaynes limestones, which comprise the core of the structure (Fig. 10.88b; Mitra 2002). The forelimb of the structure is steep to overturned. A series of small-scale imbricates cut through this limb, but the displacement on these faults is relatively small and does not control the geometry and structural relief of the structure. The tightness of the structure also results in the formation of one or more out-of-syncline thrusts on the forelimb, which terminate upward within the salt unit and downward within the Twin Creek limestones. These out-of-syncline thrusts were folded during the later stages of deformation.

The East Painter reservoir structure is a west-vergent detachment fold, formed above the hanging-wall cutoff of the Mesozoic units atop the Cretaceous detachment (Fig. 10.88b). The steep frontlimb of this structure is also cut through by a west-vergent thrust. The convergence of the two opposite-vergent structures results in significant disharmonic folding within the Twin Creek limestones and the overlying salt. Interestingly, the hydrocarbons stored in the Nugget Formation sands were sourced in stratigraphically younger but now underlying Cretaceous mudstones (Lamb 1980).

Salt-Related Traps in the Tarim Basin, China

The Tarim Basin is one of the most important hydrocarbon-bearing evaporite basins in China. It retains four salt-bearing levels, the Middle and Lower Cambrian, the Mississippian, the Paleogene, and the Neogene, which have various thickness and areal distributions (Fig. 10.89). Salt levels define various intervals of stratigraphic discontinuity across the Tarim, they define important detachment layers and intensely affect structural deformation styles in the basin.

This is especially so in the Kuqa region in the northern part of the Tarim Basin. There the Kuqa depression is a subordinate structural unit typified by numerous salt-cored structures within the larger Tarim Basin. Salt overthrusts, salt pillows, salt anticlines, salt diapirs, and salt-withdrawal basins characterise the Kuqa depression. The source layer for the deformation is the Paleogene Kumugeliemu Formation. It contains a thick succession of halokinetic salt that was first deposited in a compressional foreland. This same compressional setting continued to be active post salt deposition and drove much of the structuration across this northern part of

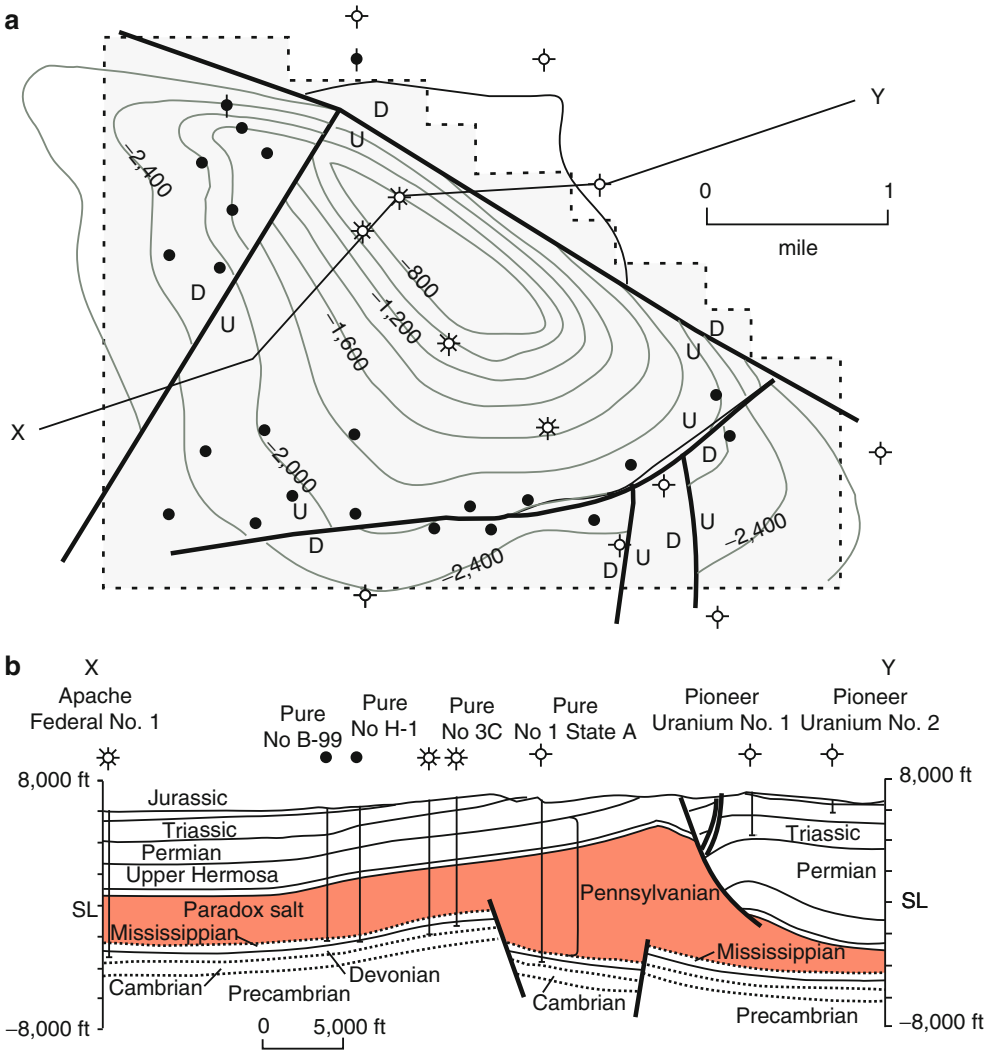

Fig. 10.87 Lisbon Field, Utah. (**a**) Depth to top of the Leadville Formation (Contours in feet subsealevel). (**b**) Regional cross section X-Y across the field showing its position beneath the seal of halokinetic Paradox Salt (After Miller 1985)

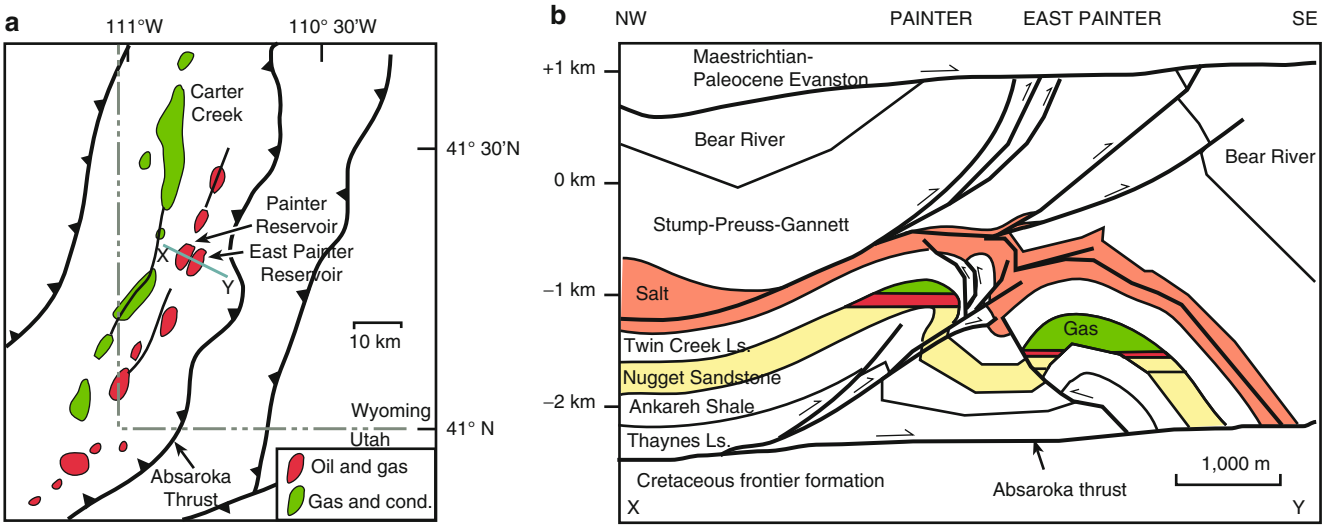

Fig. 10.88 (**a**) Geologic map of the Idaho-Wyoming-Utah fold and thrust belt showing some of the major oil- and gas-producing structures in the Absaroka thrust sheet. (**b**) Interpretive cross section through the Painter reservoir and East Painter reservoir structures (After Mitra 2002)

the Tarim basin, where a combination of salt-lubricated faulting and thrusting created the various traps, illustrated in (Fig. 10.90a–c).

Clearly, the contraction that resulted from ongoing orogeny plays a key function on the formation of various salt structures. Suprasalt growth strata thickening shows that intense salt structural deformation in the Kuqa depression occurred during the Himalayan movement from Oligocene to Holocene, with earlier structural deformation in the north and later deformation in the south of the depression. Growth sequences also record at least two phases of salt tectonism. In the Tahe area (as well as the Yingmaili and Tazhong areas) low-amplitude salt pillows are the most common salt structures, and these structures are commonly accompanied by thrust faults. There the faulting and uplifting of basement blocks controlled the location of salt structures. The differences in the geometries of salt structures in different regions show that the thickness of the salt sequences has an important influence on the development of salt-cored detachment folds and related thrust faults in the Tarim Basin (Yu et al. 2014).

Salt sequences and salt structures in the Tarim Basin are closely linked to hydrocarbon accumulations. Oil and gas fields have been discovered in the subsalt, intrasalt, and suprasalt strata. Salt deformation has created numerous potential traps, and salt sequences have provided a good seal for the preservation of hydrocarbon accumulations. Large- and small-scale faults related with salt structures have also given favorable migration pathways for oil and gas. For example, the trap style of the Dawanqi oil field in the Kuqa depression is a suprasalt faulted-anticline, controlled by salt tectonism (Fig. 10.90a). There the associated thick salt sequence is a good seal, which forces oil migrated along the Tuzimazha fault from the underlying Jurassic and Triassic source rocks into the sand reservoirs in the Neogene Kangcun Formation and moves oil into suitable reservoir sands as high as the Pleistocene sections.

But as in most oil accumulations worldwide, a subsalt trap tends to hold back larger hydrocarbon volumes. The Kela 2 structure is a subsalt imbricate pop-up structure, which is one of the largest gas fields in China with proven reserves of 284 billion m^3 and across its extent is sealed by the thick salt sequence of the Paleogene Kumugeliemu Formation (Yu et al. 2014). The structure allows the underlying Cretaceous section to fault and fracture, while the salt flows and maintains its seal integrity.

Although holding a smaller volume, the trap in Kela 3 gas field (also located in the Kuqa depression) is very interesting as it one of the few examples of a producing intrasalt field. The structure is a faulted anticline, where the reservoir is made up fine sandstones encased in the middle portion of the salt sequence in the Kumugeliemu Formation (Fig. 10.90c).

To the south of the Kuqa depression there are fields created by salt dissolution of the Mississippian-age salt of the Bachu Formation, such as the Tahe oilfield, which is mostly a subsalt hydrocarbon accumulation (Fig. 10.90d). Edge dissolution has driven overburden collapse and faulting, which is focused around the salt's dissolution edge. A salt edge allows hydrocarbons formerly draining laterally beneath a salt bed to move vertically in the overlying succession. Small-scale normal faults with 40–80-m (131–262-ft) throw are developed in the salt-edge sags in the Tahe These faults connect the deep source rocks and shallow reservoirs, and are important migration pathways (Yu et al. 2014).

Evaporite Dissolution

Collapse-related traps can form early within the depositional setting, or much later during catabaric salt removal. A dissolving subsurface salt unit creates zones of differential collapse, which can induce economic levels of fracturing in the overburden. Where the effects of a shallow dissolution edge reach the landsurface it creates a depression, which focuses deposition of sand, mud or even reefal buildups around its rim (Fig. 7.6; subsidence trough). If it does not reach the surface it still affects brittle overburden as it creates fractures that increase permeability. Either style of dissolution creates anomalous fluid movements, diagenetic haloes, and reservoir modification that can form a structural anomaly at the seismic scale. Salt dissolution breccias that define the position of former salt units or intervals of former salt cements can contribute to the permeability of the fractured overburden interval.

An association between salt collapse, fracturing and oil production is proven in the oil and gas fields of southeast Saskatchewan, southeastern Montana and southwestern North Dakota (Smith and Pullen 1967; Swensen 1967). Examples include reservoirs in Upper Devonian carbonates of the Hummingbird Field (Birdbear Formation), and the Dolphin, Fryburg, Kisbey, Flat Lake, Medoria-Scoria, Outlook, Star Valley, Tatagwa, Tule Creek, Walpole and West Hope fields. In their study of reservoir porosity in Devonian reef and bank carbonates of western Canada, Beales and Oldershaw (1969) make the observation that, "much of the so-called primary porosity in reef reservoirs may be evaporite solution porosity." Salt collapse depressions in the landscape also focused deposition of Cretaceous reservoir sands in the Mannville Formation in Westhazel Field. Subsurface salt bed leaching and collapse has also contributed to porosity distribution in various North Sea fields (Cartwright et al. 2007; Jenyon and Taylor 1983; Lohmann 1979) and to the fracturefocused creation of porosity in hydrothermal dolomites in the platform carbonates of the Rainbow/Zama Basin.

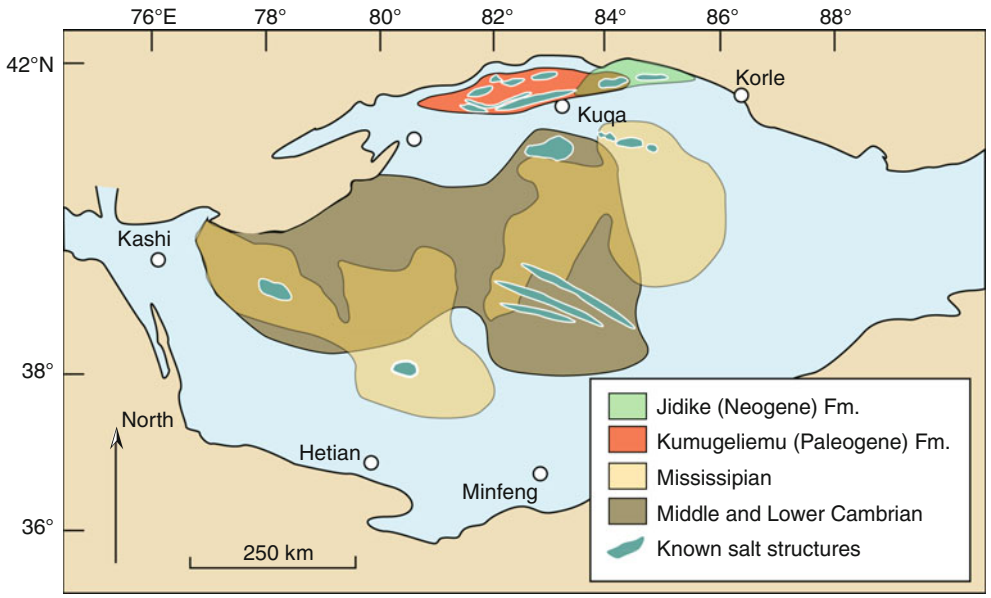

Fig. 10.89 Distribution of the 4 main levels of salt in the Tarim Basin, China, and the positions of the main salt structures (After Yu et al. 2014)

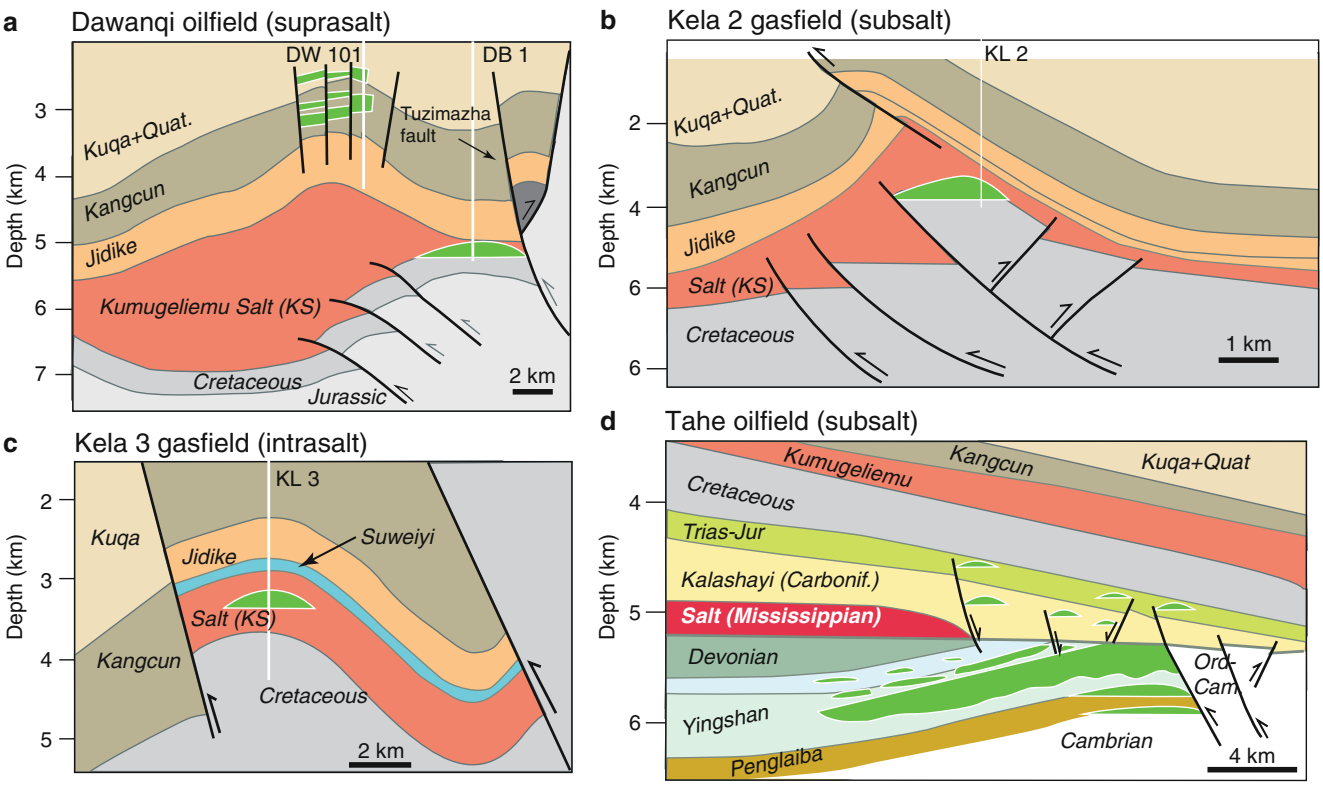

Fig. 10.90 Cross sections showing the trap styles in selected salt-related oil and gas fields in the Tarim Basin. (**a**) Dawanqi suprasalt oil field. (**b**) Kela 2 subsalt gas field. (**c**) Kela 3 intrasalt gas field. (**d**) Tahe subsalt oil field. **a** = **c** are related to the Paleogene salt that dominates the Paleogene Kumugeliemu Formation. The Tahe field is related to the dissolution edge of the salts in the Carboniferous Bachu Formation (After Yu et al. 2014)

The various salt collapse reservoirs in Devonian carbonates of Canada are typified by fractures and solution-enlarged vuggy to karstic pore systems in what are otherwise dense carbonates. These reservoirs have porosities exceeding 20–30 % and permeabilities in the range of darcies. The fields are small but their location makes them economic. Hummingbird Pool has produced more than 3 million barrels and Kisbey more than 1.6 million barrels. The Hummingbird oil pool was discovered in September 1966 on the northwest flank of the Williston Basin by drilling a semi-circular collapse-fill structure covering 2.6 km^2, thought to be a pinnacle reef prior to drilling (see Fig. 7.7 for location of Hummingbird Trough). Oil in the Hummingbird structure is produced from fractured 15 m-thick algal and bioclastic limestones of the Mississippian Charles Formation and 17 m-thick vuggy dolomites of the Devonian Birdbear Limestone. The structure was created by local solution collapse followed by complete regional dissolution during multiple episodes of Prairie Evaporite solution loss during the Late Devonian and Early Mississippian.

Synthesis of the various styles of dissolution induced traps in the Alberta Basin of Canada and the Williston Basin in the USA shows the dissolution process is broad ranging, variable in terms of timing and tied to the dissolving edge of the Prairie Evaporite (Fig. 7.7). Compactional drapes can create a rollover anticline that is closed over the dissolved edge of a residual salt body (Fig. 10.91a; Anderson et al. 1988; Anderson and Knapp 1993; Parker 1967). Local solution or collapse can form a sediment-filled sink that transforms to an inverted thick with the ongoing solution of the surrounding salt (Fig. 10.91b; a "pseudo-reef" – Anderson and Hunt 1964). Or subsidence can form a focused sand infill within a solution-induced depression on the land surface (Figs. 7.7 and 10.91c): or it can form as a remnant of a formerly widespread sand unit that was ultimately preserved only in sediment-filled depressions within the salt bed (Fig. 10.91d). Seismic is very useful in defining the lateral and vertical extent of many collapse anomalies and, if properly acquired and processed, can be used to define internal stratigraphy and reservoir development. Salt collapse structures can lead to focused oil entrapment in fractures in what otherwise may be a "tight" overburden lithology (Fig. 7.7). A breach in a dissolving salt bed can also create structural and stratigraphic closure in the overburden. This is especially so if the collapse anomaly occurs "on-salt", i.e. within a breach surrounded by, or adjacent to, the dissolving salt edge.

Ongoing fluid throughflow prior to oil emplacement in intervals above a dissolved salt bed or collapse chimney may have become pervasively cemented and thus rendered impermeable. Even so, the interval may then provide a seal for fractured and leached reservoirs still being created along the downdip side of the adjacent collapse basin. Collapse structures in the carbonate overburden may be multistage structures located "off-salt", i.e. in areas where all salt has been removed, as in the classic "Hummingbird" oil trap. Hummingbird drape was created by sequential collapse and its pinnacle-like appearance in seismic gave it the name "pseudo-reef" in early exploration programmes in the Alberta Basin (Fig. 10.91b). When dissolution is early, sediments often thicken above the areas of dissolution and thin in the areas over the remaining salt outlier. These overlying sediments can develop the same types of porosity patterns that form above salt ridges. Sometimes the salt dissolves in stages and so creates sequential thickened beds up section as the locus of salt dissolution shifts. In Fig. 10.91b, two areas of sediment thickening are created by salt dissolution; the first forms in stage 2, the second in stage 4. This and later differential compaction and drape can create reservoirs above salt remnants (high in stage 2) or by later differential compaction (stages 3 and 4). Other solution traps may be "on-salt," the result of compactional drape over a single stage fill of a salt solution trough such as at Kisbey Field (Fig. 10.91c, d).

Collapse has also created reservoirs in quartz sands such as Berry Field and the Westhazel pool in Lower Cretaceous fluvial sandstones of Alberta. These reservoirs were created by depositional focusing of fluvial sands at the migrating edge of the dissolving subsurface salt of the Prairie Evaporite (Hopkins 1987). Compared with most stratigraphic traps in Cretaceous sands in the region, the Berry Field is unusual in its occurrence on the flank of a local structural high within a larger regional structural depression. This unusual synclinal setting for the reservoir is a direct indication of its origin as a fluvial system within a landscape position controlled by salt solution.

The Westhazel General Petroleums Pool of west-central Saskatchewan, Canada, produces from the GP member of the Lower Cretaceous Mannville Group and is an excellent example of reservoir stacking in a salt dissolution trough (Fig. 10.92; Anderson and Cederwall 1993). The reservoir facies consists of fine- to medium-grained quartzose sandstones. The lateral uniformity and coarsening upward appearance of this unit and the uniform thickness of the underlying and overlying shales indicates that the General Petroleums Member was deposited in a relatively shallow, marine environment. The pool was discovered in 1971 and produced in excess of 60,000 m^3 (380,000 barrels) of heavy oil from the marine sandstones of the General Petroleums (GP) Member.

This reservoir is structurally closed across the updip, eastern dissolutional edge of the underlying Middle Devonian rock salt of the Leofnard Member of the Prairie Evaporite. The leaching of these salts occurred in post-Mannville time in the Westhazel area and caused the regional southwest dip of the General Petroleums member to be locally reversed

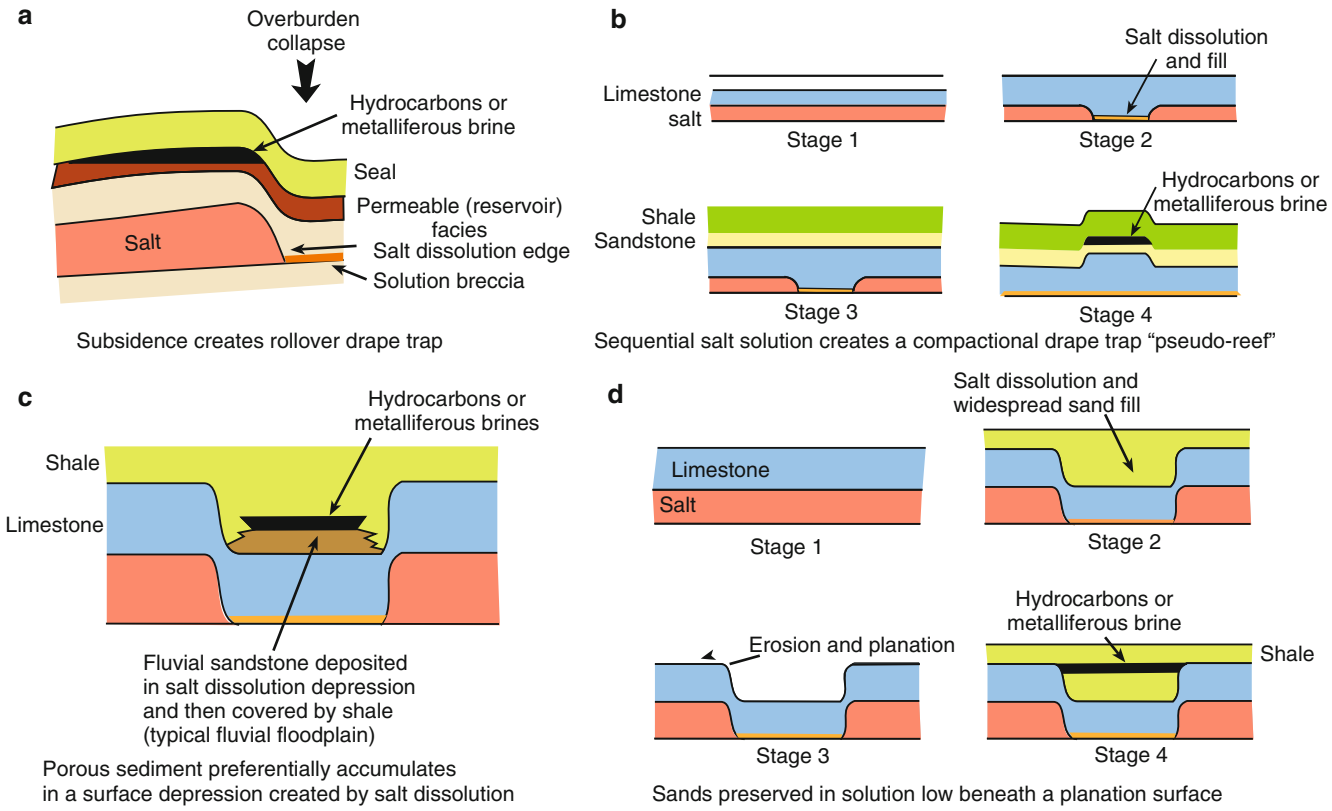

Fig. 10.91 Styles of structural and diagenetic trap created by localised salt solution (In part after Anderson et al. 1988). See text for detail of (**a**–**d**)

(Fig. 7.6). The thin, 10 m-thick reservoir facies at Westhazel does not exhibit a diagnostic signature on either seismic or gravity data. Rather, it is the updip edge of the salt, across which the reservoir is closed, that can be mapped using geophysical techniques.

On seismic data, the dissolutional edge of the Prairie salt is characterized by: (1) a subtle decrease in the amplitude and lateral coherency of the underlying Winnipegosis event; (2) a gradual thinning of key encompassing Palaeozoic intervals; (3) dip reversal along the Beaverhill Lake (Late Devonian) event; (4) dip reversal along the Mannville (Lower Cretaceous) event; and (5) time-structural "push down" of Lower Cretaceous and underlying reflections in areas of recent salt dissolution (salt is characterised by fast seismic velocities). On the gravity profile, the edge of the salt is manifested as a 1.5 mGal anomaly. The interpretation of both geophysical data sets is consistent with available geologic control. For more detailed information on salt solution traps the interested reader is referred to an excellent summary paper by Anderson and Knapp (1993).

Occasionally, the solution breccia created by the dissolution of salt can itself act as the reservoir rather than just fracturing and structuring the overburden. This is the case with Wolf Springs Field (north and south pools) and South Wolf Springs Field, located in Yellowstone County, Montana (Luebking et al. 2001). The Wolf Springs fields are unconformity-related combination structural and stratigraphic traps (Fig. 10.93; Luebking et al. 2001). The fields are located on a structural closure on the Custer anticline, where porosity and permeability development exhibits a northeast-southwest orientation perpendicular to structural strike of the anticline. The solution-collapse breccias pinch out laterally into either dense dolomites or anhydrite-plugged collapse breccias. The overlying shaly dolomite breccia of the Botts Member, located just below the Piper unconformity, and the Jurassic Piper Limestone together provide the top seal.

The Wolf Springs and South Wolf Springs fields were discovered in 1955 and 1957, respectively, and have produced more than 5.7 million barrels of oil from the Pennsylvanian Amsden Formation. Amsden reservoir rocks in the area are fractured and brecciated cherts and dolomites that occur in several laterally persistent and mappable zones (Fig. 10.93). The Amsden was deposited in a peritidal to sabkha setting, where evaporite minerals, mainly anhydrite, were once common. These evaporites were partly replaced by silica (chalcedony and chert) soon after deposition. Later dissolution of the remaining evaporites not long after the silicification event, or during the pre-Middle Jurassic unconformity, produced the solution-collapse chert breccias that now serve as

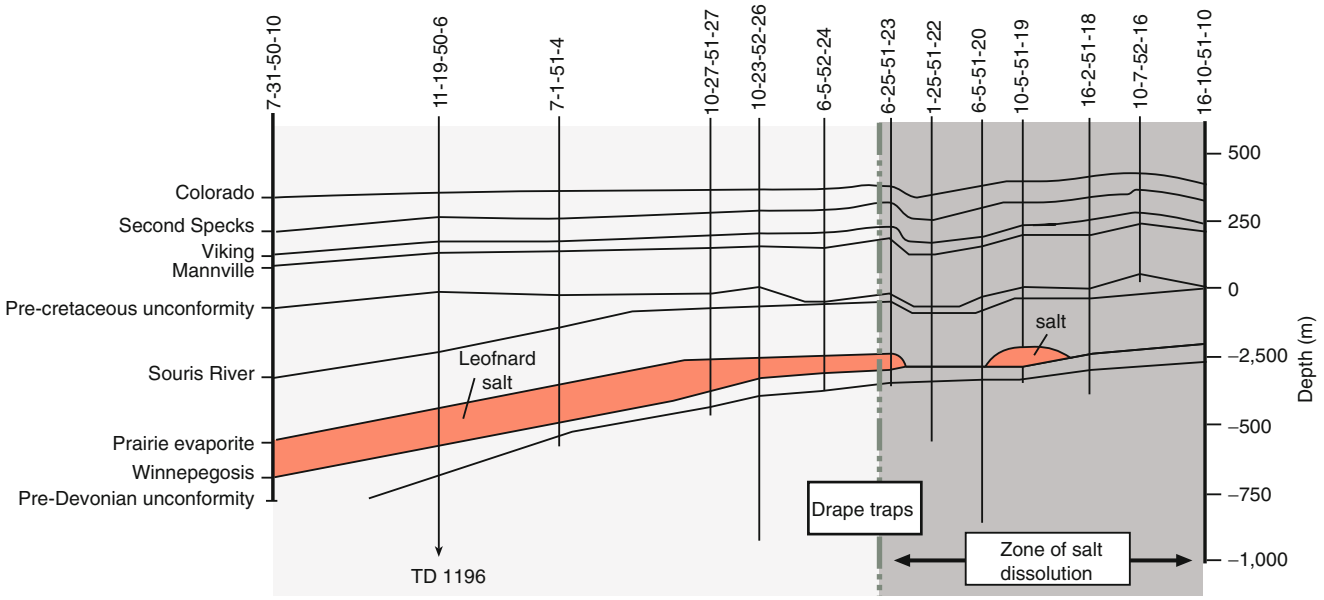

Fig. 10.92 Schematic section illustrating the eastern dissolutional edge of the Prairie Formation. The Westhazel study area straddles T50 and T51 in R23W3M – see Fig. 7.7 for location (After Anderson and Cederwall 1993)

the best reservoir facies in the field. Subtle variations in the diagenetic history of these breccias are a major factor in shaping reservoir quality. But the most impressive accumulation, worldwide, related to salt dissolution is the Athabasca oil (tar) sand accumulation.

Athabasca Tar Sands, Western Canada

The heavy-oil or bitumen reservoirs of northeast Alberta contain 1.8 trillion bbl of resources, the second largest known oil reserve after Saudi Arabia. Of this, almost 1 trillion bbl are contained in the Lower Cretaceous Wabiskaw and McMurray reservoirs of the Athabasca oil sands. The Athabasca oil sands lie close to the eastern edge of the Western Canada Sedimentary Basin (WCSB) at outcrop or a shallow depth of burial, and therefore, their location was known from direct observation even prior to the first descriptions by the Geological Survey of Canada (Fig. 10.94; Tozer et al. 2014; Broughton 2013).

The Lower Cretaceous Athabasca oil sands deposit, the largest of three in northern Alberta accumulated along a north-northwest oriented depression on the Devonian carbonate strata along the uplifted eastern margin of the WCSB. Pathways through the Devonian substrate controlled oil migrations into the overlying Cretaceous sands. The oil was subsequently biodegraded in situ into bitumen (7–9° API). The source rocks, timing of the oil migrations and bitumen formation are contentious, but there is a general consensus for the source rocks being Devonian strata to the west, and for Late Cretaceous to Early Tertiary (Laramide) oil migrations and biodegradation (Broughton 2013).

The northern one-third of the Athabasca deposit overlies a segment of a 150 km wide Middle Devonian salt dissolution trend that extends for 1,000 km along the eastern updip margin of the Middle Devonian Elk Point evaporite basin (Figs. 10.94 and 10.95). The northern Athabasca deposit and the easternmost margin of the Cold Lake deposit to the southeast are the only oil sands areas across northern Alberta to have been structurally impacted by the underlying salt removal.

Salt dissolution collapse-subsidence of Upper Devonian fault blocks underlying the Athabasca oil sands deposit has been widely accepted as the main control that configured the sub-Cretaceous paleotopography (Fig. 10.95) with multi-kilometer long troughs. This evaporite karst structuring fragmented and sagged the Upper Devonian strata, which gravity settled into salt withdrawal areas prior to the accumulation of the unconformably overlying McMurray Formation (Aptian) sands. Factors driving the collapse and the various mechanism of adjustment, such as fluvial capture in monoclinal sags, were discussed in detail in Chap. 7

The giant scale of the halite salt karst underlying the northern Athabasca deposit is widely known as one of the largest and thickest dissolution collapse-subsidence areas, as well as one of the worlds largest known stacked evaporite and collapse breccia karsts. Historically, within the industry, the salt edge is not typically modelled in terms of evaporite deposition and diagenesis, and is more generally recognized as a fault block subsidence terrain than as a

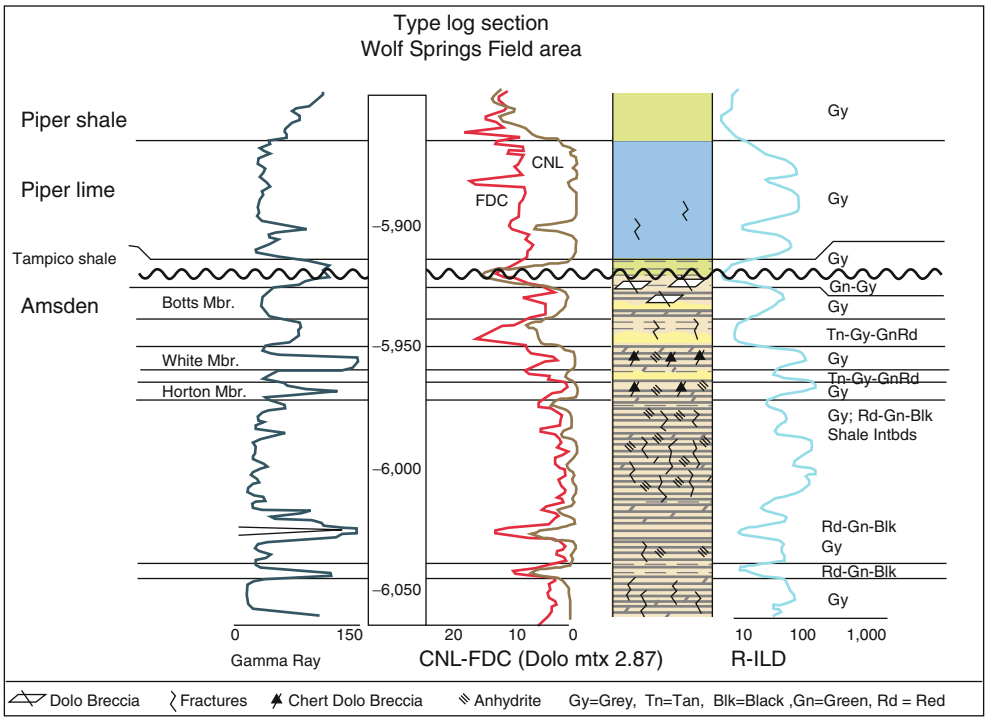

Fig. 10.93 Type log for the Wolf Springs Field area. The Botts, White, and Horton members of the upper Amsden are readily discernible as resistive kicks. The White and Horton members correspond to the zones of solution-collapse breccias. The Botts member is a shaly dolomite breccia. The lithologies shown in the Amsden and Piper formations represent compilations assembled from cores in the area (After Luebking et al. 2001)

system with pervasive faults originating as response to ongoing formation of evaporite collapse breccias. More recent work has begun to integrate the evolution of the salt dissolution edge into an improved understanding that will lead to more efficient recovery of this huge hydrocarbon resource and to better definition of subsurface areas suitable for brine waste disposal (Broughton 2013).

The sub-Cretaceous paleotopography beneath the Lower Cretaceous Athabasca oil sands, northern Alberta, shows an orthogonal lattice pattern of troughs up to 50 km long and 100 m deep between pairs of cross-cutting lineaments (Broughton 2013). These structures are likely inherited from a similar pattern of dissolution collapse-subsidence troughs in the underlying Middle Devonian salt beds. Removal of more than 100 m of halite via meteoric water crossflows has fragmented the overlying Upper Devonian strata into fault blocks and collapse breccias that subsided into the underlying dissolution troughs. An unusually low 1:2 to 1:3 thickness ratios of halite salts to the overlying strata resulted in Upper Devonian strata collapse-subsidence into underlying salt dissolution troughs being more cataclysmic during the first phase of salt removal. The second phase of slower but complete salt removal between the earlier troughs resulted in a more gradual subsidence of the overlying strata. This largely obliterated the earlier pattern of giant cross-cutting dissolution troughs bounded by major lineaments.

The collapse breccia fabrics underlying the earlier troughs differ from those areas between the troughs. Collapse breccias underlying the large troughs often have crushed fabrics distributed in zones that rapidly pinch out between fault blocks. Breccias between troughs developed as giant mosaics of detached carbonate blocks that formed breccia pipe complexes. Multiple sinkholes up to 100 m deep are aligned along multi-km linear valley trends that dissect the sub-Cretaceous paleotopography. These sinkhole trends form orthogonal patterns inherited from underlying lattice of NW-SE and NE-SW salt-structured lineaments. These cross-cutting sinkhole trends have a smaller 5 km scale reticulate pattern similar to the giant 50 km scale pattern of collapse-subsidence troughs. Other sinkholes developed as lower McMurray strata sagged when underlying Devonian fault blocks and breccia pipes differentially subsided.

Interestingly, not all hydrocarbon-reservoirs in salt entraining basins typified by stratiform breccias in carbonate platforms, are related to earth-bound dissolution processes. The Cantarell oil field in the Campeche Platform of Mexico, with a current daily production of 1.3 million barrels of oil, is probably the most voluminous oil-producing unit where reservoir fracturing is related to a bolide impact event. The K-T breccia reservoir itself, its ejecta horizon and its sealing muds are related to the same bolide event that wiped out the dinosaurs (Grajales-Nishimura et al. 2000).

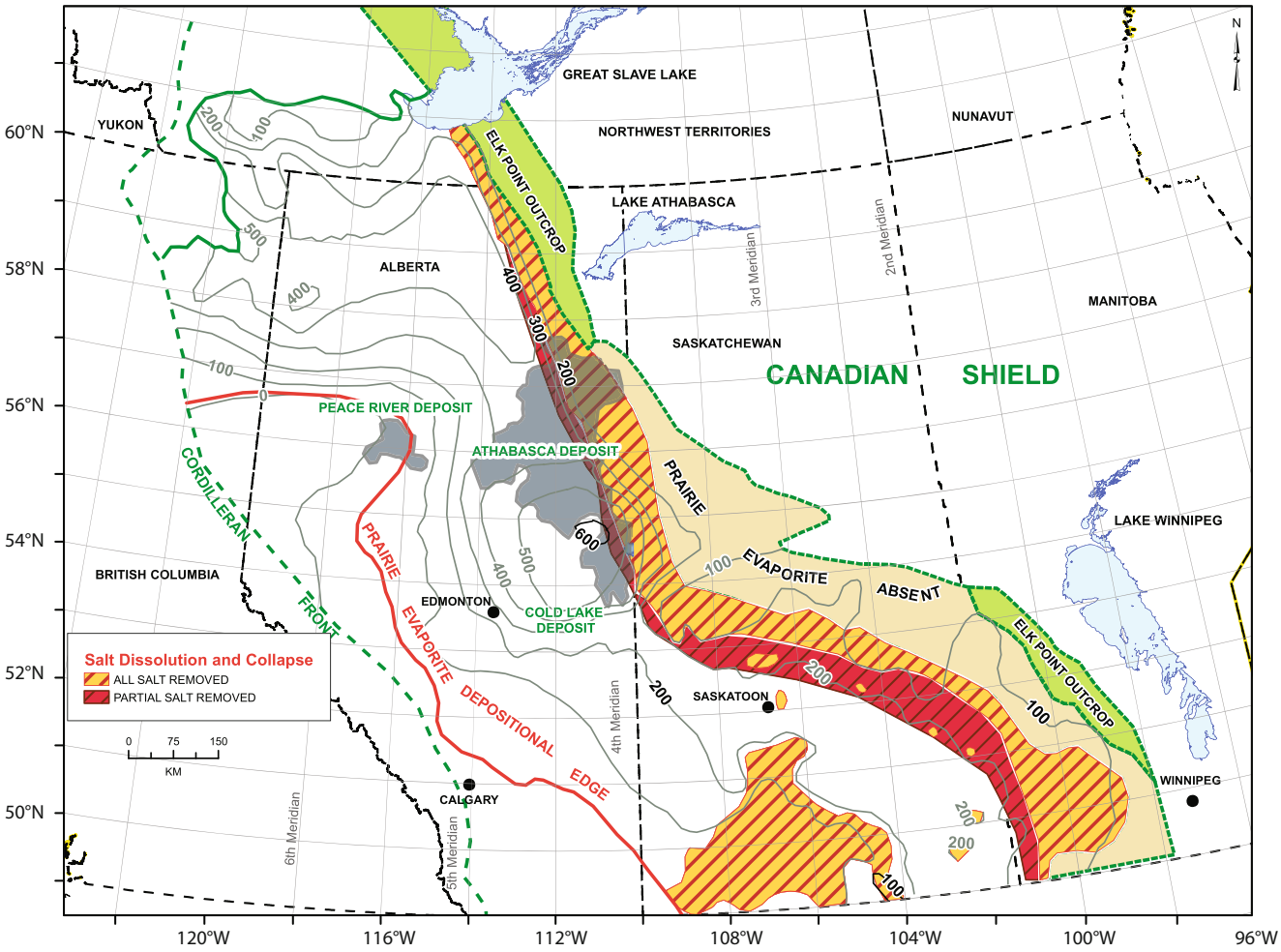

Fig. 10.94 Prairie Evaporite (Middle Devonian) salt basin extends across Western Canada with partial to complete salt removal trends typifying its salt dissolution edges. A 1,000 km long and 150 km wide salt dissolution trend underlies the northern one-third of the Athabasca oil sands deposit and the narrow eastern margin of the Cold Lake deposit to the south. Contours are 100 m (After Broughton 2013)

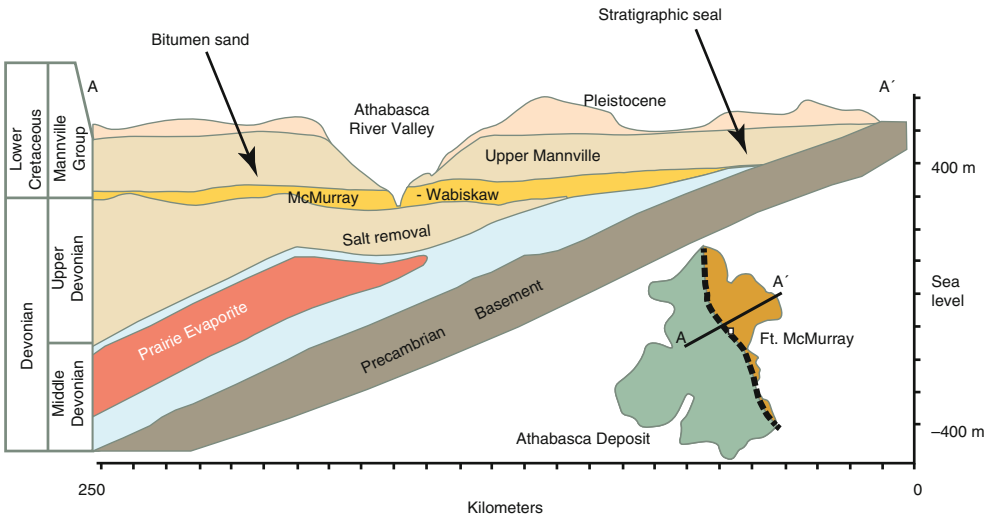

Fig. 10.95 Cross-section across the northern Athabasca oil sands deposit showing the sub-Cretaceous unconformity on the underlying Devonian strata and the salt removal from the Prairie Evaporite (After Broughton 2013; see also Chap. 7)

Potash Resources: Occurrences and Controls

11

Introduction

Natural potash evaporites are a typical part of a brine evaporation series, crystallizing at the higher concentration or bittern end, either at the surface (primary salts) or in the shallow subsurface (secondary salts). Today, bedded accumulations of primary potash evaporites are a relatively rare occurrence. Extremely high solubility of most potash salts means they accumulate in highly restricted, some would say highly continental, modern depositional settings (Cendon et al. 2003). Wherever Quaternary potash does occur naturally, as in the playas of the intermontane Qaidam Basin in China and in the Danakil Depression in the Afar Rift of Africa[1], carnallite, not[2] sylvite, is the dominant potash salt. This has led some to postulate that carnallite is the archetypal primary marine potash phase, while sylvite is a secondary diagenetic mineral formed by incongruent dissolution of carnallite. Others have argued that ancient sylvite was sometimes a primary precipitate, deposited by the cooling of highly saline surface or near surface brines and from seawater with ionic proportions different to those of today (Hardie 1996).

Phanerozoic potash salt series define two distinct time-related groupings of brines and associated minerals: $MgSO_4$-rich and $MgSO_4$-poor. Potash salts have not been recovered from Precambrian sediments, other than in minor amounts of intercrystalline cement in the latest Neoproterozoic evaporites of the Ara Salt Group of Oman and the Hanserian Evaporite Group (HEG) of the Nagaur-Ganganagar basin in India/Pakistan. No potash salt was recovered in Oman (inferred from wireline log), while the dominant potash mineral cored in the HEG is polyhalite, making it less attractive as an exploration target for fertiliser manufacture in that part of the world (Mohnot et al. 2005). All potash deposits rich in $MgSO_4$ accessories are composed of some combination of gypsum, anhydrite, polyhalite, kieserite, kainite, carnallite and bischofite. This group of $MgSO_4$-entraining salts typifies Quaternary salts in the Dallol depression of Ethiopia, the Miocene assemblages of the Ukraine and Sicily, as well as some Permian potash deposits in Europe and Russia and the few Eocambrian deposits known to exist. Potash deposits free of, or poor in, $MgSO_4$ minerals are dominated by some combination of halite, carnallite, and sylvite and typify much of the Phanerozoic rock record. This $MgSO_4$-depleted group constitutes the majority of known reserves of exploited potash, which are dominated by Devonian evaporites in Canada.

Potash is a collective term for a variety of ore-bearing minerals, ores and refined products, all containing the element potassium in water-soluble form (Table 11.1). The word "potassium" is derived from the word potash. In the 1800s the term "potash" was used to describe the mixture of potassium carbonate and potassium hydroxide crystals, which were recovered in heated iron "pots" from boiling the washings of wood or broad-leaf tree leaves "ashes," both these recovered potash salts are caustic. Lye meant sodium hydroxide and potash lye was potassium hydroxide, a higher grade product that has been used since the fifteenth century in the manufacture of higher-grade softer or facial grade soaps.

Potash minerals were mined from at-surface and nearsurface Quaternary salt beds in the Dallol region of the Danakil Depression as long ago as the fourteenth Century. In the western world, the Germans were the first to discovery subsurface quantities of potash salts in the 1850s in the Zechstein Basin and a few years later had determined the utility of potash as a fertiliser for improving plant production. The first documented use of potash as a soil fertiliser in the USA was in 1873, and since the start of the twentieth century potash

[1]The name carnallite comes from the German geologist Rudolph von Carnall (1804–1874).

[2]The name sylvite come from *sal digestevus Sylvii* (New Latin: digestive salt of Sylvius), named for the Dutch physician and chemist Franciscus de la Boë (1614–1672), a.k.a. Sylvius.

© Springer International Publishing Switzerland 2016

J.K. Warren, *Evaporites: A Geological Compendium*, DOI 10.1007/978-3-319-13512-0_11

Table 11.1 Potassium ore salts and contaminants, with K_2O equivalents

Mineral	Composition	K_2O %	Comments
Chlorides			
Sylvite	KCl	63.2	Principal ore mineral
Carnallite	$MgCl_2 \cdot KCl \cdot 6H_2O$	16.9	Ore mineral and contaminant
Kainite	$4MgSO_4 \cdot 4KCl \cdot 11H_2O$	19.3	Important ore mineral
Sulphates			
Polyhalite	$2CaSO_4 \cdot MgSO_4 \cdot K_2SO_4 \cdot 2H_2O$	15.6	Ore contaminant
Langbeinite	$2MgSO_4 \cdot K_2SO_4$	22.7	Important ore mineral
Leonite	$MgSO_4 \cdot K_2SO_4 \cdot 4H_2O$	25.7	Ore contaminant
Schoenite (picromerite)	$MgSO_4 \cdot K_2SO_4 \cdot 6H_2O$	23.4	Accessory
Glaserite (aphthitalite)	$K_2SO_4 \cdot (Na, K)SO_4$	42.5	Accessory
Syngenite	$CaSO_4 \cdot K_2SO_4 \cdot H_2O$	28.7	Accessory
Associated minerals			
Halite	NaCl	0	Principal ore contaminant
Anhydrite	$CaSO_4$	0	Common ore contaminant
Bischofite	$2MgCl_2 \cdot 12H_2O$	0	Accessory contaminant
Bloedite (astrakanite)	$Na_2SO_4 \cdot MgSO_4 \cdot 2H_2O$	0	Accessory
Loewite	$2MgSO_4 \cdot 2Na_2SO_4 \cdot 5H_2O$	0	Accessory
Vanthoffite	$MgSO_4 \cdot 3Na_2SO_4$	0	Accessory
Kieserite	$MgSO_4 \cdot H_2O$	0	Common ore contaminant
Hexahydrite	$MgSO_4 \cdot 6H_2O$	0	Accessory
Epsomite	$MgSO_4 \cdot 7H_2O$	0	Accessory
Ores			
Sylvinite	KCl + NaCl	10–35	Canada, USA, Russia, Brazil, Congo, Thailand
Hartsalz	$KCl + NaCl + CaSO_4 + (MgSO_4 \cdot H_2O)$	10–20	Germany
Carnallitite	$MgCl_2 \cdot KCl \cdot 6H_2O + NaCl$	10–16	Germany, Spain, Thailand
Langbeinitite	$2MgSO_4 \cdot K_2SO_4 + NaCl$	7–12	USA, Russia
Mischsalz	Hartsalz + Carnallite	8–20	Germany
Kainitite	$4MgSO_4 \cdot 4KCl \cdot 11H_2O + NaCl$	13–18	Italy, Ethiopia, Belarus

has been increasingly used to enhance agricultural productivity worldwide. Today, our ability to feed the world's ever-expanding population is totally dependent on the use of various soluble potash salts as plant[3] fertilisers.

This change in potash usage from an ash product to an industrial chemical/fertiliser has changed the meaning of the term potash. Since the 1950s the terms, potash or potash salts, have been used commercially as general descriptions for potassium chloride (KCl or muriate of potash – MOP), potassium sulphate (K_2SO_4 or sulphate of potash – SOP), potassium-magnesium sulphate (K_2SO_4-$MgSO_4$ or sulphate of potash magnesia), potassium nitrate (KNO_3 or saltpetre), or mixed sodium-potassium nitrate ($NaNO_3 + KNO_3$ or Chilean saltpetre). Carnallite and sylvite are the most common naturally occurring potash mineral salts, with sylvite the most economically important. Other common potassium-entraining natural evaporite salts include: kainite, kieserite, langbeinite, leonite and polyhalite (Table 11.1). Of these, carnallite, kainite, langbeinite and polyhalite when processed, can constitute potash ore minerals. Today, langbeinite ore is economically exploited only in New Mexico.

Sylvinite, a mixture of sylvite and halite, constitutes the highest-grade ore source, while MOP constitutes some 96 % of the world's current potash production. Carnallite, when present in a sylvinite ore, is considered a contaminant. Muriate of potash is also a byproduct of the processing of the natural deposits of $NaNO_3$, which historically have been mined in significant volumes from soils in the hyperarid Atacama Desert of Chile. Potassium sulphate is produced

[3]Potassium increases plant resistance to drought, frost and to a number of diseases and pests, it is essential for the development of the root system, fosters nitrogen fixation in leguminous crops, and also it improves the size, colour and sugar content of crops, such as fruits. Natural reserves of soil-potassium diminish with each successive crop. This withdrawal or "soil mining" is greatly increased and accelerated by higher yields and more intensive cropping. For example, high-yielding, short-season rice varieties in a double-cropping annual system will remove up to 36 times more potassium from soil compared to a single crop of traditional varieties. Potassium uptake by rice in a triple-cropping system will be about 50 % more than extracted by two crops annually. Although some soils are rich in potassium, many are poorly endowed and crop production thereon is unsustainable if the potassium removed by cropping is not replenished in appropriate amounts.

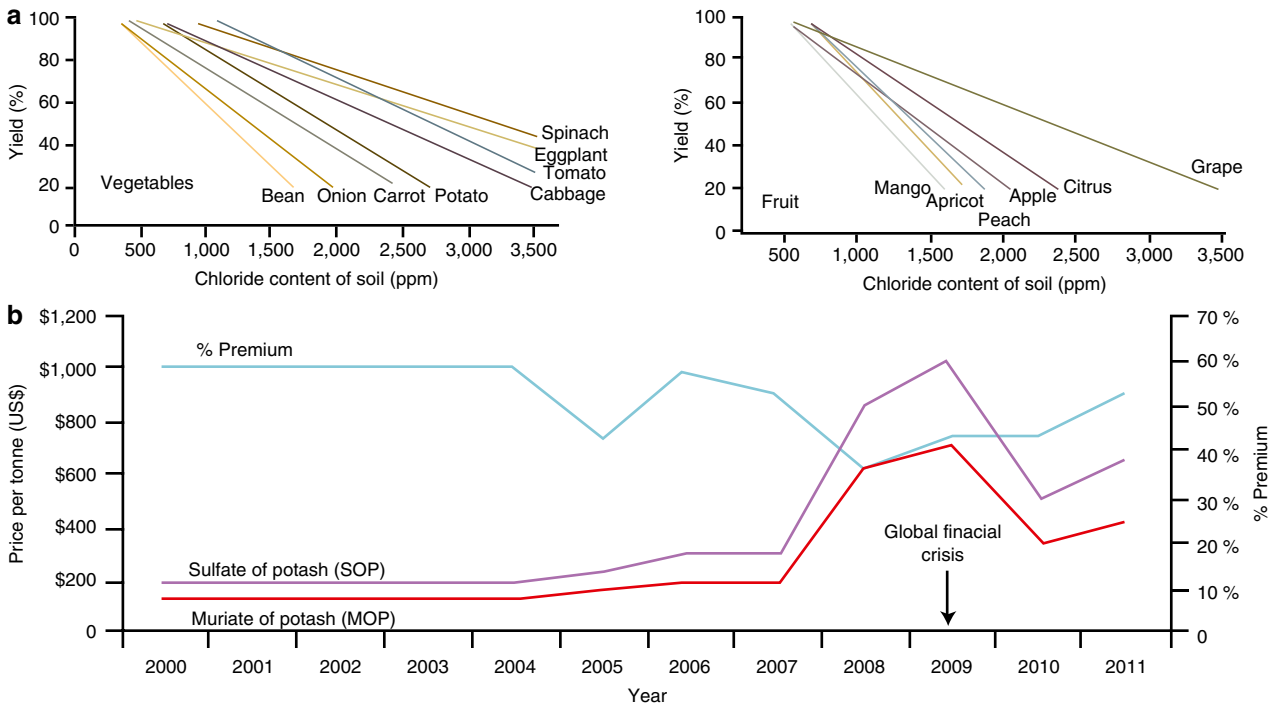

Fig. 11.1 Muriate of potash (MOP) and sulphate of potash (SOP). (**a**) Fruit and vegetables show decreasing yield with increasing chloride content in the soil. (**b**) Price comparison shown how SOP sells at a premium compared with MOP

from mined minerals in Germany and the USA and from processing of cool-climate lake brines in Canada, Chile, China, and the USA. In order to compare the various mineral sources of soluble potassium, the commodity is often listed and traded as K_2O equivalents (Table 11.1). No source of soluble potash for fertiliser actually contains K_2O as this form of potash is highly caustic and burns any plant in contact.

The fertiliser industry uses more than 90–95 % of produced potash, while the chemical industry uses the remainder in the manufacture of soaps and detergents, glass, ceramics, synthetic rubber and numerous industrial chemicals. As mentioned earlier, the main use of potash is as a source of soluble potassium, which is one of the three primary plant nutrients; the other fertilisers are fixed and soluble phosphorus and nitrogen. Mankind's use of these three nutrients, in commercial forms, started the "Green Revolution" in agriculture in the 1950s. More than 95 % of the world's potash fertiliser is today produced as muriate of potash (MOP-potassium chloride) and sylvite is the preferred ore mineral in most mines, due to relatively low processing costs. MOP fertilizer has a minimum requirement of 60 % K_2O content. Sulphate of Potash (SOP-Potassium sulphate) and Sulphate of Potash-Magnesia (SOPM-potassium magnesium sulphate), together make up around another 5 % of current fertiliser usage, and are required by some more sensitive crops where elevated chloride levels could be a problem (Fig. 11.1a). SOP has a minimum requirement of 50 % K_2O, while SOPM has a minimum requirement of 19 % K_2O content. Retailers sell potash, or potash blended with other fertilizers, in dry or liquid form.

Since 1960, the number of people on the planet has more than doubled, while the amount of arable land per hectare has halved (Fig. 11.2a). Yet the total crop or food production per capita has managed to exceed the growth in world population. Each year, potash fertiliser is used in the production of fruit and vegetables (17 %), maize (15 %), wheat (15 %), rice (14 %), sugar (4 %), cotton (4 %), soybeans (4 %) and palm oil (2 %). Our ability to continue to produce more food per capita is largely the result of the increasing use of potassium and other fertilisers and encapsulates the "Green Revolution".

Even so, the world's ever-expanding population means soil degradation now affects more than 15 % of the Earth's land area, resulting in 30 % of the world's cropland becoming increasingly unproductive, especially in the semi-arid climate belts of the Developing World, where many subsistence farmers cannot afford to buy fertiliser to boost yields (Rattan 2007). In addition, salt marshes of the temperate zones, heavily irrigated lands, and wetland rice soils are also increasingly saline, with elevated levels of sodium and chloride in the waters (Kendall and Pimental 1994; Timms 2005). Worldwide, soil degradation affects more than 15 % of the Earth's land area, resulting in 30 % of the world's current cropland currently becoming increasingly unproductive. This is mostly due to increasing soil salinity, especially in the

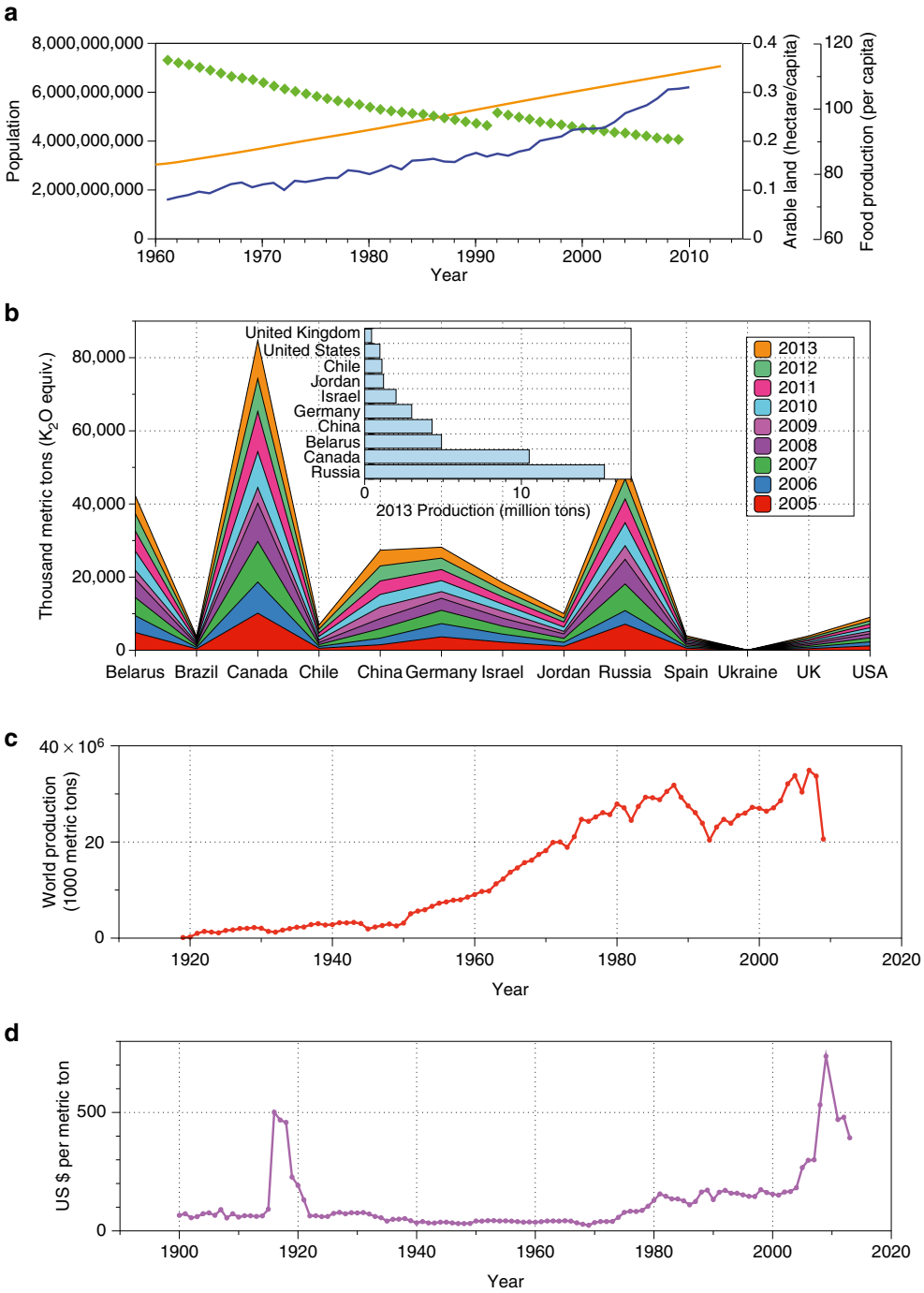

Fig. 11.2 World Statistics. (**a**) Trends since 1960 of world population (*gold line*), arable land per capita (*green diamonds*) and per capita food production (*blue line*), indexed to 100 and based on period 2004–2006 (From FAO database http://faostat3.fao.org accessed Sept 1, 2012). (**b**) Major potash producers for 1998–2010, the legend and chart match in their vertical order (Compiled from USGS on-line data tables downloaded from http://minerals.usgs.gov/minerals/pubs/commodity/potash/ last accessed 7 April, 2014). *Inset* shows 2013 production for top ten. (**c**) World potash production 1919–2010. (**d**) Price (annual average) of potash in US$ per metric ton. All potash production in thousand metric tons of K_2O equivalent showing dip in the market in 2009 due to the global financial crisis. (Potash data for **c** and were replotted using downloaded data from http://minerals.usgs.gov/ds/2005/140/ last accessed 4 April 2014)

world's semi-arid climate belts where water access is limited and irrigation, coupled with application of fertiliser, drives a combination of salinisation and groundwater depletion (Rattan 2007). Salinity induced symptoms in a crop include reduced root growth, decreased flowering, and smaller leaf size (Fig. 11.1a). When applied to the soil, SOP has a lower salinity effect on soil quality compared to MOP (potash is carried to the soil and the plant roots as a soluble sulphate versus chloride salt), and therefore is the preferred fertilizer for many saline soils around the world. For this reason there is a 40–60 % price premium for SOP over MOP (Fig. 11.1).

Through the increasing use of potash and other fertilisers, we are currently winning the battle to supply enough food to support the world's growing population, even as the quality of some soil is subject to increasing salinisation. The major cause of famine today is not lack of food in the world, rather, regional famine is often due to a combination of war, ethnic and religious conflicts. The result is lack of required infrastructure and funding at the state and regional level needed to move large volumes of food into regions that require it.

In my opinion, over the longer term, ongoing unfettered population growth is driving what will likely be a catastrophic

collapse in the world's food supply. This is true whether or not one subscribes to claims of anthropogenically-induced climate change and the possible additional stresses this will add to an already depressing picture of the future health of the world's agriculture (Fig. 11.1a). Population growth is a problem that is much harder for the world's political class to address by giving speeches and putting in place a few legislative measures to reduce anthropogenic CO_2. It requires governments to address head-on the larger and more fundamental problem of too many mouths to feed. This is a situation created by a combination of human need and superstition, a lack of social systems to support the old, and by dogma inherent in the majority of the world's religions in their support of notions of large families, a lack of support for contraception and antithetic attitudes to homosexuality.

Production and Consumption

In 2013–2014 there were 14 potash producing countries, including smaller production volumes from the Ukraine, the UK and Chile. In 2013 Russian production exceeded that of Canada, other countries in the top ten in descending order were; Belarus, China, Germany, Israel, Jordan, Chile, USA and the UK (Fig. 11.2b and inset). The volume of produced potash has been steadily increasing since records are first available in 1919 (Fig. 11.2c). There were significant drops in world production in the late 1980s and in 2009, related to world financial crises. The price of potash in the period 1900–2013 shows a serrated rise since the 1950s, directly tied to the agricultural green revolution and increasing population pressure on the world's arable land (Fig. 11.1a). This is combined with rising middle class numbers in the developing world, along with increasing consumption of animal protein.

The sharp price spike during World War 1 (1914–1918) relates to the use of Chilean salt petre (potassium nitrate and sodium nitrate) in the manufacture of gunpowder (mixture of sulfur, charcoal and potassium nitrate) and to the fact that at that time the Germans exerted control of the world's potash production, which was focused in the Zechstein and Alsace basins (Fig. 11.2d). At that time extractable deposits in the caliche soils of the Atacama Desert were known as "white gold" (Fig. 12.62). Canada, historically the world's largest potash producer, holds more than 45 % of the world's known potash reserves (Fig. 11.3a) and recovers potash by mostly conventional underground mining of bedded sylvinite deposits. Production is centred on the Devonian Prairie Evaporite in the Elk Point Basin in Saskatchewan, with lesser production in the Carboniferous New Brunswick sub-basin in the Maritime Provinces (Table 11.5). Russia is the other major potash producer at the world scale, it holds some 35 % of known world reserves including significant potential for new discoveries in the East Siberian region. Currently, Russia extracts most of its potash from the Cis-Urals region, where sylvinite is conventionally mined from the Permian Upper Kama Basin in the Solikamsk region west of the Urals. Devonian potash is also mined in the Pripyat depression of Belarus, which holds 9 % of the world's known reserves. In terms of world potash resource, Canada once again tops the bill. A combined U.S. Geological Survey and Saskatchewan Geological Survey assessment (Cocker et al. 2010) estimate known potash resources in the Prairie Evaporite Deposit to be around 88.8 billion tonnes of potassium oxide (K_2O). This estimate is higher than various previous estimates ranging from 56 to 67 billion t of K_2O. If correct, the potash resource in Saskatchewan would be sufficient to mine for several thousand years at the current production level.

Significant volumes of Permian potash are still mined from the Zechstein of NW Europe (Germany, UK and the Netherlands), while smaller amounts are mined from the northern margin of the Delaware Basin in New Mexico, USA. Oligocene potash was formerly extracted from the Rhine Graben (Alsace Basin) in France, while Miocene potash was mined until a few years ago in the Stebnik area in the western Ukraine. In Spain, in the northern part of the Ebro Basin near the border with France, potash is produced from Eocene-Oligocene lake sediments. In Utah, potash is solution mined from the Carboniferous Paradox Formation deposits and recovered from Great Salt Lake brines by solar evaporation and flotation. Israel and Jordan use similar solar technology to produce large volumes of potash from Dead Sea brines created naturally from recycled marine Miocene evaporites and connate waters buried beneath the floor of the Dead Sea. In China, various combinations of KCl and/or K_2SO_4 are recovered by processing of saline lake brines from the Qarhan and Lop Nur salt flats. In California, potash and coproducts, borax pentahydrate, soda ash and saltcake, have been recovered from various subsurface playa brines using mechanical evaporation. KCl and K_2SO_4 are byproducts of lithium processing from salar brines in the Atacama Desert of Chile, South America.

Conventional underground mining typically requires an ore grade of 14 % K_2O or higher, and bed thickness of more than 1.2 m, with some 8-m of salt in the mine back or roof (Kogel et al. 2006; p 734). The 14 % rule was established in the 1930s by operations in the Carlsbad region of New Mexico. Last century, under centrally planned economies, the East Germans and the Russians utilized mined potash levels as low as 11 % K_2O. In the USA the Carlsbad producers operated with 80–85 % recovery in the mill (some producers operated with 92 % recovery by pulling pillars). Crystallizers were first installed in the back ends of potash mills by British and French operators to capture potash from waste liquors, before dispatching wastes to the slurry piles. This raised their recovery efficiencies to as high as 92 %.

Today there are 150 countries world-wide that use potash as a major agricultural component (Fig. 11.4a; FAO 2010).

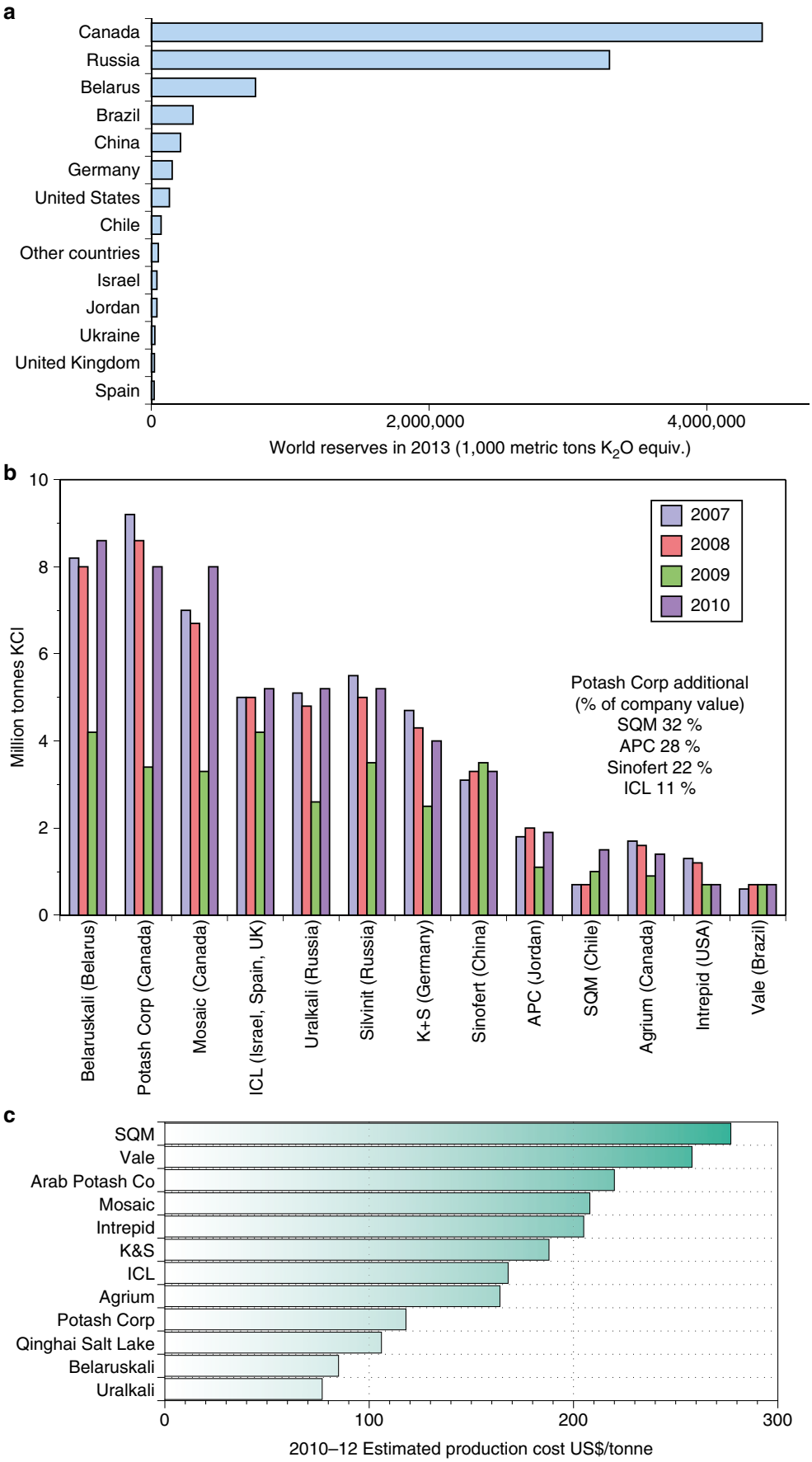

Fig. 11.3 Reserves and ownership. (**a**) World reserves as listed by USGS in 2011 in 1000 metric tonnes. (**b**) Major corporate producers of KCl in period 2007–2010, clearly showing the effects of the Global Financial Crisis in 2009. (**c**) Estimated averaged production costs (US$/tonne) for period 2010–2012, does not include freight costs and is broken down by major producers (extracted from various SaltWork database tables)

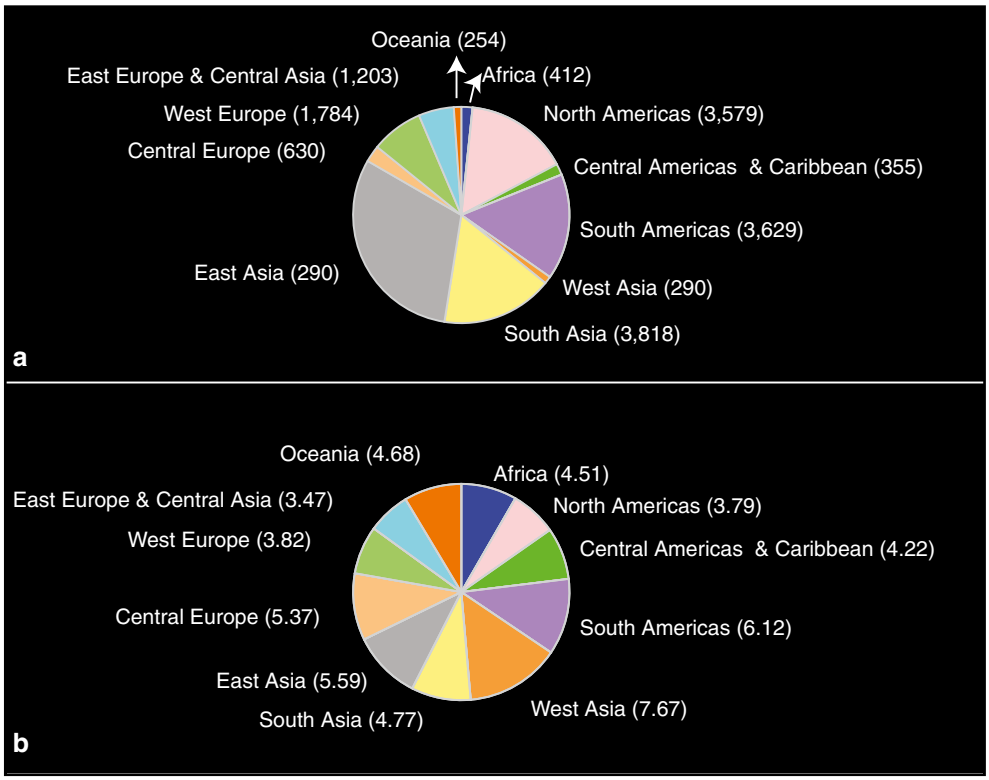

Fig. 11.4 Potash consumption. (**a**) Potash consumption by region in 2009 (in 1,000 metric tonnes). (**b**) Projected increase in demand, expressed as compound annual growth rate (%) in potash consumed (as K_2O) for the period 2010–2014 (Replotted from FAO reports 2010)

The United States is one the world's largest net consumers of potash, but produces only 23 % of the potash it consumes. Asian nations produce only 13 % of their potash demand. China and India and Brazil are the world's largest importers of potash and China's domestic production has risen over the past decade). Even so, all three have low levels of domestic production relative to demand and their rapidly growing population bases will fuel a world-scale increased demand for potash over the next decades (Fig. 11.4b).

Of current world production, just ten companies control some 90 % of the world's potash, and the five largest companies control more than 70 %, with a strong focus in ownership by Canadian and Russian companies (Fig. 11.3b). Canpotex is the world's largest exporter of potash, it was created in 1972 and is wholly owned by three Canadian potash producers (PotashCorp, Mosaic and Agrium). It even owns its own shipping fleet. Its overall share of the market is around 35 % with more than 130 customer groups in 60 countries. In 2011, Brazil, China, India, Indonesia and Malaysia accounted for some 70 % of its annual sales. In 2005, the Russian potash consortium Belarusian was formed by the merger of the Uralkali and Belaruskali (50 % stake) corporations. Until July 2013 the Belarusian Potash Company was the second largest supplier of potash to the world market and exports to more than 80 countries worldwide. Together the Canadian-Russian duopoly accounts for 70 % of global potash trade.

Historically, the world's supply of MOP has been held mostly by a few companies, whose coordinated actions in choosing to withhold supply has controlled prices. This ability to withhold supply is the result of the limited number of producers in the market and relatively high entry costs to construct a new mine (more than US$ 1–1.5 billion). Such marketing control, exerted by a few world-scale producers, is considered by some as a protectionist cartel, capable of artificially maintaining prices by controlling supply (see Javier Blas, Financial Times, London UK, August 19, 2010; al Rawashdeh and Maxwell 2014). Until recently the potash cartel was coordinated by two exporting consortia – Canpotex in North America (owned by PotashCorp, Agrium and Mosaic) and the Belarusian Potash Company in the Former Soviet Union (owned by Uralkali and Belaruskali). Through their size in the market they could act on State and Federal governments to prevent entry of new major competitors into their market. In November 2010, the Canadian potash industry successfully lobbied state and federal governments to block a $40 billion BHP Billiton bid to purchase PotashCorp (instigated in August, 2010). BHP Billiton has a worldwide policy of selling a commodity to world markets at current prices for all its commodities and to maximise the efficiencies of their operations when under price pressure. This was not a popular approach to Canpotex management in the sheltered Canadian marketplace, where historically the dominant producers have chosen to throttle production to maintain what they see as an acceptable potash price.

Unlike many other commodities such as gold and oil, which trade continuously on world markets, potash is sold

directly via negotiated contracts or by spot sales between producers and consumers, in a market where the sales price was dominated by the actions of the former duopoly. Farmers were at the delivery end of this largely consortia-controlled set of negotiations, but if they do not like the asking price, they could only choose not to fertilise their fields for 1–2 years. After this, there are substantial drops in productivity per acre. So, even when prices are high, agriculturalists must buy most years in order to maintain the required crop productivity. At times this lead to significant tensions in negotiations between suppliers and consumers of potash and to active exploration for potash outside of the holdings of the duopoly.

Each potash deposit has its own characteristics and associated mining problems that must be handled on an individual basis (Garrett 1995; UN Industrial Development Organization 1998). According to the Blas article in the Financial Times of London, mentioned earlier, not all potash operations are low cost, most high-cost production is outside of the conventional underground mines of Canada and Russia. It is in the hands of K+S in Germany, as well as mines in Spain, the UK and Israel Chemicals. Intrepid Potash, a US-based group, SQM and Vale of are also high-cost producers relative to the Canadians and the Russians (Fig. 11.3c).

Currently (mid 2014), after the vitriolic 2013[4] break-up of the Russian duopoly, Uralkali is undercutting the average world market price and is supplying bulk contract potash to India and China at around US$320–350 per tonne, leading to production cut-backs and layoffs in the Canadian industry and elsewhere (Fig. 11.3c). Over the past decade the price of potash has doubled but also fluctuated widely. At the beginning of 2008 the price rose rapidly from less than $200 a tonne to a high of $875 in February 2009. Then it dropped dramatically to an April 2010 low of $310, before recovering in 2011–2012, and relapsing again in 2013 (Figs. 11.1b and 11.2d). The potash price suffered less than other commodities during the 2009 global financial crisis, but current price projections for the next few years (2014–2016) are not optimistic, largely because of the July 2013 breakdown of the Russia Belarus cartel and the ongoing passage to the market of cheap potash. In the longer term, the per acre productivity of world agriculture must continue to increase in order to feed the world's burgeoning population, so the longterm price will slowly recovery.

Ore Extraction Technologies

There are three basic types of potash extraction in use today: (1) Conventional mining that, once the ore level is attained, can encompasses several standard mining methods, modified as necessary for specific subsurface situations, (2) Solution mining of ancient evaporites and (3) Solar processing of modern lake brines (Fig. 11.5). Solution mining typically requires lower upfront capital expenditure compared to conventional underground mining techniques, which requires significant mine development prior to production. Conversely, operating costs for underground mining techniques are generally lower, compared to solution mining and lake brine extraction processing methods, which can both be energy intensive.

Conventional Mining

For potash beds that are relatively flat and uniform in thickness, or for cutting entries to the ore zone, boring machines with two or four cutting arms have proven to be an effective and economic mining method. For moderately inclined, undulating and/or thickening-thinning potash seams, continuous miners with cutting "drums" mounted on one or two moveable arms are the most effective (Fig. 11.5). In general, two types of continuous mining machines are used: Borer miners and Drum miners. Borer miners apply uniform cutting pressure, have fixed cutting heads, and possess a higher capacity, though they only cut a fixed seam thickness and width. Drum miners have rotating cutting heads that cut sideways against the face and despite their lower capacity, are better able to adapt to changing ore thicknesses. For highly variable ore bodies, or ore with potential rock-bursts or other

[4]In July 2013, Vladislav Baumgertner, chief executive of the world's largest potash and cheapest producer, OAO Uralkali, suddenly announced, without prior warning, that he was removing his firm from one of the potash world's major price support cartels which his company had maintained with another firm, Belarusian Potash Company. As a result of his actions, Baumgertner has been ridiculed, reviled and even imprisoned for a month when he visited Belarus. Mining Weekly estimated that this decision had the effect of wiping out $18 billion in market capitalization of the major potash players, worldwide. The world of potash production and distribution has been thrown into major turmoil and a trade war between his home nation of Russia and neighbouring Belarus may very well have broken out. Baumgertner has explained his action was based on market forces (responding to cartel actions and changes in market share), which had led to a steady rise in his company's above-ground potash stocks. He believed the only way to work off those stocks was to stimulate demand by forcing prices lower. Naturally, agricultural consumers rejoiced somewhat, but for many potash producers, the decline in prices to US$325 per tonne by late October 2013 was a real profit-buster (see Table 11.3c).

Share prices of PotashCorp (POT) of Saskatchewan had been on a rollercoaster ride ever since the original price/tonne oscillations began in 2008, but, by 2013 stock prices appeared to be holding firmly between $40 and $45. This was so until the July announcement, upon which its share price immediately plunged by over 25 per cent to barely $30 per share. Part of POT's problem stemmed from their decision to dramatically increase brownfield production from 9,000,000 tonnes per year to a prodigious 17.1 million tonnes per year, by 2015. China moved swiftly to take advantage of the situation and purchased a huge block of Uralkali stock, thereby acquiring a 12.5 % ownership position and thereby gained market leverage in order to assure China of adequate potash supplies going forward.

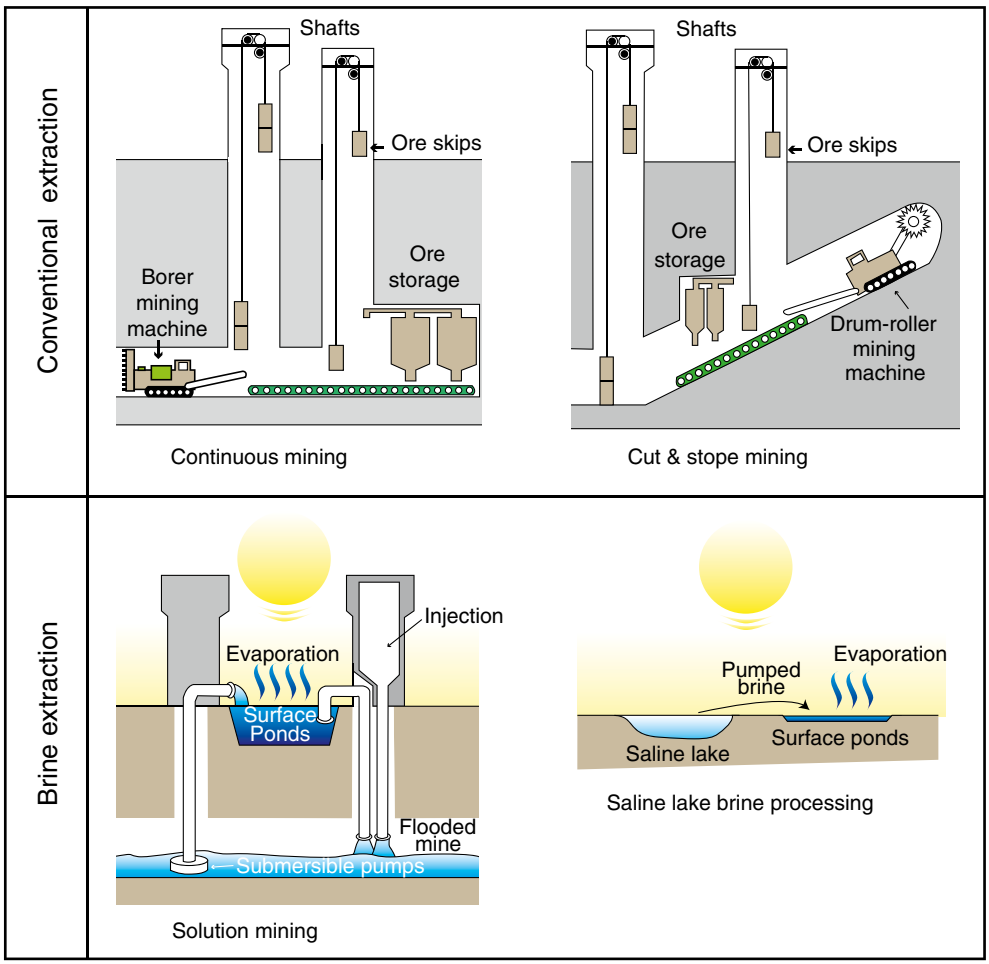

Fig. 11.5 Potash extraction techniques

special needs, drilling and blasting are still required. Blasting is most effective in managing mine sites with large variances in ore thickness, and requires less initial capital and maintenance than continuous mining, though generally results in higher costs overall.

Many potash mine configurations are conventional room and pillar designs. Stress-relief mining (multiple entries with outer yield pillars) has proven highly effective in deeper room and pillar mines, where there is a need to deal with plastic flow (of the ore and the adjacent salt host) or with unstable roof (mine back) conditions. The "room and pillar" method progresses along the potash seam, while pillars and timber are usually left standing to support the potash mine roof. Worldwide, in many shallower operations, where the original pillars collapse rapidly enough for the waste heaps to support the weight of the back, miners can return to extract ore from the pillars.

Sylvinite and langbeinite mining in Carlsbad, New Mexico, is room-and-pillar, while the Boulby mine on the eastern coast of England drives five panels with crossovers in a V-shape to redistribute the stress. Historically, Carlsbad, New Mexico potash mines (most of which are now exhausted) operated at depths between 270 and 430 m, recovered around 75 % of the ore on the first pass and attained 90 %, with the expectation of some surface subsidence on the retreating pass to mine out the pillars. Saskatchewan mines typically operate at greater depths (down to 1,000–1,100 m) with a 35–45 % recovery and typically do not utilise a retreating ore-recovery pass. Boulby mine UK also operates at a lower recovery rate (35 %) because of its greater operational depth, around 1,100 m and, due to its less than ideal back thickness, the ore zone is approached from below and ore is extracted using remote-control vehicles.

For those mines without high-pressure aquifers above the potash and with somewhat plastic overlying strata, the long-wall mining method, which allows the roof to gradually descend soon after the ore is cut, can provide very high ore recovery rates and result in high productivity. In the case of long-wall mining, the beds must be fairly uniform and continuous (very minor faulting, slumping) over the width and length of individual mining panels. Borers extract ore in very long galleries to take advantage of their cutting method, rather than room-and-pillar, which is the method typically used with drum mining. Some Canadian mines utilising

borers produce 1,200-m-long galleries with longwalls in between. Other Canadian mines use panels that have five entries per panel, with the outer two entries collapsing in 1 or 2 days (Kogel et al. 2006). Although long-wall mining can produce ores at relatively low costs per tonne, equipment and development costs can be high and the method is not as flexible as other methods. Yet, despite the high initial cost and substantial maintenance of continuous mining machines, they are incredibly efficient once in operation and are able to cut smoothly, provide low disturbance entry, and possess a very high extraction capacity. This places extraction costs in the Canadian mines of the Prairies at the cheaper end of the world's larger producers (Fig. 11.3c). In addition, the continuous mining method facilitates conveyor belt ore haulage, allowing for the near total automation of the entire ore extraction process.

For thicker or highly inclined potash seams, the open stope (successive horizontal cuts for thick beds) or cut and fill methods allow both a high ore recovery and an easy means of disposing of both waste produced underground and plant tailings (Kogel et al. 2006; Schultz et al. 2005). PotashCorp at its underground operation at Penobsquis, near Sussex in New Brunswick, Canada, mines with road headers in a cut-and-fill technique up one side of a salt anticline. Provincial environmental regulations require that no tailings pile remains on the surface, so all tailings are backfilled into the mine using a second conveyor belt system. Some German potash mines also use block-caving (benchmining and funnel-stoping) methods because potash ore is on the dipping flanks of salt domes and gangue can more readily be left underground.

Underground ore transport of potash (and in some cases the tailings return) is now accomplished almost entirely by conveyor belts. Conveyor belts may be suspended from the roof or set on the floor. For the highest capacity mines with continuous (borer or drum) mining machines, flexible belt conveyors attached to, or directly fed from, the miner, such directly feeding into a panel belt gives considerable savings. Some mines still employ either shuttle cars to take the ore from the mining machines to the feeder breaker at the panel belt, or load-haul-dump (LHD) machines that pick up ore from the floor and then haul it to a feed station. Most potash mines, because large cavities are cheaply and safely excavated in the salt host, typically have considerable underground ore storage capacity, this evens out the flow to the mill. Many of the large capacity operations also use feed bins where the ore is loaded into high-speed "skips" (elevator bins) that take the ore to the surface and dump it, with all aspects of the loading-lifting-dumping cycle now being done automatically. A few shallower mines can bring the ore to the surface with conveyor belts in long inclined tunnels.

The extraction costs of potash mining by conventional methods can vary tremendously (Fig. 11.3c). Mining is the major expense of potash production in operations that require more man-power because of low-grade ore or difficult mining conditions. For ore bodies and situations that allow high-capacity operations, mining can be somewhat less expensive than the costs of processing at the surface. Freight or transport costs are also significant, especially in markets located some distance from suppliers and is one of the major drivers for current greenfields potash exploration in Africa, Asia and South America.

Whatever the chosen production method, establishing a new conventional potash mine is associated with setup costs well in excess of a billion or more dollars (US$), so new players in the market are rare. The costs are high as the entry shaft for a new mine must be completed without water entry and is usually done via ground freezing. Once the vertical shaft is completed it is protected from water-bearing rocks by the use of tubbings, which are curved segments bolted together and sealed to form stacked rings that line the shaft. They are usually made from cast iron or steel-reinforced concrete. Such tubbed shafts generally have a diameter of 5–7 m, and can extend down to depths exceeding 1,000 m. Because of the very high costs involved in entry construction for a new potash mine, the proved amount of ore should be sufficient for at least 20 years of production (subject to a given mill size, mill recovery rate for a given ore depth and the density and origin of salt "horses"). Kogel et al. (2006) states the initial plant or mill annual capacity should be at least 300,000 t K_2O, in order to compete with a number of established plants with capacity in excess of 1 Mt.

High lead-in costs mean no significant greenfield potash project involving a conventional mine has been completed in the past three decades, although some brownfield expansion has taken place. In recent years a number of greenfield projects have been announced due to projected margin expansion and long term potash demand certainty (Tables 11.2, 11.3 and 11.5). For a conventional mine it takes 5–7 years to take a new greenfield project from conception to production. Currently the largest conventional mine in development is BHP-Billiton's Jansen project in Saskatchewan. Shaft excavation is currently underway and expected to be completed in 2016. When operational, the Jansen mine is projected by BHP -Billiton to be capable of production levels of up to ten million tonnes per year. Lead times for solution mining projects are typically shorter, on the order of 3–5 years. Currently the Legacy Facility, near Bethune Saskatchewan, is the largest greenfields solution mining plant under construction. Due to be completed by 2016, it has a projected mine life of at least 40–50 years, with a planned annual output from 2017 of 2.8 million tonnes per year (Table 11.2). Conventional brownfield mine expansion lead times are variable, most of the projects currently planned are projected to take less than 5 years. In the past few years, a lack of price stability and currently low ore prices have had a detrimental effect on the viability of some of the small to mid sized potash explorers.

Table 11.2 Active and projected solution mines that target potash extraction

Mine/property	Company	Target	Depth (m) to target	Product	Reserves (R) or inferred (I) resource or annual brine production and, where available, ore grade (K_2O %) Mt = million tonne	Extraction technique	Stage on ground in 2012
Patience Lake Solution Mine, Saskatchewan	Potash Corp	Sylvite	1,600	MOP	330,000 tonne/year 37 Mt (R)	Solution mining of flooded MOP mine	Active facility
Belle Plaine Solution Mine, Saskatchewan	Mosaic Corp	Sylvite	650	MOP	2.0–2.8 Mt/year 230 Mt (R)	Purpose-built solution mine in operation since 1960s	Active facility
Cane Creek, Utah	Intrepid Potash	Sylvite	850–1,200	MOP	60,000 tonne/year potash and 100,000 tonne/year halite (Mine had @ 25.0)	Solution mining of flooded MOP mine	Active facility
Hersey facility, Michigan	Mosaic Potash	Sylvinite	1,600–2,000	MOP	120,000 tonne/year 3,000,000 tonne/year halite	Purpose-built solution mine	Potash stream shut down in 2012, convert to halite only
Legacy Facility, Saskatchwan	K+S/Pot-ash One	Sylvinite	1,500–1,600	MOP	859 Mt(I) @ 16.4 % K_2O. From 2016, estimated production 2.8 Mt/year for 50 years	Purpose-built solution mine	Ground broken June 2012
Veendam Brine facility, Netherlands	NedMag	Bischofite, carnallitite	1,400–1,800	Magnesia and $MgCl_2$ brine	70,000 tonne/year $MgCl_2$ 160,00-tonne/year of Magnesium	Purpose-built solution mine	Active facility
Milestone Property, Saskatchewan	Western Potash	Sylvinite	1,600–1,800	MOP	708 Mt(I) @ 15.8 % K_2O	Purpose-built solution mine	Feasibility being assessed
Muskowekwan First Home Nations Project, Saskatchwan	Encanto	Sylvinite	1,200	MOP	235 Mt(I) @ 17.9 % K_2O Estimated potash extraction rate of 2.8 Mt/year	Purpose-built solution mine	Feasilbility being assessed
Spar Property (Indian Nations), Saskatch-wan	Encanto	Sylvinite	900–1,000	MOP	34 Mt(I) @ 23.8 % K_2O	Possible conventional mine	Feasilbility being assessed
Wynyard Property, Saskatchewan	Karnalyte Resources	Carnallite	900–1,100	MOP	269 Mt(I) @ 9.0 % K_2O	Purpose-built solution mine	Feasilbility being assessed
North Dakota, Burke Co., USA	Sirius Minerals	Carnallite	2,702 (Eby-1 well)	MOP	Well (TD 2,794 m) intersected 8.51 m of carnallitite @ 11.2 % K_2O and 8.6 % carnallite	Purpose-built solution mine	Feasilbility being assessed
Carnalita potash project, Sergipe, Brazil	Vale Carnalita	Carnallite	1,200–1,300	MOP	Expected full production from 2015 to 2016 of 1.2 Mt/year	Pilot plant commissioned in 2008	Expected to move to production in 2015
Sergi Potash Project	Rio Verde Minerals	Sylvinite, Carnallite	1,200	MOP	Drill hole SED-001-01 intersect Sylvinite Zone 1 from 1,189.38 m 8.27 m@13.23 % K_2O and Sylvinite Zone 2 from 1,221.868.46 m@18.31 % K_2O and carnallitite 1,257.95–1,318.98 m	Purpose-built solution mine	Feasilbility being assessed

(continued)

Table 11.2 (continued)

Mine/property	Company	Target	Depth (m) to target	Product	Reserves (R) or inferred (I) resource or annual brine production and, where available, ore grade (K_2O %) Mt = million tonne	Extraction technique	Stage on ground in 2012
Neuquén Basin, Argentina	Vale	Sylvite, carnallite	≈1,000	MOP	Upper ore zone is some 2.2–2.5 m thick analysing 28–32 % K_2O, lower up to 10–20 m thick with 20–27 % K_2O. Projected capacity 1.4–2.6 million tonnes/year. Conventional mine precluded by high geothermal gradient	Purpose-built solution mine	Feasilbility being assessed
Bleicherode Facility, Germany	Deusa International	Carnallite	450–500	$MgCl_2$ and MOP	Nameplate 100,000 tonnes/year but currently operates far below that level	Purpose-built solution mine	Feasilbility being assessed
Mengo Potash Project, Congo	Mag Industries	Carnallite	400–500	MOP	186 Mt (I) of KCl from carnallite, which is equivalent to 117 Mt (I) of K_2O	Purpose-built solution mine	Feasilbility being assessed
Sintoukola Potash Project, Congo	Elemental Minerals	Sylvinite and Carnallite	250–400	MOP	Resource 513 Mt (I) @ 15.33 % K_2O Sylvinite zones 261 Mt (I) @ 19.56 K_2O	Conventional mine more likely than solution	Feasilbility being assessed

Compiled from SaltWork database

Table 11.3 Potash extraction (active and proposed) in Quaternary saline lacustrine settings

Mine/property	Company	Target	Depth (m) to target	Product	Reserves (R) or inferred (I) Resource or annual brine production and, where available, Ore Grade (K_2O %) Mt = million tonne	Extraction technique	Stage on ground in 2012
Dead Sea (DS), Israel and Jordan	ICL (Israeli side) Jordan Arab Potash (Jordanian side)	Processing of carnallitite slurry precipitated in solar pans	DS water pumped in to pans	MOP and $MgCl_2$ brine	Israel: 3.7 Mt of KCl per year Jordan: 3.17 Mt of KCl per year	Evaporation pans as brine concentrator (fractionation) with carnallitite slurry	Active facility
Qarhan Salt Lake	Qinghai Potash Company (Sinochem)	Carnallitite, lesser sylvite	0–40	MOP	220 Mt (I) of potash (reserve and grade not available. Annual production though to be around 1 Mt of KCl. ($MgSO_4$ in other parts of depression)	Brinefield in salt flat feeding evaporation pans. Likely that cryogenesis plays a role.	Active facility
Wendover Facility, Bonneville salt flats, Utah	Intrepid Potash	Shallow poreheld saline lake brine	0–10	MOP	100,000 tonnes/year of KCl (currently is largest potash producer in USA)	Brinefield in salt flat feeding evaporation pans	Active facility (remaining life 123 years)
Dallol depression, Ethiopia	Allana Potash	Sylvite/carnallite/kainite, kieserite	60–150	MOP & possible SOP	Sylvinite: 31.3 Mt (I) @ 25.4 % KCl (16.1 % K_2O) Kainitite: 73.9 Mt @ 61.7 % kainite (≈11.1 % K_2O)	Solution Mine/ brinefield & evaporation pans	Feasilbility being assessed
Bounty Project, Pilot Valley, Utah	Mesa Exploration	Shallow poreheld saline lake brine	0–10	MOP	Nearsurface potash brine estimated to contain 5.1 million tons KCl and so have same operating life >75 years as nearby Wendover Facility (10,000 tonne/year) of SOP and 1.5 Mt halite	Brinefield with evaporation pans (similar to current Wendover facility)	Feasilbility being assessed
Lop Nur, China	Xinjiang Lop Nur Potash Co., Ltd	Shallow poreheld saline lake brine	0–70	SOP	1.7 Million tonnes/year from slurry precipitated in cryogenic surface pans, pumping brine from saline unconfined and confined aquifers. (36 Mt recover-able) 3 Mt/year in 2015	Brinefield in salt flat feeding evaporation pans	Active facility

(continued)

Table 11.3 (continued)

Mine/property	Company	Target	Depth (m) to target	Product	Reserves (R) or inferred (I) Resource or annual brine production and, where available, Ore Grade (K_2O %) Mt = million tonne	Extraction technique	Stage on ground in 2012
Great Salt Lake (GSL), Utah	Compass Minerals Group	Kainitite	GSL brine in pans	SOP	Kainite-carnallite to schoenite slurry processing to SOP 350,000 tonne/year SOP 1.5 Mt/year halite	Evaporation followed by cryogenesis in pans on lake edge	Active facility
Salar de Atacama, Chile	SQM	Shallow poreheld saline lake brine	0–40	SOP and MOP	SOP recovered from brine field during $LiCO_3$ concentration. Capacity 650,000/year	Brinefield with evaporation pans	Active facility
Sevier Lake, Utah	EPM Mining Ventures Inc	Shallow poreheld saline lake brine	0–33	SOP	Equivalent from Brine: 29.4 Mt of SOP, 32.6 Mt of $MgCl_2$ brine, 41.2 Mt of $MgSO_4$ bittern, 77.8 Mt saltcake (Na_2SO_4), 592.7 Mt of halite.	Brinefield with evaporation pans (similar to current Great Salt Lake facility)	Feasilbility being assessed
Lake Disappointment, West Australia	Reward Minerals, Ltd	Shallow pore-held saline lake brine	0–4	SOP	JORC compliant Indicated resource of 7,705 Bt at 3.17 kg/t K_2SO_4 for 24.4 Mt contained K_2SO_4	Brinefield with evaporation pans	Feasibility being assessed

Solution Mining of Potash

Solution mining entails the injection of brine solutions into underground potash-bearing salt seams (Fig. 11.5). The solution dissolves soluble potash-bearing minerals from the seam and the pregnant potash-bearing solution is then recovered to the surface for processing. Solution mining techniques, focused on caverns in halite, are discussed in detail in Chap. 13, this current section deals specifically with potash. Solution mining can substitute for conventional shaft mining in some potash deposits at depths of more than 1,100 m, which is the current limit for conventional potash mining. It is not an all-encompassing mining alternative to be used whenever potash zones are too deep or too variable for conventional mining methods. Currently, there are six active and a number of planned solution mining operations, focused specifically on potash recovery (Table 11.2). Thickness, mineralogy, and structure/ore-continuity, as well as other technical considerations of the mining operation, must be evaluated to determine the suitability of solution mining.

As well as purpose-designed facilities, a solution mining approach has been successfully employed in situations where a conventional underground potash mines was accidentally flooded and became unworkable. Of the three current potash solution mining plants in the North Americas, two recover brine from flooded mines, one in Canada (PCS-Patience Lake) and the other (Moab) in the United States. Water is injected as brine and circulated throughout the flooded mine workings, dissolving potash and salt from the original pillars and walls. The resulting dense brine sinks to the bottom of the water-filled mine cavity, is pumped back to the surface and into an evaporation pond or set of crystallizers. High capacity submersible pumps are used in these operations, for example in the PCS-Patience Lake solution mine each is pumping about 9,000 l/min.

Dissolution selectively picks up KCl over halite across the substantial surface area in the ore-zone focused flooded workings of the PCS Patience Lake Division Mine. The resulting dense brine is withdrawn from the mine sump and pumped to a large pond, which was formerly used for tailings, before being rebuilt as a set of holding and cooling reservoirs. This large pond operates each year as a cryogenic crystallizer from September through May. As warm brine from the mine flows into the pond, sylvite (not halite) crystallizes via exposure and rapid cooling of the brine beneath the cold winter air (Fig. 11.6). The sylvite precipitation process is predicated on the different temperature dependences of NaCl and KCl solubilities (Fig. 11.27). As the liquid in the surface pond cools, potash and salt crystals settle to the bottom of the pond. Residual cooled brine is then heated and reinjected into the mine to start dissolving potash again. The sylvinite slurry is harvested by floating dredges and sent to a nearby milling plant for drying, screening, and compacting.

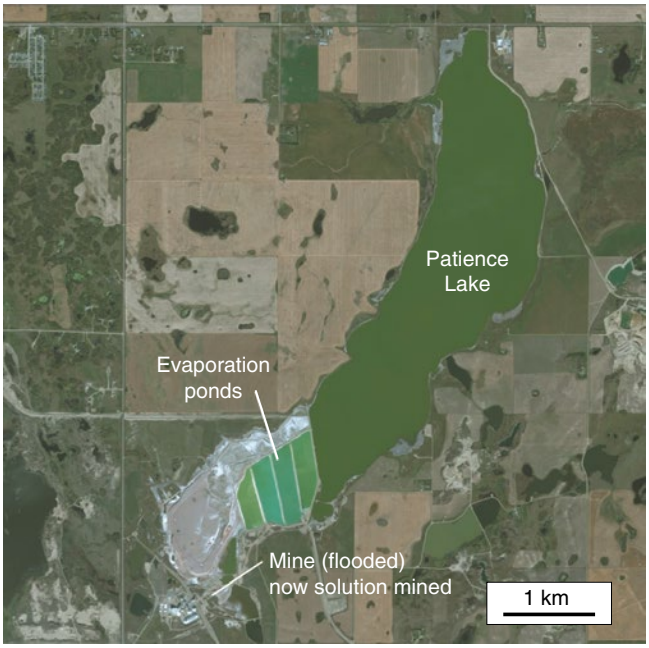

Fig. 11.6 Patience Lake – PCS solution mine, Saskatchewan, Canada

The other solution-mined facility in an intentionally flooded mine is the Moab Cane Creek Mine solution facility, Utah (USA). There potash brine is pumped to the surface to be solar evaporated and crystallize sylvinite. The sylvinite is the dry-harvested and sent to a processing plant for conventional flotation.

In contrast to the two postflood operations, the solution mine of Mosaic, near Moose Jaw, Saskatchewan (Canada), is a purpose-designed as a conventional 3-pipe string potash solution mining operation. The Moose Jaw (Belle Plaine) operation illustrates the success of a purpose-built facility as it can recover more than 2,700,000 tonnes of product a year, compared to 300,000–400,000 tonnes at Patience Lake and ≈60,000–100,000 tonnes of potash (and 210,000 t of by-product salt) at Cane Creek-Moab (Table 11.2).

The three-pipe-in-one-string solution method has an innermost pipe as the deepest pipe in the solution cavity and it is used to withdraw saturated brine from near the base of the cavity. The medial pipe is used to inject undersaturated brine into the cavity. The outermost and shortest pipe inserted into the cavity is used to maintain the uppermost pad fluid and so prevent the potentially destabilizing dissolution rise of the cavity roof (see Chap. 13 for more detail, especially Figs. 13.6, 13.7 and 13.8).

Brine production began in Moose Jaw facility the mid 1960s and was positioned to take advantage of a major thickening of the Belle Plaine Member at about 650-m depth. Brine from the well field is extracted, then evaporated in triple-effect evaporators to crystallize dissolved halite, and the brine is then cooled to crystallize the potash salts. The

residual brine is recirculated to the evaporators, although in the winter it is first sent to ponds to be further cooled and to precipitate additional potash salts.

Lake Brine Processing and Solution Chemistry

Potash is extracted from modern lake brines in two forms; MOP and SOP (Table 11.3; Fig. 11.5). In both cases, due to elevated levels of Mg or SO_4, sylvite is typically not the precipitated phase, making the production of sylvite from these facilities relatively expensive compared to conventional mines targeting sylvite ore from ancient bedded deposits (Fig. 11.3c). The largest set of lake brine potash operations is extracting sylvite from the processing of carnallitite precipitates in man-made solar ponds at the southern end of the Dead Sea. This and other lake brine operations, along with their brine chemistries, are discussed in detail later in this chapter.

Climate is critical for effective solar evaporation or cryogenic production from surface ponds, this is true whether ponds are fed modern lake brines or brines pumped from solution mine cavities. Brine brought to the surface at the Moab mine (Köppen climate BSk) evaporates completely in single ponds to precipitate a mixture of sylvite and halite. Because of its cool steppe arid climate, blue dyes added to pond brines increase solar energy adsorption and so increase brine temperature and rates of evaporation. The operations at Ogden and Wendover, Utah (Köppen Climate, Csa and BWh, respectively), use Great Salt Lake water (Ogden) or nearsurface brines and multiple ponds on the Bonneville saltflat (Wendover). Multiple fractionation ponds are used to establish brine densities for various K minerals at different stages. Efficient solar evaporation occurs during only 3 months of the year (June, July, and August) in the Utah region, with more than half the local evaporation occurring in July. During this 3-month period, low rainfall must combine with sufficient wind to keep the brine mixed and to enhance evaporation. In the potash-harvesting ponds at Moab and Wendover, both sylvite and halite drop precipitate out of the liquor. The harvest is then sent to a standard flotation-type beneficiation plant to separate the two salts.

In the Middle East, the two potash operations at the south end of the Dead Sea benefit from a hot arid climate that promotes evaporation throughout the year (Köppen climate, BSh) whereby carnallite and halite drop out of solution in harvesting ponds. In the nearby processing plant, $MgCl_2$ is leached away with freshwater, leaving a mixture of sylvite and halite. On the Israeli side, sylvite is separated from halite in three different processing plants. The oldest plant uses flotation technology. A more recent capacity expansion added a process that uses dissolution-recrystallisation. The newest plant uses a proprietary cold-crystallisation process that uses a low-heat crystallizer to produce KCl and makes the extraction process more energy and cost efficient (Fig. 11.3c).

Ore Beneficiation

With sylvite ores, the ore composition, the ore grade, the proportion of oversized particles required to allow separation of different minerals, and the type and the amount of insoluble slimes (such as clay, anhydrite, dolomite, silica, etc.) are different for different deposits and may perhaps even be highly variable within a single deposit. So, beneficiation of raw potash ore from different basins requires a somewhat different scheme and equipment for each MOP processing plant and ore source (Fig. 11.7; Perucca 2003; Schultz et al. 2005; Kogel et al. 2006; Gowariker et al. 2009). Four basic beneficiation techniques used to process MOP potash ore are: flotation, heavy media separation, electrostatic separation and thermal dissolution crystallization. The other techniques include ammoniacal leaching and gravity separation using shake tables. Ammoniacal leaching is costly and gravity separation gives only about 80 % pure concentrates.

The first step in the beneficiation of a solid potash ore is to reduce the particle size to a point where the potash is liberated from the other ore constituents, but doing so in an optimal fashion ensures crushing and grinding generates the minimum amount of fines (Fig. 11.7). Potash ore must be crushed because the sylvite (processing target) crystals are intimately intergrown with halite at the cm scale and so must be released by breaking down ore to the appropriate size (usually less than 4–5 mm). After crushing, fine particles of both ore minerals and insolubles are removed to the maximum possible extent (scrubbing and desliming), before potash separation begins.

Scrubbing involves flushing the crushed product with saturated brine. During this stage, enough fresh water is added to high carnallite ores to dissolve magnesium chloride (Perucca 2003). Scrubbing is usually accomplished in a series of highly agitated cells, normally run at high percent solids (60–70 % solids in a KCl-NaCl saturated brine), and also designed to liberate the insolubles attached to the potash particles. Two-stage scrubbing is common in mines with high levels of insolubles in the ore. After scrubbing, separation of the insolubles may be done with cyclones, siphon-sizers or wet screens, while the secondary separation is usually accomplished with hydro-separators, cyclones and thickeners. Desliming by flotation of insoluble slimes from the ore in two stages is also practiced. This method has the advantage of reduced capital expenditures for desliming equipment, but suffers the disadvantage of higher reagent costs. Successful desliming is critical, as a virtually slime-free product is necessary to optimise feed to the potash flotation stage, this minimizes reagent costs and ensures optimal potash recovery.

After desliming the feed to the flotation cells is typically chemically conditioned to further improve recovery. Coarse material is conditioned separately from fine material in order to optimise reagent usage and promote more effective coarse

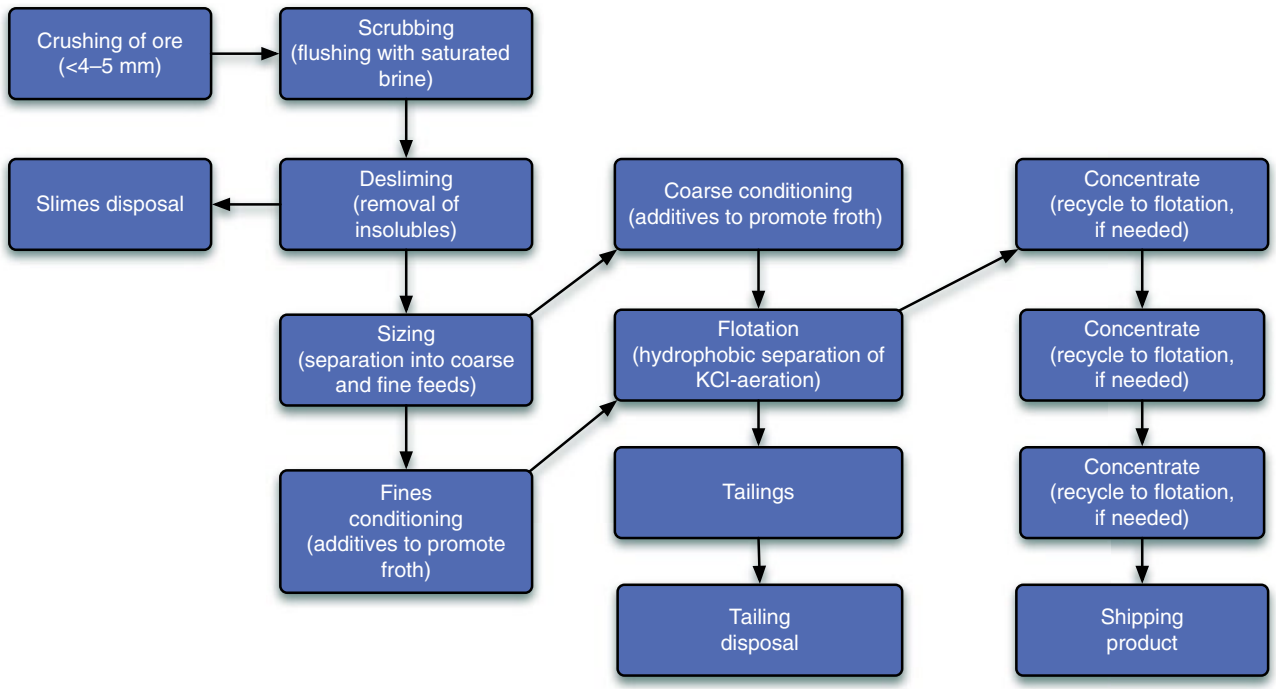

Fig. 11.7 Schematic block diagram of a conventional potash flotation plant (After Perucca 2003)

particle flotation. Both coarse and fine material is conditioned with a depressant and a potash collector. An extender oil is added to the coarse conditioner and various alcohols are normally added to promote frothing.

In potash flotation, the aim is to separate sylvite from halite using cationic collectors interacting with sylvinite feed, known as the pulp (Perucca 2003). Flotation is a selective beneficiation process that utilizes the differences in surface properties of various minerals. Sylvite (KCl) is hydrophobic and will therefore attach itself to air bubbles in an agitation cell and so can be separated from gangue material. The flotation process has advantages over hot leaching and crystallisation as it is not as energy intensive and so has a lower capital cost. In all flotation processes, the fine particles having high surface areas tend to adsorb excessive quantities of the flotation reagent, raising reagent costs and contaminating the product, hence the proportion of fines must be minimised. Post flotation, the residual slimes are finally thickened and sent to tailing areas for disposal. The most important reagents used in flotation are termed collectors. In the case of flotation of sylvinite ores, a cationic collector is added to the closely sized and deslimed ore slurry. The collectors for potash are mostly straight chain aliphatic amines derived from natural fats and oils that are neutralized by acetic or hydrochloric acid before use.

Frothers are another category of conditioning reagents used during flotation. They aid the formation and stabilization of flotation froth and typically are organic heteropolar compounds (e.g., pine oil and methyl isobutyl carbinol). Modifiers (or regulators) are another class of compounds added to the pulp to control the flotation process. In potash flotation, slime depressants such as starch, guar gum, dextrin and synthetic compounds are typically used. Once treated with a collector and a frother, the pulp is passed into an agitation cell where compressed air is introduced from the bottom. A froth of amine and entrained air bubbles carries the potash to the surface where it is mechanically swept over the side of the cell into a trough. Carnallite is avoided during mining due to its detrimental effect in the flotation process.

The concentrate from the flotation cells is made up of potash particles and brine, which are transferred to centrifuge to remove the brine. The potash solids are then moved to dryers, which heat the product to about 200 °C. The resulting dry mixture contains various sizes of product that are size-separated by huge mesh screens into standard, granular and suspension grade product. A portion of the finer product stream is typically fused under high pressure between two rollers. The resulting solid "board" is broken into pieces and sized to form additional granular potash. In some Canadian mills, finer product is dissolved in hot brine to release further small quantities of impurities. The brine is then cooled in vessels to produce a high purity white product, suitable for use in soluble fertilizer and in industrial markets.

When potash ore feeds contain sulphate minerals like kainite or kieserite, sulphate salts are floated using fatty acids or sulphated fatty acids as collectors. Potash flotation circuits

Table 11.4 Processes and costs in 2012 involved in various types of sulphate of potash (SOP) manufacture

Process method	World capacity	Process inputs	Products	Cost/t (US$)	Companies
Mannheim	60 %	MOP, sulphuric acid, energy	SOP, HCl	$700	Tessenderlo, Qingshang, Yara
MOP and Kieserite	25 %	MOP, Kieserite, energy	SOP, $MgCl_2$ brine	$350	K+S Kali
Salt lakes, Kainite-Schoenite slurry	15 %	Lake brines (saline), energy	SOP, $MgCl_2$ brine	$220	Luobupo Potash, SQM Compass Minerals
Polyhalite leach and solar concentration	In process	Polyhalite, water, energy	SOP, Kieserite	$160	IC Potash

always have both rough and clean cells. In the rough cells, as much potash as possible is made to float, while in the cleaner cells the purity of the floated product is the prime consideration. The coarse particles of the rough tailings and the tailings from the clean cells are usually re-ground to a smaller size and re-floated. With very fine ores, sometimes countercurrent flotation is used.

Another potash beneficiation process is heavy media separation, this is the technique used by the Mosaic Company in Saskatchewan. The process uses the difference in specific gravity of sylvite (SG = 1.9) and halite (SG = 2.13). In a liquid of intermediate specific gravity, halite will sink, while sylvite will float. Commercial heavy media operations use a very finely divided weighing agent, generally ferro-silicon or magnetite of 200 mesh, which is slurried to create an artificial heavy medium at the specific gravity required for separation. After separation, the magnetite or ferro-silicon is recovered by magnetic separation and recirculated to the system. In Carlsbad, one heavy media circuit separates sylvinite and langbeinite (SG = 2.83), then a second circuit separates sylvite from halite.

Electrostatic separation is a dry technique in which a mixture of minerals is differentiated according to their conductivity and is used when gangue materials are more conductive. Potash minerals are not naturally conductive, so with a potash ore feed the separation is preceded by a conducting step that induces the electrostatic charges of different magnitude for different minerals. For potash, fractional or triboelectric charging (charging via friction) is used via repeated physical contact between different materials. This separation technique was used by a number of German potash mines.

In Germany, potash ore is conditioned with aromatic and aliphatic monocarboxylic acids. The mixture is heated in a fluid bed and the relative humidity is adjusted to enhance the charging of particles. The ore is then fed to an electrostatic separator to give three fractions, namely, product, residue and middlings. The method has two advantages; cost and reduced environmental impact. Using a dry process to improve the product grade also eliminates the drying costs.

Thermal dissolution and crystallisation are possible because of the higher solubility of potassium chloride (KCl) in hot water than in cold water compared to that of sodium chloride (NaCl) which is slightly more soluble at 100 °C than at 20 °C. When a mixture of sylvite and halite is dissolved in water and heated to 100 °C, KCl is substantially in solution but not NaCl. The ore is crushed to minus 3 mesh and washed with cold water and a NaCl/KCl solution. Clays are removed by desliming and the clarified solution is then heated and used to dissolve the potash in the washed ore. Undissolved NaCl is discarded as tailings. The brine solution on cooling under vacuum separates out KCl, which is filtered, washed and dried. The remaining brine is recycled. It is once again recrystallised to meet the needs of high purity KCl.

Even though it was the preferred ore target in the 1860s in Germany, carnallite is not usually a targeted mine in any conventional mine, because; (1) Carnallite the mineral is deliquescent and so is unsuitable for use directly as fertilizer and so carnallite must be converted to sylvite, (2) Carnallite ores are lower grade (Table 11.2; K_2O of 17 %, compared with 63 % for pure sylvite), (3) Carnallite has unfavourable mechanical properties, compared to sylvite, making it more difficult to mine and, (4) Processing of carnallite to produce sylvite, produces large volumes of $MgCl_2$, which must be utilised or disposed of (Schultz et al. 2005).

Carnallite ore processing methods vary widely and depend upon accessory minerals that are associated with the ore. All the current dissolution and recrystallization methods used to convert carnallite to sylvite are energy intensive and relatively expensive. Processing of carnallite to sylvite is done commercially using carnallitite slurries produced in solar pans at the southern end of the Dead Sea. There the two general methods of carnallite processing are cold leaching and hot leaching. Cold leaching is carried at 20–25 °C, while hot leaching is done at 100 °C to dissolve $MgCl_2$, KCl and NaCl, if any (see later).

Unlike the cheaper MOP fertilizers, which can be recovered from a sylvinite ore feed by a combination of grinding and various relatively low cost flotation techniques with tailings disposal (Fig. 11.6), a conventionally mineable sulphate of potash (SOP) fertiliser ore source does not occur naturally (Perucca 2003; Gowariker et al. 2009). SOP is a commercially produced product that requires additional energy to manufacture from a potash ore source (Table 11.4). Most SOP is synthesized by heating MOP in the presence of sulphuric acid to temperatures around 650 °C in large continuous-feed furnaces (Mannheim Process). Some mines

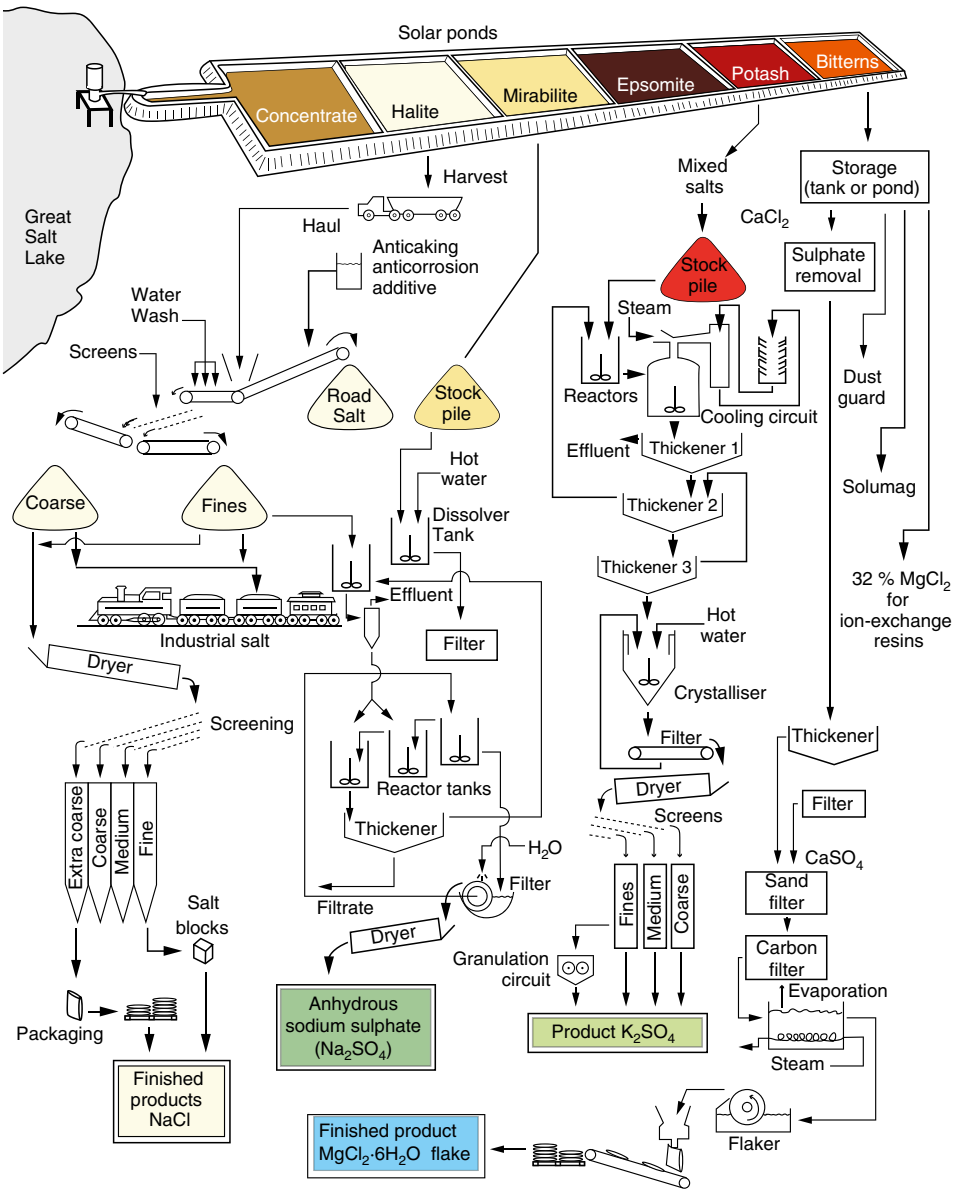

Fig. 11.8 Process stream for the manufacture of Sulphate of Potash in Great Salt Lake, Utah (After Butts 2007)

in Germany combine and process kieserite and sylvite to produce SOP. Currently the cost of production of SOP is $350–$700 per tonne using the Mannheim process, with the cost to purchase MOP making up $300–$600 per tonne of that cost.

SOP from a kainite/schoenite brine source (with lixiviation during processing) is produced from solar evaporators or crystallizers using saline Quaternary lake brines in Quill Lake in Canada, Great Salt Lake in USA, Lop Nor in China, and Salar de Atacama in Chile (where SOP production is a byproduct of lithium carbonate production). Production from three of these four lakes currently accounts for around 15 % of the world's SOP production, Quill Lake outputs are small compared to the other three. Once any halite is removed (typically via precipitation in earlier brine fractionation ponds), the kainite-schoenite slurry is processed so that kainite is converted to schoenite and then SOP crystallized from this schoenite source (Fig. 11.8). The volume of SOP production in all four regions is constrained by the chemistry the lake brines, that typically have relatively low levels of contained sulphate in the inflow waters. Because of a more favorable arid BSk climates in Salar de Atacama and Lop Nor regions, compared to the other two lake brine manufactures in Canada and the USA, it is likely that these two operations have SOP production costs of under $220 per tonne.

When langbeinite is targeted, as in the Carlsbad region today, it is separated from sylvite and halite by selective washing, froth flotation, or heavy media separation. Although processed langbeinite has a low K_2O content (23 %), it is marketed as a fertilizer or animal feed and as a source of K, Mg and S. It can also be used as a chemical feed and converted into other potash products such as SOP. Using a

mixture of mined sylvinite and langbeinite, SOP is today manufactured via a process of ion (base) exchange in the McNutt Potash region near Carlsbad, New Mexico. A drastic expansion of SOP manufacturing is proposed for the region, utilizing solar processing of a dissolved polyhalite ore.

Other than agricultural usage, soluble KCl is used as a drilling mud additive to stabilise reactive clays in oil well drilling. It is also used in aluminium recycling, in various steel heat-treating processes, metal electroplating, snow and ice melting, and water softening. Potassium chloride is used by the chlor-alkali industry to produce potassium hydroxide. The alkali potassium hydroxide is used for industrial water treatment and is the precursor of; potassium carbonate, several forms of potassium phosphate, many other potassic chemicals, and is the main ingredient in soap manufacture. The alkaline salt potassium carbonate is used with strontium and barium carbonate in the faceglass for televisions and computer monitors (used as radiation screen, but this is a decreasing use with advent of digital flatscreens), alkaline batteries, food products, pharmaceutical preparations, photography, some fire extinguishers, animal feed supplements, and as a catalyst for synthetic rubber manufacture.

The importance of potash to the future world agricultural economy means it is worthwhile gaining a detailed understanding of how potash salts accumulate in a variety of depositional and diagenetic settings. In the short term future the world's need for potash can only increase and more mineralogically diverse deposits will be utilized. Table 11.5 and Fig. 11.9 summarize the details of the various known potash occurrences that we shall discuss and interpret in the following pages. First, we shall look at some Quaternary lacustrine associations and then at the volumetrically more significant ancient (pre-Quaternary) sources of potash.

Quaternary Potash

Significant modern potash accumulations are rare: there are only two well documented examples of substantial Quaternary stratiform potash accumulating naturally, namely, the Qaidam Basin in China and the Danakil Depression in Ethiopia. Both basins, along with the anthropogenic potash pans of the Dead Sea basin are fed by calcium chloride brines with lower proportions of bicarbonate and sulphate, compared to brines derived by the evolution of modern seawater (Lowenstein and Risacher 2009; Katz and Starinsky 2009). Other modern examples, where carnallite or sylvite accumulates naturally are volumetrically minor and occur in continental lakes, playas and soils, either in ephemeral mineral efflorescences or in thin crusts Beds of potash salts can also accumulate in purpose-built pans. Such anthropogenic potash was precipitated experimentally as langbeinite by enhanced solar pond evaporation of seawater in Lake Macleod in Australia and by evaporation of continental lake and pore waters pumped into surface pans in the southern basin of the Dead Sea. In Canada, cryogenic pans are fed brines derived by solution mining and there are the dye-enhanced solar pans at Moab, Utah, which are also fed by solution-mined brines. Sylvite also occurs naturally as a widespread pedogenic salt along with nitrates in the hyperarid regions of the Atacama Desert in Chile.

Playas of the Qaidam Basin

The high plateau region of northern Qinghai-Xizang in west central China north of Tibet contains a number of large endorheic intermontane lake basins with thick fills of Mesozoic and Cenozoic nonmarine sediments (Fig. 11.10). The Qaidam (Chaidam) is one the larger such basins and its modern at-surface playas and salt lake sumps are subject to intense evaporation. Many of the drainage depressions in the basin are characterised by hypersaline brines with variable ionic proportions and, in some, there are accumulations of potash and borate-rich brines and salts. Lake Dabuxum and its surrounds in the southern Qaidam Depression is of special geological interest as it is one of the few localities in the world where quantities of potash salts are precipitating today in a number of laterally-limited groundwater sumps (Yang et al. 1995; Vengosh et al. 1995; Casas et al. 1992; Duan and Hu 2001).

Qaidam Basin is a large intermontane sedimentary and structural basin at the northern margin of the Qinghai-Tibet Plateau. With an area of 120,000 km^2, it has an extent that approaches that of some of the moderate to small ancient continental "saline giants," but the active-salt accumulating salt lakes are a much smaller proportion of the basin depression and only occupy its lower parts (Fig. 11.10). The Kunlun Mountains bound the plateau to the south, the Altun mountains to the west and the Qilian Mountains (which reach 5,000 m above sea level) bind the northern portion of the basin/plateau. Today the Qaidam Plateau (Qaidam Basin) is experiencing northeast-southwest compression, driven by the Himalayan Orogeny and expressed as active northwest-trending thrust faults, particularly along the Kunlun and Qilian Mountain fronts, with the basin sediments also cut by northeast-trending strike slip faults. The plateau centre has an average elevation of 2,800 m and contains numerous shallow to ephemeral saline lakes and dry saline pans. Its current hydrology is separated from the ocean by thousands of kilometers.

The Qaidam Basin first formed in the Jurassic, via extension in the Palaeozoic basement, when it was delineated by WNW-ESE faults. The basin was then filled by a 10-km thick succession of Mesozoic-Cenozoic terrestrial sediments. Lacustrine sedimentation began in the Early Cenozoic, but was limited to the western part of the current Qaidam

Table 11.5 Potash occurrences, listed by country, reserves listed in million tons (mt) or billion (Gt) metric tons of K_2O equivalent

Location, country	Age	Köppen	Brine source	Target unit	Comments/key reference
Potash in Congo and Gabon basins, Africa (Congo, Zaire, Angola)	Cret. Low.	–	Marine	Kouilou horizons	Carnallite, sylvinite in halite host, variable tachyhydrite (Aptian). Previously mined at Holle Mine (Republic of Congo) in 2 variable layers of 1.9 and 3 m thickness with K_2O contents of 18 and 38 % respectively with × mineable reserves of 17 and 26 mt K_2O respectively. Mine lost to flooding (breccia zone) in 1977. Future projected solution mine targeting of K and Mg brines in Kouilou evaporite horizons (De Ruiter 1979).
Neuquén and Mendoza Basins, Andes, Argentina	Cret.	–	Marine	Potash interval	Possible future solution mine. Sylvinite ore divided into 2 zones, upper zone about 3 m thick and lower about 11 m thick, average grade 20–25 % K_2O. A 1,000 m depth and high formation temperature (>50 °C) precludes conventional mine (Prud'homme and Krukowski 2006).
Pripyat Depression, Belarus	Dev., Upp.	–	Marine	Liven and Elets horizons	Livet (Frasnian) interval made up of four potash horizons with areas between 130 and 1,500 sq. km. Sylvite ore with minor carnallite in beds 4 cm to 1.5 m thick interbedded with muddy halite. Elets (Fammenian) interval >60 potash beds over 5,000 sq. km at depth of 200–3,000 m. Major potash production from Elets at average depth 480 m, grade 18 % K_2O.(Zharkov 1984).
Sergipe Basin, Brazil	Cret. Low.	–	Marine	Ibera member	Taquari-Vassouras mine targets sylvinite beds in Muribeca Fm. found in association with halite host, variable carnallite, tachyhydrite (primary textures in unit up to 90 m thick) constituting some 9 evaporite cycles deposited in an opening rift (Aptian). Tachyhydrite present (Wardlaw 1972).
Amazonas Basin, Brazil	Upp. Carb.-Perm, Low.	–	Marine	Nova Olinda Fm.	Two potential sylvinite deposits (sylvite cap to uppermost of 7 evaporite cycles) near Manaus ≈1,000 m depth, with average thickness of 2.7 m and grade 16.5 % K_2O. (Ufimian – Olenekian) (Szatmari et al. 1979)
New Brunswick Potash, Fundy Basin, Canada	Carb. Low.	–	Marine	Cassidy Lake Fm.	Formerly mined at depths 300-100 m in halokinetic salt wall, Mississippian sylvinite-halite sequence with local carnallite in Windsor Group in Moncton subbasin. (Visean) (Anderle et al. 1979; Wilson et al. 2006)
Alberta Potash Basin, Canada	Dev., Middle	–	Marine	Prairie Fm	Actively mined, some ten mines (2 solution mines) at depths between 800 and 1,000 m, region is world's major supplier of potash ore. Three potash horizons (sylvite, carnallite, halite) 20–25 m thick in upper part of Prairie Fm. (Esterhazy, Belle Plain and Patience Lake members). Dips gently to south at 1–8 m/km with potash level some 600–2,500 m below surface. Prairie Evaporite basin is a marine-fed foreland basin situated behind foreland bulge created by Antlerian orogen. (Givetian) (see text)
Quill Lake, Canada	Quat.	Dfb	Nonmarine	Recent	Saline depression in Quaternary glacial outwash. Supratill, sodium sulphate salts in lake floor beds, lake brine pumping and winter processing brine then combined with MOP (trucked in) to produce SOP (Eatock 1987).
Salar de Atacama brine, Chile	Quat.	BWk	Nonmarine	Recent	Brine Processing. Sylvinite and SOP is recovered as byproduct of lithium carbonate production (800 kt in 2004). Situated in Andean Altiplano at 2,250 m above sealevel (Garrett 2004).

(continued)

Table 11.5 (continued)

Location, country	Age	Köppen	Brine source	Target unit	Comments/key reference
Dabuxum Lake (stratoid potash) Qahran Playa, Qaidam Basin, China	Quat.	BWk	Nonmarine	Recent	Carnallite (via solar processing of lake brine along with bishofite). Transtensional basin at 2,675 m elev. The Qahran playa region is main local supplier of potash to Chinese market (annual production of 1.2 Mt K_2O). Other Quaternary K-rich lakes in Qaidam Basin include Seni Lake and Tuanje Playa (see text and Fig. 11.31).
Lop Nur, China	Quat.	BWk	Non Marine	Recent	Natural lake evaporites are a nonmarine assemblages of mirabilite-glauberitepolyhalite-bloedite-gypsum-halite. Recent evaporitic stages of the lake fill in Lop Nur contain massive amounts of glauberite and polyhalite, compared to the other salts present. Their predominance, is indicative of pervasive backreactions, as is the presence of very minor amounts of carnallite and sylvite. Lake waters are processed to produce SOP (Ma et al. 2010; Dong et al. 2012). Annual capacity 1.7 Mt. Largest set of salt ponds in world.
Dallol Saline pan, Ethiopia	Quat.	BWh	Marine	Houston Fm.	Three members; uppermost is sylvinite member up to 10 thick; intermediate is 3–24 m thick with carnallite throughout, (sylvite at its top and kainite at its base) and lower member is kainite that is 4–13 m thick. It is a Pleistocene marine-fed unit that now lies beneath continental halite in a subsealevel (−115 msl) hydrographically-isolated marine-fed rift valley, region of active volcanism and hydrothermal overprints (Garrett 2004).
Mulhouse Potash Basin, Rhine rift, France	Eoc.-Olig.	–	Marine	Upper Salt Group	Main potash target is primary sylvite bed in Salt IV in Oligocene Rupelian succession at depths between 420 and 1,100 m. Basin was a consequence of Paleogene collision between European and African plates. Periodically mined for carnallite/sylvite ore. Subsealevel rift graben was active along western sidewall of the Alpine orogen during collision of the Apulian indentor with the European passive margin (Sannoisan) (Cendon et al. 2008).
Zechstein Potash Basin, Germany	Perm. Upp.	–	Marine	Zechstein Group	Actively mined at depths between 300 and 800 m, Zechstein comprises four evaporite cycles, with potash as five ore horizons in lower three (Thuringen, Hessen, Stassfurt, Ronnenberg and Riedel) (Tatarian). Tachyhydrite present in Stassfurt (Smith and Crosby 1979; Richter-Bernburg 1986).
Dead Sea brines, Israel and Jordan	Quat.	BSh	Nonmarine	Holocene anthrop.	Brine Processing (carnallite ppt. and converted to KCl) of lake brine pumped into a series of processing pans at southern end of Dead Sea. The Dead Sea brine contains an estimate 2 Gt of dissolved KCl, 1 Gt of $MgBr_2$ and 20 Gt of $MgCl_2$. Annual production of KCl ≈ 3.4 Mt ($MgCl_2$ is coproduct) Subsealevel transtensional basin with brine surface some 415 m below sealevel. (Recent) (Zak 1997; Garrett 2004)
Sicilian Basin, Italy	Mioc., Late	–	Marine	Solfifera Series	Inactive since mid 1990s. Kainite was dominant ore mineral (manufactured potassium sulphate). Other minerals in ore were sylvite, kieserite, and bischofite in 2–30 m thick beds dipping to 60°. Piggy-back basin in thrust belt. (Messinian).

Table 11.5 (continued)

Location, country	Age	Köppen	Brine source	Target unit	Comments/key reference
Pricaspian depression, Kazakhstan	Perm. Low.	–	Marine	Potash interval	Not mined. Potash interval contains polyhalite-halite, bishofite-carnallite, carnallite-halite, interval is strongly halokinetic in central part of basin. Oil wells intersected several potash horizons in this region. (Kungurian) (Volozh et al. 2003; Garrett 2004).
Solikamsk depression, Russia	Perm. Upp.	–	Marine	Iren horizon	Bezeneski and Solimgansk mines. potash interval lies at depths of 200–500 m and is divided into lower sylvinite and upper sylvinite-carnallite, little to no $MgSO_4$ salts. Av. lower interval thickness 21 m, upper interval 60 m (Kungurian) (Zharkov 1984).
Eastern Siberia Potash Basin, Russia	Camb. Lower	–	Marine	Chara horizon	Potash lies at depths of 600–900 m and contains some ore-grade sylvite intervals (>30 % K_2O) in Usolye and Angara Fm. Not currently exploited. (Botoman – Amgan) (Zharkov 1984)
Catalonia and Navarra Potash Basins, Spain	Eoc. upper	–	Marine		Transitional from marine evaporite to continental, deposited in two depocentres in Southern Pyrenean foreland. Sylvite + halite at base of unit, carnallite + halite toward top (Bartonian). Lower sylvite member is ore bed. $MgSO_4$-free (Rosell and Ortí 1981; Cendon et al. 2003).
Khorat & Sakhon Nakhon Potash Basins, Thailand, Laos	Cret. Upp.	–	Marine	Maha Sarakham Fm.	Possible sylvinite target on basin margin. Widespread massive halite, carnallite (with local zones of sylvinite), tachyhydrite and bischofite traces of priceite/boracite. Unconformable base, interbedded with three continental redbed successions and overlain by continental deposits. Variably halokinetic toward basin centre. (Albian-Cenomanian?) (Hite and Japakasetr 1979; El Tabakh et al. 1999a; Warren 2000c)
English Zechstein Potash Basin, UK	Perm. Upp.	–	Marine	Zechstein 3	Boulby Mine in UK extracts sylvinite ore from two 6 to 8 m beds at depths between 1,000 and 2,700 m, essentially no $MgSO_4$ phases. Water inflow and instability problems (Tatarian) (Smith 1996; Woods 1979).
Carpathian foredeep, Ukraine	Mioc. Middle	–	Marine	Tyras Suite	Stebnik mine and Kalush-Golyn region. Four evaporite cycles upper three with potash; exploited potash units composed of kainite, langbeinite, kainite–langbeinite, sylvinite and carnallite rocks with layers of rock salt or interbedded clays and carbonates. Fourth bed is polyhalite. (Burdigalian-Helvetian) (Hryniv et al. 2007).
Great Salt Lake region, UT USA	Quat.	Csa	Nonmarine	Rec.	Processing of lake brines in North Arm of lake and of shallow brines in Great Salt Lake desert (Bonneville Basin) at Wendover (MgCl is coproduct). Lake surface is 1,270 m above msl (Bingham, 1980; Garrett 2004).
Paradox Potash Basin, UT, USA	Penn. Mid.	–	Marine	Paradox Fm.	Solution mining of Paradox Fm. in converted conventional mine on Cane Creek anticline at a depth of 850 m. Middle Pennsylvanian collision basin related to Marathon-Ouchita orogeny, 18 of 29 halite cycles contain potash, mostly sylvite. (Moscovian) Tachyhydrite present (Desmoinian) (Hite 1961; Williams-Stroud 1994).

(continued)

Table 11.5 (continued)

Location, country	Age	Köppen	Brine source	Target unit	Comments/key reference
Salado Potash Basin, NM, USA	Perm.-Upp. Lower Trias.	–	Marine	Salado Fm.	Resource now largely depleted, 12 potash horizons in part of Delaware Basin known as McNutt Zone (sylvite ore), few mines still active. Ore zones contain sylvite, carnallite, lesser amounts of sulphate minerals such as polyhalite and langbeinite (Tatarian – Olenekian) (Lowenstein 1988).
Michigan Basin, MI, USA	Sil. Low. -Upp.	–	Marine	Salina A-1 Evap.	Sylvinite and carnallite ore within central part of an intracratonic sag basin. Potash zone >30 m thick in central part of basin but ore concentration is erratic locally up to 40 % K_2O and as deep as 2,550 m but only solution mining is possible at these depths. (Wenlockian-Ludlovian). Tachyhydrite present (Matthews and Egleson 1974).

For overviews see Garrett (2004), Prud'homme and Krukowski (2006), Warren (2010) and references therein

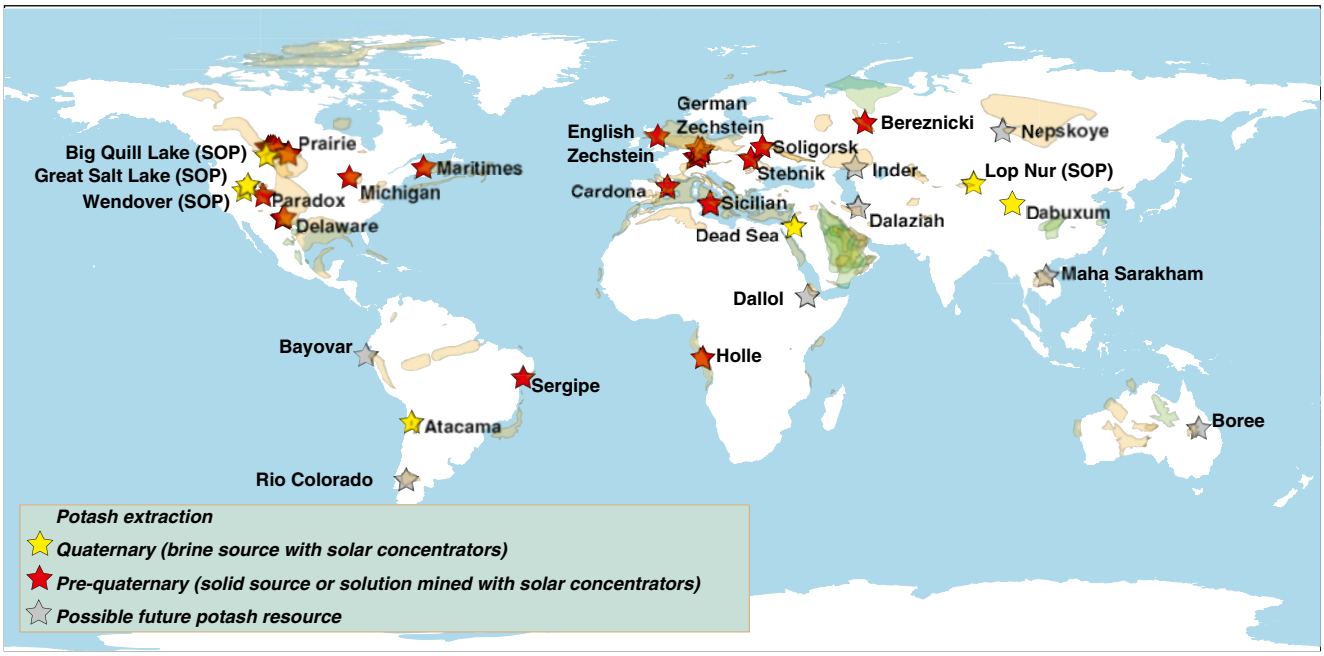

Fig. 11.9 World occurrences of potash; SOP indicates deposits where sulphate of potash is a significant part of the produced potash volume in that occurrence (occurrences and production details extracted from the SaltWork 1.8 database)

Basin (Duan and Hu 2001; Yin et al. 2008). In the Miocene the proto-Qaidam Lake expanded eastwards for some 300 km to attain its largest extent. Compressional tectonics, and the onset by 12 Ma of a relatively dry climate, broke the once continuous freshwater lake into many lacustrine sub-basins, a good proportion of which of which were saline sumps (Zhuang et al. 2011). Its active subsidence history, with more than 14 km of sediment deposited since the Oligocene, make it one of the deepest active sedimentary basins in the world (Wang and Coward 1990).

The present climate across the Qaidam Basin is arid to hyperarid (BWk), with an average annual rainfall of 26 mm, mean annual evaporation is 3,000–3,200 mm, and a mean annual temperature 2–4 °C in the central basin (An et al. 2012). Various salt lakes and playas are spread across the basin and contain alternating climate-dependent evaporitic sedimentary sequences. In the basin the various playas are surrounded by aeolian deposits and wind-erosion landforms. Overall the basin displays a typical exposed lacustrine geomorphology and desert landscape, related to increasing aridification. In contrast, the surrounding elevated highlands are mostly typified by a high-alpine tundra (ET) Köppen climate (Kottek et al. 2006).

The Qarhan saltflat/lake is now the largest hypersaline sump within the disaggregated lacustrine system that makes

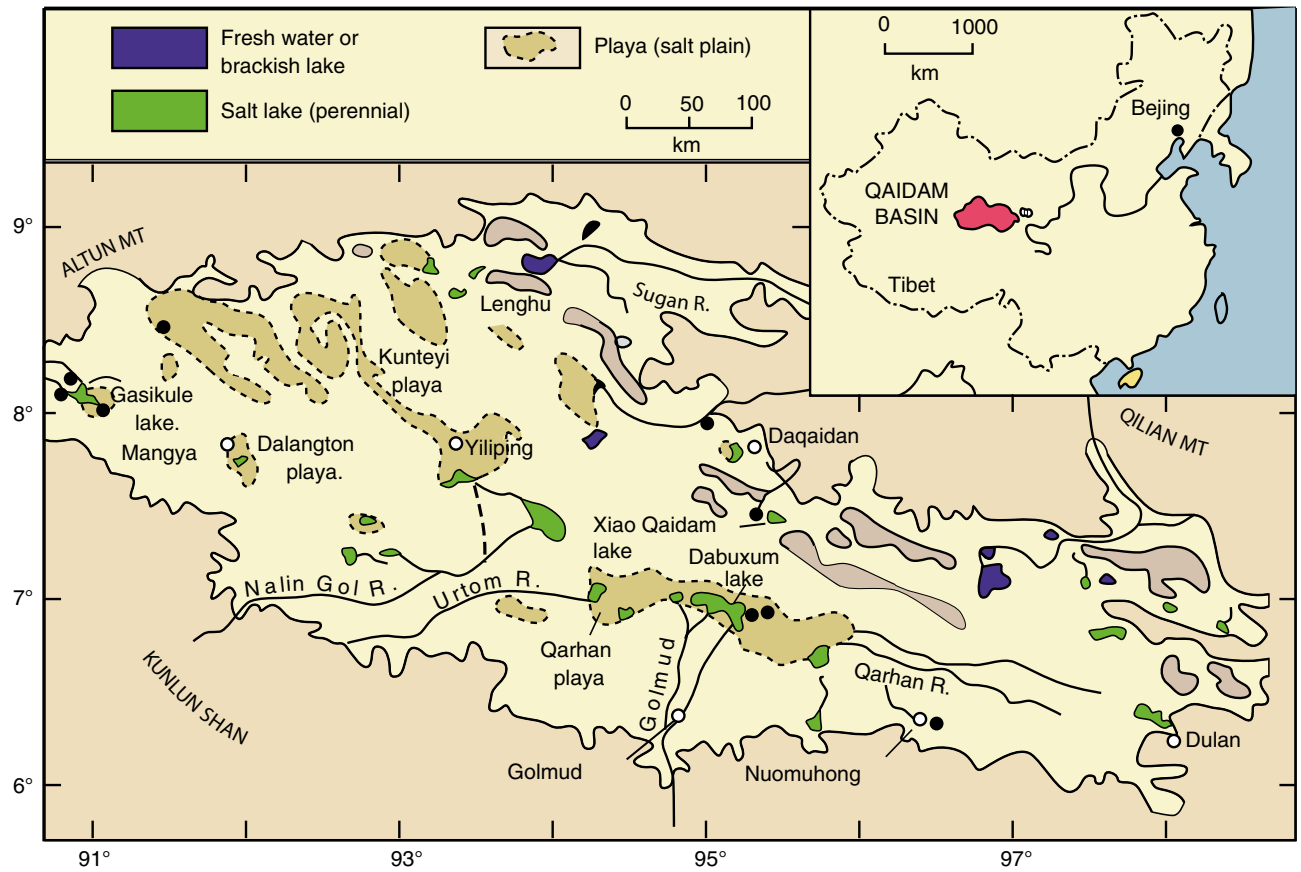

Fig. 11.10 Location of salt lakes, freshwater-brackish lakes and saltflat playas in the Qaidam Basin, China, with Dabuxum Lake located in Qahan playa in the central southern part of the map

up the Qaidam[5] hydrology. It has an area of some 6,000 km^2, is mostly underlain by bedded Late Quaternary halite (Fig. 11.11). The Qarhan depression is endorheic, fed by the Golmud, Qarhan and Urtom (Wutumeiren) rivers, and today is mostly covered by a layered halite pan crust. Below, some 0–1.3 m beneath the playa surface, is the watertable atop a permanent hypersaline groundwater brine lens.

The Qarhan Playa sump entrains nine perennial salt lakes: Seni, Dabiele, Xiaobiele, Daxi, Dabuxun (Dabsan Hu), Tuanjie, Xiezuo and Fubuxum north and south lakes (Fig. 11.11b). Dabuxum, which occupies the central part of the Qarhan sump, is the largest of the perennial lakes (184 km^2). Lake water depths vary seasonally from 20 cm to 1 m and never deeper than a metre, even when flooded. Salt contents vary from 165 to 360 g/l, with pH ranging between 5.4 and 7.85. Today the salt plain and pans of the Qahan playa are fed mostly from runoff from the Kunlun Mountains (Kunlun Shan), with a number of saline groundwater springs concentrated along the fault that defines an are of salt karst along the northern edge of the sump, especially north of Xiezuo Lake.

Bedded and displacive salts began to accumulate in the Qarhan depression some 50,000 years ago. Today, the surface salt crust consists of a chaotic mixture of fine-grained halite crystals and mud, with a rugged, pitted upper surface (Schubel and Lowenstein 1997; Duan and Hu 2001). Vadose diagenetic features, such as dissolution pits, cavities and pendant cements, form where the salt crust lies above the watertable. Interbedded salts and siliciclastic sediments underlie the crust to reach thicknesses of up to 75 m (Kezao and Bowler 1985).

Bedded potash, as carnallite, precipitates naturally in transient volumetrically-minor lake strandzone (stratoid) beds about the northeastern margin of Lake Dabuxum and as cements iLate Pleistocene bedded deposits in nearby Lake Tanje (Fig. 11.11a, b). Ongoing freshened sheetflow from the updip fans means the proportion of carnallite versus halite in the unit increases with distance from the Golmud Fan in both the layered (bedded) and stratoid (cement) modes of occurrence (Fig. 11.11c).

At times in the past, when the watertable was lower, meteoric inflow was also the driver for the brine cycling that created the karst cavities hosting the halite and carnallite cements. Solid potash salts are not present in sufficient

[5] "Qaidam" means salt marsh in Mongolian.

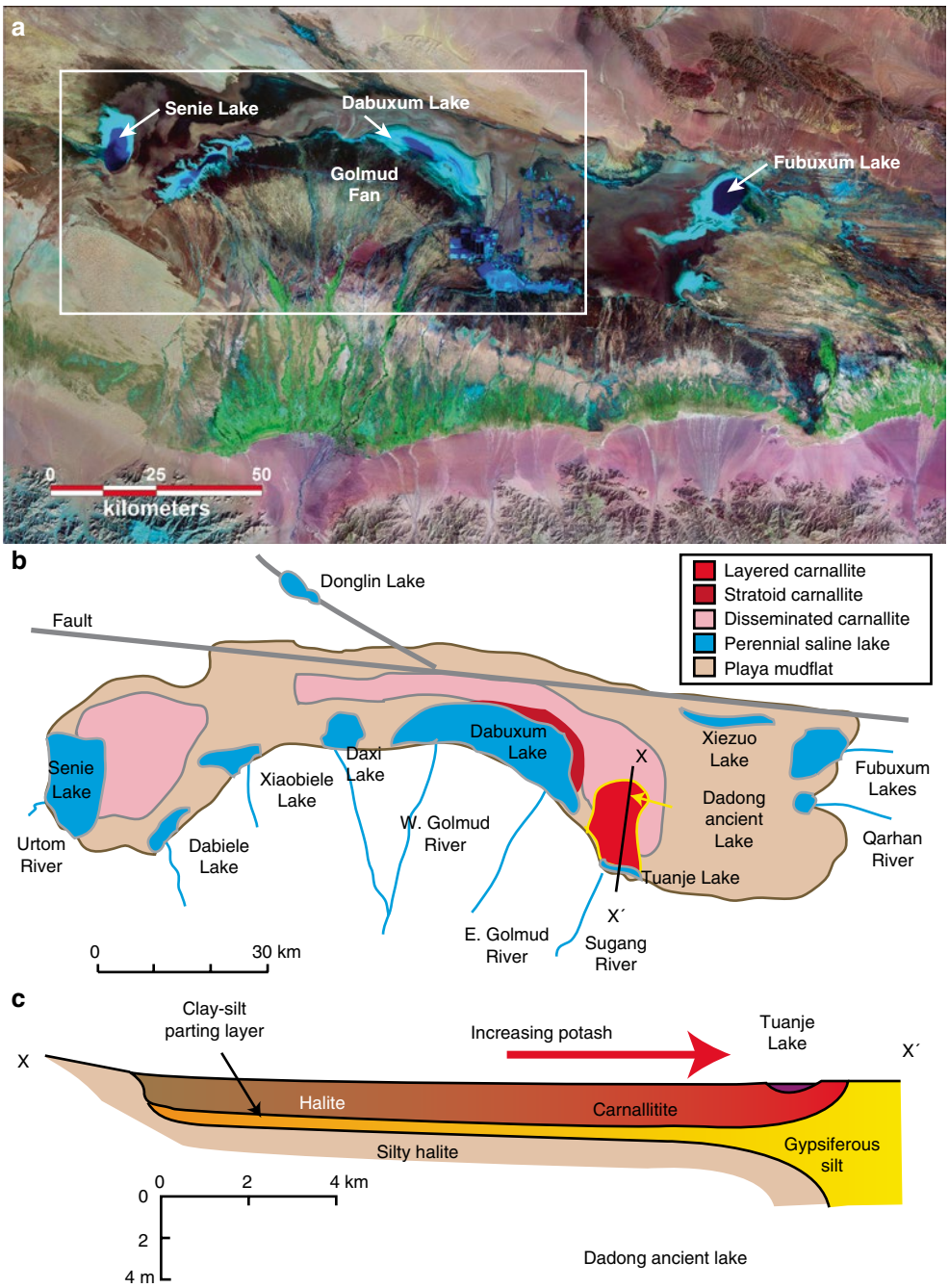

Fig. 11.11 Potash in the Lake Dabuxum region, Qarhan Playa, China. (**a**) locality map showing distribution of potash beds and lakes on the downflow side of the Golmud bajada (Landsat image courtesy of NASA https://zulu.ssc.nasa.gov/mrsid. (**b**) Potash geological plan, position indicated by white rectangle in (**a**) (After Duan and Hu 2001). (**c**) Cross section showing thickness and lateral extent of potash in ancient Lake Dadong (see b) for plan view and section location (After Duan and Hu 2001)

amounts to be quarried and most of the exploited potash resource resides in interstitial brines that are pumped and processed using solar ponds.

Compositions of fluid inclusions in primary (chevron) halite beds hosting carnallite cements in the various Qarhan salt crusts represent preserved lake brines and indicate relatively wetter conditions throughout most of the Late Pleistocene (Yang et al. 1995). Oxygen isotope signatures of the inclusions record episodic freshening and concentration during the formation of the various salt units interlayered with lacustrine muds. Desiccation events, sufficient to allow halite beds to accumulate, occurred a number of times in the Late Quaternary: (1) in a short-lived event ≈50,000 ka, (2) from about 17–8,000 ka, and (3) from about 2,000 ka till now (Fig. 11.12). Modern halite crusts in Qahan playa contain the most concentrated brine inclusions, suggesting that today may be the most desiccated period recorded over the last 50,000 years. Measurements of inclusions in early diagenetic halite that formed from shallow groundwater brines (clear halite-spar void-fill between chevrons), confirm the climatic record derived from primary (chevron) halite. The occurrence of

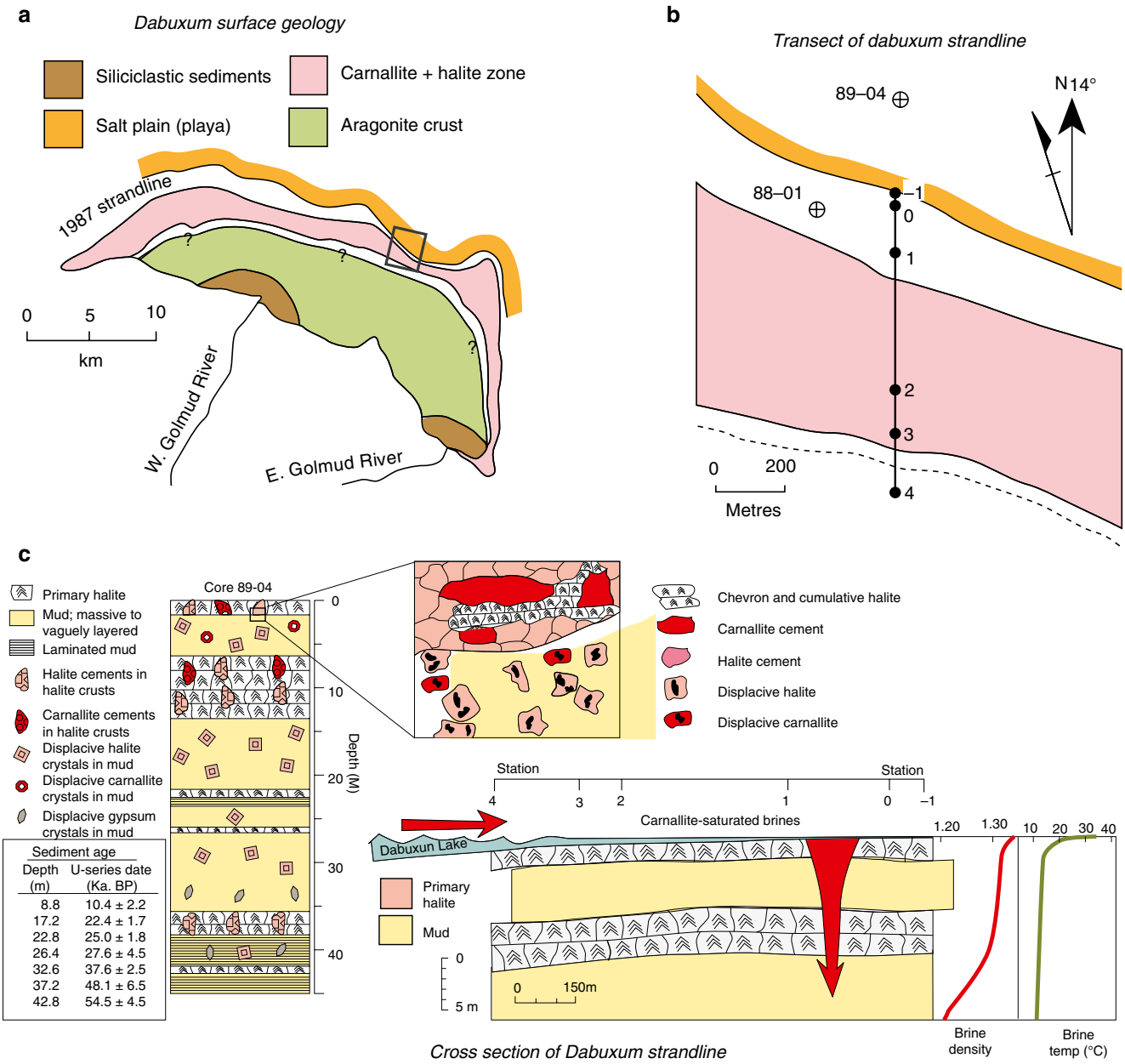

Fig. 11.12 Geology of carnallite in Lake Dabuxum area of the Qahan playa, Qaidam Basin. (**a**) Distribution of surficial sediment types also showing the position of enlarged region seen in **b** – see Fig. 11.11a for regional location. (**b**) Strandline geology of the northern shore of Lake Dabuxum showing position of coring traverse as shown as *inset* in **c**. (**c**) Cross section showing how the process of brine cooling forms carnallite cement in the karstic voids in shallow subsurface halite crusts and creates karst-filling cement textures (After Casas et al. 1992)

carnallite-saturated brines in fluid inclusions in the diagenetic halite in the top 13 m of Qahan playa sediments also imply a diagenetic, not depositional, origin of carnallite, which locally accumulated in the same voids as the more widespread microkarst halite-spar cements.

Transient surficial primary carnallite can accumulate along the strandline of Lake Dabuxum (Fig. 11.11a; Casas 1992; Van Gent et al. 2011). The greatest volume of water entering this lake comes from the Golmud River (Fig. 11.12a). Cold springs, emerging from a linear karst zone some 10 km to the north of the strandline and extending hundreds of km across the basin, also supply solutes to the lake.

The spring waters that discharge along the karst zone are chemically similar to the hydrothermal Ca–Cl sourced waters and are interpreted as subsurface brines that have risen to the surface along deep faults (Fig. 11.13; Lowenstein and Risacher 2009). Depths from where the Ca–Cl spring waters rise is not known; the subsurface of the Qaidam Basin in this region contains Jurassic and younger sediments and sedimentary rocks, up to 15 km thick, that overlie Proterozoic

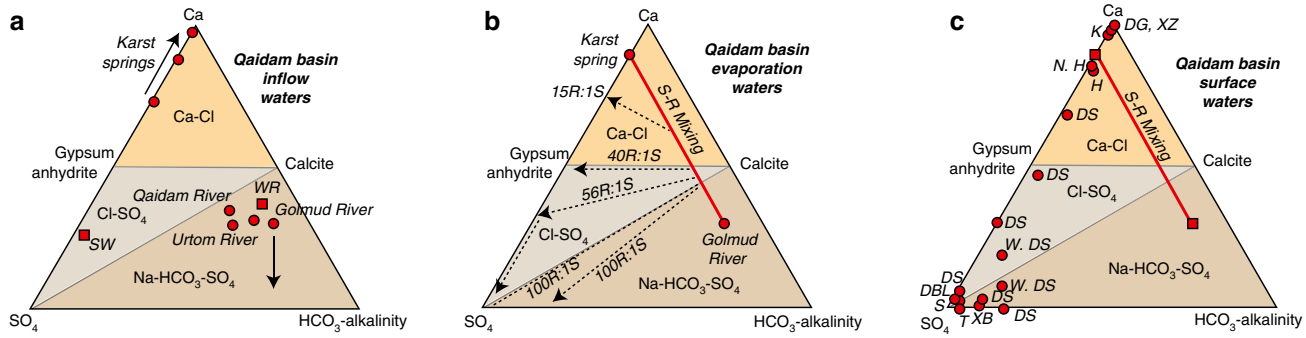

Fig. 11.13 Ternary Ca–SO_4–HCO_3 phase diagrams (After Lowenstein and Risacher 2009). (**a**) Qaidam Basin inflow water compositions. WR is world average river water, SW is Seawater. (**b**) Evaporation paths for mixtures of river water (Golmud River) and karst spring inflow. S–R is a spring water (karst spring) and river water (Golmud River) mixing line. (**c**) Qaidam Basin surface brine lake compositions (*DG* Donglin, *XZ* Xiezhuo, *NH* North Huobusun, *H* Huobusun, *K* karst brine pond, *WDS* West Dabuxun, *DS* Dabuxun, *S* Senie, *DBL* Dabiele, *XB* Xiaobiele, *T* Tuanjie)

metamorphic rocks (Wang and Coward 1990). It is also possible that Ca–Cl waters rise to the surface along a focusing permeability boundary between alluvial fan-dune sediments to the north and less permeable salt-mud sediments of Qarhan to the south. Spring inflow, whatever its flow path, has created an at-surface karst zone, focused along the main fault and defined by a series of depressions, where rising waters have dissolved soluble evaporites.

Several lakes located near this northern karst zone (Donglin, North Huobusun, Xiezhuo, and Huobusun) receive enough Ca–Cl inflow, more than 1 part spring inflow to 40 parts river inflow, to give these mixtures Ca equivalents >equivalents $HCO_3 + SO_4$ (Ca-Cl field in Fig. 11.13). With evaporation such waters evolve into Ca–Cl-rich, HCO_3–SO_4 -poor brines following precipitation of calcite and gypsum (much like seawater). The largest lake at Qarhan is Dabuxun, with its Na–Mg–K–Cl dominant brines and minor Ca and SO_4. These brines are interpreted by Lowenstein and Risacher (2009) to have formed from a mix of ≈40 parts river water to 1 part spring inflow, so that the equivalents of Ca ≈ equivalents $HCO_3 + SO_4$. Brines with this ratio of river to spring inflow lose most of their Ca, SO_4, and HCO_3 after precipitation of $CaCO_3$ and $CaSO_4$, and so form Na–K–Mg–Cl brines capable of precipitating carnallite and sylvite (Fig. 11.13). The chemical composition of surface brines in the various lakes on the Qarhan Salt plain appears to be controlled by the particular blend of river and spring inflows, which in turn is controlled geographically by proximity to river mouths and the northern karst zone with the formation of marine-like ionic proportions in some lakes.

Surface sediments of Dabuxum Lake are zoned (Fig. 11.12a, b). The southern part of the lake, closest to the Golmud River delta, is underlain by fine-grained siliciclastic sediments that pass lakeward into a centimetre-thick aragonite crusts, which floor much of the water-covered area of the lake. A small island in the centre of Dabuxum Lake is made up of mud and silt laminae coated by microcrystalline aragonite and mud chip breccias cemented with aragonite. Stacked halite pan crusts define most of the subaerial Qahan playa saltflats to the north of the perennial lake.

Surface efflorescent crusts of halite and carnallite accumulated along the edges of Dabuxum Lake from 1987 to 1989 with carnallite reaching thicknesses of up to 0.3 m along a strandline zone approximately 1 km wide. The water-covered lake area at that time was approximately 250 km^2 and waters were less than 1 m deep (Casas et al. 1992). The carnallite crust was brine-saturated, poorly cemented and had a mushy consistency. It was dominated by equigranular, anhedral carnallite crystals up to 5 mm in diameter. Thin sub-centimetre layers of very fine-grained (sub-millimetre) carnallite and siliciclastic mud occurred within the carnallite mush. Individual carnallite crystals in the mush were often linked with textures identical to rafts or films of fine-grained carnallite, which could be seen floating on the surface of the very shallow brines near the lakeshore. Rafts were being blown onto the strandline or left behind on the lake floor as the drying brine sheets retreated from the northern strand-zone of the lake. Strandline carnallites underwent extensive syndepositional diagenetic modification depending on daily temperature and weather conditions. In a single 2-week period, dominated by fine sunny weather with daily temperatures up to 35 °C, carnallite precipitated in the afternoon as rafts, or as centimetre-size, needle shaped skeletal crystals, or as efflorescent puffs of sub-millimetre crystals on evaporitic mudflats wherever the brine level was below the surface.

Light rains and strong southwest winds are common in the summer in Qaidam Basin. During such storms Dabuxum lake waters are blown over the halite-encrusted north shore and pond as thin brine sheets (Fig. 11.12b). For example, vigorous winds on 6 and 10 August 1988 shifted the northern lakeshore several hundred metres north (Casas et al. 1992).

These overlapping open lake waters were at or slightly below halite saturation and considerably below carnallite saturation. The carnallite strand zone was modified and partly dissolved after being covered by these waters, but was re-established during subsequent warm days. In a subsequent large flood, during July to September 1990, the Dabuxum Lake area expanded from 250 to 800 km^2, while the associated freshening of the expanded lake completely dissolved the carnallite crust. Clearly, surface carnallite along the north shore of Lake Dabuxum is an ephemeral strandzone sediment, with little or no preservation potential.

However, carnallite has been widely precipitated and preserved in the upper 13 m of the 45-m thick interbedded clay-halite succession that underlies the modern Lake Dabuxum strandline (Fig. 11.12c). These subsurface carnallites are diagenetic void-filling cements and displacive crystals, which indicate a carnallite distribution with a strong temperature control. As dense carnallite-saturated lake brines sank into the underlying sediment they cooled and so precipitated in pre-existing karst holes and pits in the halite bed (Fig. 11.12c; Casas et al. 1992). The voids in the halite were created by earlier lowerings of the watertable, alternating with times of freshening of the lake waters, with both events occurring numerous times prior to the accumulation of the present salt crust. This style of secondary nearsurface carnallite as early cements in the active phreatic zone is texturally analogous to much of the secondary carnallite and sylvite karst-fill fabric seen in ancient potash deposits in Thailand, Canada and the USA.

Because the majority of the carnallite in the Qarhan region is made up of patchy cement clusters hosted in bedded halite in karst cavities in the upper 13 m of the playa salt sequence is recovered via a brinefield pumping to a cluster of solar evaporators. The resulting crystal mush is scrapped and dredged from the pans by floating dredges to create the feedstock slurry for the nearby chemical processing plant that produces a combination of K_2SO_4 and KCl salt products.

Danakil Depression, Ethiopia

The Danakil Depression (aka Dallol Depression) of Ethiopia and Eritrea is an area of intense hydrothermal activity with potash occurrences related to rift magmatism, marine flooding, and deep brine cycling. It is part of the Afar Triple Junction and is located in the axial zone of the Afar rift, near the confluence of the East African, Red Sea and Carlsberg rifts (Fig. 11.14a; Holwerda and Hutchinson 1968; Hutchinson and Engels 1970; Hardie 1990). The depression is the northern part of the Afar depression and runs SSE parallel to the Red Sea coast but is some 50–80 km inland and separated from the sea by the Danakil Mountains. It is 185 km long, up to 70 km wide, with a floor more than 116 m below sea level in the deeper part of the depression. The Danakil Depression widens to the south, beginning with a 10 km width in the north and widening up to 70 km in the south (Fig. 11.14b, c). The basin floor in the northern part is the deepest and has elevations as low as 50–120 m below sealevel (Fig. 11.14c). A shallow volcanotectonic barrier behind Mersa Fatma on the coast prevents hydrographic recharge, or even substantial seawater seepage, into the current depression from waters of Howakil Bay, which is some 50–60 km WNW of Ito Aichil on the Red Sea coast.

In terms of daily temperature the floor of the Danakil is one of the hottest places on earth; year round the daily temperature is above 34 °C and in summer every day tops 40 °C, with some days topping 50 °C (Fig. 11.15). These high temperatures and a lack of rainfall place it at the hyperarid end of the world desert spectrum and make it a well known example of a BWh Köppen climate zone (Kottek et al. 2006).

A halite-floored elongate saltpan covers the deepest part of the Danakil Depression over an area some 40 km long and 10 km wide, (Figs. 11.14b, c and 11.16). The pan's position is asymmetric; it lies near the depression's western edge, some 5 km from the foot of the escarpment to the Balakia Mountains and the Ethiopian Highlands, but some 50 km from the eastern margin of the depression and today constitutes the deepest continental drainage sump of the Afar depression. The area in white shown in Fig. 11.15b, and located northeast of the main modern salt pan, is mostly an extensive gypsum plain. It defines a higher less saline lacustrine episode in the basin fill. Bedded Pleistocene evaporites may underlie the entire Danakil depression, but younger lava flows of the Aden Volcanic Series and alluvium washed in from the surrounding bajada obscure much of the older Pleistocene sedimentary series in southern part of the depression beyond Lake Assale (Fig. 11.14a).

Depositional Patterns in Outcrop

Surficial sediment distributions outline classic drawdown facies belts with a wadi fed alluvial fan fringe passing down dip into sandflats (local dune fields), dry mudflats (with springs), saline mudflats and shallow brine pans (Lake Assale). The fans are indented or locally covered by a mostly younger succession of constant-elevation marine, biochemical and evaporitic sediments fringes or "bathtub rim" facies (Fig. 11.16).

Pleistocene beds, exposed by local uplift, deflation and ongoing watertable lowering, outcrop about updip edges to the salt crusted parts of the northern Danakil, and form low flat-topped plateaus or mesas on the plain, they are the tops of alluvial fans aprons which are heavily dissected and eroded by occasional storm runoff and rainfall. This fan fringe contains relatively fresh water lenses in a desert setting that is one

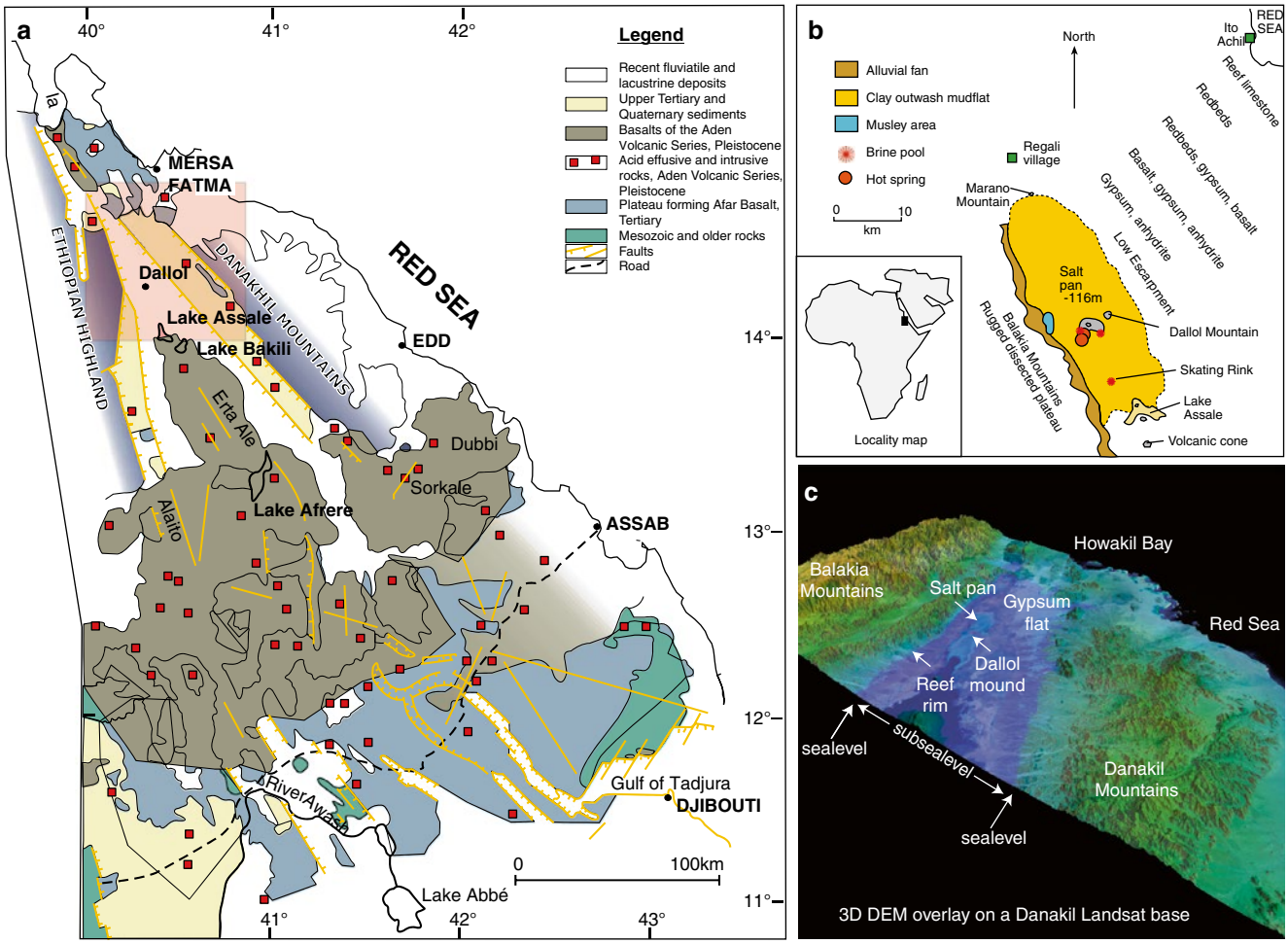

Fig. 11.14 Dallol depression, Ethiopia and Eritrea. (**a**) Regional geological setting of the triangular NNW-SSE trending Danakil rift graben (After Ercosplan 2011a). (**b**) Location and geological features of the Dallol saline pan (BWh Köppen zone; After Holwerda and Hutchinson 1968;). (**c**) 3D DEM overlay image of Danakil Depression, the colour transition from *green* to *blue* shading indicates above and below sealevel. North is toward *upper right* (Base image courtesy of NASA)

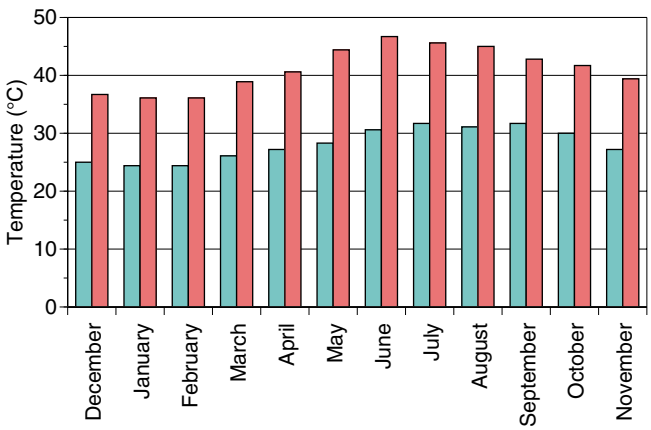

Fig. 11.15 Typical minimum and maximum monthly temperatures at Dallol, Ethiopia (Replotted from Ercosplan 2011a)

of the world's harshest (Kebede 2012) Most of the active fans line the western margin of the basin. Many of the downdip fan edges are defined by a gypsum pavement, while others, such as the Musley fan, have flowed across the pavement level and into the lower parts of the depression (Fig. 11.16).

The Musley fan characteristics are documented by the potash explorers in the basin as it offers a reliable water source for potential ore processing and so has been cored by a number of proposed water wells. Internally the fan is composed of interfingering layers and lenses of sand, gravel and clay, with highly porous intervals in the sand and gravels. Depth to the watertable varies from >2 to 60 m, and salinities from 760 ppm to more than 23,400 ppm. The principal source of recharge is flash floods, originating in Musley Canyon draining the Western Escarpment, along with minor inflows from the adjacent uplifted volcanic block and local highly intermittent rains. Of six potential water wells drilled in the fan by the Parsons Company in the 1960s, four returned water of good quality (<2,000 mg/l) while the other two had waters with salinities in excess of 20 g/l. Pump test data indicate average transmissivity of the water-bearing beds around 870 m^2/day, with salinity in the fan increasing from west to east.

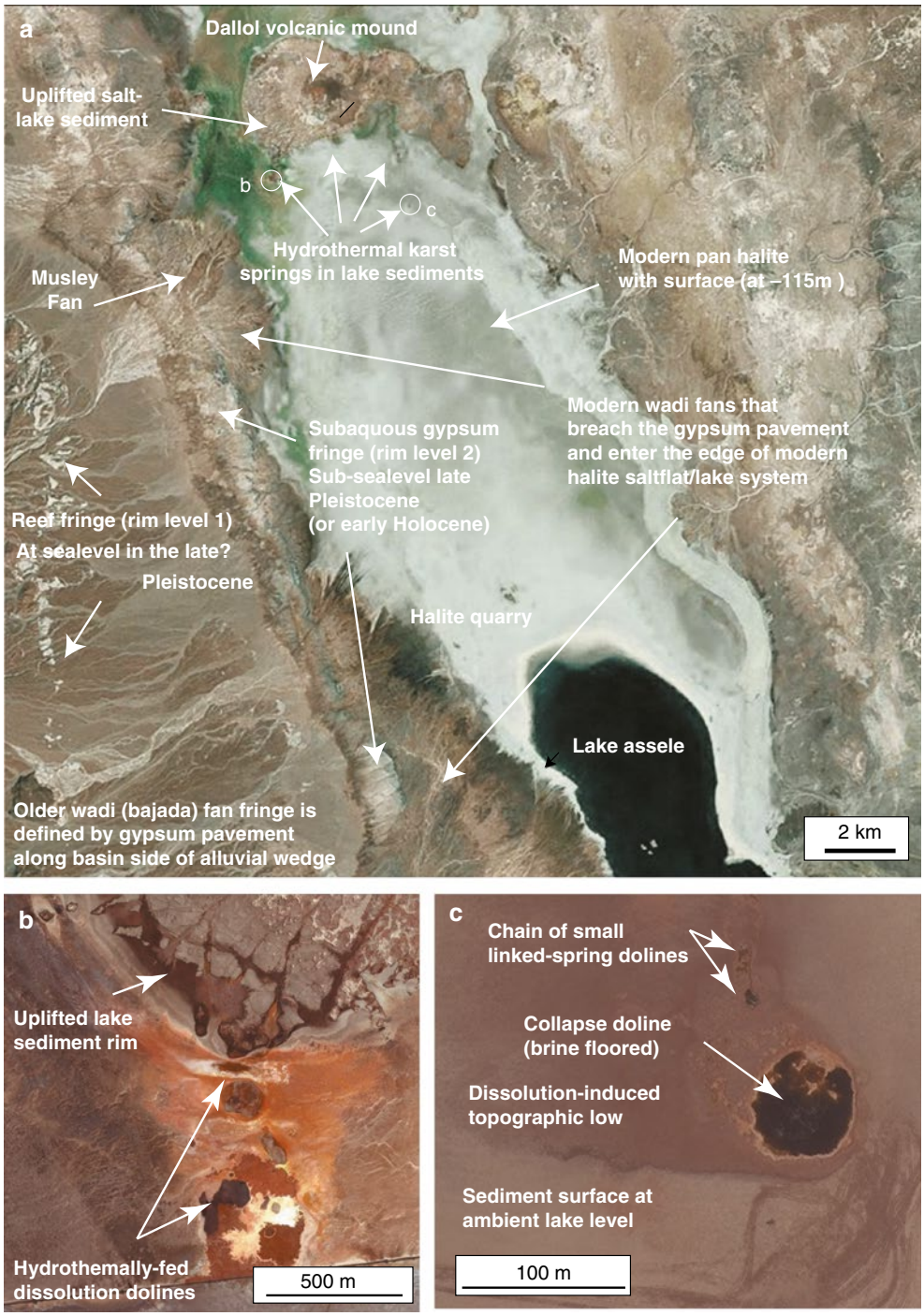

Fig. 11.16 Surficial geology of the northern Danakil depression/ (**a**) Broad-scale view showing the reef and gypsum rim and modern halite pan at successively lower elevations in the depression. Also shown is the position of the Dallol volcanic mound, its fringe of uplifted lake sediments and the associated hydrothermal springs and collapse dolines where carnallite and bischofite are precipitating, (**b**) and (**c**) Close-up views of selected hydrothermal springs and collapse dolines. Positions are indicated by *circles b* and *c* in (**a**) (scaled and interpreted Bing® images mounted in MapInfo®)

Overall, surface sediment patterns in the Danakil depression define a depositional framework of brine drawdown, related to basin isolation from an earlier hydrographic (at surface) marine connection to the Red Sea, followed by stepped evaporative drawdown. This is indicated by fringing topographically-distinct belts or rims of now inactive coralgal carbonates and gypsum evaporites (aka "bathtub ring" patterns) these were followed by the present drawdown saline-pan halite-dominant hydrology (Figs. 11.16 and 11.17a, b). The current hydrological package of sediments sits atop and postdates the Pleistocene potash hosting Lower Halite Formation and is probably equivalent to the uppermost part of the clastic overburden facies illustrated in Fig. 11.18.

In earlier work, some authors interpreted these fringing belts, especially the coralgal reefal belt, as being possibly of Pliocene or even Miocene age. However, when one looks at the stratiform nature of the outcrop trace of both the reef belt and the gypsum belt, and the carapace nature of its depositional boundaries in the field, it is immediately apparent they must be younger. Both the reefal and gypsum belts track horizontal hydrological intersections with the landscape, in

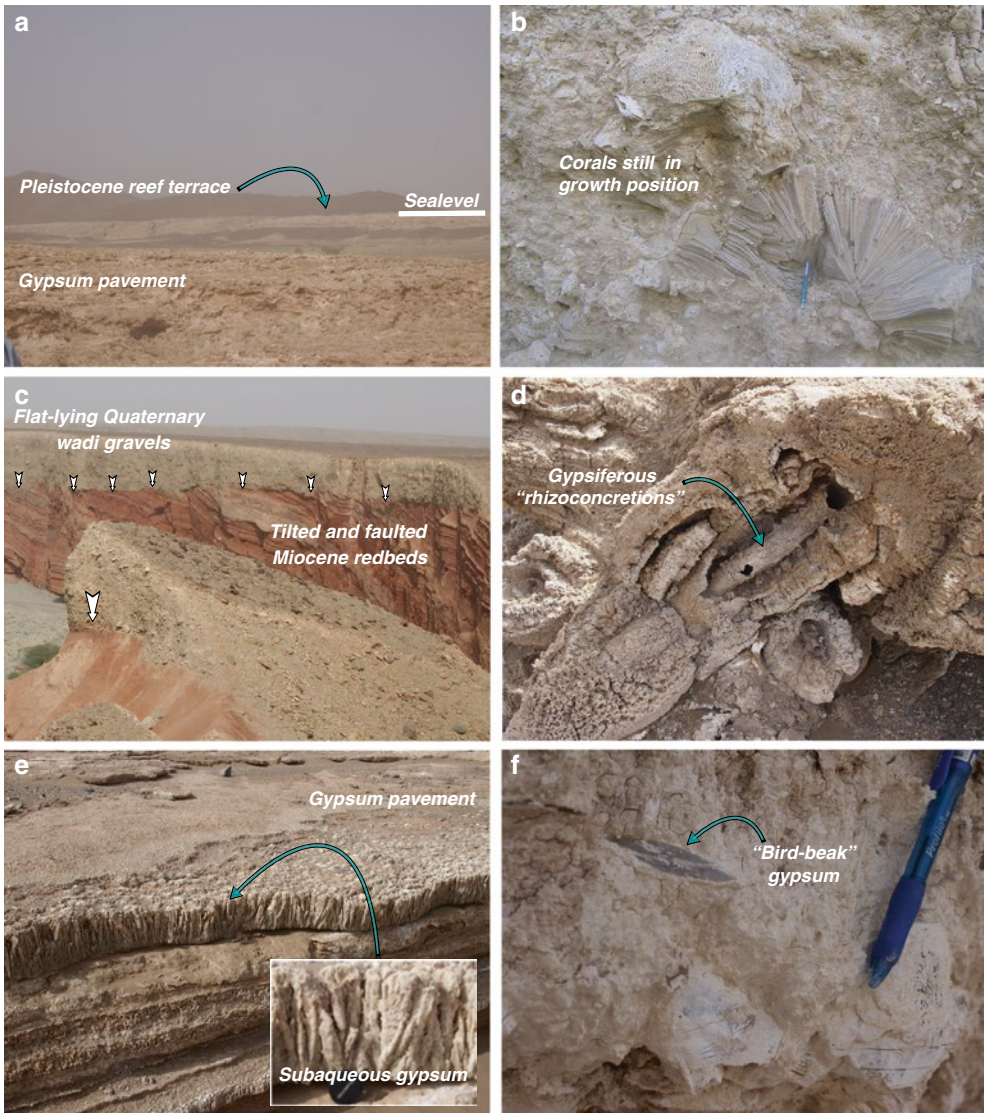

Fig. 11.17 Outcrop distribution and textures (**a**) View westward standing on the subsealevel gypsum pavement looking toward basin edge and the at-sea level Pleistocene coralgal rim (see Fig. 11.16a for map view of rim). (**b**) Coral heads in growth position in the reef rim facies. (**c**) Angular unconformity (*arrows*) separating tilted and faulted Miocene redbeds from overlying flat-bedded Quaternary wadi gravels. (**d**) Gypsiferous tufa encrustations around former tree roots. (**e**) Stacked subaqueous gypsum crystal beds in the gypsum rim. (**f**) Bird-beak displacive gypsum growing diagenetically in Pleistocene marls adjacent to rimming reef

what is an ongoing volcanogenic and tectonically active depression. When the reefal belt image is overlain by a DEM it shows the reef belt is consistently at sea level (Fig. 11.14c). If the outcrops of the reef belt and the gypsum pavement were older than late Pleistocene or Holocene, then ongoing episodes of tectonism and volcanism would have modified the elevations of the two outcrop belts in the landscape. Field visits to the Miocene section clearly show the influence of ongoing tilting and tectonism and hence why the flat-lying tops to the reef and gypsum belts imply a late Pleistocene-Holocene (Fig. 11.17c).

That is, the topographic distribution of the top of the reef facies, which lies within a metre or two of current sea level, implies that the Danakil depression had a relatively recent connection to the Red Sea. The pristine preservation of aragonitic corals and sand dollars in the adjacent marls suggest the connection was either related to the penultimate interglacial (around 104,000 years ago) or to an early Holocene transgression into the depression (Fig. 11.17b). My personal inclination is that this reef terrace is related to the penultimate sea level high (104 ka), when world sea level was a few metres above its present level. If so, there is no indication that since then the depression was ever connected at the surface to the Holocene waters of the Red Sea.

The coralgal reef terrace indicates normal marine water were once present in the Dallol depression, while the occurrences of the stratiform gypsum pavement are at a somewhat lower elevation (Fig. 11.17a). Like the reef rim, the gypsum pavement fringe defines a consistent elevated level, visible along the western margin of the present salt flat. It is the result of gypsum deposition during a period of drawdown associated with brine level stability, subsequent to the isolation of the depression from its former "at-surface" marine connection. During this time gypsum accumulated as a stack

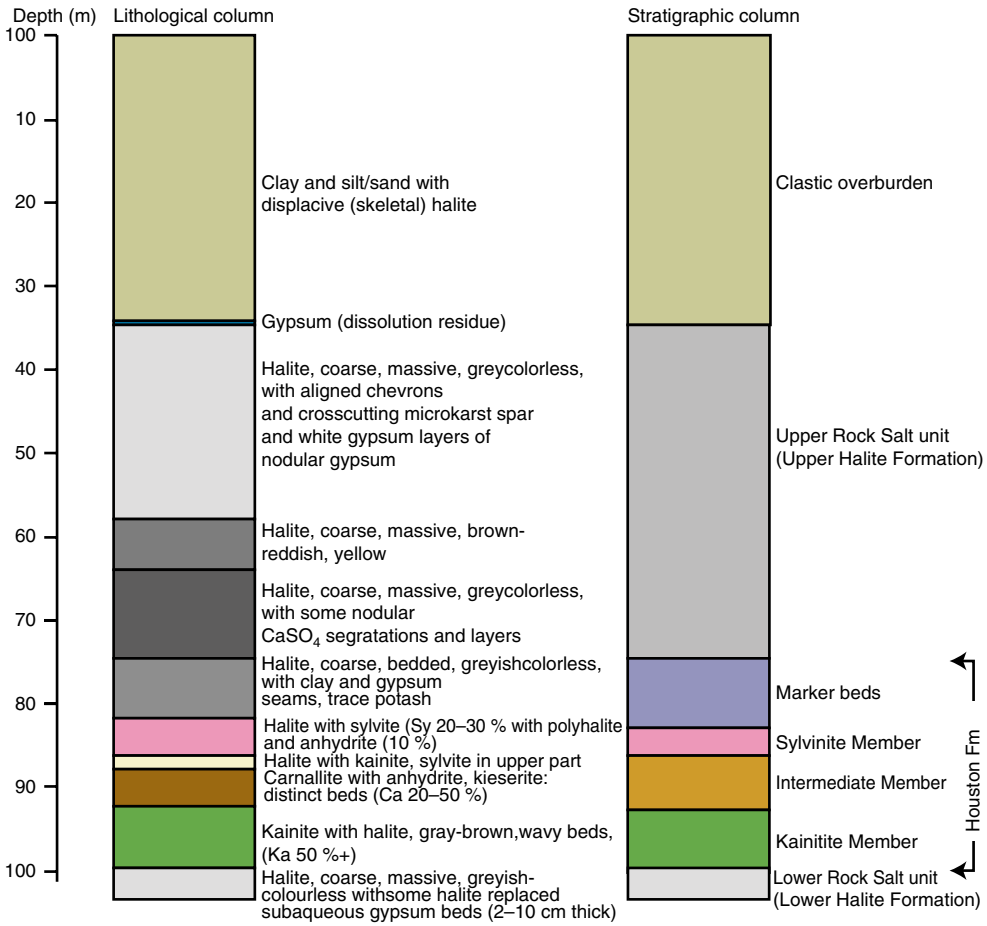

Fig. 11.18 Lithological column and stratigraphic column for the upper potash section in the Dallol depression (Based on personal study of cores and Ercosplan 2010). (See Fig. 11.20 for core-based textural details)

of subaqueous aligned gypsum beds, along with a series of gypsiferous tufas and rhizoconcretions in zones about the more marginward spring-fed parts of the gypsiferous lake margin (Fig. 11.17d, e). The evolution from marine waters that deposited the reefs and adjacent echinoid-rich lagoonal marls at a higher level in the depression (the lit zone) into a more saline capillary-fed system with no ongoing marine surface connection to the Red Sea is indicated by the diagenetic growth of large lenticular ("bird's-beak") gypsum crystals within the marine marls (Fig. 11.17f)

The current halite-dominant system is associated with even greater drawdown levels compared to the gypsum-dominant hydrology. Today's hydrology deposits a series of stacked brinepan salt sheets, which are still quarried by the local tribesmen using handtools and long trains of camels and asses to carry the mined blocks out of the quarry areas. The brine flats accumulate halite whenever the Lake Assele water line is periodically blown back and forth over the brine flat. Southerly winds occur quite often in the annual weather cycle and so the halite exploited by the tribesman is a renewable resource. Superimposed on this is occasional sheetflood event, driven by rare rainstorms and the deposition of a silt-mud layer sourced from the wadi belt. This brineflat hydrology is stable with respect to the current climate (groundwater inflow ≈ outflow). It means the current brine-flat of the northern Danakil low is accumulating salt at an even lower topographic level in the basin than the surrounding gypsum pavement, implying today's evaporites form under more arid conditions (less humid, more drawndown) than that of the gypsum pavement.

This stepped late-Pleistocene-early Holocene hydrology, captured in the modern surficial geology of the Dallol Depression, probably postdates a somewhat wetter (humid) climatic period indicated by the widespread deposition of the clastic overburden atop the Upper Halite Formation (UHF; Figs. 11.18 and 11.20). That is, the modern hydrology in present-day Lake Assale, and its adjacent saline mud flats, is not the same hydrology as that which precipitated the massive UHF cored the present clastic dominated saline pan. Texturally and hydrologically the UHF depositional system of stacked salt crusts that dominates the upper part of the UHF in the cored wells was similar to today, but a wetter moister period dominated by sheetflood clastic supply separates the two hydrological events in all the cored wells. A somewhat different marine-fed seepage hydrology formed the Lower Halite Formation (LHF) and its potash bittern cap (Houston Fm).

Table 11.6 Distinguishing features of the Lower and Upper Halite formations

Feature	Lower Halite Formation (LHF)	Upper Halite Formation (UHF)
Dominant halite style	Subaqueous, medium to coarsely crystalline, Chevron proportion increases upwards in formation.	Pan/mudflat, Coarser crystalline nearer base passes up into chevron dominate. Pristine textures.
Porosity	None to rare throughout	Yes, typically >10–15 %
$CaSO_4$ style	Anhydrite (?) crystal mantles and layers (subaqueous deposition some dissolution relicts)	Gypsum nodules with co-associated brine freshening – two styles (a) with detritals, (b) without detritals
Detrital styles (siliciclastic)	Minor aeolian settle-out, no sheetflood events	Sheetflood and rainstorm events with associated freshening and microkarsting truncations
Microkarst	Minor, only noted in halite immediately below transition to kainitite member	Multiple microkarst levels and subvertical cavity infill cements
Depositional style	Subaqueous marine fed system that shallows and brines upward into a potash association	Alternating saline pan facies, coarsely crystalline and chevron halite with increasing freshening upsection indicated by increasing levels of sheetflood clays
Potash association	Yes; depositional kainitite and reworked potash salts association (carnallite, primary and secondary, sylvite as early secondary potash minerals, with Mg salts kieserite, bischofites as co-associates)	No; little or no mineralogical evidence for bittern level salinities

Core-Based Geology

More than 970 m of halite-dominated Quaternary evaporites have accumulated beneath the present salt pan of the Northern Danakil, along with interbeds of gypsum, anhydrite and shale (Holwerda and Hutchinson 1968; Augustithis 1980). This km-thick subcropping Quaternary halite fill contains one and perhaps two or more dipping potash beds. The upper potash bed lies at a depth of 38–190 m and has been cored in a number of wells, while a lower inferred potash bed is at a depth of 596 m near the western end, but has been interpreted only from high API kicks in gamma logs run in deeper wells. The upper potash bed is the target zone for a number of minerals companies currently exploring for potash in the region. Regionally, both potash units dip to the east, and the deepest that indicators of the two units were encountered by the drill in a single well was at 683 and 930 m, respectively (Holwerda and Hutchinson 1968). The Quaternary age of the potash units, if they are marine-sourced, explains the high magnesium content of the potash bitterns depositing these evaporite as modern seawater contains high levels of Mg and SO_4 (Fig. 2.12).

My study of cores the intersected both the Lower and Upper Halite formations shows both the lower and the upper halite units retain pristine sedimentary textures with features and vertical successions that indicate distinct hydrologies during their deposition. There is no textural evidence of halokinetic recrystallization in halites any of the studied cores and published seismic also indicates consistent dips in the evaporites (Table 11.6; Figs. 11.19d, e and 11.20; Ercosplan 2010). Most of the textures in the cored potash interval indicate a subaqueous/phreatic environment, with brine reworking of a primary kainitite unit. The following paragraphs summarise my corebased observations and interpretations.

The *Lower Halite Formation* (LHF) is dominated by subaqueous halite textures and a lack of siliciclastic detritus compared to the upper Halite Formation (Fig. 11.19e). Overall, the formation is dominated by subaqueous textures and was most likely deposited in a marine-fed brine lake or seaway, which shallowed and brined upward via a gradational contact into the *Kainitite Member* (Fig. 11.20). Textures in the LHF are near identical to those in the Messinian of Spain and Sicily (Chap. 5). The mm-laminated Kainitite Member is a also subaqueous unit and was likely deposited on a pelagic bottom beneath a shallow body of marine-fed bittern waters, which never reached carnallite saturation. Above this are the variably present carnallitic *Intermediate and Sylvinitite members* and the overlying *Halite marker beds*. All retain pristine textures indicating mostly subaqueous deposition, soon followed by varying exposure and reaction to shallow phreatic brines moving across the top of Kainitite member. This shallow phreatic brine crossflow drove syndepositional mineral alteration and collapse.

Halite textures in the LHF show it did not experience this crossflow; beds are tight with primary bottom-nucleated textures dominated by coarsely crystalline beds, made up of cm-scale couplets dominated by upward pointing chevrons and mantled by thin $CaSO_4$ layers (Fig. 11.19e). This meromictic-holomictic textural association passes up into the upper part of the LHF with cm-scale alternating less-saline to more-saline episodes of evaporite precipitation, indicating an "on-average" increasingly shallow subaqueous depositional setting. The upward-shallowing, increasingly schizohaline trend is also indicated by an increasing proportion

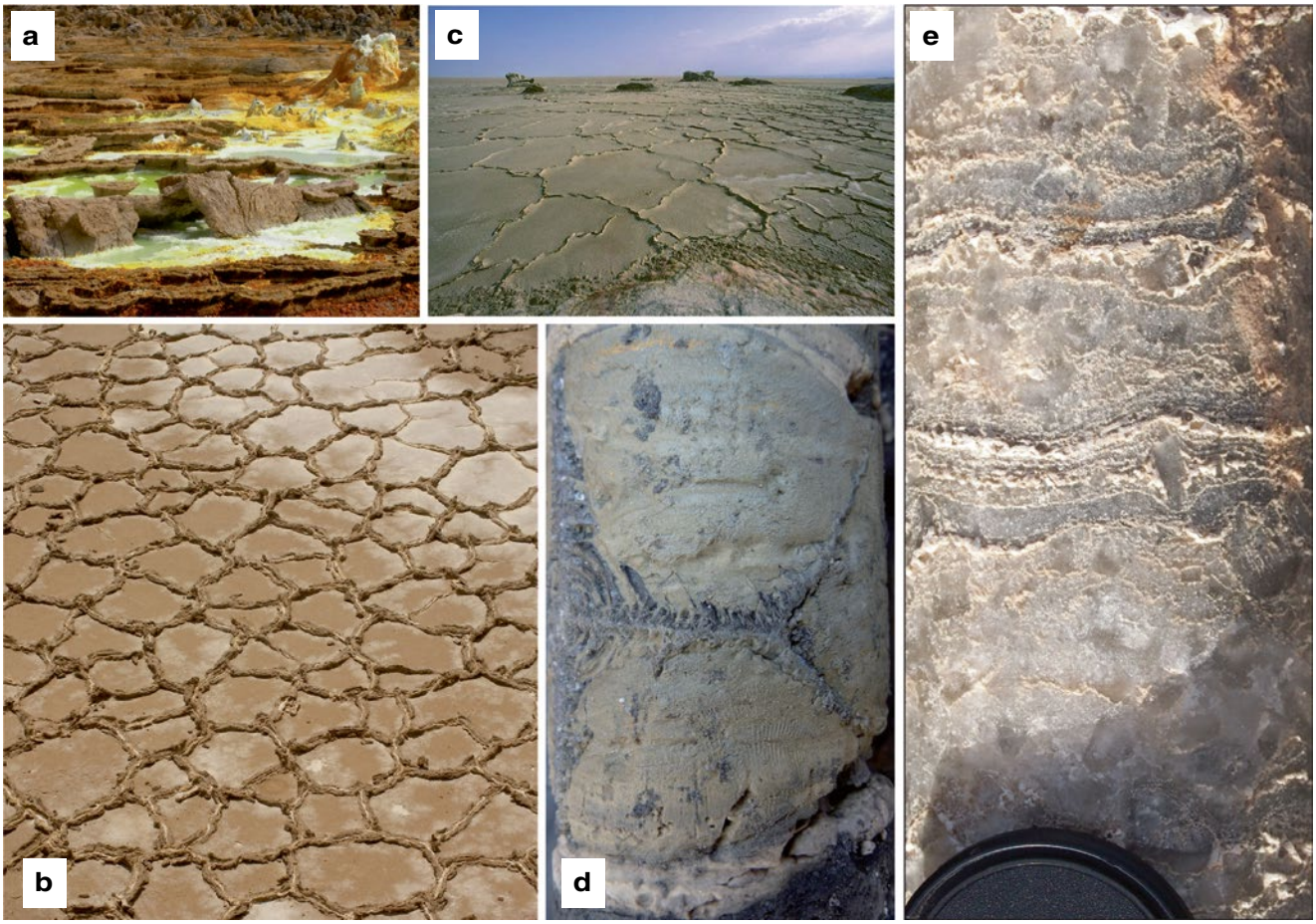

Fig. 11.19 Halite styles at the surface and in the subsurface in the Dallol depression, Ethiopia. (**a**) Salt and sulphur in hydrothermal spring region near volcanically active Dallol Mountain, a local region of salt ground collapse driven by volcanogenic uplift. (**b**) Newly-formed salt crust near Dallol Mountain. (**c**) View across the halite crusted Danakil saltflat near the margin of the Musley fan showing remnants in the mid-distance of outlier blocks of earlier evaporitic lake sediments exposed by lake floor sheet flood erosion and deflation. (**d**) Core in brine saturated clastics showing displacive halite in a silty matrix with white cm-thick $CaSO_4$ beds above and below. The core is approximately 12 cm wide and 45 m below the modern lake surface. (**e**) Subaqueous textured halite-anhydrite in core from more than 150 m below the surface in Lower Rock Salt Member (Selected images courtesy of Allana geologists Sam Baldwin and Rhys Cole)

of milky (brine-inclusion rich) chevron halite textures in the upper parts of the LHF (Fig. 11.20). The nature of the primary layering over the same interval changes from mantles (zig-zags) to flatter truncational laminae. The $CaSO_4$ layers mantle upward-aligned halites (Fig. 11.19e). The cubic crystal terminations on the halites encased in $CaSO_4$ show this is a primary texture, although similar features have been interpreted as replacive in the Permian of west Texas. Throughout the LHF there is little evidence of microkarsting (Fig. 11.20). In combination, all these pristine textures in the LHF indicate a perennial, periodically shallowing and freshening brine body. In the upper part of the unit, it shallowed to where the somewhat fresher upper water mass periodically touched down on the perennially-subaqueous depositional pavement.

Between the UHF and LHF is the potash-entraining Houston Formation (Figs. 11.18 and 11.20). It has been drilled and cored extensively and is consistently between 15 and 40 m thick (Fig. 11.18). Stratigraphically, it consists of lower Kainitite Member (4–14 m thick) atop and in depositional continuity with the LHF (more than 500 m thick). The Kainitite Member is fine-grained, laminated, locally wavy-bedded, containing up to 50 % kainite in a halite background. It is overlain by what older literature describes as the "Carnallitite Intermediate unit" (3–25 m thick). More recent potash exploration drilling has shown the Intermediate Carnallitite Member is not always present within the Dallol depression and mineralogically is at best considered as variably developed. The lower part is a carnallite-halite mixture with some kieserite and anhydrite. This passes up or laterally into kainitite with sylvite. Above the Intermediate Member is the 0–10 m thick Sylvinite Member containing 20–30 % sylvite, along with polyhalite and anhydrite (up to 10 %). This passes up into a halite-dominated unit that is known as

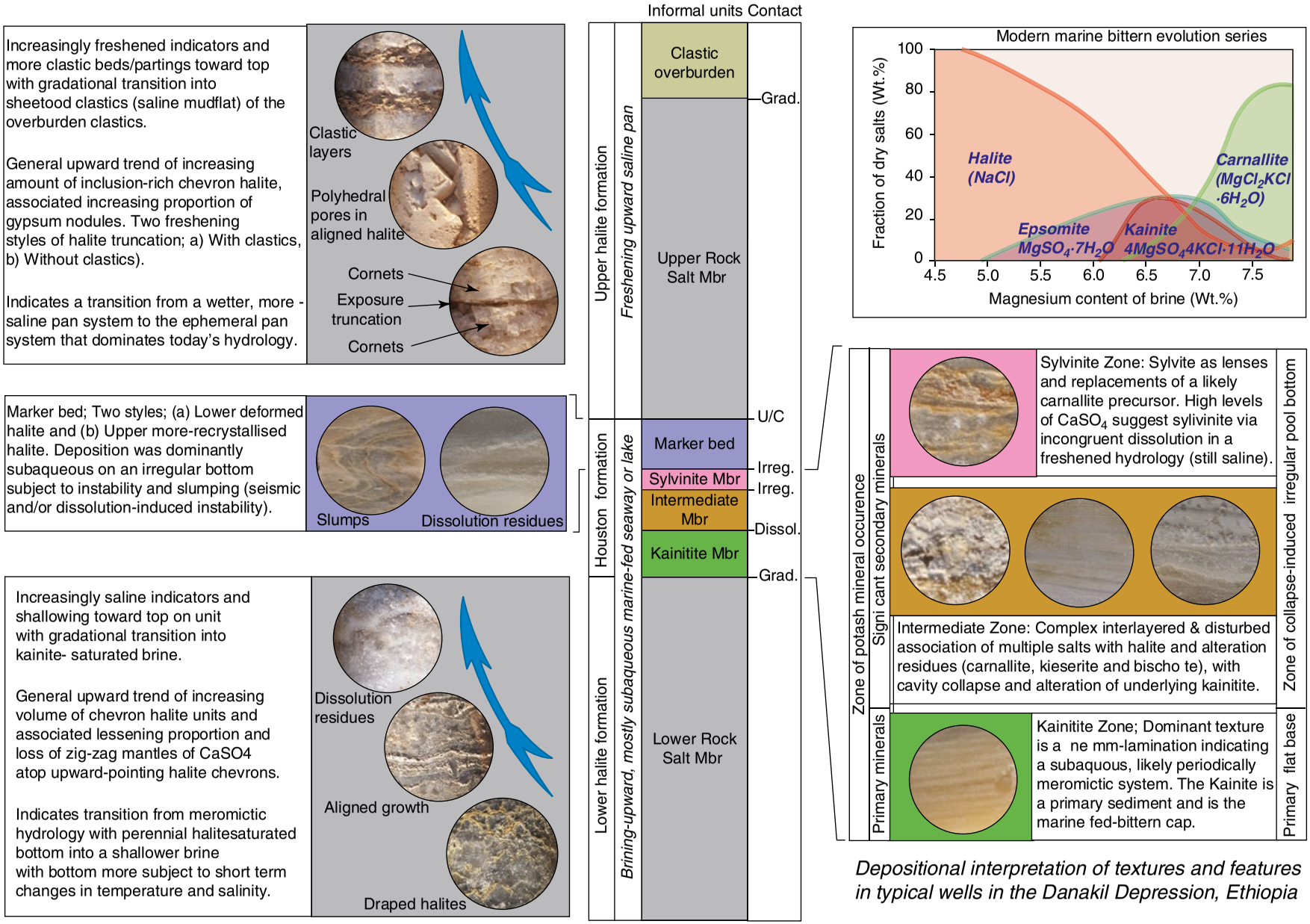

Depositional interpretation of textures and features in typical wells in the Danakil Depression, Ethiopia

Fig. 11.20 Depositional summary of the significance of sedimentary textures in a representative potash-intersecting well, Danakil Depression, Ethiopia

the "Marker Beds" because of the co-associated presence of clay lamina and bedded halite, along with traces of potash minerals. This unit then passes up in the massive Upper Rock Salt unit across an unconformity at the top of the "Marker Beds." The bedded, and at times finely laminated textures in the magnesian bittern units, are used by many to argue that the kainitite and possibly carnallitite members are primary or syndepositional precipitates.

Cores through the sylvinite member sample a range of recrystallization rather than primary textures. Three types of barren zone occur within it and are possibly related to the effects of groundwaters and solution cavity cements within the carnallitite unit, perhaps precipitated before the deposition of the overlying halites. Barren zones in the Sylvinite member are regions where: (a) the entire sylvinite bed is replaced by a relatively pure stratiform halite, along with dispersed nodules of anhydrite, (b) zones up to 23 m thick and composed of pure crystalline halite (karst-fill cements?) that occur patchily within the sylvinite bed and, (c) potash-depleted zones defined by coarsely crystalline halite instead of sylvinite. Bedding plane spacing and layering in the halite in styles a and b are similar to that in the laterally adjacent sylvite bed. Contact with through flushing freshened waters probably created most of the barren zones in the sylvinite. Fluid crossflow may also have formed the sylvite of the upper member, via selective surface or nearsurface leaching of $MgCl_2$ from its carnallite precursor (Holwerda and Hutchinson 1968). Due to its secondary origin, the proportion of sylvite in the sylvinite member decreases as the proportion of carnallite increases, along with kieserite, polyhalite and kainite.

Beneath the sylvinite member, the variably-present carnallitite member contains a varied suite of non-commercial potash minerals that in addition to carnallite include, kieserite, kainite (up to 10 % by volume) and polyhalite, along with minor amounts of sylvite. Minor anhydrite is common, while bischofite and rinneite may occur locally, along with rust-red iron staining. Sylvite is more abundant near the top of the carnallitite member and its proportion decreases downward, perhaps reflecting its groundwater origin. Kainite is the reverse and its proportion increases downward. The sylvinite member and the carnallitite member also show an inverse thickness relationship. Bedding in the carnallitite member is commonly contorted with folded and brecciated horizons interpreted as slumps. The base of the carnallitite member is defined as the level where carnallite forms isolated patches in the kainite before disappearing entirely.

The kainite member is texturally distinctive and is composed of nearly pure, fine-grained, dense, relatively hard, amber-coloured kainite with ≈25 % admixed halite. Texture and colour are characteristic of the unit, but even more so are the distinct "ruler-straight" bedding planes in the kainite, a striking contrast to the wavy, contorted and irregular bedding planes of the overlying carnallitite and sylvinite members. Core study shows the lamina style remained flat-laminar (that is, subaqueous density-stratified with periodic bottom freshening) as the mineralogy passes from the LHF up into the flat-laminated kainitite member (Fig. 11.20). Throughout, the kainitite unit shows this finely sub-mm scale layering, with no evidence of microkarsting or any exposure of the kainitite depositional surface. That is, the Kainitite Member is a primary depositional unit, like the underlying halite and still retains pristine evidence of its dominantly subaqueous depositional hydrology. The decreased proportion of anhydrite in the Kainitite Member, compared to the underlying LHF, indicates a system that on-average was more saline than the brines that deposited the underlying halite. The preponderance of $MgSO_4$ salts means the Kainitite unit like the underlying LHF formed by the evaporation of seep-supplied seawater. This situation differs from the present "closed basin" hydrology of the Danakil Depression (Hardie 1990).

The top of the Kainitite Member is typically defined by a 2–3 m-thick zone of poor core recovery (brine-cavity zone?). Sediments of the what is known as the Intermediate Member occur immediately above this zone of poor recovery. The Intermediate Member is defined by the first appearance of carnallite in the well stratigraphy. Carnallite and kieserite, along with bischofite and some halite are co-associated mineralogies above the dissolutional top to the Kainitite Member (Fig. 11.20).

Textures in cores in all intervals above this poor recovery zone indicate deposition occurred on a more irregular bottom topography (e.g. pseudo-crossbeds in kieserite beds). Ongoing bottom instability is indicated by slumps and brecciation-induced collapse zones, along with pervasive lenticular bed styles. Taken together they indicate deposition in a subaqueous brine lake or seaway, but compared to the underlying LHF sediments this brine system had a more irregular and unstable, bottom topography. This was so throughout deposition of the Intermediate member, the Sylvinite member and the overlying marker beds. Together all these members atop the LHF constitute what is known as the Houston Formation (Fig. 11.20).

The amount of anhydrite increases in these beds compared to the underlying Kainitite Member, indicating a somewhat freshened (but still hypersaline) depositional/diagenetic brine hydrology that was capable of dissolving and reprecipitating potash and magnesia as it diagenetically reworked top of the Kainitite member. This inference of an early diagenetic component to the potash distribution is reinforced by the variable presence of bischofite (up to 200 m thick units of massive bischofite have been cored in some of the wells drill by Allana Potash). Interestingly, in terms of the somewhat mobile nature of $MgCl_2$ brines both past and present, there is today a bischofite-saturated brine pool active at the surface near Dallol. It contains brine at a temperatures of 132 °C and if a stick is placed in the brine and then extracted a coat of bischofite forms immediately on exposure to the air.

The zone of potash minerals in the two units atop the primary laminated textures of the kainitite show various

secondary potash textures (Fig. 11.20). It seems much of the potash alteration occurred in the shallow subsurface in zones subject to groundwater crossflows and collapse, possibly aided by seismically induced pulses of brine crossflow. All this hydrology was subject to long term brine reflux and the brine displacement backreactions that typify all evaporite deposition, past and present.

An observation of early ionic mobility in potash zone brines in the Danakil depositional system is also not unusual in any modern or ancient potash deposit. It should not be considered necessarily detrimental to the possibility of an extensive economically exploitable potash zone being present in the Danakil Depression. As we shall see in the later sections of this chapter, all the world's exploited potash deposits, including those in the Devonian of Canada and Belarus, the Perm of the Urals and the potash bed of west Texas, show evidence of syndepositional and shallow burial reworking of potash. Early potassium remobilization has created the ore distributions in these and other mined potash deposits. Likewise lack of knowledge in terms of evaporite textures and associated hydrological controls to explain such redistributions and their polycyclic nature explains many of the problems encountered in potash exploration and exploitation (Chap. 13; case studies).

Textures and mineralogies in the *Upper Halite Formation* (UHF) define a separate hydrological association to the marine-fed LHF and Houston Formation (Table 11.6). Compared to the LHF, the UHF has much higher levels of depositional porosity, lacks high levels of $CaSO_4$, has high levels of detrital siliciclastics. This is especially so in its upper part, which shows textural evidence of periodic and ongoing clastic-rich sheetflooding and freshening (Fig. 11.20). It was deposited in a hydrology that evolved up section to become very similar to that active on today's halite pan surface. The UHF contains no evidence of salinities or textures associated with a potash bittern event and is probably not a viable exploration target for solid potash salts.

The UHF lies immediately above the halite marker bed, which defines the top of the Houston Formation, where it is highly porous, with interconnected locally-high levels of effective intercrystalline polyhedral porosity. It is a likely a still-active basal aquifer to the Upper Halite Formation (Fig. 11.20). The lower part of the UHF is dominated by a relatively pure halite, with major impurities being occasional cm-sized nodules of gypsum or coats of clastics (mostly eolian transported). Halite crystals can be cm-scale meshworks and crosscut by still-open, partially-cemented subvertical dissolution cavities. Such microkarst textures indicate that during the formation of the pan halite crystals, the water level fell below the depositional surface numerous times to become a watertable. Higher in the UHF, especially in its upper 20–30 m the amount of clastic detritus (shale bands and beds) increases, with laminated clastic units tens of centimetres to more than a metre present in its uppermost part. Some of these beds entrain gypsum nodules and displacive halites, indicating periodic intrasediment capillary evaporite precipitation, tied to subaerial exposure of the sedimentation surface. This gradational transition upward into more siliciclastics indicates a UHF hydrological system that was overall freshening upward, with the effects of rainstorms and sheetfloods coming to dominate the depositional textures in its upper parts. This upward freshening of the UHF contrasts strongly with the upward brining hydrology that characterises the mineralogies and textures of the LHF. It means substantial volumes of preserved potash salts are highly unlikely in the UHF.

Up-section in the UHF the amount of mesocrystalline chevron halite increases at the expense of the more coarsely-crystalline halite, along with upward overall increases in numbers and thicknesses of detrital beds in the halites and increasing volumes of nodular gypsum. But gypsum never makes up more than a percent or two in any of the UHF halites. The chevron units that dominate the halites in the mid and upper parts of the UHF show two styles of truncation surfaces related to short-term freshening events in the pan hydrology. They are; (1) A relatively detrital-free $CaSO_4$ enriched layer where gypsum nodules formed after rainstorm-induced freshening of pan brine sheets, without substantial sheetflow transport of clays. These layers are composed of subhorizontally scattered nodules across a break in halite crystallisation. (2) A detrital-rich horizon or break that truncates the underlying halite chevron bed. These breaks in halite sedimentation are typified by cm-thick beds of siliciclastic muds that also entrain gypsum nodules These clastics define times of sheetflood clay transport out into the saline pan and were associated with times of wadi flooding. Both types of freshened surfaces are truncations not mantles in the background salt sedimentation and so indicate meteoric influxes in the pan history. Throughout chevron deposition they formed diurnally from thin sheets of brine subject to periodic freshening and desiccation (very different to the subaqueous holomictic-meromictic hydrology of the LHF with its resulting cm-layered anhydrite mantles).

Above the UHF is a clastic unit with significant amounts of and sometimes beds dominated by lenticular gypsum and displacive halite. The widespread presence of these diagenetic salts indicate high pore salinities as, or soon after, beds that stack into the clastic unit were deposited. Some of these early diagenetic evaporite are spectacular, as seen in the displacive halite recovered in a core from the lower portion of the clastic overburden some 45 m below the modern pan surface (Fig. 11.19d).

Today hot springs, rich in basinal $CaCl_2$ and depleted in $MgSO_4$, supply and maintain the active hydrothermally-fed brine pools and karst lakes in the solution depressions near the volcanic edifices that define Dallol Mountain

(Figs. 11.16b, c and 11.19a; Carniel et al. 2010). For example, there is a small carnallite deposit known as the Crescent deposit in the vicinity of this active hydrothermal region centred on the Dallol volcanic mound. Hydrothermally-driven groundwater activity has broken up the mineralogical continuity of the nearsurface salt beds in this region and drove the formation of natural regions of ground collapse, sulphurous and acidic springs and fumaroles along with the creation or water-filled chimneys and doline sags. Occasional intense storm-driven sheet floods drive renewed hydrothermal activity, as happened in the recent floods of February 2011, when a natural collapse doline tens of metres across formed on the depression margin. It is likely that hydrothermal circulation evidenced by these intra-saltflat dolines offers an explanation for some of the unusual mineral associations recovered in some wells such as a 200 m intersection of bischofite.

Some 60 km to the southeast of the Musley area, still in Ethiopia, is Lake Afrera (Lake Giulietti), with an area of 100 km^2, a water level some 102 m below sealevel and a water mass possibly 160 m deep (not confirmed) in the lake centre. It is located immediately southeast of the active Erta Ale volcanic field of the southern Danakil. Unlike the mostly alkaline waters of the majority of saline waters of the rift lakes to the south, its waters are acidic. Both the inflowing hot springs (40–50 °C) and the brines of the lake itself are rich in $CaCl_2$ and poor in $MgSO_4$. The modern lake waters are brackish and support a few species of halotolerant fish. Halite has been manufactured for centuries by concentrating lake waters in a series of anthropogenic pans that surround much of the lakeshore. Extensive concentration and desiccation of the waters in the lake may eventually lead to deposition of an $MgSO_4$-poor series of salts, dominated by carnallite, halite and $CaCl_2$ salts. Much in the same way these $MgSO_4$-deficient salts today dominate the surface salts of the Dallol salt pan. This will be in marked contrast to the thick underlying $MgSO_4$ -rich Pleistocene evaporites of the Musley area. It seems that seawater was much more important as a brine source in the Dallol in the Pleistocene than today.

In summary, it seems that the interaction between hot basinal groundwaters and volcanic bedrock is the likely explanation of the present inflow chemistry and groundwater-driven alteration of the original carnallitite beds. Fractional dissolution of the earlier highly soluble potash evaporites, in preference to the less soluble Mg-salts, plays an important part in the formation of sylvinite at a time after the deposition of the marine-fed lower Rock Salt Member and prior to the deposition of the overlying Upper Halite bed. Many hot modern brine springs, Some of which are at temperatures or more than 120 °C and precipitating bischofite in geothermally active areas in around Black Mountain and Dallol Mountain salt lakes are also rich in $FeCl_2$, sulphur and manganese (Carniel et al. 2010) This indicates ongoing hydrothermal interactions of saline groundwaters with volcanics and gives bright red-orange and yellow colours to many of the mineral assemblages precipitating in and about active springs (Fig. 11.14a).

Inland Chotts and Coastal Sabkhas in North Africa

Chott el Djerid in southern Tunisia is an endorheic playa where ephemeral carnallite accumulates as efflorescences and rare intercrystalline cements in the uppermost parts of ephemeral halite crusts in lowermost, more central portions of the saline pan facies (Fig. 11.21; Bryant et al. 1994a, b; Swezey 2009; Stivaletta et al. 2009). The chott, with an elevation typically more than 10 m below sea level on the saltflats, has an area of approximately 5,360 km^2 in a drainage basin with an area of 10,500 km^2. Mean annual rainfall for the area is 80–140 mm, the mean annual temperature is 21 °C and evaporation, which is highest between May and September, has a mean annual value of 1,500 mm. It has an elongated arm (Chott Fejej) that stretches eastward toward the coastal city of Gabes.

Chott el Djerid is the largest in a zone of chotts formed where a series of regional aquifers emerge to create a region of discharge playas along the northeast extremity of the Bas Saharan Artesian Basin (Fig. 11.22a; Rosen 1994). It is a groundwater sump region in a tectonically quiescent area of the North African craton. The encompassing chott-hosting depression extends over much of the Saharan desert into Morocco and Libya and encloses the northern end of the Grand Erg Oriental.

The zone of chotts defines the major discharge area of the "Complexe Terminal" aquifer system, which is made up of permeable Turonian dolomites and Upper Cenomanian limestones and intercalated evaporites, along with some Mio-Pliocene sands and conglomerates (Fig. 11.22b; Swezey et al. 1999). Discharging continental groundwaters seep into the chotts beneath the edges of thin Quaternary clay aquitards that also form the impervious bottoms to much of the playa areas. The same thin clay bed facilitates temporary ponding of waters supplied by winter floods onto the central playa facies. All the chotts in the "Complexe Terminal" occupy the lowest areas on the north African interior; Chott el Melrhir in Algeria is 40 m below sea level, while in their lowermost portions Djerid and Garsa are 16 and 21 m below sea level, respectively.

The lowest and more central part of the deflationary depression that is Chott el Djerid is now a halite pan outlined by a thin ephemeral halite crust atop Quaternary clays and sand aquifers that host saline pore waters. It is surrounded by a gypsum mudflat, which in turn pass marginward into a broad evaporitic mudflat and dry sandflat. Much of the

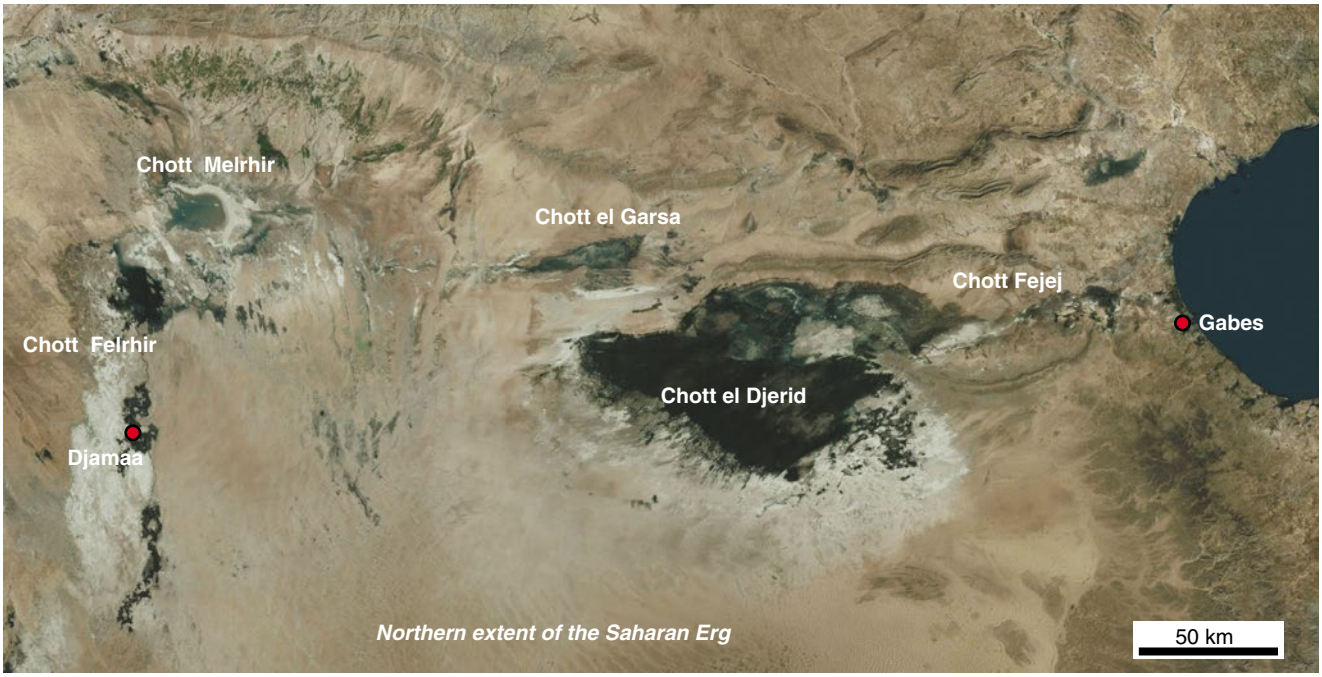

Fig. 11.21 Chott el Djerid, and other nearby chotts, Tunisia, showing the extensive saline mudflats that characterises the lowermost part of this inland depression. A surface geology map of the saline mudflat in northeastern portion of this region is given in Fig. 11.22c (Scaled Bing® image mounted in MapInfo®)

mudflat surface surrounding the halite-encrusted portion is covered by gypsum petees and adhesion ripples (Fig. 11.22c). Parts of the sandflat are transitional into aeolian-overprinted sediments with characteristic wind-blown sand streaks, wind-rippled sand sheets mounds and shadow dunes, all of which are cross cut by wadi channels that feed surface water into the central depression during times of flood. To the north, beyond the sands flats are the low-relief alluvial fans of the Atlas foothills. To the south of Chott el Djerid is the transition into the Great Eastern Erg of the Saharan Desert, the outer edges of which are characterized by low-relief, isolated sand mounds that mostly lack well-defined slip faces and are separated by interdunal sabkhas.

Like the interior salt lake basins along the southern edge of the Great Artesian Basin of Australia, the chotts are deflationary rather than accretionary depressions. They have lost something like 15–20 m of late Quaternary fill via eolian deflation to the adjacent Sahara desert erg (Blum et al. 1998). No evaporite beds occur in the 10 m of eolian-dominated Pleistocene sediments that lie atop the Miocene unconformity and beneath the ephemeral modern salt crust cap to the chott. This deflation-dominant outflow hydrology offers little preservation potential in terms of salts deposited in a surface salt crust. They cannot remain long enough in the stratigraphy to be buried. That is, periodic flooding and ongoing deflation mean there is no potential for potash preservation in this style of saline hydrology. Its sump hydrology is simply not saline enough, even though a thin salt crust cap extends for hundreds of kilometres over most of the chott surface.

Even though most of the present-day chott surface is deflationary, there is some local accretion around spring mounds, which are point sources of water escape from underlying artesian aquifers (Fig. 11.22c; Swezey et al. 1999; Stivaletta et al. 2009; Stivaletta and Barbieri 2009). Interestingly, the region around Chott el Djerid salt pan includes some of the most extensive gypsum beds in Africa (Drake et al. 2004; Barbieri et al. 2006). Regional chemical analyses show a marine signature to this pedogenic gypsum and by association the rare potash efflorescences (Gueddari 1984; Bryant 1999; Bryant et al. 1994a, b). The constituent sulphate ions are leached by deeply circulating meteoric groundwaters moving through Cretaceous and Triassic marine evaporite beds. That is, the ultimate salt source to the solutes in the nonmarine chott depression is seawater, it is just that the cycling of the marine solutes into the depression was delayed by more than 100–150 Ma, while the salt was stored in sediment beds (Drake et al 2004). In this sense the ion source to the North African gypcrete crusts are different from surface gypcretes about saline pans in the deserts of Namibia and Australia. There the recycling time from an oceanic atmospheric source is much shorter (contemporary to hundreds of years). Rare potash salts (mostly carnallite) that form ephemeral cements and efflorescences in upper parts of halite crusts and pans in Chott el Djerid have a similar longterm, ultimately marine, meteorically recycled ion sources (Bryant et al. 1994a).

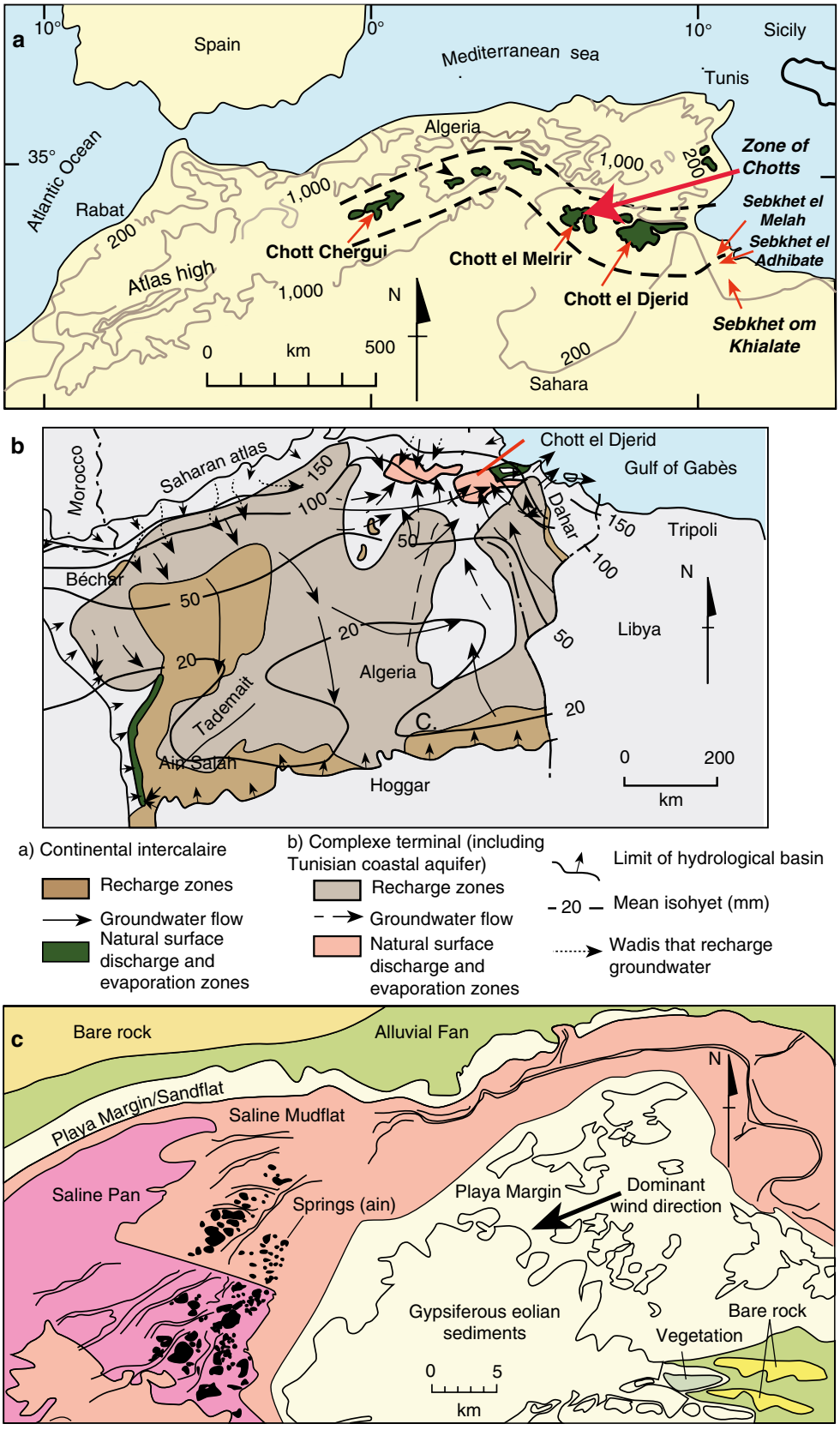

Fig. 11.22 Chott el Djerid. (**a**) Locality showing Zone of Chotts as regional groundwater outflow zone. (**b**) Regional hydrology. (**c**) Facies in northeastern corner of Chott el Djerid (After Bryant et al. 1994a)

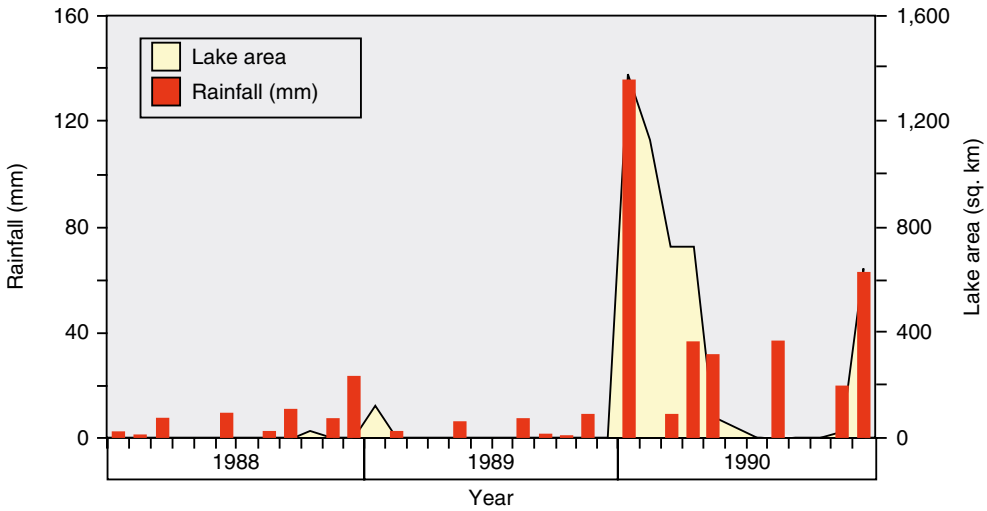

Fig. 11.23 Rainfall and lake areas recorded on the Chott el Djerid from 1987 to 1990 (After Bechtel et al. 1999)

Table 11.7 Average composition (g/l) of Tunisian chott and sabkha brines

Locality	Na	K	Ca	Mg	Cl	SO_4
Chott el Jerid	100	9.0	0.7	12	197	12
Sabkhat el Melah	45	7.7	0.2	50	200	28
Sabkhat el Adhibate	88	3.6	1.0	12.6	150	37
Sabkhat om Khialate	43	0.8	0.4	3.3	24	74

After Kbir-Ariguib et al. (2001)

A flood occurred in the northeast portion of Chott el Djerid in January 1990 after an intense storm period when more than 120 mm of rain fell (Fig. 11.23). Its aftermath showed that Chott el Djerid undergoes four evolutionary stages as it recycles and concentrates its surface and nearsurface salts. The four stages define the evolution of the chott evaporites as it desiccates from a freshwater flood sheet to desiccated salinities where small volumes of potash salts precipitate as thin efflorescent crusts and pore cements in uppermost parts of the saline mudflat. The four stages are (Bryant et al. 1994a): (1) initial flooding, (2) evaporative concentration of lake waters, (3) the movement of concentrated thin brine sheets over the playa surface as a result of wind action, and (4) total desiccation of the lake by September 1990, some 9 months after the initial flood to precipitate halite crusts with minor bittern cements.

Surface waters and seeps in the chott have a consistent Ca–SO_4–Cl rich and HCO_3–CO_3 poor chemistry, reflecting the recycling of older (Pleistocene – Cretaceous) marine evaporites within the catchment area. As the lake desiccates and shrinks, these waters concentrate to produce a Na–Mg–K–Cl–SO_4 continental brine with ionic proportions similar to those of modern seawater (Table 11.7). But the brine source is continental not marine, and the contribution from modern marine aerosols is minor (Drake et al. 2004). During desiccation, saturation of surface water was reached first with respect to gypsum and then with halite and ultimately with potash minerals. The total brine volume in the chott is $\approx 5 \times 10^9$ m^3 and average shallow subsurface salinity ≈330‰.

Pore brines tend to be more potash-rich on the western side of the Djerid playa, where the waters are more saline, while they are more sulphate-rich on the eastern side (Kbir-Ariguib et al. 2001). After complete desiccation, the main mineral phases in the crystal mush on the floor of the many saline pans across the surface of the chott are gypsum and halite. Ephemeral carnallite (not sylvite) is present mostly as pore fills in thin cm-scale cemented halite crusts, within small hematite-stained areas near the centre of the various pan depressions on the chott floor, especially on the western (sump) side of the chott (Fig. 11.22c). The carnallite redissolves with each new flood of the chott. Its mode of occurrence is typical of the hydrologically decoupled mode of salt crusts in many modern artesian fed playas and its preservation potential is very low. Such systems are not Quaternary analogs to any substantial ancient accumulation of bedded potash.

Large scale pumping and evaporation tests have been made in the chott depression (Garrett 1995). Over much of its extent the chott surface is sandy, (with a great deal of poikilotopic gypsum, including frequent large desert rose and lenticular crystals growing at or near the watertable). Such a relatively porous substrate allows high pumping rates, but limits the area in the chott suitable for solar ponds, as does the decoupled hydrology.

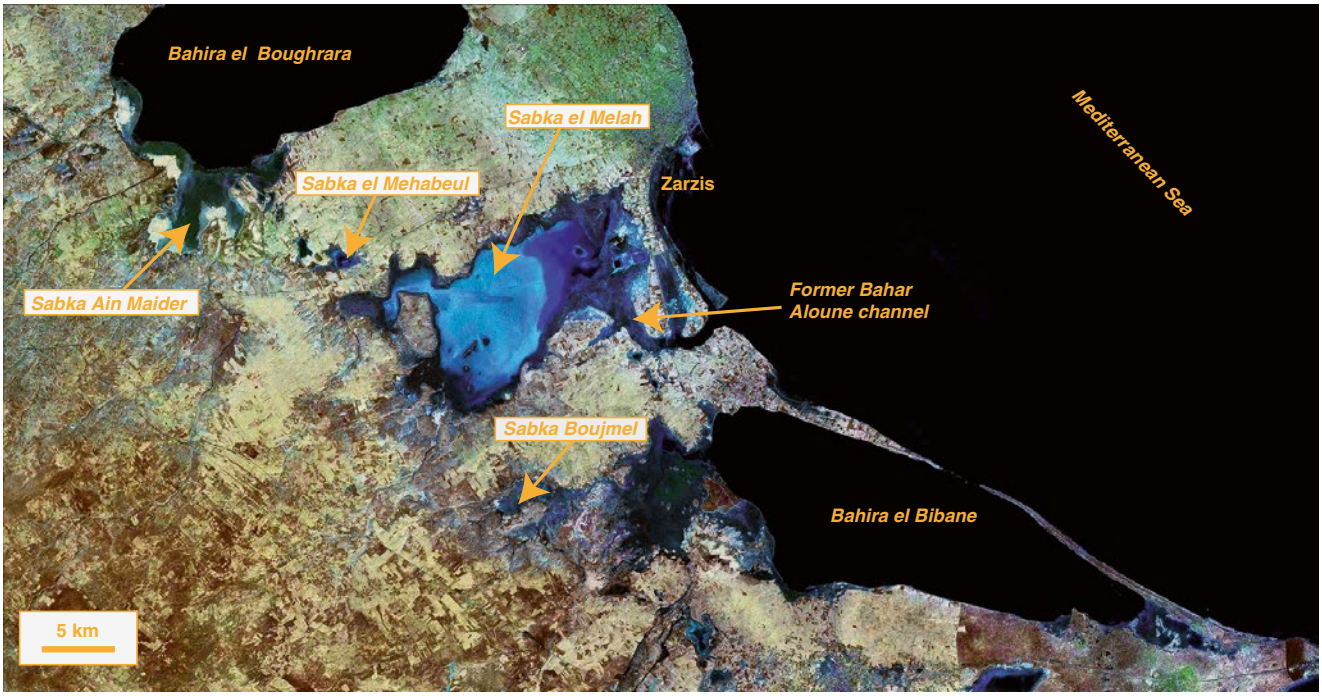

Fig. 11.24 Region of coastal sabkhas on the Tunisian coast near the town of Zarzis (Image base courtesy of NASA)

Sabkhat om Khialate with an area of 75 km^2 is another area of minor potash precipitation, once again as carnallite, not sylvite. It a small sabkha depression in the interior desert, well inland of the coastal plain and south of the coastal Sabkhat el Melah (Fig. 11.22a). Fed by continental waters, it is covered by a thin ephemeral salt crust a few decimetres thick, which contains a mixture of halite, gypsum, and thenardite (Na_2SO_4). Further toward the pan margin are thin efflorescent crusts made up almost solely of powdery thenardite with minute amounts of carnallite as a capillary precipitate.

Yet another modern area of ephemeral carnallite formation in North Africa is the near-coastal mudflats of Sabkha el Melah and the smaller nearby Sabkha el Mehabeul (Fig. 11.24; Perthuisot 1975; Garrett 1995). Both mudflats are situated on the northern edge of the Djeffara coastal plain near the town of Zarzis, Tunisia. Sabkha el Mehabeul is the more isolated of the Tunisian sabkhas; today it is a continental endorheic depression and has not been hydrographically connected to the nearby Mediterranean since the Late Pleistocene (Trabelsi et al. 2012). It retains preserved carnallite and kieserite interstitial cements in thin halite layers deposited in the last 2,000 years, along with minor occurrences of magnesite and huntite (Stengele and Smykatz-Kloss 1995; Schulz et al. 2002).

The larger Sabkha el Melah lies behind the coastal town of Zarzis and occasionally is hydrographically reconnected to the open sea by a channel that opens in times of flooding and turbulent seas (Fig. 11.24). The Holocene gypsum section beneath Sabkha el Melah is up 20 m thick and has been deposited in the last 4,000 years (Perthuisot et al. 1972; Lakhdar et al. 2006). Where freshened waters flow and seep as springs into the salt flat, typically near the sabkha edge, there are 6–8 m wide dissolution holes in the surface (moat facies). Wind action, in combination with ongoing gypsum intrasediment growth, has exposed large gypsum prisms and lenses in a deflationary crystal lag across much of the sabkha surface.

Sabkha el Melah was operated for bromine production during World War I, but no potash was recovered from their solar evaporation ponds. Brine was pumped from at least four of the larger springs into pans constructed on the sabkha surface. Garrett (1995) estimates the sabkha sediments down to about 10 m contain brines holding five million tons of equivalent KCl. However, like other sabkhas worldwide, permeabilities are inherently low and recovering the brine would be difficult. Phreatic brines in these coastal sabkhat are homogeneous and contain elevated magnesium and sulphate indicative of their marine source (Table 11.7).

Capillary evaporites in Djerid and the various coastal sabkhas are concentrically zoned within the uppermost few tens of cm of sediment beneath the ephemeral sabkha salt crusts. In all, the bittern salts only precipitate in the uppermost 0.5 m of sump sediments, via the processes of lateral capillary fractionation. Zonation is more evident in Sabkha el Melah where gypsum and anhydrite occur at the rim of the sabkha depression, while increasing amounts of halite with bitterns occurring in and beneath ephemeral crusts towards the centres (sumps) of local ephemeral saline pan depressions across the sabkha surface.

Traces of thenardite and carnallite can occur in the shallow subsurface sediments in the centres of some pans on the Melah sabkha (down to depths of a few tens of cm below the surface), but only in the innermost and lowermost sump zones of the saline pan facies. Polyhalite also occurs in the Sabkha el Melah sediments and, like similar occurrences in Ojo de Liebre Lagoon, Mexico, forms as a replacement of gypsum under the influence of increasingly saline capillary pore water (Perthuisot 1975; Pierre 1985).

The hydrographic separation of the Sabkha el Mehabeul from the ocean and Sabkha el Melah since the late Pleistocene has enabled a more advanced stage of diagenetic maturity and pore brine evolution in its sabkha fill. Anhydrite dominates over gypsum across the sabkha and the concentric zonation of the pan minerals into local depressions is much less obvious than the less saline Sabkha el Melah. Notably, in both these coastal sabkhas, carnallite, is no more than a minor mineral phase, is found co-associated with sulphate salts. All the bittern salts are dominantly part of powdery efflorescent crust salts.

To date, there has been no economic recovery of potash from saline brines held in marine coastal salt flats. This may be about to change. There are plans to develop a coastal brine recovery plant using brine held in coastal salt flats at Bayovar, Peru. Located in the coastal sandflats of the Sechura Desert (BWh climate). There the shallow coastal sediments are estimated to contain some 20 million tons of equivalent KCl, as a 0.1–0.8 % KCl brine (Garrett 1995). The higher grade reserves (0.4–0.8 % KCl) are estimated to be about half of the total reserves. Ample flat areas for the construction of solar ponds are available, but much of the shallow subsurface is quite permeable, or has many sandy beach berms zones. In mid 2012 a series of test brine wells are been pump-tested to ascertain the hydrological feasibility of potash production in a series of purpose-constructed lined pans.

The Bayovar project is unusual, and a lack of preserved bedded potash in all natural modern marine-fed depressions characterises Holocene coastal sabkhas and salinas, worldwide. Clearly, in terms of a marine-fed bedded potash deposits, the world's present day arid coastal sabkha and salina settings constitute a poor key to understanding widespread thick-bedded marine potash accumulations of the past. This relates to the fact we live in a time of icehouse earth, also lacking contemporaneous tectonically-induced saline giants.

Potash from Brine

There is no economic production from a Quaternary potash source by conventional mining anywhere in the world, rather potash is produced by brine processing in modern solar evaporation pans sourced in various saline continental lakes and playas. The world's largest Quaternary brine factories for MOP currently located at the southern end of the Dead Sea, Israel and Jordan, with a smaller MOP operation in the Dabuxum Lake area of the Qaidam Basin, China (Fig. 11.12). All locations utilise brines that are calcium-chloride rich and ultimately derived from hydrothermally-dominated inflows. These waters are pumped into solar concentrator brine pans, with a carnallitite slurry as the desired product. An even larger set of surface ponds than those of the southern Dead Sea have recently constructed for SOP production in Lop Nur region, China.

As mentioned earlier, a mother brine feed to a solar pan designed to precipitate potash salts can also be extracted by solution mining of potash horizons some hundreds of metres below the surface, as it is in operations near Moab, USA, and in the Belle-Plaine operation near Regina, Canada where a brine is recovered from the Prairie potash at a depth of 1,800 m. Often, such deep-sourced solution recovery exploits potash source beds not suitable for extractive mining due to great depth, structural complexity or propensity for water flood in a precursor conventional mine. The latter was the case at Patience Lake Mine in Saskatchewan, Canada, where two floods in the mid 1980s closed down the conventional mine operation. The former underground mine workings were abandoned and allowed to fill with water so that in 1988 the operation converted to a solution mining/brine recovery setup. Likewise, adverse mining conditions in the former Cane Creek mine led to a decision in 1970 to intentionally flood the mine and convert the subsurface operation into a solution-brine feed, sourcing saline waters for a series of at-surface purpose-built solar evaporation pans.

Dead Sea Potash, Middle East

Whatever the brine source, in order to recover potash once suitable brine is at the surface, it must be subjected to varying combinations of mechanical crystallization, natural crystallization (solar evaporation) and flotation. In the Southern Basin of the Dead Sea a series of linked fractionation ponds have been built to concentrate Dead Sea brine to the carnallite stage (Fig. 11.25a). On the Israeli side this is done by the Dead Sea Works Ltd. (DSW), near Mt. Sedom, and by the Arab Potash Company (APC) at Ghor al Safi on the Jordanian side. In both brine fields, muriate of potash is extracted by processing carnallitite slurries, created by sequential evaporation in a series of linked, gravity-fed fractionation ponds. After slurry extraction the residual brine, with a density of 1.34 g/cc, is pumped back into the northern Dead Sea basin water mass.

The area of the concentration pans is more than 130 km^2, within the total area of 1,000 km^2 that is the Dead Sea floor. The first stage in the evaporation process is pumping of Dead Sea water into header ponds to the gravity-fed series of artificial fractionation pans that now cover the Southern

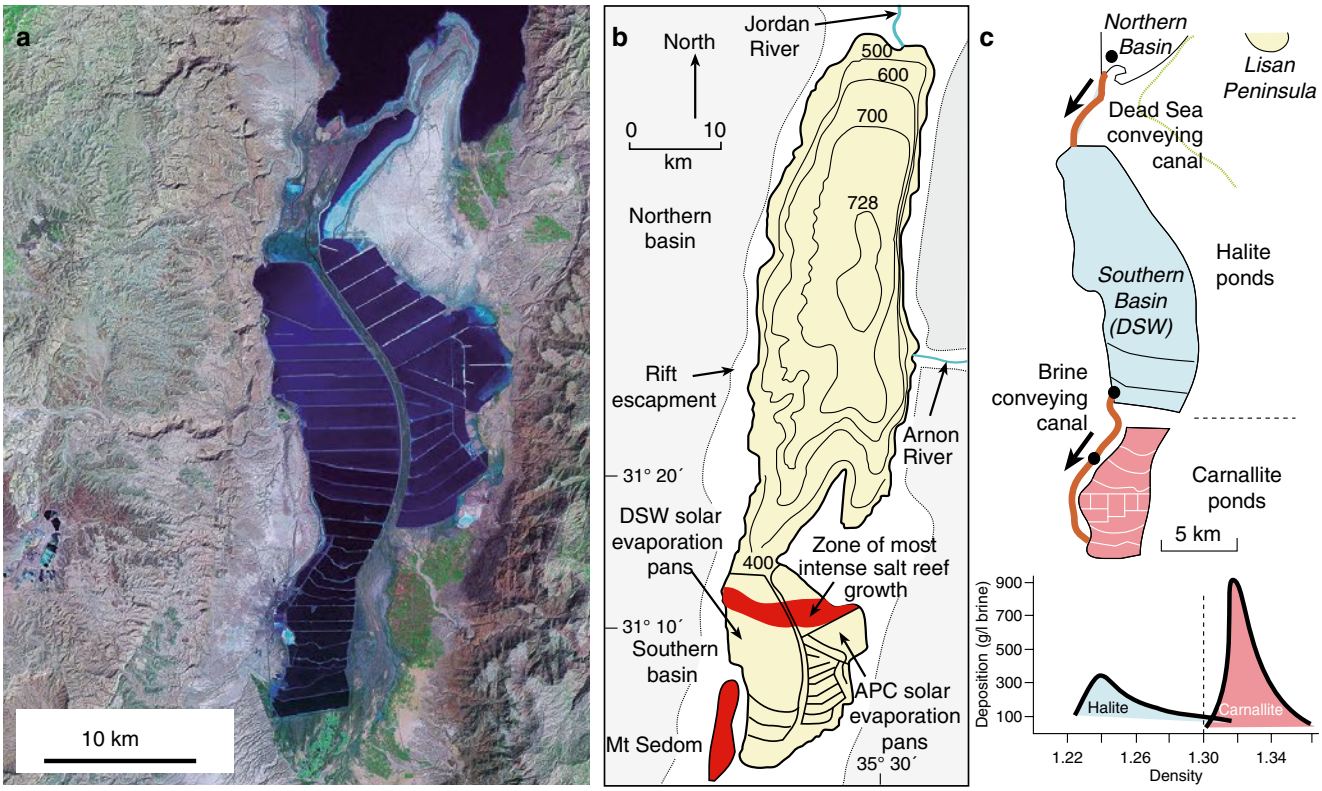

Fig. 11.25 Dead Sea Potash production. (a) Evaporation pans at the southern end of the Dead Sea (2000 Landsat image courtesy of NASA). (b) The water surface in the Dead Sea is around 417 m below sea level so the Southern Basin (elevation more than 401 m) is covered only by a thin controlled brine sheet up to 2 m deep, in a series of pans maintained by pumping of brines from the Northern Basin where waters attain depths of more than 300 m, seafloor isobaths are in metres below sea level. (c) Design of sequential evaporation pans at the Israeli Sedom plant, southern Basin of the Dead Sea colour coded to showing the relationship between increasing concentration (density) and the transition from halite to carnallite precipitation. ponds and the associated brine densities (After Karcz and Zak 1987)

Basin floor. With the ongoing fall of the Dead Sea water level over the past 60 years, brines from the Northern Basin must be pumped higher and over further lateral distances, resulting in a ongoing need for more powerful brine pumps. Saturation stages of the evolving brines are monitored and waters are moved from pan to pan as they are subject to the ongoing and intense levels of natural solar evaporation (Fig. 11.25b, c; Karcz and Zak 1987).

The artificial salt ponds of the Dead Sea are unusual in that they are designed to trap and discard most of the halite precipitate rather than harvest it. Most other artificial salt ponds around the world are shallow pans purpose-designed as ephemeral water-holding depressions that periodically dry out so that halite can be scrapped and harvested. In contrast, the Dead Sea halite ponds are purpose-designed to be permanently subaqueous and relatively deep (≈4 m). Brine levels in the ponds vary by a few decimetres during the year, and lowstand levels generally increase each winter when waste brine is pumped back into the northern basin.

As the Dead Sea brine thickens, minor gypsum, then voluminous halite precipitates on the pan floor in the upstream section of the concentration series, where the halite-precipitating-brines have densities >1.2 g/cc). As the concentrating brines approach carnallite precipitating densities (around 1.3 g/cc), they are allowed to flow into the carnallite precipitating ponds (Fig. 11.25c). Individual pans have areas around 6–8 km^2 and brine depths up to 2 m. During the early halite concentration stages a series of halite reefs or mushroom polygons can build to the brine surface and so compartmentalise and entrap brines within isolated pockets enclosed by the reefs, so preventing the orderly downstream progression of increasingly saline brines into the carnallite ponds, with the associated loss of product (Fig. 1.44).

When the plant was first designed the expectation was that halite would accumulate on the floor of the early fractionation ponds as horizontal beds and crusts, beneath permanent holomictic brine layers. The expected volume of salt was deposited in the pans each year (Talbot et al. 1996), but instead of accumulating on a flat floor aggrading 15–20 cm each year, halite in some areas built large numbers of macroscopic mounded salt reefs (aka salt mushrooms). Then, instead of each brine lake being homogenized by wind shear across these large subaqueous ponds, the salt reefs separated

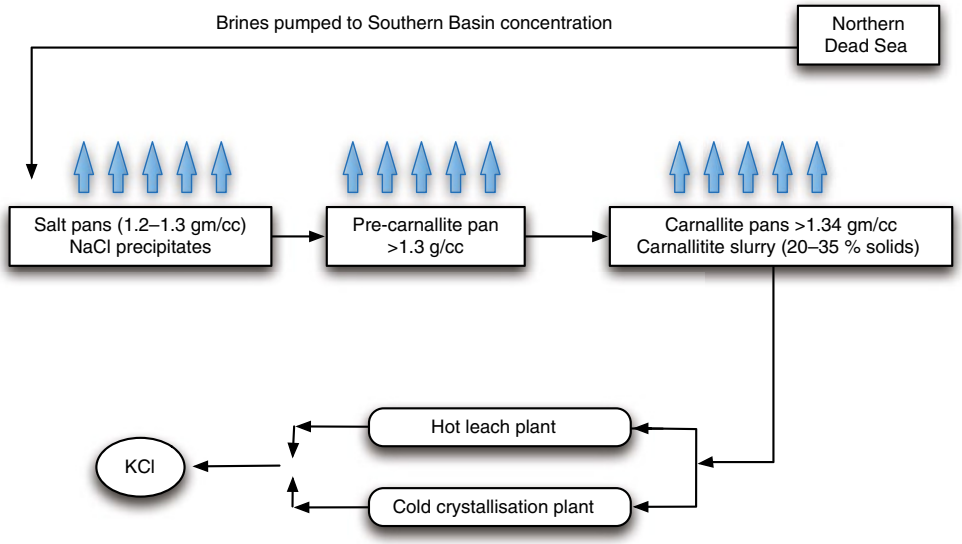

Fig. 11.26 Process stream for MOP manufacture in Dead Sea brine pans (*Blue arrows* indicate solar evaporation)

the larger early ponds into thousands of smaller polygonal compartments in which the isolated brines developed different compositions. Carnallitite slurries crystallized in inter-reef compartments from where it could not be easily harvested, so large volumes of potential product were locked up in the early fractionation ponds. Attempts to drown the reefs by maintaining freshened waters in the ponds during the winters of 1984 and 1985 were only partly successful. The current approach to the salt reef problem in the early fractionation ponds is to periodically breakup and remove the halite reefs and mushrooms by a combination of dredging and occasional blasting.

Unlike seawater feeds to conventional marine coastal saltworks producing halite with marine inflow salinities ≈35‰, the inflow brine pumped into the header ponds from the Dead Sea already has a salinity of more than 300‰. Massive halite precipitation occurs quickly, once the brine attains a density of 1.235 (≈340‰) and reaches a maximum at a density of 1.24 (Fig. 11.25c). Evaporation is allowed to continue in the initial halite concentrator ponds until the original water volume pumped into the pond has been halved. Concentrated halite-depleted brine is then pumped through a conveyance canal into a series of smaller evaporation ponds where carnallite, along with minor halite and gypsum precipitates (Fig. 11.25b). Around 300–400 mm of carnallite salt slurry is allowed to accumulate in the carnallite ponds, with 84 % pure carnallite and 16 % sodium chloride as the average chemical composition (Fig. 11.26; Abu-Hamatteh and Al-Amr 2008). The carnallite bed is harvested (pumped) from beneath the brine in slurry form and is delivered through corrosion-resistant steel pipes to the process refineries via a series of powerful pumps.

This carnallitite slurry is harvested using purpose-specific dredges floating across the crystalliser ponds. These dredges not only pump the slurry to the processing plant but also undertake the early part of the processing stream. On the dredge, harvested slurry is crushed, size sorted, with the coarser purer crystals separated for cold crystallization. The remainder is slurried with the residual pan brine and then further filtered aboard the floating dredges. At this stage in the processing stream the dredges pipe the treated slurries from the pans to the refining plant. On arrival at the processing plant, this raw product is then used to manufacture muriate of potash, salt, magnesium chloride, magnesium oxide, hydrochloric acid, bath salts, chlorine, caustic soda and magnesium metal. Residual brine after carnallitite precipitation contain about 11–12 g/l bromide and is used for the production of bromine, before the waste brine (with a density around 1.34 g/cc) is returned to the northern Dead Sea water mass. Israeli potash production currently exceeds 1.9 million tonnes per year while Jordanian production is more than a 1.7 tonnes per year. The production process continues 24 h a day, 365 days a year. The entire cycle from the harvesting to the MOP production takes as little as 5 h.

In the initial years of both DSW and APC operations, MOP was originally refined from the carnallite slurry by hot leaching and/or flotation. In the coarser-crystalline carnallitite feed, significant volumes of sylvite are now produced more economically in a cold crystallization plant (Fig. 11.26). The cold crystallization process takes place at ambient temperature and is less energy-intensive than the hot crystallization unit. The process also consumes less water but requires a higher and more consistent grade of carnallite feed (Mansour and Takrouri 2007; Abu-Hamatteh and Al-Amr 2008). Both hot (thermal) and cold production methods can be utilized in either plant, depending on the quality of the slurry feed.

Sylvite is produced via cold crystallization using the addition of water to incongruently dissolve the magnesium

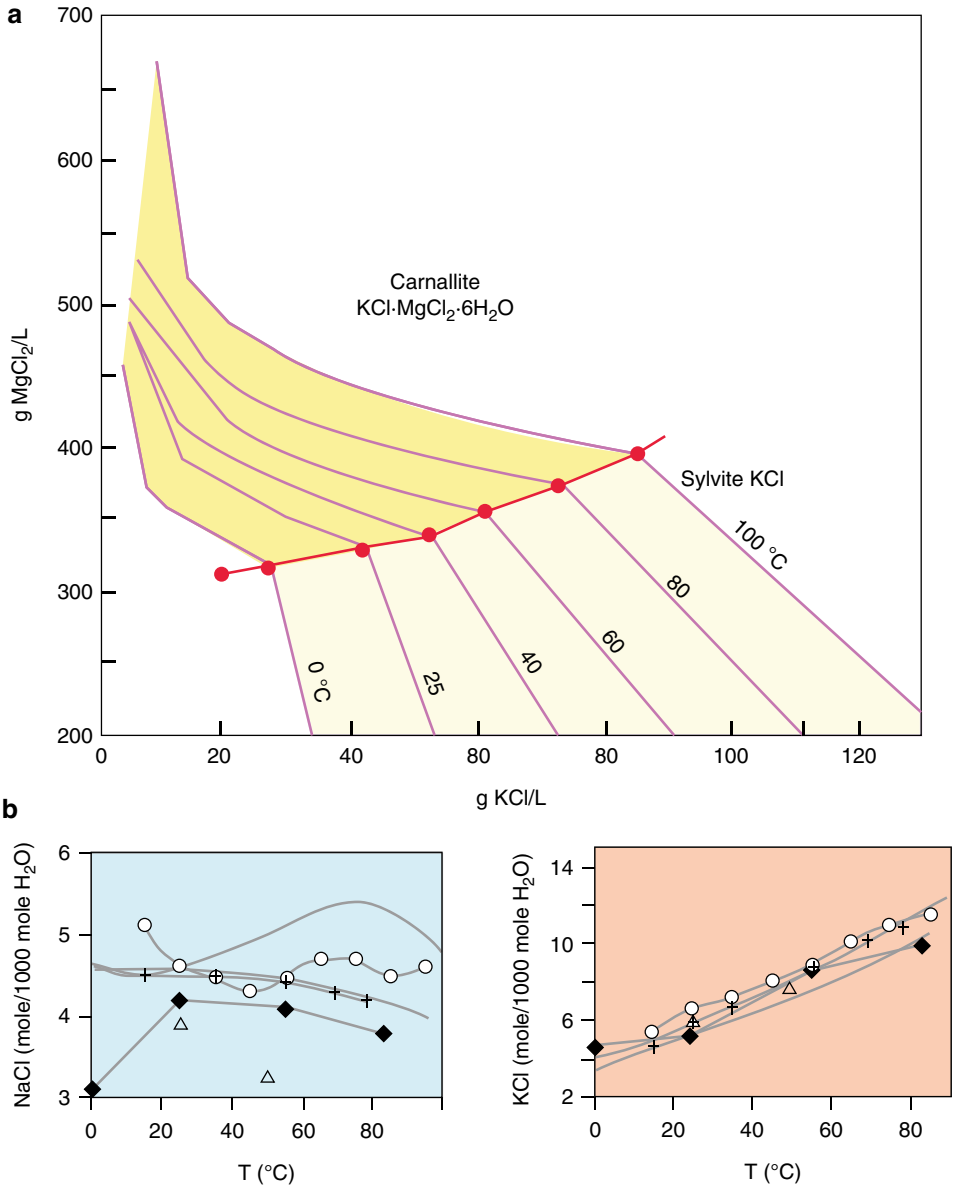

Fig. 11.27 Dead Sea potash production chemistries. (**a**) Cold Crystallization based on incongruent dissolution and illustrated by carnallite/KCl curve in the presence of 3 % NaCl (After Mansour and Takrouri 2007). (**b**) Hot or thermal crystallization is based on fact that halite solubility does not change greatly with temperature, while KCl solubility trebles over the same range (After Karcz and Zak 1987)

chloride from the crystal structure. If the carnallite slurry contains only a small amount of halite, the solid residue that remains after water flushing is mostly sylvite. As is shown in Fig. 11.27a, if the $MgCl_2$ concentration is at or near the triple-saturation point (the point at which the solution is saturated with carnallite, NaCl, and KCl), the KCl solubility is suppressed to the point where most of it will precipitate as sylvite. For maximum recovery, the crystallizing mixture must be saturated with carnallite at its triple-saturation point. If the mixture is not saturated, for example, it contains higher levels of NaCl, then more KCl will dissolve during the water flushing of the slurry. Industrially, the cold crystallizers are usually fed with both coarse and fine carnallite streams, such that 10 % carnallite remains in the slurry, this can be achieved by adjusting addition of process water (Mansour and Takrouri 2007).

Successful cold crystallization depends largely on a high quality carnallite feed. If a large amount of halite is present in the feed slurry, the resulting solid residue from cold crystallization is sylvinite, not sylvite. This needs to be further refined by hot crystallization, a more expensive extraction method based on the fact that the solubility of sylvite varies greatly with increasing temperature, while that of salt remains relatively constant (Fig. 11.27b). As potash brine is hot leached from the sylvinite, the remaining halite is filtered off, and the brine is cooled under controlled conditions to yield sylvite.

Residual brine from the crystallization processes then undergoes electrolysis to yield chlorine, caustic soda and hydrogen. Chlorine is then reacted with brine filtered from the pans to produce bromine. The caustic soda is sold, and the hydrogen is used to make bromine compounds, with the

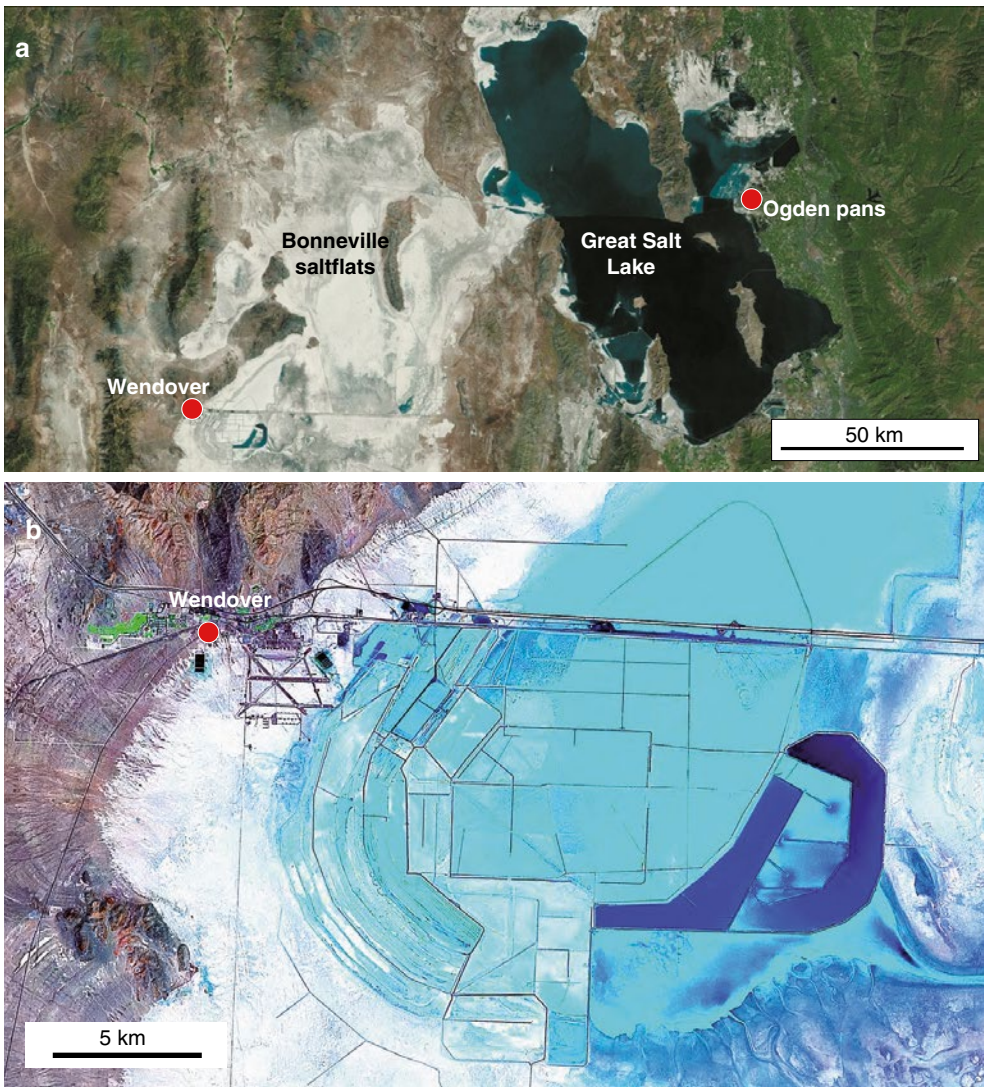

Fig. 11.28 (a) Regional map showing relative positions of Wendover (MOP) and Great Salt Lake (SOP) operations, Utah (b) Intrepid Mining's Wendover potash facility located in a drainage sump on the eastern edge of the Bonneville Salt flat, south of Interstate 80 and southeast of the town of Westover, Utah (Images courtesy of NASA and Microsoft Bing® mounted in MapInfo)

excess being burnt as fuel. Bromine distilled from the brine is sold partly as elemental bromine, and partly in the form of bromine compounds produced in the bromine plant at Ramat Hovav (near Beer Sheva). This is the largest bromine plant in the world, and Israel is the main exporter of bromine to Europe. About 200,000 t of bromine are produced each year. Residual magnesium chloride-rich solutions created by cold crystallization are concentrated and sold as flakes for use in the chemical industry and for de-icing (about 100,000 t per year) and dirt road dedusting. Part of the $MgCl_2$ solution produced is sold to the nearby Dead Sea Periclase plant (a subsidiary of Israel Chemicals Ltd.). At this plant the brine is decomposed thermally to give an extremely pure magnesium oxide (periclase) and hydrochloric acid.

In Israel, Dead Sea Salt Work's (DSW) production has risen to more than 2.9 Mt KCl since 2005, continuing a series of increments and reflecting and investment in expanded capacity, the streamlining of product throughput in the mill facilities, and the amelioration of the effects of salt mushrooms, and increased salinity of the Dead Sea due to extended drought conditions. On the other side of the truce line in Jordan, the Arab Potash Co. Ltd. (APC) output rose to 1.94 Mt KCl in 2010 (Fig. 11.2a). APC also has to remove salt mushrooms from its ponds, a process which when completed can increase carnallite output by over 50 000 t/year. The company is continuing with an expansion program aimed at increasing potash capacity to 2.5 Mt/year.

Potash from Solution Recovery Brine in Utah, USA

Potash extraction via solar pan concentration in Utah takes place near Ogden on the eastern edge of Great Salt Lake, on the Bonneville Salt Flats near Wendover, and the Cane Creek salt pans, near the town of Moab (Figs. 11.28a and 11.30). The Wendover MOP facility spans a BWk and BWh climate zone (Fig. 11.28b). The facility, owned since 2004 by

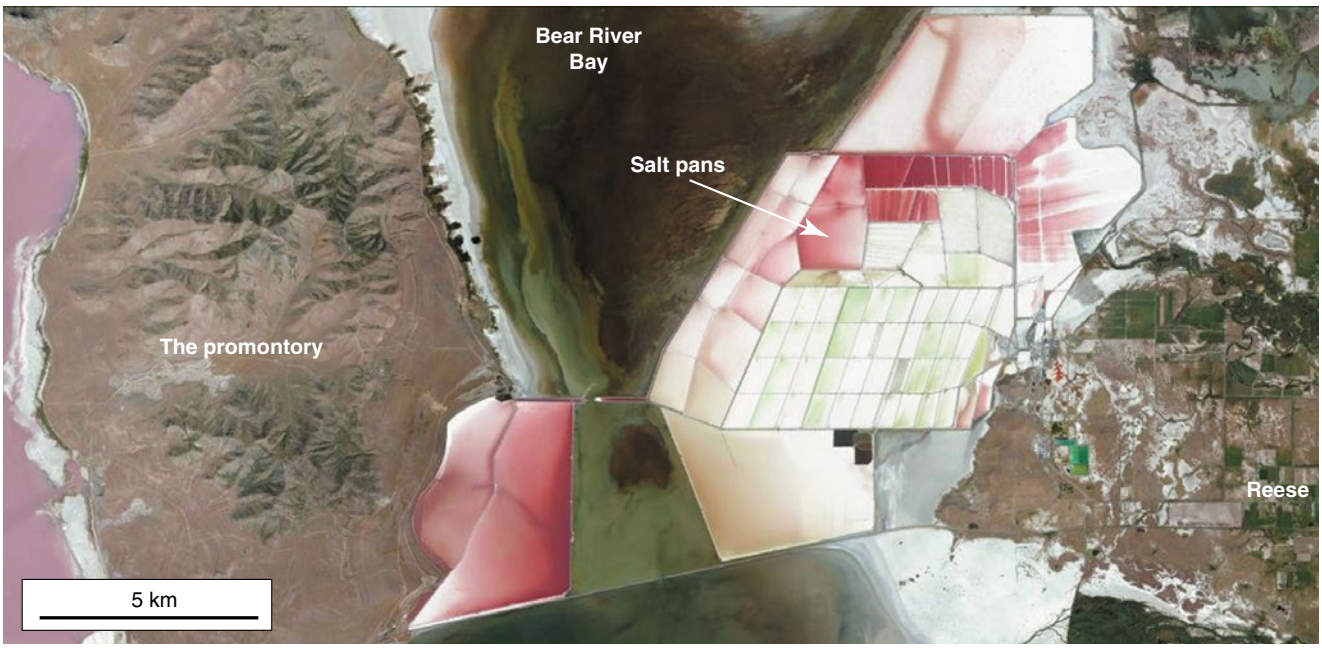

Fig. 11.29 Compass Mineral's SOP pans NE of Ogden, Utah on northeastern margin of Great Salt Lake (Microsoft Bing® image mounted and scaled in MapInfo®)

Intrepid Potash Inc., consists of a series of connected drainage ditches cut up to 2 m into the Bonneville saltflat. The saltflat occupies the western sump of a large playa located on the downdropped side of a Basin and Range boundary fault, which has more than 1,500 m of vertical displacement (Gwynn 2008; Turk 1973).

When the ditch water levels are pumped down, saltflat brines flow into the ditches as pore brines seep in from the adjacent saline lake sediments, driven by the artificially created brine head, which ranges from 1.6 to 4.5 m. Newly created ditch brine is then pumped from the collection ditches (made up of over 160 km of interconnected ditches across an area of more than 350 km^2) into concentrator ponds and allowed to season via solar evaporation. Once densities in the concentrators attain values in excess of 1.245 g/cc, they are then pumped into prepared evaporation/harvest ponds for KCl precipitation.

Sylvinite slurry, not carnallitite, is the precipitated salt in the harvest pond at Wendover (Bingham 1980). But the concentration process does not end with sylvite precipitation. Brine is pumped out of the sylvinite harvest pond into the adjacent carnallite ponds before the brine density attains values in excess of 1.257. This is the density that marks the onset of carnallite precipitation. Significantly, for the geological models of primary sylvite discussed later in this chapter, the Wendover facility is a brine fractionation system where sylvite crystallization precedes carnallite in the evaporation series.

The sylvite harvest ponds cover an area of some 3.2 km^2. Each sylvinite harvest concentrates more than 18 million cubic metres (5 billion gallons) of lake brine to make around 95,000 t of potash, making Wendover the largest single producer of potash in the United States. Once a sylvite harvesting pond is pumped down, the sylvinite mush is scrapped and transported to the processing plant for MOP manufacture via froth flotation and drying. The total period from ditch drawdown to harvest is around 180 days. Harvesting ponds are constructed with compacted floors and synthetic rubber liners. This prevents liquor loss during the seasoning cycle and allows conventional front end-loaders and scrapers to move across the sylvite-encrusted harvester pan floors, without sinking into water-saturated muddy sediments.

Prior to sylvite harvesting, residual brines are pumped into nearby carnallite ponds for further concentration and seasoning, resulting in highly concentrated brines that are then extracted and stored. These end brines in the carnallite ponds are very rich in $MgCl_2$ and are sold for use as a liquid de-icer.

The other Quaternary potash extractive facility in Utah is some 150 km from the Wendover facility and is operated by Compass Minerals (Fig. 11.28a). Brine ponds are located in two separate pond areas on the northwest and eastern shores of Great Salt Lake near Ogden, Utah and joined by a channel/levee system. Brines pumped in from Great Salt Lake are concentrated across more than 160 km^2 of ponds within a total area of some 4,100 km^2 (Fig. 11.29). Unlike Wendover, these brine ponds lie beneath a cooler Csa/Cfa Köppen climate zone, have much higher levels of sulphate in their brine feed, and utilise a seasonal brine chemistry that manufactures halite via solar evaporation in the summer and SOP from cryogenic brines in the winter.

During normal summer conditions, 90 % of the halite present in the brine is precipitated in the fractionation ponds with little contamination by other salts and it is harvested from the ponds for use mostly as de-iceing salt. Mirabilite can be a winter precipitate in the solar ponds that contain brine from ponds which had earlier precipitated halite. Once potassium salts begin to precipitate from the halite-depleted brine, it forms a complex mixture of double salts, such as kainite, schoenite and carnallite. At the same time magnesium can precipitate as bischofite, a highly hydrated magnesium chloride (Fig. 11.8). This salt sequence chemistry is one of the more complicated solar pond series of naturally-produced industrial salts in the world. Throughout the production phase of the various salts, ambient ionic compositions are monitored and brines are pumped and mixed from the various fractionation pans to maximise the production of both halite and potash salts. Ultimately the plant produces the following end products; sodium chloride, potassium sulphate, sodium sulphate and magnesium chloride hexahydrate.

Natural brines pumped into the pans from the Great Salt Lake are allowed to evaporate in a set of halite ponds until saturated with potassium salts. The residual brine is then transferred to a mixing pond where it is mixed with a second brine (from higher up the evaporation series, which contains a higher molar ratio of magnesium to potassium. This adjusted brine is allowed to evaporate to precipitate sodium chloride once more, until it is again saturated with respect to potassium salts. The brine is then transferred to another pond, is further evaporated and precipitates kainite (Fig. 11.8). Kainite precipitation continues until carnallite begins to form, at which time the brine is transferred to another pond and is allowed to evaporate further to precipitate carnallite. Some of the kainite-depleted brine is recycled to the mixing pond to maintain the required molar ratio of magnesium to calcium in the mixing pond. Once carnallite has precipitated, the residual brine is transferred to deep storage and subjected to winter cooling to precipitate additional carnallite. Cryogenically precipitated carnallite is converted to kainite by mixing it with a kainite-saturated brine.

Formerly, the salt solids were harvested from the Great Salt Lake pans using front-end loaders and trucks, similar to the Wendover facility, and transported to the processing plants (Fig. 11.8). More recently, the Behrens Trench was completed, this is a 35 km underwater canal on the floor of the Great Salt Lake that transports saturated brine product from the western shore solar ponds across the lake to its processing facilities on the eastern shore. Since 2000 the Great Salt Lake plant has produced more that 550,000 t of sulphate of potash. But, the earlier history of salt workings about the strandline of Great Salt Lake illustrate one of the major problems in solar pond extraction atop saline mudflats in continental lakes. Record floods in 1984 filled the solar ponds with fresh water and destroyed much of the levee infrastructure. Harvesting did not recommence until the early 1990s. Rapid and at times substantial changes in lake level are endemic to saline lacustrine systems and must be planned for in the development of a saltworks.

Fig. 11.30 Intrepid's Moab Potash Operation, Utah. Brines are pumped from the flooded workings of the former Cane Creek Potash Mine into the Moab solar pans, where they concentrate to sylvite saturation (Base image is courtesy of Microsoft Bing®)

Potash is also produced by evaporative concentration of solution-mined brine extracted from Pennsylvanian potash evaporites in the Paradox member of the Hermosa Formation in the now flooded Cane Creek mine, locate in an anticline in the northern part of the Paradox Basin in Utah near the town of Moab (Figs. 11.30) There are at least 29 evaporite cycles in the Hermosa Formation, which is dominated by varying combinations of limestone, dolomite, anhydrite and halite. Potash occurs near the top of 18 of these cycles, all located immediately above a thick halite bed (Raup 1966). Eleven of the 18 are of sufficient thickness and quality to be considered economic. Salt beds in the halokinetic Cane Creek anticlinal core are characterised by numerous folds discontinuities and faults, which can deepen, thicken or thin, and rotate the potash seam and alter the continuity of beds in the mine head (Fig. 11.31) The target potash bed, known as Bed 5, is a 3.4 m-thick sylvinite bed some 1,200 m below the surface in

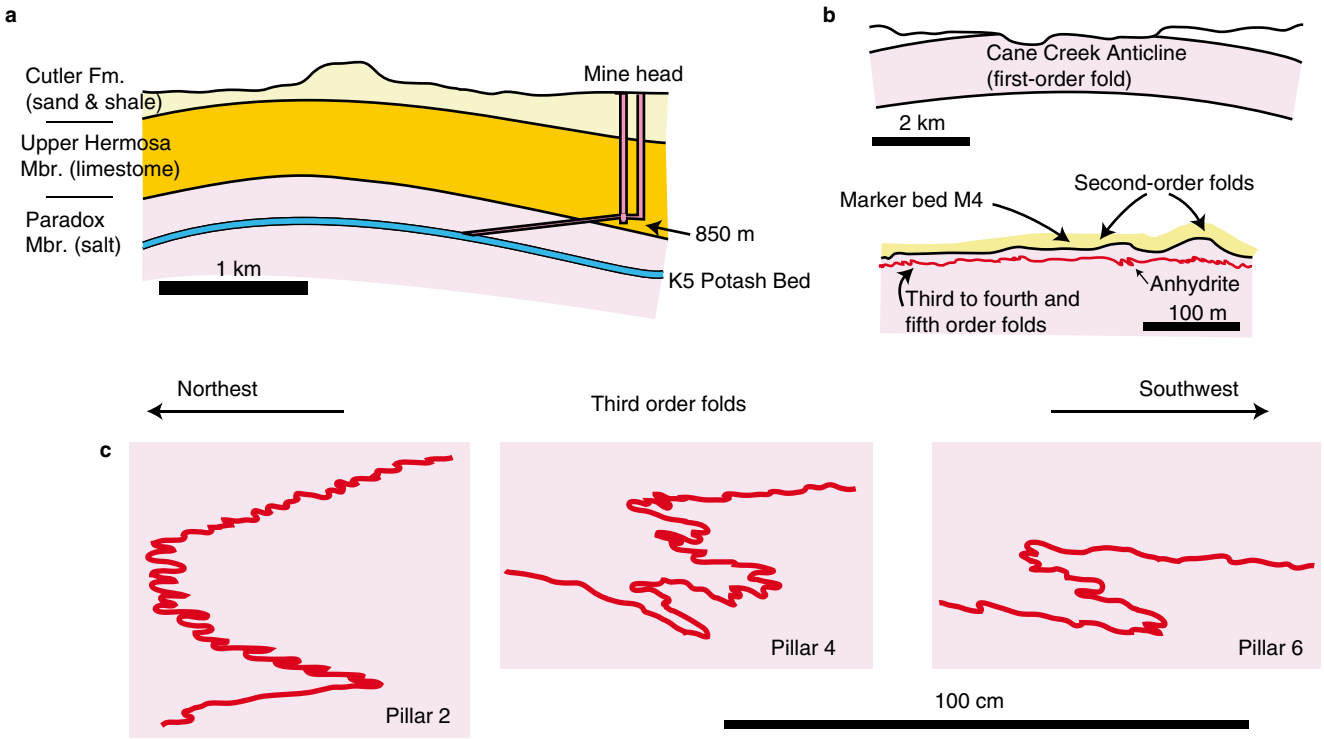

Fig. 11.31 Structural complexity in the original Cane Creek potash mine pillars before conversion to a solution feed operation (After Evans and Linn 1970). (**a**) Cane Creek stratigraphy and mine position on the anticline limb. (**b**) Fold orders in the ore zone of the Cane Creek Anticline. (**c**) Folds in anhydrite in the ore zone

the mine area and averaging 25–30 % K_2O. The depth to ore and its folded nature meant working conditions underground were difficult with mine temperatures around 35 °C or higher (Doelling and Chidsey 2000; Gwynn 1984).

The former Cane Creek mine, which began extracting ore in 1965, was never economically viable due to a combination of gassy bottom and the high degree of deformation of the target ore horizon. The target, Potash Bed K5, consists of variably dipping sylvinite layers 2.5–15 cm thick, alternating with folded anhydrite layers less than 3 mm thick. The ore horizon is overlain by 12 m of shaly dolomite and underlain by 43 m of halite. Fold wavelengths exposed in mine pillars are ≈30–120 m, with amplitudes ranging from 6 to 30 m (Fig. 11.31; Evans and Linn 1970). By 1963 some 550 km of 2.7×4.9 m rooms and entries had been completed. As well as the problems with structural complexity, a number of dangerous "gassy" intersections had occurred during the short operational life of the mine. On 28 August, 1963, 18 miners were tragically killed by a methane explosion, while constructing lateral access shafts. This calamity meant the mine was too dangerous to mine conventionally and the decision was made to convert to a solution mine.

The Moab Utah brine extraction operation began in 1972, after the conventional mine was abandoned in 1970, flooded and converted to the current solution-mined evaporation-processed operation. Colorado River water is now pumped through injection wells into the old mine workings to dissolve the potash and salt. The resulting dense brine is pumped out of sumps in the mine and piped to nearby solar evaporation ponds where the minerals are eventually harvested (Fig. 11.30).

It takes 2 years of brine seasoning in the Moab solar ponds under a BSk climate to make a potash crop. Evaporation proceeds to the point where halite drops out and the remaining potash-enriched brines are successively moved into the harvester ponds. A blue dye is added to some of the ponds to enhance solar absorption/evaporation and this makes the view from the site overview popular with photographers. There are 23 ponds, up to a metre deep, in four areas covering a total pan area in excess of 1.6 km^2 (Kogel et al. 2006). A sylvinite mixture forms in the final ponds and is harvested once a year per pond. The slurry is pumped north to the processing facility where the halite is separated from the potash by flotation. If the product cannot be harvested within 2 years the operational cycle becomes uneconomic. Potash production is roughly 60,000 t annually and around 200,000 t of halite are produced annually as a by-product.

Solution mining for potash is also profitable in other mines lost to flooding, as in Canada, where solution mining operations have been active in the abandoned Patience Lake Mine since 1988. The solution recovery process of PotashCorp in Patience Lake, Saskatchewan, uses a selective precipitation process that takes advantage of natural cooling (Kogel et al. 2006; p 735). One large final precipitation pond operates from September through May and produces around

0.4 million tonnes per year. As warm brine from the mine flows into the pond, only sylvite crystallizes on exposure to the cold winter air. Then the pond is dredged and the precipitated sylvite is dried for marketing. The process is predicated on the differing temperature dependence of NaCl and KCl solubilities (Fig. 11.27b).

Another method of potash recovery is used by the Mosaic Potash Company in Belle Plaine, Saskatchewan. This operation began in 1964 and was the world's first purpose-built solution mine operation. With an ore depth of 1,600 m it was too deep for a conventional mine. There the brine is processed using two trains of evaporators and crystallizers. Evaporators remove NaCl from the brine and KCl precipitates in the crystallizers. Annual production is 2.8 million tonnes per year. This process is more energy intensive than recovery by natural winter cooling in surface ponds.

Potash mining or recovery from brine is a possible technology of the future in areas where the potash has an $MgSO_4$ association, such as the eastern end Salt Range of Pakistan, where at a depth of 1,300 m a potash brine was recovered in a well. It is perhaps a relict bittern, first derived during deposition of the marine-fed halite beds and retained (Gill and Akhtar 1982). According to Garrett (1995) there are perhaps ten stacked potash beds within the 75 m thick upper salt formation of the Saline Series (Eocene) in the Salt Range, of the Punjab region, Pakistan. There are indications that the potash layers extend under much of the Salt Range and parts of the Potwar and Indus Plains. Drilling and salt mining operations show that the potash zones tend to be patchily distributed, occurring as lenses or beds up to 4 m thick. Kainite and langbeinite (combined) may total 80 % of the potash in some areas, with sylvite and smaller amounts of polyhalite. Astrakanite, epsomite and kieserite have also been reported. Volcanic rocks occur in the upper part of the saline series. Samples of the potash from Klewra and Nupur regions analyzed 10–14 % K_2O, 20–24 % $MgSO_4$ and 23–55 % NaCl (Garrett 1995).

Mineralogically similar, very thick, halokinetic halite deposits of Miocene age occur under the Red Sea's coastal plain between Jizan, Saudi Arabia (where they outcrop) to Safaga, Egypt, and limited potash beds have been found in some locations (Notholt 1983; Garrett 1995). Potash-enriched marine end-liquor brines characterise Red Sea geothermal springs, implying a more sizeable potash deposit may be (or once have been) present in this region. Hite and Wassef (1983) argue gamma ray logs in two drill holes in this area suggest the presence of sylvite, carnallite and possibly langbeinite.

Sulphate of Potash from Brine

Sulphate of potash is an attractive product as it does not salinise the soils as readily as muriate of potash. We have already seen how it is produced from the Ogden flats, and other continental brine lake settings. The most significant lake brine production volume comes from Lop Nur, China.

Lop Nur

Sulphate of potash (SOP) via brine processing (solution mining) of lake sediments and brines is currently underway in the Luobei Hollow region of the Lop Nur playa, in the southeastern part of Xinjiang Province, Western China (Fig. 11.32, Table 11.2). The recoverable sulphate of potash resource is estimated to be 36 million tonnes from lake brine (Dong et al. 2012). Lop Nur is in the eastern part of the Taklimakan Desert, China's largest and driest desert, and is in the drainage sump of the basin, some 780 m above sea

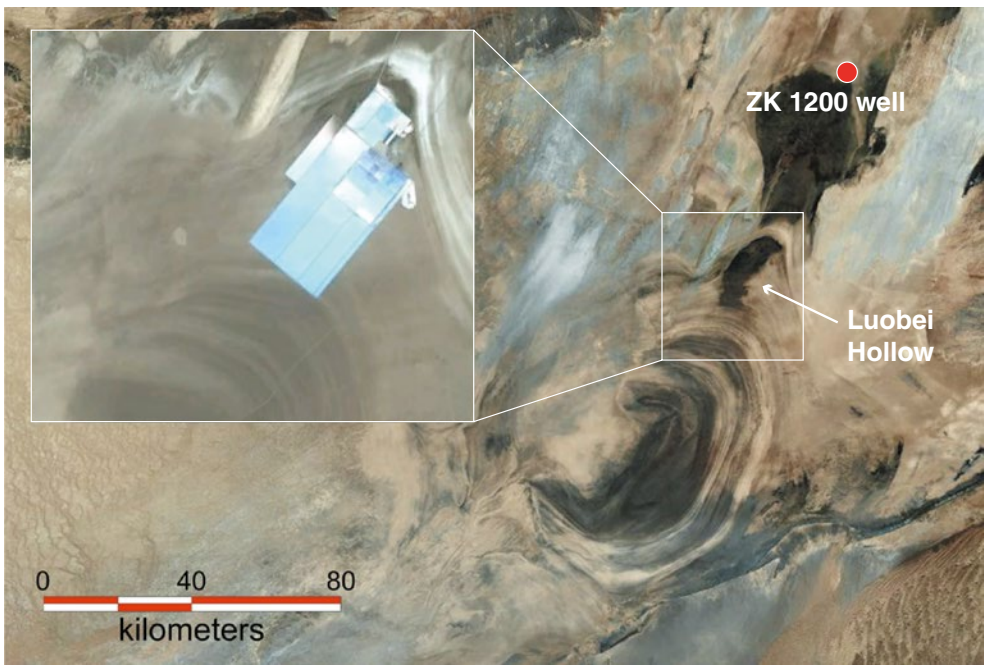

Fig. 11.32 Lop Nur playa (aka "great ear" region) eastern Tarim Basin, China before the construction of the sulphate of potash (SOP) facility. The concentric ring structure of the playa is created by successive strandline positions as the lake shrank. Inset shows the region of the SOP facility (as of July 2011) in the fault-bound Luobei sub-depression (Images courtesy of Google Earth and Bing® images, loaded into MapInfo®)

level and in a BSk climate belt. The Lop Nur depression first formed in the early Quaternary, due to the extensional collapse of the eastern Tarim Platform and is surrounded and typically in fault contact with the Kuruktagh (to north), Bei Shan (to east) and Altun (to south) mountains.

The resulting Lop Nor sump is a large groundwater discharge playa that is the terminal point of China's largest endorheic drainage system, the Tarim Basin, which occupies an area of more than 530,000 km^2 (Ma et al. 2010). The playa is the hydrographic base level to local and regional groundwater and surface water flow systems, and thus collectively captures all river and subsurface flow originating in the surrounding mountainous regions. The region has been subject to ongoing Quaternary climate oscillations, resulting in concentric strandzones on the playa surface over the last few hundred years, and widespread longer term (thousands of years) changes driving deposition of saline glauberite-polyhalite deposits, alternating with more humid lacustrine mudstones.

Presently, the Lop Nur playa lacks a longterm surface inflow and is characterized by desiccated saline mudflats and polygonal salt crusts. The upward capillary flux from the shallow groundwater helps to maintain a high rate of evaporation in the depression and drives the formation of a metre-thick ephemeral halite crust that covers much of the depression. Historically, prior to the construction of widespread irrigation systems in the upstream portion of the various riverine feeds to the depression and the diversion of water into the Tarim-Kongqi-Qargan canal, brackish flood waters periodically accumulated in the Lop Nur depression. After the diversion in flow, the terminal desiccation led to the formation of the concentric shrinkage shorelines, that today outline the "Great Ear" region of the Tarim Basin (Huntington 1907; Chao et al. 2009).

Climate is extremely arid; average annual rainfall is less than 20 mm and the average potential evaporation rates are ≈3,500 mm/year (Ma et al. 2010). The mean annual air temperature is 11.6 °C; highest temperatures occur during July (>40 °C) and the lowest temperatures occur during January (<20 °C). Primary wind direction is NE. The Lop Nor basin experiences severe and frequent sandstorms; the region is well known for its wind-eroded features, including many meso-yardangs along the northern, western and eastern margins of the Lop Nur salt plain.

Salinity and chemical composition of modern groundwater brine varies little in the "Great Ear" area and appears not to have changed significantly over the last decade (Ma et al. 2010). Dominant river inflow waters to the Lop Nor basin are of the Na–Mg–Ca–SO_4–Cl–HCO_3 type. In contrast, the sump region is characterized by highly concentrated groundwater brines (≈350 mg/l) that are rich in Na and Cl, poor in Ca and HCO_3+CO_3, and contain considerable amounts of Mg, SO_4 and K, with pH ranging from 6.6 to 7.2. When concentrated, the brine is saturated with respect to halite, glauberite, thenardite, polyhalite and bloedite (Ma et al. 2010). Groundwater brines in the northern sub-depression, the Luobei region, where potash is produced in a series of concentrator pans, is similar in chemistry and salinity to the Great Ear area (Hu and Wang, 2001). There, K-rich mother brines, that also contain $MgSO_4$, occur in pores of a widespread subsurface glauberite bed, with a potassium content of 1.4 % (Liu et al. 2008). These are the source brines pumped in to a large field of concentrator pans to produce sulphate of potash (Fig. 11.32).

Brine chemical models, using current inflow water and groundwater brine chemistries and assuming an open system hydrology, show good agreement between theoretically predicted and observed minerals in upper parts of the Lop Nor basin succession (Ma et al. 2010). Such modeling does not explain the massive amounts of glauberite ($Na_2SO_4{\cdot}CaSO_4$) and polyhalite ($K_2SO_4MgSO_4{\cdot}2CaSO_4{\cdot}2H_2O$) recovered in a 230 m deep core (ZK1200B well) from the Lop Nor basin (Fig. 11.33). Hydrochemical simulations assuming a closed system at depth and allowing brine reactions with previously formed minerals imply that widespread glauberite in the basin formed via back reactions between brine, gypsum and anhydrite and that polyhalite formed by diagenetic reaction between brine and glauberite. Diagenetic textures related to recrystallization and secondary replacement are seen in ZK1200B core, they include gypsum-cored glauberite crystals and gypsum replacing glauberite. Such textures indicate significant mineral-brine interaction during crystallization of glauberite and polyhalite.

Mineral assemblages predicted from the evaporation of Tarim river water match closely with natural assemblages and abundances and, in combination with a model that allows widespread backreactions, can explain the extensive glauberite deposits in the Lop Nor basin (Ma et al. 2010). It seems that the Tarim river inflows, not upwelling hydrothermal brines, were the dominant source throughout the lake history and that layered distribution of minerals in the cored sediments documents the evolving history of inflow water response to wet and dry periods in the Lop Nor basin. The occurrence of abundant glauberite and gypsum below 40 m depth, and the absence of halite, polyhalite and bloedite in the same sediment suggests that the brine underwent incomplete evaporation in the wetter periods Fig. 11.33). In contrast, the increasing abundance of halite, polyhalite and bloedite in the top 40 m of core from the ZK1200B well indicate relatively dry periods, where halite precipitated at lower evaporative concentrations (log = 3.15), while polyhalite and bloedite precipitated at higher evaporative concentrations (log = 3.31 and 3.48 respectively). Following deposition of the more saline minerals the lake system once again became more humid, until the anthropogenically induced changes in the hydrology over the last few decades.

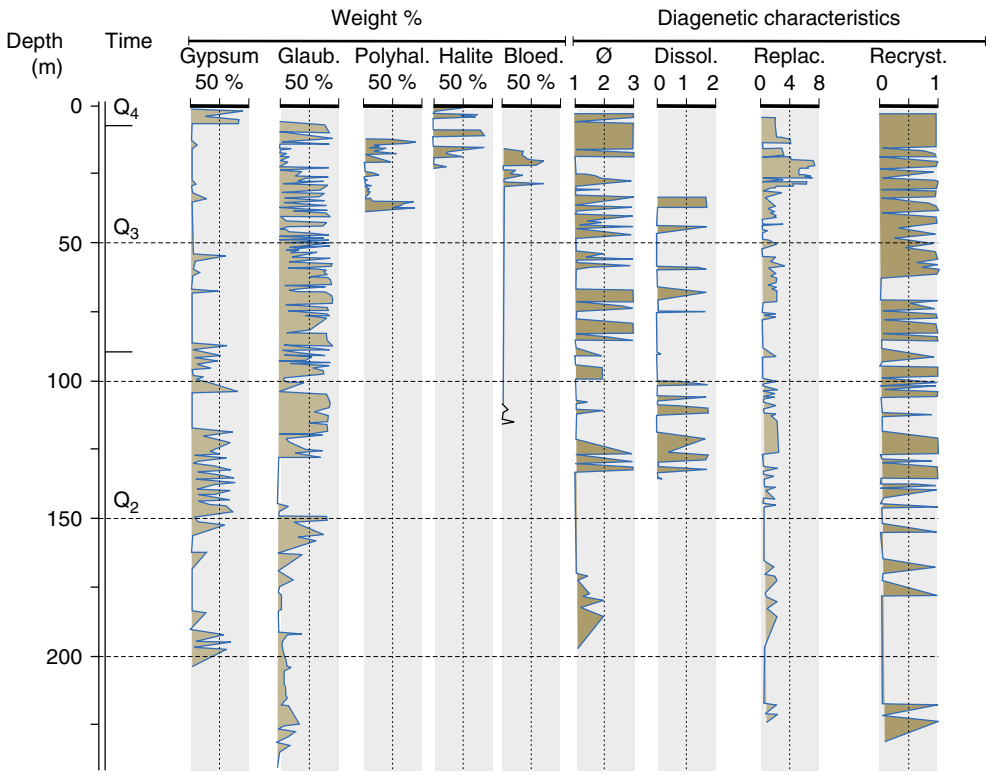

Fig. 11.33 The stratigraphic variation of salt minerals and corresponding diagenetic characteristics in Core ZK 1200B, Lop Nu Basin. See Fig. 11.32 for location. Porosity: *1*. Porosity less than 5 %; *2*. Porosity range of 10–15 %; *3*. Porosity range of 20–35 %. Dissolution: *1*. Near-surface dissolution; *2*. Deep dissolution. Replacement: *1*. Anhydrite is replaced by gypsum; *2*. Anhydrite is replaced by glauberite; *3*. Glauberite is replaced by polyhalite; *4*. Halite is replaced by polyhalite; *5*. Bloedite is replaced by polyhalite; *6*. Glauberite is replaced by bloedite; *7*. Halite is replaced by bloedite. Recrystallization: *1*. Undeveloped; *2*. Developed (After Ma et al. 2010)

The Lop Nur potash recovery plant and pan system, located in the LuoBei Hollow (Fig. 11.32, inset), utilises a brine source where the potash brine is reservoired in intercrystalline and vuggy porosity in a thick glauberite bed (as seen in Fig. 11.33). This makes the Lop Nur system unique in that it is the first large-scale example of brine commercialisation for potash recovery from a continental playa system with a non-KCl brine target. In the past similar glauberite-mirabilite hosted brines and beds have been use to recover sodium sulphate in both cryogenic and hot semi-arid desert scenarios, but these Quaternary-hosted brine systems did not target potassium sulphate (Warren 2010). In the case of the cryogenic systems in Quill Lake, Canada, small volumes of SOP are produced via mixing of a sylvite feed (trucked in to site) with a $NaSO_4$ lake brine, while the Great Salt Lake SOP brine chemistry and processing stream is described earlier in this module (Fig. 11.8).

SOP Brine Potential in the Amadeus Basin, Australia?

To the south of Alice Springs in the Amadeus Basin of Central Australia there are a number of small saline playas (areas <50 km^2) with thin ephemeral sylvite/glauberite crusts and efflorescences in an area centred on the Karinga Creek palaeodrainage (Fig. 11.34a; Arakel and Hong Jun 1994). In contrast, there are no documented sylvite or glauberite crusts in any of the larger playas of the same region, such as Lake Amadeus (area ≈ 750 km^2; Fig. 11.34b). The absence of potash precipitates in the larger playas reflects the variably decoupled nature of the inflow hydrologies to groundwater seeps in the region (Fig. 2.63; Jankowski and Jacobson 1990). Both types of playa experience the same arid (BWh) climate; median and mean annual rainfall in the region are 190 and 220 mm, respectively, mostly falling in summer (Dec.-Feb.); while annual evaporation is ≈ 3,300 mm. All the playas are ultimately supplied by a combination of surface runoff and seepage from a large regional groundwater outflow system, which discharges into this chain of playa lakes along an outflow zone that is some 500 km long (Fig. 11.34).

The difference in the mineralogy of the ephemeral surface salt crusts between the smaller and larger playas correlates with the depth to which the various playa groundwater systems tap into the regional hydrology. Throughout the artesian discharge zone, the various playa salt crusts form by capillary evaporation of resurging groundwaters. All the playa sediments entrain highly concentrated brines; typically, these are sodium-chloride rich waters with appreciable magnesium and sulphate and very low concentrations of calcium and bicarbonate. The larger playas in the chain, exemplified by Lake Amadeus, have dual shallow and deep groundwater inflow paths. The smaller playas, exemplified by Spring Lake and the Na_2SO_4 lakes of the Karinga Creek drainage system, have only shallow inflow paths. Brines in the larger playas such as Lake Amadeus are continually diluted by mixing with upwelling deep groundwaters tapping into the regional hydrology (Fig. 11.34b). This gives

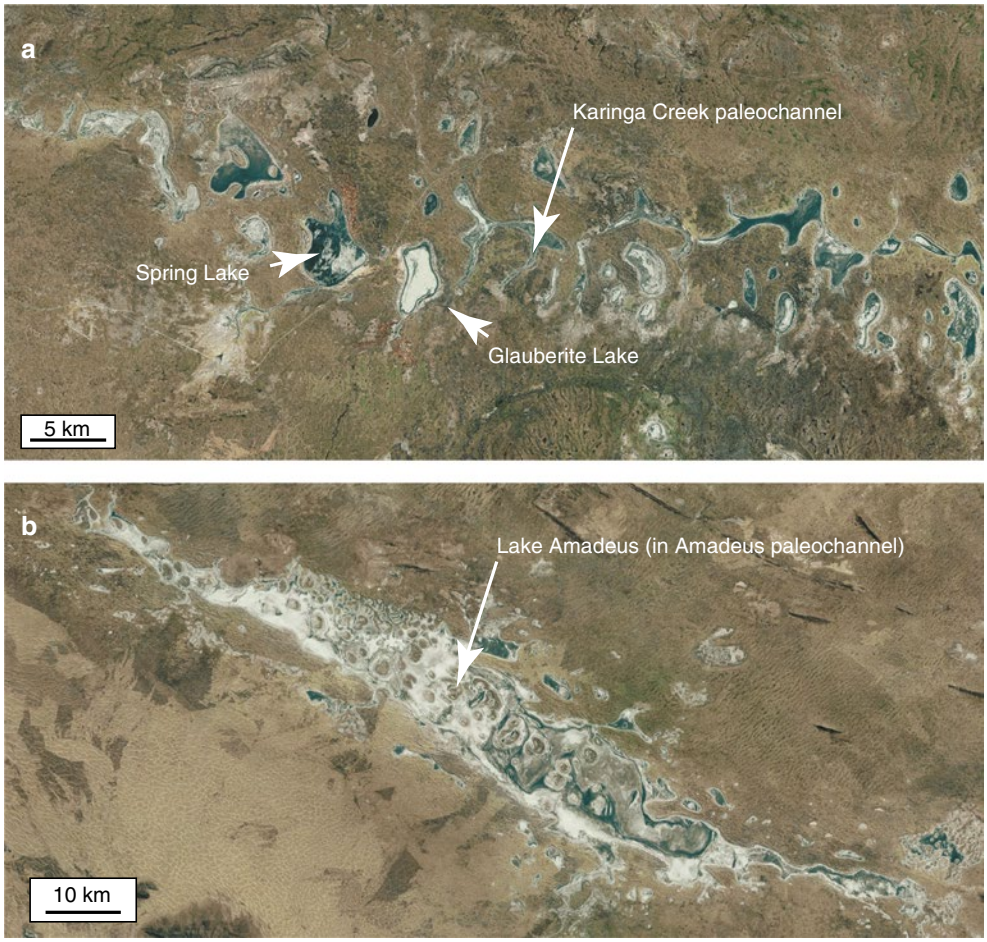

Fig. 11.34 Potash potential in palaeodrainage channels and lakes of the Northern Territory, central Australia. (**a**) Karinga Creek Palaeodrainage defined a series of local sumps with small playas draining the upper portion of the local hydrology (see Chap. 2). (**b**) Lake Amadeus; this large salt lake lies in a drainage chain that forms the central part of the 500-km long groundwater outflow belt (and palaeochannel network) along the northern edge of the Victoria desert and extends ESE into the Karinga Creek-Curtin Creek paleodrainages (Scaled Bing® images mounted in MapInfo®)

larger playas a stable recharge hydrology so that halite saturation rarely occurs within the playa sediments and thin ephemeral beds are short term features, thicker halite crusts cannot form.

In contrast, smaller playas tend to be uncoupled from the deep recharge system so pore saturation with respect to gypsum/halite is reached rapidly in the capillary zone of their mudflats (e.g. Spring Lake and Glauberite Lake). Subcropping groundwaters in both lake Amadeus and Spring Lake/Glauberite lake are undersaturated with respect to glauberite and sylvite. Yet both minerals accumulate as ephemeral efflorescent crusts about the edges of small salt lakes in the Karinga Creek palaeodrainage but not in Lake Amadeus due to its inherently higher local salinities and its rapidly transitioning lake surface, which because it is located well above the regional groundwater discharge level can attain short-term bittern saturation. The continual regional recharge from artesian waters beneath both small and larger playa depressions of this region means there is little longterm preservation of any salts, and zero potential for bedded potash preservation. However, the decoupled hydrology in the various salt lakes that define the Karinga Creek palaeochannel has the potential to supply brines that may suitable for sulphate of potash processing via anthropogenic solar pans, as is currently done in Lop Nor.

The hydrology of the large central Australian playas, and, for the same reasons, the artesian outflow hydrologies of other artesian-fed salt lakes/playas to the south such as Lake Eyre and Lake Frome are not suitable settings for the longterm natural accumulation of thick beds of potash salts. Their position in zones of regional meteoric outflow means they are too fresh and too deflationary, and the underlying groundwater prism is too fresh, to allow thick sequences of bedded salts to accumulate. Similarly decoupled seepage hydrologies are also why there are no substantial bedded accumulations of Quaternary potash in the Chotts of Tunisia. You need a deep depression with a saline feed and a stable hypersaline brine curtain to accumulate thick sequences of bedded salts, and in the case of potash salts that brine curtain must be maintained at the upper bittern end of the concentration range and preferable have a calcium chloride dominated hydrochemical makeup. Zones of shallow rising meteoric groundwaters, with typically higher levels of bicarbonate and sulphate, never underlie the sump hydrology of systems accumulating substantial volumes of potash salts (Hardie 1990).

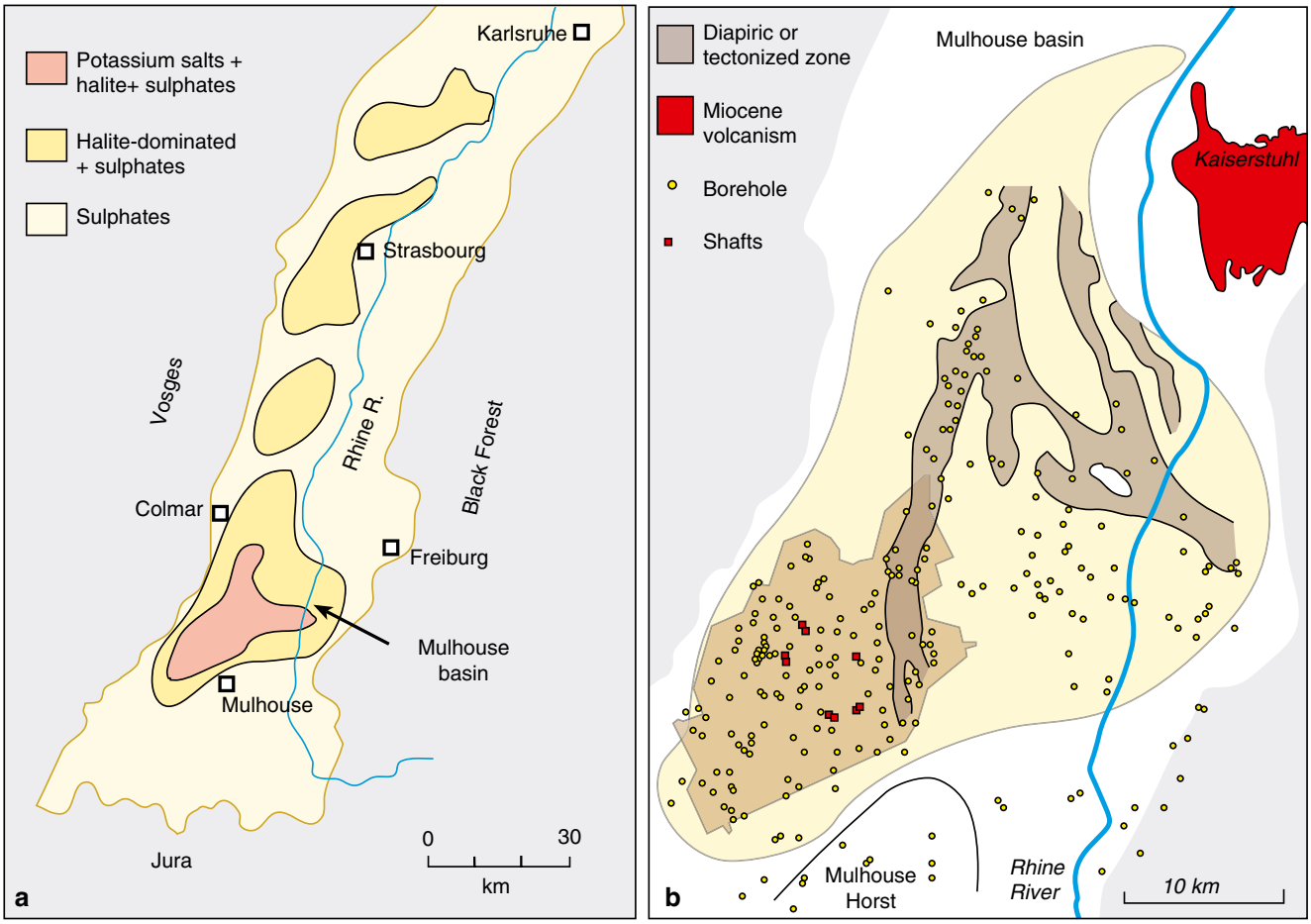

Fig. 11.35 Mulhouse Basin, Rhine Graben. (**a**) Regional distribution of salt basins showing how the potash dominant section is the southernmost of a number of small saline lacustrine deposits in the graben. (**b**) Detail of the Mulhouse (Alsace) Basin show how the exploited bedded potash area lay to the southeast of a more disturbed and diapiric zone (After Blanc-Valleron and Schuler 1997)

Ancient (Pre-Quaternary) Potash

Surface pan operations account for a little over 10 % of the world's annual potash production. The other 90 % comes from the extraction and mining of potash from ancient evaporite successions. Many ancient potash deposits accumulated as the bittern portions of marine-fed saline giants, with the larger examples forming during times of $MgSO_4$-depleted ocean chemistries and have no modern marine counterpart. We shall now look back progressively through time at some of the more important of the ancient potash occurrences.

Upper Rhine Graben, France

Until 2002 potash was conventionally mined in France in the Mulhouse basin. With an area of 400 km^2, the Mulhouse Basin (near Alsace, France) is the southernmost of a number of Lower Oligocene evaporite basins that occupied the upper Rhine Graben, which at that time was a narrow adiabatic-arid rift valley, experiencing a tectonic setting not dissimilar to the modern Danakil depression (Fig. 11.35a). The Rhine Graben is a Tertiary rift, some 150 km long and 10–25 km wide that straddles the Franco-German border as it runs from Basle in Switzerland to Frankfurt in Germany. Palaeogeographical reconstructions place a potential seaway seepage feed north or perhaps southeast of the Mulhouse basin, while marginal conglomerates tend to preclude any hydrographic connection with the ocean (Blanc-Valleron 1991; Cendon et al. 2008). Total fill of Oligocene lacustrine/marine-fed sediments is some 1,700 m thick and is dominated by anhydrites, halites and mudstones. The sequence is underlain by non-evaporitic Eocene continental mudstones with lacustrine fossils and local anhydrite. Bed continuity in the northern part of the basin are disturbed by diapiric and or erosional/fault movement and so were not considered economic targets for conventional mining (Fig. 11.35b).

The Paleogene filling of the basin is divided into 6 units; a pre-evaporitic series, Lower Salt Group (LSG), Middle Salt Group (MSG), an Upper Salt Group (USG – with potash),

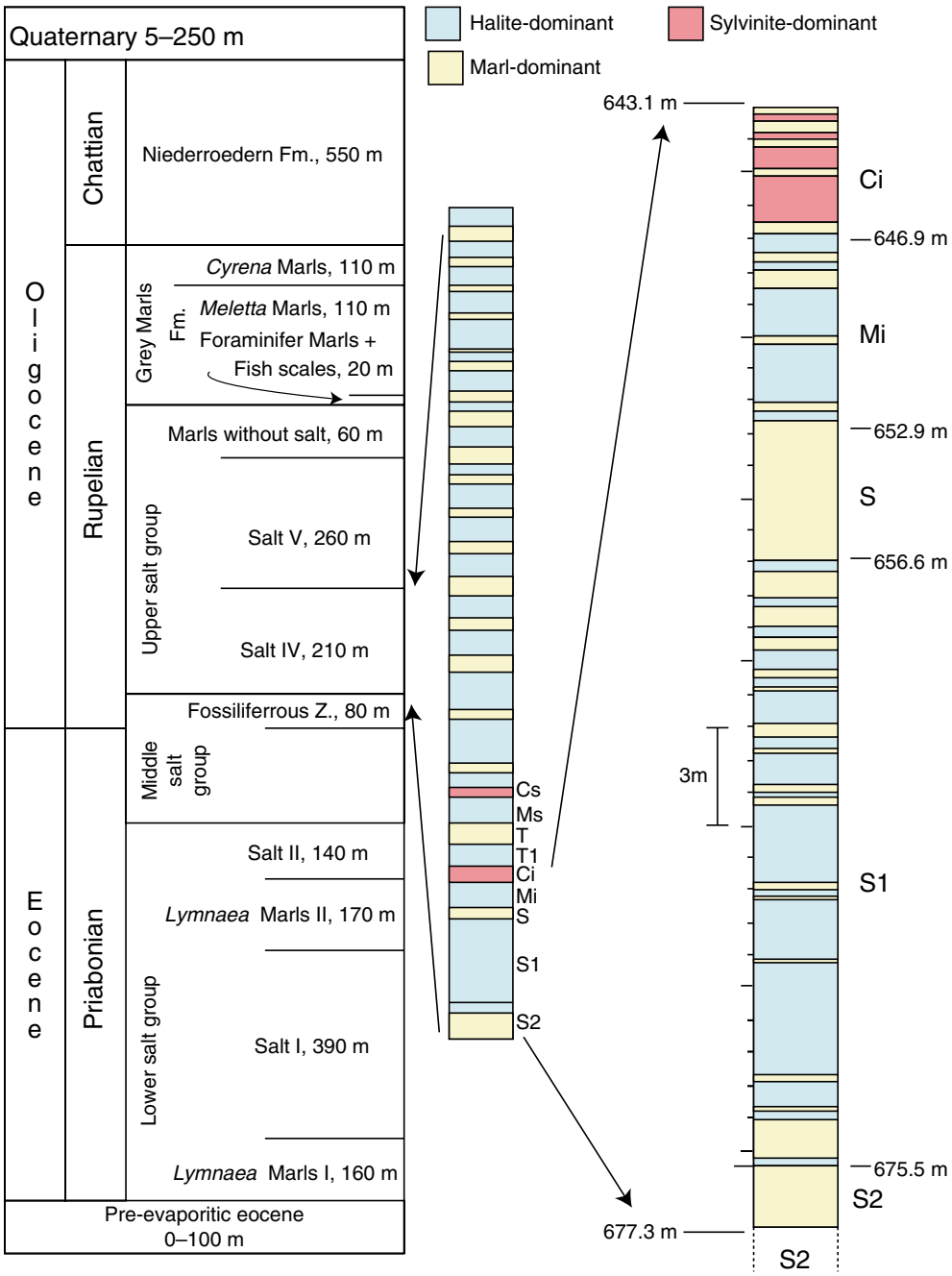

Fig. 11.36 Stratigraphy of the Mulhouse basin (After Cendon et al. 2008)

Grey Marls Fm., and Niederroedern Fm (Fig. 11.36; Cendon et al. 2008). The LSG and lower section of the MSG are interpreted as lacustrine in origin based on the scarce palaeontologic and geochemical data. However, based on the presence of Cenozoic marine nannoplankton, shallow water benthic foraminifera, and well diversified dinocyst assemblages in the Fossiliferous zone below Salt IV. Blanc-Valleron (1991) favours a marine influence near the top of the MSG, while recognizing the ambiguity of marine proportions with brackish faunas. Many marine-seepage fed brine systems have salinities that allow halotolerant species to flourish in marine-fed basins with no ongoing marine hydrographic connection. According to Blanc-Valleron and Schuler (1997), the region experienced a Mediterranean climate with long dry seasons during Salt IV member deposition.

In detail, the Salt IV member is made up of some 210 m of evaporitic sequence, with two relatively thin potash levels (Ci and Cs). The stratigraphy associated with this potash zone is, from base to top (Fig. 11.36):

S2 Unit: 11.5 m thick with well defined layers of organic-rich marls often dolomitic, with dispersed anhydrite layers.

S1 Unit: 19 m thick and made up of alternating metre-scale milky (inclusion-rich) halite layers, with much thinner marls and anhydrite layers. Marls show a sub-millimetric lamination formed by micritic carbonate laminae alternating with clay, quartz, and organic matter-rich laminae. Hofmann et al. (1993a, b) interpreted these couplets as reflecting seasonal variations. Anhydrite occasionally displays remnant swallowtail textures, which suggest that at least part of the anhydrite was primarily precipitated as gypsum. Halite shows abundance of growth-aligned primary textures, with abundant fluid inclusion banding (Lowenstein and Spencer 1990).

S Unit: Is 3.7 m thick and consists of thin marl layers and anhydrite, similar to the S2 Unit, with a few thin millimetric layers of halite.

Mi Unit: With a thickness of 6 m, it is mostly halite with similar characteristics to S1 Unit. Sylvite was detected in one sample, but its presence is probably related to the evolution of interstitial brines (Cendon et al. 2008).

Ci Unit ("*Couche inférieure*"): Is formed by 4 m of alternating marls/anhydrite, halite, and sylvite beds.

The Ti unit consists of alternating beds of halite, marl and anhydrite. The top of the interval is the *T unit*, which is similar in character to the *S unit* and consists of alternating beds of marl and anhydrite. Above this is the *Ms or upper Marl*, near identical to the *lower marl Mi.* The Mi is overlain by the upper potash bed *(Cs)*, a thinner, but texturally equivalent, bed compared to the sylvinitic Ci unit.

Thus, the Oligocene halite section includes two thin, but mined, potash zones: the Couche inferieure (Ci; 3.9 m thick), and Couche superieure (Cs; 1.6 m thick), both within Salt IV of the Upper Salt group (Fig. 11.36). Both potash beds are made up of stacked, thin, parallel-sided cm-dm-thick beds (averaging 8 cm thickness), which are in turn constructed of couplets composed of grey-coloured halite overlain by red-coloured sylvite. Each couplet has a sharp base that separates the basal halite from the sylvite cap of the underlying bed. In some cases the separation is also marked by a bituminous parting. The bottom-most halite in each dm-thick bed consists of halite aggregates with cumulate textures that pass upward into large, but delicate, primary chevrons and cornets. Clusters of this chevron halite swell upward to create a hummocky boundary with the overlying sylvite (Lowenstein and Spencer 1990).

The sylvite member of the couplet consists of granular aggregates of small clear halite cubes and rounded grains of red sylvite (with some euhedral sylvite hoppers) infilling the swales in the underlying hummocky halite. The sylvite layer is usually thick enough to bury the highest protuberances of the halite, so that the top of each sylvite layer, and the top of the couplet, is flat. Dissolution pipes and intercrystalline cavities are noticeably absent, although some chevrons show rounded coigns. Intercalated marker beds formed during times of brine pool freshening are composed of a finely laminated bituminous shale, with dolomite and anhydrite.

The sylvite-halite couplets appear to record unaltered settle-out and bottom-growth features of a primary chemical sediment that accumulated in a shallow perennial surface brine pool. The sylvite layers, like the halite layers, are interpreted as primary subaqueous deposits (Lowenstein and Spencer 1990). Based on their crystal size, the close association with cumulate halites in the sylvite layers, and the manner in which they mantle underlying chevron halites, sylvites are interpreted as precipitates first formed at the air-brine surface (or within the upper brine) that then sank to the bottom to form well sorted accumulations. Similar cumulate sylvite deposits form as ephemeral bottom accumulations on the floor of modern Lake Dabuxum in China during its more saline phases.

The current mosaic textural overprint in the Mulhouse sylvite layers was probably produced by postdepositional modification of the crystal boundaries, much in the same way as mosaic halite is formed by recrystallization of raft and cumulate halite during shallow burial. Inclusion studies in both the sylvite and the halites average 63 °C, suggesting solar heating of surface brines as precipitation took place (Cendon et al. 2008). Similar high at-surface brine temperatures are not unusual in many modern brine pools, especially those subject to periodic density stratification and heliothermometry.

Mineralogically, potash evaporites in the Mulhouse Basin in the Rhine Graben (also known as the Alsatian (Alsace) Wittelsheim Potash district) contain sylvite with subordinate carnallite, but lack the abundant $MgSO_4$ salts characteristic of the evaporation of modern seawater. The Rhine graben formed during the Oligocene, via crustal extension related to mantle upwelling. It was, and is, a continental graben typified by high geothermal gradients along its rift axis and in depositional setting is not dissimilar to the Quaternary Danakil and the Dead Sea during the deposition of the Sedom Fm. The role of its high temperature geothermal association in defining the $CaCl_2$ nature of the potash-precipitating brines versus a derivation from a $MgSO_4$-depleted marine feed is considered significant but is poorly understood (Hardie 1990). World ocean chemistry in the Oligocene is on a shoulder between the $MgSO_4$ -depleted $CaCl_2$-rich oceans of the Cretaceous and the $MgSO_4$ -enriched oceans of the Neogene (Zimmermann 2000b).

Recent work on the origin of the Mulhouse brines argues for an initial marine source but likely within a series of rift-valley basin depressions for which there was no direct hydrographic connection at the time the Middle Salt Member (potash entraining) was deposited (Cendon et al. 2008) That is, the general hydrological evolution of the Mulhouse basin is explained as a restricted sub-basin with an initial marine

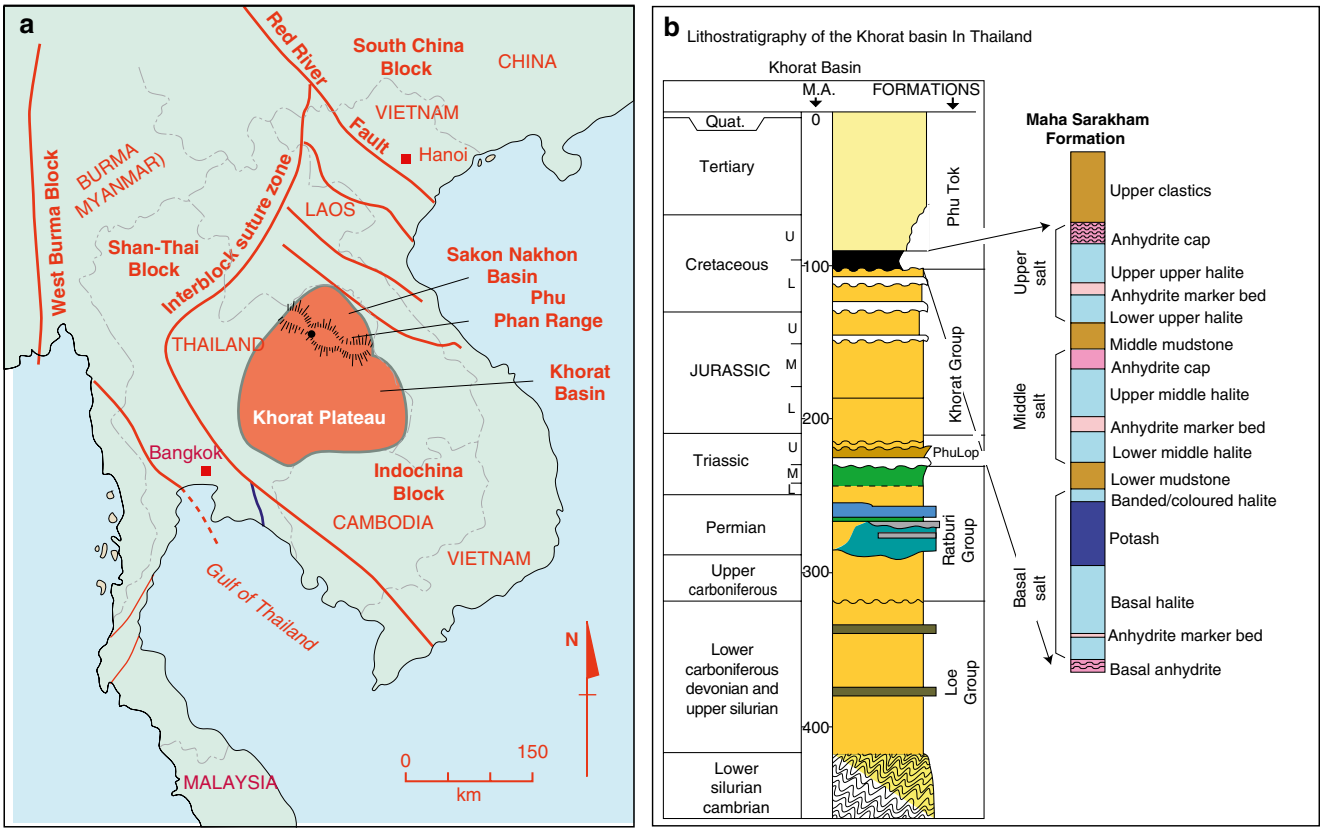

Fig. 11.37 Potash in Thailand. (**a**) Locality map showing location and tectonic setting of the Khorat Plateau, the Khorat Basin and the Sakon Nakhon Basin. (**b**) Stratigraphy of the Khorat Basin and the Maha Sarakham Formation (Albian-Cenomanian), NE Thailand (After Suwanich 1986; Mouret 1994; Racey 2009)

stage. This gradually changed to ≈40 % marine source at the beginning of evaporite precipitation, with the rest of hydrological inputs non-marine. The general proportion of solutes did not change greatly over evaporite precipitation. However, as the basin restriction increased, the originally marine inputs changed to continental or marine-modified inputs from neighboring basins north of Mulhouse basin.

Khorat Plateau, Thailand

Potash in the halite-dominated Cretaceous Maha Sarakham Formation is preserved within two structural basins: the northern Sakon Nakhon Basin (which also extends into Laos) and the southern Khorat Basin. These basins underlie much of the Khorat Plateau in NE Thailand and are separated by the highlands of the Phu Phan Range (Fig. 11.37a). It is likely that a single larger evaporite basin encompassing more than the current area of the present day Sakon Nakhon and Khorat Basins existed at the time of deposition. These deposits represent one of the last saline giants preserved in SE Asia and suggest an extreme arid period during Albian-Cenomanian time within a subsealevel marine-fed continental depression, possibly created by transpressional collision events that preceded the Himalayan Orogeny (see Morley 2012 and Racey 2009 for possible timing of various Mesozoic and Tertiary tectonic events). The evaporite sequence lacks $MgSO_4$ salts, consistent with our current understanding of the evolution of Cretaceous seawater chemistry.

The current margins of both basins are dissolutional, as are the upper and lower contacts of the salt units. If units of dolomite or anhydrite did form as platform wedges about the depositional edge of the basin, they must have been located outside the present structural/dissolution margins to the basin. More likely, thick units of dolomite or anhydrite were never present and these minerals only formed thin layers during times of short term freshening within the dominantly halite fill of the basin. Work by Racey (2009) suggests that the Khorat Group and the Maha Sarakham were originally deposited in a foreland basin setting rather than a thermal sag basin, following Late Triassic rifting. Moreover, the original site of deposition was to the north, somewhere in southern China, with the present-day location being the result of block movement along the Red River Fault coupled with a clockwise rotation of the Indochina Block (on which the Khorat Group sits) with respect to the South China Block.

In those parts of the stratigraphy largely unaffected by evaporite dissolution, the Maha Sarakham is composed of three salt beds –Lower, Middle and Upper Salt members– each overlain by a clastic mudstone –Lower, Middle and Upper Clastic members– (Fig. 11.37b). Where the Maha Sarakham has not been thinned, either by dissolution or salt flow, it is 250–300 m thick. In areas of salt dissolution it thins to <50 m, while in halokinetic regions it can be more than a 500 m thick (Figs. 7.40, 7.41a and 11.39). Evaporite minerals include halite; the sulphates gypsum and anhydrite, along with a variety of halite-hosted potash phases, dominated by carnallite and lesser sylvite with accessory tachyhydrite. Portions of the bedded halite display intricate depositional, dissolutional and diagenetic features that rank amongst the most pristine I have seen preserved in an ancient evaporite (Figs. 7.42 and 11.38).

Middle and Upper Salt members are generally flat lying and correlatable from well to well. In contrast, seismic and geomorphologic analysis shows that the Lower Salt of the Maha Sarakham has flowed in some parts of the basin so that thicknesses are much more variable from well to well (Fig. 11.39). Textures in the Lower Salt Member range from well preserved depositional textures in its upper part immediately below the potash entraining intervals to pervasive flowage features lower in the section. Petrographic evidence for salt flowage includes overburden-controlled elongate flattening of crystals and pervasive halite recrystallization that has destroyed original bedding features. In wells that sample deeper into the Lower Salt Member there is often a transition down core from pristine depositional textures into flowage textures, implying that flow into the pillows was fed mostly from the deeper parts of the Lower Salt Member. This is also consistent with the upper portions of the salt unit still being deposited while the lower parts of the same unit were flowing.

The potash interval in the upper part of the lower Halite unit of the Maha Sarakham in NE Thailand is dominated by carnallitite (up to 20–30 m thick), which forms a widespread stratiform unit along the western margins of both the Khorat and Sakon Nakhon basins. It is variably capped by sylvinite (<6 m) and typically covered by a bed of colour-banded red and grey halite (up to 6 m thick). This colour-banded halite preserves pristine depositional textures and is in turn overlain by the Lower Member.

A complete interval in the potash-entraining region at the top of the Lower Salt Member is divisible into (Fig. 11.37b):

(4) Uppermost colour-banded halite (0–6 m),
(3) Sylvinite zone (0–6 m),
(2) Carnallitite zone (0 up to 15–30 m),
(1) Lower zone of massive to bedded halite with traces of carnallite (50–300 m).

The lower zone (1), is dominated by massive, colourless, inclusion-free halite, which is made up of stacks of beds 0.2–0.5 m thick. The upper portion of this halite interval retains pristine depositional textures, including aligned bottom-nucleated chevron growth forms, clay dissolution stringers and microkarst and macrokarst pits. This halite zone is underlain by clean re-crystallized mosaic halite, which may stack into intervals that are hundreds of metres thick in halokinetic zones. Often this clean halite is dominated by biaxially flattened or necked and recrystallized lensoidal textures, a texture indicative of salt flow. Minor anhydrite stingers and nodules (≈1 cm thick) crosscut the axes of cores often with steep inclinations that also suggest flowage. This form of anhydrite is microcrystalline and lacks any of the original gypsum ghost structures so well preserved in thicker regional marker beds, especially those in the middle and upper halite members (Fig. 11.37b).

The carnallitite zone (2) is typically 15–25 m thick near the western edge of the current structural basin but can also disappear near the outermost parts of the basin where it has been dissolved by surface-driven crossflows of meteoric water. Three types of halite are found in the carnallitite zone: (a) inclusion-rich, cloudy, chevron halite; (b) clear, recrystallized, coarsely crystalline halite; and (c) granular, fine-grained halite. The first typifies preserved bottom-nucleated beds, the second typifies massive halite beds with poorly defined upper and lower contacts and suggests textures associated with macro and micro karstification, while the third type is found as disseminated halite in carnallite-filled voids. Anhydrite and other insoluble residues are scarce in the carnallitite zone. Halite that hosts carnallite is often crosscut by dissolution surfaces, clay stringers, collapsed halite beds and karst cavities can be coated with microcrystalline to coarsely crystalline carnallite (Fig. 11.38).

Many of the carnallite-filled voids are subvertical and narrow downward. In the older literature this texture was sometimes described and amoeboid potash. But much of this "amoeboid" texture is a syndepositional vadose karst fill, which prior to the precipitation of the carnallite cement was an open void. Textures in this part of the potash zone are identical to those found in the bedded potash deposits of the modern Qahan Playa and indicate the watertable was subject to large oscillations. Textures in the carnallitite interval in the Maha Sarakham show it was subject to syndepositional brine freshening, subaerial exposure and watertable lowering related to climatic changes and tectonic tilting in the depositional basin.

The sylvinite zone (a mixture of halite and sylvite) directly overlies the carnallitite zone and can be up to 6 m thick. It is not always present. Its contact zone is transitional with the underlying carnallitite zone, although sylvite crystal-clusters in the transition zone typically show sharp

Fig. 11.38 Typical multistage dissolution collapse and fill in Maha Sarakham Fm. by chevron halite. Cavities are sometimes filled by clear sylvite, not halite

non-horizontal edges. Sylvite is present in its halite host as: a) individual and small crystal clusters of up to 1 cm size, making up amoeboid-shaped forms; (b) coarsely crystalline massive beds up to 5 cm thick; (c) even layered, thick beds of up to 4 cm thick; (d) irregular medium to coarsely crystalline patches within massive halite beds and as patches sometimes rimming pre-existing carnallite crystals; and (e) massive sylvite units up to 25 cm across. In almost all cases, dark grey clayey matrix surrounds the larger sylvite crystals and/or alternates with the subhorizontal sylvite beds. Petrographically, sylvite crystals exhibit euhedral crystalline forms, either as individual crystals or as clusters of crystals.

At the transition between the carnallitite and sylvinite zones some dissolution cavities can be 25 cm across (in core) and filled with single clear sylvite crystals. Higher in the sylvinite interval the sylvite tends to occur as stratiform primary layers showing subhorizontal bedding, and ranges from 10 cm to 1 m thick. Individual primary sylvite crystals can reach up to 2 cm in size in the primary layers. Macroscopically, sylvite layers are not homogeneous and several types of sylvite may coexist within single layers along with fine clastic components and halite.

Halite beds alternating with sylvite layers range in thickness from 1 to 15 cm. Where not destroyed by the processes of dissolution and recrystallization, these halite beds can still exhibit relict bedding and occasionally are milky from inclusions in the preserved chevrons. But most of the halite in the sylvinite zone is clear and coarsely recrystallized, with geometries suggesting repeated episodes of dissolution followed by precipitation as passive void-fill cements. Traces of anhydrite are present throughout the sylvinite zone, along with traces of tachyhydrite. Anhydritic cm-diameter nodules are locally present, as are white nodules dominated by microcrystalline borate minerals (boracite and tyreskite).

More than one sylvite-rich interval may occur in the sylvinite zone. Workers in the region who have used a strict stratigraphic approach have often reported intervals with more than one sylvite layer as representing fault-repeat sections. Such an approach underscores the limitations of using a non-process based layer-cake stratigraphy in an evaporite succession. What is occurring is not associated with a fault-repeat of a single sylvite bed, but the vagaries of a sylvite-filled anastomose karst system being intersected a number of times in a single core. Contacts of many of the so-called repeat beds show classic insoluble-rich geopetal linings.

Colour banded halite (4) constitutes the uppermost part of the Lower Salt Member. It is coarsely laminated and retains pristine depositional textures (mostly chevrons) with little or no evidence of recrystallization. There is often a sharp upper dissolution contact with the overlying Lower Clastic Member, defined by a diagenetic horizon made up of anhydritic dissolution residues.

The origin of the richest sylvite zone (3) is related in part to the action of actively refluxing, possibly freshened brines working on an actively rising (pillowing) carnallite/halite precursor. For example, in the Khon Kaen region (Fig. 11.39), the Lower Salt Member has flowed into a pillow structure and the overlying strata are truncated beneath an alluvial cover. The synclinal structure associated with the rim of this pillow is also a zone where sylvinite thickens at the expense of the underlying carnallitite (Fig. 11.40a). This sylvinite is capped by the Lower Clastic Member, which is in turn capped by the

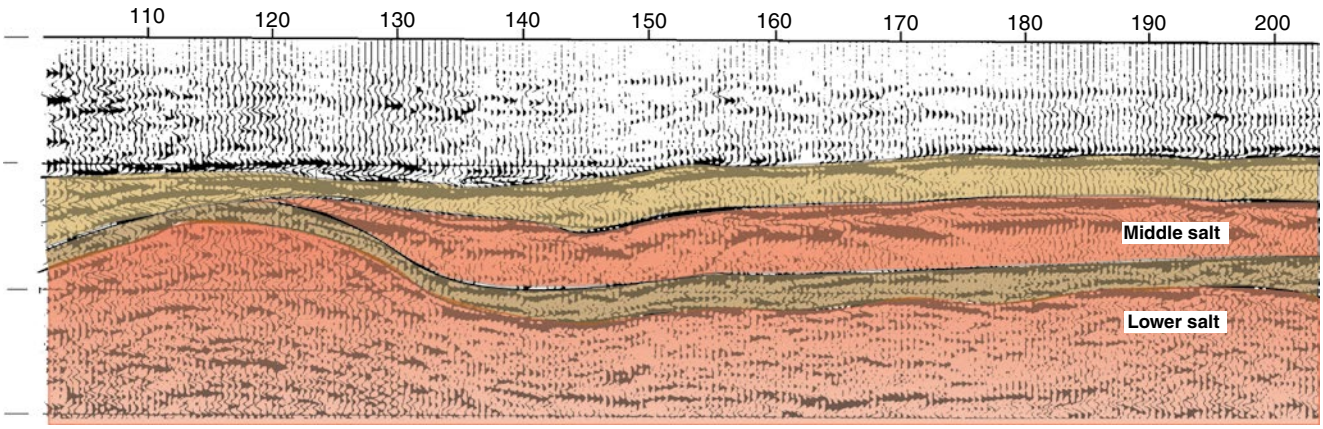

Fig. 11.39 Seismic image of Maha Sarakham Formation, from the Khon Kaen area showing a salt pillow in the Lower Salt Member and the syndepositional reduction in sedimentary thickness in units above this structure (seismic line supplied by CRA-RTZ)

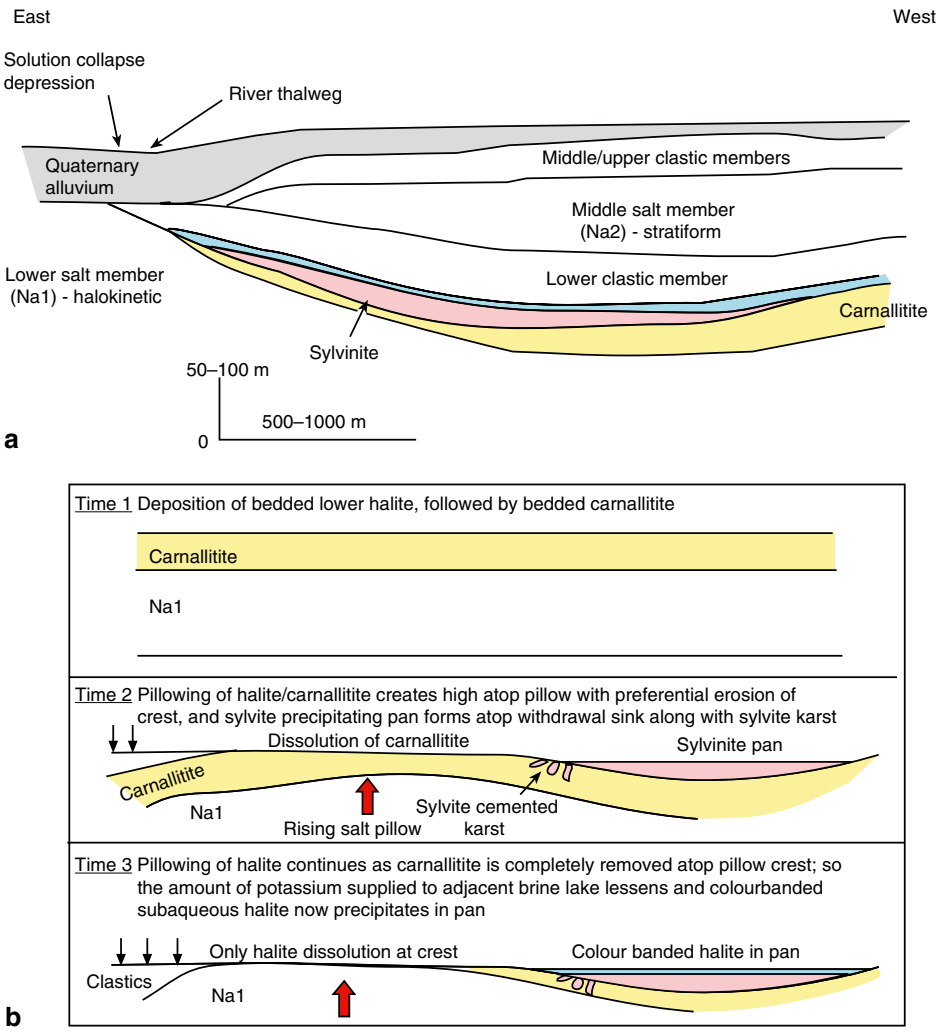

Fig. 11.40 Sylvite controls in the Maha Sarakham Formation along the western margin of the Khorat Plateau near Khon Kaen, Thailand. (**a**) Generalised schematic of current sylvite distribution based on well data in the region. (**b**) Sequential development of pillow and the erosion of crest facies controlling first the formation of sylvite and then the colour-banded halite within brine-entraining rim syncline depressions (see text for full explanation). Schematic based on author's research and field work in the region

Middle Halite Member. Core from the Middle Halite Member in this region shows predominantly undisturbed subhorizontal bedding and still retains perfectly preserved primary textures, such as chevrons and halite intercrystal karst, along with a regional dm-thick marker bed made up of subaqueous swallowtail gypsum pseudomorphed by halite/anhydrite (pers. obs. of core). At the regional scale, the halokinetic features follow curvilinear trends that are typically subparallel to

the present basin margin. Some pillows in the Lower Salt Member, especially those associated with sylvinite along the western margin of the basin, were probably syndepositionally initiated as they are truncated by sediments of the Lower Clastic Member (Fig. 11.39). Locally, other salt flow features are probably still active today, driven by laterally shifting surface river systems, including the Mekong and its tributaries. For example, $CaSO_4$ caprocks outcrop today in Laos in the erosional river-banks of the Nam Theun river one of the major tributaries to the Mekong (pers. obs.).

Initiation of the salt flow in the Maha Sarakham halite is probably diachronous and driven by sediment loading from various depocentres moving across the salt bed. In the Cretaceous the depocentres were tied to the deposition of the Lower Clastic Member and possibly the basin tilting related to the uplift of the Phu Pham ridge; today they are tied to the fluviatile deposits of the Mekong and its tributaries. Such feedback systems between depositional loading (sediment thicks) and salt buildups (pillows and anticlines) and salt dissolution characterise the western margin of the Maha Sarakham in the vicinity of Khon Kaen (Fig. 11.39). As well as being seen seismically, the relationship between surface landform and the underlying structuring of the salt can be imaged using currently available topographic maps, aerial photography and satellite imagery.

Like much of the halite in the Maha Sarakham, the petrography, depositional style and preservation quality of potash in the Lower Salt Member has been complicated by dissolution and halokinesis (Hite and Japakasetr 1979; Sessler 1990; El Tabakh et al. 1995; Utha-aroon et al. 1995). In terms of the potash minerals, carnallite dominates over sylvite through most the basin, while traces of tachyhydrite are also found preserved as enclosed euhedral to subhedral crystals in halite along with locally common boracite and priceite (up to 4 %).

Potash is widely dispersed as minor shows in the upper part of the Lower Halite unit across the basin. The only well studied and significant potash-rich zones are in the upper section of the Lower Salt Member along the western margin of the Khorat Plateau. Additional work has recently been publish by the Chinese on the equivalent marine fed potash units in the Khammuane regions of Laos (Zhang et al. 2013). Some Chinese authors assign a Paleocene (not mid Cretaceous) age for potash deposition (Tan et al. 2010). The isotopic evidence from the Laotian succession show the brine source is clearly marine (Fig. 11.41a). The actual age of the Maha Sarakham is contentious. Most workers in Thailand accept a Cretaceous age for the unit based on the assignment of a Late Cretaceous age to the overlying Phu Tok (Booth and Sattayarak 2011).

Around Vientiane, Lovatt-Smith et al. (1996) found evidence on seismic lines of an inversion event, which had created the Nam Leuk Uplift, an east–west trending feature that is bounded on its southern side variously by either a monocline

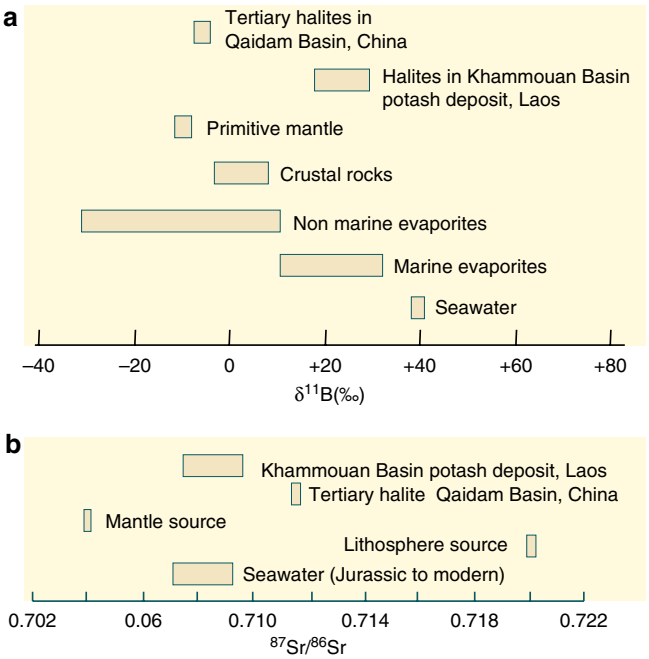

Fig. 11.41 Thangon Fm (= Maha Sarakham equiv. in Laos) isotope chemistry (**a**) Boron Isotopes. (**b**) Strontium isotopes (After Zhang et al. 2013)

or a high-angle reverse fault. They concluded that the evaporites of the Thangon Formation, which is the direct equivalent of the Maha Sarakham formation in Thailand, are essentially horizontally bedded and onlap the monocline in front of the Nam Leuk Uplift. On the basis of their seismic interpretation, which provided a mid-Cretaceous age for the Nam Leuk Uplift north of Vientiane. Lovatt-Smith et al. (1996) argued it was likely that the Phu Phan Uplift in Thailand had two stages of inversion: the first during this Mid-Cretaceous Event and the second during the Tertiary Himalayan Orogeny.

The presence of a regional unconformity at the base of the Maha Sarakham, Formation, as identified by Sattayarak et al. (1991), suggests that a deformational event did affect NE Thailand in the Mid-Cretaceous. However, although it is generally assumed that the Phu Phan Uplift was initiated in the Mid-Cretaceous, there is not yet any unequivocal evidence to support this contention. If such a regional unconformity is accepted, then the overlying Maha Sarakham and Phu Tok Formations should he regarded as separate from the Khorat Group.

The lower 100–200 m of the Phu Tok Formation (Booth and Sattayarak 2011) consists of a sequence of brick-red to red-brown clay-stones with minor siltstone and rare, thin, very fine-grained sandstone beds Overlying this is a sequence, at least 300 m thick, comprising thick beds of brick-red sandstone with large-scale high-angle cross-bedding. The lower claystone unit is interpreted to have been deposited in a very

low-energy fluvial environment, while the overlying sandstones are clearly aeolian. In many places the PhuTok Formation has been completely removed by Tertiary to Recent erosion, but in the centre of the basin seismic lines indicate that up to 500 m of section is still preserved. The original depositional thickness of the Phu Tok Formation is unknown. Hasegawa et al. (2010) have concluded from palaeomagnetic polarity studies that the aeolian beds are mid-Cretaceous (126- to 99–93 Ma), and that, at least in part the Phu Tok interfingers with the Maha Sarakham Fm.

There is little doubt that the large-wavelength folds of Khorat Group, which are such a notable feature of the surface geology of NE Thailand were initiated in the early Tertiary. The beginning of the uplift that accompanied the formation of these folds has been dated by Mouret et al. (1993) and Lovatt-Smith et al. (1996) using fission-track data at 65 Ma (earliest Palaeocene) and 60 Ma (Mid Palaeocene), respectively. Booth and Sattayarak (2011) estimate that the entire region of NE Thailand was uplifted and deeply eroded during the Tertiary, with some 1,000–1,250 m of section lost across the entire area and up to 3,000 m eroded off the Phu Ham high (which is a major inversion fold). The contentious question in terms of the Maha Sarakham age is whether its basinwide formation is related to the mid Cretaceous or Palaeocene tectonic collision event or were there aspects of evaporite deposition related to both events.

Facies geometries suggest that sylvite deposited along the western margin of the Khorat Plateau was: (a) precipitated after the deposition of the carnallitite; (b) deposited prior to deposition of the Lower Clastic Member; (c) influenced by lateral ground water inflows, probably driven by a potentiometric head generated by relative uplift of an adjacent growing salt pillow; (d) related to the cannibalisation of the uplifted carnallitite bed atop a growing salt pillow; (e) precipitated early, either as pond-bottom nucleates and floundered raft cumulates or as downward-fluxing karst-filling cements in the rising margins of the brine pool; and (f) then covered by subaqueous colour-banded halite, fed via the dissolution of halite from a now carnallitite-depleted pillow crest (Fig. 11.40b).

Sylvite precipitation was driven both by solar evaporation on the pond floor (as in the Mulhouse Basin) and by subsurface cooling of downward flushing potassium-saturated brines (as in the Qaidam Basin). Similar potash recycling into modern playa depressions in rim synclines is occurring around outcropping crests of diapirs fed by Miocene salt in the Qum Kuh region of central Iran (Warren 2008). The central Iranian potash is probably reworked from a Miocene source layer in the diapiric salt (Rahimpour-Bonab and Kalantarzadeh 2005). Diapiric potash is also hosted in the Pohl and Hormuz island diapirs in area of outcropping and subcropping Hormuz salt centred on the coastal city of Bandar Abbas. Iran. These namakier deposits present a number of problems in terms of stability and general safety if they are to be exploited using conventional mining techniques (Talbot et al. 2009a; b). Solution mining would be a more viable option.

In terms of potash exploration in Khon Kaen region and elsewhere in Thailand, it is important to note that the thickest potentially exploitable sylvinite fairways lie in rim synclines adjacent to syndepositionally breached salt pillows (Fig. 11.40a). They do not form laterally extensive horizons and are not akin to the Devonian sequences of Canada discussed later in this section. These pillows were deforming the carnallite zone and uplifting previously formed carnallite beds into a periodically freshened hydrological setting. Simultaneously, sylvite was precipitating on the pan floor and in karstic voids in the halite about the pan rim (Fig. 11.40b). It was the superimposed pillow hydrology that was karstifying the halite at the same time that the upper portion of the carnallite member was dissolving and supplying K-rich brines to the pool floor. The raising of the sedimentation surface, via pillowing, explains why some of the sylvite forms clear coarse-crystal fills in large karst holes in the halite, while other sylvite is a primary precipitate interlayered with primary halite.

The potash geology of the Maha Sarakham has a number of technological challenges for a conventional sylvite mining operation. Its geology should be carefully and publicly documented before the onset of any major mining operation. Maha Sarakham potash tends to occur in the upper part of the lower halite unit, and about the current dissolutional edge of the basin it is sometimes without a substantial thickness of halite atop the potential ore interval. Such a halite bed is a required back when mining, as it will support the mine roof as ore is extracted. Mine backs are typically more than 5–10 m of halite above the potash level in mines in Canada and New Mexico and 1–2 m in the robotically extracted potash ores of the Boulby Mine, UK. The overlying lower clastic unit in the Thai succession is typically not well-indurated sediment, so maintaining mine headwall stability will be a major consideration in mine planning.

Likewise, tilting, dissolution and flowage of the Lower Salt means some sylvite layers show bed inclinations of up to 70–80° to the drill core axis, implying sylvinite beds have dissolved or flowed. This means the bed thicknesses must be ascertained as a true thickness and not be indicated solely by assay thickness in core or wireline intersections in wells. Such high dips are also problematic in designing a mine plan utilising conventional mine equipment where access and assumptions of stratiform stratigraphy dominate.

There may be long term problems of ground subsidence and water entry in and above a shallow conventional mine within this area where depths to be mined are as shallow as 350–400 m and located a tropical Aw climate setting characterised by high seasonal rainfalls.

There is also the potential for unexpected intersection with brine-filled cavities. For decades, some of the local villagers near Ban Nonsaaeng, Sakhon Nakhon Province, have been extracting brine from cavernous regions above shallow diapir crests and using it to manufacture salt. The subsurface positions of shallow wells used in these cottage industry scale workings are largely undocumented and not subject to legislative controls. The associated at-surface solar pans are also subject to leakage that can degrade the underlying soils, drive subsidence that can damage adjacent rice paddies and aid in the formation of collapse dolines (Satarugsa 2011; Jenkunawat 2012).

To date, large-scale solution mining has not been the focus of any potash exploration programme in Thailand. All studies of the feasibility of extracting potash in the last three decades have focused on shallower areas of potash about the dissolution-overprinted basin edges, where potash tends to occur at depths more amenable to conventional mining (e.g. planned operations at Bamnet Narong and Udon Thani). Further out in both structural basins there may be some intervals of potash in the Maha Sarakham Formation that are more deeply buried and more amenable to solution mining. Some 45 km NE of Nakhon Ratchasima, there is a well-run salt solution operation (Pimai Salt Co. plant) that has sonar-monitored linked multi-pad wells that extract brine in a controlled manner to produce halite from the Maha Sarakham.

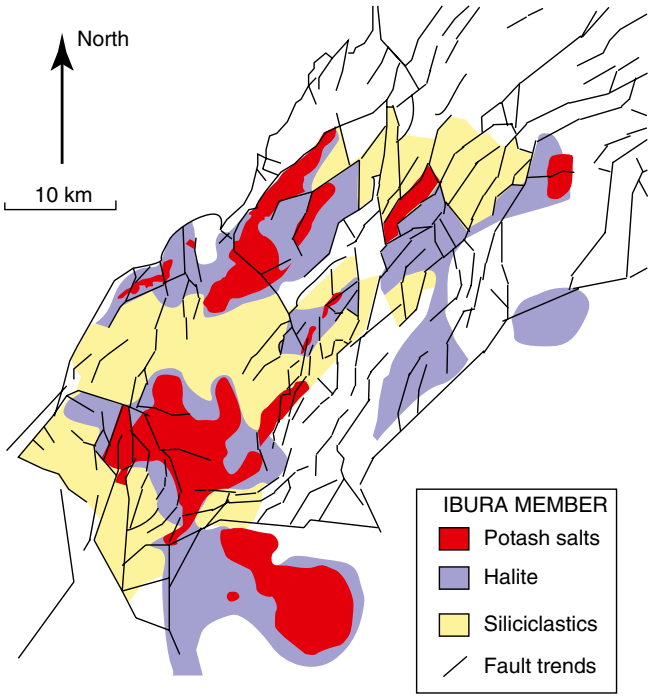

Fig. 11.42 Potash and halite distribution in the Sergipe region using a paleogeographic reconstruction (After Ecrosplan 2011b)

Cretaceous Trans-Atlantic Potash

Cretaceous (Aptian) evaporites, with bitterns, were deposited in a series of growing rifts created as Africa separated from South America. Today the remnants of these beds are to be found on opposite sides of the Atlantic in the Sergipe-Alagoas and Gabon-Congo basins (Chap. 5). In the Sergipe Basin the evaporite sequence (Ibura member of the Muribeca Formation) is a $MgSO_4$ -free potash deposit composed of stacked cycles of halite, carnallite and sylvite up to 800 m thick. Its distribution can be tied to deposition in a series of 10-km scale structural lows or sumps within a now halokinetic host and surrounded by siliciclastic aprons (Fig. 11.42).

More than 750,000 t/year of potash ore is extracted from the Ibura Member by the Companhia Vale do Rio Doce's at its conventional potash mine (Taquari-Vassouras mine) in Sergipe State. The deposit extent is relatively small and Mayrhofer (1985) estimated an *in situ* K_2O reserve of 11 million tonnes. The mine has a $174-per-ton operating cost and a projected productive life (as of 2012) of 9 years. It is owned by Petrobras, the state oil company, but leased and operated by Vale.

Depth to ore varies from 500 to 800 m, the thickness of the potash beds is uneven and ranges from 2 to 31.3 m (averaging 20.3 m). Sylvinite zones are mined as two separate layers, contain some carnallite and have an average grade around 25 % K_2O. Each layer is up to 11 m thick and they are separated by 3–6 m of barren halite. Several of the cycles in the Ibura Member are composed of thick halite (more than tens of metres thick) containing the highly soluble $CaCl_2$ mineral tachyhydrite (Fig. 11.43; Meister and Aurich 1972; Wardlaw 1972; Wardlaw and Nicholls 1972; Borchert 1977). The Sergipe deposits are characterised by thick cycles with a characteristic brining upward trend: halite (100 %) —>halite (35–90 %) + carnallite (10–65 %) —> tachyhydrite (5–100 %). Wardlaw (1972) showed that these deposits are primary as they contain bottom-growth features and primary bedding in the halite-carnallite units. Documented textures also suggest that there were episodes of syndepositional karstification and flowage within the carnallite, creating near identical textures to those seen in Thailand and the Qaidam Basin, but not yet documented as possible depositional analogs at the time when Wardlaw studied the Ibura sequence back in 1972.

In the upper part of the Ibura evaporite sequence a sylvinite bed sits atop a carnallite + halite bed and is overlain by a halite bed; a mineralogical evolution similar to that of the Thai and many other potash successions. The presence of a tachyhydrite layer just below a mine floor means that if tachyhydrite-entraining units are allowed to approach the mine floor, then there will likely be floor and mine-wall stability problems. This is always true of a tachyhydrite interval in a mined sequence, because tachyhydrite is

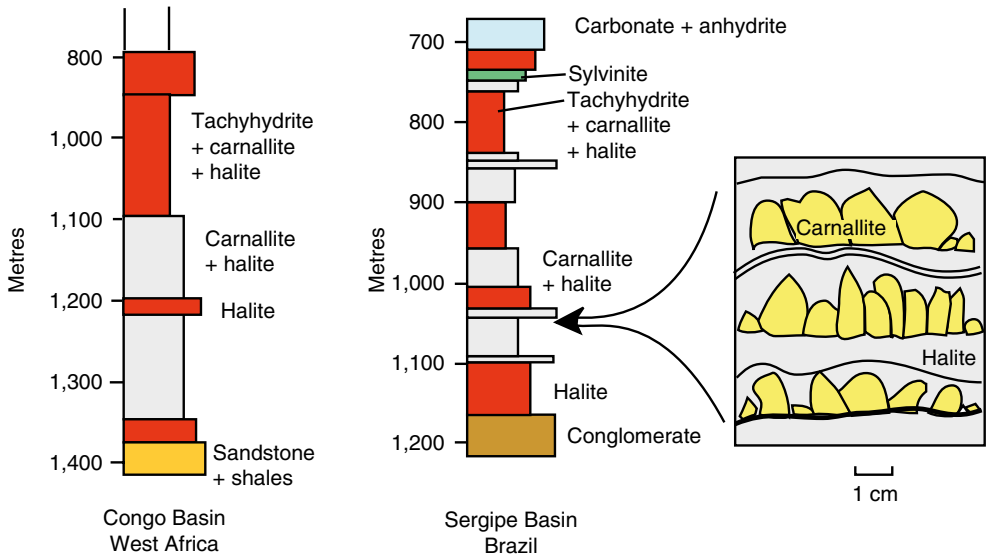

Fig. 11.43 Similarities in potash sequences from the Sergipe and Congo Basins (After Hardie 1990). *Inset* on the *right* shows primary layering and bottom-growth features of the Sergipe halite-carnallite subfacies (After Fig. 2 in Wardlaw 1972)

highly hygroscopic and has very low mechanical strength. Dangerous methane outbursts have also occurred in the Taquari-Vassouras mine when gas-filled dilation fractures were intersected (Davison 2009).

Today, away from the mined area, the various potash minerals in the Sergipe Basin show a systematic lateral zonation away from the anticlinal domes that also define the three main oil-producing structures in the Sergipe Basin. Oil-related drilling has shown that near the top of the anticlinal slope there is only rock salt, further out on the anticlinal arms there are intercalated sylvinitic layers, which in turn pass outward into carnallitic and tachyhydritic beds. There are no documented halokinetic structures beneath the anticlines and syndepositional uplift driving the leaching was perhaps related to drape over underlying horsts. This down-limb potash transition suggests that more soluble potash salts have been leached or escaped from the crests of the domes (Borchert 1977). In my opinion, given the similarity of the sequencing and layering to the Maha Sarakham and the preservation of detailed primary texture one can argue strongly for synprecipitational focusing of the ore via local halokinetic karstic reworking, as in the Maha Sarakham Fm.

Cyclic potash sequences constitute similar age beds on the African side of the Atlantic, there the beds are also free of $MgSO_4$ salts and include thick tachyhydrite or bischofite units. In and around salt domes, the Congo beds show a similar layering and downdip sequencing as in Brazil (Borchert 1977; De Ruiter 1979; Ercosplan 2007).

Within the Congo Basin the most extensive and thickest potash deposits occur in the coastal Kouilou region where ten evaporite intervals are recognised, with a cumulative thickness of potash beds of more than 100 m. Carnallite is the predominant potash mineral, while some cycles also contain bischofite and tachyhydrite, but lack substantial volumes of bedded sylvite (Fig. 11.44). The region is thought to be halokinetic, at least in part, and carnallite locally grades into sylvite in the upper parts of some beds. This implies transformation to sylvinite from a carnallitic precursor in zones of freshened water crossflow, either via incongruent dissolution, or synprecipitational karstic leaching from salt structure crests (as in the Maha Sarakham Fm).

Further inland, for 9 years in the 1970s, the equivalents of these carnallitic potash cycles were conventionally mined for sylvite in the Holle mine area in Republic of Congo, formerly Congo-Brazzaville (Fig. 11.45). Production was from uppermost sylvinite layers atop carnallite, with extraction rates around 360,000–450,000 tonne/year. Sylvinite was targeted in the second highest (9th) evaporite cycle in four separate beds. Two layers, beds 3 and 7/8 were mined at typical depths of 290–380 m, at an average grade of 18 % K_2O, over an area of 18 km^2. Bed 3, which was 10–20 below bed 8, had an average thickness of 3 m and a grade of up to 38 % K_2O with only 0.1 % insolubles.

Galleries were dug out below a 35-m to 55-m thickness of salt; the observed minimum mine head was 16 m. No faults or fractures were encountered over 8 years of operation. But on June 17, 1977, a flow ingress and a fall of materials with characteristic of the levels above the salt roof, occurred. At this specific location, the salt roof was some 70 m above the mine galleries. On June 20, a large water flow developed, and rocky blocks fell into the gallery; the inflow rate was 30 m^3/h, and the brine NaCl content had decreased drastically. By June 21, the flow rate was as much as 1,650 m^3/h and increased to 10,000 m^3/h or more on June 22. A large conical crater, 150 m in diameter and 20-m deep, developed at ground level above the mine. On June 20, 1977 water from a breached overlying aquifer termed a "clastic break-in" by the mine geologist had begun to enter the mine, accounting for the increased rate of inflow and with 36 h the mine was lost to flooding.

Prior to the final flooding ongoing geological and water problems prevented the Holle mine from ever being profitable

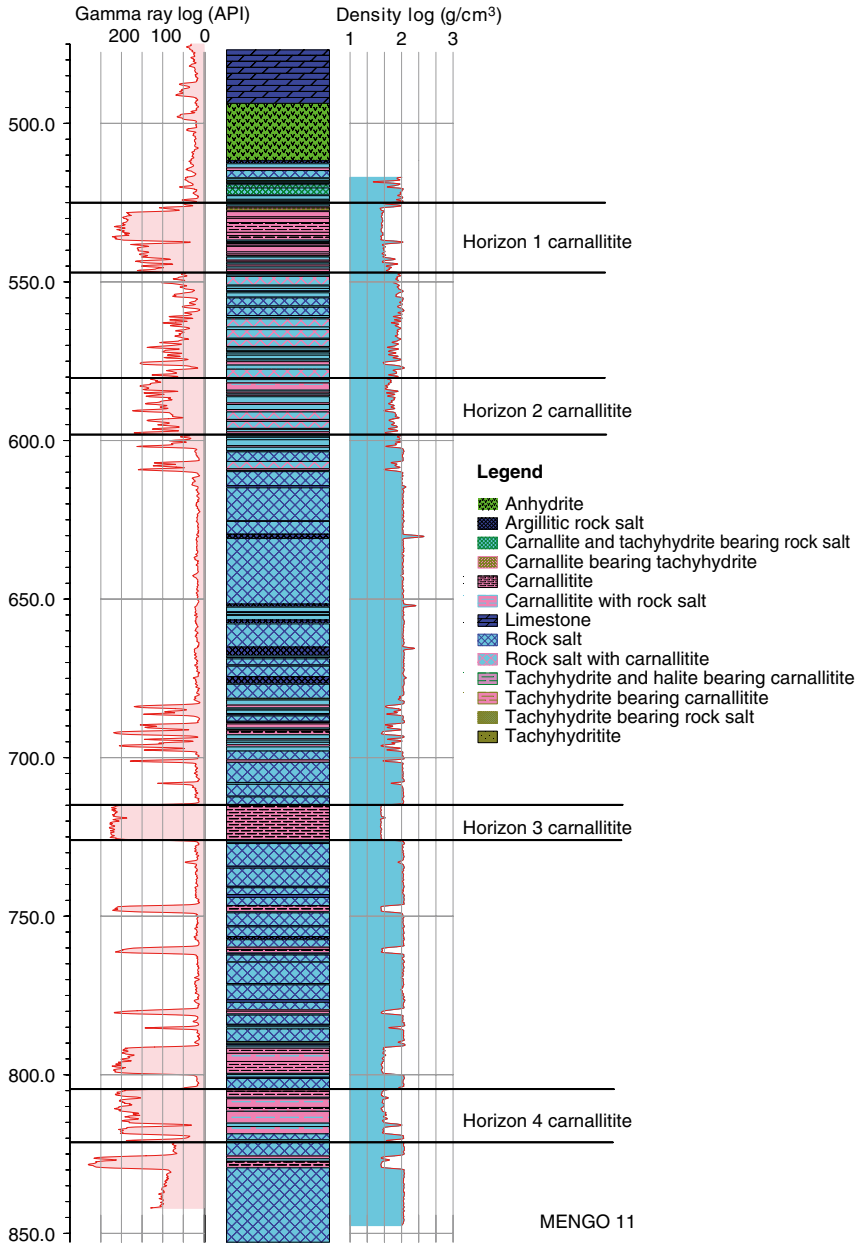

Fig. 11.44 Potash stratigraphy in the Mengo 11 well, Kouilou region, Congo Basin (After Ercosplan 2007)

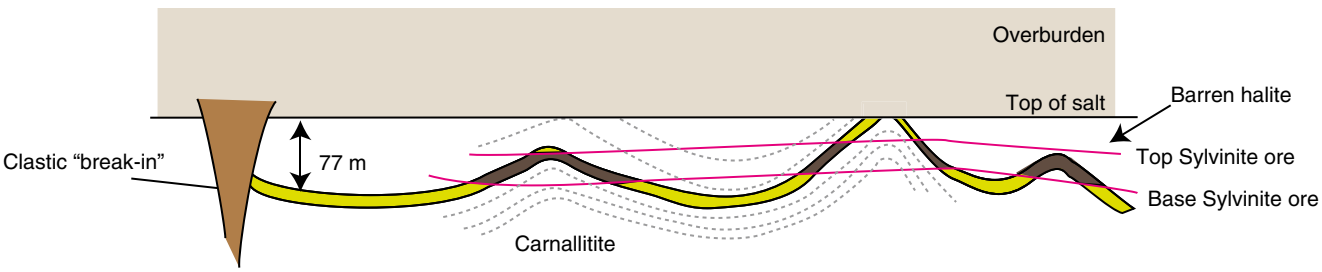

Fig. 11.45 Schematic section of Holle Mine showing discontinuous nature of sylvinite ore (After Mayrhofer 1985)

or reaching its target production level of 720,000 tonne/year. All operations at the site ceased in 1978. The shallow, discontinuous nature of the targeted sylvinite horizon in this deposit, probably means that the best way an economic recovery could be attained, in either the Kouilou or the Holle Mine areas, is via solution mining. The tropical climate of the region means energy-intensive crystallizers, rather than solar evaporite pans, would be needed to concentrate the return brines.

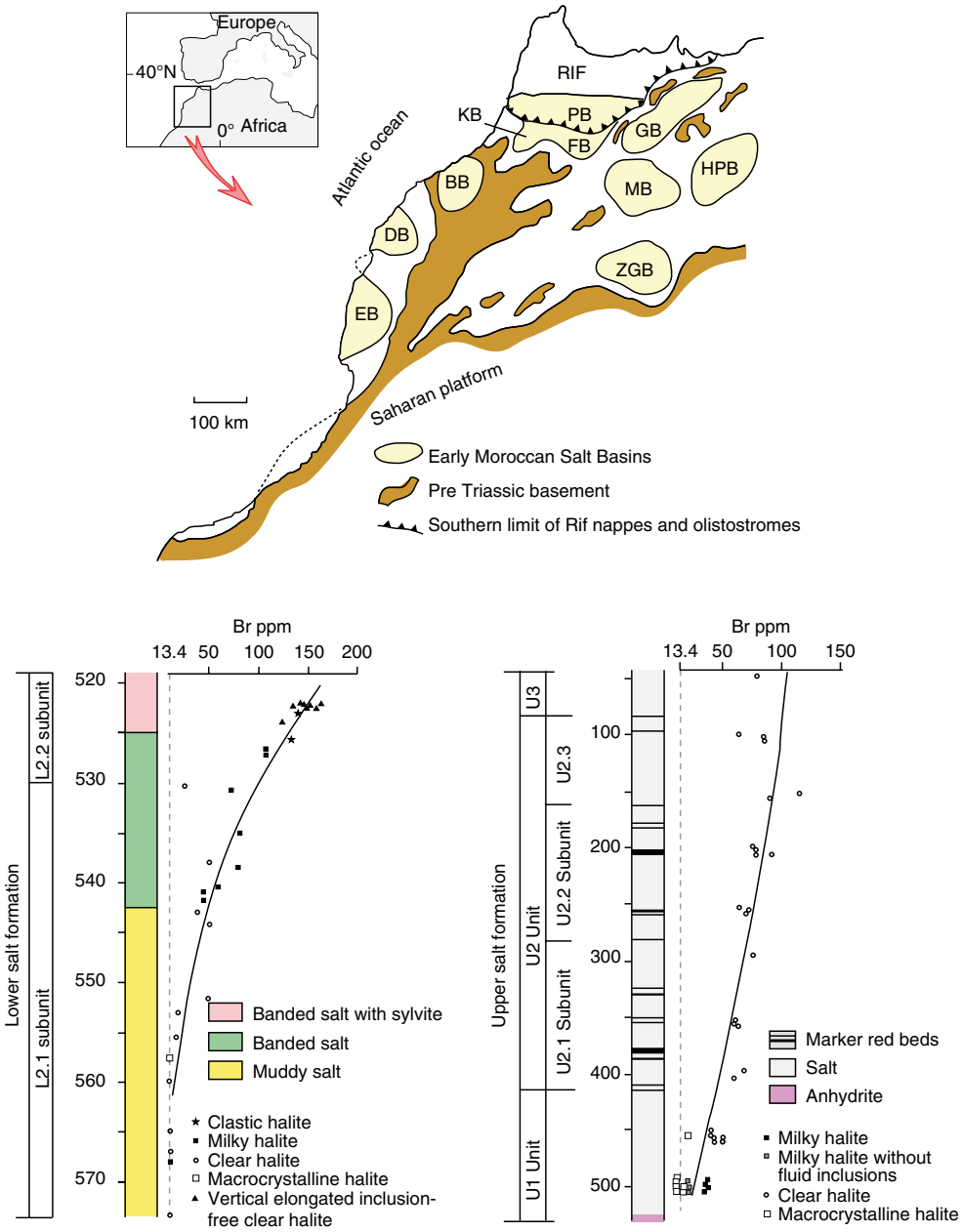

Fig. 11.46 Salt in Morocco. (**a**) Location of major Lower Mesozoic Moroccan Salt Basins. Key: *BB* Berrechid Basin, *DB* Doukkala Basin, *EB* Essaouira Basin, *FB* Boufekrane Basin, *GB* Guerif Basin, *HPB* Haut-Plateaux Basin, *KB* Khemisset Basin, *MB* Moulouya Basin, *MM* Moroccan Meseta, *PB* Prerif Basin, *ZGB* Ziz-Guir Basin. (**b**) Stratigraphy and bromine profiles from the Lower and Upper Salt Formations in the Khemisset Basin, northwestern Morocco (After Et-Touhami 1996)

Interestingly, neither the Sergipe nor the Congo potash/tachy-hydrite mineralogies can be derived from the evaporation of modern day seawater. Yet both deposits retain bottom-nucleated halite crystal fabrics and widespread tachyhydrite, implying different seawater chemistry in the Cretaceous (Fig. 11.43).

Moroccan Meseta (Late Triassic)

Salt basins formed in Morocco as rifts evolved into subsea-level intracratonic sags during the Triassic breakup of the supercontinent Pangaea. As a result, nonmarine redbeds and evaporites fill the many Late Triassic (Keuper) to early Liassic half grabens, which make up the Moroccan Meseta (Fig. 11.46a). Thick basalt flows (up to 500 m) underlie and overlie these saline deposits (Van Houten 1977; Clement and Holser 1988; Lorenz 1988; Courel et al. 2003). In four of the sub-basins, including the Khemisset Basin, evaporites interbedded with basalts carry varying concentrations of potash, but as yet none are exploited commercially. Documented sylvinite occurrences in the Meseta Basin occur at depths of 490–790 m, tend to be low grade and erratically distributed (Tortochaux 1968). These potash intervals consist essentially of halite, carnallite, sylvite and rinneite, with less than 1 % of other minerals (anhydrite, kieserite, bischofite, douglasite;

Salvan 1972). Once again, like the Cretaceous examples just discussed, this is a $MgSO_4$ -depleted potash sequence and indicate a largely marine-derived Ca-Cl brine source with ionic proportions different from today.

The most detailed work on the stratigraphy of the evaporite intervals of the Meseta to date is by Courel et al. (Courel et al. 2003) and Et-Touhami (1996), who noted up to a kilometer of red-bed fringed halite in the thicker portions of the Khemisset Basin graben. Et-Touhami (1996) focused on potash-entraining strata in the centre of the Khemisset Basin, which are Late Triassic to Early Liassic and made up of five formations (from base to top); Lower Clay Formation, Lower Salt Formation, the Basaltic Formation, Upper Salt Formation and the Upper Clay Formation (Fig. 11.46b). Potash occurs toward the top of the Lower Salt Formation (LSF). The LSF is subdivided into two informal units known as L1 and L2. The lower unit (L1) is composed mostly of red-brown chaotic mudstone interbedded with red beds, especially toward its base. The upper unit (L2) is further divided into the L2.1 and L2.2 subunits (Fig. 11.46b). Subunit L2.1 is made up of black chaotic to massive banded salt with some local inclusions of potash. Subunit L2.2 is made up of massive banded halite with potash layers (sylvite and carnallite), along with thin stringers of anhydrite and polyhalite. As in Thailand and Brazil, the sylvite unit tends to occur near the top of a colour-banded halite unit and sits directly atop a carnallitite succession. Locally the halite crystals in the carnallitite unit retain relict chevron fabrics and vertically-elongate inclusion-free halites identical to those interpreted as syndepositional relicts in the Mallowa Salt of the Canning Basin, Australia (Cathro et al. 1992). Slumps and synprecipitational karstic textures also characterise the carnallitite. A bromine profile through the LSF shows the potash was precipitated in the most saline stage of the accumulation (Br >100 ppm; Fig. 11.46b).

The LSF in the Khemisset Basin is covered by vesicular to highly altered lavas and flows of the Basaltic Formation, which also retains local lenticular intercalations of claystones, limestones and evaporites. Atop this is the Upper Salt Formation, a unit composed of generally flat lying salt beds intercalated with siliciclastic mudstones and siltstones. It is divided into Units 1–3, with local potash inclusions sometimes found in Unit 3. The bromine profile of the Upper Salt Formation shows lower concentrations than the LSF and does not appear to have attained the bittern stage for long enough periods to accumulate thick beds of potash (Br <100 ppm; Fig. 11.46b). Hence, potash occurrences noted today in the Meseta tend to be low grade and erratically distributed.

Permian Potash

The Permian was a time of widespread epicontinental salt deposition across Europe, Russia and North America in basins driven by tectonics tied to the accretion of Pangaea. Like today, it was a time of $MgSO_4$ ocean chemistry. Most of the European Permian potash occurrences centre either on sumps in the large intracratonic thermal sag basin known as the Zechstein (Lopingian), or in foreland flexures located the east of the Cis-Urals collision suture (Kungurian). The Zechstein Basin stretched from northern Britain, southeast across the North Sea through the Netherlands, Denmark, Germany and Poland to the edge of the Hercynian massifs (Harz, Rhine and Bohemian mountains). North American potash was deposited in local sumps at a time of "fill and spill" in the aulocogen known as the Delaware basin (Lopingian stage). Chapter 5 discusses the tectonic and eustatic character of these various basins.

The Zechstein salt succession of NW Europe and its bedded potash was deposited in a Late Permian intracratonic thermal sag basin, within a tectonic relaxation or regional flexure setting, related more to the aftermath of the Hercynian orogeny than to the early stages of Mesozoic extension (Geluk 1999; Van Wees et al. 2000; Scheck et al. 2003). Zechstein salt deposition took place at the onset of a time of entry of marine waters in a period of thermal subsidence lasting from Permian to Late Triassic (Littke et al. 2008). This occurred after an initial volcanic rift-associated episode during Late Carboniferous to Early Permian. In the Late Triassic, a second extensional phase affected the Zechstein basin and halokinesis was widespread. This was followed by uplift of portions of the northern part of the basin in Late Jurassic–Early Cretaceous and a phase of compression during Late Cretaceous–Early Tertiary, both events reinvigorated salt flow and remobilized potash distributions within many salt structures.

Potash extracted from the Permian Zechstein evaporites provides 20 % of the world's potash. The Zechstein succession of NW Europe was deposited in a huge drawdown seaway extending across much of modern Europe and is today made up of four evaporite cycles: the Z1-Werra Series, Z2-Stassfurt Series; Z3-Leine Series and Z4-Aller Series. Each Zechstein series has a general sequence of clastics, carbonates, one or two phases of sodium and potassium salts, regressive halite or anhydrite, and carbonate. Potash beds of Z1 and Z2 are primarily composed of sylvite (KCl), carnallite ($KCl.MgCl_2.6H_2O$) and kieserite ($MgSO_4.H_2O$) and rapid lateral changes due to halokinesis are common. The Zechstein 2 potash bed interval locally attains a true thickness of about 15 m. Permian potash worldwide tends to be associated with $MgSO_4$ salts as the Permian was the penultimate time of a $MgSO_4$ ocean, prior to the current one (Warren 2010).

German Potash (Z1, Z2 and Z3 Potash)

Six mines are currently active in three German potash districts: the Hanover district in Lower Saxony, the Calvörder

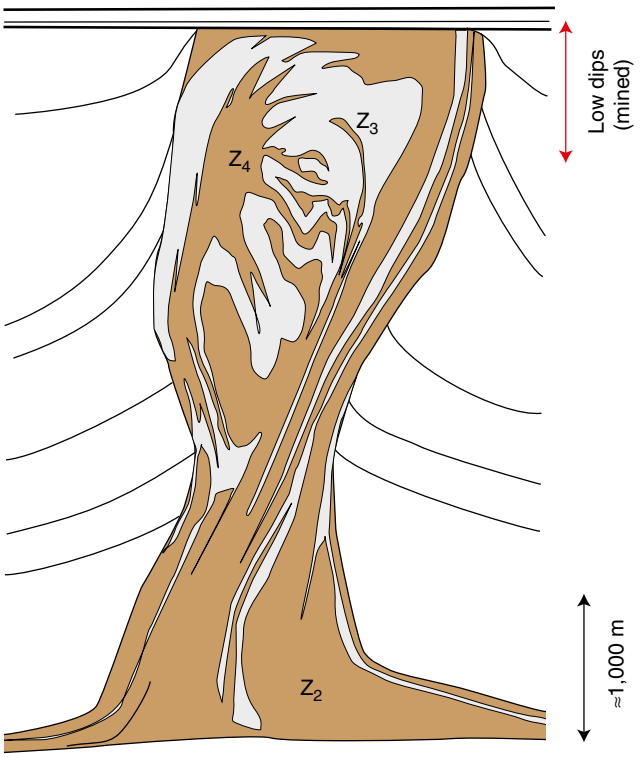

Fig. 11.47 Cross section showing geometries of the Permian Zechstein Z1–Z3 series in the salt structure that hosts the Mariaglück Mine, former West Germany (After Mayrhofer 1985)

district in Saxony-Anhalt and the Werra-Fulda district in Hesse and Thuringia. Some of these currently active German potash mines in the Stassfurt (Z2) and Leine (Z3) in the Saxony-Anhalt district are more than 100 years old. The Z3 seams are mostly sylvinite and ore zones are mostly free from higher levels of Mg-salts present in the Z2 series (carnallite and kieserite). In general, the average grade of halokinetic potash (sylvinite type) across Germany is 17–18 % K_2O, which is low by Canadian standards. However, the extracted products can be utilized economically due to proximity of the market, mining efficiencies, and high levels of government farming subsidies throughout the European community.

Two potash cycles are exploited in the Z1 in the Werra-Fulda Basin southeast of Kassel, while two potash beds in the Z2 and Z3 are mined near Hanover. Formations near Hanover in northwestern Germany occur in diapiric salt domes (Fig. 11.47). There, the salt and potash mines are located along salt walls that trend along strike for over 20 km and are 800–1,000 m wide. In the Hanover area, potash is mined between depths of 300 and 900 m, along a steeply-dipping seam some 2–30 m in width (the increased width is due to multiple, tight folds). In the southern potash-mining district of Werra-Fulda, two seams are mined at depths of 300–900 m with thicknesses of between 2 and 4 m. These seams are even lower in grade than in the Hanover area, but unit extraction costs are lower as seams gently dip and are steeply folded. However, the internal geometries of the various beds are complex and salts are usually extracted from those upper parts of the salt structures with dips that are relatively low angle (Fig. 11.47).

In Poland there are various occurrences of potash in the Zechstein series. For example, the Z1 is found at mineable depths north of Gdansk on the Leba upland, where it is made up of thin layers of polyhalite, with carnallite, kainite, glaserite and loeweite inclusions. Clay, anhydrite and gypsum are major components present with the polyhalite, which also contains smaller amounts of celestite, epsomite, halite and carbonate. In the central Polish depression the Z2 (Stassfurt) bed consists of up to 25 m of carnallite, but atop the Klodawa salt structure it has changed to 6–8 m of a high-kieserite sylvinite (Garrett 1995). Over the years many studies have been conducted on the possible utilization of these various halokinetic potash beds, but so far Polish potash has yet to be exploited commercially.

The nature of sylvite in the Polish Zechstein (Stassfurt Z2 and Leine Z3 cycles) is of broader interest than deposit occurrence, in that it illustrates the unusual thermal and reactive nature of potash salts encased in halite, both at deposition and in subsequent diagenesis. In a study of inclusion homogenization temperatures in chevron halite associated with sylvite layers, Vovnyuk and Czapowski (2007), found a thermal dichotomy in the inclusion data (Fig. 11.48). They interpret this as a combination of depositional and diagenetic signatures. The lower temperature band (53–60 °C) indicates primary halite and sylvite deposition via brine cooling within heliothermic salt lagoons and saltpan-salinas. Inclusion chemistry in the primary chevron-textured halite (group a) shows the bitterns were Na-K-Mg-Cl-SO_4 (SO_4-rich) waters, that is, brines typical of a marine oceanic source. The studied system differs in its elevated potassium contents compared to brines typical of many other primary-textured Zechstein halites. With diagenesis this has produced sylvite (also associated with daughter crystals in halite inclusions), via redeposition of locally generated potassium salts during inflow of fresh seawater into the sedimentary basin (i.e., sylvite layers via incongruent dissolution). The second brine group (group b), with somewhat higher temperatures of 85–135 °C, indicates subsequent diagenetic recrystallization of the buried halite and interlayered potash (Fig. 11.48).

Z3 – Boulby Potash, UK

Elsewhere in Europe, potash is solution mined from the Aller Series in the Veeder region of Netherlands and conventionally mined from the potash member of the Boulby Halite in the Teeside Group, with the mine located at the southeast

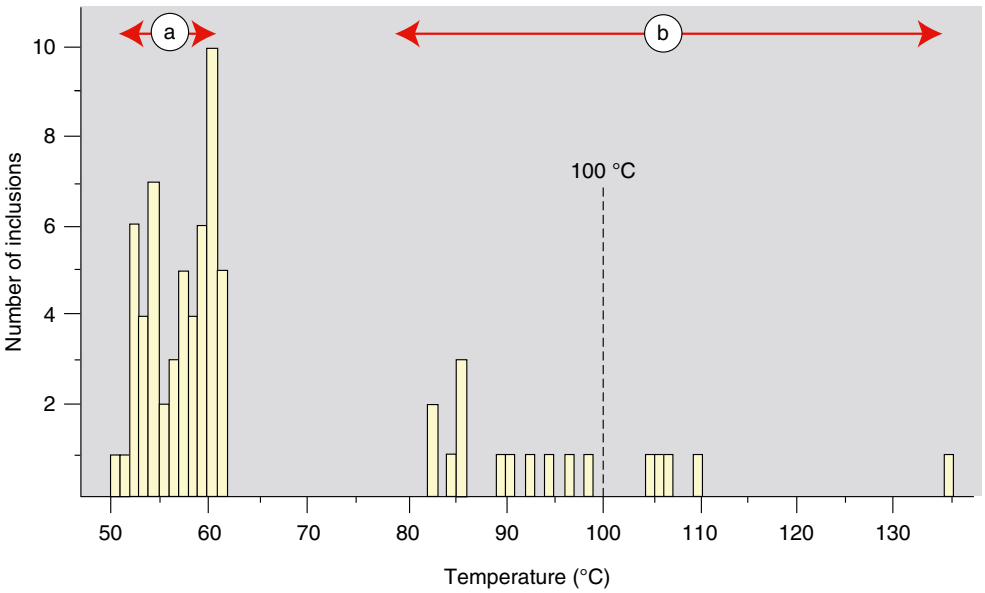

Fig. 11.48 Halite homogenization temperatures (*a*) indicate measurements that reflect the temperature of heliothemic-prone basin brines during precipitation, (*b*) homogenisation temperatures of inclusions in chevron halite from regions of halite/sylvite recrystallisation via diagenetic fluid overflow (After Vovnyuk and Czapowski 2007)

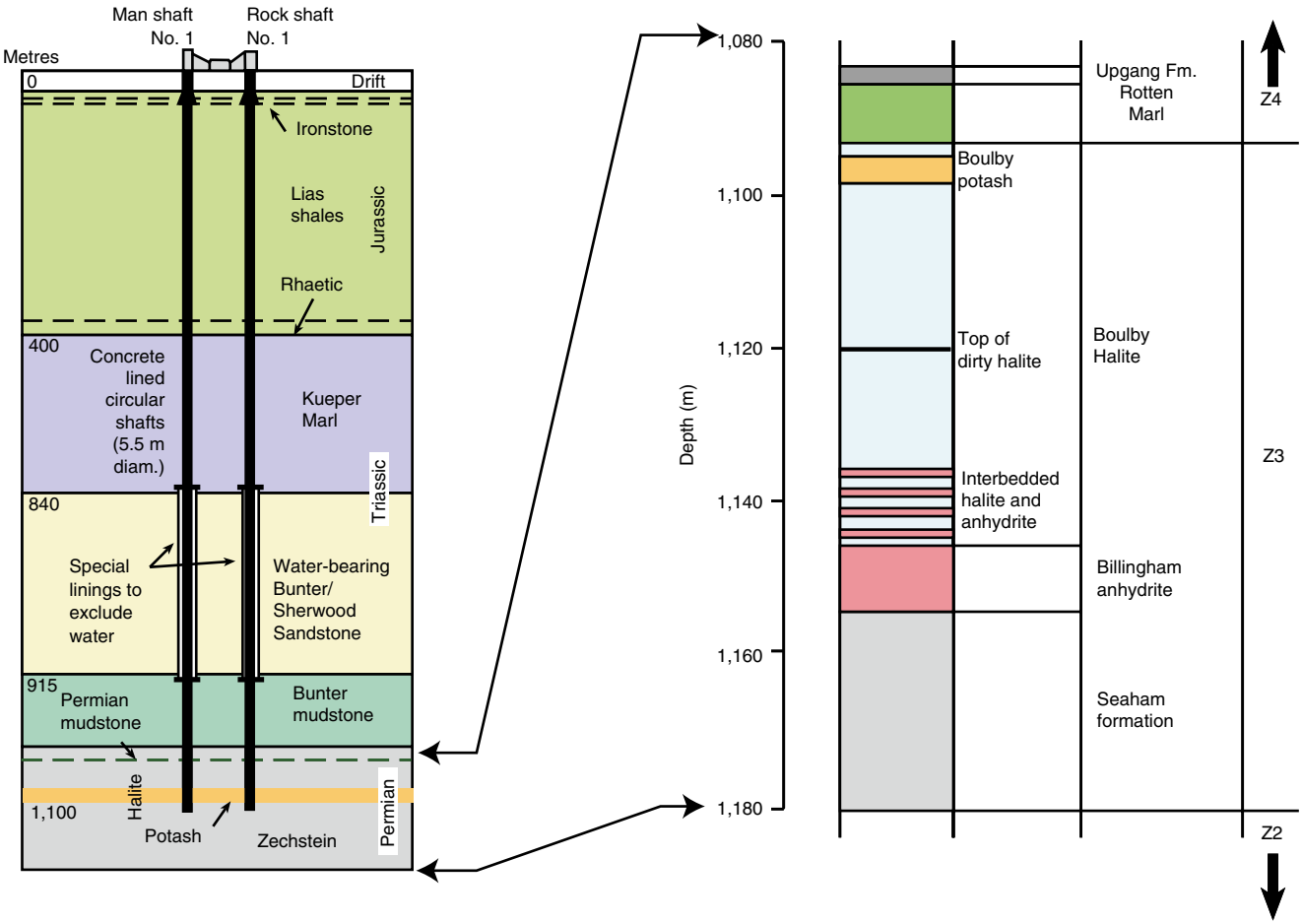

Fig. 11.49 Stratigraphy of the Boulby Mine, Sussex, UK (After Holmes 1991)

boundary of Cleveland County on the coast of NE England (Figs. 11.49 and 11.50). The Boulby mine has more than a 1,000 km of tunnels over an area measuring 8 km by 5 km, with around 50 km of new tunnels added each year. Workings extend more than 5 km under the North Sea. Today, the mine is the only exploitation of Zechstein potash in England,

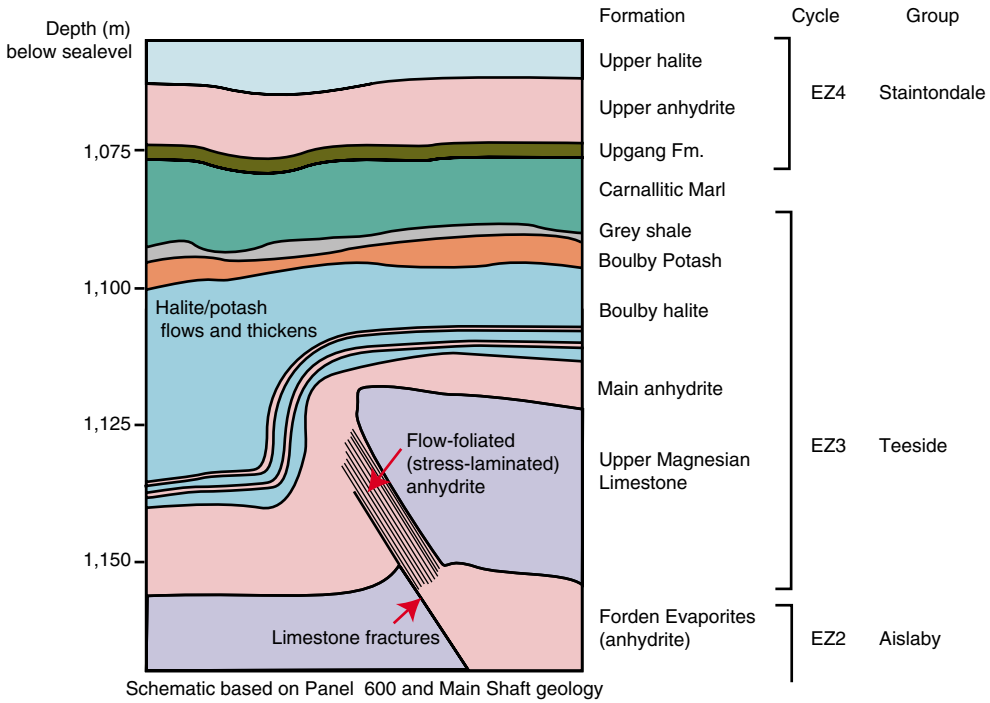

Fig. 11.50 Effect of reverse faulting (Mesozoic-Tertiary compression on the Boulby Evaporite Succession where salts tend to flow and thicken, while brittle carbonates fracture (After Talbot et al. 1982; Davison 2009)

although new mines in the same coastal region are currently under consideration. Cleveland Potash Ltd (CPL), a business unit of ICL Fertilizers, has operated the Boulby Mine for over 35 years, currently producing over one million tonnes per annum of refined KCl and 0.5 Mtpa salt. The operation extracts sylvinite from between 850 and 1,350 m and is operating is near the limit for conventional underground potash mining. It processes the ore by conventional froth flotation techniques and in April 2011 the mine also began to extract and process a polyhalite ore.

The Boulby deposit lies at the extreme western edge of the Zechstein Basin and marks one of the deeper zones of the Zechstein 3 and 4 potash (Garrett 1995). The English Middle (or Boulby) Potash bed is assumed to be a Zechstein 3 equivalent, and the Upper Potash bed (not found at the Boulby mine) to be Zechstein 4 (Smith and Crosby 1979). This consensus correlation is still used today, even though some consider the Zechstein series of England to be depositionally distinct from Germany and Poland. The Boulby Potash bed deepens to the south of the current mine workings, where the "Upper Potash" bed (Z4) is also present. Potash ore is underlain by a thick sequence of mildly halokinetic halite, which makes up the majority of the Boulby Formation (Fig. 11.49). This halite is in turn underlain by the Billingham Main Anhydrite and Upper Magnesian Limestone Formations of the Teeside Group.

The targeted Boulby Potash interval is a sylvinite with gneissic and augen-like flow textures, along with tectonically-rounded rock fragments from adjacent intrasalt beds (Figs. 11.49 and 11.50; Woods 1979; Talbot et al. 1982; Smith 1996; Davison 2009). The sylvinite has a variable bed thickness ranging from less than 1 to 20 m over lateral distances of 20–30 m, with mined units generally ranging between 0 and 8.5 m in thickness. The ore horizon essentially lacks soluble magnesium or sulphate salts, and so is an ore feed lacking many of the processing problems inherent to more magnesian potash ores currently extracted on the European mainland.

There are five distinct Boulby ore types across the more than 40 km^2 of the mine workings, all of which exhibit flow-related rapid lateral changes. An ore type can predominant over mine areas more than a kilometer across (Garrett 1995). In some zones an ore with low insolubles is found, with the gneiss-like texture of sylvite crystals being elongated in a ratio as high as 3–1, and generally with a near-horizontal bed orientation (Woods 1979). This is the ideal ore. The sylvite can be red to white, and the halite may contain considerable anhydrite and clay, or be quite pure and apparently recrystallized (Fig. 11.51). The second type of ore is similar in quality, but found in areas with folds, overturned folds (recumbent; often with a near-horizontal axis), or sheet-like with a horizontal surface (nappes). Some of the overlying salt clay, or underlying halite may occasionally be incorporated into the overfolding. The ore may be as much as 20 m thick and have a KCl content of over 50 %, probably because of sylvite's differential flow character compared to halite.

The next three ore types have purer sylvinite at their base for 0.5–1.5 m, with grey anhydritic shale on top of it. The shale contains a high percentage of crystallized or fibrous veins of sylvinite. In one of these types, shale is usually

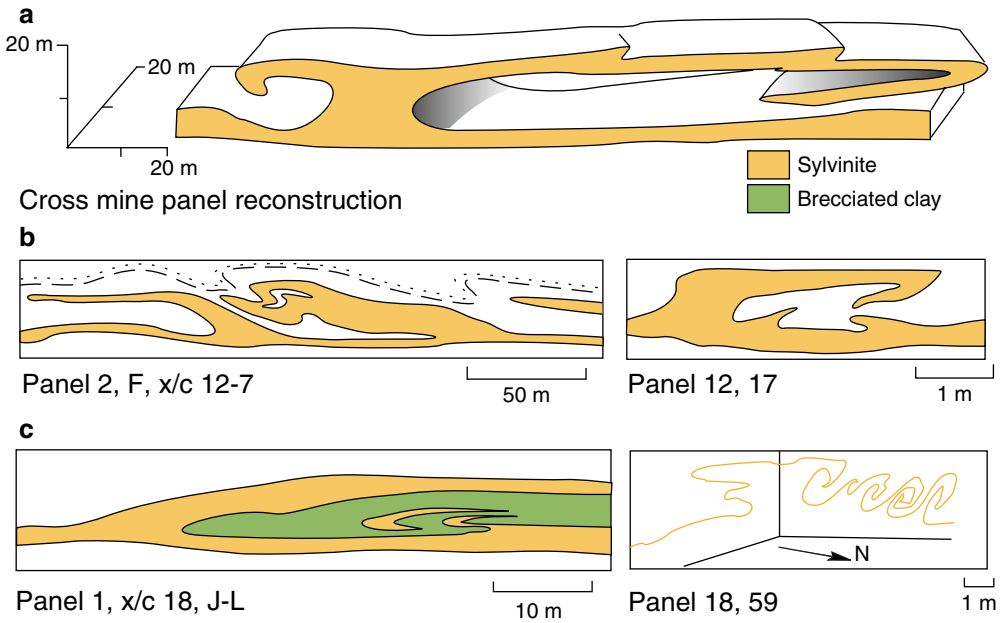

Fig. 11.51 Structural complexity of the sylvinite ore as mapped in the mine panels (After Talbot et al. 1982)

topped by the salt clay, but a displaced halite zone may also be present. The next type is similar, except sylvinite also occurs above highly veined shale, and folds and nappe structures occur, resulting in a much thicker deposit. Ore grades there often exceed 40 % KCl. The final type is also similar, but has a greater portion of halite in the upper sylvinite.

The average KCl content in the exploited parts of the Boulby Halite is 26 % KCl. As in the New Brunswick ores of eastern Canada, Boulby sylvinite ore is characterized by marked thickness changes reflecting flow thickening, related to the high differential stresses created by halokinesis in potash encased in halite (Fig. 11.50). The flow thickening of highly mobile potash intervals has locally enriched several of the ore beds to grades in excess of 50 % KCl in a process sometimes called "flow or stress refining". The same potash-related thickening is seen seismically in North Sea diapirs (Jenyon 1986).

The first of two shafts at Boulby was completed in 1973 (Fig. 11.49). It quickly became apparent that ore grade in this potash deposit, which sits atop the thick halites of the Boulby Halite Formation, was characterized by postdepositional textures indicating both brine-controlled mineral migration (early karst) and gravity-induced plastic flow especially in the sylvinite bed (Fig. 11.51). From core studies related to mine definition, Stewart (1965) estimated that the sylvite (or at least 50 % of it) in the Boulby Potash zone was derived from carnallite. This interpretation was based upon the presence of abundant halite pseudomorphs after carnallite in one core, with lesser, but still considerable volumes of similar pseudomorphs seen in each of the other three cores he examined.

Bromine analyses appear to further indicate that the Boulby sylvite was formed from carnallite (Garrett 1995). It seems that the carnallite was converted to sylvinite soon after deposition, since there is no evidence of the overlying sediments settling or being distorted by the carnallite-to-sylvite volume change. There is a distinct red halite zone in the underlying Boulby Halite, where perhaps red carnallite was converted to sylvite and then, because of a period of shallow subsurface epsomite leaching, the associated sylvite was also fractionally dissolved, leaving the zones of red halite with associated red halite-cemented caverns in the host halite. This leaching and alteration must have occurred soon after deposition because of the Upper Halite's relatively undisturbed bedding planes and structure. Calcium and magnesium-containing brine also seeps from cuts in the halite bed at the access level in the mine (below the potash level), further indicating the early removal of the last traces of kieserite by precipitation with shallow-burial dolomite conversion brines.

Deformation of the potash bed is ongoing today and has led to a number of mining problems over the years, exacerbated by high temperatures of 40 °C or more at the deepest workings (≈1,200–1,300 m below land surface), and the occurrence of local highly pressurised nitrogen gas pockets in the salt. Past mine problems include one gas blowout (in 1976) with sufficient pressure to turn a continuous miner onto its side and the need to cope with the inherently unstable geology of the salt-clay head to the mine workings. However, the high-grade of the ore, its relative simple mineralogy (no sulphates) and low dips even though halokinetic (Fig. 11.51) make processing straightforward and so the

deposit is economic. The virtual absence of magnesium minerals is particularly relevant to economic processing of the ore stream.

Locally, clay content in a projected ore zone can be anomalously high due to a combination of halokinesis and karst, which can exert a major detrimental effect on ore grade, as do unexpected elevated levels of anhydrite, magnesite, pyrite, quartz and boron minerals, which together can locally exceed 15 %.

The Carnallitic (Rotten) Marl Formation of the Staintondale Group, composed primarily of dehydrated clay minerals and halite, overlies the Boulby Halite Formation. As the name implies the Rotten Marl is a "salt-clay" bed. It tends to be structurally incompetent as it lacks any significant cementing mineral binding the soft clay. The bed is further weakened in some parts of the mine area by steeply dipping discontinuities created by a combination of flow and dissolution features. It must be well characterised before mining can proceed safely. A minimum of 1.5–2 m of salt in the mine back (roof) is maintained to ensure no significant roof collapse and the ore zone is always approached from below, not above. The Carnallitic (Rotten) Marl Formation sits in sharp contact with the overlying Upgang Formation, which in turn is overlain by the Upper Anhydrite Formation and Upper Halite Formation of the Zechstein Cycle 4 of the Staintondale Group. The Staintondale Group is in turn overlain by more than a kilometer thick Upper Permian and Triassic marine and continental clastic sediments, which include highly pressurised brines in sands of the Triassic Sherwood Formation, a unit which required expensive specialised linings when the shafts were first sank to enter the ore level (Fig. 11.49).

The Boulby potash zone is worked using a variation of the room and pillar method. Ore is extracted from the rooms (potash panels) using "continuous miner" equipment, similar to that used in coal mines. Mine development work is carried out in relatively thick stable halite beds, located some 30 m below the potash ore. Ramps are then driven upward from the development roadway level into the potash zone, which is less structurally stable. Even the access roads are liable to instability due to high lithostatic pressures at these 1,000 m + depths, so long horizontal slots are cut into roadway walls for stress relief. Although the basic concept of roadway development in salt to access room-and-pillar potash panels was sound, determining the most efficient mining system proved difficult and it was not until 1984 that mining costs were sufficiently reduced to achieve profitability. By the mid-1990s, output had stabilized at 16,000 t/day – 2.8 Mt/year from 6 production sections. To cope with greater stresses in the ore below 1,200 m and to raise output above 3 Mt/year, in 2001 the miner-operator (ICL Fertilizers; Cleveland Potash) converted its continuous miners to remote-controlled operation (so they can be used safely without prior blasting and gas relief in shaly, gassy sections of the potash ore level).

New Mexico Potash, USA

Potash is mined from McNutt Member of the Salado Formation in the Carlsbad Potash District of the Permian Basin of New Mexico (251 Ma – Lopingian). Now largely depleted the area once produced more than 70 % the potash mined in the United States. Potash was first discovered in this region in the mid 1920s during drilling for oil and the first potash mine was opened in 1931. Various potash minerals occur in 11 ore zones numbered 1–11 (in ascending order) in a 215 m thick cyclic interval known as the McNutt interval located in the middle of the Salado Formation and atop some 400–700 m of halite (Fig. 11.52: Adams 1970; Lowenstein 1987b). Zone 1 is the richest, but is now exhausted. More recent production in the 1980s and 1990s was mostly from zones 3, 5, 7 and 10, where the proportion of langbeinite is higher but, in terms of conventional mining, these levels too are now largely depleted. The areal extent of the potash is both highly irregular and in some ore zones is patchy and scattered. The number of ore beds in a vertical section can vary considerably, and their shape and location is only roughly similar. This is so even within the 1,100 km^2 area underlain by shallow, high-grade ore and designated the "Potash Area" or "Carlsbad Potash District" in 1934 by the Secretary of the Interior (this is the area in New Mexico where oil and gas drilling is largely banned). It lies at the centre of a larger 140,000 km^2 area underlain by low grades of potash and centred on the towns of Hobbs and Carlsbad, New Mexico (Fig. 11.53a). Throughout the "Potash Area", the potash ore beds are relatively flat lying, making them amenable conventional mining targets. Beds can mildly-to-moderately undulate at the sub-km scale, and locally, at a scale of tens of metres or less, there can be gradual-to-steep displacement and folding in the targeted ore beds, related to dissolution and mineralogical transformation.

Major ore minerals are sylvite and langbeinite, with accessory leonite, kainite, carnallite, polyhalite, kieserite, bloedite, halite and anhydrite (Fig. 11.52). A typical ore in zone 1 ran 60 % halite, 30 % sylvite, 5 % langbeinite, and 2 % of polyhalite and insolubles. Langbeinite ore is produced from zone 4 and mixed sylvite-langbeinite from zone 5. For example, in the former IMC Global Inc operation (now the Mosaic Potash Facility), the ore on the 900 ft (275 m) level (zone 5) is primarily sylvinite with some langbeinite. The 260 m (850 ft) level ore is langbeinite (zone 4). The 244 and 213 m (800 and 700 ft) level ores are a mixture of the two. Currently, in a nearby operation at its "East Mine," Intrepid Potash produces muriate from sylvinite ore, and sulphate of potash -magnesia from langbeinite and MOP combinations.

The potash ores in New Mexico are $MgSO_4$ associations and lie above and immediately at times basinward of the older Permian basin margin, as defined by the position of the underlying Capitan Reef (Fig. 11.53a). This location corresponds to a likely surface depression and water sink at the

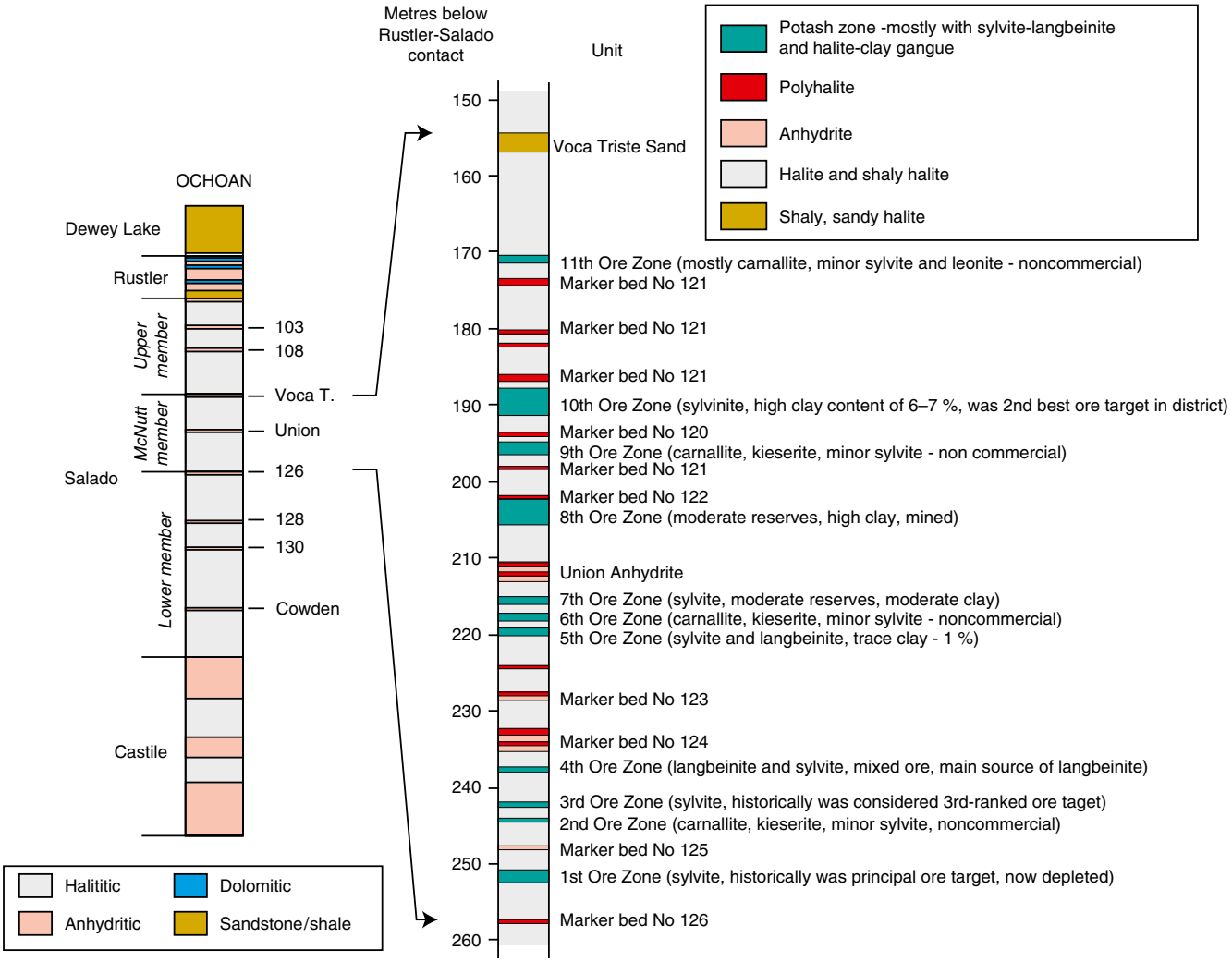

Fig. 11.52 Stratigraphy of the McNutt Potash zone in the Salado Fm, based on the main ore zone near Hobbs New Mexico (Comments on mineralogy from Griswold 1982)

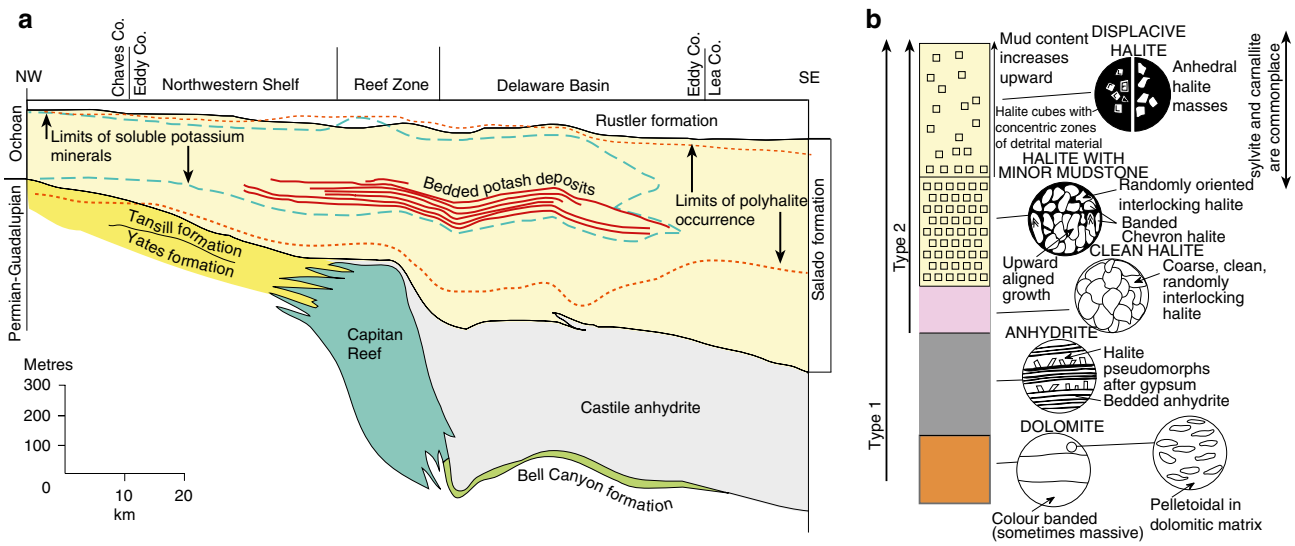

Fig. 11.53 Potash in the Carlsbad Potash District, New Mexico. (**a**) Stratigraphic section in southeastern New Mexico showing distribution of bedded potash (McNutt ore zone) about basin margin (After Bates 1969). (**b**) Idealised halite-dominated depositional cycles that host the ore beds (After Lowenstein, 1987b)

time of deposition. At the time the potash was emplaced, it was probably a zone of differential subsidence in the underlying sediment, located at the hinge between indurated platform edge carbonates and muddier basin-centre evaporites. It was also the spill point of the aggrading basin-filling evaporite cycles that make up the basinwide evaporites of the Castile and Salado formations as well as a focus for later upwellings of deeply circulated meteoric waters. The significance of fill and spill hydrology as loci of changes in evaporite mineralogy was discussed in Chap. 5 in Warren 2006. The nearby underlying Capitan Fm. reef crest acted as a focus to any subsequent rise of artesian or escaping basinal waters.

Two types of sedimentologic cycles dominate ore zones in the Carlsbad Potash District (Fig. 11.53b; Lowenstein 1987b). Type I cycles begin with mixed siliciclastic carbonate (magnesite) mudstone, followed by anhydrite-polyhalite with gypsum crystal pseudomorphs, overlain by halite and capped by muddy halite. Type II cycles begin with halite that grades transitionally upsection into muddy halite and pseudomorphs after gypsum, which retain subaqueous bottom-aligned growth habits or mechanically deposited sedimentary structures (ripples, cross beds, etc.). In the anhydrite-polyhalite parts of the cycles there are many pseudomorphs of primary gypsum textures that are now replaced by anhydrite, polyhalite, halite or sylvite. Sylvite and carnallite are most common in the muddy halite parts of the cycles where they occur as millimetre- to centimetre-sized anhedral crystals.

Both blood-red sylvite and the purple carnallite colours in the ore zones come from micrometre-sized plates of hematite (Sonnenfeld 1995). The same potash crystals may be internally zoned; with dark hematite-rich bands developed at the crystal rims, and progressively lighter bands, depleted in hematite, in the cores of the crystals. Ore zones are hosted in stacked halite beds, up to 1 m thick and contain up to 50 % sylvite and carnallite. Thin sections of the ore show poikilitic textures, with several halite crystals encased in single carnallite or sylvite crystals. The sylvite and carnallite occupy areas equivalent in size and shape to the void spaces in modern saline pan halites and are interpreted as pore-filling cements (Lowenstein and Spencer 1990).

Given that Quaternary halite beds lose porosity by 100 m depth, it is likely that the bulk of the stratiform potash ores within the McNutt potash zone were emplaced syndepositionally or very early during shallow burial. A study of the ore emplacement temperatures using brine inclusions in chevron halite near sylvite in a number of primary textured zones shows that the bulk of the crystals formed at temperatures ranging upward from 30 °C (Fig. 11.54a, b). Lowenstein and Spencer (1990) suggest that the ore-hosting halite crystallized from warm surface brines rich in KCl and that syndepositional cooling of these brines just below the surface achieved supersaturation with respect to sylvite. They concluded that the Salado sylvite did not form by incongruent dissolution of carnallite. Others have suggested that the widespread langbeinite with carnallite and the associated discontinuities in the ore beds, along with evidence of early karst features, implies that warm (>55–60 °C) geothermal brines where present at or soon after deposition of the primary salts (Fig. 11.54b; Garrett 1995).

Harville and Fritz (1986) document textures in three cores from two of the high-langbeinite beds in the third and fourth ore zones. In two of the three cores, the langbeinite conversion from sylvinite was essentially complete, but in one considerable sylvinite remained, probably because of reduced brine circulation. In one core some early diagenetic kainite was formed, typically as a rim to langbeinite, implying it formed as residual brines cooled. In all cases the adjacent anhydrite was converted to polyhalite, and the langbeinite crystal size was large, as would result from slow, intruding brine crystallization rather than primary langbeinite. We shall return to this topic of the relative importance of incongruent dissolution versus primary precipitation of carnallite verses primary sylvite as an ore-forming set of processes later in the chapter.

That the ore is early is reinforced by an argon date of 250 ± 0.6 Ma for deposition obtained from langbeinites in the McNutt ore zone, with subsequent local recrystallization events at 245 and 94 Ma (Renne et al. 2001). Like their more recent analogs, this Permian Salado potash precipitated as stratiform units in depressions in a saltern to mudflat terrain subject to exposure and shallow karsting in bedded halite beds. Much of the initial ore precipitation was driven by cooling of warm refluxing shallow brine. Later in its burial history the ore zones were subject to recrystallization from fluid crossflows (descending or ascending), most likely driven by local or region tectonic events. This explains the irregular distribution of the stratiform Carlsbad potash salts and a general lack of fine original texture in halite hosts, which away from the ore zone still retain the original chevron halite texture. It is also why the stratiform Salado potash zone ores usually cross depositional boundaries in the primary halite beds (Fig. 11.53a).

Upper Kama Potash Region, Cis-Urals Russia

The largest potash occurrence currently mined in Russia is in the Upper Kama Basin in the Perm region of Russia, some 250 km north of the town of Perm, adjacent to the Kama River and the Ural Mountains. This deposit is second in size only to the Saskatchewan deposits in Canada (although perhaps also smaller than the under explored Nepskoye potash district in Siberia to the west). In Russia the region is often called the Ural or Verkhnekamskoye potash ore district (Kovin 2011). The potash is part of the Iren Fm (Kungurian-

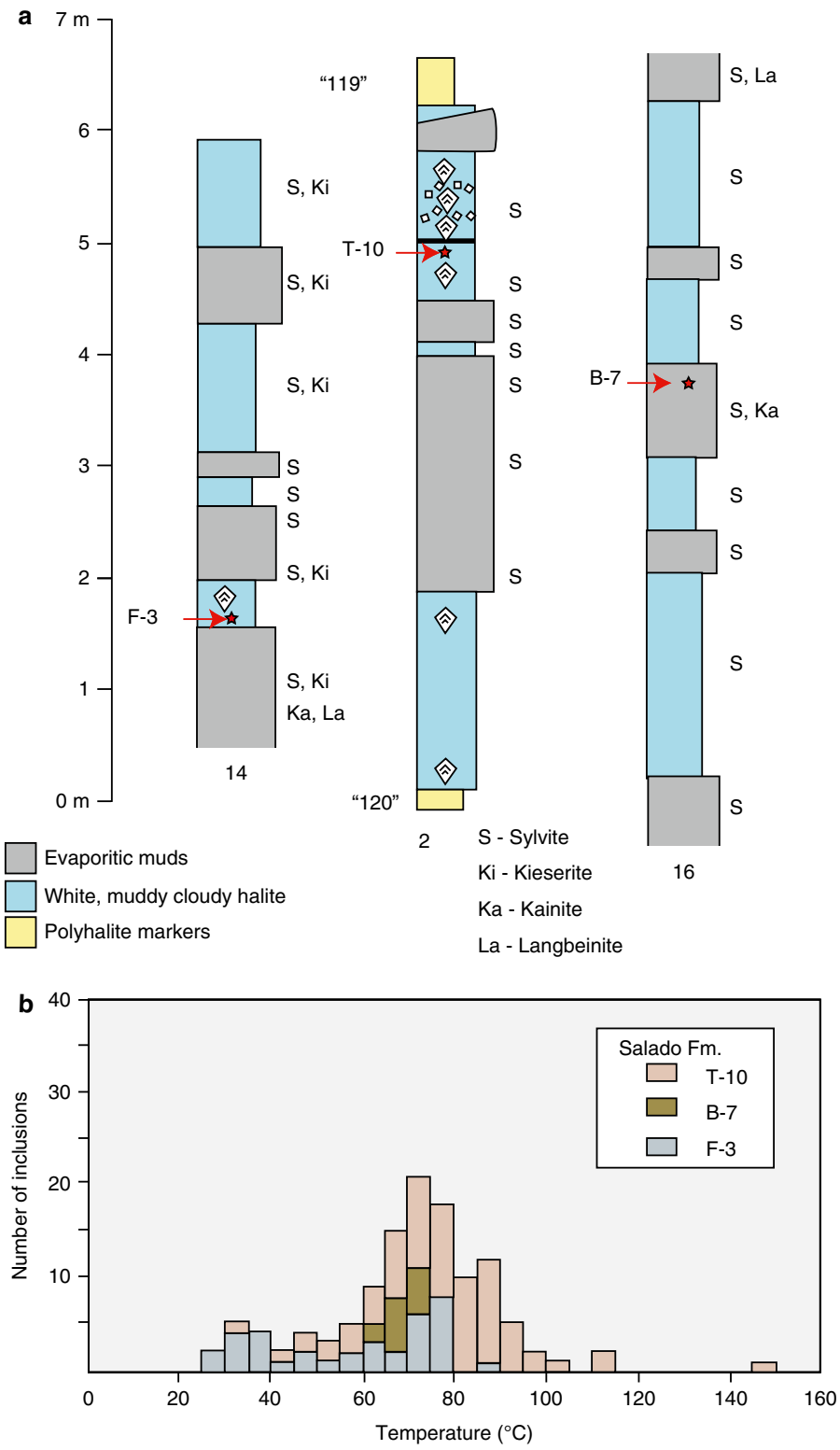

Fig. 11.54 Depositional and thermal styles in halite in the McNutt Potash Zone, New Mexico. (**a**) Measured stratigraphic sections from underground mine exposures. *Red stars* indicate chevrons sampled for inclusion analyses as shown in (**b**). *Diamond symbols* indicates chevrons, *squares* indicate cumulate halite textures. (**b**) Temperatures of dissolution of sylvite daughter crystals in 119 primary fluid inclusions in chevron halite from ore zones that contain sylvite (After Lowenstein and Spencer 1990)

Permian) and covers about 3,000 km^2 near the shallow edge of a somewhat larger megasulphate basin that is the upper part of Cis-Ural Trough (Figs. 11.55 and 11.56a, b). In the potash ore district there are 13 potentially mineable beds at depths of 200–500 m. Ground collapse and water influx are ongoing environmental problems in areas of the Kama Basin where the exploited intervals are within a few hundred metres of the landsurface; as seen in the Solikamsk 2 mine collapse in 1995 and the collapse in the 3rd Berenzki mine in 1986 (Chap. 13; Whyatt and Varley 2008).

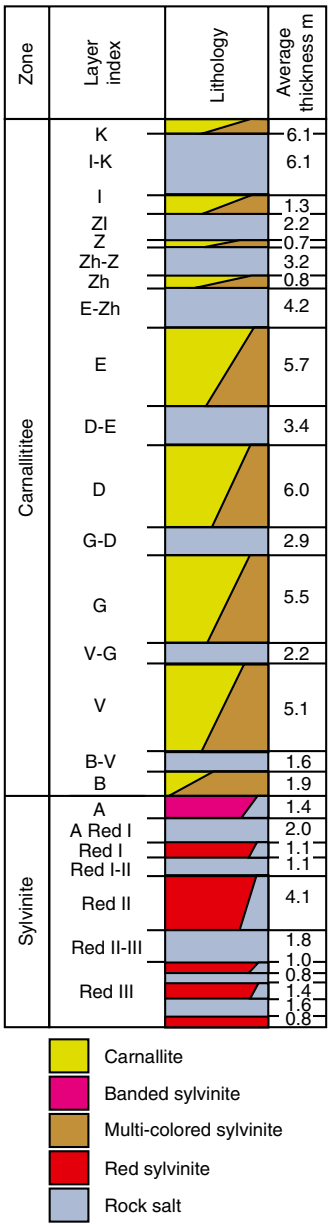

Fig. 11.55 Stratigraphic subdivision of the potash zone (After Kudryashov 2001)

Historically, the deposit's major extraction areas have been centred about the towns of Solikamsk, Bereznki and Romanovo. Annual capacity in the region is around 850,000 t/year and total mineable reserves are thought to be in excess of 3.8 billion tonnes (Fig. 11.2). The two largest potash producers in the area, both semi-privatised state enterprises, merged in 2011 to create a US$ 15 billion enterprise. The Joint Stock Company (JSC) "Uralkali", headquartered in city of Bereznki, operates in the southern part of the potash deposit, and the Joint Stock Company "Silvinit", headquartered in Solikamsk, operates in the northern area.

The Upper Kama potash deposit lies in central part of the Solikamsk (Solikamskaya) depression of the Pre-Ural foreland basin. This horizontally bedded evaporitic formation, up to 500 m thick, is composed predominantly of halite with substantial interbedded sylvinite, carnallite, clay, and anhydrite layers (Fig. 11.55). Regionally, the lower rocksalt is 250–400 m thick and is overlain by the potash-hosting sequence with a thickness of 30–125 m (Figs. 11.55 and 11.56c; Mayrhofer 1985). The Iren Fm. evaporites were deposited after the rise of the Ural Mountains in the late Carboniferous as a result of the continental collision between the East-European platform and West-Siberian plate (Kovin 2011). The evaporite formation is underlain by 2–3 km of clastic Proterozoic rocks, a Devonian reef sequence, a dominantly carbonate Carboniferous sequence, and Lower Permian sediments of up to 1 km in thickness. The Lower Permian molasse (flysch) wedge, consisting of conglomerate, sandstone and argillite beds, underlies the eastern part of the potash deposit (Fig. 11.56b). The uppermost 80–120 m of evaporite formation contains economic deposits of potash salt, which include 13 sylvinite and carnallite mineable beds and interbed halite layers.

The potash zone overlies a thick halite deposit and most recovered ores are medium grade (16–23 % K_2O). Four sylvite-rich beds (referred to as A, Red I, Red II and Red III) in the lowest part of productive strata are the principal mineable beds with typical ore grades in the medium quality range of 16–23 % K_2O (Kovin 2011; Figs. 11.55 and 11.56c). Nine carnallite beds (namely B, V, G, D, E, Zh, Z, I, K) along with halite interlayers lie on top of the 4 beds of the sylvinite layer and form a carnallite zone that ranges in thickness from 38 to 80 m. A halite layer some 20 m thick, termed the overlying rock salt, covers the potash beds, unless breached or dissolved (Kudryashov 2001). The Middle Permian terrigeneous-carbonate complex with multiple aquifer layers overlies evaporites. This aquifer system typically overlies and locally penetrates the evaporite strata with water pressures of up to 3.5 MPa, while the ore deposit depth varies from 75 to 450 m (Mayrhofer 1985).

Six of the thirteen potash beds are intermittent over 15–35 % of this area, and the principal bed that is mined, Red (KrII), has now been depleted across significant portions of the defined ore district. The ore zone dips to the west and is lost via complete dissolution to the east along a halite basin edge that has captured the Glukhaya Vil'va River (Fig. 11.56b). Even so, the remaining mineable reserves of K_2O in the ore district are still estimated to be in excess of two billion tonnes. Regionally within the Upper Kama basin there is a general tendency for the potash zone to contain 5–13 % more KCl to the south than in the north, and 1–1.5 % more KCl in the east than in the west at Solikamsk, and 5–6 % more in the east than in the west in the southern district (Garrett 1995). For example, the four beds of the Red II layer near Solikamsk average 5.2 m with 23 % KCl, and the

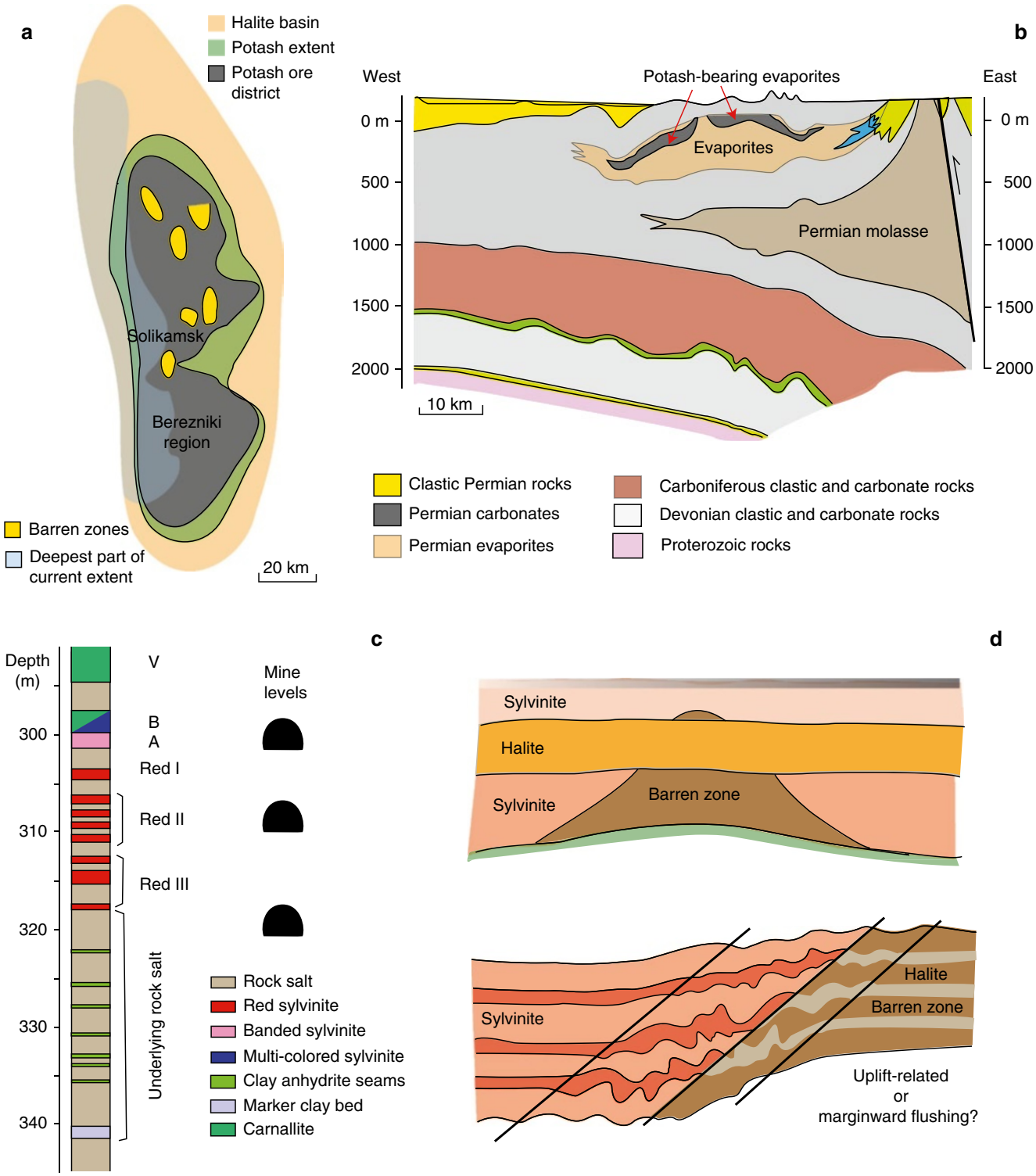

Fig. 11.56 Potash distribution and style in the Kama Basin, Cis-Urals, Russia. (**a**) Map of halite basin extent (**b**) East-west cross section showing control on faceies exterted by Urals suture. (**c**) Ore zone stratigraphy. (**d**) Geometries of barren zones (After Kovin 2011; Tret'yakov 1974; Garrett 1995)

A layer averages 1.4 m with 29 % KCl, while near Bereznki the comparable figures are 4.8 m and 32 % KCl, and 1.5 m and 43 % KCl respectively (Fig. 11.55; Garrett 1995).

The upper part of the potash deposit along with the overlaying marl, halite, clay, anhydrite, gypsum and carbonate beds of the transitional series is left un-mined to form a water

protective barrier above the mine. The average thickness of impermeable strata is 70–90 m. Insolubles are present in the ore succession, mostly as thin centimeter-scale parting seams composed of clay and anhydrite. The 1–2 m thick carbonate clay layer (referred to as "Marker Clay") located in the underlying rock salt, some 20 m below sylvinite zone, is the most stable stratigraphic marker at the Upper Kama deposit (Kudryashov et al. 2004).

Most of the historically mined beds have very gentle dips of from 0 to 4°, but folds do occur, influencing continuity of strata, as do occasional cavities and numerous barren zones (Fig. 11.56d). For example, folds in bed V have been found between 2 and 9 m in height, with a width of 8–30 m and length of 50–150 m (Garrett 1995).

The salt roof to the ore zone, averaging about 25 m, is a sometimes entirely sub-eroded. In its place is an alternating sequence of originally existing rocksalt, now mostly sub-eroded, and claystone, which changes substantially in thickness (0–80 m). This then passes up to the upper Kungur member, a lime-sand and clay-sand stratum, which is about 25 m thick. Within the mined potash beds, small quantities of trapped brines occur frequently, and there are locally significant quantities of methane and hydrogen. There are also brine-filled poorly documented disturbances in the uppermost portions of the saline formations, the watery residues from former poorly-controlled long-term solution mining of rock salt in the Soviet era (see Chap. 13; case histories). Patchy distribution of highest-grade ore, and abrupt lateral transitions are reflective of the shallow nature of the ore zone across the district, so that controlling water entry and preventing or minimising salt-karst related collapse are ongoing problems.

As previously noted, there are major zones of ore impoverishment in the Kama deposit, and the two most common styles are illustrated in Fig. 11.56d. Tret'yakov (1974) considers them to have been formed in; (1) Regions of the basin that were structurally higher during or soon after the potash deposition or perhaps located in zones that were more severely leached when the basin was reflooded, or (2), Areas where there has been later fault or karst-related fluid movement, allowing intruding formation waters to enter the deposit and leach the potash, replacing it with halite. In these barren zones the bedding planes are often missing, and the structure is that of recrystallized salt similar to the salt horses of New Mexico and Carlsbad (Tret'yakov 1974). Garrett (1995) noted that the sylvinite is thought to be richer in the areas of the deposit where there was no syndepositional subsidence (or there was even a slight upwarping), and less rich where settling (or downwarping) occurred during deposition.

The Upper Kama deposit has been subjected to major compressive regional tectonic, gravitational and mining induced forces. Extensive folding of variable amplitudes and wavelengths is characteristic of evaporite formation of the Upper Kama deposit (Kovin 2001). Predominantly, tectonic movements in the adjacent orogens governed the folding deformation of the evaporite, so that the main folds in the Upper Kama potash deposit have submeridianal orientations, perpendicular to principal lateral E–W tectonic stress caused by the Uralian Orogen. Locally, a superposition of a major tectonic stress and stress from the faults and numerous uplift structures leads to deformation reorientation or overlapping the deformational structures with different trends (Fig. 11.56d). Because of their inherently high plasticity, brittle deformation is not common in the potash zones, but occurs locally when tectonic, gravitational or mine induced stress exceeds the strength of the rock mass.

A number of discrete natural fractures and fracture systems of various scales have been observed, especially in the central part of the Upper Kama deposit. Most of these fractures are effectively healed and can be visually observed only in the non-annealed clay–anhydrite layers. Open fractures are encountered mostly in the sylvinite–carnallite zone. They usually develop with meridianal and NW–SE direction. The most intense deformations are seen in the carnallite zone, where very steep folding, tectonic brecciation and blocks of interbed rock salt are present (Kovin 2011).

Canadian Maritimes (Mississippian of Nova Scotia and New Brunswick)

The Carboniferous geology of the Maritime Provinces and Quebec is characterised by a series of northeast trending fault-bound grabens or half grabens containing clastics and evaporites (mostly halite) up to 10 km thick (Roberts and Williams 1993). The Windsor Group (Visean) in Nova Scotia and New Brunswick hosts $MgSO_4$ -poor potash evaporites of the Cassidy Lake Formation in several continental intermontane basins that were created by extension-driven post-Acadian strike-slip faulting with the salt then subject to halokinesis first by extension and then subsequent compression. The same evaporite unit that hosts the potash ore also acts as a seal to MVT deposits at Gays River and Jubilee (Fig. 11.57).

Salt deposits were first utilized in the Sussex area in the early 1800's when area residents tapped local salt springs, dried the brine to produce halite, which they then used in food preservation. Exploitable subsurface potash at New Brunswick near the town of Sussex was discovered in the 1970s by the New Brunswick Mineral Resources Branch of the Geological Survey, with the first intersection occurring in 1969–1970 during a drilling program designed to define a halite resource suitable for hydrocarbon storage. Two mines were built near the town, one in Penobsquis (aka Sussex Mine), 8 km east of Sussex, and another at Cassidy Lake (aka Potocan Mine or Clover Hill Mine), some 10 km

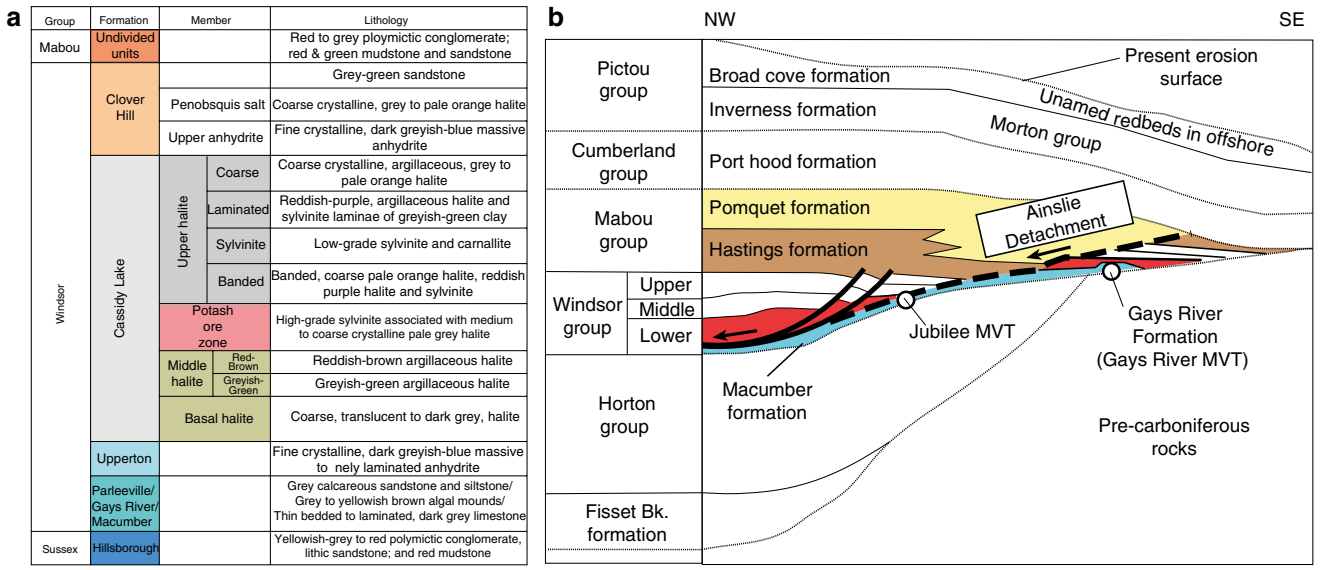

Fig. 11.57 Potash in the Cassidy Lake Formation of the Lower Windsor Group, New Brunswick and Nova Scotia. (**a**) Cassidy Lake Fm and Potash ore Stratigraphy (After Wilson et al. 2006). (**b**) Schematic cross-section of the stratigraphy and position of the regional Ainslie Detachment, in Nova Scotia, a major allochthon feature associated with salt flow and gravity gliding into the basin. Lubricating evaporites of the lower Windsor Group (Carrols Corner Formation) are shaded grey. Note the salt raft tectonics geometry with thickening of the Mabou Group in the salt-withdrawal sink. Jubilee-style base metal deposits are hosted in the salt tectonites created by the detachment. In contrast, the Gays River-style of deposit is formed at the evaporite-encased underbelly contact adjacent to the salt-encased reefal buildup. In the case of the Jubilee deposit it was focused by the feather edge of the salt unit (After Lynch et al. 1998; Warren 2000b)

southeast of the town of Sussex. Following creation of the Penobsquis Mine under the auspices of Potash Corporation of America, the Port of Saint John potash shipping terminal was constructed and potash was first shipped from New Brunswick in 1983.

The Penobsquis Mine continues in operation to the present time under the ownership of PotashCorp, which acquired the project from PCA in 1993 and until the first half of 2014 produced potash at a rate of over 700,000 tonnes per year. Cassidy Lake mine was brought into production in 1985 by Denison Mines Ltd. and Potash Company of Canada and actually outproduced the Penobsquis Mine, attaining an annual production rate of around one million tonnes of potash per year. However, massive underground flooding caused the permanent closure of the mine in 1997. In 2002, drillers for natural gas intersected another major potash deposit near Penobsquis, presently known as the Picadilly Deposit. PotashCorp has developed Picadilly to the point where a major mine is under development with production scheduled to beginning in second half of 2014. Due to lower potash prices in the second half of 2013, PotashCorp will cease production at its Penobsquis mine sometime in 2014 as it focuses future activities in the Picadilly mine and the nearby wet mill.

Of particular interest for potash extraction in New Brunswick is the Cassidy Lake Formation of the Moncton Sub-basin (Fig. 11.57a). It entrains structurally complex potash ore and, with variable dips ranging to subvertical and ore thicknesses ranging from 0 to 45 m, is much more deformed than the conventionally mined bedded potash occurrences of Saskatchewan (Fig. 11.58). Seismic and borehole evidence from the Windsor Group shows that the Cassidy Lake Formation (rock salt and potash) is separated from the underlying Upperton Formation (anhydrite) by a low-angle décollement surface marked by the presence of mylonitic salt and cataclastic limestone and anhydrite. Much of the halokinetic deformation occurred above the regional décollement separating the Cassidy Lake Formation from the underlying Upperton Formation. Deformation was syntectonically mobilised by gravity sliding, thrusting and folding atop the regional décollement surface, with the most intense deformation being taken up in the highly deformable sylvinites. Flow has been complex within the salt body itself, resulting in structural repeats of the salt stratigraphy through recumbent to inclined isoclinal folds and sheath folds (Fig. 11.58).

The Potash Ore Member in the Cassidy Lake Formation consists of cm-scale beds of halite and halite + sylvite and minor rinneite and polyhalite. The exploited ore is sylvinite, running 20–30 % K_2O with 0.5–5.0 % insolubles. Grade at Penobsquis is around 26 % K_2O and 28 % K_2O at the former Cassidy Lake mine. The Upper Halite Member atop the potash ore is between 2.5 and 20 m thick and composed of interlayered thin beds and laminae of argillaceous halite, sylvinite and claystone-anhydrite (Anderle et al. 1979). Because of structural thickening in this halokinetic salt, it entrains what is perhaps the thickest exploited bed of KCl salts in the world in a domelike anticline fold with a highly complicated

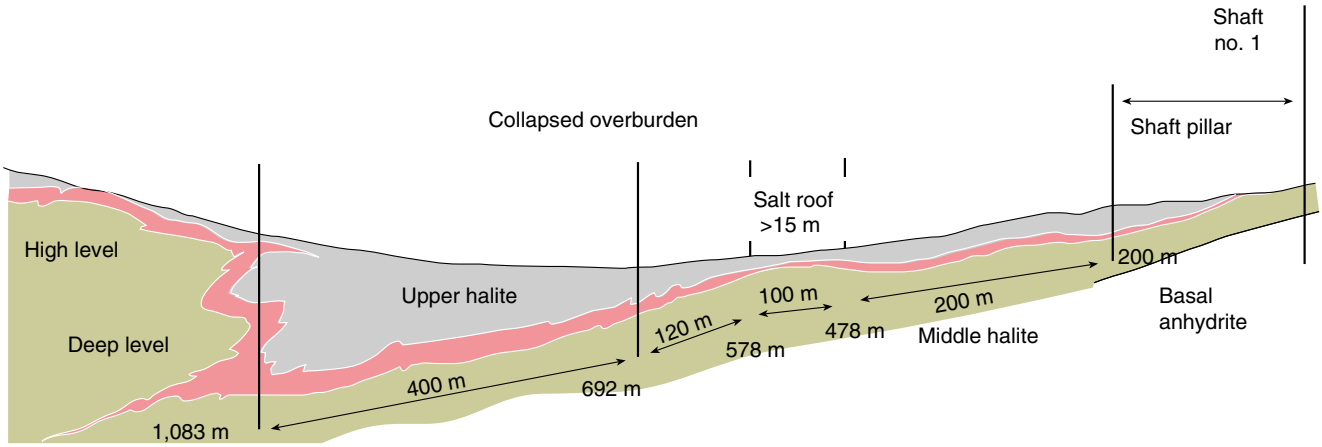

Fig. 11.58 Distribution of sylvinite ore zone (*pink*), encased in halokinetic halite an anticlinal structure in a New Brunswick potash mine. See Fig. 11.57a for stratigraphy

internal structure dominated by isoclinal and sheath folds (Roberts and Williams 1993).

The depth to ore in this structure ranges from 580 to 850 m below the surface and in thickness the ore zone ranges from a few metres to 30 m. The variable inclination and thickness of the ore zone means mining procedures are more variable than those used in extracting potash from the Prairie Evaporite. In intervals where the ore zone is relatively flat, continuous front procedures are used, similar to Saskatchewan. Where the ore zone is more steeply inclined, classic drill and blast techniques are used to extract the ore.

Salt, not potash, is the main product from Pugwash Mine, Nova Scotia, within equivalent age evaporites, but the operations in the halite show a similar structural complexity in the salt to the New Brunswick operation. Fig. 11.59 shows a refolded fold in the Pugwash Mine: the axial plane of the initial antiform (axial trace 1) was folded and the nose (axial trace 2) of the resultant synform was folded (axial trace 3). The axial planes of each of the folds have the same axial orientations as the axial plane traces of the other two clearly demonstrating an inherently high degree of plasticity during deformation (Evans 1967).

Borates are commonplace coprecipitates in particular horizons in the Cassidy Lake Formation: for example, danburite occurs in the Basal Halite; while boracite, hydroboracite, szaebelyite, hilgardite and ulexite are found in the Upper Salt Member of the Windsor Group (Roulston and Waugh 1981). Where the Clover Hill Formation overlies the Cassidy Lake Formation the contact is typically a thin "residual" bed made up of laminated clayey anhydrite, borates and quartz grains. It is not a depositional contact but the result of ongoing post deformational "sub-rosion" at the evaporite-nonevaporite interface, similar to that documented at the upper and lower contacts of the Maha Sarakham Fm. in Thailand.

In 1997, Potocan was forced to close the 890,000-t mine at Cassidy Lake, because of flooding related to intersection

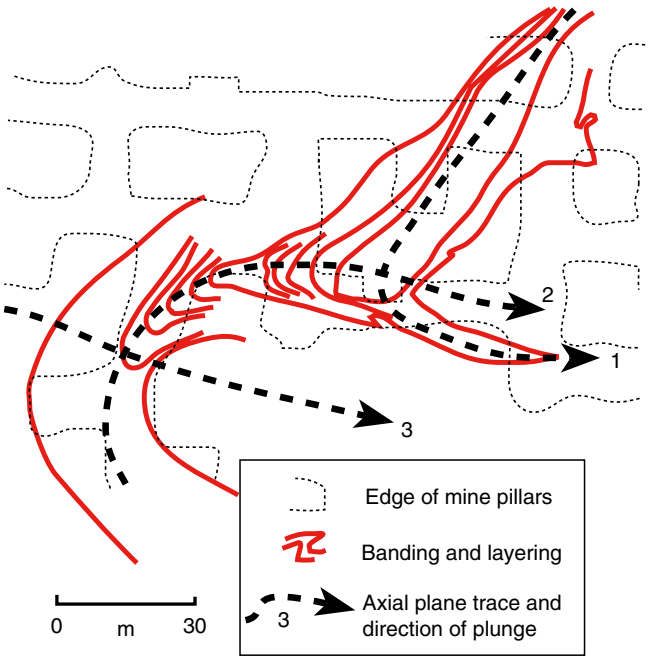

Fig. 11.59 Refolded fold in sylvite-halite, Pugwash Mine, Nova Scotia (After Evans 1967)

of an unexpected salt "horse." This leaves one conventional mine (Sussex Mine or New Brunswick Facility) currently exploiting the New Brunswick potash ore in this structurally complex region. Construction of two new shafts and an expanded mill is underway at the Sussex Mine and expected to double the current annual output by 2015 when it will become possible to produce more than two million tonne per year. There is also the possibility of a new mine in the Millstream area where there is a known 500 m thick halite with several sylvinite and carnallite intersections.

In 1998 Potash Corporation of Saskatchewan Inc. purchased both the Cassidy Lake and Sussex Mine

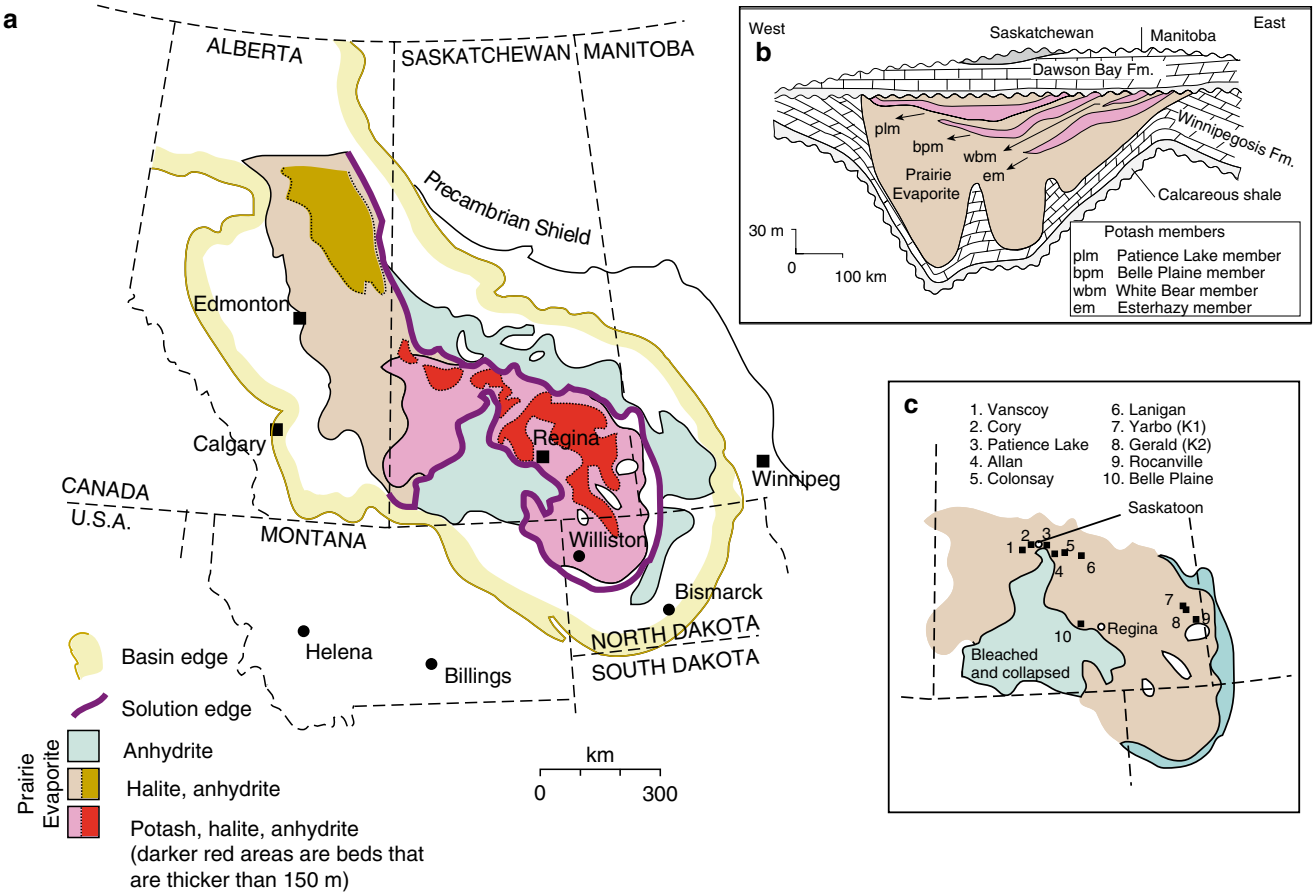

Fig. 11.60 Potash in the Elk Point Basin, western Canada. (**a**) Regional geology showing thickest salt and potash intervals in the Prairie Evaporite and its dissolution edge. (**b**) Cross section of basin showing distribution of potash members. (**c**) Map of potash mines in the basin (Compiled and modified from Worsley and Fuzesy 1979; Fuzesy 1982; Boys 1993)

properties – a flooded mine and a functioning mill. The flooded mine was renamed the Cassidy Lake Division of PCS. Today the Cassidy Lake mine acts as a brine storage facility for the nearby Penobsquis Mine. At the Cassidy Lake brine facility a small group of employees manage the company's brine pipeline to the Bay of Fundy. Each day some 300–350 tanker truckloads of brine from the Sussex mine arrive at the Cassidy Lake storage facility. The brine is a slurry of potash and brine that has been brought to surface to alleviate any water inflow problems in the Penobsquis Mine. The brine is pumped into slurry-holding lagoons where the brine is taken off and pumped via a pipeline into the Bay of Fundy near Giffin's Pond, south of St. Martin's.

West Canadian Potash (Devonian)

The Middle Devonian (Givetian) Prairie Evaporite Formation is a potash-entraining halite sequence deposited in the Elk Point Basin, an early intracratonic phase of the Western Canada Sedimentary Basin (WCSB; Chipley and Kyser 1989). It is the world's predominate source of potash. The flexure that formed the basin and its subsealevel accommodation space was a distal downwarp to, and driven by, the early stages of the Antler Orogeny (Root 2001). Devonian halite constitutes a large portion of the four formations that make up the Elk Point Group: (1) the Lotsberg (Lower and Upper Lotsberg Salt), (2) the Cold Lake (Cold Lake Salt), (3) the Prairie Evaporite (Whitkow and Leofnard Salt), and (4) the Dawson Bay (Hubbard Evaporite). Today the remnants of the Middle Devonian Prairie Evaporite Formation constitute a bedded unit some 220 m thick, which lies atop the irregular topography of the platform carbonates of the Winnipegosis Fm. Extensive solutioning of the various salts has given rise to an irregular thickness to the formation and the local absence of salt (Fig. 11.60a).

The Elk Point Group was deposited within what is termed the Middle Devonian "Elk Point Seaway," a broad intracratonic sag basin extending from North Dakota and northeastern Montana at its southern extent north through southwestern Manitoba, southern and central Saskatchewan, and eastern to northern Alberta (Fig. 11.60a). Its Pacific

coast was near the present Alberta-British Columbia border, and the basin was centred at approximately 10°S latitude. To the north and west the basin was bound by a series of tectonic ridges and arches; but, due to subsequent erosion, the true eastern extent is unknown (Mossop and Shetsen 1994). In northern Alberta, the Prairie Evaporite is correlated with the Muskeg and Presqu'ile formations. Hydrographic isolation of the intracratonic basin from its marine connection resulted in the deposition of a drawndown sequence of basinwide (platform-dominant) evaporites with what is a uniquely high volume of preserved potash salts deposited within a clayey halite host. The potash resource in this basin far exceeds that of any other known potash basin in the world (Fig. 11.2).

Above the Prairie Evaporite Formation is a series of cyclic Devonian limestones, dolomites and evaporites that make up the Dawson Bay, Souris River, Duperow and Nisku Formations. Together the Dawson Bay Formation and overlying Souris River constitute the informally named Manitoba group. The presence of the "Manitoba Group" above any potential mine is important as it entrains two halite beds: (1) the "Hubbard Salt," which is the uppermost bed of the Dawson Bay, and (2) the "Davidson Evaporite" composed of two halite beds separated by an anhydrite bed. Where present, the evaporites of the Manitoba Group form a flood protection zone, separating the Prairie Evaporite potash mining horizons from the water and brine aquifers present within the overlying Mesozoic sands. Its absence, especially of its halites, implies dissolution and removal processes have been active, so creating potential head and lateral stability difficulties in a conventional underground mine. Lying unconformably on the Dawson Group are the Lower Cretaceous sands of the Mannville Group, which are in turn overlain by younger Cretaceous shales and capped by Quaternary glacial sediments.

Potash Geology of the WCSB

Potash deposits mined in Saskatchewan are all found within the upper 60–70 m of the Prairie Evaporite Formation, at depths of more than 400–2,750 m beneath the surface of the Saskatchewan Plains. Within the Prairie Evaporite there are four main potash-bearing members, in ascending stratigraphic order they are: Esterhazy, White Bear, Belle Plaine and Patience Lake members (Fig. 11.60b). Each member is composed of various combinations of halite, sylvite, sylvinite, and carnallitite, with occurrences of sylvite versus carnallite definable with wireline signatures (once calibrated to core or mine control – Fig. 11.61; Fuzesy 1982). The Patience Lake Member is the uppermost Prairie Evaporite member and is separated from the Belle Plaine by 3–12 m of barren halite (Holter 1972). Its thickness ranges from 0 to 21 m and averages 12 m, its top 7–14 m is made up halite with clay bands and stratiform sylvite. This is the targeted ore unit in conventional mines in the Saskatoon and Lanigan areas and is the solution-mined target, along with the underlying Belle Plaine Member, at the Mosaic Belle Plaine potash facility. The Belle Plaine member is separated from the Esterhazy by the White Bear Marker beds made up of some 15 m of low grade halite, clay seams and sylvinite, The Belle Plaine Member is more carnallite-prone than the Patience Lake member (Fig. 11.61). It is the ore unit in the conventional mines at Rocanville and Esterhazy (Fig. 11.60b) where its thickness ranges from 0 to 18 m and averages around 9 m. In total, the Prairie Evaporite Formation does not contain any significant $MgSO_4$ minerals (kieserite, polyhalite) although some members do contain abundant carnallite. This mineralogy indicates precipitation from a Devonian seawater/brine chemistry somewhat different from today's.

As early as 1860, salt springs and seepages near the edge of the Elk Point Basin indicated the presence of widespread salt in Western Canada. Rock salt was first sampled in 1907, while potash beds were intersected in Saskatchewan in 1942 during the sinking of oil and gas wells. The potential of commercial grades of potash mineralisation was not recognized until 1946. Canadian potash deposits are among the richest and largest on earth, containing around five billion tons of ore in a mineable band up to 50 miles wide, which stretches some 725 km (450 miles) across the province (Fig. 11.60a). Canada today supplies more than 30 % of the world's annual potash production (Fig. 11.2).

The Prairie Evaporite Fm. is nonhalokinetic throughout the basin, it is more than 200 m thick in the potash mining district in Saskatoon and 140 m thick in the Rocanville area to the southeast. The Patience Lake member is the main target for conventional mining near Saskatoon. The Esterhazy potash member rises close to the surface in the southeastern part of Saskatchewan near Rocanville and on into Manitoba. This is a region where the Patience Lake Member is thinner or completely dissolved (Fig. 11.60b). Over the area of mineable interest in the Patience Lake Member, centred on Saskatoon, the ore bed currently slopes downward only slightly in a westerly direction, but deepens more strongly to the south at a rate of 3–9 m/km. Mines near Saskatoon are at depths approaching a kilometer and so are nearing the limits of currently economic shaft mining. The main shaft for the Colonsay Mine, which took IMC Global Inc. more than 5 years to complete through a water-saturated sediment column, finally reached the target ore body at a depth of 960 m. Such depths and a southerly dip to the ore means that the conventional shaft mines near Saskatoon define a narrow WNW-ESE band of activity (Fig. 11.60c). To the south potash is recovered from greater depths by solution mining; the Belle Plaine operation leaches potash from the Belle Plaine member at a depth of 1,800 m.

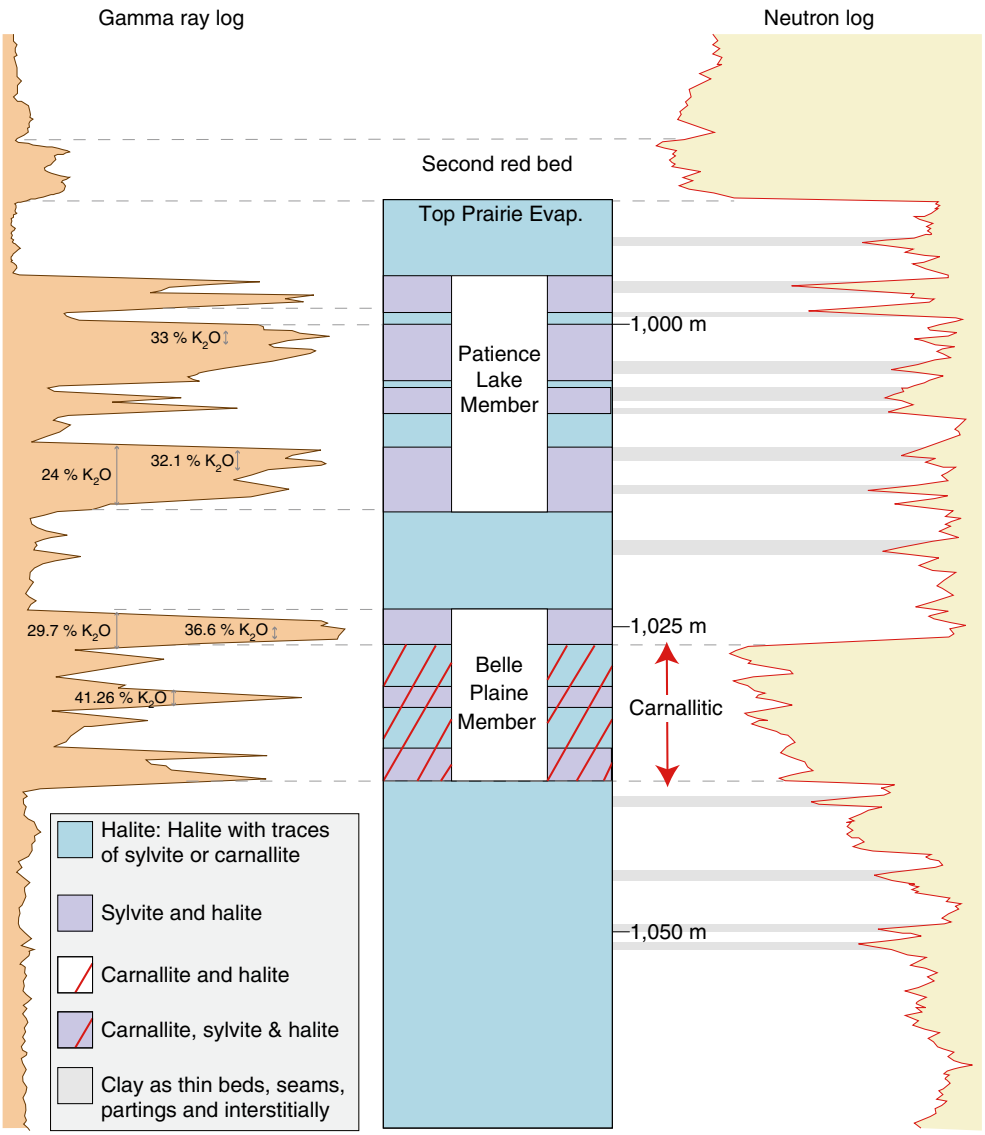

Fig. 11.61 Typical ore grades, thicknesses and wireline characteristics of the potash members in the Upper Prairie Evaporite (After Fuzesy 1982)

The Prairie Evaporite typically thins southwards in the basin; although local thickening occurs where carnallite, not sylvite, is the dominant potash mineral (Worsley and Fuzesy 1979). The Patience Lake member is mined at the Cory, Allan and Lanigan mines, and the Esterhazy Member is mined in the Rocanville area (Fig. 11.60c). Ore mined from the 2.4 m thick Esterhazy Member in eastern Saskatchewan contain minimal amounts of insolubles (≈1 %), but considerable quantities of carnallite (typically 1 %, but up to 10 %) and this reduces the average KCl grade value to an average of 25 % K_2O. The converse is true for ore mined from the Patience Lake potash member in western Saskatchewan near Saskatoon, where carnallite is uncommon in the Cory and Allan mines. The mined ore thickness is a 2.74–3.35 m cut off near the top of the 3.66–4.57 m Prairie Lake potash member. Ore grade is 20–26 % K_2O and inversely related to thickness (Fig. 11.62). The insoluble content is 4–7 %, mostly clay and markedly higher than in the Rocanville mines.

A typical sylvinite ore zone in the Patience Lake member can be divided into four to six units, based on potash rock-types and clay seams (Figs. 11.61 and 11.62a; M1–M6 of Boys 1990). Units are mappable and have been correlated throughout the PCS Cory Mine with varying degrees of success, dependent on partial or complete loss of section from dissolution. Potash deposition appears to have been early and related to syndepositional reflux. So it is cyclic, expressed in the repetitive distribution of hematite and other insoluble minerals. Desiccation polygons, desiccation cracks, microkarst pits and chevron halite crystals indicate that the Patience Lake member that entrains the potash ore was deposited in and just beneath a shallow-brine, salt-pan environment (Fig. 11.62b).

Clay seams form thin stratigraphic layers throughout the potash ore zone(s) of the Prairie Evaporite, as well as disseminated intervals, and constitute about 6 % of the ore as mined.

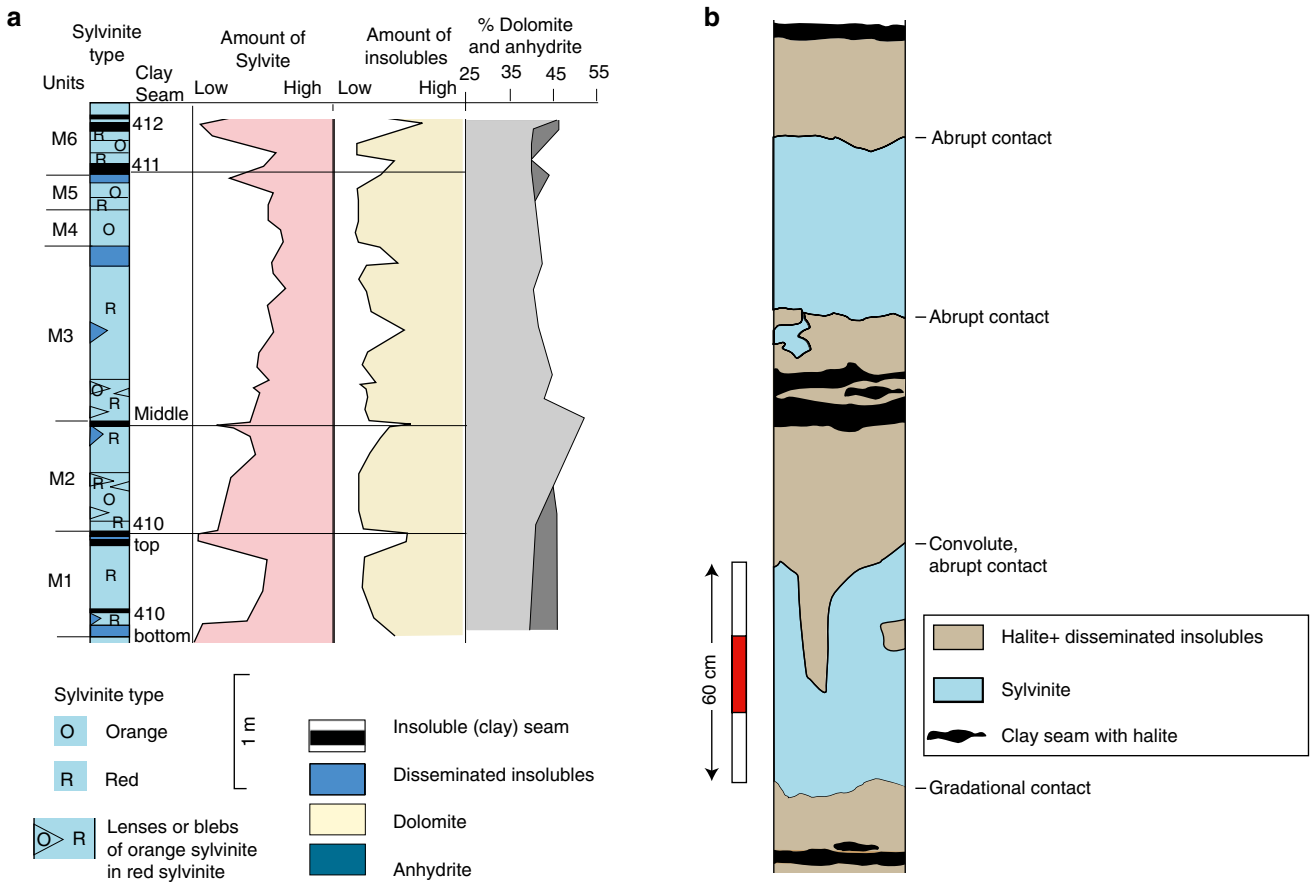

Fig. 11.62 Mineralogy and textures in the ore section in the Patience Lake member of the Prairie Evaporite Formation in the PCS Cory potash mine. (**a**) Typical mineralogy in cycles (units). (**b**) Contacts in two ore cycles showing early karst outlines (Redrawn and modified based on Boys 1990)

Insoluble minerals found in the PCS Cory samples are, in approximate order of decreasing abundance: dolomite, clay [illite, chlorite (including swelling-chlorite/chlorite), and septechlorite], quartz, anhydrite, hematite, and goethite. Clay minerals make up about one-third of the total insolubles: other minor components include: potassium feldspar, hydrocarbons, and sporadic non-diagnostic palynomorphs (Boys 1990).

Potash salts probably first formed as syndepositional secondary precipitates just beneath the sediment surface and were modified to varying degrees by ongoing fluid flushing in the shallow burial environment. The cyclic depositional distribution of disseminated insolubles was possibly due to a combination of source proximity and the strength of the winds blowing detritals out over the brine seaway. Possible intrapotash disconformities, created by dissolution of overlying potash-bearing beds, are indicated by an abundance of residual hematite in clay seams. Except in, and near, dissolution and collapse features, the secondary redistribution of insolubles, other than iron oxides, is insignificant.

Bedded halite away from the ore zones generally retains primary depositional textures typical of halite precipitation in shallow ephemeral saline pans (Brodylo and Spencer 1987). Crystalline growth fabrics, mainly remnants of vertically elongate halite chevrons, are found in 50–90 % of the halite from many intervals in the Prairie Evaporite. Many of the chevrons are truncated by irregular patches of clear halite that formed as early diagenetic cements in syndepositional karst.

In contrast, the halite hosting the potash ore layers lacks well defined primary textures. From the regional petrology and the lower than expected Br levels in halite in the Prairie Evaporite Formation, Schwerdtner (1964), Wardlaw and Watson (1966) and Wardlaw (1968) postulated a series of recrystallization events forming sylvite after carnallite as a result of periodic flushing by hypersaline solutions. This origin as a secondary precipitate is supported by observations of intergrowth and overgrowth textures (McIntosh and Wardlaw, 1968), large-scale collapse and dissolution features (Gendzwill 1978), radiometric ages (Baadsgaard 1987) and palaeomagnetic orientations of the diagenetic hematite linings associated with the emplacement of the potash (Koehler et al. 1997).

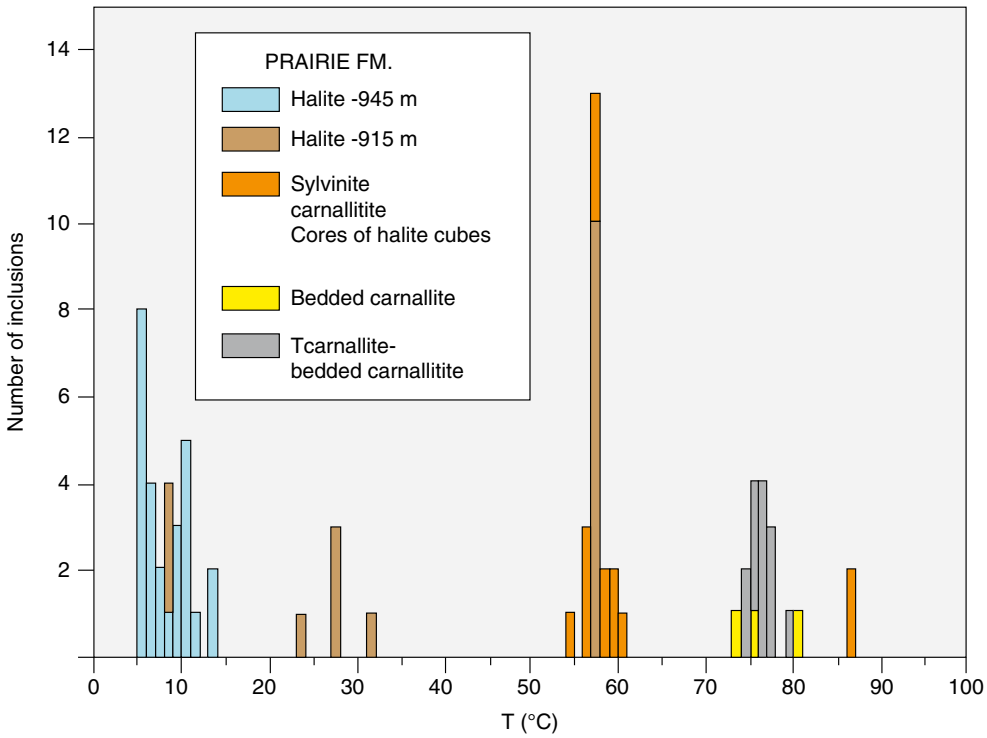

Fig. 11.63 Histogram of the temperature of dissolution of sylvite daughter crystals in fluid inclusions in halite of the Prairie Fm. from the Winsal Osler well at 915 and 945 m; sylvite daughter crystal dissolution temperatures from fluid inclusions in the cloudy centres of halite crystals associated with potash salts from other cores and sylvite and carnallite daughter crystal dissolution temperatures from fluid inclusions in fluid inclusion banded halite from bedded halite-carnallite (After Lowenstein and Spencer 1990)

Dating of clear halite crystals associated with the ore zone shows that the exceptionally coarse and pure secondary halites forming pods in the mined potash horizons may have precipitated as soon as early burial or have formed as late as Pliocene-Pleistocene. Even today, alteration and remobilisation of the sylvite and carnallite appears to be an ongoing process, perhaps related to the encroachment of the current dissolution edge or the ongoing stoping of chimneys fed by deep artesian circulation.

Halite-sylvite (sylvinite) rocks in the ore zone show two end member textures, the most common is a recrystallized polygonal mosaic texture with individual crystals ranging from millimetres to centimetres and sylvite grain boundaries outlined by concentrations of blood-red halite. The other end member texture is a framework of euhedral and subhedral halite cubes enclosed by anhedral crystals of sylvite. This is very similar to ore textures in the Salado Formation of New Mexico interpreted as early passive precipitates in karstic voids.

Petrographically, the halite-carnallite (carnallitite) rocks display three distinct textures. Most halite-carnallite rocks contain isolated centimetre-sized cubes of halite enclosed by poikilitic carnallite crystals. The halite cubes are typically clear, with occasional cloudy crystal cores that retain patches of syndepositional growth textures (Lowenstein and Spencer 1990). The second texture is coarsely crystalline halite-carnallite with equigranular, polygonal mosaic textures. The third type, which is rare, contains interlayered halite and carnallite with a primary bedding style similar to that in the Oligocene potash of the Rhine Graben. In zones where halite overlies anhydrite, most of the halite is clear with only the occasional crystal showing fluid inclusion banding.

Fluid inclusions support the notion of primary textures in the low formations temperatures in chevron halite in the Prairie evaporite and an associated thermal separation of non-sylvite and sylvite associated halite (Fig. 11.63; Lowenstein and Spencer 1990). Most fluid inclusions found in primary, fluid inclusion-banded halite associated with the Prairie potash salts contain sylvite daughter crystals at room temperature or nucleate them on cooling (halite at 915 and 945 m depth in the Winsal Osler well) In contrast, no sylvite daughter crystals have been observed in fluid inclusions outlining primary growth textures from chevron halites away from the potash deposits. This establishes that potash salts occur in stratigraphic intervals where syndepositional surface brines contained high concentrations of potassium ions and at least a portion of the potash salts formed as passive pore filling cements in a meshwork of halite. Whether the cement was sylvite or carnallite is open to interpretation (Lowenstein and Spencer 1990).

Clay minerals, which tend to occur as long continuous seams or markers in the potash zones, are mainly composed of detrital chlorite and illite and authigenic septechlorite, montmorillonite and sepiolite (Mossman et al. 1982; Boys 1990). Of the two chlorites, septechlorite is the more thermally stable. The septechlorite, sepiolite and vermiculite very likely originated as direct products of settle-out or early diagenesis under hypersaline conditions of what was

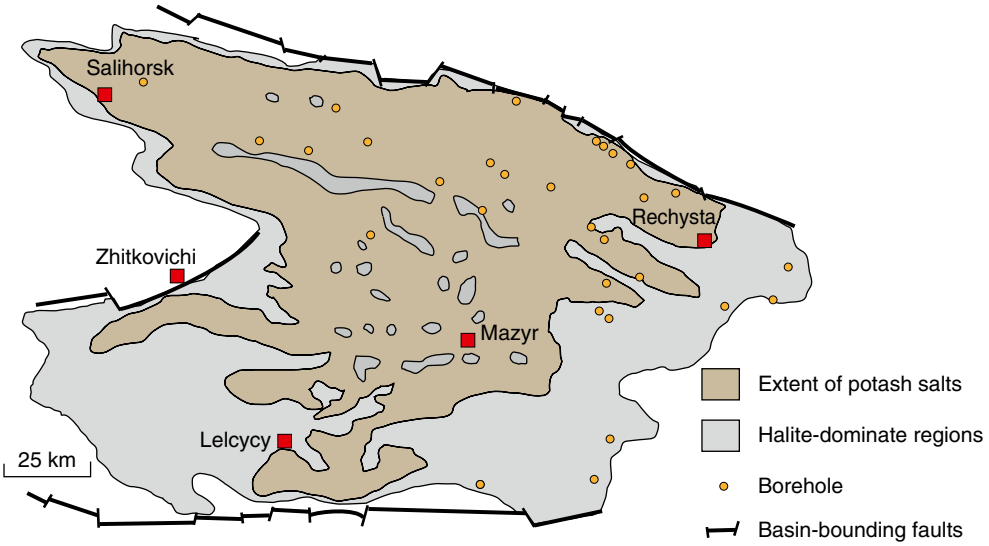

Fig. 11.64 Salt and potash extent in the Pripyat Basin (After Peryt et al. 2007)

originally eolian dust settling into a huge brine seaway. Absence of the otherwise ubiquitous septechlorite from Second Red Beds west of the zero-edge of the evaporite basin supports this concept.

The WCSB Fluids

Analysis of subsurface waters from various Canadian potash mines and collapse anomalies in the Prairie Evaporite suggest that, after initial potash precipitation, a series of recrystallising fluids had access to the evaporite minerals at various times throughout the burial history of the Prairie Formation (Chipley 1995; Koehler et al. 1997). Likewise, the Rb-Sr isotope systematics of crystal layers in both halite and sylvite indicate that the Prairie Evaporite was variably recrystallized during fluid overprint events at 371, 284, 241, 185, 147, 85, 35 and 0.5 Ma. These ages are all more recent than original deposition and correspond to ages of various tectonic events that influenced the western margin of North America.

Chemical compositions of inclusion fluids in the Prairie Evaporite, as determined by their thermometric properties, reveal at least two distinct waters played a role in potash formation: a Na-K-Mg-Ca-Cl brine, variably saturated with respect to sylvite and carnallite; and a Na-K-Cl brine that is the result of fluidrock interaction and did not result from simple evaporation of seawater to sylvite bitterns (Chipley 1995). This is supported by δD and $\delta^{18}O$ values of inclusion fluids in both halite and sylvite, which range from −146 to 0‰ and from −17.6 to −3.0‰, respectively. Most of the various preserved isotope values are different from those of evaporated seawater, which should have δD and $\delta^{18}O$ values near 0‰. Furthermore, the δD and $\delta^{18}O$ values of inclusion fluids are probably not the result of precipitation of the evaporite minerals from a brine that was a mixture of seawater and meteoric water. The low latitude position of the basin during the Middle Devonian (10-15° from the equator), the required lack of meteoric water to precipitate basinwide evaporites, and the expected δD and $\delta^{18}O$ values of any meteoric water in such a setting, make this an unlikely explanation. Rather, the δD and $\delta^{18}O$ values of inclusion fluids in the halites reflect ambient and evolving brine chemistries as the fluids in inclusions in the various growth layers were intermittently trapped during the subsurface evolution of the Prairie Formation in the Western Canada Sedimentary Basin. They also suggest that nonmarine pore water has been a major component of the crossflowing basinal brines throughout much of the recrystallization history (Chipley 1995).

Pripyat Basin (Devonian) Belarus

Pripyat Basin is the northwestern part of a larger linear sedimentary trough made up of the Pripyat, Dnieper-Donets and Donbas (foldbelt) basins (Ulmishek et al. 1994). The Dnieper-Donets and Pripyat Basins are separated by the Brahin-Loeu High. The northern and southern boundaries of the Pripyat Basin are defined by the boundary faults of a Devonian rift that was active as the potash hosting evaporites were deposited (Fig. 11.64). The basin is considered a classic example of an aulocogen and has a current area in excess of 10,000 km^2 entraining a two layered Devonian salt succession containing more than 30 potash beds, made up of sylvite and carnallite (Peryt et al. 2007; Mayrhofer 1985).

Basement to the Pripyat is an Archaean to lower Proterozoic crystalline craton sequence, which is unconformably overlain by Devonian rift-fill and later post-rift sediments (Fig. 11.65a). The thickness of Pripyat sediment fill is up to 6.5 km, thinnest in the west where it is only 2.9 km thick. There are three evaporite intervals in the Pripyat, with the halite dominant section occurring as two

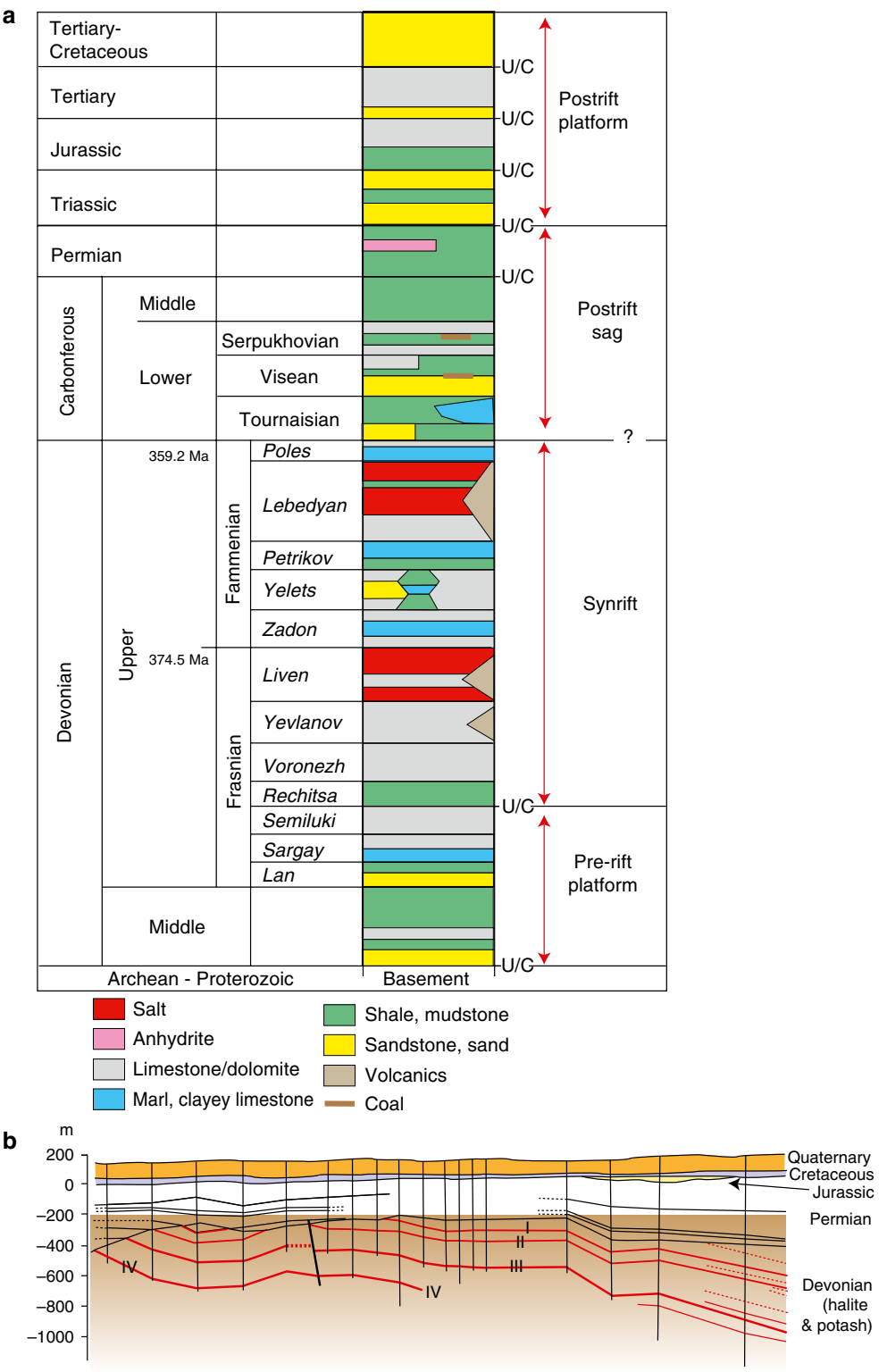

Fig. 11.65 Evaporites in Pripyat Basin, Belarus. (**a**) Basin stratigraphy. (**b**) Cross section showing potash ore layers in the upper salt unit (After Peryt et al. 2007; Mayrhofer 1985)

halite units separated by a succession of Devonian carbonates. The later Permian evaporite is an anhydrite-dominant sequence formed in association with the Uralian orogeny.

The synrift halite-dominant sequences constitute two salt formations of Late Frasnian and Late Famennian age. These salts were deposited in a hydrographically isolated stage of a deepwater marine basin, with marine brine supplied from the vast nearby epicontinental sea covering much of the East European Platform (Zharkov 1984). In contrast to the lower halite (Famennian) sequence, which contains numerous carbonate/anhydrite interbeds, the upper (Frasnian) sequence is purer in terms of its halite content and so is characterized by

Table 11.8 Stratigraphy of the Nepa Basin

Unit	Unit Index	Horizon	Horizon Index	Super horizon	Super horizon No.
Upper anhydrite	UA				
Upper rock salt	URS	5th anhydrite-halite	URS5		
		4th anhydrite-halite	URS4		
		3rd anhydrite-halite	URS3		
		2nd anhydrite-halite	URS2		
		1st anhydrite-halite	URS1		
Potassium Bearing	K	Halite "6"	H6	Rock salt with sylvite and carnallite	V
		Narigonda potassium horizon	K5		
		Halite "5–6"	H5–6		
		Uznmum potassium horizon	K5		
		Halite "4–5"	H4–5	Spotty varicoloured sylvites and carnallites	IV
		Dotkon potassium horizon	K4		
		Halite "3–4"	H3–4	Pink carnallites and sylvites	III
		Chechei potassium horizon	K3		
		Halite "2–3"	H2–3	Gray massive carnallites and sylvites	II
		Tunguaka potassium horizon	K2		
		Halite "1–2"	H1–2	Lower sylvites	I
		Bur potassium horizon	K1		
Lower rock salt	LRS	Light-coloured equigranular rock salt	LRS3		
		Green rock salt	LRS2		
		Smoky-gray rock salt	LRS1		
Lower anhydrite	LA				

After Andreev et al. (1986), Garrett (1995)

more pronounced salt tectonics, with well-developed salt domes, plugs, and swells (Fig. 11.64; Khutorskoi et al. 2010). The Famennian evaporite basin was restricted to the NW part of the depression, while the Late Frasnian evaporite deposition terminated with potash salts of sylvite composition (lack $MgSO_4$ salts).

In the northeastern part of the basin, sedimentation was accompanied by active faulting and volcanic activity, so sedimentary-volcanic sequences and alkali basalts are coeval with the evaporite sequences (as was the related hydrothermal circulation and seismicity). In contrast to the lower halite sequence, the upper sequence is characterized by more pronounced salt tectonics with well-developed salt domes, plugs, and swells.

The potash beds I-IV can be traced continuously from 485 to 1,488 m depth in the Soligorsk region as the depth to potash increases from NW to SE (Fig. 11.65b). The current mining area is situated in the northwest corner of the basin centred on Soligorsk and is divided into four large mining fields covering 640 sq km (Mayrhofer 1985). Future mines (including solution mines) are planned for the Starobin region. Potash beds (I-IV) in the Soligorsk region are no more than slightly inclined, and practically flat with respect to the potash beds II and III, which are the targeted ore beds (Fig. 11.65b). Mayrhofer (1985) estimated ore reserves in excess of 100 Mt for the region. Considerable mine-roof stress problems must be dealt with in day-to-day operations, due the clay-carnallite alternations above the lower mined section, and the ore over most of its extent has a high content of insolubles, as much as 10.7 %).

Other Significant Deposits

In addition to the exploited deposits discussed in the preceding section, there are a number of bedded or halokinetic deposits of potash that are yet to be considered economic opportunities. For example, in Nagaur-Ganganagar evaporite basin of India there are seven halite cycles of Late Precambrian or Early Cambrian age (Dasgupta et al. 1998; Banerjee et al. 1998). Sylvinite horizons are known to occur between 592 and 681 m depth, with intersections averaging 0.5 m in thickness and containing 2.5–19.2 % K (Garrett 1995). In two adjacent halite beds polyhalite occurs in layers 0.1–8.8 m thick with 0.75–8.7 % K.

By far the largest known bedded potash deposit in Russia, which is not yet produced, occurs in an immense Lower Cambrian age basin in the Siberian Platform (Table 11.8;

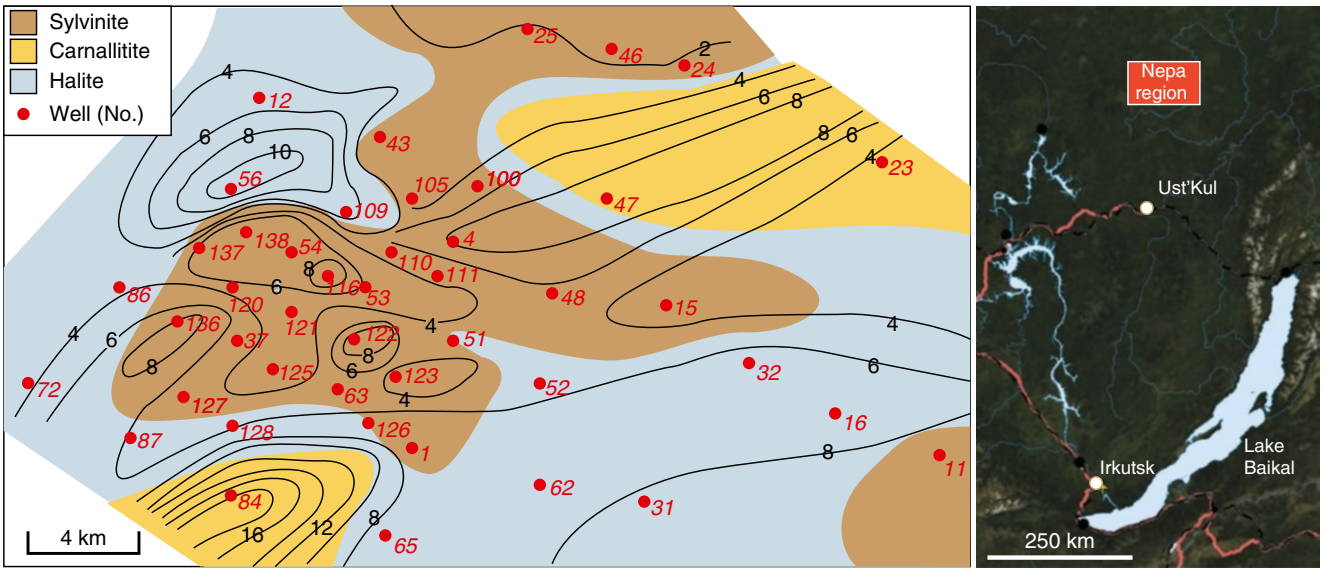

Fig. 11.66 Potash occurrence at the base of the Cambrian Angara Formation in the Nepa Region of Siberia. Note that the region posted as sylvinite carnallitite and halite is the K1 level and is isopached at the level of the K2 potash zone, this region is only some 30 km across and occurs within the red rectangle indicating the potash-rich Nepa Region (After Andreev et al. 1986; Garrett 1995)

Garrett 1995). Potash salts occur at the base of the Angara formation in what is called the sixth halite series. This basin is one of the larger potash-entraining salt deposits in the world, several times larger than the Upper Kama deposit and approaching the Prairie Evaporite in aerial extent. Plans were made in 1986 under the old Soviet regime to initiate a mining program in a section of this basin called the Nepskoye deposit, but were never implemented (Fig. 11.66; Andreev et al. 1986).

The proposed development region is near the towns of Nepa and Ust-Kut (300 km apart) in Irkutsk State. High-grade sylvinite was intersected at depths of 600–1,000 m in beds some 1.5–5 m thick over an area of more than 1,000 km^2 (Garrett 1995). The lower Bur or K1 bedded potash horizon lies at a depth of 750–960 m and is 2–18 m thick (4–6 m in the central area (Fig. 11.66; Table 11.8). Two sylvinite zones in this horizon were mapped, with the central one being 16–26 km long and 6–8 km wide. In the lower horizon (K1) the sylvinite was 1.5–3 m thick, and averaged 15–50 % KCl, 0.05–0.5 % $MgCl_2$, with 0.5 % insolubles. The overlying K2 potash zone also entrains several sylvinite beds and is some 679–880 m deep and 2.5–20 m thick. It has a 15–45 % KCl content and comparatively low $MgCl_2$ and insoluble contents. This zone represents the major potash reserves of the deposit. In the upper potash beds (K2) the sylvinite strata becomes more discontinuous, but some reasonably thick, high grade and extensive zones exist (Andreev et al. 1986).

To the south and west, between Taseyevo and Irkutsk, other large potash occurrences have been reported in the same general but poorly delineated evaporite basin. For instance, in the Kanak-Taseyevo basin, potash beds containing 3–24 % K_2O have been intersected at depths of 1,240–1,415 m (Garrett 1995). Potash beds at these depths would require a solution mining methodology, but the at-surface climate would mean either cryogenic pan processing or evaporators, making recovery more difficult and expensive.

Another significant, as yet poorly delineated, set of potash occurrences occur in the Amazon Basin, Brazil (Szatmari et al. 1979). The Amazon Basin is an intracratonic sag basin, some 2,100 km long and 300 km wide, located in the central zone of the Amazon Craton (Fig. 11.67a). It contains a number of stacked megasequence cycles ranging in age from Lower Ordovician (Autaz Mirim Member of Trombetas Formation) to Lower Permian (Andirá Formation; Gonzaga et al. 2000). The basin has a widespread Upper Cretaceous cover (Alter do Chão Formation) and was affected by widespread tholeiitic magmatic activity (Penatecaua dolerites) at about 150 Ma, making seismic-based exploration difficult especially as much of the basin still lies beneath thick jungle. Because of the recognition of this widespread igneous overprint, hydrocarbon exploration efforts were subdued since the late 1970s.

However, this large sag basin is developed on the same scale as the Alberta basin of Canada and entrains the Carboniferous (Pennsylvanian, ≈305 Ma) Nova Olinda Formation, which is made up of a large laterally extensive set of cyclic evaporite beds, dominated by interbedded combinations of anhydrite and halite (Gonzaga et al. 2000). These evaporites occur within the Carboniferous-Permian megasequence, known as the Tapajós Group, which can be up to 1,600 m thick (Fig. 11.67b: Milani and Zalan 1999). The lowest part of the megasequence is a blanket of eolian sandstones (Monte Alegre Formation), which is covered by marine-influenced carbonates and evaporites (Itaituba and

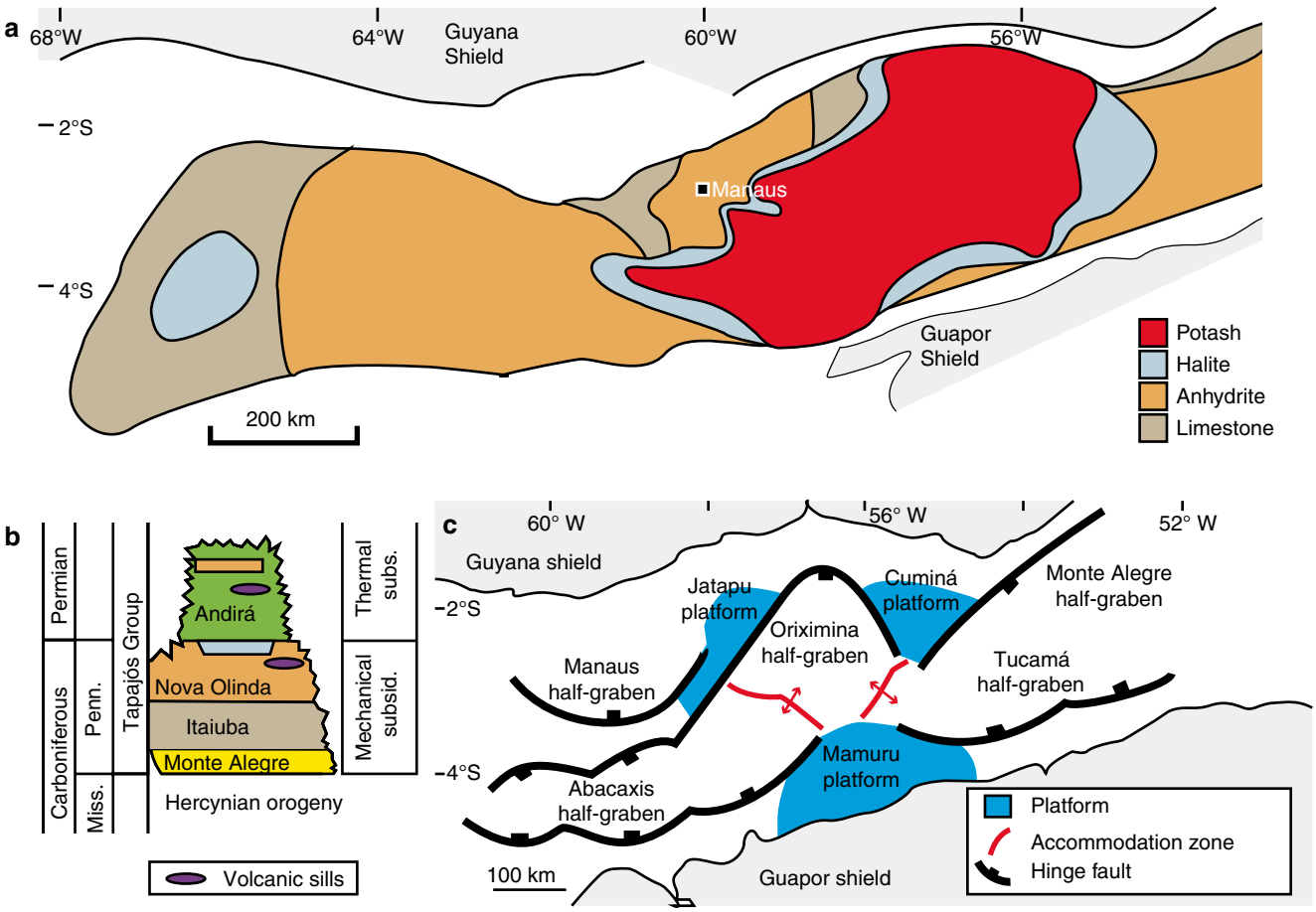

Fig. 11.67 Amazon Basin, Brazil. Amazon Basin, Brazil. (**a**) Distribution of potash and other evaporite salts in the Nova Olinda Fm (After Szatmari et al. 1979). (**b**) Relevant stratigraphy. (**c**) Basin architecture in the main evaporite area (After Gonzaga et al. 2000)

Nova Olinda Formations, respectively), along with subordinate sandstones and shales. The Tapajós megacycle is closed by a suite of Permian continental redbeds (Andirá Formation) of Permian age. Subsequent east-west regional extension facilitated a pervasive intrusion of magmatic bodies during the Early Jurassic (Penatecaua dolerites and equivalents).

Individual halite beds in the Nova Olinda evaporite cycles are 20–80 m thick, while the Nova Olinda Fm. has an average thickness of 900 m. Because of the high levels of entrained anhydrite beds in the Nova Olinda Fm., evaporite layers are not halokinetic, but are subject to collapse and flow about the basin margin in areas of intense dissolution.

Early Petrobras drilling programs conducted in the Amazon Basin from 1953 to 1963, defined the presence of halite, but did not appreciate that a number of the beds of NaCl in The Nova Olinda Formation are capped by sylvinite/carnallite beds. During the late 1960s and 1970s, higher resolution gamma ray logging tools were used, along with better mud technology and associated narrower caliper measures. This work identified a number of (0.5–2 m thick) layers of sylvinite, capping the halites (Szatmari et al. 1979). For example, the fifth and seventh depositional cycles define isolated salt sub-basins that accumulated significant potash salts in Fazendinha and Arari regions. KCl contents of these beds are between 28 and 33 % in beds some 2.47–2.65 m thick (Garrett 1995). As well as carnallite and sylvite, the potential ore intervals contain anhydrite and kieserite, but reserves are interpreted to be very large (Szatmari et al. 1979; Garrett 1995). The average ore depth at Fazendinha, the larger of the known potash area, is 1,050 m. Much of the halite and potash distribution is controlled by the underlying Basin architecture (Fig. 11.67c).

So, How Does Mineable Potash Form?

According to Braitsch (1971, p. 120), "The incongruent alteration of carnallite is probably the most important process in the alteration of potash salts." Incongruent dissolution" of carnallite is the process whereby carnallite alters to sylvite via the loss of magnesium chloride in the reaction

$$KMgCl_3.6H_2O \rightarrow KCl + Mg^{++} + 2Cl^{-} + 6H_2O$$

The reaction generates magnesium and chloride, it has been used to explain diagenetic bischofite and dolomite found is proximity to the newly formed sylvite. Bischofite is a highly soluble salt and may be metastable in many of the subsurface settings where incongruent dissolution is deemed to have occurred. In many such hydrologically active systems it may be flushed by associated brine crossflow.

Sylvite, interpreted to have formed from incongruent dissolution of primary carnallite, is reported from the Late Permian Zechstein Formation of Germany (Borchert and Muir 1964), Late Permian Salado Formation of New Mexico (Adams 1970), Early Mississippian Windsor Group of Nova Scotia (Evans 1970), Early Cretaceous Muribeca Formation of Brazil and the Gabon Basin, West Africa (Wardlaw 1972; Wardlaw and Nicholls 1972; Szatmari et al. 1979; De Ruiter 1979), Late Cretaceous of the Maha Sarakham Formation, Khorat Plateau, Thailand and Laos (Hite and Japakasetr 1979), Pleistocene Houston Formation, Danakil Depression, Ethiopia (Holwerda and Hutchinson 1968), and Middle Devonian Prairie Formation of western Canada (Schwerdtner 1964; Wardlaw 1968).

This rich literature base supports a long-held notion that there is a problem with primary sylvite as a marine salt Lowenstein and Spencer (1990)). Put simply, sylvite does not crystallize via evaporation of modern seawater at 25 °C, except under metastable equilibrium conditions (Braitsch 1971; Valyashko 1972; Hardie 1984). The sequence of bitterns crystallizing from modern seawater bitterns is illustrated in Fig. 11.68a.

The notion of sylvite via incongruent dissolution at depth is further supported by the thermodynamics of connate brines with ionic proportions of modern seawater (Fig. 11.68b; Koehler et al. 1990). Carnallite precipitating from a modern seawater bittern crystallises from a solution that has an ion activity product (IAP) within the carnallite stability field, at 1 bar pressure and approximately 30 °C (shown as point A in Fig. 11.68b). Increasing pressure, as carnallite is buried, moves the stability point into the sylvite + solution field as the carnallite sylvite boundary attains higher values of K. At a pressure of 1 kilobar, which corresponds to a lithostatic load equivalent to 2–3 km burial, the IAP position of the connate solution that first precipitated the carnallite at 1 bar, now lies in the sylvite + solution field. If equilibrium is maintained, the carnallite can react incongruently to form sylvite + solution.

So, based on this short geochemical discussion, and what we observed in our discussion of the various examples of sylvite occurrence, it seems the dilemma of primary sylvite can be solved in one of three ways. Historically, most workers have interpreted widespread sylvite as a diagenetic mineral formed by the incongruent dissolution of carnallite. Then there is the interpretation that some sylvite beds, perhaps associated with tachyhydrite, were the evaporite bittern part of a basin hydrology fed by $CaCl_2$-rich basinal

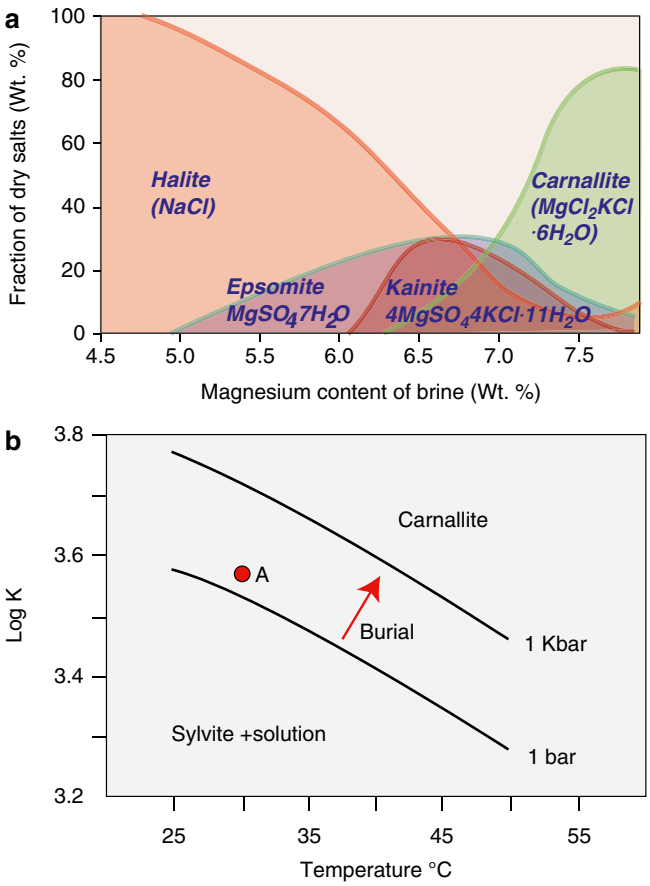

Fig. 11.68 Marine bitterns and incongruent dissolution. (**a**) Typical bittern sequence precipitated from modern seawater (After Garrett 1970a). (**b**) Phase relationship between the equilibrium constant (K) and temperature for the incongruent dissolution of carnallite to sylvite at 1 bar and 1 kbar pressures (After Koehler et al. 1990). The ion activity product (IAP) is related to the product of the concentration of Cl^- and Mg^{++} in the solution and is equal to K along the boundary between carnallite and sylvite stability fields

hydrothermal waters (Hardie 1990). The third, and increasing popular explanation of syndepositional sylvite, well supported by brine inclusion chemistry of co-associated halite, is that the chemistry of Phanerozoic seawater has evolved so that there were times in the past when $MgSO_4$ levels were lower and sylvite was a primary marine bittern precipitate (Lowenstein et al. 2001).

All views are valid within their relevant geological contexts but, if used exclusively to explain the presence of sylvite, are perhaps a little too dogmatic. My own view is that, owing to its high solubility, the various textures found in ancient potash salts reflect variegated and evolving origins that are dependent on how many times and how pervasively in its burial history an evolving brine chemistry came into contact with the potash beds (Warren 2000c). In other words, various forms and textures of potash may dissolve, recrystallise and backreact with each other from the time a potash salt is first precipitated until it is exploited.

Textural and mineralogical evolution depends on how open is the hydrology of the system at various stages during its burial evolution. Alteration can occur syndepositionally, in brine reflux or during later flushing by compactional or thermobaric subsurface waters. Tectonism (extensional and compactional) during the various stages of a basin's burial evolution acts as a bellows driving fluid flow within a basin, so forcing and speeding up the focused circulation of potash-altering waters.

A similar, but less intense, textural evolution can also be seen in the burial history of the less soluble salts. For example, $CaSO_4$ can flip-flop from gypsum to anhydrite depending on temperature, pore fluid salinity and the state of uplift/burial. This means that, as in gypsum/anhydrite sequences, there will be primary and secondary forms of both carnallite and sylvite that can alternate during deposition, during burial and during any deep meteoric flushing.

In Thailand, both primary potash precipitation and shallow diagenetic backreactions seem to have worked simultaneously with hydrologies that were first driven by early salt diapirism, that were also associated with the formation of shallow karst. Then alteration continued into deeper burial and finally during uplift, driven by the regional gravity drive of throughflushing fluids whose flow was focused along nearby clastic aquifers. The Canadian examples show how carnallite/sylvite has continued to evolve with the evolution of basinal and deeply flushing suprasalt and subsalt meteoric waters, as they came into contact with variably dissolving salt units. The Canadian potash deposits are unique in terms of their size and relative stratabound continuity, so, as part of this discussion on what make or destroys ore grade potash, we must consider why the Western Canadian Sedimentary Basin has so much more potash than any other.

Whatever model, or combination of models, is used to explain the origin of the world's major potash salts, the most important economic corollary is that, wherever a potash bed is in contact with mobile pore fluids, these highly soluble salts are continually subject to dissolution, mobilisation and reprecipitation. When trying to understand the distribution of potash ore in a halite-dominated sequence in various sedimentary and tectonic settings, the ability of the potash salts to flow, dissolve, alter and reprecipitate must be accounted for in order to create a predictive exploration model or development programme. So let us look first at controls on ore grade at the deposit scale and then at the basin and world tectonic scale.

Controls on Potash Quality: Anomalies, Leaching and Problematic Mine Waters

Just as the first rule for safe conventional halite mining is "stay in the salt," problem areas encountered in most potash mines are related to thinning or disappearing ore seams in zones showing evidence of water-related dissolution and solution collapse (Fig. 11.69; Boys 1990, 1993; Woods 1979).

Uncontrollable water inflow is the greatest threat to any operating potash mine, as can be seen in a history of loss of operational potash mines over the past four decades. In 1970 the decision was made to allow the Cane Creek (Moab) potash mine to flood, after 5 difficult years trying to deal with unexpected water inflows and ore-grade problems. In 1977 The Holle Mine in West Africa was lost to flooding. In 1986 Uralkali's Mine 3 was abandoned due to flooding. In early 1987 the Patience Lake potash mine was closed due to uncontrollable flooding. Water inflows were first encountered there during routine mining in 1975 and after a number of years of trying to cope with the inflows the former conventional underground mine was closed, allowed to flood, and a new solution mine started in 1988. The Cassidy Lake (Potacan) potash mine in New Brunswick, closed in October 1997 because of irreparable damage from severe flooding, at the time its capacity was 1.3 million tonnes. In October 2006, Uralkali's (URKA–RT) Mine 1 was closed due to flooding, with associated ground collapse, resulting in the loss of some 3 % or 1.2 million tonnes/year of global production. Today, Mosaic's Esterhazy K1 and K2 facilities are still dealing with ongoing water inflow problems. A flood at the Esterhazy complex (current capacity of 5.3 million tonnes/year) would affect some 9 % of current global capacity and it probably represents the most credible known current risk for a potash mine to flood.

In all these situations, other than intersecting old open well bores in the potash ore zone, most episodes of flooding, including the complete loss of working mines, stem from uncontrolled water inflows that follow an unexpected intersection with an anomalous non-ore zone. So in order to understand both the controls on potash ore grade and a mine's susceptibility to water inflow we must study how groundwater interacts with any potash intersection.

Increased water inflows in Saskatchewan potash mines are consistently linked to salt anomalies, that is, to natural areas of little or no potash within the potash ore bed (Gendzwill and Martin 1996). Geology of potash ore quality in three salt anomalies were studied by Boys (1990) in the PCS Cory mine, Canada, which extracts potash from the Patience Lake member of the Prairie Evaporite Formation. He defined five postburial facies in the vicinity of the salt anomalies, all related to a current or previous crossflow of water undersaturated with respect to potash (Fig. 11.69a). Where undersaturated groundwater continually interacts with a sylvinite bed it ultimately dissolves all the salts to leave behind only insoluble residues in a solution collapse breccia (facies 1). This potash-free interval is at the one end of the facies continuum defining salt anomalies in the PCS mine (Fig. 11.69a; facies 1 through 5). At

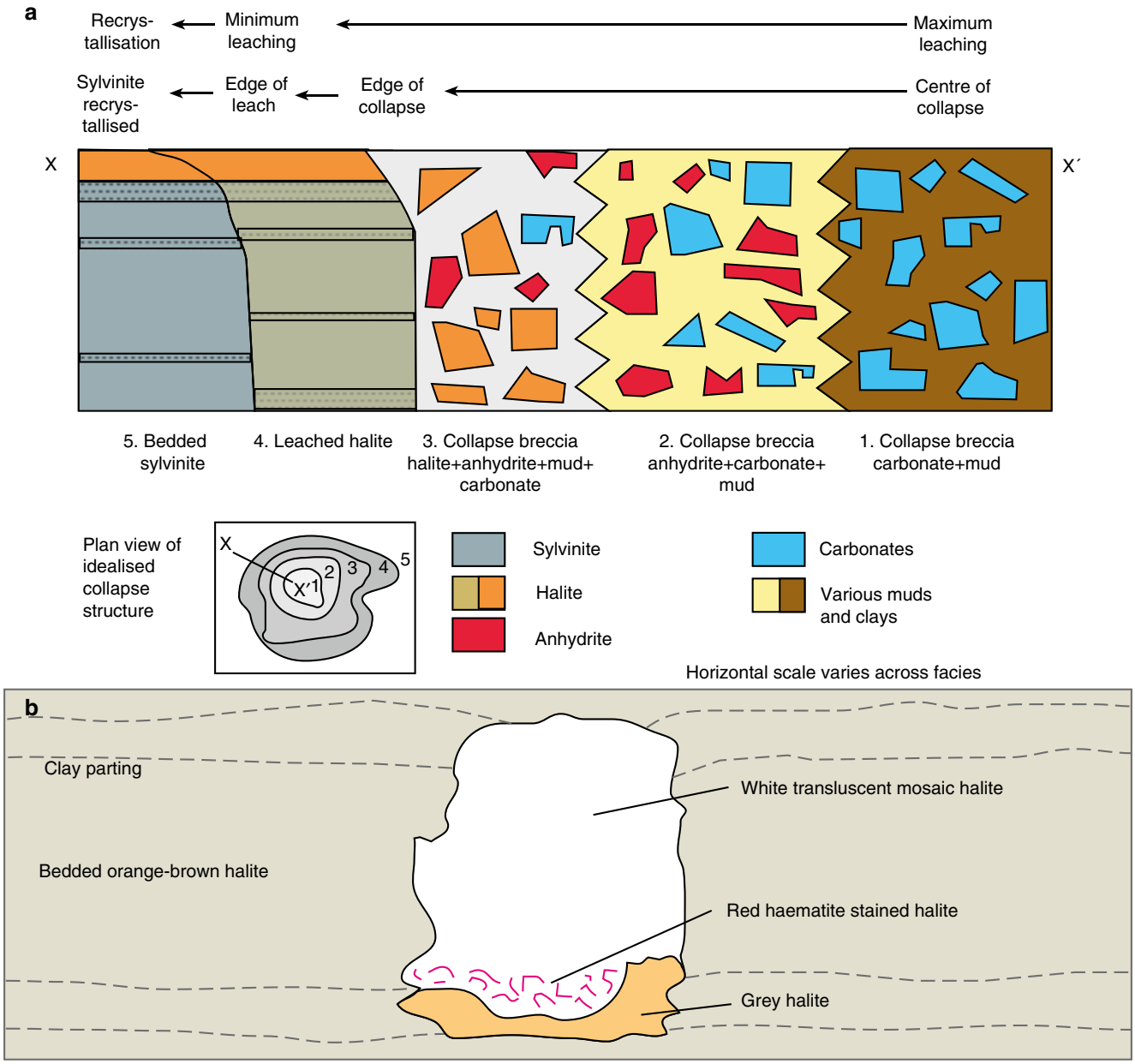

Fig. 11.69 Potash solution features. (**a**) Cross section A–A′ through half of an idealised collapse structure in the Prairie Evaporite Formation, Variable scale from 100 to more than 500 m across (After Boys 1990, 1993). (**b**) Recemented solution cavity in the Boulby Halite, Boulby Mine, UK. This interval is located below the main potash zone (After Woods 1979)

the other end of the groundwater-potash interaction spectrum are beds composed of completely recrystallized and often potash-enriched sylvinite (facies 5). These sweet spots lie adjacent to leached beds where recrystallized halite (facies 4) passes laterally into collapse breccias with blocks of anhydrite and halite (facies 3 and 2; solution residues made up of the less soluble salts), which in turn pass laterally into the most mature dissolution breccias of facies 1, where no evaporite salts remain. When a drive or a test hole passes out of the ore into facies 1 the potential for water problems is high.

In his model, salt anomalies indicate proximity to collapse structures that act as conduits for overlying (or possibly pressurised underlying?) formation waters. The crossflow drives a halo of pervasive leaching and recrystallization in the Prairie Evaporite Formation. The same fluids that cause widespread recrystallization, and possibly enrichment of the potash salts at the outer edge of the salt anomaly, also dissolve water-filled cavities in the more central parts of the anomalies. The intensity of the leaching and the geometry of the leached halo is variable, while the timing of major leaching events in the Prairie Evaporite is still poorly constrained. Boys (1990) pos-

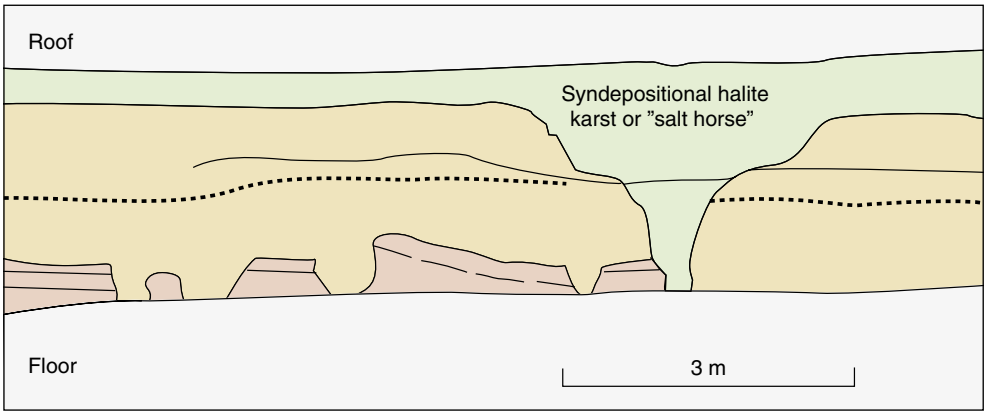

Fig. 11.70 Sedimentary structures showing the abundance of vadose textures including a downcutting "salt horse" from halite cavern infill in the Salado Formation of the Delaware Basin, as exposed in the WIPP shaft, USA (After Hovorka et al. 2007)

tulates at least two major water crossflow events in the PCS mine, possibly driven by uplift and tectonism: one occurred in the Late Devonian, the other in the Cretaceous, both are tied to the gravity-driven descent of undersaturated waters.

Similar leached solution cavity-fill features that create salt anomalies occur in the Boulby Potash Mine in the UK, although most of the features are now halite-cemented and consist of lenses of coarse pure translucent secondary halite (Fig. 11.69b). Intersected zones are up to 2 m across and typically overlie a band of halite encrusted with red hematite (Woods (1979)). The amount of anhydrite at the base of many cavities is greater than would accumulate as a simple insoluble residue implying they formed from waters close to $CaSO_4$ saturation. According to Woods (1979), the cavities formed in the subsurface from $CaSO_4$ -saturated brines that were involved in dissolving the carnallite and sylvite. The resulting brines became supersaturated with respect to $CaSO_4$ causing halite to precipitate and accumulate on the cavity floor.

At a smaller scale, I have observed similar $CaSO_4$-floored dm-scale cavities in core from the Maha Sarakham potash intervals in Thailand and in this case they formed early, syn-precipitationally to bedded sylvinite in adjacent salt withdrawal depressions (Fig. 11.38). It seems that vadose and shallow phreatic dissolution is commonplace in many potash intervals worldwide. The infill, however, is not always halite; and in Thailand, in the heavily recrystallized sylvinite zones, some of these anhydrite-floored cavities have been filled by coarse-grained clear sylvite made up of single crystals that can be more than 30 cm across.

Salt anomalies (barren zones in potash ore) also form crosscutting intervals in the Permian potash ores in New Mexico (Linn and Adams 1966). Locally called "salt horses"[6], these crosscutting irregular zones range from 0.3 to 100 m in width and 3–200 m in length. Beds in salt horses are thinner than the equivalent beds in ore. Contacts between salt horses and ore are sharp and colour of the clay changes from grey in ore to brown in salt horses, perhaps indicating more oxygenated crossflushing waters. Pods and lenses of langbeinite, leonite, kainite, recrystallized halite, and recrystallized sylvite occur in McNutt ore near the salt horses, while disseminated polyhalite of the typical marker bed is locally concentrated into intergranular seams and pods in or near horses.

According to Linn and Adams (1966) the NaCl-saturated brines creating the horses entered the ore zone from below and formed horses by the selective metasomatic leaching of sylvite. Fluid entry from below is not unreasonable in the New Mexico situation, as the potash evaporites occur along the western margin of the Delaware Basin and sit atop an aquifer that entrains deeply circulating meteoric waters. However, based on three decades of detailed geological study in the same area, both at the WIPP site and the surrounding potash mines, Hovorka et al. (2007; p. 351) conclude that the large 'salt horses' composed of relatively pure halite encountered in Salado ore zones are perhaps large halite-filled synsedimentary dissolution pits (Fig. 11.70) They go on to state that a least a proportions of geometrically similar large pits (anomalies of Boys 1993) that have been mapped in various potash mines in the Devonian Prairie evaporite may also be synsedimentary.

Effects of the leaching events that produce the salt anomalies and loss of potash in Canada or elsewhere, range from weak to strong, from selectively preserving delicate laminae and chevron textures, to deforming and destroying salt beds (Boys 1990). Good preservation of iron oxides in halite may indicate that the leaching was weak or of short duration. In many leach anomalies fed from above, salinity indicator minerals increase downward evolution in a structure, possibly because fluids exit downward and NaCl-saturated fluids tend to follow the chemical gradient provided by potash beds. Or, in my opinion, it zones downward because all

[6]"Horse" is possibly a miner's corruption of the term horst. In mining the term typically refers to a block of country rock entirely encased within a mineral lode. Horse is also a broader geological technical term to describe any block of rock completely separated from the surrounding rock either by mineral veins or fault planes.

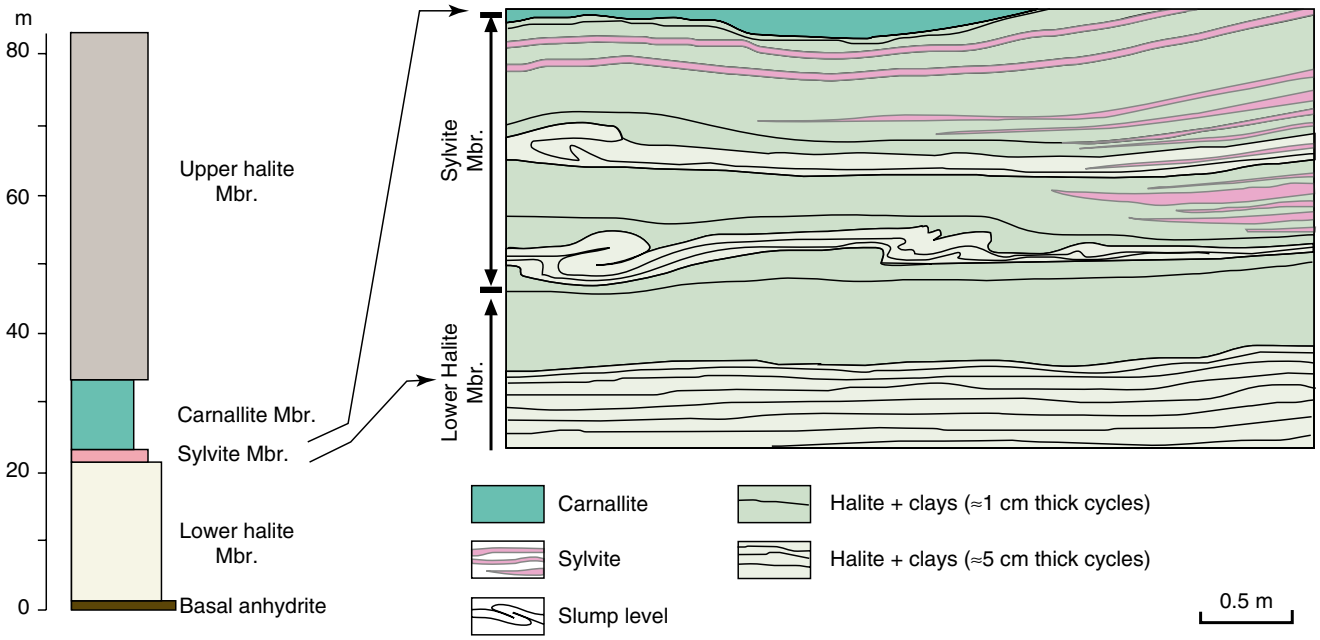

Fig. 11.71 Stratigraphy of Upper Eocene potash section based on sequence cored in Biurrun borehole and tied to a mine wall sketch from Subiza Mine, showing barren body made up of two superimposed slump structures with corresponding upper sections, where the overlapping sylvite beds evolve from absent to continuous (After Cendon et al. 1998)

brines tend to density stratify and the denser more saturated waters in a downward growing dissolution feature would tend to have ponded in its bottom (or synprecipitational sump). Early stages of stratification are seen in the perched waters on blind-bottomed sub-vertical karst holes in Mt Sedom, Israel.

Identifying proximity to a salt anomaly is obviously important in terms of ore quality and mine safety (Boys 1990). Geological indicators of proximity to a halite anomaly include: a change in insoluble seam colour from greenish-grey to mottled brown and greenish-grey (probably corresponds to increasingly oxidised fluids in the crossflow structure), unusual local increases in ore grade, large patches of sylvite-poor potash crosscutting units near the top of the ore zone, and drops in topography >10 m of the marker seams across an anomaly. For example, within 5 m of a large salt anomaly, Boys (1990) found large blebs (>200 cm^2 on the mine wall) of sylvite-poor potash that crosscut the units of an incomplete potash cycle near the top of the main ore zone. Anhydrite, a less soluble salt, is also more common in a salt anomaly than in the adjacent ore. Once into the anomaly facies, possible indicators of a nearby major collapse feature include: stretched clay seams; folded beds; small collapse features (1–20 m scale); and split clay seams with salt appearing to be injected into the seam.

In a study of "barren bodies" in the Subiza Mine, Navarra, Spain, Cendon et al. (1998) recognised a syndepositional mechanism of "salt horse" formation (Fig. 11.71). It was controlled by brine pool stratification, not various diagenetic processes tied to subsurface crossflow. The Subiza potash deposit contains a 100 m thick Upper Eocene succession of alternating claystone and evaporites (sulphate, halite, and sylvite). The evaporites accumulated in an elongated basin that is one of the depocentres within the 250 km long South Pyrenean foreland basin. Slope instability along the margin of the basin, perhaps promoted by tectonism, created mass wasting of the evaporite beds. This formed subaqueous mounds 0.5–2 m high and tens of metres across. As evaporation progressed, a stratified brine system formed and encroached over the mounds. Halite precipitated at the air-brine interface and sank to the bottom of the basin, along with terrigenous clays. Sylvite, however, precipitated only from the cooling of a lower denser bottom hugging brine. This brine was warm where it formed about the basin edge and cooled as it seeped into the deeper parts of the basin floor. As many mound crests extended into the upper less saline brine, the sylvite could not precipitate over these subaqueous highs. With progressive accumulation, the lower brine ultimately covered the mounds as sylvite beds overlapped the mound tops.

This model, however, is in my opinion problematic in terms of its hydrological restraints: it requires a hydrological system that encapsulates sylvite saturation and precipitation in the cooling lower brine with simultaneous halite precipitation in the upper brine. Such a system is extremely difficult to maintain over time frames that allow metre-thick beds of evaporites to accumulate. A more likely hydrology is perhaps a desiccating and concentrating single brine body,

which reached halite saturation at the "pond full" stages while the mounds were still covered with brine. It did not reach sylvite saturation until ongoing drying of the brine lake had lowered the level to where the crests of the mounds were exposed. Whichever model is accepted, what is most important in terms of potash geology is that breached syndepositional salt horses or barren zones are less likely to possess subsequent subsurface hydrologies that will flood mines, as compared with horsts induced by later subsurface leaching, as defined by Boys (1993). The Navarra type of salt anomaly would not be tied to a zone of potential inflow in an active mine. Using and applying it as an interpretation of salt anomalies in an ore zone outside of the region where it was documented has significant implications in terms of mine safety.

Intersecting unexpected salt anomalies, especially those associated with flowing undersaturated brines should always be noted and dealt with as early as possible in a mine plan. Otherwise these zones can impair or destroy a potash mine. In the 1970s the Patience Lake potash mine operation, located on the eastern outskirts of Saskatoon, encountered a natural collapse structure. Grouting managed to control the inflow and mining continued. Then, in January of 1986 the rate of water inflow began to increase dramatically from the same fractured interval (Fig. 11.72; Gendzwill and Martin 1996). At its worst, the fractures associated with the structure were leaking 75 m^3/min (680,000 bbl/day) of water into the mine. The water was traced back to the overlying Cretaceous Mannville and possibly the Duperow formations. Finally, in January 1987 the mine was abandoned. It took another 6 months for the mine to fill with water. Subsequent seismic shot over the offending structure suggested that the actual collapse wasn't even penetrated; the mine had merely intersected a fracture within a marginal zone of partial collapse (Gendzwill and Martin 1996). Part of the problem was that the water was undersaturated and quickly weakened pillars and supports, so compromising the structural integrity of the workings. The unexpected intersection of one simple fracture system resulted in the loss of a billion dollar mine.

Patience Lake mine now operates as a solution mine by pumping KCl-rich brine from the flooded mine workings to the surface (Fig. 11.6). The operation has a capacity to produce more than a million tonnes of potash annually. It works by circulating heated brine through the flooded mineshaft into the former workings, which extend up to 18 km from the main shaft. Heated recovered potassium-rich brines are pumped into surface crystallization ponds where the liquor evaporates and cools. Sylvite, potash, and other salt crystals form and settle to the bottom of the pond. This potash sludge is pumped from a floating dredge to the processing plan, while the cooled NaCl-saturated pond brine is reheated and re-injected into the mine to repeat the process.

Prugger and Prugger (1991) documented the successful treatment of an underground inflow into the Rocanville mine that occurred in 1984 (Fig. 11.73). In this case the mine was saved. It began when a mine entry accidentally penetrated a salt collapse structure that then began to leak brine into the mine at rates exceeding 10 m^3/min (90,576 bbl/day). Seismic showed that the structure was roughly circular and relatively

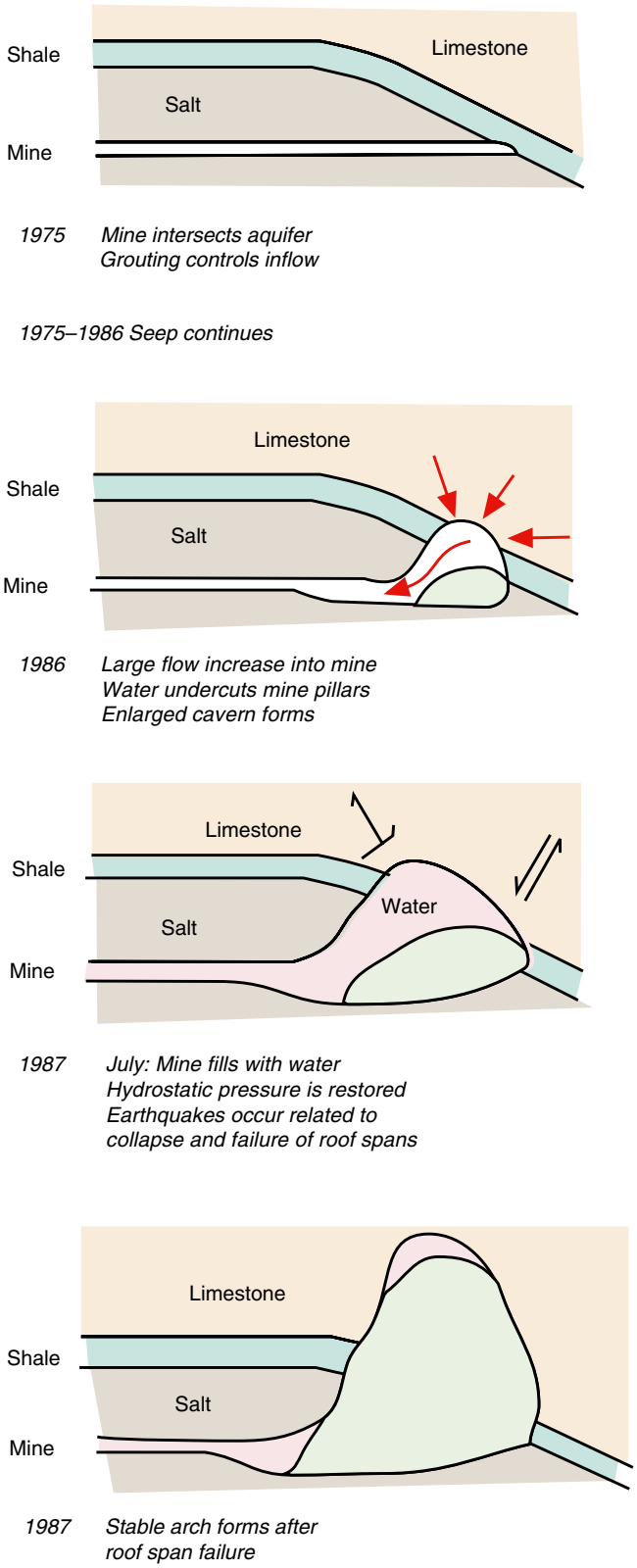

Fig. 11.72 Sequence of events controlling the flooding of the Patience Lake Mine (After Gendzwill and Martin 1996)

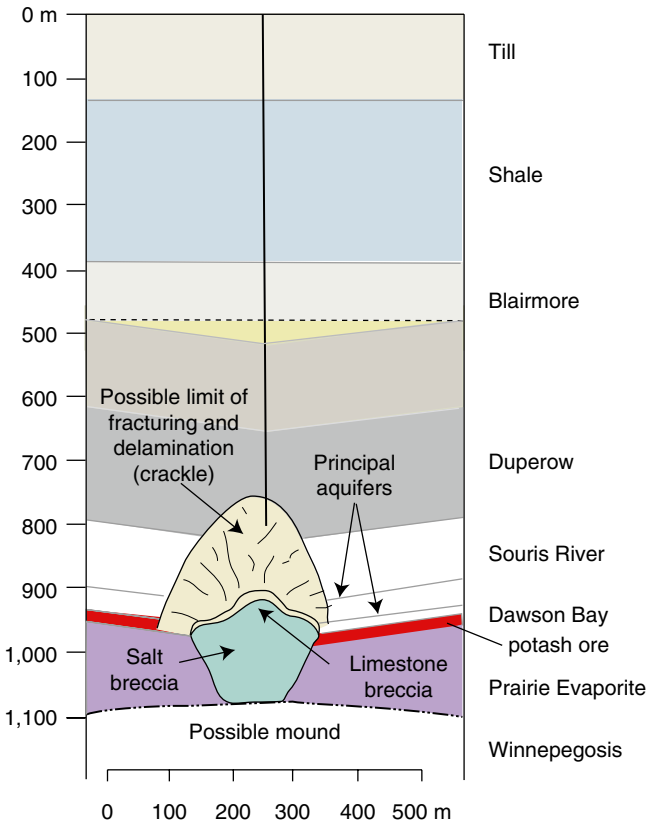

Fig. 11.73 Dimensions of the salt collapse chimney that was breached in the Rocanville Mine in 1984 (After Prugger and Prugger 1991)

small in size (300 m in diameter), and was isolated from other collapse structures. A grout well was drilled from the surface and encountered the collapse upon penetrating the carbonates of the overlying Duperow Formation, suggesting that fracturing associated with the collapse structure had extended as a blind chimney a considerable distance up from the Prairie level. Unlike the Patience Lake Mine flood, a combination of grouting and bulkhead emplacement in Rocanville succeeded in sealing off the inflow, thus saving the mine. Also unlike Patience Lake, the brine from the breached structure was halite-saturated so limiting the amount of dissolution damage. Different outcomes between the loss of the Patience Lake Mine and recovery from flooding in the Rocanville Mine may reflect the difference between intersecting a chimney that made its way to the Cretaceous landsurface and is now overlain by a wide-draining set of sediments versus intersecting a blind chimney that never broke out at the landsurface.

The notion of ore continuity in the sylvinite units of the Prairie Evaporite in the potash area of the Western Canada Sedimentary Basin is a commonly stated precept. But when the actual distribution and scale of salt horses are mapped as a mining operation proceeds it is obvious that many small 10 m-scale discontinuities are present. Sometimes they thin and degrade (Section A–A_1–A_2), other times locally enrich the ore grade (B–B_1). They are much more widespread than often considered to be present in what is the richest potash ore deposit in the world and exemplified for the lateral continuity of the ore zones (Fig. 11.74; Baar 1974). It seems that unexpectedly intersecting a salt anomaly in an ore zone can have a range of outcomes ranging from the inconsequential to the catastrophic, in part because there is more than one type of salt anomaly or "salt horse."

Figure 11.75 summarises what are considered the three most common salt anomalies and their occurrence styles are in part time-related (Boys 1990). Washouts are defined as… "salt-filled V- or U-shaped structures, which transect the normal bedded sequence and obliterate the stratigraphy" (Fig. 11.75a; Mackintosh and McVittie 1983, p. 60). They are typically enriched or filled by insoluble materials in their lower one-third and medium-coarse-grained halite in the upper two thirds. Up to several metres across, when traced laterally they typically pass into halite-cemented paleo-sinks and cavern networks (e.g. Fig. 11.75b). Most washouts likely formed penecon-temporaneous with the potash beds they transect, that is, they are preserved examples of synkarst with infilling of the karst void by a slightly later halite cement. They indicate watertable lowering in a potash rich saline sump. This was followed soon after by a period of higher watertables and brine saturations, when halite cements occluded the washouts and palaeocaverns. Modern examples of this process typify the edges of subcropping and contemporary evaporite beds, as about the recently exposed edges of the modern Dead Sea. As such, "wash outs" tend to indicate relatively early interactions of the potash interval with undersaturated waters, they may even be a part of the syndepositional remobilization hydrology that focused, and locally enriched, potash ore levels.

In a leach zone, the stratabound sylvinite ore zone has been partially or completely replaced by barren halite, without significantly disturbing the normal stratigraphic sequence (Fig. 11.75b). Some loss of volume or local thinning of the stratigraphy is typical in this type of salt horse. Typically saucer-shaped, they have diameters ranging from a few metres up to 400 m. Less often, they can be linear features that are up to 20 m wide and 1,600 m long. Leach zones can form contemporaneously due to depressions and back-reactions in the ore beds, or by later low-energy infiltration of Na-saturated, K-undersaturated brines. The latter method of formation is also likely on the margins of collapse zones, a situation typically classified as a leach-collapse anomaly (Mackintosh and McVittie 1983; McIntosh and Wardlaw, 1968).

Of the three types of salt anomaly illustrated, leach zone processes are the least understood. Historically, when incongruent dissolution was the widely accepted interpretation for loss of unit thickness many leach anomalies were considered metasomatic. Much of the inherent metasomatic interpretation was based on decades of detailed work in the various salt mines of the German Zechstein Basin. Intellectually, evaporites were considered more akin to metamorphic rocks and the term metasomatic alteration was commonly used

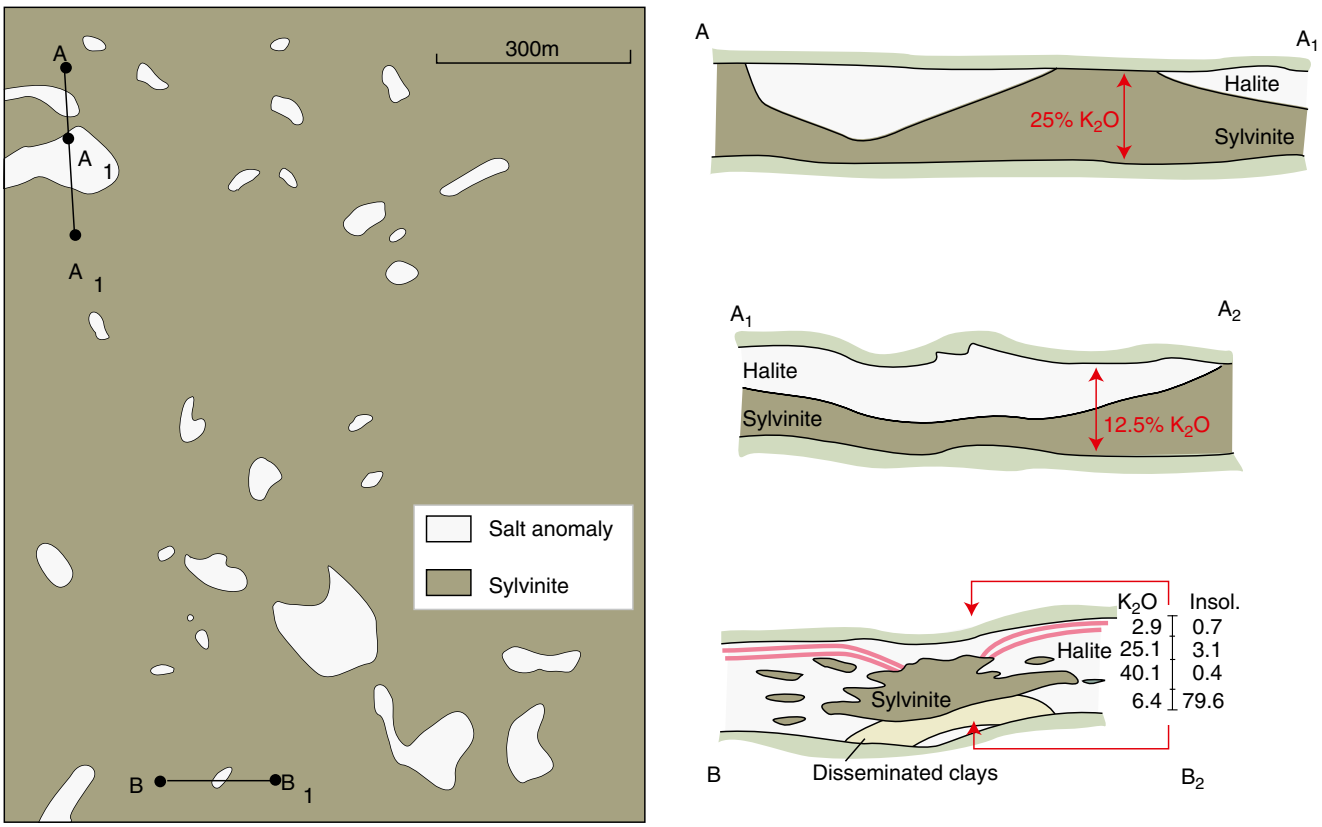

Fig. 11.74 Salt horses mapped in an ore level in a potash mine near Saskatoon, Canada (After Baar 1974). (**a**) Subsurface distribution of small scale salt anomalies mapped during mining. (**b**) Scaled cross sections of salt anomalies and associated K_2O

when explaining leach anomalies. In the past two decades, widespread observations of the preservation of primary chevron halite in most bedded evaporites have led to a reduced use of notions of widespread metamorphic-like metasomatic or solid-state alteration processes in bedded evaporites. There is just too much preserved primary texture in the bedded salt units to invoke pervasive burial metasomatism. So how do leach anomalies, as illustrated in Fig. 11.75b, occur in nonhalokinetic settings? A possible explanation is given by the depositional salt horse textures documented in the Navarra Potash Province (Fig. 11.71). There, the underlying and overlying salt stratigraphy is contiguous, while the intervening sylvite passed laterally into a syndepositional "salt horse."

On the other hand, in halokinetic situations (which characterises much Zechstein salt) solid-state alteration via inclusion related migration in flowing salt beds is a well-documented set of texture-altering processes (diffusion metasomatism). Most workers in such halokinetic systems would agree that there must have been an original stratiform potassium segregation present during or soon after deposition related to initial precipitation, fractional dissolution and karst-cooling precipitation. But what is controlling potassium distribution now is a totally recrystallised and remobilised set of textures that preserve little or no crystal-scale evidence of primary conditions. The complex layering in such deposits may preserve a broad depositional stratigraphy, but the decimetre to metre scale mineral distributions are indications of complex interactions of folds, overfolds, and disaggregation with local flow thickening.

Collapse zones are characterized by a loss of recognizable ore strata, which is replaced by brecciated, recemented and recrystallized material, with the breccia blocks typically made of the intrasalt or roof lithologies (Fig. 11.75c), so angular fragments of the Second Red beds and dolostones of the Dawson Bay Formation are the most conspicuous components of the collapse features in the Western Canada Sedimentary Basin. When ore dissolution is well developed, all the halite can dissolve, along with the potash salts, and the overlying strata collapse into the cavity (these are classic solution collapse features). Transitional leached zones typically separate the collapsed core from normal bedded potash. Such collapse structures indicate a breach of the ore layers by unsaturated waters, fed either from below or above. For example, in the Western Canada Sedimentary Basin, well developed collapse structures tend to occur over the edges and top Devonian mud mounds, while in the New Mexico potash zone the collapse zones are related to highs

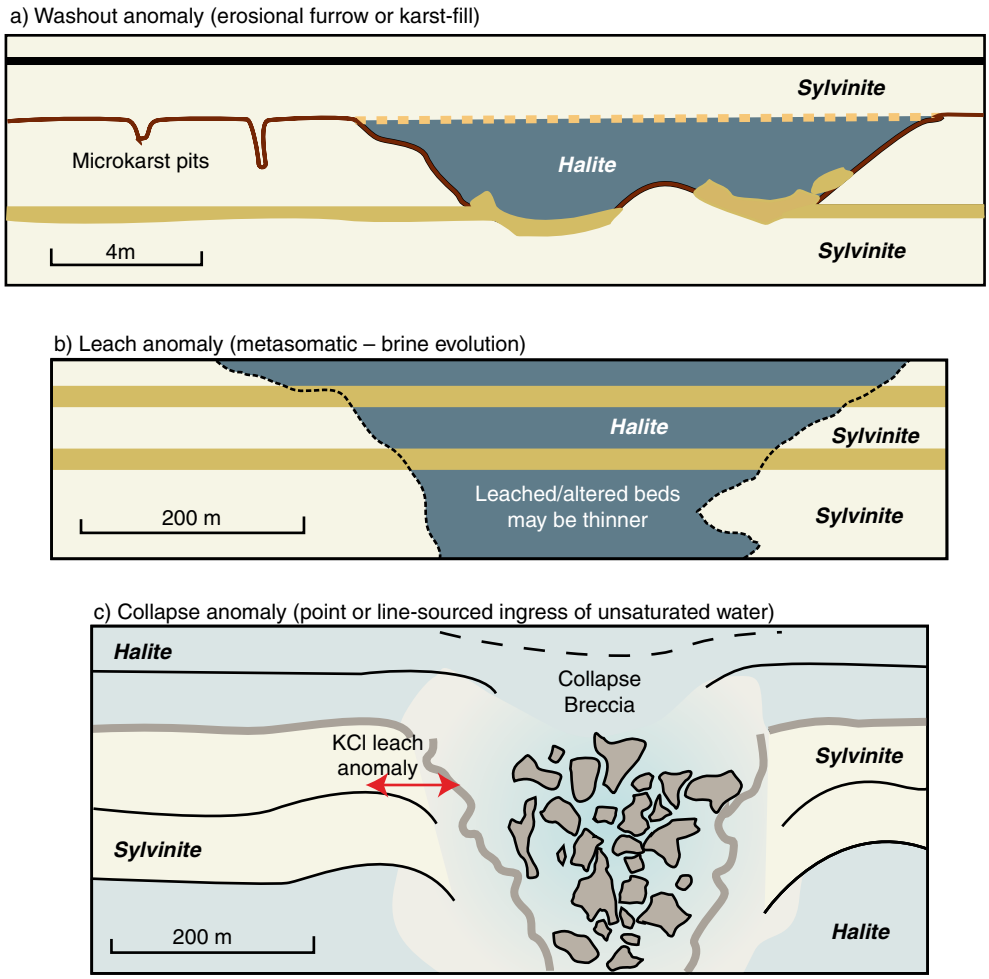

Fig. 11.75 Three main types of salt anomalies or salt horses (Based on Boys 1990 and Mackintosh and McVittie 1983)

in the underlying Capitan reef trend. Leaching fluids may have come from below or above to form collapse structures at anytime after initial deposition. When connected to a water source, these are the subsurface features that when intersected can quickly move the mining operation out of the salt into and adjacent aquifer system, a transition that led to flooding in most of the mine-lost operations listed earlier.

Clearly, identifying at the mine scale the set of processes that created a salt horse has implications in terms of its likely influence on mine stability whatever decision is made on how to deal with it as part of the ongoing mine operation. Syndepositional karst fills and leach anomalies are least likely to be problematic if penetrated, as the aquifer system that formed them is likely no longer active. In contrast, penetration or removal of the region around a salt-depleted collapse breccia may lead to uncontrollable water inflows and ultimately to loss of the mine. Unfortunately, in terms of production planning, the features of the periphery of a leach anomaly can be similar if not identical to those in the alteration halo that typically forms about the leached edge a collapse zone. The processes of sylvite recrystallization that define the edge of collapse anomaly can lead to local enrichment in sylvite levels, making these zones surrounding the collapse core attractive extraction targets (Fig. 11.69a; Boys 1990, 1993). Boundaries of any alteration halo about a collapse centre are not concentric but irregular making prediction of a feature's geometry very difficult, if not impossible. The safest course of action is to avoid mining salt anomalies but longwall techniques make this difficult and they must be identified and dealt with. There are a number of features that should be monitored in an active potash mine to help identify proximity to a salt anomaly or salt horse and minimise associated problems related to maintaining a constant ore-grade feed to the mill (Table 11.9).

Potash Occurrence and Quality at the Worldscale

The solubility of potash salts controls how and where beds are economic at the extraction scale, but are the same sets of processes, namely dilution and reprecipitation, also

Table 11.9 Features that should be monitored and mapped during both exploration for, and development of a potash deposit/mine

Feature	Problem	Related observations
Structure of the ore horizon	Faulting. folding or flowage of ore horizon complicating or precluding room-and-pillar mining method.	(a) Correlation of stratigraphy between boreholes (b) Examination of core for evidence of deformation and recrystallisation.
Stratigraphy	Incorrect correlation of ore horizons; salt thicknesses above ore are insufficient to protect deposit from water influx; slabbing, and ore dilution from clay beds above ore horizon.	Detailed core logging and correlation of beds between drill holes.
Ore depth	Low mine extraction or excessive development and mining costs.	Mining method and size of mine openings designed on basis of rock mechanics and geology.
Ore thickness	Local systematic or random thinning of ore zone.	(a) Isopach maps of stratigraphic units and mineralisation in ore zone. (b) Inspection of core for evidence of metasomatism and potash leaching, i.e., recrystallised halite, clay in intergranular clots, and horizontal mineral zoning.
Ore mineralogy	Assemblages incompatible with proposed mill circuit; certain assemblages reduce stability of mine openings, high insoluble content requires extra desliming capacity.	Determinative mineralogy of core.
Ore grade	Grade may be too low or erratic to maintain acceptable mill feed, recoverable K_2O may be significantly less than total K_2O.	Correlation and interpretation of drill hole data, comparison of chemical analyses with determinative mineralogy.
Ore continuity	Erratic barren or thin areas in ore zone.	Correlation of stratigraphic units and mineralisation in ore zones, inspection of core for evidence of recrystallisation and horizontal mineral zoning.
Ore crystallinity	Inclusion of contaminants within potash minerals, fine-grained assemblages requiring finer grind.	Correlation of microscopic examination of ore samples with chemical analyses of mineral separates.
Ore reserves	Insufficient reserves or excessive mining and milling costs.	Accurate geological description of deposit for mining and metallurgical studies.

After Adams and Hite (1983)

significant in controlling potash texture and distribution at the basin scale and defines which tectonic associations are likely to be optimal for the development of basins that entrain relatively undeformed, mineable, potash horizons?

First let us consider the some documented Quaternary potash deposits (Table 11.10), these systems can be subdivided into those where the potash minerals occur naturally at the present day landsurface, namely, Salar Gorbea-ET, Quinghai (Dabaxum)-BWk, and Chott el Djerid-BWh. Aridity in these settings ranges across polar tundra, to desert steppe, to hot dry desert. In all three cases the modern potash precipitate is carnallite, not sylvite, and it is either precipitated as ephemeral efflorescences, or occurs as a karst fill cement in a bedded halite host. In no case is Quaternary potash a marine-sourced mineral, in only two regions (Qinghai and Danakil) is the potash present in sufficient volumes to be exploited, and in neither case is the potash present as extensive at-surface beds, rather it occurs in discontinuous karst-influenced cement clusters, hosted in primary textured halite beds. In all the other listed Quaternary examples there is no natural precipitate of potash, it is anthropogenically produced in salt factory facilities operating as brine concentrators, with inflow brine feeds derived either from modern lake brines or recovered by the solution mining of ancient evaporites.

Mineralogically and topographically, there is a distinct schism in Quaternary potash associations. Muriate of potash is the dominant phase produced, or expected to be produced, in the Dead Sea and the Danakil depressions. Both deposits are forming in extreme endorheic lows on the Earth's surface (some 415 and 115 m below sea level, respectively), both are in adiabatic deserts in regions of drastic subsidence, both have brine inflows with chemistries and ionic proportions substantially influenced by the dissolution of older marine evaporites. The slightly milder BSh (hot desert steppe) setting of the southern Dead Sea versus the BWh (hot arid desert) setting of the Danakil, which encompasses the hottest place (year round) on the earth's surface, may explain why carnallite is a at-surface precipitate in the Danakil and a manufactured salt in the desert steppe climate of southern Dead Sea pans (Warren 2015a,b).

In contrast to the two listed muriate of potash occurrences, for the SOP examples the various combinations of mixed sulphate of potash salts are the precipitated precursor salts in the briney lake sediments, as well as being the manufactured product. In Lop Nur, for example the natural lake evaporites are a nonmarine assemblages of mirabilite-glauberite-polyhalite-bloedite-gypsum-halite. The evaporitic stages of the lake fill in Lop Nur contain massive amounts of glauberite

Table 11.10 Quaternary potash occurrences and producers, listed by country

Location	Tectonic setting (orogeny)	Köppen	Elevation (m msl)	Commodity (est. reserve Mt) or occurrence	Comment
Big Quill Lake, Brine plant, Canada	Canadian plain, Foreland basin to Rockies	Dfb	500	Sulphate of potash (small)	Small SOP operation near Wynyard, Saskatchewan, combines trucked-in KCl with Mg_2SO_4 from Quill Lake brine to produce K_2SO_4, for specialty fertilizers. Capacity 40,000 t/year
Salar Gorbea, Chile	Convergent. Intermontane (Andean)	ET	3,946	Local occurrence (not economic)	Carnallite cements in marginal salt crusts in two adjacent salars (Gorbea and Ignorado) with waters that are acidic, almost all other South American salars are neutral or alkaline
Salar de Atacama, Chile	Convergent. Intermontane (Andean)	BWk	2,250	Sulphate of potash (250) and MOP	Solar evaporation of brine, SOP recovered from brine field during $LiCO_3$ concentration. Capacity 650,000/year
Lop Nur, China	Convergent, Intermontane (Himalayan)	BWk	789	Sulphate of potash (36, expanding)	World's largest SOP pan facility at eastern end of Takla Makan Desert in Playa atop former delta of Tarim River
Quinghai Salt Lake, China	Convergent, Intermontane (Himalayan)	BWk	2,672	Muriate of potash (220)	Active solar evaporation of lake brines to precipitate carnallite which is processed to produce KCl
Danakil depression, Ethiopia and Eritrea	Rift (East African-Afar rift)	BWh	−115	Prospect (possible resource more than 600)	Salt mineralogy indicates a brine feed that transitioned from partial Pleistocene marine seepage to modern hydrothermal nonmarine. Active plans to solution mine and open pit mine parts of the deposit
Dead Sea, Jordan and Israel, Middle East	Transform, rift (Palestinian Transform)	BSh	−416	Muriate of potash (1,000)	Brine processing since 1955 (carnallitite slurry), Dead Sea (Israel and Jordan) supplies 10–12 % of world potash (Mg as byproduct). Ongoing problem with halite mushrooms in concentrator pans
Bayovar, brine pilot, Peru	Convergent, marine coastal (Andean)	BWh	2	Prospect	Located in coast part of Sechura Desert. Pilot plant for potash production in operation in coastal evaporators using pumped in solution brines
Chott El Djerid, Tunisia	Intracratonic sag (stable craton)	BWh	15	Local KCl effloresences (not economic)	Small hematite stained crystals of carnallite form atop 10 cm thick halite crust (documented occurrence on Sept. 1990)
Great Salt Lake, USA	Basin and Range	Csa	1,270	Sulphate of potash	Kainite, schoenite and halite in artificial concentrator pans on lake flat pans fed lake brine, slurry processed to produce SOP. Annual capacity 400,000 t
Bonneville Salt Flats, USA	Basin and Range	BSk	1,280	Muriate of potash	Output from lake flat brine trenches pumped into concentrators, brine has less sulphate and magnesium than Great Salt Lake
Cane Creek Mine (Moab salt pans), USA	Basin and Range	BSk	1,390	Muriate of potash	Solution mine in a former mine facility intentionally flooded in 1970, solution mine (Colorado river water injected, recovered mine brine now feeding solar evaporators precipitating carnallitite/ sylvinite in nearby Shafer basin. Capacity 180,000 t/year

See also Table 11.2

and polyhalite compared to the other salts present, and their predominance, is indicative of pervasive back-reactions, as is the presence of very minor amounts of carnallite and sylvite (Ma et al. 2010; Dong et al. 2012). In Great Salt Lake the SOP is produced by processing a slurry of kainite and schoenite that is the prime winter precipitate after halite has formed in

Table 11.11 Some of the world's larger ancient potash ancient potash accumulations, as discussed in this chapter and listed by age of deposit (reserves listed are in million tonnes of *in situ* K_2O, as estimated by Mayrhofer, 1985 – the Salado *in situ* estimate comes from the USGS and includes Paradox reserves)

Host formation and location	Age	Synsalt tectonics	Post-salt tectonics	Halokinesis (reserves)	Mineralogy	Comment
Prairie Evaporites in Western Canada Sedimentary Basin	Devonian (Givetian)	Intracratonic sag that was a distal foreland basin to early stages of Antler Orogeny	Ongoing distal flexural responses Laramide Orgeny	No (507,218)	Sylvite ocean	Extensive ongoing edge dissolution/recycling throughout its history.
Liven Fm., Soligorsk or Starobin deposit, Belarus, Pripyat Basin	Devonian (Frasnian)	Devonian intracratonic synrift passing into aulocogen sag basin	Polyphase former intracratonic sag inverted in Cretaceous-Tertiary	Yes (444)	Sylvite ocean	Synrift salt is actually two separate thick beds Liven (late Frasnian) and Lebeyan (Late Fammenian) Fm
Iren Fm., Upper Kama Basin, Pre Urals Trough, Russia	Permian (Kungurian)	Intracratonic sag basin related to Uralian orogeny	Polyphase, former sag inverted in Mesozoic and Tertiary	Yes (10,822)	$MgSO_4$ ocean	Currently very shallow mining operation with associated groundwater entry considerations
Zechstein salts, NW Europe	Permian (Lopingian)	Intracratonic thermal sag (post Hercynian relaxation)	Polyphase, former intracratonic sag inverted in Cretaceous-Tertiary	Yes (1,620)	$MgSO_4$ ocean	Former more extensive potash beds have been broken up by extensional and compressional halokinesis
Salado Fm., Delaware Basin	Permian (Lopingian)	Intracratonic basin flexure (downwarp) due to closure of Gondwana against Laurentia	Ongoing distal flexural responses Laramide Orgeny	No (800)	$MgSO_4$ ocean	Potash sedimentation in a fill-and-spill transition over old Capitan reef/basin margin
Brazil	Cretaceous (Aptian)	Small isolated rift-margin basin (open of South Atlantic)	Halokinesis via combination of loading and tectonic extension	Yes (100)	Sylvite ocean	Small and discontinuous, stability problems related to nearby tachyhydrite
Carpathian basin, Ukraine	Middle Miocene (Badenian)	Foreland basin form in response to Alpine orogeny	Halokinesis via combination of loading and compression tectonics	Yes (129)	$MgSO_4$ ocean	Problematic ore mineral ores association and patchy ore distribution
Brine producers	(See Table 11.6).					

the summer in the earlier concentrator pans. In Quill Lake, Canada, SOP is produced by the mixing of $MgSO_4$-rich lake brines with sylvite trucked to the lake processing plant.

In the Moab pans, muriate of potash is the product after solar evaporation, dye injection and slurry processing. The brine feed to the solar pans is not a Quaternary lake brine, but is derived from the pumped-in waters of the Colorado River, which are heated, pumped into, and flow through the flooded workings of the former Cane Creek Potash Mine, before being piped into the at-surface solar pans. In Salar de Atacama there are two potash brine processing streams in the evaporation pans, both are fed from a brine field located in the nearby natural sump: (a) One of the pan processing stream produces a KCl precipitate (sylvite and carnallite) as it is concentrated to a lithium chloride brine stage; (b) The other potash processing stream in the pans precipitates SOP with boric acid as a manufactured byproduct. The hyperarid climate at Atacama facilitates year round solar-driven production of the salts. Both the Moab and Atacama occurrences and all the other SOP Quaternary examples listed in Table 11.11 are situated in cool arid (BWk) or desert steppe (BSk) climates, or, in the case of the Great Salt Lake and Quill lake, even milder temperate seasonally arid climates. None of the SOP climates are as extreme as the MOP forming areas in the Danakil and the Dead Sea. Yet these two, and all of the Quaternary lacustrine settings manufacturing SOP, have hydrologies that are fed nonmarine brine inflow with ionic constituents very different from modern seawater.

If we look at Quaternary potash occurrences worldwide, it is clear that all modern potash is a nonmarine salt, as are many of the other economic salt-based feedstocks to the chemical industries of the world (salt cake, soda ash, borates, $CaCl_2$ and lithium brines – Warren 2010). That is, to state the obvious, all Quaternary potash producing environments are

defined by markedly nonmarine sets of environments of deposition. We should not use them as same-scale analogs for ancient marine-associated potash occurrences.

Phanerozoic potash salt beds comprise two distinct associations: $MgSO_4$ -rich and $MgSO_4$ -poor (Table 11.11). Ancient potash deposits, rich in $MgSO_4$, are composed of some combination of gypsum, anhydrite, polyhalite, kieserite, kainite, carnallite and bischofite. Potash deposits free of, or poor in, $MgSO_4$ are dominated by some combination of halite, carnallite, and sylvite. This latter group constitutes a majority of the known "*in situ*" potash reserves of the world, and is very much dominated by the Devonian evaporites of western Canada. Other than minor amounts of sylvite in the halokinetic structures in Late Neoproterozoic-Early Cambrian Ara Salt of Oman, potash salt remnants have not been recognized in Precambrian sediments. In contrast, to the markedly nonmarine locations of potash recovery from the Quaternary sources, almost all pre-Quaternary potash operations extract product from marine-fed basinwide ore hosts during times of $MgSO_4$ depleted and $MgSO_4$ enriched oceans. This time-based dichotomy in potash ore sources with nonmarine hosts in the Quaternary deposits and marine evaporite hosted ore zones in Miocene deposits and older, reflects the simple lack of basinwide marine deposits since the late Miocene (Warren 2010). As for all ancient marine evaporites, the depositional system that deposited ancient marine-fed potash deposits was one to two orders of magnitude larger and the resultant deposits were typically thicker stacks than any Quaternary potash settings. The last such "saline giant" potash system was the Solfifera series in the Sicilian basin, deposited as part of the Mediterranean "salinity crisis".

So, what are the factors that favour the formation of, and hence exploration for, additional deposits of exploitable ancient potash? First they are all basinwide, not lacustrine deposits. Within the basinwide association it seems that intracratonic basins host significantly larger reserves of ore, compared to systems that formed in the more tectonically-active plate-edge association. This is a reflection of: (1) accessibility – near the shallow current edge of a salt basin, (2) a lack of a halokinetic overprint and, (3) the setup of longterm, stable, edge-dissolution brine hydrologies that typify many intracratonic basins. Known reserves of potash in the Devonian Prairie evaporite in West Canadian Sedimentary Basin (WCSB) are of the order of 50 times that of next largest known deposit, the Permian of the Upper Kama basin, and more than two orders of magnitude larger than any other of the other known exploited deposits (Table 11.11).

Part of this difference in the volume of recoverable reserves lies in the fact that the various Canadian potash members in the WCSB are still bedded and flat-lying. Beds have not been broken up or steepened, by any subsequent halokinesis. The only set of processes overprinting and remobilizing the various potash salts in the WCSB are related to various styles and timings of aquifer encroachment on the potash units, and this probably took place at various times since the potash was first deposited, largely driven by a combination of hinterland uplift and subrosion. In contrast, most of the other significant potash basins listed in Table 11.11 have been subjected to ongoing combinations of halokinesis and groundwater encroachments, making these beds much less laterally predictable. In their formative stages the WCSB potash beds were located a substantial distance from the orogenic belt that drove flexural downwarp and creation of the subsealevel sag depression. Like many other intracratonic basins the WCSB did not experience substantial syndepositional compression or rift-related loading.

Non-Potash Salts: Borates, Na-Sulphates, Na-Carbonate, Lithium Salts, Gypsum, Halite and Zolites

12

Introduction

In Chap. 11 we focused on potash deposits and concluded that the larger accumulations of potash that dominate the rock record are marine-derived. That is, the larger potash deposits that are conventionally mined across the world accumulated in ancient tectonic (megahalite) basins with no Quaternary counterpart. We shall now discuss various accumulations of other evaporite salts and related products that are exploited as economic resources, namely the borates, Na-carbonates, Na-sulphates, lithium salts and zeolites, along with short considerations of exploited gypsum and halite deposits (Table 12.1). Other than gypsum and halite, they are typically lacustrine precipitates or brine products, formed by the evaporation of waters with nonmarine ionic proportions and in supra-sealevel depositional settings that do have same-scale pre-Quaternary counterparts (Warren 2010). The marine-derived megahalite and megasulphate deposits, which have no same-scale modern counterparts, were the focus of much of the discussion in earlier chapters. Aspects of these halite and gypsum deposits are only mentioned in passing in this chapter, via a discussion of their annual production volumes and uses, but they are the highest ranked deposits in terms of the weight utilized as mineable or extractable natural resources (Table 12.2). Next in terms of extracted volume is soda ash, then the potash salts, then with an order of magnitude less is salt cake and the borate salts.

This chapter focuses on those industrial salts derived in large part from extraction and processing of evaporite salts or associated brines. There are other industrial commodities, such as bromine, iodine and sulphur that, although intimately tied to evaporites in their natural settings, are no longer extracted via quarrying and mining. Rather these commodities, along with increasing proportions of gypsum, are synthetic byproducts of other industrial processes.

Borate Salts (Tincals)

Borate salts are least in terms of annual volumes extracted of naturally occurring nonmarine salts and of the same order of magnitude as sodium sulphate or salt cake (Table 12.2). Borate production is dominated by a few nations, with Turkey as the largest producer, followed by the USA (Fig. 12.1). Seventy five percent of the market is controlled by the two major producers, Etimine, based in Turkey, and Rio Tinto Borax with its main mine at Boron in California. The rest of the market is made up of half a dozen or so minor producers. The market is, to all intents and purposes, a duopoly. Due to economies of scale and other factors the two main suppliers have low cost bases and the other suppliers higher costs, some significantly so. The lower cost producers can compete on a worldwide basis because they can absorb the transportation costs, while the higher cost producers are mostly restricted to a geographical area, again to a greater or lesser degree determined by their underlying costs. In all world markets the two major producers are the price setters and can determine the price according to the market penetration to which they aspire. There is one very significant difference between the two major producers. Rio Tinto Borax is well into the latter part of the Boron mine life cycle, whereas Etimine's mines are in the relatively early stages of theirs. According to the Turkish Ministry of Energy and Natural Resources, Turkey has over two thirds of the world known boron resource totaling over 950 million tonnes while remaining known US resource is somewhere around 80 million tonnes.

Character, History and Processing

Boron (from the Arabic *Buraq* or the Persian *Burah* meaning white, or to glitter or shine) is a highly dispersed element in nature – averaging 3–20 ppm in the earth's upper crust, as estimated by various authors, and 4.6 ppm in seawater. It is

© Springer International Publishing Switzerland 2016
J.K. Warren, *Evaporites: A Geological Compendium*, DOI 10.1007/978-3-319-13512-0_12

Table 12.1 Uses of evaporite salts, byproducts and brines

Type	Mineralogy	Source	Uses
Rock-salt (halite)	NaCl	Halite, brine processing	Chloralkali industry for manufacture of chlorine, sodium hydroxide and other related industrial chemicals and industrial products, road de-icing, food processing, water softening, swimming pool additive, stockfeed additive
Gypsum	$CaSO_4$	Gypsum, including secondary after anhydrite	Construction industry, mostly in wallboard and plaster products, cement retardant, agricultural soil enhancer, high purity forms used in wide range of industrial processes including glass manufacture and smelting
Potash (mostly sylvite)	KCl, KNO_3, K_2SO_4	Sylvite, sylvinite, brine processing	Fertiliser (main usage), use as feedstock to chemical industry to manufacture KCl, KOH, K_2CO_3, several forms of potassium phosphate, many other potassic chemicals, drilling muds, also used in recycling alumina, electroplating, etc.
Borates	B_2O_3	Borax (tincal), boracite, colemanite, hydroboracite, kernite, ulexite	Glass, ceramics. fiberglass, textile manufacture, agricultural chemicals, pharmaceuticals, flux cleansing agent, detergents, water softener, preservative and fire retardant
Sodium carbonate (soda-ash)	Na_2CO_3	Trona, solvay process, brine processing	Glass manufacture, chemicals, soap and detergents, pulp and paper manufacture, water treatment, and flue gas desulphurization
Sodium sulphate (salt-cake)	Na_2SO_4	Mirabilite, thenardite, glauberite, brine processing	Filler in soap and detergent powder, textile and glass manufacture, pulp and paper industry, carpet fresheners
Lithium	Li	Brine Processing, hectorite in some saline clays	Production of ceramics, glass, and primary aluminium, battery technology, pharmaceutical
Calcium Chloride	$CaCl_2$	Brine processing	Deicing, dust control, road stabilization, concrete curing, oil well drilling, tire ballasting
Magnesium carbonate, Magnesium oxide, Magnesium sulphate	$MgCO_3$, MgO, $MgSO_4$	Brine Processing, magnesite, electrolytic processing	Majority used for refractories. A constituent in aluminium-base alloys, used for packaging, transportation, and other applications. Remainder is consumed in agricultural, chemical, construction, environmental, and industrial applications
Bromine (sodium bromide)	Br_2, NaBr	Brine Processing	Additive
Iodine	I_2	Brine Processing	Animal feed supplements, catalysts, inks and colourants, pharmaceutical, photographic equipment, sanitary and industrial disinfectant, and stabilizers
Ammonium chloride Ammonium sulphate	NH_4 Cl, $(NH_4)_2SO_4$	Brine Processing	Fertiliser, industrial additive

NH_4 salts are not further discussed in this paper

both a volatile and mobile element and so tends to be enriched in the later stages of both magmatic crystallization and volcanic eruptions and a few small economic deposits are found in skarns where late-stage magmas have intruded carbonates. When these primary sources are weathered in arid settings, borate evaporites can form.

Boron is the fifth element of the periodic table and is the only electron-deficient nonmetallic element. Thus, boron

Table 12.2 World production of industrial salts, all values are in 1,000 metric tons

Year	2006	2007	2008	2009	2010	2011
Salt (halite)	261,000	266,000	276,000	279,000	280,000	286,000
Gypsum	160,000	167,000	157,000	148,000	147,000	147,000
Soda-ash	43,700	46,200	47,000	44,400	48,100	51,300
Potash (K_2O eqv.)	30,400	34,900	33,700	20,800	34,100	36,400
Boron (B_2O_3 eqv.)	3,620	4,200	4.480	3,710	4,050	4,550
Salt-cake	No reliable published data; annual production is ≈4 million metric tons					

As published by US Geological Survey (USGS) and available from http://minerals.usgs.gov/minerals/pubs/commodity last accessed 4 September, 2013

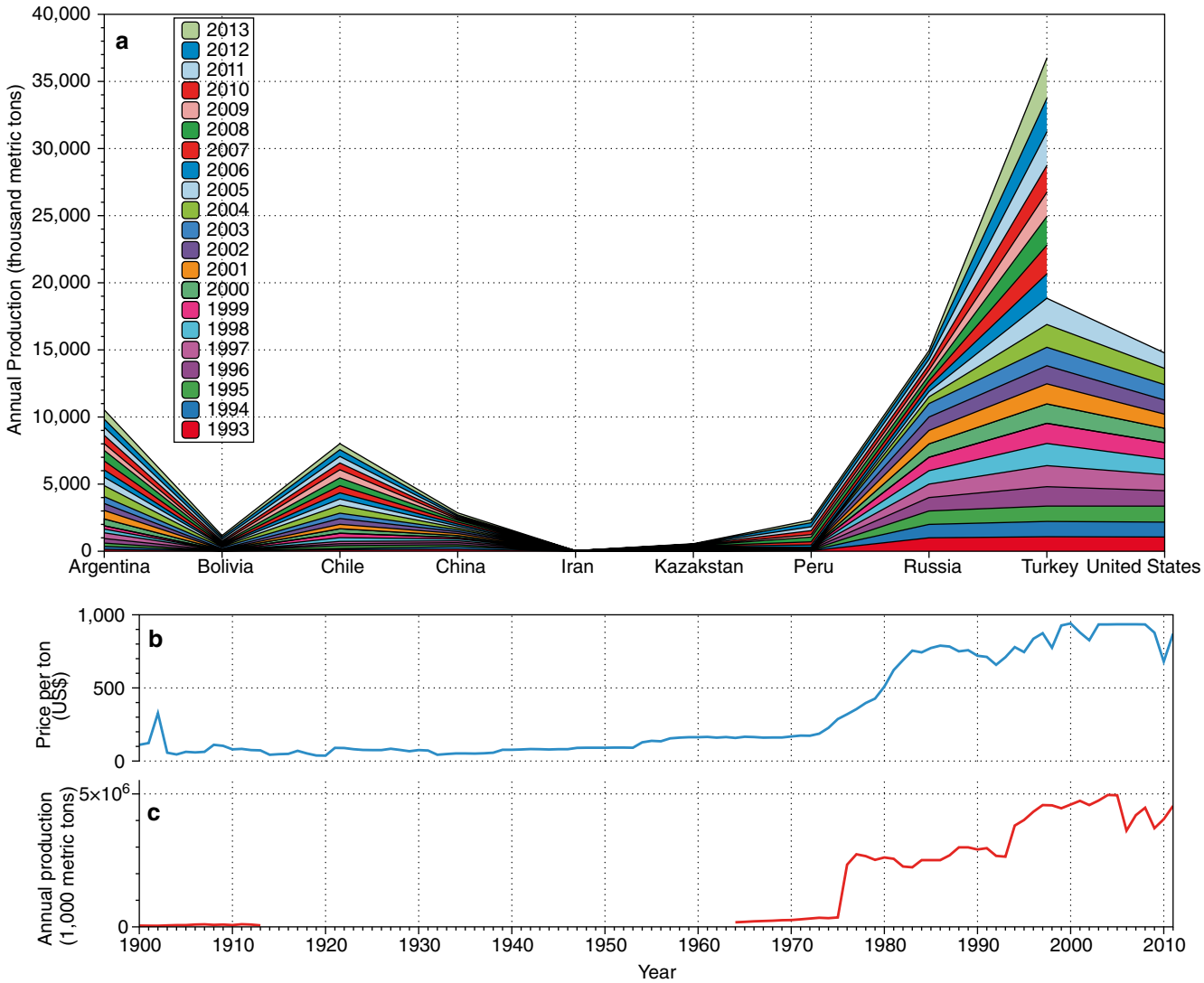

Fig. 12.1 (**a**) Cumulative area plot of borate production (1,000 metric tons of boric oxide B_2O_3 equivalent). (**b**) Price per tonne in US dollars. (**c**) Annual world production. Production figures compiled from USGS on-line data tables downloaded from. Since 2005, production data for USA in (**a**) is not listed by USGS, supposedly for reasons of commercial confidentiality needed by US companies mining borate

has a high affinity for oxygen and so forms strong covalent-bound salts known as borates. In the chemical industry borate salts are defined as minerals containing boric acid or boron-oxygen molecules (Kogel et al. 2006). As such, their purity can be expressed on the basis of B_2O_3, in combination with a major cation (typically Ca, or Na) and so borates as a

Table 12.3 Commonplace sedimentary (and metasedimentary) borate minerals with B_2O_3 equivalents

Borate Mineral	Composition	B_2O_3%	Remarks
Na Borates			
Borax (tincal)	$Na_2B_4O_7{\cdot}10H_2O$	36.5	Major ore mineral in USA, Turkey and Argentina
Kernite	$Na_2B_4O_7{\cdot}4H_2O$	51.0	Major mineral in USA, often converts to borax
Tincalconite	$Na_2B_4O_7{\cdot}5H_2O$	47.8	Intermediate or accessory mineral + manufactured endproduct
Na-Ca Borates			
Ulexite (cottonball)	$NaCaB_5O_9{\cdot}8H_2O$	43.0	Major ore mineral particularly in Turkey and South America
Probertite	$NaCaB_5O_9{\cdot}8H_2O$	49.6	Secondary/accessory mineral
Ca Borates			
Colemanite	$Ca_2B_5O_{11}{\cdot}5H_2O$	50.8	Major ore mineral, particularly in Turkey. Secondary after inyoite
Meyerhoffite	$Ca_2B_5O_{11}{\cdot}7H_2O$	46.7	Intermediate ore mineral, rarely survives at surface
Priceite (pandermite)	$Ca_2B_4O_{10}{\cdot}7H_2O$	49.8	Ore mineral in Bigadic, elsewhere minor
Inyoite	$Ca_2B_6O_{11}{\cdot}13H_2O$	37.6	Minor ore mineral
Danburite	$CaB_2Si_2O_8$	28.3	Ore mineral (borosilicate) in evaporitic skarns in Russia
Datolite	$Ca_2B_2Si_2O_9{\cdot}H_2O$	21.8	Ore mineral (borosilicate) in evaporitic skarns in Russia
Other Borates			
Sassolite	$B(OH)_3$ or $B_2O_3{\cdot}3H_2O$	56.4	Natural boric acid (fumarole, hot springs), once extracted in Italy
Ludwigite	$(Fe,Mg)_4Fe_2B_2O_7$	17.8	Accessory mineral (meta-evaporitic) association
Hydroboracite	$CaMgB_6O_{11}{\cdot}6H_2O$	50.5	Secondary ore mineral
Szaibelyite (ascharite)	$Mg_2B_2O_5{\cdot}H_2O$	41.4	Ore in Russia and China (meta-evaporite)
Suanite	$Mg_2B_2O_5$	46.3	Ore mineral Russia/China (meta-evaporite, hydrates to szaibelyite)
Boracite (strassfurite)	$Mg_3B_7O_{13}{\cdot}Cl$	62.2	Associated with potash especially in Zechstein of Europe
Pinnoite	$MgB_2O{\cdot}3H_2O$	42.5	Secondary to minor ore mineral in some saline lakes, China
Inderite	$Mg_2B_60_{11}{\cdot}15H_2O$	37.3	Commonplace in ore from Lake Inder deposit, Kazakhstan
Howlite	$Ca_2SiB_5O_9(OH)_5$	44.5	Accessory mineral
Bakerite	$Ca_4B_4(BO_4)(SiO_4)_3(OH)_3{\cdot}H_2O$	42.1	Accessory mineral
Tunellite	$SrB_6O_9(OH)_2{\cdot}3H_2O$	55.1	Accessory mineral
Tertschite	$Ca_4B_{10}O_{19}{\cdot}2H_2O$	65.1	Accessory mineral
Kurnakovite	$Mg_2B_5O_{11}{\cdot}15H_2O$	37.3	Accessory mineral

commodity are sold on the basis of their boric oxide content (Table 12.3). Only a few of the range of naturally occurring borate salts are stable over the long term (Birsoy and Özbaz 2012). Four minerals comprise more than 90 % of the borate salts used by the borate industry; the sodium borates – borax (tincal), kernite, the calcium borate – colemanite, and the sodium-calcium borate – ulexite. Water content of the various borate salts tends to decrease with burial and to increase with exposure and weathering. Borax is the primary mineral in many US deposits, but with burial and dewatering it converts to tincalconite and kernite. If kernite is exposed to weathering or crossflowing groundwater it reconverts to borax.

Currently, borax (tincal) is the preferred sodium borate ore as it needs little processing, crushes freely and dissolves readily in water with a rate of solubility that increases steeply with increasing temperature. "Tincal" is the old general name for borax in the chemical industry and is sometimes used to distinguish the naturally occurring borax ore mineral (tincalonite) from the chemically identical manufactured salt called tincal. Kernite (a source for boric acid manufacture) is present in large tonnages in the USA and Argentina. It is less

suitable as an ore salt than borax or tincalonite despite its high B_2O_3 content. Kernite has excellent cleavage, but crushes into fibres that tend to mat and clog handling equipment. It also is much less soluble in water than borax and so is less suitable as a feedstock for the manufacture of pentahydrate. Colemanite is the preferred calcium-bearing borate; it is the least soluble of the commercial borates and only slowly dissolves in water, but is highly soluble in acid solutions. Szaebelyite, a magnesium borate is the main ore mineral in the Proterozoic meta-evaporite ores of the Liaoning Province, China, while datolite was the principal ore salt in the borate skarns of Dalnegorsk in Russia (Fig. 12.2).

Because most borate salts are soluble in water, most exploitable Neogene deposits of at-surface or near-surface borate salt beds involved lacustrine deposition in arid settings that were strongly influenced by volcanic activity at the time of lake sedimentation. These deposits, which make up the majority of the world's borate reserves, tend to have abundant tuffs and basalts in the drainage basin, to have formed beneath a semi-arid climate and a precipitated from saline continental brines (Fig. 12.3). A protective layer of other impervious less-soluble evaporite salts, such as gypsum or anhydrite, typically forms a carapace that prevents subsequent redissolution.

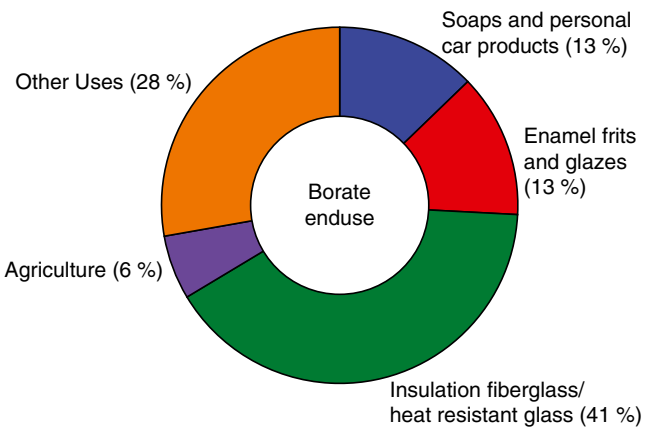

Fig. 12.2 End uses of mined borates (After Butts 2007)

In terms of dollar value, the most commercially significant boron salt is the pentahydrate ($Na_2B_4O_7{\cdot}5H_2O$; tincal), which is used is in the manufacture of borosilicate glass (fibre-glass and heat-resistant glass). Next in importance is borax ($Na_2B_4O_7{\cdot}10H_2O$; sodium tetraborate decahydrate), which is used principally in laundry products. Borax's mild alkalinity means it can emulsify oil and grease and also reduces the surface tension of water which aids in the loosening of dirt particles. It also reacts with some organics to produce esters, making it a mild bactericide. This means it has a strong but gentle cleansing action, making it suitable for personal and fabric cleansing (Fig. 12.2). Borax is also used in the manufacture of abrasives and refractories; some boride compounds have a hardness around 9 on the Moh scale and also exhibit high thermal and electrical conductivity. In agriculture boron is essential to plant growth and one of the 16 basic plant nutrition although in higher concentrations it is toxic. Use of borax as a mild antiseptic is minor in terms of both dollars and tons. Amorphous boron is used in pyrotechnic flares to provide a distinctive green colour, and in rockets as an igniter. Other boron compounds show promise in treating arthritis.

In the field of nuclear energy, boron (the ^{10}B isotope) protects personnel from the harmful effects of reactors. It has the unique property of absorbing neutrons produced by nuclear reaction without the emission of harmful secondary gamma radiation and is sold as an organic borate, made by combination with paraffin, for nuclear shielding. The elemental form of boron is also incorporated into polyethylene and rubber. Ammonium pentaborate is used in a 'poison' charge in atomic submarines. Another organo-sodium borate (Liquibor) is now in use in hydraulic brake fluids in cars to provide lower volatility and built-in corrosive protection. Boron, also, confers a low co-efficient of expansion, increases the resistance to mechanical and thermal shocks and gives a bright and pleasing appearance to glass. Borax and boric acid are used together in the manufacture of a number of boro-silicate glasses of low alkali content. Between 15 and 50 parts of borax are used to each 1,000 parts of a glass-sand batch to give enhanced properties to glass.

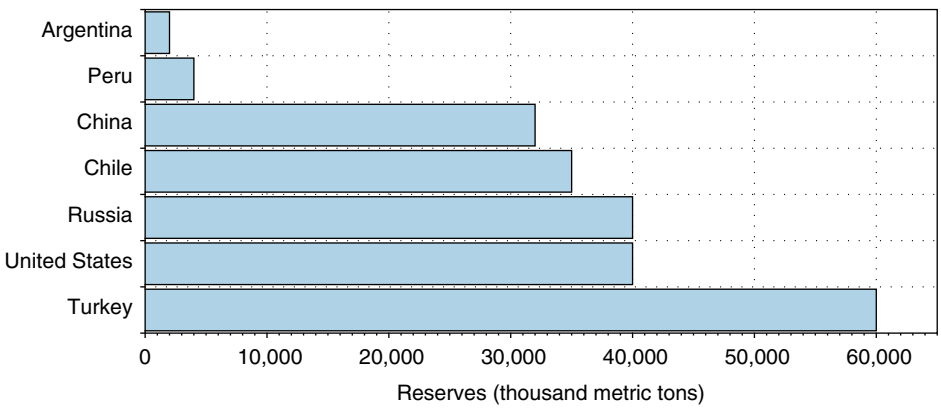

Fig. 12.3 World borate reserves as listed by USGS (http://minerals.usgs.gov/minerals/index.html last accessed April, 2014)

Boron nitride can be used to make a material almost as hard as diamond. Cubic boron nitride, commercially called 'Borazon' can withstand temperatures which are more than twice the temperature limit of a diamond (about 900 °C) and so is used as a flux in the manufacture of artificial gems. The nitride also behaves like an electrical insulator but conducts heat like a metal. It also has lubricating properties similar to graphite. Boron hydrides are easily oxidized with considerable energy liberation, and have been studied for use as rocket fuels and ignitors for fuels. Demand is increasing for boron filaments, a high-strength, lightweight material chiefly employed for advanced aerospace structures. This form of boron is similar to carbon in that it has a capacity to form stable covalently bonded molecular networks.

Historically, borates (as a component of natron salts) were used 4,000 years ago in mummification. Subsequently, borax (in a purer form than natron) was imported from the Far East for use as a gold and silver flux, first used by the ancient Babylonians. The word tincal comes from the Babylonian *tincar* meaning "Far East" and the Malay word *tingkal* meaning borax.

By the eighth century AD, the Arabs around Mecca, Medina and Baghdad were using imported borax (tincar) as a kiln additive or flux to braze or harden precious metals, especially gold. Borax glazes were used in China from AD 300, and boron compounds were used in glassmaking in ancient Rome. By the Middle Ages, borax from Tibet was regularly imported into Europe. At the time borax was very expensive, and this limited its use principally to the precious metal trade where goldsmiths used it as a soldering agent and in the refining of metals and assaying of ores. Quantities traded were small, its method of production was a tightly held secret of the alchemist's guild, and its source in the borate pavements precipitated in the salt lakes of Tibet remained a mystery until the second half of eighteenth century.

At the time of Marco Polo's travels, Tibetan borax was transported over the Himalayas into India in bags tied to the necks of sheep. Marco Polo claimed to have brought the first borates from China to Europe and his homeport of Venice became a centre for refined arts in gold, ceramics and glassware. This use of borate was a closely held Venetian "trade-secret". The price of borax remained high for hundreds of years, with refined borax fetching $3/oz in London, as late as 1790. Tibet continued to be the source of most borate into Europe until the beginning of the nineteenth century when sassolite was discovered around fumaroles in Larderello, near Pisa, Italy and production began there in 1808. Sassolite is natural boric acid and is a volcanic product that occurs in association with sulphur in the craters of volcano. As well as the Lardello deposits it was found in the Lipari Islands, southern Italy and the Tuscan lagoons, between Voltena and Massa Marittima. In all cases the boric acid condenses naturally in water and separates in large sassolite flakes which contain about 50 % of the acid.

Subsequent borate salt discoveries in the desert playas of North and South America in the 1860s to 1880s brought large volumes to the market and prices fell as manufacturing volumes increased for this once rare commodity. Today, borate's supply routes are more mundane, but the volumes consumed in the chemical industries are huge (Fig. 12.1c), with major present or past production centres in northern Argentina, Chile, southern Bolivia, Peru, southern California, eastern Russia, Turkey, and China.

US Borax, a member of the Rio Tinto Borax Group, is the largest global miner of B_2O_3, mostly of tincal ore. The company is also the world's largest manufacturer of refined borate products. US Borax supplies almost half of the world's demand for industrial and specialty borates from its Kramer borate deposit at Boron in southern California's Mojave Desert. Turkey is the world's largest producer of borate ore, mining more than 1 Mt (1.1 million st) of salable product each year (Fig. 12.1a) including refined materials from Kirka and Bandirma. This makes Turkey the second largest producer of refined boron compounds after the USA. The government organization, ETI Holding A. S., is the sole producer of Turkish borate compounds through its subsidiary Etibank A. S. Combined production of Turkey and the US accounts for more than 90 % of the global borate output.

During ore processing, advantage is taken of the solubility of borate salts, especially borax and kernite, in separating clayey material by water washing and recrystallization. Refined borax is produced by dissolving the crude material in hot water under pressure. The insoluble impurities are filtered off and the liquor is crystallized to give borax, or if boric acid is to be manufactured, the hot water solution is reacted with sulphuric acid. The reaction that takes place is as follows:

$$Na_2B_4O_7 \cdot 10H_2O + H_2SO_4 \Rightarrow 4H_3BO_3 + Na_2SO_4 + 5H_2O$$

The ulexite or colemanite mined in Turkey is shipped to many European countries for processing into boric acid and borax. Ulexite and colemanite are treated in the same manner with sulphuric acid to convert them into boric acid. If borax is to be prepared, the boric acid is added to a soda ash solution. Borax is also produced from colemanite via boiling the powdered mineral with a sodium carbonate solution for about 3 h. After filtering, the solution is allowed to crystallize to yield crude borax. Borax is recovered from the Searles Lake deposits as a by-product of potash recovery.

Geology of Borates

The major commercial borate deposits occur in a limited number of Neogene to Holocene non-marine evaporitic settings (Garrett 1998; Helvaci et al. 2012). They are always

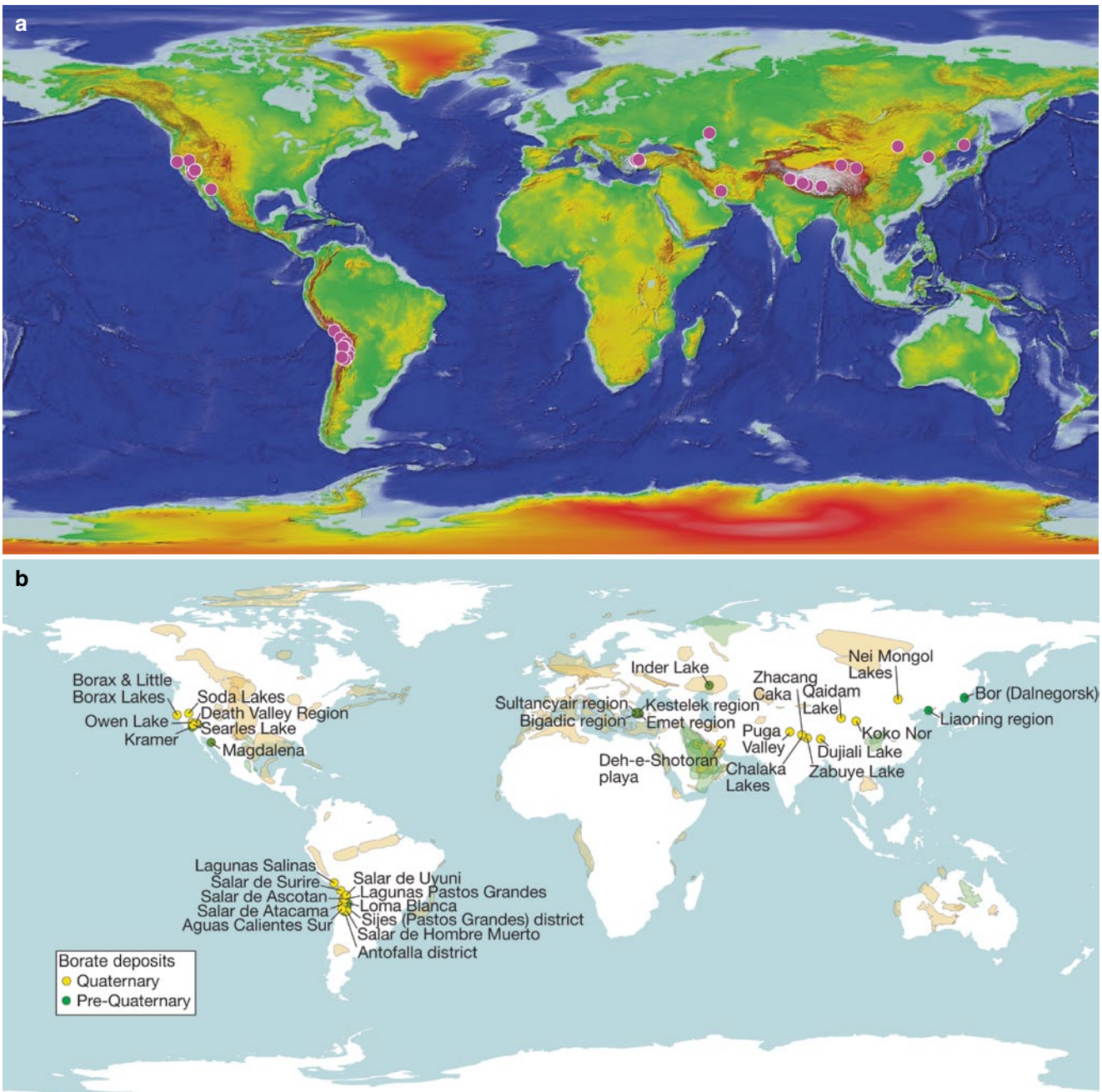

Fig. 12.4 Borate deposits. (**a**) Deposits plotted on a world topographic/tectonic base (Table 12.4). (**b**) Deposits plotted on a marine evaporite basin base, where brown shading indicates halite-dominant and green indicates megasulphate basin (After Warren 2010). Plot shows that borate deposits are better developed in volcanic-associated, active orogenic collision belts and zones of fractured continental crust. They do not occur atop or within large marine-fed mega-evaporite basins

related to volcanic rocks and pyroclastic deposits and closed-basin alkaline lakes or playas fed by hydrothermal sources (Fig. 12.5b). Borax, and to a lesser extent kernite, is open-pit mined today at the Kramer mine near Boron in California, the Sarikaya mine in Kirka ore district (Eskisehir Province, in Turkey), and Tincalayu in northern Argentina (Fig. 12.4, Table 12.4; Briggs 2007). These three saline lacustrine regions, plus the brines from Searles Lake, California, furnish the majority of the sodium borates used by chemical industry (Fig. 12.1a). Sodium borates ores are easily soluble in water, making them preferable feedstock for many end uses. Most of the larger extractive facilities also produce boric acid at nearby refineries. Colemanite is mined from several deposits in the Emet and Bigadic basins of western Turkey, one former Death Valley deposit, and small deposits in northern Argentina. This calcium borate is used in boron

Table 12.4 Borate deposits of the world, listed by country, areas and Köppen climate for Quaternary playas/salars

Location	Age	Elev. (m)	Köppen	Mineralogy/setting/comments
Loma Blanca, Argentina	Miocene (7 Ma)	3,970	–	Borax, lesser inyoite and ulexite, some kernite, minor colemanite in Sijes Fm (2.7 mt). 30 m of borate is interlayered with green-grey tuffites and clays and overlain by volcaniclastics. Active open pit. (Alonso et al. 1988; Helvaci and Alonso 2000)
Salar de Hombre Muerto, Argentina (565 km^2)	Quaternary	4,300	ET	Ulexite on playa surface and shallow subsurface, also large brine reserves (second largest playa after Arizaro in Argentine Puna region). Borate recovered as byproduct during lithium recovery (3 mt). Typical lake brine contains 230 ppm B and 540 ppm Li. Low Mg/Li. Lithium largely sourced via leaching of surrounding volcaniclastics (Garrett 1998; Vinante and Alonso 2006; Godfrey et al. 2013)
Sijes district (Monte Amarillo, Monte Verde, Esperanza, and Santa Rosa deposits), Argentina	Miocene, 5.7–6.8 Ma	4,050	–	Bedded colemanite [Monte Verde, Esperanza (upper beds)], inyoite [Monte Verde (middle beds)], and hydroboracite [Monte Amarillo (lower beds)] within the Sijes Formation (4 mt). Deposited in more than ten 1–4 km^2 sub-basins as a chain of lakes, fed via thermal springs probably opened by emplacement of the Quevar volcanic complex. Deposits change laterally from borates to gypsum (or anhydrite) to clastics or pyroclastics and are folded and dip to the east. Open pit mining (Garrett 1998; Orti and Alonso 2000).
Tincalayu, Argentina	Miocene, 5.86 Ma	3,938	–	Borax (4.8 mt) in Sijes Fm, occurs as limited zones of kernite in lower part of ore bed, or veins, ulexite nodules in clays occur above ore. Irregular borate member (folded) lies atop a halite unit (that is less than 100 m thick) and is covered by 25 m-thick pelitic member. (Ericksen 1993; Helvaci and Alonso 2000)
Lagunas Pastos Grandes, Bolivia (100 km^2)	Quaternary	4,430	ET	Brine, ulexite. Lithium and potassium recovery from lake brine is possible. This salar is slightly southwest of Uyuni, in Bolivia. There is also a Pastos Grandes in Argentina. Typical lake brine contains 230 ppm B and 540 ppm Li. (Muessig 1966; Jones and Renaut 1994; vanderVoort 1997)
Salar de Uyuni, Bolivia (9,654 km^2)	Quaternary	3,650	BWk	Ulexite (10 mt). Surface salt crust in the southern area is being mined for its ulexite content (in 1996 at a rate of 5,000 t/month), and salt has been mined from the central area since the 1500s. Typical lake brine contains 320 ppm B and 187 ppm Li (Garret 1998, 2004; Risacher and Fritz 2000)
Aguas Calientes Sur, Chile (76 km^2)	Quaternary	3,770	ET	Ulexite. Previously mined. Lake brines have elevated levels of both boron (474 ppm) and lithium (152 ppm). Possible future lithium resource. (Garrett 1998; Chong et al. 2000)
Salar de Ascotan, Chile (232 km^2)	Quaternary	3,960	ET	Ulexite. It was first Puna salar to be mined (1852), but there was no significant production until the 1880s, by 1900 it was among the world's largest producers, reaching a peak in 1913 and almost totally stopped from 1967 to 1978. Harvesting resumed in late 1990s. (Garrett 1998; Chong et al. 2000)
Salar de Atacama, Chile (3,065 km^2)	Quaternary	2,300	BWk	Natural ulexite nodules on or near parts of salar surface. Borate as byproduct during potash and lithium production via brine processing (10 m). Previously mined for borates in early part of last century. Lake brine contains up to 440 ppm B and 1,570 ppm Li. (Bobst et al. 2001; Boschetti et al. 2007)
Salar de Surire, Chile (141 km^2)	Quaternary	4,250	ET	Ulexite (5 m). Perennial lake with hot springs below, still producing ulexite via open pit method. Sporadically mined since 1880s. Lake brine contains up to 1,820 ppm B and 340 ppm Li. (Garrett 1998; Chong et al. 2000)

Table 12.4 (continued)

Location	Age	Elev. (m)	Köppen	Mineralogy/setting/comments
Liaoning Borate region, China	Paleoproterozoic	500	–	Szaibelyite (ascharite) and szaibelyite-ludwigite, with some suanite. Metasediments and metavolcanics in Liaoning and Jilin provinces. 55 underground and open pit mines in 112 separate borate deposits (12 contained 98 % of the reserves) in the Liaoning area (40 mt). (Peng and Palmer 2002)
Numerous lakes and flats, Tibet Plateau, China (>50–100 km^2)	Quaternary (<40 ka)	3,200	Dwc	Numerous (>60) low carbonate-borate lakes on Qaidam-Ziqang flats (e.g. lakes Koko and Qinghai) with B potential via brine processing. Lake waters up to 2,000 ppm B and 310 ppm Li. See Xiao Chaidam and Dujali Lake for representative deposits) Borate nodules in Qaidam saltflats are more extensive than in water-covered lake beds. (Vengosh et al. 1995; Li et al. 2001; Zheng and Liu 2009)
Xiao Chaidam (Qaidam Lake), Chaidamu Basin, China (Tibet) (51 km^2)	Quaternary	3,154	BWk	Pinnoite, ulexite, halite, minor mirabilite in perennial lake beds on edge of Quidam Basin. Upper 2.5–3.5 m are porous with gypsum and mirabilite beds, next 1–2 m contain ulexite with gypsum and lentiform mirabilite, below is 1–2 m of gray-to-black mud with gypsum. Lake brines contain up to 3,600 ppm B and 280 ppm Li. (Garrett 1998; Zheng 1997)
Dujiali Lake (Guojialin), China, (Tibet) (480 km^2)	Quaternary	4,632	ET	Borax, tincalconite. Section made up of thin beds of borax interlayered with mirabilite and trona. Lake was a major borate supplier to Medieval Europe (gold flux), salt crusts are still periodically harvested. Lake brine contains 1,540 ppm B. (Garrett 1998; Zheng 1997)
Nei (Inner) Mongol Plateau Lakes, China (up to 990 km^2)	Quaternary	998	BSk	Borax/Boric acid (byproduct of soda-ash production at lakes Chaganor (aka Qagan Nur) and Ordus lakes). Numerous borate springs in region. Lake beds typically composed of two alternating layers, one of natron, mirabilite, halite and trona, which is interbedded with black mud containing illite, some gaylussite, dolomite and calcite. (Garrett 1998; Zheng et al. 1993, 1997; Zheng and Liu 2009)
Zabuye (Chabyer) Salt Lake, China (Tibet) (251 km^2)	Quaternary	4,426	Dwc	Borax. High concentrations of the alkali metals (K, Li, Rb, and Ce) as well as borax, sodium, chloride, sulphate, and carbonate. Similar to Searles Lake. Lake brine contains 1,760 ppm B. Lithium carbonate (zabuyelite) is a natural salt precipitate in the lake. Operational lithium plant. (Wang et al. 2004; Zheng et al. 1993, 1997; Nie et al. 2009)
Zhacang Salt Lakes (Zhacang Caka), China (Tibet) (26 km^2)	Quaternary	4,962	ET	Mirabilite in uppermost sediments, as well as kurnakovite, pinnoite, inderite, ulexite. A large playa basin in interior of the Tibetan Plateau. There are three salt lakes (Lakes I, II and III) in playa, with areas between 23 and 58 km^2, and salt depths of 30 cm to 2 m. (Xiyu 1984; Zheng et al. 1993)
Puga Valley, Kashmir. India	Quaternary	4,400	ET	Kernite crusts periodically removed since 1860s. Hot springs with kernite crusts, is part of the extensive Ladakh borax spring zone. (Garrett 1998)
Deh-e-Shotoran playa, Iran	Quaternary	1,806	BSk	Ulexite. Minor occurrences of ulexite precipitated in halite-rich saline depressions in a region draining tourmaline-rich granites. (Garrett 1998)
Inder Lake, Kazakhstan (106 km^2)	Quaternary	−25	BSk	Hydroboracite is main ore mineral, also borax, colemanite, inyoite, sylvite, ulexite. Receives drainage from the borate-containing Inder salt dome and has formed a porous, 36-m deep brine-filled lake atop salt mass (1 mt) with borate veins in salt dome caprock. (Garrett 1998)

(continued)

Table 12.4 (continued)

Location	Age	Elev. (m)	Köppen	Mineralogy/setting/comments
Magdalena, Mexico	Mid-Tertiary (Miocene?)	850	–	Howlite veins in Tertiary lacustrine sediments, minor meyerhofferite and priceite. Colemanite in subsurface (high arsenic levels make processing difficult). 50 % of veins are 10–30 cm thick in pale red-green tuffaceous shales, 40 % are 1- to 20-cm beds in finegrained silty sandstone, 10 % are 1- to 80-cm beds in zeolitic or lithic tuffs (Lefond and Barker 1979)
Laguna Salinas, Peru (110 km^2)	Quaternary	4,400	ET	Inyoite, ulexite. It becomes partly flooded (50 cm deep) after the winter rains (December-March) and dries rapidly to form surface crusts containing ulexite, halite, glauber salt and thenardite. Beneath the surface are irregular 10- to 100-cm beds or lenses of ulexite (3 t). (Muessig 1958)
Bor (Dal'negorsk), Russia	Triassic?	270	–	Datolite and danburite. Rhythmically banded pyroxene-wollastonite skarn (3 stages) in Triassic limest. and siltstone intruded by Cretaceous granodiorite; Ore body is 2 km long, <500 m wide, > 1,000 m deep. Boroslilicates can occur as "giant crystals" and are cogenetic with the Pb-Zn-Ag skarns and replacements in the same worldclass ore field. Mined as open pit (54 mt) (Obolenskiy et al. 2007) Likely nomarine evaporite source for boron Baskina 2008; Dubinina et al. 2011)
Bigadic region, Turkey	Miocene, 17 Ma	444	–	Ulexite and colemanite, minor but locally significant probertite and hydroboracite, Borate beds (0.2–0.5 m thick) alternate with marl, tuff, claystone mudstone. Ulexite sits atop colemanite (330 mt) (Helvaci 1995)
Emet region, Turkey	Mid-Oligocene	1,028	–	Colemanite with minor ulexite, hydroboracite, intercalated claystones. Borate zones mostly discontinuous, nodular in beds 2–20 m thick (200 mt). (Helvaci and Alonso 2000). Proberite diagenetically replaces ulexite in the lake margins during flooding episodes of the tuff flats and there is a biogenic (bacterial) dolomite association in the lake carbonates (García-Veigas et al. 2011b).
Kestelek region, Turkey	Miocene, 17.4 Ma	748	–	Colemanite, ulexite, and probertite predominate, with coarse hydroboracite. Nodular colemanite in 5 m thick zone intercalated with volcaniclastic claystones (3 mt). (Helvaci 1994)
Kirka region, Turkey	Miocene, 17 Ma	1,000	–	Main borate minerals is borax, with lesser ulexite and colemanite (140 mt). Borate lacustrine interval is up to 145 m thick and hosts the only sodium borate orebody in Turkey, with a B_2O_3 content of 20–25 % (Helvaci and Orti 2004)
Sultancyair region, Turkey	Miocene, 20 Ma	210	–	Priceite in gypsum-clay matrix, minor howlite. District with first (1865) borate mine (underground mine) in Turkey, region is now depleted. (Helvaci 1994)
Borax Lake, California, USA (1.2 km^2)	Quaternary	500	–	Layered borax grits some 0.6–1 m below lake floor clays. Small (100 ha) shallow perennial lake, adjacent to active hot spring in recently active volcanic area. First commercially exploited deposit in US (1860s). (Garrett 1998)
Death Valley region, California, USA (54 km^2)	Quaternary	−24	BWh	Ulexite is common on the modern halite playa, along with halite, thenardite, and trona. (Crowley 1993)
Death Valley Borate deposits, California, USA	Miocene, 6–7 Ma	950	–	Colemanite with ulexite and proberite in central core. 23 deposits in area. Borates interbedded with lacustrine clays, tuffaceous mudstones, mainly in Black Mountain tectonic block (8 mt; deposits include; Biddy-McCarthy; Billie; Boraxco; Corkscrew-DeBely; Gertsley; Grand View Mine). (Tanner 2002)

Table 12.4 (continued)

Location	Age	Elev. (m)	Köppen	Mineralogy/setting/comments
Hector (Fort Cady area) Ca, USA	Miocene -Pliocene?	900	–	Colemanite intersected in a 58-m drillhole interval at 410 m depth as stacked <60 cm thick beds of spherulitic crystals in a tuffaceous clay or anhydrite rock host. Some secondary veins of clear colemanite or anhydrite and minor howlite (potential 7 mt) (Garrett 1998)
Kramer, Boron, California, USA	Miocene, 19 Ma	800	–	Borax, colemanite, kernite, tincalconite. Lacustrine deposit underlain and overlain by arkoses with Saddleback Basalt as base to deposit (46 mt) (Garrett 1998)
Little Borax (Hachinhama) Lake, California, USA (0.1 km^2)	Quaternary	400	Csb	Borax from solar evaporators on edge of small shallow (>1 m deep) perennial saline lake in volcanic crater. Operational only from 1869 to 1872, could not compete with playa ulexite deposits (Garrett 1998)
Owens Lake, California, USA (278 km^2)	Quaternary	1,081	BSk	Trona is the dominant primary sal preserved in the surface crust, also borax, some burkeite, mirabilite, natron, and thermonatrite. In winter considerable natron, glauber salt, and borax crystallize, but largely melt in the warmer summer brine (Smith and Friedman 1998). From 1915 to 1953 soda-ash was produced from brine evaporators with borax byproduct. Salts derived from leaching of nearby active geothermal springs (3 mt) (Alderman 1985; Garrett 1998)
Searles Lake, California, USA (132 km^2)	Quaternary	493	BWk	Trona is the dominant salt, also borax, some burkeite, mirabilite, natron, and thermonatrite. In winter considerable natron, glauber salt, and borax crystallize, but melt in summer. Mother brine via dissolution of buried glauberite (43 mt) (Garrett 1998; Smith 1979)
Soda Lakes, Nevada, USA (0.16 km^2)	Quaternary	1,000	BWk	Borax as minor byproduct of soda-ash brine operations in 1860s. Is a small playa adjacent to Big Soda Lake. (Garrett 1998)

See Fig. 12.4 for locations (reserves in mt (million metric tons) of B_2O_3 after Garrett 1998; for overviews see Warren 2010, Carpenter and Kistler 2006, and references within

endproducts that have a low sodium requirement, and in making boric acid.

Ulexite is the common playa (salar) or hypersaline marsh borate. It is produced commercially from numerous salars in South America and playas in the Provinces of Quinghi and Xizang (Tibet) in western China. Ancient saline lacustrine deposits 5–20 million years old— are the source of Turkish ulexite, it is found in Death Valley and in some of the ore produced in Argentina. Much of this material is ground and used as a crude product in agriculture or to manufacture boric acid.

The less easily refined magnesium borates of China occur in the Palaeoproterozoic metasediments of Liaoning peninsula adjacent to North Korea. These are mined by underground methods and refined in small, local plants to produce sodium borates and boric acid for domestic use. A unique borosilicate skarn deposit (datolite and danburite) near Dal'negorsk in fareastern Russia is open pit mined to produce boric acid. Triassic carbonates were intruded by Cretaceous granodiorites to create the borosilicate skarn. Borates from this source were once shipped by rail to western Russia and eastern Europe, when they were mines operated under the auspices of the Former Soviet Union, but more recently ore products are shipped through local ports to markets in the Far East.

Other borate deposits, some of which were once mined commercially, include the Inder region of Kazakhstan, the Stassfurt district of eastern Germany, as well as parts of northern Iran, and Yugoslavia. Numerous smaller lacustrine playa deposits are known in western United States, western Turkey, and in South America. Some of these Holocene playa deposits were extensively exploited by pioneer producers in the late nineteenth and early twentieth centuries, but are not currently in production (Garrett 1998; Warren 2010). We shall now discuss the geological detail of the more significant of these borate deposits.

Turkish Borates

Turkey has the largest known reserves of natural borate in the world. The borate region of western Anatolia has five districts, from west to east they are: Bigadic, Sultancayir, Kestelek, Emet, and Kirka, with the Kirka district containing the most mature borate mining operations (Fig. 12.5a; Helvaci and Orti 1998, 2004; Helvaci and Alonso 2000;

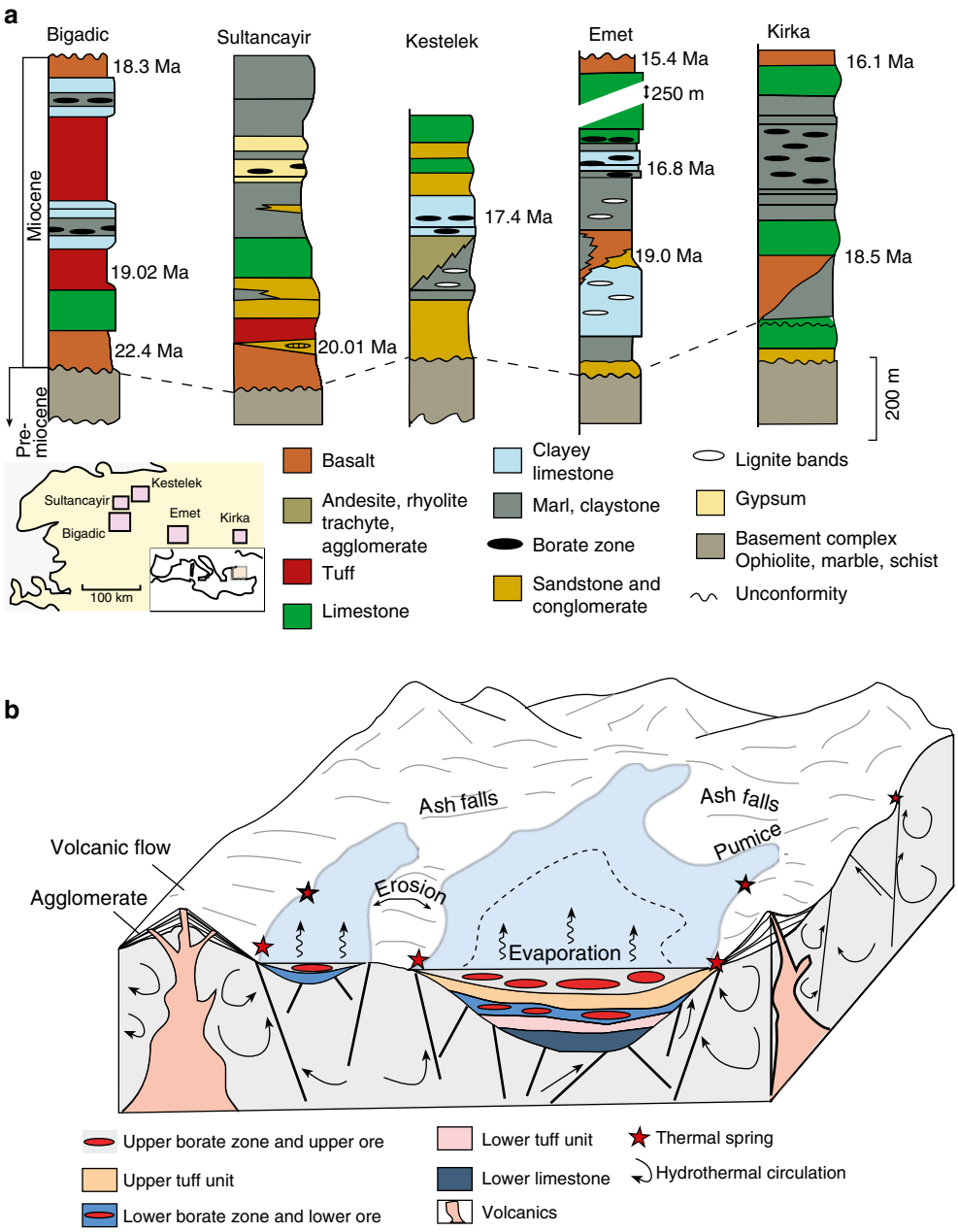

Fig. 12.5 Turkish borate deposits. (**a**) Representative sections of the various Miocene borate deposits in western Turkey. All occur in local extensional rifts in a volcanogenic continent-to-continent collision setting (After Helvaci and Alonso 2000). (**b**) Classic playa stage of the Bigadic Deposit (After Helvaci 1995). Deposition occurred under arid to semi-arid conditions within separate or interconnected shallow perennial saline lakes located in an active volcanic area within lakes, fed by borate-rich thermal springs and surrounded by saline mudflats

García-Veigas et al. 2011b; García-Veigas and Helvaci 2013). Turkish borates have been mined for the last fifteen centuries. Proven borate reserves are 532 million tonnes with total estimated reserves of 987 million tonnes. Colemanite is the major ore mineral at Bigadic, Emet, and Kestelek, ulexite at Bigadic, and tincal at Kirka. Borax and colemanite ores are refined and concentrated at the Kirka and Bandirma plants. Bigadic borates are extracted from what is likely the largest colemanite/ulexite deposit in the world, with high-grade colemanite and ulexite ores running 30 % and 29 % B_2O_3, respectively.

The Kirka stratigraphic succession comprises borates that are intimately interbedded with and penetrating into marls, claystones, zeolitized tuffs and tuffaceous epiclastic materials in bedded lacustrine sediments (Fig. 12.5a). The main boron mineral is borax with lesser amounts of colemanite, ulexite and other borate minerals. Volcano-sedimentary rock units in the Sultancayir deposit include borate-bearing gypsum intercalated in a sandy claystone unit. Calcium borates, mainly pandermite (priceite) and howlite, but also colemanite and bakerite, are interspersed within the Sultancayir gypsum. The Kestelek deposit is 27 km southeast of the town of Mustafa Kemalpasa in the province of Bursa. The borate ore zone there makes up part of an interbedded lacustrine succession of marl, limestone, tuffaceous limestone, tuff and borate layers (Fig. 12.5a; Helvaci and Alonso 2000). Borate

layers are typically hosted in clays. Colemanite is present as nodule to boulder size masses (up to 1 m in diameter), and as thin layers of fibrous and euhedral crystals. Colemanite, ulexite and probertite predominate and sparse hydroboracite is also present locally.

All the exploited Turkish borate ores were originally precipitated as early Miocene (16–20 Ma) perennial saline lake sediment within a series of northeast-southwest-trending elongate basins, which are underlain by a Palaeozoic and Mesozoic basement composed of ophiolites, marbles and schists (Fig. 12.5b; Helvaci 1995). The Bigadic, Emet and Kirka lacustrine basins of western Turkey are hosted by Tibet-type extensional graben structures. The grabens developed during Miocene continent-to-continent collision along the Izmir-Ankara suture zone, where calc-alkaline volcanism was simultaneous with borate sedimentation. This volcano-sedimentary sequence consists of (from bottom to top) basement volcanics and volcaniclastics, lower limestone, lower tuff, lower borate zone, upper tuff, upper borate zone and olivine basalt (Fig. 12.5b). Borates in the upper zone occur in units up to 30 m thick beneath a sediment cover that is 25–410 m thick, while the lower borate zone is up to 65 m thick and is found at depths between 150 and 950 m.

All these Neogene borate deposits have thin sedimentary covers and have never been deeply buried (Helvaci and Orti 1998). Borate precipitation occurred mostly in shallow to at-surface brine saturated settings, in saline lake systems encompassing a range of evaporitic settings, from stable playa mudflats to deeper perennial lakes, the latter typically preserve shoaling suceessions, changing from shallow lake to playa and mudflat. Shallowing-upward cyclicity typifies all ore beds in these deposits, which accumulated as lacustrine deposits in a hydrothermally active volcanogenic terrain (Fig. 12.5b). Colemanite tends to occupy the deposit's depositional margins, while laminated borax is more common in the centres of the lacustrine basins, with a zone of ulexite separating the two (Inan et al. 1973). This mineral zonation is syndepositional and cannot be ascribed to later burial diagenetic processes.

When details on these obviously primary to very early secondary (sabkha) deposits began to come to the world scientific literature in the mid 1970s the prevailing notion of borate ore zones as thermal replacements (mesogenetic) during somewhat deeper burial were challenged (thermal replacement models were largely based on the US deposits and the work of Foshag 1921 and Christ and Garrels 1959). When details of the primary borate textures in South American deposits became known in the mid 1980s (next section in this chapter) even some of the strongest proponents of the thermal or mesogenetetic replacement model for borate ores began to admit the possibility of a primary or syndepositional origin for the ore zonation for most of the world's borate deposits.

Borate minerals at Bigadic form two ore zones, now separated by thick tuff beds that have been transformed to montmorillonite, chlorite, and zeolites (mainly heulandite) during diagenesis (Figs. 12.5b and 12.6; Gundogdu et al. 1996; Helvaci and Orti 1998). Colemanite with lesser ulexite predominates in both zones: but other borates, including howlite, proberite, and hydroboracite are present in the lower borate zone; whereas inyoite, meyerhofferite, pandermite, tertschite(?), hydroboracite, howlite, tunellite, and rivadavite are found in the upper borate zone (Helvaci 1995). Calcite, anhydrite, gypsum, celestite, K-feldspar, analcime, heulandite, clinoptilolite, quartz, opal-CT, montmorillonite, chlorite, and illite are also found in the Bigadic deposit.

Nodules of colemanite and ulexite predominate in both borate zones at Bigadic (Fig. 12.6). Agglomerated colemanite and ulexite nodules construct alternating bedded horizons with relatively sharp boundaries. Because these minerals are readily dissolved and reprecipitated, early secondary masses of pure and transparent colemanite and ulexite are often encountered in cavities, nodules and cracks in the same ore hosts. Some nearsurface colemanite and ulexite beds are now so weathered they are completely replaced by calcite.

Colemanite nodules in both ore zones first formed as widespread secondary syndepositional precipitates in concentrated pore brines within unconsolidated gypsiferous sediments (Fig. 12.6; Helvaci and Orti 1998). Colemanite and ulexite formed mostly as interstitial growths under syn-sedimentary conditions, either as mineralogically primary or as displacive and cementing lithofacies. All crystals were later affected by waters tied to progressive compaction and the conversion of gypsum to anhydrite. Heliothermal conditions may have favoured the precipitation of colemanite over ulexite on the shallow bottom or just below the sediment surface in some density-stratified lakes. Locally, some colemanite is a secondary precipitate emplaced during early burial, its precipitation was possibly driven by compactional pore water crossflow via the (macroscopic) replacement of precursor ulexite. Early formed nodules continued to grow as the sediments were compacted to give septarian-like fracture fills. Later generations of colemanite and ulexite are found in vugs and veins and as fibrous margins of early-formed nodules. Burial diagenetic changes in the main borates include the partial replacement of colemanite by howlite and hydroboracite, and replacement of ulexite by tunellite. It is unlikely that substantial volumes of Turkish colemanite ever formed by dehydration of inyoite or by a burial driven thermal replacement of ulexite.

Proberite bands at Bigadic are found in some ulexite horizons, especially in the lower borate zone. It formed in the same chemical environment as ulexite, and according to Helvaci (1995) indicates short periods of extreme desiccation and possibly short periods of subaerial exposure within the lake centres. Euhedral tunellite formed during dissolution

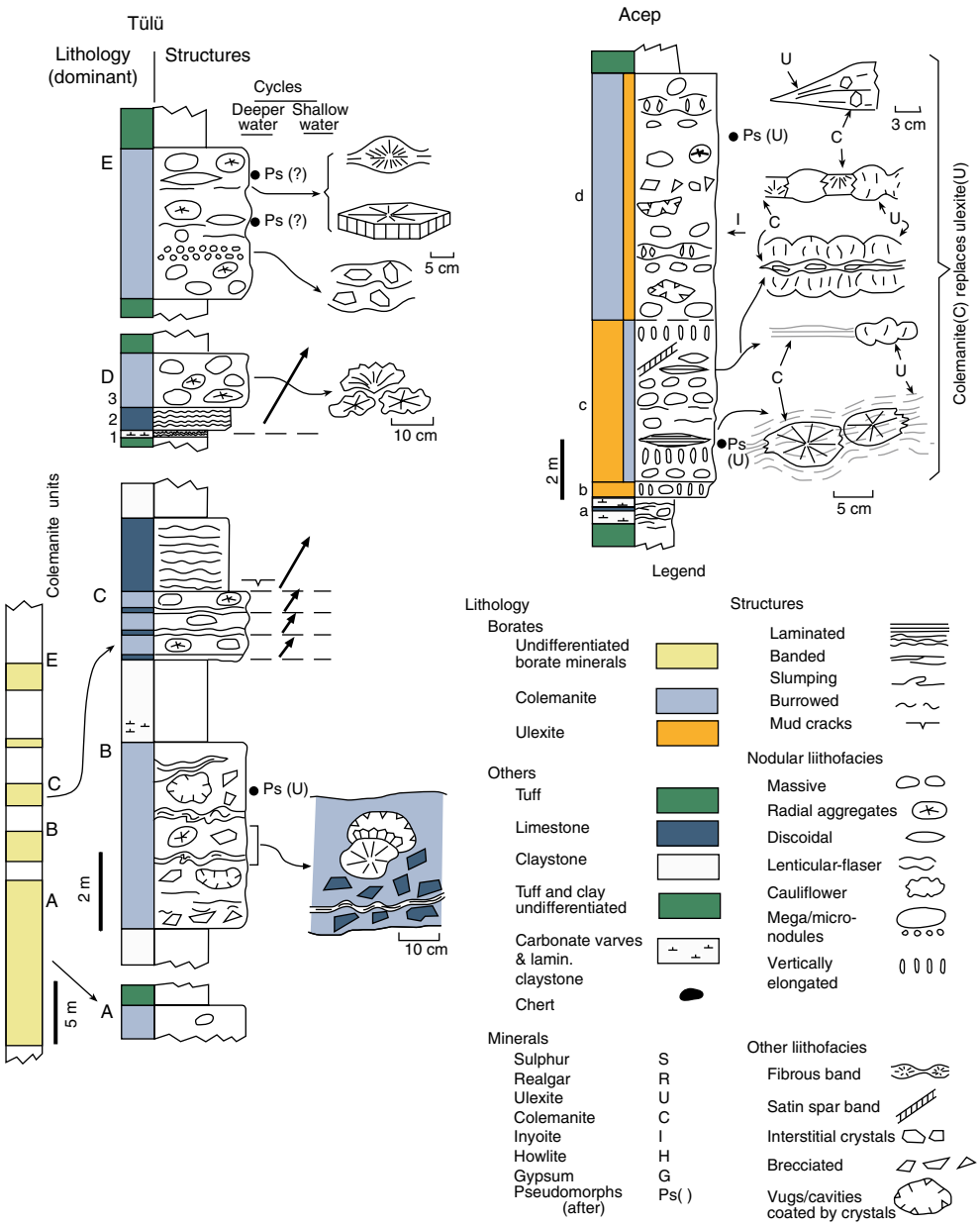

Fig. 12.6 Detailed stratigraphic sections of Tülü (lower borate unit), and Acep (upper borate unit) open pits, in the Bigadic ore district, Turkey, showing details of lithofacies, rock units, carbonate-borate depositional cycles, and the replacement of ulexite by secondary colemanite (After Helvaci and Orti 1998)

and recrystallization of some Sr-rich ulexite horizons. In the Bigadic deposits, hydroboracite formed by replacement of colemanite, with Mg ions supplied from adjacent tuffs and clays by ion exchange. Howlite grew in clay bands alternating with thin colemanite bands and coincided with periods of relatively high silica concentrations. Diagenetic processes also produced small howlite nodules embedded in unconsolidated colemanite nodules.

In contrast to the colemanite-ulexite dominance at Bigadic, laminated lacustrine borax is volumetrically and economically the most important zone in the Kirka borate deposit (Helvaci and Orti 2004; García-Veigas and Helvaci 2013), The deposit is symmetrically zoned in a lateral sense with a central body of Na borate (borax), an intermediate zone of Na–Ca borate (ulexite), and a marginal zone of Ca borate (colemanite; Fig. 12.7). The same mineral zonation is also developed in a vertical sense, although it is somewhat asymmetrical because of the presence of a discontinuous Mg borate horizon overlying the central body of borax. Older studies, based on analogies with US borate deposits, attributed the zonation to a diagenetic overprint on the margins of the original syndepositional boraxclay laminates of the lake (Inan et al. 1973). More recent work has shown that the Kirka sequences are depositionally fractionated and that the zonation represents a hydrologically controlled separation of evaporite minerals in a lake basin actively accumulating sediment (Fig. 12.7b; Helvaci and Orti 2004; García-Veigas et al. 2011b). Lateral gradients in salinity in the mudflats

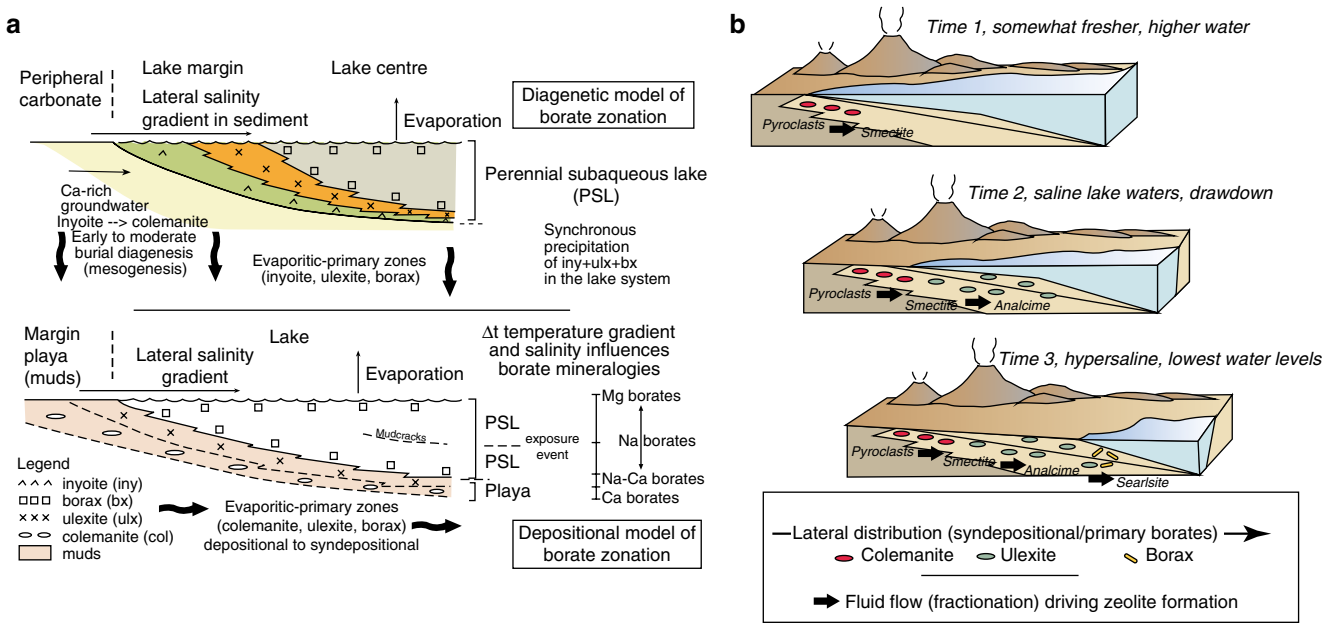

Fig. 12.7 Depositional setting and zonation of Turkish borate deposits. (**a**) Two endmember models used to explain the zonation of Turkish borates; one uses diagenetic flushing by Ca-rich subsurface waters (After Inan et al. 1973), the other explains the zonation as a depositional separation (After Helvaci and Orti 2004). (**b**) Current model that integrates depositional aspects (borates) and diagenetic aspects (zeolites) used to explain mineralogies in the various Turkish borate deposits (After García-Veigas and Helvaci 2013)

passing into the perennially subaqueous centre conditioned the concentric pattern of the facies at Kirka. Thus, the various borax lithofacies zones (chemical, clastic, mixed) seen in the central ore body reflect surface and near-surface borate precipitation in a lake that evolved with subsidence and climate. Conditions oscillated from predominantly subaqueous with variable brine depths (perennial lake stage), to an interstitial sabkha or mudflat setting (playa-lake stage). The evaporative concentration of the boratiferous waters in the lake, together with the periodic changes in temperature of the water mass, are the main controls on the crystallization of borax.

Helvaci and Orti (2004) found no petrographic evidence for a thermally induced inyoite-to-colemanite transformation, as previously proposed by the diageneticists and went on to argue that the moderate burial depths in all the various Turkish borate deposits are insufficient for the generalized transformations required by the diageneticists (Fig. 12.7a). Rather the Mg borates represent evaporitic precipitates from the fractionation of the initial boratiferous inflow, they are not burial driven reaction products between pre-existing borates and groundwaters. Thus the mineral zonation in Kirka is primary, not only for borax and ulexite in the subaqueous dominated parts of the lake, but also for both the colemanite forming the marginal playa dominated zones and for the Mg borates overlying the central body of borax in Kirka (Fig. 12.7b). This same argument of syndepositional not burial flushing can be applied to Bigadic, which is then seen to be a deposit accumulating under predominantly playa conditions (Fig. 12.5b).

Almost all workers now accept that the borax-clay laminite texture that dominates the core of the Bigadic deposit is subaqueous. Crystal outlines have a characteristic growth-aligned borax (palisade) texture in mm-cm thick layers separated by clay segregations. This is a texture similar in many ways to the hydroboracites of South American salars (Fig. 12.9) and the Kramer deposit in the USA. Borax crystals in the lower portions of the lower borate unit in Kirka show zigzag tops mantled by clay, while borax layers in the upper parts of the same unit show erosional tops. The same textural transition from zig-zag to truncation is seen in meromictic gypsum lakes as the depositional surface aggrades across the zone of saturation in a permanently subaqueous brine lake (Fig. 2.72). The nodular Turkish borate ore of the playa margin is more enigmatic; it may be an early diagenetic playa mudflat precipitate or it may be an early alteration halo created by centripetal flushing of the borax core by shallow subsurface waters. These same early pore brines that are laterally fractionating the mudflat borates are also driving clay mineral alteration of the volcanic hosts. This creates classic bull's distributions in the authigenic zeolites (Fig. 12.7b). The ultimate products are analcime and searlesite and processes involved in their formation are discussed later in this chapter

Initial volcanogenic waters that fed the alkaline perennial saline lake(s) were low in Cl and SO_4, and high in boron and Ca, with subordinate Na. Boron isotope data from the Turkish deposits are consistent with colemanite being precipitated from a more acidic brine than ulexite, with borax being

precipitated from a brine that was more basic (Helvaci 1995; Palmer and Helvaci 1995, 1997). Borax precipitation and replacement to create ore grade beds typically occurred in a laminated gypsiferous host, either syndepositionally or in very early burial, perhaps in or immediately beneath stratified brines, where solar-derived brines mixed with upwelling boron-rich hydrothermal solutions. With further burial, the anhydritization of gypsum began at depths that were less than 250 m. At the same time, anhydrite can replace some of the earlier formed more reactive borates (priceite, bakerite and howlite), along with associated celestite precipitation. Subsequent uplift and exposure of some parts of the sequence has rehydrated nearsurface anhydrite to secondary gypsum and partially transformed priceite and howlite into secondary calcite.

South American Borates

In the Andes of South America there are more than forty borate deposits hosted in Neogene volcanogenic-sedimentary rocks across an 880-km-long stretch paralleing the common borders of Argentina, Bolivia, Chile and Peru (Fig. 12.4). This area is high plateau created in the late Cenozoic in the compressional/subduction orogen that created the Andes. As in Turkey, the Andean borate province sits on a major plate suture zone. Most deposits are small aprons or cones of borax and ulexite near volcanic vents, with reserves measured in thousands of tonnes. But in the larger endorheic basins, where volcanogenic brines can pond and concentrate, there are beds of ulexite, borax and inyoite in modern and ancient salars ranging up to hundreds of square kilometers in area, with reserves measured in millions to tens of millions of tonnes. They occupy groundwater sumps formed during arid to hyperarid conditions that have prevailed in most of the Andean intermontane lows since the Miocene and appropriate sumps continue to focus borate precipitates, even today (Strecker et al. 2007; Oveyero-Toledo et al. 2009).

Two main textures typify the borate salts, both modern and ancient; (1) nodular borate locally known as "papas" (potato or cottonball borate), and (2) bedded borates usually interbedded and intermixed with lacustrine muds and locally known as "barras or bancos" (meaning beds or banks). Nodules are the preferred texture to mine as they tend to create a purer product when cleaned and air dried (can be >28 % B_2O_3; Garrett 1998).

Extraction from modern and Quaternary salars utilises ulexite or brine, while ancient (Miocene) ore is dominated by borax or tincal (see inset in Fig. 12.8a). The main ancient borate reserves lie in the Argentinian Andes, mostly in the Pastos Grandes Basin within the 1,500-m-thick volcaniclastic and lacustrine stratigraphic unit known as the Sijes Formation (Fig. 12.8). There were three major pulses of borate generation during deposition of the Miocene Sijes Formation. These pulses are easily identifiable in the central part of the basin but become indistinct and tend to thin out toward the edges (Helvaci and Alonso 2000). Along its approximately 30 km outcrop belt, the Sijes Formation is characterized by a string of variably overlapping borate lenses and is not one continuous bed. Borate-bearing members of the Sijes formation from the base to top are as follows: Monte Amarillo (Fig. 12.8b; mostly hydroboracite), Monte Verde (colemanite-inyoite) and Esperanza (colemanite). The Tincalayu and Loma Blanca areas are important regions of older borate salt units (typified by borax occurrences). Modern active salars, such as Salar di Rincón and Salar di Surire are typified by ulexite plus borax as the dominant borate salts (Helvaci and Alonso 2000; Oveyero-Toledo et al. 2009). Ulexite is also the first evaporite to precipitate in the Pleistocene Blanca Lila Formation near Salar Pastos Grandes, followed by gypsum then halite (Vandervoort 1997).

Typically, ancient South American salars with substantial borates have a central zone, consisting of a relatively thick halite, surrounded by a thinner marginal sulphate zone consisting of a variety of sulphate minerals, as well as variable amounts of halite, ulexite and other borates (Fig. 12.8a; Ericksen 1993; Helvaci and Alonso 2000). Salars that are filled mostly with gypsum lack this zonation. The borate zoning may be symmetrical (bull's-eye pattern) with sulphate surrounding a central halite core, or asymmetrical with the halite zone crowded against one side of the salar. This is also the situation in modern Salar de Atacama where tectonic tilting has displaced the lowest part of the brine sink to the southern end of the playa (see Fig. 12.51). Both the halite and sulphate zones are typically underlain by gypsum and this in turn by siliciclastics. Alternating arid and pluvial climatic episodes in the Andes since the mid-Miocene, means the playas are filled by alternating salt beds and siliciclastics (Figs. 3.48 and 3.49).

Most Neogene borate-rich salar deposits in South America have undergone relatively minor deformation since they were first emplaced. As a result, borates are extracted from a number of open pit operations in the Andean Altiplano (Alonso 1991). Borax Argentina, a member of the Rio Tinto Borax Group, extracts sodium borate ores at its Tincalayu Mine, high in the Argentinian Andes Mountains (altitude of 4,100 m). Nearby, hydroboracite is extracted at Sijes, and ulexite from two modern dry lakebeds, Salar Cauchari and Salar Diablillos, all in the Salta province. Originally developed in 1976, Tincalayu is now Argentina's largest open pit operation measuring more than 1.5 km (1 mile) across and 100 m (330 ft) deep and extracts ore at a rate of 100,000 t per year. In Bolivia, ulexite is extracted from mines in the Salar de Uyuni (Fig. 3.43). In Chile, borates are extracted from Salar de Surire; the largest Quaternary ulexite deposit in the world, with reserves reported to be ≈1.5 million tonnes of 35 % boron oxide. The salar is located some 4,250 m above

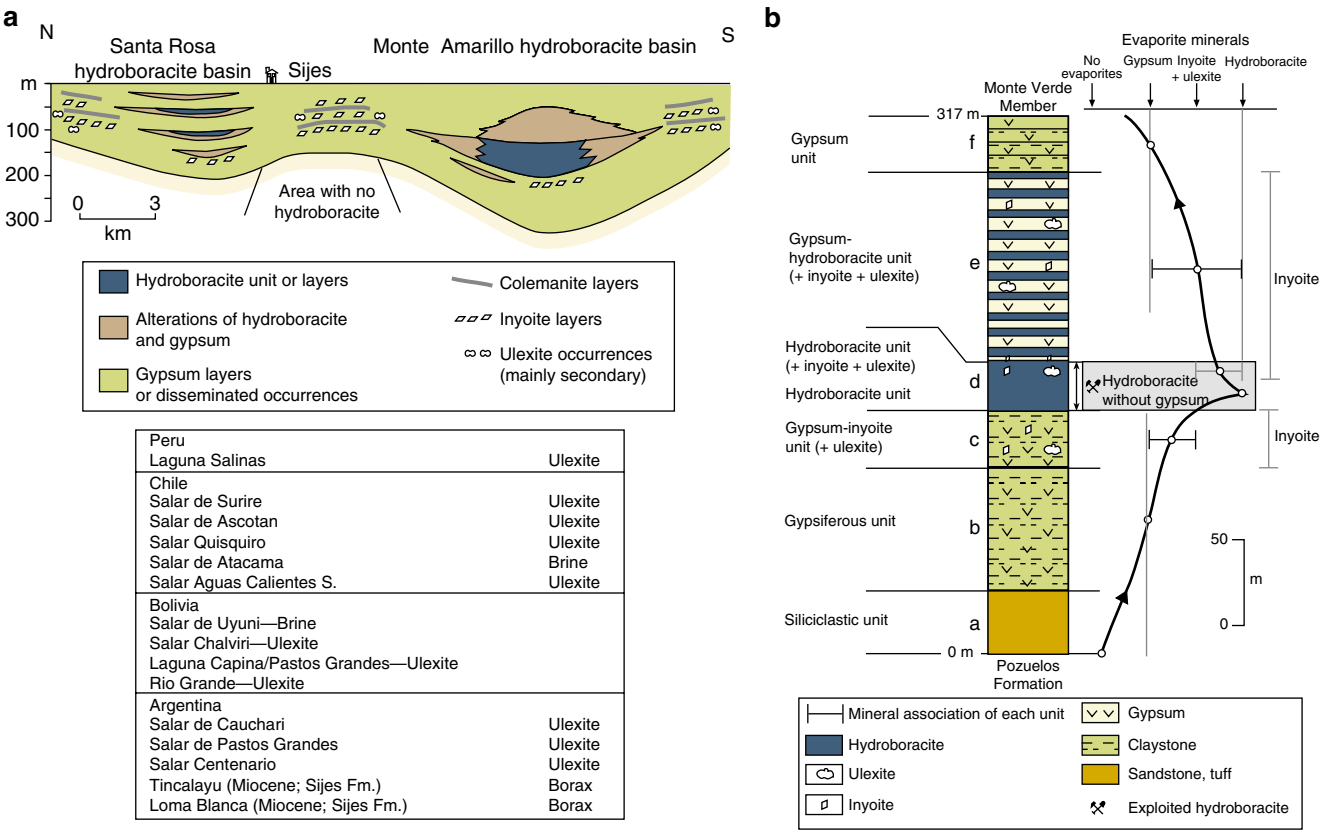

Peru	
Laguna Salinas	Ulexite
Chile	
Salar de Surire	Ulexite
Salar de Ascotan	Ulexite
Salar Quisquiro	Ulexite
Salar de Atacama	Brine
Salar Aguas Calientes S.	Ulexite
Bolivia	
Salar de Uyuni—Brine	
Salar Chalviri—Ulexite	
Laguna Capina/Pastos Grandes—Ulexite	
Rio Grande—Ulexite	
Argentina	
Salar de Cauchari	Ulexite
Salar de Pastos Grandes	Ulexite
Salar Centenario	Ulexite
Tincalayu (Miocene; Sijes Fm.)	Borax
Loma Blanca (Miocene; Sijes Fm.)	Borax

Fig. 12.8 Hydroboracite in the Monte Amarillo Member, Sijes Sierra, northern Argentina. (**a**) Borate facies distribution in the Santa Rosa and Monte Amarillo basins. *Inset* table lists significant borate occurrences. See Fig. 3.41 for locations. (**b**) Type section of the Monte Amarillo Member showing distribution of the various borate minerals and the relative position of the exploited horizon (After Orti and Alonso 2000)

sealevel and within the borders of the Monumento Natural de Surire national park of Chile.

Borate salts occurrences in South America are variously described as depositional or diagenetic, or perhaps syndepositional replacements of gypsum. A significant portion of the bedded hydroboracite is thought to be a primary precipitate in the Sijes Formation (Miocene, central Andes, NW Argentina), which is the major exploited Neogene ore target (Orti and Alonso 2000) and encompasses the largest known hydroboracite accumulation in the world. At outcrop, sulphate minerals in the Sijes Fm, are mostly secondary gypsum and minor anhydrite, while the borate minerals are hydroboracite with subordinate inyoite and colemanite, and some ulexite. Regionally, the Sijes Formation (Miocene) has four members; three of them are fine-grained siliciclastic, tuffaceous, and chemical-evaporitic in nature (the Monte Amarillo Member, the Monte Verde Member, and the Esperanza Member), while the other member is dominantly a coarse-grained siliciclastic (the Conglomerate Member). The overlying Blanca Lila Formation (Pleistocene) is made up of claystone and evaporites (including borates). Much of the exploitable hydroboracite resides in the Monte Amarillo member.

The Monte Amarillo Member accumulated in two coeval, shallow lacustrine Miocene subbasins (Fig. 12.8a): (1) The Monte Amarillo hydroboracite subbasin, and (2) The Santa Rosa hydroboracite subbasin. The Monte Amarillo hydroboracite subbasin encompasses the borate districts to the south of the Sijes village and is an area where hydroboracite has been mined since 1985. This district is located at an altitude of 3,900 m and lies near the paleogeographic centre of the Monte Amarillo subbasin. The Santa Rosa hydroboracite subbasin, includes the borate districts to the north of the Sijes village and is located at an altitude of 3,900 m. This subbasin occupies a marginal position with respect to the Monte Amarillo subbasin. In these subbasins, the hydroboracite layers are fine-grained, light brown, and difficult to break with a hammer. Because of these characteristics, they had for a long time been confused with limestones. In both subbasins, gypsum accumulated in the margins and the hydroboracite in the centres, the intermediate zones being characterized by mixed gypsum hydroboracite layers.

The type section of the Monte Amarillo Member is 317 m thick, contains an inyoite unit 36 m thick at the base, which is overlain by a hydroboracite unit 137 m thick (Fig. 12.8b; Alonso 1986). This hydroboracite unit has variable amounts

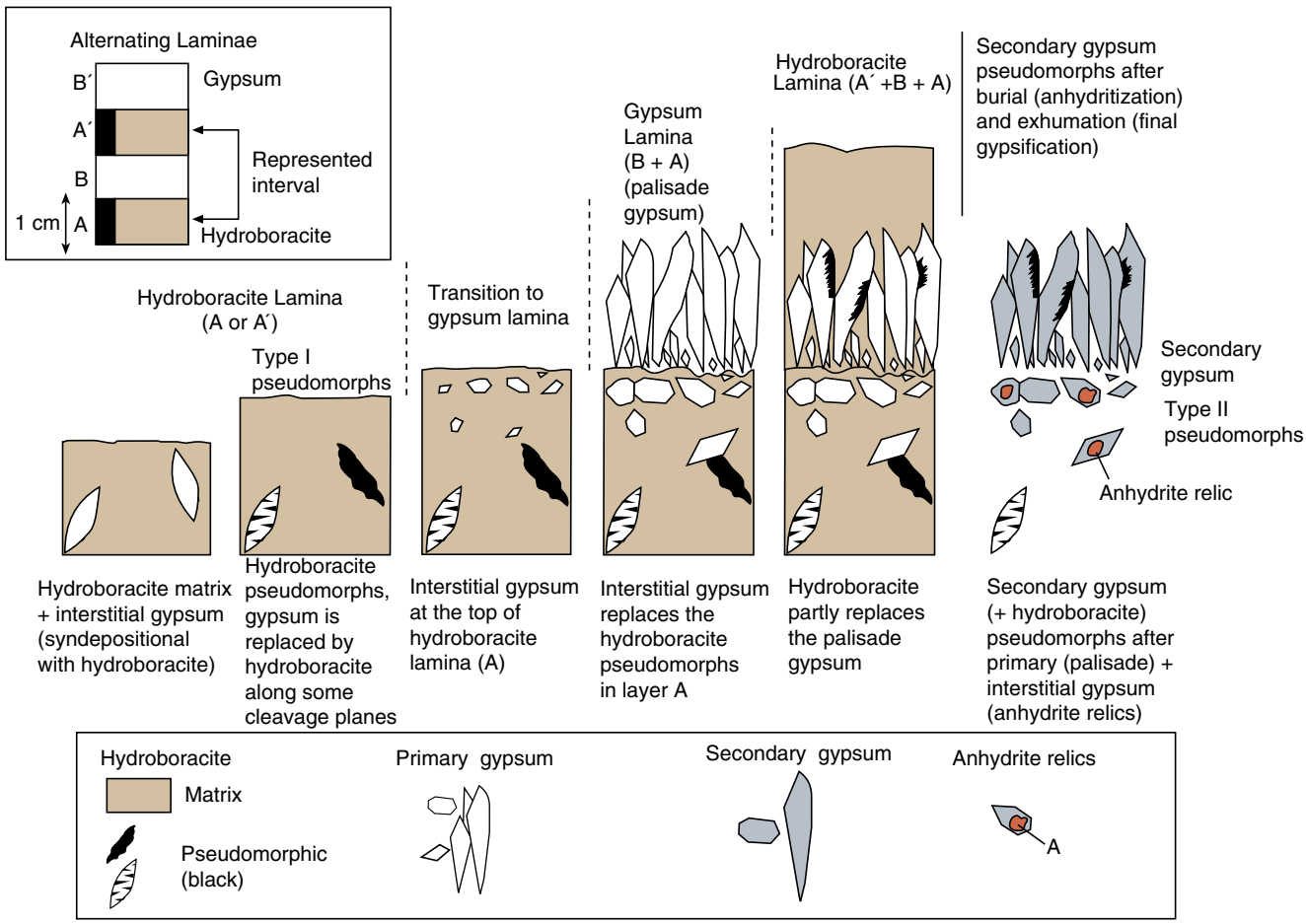

Fig. 12.9 Syndepositional formation of hydroboracite pseudomorphs after gypsum in primary hydroboracite successions composed of alternating cm-scale beds of hydroboracite and gypsum precipitates. Most of the hydroboracite is primary, not secondary (After Orti and Alonso 2000)

of inyoite and ulexite. Gypsum layers are ubiquitous in the Monte Amarillo Member. Samples of two tuff levels located close to the base and at the top of this section were dated as 6.81 ± 0.18 and 6.25 ± 0.15 Ma, respectively, which indicates a depositional period of about 630,000 years for the Monte Amarillo Member during the Upper Miocene (Alonso 1986).

Alternations between gypsum and hydroboracite laminae are present in the transition from gypsum units to hydroboracite units in the Monte Amrillo member and contain fabrics that indicate both the borates and the gypsum-anhydrite were primary or syndepositional precipitates. Fine-grained hydroboracite matrix commonly cements and partly replaces the precursor gypsarenite crystals in the gypsum laminae (Fig. 12.9; Orti and Alonso 2000). In addition, micronodules of hydroboracite can displace or replace gypsum laminae. Two styles of pseudomorphs after interstitially grown (precursor) gypsum are preserved at the mm-scale in hydroboracite laminae. Type I corresponds to hydroboracite pseudomorphs after euhedral, lenticular or tabular gypsum crystals. Many of these pseudomorphs are thin, curved, lenticular or slightly deformed, and now composed of fine-grained hydroboracite crystals. Others are made up of parallel prisms of hydroboracite that project inward from the boundaries of the pseudomorph with the centre commonly occupied by secondary gypsum bearing anhydrite relics. Parallel arrangement of the prisms suggests replacement of the precursor gypsum along the main cleavage plane (010). Type II corresponds to secondary gypsum pseudomorphs after equant to prismatic, commonly zoned (precursor) gypsum crystals. These pseudomorphs are located in the uppermost parts of hydroboracite laminae and grade into secondary gypsum pseudomorphs that constitute the overlying gypsum lamina. Type II pseudomorphs crosscut and replace type I pseudomorphs suggesting that type II pseudomorphs postdate type I.

Alternations between gypsum laminae (with aligned crystal outlines) and hydroboracite laminae imply bottom precipitation in a shallow subaqueous environment, where fine-grained, soft hydroboracite mud encased the gypsum in the laminated gypsarenites. The prevalent microcrystalline or fibrous textures of hydroboracite suggest a primary origin for these alternations in which precipitating conditions

oscillated from gypsum to hydroboracite. Hydroboracite matrix appears to have precipitated interstitially within the open fabric of the (precursor) gypsarenite under synsedimentary conditions (Orti and Alonso 2000). This precipitation, together with associated partial replacement of (precursor) gypsum crystals, occurred during the sedimentation of the overlying hydroboracite lamina (Fig. 12.9). In the hydroboracite laminae, type I pseudomorphs seem to correspond to (precursor) gypsum crystals that grew interstitially in the hydroboracite matrix when the borate concentration of the brine was relatively low. It appears that these crystals were very soon (syndepositionally) replaced by hydroboracite matrix. Flow deformation of the pseudomorphs that are formed by fine-grained hydroboracite occur between flat laminae suggesting that the replacement process took place in a soft matrix under synsedimentary conditions. However, when this replacement occurred as a growth of prisms along the gypsum cleavage planes, the pseudomorphs remained undeformed and consistent. In general, this mechanism was less penetrative, and many pseudomorphs had a mixed hydroboracite–gypsum composition. Presumably, in these mixed pseudomorphs, the anhydrite replacement of the gypsum postdates the partial hydroboracite replacement. These pseudomorphs changed to hydroboracite–anhydrite during burial, and to hydroboracite–secondary gypsum in final exhumation. Type II pseudomorphs seem to correspond to (precursor) gypsum crystals that grew interstitially toward the tops of the hydroboracite laminae during precipitation of the overlying gypsarenite layer, once again a syndepositional diagenetic process.

Beds dominated by primary gypsum (gypsarenite) and syndepositional anhydrite were first precipitated during deposition of the Monte Amarillo Member, in association with limited amounts of calcium borates (colemanite, inyoite). This was soon followed by beds containing hydroboracite (calcium/magnesium borate) and alternating gypsum and hydroboracite layers also formed. The hydroboracite at this level in the stratigraphy is mainly a primary mineral, although it also replaced some gypsum under synsedimentary conditions (Fig. 12.9). The formation of colemanite, which occurred during early diagenesis, is linked to brines precipitating calcium sulphates (gypsum and anhydrite), whereas inyoite coexisted with brines precipitating both calcium sulphate and magnesium-bearing borates. Transformations among the various borate minerals during later burial diagenesis were not detected by Orti and Alonso (2000). Primary gypsum was transformed into anhydrite from the onset of early diagenesis through to moderate burial diagenesis. The boron source of these deposits is volcanic/hydrothermal activity in the central Andes during the Miocene. Likewise, borate salt deposition in the modern salars, such as Salar el Rincón, is also syndepositional (Oveyero-Toledo et al. 2009, inset table in Fig. 12.8a and depositional detail in Chap. 3).

North American Borates

The United States is the world's largest producer of boron compounds and the second largest producer of borate ore with California' largest open pit mine working the Kramer deposit and supplying almost half of the world's borate needs. Other US producers exploit saline brines and bedded playa deposits, such as Searles Lake in California (Smith 1979) or Tertiary counterparts at Boron and the much smaller conventionally mined deposits in the nearby Death Valley area (Kistler and Smith 1983). An excellent history of the Californian borate industry is given by Beeby (2002).

The Kramer deposit (aka Boron deposit) is huge and located near Boron, California, in the Mojave Desert, some 140 km north northeast of Los Angeles and midway between the towns of Barstow and Mojave (Fig. 12.4). The total borate area (including the ulexite and colemanite[1] rims) is 8 km (east–west) by 1.6 km (north–south). The deposit within this area is about 1,600 m long, 800 m wide by 100 m thick, and consists of a lenticular central mass of borax/kernite with interbedded montmorillonite-smectite clay. Borate ore reserves exceed 100 Mt (110 million st). The original borax target was 45–305 m deep and dipped 10–15° to the south. The deposit was discovered in 1913 and was developed as an underground operation during the 1920s. It was converted to an open-pit operation in 1957. Since that time, the operation has grown to become the largest mining operation in California and is operated today by Rio Tinto Borax. The mine open cut is now more than 2.8 km wide, 3.2 km long and 230 m deep (Fig. 12.10b). Ores are part of the shale member of the Kramer beds, which include an arkose member above and the Saddleback Basalt below (Fig. 12.10a, c).

The age of the deposit is 19 ± 0.7 Ma and it defines a small subbasin in a much larger Tertiary lacustrine basin. It is encased in arkosic sands, silts and minor volcanics and limestones. Sedimentation in the basin was interrupted by flows of acidic lava (olivine basalt to latite) known as the Saddleback Basalt, it constitutes the base to the borate ore zone and also interfingers with other sediments of the basin fill. The upper part of the basalt in the mine area has fractures filled with ulexite and searlesite and its contact with the overlying sediments is defined by an "apple green" siliceous shale that contains ostracod carapaces. The colour of the shale reflects its creation by the basalt reacting with lake waters.

Barnard and Kistler (1966) defined the sedimentology of borate beds above the Saddleback Basalt (Fig. 12.10). First is a 7.6–15 m thick footwall shale, further divisible into an initial barren (≈3.7 m) shale and then a ulexite zone. This is a

[1]The mineral name colemanite is named after one of the early miners in the Death Valley region, Mr. William T. Coleman. Ulexite was named for the German chemist Georg Ludwig Ulex (1811–1883) who first discovered it.

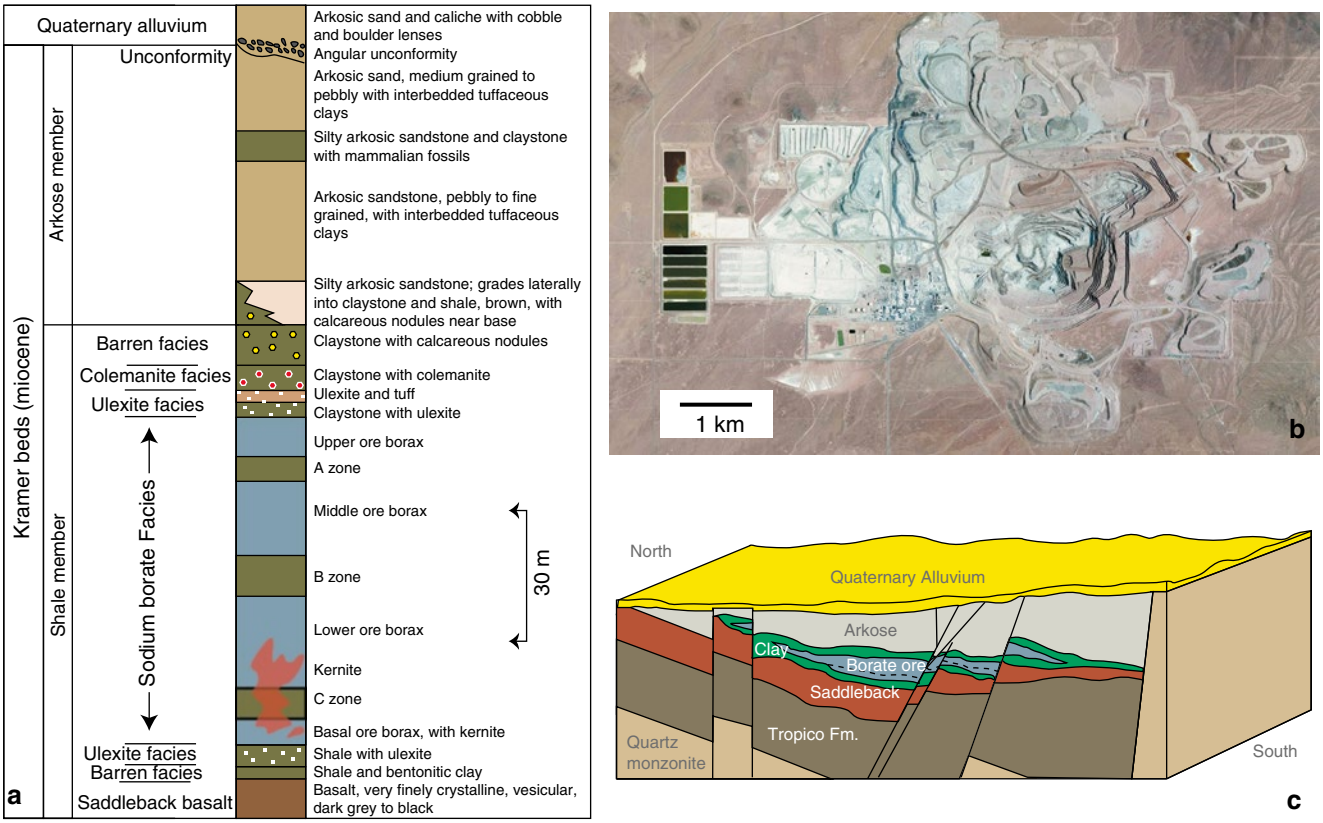

Fig. 12.10 Kramer Borate deposit, near Boron, California. (**a**) Vertical sequence in the mine pit. (**b**) Aerial view of Kramer Pit. (**c**) 3D-schematic showing borate ore distribution with respect to adjacent geology, dashed line indicates inferred extent of kernite (irregular mass in lower part of ore zone; in part after Barnard and Kistler 1996; Bowser and Dickson 1966; Siefke 1991)

layer of greenish-gray at times black fissile shale that is thinly laminated, micaceous and at times contorted. Locally it encloses lenses of arkosic sandstone and coarse conglomerate. Above this are the borax beds interbedded with clay and shale along with some beds and lenses of tuff, arkosic sand and conglomerate. The low permeability of these lacustrine shales is thought to have helped preserve the borax by preventing entry of groundwaters. Laterally and vertically away from the deposit's borax/kernite core, the borate facies changes to ulexite and colemanite, and the levels of shale interbeds and clay impurities in the borates become more significant (Bowser and Dickson 1966).

The deposit is believed to have formed in a shallow Mid-Miocene saline lake, fed by Na- and B-rich thermal springs, a response to the later stages of volcanism. Saline sodium-borate-bearing thermal spring waters, being denser, sank to the lake bottom, cooled, and precipitated borax as they cooled. The original lake position was controlled by faulting contemporaneous with the accumulation of the borax. Continued fault movement, associated with the middle Pliocene uplift of the Mojave Block, tilted and dropped the lake sediments, which are now buried by more than 760 m of late Miocene and Pliocene arkosic sediment. Older models argue that deeply buried portions of the borax deposit were altered, via water loss, to kernite at this time. Renewed movement in late Pliocene–Pleistocene uplifted the deposit and drove some erosion of the original borate so that the outer portions of the kernite facies were rehydrated at that time. The deposit was then covered by 9–21 m of Pleistocene and Recent sands and gravels (Barnard and Kistler 1966; Siefke 1991).

As well as 19 Ma Kramer deposit, across the Death Valley area, borates were also deposited 6 Ma and there are more than 23 known deposits (Garrett 1998). In all, the borate ore is contained in the lower 150 m of the 2,100 m thick Pliocene Furnace Creek Formation. The interiors of most of the ore deposits preserve unaltered bedding planes and uniform depositional patterns. There are few to no indicators of syndepositional alteration (slumps, pseudomorphs) in the centres of the deposits but considerable evidence for alteration and replacement about the deposit's edges. The agglomerated nodular structure composed of masses of acicular crystals in much of the originally exploited ore meant that earlier miners in Death Valley area described the various exposures of borate ore as cottonball or cotton-tail (like the fluffy tail of a cottontail rabbit). Regionally a series of projected shoreline

features can be traced from the Billie to the Boraxo to the Sigma-White Monster mines and residues of ancient geothermal spring mantle deposits are locally present (Garrett 1998).

One of the largest deposits in the Death Valley area was the Billie orebody (an underground mine, now abandoned), a 1,100 m long lens of ulexite, proberite and colemanite, interbedded and surrounded by limey laminated lacustrine mudstone and shale. Fault activity controlled the position of the lake-bed borates and some beds now have local dips of upwards of 45°. The Billie orebody has an average thickness of 45–55 m, a width of 220 m, and a regional dip of 20–30° toward the southeast. Reserves were of the order of 2,700,000 metric tons of ulexite-proberite at 27 % B_2O_3 and 11,000,000 metric tons of colemanite at 21 % B_2O_3 (Garrett 1998).

The borate ore zone at Billie Creek is hosted by shales of the Furnace Creek Formation and is made up of metre-scale units of nodular borate, mainly colemanite, interbedded with laminated mudstones deposited in a saline lacustrine environment during extension of the basin. The hosting laminites lack features of syndepositional exposure or wave-reworked deposition, indicating that the borate-hosting sediment first accumulated on the floor of a density-stratified perennial lake (Tanner 2002). The presence of interbedded sulphate minerals in this facies suggests that salinity in this lake was elevated. Metre-scale mounds of porous limestone with a clotted-micritic fabric define spring-apron tufas that formed where groundwater discharged along fault-fed outflows about the edge of a more saline water mass.

The exploited massive borate facies in the various Death Valley deposits are made up of thick, massive borate layers, locally containing host rock clasts with sharp to diffuse boundaries. Borate formation first took place at or below the sediment/water interface. The composition of the borate deposits in Death Valley varies from mainly colemanite to zoned accumulations, with colemanite surrounding a core of probertite and ulexite.

Many older models for the formation of colemanite in the Kramer and Death Valley deposits, prior to the 1960s argue for burial (thermal) replacement of ulexite and inyoite via flushing by "intruding warm borax solutions." High Ca/Na ratios favoured primary deposition of hydrated Ca-borates, which early workers argued were subsequently transformed by diagenetic dehydration to colemanite (Foshag 1921; Christ and Garrels 1959). This meant the gradual depletion of Ca and decreasing Ca/Na ratios in the mother brine resulted in Na-Ca-borate precipitation, while any renewed onset of elevated Ca/Na ratios again caused Ca-borate deposition.

But these older burial/thermal fluid models never clearly addressed a number of textural and conceptual problems (Garrett 2001). Namely, (1) Where did these conversion liquors come from? (2) How did they maintain their chemical uniformity? (3) How did they totally and completely pervade and replace what were impermeable salt units? (4) What was the required voluminous Ca source needed to accomplish the transformation? (5) Where did the residual brine go? In addition, why are there no widespread disruption texture and slumps structures both within and above the bedded salts and why are commonplace colemanite alteration minerals like, priceite, ginorite, nobleite and gowerite, absent?

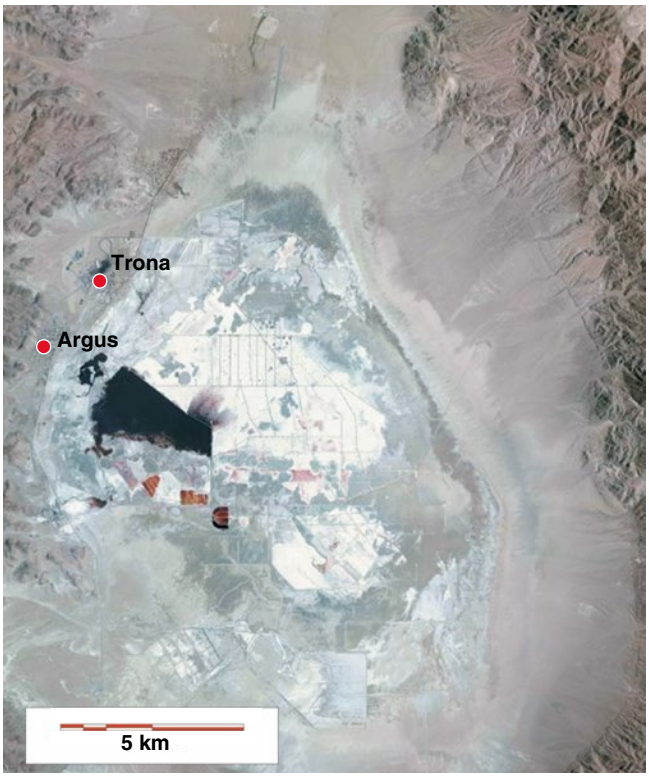

Fig. 12.11 Searles lake, California, showing that it is a endorheic basin in the Basin and Range of the USA

A similar set of problems beset the notion that the dehydration of borax to kernite indicates a deep burial conversion process. The problem as to deposition versus burial replacement for the Kramer deposit is yet to be resolved to the satisfaction of all. But, given the widespread preservation of depositional features in the Kramer and Death Valley deposits, the clearly primary nature of the various less compacted borate salt beds in Turkish deposits as likely analogs, syndepositional controls for the Kramer and Death Valley deposits are favored. This places colemanite, for example, as forming in the capillary zone of a saline lacustrine mudflat, with inyoite in the more saline perennial centre of the sump (e.g., Fig. 12.7).

Searles Lake in southeastern California is located in the lower central portion of a small block-faulted desert valley with a drainage area of 1,600 km^2 and located midway between Boron and Death Valley (Fig. 12.11). It is a likely Pleistocene counterpart to the lacustrine evaporites that

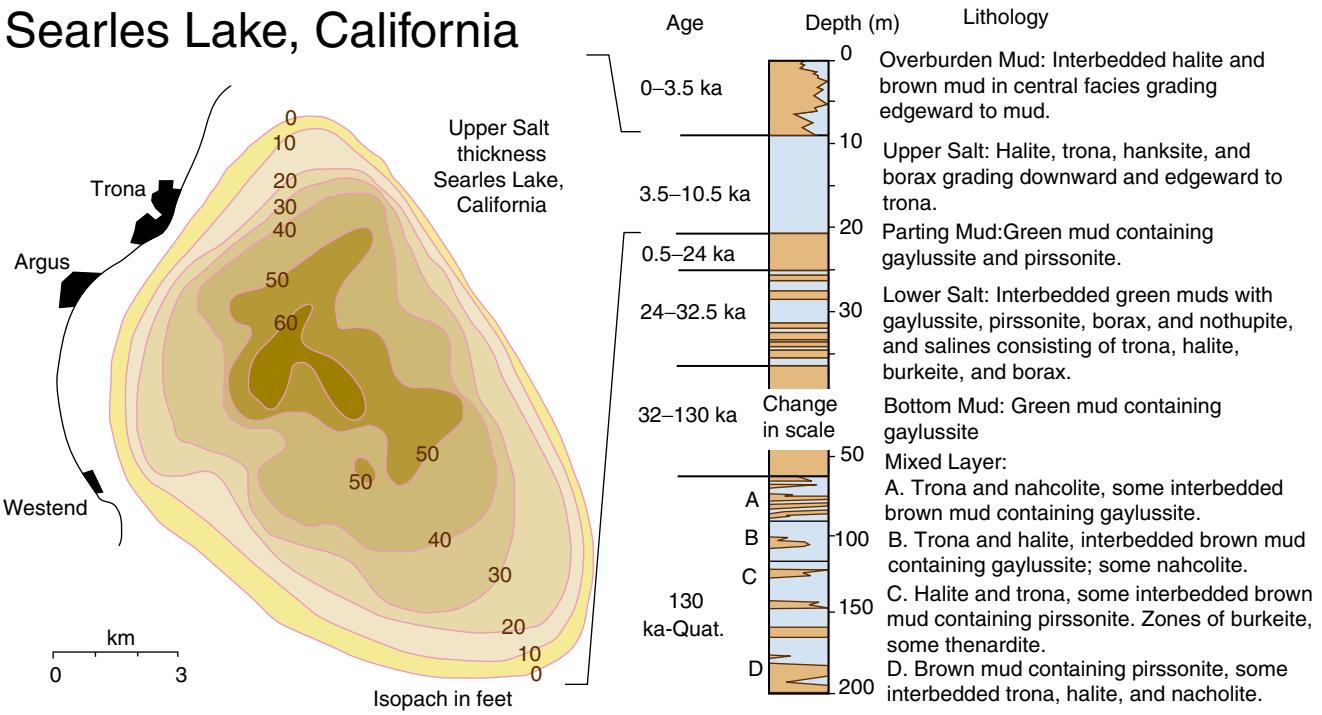

Fig. 12.12 Searles Lake, California showing isopach of the "Upper Salt" in feet as well the stratigraphy of the three salt layers and intervening clays (After Smith 1979). Note the change in scale in the vertical section at around 50 m

entrain the exploited Neogene deposits of Boron and Death Valley. The central pan, some 103 km^2 in extent, overlies a crystalline mush of mixed salts dominated by sodium carbonates, but also with borax, clays, and hypersaline interstitial brines. The brine recovery operation is a multicomponent chemical system and borax is only one of the products recovered; others include sodium sulphate, lithium compounds, potash, bromine and other salts. Boron was supplied to the lake via thermal springs along the Sierra Nevada frontal faults in Long and Owens Valleys (Smith 1979).

There are two main solution-mined salt horizons beneath the central pan: the "upper salt," some 9–27 m thick (averaging 15 m), with a brine content averaging 1.0 % B_2O_3; and the "lower salt," some 8–14 m thick, (averaging 12 m), with a brine content averaging 1.2 % B_2O_3. The upper salt is overlain by a surficial mud and salt-crust unit some 7–9 m thick and is separated from the lower salt by 3–6 m (average 4 m), of relatively impervious clays called the "parting muds" (Fig. 12.12). The upper two salt beds accumulated in the period 3.5–40 Ka. There is also a much deeper salt bed with a mineralogy dominated by trona-nahcolite-halite with lesser amounts of burkeite-thenardite.

The salt mush in both the upper and lower salt beds is quite porous (0.35–0.40) and the stored brine is pumped via a series of wells into adjacent saltworks where borate, sodium bicarbonate and sodium sulphate salts are recovered. A constant resupply of brine to the mush beds is maintained by natural recharge and percolation of dilute refinery effluent, which is pumped back into the mush beds. The two salt horizons are pumped separately as they differ somewhat in chemical makeup and therefore require different plant treatments. Historically, until 1979, the upper salt was the solution-mining target, since then the lower salt has been mined as a trona target and processed using carbonation.

Other Borate Deposits

Borates in China are found in many salt lakes on the Qinghai-Xizang (Tibet) Plateau, in cold arid conditions in lakes such as Zhacang Caka and Zabuye Caka. There typical lake waters contain 85 mg/l of boron oxide and are co-associated with elevated lithium levels (Fig. 12.55; Sun and Li 1993; Zheng and Liu 2009). The maximum value of boron oxide in such lake brines is around 1,500 mg/l. The saltflats in lakes such as these, and their borate crusts, were the original suppliers of borate salts to Medieval Europe.

However, today the largest economic borate reserves in China occur not in Quaternary/Tertiary saline lakes but in the Precambrian meta-evaporitic borosilicates in Liaoning Province. Reported reserves are 44 million tonnes of boromagnesite with 8.4 % boron oxide content. The deposits in the Liaoning Province represent 64 % of the country's total boron resources and 90 % of these deposits are associated with banded iron formations. There are more than 112 separate borosilicate deposits (12 contain 98 % of the known reserves)

in the Liaoning area on the Liaoning Peninsular in northeast China. The main ore mineral is szaibelyite (aka ascharite), along with ludwigite, with some suanite. All are Mg-borates and are hosted along with magnesite and magnetite in fractured marbles. Deposits are thought to be meta-evaporitic skarns, originally deposited as lacustrine borates interbedded with volcanic tuffs (Peng and Palmer 2002). These deposits are discussed in detail in Chap. 14 (Fig. 14.44).

The world's only exploited marine borate deposit is in the Inder district of Kazakhstan (former USSR), north of the Caspian Sea. Now-depleted mined borates formed bedded lenses up to 3 m thick and were hosted in the gypsiferous caprock in the 100+ km^2 crest of a large Permian salt dome. Ores are magnesian borates, rather than the more commonplace sodian-calcian borates typically found in modern continental salars and playas. Mineralization is centred on fractures near the top of the dome, where borates have precipitated in a matrix of gypsum, clay and anhydrite. The fluids precipitating borate are thought to be derived from geothermal springs (Garrett 1995). Boron is also periodically extracted from the brines of nearby Lake Inder. This salt lake has a m-thick surface salt crust underlain by some 30 m of brine-saturated salt, which contains potassium chlorides and bromides as well as borax (Kistler and Smith 1983). Unlike the other economic borate deposits of the world, this deposit is sourced by dissolving Permian marine salts, hence the association with the magnesian salts, and is not tied to volcanism.

Its marine origin is obvious in its boron isotope signature, which is clearly much more enriched in ^{11}B than nonmarine sediments (Fig. 2.39c; Swihart et al. 1986). The clear separation of nonmarine and marine borate salts using boron isotopes is also used to define parentage of various meta-evaporitic tourmalines in the meta-evaporites of Liaoning, China. Isotope analysis is a useful technique for determining boron source long after the original salts have evolved into lattice components of high temperature and high pressure minerals (see Chap. 14).

Borate minerals do occur in marine evaporites other than the Inder deposit, but are not known in sufficient amounts to be economic targets. For example, potash ore processing of the Zechstein potash ores in Germany leaves behind borates in the mud residues. At times this borate has been recovered as a small-tonnage byproduct (Garrett 1998). Marine borates such as priceite and howlite are present in minor amounts in the Cretaceous marine evaporites of the Maha Sarakham Fm. in Thailand, in the Mesozoic evaporites of the Atlantic margin in Nova Scotia, Brazil and West Africa, and in the Permian evaporites of the Delaware Basin, USA (Chap. 7). In all cases it seems that the levels of boron in the marine bitterns were never sufficient to create economic levels of borate salts. That seems to requires hydrothermal circulation, usually in a volcanic basin.

Evaporitic Borates and the Evolution of Life

Associated with the earliest borate minerals of the Hadean and the earliest Archaean in a period of time known colloquially as the RNA World, there is an esoteric, but nonetheless interesting, association of borate salts and evolution of the earliest lifeforms. RNA World hydrochemistry is thought to have been an important link between purely prebiotic (≈3.7 Ga) chemistry and modern DNA/protein biochemistry. Given the ambient atmospheric and hydrospheric chemistry of that time, one major concern in the evolution of early life, is the geochemical stability of ribose, which is the sugar moiety of RNA and the precursor to true DNA-based life. Prebiotic stabilization of ribose by solutions associated with borate minerals, notably colemanite, ulexite, and kernite, has been proposed by a number of workers (Fig. 12.13; Grew et al. 2011).

Although the oldest reported colemanite and ulexite are 330 million years old, and the oldest reported kernite, 19 Ma, boron isotope data and geologic context are consistent with an evaporitic borate precursor to 2,400–2,100 Ma borate deposits in the Liaoning and Jilin Provinces, China, as well as to tourmaline-group minerals at 3,300–3,450 Ma in the Barberton belt, South Africa (Fig. 12.13). The oldest boron minerals for which the age of crystallization can be determined are derived from metamorphic tourmaline species, schorl and dravite, in the Isua complex, Greenland (metamorphism between 3,650 and 3,600 Ma). Whether borates such as colemanite, ulexite and kernite were present in the Hadean (≈4,000 Ma) at the critical juncture when prebiotic molecules such as ribose required stabilization depends on whether a granitic continental crust had yet differentiated. In its absence there appears to be no means for boron to be sufficiently concentrated for low temperature borates to precipitate; the discussion continues.

Sodium Sulphate Salts (Salt Cake)

Sodium sulphate salts are similar to borates in terms of volumes extracted of naturally occurring nonmarine sodium salts (Table 12.2). Sodium sulphate salts typical of ore mineral assemblages include combinations of: thenardite, mirabilite [also called glaubers salt], glauberite, astrakanite (also called bloedite) and burkeite (Table 12.5).

Character and History

Sodium sulphate mineral assemblages show interesting stability relationships with respect to salinity and temperature, with corresponding affects on crystallization assemblages in

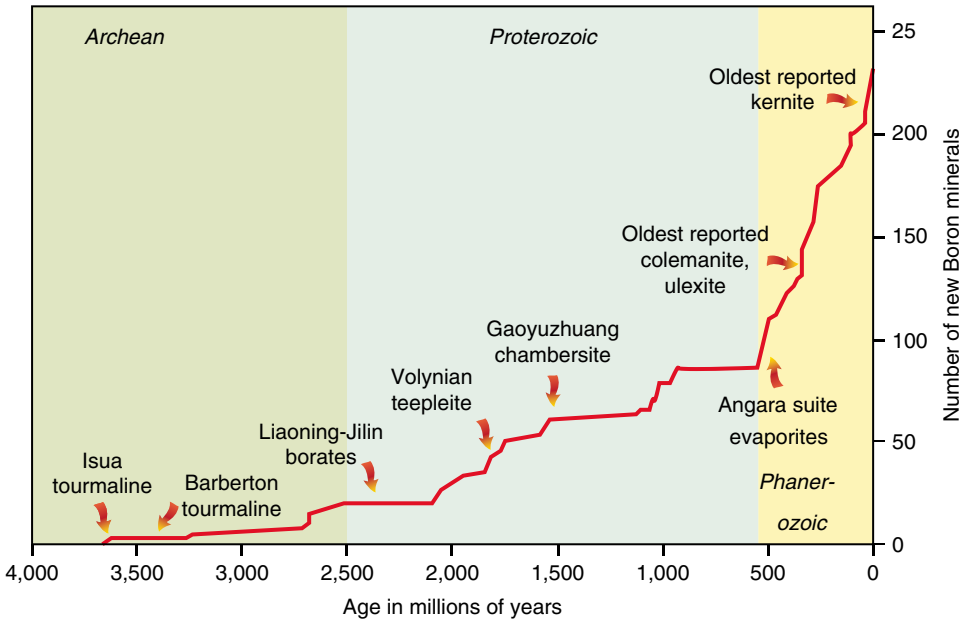

Fig. 12.13 Cumulative plot for 263 boron minerals based on reported occurrences and age determinations (After Grew et al. 2011)

Table 12.5 Minerals that contain Na_2SO_4 and percent Na_2SO_4

Mineral name	Composition	%
Thenardite	Na_2SO_4	100
Hanksite	$9Na_2SO_4{\cdot}2Na_2CO_3{\cdot}KCl$	81.7
D'ansite	$9Na_2SO_4{\cdot}MgSO_4{\cdot}3NaCl$	81.2
Lecontite	$(Na,NH_4K)_2SO_4{\cdot}2H_2O$	<79.8
Vanthoffite	$3Na_2SO_4{\cdot}MgSO_4$	78
Hectorfloresite	$4Na_2SO_4{\cdot}NaClO_3$	74.1
Sulphohalite	$2Na_2SO_4{\cdot}NaCl{\cdot}NaF$	73.9
Burkeite	$2Na_2SO_4{\cdot}Na_2CO_3$	72.8
Eugsterite (Fritzche's salt)	$2Na_2SO_4{\cdot}CaSO_4{\cdot}2H_2O$	62.3
Darapskite	$NaNO_3{\cdot}Na_2SO_4{\cdot}H_2O$	58.0
Hydro-glauberite	$5Na_2SO_4{\cdot}3CaSO_4{\cdot}6H_2O$	57.9
Glauberite	$Na_2SO_4{\cdot}CaSO_4$	51.1
Loeweite	$Na_2SO_4{\cdot}MgSO_4{\cdot}2.5H_2O$	46.2
Ferrinatrite	$3Na_2SO_4{\cdot}Fe_2(SO_4)_3{\cdot}6H_2O$	45.6
Mirabilite (Glauber's salt)	$Na_2SO_4{\cdot}10H_2O$	44.1
Bloedite (astrakanite)	$Na_2SO_4{\cdot}MgSO_4{\cdot}H_2O$	42.5
Kroehnkite	$CuSO_4{\cdot}NaSO_4{\cdot}2H_2O$	42.1
Nickelbloedite	$Na_2Ni(SO_4)_2{\cdot}4H_2O$	40.3
Sideronatrite	$Na_2Fe(SO_4)_2{\cdot}OH{\cdot}3H_2O$	38.9
Caracolite	$Pb(OH)Cl{\cdot}NaSO_4$	35.4
Palmierite	$(K,Na)_2Pb(SO_4)_2$	<31.9
Tychite	$Na_2SO_4{\cdot}2Na_2CO_3{\cdot}2MgCO_3$	27.2
Aphthitalite (Glaserite)	$Na_2SO_4{\cdot}3K_2SO_4$	21–38
Tamarugite	$Na_2SO_4{\cdot}Al_2(SO_4)_3{\cdot}12H_2O$	20.3
Natrochalcite	$Cu_4(OH)_2(SO_4)_2{\cdot}NaSO_4{\cdot}2H_2O$	18.8
Almerite	$Na_2SO_4{\cdot}Al_2(SO_4)_3{\cdot}5Al(OH)_3{\cdot}H_2O$	15.9
Mendozite (soda alum)	$Na_2SO_4{\cdot}Al_2(SO_4)_3{\cdot}24H_2O$	15.5
Natrojarosite	$Na_2Fe_6(OH)_{12}(SO_4)_4$	14.7
Noselite	$3Na_2Al_2Si_2O_8{\cdot}NaSO_4$	14.3
Slavikite	$(NaK)_2SO_4{\cdot}Fe_{10}(OH)_6(SO_4)_{12}{\cdot}63H_2O$	<4.6

Salt cake is defined as anhydrous sodium sulphate with purity less than 98 %

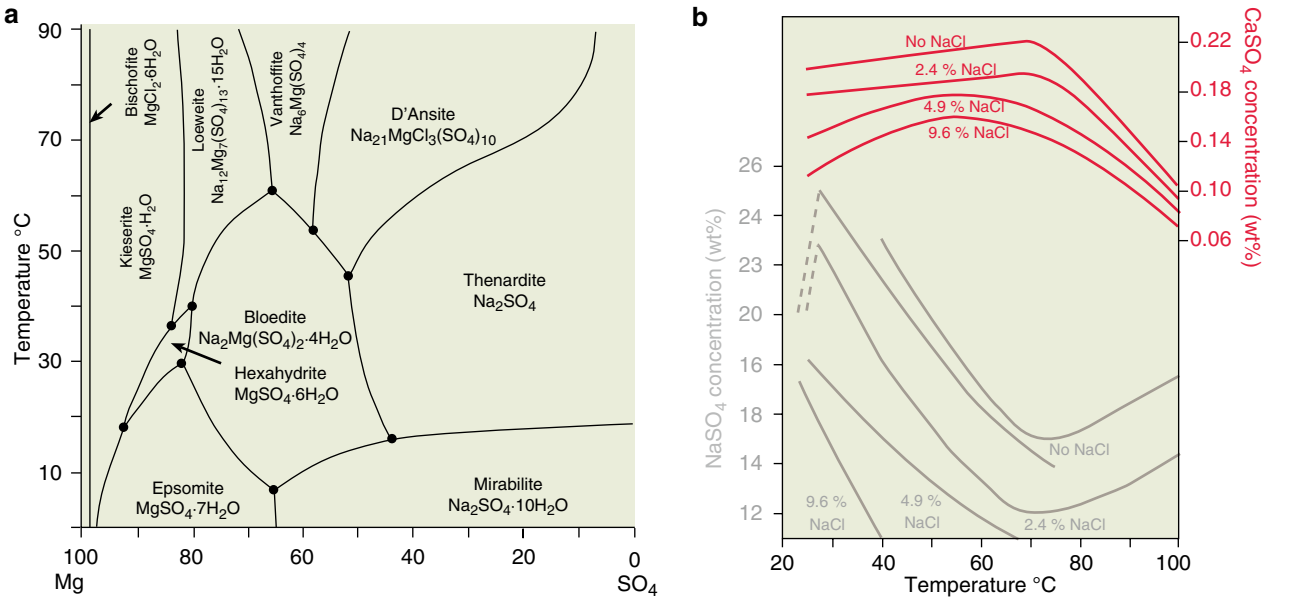

Fig. 12.14 Sodium sulphate chemistry. (**a**) Temperature dependency of Na_2SO_4 minerals in an NaCl-saturated NaCl–Na_2SO_4–$MgCl_2$–H_2O system (After Braitsch 1964). (**b**) Solubility of sodium sulphate and calcium sulphate (different scales) when glauberite and gypsum/anhydrite are both present at 20–100 °C, and with 0–9.6 % NaCl, wt% (After Garrett 2001)

natural and processed brines (Fig. 12.14a, b). Thenardite and mirabilite, respectively, are the anhydrous and decahydrate single-sodium sulphate salts and are the commercially important ore salts, with lesser production from glauberite and bloedite (astrakanite) ores. Thenardite, named for the French chemist Louis J. Thenard, is a colourless to white mineral with a specific gravity of 2.67 and a hardness of 2.5–3.0. It is stable below 33 °C and is extremely hygroscopic below 25 °C, converting to the decahydrate mirabilite (Fig. 12.14a). This mineral contains 55.9 % water of crystallization and forms opaque to colourless needle-like crystals sometimes referred to as Glauber's salt. Common nongeological usage of the term Glauber's salts can be confusing, it usually refers to mirabilite rather than glauberite (named after the seventeenth century German iatrochemist, Johann Glauber). The mineral name mirabilite comes from the Latin *sal mirabilis* or "miracle salt" possibly referring to its pharmacological use as a cathartic or laxative in the Middle Ages and its utility in treating a wide variety of gastric complaints. The mineral glauberite and Glauber's salt are two separate minerals; Glauber's salt is the industrial name for the mineral mirabilite.

Essentially all commercial deposits of natural sodium sulphate are the result of the accumulation and evaporation of continental surface waters and groundwaters in arid endorheic basins, all located in hot or cold, arid to semiarid, desert regions. Exploited Na_2SO_4 deposits can be further classified into; (1) those extracted from Quaternary-age brines hosted in crystalline beds containing mirabilite or glauberite; and (2) those found as older (Pre-Quaternary) bedded accumulations of thenardite, glauberite and associated minerals. The first category includes most of the principal economic deposits of the world. Notable among them are, the lake deposits of western Canada; the vast mirabilite-glauberite deposits of Karabogazgol on the eastern shore of the Caspian Sea, the mirabilites of Great Salt Lake, Utah; the brine deposits of Laguna del Rey in western Mexico and Searles Lake in the western USA. All these Quaternary lacustrine systems require brine reservoiring for exploitation, some also require dredging. Commercial deposits of the second category, that is, the Pre-Quaternary bedded ores, are relatively rare occurrences. Miocene saline lacustrine deposits of thenardite and glauberite are mined in Spain, while thenardite was mined at Camp Verde, Arizona, and Rhodes Marsh near Mina, Nevada. Conventional mining techniques are, or were, used for ore extraction in this group of deposits.

Quaternary sodium sulphate brines show an interesting climatic dichotomy, one group is characterised by the formation of mirabilite via brine freezing (cryogenic salts), the other by glauberite/bloedite created by the evaporation of continental brines in saline groundwater sumps in warm to hot arid deserts.

The dichotomy reflects the fact that sodium sulphate solubility in water changes as a nonlinear function of temperature (Fig. 12.14a). Below 1.2 °C, ice and mirabilite

tend to precipitate as seawater or a saline brine freezes. As the temperature increases above 0 °C, increasing amounts of hydrous sodium sulphate (as the decahydrate, mirabilite) become soluble, while the hydrous form (thenardite) becomes the precipitative phase in brines saturated with respect to the sodium sulphate salts. At 32.4 °C in pure water, a transition point on the solubility curve is reached, whereby mirabilite melts in its own water of crystallization and thenardite crystallizes. Presence of other dissolved salts changes the transition temperature and solubility characteristics of sodium sulphate due to the double salt effect. Figure 12.14b plots solubility versus temperature in terms of $NaSO_4$ and $CaSO_4$ in various NaCl solutions. It clearly shows the retrograde solubility of both salts and in part explains why glauberite is a common low temperature replacement of gypsum/anhydrite in many salt-cake beds (see discussion of double salt effect in Chap. 2).

Natural temperature drops in sodium sulphate-saturated brines in cooler climates are sufficient to allow mirabilite to crystallise in Canadian salt lakes during the autumn transition to winter, and even during cooling on summer nights in higher altitudes. In many places, mirabilite crystals redissolve into the lake brine with the next passage to warmer temperatures, this can be on the next day, or with the passage of winter into spring. This is also true of the brines in Great Salt Lake and Karabogazgol.

Natural sources of sodium sulphate make up over 60 % of world production, the balance is a synthetic byproduct of various chemical and waste recovery processes, including the manufacture of rayon, dichromate, phenol and potash. Mexico and Spain are the world's highest tonnage miners of natural sodium sulphate, followed by a group comprising the USA, Canada, Turkey and Iran (Table 12.6, Fig. 12.15). The Chinese probably manufacture the largest volume of synthetic salt-cake, although figures are not released. The

Table 12.6 $NaSO_4$ deposits, listed by country

Location (area)	Age	Elev. (m)	Köppen	Mineralogy/setting/comments/key references
Hobbs mirabilite area, Antarctica	Quaternary	174	EF	Pure bedded mirabilite to mirabilite-cemented till of Hobbs Glacier in region between glacial nose and coastline. Mainly sourced by freezing of seawater-influenced aerosols. Not exploited (4 mt). (Bowser et al. 1970)
Cerro Blanco, Argentina	Pliocene	3,926	–	Thenardite, small deposit (1.2 mt) in Upper Member of Rodeo Fm. Hosted in clay, shale, gypsum and volcanic ash. (Garrett 2001)
Florentino Ameghino, Argentina (13 km^2)	Quaternary	122	BSk	Mirabilite, halite. Four "mineralized levels" (beds) containing multiple lenses (several metres long and up to 10 cm thick) associated with similar sized lenses gypsum after anhydrite. Numerous springs. (Garrett 2001)
Rio Grande Salar, Argentina (67 km^2)	Quaternary	3,630	ET	Mirabilite/thenardite, bedded salar salts, occasional extraction (≈6,000 t/year) via trenching in Salta Province. (Garrett 2001)
Sua (Sowa) Pan, Botswana (3,306 km^2)	Quaternary	892	BSh	Brine processing active in Makgadikgadi playa. Salt-cake is possible future byproduct from brine carbonation in existing soda-ash facility. Estimated there is ≈110 mt of $NaSO_4$ in brine stored in pan aquifer. (Low et al. 2000; Eckardt et al. 2008)
Canadian saline lakes on the Great Plains Canada	Quaternary	650–712	BSk	Mirabilite/thenardite. Supratill depressions, some lakes with permanent mirabilite beds, others with ephemeral mirabilite (winter) recovery by various combinations of dredging and brine processing. Ingebright Lake (2.8 km^2, BSk) had largest reserves of the Canadian lakes (11.7 mt). Other exploited and now depleted lakes (in BSk and Dfb climate) include Big Quill Lake (7 mt), Chaplin Lake (3 mt), Dead Moose (1.6 mt), Freefight Lake (1.3 mt), Horseshoe Lake (3.7 mt), Sybouts Lake (3.3 mt), Whiteshore Lake (6.5 mt). (Last 2002)
Submergent coastal lake basins, Sachs Harbor, Canadian Arctic	Quaternary	−1.0	ET	Freezing of seawater excludes salts, generating dense brines that sink to the basin bottom (Mirabilite Lakes 1&2). Progressive freezing increases salinity of residual brines to the point of mirabilite saturation, and as a result sedimentary deposits of mirabilite (1 m-thick beds) accumulate on the basin floors. Brine formation also leads to density stratification and bottom water anoxia (Grasby et al. 2013).

Table 12.6 (continued)

Location (area)	Age	Elev. (m)	Köppen	Mineralogy/setting/comments/key references
Weldon, New Brunswick, Canada	Lower Carboniferous	4	–	Glauberite (25 mt) at 344 m depth in the lacustrine Gautreau Formation. Overlies at least 60 % of halite extent and grades into, a 13 km^2 halite deposit in the small nonmarine Weldon-Gautreau Basin. Not exploited, ≈ 25 mt. (St. Peter 2006; Webb 1977)
Salars inland of Antofagasta (>100 salars), Northern Chile (<10 km^2)	Quaternary	1,400	BWk	Mirabilite/thenardite in small playas of Atacama and Central Valley. Bedded salar salts, occasional extraction via trenching, association with pedogenic nitrate (1,200 mt). (Garrett 2001)
Chaganor Salt Lake, China (Inner Mongolia) (21 km^2)	Quaternary	968	BSk	Brine processing. Nine porous brine-filled beds of salts with 11.3 mt of sodium carbonate, and 4.5 mt of sodium sulphate. Beds of natron, mirabilite, halite, burkeite and trona interbedded with black mud containing illite, some gaylussite, dolomite and calcite. (Zheng 1997)
Beida Lake (Wadi Natrun), Egypt (1.2 km^2)	Quaternary	−23	BWh	Massive 1-m-thick thenardite below 0.5 m halite bed. Lowest lake in Wadi Natrun chain, which are spring-fed depressions sourced in Nile. No brine-based salt-cake production, historically mined (1.1 mt). (Atia et al. 1970; Nakla and Saleh 1985; Shortland 2004)
Lake Qarun, Egypt (226 km^2)	Quaternary	5	BWh	Thenardite via brine processing in El Faiyum depression, possibly not implementable as lake brine is very dilute (4 mt). (Rasmy and Estefan 1983)
N. Aral Sea, Kazak. and Uzbek. (400 km^2)	Quaternary	40	BWk	Mirabilite/thenardite in shallow bed up to 60–70 cm thick beneath 1.5–2 m gypsiferous silt in Lesser Northern Sea, processing required. Seasonal mirabilite precipitation (≈200 mt). (Crétaux et al. 2009; Zavialov et al. 2009)
Tien Shan region, Kyrgyzstan	Tertiary Late?	1,500–2,200	–	Halite with glauberite (after thenardite as it sits atop glauberite). Lenses up to 5 m thick that aggregate to a several hundred metre thick saline section hosted in more than 2,000 m of Miocene sediment. Found in various intermontane sub-basins in Kochkorka, Kegen Dzhamgol, Frunze and Naryn regions (≈4,000 mt). (Garrett 2001; Wünnemann et al. 2007)
Bacadehuachi Valley, Sonora (includes Oro Blanco Pit), Mexico	OligoMiocene	700	–	Thenardite, lesser mirabilite, hosted in fine-grained, vitreous lacustrine tuff beds, beneath dissected alluvial fan conglomerate. Lenticular beds 20 m thick, outcrops in Baucarit Group, ore zone that is 4 km wide, area 13 km^2, in block-faulted basin in Occidental Sierra Madre Mountains (100 mt). (Austin and Humphrey 2006)
Laguna del Rey, Mexico (40 km^2)	Quaternary	1,000	BWh	Targeted horizon has 50 % glauberite and 20 % astrakanite (bloedite), lesser halite, minor mirabilite. Richest bloedite is 8 m below top of salt bed Shallow lake beds ≈10 km long, 4 km wide and 35 m thick in centre. Recovery via brine pumping and processing (350 mt). (Sanchez-Mejorada 1986)
Otjiwalunda playa, Namibia (95 km^2)	Quaternary	900	BSh	Thenardite (dominant) and significant trona (lesser burkeite). 80 mt of salt-cake and 40 mt of trona. Surface salts constitute a surface and nearsurface old massive playa bed, probably strip mineable with simple flotation separation. Most of the potential ore has 2–3 % insolubles. Lies 80 km to the west of Etosha Pan. (Garret 2001)
Laguna Salinas, Peru (4.4 km^2)	Quaternary	4,200	ET	Mirabilite/thenardite (3 mt) within surface crusts on playa floor, along with halite and ulexite. Is partially flooded in winter, then dries as surface crusts form. High altitude intermontane depression in Southern Peru, potential but not developed, primary target would be borates. (Garrett 2001; Muessig 1958)
Kuchuk Lake (Ozero Kuchukskoye), Russia (178 km^2)	Quaternary	92	Dfb	Brine processing; there are also two" glassy mirabilite beds in the lake partially converted to thenardite. Upper bed is 3 m thick. Mirabilite crystallizes in winter and on cool summer evenings (converts to thenardite). Problems due to fluctuating lake levels (540 mt). (Lebedeva et al. 2008)

(continued)

Table 12.6 (continued)

Location (area)	Age	Elev. (m)	Köppen	Mineralogy/setting/comments/key references
Madrid, Ebro and Calatayud basins, Spain	Miocene, Lower	500		Thenardite, glauberite. e.g. El Castillar Mine via pillar and room mine on 5–8 m thick (Lower Saline unit) thenardite bed, processed in evaporation plant (Total 2,500 mt of $NaSO_4$; economic 272 mt). (Ordonez and Garcia 1988; Salvany et al. 2007)
Cayirhan mine (aka Kimir or Beypazari deposit), Turkey	Miocene Upper	700		Thenardite, glauberite (possibly after mirabilite). Hosted in Kirmir Fm. (up to 250 m thick) intercalated with gypsum and claystones, sits atop trona in Hirka Fm. and atop lignite deposit. (65 mt) (Orti et al. 2002; Gungdogan and Helvaci 2001)
Acigol, Turkey (Extent: Spring 100 km^2, Summer 35 km^2)	Quaternary	836	Csa	Mirabilite/thenardite via solar evaporators. Intermontane, ephemeral saline pan beds, brine ponding and processing (12.5 mt; possible 82 mt resource). Production also in nearby Lakes Tersakan (56 km^2) and Bolluk (20 km^2) within the Tuzgolu depression (10 mt). (Mutlu et al. 1999)
Kara Bogaz Gol, Turkmenistan (18,000 km^2)	Quaternary	−29	BSk	Glauberite/astrakanite via groundwater flushing (mirabilite precursor). Speculated resource of 2 billion tons of salt-cake in the Gulf (10 mt under production via brine processing). Saline lake floor beds are widespread, especially along northern margin of the gulf, which is a post-collision lacustrine foreland basin. (Kosarev et al. 2009; Kurilenko et al. 1988)
Bertram, CA, USA	Neogene	−27	–	Discontinuous thenardite/astrakanite beds, sporadically mined. Ore hosted in highly deformed gypsiferous lake beds, occasional extraction (2 mt). (Garrett 2001)
Owens Lake, USA (278 km^2)	Quaternary	1,081	BSk	Brine processing (10 mt). Dry playa in block-faulted Basin and Range valley (anthropogenic increased salinity). Natron, mirabilite and borax are all winter precipitates in lake. Trona is dominant salt in salt bed, which is some 3,500 years old, about same age as upper salt bed in Searles Lake. Was a perennial saline lake until 1917 and inflow diverted in LA aqueduct, was dry by 1922. (Alderman 1985)
Searles Lake, USA (132 km^2)	Quaternary	493	BWk	Brine extraction from two buried saline playa salt beds (halite, trona, hanksite, borax, thenardite). Both beds less than 35 ka. Brine pumping and processing (carbonation), mirabilite formerly produced by winter spraying, concentrated brine now largely depleted (434 mt). (Smith 1979)
Great Salt Lake, USA (4,998 km^2)	Quaternary	1,270	Csa	Mirabilite, brine processing (408 mt). Buried fault-bound Pleistocene mirabilite bed deposited when brine level fell rapidly at end of Provo Level time. $NaSO_4$ is also a byproduct of brine processing in Northern Arm of Lake). (Garrett 2001; Colman et al. 2002)

Reserves in million metric tons (mt) of $NaSO_4$ after Garrett 2001 (for additional overviews see Austin and Humphrey 2006; Butts and Bush 2007)

world's largest and purest exploited brine sources of Na_2SO_4 salts (as documented in the literature) occur in two saline, but climatically contrasting, Quaternary playas/lakes in arid deserts, namely; cryogenic salt in Kara Bogaz Gol in Turkmenistan (BWk) and hot desert evaporites in Laguna del Rey in Mexico (BWh; Fig. 12.16). In both, the prime target beds are dominated by glauberite/halite with lesser astrakanite (bloedite). Searles Lake in California (BWk) constitutes a third Quaternary saline lacustrine system where $NaSO_4$ is recovered via brine extraction and solar processing from a Late Pleistocene trona/halite bed that contains significant thenardite, but soda-ash, not salt-cake is the primary product. Today, all three of these deposits are in an extraction phase where brine pumping and processing rather than mining of the solid salt drives the economics. Then there are the ancient (Tertiary-age) lacustrine deposits of Spain and Turkey where glauberite and thenardite are the main ore minerals and the modern pedogenic deposits in the Atacama Desert of Chile.

Although commercial production figures and reserves are not released by the Chinese Government, it is likely that in 2012 China was the leading exporter and producer of natural and synthetic sodium sulphate in the world. Jiangsu Province is the major area for sodium sulphate production. According to the USGS it is anticipated that this area will produce 4.8 million tons of sodium sulphate annually by the end of 2014.

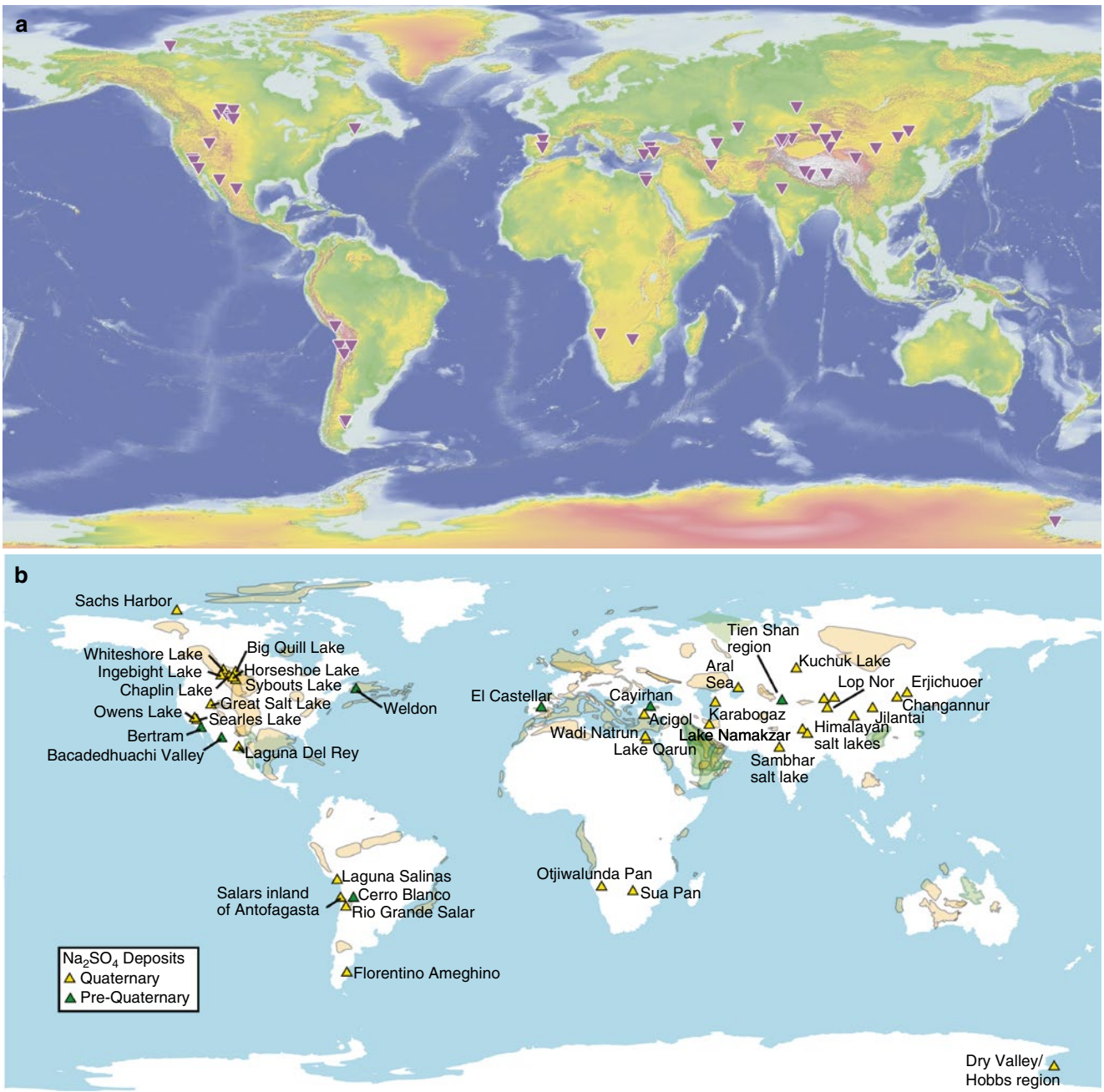

Fig. 12.15 Na_2SO_4 deposits. (**a**) Deposits plotted on a world topographic/tectonic base (Table 12.6). (**b**) Deposits plotted on a marine evaporite basin base, where brown shading indicates halite-dominant and green indicates megasulphate basin (After Warren 2010). Plot shows that borate deposits are better developed in volcanic-associated, active orogenic collision belts and zones of fractured continental crust. They do not occur atop or within large marine-fed mega-evaporite basins

As of 2008, it was estimated China represented about three-fourths of world production capacity of saltcake and more than 70 % of world production (Kostick 2012). Although data on mine production for natural sodium sulphate are not available, total world production of natural sodium sulphate is estimated to be about 6 million tons (Fig. 12.16). Today in the United States, more than one half of the total domestic sodium sulphate output is a by-product of various manufacturing processes or products including ascorbic acid, battery reclamation, cellulose, rayon, and silica pigments (Austin and Humphrey 2006). In addition, there is sizable production of sodium sulphate from other chemicals (primarily salt and sulphuric acid). Total world production of byproduct sodium sulphate is estimated to be between 1.5 and 2.0 million tons. World sodium sulphate production from natural sources probably peaked around 1970

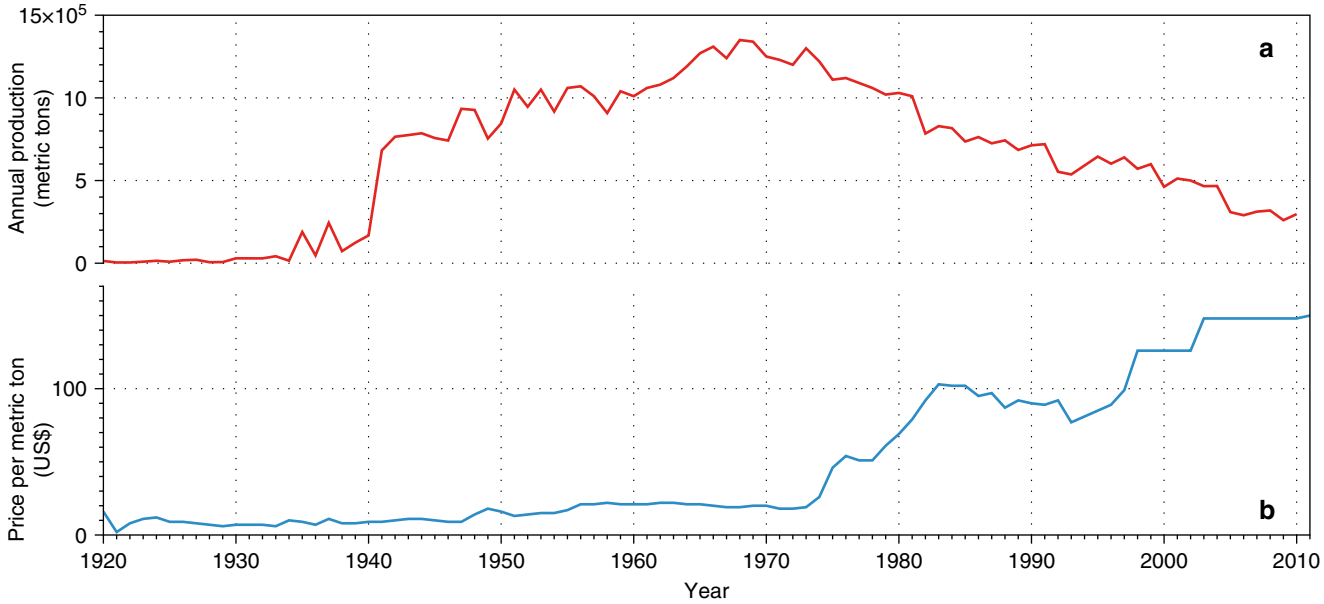

Fig. 12.16 World Production of $NaSO_4$. (**a**) Annual production in metric tons. (**b**) Price per metric ton in US dollars (**a**, **b** are replotted from USGS on-line data tables, downloaded from http://minerals.usgs.gov/minerals/index.html, last accessed May 5, 2014)

Table 12.7 World reserves of natural Na_2SO_4

Country	Reserves (1,000 metric tons)
United States	860,000
Canada	84,000
China	Not available
Mexico	170,000
Spain	180,000
Turkey	100,000
Other countries	1,900,000
World (rounded)	3,300,000

After Kostick 2012

(Fig. 12.16a) and although the absolute price shows a consistent rise since then, in terms of inflation corrected value per ton, the price has risen little since 1970. Reserves of natural Na_2SO_4, other than in China, are given in Table 12.7.

Canadian Brine Extraction

The number of saline lakes in the moraine plain of central Canada is staggering. Estimates vary from about one million to greater than ten million, with densities in some areas being as high as 120 lakes/km^2, creating a concentration and diversity of salt lake environments unequalled in the world (Last and Ginn 2005). Virtually all brine types are represented in these lakes, with Na-Mg-SO_4 chemistries dominant. Over 80 species of endogenic precipitates and authigenic minerals have been identified as lake precipitates, the most common being calcium/calcium-magnesium carbonates (calcite/dolomite) and sodium/sodium-magnesium sulphates (mirabilite/gypsum) (Fig. 12.17).

All the present and former Canadian production of sodium sulphate in southern Saskatchewan and southeastern Alberta comes from deposits that are the result of present day or earlier Holocene late autumn- early winter cooling/freezing of playa brines. Cryogenic precipitates in the ore salts are mostly mirabilitic, which may convert to thenardite with warming. Saltcake ore formation in Canada is a cryogenic, not solar evaporative, process. Most of the mirabilite-accumulating lakes are small (<100 km^2), shallow (brines <3–20 m deep), with permanent salt beds found only in the lowest portions of some of the hydrologically-closed meromictic depressions (Last 1989a, 1994). Around a hundred lakes have salt reserves of more than 100 kt of Na_2SO_4 and their combined recoverable reserves prior to ongoing exploitation were around 80–100 Mt (Fig. 12.18; Garrett 2002; Last and Ginn 2005).

Large tracts of hummocky and icethrust moraine dominate the saline lakes region where cryogenic salts precipitate in landscape sumps. In combination with the limited efficacy of fluvial processes under a subhumid to semiarid temperate climate, this geomorphology results in more than 45 % of the region being endorheically drained into perennial saline lakes in depressions in the glacial drift. Some of these depressions are elongate and probably occupy pre-ice age river valleys (Fig. 12.17; Little Manitou Lake), others were created as kettles by the melting of huge relict blocks of ice left in the moraine after the main front of the ice sheet had retreated (Fig. 12.19a, b; Freefight Lake, Ingebright Lake). Groundwater seeping from the surrounding moraine, through the underlying

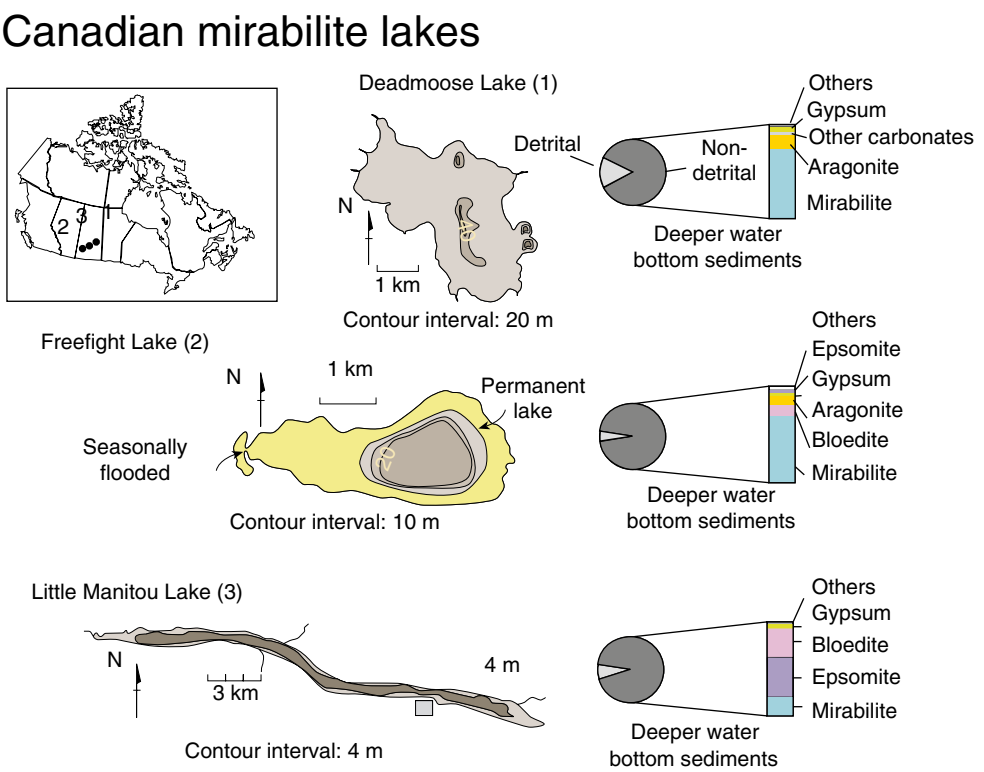

Fig. 12.17 Sodium sulphate lakes, Canada. Selected mirabilite lakes in the plains of Canada, showing bathymetry and bottom sediment composition in deeper subaqueous parts of lake floor (After Last 1994)

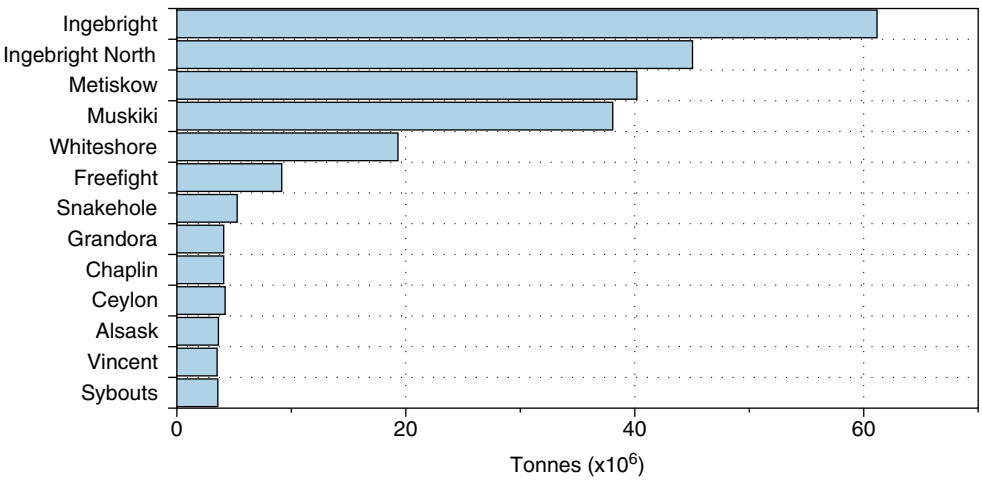

Fig. 12.18 Reserves of anhydrous sodium sulphate in the twelve largest lacustrine deposits in the northern Great Plains of western Canada. Ingebright and North Ingebright deposits have been separated but geologically are one contiguous deposit (After Last and Ginn 2005)

valley sands and across underlying bedrock, supplies much of the dissolved content, but there is still no consensus as to the ultimate origin of the sodium and sulphate (Last 1989a). The geographic coincidence of many of the more productive lakes to the subsurface solution edge of the Devonian Prairie Evaporite lead Grossman (1968) to suggest dissolution-derived salt-rich resurging groundwaters were the ultimate source. Others have argued that weathering and leaching of pyritiferous glacial flour is the likely source for the ions, independent of the underlying Devonian salts (Wallick 1981).

Before the mirabilite crusts redissolve with the passage in to the warmer lake waters of spring, these coldwater saltcake crystals can be dredged each year from suitably saline lakes. Thicker-bedded crystalline thenardite deposits (transformed from primary mirabilite) have accumulated over hundreds to thousands of years on the bottom of some of these lake depressions. Each year, they retain a saturated brine layer from few centimeters to metres deep, but the bottom waters in the shallower stratified are typically subject to seasonal warming sufficient to convert some mirabilite to thenardite/bloedite. Waters in the upper water mass of all the deeper perennial lakes are replenished annually by spring melt. Cryogenic cycling, whereby some of the mirabilite redissolves due to heating, can produce lake-bottom brines with

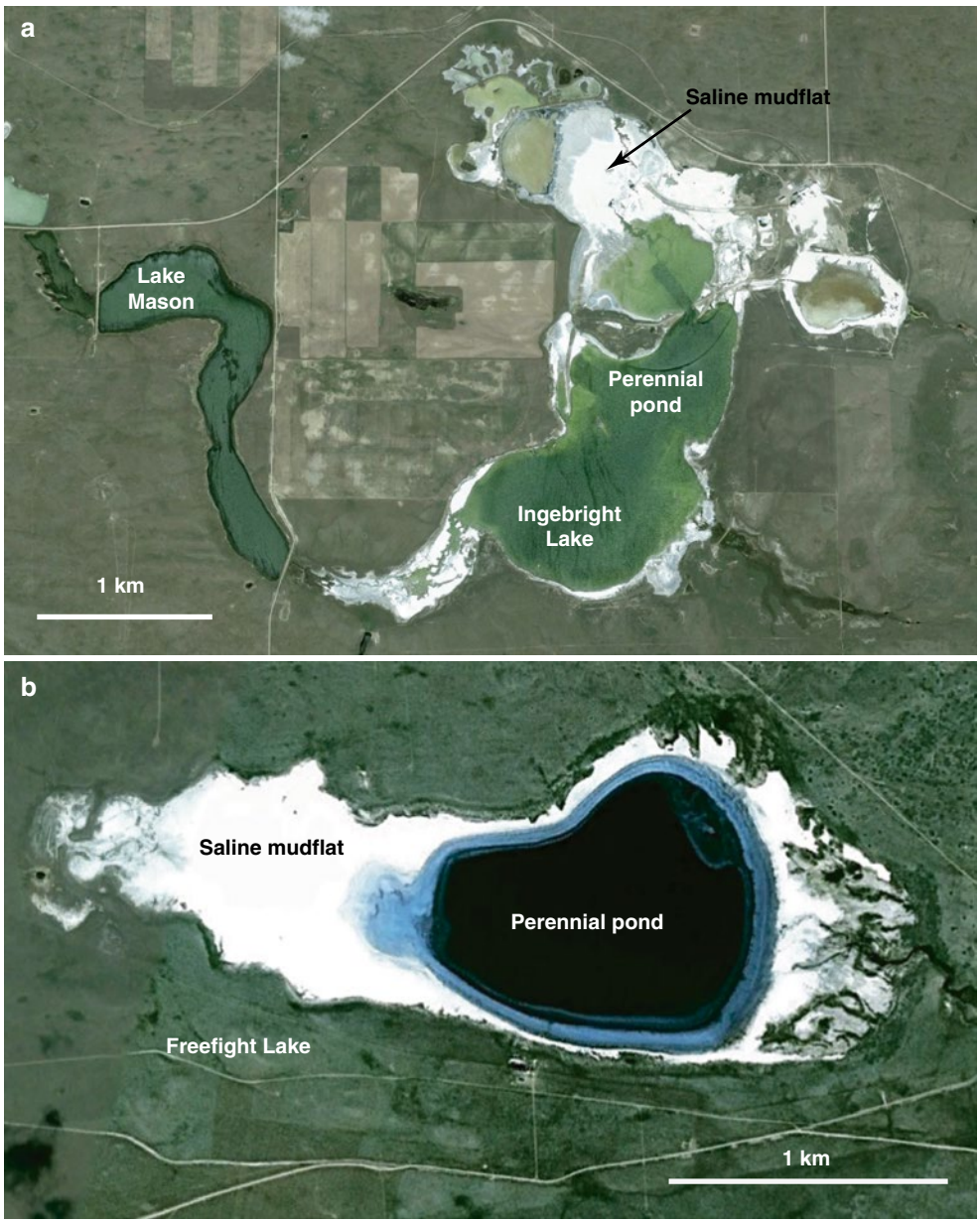

Fig. 12.19 Canadian cryogenic Lakes. (**a**) Ingebright Lake, (**b**) Freefight Lake, Saskatchewan, Canada, showing perennial lake areas and surrounding saline pan – mudflat. Two of numerous such $NaSO_4$ lakes in the Canadian Great Plain (See Fig. 12.17 for geological detail)

salinities that may exceed 400‰. This maintains a perennial curtain or plume of saturated pore brines that preserve thick saltcake beds in the lower parts of the lake depression (Fig. 12.17).

The saline lakes region of Saskatchewan encompasses some of the largest (Quill, Old Wives) and deepest (Freefight), perennial hypersaline lakes in North America, capable of accumulating bedded salts more saline than evaporitic carbonate. Ingebright Lake in southern Saskatchewan, although it is small in area (<2 km^2) has, at 25–40 m-thick, the thickest Holocene evaporite bed in North America and it is dominated by primary precipitates of thenardite, Mg-carbonates and gypsum. Ingebright Lake had the largest reserves of the various $NaSO_4$ salt lakes recently in production, but in 2005 extraction facilities were mothballed. Bed thickness once averaged 6.7 m of permanent salt, and reserves once exceeded 60 million tonnes beneath a lake area of 280 ha (Fig. 12.17; Garrett 2001). The lake and its drainage area is not large and no modern streams flow into it although it does define the termination of a glacial paleodrainage channel (Fig. 12.19a). Today, it is fed by numerous saline springs and seeps about the lake edge, including five large springs that flow year round, so supplying a dilute high-sulphate medium carbonate/bicarbonate water to the upper water mass (TDS of 2,800 ppm; Cole 1926). Subaqueous springs also cut up through the mirabilite bed that covers the lake floor. Springs tend to be cold (7 °C) in the northern part of the lake, and warmer (15–18 °C) and more saline in the south. Each winter

these more saline southern springs precipitate large ephemeral mirabilite mounds that are up to 3 m tall and 6 m across.

The fresher nature of the water supply to the northern springs means they are capable of dissolving all the mirabilite on their rise to the lake floor and so are defined by mud pipes or chimneys cutting up through the mirabilite ore bed (Last 1993a). The metres-thick mirabilite bed, which covers the perennially subaqueous lake floor, is compact and friable. In the northern part of the lake it contains numerous clay layers that are mostly cm-scale, but as thick a 1 m at the 7.6–9.1 m level in the lake (Cole 1926). In the south there is much less mud in the salt and it is more indurated. In the thicker ore bed of the southern part of the lake there are two zones where the mirabilite bed is thicker than 30 m and one borehole intersected more than 42 m of relatively pure sodium sulphate.

Two recognizable brine styles drive $NaSO_4$ precipitation and accumulation in the various Canadian lakes; intermittent saturation and permanent saturation (Last 1994). Intermittent brines form seasonally on the bottom and along the shores of the lakes. There, cryogenic mirabilite crystallizes and largely redissolves with each seasonal cycle of cooling and warming. Mirabilite precipitation-dissolution cycles in such lakes can occur in a matter of hours, but as winter sets in, redissolution wanes, causing the crusts to become thicker and more compact. Spring meltwaters in a few lakes with such intermittent brine hydrologies carry in sufficient volumes of fine detritus to mantle salts in the shallower parts of the lakes and so preserve some of the lake precipitates year round. Such beds range in thickness from less than one to several metres, they are relatively impure, and made up of thenardite interstratified with thin layers of mud, clay, and organics.

Thicker purer beds of $NaSO_4$ tend to accumulate and be preserved beneath the permanent meromictic waters of the deeper lakes. Hence, Deadmoose, Little Manitou, and Freefight Lakes are lacustrine depressions in the moraine plain where soluble and sparingly soluble $NaSO_4$ salts accumulate beneath relatively deep permanent brine bodies (up to 20 m deep; Fig. 12.17). Both Deadmoose and Freefight Lakes are hypersaline and meromictic systems, with strongly anoxic hypersaline bottom waters. Little Manitou is also hypersaline, but the seasonal density and chemical stratification in the water column usually breaks down in early to midsummer, so allowing mixing of the upper and lower water masses down to the sediment surface.

There are four distinct styles of salt occurrence in these perennial mirabilite lakes: (a) crusts and hardgrounds of the lake edge, (b) massive and bedded salts of the lake centre, (c) spring or seep deposits, (d) subsurface and groundwater related interstitial and replacive cements (Last 1989a, b). Relatively thick sections of subaqueous evaporites (mostly mriabilite/thenardite) have accumulated on the bottoms of some of these deep perennial lakes making them one of our better examples of textures in modern "deepwater" evaporites

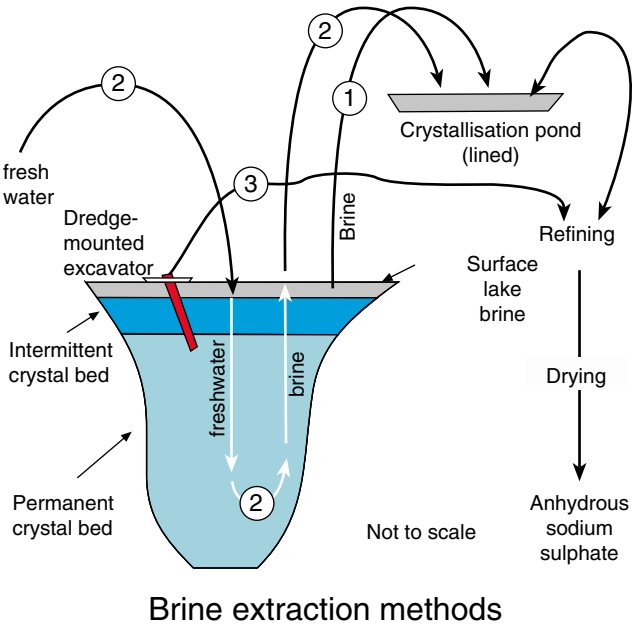

Fig. 12.20 Extraction methods in various Saskatchewan sodium sulphate deposits (After Garrett 2001); (*1*) Evaporative concentration of lake brine in crystallization pond, followed by precipitation of crystals of Glauber's salt (mirabilite) as the brine cools in autumn; (*2*) Solution mining of thick crystal beds. The return brine is treated as in *1*; and (*3*) Dredging of lake bottom crystal beds

(Last 1994). These deepwater salts are generally coarsely crystalline, massive to thickly bedded, and interfinger laterally with laminated organic-rich clays and poorly sorted carbonate-clastic debris washed in from nearshore areas. As in the Dead Sea, it seems that the deep water signature to a salt body accumulating in deeper hypersaline waters is not a laminate, but an aggregated bed of coarse crystals growing at the base of a holomictic brine column as crystal meshworks showing little or no preferred growth direction.

Today, the mirabilite extraction industry in Canada is in decline after peaking in the 1970s, most remaining commercial lakes are small, intermittently exploited and located in southern Saskatchewan. Most of the richer bedded Quaternary salt-cake has been mined. In the early days of the 1950s and 60s, operators merely mined mirabilite by scraping or blasting, later some of the mirabilite was solution mined (Garrett 2001, 2002). Traditional brine extraction involves pumping of surface brines into storage reservoirs during the summer and then allowing the lower autumn and winter temperatures to precipitate mirabilite (Fig. 12.20). The mirabilite was then trucked to the processing plant, where water of crystallization is removed and product then dried to salt cake in a rotary kiln. The largest problem for the Canadian operators was maintaining a high purity economic product that was comparable to the cheaper but higher purity product from dry playa brine leachate operations at Laguna Del Rey and the low-cost brine production and synthetic recovery plants of China.

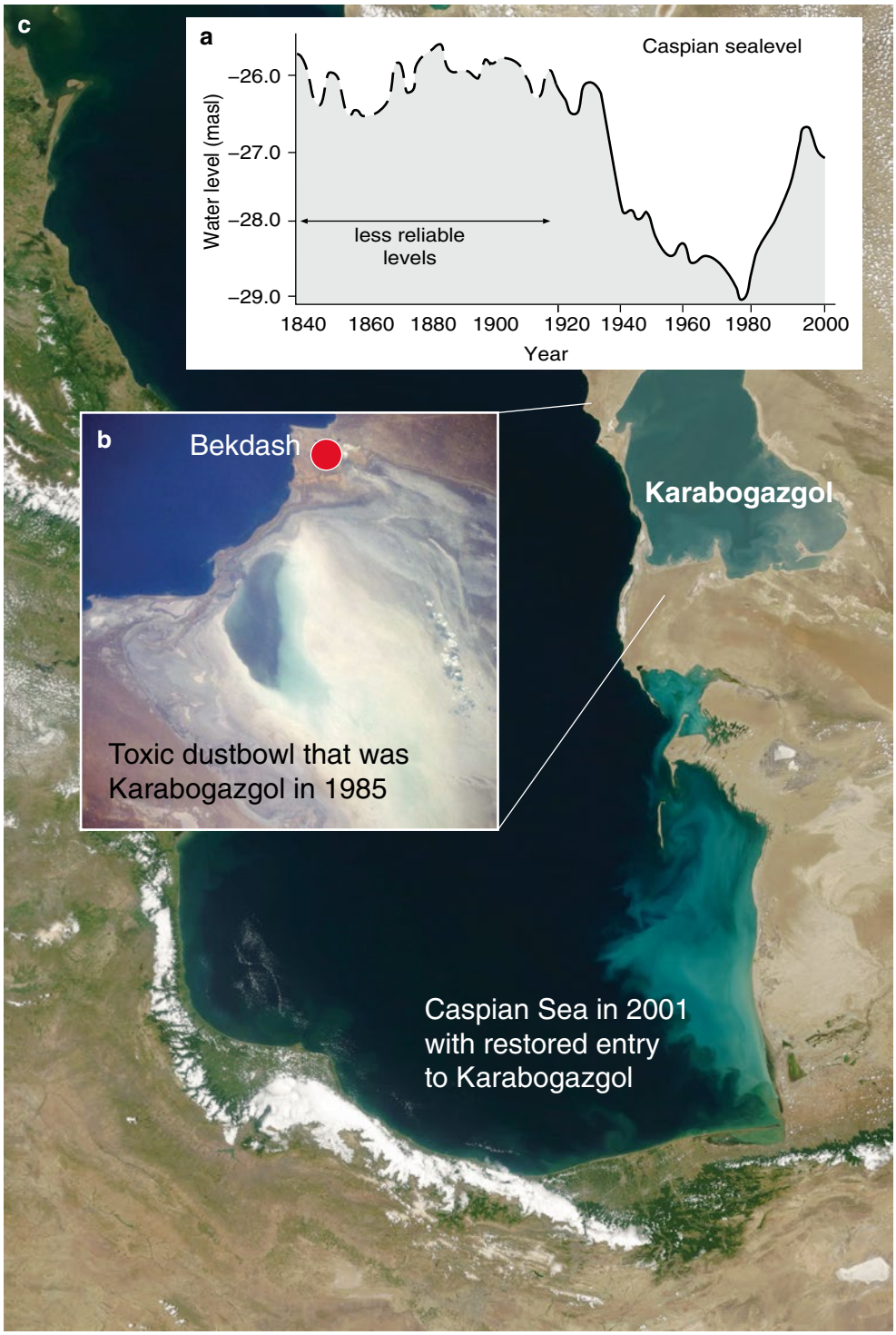

Fig. 12.21 Karabogazgol and the Caspian Sea. (*A*) Variation in the level of the Caspian Sea with the low in the period 1960–1990 driving the hydrographic isolation of Karabogazgol. (*B*) Desiccated Karabogazgol in 1985. (*C*) Water filled Karabogazgol in 2001, soon after hydrographic connection to Caspian Sea was restored

Karabogazgol Brines, Turkmenistan

Sodium sulphate occurs as mirabilite-glauberite beds in the shallow subsurface of the Karabogazgol. Karabogazgol, along with the adjacent Caspian Sea, is a lacustrine foreland remnant of the former Tethyan seaway. Kara Bogaz lies in the cool arid steppes of Turkmenistan at the edge of the Caspian Sea with a brine surface some 29 m below sea level (Fig. 12.21a). The speculated total resource beneath the lake/playa is some 2–4 billion tonnes of salt-cake (Garrett 2001). The waters of Karabogazgol are derived from the Caspian Sea via a narrow inlet that gives the Gulf its name. In the past 100 years water levels in Karabogazgol have been a metre or so less than the adjacent Caspian surface, which has fluctuated between 25 and 29 m below sea level (Fig. 12.21a).

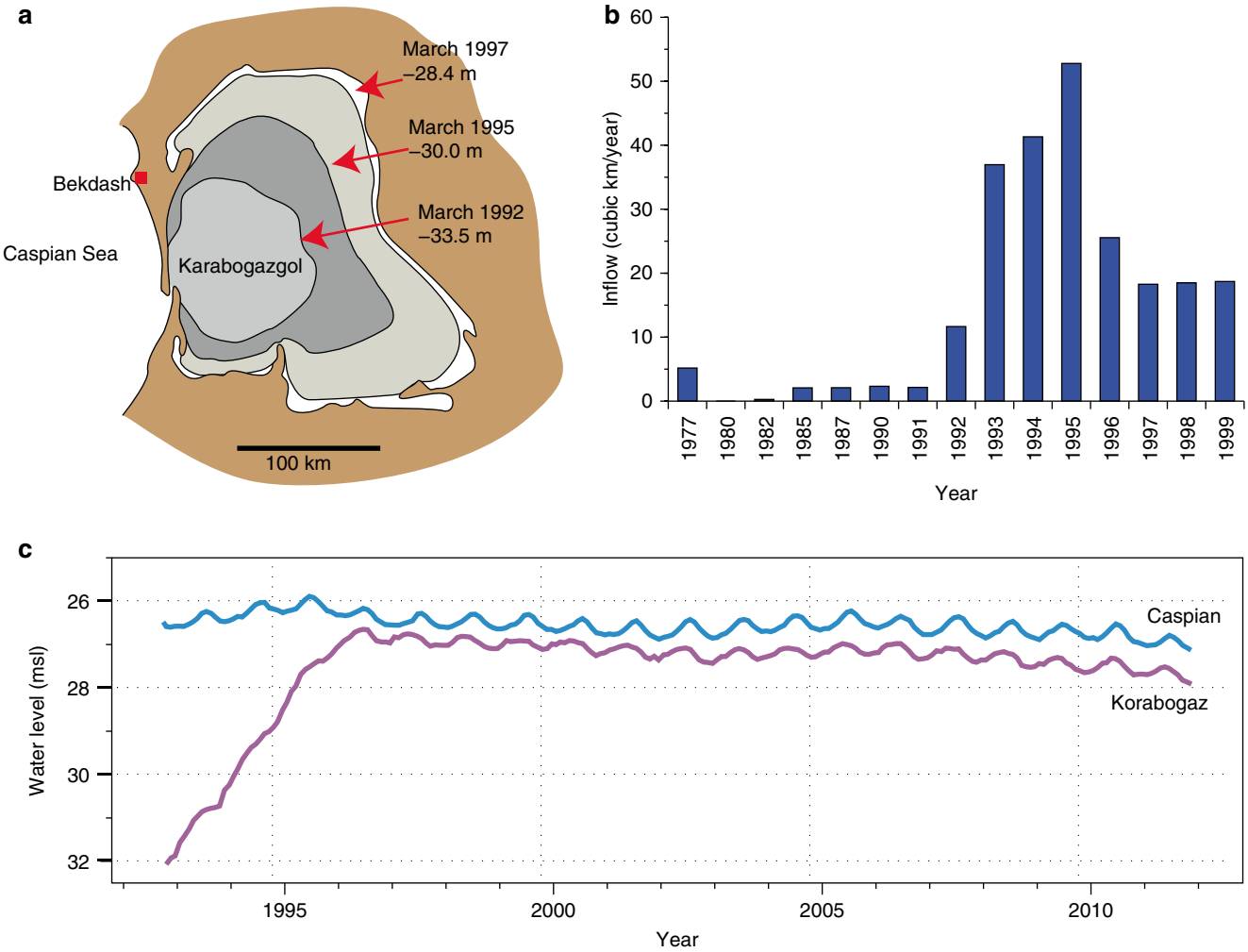

Fig. 12.22 Karabogazgol recovery. (**a**) Successive annual extents of water levels in the Gulf 1992–1997. (**b**) Annual inflow volumes through Karabogaz inlet 1977–1999. Note there was no inflow in 1980 (After Leroy et al. 2006). (**c**) Water levels in the Caspian and Korabogaz Bay in the period 1999–2011 (Replotted from data downloaded from http://www.legos.obs-mip.fr/soa/hydrologie/) (See Crétaux et al. 2011)

For much of the Holocene, Karabogazgol (Bay) has been connected via a narrow 500 m-wide inlet to the Caspian Sea, which flows water from the Caspian to Karabogazgol at a rate of 25–44 m/min. Natural inflow from the Caspian replaces water lost by evaporation from Karabogazgol (Bay) and when this happens the drawndown water level in the gulf is consistently 0.5–3 m below that of the Caspian Sea. This makes it one of the few modern examples of a drawdown basin with a highly restricted hydrographic connection between one isolated seaway and another (A_o:A_i = 2 × 10^7; Fig. 2.80). It is sufficiently restricted to allow gypsarenite to accumulate today on the brine-covered lake bottom. Water level in the Caspian Sea levels have varied considerably over the 10,000 years and so Karabogazgol repeatedly lost its hydrographic connection with the Caspian whenever water levels fell below the entrance sill. In earlier times of cooler temperatures that allowed winter freezing of a perennial water body, beds some 3–8 m-thick containing cryogenic sodium sulphate formed and are today composed of varying amounts of calcite-hydromagnesite-gypsum-halite-epsomite-mirabilite-glauberite (Fig. 12.23).

In Turkmen, Karabogazgol means "lake of the black throat," so named because the gulf is continually gulping down the waters of the Caspian. There is an interesting anthropogenic aspect to the natural loss of water from the Caspian to the Gulf and the periodic salting of Karabogazgol. Early last century (prior to 1929) the Caspian sealevel was around −26 masl and Karabogazgol was almost entirely water-filled (as it is today; Figs. 12.21a, b and 12.22a). The water-covered surface area was around 18,000 km^2 and its maximum water depth was around 9 m. The annual volume of water flowing through the inlet was high, somewhere between 18 and 26 km^3 and the difference in level between waters of the Caspian and Karabogazgol was around 0.45 m. From 1929 until 1940 there was a 1.8 fall in the level of the Caspian Sea and by 1948 the Caspian level was −27.87 m. The volume of inflow to the Gulf fell to 12–14 km^3/year by the late 1940s

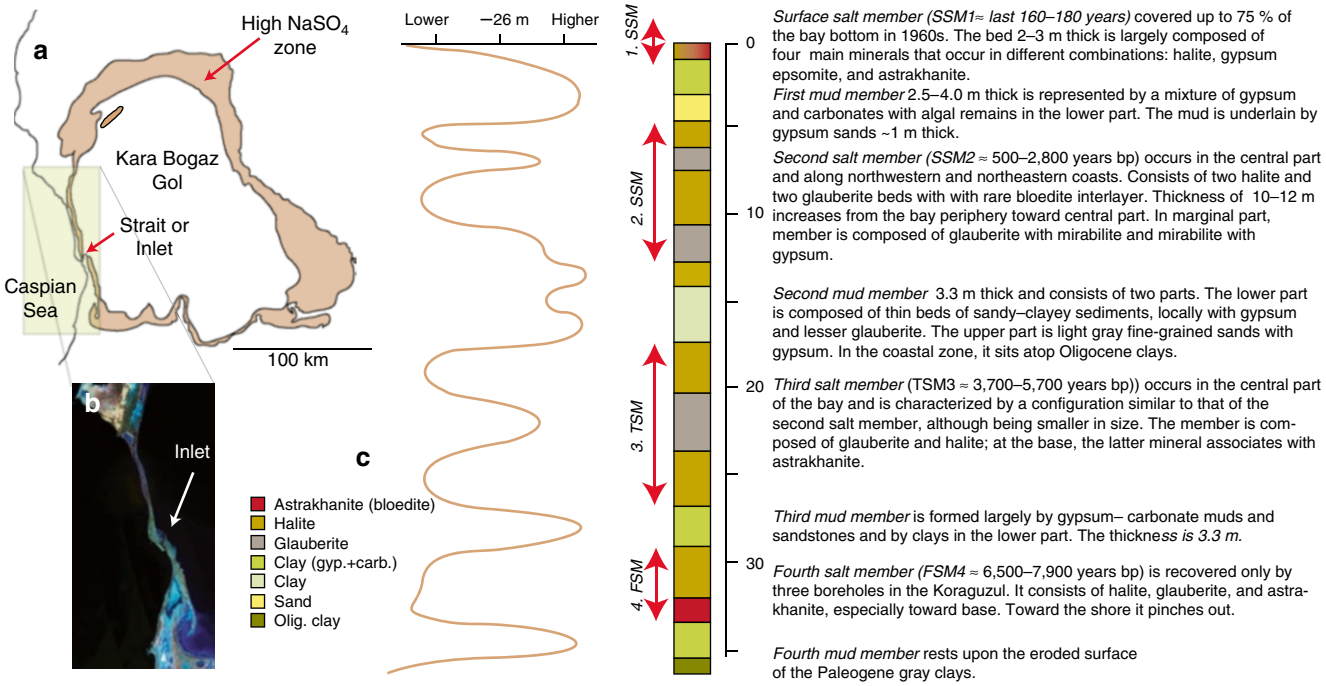

Fig. 12.23 Kara Bogaz Gol, Turkmenistan. (*A*) Plan view showing distribution of second salt member zones with higher $NaSO_4$, which tend to occur about bay margin (After Strakhov 1970). (*B*) The Landsat image insert shows detail of the narrow inlet allowing surface entry of Caspian Seawater into bay. (*C*) Typical lake stratigraphy showing thickness, relative water levels and Holocene ages of the four salt members that define the saline successions in the bay (In part after Karpychev 2007)

and to 8 km^3/year in 1956. Differences in water level between Caspian and the Gulf increased to 3.17 m in 1947 and 3.80 m in 1955. By 1957–1959 the water-covered area in Karabogazgol had fallen to around 13,000 km^2. By 1977 water level in the Caspian was −29.02 masl, it had fallen fell by more than 3 m since 1929 (Fig. 12.21a). The 1977 water surface in Karabogazgol was 4.5 m lower than the Caspian and the strandline of southern Karabogazgol had retreated by 50–60 km in 50 years. This ongoing drop in water level in Karabogazgol since 1929 meant fisheries were threatened on the Caspian side and numerous salt works had developed in the increasingly exposed and accessible brine flats.

The ongoing fall of the Caspian Sea level from 1929 and well into the 1970s, was thought by the Russian Government to be related to the continuous loss of water from the Caspian to Karabogazgol. After all, the climate in the Karabogazgol was arid, the annual evaporation rate was 1,000–1,500 mm and annual rainfall around 70 mm. Russian government scientists argued that damming the entryway would stop the Caspian spilling into the Gulf and so arrest the fall in the Caspian water level and the threat to fisheries. This notion of interfering in a natural saline system was opposed by a number of Turkmeni scientists who argued that the rise and fall of the Caspian and the variable filling in Karabogazgol were natural processes and had been noted in the texts of ancient Islamic scholars living in the region.

Ignoring the argument that rise and fall of brine level in isolated saline waters bodies, such as the Caspian, was the normal situation, a decision was made in 1977 by the central administration in Moscow that the entryway would be damned. Central administration scientists had concluded that sufficient water would remain in Karabogazgol after damming to allow the salt industry to continue its operations. The dam was not actually constructed for another 3 years. Ironically, the natural fall in the level of the Caspian had reversed in 1977 and had began to rise once more, with a corresponding rise in waters levels in the Gulf. From 1977 until 1995 the Caspian level rose by the same 3 m it had dropped since the 30s. However a decision had been made back in 1977 to dam the entryway, so in 1980, even though the Caspian water level was rising once more, Russian engineers dammed the entry strait between the Caspian and Karabogazgol.

This complete loss of hydrographic connection to the Caspian did not have the desired effect, which was by then an irrelevancy, but egos and the authority of the Russian Empire was involved. Rather, the damming of the inflow resulted in rapid desiccation of Karabogazgol, so that by 1983 only a small brine-covered area remained in the lowest part of the gulf depression (Figs. 12.22a, b and 12.23). Much of the former brine lake floor had turned into a saline dust bowl, blowing high levels of sodium salts onto downwind irrigated pasture lands. By 1984 the villages surrounding Karabogazgol had turned into ghost towns. In 1984, in an attempt to restore the ecosystem, eleven large diameter pipes were laid across the dam so that Caspian water could be pumped back into Karabogaz at a

controlled rate. In 1992, after the fall of the Soviet Empire, this approach was abandoned and the dam was completely demolished by order of the president of the newly independent Turkmenistan. As it refilled from 1992 to 1995, the gulf water level rose by some 6 m and since then its water level has once again matched that of the Caspian Sea and it is once again fulfilling its role as a natural desalinator of the waters of the Caspian (Fig. 12.22; Leroy et al. 2006; Crétaux et al. 2011).

Today, with the entryway connection to the Caspian restored, the water chemistry of the main open water body in the centre of the gulf is an Na-Mg-Cl brine, with a density of 1.2 g/cm^3, and pH values that range between 7.2 and 9 (Giralt et al. 2003). Surface water temperatures range from 4 °C in December to 25 °C in July. These temperature fluctuations are seen in the precipitation of different mineral phases during the year. Calcite, aragonite and perhaps hydromagnesite usually precipitate from lake waters in spring, gypsum in summer (via solar evaporation), and rafts, blown shoreward, into stacked crusts of cryogenic mirabilite and halite accumulate on the shores and mudflats of the embayment edge throughout the winter. Gypsum (as lenticular sand-sized grains) is the only permanent sulphate phase seen in cores sampling surface sediments from beneath today's central embaymnt water body (Giralt et al. 2003).

Below this modern hydrology, $NaSO_4$ salts occur in 4 main beds (Salt members 1–4), dominated by glauberite/astrakanite, with alteration textures suggesting a mirabilite precursor (Fig. 12.23). Three separate glauberite layers are present, a fourth lowermost layer is dominated by bloedite: the upper layer is at a depth of 0–0.3 m and is up to 3 m thick; the middle layer is at a depth of 5–8 m; and the lower layer is at a depth of 14–18 m. Gypsiferous-carbonate muds separate the salt layers by 2–5 m.

Depending on the water salinity in Kara Bogaz, the following succession of various salts have precipitated in response to increasing salinity and temperature fluctuations: carbonates–gypsum–mirabilite–glauberite–halite (in the summertime) and mirabilite (in the winter) -epsomite–astrakanite. Today, although mirabilite precipitates each winter across the Gulf, much of it is redissolved with the passage into warmer weather and drying of much of the Gulf floor. Hence, across the central parts of the Gulf, mirabilite is not currently contributing large volumes of precipitates to the at-surface gypsum bed (Fig. 12.23).

Each of the four underlying $NaSO_4$ beds is a likely remnant from cooler climatic periods over the last 10,000 years (Karpychev 2007). Then large amounts of mirabilite formed each winter, much like today but, unlike today, the cooler more humid glacial climate meant the bay was not as subject to summer desiccation. Dense residual bottom brines were perennially ponded and so preserved a summer-halite sealing bed. This allowed the underlying mirabilite/epsomite winter precipitates to be preserved across the lake floor. During the following winter the process was repeated as mirabilite/epsomite/halite beds stacked one atop the other to create a future ore horizon. In time, the combination of groundwater and exposure, especially nearer the Gulf's strandzone, converted most of the mirabilite, along with epsomite, to astrakanite, and then both phases to glauberite in the upper three beds. This explains the association of the richer glauberite zones with the lake edges (Fig. 12.23a; Strakhov 1970). Water of crystallization is released by the mirabilite to thenardite conversion, then it slightly dilutes any strong residual brine, so facilitating a high sodium-sulphate mineral and brine composition across the bay (Kurilenko et al. 1988).

Even today, a portion of the air-brine winter mirabilite precipitates do not sink, but form crystal rafts that are blown by prevailing winds to stack into crusts fringing the lake shore. Early last century the resulting strandzone mirabilite/epsomite beds were harvested by the local peasantry. In contrast to the current complete loss of mirabilite from the lake floor each summer, cooler earlier Holocene conditions favoured retention of bottom-cumulates much like winter salting in saline lakes in Canada today (Fig. 12.23). Today's gypsum/glauberite/thenardite fringes form during the summer transformation of the mirabilite, epsomite and bloedite that accumulated as windblown fringes each previous winter about the edges Karabogazgol. That is, because the climate and bay hydrology has changed over the last few thousand years, the present is not a direct key to immediate past textures and extents.

During the anthropogenic dust-bowl stage of the lake in the 1960s to 1980s a glauberite/bloedite/mirabilite/gypsum windblown mineralogy formed as capillary efflorescences were exposed across the whole exposed floor of the gulf. At that time the Karabogazgol depression was converting to a saline perennial dust bowl. But since 1992, with a return to the high water levels of today, glauberite no longer accumulates on the floor of the lake, only gypsum. The only glauberite/thenardite forming today is that accumulating about the exposed margins of the gulf where each summer high-calcium groundwaters dissolve and transform earlier winter precipitates of astrakanite, epsomite and mirabilite into capillary precipitates of glauberite/thenardite.

Natural winter precipitates of sodium sulphate salts in this natural evaporation basin have been used commercially since at least the 1920s. Back then, the produced[2] commodity was

[2]In the first decades of the twentieth century the mining of Korabogazgol (Bay) raw materials for the Russian chemical industry was based on natural processes. Year-round the upper layers of water in the bay contained sodium chloride NaCl, magnesium chloride $MgCl_2$, and sodium sulfate Na_2SO_4. Every year, in late November, when the water temperatures dropped to 5.5–6 °C, the water became saturated with sodium sulfate, and mirabilite ($Na_2SO_4{\cdot}10H_2O$) precipitated as colorless crystals on the bay bottom that were then transported by wind and wave action to the shorezone, especially during winter storms. In mid-March when the bay waters were heated to over 6 °C, the mirabilite on the bay floor began to redissolve. By July–August the entire precipitated mirabilite crop out in the bay had re-dissolved. The period from November through March was a period of "harvesting" mirabilite on the bay shores. In summer with its arid climate the remaining strandzone salt converted to thenardite Na_2SO_4 that was gathered at the end of each summer.

just whatever accumulated on the shore from winter wave action, especially on the southern shores of the Gulf during winter (Kosarev et al. 2009). The salt was scraped and harvested by hand and shipped to the Caspian using animals and barges. In the early 1930s, the port town of Karabogazgol was established on the Caspian side of the entryway, in order to trans-ship salt from the barges to the Caspian and its population grew to a peak of 7,000 in 1936. By the late 1930s, the gulf was too shallow for barge traffic and the port town of Karabogazgol was abandoned in 1941. The falling water levels in the gulf also meant that by the end of the 1930s manual collection of naturally formed salt in the southern part of the gulf had stopped as well. The industry had to shift north to its present centre located inland of the town of Bekdash, which is a town of about 10,000 people on the shores of the Caspian Sea.

Canals were built inland of Bekdash on the increasingly exposed mudflats that defined the strandzone of the Gulf. The canals were designed to feed gulf waters into large salt settling basins, which were filled with lake brines in the summer and left to cool in winter when mirabilite precipitated. Bekdash eventually became the centre of the salt-cake industry of Karabogazgol and in the 1960s and 70s supplied chemical feedstock to much of the Russian chemicals industry in the satellite states surrounding the Caspian Sea. By the end of the 1930s, the falling water level drove increased salinities and a shift toward higher volumes of sodium chloride precipitates from ponded gulf waters, an unwanted by-product in the sodium sulphate industry. Profitability fell, and the salt pan-based industry waned through the 1940s. In the 1950s, production technology shifted to extraction and processing of subsurface brines, Bekdash was reinvigorated as it had been connected to a major brine extraction site via a 24-km pipeline.

In 1963 construction began at Bekdash on a modern plant for increased year-round production of salines, independent of natural evaporation. This plant was completed in 1973. The brines for the processing plant were extracted from the buried glauberite/bloedite/epsomite beds beneath the margin of the gulf. These beds still constitute a huge potential resource containing more than 3 Gt of sodium sulphate. Currently, sodium sulphate brines are solution mined which in the 1980s used a single high capacity captive well and a mine planning approach that is a leftover from excesses of the former Soviet Union. Unlike the monitored gentle extraction of 113 l/s of intercrystalline sodium sulphate brine spread over more than 70 wells in Laguna del Rey brinefield (next section), a single well into the Karabogaz salt layers blasted out 126 l/s to a pipeline feeding the processing plant. Within the first 10 years of the brinefield operation it had largely drained all the high salinity brines from the immediate vicinity and created a short circuit for less saline brine entry into the well bore. Ongoing drawdown and associated coning meant brine strength supplied to the plant dropped to almost unusable levels. Once set up, coning from overpumping is difficult to reverse.

The highly competitive state of today's sodium sulphate industry probably means that, without new capital injection for a better planned and monitored set of brinefields and extraction wells, the Karabogaz salt industry will continue to shrink. By the end of the 1980s recommendations were being made to alleviate the problem; Kurilenko et al. (1988) proposed the following changes to the local brine industry; (1) locating and developing production wells based on optimum hydrogeology and stratigraphy, (2) lowering the brine output of every well from 500 to 250 m^3/h, and reinjecting end liquors from the plants to recharge and stabilise pay horizons.

Other substantial modern saline lakes with cryogenic saltcake potential are relatively common in the former USSR and extend from the Black Sea to western China (Fig. 12.15). Examples include Selenga Lake in the eastern Transbaikal, Lakes Azhbulat, Ebeity and Tengis in Kazakhstan, and the Batalpashinsk and Tambukan Lakes between the Black and Caspian Seas. The enormous salt cake potential of these deposits is illustrated in Lake Azhbulat where some 40 Mt of mirabilite is deposited each winter. On the Kulunda Steppe, western Siberia, lacustrine deposits consist of sodium chloride in the upper layers and mirabilite below. The largest sodium sulphate lake in the region, Lake Kuchuk, 320 km southwest of Novosibirsk, covers an area of some 150 km^2. It contains an estimated 600 Mt of sodium sulphate in brines and underlying strata and each winter between 380,000 and 640,000 tonnes of mirabilite drop out of solution.

Laguna Del Ray Brines, Mexico

Quimica del Rey, SA, a subsidiary of Industrias Peñoles, SA de CV, produces sodium sulphate from brines extracted from a playa of Laguna del Rey, located in the State of Coahuila in northern Mexico, some 150 km north of Torreon. The precipitation of the mother salt beds occurred in a hot arid desert setting and is not a cryogenic association. The brine processing plant on the lakeshore is the world's largest sodium sulphate brine facility outside of China (Fig. 12.24). Spent brine from the plant is used as raw material for the production of magnesium oxide. The playa is one the world's larger exploited bedded sodium sulphate deposits and Mexico's major sodium sulphate resource.

Today the lake is a dry playa some 10 km long and 4 km wide. It contains a captive brinefield that solution mines

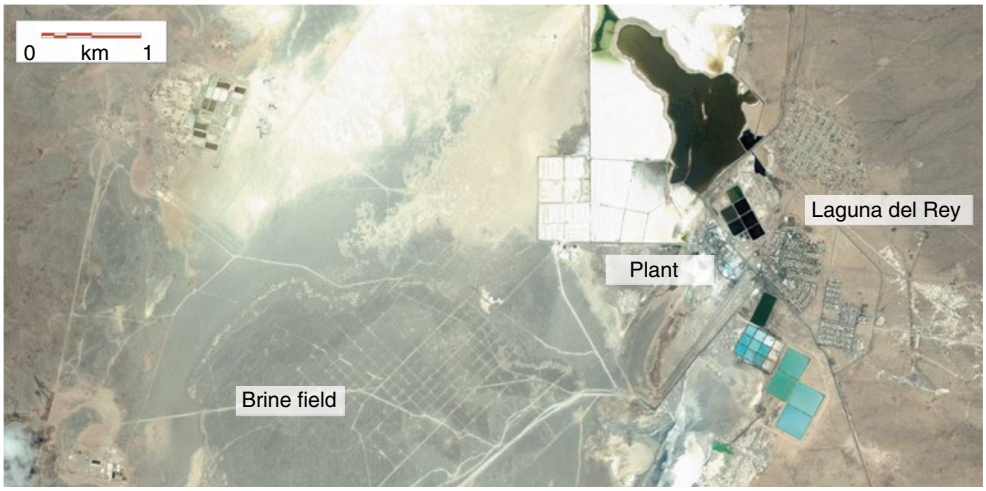

Fig. 12.24 Laguna del Rey, Mexico. Plant and brine field

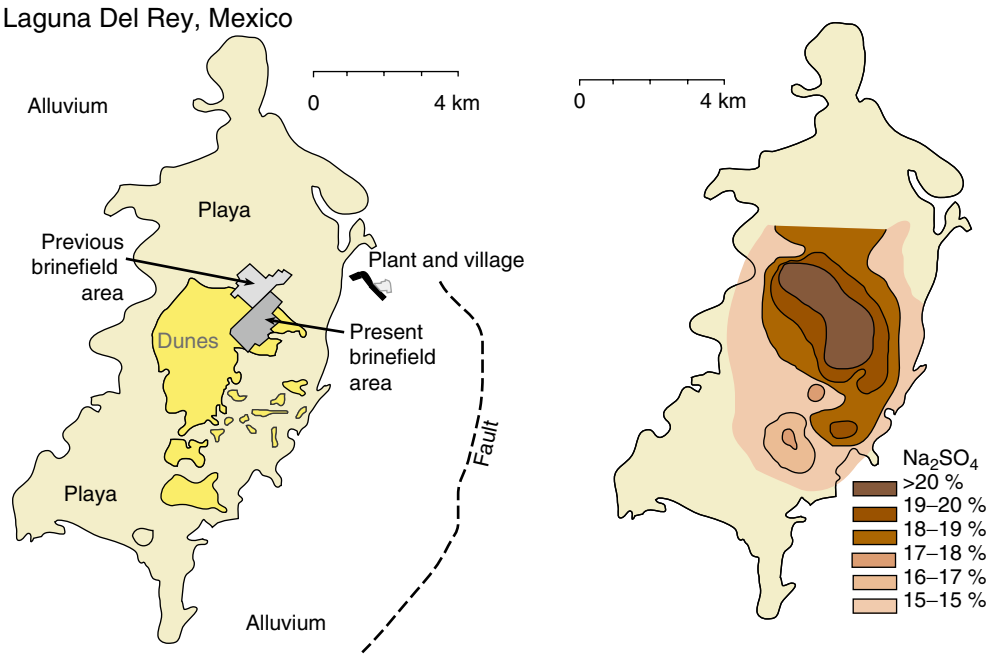

Fig. 12.25 Laguna del Rey, Mexico showing distribution of surface features and the distribution of Na_2SO_4 in brines in the exploited shallow subsurface salt bed (After Garrett 2001)

brine from a Na_2SO_4 bed containing 50 % glauberite, 20 % bloedite (astrakanite), 28 % clay and various other sodium and magnesium salts, including 1 % halite. Minor mirabilite and epsomite are locally present as a cement between the glauberite crystals (Garrett 2002). The salt body lies some 1–2 m beneath the present playa floor, with porosity around 25 %, is lenticular in cross section, dips slightly to the east and thickens to the south. It has a maximum thickness of 35 m and an area of 40 km^2 and contains a resource of some 350 million metric tons of sodium sulphate and 77 million metric tons of magnesium sulphate.

The lower parts of the modern flat playa surface, its sumps, are marked by an ephemeral halite crust, broken in places by relicts of a now largely inactive dune field. Above the halite crust is a green clay containing abundant gypsum and lesser glauberite and halite. Below the green clay is a red clay bed that immediately overlies the target salt bed. A similar, but much thicker, red clay also underlies the main salt mass. Porosity in the salt bed is filled with a brine that when pumped from this salt bed contains more than 26 % sodium sulphate (Fig. 12.25). A brinefield of more than 70 wells pumps brine to the surface from depths down to 24–25 m below the playa surface. Wells are gravel packed for the lower 12 m and the brinefield pumps around 113 l/s of 25 °C 200 g/l sulphate to the recovery plant (Garrett 2002). The ultimate source of the ions now accumulating in the playa

depression is thought to be halokinetic gypsum-capped marine evaporites and carbonates that subcrop in the surrounding highlands. Possibly this was followed by ion exchange on saline clays of calcium for sodium. The oxidation of sulphides from the large silver-lead deposit at Sierra Mojada (to the north) must have augmented the proportion of sulphate in the drainage, along with leaching some of the dolomite in the drainage area's soil, to form the high-magnesium parent brine (Sanchez-Mejorada 1986).

Brine processed at Quimica del Rey. S.A. de C.V. plant on the playa shore is hypersaline and probably saturated with more than 26 % sodium sulphate and appreciable amounts of chlorides and magnesium (Kogel et al. 2006). The brine temperature entering the plant is around 25 °C before precooling with the spent brine. The cooled brine is fed to a vacuum crystallizer where it is further cooled to 9 °C by evaporative cooling, causing Glauber's salt to crystallize. The resulting slurry is then thickened, filtered, and melted. Evaporation is accomplished in multiple-effect evaporators. Final drying is in co-current-fired rotary kilns. Part of the mother liquor is processed further for recovery of magnesia products and the balance goes to waste.

Spanish Glauberite Mines

Tertiary lacustrine sediments are the major source of sodium sulphate in Spain within three large Tertiary basins (Madrid, Ebro and Calatayud basins) that together contain as much as 3 Gt in the form of glauberite or thenardite (Table 12.8; Salvany et al. 2007; Garrett 2001). Spain probably has the largest glauberite-thenardite deposits in the world, except perhaps for the less well known Tien Shan (Kyrgyzstan) deposits. Deposits in the Madrid and Ebro basins are very well defined and many of the richer deposits are largely depleted, while the Calatayud Basin still has potential.

Spanish operations recover solid ores for processing, not brine. Ore is mined via room and pillar methods or in-situ leaching extracted via planned face retreat. The "El Castillar" mine in Toledo Province yields mostly thenardite from an ore averaging 67 % Na_2SO_4, 19 % $CaSO_4$ and 12 % clay and marl. The ore bed thickness averages 9 m and it lies atop a 13 m-thick halite bed. Glauberite is extracted also at Cerezo de Riotirón, Burgos Province, where the deposit is practically horizontal, undisturbed and made up of glauberite in four beds hosted in Miocene lacustrine marls.

The exploited salts have a primary paragenesis of glauberite + anhydrite + dolomite ± chalcedony; the secondary minerals related to hydration and incongruent dissolution of glauberite are mainly gypsum and calcite (Menduina et al. 1984; Salvany and Orti 1994). Glauberite ore types are varying combinations of: (1) massive glauberite within fining-upward sequences containing nodular anhydrite; (2) millimeter-scale glauberite layers alternating with dolomicrites; (3) single glauberite crystals dispersed in dolomicritic matrix (Fig. 12.26a). There is no mirabilite phase preserved in these deposits.

A 'perennial saline lake' model with warm extensive continental saline mudflats is typically used to explain the various glauberite deposits (Fig. 12.26b; Salvany and Orti 1994; Salvany et al. 2007). Solutes were derived from the phreatic dissolution of Mesozoic evaporites, mainly Ca-sulphates and halite, in the nearby mountains (Pyrenees and Iberian Ridge).

The concentration sequence was: carbonate, gypsum-anhydrite, glauberite, halite-polyhalite. Indicators of backreactions of glauberite with gypsum/anhydrite are commonplace via dissolution-driven interactions of primary precipitates with less concentrated (meteoric) brines and seeps from the basin margin, supplemented by occasional storm runoff. That is, some of the glauberite, anhydrite and polyhalite in the ore units is made up of early diagenetic minerals, formed via backreactions with a solid precursor (typically nodular gypsum) during early diagenesis, others are primary (Fig. 12.26; Salvany et al. 2007).

The brines that drove early alteration reacted with the solid precursor in two ways: (1) reaction of the concentrated

Table 12.8 $NaSO_4$ -bearing formations in the 3 Spanish continental basins

Basins and formations	Age	Original Mineral Association	Exploitation
Madrid (Tajo) Basin			
Saline Unit	Lower Miocene	H, Ph, Th, Gb, An, G, Dol	Active, Th-Gb
Ebro Basin (Spain)			
Cerezo Gypsum Fm.	Lower Miocene	Gb, An, G, Dol	Active, Gb
Lerin Gypsum Fm.	Basal Lower Miocene	H, Ph, Gb, An, G, Mg, Dol	Inactive, Gb, H
Falces Gypsum Fm.	Oligocene	H, Gb, An, G, Dol	
Zaragoza Gypsum Fm.	Lower Miocene	H, Gb, An, Dol, Qz	Active H, Exploratory Gb
Calatayud Basin			
Calatayud Gypsum	Lower Miocene	Th, Gb, An, G, Dol, Ar	Exploratory, Th-Gb

Mineral abbreviations: *H* halite, *Ph* polyhalite, *Th* thenardite, *Gb* glauberite, *An* anhydrite, *G* gypsum (primary), *Mg* dolomite, *Ar* aragonite, *Qz* quartz. Primary gypsum (G) refers to the deduced original mineral association. The presence of secondary gypsum in all the formations is omitted (After Salvany et al. 2007)

brine with the solid phase precipitated during episodes of lowered salinity (e.g. anhydrite alters to glauberite; glauberite alters to polyhalite), and (2) reaction of dilute brines with solid phases precipitated in episodes of higher salinity (e.g. glauberite alters to anhydrite, polyhalite alters to glauberite or anhydrite). Burial led to further transformations of gypsum to anhydrite and, during exhumation and exposure, all pre-existing sulphates (anhydrite, glauberite, polyhalite) were transformed near the surface into gypsum, which now dominates the weathered cover or carapace atop many ore profiles (Fig. 12.26a).

However, the relative proportion of primary versus secondary textured glauberite in the extracted ore, and where in the basin depositional setting was syndepositional alteration most likely, has always been a point of discussion. Detailed petrographic analysis by Salvany et al. (2007) on core from glauberite intervals in two wells sampling the Zaragoza Gypsum Formation has gone some way to defining a resolution (Fig. 12.27). They document two glauberite-halite lithofacies associations, A and B: (1) Association A is a combination of bedded cloudy halite and minor amounts of massive and clastic glauberite; (2) Association B is made up of laminated to thin-bedded, clear macrocrystalline, massive, clastic and contorted lithofacies of glauberite, and small amounts of bedded cloudy halite. Transparent glauberite cemented by clear halite, as well as normal-graded and reverse-graded glauberite textures, are common in Association B. This type of transparent glauberite is interpreted as a primary, subaqueous precipitate. Gypsum, thenardite or mirabilite are absent in either association. The depositional environment is interpreted as a shallow perennial saline lake system, in which chloride brines (association A) and sulphate-(chloride) brines (association B) are developed at different lake levels and salinities, much like the gypsum and halite facies are indicative of higher and lower lake levels in the Pleistocene evaporites of the Danakil Depression.

The geochemical study of halite crystals (bromine contents and fluid inclusion compositions) demonstrates that conditions for co-precipitation of halite and glauberite, or for primary precipitation of Na-sulphates (mirabilite, thenardite) were never fulfilled in the Zaragoza saline lake system. In my opinion, this absence of phases that had by some earlier workers been interpreted as likely co-precipitates, relates to the need for holomictic brine conditions for synchronous across-basin subaqueous halite deposition.

Weathering products of these glauberite-entraining Miocene evaporites are sometimes recycled into saline sumps in the modern landscape. For example, salt crusts covering the surface of the Salda Mediana, a seasonally dry saline lake in the arid part of the central Ebro Basin in northern Spain, consist predominantly of bloedite ($Na_2SO_4{\cdot}MgSO_4{\cdot}4H_2O$) atop a succession of evaporitic sediments dominated by gypsum (Fig. 12.28; Mees et al. 2011). In the various modern Spanish lakes, bloedite tends to occupy the sump centre, while epsomite tends to dominate the borders to the sump (Sanchez-Moral et al. 1998). The genesis of bloedite is perhaps explained by a rapid early diagenetic alteration of the previously precipitated epsomite

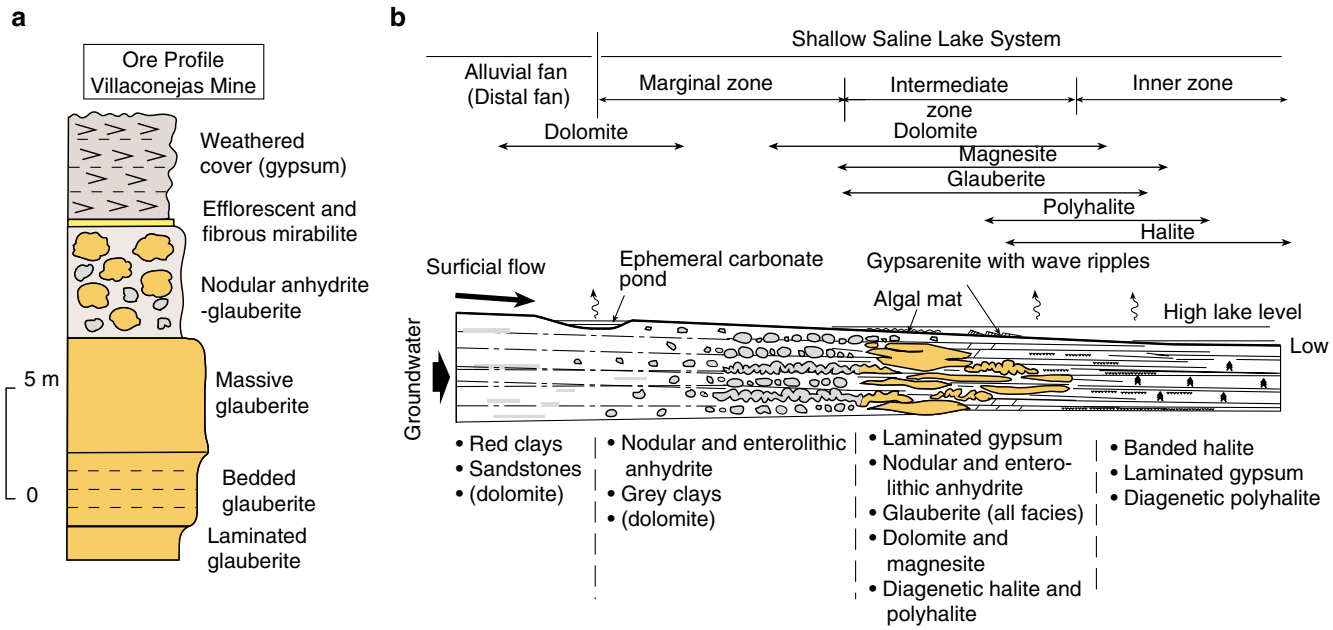

Fig. 12.26 Miocene glauberite in Spain. (**a**) Profile of the ore zone in the Villaconejas Mine, Spain. (**b**) Sedimentological model for deposition of Spanish glauberite deposits (After Salvany and Orti 1994)

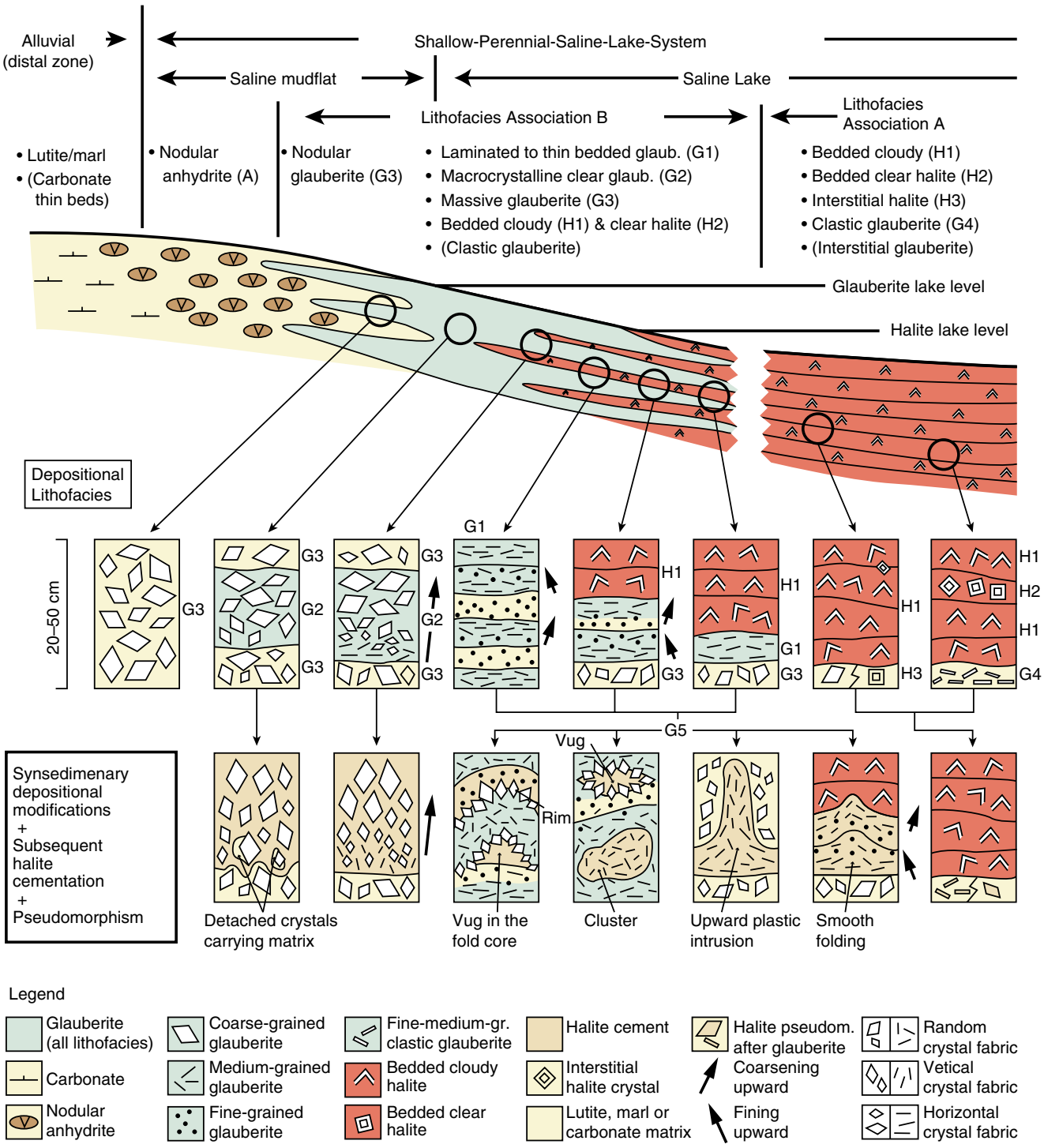

Fig. 12.27 Deposition and diagenesis in the Zaragoza Fm, Ebro Basin, Spain (After Salvany et al. 2007)

that had accumulated at the bottom ("bloeditization"), by means of a reaction with a crossflowing brine enriched in Na^+ and Cl^-. It means the replacement of epsomite, as well as some previously precipitated halite, by bloedite in the accumulated saline deposit, had also released magnesium chloride and water to the brine.

Turkish Deposits

Sodium sulphate salts are extracted from the Upper Miocene Kirmir Formation at Cayirhan Mine, Turkey (Fig. 12.29; Orti et al. 2002). Unlike the Spanish ores, thenardite (after mirabilite) is thought to be a significant depositional component of

the bedded $NaSO_4$ salts in this lacustrine ore association. However, none of the primary mirabilite remains as it has since converted to thenardite with moderate burial. The Evaporite Member of the Kirmir Formation, which is composed of secondary gypsum at outcrop, can be subdivided into a bedded lower unit and a massive upper unit (Fig. 12.29a). Most of the current outcropping and subcropping gypsum of the bedded lower unit has been transformed to gypsum during exhumation from a glauberite parent. Glauberite layers ("clear glauberite") still remain at depth, as in the Cayirhan mine, where textures suggest it was deposited as a primary, subaqueous, cumulate precipitate on the saline lake floor (Fig. 12.29b). But more typically, the glauberite textures are nodular, suggesting it was an early (syndepositional to precompaction) interstitial precipitate, indicating crystal growth occurred just below the sediment surface as passive and displacive crystals within a poorly lithified clayey magnesitic matrix. Thenardite layers in the glauberite beds in the Cayirhan mine, show disruption structures created by synsedimentary dissolution and infill (Fig. 12.29c). These structures, together with their pseudomorphic textures, suggest mirabilite was the original sodium sulphate lakefloor precipitate. If so, the current thenardite ore is a secondary phase, formed by mirabilite dehydration during early to moderate burial.

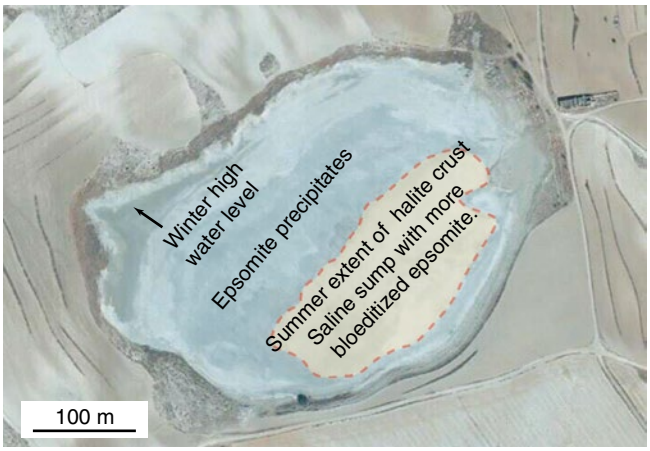

Fig. 12.28 Salada Mediana, Spain. Showing ephemeral nature of seasonal water filling that controls complex textural overprints in the bloedite-halite crust and efflorescences (Mees et al. 2011)

The massive upper unit, in which evidence of any sodium-bearing minerals is absent, is characterized by laminated to banded gypsum, with nodular gypsum dominant in the marginal areas of the evaporitic basin. Thick, clast-supported gypsum

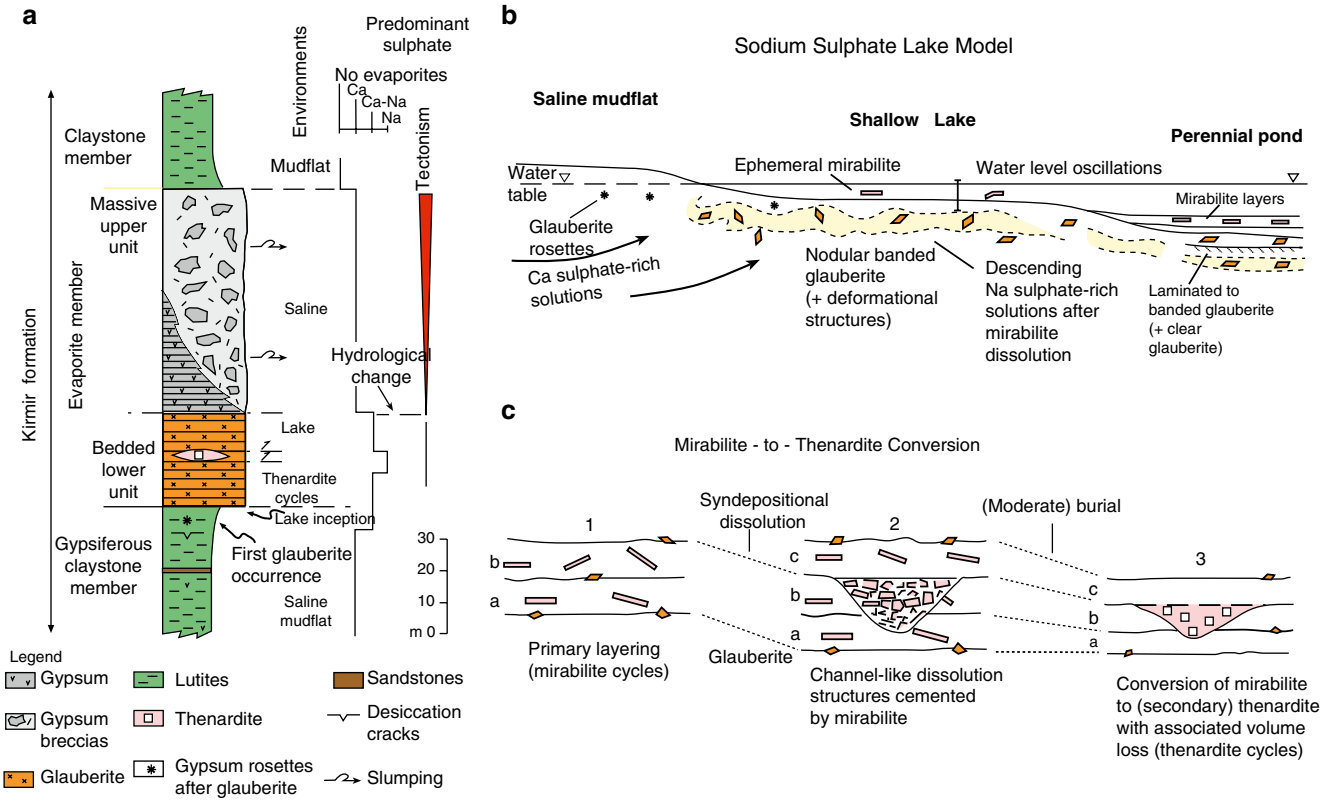

Fig. 12.29 Na-Sulphate in the Upper Miocene Kirmir Formation, Turkey (After Orti et al. 2002). (**a**) Stratigraphic occurrence and depositional setting. (**b**) Depositional settings of the lacustrine evaporative system at the time it was precipitating sodium sulphates of the bedded lower unit (Evaporite Member of the Kirmir Formation). (**c**) Interpretation of the genesis of mirabilite and its synsedimentary dissolution and final conversion to thenardite during (moderate) burial

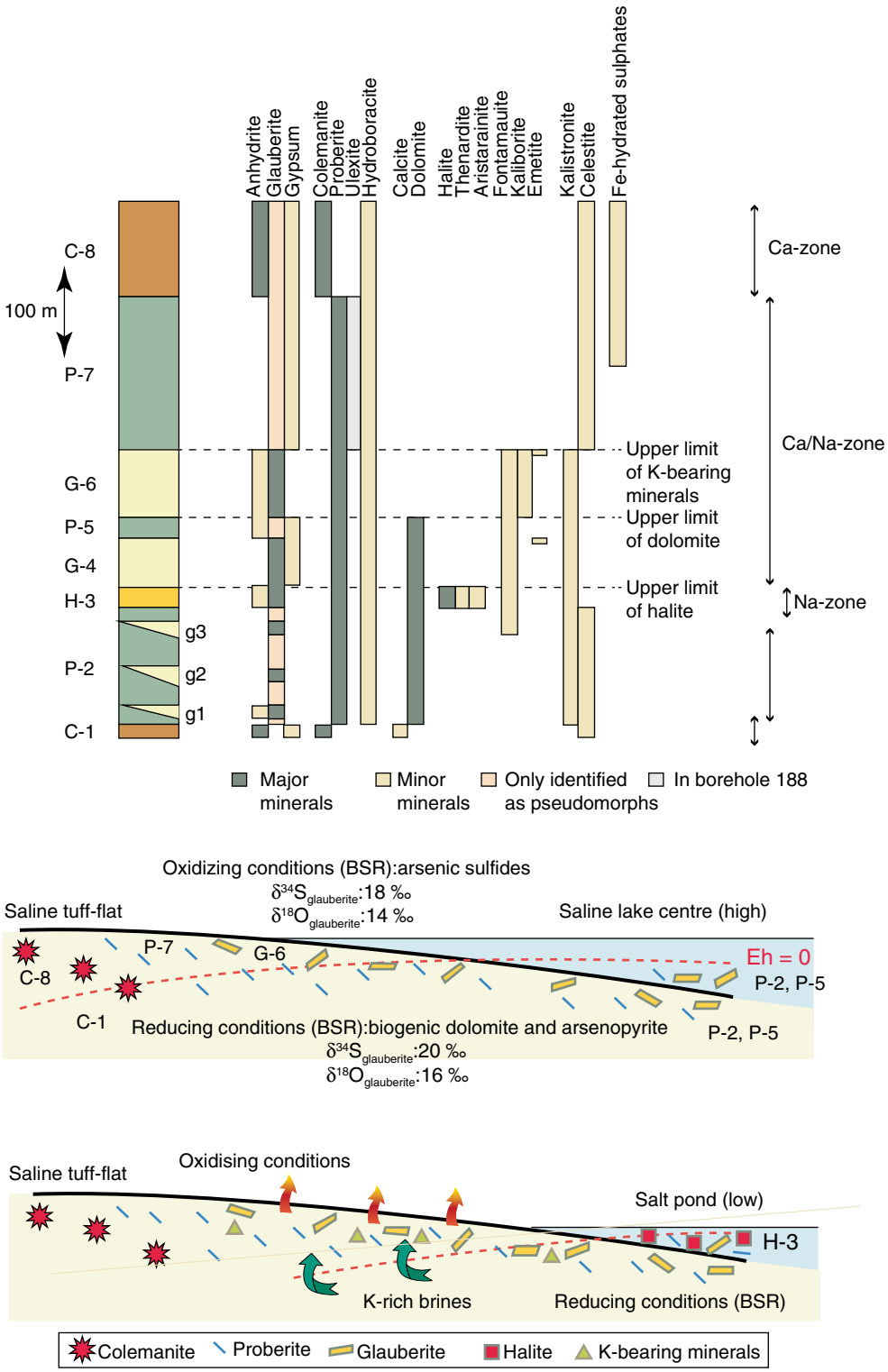

Fig. 12.30 $NaSO_4$ in Emet Basin, Turkey. (**a**) Schematic distribution of the various depositional and diagenetic evaporitic minerals with depth in borehole Doğanlar no. 2 well. (**b**) Hydrochemical and mineralogical model of evaporitic precipitation in the Doğanlar saline lake. Contrasts high water situation for predominant precipitation of the various borates and sulphates, versus more saline lower level that typifies the halite precipitation stage (García-Veigas et al. 2011b)

breccias prevail in the northern, deeper part of the basin. The brecciation of these calcium sulphate layers possibly occurred as a result of synsedimentary, gravitational slumping into the deeper parts of the perennial lake during times of lake flow instability driven by active tectonism (Orti et al. 2002).

Sodium sulphate minerals are also widespread co-precipitates with borates and glauberite, but in the Emet Basin of Turkey are diagenetic associations (García-Veigas et al. 2011b, 2013). They are part of a complex mineral association in which probertite, glauberite, and halite constitute the major primary phases (without mineral precursors) precipitated in a saline lake placed in a volcano-sedimentary context (Fig. 12.30a). Other sulphates (anhydrite, gypsum, thenardite, celestite and kalistrontite), borates (colemanite, ulexite, hydroboracite, tunellite, kaliborite

Fig. 12.31 Anthropogenic pans at the northern end of Tersakan Golu (near Tuz Golu), Turkey, used by Alkim Alkali Kimya A.Ş to precipitate thenardite (Bing® image mounted and scaled in MapInfo®)

and aristarainite), and sulphides (arsenopyrite, realgar and orpiment) are attributed to early diagenesis. So far, the Doganlar deposit is the most important deposit of probertite known in Turkey and perhaps worldwide (Fig. 12.30b).

Chemical changes in the groundwater inflow led to the precipitation of Ca-bearing borates (colemanite) in the tuff-flat environment surrounding the lake, while Na-Ca sulphates and borates (glauberite and probertite) precipitated in the centre of the lake. Fluid inclusion compositions in halite indicate that the advanced brines correspond to the Na-K-Cl-SO_4 type. During restricted stages of the saline lake, the residual brines seeped through the tuff-flat sediments, leading to transformations of previous precipitates that resulted in the formation of K-bearing minerals (Fig. 12.30b). The abundance of coccoidlike biogenic dolomite, colloidal arsenopyrite and the isotopic composition of sulphates are indicative of bacterial sulphate reduction. In contrast, arsenic sulphides are attributed to acidophilic micro-organisms in oxidizing conditions. Fluctuations of redox conditions in both free and interstitial brines control the biological influence in some diagenetic transformations.

As well as these ancient $NaSO_4$ resources, there are three Turkish playa lakes where sodium sulphate is produced from winter brine; they are Acigol, Tersakan and Bolluk and all three use the same basic production method (Fig. 12.31). Surface brine is pumped into a series of solar ponds or small depressions on the lake floor in the summer and autumn. The inflow in some is supplemented by spring or aquifer waters, as well as interstitial brine from lake bores, or seepage trenches in areas on the lake floor outside of the pans. Salinity of brine in the pans is monitored so that it does not become saline enough to precipitate halite nor fresh enough to dissolve the pan floor where a seed bed some 20–30 cm thick of thenardite (with minor mirabilite) was left from the previous year's salt harvest. As the concentrated brine cools from October to December, a 50–60 cm thick layer of mirabilite crystallizes in the centre of the ponds. From January and on into early spring the residual brine and any spring rainfall is drained from the pan. The flush of this fresher water through the lower part of the now metre-thick salt bed helps re-establish the integrity of the seed layer that will be left behind after harvesting. Any mirabilite slowly dehydrates and by the end of June the bed is largely composed of thenardite, which is scraped from the lake surface and loaded into bags.

The textural transitions associated with this process are interesting and as it ultimately forms a vadose product with textures that are somewhat different to the perennial lakes of Canada but more analogous to the Tertiary-age deposits just discussed. The mirabilite has two forms, either large thin interlocking elongate hoppers or fine radiating spherules made up of acicular crystals (Garrett 2001). The 0.6 m-thick mirabilite crust precipitated each winter is characterised by a thin uppermost layer or lamina of thenardite-mirabilite crystals, with some astrakanite. This is underlain by downward-pointing dog-tooth spar crystals of mirabilite, which constitute the bulk of the winter precipitates. They are downward-pointing as mirabilite tends to form rafts or hoppers at the contact between cool air and brine and not to grow upward from the lake floor. Below the coarse crystalline mirabilite is a thin layer of smaller equant mirabilite crystals defining the base of the winter precipitate layer. As the mirabilite bed dehydrates in the following summer, it forms small powdery crystals that are easily blown about in the wind and escape the pans. As summer temperatures reach 30–35 °C the mirabilite bed "melts" leaving behind some 15 % of its former mass as thenardite and a saturated sodium sulphate solution that then continues to precipitate more thenardite. The resulting thenardite layer is composed of hard compact transparent crystals, which can contain numerous solid phase inclusions.

Other Sodium Sulphate Deposits

Most US production of sodium sulphate comes from multi-component brine processing in Searles Lake, California. As discussed earlier in the section dealing with borates, this brine

resides in the interstices of the lake's salt beds, which contain some 369 million metric tons of Na_2SO_4 and 65 million metric tons of K_2SO_4, representing ≈35 % of the total lake brine (Fig. 12.12). These volumes rank Searles Lake as one of the world's larger exploitable sodium sulphate brine accumulations. Brine processing began in 1873 and the first sodium sulphate from brine was produced in 1914. Searles Valley Minerals, Inc. (a subsidary of the Indian Company Nirma) today operates two facilities near Searles Lake, the West End plant and the Argus plant. The West End plant is North American's only source of sodium sulphate recovered as the primary product, along with secondary soda ash and borax. Mixed brines are processed (carbonated) with carbon dioxide to precipitate sodium bicarbonate, which is then removed by filtration. The decarbonated brine is cooled three times to produce two successive batches of borax and one of Glauber's Salt (mirabilite). By heating, the sodium bicarbonate is converted to soda ash and the borax is either crystallized as a hydrate or dehydrated to its anhydrous form. The Glauber's salt is washed, melted, and recrystallized as anhydrous sodium sulphate; 99.3 % purity can be obtained in this process.

In the saline waters of the Great Salt Lake, Utah, about 12 % of the dissolved salt is sodium sulphate, representing about 400 million tonnes of potential resource. The precipitation process begins in December when brine temperatures can drop below −4 °C and mirabilite crystals begin to form as rafts atop the cold lake brines. Some sink to the lake bottom, others are blown to shore. Where the mirabilite sinks to the bottom it can by late winter form a layer, some 0.15–0.30 m thick, that extends over large portions of the lake floor, but redissolves with warming and the passage into spring. When mirabilite rafts are blown to the lake shore, it can form strandzone banks, some 0.9–1.2 m thick, extending up to 60 m inland of the lake shore and standing some 0.3–0.5 m above the water line. Due to their low density (≈1.5 g/cc) and the elevated density of the underlying formative brine (1.22–1.25 g/cc), mirabilite rafts have the propensity to form strandzone banks, both in the Great Salt Lake and, as described earlier, in Karabogazgol. By late winter, a strandline bank of mirabilite can become quite solid and resemble a large lake-edge snowbank. Then, as the spring meltwaters flood the lake and the brines warm, most of the mirabilite redissolves (Adams 1993).

Beneath the south and southeast parts of the lake there are permanent metre-thick mirabilite beds below some 0.5 m of oolitic sand. To the north, immediately west of Promontory Point, there is a much thicker accumulation of bedded mirabilite making up an irregular, 21-m-thick, mirabilite deposit, which is interlayered with clay beds between 4.5 and 9.1 m thick (Fig. 12.32). This more substantial mirabilite accumulation probably accumulated as bedded salt during colder conditions of the last glacial (probably under a meromictic hydrology similar to that in Ingebright Lake today or to Karabogazgol in an earlier glacial period). Historically, the Great Salt Lake mirabilite bed has been blasted and dredged in different parts

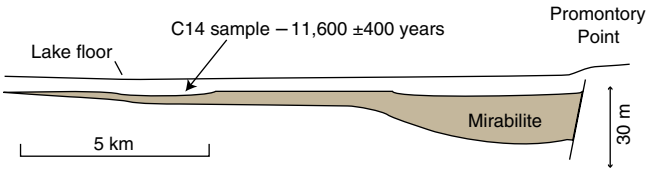

Fig. 12.32 Distribution of the mirabilite bed under the railway embankment at the northern end of Great Salt Lake (After Eardley 1962). See Fig. 4.21 for location

of the lake and a purpose-built Na_2SO_4 processing plant was set up on the shores of the lake in the 1930s and 40s.

In the recent past, the Great Salt Lake Minerals and Chemicals Corp. (Compass Minerals) made use of the annual cooling in its Great Salt Lake brine pans to manufacture sodium sulphate salts as secondary product, with sulphate of potash as the primary product (Fig. 11.28). Today the operation produces potassium sulphate, halite and magnesium chloride; sodium sulphate is no longer produced, but can be stockpiled if ever required. The first sodium sulphate production from Great Salt Lake took place in 1970 and had ceased by 2005.

Brine is pumped from the Great Salt Lake into solar evaporation ponds where sodium chloride precipitates in the summer and is also a natural summer precipitate in the lake (Adams 1938). When winter weather cools the residual brine in the pans to −1 to −4 °C, sodium sulphate crystals precipitate as mirabilite in a fairly pure state. Crystals can be picked up by large earth-moving machinery and stored outdoors each winter until further processing takes place. The harvested salt is melted and anhydrous sodium sulphate precipitated by the addition of sodium chloride to reduce its solubility through the common ion effect. The final product was 99.5 % pure $NaSO_4$. Thus, sodium sulphate can be produced in Great Salt Lake as a byproduct of the halite and potash production process (Fig. 11.8), but low Na_2SO_4 prices meant it has not been harvested for the last decade.

Ancient lacustrine deposits in the USA containing bedded sodium sulphate are considered non-commercial today, but have been mined in the past at Camp Verde, Arizona and Rhodes Marsh near Mina, Nevada, all mining ceased in 1934. The thenardite deposit at Camp Verde is the only large well-defined ancient sodium sulphate deposit in the USA, it has projected reserves ≈100 Mt (Garrett 2002). The Camp Verde deposit is unusual, because pure anhydrous sodium sulphate occurring in solid crystal form is rare (Austin and Humphrey 2006). The deposit consists of layers of thenardite and other sodium salts interbedded with clay, which form a part of the Verde Formation. The total thickness of the beds is at least 46 m. Camp Verde also has the distinction of probably being the oldest mining operation in the United States. A tunnel in one of the halite beds at the base of the deposit yielded Indian artifacts around 2,000 years old. During the fourteenth and fifteenth centuries, it was mined more intensively by the Mesa Verde and Rio Verde cliff dwellers, who removed a few thousand cubic metres.

An anhydrous natural sodium sulphate operation in China, with an annual capacity of 200,000 t, came onstream in mid 2003. The plant, operated by Dayang Chemical Limited Company, is located in Xishunhe Town, Hongze County, Jiangsu Province. The company, which is a joint venture between a Chinese company and an Indonesian firm, extracts mirabilite from a large sodium sulphate deposit in east China. Little has yet been published on the geology of this lacustrine deposit. It has a proven area of more than 8.4 km^2, and a likely reserve of up to 150 million tons. It operates, in combination with a second facility, with an annual capacity of up to 600,000 t, and has been in production since the year 2000 (operated by Jiangsu Nanfeng Chemical Co. Ltd., which is a joint venture between Shanxi Nanfeng Group and Hongze Chemical Group, which is the Chinese operating arm of the Spanish Crimidesa Group). Sodium sulphate also occurs in several of China's large soda ash deposits, such as at Chaganor (Austin and Humphrey 2006). This Pleistocene deposit is located in the central part of the Inner Mongolia Autonomous region, 80 km south east of Erlianhot. The deposit covers 21 km^2, with nine porous brine-filled beds of salts containing about 11.3 Mt of sodium carbonate and 4.5 Mt of sodium sulphate. In combination, this now makes China the world's largest natural sodium sulphate producer, with a combined capacity of some 800,000 t per year.

Sodium Carbonate Salts (Soda ash)

Worldwide, in terms of naturally-occurring salts, sodium carbonate is next to gypsum in terms of annual volumes extracted (Table 12.2). The dominant ore salt is trona. The word trona is an aphaeretic form of natrun, derivative of the Arabic word *natrun*, from which we also derive the English word natron. Mineralogically natron (not *natrun* as originally used by the ancient Egyptians and then the Arab alchemists) describes the decahydrate form of sodium carbonate and is one of a number of evaporitic sodium carbonate minerals (Table 12.9).

Table 12.9 Minerals containing sodium carbonate

Mineral	Formula	Na_2CO_3 (equiv.%)
Trona	$NaHCO_3{\cdot}Na_2CO_3{\cdot}2H_2O$	70.4
Thermonatrite	$Na_2CO_3{\cdot}H_2O$	85.5
Nahcolite	$NaHCO_3$	63.1
Bradleyite	$Na_2PO_4{\cdot}MgCO_3$	47.1
Pirssonite	$CaCO_3{\cdot}Na_2CO_3{\cdot}2H_2O$	43.8
Northupite	$Na_2CO_3{\cdot}NaCl{\cdot}MgCO_3$	40.6
Tychite	$2MgCO_3{\cdot}2Na_2CO_3{\cdot}Na_2SO_4$	42.6
Natron	$Na_2CO_3{\cdot}10H_2O$	37.1
Dawsonite	$NaAl(CO_3)(OH)_2$	35.8
Gaylussite	$CaCO_3{\cdot}Na_2CO_3{\cdot}5H_2O$	35.8
Shortite	$Na_2CO_3{\cdot}2CaCO_3$	34.6
Burkeite	$Na_2CO_3{\cdot}2Na_2SO_4$	27.2
Hanksite	$2Na_2CO_3{\cdot}9Na_2SO_4{\cdot}KCl$	13.6

Character and Extraction History

Modern sodium carbonate end usage is mostly in glass manufacture followed by chemicals, soap and detergents, pulp and paper manufacture, water treatment, and flue gas desulphurization. One of sodium carbonate's prime uses in ancient Egypt, in the form of *natrun* (a trona-halite-sodium sulphate mix) quarried from salt lakes, was as an integral part of the mummification[3]

[3] Ancient Egyptians are famous for their perfection of the art of mummification. A key ingredient in the process was *natrun*, which is composed of halite + trona + sodium sulphate (Edwards et al. 2007). The ancients knew its preservative properties rivalled those of halite and, as it also absorbs water readily, it is an excellent desiccant/ preservative of organic material. *Natrun* is found in large quantities in the beds of several Egyptian playa lakes (e.g. Wadi Natrun and El Kab, as well as Behiera in the nearby Libyan desert) and has been mined and traded from these localities for thousands of years. Writings as old as the reign of Rameses III (1198–1166 B.C.) refer to these deposits. The preservative qualities must have been immediately apparent to the ancient Egyptians from its effects on any wild life, which had died in these lakes. There is some evidence that the Egyptians artificially precipitated *natrun* by isolating shallow basins of lake waters for faster evaporation, as is still done in parts of the depression today. For purification and preservation, *natrun* was preferred over halite because it chemically attacks and destroys grease and fat and so is a superior drying agent (as is sodium borate). It is found not only in tombs and in pits, along with other discarded embalming materials, but also forms nodules and residues in the mummies themselves.

There is some debate over the method in which the *natrun* was used for mummification by the ancient Egyptians. Some argue it was used in a way similar to the contemporary method for "salting" fish. Dry *natrun* would be sprinkled over the body, perhaps with sawdust, or spread with linen cloths. Others with a more prosaic bent, believe the body was immersed in vats containing a *natrun* solution. Such a wet method would have been odiferous and accelerated putrefaction, thus counterproductive to the preservation of the body, although it makes for good Hollywood images. A dry body is also more readily bandaged as well as being more amenable to the attachment of amulets and other jewelry. Although mummification has supernatural trappings in popular culture and ancient religions, its basis is rooted in simple chemistry and processes as mundane as salting fish.

Mummification also occurs naturally in halite and trona is not necessary, although it improves preservation. In 1593 AD and again in 1616 AD several tombs encased in salt were exposed by natural salt weathering and collapse in the Hazel Mountains. When the coffins were opened by the local people of Hallein and Hallstatt, there was astonishment that the bodies inside had very well preserved soft tissues. It was the result of the hyperarid encasement in a Neolithic salt mine, but frightened religious locals insisted of prompt reburial with additional efforts to create effective seals. There was a similar popular response in 1734 AD when the salt preserved body of a man wearing mountain clothing (possibly a miner) was discovered. Fearful locals insisted on immediate reburial with no further study or observations on the remains (Aufderheide 2011). First in the winter of 1993 and later in 2004, in the modern Chehr Abad Salt Mine, near Hamzehloo, Zanjan Province of Iran, at total five salt-preserved male bodies were found in a collapsed tunnel of a former salt mine, which was active around 400 BC. The first discovery in the winter of 1993 was a salt encased bearded head and some artifacts, the later discovery, beginning in November 2004, was of the remaining bodies. It is likely all five men died in earthquake induced collapses in the salt mine (Pollard et al. 2008). Encasement in the hyperarid atmosphere of the collapsed salt mine tunnel led to mummification of the bodies.

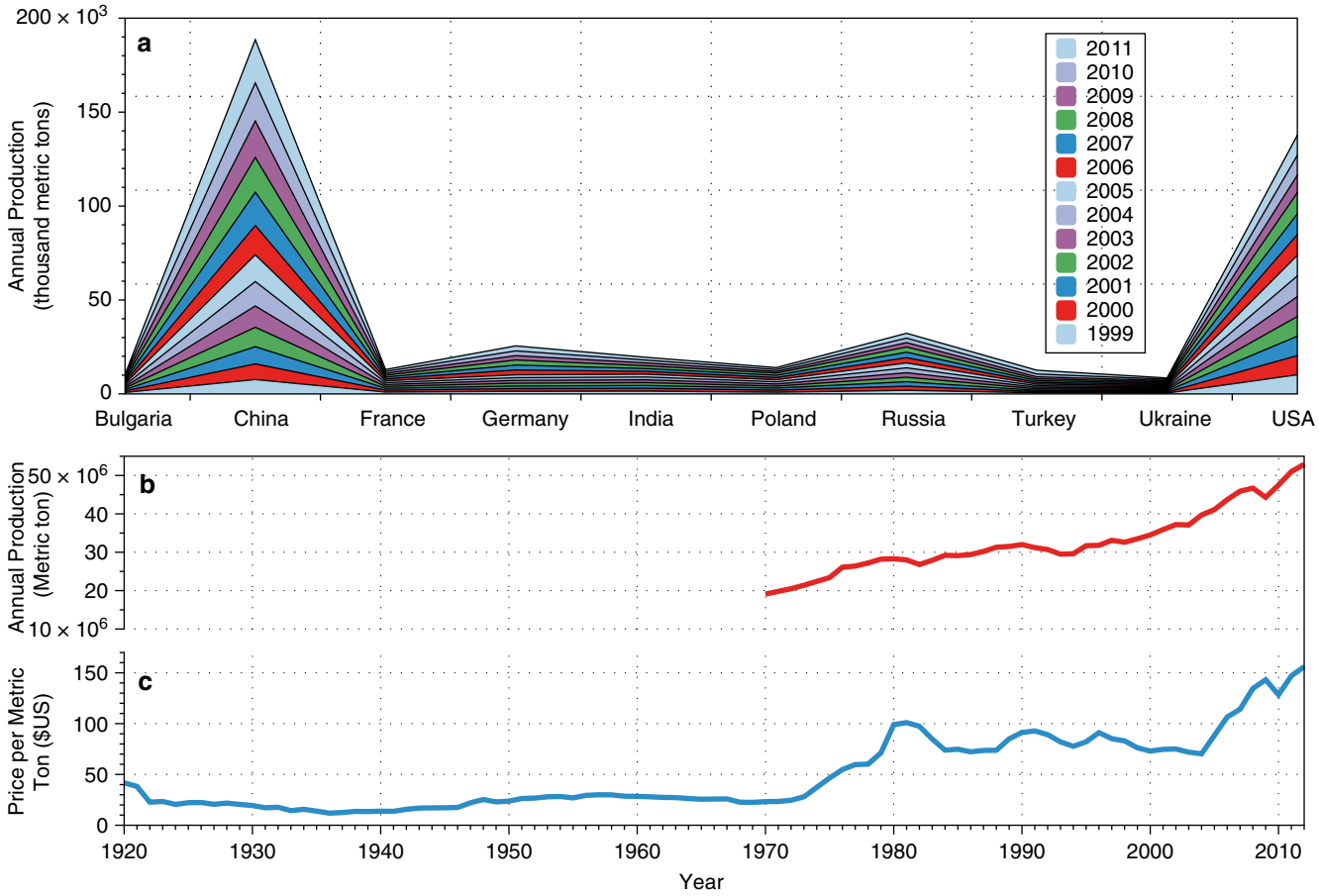

Fig. 12.33 World production of synthetic and natural soda ash. (**a**) Cumulative area plot of top producing countries, (**b**) World production (1,000 metric ton), (**c**) Price per metric ton in US dollars (Plots compiled from USGS on-line data tables downloaded from http://minerals.usgs.gov/minerals/index.html last accessed September 3, 2014)

process so body and soul could re-unite in death. Natron was also used as a flux in glassmaking in Egypt since the Badarian Period (early 4th millennium BC), indicated by the very low potash contents of glasses from that time (Dotsika et al. 2009; Shortland et al. 2006). The use of natron as a soda flux in glass manufacture is increasingly apparent in glass chemistry since the 1st millennium BC. Glass from the tomb of Nesikhons in Egypt has a low content of potash, magnesia and lime implying that the soda flux was derived from natron. Other evidence of natron use in the same period is in the chemistry of blue glass manufactured in eighth to ninth century BC at Nimrud, Iraq. Likewise, the Roman glassmaking industry seems to have been based on natron, as indicated by the low-magnesia content of Roman glass.

Until the ninth century AD, natron continued to be the basic flux material in glassmaking in the Levant, the Mediterranean, and Europe. Use of natron as the flux in glass production declines in Near East and in Europe in the ninth century AD, when it was replaced by soda-rich plant ash as a flux (Shortland et al. 2006). However, natron continued to be harvested at al-Barnuj in the Western Nile Delta, Egypt until the eighteenth century AD. From the 1920s onwards, natron was collected in the same sump area by the Egypt Salt and Soda Company. A natron occurrence in ancient Greece was mentioned by Plato in the fifth century in his writings on the Republic (Testimonium 1), it was likely harvested from Lake Pikrolimni (Dotsika et al. 2009).

Today, in many countries local supply of sodium carbonate (aka soda ash) is synthetic, created using the Solvay process, which utilizes halite and limestone as raw materials with an ammonia catalyst within the carbonating towers. Annually, roughly twice as much soda ash is produced worldwide by the Solvay process than by bedded trona extraction. Major producers using the Solvay method include; China, Germany, India and Russia (Fig. 12.33a). In 2003 Chinese production of soda ash exceeded that of the USA for the first time, and this has been the situation since then. In 2010, world soda ash production was estimated to be 47.5 Mt, which was a 7 % increase from that of 2009, indicating a rebound from the global financial crisis. The top five soda ash-producing nations accounted for 79 % of world

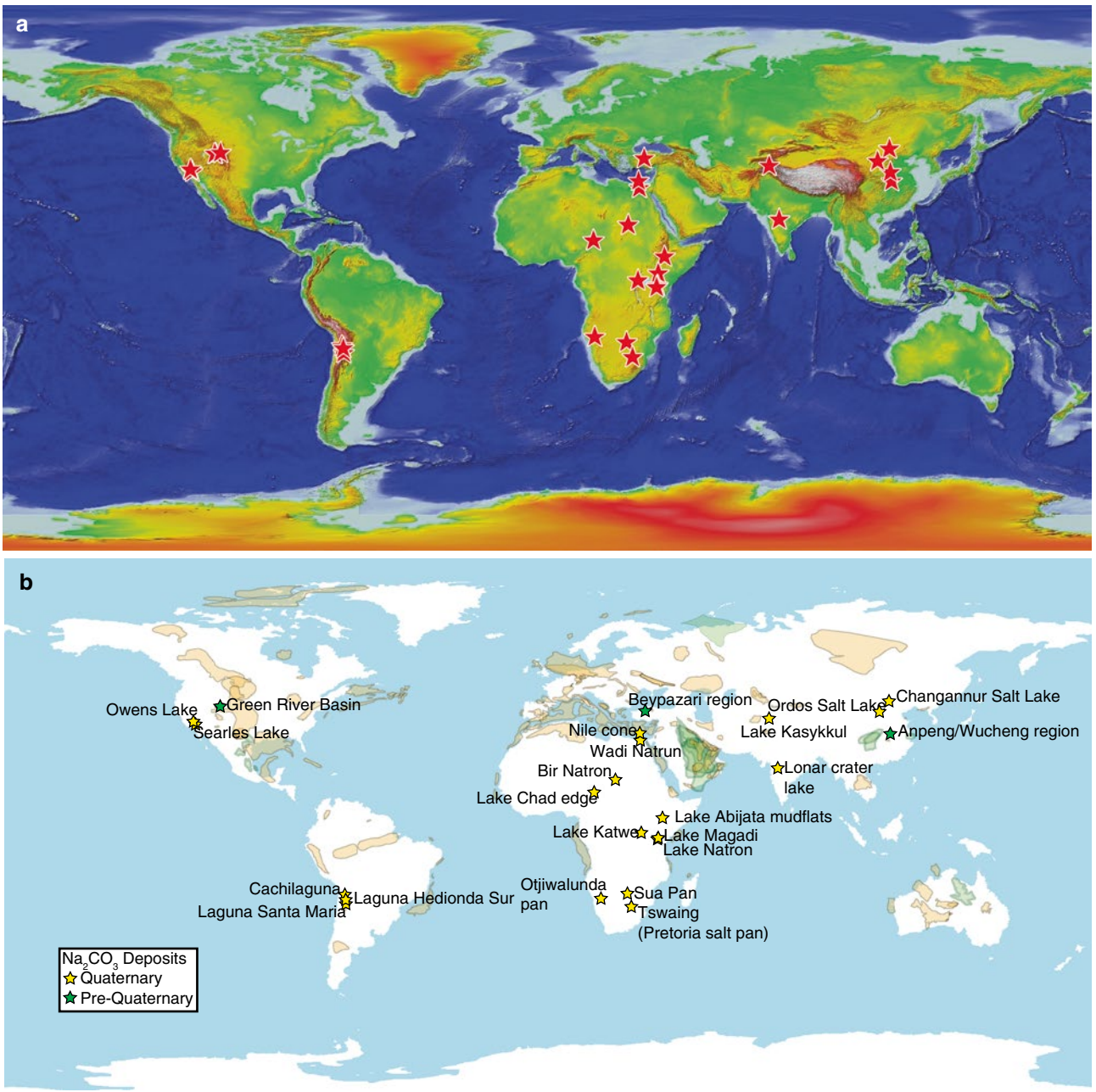

Fig. 12.34 Sodium carbonate occurrence. (**a**) Deposits plotted on a world topographic/tectonic base (see Table 12.10). (**b**) Deposits plotted on a marine evaporite basin base, where *brown shading* indicates halite-dominant and *green* indicates megasulphate basin (After Warren 2010). Plot shows that soda-ash deposits do not occur atop or within large marine-fed mega-evaporite basins

production in 2011 (Fig. 12.33; Kostick 2011). Of the 29 countries that produce natural and synthetic soda ash in 2011, the United States was the world's second-ranked producer, accounting for 22 % of total world output and producing around 10.6 million metric tons of natural soda. The USA, China and Russia combined have a 65 % share of installed world capacity. India, Germany, Ukraine, France, the United Kingdom, Italy, Bulgaria and Romania also have significant capacity.

Only Botswana, China, Ethiopia, Kenya, Turkey, and the United States produce significant quantities of soda ash from natural sources (Fig. 12.34; Table 12.10); the remaining 23 nations manufacture synthetic soda ash through various chemical processes, primarily the Solvay process. Total world natural soda ash production represented about 26 % of combined world soda ash production. A number of naturally occurring evaporite minerals contain Na_2CO_3, but only trona is economically extracted or solution mined at this time.

Table 12.10 Selected sodium carbonate occurrences, listed by country, reserves listed in million (mt) or billion (Gt) metric tons of sodium carbonate equivalent

Location	Age	Elev. (m)	Köppen	Mineralogy/setting/comments/key references
Laguna Santa Maria, Argentina	Quaternary	4,300	ET	Thin trona beds in a moderately small (19 km^2) alpine deposit some 5 km from border with Chile.
Cachilaguna (Laguna Cachi), Bolivia	Quaternary	3,650	ET	Trona, small (1.5 km^2) alkaline brine lake, brine depth ≈17 cm. Salts precipitated when lake brine freezes in winter to form a 6 to 10 cm thick crust of trona and thermonatrite (Ahlfeld and Muñoz Reyes 1955)
Laguna Hedionda Sur, Bolivia	Quaternary	4,572	ET	Trona, small (2.8 km^2) alkaline brine lake (pH 10.46) covering, average brine depth 75 cm. (Ahlfeld and Muñoz Reyes 1955)
Laguna Honda Sur, Bolivia	Quaternary	4,636	ET	Trona, small alkaline brine lake (pH 9.88) covering 30 ha (0.3 km^2), average brine depth only 10 cm. (Ahlfeld and Munoz-Reyes 1955)
Sua (Sowa) Pan, Makgadikgadi Basin, Botswana (3,307 km^2)	Quaternary	892	BSh	Deepest of a three pan complex separated by dune covered ridges. Pan surfaces of brine-saturated sand and clay layers with surface efflorescence of trona and halite. Seasonally flooded by Nata River. Trona, brine processing plant commenced operations in 1991. Salt-cake as possible byproduct. Produces 300 kty of soda-ash and 600 kty of halite for South African market. (360 Mt) (Low et al. 2000; Eckardt et al. 2008)
NE Lake Chad, interdunal pans, Chad (22,351 km^2)	Quaternary	264	BWh	Evaporation of groundwaters to form trona-halite-gaylussite crystals crusts and efflorescences in the capillary zone of interdunal depressions. Some pans with natron mixed with halite, small anthropogenic crystallizer pans in interdunal depressions (<5 km^2), NE Lake Chad. Low quality product for local consumption. (Eugster and Maglione 1979)
Anpeng Basin Trona Mine, China	Eocene	1,266		Nahcolite, trona, mirabilite, gypsum. Solution-mined, 17 nahcolite beds (0.6–3.6 m thick) mixed with sulphate- and carbonate-bearing layer in a depth of around 1,310–2,520 m. Located near Anpeng, about 35 km NW of Tongbai (Wang 1987)
Wucheng Basin Trona Mine, Henan Province China	Neogene	142		Trona, halite, lesser nahcolite (minor northupite and shortite), 36 trona beds (693–974 m deep), lower 15 beds are 0.5–1.5 m thick, thickest 2.38 m; upper 21 beds are 1–3 m thick, maximum 4.56 m, hosted and underlain by dolomitic oil shales of Wulidui Fm. Actual ore body re body contains about 77 % trona and 23 % nahcolite, and lies 650–970 m deep in beds 0.3–3.0 m thick (Youxun 1985)
Chaganor Salt Lake (Qagan Nur), China (Nei Mongol) (21 km^2)	Quaternary	968	BSk	Trona in nine porous brine-filled saline beds containing 11.3 million mt of sodium carbonate, and 4.5 million mt of sodium sulphate. Beds <10,000 years. Current lake area of 21 km^2 consisting of smaller northeastern sub-basin (East Chagannur) and a larger southwestern sub-basin (West Chagannur) joined by a narrow channel (Zheng 1997; Yu et al. 2001)
Wadi Natrun. Egypt (500 km^2)	Quaternary	−23	BWh	Natrun beds with burkeite, gaylussite, trona, halite, northupite, pirsonite, thenardite in various lakes in the depression. Exploited by ancient Egyptians. (Shortland 2004)
Nile Cone (Outer Egyptian Shelf) Mediterranean	Quaternary	down to −2,345	Marine	Trona and thenardite occur in Late Quaternary sediments cored on the outer Egyptian Shelf and the Rosetta Fan of the Nile Cone. Their distinct spatial–temporal distribution suggests emplacement by resedimentation (Stanley and Sheng 1979).
Lake Magadi, Kenya (110 km^2)	Quaternary	696	Aw	Trona, nahcolite, burkeite, magadiite, kenyaite. Contains up to 30 billion tons of trona in Holocene unit 74 km^2 area and 15–40 m thick. Current production ≈350 kty (via dredging) with ≈200 kty renewed (Jones et al. 1977)

Table 12.10 (continued)

Location	Age	Elev. (m)	Köppen	Mineralogy/setting/comments/key references
Lake Natron, Tanzania (561 km^2)	Quaternary	538	Aw	Trona/nahcolite/burkeite. A 2,100 km^2 area of northern part lake is covered by a 1.5 m thick trona bed (≈150 mt resource). (Manega and Bieda 1987)
Sasykkul Lake, Tajikistan (Pamir)	Quaternary			Small, heliothermal lake with local halite and trona precipitation. Similar alpine association to Bolivian trona lakes (Volkova 1998)
Beypazari region, Turkey	Miocene 21.5 Ma	738		Trona, halite, minor nahcolite (in lake margin). Areal extent of the trona deposit is estimated to be 8 km^2. Deposited as two fault-bound lensoidal trona bodies within a 70- to 100-m-thick zone in the lower part of a lacustrine oil shale (Lower Hirka Fm.) Total of 33 trona beds: 16 in the lower trona lens and 17 in the upper. Total thickness of the lower sequence is 40–60 m; upper trona ≈40 m. The interval between the lower and the upper trona sequence is 30–35 m. There is $NaSO_4$ in overlying Kimir Fm (Helvaci 1998; Suner et al. 2003)
Green River Fm., WY, USA	Eocene	1,900		Trona, halite, shortite, dolomitic oil shale of Wilkins Peak Member of Green River Fm over some 31,000 km^2 made up of 42 layers of crystalline trona in basin, 25 of which exceed 1 m thickness. World's largest exploited natural deposit (127 Gt of trona). Nearby in the Piceance Creek basin (18,700 km^2) is the worlds second largest known $NaCO_3$ occurrence, some 27 Gt of nahcolite and 17 Gt of dawsonite in the lower part of the Piceance River Formation (see text)
Owens Lake, CA, USA (278 km^2)	Quaternary	1,081	BSk	Trona/burkeite/thermonatrite/halite. Small playa valley in block-faulted Basin and Range region (anthropogenic salinity). (≈52 mt of sodium carbonate equivalent). (Alderman 1985)
Searles Lake, CA, USA (132 km^2)	Quaternary	493	BWk	Trona-nahcolite-halite. Two saline beds with trona-nacholite dominant in lower salt bed. Soda-ash via brine extraction and processing, salt-cake as byproduct. Playa in blockfaulted Basin and Range valley (estimated 1.06 Gt of sodium carbonate equivalent) (Smith 1979)

See also Garrett 2001; Santini et al. 2006; Kogel et al. 2006 and references therein

Nahcolite shows promise as another mineral that may be solution mined commercially in the near future (Table 12.10).

Until the 1960s, soda ash in the USA was almost totally derived from Solvay plants situated near industrial markets in the country's northeast. Today the position in the USA is reversed and natural extraction dominates due to lower extractive costs and lesser environmental impact. Trona in the USA is mined from the Eocene Green River Basin, Wyoming, or processed from lacustrine brines in Searles Lake and Owens Lake, California. The large-scale subsurface operations in Wyoming extract trona using various conventional combinations of room-and-pillar, longwall and shortwall extraction methods.

In contrast, solution mining and multicomponent recovery methods process brines extracted from trona beds in Searles Lake (Fig. 12.12). Dilute sodium hydroxide (NaOH – commonly called caustic soda) is typically injected into the lake beds to dissolve trona. The recovered solution is treated with CO_2 gas in carbonation towers to convert the sodium carbonate (Na_2CO_3) in solution to sodium bicarbonate ($NaHCO_3$), which precipitates as nahcolite and is filtered out. The crystals are again dissolved in water, precipitated with carbon dioxide, and filtered. The product is then calcined to produce dense soda ash. Sodium bicarbonate, sodium sulphate, potassium chloride, potassium sulphate, borax, and other minor minerals are produced as coproducts from sodium carbonate production from brines in Searles Lake, California. Likewise, sodium bicarbonate, sodium sulphite, sodium tripolyphosphate, and chemical caustic soda are manufactured as coproducts during processing of mined trona at several of the Wyoming soda ash plants.

There is a common misconception among some geologists that the presence of thick-bedded trona indicates a carbonatite-rift source area. Certainly, there are some geologically scenic trona deposits in the African rift, which are surrounded by volcanoes spewing natrocarbonatites; but these are volumetrically minor deposits, even in terms of the volume of rift sediment fill in the rift sump and, especially when compared to the volumes of ancient lacustrine Eocene trona in Wyoming and China, or the trona (long since

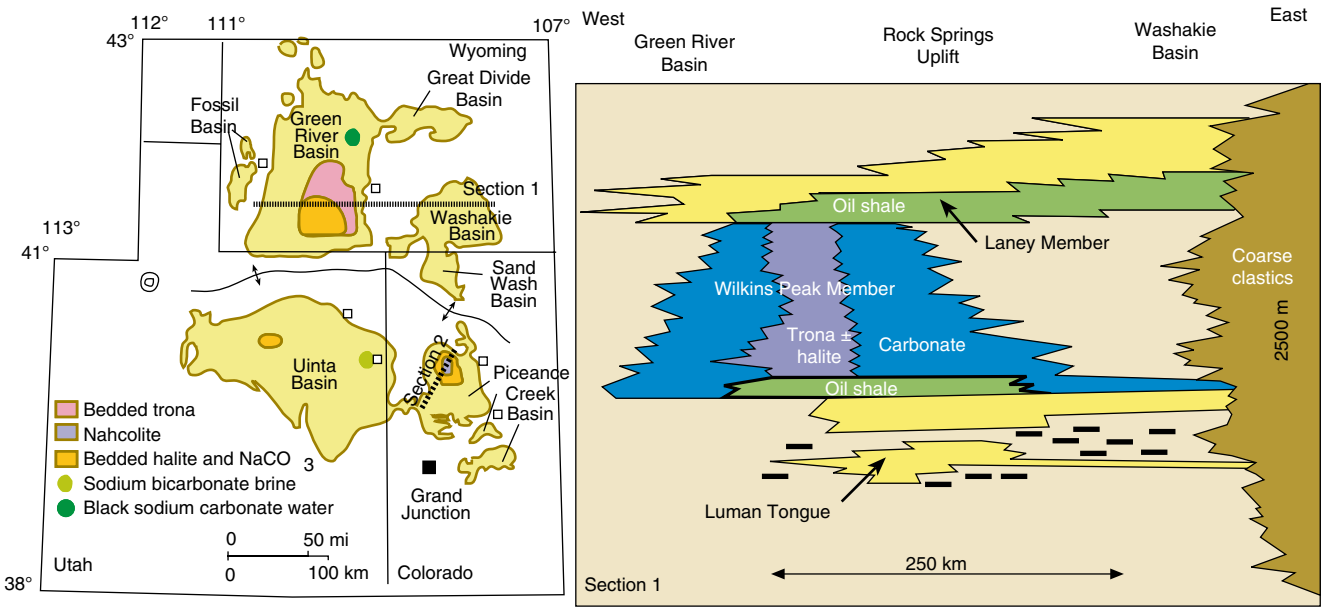

Fig. 12.35 Green River Formation. (**a**) Areal distribution and the locations of sodium carbonate deposits in Utah, Colorado, and Wyoming. (**b**) Stratigraphy of the Eocene Green River Formation showing interrelationships between various members and facies in the Green River Basin (After Dyni 1996)

dissolved) that once precipited in evaporitic seaways of the Archaean. Even today, all that is needed to form sodium carbonate brine is a suitably alkaline inflow water, depleted in sulphate and chloride. Most continental ground waters in metamorphic, volcanic, or igneous terrains can produce alkaline solutions upon evaporation (Hardie and Eugster 1970). The relative absence of chloride and sulphate in these types of rocks permits solutions to become relatively enriched in Na and HCO_3 and so follow the appropriate "closed basin" concentration pathway leading to trona/nahcolite (Fig. 2.19; pathway I). Mechanisms driving the appropriate chemical evolution leading to trona are varying combinations of mineral precipitation, selective dissolution of efflorescent crusts, degassing of brines, and/or redox reactions (Jones et al. 1977).

Groundwater percolating through siliceous soils, such as those developed on granite or windblown sand, can become highly alkaline and enriched in sodium carbonate (Garrels and Mackenzie 1981). Alternatively, very high carbon dioxide concentrations (up to 10 % in soil gas) can be the result of intense biological activity in the precipitative brine. The Pretoria pan and the Sua Pan in Botswana are examples showing elevated sodium carbonate in soil waters, so the construction of solar evaporators using this water can produce substantial volumes of trona each dry season. In soda lakes such as Lake Magadi and Lake Natron, the deposition of monomineralic beds of trona is be aided by the continual generation of biogenic CO_2 from the halobiota flourishing in alkaline lake waters (Chap. 9; The Flamingo connection).

In regions characterised by an abundance of limestone or dolomite, or even a drainage basin leaching older marine evaporites, the inflow waters to the saline depression typically contain too much chloride, sulphate, and calcium to produce a trona brine. Even in some areas draining igneous and volcanic terrains, the inflow waters mix with other basinal waters or with other rock and soil types to create a hybrid chemistry where trona cannot precipitate.

Trona in North America

The lacustrine Green River Formation (Eocene) in the Green River Basin in Sweetwater County, southwest Wyoming contains the world's largest known resource of natural sodium carbonate in the form of bedded trona (Fig. 12.35). The scale of current extraction, and the possibility for future expansion using conventional mining techniques for the various Wyoming operations is huge. For example, General Chemical's Green River Basin plant has identified trona ore reserves of more than 500 million tonnes and currently maintains more than 200 km of underground workings. Total identified trona resource in the basin is more than 47 billion tonnes, dwarfing any other known natural trona resource. For comparison, the combined identified total resource for Searles and Owens lakes is slightly in excess of 815 million tonnes. America today produces over 10 million tonnes of trona per year and is a net exporter of product.

The Eocene Green River Formation is divided in ascending order into the Tipton Shale, Wilkins Peak Member, and

the Laney Shale. The trona resource lies wholly within the lacustrine Wilkins Peak Member. The Wilkins Peak ranges from about 183 to 410 m (600 to 1,350 ft) in thickness and consists of marlstone, oil shale, trona, siltstone, mudstone, and numerous laterally persistent thin layers of tuff. These sodium carbonate-rich sediments were deposited in two large lakes that occupied several lacustrine sedimentary-structural basins in Colorado, Wyoming, and Utah (Figs. 5.12 and 12.35; Dyni 1996; Smith et al. 2008; Tanavsuu-Milkeviciene and Sarg 2012). These Eocene basins include the Green River, Washakie, and Sand Wash Basins in southwest Wyoming and northwest Colorado, the Piceance Creek Basin in northwest Colorado, and the Uinta Basin in northeast Utah. Eocene Lake Gosiute is the northern lake that once occupied the Green River, Washakie, and Sand Wash Basins. The southern lake, Eocene Lake Uinta, occupied the Uinta and Piceance Creek Basins in Utah and Colorado (Fig. 12.35a). The Uinta Mountain Uplift, an east–west positive structural element, separated the two lakes, although they may have been connected during part of their existence on the east side of the uplift. At its maximum extent, Lake Uinta covered about 57,000 km^2 (22,000 square miles), and Lake Gosiute, about 38,850 km^2 (15,000 square miles).

During much of Green River time, the lakes were hydrographically-closed with no surface outlets. The Green River Formation consists of a variety of lacustrine sedimentary rocks, including sandstone, claystone, shale, dolomitic marlstone, oil shale, and numerous, generally thin beds of volcanic tuff (Dyni 1996). Typically, the Green River sediments grade from fine-grained sandstone, mudstone, claystone, and shale in shoreward areas of the lakes into carbonate-bearing sediments enriched in organic matter toward basin centre (Dyni, op. cit.). The lateral transition from siliciclastic to carbonate-enriched rocks is also reflected in vertical sequences of the Green River Formation and equivalents in the Green River, Piceance Creek, and Uinta Basins. This indicates increasing salinity of remaining alkaline lake waters as divalent cations of calcium and magnesium were precipitated as calcite, Mg-calcite, and dolomite in lake fringe mudflats, while dissolved sodium, bicarbonate, and chloride continued to accumulate in surface and near-surface waters in saline pans in the lower parts of the basin. A lack of sulphate in the trona pans perhaps reflects bacteriogenic sulphate reduction in the lake brines, as in modern lakes in the African rift valley. Associated hydrolysis of detrital silicate minerals and glassy volcanic ash (zeolites) also contributes additional dissolved bicarbonate, sodium, and other ions to the lake brines. Tuffaceous debris amounts to roughly 5 % of the total sediments in the Green River Formation.

During drier periods these Eocene lakes shrank and large volumes of saline sodium bicarbonate minerals were deposited, either as bottom nucleates in shallow brine sheets or as displacive intrasediment nodules in mudflats. The more abundant sodium salts include trona, nahcolite, shortite, dawsonite, halite, and less commonly eitelite and wegscheiderite. The most important lake desiccation event occurred during Wilkins Peak and Parachute Creek time when vast deposits of trona and nahcolite were precipitated in the Green River and Piceance Creek Basins, respectively (Figs. 12.35 and 12.36). During two later desiccation events, nahcolite was deposited as nodules and possibly some thin beds in the Birds-nest zone in the eastern Uinta Basin, Utah. Finally, during a later desiccation event, bedded sodium salts were deposited in the Uinta Basin near Duchesne, Utah (Dyni 1996). Interbedded dolomitic oil shales separate these desiccation events and represent biochemical deposition from relatively dilute lake waters during expanded lake phases. Trona beds were deposited in the lowest sectors of the various basins during times when surface waters were extremely shallow to ephemeral with brine chemistries akin to those in modern Lake Magadi (Surdam and Wolfbauer 1975; Fischer and Roberts 1991). Centripetal groundwater inflows subsequently dissolved some of the sodium salts, as evidenced by the presence of solution breccias and solution cavities in cores collected in marginward parts of the Green River Formation. At least two areas today contain sodium carbonate brine pools of unknown size, but that are possibly exploitable brine resources (Fig. 12.35).

Currently mined trona ore in the Green River Basin is restricted to the Eocene Wilkins Peak Member of Wyoming. Culbertson (1966) defined 42 beds of trona, up to 14 m thick in the member, at depths ranging from 120 m to over 1,000 m. He numbered the thickest and economically most important of these beds from 1 to 25 in ascending order (Fig. 12.36). These trona beds are remarkable for their purity and continuity compared to other large lacustrine trona deposits elsewhere in the world. Sulphate minerals are essentially absent, and other than halite, the chief impurities are thin dolomitic marlstone stringers and vertical seams of mudstone created by extension and injection of water saturated mud. Faults cutting the trona are rare and bed dips are typically less than a degree, making them eminently suitable for mining. Toward the depocenter in the southern part of the basin some of the trona beds grade laterally into mixed halite and trona (south of dashed line in Fig. 12.36). Nahcolite is abundant in some beds in the lower part of the evaporite stratigraphy making them less suitable mining targets. Dyni (1996) also notes that nahcolite, wegscheiderite, northupite, and possibly shortite become locally abundant, as well as quartz, toward the depositional centre of the mixed halite and trona interval in bed 17 when it is traced into the southern part of the basin. Bed 17 is one of the most important ore targets as it has the greatest area in the basin.

The Wyoming trona district currently produces about 8.2 million mt (9 million tons) of refined soda ash annually from five underground mines that extract a total of about 16.3 million mt (18 million tons) of trona ore (Dyni 1996). Trona

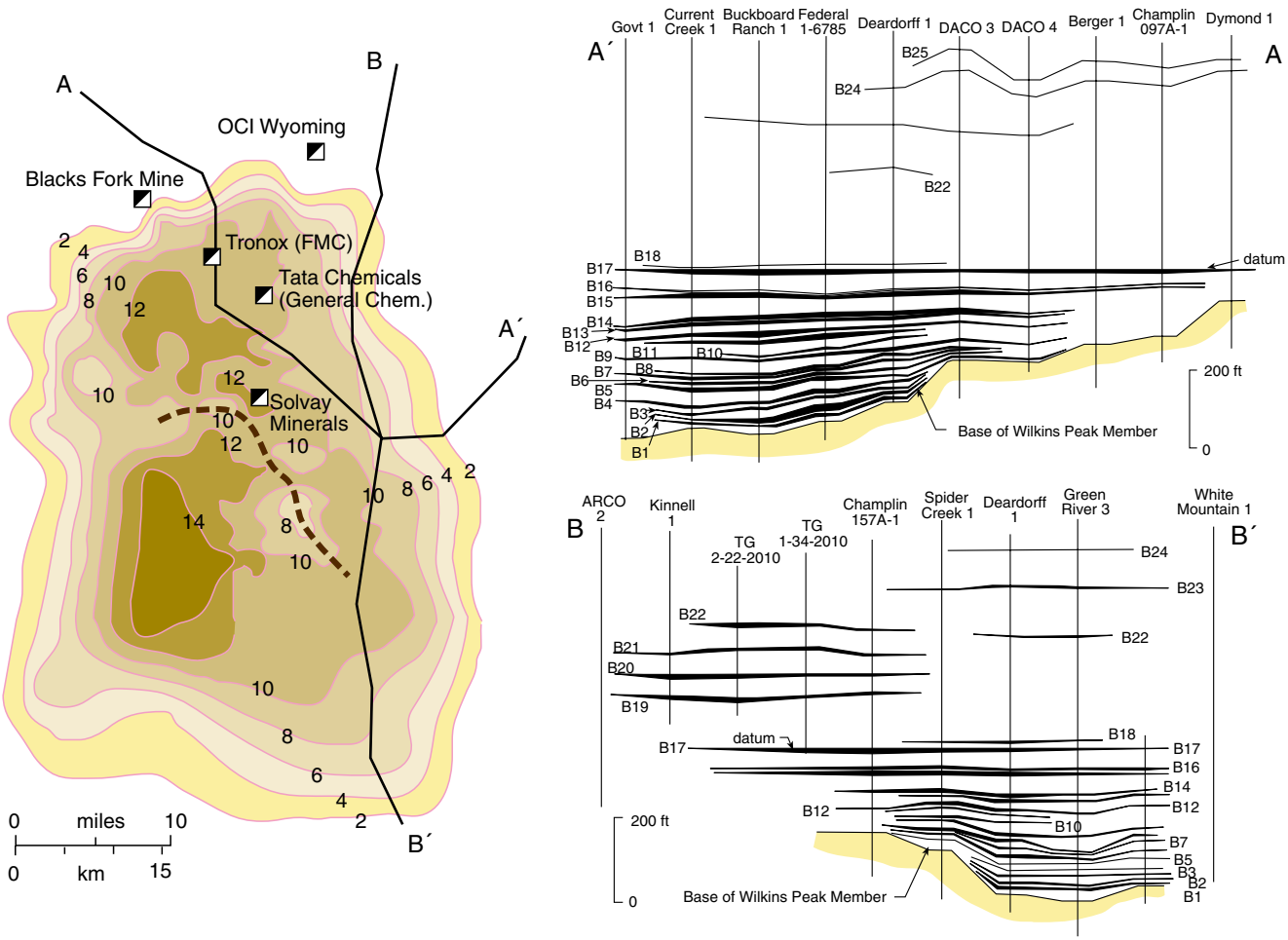

Fig. 12.36 Trona distribution in the Wilkins Peak Member of the Eocene Green River Formation in Wyoming. Isopach is of Bed 17 and is in feet. *Heavy dashed line* indicates approximate northern extent of halitic facies. Cross sections use Bed 17 as a datum; halitic facies are not shown and the wells are equally spaced in the cross sections (After Dyni 1996 and Wiig et al. 1995)

bed 17 where it is more than 1.2 m (4 ft) thick, underlies about 2,000 km^2 (775 square miles) of the basin and ranges from 1.2 to 5.2 m (4–17 ft) in thickness (Fig. 12.36; Dyni 1996). Twenty-two of the 25 numbered beds listed by Dyni (1996) are estimated to contain 115 billion mt (127 billion tons) of trona ore, or 69 billion mt (76 billion tons) of trona in beds containing less than 2 % halite. These 22 beds, where they are 1.2 or more metres (4 or more feet) thick, underlie areas ranging from 130 to more than 2,000 km^2 (50 to more than 775 square miles) at depths of 200–915 m (650–3,000 feet) below the surface. The trona contains 70.3 wt% sodium carbonate and it takes about 2 t of trona ore to produce 1 t of soda ash. Currently, Tronox (formerly FMC), Tata Chemicals, and Solvay Chemicals mine trona bed 17, Blacks Fork mines bed 20, and OCI Wyoming (formerly DC Chemicals) mines beds 24 and 25.

Mining is conventional, using vertical shafts to access the ore level and then room-and-pillar, short- and long-wall techniques (Dyni 1996). At three mines, additional sodium carbonate is recovered from wastewaters from the processing plant, which are used to slurry tailings to abandoned parts of the mines. These same waters dissolve additional trona from the pillars and are then pumped back to the surface to recover the additional sodium carbonate. This post-mining brine recovery/recycling technique has proven to be economical and will probably soon be employed by other mines in the district. Earlier attempts to solution mine trona from vertically drilled holes have been unsuccessful due to nahcolite 'blinding' (Fig. 13.11).

At the end of the millenium, a small-scale solution mining operation began in the Parachute Creek member in the Piceance Creek Basin using horizontally drilled holes with nahcolite, not trona, as the planned feed source. If the blinding problem is solved a similar horizontal drilling method may be especially useful in the southern part of the Uinta basin where the trona beds are thicker and lie at greater depths. By mid 2004 operations at this facility were scaled back and today there are no active extraction or processing activities focused on nahcolite in this area.

The Parachute Creek Member in the deeper northern part of the Piceance Creek Basin contains a saline facies,

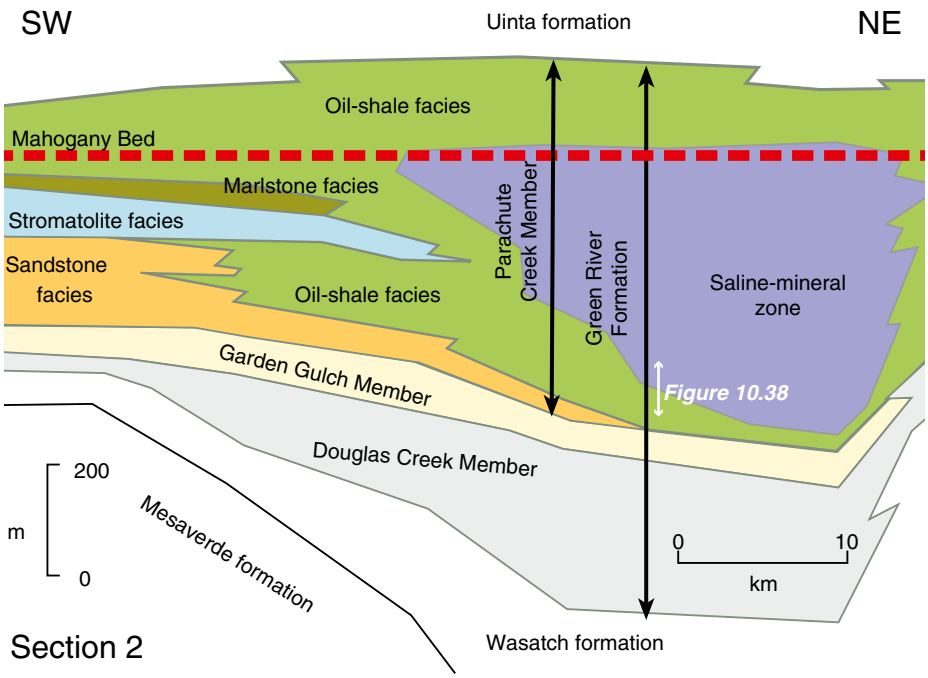

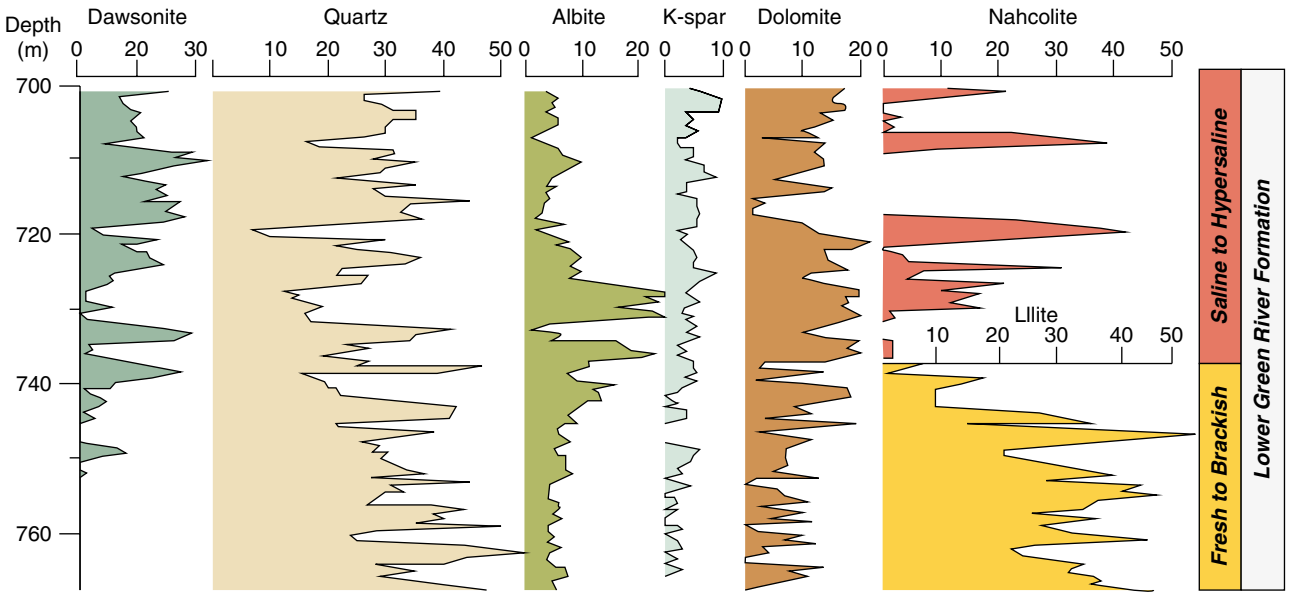

Fig. 12.37 Stratigraphy of the Eocene Green River Formation showing interrelationships between various members and facies in the Piceance River Basin (section 2). Locality of section indicated on Fig. 12.35

Fig. 12.38 Salinity-related transition to saline nahcolite-precipitating brines in Lower Green River Formation in core from the Juhan 4–1 well, Piceance Creek Basin, Colorado. Note the upward decrease then disappearance of illite as the first sodium carbonate minerals, nahcolite and dawsonite appear. The increasing salinity is indicated also by increases in dolomite and albite and a decrease in the level of quartz (After Dyni 1998)

which includes beds of nahcolite and some halite, along with scattered crystals, nodules, and coarse-crystalline aggregates of nahcolite commingled with high-grade oil shale (Fig. 12.37; Dyni 1996, 1998). Also included in the saline facies is dawsonite as microscopic crystals in the microcrystalline matrix of the oil shale. The transition into saline oil shales and into the sodium carbonate minerals nahcolite and dawsonite in the Piceance Creek Basin is a transition from brackish into saline waters, accompanied by a loss of detrital illite and an increase in dolomite and albite (Fig. 12.38; Dyni 1998).

The top of the nahcolite-bearing oil shale in the Piceance Creek Basin is a dissolution surface above which meteoric waters have dissolved nahcolite and halite forming a "leached zone" of vuggy brecciated oil shale (collapse breccia), which is up to several hundred feet thick. The leached zone extends upward into the lower part of the Mahogany oil-shale zone, a unit of high-grade oil shale traceable throughout the basin

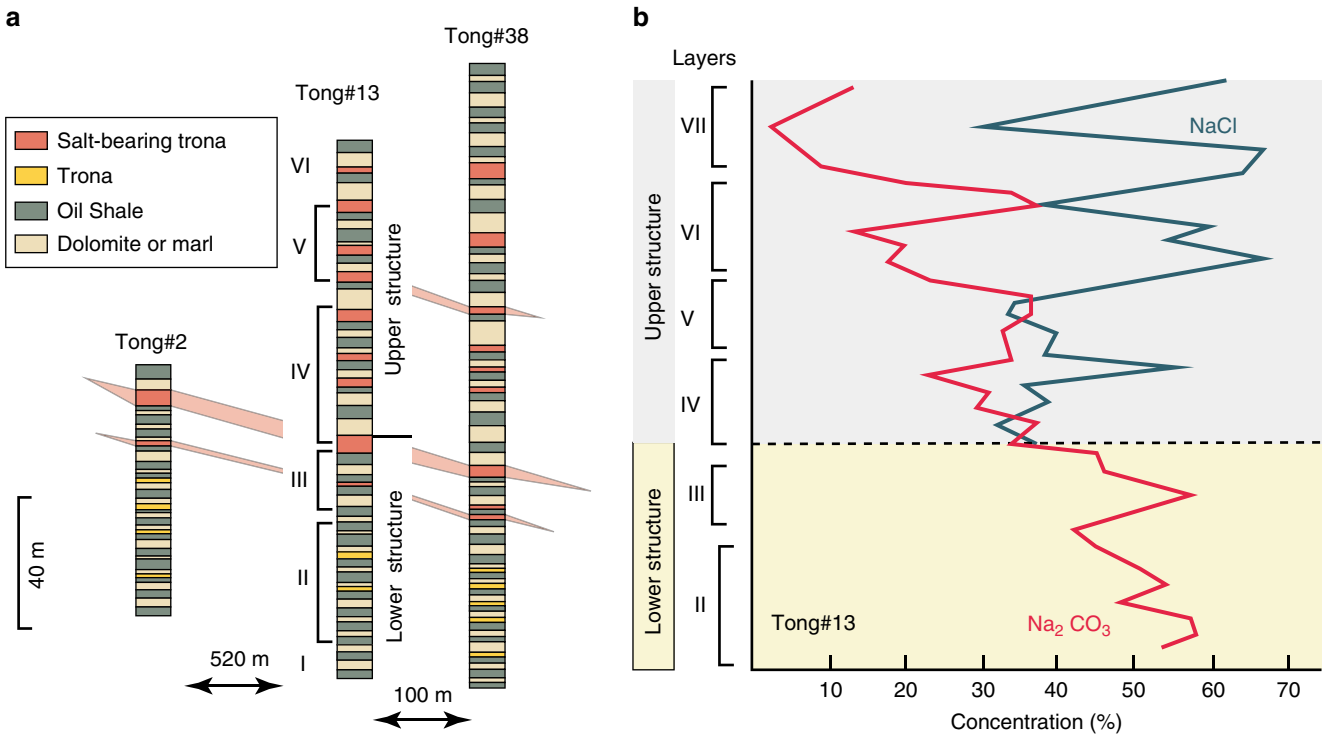

Fig. 12.39 Eocene lacustrine trona at Wucheng, China. (**a**) Layering across 3 wells in the Wucheng deposit showing purer trona in the "Lower Structure" interval of the deposit. (**b**) Detail illustrating loss of halite and increase in trona in the *lower part* of the Tong#13 borehole (After Zhang 1998)

(Fig. 12.37). The top of the leached zone is defined by the stratigraphically highest occurrence of the solution breccia (Dyni 1981). This top can be considered to be the top of the original bedded saline facies in the Parachute Creek Member, although crystal cavities and vugs are found scattered through the upper part of the Parachute Creek Member well above the Mahogany oil shale in a zone 168–335 m (550–1,100 ft) thick.

The potential nahcolite resource in the Piceance Creek basin is estimated at between 29 and 32 billion short tons (26–29 billion mt; Dyni 1996). It is unlikely that this resource will be exploited as associated oil shale cannot be removed or damaged under current sodium leasing regulations. The major part of the potential nahcolite resource, which occurs as crystalline aggregates scattered through oil shale, will be difficult to economically mine for soda ash alone. Any solution mining of nahcolite beds in this part of the basin may render portions of the overlying oil shale unsuitable for future in situ or underground mining.

Natural Soda Ash in China

In China, synthetic sources dominate the country's total soda ash production, but lesser volumes of natural soda ash are extracted via solution mining of two Eocene deposits (Wucheng and Anpeng) and winter extraction in two Quaternary salt lake systems (Lakes Changnor and Ordus; Zhang 1998).

The Wucheng trona deposit in southern Henan Province, 18 km west of Tongbai County was discovered in 1971 during petroleum exploration. This Eocene deposit lies in the central part of the Paleogene faulted Wucheng basin (Zhang 1998). Trona beds cover an area of 4.66 km^2 at depths of 643–974 m. Based on NaCl content is divided in two units: (1) The "upper structure" consists of 21 salt-bearing trona beds with thicknesses ranging from 1 to 3 m (Fig. 12.39a). The beds of the upper structure contain an average of 34.0 % total sodium carbonate and 45.6 % sodium chloride. (2) The "lower structure" consists of 15 trona beds with low halite content and thicknesses ranging from 0.5 to 1.5 m. The ore (trona beds) of the lower structure contains an average of 55.0 % total sodium carbonate and less than 0.3 % sodium chloride (Fig. 12.39b). Resources of the Wucheng trona deposit total 36.8 Mt sodium carbonate and 17.8 Mt sodium chloride.

Sodium carbonate-bearing minerals in Wucheng are mostly trona and nahcolite, typically associated with lesser amounts of shortite, northupite, and $NaCl{\cdot}Na_2CO_3{\cdot}(MgFe)CO_3$. Halite is a commingled mineral in both the upper and lower units but present in much lower proportions in units of the lower structure. The floor and roof strata of the ore units and gangue interbeds are composed of oil shale, dolomite, and marl. A representative cross section based on three

boreholes through the Wucheng trona deposit is presented as Fig. 12.39a, while sodium carbonate and sodium chloride variations within layers in the Tong #13 borehole are illustrated in Fig. 12.39b.

A trona bed in the lower structure of the Wucheng trona deposit is the target for solution mining extraction. This trona bed is made up of 38.63 % Na_2CO_3, 47.72 % $NaHCO_3$, 0.53 % NaCl, and 13.12 % H_2O (without insoluble matter). The calculated optimum concentration and consumption of caustic soda used for solution mining for this bed is optimised for various subsurface temperatures across the deposit (Chap. 13). This trona bed is separated by 450 m of impermeable dolomite, marl, and oil shale from upper aquifer strata; the floor strata are also impermeable.

The Wucheng trona deposit shows no obvious faults. Surface distance between the injection and production wells is about 100–150 m, The trona was fractured at an injection pressure of 15 megapascals (MPa), and the operating pressure kept at about 2.5 MPa. Under normal conditions, solvent is injected with a caustic soda concentration of 4–5 %. The solution obtained at the production well has a sodium carbonate content of 14–16 %. The flow rate proportion of produced solution to injected solvent is about 0.85.

The nearby Anpeng nahcolite deposit is located 60 km southwest of the Wucheng trona deposit and was discovered in 1976 during petroleum exploration (Zhang 1998). The deposit lies in the southeastern part of the faulted Paleogene Biyang basin and like Wucheng also formed as saline lacustrine precipitates in the Eocene at a time when CO_2 levels in the atmosphere were much higher than today (≈1,125 ppm; Lowenstein and Demicco 2006). The deposit consists of 17 nahcolite beds with thicknesses ranging from 0.6 to 3.6 m across an area of 8 km^2 at depths of 1,310–2,520 m. Ore targets are located in the middle, proximal middle, and upper parts of the Lower Tertiary Hetaoyuan Formation. Northwest of the main exploited area of the nahcolite beds, brines containing sodium bicarbonate and sodium carbonate occur in porous and permeable lacustrine dolomites in five layers with thicknesses ranging from 1 to 5 m. Solid minerals in the Anpeng deposit are mainly nahcolite and wegscheiderite ($Na_2CO_3 \cdot 3NaHCO_3$). The floor and roof strata and evaporite interbeds consist of dolomite, oil shale, and sandstone. The Anpeng nahcolite deposit has a likely reserve of 55 Mt sodium carbonate, of which about 2–3 % occurs in brine.

Solution mining of the Anpeng nahcolite deposit is similar to that of the Wucheng trona deposit, utilising a set of injectors and producer wells. Surface distance between injection and production wells is about 168–215 m. The dolomitic floor and roof stratum have a higher strength than nahcolite, enabling effective longterm solution mining. With injection of a 3 % caustic soda solution as a solvent, the produced solution has a sodium carbonate content of 8.5–10.1 %. The flow rate proportion of produced solution to injected solvent is about 0.82. Some nahcolite ore is contaminated by petroleum, which influences the dissolving effect. The pumped solution can contain some sodium carbonate crystals. Recently, there have been local saline groundwater breakouts that are related to escaping solution mine brines causing environmental problems via contamination of local aquifers and soil salinisation in the vicinity Cao Village (see Chap. 13; Shi et al. 2013).

The Chaganur (Chagonnor) soda ash lake deposit, discovered in 1966, is located in the central part of the Inner Mongolia Autonomous Region, some 80 km southeast of Erlianhot (Fig. 12.40a). At an elevation of 1,000 m, it is a lacustrine sump in the lowest part an arid deflation basin situated at an erg edge in the cool arid steppes (BSk) of the Inner Mongolian plateau. It is made up of a smaller northeastern sub-basin (East Chaganur) and a larger southwestern sub-basin (West Chaganur) joined by a narrow channel. Two intermittent rivers discharge into the lake, one from the northeast and the other from the southeast. The lake is also fed by direct precipitation. Chagannur is the largest of a series of 16 alkaline salt lakes in the region (e.g. Hushunur, Wulannur, Huguonur, Halefushuyingnur, Muyingnur, Wulannur, Wenduobunur, South Chaganur) that are relicts of a formerly more extensive lake (palaeolake Chagannur).

At its maximum extent, which is thought to have been during the early to mid- Holocene, this palaeolake occupied an area around 2,640 km^2. The total area of the various lakes in the basin today is ca 156 km^2 and the area of the current catchment is 2,800 km^2. The basin, which is controlled by two faults running SW-NE, is a tectonic sump with a Cretaceous bedrock of sandstone and mudstone. Annual evaporation today is ten times that of precipitation. The natural soda beds in the Chaganur lake accumulated during climatically-induced shrinkage events and occupy an area of 21 km^2 and are under-lain by some 20 m of sandy clay. The targeted deposit consists of nine soda beds with interstitial hypersaline brines that are interlayered with black muds (Fig. 12.40a).

The main minerals in the soda beds are natron and trona, with associated mirabilite and halite, and small amounts of northupite and gaylussite. The Chaganor deposit has a reserve of 11.3 Mt of sodium carbonate and 4.5 Mt of sodium sulphate. After the topsoil is removed, trona levels are quarried, bed by bed. Interstitial brine is pumped off in advance of bed removal via pumping into solar ponds where halite is recovered in the summer and burkeite in the autumn. Earthern walls are constructed to prevent surface floods entering the worked areas.

The Ordus (Ordos) alkali lakes are located on Ordus Plateau in the southwestern part of the Inner Mongolia Autonomous Region. Some of these alkali lakes are among the earliest worked natural soda ash deposits in China. The lakes lie in the Ordus Plateau region, at an elevation of

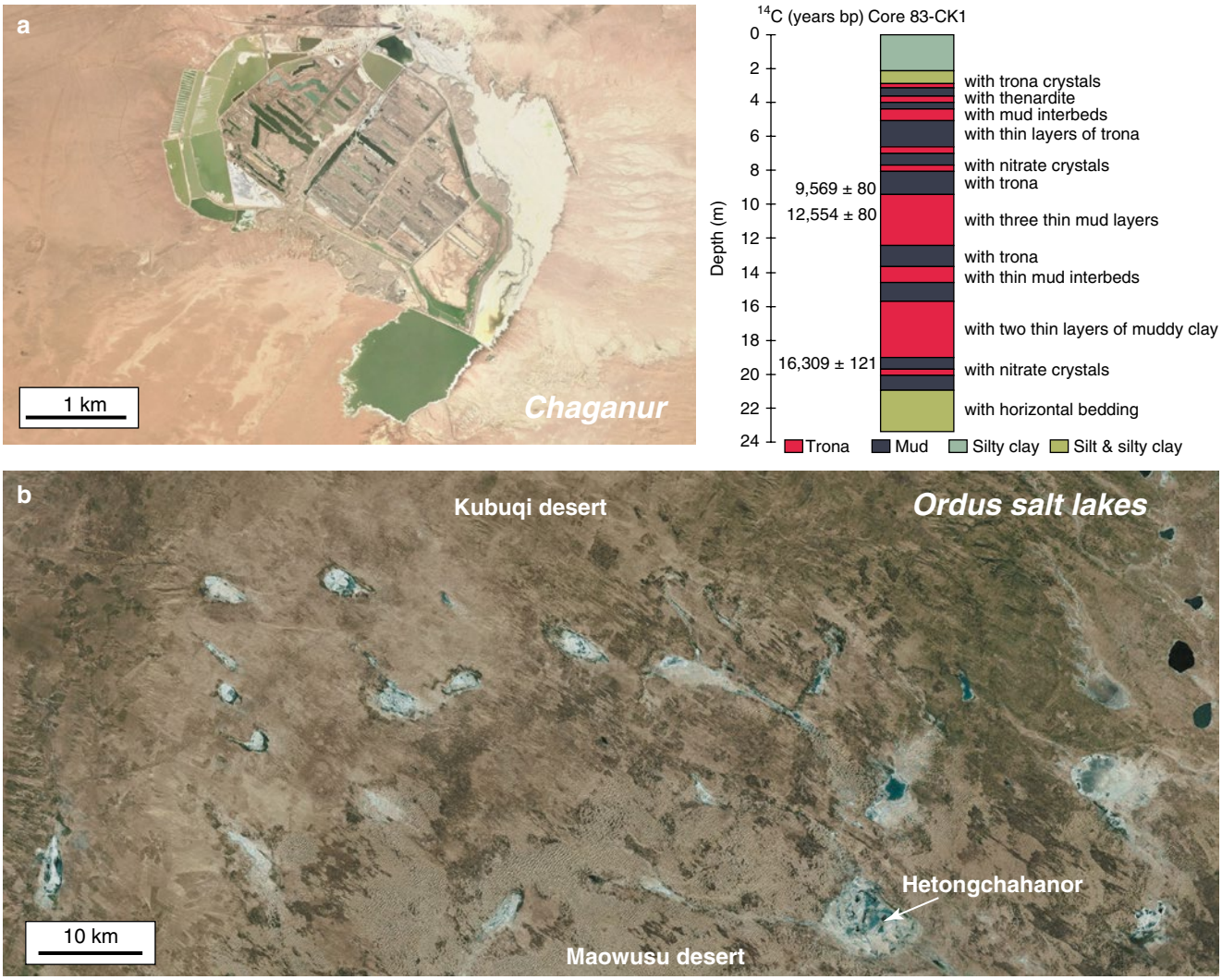

Fig. 12.40 Quaternary trona lakes, Inner Mongolia autonomous region, China. (**a**) Chagannor Lake, with geological detail of core 83-CK1 collected in the lake. (**b**) Regional view of the Ordus Salt lake system (Bing® Images mounted in Mapinfo®)

1,268–1,412 m, at the margin of the Gobi Desert in a corridor that separates two sandy deserts called Kubuqi and Maowusu. Climate is cool arid (BSk), with annual evaporation levels some seven times that of precipitation. Around ten significant alkali lakes are distributed over the two desert margins (Fig. 12.40b).

Like the other lakes of the Ordus system, the largest lake Hetongchahanor-occupies a deflation depression and is located in the northern extent of the Maowusu desert, 110 km southwest of Dongsheng. The Hetongchahanor alkali lake has an area of 29 km^2, and contains 0.4–1.0 m of perennial alkaline surface water. The ore target consists of one natural soda bed and its interstitial brine. This soda bed covers an area of 6.14 km^2, with an average thickness of 1 m, and is underlain by 1–1.5 m of sandy clay. Hetongchahanor alkali lake contains a reserve of 1.7 Mt sodium carbonate. Principal minerals are natron and trona with associated mirabilite and halite, and a small amount of gaylussite. Solar ponds have been used at Hetongchahanor to recover trona in the summer and natron and mirabilite in the winter.

Trona in the African Rift

Outside of the USA, the largest documented production of natural soda ash in Quaternary sediments is from Lake Magadi, located some 120 km southwest of Nairobi, Kenya (Chap. 4). The lake is situated in the lowest part of the East African Rift Valley and has a total area of 100 km^2, it lies in an Aw climate belt with a net evaporation rate in excess of 400 mm per year in the lake vicinity. The deposit contains more than 30 billion metric tons of trona in a bed between 7 and 40 m thick and believed to have formed in the last 9,000 years. Thermal springs, driven by the area's volcanic

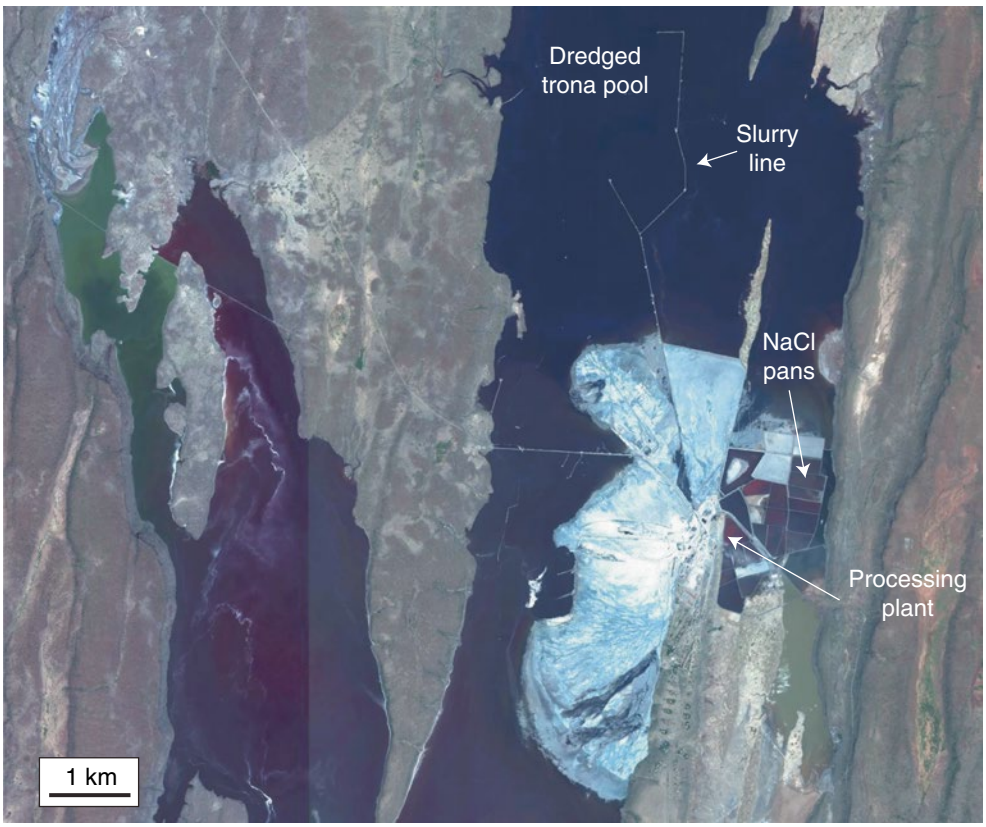

Fig. 12.41 Lake Magadi, extraction and processing areas

activity, are the major source of sodium in the lake and are sourced from a deep actively circulating groundwater reservoir. Trona precipitates in the more central areas of Lake Magadi as a bottom-nucleated crystal pavement. The annual crop is estimated at 1.5 million tonnes/year, although the bulk of this crop (≈75 %) redissolves each wet season. When trona-saturated surface brines in Magadi dry up, the brine level stays close to the trona pavement surface. Even during exceptionally dry years the brine surface drops only 1 or 2 cm into the trona bed.

Trona in Lake Magadi has been mined since 1914 and is currently quarried from the central pavement using dredging barges. Today, the facility is owned and operated by Tata Chemicals Magadi Ltd and produces around 350,000 tonne/year. As the solid material is removed by a digger belt, liquor from the surrounding trona pavement drains into the resulting cavity, forming a pool or 'paddock' in which dredges float and move forward (Fig. 12.41). Crystals of trona produced by the dredges are coarse crushed, mixed with lake liquor and pumped as a slurry back to the factory where the liquor is discarded and the crystals washed and centrifuged. Water washing reduces the sodium chloride level associated with the liquor from 11.5 % to around 0.33 %. The damp crystals are then fed into calciner plant. The crushed refined soda is then conveyed to the calciner plant. There it is fed into two large rotary kilns and subjected to a continuous flow of hot gases across a reaction bed to chemically decompose the trona (sodium sesquicarbonate) into soda ash, carbon dioxide and water vapour. This calcined material is conveyed to the grinding and screening plant, where the physical grading of the product takes place, before the product is conveyed to the storage silos, followed by packaging and transport to market.

If for any reason a dredging barge breaks down for more than a day or two, trona precipitating in the paddock about the base of the barge can lock the barge in place. This trona has to be physically chipped away before dredging operations can continue. Replenishment of trona in the lake is so rapid that at present extraction rates the Magadi trona could be considered a renewable resource.

The Lake Magadi facility also produces NaCl in a series of purpose-constructed solar evaporation ponds use to concentrated natural lake brines pumped into the pans (Fig. 12.41). Lake brines are typically saturated, with a total dissolved solids (TDS) content of approximately 32 %. Of this, sodium chloride content varies from 30 to 34 %, the rest being almost exclusively sodium carbonate compounds with some sodium fluoride in small quantities (Chap. 4).

Lake brines are pumped to pre-concentration ponds where mostly sodium carbonate monohydrate precipitates. When the remaining brine contains a 50:50 ratio of sodium chloride and sodium carbonate, it is transferred to the salt-making ponds and left to cure. With more evaporation a mixture of soda ash and halite precipitates as a 1-cm-thick layer. This

layer is manually harvested and transported to the factory for processing into various grades of sodium chloride for different salt markets.

There is additional trona production and occurrence on the African continent (Table 12.10): (1) An industrial brine processing plant on the Sua Pan in the Makgadikgadi Basin in NE Botswana (annual production around 300,000 tonne), (2) Minor production of an impure product, mostly for local consumption, from interdunal pans on the NE edge of Lake Chad, (3) Minor production form the Wadi Natrun region of Egypt, some 80 km NW of Cairo, where varying mixtures of trona + halite precipitate each summer in a series of most ephemeral lakes, including Lakes Hamra and Beida (Shortland 2004), (4) Minor production from small ephemeral lake and sodium carbonate brine occurrences spread across the rift valley of Ethiopia, especially toward the southern end of the Ethiopian rift, as in the Lake Abijata mudflats (Tadesse et al. 2003). (5) Lake Katwe, a volcanic cone lake in Uganda, which may also be suitable site for the production of small volumes of potash salts. (6) Lake Logipi, Kenya, (7) The Pretoria Salt Pan (Tswaing), South Africa, (8) Bir Natron (Al 'Atrun) in the Sudan, and (9) A poorly understood noneconomic occurrence of trona crystals recovered in a core taken from sediments of the Nile cone at water depths down to 2,500 m (Stanley and Sheng 1979). Worldwide, other natural trona and sodium bicarbonate brine occurrences include: the saline lakes of the high Andes (including, Laguna Santa Maria, Cachilaguna, Laguna Hedionda Sur, Laguna Honda Sur); Pikrolimni Lake, Greece; Lonar Crater Lake, India; and Sasykkul Lake in Tajikistan (Fig. 12.34, Table 12.10).

In summary, at the worldscale, exploited trona deposits can be grouped into two major and three minor subdivisions (Fig. 12.34, Table 12.10): (1) Eocene-Miocene lacustrine deposits formed in intermontane depressions within actively subsiding foreland depressions with relatively high relief surrounding drainage terranes, and, (2) Quaternary lacustrine deposits at the termina of hydrographically-closed drainages and further divisible into: (a) Intermontane depressions surrounded by relatively high topographic relief in the drainage basin where either (i) hot arid conditions allows bedded $NaCO_3$ to accumulate (Lake Magadi, Lake Natron, Searles Lake) or, (ii) high altitude conditions where seasonal brine freezing facilitates the formation of trona crusts (high altitude lakes of South America and the Pamirs and Nei (inner) Mongolia). Cryogenic soda-ash deposits tend to be marginally economic unless the sodium carbonate phase is a byproduct of other brine processing operations. (b) Terminal pans in lower-relief hot arid cratonic settings where a $NaCO_3$ resource resides within annually replenished $NaCO_3$ brines, often in combination with $NaSO_4$ (SuaPan, WadiNatrun, Lake Chad). Elevated CO_2 levels are common to all $NaCO_3$ settings modern and ancient; nahcolite was a typical bedded co-precipitate with trona during the peak Eocene greenhouse period when atmospheric CO_2 levels more than double that of today (Lowenstein and Demicco 2006).

$CaSO_4$ and NaCl

The depositional, diagenetic and geological settings of halite (rock salt) and gypsum/anhydrite (the most commonplace evaporite salts) were discussed in detail in earlier chapters, and will not be repeated here, only aspects relevant to economic exploitation and production are presented.

Calcium Sulphate (Gypsum)

The predominant use of gypsum since ancient times has been as a construction material (Kogel et al. 2006). The word gypsum is derived from the Greek word *gupsos* and the Arabic *jibs*, both meaning "plaster" and used in reference to calcined gypsum. The deriviation probably comes from the ancient Greeks; the Greek words "*epseo*" means burning or cooking and "*ge*" means earth ("*gepseos*" originally meant chalk).

Character and Extraction History

Gypsum's utility to the construction industry stems from its hydrated character. When gypsum is calcined at 160 °C it loses 1.5 mol of its combined water to form calcium sulphate[4] hemihydrate ($CaSO_4 \cdot 1/2H_2O$); stucco or "Plaster of Paris." When mixed with water the hemihydrate can be spread, cast or molded into the desired form, which then sets to a rocklike hardness. The name "Plaster of Paris" comes from gypsum quarries in the Montmartre district of Paris, which have furnished calcined gypsum to much of Europe since the Middle Ages. When calcined gypsum is added to water, spread between sheets of heavy paper and allowed to set, it makes the plasterboard or wallboard used worldwide in the "dry wall" industry. Uncalcined finely crushed gypsum and anhydrite are used as retarding agents in Portland cement; the set of the cement is slowed, but the tensile strength is not lessened.

The oldest traces of plaster renders are 9,000 years old, and were found in Anatolia and Syria. We also know that 5,000 years ago, the Egyptians burnt gypsum in open-air fires, then crushed it into powder, and finally mixed this powder with water to make jointing material for the blocks of

[4]Calcium sulphate has several forms, ie, calcium sulphate dihydrate ($CaSO_4 \cdot 2H_2O$; commercially known as gypsum), calcium sulphate anhydrous ($CaSO_4$; anhydrite), calcium sulphate hemihydrate ($CaSO_4 \cdot 1/2H_2O$), present in two different structures, α-hemihydrate and β-hemihydrate (commercial name of β-form: stucco or plaster of Paris).

their monuments, such as the Cheops Pyramid in 3500 BC. The writer Theophraste (372–287 BC) described quite precisely the fabrication of plaster as it was done at that time in Syria and Phoenicia. Hydraulic gypsum mortar was used in medieval times in castles and fortresses in what today is Germany. Remnants of walls constructed with hydraulic gypsum mortar have existed for centuries in the Hartz Mountain region of Germany. The ancient Greeks also used gypsum, in particular large plates of clear gypsum as temple windows. When the sun is viewed through relatively large plates of clear gypsum it takes on the appearance of the moon, hence the term selenite to describe this form of gypsum.

The industrial development of gypsum plasters is difficult to trace, but by the late 1800s a commercial process had been developed to slow the setting times, thereby allowing widespread use of finishing plaster in the construction industry. Prefabricated wallboard panels were developed in 1918, but were not widely used until the great construction boom after World War II (Adams 1993). Before that time, plastered walls were more common in residential and commercial construction.

Production

Global crude gypsum production in 2009 was estimated by Crangle (2009) to be 149×10^9 metric tonnes, representing a decrease of 5 % compared with that of 2008, when production totaled 157×10^9 metric tonnes (Fig. 12.42; pre world global financial crisis). In 2009, 87 countries produced significant quantities of gypsum, 10 of which accounted for 74 % of the total world production (Fig. 12.42a). In 2008 (the last year reliable worldwide end use data is available), cement manufacture accounted for up to 60 % of worldwide gypsum consumption, while plaster products, including wallboard, accounted for approximately 30 % of all consumption.

China was the leading producer of crude gypsum in 2011 with an estimated 45 Mt, followed by Iran with 13.0 Mt, Spain with 11.5 Mt, the United States with 10.4 Mt, Thailand with 8.5 Mt, Mexico and Japan with 5.8 Mt each, and Italy with 4.1 Mt (Fig. 12.42a). Given the likely longterm ongoing expansion in China's economy and its respective construction and infrastructure demands, China will likely continue to be the world's leading gypsum producer in the near future. Much of the Chinese production is an industrial byproduct

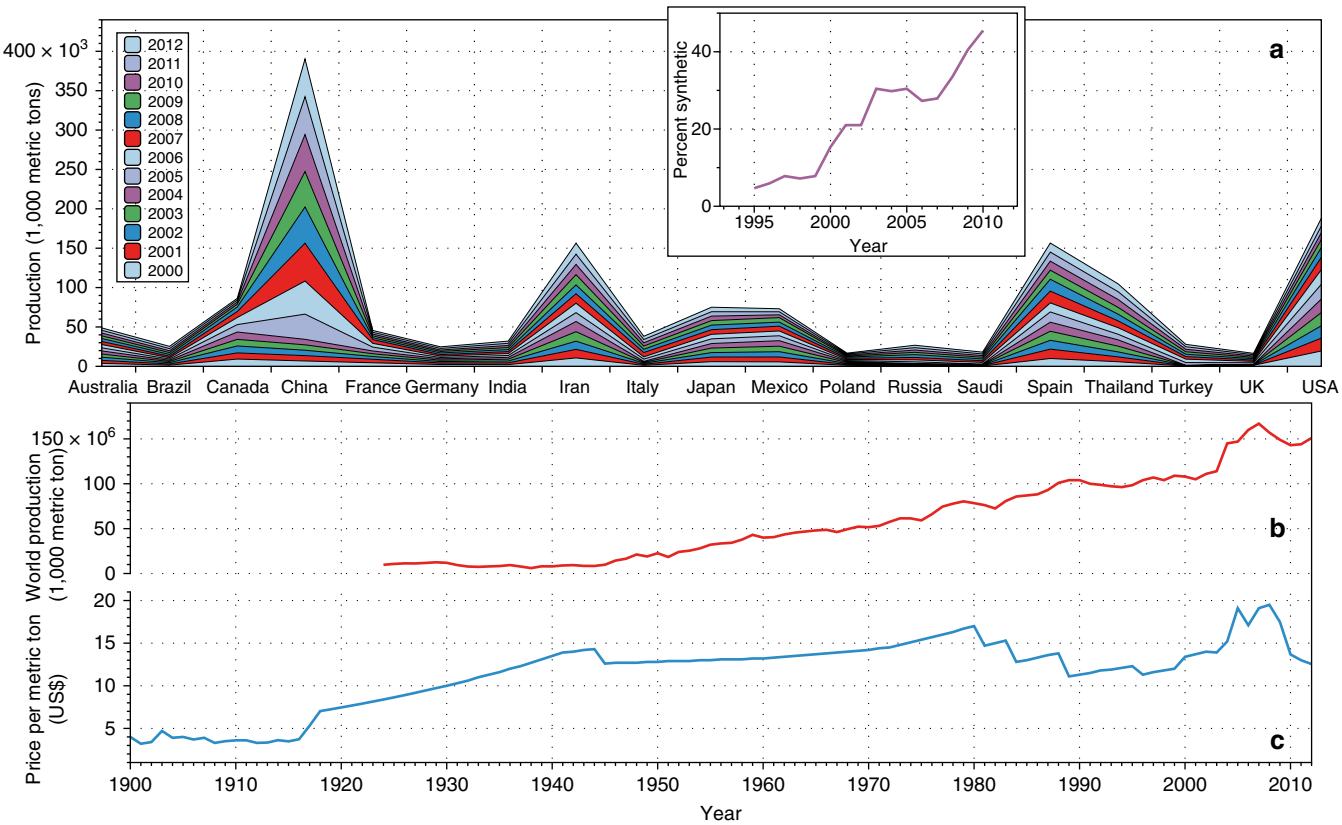

Fig. 12.42 Gypsum Production. (**a**) Cumulative area plot of annual production of top producing countries (in 1,000 metric tons). The drastic increase in Chinese production since 2004 is not as large as it seems in the figure, but indicates a more realistic set of estimates of China production by USGS since that time. Inset shows percent of world production that is synthetic (largely in China). (**b**) World production from 1924 to 2012 (1,000 metric tons), (**c**) Price per tonne in US dollars from 1910 to 2012 (Compiled from USGS on-line data tables downloaded from http://minerals.usgs.gov/minerals/index.html last accessed April 18, 2014)

and Chinese utilization of synthetic gypsum in wallboard and other construction material is increasing.

Use of gypsum wallboard is increasing worldwide, but only industrialized nations have the majority of their gypsum consumed in the manufacture of wallboard products. In developing countries, especially in Asia and the Middle East, the majority of gypsum is consumed in the production of cement or plaster products. Because some gypsum producers, especially in the developing world, manufacture gypsum products onsite, or nearsite, and intermittently, this product volume goes unreported. Accordingly, Crangle (2011) notes that world production levels are probably underestimated in USGS compilations, as illustrated in Fig. 12.42.

Use of gypsum plaster or wallboard in the construction industry also acts to improve fire protection in a building. Back in the 1600s, Louis XIV issued an edict stipulating that all wooden buildings must be covered inside and out with a layer of gypsum plaster. It is doubtful the mechanism of fire protection by gypsum was fully understood at the time, but considerable protection of the building ensued. At the very least, gypsum plating leads to compartmentalization of a fire, which in the typical wooden dwelling of the seventeenth century was a tremendous advance in fire protection and control.

When applied as soil conditioners, gypsum and anhydrite can have beneficial effects. They decrease the salinity of salty soil, improve the permeability of clayey soil and provide sulphur, calcium and catalytic support, so decreasing fertilizer use and maximizing the economics of crop production. Uncalcined gypsum is also used as a filler in a diverse range of products including paint, paper and toothpaste, as a flux in the smelting of certain nickel ores, in the manufacture of crayons, in asbestos packing gaskets and when in the form of alabaster[5] as a medium for sculpting. Other minor uses for calcined gypsum include dental plaster, modelling casts, moulds, surgical casts and drilling mud additives. Gypsum is also added to tofu to improve its stability and is probably one of the main sources of calcium for many people in SE Asia, who tend not to consume large volumes of dairy products.

Natural anhydrite is also crushed to less than 7 mm (30 % of which is dust), then mixed with water and an accelerator (Fe_2SO_4 and K_2SO_4), to form quick-setting, high strength roadside packs. Aerated anhydrite products are sometimes used to fill cavities in mines or in spaces above road arches. Anhydrite has also been used as a filling and packing material in the coal mining industry of West Germany since the mid 1960s.

Current natural $CaSO_4$ production is either from quarrying or mining. In North America and Europe, gypsum is mined at relatively shallow depths in areas where ancient buried anhydrite beds or diapir caprocks have reconverted to gypsum during uplift and erosion. The Maritimes region of eastern Canada and the USA produces the most gypsum from a single area in the world, with more than 6 million metric tonnes extracted each year from Mississippian strata of the Windsor Group. There is also substantial US production from Tertiary playa deposits in the Salton Trough, California. Spain is Europe's leading gypsum producer, with the main production from bedded Tertiary lacustrine deposits. In Germany, the greater volume of its gypsum is mined from the rehydrated caprock crests of near surface salt structures of Permian Zechstein salt. Secondary targets are the Middle Muschelkalk and minor production comes from the Keuper. In the UK, the most important beds are Permo-Triassic in age, except for those in Sussex, which are Jurassic.

In the southern Hemisphere, substantial volumes of high-grade gypsum are quarried, processed and shipped from Holocene coastal lakes in southern (>1,000,000 tonnes/year) and western Australia (300,000–500,000 tonnes/year). This production supplies the construction industry of Australia and many other parts of Southeast Asia. Small amounts of coarsely crushed gypsum are used as a cheap aggregate to pave unsealed minor roads in many places in southern Australia. Under the region's semi-arid to arid climate gypsum aggregate tends to compact and set into a hard flexible crust.

Synthetic gypsum is produced by a variety of industrial processes (Kuntze 2009). Most synthetic gypsum is the result of a neutralizing reaction between sulphate and calcium ions, as in the manufacture of phosphoric acid or titanium dioxide. Likewise, most chemical processes that use sulphuric acid to digest rocks result in acidic fluids that must be neutralised before they can be recycled or safely discarded. Limestone is the most common neutralising agent and synthetic gypsum is typically produced in the neutralising process. As mentioned previously, synthetic gypsum is chemically identical to natural gypsum and has the same crystal structure. Usually it has a higher dihydrate content and purity than most natural gypsums, but its impurities distributions are different and in some synthetic gypsums that can be of environmental concern.

Hence. despite the availability of synthetic gypsum as an industrial byproduct for more than half a century, there was an initial reluctance in North America and other places in the developed world to use synthetic material in wallboard manufacture. Nevertheless, over the past 20 years, due to increasing availability there has been a considerable change in attitude toward the use of synthetic gypsum, especially that sourced by desulphurization of flue gases at coal-fired power plants.

The price of crude gypsum fell in 2009 as the gypsum industry is closely tied to the construction industry (Fig. 12.42c). Even as the world economy improves, post the

[5] Alabaster is a form of gypsum that is massive, fine-grained, granular and compact; the name is related to a place in ancient Egypt called Alabaston, where this mineral was quarried for sculpturing.

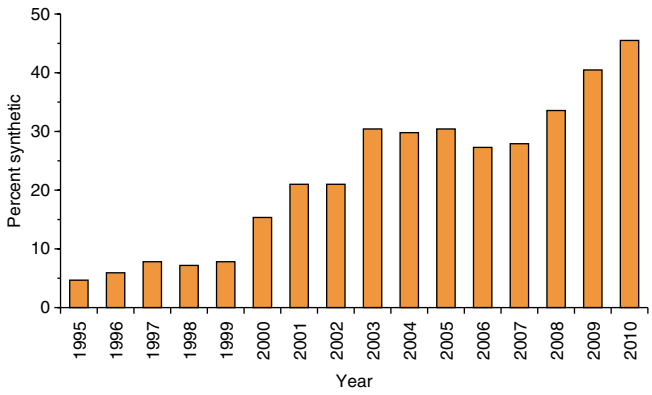

Fig. 12.43 Synthetic gypsum as a percentage of total gypsum ore used to manufacture gypsum panels in the United States 1995–2010 (Replotted from data on http://www.gypsumsustainability.org/recycled.html)

2009 financial crisis, it is unlikely there will be any substantial increases in price. This is because the market is being increasingly supplied and saturated by cheap synthetic gypsum. Increasing long-term use of synthetic gypsum derived from flue gas desulphurization (FGD) will continue to increase worldwide as more coal-fired electric powerplants convert their desulphurization processes to produce marketable gypsum (Crangle 2011). For example, most coal-burning powerplants in the United States are required by the U.S. Environmental Protection Agency to install sulphur dioxide scrubbing systems. This has created a significant source of gypsum, at a lower price than the cost of its mined counterpart, and in the past two decades has led to the construction of wallboard production facilities adjacent to coal-fired powerplants across the USA (Fig. 12.43). An estimated 250 million metric tons per year of synthetic gypsum is generated worldwide (Crangle 2011). Synthetic gypsum that is suitable for use in wallboard includes flue-gas desulphurization (FGD) gypsum, fluorogypsum (byproduct of fluoric acid manufacture), citrogypsum, and titanogypsum. Phosphogypsum (byproduct of phosphoric acid manufacture from apatite or phosphorite) on the other hand must be disposed of rather than used, due to unacceptable levels of deleterious impurities, such as radon and radionuclides.

Rock and Pan Salt (Halite)

The word halite comes from the Greek *hals* meaning salt. Annual world production of salt has today reached more than 280 billion tons (Fig. 12.44). Approximately one third of the total is produced by solar evaporation of seawater or inland brines; another third is obtained by mining of rock salt deposits. The balance is obtained from processing of recovered brines, mainly via solution mining.

Usage History

Sodium chloride (halite), the most common industrial evaporite salt, is used in some form by virtually every person in the world. There are more than 14,000 reported usages of halite and more than 30 references to salt in the Bible. Halite has long played a very important role in human affairs. Some 3,200 years ago Bronze-Age Celtic miners were extracting salt near Hallstatt in Austria, from a network of several kilometres of galleries up to 300 m below the surface. Two thousand seven hundred years later some ten pages deal with salt in the "De Re Metallica" by Georgius Agricola (Georg Bauer), both in terms of mining it and producing it from seawater. Published in 1556, his was the first book on mining to be based on field research and observation. Until the nineteenth Century and the advent of refrigeration, salt's main uses were as a preservative and as a much sought after additive to flavour foodstuffs (Kurlansky 2002). Without salt, the human metabolism cannot function. Even today, most people think of salt in terms of sprinkling it on their food, or in colder climates they may also think in terms of road de-icing. These are in fact lesser modern usages of halite; its main use is as a feedstock in the chemical industry.

The human body's need for salt gave it military significance; the earliest recorded war over access to a supply of salt was over a salt lake in China in 3000 BC. The words, 'war' and 'peace' originate from the words for salt and bread in ancient Hebrew and Arabic. In the American Civil War the salt production facilities in Saltville, Va., Virginia's Kanawha Valley and Avery Island, Louisiana, were early targets of the Union Army. The North fought for 36 h to capture Saltville, Va., where the salt works were considered crucial to the Rebel army – so crucial that Confederate President Jefferson Davis offered to waive military service to anyone willing to tend coastal salt kettles to supply the South's war effort. In addition to dietary salt, the Confederacy needed this precious mineral to treat wounds, tan leather, dye cloth for uniforms and to preserve meat and other foodstuffs. Thousands of Napoleon's troops died during his retreat from Moscow, because, for lack of salt, their wounds would not heal.

Early hominids lived on the edge of the saline Lake Olduvai (Hay and Kyser 2001) and salt was part of their diet. In ancient Greece it was so valuable that the slave trade involved an exchange of salt for a slave and gave rise to the expression, "not worth his salt." Some 4,700 years ago the Peng-Tzao-Kan-Mu was published in China. It is probably the earliest known treatise on pharmacology, with detailed discussions of the palliative and curative powers of more than 40 kinds of salts, including descriptions of two methods of recovering usable salts from brine. In 2200 BC the Chinese emperor Hsia Yua declared than Shandong Province must supply the Imperial Court with salt. An ancient Chinese philosopher once called salt "the sweetest thing on earth."

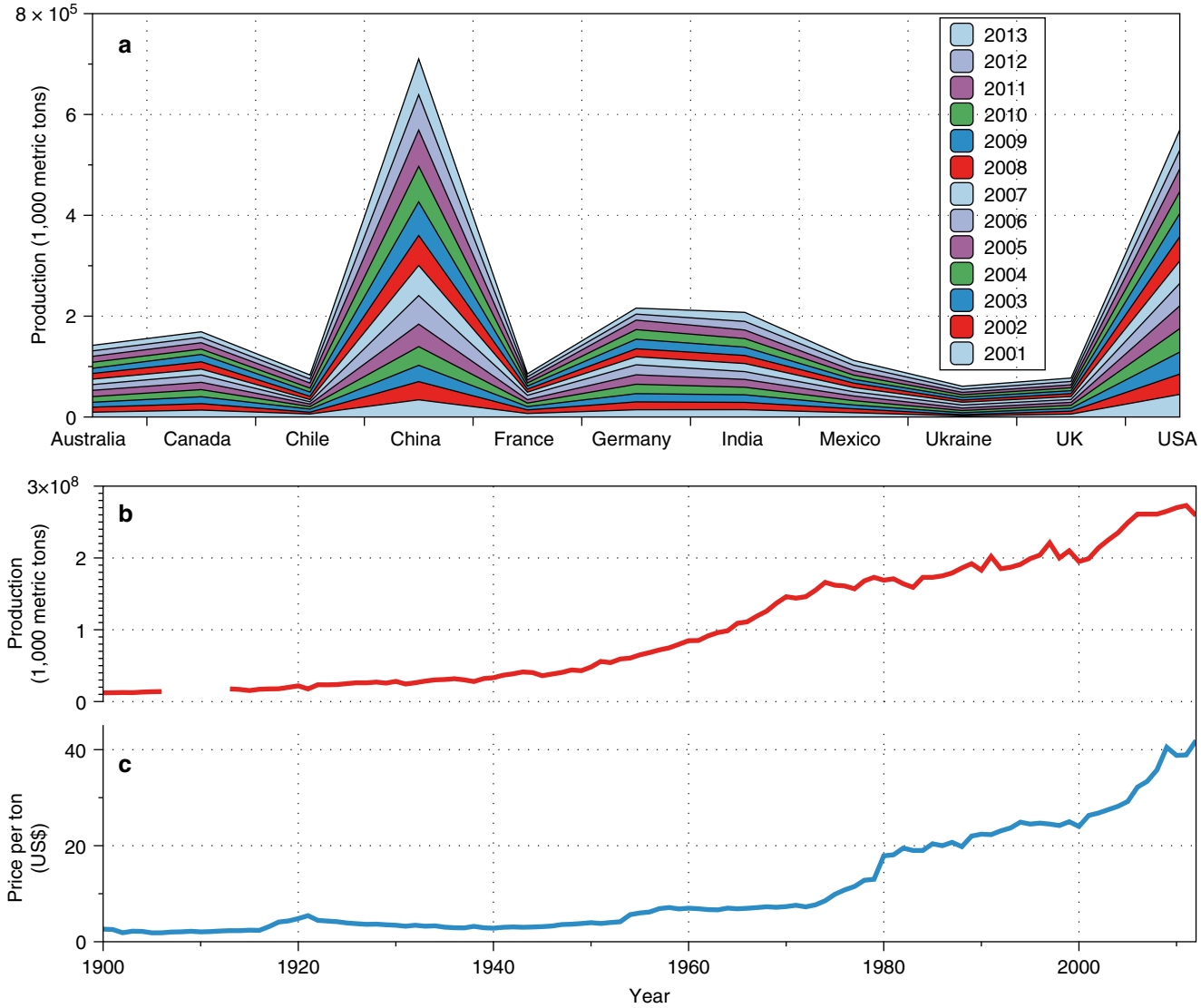

Fig. 12.44 Salt Production. (**a**) Cumulative area plot of top salt-producing countries (1,000 metric tons). (**b**) Salt production from 1900 to 2012. (**c**) Price per tonne in US dollars (Charts compiled from USGS on-line data tables downloaded from http://minerals.usgs.gov/minerals/index.html last accessed April 10, 2014)

In Europe, the first recorded industrial production of pan salt took place in Italy some 2,500 years ago when Ancus Martius, one of the early Roman kings, began letting seawater into an enclosed basin, then allowing the sun to evaporate the water to create a salt residue. The importance that Rome attached to the salt works and port at Ostia was such that the main highway along which the salt was carried to Rome was called the Via Salaria. Like Venice after it, the city of Rome based much of its early commerce on trading salt. Special salt ration equivalents, paid to early Roman soldiers, were known as "salarium argentum", the forerunner of the English word "salary." With a near monopoly on supply to Rome, the traders in the port of Ostia raised the salt price so high that the state was forced to take over the industry in 506 BC.

When Julius Caesar landed in Britain in 55 BC, he brought his salinators with him, but found that even the backward Britons were extracting salt by pouring brine on to hot stones. The Romans, however, used iron pans in which they boiled the brine, and Caesar established a brine-based salt works in Cheshire and subsequently in other localities. The towns in Britain where salt was made can be distinguished to this day by the termination "wich", an Anglo-Saxon descriptor for a place where salt was made and includes towns like Greenwich, Ipswich, Droitwich, Northwich and Middlewich.

Merchants in twelfth-Century Timbuktu in Africa, the gateway to the Sahara Desert and the seat of renowned scholars, valued salt as highly as books or gold. In Tibet, Marco Polo noted that tiny cakes of salt, manufactured from salt lakes in the high plains of Tibet were pressed with images of

the Grand Khan and used as coins. Salt is still carried by camel trains and still used as money among the some of the nomadic tribes of the Sahara and Ethiopia's Danakil Plains. The ancient Maya made salt at Salinas de los Nueve Cerros, Guatemala, an area where natural salt springs flowed into a river gully, giving easy trading access to downstream customers. This site was the only large-scale source of salt for the interior Lowland Maya. Maya technology included solar evaporation and firing of brine from salt springs in special large ceramic bowls that are the largest receptacles ever found in any Maya sites.

Salt's economic value meant it was taxed by governments from the ancient Chinese and Romans to late medieval Europe. In 2200 BC the Chinese Emperor Hsia Yu levied a salt tax as one of the world's first documented taxes. Mary Queen of Scots was perhaps the first European head of state to have the idea of making salt a source of governmental revenue. She granted a patent to an Italian to make salt in Scotland and then placed a heavy tax on it, which she appropriated to herself. Elizabeth, Queen of England, and Mary's lifelong "dear sister" and eventual executioner, thought this an excellent idea and likewise taxed English salt making. Salt tax was a source of great resentment to everyone, English and Scots alike, and smuggling grew to alarming proportions. In 1785, the Earl of Dundonald wrote that every year in England, 10,000 people were arrested for salt smuggling. During Queen Anne's reign, the salt tax rose to £30 a ton, an enormous amount of money in those days. The whole of England arose in rioting protest, with the result that the salt tax was finally abolished.

In Burgundy, salt was taxed at more than 100 % as it came from the salt-works. This tax was extended to the whole of France when Burgundy was absorbed and the notorious salt tax "la gabelle" became a necessary input to the government's finances. Cardinal Richelieu said that salt was as vital to France as American silver was to Spain. The repeal of the salt tax was a major goal of the revolutionaries of 1789, but Napoléon restored the salt tax to pay for his foreign wars as soon as he became Emperor and the impost continued until 1945 to feed French government coffers. It is said that income from a salt pan in southern Spain largely financed Columbus' voyages. The Erie Canal, an engineering marvel that connected the Great Lakes to New York's Hudson River in 1825, was called "the ditch that salt built" as salt taxes paid for half of the cost of construction. The "Great Hedge of India," the mid-eighteenth century colonial equivalent of the Great Wall of China, stretched 3,700 km from the western border of Punjab down to the Bay of Bengal. It was manned by 12,000 men and planted by the British to minimise salt smuggling into Bengal and enforce the collection of the Indian salt tax. As late as the 1940s, the people of India under the leadership of Mahatma Gandhi protested British taxes on salt supply. In 1930 he led a 200-mile march to the Arabian Ocean to symbolically collect untaxed salt for India's poor.

Salt, because of its value in the ancient world, still has religious significance. Ancient Greek worshippers consecrated salt in their rituals. Jewish temple offerings included salt; on the Sabbath, Jews still dip their bread in salt as a remembrance of those sacrifices. Covenants in both the Old and New Testaments were often sealed with salt, explaining the origin of the word "salvation." In the Catholic Church, salt was or is used in a variety of purifying rituals. Jesus called his disciples "the Salt of the Earth", a statement that was commemorated by the Catholic church until Vatican II, by placing a small taste of salt on a baby's lip at his or her baptism. In Leonardo Da Vinci's famous painting, "The Last Supper," Judas Escariot has just spilled a bowl of salt – a portent of evil and bad luck. In Buddhist tradition, salt repels evil spirits. That's why in some Asian cultures it can still be customary to throw salt over your shoulder before entering your house after a funeral: it scares off any evil spirits that may be clinging to your back. In 1933, the Dalai Lama was buried sitting up in a bed of salt. Shinto religion also uses salt to purify an area. Before sumo wrestlers enter the ring for a match – which is actually an elaborate Shinto rite – a handful of salt is thrown into the centre to drive off malevolent spirits. In the American Southwest, the Pueblo worship the Salt Mother. Other Native American tribes had significant restrictions on who was permitted to eat salt. Hopi legend holds that the angry Warrior Twins punished mankind by placing valuable salt deposits far from civilization, requiring hard work and bravery to harvest the precious mineral.

Today, halite is a cheaply produced commodity extracted either from mines or saltpans. In the production of table salt, processing, packaging and marketing are the major costs. An exception to the low sale price of modern salt is "Fleur de Sel de Geurande" a delicate gourmet form of white seasalt that is still hand-produced (for the correct "feel on the tongue") in the fens along the coast of Brittany. It costs ≈ US$40–50/kg and is produced by "paludiers" only on suitable summer days when halite rafts can be raked from the brine surface of specially maintained coastal salt pans, which are floored with grey clay. According to the local legend it only forms when the wind blows from the east (from the sea). It and the cheaper grey salt (sel gris), which is scraped from the pan floors and also prized by gourmands, has been produced this way since Pre-Roman times. Impurities like this clay are called grey spot or black spot in highly efficient mechanised production plants elsewhere in the world and are considered undesirable in the end product. It says something about our notions of luxury, French culinary marketing skills, and perhaps the gullibility of middle-class gourmands with too much money and time on their hands, that each year the gourmet industry successfully markets dirt-polluted variable-quality salt for top prices.

Production

The largest volumes of salt production are concentrated in 15 nations, which together produce more than 80 % of the world's total production (Fig. 12.44a). China today is the dominant salt producer, followed by the United States. In 2012, estimated salt production in China was about 70 million tonnes, or about 26 % of total world output compared to the US with 14 % of the world's production. Most countries possess some form of salt production capability, with production levels set to meet their own domestic requirements and with additional quantities available for export to other countries.

World resources of rock salt and sea salt are practically unlimited and total production levels continue to rise as the human population rises (Fig. 12.44b). The majority of usage worldwide is in the chemical industry, some 60 % of total rock salt production is processed to supply sodium and chlorine chemicals that are then used to manufacture a multiplicity of products (Kogel et al. 2006). The principal basic chemicals, chlorine and sodium hydroxide (caustic soda) are manufactured from brine via electrolysis. Sodium chloride is reacted with limestone in the Solvay process to produce sodium carbonate (soda ash), and with sulphuric acid to produce hydrochloric acid and sodium sulphate (salt cake). The chloralkali industry also uses substantial quantities of salt. Most of its output is polyvinyl chloride and vinyl chloride monomers; chlorine is another product. The second largest user of salt is mankind itself. Humans metabolise around 30 % of the total salt produced to support their physiological functions and eating habits. Salt for food is probably the most "taken for granted" commodity in the world today, available from thousands of sources in hundreds of qualities as table, cooking and industrial salt for food production. Salt usage in the northern hemisphere increases in the winter months when salt is used to de-ice frozen roadways (≈10–15 % of world annual production).

Important commercial rock salt deposits are found in the Silurian of northeastern North America; the Devonian of western Canada (also a major producer of potash); the Permian of Russia, western Europe, the midwest of North America, the Jurassic of the US Gulf Coast and the Miocene of the Middle East. In Europe and North America the salt is recovered either by hard rock mining (mostly room and pillar methods) or by solution mining. In warmer climates, such as Australia, Spain, Mexico and the inland deserts of China, large volumes of salt are recovered by solar evaporation of seawater, or less commonly of inland playa waters. The term sea salt is sometimes applied to this type of salt to distinguish it from rock salt, which tend to be mined,

The advantage of salt manufacture via large scale marine-fed solar evaporation ponds in arid coastal settings is the ability to control purity and consistency of the feedstock flowing to the processing plant, as well as the relatively low energy costs involved in sea-salt manufacture (sun and wind) compared with conventional mining techniques used to extract rock salt. Modern computer-configured and -monitored saltworks in Australia and Mexico used automated logger measurement of the salt pan climate and the state of the brines in the various pans in order to a produce a high quality, high volume, consistent NaCl feedstock. These high volume industrial sea-salt plants in Mexico and Australia supply a consistently high volume, high quality, low-impurity product to the world's chemicals industries. Smaller "cottage-industry" pans or saltworks are commonplace around the world, but with lesser quality monitoring, they tend to produce a range of lower volume and lower quality salts.

Climate distributions plotted against annual production of coastal solar saltworks suggests a relatively narrow climatic range for the more efficient high-volume producers. The majority of the high volume saltworks (with annual production more than 1–2 million tonnes) are located in arid coastal climates typified by hot arid desert (BWh) or hot arid steppe (BSh) zones (Table 12.11, Figs. 12.45 and 12.46).

The largest and most efficient producers of seasalt are located in the BWh climate zones of Mexico and NW Australia, and significant cumulative production also comes from numerous but smaller coastal salt farms in BSh zones along the Gujarat coast of India (Fig. 12.45). In the past, much of the Indian coastal salt production on the Gujarat coast and in southern India has been a village industry, with little control on overall quality or volume of output. That is changing, but not without local political implications, as the Indian salt industry moves toward larger more efficient pans and less labour intensive modes of harvesting.

Outside of these three main regions of high volume production, there are other salt plants with significant annual production volumes, also located in hot coastal desert steppe settings (BSh), as in the Macau region of coastal Brazil and Shark Bay, Australia (Fig. 12.46; illustrates regions with $>10^6$ tonne/year production, the background zone with these higher production volumes is shaded brown in the figure). Unlike the cooler climates of the suprasealevel nonmarine evaporites (that constitutes the natural sources of saline borates, soda ash and salt cake), the cooler arid coastal climates (BWk and BSk) do not host the huge production volumes that are accomplished in the hot arid coastal deserts and steppes. Even so, locally some large volumes are possible in somewhat cooler coastal climes, as in the Cabo del Gata plant (BSk) in the Almeiria region of Spain (Table 12.11). The Morton Saltworks on Great Inagua Island (Aw) with annual production near 1 million tonnes is the largest producer in an oceanic seasonal semiarid climate zone that typifies the south Caribbean and the Netherland Antilles.

Any salt harvest in a cooler BSk or Cs coastal climate is more subject to vagaries in meteoric inflow volumes and

Table 12.11 A list of active halite production facilities in sea-fed anthropogenic salt pans tied to Köppen climate at the site and its annual production (tonne/year)

Key	Name	Country	Köppen	Annual production (tonnes)
1	Newark Saltworks (Morton Salt), California	USA	Csb	650,000
2	Western Salt, Chula Vista saltworks, California	USA	BSk	75,000
3	Guerrero Negro (Exportadora del Sal), Baja California	Mexico	BWh	7,000,000
4	Salinera Del Istmo (Oaxaca)	Mexico	Aw	220,000
5	Ind. Salinera de Yucatan (saltworks)	Mexico	As	500,000
6	Great Inagua Island, (Morton Bahama Salt Co.- K&S) saltworks	Bahamas	Aw	1,000,000
7	Bonaire Cargill saltworks (Oranje Pans)	Neth. Antilles	Aw	400,000
8	Cabo Rojo saltworks	Puerto Rica	Aw	13,600
9	Salinor Saltworks, Macau	Brazil	BSh	2,000,000
10	Kaolack Salt works	Senegal	BSh	45,000
11	Salinas de Janubio, Lanzarote Islands	Canary Islands	BWh	10,000
12	Batz Sur Mer (Company Bourdic)	France	Cfb	12,000
13	Cabo de Gata, Almeria	Spain	BSk	1,000,000
14	Torrevieja saltworks	Spain	BSk	250,000
15	Santa Pola and Bras del Port saltworks, Alicante	Spain	BSk	100,000
16	Pambros saltworks, Accra	Ghana	Aw	250,000
17	Salines de la Trinitat saltworks	Spain	Csa	20,000
18	Uigues-Mortes saltworks, Camargue	France	Csa	250,000
19	Salin de Giraud saltworks	France	Csa	340,000
20	Berre saltworks, Marseille	France	Csa	45,000
21	Sousse saltworks	Tunisia	BSh	125,000
22	Sfax saltworks	Tunisia	BSh	330,000
23	Salina Di Cervia	Italy	Cfa	50,000
24	Cape Cross	Namibia	BWk	40,000
25	Walvis Bay Saltworks	Namibia	BWh	450,000
26	Swakopmund saltworks (Panther Beacon)	Namibia	BWk	150,000
27	Veldrift (Khoisan) saltworks	South Africa	BSk	3,000
28	Mesolonghi saltworks	Greece	Csa	120,000
29	Coega saltworks, Port Elizabeth	South Africa	Cfa	45,000
30	Megalon Embolon saltworks, Levos Island	Greece	Csa	40,000
31	Burgas saltworks	Bulgaria	Cfa	60,000
32	El Nasir, salines, Burg el Arab Salines saltworks	Egypt	BWh	100,000
33	El-Mex Salines saltworks, Alexandria	Egypt	BWh	1,400,000
34	El-Mex Salines saltworks, Port Said	Egypt	BWh	350,000
35	El Nasir, salines, Sebika Saline, Arish, North Sinai	Egypt	BWh	1,000,000
36	Eilat saltworks	Israel	BWh	150,000
37	Massawa Salina Salt Works	Eritrea	BWh	80,000
38	Asseb Salt Works	Eritrea	BWh	150,000
39	Kandla coast, Rann 0f Kutch, Gujarat State	India	BSh	4,000,000
40	Gujarat Coast, Vagra and surrounds	India	BSh	3,000,000
41	Vendaraniyam saltworks	India	Aw	40,000
42	Useless Loop Saltworks, Shark Bay	Australia	BSh	1,500,000
43	Lake Macleod, Cape Cuvier saltworks	Australia	BWh	1,600,000
44	Onslow saltwarks	Australia	BWh	2,500,000
45	Dampier saltworks, Karratha	Australia	BWh	4,200,000
46	Dampier (formerly Cargill) saltworks, Port Hedland	Australia	BWh	3,200,000
47	Salt manufacture site, ancient China, Bo Hai Bay	China	Cwa	1,000
48	Dry Creek, Cheetham Salt – Penrice Soda Products, Adelaide	Australia	Csb	700,000
49	Cheetham saltworks, Port Alma, Queensland	Australia	Cfa	200,000

Key column refers to locations in Fig. 12.45

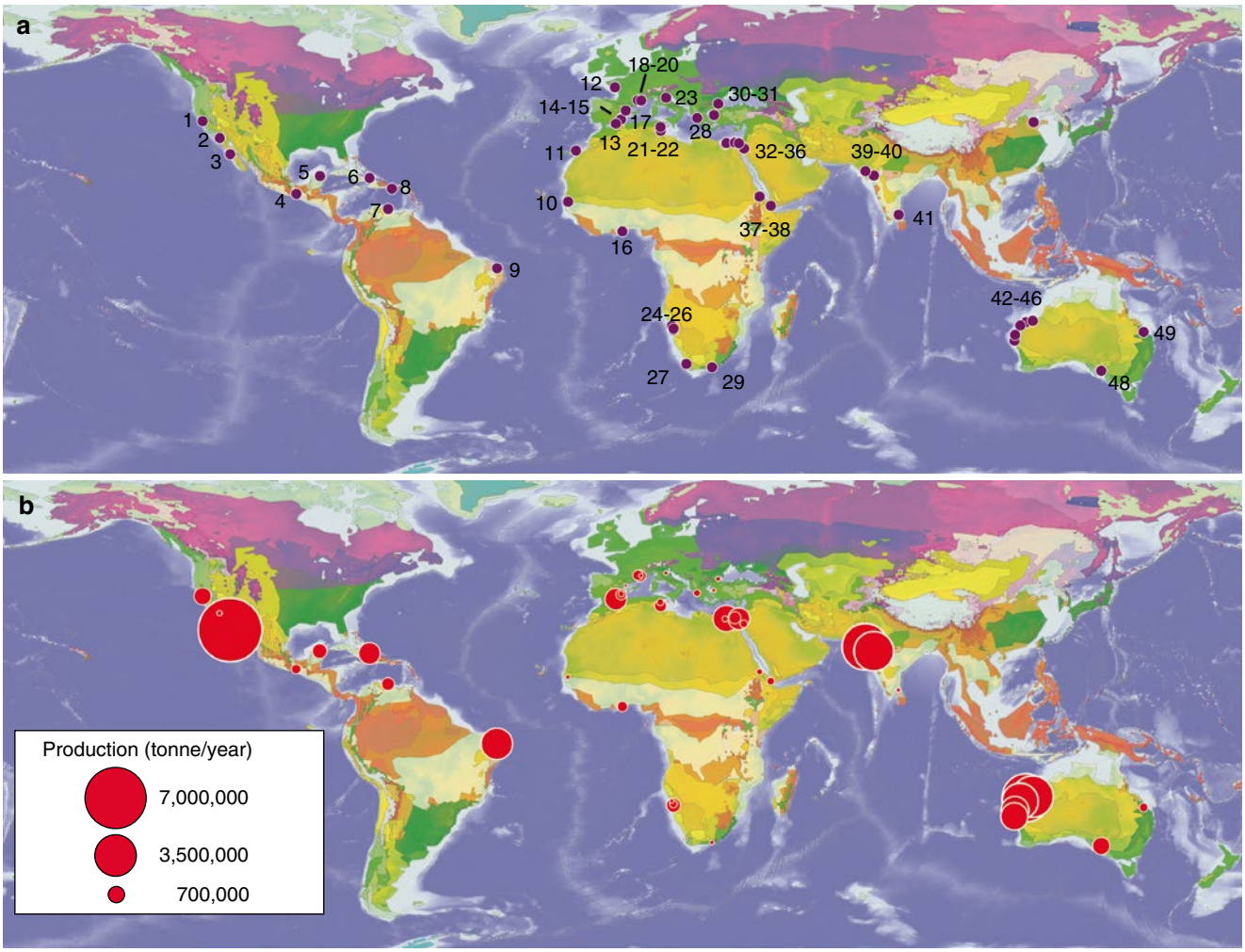

Fig. 12.45 Anthropogenic seawater-fed coastal salt pans. (a) Locations of salt pans, numbers refer to key code listed into Table 12.11. (**b**) Annual production of salt (NaCl) at various sites, as listed in Table 12.11. Base is colour-coded Köppen zones. Data extracted and replotted from SaltWork database, version 1.7, with permission

lower evaporation rates, so many of the viable saltworks in these somewhat cooler moister coastal climates are compensated by proximity to markets. For a transport-cost controlled product these lower-volume manufacturing facilities can be economic, even though they must deal with a more impure product and a longer time to harvesting.

Usually, there are semipermanent dm-cm thick natural salt crusts along BWh coastal regions in regions of low permeability seepage mudflat sumps areas outside the landscaped anthropogenic pans. These coastal sabkha crusts remain until waters from an occasional cyclone or hurricane passing over the area supplies enough surface runoff to dissolve the surface salt, including potential harvest salt in the nearby crystallizers. After the flood, this dissolved halite then reprecipitates a few months later. In contrast, in milder and moister BSk and Cs regions, any remnant halite in a crystallizer after a salt harvest, along with any natural salt efflorescences covering mudflats outside the crystallizer pans, dissolve each year with the onset of seasonal rain and will not reform until the next dry season.

Time to harvest from first inflow lagoons (pre-concentrators) to crystallizer pans gets longer as the climate gets milder. For example, in the solar saltworks that operated in South San Francisco Bay (Csb) it took 5 years to move seawater from the initial concentrator lagoons to the final crystallizers. In the BWh settings of Mexico and NW Australia it takes less than a year. Longer residence times can detrimentally affect the quality and volume of the halite product and salt from these plants typically has higher levels of impurities. As coastal climates where salt is manufactured get cooler and wetter it may require more expensive artificial means (e.g. fans, lifting pumps and cyclonic dryers) to maintain conditions suitable for salt precipitation (Fig. 12.45b).

This is why older and climatically less efficient salt plants in the northern Mediterranean and southern France cannot compete with the chemical quality (consistent product purity)

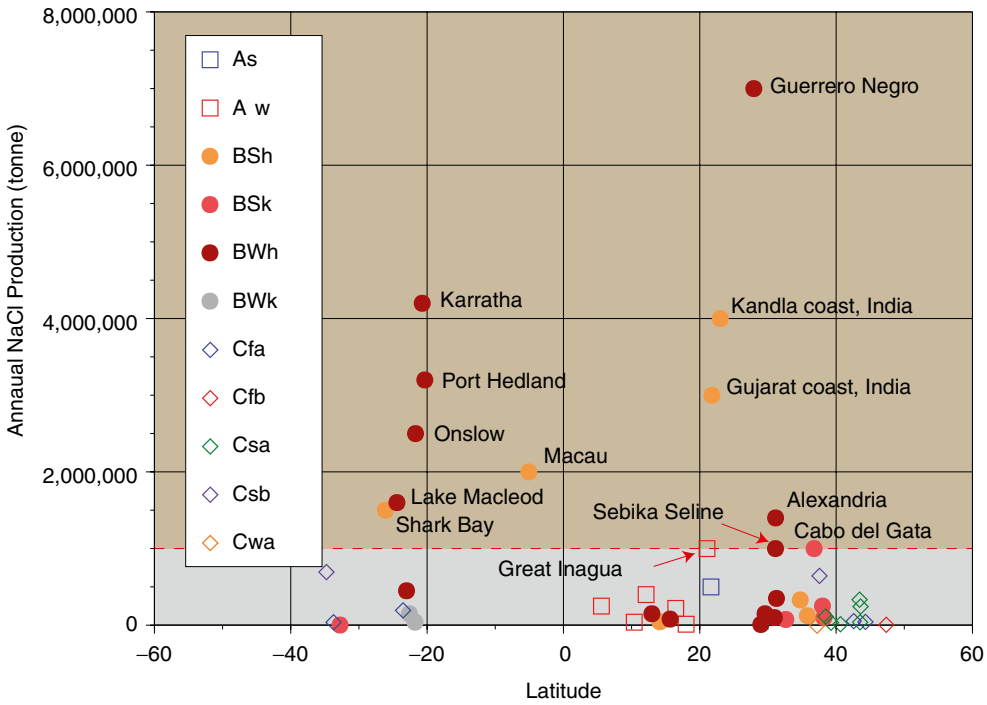

Fig. 12.46 Annual production versus latitude and Köppen climate setting of anthropogenic seawater-fed salt works listed in Table 12.11 and illustrated in Fig. 12.45

of the industrial product maintained by high volume suppliers of NaCl in the BWh climate belts. Many of the NaCl manufacturers in solar saltworks, based in small coastal pans in less climatically efficient areas, today emphasize their "green" and "buy local" credentials. Their inflow concentrator lagoons are mostly monitored wildlife sanctuaries in part to maintain subsidies and other governmental support. In some regions of Europe the remaining local salt industry maintain an even more labour-intensive high-value cottage-industry with a specialised consumer-quality image for their sea salt manufacture (paludiers). As mentioned earlier, annually they harvest small volumes of high-value gourmet salt for specialized use in the food industry (marketed as flaked salt, grey salt and Fleur del Sel). Chemically these products are less pure than that of the larger volume industrial manufacturers, but to a gourmand a little clay in the final product and a variable crystal size, with many of the larger halite hopper rafts preserved, gives it "on-the-tongue character" for which they are more than happy to pay a premium price.

Worldwide, all the high volume saltworks with annual production of more than a million tonnes/year are located on coasts in the Trade Wind belts, which are latitudinally-limited arid regions beneath bands of cool dry descending air in the subtropical arms of Hadley cells. Such regions sit on either side of the equatorial divergence as two BW climate bands, meandering along in two subparallel arid belts centred on regions some 20–35° north and south of the equator (Fig. 12.46; see also Chap. 2).

Today, there is only one high volume solar seasalt producer (output more than 1,500,000 tonnes/year) located outside the Trade Wind belt. It is centred on the Salinor saltworks in the Nordeste region near Macau, on the coast of NE Brazil and is only some 5° south of the equator, but is located in a local BSh setting (Fig. 12.46). There is another even hotter and drier anomalous coastal zone (BWh) outside the Trade Wind belt at 6°S south of the Equator on the coast of the Sechura Desert of NE Venezuela. There the Bayovar solar brine plant is in the early stages of construction and pilot solar plants have already recovered sylvite and carnallite from pans that focused and ponded shallow mudflat brines. Both the Bayovar and Macau regions are considered anomalous in terms of a north-to-south latitudinal zonation in the earth's broad scale climate zones. The Nordeste region, with its relatively high population density, has been classified as an El Niño "hotspot" in that drought stress is an ongoing climate hazard.

Both regions are arid responses to seasonal changes in oceanic circulation interacting with onshore climate. In either region the precise causes driving aridity are not fully understood, like much of our understanding of the controls on long and short term variations in the world's climate. Aridity in the Nordeste region involves the seasonally changing position of the subtropical high-pressure system over the Atlantic Ocean, the position of the advance and retreat of the intertropical convergence zone or ITC (hence the El Niño designation of the Nordeste climate hazard, even though it is on the Atlantic Ocean – Oliver 2005, p. 678) and the interaction of air circulation patterns with local topography. Causes of aridity over the Bayovar region are equally problematic. The location is such that onshore trade winds, local

mountains, and the anticipated presence of the ITC should provide copious rainfall, but it does not. In spring (the driest season) a deep easterly air flow prevails with a divergence up to at least 2,000 m elevation to give rise to subsidence of a dry air mass. In summer the ITC is absent and the subsidence continues, although not as severe as in the spring, and some rain can fall (Oliver 2005). Winter, like autumn can be somewhat moister in the Bayovar region, but subsidence still continues to minimize the influx of moisture-carrying air from the oceanic side, hence the formation of the Sechura Desert.

Reasons for the tie between large volumes of bedded seasalt production and hot arid coastal desert climates in both natural and anthropogenic marine fed saltworks are axiomatic (Table 12.11 and Fig. 12.46). The corollaries are also of geological interest. By definition, a marine seepage system has continual access to a huge isochemical brine reservoir (the sea). But water cannot flow uphill, so providing a linking aquifer exists to a closed subsealevel natural coastal depression (coastal salina) (or in the case of anthropogenic salt pans a pumping station to pump seawater uphill into the pans), then the water supply to a marine-fed hydrology is not a limiting factor. Seepage resupply continues until the coastal inflow system attains a sediment level and a natural hydrological equilibrium where inflow = outflow, as in modern Lake Macleod, which is the largest natural halite-filled coastal salina in the world, there the natural sediment surface has stabilised at around 0.5–1 m below mean sea level.

Interestingly, Quaternary continental salt sumps are five to ten times larger in area and the salt volumes much greater than Quaternary coastal systems (Chap. 5). Also, unlike coastal anthropogenic and natural halite-filled salinas that accumulate the greatest salt volumes in hot arid coastal deserts (BWh), our most voluminous natural lacustrine examples accumulating bedded salts are located in high-altitude high-relief, steppe climates (BSk), such as Salar di Atacama and Salar di Uyuni. Large volumes of halite and other salts do not accumulate in hot arid continental-interior deserts (BWh). This is because in terrestrial BSk sump settings, the ponded moisture input levels are higher than in terrestrial BWh settings, evaporation rates are less and at- or near-surface residence times of saturated brines are longer. Hence, no marine-fed modern natural coastal salina or a continental interior saline lacustrine system can offer a same-scale analog to the inflow hydrology of an ancient marine seepage-fed evaporite drawdown basin (Chap. 5 – basinwide and saltern systems).

Lithium and $CaCl_2$ Brines, Iodine and Bromine

So far we have considered salt resources as dominantly solid salt systems where targeted beds (various borates, $NaSO_4$ and Na_2CO_3 salts) are present, while their interstitial brines are saturated with the same set of ions. Production is both by extraction of the solid product (ore) and/or the extraction and processing of associated interstitial brines to produce the targeted salts. But there is another group of subsurface-derived saline products where, due to high levels of the targeted cations in the hypersaline interstitial waters, the targeted element or its salts, can be extracted from the processed brine, even though no solid salt of the targeted product is present in the ore horizon. These targeted products are lithium carbonate and calcium chloride brines, iodine and bromine. Figure 12.47 plots distribution of current and future resources for lithium and calcium chloride brines.

Lithium Brines

Historically, until the electronic revolution, lithium located near the top of the periodic table, was of little economic interest. With an atomic number of 3 and a atomic weight of 6.9, lithium is exceptionally small and light, with a high charge/radius ratio. Lithium compounds are consumed in the production of ceramics, lubricants, glass, and primary aluminium (Fig. 12.48). Its high specific heat capacity and high electrochemical potential, make lithium ideal in heat transfer technology where it is used in welding and metallurgical applications. High electrochemical potential and light weight make it amenable to battery applications. Compared to nickel metal hydride batteries, the type of battery currently powering most hybrid electric vehicles, Li-ion batteries are lighter, less bulky, and more energy efficient. Lithium batteries have three times the energy of nickel hydride at one-third of the weight, and they operate at very low temperatures with a longer battery life. Growing use of lithium in batteries for electric vehicles is expected to make this usage the main market for lithium in the twenty-first century (Kesler et al. 2012; Grosjean et al. 2012).

Production

Lithium occurs in more than 140 minerals, with conventionally mined production of lithium ore concentrates mostly from nonevaporitic spodumene ($LiAlSi_2O_6$) and petalite ($LiAlSi_4O_{10}$) in pegmatites. Currently, there is no known economic process for extracting lithium from lithium-bearing clays, but if the technology develops these too may be future conventional mining targets. The breadth of mineral occurrences of lithium is seen in the etymological derivation of lithium. It comes from lithos (Greek for stone) and -ium referring to the fact that this element was first found in minerals, while its cognates sodium and potassium were first found in plant ashes (Senning 2007). Three major lithium miners supply the majority of worldwide demand for solid lithium ore concentrates (Table 12.12). They are; Sons of Gwalia in Australia (largest), Tanco in Canada, and Bikita

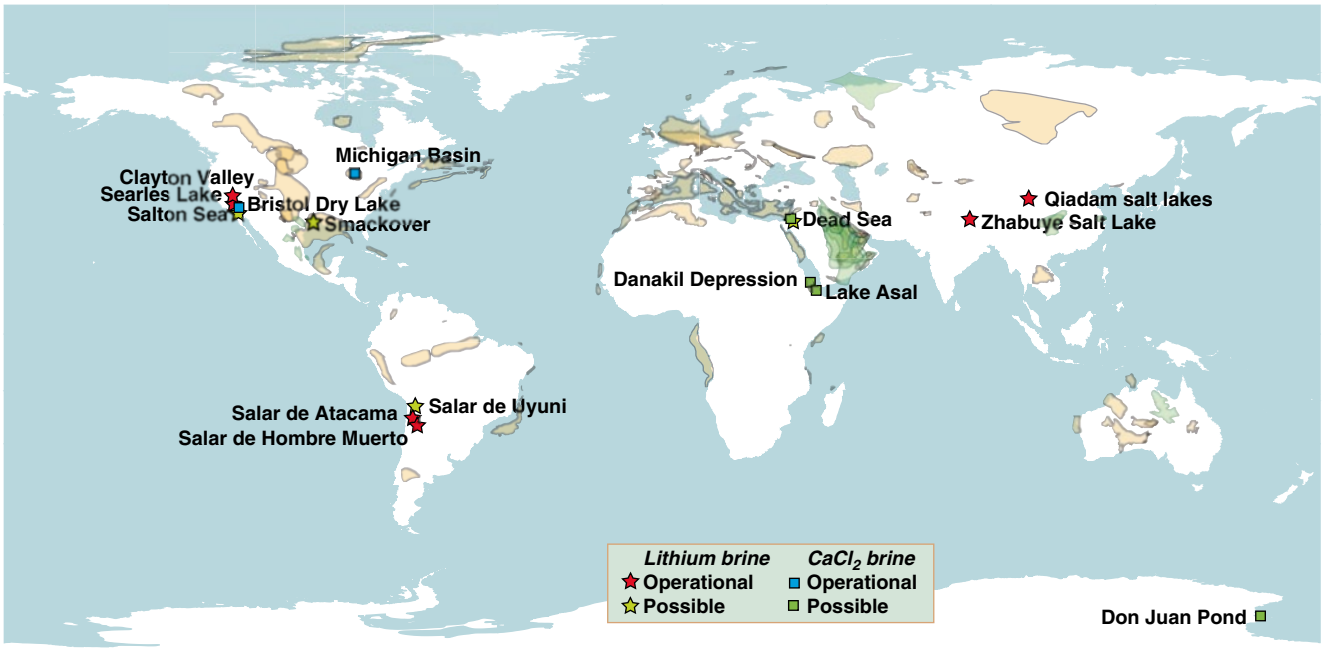

Fig. 12.47 Lithium and $CaCl_2$ brine occurrences. Red stars indicate operations that are extracting (or have extracted) lithium brines in a saline setting. Green stars indicate locations of possible future lithium brine resources. Blue square indicates an active $CaCl_2$ brine operation, *green squares* indicate other sites of $CaCl_2$ that may be a future possible $CaCl_2$ brine resource. The *brown and green shaded zones* indicate the positions of ancient marine halite and sulphate basins, respectively (See Tables 12.12, 12.13 and 12.14 for occurrence details)

Fig. 12.48 Current lithium uses

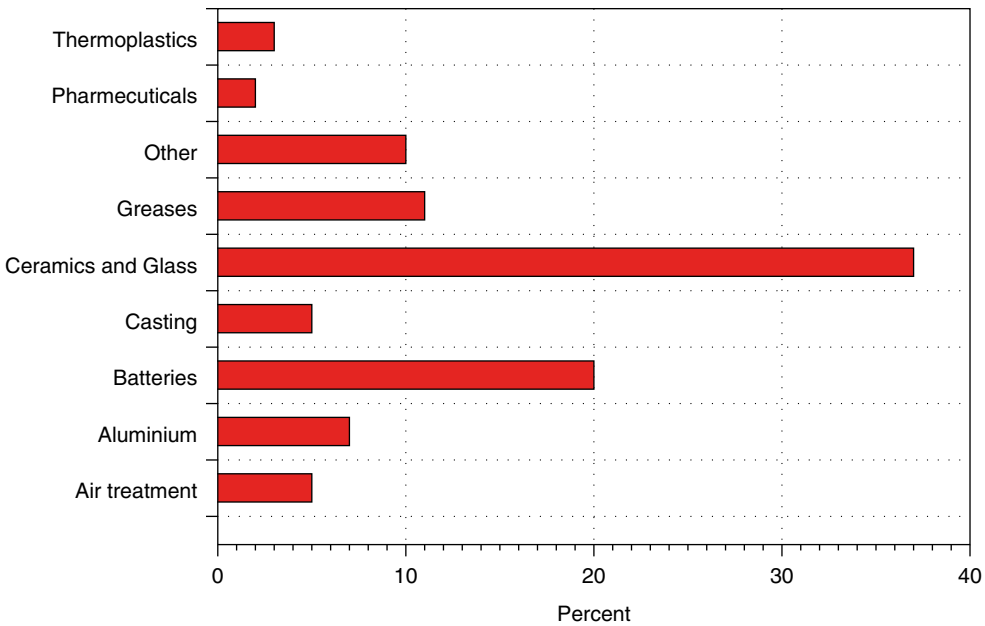

Minerals in Zimbabwe, with combined production form these sources in 2010 at more than 350,000 t.

To produce lithium carbonate from spodumene, the material is pulverized, calcined at 1,100 °C, treated with sulphuric acid, dissolved in water, separated from aluminium, and precipitated with soda ash. Energy expended in the heating and dissolution required in this processing stream make it more expensive compared to lithium brine processing. However, this cost differential is somewhat ameliorated by the higher concentration of lithium in pegmatites compared to brines.

In his 1992 book "La Industria del Litio en Chile," P. Pavlovic estimated the cost to produce a kilogram of Li_2CO_3 from Bessemer City spodumene pegmatite (North

Table 12.12 Estimate of world in-situ lithium resource

Deposit	Country	Type	Average concentration (% Li)	In situ resource (Mt Li)
Uyuni	Bolivia	Brine	0.0532	10.2
Atacama[1]	Chile	Brine	0.14	6.3
Kings Mountain Belt	United States	Pegmatite	0.68	5.9
Qaidam[1]	China	Brine	0.03	2.02
Kings Valley	United States	Clay	0.27	2.0
Zabuye[1]	China	Brine	0.068	1.53
Manono/Kitotolo	Congo	Pegmatite	0.58	1.145
Rincon	Argentina	Brine	0.033	1.118
Brawley	United States	Brine	–	1.0
Jadar Valley	Serbia	Clay	0.0087	0.99
Hombre Muerto[1]	Argentina	Brine	0.052	0.8
Smackover	United States	Brine	0.0146	0.75
Gajika	China	Pegmatite	–	0.591
Greenbushes[1]	Australia	Pegmatite	1.59	0.56
Beaverhill	Canada	Brine	–	0.515
Yichun[1]	China	Pegmatite	–	0.325
Salton Sea	United States	Brine	0.02	0.316
Silver Peak[1]	United States	Brine	0.02	0.3
Kolmorzerskoe	Russia	Pegmatite	–	0.288
Maerking[1]	China	Pegmatite	–	0.225
Maricunga	Chile	Brine	0.092	0.22
Jiajika[1]	China	Pegmatite	0.59	0.204
Daoxian	China	Pegmatite	–	0.182
Dangxiongcuo[1]	China	Brine	0.04	0.181
Olaroz	Argentina	Brine	0.07	0.156
Other (producing)[1]	8 deposits in Brazil, Canada, China, Portugal	Pegmatite	–	0.147
Goltsovoe	Russia	Pegmatite	–	0.139
Polmostundrovskoe	Russia	Pegmatite	–	0.139
Ulug-Tanzek	Russia	Pegmatite	–	0.139
Urikskoe	Russia	Pegmatite	–	0.139
Koralpe	Austria	Pegmatite	–	0.1
Mibra	Brazil	Pegmatite	–	0.1
Bikita[1]	Zimbabwe	Pegmatite	1.4	0.0567
Dead Sea	Israel	Brine	0.001	–
Great Salt Lake	United States	Brine	0.004	–
Searles Lake	United States	Brine	0.005	–
Total				38.68

After Gruber et al. 2011
The technology does not yet exist to economically extract clay-bound lithium
Mt million tonnes
[1]Indicates current producer

Carolina), hectorite-hosted Silver Peak brine (Nevada) and Salar de Atacama halite-hosted brine (Chile) as US$2.45, $1.65 and $1.10, respectively. Today, the even higher costs of energy compared to solar evaporation make it relatively much more expensive to process spodumene. But, compared to suitable rock (spodumene) sources, the distribution of known suitable lithium-entraining brine lakes is limited. In addition, the future exploitation of solid versus liquid sources will depend on the world's need for lithium batteries, versus conventional hydrocarbon-derived energy. Likely, the known pegmatite sources will continue to be exploited for the foreseeable future and a number of the larger solid ore deposits, compared to brine sources, are located in regions that are less susceptible to issues of sovereign risk (Kesler et al. 2012).

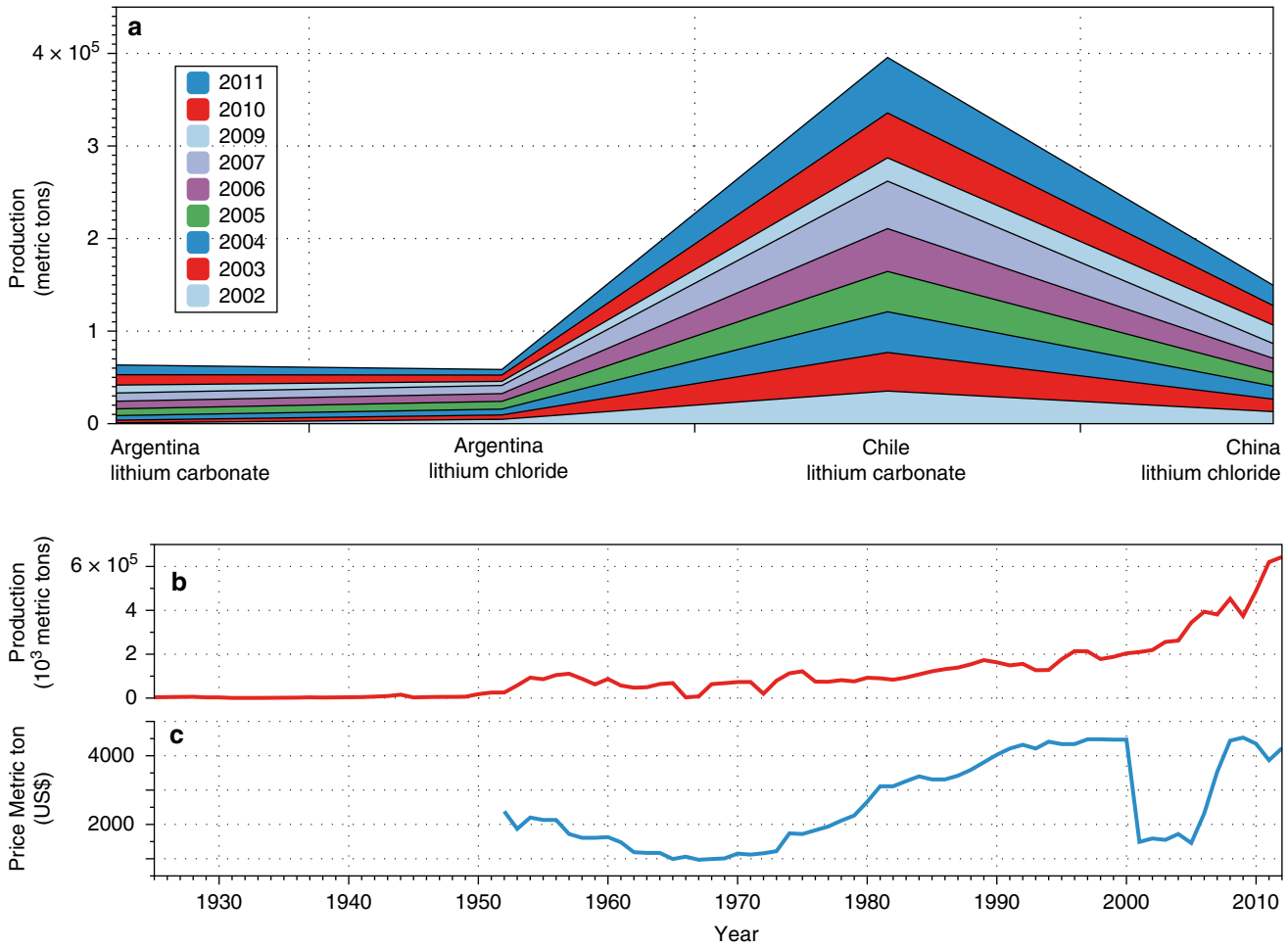

Fig. 12.49 Lithium brine production. (**a**) Cumulative area plot of annual production of lithium salts from brine producing countries in metric tons. USA also produces lithium from brine, but figures not made public, they are less than other countries listed. (**b**) World production from 1925 to 2011 (metric tons, includes both brine and spodumene sources), (**c**) Price per metric ton in US dollars from 1954 to 2010 (Compiled from USGS on-line data tables downloaded from http://minerals.usgs.gov/minerals/index.html last accessed April 28, 2014)

The price of lithium carbonate (in adjusted or relative dollars) steadily declined from 1954 to 1998, as new South American production began at Atacama in 1984 and Hombre Muerto, Argentina, in 1997. Beginning in 2003, the price of lithium carbonate (in relative dollars) increased until 2008 (Gruber et al. 2011). In 2009, however, the price of lithium carbonate decreased by 25 %, likely due to decreasing demand and possibly due to SQM's September announcement that it would reduce the price of lithium by 20 %.

Cheaper prices and abundant supply in the previous decade meant there was a move away from ore to brine as the major source of lithium. Today, Chilean and Argentinian salars, along with Chinese (Tibetan) salt lakes are the dominant brine sources, with significant brine reserves in Salar de Atacama (Figs. 12.49a–c and 12.50a, b; Tables 12.12 and 12.13). Today there are substantial lithium carbonate brine operations in Salar de Atacama, Chile and Salar del Hombre Muerto, Argentina, and Dabuxum Salt Lake in China, along with smaller volumes recovered from multicomponent brine operations in Searles Lake, California, and Clayton Valley, Nevada (Figs. 12.49 and 12.50). Salar operations in South America can now produce lithium throughout the year, whereas historically the brine extraction operations were seasonal and subject to downtime related to periodic salar floods.

The highly competitive nature of the current supply market makes some published lithium figures suspect. It is a market where availability of known reserves exceeds projected needs by a ratio of more than 2:1 and lithium carbonate from brine is perhaps now supplying as much as 60–80 % of the world's needs. A ready cheap supply of lithium from brine operations led to a fall in the real price of lithium by up to 50 % in the late 1990s. Increasing use in battery manufacture accounts for much of the price recovery since the mid 2000s (Fig. 12.49b, c). Even so, the market today is still highly competitive with some more expensive spodumene operations and low capacity brine operations closing each year. United

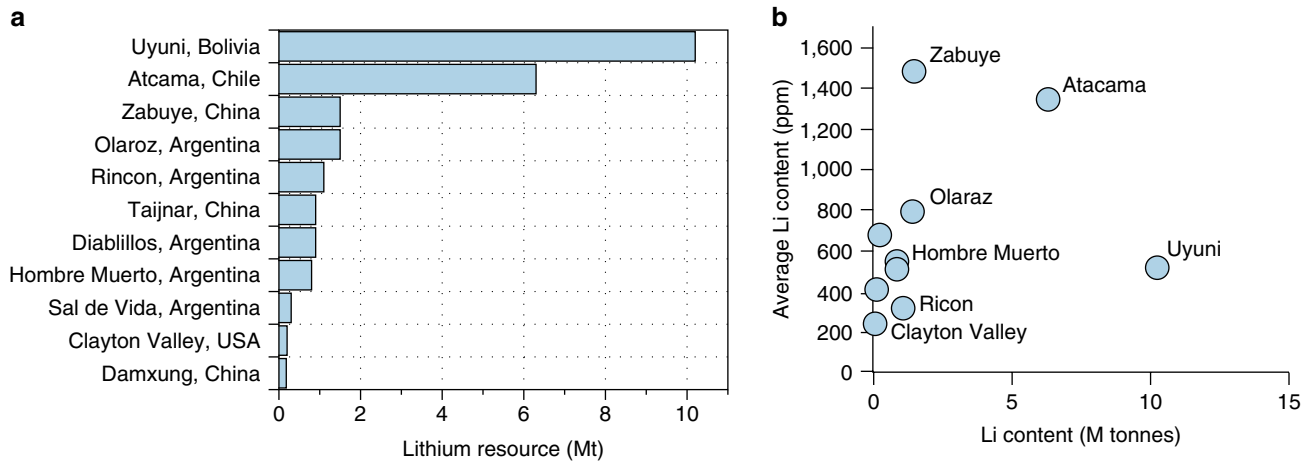

Fig. 12.50 Lithium resource. (**a**) Estimated lithium resources (Mt Li) for brine deposits. (**b**) Average lithium concentration vs. lithium content (endowment) for brine deposits based on Kesler et al. (2012)

Table 12.13 Lithium-enriched brine occurrences, mostly in Quaternary saline settings (many lithium-rich brine occurrences are closely association with saline borate deposits, as listed in Table 12.4)

Location, Country (area)	Elev. (msl)	Köppen	Comments
Salar de Hombre Muerto, Argentina (565 km^2)	4,300	ET	Lithium carbonate brine processing; Rather than solar evaporation, FMC use a proprietary alumina adsorption system to directly extract lithium from the salar brine. Nodular ulexite is commonplace on the salar and in shallow subsurface. A porous halite bed (15 % Ø) some 40–50 m thick extends across much of the salar. Pore brines are principally sourced from lithium-containing hot springs and seeps, fed by groundwaters that leached surrounding volcaniclastics. Average Li levels in the brine ≈520 ppm. Brine in the salar is usually within 20 cm of the salar surface, and appears to be relatively constant in composition to depths of at least 15 m. (Vinante and Alonso 2006; Godfrey et al. 2013)
Salar de Uyuni, Bolivia (9,654 km^2)	3,650	BWk	Planned lithium carbonate brine processing facility. Typical sediment thickness is 121 m, made up of 11 variably porous (0–30 % Ø) halite beds separated by layers of mud and sand. Ulexite is present. The upper halite bed is porous and is the currently targeted bed, it is around 11 m thick across much of the salar. Brine is always within 5–20 cm of the surface and contains 80–1,150 ppm of lithium, averaging 321 ppm Li; a limited area in the southeast corner averages 625 ppm. Pore brines are principally sourced from lithium-containing hot springs and seeps. Mg/Li ratios are three times that in Salar de Atacama making Li extraction much more difficult. A similar processing problem occurs at the nearby Salar de Rincon, where Admiralty Resources plan to pretreat the raw brine with calcium hydroxide to reduce the magnesium content before pan evaporation commences. Compared to Atacama and de Hombre Muerto, the lesser thickness of porous halite (11 m versus 35 m), the lower Li, and higher Mg content in the brines have made this salar a less attractive resource. (Risacher and Fritz 2000; Ericksen et al. 1978; Risacher et al. 2003)
Salar de Atacama, Chile (3,065 km^2)	2,250	BWk	Lithium carbonate extraction via solar concentration of extracted and ponded salar brine. Sediment fill thickness is more than 950 m of intercalated halite and lacustrine muds. Nearsurface salt unit is very porous (30, 20, 15 and 5 % at 0–0.5, 0.5–2, 2–25 and 25 m depth, respectively; average of 18 % in upper 25 m), and brine-filled from about 0.6–35 m. The porosity decreases rapidly to nearly zero after about 35–40 m depth. The brine is saturated with halite, and contains variable concentrations of lithium, potassium, magnesium, sulphate and borate in different locations in the Salar; Lithium concentration varies from about 1,000–4,000 ppm, and averages over 1,500 ppm for the two commercial lithium operations on the Salar. SQM's production costs estimated $1,260 per ton of lithium carbonate, historically it has sold that ton for up to $12,000. Unusual compared with other Puna salars as it contains no borate beds. (Boschetti et al. 2007; Risacher et al. 2003).

Table 12.13 (continued)

Location, Country (area)	Elev. (msl)	Köppen	Comments
Zabuye (Chabyer) Salt Lake, western Tibet, China (251 km^2)	4,426	Dwc	Currently under expansion, a 5,000 tpy $LiCO_3$ plant began operations in 2005. Complex perennial brine; Li from 500 to 1,000 ppm, the lake centre brine is saturated with both halite and potassium sulphate, during solar evaporation lithium starts to crystallize around two-fold concentration. Unique saline lacustrine system in that $LiCO_3$ is a natural precipitate about lake strandzone. (Zheng and Liu 2009; Nie et al. 2009)
Dabuxum/East Taijinaier Lakes, China (350 km^2)	3,200	Dwc	Potash brine operation via extraction and solar concentration since mid 1980s, a 35,000 tpy $LiCO_3$ plant began operations at Golmud in 2007, but will not reach full capacity for a number of years. A 8–13 ppm Li brine is pumped into solar evaporation ponds where the final potash end-liquors (carnallite) contain around 120 ppm Li. (see text and Yu et al. 2013)
Dead Sea, Israel, Jordan (1,023 km^2)	−415	BSh	Possible future resource. The $MgCl_2$-rich lake brine is currently pumped into large solar ponds to produce potash (carnallite) and magnesia in both Israel and Jordan (Mg and Br as byproducts). Pond end-liquors contain about 30 ppm Li, but high Mg content make Li extraction problematic. (Garrett 2004)
Clayton Valley Playa, Nevada, USA	1,300	BWk	Lithium carbonate operation started in 1966 (then Li in brine was 360–400 ppm, today ≈230 ppm). Brine level (WT) was sometimes as low as 15–76 m beneath the playa floor. Brine wells were pumped into solar ponds where Li concentration reached 5,000 ppm, then sent to Li recovery plant. Current lower Li levels make this operation unattractive compared to South American salars. Hectorite clays ($Na_{0.33}(Mg,Li)_3Si_4O_{10}(F,OH)_{2)}$ found in playa formed by interaction of playa brine with smectitic clays (Davis et al. 1986)
Great Salt Lake, USA (4,998 km^2)	1,280	Cfa	Possible future resource. The lake brine Li concentration varies widely with the climate cycle, the southern brine contains up to 18 to 43 ppm Li, and the northern brine from 40 to 64 ppm Li. The commercial magnesium plant's solar pond end-liquor often contains about 600 ppm Li, while the potassium sulphate plant has achieved values of 700–1,600 ppm Li, but high Mg content make Li concentration and extraction problematic from either brine source. (Garrett 2004)
Searles Lake, USA (100 km^2)	490	BWk	Lithium carbonate manufacture as byproduct from salt-cake and soda-ash processing via brine extraction from two porous halite layers and subsequent solar concentration. Li plant operated from 1951 to 1978. In the central section of the lake the brine contained an average of 50–80 ppm Li, which graded to 10–70 ppm Li near the lake edges. The high salinity brine resource beneath the lake is now largely depleted, Li content is probably too low and volumes too small to make this a viable future $LiCO_3$ resource. (Garrett 2004)
Salton Sea, USA	−70	BWh	Possible future resource, situated in a very large geothermal brine field hosted in porous saline sediments at a depth of about 500–3,000 m. Brine is a hot (100–400 °C) NaCl solution carrying elevated levels of metals, including from 100 to 400 ppm Li (200 ppm average). Many difficulties to be overcome in terms of rigid environmental restraints, elevated Mg and other metal content in the concentrated brines and land access needed to construct solar evaporators. (McKibben et al. 1987; Garrett 2004)
Smackover oilfield brines, Arkansas, USA	–	–	Possible future resource, Smackover reservoirs in both Texas and Arkansas have Li content of 50–572 ppm, in one zone in Texas the brine averages 386 ppm Li, while Arkansas a brine averages 365 ppm. Brines occur at 1,800–4,800 m depth and are currently commercially processed to extract bromine before re-injection (these brines currently account for 40 % of world Br production). (Garrett 2004)

For additional overviews see Garrett (2004), Kunasz (2006) and Kogel et al. (2006)

States production from brine was surpassed in 1998 by Chile and today only one lithium carbonate focused brine operation is still active in the USA. The United States remains the world's largest consumer of lithium.

Production from pore brines in South American salars dominates current world lithium brine production, with Chile and Argentina producing some two-thirds of the documented brine production (Figs. 12.48a and 12.49a, b). Most lithium

Table 12.14 Lithium contents of some salar and playa brines

Location	Country	Lithium (ppm)	Reference
Salar de Atacama	Chile	1,000–7,000	Risacher and Alonso (1996)
Salar del Hombre Muerto	Argentina	100–700	Saller and O'Driscoll (2000)
Salar de Uyuni	Bolivia	100–500	Risacher and Fritz (2000)
Lake Zabuye	Tibet	700–1,000	Chen (1986)
Clayton Playa, Nevada	USA	100–300	Davis et al. (1986)
Searles Lake, Ca	USA	70	Kunasz (1983)
Great Salt Lake, Utah	USA	30–60	Kunasz (1983)
Qinghai Lake	China	100	Kunasz (1983)

salts are highly soluble in natural brines and tend stay in solution although some can be to be absorbed on playa clays, as in the hectorite beds in Clayton Playa, Nevada. Interestingly, lithium carbonate (zabuyelite) is a natural precipitate from the high-altitude hypersaline waters of Lake Zabuye in Tibet.

Geological Setting of Li Brines

Only the geology of the brine sources and associated saline sediment host is discussed in detail in this section, the interested reader is referred to Garrett (2004), and Kesler et al.(2012) for a full discussion of all lithium raw materials. Subsurface lithium in playa sediments typically occurs either as a brine component (Tables 12.13 and 12.14; Fig. 12.50) or as lithium bearing minerals in saline clays such as hectorite [$Na_{0.33}(Mg,Li)_3Si_4O_{10}(F,OH)_2$] a clay mineral of the smectite group where the replacement of aluminium by lithium and magnesium is essentially complete or jadarite [$LiNaB_3SiO_7(OH)$], a newly recognized mineral with up to 5.7 % Li and 14.7 % B. Jadarite[6] is associated with borate salts such as colemanite in the Oligocene-Pliocene host lacustrine sediments in its type area in the Jadar Valley in Serbia (Stanley 2007). Hectorite is probably associated with crossflows of moderate salinity hydrothermal waters, while jadarite requires hypersaline hydrothermal waters to form. To date an economic technology for extracting lithium from saline clays, rather than brine, is yet to be developed.

Hectorite is still mined periodically (not as a lithium source) in its type area, near Hector, California. It has a soft, greasy texture, a candlewax-like appearance and feels like modelling clay when squeezed between the fingers. As a colloid, hectorite's unique thixotropic properties for emulsion stabilizing, gelling, suspending, binding, bodying and disintegrating, means it sells for more than US$2,000 a ton. Associated authigenic clays include stevensite and saponite and in its type area it lies adjacent to a colemanite deposit. Hecorite, along with associated authigenic clays and zeolites, is the diagenetic result of alkaline brines flushing highly labile volcaniclastic playa sediments. A similar moat/fault genesis explains the lithium-rich hectorite clays in King Valley, Nevada. There, layers of hectorite occur in a sequence of sedimentary and tuffaceous rocks in moat sediments along the western side of the McDermitt caldera (Kesler et al. 2012). As in the type area in California, hectorite is the main clay mineral in a sequence of altered volcanic ash beds that are interbedded with lake sediments and travertines, along an 8 km fault zone. King Valley hectorite again formed through hydrothermal alteration of volcanic ash by moderately saline hydrothermal fluids moving up fault zone. None of the clay-bound lithium occurrences are currently exploited as a lithium source.

Lithium in Andean Salars

The situation is very different with respect to lithium-entraining saline lacustrine pore brines. In the last two decades Chile has emerged as the most important lithium carbonate producer from a lake brine, largely through the exploitation of Salar de Atacama, Chile (Figs. 12.51 and 12.52) followed by China with operations focused in the Qaidam Basin. Salar de Atacama lies on the Tropic of Capricorn at an altitude of 2,300 m in the Desierto de Atacama, some 200 km inland from Antofagasto. In its more central portions this salt-encrusted playa contains a massive halite unit (nucleus) that is more than 900 m thick, with an area ≈1,100 km^2. Fringing saline muds, with an area ≈2,000 km^2, surround the nucleus (Fig. 12.51a, b).

The current salt crust atop this halite nucleus contains a sodium chloride interstitial brine that is rich in Mg, K, Li, and B (Alonso and Risacher 1996). Lithium contents of the pore brines range from 200 to 300 ppm in the marginal zone, some 500–1,600 ppm in the intermediate zone and 1,510–6,400 ppm in the salt nucleus (Fig. 12.51c). The nucleus zone averages 4,000 ppm lithium and is asymmetric with respect to the salar center due to the sump offset via ongoing faulting (Chap. 3). Main inflows to the salar

[6]Jadarite was discovered by Rio Tinto in November 2006, in drill core from the Jadar Valley, Serbia. Jadarite's chemical formula is very close to the formula ("sodium lithium boron silicate hydroxide with fluorine") invented for the fictional substance kryptonite in the 2006 film *Superman Returns*, although jadarite lacks fluorine and is white not green. This coincidence in chemistry attracted significant mass-media attention, following its discovery.

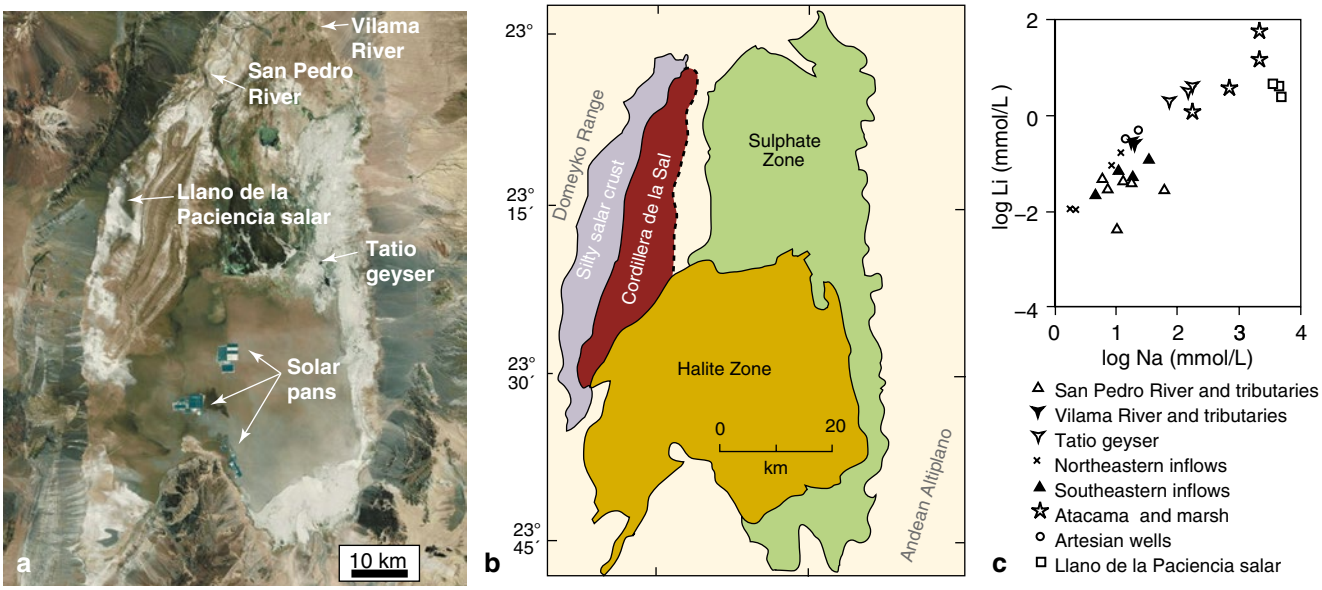

Fig. 12.51 Lithium brines in Salar de Atacama, Chile. (**a**) General overview of Salar de Atacama, Chile, showing centripetal endorheic drainage (Bing® image scaled and mounted in MapInfo®). (**b**) Surface geology showing nearby Neogene evaporite outcrops in the Cordillera de la Sal. (**c**) Lithium content of wells in the halite nucleus and other nearby brine sources (After Carmona et al. 2000)

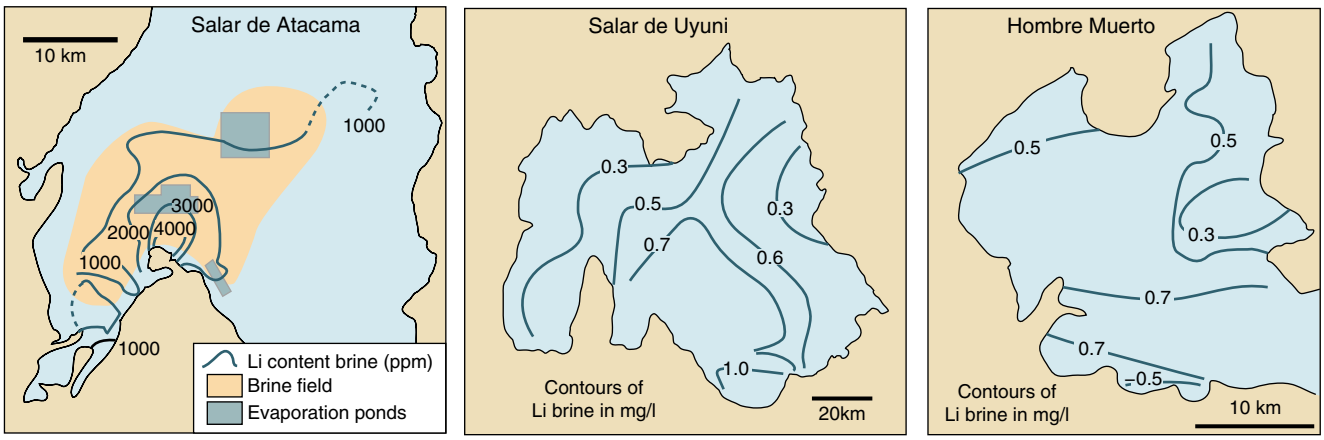

Fig. 12.52 Selected South American salars showing variations in Lithium in near surface pore brines (After Kesler et al. 2012)

drain volcanic formations of the Andean Highlands located to the east of the basin. Salts dissolved in inflow waters have a double origin. Weathering of volcanic rocks supplies K, Li, Mg, B and, to a lesser extent, Na and Ca. Leaching of ancient halokinetic evaporites sourced in a mother salt layer beneath the volcanic formations provides additional amounts of Na, Ca, Cl, SO_4 to the most saline inflow waters. The mass-balance of the upper halite nucleus in the salar shows a strong excess of NaCl with respect to the bittern solutes Mg, K, Li, B. According to Alonso and Risacher (1996) this suggests that the nucleus did not originate from evaporation of inflow waters similar to the present groundwaters. Rather the excess of NaCl is due to NaCl-rich inflow waters that formerly drained the Cordillera de la Sal, a Tertiary-age evaporitic ridge along the western rim of the present-day salar.

Although annual salt accreation rates in the nucleus facies can be as high as 5–6 cm/year (Ruch et al. 2012), the average sedimentation rate of halite in the lake centre is ≈0.1 mm/year, based on the age of an ignimbrite interbedded with the salt. This slow aggradation rate implies a climatic setting of long dry periods and inactivity alternating with short wet periods during which large amounts of water, and so large amounts of salt, accumulated in the basin centre. The lack of peripheral lacustrine deposits and the high purity of the salt also suggest that the main salt unit is not the remnant of an ancient deep saline lake, but originated mostly from evaporation of waters supplied by subsurface and subterranean saline seeps.

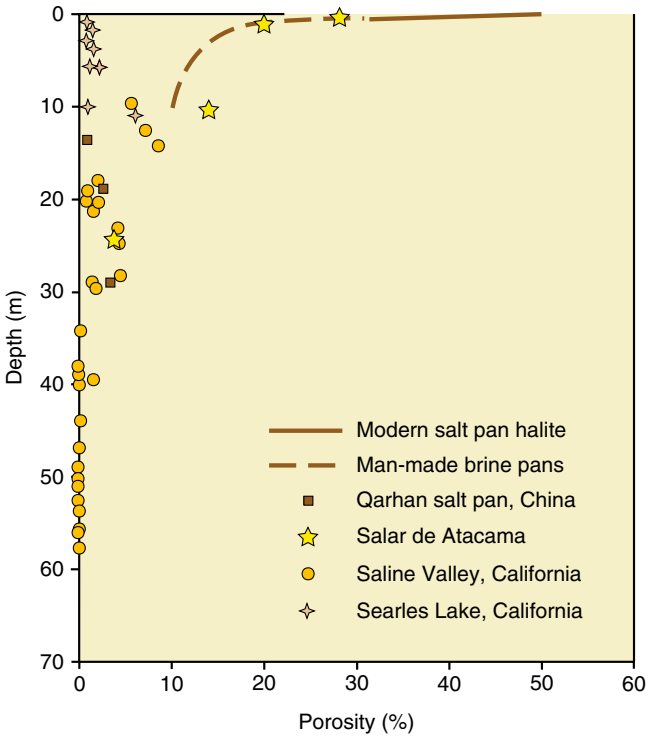

Fig. 12.53 Porosity loss with depth in bedded halite from saline pan and salar deposits (In part after Casas and Lowenstein 1989)

Brines are pumped from 30 m deep boreholes in the salt nucleus into solar evaporation ponds. In the ponds the liquours are concentrated by a factor of 25, generating a final brine strength of 4.3 % Li. During evaporation processing and the production of potassium chloride and potassium sulphate the ion ratios are constantly monitored and adjusted to avoid the precipitation of lithium potassium sulphate. When soda ash (sodium carbonate) is added to the concentrated brines, lithium carbonate drops out (Fig. 12.55c). The high initial lithium content of the Atacama brines and the extremely arid setting (3,200 mm pan evaporation and <15 mm precipitation) means that only 90 ha of evaporation ponds are required for one of the current brine operations on the salar, this is only 5 % of the area required at Clayton Valley, Nevada (Fig. 12.52a). Borate (as perborate) is recovered at levels of 0.84 g/l during lithium extraction. Increasing volumes of lithium are also produced by new salar brine processing facilities in Salar de Hombre Muerto, Argentina and Salar de Uyuni, Bolivia. In Lake Zabuye, China, the seasonal cooling of lithium-rich lake brines leads to the natural precipitation of lithium carbonate (Fig. 12.55d).

Porosity levels in a host halite aquifer are a major constraint on potential economics of any salar or salt lake lithium brine resource. Most halite units lose their effective porosity and permeability by depths of 50–60 m (Fig. 12.53). Thus, most Quaternary lithium brine operations hosted in a halite bed/aquifer will have an economic basement to brine recovery at around this depth. It is unlikely that recovery operations in Salar de Atacama and planned projects in Salar de Uyuni can recover economic brine volumes at much greater depths. There may be a 900 m thick halite-dominant succession infilling Salar de Atacama and a number of halite beds to a depth of 120 m in Salar de Uyuni, but economic porosities in the halite will likely only be present in the upper portions of the halite fill in both salars.

Postulating likely lithium resources, in a salar of a salt lake, to depths greater than 50–60 m should only be done after salar-hydrology-aware drilling has established the presence of economic permeabilities in the hosting halite aquifer and this is likely related to the presence of active faults (see below). Such measurements require drilling and sampling equipment that facilitate reliable "in-situ" determinations of porosity and permeability in the halite mass and Li measurements in the brine that are related to actual content at the level of measurement, with minimal contamination by waters from outside the measured horizon.

Clayton Valley, Nevada

Lithium carbonate is still produced from playa brines in Searles Lake, California and Clayton Valley (Silver Peak playa), Nevada. Historically, the Clayton Valley playa produced about one-third of the US lithium requirements, but its economic viability is now suffering from fierce market competition and a largely depleted brine supply. Originally, the central valley area contained 100–800 ppm Li, and the discovery well at 229 m depth contained 678 ppm when pumped at 450 gpm (Garrett 2004). The average brine analysis when commercial production of lithium carbonate began in 1966 was about 400 ppm (Fig. 12.54). Since that time it has been slowly declining, and in 1998 the concentration was about 100–300 ppm Li (averaging 160 ppm, Harben and Edwards 1998).

The Silver Peak playa has an area of 50 km^2 and an elevation of 1,300–1,400 m (Fig. 12.54). It lies in the rain-shadow of the Sierra Nevada, with an annual rainfall ≈130 mm and an evaporation rate of ≈1,380 mm. Near surface sediments consist of a mixture of clays (smectite, illite, chlorite, kaolin) and salts (halite and gypsum) and widespread pedogenic calcite. Lithium in the brines is from weathering and leaching of volcaniclastics in Tertiary Esmeralda Formation and Quaternary ash-fall tuffs (Davis et al. 1986). Lithium content is highest on the eastern side of the playa adjacent to the outcropping marls of the Esmeralda Fm. Before it is leached, lithium is held in the clay fraction of the playa sediments and is probably part of the clay structure (hectorite is a widespread minor component in the Clayton Valley clays).

Lithium-rich brine feed to the plant, averages 0.023 % (230 ppm) lithium in a background NaCl concentration of

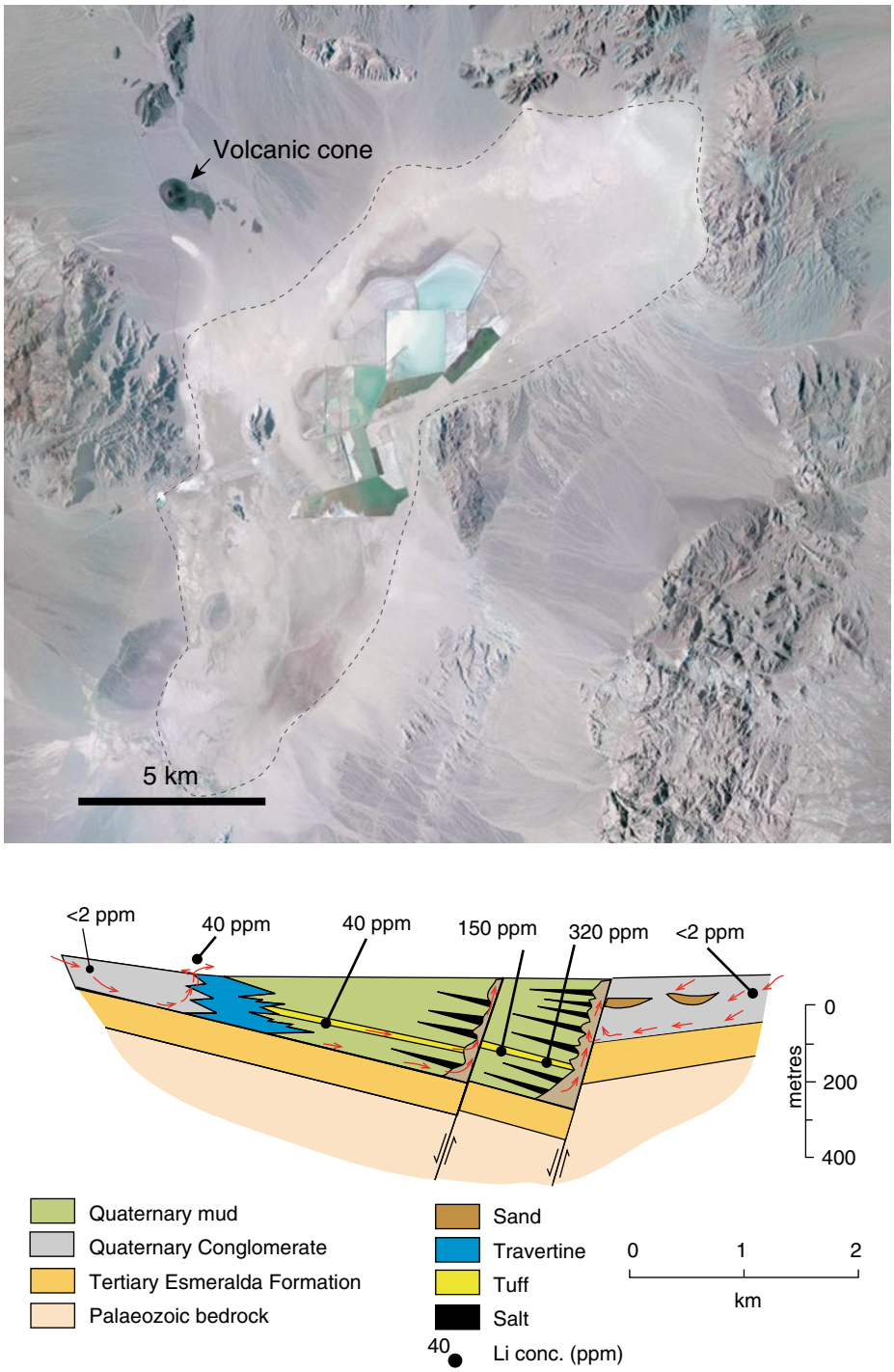

Fig. 12.54 Plan view and generalised cross section of Clayton Valley (Silver Peak) Playa, Nevada. Basin is hydrographically closed with a recent volcanic cone in bajada to northwest of playa depression. Cross section shows the relative position of the major tuff-bed aquifer, inferred directions of groundwater flow and representative lithium concentrations (ppm) in the various aquifers and springs (In part after Davis et al. 1986)

200,000 ppm, is pumped from depths of 100–300 m in the Clayton Valley (Silver Peak) playa via a number of gravel-packed wells. The lithium (and potassium) in the deposit probably originated from currently flowing hot springs along the Silver Peak Fault, with the current brine composition being a blend of evaporated water from these springs and surface and ground water that drains into the basin (Garrett 2004). Springs flow at 10–20 gpm and contain 9,280–10,000 ppm Na, 786–826 ppm K and 24–43 ppm Li (Fig. 12.54; Table 12.14). Unusually high brine temperatures in some areas of the deposit (up to 44 °C at fairly shallow depths ≈25 m) tend to support a geothermal origin for the lithium. Some of the brine feed shows elevated levels of radon gas.

Pumped brine progresses through a series of fractionating evaporation ponds (Fig. 12.54; Zampirro 2004). Lithium

concentration in the liquor increases to 6,000 ppm over the course of 12–18 months in the solar evaporation pans. When the lithium chloride level reaches optimum concentration, the liquor is pumped to a recovery plant and treated with soda ash to precipitate lithium carbonate, which is then removed through filtration, dried, and shipped. Lithium from brine, when the Clayton valley first produced product in the 1970s, was a unique deposit. It established the technology and economic viability of lithium recovery from brine that led to the development of brine production from the salars of South America, which now dominate world production of lithium from brine.

Lithium in Chinese Salt Lakes: Zabuye and Qaidam Basins

The lithium brine resource of China is held mostly stored in two saline lake regions in high altitude zones, Lake Zabuye on the Tibetan Plateau and four salt lakes in the Qaidam Basin on the Mongolian Plateau (Figs. 12.47 and 12.50). Something like 80 % of brine lithium resource found in China is contained in the four salt lakes of the Qiadam: Bieletan (BLT), DongTaijinaier (DT), XiTaijinaier (XT) and Yiliping (YLP). Zabuye lake on the Tibetan Plateau is probably the most geologically interesting as the Li content of the lake waters are so elevated that it is the only know lacustrine location where lithium carbonate, zabuyelite, is an exploitable natural precipitate (Nie et al. 2009).

Lake Zabuye, is located some 1,000 km west of Lhasa, the Tibetan capital and lies in the ET Köppen high altitude climate zone of the Tibetan Plateau (Fig. 12.55a). When artificially concentrated, the crystallization sequence of primary salts from Zabuye lake brine at 25 °C is (Fig. 12.55b):

$$\begin{aligned}&\text{halite}\left(\text{NaCl}\right) \rightarrow \text{aphthitalite}\left(3\text{K}_2\text{SO}_4 \cdot \text{Na}_2\text{SO}_4\right)\\&\quad \rightarrow \text{zabuyelite}\left(\text{Li}_2\text{CO}_3\right) \rightarrow \text{sylvite}\left(\text{KCl}\right)\\&\quad \rightarrow \text{trona}\left(\text{Na}_2\text{CO}_3 \cdot \text{NaHCO}_3 \cdot 2\text{H}_2\text{O}\right) \text{and}\\&\qquad \text{thermonatrite}\left(\text{Na}_2\text{CO}_3 \cdot \text{H}_2\text{O}\right)\end{aligned}$$

The lake's brine is naturally supersaturated with NaCl and other salts, so millions of metric tons of halite, potash, trona, and other minerals have accumulated on the bottom of the lake in the past few thousand years (Zheng et al. 1987; Zheng and Liu 1989). Zabuye Lake is of significant economic value as it is a new type of exploited saline lacustrine deposit that contains lithium and borate salts in addition to significant volumes of potash, halite, natron and Glauber's salt. Lake waters also retain elevated levels of caesium, rubidium and bromine. Lake levels can vary by metres each year; in 2008 the water level was some 4,422 m above sea level. At this level, the lake's area is approximately 247 km^2 and its salinity varies from 360 to 440‰, depending on seasonal differences in water input and evaporation rate. Lithium carbonate and sylvite precipitate, via a combination of brine concentration and cooling, but can also be induced by the addition of soda ash (Fig. 12.55c, d).

Detailed sedimentologial and hydrological work in the Qaidam by Yu et al. (2013) has shown that: (1) Some 748.8 tonnes of lithium is transported annually into the lower catchment of the four salt lakes via the Hongshui-Nalinggele river (H-N river in Fig. 12.55e), which is the largest river draining into the Qaidam Basin, (2) Li^+-rich brines are formed only in those salt lakes in the Qaidam that are associated with inflowing rivers with Li^+ concentrations greater than 0.4 mg/L, and (3) the water Li^+ concentration is positively correlated with elevated levels in both the inflowing river and the associated subsurface brine. Their findings clearly show that long-term input of Li^+ from the Hongshui-Nalinggele river controls the formation of lithium brine deposits. They conclude that the source of the lithium in the lake brines is ultimately from hydrothermal fields where two active faults converge in the upper reach of the Hongshui River. These hydrothermal fields are associated with a magmatic heat source, as suggested by the high Li^+ and As^{3+} content water in geysers. Based on the assumption of a constant rate of lithium influx, they estimate that the total reserves of lithium in the Qaidam were likely formed since the postglacial period. Their field mapping and coring indicates that lithium reserves in each of the four salt lakes depend on the influx of Li^+-bearing water from the H-N River. The data also suggest that during the progradation of the alluvial Fan I, the Hongshui-Nalinggele drained mostly into the Bieletan salt lake until the Taijinaier River shifted its watercourse to the north and began to feed the salt lakes of the DongTaijinaier, XiTaijinaier and Yiliping salt lakes, while also driving Fan II progradation (Fig. 14.55e). One of their major findings in terms of Lithium enrichment is the importance of the contrasting hydroclimatic conditions between the high mountains containing ice caps and the terminal salt lakes. The greater than 4,000 m of relief in the watershed enables a massive amount of ions, such as K+, to be weathered and transported, together with detrital material from the huge, relatively wet alpine regions to the hyperarid terminal basins, where intense evaporation rapidly enriches the lake water, resulting in evaporite deposition and associated K+ and Li^+ rich brine deposits.

In summary, characteristics that appear to be essential to define a potential lithium carbonate brine resource are; (i) an arid climate and, (ii) a closed, tectonically active basin e, with significant elevation and tectonically active that can entrain brines with elevated lithium contents (Fig. 12.56a; Bradley et al. 2013; Yu et al. 2013). Sources of lithium can be deeply circulated magmatic or basinal fluids. Magnesium levels in the brine should not be too high as this complicates brine processing. A co-occurring potash resource, extractable from the same brine, if present typically reduces processing costs. Another possible requirement—or at least a favourable characteristic—is elevated heat flow, as evident from young volcanoes or hot springs and the associated increase in Li-rich juvenile waters flushing the surrounding

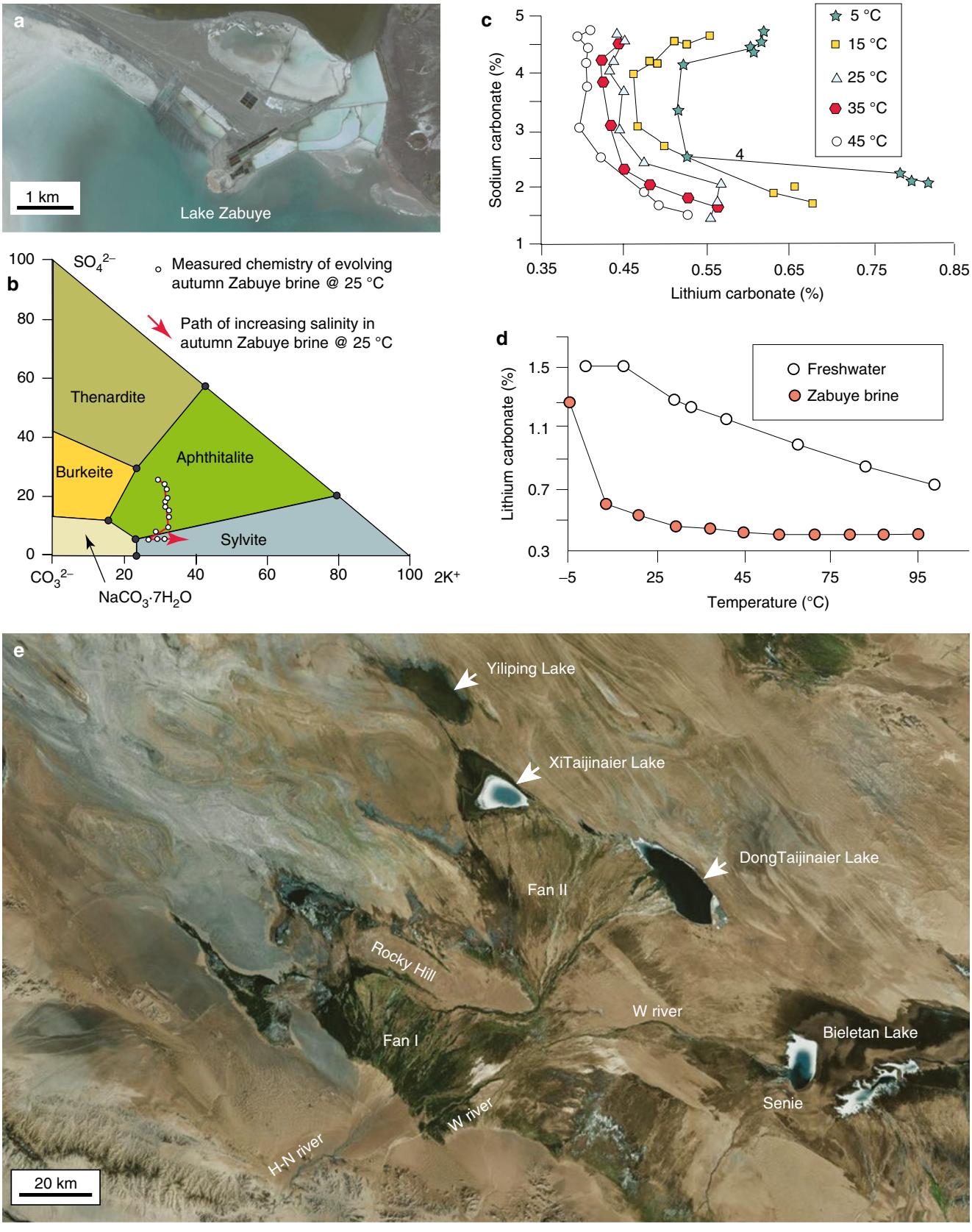

Fig. 12.55 Lithium brine lakes China. (**a**) location of Li plant on northern shore of Lake Zabuye, Tibetan Plateau. (**b**) Brine evolution pathway (After Nie et al. 2009). (**c**) Lithium carbonate solubility with respect to temperature. (**d**) Lithium carbonate solubility with respect to sodium bicarbonate content at various temperatures (After Sha et al. 2009) (**e**) Lithium lakes and supplying rivers and fans in Qaidam Basin (After Yu et al. 2013). The Golmud potash lakes and brine plant lie to the east of Lake Senie (See Fig. 11.11)

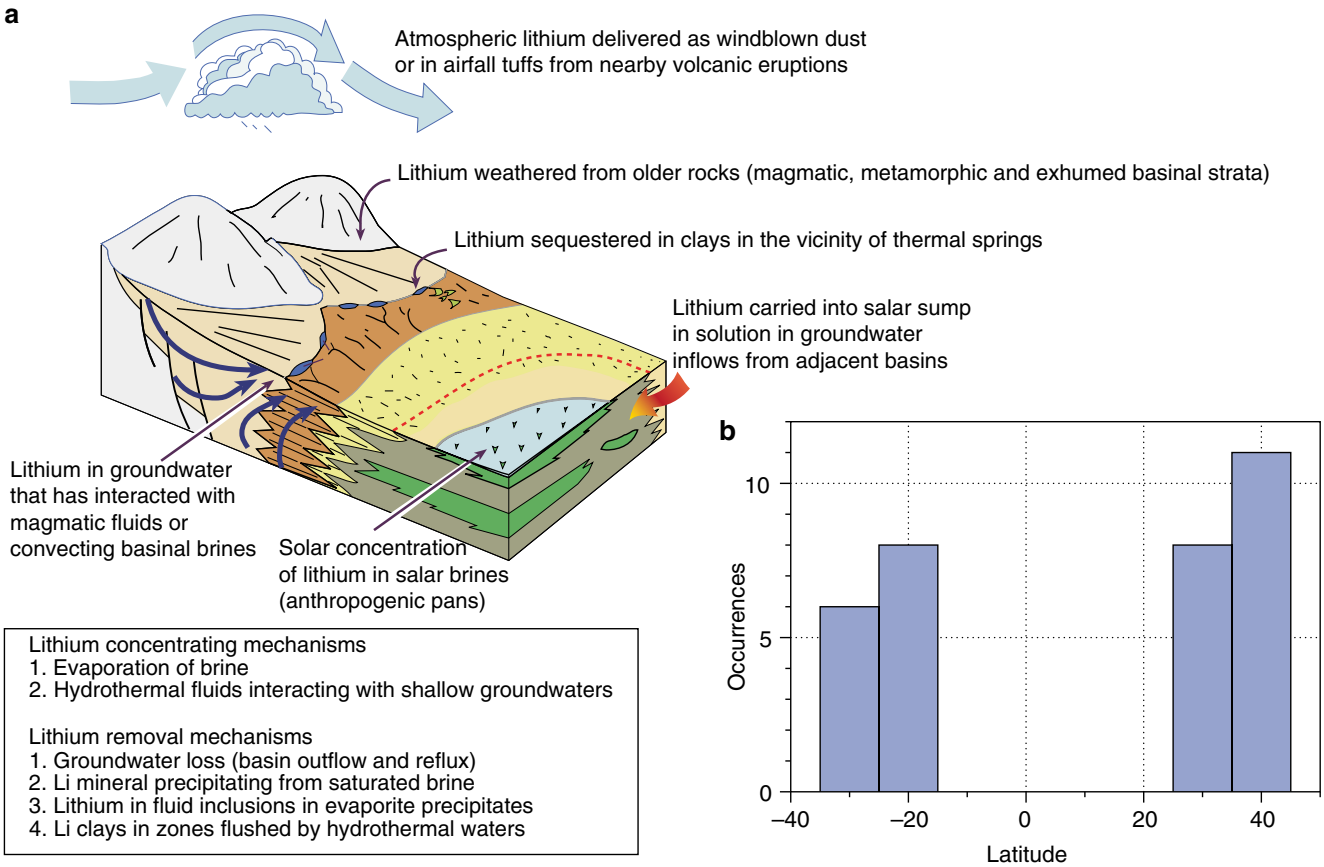

Fig. 12.56 Lithium controls and distribution. (**a**) Summary of mechanisms controlling lithium in a salar setting. (**b**) Latitudinal distribution of modern lithium brine occurrences (Replotted with permission from SaltWork database version 1.6- see also Fig. 12.47)

drainage basin beneath the Andean Altiplano. Volcanigenic source rocks in the lake drainage, such as felsic, vitric tuffs that have abundant and readily leached lithium are favourable, but perhaps not essential, since lithium is present in most crustal rocks at tens of parts per million (ppm). Another possible favourable indication of lithium brines is the existence of hectorite or jadarite in associated clays in the bajada rims. Active faulting appears to be involved in forming a suitable spring-fed hydrology for all known economic lithium brine basins. Fault-related subsidence also creates accommodation space, without which only a thin veneer of arid basin sediments and brines can accumulate. Thus, a thick basin fill is needed to provide an aquifer of sufficient volume to hold a viable lithium brine resource.

In contrast, shallow, superficial basins in intracratonic regions such as the Sahara Desert and most inland Australian deserts largely lack active fault control and associated rapid subsidence and so are not known to be prospective for lithium brines. As well as the aquifers, salt fills in some lithium basin sumps are cut by active intrabasinal faults (known from boreholes and seismic) but have no surface expression due to rapid infill and levelling of the accommodation space by salt precipitation. Significantly, the brine pools in ClaytonValley, Salar deAtacama and the Qaidam sumps are localized along active intrabasinal faults, which also control the distribution of aquifers and influence groundwater movement patterns, as well as the position of maximum stacking of concentrates and brines in the halite nucleus, along with porosity retention levels in the subsurface halite host (Chaps. 2 and 3; Zampirro 2004; Jordan et al. 2002). A plot of known Quaternary-hosted lithium brines also shows that these accumulations are latitudinally restricted to cool arid belts within endoheic brine sumps that are surrounded by high altitude drainage basins (Fig. 12.56b; Warren 2010).

$CaCl_2$ Brines and Minerals

Calcium chloride is produced in commercial amounts using many different procedures: (1) refining of natural brines, (2) reaction of calcium hydroxide with ammonium chloride in Solvay soda ash production, and (3) reaction of hydrochloric acid with calcium carbonate. The first two processes account for over 90 % of the world's total calcium chloride production Historically, natural brines sources have been the dominant source. There is currently an excess of capacity in the

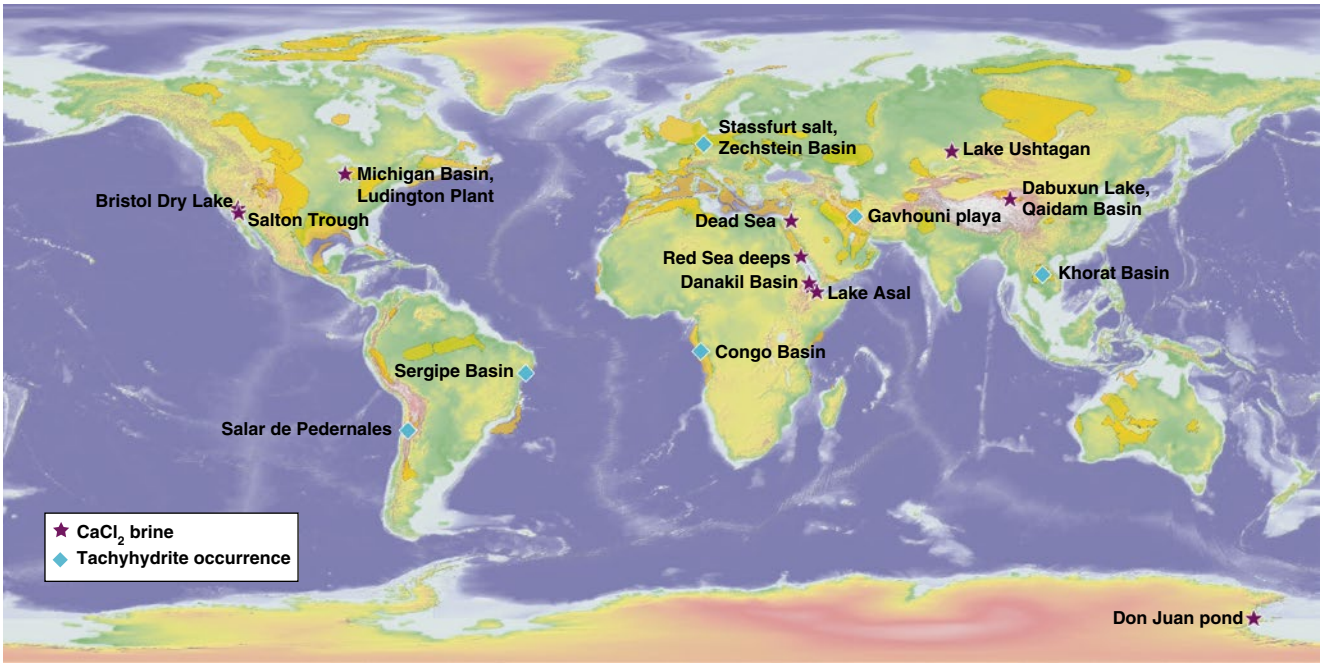

Fig. 12.57 Occurrences of tachyhydrite and calcium chloride brines. Only the Cretaceous occurrences in circum Atlantic Salt basins and the Maha Sarakham are sufficient to be considered bedded or stratabound

calcium chloride industry, a situation which is only expected to become more acute as additional synthetic or byproduct capacity increases.

More than 50 % of $CaCl_2$ use is for deicing during winter, roadbed stabilization, and as a dust palliative during the summer. It is also used as an accelerator in the ready-mix concrete industry, where there is concern about its usage because of possible chloride-induced corrosion of steel in highways and buildings. Calcium chloride is also widely used to increase mud fluid densities in oil- and gas-well drilling.

Most natural calcium chloride brines are derived from a hydrothermally-modified marine waters or from resurging deep basinal brines/formation waters. Volumetrically, the largest volumes $CaCl_2$ occur in relatively dilute, oceanic $CaCl_2$ brines that are the result hydrothermal circulation and thermally-driven alteration of mid-ocean ridge lithosphere. These $CaCl_2$ waters occur in and near active fracture zones, wherever seawater interacts with labile basalt (oceanic crust) at elevated temperatures and coverts a connate hydrothermal brine from a Na-Mg-Cl water into a low-salinity Na-Ca-Cl brine, depleted in Mg and SO_4. Similar hydrothermally-driven alterations of continental basalts, driven by deeply circulated seawater, forms modern $CaCl_2$ brine feeds to the active continental Danakil rift valley where potentially economic volumes of potash are found. The only current commercially, exploited natural $CaCl_2$ brine source is in Bristol Dry Lake, California (Fig. 12.57, Table 12.15).

Found in association with some highly-saline calcium chloride brines are two indicator $CaCl_2$ evaporite minerals, namely tachyhydrite and antarcticite. Bischofite is sometimes a co-precipitate with tachyhydrite and is indicative of mother brines with higher $MgCl_2$ contents (Fig. 12.57). Halite-encased tachyhydrite ($CaMg_2Cl_6{\cdot}12H_2O$) is a rare bittern mineral phase in some evaporites across much of the Phanerozoic. Along with carnallite ($KCl{\cdot}MgCl_2{\cdot}6H_2O$) and bischofite ($MgCl_2{\cdot}6H_2O$), it typifies highly saline marine bittern assemblages in some, but not all, ancient basinwide potash-rich evaporite systems that are $MgSO_4$ poor. They include: Silurian potash of Michigan Basin; Carboniferous potash in the Canadian Maritimes and the Paradox basin; Permian Zechstein 2 Stassfurt potash seams in Stassfurt, Germany; Triassic Saharan potash of North Africa; Cretaceous potash evaporites in Brazil, Gabon and Thailand and Oligocene potash in the Rhine Graben. Outside of these deposits, tachyhydrite-bearing successions are much less common within this broader $MgSO_4$-poor group of ancient potash deposits (see Chaps. 2 and 11 for the detail).

To form antarcticite ($CaCl_2$)$\cdot 6H_2O$ at the bittern stage, a $CaCl_2$ brine must be depleted in Mg, otherwise tachyhydrite forms, along with carnallite and bischofite. These three chloride bittern salts are not part of the bittern suite precipitated from today's $MgSO_4$ oceans, where sulphate and magnesium levels are too high relative to calcium. But carnallite and tachyhydrite were more common precipititates in the bittern stages of ancient $CaCl_2$ or $MgSO_4$-depleted oceans at times when rates of seafloor spreading, and hence volumes of through-circulated seawater, were greater than today (Fig. 2.45). It seems that most the highly saline calcium chloride brines form in sedimentary basins with a thick evaporite

Table 12.15 $CaCl_2$ brines in Quaternary saline settings; $CaCl_2$ brines and tachyhydrite in ancient evaporite deposits tend to typify times of $CaCl_2$ oceans, as listed in Fig. 12.57

Location, Country (area)	Elev. (msl)	Köppen	Comments
Don Juan Pond, Lake Vanda, Antarctica (<1 km^2)	90	EF	Very small saline lake (<1 km^2) and only of academic interest. Unusual association of low $MgCl_2$ levels in this $CaCl_2$ brine. Calcite, gypsum, mirabilite, antarcticite are lake floor precipitates. See earlier mirabilite discussion for deposit details. (Torii and Ossaka 1965; Horita 2009)
Lake Asal, Djibouti (54 km^2)	−155	BWh	Possible future resource. Lake precipitates halite and gypsum and is fed in east by hydrothermally-altered $CaCl_2$-rich modified seawater (Manda springs; 40–80 °C) seeping through recent fault zones in Dahla Basalt ridge (salinities >100,000 ppm). Lake waters are less enriched in Ca relative to springs due to widespread precipitation of subaqueous gypsum on perennial lake floor. (Stieljes 1973, Castanier et al. 1992; Garrett 2004)
Danakil depression, Ethiopia	−77 and −118 resp.	BWh	Possible future resource. Lake Afrera (Lake Giulietti; −77 m, 115 km^2) is largest perennial saline lake in Danakil depression, water depth of over 100 m situated in an actively rifting area in the centre of the Danakil Depression and surrounded by active volcanic peaks. A number of calcium chloride-containing hot springs (40–50 °C) flow into the southwest edge of Lake Afrera, and the lake appears to occasionally drain into the nearby Dallol Salt Pan (−118 m, 344 km^2). Inflow water is hydrothermally-altered seawater. In the northern portion of the Danakil Depression, bischofite and carnallite precipitate from a 130 °C $MgCl_2$ brine that emerges from the Black Mountain hot spring, although bischofite quickly deliquesces to sylvite upon exposure to the atmosphere. (Hutchinson and Holwerda 1968, Augustithis 1980)
Dead Sea, Israel, Jordan (1,023 km^2)	−415	BSh	Possible future resource. Ca and $MgCl_2$ brine tied to carnallite and bischofite precipitate stages in artificial pans and then can be used to manufacture $MgCl_2$. Dead Sea is a nonmarine, fault-bounded evaporite basin that contains $CaCl_2$-rich and SO_4- and $CaCO_3$-poor waters, supplied by the Jordan River and a number of hydrothermal springs., Most of the solutes come from hydrothermal spring waters that have leached earlier Miocene marine evaporites. These hydrothermal brines are enriched in $CaCl_2$, have a chlorinity that is eight times that of seawater, and are rich in the heavy metals; iron, manganese, lead and zinc. (Gavrieli et al. 2001)
Bristol Dry Lake, California, USA (200 km^2)	180	BWk	Active $CaCl_2$ brine extraction and processing. Unusual nonmarine association of low $MgCl_2$ levels in a $CaCl_2$ lake brine. Main evaporites are gypsum, anhydrite, and halite with rare antarcticite, celestite ($SrSO_4$), bacterial calcite, and possibly chlorocalcite ($KCaCl_3$). Bristol Dry Lake is mined for its chloride brines and is thus covered with pits and trenches. Antarcticite was identified in one trench that was 3 m deep, 20 m long, and contained a 10–25 cm deep pool of $CaCl_2$ brine. The base of the pit was a massive halite deposit with acicular groups of antarcticite protruding outward from the halite and within the brine. Evaporative concentration of this brine in the arid cool winter climate with temperatures well below 30 °C allowed antarcticite to precipitate. (Dunning and Cooper 1969; Garrett 2004)

For additional overviews of geology of deposits see Garrett (2004) and Kogel et al. (2006)

near the base of the sediment fill. But, as Fig. 12.57 illustrates, not all are basins with highly saline $CaCl_2$ brines are co-associated with bedded tachyhydrite occurrences in the buried and dissolving evaporite units.

Textures recovered in core, and visible in mine walls in Brazil, indicate this tachyhydrite was a primary bedded precipitate in those circum-Atlantic Cretaceous evaporites with stratiform tachyhydrite units in these potash beds (Fig. 11.43;

Wardlaw 1972). The Cretaceous world ocean at the time this tachyhydrite precipitated was typified by $MgSO_4$-free marine bitterns. Yet, as Fig. 12.57 shows, tachyhydrite does not occur as a bittern phases in many other potash sequences deposited in basinwide settings at other times of $CaCl_2$ oceans (e.g. the Devonian of Canada, the Silurian of the Michigan Basin). This has led to the argument that stratabound tachyhydrite in potash beds indicates a hydrothermal/basinal source for the mother brine; as such the presence of tachyhydrite is not necessarily indicative of a $MgSO_4$-depleted marine feed to the basin (Hardie 1990).

Today, large volumes of relatively dilute, oceanic $CaCl_2$ brines form via hydrothermal circulation and thermally-driven alteration of mid-ocean ridge (MOR) lithosphere. These $CaCl_2$ waters occur in and near active fracture zones, wherever seawater interacts with labile basalt (oceanic crust) at elevated temperatures and coverts the circulating fluid from a Na-Mg-Cl water into a low-salinity Na-Ca-Cl brine, depleted in Mg and SO_4. Similar hydrothermally-driven alteration of continental basalts via deeply circulated seawater interactions forms modern $CaCl_2$-rich brine seeps, for example, within the thermally active continental Danakil rift valley (Hardie 1990).

There may be an additional factor at work here in terms of our recognition of tachyhydrite's basin-by-basin distribution and that is tachyhydrite's high solubility in most subsurface waters and drilling muds. Even the name, tachyhydrite, was chosen from the Greek *tachy hydros* for "*swift water*" to indicate its rapid deliquescence on exposure to atmospheric conditions. This property means that any ground-up remains (rock chips) of tachyhydrite in the return mud stream of a conventional drilling operation typically do not make it to the surface. So, there may be more tachyhydrite occurrences in deeply buried basin evaporites than the few currently documented. Ancient tachyhydrite has only been found encased in halite in recovered cores and mine walls, never drill cuttings, and its presence or absence can be easily misinterpreted in wireline logs, especially when drilling through thick salt masses in the search for oil and gas (companies tend to run a more limited log suite in thick salt units).

Tachyhydrite's lack of shear strength and extremely high solubility makes mining the associated potash difficult, it leads to head beam and floor stability problems in conventional underground mines in Brazil and West Africa. Holle, a West African potash mine in the 1970s, was never economic and was lost to flooding after a few years of conventional mining and the Brazilian mine has ongoing floor and wall stability problems ties to tachyhydrite-induced heave. Today, solution mining is proposed and a more effective means to exploit areas of Cretaceous potash associated with tachyhydrite beds, as in Aptian halite-potash associations on both sides of the Atlantic.

Not only is tachyhydrite highly soluble, it is highly reactive whenever in comes into contact with subsurface bitterns. Based on its occurrence in the Permian Stassfurt series in Germany, D'Ans (1961) suggested that much of the widespread polyhalite found in the $CaCl_2$ brine-rich parts of the Zechstein Basin was a reaction product indicating former tachyhydrite. He noted that, at temperatures higher than room, there is a reaction between gypsum/anhydrite, sylvite and tachyhydrite-bischofite, or their dissolution-related brines, which removes tachyhydrite to form diagenetic polyhalite and calcium chloride brines;

$$CaMg_2Cl_6 \cdot 12H_2O + 4KCl + 8CaSO_4 \rightarrow 2CaSO_4Mg(SO_4)4(H_2O)_2 + 5CaCl_2 + 4H_2O$$

This was the mechanism suggested by Manheim (1974) to explain the lack of tachyhydrite and the formation $CaCl_2$-rich brines that characterize hydrothermal pore waters circulating in sediments associated with buried Miocene evaporites along the deep axial trough of the Red Sea.

Natural modern tachyhydrite is documented only in a few hypersaline settings and never in a bed with primary precipitation textures. Tachyhydrite occurs seasonally as a minor interstitial cements and efflorescences, along with antarcticite (the hexa-hydrate form of calcium chloride), in the modern ephemeral halite crusts, atop sabkhas, of the Gavkhoni Playa (BWk), southeast of Isfahan, Iran (Pakzad and Ajalloeian 2004) and perhaps the Abu Dhabi sabkha (Wood et al. 2005). One occurrence of the dihydrate form of calcium chloride (sinjarite; $CaCl_2 \cdot 2H_2O$) has been documented as small rare pink crystals in wadi sediments of Sinjar town, west of Mosul city, Iraq (Aljubouri and Alddabbagh 1980).

Much of the elevated ionic content of various Iranian playas in the Great Kavir is due to salt dissolution of the crests of nearby at- or near-surface diapirs and namakiers, where the mother salt sourced in halokinetic Miocene marine salts (Warren 2008). These outcropping diapirs have carried carnallite and sylvite remnants to the namakiers that now reside at the surface (Rahimpour-Bonab and Kalantarzadeh 2005). Tachyhydrite is also found as white feathery efflorescences within waste piles at an abandoned borate working along the southwestern margin of Salar de Pedernales, Chile (a BWk location very near the ET climate boundary; Ericksen and Salas 1989).

It seems that tachyhydrite's high solubility means it has little or no preservation potential as a solid salt in any modern at-surface depositional setting; in the Peruvian case it is a winter precipitate that disappears with the end of winter. In Abu Dhabi it, along with other highly soluble salts in the salty surface efflorescences, can disappear in morning dew (Warren, pers. obs.). In both the Iranian and the Peruvian setting the climate is cool and elevated. The arid desert

environments where bedded subaqueous-textured tachyhydrite accumulated in the drawndown Aptian seepage basins of the opening Atlantic were very different to its occurrence in the evaporite settings of today.

The purest $CaCl_2$ mineral precipitates (antarcticite and sinjarite) are rare occurrences as crystalline beds anywhere in today's hypersaline lakes. None have been documented in ancient salts, except as a volumetrically insignificant mineral phase in brine inclusions in both sediments and igneous rocks, even in basins with highly saline $CaCl_2$-rich pore fluids. Antarcticite in Holocene occurrences in saline settings requires a Ca-enriched mother brine that is completely depleted in sulphate. Otherwise gypsum precipitates, and in so doing removes all the calcium from concentrating brine, well prior to the bittern stage. There are only two known modern hypersaline saline deposits where the pure $CaCl_2$ mineral antarcticite ($CaCl_2{\cdot}6H_2O$) is present as thin crystal beds and effloresences; they are, Bristol Dry Lake (BWh) in California and Don Juan Pond (EF) in the Dry Valleys, near Lake Vanda in Antarctica (Dunning and Cooper 1969; Horita 2009). Both saline lakes possess similar $CaCl_2$-enriched, $MgCl_2$-depleted chemistries and are fed by hydrothermal waters. In Bristol Dry Lake the concentration process is driven by solar evaporation, while cryogenesis is the main driver in Don Juan pond. Only in Bristol Dry Lake is a $CaCl_2$ brine is commercially extracted.

The high solubility of $CaCl_2$ minerals means that, with the exception of some parts of the Aptian Atlantic potash association, even in past times of likely $CaCl_2$-rich oceans, calcium chloride minerals are relatively rare as primary-textured occurrences in solid salt beds. On the other hand, $CaCl_2$ brines are commonplace in basinal or formation waters in many Phanerozoic sedimentary basins entraining thick sequences of dissolving ancient salt. For example, since 1914, $CaCl_2$ brines have been extracted from Silurian strata adjacent to Salina Salt of the Michigan Basin USA (Garrett 2004). These brines are recovered from Detroit Group sediments that overlie the Silurian Salina evaporites. Based on fluid inclusions in primary halite chevrons in the Salina Salt, the Silurian was a time characterized by a $CaCl_2$-enriched $MgSO_4$-depleted ocean (but no tachyhydrite is known from Silurian strata – see Chap. 2). The porous 0–90 m thick Sylvania Sandstone lies at the base of the Detroit River Group, while the remainder of the Group consists of 0–350 m of variably porous carbonates (Garrett 1995, 2004). Both contain $CaCl_2$-rich brines and extend across some 40 % of the Michigan Basin at depths of from 300 to 1,400 m. Brine concentration and the relative amount of $CaCl_2$ increases with depth. Typically, the brines are only considered to be of economic importance below about 880 m. In carbonate hosts, the $CaCl_2$ content varies from 3 to 23 % and KCl from 0.2 to 2.9 %, usually increasing in concert with concentration, as the NaCl content decreases. $CaCl_2$ content in the Sylvania Sandstone varies from 14 to 22 %, KCl from 0.6 to 2.1 %, and both are more uniformly concentrated compared to the carbonate hosted brines (Fig. 12.43; Garrett 2004).

Historically, before micro-inclusion studies of chevron halite showed that the ionic proportions of seawater likely varied across the Phanerozoic, the various $CaCl_2$ basinal brines occurrences in Silurian and Cretaceous strata were explained as an indicator of widespread dolomitisation and other diagenetic reactions, which preferentially extracted magnesium from pore waters. Since then, some authors have argued that $CaCl_2$ enrichments in many ancient basinal brines, including brines in the Detroit group are partial leftovers of primary seawater chemistries (Lowenstein and Timofeeff 2008). That is, Ca-enriched ($MgSO_4$-depleted) pore brines are indicators of ancient $CaCl_2$ oceans, with the pore brines being remnants from time the enclosing evaporitic and marine sediments were deposited (relict or connate brines). Others, such as Houston et al. (2011), conclude this is not necessarily so, they agree that there are two end-members typifying highly saline subsurface brines. But they conclude that end member chemistries relate to either substantial subsurface halite dissolution, or to preservation of early reflux-related seawater. Houston et al. (2011) go on to argue that $CaCl_2$-enriched formation water chemistries from many basins worldwide, including the Michigan Basin, do not support an interpretation[7] of variation in ionic proportions in seawater across the Phanerozoic. They find that $CaCl_2$-rich brines formed either by dissolving bittern salts in the subsurface, or simply lost water in the subsurface after significant rock-fluid interaction had taken place. Water loss might be achieved by interaction with a gas phase in the elevated temperatures of deep burial or, alternatively, water may have been lost to clays. Both these mechanisms would have the effect of dehydrating (concentrating) the brine.

However, whatever the mechanism, it does seem that there is a Quaternary continental/pre-Quaternary marine dichotomy in the nature and distribution of $CaCl_2$ brines and the associated antarcticite/tachyhydrite minerals, as there is for the world's potash deposits ($MgSO_4$-enriched versus $MgSO_4$-depleted). There are no documented examples of pre-Quaternary bedded antarcticite. Today antarcticite either precipitates in the hot-arid Bristol Dry Lake or the icecap-polar setting of Don Juan Pond, neither is associated with brine sourced in seawater or derived by the recycling of older ("connate") marine evaporite successions. Other present-day examples of regions with somewhat enriched $CaCl_2$ surface waters, lack both tachyhydrite and antarcticite precipitates,

[7]In the context of past seawater chemistries it is important to note that this discussion of brine origin concerns interpretation of proportions of ions present in porous non-evaporite sediment hosts. It is totally separate to interpretations of past seawater chemistries based on analyses of inclusions held in primary chevron halite crystals sampled from a impermeable bedded salt mass. In this latter case the ionic proportions of the ambient seawater concentrate are unequivocally preserved.

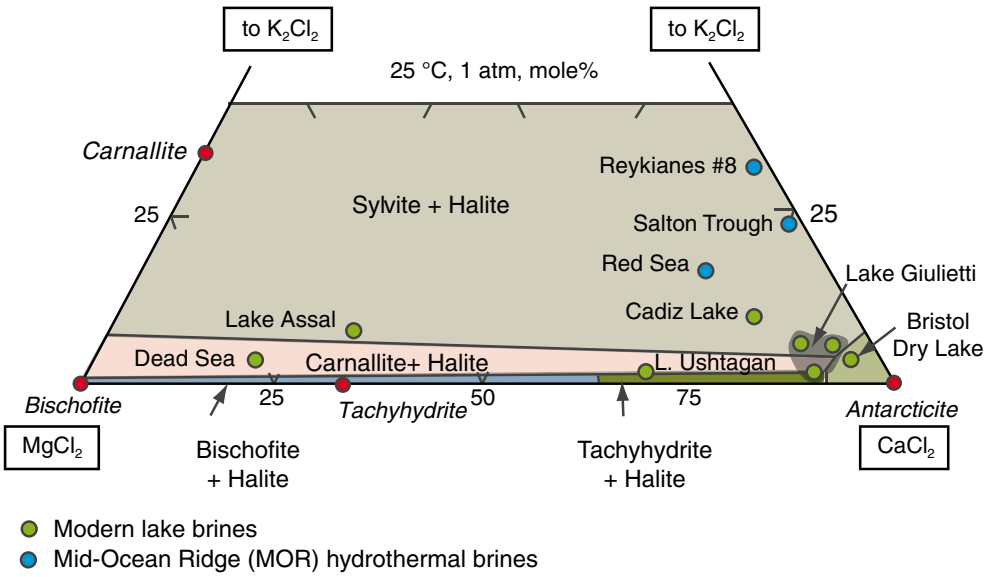

Fig. 12.58 Phase relations and brine chemistry of modern $CaCl_2$ brine associations in the system $CaCl_2$-$MgCl_2$-KCl-NaCl-H_2O at halite saturation, 25 °C, and 1 atm total pressure (After Hardie 1990)

and contain higher levels of Mg that are tied to deeply circulated marine/hydrothermal waters and variable interactions with $MgSO_4$-enriched marine salts (Fig. 12.58; e.g., Lake Asal and the Dallol Salt Pan). $CaCl_2$ brines of the Dead Sea and the Red Sea show even more elevated levels of $MgCl_2$ as they are derived, at least in part by the fractionated dissolution of bedded and halokinetic Miocene marine evaporites. The Mg-rich clay palygorskite is co-associated with these brines in the subsurface of the Red Sea and the Dallol.

In contrast, tachyhydrite in some ancient marine-fed basinwide evaporite associations is found as somewhat rare, but at times bedded, units in the bittern-rich portions of the halite succession (Fig. 12.57; Table 12.14), as in the Cretaceous basinwide evaporites of Brazil, the Congo and Thailand, and as a cementing phase in the Permian Stassfurt 2 in the Zechstein (where it is commercially extracted in association with $MgCl_2$ brines). All the ancient tachyhydrite examples mentioned above, are associated with the presence of widespread potash within adjacent salt beds. However, there are many other even larger ancient potash deposits, such as the intracratonic Alberta and the Kama basins where no tachyhydrite is documented. It seems that the precipitation of bedded tachyhydrite is not just favoured by times of $CaCl_2$ oceans, it also requires additional input from saline hydrothermal/basinal waters. Such settings are most likely in the transition phases in an actively-opening hydrothermally-influenced continental rift as passes into the marine seepage realm at a time when the adjacent ocean was a $MgSO_4$ -depleted system.

Iodine

The name iodine comes from the Greek word *iodes*, for "violet-like." Iodine was discovered by Bernard Curtois toward the end of 1811 or early 1812 when, while attempting to minimise pot corrosion in a seaweed processing saltpetre factory where he was employed, he decided to understand the violet vapours he observed rising from heated saltpetre pots and associated purple crystals sublimating on cooler surfaces (Lauterbach 2007).

Iodine at 0.46 part per million in the Earth's crust is one of the scarcest of nonmetallic elements in the total composition of the earth; it is the sixtieth element in order of world element abundance. Although not abundant in terms of quantity, iodine can be found almost everywhere on the earth. It is present in rocks, soils, water-bodies, plants, animal tissues, and foodstuffs. Natural commercial surface deposits contain iodates such as lautarite $Ca(IO_3)_2$ and dietzeite $Ca(lO_3)_2$. (CrO_4). Except for the possible occurrence of elemental iodine vapour in the air near certain iodine-rich volcanic springs, iodine never occurs naturally in its elemental form. It is always found in combination with other elements, either as inorganic salts or rather complex organic compounds, such as thyroxin. Organic-rich sedimentary rocks represent the Earth's dominant iodine reservoir and marine organic matter contains high ppm-levels of both I and Br (Collins et al. 1971; Kendrick and Burnard 2013). Ongoing subsurface fluid interaction with organic matter does not influence salinity but represents the dominant control of fluid I/Cl, and can exert a significant influence on the Br/Cl ratio.

Wherever iodine occurs naturally, its quantities are generally exceedingly small, and very sophisticated chemical methods are required to detect it. Only a few natural substances characteristically contain iodine in relatively large quantities (Lauterbach 2007). These are: marine seaweeds and sponges, subsurface waters in deep oil wells or mineral springs and in natural deposits of sodium nitrate, ("caliche ore" or saltpetre) in the northern part of Chile. In all natural

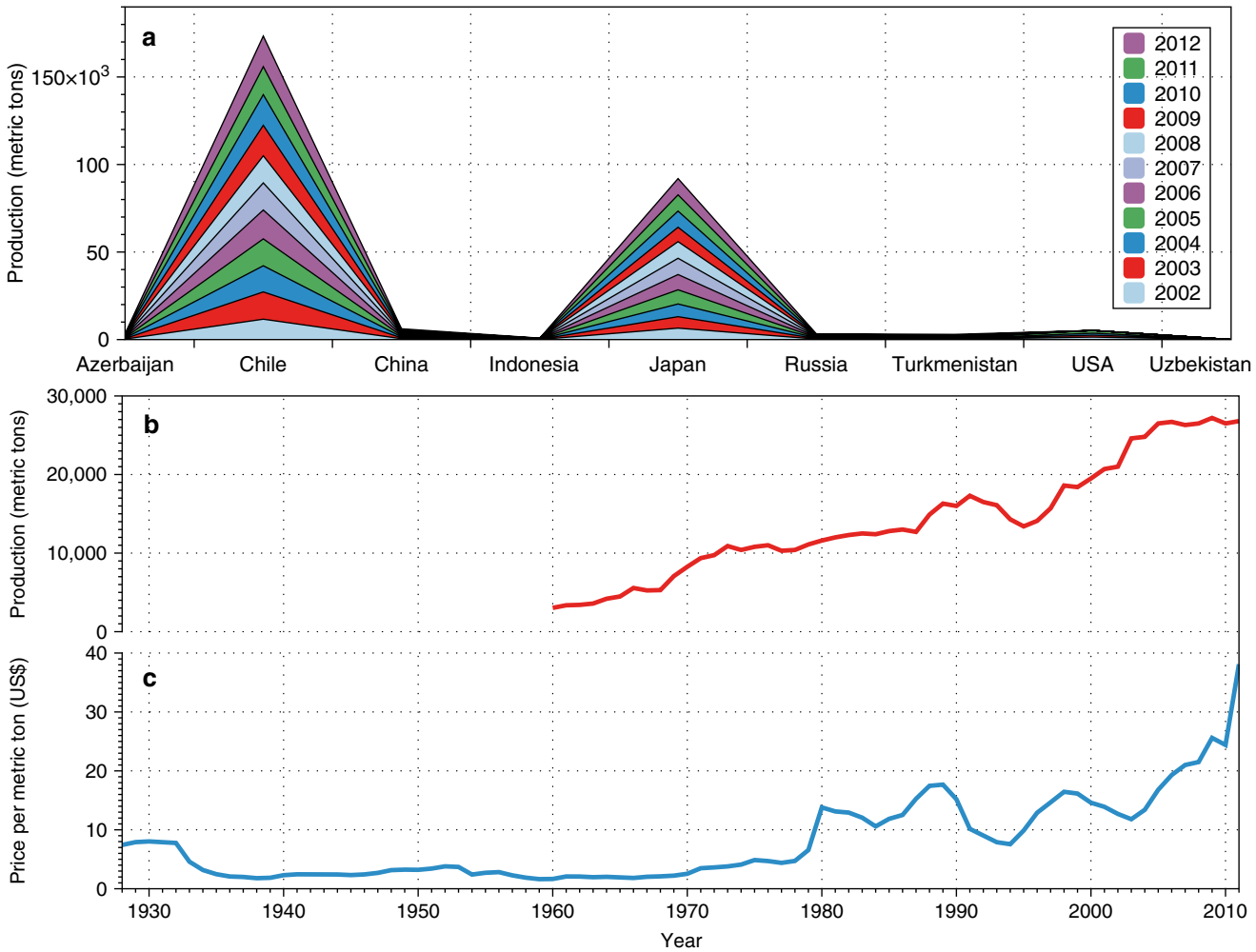

Fig. 12.59 Iodine production. (**a**) Cumulative area plot of annual production of major iodine producing countries in metric tons. USA figures not made public since 2006. (**b**) World production from 1960 to 2011 (metric tons), (**c**) Price per metric ton in US dollars from 1927 to 2011 (Compiled from USGS on-line data tables downloaded from http://minerals.usgs.gov/minerals/index.html last accessed September 4, 2013)

examples, other than the Chilean iodates in caliche, the proportion of iodine is small, rarely exceeding 2,000 ppm (Lauterbach 2007). Oilfield brines in Louisiana, California, and Michigan contain 30–40 parts per million iodide, while some Japanese subsurface brines contain up to 100 parts per million. Iodine makes up only 0.05 ppm in seawater, but some seaweeds concentrate iodine up to 0.45 % (4,500 ppm) of their dry weight.

Iodine is quarried and extracted from hypersaline lakes and saline desert soils of the Atacama Desert in Chile, or recovered from saline subsurface brine associated with natural gas production (e.g. southern Kanto gasfield, Japan) and from deep highly-saline oilfield brines in the USA (e.g. Woodward Shale, Oklahoma: Moran 1996). Chile today controls around 58 % of the world iodine capacity, Japan 21 %, and the USA around 5 % (Fig. 12.59). In 2012, global crude iodine production was estimated at around 28,700 metric tons and was carried out in only nine countries: Chile, Japan, USA, China, Turkmenistan, Azerbaijan, Indonesia, Russia and Iran (Fig. 12.59a). Chilean reserves are vast, but producers can experience climate-related or other anthropogenic variations in ore quality that can affect production costs and iodine price (Angulo 2011).

High levels of Na_2SO_4 in the Chilean processing feedstock can be detrimental and this delayed the opening of the new iodine processing at the Aguas Blancas mine in northern Chile. Reserves of iodine-rich brines are also huge in Japan, and considered near-inexhaustible at current extraction rates. Japanese production is limited. however, by problems of land subsidence and the occasional earthquake. Compared with Japanese and Chilean reserves, the US reserves are much smaller, but are still estimated to be sufficient for domestic use for another century at current production rates. Mid nineteenth century, small, but commercial, amounts of iodine were produced from the ash of seaweed collected of the coast of Great Britain (Rosenfeld 2000). World iodine

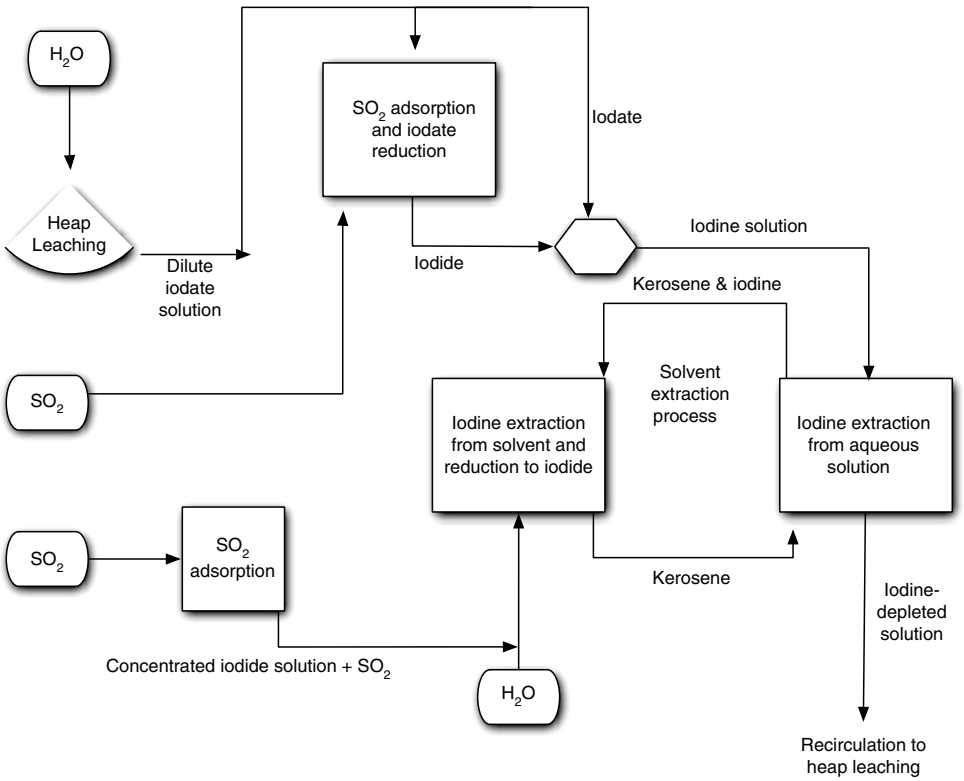

Fig. 12.60 SQM's heap leaching of caliche tailings for iodine recovery from dilute iodate solutions in the Atacama Desert, Chile (After Lauterbach 2007)

production has not risen greatly since the mid 2000s, current annual world production is about 28,000 metric tons (Fig. 12.59b; Angulo 2011).

The method of iodine extraction depends on the source of the iodine. From Chilean saltpeter beds, sodium iodate is dissolved by an alkaline solution, converted to iodide ion by reaction with sodium hydrogen sulphite, and iodine is then precipitated by adding iodate solution (Fig. 12.60). From brines, the iodide ion is converted to iodine by reaction with chlorine. Air blown in through the solution collects the iodine, which then precipitates, while purification is by resublimation. In an alternate method the iodide ion is precipitated with silver ions, reacted with iron to make iron iodide, and reacted with chlorine to produce iodine. Another method uses an ion-exchange resin to collect the iodine after it has reacted with chlorine.

Iodine prices were largely stable around US$32/kg throughout 2010 and the beginning of 2011 (Fig. 12.59c). In March of that year, prices went from US$33/kg to US$97.5/kg on the spot market because of the Japanese earthquake and a later a seasonal production drop off in South America. A further factor was that Cosayach of Chile idled a significant proportion of its capacity because of lack of water, following the closure of illegal water wells.

Chile is the largest producer of iodine in the world and the sole producer of commercial quantities of natural iodine from a non deep-brine source, namely naturally occurring iodate salts (Table 12.16). Historically, iodine in Chile was recovered either as a byproduct in the processing of nitrate saltpetre deposits, or by leaching of nitrate tailings heaps (Fig. 12.60; e.g. at Coya Sur, in northern Chile- see nitrates in following section). Today iodates in the Atacama, rather than nitrates, can be prime target in some Atacama operations as at Aguas Blancas. The nitrate fields are mostly located in the Central Valley of Chile, called Pampa del Tamarugal, which lies between the relatively low Coastal Range to the west and the high Andes mountains to the east (Fig. 12.62).

The most likely ultimate source of Chilean iodine is thought to be iodine-rich organic films on the ocean surface. This organic scum is carried inland, along with nitrogen, as aerosols and sea spray (Fig. 2.29). Alternatively, some have argued the dominant iodine source in the Atacama caliche is from the gases and sublimates associated with Andean volcanism others have argued it is sourced by the weathering of uplifted Jurassic sediments. Once at or near the hyperarid land surface, iodates and nitrates are leached and transported by groundwaters to ultimately concentrate in pedogenic profiles (Ericksen 1993). Iodine salts in caliche ores, are largely present as the oxidized iodate minerals; lautarite (CaI_2O_6) and dietzite ($7CaI_2O_6{\cdot}8CaCrO_4$) (Table 12.16). Ore layers are 1–3 m thick and overburden is less than 1 m. The nitrate deposit in the Atacama Desert, with which it is associated, is huge, measuring some 15–75 km across and paralleling the coast for more than 720 km (Fig. 12.62). Processing of the quarried nitrate ore to produce an iodate concentrate involves

Table 12.16 Typical iodate, nitrate, borate and other minerals in the Atacama Desert, Chile

Halides	
Halite	$NaCl$
Nitrates	
Nitratite (soda nitre) -main ore	$NaNO_3$
Nitre (saltpetre) – secondary salt	KNO_3
Darapskite – Minor salt	$Na_3(SO_4)(NO_3)\cdot H_2O$
Humberstonite – Minor salt	$K_3Na_7Mg_2(SO_4)_6(NO_3)_2\cdot 6H_2O$
Iodates and chromates	
Lautarite	$Ca(IO_3)_2$
Bruggenite	$Ca(lO_3)_2\cdot H_2O$
Dietzeite	$Ca(lO_3)_2\cdot(CrO_4)$
Hectorfloresite	$Na_9(IO_3)(SO_4)_4$
Fuenzalidaite	$K_3(Na,K)2Na_3Mg_5(IO_3)_6(SO_4)_6\cdot 6H_2O$
Tarapacaite	K_2CrO_4
Lopezite	$K_2Cr_20_7$
Borates	
Ulexite	$NaCaB_5O_9\cdot 8H_2O$
Probertite	$NaCaB_5O_9\cdot 5H_2O$
Ginorite	$Ca_2B_{14}O_{23}\cdot 8H_2O$
Hydroboracite	$CaMgB_6O_{11}\cdot 6H_2O$
Kaliborite	$HKMg_2B_{12}O_{16}(OH)_{10}\cdot 4H_2O$
Colemanite	$Ca_2B_6O_{11}\cdot 5H_2O$
Sulphates	
Thenardite	Na_2S0_4
Glauberite	$Na_2Ca(SO_4)_2$
Bloedite	$Na_2Mg(SO_4)_2\cdot 4H_2O$
Kieserite	$MgSO_4\cdot H_2O$
Epsomite	$MgS0_4\cdot 7H_2O$
Gypsum	$CaSO_4\cdot 2H_2O$
Anhydrite	$CaSO_4$
Bassanite	$2CaS0_4\cdot 0.5H_2O$
Polyhalite	$K_2Ca_2Mg(S0_4)_4\cdot 2H_2O$

After Garrett 1985

crushing, leaching with fresher water, thickening, filtration, and calcium iodate (with sodium nitrate) precipitation. Many of the iodine plants use solar evaporation ponds to thicken the leachate prior to processing (Fig. 12.60).

Like the coastal desert association of iodine in the hypersaline Chilean deposits, most of the iodine in highly saline subsurface brines of marine sedimentary basins ultimately comes from an organic source (Worden 1996). In fact, many such subsurface waters are enriched in iodine by up to three orders of magnitude relative to modern seawater evaporated to the same concentrations. Iodine enrichment in brines is often tied to proximity to hydrocarbon pools and iodine increases in concentration in pore waters with increasing depth of burial at a faster rate than bromine (Martin et al. 1993a).

Iodine is used in a diverse range of applications by a wide variety of industries. Around half is used in applications directly related to human health, for example x-ray contrast media, iodophors (biocides) and iodine supplements and pharmaceuticals. Most of the remainder is in industrial applications such as optical polarising film (OPF) for liquid crystal displays (LCDs), catalysts, heat stabilisers and the production of fluorine derivatives, along with animal feed supplements, catalysts, inks and colourants. For the next 5 or so years, world demand for iodine is forecast to rise due to expanding usage mostly in the x-ray contrast media, OPF and biocide markets. Demand for iodine in OPF will continue to grow until the end of the decade, but after that LCDs are expected to face increasing competition from technologies that do not use OPF such as OLED.

Healthwise, a worldwide effort is underway to eliminate iodine-deficiency disorders by fortifying world salt supply with iodine. Iodine deficiency[8] is the Developing World's leading cause of mental health problems along with more subtle associated problems such as clumsiness, lethargy, and reduced learning capacity. Endemic cretinism manifested in mental retardation, deaf muteness, blindness, crosseye, and growth lag, are created in areas where pregnancy occurs in the presence of an iodine deficit. Globally, more than 2.2 billion people live in iodine-deficient areas, especially in mountainous areas located well away from the sea coast. Iodine is an essential part of the thyroid hormone, a substance that contributes to brain development during foetal life and later metabolism.

In Tibet for example, some remote mountain villages have birthing data that show 13 % of newborns suffer from cretinism. This is because of low iodine levels in the soils and the fact that local salt is harvested from salt lakes where glaciation and deep weathering have long ago removed iodine from soils and associated salts. Unlike seasalt, the present soil waters and runoff, that ends up collecting and evaporating in the salt lakes, contains little or no iodine (Lee 2001). Salt harvested from the Tibetan lakes, when carried to the villages and sold, is 50 % cheaper than salt that has been fortified (sprayed) with iodine. A lower cost makes natural local salt a more attractive product to peasants in the villages, most of whom are subsistence-level farmers. Harvested salt is usually bartered or exchanged for an equivalent weight in rice. In an attempt to improve the health of the people, selling non-iodised salt has been made illegal by the Chinese government. But a lower price and the fact that the salt

[8]The human body contains approximately 5 mg of iodine, which functions only in the iodine-containing thyroid hormones. In 1990, the United Nations and WHO estimated that about one billion people are at risk for iodine deficiency disorders (IDD), 211 million with goiter (enlargement of the thyroid gland), 5.1 million with severe cognitive and neuromotor deficiencies (cretinism), and many more with less severe neuropsychological defects.

harvesters usually barter their salt for an equivalent weight in rice, and have done so for hundreds of years, make the harvested natural salt more attractive than the more expensive iodized product. To maintain their own subsistence level livelihoods, the salt harvesters have spread and encouraged rumors that animals and people fed iodized salt will be infertile.

In rural China and Mongolia, the Chinese government's policy of introducing iodized salt to the agrarian population has been much more successful than in religious regions of Tibet. In the 1980s the rates of goiter (indicated by an enlarged thyroid and an indicator of iodine deficiency) in the general population of China were as high as 40 %. By making non-iodized salt illegal and keeping the price of the iodized salt low, the current rate of goiter in the general Chinese population is now somewhere near 5 %.

Iodization programs in salt and milk products in the western world since the 1920s had largely eliminated the problem of iodine-deficiency by the 1960s. Ironically, in some in parts of the western world now lacking a government-enforced iodine program, the populist anti-science "new-age" push for healthier back-to-nature, vegan and organic food products is an evergrowing and ever more profitable market trend. Accordingly, there has been a move away from iodized salt and iodized milk to make it more "natural." Now the rate of incidence of iodine-deficiency in the general population, and in children especially, is growing once more in many parts of the developed world.

For example, in Australia in 2003 the iodine intake in the population was half what it was 5 years earlier, but most Australian adults were unaware they were recreating the problem of iodine-deficiency in their children (Li et al. 2001). Based on a more recent 2010 WHO study, it appears the problem in Australia has grown even further (Sydney Morning Herald Newspaper, Oct 10, 2010). The WHO study, which focused on almost all the babies born in the state of Victoria from 2001 to 2006, found clear signs of iodine deficiency in many Australian newborns. About 26,000 of the 368,000 newborns, or about seven per cent, were found to have elevated concentrations of thyroid-stimulating hormone (TSH) caused by the body's compensatory response to a poor intake of iodine. A smaller NSW-based study found 5–8 % of newborns in that state from 1998 to 2000 were iodine deficient. The WHO considers a population to be iodine deficient if more than three per cent of neonatal blood samples show elevated TSH concentrations. New-age anti-science and anti-industrial mantras, now followed by an increasingly scientifically-uninformed proportion of the Australian adult population, have returned the status of Australia's newborn population to that of "iodine deficiency." Some states in Australia are now considering legislation to make iodized flour mandatory in bakery products.

Bromine

Bromine has an abundance of 2.5 parts per million in the Earth's crust, ranking it forty-sixth in order of abundance of the elements. It is more prevalent in the oceans, at 65 ppm. The name bromine comes from the Greek *bromos* meaning stench. Bromine was discovered in 1825 when Antoine Balard extracted it from seawater bitterns. The United States and Israel dominate the world's elemental bromine output of about 5.2 million tonnes (5.7 million st). Azerbaijan, Ukraine, France, United Kingdom, China, Japan and India contribute most of the rest. Bromine is recovered from modern brines in Searles Lake and the Dead Sea, as well as from formation waters in the Gulf of Mexico and the Michigan Basin, and seawater in Japan and Spain (Fig. 12.61). For example, a brine averaging 5,000 ppm Br is recovered for processing from depths around 2,500 m in the upper Reynolds Oolite Member of the Upper Jurassic Smackover Formation in Union Co, southern Arkansas (Kyle 1991). The elevated Br content in this brine indicates natural leaching of the underlying Louann Salt.

Since 1957 bromine has been produced at Beersheva, Israel, as a byproduct from bitterns associated with potash, chlorine and caustic soda production. There, and in the Jordanian salt works on the other side of the border, solar evaporation concentrates lake brines pumped from the Dead Sea ($Br \approx 4{,}000$ ppm). After the potash slurry is processed, residual bitterns are treated with chlorine to recover bromine. Bromine-free bitterns are then further processed to recover magnesium. The Dead Sea effluent feed-brine for bromine recovery contains 11,000–12,000 ppm of bromine and is one of the richest bromine brine feeds currently in commercial operation. Brine reserves are huge, with the Dead Sea waters containing more than 1 billion tonnes of bromine. In Germany, bromine is produced as a byproduct of potash mined from the Zechstein salt.

Since 1973, when the United States produced 71 % of the world supply, its market share has decreased; a result of local environmental constraints and the emergence of Israel as the world's largest producer. Israel, the United States, Jordan, China, Japan, and Turkmenistan, in descending order, had the leading bromine production capabilities in 2010, although none of these countries operated at capacity in that year (Fig. 12.61; Ober 2011).

Traditionally, the major market for bromine was in the production of ethylene dibromide; a lead scavenger in gasoline antiknock compounds. However, this market has been in decline over the past four decades, and is now very small, as more and more countries legislated to require catalytic converters in all new cars and the use of lead-free gasoline. Flame retardant is now the largest end use and accounts for more than 30 % of the US bromine market. Other uses include intermediates in chemical manufacture of dyes,

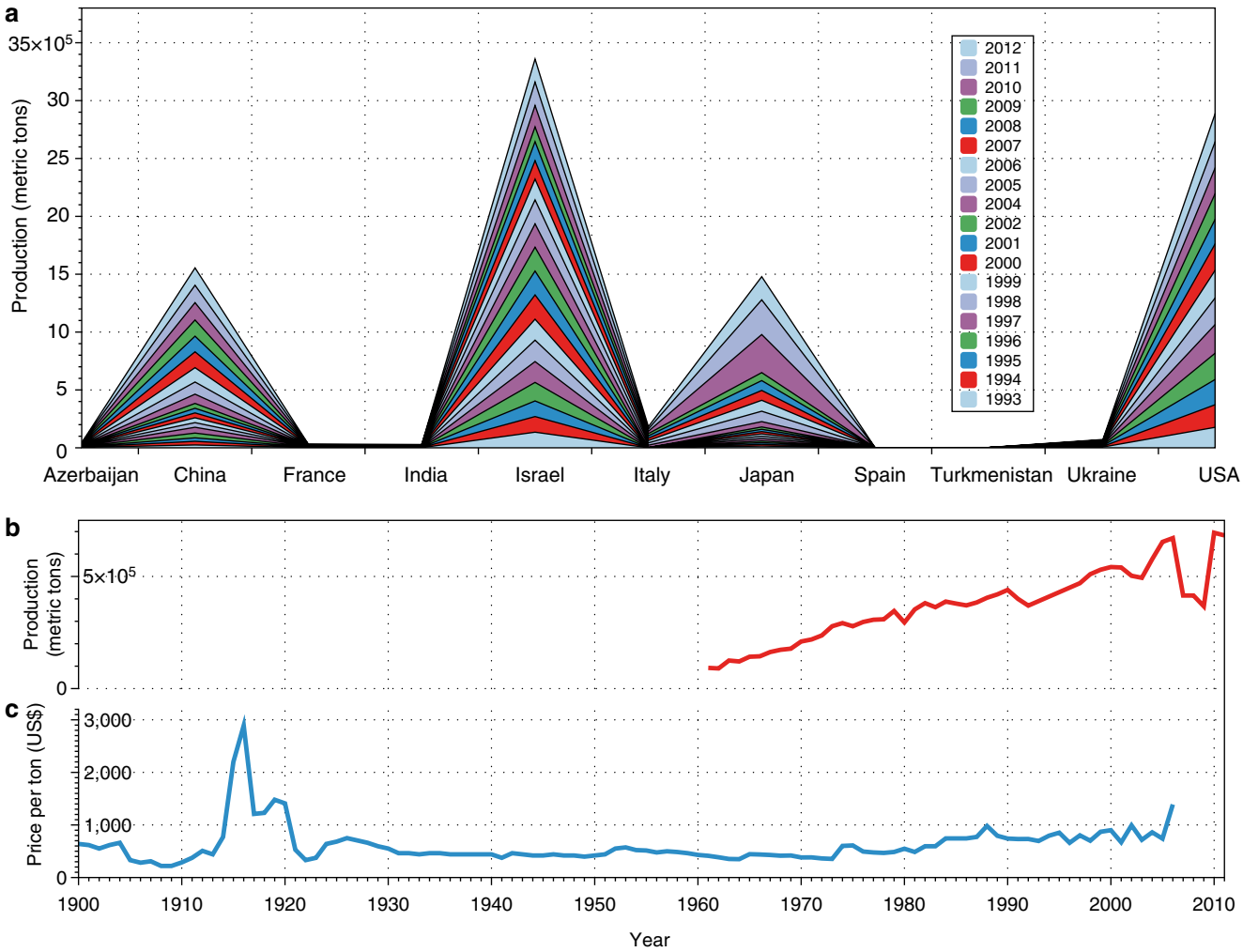

Fig. 12.61 Bromine production. (**a**) Cumulative area plot of annual brine production of major producing countries in metric tons. USA figures not made public since 2006 and so not plotted. (**b**) World production from 1960 to 2011 (metric tons), (**c**) Price per metric ton in US dollars from 1900 to 2006, since 2006 prices withheld for reasons of commercial confidentiality (Compiled from USGS on-line data tables downloaded from http://minerals.usgs.gov/minerals/index.html last accessed April 21, 2014)

fragrances and pharmaceuticals; it is also used in photographic compounds, as bleach, as an additive in drilling fluids, and in the production of methyl bromide, a pre-plant soil fumigant. The market potential for bromide-based technologies to remove mercury emissions at coal-fired powerplants is an area of potential growth for the industry. Bromine use in commercial film processing continues to decrease as digital photography expands.

Nitrate Salts (Nitratite and Saltpetre)

The word nitre and the entomological derivatives nitrogen and nitrate ultimately come form the ancient Egyptian for nitre salts, *ntry*. Nitrogen is abundant on and near the earth's surface where it makes up 78 % of the world's atmosphere. It, along with potassium and phosphorus, make up the three essential plant nutrients driving the "green" agricultural revolution of th past 60 years. Natural deposits of nitrate are rare because of the extreme solubility of nitrate salts in water; synthetic sources of nitrate today far outweigh the natural sources, with natural sources today supplying less than 0.3 % of the world's nitrogen needs.

Nitrate salts precipitate as efflorescent crusts in several of the world's deserts including; the Egyptian and Namibian Deserts, the Gobi desert, the Abu Dhabi sabkhas and deserts of the Mojave and Death Valley. Small amounts of nitrate salts have also precipitated in the cryogenic deserts of Antarctica. Natural nitrate salts are only present in mineable quantities in the Atacama Desert of Chile, where deposits occur in a narrow zone between the low-lying Pampa del Tamarugal to the east and the hills of the Coastal Range to the west (Fig. 12.62a; Table 12.16; Ericksen 1981, 1983; Searl and Rankin 1993). This area contains nitrate-rich soft

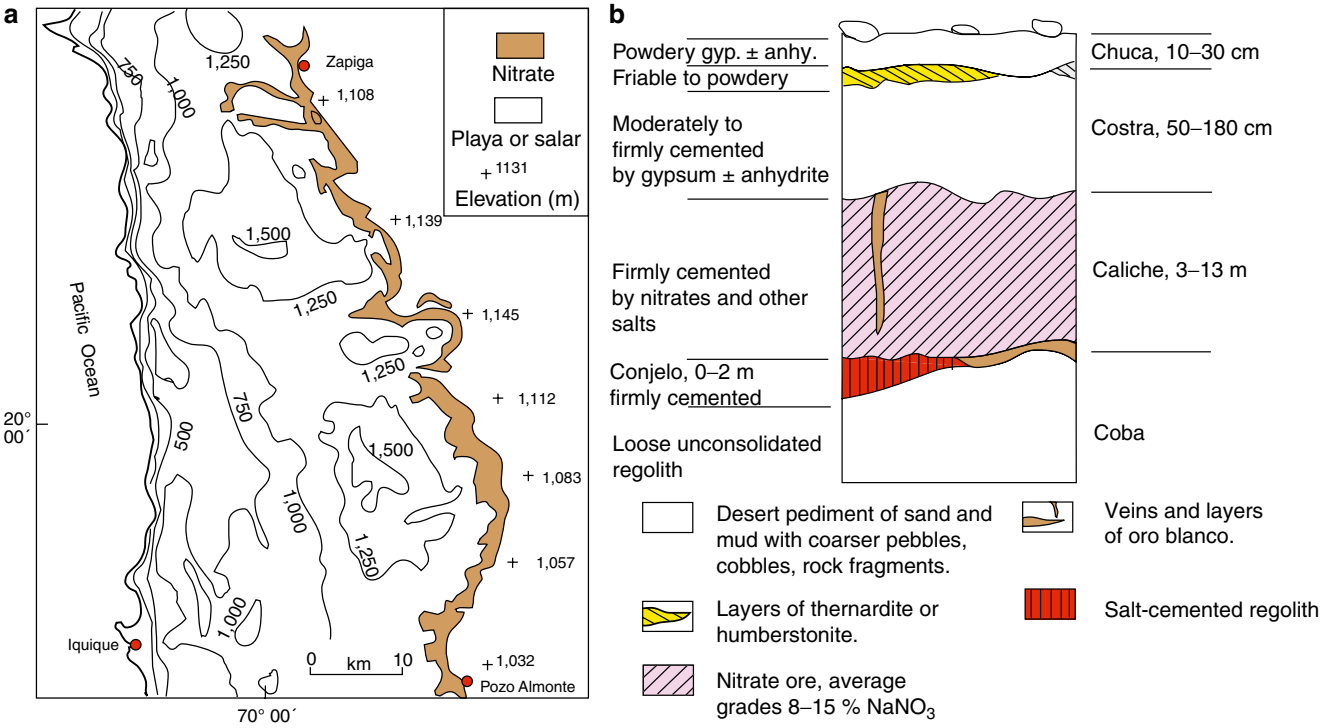

Fig. 12.62 South American nitrates. (**a**) Sketch of northernmost Chilean nitrate field, which is located along the eastern side of the Coastal Range, and marginal to salars and clay playas on the western side of Pampa del Tamarugal. (**b**) Typical regolith profile through alluvial-type nitrate deposits in a Chilean nitrate field (After Ericksen 1993; Ericksen and Mrose 1972)

soils, as well as surfaces encrusted with nitrate-bearing salts, saline-cemented regolith, and nitrates accumulating in closed basin playas or salars. Commercial concentrations develop in and atop weathered rock types ranging from granite to limestone and shales. Nitrates can be found in all topographic positions from hilltops to hillsides to playa and valley floor. The richest accumulations tend to be on the lower slope of hills situated marginal to salars and playas (Ericksen 1993).

Prior to the invention of synthetic nitre sources by Germany in the First World War, the Chilean nitrates were the main source of salt petre[9] in dynamite, and other explosive nitrate-based derivatives like nitroglycerine or glycerol tri-nitrate, nitrocellulose, nitroglycol, ammonium nitrate, etc. At its peak in the first 20 years of last century there were more than 250 actively mined concessions in the Atacama Desert, with production of 4 million tonnes/year and a local population of more than 250,000 people. At the time, the local name for the nitrate ore was "*oro blanco*" or white gold. By the 1960s synthetic worldwide production of nitrate and ammonia fertilizers meant there was no longer a viable economic base in the Atacama sufficient to support the nitrate boom towns of the first 20 years of last century; the last major mining town in the Atacama closed in 1960. Since then, the mining towns of Humberstone and Santa Laura have been declared World Heritage Sites. Total nitrate production from 1830 to 1970 in this region amounted to 135 million tonnes of $NaNO_3$. By 1980 the Chilean nitrates were only 0.14 % of the world market for fixed nitrogen.

Two major types of nitrate ore have been recognized in the Atacama desert (Ericksen 1983; Ericksen and Mrose 1972): (1) Regolith cement ("alluvial caliche") and (2) Impregnated bedrock ("bedrock caliche"). A typical alluvial caliche consists of various zone, at the top is *chuca*, a powdery to poorly cemented surface layer up around 10–30 cm thick (Fig. 12.62b). This consists of friable silt, sand, rock fragments and some gypsum and anhydrite. It is a surface soil from which a large portion of the soluble saline material has been leached and to which eolian silts have accumulated. It may contain a layer of soluble salts, including thenardite, bloedite and humberstonite. Beneath this, typically, is the 0.5–2.0 m thick transitional *costra* zone, which is moderately

[9]Nitre (sometimes called saltpetre) is a naturally occurring nitrate. The name saltpetre comes from medieval Latin "sal petrae" meaning "stone salt". The saltpetre terminology can be confusing as there are types of saltpetre, namely, (1) Ordinary saltpetre, or potassium nitrate (KNO_3) and generally referred to as 'saltpetre' without any prefix – it was the active gunpowder component that in Medieval times was derived from dung heaps and other decomposing organic material; (2) Chilean saltpetre or "cubic nitre" or "soda nitre" or "nitratine" or sodium nitrate ($NaNO_3$), this is the focus of our discussion as it is the predominant nitrate salt in the Atacama Desert; (3) Lime saltpetre or wall saltpetre or calcium nitrate [$Ca(NO_3)_2$] or Norgessalpetre (Norwegian saltpetre) or kalksalpetre – a rare efflorescent salt in natural state.

to firmly cemented with polygonal or "ped" structures. It in turn is underlain by the 1–3 m thick '*caliche*' zone, which is firmly cemented and contains layers of high-purity, white, nitrate-rich material called "caliche blanco". The caliche grades downwards into *conjelo* (saline-cemented regolith containing little sodium nitrate) or into *coba* (loose, uncemented regolith).

In contrast, bedrock caliche consists of saline impregnations and layers (from a few centimeters to several tens of centimeters in thickness) where crystallization processes have gradually forced open cracks and fissures in the matrix (Ericksen and Mrose 1972). In some cases the fractured bedrock may be so altered that it has converted into a mosaic of isolated rock fragments in a matrix of "caliche blanco".

There are a few small-scale nitrate mines still operating intermittently in the Atacama Desert, including Santa Maria, which is an open pit scrape extracting nitrate ore from stratiform pedogenic seams, just below the desert surface (Callao et al. 2002). Ores are hosted mostly by breccias or sandstones (volcaniclastics and tuffs) with the ore minerals occurring as mm-metre scale rinds about breccia or sandstone clasts. Nitrate contents in the ore seams vary between 7.5 and more than 20 wt% and NaCl between 8.6 and 40 wt%. Locally abundant are the sulphates thenardite, anhydrite, bloedite, polyhalite, hexahydrite and glauberite, which reflect part of 7.5–19.7 wt% content of Na_2SO_4. Other salts present as minor contents include a variety of sulphates (kieserite, woodwardite, loeweite); nitrates (humberstonite, darapskite and nitre); borates (calciborite, strontio-borite); chlorides (sylvite, nantokite) and iodates (bruggenite). The IO_3 content varies between 0.026 and 0.074 wt%. Other intermittently active nitrate quarries in the northern Chilean desert include Pedro de Valdivia and Pampa Blanca.

The micromorphology of nitrates from the Antofagasta region is described and illustrated by Pueyo et al. (1998), but overall the amount of information available on this aspect of caliche deposits is modest. The main features that can be noted are: (a) frequent complex mixing of crystals of different composition, with, for example, layers of that mixtures of relatively pure sulphate minerals (humberstonite, bloedite, etc.); (b) evidence for multiple episodes of precipitation and dissolution (e.g. solution cavities), and formation of desiccation polygons; (c) evidence for repeated fracturing and displacive growth, including the incorporation of microscopic fragments of saline minerals into larger crystals or grains of soda niter and halite; (d) incorporation of silt and other detrital material, together with remains of birds (feathers, guano, egg fragments, etc.; Ericksen 1981, p. 18); (e) presence of veins of purer nitrate (Ericksen and Mrose 1972); (f) evidence of extensive fracturing in the vicinity of faults; (g) formation of hard, spheroidal cakes of anhydrite, called *losa*, probably produced at the surface by prolonged slow leaching (Ericksen 1981); an (h) presence of small, length-slow chalcedony nodules.

Chilean nitrate ores have an average composition of: 7–10 % $NaNO_3$; 4–10 % NaCl; 10–30 % Na_2SO_4; and 2–7 % Mg, Ca, K, Br, and I (Ericksen 1983; Searl and Rankin 1993). The dominant nitrate in the Atacama is mostly nitratite (aka soda nitre or Chilean saltpetre, as distinct form KNO_3 known as saltpetre or common saltpetre). A number of other unusual highly soluble salts have also accumulated in the caliche ore, along with the nitrates, and include iodates, perchlorates, chromates and dichromates, as well as the more familiar borates, sulphates and chlorides (Table 12.16). The Atacama is the only known region in the world that contains natural perchlorate. Salts form at the more saline end of a vadose/phreatic precipitation sequence made up of progressively more soluble evaporitic minerals: silicates (zeolites); calcite; Ca-, Na-, (K-) and Mg-sulphates; Na- and K-Mg-nitrate-sulphates; nitratine; and small amounts of iodates, Na- and K-Mg-iodate-sulphates, chromates, borates and perchlorates (Pueyo et al. 1998). Two specific precipitation trends were distinguished within this more general regional sequence; a Na-trend characterised by an association of glauberite-darapskite-(hectorfloresite), and a K-Mg-Na-trend related to bloedite-polyhalite-humberstoniteniter-(fuenzalidaite).

What is most amazing about the Atacama nitrates is the age of the desert host and stability of its geomorphic features; some nitrate soils are thought have been at the surface since the mid-Miocene, so allowing the gradual buildup of large volumes of pedogenic and atmospheric salines in the soils including the exploited nitrates (Alonso et al. 1991). The Atacama Desert is one of the driest places on Earth, its hyperaridity is the result of the rainshadow effect of the High Andes and the strong atmospheric temperature inversion along the coast (Chap. 2). Average annual rainfall in the Atacama Desert is less than a centimetre, and as much as 20 years can pass between rainstorms, with similar conditions prevailing since the middle Miocene.

The unusual mineralogy of the nitrate ore reflects the extreme chemical evolution of the precipitating brines through multiple episodes of salt precipitation and remobilization during transport to the nitrate horizons. The ultimate source of the nitrate is atmospheric nitrogen, first carried inland as nitrate in sea fogs (Rech et al. 2003; Ericksen 1993). These dense coastal fogs or low clouds, locally known as *camanchaca*, sweep inland from the Pacific Ocean, covering the nitrate area nearly every night-early morning during the winter months of June to August, and usually precipitating some condensate on the soil surface (Garrett 1985). The fogs in most areas generally do not extend farther east than the central valley of Pampa del Tamarugal but do fairly completely cover the nitrate zone (Fig. 12.62a). The marine biogenic nitrates and iodates carried inland by these fogs are then mobilised from the soil moisture zone into the vadose (caliche) zone during rare but perhaps intense rainfall events that occasionally flood this hyperarid desert.

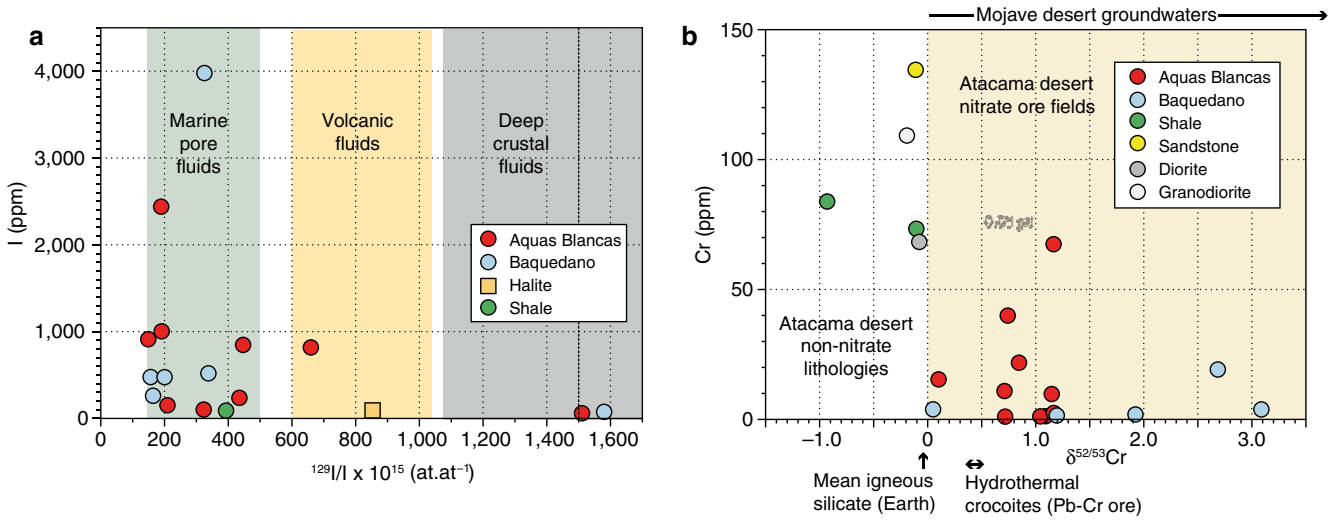

Fig. 12.63 Isotope indicators in nitrates of the Atacama Desert, northern Chile. (**a**) $^{129}I/I$ ratios of nitrate sample (AMS—accelerator mass spectrometry) plotted against iodine levels (ppm). Vertical dashed line shows pre-anthropogenic surficial/atmospheric iodine ratio ($1{,}500 \times 10^{-15}$). (**b**) $\delta^{53/52}Cr$ of nitrate samples plotted against Cr levels (ppm). Also plotted are Mojave Desert (western USA) groundwater values as well as mean values for igneous silicate earth and hydrothermal crocoites (Plots are compiled from geochemical spreadsheets stored in GSA data repository for Pérez-Fodich et al. 2014)

Upwelling coastal waters off Chile, and associated coastal fogs, can contain high concentrations of nutrients and dissolved solutes. The average concentration of dissolved solutes in Chilean coastal fog are: 9.1 ppm SO_4; 0.8 ppm NO_3; 1.8 ppm Cl; 4.81 ppm Na; 0.4 ppm K; 1.0 ppm Ca; 0.6 ppm Mg. Sea spray moves these solutes as aerosols into the coastal fog, while the sulphate in sea spray comes mostly from outgassing of biogenic marine sulphur (Chap. 2). As sea fog moves inland over the Atacama, it settles and evaporates, so depositing its dissolved solutes into the soil moisture zone, which are then fractionated by pedogenic and downslope meteoric processes. To form an ore grade nitrate buildup in the soil requires multiple pedogenic fractionation episodes that are driven by dissolution, reprecipitation and recrystallisation within hyperarid desert soils. Millennia of these processes vertically separates the highly soluble nitrate salts from less soluble sulphate salts in the overlying profile (Fig. 12.62b).

Once the nitrates and iodates arrive in the soil moisture zone via a combination of sea fogs, runoff and volcanic sublimates, they are reworked into the groundwater system. The parental brines for the richer nitrate deposits are the hypersaline discharge portions of the regional vadose/phreatic system, which Pueyo et al. (1998) consider to be older than 6 Ma. At that time the main physiographic features were similar to today, but the climate was more humid. Precipitating parental waters were derived from a variety of meteoric sources: westward flowing Andean groundwater, coastal fogs, occasional rainfall and Andean-derived surface floodwaters. Evaporation in a background of shallow watertables and hyperaridity was involved in the nitrate paragenesis; it is the only mechanism effective enough to saturate a brine with these very soluble supersaline minerals (Garrett 1985). Nevertheless, most of the nitrate ores do not show typical displacive nodular and enterolithic evaporitic textures, rather, the salts tend to passively infill veins, fractures or pre-existing matrix porosity and the various salts have largely accumulated through passive growth. Locally, some of the host silicate and carbonate lithologies have also undergone a small degree of active salt replacement.

Isotopes of iodine and chromium indicate multiple and complex sources for the various elemental components in the Atacama nitrate ores (Fig. 12.63; Pérez-Fodich et al. 2014). Isotopic ratios of iodine held in the nitrate ores ($^{129}I/I \approx 150$–600×10^{-15}) share similarities with deep sedimentary (marine) pore waters and shales, and are significantly different from the pre anthropogenic atmospheric iodine ratios (Fig. 12.63a; $^{129}I/I \approx 1{,}500 \times 10^{-15}$). Such dominantly low ratios in the majority of nitrate ore values, likely rule out a prevalent atmospheric/eolian source for most of the I and point toward an old I source. It is likely that much of the iodine in the nitrates was leached from Jurassic marine sediments that are exposed along the eastern margin of the Atacama Desert. The few samples showing higher $^{129}I/I$ ratios (~600–$1{,}580 \times 10^{-15}$) are perhaps indicative of the influence of meteoric water with high pre-anthropogenic $^{129}I/I$ ratios, related to infrequent moisture and flooding events, associated with increased precipitation in the High Andes, as occurred 16–10 ka and led to increased groundwater recharge.

The positive and highly fractionated $\delta^{53/52}Cr_{SRM979}$ values (+0.7‰ to +3‰) are indicative of Cr enrichment relative to

Table 12.17 Sedimentary minerals and deposit types used as a source for magnesium oxide or magnesium metal

Mineral	Formula	Deposit exploited
Magnesite	$MgCO_3$	Sparry or cryptocrystalline
Dolomite	$Ca_{(1-x)}Mg_x(CO_3)_2$	Not utilized
Brucite	$Mg(OH)_2$	Weathering byproduct
Brunnerite	$Mg_{(1-x)}Fe_x(CO_3)_2$	Sparry (magnesite associated)

the mean value of silicate Earth reservoirs (Fig. 12.63b; Pérez-Fodich et al. 2014). This highly fractionated Cr isotope signature in Atacama's nitrates, with respect to common Cr sources such as igneous rocks and marine shales is strong evidence of extensive Cr redox cycling from its source to the final deposition in the nitrate salts. This set of highly fractionated $\delta^{53/52}Cr_{SRM979}$ values are comparable to groundwater $\delta^{53/52}Cr_{SRM979}$ values in the arid hydrology the Mojave Desert, California and argues for a similar origin.

Pérez-Fodich et al. 2014 use isotope values in the Aguas Blancos and Baquedano nitrate ores to argue for a multisource genetic model. If so, extensive pedogenic nitrate accumulations are the result of long-lived, near-surface mineral precipitation, driven by groundwater evaporation (chromates, iodates) coupled with dry atmospheric supply (nitrates, perchlorates) and sea spray inputs (sulphates, chlorides), deposited by an evaporite hydrology triggered by increasing aridity and tectonic uplift in the late Miocene to early Pliocene. That is, the unique nitrate deposits that constitute a large and near-continuous, 700-km-long by 20-km-wide pedogenic salt belt are the result of an unusual convergence of common physical-chemical processes where an ideal combination of geologic, tectonic, hydrologic, and climatic has occurred. The nitrate belt defines the hyperarid portion of a convergent margin, undergoing rapid uplift since the late Miocene to hinterland elevations sufficient for exhumation and weathering of Jurassic marine sequences, and enhanced large-scale groundwater flow toward the Central Basin.

Magnesite and Magnesia Salts

Magnesium is the eighth most abundant element in the earth's crust (2.4 %) and is widely distributed in numerous minerals. Magnesium is named after ancient *Magnesia*, a district in Thessaly, Greece. Among the more commercially important magnesium minerals are magnesite, brucite, dolomite, olivine, talc and serpentine (Table 12.17), as well as the magnesium sulphate and chloride salts recovered from natural brines and concentrated seawater (e.g., epsomite, bischofite, carnallite). World resources of magnesite, dolomite and magnesium-bearing evaporite minerals are enormous. Magnesium-bearing extractable brines are estimated to constitute a potential resource measured in billions of tonnes, and in the near future magnesium will be economically recovered from seawater off arid coasts.

As well as being extracted by concentrating seawater, magnesium is also produced by processing of continental evaporitic and subsurface basinal brines in the USA, the Netherlands, Israel and Mexico. In the Netherlands the brine is formed by solution mining of magnesium/potassium-bearing horizons (carnallite, bischofite and kieserite) in the Permian Zechstein section (Fig. 13.6). Mg-rich continental brines of the Dead Sea are also processed for magnesium after bromine is extracted. When pumped into the saltworks, Dead Sea brine already contains 42,430 ppm of magnesium (30 times seawater levels), which when evaporated and processed produces caustic-calcined and dead-burned magnesia,[10] along with small amounts of magnesian chloride.

Electrolytic processes recover much of the world's currently produced magnesium. The majority of magnesium compounds are used for refractories in the die casting industry. Due to an inherent high strength to weight ratio, usage in the automobile industry is expected to double in the next decade. Currently, the aluminium industry is the largest consumer of magnesium, where it is a constituent in aluminium-base alloys used for packaging, transportation, and other applications. The remainder is consumed in agricultural, chemical, construction, environmental, and industrial applications. Annual world magnesia production (from magnesite) is more than 3.1 Mt (3.4 million st), mostly from China, USA, North Korea, Russia and Turkey. Although no specific production figures are available, China and the United States probably account for more than one-half of the world's capacity for the production of magnesium compounds from seawater and brines.

Geological occurrences of magnesite are either microcrystalline (micritic) or macrocrystalline (sparry), as illustrated in Table 12.18. Within this classification framework there are four end member types (named using European examples, Pohl 1989). They are; Kraubath, Bela Stena, Greiner and Veitch.

[10] *Dead–burned magnesite* (or refractory magnesia) refers to the granular product produced by firing magnesite, magnesium hydroxide, or other materials reducible to magnesia at temperatures in excess of 1,450 °C.

Calcined magnesia is the result of 800–1,000 °C heat being applied, frequently in a rotary kiln, to magnesite or other materials reducible by heat to magnesia. It is heated to such a degree that less than 10 % ignition loss remains and the product displays absorptive capacity or activity. *Fused magnesia* is produced by heating high grade magnesite to a molten state for up to 6 h in electric arc furnaces to temperatures approximately 3,000 °C. The resultant product, at 96–98 % MgO, has a favorable high density of 3.50 g/cc and relatively high chemical stability, strength, and resistance to abrasion.

Table 12.18 Classic styles of magnesite occurrence, based on type settings in Europe

	Ultramafic-hosted	Sediment-hosted
Ultrafine-grained (cryptocrystalline to microcrystalline)	Kraubath	Bela Stena
Coarse-grained (sparry)	Greiner	Veitch

After Pohl (1989)

1. Kraubath-type, consisting of cryptocrystalline (or microcrystalline) high-purity, snow-white, magnesite forming veins and stockworks related to hot spring alteration of ultramafic rocks (e.g. Neogene alpine fault zones in southern Europe).
2. Bela Stena-type, consisting of fine-grained, high-purity, nodular, massive, banded, brecciated or vuggy magnesite forming lensoidal or irregular bodies grading into well-defined seams (less commonly sinter deposits) within mainly clastic lacustrine Tertiary-age sediments developed close to ultramafic outcrops.
3. Greiner-type, consisting of sparry, ferroan magnesite–talc or ferroan magnesite–chlorite assemblages (up to 70 % granular magnesite) formed by carbonation of ultramafic rocks.
4. Veitch-type, consisting of sparry, high-purity magnesite associated with bedded siliciclastic and carbonate rocks, and commonly forming very large deposits (130 Gt in Liaoning deposits in China) and depositionally related typically to original marginal marine deposition (e.g. partial analogies to Coorong area in South Australia), typically with regional metamorphism or hydrothermal replacement of a limestone precursor (with dolomite as an intermediate stage).

Overlaying this classic subdivision based on the geology of type magnesite deposits, there are three geologic modes of sedimentary-associated magnesite occurrence: (1) Small scale micritic deposits accumulating in Quaternary alkaline lake and mudflats in climates ranging from hot arid to cold temperate (Table 12.19); (2) Laterally continuous, stratiform sedimen-thosted deposits, which can be cryptocrystalline (micritic) or coarsely crystalline (sparry). Sparry deposits tend to occur more frequently in Precambrian strata; (3) Clustered hydrothermal deposits that form sparry magnesites at or near ultramafic complexes of all ages. Weathered cryptocrystalline magnesite stockwork deposits (Kraubath style) hosted in serpentinites and dunites are commercially exploited in the Yerakini mine, Greece. Similar cryptocrystalline deposits, hosted in dunites, are mined in southern Salem district of Madras state, India. Further discussion of style 3 (Kraubath and Greiner styles) and variably developed pedogenic textures lies outside the evaporite focus of this book and the interested reader is referred to Pohl (1990).

Sparry style 2 occurrences constitute a large portion of current refactory magnesia ores. Style 1 deposits offer small-scale analogs for the sort of low temperature brine chemistry that has produced many sedimentary magnesite deposits. It suggests a requirement of waters enriched in magnesium, commonly hypersaline, and an association with microbes (Table 12.19). Within Style 2, magnesite occurs in two commercially exploited forms, coarse crystalline (sparry) magnesite -Veitch style- and cryptocrystalline magnesite -Bela Stena style- (Table 12.18; Pohl 1989). Sparry magnesite deposits tend to be larger and purer (70–90 % $MgCO_3$) than most cryptocrystalline magnesite deposits (purity <12 %$MgCO_3$) and are the preferred ore deposit style, worldwide. Much of the world's sediment-hosted coarsely crystalline magnesite is Precambrian and typically occurs as variations on a theme of fault-controlled, high temperature, hydrothermal alteration of dolomitic shelf sediment.

Modern cryptocrystalline sedimentary magnesite occurrences are nonmarine bedded, micritic, laterally limited and lacustrine; most ancient sedimentary magnesites are marine-associated, stratiform, microsparry to sparry, laterally and vertically extensive, and diagenetically altered. As with ancient evaporitic dolomite and ancient marine-fed evaporites, there are fundamental problems when comparing brine chemistries of recent and ancient sedimentary magnesite deposits. Today cryptocrystalline magnesite is mostly a nonmarine saline lacustrine precipitate with precipitation increasingly being interpreted and bacterially mediated (Table 12.19; Gierlowski-Kordesch 2010; Armenteros 2010; Sanz-Montero and Rodriguez-Aranda 2012). For an excellent and readily accessible summary of precipitative settings of modern magnesian carbonates see Deelman (2011).

Magnesite is easily manufactured in the lab using inorganic chemical techniques, but as for inorganically produced dolomite, natural magnesite requires temperatures much too high to be realistic in a modern marine sedimentary system. Likewise there are intrinsic problems with comparisons of scale and diversity modern and ancient, leading to interpretations of ancient magnesite origins in terms of "solving the magnesite problem." Some authors have suggested that Precambrian magnesite was a primary evaporitic marine carbonate, or even a normal marine mineral (Frank and Fielding 2003).

Major Phanerozoic cryptocrystalline sedimentary magnesite deposits occur in Australia and Turkey, where most occurrences are considered potential, rather than actual, ore deposits. Worldwide, almost all Phanerozoic cryptocrystalline magnesite sediments are either sepentinite-hosted stockworks (Kraubath style) or lenses of evaporitic lacustrine sediments in serpentinite terrains. The huge Tertiary lacustrine/pedogenic cryptocrystalline lacustrine deposits in the vicinity of Rockhampton, Australia, are a possible exception, as are the Neogene huntite-magnesite-hydromagnesite lacustrine deposits in the Kozani Basin, Northern Greece, the Bela

Table 12.19 Selected examples of Holocene occurrences of sedimentary magnesite

Location	Style	Reference
Coorong lagoon, southern Australia (Csb)	Primary magnesite precipitates (with magnesian dolomite) in a number of hypersaline-schizohaline coastal lakes fed by continental brines. Nearby lakes contain hydromagnesite-aragonite associations.	Alderman and von der Borch (1963), Warren (1990)
Clipperton Atoll, Pacific Ocean (mid oceanic; BSh?)	Magnesite occurs at the bottom of the atoll lagoon. Some 2,850 years ago the lagoon became sufficiently isolated to be density stratified. At present the upper 14–15 m of the water column has a salinity of 14‰, while the underlying water mass up to a maximum depth of 34 m is marine (salinity of 33–34‰).	Bourrouilh-Le Jan et al. (1985)
Lake Bonneville, Great Salt Lake depression, Utah (BSk)	Magnesite was found in association with aragonite and dolomite in five cores taken through saline laminites near the shore of former Lake Bonneville. The dark layers contain about twice as much magnesium as the light layers. The light-coloured laminations contain more clay minerals than carbonate.	Graf et al. (1961), Bissell and Chilingar (1962)
Lake Yao, Chad (BWh)	Magnesite occurs in beaches of Lake Yao, a saline lake in northern Chad. Occurs in a sequential paragenesis going from the lake up to the beach: changes from calcite, aragonite, magnesium calcite, dolomite, huntite, magnesite, sodium carbonates (nahcolite, thermonatrite, trona), sodium sulphates (burkeite, thenardite), halite and sylvite. Accompanying brine has pH ≈ 10.	Gac et al. (1977)
Lake Walyungup, (coastal lake) Western Australia (Csa)	Hydromagnesite in the littoral zone replacing aragonite, particularly within the mesoclot fabric of stromatolites, but also in sediments (strandline and dune sand, crusts) derived by erosion of stromatolites.	Coshell et al. (1998)
Playa Pito, Playa Gualla, and Laguna Gallocanta southeast of Zaragoza, Spain (Cfb)	Diagenetic association with dolomite, calcite, gypsum, halite, thenardite, and bloedite, increases with depth (from 5 to 30 %). Tends to form in mixing zone about playa edge where hypersaline lake brines mix with brackish groundwaters.	Pueyo-Mur and Inglés-Urpinell (1987)
Tuz Gölu, Turkey (Csa)	Magnesite and huntite are early diagenetic minerals in saline mudflat formed by transformation of dolomite in the presence of pore fluids with a high Mg/Ca ratio.	Irion and Mueller (1968), Camur and Mutlu (1996)
Sabkha El Melah, Tunisia (BSh)	Minor phase in coastal sabkha, probably replacing aragonite.	Perthuisot et al. (1972)
Sabkhat of Abu Dhabi (BWh)	Magnesite is a minor phase (possibly after huntite) found only in the upper 10–20 cm of the Abu Dhabi supratidal.	Kinsman et al. (1967), Bush (1973)
Salda Gölu, Turkey (Csa)	Extensive areas of hydromagnesite shorelines and basin centre turbidites formed by mechanical breakdown of hydromagnesite microbialites.	Braithwaite and Zedef (1994), 1996
Saline lakes, British Columbia, Canada (Dfc)	Simple monomineralic biolaminated carbonate or sulphate layers as well as beds and mounds composed of complex mixtures of aragonite, magnesite, hydromagnesite, mirabilite, gypsum, epsomite, and/or bloedite.	Last and Vance (1997), Power et al. (2014)

Stena region of southeastern Serbia and the lacustrine magnesites in the Acıgöl Basin, southwestern Anatolia, Turkey (Stamatakis 1995; Alçiçek 2009). Extensive drilling in eastern Australia in the 1980s, centred on Rockhampton, outlined several large lacustrine magnesite deposits, namely; Marlborough, Kunwarara, Merimal and Yamba. Of these, the largest, but as yet not yet fully realized, economic accumulation is the Kunwarara deposit (Fig. 12.64). It contains some 550 million tonnes of potential magnesite ore, including 260 million tonnes in a soil-covered nearsurface "blanket" ore composed of 40–45 % cryptocrystalline magnesite.

The Kunwarara deposit, situated some 60 km northwest of Rockhampton, has a proven area of 31 km^2 making it one of the world's largest deposits of cryptocrystalline magnesite, and is the only major source of lacustrine magnesite in Australia. The deposit, which has been intermittently mined

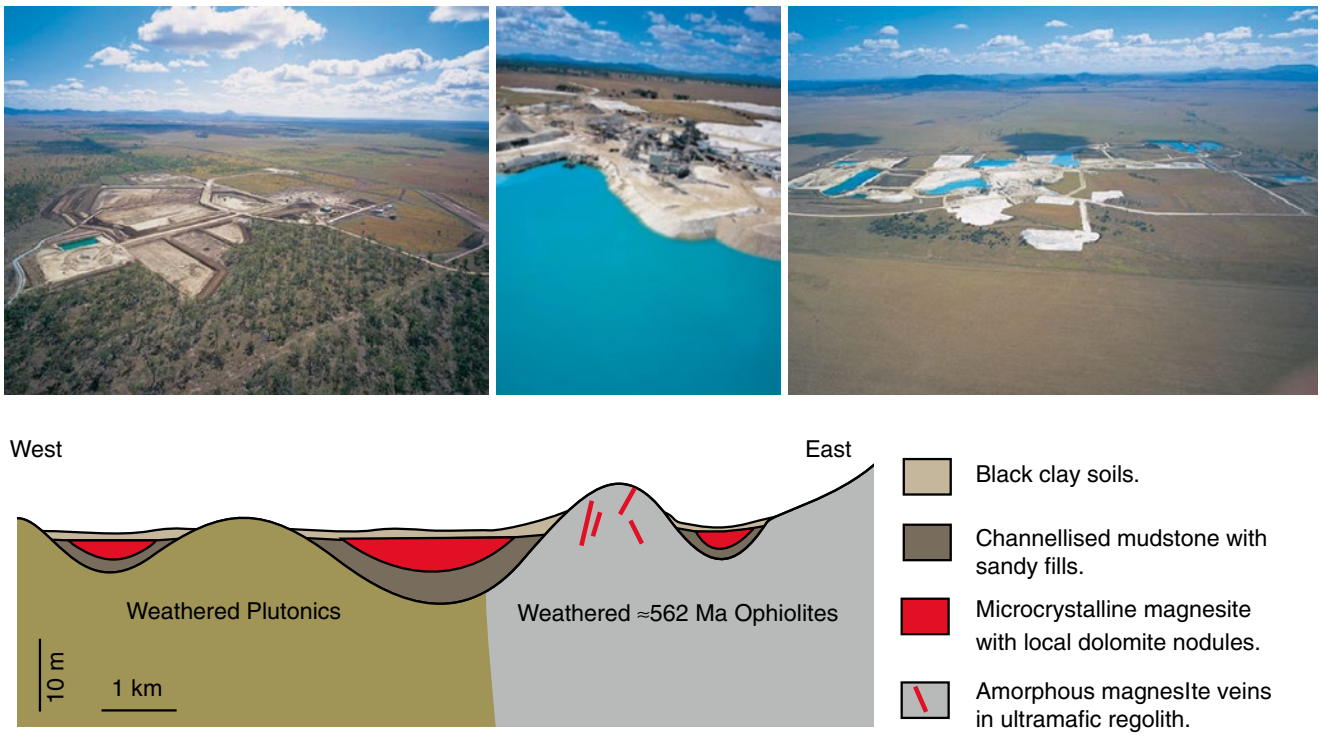

Fig. 12.64 Kunwarara magnesite, Queensland, Australia, showing general mine views and a magnesite distribution schematic cross section of regolith over the Marlborough ophiolite complex

on a small scale since 1991, has an inferred resource of 1.2 billion tonne magnesite concentrate at 20 % $MgCO_3$ cutoff, for 345 mt Mg (Milburn and Wilcock 1998). All this magnesite is stratiform, micritic and shallow, making it readily accessible to open pit access (Fig. 12.64). It is a blanket deposit varying in thickness from 1 m to 26 m, with an average thickness of 7.75 m. It lies below a humus-rich black clay ranging in thickness from 0.4 to 12 m, with an average thickness of 7.75 m (Fig. 12.48; Burban 1990; Hill 1993; Milburn and Wilcock 1998).

Most of the Kunwarara magnesite is in mm-metre diameter nodules and lumps, in a matrix of soft magnesitic mudstone, which is underlain by dolomitic mudstone, sandstone or gravel. The deposit is thought to have formed via secondary alteration of magnesian-rich lacustrine sediments. In the Marlborough area, economic magnesite occurrences are more lenticular and occur in paleochannels in the regolith, as well as in nodules, veins and stockworks in the weathered zone of ultramafic basement rocks. The formation of all the Queensland magnesite deposits involved erosion of deeply weathered lateritic soils on magnesium-rich serpentinites with subsequent deposition as fluvial/lacustrine sediments, which were then subject to further evaporatively-driven pedogenic enrichment.

A partial modern analogue for Kunwarara is the magnesite-rich lake sequence of Salda Golu in southern Turkey (Fig. 4.32; Schmid 1987). Based on this comparison, the following conditions are thought to have formed the Kunwarara deposits:

- Deep weathering of primary stockwork-bearing serpentine rocks and subsequent erosion by heavy rains.
- Water and groundwater transport of eroded and dissolved magnesian materials into a lake depression.
- Deposition and crystallization of magnesite muds in an ephemeral mudflat (capillary evaporation). Agglomeration of material into cryptocrystalline nodules.
- Periodic waves and sheet flooding carries away non-crystallized impurities such as SiO_2, Al_2O_3 and CaO.
- Flushed impurities deposited in adjacent shallow lakes, which, with a lowering of lake levels, then acted as matrix for later magnesite nodules.
- Magnesite layers were compacted and covered by soil. Pedogenesis also formed a silica-rich skin on the nodules, while pedogenic magnesite continued to crystallise in the nodular horizons.

In contrast to the meteoric supply and precipitation of micritic magnesite in Tertiary lake depressions, much of the cryptocrystalline sedimentary magnesite in Precambrian sediment is thought to be a primary precipitate from marine-fed brines. The "Magnesite Problem" is most obvious when comparing the disparity between the abundance of primary or syndepositional cyptocrystalline magnesite in

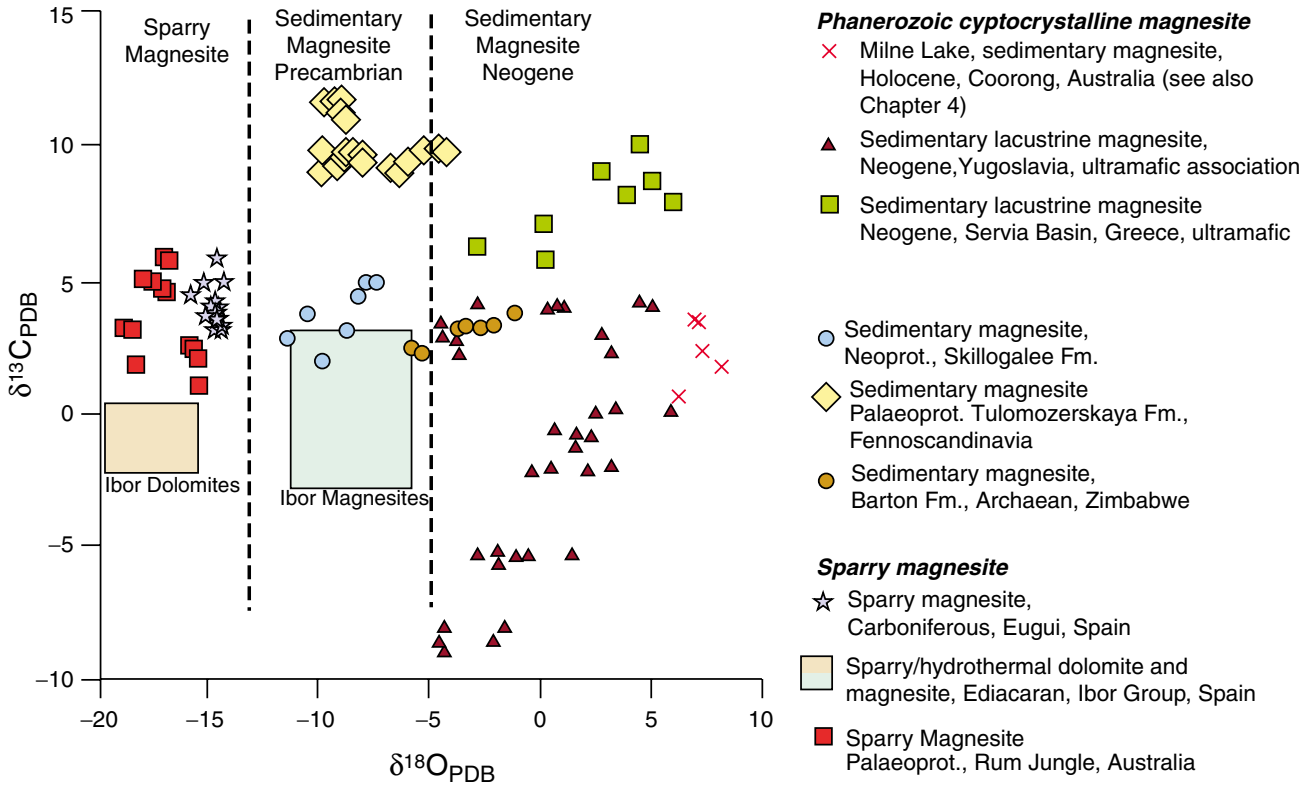

Fig. 12.65 Stable isotope signatures of sparry, lacustrine and cryptocrystalline Precambrian magnesites (In part after Melezhik et al. 2001; Herrero et al. 2011)

Precambrian restricted-marine settings and the paucity of cryptocrystalline magnesite in similar modern marine-fed evaporitic settings. The disparity probably reflects differences in the ionic proportions in Precambrian and modern oceans, especially the relative lack of sulphate and calcium, as well as extreme carbonate saturation in Precambrian oceans (Chap. 2).

Well-documented examples of widespread Precambrian magnesite are the Paleoproterozoic Tulomozerskaya Formation of the Fennoscandinavian Shield (Melezhik et al. 2001), the Ediacaran Ibor Group of western Spain (Herrero et al. 2011) and Neoproterozoic Skillogalee Formation of the Flinders Ranges in southern Australia (Frank and Fielding 2003). The latter is intermittently exploited in a small way (≈10,000 t/year). In the vicinity of Leigh Creek an inherently high purity gives the Skilogalee the potential for much higher levels of exploitation (Keeling and Mauger 1998). Outcrops of Skillogalee magnesite across the Flinders Ranges show very well preserved primary structures. In contrast, metamorphism and coarser recrystallization has destroyed more of the fine primary detail in the Fennoscandinavian magnesite strata. Yet, both areas still retain abundant textures from their primary marine-fed evaporite association (stromatolites, mudcracks, tepees, evaporite pseudomorphs, intraclastic horizons, dissolution breccias).

Some highly metamorphosed Precambrian sparry ore deposits are huge; a single magnesite-bearing zone in Liaoning Province of China is approximately 60 km long and has an outcrop width of 1–2 km. It is known to continue further to the north-east and reportedly contains some 2.5 Gt of ore (Qiusheng 1988). There are 17 moderate to large deposits and many smaller ones in the district. The magnesite bodies are stratiform, concordant with the bedding in the host dolomites, and have an average thickness of 100 m. Minor amounts of talc, tremolite, quartz, dolomite, calcite and pyrite accompany the magnesite. The magnesia content is very uniform. This, and the excellently preserved sedimentary structures, such as hail pits on bedding surfaces and slump folds, that have been found, and stable isotopic investigations, suggested to Qiusheng (1988) that the deposits are of primary saline sedimentary origin. They are associated with the siliceous metaborate marble-hosted meta-evaporites discussed in Chap. 14.

A comparison of stable isotope signatures from various types of magnesite deposits shows a clear separation in oxygen isotope signatures between Neogene lacustrine magnesites, Precambrian cryptocrystalline magnesites, and Precambrian sparry magnesites, with each group showing successively more negative values (Fig. 12.65). This difference, at least in part, reflects the higher hydrothermal

temperatures that characterise the sparry magnesite association. Within the cyptocrystalline magnesites it also reflects the likelihood that Precambrian carbonates have in general experienced higher burial temperatures for longer periods than Neogene lacustrine precipitates (Melezhik et al. 2001). Carbon isotope signatures are much more variable and relate in part to the variable supply of carbon from pre-existing carbonate minerals, levels of organic contribution and amounts of meteoric input.

Sulphur Salts (Brimstone)

Sulphur, a nonmetallic element, is the second element of Group 16 (VIA) in the periodic table, coming below oxygen and above selenium. In massive elemental form, sulphur is often referred to as brimstone. The name comes from the ancient Latin *sulpur*, referring to it as the stone that burns. Sulphur is one of the most important raw materials of the chemical industry and of prime importance to the fertilizer industry. Its consumption is generally regarded as one of the best measures of a nation's industrial development and economic activity (Anonymous 2007). Sulphur may be found alone as native or elemental sulphur, or as a gregarious element in combination with many other elements, including metal sulphides and evaporitic sulphates. In nature it is a common byproduct of bacterial and thermochemical sulphate reduction with the sulphate supplied by dissolving anhydrite or gypsum. In the chemical industry it is mostly a byproduct of metallurgical and hydrocarbon processing.

Usage History and Industry Trends

Native sulphur was known to the ancients as brimstone or "the stone that burns," in Christian mythology it was said to "fuel the Fires of Hell." Much of the following discussion of sulphur's historical uses comes from Wilburn et al. (2001). Early man used sulphur as a colourant for cave drawings, as a fumigant, in medicine, and as incense. By 2000 BC, the Egyptians began using sulphur in the bleaching of linen textiles. Homer refers to its use as a fumigant in the Odyssey. During the Peloponnesian War, in the fifth century BC, the Greeks used burning sulphur and pitch to produce suffocating gases. The Romans combined brimstone with tar, pitch, and other combustible materials to produce the first incendiary weapons. This technology was lost in the "Dark Ages." Muslims, through the use of alchemy during the "Golden Age of Arabic Science" around AD 700, probably were the first to produce sulphuric acid and this is today the major use of sulphur. Sulphuric acid is a chemical workhorse throughout the world's chemical industries. Early uses of sulphur were relatively limited in terms of quantities and the small quantities needed were mined, typically from volcanic vent deposits.

Sulphur is a necessary ingredient in gunpowder, which was developed by the Chinese during the time of Confucius (557?–479 BC). Crusaders returning from the Holy Land in the early 1300s brought with them the knowledge of gunpowder. Gunpowder was first used effectively in Europe at the Battle of Crécy (1346). Its introduction led to profound social and political changes and for the first time made sulphur an important tradeable mineral commodity. Sicilian sulphur deposits, hosted in Messinian evaporites, satisfied European demand throughout the Renaissance and continued to supply much of the world's sulphur into the last century. But attempts to stabilize the price of Sicilian sulphur at high levels by French controlling interests in 1838 led to the development and use of alternative sources.

In 1833, a French chemist, Michel Perrett, developed an economical method of obtaining sulphur dioxide by roasting pyrite. His invention led to the development of a rotary furnace in 1870 that made pyrite a profitable raw material for sulphuric acid production. By 1880, sulphuric acid throughout the world was being produced from pyrite, except in the United States where import tariffs on iron and copper sulphides prevented a shift away from native sulphur. These import tariffs were removed in 1890 and 1894 respectively, and by 1900 burnt pyrite had become the principal acid–making material in the United States.

Native sulphur deposits occur in a number of evaporite basins in America and Europe, and several attempts were made to mine sulphur from salt dome cap rock in Louisiana between 1870 and 1890 using conventional underground mining techniques. These efforts were all frustrated by the patchy nature of caprock sulphur ore and collapse-prone overburden. In 1894, Herman Frasch developed a method of recovering native sulphur using hot water and compressed air. It is a form of chemically-targeted solution mining and comprises a well made up of three concentric pipes (casing) ending in the ore zone. Pressurized superheated water is pumped down the outermost pipe in the string. The resulting steam melts the sulphur, while air pressure applied via the innermost pipe forces the molten sulphur to the surface via the intermediate space in the pipe string. Sulphur was first commercially obtained using the Frasch method in 1895 by the Union Sulphur Company at Sulphur Mines dome, Calcasieu Parish, LA. The Frasch method was also employed in 1912 at Bryan Mound, Brazoria County, Texas, and later at many other domes scattered about the US Gulf Coast.

Worldwide, documented resource of elemental sulphur amounts to about 5 billion tonnes (Fig. 12.66). It occurs in evaporite and volcanic deposits, or as sulphur associated with natural gas, petroleum, tar sands, and metal sulphides. Current uses for sulphur are: phosphate fertilizer production – 70 %;

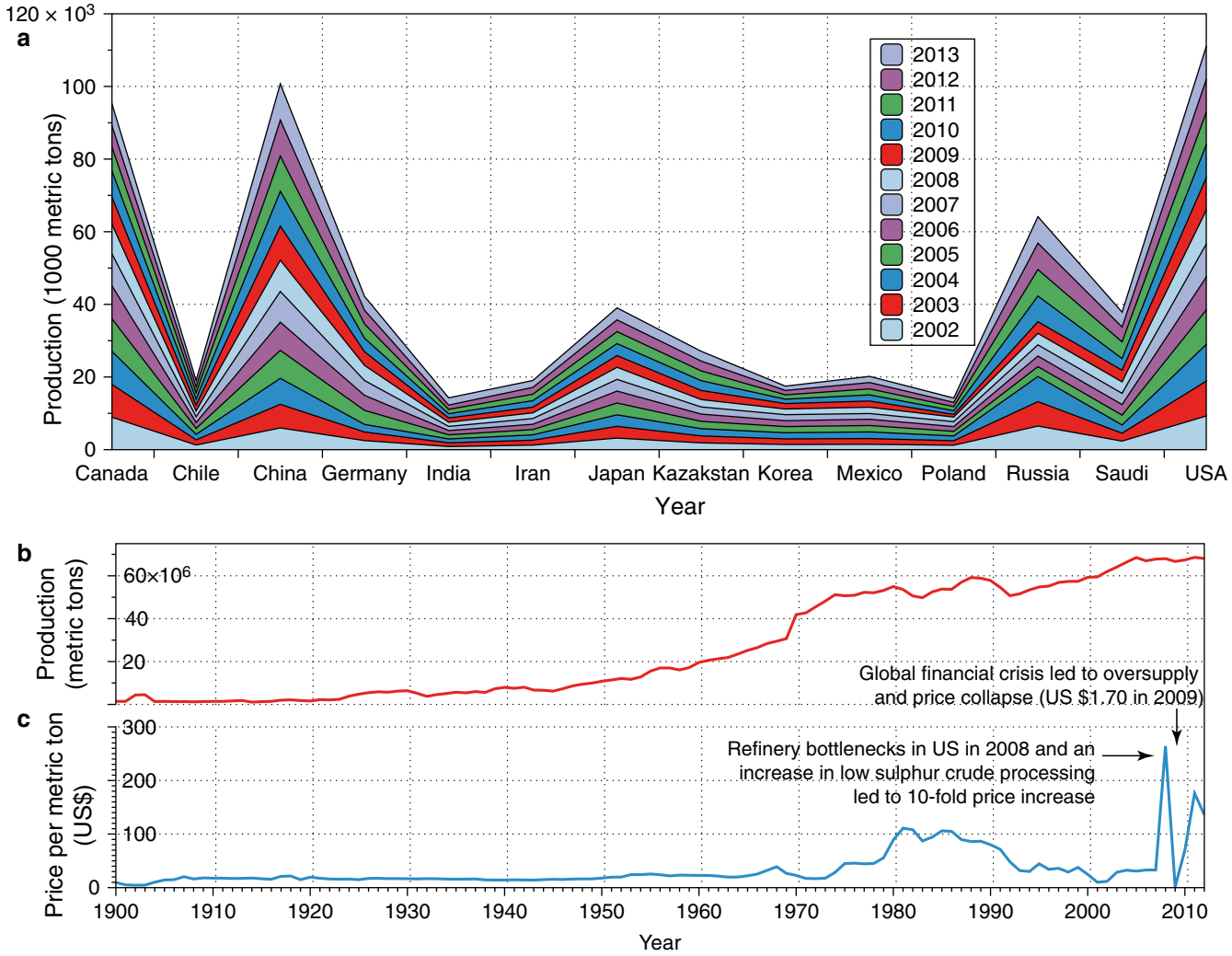

Fig. 12.66 Sulphur production mostly as byproduct of petroleum processing. (**a**) Cumulative area plot of annual production in major producing countries in metric tons (See Fig. 12.67 for manufacture-process proportions). (**b**) World production from 1900 to 2011 (metric tons), (**c**) Price per metric ton in US dollars from 1900 to 2012 (Compiled from USGS on-line data tables downloaded from http://minerals.usgs.gov/minerals/index.html last accessed April 29, 2014)

petroleum alkylation catalysis (the conversion of one kind of hydrocarbon into another) – 15 %; metals industry processes (leaching and pickling) – 7 %; chemicals – 4 %: and other uses – 4 % (Fig. 12.67; Ober 2000).

Worldwide, the production of mined or extractive sulphur has been falling since the mid 1980s, as has the price per ton. During 2009 and the global financial crisis, the price per ton at $1.70 reached a record low but has since recovered (Fig. 12.66c; Apodaca 2012). Most sulphur is today produced either as a byproduct in hydrocarbon processing or as a metallurgical byproduct (Fig. 12.67). Poland is the only country still producing substantial quantities of native sulphur from evaporite-related deposits, using either the Frasch method or conventional mining. In August 2000, Freeport Sulphur closed its Main Pass Mine, offshore Louisiana, which was extracting sulphur from diapiric caprock, this facility was the last remaining Frasch mine in the USA. At the time it ceased operation it was the largest offshore structure in the Gulf of Mexico and the largest mine worldwide utilising the Frasch process.

In the previous year, Freeport had closed the Culberson Mine in West Texas, which was the last mine in the onshore of the USA using the Frasch method to recover sulphur from bacteriogenic deposits hosted in bedded Permian evaporites. Polish Frasch sulphur production still hovers around 1,000 metric tons per year, although this production is now threatened by low international prices, due to saturation of the market with byproduct sulphur. Today, small quantities of native sulphur are still mined in Asia, Europe, and North and South America. The use of pyrite as a sulphur source has significantly decreased in the last two decades because of pollution concerns. China, South Africa, and Spain are now

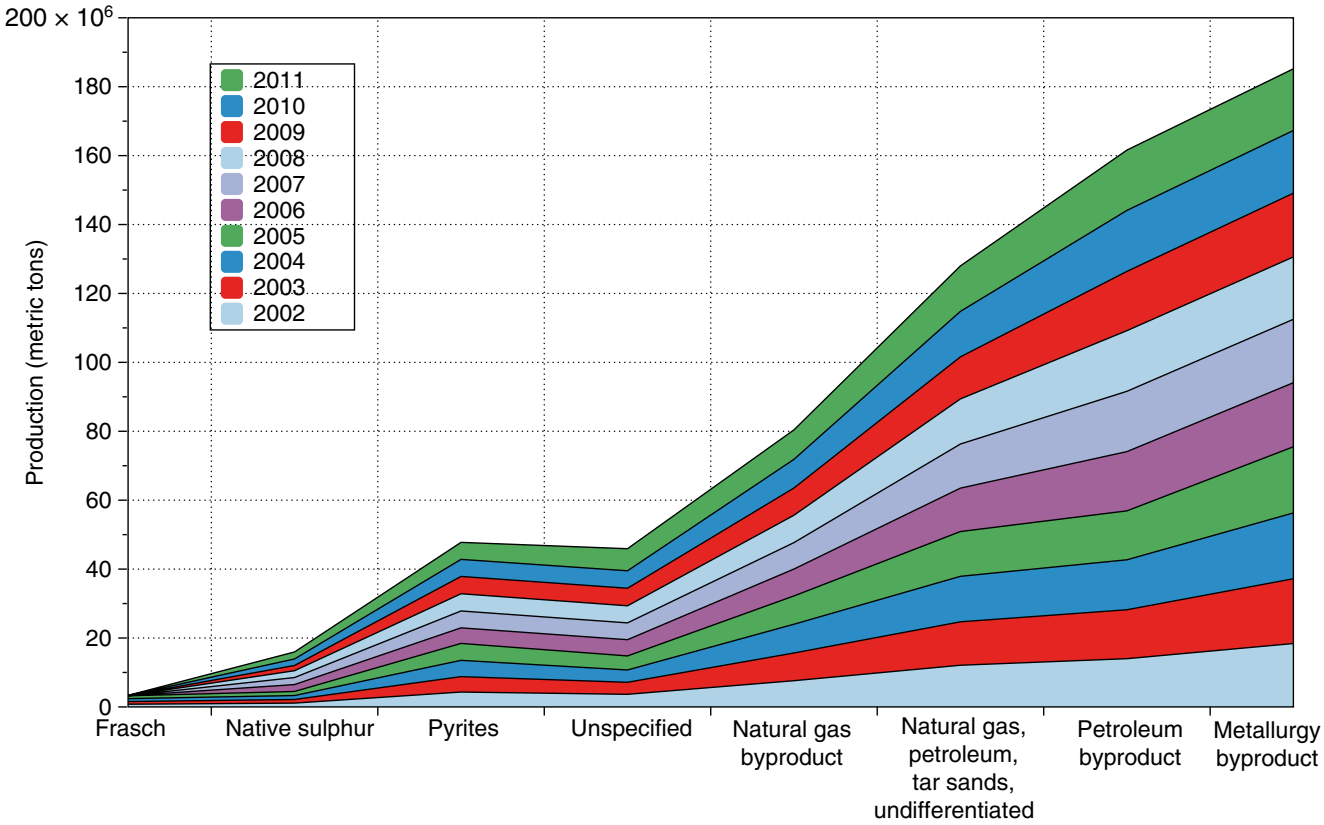

Fig. 12.67 Processes of sulphur manufacture – worldwide from 2002 to 2011 (in 1,000 metric tons). Dominance as a product of hydrocarbon and matallurgical processing is clear (Compiled from USGS on-line data tables downloaded from http://minerals.usgs.gov/minerals/index.html last accessed April 29, 2014)

the only countries in the top 15 sulphur producers whose prime sulphur source is pyrite; together these three nations account for more than 80 % of all pyrite-based production (Apodaca 2012).

Although mined sulphur production is decreasing worldwide, world production of recovered (byproduct) sulphur is increasing (Fig. 12.67). The growth comes mostly from sulphur recovery from sour gas processing plants and from the refining of sour crude oils, especially the sulphur-rich hydrocarbons of the Middle East and Canada. Chemically recovered elemental sulphur is now the predominant sulphur source in Canada, France, Germany, Iran, Russia, Saudi Arabia, and the United States, and an important sulphur source in Japan and Mexico (Fig. 12.66a). In many countries this form of sulphur is recovered in compliance with environmental regulations that restrict the sulphur content of the fuels sold or used by a processing facility. Growth in sulphur recovery continues to outpace sulphur demand, resulting in increased stocks worldwide, as increasingly stringent environmental regulations force producers to limit atmospheric emissions of sulphur dioxide.

In addition to the currently known native sulphur resource, the amount of natural sulphur held as sulphate in gypsum and anhydrite is almost limitless. Some 600 billion tonnes are contained in coal, oil shale, and shale rich in organic matter, but low-cost recovery methods are lacking.

Types of Natural Sulphur Deposits

Most large nearsurface accumulations of natural sulphur are the results of chemoautotrophic bacteria living on hydrocarbons or organic matter and dissolving anhydrite/gypsum, either in diapiric caprocks or in stratiform layers near the dissolving edges of anhydrite/gypsum beds (Ruckmick et al. 1979). Such deposits are classified as bio-epigenetic and are intimately linked to the formation of microbial calcite. Bacteriogenic production can take place up to a kilometer or more below the landsurface. The same bacterial sulphate reduction process also forms much smaller volumes of native sulphur in modern anoxic marine or lacustrine muds, termed biosyngenetic deposits by Ruckmick et al. (1979). Thermogenic deposits of molten sulphur precipitate as via thermochemical sulphate reduction at much higher burial temperatures in association with

natural sour gas (Chap. 9). There are also deposits of native sulphur in volcanic terrains, usually as vein and fracture fills; a few still are mined in a small way and may be locally important, especially in the developing world. Lastly, there is oxidative native sulphur, which according to Ruckmick et al. (1979) is widespread but typically creates small sulphur occurrences. This type of sulphur forms wherever hydrogen sulphide (regardless of origin) is oxidized. An example would be the dispersed native sulphur that occurs in the Carlsbad and Lechuguilla caves in New Mexico. We shall only discuss bioepigenetic occurrences in this chapter. Thermochemical sulphur occurrences are typically to deep to have ever been viable extraction targets and the formative mechanisms were discussed in detail in Chaps. 7 and 9.

Biology of Native Sulphur

Native sulphur is microbially produced from calcium sulphate via bacterial degradation (sulphate reduction) of anhydrite and gypsum in the presence of organic matter or hydrocarbons at temperatures of up to 110 °C;

$$CaSO_4 \cdot 2H_2O + \text{hydrocarbons} \rightarrow H_2S + CaCO_3 + H_2O$$

Sulphate-reducing bacteria chemoautotrophically metabolise migrating hydrocarbons and sulphate minerals within the evaporites to produce hydrogen sulphide and vuggy bacteriogenic calcite. Infiltrating meteoric water then oxidises the H_2S to form elemental sulphur. The reaction takes place in the mixing zone between shallow meteoric waters and deep basin fluids in both bedded and diapiric $CaSO_4$ precursors (Aref 1998b). Fine specks of sulphur and calcite replace gypsum in the early stages. With increasing replacement, sulphur and calcite form networks and patches within the gypsum (rehydrated anhydrite), which expand until gypsum remains only as relict splotches in a massive vuggy bioepigenetic calcite with pores lined with sulphur.

Dominant species of sulphate-reducing bacteria acting on the $CaSO_4$ change with salinity and temperature (Chap. 9); *Desulphovibrio desulphrican* is active at shallow subsurface temperatures, *Desulphovibrio orientis* is active at moderate burial temperatures and *Clostridium nigrificans* dominates in hotter conditions. These bacterial reducers consume organics or hydrocarbons as a source of energy, but use sulphur instead of oxygen as a hydrogen acceptor and so produce hydrogen sulphide, calcite and water as byproducts. In addition to West Texas and the Gulf of Mexico, large deposits of bioepigenetic sulphur replacing gypsum/anhydrite occur in the Mishraq sulphur deposits (Barker et al. 1979), in the Polish sulphur deposits (Pawlowski et al. 1979), and in the Gulf of Suez (Youssef 1989; Aref 1998b). In the past all these deposits have been mined.

Occurrences and Textures

In sulphur-entraining caprocks atop diapirs in the Gulf Coast and Mexico, the $CaSO_4$ ore host is first created by dissolution of halite in the rising salt stem (Chap. 6). This leaves behind a residual carapace or caprock of anhydrite that phreatic groundwater flushing then converts to gypsum at shallower depths (Fig. 12.68a; Ruckmick et al. 1979). In the stratiform sulphur ore district of Culberson County, West Texas, requisite ore-forming fluids, including basinal hydrocarbons and deeply circulating meteoric groundwaters, migrated upward from underlying carrier beds, along steeply dipping normal faults, into the Salado Formation host (Fig. 12.68b). Likewise, native sulphur occurs in the Red Sea Coast at Ras Gemsa, where an uplifted horst block, containing middle Miocene oil and gas bearing strata, is overlain and sealed by evaporite-carbonate layers (Youssef 1989). In all cases, the native sulphur resides in pores and vugs of bio-epigenetic limestone beds.

In its unaltered subsurface state the Castile Formation of the Delaware Basin is made up of stacked laminar anhydrite beds. The unit's underside acts as a seal and a focus for hydrocarbons seeping up from the oil kitchen in the deeper parts of the Delaware Basin and for deeply circulating meteoric waters (Fig. 12.68b). Previously mineralised castiles now outcrop and subcrop about the edge of the Delaware Basin. The trap was naturally prepared for sulphur accumulation by a series of faults and collapse anticlines, activated or reactivated by evaporite dissolution about the basin edge. These extensional fractures acted as hydrological foci during the creation of porous dissolution collapse breccias or chimneys that crosscut the anhydrite beds of the Castile and the overlying Salado and Rustler formations (Fig. 12.68b). Once a dissolution breccia/karst system was created toward the basin margins, it focused the ascent of petroleum-bearing waters from the underlying carrier beds (Bell Canyon Sandstone aquifer). As hydrocarbon-bearing waters flushed through the breccia, sulphate-reducing bacteria converted anhydrite to limestone and deposited sulphur in newly created fractures and vugs.

Locations of stratiform sulphur in this style of deposit are always structurally controlled and initiated during regional bathyphreatic speleogenesis (Stafford et al. 2008a, b). Individual sulphur deposits in West Texas are generally small, although the now closed Duval Mine in Culberson County, Texas, had original sulphur ore reserves of more than 55 Mt, between depths of 70 and 380 m (Davis and Kirkland 1979). The Fort Stockton Mine in Pecos County was located on the culmination of a leaky northwest-southeast trending anticline in the Salado Formation with a structural closure of 20 m (65 ft) in mine area (Fig. 12.69; McNeal and Hemenway 1972). Sulphur ore was largely confined to diagenetic limestone hosts that made up the A, B, and C units. Tops of the B

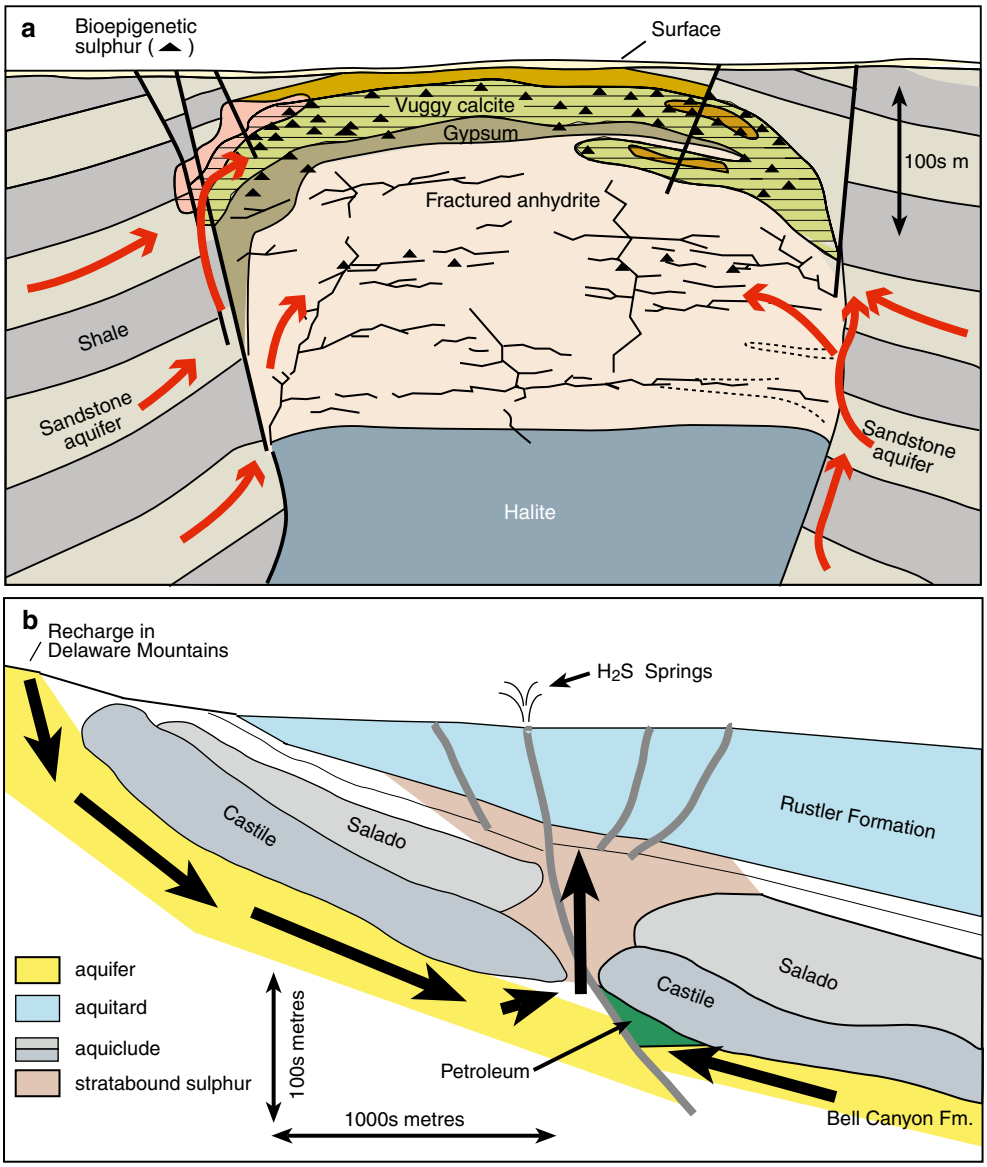

Fig. 12.68 Conceptual models for the origin of evaporite-related elemental sulphur. (**a**) Genetic model for diapir caprocks. (**b**) Genetic model for stratabound or stratiform sulphur and the formation of subsurface castiles in the Permian Castile Formation of West Texas and New Mexico (After Ruckmick et al. 1979)

and C units were defined by radiogenic clay marker beds and the top of the A was defined as the top of the Salado Formation. Sulphur in the ore zones sat mostly within dispersed vugs, fractures and fenestra in solution collapse breccia units, so it was more amenable to Frasch processing rather than conventional mining. As the ore was mined by steam injection, the more permeable megavug, mesovug and megafenestral ore zones were prime targets in the steam-mined interval. Intervals with mesointercrystalline and mesofenestral porosity greatly increased the efficiencies of recovery by facilitating improved steam circulation through sulphur-impregnated intervals.

Similar stratiform sulphur occurs along the Red Sea coast of Egypt where accumulations range from small and non-commercial (Gebel Abu Gerfan and Ras Dip) to economic deposits (Gemsa; Aref 1998b). Sulphur crystals vary in morphology, colour, and size, it forms fine disseminations at Abu Gerfan, Gemsa and Gebel El Zeit; fracture and cavity fillings at Gemsa and Little Zeit; and sulphur nests at Gemsa and Shagar. The size of the sulphur aggregates ranges from a few millimeters to 5 cm diameter and crystal morphologies range from anhedral to subhedral to euhedral orthorhombic. Occurrences vary in colour from clear or turbid yellow crystals that may be encrusted with bitumen, to brown or black bitumen-stained sulphur varieties. Within outcropping calcite castiles along the Red Sea coast these epigenetic sulphur crystals can fill vugs or fractures in the host rocks, or they can replace gypsum or anhydrite along cleavage planes or intercrystalline crystal boundaries. They also may pervasively replace gypsum and calcite units to form network or meshwork patterns.

Bio-epigenetic sulphur was mined in Poland as early as the fifteenth century, and although declining, annual sulphur

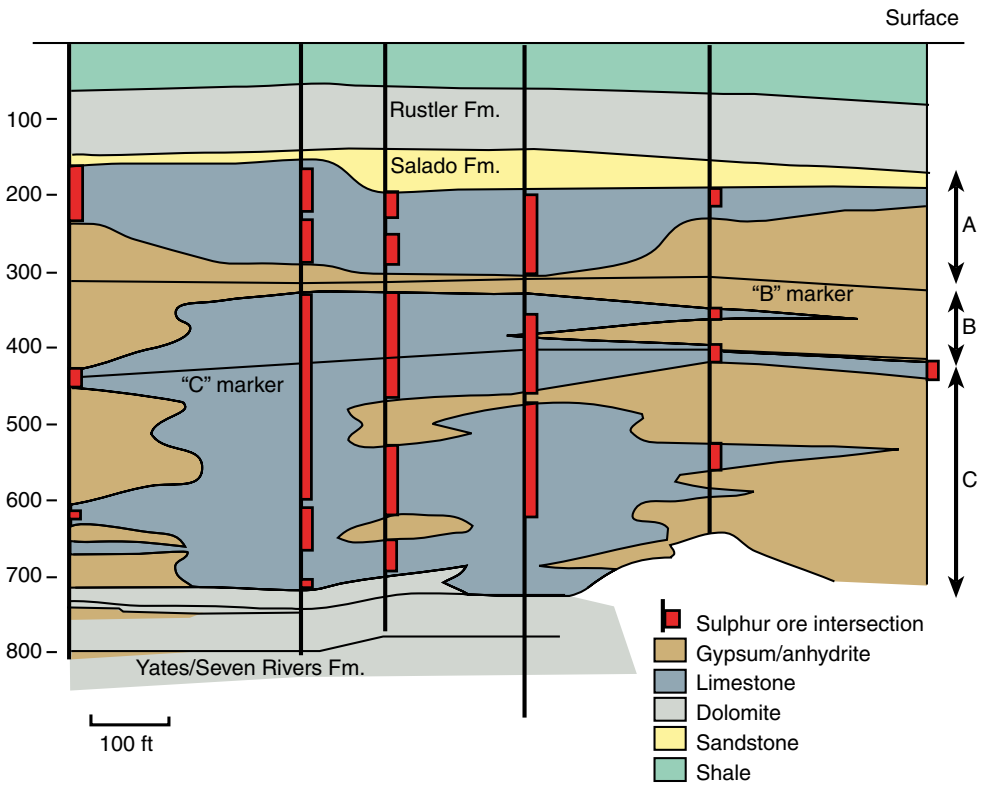

Fig. 12.69 West-east cross section through the Fort Stockton anticline showing sulphur occurrence is largely confined to the dissolved and bacteriogenically reworked remnants of the Castile and Salado Formations (After McNeal and Hemenway 1972)

production in Poland still exceeds a million metric tons. Native sulphur deposits today occur beneath fluvioglacial outwash in the Vistula Valley, some 190 km south of Warsaw, and in the area around Lublin. All deposits lie within a Middle Tortonian gypsum host and are part of the 3,000 m thick fill of Miocene sediments that accumulated during the Alpine Orogeny in the foredeep north of the Carpathian Front (Chap. 12).

Polish sulphur is either extracted by conventional open-pit mining or by the Frasch hot-water/steam method (Pawlowski et al. 1979). The sulphur occurs in several styles; the most commercially important is as disseminated microcrystalline sulphur in a fine-grained poorly lithified calcitic marl host. This form of sulphur makes up 15 to 80 % of the exploited rock mass and averages 30 %. It is pale coloured and may occur in rounded concretionary masses, in thin irregular stringers, or in thick masses of high purity. A secondary ore mode is as coarser recrystallized forms that are bright yellow and typically occurs as crystals lining vugs and along fractures and seams. Masses of this coarsely crystalline form commonly grade into the microcrystalline form. Non-commercial occurrences constitute finely divided sulphur in interstices in growth-aligned bottom-nucleated gypsum crystals and as dispersed sulphur cements in sandstone beds. Both styles contain less than 15 % sulphur in forms that are difficult to concentrate.

The main difference between North American, Polish and Red Sea sulphur occurrences is that the ore host is rehydrated and exhumed anhydrite in North America, while the Polish and Red Sea ore hosts have never been sufficiently buried to convert primary gypsum to anhydrite. This is also the case in the sulphur deposits of Sicily, which are hosted in Messinian gypsum with immature hydrocarbons bleeding from the mine walls (pers. obs.).

Bacterial reduction of sulphate in all native sulphur ore hosts causes significant depletion of $\delta^{34}S$ in H_2S relative to the parent sulphate and a similar depletion in the sulphur derived from it (Thode and Monster 1973). Reoxidation of sulphide to sulphate or sulphur by O_2 in the fluid mixing zone does not cause significant isotopic fractionation. Hence the lighter sulphur isotopic composition of oxidative sulphur in Guadalupe Mountain caves ($\delta^{34}S_{CDT} = -25.8$) and in the stratiform sulphur of the Culberson mine (–4.7‰) (Hill and Forti 1997). The light carbon isotope signature of epigenetic calcite in the Culberson mine also indicates a hydrocarbon source ($\delta^{13}C_{PDB} = -44.2$ to –18.6‰; Hill 1995). The depleted $\delta^{13}C_{PDB}$ values are significantly lower than would be expected in marine carbonates, which typically fall in the range –4 to +4‰.

Zeolites – Molecular Sieves

Zeolites are aluminosilicate minerals that occur as low-temperature (generally less than 200 °C) alteration products of volcanic and feldspathic rocks. Like clays, zeolites are hydrated aluminosilicates made up of alkaline and alkaline

Table 12.20 Properties of some important zeolites

Mineral structure (channel size in angstroms)	Typical unit cell content	Void volume	Specific Gravity	CEC (meq/g)
Group 1: Single 4-ring				
Analcime (1.6 × 4.2; irregular)	$Na[AlSi_2O_6]\cdot H_2O$	0.18	2.24–2.39	4.54
Phillipsite (4.2 × 4.4)	$(K,Na,Ca_{0.5},Ba_{0.5})_x[Al_xSi_{16-x}O_{32}]\cdot 12H_2O$	0.31	2.15–2.20	3.87
Laumonite (5.0 × 5.3)	$Ca_4[Al_8Si_{16}O_{48}]\cdot 18H_2O$	0.34	2.20–2.23	4.25
Group 2: Single 6-ring				
Erionite (3.6 × 5.2)	$K_2(Na,Ca_{0.5})_8[Al_{10}Si_{26}O_{72}]\cdot 30H_2O$	0.35	2.02–2.08	3.12
Group 3: Double 4-ring				
A (Linde: 4.2)	$Na_{12}[(AlO_2)_{12}]\cdot 27H_2O$	0.47	1.99	3.12
Group 4: Double 4-ring				
Chabazite (3.7 × 4.2)	$(Ca_{0.5},Na,K)_4[Al_4Si_8O_{24}]\cdot 12H_2O$	0.47	2.05–2.10	3.81
Group 5: Complex 4–1, T_5O_{10}				
Natrolite (2.6 × 3.9)	$Na_2[Al_2Si_3O_{10}]\cdot 2H_2O$	0.23	2.20–2.26	5.26
Group 6: Complex 5–1, T_8O_{16}				
Mordenite (2.9 × 5.7)	$(Na_2,Ca,K_2)_4[Al_8Si_{40}O_{96}]\cdot 28H_2O$	0.28	2.12–2.15	2.29
Group 7: Complex 4-4-1, $T_{10}O_{20}$				
Clinoptilolite (3.9 × 5.4)	$(Na,K,Ca_{0.5},Sr_{0.5},Ba_{0.5},Mg_{0.5})_6[Al_6Si_{30}O_{72}]\cdot$ ~$20H_2O$	0.34	2.16	2.54

In part after Breck 1974

earth metals. Their varying tetrahedral structures break them down into seven related aluminosilicate groups, each with some non-claylike properties (Table 12.20). Most clays have a layered crystalline structure and are subject to shrinking and swelling as water is absorbed and removed between the expanding and contracting lattice layers. In contrast, zeolites lack this expandable layered lattice. Rather, they have a rigid, 3-dimensional crystalline structure consisting of a network of interconnected tunnels and cages, separated by tetrahedal latticework. Water moves freely in and out of these pores, while the zeolite framework remains rigid. A dehydrated zeolite framework, with its honeycomb of passageways, is capable of absorbing large quantities of fluids and gases in place of the removed water, without ever changing volume. In fact, the word zeolite comes from the Greek *zein* meaning "to boil" (lit. *boiling rock*) and was given its name by Swedish mineralogist Axel Fredrik Cronstedt who had seen water boiling out of the rock pores when it was heated, but without obvious changes in rock volume.

As of 2008, 175 catalogued unique zeolite frameworks had been identified, 40 of which are naturally occurring. Their rather unusual cage- or sieve-like lattice structure gives zeolites some useful characteristics (Table 12.20: Breck 1974):

- a high degree of hydration;
- a rigid structure with a low density and large void volume when dehydrated;
- a stable crystal structure when dehydrated;
- a set of mineral specific cation exchange properties;
- a set of uniform molecular-sized channels in many dehydrated crystals;
- a controlled variable set of physical properties such as electrical conductivity;
- an ability to adsorb selected gases and vapours;
- catalytic properties.

Because each member of the zeolite family has a unique aperture size, the molecules admitted to the framework are restricted to those of appropriate dimensions. This selective nature of the various zeolite structures makes them extremely useful as molecular sieves, with numerous industrial applications.

Zeolites also have the ability to exchange cations, whereby one charged ion is exchanged for another in the crystal structure. The ability of a zeolite to do this is measured by its cation exchange capacity (CEC; Table 12.20). Compared to clays, zeolites have high CEC's, which are lattice specific and reflect varying degrees of alumina substitution for silica in the lattice tetrahedra to create lattice specific zones of surface charge. Exchange sites on natural zeolites are primarily occupied by three major cations: potassium (K), calcium (Ca), and sodium (Na), although other elements such as magnesium (Mg) may also be present. Exchange sites on a particular zeolite may contain nearly all K, nearly all Na, some Ca or Mg, or a combination of these, and this controls which zeolites are suitable for a particular application.

Usage and Production

The primary use for zeolites is in laundry detergents. The mineral's porous nature allows particles of dirt and contaminants to be captured in the wash cycle and then rinsed away

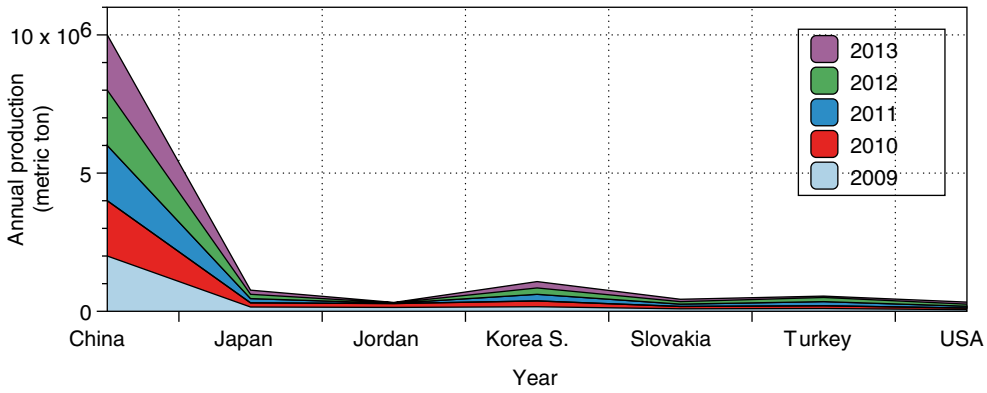

Fig. 12.70 Estimates of country by country annual production of zeolites. Subject to error as some countries producing substantial zeolite volume do not compile estimates (Compiled from USGS on-line data tables downloaded from http://minerals.usgs.gov/minerals/pubs/commodity/zeolites/ last accessed May 5, 2014)

in the rinse cycle. Other common household uses are as aquarium filters and cat litter. Zeolites are also used extensively within the medical profession as sieves to filter and purify air to make medical grade oxygen. In agriculture, zeolites are used as preservative agents (desiccants), soil conditioners, fertilizer extenders, herbicides, pesticide and fungicide carriers, animal food additives and odor controllers. Zeolites with K exchange sites are useful as longterm K-release fertilizers. Other uses include dimension stone, lightweight aggregate, pozzolan and numerous filtration/treatment uses, such as natural gas purification, nuclear waste treatment and disposal, and oil spill, sewage and effluent cleanup. Chabazite is used to remove CO_2 and H_2S from sour natural gas, while clinoptilolite can remove ammonia in tertiary sewage treatment and is also used for odor control in pet-litter. It also relieves ammonia stress in cud-chewing animals and it can strip base metals from effluents. Clinoptilolite is also highly effective in the cleanup of radioactive waste as it strongly adsorbs strontium and caesium, two of the longest-lived radioactive ions. It was used in the cleanup of Three Mile Island spill and was fed to children affected by the Chernobyl disaster.

World reserves of natural zeolites have not been reliably estimated and plots of production, as in Fig. 12.70 are subject to error (Vitra 2014). Deposits occur in many countries, but companies rarely, if ever, publish reserve data. Further complicating estimates of reserves is the fact that much of the reported world production includes altered volcanic tuffs that contain low to moderate concentrations of zeolites. These typically are used in high-volume construction applications, and therefore some deposits should be excluded from reserve estimates because it is the rock itself and not its zeolite content that makes the deposit valuable.

Countries mining large tonnages of zeolites typically use them in low-value applications. The ready availability of zeolite-rich rock at low cost and the shortage of competing minerals and rocks are probably the most important factors encouraging its large-scale use. It is also likely that a significant percentage of the material sold as zeolites in some countries is ground or sawn volcanic tuff that contains only a small amount of zeolites. Examples of such usage are dimension stone (as an altered volcanic tuff), lightweight aggregate, pozzolanic cement, and soil conditioners. Where zeolite figures are more reliably estimated the reserves are substantial. For example, some 120 million tons of clinoptilolite, chabazite, erionite, mordenite, and phillipsite is present in near-surface deposits in the Basin and Range province in the United States (Vitra 2014). Resources in the United States may approach 10 trillion tons for zeolite-rich deposits.

Geological Controls on Saline Zeolitisation

There are six major geological settings where zeolites are found, of which saline lacustrine settings are one (Table 12.21). Most zeolites are altered volcaniclastics, with the larger number of exploited zeolite deposits formed by groundwater flushing of volcaniclastics within saline lacustrine settings (Surdam 1981). These are ideal settings as they are characterised by hydrologies that force alkaline lake and pore brines to interact and alter trachyte glass (Fig. 12.71). Zeolites are not preserved in rocks where metamorphic grade exceeds zeolite facies and so their occurrence decreases with age. More than 30 different zeolite minerals have been identified in Cenozoic rocks, only 7 in Mesozoic strata, 2 in the Early Palaeozoic, 4 in the Late Palaeozoic, one in the Neoproterozoic and none in the Archaean (Iijama 1980). The interested reader is referred to Mumpton (1983) or Iijama (1980) for a full discussion of all the geological settings forming zeolites, in the following section we shall only consider natural zeolites formed in saline lacustrine settings.

Natural zeolites in saline settings typically form via the reaction of pore waters with labile material, typically volcanic glass, but also with poorly crystalline clay, plagioclase or silica. Factors influencing zeolite mineralogy are salinity, pH, ratios of alkali and alkaline-earth ions in the pore waters, along with temperature, pressure and partial pressure of water in the fluid-filled pore spaces. Zeolitization is favoured by higher pH in waters interacting with volcanics and by elevated ratios of Mg compared to Na, K and Ca, conditions

Table 12.21 Geological occurrence of some natural zeolites

Mode of occurrence	Temp. (°C)	Zeolite species	Examples
Alkaline saline lake and percolating groundwater, semi arid (in basic tephra)	20–50	Ph, Cp, Ch, Er, Mo, Gi, Fa, Go, Na, An, (He)	Zeolitic tuffs of ancient Lake Tecopa, Shoshone, California
Percolating groundwater in a semi-arid setting (in acid tephra – vitric tuff)	20–50	Ph, Cp, Er, Mo, Fe, Th, Me	Altered tuffs of the John Day Formation, central Oregon
Nearshore or deep sea volcaniclastic sediment halmylosis	4–50	Ph, Cp, (An)	Massive, clinoptilolite-rich tuff near Kurdzali, Bulgaria
Shallow burial diagenesis (low-temp. hydro-thermal)	25–100	Sc, He, St	Massive, clinoptilolite-rich tuff near Kurdzali, Bulgaria
Deep burial diagenesis (mod. temp. hydro-thermal)	100	La, An	Massive, clinoptilolite-rich tuff near Kurdzali, Bulgaria
Low grade metamorphic (high temp. hydro-thermal)	>200	Wa, Yu, An	Altered tuffs and sandstones Wairakei, New Zealand
Magmatic primary	high	An	Nishi-Iburi District, Hokkaido, Japan

In part after Iijama 1980; Mumpton 1983
Ph phillipsite, *Cp* clinoptilolite, *Ch* chabazite, *Er* erionite, *Mo* mordenite, *Gi* gismondite, *Fa* FaHe: heulandite, *Th* thomsonite, *Me* mesolite, *Sc* scolecite, *St* stilbite, *La* laumontite, *Wa* waira, *Yu* yugawaralite

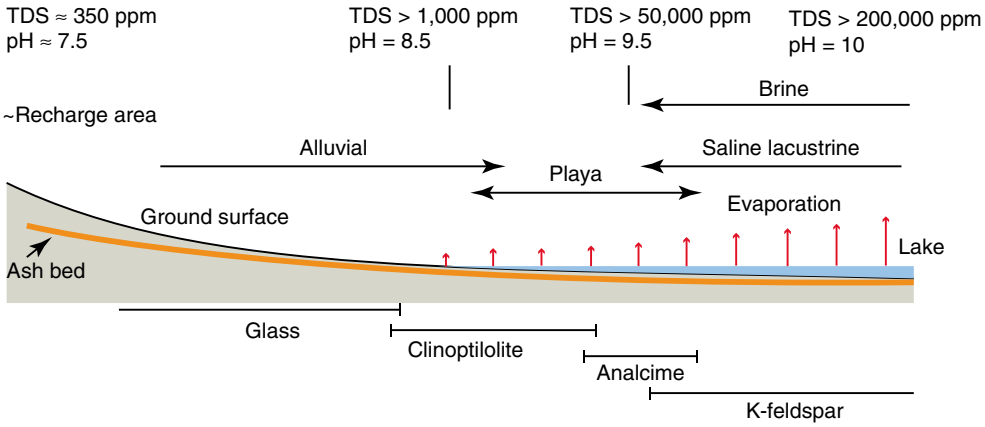

Fig. 12.71 Zeolite distribution in relation to the pore brines in a saline lacustrine system that are driving the alteration of the volcanic glass. *TDS* total dissolve solids (After Deer et al. 2004)

that typify saline groundwaters in many closed hypersaline basins, especially in tectonically active depressions (continental rifts and collision belts). A preponderance of sodic-rich zeolites such as analcime, mordenite, phillipsite, natrolite and clinoptilolite is probably a more common outcome in evaporitic, compared to nonevaporitic, zeolite associations, reflecting high levels of Na in most saline brines. Chemical composition of the protolith glass, grain size and permeability of the host vitric tuff, are additional factors controlling the mineralogy of a zeolite, pH of the flushing solution is the most important (Hay 1981; Hall 1998).

Volcanic glass in a saline mudflat hydrology is most readily altered near the watertable as alkalinity increases via evaporative pumping and an aluminosilicate gel forms. Once pore brines become alkaline (pH >9–10), zeolites begin to crystallise (Fig. 12.71). Mariner and Surdam (1970) showed experimentally that the rate of dissolution and hence alteration of rhyolitic glass increases 20-fold as the pH is raised from 8.5 to 11.5. Initial surface waters and groundwaters in many volcanic areas are acidic, but zeolitisation requires neutral to alkaline (bicarbonate-bearing) conditions. Before zeolitisation can take place, acidic interstitial water must be removed or neutralized. This can occur via deposition or redeposition of ash in a standing body of alkaline water (not uncommon in saline depressions), or if there is reheating of ash via hydrothermal circulation pushing alkaline saline groundwater through the ash bed. Alkaline water can come from leaching of overlying or neighboring limestone. Arid hypersaline depressions are associated with density-induced circulation cells that favour the replacement of original acidic pore water with more alkaline brackish to hypersaline brines (Fig. 12.72).

Saline-alkaline lake chemistry evolves through time. Clinoptilolite forms early or more marginally in the region of more dilute waters, which tend to contain Ca^{++} along with K^{+} and Na^{+}. As the lake waters become more alkaline, due to ongoing evaporation and precipitation of Ca^{++}- bearing minerals, chabazite, phillipsite and erionite become stable digenetic products. The proportion of clinoptilolite decreases as lake waters become more enriched in K^{+}. As the waters continue to evolve and become richer in Na^{+}, analcime becomes stable (Fig. 12.71). This creates a bull's-eye pattern of

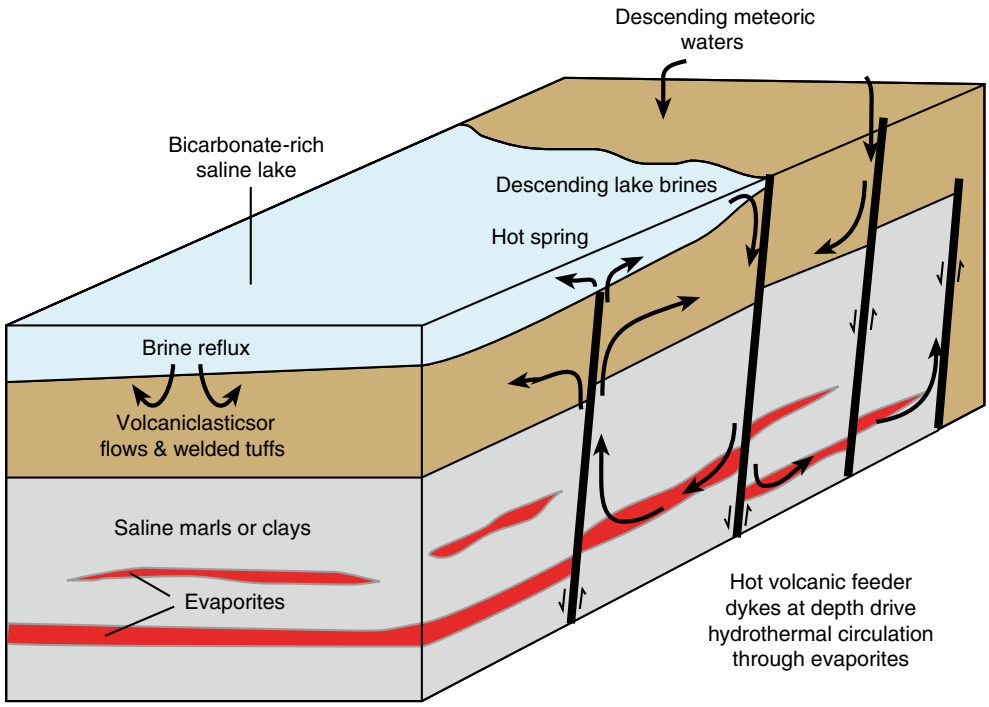

Fig. 12.72 Schematic showing possible circulation mechanism in a saline lacustrine system where volcanics are altering and weathering to various zeolites

zeolites in the saline lake. Phillipsite is stable at lower silica activities, in equilibrium with quartz, while erionite requires silica activity equivalent to cristobalite. Erionite, phillipsite and clinoptilolite are replaced by authigenic orthoclase (K-feldspar) where the K^+ concentration is high.

Zeolites can also form rapidly in alkaline soils not directly flushed by lake waters, but wherever vadose flushing tends to reduce the amount of acidic pore water (Hay 1963; Renaut 1993). The reaction of volcanic glass with crossflowing water can itself conducive to a rise in pH as the dissolution mechanism involves cation exchange reaction at the glass surface, whereby H_3O^+ enters the glass from the solution, while Na and K enter the solution from the glass (Casey and Bunker 1990).

Saline lacustrine zeolites are commonplace in: (1) endorheic alkaline basins in block-faulted terrains (such as the Basin and Range province of the USA; Sheppard and Gude 1968), (2) in trough valley depressions associated with rifting (such as Lake Magadi or Lake Bogoria in the Eastern Rift Valley of Kenya; Surdam and Eugster 1976), or (3) in Tibet-type grabens forming depressions in compressional terrains (such as Emet and Kirka basins, Turkey; Gundogdu et al. 1996). Most saline Neogene basins that retain exploitable volumes of zeolites still retain large volumes of highly reactive, silica-rich, vitric, volcanic material and evaporite beds. Bedded evaporite levels or their dissolution residues in a volcanic terrain are the product of a density-driven through-flushing brine system that displaced the original acidic waters. Hence, in terms of exploration for zeolites, evaporite horizons are excellent pointers in a basin to a level in the stratigraphy where ash alteration and zeolites are likely.

Zeolites precipitate in volcanic hosts in timeframes measured in thousands to hundreds of thousands of years, depending on brine alkalinity, the precursor mineralogy and the climate (typically semi-arid rather than hyperarid). Groundwaters driving zeolite formation in saline settings are typically sodium-rich, often with elevated carbonate-bicarbonate contents and a pH level maintained above 9 (soda lakes). Favorable hostrocks are freshly deposited rhyolitic to dacitic, vitric tuffs, especially those levels of the volcaniclastic succession time equivalent to alkali-rich saline mudflats and saline pans. Saline aluminosilicate gels (kenyaite, magadiite) can form pointer minerals at these levels and can act as zeolite precursors. Associated saline rocks can be bedded evaporites (trona, halite, borate), with interlayered mudstones, oil shales, diatomites (which can be an additional silica source in many alkaline lakes), bedded or nodular Magadi-style cherts and volcaniclastic conglomerate/sandstone.

Zeolitic alteration haloes in exposed marginward saline sediments of Lake Bogoria in the Kenya Rift Valley provide a useful Quaternary analog for many older saline lacustrine zeolites (Renaut 1993; Owen et al. 2008). Late Quaternary fluviolacustrine siltstones, mudstones and claystones (Loboi Silts) make up the northern margins of this saline, alkaline lake and contain up to 40 % authigenic analcime and minor natrolite (Fig. 12.73a). The zeolitic sedimentary layers are reddish brown and up to 1 m thick. The amount of analcime increases upward in the profile, but decreases with distance from the saline lake (Fig. 12.73b). Altered sediments hosting the zeolites show many pedogenic features including; zeolitic

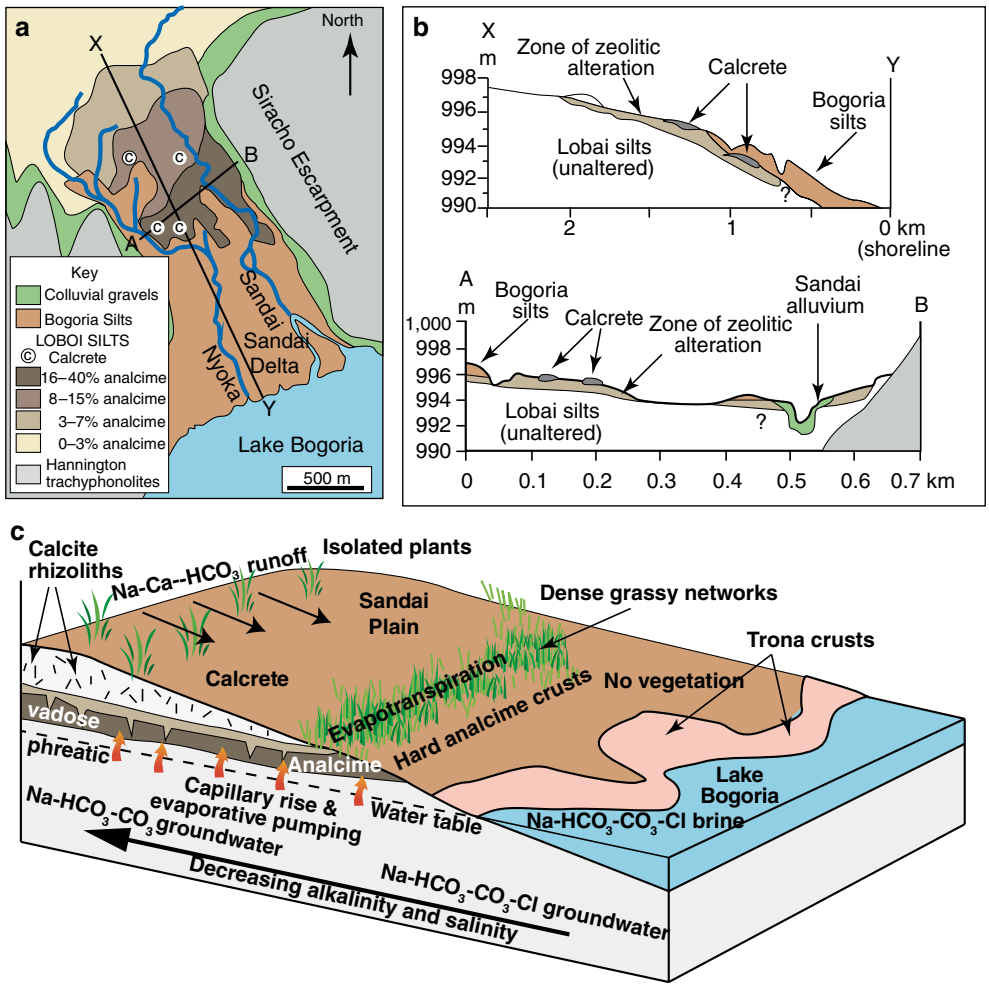

Fig. 12.73 Lake Bogoria, African rift. (**a**) The Sandai Plain, showing the sediment distribution and the variation of analcime concentration in the upper 10 cm of the Loboi Silts. (**b**) Cross-sections show thickness of zeolitic alteration and relationship of the zeolitic profile to the Bogoria Silts. (**c**) Schematic showing zeolite and rhizolith formation on Sandai Plain. Saline, alkaline groundwater is subject to capillary rise and evaporative pumping. In upper profile vadose waters react with labile clastics to produce zeolites. Infiltrating Ca-bearing surface waters precipitate calcite upon mixing with saline alkaline waters, or following evaporative concentration and CO_2 degassing (After Renaut 1993; Owen et al. 2008)

root mats, rootmarks, concretions and carbonate rhizoliths. Residual patches of calcrete locally cap the zeolitic rocks. The zeolitic profile about the edge of Lake Bogoria is interpreted as an exhumed palaeosol, which defines a former landsurface on the saline mudflat of the paleolake, no some 10 m above the present water level.

Analcime in the Bogoria mudflat is made up of submicroscopic (0.5–2.5 μm) subhedral and euhedral crystals, which have an average Si/Al ratio of 2.33 (as determined by X- ray micro-analysis) or 2.18 (as determined from the d-value of analcime peak). Analcime formed diagenetically in these lake-marginal sediments via reaction of silicate detritus with alkaline Na_2CO_3 rich pore waters, which had concentrated during sabkha-like capillary evaporation and evapotranspiration.

Poorly ordered clay minerals were probably the main matrix reactants. Authigenic illite may have been a byproduct of the reactions forming the analcime. The saline pore waters of the mudflat probably supplied additional Na, and possibly K and SiO_2 to the process of zeolitisation. Calcrete and rhizoliths formed during or shortly after the main period of zeolitisation with the Ca sourced by dilute runoff and seepage waters (Fig. 12.73c). Authigenic smectite was precipitated in open pores following analcime formation. Zeolites have formed in similar saline mudflat settings in other nearby alkaline lakes such as Lake Magadi, where zeolites are associated with magadiite nodule.

Microcrystalline zeolite-bearing vitric tuffs, chiefly composed of analcime, chabazite, clinoptilolite, mordenite, phillipsite and sometimes erionite, are typical of mined saline lacustrine zeolites worldwide. Ore deposits are typically layered and may consist of one to several stacked zeolite layers separated by sub-economic or barren beds. Cutoff grade for zeolite ore varies greatly depending on mineralogy and cementation intensity. For example, a 10–20 cm thick ore bed at Bowie in North America contains 60–80 % chabazite. This zone would not be economic if the main ore mineral was clinoptilolite. Most commercial clinoptilolite deposits contain between 50 and 90 % zeolite.

Large-scale commercial exploitation of saline lacustrine zeolites currently takes place in the Basin and Range province of the United State (Surdam and Sheppard 1978), the Andes (Hartley et al. 1991) and in Tibet. For example, zeolites are extracted from saline lacustrine strata in the San Simon Valley, Arizona. The valley is underlain by 700 m of Pliocene

to Holocene flat-lying fluviatile and lacustrine rocks. Ore horizons occur within what is known as the "older alluvial fill," which is a zeolitized Pliocene tuff and part of a more regional tuff marker bed within the Green Lake Beds (Sheppard et al. 1978). Thickness of individual zeolitic tuff layers ranges from 10 cm to 10 m with areal extents from tens to hundreds of square kilometers. The most common zeolites in this succession are chabazite, erionite and clinoptilolite, with small quantities of analcime in the southern part of the deposit. Parent materials include volcanic glass, biogenic silica, clays, plagioclase and quartz. Non-zeolite authigenic minerals in the tuff include smectite clays, calcite, halite, gypsum and/or thenardite. Chabazite, the main commercial mineral, constitutes up to 80 % of the bed in the ore zone.

These zeolites crystallized after the accumulation of volcanic ash as throughflushing saline alkaline groundwaters reacted with the ash in the lake mudflat (Fig. 12.71). Factors controlling intensity of alteration in the Green Lake Beds included the original lake bottom topography, depth and cation content of the saline-alkaline lake waters and proximity to postdepositional erosion surfaces (Eyde and Eyde 1987). Zeolitic alteration ceased when an extensive system of younger paleochannels deeply eroded the Green Lake Beds. Erosion indicates a change in the base level and a fall in groundwater level that removed the beds from the zone of active saline flushing. Erosion left only a few dissected remnants of the original tuff marker so that the "high grade zeolite bed" now outcrops in the various channel walls, where it is now mined. Former channels and the Green Lake Beds are now overlain by a section of halite-cemented brown mudstone known as the Brown Lake Beds, which largely prevented any later surface-driven meteoric alteration of the zeolites.

Throughflushing saline waters will first generate analcime and then K-feldspar with more complete alteration. In ancient zeolitized lacustrine deposits this is reflected in a commonplace transition from unaltered finely crystalline volcaniclastic glass and tuff near a palaeostrandline, through a series of immature alkaline silicic zeolites to analcime to potassic and sodic authigenic feldspars in the lake centre (Eugster 1986; Hay et al. 1991). Volcanic glass is initially converted to zeolites such as clinoptilolite and mordenite before being altered to analcime. Under ultrasaline conditions when the K/Na activity ratio is sufficiently high (from earlier halite precipitation), analcime is then converted to K-feldspar. Tuff beds deposited during the most saline and alkaline phase of Lake Gosiute in the Eocene Green River Formation typically exhibit such K feldspar alteration. Beds that remain soaked in somewhat less saline brines still remain at the analcime alteration stage (Smith et al. 2003).

Likewise, basin-centre Quaternary deposits in the various saline east African rift valley lakes typically exhibit more alteration toward the lake centres, suggesting that as Pleistocene saline lakes shrank and concentrated, sediments in the lowest (central) positions were more exposed to increasingly saline and alkaline fluids. For example, in Lake Naivasha, Kenya, low lake levels are represented by the presence of chabazite and phillipsite, with even greater aridity indicated by clinoptilolite and analcime (Trauth et al. 2001). Analcime is also common in sodium-rich alkaline desert soils.

Such pointers to the intensity of alteration also outline Cretaceous Lake T'oo'dichi' in the Four Corners region of the USA (Fig. 12.74; Turner and Fishman 1991). This large alkaline saline lake occupied the entire eastern part of the Colorado Plateau region during deposition of the Brushy Basin Member of the Upper Jurassic Morrison Formation. At its maximum it extended from Albuquerque, New Mexico, to Grand Junction, Colorado, and occupied a region that encompassed the San Juan and ancestral Paradox basins, making it one of the largest ancient alkaline, saline lakes known; it was more than twice the size of Eocene Lake Uinta. As yet, zeolites have not been found in sufficient quantity to be exploited in this ancient lake system.

The lake was typically shallow and frequently evaporated to dryness, although the watertable was probably never far beneath the surface and widespread bedded salt did not form (Fig. 12.74; Turner and Fishman 1991). Intermittent streams carried detritus from source areas to the west and southwest far out into the lake basin, a reflection of a low depositional gradient and the ephemeral brackish nature of the lake. Prevailing westerly winds carried silicic volcanic ash to the lake basin from an arc region to the west and southwest. A lateral hydrogeochemical gradient, characterized by increasing salinity and alkalinity from the margin of the lake to the centre, developed in pore waters of the lacustrine sediments and resulted in alteration of the ash to a variety of authigenic minerals that define concentric zones within the lake basin. The basinward progression of diagenetic mineral zones is smectite to clinoptilolite to analcime ± potassium feldspar to albite in the lake centre. A concomitant lateral zonation of mixed-layer illite/smectite developed, from highly smectitic in the outermost zones to highly illitic in the central zone (Fig. 12.74).

Authigenic albite and illitic mixed-layer clay, minerals typically thought to require elevated temperatures for formation in non-saline burial settings, crystallized during early diagenesis at syndepositional temperatures in the lacustrine sediments of Lake T'oo'dichi'. Other examples of syndepositional authigenic albite are documented in saline lacustrine sediments of the Eocene Green River Fm. (Cole 1985), Miocene tuffs near Boron, California (Williamson 1987) and albite rims to evaporite pseudomorphs in the Triassic lacustrine mudstones of the Passaic Formation of the Newark Basin (El Tabakh et al. 1997).

Throughout burial, and on into the zone of metamorphism, zeolites can continue to react with evolving pore

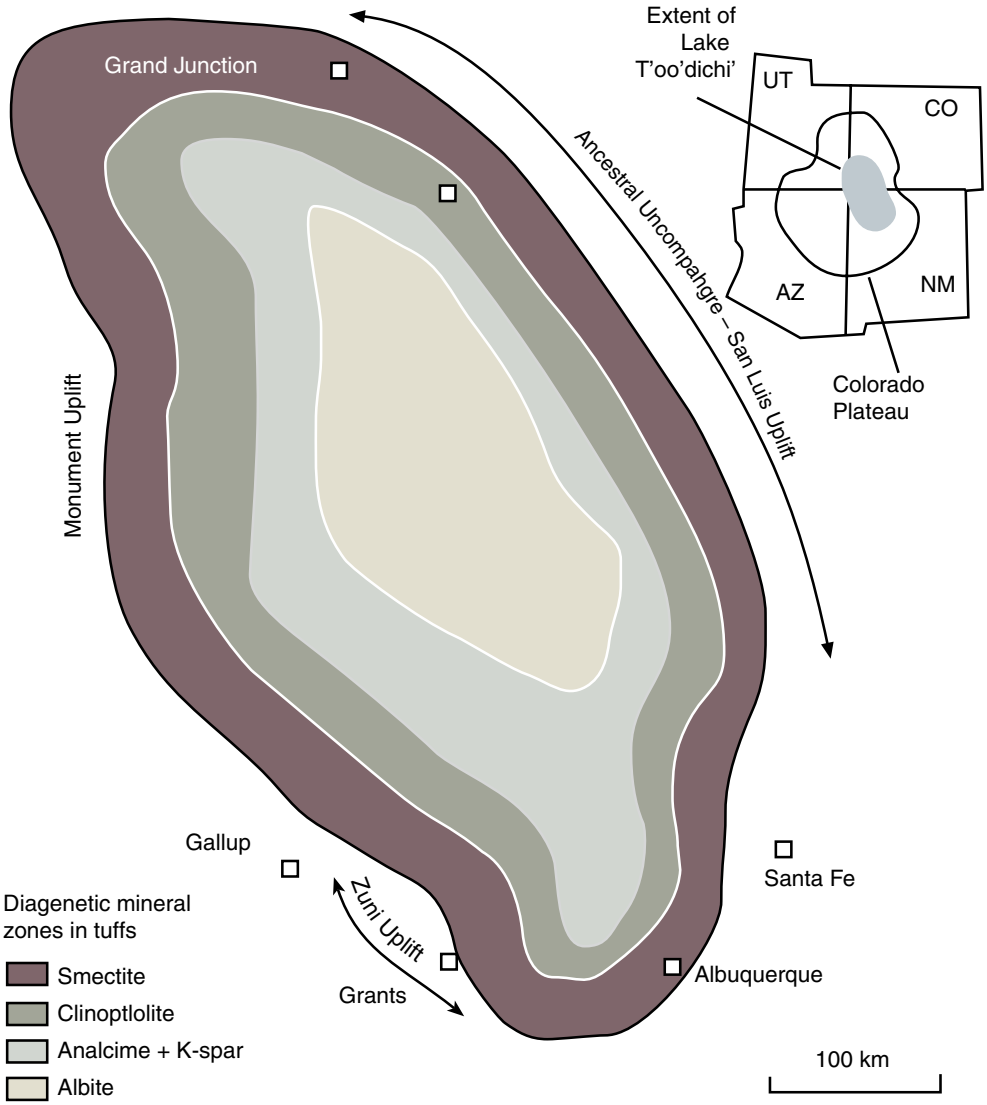

Fig. 12.74 Basinward progression of concentric alteration haloes in the tuff lithofacies in the lacustrine Brushy Basin Member of Jurassic Lake T'oo'dichi' (After Turner and Fishman 1991) This ancient alkaline lake occupied the combined San Juan-Paradox Basin area and was bound by structurally active uplift areas (related to an active volcanic arc that lay to the west)

fluids as new minerals are formed by the replacement of earlier zeolites. Ongoing alteration in deep burial also explains the abundance of albitised metasediments and metavolcanics in meta-evaporitic settings and the loss of natural zeolites with increasing geological age.

But not all sodic zeolites in saline lakes need labile volcaniclastic precursors. Analcime occurs in the basal anhydrite of the Navarra potash in a late Eocene basin that contained no volcaniclastics. Rosell and Orti (1980) interpreted it as a result of the interaction of highly concentrated brines with detrital clays. Likewise, authigenic analcime (±morganite) is forming today in early to mid Pleistocene playa muds in deflation playas, such as Lake Lewis in central Australia,. The zeolites are hosted in endorheic saline clays, within saline hydrologies that do not interact with labile volcaniclastics (Fig. 12.75; English 2001). Lake Lewis playa in the Northern Territory lies in a hydrologically closed intermontane basin in a low relief terrain in which clay-rich paleolacustrine sediments are infused with highly evolved sodic brines. Near-stagnant lake waters, fed by groundwaters flowing through the Proterozoic Arunta granite-gneiss terrain and through arkosic alluvium and its weathering products, source the silica and sodium needed to precipitate analcime. Supersaturation of groundwaters with respect to SiO_2 and the availability of catalytic ions, coupled with high rates of evaporation, favours precipitation of opal and chalcedonic silica from solution near the groundwater discharge zone about the lake strandline. Moganite, a distinctive silica polymorph that is commonly associated with evaporites, is amongst the various silica species precipitated in association with the analcime (Chap. 7).

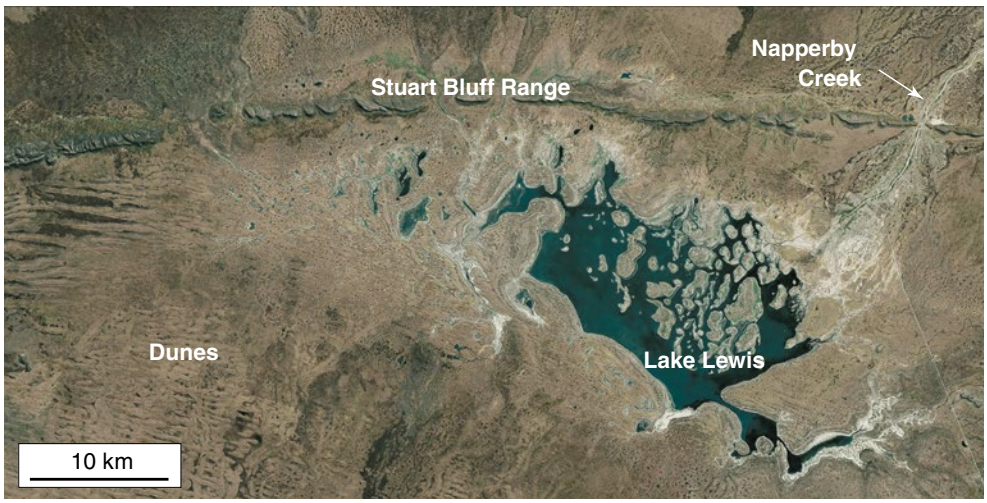

Fig. 12.75 Lake Lewis, Central Australia, where analcime and moganite are precipitating in the Early to Mid Pleistocene Anmatyerre clay (Bing® image mounted and scaled in MapInfo)

Downgradient from the zone of silica precipitation, beneath the playa proper, the brines become SiO_2-deficient. Long periods of weathering and diagenesis of the lacustrine clays, immersed in semi-stagnant brines, has transformed detrital minerals into amorphous or gelatinous aluminosilicates. Hence, various aluminosilicate phases have become metastable in the longterm presence of evolved SiO_2-deficient interstitial brine. Analcime is stable in this relatively stagnant Na-rich brine and is crystallizing authigenically below the watertable from these amorphous and gelatinous aluminosilicates in the more central parts of the lake depression. No volcanic rocks or pyroclastic sediments are involved in this diagenetic occurrence of analcime. The appearance of analcime in Lake Lewis probably commenced within the last 100,000 years and is ongoing (English 2001).

Summary

The greater majority of nonpotash bedded salt resources (borates, sodium carbonates or sodium sulphates) accumulated in continental lacustrine or playa settings. They owe their existence to the unusual ionic compositions that come from groundwater leaching under highly arid conditions, in appropriate bedrock terrains. Quaternary continental examples have same scale and same ionic proportions in the brines as their ancient lacustrine counterparts (Chap. 5).

Simple marine geochemistry shows that these types of lacustrine deposits can not form by simple evaporation of Phanerozoic seawater. Phanerozoic seawater simply never had the ionic proportions necessary to precipitate borates, nitrates, sodium carbonates or sodium sulphates. This chemical evolution can only happen with nonmarine brines, typically where nonmarine waters drain into an arid, highly isolated depression in the continental landsurface. The effect of isolation and concentration in producing appropriate brine chemistries is often enhanced by the presence of nearby mountains. Mountains act both to form a rain shadow zone and to create topographic head, which drives deep circulation of meteoric groundwaters. In endorheic continental lakes in both extensional rift valleys and collision belts, the creation of the mountains is tied to an active tectonic regime and volcanism, which in turn tends to create enhanced hydrothermal circulation and labile volcaniclastic aquifers in hydrographically closed depressions where the saline waters are ponding. Borates, for example, form via the lacustrine concentration of spring inflows that have passed through active volcanogenic terrain. Likewise, the trona beds of Lake Magadi reflect nonacidic groundwater and hydrothermal/basin brine leaching (low sulphate, high bicarbonate waters).

Most of the non-potash deposits discussed in this chapter are nonmarine lacustrine associations, and so are a distinct association from the ancient marine-fed potash deposits discussed in the preceding chapter (Table 12.21). This situation is most obvious in the various South American salars that contain economic brine associations of boron and lithium. They lie in intermontane depressions with floors that are thousands of metres above sea level, yet they drain and pond hypersaline waters for long periods of time, sufficient to allow salt beds hundred of metres thick to accumulate. Likewise, mountains and volcanoes influenced local climate and helped create the Neogene successions of NE Turkey and the Basin and Range playas in the USA. Long-term aridity for more than 6 Ma tied to rain shadow effects, in combination with offshore upwelling, explains the hyperarid nitrate regolith of Atacama Desert.

The high solubility of the nonpotash salt resources, and their formation as lacustrine, not marine, precipitates explains their limited thicknesses, their mostly Neogene ages and their relatively small size compared to marine evaporites (Table 12.22). Self-evidently, a lacustrine depositional setting, with its inherent lack of a huge isochemical brine reserve (seawater), means

Table 12.22 Summary of non-potash evaporite characteristics

	Commodity	Hydrologic situation	Brine source	Depositional associations	Exploration characteristics
NONMARINE (lesser ancient evaporite systems)	Borate	Suprasealevel intermontane hydrographically closed continental depressions ACTIVE SAME-SCALE AS PRE-QUATERNARY COUNTER PARTS	Nonmarine brine, typically with volcanogenic leachates	Neogene lacustrine underfilled basin in cooler but arid conditions, generally in high elevation intermontane fault-bound depressions. A few borate deposits also found in older meta-evaporitic and igneous associations	Continental interior lacustrine. Best developed in Neogene continent-continent collision belts and/or continent/ocean plate subduction zones with active magmatism. Not located within or atop ancient marine mega-evaporite basins
	Sodium Sulphate (salt-cake)		Nonmarine brine	Neogene lacustrine underfilled basin. (1) Solar concentration of surface brines with associated increasing temperature in endorheic continental playa depressions, (2) The winter onset of saline brine cooling in local depressions	Continental interior lacustrine. Not located within or atop ancient marine mega-evaporite basins. Basin drainage must be high sulphate, e.g. from dissolution of older evaporites, cation exchange, volcanics or pyrite oxidation.
	Sodium Carbonate (soda-ash)		Nonmarine brine with elevated CO_2 levels	Neogene lacustrine underfilled basin. (1) Eocene-Miocene intermontane depressions in actively subsiding foreland depressions with relatively high relief surrounding drainage terranes, (2) Quaternary lacustrine deposits at termini of hydrographically-closed drainages in: (a) Intermontane depressions surrounded by relatively high topographic relief and, (i) hot arid conditions or, (ii) high altitude conditions. (b) Terminal pans in lower-relief hot arid cratonic settings where $NaCO_3$ resource resides within annually replenished $NaCO_3$ brines, often in combination with $NaSO_4$.	Continental interior lacustrine. Not located within or atop ancient marine mega-evaporite basins. Sodium must be present (ionic exchange) with appropriate labiles in abundant quantities along with elevated levels of CO_2. Nahcolite was a typical bedded co-precipitate with trona during the peak Eocene greenhouse period when atmospheric CO_2 levels more than double those of today. Trona-nacholite, along with halite and not gypsum, were the dominant Early Archaean evaporite salts.
	Lithium Brines		Nonmarine	As for borates	As for borates

(continued)

Table 12.22 (continued)

	Commodity	Hydrologic situation	Brine source	Depositional associations	Exploration characteristics
MARINE (dominant ancient evaporite systems)	Mega-evaporite (especially thick halite intervals) but also mega-sulphate and mega-potash beds	Subsealevel, hydrographically-closed marine-seepage depressions, occasional breaching of barrier NO CURRENTLY ACTIVE SAME-SCALE QUATERNARY COUNTER PART	Marine brine. Alternating $MgSO_4$ and $CaCl_2$ ocean chemistry in the Phanerozoic tied to variable rates of seafloor spreading and platform dolomitisation	Continent-continent proximity. Megahalite and megasulphate beds deposited in: (1) Soft suture collision basin (2) Opening rift to incipient ocean basin (3) Intracratonic sag basin (4) Strike-slip depression (smallest of the associations)	Marine mega-evaporite basins in zones of appropriate tectonics and climate, Late Neoproterozoic to Neogene at plate margins or intracratonic sags. Thick halite beds in this association subject to early halokinesis due to syndepositional tectonics, rapid subsidence and sediment loading (except in intracratonic settings where superimposed tectonism drives salt flow).
	Mega-sulphate			(1) Periplatform saltern and mudflat beds intercalated with open marine platform/shelf carbonates (2) Intracratonic sag with 10 m + thick sulphate typically intercalated with halite and evaporitic carbonates of equivalent or greater thickness	Epeiric platforms favouredby greenhouse eustasy.
HYBRID	$CaCl_2$ brines	Subsealevel or basinal	Marine/hydrothermal	Low Mg $CaCl_2$ salts in underfilled continental lacustrine depression. High Mg $CaCl_2$ salts in marine evaporite association	Typical subsurface connate association with marine evaporites, especially if ancient salts from a $CaCl_2$ oceans are present.

total bed thicknesses and salt volumes will always be less than that of bedded salts accumulating in marine-fed saline giants. Inherent high solubility of lacustrine salt beds (trona, mirabilite, glauberite) in a hydrology susceptible to drastic changes in water supply and watertable, means lacustrine salts are rarely found in rocks with pre-Cenozoic ages. The Proterozoic borates of Liaoning Province are an obvious exception. The impervious nature of this succession, its metavolcaniclastic host, and the formation of a silicified envelope around the borates, relatively soon after their precipitation, allowed these salts to be preserved, although as a meta-evaporite.

As a rule of thumb for salt exploration for borates, soda ash, salt cake, lithium brines and zeolites in a frontier area, those arid basins with post Mid-Tertiary ages should be considered much more prospective than any older basins. You should not expect to find trona or thenardite or other soluble lacustrine phases preserved in large volumes in Palaeozoic saline successions and will probably not find them at all in Precambrian strata, at least not without a meta-evaporite silica-genesis and a co-transformation of host mineral phases into tourmalines white micas and scapolites.

Solution Mining and Salt Cavern Usage

13

Introduction

Salt solution mining is just what it says, the mining of various salts by dissolving them and pumping the resulting brine to the surface where it is concentrated or processed to recover the desired chemical products. Actual dissolution and recovery methodology is predicated on the solubility of the targeted salt, A "rule of thumb" in the solution mining industry is that every 7–8 m^3 of freshwater pumped into a cavity will dissolve 1 m^3 of halite. Water or undersaturated brine is injected through a purpose-designed well drilled into a salt mass to etch out a void or cavern. The resulting "almost saturated" brine is then extracted for processing. The technique usually targets salts at depths greater than 400–500 m and down to 2,000 m (Fig. 13.1). The current deepest salt solution operation is in the Barradeel concession in northern Netherlands in Zechstein Z2 salts and operating at depths around 2,800 m (Geluk et al. 2007). At depths greater than 2,000 m ongoing salt creep tends to reduce cavern size. Some operating brinefield caverns are as shallow as 150 m, but this can lead to catastrophic chimneying and stoping in sediments above cavity. With deeper operations the landsurface tends to subside into a bowl of subsidence, as it does above many conventional mines. Cavern shape and the upward rise of the cavern roof is today controlled by an inert fluid blanket pumped in and maintained at the top of the zone of active brine creation. Early solution wells did not use this blanket technology. In the 1800s and extending into first half of last century many brinefield operators perceived surface sinks, collapses and regular abandonment of caved wells as normal, during the operational life of a saltfield. Attitudes in the mining community today, across all types of exploration and production, are much changed.

In a solution mining saltworks, where production of various chemical salts is the main aim, saline brine is withdrawn from the expanding cavern and often pumped into solar evaporation pans to manufacture salts of designated grade, mineralogy and quality. Brine product from the pans, either solids or slurries, or a brine feed direct from the solution cavern, is piped to a nearby chemical processing plant designed for particular chloralkali, magnesia or other chemical products. Wells located near the site of a chemical plant and designed to capture brine of a particular chemistry are called captive brine wells.

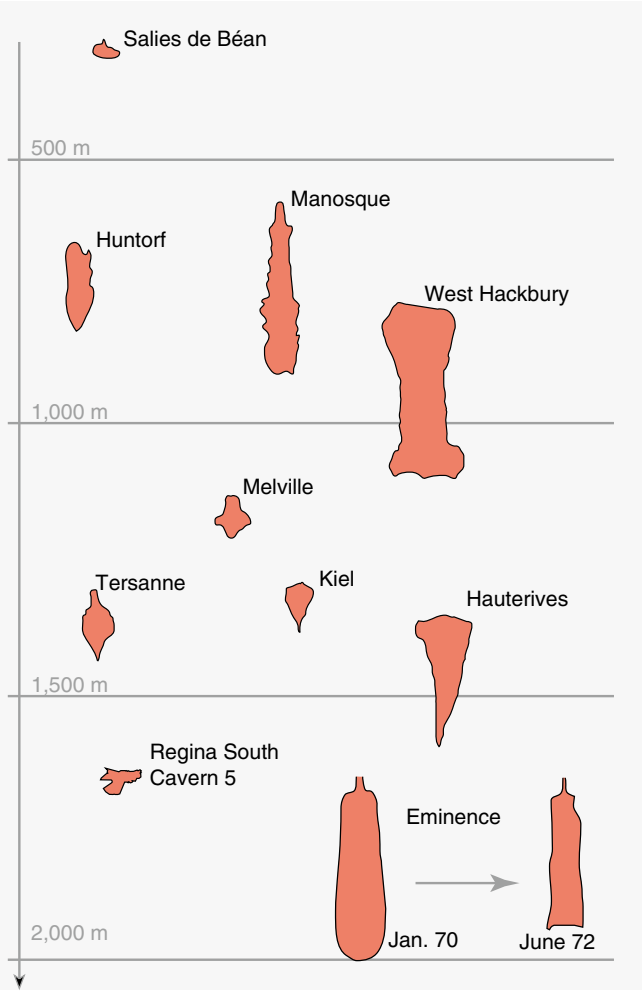

Fig. 13.1 Depth profiles of various salt caverns, all are in salt domes except Regina South and Salies de Bean, which are in bedded salt. Eminence shows the volume changes after 18 months due to salt creep (see Fig. 13.55)

© Springer International Publishing Switzerland 2016

J.K. Warren, *Evaporites: A Geological Compendium*, DOI 10.1007/978-3-319-13512-0_13

The advantage of solution mining over conventional salt mining or surface evaporation pans is that product quality and the extraction operation is not as subject to the vagaries of climate or rock strength. Specific subsurface mineralogies can be targeted by the well bore to obtain a specific feedstock or chemical product, without the need to get men and equipment from the surface to the mine face. Solution mining can exploit folded and disturbed beds or deep-lying salt strata, situations not easily mined using conventional techniques. The main limitation of the solution mining method is an inherent outcome of a need for a significant volume of undersaturated water to be pumped into a salt bed and returned to the surface for processing. There is always a need to manage spent brine in an environmentally aware manner (Yanosky and Kappel 1997).

As well as halite, which historically has been the most common commercial target, other solution-mined salts include; potash (sylvite, sylvinite, carnallite), trona/nahcolite (sodium carbonate/sodium bicarbonate), borates (borax, ulexite, colemanite), sodium sulphates (mirabilite, thenardite) and magnesium chlorides. Today the cavern produced by solution mining can have a greater value than the extracted brine, particularly for a ubiquitous salt like halite. If appropriately designed, a cavity can be used for hydrocarbon or waste storage and even for energy storage/generation. In the future it is likely salt caverns will be used for hydrogen storage as part of an energy storage grid, fed by renewable energy sources (e.g., storage of energy output from wind and solar energy; Ozarslan 2012).

Diapiric salt masses tend to be the preferred medium for solution mining as the salt mass undergoing designed dissolution is typically large, thick and tends toward internal homogeneity. This makes it easier to purpose design in terms of both cavern shape and volume. Bedded salts tend to be less vertically homogenous and so more subject to differential caving and roof collapse in the life of a cavern. Ongoing improvements in directional and horizontal drilling mean bedded deposits can now be more reliably exploited. Rather than the brine product, more and more the cavern itself and its use as a storage vessel, is the rationale for solution mining. Many salt masses, especially in regions of relatively shallow salt or hydrocarbon interest have been drilled and exploited for more than a century and a half. In the 1800s and the first half of last century, well positions, completions and abandonment procedures were poorly documented and controlled. This has led to many of ground stability problems discussed later in the chapter.

The Solution Mining Process

Solution mining is an alternative to mechanical excavation of salt ores (Richner et al. 1992). Since most waste components in solution mining are not soluble they are left behind to settle to the bottom of the expanding cavern, as the brine product is removed to a surface processing facility. Unlike conventional mining, there are no large above-ground waste piles and tailings impoundments. However, the possibility of collapse and karstification atop brinefields means contamination and brine leakage into nearsurface and surface waters are potential problems. Monitoring of landsurface stability reduces the possibility of uncontrolled cavity collapse and associated environmental degradation.

History of Salt Solution Wells

The Chinese have been using brine wells and a form of salt solution mining, for more than 2,000 years (Flad et al. 2005; Kuhn 2004; Zhong and Huang 1997; Vogel 1993; Yoshida 1992; Yuanxiong and Chengxun 1983). Designed-use shaft wells were sunk as early as 220 BC in the Szechuan and Yunnan provinces (Table 13.1). By 1035 AD the Chinese in the Szechuan area were using percussion drilling to recover deep brines, a technique that would not come to the West for another 600–800 years (Fig. 13.2). European travellers to China in 1400–1700 AD reported salt and natural gas production from dense networks of brine wells. Some of the wells had been sunk deeper than 450 m and at least one well was more than 1,000 m deep (Table 13.1). Salt production in China at that time was prodigious, with more than 10,000 wells in operation. Marco Polo reported annual production in a single province of more than 30,000 t.

Practically all the materials used in Chinese brine recovery wells, including ropes, casing and derricks, were made from wood or wood fibre, mostly bamboo. Bamboo is salt resistant, while salt and brine kills microbes and algae that would otherwise cause it to rot. Pipeline joints were sealed by mud or a mixture of lime and tung oil. Manpower was used both to power the drilling process and to raise the brine. A sharp iron wedge bit (resembling a spade or shovel) was suspended on a levered rope at the end of a bamboo cable so that it kept pounding and pulverising the rock at the bottom of the drill hole (Fig. 13.2a inset). At the surface the drilling

Table 13.1 Maximum well depths attained since 221 BC using bamboo drilling technology in China

Royal empire	Time period	Well depth (m)
Qin Dynasty	221–206 BC	30.0
Han Dynasty	206 BC–220 AD	138.2
Tang Dynasty	618–907 AD	248.8
Song Dynasty	960–1280 AD	276.5
Ming Dynasty	1368–1644 AD	311.0
Qing Dynasty	1736–1796 AD	530.0
	1796–1821 AD	797.8
(Xinghai well)	1821–1851 AD	1,001.4
	1851–1861 AD	1,045.0
	1875–1908 AD	1,119.0

After Ruilin (1997)

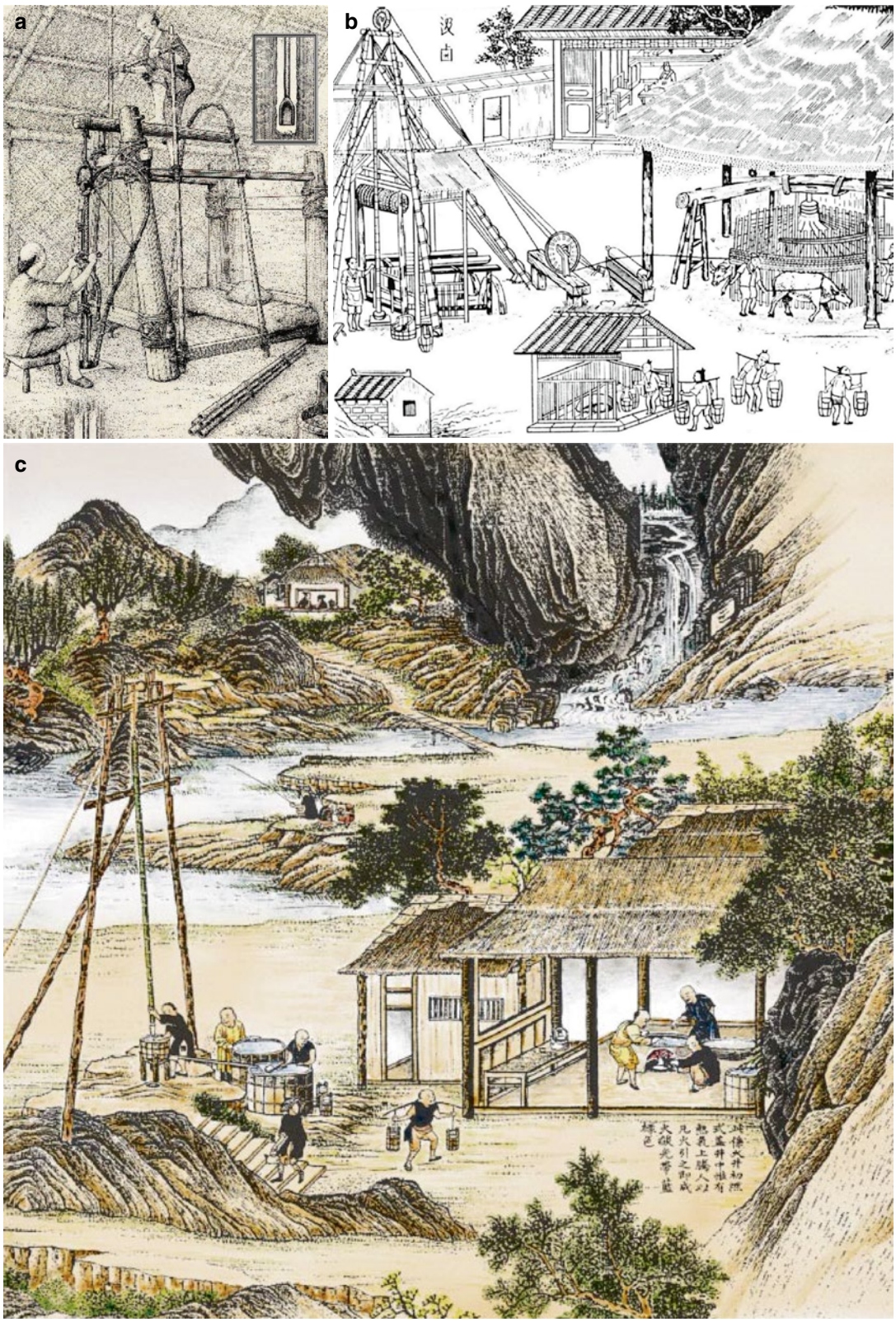

Fig. 13.2 Solution mining and brine recovery technology in saltworks of the Szechuan region of China in the mid-eighteenth century. (**a**) Man-powered percussion drilling using a human-weighted lever system to raise the drill bit. *Inset shows* typical spade like iron drill bit that was suspended on bottom of bamboo drill string. (**b**) Animal-powered hoisting of brine from a salt well showing use of flexible bamboo cable wrapped on spindle. (**c**) Transfer of brine to iron pans for boiling of the brine product and recovery of salt. Boiling plants often using piped natural gas (No bamboo piping from well head to boiling house is shown in this image) (From the annals of Salt Law of Sichuan Province)

tool and drill string (flexible bamboo cable) were suspended from the end of a "spring pole." The raising and lowering of the percussion head at the base of the hole was supplied either by workmen running up a short incline and jumping down, one after the other, onto a small platform attached to the spring pole or by a single workman alternately standing on a wooden lever pole and stepping off (Fig. 13.2a; Deutsch 1978). As the drill assembly was raised after each descent another worker rotated the drill string assembly so it would strike the base of the hole in a different position. After 3–5 years, a successful well could have penetrated up to several hundred metres to intersect a brine or natural gas target. In 1835, the Xinhai well reached a depth of more than 1 km using this bamboo percussion technology (Table 13.1). Interestingly, the deepest percussion well in Europe around the same time was in Germany, where a percussion well reached 535 m in 1835. A likely reason for this shallower depth was that the Europeans used rope to suspend the drill tool, while the Chinese used flexible bamboo cable.

Periodically, pulverised rock was bailed from the base of the deepening hole. This was done by pouring water down the hole to create a slurry. The slurry was extracted by lowering a weighted hollowed-out bamboo pipe with an interior leather flap on its lower end. When lowered into the slurry the flap would open and jigging the pipe up and down when on the base of the hole forced rock slurry into the pipe. Then the pipe was raised with the weight of the slurry forcing the leather flap closed.

Later, once the hole had achieved its target depth, brine in the Szechuan area was often recovered from the well by the same means, namely, using a long bamboo bailer with a leather valve at its bottom. When a brine-filled tube was suspended over a nearby storage tank, a poke from a stick would open the valve releasing the brine (Fig. 13.2b). Alternatively, a section of bamboo with pith left in place was cut by a series of holes located just below each pith level creating a series of small buckets. The weighted bailer was lowered into the brine pooled at the base of the brine well and brine flowed into the holed pith sections. Then the bailer was raised and inverted over the storage tank.

Often the storage tank was connected by bamboo piping to the salt boiling house (Fig. 13.2c). Other bamboo pipes, located just below a natural gas wellhead were used to capture escaping methane and pipe it to the boiling house to fire the salt crystallisers (iron pans).

From the flexible bamboo pipe (cable) technology developed at the Szechuan brine works, Chinese throughout the country learned to build irrigation and plumbing systems (Kurlansky 2002; Zheng and Palmer 2009). Farms, villages, and even houses were fitted with bamboo plumbing. By the time of the Norman conquest of England, Su Dongpo, a bureaucrat born in Sichuan, was building sophisticated bamboo urban plumbing networks. Large bamboo water mains were installed in Hangzhou in 1089 AD and in Canton in 1096 AD. Holes and ventilators were installed for dealing with both blockages and air pockets.

In Europe, near Lorraine, France, much simpler designed-usage brine shaft wells were sunk by hand as early as 858 AD (something the Chinese had been doing since at least 250 BC). In 1381 AD the Duke of Lorraine, the Bishop of Metz and the Duke of Bar, formed a salt cartel that operated brine wells at Chateau-Salins and Salonne (Deutsch 1978). By 1740 brine was raised in the region using horse-driven pumps and in 1758 steam-driven pumps were drawing brine from wells that were more than 100 m deep. By 1839 salt was being directly mined in an underground operation at Dienze that employed over 400 miners. By 1830 in the USA there were more than 60 brine wells in operation in Kanawha region near the confluence of the Kanawha and Ohio rivers. Numerous brine wells were in operation in New York State by 1880, while large-scale brine recovery operations in the various playas of the Basin and Range were underway by the early 1900s. Today, steel-cased brine wells are consistently drilled to depths of more than 1–2 km to extract brine product or to excavate custom-built salt caverns for hydrocarbon or waste storage.

Well and Cavern Design

The design of a salt solution well consists of two or more columns of steel pipes (casing strings) with the smaller inside the larger. Fresh water or undersaturated brine (feed solvent), needed to drive the solution process in an expanding cavern, is pumped into the well to create a cavity in the targeted salt. The resulting brine is then returned to the surface for processing and recovery.

The first step in solution mining salt is to drill an appropriate diameter borehole, large enough to accommodate all the required pipes (casing). This means solution wells are wider than most oil and gas or water wells. Near the surface, the borehole is widest to allow for installation of several concentric layers of pipe casing (Fig. 13.3). The outermost layer of casing, known as the surface casing, is cemented in place to prevent any leakage and contamination of nearby groundwaters. Surface casing does not typically extend all the way down to the cavern roof. The final casing string (or long string casing), which is also cemented in place, is set at some depth below the top of the target salt so that during dissolution a reasonable thickness of salt remains in place as a salt roof to the expanding solution cavity. In modern wells there is another string immediately inside the outer casing string that controls the thickness of the fluid blanket.

Generally, one or more non-cemented casing strings, the tubing strings, are placed inside the final casing string. In modern designed-use caverns, non-cemented casing or

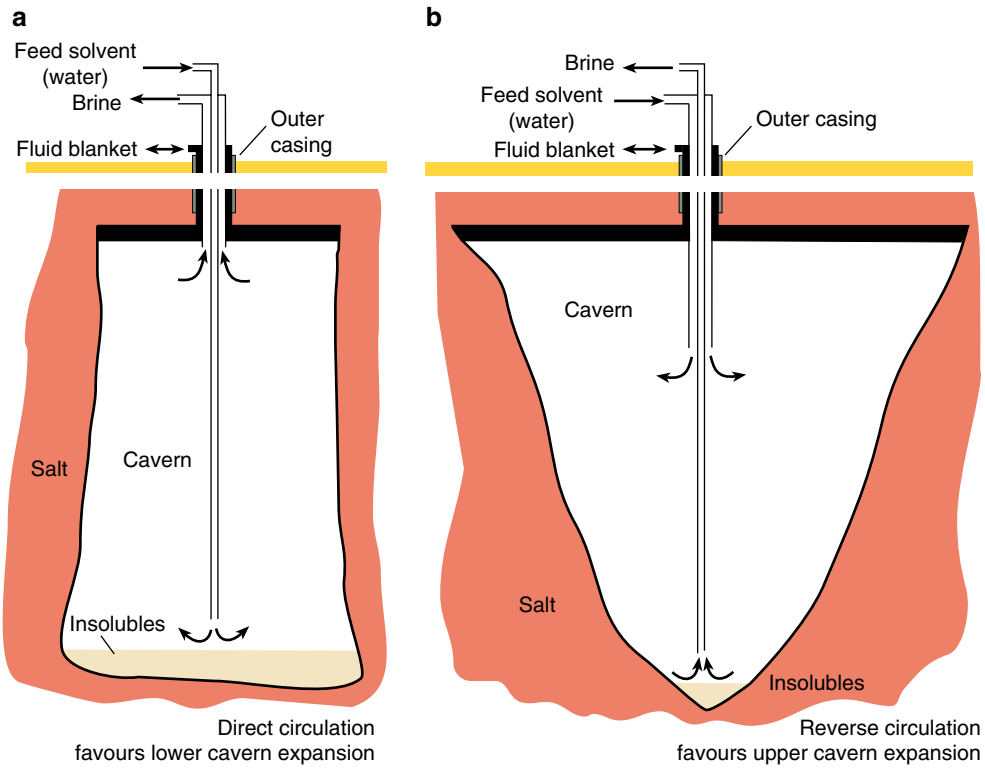

Fig. 13.3 The solution mining process. (**a**) Direct brine circulation where feed solvent is injected through the tubing string and brine is withdrawn through the annular space between the tubing string and the final casing. Cavern shape tends toward cylindrical with slightly expanded lower section. (**b**) Reverse-circulation where the feed solvent enters the cavity through the annulus and brine is withdrawn through the tubing string. Cavern tends to be wider at top than base ("morning glory"). In both cases the outermost casing allows feed of the blanket solution into the uppermost part of the cavern, so protecting the cavern roof. Varying the volume of blanket in the cavern can be used to help shape the cavity

tubing strings first extend to a depth near the planned based of the cavern. Under this design scenario, strings can be rotated and raised (snubbed or pulled) as the cavern grows and the bottom fills with insoluble debris. Depending on the size of the cavern and the amount of impurities present, more than 20 m of impurities (dolomite-anhydrite residues and fragmented roof blocks) can sit on the bottom of an active solution cavern (Crossley 1998; Tomasko 1985). Some older interconnected multi-well brinefields did not have non-cemented strings in each well.

Salt subjected to undersaturated crossflow in an expanding solution cavity tends to leach 1.5–2 times faster vertically than horizontally (fresher water is less dense than brine and tends to accumulate in the upper part of a cavity). Vertical leaching tends to be even faster if there are gas inclusions in the cavity waters, giving it even greater buoyancy. An inert low-density fluid blanket is usually pumped into a solution cavern to prevent rapid upward stoping and ultimate collapse of the cavern roof into the growing cavity, along with its cemented casing string. Roof blanketing, sonar imaging and designed cavern shaping typify most contemporary commercial solution mining operations.

Blanketing fluid is inert so it does not dissolve the target salt, and is always less dense than the feed solvent or the produced brine. It always floats to the top of the cavern where it insulates the roof from the effects of dissolution. Older blankets were one of a number of different types of oil, typically diesel or crude, but today are increasingly composed of other fluids including LPG, nitrogen and compressed air. Nitrogen and less often compressed air tend to be the fluids of choice as they do not have the environmental and safety issues associated with a hydrocarbon blanket. Generating a blanket requires the addition of a devoted column of pipes in the well string and the blanket is usually pumped in/out via the annular space between the outer and middle casing pipes (Fig. 13.3).

There are several methods for developing and shaping caverns. In the direct circulation method, feed solvent is injected through the tubing string and brine is withdrawn through the annular space between the tubing string and the final casing (Fig. 13.3a). In the reverse-circulation method, feed solvent enters through the annulus and the brine is withdrawn through the tubing string (Fig. 13.3b). As less dense water in a salt cavern tends to float on a more concentrated brine, a "morning glory" type cavity with a much wider top than base is likely to be formed by what is called reverse circulation, especially in cavities grown without the aid of a fluid blanket. A more cylindrical cavity is formed by direct circulation. During cavern excavation, the volume of the blanket fluid is increased or decreased to help shape the cavity.

Detailed discussion of the engineering aspects involved in well design and cavern shaping is largely outside the geological focus of this book. Various authors, such as Remson et al. (1966), have outlined the general procedures for controlling the shape of the solution mine cavities, and many articles, such as that of Shock (1985) and Jacoby (1974),

have been written on basic solution mining techniques for various salts. Extensive bibliographies also have been prepared on solution mining, such as those by Dahl (1985) and Nigbor (1982). Combinations of these various methods and other more complicated solution mining approaches are now well understood and can be used to obtain any desired cavern geometry or well-to-well interconnections (API 1994).

If a particular brine product is the goal of a solution mining operation, rather than the cavern itself, then the extracted brine typically is evaporated or treated at the surface to produce a crystallized product. In this case an "almost saturated" brine product is mandatory in the rising casing string. Dilute brine is too expensive to process, while supersaturated brine can block the raising string with unwanted precipitates. When a single hole solution mining well is first drilled, the flow rate through the cavity and up the pipe is usually kept very low to maintain higher levels of brine concentration. As the surface area of the cavity and the cavity volume increase with time, the extracted brine flow rate can be progressively raised. In a year or so comparatively high flow rates can be maintained. The life of a successful brine well can be quite long, up to 30–40 years. If the solution process is maintained from a single well the area around the well will eventually subside, or the borehole roof carrying the casing strings will weaken and cave, disrupting the brine flow. Even if the roof doesn't cave, salt will dissolve from around the casing string and it will eventually corrode and fall into the cavity.

Historically, until the 1950s in the West and much later in the former Soviet Union, captive wells designed for brine recovery and not for storage were expected to be abandoned or to fail. Most such wells started out as reasonably good producers, but ultimately failed by breakage or damage to the casing string by corrosion, by roof caving or by subsidence-related shearing/collapse of the casing string (Deutsch 1978). Failure could occur soon after a well evolved into a high-capacity performer or decades later. Most brinefield operators learnt that many of their oldest wells were their most reliable producers. Many captive brinewells "die" during their "infancy," but if they live through the usual "childhood diseases" of roof collapse and casing shear, the chance of failure lessen as they get older. Some older brinefield wells in bedded salts, that is, wells that had produced for 20–30 years, seemed to be immune to caving and were abandoned only when the target salt layer was exhausted.

Predicting which wells survive in a brinefield is difficult. An analysis of some 60 wells drilled between 1,887 and 1,925 clearly shows this trend of long-lived survivors (Fig. 13.4). One possible explanation for "long-life" wells is that early cave-ins distributed fallen rock in such a way that the lowest part of the tubing string was protected from damage by later cave-ins. Alternatively, as the roof of a growing salt cavity reached a greater and greater span, it could either cave with serious results for the well, or it could very gradually subside

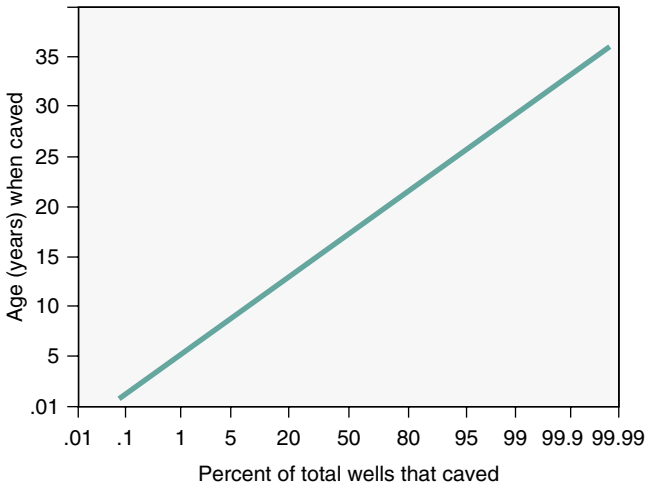

Fig. 13.4 Schematic of the "life expectancy" of a set of brine wells (Deutsch 1978)

until it was supported by silt or projections and debris at the bottom of the cavity. A brine well in the latter situation would continue to be a good producer, even with a very shallow cavity. Well failure or poor performance is somewhat random in nature, and can occur unexpectedly. Consequently, and because of slow initial production rates, most captive brinefield operators employ many wells, abandoning nonproducers and bringing new ones on-line.

In all cases, mud and other insolubles, as well as some salt falls accumulate as muddy breccias at the base of the expanding cavity. In wells where salt layers other than halite are the target and are encased in thick halite, the initial borehole is typically drilled through the target bed(s) to some distance into the underlying halite mass. As the cavity then expands, it creates a sump below the target bed where insolubles can accumulate. In any solution cavity it will be necessary to raise the bottom casing string (snubbing) above the level of the insolubles, otherwise the well will need to be plugged and abandoned. This is also true if the casing has been severely bent or damaged by the rock-falls from the roof. Normally these problems occur very slowly, and the cost of the initial capital and well operation is such that the total mining expense is very low compared to conventional room and pillar extraction.

Many land areas above brinefields, which were active in the eighteenth or nineteenth centuries and were over-exploited, are today subject to collapse. But few records of well placement or even the position of the brinefield were kept in older areas of extraction (as in Hutchinson, Kansas – see case histories later in this chapter). This leads to all manner of environmental and civil engineering problems in the vicinity of many former brinefields. But not all engineering and subsidence problems in areas of nearsurface salt are anthropogenic (Table 7.10). Salt dissolves and the large collapse cavities form naturally at the landsurface in time scales measured in days or

weeks. Outside of areas atop poorly managed or historical brinefields, separating anthropogenic sinkholes from natural dissolution cratering is very difficult. A cynic might conclude that many causative interpretations depend in large part on which interest group is paying the consultancy bill.

Solution Well Styles

Various techniques have been employed in brinefields over the last 150 years to improve brine production costs and to increase the amount of brine produced per well. Today the dissolution process for single wells can involve multiple concentric or independent tubing strings, various fluid injection/production depth combinations, as well as several different roof-protection combinations involving blankets of different types of hydrocarbons including crude oil, LPG, and gases such as nitrogen and CO_2. Blanket design now also includes solids such as floatable cements and hollow spheres (Richner et al. 1992). Multiple-well interconnections can be achieved in a planned manner using appropriate geological understanding along with combinations of roof padding, well deviation/ horizontal drilling and hydraulic fracturing.

Expert design of solution wells is for the most part dependent on geological understanding of the salt to be exploited. Required knowledge includes: dip and thickness variations of the target bed; mineralogical composition, homogeneity, insoluble levels and dissolution behaviour of the target salt bed and adjacent salt layers; distribution and mineralogy of intrasalt beds; structural integrity of confining beds. Caverns engineered in salt domes tend to be more reliable and predictable structures than caverns engineered in bedded salts and are more suited to product storage especially if the product is stored under pressure. Compared to dome salt, bedded salt in the vicinity of a solution well tends to be thinner and bound above and below by more permeable formations. Bedded salt is also more likely to enclose layered intrasalt beds with varying levels of solubility and fracture intensity (anhydrite, shale and dolomite intrabeds) and so tends to supply significantly higher quantities of impurities to the cavity floor. The most stable cavern shape for purpose-designed storage resembles a giant carrot or cucumber embedded deep in a mass of salt. This ideal shape is next to impossible in bedded salt, and to continue the vegetable garden analogy, jack-o-lantern pumpkins are a more likely outcome.

Historically, the earliest single wells had top injection (reverse circulation) and no roof pad or blanket. This style of well is known as a "Tully method" well and also are described as "top-injection," "casing-injection," "direct-circulation" and topwater injection" wells. Tully-method wells had the advantage of low investment costs along with rapid development of saturated brine flow (Richner et al. 1992). Unfortunately, this technique tended to create unstable morning-glory caverns subject to roof failure and their design inherently limits brine recovery to the upper portions of any targeted salt mass. Casing damage was likely even in the very early stages of cavern growth. "Tully" wells are not used today and belong to a time in human history when landscape damage was seen as a positive indicator of "progress." In the 1920s and 30s "Detroit-method" wells, with direct circulation via a bottom tubing injection, became the preferred method for excavating single well brine producers as they tended to create more stable cylindrical caverns, less subject to early collapse and loss of the well. Detroit-method wells are also referred to as "bottom water injection," "tubing injection" or "reverse circulation" wells.

In the 1930s the "Trump" method, a multiple well technique, was introduced to exploit bedded salts. It involved direct circulation and the use of a roof pad or blanket (Fig. 13.5. Multiple wells were completed near the base of the targeted salt formation. The aim was to create large diameter undercuts near the base of the target salt bed and then allow the undercut caverns to expand beneath their blankets until adjacent cavities met. Historically, wells utilising the Trump method were between 61 and 183 m apart. Once an interwell connection occurred, the wells were changed from two independent circulation wells, into two-well or multiple-well operations. One (or more) well(s) became the injector(s) for feed solvent and the other(s) became the brine producer(s) (Fig. 13.5). In this way the salt formation between the two wells was more efficiently recovered by the rising cavity roof and the per well brine production rates and tonnages were markedly improved compared to the older single "Tully" method wells. Using the Trump method entails a 12–24 month period of cavern development during which arrangements must be made for the usage or disposal of unsaturated brine.

Henderson (1974) reviewed this multiwell method of solution mining for halite targets. For maximum efficiency, he recommended a 91 m well spacing in bedded salt and about 18 months from the onset of feeder brine pumping to a time when an appropriate and consistent quality brine product could be recovered. He noted that cavity development and brine field subsidence in general can be controlled to a greater degree using the "Trump" procedure rather than a single Tully well. It entails relatively low production costs and high flow rates per mature well. However, the padded rising roof of the cavity is not a structurally competent shape, and roof falls ultimately occur. Constant raising of the casing is often required, especially in the downdip feed wells. The production or uphole wells are particularly vulnerable, and generally weaken and fail first (see the Romanian SALROM disaster in case studies).

Specific examples of the mining of very thin beds of salt using one- or two-hole methods were reported from a brinefield in China by Yuanxiong and Chengxun (1983). Single-well, nonblanketed, production of a salt bed 1–6 m thick at a

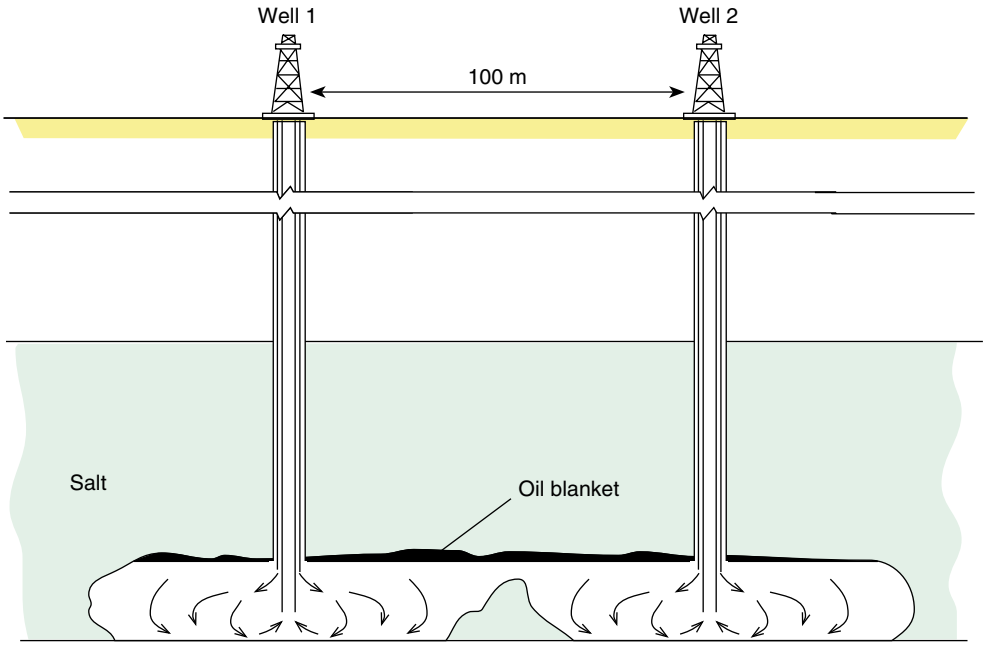

Fig. 13.5 Solution mining by joining wells by using an oil pad or blanket in combination with reverse circulation (After Henderson 1974)

depth of over 1,000 m in 12 wells over a 5-year period averaged 20,000–30,000 t/year of salt per well (maximum 70,000 t/year), with a well life of 4–8 months. Both the casing and tubing tended to deform, bend, and break from roof falls. Well life was longer in zones with a more stable roof. However, when oil pads were employed on a single two-pipe well 935 m deep within a 17-m-thick salt, the well was fairly quickly producing 50 t/day of salt as a saturated brine. Well life and productivity were much improved. Two other wells were then connected by using oil pad control to test against the single well extraction method. The wells were 1,042 m deep, 71.7 m apart, and operating in a salt bed some 17–20 m thick. Cavity height during excavation was maintained about 2 m above the base of the salt. By 100 days the flow rate in each well was 10 m^3/h with an "almost saturated" exit brine, and in 500 days the wells were interconnected. In a third set of wells at 1,004 m depth, 16-m-thick salt, and 68-m spacing, it only took 180 days to make the connection. About 26,000 t of salt were "wet mined" in making each cavity, and the daily salt output was 300–400 t/day per well at the end of this period. Blanketed reverse circulation (top injection, bottom production) was employed to better control roof height and allow faster horizontal cavity growth. Over 50 % recoveries of the entire thin salt beds were obtained with excellent economics and minimal surface subsidence using this procedure.

Today, most single well solution mining operations utilise a modified annular injection method, known as variable point injection, where both the tubing string and the casing string are positioned near the lowermost level of salt to be dissolved. Undercuts of more than 100 m diameter are achieved using a gaseous or liquid roof pad. In captive wells, brine production rates of more than 13 l/s have been obtained once the blanket is withdrawn. As solution proceeds both the tubing string and the casing strings are raised clear of the accumulating insolubles (snubbed). This type of well is also capable of achieving planned-cavity shapes suitable for waste storage.

An interesting test of the efficiency of both single-well and two-connected-wells solution mining systems targeting a thin bed of sodium borate was described by Taylor (1970). An 8.8-m thick layer of borate ore, which was 107 m below the land surface with a 72 % ore grade, was solution-mined in a series of tests. At the completion of the tests the cavities were physically mined (entered) and inspected. No roof padding was employed during the tests. Hot water at 102–110 °C was injected as a feed into the 21 °C formation and a 15 l/min flow produced an "almost saturated" borax solution with an exit temperature around 77 °C. As the test progressed, feed temperature was steadily decreased and the allowable flow rate of the saturated solution steadily increased. On later cavern entry it was found that broad morning glory holes had formed and large amounts of insolubles had accumulated on the cavern floor. Clay and shales from the roof had fallen as intraclasts with a "sand and gravel" structure. Cavity bottoms were dominated by this material, rather than by fine bottom slimes usually postulated to dominate cavity bottoms. Some slabs of borate remained encased in the pile of insolubles, where they remained buried as unleached blocks.

Techniques in Potash Operations

Texas Gulf solution mines potash-rich brine from deformed salt beds in the Paradox Formation at Moab, Utah and then uses solar concentrators to achieve a product appropriate for

processing Fig. 11.30). The IMC Kalium operation near Moose Jaw, Saskatoon, recovers potash brine by solution mining a sylvinite bed (Belle Plain Member) 9–15 m thick at a depth of 1,650 m using a patented solution and recovery method (Fig. 11.61). To capture the ore, hot undersaturated brine feed is pumped into the dissolution cavity. Concentrated potash brine is then returned to the surface processing plant, which uses a sequential evaporation-crystallization process to recover potash and recycle hot NaCl-rich brine to the subsurface for another leach cycle. In the dry steam driven evaporation stage in the processing plant, moisture is removed and the recovered brine is brought to saturation point. But halite and sylvite have different temperature responses (Fig. 11.68b). Halite is crystallized first by evaporating the recovered brine, then potash is recovered by cooling the remaining hot, saturated solution.

In conventional solution mining of potash intervals, all of the halite in the dissolution cavern must be leached along with the potash in order to keep the face of the solution cavity open and dissolving rapidly. Otherwise, a buildup of salt and insolubles on the active dissolution face cause blinding. Bottom casings are raised (snubbed) periodically to keep above the buildup of insolubles. In all solution brine operations, including those targeting potash intervals, flow rates are kept low enough to produce a transparent "almost saturated" brine. Because the targeted potash bed is typically thin with respect to the halite host, well capital and operating costs are comparatively high, but are reported to be still less than conventional potash mining. Relevant published potash solution mining articles and processing patents include; Bach et al. (1985), Day (1967), Dillard et al. (1975) and Schlitt (1982) (Fig. 13.6).

Carnallitite, like trona, shows incongruent solubility so that in beds composed of mixtures of carnallite, sylvite and halite, the sylvite tends to be left behind as a less soluble component that can slow the rate of dissolution (surface blinding; Fig. 13.7). Furthermore, the solubility of halite, sylvite, and kieserite is very low in strong $MgCl_2$ solutions and this limits exploitation in intervals where these minerals are co-associated.

The NedMag solution mining facility near Veendam in the Nederlands produces magnesium from magnesium chloride brine by solution mining a Zechstein salt dome, targeting beds that are a mixture of carnallite ($KCl \cdot MgCl_2 \cdot 6H_2O$), bischofite ($MgCl_2 \cdot 6H_2O$) and halite (NaCl), with some sylvite (KCl) and kieserite ($MgSO_4 \cdot H_2O$). Target intervals at Veenham average 100 m (combined) thickness at depths, dipping around 20°, at depths between 1,400 and 1,800 m. About a 100 m of halite lies above the target magnesium salts and more than 1,400 m

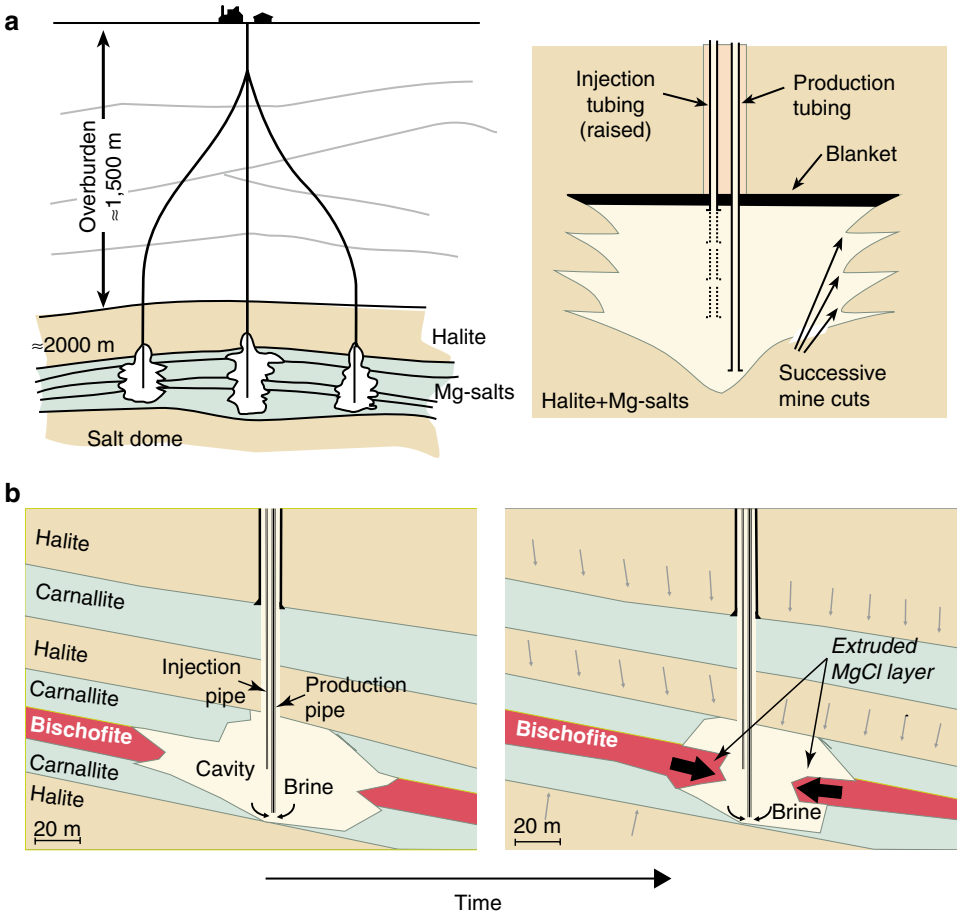

Fig. 13.6 Squeeze mining (**a**) Schematic of deviated wells in magnesium salts at the NedMag plant in Veendam, Netherlands, showing solution mining method of upward retreating successive cuts with positions controlled by the blanket (After Currie and Walters 1985). (**b**) Squeeze mining method utilised at Veendam targeting bischofite layers (in part after Drijkoningen et al. 2012)

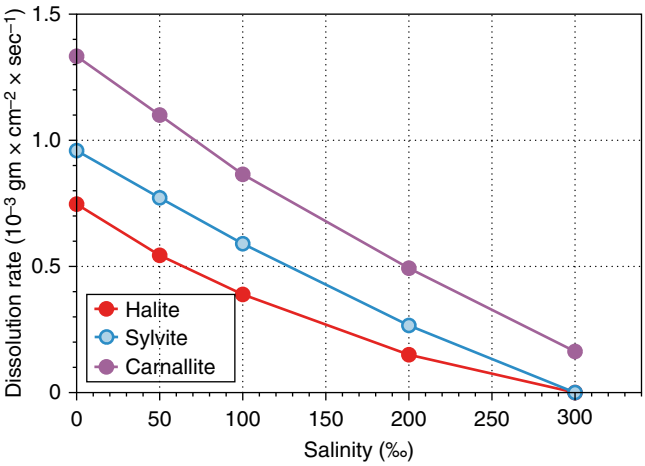

Fig. 13.7 Solubilities in water of the three main potash minerals at 25 °C

occur below (Fokker 1995). Beds were accessed by a total of 12 solution wells drilled between 1972 and 1991. Nine of these wells were still operational in 2000 with average brine production per well around 25 m^3/h. NedMag has recently excavated one of the deepest solution mining cavities in the world at 2,890 m. Each year the NedMag plant produces in excess of 200,000 tonnes of high purity synthetic dead-burned magnesia and more than 70,000 tonnes of magnesium chloride in liquid or solid form. A similar solution-mined operation producing $MgCl_2$ brine by targeting bischofite beds is planned for a large deposit near Volgograd in Russia.

The mining procedure at Veendam utilizes a backstepping solution cavity method (Fig. 13.6a; Fokker 1995). Cavity extent is limited to ≈ 100 m diameter (perhaps now extended to 150 m), and the brine is maintained at the original downhole (lithostatic) pressure. Wells are designed to be plugged and abandoned at full pressure. During production the magnesium salt-rich layers are preferentially dissolved, leaving behind many halite balconies on the cavity walls. Eventually the balconies collapse. This creates considerable insoluble rockfall and mud deposition on the cavity floor, compared to conventional cavities that target homogenous halite. Dealing with this extra volume of collapse debris requires frequent raising of both the injection (to control the cavity diameter) and the withdrawal pipes (to prevent blockages; Fig. 13.6a).

Cavern pressures are kept relatively low in the producing caverns (average of 10 MPa or 100 bars) and well below the far field rock stresses. This facilitates salt creep into the cavern, but the lower viscosity of the magnesium salts compared to halite means they are preferentially squeezed like toothpaste into an active solution cavern at a rate far greater than the creep of the adjacent halite (Fig. 13.6b). Hence, the bischofite beds supply far greater volumes to the dissolution cavern than the adjacent halite beds, with convergence rates contributing 30–40 % of the produced MgCl-brine volume. This method has been called "squeeze mining" and the brine product from squeeze caverns can be very pure. For example, four wells producing brine from "squeeze caverns" at Veendam are almost saturated with respect to bischofite, rendering a high quality brine product with less than 1 % by weight of non-magnesium chloride salts.

Although the degree of creep is not well understood, it has been established that halite shows a much lower creep than carnallite, which in turn shows a much lower creep than bischofite (Fig. 13.6b; Drijkoningen et al. 2012). Although the strain rate depends on differential stress, the strain rates can be estimated very roughly, in order of magnitude, as 1:10:100, respectively. The bischofite will therefore creep towards the caverns, resulting in a gradual thinning of the salt layer. Bischofite will creep due to pressure difference between lithostatic pressure depending on the depth and the pressure applied in the cavern.

In the development of cavities it is important to note that squeeze mining has a different effect than conventional solution mining under lithostatic conditions, because part of the created brine is replaced by solid salt. This enables production of more salt from the same cavern (Drijkoningen et al. 2012). A counter-effect is that squeeze mining leads to a more rapid surface subsidence than conventional lithostatic mining, in which there is no net volume change in the salt layers. The squeeze mining leads to extra deformation of the overburden, which in turn causes extra subsidence of the Earth's surface. Dutch regulations now impose a maximum subsidence of the surface of 65 cm for this mine, limiting production in the future.

By carefully maintaining the proper $MgCl_2$ concentration in the Veendam cavern brines and monitoring solution flow rates using variably pressurised waters, NedMag has minimised blinding in bischofite beds (Steenge 1979). For successful magnesium chloride recovery, the solution rate, the dissolving surface and the produced brine at Veendam must be maintained at all times at an 'almost saturated" condition. The operations at Veendam are a worldclass example of targeted and monitored solution mining with a set of process technologies specifically designed for the brine product. Historically, high levels of carnallite in some potash beds in the Zechstein have made them a poor choice for a KCl targeted beds in both solution and conventional mining operations. But NedMag has recently begun to use a patented process to produce brines that are also saturated with respect to carnallite from carnallitic beds previously considered subeconomic.

Lithology Effects Shape

So far, much of our discussion of shapes of solution cavities has assumed that the thick salt targeted for dissolution is relatively homogenous. But halite masses typically contain

thinner intercalated layers, composed either of less soluble salts, such as anhydrite or dolomite, or of more soluble salts, such as carnallite or bischofite (as at Veendam). An assumption of target bed homogeneity in solution planning can lead to problems during the leaching process.

With less soluble salt layers intersecting a cavern edge there is a tendency to form unsupported ledges and bevels, which eventually collapse to the floor of the expanding cavity. This can damage the roof in the vicinity of the feeder pipe, break the drill string, or force the operator of a suitably designed well to raise the well pipe off the former cavity floor (snubbing). In the case of more soluble beds, their rapid solution can leave behind blocks of unstable halite, which have a propensity for collapse, or it can lead to cavity shapes that become enlarged in one direction and encroach on the structural integrity of the well design, especially when there are adjacent solution cavities.

The best-studied and modelled examples of lithology variation effecting cavity shape come from the monitored cavities in the Zechstein salts of onshore Germany (Wilke et al. 2001). Of the four major Zechstein formations in the northwest European Zechstein basin, the Stassfurt formation (Zechstein 2) occurs in sufficient thickness (more than 800 m), to flow in to salt pillows and diapirs and so is the most important target unit for solution-leached caverns in this part of Europe. The underlying units of Werra formation, along with older salt units of the Rotliegende, are typically inactive and many beds are still attached to the basement. Salt of the overlying Leine formation (Zechstein 3) contains relatively thick beds of anhydrite and dolomite. It has an original thickness of 200 m, lies above the Stassfurt formation and is typically caught up in the Zechstein flows, but it needs the underlying thick halite of the Zechstein 2 to flow and carry it along.

High quality documentation of the internal structures of the German diapirs during potash mining has produced an excellent data set on which to model the likely geological complexity of these Zechstein structures (Fig. 11.47). This work caused the German salt experts, Richter-Bernberg and Horfrichter to conclude that of the Z2 and the Z3 series, the Hauptsalz member of the Stassfurt formation is most suitable for designed-use cavern construction and that the upper part of Stassfurt be avoided where possible due to inherently higher proportions of highly soluble potash and magnesium layers. Likewise, the overlying Hauptanhydrit of the Z3 has a propensity to create unstable anhydrite blocks during halite leaching and is not considered suitable for controlled cavity creation. Since their pioneer work, the goal has been to avoid solution mining in this transition zone between Zechstein 2 (Stassfurt Formation) and Zechstein 3 (Leine Formation). Nevertheless, several caverns have been leached in these strata, some without any problems, others with intensive preferred leaching directions (Fig. 13.8a, b; Wilke et al. 2001).

Structural elements in salt diapirs, largely crystal size and anhydrite distribution patterns in non-potash containing intervals lead to slight changes in cavern development. For this reason a sonar-measured cavern shape can be used to re-interpret a preexisting geological map. For example, the horizontal section in Fig. 13.8c outlines the contact between the Kristallbrockensalz (Z2A-HS3) and the Streifensalz (Z2-HS2), which leaches slightly faster due to its finer halite crystal size and more widely dispersed insolubles. Figure 13.8a, b are examples of preferred leaching along a relatively undisturbed potash seam. It lies several metres above a previously interpreted contact between the Kristallbrockensalz (Z2-HS3) and the Streifensalz (Z2-HS2). This later geological interpretation along the borehole provoked concerns that the potash layer would be intersected as cavern proceeded and led to a modified plan for cavern creation.

Experience in this terrain has shown that where potash layers of the Kaliflöz Stassfurt cross the drill axis a number of times it is not possible to perform a controlled leaching in one step. Rather, the leach design has to be planned as a number of mining steps to avoid a premature achievement of the maximum allowed cavern diameter in the vicinity of the potash layers (Wilke et al. 2001).

Such a controlled leaching program, tied to lithological variation, is called blanket management and proceeds in a series of back steps as described by Wilke et al. (2001); Fig. 13.9:

- Blanket depth is kept below the 50° dipping potassium seam at a distance such that the expanding cavern wall will not touch the seam while it is expanding towards the maximum allowed diameter.
- After reaching 80 % of the planned cavern volume below the seam, the blanket is raised to a position slightly above the dipping seam to allow some upwards leaching along its occurrence.
- After some weeks of development of the original borehole, the blanket is pumped down to once again cover the more soluble part of the leached section.
- Continue leaching and continuously add "oversize" amounts to the blanket to be sure the more soluble section is covered.
- Raise the blanket to prepare a new leaching step, before snubbing the pipes. Maintain the blanket in the section of the potassium seam to continue protecting that area.
- Change the injection point depths shortly before the maximum diameter is reached below the seam and while the production point is still sufficiently deep to approach to the maximum allowable shape in this part of the cavern. All the upper section of the cavern is then allowed to expand toward planned diameter.

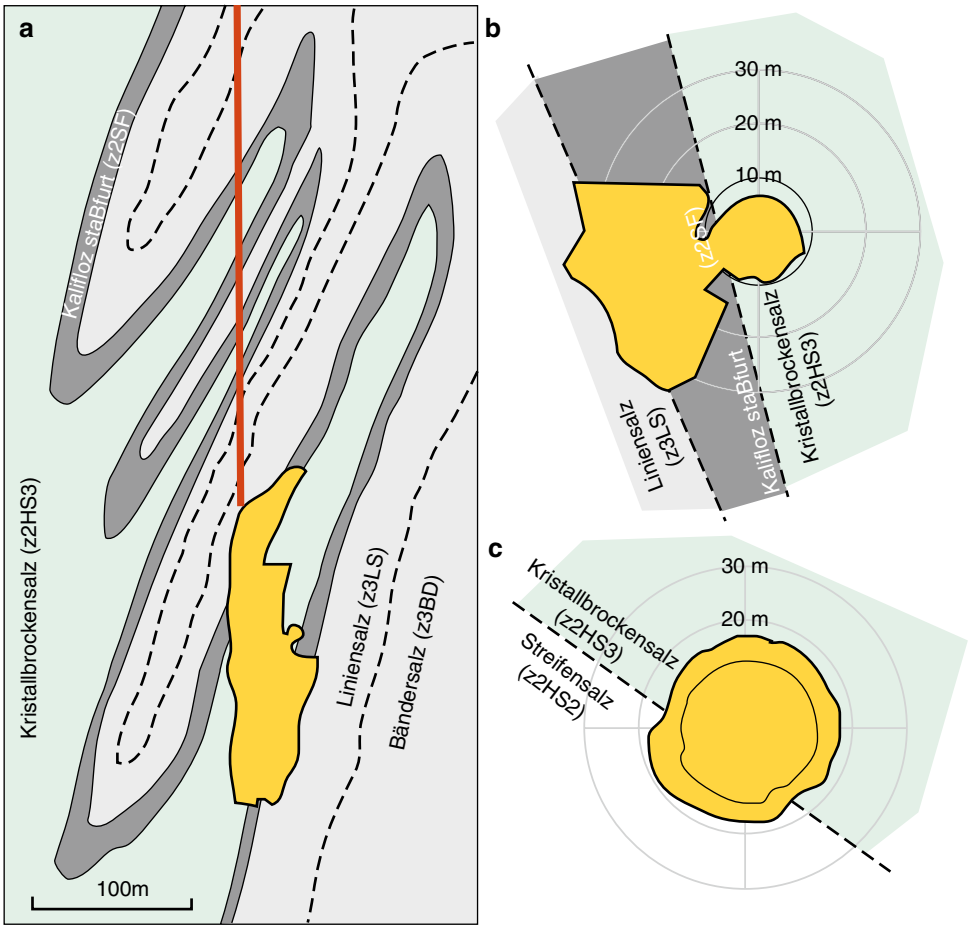

Fig. 13.8 Effect of salt geology on cavern shape in diapiric Zechstein Salt. (**a**) Vertical section through a cavity in Zechstein Salt in Germany showing preferential enlargement into potash-rich Kaliflöz Stassfurt horizon (*shaded grey*). (**b**) Horizontal slice showing strongly asymmetrical shape formed as cavity develops preferentially into the potash facies of the Kaliflöz Stassfurt. (**c**) Horizontal slice in a cavity in two halite lithologies where differences in crystal size and proportion of insolubles create a slight asymmetry that is maintained during growth (After Wilke et al. 2001)

In the case of caverns intersecting highly soluble intrasalt beds it is especially important to create "as much as possible" cylindrical caverns below the level of any seam. This approach means that the largest allowable storage volume is created inside the project's rock mechanical parameters. At the same time the cavity shape must be monitored often enough to avoid uncontrolled expansion in the highly soluble (potash) layers.

Well Pad Design

Some modern brinefields and storage sites are made up of single wells with concentric casings extending into individual caverns. Others consist of several adjacent brine wells extending into a single large cavern. Yet others create multiple caverns off a cluster pad. Brine is withdrawn either through the outer concentric casing in a single well cavern, or through a separate casing in a multiple well cavern. Once active, the size and shape of solution-mined caverns can be measured and controlled with cavern sonar and operating techniques (Crossley 1997, 1998).

Single drill pads typically sit atop vertical wells, they offer maximum flexibility in cavern depth range and minimisation of hole damage (Fig. 13.10). Snubbing or pulling pipe is relatively straightforward in a vertical well due to low frictional losses. There is minimal borehole contact and good control on any twisting of the drill string needed to free it if it has become stuck. In all solution wells the initial borehole shape is important as it can strongly influence the shape of the subsequent cavern. Vertical holes suffer minimal borehole asymmetry, which is often created by excessive one-sided hole wear during the drilling phase of an inclined well.

Cluster well pads allow multiple caverns to be created beneath a large pad and are a cheaper alternative to single well pads (Fig. 13.10b). They have lower infrastructure costs and land area requirements, they need only a single access road, one field pipeline for the brine product, one set of power supply cables to the pad, and the surveillance of only one site. However, compared to single well pads, they suffer from less flexibility in ongoing planning and maintenance. The need for directional drilling and the degree of deviation means it may be difficult or even impossible to turn the leaching strings or the cables after a cluster pad well is activated. Rotating a tubing string is a technique frequently used to free the coupling on the last cemented casing shoe if it has become stuck during production.

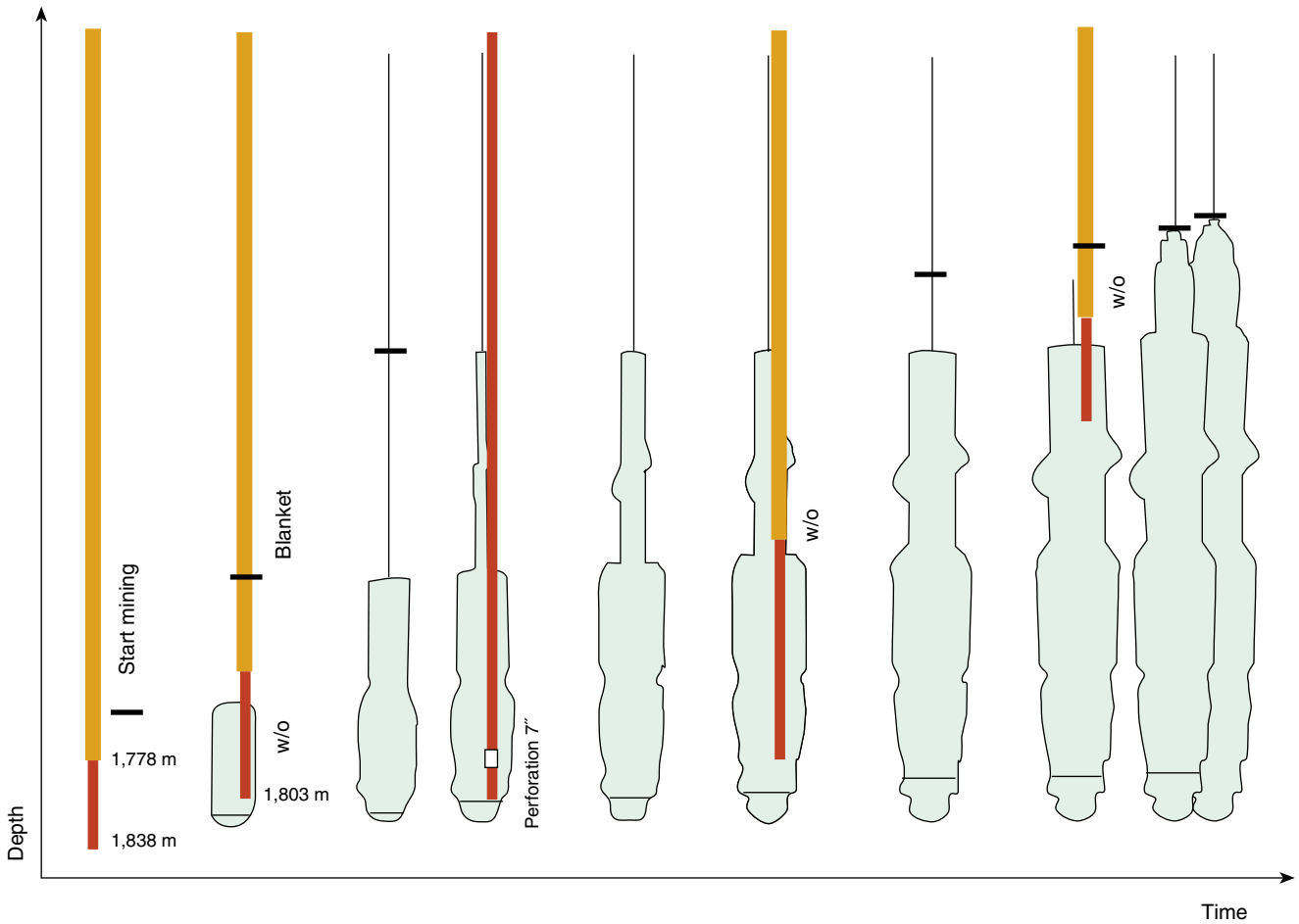

Fig. 13.9 Solution mining for a gas storage cavern using a blanket management plan designed to control breakout across an inclined potash bed that cuts the storage cavern twice along its planned length (as shown in Fig. 13.8a). The scheme uses a combination of blanket management and sequential snubbing. See text for details (After Wilke et al. 2001)

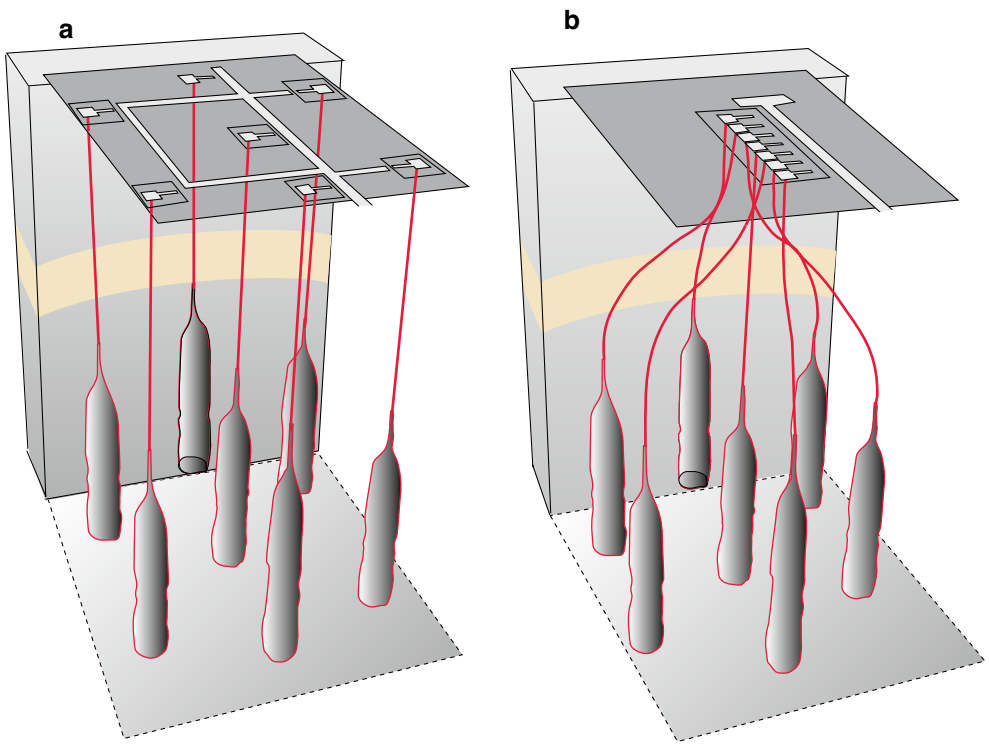

Fig. 13.10 Well pad design. (**a**) Single well pads. (**b**) Cluster pad

Once a cluster well group is completed is difficult to later modify production casings, but this can be an ongoing need in some hydrocarbon storage caverns. Cluster wells, which require an S-shaped drilling path, may not be feasible in regions where the targeted salt is shallow. Cluster pads only work if target salt bodies are more than 600–700 m below the surface. A rough rule of thumb is that directed drilling can give deviations of some 1.5° every 10 m of vertical depth.

Casing couplings should be engineered in the early stages of well completion design and are a critical feature in most cluster pad wells, especially those used for hydrocarbon storage. Once operational, it is virtually impossible to turn the leaching string in a deviated well. To compensate, the outermost leaching casing should be fitted with an integral coupling below the casing shoe of the last cemented casing string. That way, couplings do not stick in the vicinity of the casing shoe. When a cavern is to be used for gas storage the more expensive option of integral couplings should be included in design of the brine withdrawal string. This prevents the sticking of casing in the vicinity of the production-string casing shoe. If a cavity is to be used for gas storage, the brine withdrawal string must be raised under gas pressure as the cavern is first filled with gas.

Deciding on single well pads versus cluster pads influences the design of the casing string and the completion specifications. With a cluster pad the likely depth and homogeneity of the target salt must be known prior to the commencement of drilling. Successful directional drilling of S-shaped wells is best achieved using measurement while drilling (MWD) techniques. MWD techniques are now standard methods in the oil and gas industry and should perhaps be more widely considered for single well pads. MWD allows the operator to better deal with any unexpected deviations encountered during the drilling of vertical or inclined wells.

Blinding and Phase Chemistry

Halite is the targeted salt for most solution-mined brinefields and is one of the simplest chemical systems to cope with in the subsurface. Thick halite deposits, if associated with only carbonate and calcium sulphate impurities, are chemically well behaved during dissolution and their basic brine chemistry was discussed in Chap. 2. But today, there are a growing number of solution mining operations that target salts with more complex dissolution chemistries, such as the borate or sodium carbonate salts, where covering or blinding the cavern surface with a layer of less soluble salts is a strong possibility.

All non-halite salt targets require a predictive understanding of brine phase chemistry. The intricacies of phase chemistry of brines and salts is largely outside the evaporite focus of this book and a detailed consideration of the various precipitation outcomes requires a book in its own right (see Usdowski and Dietzel 1998). To illustrate what is possible we will look at some of the complexities and possible problems using current understanding of simple phase equilibria and dissolution kinetics for trona (After Haynes 1997). Searles Valley Minerals (Nirma) currently solution mines soda ash at Trona, California and until recently American Soda operated a directionally drilled solution mine facility for a nahcolite target bed in Colorado.

Phase Chemistry – Trona Solution Mining

The ternary phase equilibria of the sodium carbonate system Na_2CO_3–$NaHCO_3$–H_2O is temperature dependent (Haynes 1997 see also Fig. 2.20a). When trona is dissolved in pure water it follows the dissolution path A-A' (Fig. 13.11a). If the system is at 40 °C, an undersaturated brine following the trona dissolution path will encounter the 40 °C isotherm at X. Further trona dissolution means the brine is now supersaturated with respect to nahcolite. At some point this mineral begins to drop out of solution, while the brine follows the path X – Y. At Y, solid nahcolite, solid trona and a brine liquor corresponding to point Y (17 % Na_2CO_3 and 5.6 % $NaHCO_3$) are all in equilibrium. A similar precipitation sequence will occur at other temperatures from 25 to 87 °C, showing that sodium carbonate solubility doesn't change much over this range, while the wt% of bicarbonate doubles in the residual brine (Y to Z). Wegscheiderite forms above 87 °C (Fig. 13.11b). The formation of the less soluble nahcolite is the reason many early field tests attempting to solution mine trona typically mention "blinding" of the dissolution surface whereby a coat of nahcolite forms atop the dissolving trona, slowing or preventing further dissolution.

"Blinding" problems can be avoided if temperatures for brine extraction are kept high or if the feed solvent is not pure water but a solution of Na_2CO_3. The effect of high temperature can be seen as a byproduct of shale-oil recovery experiments conducted by Shell Oil in the Piceance Creek Basin. In 1970–72, the Company experimented with warm water and steam injection in an attempt to recover oil from nahcolite-bearing oil shales of the Parachute Creek Member on a 10-acre site in Rio Blanco County, Piceance Basin Colorado. In addition to the expected oil, Ireson (1990) reported that large amounts of sodium carbonate brine were co-produced at higher recovered brine temperatures (Fig. 13.12).

In 1990, solution mining of Boies nahcolite bed began near Rifle, Colorado. Where mined, the Boies bed is about 7.6 m (25 ft) thick and at a depth of 610 m (2,000 ft; Day 1974). Such a thin target bed means solution mining is most efficient if it involves directional drilling. A vertical hole is sunk to a 100 m or so above the target bed, the hole is then turned so it enters the target bed at a slight angle and then is drilled horizontally along the base of the bed. Hot water is then injected into the bed to dissolve the nahcolite and form an expanding cavity. Sodium carbonate brine is recovered

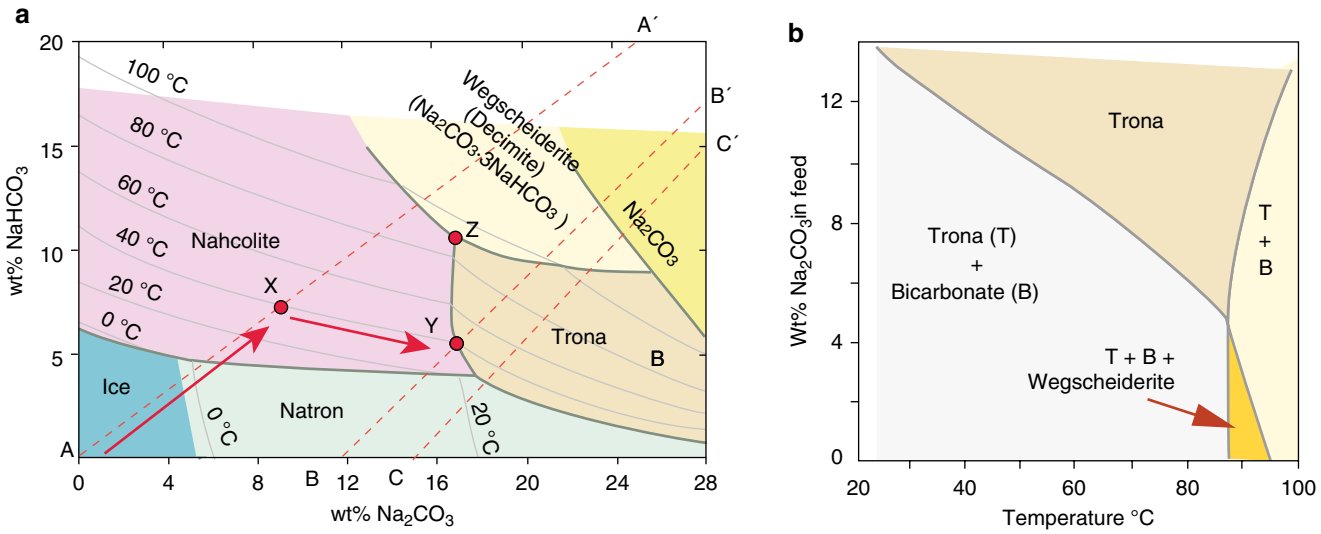

Fig. 13.11 Trona stability (After Haynes 1997). (**a**) Stability of major sodium carbonate minerals in the temperature range 0–100 °C. (**b**) Stability fields of various precipitates, trona is in excess in all phases

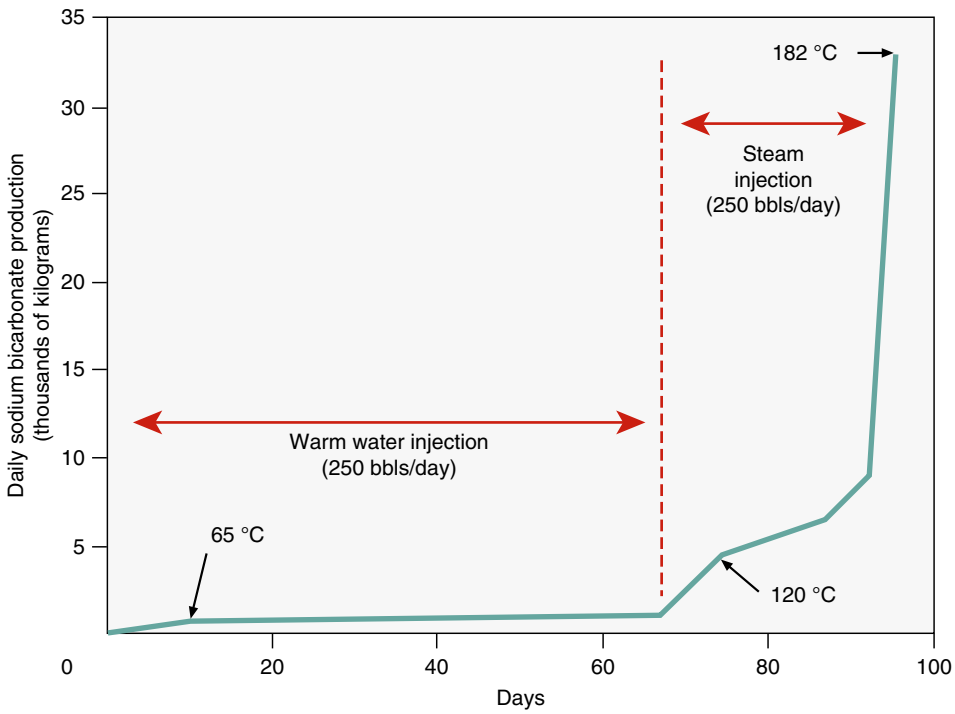

Fig. 13.12 Daily production of sodium bicarbonate from Shell's shale-oil recovery experiment in the Piceance Creek Basin, Colorado (From Ireson 1990)

from another vertical hole drilled into the cavity some hundreds of feet from the injection hole.

Until 2004, American Soda PPL solution mined nahcolite using this hot extraction method on a lease near Parachute, Colorado and adjacent to White River Nahcolite's property. First, pressurized hot water was injected into bedded nahcolite at depths of some 450–600 m subsurface. Nahcolite was returned to the surface as a highly saturated $NaHCO_3$ solution. In the first quarter of 2002, the company drilled 26 wells but anticipated that as the solution cavities expanded, production would be maintained using half that number. Idle wells were to be held in reserve to ensure an uninterrupted source of feed brine. At the brinefield plant, CO_2 was stripped from the well liquor ahead of pipeline transport. This created a brine solution more suitable for pipeline transport and also gave a relatively low-cost source of CO_2. Brine was pumped 70 km (44 miles) from the brinefield to the Parachute Creek processing plant using an insulated, pressurized, closed-loop pipeline. At the plant, the incoming brine passed through crystallisers, was dried and packaged for shipping. Recycled

hot water from the processing plant was then piped back to the minesite to leach more nahcolite. The 1,000-acre upper site was the prior location of Unocal's shale oil upgrading plant and much of the former infrastructure was used by American Soda. Unfortunately, the operation was deemed uneconomic and was shut down in late 2004.

Solution mining nahcolite in the Piceance Creek Basin suffers some unusual problems that can be expensive to control (Dyni 1996). Problems include: (1) Cavern shapes in the Boise must be tightly controlled and regularly monitored as the Boise bed is very close to a natural dissolution surface in the immediate overburden, a breakthrough into this overlying water-bearing leached zone would be detrimental to controlled solution mining in the target bed; (2) The Boise bed actually consists of two nahcolite beds, the lower one is thinner and also contains halite, so exact bed targeting is very important both during directional drilling and in cavity expansion during production; (3) The Boies bed grades laterally into mixed halite and nahcolite toward the basin's chemical depocentre, accidentally dissolving halite in this region would contaminate brine product with high levels of sodium chloride; (4) Oil shale which overlies the Boise Bed cannot be mined or damaged under current sodium leasing regulations. Given the major part of the known nahcolite resource today occurs as crystalline aggregates scattered through oil shale, it difficult to target mine for soda ash alone. Current legislation makes the solution mining of soda ash difficult, if not impossible, over much of the extent of the Boise Bed as it could render parts of the overlying oil shale unsuitable for future in situ leaching or underground mining. Under current legislation, any oil shale that is damaged by solution mining must be stockpiled for future oil recovery.

A possible future method to solution mine trona, not nahcolite, could use an initial feed solvent that contains Na_2CO_3 in solution (Haynes 1997). For example, a 15 wt% Na_2CO_3 solution proceeds along the line C-C' in Fig. 13.11a. This intersects the 40 °C isotherm well into the trona stability field and no sodium bicarbonate (nahcolite) will form. The line B-B' separates fields at 40 °C where nahcolite and trona are likely precipitates and corresponds to a value of 11.9 wt% Na_2CO_3 on the abscissa. This is the minimum feed solvent composition that will insure that no nahcolite is precipitated during the dissolution process. Critical "excess carbonate lines" were similarly determined by Haynes (1997) at other temperatures and are plotted as the solid phase existence fields of Fig. 13.11b. Trona is present in all stability fields as it is the excess phase.

Another way to avoid nahcolite blinding in a trona target bed is to maintain a caustic solution for the feed (Haynes 1997). The phase relationships in Fig. 13.11 are well known to the trona industry but their utility is greatly lessened in situations where impurities are present in the dissolving trona or in situations where other reagents need to be introduced to the solvent feed (see Haynes 1997 for details). Clearly, an understanding of the phase equilibria and temperature susceptibility of any targeted salt system is fundamental to any successful solution mining operation.

Use of Salt Caverns

Subsurface salt is an appropriate medium for enclosing and storing of a range of materials from artwork, to hydrocarbons, to industrial and nuclear waste to CO_2. Former salt mines offer a constant temperature and low humidity in which waste, munitions, paper and computer records, and works of art may be stored. For example, Winsford Mine in Cheshire, with around 26 million m^3 of space, is used for the secure, long-term and 'active' storage of a wide range of documents and sensitive or fragile materials (Evans et al. 2009). Part of Winsford Mine is also used for the disposal (and is therefore regulated as a landfill site) of up to 100,000 tonnes of selected hazardous wastes such as contaminated soils and residues from the nonferrous metals and chemicals industries.

Less and less the rationale to create a solution mined salt cavern is the production of brine or a particular chemical feedstock. In the past few decades, the number of purpose-built storage caverns, shaped using solution mining techniques, has expanded rapidly and an industry centred on the construction of salt caverns for hydrocarbon and waster storage has evolved and continues to expand (Thoms and Gehle 2000a, b). Today's commercial brine producers are also aware of potential storage opportunities, they still use controlled solution mining techniques to produce their required brine feed, but at the same time their ultimate goal is to produce a tight cavern suitable for future hydrocarbon or long-term waste storage (Table 13.2).

Energy Liquids & Compressed Air Storage

Crude oil or unrefined petroleum and light hydrocarbons can be safely stored below ground in liquid form in brine-compensated salt caverns (Table 13.3; Veil et al. 1996; Grappe 2000; Thoms and Gehle 2000a). Light hydrocarbons currently stored in salt caverns include propane, butane, ethane, ethylene, and other products extracted by refineries that can be transported and stored as liquids. In recent years natural gas[1] has been stored in salt caverns in increasing volumes, this entails much higher storage pressures and a greater need

[1]Natural gas is a naturally occurring mixture of hydrocarbon gases, principally methane with lesser quantities of ethane, propane, butane, and other gases.

Table 13.2 Use of salt caverns as storage facilities

Cavern Usage	Product stored	Distribution and specifications	Operational mechanism
Hydrocarbons	Liquid hydrocarbons-Crude oil, distillate, naptha, etc.	More than 16 storage sites encompassing more than 190 caverns. Largest volume stored in USA (SPR), storage also in France, Mexico and Germany.	Due to reduced compressibility but relatively low density of product and immiscibility with water, caverns are operated by a brine compensation mechanism. This requires above ground facility (ponds) for storing excess brine when the caverns are filled with hydrocarbons. Brine compensation enlarges the cavern during each recovery cycle, hence cavern shape must be continually monitored throughout life of facility. Less pressure variation occurs in caverns used for liquid storage compared to gas, so caverns can be much larger for liquid storage (more than 1 million m^3) in a single cavern. Salt creep is less critical for liquid storage compared to gas.
	Liquefied hydrocarbons-LPG, ethylene, ethane	Around 110 storage sites with over 190 caverns. Major sites in Sarnia (Canada) and Mount Belvieu (USA). Sites also in Morocco, France and Germany.	
Compressed air storage	Energy generation via electrical demand-peak shaving	Two plants currently in operation worldwide- Huntorf Germany and Alabama Electric Cooperative, USA.	Air is compressed and stored in a salt cavern using cheap electricity. Then stored air is expanded through a gas turbine to produce high value, peak electricity. Caverns cycle daily.
Waste storage	Industrial waste	Limited number of facilities in operation in USA and Europe, most caverns used to store oil-field wastes or industrial chemicals.	Waste is stored as a "final repository" hence cavern must be emptied prior to filling with pelleted waste (avoids groundwater contamination), or an inert blanket of suitable density must be used to separate waste (pasty consistency) from the brine. Waste is also stored as both "inerted" bulk material and in containers in old salt mines in Germany.
	Nuclear waste	Operational site at WIPP, New Mexico, USA. Waste is isolated by plugs made from a crushed mix of salt and compacted clay.	Purpose built facility using conventional mining in a salt bed rather than a solution-leached cavern in a salt dome as there is a legislated requirement for reversibility of nuclear storage and site stability for at least 10,000 years.

After Grappe (2000)

Table 13.3 Hydrocarbon storage (1,000 m^3) in salt caverns, xxxx indicates storage but volumetric data is not available

Country	Light hydrocarbons	Crude oil	Natural gas
Canada	6,620	–	552,720
Denmark	–	–	xxxx
France	xxxx	–	xxxx
Germany	xxxx	xxxx	5,040
Iraq	xxxx	–	–
Mexico	–	1,500	–
Morocco	xxxx	–	–
Poland	–	–	143,000
Russia	465–750	–	60–180
USA	85,220	102,100	3,423,250

After Thoms and Gehle (2000a)

for pressure integrity in the access well(s) and couplings compared to liquids storage. Natural gas is a clean burning energy source and has become a prime source of energy worldwide, especially in gas-fired power plants, which now constitute some 25 % of gas usage in the United States (Thoms and Gehle 2000a). Earlier last century natural gas was flared as a oilfield byproduct. By the 1970s it was thought to be in short supply, but it is now known to exist in adequate volumes for the foreseeable future.

As early as 1916 there was a German patent taken out to cover the solution mining of salt caverns for the storage of crude oil and distillates. The earliest oil storage in caverns was in bedded salt in Canada early in World War II. A few years later, by 1949, liquefied petroleum gas (LPG) was stored in caverns in bedded Permian salts near Kermit, Texas. Crude oil was stored in salt caverns in England during the "Suez Crisis" in the 1950s. In 1975, the US Congress created the Strategic Petroleum Reserve (SPR) program to provide sufficient petroleum reserves to reduce the impact of interruptions to future oil supplies. The SPR today consists of more than 60 caverns in domal salt bodies across the United States, with a total capacity of 680 million barrels (108×10^6 m^3).

The first storage of natural gas in a salt cavern was at Unity Saskatchewan in 1959, followed soon after in 1961 in Marysville, Michigan USA. Gas storage caverns were first purpose engineered in 1963 in Saskatchewan, Canada, in bedded Devonian salt at depths of 1,100 m. This was followed in 1964 by the first purpose-engineered gas cavern in a salt dome at Eminence, Mississippi, at a depth of 1,740–2,040 m (Fig. 13.1). European gas storage in salt domes began in Tersanne, France in 1970 at depths of 1,400–1,500 m and near Kiel, Germany in 1971 at depths of more than 1,300 m.

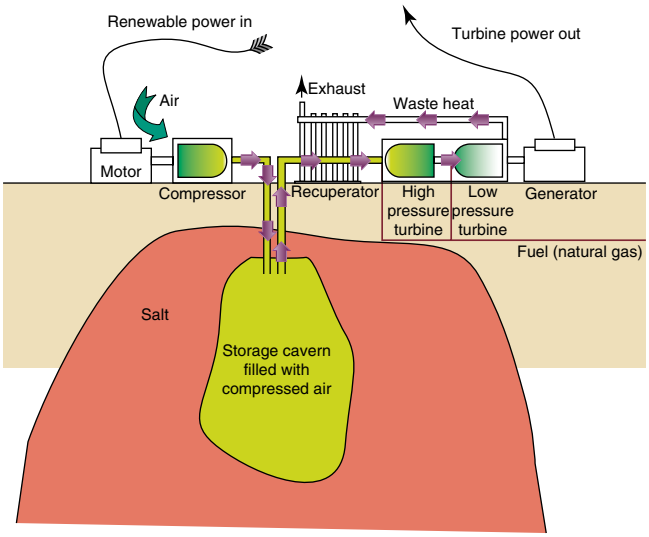

Fig. 13.13 Schematic of processes in a compressed air energy storage facility

Compressed air energy storage (CAES)[2] for peak electricity generation began in 1978 in as purpose built salt cavern Huntorf dome near Hamburg, while in 1991 a second CAES plant was commissioned in the McIntosh salt dome, near Mobile, Alabama (Fig. 13.13). Huntorf was designed for peaking and black-start[3] applications, it was initially designed with a storage volume capable of 2 h of rated output. The plant has since been modified to provide up to 3 h of storage and has been used increasingly to help balance the rapidly growing wind output from North Germany. The 110 MW Macintosh plant was built by the Alabama Electric Cooperative on the McIntosh salt dome in southwestern Alabama It was designed for 26 h of generation at full power and uses a single salt cavern (560,000 m^3) designed to operate between 45 and 74 bar. Although the McIntosh plant experienced significant outages in its early operation, the causes were addressed through modifications of the high pressure combustor mounting and a redesign of the low pressure combustor. These changes enabled the McIntosh plant, over 10 years of operation, to achieve 91.2 and 92.1 % average starting reliabilities with 96.8 and 99.5 % average running reliabilities for the generation and compression cycles, respectively.

[2]Compressed air energy storage (CAES) is a way to store massive amounts of renewable power by compressing air at very high pressures and storing it in large underground caverns (or depleted fields or aquifers). Compression and underground storage takes place at times of excess energy generation (aka peaking). The compressed air is later released and run through turbines to generate power when wind turbines and solar plant outputs are reduced and power is needed.

[3]Black start is the ability of a plant to start up during a complete grid outage. Because nuclear power stations require some power to resume operation, the Huntorf plant was built in part to provide black-start power.

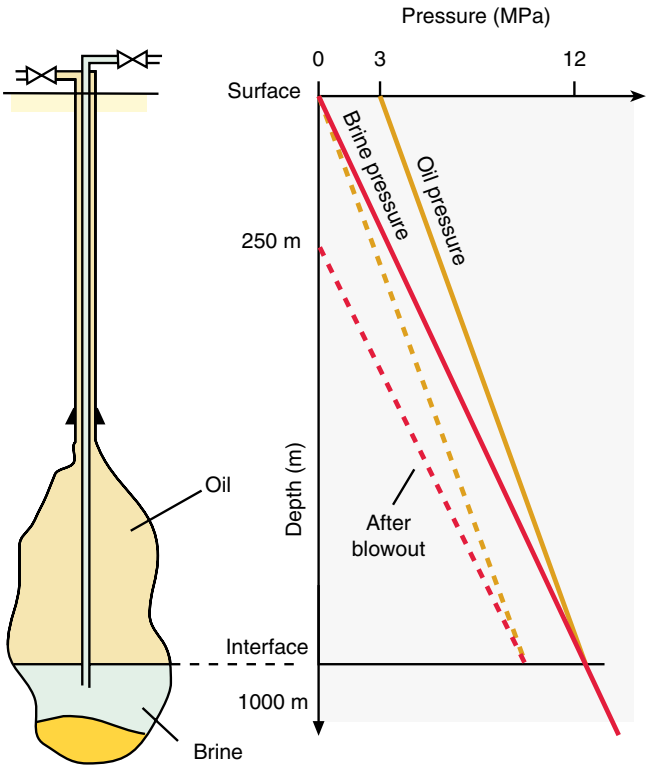

Fig. 13.14 Typical pressure regime in a salt cavern used for oil storage. Situation after a blowout is graphed as dashed lines (After Bérest and Brouard 2002)

Hydrocarbons in a salt cavern are stored in what is in effect a pressure vessel, where high pressure fluids are contained within a stiff impervious envelope using a system of pipes and valves that allow fluids to be placed, sealed and periodically withdrawn from the cavity. Salt caverns differ from standard surface storage tanks in the following way (Bérest and Brouard 2003):

1. The "container" consists of the access well and the cavern proper. Typically, the height (depth) of such a system is ≈ 1 km. The access well(s) is equipped with several casing strings or tubes, one inside the other, containing fluids (brine and hydrocarbons) at different densities. Even small differences in fluid densities result in very different column weights within the concentric annuli that make up the well. At the same depth, the gap between fluid pressures in adjacent annuli can be several MPa (Fig. 13.14). If the concentric fluids accidentally come into direct contact it creates unstable situations where accidents, such as blowouts and spills, are more likely.
2. The volume of a storage cavern is very large (up to 1,000,000 m^3). Even a small pressure drop in the cavern results in a significant change in the volume of the stored product. Liquid compressibility, a typically negligible consideration in most above-ground storage tanks, plays a significant role in the safe operation of large underground caverns.

Interactions between these two factors explain most industrial accidents involving hydrocarbons in salt caverns (see case histories).

Storage facilities for liquids (oil, naphtha, kerosene, gasoline) and liquefied hydrocarbons (LPG, ethylene, propylene) are operated by the "brine compensation" method. As brine is injected through a central tube at the bottom of the cavern, an equivalent volume of product is withdrawn through the annular space between the steel cemented casing and the central brine tube. When the cavern is idle, the brine is at atmospheric pressure at ground level. In the brine tube, however, the pressure is in proportion to the depth and specific density of brine, which is around 1,200 $kg \cdot m^{-3}$ (Fig. 13.14). If the interface between the oil and brine is 1,000 m below ground level, the pressure in the brine column at this point is approximately 12 MPa. Brine pressure and product pressure are equal at the interface in the cavern between brine and product. Above this point, the pressure in the product-filled annular space reduces gradually, and more slowly than in brine because the density of the stored product is lower (of the order of 900 $kg \cdot m^{-3}$ for oil, and 500 $kg \cdot m^{-3}$ for LPG).

Thus at any given depth, the pressure in the annular space containing the product is higher than the pressure in the central brine-filled tube. The difference is greatest at ground level, where in a 1 km deep example it is 3 MPa (for oil storage) or 7 MPa (for LPG storage). At the wellhead, the stored product applies pressure to the valve controlling the annular space. If this valve fails, the product is ejected suddenly, and the brine level in the central string drops until a new pressure balance is reached (see West Hackberry blowout in case histories).

For a valve failure in an oil-storage cavern, with an oil density of 900 $kg \cdot m^{-3}$ and with the initial brine oil storage interface at a depth of 1,000 m, the top level of the brine in the central tubing will come to rest at a depth of 250 m below the surface (Fig. 13.14; Bérest and Brouard 2003; Bérest et al. 1999). The weights of the brine column and the oil column will then be equal at the interface depth in the cavern. If both fluids were incompressible, the volume of expelled oil following valve failure would be small because the central tube capacity in the access well is only a few tens of litres per metre length of casing. In reality, due to differences in liquid compressibility in oil and brine in the cavern itself, much more oil is expelled. The compressibility factor of brine is $Bb = 2.7 \times 10^{-4}$ MPa^{-1}; the compressibility factor of the cavern is $Bc = 1.3 \times 10^{-4}$ MPa^{-1} (this figure can vary, depending on the elastic properties of rock salt and the cavern shape; see Bérest et al. 1999.); and the compressibility factor of the oil is $\approx Bo = 6 \times 10^{-4}$ MPa^{-1}. If y is the ratio between the stored-oil volume and the cavern volume, the global compressibility is;

$$B = B_c + yB_o + (1-y)B_b.$$

Following the wellhead valve failure, the pressure of the entire body of stored fluids (oil and brine) will be reduced by $\Delta P = 3$ MPa (in a 1 km deep example). If the cavity contains $V = 500{,}000$ m^3 of oil and very little brine ($y \approx 1$), then, because of the compressibility, the amount ejected will be;

$$B \cdot V \cdot \Delta P = \left(6 \times 10^{-4}\ MPa^{-1} \times 500{,}000\ m^3\right) \times 3\ MPa = 900\ m^3.$$

For liquefied product, a limited amount of LPG would first be expelled in liquid form. (However, this amount will be larger than in the case of oil, as the compressibility factor of LPG is larger, $Bp = 3 \times 10^{-3}$ MPa^{-1}). This liquid would evaporate gradually after running over the ground, and a heavier-than-air gas cloud would form. Accidental ignition of such a gas cloud is likely (see Brenham explosion in case histories).

Brine pumped into a cavern to compensate for displaced product must be less than totally saturated with respect to the encasing salt. This prevents any salt crystallising in the access casing, but it also leaches salt from the cavern wall. Regular product cycling using brine compensation increases the size of a salt cavern. Caverns used by oil storage companies in North America typically increase in size by about 1–2 % a year. Some of the older caverns in the USA and Canada are now twice as large as when they were first filled (Figs. 13.14 and 13.15).

Unfettered enlargement of a storage cavern can evolve into a stability problem as the retreating salt roof and walls are increasingly susceptible to sloughing, caving, fusion and associated damage to the long casing string. Cavern expansion has led to industrial accidents at some storage facilities and during the 1980s emphasized the need for better legislative definitions of safe storage and cavern life in the USA (see Mineola fire in case histories). The worst case expansion scenario is total roof failure and the formation of a sinkhole connecting the surface to the underlying storage cavern. This is highly unlikely in modern, well-maintained and monitored storage facilities around the developed world. The recognition of such a possibility required the complete drainage of the former SPR facility on Weeks Island, Louisiana (see case histories).

Natural gas storage caverns operate under much higher pressures than those storing liquid hydrocarbons. Internal pressure not brine compensation cycles the stored product. Purpose designed salt caverns are ideal for the storage of natural gas, especially when excavated in salt domes. They are stable and will not disintegrate in an explosion. They are safe and out of sight and so can be located near demand centres. They act as huge pressurised cavities with low gas

cushion[4] requirements of around 33 % of the total storage volume (Table 13.4). Unlike other gas storage facilities above and below ground, a salt cavern also offers very high deliverability and rapid product cycling. Caverns deal readily with peak demand, gas shaving and any rapid demand fluctuations. Operators can change from injection to withdrawal in 15 min and back to injection in 30 min. The main disadvantage to natural gas storage in a solution cavern is the relatively high cost of construction compared to other forms of underground storage using depleted oil and gas fields or suitable aquifers (Barnes and Levine 2011). But purpose-built salt cavity facilities are consistently safer and cleaner than all other types of underground and above-ground storage. The relative proportion of gas that is stored in salt caverns in the United States is increasing over volumes stored in aquifers and depleted fields (Fig. 13.16).

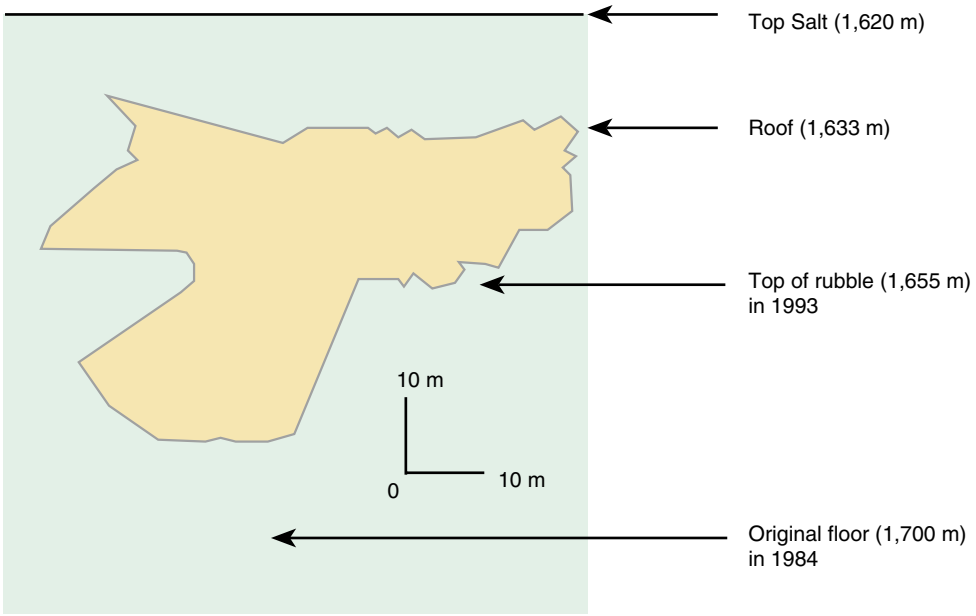

Fig. 13.15 Outline (cross section) as of 1993 of Cavern 5, Regina South, leached into the bedded salt of the Devonian Winnipegosis Salt, Canada. It is one of a number used for brine-compensated gas storage. Changes in floor level show how its shape has changed since 1984 (After Crossley 1998)

[4]Cushion gas is the volume of gas needed to fill a subsurface storage facility to where the gas pressure is sufficient to supply a significant flow of gas to the surface.

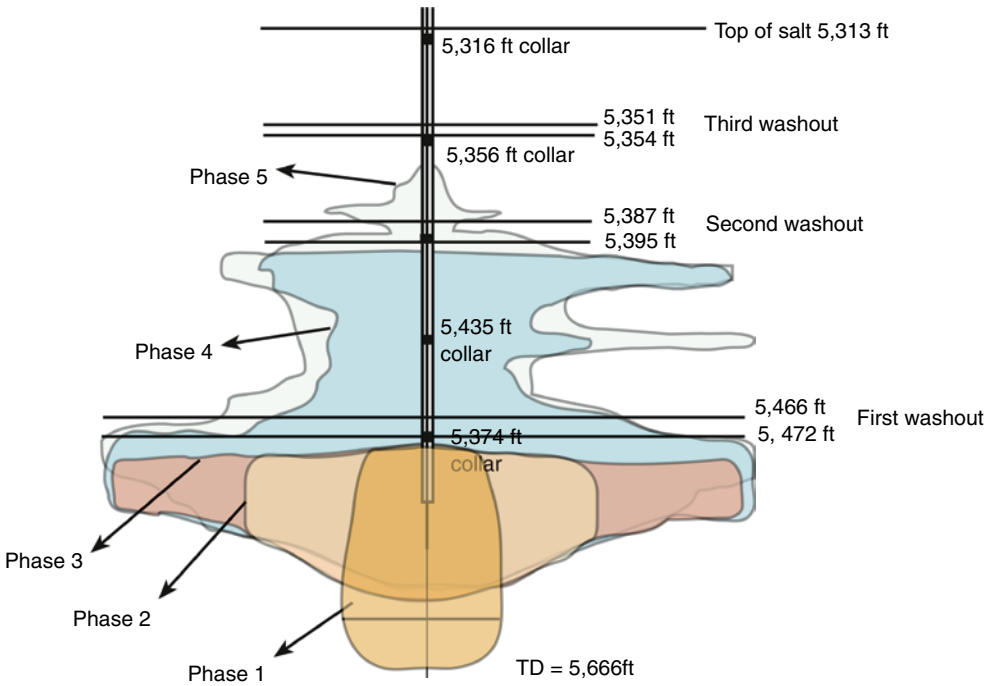

Outline (cross section) of Cavern 5, Regina South cavern field, leached into the bedded salt of the Devonian Winnipegosis Salt, Canada. Shows changes in cavern shape over time (Phase 1–5) due to ongoing brine compensation (After Crossley 1998)

Table 13.4 Cushion and cycle time requirements for underground gas storage operations

Type	Cushion to working gas ratio	Injection period (days)	Withdrawal period (days)
Aquifer	Cushion is 50–80 %	200–250	100–150
Depleted oil/gas reservoir	Cushion 50 %	200–250	100–150
Salt cavern	Cushion 20–30 %	20–40	10–20

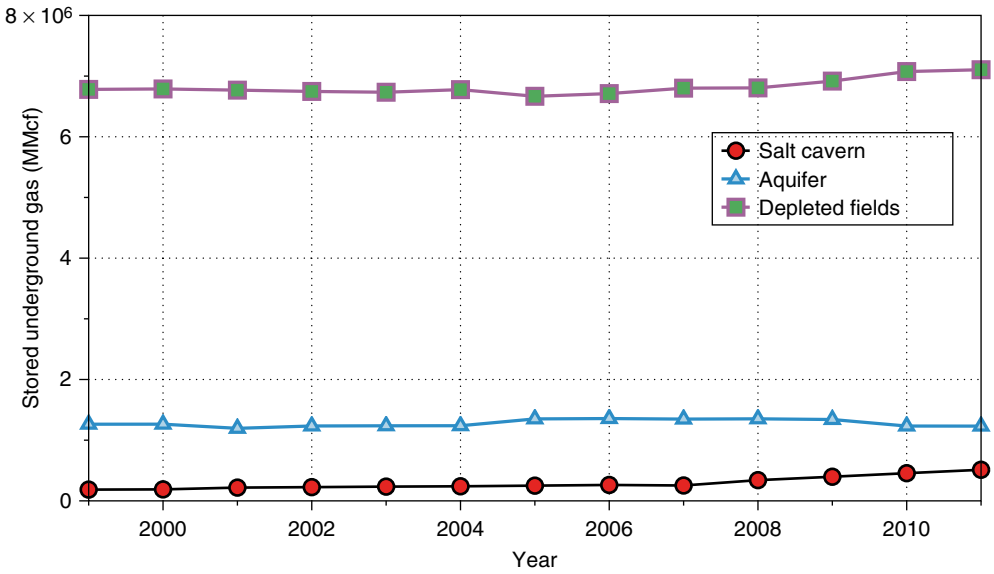

Fig. 13.16 History of the volume of natural gas stored underground in the USA and contributions of different modes of storage (Replotted from data downloaded from the US Energy Information Administration website <http://www.eia.gov>. Last accessed September 15, 2013)

As an example of cost, consider the purpose built "Big Hill" storage facility in Texas; completed in 1992, it is a 14.3 million cubic metre, solution-mined cavity operated under the U.S. Petroleum Reserve. The leaching cost (in 1992 dollars) was ≈$1.80 per cubic metre of salt excavated, and the total cost of the project (including land acquisition, design, site development, pipeline development, drilling, hydrocarbon interfaces, etc.) was $21.80 per cubic metre. Part of the higher cost for salt caverns reflects the need for controlled circulation and safe disposal of large volumes of cycled water required during the construction stage. But construction and maintenance costs are low compared with above ground storage facilities, which also suffer from much lower cycling rates, storage volumes, a higher likelihood of catastrophic damage during an accident and a need for higher gas cushions.

Hence, once in operation, a gas storage cavern has several advantages over depleted oil/gas field or aquifer storages. Purpose engineered salt caverns are integral structures that allow very little of the injected natural gas to escape from storage unless specifically extracted. If well designed with an adequate salt buffer between cavities, the walls of the salt cavern are strong and impervious to gas over the lifespan of the storage facility.

However, salt caverns are usually much smaller than depleted gas reservoir and aquifer storage facilities. A salt cavern facility may occupy only 1 % of the area taken up by a depleted gas reservoir facility. Consequently, salt caverns cannot hold the large volumes of gas necessary to meet base load storage requirements. Deliverability from salt caverns is, however, much higher than for either aquifers or depleted reservoirs, making them more cost effective. This high deliverability allows the gas stored in a salt cavern to be withdrawn and replenished more readily and quickly. This quick cycle-time is useful in emergency situations or during short periods of unexpected demand surges.

Life expectancy of a storage cavern may be as little as 40 years for existing caverns made with older solution leach technologies, or a century or more in purpose-engineered facilities constructed with current technologies. Deep caverns in thicker relatively homogenous salt bodies (as typifies many salt domes) are the safest hydrocarbon storage facilities currently known for natural gas and liquids.

Waste Disposal

Salt caverns can be used for the safe disposal of various types of hazardous waste (Table 13.2; Grappe 2000; Dusseault and Davidson 1999). Until recently, the major users of solution caverns as waste repositories were within the same salt-based and hydrocarbon-based industries that generated the cavities.

Nonradioactive Waste Disposal

Since 1959, alkali wastes from local "soda ash" production has been pumped back into "worked out" solution caverns of the Holford brinefield, located some 30 km south of Manchester, England. The Holford brinefield operator is authorised to dispose of 200 t per day of brine mud solids from the purification of crude brine, and 250 t per day of alkali wastes from local soda ash production. In addition, the operator is authorised to dispose of organic residues from the production of perchloroethylene, trichloroethylene, and other related chlorohydrocarbons into specially designated caverns that contain alkaline material designed to neutralise any free acid in the wastes. Brine displaced from the caverns by the emplacement of solids is used to slurry additional solids back to the caverns. The US salt mining industry also disposes of impurities generated during above-ground brine purification processes into salt caverns. Wassmann (1983) reported that the Dutch pumped wastes from a brine purification plant in to a nearby salt cavern. Concentrated magnesium chloride brine has also been stored in caverns in the Nederlands. In Mexico, sulphate purged from salt evaporators is being disposed of in salt caverns.

In addition to brine wastes, salt caverns are now also used to dispose of oilfield wastes. The state of Texas recently legislated that six salt caverns can be used for the disposal of nonhazardous oilfield waste and one cavern for the disposal of naturally occurring radioactive waste. The states of Louisiana and New Mexico are developing similar legislation. Canada has recently authorised disposal of oil field wastes into several caverns near Edmonton and Unity, Saskatchewan. Oil field products slated for disposal in salt caverns include; used drilling fluids, drill cuttings, completion and stimulation waste, produced sand, tank bottoms, and soil contaminated by crude oil or produced water.

Disposal caverns used in hydrocarbon waste disposal act like large oil/water/solids separators. The solids in the incoming waste settle to the bottom of the cavern while the lighter oils and hydrocarbons rise to the top of the cavern, where they can be removed. Incoming waste displaces clean brine, which is either sold as a product or disposed of. Cavern pressure integrity in a cavern to be put to such a use should be defined, tested and access controlled before the cavern is filled with oil field waste. It should be regularly monitored throughout the waste emplacement cycle, and optimally, for some period of time after waste emplacement has ended and before the cavern is finally sealed.

The main concern in any waste liquid storage is what will be the longterm response of the cavern once it is filled. Will it maintain its integrity for hundreds or even thousands of years? In a detailed study of rock property responses based on more than a decade of detailed rock mechanics studies in the laboratory, in the field and in abandoned salt cavities, Bérest and Brouard (2001) concluded that storing hazardous waste in salt caverns is an appealing solution when the toxicity of the waste vanishes after a few decades or centuries.

A suitable selection of cavern fluid pressure in the storage cavity will prevent too fast a convergence rate and allow a small amount of rock-mass fluid flow to be directed toward the cavern, preventing any fluid seepage from the cavern. Bérest and Brouard (2001) recommend that such storage facilities be shallower than 1,000 m to minimise the effects of creep and published cavern convergence curves for both a brine and a fuel-oil support medium (Fig. 13.17). As is to be expected, cavern convergence or creep rates are much higher when less dense fuel oil rather than brine is the support medium in the cavern.

Radioactive Waste

Radioactive waste disposal in salt caverns is much more problematic as toxicity can remain for millennia and stability must be maintained across such timeframes. Such timelengths include the possible to and fro of icesheets over much of North America and Europe. A key question to be resolved is whether medium and high level waste should be stored above or below the watertable.

Mainland Europe has adopted rigorous technical regulations for hazardous waste management. Germany, for example, requires that all waste, which cannot be stored for extended periods above ground without posing a serious threat to the biosphere, even after undergoing treatment, should be stored underground in suitable geologic formations. In the early 1960s the German Federal Government (former West Germany) decided that radioactive waste is to be stored exclusively in deep geological formations of the continental crust. Whereas the German nuclear industry was to be responsible for waste processing, intermediate disposal and conditioning, the German Government was to be responsible for final disposal. To this end the German Government contracted DBE, a company especially founded for this purpose in 1979, to plan, construct and operate the final radioactive waste repositories of the German Government. Until unification, DBE activities centred on the Gorleben and Asse salt domes and on the Konrad iron ore mine. Up to 1979, the Asse facility was also used as an experimental final repository for low-level wastes. In the following two decades the focus of experimental studies shifted to the purpose-designed Gorleben facility in the Gorleben salt dome.

Since March 1999, the WIPP site in New Mexico, USA, has been receiving radioactive waste for storage. This is a purpose-built salt cavern constructed by conventional mining techniques in bedded salt, not by solution mining. Like an unpressurized solution cavern, it is subject to the same creep, closure, temperature and pressure considerations and its depth of some 500 m below the surface places it in a depth range where karst penetration and lateral discontinuities including upward stoping chimneys are possible, if highly

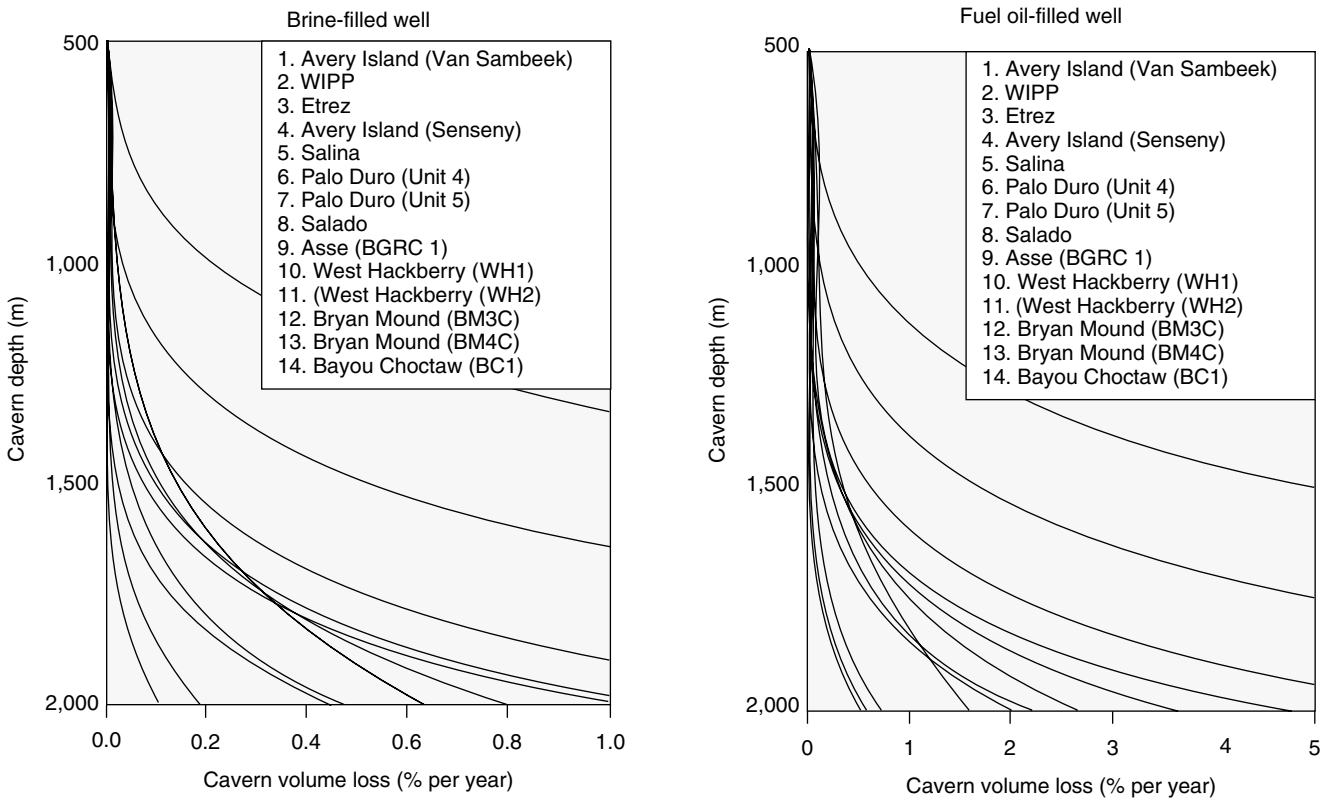

Fig. 13.17 Calculated annual convergence of a sealed salt cavern filled with brine or fuel oil and expressed as percent volume loss (Bérest and Brouard 2001)

unlikely, in the next few hundred millennia. At this stage no salt solution cavern is used for nuclear waste storage in the USA, because of a legislated requirement for reversibility (Grappe 2000). Unfortunately in some ways, much of the research effort by the DOE in the USA has focused on the relatively shallow WIPP site in a region of chimneying and deep subsalt artesian circulation and not on the development of deep purpose-built storage caverns in diapiric salt. Then again, no-one wants a radiogenic waste storage facility in their backyard across the much more highly populated Gulf of Mexico rim where salt structures subcrop.

In the context of the ability of diapiric salt caverns to safely store nuclear waste in a cavern space with adequate confinement and salt cover it's worthwhile looking at the response of salt caverns to nuclear detonations (Thoms and Gehle 2000a). Two 5-kt devices were detonated in salt as events within the "Ploughshare" and "Project Dribble" test programs. The event "Gnome" of Ploughshare took place in 1961 in bedded salt near Carlsbad, New Mexico, and the event "Salmon" of Project Dribble occurred in 1964 in the Tatum Dome near Hattiesburg, Mississippi. Three additional events involving explosions of natural gas were performed in the cavity in the Tatum salt stock first created by the Salmon event. The salt stock completely contained all the blasts and the original cavern was only enlarged by 17 m (55 ft) by the original nuclear explosion. To date no leakage of radioactivity has been reported atop the Tatum dome. It seems salt domes maintain seal integrity even when subject to the rigours of nuclear explosions within the cavern!

The suitability of purpose-built caverns deep in salt domes for the disposal of hazardous chemical and even low level nuclear wastes has been recognised by governments and companies worldwide, but applications to construct such waste disposal facilities have also raised such strong public objections that few permissions have been given anywhere in the developed world. As that famous German, Chancellor Bismarck, once said, "When a man says he approves of something in principle, it means he hasn't the slightest intention of putting it into practice."

Problems in Salt Solution Mines, Conventional Mines, Well-Bores and Storage Facilities

Dissolution and collapse of nearsurface and at-surface salt is a natural and ongoing process. When such salt bodies are penetrated by drilling or parts of the salt mass are extracted in a poorly supervised fashion, the resulting disturbance can speed up natural solution and collapse, sometimes with

Fig. 13.18 Locations of some of the anthropologically-facilitated problem areas in the circum-Atlantic that are discussed in the following pages. This map does not show that these areas are more subject to problems than other areas in the world that are underlain by shallow salt. Only that in these areas the political systems are such that it allows public documentation and discussion of the potential problems. All these areas are also in regions where natural salt collapse is ongoing

unexpected environmental consequences (Fig. 13.18; Table 13.5). In this context, and as a justification for the following section, it is of interest to quote part of the introduction in a paper by Zuber et al. (2000) dealing with flooding and collapse events in Polish salt mines.

"Catastrophic inflows to salt mines, though quite frequent, are seldom described in literature and consequently students of mining and mine managers remain, to a high degree, ignorant in this respect. Contrary to common opinion, inflows are seldom caused by unavoidable forces of nature. Though some errors were unavoidable in the past, modern geophysical methods are, most probably, quite sufficient to solve the majority of problems (e.g., to determine a close presence of the salt boundary). Detailed study of the recent catastrophic floods, which happened in Polish salt mines, shows that they usually occur, or have strong negative impacts, due to human errors. Most probably similar human errors caused catastrophic inflows to salt mines in other countries. It seems that a knowledge of the real history of catastrophes, better education of mine engineers and the application of modern geophysical methods could lead to the reduction of floods in salt mines."

Case Histories: Caving Brinefields

Abandoned brine fields can be areas with major environmental problems as many old wells are undocumented and unmonitored. Like areas of natural solution collapse (Tables 7.9 and 7.10), they can become zones of catastrophic ground failure, this is especially problematic if located near cities or towns (Table 13.5). Some of the most outstanding examples of how not to solution mine a resource and how not to control ground subsidence effects are to be found in east European countries that are still trying to deal with the environmental outcomes of being former satellite states of the Soviet Union. But caving problems have been tied also to mines and boreholes in the United States and Canada, once again human error, greed or ignorance has created many of these problem structures.

Ocnele Mari Brinefield, Romania

SALROM, a government-owned company, solution mines Badenian (Miocene) halite in the Valcea Prefecture of Romania (Fig. 13.19). Production from Field 2 was shut down on March 5, 1991, when earth vibrations were noted by SALROM workers. A subsequent sonar survey showed that poorly monitored brinefield leaching between 1971 and 1991 had created a gigantic merged cavern as salt pillars separating adjoining caverns were inadvertently dissolved (Fig. 13.20); the upper parts of the captive boreholes 363, 364, 365, 366, 367 and 369 had merged into a common cavern. The cavern was filled with some 4.5 million cubic metres of brine, was less than a hundred metres below the landsurface, was more than 350 m across and was overlain by loosely consolidated sandy marls (von Tryller 2002; Zamfirescu et al. 2003). The cavern was overlain by a bowl of subsidence and, even though mining operations in the region of the cavern completely stopped in 1993, the ground above continued to subside to a maximum of 2.2 m prior to the September 2001 collapse. In the period 1993–2001 the cavern continued to enlarge and the northern part of the cavity expanded by some 25–35 m (see inset in Fig. 13.20 showing sonar surveys 1995–2001).

The 1993 sonic survey of the cavern showed it was so large and shallow that its roof must ultimately collapse, predicting when was the unknown. The fear was that if it collapsed catastrophically, it could release a flood of at least a million cubic metres of brine. Brine could be released either

Table 13.5 Collapse and subsidence vents associated with brinefields

Location	Timing and size	Explanations & implications	Reference
Ocnele Mari Brinefield, Romania	Partial collapse of the roof of a much larger solution cavern occurred on 12 September 2001, it formed a large collapse crater and forced a brine flood down a nearby valley. Subsequent collapse and flooding occurred on July 15, 2004.	Poorly monitored salt leaching under the former Soviet regime between 1970 and 1993 created a gigantic cavern as salt pillars separating adjoining caverns were inadvertently dissolved and the cavern roof migrated toward the surface. The resulting cavern was filled with 4 million cubic metres of brine and was more than 350 m across. It broke through to the surface at its northern end in 2001, with further collapse in 2004.	von Tryller (2002)
Ground subsidence in brinefields near Krakow, Poland (Lezkowice/Barycz brinefields)	At the Barycz brinefield, 33 sinkholes up to 27 m wide and 27 m deep appeared between 1923 and 1993, the region is subject to numerous landslides.	A large deep sinkhole formed between 1984 and 1986 above the Lezkowice brinefield. Pollution of the groundwater system via poorly managed wells and broken pipes allowed high salinity waters to reach the nearby Raba River. In 1983 the river salinity reached 206 mg/l.	Garlicki (1993), Zuber et al. (2000)
Collapse at Compagnie des Salins Gellenoncourt saltworks near Lorraine, France	On March 4, 1998, a sinkhole more than 50 m across and 40 m deep formed atop the SG4 and SG5 brinefield caverns, France. It was an induced collapse.	The SG4 and SG5 caverns, drilled in 1967, unexpectedly joined in 1971. By 1982 the salt cushion in the roof had dissolved out putting the cavity roof in direct contact with a 25 m thick marl. In October 1992 the marls broke free, exposing a large section of the cavity roof to direct contact with the brittle Dolomite de Beaumont. Collapse was induced by enlarging the cavity by injecting 300,000 m^3 of fresh water.	Buffet (1998)
Cargill saltworks collapse, near Hutchinson, Kansas	Collapse started on October 21, 1974. Within 4 h the crater was 60 m across and after 3 days had created a circular depression some 90 m in diameter and nearly 15 m deep.	Uncontrolled brine extraction since 1888 certainly contributed to the Cargill collapse. Post-mortem analyses showed that several warning signs, especially an enlarging bowl of subsidence, had been noted, but ignored. After the collapse the brine field and the loss of part of the saltworks infrastructure the brinefield was abandoned.	Walters (1978), Hendron and Lenzini (1983), Dyni (1986)
Brinefield sinkholes at Windsor, Ontario and Point Hennepin, Michigan	On February 19, 1954, near Windsor, a water filled depression some 120–150 m across and up to 7.5 m deep formed within a few hours, destroying much of the surface plant. On January 9, 1971 at Point Hennepin the first collapse crater formed, after a few months it stabilized with a diameter of 65 m. A second crater developed in April and May 1971 measuring some 120 m across, with a depth of 35 m.	The similarity in the geology of the Windsor and the Detroit sites as well as the rapidity of the collapse, along with the size and steepness of the collapse craters, led Nieto and Russell (1984) to question the collapse mechanism of Terzaghi (1971). They argued his notion of steep upward caving from more than 300–400 m below the surface and centred on solution caverns in the Salina Salt could not explain the craters or their subsidence history. Instead, they proposed a collapse scenario based on a loss of cohesion in pressurised Sylvania sandstone and in the presence of water.	Terzaghi (1971), Nieto and Russell (1984)
Retsof Mine collapse, New York State	Loss of the Retsof Salt Mine began with a magnitude 3.6 earthquake in the early morning hours of March 12, 1994. Two large, circular collapse features some 100 m apart developed a month apart at the land surface above two collapsed mine rooms.	Catastrophic breakdown driven by collapse of a small pillar and panel section in the mine some 340 m below the surface. Collapse of the "back" was accompanied by an initial inrush of brine and gas (methane) into the mine and by a sustained inflow of water via the overlying fractured limestone. A month later on April 18 an adjacent mine room collapsed.	Gowan and Trader (1999), Payment (2000)

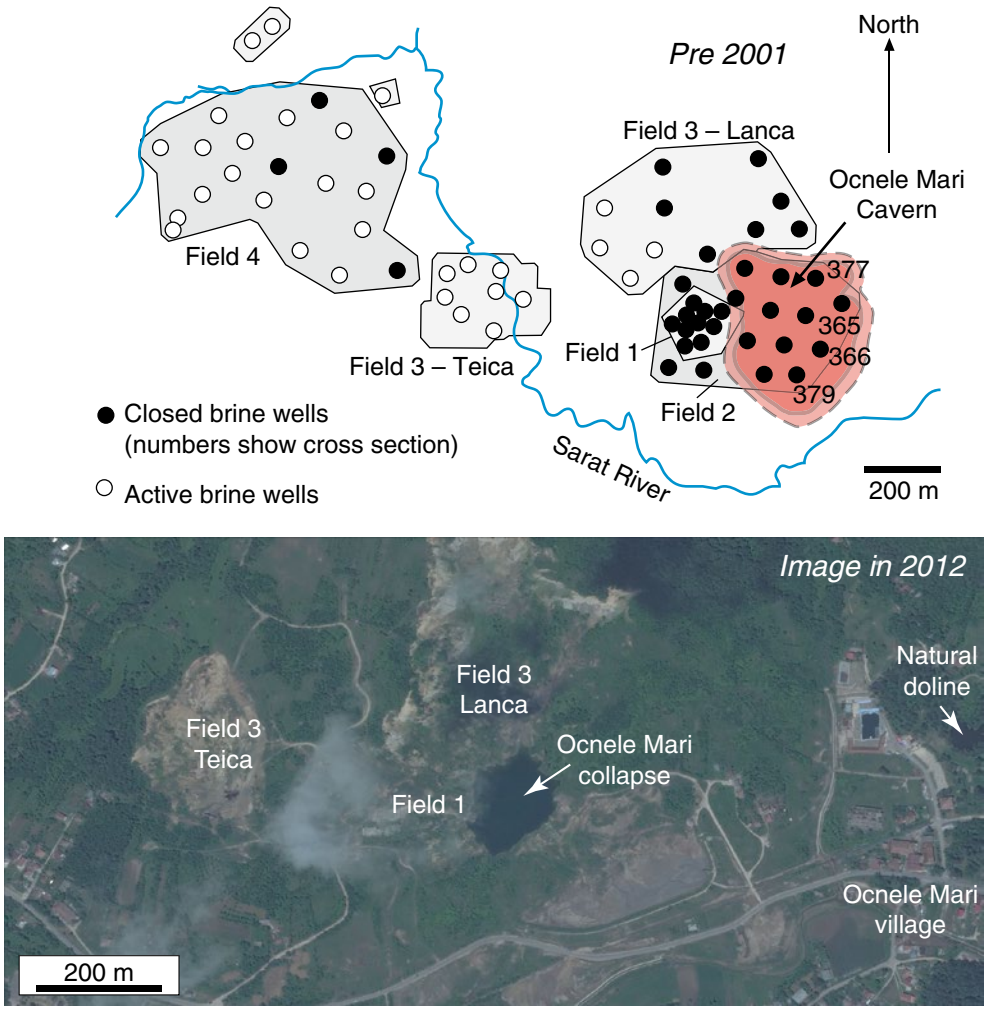

Fig. 13.19 Ocnele Mari brinefield, Romania. Locality maps showing various active and inactive brinefields as well as the likely extent of the large solution cavern defined by SOGON. Line drawing is situation pre 2001, while the lower image was captured in 2012

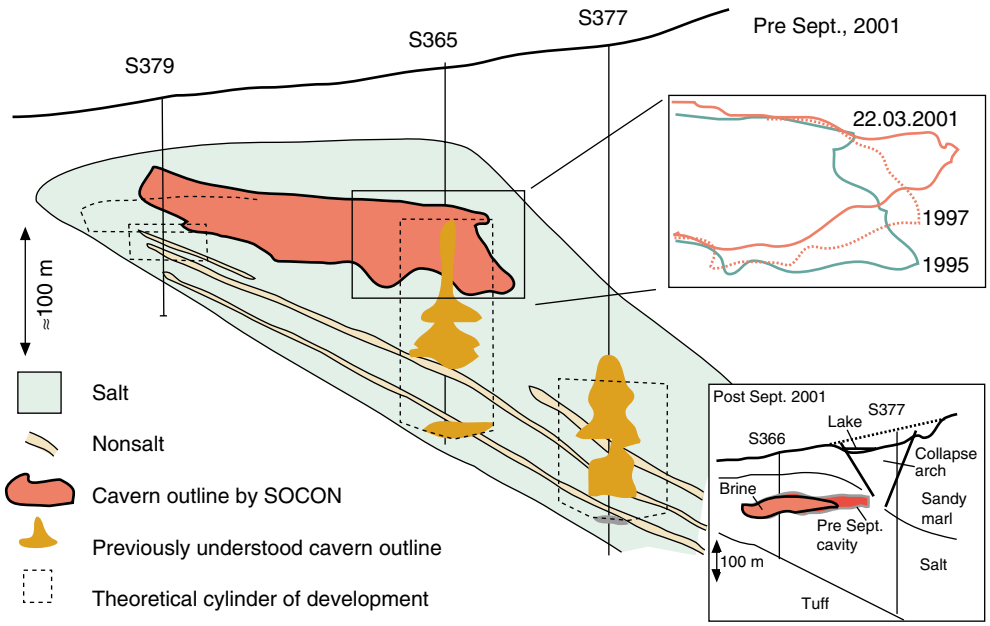

Fig. 13.20 Ocnele Mari brinefield, Romania. Interpretive cross section showing locality of cavern and proximity to land surface, the *inset shows* sonar defined outlines and the upward migration of the cavern from 1995 to 2001. This ultimately led to a partial collapse of the cavern roof in this zone on September 12, 2001, as seen in *lower inset* (Redrafted from SMRI data files at <http://www.solutionmining.org>, von Tryller (2002), Zamfirescu et al. (2003))

over several hours (least damaging scenario) or instantly forming a wave of escaping water several metres high that would flood the nearby Sarat River valley for many kilometres downstream. There were 22 homes on top of the cavern that would be immediately affected; also at risk were the hundreds and perhaps thousands of residents in the area of the saltworks and river valley below, as well as the local ecology and the civil/industrial infrastructure. Ongoing brine delivery from other nearby operational SALROM caverns to the large Oltchem and Govora chemical plants would also be disrupted. When collapse did ultimately occur (twice in the period 2001–2004), each episode took place over a number of hours and so a catastrophic wave of water did not eventuate.

According to SMRI (Solution Mining Research Institute), there was no good engineering solution to prevent the Ocnele cavern roof from collapsing. Prior to collapse, brine in the cavern exerted pressure against the roof helping to hold it up; removing even a small amount of brine would remove hydraulic pressure that could possibly trigger a catastrophic collapse. Nor was it practical to fill the cavern with sand and industrial wastes as suggested by the Romanian government. It would take too long and it was unsafe to place men and equipment on top of the still expanding cavern. Even if it could be done, only the areas directly below the injection wells would be filled. The best solution was to construct a dam as close to the cavern as possible, and then perhaps trigger a controlled collapse by pumping out the cavern brine.

A partial collapse of the cavern roof atop well 377 occurred on 12 September of 2001, the ensuing brine flood killed a child and injured an older man. The collapse began at 7 pm with brine spilling out of wells 365 and 367. Southward of well 377 a collapse cone some 10 m across started to form and fill with brine. The cone continued to expand and fill with water until its southern lip was breached. Water spilled out of the cone and down the hill slope. The flow rate of the expelled flow reached a maximum of 17 m^3/s at 3 am on September 13th, with flow continuously exceeding 10 m^3/s for a period of more than 6 h around that time. By 7 am flow was down to 4–5 m^3/s and by 7 pm, 24 h after the flow began the flow rate was 0.4–0.5 m^3/s. Some 24 h after the onset, roof collapse had formed a water-filled lake with an area of 2.4 ha (Fig. 13.19; Zamfirescu et al. 2003).

A second roof collapse occurred on July 13, 2004. Realitatea Romaneasca, Romania, reported that ground collapse occurred on 9:30 pm July 13, 2004, possibly triggered by heavy, recent rains. The wellhead of bore 365 was destroyed in this collapse and many other well heads in Field 2 had been destroyed by ongoing subsidence in the period 2001–2004. This collapse was the culmination of a series of collapse-related events that began on Monday July 11. It was planned that a purpose-built earthern dam would contain the brine flood. But when the roof fall occurred at 9:30 pm, the dam was breached 30 min later by some 250,000 m^3 of salt water. Flow rate through the breach reached a maximum of 6 m^3/s. Collapse did not occur until just after local authorities had evacuated people from 50 homes in the area around the cavern. Most of the brine forced out by the roof collapse escaped into the Sarat (Olt) River. The government attempted to dilute the effects of this flush of salt water by releasing fresh water into the river from nearby dams. Fortunately, unlike the 2001 event, there was no loss of life.

Subsidence in Old Belvedere Spinello, Italy

The Old Belvedere Spinello brinefield is located near Crotone, in southern Italy and exploited the salts of the Messinian series and is transgressively covered by a number of Plio-Pleistocene alternating sandy clay units. Originally the Belvedere Spinello brinefield was operated via brine wells interconnected by hydraulic fractures. This area, now referred to as the "Old Mine," was operational in the 1970s and 1980s, exhibits subsidence effects ranging from sinkholes to bowl subsidence and landslides (Fig. 13.21). Salt strata do not outcrop in the valley and are folded in an anti-

Fig. 13.21 Sinkholes in an anthropogenically-induced cone of collapses in the "old mine area" in the upper valley of the former Belvedere Spinello brinefield, Italy (Scaled Bing® Image mounted in MapInfo)

cline with a NNE to SSW oriented axis. The brinefield, which is no longer active, sat atop this anticline and was located over two main Messinian salt layers, the first or upper, was targeted for solution mining. It is made up of breccia (clayey marl, gypsum, etc.), cemented by salts, mostly halite; it has a halite percentage of about 60 and an average thickness of about 150 m. The depth from the ground level of the surface to this layer varies from 200 to 600 m (Fig. 13.22). The brinefield occupies a valley atop a salt anticline which is asymmetrical; its western side is vertical, or locally overturned, while the eastern side grades eastward with an inclination of 15–20° (Fig. 13.22b). The character of the exploited salt varies down the valley from a modestly deformed bi-crested salt anticline in the "Old Mine" area to a laterally compressed and thickened domelike anticline lower down the valley in what is called the "New Mine" area. Brinefield mining began in the 1970s over the less deformed salt in the upper valley and gradually moved down the valley toward thicker more deformed salt (indicated by the southern area dominated by Ba-numbered wells in Fig. 13.22).

Relatively strong formations overlie the less deformed salt of the "Old Mine" brinefield area. Over the more recently mined domelike salt targets, located further down the valley, these brittle formations are replaced by relatively weak overburden strata. For a short distance on one side of the valley near the "Old Mine area" the crest of the salt anticline lies against a fault running beneath the toe of a steep hill. From this point the top of the salt dips steeply in the direction of brine wells located some distance away in the valley axis.

The first sinkhole surfaced in January 1983 around well 5. After the collapse, a circular doline opened in the ground, with a diameter of 50 m and an area of about 2,000 m and filled with brine to a depth of 6 m. Subsequent erosion of the soft materials of the walls progressively refilled much of the doline. The initial volume of brine was about 20,000 m^3, with a TDS of 30 g/l (Gisotti 1991).

A second sinkhole (now filled) appeared in April 1984, to the east of Colle Barretta, near the south-western edge of the brine field and more than 360 m from the nearest active brine well of the "Old Mine" area. It formed at the foot of the hilly slope of Barretta Hill, causing a catastrophic landslide into the water-filled sinkhole, with consequent violent expulsion and projections of a significant volume of brine. Around 100,000 m^3 of brine was released in this flood, first into the river bed of Fosso Barretta, then onto the plain of the Neto River, extending across an area of some 120 ha. Brine flowed into the fluvial stream of Neto River, polluting it, and also polluting the local ground waters via percolation. The salinity of fluvial waters, immediately after the brine flood, reached values of 19.7 g/1. Step by step, the salinity has returned to normal values.

This destructive sinkhole formed along the Timpa del Salto fault, so putting into contact the "marly clay of Cutro" (that suffered the majority of the sliding), on the downthrown side, to the "Molasse of Scandale" on the upthrown

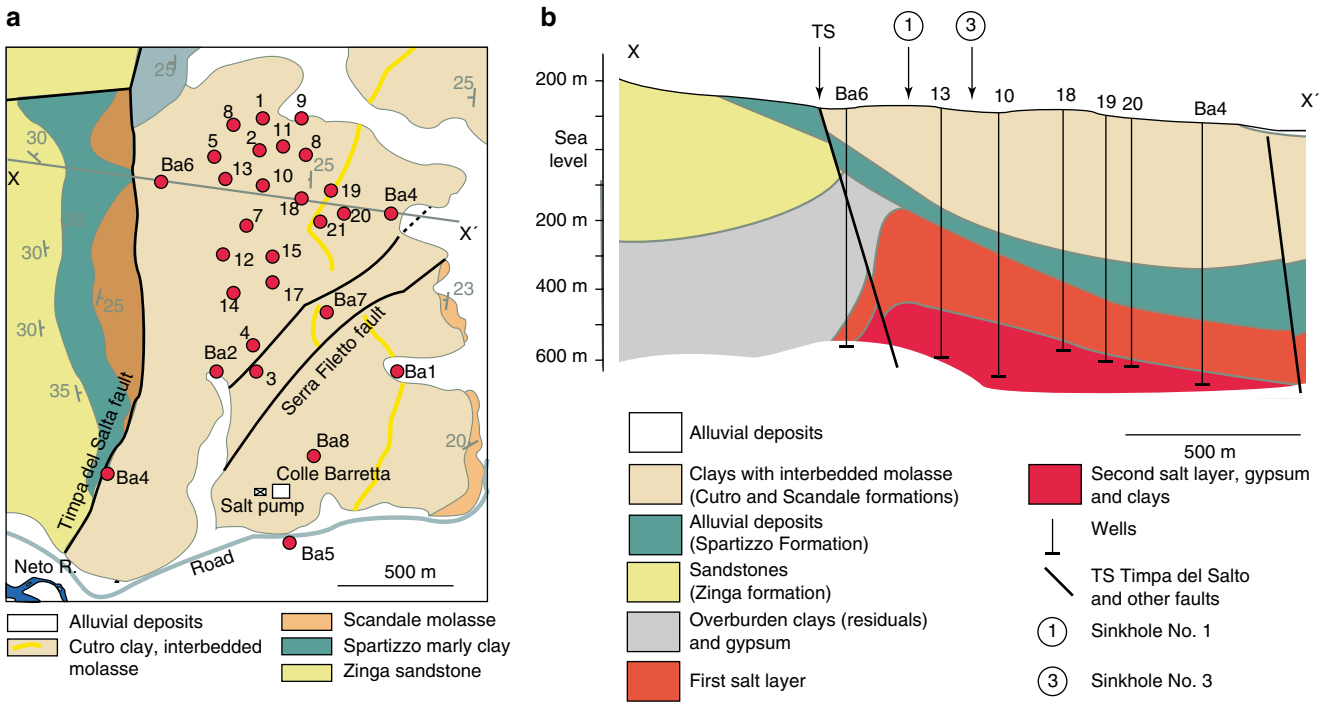

Fig. 13.22 Belvedere Spinello brinefield, near Crotone, Italy. (**a**) Geological map. (**b**) Geological cross section X-X′ (After Gisotti 1991)

side. Material caught up in the landslide had a volume less than the landslide body; meaning that the missing rock filled the sinkhole in response to the collapse of the stoped roof to the induced subterranean cavity. The centre of this collapse was not immediately above any of the producing wells; salt solutioning had apparently migrated within the salt formation for a considerable distance laterally from the brine wells to where it had dissolved a large cavity at the toe of the hill. After the landslide and the consequent brine flood, saltworks operations were interrupted, and began again in the first months of 1987 with improved monitoring of all wells.

In September 1986, a third sinkhole formed on a quite steep hilly slope in the area of Barretta Asciutta of the Old Mine" area, located in a triangle with vertexes defined by the wells 13, 10 and 7 (Gisotti 1991). This new collapse doline (Sinkhole 3) was 200 m away from the first sinkhole, which was close to the well 5, and once again located in the "marly clays of Cutro" (Fig. 13.22). Initially, the collapse doline diameter was ≈ 30 m and the bottom was covered by a small brine lake, with a depth to the surface of this water body some 20 m below the doline edge. The width of the sinkhole increased because of subsequent collapses, and the brine dispersed back underground and so that the diameter of the hole evolved to about 50 m, with an area of about 8,000 m^3 and a depth around 25 m. Today all these dolines in the "Old Mine" area are water filled (Fig. 13.21). No further sinkholes appeared in the more recently mined end of the brinefield, probably due to its relatively weak overburden. Instead, gradual bowl subsidence dominates this part of the field. Solution mining continued until 2008 in what was called the new Belvedere Spinello Brinefield using a number of single-well, sonar-monitored salt caverns (Guarascio, et al. 1995). The brinefield is no longer active.

Brinefield and Mine Collapse Near Krakow, Poland

A former salt mining region, including the World-Heritage Wieliczka Mine, lies close to Krakow in south of Poland, has been mined since the thirteenth century. There are two main problem sites, Barycz/Wieliczka and Lezkowice. The Lezkowice site is east of Krakow and lies about 10 km east of Wieliczka city. The Barycz site, located to the immediate west of Wieliczka Mine, covers an area of one square kilometre, and is two kilometres wide at its maximum extent (Fig. 13.23). It was first solution mined in 1923. Miocene salt at Barycz is relatively flat lying, around 30 m thick, and some 230–280 m below the land surface. Salt at Lezkowice is steeply dipping and can be found as patchy subcrops as shallow as 40 m below the surface. Salt was solution mined at Lezkowice from the nearsurface to depths of more than 450 m. Both sites are covered by 15–20 m of unconsolidated Quaternary sediments (sands, gravels and peats).

At its most active the Barycz brinefield consisted of more than 900 solution wells about 50 m apart. In 1993 after 70 years of exploitation the field had produced some ten million tons of salt, equivalent to a unit 3 m thick across the whole of the exploited area. There was significant surface subsidence in the brinefield from the onset of solution mining, with ground displacements of 10–30 cm noted between 1926 and 1934. Thirty three sinkholes up to 27 m wide and 27 m deep appeared in the brinefield between 1923 and 1993, and the region was subject to numerous landslides. By 1993, the brinefield was exhausted and the landsurface was pock-marked by stagnant brine-filled subsidence cones and sinkholes, often centred on abandoned wells. As the land is considered unusable for agricultural purposes, it is currently used as a waste dump by the nearby town of Krakow (≈800,000 inhabitants) (Fig. 13.23).

Fig. 13.23 Location of former Barycz brinefield (*shaded*) and the Wieliczka salt mine. Bing® image mounted and scaled in MapInfo®

Unfortunately, although the Barycz and Wieliczka areas are separated by a shallow salt ridge, the world heritage Wieliczka Mine with its unique salt sculptures and carvings in the upper levels of the mine, lies less than a few kilometres from the Barycz brinefield. Throughout its history, the mine has been subject to flooding and freshwater influx. Even though a dehumidification program for the mine air has now removed the sculptures and carvings in the mine from the endangered sites list, it is in a constant state of possible destruction by flooding (Zuber et al. 2000). Exploited Miocene salt in Wieliczka mine is made up of two intervals: the lower one consists of layered salt which was strongly tectonically deformed, while the upper interval consists of salty clays with large salt blocks (Fig. 13.24). The salt deposit, and the adjacent flysch sediments were overthrust from the south and are relatively well documented by the mining operations. Tertiary-age water-bearing Chodenice beds make up the northern boundary of the deposit and are much less well studied. They consist mainly of clays, slightly cemented sandstones and sandstone conglomerates that were probably strongly fractured during Miocene folding (Fig. 13.24). The main water inflow into the mine network occurs along the southern boundary with the Chodenice beds.

Seven centuries of exploitation in the Wieliczka Mine, beginning in the thirteenth century, has created more than 2,000 chambers with the total volume of about 7.5×10^6 m^3 and over 190 km of galleries in nine main levels and several local midlevels. Throughout the 700 years of mine history there were many catastrophic intrusions of water and loose sand, largely caused by a lack of knowledge of the boundary of the salt and the high permeability of adjacent rocks.

Zuber et al. (2000) gives a simplified historical record of inflow rates to the mine in m^3 day^{-1} as: 6 in 1381–1819, 31 in 1820–1919, 50 in 1925–1960, 135 in 1960–1971,

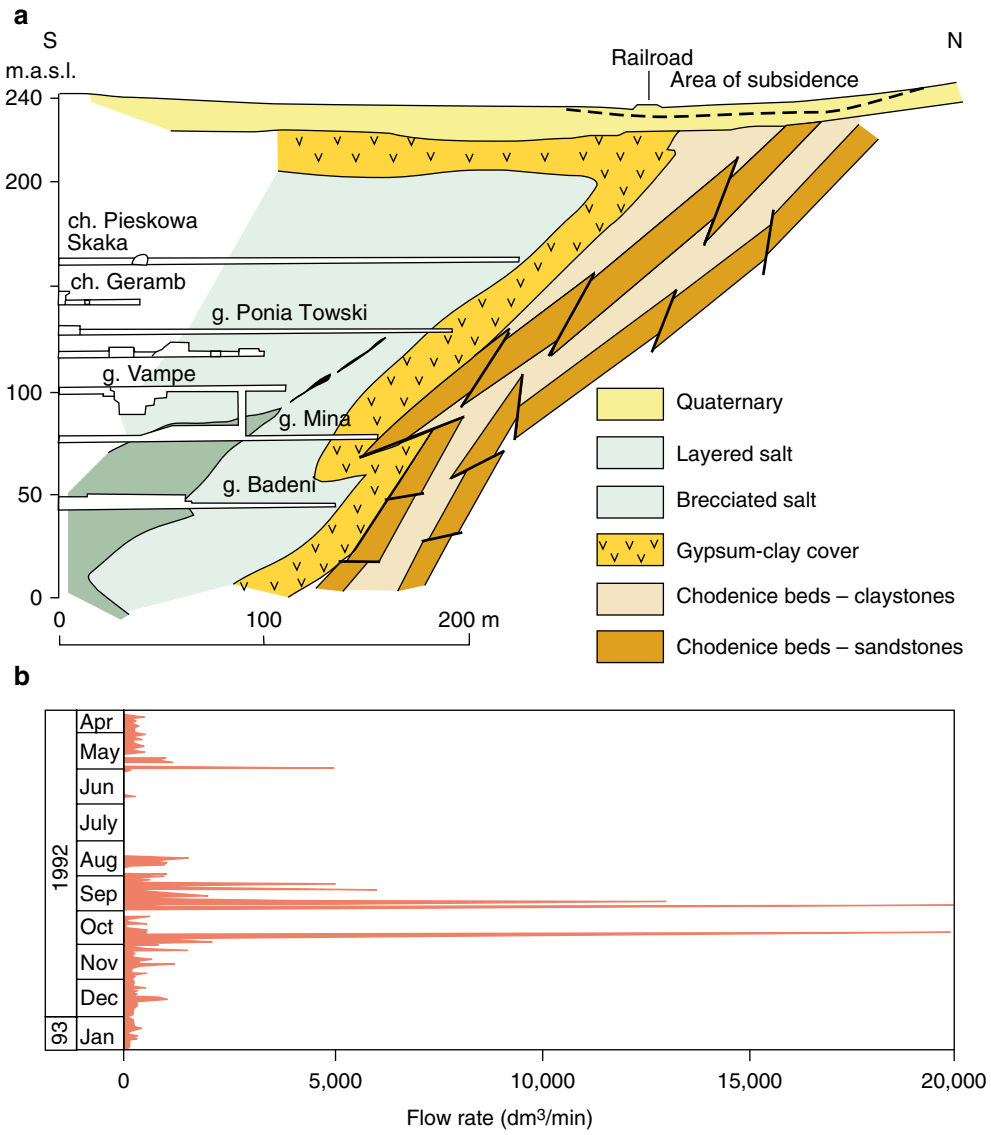

Fig. 13.24 (**a**) Wieliczka Mine cross section through the northern boundary in the region of the Mina Gallery. (**b**) Inflow rates into the Mina Gallery during 1992–93 (After Garlicki and Wilk 1993; Zuber et al. 2000)

500–418 in 1972–1991, and about 900 in 1992. In 1991, there were about 260 inflows with very low flow rates and several larger inflows at the fourth, fifth, sixth and seventh mine levels. These large inflows considerably increased the total water inflow to the mine in the last several decades. One of the most catastrophic inflows started in 1992 in the Mina gallery at the fourth level and was so intense that the lower flooded sections of the mine had to be abandoned (Fig. 13.24b). Shortly before the First World War that gallery had crossed the salt boundary and stopped 20 m beyond the salt deposit in gypsum and clay cover (Fig. 13.24a). After the Second World War, the gallery was not accessible due to rock falls, and slag used to fill in the Dunajewski chamber cut across the Mina gallery. Water was seeping downward through the slag deposit and exiting at the fifth level (Badeni gallery) at a rate of 4–5 l per minute and TDS of 300 g/l (Zuber et al. 2000).

Serious trouble with inflows started during a reconstruction of the Mina gallery aimed at ponding the inflow behind a dam where it could be pumped from the mine. A catastrophic influx began on the night of 13 April 1992 when the flow rate increased to 200–300 l per minute (290–430 $m^3\,day^{-1}$), i.e., nearly equal to the sum of all other inflows to the mine at that time. Pumps then in use were not able to pump it out. In consequence, the gallery was filled nearly to the ceiling with water and mud, but the water drained or was pumped out after a few days. An even more catastrophic flood began on September 13, 1991 and overwhelmed the pumps and the newly constructed dams. Influxes exceeded 10,000 l per minute. Inflows to the Mina Gallery continued to show a similar pulsing, well into 1993 (Fig. 13.24b). Operations in the lower levels ceased soon after and the mine today is no longer exploiting solid salt although brine pumping still takes place. This extraction is expanding the proportion of cavities in the lower levels of the mine and will ultimately destabilise the tourist areas. But if brine is not removed and processed, the resulting rising waters will also enter the tourist levels of the mine.

The pore pressure release created by the flooding drove considerable subsidence at the surface (Zuber et al. 2000; Perski et al. 2009). Walls surrounding a historic Franciscan monastery partially caved and huge cracks appeared in the walls of the buildings both inside the monastery itself and around it, making some sites structurally unsafe. In October 1992 the surface subsidence in the wake of the successive floods was as deep as 0.5 m.

The pulsed nature of the inflow prior to the final flood argues for more than one water source to the Mina level (Zuber et al. 2000). Initially, the Chodenice beds in the vicinity of the Mina gallery were drained of water, then either waters stored in the Chodenice beds west and east of the Mina gallery were drained, or there was a hydraulic contact established with the sands of the Tertiary Grabowiec beds (Fig. 13.24a). The Grabowiec beds are mostly confined aquifers filled with Holocene waters. In any case, the increased influx at the Minas level did not influence the flow rate of other inflows, and the local recharge, especially within the subsidence cone atop the mine, was negligible.

The pulsed character of the measured inflow was probably driven by natural instability of adjacent rocks, and by unsuccessful attempts to stop the inflow. Wash out (suffosion) periods occurred during times with high inflow rates. These were followed by land subsidence, which led to clogging (colmatation) when the flow rates and hydraulic pressures dropped (Zuber et al. 2000). A temporary colmatation lead to an increase of the watertable level in the Chodenice beds, this drove an increase in hydraulic head until pressure breakout occurred and the whole cycle repeated.

That the pulsing process is quite complicated is shown by differences in water levels observed in a number of boreholes in the northern region of the mine adjacent to the Mina gallery (Garlicki et al. 1996). In general, when the water pressure builds-up sufficiently, dams, or any other anthropogenic sealing structures in this area of the mine are easily destroyed or moved from their positions because they cannot be anchored in stable rocks. The Chodenice beds are naturally unstable and additionally deformed and weakened by ongoing exposure to water crossflows. If the exiting water is recharged indirectly through the Grabowiec sands, the inflow rate to the mine can perhaps be reduced, but only if their basal sections are sealed in the region of the contact with the Chodenice beds. If the water comes from the distant parts of the Chodenice beds, the inflow rate can be reduced by pumping in wells installed at distances sufficient to avoid further rock destabilization in the vicinity of the gallery. Undoubtedly, any such operation would be a very expensive undertaking.

When the inflow to the Mina gallery developed to catastrophic dimensions in the early 1990s, the mine management showed a remarkable lack of scientific or engineering sophistication and no understanding of simple hydrological principles. They called on and paid generously for dowsing and witching methods to solve the flooding problem. The dowsers claimed that an underground "river" flows through the mine at the rate of 1.5 m^3/s. Following the advice of witches and dowsers, a 100-m-long trail was buried about 1 m below the ground surface, it was supposed to stop the inflow of the underground "river" at a depth of 170 m, and to change the "rivers" flow direction upwards (Zuber et al. 2000). Today, the flooding of the lower mine continues, the tourist region of the mine area is still under constant threat of renewed flooding, but the witches and dowsers are happy and counting their spare zlotys.

Depletion of the Barycz brinefield meant that in order to maintain a feedstock for nearby chemical industries the saltworks needed to shift to the Lezkowice site in 1968. There the brinefield wells were sited 35 m apart with a 300 m wide

"exclusion" zone between the brinefield and the nearby Raba River (Fig. 13.25). Brine well production was supposed to be limited to 8–10 years and the cavities monitored by sonar to prevent the problems experienced at Barycz. Exploitation actually continued unabated for 20 years until January 1988 when the brinefield was finally shutdown. Over-exploitation led to the fusion of numerous cavities, the unfettered escape of brine into the environment and the nearby Raba River. Some 5.1 million tons of salt were extracted over the 20 year life of the brinefield (corresponds to 17 million cubic meters of brine product). In an attempt to prevent further ground collapse, loam and ash waste from a nearby power station were injected into some of the cavities. Even taking into account the re-injection of some 1.10 million cubic meters of waste, the cumulative volume of the cavities remaining beneath the Lezkowice site in 1990 was of the order of 1.45 million cubic metres.

Subsidence measurements were made at Lezkowice from the beginning of the exploitation in 1968. Measurements carried out between 1974 and 1988 show two principal zones where subsidence exceeds 80 cm (Fig. 13.24a; Garlicki 1993). The most significant area of subsidence lies at the centre of the brinefield, but extends beyond the exploited zone, in particular in the northeast. Subsidence reaches 1.20 m in the brinefield centre. The second major subsidence zone, where subsidence was higher than 80 cm, is located in the northern part of the brinefield. There is a third zone of subsidence with depressions of more than 50 cm to the east of the former brinefield.

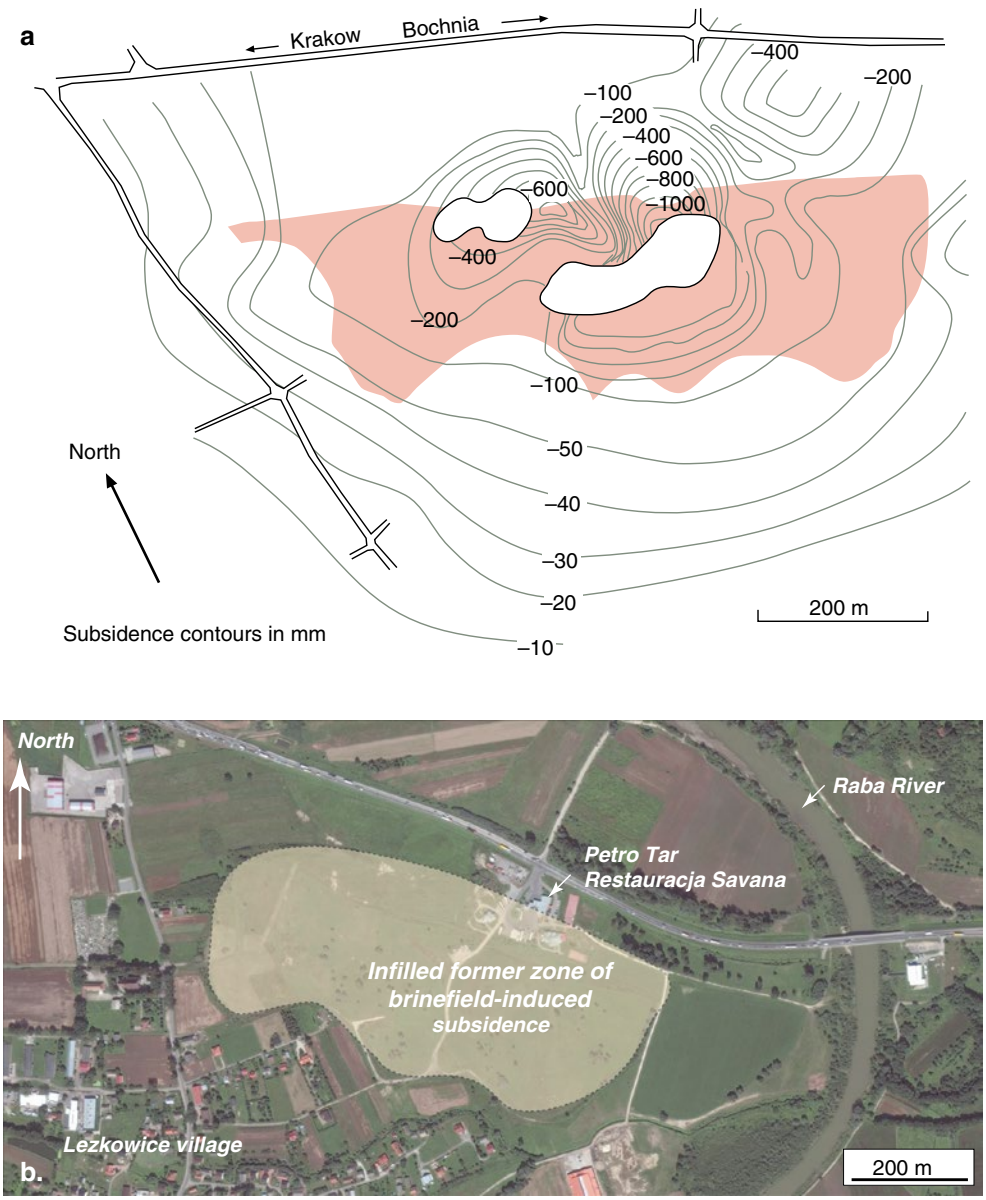

Fig. 13.25 Lezkowice brinefield site, Poland. (**a**) Subsidence at the between 1974 and 1988, contours in mm. Area of the former brinefield is shaded pink (After Garlicki 1993). (**b**) Situation in 2012 following infill of subsidence cone and construction of commercial sites (including a roadside petrol station) above the former cone of subsidence. Bing® image mounted and scaled in MapInfo®

Between August 1988 and June 1991, subsidence increased by 40 cm in the western part, and 80 cm in the central part; sagging in the central part had lengthened along an east-west axis and the depression bowl had migrated 150 m east. The first large deep (22 m) sinkhole at Lezkowice started to form in 1984, and continued to grow until 1986. After the first few months, the sinkhole was filled by the brinefield operator with more than 250,000 m^3 of sandy and argillaceous waste materials. Another large sinkhole formed nearby between 1988 and 1989, but it was no more than 3 m deep. Still more sinkholes appeared between 1988 and 1990 with a total a volume of more than 300,000 m^3, all were filled using waste residues.

Garlicki (1993) estimates that the large deep sinkhole, which formed between 1984 and 1986, was a response to the uncontrolled dissolution of a steeply dipping layer of salt that lay no more than a few metres beneath the Quaternary cover. There was significant salinization of the Quaternary aquifer in the region due a combination of brine leakage from poorly maintained pipelines and casings, and the uncontrolled solution flushing of shallow salt. The resulting brine percolated through sands and gravel aquifers and easily breached the "exclusion" zone to reach the River Raba. River salinity reached 206 mg/l in 1983 but returned to lower levels after the operator drilled drainage sumps.

Induced Collapse, Gellenoncourt Saltworks, France

Gellenoncourt is one of three sites that exploit halite beds of the Lower Keuper in the eastern part of the Paris Basin. The deposits extend from Cezanne in the west to Nancy with a length of 250 km and a width of 50–70 km. Salt production utilising solution mining techniques is focused on three sites along the Meurthe river, which all lie immediately to the east of Nancy.

On March 4, 1998, a sinkhole more than 50 m across and 40 m deep formed atop the SG4 and SG5 brinefield caverns in the Gellenoncourt saltworks near Lorraine, France (Fig. 13.26; Buffet 1998). It was an induced collapse designed to prevent a possible uncontrolled future ground collapse. The problem started in 1967 with the beginning of the exploitation of Triassic salt layers in the Keuper Fm. In total the Keuper is more than 150 m thick with five salt layers at its base, passing up into variegated and poorly consolidated marls and sandstones and capped by the Dolomite du Beaumont. The top of the salt is some 220 m below the surface and divided into 5 beds numbered 1–5 from top to bottom, with the solution mining program designed to leach beds 1 through 3 in the region of SG4 and SG5 caverns (Fig. 13.27). Five wells, SG1 to SG5, were joined using hydrofracturing in February 1967. Theoretically, the process was designed to leave a substantial salt pillow atop all the cavities and so separate the solution cavities from the overlying marls (Fig. 13.27; 1967–1971). The SG4 and SG5 caverns unexpectedly joined in 1971. Brine injection to these two wells was stopped, but crossflowing brines flowing to the producing SG1 well continued to excavate these two caverns. By 1982 the salt cushion in the roof of the SG4-SG5 cavern had completely dissolved away, placing the cavity roof in direct contact with the base of the marls.

From 1982 until October 1992 there was no further upward growth of the cavern roof. Then a 25 m-thick section of the variegated marls in the roof broke free and fell to the

Fig. 13.26 Gellenoncourt brinefield, France. Shows the position of the induced collapse dolines in the region of the former SG4 and SG5 brine wells (Bing® image mounted and scaled using MapInfo® software)

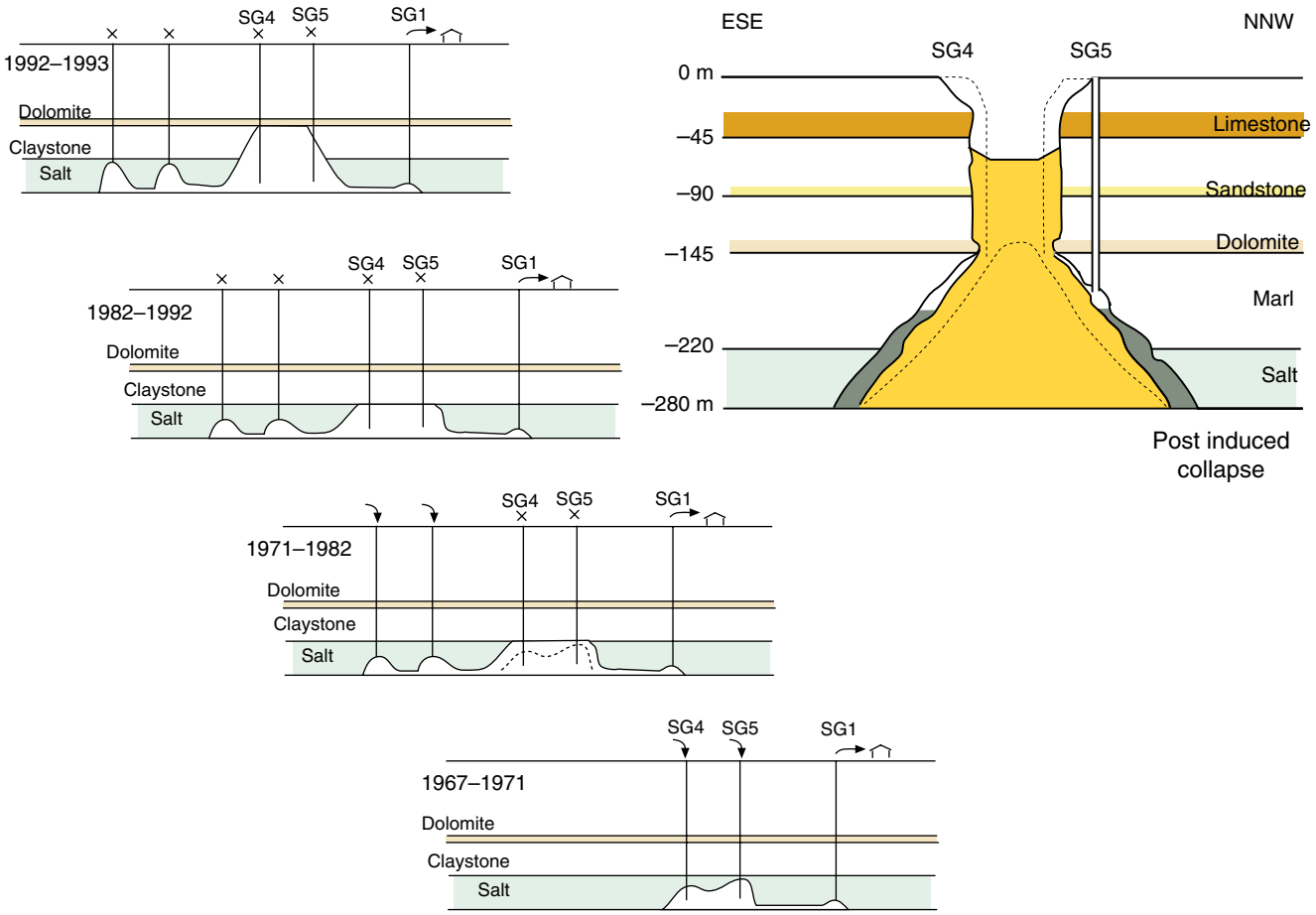

Fig. 13.27 Series of chronological panels showing the evolution of the SG4-SG5 cavity in the Gellenoncourt saltworks, France. The larger panel shows the shape and size of the final induced collapse crater (After Buffet 1998)

cavern floor, leaving a large section of the cavity roof in direct contact with the brittle Dolomite de Beaumont. This stiff dolomite layer prevented any further immediate collapse of the roof and consequent propagation of the cavity to the surface. But continued growth of the roof span beneath the dolomite would mean a later, larger, perhaps catastrophic collapse. In 1995 the operator tried to induce a controlled collapse by placing a submerged pump in the cavity and pumping out brine to create an exposed upper face. But this didn't work. The next approach was to further enlarge the roof span by injecting 300,000 m^3 of freshwater into the cavity. Collapse occurred on March 4, 1998, forming a 50 m wide crater. To protect the surrounding countryside from any brineflood damage a dam was constructed to capture any brine overflow, but in the actual event it was not needed.

Solution Mining Induced Ground Collapse, Tusla

Salt mining induced ground subsidence is a major hazard in the city of Tuzla (Northeastern sector of Bosnia and Herzegovina) and its surroundings since 1950, when salt solution mining began (Fig. 13.28; Mancini et al. 2009).

The exploited salt is a Tertiary bedded deposit (Eocene to Miocene) with five salt horizons lying at an average depth of 300 m. It covers a limited known area of only 1.5 km^2 (Fig. 13.28). In the 1990s the original Tusanj site in Tuzla was expanded to include the Tetima brine field, which was known to have high quality and large thicknesses of salt down to depths of 900 m, separated from one another by interbeds of banded marls, impure salt and clay horizons. The mining operations had been conducted for hundreds of years at depths starting from 170 m, but it was the large volumes extracted in the 1990s that caused massive surface subsidence and damage.

Analysis of topographical data collected during two periods: from 1956 to the Balkan War, and from 1992 to 2003 shows cumulative subsidence as high as 12 m across the whole period. It has damaged buildings and infrastructure across an area that includes a large portion of the historical town. Human-induced subsidence, with rates up to 40 cm/year in the most developed areas, were documented by GPS-based monitoring that began in 2004. It defines a decrease in subsidence rate to 20 cm/year in the past few years, and this decrease is directly related to reduction in rates of salt exploitation.

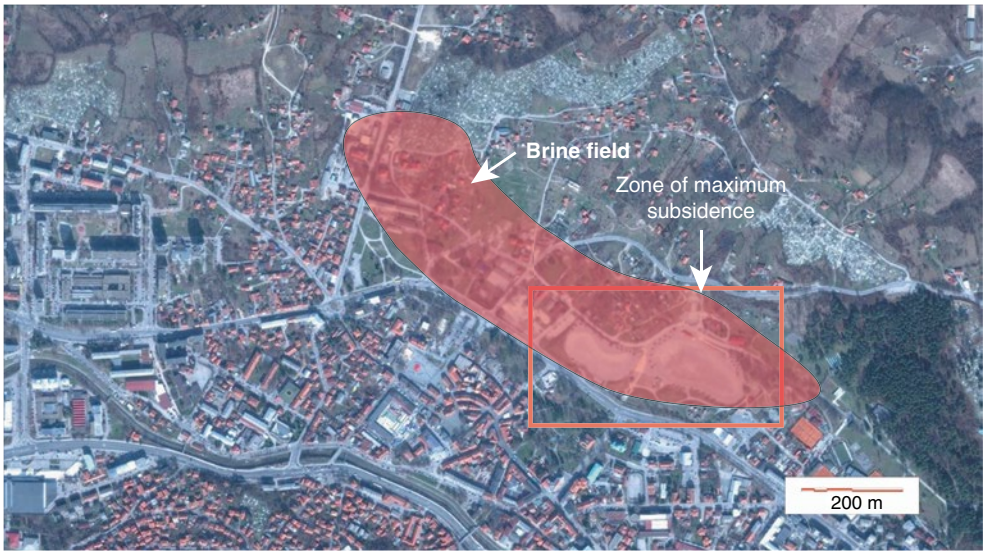

Fig. 13.28 Tusla city, Bosnia-Herzegovina, showing zone of maximum solution induced subsidence (*rectangle*) in relation to the brine field (Based on information in Mancini et al. 2009). Bing® image mounted and scaled in MapInfo®

That is, Mancini et al. (2009) show that there is close correlation between the average subsidence rate and the annual amount of salt extracted. The most intense period of damage occurred under Soviet domination and so destructive events are poorly documented in the state records. Something like 2,350 apartments were demolished by 1979 and 10,000 people lost their homes with a further loss of 1,500 buildings in the following 2 years. Today, the same region of maximum subsidence has been converted to public space with the subsidence depression in the zone of maximum subsidence used as a swimming pond, surrounded by parklands (Fig. 13.28).

Solikamsk and Bereznki Mine Collapses, Russia

Collapse of the Solikamsk-2 potash mine, Verkhnekamsky deposit, in the Upper Kama district of western Ural, Russia, resulted in a 4.7 magnitude seismic event on January 5th, 1995 and 4.5 m of surface subsidence (Fig. 13.29a, b; Whyatt and Varley 2008; Malovichko et al. 2001). Underground, the mine roof collapsed over an area measuring 600 m by 600 m. The event released an estimated 900,000 m^3 of gas (a mix of methane, hydrogen, carbon dioxide, carbon monoxide and other gases) that in turn led to gas explosions on the following day. Timely placement by the operators of a "significant volume" of backfill is credited with preventing further catastrophic consequences. There were subsequent collapses nearby in 2007 and 2014 (see www.saltworkconsultants.com).

The mined salt is of Middle Permian (Kungurian) age and located in one of six sub-basins extending from the Urals foreland to the Caspian basin. Sylvinite (potash) in the collapse area was extracted from 2 to 3 beds, with 10–16 m of total extraction height (Fig. 11.56). The mine used a panel system of rooms and pillars under 200–400 m of overburden. Rooms were 13–16 m wide and pillars 11–14 m wide by 200 m long.

A "rule of thumb" used across the Upper Kama district is that surface subsidence typically reaches 50 % of excavation

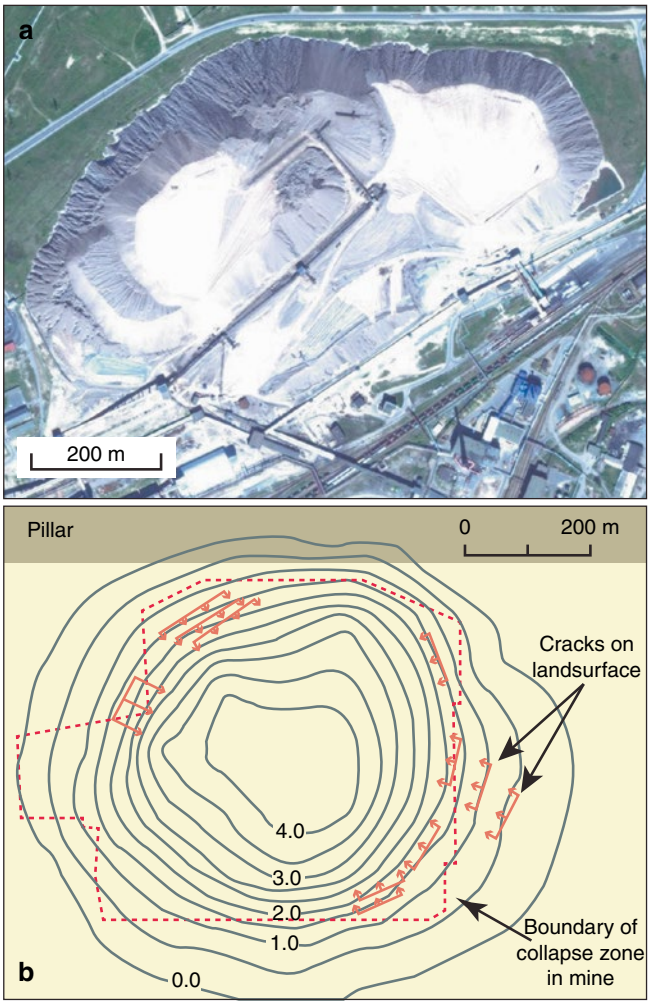

Fig. 13.29 Solikamsk-2 collapse, Urals. (**a**) View of collapse crater (Bing® image mounted in Mapinfo®). (**b**) Landsurface collapse contours in metres and the extent of the collapse zone in the mine (After Malovichko et al. 2001)

height 48 months after excavation. The collapse event in 1995 occurred 15 years after mining began, and 7 years after mining was completed beneath the collapse area. The unusual delay in subsidence implies extensive bridging of overburden, consistent with the uncommonly high release of seismic energy. The next largest collapses occurred in 1993 and 1997 with seismic magnitudes of 2.6 and 2.8, respectively.

An earlier collapse in the nearby 3rd Bereznki potash mine in July 25, 1986 is another interesting case of sinkhole formation from a mine operating at relatively shallow depths (Andrejchuk 2002; Whyatt and Varley 2008). Potash extraction was active at depths of 235 and 425 m below surface, where the targeted ore zone was overlain by a 100 m thick "salt complex" made up of halite and carnallite beds, overlain in turn by clays, carbonates, aquifers and sediments. Mining created "yield pillars," with 5.3 m wide rooms, 3.8 m wide pillars and a 5.5 m mining height. After mining, conditions in mined-out areas were described as, "pillars crushed and roofs sagged."

Observations of significant brine leakage into the 3rd Bereznki potash mine workings at a depth of 400 m indicated a loss of hydraulic control as early as January of 1986 (Andrejchuk 2002; Andrejchuk et al. 2000). This was a prelude or warning of massive dissolution occurring in the 90 m interval of salt overlying the potash level. Some 7 months later a large cavity had formed in the sandstone/limestone overburden, which was nearly 200 m thick. In the mine it appeared the water inflow situation remained relatively stable, at least until July. Failure of the mine head then occurred, the result of a cavity that had migrated vertically through more than 300 m of limestones, mudstones and sandstones. Final stoping was indicated by the near instantaneous appearance of a caprock sinkhole, which was 150 m deep and 40–80 m across and located at the top of a stoping breccia pipe or chimney of the same dimensions. Failure of this sequence began at 18:30 h with "clearly felt underground shocks" culminating with a final collapse at midnight, which was accompanied by an explosion with "flashes of light." Roof stoping over the pipe in the final stages before the cavity daylighted took only 12 days to migrate through the last 100 m of mudstone (Waltham et al. 2005). This very high rate of stoping was aided by structural weakness in a fracture zone along a local fold axis.

Retsof Mine, New York State, USA

The 1994 flooding of the Retsof Mine, New York State USA, took place over a period of weeks. Prior to abandonment, the 24 km^2 area of subsurface workings made it the largest underground salt mine in the USA and the second largest in the world (Figs. 13.30 and 13.31). It had been in operation since 1885, exploiting the Silurian Salina Salt and each year it produced a little over three million tons of halite. It supplied more than 50 % of the total volume of salt used to deice roads across the United States.

The eventual loss of the Retsof Salt Mine began in the early morning hours of March 12, 1994, with a magnitude 3.6 earthquake. The quake was caused by the catastrophic breakdown of a small mine pillar and panel section some 340 m below the surface and was accompanied by surface collapse of an area atop the mine that was some 180 by 180 m across and 10 m deep. This all occurred at the southern end of the mine near the town of Cuylerville. A month later, on April 18, an adjacent mine room collapsed to form a second collapse crater (Fig. 13.30). The initial March 12 collapse in the mine was accompanied by an inrush of brine and gas (methane) and by a sustained intense inflow of water at rates in excess of 70 m^3/min, via the overlying now fractured limestone back (Gowan and Trader 1999).

In a little more than a month, two steep-sided circular collapse features, some 100 m apart, had indented the landscape above the two collapsed mine rooms (Fig. 13.31). The northernmost feature, which was more than 200 m across, included a central area that was about 60 m wide and had subsided about 6–10 m. The southernmost feature, which was about 270 m in diameter, included a central area that was about 200 m wide and had subsided about 20 m (Fig. 13.30).

Fig. 13.30 Location of the collapse dolines atop the former Retsof Mine to the east of the town of Cuylerville. The doline occupies a pre-existing low that had also captured Beard Creek (Bing® 2012 image mounted and scaled in MapInfo®)

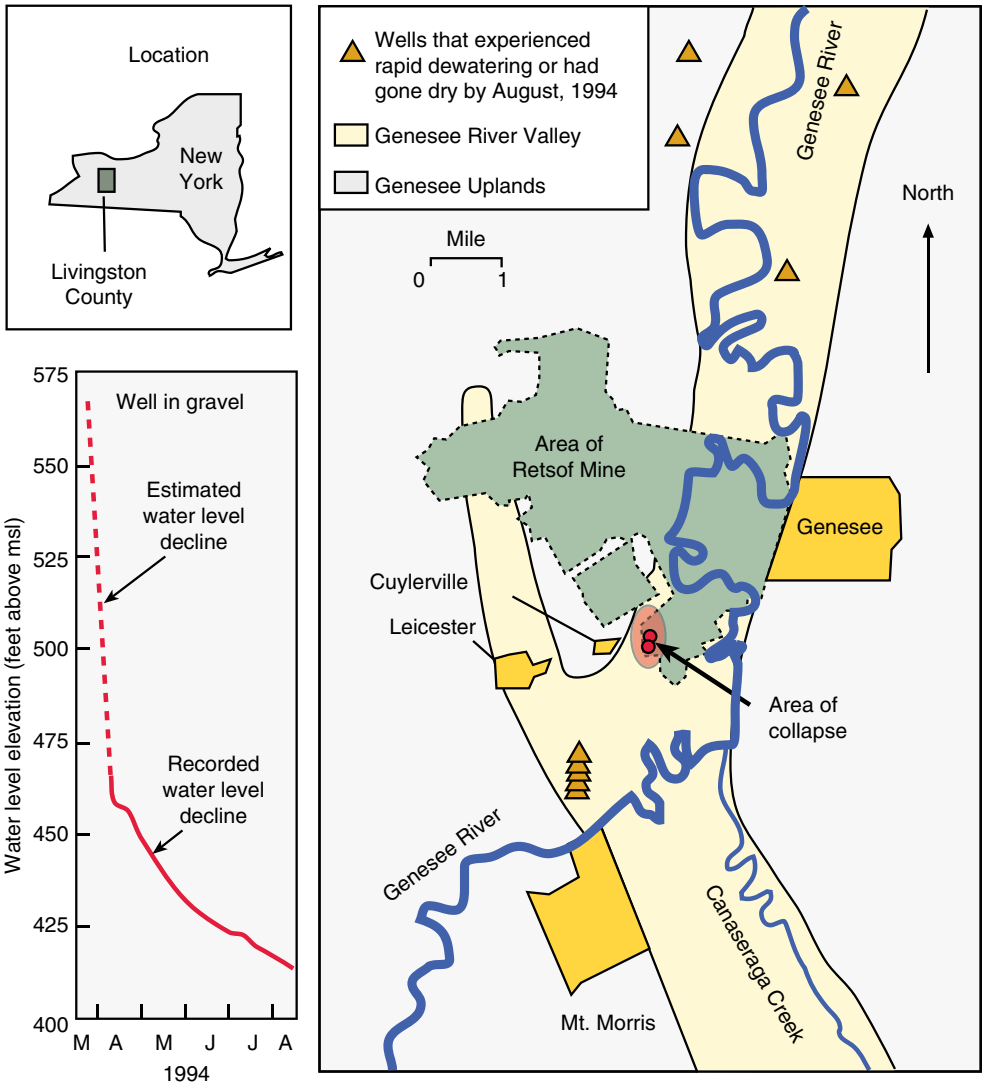

Fig. 13.31 Locality plan of the Retsof mine and the area of collapse along with a selected hydrograph from a well in the Genesee River valley (March 12 to August 12 1994; after Tepper et al. 1997)

Fractures extending up from the broken mine back created hydraulic connections between aquifers, which previously had been isolated from each and so provided new high volume flow routes for rapid migration of perched groundwaters into the mine level.

Water flooded the mine at rates that eventually exceeded 60,000 l per minute and could not be controlled by pumping or in-mine grouting. Within weeks the entire mine was flooded. Associated aquifer drawdown caused inadequate water supply to a number of local wells in the months following the collapse; some dried up (Fig. 13.31; Tepper et al. 1997). Aside from the loss of the mine and its effect on the local economy, other adverse effects included abandonment of four homes, damage to other homes (some as much as 1.5 km from the sinkholes), the loss of a major highway and bridge, loss of water wells and prohibition of public access to the collapse area. Land subsidence, possibly related to compaction induced by aquifer drainage to the mine, even occurred near the town of Mt. Morris some 3 miles southwest of the collapse area.

Post-mortem examination of closure data from the two failed mine panels showed an anomalous buildup of fluid pressure above the panels in the period leading up to their collapse. The initial influx of brine and gas following the first collapse coincided with the relief of this excess pressure. Gowan and Trader (1999) demonstrated the existence of pre-collapse pressurized brine cavities and gas pools above the panels and related them to nineteenth-century solution mining operations. They also documented widespread natural gas and brine pools within Unit D of the Syracuse Formation approximately 160 ft above the mined horizon in the Retsof Mine. The satellite image also shows the collapse occurred along the landscape low that was the Beard Creek valley (Fig. 13.30). Brine accumulations apparently formed in natural sinks, long before solution mining began in the valley, driven by the natural circulation and accumulation of meteoric waters along vertical discontinuities, which connected zones of dissolving salt to overlying fresh water aquifers.

Sinkhole Problems Cargill Saltworks, Kansas

A number of sinkholes appeared in the 1950s and 1970s around brine wells near Hutchinson, Kansas, an area where numerous wells and mines were extracting brine from bedded Permian salts as long ago as 1887. The Cargill south collapse sink near Hutchinson, Kansas, started to form on October 21, 1974. Within 4 h it was 60 m across, after 3 days it had created a circular depression some 90 m across and nearly 15 m deep (Fig. 13.32). The initial collapse left the tracks of the Missouri-Pacific Railroad spectacularly suspended 6 m above the water that accumulated in the sinkhole. There was no loss of life at the site.

Fig. 13.32 Location of the 1974 collapse doline to the south of the Hutchison Salt Mine (2012 Bing® image mounted and scaled in MapInfo®)

The Permian Hutchinson salt at this site is about 105 m thick and occurs at a depth of some 130 m (Martinez et al. 1998). The salt is overlain by 110 m of Permian shales, and these, in turn, are covered by about 20 m of water-saturated, loose Quaternary sands (Fig. 13.33a, b). Locations of some of the earliest brine wells in this property are unknown, and the early dissolution methods were not documented (see Hutchinson gas explosion). The sink developed in an area that was part of an active brine field at the time of collapse and would have included both operating and abandoned wells. Embraced within the sinkhole itself was a captive brine well that was drilled in 1908 and plugged and abandoned in 1929.

Earlier uncontrolled brine extraction in the region since 1888 certainly contributed to the Cargill collapse (Fig. 13.33a). Post-mortem analysis showed that several warning signs, especially an enlarging bowl of subsidence, had been noted, but ignored. Post-event drilling revealed a large elongate solution gallery underlay the crater (Dyni 1986; Hendron and Lenzini 1983; Walters 1978). The cavern paralleled a line of brine-producing wells that were hydraulically connected. Prior to collapse the span of the cavern roof was more than 400 m long and a little less than 90 m wide.

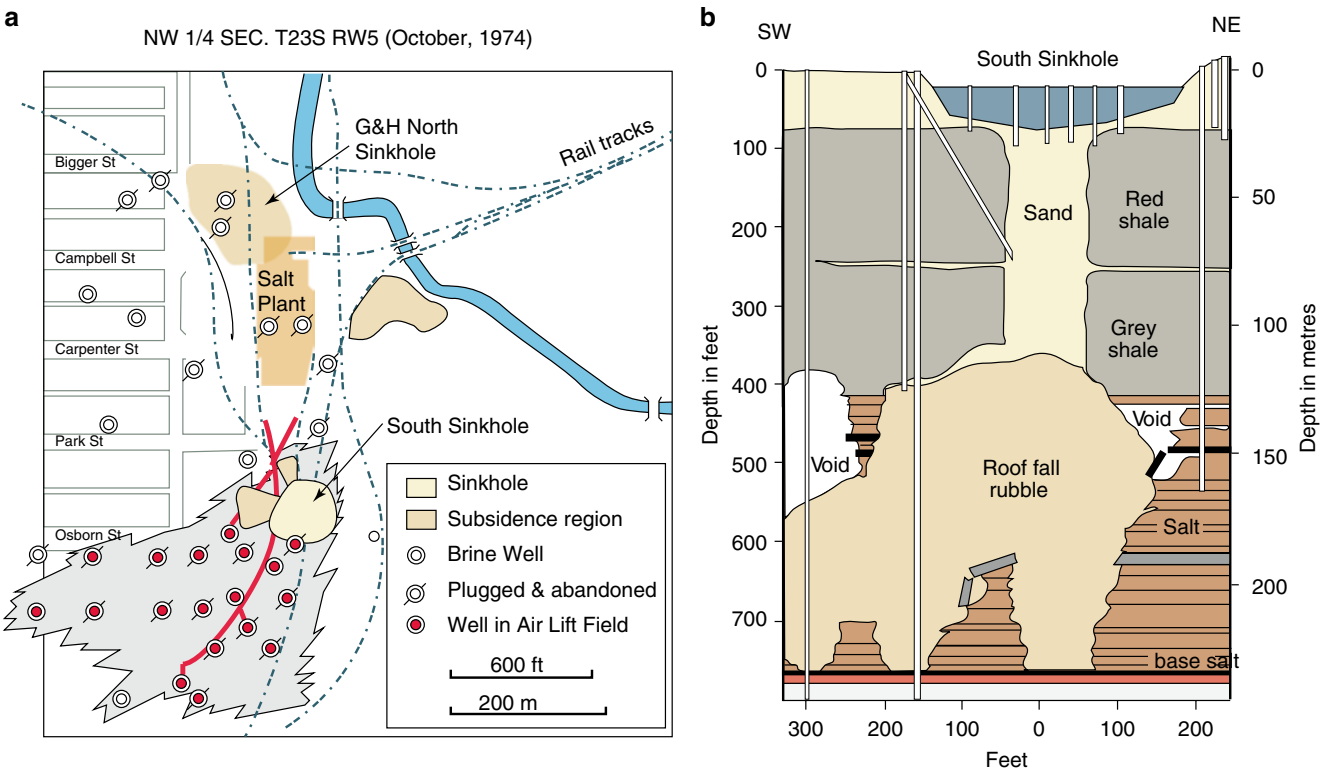

Fig. 13.33 Cargill Salt collapse. (**a**) Plan view of the collapse at the time the South Sinkhole formed in October, 1974. Grey shaded area outlines the approximate extent of the Air Lift brinefield. (**b**). Cross section through South Sinkhole at the Cargill collapse site showing the fused solution voids in the Permian Hutchinson Salt, which led to catastrophic cavern roof collapse (After Walters 1978)

This growing roof span had ultimately exceeded the bridging capacity of overlying Permian shales. Successive overlying rock layers collapsed into the stoping cavity atop the salt, forming an expanding bowl of subsidence at the surface, until the uppermost shale layer finally dropped into the water-filled void. At this point, loose water-saturated Quaternary sands quickly sank into the cavity, creating the surface sink. The sand continued to flow until it filled a subsurface chimney some 30 m in diameter (Fig. 13.33b).

This, and other nearby sinkholes in the Hutchinson region, formed atop breached salt caverns where bedded salt lay at shallow depths in areas with easily broken shaly overburden. As a result of numerous collapses, the State of Kansas now requires caverns created by solution wells to be acoustically monitored and a salt roof of at least 12 m be maintained over captive brine caverns.

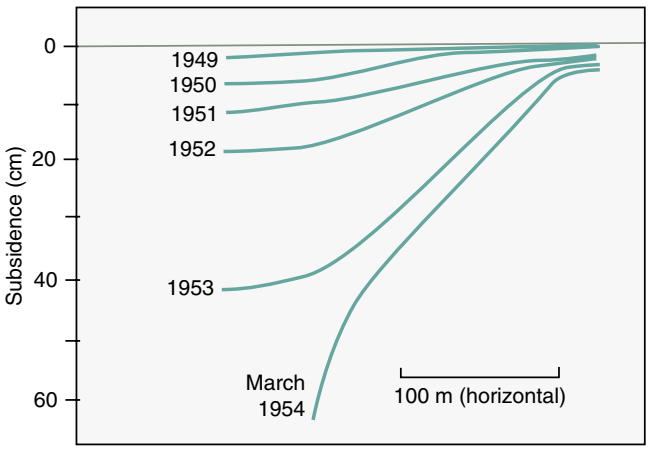

Fig. 13.34 Subsidence profile over the margin of the collapse zone in Windsor, Ontario (After Terzaghi 1971)

Brinefield Subsidence, Windsor, Ontario

Subsidence identified in 1948, followed by collapse in 1954, destroyed a portion of the suprastructure in the brinefield of the Canadian Salt Company near Windsor, Ontario. It was the end result of solution mining of the Silurian Salina salt for a period of 50 years. The first well in the brinefield was drilled in 1902, but intensive exploitation began in 1922, from 1922 to 1953 some 25 wells were drilled. Most were completed in the "Lower Salt" at depths around 480 m (Terzaghi 1971). Wells were typically cased and cemented to depths below the base of the "Middle Salt," between 370 and 390 m. All of the early captive wells circulated water without a blanket, so dissolution tended to be rapid, upward stoping and poorly constrained.

Prior to the 1954 collapse, an area that was some 300 m across had subsided some 40 cm over a period of 5 years. Cracks in several buildings on the site were first noted in 1948 and measurements were then made of the subsidence cone up until the collapse. During the first 2 years of monitoring (1948–1950) maximum subsidence was 6.3 cm (Fig. 13.34). The general trend over the 5 years of monitoring was that the cone of subsidence was becoming increasingly deep at increasing speed. By the fifth year of monitoring the depth of the basin had increased another 23 cm making for a total drop of 40 cm in the landsurface since the beginning of monitoring. The rate of subsidence climaxed on February 19, 1954 with a catastrophic failure when a water-filled depression, some 120–150 m across and up to 7.5 m deep, swallowed much of the surface plant. Prior to the 1954 collapse an estimated 4.25×10^6 m^3 of salt had been dissolved. Contrary to the initial expectations voiced in 1948, collapse was not centred on wells of the brinefield, but beneath the saltworks itself.

The February 19, 1954, collapse event was spectacular, the 9 h it took to pass to completion shows how quickly such events can proceed, once the collapse chimney reaches the land surface. The first signs of a pending collapse were noted between 8 and 9 am with small ground tremors and vibrations. By 10:30 am it was obvious a crater was forming in the centre of the bowl of subsidence, which was visibly sagging. Around midday the crater started to fill with water, first by draining a nearby marsh and later with water from broken pipes. Around 1:15 pm there was a rapid 1 m drop in the ground defining the edge of the crater, accompanied by a 1.2 m high water spout issuing from a crack along part of the crater edge. Throughout the early afternoon other cracks and water jets appeared. The escaping waters were black and smelt of H_2S. By the mid afternoon the collapse had ceased and had constructed a 150 m wide water-filled sinkhole in the middle of a 600 m wide cone of subsidence.

Sinkholes in the Detroit River

Early in 1971 several sinkholes developed in and around Hennepin Point and on nearby Grosse Isle in the brinefield of the BASF Wyandotte Corporation (Landes and Piper 1972). Both sites are located next to the Detroit River, SE Michigan, near Detroit and 10 km downriver from the Windsor collapse site. The sinkholes were the result of 30 years of solution mining of the "Lower Salt" of Silurian Salina Group salts at depths of more than 320 m. Production of brinefield salt at Point Hennepin began in 1943 using unblanketed brine wells. Salt cavities quickly met to form larger cavities. The largest was made up of two galleries called the Northern gallery and Central gallery. Ground subsidence atop this large cavity was first noticed in 1960. The rate of subsidence was constant until the end of 1967. From then it accelerated until the first collapse crater formed above the Northern Gallery on January 9, 1971. Its subsidence history is near identical to the 1954 Windsor site. After a few months of expansion, this first crater stabilized with a diameter of 65 m. In April and May 1971 a second crater then developed above the Central gallery. This crater, some 120 m across and up to 35 m deep, was larger than that above Northern gallery. By May, another companion crater, some 60 m in diameter, had formed next to the larger sinkhole.

The similarity in the geology of the Windsor and the Detroit sites, as well as the rapidity of the collapse, along with the size and steepness of the collapse craters, led Nieto and Russell (1984) to question the upward caving or stoping collapse mechanism of Terzaghi (1971). They argued his notion of steep upward propagation and caving from more than 300–400 m below the surface could not explain the steepness of the three surface craters or their rapid, near catastrophic subsidence. Instead, they proposed a collapse scenario based on loss of cohesion in the Sylvania sandstone layer some distance atop the Silurian salt bed. Their collapse scenario is now accepted for both the Windsor and Point Hennepin events (Fig. 13.35).

Intensive solution leaching of the lower layer of Salina salt, and to a lesser degree the two other salt beds in the Salina Group, formed a basin of subsidence in the overlying strata. At the landsurface this cone of subsidence was initially small and slowly evolved outward. It became unstable when it had attained surface slopes of more than 2 mm/m and a diameter of more than 500 m. As the cone expanded out and up, strata atop the growing cavity salt cavity responded by downwarping elastically into the underlying cavity and then fracturing, but not necessarily collapsing. Downwarping created compressive stresses in the higher part of each cohesively downwarping overburden unit. Expanding joints in the lower part of each unit took up the corresponding tensile stress. Compression increased in the higher part of each layer until it reached its compressional limit, the layer then fractured. Like the adjacent carbonate beams, the Sylvania sandstone bed initially deformed elastically until a rupture, driven by internal compression, formed in the higher part of the bed.

What was different in the collapse-response in the Sylvania layer compared to the limestone beams atop the cavity was its fracture response to compressional stress. When plugs of the Sylvania sandstone were subjected to triaxial compression testing, it was found the plugs failed by pervasive grain rotation, not by fracture (in contrast, plugs of the underlying dolomites all failed by fracture). Instead of a cracked plug at the end of a test, what was left in the stress jacket after a test of Sylvania Sandstone was freeflowing sand grains. In the real world, a network of growing fractures and solution channels in the underlying Bois Blanc and Bass Island formations allowed the disaggregated Sylvania sands to infiltrate into the saltwork galleries. Collapse of overburden into resulting cavities in the Sylvania then followed. The catastrophic collapse of the landsurface was facilitated by expanding shallow cavities in the sandstone, not the deeper cavities in the Salina Salt. A similar pervasive loss of mechanical strength can occur in oil reservoir intervals across zones that were formerly partially-cemented by halite and where significant volumes of hydrocarbons were extracted to be replaced by undersaturated pore waters (pers.obs.).

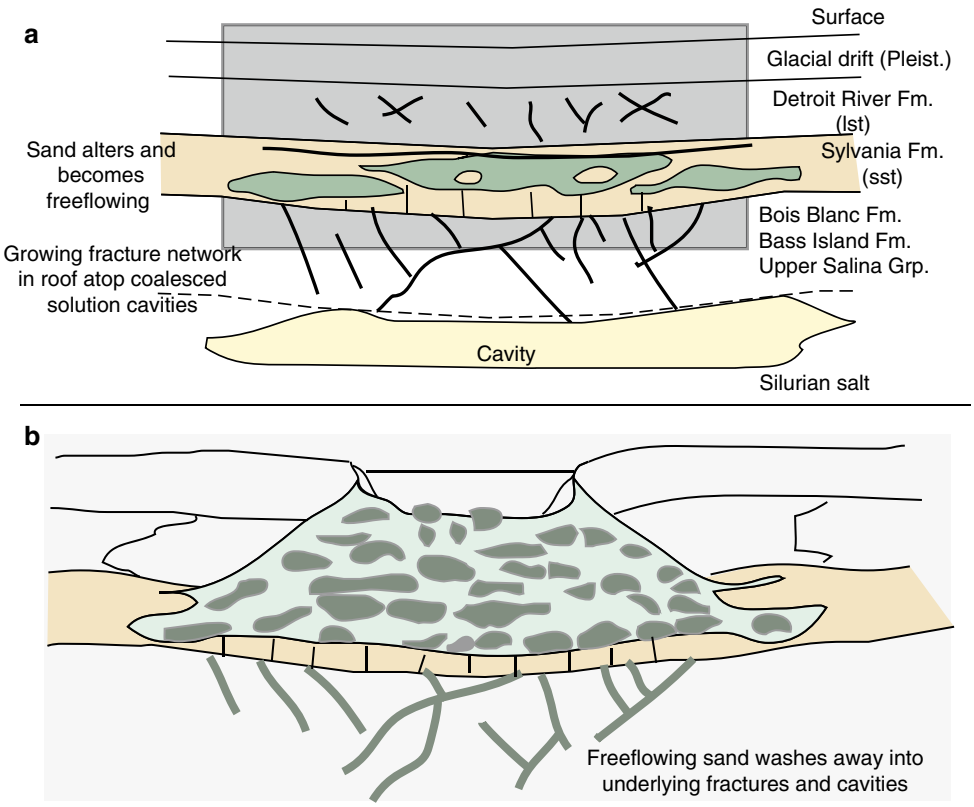

Fig. 13.35 Collapse mechanism for the Windsor and Detroit events. (**a**) A growing cone of subsidence causes fractures in the carbonate overburden and pervasive disaggregation and cavity growth in the Sylvania sandstone. (**b**) Catastrophic collapse of the overburden into cavities in the Sylvania sandstone not into cavities in the Salina salt drives sinkhole formation at the landsurface (in part after Nieto and Russell 1984)

Case Histories: Caving and Leaking Wells

Petroleum-industry activities have unintentionally aided and produced dissolution cavities via exploration, production or brine disposal wells drilled in, or through, subsurface salt units (Table 13.6; Martinez et al. 1998). Ongoing corrosion of access wells to storage caverns, or the continued expansion of caverns as stored product is cycled, can have unexpected and sometimes devastating results. If a storage cavity becomes too large for the roof to be self-supporting, successive roof failures may cause cavities to migrate upward and breach the land surface. Documented surface collapses and sinks, which can be directly related to oil drilling and poor brine disposal practices, tend to involve boreholes drilled long ago, typically in the 1920s to 1950s. This was at a time of different public perceptions of development and long before the application of modern engineering safeguards pertaining to drilling-mud design, casing placement and the use of salt-tolerant cements. It can be more than 30 or 40 years after a well was plugged and abandoned before the problem becomes obvious at the surface. In the future there will be more problems related to old wells that intersected evaporites.

Permian Basin, Ground Stability Problems, Southwest USA

Wink Sink (aka Wink Sink No. 1 sinkhole), located 3 km north of the town of Wink in Winkler County, Texas, formed in early June, 1980, and is centred on an abandoned oil well within the giant Hendrick oilfield (Fig. 13.36). Hendrick 10A had produced oil from 1928 to 1951 and was the foci of the sink crater, while a second nearby operational oil well was plugged and abandoned, soon after the collapse began (Fig. 13.37). Wink Sink No. 1. first formed on June 3, 1980 and within 24 h had expanded to a maximum width of 110 m. Two days later, the maximum depth of the sinkhole was 34 m with a volume estimated at 159,000 m^3 (Johnson 1987, 1989). The collapse was the surface expression of an underlying dissolution cavity that had migrated upward by successive roof failures until it breached the land surface. The instigating cavity had first developed in halite beds of the Permian Salado Formation, some 400 m below (Fig. 13.37).

The location of Wink Sink atop the Guadalupian Capitan Reef trend (pressurised artesian aquifer) places it in a region of natural ongoing dissolution of salt and associated chimneying, which first occurred atop the reef aquifer as early as Salado time (Fig. 7.12). Wink Sink lies in an evaporite karst region where water filled sinkholes as large as, and larger than, Wink Sink are a natural part of the landscape of the Permian Basin (e.g. water-filled sinkholes that make up the various lakes in Bottomless Lakes State Park, New Mexico). Such structures were collapsing long before the arrival of man. Sediments in collapse chimneys in the vicinity of Wink Sink indicate salt-related caving events had occurred at various times from the late Permian, to Triassic, to the Cenozoic (Johnson 1987; Baumgardner et al. 1982). But the natural processes of salt dissolution, cavity growth and resultant chimney collapse were perhaps accelerated by drilling and inappropriate well management practices in the immediate area of the Wink sinkhole centred on the Hendrick 10A well.

Drilling and completion of the Hendrick well 10A during the late 1920s was consistent with standard industry practices of the time (Fig. 13.37a). But in retrospect, several factors and events related to the drilling and ongoing exploitation of the borehole probably contributed to development of a surface sink, centred on the well. These include the probable use of a fresh-water drilling fluid, use of nitroglycerine to straighten the hole, the strong possibility of poor cement jobs that inadequately sealed off the salt beds behind the casing, possible corrosion of casing and cement fretting by salt water, and the removal of some critical casing during the final plugging of the well in 1964.

Poor cement jobs and fractures in cement linings behind the well casing opened a vertical pathway for movement of undersaturated fluid up or down the borehole surrounds (Baumgardner et al. 1982). Surface casing in the well was originally set at a depth of 122 m, approximately at the base of the Santa Rosa fresh-water aquifer. If the casing were set too shallow to seal off the aquifer, or if undersaturated waters were present in some of the siltstone or sandstone beds of the underlying Tecovas Formation, undersaturated waters would have leaked into the borehole surrounds (Fig. 13.37b). Also, the cement job at the base of this surface casing in 1928 was probably not suitable for the subsurface conditions. It was done at a time when salt-tolerant cements were not yet in use. Fracturing of the original cement possibly occurred during later workover, re-entry, and plugging operations. Fractures could have focused water flow from the Santa Rosa into the borehole surrounds at the level of the Salado Salt (Fig. 13.37c).

Baumgardner et al. (1982) pointed out that the absence of cement plugs or cement linings in the Hendrick 10A borehole below a depth of 669 m during the period from 1928 to 1951 would have allowed water to move upward under artesian pressure from the Guadalupian aquifer at the base of the Salado Formation. In my opinion, this is the more likely mechanism driving dissolution as it creates a density inversion in the hydrology that moves fresher waters upward into the salt. Contamination from above requires the less saline (lighter) waters of the Santa Rosa aquifer to displace brine (denser). Casing in the well may have also been perforated by corrosion. In addition the pumping of large amounts of saline water between 1928 and 1951, when it was used as a brine well, would have caused a substantial crossflow of undersaturated water and aided further corrosion of the casing (Hendrick Field brines ranged from 5,000 to 48,000 ppm dissolved solids; Johnson 1987).

Table 13.6 Events associated with oil wells or storage

Location	Timing and size	Explanations and implications	Reference
Haoud Berkaoui oilfield, near Ouarlaga, Algeria	In October 1986 a crater 200 m in diameter, 75 m deep formed. It has expanded until now, when the cavity is more than 230 by 600 m across. Its outward progression is still continuing at a rate of 1 m per year (denoted by environmentalists to be the "largest anthropogenic sinkhole in the world").	In 1978, an oil exploration well with a 2,500 m Ordovician target was abandoned because of stability problems in Triassic salt at a depth around 650 m. The well was abandoned without casing near the bottom of the well. A second well was drilled in 1979 located 80 m from the previous well. In March 1981, the lining of this well broke because of cavity formation at around 550 m, which is the level of salt. In October 1986 a surface crater formed, centred on these two wells. Dissolving salt may be salinising the crossflowing artesian waters, leading to undocumented, but possible, degradation of freshwater oases in the region.	Morisseau (2000)
Wink Sink, Texas, and Whitten Ranch Sink, New Mexico	On June 3, 1980 the Wink Sink formed a 110 m wide and 34 m deep collapse crater. It was centred on the Hendrick 10 A well in the Hendrick oil field. Whitten Ranch Sinkhole or collapse crater formed sometime between August 31 and September 5, 1998 and was up to 23 m wide and 33 m deep.	It appears likely that the natural processes of salt dissolution, cavity growth and resultant chimney collapse atop the Permian Capitan reef were accelerated by oil drilling and extraction activity in the immediate area of the sinkholes in the early part of last century. Large water filled sinkholes (as in the "Bottomless Lakes" of New Mexico) are a natural part of the landscape in the region and were collapsing long before the arrival of man.	Baumgardner et al. (1982), Powers (2000), Johnson (2001)
Panning Sink, Kansas	It formed in April 1959 with a diameter of 90 m and had a water surface more than 18 m below the sinkhole lip.	Formed by subsidence and collapse around an already tilted and abandoned salt-water-disposal (SWD) well – Panning 11A.	Walters (1978, 1991)
Lake Peigneur, Jefferson Island Louisiana	On November 20, 1980, Lake Peigneur disappeared in hours as it drained into an underlying salt mine cavern. Within hours, a collapse sink-hole 0.91 km^2 in area developed in the SE portion of the lake and in 12 h the underlying mine had flooded, some 2 days later the lake had refilled with water.	An oil well being drilled from barges and platforms in lake intersected an abandoned part of an active salt mine in the salt dome that underlies the lake. Water from the lake and the intervening natural collapse features entered the mine workings. Peigneur Lake itself is a natural dissolution depression.	Autin (2002), Thoms and Gehle (2000b), Thoms and Gehle (1994)
Sinkhole atop Weeks Island, storage facility, Louisiana	An active sinkhole some 10 m across and 10 m deep, first noted near the edge of the SPR facility in May 1992. A second, much smaller sinkhole was noticed early February 1995, but it lay outside the area of cavern storage.	The sinkhole led to the decision to drain the facility of its hydrocarbons. Drainage and remediation was completed in 1999 at a cost of US $100 million. This facility was not purpose built, but was an old salt dome mine facility. In hindsight, based on an earlier event, one might fault the initial DOE decision to select this mine for oil storage. A groundwater leak in the mine in 1978 may have been a forewarning of events to come. Injection of cement grout into the flow path controlled the leak at that time, but it could just as easily have become uncontrollable and formed a sinkhole.	Neal and Meyers (1995), Bauer et al. (2000)
Mont Belvieu sinkhole, Texas	July 30, 1993 a sinkhole crater formed between two brine storage wells. The crater stabilized in a few hours with a diameter of 12 m and a depth of 6 m. It was filled with sand a few days later.	Large volumes of brine are periodically cycled in and out of the brine cavern in the caprock. It is used to drive the withdrawal of the stored hydrocarbons in other deeper storage caverns. Using a system that stores saline brine in a caprock, even without the possibility of the collapse of a brine well, means there is a possibility of groundwater contamination from leaked storage brines.	Cartwright et al. (2000)

See text for full description of these and other sinkholes

Fig. 13.36 Sinkhole breakouts in the Wink sinks, Permian Basin, West Texas. Wink Sink No 1 reached the landsurface in 1980, No. 2 in 2002 (Bing® image mounted in MapInfo® software)

Wink Sink No. 1, which broke through to the surface in 1980 was largely inactive for the next 20 years, but in May, 2002 a new sinkhole formed less than 2 km south of Wink Sink No. 1. It was named Wink Sink No. 2 and was significantly larger than its predecessor, with a maximum width of 238 m and an estimated total volume of 1.3 million cubic meters (Fig. 13.36). It developed some 400 m west of a number of existing natural dolines and caprock collapse sinkholes. Both Wink #1 and #2 sinkholes are assumed to have formed by dissolution of salt beds in the Upper Permian Salado Formation.

The problem of rapid wellhead collapse and sinkhole formation continues throughout many areas of New Mexico and Texas typified by shallow Permian salt and poorly monitored brine solution cavities (Land 2013). For example, around 8:15 on the morning of July 16th, 2008, a driver for Jim's Water Service, a local oil field service company based in Carlsbad, NM, was inspecting a brine well (BW-005) located on state trust land, near Artesia, some 35 km northeast of Carlsbad. While on location, the driver noticed a significant amount of dust in the air in the vicinity of the well, he then heard a rumbling noise and saw a large ground crack propagating toward him. He quickly vacated the site. Minutes later, a large sinkhole (now known as the JWS sinkhole) abruptly formed, engulfing the brine well and associated infrastructure (Fig. 13.38).

The well operator had been solution mining the Salado Formation by injecting fresh water and circulating it through the 86 m thick section of halite until the water reached saturation. The resulting brine was then sold as oil field drilling fluid. BW-005 was originally drilled as an oil and gas exploration and production well in 1955 with cable tools to a total depth of 1,191 m (3,909 ft). The well was plugged and abandoned in 1955. The well was reentered and recompleted as a brine well in 1978. The Salado Formation was encountered at approximately 121 m (397 ft) below ground surface (BGS). BW-005 was operated as a single well system with a single tubing configuration using direct circulation until 1986, when it was switched to reverse circulation (Fig. 13.3). No sonar surveys were ever run to map the cavern. Based on incomplete production data, the New Mexico Oil Conservation Division (NMOCD) estimated that the total brine production at BW-005 was approximately 8 million barrels and that the cavern volume was approximately 1.3 million barrels.

Initially, JWS sinkhole, was several tens of meters in diameter and filled with water to a depth of ~12 m below land surface (Land 2013). Large concentric fractures developed around the perimeter of the sink, threatening the integrity of County Road 217, some 100 m away (Fig. 13.38). By July 24 the originally vertical walls of the sinkhole had begun to collapse, and the sink continued to grow in diameter over the course of the next 2 weeks. By July 28, the walls of the sink had developed an angle of about 45° to within ~10 m below ground level, above which the sides of the sink were vertical, and the water originally visible in the base of the cavity had subsided into the subsurface. As there are no significant sources of groundwater at shallow depths in the immediate vicinity of the JWS sink, the water is assumed to have been solution mining fluid that was forced up the stoping debris chimney in the initial stages of collapse. The same water is now stored in pore spaces of the resulting collapse breccia, and in shallower porous zones of the overlying Rustler and Dewey Lake Formations. By end July, the sinkhole had attained a diameter of ~111 m and a maximum depth of ~45 m. It has since been filled by the operator.

On November 3, 2008, less than 4 months after the JWS collapse, another brine well-centred sinkhole broke out at the surface north of the small community of Loco Hills, in northern Eddy County, New Mexico. Centred on the Loco Hills Water Disposal Service (BW-021) brine well, it formed a sinkhole of similar dimensions to the JWS doline, it is now

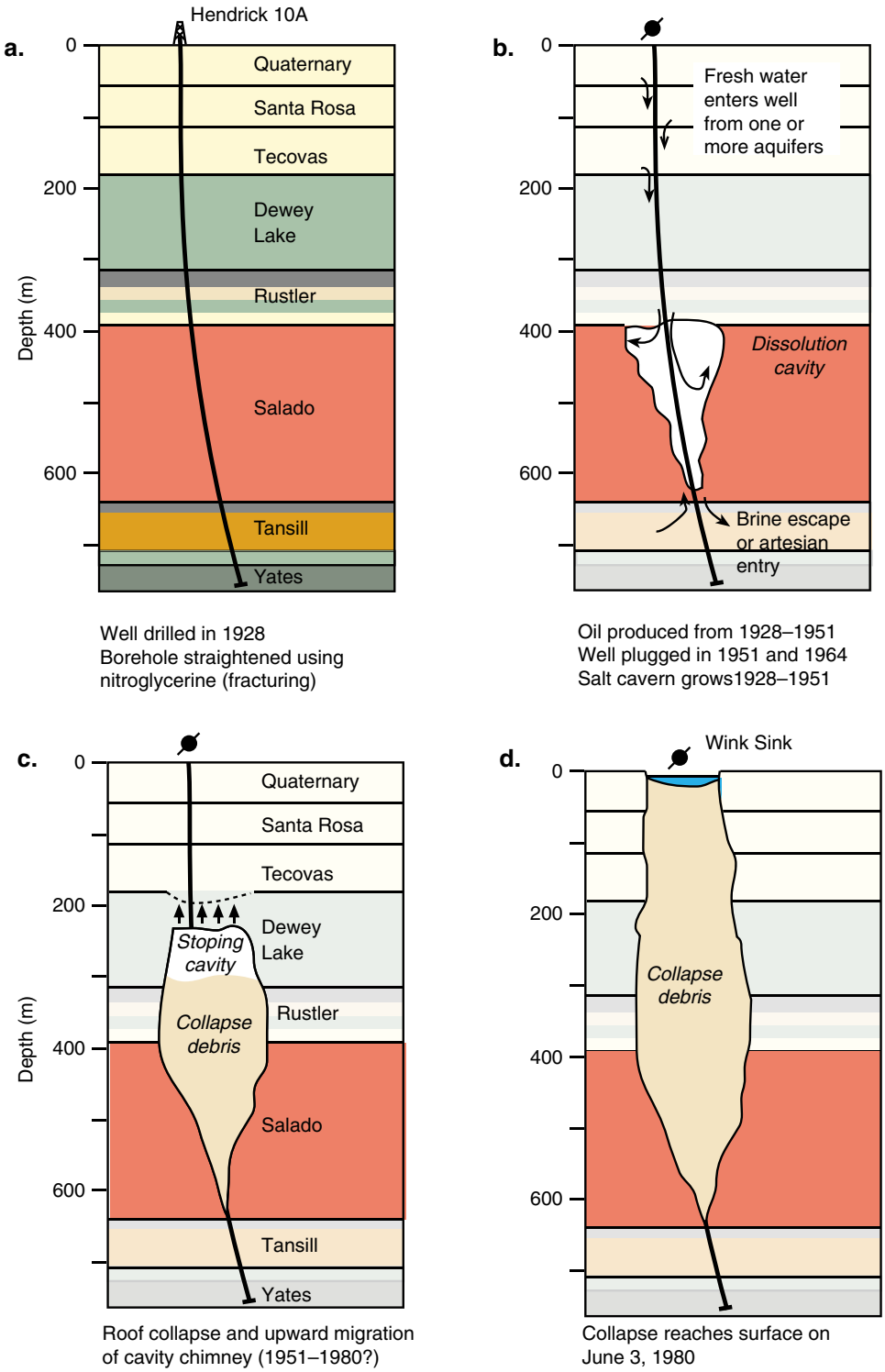

Fig. 13.37 East–west section through Hendrick well 10-A in Wink Sink, West Texas (After Johnson 1987). Undersaturated meteoric and artesian water circulated along borehole margins to dissolve the salt and create a salt cavern, which migrated to the land surface by successive roof failures ("chimneying"). See text for detailed discussion of stages (**a**–**d**). See Fig. 7.12 for location of the Wink Sink

back-filled. The BW-021 well was originally drilled as an oil and gas exploration and production well and was converted into a brine production well approximately 25 years ago. It was operated as a single well system with a single tubing configuration using reverse circulation. The casing shoe was set at 126 m (415 ft) BGS above the salt, which occurs at 143 m (470 ft) BGS. (It is not clear whether the exploited salt was part of the Rustler or Salado Formation, or both). The production tubing was set at 274 m (900 ft) BGS. The last sonar log of the well was completed on February 7, 2001. Based on incomplete production information, NMOCD estimates that the total brine production at BW-021 was

approximately eight million barrels and that the cavern volume was approximately 750,000 barrels.

BW-021 was plugged and abandoned at the time of the collapse and was being visually monitored for subsidence.

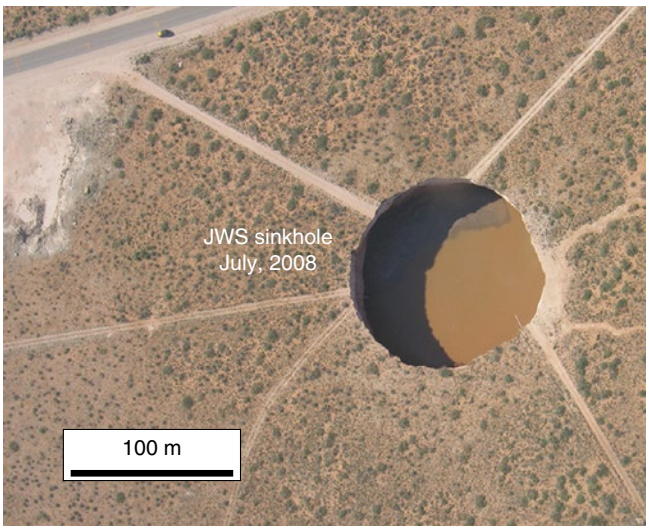

Fig. 13.38 JWS collapse doline, New Mexico, soon after collapse when solution brines are still visible in base of collapse. Bing® image mounted and scaled in MapInfo®

NMOCD had ordered the operator to plug and abandon the well. The well had failed an formation integrity test on June 18, 2008, as part of a statewide review of brine wells conducted in the aftermath of the JWS collapse. The well had previously passed a 5-year MIT of the casing in 2006 (Land 2012, 2013).

Like the JWS collapse, the Loco Hills sinkhole was likely a result of overly aggressive solution mining of the Salado Formation using unblanketed circulation methods. Then in July, 2009, another sinkhole abruptly formed near Denver City, Texas, ~115 km east of Loco Hills. The Denver City sinkhole was also the product of a solution mining operation.

During a well review program across New Mexico, instigated by the JWS sinkhole, the I & W brine well facility was identified within the city limits of Carlsbad as a potential problem, it had a similar geologic setting and pumping history to the already collapsed JWS and Loco well heads (Fig. 13.39a). The I & W brine facility originally involved two wells, which conducted solution mining of the Salado Formation almost continuously since 1979. Eugenie #1 well was drilled first with the intent of being a single-well brine producer. However, after a short period of poor production, Eugenie #2 was drilled approximately 100 m to the north-

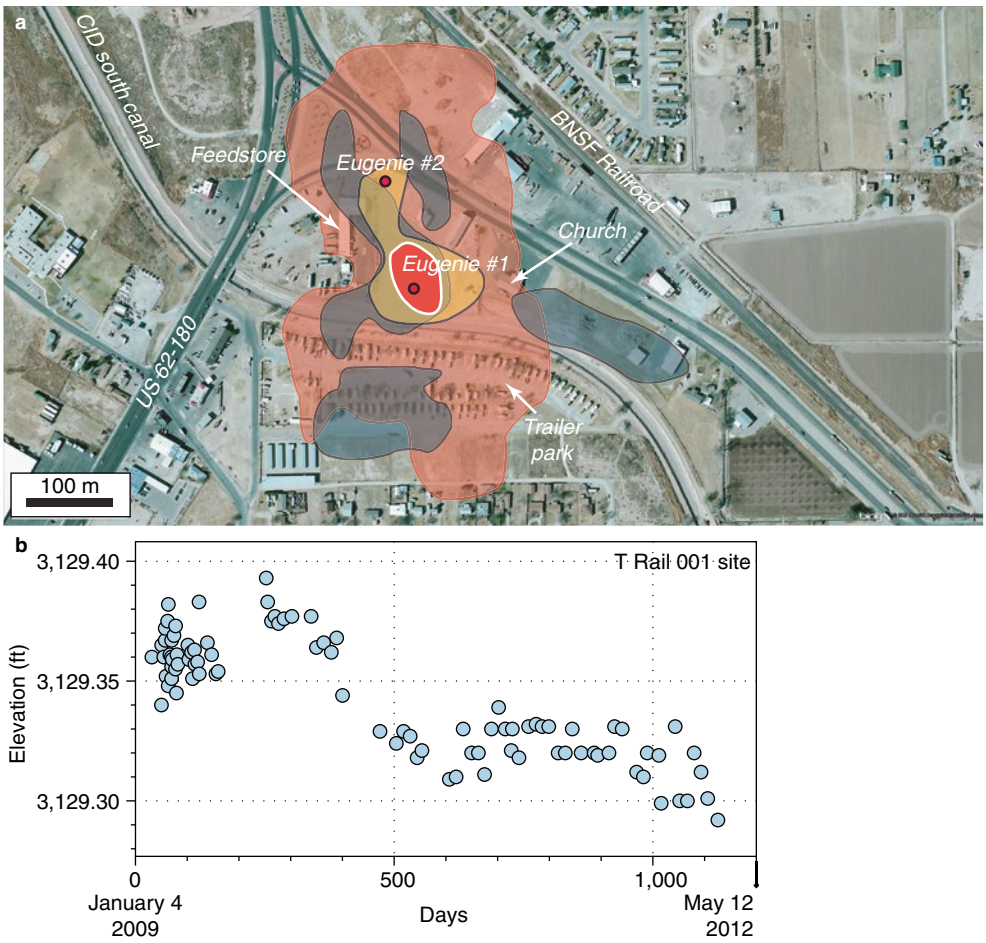

Fig. 13.39 Potential problems in Carlsbad New Mexico. (**a**) Region of possible subsidence and collapse in south Carlsbad City, New Mexico. *Pink region* outlines the area where magneto-telluric surveys identified subsurface void thickness greater than 3 m. *Orange shading* identifies extent of region where a cavern signature was identified on seismic, while the *white-rimmed ellipse shows* region of maximum seismic disturbance within this region *Grey areas* indicate low resistivity (high conductivity regions defined by electrical resistivity survey (All regions are replotted from Land (2013) using a Bing® image base and MapInfo® software). (**b**) Subsidence monitoring at the TRail site from January 2009 to early 2012

west as a freshwater injection well. The two wells were connected by hydraulic fracturing, and brine was produced from Eugenie #1. After June 2000, Eugenie #2 was shut in, and solution mining was conducted as a single-well operation through Eugenie #1, wherein freshwater was injected through the annulus and brine withdrawn through suspended tubing (Goodman et al. 2009). This is the ideal set-up to created poorly controlled upward stoping "morning glory" cavities (Fig. 13.3).

Unlike the JWS and Loco Hills sinkholes, which are located in relatively remote areas in northern Eddy County, the I&W operation is sited in a more densely populated area within the city of Carlsbad, near the BN&SF rail line and the intersection of two major highways known as the "South Y." The Carlsbad Irrigation District (CID) South Canal is approximately 50 m south of the Eugenie #1 wellhead, and the immediate area also includes a feed store, truck stop, mobile home park, and Jehovah's Witness church (Fig. 13.39a). A catastrophic collapse in this area would inflict extensive damage to individual property and civic infrastructure. Following the collapse of the JWS sinkhole, the New Mexico Oil Conservation Division ordered closure of the I&W brine well and initiated site characterization, which has determined the likely presence of a significant solution cavity beneath the region. As yet, possible still-rising solution cavities have not surfaced or created any damage to the town's infrastructure, but ongoing ground monitoring and emergency procedures are now in place (Fig. 13.39b).

Market value of brine is relatively low, but is a steady source of income in an oilfield region, when nearby wells are being drilled. In New Mexico, extracted brine typically sells for less than two dollars per barrel and monthly statewide brine production in 2011 in New Mexico exceeded 200,000 barrels per month. Brine extraction operations there have almost exclusively been owned and run by trucking companies. Oversight of brine wells by the Oil Conservation Division was accomplished under provisions of the federal Underground Injection Control program and the New Mexico Water Quality Control Commission regulations. Both these enforcement mechanisms are primarily concerned with the protection of groundwater quality, not cavern monitoring. In the "reverse" circulation method, fresh water is injected down the annulus and the brine is extracted through the tubing. The reverse circulation method was rationalised as more protective of any fresh water zones above the Salado Formation because in the event of a casing leak, fresh water would leak into the fresh water zone rather than brine. However, as mentioned earlier, in imperfectly monitored situations, this is the ideal set-up to created poorly-controlled upward-stoping "morning glory" cavities.

It is not just oil and gas related wells in New Mexico that can facilitate ground stability problems in areas of shallow evaporite karst. Water wells can also focus the formation of sinkholes. Powers (2000) argues it was an improper casing seal in an artesian water well that focused rising waters and instigated the Jal collapse doline, New Mexico. This was the Skelly Jal Water System #2 well, which penetrated the Salado Formation to access the pressurised Capitan Reef aquifer at around 100 m. It was the centre to the Jal sinkhole (aka Whitten ranch Sinkhole), which was some 25 m across and located 13 km north-northwest of the township of Jal. Local ranchers Jimmy and Linda O'Rear noticed a small surface opening on August 31, 1998, at the site of the collapse. On the morning of September 5, they discovered the full-sized sinkhole (Fig. 13.40).

Clearly drilling, completion, plugging and brine extraction procedures in the Permian Basin can combine to create borehole-focused conduits that enable fresh water to better circulate in the vicinity of the well and so dissolve salt. This is

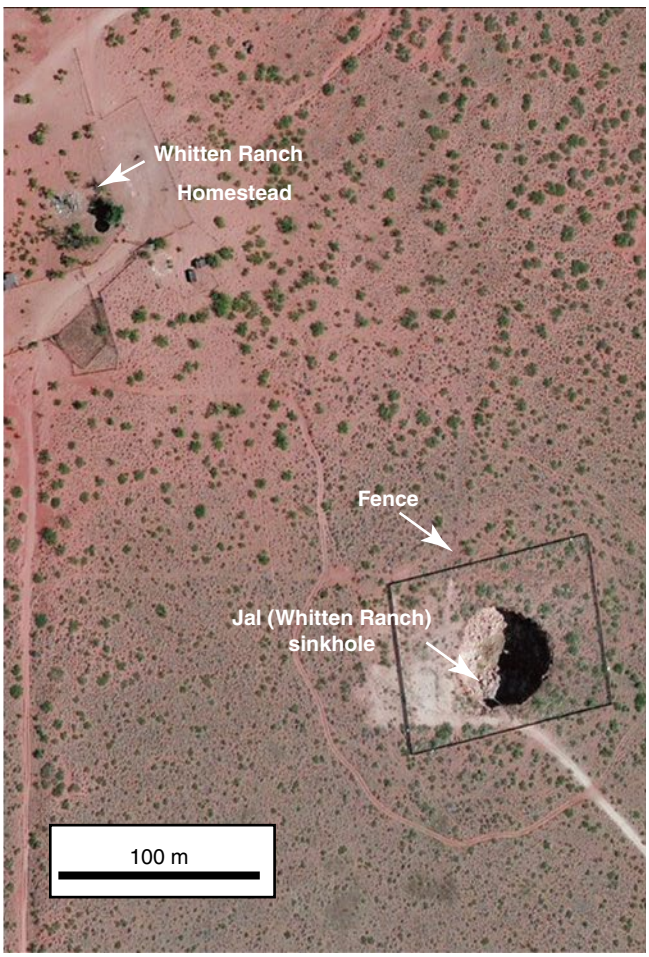

Fig. 13.40 Jal (Whitten Ranch), New Mexico, sinkhole reached the landsurface in 2008 (Bing® image mounted in MapInfo® software)

especially so in unmonitored and poorly regulated brine extraction scenarios without suitable geological overview. The potential for surface collapse is greater in hydrological settings of subsalt pressurised (artesian) aquifers. When an expanding dissolution cavity is large enough, the roof fails and overlying strata collapse, often catastrophically into the cavity. The collapses in Texas and New Mexico underline the importance of having legislation in place that defines and enforces appropriate well design specifications, reliably monitors solution cavity maintenance during well life, and emphasizes the need for adequate plugging and abandonment procedures, specifically designed for wells passing through salt intervals.

Panning Sink, Barton County, Kansas

Panning Sink on the Panning Lease reached the surface on April 24, 1959 in an area of subsidence and collapse, centred on an already tilted and abandoned salt-water-disposal well (Fig. 13.41). The Panning 11A well had been abandoned in the previous January because of uncontrolled well-head tilting. Walters (1978) reported that the 90-m-wide water-filled sinkhole formed in about 12 h, with a water surface more than 18 m below the lip of the sinkhole. Four days later the diameter of the sinkhole had not increased, but the water surface was only 3.5 m below the crater edge.

The suspect well, originally drilled as an oil producer in 1938, penetrated 91 m of Permian Hutchinson salt at a depth of 298 m on its way to the Arbuckle Group reservoir. Freshwater drilling fluids used in drilling the well dissolved the salt in the borehole to an excessive diameter (≈1.4 m) and this washed-out zone was not cemented behind the 15.2-centimeter-diameter casing. Conversion of the borehole to an salt-water-disposal well from 1946 to 1958 injected a large quantity (≈1.6 × 10^6 m^3) of unsaturated oilfield brines (with a total concentration around 28,000 ppm) into the well and so further dissolved the salt behind the well casing. Disposal was supposedly into the Arbuckle Group dolomite at a depth of 995 m. In 1949, the tubing was removed, and water was injected directly down the 15.2 cm casing. Ongoing exposure to this undersaturated brine formed a large cavern, and with successive roof falls as the void migrated upward to ultimately cause the surface crater.

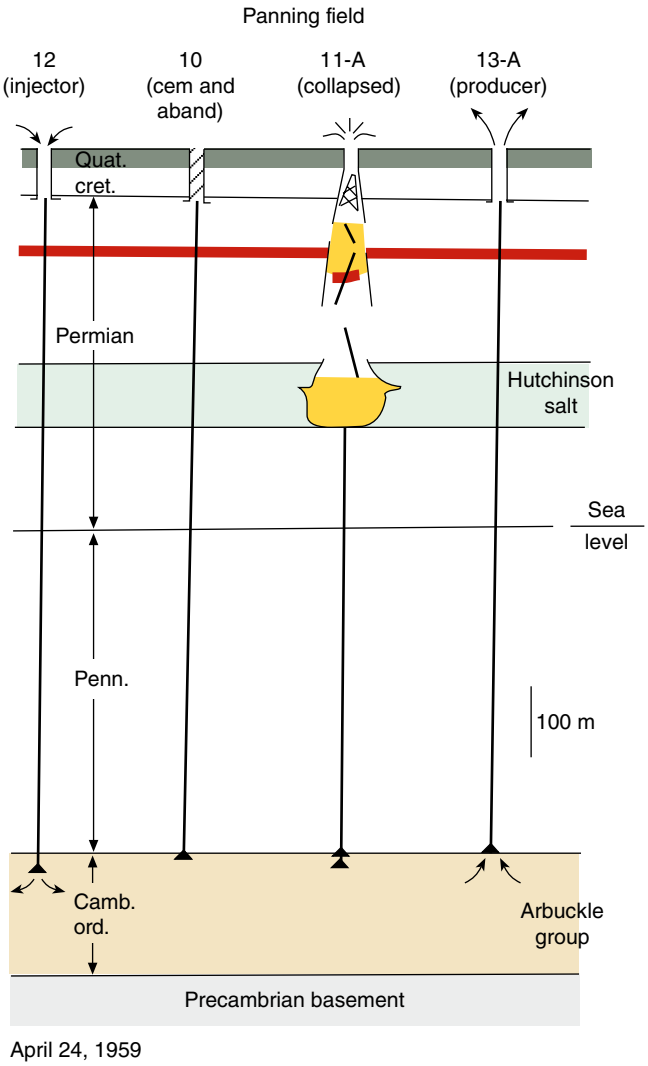

Fig. 13.41 Schematic cross section through Panning Field, Kansas, showing the situation on April 24, 1959 (After Johnson 2001; Walters 1978)

Gorham oil Field and I-70, Russell County, Kansas

Gorham oil field, a former giant field in Russell County, Kansas, is the site of slow subsidence of a major highway (Interstate 70) above salt-dissolution zones in the Permian Hutchinson salt (Fig. 13.42a; Croxton 2003; Walters 1991; Knapp et al. 1989). A series of oil wells, drilled on four-hectare spacing in the 1920s through the 1940s, penetrated 75 m of salt at a depth of 390 m (Fig. 13.42b). Gorham field produced more than 100 million barrels and the wells are now plugged and abandoned. Corroded casing has been left in some of the boreholes at depths above, within, and below the salt unit. As a result of what appears to be improper plugging of these abandoned oil wells, unsaturated water probably has flowed down some of the boreholes and has dissolved large volumes of the salt. Subsidence was further aided by disposal of waste oilfield brines that were re-injected when unsaturated with respect to halite.

Initial studies of the area (before road construction) did not reveal subsidence along the proposed alignment of 1–70 through the Gorham oil field, and final grading for the new highway was completed in 1966 (Fig. 13.42; Croxton 2003). Subsidence of 1–70 pavement subsequently occurred at several sites along the highway, with principal sites being the Witt sink and the Crawford sink (located some 5–6 km east of the town of Gorham). Subsidence had occurred at rates of 10–15 cm/year, and by 1971, the lanes had dropped so much that they had to be

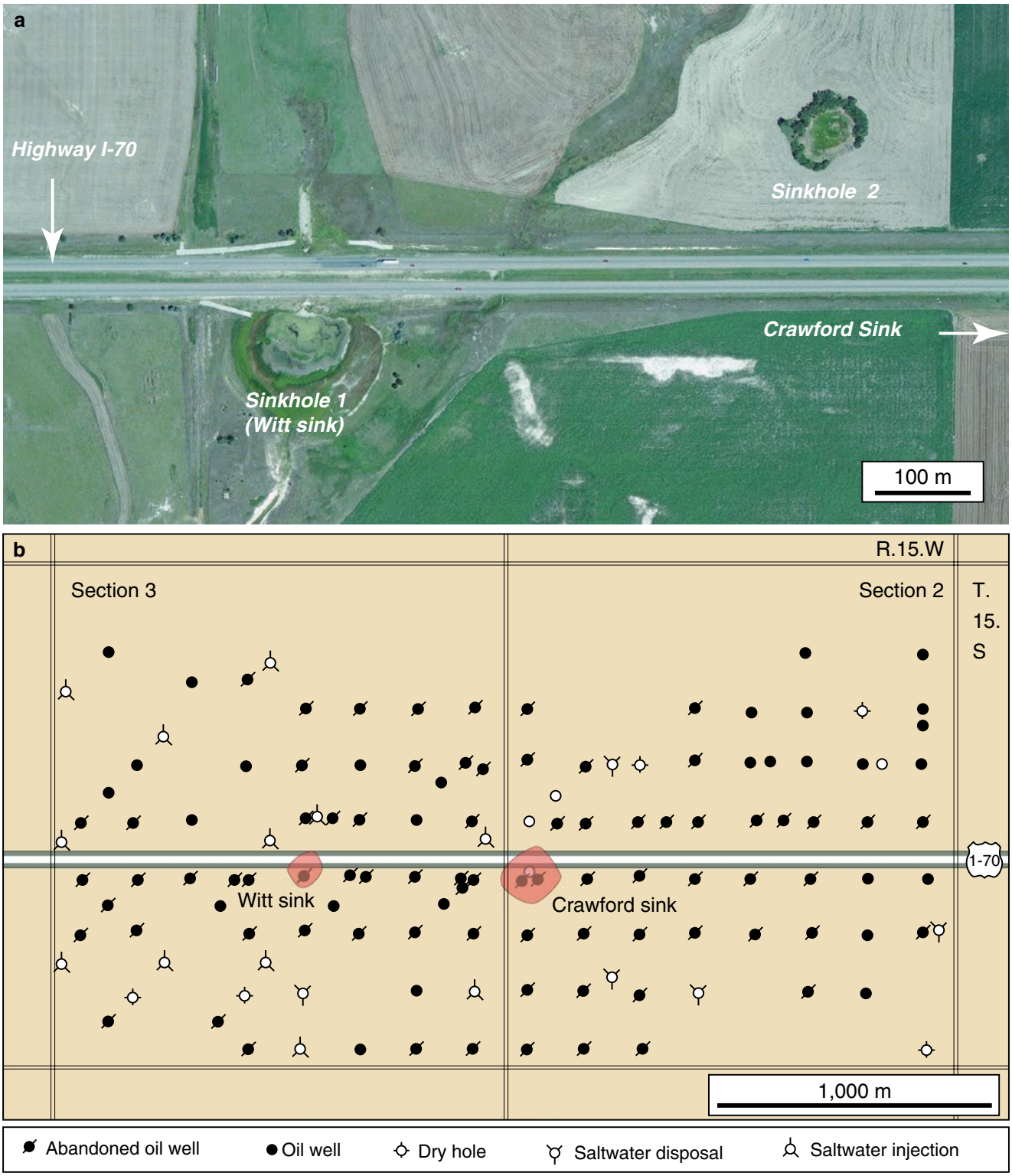

Fig. 13.42 I-70 sinkholes east of Gorham city. (**a**) Sinkholes in a cone of subsidence defined by where Witt Sink intersects Interstate-70 (scaled Bing® image mounted in MapInfo® software). (**b**) Distribution of Gorham and Witt sinks with respect to the various wells of the now depleted Gorham oilfield, some 6 km east of Gorham, Kansas (in part after Knapp et al. 1989)

regraded; paving was raised by some 1.5 m at both sinks, at a cost of US$220,000. By 1984, the lanes at the Witt sink had again subsided nearly 2.5 m and a line-of-sight problem arose because cars down in the sink could not be seen by oncoming traffic. Witt sink was again regraded and repaved in 1986 at a cost of nearly US$500,000.

Further attempts to remedy the problem were carried out in 1986 and 1988 when a borehole was drilled adjacent to the abandoned oil well thought to be the cause of the Witt sink. Cement with additives was injected into the well to try to plug the old well at the base of the salt. Although the plugging appeared to stop the settling for about 6 months, subsidence then resumed at a rate of 12–15 cm/year. Present plans call for continuing to regrade the lanes of 1–70, as needed, because an economical solution to the subsidence problem has not been found (Croxton 2003).

The highway in the vicinity of the Witt sink can be regraded as many times as necessary. The highway in the vicinity of Crawford sink is a different matter as it is located near where a local road passes over the interstate, via a road bridge. This section of highway cannot be successively regraded because of clearance and line-of-sight requirements under the nearby bridge. The bridge is sinking, too; one end has dropped over 6 ft since it was built in 1965. At the south abutment, the east curb is now 2 ft higher than the west curb. Yet, about the only indication that the bridge is under any stress at all are narrow cracks in the curbs just over the piers. Something will eventually have to be re-engineered at the Crawford sink site. This will probably happen when the bridge finally subsides enough to become a sight distance problem for traffic on I-70, or water will begin to cover the highway during storms.

In a geophysical study of this, and other areas of Kansas subject to salt-related subsidence, Knapp et al. (1989) note that poor well completion and disposal practices tend to exacerbate a natural set of subsidence problems that predate human settlement, let alone the activities of the oil industry.[5]

[5]On completion of this section of highway, and the subsidence that followed, the press and the locals were quick to blame the subsidence on the oil industry and poor drilling practice, with subsequent questions as to the competency of the engineering studies done prior to highway construction. When geology crews began their preliminary studies for this section of 1–70 in the early 1960s, there was a large pond along the right-of-way, some six miles west of Russell. They noticed that the pond appeared rather deep, and although it was situated in a streambed, apparently it had no dam. Asking around among local residents, Highway Commission geologists were told that the pond had always been there. An 83-year-old woman who had lived in the area all of her life reported that there had been a pond in that location ever since she could remember (pre-oilfield!). So little additional planning as to its origin was given. During construction, the Crawford and Witt sinks were filled in and the highway was built, along with a nearby bridge to carry county traffic over the interstate. Final grading for the new lanes was finished in the spring of 1966 and the subsidence problems began.

Despite these and other salt-related problems, incidents of rapid dissolution induced subsidence atop wells drilled through the Hutchison (Wellington) Salt and equivalents are rare events. In Kansas the ratio of wells intersecting salt and being associated with at-surface subsidence is something like 1:10,000 (Walters 1978, 1991).

Sinkholes at Bayou Corne (2012) and Bayou Choctaw (1954) Domes, Louisiana

In spring 2012, residents of a rural community near Bayou Corne in Louisiana's Assumption Parish noticed gas bubbles rising to the surface in some bayous. Shortly thereafter, a series of small earthquakes shook the area, prompting state officials to investigate. In early August 2012, a sinkhole, some 110 m across, surfaced adjacent to in the property of the Texas Brine Company, which operates the surrounding brine extraction (solution mining) facility (Fig. 13.43). On August 3, 2012, Louisiana Governor Bobby Jindal declared a statewide emergency, and local officials in Assumption County ordered the mandatory evacuation of about 300 residents from more than 150 homes located about a half-mile from the sinkhole. The sinkhole is unusual in that the salt breach has occurred on the sidewall of the intradome solution cavity, not the typical sinkhole position above a solution cavity (Jones and Blom 2014).

The cause of the sinkhole is likely related to uncontrolled stoping or a wall breach in one of two Texas Brine LLC's storage caverns, located near the edge the Napoleonville Salt Dome. The top of the dome is some 210 m below the surface. Much of the attention has been focused on the Oxy Geismar Well No 3, and associated solution cavity, as being the likely facilitator of the collapse (Jones and Blom 2014; Nunn 2013). The Oxy Geismar Well No. 3 was first permitted on April 15, 1982 for the mining of salt water brine from the Napoleonville Salt Dome. A 2007 sonar survey indicated the top of cavern was around 1,031 m, the base of cavern around 1,707 m with a cavern diameter of more than 61 m.

In early September 2010, Texas Brine began reworking the cavern well, milling a section of salt higher than the existing cavern roof, then at 1,036 m, to test if the upper strata could be solution mined and so expand the storage capacity. A Louisiana Department of Natural Resources (LDNR) permit for that work was issued in May 2010. In 2011, the well failed a pressure test implying that the integrity of the well had been lost. It has since been interpreted that the solution cavity was likely in a previously unrecognised salt overhang. Texas Brine LLC sent a letter to LDNR

Once again it seems Hutchison Salt in the Gorham region likely was dissolving naturally with a typical landscape sink expression. If word of mouth recollection was correct, then sinks were present in the area prior to both the oil field and highway construction. Then again, as all lawyers know, it is hard to sue mother nature.

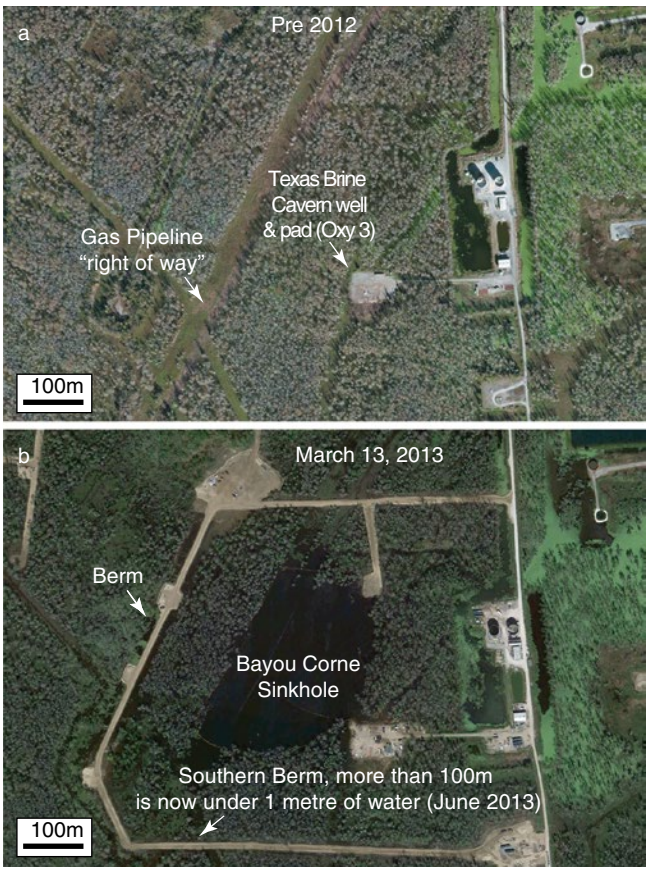

Fig. 13.43 Zone of subsidence and collapse in water saturated Bayou Corne region, Louisiana. (**a**) Situation pre the sinkhole breaching the surface. (**b**) Situation on and after March 13, 2013 (Bing® base images mounted and scaled using MapInfo® software)

reporting the failed test and expressing concern over the possibility that "a breach out of the salt dome appears possible." On June 6, 2011, the well bore above the cavern was plugged with cement.

On August 13, 2012 the LDNR-Injection and Mining Division approved Texas Brine LLC's permit to drill a new well into the company's abandoned brine cavern in order to determine the structural status of the cavern and what pressures, gas or brine it contained. Sonar, run on September 24, confirmed that the cavern floor was at 1,220 m, some 400 m above the depth recorded prior to the closure of the cavern in 2011. On September 24, 2012, Texas Brine LLC issued a statement claiming that regional seismic activity had caused the cavern failure. On September 25, USGS consensus was that the seismic activity detected in the area was a consequence of the cavern collapse, not the cause of the collapse and the formation of the sinkhole/slurry area.

As of early 2015, the sinkhole is still actively subsiding and expanding (Fig. 13.43). On June 4, 2013 a 100 m long portion of a berm, constructed to help retain sinkhole waters, slipped into the sinkhole. Earlier an excavator platform was swallowed by the expanding sinkhole. In May 2013, the deepest part of the sinkhole collapse cone was some 53 m deep. The lawyers have yet to have their day in court, nor has the scientific work been completed on cause of the collapse, so a fact-based final understanding of the sinkhole, and how much the driving force for the at-surface cavity was anthropogenic versus enhanced natural, has yet to be finalised. It does appear that seismic monitoring and geological assessment lacked some finesse and the remilling of Oxy 3 was perhaps more driven by profit than any forward looking technical understanding (Newsweek, 20 Dec., 2013) Unfortunately, this brine extraction facility has drawn into question the integrity of the much larger Napoleonville storage cavern region. Once again, we see what can happen when a solution cavity (or a drive in a mine) is allowed to approach the edge of a salt mass.

In January 1954, there was a similar collapse when the "No. 7 brine well" atop the Bayou Choctaw salt dome, Louisiana, collapsed during brine production, probably because of loss of its salt roof atop a growing solution cavern. It is one of the few caverns in domal salt that has failed completely and catastrophically and, along with Lake Peigneur, its documented collapse is one of the most dramatic. In 1954, it occurred at a time before sonar monitoring and controlled brining, when landscape damage was an expected consequence of solution mining.

Immediately prior to its collapse the cavern generated by Brine Well No. 7, Choctaw Bayou, had no salt roof and a "morning glory" dissolution cavity had leached upward through the caprock, allowing the overburden to collapse directly into the cavern. It didn't take more than about a day for a water-filled 240 m (800 ft) diameter collapse doline/sinkhole to form. A rig that was producing brine at the time fell into the collapsing depression and was never seen again. (Stanczuk, et al. 1976; Neal et al. 1993). Today it is still a circular structure, filled with bayou water, and known as Cavern Lake. It defines the northeastern corner of the area occupied by the facilities of the Choctaw Bayou Strategic Petroleum Reserve (Fig. 13.44).

Grand Saline Sinkhole, Texas

On April 26, 1976 the Grand Saline sink emerged at the surface within the city of Grand Saline, Texas (Dunrud and Nevins 1981). The sink occurred at the site of a former brine well, which had penetrated the top of the Grand Saline salt dome at a depth of 60 m, and had produced brine from 1924 through 1949. The salt is overlain by some 50 m of Eocene claystones and 10 m of unconsolidated Quaternary silt and clay. Failure occurred in two stages. First a sinkhole 4–6 m in diameter and more 15 m deep opened at 24 Tremont Street. Second, the hole rapidly widened as rim slabs toppled in and in a few hours the collapse reached an at-surface diameter of 15 m. The sink displaced a total volume of 8,500 m^3 of silt and clay into the underground cavity. A house was

Fig. 13.44 A zone of subsidence and collapse occupies the crest of Bayou Choctaw salt dome. Visible in the image are Cavern Lake, which is the water-filled circular structure that occupies the former position of brine well No. 7. It is located northeastern edge of the Choctaw Bayou Strategic Petroleum Reserve facility (Bing® base image mounted and scaled using MapInfo software)

endangered by this collapse and, during the collapse, a pipeline broke and sewage flowed into the sinkhole. Earlier, in 1948, a similar-sized sinkhole had formed just to the east of the Grand Saline Sink.

Haoud Berkaoui Oilfield, Algeria

Located in the Sahara, some 32 km southwest of Ouargla City, the Haoud Berkaoui oilfield is an area of subsidence where numerous exploration and development wells were completed in the 1970s. Of these, the OKN32 and OKN32BIS wells have collapsed into an expanding collapse doline. It surfaced in October 1986 when a crater, some 200 m across and 75 m deep, formed (Morisseau 2000). Today the solution cavity continues to expand and is now some 230 by 600 m across. Its outward progression is continuing at a rate around 1 m per year. The collapse is centred on two oil wells drilled in the late 1970s. The problem began in 1978, when the OKN32 oil exploration well was abandoned because of stability problems in Triassic salt at a depth around 650 m. The target was an Ordovician sandstone at a depth of 2,500 m. Because of the technical problems associated with significant caverns at the level of the salt, the well was abandoned without casing being set in the salt, probably facilitating the escape of artesian waters (Morisseau 2000; Bouraoui et al. 2012).

When it reached the 600 m level, the well had already passed through 50 m of anhydrite (220–270 m depth) along with interbedded anhydrite clay and dolomite 270–450 m depth). These are evaporite sediments that, in their undisturbed state, can act as aquicludes or aquitards to any access by unconfined phreatic groundwaters, although at such shallow depths the evaporite beds are likely also to be variably overprinted by active-phreatic dissolution processes. Prior to drilling it was thought that the Senonian halite extended continuously to a depth of 600 m in the well and in turn was underlain by 50 m of anhydrite (600–650 m depth). Below the halite-anhydrite is an artesian aquifer (Albian) with a natural hydraulic head that is larger than the surface aquifer head by 2.5 MPa (Morisseau 2000)

In 1979 a second well, OKN32BIS, was drilled located some 80 m from the previous well and it successfully obtained its Ordovician target. But in March 1981, the lining of this second well broke, probably because of cavity collapse at a level around 550 m (once again the regional level of salt) and the well was lost. Five years later, on October 1 1986, a large surface crater formed, centred on these two wells. The initial at-surface diameter was 200 m and it was 75 m deep, today it is even larger (Fig. 13.45). Cavern diameter below the stope breakout at that time was estimated to be 300 m and water flows to be around 2,000 m^3/h.

Since the initial stope breakout, leaching has become progressively less effective and expansion rates have slowed (Morisseau 2000). This is because cavern growth and water outflow flow are thought to take place preferentially near the centre of the collapse, which is now far from the collapsing cavern walls Dissolving salt may be salinising the crossflowing groundwaters, leading to undocumented, but possible, ongoing degradation of freshwater oases in the region. Continuing expansion is evidenced by the development of fresh centripetal cracks about the expanding collapse margin. Using MT-InSAR analysis, Bouraoui et al. (2012) documented ongoing subsidence near the crater, with an average subsidence of 4 mm per year (between 1992 and 2002). The zone of current zone of subsidence is centred on the OKN32 location and is slowly migrating north east.

Fig. 13.45 Haoud Berkaoui collapse doline in 2010. Note the centripetal fracture mesh indicting subsidence and collapse is ongoing (Image from Microsoft ®Bing mounted and scaled in MapInfo®)

As in the USA, the loss of these wells, in this case during their active life, emphasizes the need for caution when planning well abandonment in a salt bed, especially when it is highly likely that the salt is acting as a seal, or at least an aquitard, to a regional artesian system. The fact that the first well (OKN32) was lost during drilling argues that a natural breach or cavity was already present in the salt bed and perhaps was already stoping its way to the surface. It is also possible that the inappropriate completion and cementation of casing levels, prior to the well's abandonment, may have accelerated cavity expansion. In hindsight, the loss of the second well some 5 years later was highly likely as was catastrophic cavity collapse 5 years after that; the OKN32BIS wellhead was situated only 80 m from OKN32 and was dealing with the same cavern-ridden salt geology.

Lake Peigneur, Louisiana

On November 20, 1980, one of the most spectacular sinkhole events associated with oilwell drilling occurred atop the Jefferson Island dome just west of New Iberia. Lake Peigneur disappeared as it drained into an underlying salt mine cavern and a collapse sinkhole, some 0.91 km^2 in area, developed in the SE portion of the lake (Fig. 13.46; Autin 2002). In the 12 h following the first intersection the underlying mine had flooded and the lake was completely drained.

Lake Peigneur is a natural water-filled salt solution depression atop the Jefferson Island salt dome, which is one of the salt-cored islands in the Five Islands region of the Gulf Coast (Fig. 7.18a). The lake is about 2.4 km in diameter, has a bean-shaped configuration, with a topographic promontory along the southeast shore of the lake rising to more than 23 m above sea level and the surrounding delta plain. Nearby was the site of the infrastructure of the Jefferson Island salt mine (Fig. 13.47a).

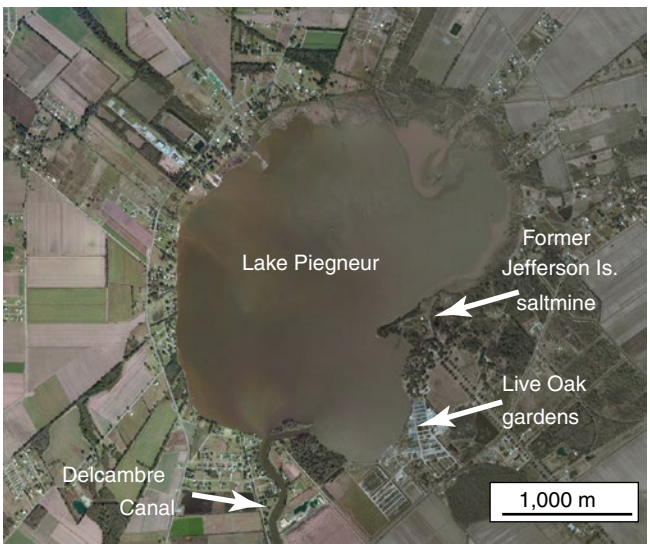

Fig. 13.46 Lake Peigneur, Louisiana (Scale ®Bing image mounted in ®MapInfo)

Drainage and collapse of the lake began when a Texaco oilrig, drilling from a pontoon in the lake, breached an unused section of the salt mine some 1,000 ft (350 m) below the lake floor (Fig. 13.47b). Witnesses working below ground described how a wave of water instantly filled an old sump in the mine measuring some 200 ft across and 24 ft deep. The volume of floodwater engulfing the mine corridors couldn't be drained by the available pumps. At the time of flooding the mine had 4 working levels and one projected future level. The shallowest was at 800 ft, it was the first mined level and had been exploited since 1922. The deepest part of the mine at the time of flooding was the approach rampways for a planned 1,800 ft level. In 58 years of mine life some 23–28

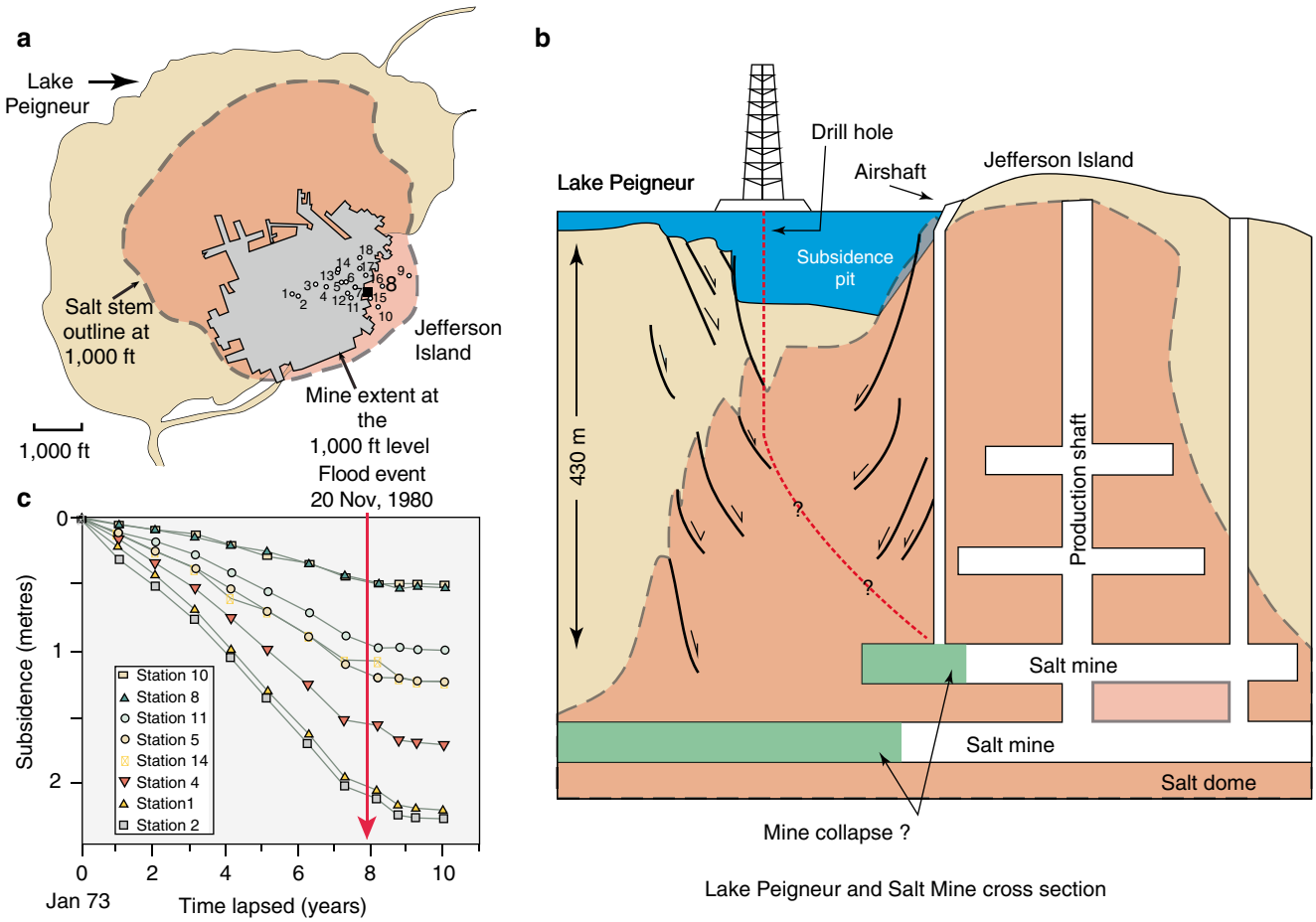

Fig. 13.47 Lake Peigneur, Jefferson Island, Louisiana. (**a**) Plan view showing the extent of Lake Peigneur and the position of the surface monitoring stations (1–18) with selected data plotted as (**c**). Also shown is the extent of the mine workings at 1,000 ft subsurface and the outline of the salt stem at the same level. *Black square* indicates the position of the now flooded No. 1 production shaft. (**b**) Cross section showing the cause of the flooding of the mine and the temporary draining of the lake (in part after Keller and Blodgett 2006) (**c**) Ten years of surface subsidence data showing the drastic decrease in subsidence that followed the flooding of the mine workings (see Fig. 7.18 for locality; after Thoms and Gehle 1994)

million m^3 of salt had been extracted. Prompt reaction to the initial flood wave by mine staff allowed all 50 personnel, who were underground at the time, to escape without anything more than a few minor injuries.

The rapid flush of lake water into the mine, probably augmented by the drainage of natural solution cavities in the caprock below the lake floor, meant landslides and mudflows developed along the perimeter of the sinkhole, and that the lake was enlarged by 28 ha. The surface entry hole in the floor of Lake Peigneur quickly grew into a half-mile-wide crater. Eyewitnesses all agreed that the lake drained like a giant unplugged bathtub—taking with it trees, two oil rigs (worth more than $5 million), eleven barges, a tug boat and most of the Live Oak botanical gardens. It almost took local fisherman Leonce Viator Jr. as well. He was out fishing with his nephew Timmy on his fourteen-foot aluminium boat when the disaster struck. The water drained from the lake so quickly that the boat got stuck in the mud and they were able to walk away! The drained lake didn't stay dry for long, within 2 days it was refilled to its normal level by Gulf of Mexico waters flowing backwards into the lake depression through a connecting bayou (Delcambre Canal, aka Carline Bayou). But, since parts of the lake bottom had slumped into the sinkhole during the collapse, the final water level in some sections was higher than before relative to previous land features. It left one former lakefront house aslant under 12 ft of water.

Of course, an anthropogenically induced disaster like this attracted the lawyers like flies to a dead dingo. On 21 November 1980, the day after the disaster, Diamond Crystal Salt filed a suit against Texaco for an unspecified amount of damage. On 25 November, Texaco filed a countersuit against Diamond Crystal. The Live Oak Gardens sued both Diamond Crystal and Texaco. Months later, the State of Louisiana was brought into the suit since the incident occurred on state land. One woman sued Texaco and Wilson Brothers (the

drillers) for $1.45 million for injuries (bruised ribs and an injured back) received while escaping from the salt mine. Less than a week before the scheduled trial, an out-of-court settlement was reached between the major players. Due to human error, related to a triangulation mistake when siting the drilling barge, Texaco and Wilson Brothers agreed to pay $32 million to Diamond Crystal and $12.1 million to the Live Oak Gardens.

An ongoing environmental catastrophe that was anticipated by environmental groups at the time of the accident never materialized. The lake quickly returned to its natural freshwater state and with it the wildlife was largely unaffected. Nine of the barges eventually popped back up like corks (the drilling rigs and tug were never to be seen again). The torrent of water helped dredge Delcambre Canal so that it was 2–4 ft deeper. And of course, the former 1 m deep Lake Peigneur was now 400 m deep in the vicinity of the borehole!

Interestingly, the filling of the mine workings with water drastically slowed the rate of land subsidence atop the mine (Fig. 13.47c). Measurements had been carried out between 1973 and 1983, some 7 years before the accident and continued for 2 years afterwards (Thoms and Gehle 1994). Slowing reflects the post-accident reduction in the total pressure exerted on the roof of the mine to half its pre-accident levels. Prior to the accident there was no hydrostatic pressure to alleviate some of the lithostatic pressure exerted by the weight of the overburden and so land subsidence above the mine workings was relatively rapid.

Although this incident is not directly related to any solution mining operation and no human lives were lost (although three dogs perished), it clearly illustrates the speed of potential leakage following a breach in a cavern roof in any shallow storage facilities filled with low density fluids. It also illustrates the usual cause of such disasters – human error in the form of a lack of due diligence, a lack of forward planning and a lack of communication between various private and government authorities. It also illustrates that filling a solution cavity with water slows the rate of subsidence atop a large salt cavity and that waters after the disturbance will return quietly to a state of density stratification.

The incident had wider resource implications as it detrimentally affected the profitability of other salt mines in the Five Islands region (Autin 2002). Even as the legal and political battles at Lake Peigneur subsided, safe mining operations at the nearby Belle Isle salt mine came into contention with public perceptions questioning the structural integrity of the salt dome roof. Horizontal stress on the mine shaft near the level where the Louann Salt contacts the overlying Pleistocene Prairie Complex had caused some mine shaft deterioration. Broad ground subsidence over the mine area was well documented and monitored, as was near continuous ground water leakage into the mine workings. The Peigneur disaster meant an increased perception of continued difficulty with mine operations and an increased risk of catastrophic collapse was considered a distinct possibility. In 1985, a controlled flooding of the Belle Isle salt mine was completed as part of a safe closure plan.

Subsidence over the nearby Avery Island salt mine (operated by Cargill Salt) has been documented since 1986. This is oldest operating salt mine in the United States and has been in operation since the American Civil War; and after the Lake Peigneur disaster the mine underwent a major reconstruction and safety workover. Mine management and landowners did not publicly disclose the technical details of rates of subsidence, but field observations revealed the nature of the subsidence process. Subsidence along the mine edge coincided with a topographic saddle above an anomalous salt zone located inside the mined salt area, ground water had seeped into the mine, and there were a number of soil gas anomalies associated with the mine. Small bead-shaped sinkholes were initially noticed in the area in 1986, then over several years, a broad area of bowl-shaped subsidence and areas of gully erosion formed (Autin 2002). Reconstruction has now stabilised this situation. Much of the subsidence on Avery Island was a natural process that occurs atop any shallow salt structure. Dating of middens and human artifacts around salt solution induced water-filled depressions atop the dome shows dissolution-induced subsidence is a natural process that extends back well beyond the 3,000 years of human occupation documented on the island.

Compared to the other salt domes of the Five Islands, Cote Blanche Island has benefited from a safe, stable salt mine operation throughout the mine life (Autin 2002). Reasons for this success to date are possibly; (i) mining operations have not been conducted as long at Cote Blanche Island as other nearby domes, (ii) the Cote Blanche salt dome may have better natural structural integrity than other islands, thus allowing for greater mine stability (although it too has anomalous zones, a salt overhang, and other structural complexities), and (iii) the salt is surrounded by more clayey (impervious) sediments than the other Five Islands, perhaps allowing for lower rates of crossflow and greater hydrologic stability.

Groundwater Breakout Tied to Anpeng Trona, China

At a depth of more than 2,000 m, the Anpeng trona salt mine, China, exploits the deepest and second largest trona deposit yet discovered in the world. The mine is located in hilly country and is solution mining Eocene sediments in the fault-bound Biyang depression, via a linked series of injector and extractor wells (Chap. 12). Since October 2008, groundwater bursting or breakout has occurred, even under rainless weather conditions in and around Cao Village, Anpeng, Tongbai County. These saline breakouts have caused severe

salinization of the land, which currently has an area of over 300,000 m^2. Water from some drinking wells has also become contaminated and nonpotable.

A systematic study of the geological conditions, operation of the mines, the hydrogeochemistry of groundwater bursts shows leaked solution waters are the source of the groundwater bursts (Shi et al. 2013). Over the 40 years of mine operations, natural and induced fractures, cracks, faults, and leaking brine wells have formed connections with one another. Previously unrecognised water leakages of saline mine waters have welled up and recharged shallow aquifers, before finally reaching the ground surface as groundwater bursts, where pressurised escaping waters can form fountains up to a metre tall.

Case Histories: Storage Cavern Problems

The world's demand for fuel means it must be held in sufficient quantities near centres of distribution so as to insure security of supply. Deciding where and how mankind stores substantial volumes of hydrocarbons (or in the future the much more volatile hydrogen) in or near populated areas will always be a problem. There have been a few accidents in below ground storage facilities and some are described in this section. However, when the environmental and safety records of above and below ground fuel storage facilities are compared, the below ground facilities are an order of magnitude safer and less environmentally hazardous. Problems with storage caverns in salt hosts are related either to the utilisation of non-purpose built caverns or to human error and poor management practices (Fig. 13.7).

Weeks Island, Louisiana

The Weeks Island Strategic Petroleum Reserve (SPR) facility on Weeks Island, Louisiana, is some 30 km SE of Jefferson Island (Fig. 7.18). Like other salt-cored islands, the landscape shows a variety of surface features indicative of ongoing salt dissolution such as dolines and linear valleys atop shear zones (Fig. 13.48a). It utilized abandoned room and pillar caverns of the Morton Salt Company mine and so was unusual compared to other purpose-built storage caverns of the Strategic Petroleum Reserve (SPR). It was purchased in the 1970s, a time that was early in the annals of the SPR and at the height of the 1970s oil crisis. Occupying a former salt mine it was the shallowest of all the SPR facilities across the USA (150–220 m below the land surface). It was not a custom built facility, nor was it constructed by solution mining technologies.

Following oil fill in 1980–1982, the facility stored some 72.5 million BBL of crude oil in abandoned mine chambers. Then in November 1995, the Department of Energy (DOE)

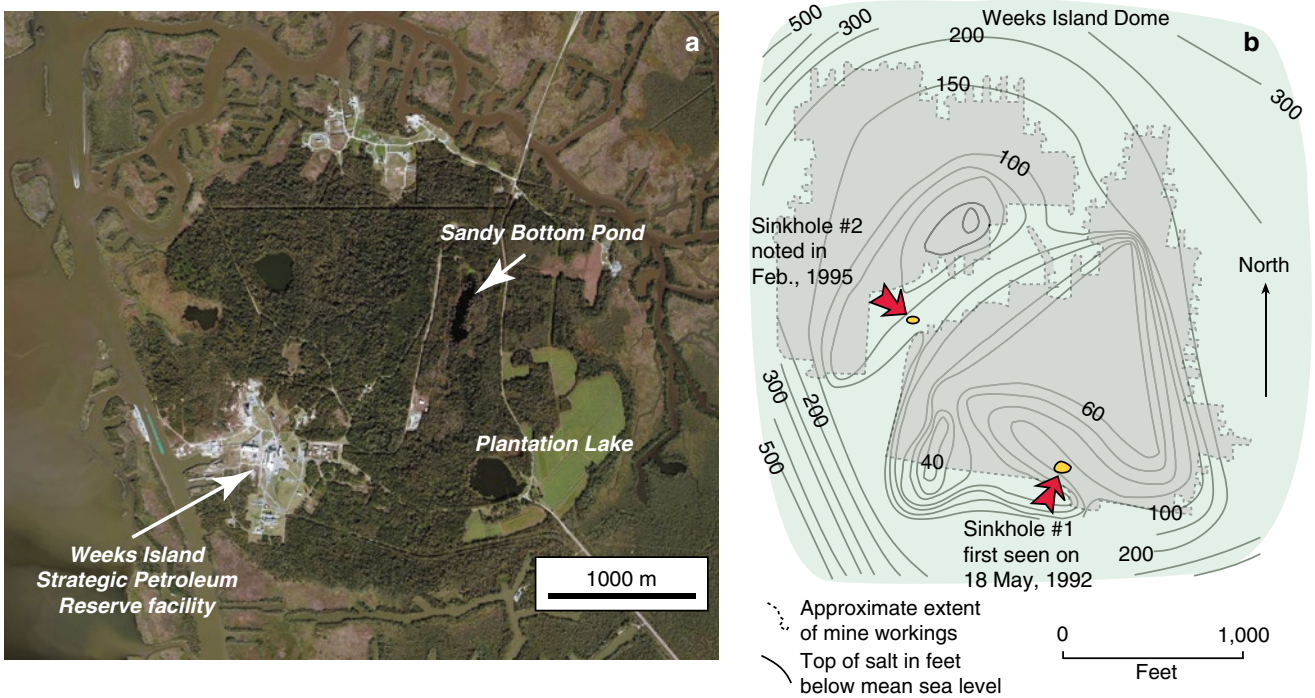

Fig. 13.48 Strategic Petroleum Reserve facility, Weeks Island, Louisiana. (**a**) Location of SPR facility and the presence of natural water-filled collapse dolines. Bing® image mounted and scaled in MapInfo®. (**b**) Top of salt contours showing how sinkholes developed in depressions atop the upper part of the salt. The sinkholes occur in regions near the edge of the cavern, with the potential for foundering of the cavern roof into the chambers of the former Morton Salt mine

initiated oil drawdown procedures, along with brine refill and oil skimming, plus numerous plugging and sealing activities. In 1999, at the end of this recovery operation, about 98 % of the crude oil had been recovered and transferred to other SPR facilities in Louisiana and Texas; approximately 1.47 MMBL still lies in the now plugged and abandoned cavern system.

The cause of this drainage and abandonment was an active sinkhole some 10 m across and 10 m deep, first noted near the edge of the SPR facility in May 1992 and perhaps reaching the surface about a year earlier. However, the growing depression was located on the south-central portion of the island, directly over a subsurface trough, which is obvious in the top-of-salt contour based on mine records (Fig. 13.48b; Neal and Myers 1995). Earlier shallow exploratory drilling around the Department of Energy service and production shafts in 1986 had identified the presence of irregularities and brine-filled voids along the top of salt in this region. A second, much smaller sinkhole was noticed in early February 1995, but it did not constitute a serious threat as it lay outside the area of cavern storage.

Neal (1994) pointed out that Kupfer's 1976 map of that part of the mine located beneath the first sinkhole showed black salt. Regionally, black salt in Gulf Coast salt mines is often associated with anomalous leach-zones, indicating zones where salt was subject to unpredictable movement and sometimes to collapse. The volume of this sinkhole (estimated as 650 m^3 when first noted), its occurrence over a trough in the top of salt, and its position directly above the oil-filled mine caverns, meant it was of concern to the SPR authorities, especially in terms of the stability of the roof of the storage cavern. This feature did not form overnight, it lies atop a shear zone that formed during the diapiric rise of the salt and capped by a rockhead valley containing Pleistocene sediment fill. Salt extraction probably created tension across the shear zone, thereby favouring fracture enlargement, as early perhaps as 1970 (Fig. 13.49; Waltham et al. 2005). Eventually, an incursion of undersaturated groundwater traversed the fracture zone across some 107 m, from a level equivalent to the rockhead down to the mine where it emerged. Over time, ongoing dissolution enlarged a void at the top of the salt, creating the collapse environment for the sinkhole that was noted at the land surface in 1991. Investigations undertaken in 1994 and 1995 into the cause of active at-surface sinkholes verified that water from the aquifer above the Weeks Island salt dome was seeping into the underground oil storage chamber at the first sinkhole site (Figs. 13.48 and 13.49; Neal and Myers 1995; Neal et al. 1995, 1997). Drainage and decommissioning of the Weeks Island facility followed.

Beginning in 1994, and continuing until abandonment of the facility, saturated brine was injected directly into the throat of first sinkhole, which lay some 75 m beneath the surface. This essentially arrested further dissolution and

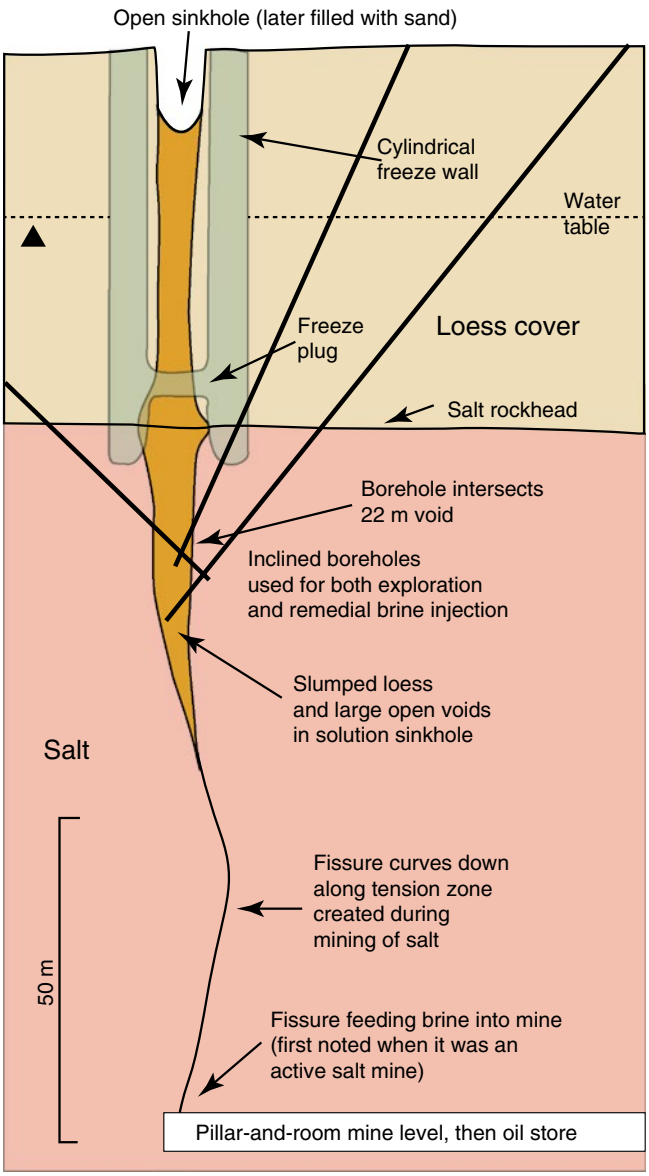

Fig. 13.49 Schematic section through the main Weeks Island sinkhole and its remedial freeze curtain (After Waltham et al. 2005)

bought time for DOE to prepare for the safe and orderly transfer of crude oil to another storage facility. To provide added insurance during the oil transfer stage, a "freeze curtain" was constructed in 1995. It consisted of a 54 well installation around the principal sinkhole, which froze the overburden and uppermost salt to a depth of 67 m (Fig. 13.49; Martinez et al. 1998). Until the mine was completely filled with brine and its hydrocarbons removed, this freeze wall prevented groundwater flow into the mine via the region of black salt around the sinkhole. Dealing with this sinkhole was costly. Mitigation and the removal and transfer of oil, including dismantling of infrastructure (pipelines, pumps etc.), cost a total of nearly US$100 million; the freeze curtain itself cost nearly $10 million.

In hindsight, based on an earlier leak into the mine, while it was an operational mine, and the noted presence of black salt in a shear zone in the mined salt, one might fault the initial DOE decision to select this mine for oil storage. In 1978 groundwater had already leaked into a part of the mine adjacent to the sinkhole and this was forewarning of events to come (Martinez et al. 1998). Injection of cement grout into the flow path controlled the leak at that time, but it could just as easily have become uncontrollable and formed a sinkhole then. But in 1978 the technology needed to understand the salt physics, salt solution and mine conditions and so predict future events had not been developed. The world, and the United States, was in the middle of an oil crisis and as a former US President once observed, "It's hard to drain the swamp when you're up to your arse in alligators!"

Gas Escape, Explosions and Fires from Cavern Leaks

Almost all the explosions and fires described in this section are caused either by human error, poor forward planning, a lack of due diligence by the storage company or operator or a combination of these factors (Table 13.7; Yang et al. 2013). In all cases the salt caverns themselves did not fail. In spite of these accidents, cavern storage is still one of the safest ways to store what are very large volumes of highly explosive materials. Consequences are far graver, and death rates orders of magnitude higher, when explosions and fires have occurred in above ground fuel storage tanks and facilities (Evans et al. 2009).

The West Hackberry Explosion

On September 21, 1978 a blowout and explosion occurred at the West Hackberry salt dome storage facility in southern Louisiana (USA). It killed one worker, released 10,000 m^3 of oil to the surface and cost US $14–20 million (1980 dollars) in cleanup and remediation. The incident occurred during workover operations on one of the access wells to the No. 6 cavity.

Understanding the causes of the explosion requires a few background comments on casing strings in the well and the workover specifications (Fig. 13.50). The well completion was made up of an outer 12.75-in (32.4 cm) casing string cemented to a depth of 2,632 ft (816 m). Cemented inside was another 9.62-in (24.4 cm) diameter casing string some 2,603 ft (807 m) long. This was probably added after the "initial" completion to improve oil tightness when the cavity was converted to oil storage. An innermost 5.5-in (14 cm) diameter pipe string was used to withdraw brine whenever oil was pumped in to the cavity (see Fig. 13.50).

On the day of the explosion the workover consisted of withdrawing the 5.5-in innermost tubing string, repairing a leak on the 12.75-in casing, and reinforcing the wellhead equipment. To accomplish this, the annular space between the innermost pipe string and the 9.62-in casing had been filled with high viscosity mud. This was designed to bring wellhead pressure in the oil string to zero. Once the annular space was filled, a packer was set at the bottom of the 5.5-in brine pipe to seal it off from the cavity. Work then commenced on pulling the innermost 5.5-in pipe; however, after 14 pipe lengths had been stacked, the packer slipped as increasing differential pressure started to push it up to the surface. As the packer rose, the pressure (brine to oil differential) on it increased. Soon the packer shot up and out on to the surface, forming an oil geyser (blowout) that continued until the pressure differential had dissipated. By that time an estimated 72,000 barrels (10,000 m^3) had shot up into the air, caught fire and killed one of the drilling crew.

A poor understanding of the pressure distribution in the fluid columns when the workover was designed is the main reason for the incident. As planned, the workover was extremely delicate, it was attempted without drawing down the oil pressure in the cavern. As the oil was under high pressure (sealed in by viscous mud in oil feeder casing) as the workover began it was liable to expand violently if any mishap upset the status quo. Injecting the viscous mud at the top of the well was a good precaution against any failure of the topside valve on the oil-filled annular space, but it had absolutely no effect on the dangerous situation at the bottom of the cavity and if the packer failed, which it did, there was no way of preventing a blowout.

A comprehensive but simple precaution would have been to release the pressure on the oil in the cavity by drawing down the top surface of the brine in the access well to about one quarter of its total original height. The volume of oil needed to be withdrawn was, of course, exactly equal to the volume that was expelled in the blowout. This relatively small volume of oil could easily have been stored temporarily in another cavity on the site. So doing would have rendered the workover situation entirely safe.

The Brenham Explosion

A disastrous explosion occurred on April 7, 1992, following the outflow of LPG onto the surface from a well atop a storage cavern in the Brenham Salt Dome. The blast occurred some 110 km northwest of Houston. It killed a 6-year old boy and two adults, injured 21 persons, damaged more than 40 homes and snapped trees like matchsticks, while denuding acres of rolling farmland. In all it caused an estimated US$ 9 million in damage to property within a 5 km radius. Seismographs at three Texas universities within 120 km of the scene recorded surface tremors ranging from 3.5 to 4.0 on the Richter scale. Windows were rattled in homes more than 200 km away.

The Brenham storage facility consisted of a 380,000-bbl (60,000-m^3) cavern filled with LPG (a mixture of propane, ethane, n-butane and other gases). The cavern was linked to

Table 13.7 Accidents associated with oil and gas storage facilities

Storage cavern	Time and place of accident	Reserve resource	Accident description	Accident cause	Economic loss	Number of casualties	Influence scope
Petal City	1974, Mississippi, USA	Liquid butane	Fire & explosion	Human error leading to overfilling	Homes destroyed within 7 km	24 injured	Influence range was 7 km, 3,000 evacuated
West Hackberry	1978, Louisiana, USA	Petroleum	Fire & blowout	Packer failure during repair of casing	72,000 bbls (about 11,446 m^3) crude oil leaked, US $ 14–20 million loss in total	1 fatality, 1 injured	Influenced area was 90,000 m^2, environment polluted
Mont Belvieu	1980, Texas, USA	Liquid propane	Fire & explosion	Casing failure-corrosion	23 million m^3 of propane loss	At least 1 fatality	75 families (300 people) evacuated for 180 days
Conway	1980–2002, Kansas, USA	Liquid propane	Gas leaking into the groundwater	Hydrated cap rock	Gas found in wells and local groundwater possibly caused by wet rockhead	None	Area near the storage cavern, 30 homes bought, 110 people relocated
Mont Belvieu	October, 1984, Texas, USA	Liquid propane	Fire & explosion	Casing failure	Several million US $ loss	None	
Mont Belvieu	November, 1985, Texas, USA	Liquid propane	Fire & explosion	Transmission pipeline cut off	110 m^3 of propane consumed and a large amount of propane leaked	2 fatalities	More than 17,000 evacuated
Viriat	1986, France	Ethylene	Gas cloud	Ground facilities broken	All gas leaked	None	
Teutschenthal	1988, Halle, Germany	Ethylene	Surface dome and crack	Casing broken	60–80 % of ethylene leaked	None	An area of approximately 8 km^2 evacuated
Clute	1988–1989, Texas, USA	Ethylene	Gas escaping	Drilling operation resulting in tightness failure	About 20,000 m^3 of ethylene loss	None	10 families evacuated
Brenham	1992, Texas, USA	Liquefied petroleum gas (LPG)	Fire & explosion	Overfilling and valve failure	332,000 barrels (about 52,500 m^3) US$5.4 million & US$1.38 million punitive damages awarded	3 fatalities, 23 injured	About 3 km radius of plant, 26 homes destroyed
Mineola	1995, Texas, USA	Propane	Fire underground and on the surface	Pillar cracks	Cavern cycling connected adjacent cavities, pressure buildup and casing leak	None	The two caverns and region within 15 m on the surface
Yaggy	2001, Kansas, USA	Natural gas	Fire & explosion	Casing bend and damage	About 5,600,000 m^3 natural gas loss. Gas surfaced in old brine pipeheads. US$800 million law suit	2 fatalities	Part of the town influenced, some 250 people evacuated
Fort-Saskatchewan	2001, Saskatchewan, Canada	Ethylene	Fire lasting 8 days	Failure of pipeline connecting two caverns	14,500 m^3 ethylene loss in	None	Area near the plant
Magnolia	2003, Louisiana, USA, near Napoleonville	Natural gas	Gas escaping	Casing crack	More than 1,000,000 m^3 natural gas leaked	None	About 30 people evacuated from Grand Bayou
Odessa	2004, Kansas, USA	Liquid propane	Gas escaping	Ground facilities broken	More than 100 t (about 90,000 kg) liquid propane leaked	None	
Clute	2004, Texas, USA	Ethylene	Fire & explosion	Drilling operation resulting in tightness failure		None	10 families evacuated
Moss Bluff	2004, Texas, USA	Natural gas	Fire & explosion (300 m high flame)	Brine pipe corrosion, well casing separation	At least 36 million US $ loss in gas inventory	None	Influence range was 120 m, 1,000 people within 5 km evacuated

After Yang et al. (2013), Evans et al. 2009)

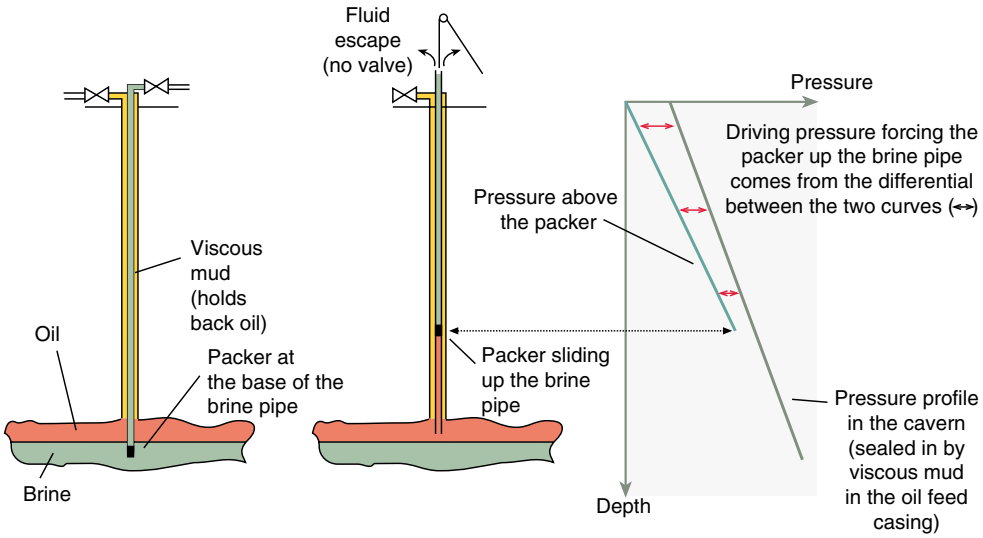

Fig. 13.50 Schematic of the pressure differentials that caused the West Hackberry blow out and explosion (see also Fig. 13.14)

ground level by a 13-3/8-in diameter, 2,702-ft long cemented casing (Fig. 13.51). A central brine pipe (2,871-ft long) allowed injection and withdrawal of brine. LPG was injected into, or withdrawn from, three distinct pipelines. Brine was provided by two above-ground brine ponds. The wellhead was equipped with a shutdown valve. The Brenham station was operated remotely by a dispatcher in Tulsa, Oklahoma (Bérest and Brouard 2003).

At 5:43 am on April 7, 1992, additional LPG was injected in the cavern. The brine/LPG interface unexpectedly reached the 1-in diameter weep hole located in the lower part of the central tubing, some 1 ft above the tubing base. The weep hole was supposed to provide warning in case of imminent overfilling. LPG flowed into the central brine tubing, leading to lower density in the fluid in the central column, partial vaporization and expansion of the lighter gases, a pressure drop in the cavern and, ultimately, a large flow of gas through the weep hole and the tubing base alike.

Brine, followed by liquefied gas, daylighted at the brine pond surface. Back-calculation proved that 3,000–10,000 bbl (500–1,600 m^3) of liquefied gases were expelled via the ponds. The release of gas into the atmosphere activated gas detectors at ground level. (Such activation was apparently a relatively frequent event at this station, and alarms were often unrelated to an actual gas leak). The dispatcher in Tulsa was not able to interpret correctly the somewhat confusing information delivered by the telemetric system – a unique signal was sent, whatever had activated a number of detectors. The shutdown valve (or cavern safety valve) was assumed to have immediately reacted to the high pressure level (100 psi) in the brine tubing at the wellhead, but the system failed.

A subsequent National Transport Safety Board (NTSB) investigation confirmed the local operator had overfilled the storage cavern to where LPG had escaped into an adjoining brine storage pit through the brine injection system via an open valve. Product had then evaporated and, being heavier than air, formed a low-lying cloud 30 ft high and several hundred yards long. At 7:08 am the "mushroom-shaped" vapour cloud was ignited by an automobile driving into the foggy cloud near the storage facility.

According to the NTSB report, Mapco (the operator of the facility) was not aware of the volume of product in storage at the site. Some 338,995 barrels were actually stored instead of the 288,000 bbl estimated by Mapco. NTSB concluded that the management procedures had lacked oversight adequate to confirm employee measurements. Nor did the company have the ability to balance cavern receipts against withdrawals. In addition, employee measurement procedures did not adequately take into account specific gravity variations of the NGLs in storage.

Aside from the computation errors, NTSB said other contributing factors included:

(a) Inadequate positioning of the brine pipe weep hole – in a post accident redesign it was moved to 6 ft above the base of the brine pipe,
(b) A lack of several fail-safe features on the cavern's shutdown system – this system had included a brine pressure-sensing line designed so that when a large pressure build-up was sensed in the brine line it switched a spring that, when triggered, sent an electrical signal in a chain containing a fusible link whose fusion should have closed the brine safety valve and so prevented product leakage back up the brine pipe. It is extremely likely than one or two manual valves were closed on this sensing line at the time of the explosion, isolating it from the main body of the brine pipe, so making the emergency shutdown system ineffective. Ironically, the shutdown valve was activated when heat from the explosion burned

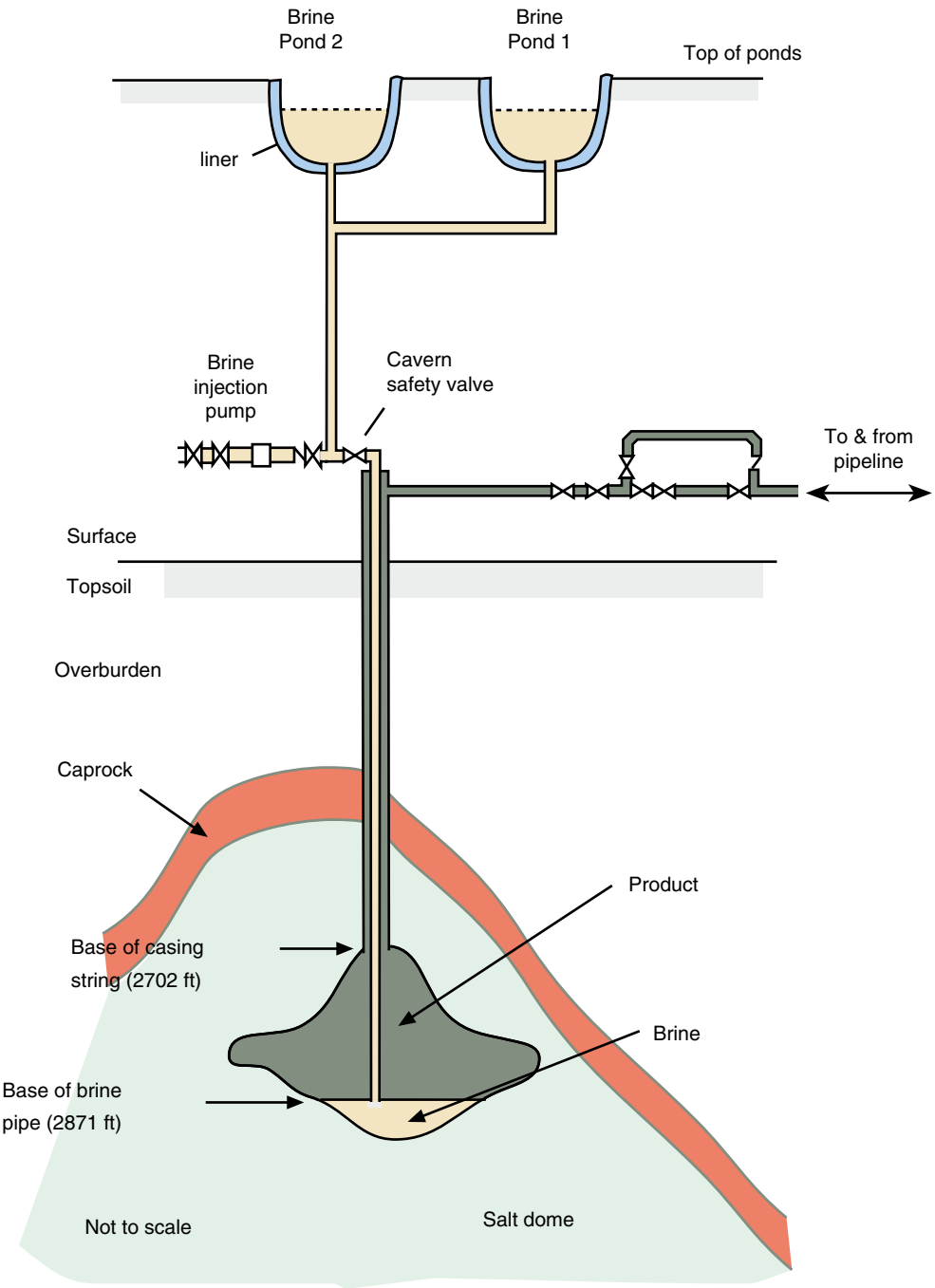

Fig. 13.51 Schematic of the situation at the time of the Brenham explosion

the fuse and triggered valve closure (it shut the barn door after the horse had bolted).

(c) Inadequate emergency response training and procedures, along with poor communication among Mapco employees responding to the alarms and to the obvious surface emergency.

Early media coverage sensationally reported that "A Salt Dome Has Blown Up". However the cavern storing the leaked liquids later passed a mechanical integrity test and is still in use today. It was operational supervision and safety procedures that failed dismally, not the cavern. After this accident, the Railroad Commission of Texas issued new regulations (effective in 1994) mandating that LPG storage caverns be protected by at least two overfill detection and automatic shut-in methods.

Barber's Hill Explosion and Collapse

On October 3, 1980 a gas-fed explosion occurred in a residence in Mont Belvieu, a Texan town that sits atop the Barbers Hill diapir, some 60 km west of Houston. Barbers Hill dome is the largest subsurface LPG storage facility in

the U.S. with over 126 active solution-mined caverns storing between 75 and 300 million barrels of light hydrocarbon products. The explosion was ignited by a woman who sustained burns when turning on her dishwasher. A spark from the dishwasher had ignited gas that had accumulated in the foundation of the house.

Two weeks earlier, on September 17, 1980, a drop in pressure had been recorded in one of the nearby cavities storing liquefied petroleum gas (70 % ethane, 30 % propane). The cavern was emptied of product and filled with brine. Subsequent investigation showed a leak had occurred through a corroded casing joint in the access well in the vicinity of the porous anhydrite caprock (Fig. 13.52). The well in question had originally been drilled in 1958. Leaking gas seeped through the surrounding soil to accumulate in the foundations of the residence where the explosion occurred. In the days that followed, gas daylighted haphazardly in residential areas around the site of the original explosion. Holes were drilled into the watertable to find and vent pockets of gas. Residual gas saturations in the soils forced the evacuation of 73 families for nearly 7 months and a drastic fall in property values.

Because of its low density, propane tends to rise to the surface, either through the cement along the outside of the casing or by dispersing in the overlying ground surrounding a breach (Bérest and Brouard 2003). This happens, for example, if escaping gas intersects a sufficiently pervious water-bearing layer just below the surface. The gas can accumulate in building foundations, emerge at streams and similar low-lying ground or come up through faults and joints, daylighting at the surface several hundred meters from the well head. To minimise this potential problem, the architecture of the access well is of utmost importance. In the Mount Belvieu situation, if the two last cemented casings been anchored in the salt formation and not into the anhydrite cap, the propane leak would have been channeled in the cemented annular space between the two casings, with considerably lesser consequences (Thoms and Kiddoo 1998).

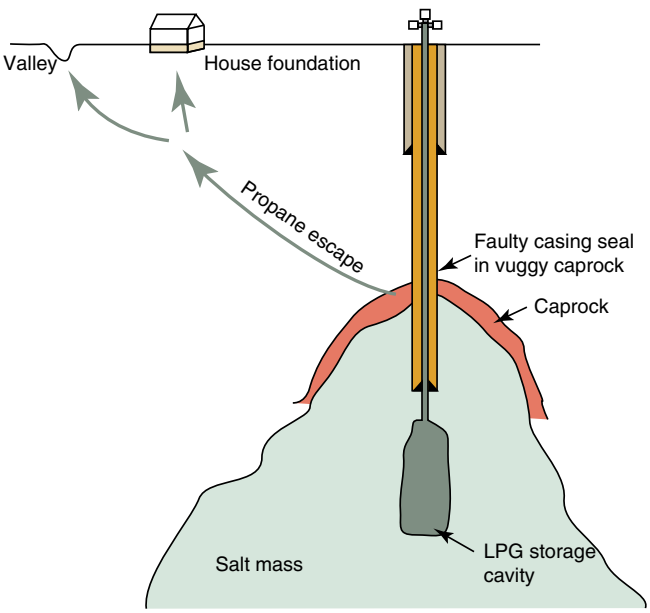

Fig. 13.52 The Mont Belvieu (Texas) 1980 accident. After 22 years of operation, the last cemented casing became leaky. In Texas, more recent wells must be equipped with two casing strings into the salt (After Bérest and Brouard 2003)

A few years later, on July 30, 1993, there was another event that further lowered Mont Belvieu property values. In a few hours a sinkhole crater formed between two brine wells in the EGP Fuel Storage facility (Cartwright et al. 2000). The crater stabilized with a diameter of 12 m and a depth of 6 m. A well that was near the problem site had to be abandoned after the sinkhole formed. It was not a hydrocarbon storage well so the environmental implications of a collapse-induced abandonment were not as significant it would have been for a failed hydrocarbon cycling well. The cause of the sinkhole is contentious but it is thought that brine cycling in the two wells may have contributed to the collapse. Detailed subsidence work in the cone of subsidence about the sinkhole suggest that it was probably there prior to the collapse and, if it had been monitored, the data could have been used as an indicator of the likelihood of collapse (Cartwright et al. 2000).

Brine injection that drives brine compensated withdrawal of the stored hydrocarbons periodically requires large volumes of brine in short time frames. But in Mont Belvieu there was not sufficient above ground infrastructure to store the large volumes of brine needed for product cycling. To give access to large volumes of brines quickly, brines were pumped down dedicated brine storage wells with bases in shallow caprock caverns. Wells adjacent to 1993 Mont Belvieu sinkhole were two such wells that had stoped toward the landsurface, perhaps facilitated by ongoing brine cycling.

Mineola Propane Fire

In 1995 there was an underground fire that burned for several days at a salt dome storage cavern operated by Suburban Propane near Mineola in East Texas, some 145 km east of Dallas. The cavern in which the blow-out occurred extended from 1,200 to 2,500 ft (350–750 m) subsurface. The blowout occurred when a salt wall separating two storage caverns had become so thin from the enlargement associated with brine compensation (product cycling) that it cracked (Gebhardt et al. 2001). This allowed stored propane product to flow from one cavern to an adjacent cavern that was empty of product and undergoing testing. Pressurised nitrogen was being injected into the adjacent brine filled cavern as part of a standard mechanical integrity test. The testing may have contributed to the penultimate pressure buildup that allowed propane product to leak into shallow depths via a casing leak

(Bérest and Brouard 2003). The leaking well had originally been drilled as an oil producer in the late 1950s, four decades before the accident. Liquified gas escaped through the soil in a halo that extended as far as 100 ft from the well. The escaping gas ignited and burned releasing heavy black smoke. Extinction of the fire was not a viable option, as dangerous re-ignition and flash back was likely. The innovative kill techniques applied to this well are described in Gebhardt et al. (2001).

There are potential problems with longterm intercavern integrity as all salt caverns will enlarge during product cycling, so the Texas Railroad Commission now legislates what is an acceptable degree of enlargement before a storage cavern must be plugged and abandoned.

Hutchinson Explosion

On January 17, 2001, a gas explosion and fire destroyed two businesses in downtown Hutchinson in central Kansas (Allison 2001). The next day in the Big Chief mobile home park 3 miles away another explosion occurred and 2 residents died of injuries received. The explosions were tied to geysers spewing gas and water, and their appearance caused the excavation of hundreds of Hutchinson residents. Pathways to the landsurface at both explosion sites and to the various active geysers across town were directly tied to undocumented and abandoned wells that were once used to solution mine the Hutchinson Salt.

The January 17–18, 2001 eruptions of gas and brine, driving 30-ft (10 m) geysers in the town, resulted from the loss of 143 MMcf of gas from the Yaggy natural gas storage facility located 7 miles down the road from the town community of 40,000 people (Fig. 13.53). Oneok Inc., owned and operated the Yaggy field through a subsidiary company called KGas. Upon review of pressure records, KGas officials realized that the S-1 cavern had probably been leaking at a low level, at least since the pod of caverns had been refilled with natural gas on January 14, and perhaps much longer, perhaps since the initial well workover in the 1990s. At the time of the refilling, technicians did not think much of a minor pressure drop, as it was a routine situation associated with filling the cavern. When the caverns are pressurized, the natural gas is compressed, raising its temperature. Once in the caverns, the pressurised gas begins to cool and condense, resulting in a slight pressure decrease. It was common practice to then "top off" the cooled caverns with additional gas to fill the caverns to the final storage pressure.

The Yaggy field of salt caverns was originally developed in the early 1980s to hold propane. Wells were drilled to depths of about 650–900 ft (200–300 m), into the lower parts of the Hutchinson Salt Member and cased with steel. The roof of each cavern was about 40 ft (12 m) below the top of the salt layer. The company had difficulty making a financial success of the operation and eventually ceased operations. All of the storage wells were filled with brine and then plugged by partially filling them with concrete. KGas acquired the facility in the early 1990s and converted it to natural gas storage (by definition this is a pressurized storage system). Plugged wells were drilled out to return the feeder

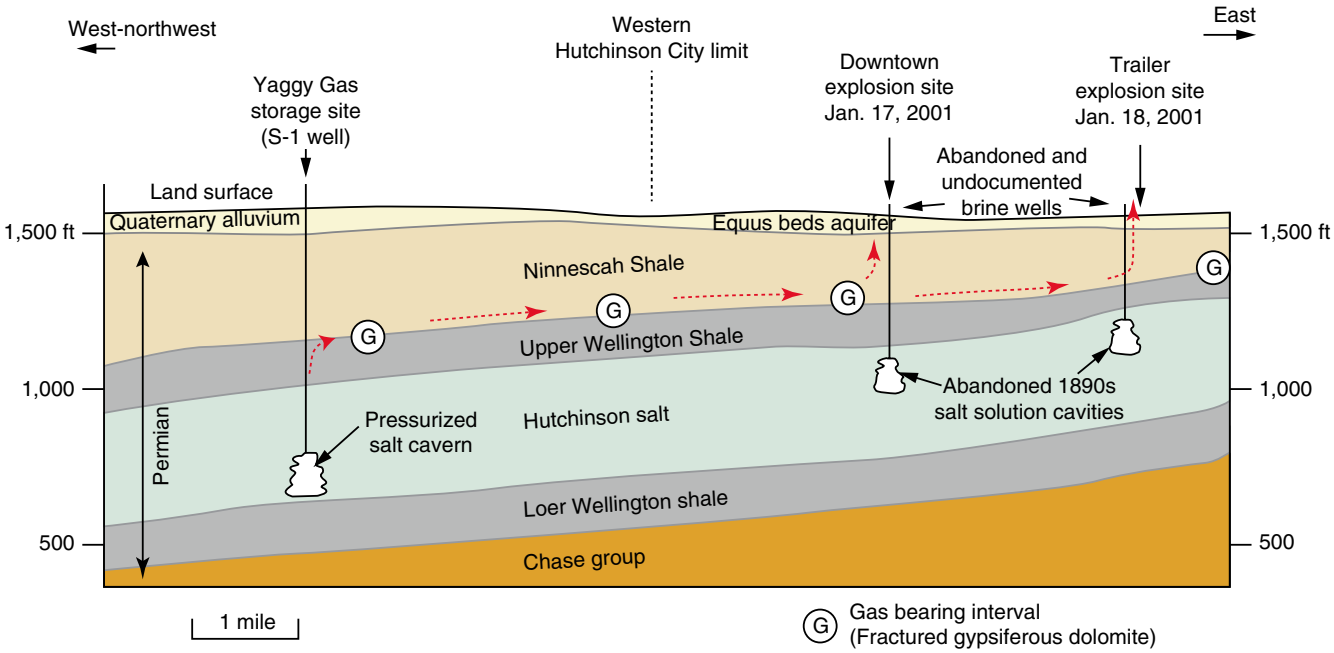

Fig. 13.53 Hutchinson, Kansas January 2001 gas explosion, explanatory cross section (Redrafted and modified from image downloaded on June 4, 2013 at <http://www.kgs.ku.edu/Hydro/Hutch/GeneralGeology/index.html>)

wells and caverns to use. At the surface the wells in the Yaggy facility are 300 ft (90 m) apart. At the time of the crisis, Yaggy had about 70 wells, of which 62 were feeders to active natural gas storage caverns. More than 20 new wells had been drilled and were being used to create new caverns for expansion of the field storage capacity.

At full capacity, the field could hold 3.5 billion cubic feet (Bcf) of gas at pressures of about 600 lb per square inch and at the time of the accident it was supplying up to 150 MMcf (million cubic feet) of gas per day. Yaggy is the only natural gas storage field in salt caverns in the state of Kansas. Other salt caverns in Kansas are used for brine-cycled storage of liquid hydrocarbons, such as propane, at much lower pressures than the natural gas at Yaggy.

Records show that when KGas drilled the concrete out from the well casing in S-1 well to return the well to operation, they encountered a steel casing coupler that was dropped into the concrete in the well during the plugging operations (Allison 2001). During the workover this object may have deflected the drill bit against the side of the well casing damaging and weakening it. A post accident down-hole video in S-1 shows a large curved slice in the casing at that depth. The city's geological consultant described it as looking "like a kitchen knife cutting into a can." Prior to the Yaggy facility approval by state authorities the S-1 had a satisfactory casing pressure test, as required by the Kansas Department of Health and Environment. The test was though to demonstrate the integrity of the casing at that time. However, the well at the depth of the leak was never tested to the maximum pressure that would be experienced in service.

The route followed to the surface by the escaping gas is not completely documented. Initial seismic surveys in early February 2001 at first indicated a possible subsurface sand channel through which the escaping gas flowed up from the storage facility. But that was not borne out by a study of regional well logs or the 22 % success rate in drilling for suspected gas pockets (Watney et al. 2003) or subsequent seismic interpretation (Nissen et al. 2004). The most likely candidate carrier is thought to be a fractured intrasalt gypsiferous dolomite layer that pinched out northwest against the tight shales, and so facilitated drainage to the crest of the anticlinal culmination that underlies the town of Hutchinson (Fig. 13.53).

There are more than 600 NGL-LPG salt storage caverns in bedded Hutchinson salt in the state of Kansas, the most of any state in the USA. Kansas also has plans for more natural gas storage caverns, although Gulf Coast salt dome caverns are 10–20 times larger. The mix of bedded salt and permeable rock formations (perhaps even intrasalt) around Hutchinson region, the presence of natural dissolution irregularities and the fact that Hutchinson has been an area of solution mining since the late 1800s is a real problem for storage of high-pressure fluids. Once the S-1 well was breached, numerous unplugged brine wells that were long ago drilled within the Hutchinson Salt and abandoned, without appropriate documentation, routed the escaping gas to the surface. Such wells are directly tied to the downtown fire that first heralded the problem, and to the two deaths that occurred in the explosion in the mobile home park a few days later. Work since the explosion has pointed out numerous problems to be addressed in a region of bedded salt that appears in many ways not to be a suitable site for future natural gas storage projects. Even so, the salt storage cavern itself did not leak, the access piping was the problem due to well workover damage.

After the accident, poor regulation and the small inspection staff numbers in the state of Kansas (compared to neighboring states) were incriminated by several experts (Bérest and Brouard 2003). New sets of regulations were discussed and legislated, including mandatory double casing in wells, corrosion control, well conversion restrictions (salt caverns designed to store LPG should not be converted to store natural gas, and cavern wells that have been plugged cannot be reopened and used again), maximum pressure limit of 0.76 psi/ft ($1.73\ 10^{-2}$ MPa/m) and new testing requirements, such as a leak test should be performed every 5 years.

CO_2 Outburst, Menzengraben Potash Mine, E. Germany

An intense outburst of carbon dioxide took place on 7 July 1953 in the vicinity of the Menzengraben potash mine of the former East Germany (Hedlund 2012). This disaster occurred in a salt mining region known to be gassy, and prone to CO_2 rock-burst problems (Table 13.8). The gas escaped from the #2 Shaft House immediately after a scheduled underground blast at 11:35 pm on the evening of July 7, 1953. As a result of the gas escape some 12 people died above ground from CO_2 -induced asphyxiation, many died in their sleep. No-one died underground as, due to the gassy nature of the extracted salt, it was standard practice to bring all staff above ground prior to a blast. For 25 min after the scheduled blast, a large amount of CO_2 blew with great force out of the mine shaft. Outside, it was a still night with no wind, allowing concentrated CO_2 to accumulate in a nearby valley, leading to multiple asphyxiation casualties.

Based on a review of concentration-response relationships, the location of victims, and other information, Hedlund (2012) concluded that concentrations of 10–30 % carbon dioxide occurred up to 450 m from the point of release at the shaft house, for at least 45 min, with some 1,100–3,900 tonnes of CO_2 blown out of the mine, at "blow-out" intensities estimated to be 4 tonnes per second. The majority of the gas escaped via a near-vertical high-velocity jet, with only little loss of momentum due to impingement. The nature of the escape and the ability of the gas to pond is relevant to planned CO_2 sequestration facilities, worldwide. The largest natural CO_2 induced

Table 13.8 Reported salt burst and CO_2 release volumes resulting from CO_2 outbursts in the Werra District

Date	Mine	Salt burst (tonnes)	CO_2 released (m^3)
27 November, 1908	Dietlas	2,700	18,000
15 April, 1938.	Marx-Engels	7,000	Not stated
31 November, 1938	Ernst Thalmann	15,000	200,000
29 January, 1942	Menzengraben	5,000	75,000
3 June, 1943	Menzengraben	18,000	450,000
10 May, 1950	Marx-Engels	20,000	Not stated
13 October, 1951	Menzengraben	13,000	200,000
7 July, 1953	Menzengraben	65,000	700,000
15 October, 1957	Menzengraben	22,000	400,000
21 August, 1981	Not stated	6,000	1,000,000
25 May, 1984	Not stated	110,000	2,300,000

After Hedlund (2012)

Table 13.9 Problems in pressurized storage caverns (see text)

Storage cavern	Time and place of accident	Reserve resource	Accident description	Accident cause	Economic loss	Influence scope
Kiel	1967, Germany	Natural gas & hydrogen	Volume lost 12.3 % after 45 days	Excessive creep of salt, operating at too low pressure	Cavern failure (reduced capacity)	The cavern
Eminence	1970–1972, Mississippi, USA	Natural gas	Volume lost more than 40 %	Excessive creep of salt, operating at too low pressure	Cavern failure (reduced capacity)	The cavern
Stratton Ridge	1990s, Texas, USA	Natural gas	Cavern abandoned, ground subsidence, settlement rate 40 mm/a	Excessive creep of salt and in wet condition	Cavern failure	Ground above the caverns
Bayou Choctaw	1954, Louisiana, USA		Cap rock collapsed, ≈245 m diameter lake formed on the surface	Human error	Cavern failure	Ground above the caverns
Clovelly	Louisiana, USA	Oil storage	Cavern in salt overhang dissolved into cap rock	Thin cap rock, inadequate salt buffer	Cavern abandonment	The cavern
Napoleonville Bayou Corne	2012-ongoing, Louisiana, USA	Brine cycling	Cap rock with large voids, unexpected shale layers in salt edge leading to collapse	Cap rock failure, inadequate salt buffer	Cavern abandonment, loss of brine storage	The cavern and ground above

disaster occurred in 1986 in the vicinity of Lake Nyos (Cameroon), when a CO_2 plume was released from lake bottom sediments. The gas plume had a likely volume of 1.5 million tonnes and spread up to 25 km from the release point, hugging the lower parts of the landscape and killing an estimated 1,700 people, along with large numbers of livestock.

Recognising and Preventing Potential Cavern Problems

Three factors can contribute to the breaching and collapse of solution-mined cavities, namely creep, uncontrolled leaching, and the presence of anomalous zones in what had been assumed to be homogenous salt (Table 13.9). Anomalous zones may be unexpected regions of highly soluble salts (potash salts), of fractured intrasalt beds, or zones of much older natural leaching (e.g. black salt), which may contain pressurized brine or gas (methane or nitrogen). In brinefields and some salt mines the anomalous zones tend to occur near intersections with poorly documented older well bores. The same set of factors generates many of the operational problems in conventional salt mines (Chaps. 11 and 12).

Salt Creep

The principal factors influencing the rate of salt creep are; (a) cavern depth and overburden characteristics; pressure and temperature gradients, (b) internal cavity pressure, (c) cavern shape,

(d) salt properties (e.g., variations in halite crystal size, moisture content). Left alone, and not subject to fresh water incursion, salt (especially carnallite and bischofite salt) will creep into an unbreached storage cavern until differential pressures are equalised. Salt cavities in homogenous halite hosts are generally stable at depths between a few hundred metres and about 2,000 m depth (Figs. 13.1 and 13.54). Below that depth there is an elastic-plastic transition zone for salt behaviour somewhere below 1,000–2,000 m. Cavities below this can be relatively unstable and show large volume decreases through rock creep; with the transition depth depending on the composition of the salt, the geothermal gradient and the overburden pressure. Effects of salt cavity creep, due to inadequate internal pressuring, were first noted in the 1970s by the operators of some large purpose-built storage caverns. The Eminence cavern in Mississippi, built at 1,700–2,000 m, lost 40 % of its volume in just 2 years post-construction, while Tersanne in France lost 30 % to salt creep (Fig. 13.55). Such losses in storage capacity were potentially expensive, but when adjustments were made to cavern depths and minimum gas storage pressures, the volume loss stopped. Today both facilities are still operational and have recovered much of their initial volume loss (Thoms and Gehle 2000a). Salt creep occurs at slower rates above the transition zone; measured rates are mm – cm per year in salt mines in Kansas and Texas with depths up to 600 m.

Like mines, salt cavities built above or within the transition zone can be extremely stable and when properly located, designed and operated may lose only a few percent

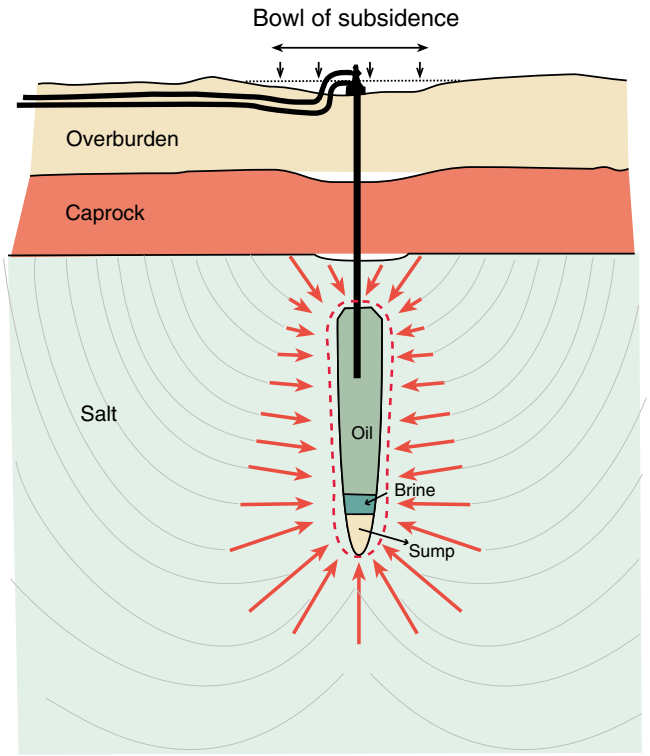

Fig. 13.54 After the cavern has formed and is filled, salt creep causes the cavern to shrink from its original size (*dashed shape*) into a somewhat smaller configuration. This induces subsidence and possible collapse in the zone above the cavern. At the surface this process forms a "bowl of subsidence" (in part after Thoms and Gehle 2000a)

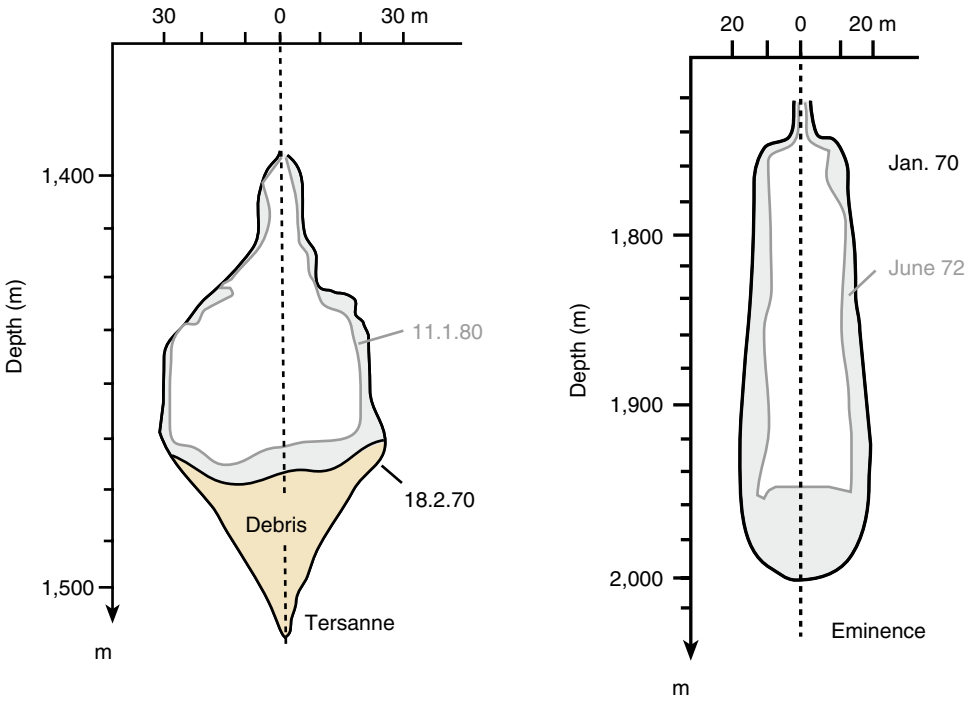

Fig. 13.55 Creep effects in Tersanne (France) and Eminence (Mississippi) showing shrinkage with time (*Brown shading* indicates the distribution of insolubles in the Tersanne cavern)

volume a year. Some cavities in salt above the transition zone can remain remarkably stable even if emptied of product. For example, in the 1950s, a lenticular cavern with a roof span 366 m was excavated by solution mining in the Bryan Mound salt dome in Texas, which is also the site for the later Strategic Petroleum Reserve programme. The cavern has an unusual shape compared to the "carrot" shape of later purpose-designed caverns in the Mound. It had an average depth of 550 m, a cavity height of 55 m and an unsupported span of more than 360 m After excavation, it was filled with LPG but subsequently lost wellhead pressure and so was abandoned (emptied). Thirty years later, measurements indicated that this cavern is still remarkably stable, having lost only about 4 % of it total volume since abandonment.

Salt creep is accelerated by large differences between natural lithostatic pressure (in the salt) and the pressure in the cavern. The rate of creep also depends on variations in the proportions and physical properties of the various salt minerals and the configuration of nearby nonevaporites (e.g. carbonate, anhydrite or potash beds in halite). To minimise creep, operational pressures in a fluid-filled storage cavern should be as high as allowed, this is especially true in facilities used to store natural gas. But this may encourage leakage and gas loss in facilities lacking structural integrity (see Hutchinson explosion in case histories).

When a cavern is active, overburden creep will typically drive ongoing subsidence at the landsurface in the form of a subsidence bowl or depression (Fig. 13.54). The length of the delay between creep into a cavern and its expression at the surface depends upon cavern depth, mode of cavern operation, thickness of salt cover and character of overburden materials or roof beams (Neal 1991). Ground effects atop shallow caverns usually show up more quickly than those above deeper caverns, subsidence over some storage caverns has been detected only after a decade or more of operation (Thoms and Gehle 2000a).

Salt Falls Versus Roof Collapses

Salt fall from the cavern roof, as distinct from catastrophic roof collapse and chimneying, occurs frequently in most caverns especially in bedded salt. In a storage cavern it is part of the preliminary construction/leaching phase and also occurs during later storage cavern expansion driven by product cycling. Providing an adequate salt pillow is left as part of the cavern's design, roof falls are not considered detrimental by most operators, as they generally do not greatly affect containment volume. They may sometimes damage casing strings "hanging" from the roof of the cavern.

Most damaging to a salt cavern and possibly to the surface environment is total collapse of a cavern's roof span. It may ultimately lead to the formation of a collapse sinkhole at the landsurface. Such surface expressions atop a brinefield may be delayed for some time after operations have ceased. Typical causes of sinkholes in brinefields are uncontrolled solution leaching, the unexpected of intersection of soluble (potash-rich) seams in the salt roof, or the presence of natural brine lenses from natural karstification near the outer parts of a salt mass (see case histories).

Figure 13.56 illustrates the range of probabilities for salt fall and collapse in salt cavities: (a) is an intact cavern with adequate salt cover – salt falls are a part of the operational running of the cavern, (b) is a breached cavern with a strong roof, still capable of spanning the cavern – ultimately ongoing salt solution it will drive it into a breached system, while (c) illustrates a breached cavern system that may soon develop into a sinkhole at the surface – it is the result of total salt removal beneath a weak cavern roof.

Ongoing brine compensation (product-cycling) means any storage cavern has the potential to expand until it collapses. To prevent potentially dangerous collapses and product leakage, the shape of a storage cavern must be monitored throughout its life. Some materials found above salt formations, such as reactive shales exposed to brine, may take time

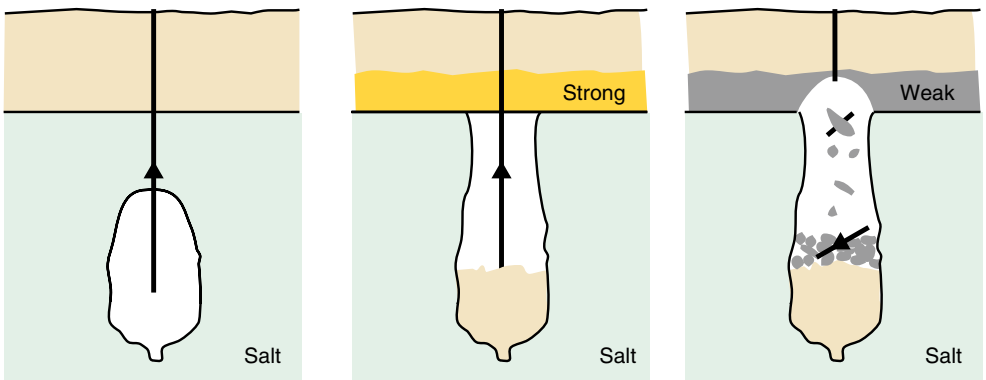

Fig. 13.56 Preservation of a salt roof or the presence of strong overburden spanning the cavern roof makes cavern collapse less likely

to weaken. This means there will be a delayed collapse event, it can occur years after the cessation of solution operations. Occasionally the salt roof to a cavern in stage (b) may be taken out with the intent of instigating collapse (see the SG4 case history). Deliberate oversolutioning is being considered to create desirable wetlands via sinkholes in the former ICI brinefield near Teeside, England.

Ground Subsidence

Salt creep means the ground surface over an intact cavern will deform into a shape resembling a wide shallow bowl, hence the name bowl subsidence. Bowl subsidence over intact salt caverns is a response to movements at depth, which are transferred to the surface with diminishing amplitude over a wide cone of influence. Subsidence of the landsurface above a salt cavern is normal and to be expected, especially above shallower storage caverns (Fig. 13.57; Table 13.10). This surface response is similar to "trough subsidence" at the surface above "long-wall" or "room and pillar" mining operations. As the boundaries of such mines advance the accompanying ground movements manifest as moving linear depressions in the landscape called areas of trough subsidence by mining engineers. Bowl subsidence above a salt cavern is not a problem unless the roof span breaches and the rate of ground subsidence increases.

Measured land subsidence rates vary above salt caverns constructed for storage of US Strategic Petroleum Reserve (SPR). Rates atop storage domes in the 1980s ranged up to 40–50 mm/year in SPR facilities in Texas and Louisiana (e.g. Fig. 13.57a). Rates above the much deeper Tersanne cavern in France are much lower ≈6–8 mm/year than those of the Gulf Coast (Fig. 13.57b), even after the cavern had shrunk relatively rapidly in the 1970s (Fig. 13.55). Since the late 1980s, almost all purpose-built storage caverns have been filled and maintained at higher pressures than in the 1970s. Pressurizing has mitigated salt creep and surface subsidence effects in land areas atop many of these domes (Thoms and Gehle 2000a).

For example, the Bryan Mound Dome, located southeast of Houston on the Texas Gulf Coast, was one of the first domes to host SPR caverns. The SPR site's subsidence rate was 24.4–36.6 mm per year from 1982 to 1988; when subsequently pressurized from 1988 to 1994 the subsidence rate fell to 6.1–24.4 mm per year; and was 3.1–15.2 mm per year from 1994 to 1999. That is, the median subsidence rate atop Bryan Mound decreased by 70 % following the increase in cavern pressure. Rates at the more recently constructed Big Hill SPR site ranged from 6.1 to 15.2 mm per year from 1989 to 1994; and from 6.1 to 9.1 mm per year from 1994 to 1999. By contrast, the subsidence rate at another SPR site, West Hackberry, was still high, approximately 76.2 mm per year

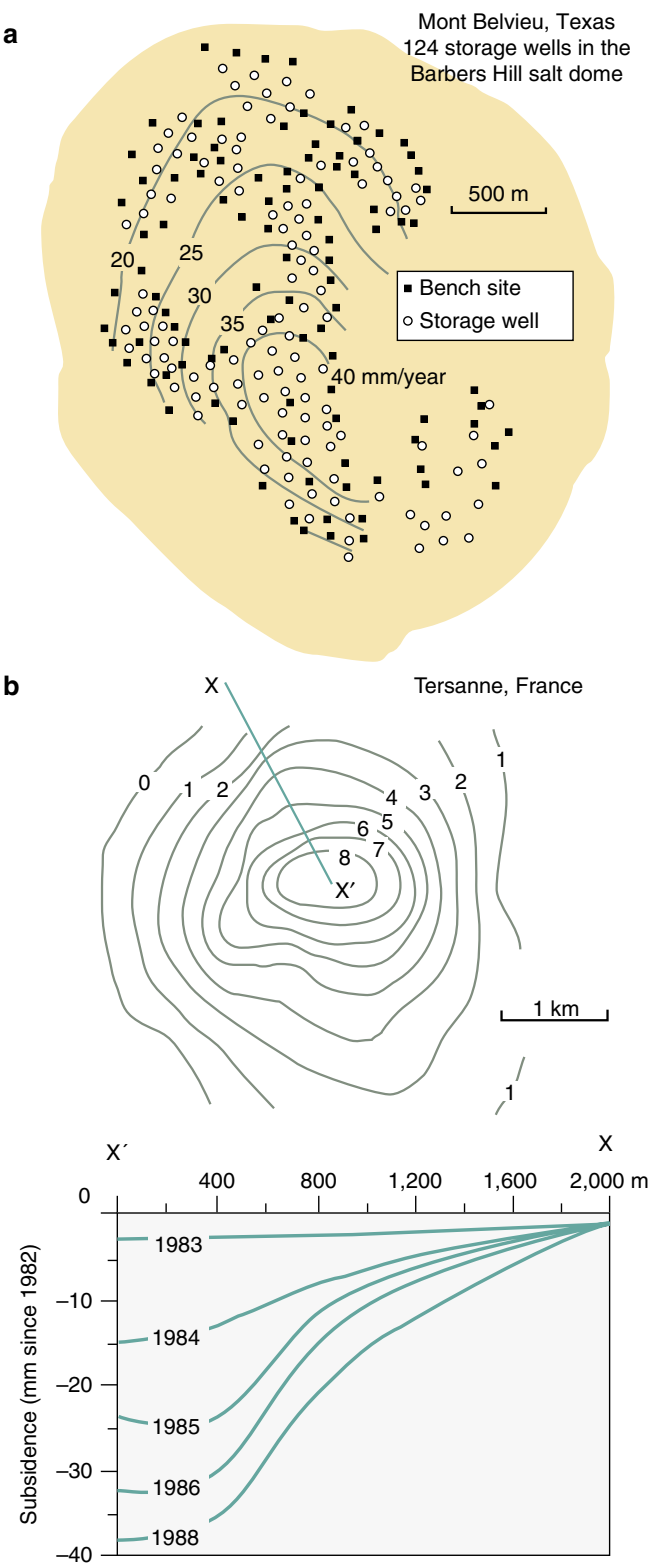

Fig. 13.57 Landsurface subsidence above storage caverns. (**a**) Subsidence contours in mm/year atop the Barbers Hill salt dome in the vicinity of Mont Belvieu, Texas (After Ratigan 1991). (**b**) Subsidence contours in mm/year atop the Tersanne storage cavern, France. Lower panel plots successive subsidence profiles from 1983 to 1988 along the line X-X' (After Bérest and Brouard 2003; Durup 1991)

Table 13.10 Examples of ground subsidence problems above salt caverns

Storage cavern	Time and place of accident	Reserve resource	Depth	Accident description	Accident cause	Influence scope
West Hack-berry	1970s, Louisiana, USA	Petroleum	750–1,400 m	Surface settlement rate 75 mm/a	Excessive creep of salt	Influence range about 750 m
Tersanne	1970–1980, France	Natural gas	1,860 m on average	Effective volume loss 35 %, settlement rate 40 mm/a	Excessive creep of salt	Influence range about 2,000 m
Bryan Mound	1982–1998, Texas, USA	Petroleum	640–1,250 m	Surface settlement rate 36 mm/a	Excessive creep of salt	Influence range about 600 m
Mont Belvieu	1988–1993, Texas, USA	Liquid propane	750–1,700 m	Surface settlement rate 20–40 mm/a	Excessive creep of salt	Influence range about 1,500 m
Big Hill	1989–1999, Texas, USA	Petroleum	1,350 m on average	Surface settlement rate 90 mm/a	Excessive creep of salt	Influence range about 1,000 m

After Yang et al. (2013)

after pressurization. The reason for the much lower rate at Big Hill is thought to reflect the very thick (300 m +) brittle caprock covering the Big Hill salt stock (Linn and Culbert 1999; Bauer 1999).

Estimates of rates of acceptable bowl subsidence atop product cycling caverns can be calculated using influence functions based on linear elasticity, the same mathematics used by mining engineers. This works well if the displacements are small, continuity prevails, and if appropriate effective reaction moduli can be estimated for the various inhomogeneous overburden materials above the caverns. Assumptions of mathematical linearity are often incorporated into methods for fitting subsidence models to existing databases in order to predict future trends of subsidence over cavern fields. But different leaching rates and inhomogeneous distributions of subsurface features means predictions are often of limited use. Sophisticated three dimensional finite element computer programs have been used to analyse subsidence over brinefields incorporating closely spaced caverns with relatively complicated subsurface geometries (see Kunstman and Mazur 2000). More recently 4D seismic approaches (Drijkoningen et al. 2012) and ERS radar interferometry (Raucoules et al. 2003) have been found to be feasible monitoring techniques.

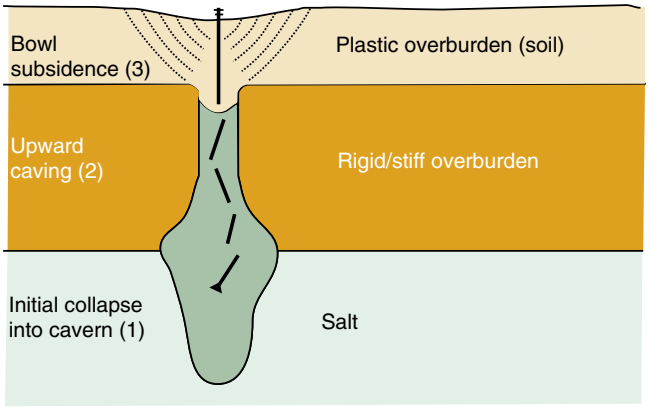

Fig. 13.58 Three stages of cavern collapse and sinkhole growth (After Thoms and Gehle 2000a)

Surface Indicators of Breached Caverns

Measuring subsidence above an active storage cavity over a number of years is a useful tool to monitor the state of the cavern and the likelihood of any sinkholes appearing at the surface. Subsidence over breaching caverns, where the integrity of the roof span is finally lost, generally involves three stages (Fig. 13.58; Thoms and Gehle 2000a): (1) initial overburden collapse into breached cavern; (2) upward caving via "chimneying" through indurated strata (which engineers sometimes describe as "stiff soils"), and (3) transition to bowl subsidence in more plastic soils near the surface. Following initial roof span collapse, local conditions determine whether caving or bowl subsidence will dominate. After an initial breach and collapse, Stage 2 caving stopes vertically through indurated strata as an upward migrating cavity atop a growing chimney. The cavity diminishes in height as it rises because of the bulking of caved materials into the stoping chimney. In Stage 3 the caving mechanism transforms into bowl subsidence as more plastic horizons (weathered strata and soils) are encountered nearer the surface. Breached caverns typically manifest at the surface as relatively deep subsidence bowls, sometimes with sinkholes near their centres.

Stage 2 caving can be bypassed or be arrested if the breached cavern is overlain only by plastic overburden or the cavern is too small to contain all the bulking debris from the overlying strata. In the latter case, the bulking materials fill the cavity to where they can support the roof once more, so arresting further upward migration. Localized bowls of subsidence will usually be seen at the surface over the arrested cavity. With time, the bulked materials may consolidate and allow some additional upward migration of the cavity, and so drive additional subsidence.

Among the various subsidence features, sinkholes are of greatest concern as they are rapidly expressed surface features of typically downdropped plugs of surface material encircled by near vertical sides. They occur when Stage 2 caving dominates all the way to the surface. Concentric fissuring and collapse of the landsurface atop a sinkhole can form within hours of the structure first breaking through to the surface. Overburden materials rapidly slip and fall into the growing water-saturated core with a huge potential for property damage and even loss of life (see case histories).

Monitoring and Minimizing Collapse

Subsidence effects, and even active sinkholing were once ignored by brinefield operators but changes in rates of subsidence, along with sonar monitoring of cavern shape, are now used as indicators of the state of the cavern. Responsible operators now conduct periodic or continuous subsidence surveys, and if anomalous effects are recognised, preventative action can be taken.

Routine monitoring of subsidence over storage cavern fields can be performed with conventional land surveying methods. A network of reference points or bench monuments is set up that effectively spans a brinefield or storage facility (Figs. 13.57a). A tie-in is often made to an established reference point located some distance away from the influence of the field. Differences in elevations of points over time intervals between surveys can then be interpreted as velocities of vertical movement (Fig. 13.57b). It is important to perform surveys at about the same time each year to minimize effects of natural seasonal factors, e.g., soil temperature and rainfall. For some cavern fields, it may be more efficient to make use of the Global Positioning System (GPS) for subsidence monitoring. Regulatory agencies often require that subsidence over storage caverns be routinely monitored and reported. Standard techniques for this purpose are given in Swarts (1993), Watts (1991) and Wong (1982).

More sophisticated automated methods for monitoring subsidence are justified when there is a significant risk of environmental or property damage, as in an area where there is a high probability of sinkhole development in close proximity to residences or storage pipelines and other infrastructure. Such a system might consist of an array of strategically placed tiltmeters, geophones, and inclinometers, with remote read-out and telemetry components (as is currently done for the subsidence cone associated with the Eugenie wells in Carlsbad, new Mexico). This system should be capable of collecting and sending data to a comprehensive analysis station at selected time intervals or when activated by a precursor event. Significant events may consist of accelerating localized surface movements, microseisms, and fissures.

Monitoring ground subsidence and cavern shape allows a cavern operator to minimize the effects of subsidence by:

Minimising subsidence from salt creep – As noted earlier, salt creep into caverns causes longterm bowl subsidence at the surface. It follows that bowl subsidence can be mitigated by minimizing salt creep in caverns. The most direct method for minimizing salt creep in existing hydrocarbon storage caverns is to operate them at the highest practical pressures at all times. The determination of the highest practical cavern pressures and operating schedules will involve consideration of site-specific cavern rock mechanics, economic and regulatory factors, as well as the potential impact of subsidence (Rokahr et al. 1998).

Maintaining adequate salt cover – In order to avoid possible collapse that might ultimately lead to sinkholes, an adequate salt cover must be maintained over salt caverns during solution mining and product cycling. Regulatory agencies generally now require that caverns be monitored to ensure that an adequate salt roof is maintained above caverns. Downhole "wireline" logging technology, e.g. sonar, is available to periodically check shapes and sizes of caverns and the location of the salt roof (Crossley 1998).

Natural or Anthropogenic Subsidence?

Figure 13.59a, b illustrates the long-term and ongoing effects of salt extraction and the utility of surface mapping in defining potential problem sites associated with long defunct solution mining. It is a subsidence map of the of the Muttenz-Pratteln area, Switzerland, a region where the solution mining of Triassic Keuper Salt ceased more than a century ago, yet ground subsidence is ongoing (Zechner et al. 2011). Recent land subsidences were surveyed at six separate locations, diameters of the affected surface areas ranging from 100 to 1,500 m, and corresponding subsidence rates reaching more than 100 mm/year (Fig. 13.59a). Of the six sites, three sites could be outlined where land subsidence was likely due on ongoing responses to salt solution mining. The others including the Lachmatt area were subsidence is greatest are likely responses to natural processes. For the natural occurrences, the authors conclude the most sensitive factor for the dissolution rate and related subsidence rate is the structure or dip of the halite formation, which leads to an increase of dissolution rate with increasing dip. This is due to the increased density of the brine, an intrinsic meteoric flow dynamic develops, which follows the direction of the dip.

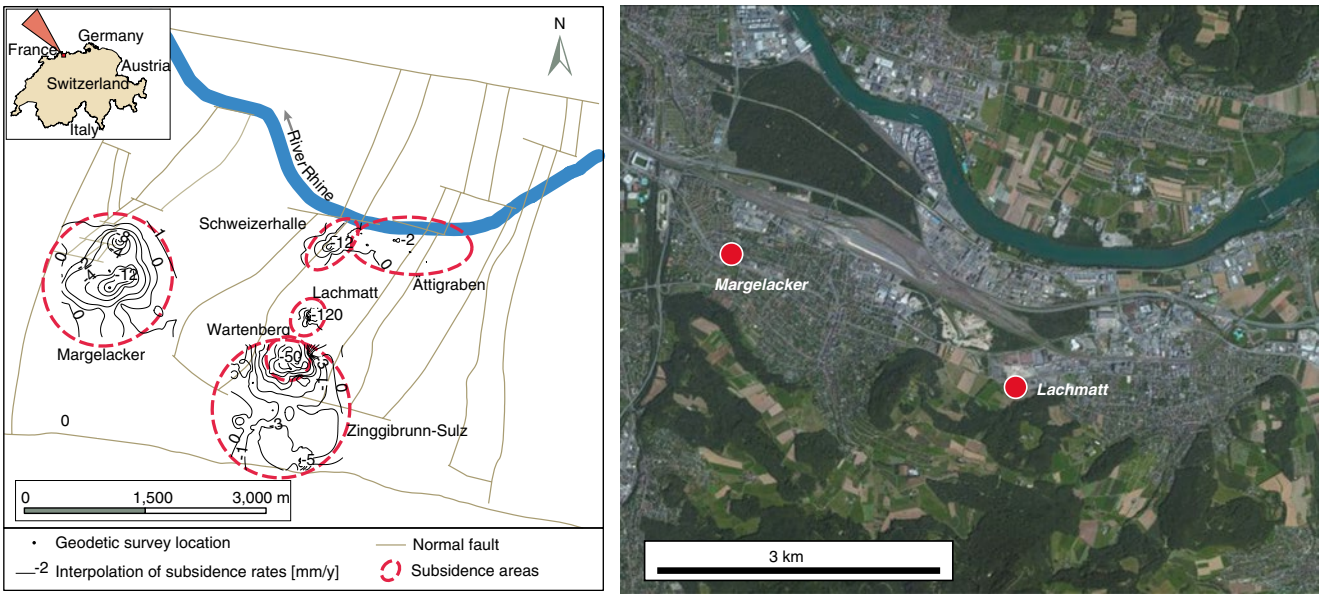

Fig. 13.59 Map of the Muttenz-Pratteln area, Switzerland. Solution mining in the area largely ceased 100 years ago. Interpolation of subsidence rates between 1975 and 2000 (averaged over 25 years), showing zone of greatest subsidence is centred on the Lachmatt area, a region with a subsidence cone unrelated to sites of former solution mining (After Zechner et al. 2011). Bing® image mounted and scaled in MapInfo®

So How Stable is a Storage Cavern?

Sites that are most suitable for a storage cavern lie within relatively homogenous regions of salt located deep in a diapiric salt mass, typically more than a kilometre below the landsurface and hundred of metres below the upper surface of the salt. Even today, many salt caverns used for various types of storage were first used for the commercial production of brine or hydrocarbons, although the number of purpose-built facilities increases year by year. Some older caverns now have shapes and spans or are at shallower depths that make them marginally suitable for future storage or waste disposal. Likewise, the access wells to these caverns were drilled some time ago and suffer the effects of chemical corrosion and older cement technologies. These older non-purpose built caverns do however make excellent "in-situ" laboratories to test the strength and integrity of salt formations. For example one brine cavern in the Bryan Mound Dome in Texas has a roof span of 335 m, yet it has not collapsed (Thoms and Gehle 2000a).

Natural gas storage caverns, with their inherent need for the deep cycling of internal pressures, place much greater demands on the integrity of the surrounding salt than caverns used for liquids storage. Salt cavities for natural gas storage were first designed with relatively small storage volumes but designs over the last three decades have increased in size. In Germany the maximum permitted volumes of gas for storage in salt caverns started at 350,000 m^3, increased to 500,000 m^3 and for the past 10 years has been set at 700,000 m^3. In the US cavern volumes for gas storage are not specifically regulated, but a design-specified cavern for natural gas storage with a volume of 15 MM bbl (6.5 Bcf) and a roof span of more than 100 m is now underway in the Napoleonville Dome in south Louisiana.

Cavern Plugging

The are a number of factors related to prior use and to long term salt creep that must be considered in designing effective closure or cavern plugs. For example during its operational life, episodes of low storage pressure can accelerate creep closure of a cavern, transmitting tensile strain to the casing. High storage pressure can cause increased permeability of the salt, by induced microcracks, which can result in migration of the stored gas into the salt, and possibly macro-fractures or casing shoe fracture. Hence, when a salt cavern used for hydrocarbon storage reaches the end of its life, it must be plugged in a way that does not allow for any later environmental degradation.

Wells creating and/or feeding a salt cavern can not be plugged using the same relatively straightforward methods used to seal an oil or gas well that has reached the end of its useful life. Oil and gas wells are usually sealed by simply installing a "plug" of alternating intervals of different grouts. Sealing and abandoning a brinewell or a salt cavern is not the same as plugging an oil and gas well for two main reasons (Fig. 13.60; Ratigan 2000):

1. Brine wells are generally completed with much larger casings than oil and gas wells.
2. The fluid pressure in the abandoned salt cavern is still joined to the casing string and it rises after plugging.

The first is not a significant deterrent to plugging and abandoning a storage well, appropriate modern grouts and methods are offered by most service companies. Essentially all of the uncertainties associated with cavern sealing and abandonment are a direct result of the second factor, rising fluid pressure and its effects on the access well(s).

Once a cavern is sealed and abandoned, salt begins to flow or creep into the opening and continues to flow until pressure differences between the salt and the cavern interior vanish. Plugs in former access wells to abandoned caverns must be capable of maintaining seal integrity and of holding back this pressure, otherwise brine or stored waste product may be squeezed back up the well bore via microcracks and seals. Fluid flow paths out of the cavern are schematically depicted in Fig. 13.60, while Table 13.11 summarizes the effects of the various processes contributing to fluid flow and pressure changes in a sealed salt cavern (Ratigan 2000).

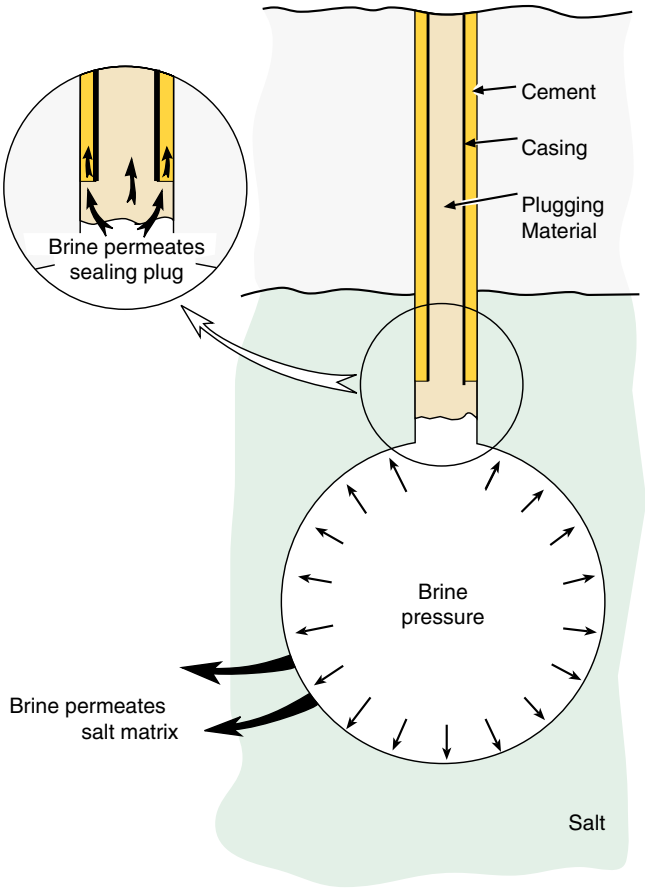

Fig. 13.60 Factors influencing cavern integrity once a cavern has been plugged and abandoned (After Ratigan 2000)

It is not just salt creep that increases the fluid pressure in an abandoned cavern. Solution mining and product cycling results in a significant disruption of the thermal environment in the salt. Feed solvent injected into the formation to create the cavern is almost always cooler than the salt formation, as is most stored product or waste. Continual leaching of a cavern to its final shape can result in a significant cooling of the salt surrounding the cavern, particularly near the cavern boundary. Unless a cavern has been inactive for a long period of time (tens of years), the fluid in the cavern will be at a lower temperature than the "pre-cavern" temperature of the rocksalt. Thus, when the cavern is sealed, heat will flow from the salt mass to the cavern fluid and its temperature will rise in response. A rise in fluid temperature expands the fluid volume and, since the cavern is sealed, the cavern fluid pressure will rise.

Unless the cavern was idle for some years prior to its plugging, cavern fluid is not 100 % saturated with sodium chloride. Salt dissolution may occur after a cavern is sealed and tends to lessen the effects of pressure rise. So, even after sealing, dissolution of the cavern wall continues until the enclosed fluid approaches halite saturation. This increases the cavern volume and so tends to decrease the cavern fluid pressure. Salt dissolution is an endothermic chemical reaction, which further reduces the temperature of the fluid, and so further reduces fluid pressure in the cavern.

A number of other interactive processes can effect the stability of a storage cavern and its plugged entry hole, depending on the nature of any waste stored in a sealed cavern. Differential settling and compaction cause the various wastes

Table 13.11 Factors influencing fluid pressure in a plugged cavern

Process	Influence on fluid pressure	Time scale
Salt creep	Increases cavern fluid pressure at a monotonically decreasing rate	Majority of the pressure rise occurs years to tens of years after sealing
Fluid heat transfer between salt and cavern	Causes cavern fluid expansion and increases cavern fluid pressure at a decreasing rate	Majority of pressure rise within tens of years to many tens of years after sealing
Salt dissolution and cavern fluid saturation	Increases cavern volume and decreases fluid temperature, which in turn, causes a decrease in fluid pressure	Majority of pressure decrease within years after sealing
Cavern fluid escape into salt	Decrease in cavern fluid pressure	Continues indefinitely
Cavern fluid escapes via sealing plug/or casing cement	Decrease in cavern fluid pressure	Continues indefinitely

After Ratigan (2000)

pumped into the cavern to separate into layers. Various chemical reactions can then occur within or between layers of waste, or between the waste and the surrounding salt. All can cause unexpected pressure build-up and so drive fluid penetration of the plug seal. Gas can also be produced in a sealed storage cavern, either by bacterial degradation of waste materials or by natural degassing corrosion of the surrounding salt. This too leads to a buildup in fluid pressures and places increased stress on the cavity plug and the cavern walls.

Even though salt has extremely low permeabilities, pressurised cavern fluid may slowly seep into the surrounding salt. This will reduce the volume of fluid in the cavern, and thus help ameliorate the pressure exerted on the salt by the cavern fluid. However, the entry of cavern fluids into the salt will also alter the salt matrix stresses, increase the rate of creep and the intrinsic permeability of the salt.

Before a cavern is sealed, the amount of cavern fluid that permeates the salt cavern walls is negligible. After the cavern is sealed and the cavern fluid pressure rises, the amount of cavern fluid that permeates the cavern wall must increase, both because the pressure gradient (driving the fluid transport) increases and because the salt permeability increases. If the cavern fluid pressure cannot be reduced sufficiently through the diffusional flow it is possible that fractures could develop in the salt. This would in turn reduce the cavern fluid pressure, but obviously increases the likelihood of a possible leak of cavern fluid into adjacent formations. Whether or not a fracture or fractures develop depends on the rate of cavern fluid pressurization. Low pressurization rates would not be expected to result in fracturing of the salt, rather the salt would flow and anneal. Very high rates of pressurization might well produce a brittle fracture.

But, as mentioned earlier, the salt itself is probably not the weakest link in terms of seal integrity. Pressurized cavern fluid will tend to first breach or fracture the sealing plug/casing shoe. Diffusional or fracture-induced flow could then occur through the sealing cement plug or the cement between the salt borehole wall and the deepest casing (Fig. 13.60 inset).

As well as dissolution creating potential seal problems, there is also the longer term problem of ongoing local rise of smaller salt spines within a diapir, which can shear casing and allow a breach to form in the well string. This was the situation in the at-surface well collar in well S-5 in the Sour Lake oilfield atop the Sour Lake diapir in Hardin County, Texas (Looff 2001). In 1998 the well casing sheared, driven by a rising spine of salt in what was overall a degrading or dissolving diapir crest. The 13 5/8-in. casing string, set in salt caprock, was being pushed upward inside the 16 in. casing. This fractured the cement between the two strings and the 16-in. casing string, that had been welded to the wellhead, which was sheared off its foundation as it was displaced upward by several inches.

Storage in salt creates a complex situation with various processes and mechanisms driving cavern pressures in opposite directions. A study of the stability of such systems is a study in multivariate rock mechanics, grout physics and pore fluid chemistry, well beyond the geological/sedimentological emphasis of this book (see Munson 1997; Lee and De Souza 1998 for a discussion of some of the basic considerations). As yet, our models of salt and grout response of time frame of hundreds or even thousands of years do not allow us to reliably predict exact conditions under which pervasive fracturing or leakage will occur. Accordingly, most storage facilities are "over-engineered" to reduce the possibility of longterm failure (Ratigan 2000).

Summary

Solution mining with appropriate monitoring and timely plugging offers major advantages in generating chemical feedstock compared to room-and-pillar mining techniques. Drilling injection and production wells cost less than sinking deeper shafts and opening underground workings. It also provides safer operating conditions as underground miners are not needed.

In terms of problems with solution cavities and storage facilities it is important to note that a salt mass used for storage has never failed or leaked. The weak point in these systems is wherever "the outside has access to the inside," so problems tend to be mostly in the well, its casing and its grout, or where uncontrolled cavity expansion breaches a salt edge. Almost all the problems related to well and cavity failure are more a matter of human error, either by negligence, or a lack of understanding by on-the-ground personnel. There is the same general rule of thumb when it comes to salt cavities and salt mines and that is, "keep it in the salt!" Most failures and breaches occur when a leaching or a mining operation allows the cavity to contact the edge of the salt. There undersaturated water crossflows can exaggerate any uncontrolled dissolution problems.

The rapidly expanding technologies of deep purpose-built and monitored storage caverns located well within geologically suitable salt masses, will lead to future safer storage of hydrocarbons and hazardous wastes. Almost all the problems documented in the USA and elsewhere come from storage operations utilising caverns constructed by earlier less-defined solution methods. Even so, in all the incidents related to various storages in salt caverns the integrity of the cavern has never been threatened by any accident. All incidents to date can be traced back to poor management practises or utilisation of facilities that are not necessarily suitable. Purpose-built salt caverns are probably one of the safest ways to store hydrocarbons and dispose of hazardous materials.

Meta-evaporites

14

Introduction

Evaporite salts can survive well into the metamorphic realm, but are altered, recrystallised or transformed into new minerals. And so, beyond the early greenschist phase, little or nothing of the original sedimentary mineral phase remains with the possible exception of anhydrite (Table 14.1; Spear 1993). Consider "the before and after" situation as a sequence of evaporite-entraining sediments passes into the metamorphic realm. Under a likely "before" regional metamorphism scenario, a typical buried marine evaporite body occupies a continental margin position, is hundreds of metres thick, tens to hundreds of kilometres wide, perhaps with halokinetic geometries and an extensively tilted and faulted overburden. Halite typically makes up more than 60–80 % of the total rock salt volume in a basinwide unit. This halite is likely to be interlayered with anhydrite, bitterns, magnesian carbonates and siliciclastic clays. "After" metamorphism, typically driven by subduction and continent-continent collision, the end product of this once dominantly NaCl body of rock is a series of sodic and magnesian aluminosilicates, magnesites, calc-silicates and marbles with local zones of potassic enrichment. The immediate question is, where did all that salt and the associated volatiles (Cl, CO_2, SO_3) go?

Some salt components may still reside in meta-evaporite indicator minerals, such as sodic or magnesian talc, lazurite, marialitic scapolites or tourmalinites. The remainder went elsewhere, perhaps as the transforming evaporite mass generated metalliferous volatile-entraining brines. The presence of volatiles and their mobilization in metamorphic transformation is typical of meta-evaporite associations. A relatively open system of hydrofractures and shear strength contrasts in the form of fault/shear-related fluid/volatile conduits was already present in the evaporitic protolith and encouraged by the polyhedral transformation of the NaCl lattice as it enters the greenschist pressure realm.

Such a "leaky" prognosis is a somewhat different subsurface scenario from the classic isochemical paradigms and closed chemical system assumptions that permeate much of the older metamorphic literature. More recent work has challenged and displaced the classic "no loss" and homogeneity assumptions in metamorphic mineral phase evolution (Yardley and Graham 2002; Putnis and Austrheim 2010). This is especially so when evaporites enter the contact, dynamic, hydrothermal and regional metamorphic realms. So first, a few definitions relevant to the metamorphic realm, then we shall consider in detail the role of evaporite salts as they evolve, dissolve, transform and release volatiles within the metamorphic milieu.

Dynamic metamorphism is associated with localised zones of high to moderate strain, such as fault zones, with textures that evolve with greater depth and pressure (Fig. 14.1a). Cataclasis, crushing and grinding of rocks into angular fragments, occurs in dynamic metamorphic zones, engendering a variety of evolving cataclastic textures. Salt bodies are an exception as a salt body is already ductile within tens of metres of the earth's surface (Chap. 6). Textures of dynamic metamorphism in the non-evaporites experiencing ever greater burial are dependent on the depth, while the temperature and confining pressure determine the deformation mechanisms which predominate (Fig. 14.1a). Generally, at depths less than 5 km, dynamic metamorphism is not operating in non-evaporites because the confining pressures are too low to produce frictional heat. Instead, brittle deformation dominates and zones of breccia or cataclasites can form as the mother rock is locally milled and broken into random fragments. At greater depths, the angular non-evaporite fragments in faults transit into ductile shear textures and into mylonite zones. Within a depth range of 5–10 km pseudotachylite can form in non-evaporites under shear, confining pressures are now enough to prevent brecciation and milling, but energy is still largely focused into discrete fault planes. Frictional heating in this case may locally melt the rock to form pseudotachylite glass. Within the depth range of 10–20 km, deformation is governed by ductile deformation conditions extending beyond the confines of individual fault damage zones and hence frictional heating is dispersed throughout shear zones. This results in a

© Springer International Publishing Switzerland 2016

J.K. Warren, *Evaporites: A Geological Compendium*, DOI 10.1007/978-3-319-13512-0_14

Table 14.1 Metamorphic facies and typical associated mineral phases see also Fig. 14.1

	Pelite	Calcareous	Mafic	Ultramafic
Zeolite	Illite/phengite + chlorite + quartz	Calcite and/or dolomite	Ca-zeolite + chlorite + albite + quartz	Lizardite/ chrysotile + brucite + magnetite
±	Kaolinite	Quartz	Prehnite, analcime, pumpellyite	Chlorite, carbonate
Prehnite-pumpellyite	Phengite + chlorite + quartz	Calcite and/or dolomite	Prehnite + pumpellyite + chlorite + albite + quartz	Lizardite/ chrysotile + brucite + magnetite
±	Pyrophyillite, paragonite, k feldspar, stilpnomelane, lawsonite	Quartz	Aactinolite, stilpnomelane, lawsonite	Antigorite, chlorite, carbonate, talc, diopside
Greenschist	Muscovite + chlorite + quartz	Calcite and/or dolomite	Chlorite + epidote + albite	Antigorite + diopside + magnetite
±	Biotite, K-feldspar, chloritoid, paragonite, albite, Mn-rich garnet	Quartz, talc, actinolite	Actinolite, biotite	Chlorite, brucite, olivine, talc, carbonate
Amphibolite	Muscovite + biotite + quartz	Calcite and/or dolomite	Plagioclase + hornblende	Olivine + tremolite
±	Garnet, staurolite, kyanite, sillimanite, andalusite, cordierite, chlorite, plagioclase, K-feldspar	Quartz, tremolite, diopside, fosterite, phlogopite, epidote, grossular, scapolite, vesuvianite	Epidote, garnet, orthoamphibole, cummingtonite	Antigorite, talc, anthophylite, cummingtonite, enstatite
Granulite	K-feldspar + plagioclase + sillimanite + quartz	Calcite and/or dolomite	Orthopyroxene + plagioclase	Olivine + diopside + enstatite
±	Biotite, garnet, kyanite, cordierite, orthopyroxene, spinel, k corundum, sapphire	Diopside, fosterite, wollastonite, scapolite, spinel monticellite, periclase, grossular	Clinopyroxene, hornblende, garnet	Spinel, plagioclase
Blueschist	Phengite + chlorite + quartz	Calcite and/or dolomite	Glaucophane/crossite + lawsonite/epidote	Antigorite + olivine + magnetite
±	Albite, jadeite, lawsonite, garnet, chloritoid, paragonite	Quartz, aragonite, phengite	Pumpellyite, chlorite, garnet, albite, aragonite, phengite, paragonite, chloritoid	Chlorite, brucite, talc, diopside
Eclogite	Phengite + garnet + quartz	Calcite and/or dolomite	Omphacite + garnet + rutile	Olivine

After Spear (1993)

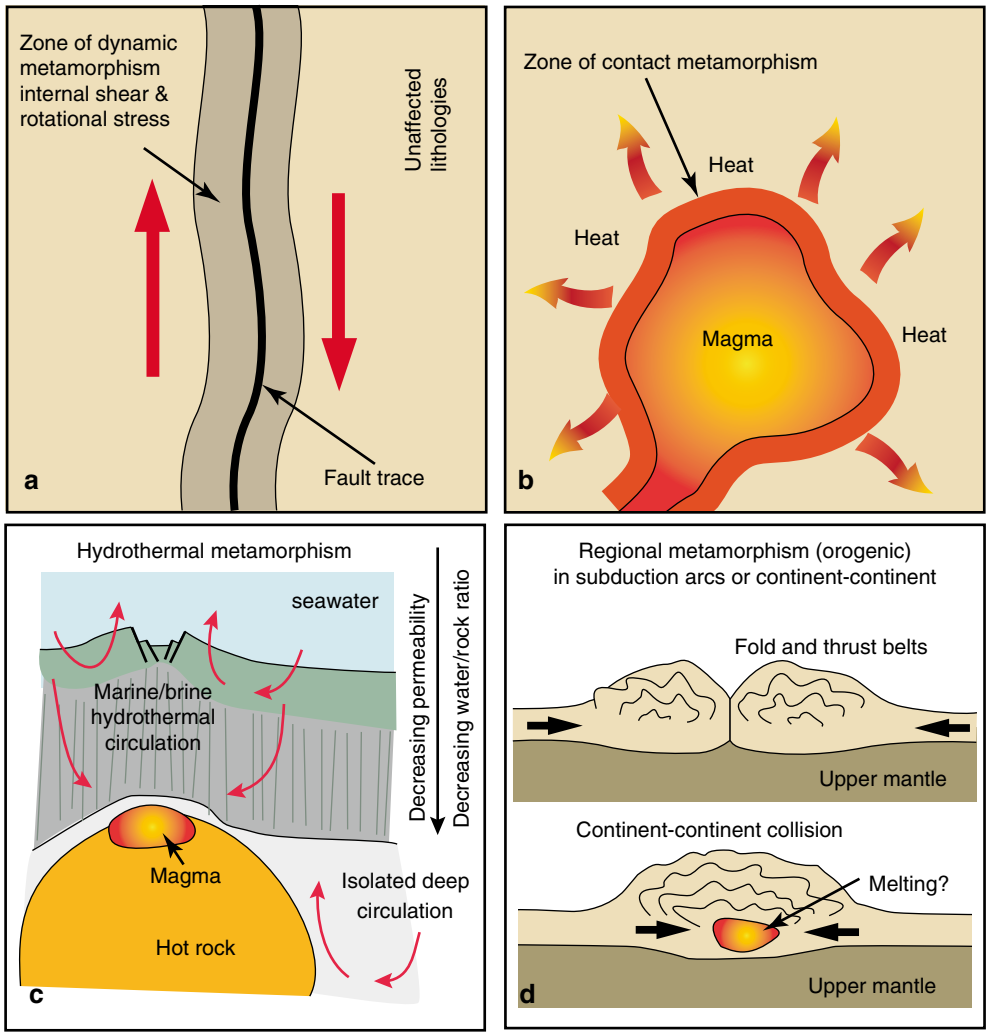

Fig. 14.1 Types of metamorphism. (**a**) Dynamic metamorphism. (**b**) Contact metamorphism. (**c**) Hydrothermal metamorphism. (**d**) Regional metamorphism. The various types are not mutually exclusive. (**a**, **b**) Tend to be more local features (tens of metres to tens of kilometres) (**c**, **d**) develop at the plate tectonic scale (tens to hundreds of kilometres)

weaker local thermal imprint and distributed more deformation. Here, deformation forms mylonite in the nonevaporites, with dynamothermal metamorphism occasionally driving the growth of porphyroblasts in the mylonite zones.

Contact metamorphism occurs typically around intrusive igneous rocks as a result of the temperature increase caused by the intrusion of magma into cooler country rock. The area surrounding the intrusion where the contact metamorphism effects are present is called the metamorphic aureole. The resultant metamorphics are typically classified as hornfels (Figs. 14.1b and 14.2).

Hydrothermal metamorphism is the result of the interaction of a rock with a high-temperature fluid of variable composition (Fig. 14.1c). The difference in composition between existing rock and the invading fluid triggers a set of metamorphic and metasomatic reactions. The hydrothermal fluid may be magmatic (originate in an intruding magma), circulating groundwater, or ocean water. Convective circulation of hydrothermal fluids in the ocean floor basalts produces extensive hydrothermal metamorphism adjacent to spreading centres and other submarine volcanic areas. The fluids eventually escape through vents in the ocean floor known as black smokers (Chap. 16).

Regional or Barrovian metamorphism covers large areas of continental crust typically associated with mountain ranges, particularly those associated with convergent tectonic plates or the roots of previously eroded mountains. The collision of two continental plates or island arcs with continental plates produce the extreme compressional forces required for the metamorphic changes typical of regional metamorphism. These orogenic mountains are later eroded, exposing the intensely deformed rocks typical of their cores. The conditions within the subducting slab as it plunges toward the mantle in a subduction zone also produce regional metamorphic effects and constituent the setting where many of the examples discussed in this chapter were formed (Figs. 14.1d and 14.2).

What effect did the flow/loss of significant volumes of metasomatic fluid/brine have on surrounding lithologies as they were released by the transforming evaporite minerals?

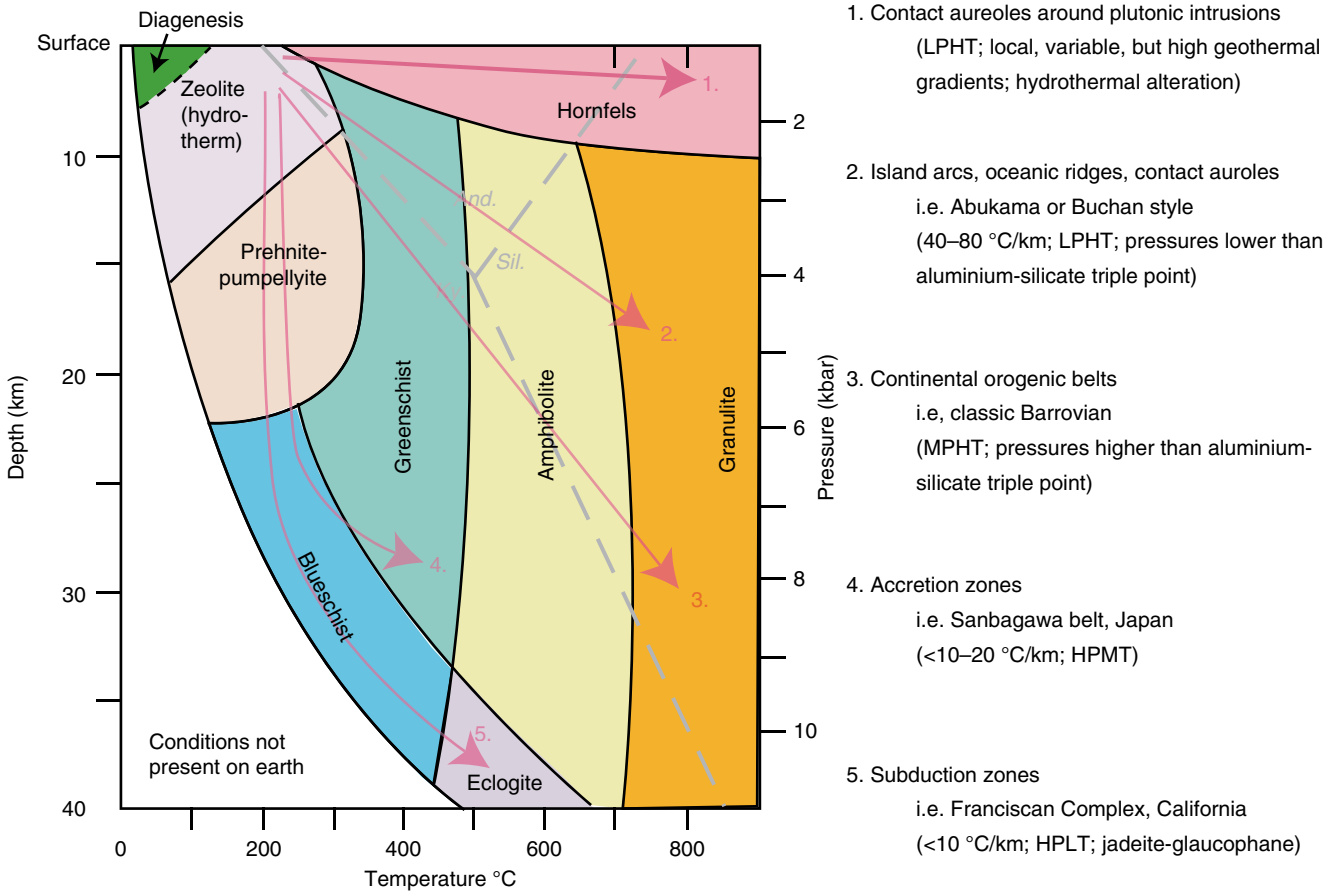

Fig. 14.2 Metamorphic facies in a depth, pressure temperature framework. *Numbered arrows* and the *adjacent listing* indicate typical facies evolution pathways (tied to geothermal gradients). *Dashed grey lines* indicate Kyanite (*Ky*) Andalusite (*And*) and Sillimanite (*Sil*) stability fields often used to help assign metamorphic grade. Refer to Table 14.1 for typical mineral associations in these facies (note this figure is constructed with isochemical or closed system assumptions)

Where, when and how did diagnostic meta-evaporite minerals precipitate? This chapter attempts to address some of these questions, while Chap. 16 addresses matters related to sulphide mineralization associated with meta-evaporites and contact/hydrothermal metamorphism.

It must be noted that the relevant literature base dealing with the "after evaporite" is sparse when compared with the mainstream literature in metamorphic petrology, and is at times contradictory (e.g., whiteschist discussion in Gebauer et al. 1997). Much of the metamorphic literature, and the associated structural literature, in meta-evaporite terranes seems to assume that prior to metamorphism all evaporitic protoliths were flat bedded, stratabound and little altered. This does not reflect the sedimentological reality that, prior to the onset of metamorphism in evaporitic basins there were:

- Steeply dipping blocks and folds in the brittle overburden and many of these structures were decoupled from basement features across widespread extensive low and high angle shear zones (décollements and shears, minibasin peripheries).
- Widespread breccias and alteration haloes defined the position of former salt units (dissolutional, halokinetic, fault plane breccias, welds and rauhwacke).
- Prior to the onset of metamorphism, pervasive alteration haloes (generally ferroan) had already formed, typically with nonstratiform geometries. They outlined hydrological conduits associated with salt sheets and welds, diapirs and faults.
- Magnesium and iron were replacing and altering adjacent sediments, with alteration beginning the time the evaporites were first deposited (e.g. reflux dolomites, ferruginized haloes, zeolites) and continuing into the metamorphic realm.
- Sodic and potassic alteration haloes in adjacent finer-grained sediments were already widespread, as were burial cements and replacements within coarser-grained non-evaporite units.

To make better sense of the influence of evaporites in some all types and scales of metamorphism of dynamic, contact hydrothermal and regional, these sedimentologic axioms need to be integrated into metamorphic/structural mineral evolution models and paradigms.

World-Scale Tectonism

Metamorphism occurs once the thermobaric regime, and associated diagenetic realm, passes with depth and increasing temperature and pressure, into the zone of metamorphism. Figure 14.2 encapsulates the pressure and temperature fields of the metamorphic regime (Yardley 1996). I have reversed the depth and pressure axes in this and some other P-T-Depth figures in this chapter from those used by some metamorphic petrologists to make it more familiar to the burial perspective to a sedimentologist (y axis goes from shallow to deep).

Regional zones of increasing metamorphic grade can be classified into metamorphic facies that represent limited ranges of burial depth, temperature, pressure, and water content in the crust. Zones of local or contact metamorphism are encapsulated in the hornfels (granofels) facies. Five major metamorphic facies of regional metamorphism are recognized (Fig. 14.2). The zeolite facies is characterized by the development of zeolite minerals in sediments and volcanics and reflects temperatures generally less than 200–250 °C and burial depths up to 10–15 km (Chap. 11). The succeeding greenschist facies is characterized by the development of chlorite, actinolite, epidote, and albite in mafic volcanics, and muscovite -biotite in pelitic rocks (Table 14.2). Albitization is also a widespread meta-mineral phase where halite and sodium bicarbonate salts are transformed within the greenschist realm.

Blueschist-facies assemblages tend to form in subduction zones with archetypal high pressures (>6–8 kbar[1]) and low temperatures (<400 °C); typical minerals are glaucophane, lawsonite, and jadeite. The amphibolite facies is characterized by kyanite, staurolite, and sillimanite in metapelites and plagioclase and hornblende in mafic rocks. The highest-grade rocks occur in the granulite facies, which is characterized by the sparsity or absence of hydrous minerals and the appearance of pyroxenes and a lack of preserved sedimentary evaporite salts, with the possible exception of anhydrite.

Clearly there are different geothermal gradients tied to different regional metamorphic associations (indicated by arrows 1–5 in Fig. 14.2). Within a plate tectonic paradigm, subduction and accretion terranes are typified by high pressure and high to moderate temperatures (arrows 5 and 4, respectively). Continental orogenic belts (continent-continent collision zone) are characterised by high temperatures and moderate pressures (arrow 3), while island arc metamorphism is characterised by high temperatures and low pressures (arrow 2). Zones of contact metamorphism (hornfels) show a wide range of temperatures at relatively low pressures and shallow depths (arrow 1). Variable temperatures and pressures in the zone of contact metamorphism can drive some types of hydrothermal circulation and associated precipitation and alteration haloes. The influence of evaporites, and associated saline basinal brines, in this setting is well documented, for example, by Barton and Johnson (1996).

In terms of thick widespread masses of evaporites evolving into meta-evaporites, the prime zones of interest are areas of hydrothermal circulation associated with contact metamorphism and zones of continent-continent collision. Thick widespread salts tend not to form in Proterozoic and Phanerozoic marine island arcs as the conditions are not typically hydrographically restricted, and likewise evaporites are not found in deepwater open marine settings (Chap. 5). That is, masses of sedimentary evaporites (or consequent meta-evaporites) are typically not part of any sediment pile found in open marine island arc/accretionary orogens (unless the suture zone was a restricted zone between two or more microcontinents, which facilitated hydrographic isolation).

Regionally extensive meta-evaporites are typically derived from thick widespread evaporite protoliths first deposited in the early stages of continental rifting or later in foreland basins tied to zones of continent-continent collision. Such thick sedimentary salt masses tend to form at the world-scale in predictable positions within the Wilson Cycle; early rift or continent-continent collision. Both are tectonic regions where substantial volumes of magma emplacement are likely. Then there is a third region of broad scale metamorphism, namely anorogenic prograde metamorphism. These are typically regions of high temperature, low pressure characterised by temperatures in excess of 600 °C, with pressures less than 5 kb. This third metamorphic grouping is typically tied to long-lived thermal anomalies tied to a mantle plume acting as the primary heat source. This third grouping is considered to have been the driver for the creation of many Archaean granite terranes such as in the eastern Yilgarn Block, Australia

During Phanerozoic and Proterozoic continental orogenies (continent-continent collision), lateral movements of the Earth's crust moved segments of continental crust into highly deformed and thickened regions known as orogenic belts (arrow 3 in Fig. 14.3). But there is a dilemma within this tripartite metamorphic frame that shades the interpretation paradigm for many meta-evaporites successions, namely, more than 50 % of the documented meta-evaporites are older than Neoproterozoic (Fig. 14.4). They occur in host successions where the precursor salts are long gone and plate tectonic models are less secured in the processes and rate of today's geosystem. That is, seems that the further back in time we look, the earth's crustal process paradigm is more and more related to a hotter mantle and a less evolved atmosphere/ocean and a somewhat different set/rates of plate tectonic paradigms.

[1]Pressure units: 1 bar = 100 kPa = 0.987 atmospheres and 1 kilobar = 1,000 bars = 100 MPa

Table 14.2 Examples of some meta-evaporite processes and indicator minerals

Process (indicator mineral)	Example	Reference
Scapolitization (scapolite) $(Na,Ca)_4[(Al,Si)_4O_8]_3(Cl,CO_3)$	Betic Cordilleras, southern Spain	Torres-Roldan (1978), Gómez-Pugnaire et al. (1994)
	Corella and Staveley Formations, Mt Isa Block, Australia	Oliver (1995), Stewart (1994a, b)
	Seve Nappe Complex, northern Sweden	Svenningsen (1994), Frietsch et al. (1997)
	Proterozoic Bamble and ModumKongsberg sectors, South Norway	Engvik et al. (2011)
	Wernecke breccia complex, Yukon Canada	Hunt et al. (2005), Kendrick et al. (2008)
	Paleoproterozoic magnesites, Ceara, NE Brazil	Parente et al. (2004)
	Granulite complex, Dronning Maud Land, Antarctica	Markl and Piazolo (1998)
	Zambesi Orogenic Belt, Zambia	Hanson et al. (1994)
Albitization (albite) $NaAlSi_3O_8$	Proterozoic Paranoa Group, Goias, Brazil	Giuliani et al. (1993)
	Olary Block, Australia	Cook (1992), Cook and Ashley (1992)
	Starra Gold deposit, Cloncurry region, Australia	Davidson et al. (1989)
Sodic talcs and/or phlogopites	Metapelites, Tell Atlas Algeria	Schreyer et al. (1980)
	Manganese-rich talc, Fowler Talc Belt, New York	Ayuso and Brown (1984)
	Sodic talc- kyanite, Sar-e-Sang, Afghanistan	Schreyer (1977)
	Permian evaporites, New Mexico and Carboniferous evaporites, Nova Scotia	Bailey (1949), Evans (1970), Gresens (1978)
Stratiform anorthositization (plagioclase) $(Na,Ca)Al(Si,Al)Si_2O_8$	Grenville Series, New York	Gresens (1978)
	Oaxacan granulite, Mexico	Ortega-Gutierrez (1984), Dostal et al. (2004)
Tourmalinitization (tourmaline) $Na(Mg,Fe)_3Al_6(BO_3)_3(Si_6O_{18})(OH)_4$	Barberton Greenstones, South Africa Willyama Supergroup, Broken Hill Block, Australia Liaoning borates, China	Byerly and Palmer (1991) Slack et al. (1989) Plimer (1988) Peng and Palmer (1995)
Lapis Lazuli (lazurite) $(Na,Ca)_8(AlSiO_4)_6(SO_4,S,Cl)_2$	Sar-e-Sang whiteschists, Afghanistan Baffin Island, Canada Edwards, New York	Faryad (2002) Hogarth and Griffith (1978) Hogarth (1979)
Columbian emerald (gem-tourmaline)	Columbia, S. America	Giuliani et al. (1995)
Marble-hosted rubies in Southeast Asia	e.g. Jegdalek Fm (Afghanistan); Mogok Fm. (Myanmar)	Garnier et al. (2008)

Although this table lists separate examples of indicators, most examples have multiple indications in the same deposits for example, scapolite and albitite are common co-associated mineral phases

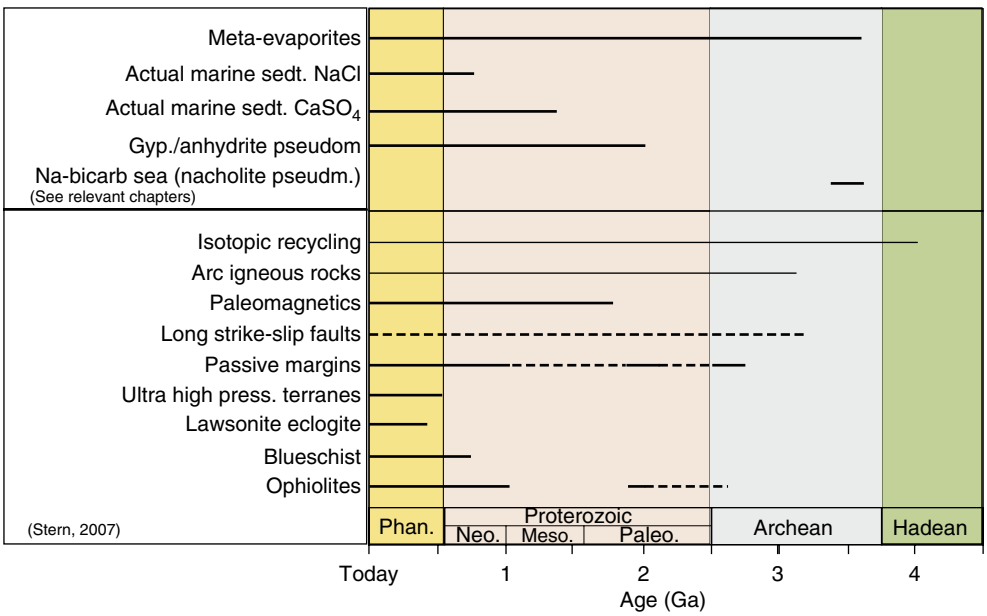

Fig. 14.3 Plate tectonic indicators and evaporite occurrences through time. *Solid lines* indicate features that are well documented, *thin lines* indicate more ambiguous indicators of plate tectonics that are well dated. *Dashed lines* indicate lesser degrees of confidence about the indicator and/or its timing (In part after Stern 2007)

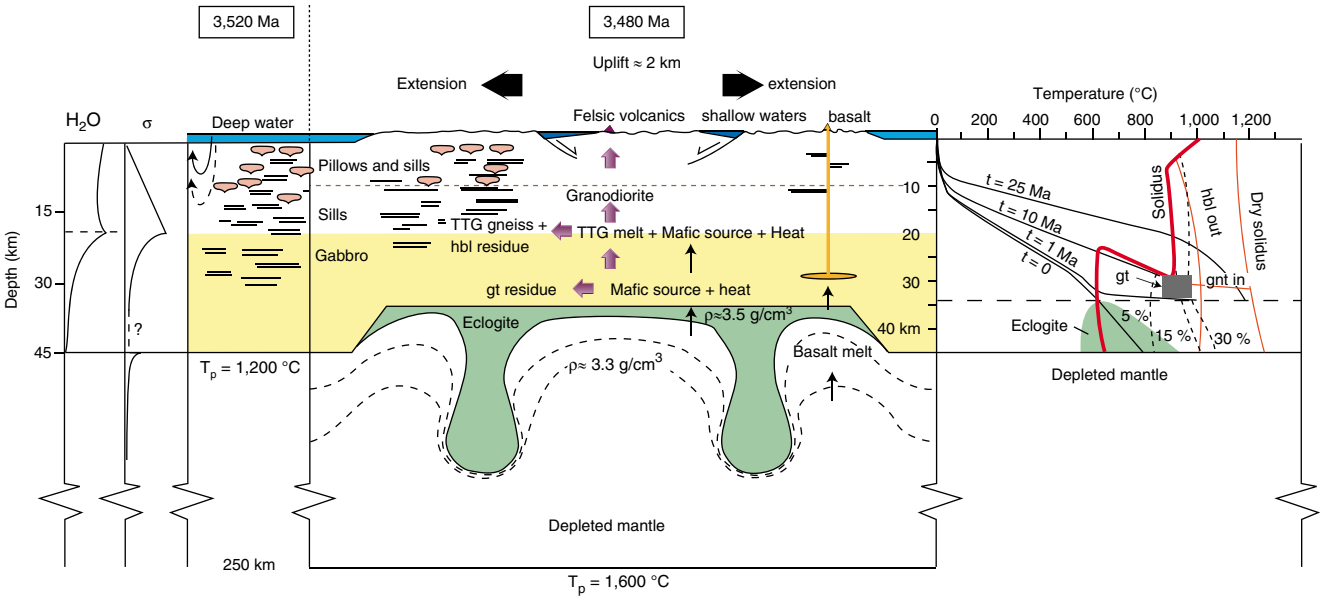

Fig. 14.4 Model for delamination of thick oceanic crust in the Middle Archaean based on Pilbara Craton geology, Australia (After Zegers and van Keken 2001). Partial melting in mantle with potential temperature (Tp) of 1,600 °C leads to thick oceanic crust (45 km) and thick depleted mantle (200 km), shown on left. Oceanic crust, corresponding to 3,520 Ma Coonterunah Succession in Pilbara craton, is hydrothermally altered by circulation of seawater. Qualitative water content is shown as a plot of H_2O. At ca. 3.49 Ga, lower oceanic crust, which has been metamorphosed to eclogite, delaminates from ductile middle crust. Eclogite is replaced by depleted mantle, forming basaltic melt by pressure-release melting. Overlying oceanic crust is intruded by these melts and conductively heated, resulting in melting of mafic protocrust to form TTG (tonalite, trondhjemite, and granodiorite) melts. Delamination of 10 km of eclogite results in ~2 km of uplift and associated extension in brittle upper crust. At right, solidus and melt contours are shown for dehydration-melting of amphibolite (*hbl*) in combination with estimated geotherms (based on conductive heating) in thick mafic protocrust before delamination, directly after delamination, and 10 and 25 m.y. after delamination. Garnet (*gt*) is formed in residue indicated by shaded rectangle in pressure-temperature condition diagram

Many Meta-evaporites are Pre-Neoproterozoic

Phanerozoic is the time frame encompassing almost all examples of preserved salts and known variations in oceanic chemistry and well-documented plate tectonic paradigms controlling metamorphic setting (Chap. 5). But more than 50 % of documented meta-evaporites are older than 1 Ga and occur within Precambrian mobile belts circumferential to Archaean craton cores. These are regions where no preserved primary salt remains. So, before discussing meta-evaporites in detail, we must consider the relevant time-based process/tectonic frame and ask; (a) What is a craton and, (b) How do models of craton formation and accretion relate to evolving styles of plate tectonism and evaporite metamorphism across deep time?

Precambrian cratonic regions have long been recognized as an important part of continental crust evolution, but looking back though a complex polycyclic igneous/metamorphic veil in order to interpret formative processes for older metaevaporite successions, means cratonic origin and accretionary evolution must be understood. Formation and preservation of cratons is a topic of ongoing and sometimes fierce geological debate. For example, in the Archaean terranes at Isua in Greenland, textures long considered as indicating the earliest sedimentary conglomerates and quartzites in the world, are now considered by others to be the relicts of tectonism and myolinitisation and not sedimentary remnants at all (see Eriksson et al. 2004; Chap. 2.2). If so, then arguments of the timing and origin of the hydrosphere using these rocks are even more enigmatic than the initial contentious argument of Appel 1984 that the stratiform tourmalinites at Isua indicated an evaporitic boron-rich precursor.

Cratons constitute the cores of today's continents and are characteristically composed of ancient crystalline basement crust, dominated by lightweight felsic igneous rocks, such as granites and granodiorites. The term craton (from the Greek, *kratos* for strength) describes old and stable parts of the continental crust that have survived the merging and splitting of continents and supercontinents (plate tectonics) and so encompass the world's oldest rocks. Cratons have thick lithospheric roots and are underlain by anomalously cold mantle corresponding to lithosphere more than twice the typical 60-mile (100 km) thickness of mature oceanic or non-cratonic, continental lithosphere (Condie 2004). But if cratons encompass the world's oldest rocks (>3.5 Ga), why were cratonic cores not destroyed by the dynamism of the recycling process that is inherent in modern plate tectonics?

Condie and Kröner (2008) argue that modern plate tectonic processes were operational, at least in some places on the planet, by 3.0 Ga, or even earlier, and that they became widespread by 2.7 Ga. They explain scarcity of complete ophiolite sequences before 1 Ga as indicating thicker oceanic crust, with preservation of only the upper, basaltic unit. They also argue that the apparent absence of blueschists and ultrahigh-pressure metamorphic rocks before ≈1 Ga indicates steeper subduction geotherms and slower rates of uplift at convergent margins.

In contrast, Stern (2007) defines plate tectonics as the horizontal motion of Earth's thermal boundary layer (lithosphere) over the convecting mantle (asthenosphere), and so it is a world-scale system or set of processes mostly driven by lithosphere sinking (subduction pull). He argues that the complete set of processes and metamorphic indicators, associated with modern subduction zones, only became active at the beginning of the Neoproterozoic (≈1 Ga). Stern interprets the older record to indicate a progression of tectonic styles from active Archaean tectonics and magmatism (greenstone belts), to something akin to modern plate tectonics at around 1.9 Ga. If so, then modern world-scale plate tectonics only began in the Neoproterozoic, with the advent of deep subduction zones (blueschists) and associated powerful slab pull mechanisms (Fig. 14.3). Flament et al. (2008) argue that the world's continents were mostly flooded (water-covered) until the end of the Archaean and that only 2–3 % of the Earth's area consisted of emerged continental crust by around 2.5 Ga.

It is very likely that the Archaean Earth's surface was broken up into many smaller plates with volcanic islands and arcs in great abundance (greenstone terranes). Small protocontinents (cratons) formed as crustal rock was melted and remelted by hot spots and recycled in subduction zones. There were no large continents in the Early Archaean, and small protocontinents were probably the norm in the MesoArchaean, when the higher rate of geologic activity (hotter core and mantle) prevented crustal segregations from coalescing into larger units (Figs. 14.3 and 14.4). During the Early-Middle Archaean, Earth's heat flow was almost three times higher than it is today, because of the greater concentration of radioactive isotopes and the residual heat from the Earth's accretion (Eriksson et al. 2004). There was considerably greater tectonic and volcanic activity; the mantle was much more fluid and the crust much thinner (Zegers and van Keken 2001; Ernst 2009; Flament et al. 2008). This resulted in rapid formation of oceanic crust at ridges and hot spots, and rapid recycling of oceanic crust at subduction zones with oceanic water cycling through hydrothermally active zones somewhat more intensely than today. Felsic protocontinents (cratons) probably formed atop Archaean hot spots from a variety of sources: mafic magma melting more felsic rocks, partial melting of mafic rock, and from the metamorphic alteration of felsic sedimentary rocks. Although the first continents formed during the Archaean, rock of this age makes up only 7 % of the world's current cratons; even allowing for erosion and destruction of past formations, evidence suggests that only 5–40 % of the present continental crust formed during the Archaean.

Whatever and wherever the onset of Archaean evaporite deposition, all agree that the mechanisms and aerial proportions world-scale plate tectonism were different in early earth history compared to the Phanerozoic. The current argument as to how different is mostly centred on when earth-scale plate tectonic processes became similar to those of today. Give much higher crustal heat flows, it is likely that hydrographically isolated subsealevel depressions, required to form widespread marine evaporites, were more localised in the Archaean than today and possibly more susceptible to hydrothermal metamorphism. Appropriate restricted brine sumps would have tended to occur in magmatically-induced uplift zones, with crestal subsealevel grabens, which were hydrographically isolated by their surrounds created by supra-sealevel uplift. Once deposited, the higher heat flow in Archaean crust and mantle would also have meant evaporites masses were more rapidly recycled by diagenetic and metamorphic processes than today.

By definition, a craton is an isostatically positive and tectonically stable portion of the world's continental crust, relative to adjacent orogenic belts. This is why evaporite masses, with a need for subsealevel seepage are not typically found atop cratons throughout the Phanerozoic (with the exception of the aulocogen zones in the Amazonian and the Siberian cratons). To have survived without being recycled, a craton core must have deep roots that extend down into the mantle. Mantle tomography shows that cratons are underlain by anomalously cold mantle, corresponding to lithosphere more than twice the approximately 100 km thickness of mature oceanic or noncratonic continental lithosphere. With roots at that depth, it could be argued that some cratons might even be anchored in the asthenosphere. Mantle roots must be chemically distinct because cratons have long-term neutral or positive buoyancy, and an intrinsically low density required to offset any density increases due to geothermal contraction across billions of years. Otherwise, cratons would have been destroyed/recycled by ongoing Proterozoic and Phanerozoic plate tectonism.

Samples of these mantle roots are contained in peridotites, delivered to the intracratonic surface as inclusions in diamond-bearing kimberlite pipes. These inclusions have densities consistent with a low density craton composition and are composed of mantle material that are residuals from high degrees of partial melt (Fig. 14.4). For example, harzburgite peridotites represent the crystalline residues after extraction of melts with compositions indicative of basalt and komatiite. The question is, how did these low density

mantle roots, now below the cratons, form, and what types of processes instigated them and allowed their longterm preservation?

Models based on the uniformitarian extrapolation of present-day arc volcanic and mantle plume processes to a hotter early Earth do not adequately explain the geology of early to Middle Archaean cratons. Alternate plate-scale mechanisms are needed to explain the formation of the earliest continental crust. In the Archaean the formation of continental crust was probably driven by delamination of the lower eclogitic part of an oceanic plateau-like protocrust, which was much thicker than today's oceanic crust. Such delamination resulted in local uplift, extension, and the production of tonalite, trondhjemite, and granodiorite (TTG) suites, as recorded in Middle Archaean cratons of NW Australia and South Africa. These are both areas where trona pseudomorphs typify meta-evaporite phases in the adjacent greenstone sediment suites (Chap. 2).

In the Pilbara craton the delamination occurred ≈3.49 Ga, just before the production of voluminous TTG melts between 3.48 and 3.42 Ga (Fig. 14.4; Zegers and van Keken 2001). Delamination resulted in rapid uplift, extension, and voluminous magmatism, which are all features of the 3.48–3.42 Ga Pilbara succession. As the delaminated portion was replaced by hot, depleted mantle, melts were produced by both decompressional melting of the mantle, resulting in high-MgO basalts (this is the Salgash Subgroup in the Pilbara craton), and melting of the gabbroic and amphibolitic lower crust, so producing TTG melts. Partial melting of the protocrust to higher levels can be envisaged as a multistep process in which heat was conducted to higher levels and advection of heat occurs by intrusion of partial melts in subsequently higher levels (indicated by purple arrows in Fig. 14.3). TTG melt products that were first intruded were subsequently metamorphosed and possibly partially melted, as can be inferred from the migmatitic gneisses of the Pilbara. This multistep history explains the complex pattern of U-Pb zircon ages of gneisses and granodiorites found within the Pilbara batholiths and the range in geochemical compositions of the Pilbara TTG suite.

Simple mass- and heat-balance considerations suggest that delamination of a 10-km-thick eclogite layer would have led to up to 2 km of crustal uplift and that the conducted and advected heat would allow mid-crustal melting and TTG production within 10–20 m.y. after delamination, which is consistent with the geologic evidence in the Pilbara and Barberton cratons (Fig. 14.4; Zegers and van Keken 2001). To produce 10 km of TTG melt from 30 km of mafic protocrust, an average of 30 % partial melting is required. Melting contours in Fig. 14.4 show that the 30 % melt contour is exceeded with the high temperatures reached in the lower and middle crust.

Between 875 and 980 °C, garnet is formed in the residue after partial melting of amphibolite (indicated by grey rectangle in Fig. 14.4), and depending on the garnet content, the residue can have a density of 3.35–3.50 g/cm^3. This high density will lead to a renewed delamination event and subsequent uplift, extension, and magmatism. At lower depth, the residue will consist of hornblende, plagioclase, and clinopyroxene. TTG production will eventually cease when the heat effects of delamination have dissipated and when no new garnet residue is produced to cause further delamination, because the crust is too thin (<30 km) to be in the garnet stability field. In the Pilbara craton, the entire range of U-Pb ages of the TTG event spans from 3.49 to 3.42 Ga in the TTG suites and volcanic rocks, but two age spikes at 3.47 and 3.45 Ga may each represent a delamination event, the second one indicative of a garnet residue event.

The eclogite-delamination model of Zegers and van Keken (2001) explains a wide range of observations in Middle Archaean cratons that have been insufficiently explained when subduction models and modern plate tectonic analogs are applied to these ancient cratons. Delamination explains; (1) the compositional difference between subcratonic Archaean and post-Archaean lithospheric mantle (as sampled in peridotites) and the spatial and temporal link between Middle Archaean crust and depleted mantle, (2) the seismically inferred thinner continental crust and absence of the basal high-velocity layer in Middle Archaean cratons (i.e. the deep roots), (3) coeval TTG melt occurring over large areas (>20,000 km^2 in the Pilbara), (4) substantial uplift, extension, and core-complex formation during intrusion of TTG suites and juxtaposition of high-grade gneisses with low-grade greenstones with preserved shallow water textures and meta-evaporites (that would have required hydrographically isolated depressions), and (5) the nonlinear arrangement of volcanic rocks, structures, and metamorphism (including the creation of highly sodic meta-evaporitic protoliths).

Key to the formation of early Archaean evaporites, which indicate a sodium bicarbonate ocean at that time (Fig. 2.48) is the observation that delamination led to up to 2 km of crustal uplift. This would have driven some regions of what were submarine sedimentary systems into suprasealevel positions, so creating the potential for hydrographically isolated – subsealevel marine seepage sumps in those portions of the uplifted crust above the zones of delamination. It also explains the centripetal nature of much shallow marine sedimentation of that time. This is cardinal at the broad tectonic scale when comparing the distribution of Archaean and Phanerozoic evaporites. Most Archaean evaporites are underlain by layered igneous complexes that were dominant across the greenstone seafloor. Uplift and the local accumulation of sodium carbonate evaporites occurred in a depositional setting that was dominated by volcaniclastics,

hydrothermal vents and extensional tectonics. Tectonic patterns in these settings have a strongly vertical flavor. In contrast, Phanerozoic salts formed from marine waters with a NaCl dominance with minor bicarbonate compared to calcium, and located mostly in subsealevel sumps formed at interacting plate margins where the dominant tectonic flavor is driven the lateral movement of plates atop a laterally moving asthenosphere.

Across the Earth's 3.5 Ga sedimentary record, not only has ocean chemistry evolved (Chap. 2), the earth's lithosphere/plate tectonic character has also evolved (Eriksson et al. 2013). The further back in time, the less reliable is the application of the current plate tectonic paradigm with its strongly lateral movements of crustal blocks and associated plate-scale evaporite basin controls. This is a system where subsealevel continental rifts and continent-continent collision belts favour the formation of mega-evaporite basins (Fig. 14.3). Instead, in a substantial portion of the 2 billion year history that is the Archaean, evaporite deposition was favoured by hydrographic isolation created by stronger vertical movement of earth's crust related to upwelling mantle plumes. There is still no real consensus as to actual time when plate tectonics, as it operates today, actually began but there is consensus that the present (in terms of plate tectonics and evaporite distribution) is not the key to much of the Archaean (Stern 2007; Rollinson 2007).

Protoliths Across the First 2 Billion Years

Key to the understanding the formation of Archaean meta-evaporites is whether the Archaean Earth was a waterworld in which only a few small landmasses (mafic or felsic) breached the surface of a global ocean; or did higher mantle temperatures and more vigorous convection produce more extensive networks of emergent mountain ranges and plateaus, possibly emergent atop mantle plumes, zones of delamination, or along the mid-ocean ridges? Whatever scenario is correct, tectonic settings, sedimentation styles, mineral proportions and lateral extents of marine evaporite protoliths were not the same in the Early-Middle Archaean as in the Phanerozoic. They evolved though time into associations more akin those at the surface of a cooler and increasingly oxygenated surface that typifies the Neoproterozoic and Phanerozoic earth (Ernst 2009). Yet there is clear evidence of evaporite episodes in the metasediments of Early Archaean greenstone terranes, both as meta-evaporite minerals (e.g. stratiform scapolites, tourmalinites and albitites) and nahcolite/trona/halite pseudomorphs in chert masses and mudstone hosts (Fig. 14.5). Archaean evaporite mineralogies reflect precipitation under much hotter surface and mantle conditions beneath a CO_2-enriched atmosphere (Chap. 2; Lowe and Tice 2004).

Very thick sections of mostly submarine mafic, and subordinate ultramafic, volcanic rocks, and mostly younger subaerial and submarine felsic volcanic rocks and sediments were oppressed into complex synforms between rising young domiform felsic batholiths mobilized by hydrous partial melting in the lower crust (Hamilton 1998). Upper-crust granite-and-greenstone terrains underwent moderate regional shortening, decoupled from the lower crust, during compositional inversion accompanying doming, but cratonization soon followed. Tonalitic basement is preserved beneath some greenstone sections but supracrustal rocks commonly give way downward to correlative or younger plutonic rocks. Stable convective mantle plume cells probably did not yet exist in the early to mid Archaean, and developing continents were concentrated in cool regions. Hot-region upper mantle was partly molten, and voluminous magmas, mostly ultramafic, erupted through many ephemeral submarine vents and rifts focussed at the thinnest crust. Surviving Archaean crust is typically from regions of cooler, and more depleted, mantle, wherein greater stability permitted uncommonly thick volcanic accumulations from which voluminous partial-melt, low-density felsic rocks could be generated.

Within this predominance of various types and styles of lava flows and magmas, four types of sediments typify Archaean greenstones that were the at-surface areas both between and onlapping the proto-sialic crust (Lowe 1994). In order of decreasing importance, they were; volcaniclastic, chemical, biochemical, and terrigenous sediments. Volcaniclastic sediments (including greywackes) range from mafic to felsic in composition and were typically deposited as turbidites, implying subaqueous sedimentation beneath an extensive hydrosphere. Whether the subaqueous setting of the early Archaean was marine in the sense of a large contiguous mass of water covering much of the earth's surface or whether surface water was present as more localized "super-lakes" perhaps residing in huge bolide depressions, is a still a matter of debate, as is when in the Early Archaean the world's surface hydrography can first be called truly oceanic (Awramik and Buchheim 2009).

Layered chert and banded iron formation are the most important nonclastic sediments in Archaean greenstone belts. Relict detrital textures in some cherts indicate that many Archaean cherts are silicified clastic sediments and volcanics. This style of hydrothermally driven chertification/silicification is not as prevalent in the cooler sedimentary basins of today. Few, if any, Archaean cherts appear to represent pelagic "marine" biochemical sediments, which today are the dominant modern style of sedimentary chert precipitation. Many Archaean cherts are local lenses and were probably tied to hydrothermal vent deposits. Low $\delta^{18}0$ values in many Archaean cherts support such a volcanogenic/high temperature origin (Knauth and Lowe 2003). A lack of sulphate in the world's anoxic oceans probably meant

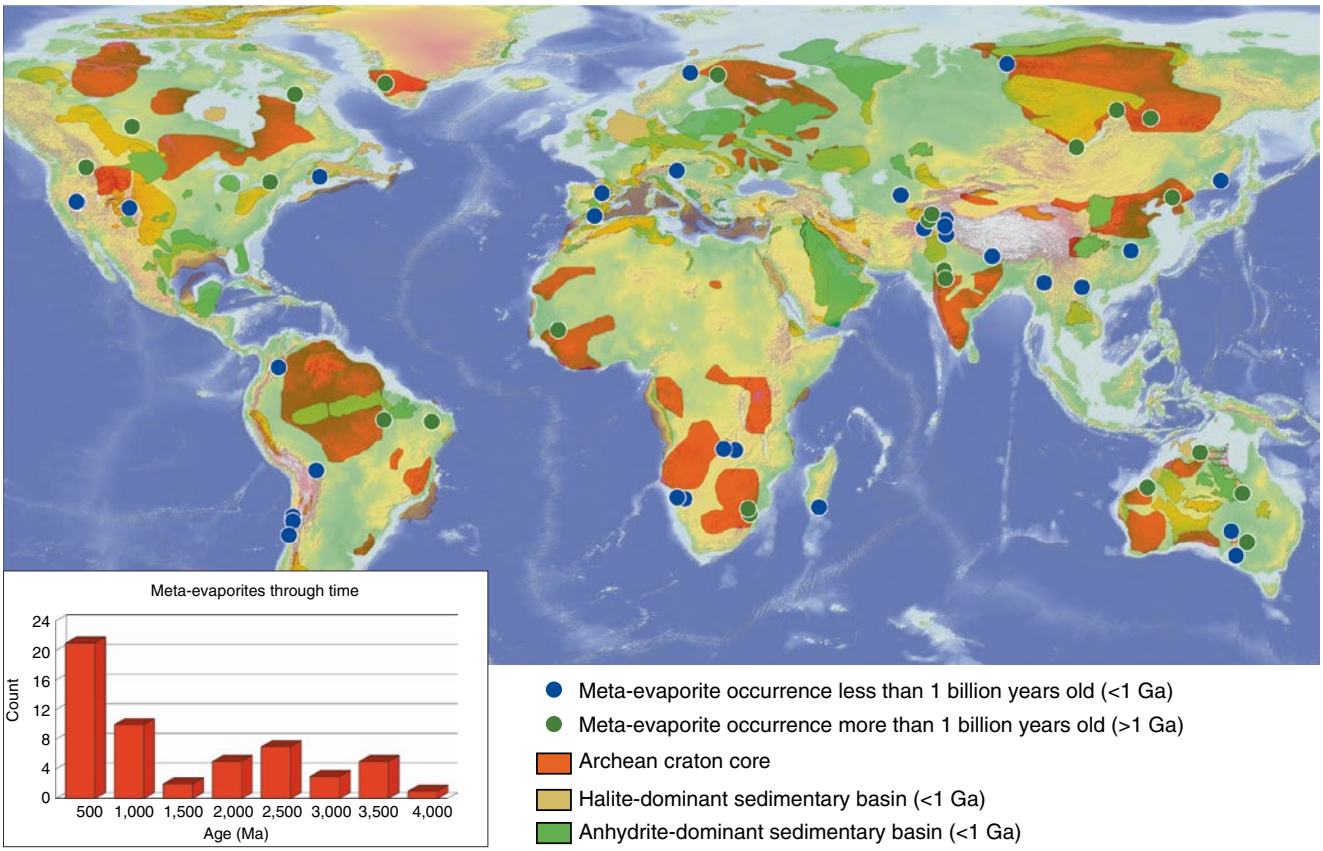

Fig. 14.5 Meta-evaporite occurrences, older and younger than 1 Ga, overlain on distribution plots of Archaean cratons, halite-dominant and anhydrite-dominant sedimentary basins. *Inset* shows age distribution of the occurrences in 500 million year blocks (Data replotted, with permission, from SaltWork database version 1.6. Details of individual plots are given in the various tables in this chapter)

marine hydrothermal anhydrite was less common as a convective oceanic salt than in modern marine hydrothermal vents and VHMS deposits.

Worldwide, the most widespread Archaean depositional environment, especially in early Archaean greenstone terranes, was the mafic plain environment (Condie 2004; Lowe 1994). In this setting, large volumes of basalt and komatiite were erupted to form widespread mostly submarine mafic plains characteristic by ubiquitous pillow structures in the lava interlayers. A second significant sedimentary environment was a deepwater, nonvolcanic setting, where chemical and biochemical cherts, banded iron formation, and carbonate laminites were deposited. The typical lack of evaporite indications in these mostly deepwater sediments indicates an ongoing lack of hydrologic restriction while the sediments were accumulating (waterworld association). The third association, a greywacke-volcanic association becomes more widespread in late Archaean greenstones, which typically sit stratigraphically atop mafic plain units. This association is composed chiefly of greywackes and interbedded calc-alkaline volcanics. It was perhaps deposited in or near island arcs and it too typically lacks widespread indicators of former marine evaporites. Fluvial and shallow-marine detrital sediments, were probably deposited locally in Archaean pull-apart basins, and mineralogically mature sediments (quartz arenites, etc.) typified the shallowest to emergent parts of continental rifts that constructed the last two of the three sedimentary environments within greenstone terranes.

Also associated with a surfacing seafloor, in regions such as the Pilbara, are particular chert and volcaniclastic layers that preserve evidence of shallowing in the form of mud cracks, wave ripples, tidalites interbedded with hyaloclastics, vuggy cherts, banded iron formations, carbonates and thick now-dissolved and altered evaporite masses (breccias), perhaps residues of beds formerly dominated by sodium carbonate salts. Strelley Pool chert in the Warrawoona Group, preserves many silicified examples that retain fine detail of primary textures such as mud cracks, oolites, and evaporite crystal casts and pseudomorphs, all indicating shallow-water to emergent deposition atop the mafic plain. In terms of crystal outlines there are rare casts of possible gypsum crystals (Chap. 2), more typically, they indicate bladed bottom-nucleated nahcolite, trona and in some instances, halite pseudomorphs (Fig. 14.6). These cherty units must have risen, at least locally, to shallow near-sealevel depths and at time become emergent, allowing local hydrographically-isolated

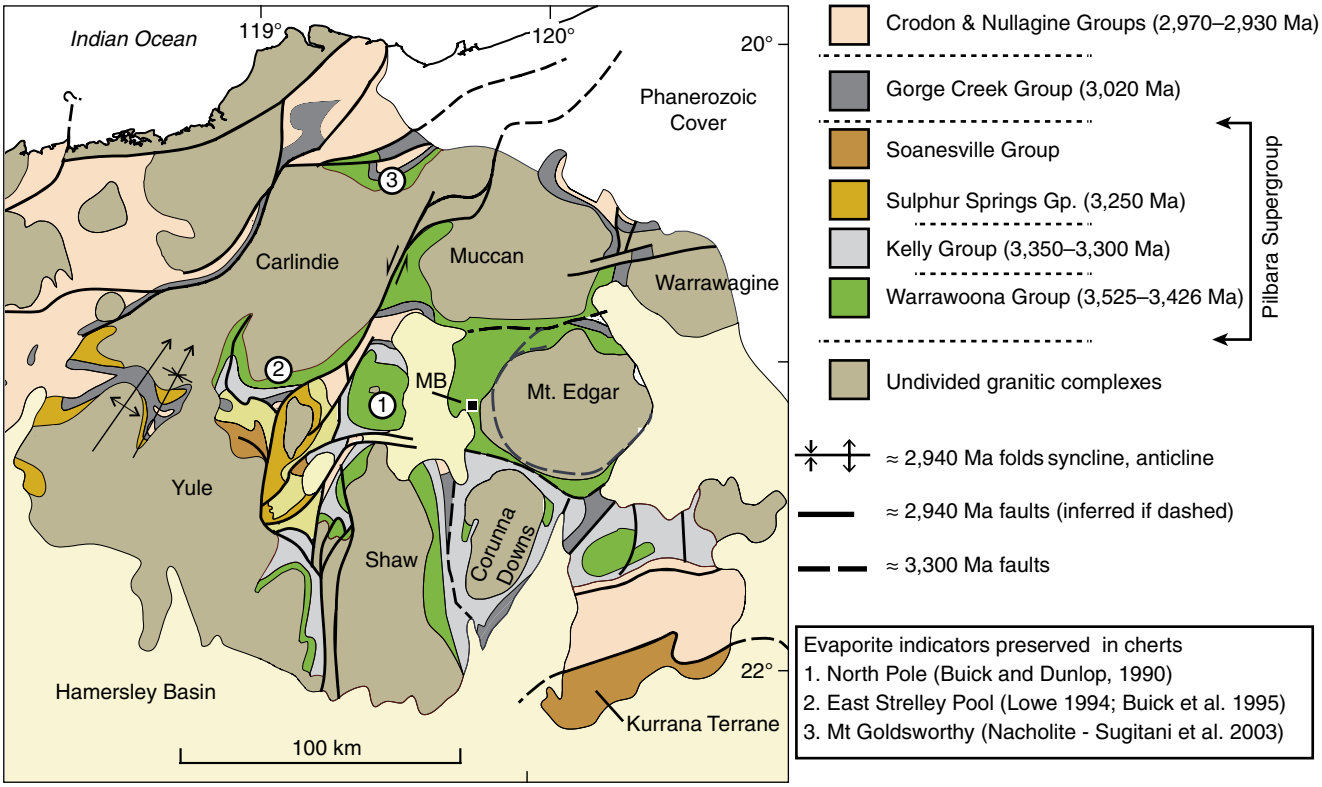

Fig. 14.6 Simplified geological map of the East Pilbara terrane, northwest Australia, showing main granitic domes and the Archaean synformal sediment fills in the interdomal regions (*greenstone*). Also illustrated are documented occurrences of evaporite indicators in chert (In part after Van Kranendonk et al. 2007)

lacustrine/rift evaporite deposition or precipitation of local seepage drawdown salts (Fig. 7.98). Associated primary-textured carbonate and baryte layers interbedded with the cherts are typically minor, bottom-nucleated baryte textures that may represent hydrothermal vent deposits.

High solubility of any sodium bicarbonate and/or halite salts in what was a hotter burial system strongly influenced by hydrothermal circulation, meant most original evaporite salts were not preserved, unless silicified in early burial. But their presence as pseudomorphs in less altered greenschist terranes intercalated with volcanics, such as in the Yilgarn, Pilbara and Kaapvaal cratons, clearly shows two things; (1) at times in the early Archaean there was sufficient hydrographic restriction to allow marine sodian carbonate and sodian chloride evaporites to form and (2) this marine restriction/seepage inflow was probably driven by ongoing volcanism and associated uplift, with evaporites restricted to particular basinwide stratigraphic indicator levels.

In the East Pilbara, the early Archaean evaporite stratigraphic level is the Strelley Pool chert, in the Warrawoona group (Fig. 14.6). This is also the level with some of the earliest indications of cellular lifeforms (Wacey 2009). For the evaporites, it marks the hydrological transition from open marine seafloor to a restricted hydrographically-isolated marine-fed sump basin, surrounded by granite-cored highs with the required uplift likely driven by delamination at the level of the mantle transition (Figs. 14.4 and 14.6). Given the intimate association of chemical sediments to volcanism in early Archaean greenstone basins, and the sodium bicarbonate ocean chemistry then, compared to the Phanerozoic evaporite hydrochemistries, we can expect a higher proportion of CO_2 volatilization and a higher boron content (tourmalinites) in early Archaean and perhaps even Paleoproterozoic meta-evaporite assemblages.

Some authors have noted that there are no widespread marine evaporites in the Archaean and in the sense of actual preserved salts, this is true. But when one considers that the Archaean crust was much hotter than today and hydrothermal circulation was more active and pervasive, then burial preservation seems highly unlikely. Even in the Neoproterozoic, only minor volumes of the original salt masses remain (Hay et al. 2006). The lack of preserved salts in earlier Precambrian strata is more a matter of great age and polycyclic metamorphic alteration. The mode of alteration associated with the nahcolite-dominant marine systems associated with a sodium-chloro-bicarbonated ocean versus the halite-$CaSO_4$ dominated marine evaporites associated with the Na-(Mg)-Cl-(SO_4) ocean of the Proterozoic and

Phanerozoic is still not widely discussed or understood. We shall come back to this topic of Archaean versus Proterozoic-Phanerozoic meta-evaporites and their alteration dissolution later in this chapter and in subsequent chapters dealing with controls on the formation of Precambrian base and precious metal deposits.

Metamorphism: Onset and Evolution

The temperature separating the diagenetic from the metamorphic realm is thought to be ≈200 °C. Conceptually, it is difficult to separate the high temperature end of the zone of diagenesis from the zone of metamorphism. In the more advanced stages of burial diagenesis many clays become unstable as they convert to interlayered mixtures of chlorite and illite, often associated with kaolinite. These mineralogical changes in clays occur in both the late diagenetic and the early metamorphic realms and are associated with the ongoing loss of pore fluids, including generation of volatiles such as CO_2, H_2S, Cl and CH_4. Hence the rock matrix chemistries, especially in evaporitic settings, cannot be interacting isochemically at this time; there must be a flow of fluid and ionic components in and out of the system.

Thrust Belts; Dynamic or Regional Metamorphism

Some metamorphic petrologists use the term anchizone (anchimetamorphic) to describe the subsurface region where chlorite-illite diagenesis is transitional into the prograde metamorphic realm, and the term epizone for the succeeding lowest grades of prograde metamorphism in which illite is largely replaced by muscovite or white mica in a process described as sericitization. Very fine-grained white micas of epizonal slaty rocks are known as sericites, with the dominant constituent typically phengite, a variety of muscovite. The degree of illite[2] crystallinity is often used by metamorphic petrologists to help define the early stages of metamorphism.

Where studies of illite crystallinity (IC) have been conducted on evaporite-encased clay samples, the outcome, while fitting the general paradigm of increasing illite crystallinity with regional temperature gradient, is a little more complicated due to various combinations of salt-edge fluid focus, halokinesis and higher thermal conductivity in NaCl masses. Spötl (1992) studied clay mineral assemblages in Upper Permian evaporites (Alpine Haselgebirge Formation) of the Northern Calcareous Alps in Austria. Using fresh samples from a salt mine from Hall in Tyrol, he found that illite crystallinity was strongly dependent on the host lithology (Fig. 14.7). Illite from muddy halite indicated an incipient anchizonal overprint (boundary is defined by $\Delta°2\theta$ mean $= 0.42 \pm 0.02$). Illites from intercalated mudrocks and sandstones were less crystalline and averaged higher $\Delta\ °2\theta$ values of 0.47 ± 0.01 and 0.56 ± 0.03, respectively. Thus, illites in these lithologies are significantly less evolved compared with intercalated muddy halite samples and indicate nonmetamorphic (diagenetic) conditions. Spötl postulates that the crystallinity in the muddy halites reflects either higher potassium content and hence greater supersaturation with respect to muscovite transformation in highly saline pore brines, or, a thermal anomaly tied to nearby diapiric ascent.

In a subsequent related study, Spötl and Hasenhüttl (1998) compared IC values and levels of vitrinite reflectance across a number of Haselgebirge localities, mostly using samples collected in salt mines, including the Hallstatt Mine site (Fig. 14.7b). They identified a general relationship between the two determinations, showing that decreasing IC values were tied to increasing temperatures of alteration/diagenesis/onset metamorphism, indicated by the higher vitrinite values. Across the Haselgebirge there were significant ranges of both values, as is to be expected given the tectonic melange origin of the Haselgebirge. As we saw in Chap. 7, it contains a mixture of clasts and fragments in a flowing salt matrix, some clasts had experienced greater degrees of thermal alteration before being mobilised as the surrounding tectonised salt moved to a shallower cooler depth.

When illite crystallinity was measured in bedded Permian–Triassic sediments (Bellerophon/Weren) of varying carbonate/siliciclastic content, recovered in the Gartnerkofel-1 Core (Carnic Alps, Austria), values appropriate to the anchizone (onset of metamorphism) were restricted to the oolitic carbonates of the Tesero horizon (Fig. 14.7c; Schramm 1991). In general, below the PermoTriassic contact, samples with lower carbonate contents had lesser IC values, and most sampled sediments had yet to reach the metamorphic realm. The exception occurs at the Permo-Triassic boundary in the 6.5 m thick Tesero Horizon. Schramm (1991) notes that regional burial and heatflow cannot explain these elevated values, especially as IC values in the underlying Bellerophon Fm are not anchimetamorphic. He concludes the IC values in the Tesero Horizon were inherited from detrital micas, which had retained anchi-metamorphic IC values. A possibility of evaporite-focused thermal fluids is mentioned as another possible explanation but Schramm went on to favour the detrital

[2]The illite lattice is structurally very similar to muscovite and it tends to transform to muscovite with increasing metamorphic grade. The Illite crystallinity or Kübler index is experimentally determined by measuring the full width at half maximum for the X-ray diffraction reflection peak along the (001) crystallographic axis of the illite sample. This value is an indirect measurement of the thickness of illite/muscovite packets, which denote change in metamorphic grade.

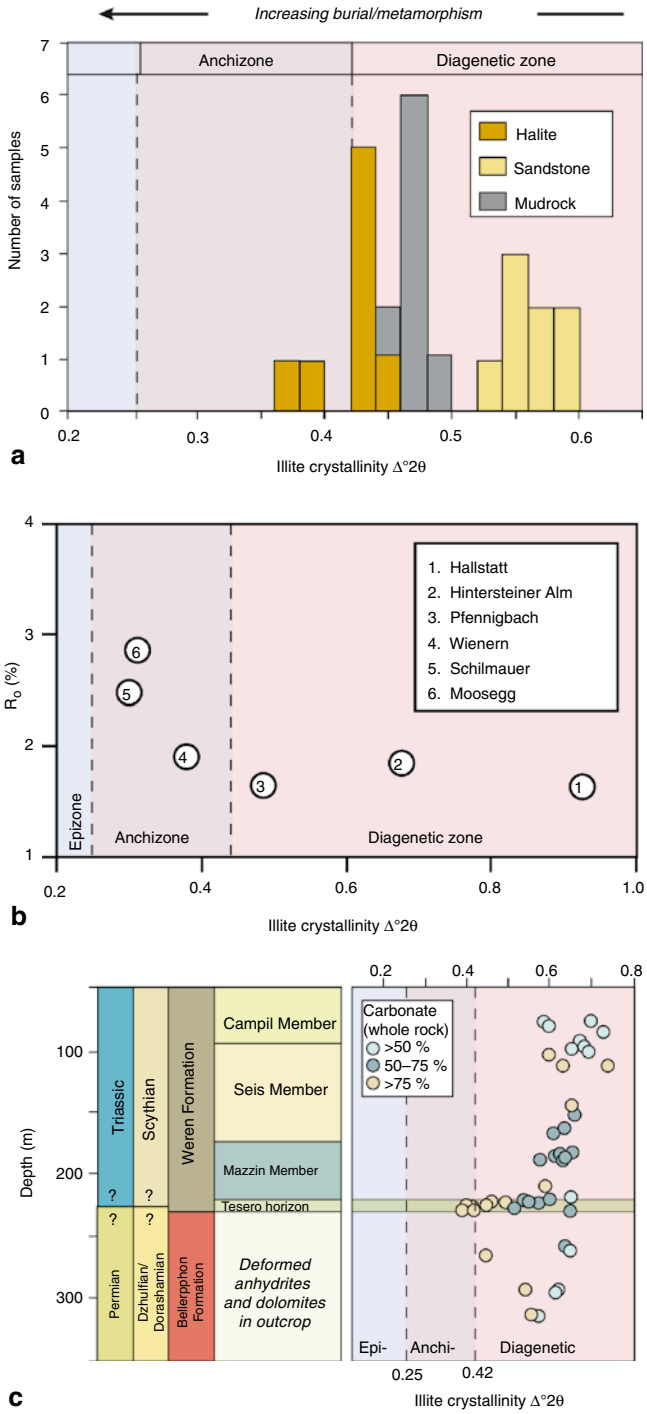

Fig. 14.7 Illite crystallinity (Δ °2θ) (**a**) From the <2 μm fraction of samples from evaporitic facies in Hall in Tyrol. Note that different lithologies from the same region show distinct crystallinities (After Spötl 1992). (**b**) Comparison of IC and vitrinite reflectance values for the six localities of the Haselgebirge mélange in the Alps (After Spötl and Hasenhüttl (1998). (**c**) IC values in core from Gartnerkofel-1 well, (Carnic Alps, Austria) sampling the contact between the deformed anhydrites residues and dolomites of the Permian Bellerphon Formation and the overlying Triassic succession with anchiomorphic values restricted to the oolitic carbonates of the Tesero Horizon (After Schramm 1991)

inheritance mechanism. In my opinion, evaporite focusing of thermal fluids is the more likely explanation, making it an example of focused hydrothermal metamorphism or alteration. The Tesero Horizon sits directly atop the Bellerophon evaporitic succession and the contact would have acted as a relative aquifer, focusing crossflows of hot halokinetic/dissolution brines as they rose along the tectonically active contact.

In contrast to higher temperature indications in anchizonal halites, as seen in Fig. 14.7a, inclusion-derived temperature measurements in halites in nearsurface exhumed evaporites in the Himalayas are preferentially overprinted by exhumation effects (telogenesis). They tend to indicate the cooler recrystallization temperatures associated with exhumation-related meteoric flushing and so do not indicate maximum burial temperatures. Maximum burial indicators are better preserved as illite crystallinity indices in the shales, which unlike the salts do not so readily transform during uplift and recrystallisation in the telogenetic realm.

In parts of the Himalayan foldbelt, Neoproterozoic evaporites and intercalated clays, which have passed through the early greenschist realm, now constitute outcrop and subcrop in the Chamba and Kashmir regions (Singh and Singh 2010). Depositionally, these Neoproterozoic evaporites were coeval with the Hormuz-Ara salts of Pakistan, Iran and Oman. The evaporite-bearing succession crops out as an association of phyllite, quartzite and carbonate, adjacent to the main boundary thrust of the Lesser Himalayas. The illite crystallinity index (KI), measured from the illite peaks of the clay minerals in beds that are separate from the evaporite rocks indicate near epizonal conditions and a maximum temperature ≈300 °C, as do the anhydrites (Fig. 14.8a). Microthermometric measurements on fluid inclusions in intercalated dolomites show a range of homogenization temperatures from 220 to 280 °C, well within the temperature range of anchizone metamorphism (Fig. 14.8b). The dolomites also show highly negative $\delta^{18}O_{PDB}$ signatures (av. = −15.5‰), which probably relate to diagenetic overprints during deep burial.

In contrast, the associated halite intervals, which were texturally transformed a number of times after their precipitation, have retained only the those temperature indicators developed during last one or two phases of telogenetic alteration, deformation and recrystallisation (Fig. 14.8b). As we saw in Chap. 7, this is an indication of an inherent high degree of shallow subsurface reactivity and solubility in halites flushed by shallow subsurface and surface meteoric waters. An inclusion-derived final temperature range of 42–78 °C in these outcropping gypsums and halites gives a thermal approximation that is not in concordance with the thermal history of the basin, but is related to telogenetic conversion of anhydrite into gypsum and pervasive recrystallization of halite during exhumation.

Using highly saline inclusions in vein quartz in the Apuan Alps metamorphic complex of Northern Italy, Montomoli et al. (2005) document the migration of halite-derived brines into subthrust sericitized metamorphic lithologies. Fluid inclusions, which are trapped in quartz crystals in syn-tectonic veins, are oversaturated in NaCl at room temperature with salinities ranging from 29.5 to 37 wt.% NaCl equiv. The isochore of the earliest trapped fluid inclusions (type IA; primary inclusions in fibrous quartz of A veins), coupled with mineralogical geothermometric data, constrains the pressure temperature conditions of the quartz to around 325–300 MPa and 370–380 °C during the late-D1 phase. Subsequent trapping of inclusion types IIA, IIB, IIIA, IIIB and VB in the two vein sets probably occurred during a pressure-temperature decrease, down to 220–245 MPa and 260–270 °C, at a lithostatic thermal gradient of 30 °C/km (Fig. 14.9a). Type IVB inclusions were probably trapped at even lower pressures (between lithostatic and hydrostatic conditions) during cementation driven by transient pressure drops resulting from fault-valve action.

The resulting fluid circulation model proposes that the high-salinity fluids found in the syn-tectonic veins, along with the high-salinity and NaCl-rich nature of the trapped fluids are the result of the original metamorphic fluids interacting with evaporite levels present at the base of the Tuscan Nappe, which overlies Apuan Alps metamorphic units (Fig. 14.9b). These hypersaline evaporite-derived fluids had infiltrated downward during metamorphism, possibly through shear zones crosscutting the stratigraphic sequence, into the syn-tectonic veins and interacted with the host-rocks to produce local element mobilization and their precipitation in the vein minerals, which reflect the quartz dominant mineralogy of the host-rocks.

Instead of illite crystallinity, the diagenetic to metamorphic transition is sometimes defined as the subsurface interval where all sedimentary porosity and permeability is lost (Phillips et al. 1994). That is, at burial depths where sedimentary porosity is significant, diagenetic fluids are likely to dominate. Once compaction and authigenic cementation occludes this porosity to negligible levels, there is little capacity to retain either diagenetic fluids or significant permeabilities and so the strata pass into the realm of metamorphism.

This definition is based on the assumption that in metasediments, unless there is evidence to the contrary, one generally assumes that with the loss of diagenetic permeability, the system can be approximated as a near isochemical closed system. Evolving mineral phases then reflect successive equilibria tied to changes in temperature and pressure, with little change in the molecular components that make up the whole rock chemistry. This is, after all, the basis for the application of phase diagrams in classic metamorphic petrology. More recent work has showing that most metamorphic systems have some degree of fluid throughput, especially those involving metasediments and decarbonation reactions or within protoliths containing high levels of other volatiles such as coals or evaporites (Yardley and Lloyd 1995; Yardley

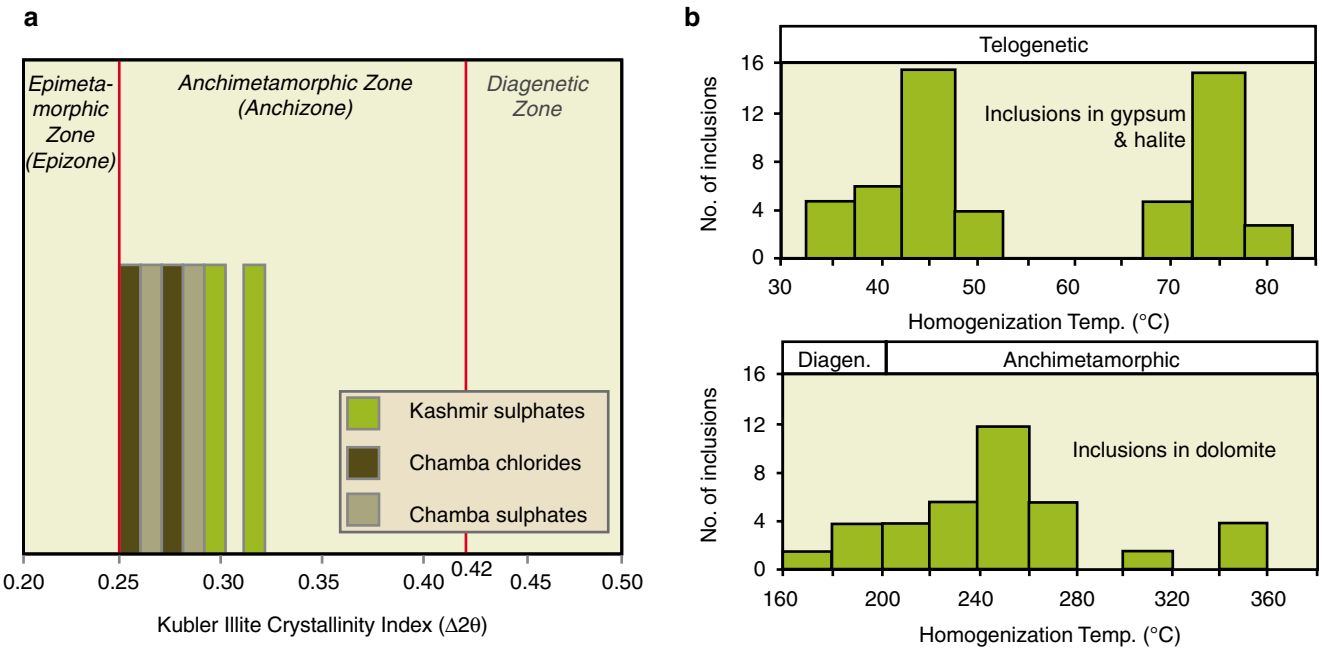

Fig. 14.8 Metamorphic indicators in the Neoproterozoic evaporitic succession in the Lesser Himalayas (After Singh and Singh 2010). (**a**) Illite crystallinity indices from clays encased in halite and $CaSO_4$ phases indicating anchizonal metamorphism. (**b**) Microthermic measurements in dolomites indicative of anchizonal temperatures and in evaporites indicative of telogenetic recrystallization

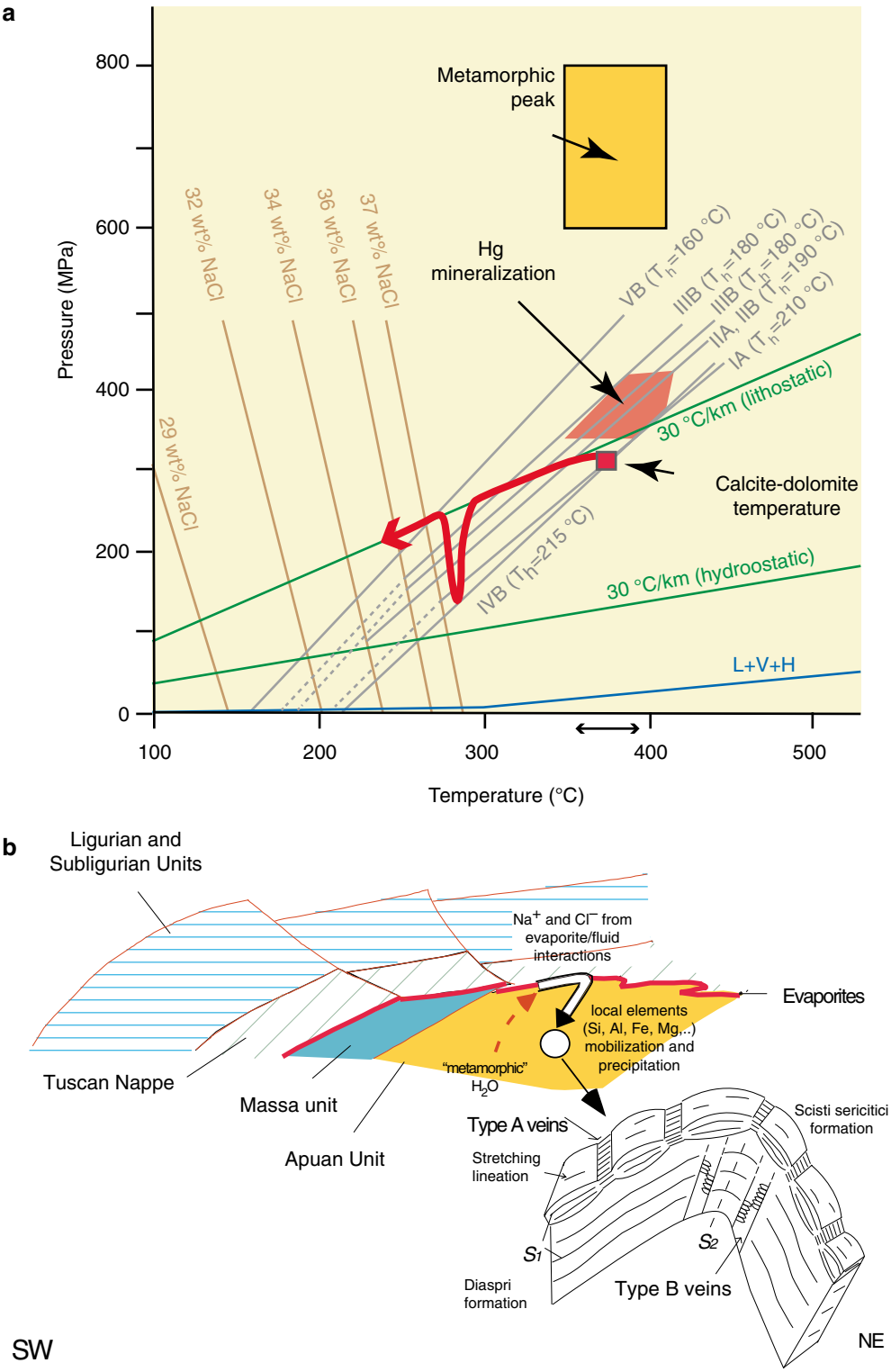

Fig. 14.9 Saline brine geothermometry, Apuan Metamorphic Complex, Italy (After Montomoli et al. 2005). (**a**) Pressure–temperature diagram from quartz vein inclusions (Types I-V) showing the representative isochores (*dashed lines* in the halite + liquid field, *light continuous lines* in the liquid field), the halite liquidi (*grey lines*) for the average salinities of the different inclusion types, and the liquid + vapour + halite (L + V + H) curve. The 30 °C/km lithostatic and hydrostatic gradient (*green lines*) are plotted as are the temperature ranges computed using the chlorite geothermometer (*black double-ended arrow*) and estimated temperature ranges for the D1-phase in the central-northern part of the complex calculated using the calcite–dolomite geothermometer (*red double ended arrow*). The *red square* indicates the pressure–temperature conditions determined from the IA-fluid inclusion representative isochore and from geothermometric estimates for the late-D1 phase. The *thick red arrow* indicates the proposed pressure–temperature evolution of the metamorphic fluids flowing in the syn-tectonic veins. Temperature-pressure field at peak metamorphism in the complex is also shown. (**b**) Schematic showing the fluid migration path for the high-salinity fluids of the Apuan Alps. Schematic block diagram (*bottom right*) shows relationship between the two vein types and the main structural elements (*S1* foliation associated to the first folding phase, *S2* foliation associated to the second folding phase)

2013). The loss of volatiles from metamorphosing evaporites, described in the first paragraphs of this chapter, means an assumption of a closed system is not appropriate for areas adjacent to, or interbedded with, thick successions of evaporites entering the realm of metamorphism.

Porosity and permeability loss in the diagenetic realm is directly related to increasing burial in all sediments, except for some evaporite salts, where permeability is lost very early but regained at greater burial depths. In bedded halite, all effective porosity and permeability in a halite bed is lost

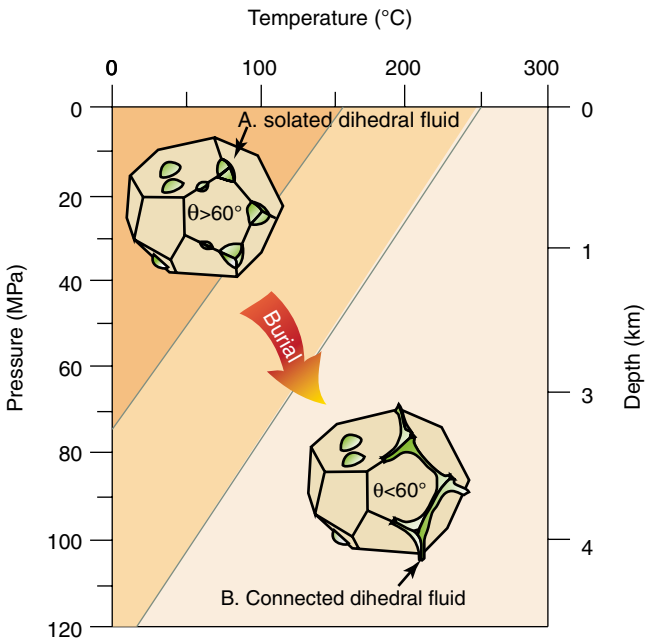

Fig. 14.10 Effect of dihedral angle on pore connectivity in texturally equilibrated monomineralic and isotopic polycrystalline mosaic halite. *Background shading* shows two polyhedral porosity fields and transition zone calculated for the Ara Salt (black salt or leaking halite plots in transition zone), Oman. (**a**) Isolated porosity for dihedral angle >60°. (**b**) Connected polyhedral porosity for dihedral angle <60° (After Lewis and Holness 1996; Kukla et al. 2011b)

by 100 m burial at temperatures that are less than 50 °C. Anhydrite beds are typically tight by 500–1,000 m depth. This, and halite's ability to flow rather than fracture, is why evaporites constitute such excellent hydrocarbon seals throughout the diagenetic realm (Chap. 10).

More deeply buried halite may regain permeability during halite recrystallization due to a change in the halite-brine dihedral angle at depth (Lewis and Holness 1996). At temperatures <100–150 °C the contact angle between halite and brine is 70 °C (Fig. 14.10a). Under laboratory conditions this contact angle equates to maintenance of closure of grain polyhedral boundaries by halite precipitation, and so at such low temperatures salt is impermeable (Schenk and Urai 2004; Lewis and Holness 1996). In this temperature range the small amounts of brine present in the salt are distributed in micrometer-sized isolated fluid inclusions. At temperatures >100 °C and pressures of 70 MPa or more, the dihedral angle decreases to values <60 °C, driving a redistribution of the fluid into a thermodynamically stable network of connected, fluid filled channels at grain boundary triple junctions. This transition may be related to the observation by Peach and Spiers (1996) that during natural deformation of rocksalt at great depths it undergoes natural hydraulic fracturing or dilatancy. The transition is also used to explain the occurrence of black (bitumen-charged) salt in the Ara Salt of Oman (Kukla et al. 2011b).

Once this recrystallization occurs, mosaic halite loses its ability to act as an aquitard and may instead act as a permeable conduit for escaping formation waters (Fig. 14.10b). According to Lewis and Holness, the depth at which the recrystallization occurs may begin as shallow as a few kilometres. But, their pressure bomb laboratory-based experiments did not completely encompass the ability of natural salt to pressure creep and self-seal by longer-term diffusion-controlled pressure solution (Chap. 6). Even if the changing dihedral angles alter and open up permeability at such shallow depths, there is no guarantee that subsequent flowage associated with pressure solution will not re-anneal these new pores. The ability of salt to continue to act as a highly effective hydrocarbon seal to depths of 8–10 km means, in my opinion, that bedded salt does not become a relative aquifer until depths of 6–10 km or more, and probably at burial temperatures that mean the sequence is entering the greenschist realm. In extreme overpressured situations the transition can be much shallower, as in the 40–50 m thick black salt rims that typify the salt-encased hydrocarbon-charged carbonate stringers in the Ara Salt of Oman (Kukla et al. 2011b). Once it does transform into polyhedral halite, a former aquiclude becomes an aquifer flushed by chloride-rich brines, likely carrying other volatiles.

A release of entrained inclusion (±intercrystalline) water at temperatures >300–400 °C (early greenschist) influences the textures of deeply buried halite. Most of the inclusions in chevron halite and other inclusion-rich cloudy primary salts are due to entrained brine inclusions and not mineral matter. Figure 14.11 plots the weight loss of various types of halite during heating. It clearly shows cloudy (inclusion-rich) halite releases up to five times more brine (0.2–0.5 wt%) than clear coarsely crystalline halite. An analysis of all fluids released during heating shows carbon dioxide and hydrogen contents are much lower than the water volumes: $CO_2/H_2O < 0.01$ and $H_2/H_2O < 0.005$. Organic compounds, with CH_4, are always present (<0.05 % H_2O), and are twice as abundant in cloudy halite. There are also traces of nitrogen and, in some samples, hydrogen sulphide and sulphur dioxide (Zimmermann and Moretto 1996).

Nitrogen is released below 240 °C and is probably of atmospheric origin. Most of the water is expelled from 330 to 410 °C, corresponding to the decrepitation of inclusions (Fig. 14.11). Likewise, CO_2 liberation occurs mainly between these temperatures. Above 420 °C an additional part of the weight loss comes from carbonate dissociation through heating. Hydrogen is extracted continuously from 200 to 460 °C, even though an evolving salt crystals water content is less than 0.5 %. Most of the hydrogen originates from dissociation of organic matter present in the halite crystals as well as from water reduction during heating (inclusion release; Zimmermann and Moretto 1996).

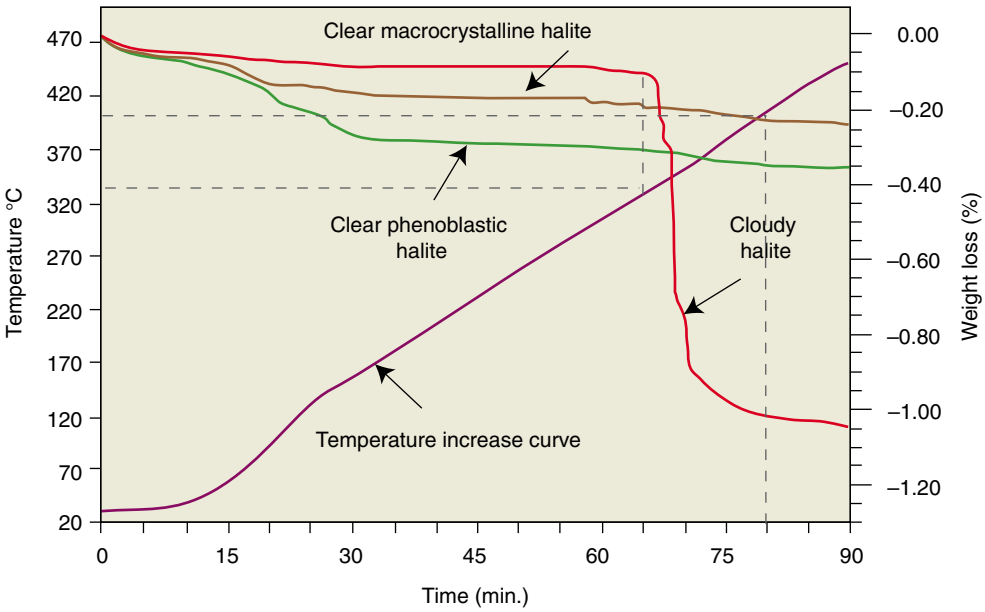

Fig. 14.11 Weight loss of three pure halite samples upon heating from ambient temperature to 470 °C. Most of the weight loss corresponds to water loss from entrained inclusions, which are more common in cloudy halite (After Zimmermann and Moretto 1996)

Halite as a distinct mineral phase is rarely recovered from metamorphic rocks beyond the early greenschist realm and is no more than an extremely rare mineral phase in granulites (Newton et al. 1998). Both the polyhedral transformation and the dehydration/alteration of cloudy salts may explain why, even though the associated temperatures in granulites are well below halite's melting point of 750–800 °C. As halite recrystallizes, via compaction-related generation of intercrystalline polyhedral porosity, the increasingly permeable halite bed is being flushed by waters from adjacent devolatising and altering meta-sediments. These waters further aid in removing and altering the highly soluble halite phase. Through its dissolution and metamorphism, halite can generate zones of extensive sodic metasomatism in nearby meta-sediments. The same chloride-rich fluids may also flush metals from adjacent beds and then carry them into contact with reducing intervals, such as graphitic schists, where metal sulphides or oxides crystallize in suitably prepared ground or pressure shadows. We shall discuss the economic significance of this transformation in detail in the next chapters, which deal with the genesis of ore deposits associated with present and former evaporites.

A thick anhydrite mass does not dissolve or transform as readily as halite entering a greenschist zone, recrystallised anhydrite is known to survive into high grades of metamorphism (Butchins and Mason 1973; Serdyuchenko 1975; Markl and Piazolo 1998). For example, hornfelsic anhydrite, interbedded with anhydrite-cemented shale breccias formed by evaporite solution collapse, is found at 1 km depth in the Magmamax 11 well in the central part the Salton Sea geothermal system (McKibben et al. 1988a, b). Massive anhydrite is found in association with copper mineralisation in the Mt Isa inlier (Wilde et al. 2006). Thick beds of recrystallised sedimentary anhydrite occur in amphibolite grade Mesoproterozoic metasediments at Balmat, New York (Whelan et al. 1990) and granulite grade Neoproterozoic metasediments in Central Dronning Maud Land in East Antarctica (Markl and Piazolo 1998; MacGregor et al. 2013). Nonevaporitic anhydrite can also form as a hydrothermal precipitate from heated seawater, and will be discussed fully in Chap. 16, this chapter focuses on metasedimentary anhydrite.

As noted earlier, evaporite-associated rock matrix chemistries cannot be interacting isochemically: there must be a flow of fluids and ionic components in and out of the system to explain the near-complete loss volatiles (Cl, CO_2, SO_3 and H_2O) during metamorphic transformation of evaporite salts. However, the presence of a likely meta-evaporitic mineral assemblage, such as NaCl-scapolite with dravite-uvite tourmaline, does not, by itself, indicate an undeniable evaporite protolith. Hydrothermal waters associated with late cooling stages of magmatic intrusions can also drive sodic alteration and scapolitization, as well as dissolve and mobilise salts in the adjacent country rock. Ideally, there should be further evidence to support a meta-evaporitic interpretation such as:

- Strict stratigraphic/halokinetic control on the occurrence of meta-evaporite mineral phases and haloes (Hietanen 1967; Sharma 1981);
- The presence of recognisable salt pseudomorphs, such as hoppers, in less metamorphosed stratigraphic equivalents (Grotzinger 1986a, b);
- Hypersaline fluid inclusions in the assemblage (Roedder 1984a, b);
- The occurrence of abundant associated Mg- and Cl-rich biotite (Moine et al. 1981).

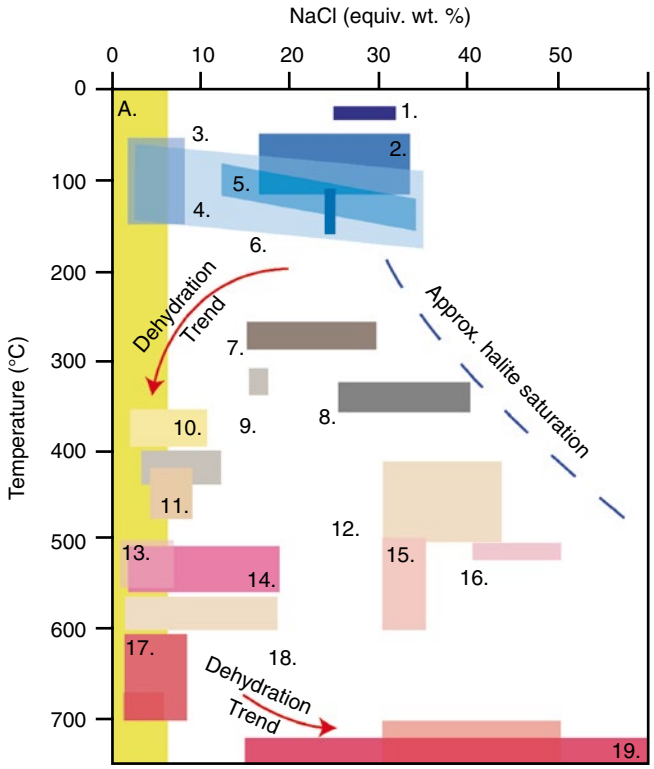

1. Brines in Permian evaporites, Salado Fm, New Mexico
2. Southern North Sea formation waters
3. Northern North Sea formation waters
4. Central North Sea formation waters
5. Mississippi oil field brine, sediments above Salt Dome Basin
6. Cements in Lower Cretaceous arkoses, offshore Angola
7. Thrust belt fluids, quartz veins in Mesozoic sediments, Pyrenees
8. Columbian emerald-bearing veins in evaporitic metasediments
9. Post-metamorphic Alpine Clefts, central European Alps
10. Syn-metamorphic quartz veins, Harlech Dome, North Wales
11. Veins in metasediments, Lukmanier Pass, Switzerland
12. Damara belt metasediments, Namibia
13. Veins in Waterville Fm. metasediments, Maine
14. Veins in Sangerville Fm. metasediments, Maine
15. Veins in metasediment, Vermont
16. Veins in dolomitic marble, Campolungo, Italy
17. Veins in Dalradian metasediments, Connemara, Ireland
18. Eclogite, Dora Maira Massif, Italy
19. UHP Eclogite, Dabie Shan, China

A. Encloses all athe low salinity fields of formation waters, springs and metamorphic fluids hosted by sequences of oceanic or accretionary prism origin.

Fig. 14.12 Temperature–salinity plot for formation waters and metamorphic fluids hosted by sequences deposited in epeiric seas and at continental margins (After Yardley and Graham 2002). Boxes reflect the range of data from each of the numbered sources listed, many of the meta-evaporite examples are discussed later in this chapter The box, designated A, clearly shows that meta-oceanic and meta-accretionary wedges lack high NaCl/salinity waters. The *red arrows* show (i) the typical dehydration trend in metamorphic successions lacking a widespread evaporite protolith and (ii) the high salinity rehydration trend within deeply buried successions subject to the elevated temperatures and high salinities created in volatiles released during by eclogite formation (not necessarily evaporitic protolith)

Ongoing progressive regional metamorphism of an evaporitic halite-entraining sequence leads to a removal of water, CO_2, Cl and other volatile components. The greatest expulsion volume of volatiles from an altering rock salt mass and the ultimate disappearance of halite occurs in the lower grades of metamorphism (greenschist). The H_2O, CO_2, Cl°, CH_4, etc. then migrates, as the fluid carries away large quantities of dissolved ions, particularly Na^+ and Cl^-. Fluid released during devolatilisation of meta-evaporites is typically saline and chloride-rich with an innate ability to leach and transport base and precious metals as chloride complexes. The resulting metamorphic minerals, dominated by sodic phases, can create zones of widespread scapolitization or albitization (Kwak 1977; Moine et al. 1981; Rozen 1979). These same metamorphic associations tend to entrain minerals and inclusions with high NaCl contents (Fig. 14.12; Yardley and Graham 2002).

What is most interesting from the work of Yardley and Graham (2002) and illustrated in Fig. 14.12 is that with nonevaporitic protoliths the salinities of metamorphic fluids show some overall trend to lower values at higher metamorphic grades, but in evaporite-bearing protoliths, the opposite trend is present. Sedimentary sequences deposited in oceanic and accretionary settings invariably yield low-salinity metamorphic fluids (<7 % wt.% NaCl; Box A in Fig. 14.12). In contrast, sedimentary sequences deposited mostly on continental crust, and including products of shallow water deposition, typically (though not invariably) give rise to relatively saline metamorphic fluids. Yardley and Graham's conclusion, that the general pattern of pore fluid salinities persists from the diagenetic into the metamorphic realm, has important implications for both metamorphic and ore-forming processes in the crust. Firstly, interpretations of metamorphic phase equilibria should consider the nature of the original sedimentary sequence; for shallow water sequences, it is essential to test for possible high fluid salinities, since these give rise to substantial deviations from the simple mixed-volatile fluid model normally used by metamorphic petrologists. Secondly, salinity is a fundamental control on the ability of fluids to transport many ore-forming elements. They go on to state that this difference is almost certainly related to the original distribution of evaporites and/or connate brines in the protolith.

In terms of migration of metals complexed by chloride and leading to the formation of base metal deposits, it is more likely that high-chloride diagenetic and metamorphic waters derived from alteration of evaporites, will tend to occur in metamorphosed saline passive-margin and intracratonic sediments. Evaporite influences are less likely in pore waters systems in oceanic and accretionary orogenic prisms. There the volatiles will tend to come from seawater and magmatic/hydrothermal sources. In the next two chapters we will focus on the importance of understanding the likely nature of the protolith when developing base and precious metal exploration models in metamorphic terranes. For now, let us now look at some of the more common evaporite indicator minerals and associations in the metamorphic realm.

Meta-evaporite Mineral Associations

Generally, metamorphic minerals with an evaporite protolith tend to be enriched in minerals entraining sodium, potassium and magnesium. They can entrain high levels of volatiles (Cl, SO_3 and CO_2) as well as elevated levels of boron, all features, along with high salinity in the associated metamorphic fluids, which are indicative of their evaporitic origins (Table 14.2; Fig. 14.12). Sodium tends to come from the dissolution of salts, such as halite or trona; while magnesium tends to be remobilized from earlier diagenetic minerals, such as reflux dolomites and magnesium-rich evaporitic clays. Boron in tourmalinites may have come from a colemanite/ulexite lacustrine precursor. Once direct evidence of a salty protolith is largely removed via fluid dispersion and ongoing loss of volatiles, the palaeo-evaporite indications are largely restricted to mineralogic associations, along with an occasional textural relict of an evaporitic breccia bed, rauwacke or salt weld.

Evidence of early stages in a evaporite-fed sodic transformation can be seen in the sodic phlogopites (phlogopite = magnesian mica) and sodian aluminian talcs in the metapelites of the Tell Atlas in Algeria (Schreyer et al. 1980). Evaporitic sulphate crystals are pseudomorphed in the NaCl-scapolite-dominated sequences of the Cordilleras Beticas of Spain (Gómez-Pugnaire et al. 1994). Rocks of higher temperature and pressure facies, such as the massive stratiform anorthosites in the Grenville Precambrian Province of North America, have been interpreted as possible meta-evaporites (Gresens 1978), as have the anhydrite-containing Mesoproterozoic calcsilicates in the Oaxacan granulite complex in southern Mexico (Ortega-Gutierrez 1984) and the pervasive scapolites in the Neoproterozoic Zambesian orogenic belt of Zambia (Hanson et al. 1994). Subsequent work on the Grenville and Limpopo anorthosites, although still allowing for a metasedimentary protolith, have concluded an igneous source of volatiles is more likely (Barton 1996; Moecher et al. 1992; Peck and Valley 2000; Glassley et al. 2010). Defining the likelihood of a evaporite protolith becomes increasing difficult as the metamorphic grade increases. Once a metamorphic rock enters the granulite facies, its protolith interpretation is typically much more contentious (e.g. the evaporite versus carbonatite interpretations in the Oaxacan granulites, Mexico).

Scapolite and Scapolitization

Like feldspar, the term scapolite describes a solid solution series. The sodium-chloride-rich end member is called marialite [$Na_4(Al, Si)_{12}O_{24}Cl$] and the calcium-carbonate-rich end member is meionite [$Ca_4(Si, Al)_{12}O_{24}(CO_3,SO_4)$]. The sulphate ion shown in the meionite formula is typically barely more than a trace, even in meta-evaporites; but is found in far greater percentages than the occasional fluorine or hydroxide interlopers in the scapolite lattice. The structure of scapolite is similar to some feldspathoids in that it is composed of large open spaces in the framework of silicate and aluminium tetrahedrons. These open spaces are large enough to cage large diameter ionic groups. So, a scapolite lattice can be described in terms of four-membered tetrahedral rings [(Si,Al)—O], linked together to form an open chain framework that is parallel to the c axis. A large subspherical opening is located at the fourfold axis and is surrounded by four oval shaped channels running parallel to the c axis [001]. This large cage is occupied by the Cl, CO_3, and SO_4 anions, whereas the channels host Na, Ca, and minor K cations (Fig. 14.13a).

In general, for each metamorphic grade, the variation in the amount of Cl in the scapolite suggests a local control (Table 14.3). In a scapolite-biotite assemblage, elevated levels of Cl indicate a high NaCl activity at the time of their crystallization from a likely evaporitic/feldspathic precursor (Orville 1975; Ellis 1978; Vanko and Bishop 1982; Mora and Valley 1989).

Marialitic scapolite grows at temperatures around 400 °C and NaCl-H_2O fluids, containing more than 40 mol% NaCl, are needed to stabilize the marialite (Vanko and Bishop 1982). The Na and Cl in the scapolite lattice may have been derived from sedimentary halite, or introduced from an outside source such as Cl-rich hydrothermal or sedimentary brines.

The distribution of scapolite lenses and layers in outcrop is often the best evidence for the origin of the scapolite (Hietanen 1967). Scapolites derived from hydrothermal brines tend to be in haloes around intrusives, while basinal brine chlorine tends to form replacement fronts associated with faults, shears and other conduits (Owen and

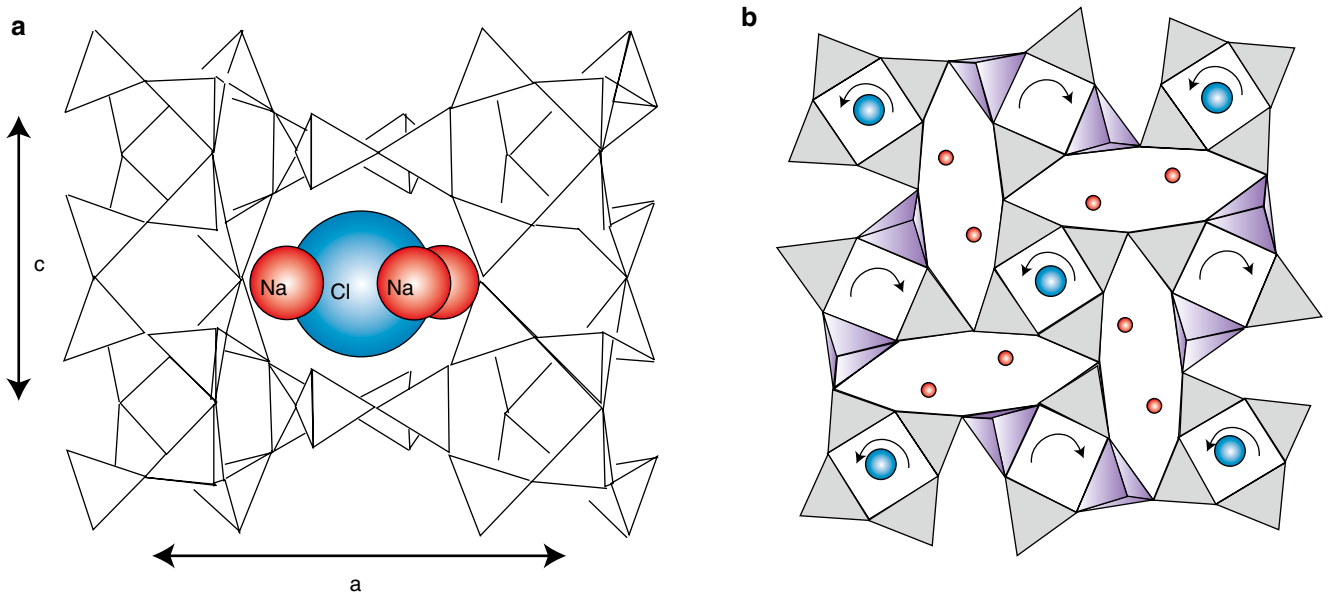

Fig. 14.13 Scapolite structure. (**a**) The [100] projection of the structure of marialite showing the cage-like structure and the linkage of the (Si,Na)—O tetrahedra parallel to the c axis. (**b**) [001] projection of the crystal structure of scapolite. Small circles represent cations (Na), larger circles represent anions (Cl). The *arrows* indicate the sense of rotation of the four-membered tetraheda rings with increasing pressure, this compaction releases the Na and Cl ions from their lattice cages (Modified from Comodi et al. 1990)

Greenough 1999). Conversely, where scapolite is distributed as fine-scale interbedded units of scapolite-bearing and scapolite-free layers that differ only in their Cl content, it argues strongly for an *in situ* salt precursor. This section will focus on scapolites interpreted as metaevaporites in continental regions with a significant sedimentary halite protolith (Table 14.3). For scapolite-anhydrite exhalites formed in seawater-influenced hydrothermal systems, Jiang et al. (1994) or Kribek et al. (2002) are good starting points, for nonevaporitic scapolitic skarns see Pan et al. (1994).

Its cage-like lattice structure means that scapolite acts as a source or sink for a number of volatile species in the metamorphic realm (Cl^-, CO_3^{2-} and SO_4^{2-}). Once a metasedimentary sequence passes beyond the early greenschist stage, scapolite takes over from halite as the most likely potential source for chloride volatiles. As metamorphic grade increases, pressure increases, and the lattice compresses by rotating its tetrahedra (Fig. 14.13b; Comodi et al. 1990). As this happens the Cl^- content of the scapolite decreases as the squeezed lattice releases Cl^- and other stored volatiles in the large diameter lattice cages. Meier (1979) highlighted the importance in Precambrian terranes of scapolite, scapolite-diopside, and scapolite-diopsideamphibolite-feldspar assemblages as ongoing saline (volatile) sources, long after halite disappeared in the early greenschist realm. Mora and Valley (1989) rejected the notion that most scapolitic assemblages were the result of Cl-rich fluid infiltration/metasomatism mostly tied to late-stage magmatic brines, instead they concluded that most metamorphic scapolite formed by the reaction of plagioclase with calcite and halite.

Whatever the ultimate Na and Cl source, most scapolite forms via the metamorphic alteration of plagioclase feldspar. As a consequence, albitization and scapolitization are typically co-associated metamorphic outcomes. The entire scapolite series can be considered to be analogous to the plagioclase series (Fig. 14.14a). If the formula of marialite is written as $3(Na(Al, Si)_4O_8)NaCl$, it is clear how well it matches the formula of the sodium-rich plagioclase, albite, $NaAlSi_3O_8$. A similar look at meionite's formula, $3(Ca(Al,Si)_4O_8)CaCO_3$, shows that it too is near three times the formula of anorthite, $CaAl_2Si_2O_8$. Along these lines, Reinhardt (1992) noted the formation of scapolite in metaevaporitic terranes of the Mary Kathleen region, Australia, can be expressed by end member reactions noted in Orville (1975):

$$3\text{Albite} + \text{NaCl} \leftrightarrow \text{Marialite}$$

$$3\text{Anorthite} + \text{CaCO}_3 \leftrightarrow \text{Meinonite}$$

$$\text{Anorthite} + \text{CaSO}_4 \leftrightarrow \text{SO}_3 - \text{Meinonite}.$$

Addition of the extra sodium chloride or calcium carbonate occurs during metamorphism, as do substantial alterations of the original lattice structure during ongoing compression. Although nearly pure albite and anorthite specimens are sometimes found in nature, pure forms of meionite and

Table 14.3 Worldwide examples of scapolites and scapolitization

Occurrence	Age	Features	Reference
Scapolite-bearing Rocks from Lapis Lazuli Deposits at Sar e Sang, Afghanistan	Neogene cooling	E. Scapolite and other halogen-rich minerals (phlogopite, amphibole, apatite, titanite and clinohumite) occur in some high-pressure amphibolite facies calc-silicates and orthopyroxene-bearing rocks. Peak P-T metamorphic conditions are 750 C and 1.3–1.4 GPa. Protolith was evaporite-bearing carbonates now indicated by scapolite, F- or Cl-rich apatite, and amphibole forming bands and layers or hosted in veins crosscutting sodalite group minerals, including lapis lazuli	Faryad (2002)
Contact metamorphicmetasomatic halo, Italian Mountain granite intrusion, Gunnison Co., Colorado	Eocene (latest)	E. Near- vertical Pennsylvanian black shales and carbonates along the west margin of the intrusive were converted to phlogopite-diopside-andalusite hornfels and scapolitediopside skarns with minor analcime Dissolution of once nearby halite or saline surface waters or shallow groundwaters moving south from the Eagle Basin supplied the NaCl	Mauger (2007)
Andean Iron belt southwest of Mendoza, Argentina.	Cretaceous	Granite-related skarn overprints the earlier diorite-related skarn and consists of garnet + clinopyroxene + scapolite (Me_{28-36}) quartz alkali feldspar endoskarn and a zoned exoskarn with proximal garnet clinopyroxene quartz, intermediate green garnet + clinopyroxene, and distal scapolite (Me_{25-36}) ferroactinolite pyrite veins	Pons et al. (2009), Franchini et al. (2007)
Andesitic volcanics in the Ningwu terrestrial basin, East China	Cretaceous	E. Iron oxide-apatite deposits with abundant scapolite in albitized breccia skarn zones composed of diopside-magnetite-scapolite, magnetite-apatite-diopside-calcite, quartzpyrite-hematite-kaolinite-anhydrite-carbonate Overlain by evaporitic Triassic lacustrine redbeds	Mao et al. (2008)
Magnetite iron ores, Anatolia region, Turkey	Cretaceous	E. Volcanic or subvolcanic rocks and are associated with a voluminous scapolite ± amphibole ± biotite alteration, derived from Late Mesozoic brine infiltration	Marschik et al. (2008)
Cordilleras Béticas, Spain	Alpine metamorphism	E. Permo-Triassic pelite-carbonate rock series (with intercalated evaporites and metabasitic rocks) in the, was metamorphosed during the Alpine metamorphism at high pressures (P_{min} near 18 kbar) Scapolite, rich in NaCl (Ca/(Ca + Na) mol% 24–40) and poor in SO_4, with Cl/(Cl + CO_3) ratios between 0.6 and 0.8, formed as porphyroblasts, sometimes replacing up to 60 % of the rock in a late stage of metamorphism (between 10 and 5 kbar, near 600 °C)	Gómez-Pugnaire et a. (1994)
Muzkol metamorphic complex in the Central Pamirs, Tajikistan	Alpine metamorphism	E. Calcite marbles contain corundum together with muscovite, scapolite, and biotite, with the scapolite is rich in marialite (60–75 mol %). The isotopic-geochemical characteristics numerical simulations of the fluid-rock interactions indicate that the corundumbearing metasomatic scapolitic rocks developed after originally sedimentary Phanerozoic carbonate rocks, with the desilicification of the terrigenous material. Neogene cooling age in Archaean-age host	Dufour et al. (2007)
Humboldt lopolith, N.W. Nevada	MidJurassic	E. Scapolite occurs: (1) as a pervasive replacement of plagioclase in gabbro, diorite and extrusive rocks; (2) as a poikiloblastic mineral in scapolite dykes; and (3) as a fracturefilling mineral with analcite, albite and sphene in scapolite veins. The likely source of Na and Cl is pre-existing evaporites or evaporite brines derived from wallrocks. Salinity may have been increased sufficiently to stabilize scapolite by hydration of dry magmas, possibly aided by hydrothermal boiling. Marialitic scapolite grew at temperatures around 400 °C from NaCl-H_2O fluids having more than 40 mol% NaCl (conditions needed to stabilize the scapolite)	Vanko and Bishop (1982)
Scapolite pegmatite from the Minas fault at McKay Head, Nova Scotia	Carboniferous	E. Pegmatite cutting chlorite schist in the Minas fault at McKay Head, Nova Scotia, consists of Cl-rich (2.7–3.8 wt.% Cl) marialitic scapolite (EqAn(21–32)) with interstitial, apparently primary analcite, hematite and rutile, and later (including vug-lining) analcite, pyrite, chlorite, titanite and calcite, and cross-cutting epidote veins. Derived from highly sodic hydrothermal solutions from early Carboniferous evaporites of the Windsor/Horton groups. Compositionally-similar fluids, also related to an evaporite source, may be responsible for a regional, early Carboniferous Na-metasomatic event that altered a suite of alkaline granitoid intrusions shortly after their emplacement	Owen and Greenough (1999)

Dolomite marble, Prosetin (Olesnice Unit, Moravicum), Czech Republic	Late Palaeozoic	E. Scapolite ($Me_{41–49}$) in Is rich in Cl (1.30–2.20 wt. %), does not contain SO_3 and forms small as nests, containing also phlogopite and zoisite. Host-rock mineral association suggest prograde metamorphic growth and support a meta-evaporitic origin of the plagioclase-muscovite-scapolite rocks. See also, Kribek et al. (2002)	Opletal et al. (2007), Bacik et al. (2012)
Scapolites in the Metamorphic Mozambique Belt, Africa	Neoproterozoic	E. Scapolitic meta-evaporites intercalated with metasomatized graphitic rocks such as graphitic gneiss and calc-silicates. Tsvorite gemstone association	Feneyrol et al. (2013)
Ketri Copper Belt, Rajasthan, NW India	Neoproterozoic	E. A 50 km wide by >100 km zone of calc silicate and albite-hematite alteration overprints and cross-cuts metamorphic fabrics. Calc silicate alteration comprises coarsegrained clinopyroxene – hornblende – epidote – apatite – scapolite – titanite – magnetite, whereas albite – hematite alteration comprises assemblages of albite – amphibole hematite – magnetite – calcite, with variable K-feldspar, biotite, epidote, scapolite, titanite, apatite and fluorite, and locally abundant pyrite and chalcopyrite. Calc silicate alteration occurs on the margins of the Khetri Copper Belt, whereas albite-hematite alteration forms a central core to the Belt and locally overprints calc-silicate assemblages	Knight et al. (2002)
Mary Kathleen Foldbelt, Queensland, Australia	Mesoproterozoic	E. Intrusion of Wonga Batholith and equivalents were emplaced between 1,760–1,720 Ma coincident with the Wonga extension. This was accompanied by widespread NaCl scapolitization, skarn development and Na-(Ca)-K metasomatism. The highly evaporitic Corella Fm was the source of salt driving the chemistry of this metasomatic event	Ramsay and Davidson (1970), Oliver et al. (1992), Hammerli et al. (2014)
IOCG associations, Fennoscandian Shield, Norway	Mesoproterozoic	E-Scapolite formed during repeated extensional and compressional events at 3.1–1.8 Ga, and is part of an iron ore province characterized by regionally developed albite and scapolite alteration and the occurrence of world class Fe-oxide (e.g. Kiirunavaara)	Martinsson et al. (2008), Frietsch et al. (1997)
Sveconorwegian metamorphic event, Southern Norway	Mesoproterozoic	E. Scapolitization was associated with veining, and was followed by albitization, transforming metagabbros pervasively over large areas. Plagioclase was replaced by Cl-rich scapolite (Me_{19-42}) reflecting Cl-saturation, while K- and Mg-saturation produced phlogopite, enstatite, sapphirine and rare corundum The sodic brines responsible for this alteration were probably evaporite derived and remobilised	Engvik et al. (2011)
E. Blackbird District, East-Central Idaho, USA	Mesoproterozoic	E. Thrust faulting juxtaposed meta-evaporite layers in the Mesoproterozoic Yellowjacket Formation over Blackbird district host rocks that facilitated chemical exchange between juxtaposed units resulting in leaching of critical elements (Cl, K, B, Na) from meta-evaporites to produce brines, mineralisation and scapolites	Lund et al. (2011)
Wernecke Breccia, Wernecke Mountains, Canada	Mesoproterozoic	E. Scapolites in the regionally-distributed brecciation in the; associated with hydrothermal alteration with saline brines from former salt décollement, now rauhwacke	Kendrick et al. (2008)
Lutzow-Holm Complex, East Antarctica	Paleo to Mesoproterozoic	E. Spectacular reaction textures in poikiloblastic scapolite boudins, within outcropping marbles. Core composition of scapolite poikiloblasts (Scp(I)) are marialitic (Cl = 0.7 apfu) whereas rims in contact with biotite or clinopyroxene are meionite rich. Finegrained recrystallized equigranular scapolite (Scp(II)) shows prominent chemical zoning, with a marialitic core and a meionitic rim (Cl = 0.36 apfu). Scapolite poikiloblasts are traversed by Scp(III) reaction zones along fractures with compositional gradients	Satish-Kumar et al. (2006)
Aravalli metasediments, NW India:	Paleoproterozoic	E. Scapolite occurs in succession dominated by amphibole-bearing dolomitic marble and albite-rich quartzo-feldspathic rocks (QFR). The presence of vugs, believed to be after dissolution of halite patches, coupled with the development of scapolite-bearing assemblages in dolomite marble, occurrence of tourmaline-rich mineralized rocks and very high Na content of carbonates and QFR indicate hypersaline depositional environment for the protolith	Golani et al. (2002)
Carajas Mineral Province, Brazil	Archaean	E. Tourmaline pre-dates mineralization, and is abundant as coarse porphyroblasts or fine-grained layers alternating with albite, quartz, and scapolite in sodic-altered mylonitic metavolcanic rocks. These rocks have been subjected to an early sodic alteration (albite and scapolite) followed by more pervasive and widespread potassium and chlorite alterations, silicification, carbonatization, and minor epidotization. K alteration is accompanied of magnetite formation	Xavier et al. (2008)

E indicates a meta-evaporite association

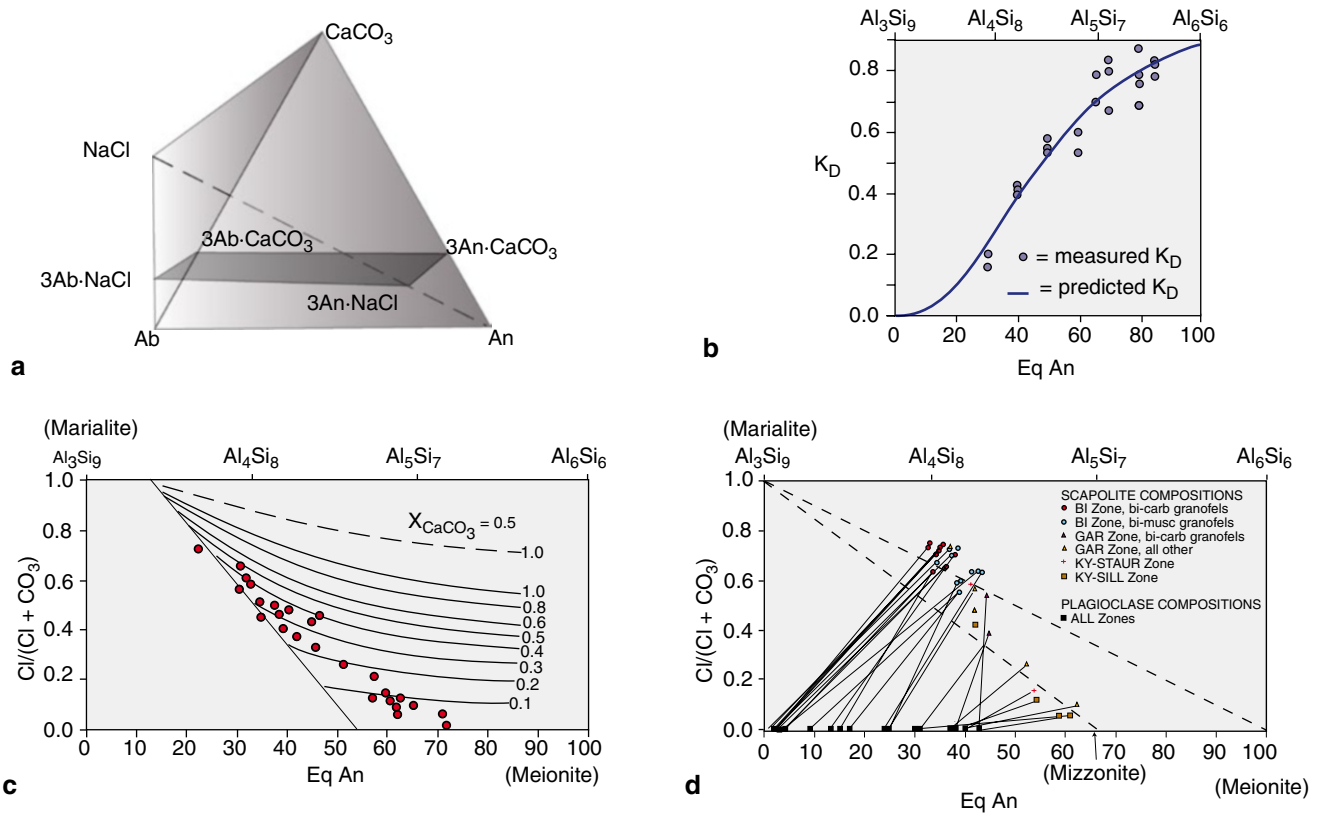

Fig. 14.14 (**a**) Compositional space for marialite-meionite. The shaded region is the theoretically possible plane of scapolite compositions (*Ab* albite, *An* anorthite). (**b**) Measured values of K_D for the reaction $NaCl_{(scap)} + CaCO_{3(fl)} = CaCO_{3(scap)} + NaCl_{(fl)}$ at 750 °C and 4,000 bar plotted against EqAn. The predicted line $LnK_D = (-0.0028)[Al/Al+Si]^{-5.5580}$ is shown for comparison. (**c**) The correlation between scapolite composition and fluid composition at 750 °C and 4,000 bar predicted by the equation $LnK_D = (-0.0028)[Al/Al+Si]^{-5.5580}$. Lines of equal $NaCl/(NaCl+H_2O)$ in coexisting fluid are shown. The compositions of natural scapolites are shown as *black dots*. (**d**) Compositions of coexisting scapolite and plagioclase in the Wallace Formation, Idaho. Plagioclase compositions are plotted along the horizontal axis. *Dashed lines* are solid solutions between marialite, meionite and mizzonite. In general, Cl in scapolite decreases with increasing metamorphic grade; but compositional variations within each grade suggest local control of fluid and scapolite compositions (**b** and **c** after Ellis 1978; **d** after Mora and Valley 1989)

marialite are unknown. Natural scapolites have compositional limits between 17.4 and 87.3 % of the meionitic component (Me) calculated as

$$Me = \frac{[Ca + Mg + Fe + Mn + Ti]}{[Ca + Na + K + Mg + Fe + Mn + Ti]}$$

Marialite corresponds to the compositions $Me_{0\text{-}20}$, and meionite to $Me_{80\text{-}100}$. Intermediates $Me_{20\text{-}50}$ and $Me_{50\text{-}80}$ are known as dipyre and mizzonite, respectively.

Minerals of the scapolite group have received considerable attention in metamorphic petrology due to their rather wide field of stability, which extends from late diagenetic to high temperature and high pressure crustal conditions. An understanding of variations in NaCl-scapolite (marialite) and $CaCO_3$-scapolite (meinonite) mineralogy is useful when studying the relationships between scapolite-plagioclase-halite reactions, metamorphic conditions, and the nature of the fluid phase.

Ellis (1978) considered the equilibrium between scapolite and a fluid, for a scapolite of fixed EqAn content, from exchange of the NaCl components:

$$NaCl_{(scapolite)} + CaCO_{3(fluid)} = CaCO_{3(scapolite)} + NaCl_{(fluid)}$$

at 750 °C and 4 kbar:

$$KD = \left[\left(X^{Scap}_{CaCO_3}\right)\left(X^{fluid}_{NaCl}\right) / \left(X^{Scap}_{NaCl}\right)\left(X^{Calcite}_{CaCO_3}\right)\right]$$

where X^i_j is the mole fraction of NaCl or $CaCO_3$ (i) in the respective phases (j). This he fitted to an expression

$$\ln K_D = -0.0028\left(X_{Al}\right)^{-5.5580}$$

where X_{Al} is the atomic Al/(Al+Si) ratio in scapolite (Fig. 14.14b). He went on to suggest that if the mixing is ideal, the activity of NaCl in fluids coexisting with scapolite grown at

temperatures and pressures, other than those of the experiment, can be calculated from this equation for K_D (Fig. 14.14c). This implies that Cl-poor natural scapolites coexisted with fluids low in NaCl and that regional occurrences of Cl-rich scapolites are likely to represent metamorphosed evaporite sequences.

Experimental results of Ellis (1978) were used by Mora and Valley (1989) and Oliver et al. (1992) in studies of meta-evaporite paragenesis to estimate the salinity of the metamorphic fluids based on the composition of Cl-bearing scapolite. Mora and Valley found that abundant Cl-rich scapolite and biotite in the Wallace Formation, Idaho, indicate high Cl activities during greenschist-through amphibolite-facies regional metamorphism of evaporite entraining metasedimentary rocks (Fig. 14.14d).

In general, Cl in scapolite decreases with increasing metamorphic grade; but compositional variations within each grade suggest local control of fluid and scapolite compositions probably related to the original distribution of halite in the sequence. The abundance of Cl-rich phases decreases abruptly with the appearance of zoisite-bearing assemblages, suggesting infiltration of low-Cl H_2O at higher metamorphic grades. The occurrence of buffered activity gradients in Cl, as indicated by scapolite and biotite compositions, also suggests that metamorphic fluid flow was highly channelized and aqueous fluid-rock interaction was limited. Similar channelisation defines scapolite distribution in the meta-evaporitic Corella Formation in the Mt Isa inlier.

Scapolite is a common mineral in the Lower Proterozoic metamorphic rocks of the Mary Kathleen area, Queensland. Australia (Ramsay and Davidson 1970). There, its occurrence in a wide range of host rock compositions, calcareous and non-calcareous metapelitics, acid and basic metavolcanics, and metadolerites, made it one of the first areas where the detailed relationships between scapolite composition and saline rock compositions were explored. The grade of metamorphism throughout is amphibolite facies. Calcareous metapelites are very sodic, and scapolite in the calcareous metapelites is more marialitic than that in intercalated low-calcium equivalents. The scapolite composition in all groups of meta-igneous rocks in the region varies through a similar range and is opposite to that of the metasedimentary group. Ramsay and Davidson (1970) concluded that the metasedimentary scapolite originated by isochemical metamorphism of shales and marls containing evaporitic halite, the local abundance of which was the main control on the composition and distribution of the scapolite. Thus the calcareous shales, which contained considerable halite, crystallized as marialitic scapolite (Me_{32}-Me_{52}), while the low-calcium equivalents formed a meionitic scapolite (Me_{50}-Me_{60}). In contrast the scapolite in the meta-igneous rocks formed metasomatically during regional metamorphism by the introduction of volatile-rich fluids derived from the adjacent evaporitic sediments (see later for more detail).

In applying geothermic postulates to their Cl-rich scapolites, Mora and Valley (1989) recognized limitations in the work of Ellis (1978), such as too high a temperature in the experiment for many meta-evaporites, and the high degree of uncertainty in terms of the nature and composition of the NaCl-H_2O-CO_2 fluid including the degree of immiscibility.

Generally, at temperatures up to 400–500 °C, the NaCl in scapolites may be derived directly from solid halite or associated highly-saline NaCl waters, that is, it is associated with the reaction:

$$\text{NaCl} + \text{plagioclase} + \text{calcite} \rightarrow \text{scapolite}.$$

At higher temperatures, the production of H_2O and CO_2 from devolatilisation reactions in adjacent metasediments tends to dissolve the remaining solid halite (Skippen and Trommsdorff 1986; Oliver et al. 1992). Scapolite growing in palaeo-evaporitic metapelites at temperatures above 400–500 °C is probably not in equilibrium with halite but with a halite-undersaturated NaCl-bearing fluid. Some minor dispersed halite may remain up to the melting point of halite at 750–800 °C. For example, minor solid inclusions of halite have been found in several samples of calcsilicate rocks from Switzerland and northern Italy that have been metamorphosed to lower amphibolite grade, with the development of talc and tremolite. Such idiomorphic crystals and dendrites of halite have been analysed and show a range of compositions in the system NaCl-KCl, which indicate temperature maximums greater than 500 °C and pressures of 2 kbar or higher (Trommsdorff et al. 1985).

Gómez-Pugnaire et al. (1994) found that the existing well-studied relationships and assumptions of the alliance between scapolite, calcite and plagioclase (e.g. Aitken 1983) were not the explanation of the meta-evaporitic scapolites of the Cóbdar region of Spain. There biotite, not albite, was involved with halite in scapolite formation and the scapolite is a retrograde mineral phases. This Permo-Triassic pelite-carbonate rock series (with intercalated metabasitic rocks) in the Cordilleras Beticas, Spain, was metamorphosed during the Alpine metamorphism with peak metamorphism at eclogite facies with high pressures (P_{min} near 18–22 kbar) and relatively low temperatures (≈650 °C). These evaporitic metapelites have a whole rock composition characterised by high Mg/(Mg + Ca) ratios >0.7, variable alkaline and Sr, Ba, contents, but are mostly K_2O rich (<8.8 wt%). The F (<2,600 ppm), Cl (<3,600 ppm), and P_2O_5 (<0.24 wt%) contents are also high. The pelitic member of this series is a fine-grained biotite rock, where kyanite-phengite-talcbiotite clusters in pseudomorphs developed in the high pressure stage. Albite-rich plagioclase was formed when the rocks crossed the albite stability curve in the early stages of the uplift. Scapolite, rich in NaCl [Ca/(Ca + Na) ≈ 24–40 mol%] and poor in SO_4, with Cl/(Cl + CO_3) ratios between 0.6 and 0.8, formed as porphyroblasts, sometimes replacing up to

60 % of the rock in the later decompressional stage of metamorphism (between 10 and 5 kbar, near 600 °C).

That is, the Spanish scapolites are rich in Na and poor in CO_3. Plagioclase is not consumed by scapolitization; but biotite, the most important matrix material, almost completely disappears in areas of scapolite blastesis. Gómez-Pugnaire et al. (1994) conclude that these Spanish scapolites formed during retrograde metamorphism from a biotite precursor by the reaction:

$$\text{Al-biotite} + \text{CaCO}_3 + \text{NaCl} + \text{SiO}_2 = \text{Al-poor biotite} + \text{scapolite} + \text{MgCO}_3 + \text{KCl} + \text{MgCl}_2 + \text{H}_2\text{O}$$

The rocks, even though at amphibolite grade, still retain well preserved sedimentary indicators of former evaporites, such as pseudomorphs after sulphate evaporites, which are now composed of talc, kyanite-phengite-talc-biotite, and quartz. In addition, there are relicts of baryte, anhydrite, NaCl and KCl still present in the rock matrix. All the metasedimentary evidence indicates a salt-clay mixture as the protolith, which was dominated by illite, chlorite, talc, and halite. Calculated fluid composition in equilibrium with scapolite indicates varying salt concentrations in the fluid, and the distribution of Cl and F in biotite and apatite also indicates varying fluid compositions possibly inherited from the metasedimentary protolith.

Br/Cl ratios were recognised by Pan and Dong (2003) to closely reflect those of its co-existing melts and fluids and so are useful indicators of likely scapolite protoliths and sources of any associated ore-forming fluids, even at amphibolite grade metamorphism. Cl/Br values of marialite in the Tieshan deposit are considerably higher than seawater, but can be explained by the dissolution of halite and sylvite as the mode of origin of the hydrothermal metamorphosing brines (Fig. 14.15a). Likewise, Cl/Br values of scapolite-group minerals in exoskarns of the Nickel Plate deposit are close to those of the Tieshan deposit, and according to Pan and Dong (2003) indicate a similar meta-evaporitic origin. Interestingly, the Nickel Plate gold deposit, some 240 km east of Vancouver, is one of the largest and most important gold-skarn deposits in British Columbia, having produced some 49 tonnes of gold, which is approximately half of all the gold produced from skarns in British Columbia (Pan et al. 1994). The increase in Cl/Br from endoskarn to exoskarn in the deposit is readily attributable to an increased involvement of magmatic H_2O in the former, while the exoskarn values indicate involvement of metamorphosed Triassic evaporites. Similarly, a wide variation in Cl/Br in scapolite-group minerals from the Grenville deposits of Ontario (Fig. 14.15b) is consistent with varying degrees of mixing of

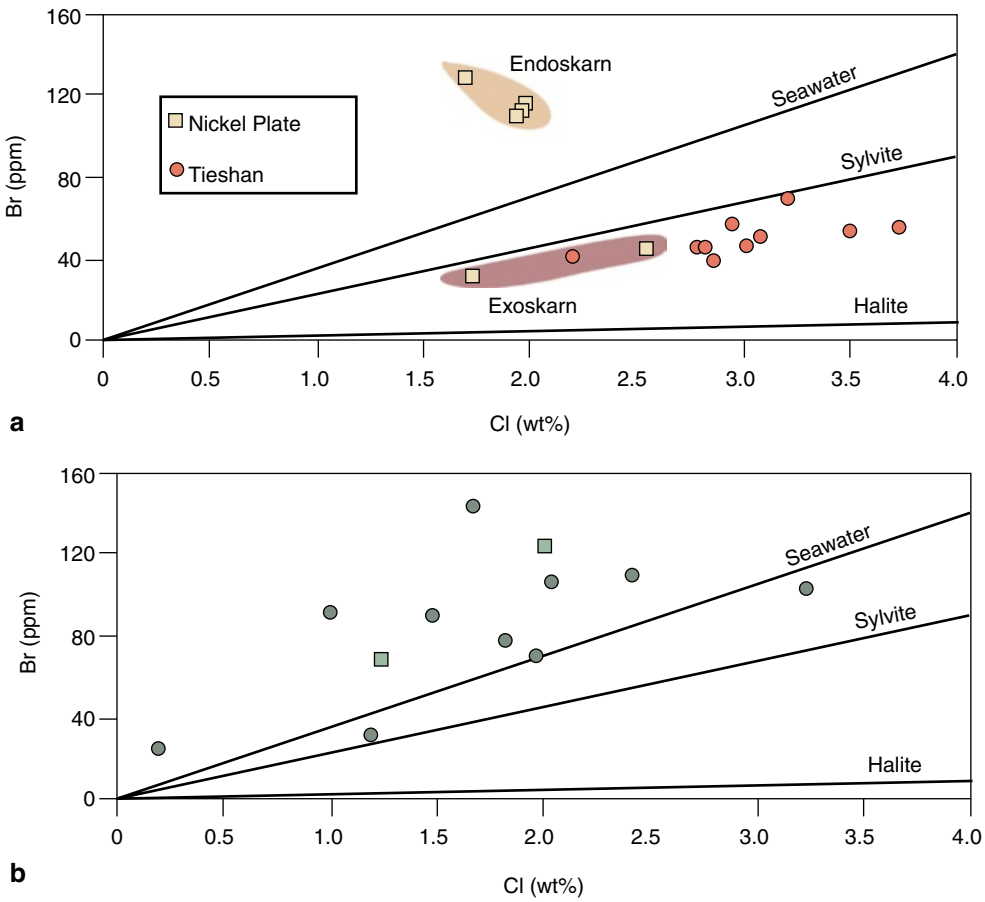

Fig. 14.15 Br (ppm) versus Cl (wt%) plots illustrating scapolite group minerals from: (**a**) the Tieshan, China and Nickel Plate, British Columbia, skarn deposits, and (**b**) the Grenville, Ontario-Quebec, pegmatite, skarn, and vein deposits (Replotted from Pan and Dong 2003)

hydrothermal fluids derived from magmatic sources and associated variably evaporitic sedimentary rocks. In a recent study of scapolites in the Mary Kathleen region, Hammerli et al. (2014) used Br/Cl signatures to refine brine origins and likely protoliths in this amphibolite-grade terrane (see later).

Albitites and Albitization

The process of albitization describes any system of sodic alteration (secondary mineral formation) where the effected rock is partly or completely replaced by albite. Albite-rich rocks are typically termed albitites, but are sometimes referred to as "adinole," "albite felsite," "albite fels" and "alitolite" (Kalsbeek 1992). Albitization can overprint all rock types, sedimentary, metamorphic and igneous, and the sodic solutions driving the albitization can be derived from magmatic solutions or an evaporitic protolith (e.g. Frietsch et al. 1997; Oliver et al. 2004). Oliver et al. (2004) argues albitization, as it is tied to sodic fluids that leached metals, is part of the ore-forming process in the metasedimentary section of the Cloncurry region. Worldwide, albitites occur in intimate association with Iron-Oxide-Copper-Gold (IOCG) deposits and with mineralised zones in the Broken Hill and Cloncurry regions (Chap. 16). As such, there are numerous widespread examples of albitites in Proterozoic and Archaean terranes (Table 14.4).

Albite, the mineral, is one end-member of the plagioclase feldspar series with anorthite constituting the other (Fig. 14.16a). Other members of the plagioclase series (oligoclase, andesine, labradorite, bytownite and anorthite) are defined by variable rations of Na/Ca. Albite is also one end member of the alkali feldspar series with orthoclase as the other, with constituent members of the alkali series being anorthoclase and sanidine and subdivided based on the Na/K ratio. Albitization is a worldwide replacement mechanism and albitites have formed throughout earth history in a wide variety of igneous, hydrothermal and metasedimentary settings (Table 14.4). Albite's thermal stability field, like scapolite, is now thought to encompass temperatures ranges from the early diagenetic (≈40–60 °C) well into the amphibolite facies (≈600 °C). Albitite is often associated with scapolite and mineralogical similarities between the two mineral series were noted in the previous section.

Proposed sources for the Na-rich brines that drive albitisation in the metamorphic realm include: (1) leaching of halite from exhalatives (Bierlein et al. 1996); (2) Dissolution of evaporites (Bierlein et al. 1996); (3) Dehydration reactions (Clark et al. 2005); (4) Magmatic fluids; (5) Fluids derived form the devolatilisation of volcanics; (6) Seawater interactions; (7) Intraformation Na-rich brines (8) Surface-driven infiltration of dense hypersaline brines. Much of the following discussion is centred on albitites tied to evaporites and hypersaline brines, my intention is not to make the case that the majority of the world's albitites are tied to evaporites, clearly there are numerous examples where they are not; but the focus of this chapter is meta-evaporites and for this book is evaporites. For a broader discussion of albitites in a metasomatic[3] framework see Yardley (2013), and work without a focus on deposits tied to evaporites and their dissolution/alteration products, the reader is referred to papers such as Castorina et al. (2006), or Azer et al. (2010) and the references therein.

In the diagenetic realm, halite dissolution supplies much of the sodium for albitization, while the albitisation of pre-existing sedimentary feldspars is an important source of Ca to basinal brines. These brines continue to be important in the metamorphic realm (Fig. 14.12; Yardley 2013). Ramseyer et al. (1992) noted that deeply buried plagioclase grains in sandstones are commonly albitised, especially when bathed in more-saline basinal brines. For example, massive albitization of feldspars (both plagioclase and alkali feldspar) occurred during burial diagenesis at depths greater than 4,000 m in the Oligocene Frio Formation (Texas) over much of its extent in the Gulf of Mexico. Albitization was intimately associated with the circulation of Na–Ca–Cl basinal brines and is tied to its sodium supply via massive dissolution of deeply buried salt (Land and Milliken 1981). Albitization has developed in several other sandstone formations of the Gulf Coast Tertiary between 2,500 and 2,870 m depth at temperatures between 110 and 120 °C and can supply Ca to the basin brines (Fig. 14.16b; Boles 1982). Quartz and albite also formed diagenetically in Devonian limestone's of the Belgian Ardennes during burial diagenesis at temperatures less than 90 °C (Molenaar and de Jong 1987).

Albitization did not begin in Tertiary clastic reservoir sandstones in the North Sea at depths less than 2,000 m and at 65–145 °C (Saigal et al. 1988; Aagaard et al. 1990; Morad et al. 1990). Consequently plagioclase albitization is seen from a sedimentological viewpoint as occurring during in burial diagenesis and is driven by the circulation of saline basinal brines at temperatures between 75 and 160 °C (Ramseyer et al. 1992; Saigal et al. 1988; Aagaard et al. 1990; Morad et al. 1990; Ben Baccar et al. 1993). These sodic brines tend to be well developed in basins with thick deeply buried halite masses subject to burial dissolution (e.g. examples 1–6 in Fig. 14.12).

[3]Metamorphism and metasomatism both involve the re-equilibration of mineral assemblages due to changes in pressure, temperature and/or chemical environment. Both processes involve material transport but on different length scales, so every metamorphic reaction is metasomatic on a local scale. Fluids provide a transport mechanism which is orders of magnitude faster than solid state diffusion and induce re-equilibration through dissolution of parent phases and reprecipitation of products (Putnis and Austrheim 2010).

Table 14.4 Worldwide examples of albitites

Time	Africa	Americas	Asia	Australia	Europe and adjacent
Mesozoic/ Cenozoic	Hercynian of northern Africa (Hill 2003)	Chilean coastal batholith (E – Chiaradia et al. 2006); Chilean Coastal Cordillera (Hopper and Correa 2000) Hanging wall association to Columbian emerald occurrences (Branquet et al. 1999)	Ningwu Basin, Cretaceous, China (Mao et al. 2008); Mlakawa albitite, NE Iraq (Mohammad et al. 2007)	–	Stratabound Zechstein Copper deposits, Poland (E – Kucha and Pawlikowski 1986); Morvan Massif, France (*E* – Parcerisa et al. 2010) Volcaniclastics in vicinity of the Gemsbach fault zone (E – Brockamp et al. 1994); Northeast German Basin (Paulick and Breitkreuz 2005); Streltsovka U-deposit (Chabiron et al. 2003)
Palaeozoic	Hercynian sandstones, North Africa (Hill 2003)	Spruce Lake Nappe, Northern New Brunswick, Canada, (445–425 Ma; Van Staal et al. 2001)	Later Caledonian alteration, Bayan Obo, North China (E?- 555–420 Ma; Smith and Chengyu 2002)	(E) Carbonatite diatreme, Umberatana, South Australia (E – Lottermoser 1988) Blue Tier Batholith, NW Tasmania (Sun and Higgins 1996)	Menheniot, Porthleven, Cornwall, and Palaeozoic sediments in the Western Approaches, UK (E – Gleeson et al. 2001); Eastern Belgium (Heijlen et al. 2001) Hercynian granodiorites, Sardinia (Fiori and Grillo 2002)
Neoproterozoic	Kimbambale basalts, central Shaba, Zaire (E – Kampunzu et al. 2009) Damara Belt, Namibia (E – Chetty and Frimmel 2000; Frimmel and Jiang 2001)	Indian Head Range, Newfoundland (E? – Owen et al. 2003)	Bayan Obo, North China (E? – Smith and Chengyu 2002) Wai Tarr Albitite, Sinai (605 ± 13 Ma; Azer et al. 2010)	Copperhead Albitite 'Carbonatite' Complex (860–800 Ma; Rugless and Pirajno 1996)	Albitites, scapolites and tourmalinites in the Svratka Window, near Prosetín (Olešnice Unit, Moravicum, Czech Republic (E., Bacik et al. 2012)
Mesoproterozoic		Albite gneisses, northeastern Adirondack Mountains, New York (Whitney and Olmsted 1988) Belt-Purcell Basin, vicinity Sullivan Mine, Canada (E – Jiang et al. 1999)	Bastar Pegmatites, Central India (1,345 ± 22 Ma; Lamba and Agarkar 1988)	Fluid flow, Olary region, SA (E? – Clark et al. 2005); Gawler Craton, SA (E – 1,570–1,595 Ma; Corriveau 2007; Davidson et al. 2008)	Albitites formed in the Sveconorwegian metamorphic event, Bamble and ModumKongsberg sectors, South Norway (E- Engvik et al. 2011)
Paleoproterozoic	Faleme, Eastern Senegal (E – Bassot 1997); Phalaborwa deposit, South Africa (≈2,060 Ma; Harmer 2002; Corriveau 2007); Corriveau et al. 2009)	Wernecke Mountains, Yukon, Canada (E Hunt et al. 2005) Wollaston Domain, Precambrian Shield, northern Saskatchewan, Canada (Giblin and Appleyard 1987)	Aravalli Metasediments (E – 2.3–2.6 Ga; Golani et al. 2002) Fe-Cu deposits in Kangdian region, SW China (E – Zhao and Zhou 2011)	Curnamona-Broken Hill region, SA-NSW (E – 1,580–1,700 Ma; Conor and Preiss 2008; Cook and Ashley 1992) MacArthur Basin (E – 1,640–1,680 Ma; Davidson 1998) Eastern Foldbelt, Mt Isa Inlier (E – 1,640–1,680 Ma; Rubenach et al. 2008; Polito et al. 2009)	Northern Fennoscandinavia (E – 1.9 Ga; Frietsch et al. 1997) Kiruna region ,e.g. Kiirunavaara Deposit, Norway (E – Gleeson and Smith 2009); Disko Bugt region, Greenland (E – Kalsbeek 1992; Ryan and Escher 1999)
Archaean	Pietersburg granite-greenstone terrane, South Africa (Barton et al. 1990) Murchison Greenstone Belt, Transvaal, (Nwe and Morteani 1993) Kilo-Moto Au district Democratic Republic Congo (Milesi et al. 2006)	Igarapé Bahia, Carajas, Northern Brazil (E – Dreher et al. 2008)	–	Yanda Greenstone Belt, WA (Eilu et al. 2001)	–

E indicates albitites with a likely meta-evaporite association

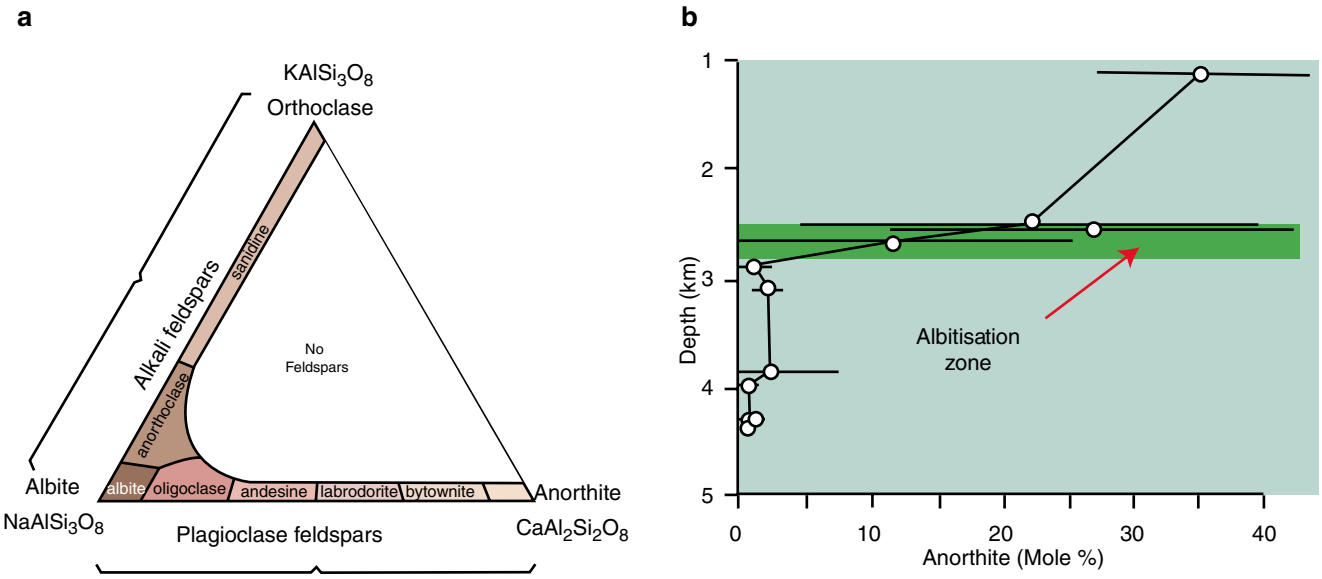

Fig. 14.16 Feldspar and albitisation. (**a**) Feldspar mineral series. (**b**) Increasing albitization of anorthite feldspar with depth in the Frio and Wilcox sandstones, Gulf of Mexico. Significant increase in albitization at 2,500–3,000 m depth (After Boles 1982)

An interesting variation on this burial diagenetic sedimentary story is seen in igneous strata that make up the Hercynian Morvan Massif (Parcerisa et al. 2010). The Massif, in the northern part of the French Massif Central, consists of granite and some rhyolite. A Triassic erosional unconformity sits atop the massif, which is in turn covered by Mesozoic sediments of the Paris Basin (Fig. 14.17). Igneous rocks of the Morvan Massif show strong alteration via; (1) the pseudomorphic replacement of the primary plagioclases with albite, (2) the pseudomorphic replacement of primary biotite with chlorite and, (3) minor precipitation of neogenic minerals like albite, chlorite, apatite, hematite, calcite and titanite. The geometry and arrangement of these alterations indicates the likely diagenetic control on their development. Some altered facies are pervasive in the massif; others are restricted to centimetric to metric-wide joints and imply fluid-flow phenomena. Moreover, the alteration facies show a clear depth-related succession with strongly altered facies at the top of the massif and immediately below the unconformity, while the intensity of alteration weakens with depth. This points to a genetic relationship of albitization to the Triassic unconformity.

Regionally, the distribution of the alteration halo, which overprints a variety of Carboniferous igneous and volcanic formations beneath the Jurassic sedimentary cover, is tied to the presence the Triassic unconformity (Fig. 14.17b, c, but not 14.17a) and not to fluids from the emplacement of the granite massif. Parcerisca et al. (2010) noted an even more interesting result; the alteration haloes are Triassic (not Hercynian), and so have the same age as the unconformity not the emplacement time of the basement. Taking into account all these geological constraints, and the widespread evidence of former now dissolved Keuper halite beds atop the unconformity, Parcerisca et al. (2010), proposed that albitization of the Morvan Massif was developed under low temperature diagenetic conditions, which were tied to a brine hydrology related to the Triassic paleosurface and not to contact metamorphic fluids related to the emplacement of the granite massif (Fig. 14.17c).

Across the metamorphic realm, examples of albitization abound, especially in the Precambrian, some with their sodium supply tied to meta-evaporites, others tied to magmatic fluids (Table 14.3). Compared to Phanerozoic examples, a direct tie to evaporites is less obvious in most of the Precambrian cases listed in Table 14.3. There are a number of reasons for this. First, the further back in time, and/or the higher the metamorphic grade or temperature of formation, the less likely it is that *prima facie* evidence is preserved of the primary mineral phases that tie to the source the sodic solutions responsible for the albitization. Second, beyond the Paleoproterozoic, the less likelihood there is of direct analogs to models within a framework of modern plate tectonic analogs to explain the source of sodium; this is true for both the igneous and meta-sedimentary fluid explanations. Third, as yet, there is no consensus in terms of world-scale models of plate movement and driving forces for basin scale sodic fluid movement in the early Archaean world (Ernst 2009 and earlier discussion in this chapter).

But there is direct evidence in preserved metasediment-volcanic greenschist associations that the Archaean greenstone world was a much more volcanigenically-driven system than today, and that Na-carbonates were likely the dominant evaporite marine precipitates. The question to be considered in the various Precambrian albitite associations is

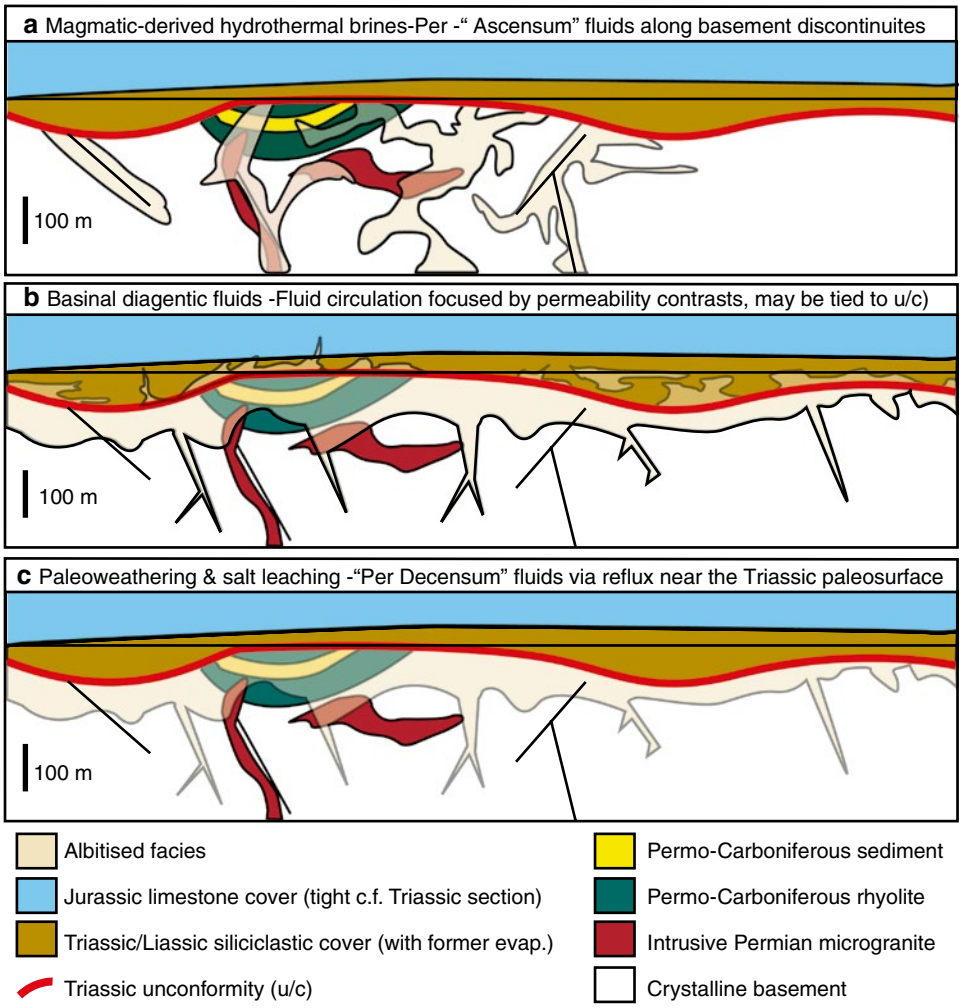

Fig. 14.17 Distribution of the albitised facies relative to three possible hypotheses as to the origin of the albitization: (**a**) Sodic solutions are hydrothermal brines associated with later stages of emplacement of igneous bodies and formed prior to the formation of the unconformity and deposition of Triassic sediments. Albitite geometries are related to fault and shear discontinuities within the basement and do not need to be located near the Triassic unconformity, (**b**) Sodic solutions are associated with Na-Ca-Cl basinal brines derive from deep subsurface dissolution of salt. Solutions flow preferentially along permeable sands beneath a relative seal created by the overlying Jurassic carbonates. Albitite geometries are preferentially developed near the contact of the sandstone aquifer and the crystalline basement. (**c**) Sodic solutions are derived via early salt leaching or supergene solutions, so the albitites form a reflux halo at the upper part of the massif, immediately below the unconformity and/or the position of former Keuper salt beds (In part after Parcerisa et al. 2010)

how important was an evolving and very different seawater chemistry to the volume of salts precipitated. Unfortunately, we are trying to decipher a system where time and metamorphism means that primary sodic salt phases and or igneous indicators have long since passed into the realm of polyphase metamorphism, within the various cratonic blocks that now constitute the cores of the world's continents.

Within this metamorphic cloud, Proterozoic albitite associations perhaps retain textural and chemical associations that are more indicative of the primary origin of many albitites that the Archaean association. It may be that the Proterozoic associations, formed in a plate tectonic system more akin to that of today, are also more readily interpreted in terms of formative processes than albitites of the Archaean greenstone world. For example, the Paleo- and Mesoproterozoic metasedimentary/metavolcanic units of the meta-evaporitic Willyama Supergroup of the South Australian Curnamona Province are considered prime examples of regional scale Proterozoic albitization. Petrographic, geochemical and SEM-BSE/edx studies by Schmidt-Mumm and Conor (2008) and Heimann et al. (2013) show that mineral replacement in the albitised units in this succession initially affects plagioclase, followed by K-feldspars, micas and finally Fe-oxides. Replacement thereby progressively reduces K, Ca, Mg, Fe and Ti, the traces of lithophiles (Ba, Sr, Rb, Th, Nb), siderophiles (Co, Ni) and chalcophiles (Cu, Zn, Pb) by orders of magnitude. With progressive intensity of albitization, the light REE are depleted preferentially over the heavy REE, but in intense albitization all REE are depleted.

At the same time, Na (and Al) are enriched while the mobility of Si is conservative and dependent on the affected lithologies, Zr appears the least mobile element. Endproducts of progressive replacement are trace element poor, Na-rich end-member albites and a highly charged, metal-rich fluid. The subsurface course these fluids take can be traced in the form of breccia pipes and dykes with a distinct FeOx-rich, calc-silicate (actinolite, clinopyroxene) bearing matrix. In my opinion, some of these breccias, where I have visited field sites in the Olary Province, do not preclude a halotectonic rather than a purely structural focus during formation. Such breccias, with analogous occurrences in the Cloncurry (Qld, Australia) and Wernecke Mts (Canada), are distinctly

enriched in Fe, Mg, Ca and K and are strongly positively anomalous in Ba, Sr and Rb, Cu, Pb and Zn as well as the REE elements, emphasizing the mineralising potential of the involved fluids. Electron microprobe and Laser Ablation ICP-MS analysis show that these metasomatic reactions gradually affect individual grains, while the influx of Na-rich fluids occurs along microfractures and crystal cleavage plains.

The effects of albitization are well documented in the Olary region, but the driving mechanisms for Precambrian albitization are not (see discussion in Conor and Preiss 2008). The same is true for other areas of Proterozoic and Archaean albitization (Kalsbeek 1992; Dreher et al. 2008). We shall return to this question of sources of sodic solutions when discussing specific Proterozoic and Archaean meta-evaporite examples later in this chapter.

Tourmaline and Tourmalinisation

Tourmaline precipitation encompasses temperatures of ≈150 to >900 °C, pressures of ≈6 MPa to >6 GPa and it can equilibrate with a wide range of geological fluids from the diagenetic to metamorphic, and precipitation sites can include low temperature caprocks atop salt allochthons such as the Challenger Knoll (Henry et al. 2008; Henry and Dutrow 2012). Boron in tourmaline in many meta-evaporite associations comes from the borate salts, while boron is ultimately produced by cosmic ray spallation and not by stellar nucleosynthesis. Hence, B is a low-abundance element in both the solar system and the Earth's crust and is concentrated by the water-solubility of its more common naturally occurring compounds, namely, the borate minerals (such as; borax. colemanite and ulexite – Chap. 12).

Tourmalinite is a common gangue in many massive sulphide and sedex deposits, where hydrothermal alteration associated with seawater convection can be a significant mineralization process (Chap. 16; Palmer and Slack 1989). Tourmaline as dravite and schorl occurs in tourmalinite in the Isua complex, Greenland, which with an age of some 3,650—ca. 3,600 Ma (metamorphic age) is probably the oldest boron mineral reported to date. Tourmaline, the mineral, is typically classified as a semi-precious stone, and gemstone forms come in a wide variety of colours from black to green to red to blue. The name tourmaline comes from the Sinhalese word "*Thuramali*," which is applied to different gemstones found across Sri Lanka.

Borate evaporites (the ultimate borate source for much metaevaporitic tourmaline) are today associated with lacustrine depressions created within zones typified by convergent continental tectonics (Chap. 12). Convergent tectonics is also a commonplace association for tourmaline precursor fluids in metavolcanic and meta-igneous deposits. But, as for albitite, there is a time-based dichotomy in the relative abundance of tourmaline, with tourmalinites with metasedimentary associations being more common in Precambrian protoliths. This is another line of evidence that there were differences in plate tectonic settings and boron fluid distributions in the early Precambrian compared to the Phanerozoic.

Tourmaline, the mineral, encompasses a complex series of aluminium borosilicates with the general formula: $XY_3Al_6Si_6O_{18}(BO_3)_3(OH,F,O)_4$. X represents large cations such as calcium, sodium and/or rarely potassium, while the Y cation represents smaller cations such as iron (+2 and/or +3), magnesium, aluminium, lithium and/or manganese (Table 14.5; Fig. 14.18). The aluminium in the Al_6 site can be substituted for, on a limited basis, by iron and more rarely chromium or vanadium. Fluorine and oxygen substitute for hydroxide in a few of the members and then only to a limited extent. For a full discussion of the various petrogenetic indicators in the tourmaline lattice see Henry and Dutrow (2012).

Table 14.5 Typical members of the tourmaline mineral series

End member	Formula
Schorl*	$NaFe^{2+}Al_6(BO_3)_3Si_6O_{18}(OH)_4$
Dravite*	$NaMg_3Al_6(BO_3)_3Si_6O_{18}(OH)_4$
Oxy-dravite*	$Na(MgAl_2)(MgAl_5)(BO_3)_3Si_6O_{18}(OH)_3O$
Povondraite*	$NaFe^{3+}{}_3Fe^{3+}{}_4Mg_{2)}(BO_3)_3Si_6O_{18}(OH)_3O$
Tsiliasite	$NaMn_3Al_6(BO_3)_3Si_6O_{18}(OH)_3$
Elbaite	$Na(Li,Al)_3Al_6(BO_3)_3Si_6O_{18}(OH)_4$
Ferridravite	$NaMg_3Fe^{3+}{}_6\ (BO_3)_3Si_6O_{18}(OH)_4$
Buergerite	$NaFe^{3+}{}_3(BO_3)_3Si_6O_{22}F$
Liddicoatite	$Ca(Li,Al)_3Al_6(BO_3)_3Si_6O_{18}(OH)_4$
Uvite	$CaMg_3(MgAl_5)(BO_3)_3Si_6O_{18}(OH)_4$

Minerals marked with an asterisk are considered by Henry et al. (2008) to be significant in many meta-evaporitic tourmaline associations

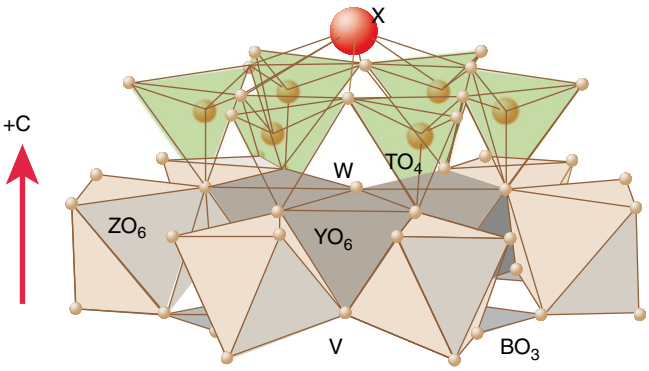

Fig. 14.18 Lattice structure of tourmaline as viewed perpendicular to the c-axis. Tetrahedra (TO_4) of the six-membered ring point in the same direction, parallel to c, to produce the crystallographic asymmetry. The polyhedra, X cation and V/W anions are labeled consistent with the structural formula. Octahedra, YO6 and ZO6, are shown together with the BO_3 site (After Henry and Dutrow 2012)

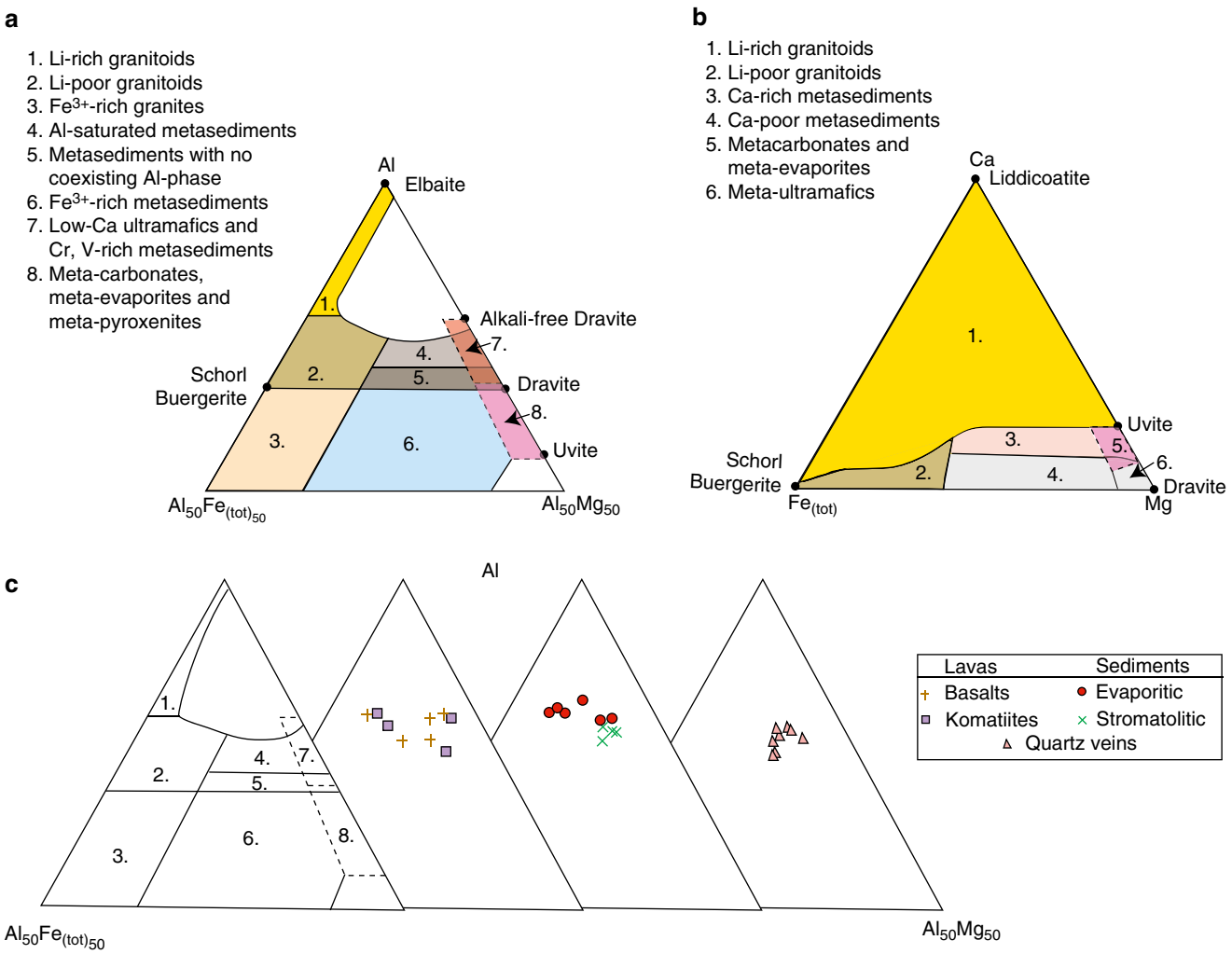

Fig. 14.19 Tourmaline composition. (**a**) Al-$Fe_{(Tot)}$-Mg diagram in molecular proportions for tourmalines, showing compositional range of various metasedimentary and igneous rock types, note overlap of fields 4 and 5 with field 7 (After Henry and Guidotti 1985). (**b**) Ca-$Fe_{(tot)}$-Mg diagram in molecular proportions for tourmalines showing compositional range of various rock types, note overlap of field 4 with field 6. Note povondraite previously called ferric dravite (After Henry and Guidotti 1985). (**c**) Compositional variations of various Barberton craton rocks using plot of A for comparison (After Byerly and Palmer 1991)

Three solid solution series characterise the most common tourmalines in nature (Fig. 14.19a, b):

- Between the Fe-rich (schorl) and the Mg-rich (dravite) tourmalines,
- Between schorl and the Li-rich (elbaite) tourmalines, and,
- Between dravite (Na>Ca) and uvite (Ca>Na) tourmalines.

The dravite-uvite series, is typical of tourmalines with metaevaporite and/or metacarbonate affinities and has end member compositions: dravite [$NaMg_3Al_6Si_6O_{18}(BO_3)_3(OH)_4$], and uvite [$Ca(Mg,Fe)_3MgAl_5Si_6O_{18}(BO_3)_3(OH)_4$]. Ayuso and Brown (1984) and Henry and Guidotti (1985) also demonstrated that tourmalines associated with meta-evaporites and metacarbonates in Precambrian sequences in North America are Mg-rich members of the schorl-dravite series, with significant Ca-uvite components.

Henry et al. (2008) note that the meta-evaporitic tourmalines are generally sodic, magnesian, moderately-to-highly depleted in Al, and enriched in Fe^{3+} and O-W^{2-} (calculated). They typically follow a trend along a join between "oxy-dravite" [$Na(Mg_2Al)(Al_6)(Si_6O_{18})(BO_3)_3(OH)_3O$] and povondraite [$NaFe_3^{3+}Fe_4^{3+}Mg_2Si_6O_{18}(BO_3)_3(OH)_3O$] (Fig. 14.19a). Tourmalines occurring in the highly magnesian high-pressure rocks (whiteschists and pyrope-coesite rocks) are distinctly more magnesian and fall close to the dravite and "oxy-dravite" compositions. These latter tourmaline compositions likely reflect the metasomatic processes that produced these more unusual bulk compositions and/or the influx of a reactive fluid that eliminated any earlier chemical signatures of meta-evaporitic fluids or protoliths.

As for stratabound tourmalinites, any restriction of these boron-rich minerals to particular stratiform units in a layered metamorphosed sequence strengthens a likely metasedimentary, possibly evaporitic, protolith (Abraham et al. 1972). However, even in meta-evaporitic settings, the boron ultimately captured in stratiform tourmalines may have come from:

(i) The diagenetic or regional metamorphic alteration of originally bedded borate mineral deposits (e.g., meta-borates in eastern Liaoning, China: Peng and Palmer 1995);
(ii) From hydrothermal activity in areas underlain by dissolving continental evaporites, such as early rift basin activity (such as in the Willyama complex: Slack et al. 1993); and
(iii) From ongoing submarine fumarolic and hydrothermal activity (exhalites) independent of any evaporitic contribution (Byerly and Palmer 1991).

Tourmalinite association (i) may well pass to (ii) as a continental rift basin evolves into a passive continental margin and then into convergence/collision (Wilson Cycle). Association (iii) can occur in volcanogenic rifts with or without the presence of borate evaporites.

The utility of tourmaline end-member concepts and compositional field divisions, as illustrated in Fig. 14.19, is only as good as our understanding of the chemical system that they represent. The tourmalines in sediments and lavas from the Archaean Barberton greenstone belt in South Africa are typical of the compositional variations seen in Precambrian metamorphics from across this region (Fig. 14.19c; Byerly and Palmer 1991). Using a standard Al-$Fe_{(tot)}$ -Mg plot places many of the Barberton samples in the field of immiscibility between dravitic and elbaitic tourmalines (Fig. 14.19c). The remainder plot in the Al-saturated metasedimentary field and are well away from the uvite compositional field. Only the Barberton tourmalines associated with meta-stromatolites and quartz veins show a degree of Mg enrichment and largely plot outside the standard metaevaporite-metacarbonate field, yet they occur in metasedimentary hosts that are considered evaporitic based on associated scapolites, evaporite pseudomorphs and isotopic compositions.

In my opinion, this quandary underlines a difficulty that seems to pervade the metamorphic literature, namely simplistic notions of the homogeneity of the sedimentary protolith. In terms of a tourmaline precursor, not all borate evaporites contain high levels of calcium, and most mined borate salts contain little or no magnesium (see borates in Chap. 11). This means the magnesium component in the protolith to meta-evaporitic tourmalines comes mostly from the host sediments that entrain the borate salts. There can be only a very minor contribution from the borax salts. If the host matrix contains dolomites and other carbonate minerals and the borate salts are dominated by colemanite or ulexite (major ore minerals in Turkey) then there will be a high level of Mg and Ca in the system and Mg-Ca rich sodic tourmalines minerals will form. But, it is worth noting that there is not any calcium in lacustrine borates composed of borax or kernite (major salts in the US borate deposits). In many borate deposits the host volcanogenic matrices are labile, and so are altered to be dominated by aluminosilicate clays (such as smectite), with some zeolites. Analcime, a common alteration product, for example, contains no Mg (see Chap. 11). Without evaporation of appropriate low salinity bicarbonate-rich inflow waters in the depositional basin, the levels of magnesium and calcium carbonate in the protolith matrix may be quite low. When borate salts in such a systems start to metamorphose and supply ions that will precipitate tourmaline, there may be little or no Ca or even Mg supplied to the system. The result will be meta-evaporitic tourmalines that do not plot in field 4 of Fig. 14.19b.

A more reliable way to determine a likely meta-evaporite protolith to some tourmalines and tourmalinites, based on chemical composition, is perhaps via a Na, Fe^{3+}, ^{W}O crossplot. Henry and Dutrow (2012) found low-temperature tourmalines that developed in hypersaline environments (e.g. salt dome caps) have distinct chemical characteristics of high Na, Fe^{3+} and ^{W}O (i.e. the W site occupied by oxygen as illustrated in lattice structure in Fig. 14.20), and follow a trend between oxy-dravite, and povondraite (O-P trend) (Fig. 14.20a, b). They argue this compositional trend can be used as a guide to indicate tourmaline development within low-temperature hypersaline environments and appears to be diagnostic of an oxidizing environment with high Na in the fluid and high salinity with the resulting reduction of the activity of H_2O. The same O-P trend is retained in some meta-evaporite deposits that are relatively high grade, as in Namibia (Fig. 14.20c). The same signature is also found in tourmalines from some types of economically important precious metal deposits, typically tied to meta-evaporites (see later).

But perhaps the most reliable method to distinguish between possible origins of meta-evaporitic tourmalines and tourmalinites is to measure their $\delta^{11}B$ isotopic signature (Fig. 14.21). Palmer and Slack (1989) described how boron isotopic signatures vary in a predictable manner in deposits ranging from primary borate salts to meta-evaporites. Tourmalinites associated with marine evaporites have a positive $\delta^{11}B$ signature near +10‰, tourmalinites associated with mafic volcanics have a signature near −2‰, tourmalinites from continental margin sediments have values near −15‰, while tourmalinites derived from nonmarine evaporites have very negative isotopic signatures near −20‰.

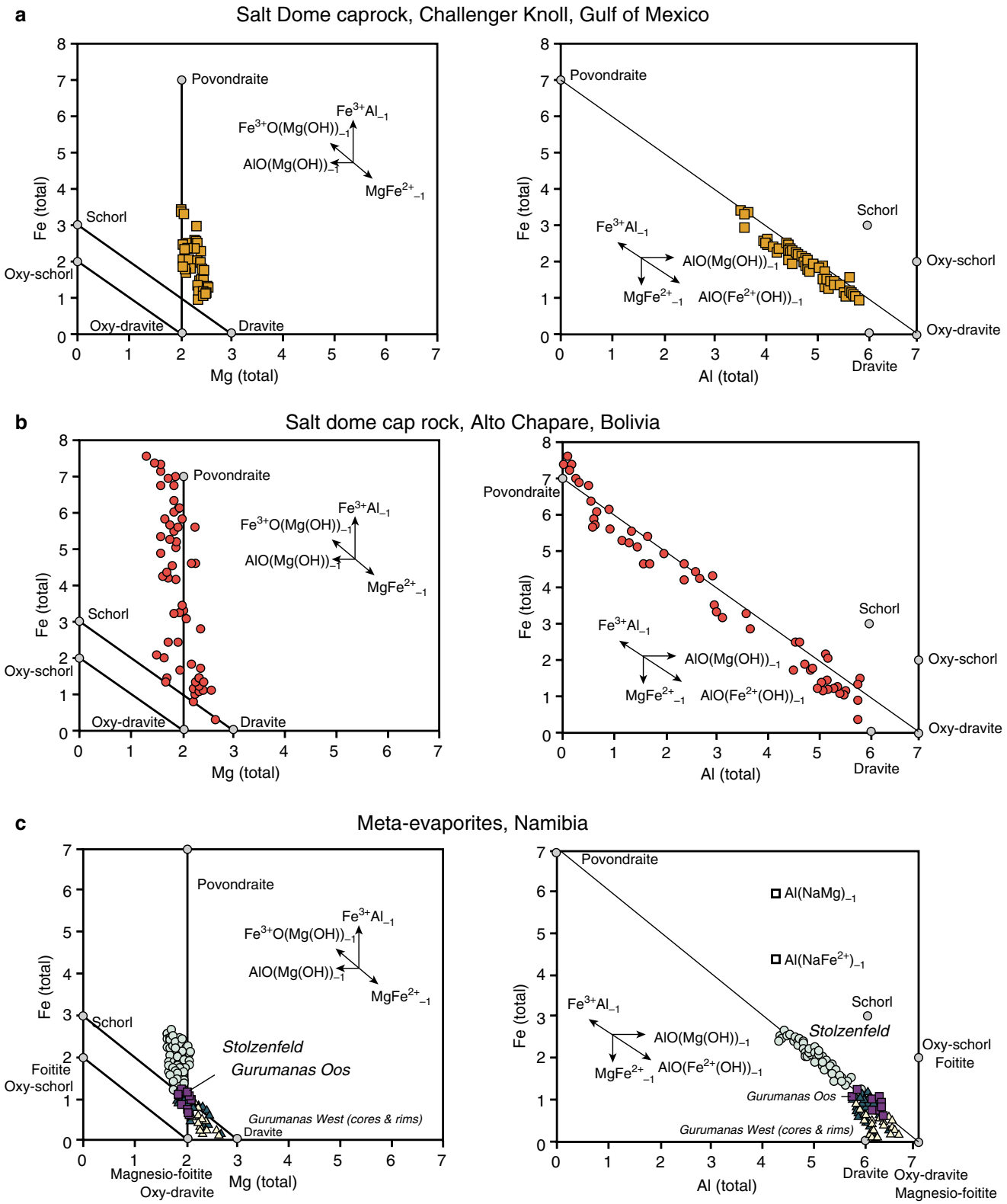

Fig. 14.20 Tourmaline components indicative of evaporite association (After Henry and Dutrow 2012). The covariant lines represent joins between selected tourmaline end members – indicated compositions cover the complete range from "oxydravite"/dravite to povondraite -see text. (**a**) Compositional variations Mg vs. Fe(total) and Al vs. Fe(total) diagrams of low-temperature tourmaline (<150 °C) found in the cap rock of the Challenger Knoll salt dome in the central Gulf of Mexico. (**b**) Compositional variations Mg vs. Fe(total) and Al vs. Fe(total) diagrams of low-temperature tourmaline found in the cap rock of the Alto Chapare salt dome, Bolivia. (**c**) Compositional variations Mg vs. Fe(total) and Al vs. Fe(total) diagrams for tourmaline found in three tourmalinite localities associated with metamorphosed evaporite deposits in Namibia. The three meta-evaporite localities are labeled and have different symbols. The green triangle for the Gurumanas West locality represents generation-2 rim compositions. As in (**a**, **b**), the array of data is generally along the "oxy-dravite"–povondraite join and is most consistent with operation of the $AlFe_{-1}$ substitution except for the Gurumanas West rims that exhibit $Mg(OH)(Fe^{3+}O)_{-1}$ and $MgFe_{-1}$ substitutions as well. These Namibian tourmalines are mostly classified as "oxy-dravites", but some are dravites

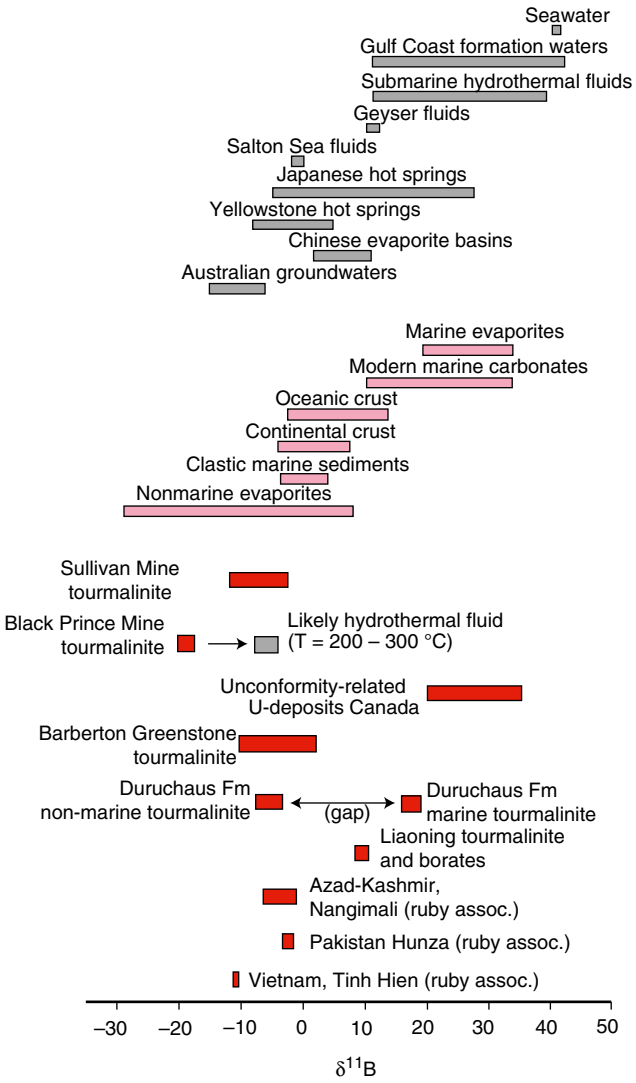

Fig. 14.21 Boron isotopic composition of tourmalines in the Black Prince Mine, Broken Hill District, Australia, the Barberton greenstone belt, South Africa, the Duruchaus Fm, Namibia and the Lianong region, China and various ruby associations in SE Asia (*solid red boxes*) compared with typical values for various boron sources; *Grey boxes* indicate fluids, *pink boxes* indicate solids (After Slack et al. 1989; Byerly and Palmer 1991; Peng and Palmer 1995; Sun 2007; Garnier et al. 2008)

Using this approach implies a likely nonmarine evaporite protolith for the Paleoproterozoic tourmalinites of the Black Prince Mine in the Broken Hill District, while samples from the Barberton Greenstone Belt indicate a mixed volcanic and sedimentary protolith. Sun (2007) showed how stratabound tourmalinites in the Neoproterozoic Duruchaus Fm of Namibia preserve separate marine and nonmarine meta-evaporite signatures. The nonmarine Duruchaus tourmaline association is tied to the early rift stage of the protolith basin, while the marine signature is related to later meta-evaporites formed in the incipient oceanic setting of the widening rift. A similar "rift-to-drift" evolution was used to explain the dichotomy of boron isotope values in the Houxianyu meta-borates of the Liaoning region, China (Jiang et al. 1997).

One of the more interesting examples comes from the Sullivan Mine in British Columbia (Fig. 14.22; Jiang et al. 1999). The Sullivan Pb–Zn–Ag deposit is a giant, SEDEX-type sulphide orebody lying conformably within clastic metasedimentary rocks of the Middle Proterozoic Aldridge Formation in the Belt–Purcell Supergroup. The orebody is divided by an irregular transition zone into a western massive sulphide body and an eastern body of bedded sulphides and intercalated clastic metasedimentary rocks. Underlying this orebody is a large, funnel-shaped tourmalinite alteration pipe. The shallow part of this pipe, <30 m from the base of the massive orebody, comprises tourmalinized fragmental breccia and conglomerates, which locally contain disseminated or stockwork of the same composition as the underlying metasedimentary rocks; no foreign clasts have been identified, implying the breccia is locally derived. Chlorite–pyrrhotite alteration is present in the uppermost portion of the tourmalinite pipe, just below the massive pyrrhotite body. The chlorite–pyrrhotite-altered rocks are in contact with, and locally cut, the footwall tourmalinites (Fig. 14.22b). The most abundant altered rock overlying the deposit contains an albite–chlorite–pyrite assemblage that forms an irregular alteration zone that overprints hangingwall tourmalinites and massive sulphides. Shortly after deposition of the Aldridge Formation, a series of gabbroic sills and dykes intruded into the partly consolidated sediments and the zircons in the sediments give a U-Pb age of 1,468 ± 3 Ma. The regional metamorphic grade at Sullivan is middle to upper greenschist, with inferred temperatures and pressures of 450 °C and 3.8 kb, respectively. Toumalinites not only typify the footwall they also occur, though in lesser volumes, in the hanging wall.

The $\delta^{11}B$ values across the footwall and hanging wall range from −11.1 to −2.9‰ (Fig. 14.23a). Jiang et al. (1999) conclude that the major control on the overall $\delta^{11}B$ values in the Sullivan tourmalinites is boron source. As can be seen in Fig. 14.23a, boron isotope data at Sullivan are consistent with possible boron derivation from leaching of footwall clastic sediments. However, the great abundance of tourmaline in the Sullivan deposit suggests that the local clastic sediments were not the most important source of boron, Jiang et al. argue that nonmarine evaporites, once buried deep below the orebody, are the most viable source of this additional boron. They go on to note that some of the spread in boron isotope values may reflect a degree mixing of boron from these two sources.

Another illustration of the utility of boron isotopes in deciphering the evolution of tourmalines comes from the Jaduguda U (–Cu-Fe) deposit, Singhbhum shear zone, India (Fig. 14.23b; Pal et al. 2010). The ≈200 km long and ≈1–5 km wide Singhbhum shear zone occurs close to the

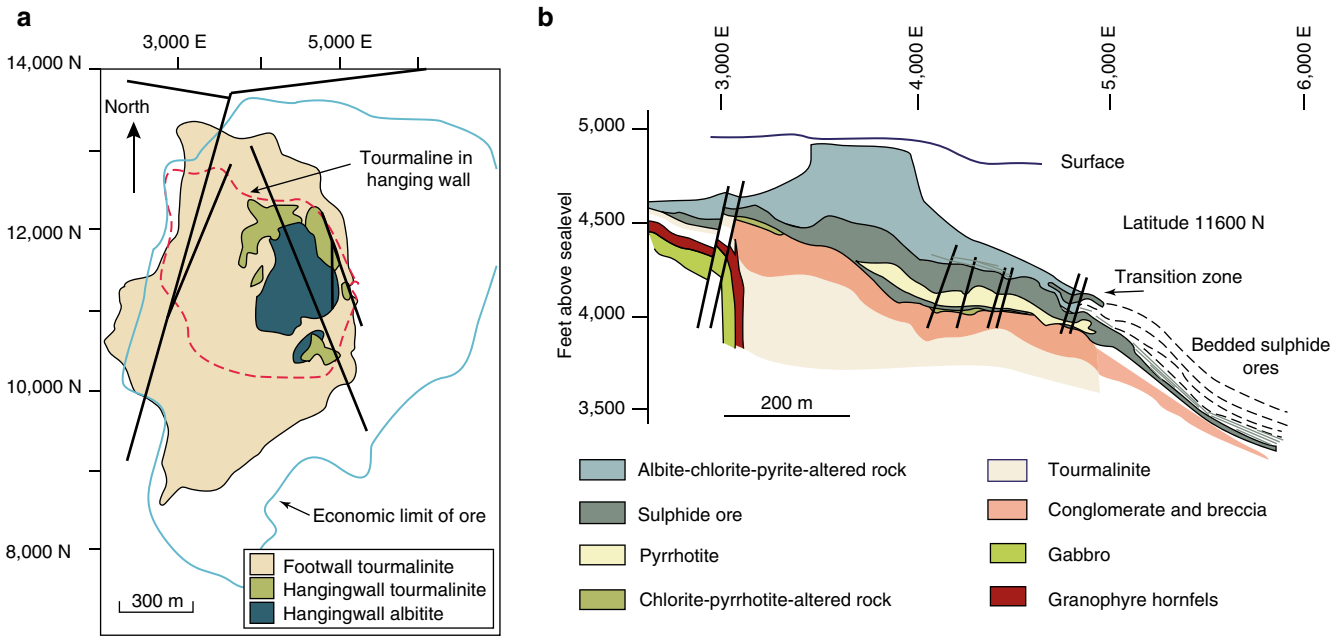

Fig. 14.22 Geology of the Sullivan Pb–Zn–Ag deposit, British Columbia (After Jiang et al. 1999). (**a**) Simplified plan of the deposit showing the projected distribution of hanging wall and footwall tourmalinites, and hanging wall albitites. (**b**) Geological cross-sections of the Sullivan Pb–Zn–Ag deposit showing the distribution of sulphide ore, footwall tourmalinite, hangingwall albite–chlorite–pyrite-altered rock, and the tourmalinite that underlies much of the ore deposit

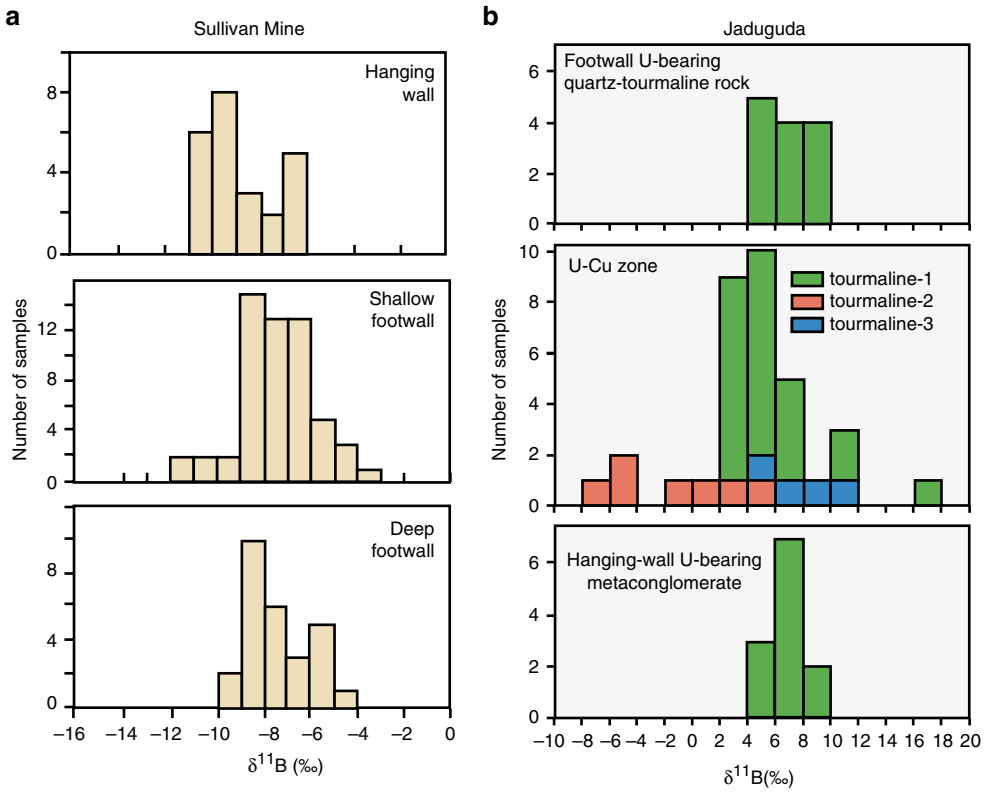

Fig. 14.23 Frequency histogram of boron isotope compositions of tourmalines. (**a**) Sullivan Mine, British Columbia with separate plots in samples from the hanging wall, the shallow footwall <30 m below the sulphide orebody and the deep footwall, see Fig. 14.22b) for geological section (After Jiang et al. 1999). (**b**) Jaduguda U-(Cu-Fe) deposit, India, with separate plots from the footwall U-bearing quartz–tourmaline rock, the U–Cu zone and the hanging-wall U-bearing metaconglomerate. Note the similarity in isotopic compositions of Tourmaline-1 in all zones and a distinctly lighter isotopic signature of Tourmaline-2 (rims/fracture-filling) in the Cu–U zone. Tourmaline 1 boron is interpreted as having a marine evaporitic source. Post deformation Tourmaline-3 displays similar isotopic compositions as that of Tourmaline-1 (After Pal et al. 2010)

boundary between the Archaean Singhbhum cratonic nucleus (3.3–3.5 Ga) on the south and the Proterozoic North Singhbhum Fold Belt on the north. Along the shear, polymetallic ores are hosted in altered, sheared and metamorphosed volcano-sedimentary rocks, and the associated geological complexity has lead to a confusion of ore genetic models for the Jaduguda deposit. A characteristic of the mineralization is the presence of tourmalinite, which is spatially associated with U and Cu mineralization in all rock types, with tourmaline locally exceeding 50 vol.%. The chemical and B-isotopic variations in the tourmalines provide important constraints on fluid source(s) and ore deposit affinity. Tourmaline grew in three different stages across the U-Cu ore zone and adjacent footwall and hanging wall meta-sedimentary rocks. Pre-kinematic tourmaline-1 is represented by fractured and porphyroblastic grains, it is ubiquitous in the wall rocks and the U-Cu zone. Syn-kinematic tourmaline-2 and post-kinematic tourmaline-3 are found exclusively in the U-Cu zone, where intense shear deformation has focussed fluid flow, alteration and metamorphism. All tourmalines belong to the alkalic group and most are dravitic.

The overall range of $\delta^{11}B$ values from −6.8 to +17.2‰ is broad and relatively undiagnostic. However, when broken down by tourmaline type, the positive values of tourmaline-1 are irrespective of host rock and ore association (U or U + Cu), and range between +2.3 and +17.2‰ (n = 44). The calculated $\delta^{11}B$ values of fluid in equilibrium with this tourmaline (for mineralization temperatures of 300–450 °C) range from +4 to +20‰. The $\delta^{11}B$ values of syn-kinematic tourmaline-2 are much lower than tourmaline-1, between −6.8 and +4‰ (n = 7) and the corresponding fluid $\delta^{11}B$ values are −4.8 + 6‰. The high values of $\delta^{11}B$ for tourmaline-1 and associated early fluid suggest a marine evaporite or basinal brine was the source of boron, and this fits with abundant mineralogical and geochemical evidence for highly-saline fluids during mineralization (Pal et al. 2010). The isotopically lighter fluid associated with tourmaline-2 and related syn-kinematic mineralization/mobilization was likely derived from the metamorphic volcano-sedimentary rocks with high fluid/rock ratios in and around the shear zone. Postkinematic tourmaline-3 is compositionally and isotopically $\delta^{11}B$ = +4 to +11.1‰ (n = 5) similar to tourmaline-1 in the same samples, suggesting it formed by local recrystallization of the earlier tourmaline or from a renewed influx of saline fluids, similar to those which formed the pre-kinematic mineralization. Given the complexity of deciphering primary fluid sources in metamorphic terranes, clearly the isotopic method is the better tool compared to bulk mineral composition.

At the world scale of plate boundary interactions, it is clear that tourmaline is a common occurrence in Phanerozoic and older hydrothermal systems in both marine and nonmarine settings. This is also indicative of the distribution of boron in the lithosphere Phanerozoic systems where the higher boron content of melts and associated exhalative associations is the result of melting of accretionary wedge sediments. There, in accretionary wedges, absolute boron levels are elevated by the photosynthesizing activities of plankton. Hence, boron tends to accumulate in pelagic sediments, compared with oceanic crust (boron is one of the seven food elements required by all phytoplankton; Park and Schlesinger 2002).

When this accretionary prism sediment is subducted it releases aqueous fluids as it moves deeper and ultimately into the zone of melting. The derived melts move boron back to the earth's surface and into renewed zones of intermontane deposition, via hydrothermal springs and seeps, especially in zones of active fluid circulation within rhyolite/andesite terranes. It is in these intermontane depressions that continental borate evaporites tend to accumulate with their characteristically negative $\delta^{11}B$ signatures (Chap. 12).

There is a relationship between boron isotope composition and depth to the Benioff zone. Field studies in subduction zones from Izu-Bonin, the Kuriles, Eastern Kamchatka, and the Central Andes consistently show that boron concentrations and $^{11}B/^{10}B$-ratios in volcanic arcs are high close to the trench and systematically decrease across the arc with increasing distance from the trench, corresponding to increasing depth of the Wadati-Benioff zone (Wunder et al. 2005). For each subduction zone, there is a systematic variation of $\delta^{11}B$ in the volcanic arc versus depth to the Wadati-Benioff zone (Fig. 14.24). In old cold slabs, such as Izu-Bonin and the Kuriles, the trend is significantly flatter, compared to the younger, hotter slabs of Eastern Kamchatka and the Central Andes. These trends are interpreted as resulting from continuous dehydration reactions within the slab and may trace the particular thermal structure of each slab.

Within the zone of metamorphism related to the subduction zone in accretionary orogens it seems that, because of its high modal abundance, potassic white mica (containing up to 270 ppm B), is probably the most important boron reservoir during subduction of oceanic sediments and altered basalts. It dominates the boron budget within the subducting slab, even in the presence of tourmaline and amphibole, which can contain B-concentrations up to 63 ppm (Wunder et al. 2005 and references therein). Moreover, this white mica is stable to depths of 300 km in cold subducting slabs where, with enhanced subduction, its modal amount is continuously decreased and its composition shifted towards phengitic mica as boron is released.

Thus, it seems Phanerozoic marine tourmalinites, based on a study of boron distribution in modern ridge and subduction settings, typify accretionary orogenies (Fig. 14.24). However, the listing of older documented metasedimentary

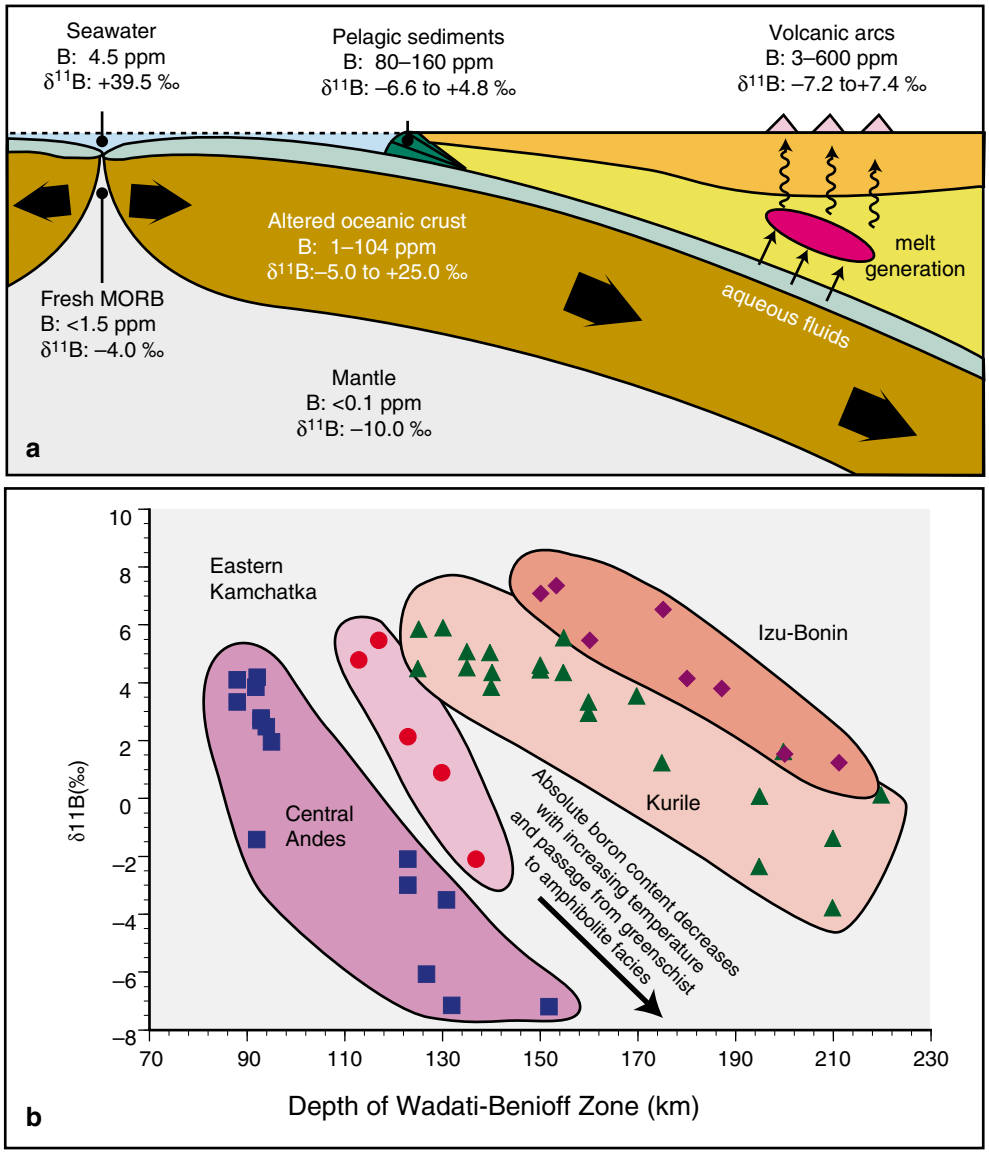

Fig. 14.24 Boron redistribution in subduction/accretionary orogeny. (**a**) Schematic cross section through a subduction zone with ranges of boron concentrations and $\delta^{11}B$-values typical for mantle, oceanic crust and convergent margin reservoirs. (**b**) Plot of $\delta^{11}B$-values of volcanic arcs versus depth of the respective Wadati-Benioff zone for four subduction zones. Izu-Bonin, Kuriles, Eastern Kamchatka, Central Andes (After Wunder et al. 2005)

tourmalinites in the same table shows a correlation of older boron/tourmalinite occurrences with Precambrian meta-evaporites, meta-carbonate and metavolcanic associations many of which are not tied to subducting oceanic plates. Rather many older tourmalinite/boron deposits occur in association with what appear to be massive sulphides in continental extensional rifts, as well as with some Proterozoic IOCG deposits, which tend to form in continental anorogenic settings (Chap. 16). Neither are directly tied to arc subduction, but rather to early extensional phases, or to zones of continent-continent collision (Table 14.6). Analogs to these settings would be perhaps be the African rift and the Alpine-Zagros orogenic belts. In addition, the numerous occurrences of metasedimentary tourmalines in Early Archaean terranes, and once again raises the question of what were the controls on boron levels and its distribution within a much hotter Archaean earth interior, prior to the evolution of the nitrogen fixation process in phytoplankton?

Table 14.6 Worldwide examples of toumalinites

Time	Africa	Americas	Asia	Australia	Europe and adjacent
Mesozoic/ Cenozoic	–	(E) Tourmaline in salt diapir caprocks, Challenger Knoll, Gulf of Mexico (Henry et al. 1999). (E?) Jurassic Light Creek Stock (Stephens and Dilles 2008)	Tourmalinite (Jurassic) from Chitral, northern Pakistan (Zahid and Moon 1999). Tourmalinite, Yozgat Batholith, Central Anatolian core complex, Turkey (Isik et al. 2004)		(E) Triassic NevadoFilábride Complex, SE Spain (Torres-Ruiz et al. 2003a, b). (E) Tourmalinite pebbles from Lower Triassic and Upper Cretaceous of W. Carpathians, Slovakia (Bacik et al. 2008)
Palaeozoic	–	(E) Tourmaline in Locotal Breccia, Alto Chapare, central Bolivian Andes (Zacek et al. 1998)	(E) Caledonian tourmalinites in Sar-e-Sang region, Afghanistan (Grew 1988). (E) tourmalinized albitic breccia lenses in Devonian Changba Sedex Pb-Zn deposits, Qinling orogenic belt, China (Ma et al. 2004)	Tourmalinite cap to Rosebery Zn-Pb-Cu-AgAu deposit (Plimer and Lees 1988)	Siluro-Devonian in Caledonides of SE Ireland (McArdle et al. 1989). (E) Early Palaeozoic meta-sediments of the Arzberg Series, W. Germany (Abraham et al. 1972). (E?)Tourmalinites in Austro-Alpine crystalline complex, Austria (Raith 1988)
Neoproterozoic	(E) Tourmalinites in Duruchaus Fm, Namibia (Henry et al. 2008; Sun 2007). (E) Tourmalinites in Nchanga Cu-Co deposit, Zambia (McGowan et al. 2006; Zacharias et al. 2005). (E) Tourmalinites in metapelites, Sikait area, Egypt (Harraz and El-Sharkawy 2001)	(E?) Tourmalinites in the Eastern Sierras Pampeanas, Argentina (Tourn et al. 2004). (E) Tourmalines via recurrent hydrothermal highly saline brine episodes driving U deposition and recrystallization with later remobilization along roll-fronts (0.4 Ga to near present) (Mercadier et al. 2012)	(E?) Tourmalines (gem quality) in Sri Lanka, part of Pan African mineral belt (Dissanayake and Chandrajith 1999)	(E) Willouran metasediments, Adelaide Foldbelt (Crawford and Hilyard 1990)	–
Mesoproterozoic	Stratiform tourmalinites in Mid-Proterozoic Bushmanland Group, Namaqua Mobile Belt, South Africa (Willner 1992)	(E) Grenville complex, New York (Ayuso and Brown 1984; Henry and Guidotti 1985). (E) Sullivan ore body, British Columbia (Conly 1995; Jiang et al. 1999)	(E)Tourmalinites in Sargipali Cu-Pb deposit (1.66 Ga), Eastern India (Vishwakarma 1996)	(E) Tourmalinite in the Blengsvatn, southern Norway (Visser et al. 1999)	–
Paleoproterozoic	(E) Stratiform tourmalinites in Schists de la Daléma (2.1 Ga), Mali (Ndiaye and Guillou 1997). Tourmalinite pebbles in hanging wall of Loulo gold deposit (Dommanget et al. 1993)	(E) Stratiform tourmalinites in the Papaskwasati Fm., Aphebian Mistassini Group, Quebec (Chown 1987)	(E) Stratiform tourmalinite in Aravalli Group, NW India (Golani et al. 2002). (E) Tourmalinites in Houxianyu borate deposit, eastern Liaoning, China (Jiang et al. 1997; Peng and Palmer 2002). (E?) Stratiform tourmalinite in Sibao Group, Guangxi Province, China (Jingwen 1995)	(E) Stratiform tourmalinite, Rum Jungle, NT, Australia (Bone 1988). (E) Willyama Supergroup, Olary Province (Slack et al. 1993; Cook and Ashley 1992; Plimer 1988, 1994). Tourmalinite in Golden Dyke Dome (Plimer 1986)	(E) Tourmalinites in Lapponian and Scevofennian Sulphide deposits, Northern Fennoscandia (Frietsch et al. 1997; Martinsson et al. 2008)
Archaean	Early Archaean tourmalinite, Barberton Greenstone Belt, South Africa (Byerly and Palmer 1991; Kalbskopf and Barton 2003)	(E) Tourmalines of Igarapé Bahia Cu-Au deposit (2,750 Ma), Brazil (Dreher et al. 2008; Xavier et al. 2008)	(E) Phase 1 and phase 3 tourmalinites in U-Cu-Fe Singhbhum shear zone, eastern India, (Sengupta et al. 2005; Pal et al. 2010). Hosts the oldest and most productive uranium mine in India	(E?) Big Bell and Mt Gibson gold deposits, Yilgarn, Australia (Jiang et al. 2002)	Stratabound tourmalinite and scheelite in altered Archaean komatiites, West Greenland (Appel 1994, 1995)

E indicates tourmalinites with a meta-evaporite association

Sodian Phyllosilicates and Talc

In the Triassic meta-evaporites from Derrag, in the Tell Atlas of Algeria, sodian phlogopite occurs naturally as an unusual meta-evaporitic product in a sugary dolomite matrix, which also hosts other magnesian phyllosilicates, as well as large porphyroblasts of albite, dravite-uvite tourmalines, quartz, scapolite, magnesite, rutile and pyrite (Schreyer et al. 1980). There the phlogopite[4] has a microprobe-determined chemical formula that is close to ideal $NaMg_3[AlSi_3O_{10}](OH)_2$, with some possible addition of lithium. Crystals are invariably coated with thin rims of the more typical potassium phlogopite and these rims probably prevented the retrograde hydration of the sodian phlogopite. The phlogopite coexists with an enigmatic talc-containing phase called kulkeite.

Kulkeite is an unusual sodian phyllosilicate mineral in this Triassic sequence, and it appears to be associated with the metaevaporites. It is an ordered 1:1 chlorite/talc mixed-layer mineral that forms platy, colourless, porphyroblastic, single crystals in its low-grade sugary dolomite host (Schreyer et al. 1982). From microprobe analysis kulkeite's empirical formula is $(Na_{0.38}K_{0.01}Ca_{0.01})(Mg_{8.02}Al_{0.99})[Al_{1.43}Si_{6.67}O_{20}](OH)_{10}$ with some variation in Na, Si and tetrahedral Al.

Both the sodian phlogopite and the kulkeite formed during low grade metamorphism of an evaporite protolith at temperatures that did not exceed 400 °C. According to Schreyer et al. (1980, 1982) these meta-evaporitic aluminosilicates are the first known natural examples of sodian phlogopite and the first documentation of an aluminosilicate showing a regular mixed interlayering between chlorite and talc (Fig. 14.25a). Both occur in dolomites interbedded with clays and thick salts, which were originally buried to depths varying from 2 to 10 km and then returned to the surface by halokinesis. The close proximity of clastic silicate rocks with dolomite and salt (mostly halite but with some K, Mg salts), as well as deep burial prior to exhumation, are thought to have been responsible for this meta-evaporite association. It is a somewhat more evolved metamorphic-halokinetic system than that in the Flinders Ranges, Australia (Chap. 7).

Sodic talc- kyanite is another likely meta-evaporite indicator in the Derrag (Schreyer 1977; Schreyer and Abraham 1976). Once again, fluid-driven chemistries of meta-evaporitic sequences do not fit easily into a conventional isochemical analysis of regional metamorphism. Meta-evaporites in the Sar-e-Sang region of Afghanistan exhibit mosaic equilibria across small volumes (in the cm^3 range) within a talc-kyanite schist (whiteschist) host. The microscale mineral variations are characterised by variations in mineral assemblages conventionally attributed to vastly different pressure/temperature conditions during regional metamorphism.

On the basis of petrographic and microprobe studies, these assemblages are attributed to three consecutive stages of metamorphism of a chemically exceptional rock with a composition that falls largely into the model system MgO-Al_2O3-SiO_2-H_2O (Fig. 14.25b; Schreyer and Abraham 1976). Stage 1, typified by Mg chlorite-quartz -talc and some paragonite, was followed during stage 2 by talc-kyanite, Mg gedrite-quartz[5] and the growth of large dravites. Microprobe analyses of the phases gedrite and talc indicate variable degrees of sodium incorporation into these phases according to the substitution NaAl— >Si. In stage 3, pure Mg cordierite formed with or without corundum and/or talc, and the kyanite was partly converted into sillimanite. Pressure and temperature during this final stage of metamorphism was near 5–6 kb and 640 °C.

Schreyer and Abraham (1976) concluded that chemical variations in the metamorphic fluids were generated by progressive metamorphism and mobilisation of an evaporite deposit. Relict anhydrite and gypsum still occur in the Sar-e-Sang area. Whiteschists and the associated lapis lazuli deposits of the region are part of a highly metamorphosed evaporitic succession (see discussion of lapis lazuli in the gem section of this chapter). Salts have largely vanished due to ongoing melting and volatilizations. The preservation of the three stage succession of mineral assemblages, across such small scales and yet related to each other through isochemical reactions, means that the main factors governing the metamorphic history of this whiteschist were compositional changes of the coexisting fluids with time. Under this scenario any pressure-temperature variations were subordinate and the chemistry of the fluids evolved as the evaporites underwent metasomatic alteration.

The sedimentary pelitic layers of this evaporitic sequence first underwent a period of metamorphism in which fluid pressures approached lithostatic (stage 1). Subsequently at higher metamorphic grades, with the beginning of mobilisation of the salts, the metamorphic fluids became increasingly enriched in ions such as Na^+, Mg^{2+}, Cl^-, SO_4^{2-}, BO_3^{3-}, etc., so that water fugacity dropped considerably. This period is represented by stage 2 of the whiteschist metamorphism and was characterised by strong metasomatism that led, for example, to the growth of dravite and the amphibolite, gedrite. The physical and chemical character of stage 3 is less clearly defined. Kyanite/sillimanite inversion requires an increase in temperature or a decrease in pressure, or both; but changes in the composition of a coexisting gas phase may have played an additional role in the formation of cordierite.

[4]Phlogopite is a yellow, greenish, or reddish-brown member of the mica family of phyllosilicates that is also known as magnesium mica.

[5]Gedrite is a silicate mineral of the amphibole group with formula: $(Mg;Fe^{2+})^2[(Mg;Fe^{2+})3Al_2](Si_6Al_2)O_{22}(OH)_2$

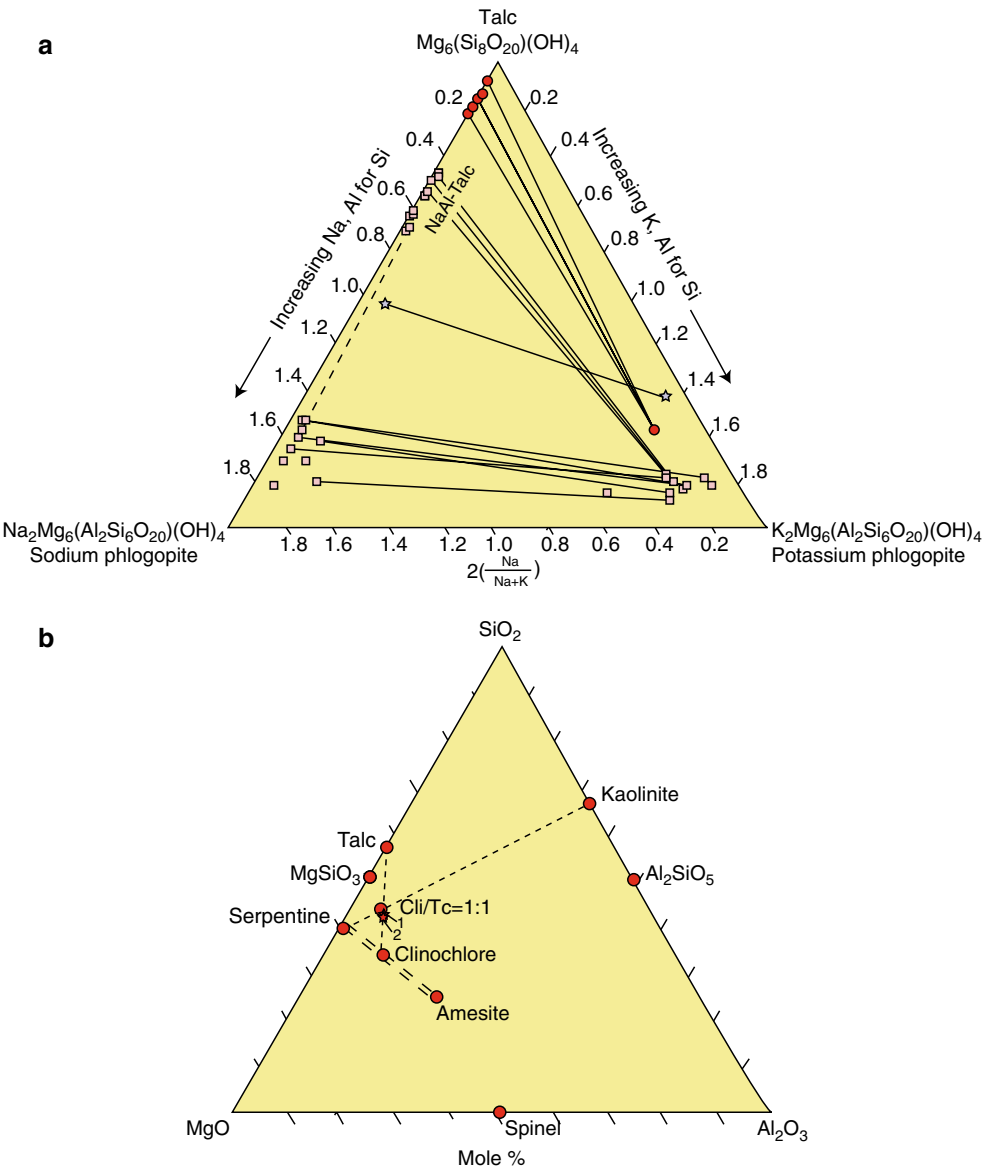

Fig. 14.25 Sodian phlogopite, talc and kulkeite. (**a**) Ternary system sodium phlogopite – potassium phlogopite talc. *Squares* represent the 10 analyses from phlogopitic micas and the sodian aluminian talc. *Circles* indicate minerals from the Sar-e-Sang, Afghanistan, whiteschist (Schreyer and Abraham 1976), *stars* plot one set of coexisting micas from Post Pond, Vermont, metavolcanics. *Solid lines* connect coexisting phases, while the *dashed tie line* between talc and a sodium phlogopite represents the assemblage spread before the growth of potassium phlogopite (After Schreyer et al. 1980). (**b**) Ternary plot of the system MgO-$A1_2O_3$-SiO_2-H_2O projected onto the water-free base showing some relevant crystalline phases, the location of a theoretical 1:1 clinochlore/talc mixture, and the analysed compositions of kulkeite indicated by *stars 1* and *2* (After Schreyer et al. 1982)

The meta-evaporite-derived assemblage in Afghanistan may in a single thin section entrain mineral assemblages that conventionally would be assigned to the greenschist facies, the hornfels facies, and to a high pressure (amphibolite) regime. The assemblages are in effect a mosaic equilibria that reflects changes in fluid composition generated from a metamorphosing evaporite pile over time and only to a lesser degree by regional evolution of total temperature and pressure. Once again, evaporites generate unusual responses compared to the general responses of metasediments.

In a refinement paper discussing the likely relationships between evaporites and whiteschists, Franz et al. (2013) note that whiteschist mineral assemblages are stable up to pressures of more than 4 GPa, but may already form at pressures of 0.5 GPa. Their formation largely depends on the composition of the protolith and requires elevated contents of Al and Mg as well as low Fe, Ca, and Na contents, as otherwise chloritoid, amphibole, feldspar, or omphacite are formed instead of kyanite or talc. They go on to note that the stability field of a whiteschist mineral assemblage strongly depends on XCO_2 and fO_2: at low values of XCO_2, CO_2 binds Mg to carbonates strongly reducing the whiteschist stability field, whereas high fO_2 enlarges the stability field and stabilizes yoderite [$Mg(Al, Fe^{3+})_3(SiO_4)_2O(OH)$].

The scarcity of whiteschist is not necessarily due to unusual P–T conditions, but to the restricted range of suitable protolith compositions and the spatial distribution of these protoliths: (1) continental sedimentary rocks and (2) hydrothermally and metasomatically altered felsic to mafic rocks. They argue continental sedimentary rocks that may

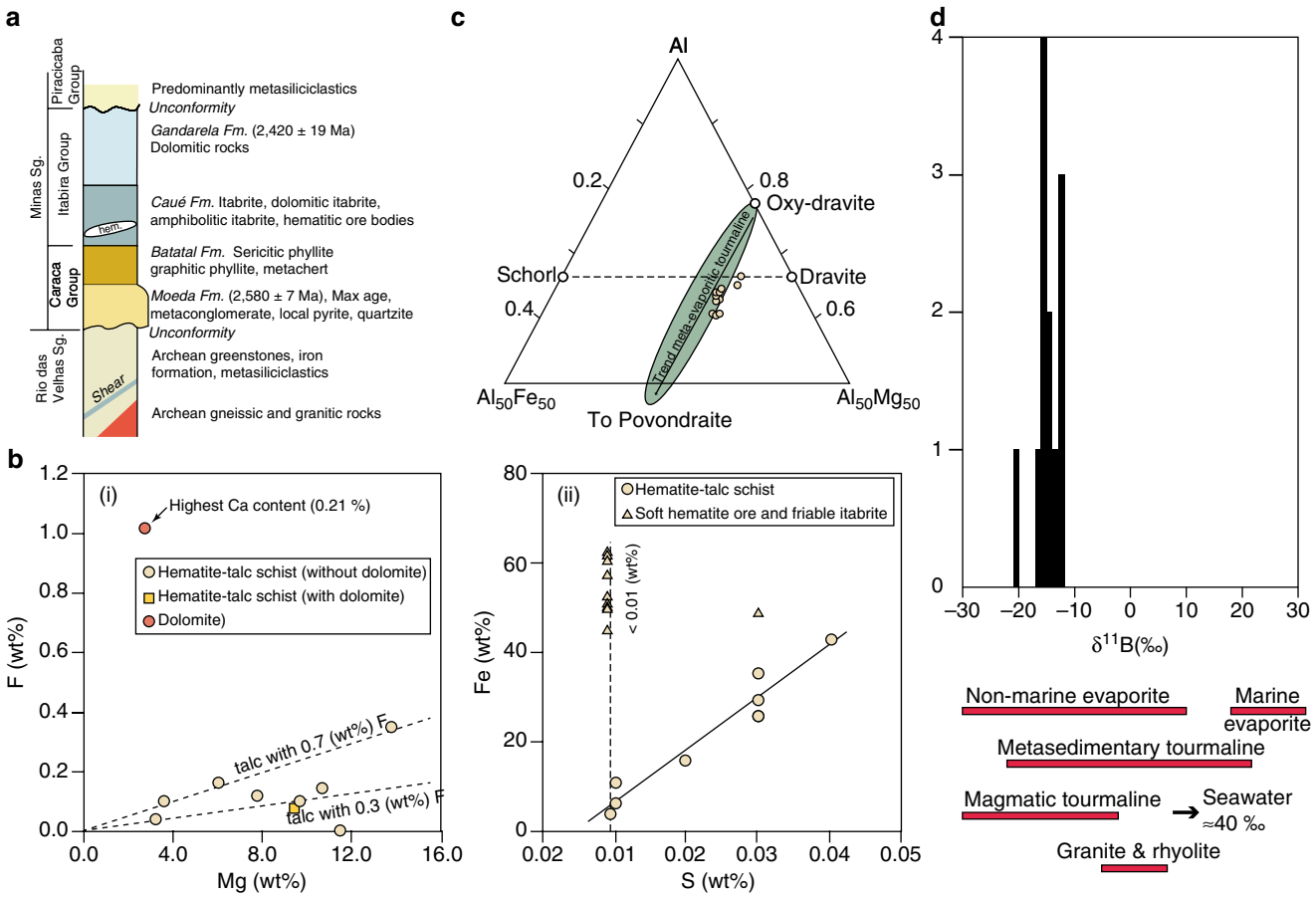

Fig. 14.26 Talc-tourmaline interrelationships in the Gongo Soco deposit, Minas Gerais, Brazil (After Cabral et al. 2012). (**a**) Lithostratigraphic column emphasising the Caraça and Itabira groups of the Minas Supergroup. (**b**) Diagram for whole-rock contents of Mg vs. Fluorine. Talc is the dominant F-bearing mineral and most samples plot within, or near, the limits defined by the *dashed lines* in (*i*). These lines represent the minimum and maximum contents of fluorine measured. (*ii*) Diagram for wholerock contents of S vs. Fe. The elements show a strong positive correlation (regression line) in samples of hematite–talc schist. Other Fe-rich rocks from Gongo Soco, which were previously analysed using the same analytical techniques, are plotted for comparison as triangles showing the S-Fe relationship only typifies the hematite-talc schist. (**c**) Upper portion of an Al–Fe–Mg ternary diagram for tourmaline within the hematite–talc schist. Meta-evaporitic tourmaline typically follows a trend along the join line between "oxy-dravite" and povondraite (see Fig. 14.20). (**d**) Histogram of tourmaline $\delta^{11}B$ value for hematite–talc schist in Gongo Soco, compared to $\delta^{11}B$ some in some known reservoirs (see Fig. 14.21). Tourmaline composition illustrates a range of negative $\delta^{11}B$ values, and this together with the abundance of fluorine- bearing talc at Gongo Soco, favour a nonmarine evaporitic reservoir supplying the talc-mineralising fluid system

produce whiteschist mineral assemblages typically have been deposited under arid climatic conditions in closed evaporite basins and may be restricted to relatively low latitudes. These rocks typically contain large amounts of palygorskite and sepiolite. Franz et al. (2013), conclude whiteschist assemblages typically are only found in settings of continental collision or where continental fragments were involved in subduction.

Talc, $Mg_3Si_4O_{10}(OH)_2$, is typically interpreted as a high-temperature mineral that forms from hydrothermal alteration or metamorphism of Mg-rich and ultrabasic rocks (Tosca et al. 2011). Lower temperature reactions can also produce talc-bearing assemblages, for example through the weathering of serpentinite deposits. It can also occur as an authigenic component in evaporites that have yet to experience metamorphic grade burial temperatures and pressures. Talc has been recorded in Permian evaporites from New Mexico (Bailey 1949; Bodine 1983), in Carboniferous evaporites in Nova Scotia (Evans 1970) from the Eskdale boreholes in NE Yorkshire (Scrivener and Sanderson 1982) and in Neoproterozoic carbonate successions (Tosca et al. 2011).

In Yorkshire it occurs as minor quantities of isolated flakes in the halite-rich parts of four evaporite breccia beds that also contain minor anhydrite, dolomite and quartz. In the Yorkshire deposit, the mineral is always enclosed by halite, but in New Mexico it is also found in the cleavage cracks of sylvinite and polyhalite. Both of

these localities are associated with magnesium-bearing salts such as carnallite and kieserite. In the case of the Yorkshire deposits, the nature of the sediments enclosing the evaporites and in the breccia suggests a salt flat or sabkha environment of deposition. There is no evidence that the talc is depositional and Scrivener and Sanderson (op. cit.) suggest that postdepositional hypersaline conditions permitted the diagenetic reaction of dolomite with silica to form talc (Bodine 1983). Given the appropriate seawater brine chemistry, as occurred at times in Neoproterozoic carbonate platforms, talc may also form during very early diagenesis of marine carbonate sediments independent of the need for hypersaline Mg- and silica-rich high-pH brines (Tosca et al. 2011).

Meta-evaporitic talc mineralisation has formed a hematite–talc schist between soft hematite ore and dolomitic itabirite[6] at Gongo Soco, Quadrilátero Ferrífero of Minas Gerais, Brazil (Cabral et al. 2012 Fig. 14.26). Hosted in the Archaean Caué Formation, it is one of numerous iron-ore deposits of the Quadrilátero Ferrífero situated in the southernmost part of the São Francisco Archaean craton, which is edged by orogenic belts of Brasiliano age, i.e. ~0.6 Ga. The talcose schist is enriched in F and has a constant Fe/S ratio (Fig. 14.26bi, bii; respectively). Electron-microprobe analyses indicate trace amounts of S in different generations of hematite. The whole-rock Fe/S ratio possibly represents sulphate S from hematite-hosted fluid inclusions. Fluid inclusions in foliation-overprinting hematite and chlorite geothermometry from talcose rocks suggest, respectively, temperatures from <200 to ~300 °C. Tourmaline, a rare mineral in the hematite–talc schists, belongs to the alkali group and falls in the dravite compositional field and plots along the meta-evaporitic "Oxy-dravite-povondraite" trend (Fig. 14.26c). Boron-isotope determinations of tourmaline crystals, using secondary ion mass spectrometry, vary from −20 to −12‰ $\delta^{11}B$ (Fig. 14.26d). This compositional isotopic range, the fluorine rich nature of the talc and the trend in tourmaline chemical composition, all suggest a meta-evaporitic origin. That is, a non-marine evaporitic setting is the most likely source of acidic, highly oxidising fluids, which resulted in the abundant F-bearing talc and the presence of otherwise immobile Ti in the hematite. Oxidising brines were channelled along shear zones and converted dolomitic itabirite into the Gongo Soco soft hematite and the talc mineralisation. The latter is envisaged as the hydrothermal wall-rock alteration of dolomitic itabirite, which gave rise to the soft hematite ore (Cabral et al. 2012).

[6]Itabirite, is a banded-quartz hematite and hematite schist, constituting a laminated, metamorphosed oxide-facies iron formation in which the original chert or jasper bands have been recrystallized into layers made up of distinct crystals of quartz and the iron is present as thin layers of hematite, magnetite, or martite.

Precious Stones as Meta-evaporites

Base and precious metals are not the only ore deposits formed in association with meta-evaporites, some gemstones can also have meta-evaporite affinities. We have already seen that tourmaline is a semi-precious stone. Precious stones[7] and gems are rare by definition and need exceptional geologic conditions that give rise to gem-quality materials. These conditions may include the availability of sometimes uncommon major constituents, the presence of adequate chromophores[8] limited concentrations of undesirable elements, open space, an environment conducive to forming crystals of sufficient size and transparency. This general statement of requirements to form a precious stone also encapsulates why some gems have meta-evaporitic associations. As we have seen, halite and most other evaporite salts disappear or transform into other mineral phases by the early greenschist phase. As this happens the dissolution/transformation releases a pulse of hot basinal chloride waters that can leach/carry elements such as beryllium, chromium and vanadium (chromophores) from any adjacent organic-rich shales. Trace elements also tend to be enriched in the more evolved depositional brines that precipitated the latter minerals in any evaporite precipitates. At the same time as halite dissolves or transforms, anhydrite layers and masses typically remains into the more evolved portions of the metamorphic realm (amphibolite-granulite facies). The volume loss associated with the dissolution/transformation of meta-evaporites facilitates the formation of open space (sometimes pressurized) as veins and fractures that then allow the free growth of the precious stone or gem material.

Many natural gemstone settings are not evaporite-associated, the following section discussed those that are. Interestingly, the common link between most natural gem-forming environments is a hydrous, typically saline to hypersaline, solution that is able to precipitate a crystal in a void from a fluid that contains elevated and unusual levels of particular constituents, including chromophores; hence pegmatites, volcanics and meta-evaporites are the most typical hosts for natural gemstones.

[7]The Ancient Greeks, distinguished between precious and semi-precious stones; similar distinctions were made in other ancient cultures. In modern usage, the precious stones are diamond, ruby, sapphire and emerald, with all other gemstones being semi-precious.

[8]Chromophore; is the part of a gem lattice responsible for its colour. A gem's colour arises when a molecule absorbs certain wavelengths of visible light and transmits or reflects others. It is a structural feature in the lattice indicative of the presence of a gem-specific electron configuration of the ions in its crystal lattice; such as transition metal ions (Cr, V or Fe) occupying several different coordination sites. For example, ferrous iron (Fe^{2+}) or ferric iron (Fe^{3+}), the ferrous ion in peridot causes the green colour and ferric ion causes the yellow colour in chrysoberyl. This colour effect has important uses in heat-treatment gemstones such as blue colour in heat-treated sapphire.

Lapis Lazuli

Lapis lazuli is made up not of a single mineral but an accumulation of minerals; it is mostly composed of lazurite $(Na,Ca)_8(AlSiO_4)_6(S,SO_4,Cl)_{1-2}$ typically 30–40 % (Table 14.7). Lapis gemstones also contains calcite (white veins), sodalite (blue), and pyrite (gold flecks of colour). Dependent on metamorphic history and protolith chemistry, other common minerals in lapis include; augite, diopside, enstatite, mica, haüyanite, hornblende, and nosean. Some specimens also contain trace amounts of the sulphur-rich mineral lollingite (*var.* geyerite). Lazurite is a member of the sodalite group of feldspathoid minerals (Table 14.7). Feldspathoids have chemistries that are close to those of the alkali feldspars, but are poor in silica. If free quartz were present at the time of formation it would react with any feldspathoid precursor to form a feldspar. Natural lazurite contains both sulphide and sulphate sulphur, in addition to calcium and sodium, and so is sometimes classified as a sulphide-bearing haüyne (Fig. 14.27a). Sulphur gives lazurite its characteristically intense blue colour, it comes from three polysulphide units made up of three sulphur atoms having a single negative charge. The S_3- ion in the sulphur has a total of 19 electrons in molecular orbitals and a transition among these orbitals produces a strong absorption band at 600 nm, giving a blue colour with yellow overtones. The intensity of the gem's blue is increased with increasing sulphur and calcium content, while a green colour is the result of insufficient sulphur (O'Donoghue 2006, p. 329).

Other members of the sodalite group include sodalite and nosean (Table 14.7). Sodalite is the most sodium-rich member of the sodalite group and differs from the other minerals of the group in that its lattice retains chlorine. Interestingly, sodalite can be created in the laboratory by heating muscovite or kaolinite in the presence of NaCl at temperatures of 500 °C or more. In the literature, the commonly accepted origin of lazurite is through contact metamorphism and metasomatism of dolomitic limestone. Such a metasedimentary system also requires a source of sodium, chlorine and sulphur; the obvious source is interbedded evaporites in the protolith, as is seen in plots of its molecular constituents (Fig. 14.28; Aleksandrov and Senin 2006).

Lapis lazuli from the Precambrian of Baffin Island, Canada (Fig. 14.27a), and from Edwards, New York, are metaevaporites, as are the lapis lazuli deposits at Sar-e-Sang in the Kokcha valley, Afghanistan and the lapis deposits in Liadjuar-Dara region ("River of Lazurite") at an altitude of 5,000 m in the Pamir Mountains, Tajikistan (Webster 1975). Throughout history its bright blue colour has made lapis, mostly from Sare-Sang, a valued gem commodity. First mined 6,000 years ago, the Sar-e-Sang lapis was transported to Egypt and present day Iraq and later to Europe where it was used in jewellery and for ornamental stone[9] Europeans even ground down the rock into an expensive powdered pigment for paints called "ultramarine".

Lapis deposits in Lake Harbour on Baffin Island and in the Edwards Mine, New York, were produced by high grade metamorphism of an evaporite-marble protolith (Hogarth and Griffin 1978). The anhydrites preserved near Balmat are also part of this sequence and are discussed separately later in this chapter. On Baffin Island the two main lapis lazuli lenses, some 1.6 km apart, lie at the structural top of two sequences of dolomitic marble, the thicker lens being approximately 150 m across (Fig. 14.27b). The elongation of both lenses parallels the local layering and foliation and shows a well-developed layering parallel to the regional foliation, implying a sedimentary protolith to the deposits. The Main and Northern bodies constitute diopside–lazurite rocks of variable gem quality and are localized in marbles among biotite gneisses. The Main (Southern) occurrence is as long as 170 and 6 m thick. In these deposits, sheets of high-quality lazurite (up to 1 m thick) contain variable amounts of relict diopside and plagioclase, as well as newly formed haüyne, nepheline, or phlogopite. The quantitative proportions of these minerals define the colour of the rock, which becomes more intense with heating. The Northern occurrence (25 × 36 m in size) is less productive than the Main occurrence and consists of small (no more than 1 m) lenses with disseminated lazurite, which imparts a bluish green colour to the polished surface of the rock. Chlorine and sulphur in the various lazurites, accessory pyrite, and pyrrhotite were

[9]Lapis is the Latin word for "stone" and lazuli is the genitive form of the Medieval Latin *lazulum* meaning blue, which was taken originally from the Persian *lāžaward*, the name of a place where lapis lazuli was mined. Taken as a whole, lapis lazuli originally meant "stone of Lāzhward." With time, the name of the place came to be associated with the stone mined there and, eventually, with its bright blue colour. Lapis lazuli's use as jewellery can be traced back to the 5th millennium B.C.E. with the discovery of beads at a cemetery outside the temple walls of Eridu (Sumer) in southern Babylonia (Von Rosen 1990). To the ancient Egyptians, it was considered a gem representing the skies or heaven, thus was thought to denote light, truth and wisdom. It was thus often shaped into eye-shaped gems and was worn by judges in ancient Egypt. A lapis amulet graced the brow of Ra. Lapis is noted in Revelations in Christian mythology as a stone in the Breastplate of Aaron. In China, lapis was worn during the Manchu dynasty for services in the Temple of Heaven. The Romans and Greeks used it as a cure for fever and melancholy.

The Sar-e-Sang region has supplied much of the gem quality lapis to the world. One of the first European explorers to the region (Wood 1841) described mining methods in use at that time. Camel-thorn and tamarisk twigs were collected from the valley below and carried up the steep path to the mine. When sufficient fuel had been collected, it was piled against the rock face and a fire was lit. When the rock was hot, cold water, which also had to be carried up the steep 350 m ascent from the valley floor, was thrown onto it. The rock cracked and split, enabling further work to be done with the primitive tools available (pick, hammer and chisel) in order to extract the lapis lazuli from its marble host rock.

Table 14.7 Feldspathoids and lapis lazuli

Others	Nepheline	$8[(Na,K)AlSiO_4]$	Si depleted lavas where Na rather than K
	Cancrinite	$4[(Na_6,Ca)_2(SiAlO_4)6(CO_3,SO_4, Cl)2{\cdot}nH2O]$	Effervesces with HCl; Si depleted lavas
	Leucite	$16[KAlSi_2O_6]$	Carbonatite component Si-depleted
Lapis lazuli components	Sodalite	$Na_8Cl_2(AlSiO_4)_6$	Royal blue colour, mineral of sodalite group; *Var*. hackmanite is tenebrescent
	Haüyne	$(Na,Ca)_8(Al,Si)_{12}O_{24}(Cl,SO_4)$	Variable colour, mineral of sodalite group, aka roeblingite
	Nosean	$Na_8(SO_4)(AlSiO_4)6{\cdot}H_2O$	Variable colour, solid solution series between nosean and hauyne, mineral of sodalite group, aka noselite
	Lazurite	$(Na,Ca)_8(Al,Si)_{12}(O,S)_{24}(SO_4)(Cl,OH)_2$	Ultramarine, mineral of sodalite group, bulk of the mineral constituents in Lapis lazuli. That name is from the Persian *lazward* for blue

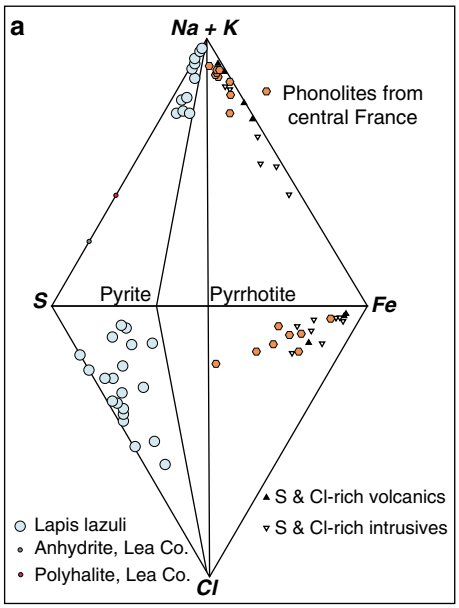

Main occurrence	North occurrence
Principal minerals (typically >0.3 %)	
Pyroxene (diopside)	Pyroxene (diopside)
Lazurite	Lazurite
Calcite	Calcite
Nepheline	Plagioclase (oligoclase)
Phlogopite	Scapolite (mizzonite)
Amphibole (pargasite)	Amphibole (edenite-pargasite)
Plagioclase (oligoclase)	Phlogopite
Sodalite (hackmanite)	Sphene
Pyrite	
Minor minerals (typically <0.3 %)	
Pyrrhotite	Apatite
Apatite	Pyrite
Sphene	Graphite
Graphite	Pyrrhotite
Zircon	Betafite (?)
Allanite	
Chalcopyrite	
Molybdenite	
Secondary minerals	
Natrolite	Hematite
Tetragonal natrolite	Thomsonite
Aragonite	Gonnarite
Hematite	Leucoxene
Goethite	Tetragonal natrolite
Leucoxene	
Cancrinite	

Fig. 14.27 Lapis Lazuli and Baffin Island. (**a**) Collateral compositional diagram, showing the relation between chlorine, iron, alkalies and sulphur for lapis lazuli from Baffin Island and Slyudyanka as well as alkalic igneous rocks and typical Permian evaporites for comparison. (**b**) Baffin Island, map of the Main (South) occurrence shows the lapis lazuli distribution is stratiform within its dolomitic marble host. Also listed are major and minor mineral phases for the Main (South) and North occurrences (After Hogarth and Griffin 1978)

derived from metamorphosed gypsum-, anhydrite-, and evaporitic-carbonate protoliths (Hogarth and Griffin 1978).

In the Lake Baikal lazurite occurrences, there is once again a strong association between marble of the Perval'na Group and lazurite occurrence (Fig. 14.28a). For example, the Slyudyanka deposit is hosted in diopside skarns and spinel–forsterite calciphyres developed from metamorphically evolved evaporitic dolomites (Aleksandrov and Senin 2006). The Slyudyanka deposit shows clearly pronounced metasomatic zoning, which was associated with the prograde magnesian skarn stage and was overprinted by retrograde postmagmatic assemblages, which were formed together with lazurite-bearing rocks under the influence of saline alkaline S–Cl-bearing hydrothermal solutions. These solutions also caused microclinization of blocks of leucocratic granite with the formation of lazurite in the some of the inner skarn zones. Potassium solutions caused phlogopitization of the host rocks.

Likewise, scapolite and magnesian whiteschists are typically saline mineral phases in the classic deposits of the Sare-Sang District (Fig. 14.28b; Faryad 2002). There the lapis is composed of a combination of lazurite, diopside, calcite and pyrite and occurs in beds and lenses up to 4 m thick within a scapolitic magnesian-marble skarn near the centre of the

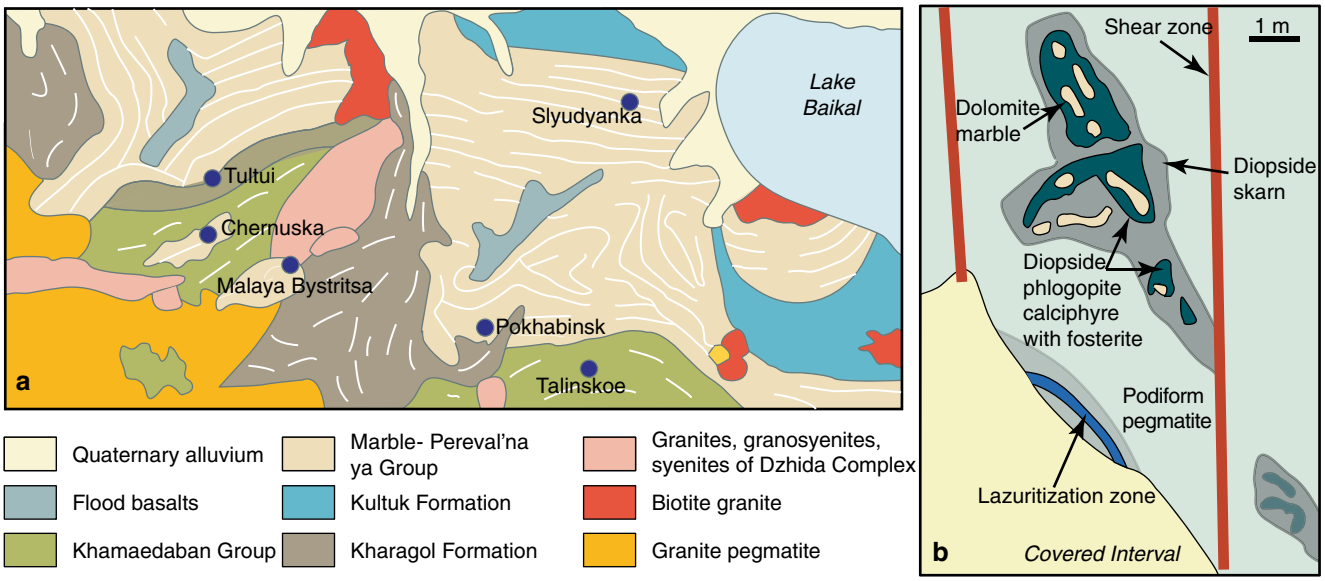

Fig. 14.28 Lapis Lazuli geological setting. (**a**) Geological map of the lazurite-bearing region in the southwestern Baikal area, also showing positions of main deposits and structural trend lines. (**b**) Geological detail of a lapis occurrence at Sar-e-Sang Afghanistan (After Aleksandrov and Senin 2006)

Hindu Kush granitic massif. It is typically interlayered with, or forms veins and lenses within its gneissic and pegmatitic host. Lens-shaped lodes are typically hosted in orthoclase–microcline–perthite hornfels containing albite and quartz (Fig. 14.28b). Lazurite bodies at the Sar-e-Sang deposit are associated with diopside metasomatites bearing nepheline, pale blue haüyne, and blue lazurite. Some lazurite-rich zones can contain up to 40–90 vol % lazurite. The rocks also contain diopside, haüyne, afghanite, and nepheline, as well as disseminated pyrite replaced by pyrrhotite. Pockets of near pure lapis lazuli can be up to 40 cm across and occasionally up to a metre.

Lapis lazuli in the North Italian Mountains of Colorado occurs in impure marbles in a meta-evaporitic skarn near the contact with the Eocene-age quartz monzonite and quartz diorites of the Italian Mountain stocks (Hogarth and Griffin 1980; Mauger 2007). There near vertical Pennsylvanian black shales and carbonates along the west margin of the intrusive have been converted to phlogopite-diopside-andalusite hornfels and scapolite-diopside skarns with minor analcime. Compared to Sar-e-Sang, lapis in this lapis in this skarn deposit is of inferior quality. It forms as deep blue lazurite granules in fine-grained forsterite-Ti phlogopite-calcite skarns and calcite marbles with diopside, Ti-phlogopite and pyrite. The hosting sediments along the NE margin of the pluton are Mississippian limestones and Devonian sandstones, while the NaCl came from dissolution of once nearby halite or dissolution-derived saline surface waters and shallow groundwaters moving south from the Eagle Basin.

High quality lapis is also mined from a limestone-granite skarn contact in the Chilean Andes (3,500 m elevation) in the headwaters of the Cazadero and Vias river, Ovalle, Coquimbo, Chile. The lapis there is good quality, although somewhat paler than Sar-e-Sang and, like the Baikal lapis deposits of Russia, is associated with wollastonite not diopside, making it a less attractive gem. The Chilean lapis occurs in an association of phlogopite, sodalite, calcite and pyrite (Coenraads and de Bon 2000).

Columbian Emeralds

Colombian emeralds[10] are meta-evaporitic gems formed via mixing of fault-focused hypersaline basinal solutions released during the subsurface dissolution and alteration of evaporites (Ottaway et al. 1994; Giuliani et al. 1995, 2000; Branquet et al. 1999; Banks et al. 2000; Groat et al. 2008). Emeralds occur within carbonate-silicate-pyrite veins and breccias hosted in black shales and limestones, tied to occurrences of hydrocarbons/bitumens. Gem fields constitute two zones, the eastern and western emerald zones, some 80 km apart in the Eastern Cordillera of Columbia (Fig. 14.29). The Columbian emerald fields supply more than 60 % of the world market (Groat et al. 2008).

The western zone crops out in the core of the Villeta anticlinorium (Fig. 14.29a; Branquet et al. 1999). The sedimentary series that enclose the emerald deposits (Fig. 14.29b) are a few hundred meters thick and are composed of, from bottom to top: (1) micritic, largely dolomitic limestones (Rosablanca Formation, Valanginian-Hauterivian); (2) calcareous black shales (Hauterivian); and (3) siliceous black shales that form the base (Hauterivian) of the thick mudstones (Barremian-Aptian) of the Paja Formation. Most of the emeralds are found in hydrothermal breccias or in

[10] Emerald is a brilliant, grass-green variety of beryl [$Be_3(Al,Cr)_2Si_6O_{18}$], highly favoured as a gemstone. Green colour is caused by trace of chromium (Cr^{3+}) and vanadium (V^{3+}) ions.

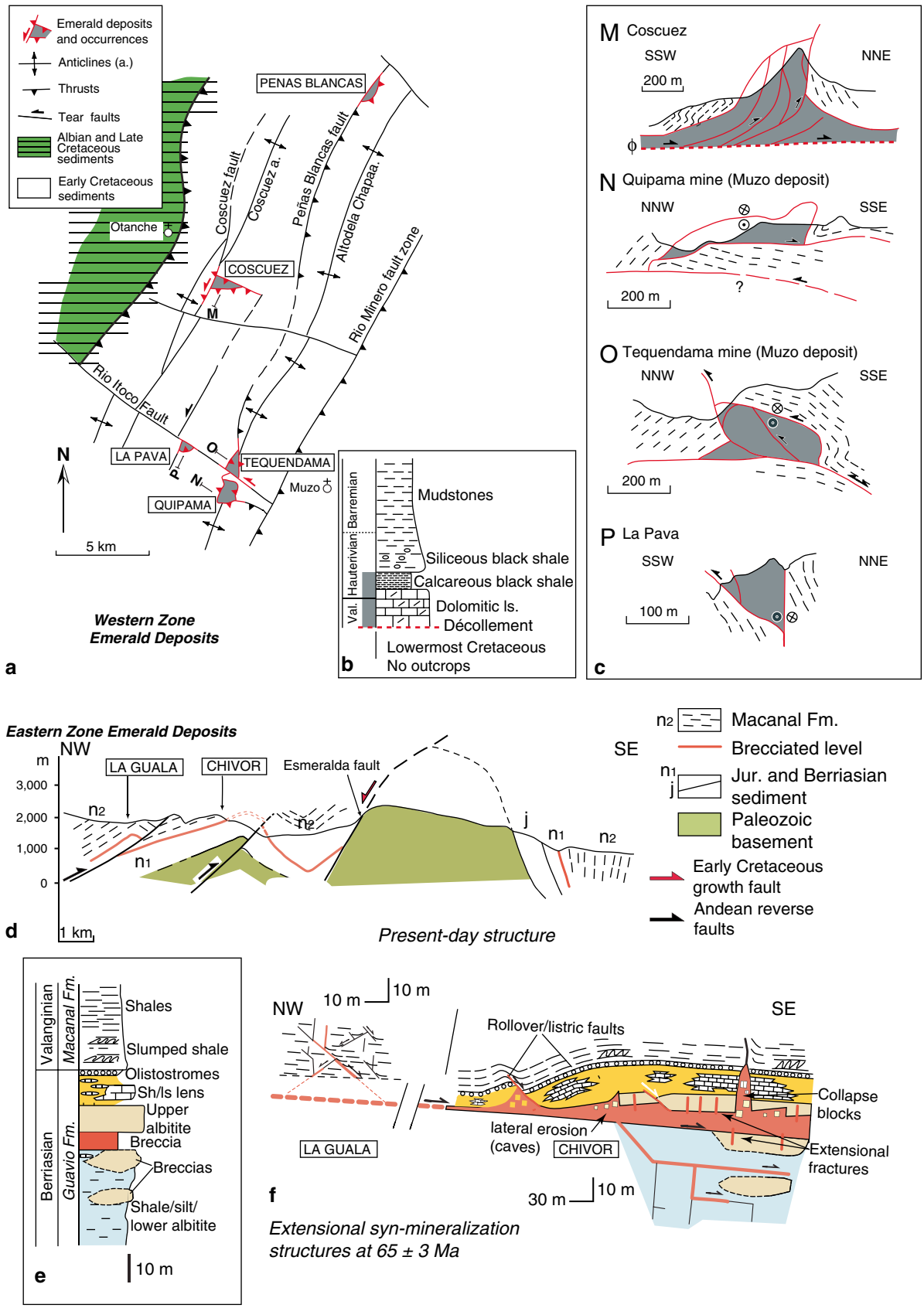

Fig. 14.29 Structural and regional geology of Western (**a**–**c**) and Eastern (**d**–**f**) emerald districts. (**a**) Structural map of the Western Zone Emerald deposits. (**b**) Schematic lithostratigraphic log. (**c**) Cross sections (see **a** for locations) of emerald deposits marked *M*–*O*; dolomitic limestone and calcareous black shale in *grey*, and hydrothermal breccias marking thrust and fault planes in *red*. (**d**) Regional section showing current structure and distribution of breccia levels (*red*). E > Schematic lithostratigraphic log of Chivor deposit. (**f**) Extensional synmineralisation structure in pre-Andean attitude. *Red* shows main brecciated level and associated mineralised faults and fractures (After Branquet et al. 1999)

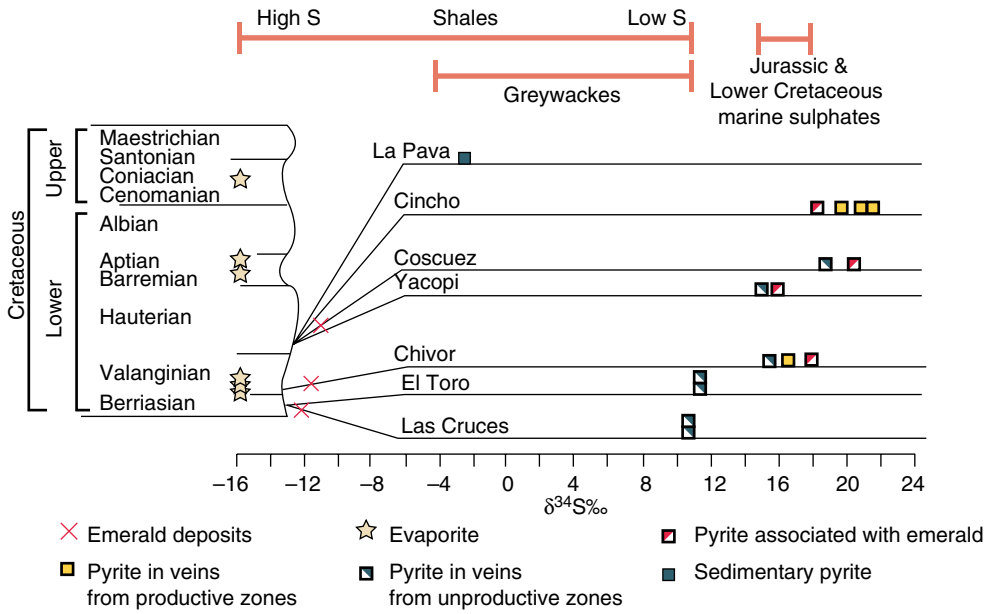

Fig. 14.30 Lithostratigraphic chart locating the main emerald deposits from eastern and western Columbia. Sulphur isotope $\delta^{34}S_{CDT}$ values of pyrites within productive and unproductive intervals plotted against potential sources of sedimentary sulphur (After Giuliani et al. 1995)

carbonate-pyrite veins developed within both dolomitic limestones and calcareous black shales.

The deposits are hectometer-sized at most and display numerous folds, thrusts, and tear faults. All the tectonic contacts are marked by centimeter-to meter-thick hydrothermal breccias that are cataclasites with clasts of black shales and albitites (i.e., massively albitized shales) within a carbonate-albite-pyrite cement. These breccias derived from a fluid-rich pulp (Branquet et al. 1999). Part of the overpressured fluid escaped and triggered intense hydraulic fracturing in surrounding rocks, especially along tear faults. In each deposit, there is evidence of complex deformation that resulted in polyphase duplex structures. For example, in the Coscuez deposit, the ore-hosting N30°E verging folds and thrusts were a response to movement on the sinistral N20°E trending Coscuez tear fault (Fig. 14.29c).

In the eastern zone (Fig. 14.29d), Andean thick-skinned tectonics are responsible for the main deformation observed on regional cross sections through the Eastern Cordillera and adjacent Llanos foothills. This Andean deformation corresponds mainly to reverse faults (with an overall vergence to the southeast) and folds affecting the Palaeozoic basement and its Cretaceous-Tertiary sedimentary cover. Some of these faults are inverted Early Cretaceous growth faults. The Esmeralda fault likely represents the preserved part of an Early Cretaceous normal fault (Fig. 14.29d). As the result of Andean thick-skinned tectonics, the Chivor emerald deposit is located on a gently northwest dipping monocline situated on the western flank of a large, N30°E-trending, upright fold, devoid of cleavage.

The enclosing sedimentary series (Fig. 14.29e) correspond to the upper part of the Guavio Formation (Berriasian), which unconformably overlies the Palaeozoic basement and is overlain by the shales of the thick (2,900 m) Valanginian Macanal Formation. The series hosting the emerald-bearing veins and associated hydrothermal breccias are composed of, from bottom to top: (1) shales and siltstones that are locally massively albitized (lower albitites); (2) a 1–10-m-thick, stratiform brecciated level, largely made of hydrothermal breccia after a former evaporite level; (3) an albitized and carbonatized sequence (upper albitites) that is white and initially contained anhydrite beds (as evidenced by phantom nodules, chicken-wire, and tepee structures); and (4) bioherms of micritic or shelly limestones grading vertically and laterally into black shales intercalated with calcareous pebbly mudstones and olistostromes.

Within the brecciated level, disrupted blocks of the hanging wall (albitites, black shales, limestones) and caving structures are evidence for the collapse of the roof. Thus, the dissolution of an evaporitic horizon (probably initially dominated by halite) appears to be a major process controlling the formation of the brecciated level. The stratiform association of evaporites, limestones, albitites, and the brecciated level is consistent across tens of kilometres around the Chivor deposit, owing to its folding by the Andean phase. All the emerald deposits of the Chivor mining district are located within or just above this regional level, and so define a stratigraphic emerald horizon (Fig. 14.29f).

Mineralizing fluids were derived via interaction of low-salinity fluids with primary halite and anhydrite, tentatively assigned to the Carib Halite Formation (Higgs 2009). The source of beryllium is thought to be the encasing black shales, while the sulphide-sulphur is evaporitic (Fig. 14.30). Organic matter, including bitumen, occurs both in the black

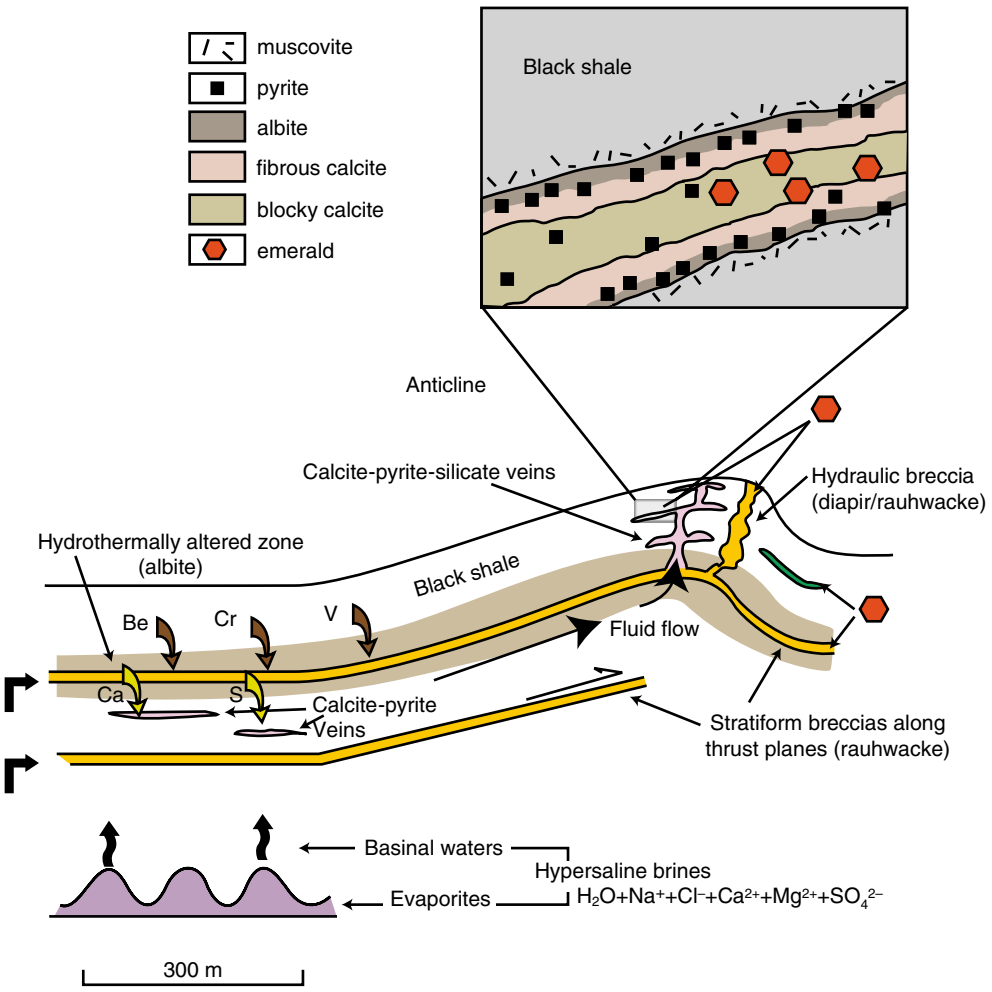

Fig. 14.31 Model of formation of Colombian emeralds. Emeralds were hydrothermally formed during thrusting and folding of black shales in a salt lubricated rauhwacke system. Highly reactive hypersaline brines, generated by circulation of hot basinal waters passing through and dissolving halokinetic evaporite beds, meant chloride-rich brines passed from thrust planes to drive wall-rock metasomatic alteration in zones immediately adjacent. By this process, Be, Cr and V were mobilised, and could then precipitate emeralds in extensional veins and hydraulic breccias (rauhwacke), which are also rich in calcite and pyrite (Compiled from sketches by Ottaway et al. (1994) and Cheilletz and Giuliani (1996))

shales and in the emerald-bearing hydrothermal veins. Organic matter is found in hydrothermally altered and unaltered forms and in primary fluid inclusions in the emeralds. Infrared microscopy of the hydrothermal bitumens revealed the absence of aliphatic and aromatic bands and the disappearance of oxygen functional groups. Rock-Eval analyses (hydrogen index (HI) <1; 19< oxygen index (OI) <61), as well the elemental H/C ratio (HI <1) of the bitumens, confirm the intense cracking suffered by the original organic matter during thermal alteration associated with emerald formation.

Fluids trapped as inclusions in the emeralds, dolomites and pyrites consist predominantly of Na-Ca-Cl brines, with some KCl. The Na-Ca-K chemistry of the inclusions supports an evaporitic parent for the hydrothermal fluids; fluid inclusion salinities in the emeralds range from 25 to 40 NaCl wt% equiv. (Giuliani et al. 2000; Banks et al. 2000). Emerald mineralization in the western zone is dated at ≈35 Ma, while eastern zone mineralization is 30 Ma older. Crush leach analyses of electrolytes in fluid inclusions within emeralds, quartz, calcites, dolomites and fluorites from both zones, demonstrate that parent brines in each region range between two extremes (fluid 1 versus fluid 2) with many samples yielding intermediate compositions. Fluid 1, found mainly in emerald-hosted fluid inclusions, is dominated by NaCl with high Cl:Br ratios indicating that the salinity was derived by dissolution of halite, most probably from local, now dissolved, salt beds. Fluid 2, found mostly in quartz hosted-fluid inclusions, is of similar salinity but contains less Na and significant concentrations of Ca-K-Fe-Cl and other cations. It has lower Cl:Br ratios, and so is more comparable with formation waters, but is inferred to have obtained part of its salinity by halite dissolution.

Bivariate plots of most cations show linear or sublinear trends, regardless of the mineral hosting the inclusions or the locality from which the samples originated, demonstrating that mixing of the two saline fluids has occurred. Because the same two fluids occur in both eastern and western zones, despite the difference in space and time for the mineralization, it is inferred that fluid compositions were rock-controlled via similar interactions with dissolving evaporites and black shales in both instances. It is proposed that beryllium was transported as Be-F complexes in the NaCl-fluid,

and was precipitated as emerald after mixing with the calcic brine caused precipitation of fluorite (CaF_2) and parisite, $[(Ce,La)_2Ca(CO_3)_3F_2]$.

The $\delta^{34}S$ values of H_2S in solution is in equilibrium with pyrite from six emerald deposits ranging from 14.8 to 19.4‰, whereas sedimentary pyrite from the enclosing black shales yields a $\delta^{34}S$ of −2.4‰ (Fig. 14.30; Giuliani et al. 1995). The narrow range in $\delta^{34}S_{H2S}$ between the different deposits suggests a uniform and probably unique source for the sulphide-sulphur. Elevated $\delta^{34}S_{H2S}$ values suggest non-participation of magmatic or Early Cretaceous black-shale sulphur sources. Salt diapirs occur in the emeraldiferous areas and the most likely explanation for high $\delta^{34}S$ involves the reduction of sedimentary marine evaporitic sulphates (Fig. 14.31). This emerald-deposit type is a mesothermal meta-evaporite deposit (300 °C) produced through thermochemical reduction of diapir-derived sulphate-rich brines to hydrogen sulphide by interaction with organic-rich strata.

Emeralds grew hydrothermally during thrusting and folding of black shales in a salt lubricated rauhwacke system. Highly reactive hypersaline brines, generated by circulation of hot basinal waters passing through and dissolving halokinetic evaporite beds, created chloride-rich brines that passed from thrust planes to drive wall-rock metasomatic alteration. By this process, Be, Cr and V were mobilised, and could then precipitate emeralds in extensional veins and hydraulic breccias (rauhwacke), which are also rich in calcite and pyrite.

A similar mesothermal metamorphic model is used to explain emeralds hosted in the Red Pine Shale, within the South Flank fault zone of the Uinta Mountains of Utah (Keith et al. 1996). The host rock is a 1 km thick, black (organic-bearing) Proterozoic shale sequence, with thin interbedded arkoses. As in Columbia, abundant pyrite, baryte, vein quartz, blocky and fibrous calcite veins, along with bleached shale and green mica, are present along and about the fault zone, and within the Cr-rich (up to 200 ppm) Red Pine Shale. As in Columbia there are no granitoid or intermediate intrusions within 50 km of the area, and no geophysical evidence to indicate that the alteration is associated with concealed igneous activity (Keith et al. 1996).

The isotopic composition of pyrite from the South Flank fault zone ($\delta^{34}S = +4.6$ to $+4.2$‰) is similar to the isotopic signature of sulphur in nearby Tertiary oil field brines (≈ +5‰). These brines are present near the base of the Uinta Basin succession, within the Wasatch Formation and the highly evaporitic Green River Formation. The deepest portion of the asymmetric Uinta basin is bounded by normal and reverse faults that were active during uplift of the Uinta Mountains. Consequently, the hydrothermal fluid, responsible for alteration of the Red Pine Shale, may be similar to that forming the Colombian emeralds. According to Keith et al. (1996), their data suggests that an external hydrothermal fluid (a highly saline, probably Tertiary age basinal brine) mixed with other subsurface waters along the fault zone. As these basinal fluids reacted with feldspar or calcite cements, they formed the sparse emerald and other alteration products now found in their Proterozoic host shales.

Rubies in SE Asia

Ruby is the red-pink transparent gem form of the mineral corundum ($2[Al_2O_3]$), with intensity of its red colour related to trace amounts of chromium[11] oxide. The coloured gem varieties of corundum include; white sapphire (colourless), ruby (red), pigeon's blood (deep red), sapphire (blue), golden sapphire (yellow), green sapphire (green), as well as olive green, purple and violet (violet sapphire). Corundum is found as highly valued rubies in Myanmar and Thailand, and as sapphires in Sri Lanka and Cashmere-India, as well as in lesser quality gem deposits in Australia, Tanzania, Cambodia, Russia, Thailand, Malagasy, Nepal, Malawi, and the USA (Manutchehr-Danai 2005).

Marble-hosted ruby deposits today represent the most important source of coloured gemstones in Central and South East Asia (Garnier et al. 2004, 2008). These deposits are located in the Himalayan belt and formed during the Tertiary collision of the Indian plate in its northward movement into the Eurasian plate (Fig. 14.32a). SE Asian rubies are spatially related to granitoid intrusions and are hosted in evaporite-entraining platform carbonates that have experienced high-grade metamorphism. All occurrences are located close to major tectonic features active during Himalayan orogenesis, either directly in suture zones in the Himalayas, or in shear zones that guided extrusion of the Indochina block after the collision in South East Asia. Ar-Ar dating of micas syngenetic with the rubies, and U-Pb dating of zircon inclusions in the rubies, show that these deposits formed during Himalayan orogenesis and associated extensional tectonics active between the Oligocene and the Pliocene, in a belt from Afghanistan to Vietnam. These ruby-bearing marbles lie in the amphibolite facies (T = 610–790 °C and P ≈6 kbar).

[11] Chromium is the chromophore in both ruby and (most) emerald. In ruby, the details of the atomic environment and local charges around the chromium ion result in a strong interaction, equivalent to a small "cage" around the ion. This induces light absorption at high energy, and hence most of the transmission is at low energy, in the red part of the visible spectrum. The opposite occurs in emerald, in which the local environment is more relaxed, resulting in a looser "cage" around the chromium ion. The absorption is at lower energies, which results in the well-known emerald-green colour (Groat and Laurs 2009).

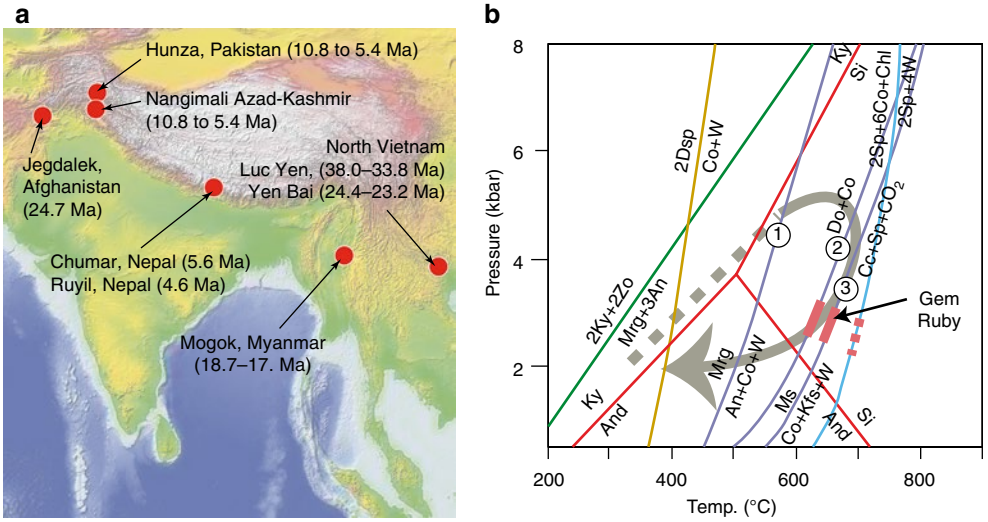

Fig. 14.32 Meta-evaporitic rubies in SE Asia (After Garnier et al. 2008). (**a**) Location and age of various gem ruby fields in SE Asia. (**b**) P-T evolution showing corundum formed during the prograde metamorphic P–T path (*dashed thick grey line*) and then during the retrograde stage (*solid grey line*) from the destabilization of different mineral assemblages as drawn in this P–T sketch: *1* from margarite, then *2* from micas, and *3* from spinel. At this stage, corundum is destabilised at lower temperature and pressure in margarite and then diaspore. Gem ruby formed at a pressure between 2.6 and 3.3 kbar and temperature between 620 and 670 °C (*pink rectangles*). Abbreviations: *An* anorthite, *And* andalusite, *Cc* calcite, *Co* corundum, *Do* dolomite, *Dsp* diaspore, *Kfs* K-feldspar, *Ky* kyanite, *Mrg* margarite, *Ms* muscovite, *Si* sillimanite, *Sp* spinel, *W* water

Fluid inclusions in the various gem rubies from the Jegdalek, Hunza and northern Vietnamese deposits indicate retrograde metamorphism; 620< T <670 °C and 2.6 <P <3.3 kbar (Fig. 14.32b; Garnier et al. 2008). Whole rock analyses of nonruby-bearing marbles show they contain enough aluminium and chromiferous elements to produce all the ruby crystals that they host. As protolith, these carbonates contained Al- and chromiferous-bearing detrital materials, probably clays, which were deposited on the platform as the same time as the mostly carbonate matrix along with locally enriched levels of organic matter.

In addition, the consistency of (C, O)-isotopic values of carbonate in the marbles shows marbles developed in a closed fluid system, and were not infiltrated by externally-derived fluids. The carbon isotopic composition of graphite in the marbles underlines its organic origin and that it exchanged C-isotopes with the adjacent carbonates during its metamorphic evolution. Earlier, less evolved examples of this isotopic exchange, with temperatures still in the upper diagenetic realms are seen in Permian Carbonates of the Saraburi region, Thailand (Warren et al. 2014). Moreover, the O-isotopic composition of ruby across SE Asia was buffered by metamorphic CO_2, released during devolatilisation of marble, while the H-isotopic composition of associated mica is consistent with a metamorphic origin for water now in equilibrium with the micas. The boron isotopes from tourmalines associated with the rubies indicates a likely nonmarine evaporite source for the boron (Fig. 14.33; Garnier et al. 2008).

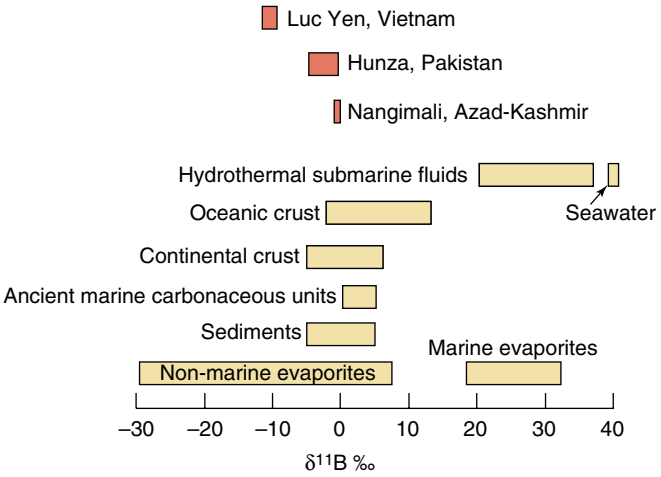

Fig. 14.33 Boron isotopic compositions of tourmaline associated with ruby in marbles compared to other typical boron sources and associations (After Garnier et al. 2008)

Garnier et al. (2004, 2005) note that the ruby-bearing marbles from Nangimali, in the Azad-Kashmir deposits of Pakistan, contain, besides phengite, atypical mica intergrowths with paragonite, phlogopite and aspidolite (sodium phlogopite). Both phlogopites, although intimately linked and coexisting with paragonite, are fluorine rich, in contrast to the phengite and paragonite. The phengite is either associated with phlogopite or can be isolated. The presence of aspidolite in these ruby-bearing marbles,

together with NaCl solid inclusions and the presence of anhydrite, further strengthen the notion that evaporites were involved in the genesis of these gem corundums.

In summary, Southeast Asian rubies formed during the retrograde portion of the metamorphic path, mainly by destabilization of muscovite or spinel. The metamorphic fluid system was rich in CO_2 released from devolatilisation of carbonates, and in fluorine, chlorine and boron, probably released from molten and altering Cretaceous or Precambrian and even Permian salt masses (NaCl, KCl, $CaSO_4$) caught up in the orogeny. Garnier et al. (2008) emphasise that evaporites are key to explaining the formation of rubies and emeralds in this gem-rich region of southeast Asia. Molten salts mobilized the *in situ* Al and metal transition elements that were contained in the host marbles, leading to crystallization of the rubies.

Tsavorite and Tanzanite

Tsavorite,[12] the vanadian variety of green grossular garnet, is a high value semi-precious gemstone. Currently it is hosted exclusively in metasedimentary and largely meta-evaporitic formations within the Neoproterozoic Metamorphic Mozambique Belt (Feneyrol et al. 2013). Deposits are mined in Kenya, Tanzania and Madagascar and other occurrences in the belt are located in Pakistan and East Antarctica. All are located within metasomatized graphitic rocks, such as graphitic gneiss and calc-silicates, intercalated with meta-evaporites. Tsavorite is found as primary deposits either in nodule (type I) or in quartz vein (type II), and in placers (type III). The primary mineralizations (types I and II) are controlled by lithostratigraphy and/or structure (Fig. 14.34).

For the African occurrences, the protoliths of the host-rocks are either anhydrite or baryte, both hosts were deposited at the beginning of the Neoproterozoic within a saline marine coastal sabkha environment, deposited at the margin of the Congo–Kalahari cratons. Subsequently, during the East African–Antarctican orogeny, these saline sediments experienced high amphibolite to granulite facies grade metamorphism, with the formation of the tsavorite occurring between 650 and 550 Ma. Nodules of tsavorite formed during prograde metamorphism, with calcium supplied by metamorphosing sedimentary sulphates and carbonates, whereas the alumina, silicates, vanadium and chromium come from a clay-chlorite protolith (Fig. 14.34). Veins formed during deformation and shearing of the metasedimentary platform were partially filled with tsavorite and other metamorphic phases. Further metasomatism occurred subsequent retrograde metamorphism with ongoing reactions with pore waters.

All the metasedimentary sequences today are still characterized by the presence of evaporitic minerals, such as gypsum and anhydrite, and scapolite. Evaporites are essential to tsavorite as they provide calcium and facilitate the mobilization of all the chemical elements for tsavorite formation. The H_2S–S_8 metamorphic fluids characterized in primary fluid inclusions of tsavorites and the $\delta^{11}B$ values of coeval dravite consistently around $-20‰$ confirm the marine evaporitic (high salinity) origin of the fluids. The V_2O_3 and Cr_2O_3 contents of tsavorite range respectively from 0.05 to 7.5 wt.%, while their $\delta^{18}O$ values are in the range of 9.5–21.1‰.

The genetic model proposed for tsavorite is metamorphic, based on chemical reactions developed between an initial assemblage composed of gypsum and anhydrite, carbonates and organic matter deposited in a sabkha-like sedimentary basin (Fig. 14.34; Feneyrol et al. 2012, 2013). Two kinds of nodules were likely precursors to tsavorite and both were hosted in an evaporitic protolith: (i) nodules Type N_I were initially anhydrite concretions within silica-rich shales; (ii) nodules Type N_{II} were initially baryte concretions located within calcareous shales. Both types of shales contained V(−Cr)-rich clays and organic matter.

At the beginning of the prograde metamorphism (stage 2), the hosting shales turned into schists, and V(−Cr)-rich clays and organic matter transformed into respectively V(−Cr)-rich micas and graphite. For the crystallisation of tsavorite in nodules Type N_I, Si and Al come from the schist, and V and Cr from the clays and transported into the anhydrite core where it forms tsavorite utilising Ca from the evaporitic sulphate, following the equation;

$$3CaSO_4 + 2Al_3 + 3SiO_2 + 6H_2O \rightarrow Ca_3Al_2\left(SiO_4\right)_3 + 6O_2 + 3H_2S + 6H^+.$$

H_2S is trapped in fluid inclusion cavities during the growth of tsavorite, while the sulphur is expelled into the schist to form pyrite. At the end of the prograde metamorphism, most of the anhydrite had been replaced by tsavorite, which is also present as small crystals scattered in the evaporitic rims. During retrograde metamorphism, these crystals are rehydrated and change in the rims into vanadian zoisite.

[12] Tsavorite (also spelled tsavolite, and tsavolithe) is a transparent, bright green to emerald green variety of grossular garnet $Ca_3Al_2(SiO_4)_3$ coloured by chromium and vanadium. RI: 1.734–1.744. SG: 3.68. H: 6½–7. Originally discovered in 1967 by British-born gemmologist Campbell Bridges and described from the Tsavo National Game Park in Kenya, from which it took its name, this green vanadium-bearing (goldmanite-component) grossular garnet, with minor chromium, is more prevalent in Tanzania, with current production from Tunduru, Ruangwa, Umba, Merelani Hills and Komolo, which has outstripped production from Kenya. Also found at Gogogogo, Madagascar, and in the Swat region, Pakistan. In 2009, Campbell Bridges was ambushed and killed by a Kenyan mob, who were illegally mining the gem on his property.

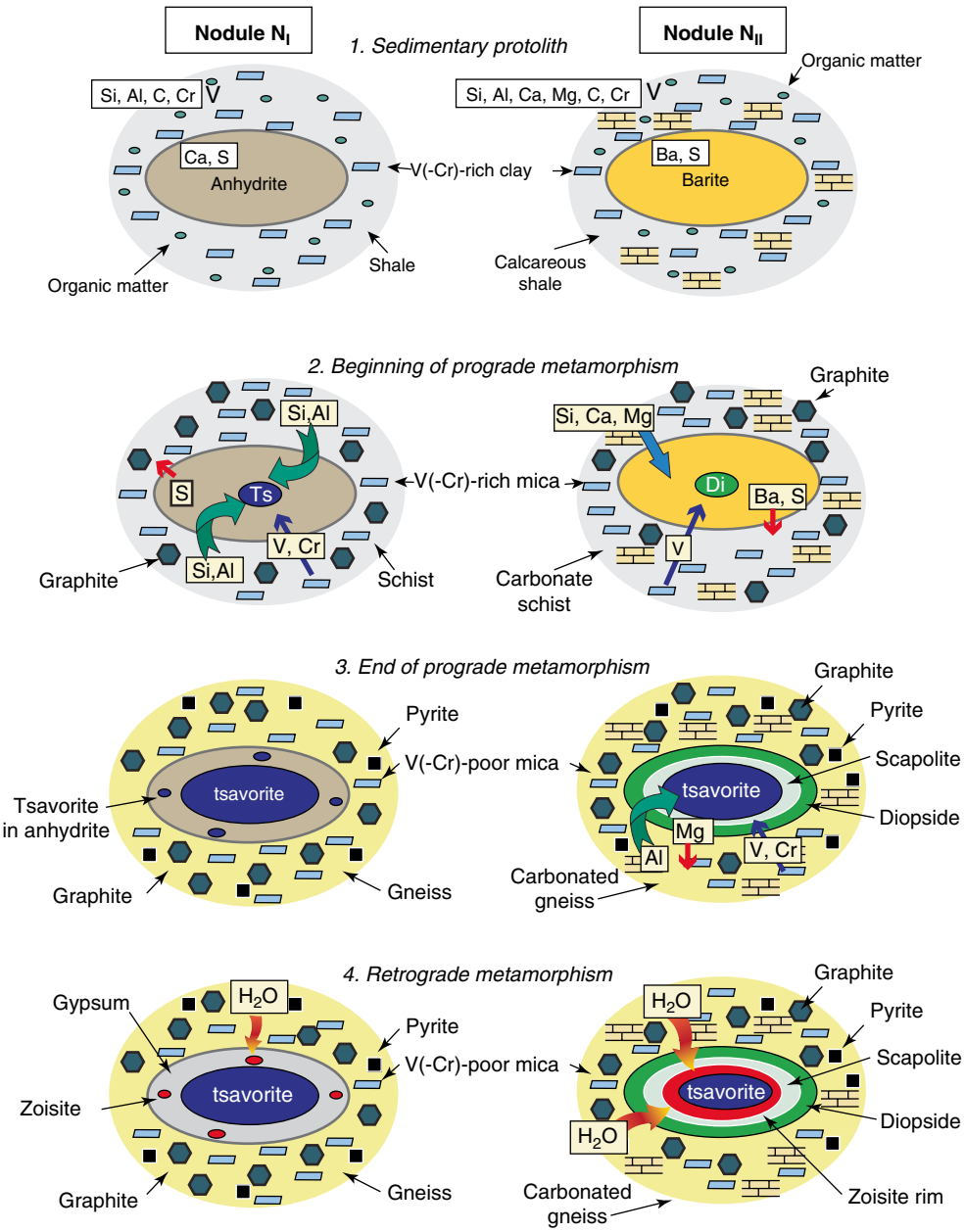

Fig. 14.34 Schematic representation of the formation of tsavorite-bearing nodules (type I and II). See text for details (After Feneyrol et al. 2013)

For the crystallisation of tsavorite in Type N_{II} nodules, Ca and Mg came from the carbonates and Si is transported towards the central part of the nodule, replacing baryte with diopside. A minor amount of vanadium is sourced from the micas and had been incorporated into the diopside core. Ba and S were expelled into the schist, the latter forming pyrite. Then the diopside core increased until replacing all the baryte. Transport of Al, V and Cr from the schist into the core led to the formation of tsavorite following the reaction;

$$3CaMgSi_2O_6 + 2Al_3^+ \rightarrow Ca_3Al_2\left(SiO_4\right)_3 + 3SiO_2 + 3Mg^{2+}.$$

Tsavorite and diopside interacted then to form scapolite following the reaction;

$$2CaMgSi_2O_6 + 2Ca_3Al_2\left(SiO_4\right)_3 + 2SiO_2 + 2CO_2 + 4Al_2O_3 \rightarrow 2Ca_4Al_6Si_6O_{24}CO_3 + 2MgO.$$

Hence, primary deposits of tsavorite are of two types, both with predictable occurrence positions in the field, which can be used to construct useful exploration paradigms (Fig. 14.35). Type I nodules occur in meta-evaporite beds creating stratiform units, intercalated within the metamorphic series and more precisely in Ca-dominated rocks such

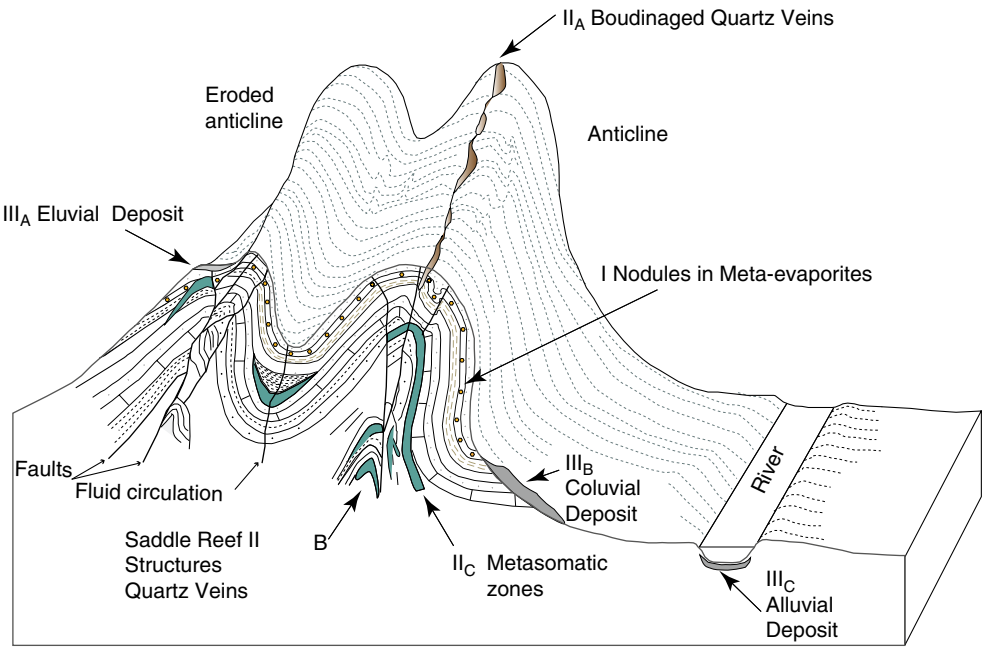

Fig. 14.35 Schematic cross-section of the different types of tsavorite deposits in the Neoproterozoic Metamorphic Mozambique Belt (After Feneyrol et al. 2013, and references therein)

as carbonate gneiss and calc-silicates with intercalations of marble (as in Kenya, Madagascar, part of Tanzania and Antarctic deposits). Type II associations occur where the metamorphic formations are affected by tight ductile isoclinal folding and shearing. The tsavorite occurs in quartz veins located at the hinges of the sheared isoclinal folds (Type IIA) and within 'saddle reef' structures (Type IIB). In this situation, deformation and shearing are associated with fluid circulation and percolation in the tectonically-opened structures. The metamorphic rocks undergo metasomatic phenomena such as pyritisation, graphitisation, silicification and carbonatisation, sometimes with precipitation of tsavorite (Type IIC). This type of deposit is found in the Lelatema area and Ruangwa in Tanzania, and in Pakistan.

Secondary tsavorite deposits (Type III) result from the erosion of the primary ones. Three secondary (reworked) sub-types are described: (i) sub-type IIIA corresponds to eluvial deposits such as those found in the Merelani area and in Kenya; (ii) sub-type IIIB is colluvial deposits such as those located in the Merelani area and in Kenya; (iii) sub-type IIIC is alluvial deposits forming the placers of Tunduru and Umba in Tanzania.

During retrograde metamorphism, hydration of both tsavorite and scapolite can lead to the formation of zoisite ($4[Ca_2Al_3(O/OH/SiO_4/Si_2O_7)]$), a member of the epidote group, which can become another gem mineral, known as Tanzanite.[13] In the Merelani region of Tanzania, veins containing tanzanite and tsavorite garnet have resulted from pegmatitic and hydrothermal fluids reacting with medium- to high-grade meta-evaporitic rocks along the crests of folds (Fig. 14.35). The faceted crystal form of many of the tanzanites is a result of their growth into dissolution cavities in the anhydrites and gypsums, fed by undersaturated mineralizing solutions and free of interference from other minerals. The zone of mineralization with such excellent gems is only a few metres wide but extends for about 9 km and includes other spectacular gem growths such of chrome tourmaline and chrome diopside. To date the known occurrences of gem quality tanzanite are restricted to the Merelani area.

Elevated Magnesium Levels in Metasediments

So far in our discussion of mineral phases that imply an evaporite protolith, we have largely focused on those mineral phases that retain evidence of the actual ionic components of the original evaporite salt; scapolite (Na, Cl, S from SO_4) albite (Na) and tourmaline (B and Na), sodian phlogopite and kulkeite. But there are also a number of commonplace metamorphic minerals, derived from an

[13] Tanzanite; a commercial term for cut zoisite; transparent blue to violet gem, pleochroic variety of zoisite, which exhibits strongly trichroic properties in deep blue, deep red, and greenish yellow. Optics; α:1.692, β:1.693, γ:1.700. Birefringence: 0.009. Dispersion: 0.019. SG;3.38. H;6–7. Currently, high quality gem forms are considered to be a thousand times rarer than diamond, but its relative softness keeps the price (hundreds to thousands of dollars per carat) far below that of fine diamond. Tiffany & Co. coined the name tanzanite for blue zoisite as they considered the term "zoisite" sounded too much like "suicide."

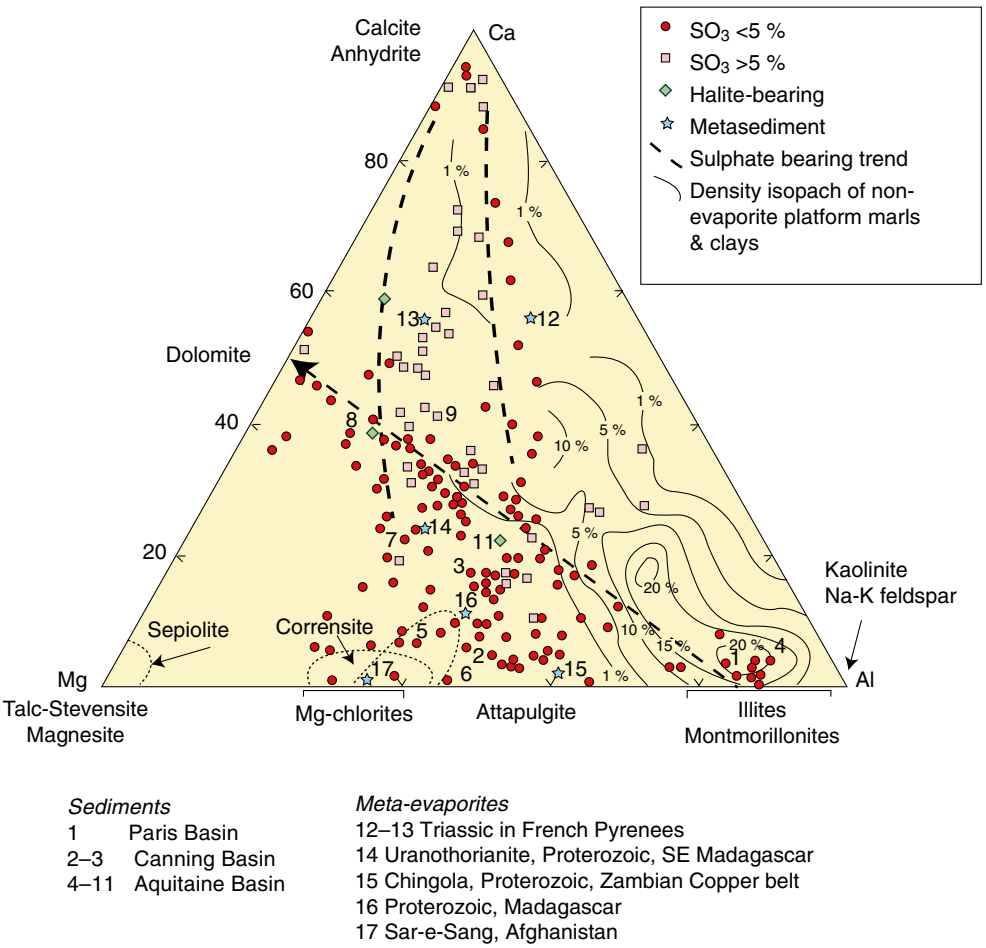

Sediments
1 Paris Basin
2–3 Canning Basin
4–11 Aquitaine Basin

Meta-evaporites
12–13 Triassic in French Pyrenees
14 Uranothorianite, Proterozoic, SE Madagascar
15 Chingola, Proterozoic, Zambian Copper belt
16 Proterozoic, Madagascar
17 Sar-e-Sang, Afghanistan

Fig. 14.36 Al-Mg-Ca diagram (milliatoms) showing the discrimination between the studied evaporitic rocks and shales and marls from common platform series (indicated by density occurrence isopachs of 120 samples). The evaporitic argillites and marl clearly exhibit higher Mg contents due to abundant magnesian clays while dolomite is the main carbonate. Sulphate-bearing rocks trend toward the Ca apex (calcite-anhydrite) and follow a trend (*dashed lines*) indicating the high Mg content of their clay fraction compared with nonevaporitic platform sediments (After Moine et al. 1981)

evaporitic protolith, that do not retain evidence of elevated levels of the ionic components in the salt protolith. Rather these meta-evaporites retain evidence of their genesis in the form of elevated levels of magnesium, which was originally deposited as magnesian interbeds (e.g., dolomite cements in interbedded clays or palygorskite) or in the periphery of the actual chloride salt mass. Such associations are much more enigmatic in terms of deciphering their meta-evaporitic protolith.

In a attempt to better define the significance of this association, Moine et al. (1981) geochemically analysed a selection of evaporitic and nonevaporitic sediments and then plotted the results as a Ca-Mg-Al triangular plot. They chose these three apices as they felt these were components that would be the least affected by subsequent metamorphism. Volatiles and the alkali elements were considered more likely to enter into a fluid phase and so perhaps lost from the system. Their triangular diagram (redrafted as Fig. 14.36) locates clay minerals along the Al-Mg edge, while the most widespread minerals in common shales, i.e. illites, smectites and kaolinite, fall near the Al corner. Chlorite, corrensite and attapulgite are located in the centre of the Al-Mg edge, while sepiolite, talc, Mg-smectite and magnesite lie close to the Mg apex. The location of dolomite, calcite and gypsum/anhydrite cluster in their respective Ca and Mg:Ca = 1:1 positions.

From their analyses, it is clear that, except for sulphate-bearing rocks, samples from evaporitic sedimentary series (red dots) are readily distinguished by their higher Mg contents from the non-evaporitic platform sediments (indicated by occurrence isopleths). The boundary between the two sets lies in the area occupied by the non-evaporitic dolomitic marls (where illite is the most common clay mineral). Where some of evaporite samples plotted in the field occupied by the non evaporite population (right side of triangle), they tend to be argillites and calcitic marls deposited along the borders of the various evaporitic basins (Moine et al. 1981). The presence of alkalis in some highly terrigenous or volcano-sedimentary formations complicates matters when isochemical comparisons are made to meta-evaporite geochemistry.

As expected, sulphate-bearing evaporitic sediments are mainly situated in a zone departing from the above-mentioned population and trending towards the Ca apex. When considering only the Al, Ca and Mg components, they seem to have the same composition as numerous common marls and

carbonate rocks. Nevertheless, as shown in Fig. 14.36, there is a definite trend for sulphate-bearing sediments to be related to variable proportions, of calcium sulphate and magnesium-rich clay minerals (indicated by field enclosed in dashed lines).

Interestingly, when meta-evaporite geochemical components are plotted using the same the same triangular axes (points 12 through 17 in Fig. 14.36) they overlap the geochemical fields of the unmetamorphosed evaporitic sediments and do not plot in the Al rich region of the nonevaporites (see Tables 1–4 in Moine et al. (1981) for the full geochemical breakdown of samples from sites 12–17). Assuming an isochemical transformation from an evaporite precursor, Moine et al. (1981) argued this Mg-dominant distribution strengthens an interpretation of a likely evaporite protolith. It should not be used as a sole indicator of a metamorphic rocks parenthood and should always be supplemented with other lines of argument.

Meta-evaporite Examples

The preceding discussion clearly shows that meta-evaporite interpretations are typically not based on the presence of actual salts but on the recognition of alteration products related to the mobilisation, volatilizations and dissolution of the precursor salts. What follows is a discussion of a number of meta-evaporitic terranes. The order of presentation is not chronological but rather in terms of the strength or the reliability of the meta-evaporite interpretation. Ancient meta-evaporite localities range from archetypical occurrences, with excellent preservation of the evaporite salts or their pseudomorphs, along with widespread sodic and potassic aluminosilicates, through to inferred areas with little more evidence for meta-evaporites than the presence of occasional sodic, magnesian and chloride-rich mineral phases. Broadly, a separation between examples where the tie to an evaporite protolith is obvious, versus examples where the tie to an evaporite protolith is more subtle, roughly corresponds to meta-evaporites in the greenschist versus the amphibolite/granulite realms, respectively.

Examples in the Greenschist Realm

Metasediments in the greenschist realm tend to retain many of the sedimentary and diagenetic indicators of their evaporite protolith including: lamination, bedding, silicified and calcified evaporite casts, salt residues, dissolution breccias, salt welds, mineral haloes and halokinetic/rauhwacke geometries; making the tie to an evaporite protolith quite obvious. This is especially so when there are abundant mineralogical daughter products, such as scapolite, tourmaline and phlogopite/talc associated with stratabound zones entraining these textural indicators. Because of their obvious ties to evaporites, some examples of chloride-rich greenschist realm meta-evaporites were discussed in the rauhwacke section of Chap. 7. Such examples include the Roan breccias of the Katangan copperbelt and the Callanna breccias of the Flinders Ranges, these examples will not be considered again here.

Anhydrite in Greenschist Conditions, Salton Sea

The Salton Trough is a continental rift zone at the head of the Gulf of California (Fig. 9.73a), It defines the transition from the offshore divergent tectonics of the East Pacific Rise to the onshore strike-slip dextral tectonics of the San Andreas Fault System (Fig. 14.37a; Patrick Muffler and White 1969; McKibben et al. 1988a, b; Osborn 1989). Infilling of the rift by the bi-polar Colorado River delta for the past 4 Ma has isolated the northern part of the trough, forming the closed Salton Basin in an orographic desert (McDougall 2008). The current Salton Sea was created anthropogenically in 1905 when a canal, designed to bring irrigation water from the Colorado River into the Imperial Valley, was breached during spring floods. The entire volume of this large river was then channelled into the Salton Sink, which at the time was an evaporitic mudflat/pan with a surface more than 100 m below sea level. It was 2 years before the breach was plugged and the river diverted back to its natural course, but, by that time the Salton Sink had become the Salton Sea, a huge saline inland lake extending over several hundred square kilometres. Much of the salinity was the result of dissolution of the salt crust that previously occupied the lower portions of the sink.

Although this transformation was anthropogenic, the underlying Quaternary fill preserves a similar set of pan to saline lake alternations. High evaporation rates combined with an extremely variable hydrologic budget resulted in episodic infill by saline lake and lacustrine evaporite sediments. Within the Salton Sea geothermal system (SSGS), rapid subsidence and rift-related magmatic intrusions at relatively shallow depth make up an arc of five Quaternary rhyolite domes. Related convective heating has flushed Plio-Pleistocene and younger sediments (fluvial and lacustrine deltaic matrices in a rift fill up to 1–4.5 km thick) with hypersaline chloride- and metal-rich brines, containing up to 26 wt% of dissolved solids (Fig. 14.37a, b). Seeps of mud, gas (CO_2) and dominantly polyaromatic hydrocarbons are common in this geothermal field, where wells drilled for geothermal power record temperatures of up to 350 °C at depths ranging from 1,500 to 2,500 m (Svensen et al. 2007; Mazzini et al. 2011). Hydrocarbons appear to originate from hydrothermal heating rather than

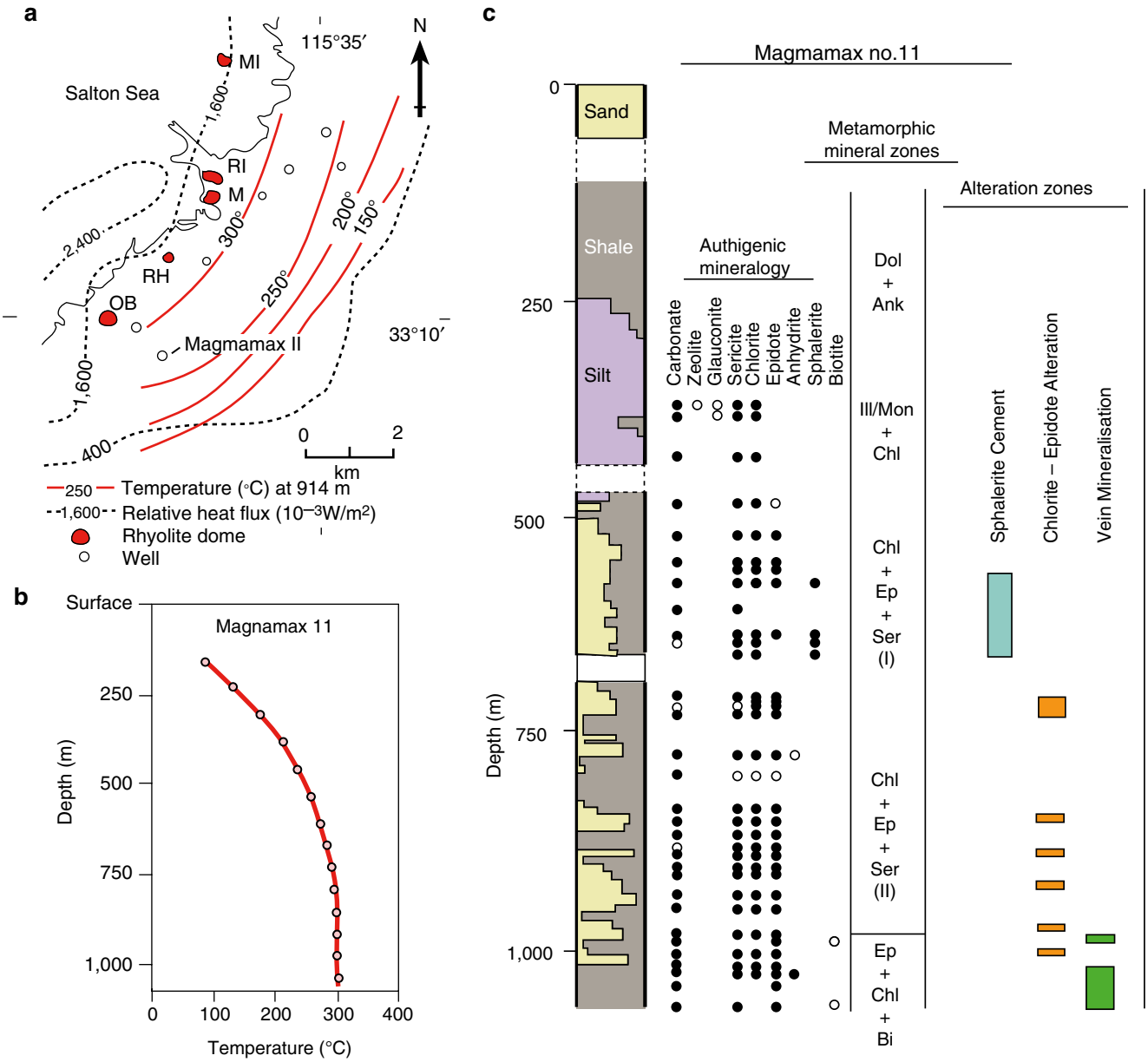

Fig. 14.37 Magmamax 11, Salton Sea. (**a**) Salton Sea geothermal field showing location of various geothermal wells including Magmamax 11. Also shown are the isotherms at 914 m (3,000 ft) and contours of relative heat flux. *Red* areas indicate Quaternary rhyolite domes extruded onto the lacustrine sediments (*OB* Obsidian Butte, *Rh* Red Hill, *RI* Red Island, *MI* Mullet Island. (**b**) Downhole temperatures from Magmamax 11. Bottom hole temperature is 305 °C. (**c**) Sediment types and alteration zones in Magmamax 11 well. *Solid circles* indicate major authigenic phases; *open circles*, minor phases. Abbreviations: *dol* dolomite, *ank* ankerite, *ill* illite, *mon* montmorillonite, *chl* chlorite, *ep* epidote, *ser* sericite, *bi* biotite, *I* epidote detectable by XRD only, *II* epidote detectable optically (After McKibben et al. 1988a, b)

thermal maturation of organic compounds via burial (Svensen et al. 2007).

In 1962, over a 3-month period, fluid discharge from Salton Sea boreholes at temperatures of 130–170 °C precipitated several tonnes of sulphide minerals and opaline silica having a bulk composition of up to 20 % Cu, 7 % Ag, and 7 % Fe (Weissberg et al. 1979). An estimate of the size and content of the saline brine reservoir by White (1981) gives the following: 5 Mt of Zn metal, 9 Mt of Pb, 120,000 t of As, 60,000 t of Cu, 20,000 t of Cd and 10,000 t of Ag, contained in a brine volume of about 11.6 km^3 to a depth of 3 km and with a mean reservoir temperature of 300 °C. The relevance of this meta-hydrothermal hydrology to sedex systems is discussed in detail in the next chapter.

Where flushed by hot hydrothermal waters, saline Salton Sea sediments are metamorphosed, typically to greenschist facies mineral assemblages: actinolite-quartz-epidote-biotiteandradite (Fig. 14.37c; Patrick Muffler and White

1969). Cores recovered from a depth of 3 km or more contain dual-amphibole assemblages marking the transition from greenschist to amphibolite facies, as well as intergranular hydrothermal anhydrite. Calcic amphiboles with up to 2.7 wt.% Cl occur in meta-sandstones, metabasites and veins at depths between 3,100 and 3,180 m where the temperatures are in excess of 350 °C (Enami et al. 1992). There the Cl-bearing amphiboles range in composition from hastingsitic (Cl >1 wt.%) to actinolitic (Cl <0.5 wt.%). These amphiboles formed by reactions involving high-salinity geothermal fluids, with 15.4–19.7 wt.% total dissolved Cl. Coexisting phases include quartz, plagioclase, K-feldspar, epidote, clinopyroxene, apatite, and titanite.

Gypsum/anhydrite are significant components in the shallow relatively-impervious 200–300 m thick caprock to the Salton Sea Geothermal System (SSGS; Younker et al. 1982). Stratiform calcium sulphate units are commonplace in drill cores recovered in the upper few hundred metres of the SSGS. They were deposited in various playa-sabkha subenvironments, with laminated to massively bedded sulphates deposited subaqueously in perennial and ephemeral saline lakes. Gypsum (now pseudomorphed by anhydrite) was precipitated within fluid-saturated sediments in lake-fringing saline mudflats and nodular sulphates were formed in the capillary zone of surrounding dry mudflats (McKibben et al. 1988a, b).

Gypsum is the only primary evaporitic sulphate found in the SSGS, but it undergoes dehydration to anhydrite at 80–105 °C and is largely converted by burial depths of 200–250 m. The resultant interlocking texture in the anhydrite beds lowers permeability and enhances the sealing qualities of the caprock. Diagenetic anhydrite dominates the $CaSO_4$ phase to the base of the SSGS caprock at depths of 340–370 m. Below this depth, the anhydrite and calcite proportions lessen as the proportion of the cementing metamorphic minerals epidote and silica increase (Younker et al. 1982).

Fluid inclusions in the gypsum contain 4–12 wt.% equivalent NaCl fluids (Osborn 1989). Gypsum dehydration apparently dilutes these fluids, forming inclusions in anhydrite that contain <4 wt.% equivalent NaCl fluids. Fluid inclusion homogenization temperatures closely parallel the thermal profile measured in boreholes, implying continual recrystallization of anhydrite to maintain thermal equilibrium with the prevailing geothermal gradient. Continuous recrystallization allows heterogeneous mixing of relatively dilute fluids from inclusions with more concentrated geothermal brines, producing inclusions containing fluids ranging from 13 to 25 wt.% equivalent NaCl. These coexist spatially with 25 wt.% equivalent NaCl geothermal brines.

The initial result of increasing temperature is a hornfelsic to granofelsic recrystallization texture in the anhydrites, which are evolving into hydrothermal anhydrites. Bedded anhydrite is still present as a 0.6 m unit at a depth of 1,000 m and a temperature of 305 °C in the Magmamax 11 well (McKibben et al. 1988a). At that depth most of the remaining anhydrite is made up of interlocking granular anhedral grains (burial anhydrite), which alternate with marly and pelitic laminae that surround small anhydrite nodules and clusters (Fig. 14.37c). Any original small-scale sedimentary growth banding and other depositional textures in the original evaporites has been largely obliterated by hydrothermally-driven metamorphic recrystallization. Shales in a 0.8 m thick section immediately below this anhydrite are extensively brecciated, forming angular fragments cemented by clean, coarse anhydrite. The angular nature of the shale breccia fragments, their sharp contact with the anhydrite cement and the lack of fine matrix between them implies that they were brecciated after lithification of the original mudstone. The burial-related breccia is interpreted as the result of halite dissolution and is thought to indicate the process that sourced much of the high salinity chloride brine beneath the caprock in the SSGS (McKibben et al. 1988a). The notion of the dissolution at depth of former halite beds to supply much of the deeper high salinity brine is further reinforced by the work of Bozkurt (1989). He recognized widespread halite relicts in calcite at 1,240 m depth and interpreted this halite as a remnant of once more-extensive beds.

Below the breccia zone in the Magmamax 11 well is a 4.7 m thick sequence of thin interbedded anhydrite and shale. The layers of anhydrite are composed of a mosaic of interlocking grains. Isolated coarse crystals of anhydrite occur scattered throughout the shale layers, possibly representing hydrothermal porphyroblasts or pseudomorphs formed in place of former gypsum crystals.

The Salton Sea geohydrology demonstrates a system where diagenesis and metamorphic interactions are tied to the temperature regime, which is ultimately a response to magmatic heating. It shows how not only is evaporite recycling an integral part of the evolution of the metamorphic fluids but the hot temperatures in young sediment drives hydrothermal cracking and so creates hydrocarbons as one of the volatile components in the metamorphic milieu, aiding in the leaching and transport of redbed metals (Fig. 14.38). Igneous emplacement sets up a number of hydrogeochemical effects and metamorphic alteration haloes in adjacent evaporitic sediment columns, as seem in the SSGS. This has significance in understanding precipitation mechanisms for some base and precious metals, so we shall return to this topic in Chap. 16.

Metaplaya Sequences, Damara Orogen (Namibia)

Evaporitic metaplaya strata, up to 1,000 m thick, typify the Neoproterozoic rift sediments of the Duruchaus Formation in the Damara Orogen, Namibia (Behr and Horn 1982; Schmidt-Mumm et al. 1987). The Damara is part of the principal PanAfrican orogenic belt in south-

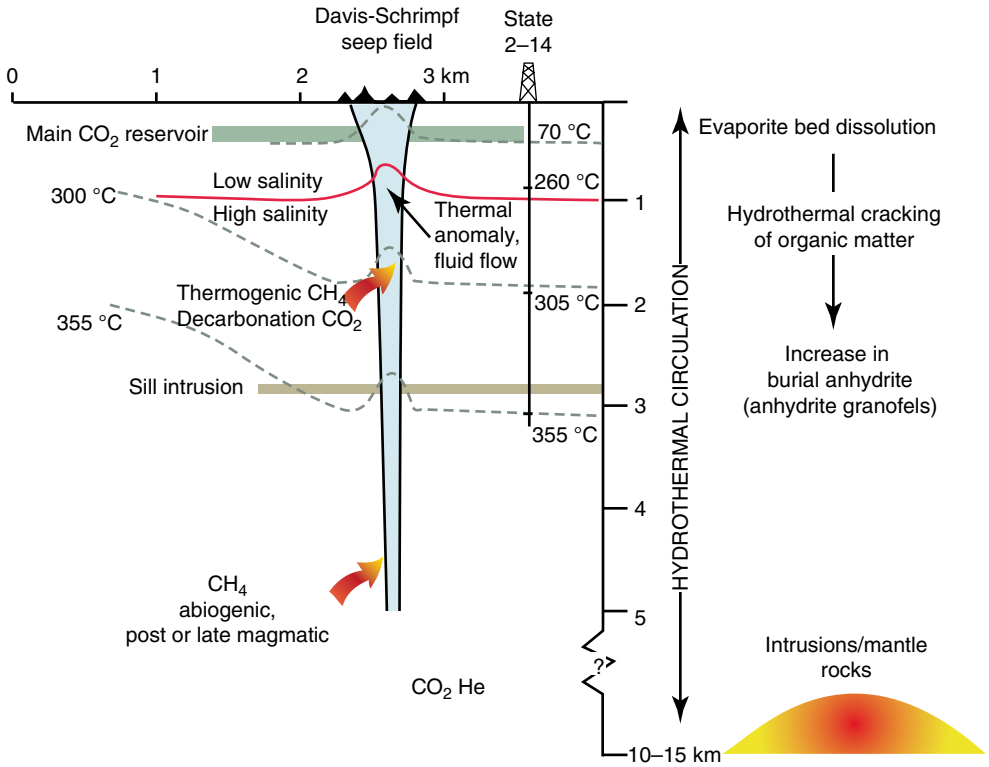

Fig. 14.38 Schematic section of the geothermal regime in Salton Sea, southern California, showing distribution of burial anhydrite and likely sources of the seep gases. Hydrothermally driven circulation of shallow meteoric fluids and dissolution/interaction with buried evaporites and associated brines controls much of the pore fluid geochemistry. A minor proportion of pore waters may have a deeper (juvenile?) origin (In part after Mazzini et al. 2011)

western Africa, reaching from the West Congo Belt in the north to the Lufilian/Zambezi, Kaoko, Damara, Gariep and finally the Saldania Belt in the south. Across the paleo-Atlantic, it faced the Ribeira-Brasilia belts and possibly the Cuchilla Dionsio-Pelotas magmatic terrane (Fig. 14.39; Frimmel et al. 2011). Its geological evolution preserves evidence Neoproterozoic breakup of Rodinia when the evaporites were formed, followed by the Cambrian accretion of Gondwana that in combination define one of the most significant supercontinent cycles in Earth history.

Evaporite deposition occurred in a widening aulocogen as a consequence of the initial breakup of the Rodinian supercontinent, some 870–740 Ma, and took place in lacustrine, playa-lake and arid fluvial settings, while overthrusting of the same evaporite deposits occurred later during the Pan-African Orogeny, 650–450 Ma. This orogenic belt, like the nearby Lufilian (Katangan) copper belt, shows an association of meta-evaporites with base metal mineralization (Chetty and Frimmel 2000), this aspect will be discussed in the following chapters.

Microthermometric fluid inclusion studies in these rocks show that two distinctly different fluid systems were active during the tectogenesis of the Damara Orogen, resulting mainly in (a) the emplacement of large bodies of quartz-dolomite plugs and dykes, and (b) the support of the extensive nappe tectonics (Naukluft Nappe, Kudos Nappe) and related mineralisations (Schmidt-Mumm et al. 1987). As a first approximation, the two systems are considered a low-salinity and a high-salinity system, which can be related to different formational conditions (Fig. 14.40). The low-salinity system is related to metapelites and metapsammites, derived from the thick geosynclinal (deeper water) sequence that was deposited in the Damara trough. The high salinity system is derived from dewatering of a sedimentary sequence containing significant continental rift/playa evaporites and cyclic pelitic-dolomite layers, intercalated with psammites (Nosib Group, Duruchaus Facies, Kamtsas Facies).

The likely continental rift playa protolith is indicated by morphologically well-preserved pseudomorphs of Na-carbonates (shortite, trona, gaylussite), borates (borax, colemanite, ulexite) and sulphates (thenardite, gypsum, baryte). All indicate a meta-evaporitic sodium bicarbonate entraining precursor, as do laterally extensive albitites and tourmalinites (Fig. 14.41). All of the pseudomorphs are now composed of microcrystalline albite with varying amounts of dolomite, calcite, tourmaline, rutile and chloritoids.

Ferroan dolomite is the most important carbonate phase in the region and at least five generations of dolomite can be distinguished in the area (Behr et al. 1983). The oldest is micritic dolomite, which is subsequently overprinted by successive coarser-grained dolospars. The composition of the dolomites varies markedly. Groups of $Ca_{90}Mg_{10}$, $Ca_{70}Mg_{30}$ and $Ca_{55}Mg_{45}$ carbonates were identified that also contained 5 % to more than 10 % FeO. Calcite occurs only locally and appears to be a product of dedolomitisation or

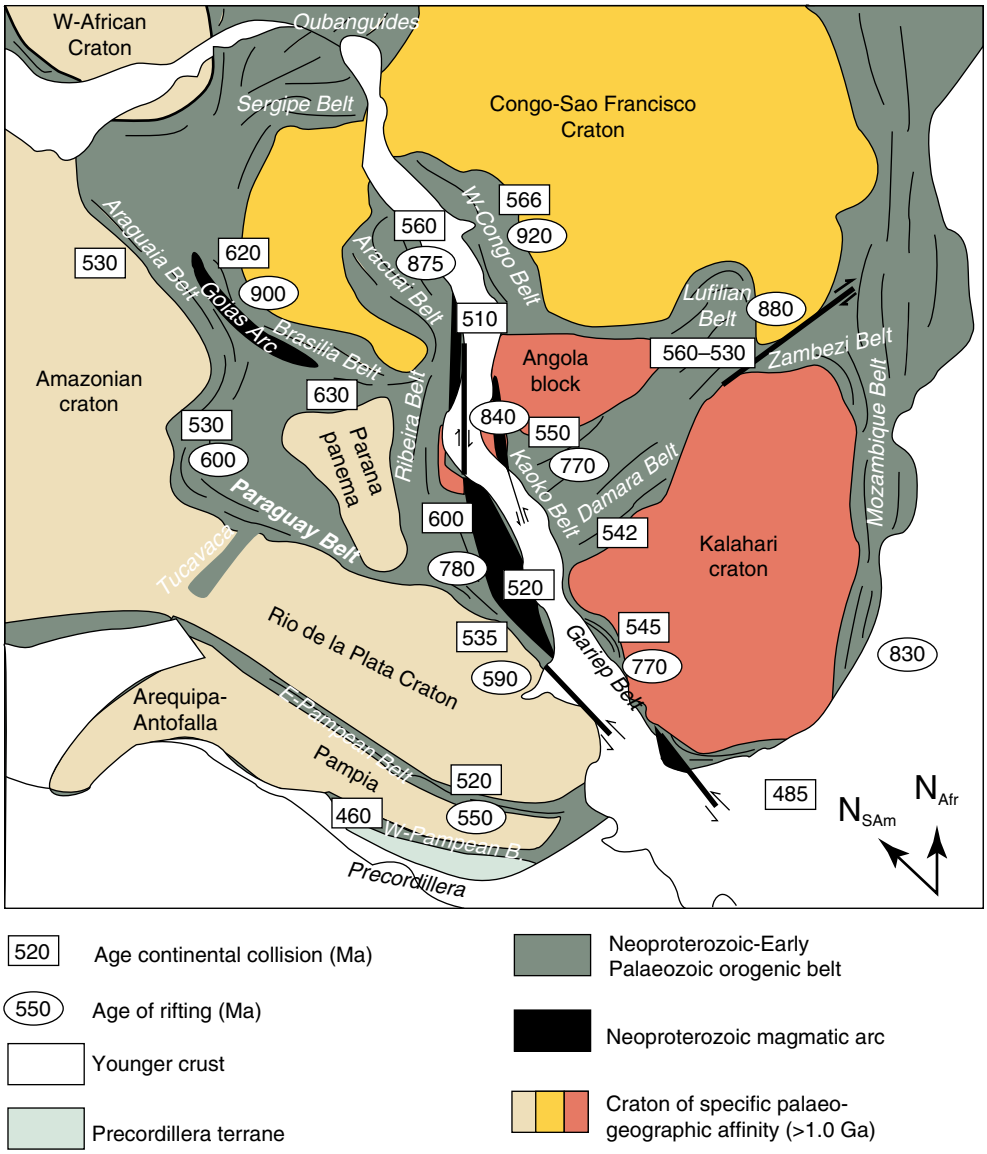

Fig. 14.39 Position of Neoproterozoic fold belts and magmatic arcs between the various cratonic blocks of southwestern Gondwana. The timing of basin opening and closure in each belt is indicated. Note that the cratonic affinity of the Parana-Panema Block is unresolved and shown here only tentatively (After Frimmel et al. 2011)

hydrothermal alteration associated with the later stages of dolomitisation

A high NaCl content in the protolith is indicated by numerous horizons dominated by Cl-scapolite with thicknesses up to several metres (Fig. 14.41a). Scapolite is best developed in dark grey dolomitic mudstones in the upper part of the Duruchaus Formation (Facies E). It is associated with albite, phlogopite and quartz; dolomite exceeds albite, and phlogopite can comprise up to 30 % of the total rock. Individual scapolite crystals are subhedral, up to 2 cm long and can make up to 80 % by volume in some layers. The scapolitic dolomites still preserve mud cracks, depositional laminae and ripples. The scapolite typically replaces calcite and phlogopite and is often associated with newly formed sparry dolomite. Average make-up is SiO_2 52–54 %, Al_2O_3 21–25 %; Na_2O 8–9 %, CaO 9–10 %; SO_3 0.7 %; Cl 2.5 %. Meionite content is calculated as 45–50 %. Behr et al. (1983) postulate the reaction:

$$\text{phlogopite} + \text{albite} + \text{NaCl}_{(aq)} + \text{calcite} \rightarrow \text{scapolite} + \text{dolomite}$$

Both the chlorine and the sodium were supplied by the metamorphism of calcareous shales containing varying amounts of halite, and were not from a magmatic source.

Laminated albite-dolomite rocks (albitites or albitolites) are also commonplace and are characterised by albite crystals up to 5 cm long (Facies D). Albite can make up more than 80 % of the rock by volume, and dolomite proportions range up to 40 % of the rock volume. Quartz, minor biotite and metamorphic muscovite are the other rock-forming minerals. Lamination is often distorted and brecciation is also widespread, possibly indicating the removal of former evaporites. The albite is usually crypto-

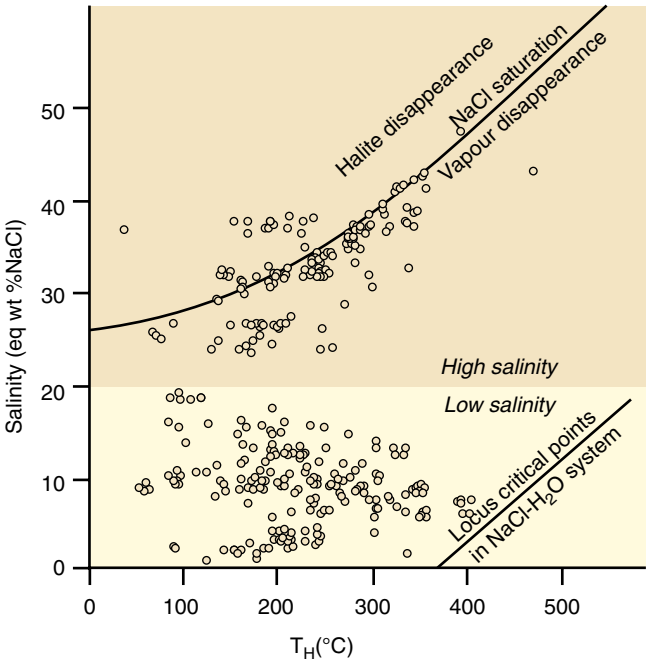

Fig. 14.40 Salinity versus total homogenisation temperature (*TH*) in the low- and high-salinity fluid systems the Damara Orogen. For highly-saline inclusions (>20 %) homogenization temperatures of daughter minerals of *cubic shape* were used to determine the salinities. For low-salinity inclusions (<20 %) values were determined from freezing data (After Schmidt-Mumm et al. 1987)

to microcrystalline (10–30 μm) and is almost pure (CaO ≈0.3 %; K_2O ≈0.1 %). Occasional larger albite crystals occur as lath-like forms (up to 500 μm) in brecciated zones. Only simple albite twins have formed and Roc-Tourne twins, so common in authigenic albites, were not found in the region. Albite is thought to have formed during late diagenesis and the onset of metamorphism in the evaporite successions from: (1) clay minerals, (2) evaporites and (3) the alteration of tuffs (Behr et al. 1983). Albite can form in the presences of saline highly alkaline waters in the following fashion:

$$\text{illite} + \text{NaCl}_{(aq)} + \text{SiO2}_{(aq)} \rightarrow \text{NaAlSi}_3\text{O}_8 + \text{HCl}_{(aq)} + \text{H}_2\text{O} + \text{KCl}_{(aq)}$$

The liberated HCl was buffered by carbonates in the matrix as the protolith was replaced by albite, a similar evolution to that documented in Triassic salts of north Africa (Kulke 1978). This style of albitization is largely restricted to the pelitic sediments of the Duruchaus Formation, and these albites typically includes relics of sericite.

Primary sodic salts in alkaline playas, such as gaylussite and trona, typically transform during dewatering to pirssonite and then to shortite. As burial proceeds and

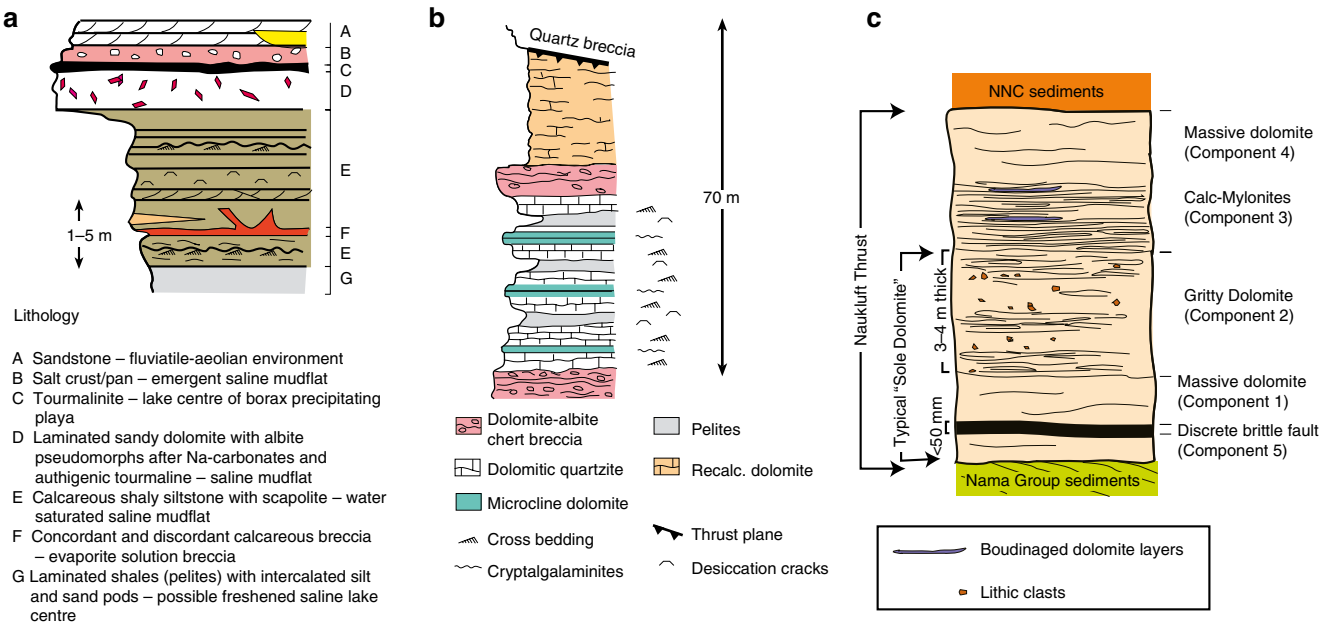

Fig. 14.41 Stratigraphy of the metasediments and thrusts associated with the Duruchaus Formation, Namibia. (**a**) Idealised vertical sequence of the metaplaya sequence, Geelkop Dome, Damara showing distribution of meta-evaporite indicators in the profile. (**b**) Generalised section of the Naos Farm dolomite sequence showing position of microcline dolomite and breccias, which indicate former evaporite horizons (**a**, **b** after Behr et al. 1983). (**c**) Schematic tectonostratigraphic section showing the five components of the Naukluft Thrust (After Miller et al. (2008). The Sole Dolomite is represented by *components 1 & 2*. Not all five components are always present and the "brittle" fault (*component 5*) may cut through at any tectonostratigraphic position, although it typically occurs within *components 1 & 2*

temperatures increase, the shortite typically transforms to albite via:

$$Na_2Ca_2(CO_3)_2 + 2Al_3OOH_{(aq)} + SiO_{2(aq)} \rightarrow 2NaAlSi_3O_8 + 2CaCO_3 + H_2O + CO_2$$

Carbonate liberated by this reaction is typically preserved as calcite and dolomite within albite pseudomorphs of the former sodium salts.

Albitites with a tuff precursor typically form dm-thick albite layers and tend to be associated with volcanics on the southern Damara margin, a similar genesis has been proposed for the widespread albitites of the Broken Hill – Olary region in Australia (see later). The pervasive recrystallization associated with this transformation means relict shard textures or analcime and other zeolites are no longer present. However, this form of albitite typically retains elevated levels of detrital rutile and biotite. The proposed reaction is:

$$\text{tuffitic glass} + \text{Duruchaus brines} - (\text{pH} > 9) \rightarrow$$
$$\text{Na - Al - Si(gel)} \rightarrow \text{zeolites} - (+\text{Na}) \rightarrow$$
$$\text{analcite} - (90^\circ\text{C}; + SiO_2) \rightarrow \text{albite 2}$$

Microcline is another conspicuous mineral in Duruchaus sediments and is especially obvious in the Naos dolomite sequence that occurs toward the top of the Duruchaus Formation (Fig. 14.41b). Microcline is present in a number of forms: (1) as microcrystalline anhedral crystals in the albite-phlogopite-quartz matrix of the pelites; (2) as rosette-like pseudomorphs after gypsum in evaporitic mudflat facies sediments; these crystals are up to 3 cm long and are often arranged perpendicular to bedding planes in cryptalgal laminites; (3) as planar, up to 1 cm long crystals in dolomite layers of calcareous shales; (4) as crystal linings in quartz-filled shear fractures; and (5) as hydrothermally formed stratiform veins, opened by hydrofracturing and the intrusion of a carbonate mush. Most of the microcline has an adularian habit with individual crystals having a dirty core and clear rims. It is interpreted by Behr et al. (1983) to have formed via hydrothermal crystallization at the end of deformation stage.

Also within this meta-evaporite sequence are stratiform tourmalinites up to several metres thick that can be traced over areas measured in tens of kilometres and extending continuously for more than 20 km (Facies C; Behr et al. 1983; Sun 2007). Electron microprobe analysis shows that they are dravites with a significantly high Mg content [average Fe/(FeO + MgO) = 0.28]. The sedimentary precursor of these tourmalinites is seen in their well-preserved finely laminated primary bedding along with preserved dewatering and cross-bedded structures, with some intervals also associated with albitites containing pseudomorphs. Some of the tourmalinite is made up of fine alternating laminae of tourmaline and albite. These units are interpreted to indicate times of hot spring activity and were associated with times of widespread borate deposition in the playa. Tourmalinites are of high economic significance in the area as they are commonly associated with stratabound accumulations of Cu, Au, Ti, U and megaquartz (Chetty and Frimmel 2000).

Metamorphism of the playa sediments, as deduced from the biotite isograd of the intercalated pelitic siltstones, and temperature-depth estimates, indicated by the CO_2 and H_2O-NaCl isochore intersections, attained temperatures of 550 °C at depths of 5–8 km burial (middle-upper greenschist facies). During this rise of temperature the large fluid volume in the enclosing dolosparite caused, by aquathermal pressuring, a mechanical destruction of the grains and a liberation of the fluid phases (Behr and Horn 1982). Additional fluids were liberated by the dehydration of the Na-carbonates, Na-silicates and Na-sulphate minerals that were concentrated in particular layers. This abnormal fluid pressure broke up the palaeoevaporite layers to form a highly mobile cataclastic sludge. Preserved fragments within the sludge range from several cubic micrometres to metres.

This process of palaeo-evaporite fluidization seems to have been initiated by the rapid overthrusting of nappes composed of hot (≈540 °C) metasediments that were squeezed out of the Khomas Trough during the Damara Orogeny. Nappe emplacement formed a hot lid some 5 km thick atop the cooler meta-playa sediments (Fig. 14.42). The underlying mobile carbonate sludge, enriched with palaeo-evaporite pseudomorphs, was partly squeezed into the thrust plane of the Khomas Nappe. Three sequential stages of brecciation were distinguished (Behr et al. 1983; Schmidt-Mumm et al. 1987):

1. A stratiform breccia formed by dewatering of water-rich evaporites in layers now enriched in palaeo-evaporitic pseudomorphs.
2. With increasing mobilisation of the saline fluids a stronger style of brecciation occurred. It was associated with aquathermal pressuring due to abnormal pore pressures and it created strongly and mostly internal hydrofractured concordant units.
3. At the final stage a very ductile discordant breccia containing xenoliths of the wall rock formed. It intruded the wallrock along faults, fissures and bedding planes.

A further breccia evolved from the type-(c) breccia that, along with diapiric ascent of the breccia mush, was intruded into the contact zones with the basement nappes. By acting as a lubricant it re-initialised or further enhanced the southwest-directed movement of the nappes (Fig. 14.42). The associated flushing of large volumes of hypersaline and alkaline solutions resulted in a strong hydrothermal and metasomatic alteration of the country rock along with mineralization of large quartz-

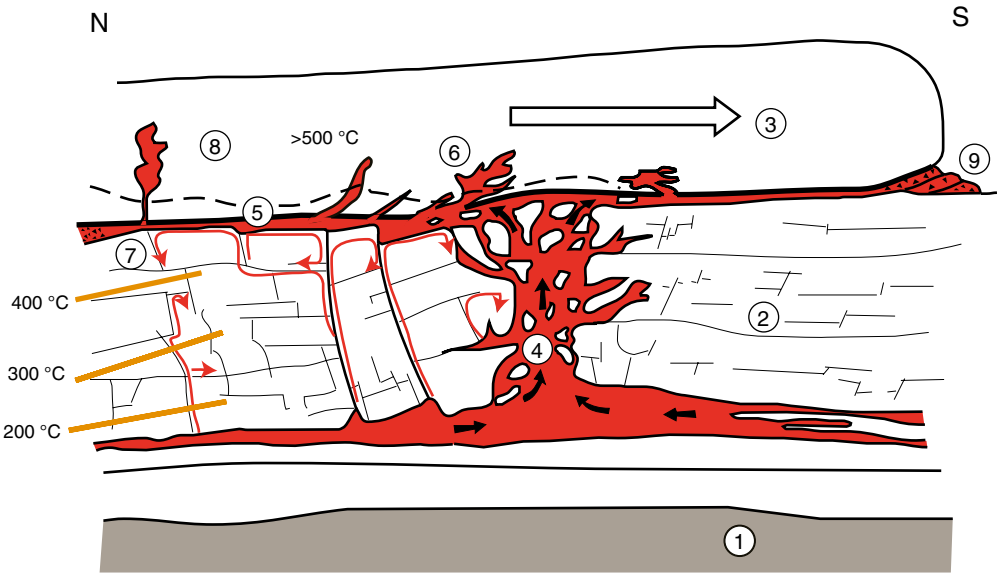

Fig. 14.42 Processes associated with the hot Kudis Nappe (>500 °C) overriding the somewhat cooler Duruchaus Formation. *1* basement, *2* Duruchaus Formation, *3* Kudis Nappe, *4* discordant breccia, *5* carbonate-quartz breccia and sole dolomite, *6* breccia injected into faults and shear planes of Kudis rocks, *7* zone of strong hydrothermal metasomatic reactions liberated by dewatering of evaporite horizons, *8* pipes plugs and veins filled by quartz precipitates derived from highly saline hydrothermal solutions, *9* breccias generated by overriding nappes (After Schmidt-Mumm et al. 1987)

carbonate bodies. Single quartz crystals within these mineralizations can have crystal faces up to 50 m across and are intergrown with large dolomite crystals up to a metre long.

In a related study, Viola et al. (2006) examined the Naukluft Nappe Complex (NNC), which forms a far-travelled fold and thrust belt klippe in the southern Pan-African Damara Belt in central Namibia, with a SE-directed displacement between 50 and 80 km. This section is less metamorphosed than the equivalent Duruchaus Fm to the north. The entire nappe stack was thrust along an out-of-sequence, nearly planar, horizontal structure, the Naukluft Thrust. The thrust zone consists of several distinct lithological components whose typical distribution, when all present, from bottom to top is (1) a massive, ochreyellow weathering dolomite; (2) a polymict gritty dolomite (called in the past Sole Dolomite), (3) strongly foliated and isoclinally folded calc-mylonites, and (4) an upper massive dolomite. In addition, a discrete (<50 mm thick, often >10 mm thick) planar brittle crosscutting fault association (component 5) can occur at any level within this sequence (1–4) but is most typically found in a basal position (Fig. 14.41c). Viola et al. (2006) concluded that the gritty dolomite formed by progressive cataclasis of a massive dolomite. They note that clasts of gritty dolomite are observed randomly oriented within a similar gritty dolomite matrix, suggesting multiple pulses of brecciation and self-brecciation (or, in my opinion, the loss of a substantial volume of pressurized halokinetic halite that once occupied the thrust plane). The gritty dolomite locally forms injection veins into the calc-mylonites, and these veins are themselves boudinaged, which they interpret as the result of broadly coeval cataclastic and ductile deformation. The evolution of structures within the thrust zone is linked to the presence and flow of overpressured pore fluids.

Based on their field observations, Viola et al. (2006) suggest that there were several pulses of fluid-induced brittle deformation that were overprinted, in a cyclic fashion, by ductile structures formed during the emplacement of the nappe edifice. Their interpretation is not related to the notion of a salt lubricated thrust and they did not consider that most of the textures in this association are classic rauhwacke, with numerous indicators of the former presence of evaporites within and about the thrust planes. Their paper is a very good example of how interpretations in thrust terranes in metamorphic settings, even low grade metamorphic settings, tend to ignore ubiquitous sedimentological analogue evidence of transcurrent and diagenetic textural overprints, now so well documented in salt allochthon terranes.

Miller et al. (2008) studied the same thrust using an isotopic approach to better understand the nature of the Naukluft Thrust (Fig. 14.43). They too found that the thrust tectonostratigraphy comprises three dolomitic components, a calc-mylonite horizon, and a discrete brittle fault (Fig. 14.41c). Stable isotope data indicate that the leading edge of the thrust is characterized by positive $\delta^{13}C$ values, whereas the trailing edge is characterized by negative $\delta^{13}C$ values. There is also a significant range in the $\delta^{18}O$ values over 15‰ in different sections, with the leading thrust edge showing a larger range than the trailing edge. The measured $\delta^{18}O$ values are characteristic of burial dolomites and secondary dolomitisation, as indicated by the presence of dolomite networks above and below the Naukluft Thrust zone. They interpret the large range in $\delta^{18}O$ values and variations in $\delta^{13}C$ versus $\delta^{18}O$ patterns to be the result of interaction between the precursor to the Naukluft Thrust zone dolomites and fluids derived from different footwall lithologies.

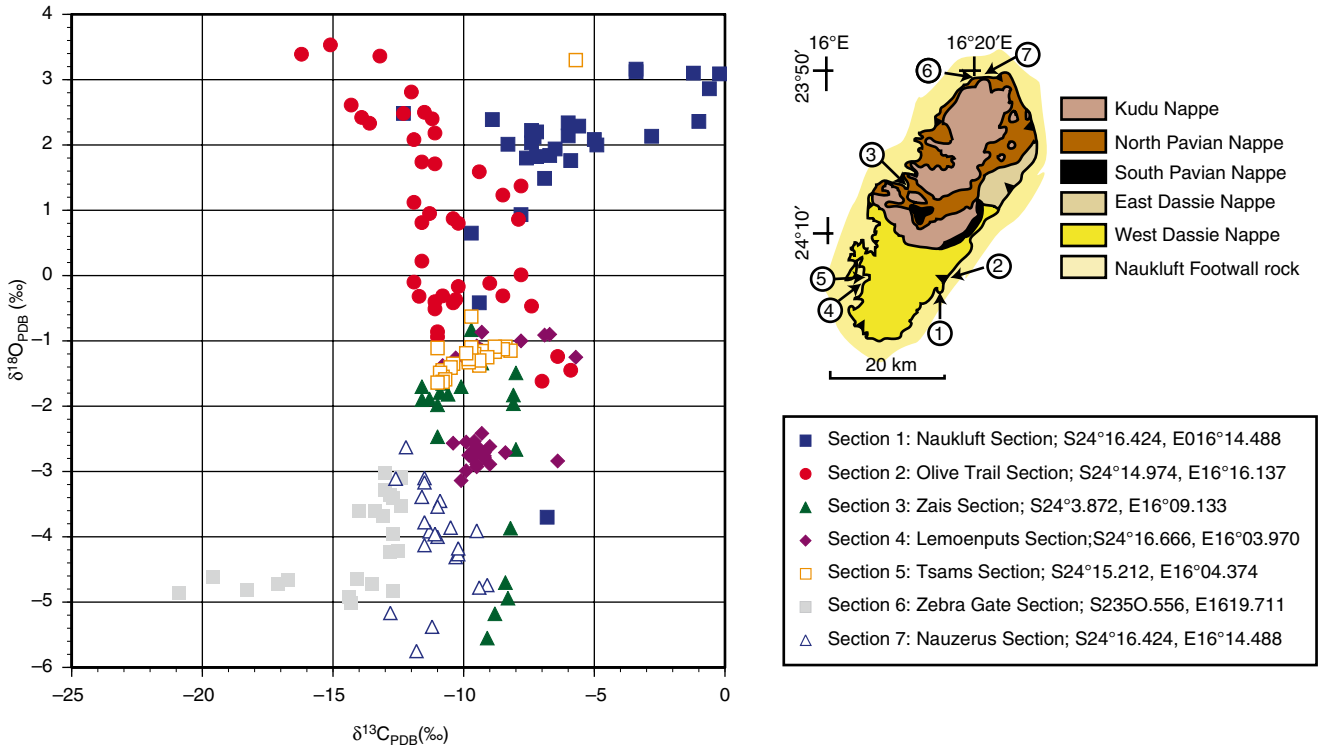

Fig. 14.43 Stable isotopes, Naukluft thrust, Namibia. Leading edge of thrust (*sections 1 &2*) show positive carbon values compared to trailing edge (*sections 3–7*). *Inset* shows Geology of the Naukluft thrust (Isotopic values replotted from Table 2 in Miller et al. (2008))

$^{87}Sr/^{86}Sr$ isotope ratios indicate that some portion of the dolomitizing fluids was derived from the basement. Although their model of the thrust and the associated dolomitisation does recognise the likely role of dissolved evaporites and multicyclic generation of the dolomitizing fluids, once again, the strong likelihood that the thrust plane was a former salt-lubricated allochthon surface is largely ignored. Their conclusion was that an original carbonate-dominated horizon existed prior to thrusting and that the basal thrust of the nappe complex exploited this horizon.

The Damara region is an interesting meta-evaporite terrane for a number of reasons: it provides excellent evidence of how sodic metasomatism is controlled by former evaporites; it offers outcrop examples of crosscutting evaporite-derived hydrothermal breccias with both diapiric and thrust-lubricated (rauhwacke) geometries; and it shows how dravite-tourmalines and albitites in greenschist facies successions can be directly related to former borate, sodium sulphate and halite salts in lacustrine settings. What is yet to be considered is how much of the metasomatism, brecciation and diapirism was related to replacement and haloes set up during the rift stage then overprinted and reworked during the subsequent orogeny. This distinction has obvious economic implications in terms of localities of prepared ground for sulphide emplacement as discussed in the next chapters.

Examples in the Amphibolite/Granulite Realm

Remnants of sedimentary evaporite salts, with the possible exception of exception of sedimentary anhydrites, do not seem to occur in metasediments that have reached amphibolite or granulite grade. It may be that the mechanical buoyancy and high solubilities of halite beds prevent them from reaching the deep-crustal milieu (Newton et al. 1998) or it may be that evaporites were transformed to meta-evaporite daughter products on attaining the greenschist realm (this chapter). It is also likely that disseminated salts or diagenetic apatite in metasediments are important sources of saline fluids capable of flushing and carrying metals in rocks that attain the amphibolite and granulite grades (see next chapter for details). This would explain observations, such as those by Touret (1985), who noted that hypersaline fluid inclusions in metamorphics of the Bamble granulite terrane in southern Norway are more abundant in marbles, metapelites and metavolcanics, compared to orthogneisses in the same terrane.

Borates of Eastern Liaoning, China

Paleoproterozoic boron deposits in eastern Liaoning, China, are now considered to be meta-evaporites that have formed with little or no fluid input from the granites of the region (Peng and Palmer 1995; Jiang et al. 1997). The borate minerals of economic interest are suanite ($Mg_2B_2O_5$),

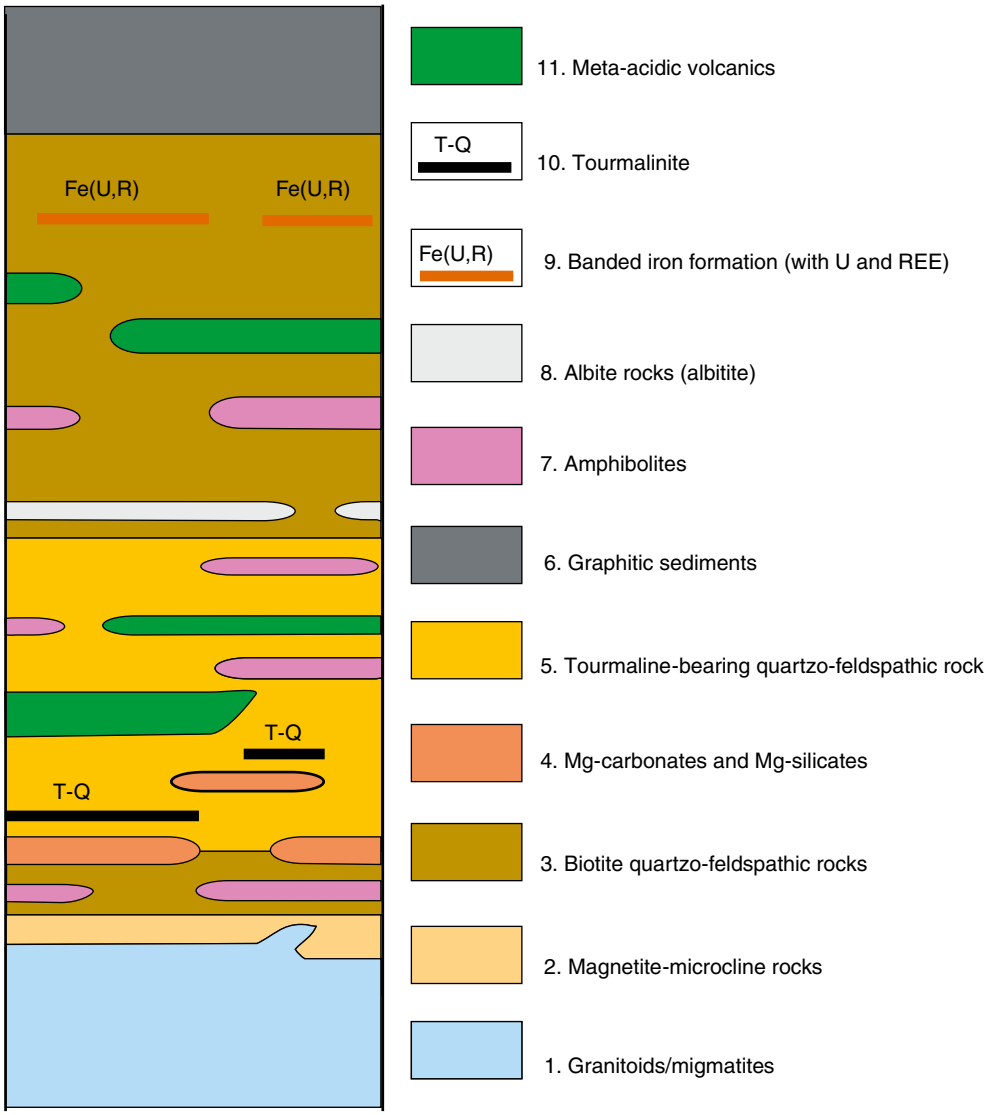

Fig. 14.44 Generalised stratigraphic section through the Liaoning borate deposits (After Peng and Palmer 1995). Various proportions of the numerically listed lithologies (1–10) make up the metamorphic facies types I (lowest) through VI (highest)

szaebelyite or ascharite ($Mg_2B_2O_5{\cdot}H_2O$), and ludwigite [$(Fe, Mg)_4Fe_2B_2O_7$]. The borates are hosted within crystalline Mg-silicate and Mg-carbonate rocks, but exhibit laminar textures implying a sedimentary precursor.

A generalized stratigraphy (from the base up) in of the Liaoning area is comprised of (Fig. 14.44; Peng and Palmer 1995): (I) Magnetite-microcline rocks (that have undergone varying degrees of metamorphism) – this unit forms the base of the borate-bearing sequence, it is dominated by microcline and contains up to 5 % magnetite. (II) Biotite-quartz-feldspar (largely microcline) rocks, and where biotite is more abundant are locally termed leptite or leptynite (≈granulite). The leptites and leptynites are remarkably K- and Na-rich, with the two elements negatively correlated. In a Na/Al–K/Al diagram, the rocks fall along the line of Na/Al = 0.9 and K/Al = 1.0 (Fig. 14.45), which is consistent with evaporite-related clastic meta-sediments (Moine et al. 1981; Cook and Ashley 1992). Tourmaline may be present locally, but only in trace amounts. (III) Mg-silicates (that have undergone varying degrees of serpentinisation) intercalated with magnesite marble – these marbles are the exclusive hosts to the borate ores and range in thickness from 15 to 160 m. In some areas the borates are present as breccias within otherwise bedded rocks and many of the blocks are laminated. Phlogopite is present in both marbles and Mg-silicate rocks and can be up to 10 % by volume of the rock. (IV). Tourmaline-bearing biotite-quartz-feldspar rocks are locally common – except for the abundant tourmaline, this lithology has the same mineralogy as the underlying leptites and leptynites. Units with abundant tourmaline tends to overlie borates and are used as an indicator of nearby ore. (V) Albite rocks may contain up to 90 % albite (albitites). They overlie the tourmaline-bearing unit and define the upper limit of the boron-bearing sequence. (VI) Graphitic gneisses – an unconformity may separate this unit from the borate bearing sequences. It is sometimes finely laminated and is interpreted as having a sedimentary

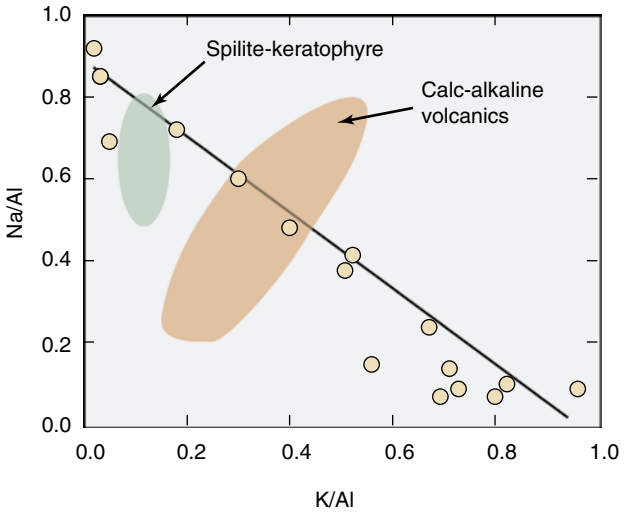

Fig. 14.45 Na/Al vs K/Al diagram of the evaporite-brine influenced pyroclastic assemblages in the Liaoning borate deposits. For comparison the general plot fields of -calc-alkali volcanics and spilites and kerotophyres are also shown (After Peng et al. 1998)

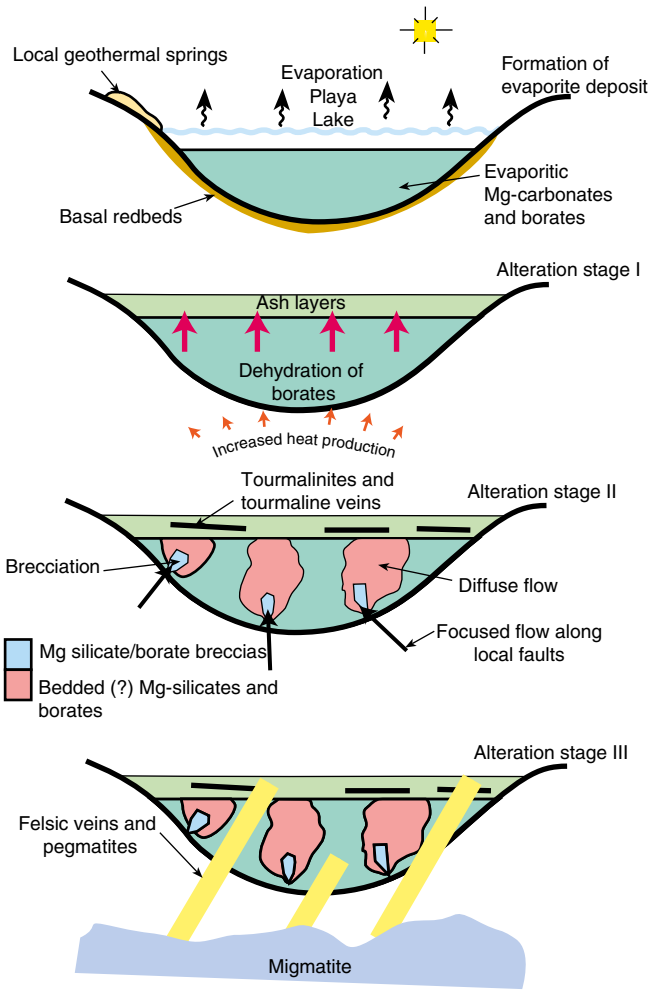

Fig. 14.46 Alteration model of lacustrine borates, Precambrian Liaoning borate deposits, China (After Peng and Palmer 1995, 2002)

protolith. Amphibolites are intercalated throughout the sequence but rarely exceed 10 m in thickness and consist almost entirely of hornblende and albite.

The borate-bearing rocks comprise much of the Liaohe Group and are overlain by graphitic gneisses with intercalations of dolomitic marbles of the Gaojiayu Formation. The thicknesses of the units vary considerably between different areas as the whole sequence has experienced intense folding and faulting, such that the true nature of the original stratigraphic column is often obscured at individual sites.

The Liaoning borates experienced several postdepositional metamorphic episodes (Fig. 14.46):

- *Stage I* The first of these prograde metamorphic events was associated with the widening of the rift basin, which led to increased geothermal gradients.
- *Stage II* This resulted in expulsion of Si-rich brines from the underlying sediments to form Mg-silicates by the alteration of lacustrine magnesite. In some places this alteration was via vigorous focused flow, which led to the development of fluidised breccias. Elsewhere in the deposits, where the fluid flow was more diffuse, this led to the replacement of carbonate in the bedded carbonate-borate evaporites on a lit-par-lit basis.
- *Stage III* At the height of metamorphism felsic veins cut through the deposits producing tourmaline-quartz rims to the veins. Subsequent deformation led to intense faulting and folding of the ore bodies.

Parental fluids for the borate and carbonate evaporites may have been originally derived from the evaporation of surface waters fed by geothermal springs associated with local volcanic activity. They have strong affinities both with the Tertiary borate deposits of Turkey (see Chap. 11) and the metasediments of the Damara Orogen (Jiang et al. 1997). Previously the Liaoning deposits were considered to have formed as skarns or as metamorphosed volcanogenic exhalative deposits. A skarn origin is now known to be incompatible with their boron isotopic signature (Fig. 14.21; Peng and Palmer 1995). A direct volcanogenic exhalative model is unlikely, as borate minerals are simply too soluble to precipitate directly into a standing fresh to marine water body fed by non-evaporated hydrothermal fluids. A concentration phase associated with solar evaporation is needed to explain the borate protolith.

In summary, Peng and Palmer (2002) reported geological, geochemical, and boron isotope data in the Liaoning-Jilin area that defines a plate-scale tectonic scenario overprinting a non-marine evaporite protolith deposited in playa lakes some 2,400–2,100 Ma ago. These evaporites were recrystallised under greenschist- to amphibolite-

facies conditions around 2,100–2,000 Ma to form siliceous borate assemblages dominated by szaibélyite, suanite and ludwigite. The protolith first experienced subduction of oceanic crust below an Archaean craton, then continental collision and lastly development of extensional basins analogous to the Cenozoic basins that contain evaporitic borates in Turkey and Argentina (Peng and Palmer 2002). Liaoning borate ore bodies differ from economic borate deposits elsewhere in the world in two important respects. First, the deposits are Precambrian, whereas most of the world's other major exploited borate deposits are located in Neogene (or younger) lacustrine sediments. Second, these borates are siliceous meta-evaporites and, with the exception of a few small skarn deposits in Russia, all other major economic boron deposits in the world are sedimentary (Chap. 12).

Grenville Complex, St Lawrence County (USA)

Northwest of New York, beneath the Adirondack Lowlands, is a 5–6 km thick Mesoproterozoic Grenville Series of metasediments and metavolcanics (Whelan et al. 1990). It is part of the Grenville Orogenic belt, a remnant of a large hot long-duration collisional orogen (Rivers 2009). At the orogen scale, Grenvillian metamorphism can be subdivided into two spatially and temporally distinct orogenic phases, a relatively high temperature Ottawan (c. 1,090–1,020 Ma) phase in the hanging wall of the Allochthon Boundary Thrust, and a relatively lower temperature Rigolet (c. 1,000–980 Ma) phase in the hanging wall of the Grenville Front (Fig. 14.47; Krauss and Rivers 2004; Rivers 2009).

The Grenville Series in the Balmat region is made up of the Upper and Lower Marbles separated by some 750 m of the Popple Hill Gneiss and underlain by the Hyde School Gneiss (Fig. 14.48a; Doe 1960; Whelan et al. 1990). Amphibolite to granulite facies metamorphism of the Grenville Series occurred about 1,050 Ma, along with emplacement of the sulphide ores, with peak conditions near the town of Balmat reaching 6.6 kb and 625 °C. There are four phases of deformation in the Balmat region. The Grenville Series is host to some unusual iron-sulphide-rich metasediments with some intervals of more than 10 m thick exceeding 70 % pyrite and containing significant stratiform anhydrite (Zimmer 1947). There are also numerous small-scale Pb-Zn occurrences in the region, which are interpreted as metamorphosed and partially remobilized MVT deposits (Fig. 14.48b; see Chap. 14).

In addition to preserved anhydrites, the Upper Marble also contains a number of other indicators of meta-evaporites, including magnesian tourmalines and local scapolites. But the most impressive are stratiform sections that are more than 50 % recrystallised anhydrite. Detailed mapping in the Balmat mine and associated drilling allows the Upper Marble to be subdivided into 16 units, numbered from oldest to youngest (Fig. 14.48a, b). In general, the sequence is composed of alternating fairly pure dolomites and quartzose calcsilicate-rich dolomitic marble. Units 1, 3, 5, 7, 9 and 12 are typically >95 % dolomite (Whelan et al. 1990). Lenses and layers of anhydrite occur in unit 6 and 10 through 14, and may be up to 50 % of the unit by volume. Brownish in unit 6, elsewhere the anhydrite is usually pale to deep lavender. Quartz and diopside may be present in the lenses, along with minor tremolite, talc, calcite, phlogopite and pyrite. The thickest lenses occur near the base of unit 6 (15–20 m) and unit 11 (40–60 m). Plastic deformation has thickened the lens in unit 11 to more than 300 m in the hinge zone of the Fowler syncline (Unit 11a in Fig. 14.48b). The anhydrite lenses in units 10, 12, 13 and 14 are 1–15 m thick. $\delta^{34}S_{anhy}$ values in the oldest anhydrite lens (Unit 6) average 8.2‰; while progressively younger lenses average 19.6, 27.2, 26.8 and 19.1‰ (Fig. 14.49; Units 10, 11a 12 and 13/14, respectively; Whelan et al. 1990). The thickest and isotopically heaviest lens (unit 11a) displays a coincident up section increase in $\delta^{34}S_{anhy}$ (24.1–30.2‰) and $\delta^{18}O_{anhy}$ (19.8–22.5‰) values. These increases and the overall ^{34}S enrichment indicate the evaporitic anhydrite precipitation was concurrent with widespread bacterial sulphate reduction in the depositional basin. A similar increase in $\delta^{34}S$ values of biogenic pyrite (total range, −31.6 to 12.9‰) and decrease in $\delta^{13}C$ values (total range, −3.7 to 5.1‰) of the marble carbonate are also consistent with bacterial reduction. Whelan et al.

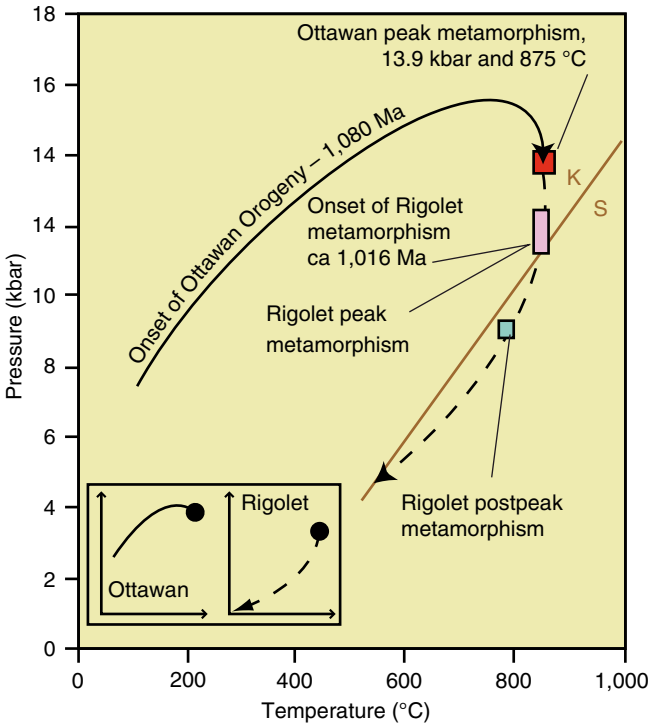

Fig. 14.47 Grenville Series. Pressure – Temperature evolution, showing two stage history (Krauss and Rivers 2004)

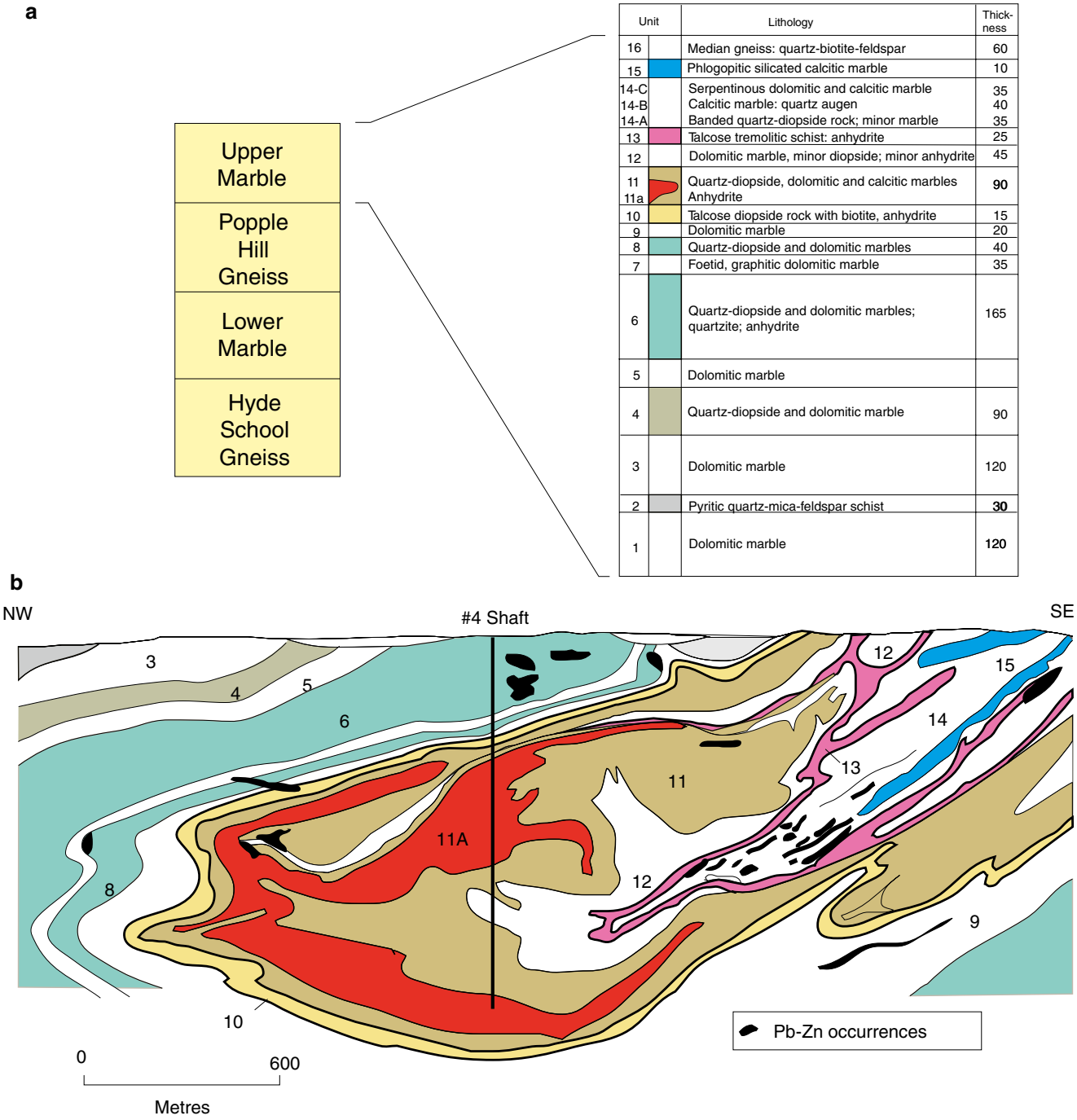

Unit		Lithology	Thick-ness
16		Median gneiss: quartz-biotite-feldspar	60
15		Phlogopitic silicated calcitic marble	10
14-C 14-B 14-A		Serpentinous dolomitic and calcitic marble Calcitic marble: quartz augen Banded quartz-diopside rock; minor marble	35 40 35
13		Talcose tremolitic schist: anhydrite	25
12		Dolomitic marble, minor diopside; minor anhydrite	45
11 11a		Quartz-diopside, dolomitic and calcitic marbles Anhydrite	90
10		Talcose diopside rock with biotite, anhydrite	15
9		Dolomitic marble	20
8		Quartz-diopside and dolomitic marbles	40
7		Foetid, graphitic dolomitic marble	35
6		Quartz-diopside and dolomitic marbles; quartzite; anhydrite	165
5		Dolomitic marble	
4		Quartz-diopside and dolomitic marble	90
3		Dolomitic marble	120
2		Pyritic quartz-mica-feldspar schist	30
1		Dolomitic marble	120

Fig. 14.48 Geology of the Upper Marble. (**a**) Stratigraphy of the Upper Marble. (**b**) Cross section of the Upper Marble, also showing location of the many Pb-Zn ore bodies in the region (*black*). Where unit 11 is more than 50 % anhydrite it is shaded *red* (After Whelan et al. 1990)

(1990) interpret the isotopic data as indicating a protolith of biogenic-sulphide rich sediments. The anhydrite lenses were deposited in a restricted basin, which was also the site of accumulation of highly saline brines and extensive bacterial sulphate reduction. The low $\delta^{34}S$ and high $\delta^{18}O$ in unit 6 are interpreted as episodes of oxidation of biogenic H_2S in the surface waters. They also infer a likely sedex setting for the precipitation of the widespread sulphides.

In a later study, Hauer (1995) argues that mineral composition, trace element and isotopic (O, C, and Sr) data show that the largely dolomitic rocks below the main anhydrite horizon (unit 11a of the Upper Marble) experienced open-system diagenesis, whereas the rocks above unit 11a experienced closed-system diagenesis. This diagenesis was accomplished penecontemporaneously by seawater-dominated fluids. Differences in the history of the Upper

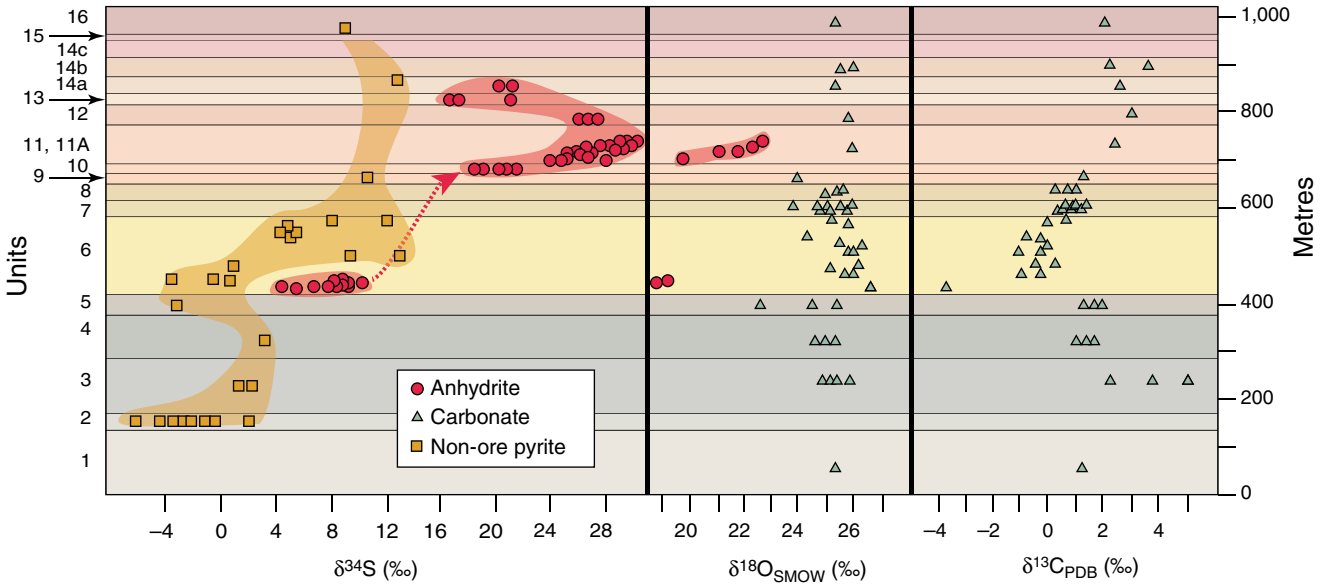

Fig. 14.49 The $\delta^{34}S$, $\delta^{18}O$ and $\delta^{13}C$ values of anhydrite, non-ore sulphide and carbonate within the Upper Marble in the Balmat stratigraphy (see Fig. 14.48) (After Whelan et al. 1990)

Marble below and above 11a are supported by differences in published Pb data for sphalerite in the Balmat Zn-Pb ores. Hauer (op. cit.) also concludes that most Upper Marble quartz originated as early diagenetic chert and that increases in aluminosilicate mineral abundances just below unit 11a are related to the tectonic events that caused the basin restriction and also drove anhydrite deposition.

Anhydrite presence has also played a significant role in the highly remobilised distribution of the ore bodies (Corriveau et al. 2007). The Balmat Pb-Zn orebodies occur within an overturned isocline in which the anhydritic units (11–13) show clear evidence of significant flow-related changes in thickness compared to other units in the metamorphic strigraphy (Fig. 14.48b). Large ductility contrasts between anhydrite and calc-silicate units led to the development of axial planar macrofractures that evolved into tectonic slides (de Lorraine 2001). Conformable massive sphalerite-pyrite-quartz lenses and layers contained with the three hosting stratigraphic units probably served as the loci for development of some of the minor or parasitic folds and the tectonic slides associated with the main syncline. Sphalerite was extremely mobile during peak metamorphism (650–700 °C and 6.5 kb) and locally flowed from the massive sulphide "parent" bodies into thin but extensive, cross-cutting ductility-contrast-induced "macrofractures" at points where macrofractures happened to transect the parent stratiform bodies. Spectacular excursions or remobilizations of "daughter" ore into macrofractures occurred locally with sulphide apparently flowing radially outward as far as 2 km away from source bed or parent ore masses. The bulk of remobilized sulphides remained within 0.5–1 km from the parent orebodies. According to Corriveau et al. (2007, 2009), such spectacular ore remobilization may have framed current perception that metamorphosed orebodies are remobilized significantly, however, this is not the norm as exemplified by well preserved stratigraphy even in marble successions (Gauthier et al. 2004) and is probably indicative of a propensity for greater mobilisation in the near fluid milieu created by deforming evaporites.

Mt Isa Inlier, Northern Australia

The Mount Isa Inlier is an extensive area of exposed midProterozoic rocks in northwest Queensland, that is part of a broader mineralised Proterozoic association extending southeast from the Pine Creek region, across the McArthur Basin the Lawn Hill Platform and into the Mt Isa Inlier (Fig. 14.50) the geology is attributed to attributed to early–mid Proterozoic tectonostratigraphic cycles (Fig. 14.51; Murphy et al. 2011; Blenkinsop et al. 2008). It contains a number of large Pb-Zn and copper accumulations, including the worldscale Mt Isa deposit. In this section we shall document the meta-evaporite nature of much of the ore-hosting matrix in the various blocks of the Mt Isa Inlier. In Chap. 15, the mineralisation aspect is discussed further, as it relates to halokinesis along with halite dissolution breccias after salt allochthon tiers, and the narrow polycyclic timing of mineralization, focusing on less metamorphosed examples, especially, the HYC deposit in the McArthur River Basin and the Century Deposit on the Lawn Hill Platform.

The Mt Isa inlier has conventionally been divided into three north–south trending tectonic units on the basis of major faults or fault zones (Fig. 14.50; Blake and Stewart

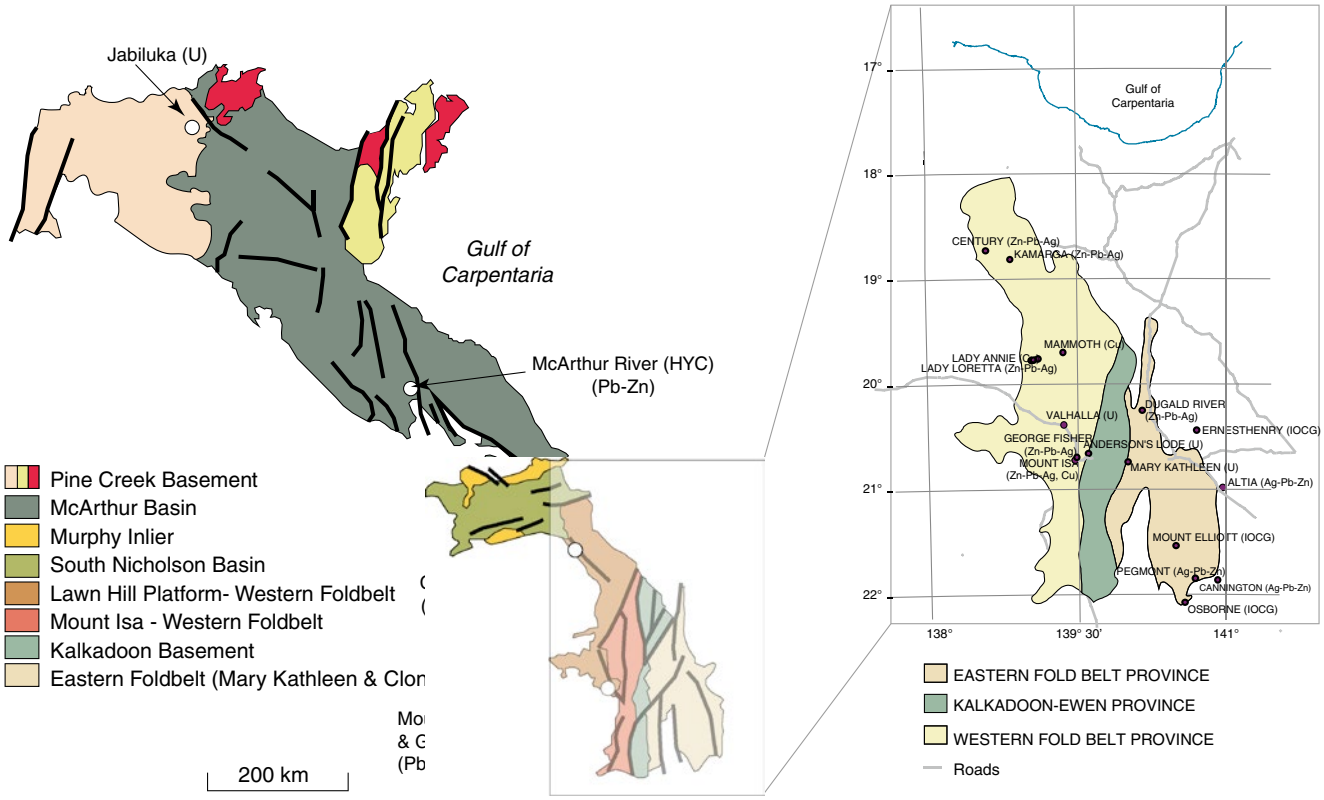

Fig. 14.50 Geological associations and provinces in the Mt Isa – McArthur Basin – Pine Creek region (Refer to Fig. 14.51 for space-time summary). Expanded view shows distribution of significant metalliferous occurrences in the region of the Mt Isa Inlier, which is made up of a central Kalkadoon-Leichhardt basement block, flanked by the eastern and western foldbelts, with significantly higher metamorphic grade defining the eastern foldbelt (After Hutton et al. 2012; Wilde 2011)

1992), namely: the Western Foldbelt (comprised of the Lawn Hill Platform and the Leichhardt River Fault Trough); the central KalkadoonLeichhardt Belt; and the Eastern Foldbelt (higher metamorphic grade, made up of the Mary Kathleen and Cloncurry districts). Across the region, remnants of the first depositional cycle form the basement to the Isa Inlier and were metamorphosed to amphibolite facies during the Barramundi Orogeny at ca. 1,900–1,870 Ma (Fig. 14.51).

The 'Barramundi Orogeny' rocks underlie the "cover sequences," which historically within the Inlier were considered to make up the "Eastern Fold Belt" and the "Western (foldbelt?) Succession" ranging across 1,550–1,800 Ma rocks. Recent geochronological, sequence stratigraphic and structural studies within the western half of the inlier have revealed that basin formation and sedimentation was more complicated than the three sequences model and that mineralization across the region is hosted in metasediments that were deposited within a relatively narrow age range between ca. 1,680 and 1,590 Ma (Foster and Austin 2008; Southgate et al. 2013). The succession is now regarded as a series of superposed basins: the 1,800–1,750 Ma Leichhardt, 1,730–1,670 Ma Calvert and 1,670–1,575 Ma Isa superbasins (Jackson et al. 2000).

Current understanding of the chronostratigraphic breakdown at the group level, and the associated igneous and orogenic events, is summarised in Fig. 14.51. This space-time plot shows a lithological spread across space-time of the three superbasins that constitute the McArthur- Mt Isa region, namely the Leichhardt, Calvert and Isa Superbasins, for which there is a spread of interpretations as to basin genesis (Murphy et al. 2011 and references therein):

1. Intra-continental rifting, punctuated by contraction, with a mantle plume that generated the flood basalts in the Leichhardt Superbasin;
2. Continental back-arc setting, punctuated by contraction due to accretion events along the plate boundary. In support of this model, trace-element geochemistry of mafic rocks mostly indicate a subducted slab component;
3. Rift to rift-drift and passive margin development, not punctuated by contraction, but by differential uplift and block rotation, particularly during the Calvert Superbasin;
4. Later in the history, ramp and strike-slip basins developed during Isa Superbasin infill, this was related to subduction in the south or

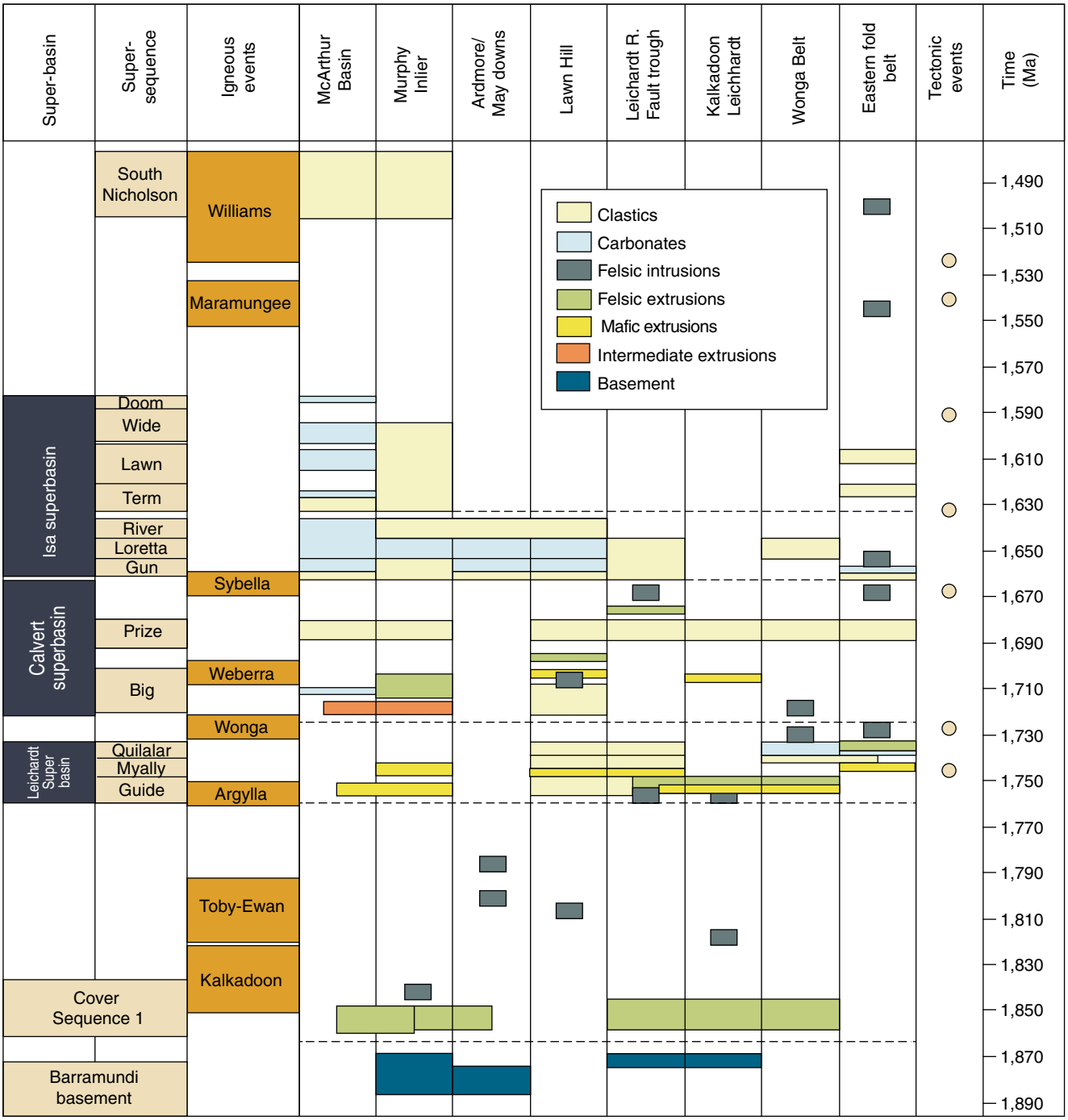

Fig. 14.51 Tectonostratigraphic evolution of the successions of the Mt Isa -McArthur River region (After Murphy et al. 2011)

5. Foreland basin development during deposition of the upper part of the Isa Superbasin. This was related to continental collision during the Isan Orogeny.

The Mount Isa Pb-Zn-Ag-Cu deposit is located in the Leichhardt Fault Trough, in the Gun Group, and hosted in the laminites of the Urquhart Shale. It contains a global resource of 255 Mt at 3.3 % Cu; while the Pb-Zn-Ag deposit contains 150 Mt at 7 % Zn, 6 % Pb, 150 g/t Ag in 10 strata-bound lenses in an en echelon arrangement around the silica-dolomite hosted copper deposits. The deposit contains 10 strata-bound Zn-Pb-Ag orebodies in an en echelon array. According to Davis (2004) the extremities of the orebodies correlate with F4 folds, and high-grade shoots are centred on F4 hinges and short limbs that contain older F2 folds (Fig. 14.52a).

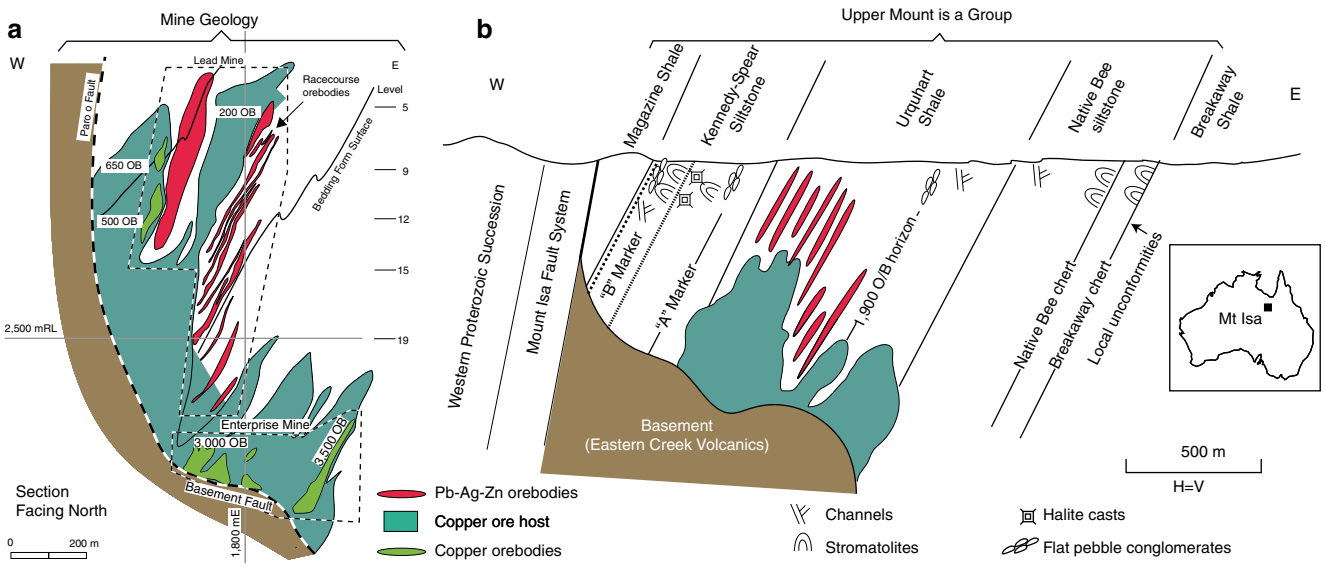

Fig. 14.52 Geology of the Mt Isa Cu-Pb-Zn ore deposit. (**a**) Ore distribution in a north-facing mine section (After Davis 2004). (**b**) Idealised E-W cross-section through Upper Mt Isa Group formations hosting the showing occurrences of various evaporitic indicators in the sequence (After Neudert 1986). *Inset*: locality map

Several major sedimentary sequences in the Mt. Isa inlier, including the ore-hosting Urquhart Shale (calcareous siltstones and shales at greenschist grade) in the western Succession and the more metamorphosed Corella Fm. and Staveley Fm. in the eastern foldbelt, all contain relict evaporite pseudomorphs or meta-evaporites indicators (Stewart and Blake 1992; Stewart 1994a, b). The sequence in the vicinity of the Mt Isa mine (Western Succession) has undergone several deformations within low greenschist facies (chlorite grade) metamorphic conditions (McClay and Carlile 1978). The deformations were not penetrative and a slaty cleavage is only well developed in the more argillaceous beds. Thus primary bedding and many other sedimentary textures are still visible in the Urquhart Sahle and adjacent lithologies, including widespread evaporite pseudomorphs, and other hypersaline indicators, such as tepees, stromatolites and dissolution breccias, (Fig. 14.52b; Table 14.8; Neudert and Russell 1981; Neudert 1986). The influence of evaporites in the Mt. Isa Inlier Cu-Pb-Zn mineralization was ongoing from the diagenetic into the metamorphic realms. Large anhydrite-baryte bodies remain in the subsurface at the northern end of the Mount Isa copper ore body (Wilde et al. 2005a, 2006). There is ongoing debate as to whether this anhydrite is a recrystallised depositional relict or is a hydrothermal anhydrite.

Likewise there is ongoing debate as to the nature of the Paroo Fault, which is widely accepted as having acted as the main conduit/focus for mineralising fluids in the Mt Isa ore (Fig. 14.52a; Long 2010). But, whether these solutions arrived when the Paroo Fault was a bounding fault to a deep seafloor minibasin, with a salt allochthon focused transport mechanism, or if was independent of any evaporite influence and was a purely structural feature focusing mineralising fluids is not yet resolved.

Mary Kathleen (Eastern) Foldbelt

The lowermost part of the Eastern Succession stratigraphic sequence (Argylla Formation, Ballara Quartzite, Corella Formation) is intruded by the Wonga Batholith, comprising bimodal intrusive rocks in the Mary Kathleen Fold Belt (Fig. 14.53a; Hammerli et al. 2014). The batholith crops out in a north– south linear zone about 200 km long and 10–20 km wide. Intrusive rocks of the batholith are subdivided into two groups based on their deformational style. The strongly foliated Wonga Granite Suite occurs in the central part of the batholith (the Wonga Belt), and is interpreted as intruding high-strain zones below a regional detachment (i.e. the lower plate). Lower plate magmatic rocks were intruded contemporaneously with shearing and the overprinted results of this process encompass various granites as well as dykes of metadolerite (now amphibolite). These rocks have experienced varying degrees of ductile deformation and some are extensively mylonitised. Mylonitic fabrics give either a top-to-the-north (Holcombe et al. 1991, 1992) or top-to-the-south sense of shear (Pearson et al. 1992; Gibson et al. 2008) and indicate amphibolite-facies conditions as they formed.

In contrast, deformation in the upper plate was accompanied by development of more brittle structures, including normal faults that root downward into the mid-crustal detachment. Metamorphism associated with initial upper-plate extensional deformation rarely exceeded greenschist facies,

Table 14.8 Sedimentary features at Mt Isa and their significance

	Sedimentary features of the Mt Isa Group				Environmental interpretation						
		Unit			Water depth				Salinity		
		Native Bee Siltstone	Urquhart Shale	Kennedy-Spear Siltstone	Emergent	Semiemergent	Shallow	Deep	Hypersaline	Penesaline	Fresh to normal
	Stratiform sheets	X		X		X	X				
	Ridge-rill structures	X				X					
Stromatolites	Domes			X		X	X				
	Rings and open rings			X	X	X					
	Ridge structures			X	X	X					
Evaporites	Discoidal gypsum		X	X						X	
	Anhydrite laths		X							X	
	Halite casts			X					X		
Sedimentary structures	Large-scale crossbeds	X	X	X		X	X				
	Small scale crossbeds	X	X	X		X	X	X			
	Stromatolite pebbles	X		X	X	X	X				
	Carbonate-intraclasts	X	X	X	X	X					
	Tepees	X			X						

with subsequent amphibolite-facies metamorphism related to later events. Along with the intervening detachment, upper and lower plate rocks were deformed into a series of upright, north–south trending D2 folds during east–west shortening accompanying the ≈1,600 Ma Isan Orogeny (Fig. 14.53b). This event post-dates extensional shearing by more than 100 Ma. By contrast, the flanking and less-foliated Burstal Igneous Suite is located in the lower strain and originally also less intensely metamorphosed upper plate above the regional detachment (Holcombe et al. 1992). Wyborn (1988) interpreted magmatism as occurring in both domains from about 1,760–1,720 Ma during an episodic period of extension known as the Wonga Extension Event.

Work by Neumann et al. (2009) refined the duration of this extension event to between 1,780 and 1,740 Ma. They demonstrated that the initial stages of this tectonomagmatic event are coincident with mafic magmatism, basin formation and rapid sedimentation of the ≈1,780–1,765 Ma Myally Supersequence of the Leichhardt Superbasin in the adjacent Leichhardt River Fault Trough. That is, deposits of the Ballara Quartzite and Corella Formation represent a period of sag-phase sedimentation during the later part this event, and that these units are likely equivalent to the Quilalar Supersequence of the Leichhardt River Fault Trough (Fig. 14.51). These correlations permit the equivalent sections of the Eastern and Western Successions of the Mt Isa Inlier to be correlated from 1,780 Ma. Locally, the Corella Formation is intruded by 1,740 Ma granites, suggesting that at least the lower parts of this package were deposited during the 1,780–1,740 Ma extensional event. That is the original evaporites, now seen as meta-evaporite remnants in the Corella Formation in the eastern foldbelt were originally deposited as "rift to drift" evaporites.

So, regionally, the Mary Kathleen Foldbelt (Eastern Succession) is composed of: (1) meta-evaporites and meta-carbonates of the Corella Formation (deposited 1,738–1,750 Ma), or (2) meta-granites and metadolerites (Oliver and Wall 1987; Foster and Austin 2008; Neumann et al. 2009). Metamorphic grade ranges from upper greenschist to upper amphibolite and the succession is intruded by batholithic late- to post-tectonic granitoids. Evaporites and carbonates (their bitterns and their daughter products) in these metasediments acted as ongoing sources of saline fluids during a protracted series of tectonothermal events and were integral to the creation of widespread hydro-brecciated textures. One wonders how much of the brittle to ductile

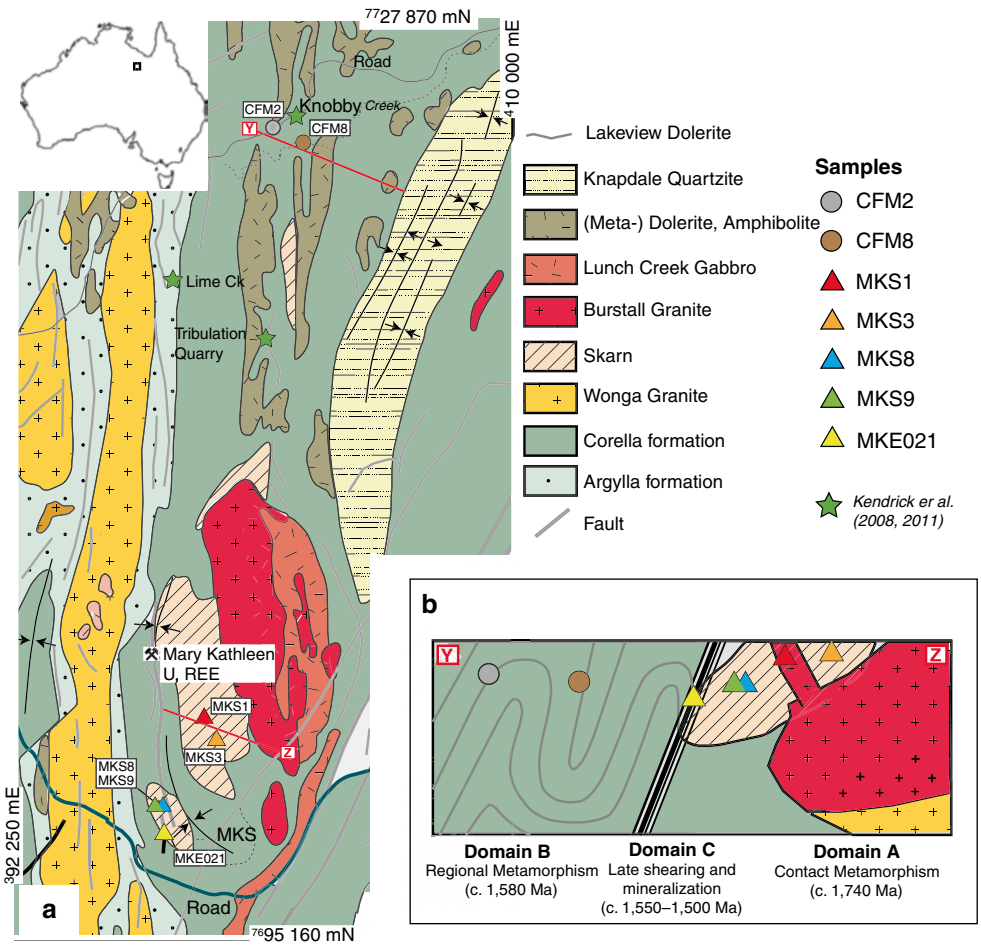

Fig. 14.53 Geology of the Mary Kathleen Foldbelt. (**a**) Map. (**b**) Section (After Hammerli et al. 2014)

transition at the base of the Corella reflects, at least in part, the influence of a brittle-ductile discontinuity associated with the presence of a thick former salt unit at the transition boundary.

For example, the fluid evolution history in the Cloncurry district is characterized by early high temperature and low salinity to late low temperature and high salinity fluids given an association that is distinct from many intrusion-related hydrothermal systems elsewhere in the world (Xu 2000). The ubiquitous presence of low-temperature (T <200 °C) $CaCl_2$-bearing inclusions is a remarkable feature of the mid-Proterozoic Cloncurry hydrothermal system (Fig. 14.54). It is interpreted to be a result of the interaction between widespread dissolving metaevaporites and downward penetration of deeply-circulating meteoric water. The transition from early hotter magmatic and/or metamorphic fluids to cooler late meteoric water is ascribed by Xu (2000) to the shift of the crustal level during exhumation.

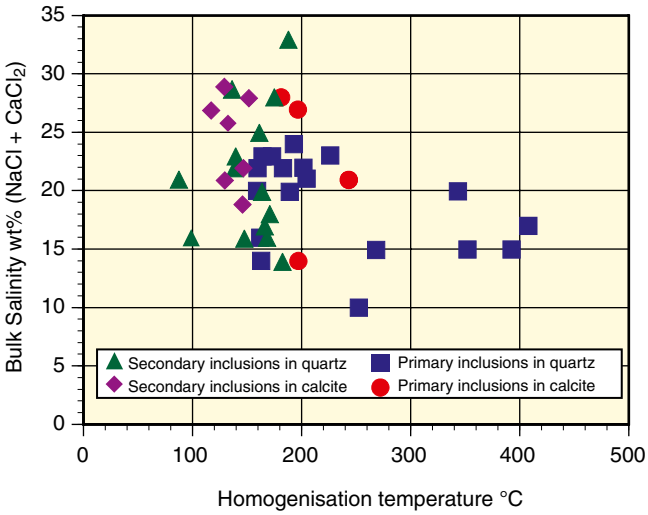

Fig. 14.54 Plot of homogenization temperatures T_h versus bulk salinities (wt.% NaCl + $CaCl_2$) of $CaCl_2$-bearing inclusions. Note the overall negative correlation between them and rapid change in Th, illustrating a fluid mixing between hot magmatic fluid and downward circulating cold $CaCl_2$ brines (After Xu 2000)

Diagenetic sulphides, Corella evaporites and associated bitterns have been extensively remobilized so that only meta-evaporite indicators, such as scapolites, albites and tourmalines, remain (Phillips et al. 1994; Oliver et al. 1994). Accordingly, the assignment of an evaporitic protolith to particular levels in this metasedimentary succession is more contentious than the Urqhardt Shale in the Leichardt Fault trough. However, noble-gas and halogen data suggest evaporite-sourced bittern brines in the sedimentary portion of the Corella protolith were significant contributors during late-Isan Orogeny albitisation in the Mary Kathleen Foldbelt and were present throughout much of the Cloncurry District during the Isan Orogeny (Fig. 14.55; Kendrick et al. 2008, 2011).

An evaporitic origin for the metasediments of Corella Formation was first postulated by Ramsay and Davidson (1970). High fluid salinities in the Corella Formation are indicated by Cl-rich biotite, amphibole, and scapolite (Fig. 14.56; maximum Cl contents: 0.60 wt%, 1.24 wt%, 3.67 wt%, respectively). Some SO_3 is present in almost all samples implying the former presence of $CaSO_4$. Reinhardt (1992) showed that the Corella Formation in the Rosebud Syncline now consists of interlayered Al- and Mg-rich metapelites, Ca-rich rocks, feldspathic schist, and scapolite schists that were originally deposited as pelite-carbonate-evaporite sequences in a Mid-Proterozoic ensialic rift basin. Widespread evaporite deposition took place in the final stage of rift sedimentation within a hypersaline shallow-water

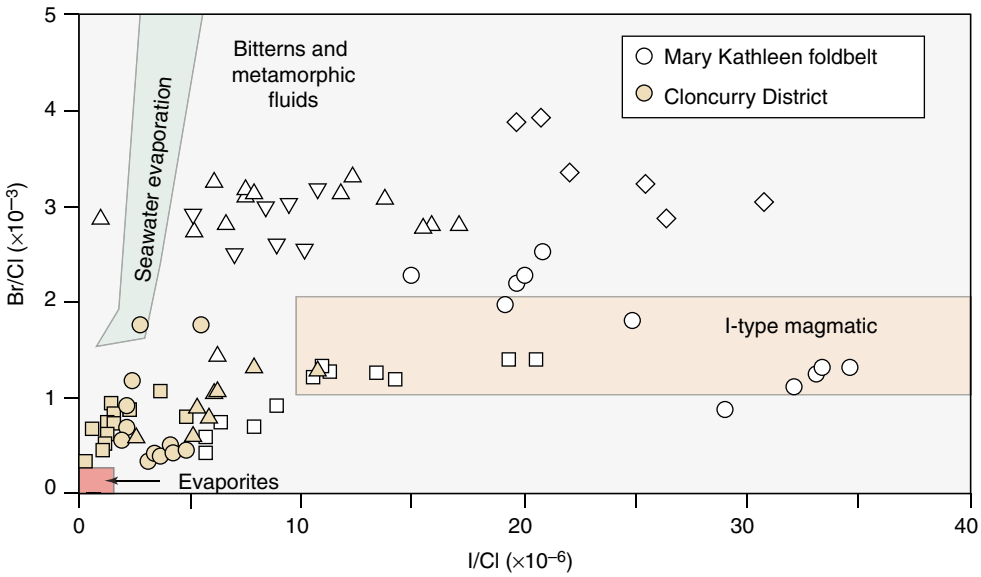

Fig. 14.55 Fluid inclusion halogen signature associated with albitisation in the Mary Kathleen Fold Belt (*open symbols*) and Cloncurry District (*closed symbols*). The Cloncurry District fluids have fractionated halogen signatures characteristic of fluid interaction with meta-evaporitic scapolite (After Kendrick et al. 2008)

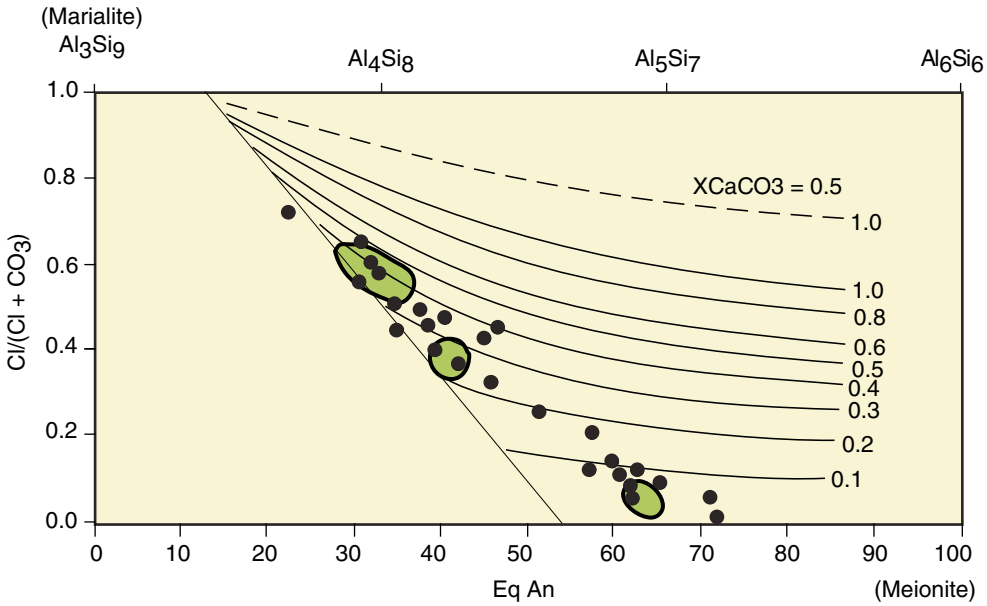

Fig. 14.56 Compositions of scapolites (low F/R group) from a single outcrop (*shaded zones*) in the Mary Kathleen Foldbelt are plotted on the equivalent anorthite/fluid salinity plot. *Black circles* are data points from Ellis 1978 (After Oliver and Wall 1987)

environment (Neumann et al. 2009). The compositional variation of scapolite in the Rosebud Syncline on a layer-to-layer scale excludes large scale infiltration of externally derived fluids in the metasediments, but suggests variable proportions of evaporitic minerals in different layers and small scale variations of fluid salinity during metamorphism.

With burial, the Corella Formation evolved in concert with its distinctly saline fluid suite under P-T conditions that initially were perhaps close to those of peak metamorphism. This pulse of sodic immersion first occurred during the extension phase (1,760–1,730 Ma), and was coincident with intrusion of voluminous granitic and doleritic magmas (Wonga Suite) at ≈5–10 km depths into the carbonate-evaporite-dominated Corella Formation (Fig. 14.57a; Oliver et al. 1994; Oliver 1995). Widespread high-temperature metasomatism ensued, involving scapolitization in dolerites, formation of albite-scapolite shear zones in granite, exo- and endoskarn formation, and a zone of K-Na-Ca alteration in the lowermost Corella Formation.

Granites and dolerites were altered to an unusual Na-Ca-rich bulk composition, reflecting infiltration of highly saline, chemically reactive externally-derived sodic fluids. The alteration products and their distribution suggest not only reaction of magmatic/aqueous fluids with the saline country rocks but also extensive halite alteration/dissolution and hydrothermal recirculation of saline fluids back into the intrusive bodies. According to Oliver and Wall (1987) the bulk of fluid flow occurred at high temperatures (500–700 °C), and the major element and isotopic fronts within the metasediments were generally not smoothed out by the effects of temperature gradients.

Oliver and Wall (1987) divided the lithologies of the Mary Kathleen Foldbelt into two distinct groups: a low fluid/rock (F/R) group and a high F/R group. The low F/R group is comprised of large areas of pristine metasediments showing evidence for internal buffering of fluid composition, as shown by $\delta^{18}O$ and $\delta^{13}C$ signatures typical of metamorphosed marine carbonates. In these low F/R metasediments the progress of calcsilicate reactions, and scapolite compositions vary greatly between adjacent layers. In contrast, the high F/R group is an assemblage developed in pretectonic intrusive rocks, as well as in metasomatic zones of calcsilicates around the margins of the intrusives (Fig. 14.57b). This group is characterised by scapolitised metadolerites, albitised calcsilicates, and large calcite pods and veins with ^{18}O- and ^{13}C-depleted values. This group indicates localized throughput of predominantly externally-derived hypersaline fluid, at high F/R ratios. It accompanied the initial metamorphic peak of 560–630 °C and 3–4 kbar and subsequent cooling.

Scapolitic layers in the foldbelt comprise approximately 40 % of the metasedimentary sequence (low F/R group; Unit A and B in Fig. 14.57b). and scapolitic modes are typically in the range 5–35 %, with average chlorine contents ≈1.5 % (Fig. 14.56). Plots of Mary Kathleen Foldbelt metasediments compared with plots from the experimental work of Ellis (1978) indicate that fluids in equilibrium with the chloride-rich scapolites must have been hypersaline, particularly in calcite-bearing metasedimentary assemblages, with >30 mol% NaCl equivalent (Fig. 14.56; Oliver and Wall 1987). Abundant three-phase halite-bearing primary fluid inclusions in scapolite, amphibole and quartz are further evidence of synmetamorphic hypersaline conditions. The Cl content in units A and B (low F/R) varies widely, even in individual outcrops, indicating small-scale salinity gradients associated with the original Cl content of

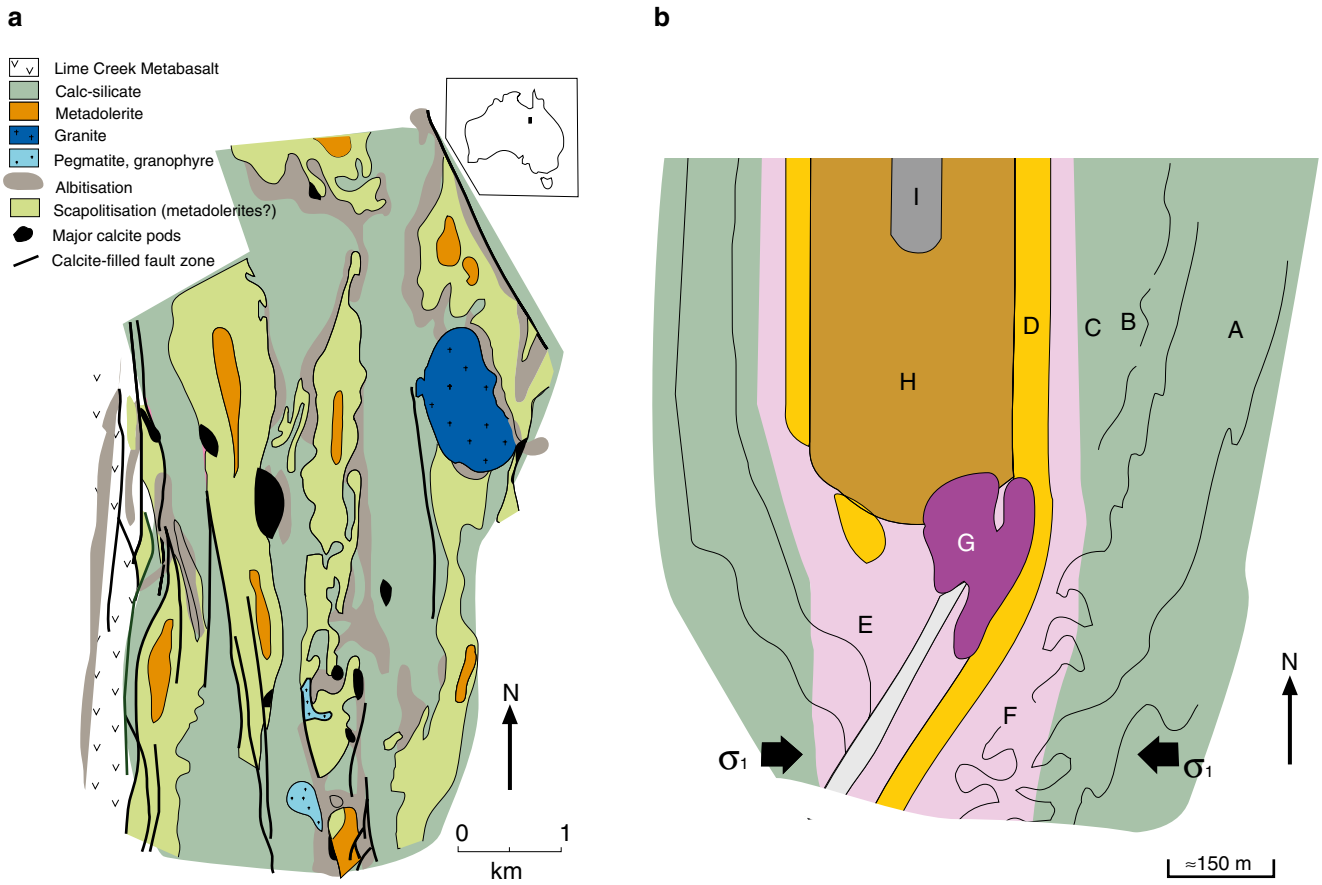

Fig. 14.57 Geology of Mary Kathleen Foldbelt. (**a**) Portion of the foldbelt showing distribution of pristine calcsilicate relative to albitised equivalents, shear zones, and scapolitised metadolerites. *Inset* shows locality of foldbelt. (**b**) Model of influence exerted by competent meta-intrusive units on localisation of fluid flow. Unit *A* is pristine calcsilicates; *B* is zone of boudinage and minor veining in zones of high differential stress; *C* is albitised and brecciated calcsilicates (failure adjacent to shear zone); *D* is albite-calcite shear zones; *E* is strain-shadow zone – abundant calcite veins and albitite breccia; *F* is refolded brecciated folds in albitised calcsilicates; *G* is large calcite pods in tensile and shear zones; *H* is scapolitised orthoamphibolite; *I* is scapolite poor metadolerite (After Oliver and Wall 1987)

the metasedimentary protolith are still retained in the sequence (Fig. 14.57). Similarly, the highly variable Cl content in the biotites in units A and B suggests a protolith differential in the low F/R group. The original proportion of halite was at least 15 % of the sedimentary sequence and probably much higher, especially if the effects of diagenetic dissolution and the likely inefficiencies of halite incorporation into scapolite are considered.

Major competency contrasts between meta-intrusive and calcsilicate metasediments of the Corella Fms influenced stress and strain patterns around the igneous bodies, which in turn controlled fracture permeability and the focusing of the interacting metamorphic fluids (Fig. 14.57b). The relatively brittle behaviour of the meta-intrusive rocks favoured the development of small-scale fracture permeability and consequent pervasive alteration of these bodies. Calcite vein systems (Units C and D) and intensely albitised calcsilicate breccias (Unit E) are localized in shear zones and dilatant areas around the meta-intrusives, either where shear stresses were high or where all stresses were low, resulting in shear and tensile failure, respectively (Units F and G). Thus, permeability enhancement, and the development of major fluid pathways during regional metamorphism of the terrane, is systematically related to variations in the stress field accompanying deformation. Oliver et al. (1994) favour a model where fluid was preferentially channelled along specific permeable conduits, including former evaporite layers, before interaction with the now exposed altered rocks. Fluid was probably driven by both convective circulation and dilatancy-related deformation accompanying emplacement of magmas into a major crustal extensional décollement.

Regionally, the halites and subsequent scapolites of the Corella Formation evaporites played an ongoing role over more than 600 million years of metasomatic alteration in the Mary Kathleen Foldbelt. There were four phases of deformation-related hydrothermal activity in the region (D1-D4), which occurred over a time range from at least 1,750–1,100 Ma, and all were associated with evaporite-derived

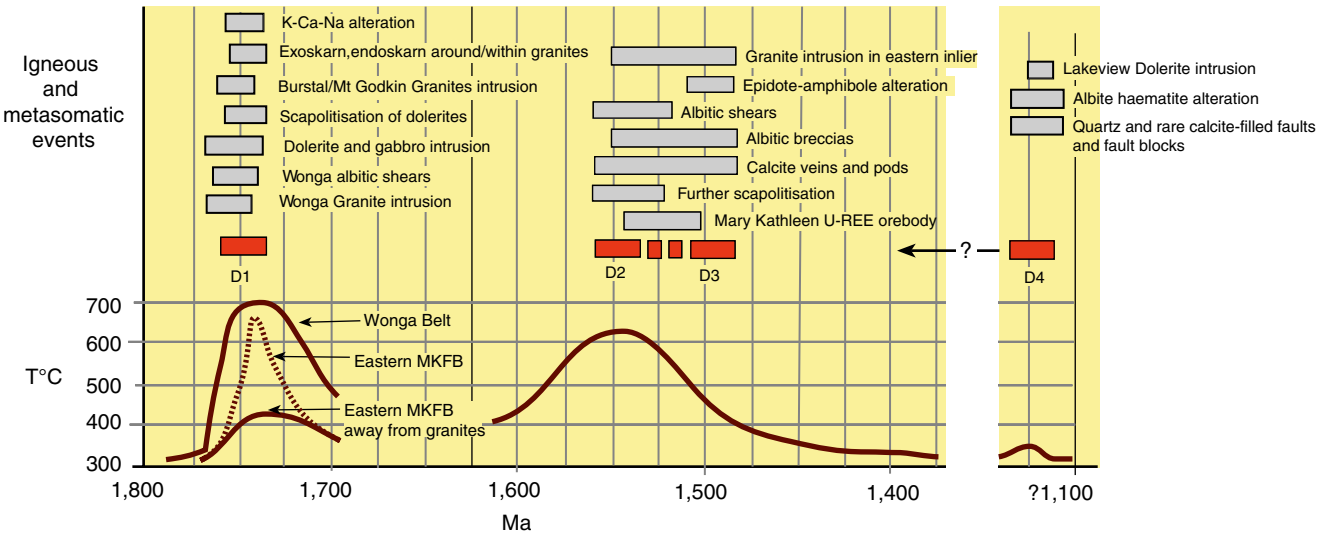

Fig. 14.58 Hydrothermal history of the Mary Kathleen Foldbelt (MKFB), the time-temperature lines are poorly constrained by available geochronological data and are schematic (After Oliver 1995)

saline fluids (Oliver 1995). The Na–Cl brine source of much of these highly saline metasomatic fluids was halite in the Corella Formation, its halokinetic derivatives, and subsequent scapolites.

In Phase 1, deformation, contact metamorphism, and metasomatism, accompanied the emplacement of the Wonga Batholith along with related mafic and felsic intrusives (1,750–1,730 Ma; Fig. 14.58). This occurred not long after the deposition of the volcano-sedimentary package that included the evaporitic protolith to the Corella Formation (1,750–1,738 Ma; Foster and Austin 2008). It involved fluid pathways related to emplacement of intrusions in and above a major crustal subhorizontal extensional shear zone where a predominantly ductile lower plate -Wonga Belt- was flanked by a predominantly brittlely deformed upper plate -Corella Formation. Intrusive rocks and contact aureoles formed discrete kilometre-scale bodies within the Corella Formation during Phase 1. As a consequence, fluid flow during Phases 2 and 3 (regional deformation and amphibolite-facies metamorphism) was localized around the boundaries of these very competent Phase 1 intrusions and contact metamorphic aureoles (Fig. 14.57b). Fluids infiltrating the rocks during Phases 2 and 3 were complex externally derived $NaCl$-$CaCl_2$-KCl-H_2O-CO_2 brines that may have undergone phase separation. This fluid flow culminated in the formation of widespread calcite vein systems (with copper) and the Mary Kathleen U-REE vein-style orebody. Mineralization was sufficiently localized by the pre-existing structural heterogeneity that many parts of the Corella Formation did not experience significant fluid flow at this time (perhaps a reflection of intrinsically lower permeability in meta-evaporite intervals not adjacent to the intrusive). Phase 4, post-metamorphic oxidising alteration (D4), was localized around major predominantly crosscutting strike-slip faults. These faults are very large with apparent strike-slip displacements of 5 to >40 km and define the most obvious crosscutting regional geological features.

Using halogen ratios in the metamorphic and hydrothermally derived scapolite from a range of rock-types in the Mary Kathleen fold belt, Hammerli et al. (2014) argue that the dominant metamorphic interactions were between bittern-grade formation waters and magmatic-hydrothermal fluids derived from granite plutons (Fig. 14.59). They conclude that halite-dissolution supplied at best only minor chlorine to fluids in the foldbelt. Chlorine/bromine ratios in metamorphic scapolite indicate that fluids were dominantly derived from basinal brines formed from sub-aerial evaporation of seawater beyond the point of halite saturation. This bittern fluid infiltrated the underlying sedimentary sequences prior to regional metamorphism. Zoned scapolites in a major late-metamorphic mineralized shear-zone record three discrete pulses of magmatic and metamorphic fluid, and suggest that fluid mixing assisted mineralization along and around this shear-zone (Fig. 14.57b). This interpretation is predicated on their conclusion that Cl and Br do not fractionate when incorporated in scapolite. Furthermore, they found unaltered rims of heavily retrogressed scapolite show indistinguishable Cl/Br signatures compared with fresh grains from the same sample, indicating retrograde metamorphism did not significantly affect Cl and Br signatures in scapolite group minerals, hence the halogen ratios are indicators of the protolith (Fig. 14.59; Hammerli et al. 2014).

Staveley Formation

The Staveley Formation (Eastern Foldbelt) was once thought to be part of the Mary Kathleen Group and indicated a conformable meta-evaporitic (middle-upper greenschist to amphibolite) transition between the Corella Fm and the Marimo Shale (Stewart 1991, 1994a, b; Krcmarov and

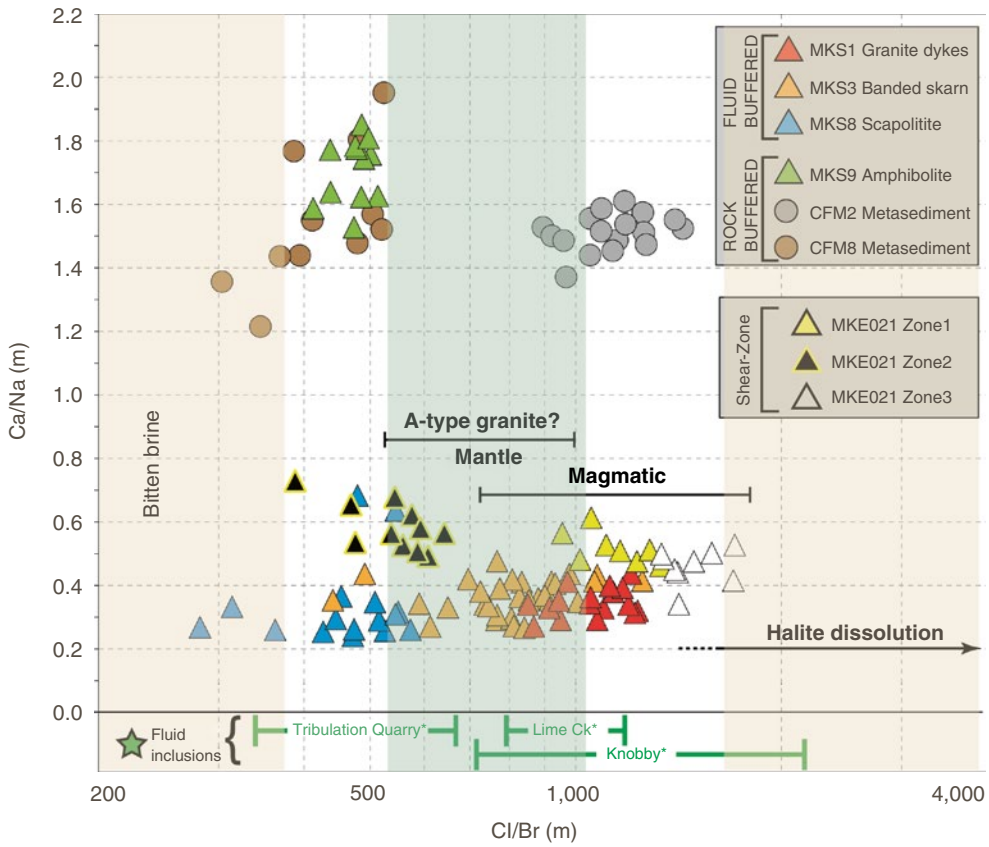

Fig. 14.59 Molar Ca/Na ratios v. molar Cl/Br ratios of fluid-buffered scapolite samples (MKS1, MKS3 and MKS8) and rock-buffered scapolite samples (MKS9, CFM2 and CFM8). Rock buffering leads to high Ca/Na ratios in scapolite. The Ca/Na variation in sample CFM8 might be due to small-scaled local equilibria. The fluid-buffered scapolite compositions fall on a fluid mixing trend between magmatic and bittern brine fluid. Plot fields of molar Cl/Br ratios of typical magmatic fluids, mantle fluids, Br-enriched bittern brine fluids and typical halite dissolution fluids are shown as shaded areas. (Figure is after Hammerli et al. 2014; Data on fluid inclusions shown in the lower part of the figure are from Kendrick et al. 2008, 2011)

Stewart 1998). More recent work by Foster et al. (2008) has shown that it is probably younger (1,610–1,675 Ma) and should be removed from this lower evaporitic grouping. It is now considered equivalent in age to the Urquhart Shale of the Western Foldbelt that hosts the Mount Isa mineralisation.

South of Cloncurry, chalcopyrite (cobaltiferous)-pyrite mineralization occurs as disseminations in pre- and syntectonic breccias in the Staveley Formation, and within disaggregated silica pseudomorphs (after thinly bedded evaporitic sulphate beds) that are associated with dolomitised limestone-calcilutites. Although this mineralization may be partly diagenetic in origin, the 200 m-thick meta-evaporitic packages are also host to a locally widespread (2–4 km long and 200 to >500 m wide) and pervasive 'redrock' styled microcline-dolomite ± hematite alteration. Within this gross alteration package there also seems to be a consistent association with narrow (10–100 m wide) linear (stratabound) semi-massive magnetite-hematite-microcline and quartz-chalcedony replacement zones. The economic significance of mineralised haematitic intervals (ironstones) in evaporitic terranes and gold deposits, such as Starra, is discussed further in Chap. 16.

Like much of the Corella Formation, the meta-evaporitic Staveley Formation experienced dissolution/alteration, paleosolution karsting (breccias), and tectonic brecciation, such that the precursor lithological details were progressively obliterated even prior to entering the metamorphic realm. The post-diagenetic to post-tectonic fluid pathway development and metasomatic alteration history of this important lithostructural package of rocks in the Eastern Succession has been traced by Stewart (1994a, b). He proposes that both the base of the Marimo Shale and parts of the underlying evaporitic-limestone dololutite have acted as conformable fluid pathways for hydrothermal and (perhaps) diagenetically derived, Cu-Au-(±Co ± As)-K-Na-Ti-REE bearing fluids and brines.

Evidence for the evaporite protolith in this amphibolite grade sequence, where the actual salts have long since disappeared, is not just mineralogical but also textural. Stewart's (op. cit.) documented evaporite indicators in the Staveley Formation include (Fig. 14.60):

1. Disaggregated chert nodules: 2–6 cm thick beds of 2–3 cm spheres comprising a collection of fragment-supported chert discoids, shingles, 'shards' and nodules with an ankerite feldspar matrix.
2. Enterolithic layers: chert nodule trains and contorted cherty nodule layers with overlying feldspathic dolomite laminae draped around nodules and slumped between them.
3. Beds of disseminated nodules and angular chert fragments with a sparry dolomite-quartz cement.

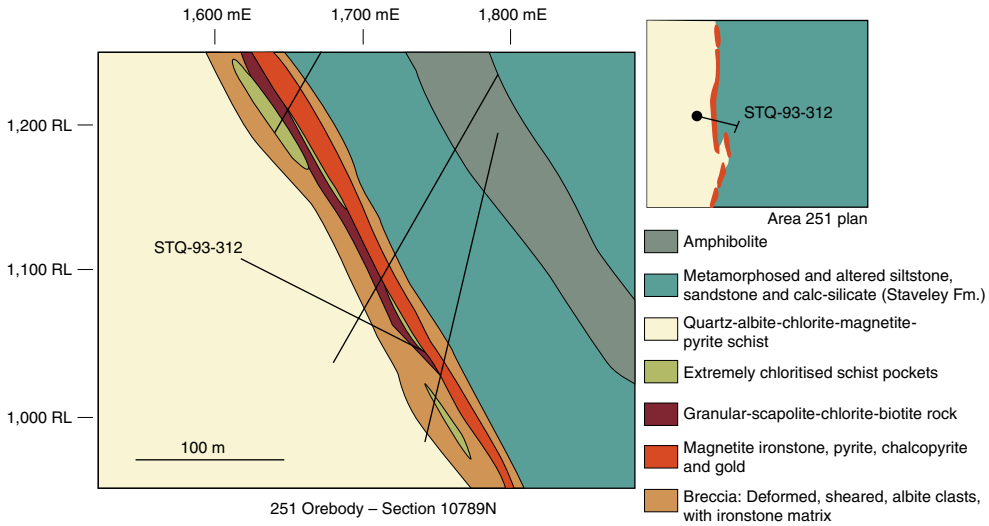

Fig. 14.60 Starra Cu-Au deposit. Cross section through 251 orebody, drill hole STQ-90-312, showing relationship between Staveley Formation, brecciated shear, ironstone lenses and Cu-Au mineralisation (After Rotherham 1997)

4. Cauliflower-textured and embayed nodules with contorted internal bands of cryptocrystalline (20 μm sized) chert.
5. Abundant hypersaline fluid inclusions (including halite crystals).
6. Displacive upward growth textures of nodules and discoids, alignment of nodule shards along low-angle cross bedding.
7. Lenticular and discoidal voids in shales. Shingle beds. Chickenwire or cottage cheese textures. Desiccation cracks. Soft sediment slumping.
8. Halite and scapolite pseudomorphs.

He shows how shallow-marine? evaporitic sulphates of the Staveley Fm. underwent Ca-Mg-Fe carbonate metasomatism and copper enrichment during diagenetic disintegration of the sulphate forms prior to general silicification.

To date workers on the various Mt Isa inlier lithologies, including the Staveley Fm., have largely ignored the possibility that halokinetic horizons in the protolith form long-lived zoned of ductility contrast (including primary and secondary salt welds, as well as fault welds) that focused various fluid conduits and channel-ways (Chaps. 15 and 16).

Willyama Supergroup: Olary and Broken Hill

The Mesoproterozoic Willyama Supergroup is part of the Curnamona Province and straddles the border between far western New South Wales and eastern South Australia (Fig. 14.61). It entrains Early to Middle Proterozoic metasedimentary and minor meta-igneous rocks that have a total stratigraphic thickness estimated at 7–9 km. It is subdivided into several structural blocks dominated by the Broken Hill and Euriowie Blocks in NSW and the Olary Block in South Australia (Figs. 14.61 and 14.62; Stevens et al. 1988). Late Proterozoic (Adelaidean) sedimentary cover separates the Euriowie and Broken Hill Blocks, while the Broken Hill and

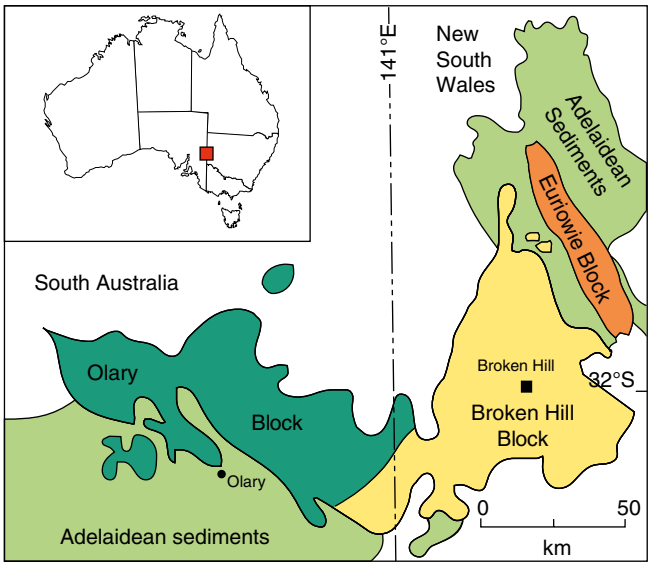

Fig. 14.61 Location of the Willyama Block, made up of the Olary Block and the Broken Hill Block

Olary Blocks are separated by Cenozoic cover in the north and an inferred fault in the south.

As well as being pervasively metamorphosed (amphibolite to granulite facies), the Willyama Supergroup is intensely mineralised. In the Olary Block copper and uranium deposits are the most significant, with lesser iron, barium, cobalt, tungsten, gold and fluorite. In the Euriowie Block tin deposits are the most significant and common, while minor deposits of lithium, niobium, tantalum, copper and iron are also present. The Broken Hill Block is dominated by deposits of lead, zinc and silver with lesser tungsten, copper, iron, cobalt, gold, nickel, platinum, tin, beryllium, uranium and fluorite. This block includes the 250 Mt of ore in Broken Hill lead-zinc-silver body, which is also the world's largest known Pb–Zn–Ag deposit.

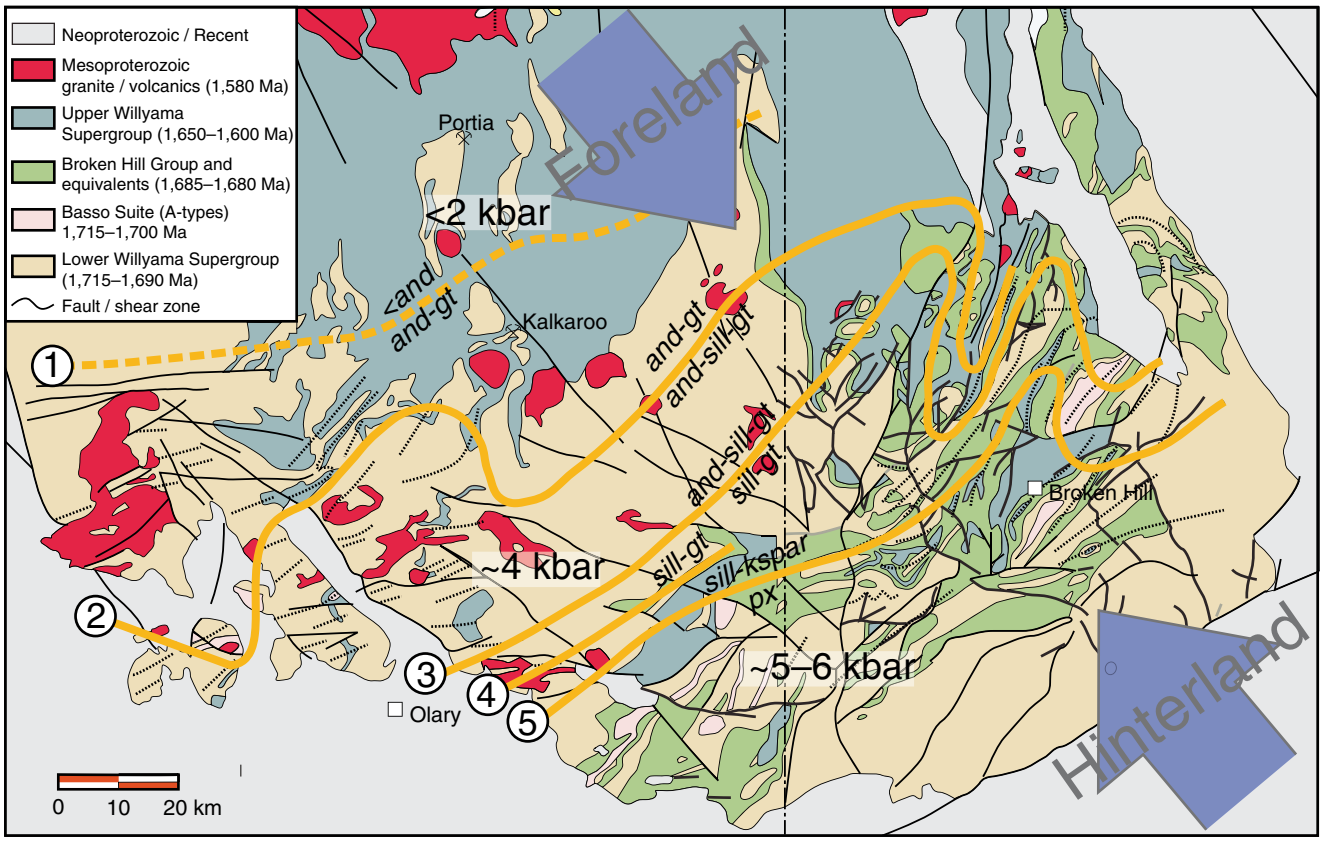

Fig. 14.62 Map of southeastern Curnamona Province showing the distribution of deformation and metamorphism associated with the 1,600–1,580 Ma Olarian Orogeny. The intensity of tectonism decreases toward the NW, suggesting the orogen may have had a NW–SE component of tectonic transport. The *dotted black lines* indicate axial traces of D2 folds which have upright to reclined orientations and deform earlier low-angle large-scale folds that invert large areas of the stratigraphy. The numbered lines (1–5 represent isograds of increasing metamorphic intensity. The ≈1,580 Ma granites immediately postdate the penetrative deformation (*and* andalusite, *gt* garnet, *Kspar* K-feldspar, *px* pyroxene, *sill* sillimanite) (After Hand et al. 2008)

The Willyama Supergroup metasediments are thought to have been deposited in an ensialic intracontinental rift zone (Conor and Preiss 2008; Barovich and Hand 2008). Multiple tectonic episodes during the ≈1,600 Ma Olarian Orogeny and the ≈500 Ma Delamerian Orogeny have dismembered and inverted the stratigraphy and metamorphosed the succession well in to granulite facies (Fig. 14.62). Lithologies in the Olary Block indicate rift margin-related conditions, whereas the majority of lithologies in the Broken Hill Block indicate more central and deeper water portions of perhaps the same progressively developing rift system (Willis et al. 1983; Plimer 1984, 1985; Vernon and Williams 1988; Slack et al. 1989; Cook and Ashley 1992; Cook 1993; Bierlein et al. 1995; Barovich and Hand 2008). Due to pervasive intense deformation and high grade regional metamorphism any primary evaporites in the rift and halokinetically mobilised into the deeper water slope and rise sediments have long since been destroyed and only subtle indications remain (Cook and Ashley 1992), such as boron isotope signatures in tourmalines (Slack et al. 1989) and the meta-evaporite associations in some stratiform scheelites (Plimer 1994).

Olary Block

The Willyama Supergroup in the Olary Block, west of the Broken Hill Block, consists of upper greenschist to amphibolite grade metamorphosed sedimentary and minor igneous rocks. The sequence is dominated by meta-clastic and meta-chemical sediments (evaporites and exhalites; Lottermoser and Ashley 1996; Conor and Preiss 2008; Heimann et al. 2013). Using lithological, geochemical and fluid inclusion data, Cook and Ashley (1992) first demonstrated the widespread importance of meta-evaporite associations within the Willyama Supergroup in the Olary Block.

The stratigraphic succession in the Olary Block displays a change in general composition from quartzo-feldspathic at the base through calcsilicate-rich to pelitic at the top (Fig. 14.63; Clarke et al. 1987; Forbes 1991; Cook and Ashley 1992). The Composite Gneiss Suite is the basal unit and is made up of crudely layered coarse-grained quartz-feldspar-biotite ± sillimanite ± garnet gneiss (migmatic). It grades into psammopelitic and pelitic schists, implying a sedimentary precursor; but there are zones exhibiting complete conversion, via *in situ* migmatites, into banded, migma-

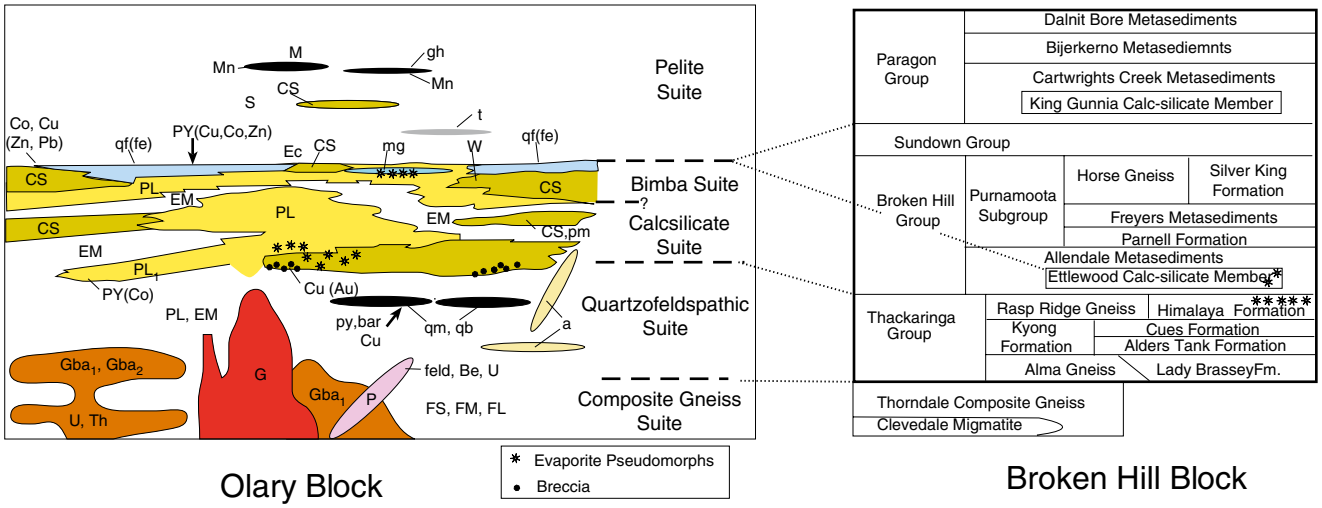

Fig. 14.63 Mineralisation types and stratigraphic sequences in the Olary Block and Broken Hill Block comprising the Willyama Supergroup (After Cook and Ashley 1992). Abbreviations; *S* psammitic schist, *M* psammopelitic schist, *EM* psammopelitic and pelitic rocks, *PL* plagioclase rock (albite-quartz rock), *PL1* pyritic albite-quartz rock, *FS* psammite-rich composite gneiss, *FM* psammopelite-rich composite gneiss, *FL* composite gneiss with leucocratic layers, *CS* calcsilicate rock, *PY* pyrite-rich rock, *Ec* carbonaceous pelite, *P* pegmatite, *G* post-tectonic granite, *Gba1* early syntectonic granite (pink porphyritic), *Gba2* early syntectonic granite (sodic), *a* amphibolite, *qf(fe)* quartz-Fe sulphide rock (Bimba horizon), *mg* magnetite-garnet rock, *qm* quartz-magnetite rock, *qb* quartz-baryte rock, *gh* garnet-quartz rock, *W* scheelite, *t* tourmalinite, *pm* piemontite-bearing rock

titic and locally massive leucocratic granitoids with intrusive characteristics (Fig. 14.64; Cook and Ashley 1992).

This is overlain by the laterally extensive Quartzofeldspathic Gneiss Suite, which is dominated by massive to layered quartz-albite and quartz-K-feldspar gneiss. These rocks have a felsic volcaniclastic precursor (Cook and Ashley 1992) and are locally intercalated with pelitic mica schists, quartzites and calcsilicate-rich layers. Radiometric U-Pb dating of zircons gives ages of 1,699 ± 10 and 1,703 ± 6 Ma for samples from a felsic metavolcanic rock and a co-magmatic granitoid (Cook 1993). Minor rock types include quartzite, laterally discontinuous horizons of quartz-magnetite-hematite and quartz-magnetite-baryte rocks along with rare amphibolite and tourmalinite.

The overlying Calcsilicate Suite is characterised by calcsilicate-bearing albitites, grading into pure calcsilicate rocks. Unusual chemical sediments of possibly exhalative hypersaline origin, such as scheelite-bearing rocks, hematite-rich banded iron formations and Mn-rich rocks, are common in this laterally extensive suite. Cook and Ashley (1992) proposed an evaporitic origin for the albitite- and calcsilicate-rich metasediments on the basis of their textures, mineralogy and calcsilicate pseudomorphs after dolomite and gypsum. Rocks of sodic composition abound, represented by albite-quartz-rich rocks (+calcite, actinolite, epidote, garnet, clinopyroxene), and are inferred to represent metamorphosed analcite-rich strata of felsic volcaniclastic provenance, with variable proportions of evaporitic carbonates. Rocks in the Olary region thought by Cook and Ashley (op. cit., p. 218) to be meta-evaporitic carry a distinctive suite of minerals including; albite, K-feldspar, amphiboles, clinopyroxene, scapolite, garnet, calcite, phlogopite, tourmaline, titanite and apatite, with several phases rich in fluorine and chlorine. Zoned amphibole grains (e.g. core-rim variations of F: 0.3–0.4 %, Cl: 0.04–0.22 %, Na_2O: 0.76–1.56 %, K_2O: 0.32–1.41 %) coexisting with pyrite indicate substantial enrichment of dissolved volatiles in the fluid phase during prograde metamorphism, presumably derived from the breakdown of former Na-, K-, and Cl-rich minerals. Phlogopite and titanite contain up to 3.50 and 2.31 %F, respectively. Scapolites are Cl-rich, containing up to 2.66 % Cl (mean 2.46 %). Feldspars are near end-member albite (usually exceeding Ab_{97}) and microcline, with the latter containing up to 4 % celsian.[14] Garnet composition is principally dependent on whole-rock Mn content, due to the strong partitioning of Mn into the garnet; low Mn rocks contain grossular-andradite types, whereas manganiferous samples (>0.8 % MnO) contain spessartine-grossular-andradite + calderite. Amphibole compositions include actinolite, edenite, and various hornblendes and clinopyroxenes are of the diopside-hedenbergite series. Tourmaline is dravite-schorl and occurs with end-member fluor-apatite. In addition, gypsum was recognized as pseudomorphic moulds and as epidote pseudomorphs in the rocks of the Calcsilicate Suite and in Bimba Iron Formation.

Whole rock analyses where substantial alkali enrichment is evident provide additional support for evaporitic condi-

[14]Celsian is an uncommon feldspar mineral, a barium aluminosilicate, $BaAl_2Si_2O_8$. It is a metamorphic mineral that may indicate an exhalative hydrothermal precursor.

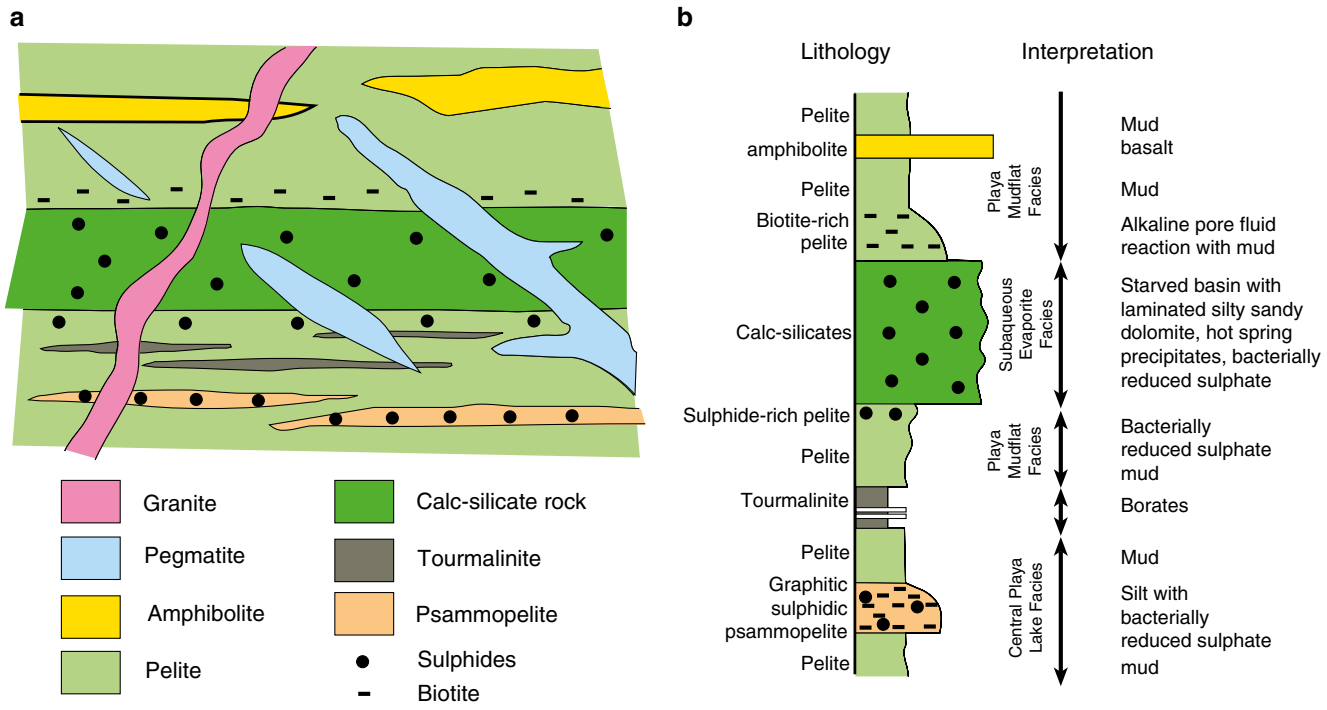

Fig. 14.64 (**a**) Schematic of stratigraphic relationships between the stratiform scheelite-bearing calcsilicate rocks and other lithologies in the Lakes Nob region of the Broken Hill Block. (**b**) Palaeolimnological interpretation of the observed sequence in the Allendale metasediments and the Ettlewood Member at Lake Nob (After Plimer 1994)

tions during deposition of some strata, other elements typically vary as a function of dilution by SiO_2 (Cook and Ashley 1992). Pseudomorphs after carbonate were also observed in calcsilicate-bearing quartz-albite rocks of lower metamorphic grade and interpreted to be pseudomorphs after dolomite that was transformed during prograde metamorphic reactions. The presence of halogen-rich minerals in a distinctive sodic mineral assemblage, in addition to hypersaline fluid inclusions, pseudomorphic voids and minerals after gypsum and carbonate, tourmalinites with isotopically light boron, imply a nonmarine evaporite protolith.

A transition from generally magnetite-bearing to sulphide-bearing strata defines the passage from the Calcsilicate Suite into the overlying quartz-feldspar-calcsilicate-carbonate-sulphide-bearing Bimba Suite. The Bimba Suite is a thin (<50 m), laterally continuous unit that, due to the widespread occurrences of stratiform Fe-dominated sulphides, is the focus of metal exploration interest in the Olary Block. Oxidation of sulphides (dominantly pyrite and pyrrhotite), calcsilicates and carbonates has led to distinctly gossanous surface exposures typically associated with anomalous Cu, Zn, Pb, Co, As, Ag, Au, Mn, Ba, W, Mo, Bi and U.

The uppermost unit of the Willyama Supergroup metasediments in the Olary Block is the widely distributed Pelite Suite. It is made up of quartzmica-garnet-andalusite-sillimanite-tourmaline schists, which are interbedded with layers of coarser-grained quartzo-feldspathic meta-siltstone and quartzite. Lenses of Mn-rich banded iron formations and garnet-quartz rocks occurring at the base or within the lower parts of the Pelite Suite imply continuing exhalative activity during deposition of this unit (Cook and Ashley 1992).

In addition to recognizable metasediments, at least four phases of widespread emplacement of granitoids have been identified, ranging from pre- through syn- to post-high grade metamorphism in age (Cook and Ashley 1992). Five deformational episodes (D_1-D_5) are recognized throughout the Olary Block (Berry et al. 1978; Clarke et al. 1987). Events D_1-D_3 only affected the Willyama Supergroup and some granitoid units. They occurred during the Middle Proterozoic Olarian Orogeny at about 1,600–1,580 Ma. Events D_4-D_5 also deformed the Adelaidean sequence during the Delamerian Orogeny (500 Ma; Preiss 1987).

Broken Hill Block

The Willyama Supergroup in the Broken Hill Block has undergone regional low-P/high-T prograde metamorphism. A series of prograde metamorphic zones is present, grading from upper greenschist to lower amphibolite. As in the Olary Block, the presence of former widespread evaporites in the district can only be inferred on the basis of indirect lithologic, chemical, and isotopic data (Slack et al. 1993). Lithologic evidence for former evaporites includes the occur-

rence of bedded albitites in the Himalaya Formation at the top of the Thackaringa Group, which are believed to represent clastic sediments or tuffs that were largely altered to analcime in an alkaline lake setting (Fig. 14.64; Plimer 1977; Stevens et al. 1988). Other evidence for evaporites and/or nonmarine depositional settings comes from (Slack et al. 1993):

- The presence of abundant scapolite locally in the Ettlewood Calcsilicate Member at the base of the Broken Hill Group, which in correlative rocks of the adjacent Olary Block in the South Australia and contains up to 2.7 % Cl (Cook 1992; Cook and Ashley 1992);
- Abundant magnetite disseminated in some quartzofeldspathic rocks of the Thackaringa Group suggesting protoliths of oxidised red beds;
- Quartz-muscovite nodules in the Rockwell area (Himalaya Formation) that have crystal forms suggesting pseudomorphic replacement of gypsum by silica in nonmarine evaporitic environments.

Quartz-albitites in the Thackaringa Group occur below the Broken Hill Main Lode (Fig. 14.63), while psammopelitic units occur above and below the quartz-albitites. The albitites are light coloured and comprise uniformly grained quartz + plagioclase (An_{8-15}) + minor biotite and pyrite locally interlayered with micaceous paragneiss. They have unusually high SiO_2, Na_2O contents, and very low CaO, MgO, K_2O (all <1 %), Pb and Zn (<20 ppm) contents compared to surrounding units. Complex zircon populations occur in the quartz-albitites (Love 1992; Nutman and Ehlers 1998). The protolith of these rocks has been subject to longterm debate, although hypersaline fluids figure in most accounts. Suggested protoliths include: rhyolites, tuffs, clastic sediments (arkoses) or evaporites, with tuffs flushed by hypersaline brines the most popular model. Altered rhyolite or rhyolitic tuffs are a possible protolith, but they would have had a very special composition (to justify the unusually high Si and Na content of the consequent quartz-albitites). An igneous precursor does not easily account for the detrital zircon populations that occur within the albitites. An arkosic protolith can account for the detrital zircons, but would require an unusually albite-rich source region or extensive post-depositional alteration.

Whatever the precursor, metasomatism and/or analcimitization have altered significant portions of the protolith. Analcimization is common in saline lakes and analcimization of tuff was first suggested for the Broken Hill albitites by Plimer (1977). An analcime-rich saline precursor is attractive as it explains the high Na content along with the occurrence of scapolite and saline fluid inclusions and the detrital zircons. Prograde metamorphism (at T >200 °C) of a quartz-analcime rock would readily produce a quartz-albitite. However, analcime-rich rocks can be produced from tuffs, argillic or arkosic sediments (rhyolite *sensu stricto* probably being too massive to react). A mix of unanalcimized tuffs and arkosic sediments in a saline continental lacustrine rift setting explains most of the characteristics of the quartz-albitites in the Broken Hill Olary region.

The former presence of evaporites at the time of albitite formation is also suggested by the occurrence of chemically unusual halide minerals in the main Pb-Zn-Ag lodes at Broken Hill (Slack et al. 1993). The oxidised ores of the main lodes are famous for containing an unusual suite of secondary halides including: ioargyrite [AgI], bromargyrite [AgBr], marshite [CuI], miersite [(Ag,Cu)I], and embolite [Ag(Cl,Br)]. These halides were reportedly concentrated at the base of the gossan, above the supergene ores and formed following the weathering of the main ore loads in the Permian and/or Tertiary. Most workers have assumed that the source of the Cl, Br, and I within oxidised ores in such desert environments is from exotic groundwaters or seawater-derived salt spray, with little if any contribution from the protolith. Similar iodine and nitrate accumulations in the soils of the hyperarid Atacama Desert, South America, are discussed in Chap. 11. Slack et al. (1993), argue that in the case of Broken Hill a local bedrock or protolith source is equally plausible, if not compelling. They also contend that much of the sulphur in the Pb-Zn-Ag ores may also have come from nonmarine evaporites.

Tourmaline-rich rocks are widespread, but minor, lithologies within the Early Proterozoic Willyama Supergroup in the Broken Hill district (Fig. 14.64a). Tourmaline concentrations occur in stratabound and local stratiform tourmalinites, clastic metasedimentary rocks, quartz-gahnite lode rocks, stratiform Pb-Zn-Ag sulphide ores, garnet quartzites, stratabound scheelite deposits, quartz-tourmaline nodules, discordant quartz veins, and granitic pegmatites. Most of the tourmaline-rich rocks are within the Broken Hill Group that hosts the main Pb-Zn-Ag ores.

Combined field and geochemical data indicate that the tourmalinites represent normal clastic sediments that were metasomatically altered by boron-rich hydrothermal fluids at or below the sediment-water interface. Slack et al. (1993) suggest the hydrothermal system(s) acquired abundant boron by leaching evaporitic borates within the Thackaringa Group, the stratigraphic sequence that underlies the Broken Hill Group and hosts most of the tourmaline concentrations. They argue that evaporites of the Thackaringa Group provided a source of readily extractable boron for formation of the tourmalinites and also acted as a source for the fluoride, sulphur, and perhaps the carbonate in the main lodes; such evaporites may have been critical for increased metal chloride complexing and transport necessary for deposition of the high-grade Pb-Zn-Ag ores.

Plimer (1994) interprets scheelite ($CaWO_4$ and an ore of tungsten) in the Willyama Supergroup -Allendale calcsilicates-

to be part of a metamorphosed sequence of intracontinental rift sediments, volcanics and hot spring precipitates. Scheelite and the calcsilicate host, which is enriched in F and Zn, constitute a conformable sequence of carbonaceous-sulphidic metabolites, tourmalinites, and amphibolites. It overlies a gneiss-metasediment sequence, part of which (Ettlewood calcsilcates) is interpreted as meta-evaporitic (Fig. 14.64b). The distribution of scheelite is unrelated to syntectonic pegmatite or posttectonic granitic rocks. The scheelite underwent only minor remobilization during tectonism. Plimer (op. cit.) interprets the calcsilicate rocks as dolomitic limey sediment that formed part of a playa-lake sequence into which B, W, Zn, and F-rich alkaline hot springs debouched (Fig. 14.64b). Coeval sudden deepening, an increased geothermal gradient, deposition of the Broken Hill Pb-Zn-Ag sulphide orebodies, and siliceous exhalite deposition all occurred after deposition of the evaporite sequence. Thus components for the highly saline Broken Hill Pb-Zn-Ag ore fluid may have been leached from the underlying evaporites and redeposited higher in the stratigraphy.

Although not considered in the current interpretations of the Broken Hill Block, it is interesting to postulate, what was the evaporite distribution in the Broken Block prior to its entrainment and alteration/destruction in the metamorphic realm? Much of meta-sediment in the Broken Hill Block is interpreted as accumulating in a deepwater setting within an evolving rift to passive margin association. If evaporites were part of this association, it is highly likely that at the time of such widespread deep water sedimentation any subjacent salt masses were allochthonous halite tongues, as was the case in the Mt Isa Inlier (Warren 2000a). These salts were sourced from a thicker older halokinetic mother salt horizon deposited in an earlier stage of rifting. Prior to onset of its flow, it was a unit situated deeper in the rift fill and perhaps updip in the basin fill, leading to gravity-glide shear-related emplacement, much like the Louann Salt in the modern Gulf of Mexico and the Aptian-sourced salt allochthons of offshore Brazil, or the Atlantis II deep region in the Red Sea.

Pine Creek Inlier, Northern Territory

The Pine Creek Inlier is a major mineral province in the Northern Territory, Australia, and covers an area of some 66,000 km^2 (Fig. 14.50 for location). It entrains Archaean and Paleoproterozoic rocks surrounded by subhorizontal strata of several intracratonic sedimentary basins that range in age from Mesoproterozoic to Mesozoic. It entrains the Alligator River, Rum Jungle and South Alligator Valley uranium provinces and the overlying Pine Creek Gold mineralization (Needham 1988; Pirajno and Bagas 2008; Hollis and Wygralak 2012). Pine Creek metasediments record four phases of moderate to tight folding, including two isoclinal folding events. An eastward increase in metamorphic grade is also apparent (Ferguson 1980). Lower greenschist facies metamorphism was coincident with folding in the western and central parts of the Inlier, but reached regional amphibolite (Barrovian) facies grade in the western region of the Inlier adjacent to the Kakadu Shelf in the final folding phase (≈1.8 Ga). There the metasediments were migmatised to form the gneissic outer parts of the Nibuwah Complex (Worden et al. 2008).

Evaporite pseudomorphs after gypsum (lenticular) and halite (cubic) were noted in the coarsely crystalline magnesite and dolomite rocks in the Rum Jungle and Alligator Rivers uranium fields Northern Territory; in the Celia and Coomalie Dolomites at Rum Jungle, and the Cahill Formation in the Alligator Rivers region of the Pine Creek Geosyncline (Fig. 14.65a; Crick and Muir 1980; Muir 1987).

These rocks are now marbles in the middle to upper greenschist facies, but they still retain recognisable sedimentary features including algal bioherms. Stratiform and domal stromatolites are common, with some domes reaching 1.5 m in height with a similar diameter; *Conophyton* bioherms are also well developed. The stromatolites may also preserve evaporite casts after gypsum and are interbedded with non-stromatolitic carbonates that contain crossbeds, ripples, scour surfaces, intraclast breccias and tepee structures (Fig. 14.65a). Possible evaporite casts in the magnesite marbles are characterised by blade shapes and discoidal shapes up to 1 cm long. Cruciform and swallowtail twin forms are also present in the magnesite marbles. Orthorhombic shapes and cubes after halite are also abundant.

However, Bone (1983) in a study of inclusions in the discoidal forms of magnesite from Rum Jungle concluded that the discoids and the cube shapes were a high temperature form of magnesite that formed above 150 °C and not evaporite pseudomorphs. Muir (1987) countered this argument with the observation that identical discoidal pseudomorphs after gypsum can be found in the Amelia Dolomite in the McArthur Basin in strata that have never been subjected to temperatures of more than 100 °C. Further evidence for an evaporite association is adduced from the co-presence of lutecite, a variety of length-slow quartz that pseudomorphs anhydrite.

Work by Aharon (1988) on the same magnesites showed that they are replacement fronts. Magnesite beds up to 700 m thick from the Lower Proterozoic rocks of the Rum Jungle Uranium Field yielded $\delta^{18}O$ and $\delta^{13}C$ compositions of +11.2 to +14.6‰ (SMOW) and +1.0 to +5.8‰ (PDB), respectively (Fig. 14.65b). Dolomites in the same region yield $\delta^{18}O$- and $\delta^{13}C$-values of +11.7 to +21.9‰ and −4.0 to +2.9 ‰, respectively, and show an ^{18}O enrichment gradient away from the magnesite. Fluid-inclusion homogenization temperatures, used in conjunction with the isotope determinations and an approximate magnesite-water equation, indicate that magnesites were formed in the temperature range of 100–200 °C from fluids that became progressively enriched in ^{18}O. He argues the results support an epigenetic-metaso-

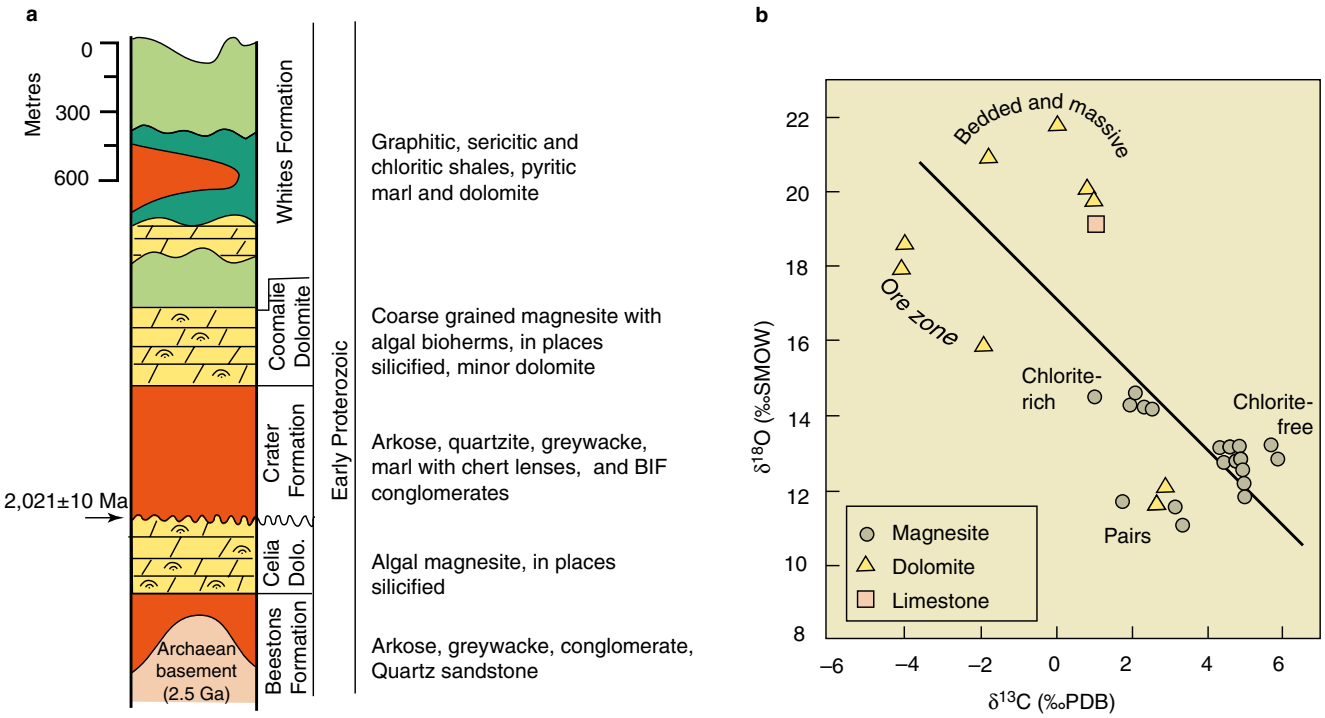

Fig. 14.65 Magnesites in the Rum Jungle Uranium Field, Northern Territory, Australia. (**a**) Stratigraphic column. (**b**) Carbon and oxygen isotope crossplots of magnesites and coeval dolomites (After Aharon 1988; Worden et al. 2008)

matic replacement model of dolomite by magnesite under the influence of invasive hot Mg-rich basinal fluids.

My own work on Proterozoic sparry magnesite elsewhere in northern Australia supports the conclusions of both Aharon and Bone. That is, the discoidal magnesites are a diagenetic replacement in a nonevaporitic platform carbonate host. In addition, my proprietary work, in selected areas also implies that these sparry magnesites are ultimately tied to evaporites. They likely do not indicate the depositional magnesite association postulated by Crick and Muir (1980). Rather, they are related diagenetic alteration fronts driven by deep subsurface dissolution of halokinetic evaporites that then supplied metalliferous chloride brines into fault conduits. In my opinion these sparry magnesites are hydrothermal pinolitic structures that were fed via fault conduits, many of which were created or reactivated by the flow of underlying salt as the basin underwent extension (Chap. 15). Similar pinolitic carbonate cements and replacements associated with faults, tied to rifting episodes, occur in other Precambrian basins in Northern Australia and the Flinders Ranges, South Australia. There are also strong similarities with Phanerozoic peridiapiric metasomatic cements in North Africa and Europe.

There are also tourmalinites in the lower metasedimentary sequence in the Rum Jungle region of the Pine Creek Inlier, mostly within the Beestons Formation, but also in the marbles of the Celia Dolomite (Fig. 14.66; Bone 1988). Although common in these Archaean metasediments, Rum Jungle tourmalinites can be difficult to recognise in the field, leading to misidentification in the Rum Jungle as amphibolites, mafic schists, actinolite schists, chert and, in the case of the leucocratic tourmalinites at the base of the Crater Formation, scapolite. In the Beestons Fm. it occurs as a conformable banded quartz-tourmaline lithological unit comprising at least 15 % and as much as 50 % of the rock. Within what are the oldest recognisable metasediments (arenites of the Beestons Fm and magnesites of the Celia Dolomite) it occurs as distinct lenses, as facies equivalents of quartz-magnetite units and mafic schists (tuffs?) and distal equivalents of polymetallic sulphides. Distinct layering, slump folding, rip-up clasts and the association with diagenetic pyrite suggest a sedimentary protolith. At the micro-scale the en-echelon fracturing of the fine-grained, light green tourmaline crystals supports pre-deformation formation. The crystals are optically and chemically zoned parallel to the c axis, with irregular growth lamellae width — which supports a pre-regional metamorphic origin. Analyses show the tourmaline to be the Mg-rich variety “dravite”.

In terms of depositional setting, parallels are drawn with tourmalinites showing a similar age and metasedimentary association in the metasediments of the Broken Hill Block (Bone 1988). The tourmalinites in the Pine Creek Inlier indicate a borate-rich protolith, possibly a lacustrine, shallow water, evaporitic setting in the sumps of a continental rift. Suitable B-bearing fluids were generated by hot spring activ-

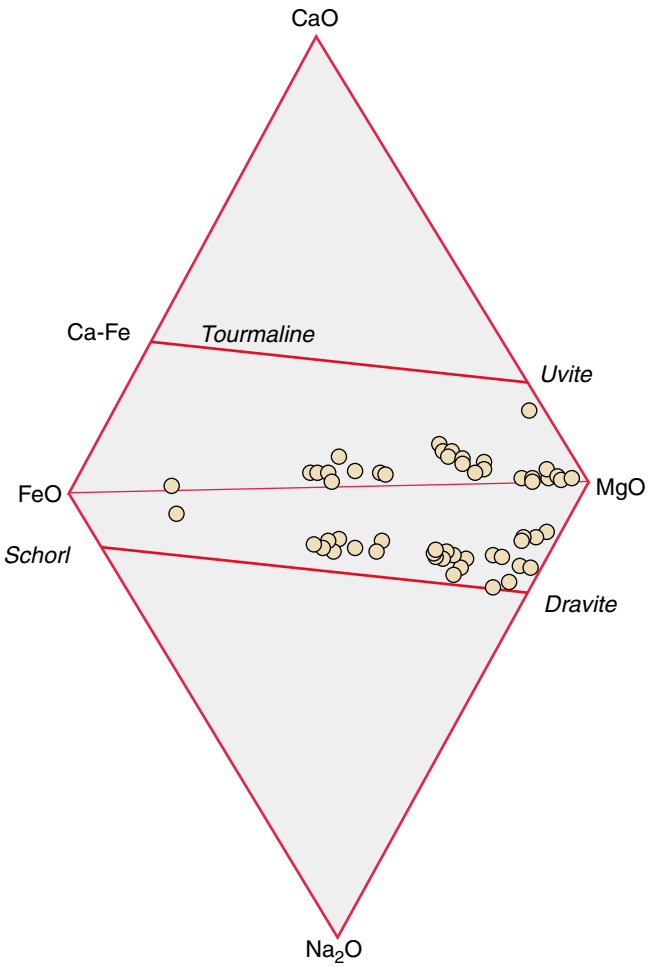

Fig. 14.66 Rum Jungle tourmaline geochemistry (After Bone 1988)

ity and mobilized by CO_2-rich fluids. Localised hot-spring activity contributed B-bearing fluids which precipitated chemical sediments according to the pertaining pH, temperature etc. Thus, diagenetic metaevaporitic alteration produced the stratabound tourmalinites of the Pine Creek Inlier

Meta-evaporites, Seve Nappe, Sarek Mts., Swedish Caledonides

The Seve Nappe Complex in the Scandinavian Caledonides preserves a portion of the fragmented Neoproterozoic continent-ocean transition between Baltica and the Iapetus Ocean. This passive margin was fragmented and thrust eastwards over the Baltic Shield during subsequent Caledonian orogenesis. The individual thrust sheets in the Seve Nappe Complex went through different P-T-depth evolutions, resulting in dramatic metamorphic contrasts where eclogite-bearing nappes are juxtaposed with nappes showing no evidence of Caledonian deformation or metamorphism in their interiors (Svenningsen 2001).

Such a nappe, with little or no evidence of Caledonian deformation, is the Sarektjåkkå Nappe. There, in the Caledonides of northern Sweden, meta-evaporitic stratiform magnesite and scapolite are hosted by diabase and amphibolite derived from diabase, (Fig. 14.67a, b: Svenningsen 1994). The Sarektjåkkå Nappe is dominated Nappe is dominated by a metasedimentary sequence, the Favoritkammen Group, that has been intruded by vast amounts of diabase as single or sheeted dykes, which now constitute up to 70–80 % of the nappe (Fig. 14.68; Svenningsen 1995). The diabase yields a Sm-Nd isochron of 573 ± 74 Ma and is related to the 608 Ma opening of the Iapetus seaway (Nystuen et al. 2008). Because the Sarektjåkkå Nappe largely escaped penetrative Caledonian (Silurian) deformation, it still preserves recognizable igneous and sedimentary elements that are linked to the evolution of the pre-Caledonian rift margin, while the sheeted dyke complex is interpreted to represent the early stage of seafloor spreading.

Magnesite and scapolite layers in the Favoritkammen Group are part of the Spika Formation. Locally the Spika Formation retains sedimentary structures, such as cross-lamination in psammitic beds, dewatering pillars and soft sediment convolute folds in former calcarenite layers. More typically, the ductility of the carbonate bed and contrast between layers of differing compositions of scapolite dolomite and magnesite means that pervasive deformation and shearing has destroyed much of the primary sedimentary structures.

The purest magnesite in Sarek is found in the Äpar Quarry, situated in a carbonate/calcsilicate lens on the northern slope of the Äpar massif (Fig. 14.67b). There it is composed of pure sparry white magnesite and has a visible area of 2,500 m^2 and has the shape of a 120 by 40 m flat-lying cigar. The Äpar magnesite is hosted by massive grey diabase and is the only known deposit of pure magnesite in the region.

Two horizons of the Spika Formation in the Äpar Magnesite Quarry contain matrix-supported intraformational breccias with intraclasts, which are interpreted as evaporite solution collapse breccias (Svenningsen 1994). This is supported by the presence nearby of carbonate pseudomorphs after anhydrite nodules. The magnesite rock is conformable with the underlying calcsilicate layers and the contacts are gradual, indicating that the magnesite was not created by metasomatic alteration derived from the diabase. Rather, the rock reflects an original sedimentary magnesite deposited in what was a Coorong-Marion Lake like hydrology.

The Spika Formation was deposited in an evaporative setting characterised by alternating influxes of continental (magnesian carbonate) and marine-fed evaporites (halite and anhydrite/gypsum) in rift-related Neoproterozoic basins (Svenningsen 1995). The overall stratigraphy of the Favoritkammen Group indicates a progressively deepening, increasingly marine-fed basin, consistent with deposition in a developing rift basin.

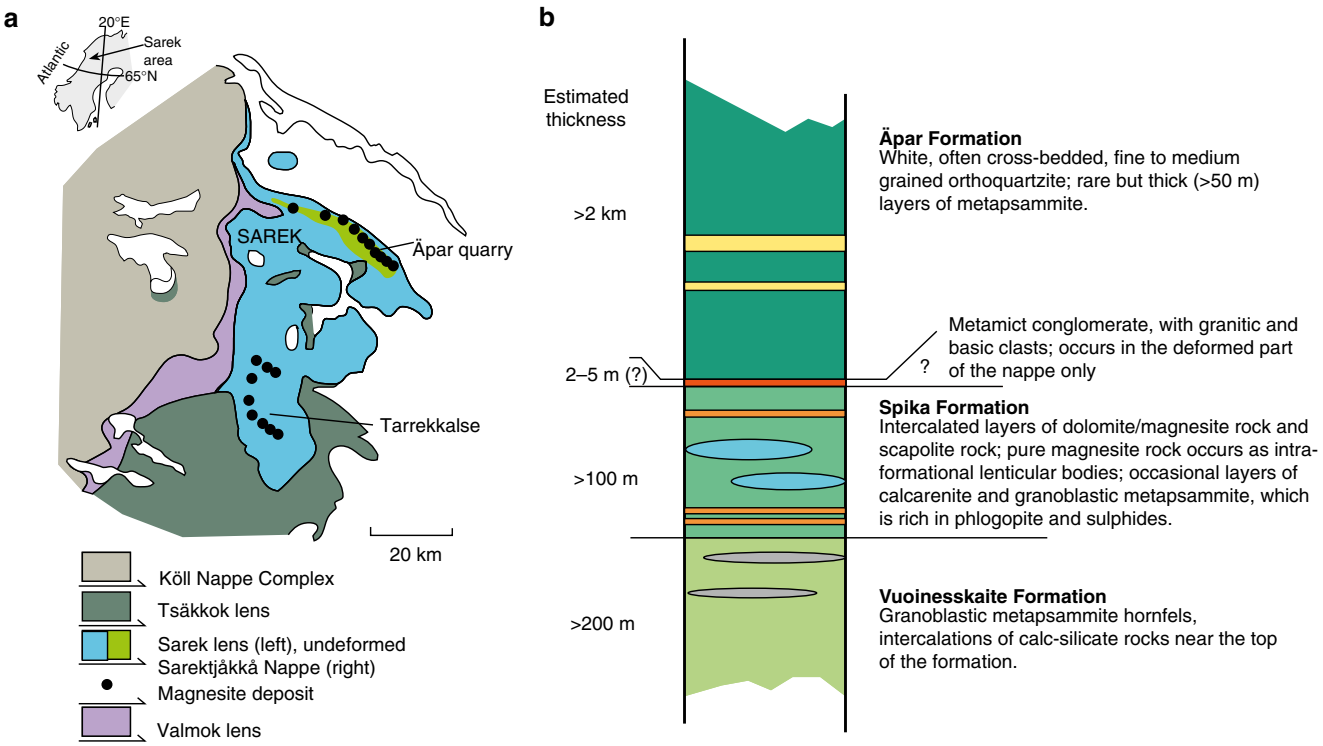

Fig. 14.67 (**a**) Tectonostratigraphic and location map of the Sarek National Park and adjacent areas. All the magnesite deposits occur in the Sarektjåkkå Nappe. (**b**) Generalised stratigraphy of the Favoritkammen Group. The sequence is dismembered by enormous quantities of diabase dykes, and so thicknesses are no more than estimates (After Svenningsen 1994)

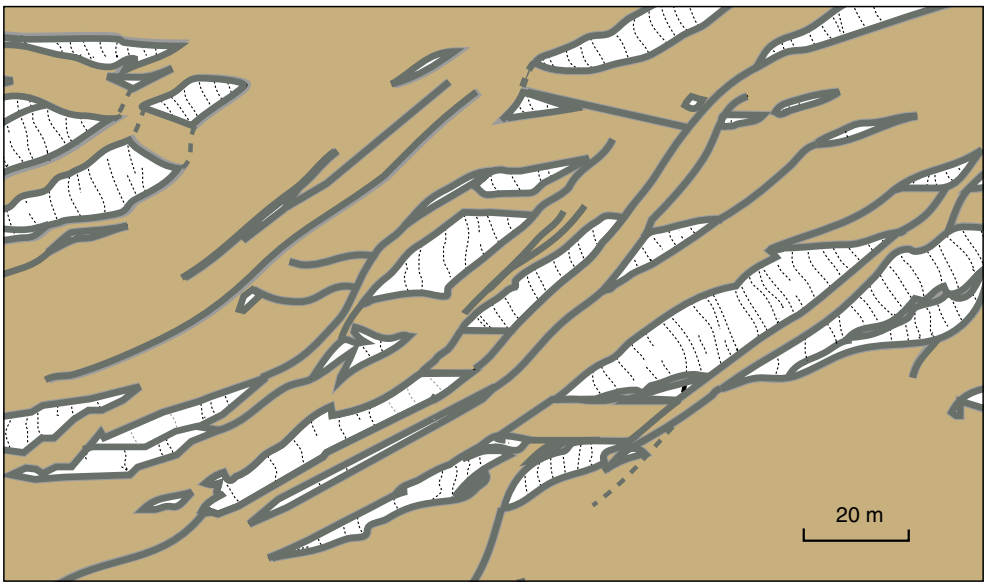

Fig. 14.68 Typical sediment-dyke pattern from the central, undeformed part of the Sarektjåkkå Nappe (Favoritkammen Ridge east of Äpar quarry). Diabase dykes are stippled *grey*, with chilled margins. Vertical bedding attitude in sediment (Äpar Formation) is also indicated. Diabase is more than 70–80 % of rock volume, yet bedding is still recognizable in metasediment blocks (After Svenningsen 1994)

The evaporitic sequence was altered to scapolitic marbles during subsequent thermal metamorphism. Diabase dykes that cut the Spika Formation drove regional thermal metamorphism, but were not responsible for the magnesite formation. The magnesites were recrystallised during thermal metamorphism but were perhaps a product of the Neoproterozoic magnesite ocean, perhaps akin to sedimentary magnesites so prevalent in similar age lithologies in the Flinders Ranges of South Australia (Frank and Fielding 2003). In summary, the metamorphic lithologies of the Sarektjåkkå Nappe record the evolution of a Neoproterozoic rift passing into a passive margin. That passive margin was subsequently detached and thrust over the Baltic Shield during the Caledonian (Silurian) Orogeny.

Oaxacan Granulites, Mexico

Two origins have been proposed for Oaxacan calcareous rocks in the ~1 Ga Oaxacan Complex of southern Mexico: (1) a meta-sedimentary origin with an evaporitic protolith first deposited in a passive-margin tectonic setting (Ortega-Gutierrez 1984); or (2) a meta-igneous origin as carbonatites (Melgarejo and Prol-Ledesma 1999). Metasomatism is a third possibility (Dostal et al. 2004).

The Oaxacan calcareous rocks contain from 10 to >90 vol% carbonate and were subdivided by Ortega-Gutiérrez (1984), using modal composition, into marbles (>50 vol% carbonates) and calc-silicates (10–50 vol% carbonates). Layers in this high grade (granulite) sequence constitute either concordant (<200 m thick) or discordant bodies up to 4 m thick. Discordant calcareous rocks are dyke-like mostly marble intrusions with xenoliths of calc-silicate and/or host rocks, whereas the concordant bodies are made up of both calc-silicates and marbles.

These calcareous bodies occur with in the upper "paragneiss" thrust slice that dominates the northern Oaxacan Complex (Fig. 14.69a; Dostal et al. 2004). This slice was intruded by within-plate, ≥1,140 Ma charnockites and meta-syenites (Keppie et al. 2003) and was involved in two tectonothermal events, the ~1,100 Ma Olmecan event, and the ~1,005–980 Ma Zapotecan event. The latter involved polyphase deformation under granulite-facies metamorphic conditions (Fig. 14.69b; Solari et al. 2003). Peak granulite facies metamorphism reached 700–750 °C and 7.2–8.2 kbar. The concordant calcareous lenses contain Zapotecan foliations and folds, and although the discordant bodies cut across these ductile structures, they record the granulite facies metamorphism, indicating that the high-grade metamorphism outlasted the deformation. Titanite and phlogopite from these discordant calcareous bodies have yielded ages of 968 ± 9 Ma (concordant U-Pb age) and 945 ± 10 Ma ($^{40}Ar/^{39}Ar$ laser fusion analyses), respectively, which have been interpreted as dating cooling through 660–700 °C and ~450 °C.

Host rocks in the thrust slice are of mostly mafic and felsic granulite anhydrous phases and include quartz, plagioclase (typically antiperthitic), hypersthene, clinopyroxene, garnet, alkali feldspar (perthite and mesoperthite), opaque minerals (ilmenite), and a variable amount of titaniferous hornblende and biotite. Hydrous phases, including hornblende and biotite, are in textural equilibrium with the anhydrous minerals (Mora et al. 1986). In places, the Oaxacan rocks are composed of mineral assemblages containing biotite, amphibole, plagioclase and opaques, indicative of only upper amphibolite facies–grade metamorphism.

High abundance of meionitic scapolite, dolomite, phlogopite, albite, and K-feldspar in the Oaxacan carbonate bodies supports a saline precursor, but all traces of primary salts have been lost by partial melting and volatile expulsion during attainment of the successions high metamorphic grade (granulite). The marialitic nature of the scapolite minerals implies the presence of Cl and Na in the protolith. Albite, K-feldspar, phlogopite, and cancrinite contain elevated concentrations of alkalis, whereas, dolomite, forsterite, clinopyroxene, and amphibole are rich in Mg, and sulphides are rich in sulphur. Rare anhydrite, now mostly present as gypsum pseudomorphing the anhydrite, remains in these metasediments, with outlines indicating that the anhydrite was in textural equilibrium with granulitic carbonate (Ortega-Gutierrez 1984).

Tourmaline is absent in Oaxacan rocks and has its absence has been used by those favouring non-evaporitic precursor for the required high salinity fluids. It is true that borates are enriched in the salts that are some of the last minerals to precipitate from seawater, but most substantial accumulations of borate salts tend to be in a nonmarine continental volcanogenic association (Chap. 11). A lack of tourmaline in the Oaxacan assemblages may indicate an evaporite protolith that was marine and never contained high levels of boron. An alternative explanation for the absence of tourmaline in the Oaxacan Complex may be thermal instability of the tourmaline under the low water pressures characteristic of granulite facies (Dostal et al. 2004). Boron, if originally present, perhaps migrated with the fluid and melt phases to lower temperature and wetter zones of the orogen. Low contents of boron may also indicate that the source of the Oaxacan carbonate rocks was non-granitic. The marbles were probably derived from impure limestones and evaporites whereas the protolith to the calc-silicate rocks were calcareous sediments with higher contents of silicates (Fig. 14.70). The common presence of spinel may indicate some silica-poor, bauxitic component in the clay fraction, and thus probably highly weathered source rocks (Dostal et al. 2004).

Scapolitic Meta-evaporites, Rajasthan, India

Paleoproterozoic metasediments of the Aravalli group (2.2 Ga) of the Aravalli craton and contain a sequence of granulites that likely have an evaporite protolith (Sharma 1981; Golani et al. 2002; Knight et al. 2002; Fareeduddin et al. 2010). The Aravalli Craton preserves an uninterrupted Archaean succession from 3.3 to 2.5 Ga as well as two significant intersecting Proterozoic foldbelts; the Paleoproterozoic Aravalli foldbelt and the younger Meso-Neoproterozoic Delhi foldbelt. The 60-km long Salumber Ghatol belt constitutes the easternmost sector of the Aravalli foldbelt. It has undergone polyphase deformation and a single metamorphic recrystallisation event at greenschist grade. It contains several Cu-Au deposits, including; Bhukia, Dugocha, Hinglaz, Mata, Timran Mata, Manpur, Kukra and Rajpura.

Electron-microprobe analyses of coexisting phases from a scapolite-garnet-epidote-calcite-plagioclase-amphibole-pyroxene (sphene-hematite-magnetite) rock of the Aravalli group in Karera area show that chlorine is an important con-

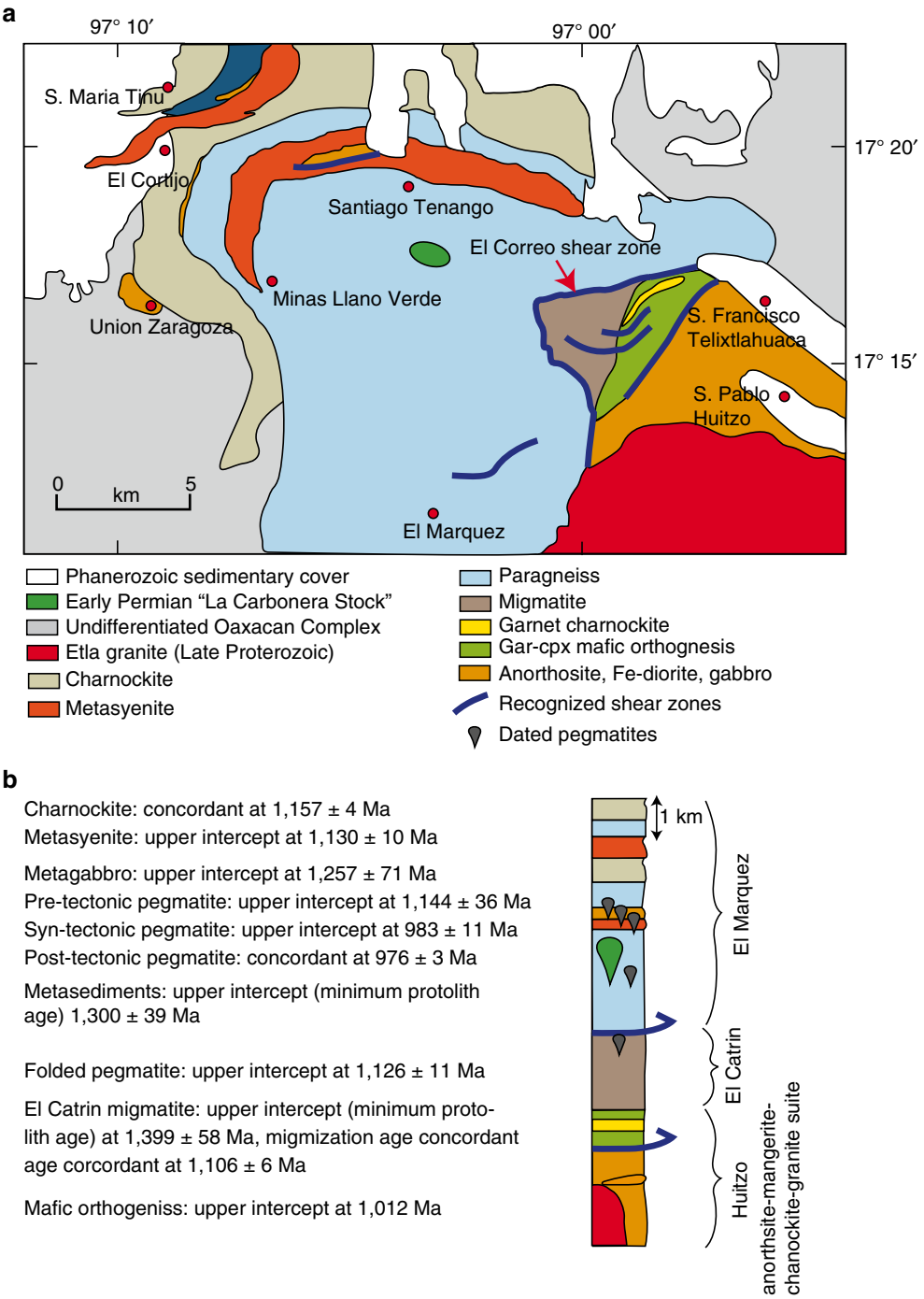

Fig. 14.69 Geology of the Oaxacan Complex. (**a**) Geological map of the northern Oaxacan Complex (**b**) Structural section of the northern Oaxacan Complex showing the location of the sampled calcareous intrusions; Huitzo, El Catrin and El Marquez refer to three thrust sheets of the Oaxacan Complex (Modified after Solari et al. 2003; Dostal et al. 2004)

stituent of both scapolite ($Me_{71.3}$) and amphibole in this succession (Sharma 1981). The amphibole also contains an unusually high K_2O (3.7 wt.%), and is a chloro-potassian hastingsite. The epidote contains 41 % pistacite and shows complete substitution of Al by Fe^{3+} in the M_2 site and to some extent also in M_1 and/or M_3 sites. The garnet is also rich in ferric iron and has a molecular composition $Pyr_{23}Alm_{8.5}Gro_{13}And_{54.5}Sp_{1.0}$. The pyroxene is dominantly a hedenbergite.

Geothermometry, based on the fractionation of Na and Ca between scapolite and plagioclase, yields metamorphic temperatures of around 700 °C, which are in agreement with those obtained by other mineral equilibria in the associated pelitic assemblages. Sharma (1981) argues that phase relations and textural as well as geological criteria exclude metasomatic processes or a magmatic source. He favours equilibrium recrystallization of the scapolite-bearing assem-

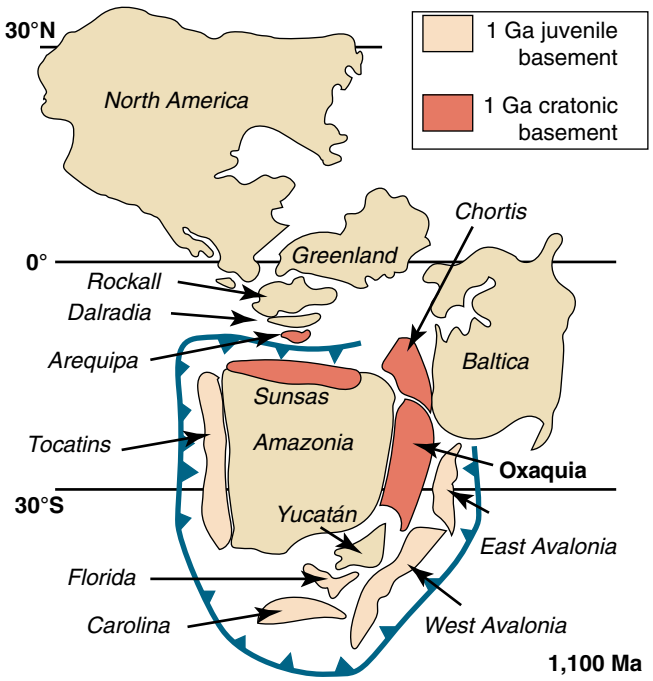

Fig. 14.70 Reconstruction of Rodinia around 1,100 Ma, showing the location of Oaxaquia, Mexico as part of a 1 Ga belt on the margin of Amazonia. Note that meta-evaporitic carbonates in Oaxaquia lie between 10° and 35°S encompassing the latitudinal limits for the formation of Phanerozoic marine evaporites, as discussed in Chap. 5. The *barbed line* define the relevant subduction zone with triangles on the upper slab (After Dostal et al. 2004)

blage with the chlorine derived from an evaporite unit in the Aravalli protolith.

The interpretation of an evaporitic protolith to the Aravalli metamorphics is strengthened by Golani et al. (2002) in their detailed geochemical and isotopic study of marbles associated with the Bhukia gold prospect. Their evidence for meta-evaporite includes:

1. Presence of dissolution 'pits' and cavities in the dolomitic marble, and a Na content (Av. = 5,013 ppm) that is significantly higher than the 1,000–3,000 ppm range for hypersaline and evaporitic (sabkha) environments and much above the 1,000 ppm level reported for normal marine sedimentary carbonates. High Na/K ratio of Bhukia rocks is comparable to carbonate lithologies in some of the large soda lakes of the world. High sodium content is also a characteristic feature of the QFR (quartzo-feldspathic rock) unit. The possibility of non-evaporitic soda metasomatism in the carbonate-QFR (±tourmalinite) litho-association is ruled out on the strength of; (a) well-bedded nature of lithological units, (b) consistent presence of Na throughout the deposition of host-rock litho-association and, (c) purity of albite feldspars, all features considered to be diagnostic of sedimentary feldspars in evaporitic settings.
2. Mineral analyses of brown biotite, a common mineral in the Bhukia Gold Prospect rocks, show that it is phlogopitic in composition. Phlogopite has been cited as an important index mineral in most of the meta-evaporitic sequences (Moine et al. 1981).
3. Development of widespread scapolite-bearing calc-silicate assemblages in Bhukia carbonates indicate an evaporitic affinity (Serdyuchenko 1975).
4. Presence of tourmaline, its common occurrence as disseminations in the quartzo-feldspathic facies and in thin tourmalinite bands, indicates a high boron flux in the protolith; as is also the case in meta-evaporites of China (Peng and Palmer 1995) and Australia (Cook and Ashley 1992). The extremely low Fe/Al ratio (mean 0.15) in the Bhukia tourmalines is far below the 38.5 level (range 10.5–62.2), reported for submarine hydrothermal deposits, but similar to values from Proterozoic meta-evaporitic sequences of China with Fe/Al ratio ranges from 0.29 to 0.87 (Fig. 14.71a; Av. = 0.48; Jiang et al. 1997).

Likewise, the geochemistry of the Ghagri tourmalinites, which are interlayered with copper sulphides, indicates a likely metaevaporitic precursor (Fareeduddin et al. 2010). These tourmalinites include a major povondraite component and follow an 'oxydravite' – povondraite crystallization trend indicative of a hypersaline saline precursor (Fig. 14.71b, c), as defined in Namibian meta-evaporitic equivalents (Henry et al. 2008).

Isotopic compositions of the Bhukia meta-sediments also support the notion of an evaporitic protolith, but also contains evidence of mixing with mantle derived fluids (Fig. 14.71d; Golani et al. 2002). Bhukia carbonates are characterized by $\delta^{18}O$ values ranging from +15.3 to +26‰$_{SMOW}$, which are slightly depleted when compared to typical Palaeoproterozoic marine carbonate compositions (Golani et al. 2002). The C- and O-isotopic compositions are non-correlative, however, the $\delta^{13}C$ values show a bimodal distribution ranging from −4.1 to +0.3‰$_{PDB}$, allowing the discrimination into two groups (Fields I and II) each with closely similar C-isotopic ratios (Fig. 14.71d). The narrow range of C isotopic ratios for Field II carbonates indicates unmodified compositions, while the spread in O-isotopic ratios for Field I indicates slightly modified $\delta^{18}O$ values as a result of evaporative conditions (trend A) and high temperature burial and/or exposure to meteoric waters (trend B; Golani et al. 2002). The Field I carbonates with similar C- and O-isotopic ratios are interpreted to best approximate the unmodified marine sedimentary carbonate signatures and closely compare with values in the Aravalli stromatolitic phosphate-bearing carbonates of Udaipur area.

In the absence of any evidence of algal activity in the Bhukia area, the Field II representing 'lighter' carbon component (mean value −3.1‰$_{PDB}$) may either indicate

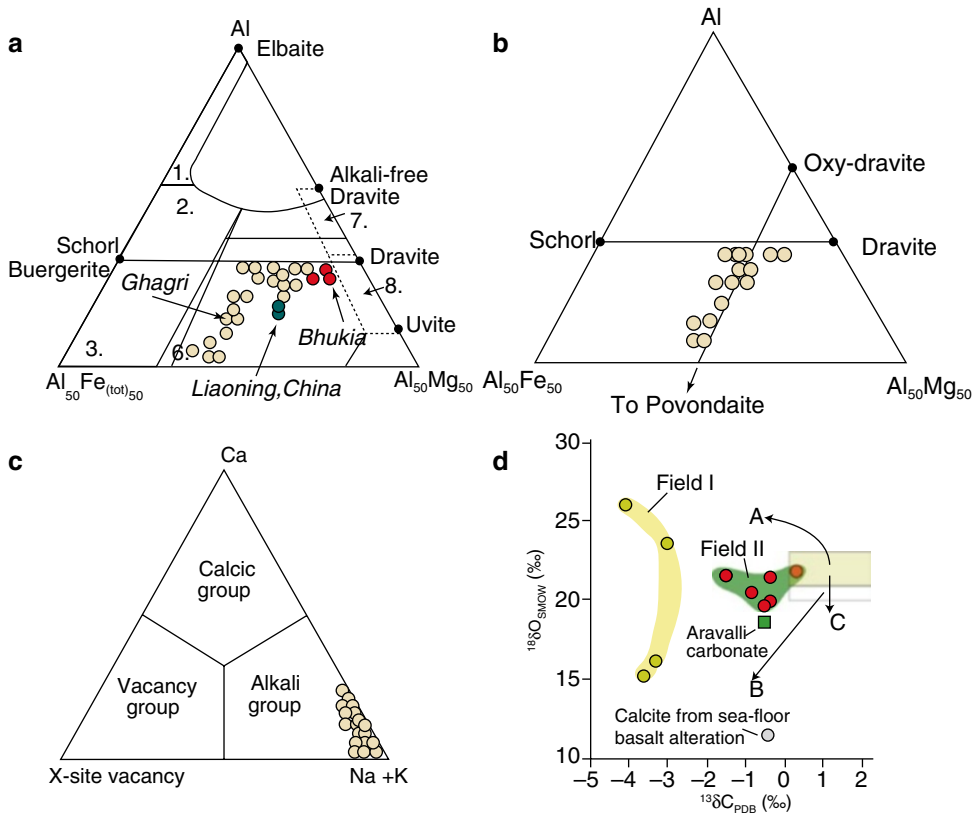

Fig. 14.71 Geochemistry of Aravalli metasediments (After Golani et al. 2002; Fareeduddin et al. 2010). (**a**) The Al-Fe-Mg (molecular proportions) plot for tourmaline of Bhukia and Ghagri areas. Note a similarity with meta-evaporitic tourmalines from Liaoning, China (see Fig. 14.19 for explanation of fields 1–7). (**b**) Ghagri values plot on the Oxy-dravite to Povondraite line indicating a meta-evaporite protolith. (**c**) Ca-X-site vacancy – Na+K plot for Ghagri samples, all samples plot in the apex of the alkali group field. (**d**) Plot of C and O stable isotope values in Bhukia carbonates. *Field I* carbonates show normal sedimentary values while *Field II* are close to mantle values. *Dashed box* represents the average sedimentary carbonate composition; alteration trends resulting from evaporitic modifications are shown as *arrows*; *A* high-temperature burial, *B* exposure to meteoric waters and *C*- weathering average composition of Aravalli carbonates of Jhamarkotra Formation and calcite from sea-floor basalt alteration are plotted for comparison

decarbonation due to thermal metamorphism or a mantle-derived carbon component. Despite evidence of high-grade metamorphism, such as development of spherulitic graphite in arsenopyrite (Golani et al. 1999) and occurrence of rare fine graphitic flakes in QFR unit, Golani et al. (2002) interpret the negative $\delta^{13}C$ values in terms of mantle affinity as, being homogeneous, they can be considered unmodified. Bhukia $\delta^{18}O$ values (mean +20.6‰$_{SMOW}$) are close to the low-grade Proterozoic evaporitic carbonates of Lomagundi (+22.6‰) and Karnataka (+21.6‰). Thermal decarbonation would normally result in lowering of both $^{13}C/^{12}C$ and $^{18}O/^{16}O$ ratios (Shieh and Taylor 1969; Bottinga 1969).

It is clear from the foregoing discussion that the metasedimentary host-rocks of gold-sulphide mineralization were deposited in a hypersaline to evaporitic environment (Field I). In contrast, the $\delta^{13}C$-depleted Bhukia carbonates of field II appear to be consistent with values in other Archaean greenstone- hosted gold deposits (Groves et al. 1988). These more $\delta^{13}C$ negative values are attributed by Golani et al. (2002) to a mantle source. They argue that this mantle flux emanated through palaeofaults and ultimately derived either from the granite–greenstone substratum or through the coeval carbonatite magmatism (2.27 Ga) in the adjacent areas. We shall deal with the copper-gold-metaevaporite association in more detail in the next two chapters.

Sulphide-Anhydrite Archaean Carbonates, Brazil

Anhydrite occurs in Archaean carbonates that host sulphidesulphate phases in high-grade metamorphics in the Caraíba gneiss-granulite complex in central Bahia State, Brazil (Fig. 14.72a; Leake et al. 1979; Oliveira and Tarney 1995). The region includes the Caraíba Mine, the largest copper deposit in Brazil. Caraíba metasediments (marbles, calcsilicates, metapelites) are crosscut by younger granitic gneisses (≈2.0 Ga) and by K-rich zones. The anhydrite-

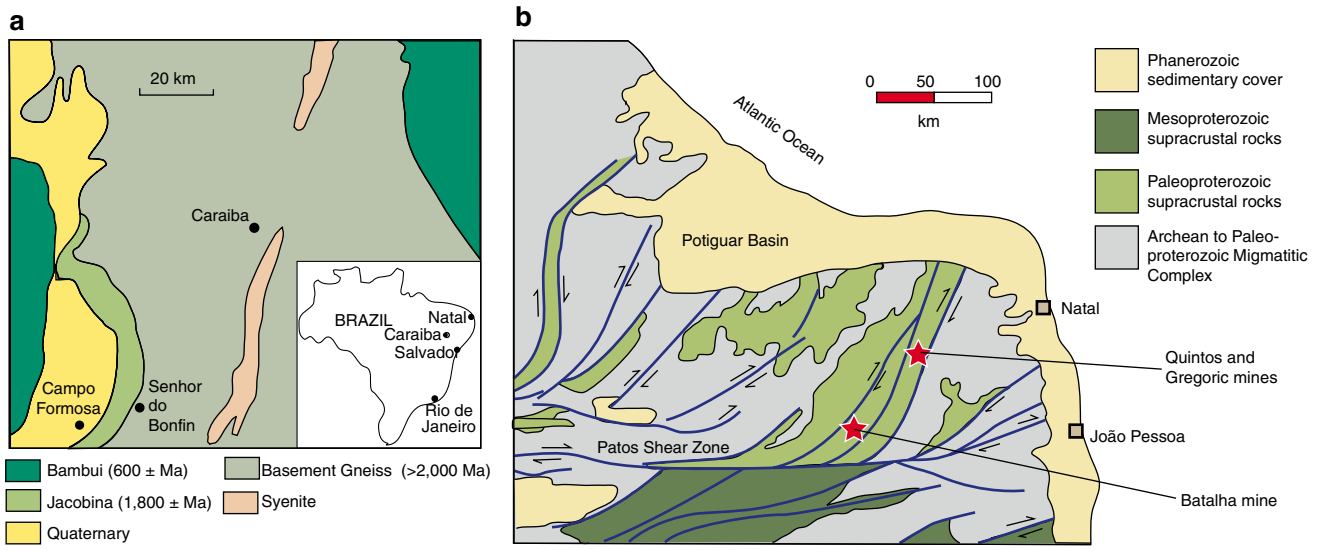

Fig. 14.72 Geological setting of the Paleoproterozoic/Archaean meta-evaporites and tourmalines in the Brazilian craton. (**a**) In the vicinity of the Caraíba copper mine in Archaean basement gneiss (After Leake et al. 1979). (**b**) Tourmaline mines in the Serido foldbelt (*red stars*) (Scares et al. 2008)

entraining metasedimentary sequence is dominated by calcsilicates with varying mineral assemblages (Sighinolfi et al. 1980):

1. diopside (≈90 %), green spinel, apatite and sphene;
2. diopside, calcite microcline;
3. diopside, anhydrite microcline;
4. diopside, anhydrite, calcite, forsterite.

Assemblages (2)–(4) contain varying amounts of phlogopitic marble and scapolite occurs locally. The anhydrite-bearing assemblages occur as layers (0.05–0.5 m thick) within the metasedimentary sequence. The anhydrite forms large crystals in the layers or forms fine-grained aggregates that fill cracks and microfractures. Textural evidence shows the anhydrite growth was associated with formation of phlogopitic mica (Sighinolfi, et al. 1980). The common occurrence of anhydrite in both marble and diopsidite led Leake et al. (1979) and Sighinolfi et al. (1980) to propose an metaevaporitic protolith.

Almost all the high grade metamorphic rocks in the Caraíba area have been heavily metasomatised and deformed, so that determining the ultimate origin of the anhydrite is beset with difficulty. The textural evidence is inconclusive. Anhydrite distribution in the layers appears sometimes to have been little affected by metamorphism, but there is also extensive anhydrite crystallization along cracks and fractures. The abundance of the anhydrite-mica association indicates its active participation in metasomatism but does not directly infer an evaporite protolith. The additional possibility of hydrothermal anhydrite has not been addressed.

Lindenmayer (1981) described relict cumulus textures in some gabbros associated with the Cu-bearing norites-hypersthenites in the Caraiba Mine area and found possible clinopyroxene exsolution lamellae in hypersthene. On the basis of chemical data and cross-cutting relationships deduced from drill cores, she concluded that the ore-hosting rocks are intrusive and evolved through fractional crystallization of a previously differentiated Fe-Ti-rich tholeiitic liquid, and that the hypersthenite-norite-gabbroanorthosite sequence might well represent the original igneous stratigraphy. She also suggested that some anhydrite-bearing marble and calcsilicate-rocks could have supplied sulphur to form part of the sulphides. The influence of entraining evaporites on magma sulphide chemistry is discussed in more detail in Chap. 16.

Interestingly, many different coloured tourmalines are found in the Paleoproterozoic meta-evaporitic successions in Bahia State to the northeast of the Caraiba Mine (Fig. 14.72b; Scares et al. 2008). Today the pink, blue and green gems are particularly popular. In 1988, miners discovered gem tourmaline in pegmatite veins of the Batalha Mine that were unlike any that they had ever seen before (Wilson 2002). The new type of tourmaline, which soon became known as Paraiba tourmaline, comes in incredibly vivid blues and greens, related to elevated levels of Cu (±Mn) in the lattice. The demand and excitement for this new material grew in the early 1990s when better specimens were soon fetched more than US$10,000 per carat, today better specimens can fetch in excess of US$20,000 per carat.

Implications

Meta-evaporites are not simple rock systems, their interpretation involves more than just recognising sodic or magnesian metamorphic minerals. This must be done in conjunction with a full description of the geometries of these phases and the recognition that the evaporites and their subsequent minerals are altered many times during their metamorphic history, often in ways that do not fit the isochemical paradigms of classic metamorphic petrology. The following questions should always be asked of potential meta-evaporite sequences:

- Are the minerals distributed in a fashion that reflects a stratiform or a halokinetic precursor?
- Are breccias present that contain nodules and other textures indicative of former evaporites?
- Do the breccias reflect a halokinetic precursor or was the brecciation a later fluidisation event (rauhwacke), perhaps associated with compression and overthrusting centred on evaporite -rich horizons that were undergoing metamorphism?

Evaporites undergoing metamorphism release large volumes of volatile-rich fluids, which are typically saline chloride solutions with elevated levels of sodium and magnesium as well as chromatophore metals that may colour gemstones growing in ductile meta-evaporitic hosts.

Many of these fluids have the capacity to mobilise and flush metals from adjacent strata that often include metalliferous metabasites. Thus meta-evaporites or their residues are often part of a metallisation series in a metamorphic terrane. The processes and styles of these evaporite-metallogeny associations are discussed further in the next chapters.

Lower Temperature Metals in an Evaporitic Framework

15

Introduction

Most subsurface evaporites ultimately dissolve and, through their ongoing dissolution and alteration, can create conditions suitable for metal enrichment and entrapment in subsurface settings ranging from the burial diagenetic through to the metamorphic and igneous realms. Within this framework, this chapter explores relationships between evaporites and lower temperature ore deposits, where ore is defined as a mineral, or an aggregate of minerals, from which a valuable constituent, especially a metal, can be profitably mined or extracted. The next chapter explores the significance of dissolving and altering evaporites in ore deposits formed in the higher temperature igneous and metamorphic realms.

An overview of a selection of the large-scale ore deposits associated with hypersaline brines and dissolving/altering salt masses, plotted on a topographic and salt basin base, shows that the many evaporite-associated ore deposits lie outside areas occupied by actual evaporite salts (Fig. 15.1). Rather, they tend to be at or near the edges of a salt basin or in areas where most or all of the actual salts have been long gone (typically via subsurface dissolution or metamorphic transformation). This is why the metal-evaporite association is not widely recognised by the economic geology community. Without the conceptual tools to recognise the former presence of evaporites (Chap. 7) and meta-evaporites (Chap. 14) the significance of disappearing salt masses, in focusing and enhancing metal precipitation via the creation of chloride-rich brines, is not obvious.

We have already discussed ore deposits where the evaporite minerals constitute the ore, or have transformed into gemstones (Chaps. 11, 12, and 14). Earlier papers by Kirkham 2001 and have noted parts of this association in the metals realm (Fig. 15.1), but have focused on the ore deposits themselves. This chapter and the next will approach this problem a little differently. We shall place the various base and precious metal deposits in the framework of our deeper understanding of evaporites and their residues and then use this understanding to pigeonhole the deposits. So, in this chapter we will focus on stratabound Cu, Pb-Zn and U associations in the low temperature realm (diagenetic and lower end of greenschist grade ores). The next chapter will focus on metalliferous ores (both gold and base metals) formed in those higher temperature igneous and metamorphic realms that have interacted with evaporites.

Let me clearly state at the outset of this discussion that I am not saying all large metal accumulations require evaporites or the highly-saline subsurface fluids that they can generate, although some recent papers do argue for a widespread role of evaporites in the Pb-Zn association (Fusswinkel et al. 2013; Wilkinson et al. 2009). This and the next chapter are only about those deposits where evaporites have contributed to the metal accumulation in some way. However, as the various tonnage-grade plots in this chapter and the next show, many accumulations with an evaporite association tend to plot at the larger end of their respective groupings.

High levels of metals in all ore deposits, like thick salts in evaporite basins across the sedimentary realm, are responses to unusual conditions, related to fortuitous associations of local and plate-scale tectonics and fluid systems. To become an ore deposit, metals need to build, at specific precipitation sites, to levels well above that of their background presence in the carrier brines. This typically requires a chemical interface that can be related to salinity/oxidation levels, or cooling/heating interfaces. As such, it is no surprise that the same process sets created by conductivity and salinity/oxidation levels tied to dissolution and reprecipitation of minerals are likely to be associated with conduits created by the passage of pore waters from altered buried evaporites and hydrothermal salts (e.g., Fusswinkel et al. 2013). As for the salts that accumulate in ancient evaporite basins, we can place ore deposit frequencies in a time and plate tectonic framework and so perhaps better understand and predict occurrences (Fig. 15.2; Groves et al. 2005).

Not all sediment-associated ore deposits are associated with evaporites. Only in those ore deposits that are classified as anorogenic and/or continental margin can subsurface evaporite masses be involved in the same unusual

© Springer International Publishing Switzerland 2016

J.K. Warren, *Evaporites: A Geological Compendium*, DOI 10.1007/978-3-319-13512-0_15

Fig. 15.1 A selection of metalliferous ore deposit provinces where formation is tied to the presence of hypersaline brines and/or evaporites (In part after Kirkham 2001; see also Table 15.1 and text in this chapter and the next for further explanation of the various deposits). Also, positions of the world's larger halite-dominated basins are plotted as *orange-coloured* areas, anhydrite-dominated as *green*

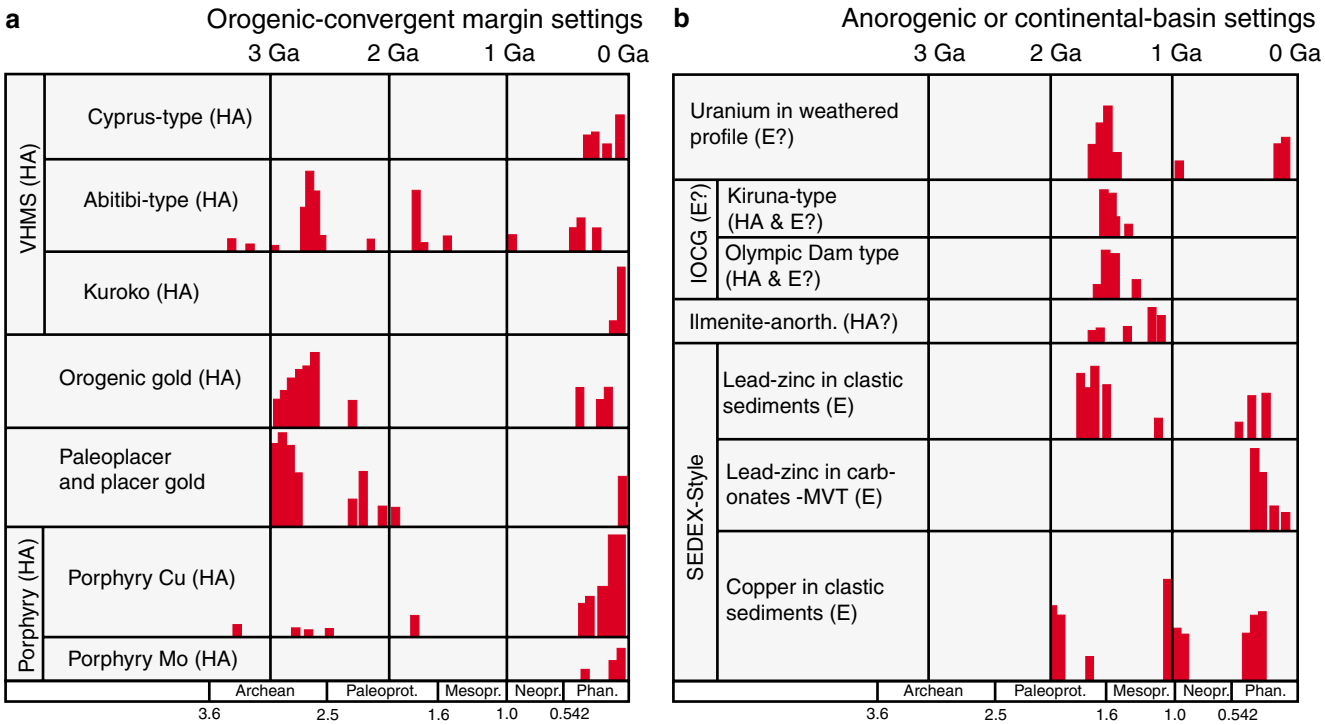

Fig. 15.2 Ore deposit occurrences across geological time (Modified from Groves et al. 2005; see Meyer 1988 for more detail and other igneous subsets). (**a**) Orogenic convergent margins, (**b**) Anorogenic or basin collision settings. *E* indicates direct evidence of evaporites or derived brine in the formative processes associated with some of the examples of this deposit style. *E?* indicates the presence of hypersaline brine associated with the formative ore process. Such brines may be magmatic or sedimentary/hydrothermal. *HA* indicates the presence or former presence of hydrothermal or igneous anhydrite precipitated by non evaporitic processes

concentration and alteration conditions that lead to the creation of metalliferous ore deposits (indicated by E in Fig. 15.2). At other times mineral salts, such as anhydrite, can be an integral part of the ore accumulation, but their occurrence may be unrelated to aridity. Rather, they are burial or magmatic hydrothermal salts formed by high salinity conditions inherent to the ore forming environment, as in the formation of carbonatites (e.g. Afrikanda and Bayan Obo; Wu 2008) and pegmatites (hydrothermal anhydrite is indicated by HA in Fig. 15.2). In such hot subsurface settings the role of any buried "true" evaporite may be, via its dissolution or alteration, to aid in the

creation of highly-saline high-temperature basinal brines. These brines can then act as either enhanced metal carriers or fixers.

The role of evaporites creating metalliferous ores is twofold; (1) In solution (halite-dominant precursor) they can act as chloride-rich metal carriers and (2) Locally, as beds or masses (especially of $CaSO_4$), their dissolution products, especially if trapped, can supply sulphur (mostly as bacteriogenic or thermogenic H_2S) and also set up chemical interfaces that act as foci in the setup of brine mixing conditions suitable for precipitation of metal sulphides or native elements. Hence, many evaporite-associated ore systems tend to be epigenetic, rather than syngenetic (Table 15.1). Subsurface salt beds and masses are merely the solid part of a large ionic recycling system, dissolved metals are another part and zones of mixing between the two are typically sites where ores tend to accumulate.

At the world-scale, both systems are driven by plate tectonics. Halite-dominated sequences, deposited in the drawdown basin centres, tend to dissolve in burial, and so supply chloride ions to the brine system. Salt beds that are thick enough tend to flow and so focus the upward and centripetal passage of basinal and hydrothermal fluid flows. Dissolving gypsum or anhydrite beds, typically deposited higher on the basin platform or diagenetically accumulated along salt dissolution edges and touchdowns can supply sulphur, via bacterial or thermochemical sulphate reduction, while simultaneously focusing metalliferous brine flows into the precipitation interface.

When the chemistries of the dissolving salt beds and the metal carriers interact so that redox fronts, salinity contrasts, and other precipitative interfaces are set up, an ore deposit can form. Thus, in base and precious metal exploration in evaporitic terranes, we are ultimately searching for those parts of a subsurface ionic cycling system where the salt dissolution, salt beds and metal systems have interacted to create economic levels of metalliferous precipitates.

Conceptually, this evaporite-related notion of regional fluid flow in a sedimentary/metasedimentary host is somewhat different to the internal process and local mineralised

Table 15.1 Classic classification of ore deposits into epigenetic and syngenetic (e.g. as used by Evans 1993). The effects of evaporites within this type of classification ranges across many subdivision -see text

Epigenetic Mineral deposit formed much later than the rocks which enclose it	Porphyry Large, low grade, usually associated with porphyritic intrusive body	Cu-Mo Cu (−Au) Mo (−W)
	Skarn Deposits formed by replacement of limestone by ore and calc-silicate minerals, usually adjacent to a felsic or granitic intrusive body	W-Cu (−Zn, −Mo) Zn-Pb-Ag (−Cu, −W) Cu (−Fe, −Au, −Ag, − Mo) Fe (−Cu, − Au) Sn (−Cu, −W, −Zn) Au (−As, −Cu)
	Vein Fracture filling deposits which often have great lateral and/or depth extent but which are usually very narrow	Hypothermal –Cu (−Au) Mesothermal –Cu-Pb-Zn-Ag-Au Epithermal –Au-Ag (−Hg)
	Mississippi Valley Type Named for the region where they were first described, these deposits formed within porous carbonate rocks (limestone reefs or caves)	Pb-Zn deposits with low Ag values
	Stratiform sediment-hosted redbed Cu	Cu
Syngenetic Mineral deposit which formed at the same time as the rocks that enclose it	Volcanic Massive Sulphide (VMS) These deposits formed as massive (over 60 % sulphide) lens-like accumulations on or near the sea floor in association with volcanic activity	Felsic volcanic hosted –Cu-Pb-Zn-Ag-Au Mafic volcanic hosted –Cu (−Zn, −Au) Mixed volcanic/sedimentary – Cu-Zn (−Au)
	Sedimentary Massive Sulphide (SedEx) Deposits formed by hydrothermal emanations on or near the sea floor in association with the deposition of sedimentary rocks	Pb-Zn-Ag Ba
	Magmatic-layered mafic intrusion During the crystallization of a magma, usually mafic or ultramafic, heavy, metal-rich liquids settle and accumulate at specific sites, often at the base, within the intrusion	PGM (Platinum group metals) Chromite Ni-Cu (−PGM)
	Placer Formed within sediments by the concentration of heavy resistant minerals by stream or wave action	Au, diamond, cassiterite

halo models that dominate our understanding of those world-class ore deposits related to the interior workings of igneous systems. The latter are known as orthomagmatic systems and encompass the majority of the deposits listed in Fig. 15.2a. There, interior igneous processes of fractional crystallisation and liquid immiscibility largely control ore formation in a framework of the evolution of world-scale tectonics across time, from Archaean greenstones to those of present-day plate tectonism. Examples where buried evaporites have been assimilated into a magma chamber are discussed in the next chapter. Then there are the various ore deposits that are external to (paramagmatic) or unrelated to the emplacement of igneous bodies (nonmagmatic). In both cases, the mineralisation is typically part of an ongoing longterm sedimentary burial history, tied to dissolving and flowing masses and associated hydrothermal circulation.

So, this chapter focuses on nonmagmatic ore deposits. The conceptualization of metal sources in a framework of orthomagmatic versus paramagmatic versus nonmagmatic is important as it either ties the deposit style to times and locations of magmatism and associated metal/heat brine sources or, in nonmagmatic settings, it does not.

Evidence for hydrothermally-induced low-moderate temperature mineralisation is often best preserved in textures in the hydrothermally altered rock matrix, typically located outside the actual ore deposit (in its hydrothermal alteration halo). From the hydrothermal perspective, one should see the role of evaporites and metal sulphides as each contributing its part to a larger scale "mineral systems" paradigm, much in the same way as, in a petroleum system, the integration of concepts of source, carrier, seal and trap are fundamental requirements to understand and predict economic oil and gas accumulations.

This ore systems approach is not fully encompassed in a number of economic geology studies that use sequence stratigraphic sedimentological approaches for ore deposit prediction in greenschist terrains (Ruffell et al. 1998; McConachie and Dunster 1996). In my opinion, this approach can shift the interpretation paradigm too far into the depositional realm. The problem with classic sequence stratigraphic approaches, when trying to understand ore genesis, is that sequence stratigraphy does not handle well the concept of a mobile ephemeral subsurface salt body that climbs the stratigraphy via autochthonous and allochthonous process sets (halokinesis). As the salt flows, it dissolves and so brings with it the associated epigenetic influences of brine-driven diagenesis and metasomatism. Current sequence stratigraphic paradigms in the economic geology realm are dominated by the assumption that the geometry of the units in the depositional system, and associated fault characteristics, are relatively static within the buried sediment prism. Yet, in terms of most sediment-hosted hypersaline ore deposits, what is most important in understanding the metal-evaporite association is the understanding of; (1) evaporite dissolution and halokinesis, (2) Migration of subsurface fluids, (3) creation of nearsurface redox fronts along with, (4) the opening and closing of fault/shear focused fluid conduits, typically tied to, the coming and going of bedded and halokinetic salts. These factors, rather than primary sediment wedge geometries, are the dominant controls as the mineralising system passes from the diagenetic into the metamorphic realm.

It is interesting that in a benchmark paper, discussing and classifying the world's ore deposits in a plate-tectonic-time framework, Groves et al. (2007) list almost all the major ore categories shown in Fig. 15.2b as belonging to the group of "…sediment-hosted deposits of non-diagnostic or variable geodynamic setting." Into this category they place all stratiform to stratabound sediment-hosted deposits with variable proportions of Pb, Zn, Cu (including Zambian Copper belt, Kupferschiefer and SedEx deposits). They go on to note (p. 26) that, although there is general agreement that the majority of these various deposits formed during active crustal extension, either in intracratonic rift basins or in passive margin sediment hosts, there is considerable controversy concerning their broader scale tectonic setting at the time of mineralisation and the driving force for hydrothermal fluid flow at the time of their mineralisation.

Perhaps this lack of model specificity in the varied interpretations of sediment-hosted deposits reflects the fact that one piece of significant information is missing from many ore genesis models. Namely, that the greater majority of these poorly classified sediment-hosted deposits sat atop, or adjacent to, or beneath, what were once thick evaporite sequences. It was the dissolution of these salt masses, either bedded or halokinetic-allochthonous, that focused much of the ore-fluid flow in the sedimentary-diagenetic realm. The loss of salt as the basin sediments passed from the low temperature diagenetic into the metamorphic realm, and as metalliferous fluid flow was focused into permeable conduits about or above the dissolving and retreating, or flowing salt edges, is how salt-related ore deposits form.

This is why the majority of these deposits tend to occur outside salt basins that retain substantial salt masses still in the diagenetic realm (Fig. 15.1). They are a response to the dissolution of evaporites, or the residual seawater bitterns created in underlying and subjacent settings as the salt beds were deposited, not the presence of evaporites. As we saw in the previous chapter in our discussion of Proterozoic and Archaean meta-evaporites, in most Precambrian evaporite associations the original salt mass is long gone from the hosting succession, via varying combinations of halokinesis, dissolution and metasomatism. Ore deposits of this age tend to be linked to evaporite alteration products and residues and rarely preserve actual sedimentary salts (other than local remains of hydrothermal anhydrite). In younger Phanerozoic

deposits, such as Kupferschiefer, the Atlantis II deep and Dzhezkazgan, portions of actual salt (brine source) remain in the more deeply buried parts of the basin.

Metal sulphide precipitates are not rare or unique in the subsurface diagenetic fluid milieu, what is important in prediction of ore-grade levels of metal sulphide buildups is understanding where and why the metal precipitation system was focused into particular structurally-controlled positions. That is, evaporite associated ore deposits are no more than ancient subsurface hydrology-specific associations where the precipitation system was stable enough, for long enough, to allow ore-grade levels of metals sulphides to accumulate from carrier brines. As such, they are part of the ore-forming process set, spread across the epigenetic and syngenetic realms (Table 15.1). They were part of the regional evolution of the fluid plumbing from time of deposition, into burial, and on into the realm of metamorphic transformations. This means to holistically understand the ore system in an evaporite-entraining system one must integrate local ore paragenesis with various aspects of the basin-scale geology, sedimentology, sequence stratigraphy, diagenetic metamorphic-igneous facies, fluid flow conduits and structural evolution of the evaporitic basin.

A Little Classification/Exploration Philosophy

Personally, I do not find much benefit in trying to create an exploration paradigm using the currently accepted somewhat generalised SSC, MVT or SedEx groupings that capture most low temperature base metal deposits. All the current compilations of Stratabound Sedimentary Copper (SSC), Mississippi Valley Type (MVT) and Sedimentary Exhalative (SedEx) deposits tie a very broad range of range of stratiform deposit styles into general association of metal precipitation occurring in sediment hosts, which may be redbeds, shelfal carbonates or deeper/quieter water laminites (as an example see the excellent compilation of Cox and Singer 2007). All these deposits are thought to form in low temperature settings, still largely in the thermal range of diagenetic (not metamorphic) geosystems, and are fed and bathed in cross-flowing basinal basement brines. Once formed, subsequent structuration and metamorphism can enhance ore quality.

Some SSC, MVT and SedEx models have the fluids escaping from the basin during basin subsidence, others call upon deep meteoric circulation driven by basin collision and uplift of the basin margin, still others draw upon the convection of basinal brines beneath evaporite seaway sediments and or the mixing of basinal and basement brines. None are rock texture specific, so making the use of applied targeting approaches problematic, if based on textures seen in outcrop, or recovered in core.

I am not saying the varied interpreted process sets, that explain the SSC, MVT and SedEx deposits, are wrong, only that the current classification sets are so broad that, when exploring, they lack the ability to make specific on-ground target predictions. Other than a general notion that most of these deposits are typically tied to faults acting as fluid conduits, there is little commonality in rock textures and lithologies across the host rock spectrum. That is to say, most of the host rock textures are extensive, but the faults are local, so we tend to target the fault or a set of fault trends, hoping to find mineralisation. Geochemistry of various sorts is the tool used to highlight areas of "on ground" interest and specify more targeted drilling; typically host rock textures do not play much of a role as part of the exploration paradigm.

But, if we can establish that evaporites (bedded or halokinetic) or their residues acted as foci to mineralisation in some types of SSC, SedEx and MVT deposits then, through recognition of positions of former evaporites either in outcrop or core we can establish additional targeting parameters to define where these masses have intersected or interacted with fluid-carrying faults. This gives us an improved ability to predict that ores are more likely to be found at or near the intersections between faults and evaporites or their residues. So for a subset of SSC, MVT and SedEx deposits (the evaporite-related subset) we then have the ability to more reliably locate and orient drilling sites and drilling grids.

Unfortunately, modelling paradigms in classic economic geology typically concentrate on particularized ore parageneses and the detailed measurement of trace/rare-earth element constituent levels, which are tied to metal sulphide emplacement, within and about an ore deposit (aka the "indicator halo"). When exploring for new deposits, this halo understanding and associated data trends are used in designing geochemical and remote sensing approaches. Inherently, this approach is most fruitful in brownfields expansion studies, it gives the more localised understanding needed to predict ore extensions and hence where to extend the current mining operation. But in greenfield areas, where predictive regional models are needed, it leads to less predictive ore exploration paradigms, other than a general concept of… "let's grid-drill (typically air-drill) around that fault with the gossan, or in the region of the associated soil anomalies, and see what we get back in the plots of the geochemical analyses of the rock flour".

With this in mind, I propose a somewhat different classification for those sediment-hosted (this chapter) and igneous-related (next chapter) ore deposits that can be linked to evaporitic associations, which are indicated by remnant salt bed and masses, their residues or their alteration products. It focuses on the nature of the evaporite, or former evaporite, (bedded or halokinetic residues) and the

ore deposits position relative to the former salt bed or salt mass. When classifying these ore deposits at the intrabasin scale, I ask; where in earth-space were these evaporite-associated metalliferous ore deposits located (within the diagenetic and early metamorphic evolution of the evaporite mass)? And I answer in terms of the following criteria:

(i) Is the ore deposit related to stratiform or halokinetic (allochthon) salt beds/masses and/or their residues?
(ii) Is the ore deposit in a; subsalt (below a thick >50–100 m salt bed/mass), intersalt (interbedded with ≈2–10 m thick salt beds) or suprasalt position (above a thick >50–100 m salt bed/mass)?
(iii) What was the likely dominant mineralogy in the former now dissolved salt mass (halite, anhydrite, trona, nahcolite, etc.)?

For the plate tectonic framework, I ask:

(i) What was the plate tectonic setting at the time these ore deposits formed; convergent, divergent, intracratonic sag or strike slip?
(ii) Does it relate to the plate tectonic association of the interacting evaporites? If yes, then: What was the depositional style of the host sediments (shallow or deep water; marine or nonmarine)? This also relates to the style, scale and geometry of the salt-related plumbing at the time of interaction/ dissolution: Was it a saltern or a basinwide salt unit, was it interbedded, massive stratiform or halokinetic? If halokinetic, was it autochthonous or allochthonous?
(iii) Was there a single metalliferous fluid or multiple fluids linked to the mineralisation/diagenetic history? Was the fluid source a burial water, or a magmatic or a metamorphic fluid, or was it some type of hybrid?
(iv) Was the deformation history of the deposit simple or complex and does it relate to the metamorphic grade or early structural controls, including halokinetic structuration of the salt overburden?

The resulting illustrative listing of some nonmagmatic deposits given in Table 15.2 is by no means comprehensive. It showcases only some of the more well-known Phanerozoic and Proterozoic examples where actual salts, or obvious residues, are still present. In the next chapter I shall expand on it as we develop paramagmatic and orthomagmatic models. For the deposits listed in Table 15.2 the depositional and diagenetic conditions are reasonably well understood in terms of atmospheric, marine and subsurface pore fluids conditions, most of these examples formed within subsurface basin chemistries somewhat similar to those seen today.

Evaporite-Related Metalliferous Brines?

Before we classify and discuss evaporite-linked ore deposits, we need to discuss in general terms how metals are sourced, transported and fixed in the various subsurface fluids found in sedimentary basins containing thick successions of dissolving evaporite salts. Chloride complexes, not organometallic or bi-sulphide complexes are what transports the greater volume of base metals through the pore spaces in the diagenetic realm of today's sedimentary basins (Kharaka and Hanor 2003). Through the inherently high pore brine densities created by subsurface halite dissolution, such high-chloride basinal brine densities can drive metal leaching waters deep into the understrata, including crystalline basement (Chap. 8; Koziy et al. 2009; Fusswinkel et al. 2013).

Also aiding the creation of metalliferous brines in the diagenetic realm is the sequential release of a metal series as organic-rich shales are subject to burial compaction under increasing temperature and pressure (Table 15.3; Wallace et al. 2002). The evolution parallels the maturation/generation of first liquid and then gaseous hydrocarbons (Chap. 9). Released metals are dissolved in the basin's aqueous (chloride-rich) fluids via a sequence of thermochemically controlled metal-maturity windows. That is, metals are released from maturing shale/mudstone source rocks in a progressive sequence, determined by ion concentrations and degree of association of ion complexes (Helgeson 1969), so that metals of similar ionic strengths and ionic diameters are released together. The temperatures at which these metal suites are released overlap, but the release from the shaly diagenetic sources follows a consistent pattern with increasing depth of burial.

As well as this grey-bed leaching, metals can also be leached diagenetically via redbed alteration in evolving saline oxidised nonmagmatic brine systems. In paramagmatic systems, igneous bodies can act as an additional source of brine products, as can leached volcaniclastics. Once released, as in a petroleum system, there must be carrier beds for the metalliferous brines, along with focusing mechanisms and then traps and seals to focus accumulations. As we shall see throughout this chapter and the next, this is how subsurface salt masses make substantial contributions to the formation of an economic metal accumulation. Before, or as, subsurface evaporite salts disappear, they generate various brine chemistries that can transport, seal, trap, focus and precipitate ore. Thus, a buried evaporite unit can act as:

(i) *An ionic source* – As the salt dissolves or alters it acts as a brine or volatile source feeding into the basin hydrology. It can supply economically important ions that, depending on the dissolving mineralogy, may be chloride-rich or a source of sulphur and so act as both a leacher and transporter of metals.

Table 15.2 Classic ore deposit breakdown (stratiform redbed-related Cu versus MVT Pb-Zn deposits) of some of the many Phanerzoic-Neoproterozoic base-metal deposits formed in the diagenetic realm in association with bedded, dissolving and flowing evaporites, mostly in situations where actual salts or remnant salts are still present. More comprehensive lists and discussions of less obviously evaporite-linked ore deposits are discussed later in this chapter and the next

Deposit, location (age of host)		Reserve (10^6 tonnes)	Cu (%)	Pb (%)	Zn (%)	Evaporite role (relative position and mechanism)	Evaporite association
Deposits associated with bedded evaporites or their residues							
Redstone River, Canada (Neoproterozoic)	Stratiform -sediment hosted copper (redbed) deposit	Small	2.7	–	–	Intersalt stratabound with subsalt focus to upwelling brine	Redbeds with bedded algal limestone host and abundant nodular $CaSO_4$
Creta, Oklahoma, USA (Permian)		1.9	2	–	–	Intersalt bedded (breccia), adjacent redox precipitates	Redbed – evaporitic mudflat host with abundant nodular $CaSO_4$
Corocoro, Bolivia (Eocene)		≥7	≈5	–	–	Intersalt bedded (breccia), brine reductant	Redbed – greenbed host with gypsum and baryte in veinlets and disseminated nodules
Nanisivik, Baffin Island (Mesoproterozoic)	Mississippi Valley Type deposit	6.5	–	1.5	12	Intersalt?, bedded	Host is a stratiform karst cavern: evaporites and pseudomorphs in lateral equivalent beds
San Vincente, Peru (Triassic – Jurassic)		12	–	1	12	Intersalt, bedded. Local supplier of sulphur via TSR	Ore hosted in cryptalgal laminites with pseudomorphs after $CaSO_4$ in barrier-lagoon host
Cadjebut, NW Australia (Devonian)		3.8	–	17 % (Pb + Zn)		Intersalt, bedded (breccia). Local supplier of sulphur via TSR	Bedded anhydrite as lateral equivalent to each ore lense and linked by evaporite dissolution breccias
Largentiére, France (Triassic)		9.6	–	0.7	3.7	Intersalt	Disseminated $CaSO_4$ cements and nodules within evaporitic lagoonal beds
Peridiapiric deposits associated with halokinetic evaporite masses or their residues							
Atlantis II Deep, Red Sea (Holocene)	Stratiform redbed -related copper deposit	150–200	0.8	Yes	5–6	Suprasalt allochthon acts as focus to resurging Cu-Zn-Cl brine (salt partially covers ridge basalts)	Dissolving salt allochthon underbelly supplies Cl-rich metalliferous brine to deep seafloor brine lake. Hydrothermal anhydrite is interbedded with laminites
Kupferschiefer-style, Lubin, Poland (Permian)		≈2,000	>2	–	–	Subsalt, stratiform with brine focus creating the Rote Faule contact and adjacent redox precipitates	Anhydrite and halite in Zechstein hangingwall and anhydrite in Rotliegende footwall – redbed ore source
Kupferschiefer-style, Mansfeld, Germany (Permian)		≈7.5	≈2.9	–	±1.8	Subsalt, stratiform with brine focus	Anhydrite and halite in Zechstein hangingwall and anhydrite in Rotliegende footwall – redbed ore source
Dzhezkazgan, Kazakhstan (Carboniferous)		≈400	1.5	0.1–1.0	–	Suprasalt diapiric, anticlinal focus to brine flow	Interbedded redbed and greybed host with $CaSO_4$ and halite in underlying salt anticline and lateral equivalents
Dongchuan deposits, China (Mesoproterozoic)		10–100	1.0–1.5	–	–	Suprasalt allochthon or intrasalt breccia. Allochthon acts as focus to resurging metalliferous brine	Stratabound ore in cryptalgal laminites adjacent to diapiric breccia
Lisbon Valley, Utah, USA (Cretaceous)		Small >0.15	1.4	–	–	Suprasalt allochthon, salt movement creates orehosting faults in overburden	Ore in vein and pore fills adjacent to faults created by halokinesis
Jubilee, Nova Scotia (Carboniferous)	Mississippi Valley Type deposit	Not economic	n/a	n/a	n/a	Subsalt allochthon (tectonic breccia) stratiform, subsalt focus to brine flow	Interstratified fractured carbonate and anhydrite ore host created by regional salt-induced gravity slide
Gays River, Nova Scotia (Carboniferous)		2.4	–	8.6	6.3	Subsalt with subsalt focus to upwelling brine. Local supplier of sulphur via TSR	Anhydrite both within main ore zone and as cement in disseminated ore
Bou Grine, Tunisia (Cretaceous)		7.3	–	2.4	9.7	Suprasalt, peridiapiric, brine focus via halokinesis	Ore in peridiapiric organic-rich pyritic laminates adjacent to halite allochthons
Gulf Coast USA (Tertiary)		Not economic	n/a	n/a	n/a	Suprasalt allochthon capstone, brine focus via halokinesis	Anhydritic caprock undergoing bacteriogenic alteration in association with reservoired hydrocarbons

Table 15.3 Temperature ranges associated with various metal releases in an organic-rich shale undergoing burial diagenesis

Metal maturity window	Temperature (°C)
U-V-(Th)	35–100
Au-PGE	60–110
Cu-Ag	60–120
Pb-Zn	70–180
Au-Co-Au	175–275

After Wallace et al. (2002), Helgeson (1970)

(ii) *A seal and* trap – Thick evaporite units act as a seal, limiting or preventing the free vertical escape of basinal, hydrothermal, hybrid or upwelling meteoric waters. Given the right geometry, an evaporite unit can also act as a fluid barrier that, until it is breached, can pond or hold back buoyant metalliferous basinal waters and hydrocarbons.

(iii) *A* precipitative *focus* – Breach points or brine mixing zones tied to the edges of a dissolving evaporite mass (i.e. the edge of bed or the edge of a salt body created by flowage, décollement, or faulting). The edge to an impervious salt mass tends to focus the escape/mixing of pressured subsurface waters into the zones above, within or sometimes even below the breach (Chap. 8). Additionally, hot metalliferous basinal water, escaping via a breach or conduit into a nearsurface and surface setting, can create brine ponds and replacement haloes about, near or atop the escape conduit.

Even after the actual salts have long gone, a zone of dissolution residues can act as an aquifer or focus for ongoing metalliferous brine flow. Recognising the process and timing under which an evaporite disappears or its residues become an aquifer is often the most important step in understanding the evaporite ore deposit link. This is especially true of ore deposits hosted in Proterozoic and Archaean rocks and metasediments where no actual salts remain, only indicators of the former evaporite protolith. Such saline metalliferous flow paths may at times be indicated by the presence of hydrothermal zebra dolomites (Diehl et al. 2010).

To better define the role of the various metal-carrying chloride brines in evaporitic basins, we will first discuss the nature and chemistry of modern subsurface basinal brines, then chemistries suitable for metal precipitation and then look to likely examples of resultant ore deposits in the sedimentary and greenschist realms.

Modern Basin Brines: Composition

Sampled deep formation waters, in particular oilfield brines, vary widely in salinity, composition and their metal-carrying capacity (Chap. 8). Most deeper saline brines, even if not carrying hydrocarbons, tend to be anoxic or, at best occasionally dysaerobic. That is, levels of dissolved oxygen in subsurface petroleum-related waters are always low and typically undetectable (Collins 1975, p. 159). Shallower, primary reflux brines can retain somewhat higher oxygen levels, but, significant dissolved oxygen levels in a brine occur only where subsurface waters are in hydrodynamic connection with the surface and are actively receiving a surface-recharge (Collins 1975, p.301). Kuznetsov (1957) measured the dissolved oxygen content in brines from wells in the Groznyv oil district and found up to 10.6 mg/l at a depth of 249 m. He also found that in general, dissolved oxygen was found only in the zone of active water circulation (surface recharge) and was lacking in zones of stagnant phreatic waters and below. This general observation has important implications in understanding depth-related controls on distribution of Rote Faule related ore zones, such as in the Kupferschiefer copper deposits of NW Europe (discussed later).

In the deeper portions of most saline basins, the dominant anion is Cl and the dominant cations Na and/or Ca (Houston et al. 2011). Elevated levels of chloride in modern basinal brines are typically created by some combination of subsurface dissolution of halite (aka secondary brines; Land 1995a, b) and infiltration of subaerially evaporated seawater (aka primary brines or reflux brines; Carpenter 1978). Both are subject to further alteration in ionic proportions in response to other ongoing water-rock interactions, such as albitisation at lower salinities and dolomitisation at moderate salinities (Houston et al. 2011).

In general, the salinity of modern basinal brines increases with depth, especially in basins entraining thick deeply-buried salt masses (Fig. 15.3; Kharaka and Thordsen 1992). Basinal pore water salinities are typically higher than seawater (35 g/l) and range to over 350 g/l in basins with thick partially-dissolved basal salt units. In some basins there is a progressive increase in salinity with depth, in others, especially in Tertiary basins with thick dewatering shale units, there may be a reversal of this trend with depth (California and South Louisiana basins in Fig. 15.3). The salinity of a Na–Cl or Na–Ca–Cl brine can be estimated from its chlorinity by the relationship; salinity $\approx$ 1.7 chlorinity. This is the basis for most of the salinities estimated from oilfield waters and plotted in Fig. 15.3 (Hanor 1996).

Inorganic (Halogen) Components in Basinal Brines

Most basinal brines of moderate salinity are dominated by dissolved Na and Cl and, as salinity increases, there is a progression from Na-Cl to Na-Ca-Cl to Ca-Cl brines (Kharaka and Hanor 2003; Houston et al. 2011). Chloride is the dominant anion in formation waters with salinities greater than 20,000 mg/l, while a transition zone between 20,000 and 10,000 mg/l defines a total dissolved solid (TDS) boundary

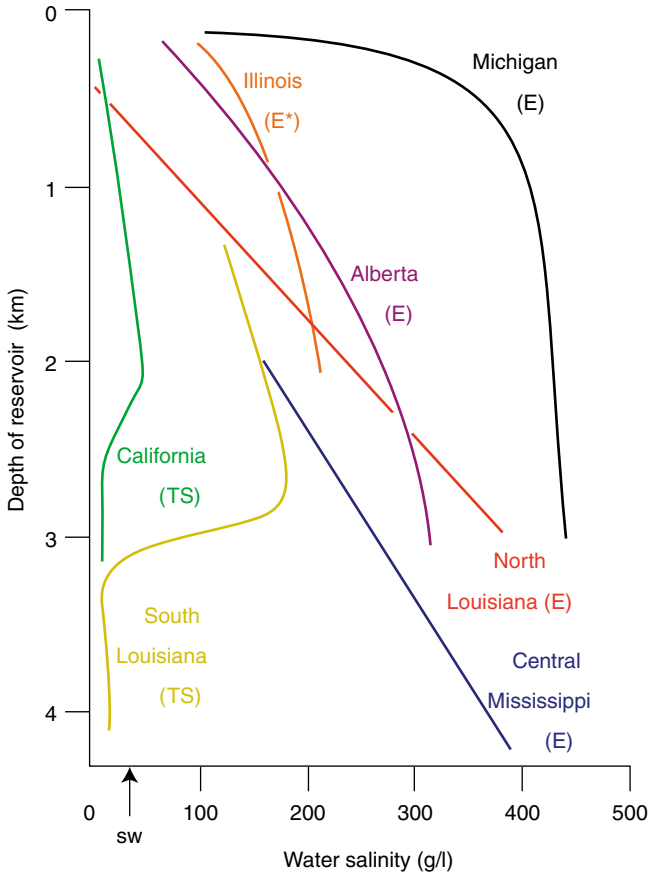

Fig. 15.3 Salinity to depth profiles in selected basins (After Kharaka and Thordsen 1992) *E* evaporitic, *E** former, now dissolved evaporite, *TS* Tertiary shale-rich basin. *Sw* indicates seawater salinity

below which the dominant anion is either bicarbonate, sulphate, or acetate (Fig. 8.40). Sodium is the dominant cation in basinal brines with salinities less than 300,000 mg/l. In general, the relative proportion of Na to K, Ca, or Mg decreases with increasing salinity and Ca becomes the dominant cation in basinal brines having salinities in excess of 330,000 mg/l TDS. Between 300,000 and 330,000 mg/l TDS, the dominant cation is either Na or Ca. Houston et al. (2011) show that most highly saline oilfield formation waters have cation chemistries controlled by chemical equilibration with the host rocks. Thus basinal fluids are almost invariably enriched in Ca relative to Na, when compared to evaporated modern seawater of similar chlorinity. This is the result of ongoing diagenetic mineral-fluid interactions in the subsurface and $CaCl_2$ brines are the result.

Evaporites are important contributors to the major ion chemistry of basinal brines through a combination of early brine reflux, ongoing nearsurface and, more importantly, subsurface dissolution/alteration (Houston et al. 2011; Hanor and McIntosh 2007). The chemical make-up of a subsurface brine depends on the mineralogy of the dissolving salt sequence and labile components in other sediments in the basin. Thick beds of dissolving halite (the most common Phanerozoic evaporite salt) generate regional chloride-rich brines. Leached anhydrite/gypsum successions are likely to develop sulphate- or sulphide-enriched waters, depending on the oxidation state of pore waters at the site of dissolution. Associated brine reflux during subsurface dissolution can drive convective circulation cells, as well as leach and transport metals, within and through the adjacent sediments. Ongoing reaction of this reflux brine with the nonevaporite matrix in nearby beds modifies overall brine chemistry (see Chap. 8).

Ongoing interaction with a dissolving salt mass is seen in the halogen water chemistry (Cl, Br, F, I) of Phanerozoic sedimentary basins. According to Worden (1996), the key geological parameters influencing chlorine and bromine (and possibly fluorine) concentrations in the basinal waters are, in order of importance: (1) Presence of salt in the basin, (2) Age of the aquifer unit, and (3) Kerogen type within any significant organic-rich rocks in the basin. Worden concluded the presence of salt in a basin means that any connate water contributing to the basin water chemistry is hypersaline. More importantly, he showed that most high chlorinity subsurface waters are not connate (i.e. not preserved seawater), but are generated though pore-water salt bed interaction during burial (e.g., Ferguson et al. 1992, 1993; Land 1995a, b).

Worden 1996 found that brines in Tertiary-age basins typically have much lower chlorine and bromine concentrations than pore waters in Mesozoic or Palaeozoic rocks. This age separation may simply reflect the different amount of time the basinal waters had to interact with any buried salt beds or that the effects of shale dewatering tends to dominate in rapidly subsiding mud-rich portions of Tertiary sedimentary basins (Fig. 15.3; California and South Louisiana basins).

Dominance of type II marine kerogen in a basin leads also to a higher bromine concentration in the basinal waters. According to Worden this may reflect the dominance of marine influences in a type II entraining basin, which in turn is more likely to lead to greater volumes of salt deposition compared with a basin dominated by terrestrial/meteoric inflows. Iodine concentrations in subsurface waters are independent of all these parameters. He found that other geological parameters, such as depth of burial, temperature, basin-forming mechanism and reservoir lithology, exerted no recognisable influence upon halogen concentrations.

In general, the pH of subsurface waters decreases with increasing salinity from values of approximately 8 for salinities near 20,000 mg/l to values between 3 and 4 for halite-saturated brines with salinities near 330,000 mg/l, thus most Na–Cl and Na–Ca– Cl brines have a pH in the 4–8 range (Fig. 8.40). Acidity, and hence the ability to leach and carry metals, can be augmented by the presence of dissolved organic acids, and CO_2, but the proportion of both, relative to

chlorinity, tends to drop off with increasing salinity (Fig. 15.5a). Outside of oilfield waters, true *in situ* pH values in deep subsurface brines are not well known, nor are the relative contributions of the various diagenetic processes that create and maintain acidity. Whatever the other possible carriers in a basinal or hydrothermal water it has been known for 40 years that elevated salinity (chlorinity) is the key to metal transport in the sedimentary diagenetic realm.

Metals, Ligands and Salinity

Oil field brine chemistry, including Holland's (1972) now-classic experiments, show that the solubility of metals such as Pb, Zn, Mn, and Fe varies as an exponential function of the chloride ion (Cl^-) concentration or salinity of the fluid and temperature (Figs. 15.4 and 15.6a). Both natural pore fluid chemistry and laboratory experiments show aqueous solutions tend to contain other dissolved ingredients that metals can bond to, thereby promoting metal dissolution. For example, the solubility of a mineral such as galena (PbS) in pure water, even at high temperatures, is extremely small. Wood and Samson (1998) calculated that the amount of Pb that could be dissolved in an aqueous solution (with 10^{-3} molal H_2S and in equilibrium with galena at 200 °C) would be a trivial 47.4 ppb. If 5.5 wt% NaCl is added to this solution, the solubility of Pb at the same temperature increases significantly to 1,038 ppm and will continue to rise with increasing temperature (Fig. 15.4).

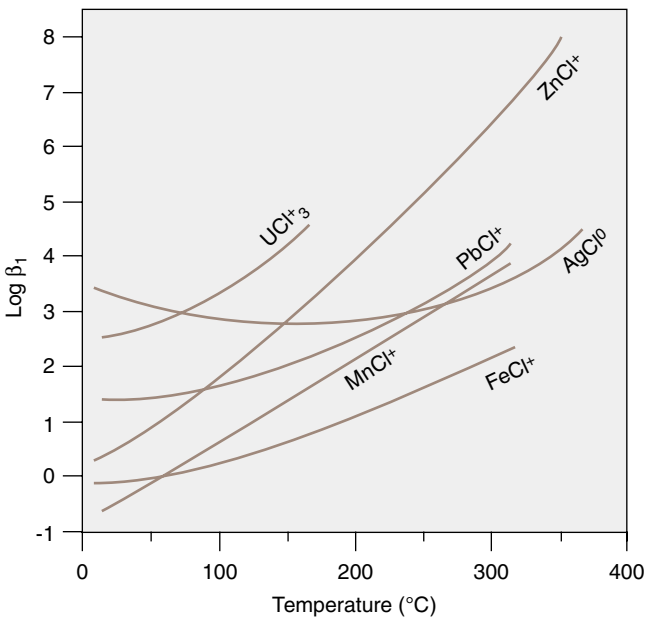

Fig. 15.4 Plot of the effective stability of a metal complex (expressed in terms of β_1, which is the equilibrium formation constant) versus temperature (After Seward and Barnes 1997). The stabilities of metal–chloride complexes shown increase by several orders of magnitude as temperature increases, as will their solubilities in aqueous solution (Redrawn from Robb 2005)

In addition to Cl^-, a variety of different ligands (electron donors or electronegative ions with lone pairs of valence electrons) will affect the solubility of metals in solution (Robb 2005). Ligands (particularly those that are chloride-associated in the high salinity sedimentary realm) combine with metallic ions by the formation of a coordinate bond, which is a type of covalent bond where the shared electron pair is provided by one of the participating molecules (the ligand in this case) rather than the normal situation where the shared electrons are supplied from each of the two participating components. A ligand that promotes the formation of complexes by coordination bonding will typically increase the solubility of metals in aqueous ore-forming solutions (Fig. 15.4).

How metals go into solution in basinal and hydrothermal fluids can be understood using the concept of Lewis acids and bases (Robb 2005). Conventional acids and bases are defined as substances capable, respectively, of contributing H^+ ions to, or taking up H^+ ions from, a solution. In contrast, Lewis acid/base concepts are applicable to subsurface fluid situations where H^+ ions are not present, and this has particular relevance to geological situations (Gill 1994). A Lewis acid is defined as an atom or molecule that can accept a lone pair of valence electrons, whereas a Lewis base can donate an electron pair to a bond.

"Hard" Lewis acids are strongly electropositive metals (with high charges and/or small atomic radii) such as the alkali and alkaline earth metals (e.g. Na^+, K^+, Mg^{2+}, Ca^{2+}) that form ionic bonds with strongly electronegative elements, like oxygen (O^{2-}). "Soft" Lewis acids have an abundance of easily accessible electrons in their outer shells and prefer to form covalent bonds with soft bases (Table 15.4, Robb 2005). Soft acids are typified by the chalcophile metals (i.e. those that have an affinity with sulphur, such as Cu, Pb, Zn, Ag, Bi, Cd), which tend to form covalent bonds with ligands of low electronegativity, such as S^{2-}. The principle stating that, in a competitive situation, hard metals (acids or electron accep-

Table 15.4 Classification of selected metals and ligands in terms of Lewis acid/base principles

Hard metals	Borderline	Soft metals
Li^+, Na^+, K^+, Rb^+, Cs^+, Be^{2+}, Sr^{2+}, Ba^{2+}, Fe^{3+}, Ce_4^+, Sn^{4+}, Mo^{4+}, W^{4+}, V^{4+}, Mb^{4+}, As^{5+}, Sb^{5+}, U^{6+}	Divalent transition metals Zn^{2+}, Pb^{2+}, Fe^{2+}, etc.	Au^+, Ag^+, Cu^+, Hg^{2+}, Cd^{2+}, Sn^{2+}, Pt^{2+}, Pd^{2+}, Au^{3+}, Tl^{3+}
Hard ligands	**Borderline**	**Soft ligands**
NH_3, ***OH***$^-$, F^-, NO_3^-, CH_3, COO^-, CO_3^{2-}, SO_4^{2-}, PO_4^{3-}	***Cl***$^-$, Br^-	***HS***$^-$, I^-, CN^-, H_2, S, S_2, O_3^{2-}

After Robb (2005) and references therein
Major ligands in basinal and hydrothermal waters shown in bold italic text

tors) will tend to complex with hard ligands (bases or electron donors), and soft metals with soft ligands, is commonly referred to as Pearson's Principle, and underpins the solubility behaviour of metals in hydrothermal and basinal waters and the notion that different leach lithologies provide different metal proportions in the leachate fluids, which is the basis for Fig. 15.4.

A "borderline" category is added to accommodate the fact that some metals (such as Fe and Pb) can complex readily with both hard and soft ligands, forming a range of minerals such as sulphides (pyrite FeS_2, galena PbS) and carbonates (siderite $FeCO_3$, cerrusite $PbCO_3$). Likewise, Cl^- can be an effective complexing agent for both hard and soft metals, and therefore promotes the solubility of a wide range of metals in hydrothermal aqueous solutions.

The classification of aqueous ionic species into hard and soft Lewis acids/bases assists considerably in understanding the nature of metal–ligand complexation, and, therefore, the controls on solubility, in basinal/hydrothermal solutions (Robb 2005; Seward and Barnes 1997; Wood and Samson 1998). In addition, it is well known that temperature plays a very important role in determining the degree to which metals enter solution. In most cases stabilities of metal–ligand complexes such as $PbCl^+$ and $ZnCl^+$ will increase by several orders of magnitude as temperature increases from ambient values to 300 °C (Seward and Barnes 1997). This is illustrated, together with data for other metal–chloride complexes, in Fig. 15.4. By contrast, an increase in pressure will have the opposite effect to temperature and the stabilities of metal–ligand complexes will tend to decrease because of bond dissociation and the formation of free metal ions. In general, however, the effect on solubilities of pressure increases are minimal and more than offset by the significant changes associated with temperature increases (Seward and Barnes 1997).

So let us now consider the significance of Lewis principles in the transport of the base metals (Cu, Zn and Pb) in the lower temperature sedimentary brine settings discussed in this chapter. In subsurface brines, copper occurs in both Cu^+ and Cu^{2+} valence states, although the monovalent state is predominant in most hydrothermal and basinal fluids (Robb 2005). It is a relatively soft Lewis acid and forms stable Cu^+ chloride and Cu^+-bisulphide complexes, as well as Cu^+-hydroxide complexes if other ligands are not available. Movement of copper in basinal solutions occurs under a wide range of conditions and is most likely to carried as Cu^+–chloride complexes in the form $CuCl^{2-}$. Although copper–bisulphide complexes will form in high-sulphur environments, they are not likely to play a significant role in most hydrothermal/basinal brine ore-forming environments where chloride dominates.

The dominant divalent zinc cation, Zn^{2+}, is a borderline Lewis acid that complexes with a variety of ligands, including Cl^-, HS^-, OH^-, HCO_3^-, and CO_3^{2-} (Robb 2005). At relatively low temperatures and high pH, and in fluids with high bisulphide concentrations but low salinities, a variety of Zn^{2+}-bisulphide complexes are stable, including $Zn(HS)_2$, $Zn(HS)_3^-$, and $Zn(HS)_4^{2-}$. In contrast, at higher temperatures and salinities and under more acidic conditions, a host of chloride complexes predominate, including $Zn(Cl)^+$, $Zn(Cl)_2$, $Zn(Cl)_3^-$, and $Zn(Cl)_4^{2-}$.

Lead is the softest of the borderline Lewis acids and forms stronger bonds with Cl^- and HS^- ligands than with OH^- or HCO_3^-. The valence state and complexing behaviour of lead is very similar to that of zinc. Pb^{2+}-bisulphide complexes are more stable than chloride complexes in low temperature, neutral to alkaline, low salinity solutions. Different Pb^{2+}-bisulphide complexes form as a function of pH, and these include $Pb(HS)_2$ under acidic conditions and $Pb(HS)_3^-$ at higher pH (i.e. >6). At higher temperatures and lower pH, however, a variety of Pb^{2+}chloride complexes form and these include $Pb(Cl)^+$, $Pb(Cl)_2$, $Pb(Cl)_3^-$, and $Pb(Cl)_4^{2-}$. Pb^{2+}-carbonate or Pb^{2+}-bicarbonate complexes can form in CO_2-bearing fluids but their solubilities are typically low and they are unlikely, therefore, to have relevance in ore-forming processes.

There is also compelling evidence that lead, and to a lesser extent zinc, can be transported by organo-metallic complexes (Table 15.5), especially in relatively low temperature environments such as those related to the formation of some Mississippi Valley type Pb–Zn deposits, where the hydrothermal/basinal fluids are known to contain hydrocarbons. The acetate ligand (CH_3COO^-) is one of a number of organic molecules that have been implicated in base metal transport, others include thiols and sulphur-bearing organic compounds.

Organic Components in Metalliferous Brines

Concentrations of carboxylic acid anions in modern petroleum field brines are highly variable with respect to their major known controls, including age and temperature of reservoir rocks, type and amount of kerogen in source rocks, and the nature of metastable equilibria and water rock interactions that characterize organic-matter interactions in the reservoir (Seewald 2003). Although concentrations vary with temperature and reservoir depth for any given petroleum field, maximum values are generally present in Cenozoic-age reservoir rocks of moderate salinities in the temperature range 80–120 °C (Fig. 15.5a, b; Kharaka and Hanor 2003; Seewald 2003). Within such brines, monocarboxylate anions (mainly acetate, propionate, butyrate, n-valerate) and dicarboxylate anions (mainly malonate, succinate, glutarate, maleate) are the dominant organic acid species. These organic acids are typically detected in moderate salinity formation waters, associated with petroleum, and mostly reside in reservoirs with temperatures ranging from 20° to 200 °C

Table 15.5 Modern oil field brines constituents and their Pb-Zn contents

Parameter	Low ΣH_2S, high trace metal content (brine 1)	Low ΣH_2S, low trace metal content (brine 2)	High ΣH_2S, low trace metal content (brine 3)
Temp (°C)	50 to 250	50 to 250	50 to 250
TDS (mg/l)	100,000 to 330,000	20,000 to 330,000	20,000 to 330,000
ΣCl^{-1} (mg/l)	60,000 to 210,000	12,000 to 210,000	12,000 to 210,000
pH	4 to 6.5	4 to 8	4 to 8
[a]ΣH_2S (mg/l)	<0.1	<1.0	1.0 to 1,000
[a]Σm_{H_2S}	$<10^{-5.5}$	$<10^{-4.5}$	$<10^{-4.5}$ to $10^{-1.4}$
[b]ΣSO_4 (mg/l)	0.1 to 1,000	0.1 to 10,000	0.1 to 1,000
[b]Σm_{SO4}	10^{-6} to 10^{-2}	10^{-6} to 10^{-2}	10^{-6} to 10^{-2}
[c]Σmonocbx (mg/l)	<1.0 to 300	<1.0 to 10,000	<1.0 to 10,000
[c]$\Sigma m_{monocbx}$	$<10^{-4.8}$ to 0.005	$<10^{-4.8}$ to ≈0.15	$<10^{-4.8}$ to ≈0.15
[d]Σdicbx (mg/l)	<1.0	<1.0 to 2,600	<1.0 to 2,600
[e]Σm_{dicbx}	$<10^{-5}$	$<10^{-5}$ to 0.025	$<10^{-5}$ to 0.025
[e]$\Sigma m_{Cl}/Sm_{Cbx}$	>340	8 to >1,000	8 to >1,000
$\Sigma m_{monocbx}/Smd_{icbx}$	≈30 to 300	>20	>20
Pb (mg/l)	5 to 70 (cluster)	<1.0 (cluster)	<0.1 (cluster)
Pb (mg/l) range	1 to 111	BDL to 0.9	BDL to 0.9
Zn (mg/l)	15 to 250 (cluster)	<1.0 (cluster)	<0.1 (cluster)
Zn (mg/l) range	1 to 575	BDL to 0.9	BDL to 0.9

After Giordano (2003)
Cluster indicates most common values observed for modern petroleum field brines not the total range
BDL below detection limit, usually less than about 0.01 mg/l
Explanation of selected parameters
[a]Total dissolved inorganic sulphide defined as $\Sigma H_2S = H_2S + HS^-$ (mg/l) and $\Sigma m_{H_2S} = m_{H_2S} + m_{HS}$ (mol kg21)
[b]Total dissolved sulphate is defined as the sum of all dissolved sulphate species in mg/l (ΣSO_4) and as the molal sum of all dissolved sulphate species (Σm_{SO4}) in mol kg^{-1}
[c]Total monocbx = sum of monocarboxylate anions, as listed by Giordano (2002) in mg/l (Σmonocbx), while $\Sigma m_{monocbx}$ = total molality of dissolved monocbx in mol kg^{-1}
[d]dicbx = sum of dicarbonxylate anions, as listed by Giordano (2002) in mg/l (Σdicbx), while [e]Σm_{dicbx} = total dissolved dicbx in mol kg^{-1}

(Kharaka et al. 2000). At higher temperatures they are destroyed by various decarboxylation reactions with CO_2 as the ultimate byproduct (Seewald 2003)

Plots of organic acid (carboxylate anions) concentration versus salinity in this temperature range show a pronounced decrease in organic acid concentration with increasing salinity (Fig. 15.5a; Hanor 1994a, b). Highest concentrations are found in pore waters with salinities less than 30,000 mg/l, while these species do not appear to be major constituents of petroleum field brines having salinities that exceed 100,000 mg/l. The total concentration of monocarboxylate anions ($\Sigma_{monocbx}$) in modern petroleum-field brines is generally less than 100 mg/l, however, many brines have concentrations in the 100–5,000 mg/l range (Table 15.5). The dominant monocarboxylate anion in most petroleum-field brines is acetate, followed in order of decreasing concentration by propionate, butrate, and valerate. The highest concentration of acetate reported in a subsurface water is 10,000 mg/l but values above 5,000 mg/l are very rare (Lundegard and Kharaka 1994; Kharaka et al. 2000).

Typically acetate comprises 80–90 % of the total monocarboxylate species (Giordano and Kharaka 1994). The dominant dicarboxylate species in modern petroleum-field brines are malonate, succinate, and glutarate. Each of these species is not likely to have concentrations greater than about 100 mg/l, but controversially high values for oxalate (494 mg/l) and malonate (2,540 mg/l) have been reported (MacGowan and Surdam 1988). Reported total dicarboxylate anion concentrations (Σ_{dicbx}) range from 0 to 2,640 mg/l but values higher than 300 mg/l are very rare.

Typically, brines high in dicarboxylate anions are also high in monocarboxylate anions; however, brines high in monocarboxylate species are not always enriched in dicarboxylate anions. The total dicarboxylate anion concentration is typically less than 5 % of the total carboxylate concentration for modern petroleumfield brines. Thus, the ratio of total monocarboxylate anions to total dicarboxylate anions ($\Sigma m_{monocbx}/\Sigma m_{dicbx}$) for modern basinal brines is nearly always greater than 20 and even higher in some brines with high trace metal contents (Table 15.5).

Basinal Brines: Metal Carrying Capacity

The presence of halite (or indicators of its former presence) in a basin fill announce that, if metals were present in sufficient volumes in adjacent strata to become leachates, then

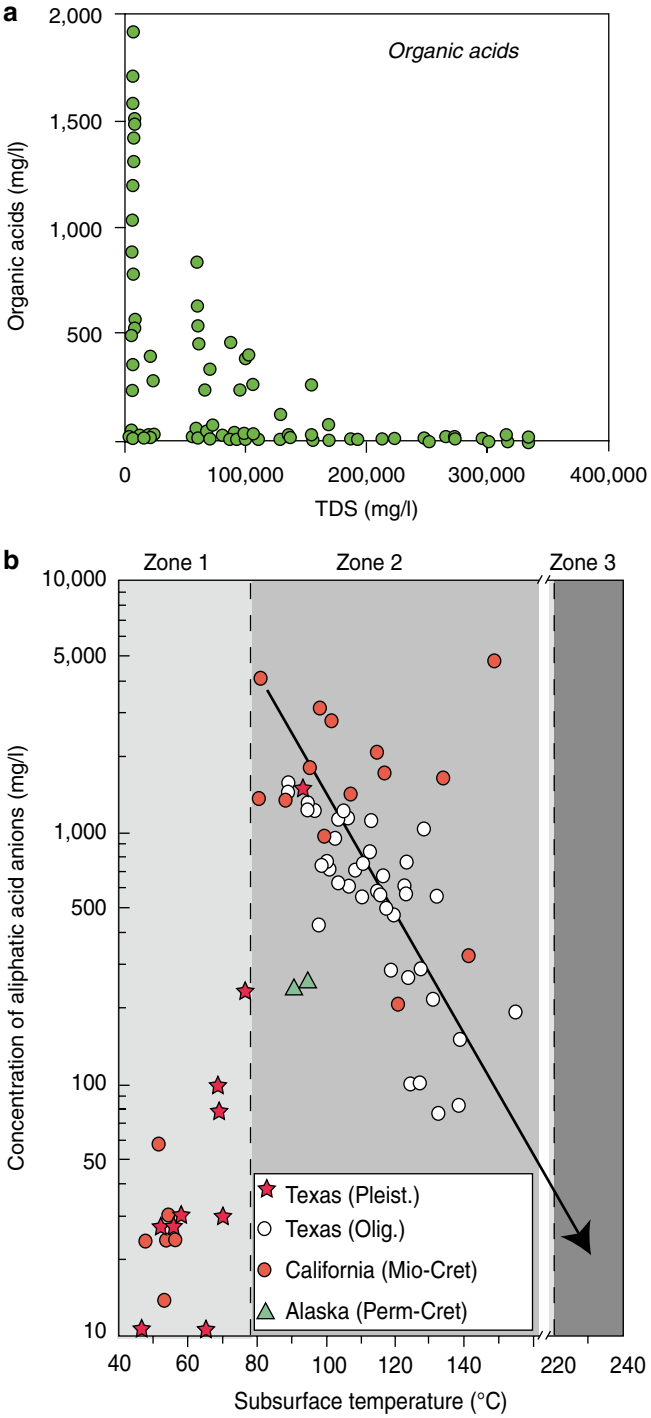

Fig. 15.5 Organics in basinal brines. (**a**) Organic acids in saline brines (After Hanor 1994a, b). (**b**) Concentrations of aliphatic acid anions (C_2–C_5) in formation waters from three sedimentary basins typified by moderate salinities. The highest concentrations are at 80–120 °C and then decrease with increasing temperatures, as indicated by *arrow*, note the scale break at 160 °C (After Kharaka and Hanor 2003)

metal transport as chloride complexes in high salinity brines was highly likely at some stage in the diagenetic history of the basin. Modern basinal pore brines, located near dissolving evaporites, are chloride-rich, somewhat acidic and in some settings, slightly oxidising. They can carry elevated levels of metals as they become more saline, and so act as potential metal "leachers and carriers" in the subsurface hydrology. In order to qualify as a potential ore carrying fluid, a basinal fluid must contain on the order of 1 mg/l or more of the dissolved metal in question (Eugster 1989; Hanor 1994a, b). Most basinal brines that achieve Pb, Zn or Cu values at or above this level have pore salinities that are typically in excess of 200,000 mg/l, with their entrained base metals carried as chloride complexes (Fig. 15.6a). These saline waters also tend to be acidic and have lower levels of organic acids when compared to their less saline counterparts (Fig. 15.5a).

Sediments as Metal Sources

Much of the base metal content, including copper, in low temperature ore deposits in sedimentary basins has an intrabasinal nonmagmatic source. Some researchers propose that the metals in basinal brines are derived either from the alteration and leaching of feldspars and clays that supply most of the iron, lead, barium and strontium, or from the alteration of carbonates to supply most of the zinc (Land and Prezbindowski 1981; Sverjensky 1986; Kharaka et al. 1987). Others workers conclude that leaching of iron-oxide-hydroxides from a redbed parent can source many metals (Carpenter et al. 1974). When incorporated as detritus in first-cycle redbeds, copper-rich mafic rocks such as basalt, or copper-rich mafic minerals (such as hornblende, pyroxene, biotite, oxides and sulphides) in felsic rocks, are ideal copper sources (Fig. 15.7; Kirkham 1989; Brown 2005, 2006). Flushing of metals sequestered into organic-rich evaporitic mudstones are yet another possible source for base-metals (Table 15.3).

Dissolving evaporite beds themselves have also been evoked as possible metal sources. Thiede and Cameron (1978) argued that Cu remains in solution during the initial evaporation process; whereas Pb and Zn enter solid precipitates, such as gypsum and anhydrite. Later dissolution of such evaporites generates a metal source enriched in Pb and Zn and depleted in Cu. More recent models have proposed it is not the evaporites, but the residual bitterns, that have sank (refluxed) into underlying and adjacent sediments, which act as the source of metals in diagenetic-realm base-metal accumulations for lead and zinc in MVT style deposits; for example, in Ireland and Arkansas, (Wilkinson et al. 2009; Kendrick et al. 2011).

Sverjensky (1989) further refined earlier brine transport models by demonstrating that significant water-rock interaction takes place as warm, subsurface chloride-rich brines traverse and interact with various deep aquifers. He concluded that, depending on the dominant lithology of the aquifer traversed by the chloride-rich brines, a single highly saline

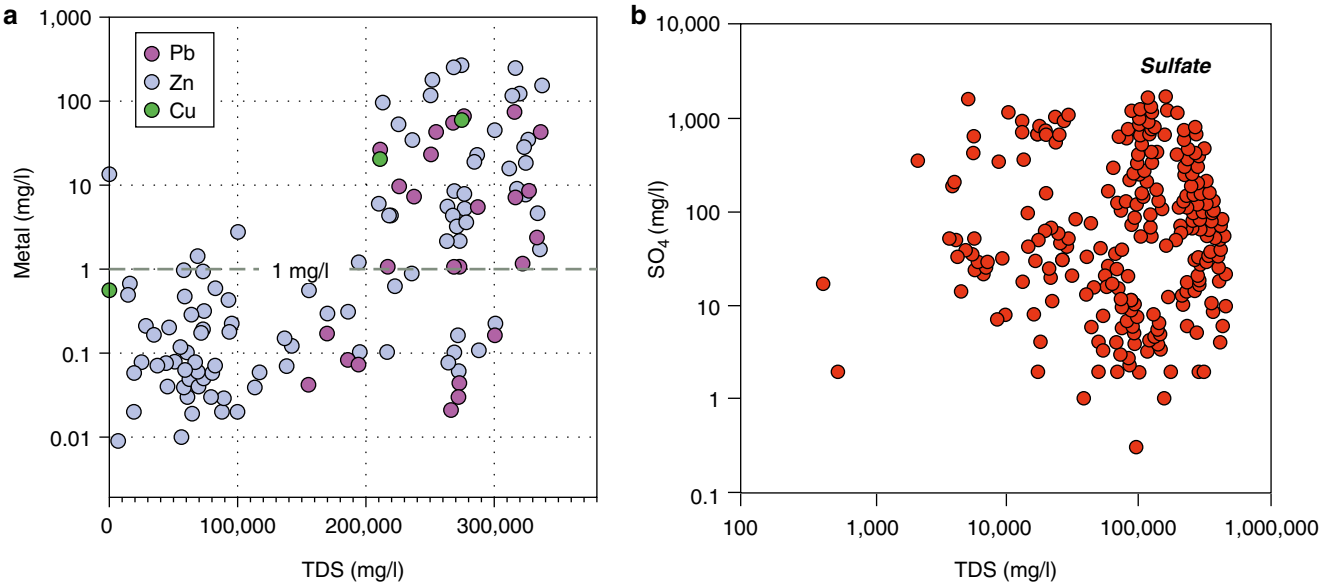

Fig. 15.6 Components of high-salinity basinal brines (After Hanor 1994a, b). (**a**) Metal content of subsurface waters showing elevated metal contents (>1 mg/l) in more saline (chloride-rich) pore waters. (**b**) Sulphate as a function of salinity

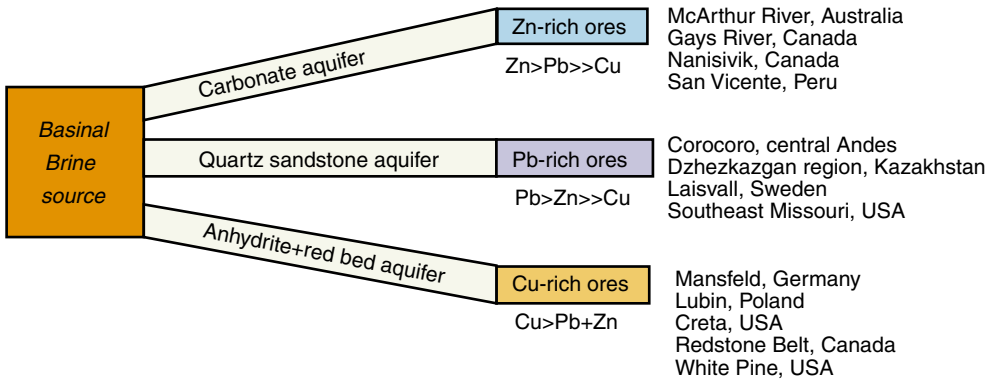

Fig. 15.7 Influence of flushed matrix mineralogy on the base metal precipitated (After Sverjensky 1989)

basinal brine may evolve chemically to become the ore-forming fluid for a wide range of sediment-hosted base-metal sulphide deposits. Migration through carbonate, quartz sandstone, or anhydrite + redbed aquifers could result in the formation of Zn-, Pb-, or Cu-rich deposits, respectively (Fig. 15.7).

As a starting point he considered a typical chloride-enriched basinal brine that was initially saturated with galena, chalcopyrite, muscovite, kaolinite and quartz, but undersaturated with respect to sphalerite, with up to 1 mg/l Pb, 0.1 mg/l Cu and 5 mg/l Zn. Passage of this fluid through a carbonate-cemented aquifer produces a metalliferous brine characterised by high Zn/Pb and (Zn + Pb)/Cu ratios. Transport of the same fluids through a quartz-cemented sandstone exhausts the buffering capacity of the aquifer relatively quickly, so that any mineral accumulations precipitated from the resulting waters are galena-rich. Maintenance of the oxidation state in a typical basinal brine near the hematite-magnetite buffer prevents copper mobilisation (solubility of Cu in a typical basinal brine is ≈ 0.07 mg/l).

Geochemical sampling by Wilde et al. (2005b) in the Canning Basin of West Australia confirms the theory outlined by Sverjensky (1989). Lead isotope and permeability/porosity data indicate that Carboniferous and Devonian feldspar-rich sandstones and siltstones are the most likely reservoirs for ore-forming brines and metals in the various Pb-Zn deposits of the eastern Canning Basin. The Anderson Formation and Tandalgoo Sandstone are characterized by extreme depletion in Pb and Zn relative to Cu (Fig. 15.8). Conversely, limestones and dolomites in the Devonian and Carboniferous rift-fill are enriched in Pb and Zn relative to Cu. This enrichment, is interpreted as due to hydrothermal circulation of chloride-rich waters derived from deep dissolution of the Mallowa salt mass. If so, it explains the numerous MVT deposits hosted in carbonate rocks of the eastern margin of this Carboniferous-Devonian rift-fill.

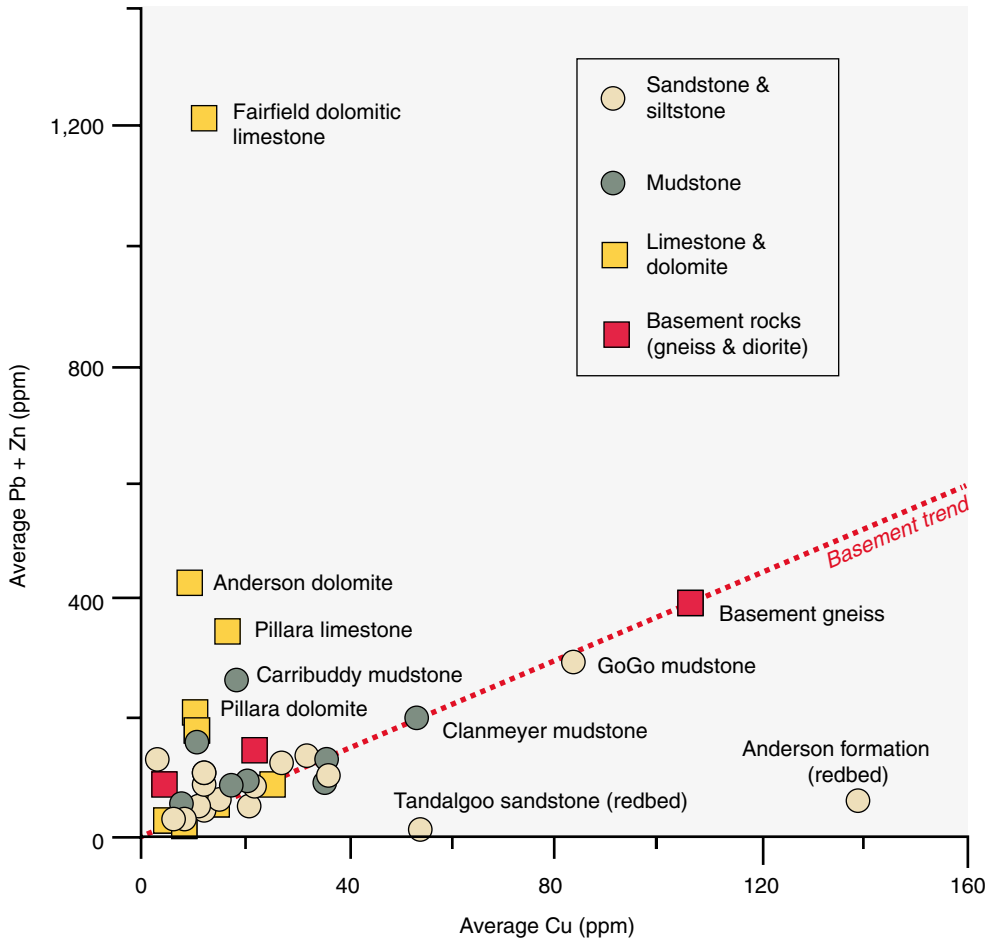

Fig. 15.8 Average base metal concentrations in various stratigraphic units of the Fitzroy Trough and Lennard Shelf in the Canning Basin, Australia (Wilde et al. 2005b)

In a variation on the same theme of metalliferous saline brines tied to leached sediments, and the corollary that magmatic heat may enhance convective circulation of basinal brines, but not supply the metals in some paramagmatic sediment-hosted ore deposits, Tornos and Heinrich (2008) have shown that shales interacting with highly saline chloride-rich basinal brines are the main suppliers of metals to the massive sulphide deposits of the Iberian Pyrite Belt (Fig. 15.9). Historically, these deposits were interpreted as volcanogenic-hosted massive sulphide (VHMS) deposits, and related to hydrothermal oceanic-rift analogs, such as the Tag Mound or the massive sulphides of Cyprus, where the metals have a magmatic source. But veinstyle deposits and other indicators of magmatically-sourced fluids, typically associated with this style of VHMS deposit, are largely lacking in the massive sulphides of the Iberian pyrite belt. Tornos and Heinrich (2008) argue that the deposit hydrology and textural/geochemical signature is more akin to that of the Sullivan and McArthur River styles of ore deposit. There, brine pools tied to focused upwelling and venting of hypersaline basinal waters into closed depressions on deep seafloor were the driving mechanisms creating the SedEx deposits.

Mildly reducing redox conditions, imposed by equilibration with a muddy metal source was most critical factor in the formation of such an effective ore-forming fluid system (Fig. 15.9). Relatively metal-rich, but organic-poor, pyrite-bearing shales, undergoing dewatering and interaction with hypersaline saline pore fluids created an effective source for the generation of sulphur-deficient, but relatively iron and base metal-rich, chloride brines (Fig. 15.9a). When temperatures are in excess of 330–340 °C, even copper becomes highly mobile in high salinity subsurface waters passing through compacting shales (Fig. 15.9a and Chap. 16). Thus, Tornos and Heinrich (2008) proposed that the giant deposits of the Iberian Pyrite Belt owe their existence not to exceptionally metal-enriched magmatic fluids, but to the existence of a fairly ordinary, but volumetrically large (with depletion ratio of 1:200), metal source in these reactive fine-grained (high grain-surface areas) siliciclastic sediments, flushed by chloride-rich evaporite-dissolution-derived basinal brines. The convective fluid flow system may be tied to an underlying igneous heat source driving the regional fluid flow, but ore focusing and metal transport is more dependent on a particularly efficient mechanism of sulphide precipitation, driven by mixing and reduction of the metalliferous brine

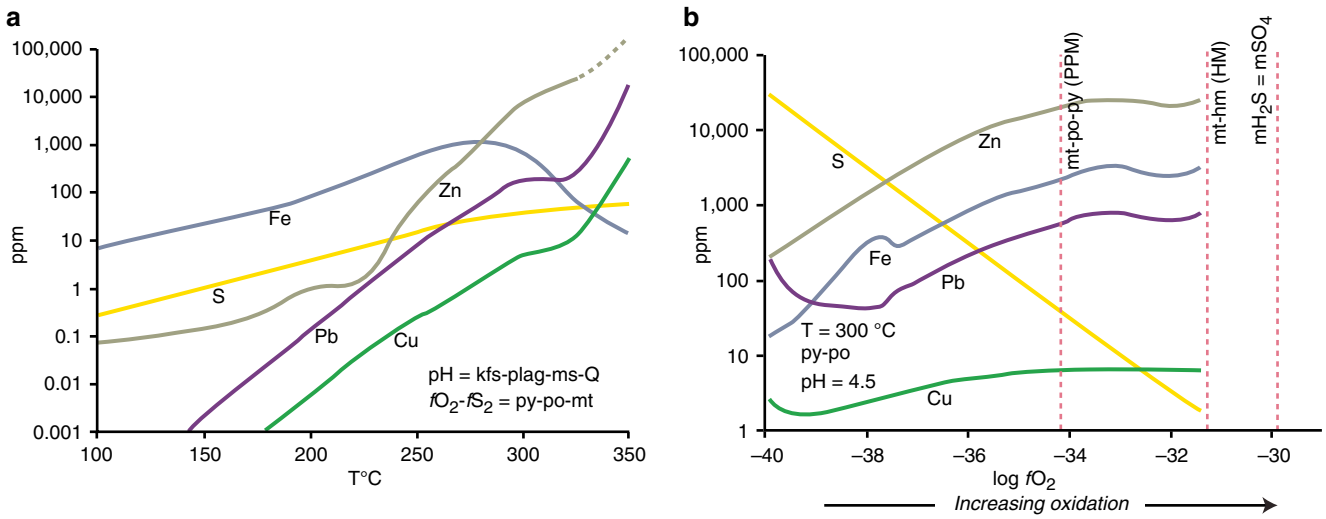

Fig. 15.9 Metal solubility and fixation in shale as related to sulphur presence (After Tornos and Heinrich 2008). (**a**) Base metal and sulphur solubility as a function of temperature between 350 and 100 °C at a pH buffered by the mineral assemblage observed in shales, for a total salinity of 9 wt.% NaCl equivalent and the fO_2 –fS_2 conditions defined by the pyrite–pyrrhotite– magnetite equilibria. Base metal solubilities are calculated in equilibrium with excess sphalerite, galena and chalcopyrite. Mineral abbreviations are; *hm* hematite, *mt* magnetite, *py* pyrite, *po* pyrrhotite, *kfs* K feldspar, *plag* plagioclase, *Ms* muscovite, *Q* quartz. (**b**) Reduced sulphur (*S*) and metal solubility in a shale-buffered reservoir at 300 °C showing the strong dependence on the redox conditions. Calculations performed at a constant pH of 4.5 and the fS_2 controlled by the pyrite–pyrrhotite equilibrium. The H_2S:SO_4 boundary is that defined by equal molalities of reduced and oxidized sulphur species

with H_2S-rich fluids at or near the seafloor (Fig. 15.9b; see later SedEx discussion). We shall come back to this notion of chloride-rich basinal brines transporting and fixing metals a number of times in this chapter, as we develop arguments in support of dissolving salt masses aiding in the focusing and trapping of brines and their outflows.

Similar redox-controlled mineral equilibria are imposed when saline chloride-enriched basinal fluids are buffered by typical continental basement rocks (Fig. 15.7). This is how copper can be mobilised and leached from the sediment, along with Pb and Zn. At redox conditions near and above the hematite–magnetite buffer, sulphate becomes the main sulphur species. This defines another diagenetic fluid environment proposed by Cooke et al. (2000) for base metal transport in sediment-hosted deposits overlying oxidized sequences, as at McArthur River (Australia). Leaching of retrograde minerals and possibly residual salts from a magmatic or metamorphic protolith are expected to generate similar, variably metal-rich, but relatively sulphide-deficient, fluids. Thus, according to Tornos and Heinrich (2008) the existence of mildly-reducing saline sedimentary brines in sedimentary hosts, not magmatic waters, can be the dominant chemical control in sourcing metalliferous fluids linked to many volcanogenic, Irish-type or SedEx deposits. Many of these brine-related deposits are known to precipitate their metal load in response to biogenic or thermochemical sulphide addition at the ore deposition site. Typically this took place within depressions on seafloor with their downslope precipitative positions maintained by a combination of extension, gravity gliding and halokinesis, and sometimes by more updip via interaction with bedded platform anhydrites.

At the contact of an evaporitic sedimentary basin with its underlying basement, dense chloride brines derived from dissolution and reflux beneath thick salts can leach metals from the underlying basement and then convectively transport them into a metal-fixing redox front. Such brines leach a variety of metals from underlying igneous and metamorphic rocks and worldwide are responsible for a number of large unconformity-associated uranium deposits and SedEx deposits (Fusswinkel et al. 2013; Wilkinson et al. 2009; Boiron et al. 2010; Koziy et al. 2009).

Carrier Brines (Eh, pH and Chlorinity/Salinity)

Numerous experimental studies have shown that chloride complexes are effective ligands for Zn and Pb in low temperature basinal brines. Bisulphide and organic complexes are less effective, particularly in moderate to highly saline pore fluids in sediments in the presence of abundant Na and Ca (Giordano 1985; Barrett and Anderson 1988; Sicree and Barnes 1996). The presence of reduced sulphur in MVT and other basinal brines (typically a H_2S association) greatly reduces the solubility of chloride-complexed Pb and Zn (Fig. 15.10b and Table 15.5; compare Pb and Zn contents with respect to ΣH_2S in brines 1 and 3). Hence, the widely accepted model for formation of MVT deposits via saline basinal brines transporting metals to local areas containing reduced sulphur where the metals are fixed as solid metal sulphide phases (Anderson 1983; Anderson and Macqueen 1988).

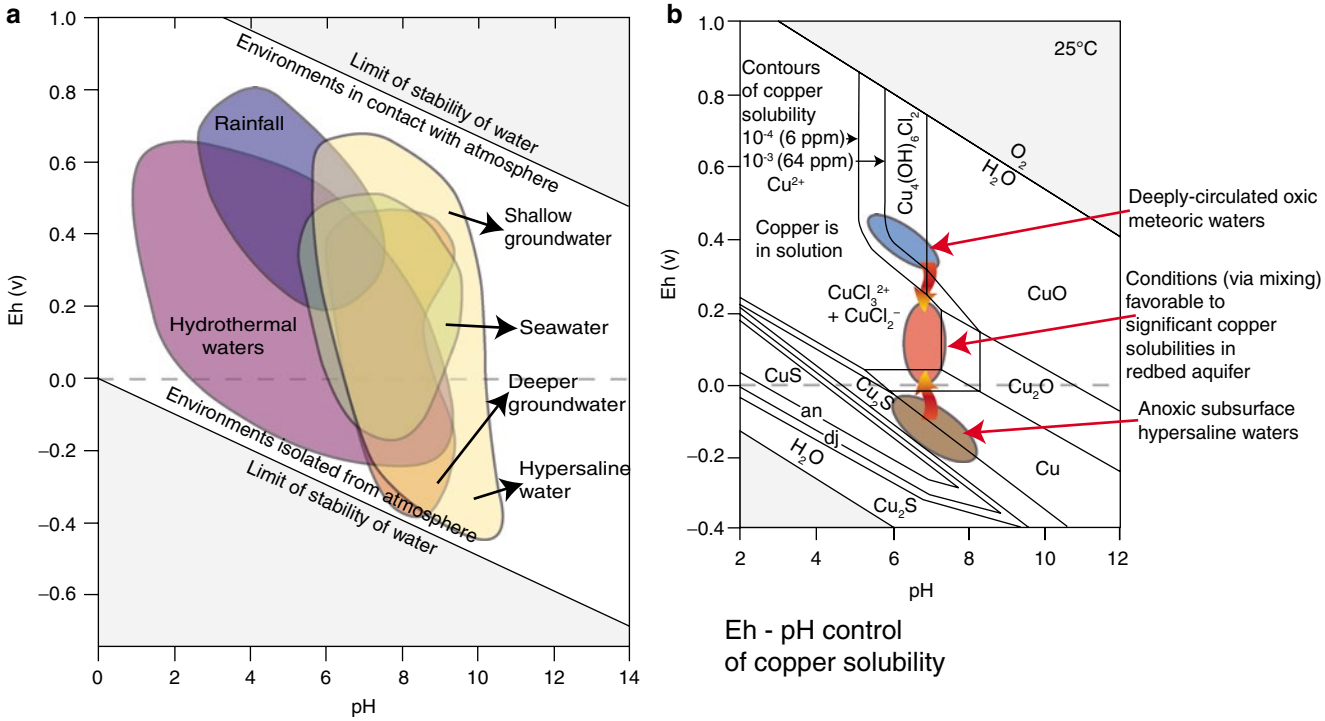

Fig. 15.10 Redox and copper solubility. (**a**) Eh-pH diagram with occurrence fields of various surface and subsurface waters plotted. (**b**) Solubility of copper as cuprous chloride complexes in a low-temperature brine, showing how a Cu-transporting brine(slightly oxidising and neutral pH) in a redbed succession is in part created by mixing of deeply circulating oxygenated meteoric and anoxic saline subsurface waters (In part after Rose 1976; Brown 2006). *CuS* covellite, *Cu_2S* chalcocite, *Cu* copper, *Cu_2O* cuprite, *CuO* tenorite, *$Cu_4(OH)_6Cl_2$* malachite

In terms of potential Pb and Zn carriers, there are three main types of basin brine in today's sedimentary basin, only one carrier has elevated levels of Pb and Zn (Table 15.5; Giordano 2003). The table shows the specific inorganic and organic fluid parameters that influence the concentration of Pb and Zn in these subsurface waters. Modern oilfield brines are bimodal in terms of total reduced sulphur content (ΣH_2S). Low H_2S brines have ΣH_2S values less than 1.0 mg/l, with the majority showing values less than 0.02 mg/l and often showing values below the detection limit (Giodarno 2003 and references therein). Not all low H_2S chloride-rich brines carry elevated levels of Pb and Zn, only those that have passed through strata containing leachable levels of these base metals.

High H_2S brines have ΣH_2S concentrations greater than 1.0 mg/l, with the highest concentrations approaching 1,000 mg/l, especially in the vicinity of active fault conduits carrying these H_2S-rich waters (see Wade et al. 1989; Moldovanyi and Walter 1992). In high H_2S formation waters, the most commonly observed ΣH_2S values are in the 10–600 mg/l range (see also Chap. 9). Total sulphate concentrations in modern petroleum-field brines rarely exceed 1,000 mg/l and are more typically in the 0.1–250 mg/l range (Fig. 15.6b; Kharaka and Hanor 2003). There is no statistical correlation between the concentration of SO_4 and chlorinity or salinity, although there appears to be a broad inverse correlation between ΣH_2S and ΣSO_4, indicating a likely relation to subsurface sulphate reduction (Fig. 15.6b; Hanor 1994a, b).

The ability of chloride-rich basinal brines to become ore forming fluids, capable of carrying and precipitating Pb-Zn minerals, is well illustrated by the Na-Ca-Cl oil field brines in the Cheleken region of Turkmenistan (Lebedev 1972). These brines contain up to 10 mg/l Zn + Pb and deposit native lead, sphalerite, galena and pyrite in the well pipes and holding tanks at rates considered analogous to ore formation. Some Na-Ca-Cl oil field brines in Jurassic and Cretaceous formations in the Salt Dome Basin of central Mississippi, USA, have total dissolved solid contents up to 350,000 mg/l, densities that exceed 1.2 g/ml, and contain up to several hundred mg/l of Pb + Zn (Fig. 15.6a; Carpenter et al. 1974; Kharaka et al. 1987). Both these highly metalliferous brines systems occur in regions underlain by thick dissolving evaporites with dissolution plumes moving through adjacent metal-carrying sediments (Chap. 8).

Similarly, sphalerite and galena scale is forming today in the pipes of producing geothermal wells in the Asal Rift in the Republic of Djibouti, Africa (D'Amore et al. 1998). Sulphide precipitation starts at the flash level (where hot pressurised water converts to steam), located at 850 m depth where temperatures are close to 260 °C, and extends deeper into the main reservoir. The main geothermal reservoir is located at depths

between 1,000 and 1,300 m with temperatures between 260 and 360 °C. Seawater seepage, with additional ionic input from dissolving salt beds, is the main source for the chloride-rich metalliferous brines in the field. As a result of sulphide precipitation, about 90 % of H_2S is removed from the original fluid before it is discharged at the surface. Brines produced in the Asal thermal field all have salinities in excess of 100,000 ppm, with a low gas content of the order of 0.6 mmol/mol.

If the subsurface brine migrates though a red bed succession that contains hematite and/or anhydrite, the oxidation state and the SO_4^{2-}/H_2S ratio of the fluid is increased by mixing of oxygenated groundwaters and anoxic brines and by reactions such as:

$$CaSO_4 = Ca^{++} + SO_4^{2-}$$

$$4Fe_2O_3 + H_2S + 14H^+ = 8Fe_2^{+} + SO_4^{2-} + 8H_2O$$

The migration of this moderately oxidising saline fluid through a red bed can then scavenge the necessary Cu, Zn and Pb to form a mineralising fluid with elevated Cu content where Cu > Pb + Zn (Fig. 15.10; see also Rose 1976; Brown 2006). Redox conditions of $\log f_{O2} > -46$ at 125 °C are necessary in the brine to mobilise copper as cuprous chloride complexes (see Rose 1976 for relevant discussion). This explains the common association of copper sulphides with redox haloes adjacent to leached redbeds in evaporitic basins (see later).

So far, we have discussed slightly-acidic metal-rich saline chloride brines. However, high salinity in a subsurface water, by itself, does not guarantee a high dissolved metal content, nor are metals always carried in the subsurface as chloride complexes in saline acidic brines. A large number of saline basinal brines and formation waters are low in metals and high in dissolved sulphides (Table 15.5). Figure 15.6a clearly shows that many highly saline subsurface waters in sedimentary basins worldwide contain <1 ppm metal. Such waters become metal-rich and sulphide-poor only when they flush germane metalliferous sediment, such as redbeds, metal-rich shales or hydrothermally altered basalts (Ellis 1968; Coveney 1989). Metal leaching and chloride transport from such metal sources involves desorption of loosely bound metals, release of metals on mineral recrystallisation or replacement, or release of metals to the brine from metal-organic complexes through thermal alteration or thermal destruction of such complexes (Carpenter et al. 1974; Gize et al. 1991).

Acidification is an essential step in the acquisition of metals in brines during dissolution or alteration of aquifer minerals. Chloride-rich, high salinity basinal fluids may become acidified by pyrite oxidation, by decomposition of organic matter, or by the precipitation of Mg silicates, such as smectite or chlorite. Organic acids may also play an important role in leaching the metals from metalliferous source beds (Raiswell and Al-Biatty 1992). In contrast, Eugster (1985, 1989) argued that not all metalliferous brines are acidic. He notes that in a Green River style of ore deposit (a category in which Eugster includes the Mt Isa and Dugald River deposits of Australia) the brines were alkaline, with pH values of up to 11. If so, then metals were carried not as chloride complexes, but as hydroxy or carbonate-complexes. Such non-chloride waters are generated today in saline continental rift lakes where sodium bicarbonate evaporites dominate, there is no primary gypsum, and the lake evolves by the evaporation of source waters that drain adjacent basic igneous or metamorphic terranes (see Chaps. 2 and 3 for a discussion of nonmarine brine evolution).

So far this discussion is largely theoretical or based on analogy with modern basinal and oil field brines. But with improvements in microsampling and laser-ablation inductively-coupled plasma mass spectrometry techniques it has become possible to study the hydrogeochemistry of metal precipitating brines by analysing the chemical makeup of individual brine inclusions in zoned quartz and sphalerite crystals and so map the evolution of the metal reprecipitating brines (Wilkinson et al. 2009; Fusswinkel et al. 2013). A study of fluid inclusions in sphalerite and a comparison with co-associate inclusions in quartz crystals from two geographically separate Pb-Zn MVT deposits in Ireland and Arkansas showed that the metal contents of the sphalerite are up to two orders of magnitude higher than associated quartz (Fig. 15.11). The difference between sphalerite and associated quartz is much higher than previously thought and strongly suggests ore formation is linked to an influx of anomalously metal-rich fluids into subsurface systems, dominated by basinal fluids that are otherwise barren of metals. It could be argued that the fluid inclusions in quartz represent spent ore fluids, trapped after sulphide precipitation had already taken place. This is thought to be unlikely in the Irish deposits because the quartz was sampled from largely barren vein systems that formed beneath the ore deposits, in hydrothermal upflow zones, and the fluids show no signs of having substantially cooled or mixed (Wilkinson et al. 2009). A metal-pulse model for ore fluids has now been shown to be true of MVT deposits based on inclusion chemistry at the microscale, rather than just inferred, as was done in many previous mineralisation transport models.

In the Tri-State MVT district, Wilkinson et al. (2009) found sphalerite- and quartz-hosted brine inclusions show distinct halogen signatures, indicating that the fluids had separate origins. Fertile ore fluids appear to have originated during strong evaporation of seawater at Earth's surface, before later burial and expulsion. This contrasts with the barren fluids that evolved from less strongly evaporated seawater. The metalliferous fluids were linked to the arid paleoclimate and the specific characteristics of the sedimentary aquifer within which they were trapped.

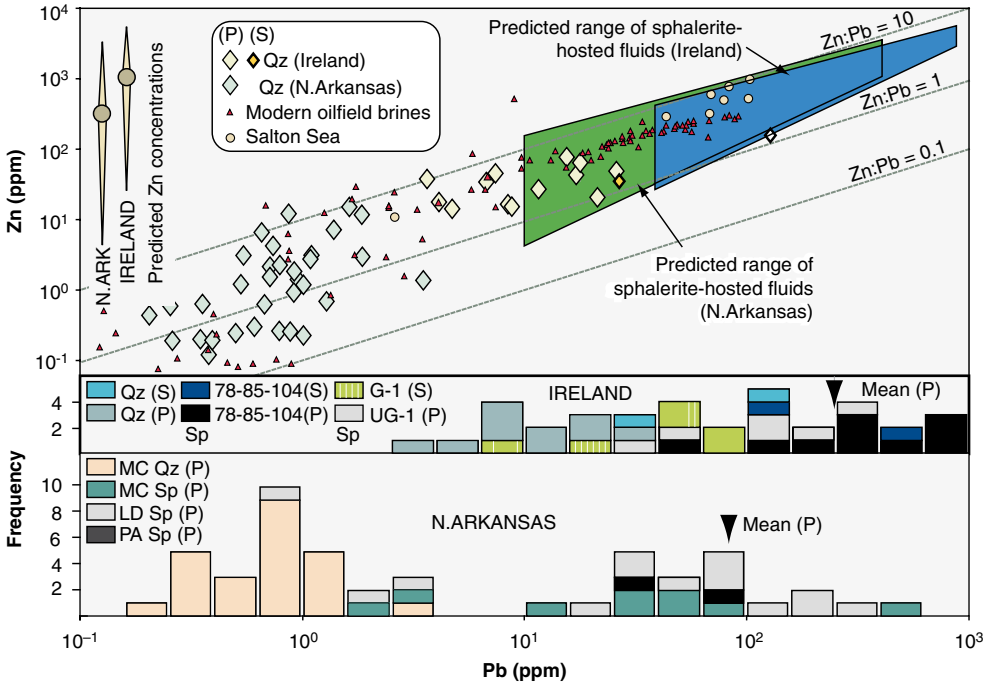

Fig. 15.11 Metals concentrations in natural subsurface waters (After Wilkinson et al. 2009). Concentrations of Zn versus Pb in quartz-hosted fluid inclusions and histograms showing measured Pb concentrations in quartz- and sphalerite-hosted inclusions from Irish and North Arkansas MVT deposits, compared with natural brine data from broadly analogous environments (subsurface Salton Sea and oilfield waters). Predicted Pb-Zn covariation for sphalerite-hosted inclusions indicated by shaded fields, based on the extrapolation of empirical Pb-Zn concentrations. All data sets have values that fall in the "high-metal" fluid fields, suggesting that they are anomalously metalliferous and indicative of viable ore-forming fluids. Typical Zn:Pb ratios (by mass) for natural fluids are in the range of 1–10 (*dashed grey lines*) are shown and all tend toward higher values at elevated concentrations. Also plotted are data points from the Northern Arkansas MVT dataset with low detected Pb are inferred secondary inclusions (S vs P for primary inclusions). *Qz* quartz, *Sp* sphalerite, Deposits plotted are *MC* Monte Cristo, *PA* Philadelphia, *LD* Lucky Dog

In a refinement of this halogen approach to the interpretation of the nature of ore fluids in quartz-fluorite-baryte-Pb-Zn vein system, Fusswinkel et al. (2013) concluded mineralisation can be related to the mixing of two evaporite-related brines (Fig. 15.12). Post-Variscan Mesozoic vein-type Pb-Zn mineralization is widespread in large parts of western and central Europe, including Variscan basement complexes of Germany, France, England, and Spain. In Germany, the vein-hosting crystalline basement is unconformably overlain by Permian and Lower Triassic redbed sedimentary rocks and Middle Triassic to Jurassic carbonates with intercalated claystones and evaporites. Utilising laser ablation analysis of inclusion trails in zoned vein quartz crystals they found evidence of two end-member hypersaline brines, one was metal rich, the other metal poor (Fig. 15.12a).

They determined simultaneously the ore metal concentrations and the Cl/Br ratio in texturally well constrained inclusion assemblages from this basement-hosted quartz-fluorite-baryte-Pb-Zn vein system. There is an inverse correlation between the Pb + Zn concentrations and the Na/Ca and Cl/Br mass ratios in the fluid inclusions, respectively (Fig. 15.12b, c). This is clear evidence of mixing of a basement-derived metal-rich hypersaline brine and a metal-poor formation brine that acquired its salinity from halite dissolution in Triassic evaporites of the sedimentary cover (high Cl/Br and Na/Ca ratios are indicative of brines derived from subsurface halite dissolution, see Chap. 8). This mixing of two distinct brines with comparable salinity is recorded during the growth of individual quartz crystals containing small galena inclusions, demonstrating the transient and episodic nature of fluid mixing during mineral deposition. Once again, this reinforces the observation of Wilkinson that at the microscale there is a pulsing of metal supply in an ore precipitating system in the diagenetic realm. It points to the importance of syndepositional metalliferous bitterns sinking into the underbelly sediments as salt successions precipitate in saline giant settings (the brine curtain – Chap. 5).

Metal Fixers

Metal transport-precipitation models breakdown into three end-members; (1) Mixing model, (2) Sulphate reduction model and, (3) Reduced sulphur model

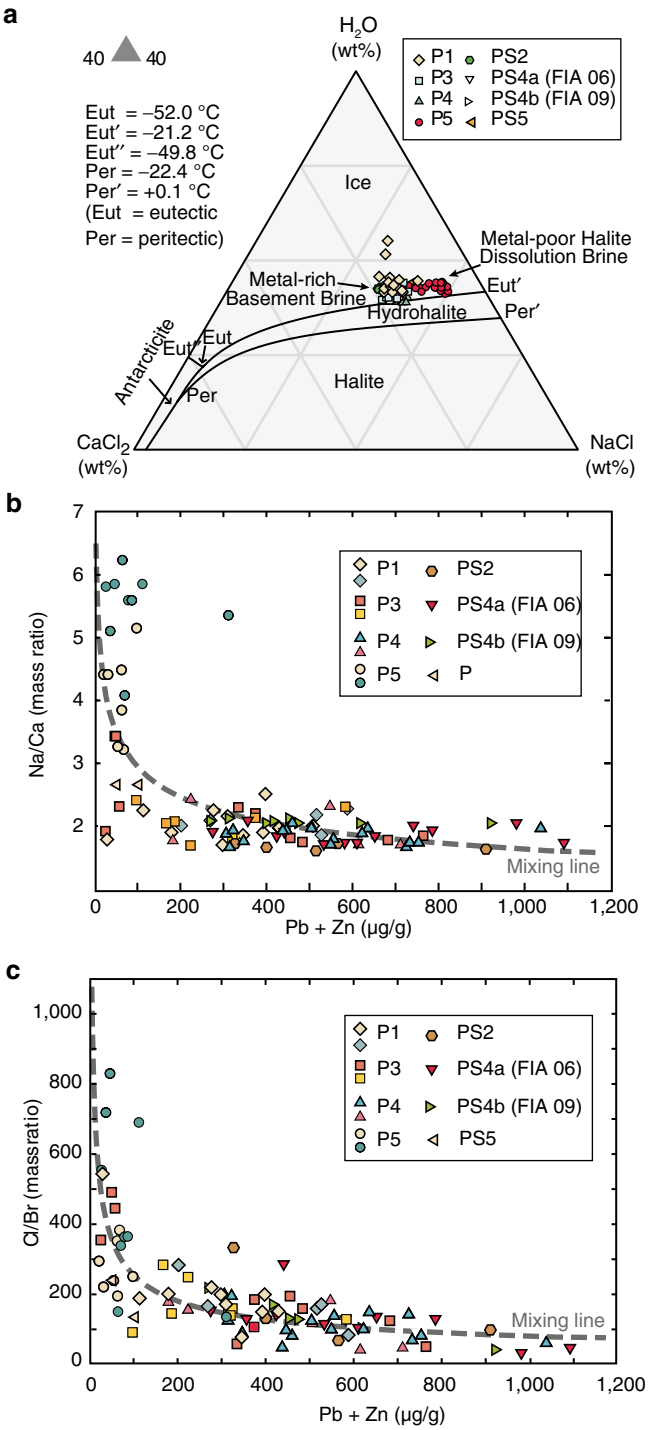

Fig. 15.12 Evaporite brine mixing creates metalliferous brines (After Fusswinkel et al. 2013). (**a**) Fluid composition in ternary H_2O-NaCl-$CaCl_2$ system as determined by microthermometry, showing close overlap of two brine end members (metal-rich and metal-poor) in terms of their major element composition. *P* primary, *PS* pseudosecondary, *FIA* fluid inclusion assemblage. (**b**) Microanalysis of single fluid inclusions shows close correlation between total base metal content (Pb+Zn) and Ca/Na ratio. *P* primary, *PS* pseudosecondary, *FIA* fluid inclusion assemblage. (**c**) Close correlation between Pb+Zn and Cl/Br ratio, resulting from mixing of two brines with similar total salinity (**a**). (**c**) Major variation of total metal content at constant Pb/Zn ratio reflects mixing of metal-bearing brine with metal-depleted fluid. Upper and lower paired symbol shapes denote laser ablation analyses performed with full and reduced element suites, respectively

Table 15.6 Widely accepted models for transportation and precipitation of base metals in low temperature (<250–300 °C) basin burial settings

Transportation of ore-forming constituents	Precipitation mechanisms
Mixing model Base metals transported by saline Cl-rich fluids without significant sulphur content	(i) Mixing with fluids containing H_2S (ii) Replacement of diagenetic iron sulphides (iii) Thermal degradation of organic compounds releasing sulphur (iv) Mixing of two hypersaline Cl-rich brines, one is metal-depleted the other is metal-rich
Sulphate reduction models Base metals transported together with sulphate in the same fluid	Reduction of sulphate by reactions with organic matter or hydrocarbons, especially methane (bacterial of thermogenic sulphate reduction)
Reduced sulphur model Base metals transported together with reduced sulphur in the same solutions	(i) Cooling (ii) Dilution (iii) Change in pH

(Sverjensky 1986; Table 15.6). According to the most commonly accepted mixing models, base metals are transported in one fluid and sulphide is transported separately in another fluid, while precipitation occurs where the two fluids mix (e.g. Anderson 1975; Beales and Jackson 1966). Related theories, encompassed by the mixing model, hypothesize that the source of reduced sulphur encountered at the precipitation site was in the form of H_2S, diagenetic iron disulphides, or sulphur associated with petroliferous materials. In the sulphate reduction model, base metals are transported in fluids along with sulphate, rather than sulphide, and precipitation is driven by a sulphate reduction reaction, whereby sulphate is reduced to sulphide, typically via oxidation of organic matter or methane (e.g. Anderson 1983; Powell and MacQueen 1984). According to the third model, the reduced-sulphur model, base metals and reduced sulphur are transported together in the same fluid, with precipitation driven by varying combinations of pH change, cooling, dilution (e.g. Helgeson 1970; Anderson 1973; Sverjensky 1989). All three precipitation interfaces in these models are typically tied to redox fronts and often relate also to pore water salinity/density mixing interfaces.

Copper minerals precipitated at a diagenetic redox front are predominantly Cu-sulphides (covellite (CuS), chalcocite (Cu_2S), chalcopyrite ($CuFeS_2$), and bornite (Cu_5FeS_4), depending on the concentration of ions in solution and Eh–pH conditions (Fig. 15.10a: Rose 1976; Wodzicki and Piestrzynski 1994; Brown 1997; Robb 2005; Asael et al. 2009). Subsequent reoxidation of the sulphides may lead to the formation of Cu(II) minerals, such as; malachite ($Cu_2(CO_3)(OH)_2$), paratacamite, ($Cu,Zn)_2(OH)_3Cl$), brochantite ($Cu_4(SO_4)(OH)_6$) and chrysocolla $(Cu,Al)_2H_2Si_2O_5(OH)_4{\cdot}n(H_2O)$. Typically, the formation of redox fronts is attributed to the interface between a fresh meteoric and a saline water mass (Fig. 15.10b). But as

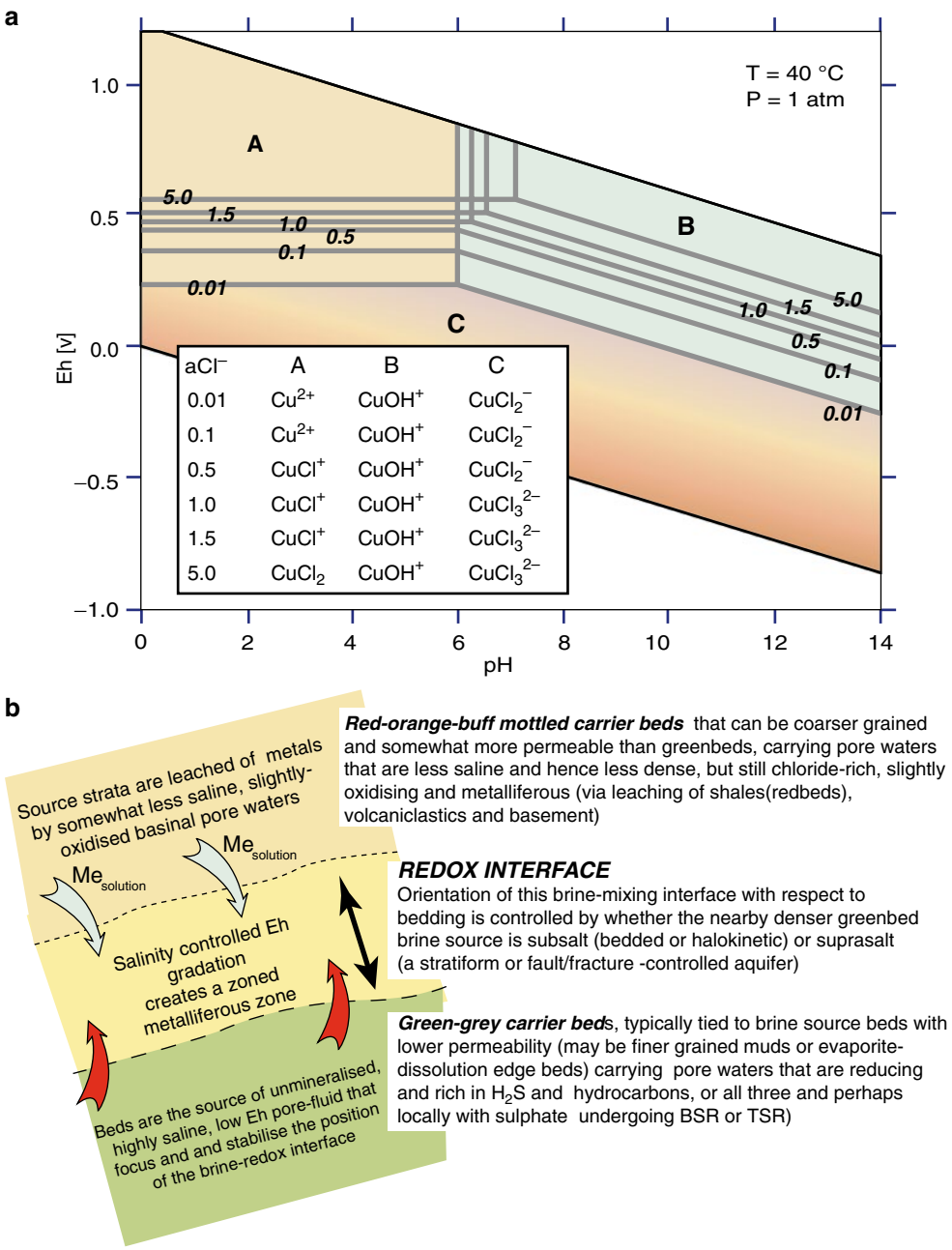

Fig. 15.13 Metal sulphide 'fixing' at redox interfaces (**a**) Eh–pH diagram showing the changes in the copper-chlorine speciation in solution and the position of the equi-concentration boundaries between the different copper complexes (ligands) at varying values of the chlorine activity aCl^- (After Asael et al. 2009). (**b**) Brine mixing between two saline water masses that are typical in the vicinity of buried and dissolving evaporites. One brine is less dense, metalliferous, somewhat acidic and slightly oxidising, the other somewhat more saline, denser, anoxic and likely carrying hydrocarbons and H_2S. (also does not destroy any organic matter in carrier beds as it is a "pickling" brine -Chap. 8)

the variations in the a, and c plot fields in Fig. 15.13a show, they can also be set up at interfaces between,; (1) dense highly saline reduced brine masses (in the immediate vicinity of a dissolving salt mass) and (2) an adjacent, still saline, but somewhat less so, chloride-dominant basinal brine that is also slightly oxidising and slightly acidic and capable of leaching copper. For example, compare the saline plot fields in Fig. 15.10b and their positions in 15.13a when aCl^- is in the range >4–5. This notion of dissolving evaporites contributing to the leaching, transport and fixing of copper sulphides is not new, aspects of it were detailed by Rose (1976).

Redox fronts and density-driven mixing interfaces in the shallow to deep subsurface are consistently located about the edge of dissolving salt beds and halokinetic salt masses, or the related brine plumes (Chap. 8). These interfaces play a significant role in localising and focusing metal precipitation in many evaporite-associated metal accumulations (Fig. 15.13b). For example, the inherent highly saline and reducing conditions adjacent to and beneath a salt bed, salt structure or an at-surface brine pool are created by the high salinity of the pore fluids in the vicinity of an evaporite unit and the likely co-occurrence of elevated levels of organics (Chap. 9). Further away from the dissolving salt mass the pore waters are typically still saline, although in some cases can be lower salinity waters, that are somewhat more acid and slightly oxidising (e.g. Fig. 15.13b). Thus, the conditions suitable for the fixing of metal sulphides in zones of mixing between the two water masses, where redox interfaces form,

can be present from the time of deposition of the sedimentary host through to the metamorphic realm. This dissolution/density style of redox front precipitation is relevant to most sediment-hosted ore deposits found in evaporitic basins and encompasses formative mechanisms in stratiform Mississippi Valley-type Pb-Zn, redbed-related base metal, and salt allochthon related base metal accumulations.

Redox fronts are typically indicated by a greenbed-redbed halo (reduced-oxidised iron) adjacent to a dissolving salt bed or its dissolution breccia. When such a redox interface is set up, between a reduced brine halo and slightly more oxygenated and acidic set of somewhat less saline basinal waters, it creates redox conditions suitable for base metal precipitation (Fig. 15.13b). For example, the reflux underbelly and edges of dissolving sequences of bedded or halokinetic salt masses tend to focus and deflect the escape of basinal or meteoric water along the underside or the feather-edge of a dissolving evaporite (see Rote Faule discussion in next section). At the same time, ongoing dissolution maintains a stable and continually renewed source of reduced anoxic brine, a near salt edge situation which survives as a relatively stable interface until the evaporite bed is leached or breached. Ongoing halokinesis, which tends to maintain salt supply over longer time frames than a dissolving salt bed edge, can further stabilise the long term position of the dissolution front in earth-space. Dissolving BSR- or TSR- sulphate evaporite sites, pyrite, or hydrocarbons on the reducing side of such redox fronts are possible sources of sulphur.

In this context it is important to note that redox fronts are not unique to evaporite dissolution zones. But what is unusual about subsurface evaporite-dissolution zones in terms of any associated mineralised redox zones is the long term chemical stability it maintains. Even as evaporites are precipitating, they are associated with a bittern or reflux underbelly that can persists for long periods, long after salt deposition has ceased (Chap. 8). And, once buried, the dissolving salt edge of a thick halokinetic salt bed or mass can maintain a redox interface in subsurface earth space over long time intervals, via replenishment from inflowing salt. Likewise, the same salt flow can maintain seismically-pumped suprasalt extension faults. At the same time, away from the salt edge or touchdown weld, dissolution of the underbelly of the salt mass aides circulation and high chloride content in density-driven convective brine flows (Fig. 8.18). Salt-floored extensional faults passing out into the upper side of a salt mass can also act as conduits for significant volumes of dense anoxic brine that also supply seafloor brine lakes or sumps (DHAL). The sump positions are stabilised by their location atop salt withdrawal sinks and so create stable seafloor positions for the formation of the laminites that constitute the prepared ground for many SedEx deposits.

In my opinion, this stabilization of the redox/mixing front may explain why, worldwide, in a plethora of subeconomic to small scale examples of redox-related Cu-segregations and small-scale Pb-Zn associations, almost all giant stratiform redbed copper and Pb-Zn deposits can be tied to structures with current, or former, evaporite-induced redox interfaces, typically located near or adjacent to present or past halokinetic salt masses. Brines from dissolving evaporites are not the source and, sometimes, not even the carriers of metals. Rather, dissolving evaporite masses are the stabilisers, both geographically and chemically, for the chemical/density subsurface interfaces that precipitate the various metals and/or act as hydrological termination sites to carriers of sulphur to the precipitation site.

Low Temperature Sediment-Hosted Ore Deposits (Evaporite-Related)

Work over the past four decades has shown many sediment-hosted stratiform copper deposits are closely associated with evaporites, or indicators of former evaporites, as are a number of SedEx and MVT deposits (Fig. 15.1). Some ore deposits discussed in this chapter still retain the actual salts responsible for the association, especially gypsum or anhydrite relics, in close proximity to the ore. Such deposits include the Zambian and Redstone copperbelts, Creta, Boleo, Corocoro, Dzhezkazgan, Kupferschiefer (Lubin and Mansfeld regions), Largentière and the Mt Isa copper association. All these accumulations of metals are associated with the formation of a burial diagenetic redox/ mixing front, where either copper or Pb-Zn sulphides tended to accumulate (Fig. 15.14).

However, examples discussed in detail in the remainder of the chapter and the resulting classification of low-temperature base metal associations is not inclusive of all styles of base metal associations in stratiform sediment-hosted Cu, SedEx and MVT settings. It only considers examples where a tie to evaporites and associated brine fluid sourcing or focusing is obvious (Table 15.2).

One of the metalliferous deposits with an obvious tie to evaporites is the modern metalliferous deep of the Red Sea, focused on the Atlantis II Deep. It is a modern example of a metalliferous laminite forming in a brine lake sump on the deep seafloor where the brine lake and the stabilisation of the precipitation interface is a result of dissolution of adjacent halokinetic salt masses. Most workers classify the metalliferous Red Sea deeps as SedEx deposits, but the low levels of lead and high levels of copper, along with its stratigraphic position atop seafloor basalts, place it outside the usual Pb-Zn dominant system that typifies SedEx deposits. Some economic geologists use the Atlantis Deeps as analogs for volcanic massive sulphides and some argue it even illustrates aspects of some stratiform Cu accumulations. Many such economic geology studies have a propensity to ignore the elephant in the room, that is the Red Sea deeps are the result

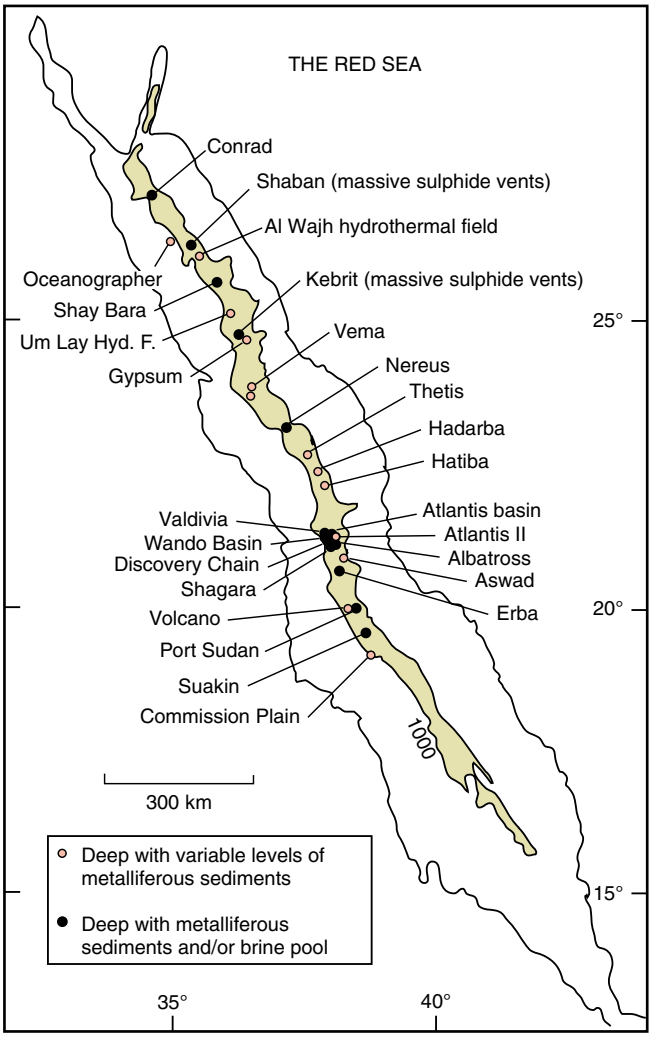

Fig. 15.14 Locality map of deeps along the Red Sea showing different characteristics, metalliferous versus brine (In part after Blum and Puchelt 1991)

of a large Tertiary-age halokinetically plumbed seafloor brine association.

In my mind what is most important about the brine lakes on the deep seafloor of the Red Sea is the fact that they exist with such large lateral extents only because of dissolution of the hosting halokinetic slope salt mass. Seismic surveys conducted in the past decade in the Red Sea show extensive salt flows (submarine salt glaciers) along the whole of the Red Sea Rift (at least from 19 to 23°N; Augustin et al. 2014). In places, these salt sheets flow into and completely blanket the axial region of the rift. Where not covered by namakiers, the seafloor comprises volcanic terrain characteristic of a mid-ocean spreading axis. In the salt-covered areas, evidence from bathymetry, volume-balance of the saltflows, and geophysical data all seems to support the conclusion that the sub-salt basement is also basaltic in nature and represents oceanic crust (Augustin et al. 2014).

The variably metalliferous seafloor deeps or deepsea hypersaline anoxic lakes (DHAL) are part of a world association of DHALs that form in association with shallowly-buried dissolving salt masses. But, what makes the Red sea deeps unique is that they can host substantial amounts of metal sulphides. And, as Pierret et al. (2010) show, a Red Sea deep without the seafloor brine lake, is not significantly mineralised. It is the intersection of the DHAL setting with an active midocean ridge (ultimate metal source) that explains the size and extent of the Atlantis deposit. Its salt-dissolution related hydrology changes the typical mid-ocean massive-sulphide ridge deposit (with volumes usually around 300,000 and up to three million tonnes; Hannington et al. 2011) into a more stable brine-stratified bottom hydrology, which can fix metals over longer time and stability frames, so that the known sulphide accumulation in the Atlantis II Deep has a reserve that exceeds 90 million tonnes.

The Atlantis II deep offers an evaporite-specific exploration paradigm for large-scale ancient counterparts. Accordingly, we shall discuss modern metalliferous laminites in the Red Sea DHALs separately to other evaporite-associated Cu, Pb-Zn and U deposits described in this and the next chapter. I offer it as our first example of the importance of nearby dissolving evaporites in stabilising the mineralisation interface in this case in a region adjacent to a volcanogenic/rift/hydrothermal heat source.

Red Sea – Modern Metalliferous Brine Lake Laminite Beds

The Red Sea is a young intracratonic basin atop a region of the crust that is currently transitional from continental to oceanic rift. It contains a thick sequence of middle Miocene evaporites formed in the early stages of ongoing rifting that is separating the African and Arabian plates. This same rifting facilitates formation of new basaltic ocean floor below the axis of the growing rift basin (Ehrhardt et al. 2005). Beneath waters more than a kilometre deep, along the deep rift axis there are numerous brine pools and deeps, some of which are underlain by metalliferous sediments (Fig. 15.14; Blanc and Anschutz 1995; Blum and Puchelt 1991).

Economically, the most important brine pool is the Atlantis II Deep; other smaller deeps, with variable development of metalliferous muds and brine sumps, include; Commission Plain, Hatiba, Thetis, Nereus, Vema, Gypsum, Kebrit and Shaban Deeps (Fig. 15.14). Laminites of the Atlantis II Deep are highly metalliferous, while the Kebrit and Shaban deeps are of metalliferous interest in that fragments of massive sulphide from hydrothermal chimney sulphides were recovered in bottom grab samples (Blum and Puchelt 1991). All brine-filled deeps are located in depressions or brine sumps along the spreading axis, in the region

of the median valley. Most of these axial troughs and deeps are also located where transverse faults, inferred from bathymetric data, seismic, or from continuation of continental fracture lines, cross the median rift valley in regions that are also characterised by halokinetic Miocene salt. Not all deeps contain brine sumps and not all brine sumps overlie metalliferous laminites.

The Conrad Deep, one of the northernmost deeps, illustrates the plate tectonic transition from continental rift to open ocean seafloor and the transition to a passive margin. Seismic across the deep shows how new seafloor ridge basalts have interacted with and penetrated the halokinetic Miocene salt mass (Fig. 15.15; Ehrhardt et al. 2005). Likewise, the Thetis and Atlantis II deeps are intimately tied to halokinesis (Mitchell et al. 2010; Feldens et al. 2012). Of the three well-studied deeps or DHALs along the Red Sea axis, only Atlantis contains significant volumes of metalliferous laminites. Interestingly, where seismic is available it clearly shows diapiric salt, not basalt underlies the deeps (Fig. 15.15a). This is in marked contrast to the typical basalt-dominant understory interpetations that dominate older pre-seismic schematics in the economic geology literature (e.g., Fig. 5.16b).

Three conditions favour the formation of the brine-filled deeps: (1) The Red Sea is a narrow depression only 200 km wide, with water circulation to the south limited by a shallow subsea sill near the connection with the Indian Ocean. (2) The surrounding hot arid desert hinterland facilitates a low levels of clastic and nutrient input so clastic and pelagic accretion rate are very low along the axial part of the rift; this prevents clastic dilution of DAHL sediments and allows hydrothermal solutions and their precipitates to be important aspects of sedimentation in the deeps. Hydrothermal outflows are perhaps focused by transverse-fault damage zones interacting with mobile gravity glide salt masses to influence the topography of the seafloor and create hydrographically open or closed seafloor depressions. (3) Nearby dissolving halokinetic salt contributes huge volumes of chloride-dominant hydrothermal and basinal brine into the irregular bottom topography it creates (Ehrhardt et al. 2005; Mitchell et al. 2010; Feldens et al. 2012). Many deeps are filled by permanently-stagnant brine pools, derived either directly from the dissolution of nearby evaporites or overspill from adjacent brine pools. Others deeps, filled by episodic hydrothermal brine seeps, may have been intermittently influenced by

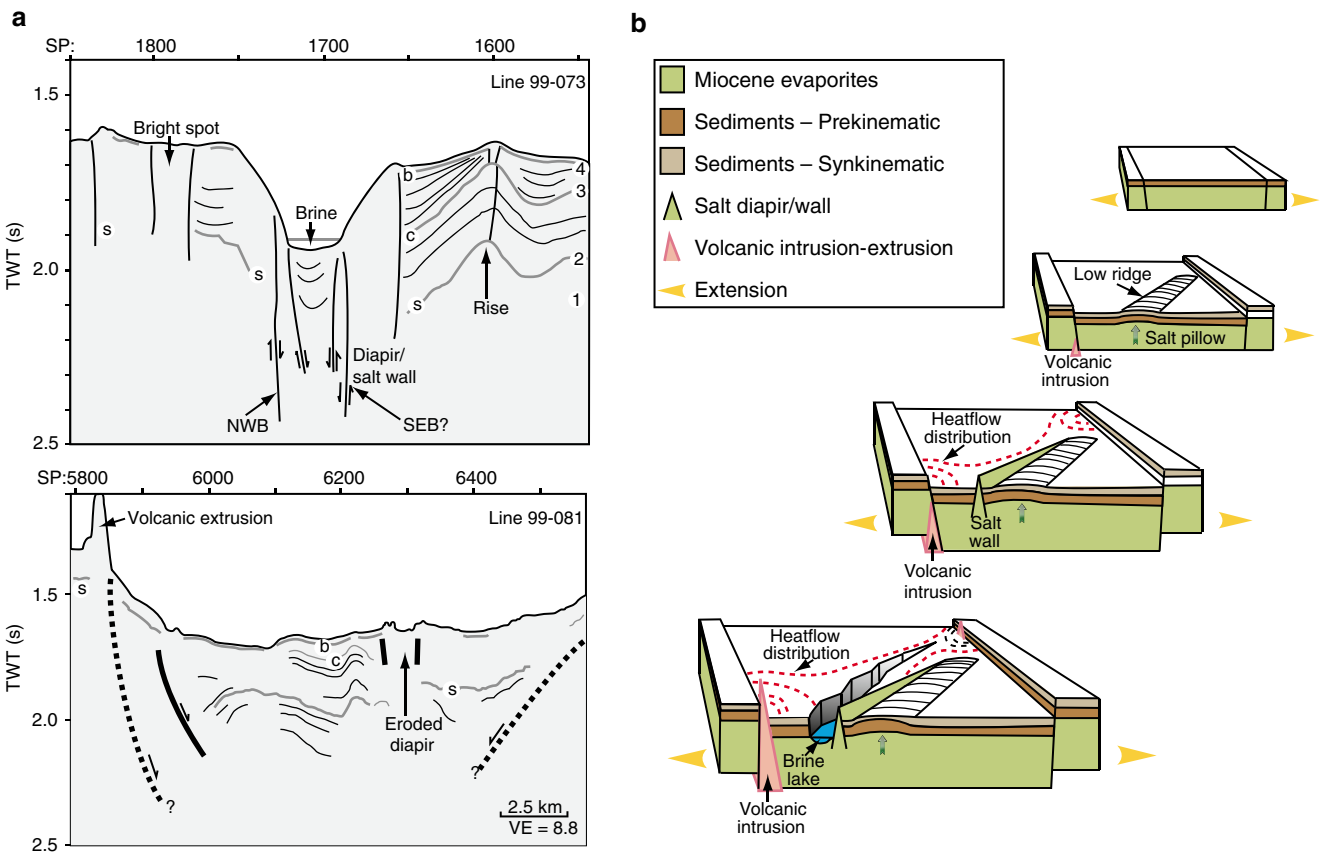

Fig. 15.15 Conrad Deep at the northern end of the axial rift in the Red Sea. (**a**) Representative seismic showing the association of extension, diapirism and volcanism as the deep forms. Some structures are active some are collapsing. Collapsed structures probably contribute to formation of brines and brine pools. (**b**) Evolution of the features in the Conrad Deep as it experiences ongoing extension (After Ehrhardt et al. 2005)

hydrothermal convection within the bottom brine mass. Still others, such as Thetis deep, show little evidence of ever acting as a seafloor sump for ponded brine.

Atlantis II Deep, Red Sea

The Deep is roughly elliptical in shape, 14 km long, 5 km wide and is located in the most geothermally active part of the central Red Sea (Fig. 15.14). The bottom of the brine pool is 2,200 m below sea level and is surrounded by thick sequences of halokinetic Miocene evaporites and thin veneers of Pliocene Recent clastics (Fig. 15.16a). Through subsurface dissolution and convective flushing, these Miocene evaporites supply ions to the seafloor and to high salinity brines caught up in hydrothermal flow cells beneath the flowing and dissolving underbelly of the salt units. Hot hybrid brines ultimately discharge onto the floor of the Deep, and settle into the lower part of the main depression to form a two layered brine pool that is some 200 m thick and is underlain by hypersaline metalliferous muds (Fig. 15.16b). For example, the southwest portion of the Atlantis II Deep contains 150–200 million tonnes of unconsolidated mud averaging 5–6 wt% Zn and 0.8 wt% Cu on a dry salt free basis. These tonnages rival some of the larger SedEx deposits in the world and represent the only known deposit of Fe, Mn, Zn, Cu, Ag and Au of economic proportions currently forming on the sea bottom (Shanks III 1983; Backer and Lange 1987).

The Deep was first discovered in 1966, it contains about 5 km^3 of brine, stratified into distinct dense and convective layers of differing temperature and chlorinity. The lower brine body has an area of 1.8 km^2 and is about 150 m thick atop a sea bottom as deep as 2,040 m (Figs. 15.16b). Distribution of bottom sediment facies is directly tied to the properties of the overlying brine column (Fig. 15.16b). In 1977 the bottom brine had a temperature of 61.5 °C, a chlorinity of 156‰, and contained no free oxygen. The overlying 50-m-thick brine layer, called the Transition Zone, was at 50 °C with 82‰ chlorinity. This partially oxygenated upper brine was a transitional zone of mixing between the lower brine and overlying normal seawater. (Anschutz and Blanc 1996; Hartmann et al. 1998).

Since the 1960s the temperature of the lower brine mass has been steadily rising. By 2008 the temperature in the bottom brine of the SW basin was 67.5 °C (Fig. 15.17). The structure of the lower transition zone, between about 1,990 m water depth and highly saline bottom brine has changed significantly, by the mid 1990s, when it contained two convective layers with nearly constant internal temperatures (61° and 55 °C, respectively). Since then temperature in the thick lower convective layer in the Atlantis II Deep has continued to increase but at a somewhat lower rate of 0.1 °C/year. Clearly, the temperature of all four convective layers in the deep have increased since the 1960s at the same rate across all four layers (Fig. 5.17). Based on the observed changes, Swift et al. (2012) concluded that diffusive vertical heat flux between the various convective layers is rapid on time scales of 3–5 years and that heat is being continually lost from the brine pools to overlying Red Sea Deep seawater. Heat budgets suggest that the heat flux from hydrothermal venting has today decreased from 0.54 GW to 0.18 GW since 1966.

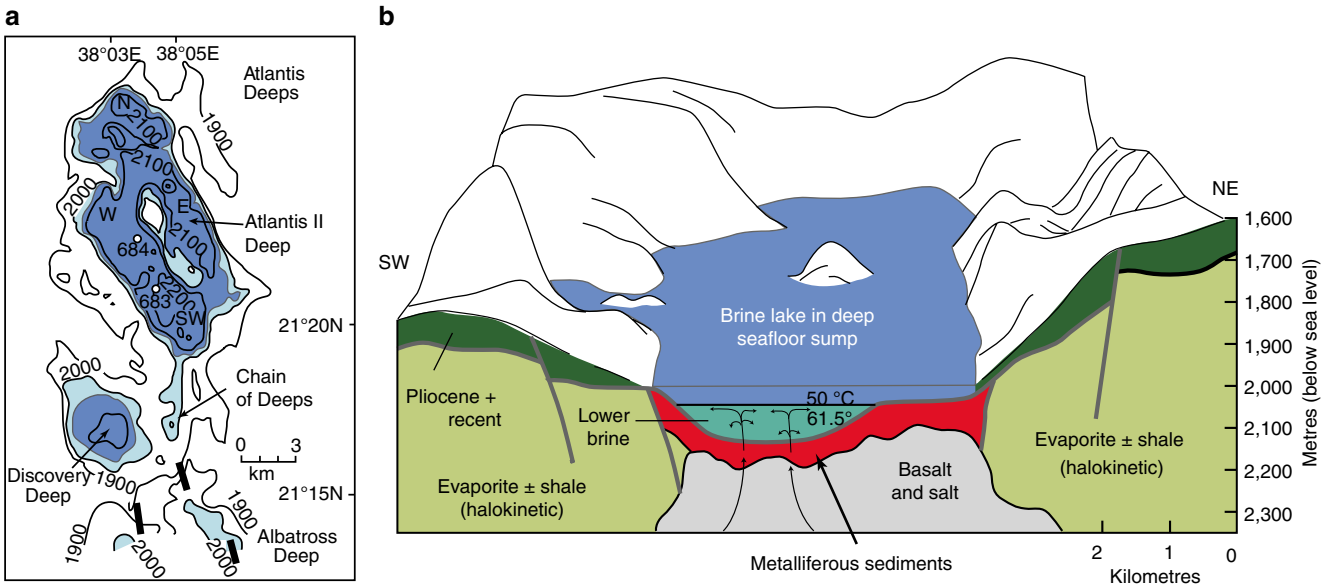

Fig. 15.16 Atlantis II Deep region, Red Sea. (**a**) Bathymetry of the Atlantis II deep and adjacent seafloor depressions, contours in metres (After Anschutz and Blanc 1995). (**b**) Schematic showing relationship of Atlantis brine lake (DHAL) to adjacent dissolving masses of halokinetic Miocene salt (After Anschutz and Blanc 1995)

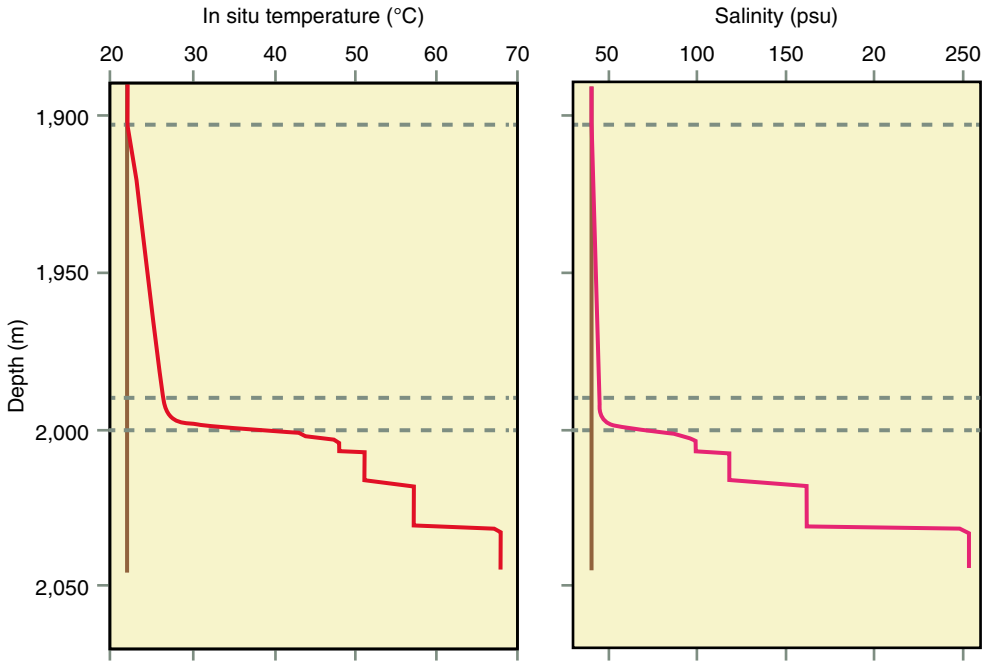

Fig. 15.17 Temperature and salinity profiles in 2008 in the Atlantis II Deep (After Swift et al. 2012). *Dashed lines* indicate the depths of bottom ridges controlling the brine lakes

Clearly, the venting of highly saline hydrothermal brines into the brine lake over the past 40 years has been continuous, but at a variable rate.

What is most significant geologically and mineralogically is the long term stability of this dense halokinetically-derived lower brine mass, with temperatures favouring anhydrite over gypsum precipitates, and its ongoing hydrochemical isolation from the overlying normal seawater column. For the last four decades, almost all additional heat and salt supplied to the Deep has been confined to the depression sump and it drives an increase in temperature in bottom waters. That is, very little heat is dispersed into the overlying seawater (Anschutz and Blanc 1996; Swift et al. 2012). The rate of heat input to the Deep was near constant during the period till 1996 and amounted to 0.54×10^9 W, which drove the documented rise in bottom-brine temperature. Salt input from the hydrothermal influx was also constant, and equalled 250–350 kg/s.

The effect of longterm brine pool stability is the precipitation of sulphide minerals at the Deep's redox interface, which is defined by the halocline contact with the overlying seawater column, and the subsequent accumulation of some rather unusual sulphide-rich saline bottom sediments. Interestingly, base metal laminites are not present on the floors of other deeps, such as Thetis, which lack a longterm brine sump (Pierret et al. 2010). The laminated nature of metalliferous sediment on the deep sea floor in the Atlantis II Deep is directly related to the oscillating nature of the overlying brine and its halocline interface (Fig. 15.18).

In the last 28,000 years some 10–30 m of the oxidic-silicatic-sulphidic laminites, along with hydrothermal anhydrites, have accumulated beneath the Atlantis brine lake, atop a basement composed of a mixture of basaltic ridges and halokinetic salt (Shanks III and Bischoff 1980; Pottorf and Barnes 1983; Anschutz and Blanc 1995; Mitchell et al. 2010; Feldens et al. 2012). Metalliferous sediments beneath the floor of the deep are composed of stacked delicately banded mudstones with bright colours of red, yellow, green, purple, black or white, indicating varying levels of oxidised or reduced iron and manganese related to varying oxidation levels and salinities in the overlying brine column. Sediments are typically anhydritic and very fine grained, with 50–80 % of the sediment less than 2 μm in size. Intercrystalline pore brines constitute up to 95 wt% of the muds, with measured pore salinities as much as 26 wt% and directly comparable to the salinity/density of the overlying brine (Fig. 5.18; Pottorf and Barnes 1983).

The sulphide-rich layers are a metre to several metres thick and form laterally continuous beds that are several kilometres across. Sulphides are dominated by very fine-grained pyrrhotite, cubic cubanite, chalcopyrite, sphalerite, and pyrite, and are interlayered with iron-rich phyllosilicates (Zierenberg and Shanks III 1983). Sulphur isotope compositions and carbon-sulphur relations indicate that some of these sulphide layers have a hydrothermal seawater component, whereas others were formed by bacterial sulphate reduction centred in the interface. Ongoing brine activity began in the western part of the Deep some 23,000 years ago with deposition of a lower and upper sulphide zone, and an amorphous silicate zone (Fig. 15.19). The metalliferous and nonmetalliferous sediments in the W basin accumulated at similar rates, averaging 150 kg/k.y./m^2, while metalliferous sediments in the SW basin accumulated at a higher rate of

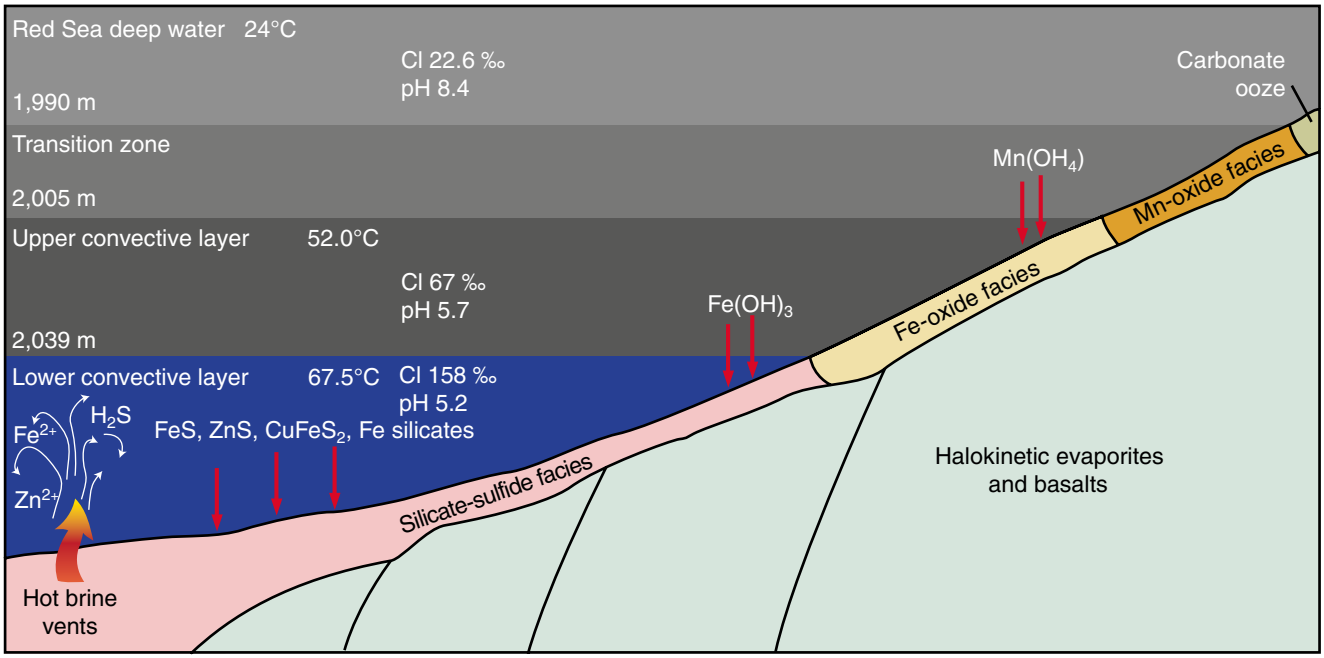

Fig. 15.18 Summary of the oceanographic and physical conditions in the Atlantis II Deep, Red Sea; not to scale (After Hovland et al. 2006b)

700 kg/k.y./m^2 (Fig. 15.19; Anschutz and Blanc 1995). The lowermost unit in the pile in the W basin consists mainly of detrital biogenic carbonates, with occasional thin beds of red iron oxides (mostly fine-grained hematite) or dark interbeds entraining sulphide minerals.

Hydrothermal anhydrite in the Atlantis II sediments occurs both as at-surface nodular hydrothermal beds around areas where hot fluid discharges onto the sea floor and as vein fills beneath the sea floor (Degens and Ross 1969; Pottorf and Barnes 1983; Ramboz and Danis 1990; Monnin and Ramboz 1996). White nodular to massive anhydrite beds in the W basin are up to 20 cm thick and composed of 20–50 μm plates and laths of anhydrite, typically interlayered with sulphide and Fe-montmorillonite beds. The central portion of individual anhydrite crystals in these beds can be composed of marcasite. The lowermost bedded unit in the SW basin contains much more nodular anhydrite, along with fragments of basalt toward its base. Its 4-m + anhydritic stratigraphy is not unlike that of nodular sekko-oko ore in a Kuroko deposit, except that any underlying volcanics are basaltic rather than felsic (see Chap. 16).

The anhydrite-filled veins that crosscut the laminites act as conduits by which hot, saline hydrothermal brines vent onto the floor of the Deep. Authigenic talc and smectite dominate in deeper, hotter vein fills, while shallower veins are rich in anhydrite cement (Zierenberg and Shanks III 1983). The vertical zoning of vein-mineral fill is related to heating haloes tied the same ascending hydrothermal fluids, with stable isotope ratios in the various vein minerals indicating precipitation temperatures ranging up to 300 °C.

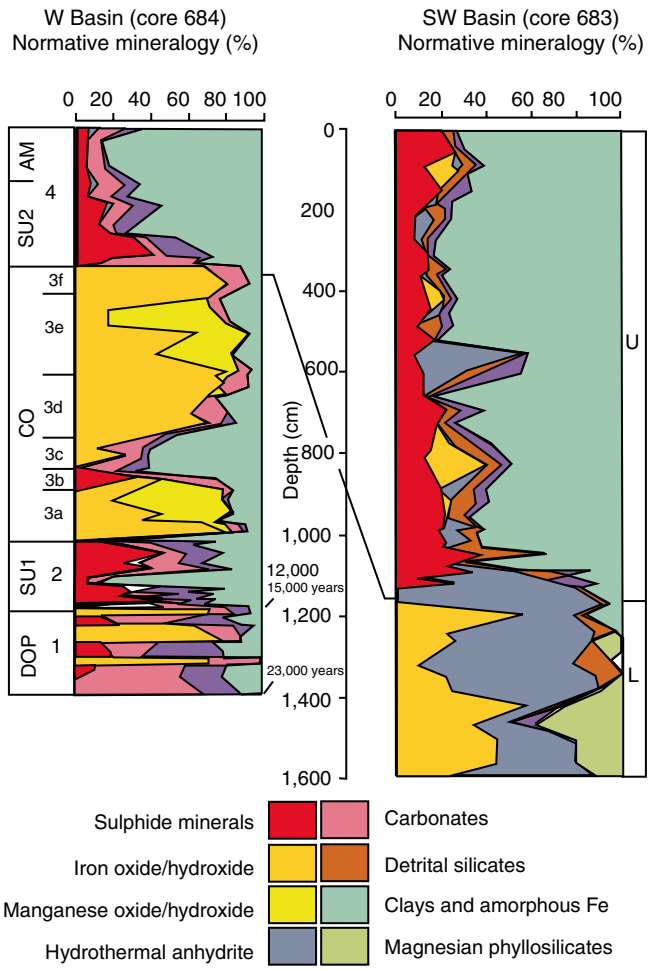

Fig. 15.19 Atlantis II Deep, Red Sea showing mineralogical proportions in cores from W and SW basins (After Anschutz and Blanc 1995)

Because of anhydrite's retrograde solubility, it can form by a process as simple as heating hydrothermally-circulating seawater to temperatures in excess of 150 °C. Pottorf and Barnes (1983) concluded that the bedded anhydrite of the Atlantis II Deep, like the vein fill, is a hydrothermal precipitate. Based on marcasite inclusions in the anhydrite units, it precipitated at temperatures down to 160 °C or less. At some temperature between 60 and 160 °C, probably close to 100–120 °C, hydrothermal anhydrite precipitation ceased. Thus, anhydrite distribution in the Atlantis II deep is related to the solution mixing and thermal anomalies associated with hydrothermal seawater circulation.

The fact that Holocene sediments in the Atlantis II Deep contain sulphate minerals and that particulate anhydrite is still suspended in the lower brine body strongly suggests that anhydrite is stable in the temperatures found at the bottom of the water column or is at least only dissolving slowly. These conclusions were clarified by Monnin and Ramboz (1996), who found that the Upper Convective Layer (UCL; or Transition Zone) of the Atlantis II hydrothermal system was undersaturated with respect to hydrothermal anhydrite throughout their study period, 1965–1985. The system reached anhydrite saturation in the lower brine only for short periods in 1966 and 1976.

What distinguishes the hydrothermal salts and sediments in the Atlantis II Deep from the much smaller hydrothermal accumulations in volcanogenic hosted massive sulphide (VHMS) deposits (Chap. 16) is that the hot metalliferous brines now found on the seafloor achieved their elevated salinities, temperatures and acidic saline chemistries via hybrid hydrothermal circulation through both seafloor basalts and dissolution of the edges and underbellies of halite in nearby halokinetic Miocene salt masses. Heat to drive this circulation probably came from the hot basaltic rocks emplaced in the slowly spreading axial zone, while most of the chloride and fluid focusing was due to circulation of marine-fed hydrothermal brines with significant, if not dominant contributions from nearby dissolution of halokinetic salt tongues. Thus, a seawater/brine flushing of newly formed basalts, as well as of Miocene evaporitic sediments atop and below the halokinetic salt, both contribute metal to the brine pool. This is clearly seen in studies of lead isotopes in the brine pool laminites, which indicate that a substantial portion of the lead came from the Miocene evaporites and their associated clastics and not from the basalts (Dupre et al. 1988).

As in anoxic halokinetic brine pools (DHALs) that typify halokinetic brine sumps on suprasalt seafloors elsewhere in the world (such as in the Mediterranean and the Gulf of Mexico), the reduced sulphur in the shallow pore brines and the bottom brine layer in the deep were mostly derived from bacteriogenic reactions, using seawater sulphate and entrained organic matter. This created conditions suitable for widespread metal sulphide precipitation at the halocline, in the brine column, and in brine-saturated sediments beneath areas covered by stable anoxic H_2S-enriched brines. Brine pool stability and an associated lack of mixing with overlying seawater (due to density/salinity stratification) allowed metal sulphides to accumulate as laminites across large areas of the brine pool floor and not just near vent localities. Hence, the larger volume of the metal resource and the greater dispersal of metal sulphides in the Atlantis II Deep compared to the much smaller near-vent precipitation sites typical of VHMS deposits, such as TAG Mound, the smokers of the east Pacific rise, and Kuroko- and Cyprus-style deposits (see Chap. 16). It is the hydrological and hydrogeochemical effects of the dissolving halokinetic evaporites that distinguish this style of hydrothermal "SedEx" precipitate from less stable seafloor brine pools, tied to much smaller open marine VHMS deposits.

Kebrit and Shaban Deeps, Red Sea

Massive sulphides dredged from the Kebrit Deep (Arabic for sulphur) represent black smoker fragments, novel to most Red Sea brine pool deposits (Fig. 15.14; Blum and Puchelt 1991). TV camera observations at 1,366 m depth in the Kebrit Deep, and just above the seawater/brine interface at 1,370 m, imaged some 40+ inactive smokers. Brines below the interface in Kebrit Deep at a depth of 1,373 m have a temperature of 24.3 °C and a salinity of 256‰, making this pool as saline but somewhat cooler (in the gypsum, not anhydrite, temperature field) than the Atlantis II deep. Above the interface the Kebrit brine has a temperature of 21.5 °C and a salinity of 41.9‰. According to Hartmann et al. (1998) there were no significant changes in temperature, brine level or chlorinity over the preceding 23 years. The transition in the column from high saline bottom brine to normal seawater salinity probably extends over a depth of only a few decimetres or less. As in the Atlantis II Deep, the dissolution of nearby Miocene evaporites accounts for the very high salinities in the bottom brine layer.

Piston core sampling in the Kebrit Deep revealed stratified somewhat metal-enriched sediments in the upper portions of the sedimentary column, while box and dredge sampling recovered specimens of elemental sulphur, sulphide and sulphates. These recovered sulphides consist primarily of Fe- Zn- and Pb-bearing phases that can be tar and asphalt impregnated. They were probably derived by hydrothermal cracking of organics held in adjacent sediments, where TOC values are more than 4 % in Kebrit and can be higher than 8 % in Shaban cores (Fig. 15.20 – see also Chap. 9). The sphalerite typically forms banded colloform nodules. Concentration of Ni in discrete bravoite [$(Fe,Ni,Co)S^2$] aggregates points to brine leaching of nearby basalts as a source for at least some of the metals in the brine pool. Unlike the Atlantis II Deep, Cu-sulphides are virtually absent from the paragenesis. This, and the presence of gypsum

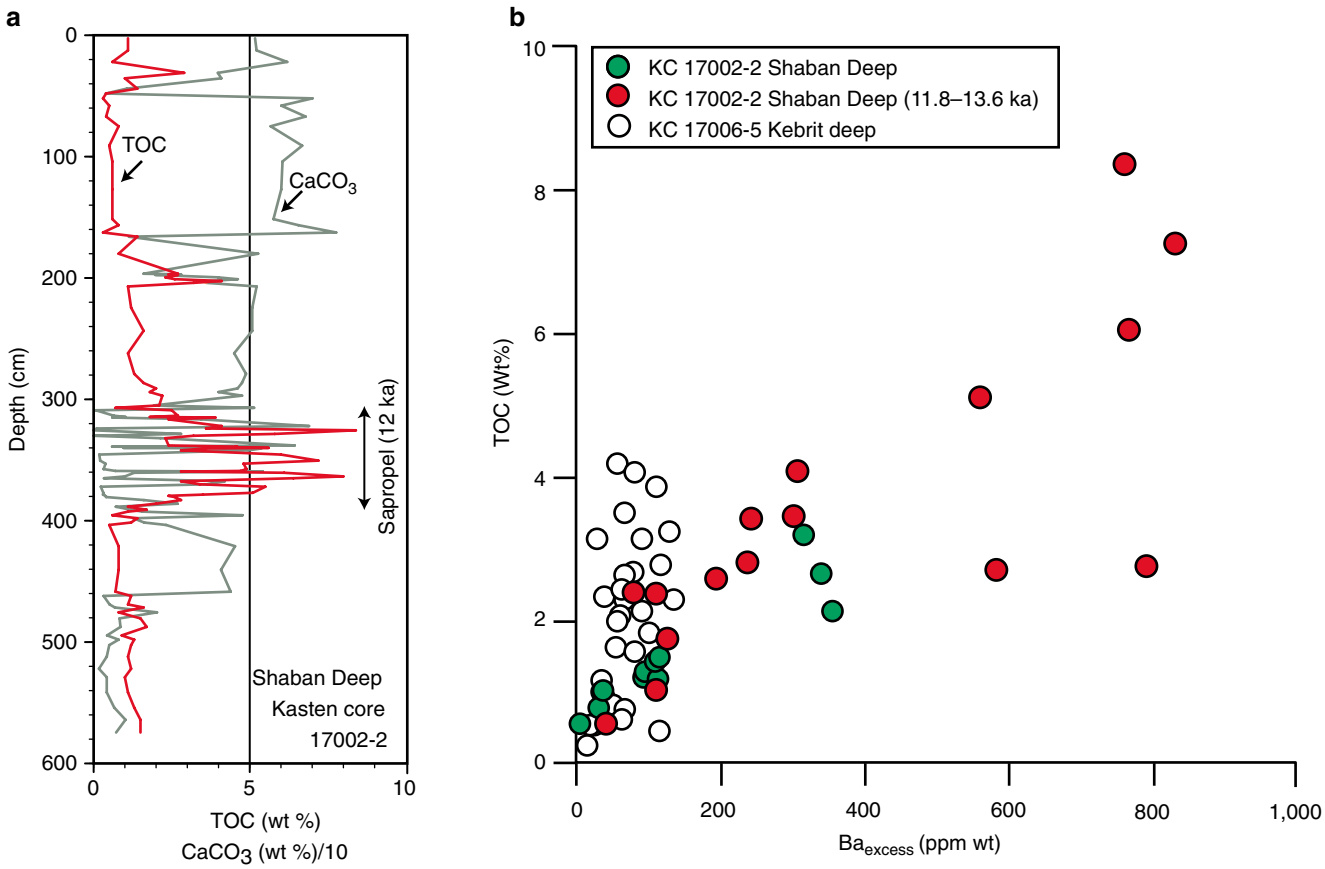

Fig. 15.20 Organic matter in the Shaban and Kebrit deeps. (**a**) TOC and $CaCO_3$ contents in the upper 6 m of the KC 17002–2 core from Shaban deep showing elevated content in the laminites (deposited 11.8–136.6 ka). (**b**) Crossplot of TOC versus Ba_{excess} in select core intervals (After Botz et al. 2007)

rather than anhydrite interlayers in chimney fragments points to formation of metal sulphides at lower temperatures compared to the Atlantis II Deep. Sulphide layering in the chimneys shows classic zonation, with Zn-bearing phases preferentially lining the interiors of the chimneys while pyrite is dominant in the outer portions.

The bottom brine layers in the Shaban Deep in the northern part of the Red Sea are 200 m thick, but the brines are only 2–3 °C warmer than the normal bottom waters (Cocherie et al. 1994). An insignificant decrease in temperature (to about 24.1 °C) occurred in the upper brine since detection of the Shaban Deep in 1981 and no changes were found for the brine-seawater level (Hartmann et al. 1998). The bottom sediment in the Shaban Deep is somewhat unusual compared with other brine pool sediments in the Red Sea in that the sediment consists almost entirely of biodetrital silicate mud (diatomaceous), with occasional volcanic glass fragments and only a thin (4 cm thick) hydrothermal sediment layer, along with intervals with more than 50 % biodetrital carbonate (Fig. 15.20a; note the plotted $CaCO_3$ values are reduced by an order of magnitude to allow plotting on the same scale as the TOC values). This biodetrital lithofacies is similar to the more oxidised layer in the western part of the Atlantis II Deep that lies beneath the metalliferous sediments and similar to the biogenic sediments found on the deep seafloor above the zone defined by the more saline portions of the brine lake (Fig. 15.18). This biogenic layer in the Shaban Deep overlies a tholeiitic ferro-basalt with transitional affinities, it too is different from the typical tholeiite basalt found further south. Thus, the Shaban Deep, the northernmost deep in the Red Sea rift, represents a very recent stage of oceanic opening. The lack of pervasive hydrothermal signature in the Shaban Deep compared with the Atlantis II Deep is also seen in both the Sr-Nd isotopes and the rare earth element signatures (Cocherie et al. 1994). Metal sulphides in Shaban Deep are less frequent than those in Kebrit, with framboidal pyrite being the dominant ore mineral.

Gypsum occurs in the bottom sediments of both the Shaban and Kebrit deeps, as both euhedral prisms and lenticular forms, up to several centimetres across. Crystals often interpenetrate the sediment layering to construct classic "desert rosette" morphologies, especially in the Kebrit Deep, where gypsum is commonplace. Deeper coring has yet to be undertaken in either of these deeps, but it is likely that this gypsum forms atop areas of subcropping and dissolving autochthonous salt in the same way morphologically

identical gypsum forms in sediments atop areas of dissolving halokinetic salt in DHAL settings worldwide.

Sulphur isotopes from gypsum in the rosettes in Kebrit Deep have values in the range +25.1‰ to +30.0 ‰. These values exceed those of normal seawater-sulphate-derived gypsum and imply a significant input of bacteriogenically fractionated residual seawater sulphate. Some samples show intimate intergrowths of idiomorphic gypsum and spongy sulphide, pointing to coprecipitation of both minerals from the same hydrothermal fluid in the presence of possible bacterial mediators. Inclusion studies show rather low sulphide and sulphate precipitation temperatures of 110–130 ° C in the Kebrit brine pool and 100 ° C in the Shaban Deep. In either deep, the gypsum, like the anhydrite in the Atlantis II deep, is not a true solar-derived deepwater evaporite, but a hydrothermal or burial salt.

There is a very interesting organic-rich laminite in the Shaban Deep with TOC values in excess of 5 wt%, qualifying it as a sapropel (Fig. 15.20a). The same interval also shows cemented carbonate layers between the organic-rich layers and elevated levels of Ba tied to elevated TOC (Fig. 15.20b). The organic signature in this 11,800–13,600 year old sapropel is largely unoxidised as it is bathed in hypersaline pore waters (Botz et al. 2007). The excellent correlation between TOC content and barium content suggests the sapropel formed via a productivity pulse in the basin arguing organic productivity not hydrothermalism controls the organic and Ba content of the Shaban sediments.

Red Sea Summary

Stable stagnant brine pools have developed in sea floor depressions along the medial ridge of the Red Sea, in close association with dissolution of adjacent thick halokinetic evaporites. Hot metalliferous brines focused by salt allochthons and escaping into the lower convective layers of these pools become widely dispersed across the extent of the deepwater brine pool with the richest metalliferous laminites (Atlantis II Deep), corresponding to a brine lake (DHAL) positioned in the most geothermally active position in the axial trough. The Atlantis II brine lake also contains the hottest brines. During active venting of metalliferous brines, the presence of a longterm brine pond facilitated stable anoxia at the sea bottom, as well as intra-brine-pool convection and the dispersal of metalliferous brine away from the immediate vent area. Diffusive mixing at the halocline atop the brine pool precipitated metal sulphides, mostly as pyrite framboids that then sank to the bottom carrying with them dispersed organic water. Thus, the longterm presence of a stable bottom brine lake increases the area of prepared ground for any subsequent Fe, Pb, Zn and Cu emplacement.

Ongoing dissolution of adjacent thick halokinetic masses not only enhances the permanency of the brine pool, it also raises the metal-carrying capacity of chloride-rich hydrothermal brines as they convect through and flush adjacent sub-salt and suprasalt sediment and volcanics, before ultimately venting and residing in the brine lake. That is, the high chloride levels in the circulating brine increases the reaction rate of any saline fluids flushing metals from the basaltic basement and suitable first-cycle sediments. The presence of a dissolving salt aquiclude atop seafloor basalt also focuses reflux driven hydrothermal vent fluids into the outflow zones about the edges of the stable brine pools. The now increasingly documented role of salt allochthons as the dominant control on the location of the deeps on the Red Sea floor, means it is likely that synkinematic salt gliding drives restriction and brine focusing on the sea floor depressions. However, the presence of salt allochthons is a focus for the mineralisation site (trap or seal), but salt focusing is not directly sourcing the metals found in some of the Deeps. If it was then sediment fills in all brine-filled deeps along the Red Sea axis would be metalliferous. Rather there is still a need for a focused deeper mantle-source convection to source the metals ultimately held in this type of deposit.

Stratiform Copper Deposits (Salt-Related)

Sediment-hosted stratiform copper deposits comprise disseminated to veinlet Cu and Cu-Fe sulphides hosted in siliciclastic or dolomitic sediments. In this chapter I am using the term "sediment-hosted stratiform copper" (SSC) as defined by Kirkham (1989). It encompasses a group of Cu deposits that are not truly stratiform in that they may cut the stratigraphy either locally or regionally. Yet, locally, most of these deposits are not only stratabound (confined to a particular stratum), but are more or less concordant or peneconcordant, either with bedding or with the edge of a salt mass or its residues (stratiform).

SSC deposits worldwide rank second only to porphyry copper deposits in terms of copper production and they represent the most important global source of cobalt (Figs. 15.21 and 15.2). Together, SSC deposits account for some 23 % of the world's Cu production and known reserves, as well as being significant sources of Co and Ag. Small SSC deposits of various ages are commonplace, but large sediment-hosted stratiform copper deposits are rare (Hitzman et al. 2005; Brown 1997). Within the supergiant grouping, three evaporitic basins, that contain enormous Cu deposits, dominate (>24 million metric tons -Mt), they are; (1) the Permian Basin Kupferschiefer of central Europe, (2) the Neoproterozoic Katangan Basin in central Africa, and (3) the Paleoproterozoic Kodaro-Udokan in Siberia (Fig. 15.21 and Table 15.7). Ore hosts in this group of supergiant deposits span lithologies that range from carbonates to siliciclastics and all the larger accumulations are associated with halokinetic evaporites or their residues.

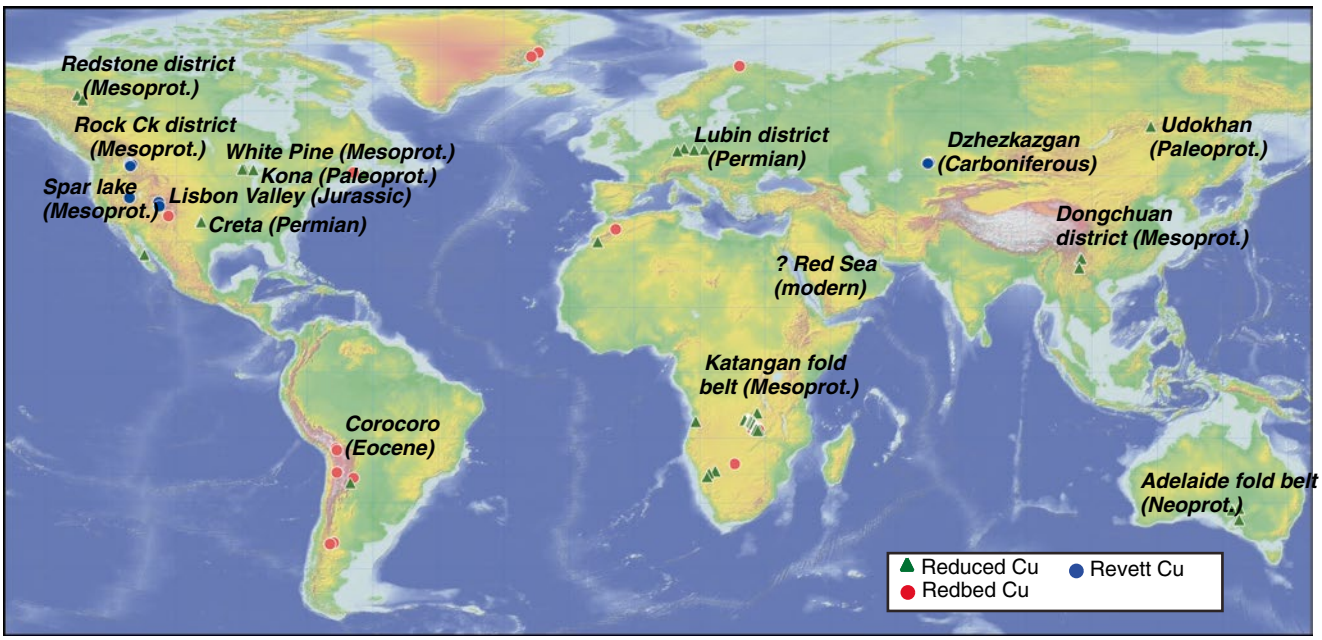

Fig. 15.21 Sediment-hosted stratiform (SSC) Cu deposits with Cu reserves of more than 1 million tonnes and discussed in this chapter (see also Fig. 15.22) (Data points extracted from Cox et al. 2007 and Salt Work database version 1.6)

Table 15.7 Selected evaporite-related sediment-hosted stratiform Cu (SSC) deposits related to salt style and position relative to the salt mass. In many cases the salt bed or mass is partially or completely dissolved and only residues remain. Only deposits still in the diagenetic realm were selected in this listing

Ore deposit position	Bedded salt	Halokinetic (peridiapiric) salt
Suprasalt and or its residues		Lisbon Valley Utah Flinders Ranges, South Australia Dongchuan, China Dzhezkazgan, Kazakhstan
Inter or lateral to salt edge and/or its residues	Corocoro Redstone, NWT	Katangan Copperbelt (Kipushi) Atlantis II Deep?
Subsalt or its residues	Creta, USA	Kupferschiefer (Lubin district)

The problem with exploration-based targeting of this group of copper deposits, especially when they are associated with now dissolved evaporites, is that we are looking at metal precipitation mechanisms that are diagenetic and dynamic. Ore positions are typically a reflection of a once rapidly evolving basin/ brine hydrology, which now is much less active. Accordingly, the various copper ore precipitates are concordant with paleopermeability trends and chemical interfaces, but they are not always concordant with regional depositional bedding. Thus, to predict positions of likely evaporite-associated stratiform copper occurrences within a basin, one must understand not just local depositional geometries, but also the subsequent diagenetic history, as well as likely focusing and trapping geometries created by interactions between redox interfaces and dissolving evaporite masses. The latter, now largely dissolved, evaporite masses were likely halokinetic in the case of the larger deposits and some masses were possibly allochthonous, as they are in a number of the larger SedEx deposits. The positions of former salt masses are now likely indicated by residues and alteration products, rather than actual salts.

Current classifications of SSC deposits do not place them in an understood evaporite framework, and the proximity of most larger deposits to halokinesis at some time in their burial evolution, is rarely noted. Many current classifications do, however, note the typical association of redbed Cu with present or former evaporites, but then tend to mismatch brine settings and associations, making the noted evaporite association useless as a pointer to mineralised positions. So, to simplify and better understand the diagenetic processes associated with copper ores tied to evaporite evolution, I have decided to steer away from the classic subdivisions of sediment-hosted Cu deposits; other than noting at the start of this section that this group of SSC deposits is currently subdivided in the literature into Reduced copper, Redbed copper and Revett copper (as illustrated in Figs. 15.21 and 15.22). According to Cox et al. (2007) these are three subtypes of sediment-hosted copper deposits show significant differences in tonnage and copper grade which can be used to help separate the three groups. In their world GIS compilation of SSC deposits they list 56 reduced-facies Cu deposits, 32 redbed Cu deposits, and 15 Revett Cu deposits. They conclude that the three types differ in the strength and efficiency of the reductant at the site of

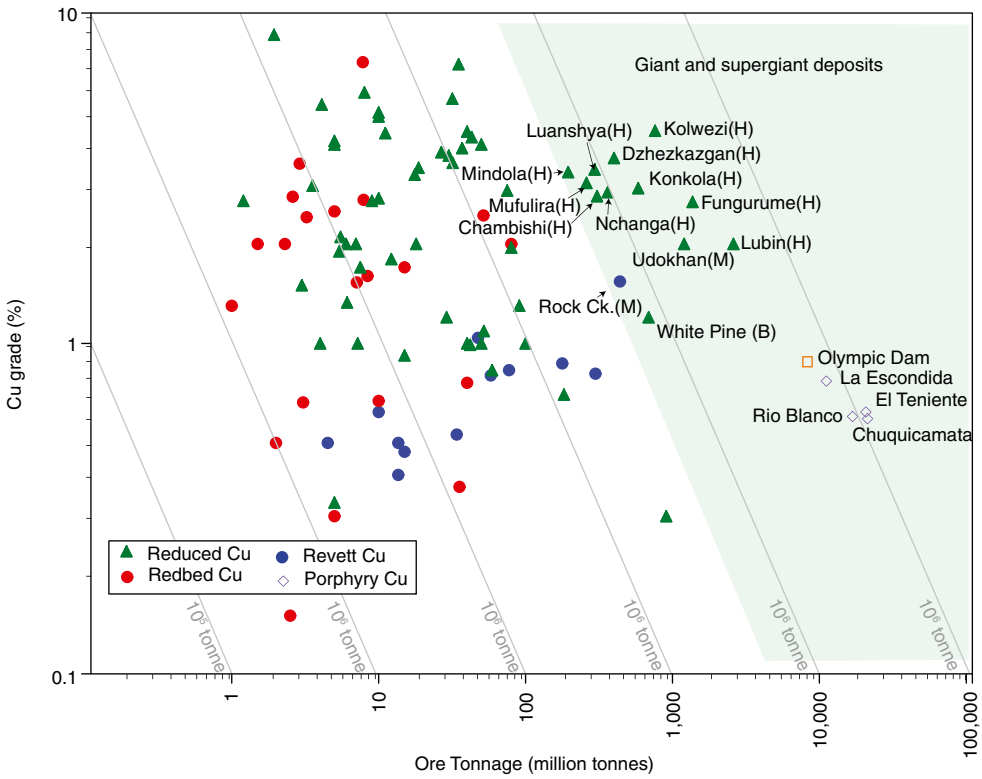

Fig. 15.22 Resource plot for sediment hosted stratiform copper deposits. Halokinetic association indicated by *H*, bedded evaporite association by *B* and metamorphic evaporite association by M (Plotted data values were extracted from Cox et al. 2007, integrated with the SSC evaporite association GIS base and classification extracted from the SaltWork database version 1.6). Also shown is Olympic Dam (IOCG) and the four largest Porphyry-Cu deposits

deposition. In classic SSC classifications, the reductant the reduced-facies deposits is a marine or lacustrine fine-grained sediment, containing abundant organic matter. In redbed deposits, the reductant is more weakly distributed, usually represented by patches of organic debris in sandstone. In Revett Cu deposits, the reductant is broad and diffuse and in some Phanerozoic deposits can be shown to be gaseous or liquid hydrocarbon, or sulphide-rich sour gas.

I shall not use this three part terminology in this chapter as it does little to improve our understanding of the role of dissolving salt in focusing and trapping processes associated with ore creation within the group of salt-related copper deposits that we will discuss. In terms of understanding how these deposits relate to evaporite-derived brines and dissolution foci, the classic classifications confuse a significant factor of prime exploration importance, namely where did the deposit form in relation to the associated evaporite mass and the redox front created by subsurface salt dissolution.

So, instead, I shall subdivide and discuss representative stratiform Cu deposits using an understanding of halokinetic and bedded salt associations. It is based on the geometry of the adjacent salt mass, or its residues, and the relative position of the ore deposits with respect to the salt mass (Tables 15.2 and 15.7; subsalt, intrasalt or suprasalt). I shall consider the halokinetic examples first, as they tend to be worldclass and currently exploited. Accordingly, the three dimensional aspects of many of the facies and structural indicators for associated salts in the halokinetic group are well mapped, if not well understood in terms of process significance.

Typing a deposit to its evaporite style makes it easier to illustrate and understand the formative brine fluid hydrologies. Interestingly, almost all the world's giant and supergiant SSC's have a halokinetic evaporite basinwide association, rather than a bedded platform evaporite association (Fig. 15.22). After discussing the various halokinetic associations, I will consider sediment-hosted Cu deposits tied to the bedded salt associations. This latter group tend encompass much more numerous, but smaller, examples of copper accumulations. Worldwide, they are patchily distributed, so deposit details are not as well documented (Fig. 15.21).

By itself, this two-part breakdown into halokinetic versus bedded and the understanding of extension, compression, and structuration that is associated with an evaporite/brine genesis, become exploration pointers or paradigms. So, as a rule of thumb in a greenfield area, when looking for the larger SSC's, one should first focus on localities where the "prepared ground" units (organic shales or former hydrocarbon traps) lie adjacent to stable halokinetic salt or rauhwacke masses, not to stratiform bedded salt associations. The latter tend to be smaller. We shall revisit this observation, but with understanding, after we have studied some representative examples (Table 15.7).

Stratiform Cu Halokinetic-Salt Associations

Within the sediment-hosted Cu association there are two styles of halokinetic salt: (1) Deposits where substantial volumes of the halokinetic salt are nearby, such as the

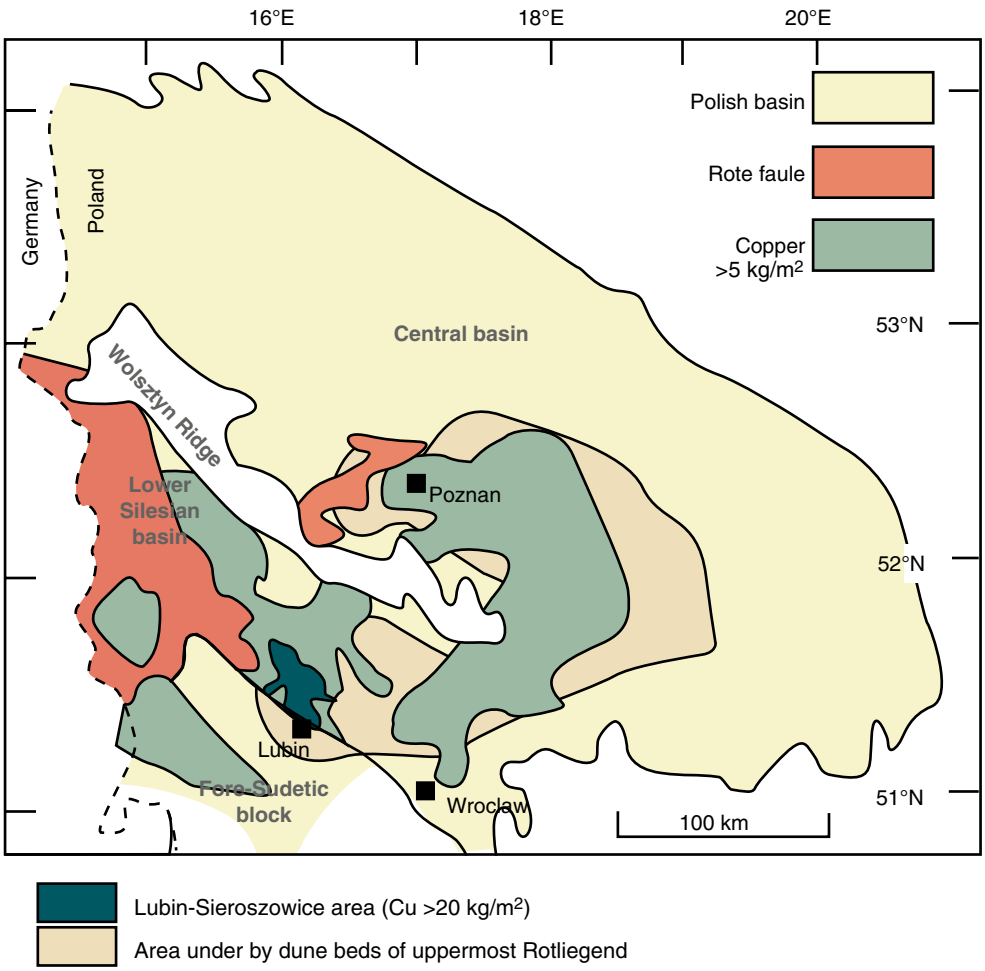

Fig. 15.23 Distribution of the Kupferschiefer copper deposits in Poland (After Oszczepalski and Blundell 2005)

Kupferschiefer, Lisbon Valley and the Dzhezkazgan deposits and, (2) Deposits where flowing salt was once present but now is indicated by dissolution remnants, typically now in thrust terranes, but often showing evidence of an early gravity gliding stage of mineralisation later overprinted compressional thrusting, given a rauhwacke association to the current outcrop/subcrop expression. Widespread examples of type 2 deposits, where salt is no longer present, typify the Katangan copperbelt, copper in the Mt Isa mine region and the numerous small suprasalt Cu occurrences in the Flinders Ranges, South Australia (see Chaps. 6 and 7 respectively for the geological background to these rauhwacke associations).

In this section I have chosen worldclass examples to illustrate Cu accumulations where dissolving halokinetic salt masses played a role, both in generating metalliferous saline brines, and in focusing the ore precipitation process at a salt-dissolution induced stable redox front. They are (Table 15.7);

(a) Subsalt – Kupferschiefer in Poland and Germany.
(b) Suprasalt -Dzhezkazgan and Lisbon Valley.
(c) Intersalt or halokinetic salt residue associated – various examples in the Donchuan District and Katangan Copper belt and their more metamorphosed equivalents (Udokhan)

Kupferschiefer/Rote Faule, Lubin Region, Poland

The world's largest sediment-hosted stratiform copper accumulation is a subsalt copper association, centred on the Kupferschiefer shales in the Lubin-Sieroszowice copper district, Poland (Fig. 15.23). Near the ore zone, is a partially dissolved thick mass of halokinetic Zechstein salt. Facies distribution preserves *prima facie* evidence of the influence of a salt mass, both deeper in the basin where it acts as a source of dissolution-related basinal brines and nearer the basin margin where it focused the set-up of a halokinetically-stabilised brine-mixing redox front.

Mineralisation typically occurs in reduced, Zechstein-capped beds at the top of a thick continental volcanic and redbed Rotliegende sequence, which was deposited within a continental Permian rift basin known as the Polish Trough. This is a generally north-west trending basin and is the south-eastern extension of the main evaporite-filled

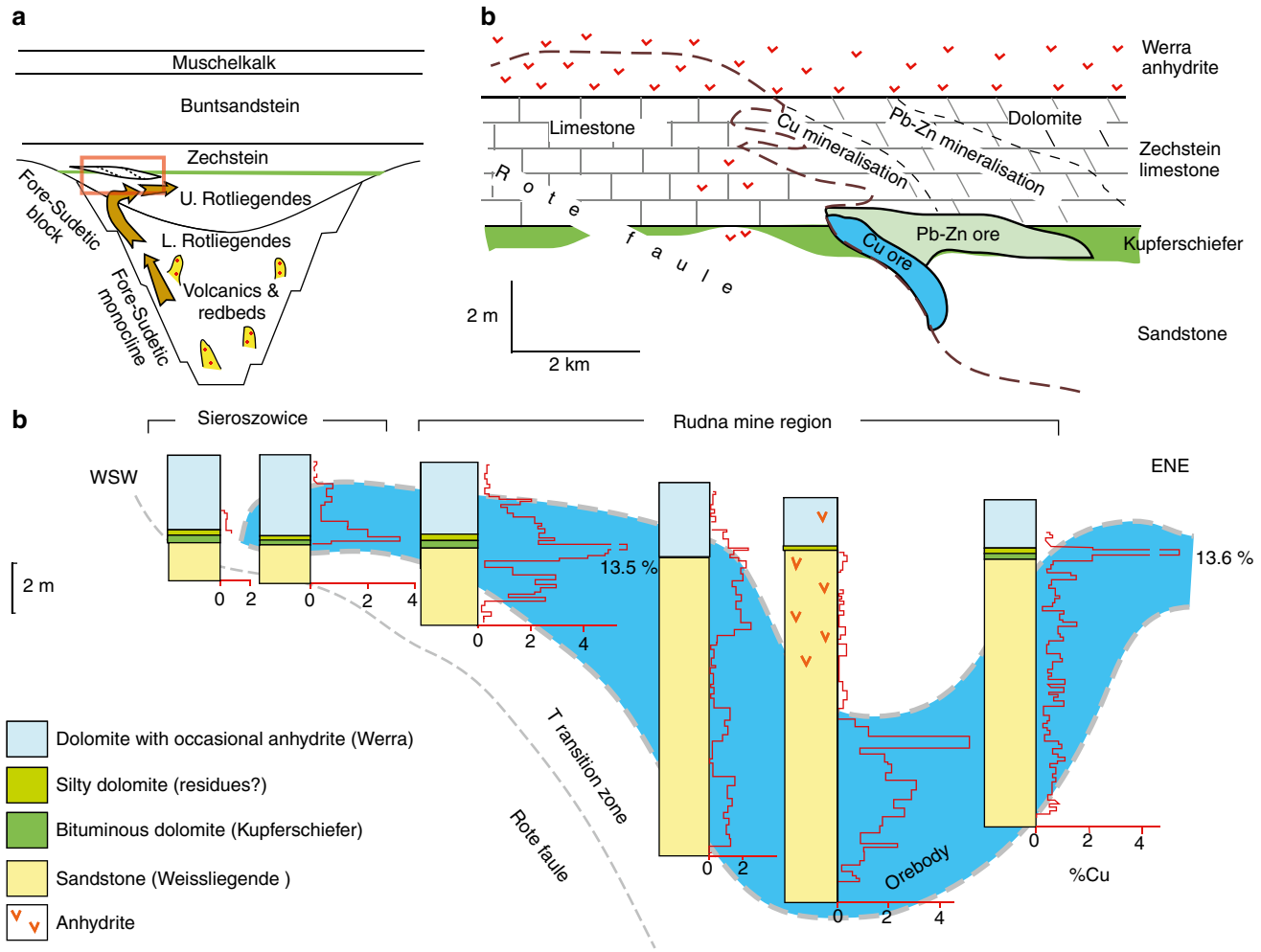

Fig. 15.24 Rote Faule and its influence on Kupferschiefer mineralisation in the Lubin copper district, Poland. (**a**) Regional schematic showing focus of upwelling of convective basinal waters toward basin edge and the Rote Faule Zone. (**b**) Enlargement of Rote Faule area outlined in **a**, showing how the resultant mineralisation cross cuts the stratigraphy. (**c**) Distribution of Cu in the Lubin ore zone, shows higher Cu enrichment in Kupferschiefer with Cu values in excess of 13 %, but the greater thickness and volume of ore in the Lubin district resides in the Upper Rotliegende sandstone, beneath a Werra Anhydrite seal (Modified from Jowett 1992; Vaughan et al. 1989; ore assays and associated stratigraphy after Wodzicki and Piestrzynski 1994)

(Zechstein Series) halokinetic Southern Permian Basin (Fig. 15.23; Krzywiec 2004). The mineralised district lies along the southern edge of the halokinetic Zechstein sequence and is also proximal to the basin margin of the Lower Silesian Basin to the south. The ongoing ability of flowing salt to maintain its seal capacity and its diagenetic interfaces in earth-space adjacent to a basement high, even as the salt was dissolved and deformed, is in my opinion the reason why the Lubin-Sieroszowice District is world-class. It has 2,369 Mt of ore, made up of 47.07 Mt Cu @ 1.3–2.6 %, 135,000 t Ag @ 30–80 g/t (Oszczepalski and Blundell 2005).

Stratabound Cu–Ag Kupferschiefer deposits were long considered classic examples of syngenetic mineralisation, driven by syndepositional bacterial sulphate reduction (e.g., Wedepohl 1964). However, detailed work in Poland in the last few decades has shown that the Cu mineralisation cuts depositional boundaries (Fig. 15.24). Levels of mineralisation in the Kupferschiefer Rote Faule interval in the Lubin-Sieroszowice district are typically far higher than background levels in the Kupferschiefer shale (Fig. 15.24c) It should be pointed out that the using term shale in this context to imply a terrigenous sediment is a misnomer, the Kupferschiefer is actually a finegrained (micritic) organic-enriched, finely laminated dolomite mudstone, often with no more than minor amounts of terrigenous material.

Locally, mineralisation transgresses depositional boundaries as it is tied to the Rote Faule/saline brine interface and not to the depositional pattern or solely to the distribution of the Kupferschiefer shale. Thus copper ore in the Lubin

district is not just hosted in the organic laminites of the Kupferschiefer and the Zechsteinkalk, it also occurs in parts of the Weissliegend aeolian sandstone, a unit that at the time of deposition in a desert sand sea was exceptionally free of organics, organic laminites and pre-ore sulphides (Figs. 15.23 and 15.24b, c).

To the dismay of many syngeneticists, this depositionally organic-clean aeolian sandstone hosts half the economic Cu-sulphides in the Lubin-Sieroszowice copper district. That is, the richest intervals of mineralisation define low-angle transgressive metal zones tied to the redox edges adjacent to diagenetic Rote Faule units (Jowett et al. 1987; Jowett 1987, 1989, 1992; Oszczepalski 1989, 1994; Vaughan et al. 1989; Hammer et al. 1990; Kucha 1990; Bechtel and Hoernes 1993; Wodzicki and Piestrzynski 1994; Bechtel et al. 1995; Heppenheimer et al. 1995; Speczik 1995; Sun et al. 1995; Large et al. 1995; Large and Gize 1996). The overlying evaporitic Zechstein sediments enhanced and focused the precipitation of base metals, both by forming prepared ground at the time of deposition (pyritic and organic-rich evaporitic laminite host), and by creating a stable dissolution hydrology during diagenesis, which focused the greater volumes of economic mineralisation into a redox zone immediately below the main evaporite mass and adjacent to the Rote Faule boundary.

The mesohaline setting of the Kupferschiefer laminites created much of the "prepared ground"- organic-rich laminites below thick salt that would later control much of the mineralising fluid flows and interfaces. Away from the zone of organic degradation associated with the Rote Faule, the degree of methylation of 2-methyl-2-trimethyl-tridecylchromans (MTTC) in the shales indicate original euryhaline to mesohaline (30–60‰) salinity during subaqueous laminite sedimentation. An abundance of biomarkers, derived from green/purple sulphur bacteria, suggests H_2S saturation of the anoxic bottom waters and maximum water depths below 100 m. These organisms lived near the boundary between the photic zone and the anoxic (euxinic) bottom water at depths of 10–30 m. Primary production in the upper water column was dominated by photosynthetic cyanobacteria or green algae. In the sediment, sulphate reduction was driven by the availability of abundant sulphate and organic detritus settling from the overlying water column. Methanogenesis was active mostly during early Kupferschiefer deposition; it is indicated by the light carbon isotopic composition of the organic matter that originated from recycling of CO_2, which was generated by methane-oxidizing bacteria in the water column (see Chap. 9 for detail).

Kupferschiefer matrix was deposited mostly from suspension load in density-stratified subaqueous lacustrine/restricted marine-fed brine lakes and seaways with reducing anoxic bottom waters (Glennie 1989a, b). Higher energy sediments were deposited in shallower shorezone areas about the basin edge or atop basement highs. The anoxic organic-rich laminates of the deeper water areas quickly became the hosts to syndepositional bacterially mediated pyrite framboids (Sawlowicz 1992). Regionally, much early metal sulphide precipitation was dominated by this pyrite. Only locally was there any early Cu or Zn enrichment as this pyrite and the associated organics were replaced by base metal sulphides, which were further concentrated in regions adjacent to Rote Faule intervals (Sawlowicz 1992). This type of enrichment is sometimes call a two-fluid or multiple-fluid ore forming process.

The high mineral content of the Kupferschiefer was attained via a three-step process (Sun and Püttmann 1997): (1) framboidal pyrite and pyrite precursors were precipitated by bacterial sulphate reduction during deposition of the sediment; (2) pyrite and pyrite precursors were largely replaced by mixed Cu/Fe minerals and by chalcocite during early diagenesis; and, (3) in those intervals with very high Cu contents (>8 %), the amount of reduced sulphur from Fe-sulphide precursors was not sufficient for precipitation of Cu and other trace metals. In this part of the profile, thermochemical sulphate reduction (TSR) occurred after pyrite replacement, as is indicated by the presence of pyrobitumen and sparry calcite.

The maturation profiles of the kerogens in the ore zone and the adjacent Rote Faule show the Rote Faule kerogen to be highly oxidised and degraded compare to kerogens in the ore zone (Fig. 15.25a; Bechtel et al. 2002). Likewise, the stable isotope profiles across the mineralised zone imply increasing oxidation in the Rote Faule (Fig. 15.25b). Biomarker profiles within the mineralised zones also imply hydrothermal alteration has occurred within locally elevated temperature regimes. Some aspects of the profiles are similar to those of hydrothermal-cracked hydrocarbons in the modern Guayamas Basin (Rospondek et al. 2007). All this is consistent with the model of Brown (2006) arguing for a mixing of reduced metalliferous basinal fluids and surface-derived, somewhat more oxidised, saline waters and indicated by Rote Faule (Fig. 15.24). According to Brown, the descending oxidising waters become more saline by coming into contact with buried evaporites (in this case it would have been the underside of the adjacent Zechstein salt seal), or in some cases he argues the surface-derived fluids are reflux brines.

Rote Faule ("red rot") describes a non-mineralised diagenetic zone and loosely encompasses barren red-coloured rocks typically found in the vicinity of high-grade ore. That is, it describes an oxidised haematitic interval that is adjacent to reduced highly mineralised intervals throughout the Lubin-Sieroszowice copper district. Levels of mineralisation in the Kupferschiefer adjacent to a Rote Faule interval are typically far higher than background levels in the

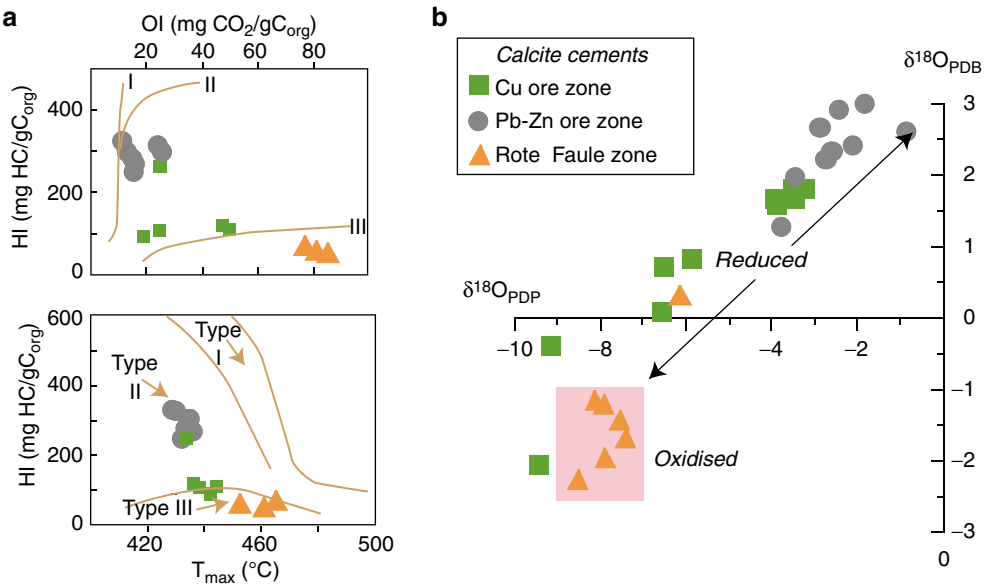

Fig. 15.25 Organic character in the vicinity of Rote Faule. (**a**) Upper figure is a modified van Krevelen diagram plotting Rock-Eval pyrolysis of samples from Kupferschiefer strata Lower figure shows relationship between hydrogen index (*HI*) and temperature as measured by maximum pyrolysis yield (*Tmax*) of the same Kupferschiefer strata. Maturation pathways typical for the different kerogen types are shown in both figures (**b**) $\delta^{13}C$ versus $\delta^{18}O$ plots of calcite cements in the Kupferschiefer in the vicinity of the Rote Faule of SW Poland (After Bechtel et al. 2002)

Kupferschiefer shales (Fig. 15.24c). Rote Faule is a diagenetic unit that is not formation specific and occurs in the Weissliegend, Kupferschiefer and Zechsteinkalk strata, wherever various types of red colour ("red rot") have been created by the diagenetic formation of disseminated authigenic hematite and goethite. Pyrite, and the original organics of the Zechstein carbonate and the Kupferschiefer mudstones, are oxidised and largely removed in Rote Faule intervals, while the economic sulphides of Cu and Pb-Zn have been largely leached and deposited in adjacent areas (Oszczepalski 1989). The organic degradation associated the development of more oxidised and leached Rote Faule is clearly seen in the degradation of the kerogen within this zone (Fig. 15.25a).

The development of Rote Faule interval indicates the oxidised portion of a redox front. In Poland, it is located near the basin margin at the top of the thick redbed sequence, which during burial dewatering was flushed by upwelling basinal waters (Fig. 15.24a). Ore sulphides occur on the far side of this subhorizontal oxidation-reduction front (Fig. 15.24b; or, in the words of the poet Byron, "a gilded halo hovering around decay"). Thus Rote Faule zones outline redox interfaces, centred immediately updip of the outflow positions of salt-seal focused hydrological conduits which carry ascending, highly saline, basinal chloride-rich brines. They define the mixing zones between ascending basinal waters and telogenetic waters of the basin margin, so that the sulphides are arranged in three distinct haloes around "Rote Faule", in the order Cu, Pb and Zn (Fig. 15.24c). Thus, around and above the Rote Faule, base metals are zoned laterally and vertically in successive mineralisation belts of chalcocite, bornite, chalcopyrite, galena and sphalerite.

Mineralisation in Kupferschiefer-style deposits transgresses depositional facies as it is tied to the Rote Faule/upwelling saline brine interface and not to the depositional pattern. That is, Kupferschiefer shales may constitute the richest prepared ground in terms of their inherently high organic content, but volumetrically are not necessarily the best ore hosts. The likely seal to gases (mostly methane), trapped in the Weissliegend sandstones, was the overlying Zechstein evaporites. Throughout Europe, and in the offshore southern Zechstein Basin in North Sea, the Weissliegend is a significant gas reservoir. In Poland, the entrained gases are mainly methane and nitrogen and are often found in the same localities as significant sulphide concentrations (Peryt 1989). These deposits cannot be mined unless vented by Alpine-age faults, as they have been in the worldclass Lubin district. Venting of this gases is tied to the dissolution-driven destruction of the Zechstein salt seal. As in the rest of Europe, the methane was largely sourced in the underlying Carboniferous coal beds and variably trapped beneath the Zechstein evaporite seal.

Geometries of mineralisation show that the underside of the Zechstein evaporites acted as a longterm seal, which focused and locally ponded or trapped the upwelling basinal waters within the immediately underlying Kupferschiefer or its lateral equivalents in the Weissliegend (Fig. 15.24c). It also acted as a pressure seal that aided hydrofracturing within the maturing organic laminates of the Kupferschiefer, as evidenced by numerous sulphide-calcite veinlets in the Kupferschiefer. An inherent lack of permeability in widespread thick evaporites also meant the upper side of the Zechstein salt beds prevented vertical/downward percolation of fresh oxygenated waters, which would otherwise have destroyed the stability of the redox interface (mixing zone) along the edge/underside of the dissolving salt bed (the "block of ice" model for salt dissolution).

Dissolving Zechstein evaporites (including basinwide sulphates) atop the Kupferschiefer laminates acted both as a

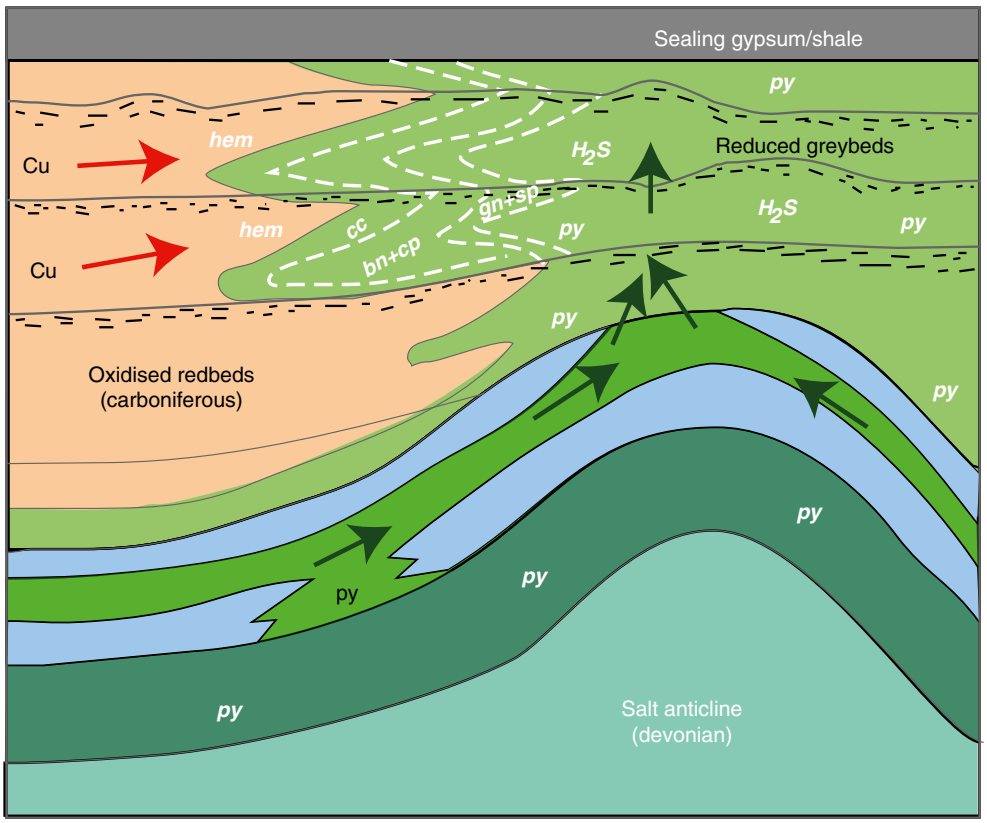

Fig. 15.26 Highly schematic cross section of the Dzhezkazgan region showing Cu zonation at the redbed/greybed interface (After Kirkham 1989)

burial seal to escaping basinal brines (and gases) and as an ongoing focus to descending oxidised brines. The mixing zones (often structurally controlled by reactivated faults), were not where the most significant regional mineralisation took place. It was the presence of an adjacent slowly dissolving salt mass that enabled longterm maintenance of the redox interface between the anoxic hydrology of the Kupferschiefer laminates and the more oxidising metalliferous water of the Rote Faule and so created the worldclass ore deposits of the Kupferschiefer. Similar evaporite-enabled focusing of redox interfaces have created the somewhat smaller ore zones of the Harz Mountains and the Spessart ore district, Germany (Wedepohl and Rentzsch 2006; Wagner et al. 2010).

Dzhezkazgan Region, Kazakhstan

The Dzhezkazgan copper deposit is a halokinetically focused suprasalt sandstone-hosted deposit (Fig. 15.26 and Table 15.7). It is located in a graben near the southern closure of a PermoCarboniferous basin, at the northern edge of the first-order Chu-Sarysu Basin of central Kazakhstan. The Basin contains several stratabound Cu and also Pb-Zn and U zones (Cu mineralisation is present in stacked sandstone beds throughout a 70 km long belt with an area of 600 km^2) of which the Dzhezkazgan ore field is the largest. Ores are hosted in Middle to Late Carboniferous continental successions of conglomerate, sandstone, shale and evaporites (Gablina 1981; Susura et al. 1986). Reserves estimates for the Dzhezkazgan deposit, but based on questionable Soviet era data, are around 400 million tonnes, with a copper grade of 1.5 % (Kirkham 1989). The depositional setting of the host was an intermontane closed-basin, which was made up of deltaic-lagoonal, alluvial and saline lake sediments.

Hosts to the ore are siliciclastic redbeds that are laterally equivalent to bedded evaporites and underlain by Early Carboniferous organic-rich sediments (presumed source rock) and sealed by shaly carbonates. The main copper sulphide and pyrite orebodies are tied to fault feeds that occur on or near the greenbed crest of an anticlinal trap, located along the flanks of a basement high, and sitting atop a salt ridge (Fig. 15.26). The host redbed sandstones become more evaporitic basinward and coarser-grained toward a pinchout along the basement highs. The mineralised sandstone is pyritic, with reduced pore fluids created by entrained hydrocarbons and high salinities. In contrast, the interbedded shales are red due to more oxidising pore fluids. These redbeds were in part derived from continental volcanics.

The mineralised system is carried by 10 cupriferous stratabound bands, within the 380 m thick Dzhezkazgan Formation. Only a limited number of these mineralised bands are of ore grade at a given point in the regional Cu trend. The mineralised system covers an area of approximately 120 km^2, extending down dip to a depth of 1,000 m

Table 15.8 Stratigraphic column of the Dzhezkazgan copper district

	Unit	Comments
Permian	H5	30–2,500 m thick – marl, and interbedded marl and interbedded 20–30 m thick salt beds. A major 1,000 m thick salt bed found in the middle of the unit. This unit is widely developed above and to the south of Dzhezkazgan.
	Black pyritic unit	Average 0.2 m thick – a Kupferschiefer type pyritic and carbonaceous (2–5 % TOC) shale layer. This unit is absent at Dzhezkazgan, but is found in the Tengiz Basin, 350 km to the north, where it contains Cu mineralisation. In the Dzhezkazgan area the units above and below the position of the absent shale are red and lacustrine
	H4	600–800 m thick – red beds, which have the same ratios of conglomerate: sandstone: siltstone as the Dzhezkazgan Formation, but with no reduced grey or green intervals and patches. There are also no carbonates. Halite and sylvite layers are found low in the unit in the main basin to the south of Dzhezkazgan, while some methane, helium and nitrogen accumulations have also been encountered within it, less than 30 km to the south of the mine;
	Sulphate unit	0–100 m thick – a discontinuous gypsum rich band up to a maximum of 100 m in thickness, containing 3–5 % $SrSO_4$
	H3	Dzhezkazgan Fm. to 380 m thick – which hosts the Cu mineralisation of the major Dzhezkazgan orebodies. This unit comprises a red, continental sequence of conglomerates, sandstones and siltstones, which has been locally reduced to a grey or greenish-grey colour in the vicinity of the orebody. The reduced beds consist of compact, uniform, fine-, medium- and coarse-grained rocks with a grey and greenish-grey colour. They contain angular 0.25–0.6 mm, and rarely up to 1 mm, clasts of feldspar and quartz in a fine siliceous-carbonate matrix. The grey sandstones are characterised by a clear stratification, emphasised by intercalations of the red varieties. Grey siltstones are rare. The red siltstones and sandstones are distinguished only by the somewhat smaller clasts and by the clay-carbonate content of the matrix. The ratio of green: red lithologies is approximately 1:1. The ratio of sandstone: siltstone is 1:1, and conglomerate:sandstone 1:30. Variable amounts of 'gypsum' impregnate the sandstones. Conglomerates are present as both intra- and inter-formational varieties. The former are generally 0.8–2 m thick, locally grading laterally into sandstone and sometimes into siltstone. The clasts are usually 0.5–1 cm in diameter and rarely up to 5 cm, comprising locally sourced rock, in a matrix of the enclosing sandstones. The interformational conglomerates have angular exotic clasts
Carboniferous	H2	Lower Member, 3,000 m thick – marine limestone to clayey-limestone or marl, with minor intercalated dolomite. Amorphous pyrite occurs within the marls. – Upper Member, 200–500 m thick – shallow water, terriginous-derived, fine grained calc-siltstone and mudstone, grading to calcarenite. In the top sections lenses of Cu mineralisation up to 20 cm thick may be found at the contact with the overlying Unit H3. This interval is characterised by thin banding and black sandstones;
	H1	Marine limestone – up to 3,000 m thick
	Transition bed	A thin, discontinuous dolomite found at the transition from the Devonian to the Carboniferous, marking the beginning of marine conditions. There is minor Pb/Zn mineralisation and concentrations of Ba and Sr on its lower contact
Devonian	F4	2,000–2,500 m thick – red terrigenous sandstone and siltstone with salt beds and domes
	F3	800–1,200 m thick – andesite, basalt and rhyolite belonging to the middle Devonian volcanic arc
	F2	Continental red beds
	F1	Rhyolite, andesite and basalt, resting on lower Devonian granites
Unconformity		
Ordovician		Grey marine sediments of indeterminate thickness

After Porter (2004)

on its southern margin. Within the cupriferous bands, there are a series of large, elongated, partially overlapping orebodies, developed at a number of different levels, covering much of an approximately 9×6 km area. In that area the ore-bearing Middle-Upper Carboniferous Dzhezkazgan Suite comprises rhythmically alternating gray and red lithic sandstone units that change facies laterally into saline siltstone.

The paleo-environment is interpreted by Gablina (1981) as a closed saline intermontane basin with alluvial, deltaic-lagoonal and saline lake facies. There are 50+ red-gray interbedded cycles in the Dzhezkazgan Formation, each 2–42 m thick, with variable colouration and mineralisation attributed to post-lithification basin brines moving updip along with hydrocarbon and H_2S. The source of Cu is unclear, typically it is attributed to the saline leaching of the regionally distributed Devonian-Lower Carboniferous andesitic volcanics of the Central Kazakhstan Andean-type margin (the Balkhash porphyry-Cu province), which is broadly contemporaneous with the Cu sandstones and located several hundred kilometres further east (Table 15.8). The mineralisation/depositional association shows some affinities with the Eocene Corocoro copper-hosting system in the Andes. The hosting sedimentary strata are gently open-folded and block faulted with much of the structuration in the area controlled by halokinesis.

Interestingly, there is a strong laterally and vertically zoned impregnation of gypsum and halite within mineralised sections of the Permo-Carboniferous cover sequence. Within the Dzhezkazgan area, the red units contain appreciable 'gypsum' within Unit H3, the Dzhezkazgan Formation (Table 15.8; Porter Geoconsultancy 2004). Away from ore, on the shared limb of the Dzhezkazgan Syncline and the adjacent Zhaniu Anticline, where the sequence is almost completely oxidised, all ten units that are mineralised within the ore zone contain abundant 'gypsum.' However, within the sulphide-bearing reduced rocks in the immediate vicinity of Dzhezkazgan, there is little to no gypsum, although it is present within interbanded red lithologies, particularly in the section above the orebodies. Within the sulphide-bearing reduced rocks the cement is mainly carbonate, rather than gypsum. This is taken to imply that the sulphur of the 'gypsum' has been consumed in the formation of sulphides.

There is also a lateral 'primary' variation in authigenic gypsum content. To the south into the Dzhezkazgan Saryzu Trough, the proportion of the red sequence containing gypsum decreases, as does the gypsum content. Similarly, to the north into the Dzhezkazgan Syncline the number of units and thickness of gypsum impregnation decreases, although on the margins of the syncline appreciable amounts are still present. Mineralisation is also present in these same zones. However, despite the drop in levels, regionally 'gypsum' is a relatively constant component of Unit H3.

Within Unit H3, the 'gypsum' is pseudomorphed by $SrSO_4$, with the sequence containing 6–8 % of celestite over thicknesses of 50–80 m. Higher in the sequence, at the base of the exclusively red bed Unit H4, a thick band of gypsiferous marl contains 3–5 % $SrSO_4$. Higher still, in Unit H5, halite and sylvite are abundant, with little or no associated gypsum.

According the Porter Geoconsultancy (2004) it is likely that there is a relationship between the development of sulphides and the presence of pre-existing authigenic sulphate, which is possibly also concentrated in structural positions. Little hydrocarbon remains in the sulphide zone, probably also having been consumed in the production of carbonates and sulphide through the thermochemical reaction/combination with the sulphates. Hydrocarbons are exploited within the main Dzhezkazgan Saryzu Trough to the south, trapped within Unit H4.

Gablina (1981) suggested that an early salt weld juxtaposed fluids of the marine/evaporitic rocks and lowermost redbeds that overlie the salt anticline. Bed geometries illustrated in Fig. 15.26 suggest this weld is halotectonic. The breach allowed hydrocarbon-bearing basinal waters to migrate vertically into the overlying redbeds, where H_2S was produced by thermochemical or bacterial sulphate-reduction. Extensive precipitation of copper and other metals occurred at the regional redox front separating reducing evaporite-fed brines and adjacent red beds.

If so, the role of the catagenically dissolved evaporites was to supply reduced brines and to create precipitation foci, atop a halokinetically controlled salt anticline. The precipitation mechanism and the metal zonation is the same as in the Kupferschiefer model, but in this case the relative position of the evaporite and the redbeds are adjacent and domal, rather than salt dissolution edge. The main evaporite bed lies below the redbeds, which are the ultimate source of the metals. Although the mineralised beds are stratiform, this deposit is really a result of halokinesis; a similar, but less economically significant, analogue is to be found in the Lisbon Valley, USA.

Copper in the Lisbon Valley, Utah

The ore deposits of the Lisbon valley are another example of halokinetic suprasalt deformation controlling structure and hence the position of redox mineralisation. Compared to Dzhezkazgan, the deposits are much smaller (34 Mmt @ 0.53 %). Cu(±Ag). Ores in Lisbon Valley occur along suprasalt extensional faults, in redbed sediments of the Paradox Basin and in coal-bearing horizons of the overlying Cretaceous Dakota Sandstone in SE Utah and SW Colorado (Fig. 15.27a). Deposits of this type occur at Salt Valley and Paradox Valley, with the largest deposits in the Lisbon Valley (Fig. 6.83; Morrison and Parry 1986). Cu is found as vein fillings, sandstone pore fillings, and as replacement of coalified plant fossils. The deposits are clearly related to halokinetically-induced faults (Fig. 15.27b, c). The largest deposits, Big Indian and Blackbird, occur along the Lisbon Valley fault in coaly horizons of the Cretaceous Dakota Formation. Almost all the mineable copper ore occurs within several hundred metres of either the Lisbon Valley fault or other major suprasalt fracture zones.

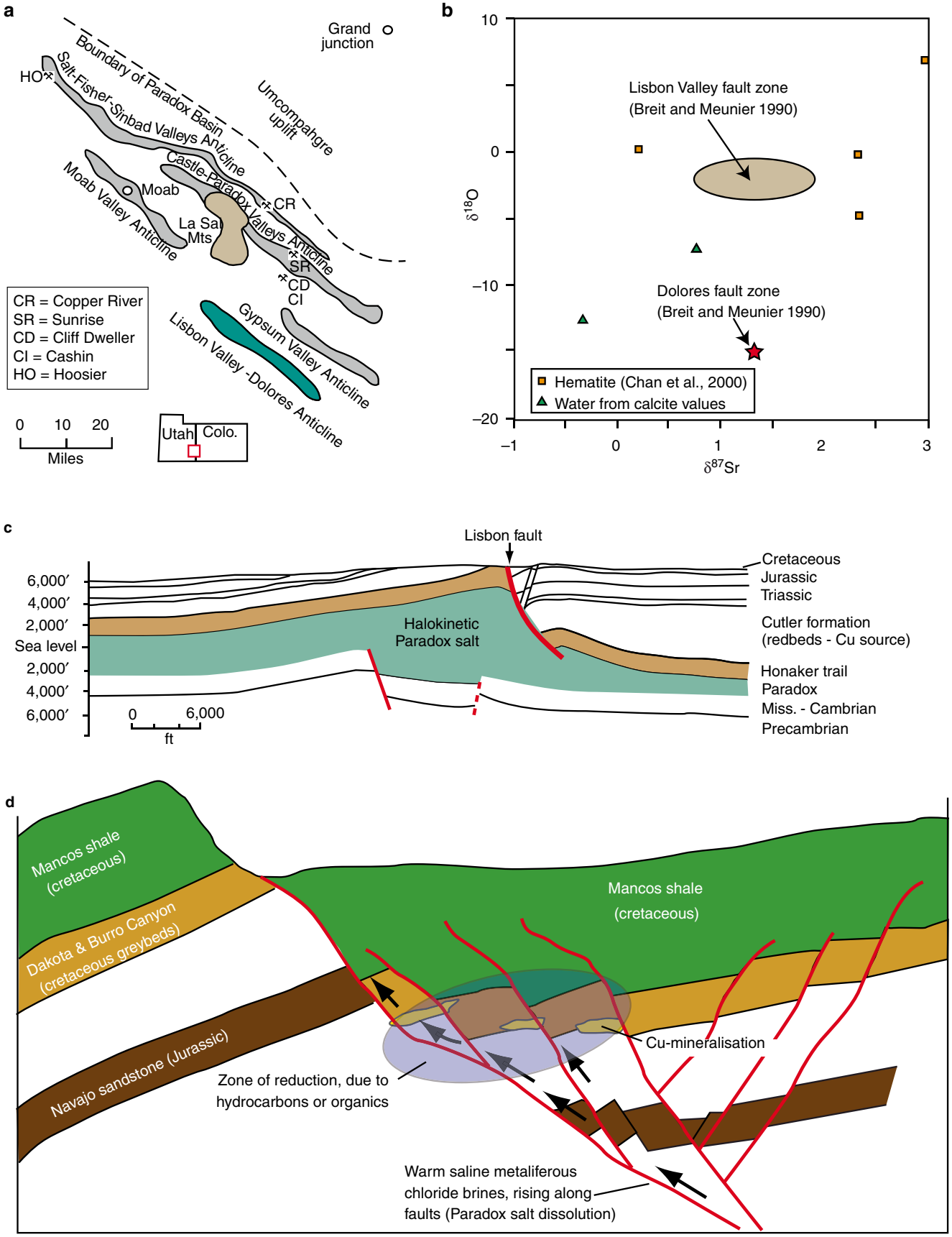

Fig. 15.27 Copper in Lisbon Valley salt anticline, Utah. (**a**) Regional distribution of salt anticlines (see also Fig. 6.83), (**b**) Isotope character of hematite and calcite. (**c**) Cross section of Lisbon Valley salt anticline. (**d**) Detail of crestal position of Lisbon Fault showing distribution of Cu ore (After Morrison and Parry 1986; Kirkham 1989)

All the deposits in the area are related by geologic setting as well as ore and gangue mineralogy (Morrison and Parry 1986). Fluid inclusions, mineral chemistry, and C-O stable isotopes in calcite gangue associated with Cu ores at Lisbon Valley suggest they formed via subsurface mixing of two diagenetic waters. Fluid temperatures ranged from 72 to 103 °C, while salinities were 5–20 equiv. wt % NaCl during calcite deposition. Saline, salt dissolution-influenced basinal fluids migrated upward along fault zones, and upon mixing with shallower reduced Ba-rich groundwater deposited ore and gangue minerals. Mineral precipitation was induced by the combination of reduction and dilution of upwelling basinal brines.

The metal-carrying fluid probably originated in the redbed aquifers of the Permian Cutler Formation. The brines may have equilibrated for long periods in these Cutler Formation aquifers and only been released during faulting driven by halokinetic activity during the Late Cretaceous – Early Tertiary Laramide orogeny. Then faults, such as the Lisbon Valley Fault, breached the redbed aquifer and so allowed pressurised, heated metalliferous fluids to escape upward along the faults until they encountered permeable units replete with reductants, such as in the Dakota and Wingate Sandstones (Kirkham 1989).

In my opinion, the role of salt has not been given the importance it deserves in the explanation of mineralisation in a Lisbon-Valley style deposit. The style of faulting that focuses the mineralisation is a response to movement on the underlying active salt structure (Fig. 15.27b, c). The ongoing dissolution of this underlying salt also supplied the chloride-rich brines that maintained the interface with leached the metals from adjacent redbeds. It also created the thermal and brine density contrasts that drove the convection and metal enrichment of this brine. Without halokinesis and salt dissolution there would be no focusing into this structurally controlled deposit. Nor would there be any long-term maintenance of the redox haloes about the faults that allowed this deposit to accumulate. Without the underlying halokinetic salt, economic levels of copper sulphides simply would not be there. As is to be expected, this cupriferous flow regime is very similar to, although less prolific than, those of the Dzhezkazgan region. The patchy ore distribution means the various Lisbon Valley deposits are classified as Revett- style Cu deposits.

The same brine-related redox hydrology is also responsible for a number of uranium deposits in the area (Lisbon Valley, White Canyon, Monument Valley) totalling some 42.5 Kt of produced uranium (Dahlkamp 1993). Tabular uraniferous orebodies are peneconcordant with bedding and located in channel sandstones rich in coalified plant trash, mostly in the in fluvial channels of the Shinarump Sandstone member of the Triassic Chinle Formation, with some reworking into exposed or subcropping positions atop the salt anticline into the Permian Cutler sandstones (Reynolds et al. 1985).

Dongchuan Copper, China

Stratabound sediment-hosted copper deposits, associated with a widespread halokinetic breccia unit, occur in a 450 km long rift in the Yunnan Province of China (Huichi et al. 1991). The Dongchuan area is the largest of five copper mining districts in this north-trending rift, which contains sandstone, shale, and carbonate rocks of the Dongchuan Group, deposited in this late Paleoproterozoic rift as it was transitioning into a passive margin (Fig. 15.28; Zhao et al. 2010; Wang and Zhou 2014).

Deposits in the area range from 10 to 100 million tonnes of ore with ore grades of 1–1.5 %. Three formations, totalling some 1,200 m, contain the copper deposits mostly in the lower part (Fig. 15.29). They are from top to bottom: the Etouchang (Heishan) Formation, mainly a carbonaceous slate; the Laoxue Formation, mainly a stromatolitic dolostone; and the Yinmin Formation, chiefly purple slate and sandstone. These formations are crosscut by breccia and mafic igneous rocks.

Numerous transtratal breccia bodies occur in the Dongchuan Group, particularly within the Yinmin Formation, and are collectively known as the Yinmin Breccia (Fig. 15.29). They are made up largely of clasts derived from the Yinmin Formation that are cemented in a matrix of rock flour and possibly hydrothermal minerals (e.g. quartz, feldspar, carbonate and biotite). The mechanism of brecciation is still unclear, but is likely due to halokinesis sourced in what were once thick mother salt beds in the lower part of the Yinmin Formation. Post emplacement, there were one or more leaching/dissolution episodes (coupled with a hydrothermal overprint), creating textures similar to, but more metamorphically evolved than seen in the Neoproterozoic diapiric breccias exposed in the Flinders Ranges, Australia. Another example of halokinetic focusing in China, but in a much more highly metamorphosed milieu is seen in the Palaeoproterozoic Fe-Cu sulphide and borate deposits in eastern Liaoning, Northeastern China (Chap. 14; Wang et al. 1998a).

Clasts of igneous rocks are locally present in the Yinmin breccia, suggesting that at least some breccia bodies postdate the igneous intrusions and were carried higher into the stratigraphy via salt flow. This is consistent with field relationships in which a number of gabbro bodies appear brecciated (Zhao et al. 2010). It is also consistent with the common association with gabbros and dolerite blocks in halokinetic breccias that define outcrops of Miocene salt in the Middle East (Chap. 7). The position of the former mother salt mass in the Yinmin Fm redbeds is also consistent with it once being a basinwide halite bed that formed during the rift to drift transition indicated by the passage from rift redbeds of the Yinmin formation to passive margin marine carbonates of the overlying Luoxue Formation.

Numerous sedimentary-hosted stratiform copper deposits, known as the “Dongchuan-type” Cu deposits in Chinese literature, are hosted within dolomites, typically near the

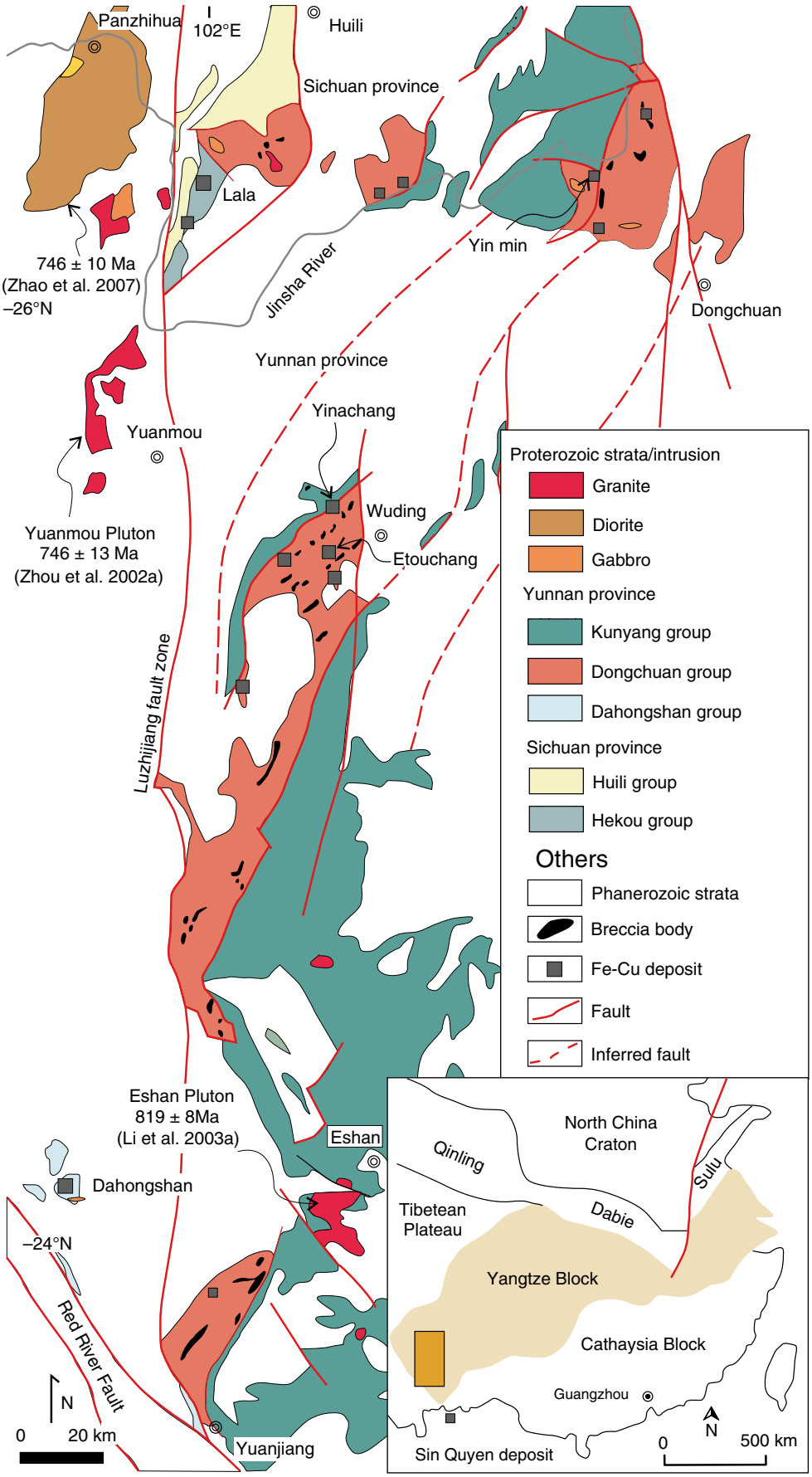

Fig. 15.28 Geological map showing the distribution of Proterozoic strata, granites and gabbros in the SW Yangtze Block, of southeastern China, while inset shows position of the Yangtze block in a simplified tectonic map of China (After Zhao et al. 2010)

contact between the Yinmin and Luoxue Formations and often associated with Yinmin breccia. Vein type ore bodies account for only 3 % of the total ore reserves in the area. Stratabound ores characteristically occur as disseminations of sulphides along stromatolitic algal layers. Locally, highgrade vein-type ores crosscut the dolostone. Both ore types contain bornite, chalcopyrite, chalcocite, and other minerals. Fluid inclusions in quartz veinlets contemporaneous with the copper mineralisation contain liquid, vapour and daughter minerals: NaCl, $CaCl_2$, KCl and $BaCl_2$. The inclusions homogenise between 200 and 280 °C.

Hot reducing chloride-rich brines, circulating and cycling upward along the flanks of the diapir, leached copper from the oxidised Yinmin Formation and carried it to the base of the overlying Laoxue Formation (Huichi et al. 1991; Wu Moude and Li Xiji 1981). There sulphide-rich fluids were formed by reaction of evaporitic sulphates with decayed organic matter in the dolostones. Copper sulphide deposition in the dolostones resulted from the mixing of these fluids. Continued circulation leached all of the remaining salt from the diapir, and the overlying and surrounding rocks collapsed to form the current breccia masses.

Cu-sulphides were precipitated at two sites: (1) as breccias, lenses, and veins around fluid-venting centres tied to the breccias; and (2) as stratiform pyrite-chalcopyrites, which are associated with anhydrite located distal to the salt domes (Fig. 15.30). Within each mining district the proximal ores are associated with brecciated, albite-and tourmaline-rich metasediments. The sulphides in the proximal ores have $\delta^{34}S$ values of 14.6‰–12.7‰, whereas the distal ores have $\delta^{34}S$ values of 2.6‰–14.5‰ for the sulphides and 7.9‰–19.0‰ for the anhydrite; suggesting a sulphate-dominated sulphur source, with the pyrite $\delta^{34}S$ variations arising mainly from decreasing temperatures away from the

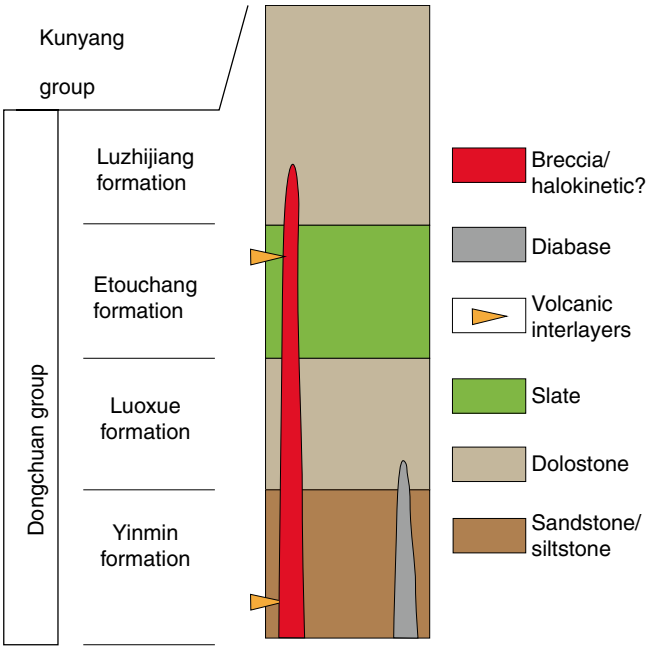

Fig. 15.29 Stratigraphy of the Dongchuan Group showing crosscutting (halokinetic?) distribution of breccia bodies

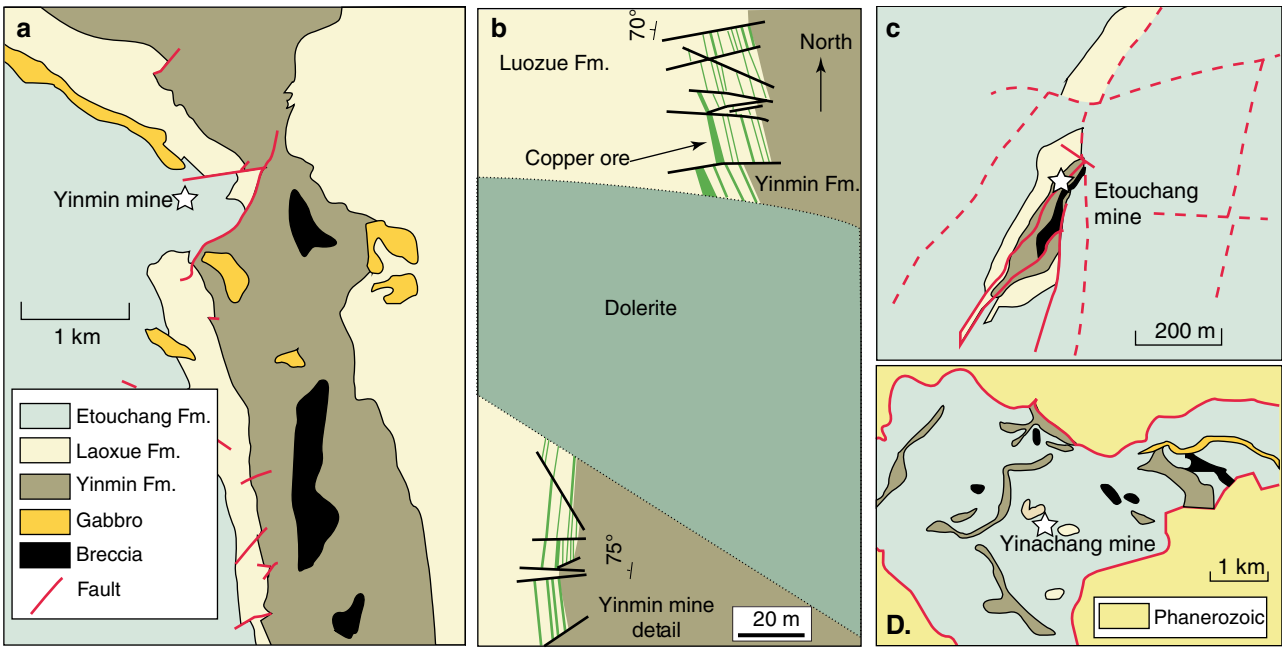

Fig. 15.30 Geological map of (**a**) Yinmin mine in Dongchuan area, (**b**) Detail from an audit in the Yinmin mine, (**c**) Etouchang mine area, (**d**) Yinachang mine area (After Zhao et al. 2010, 2013)

centres of the deposits. According to Wang et al. (1998a) the origin of the deposits is best described by a model in which sulphate-carbonate rocks were deposited in peridiapir sinks during salt diapirism. The salt domes then acted as foci for subsequent hydrothermal venting of chloride-rich metalliferous fluids and the adjacent peridiapir sediments became the centres of sulphide mineralization. The sulphides precipitated during interaction of the reduced, metal-bearing hydrothermal fluids with the *in situ* sulphates, which acted as the major *in situ* source of evaporitic sulphur.

At the broader scale the Dongchuan deposits can be related to the Dahongshan deposits, via a common paragenetic history, constituting a wider group of Paleoproterozoic Fe-Cu deposits, in the Kangdian region of SW China (Fig. 15.28; Zhao and Zhou 2011). The Dongchuan Group is composed of siltstone, slate, and dolostone with minor volcanic rocks, whereas the Dahongshan Group has undergone lower amphibolite facies metamorphism and consists of quartz mica-schist, albitite, quartzite, marble and amphibolite with local migmatite. Deposits in the Dongchuan Group are commonly localized in the cores of anticlines, in fault bends and intersections, and at lithological contacts. Orebodies are closely associated with breccias, which are locally derived from the host rocks. Fe-oxides (magnetite and/or haematite) and Cu-sulphides (chalcopyrite, bornite) form disseminated, vein-like and massive ores, and typically fill open spaces in the host rocks. The deposits have extensive albite alteration and local K-feldspar alteration overprinted by quartz, carbonate, sericite and chlorite.

Deposits in the Dahongshan Group have orebodies subparallel to stratification and show crude stratal partitioning of metals. Fe-oxide ores occur as massive and/or banded replacements within the breccia pipes, whereas Cu-sulphide ores occur predominantly as disseminations and veinlets within mica schists and massive magnetite ores. Ore textures suggest that Cu-sulphides formed somewhat later than Fe-oxides, but are possibly within the same mineralization event. Both ore minerals predated regional Neoproterozoic metamorphism. Both orebodies and host rocks have undergone extensive alteration of albite, scapolite, amphibole, biotite, sericite and chlorite. Silica and carbonate alterations are also widespread. Ore-hosting strata have a LA-ICP-MS zircon U–Pb age of 1,681 ± 13 Ma, and a dolerite dyke cutting the Fe-oxide orebodies has an age of 1,659 ± 16 Ma. Thus, the mineralization age of the Dahongshan deposit is constrained at between the two.

All ores from the Donchuan and Dahongshan groups have high Fe and low Ti, with variable Cu contents. Locally they are rich in Mo, Co, V, and REE, but all are poor in Pb and Zn. Sulphides from the Fe–Cu deposits have $\delta^{34}S$ values mostly in the range of +2 to +6 per mil, suggesting a mix of several sources due to large-scale leaching of the strata, with the involvement of evaporite-derived brines across all ore types (Zhao and Zhou 2011). Isotopic dating and field relationships suggest that these deposits formed in the late Paleoproterozoic. Ore textures, mineralogy and alteration characteristics are typical of IOCG-type deposits and thus define a major IOCG metallogenic province with an evaporitic association. We shall come back to evaporitic associations in some IOCG deposits in the next chapter

The Paleoproterozoic rift-related sedimentary sequences of the Dongchuan Group, South China, today constitute one of the largest SSC districts in the world (Zhao et al. 2013). One of the largest deposits in the Donchuan district, is the Yinmin deposit, which shows stratiform Cu orebodies intruded by dolerite dykes, which have a U-Pb age of 1,701 ± 28 Ma (Fig. 15.30a, b). This is slightly younger than the ore hosting strata which include a tuff with a zircon U-Pb age of 1,742 ± 13 Ma. Sulphides in the ore yield ages around 1,600 Ma, thus the Yinmin mineralisation and by inference other Cu deposits in the Dongchuan district correspond to a late Paleoproterozoic rifting event, likely tied to the breakup of the Columbia supercontinent (Wang and Zhou 2014). Zhao et al. 2013, argue this timing further supports the notion of genetic and temporal links between episodes of more intense formation of SSC's and the breakup of supercontinents. In my mind, this also supports the redox interface association with proximity to flow and dissolving halokinetic salt acting as deposit foci to adjacent leached redbeds. Thick and widespread halite supergiants are tied to supercontinent rifting events, last seen in the Phanerozoic in the Pangean break-up (Chap. 5) and by default to depositional systems that have redbeds and thick halokinetic-salt masses at the base of the rift succession

Zn-Cu-Pb Kipushi Deposit, Africa

The Neoproterozoic metallogenic province of Central Africa contains rich stratiform concentrations of Cu and Co in both the Shaba Province (Shaba cupriferous arc – Zaire) and Congo-Zambian copper belts (Cailteux 1994; Kampunzu et al. 2009). Both provinces retain substantial evidence of meta-evaporites. For example, scapolite is widespread in amphibolite-grade calcsilicate rocks and marbles in Katangan rocks of the copper belt and in the central provinces in Zambia. Ramsay and Ridgway (1977) point out that "scapolite is rarely found in such abundance and Zambia must be one of the major scapolite provinces in the world." Munyanyiwa (1990) argues for an evaporite precursor to this scapolite, he also notes that metasedimentary anhydrite is still present in parts of the Katangan succession in the copper belt. We shall look in detail at the Kipushi deposit, but it is indicative of facies association in many other similar perhaps more metamorphosed copper deposits in the region. Much of the following description is taken from Kampunzu et al. (2009), Van Wilderode et al. (2013), (Heijlen et al. 2008) and references therein.

The Kipushi Zn-Pb-Cu deposit, hosted in Nguba Group strata is located in the northern extension of the central African Copper Belt in southeastern Zaire. Kipushi is perhaps the most significant Zn–(Cu)–Pb carbonate-hosted deposit in the Copperbelt of Central Africa with total metal production of 6,622,116 t Zn and 4,082,275 t Cu from 1922 to 1993 when operations were suspended. The in-situ ore grade averaged 11.03 wt.% Zn and 6.80 wt.% Cu. Ore has been proven to a depth ≈ 1,800 m, but mine development stopped at 1,250 m depth. The remaining ore resources down to the 1,500 m level are estimated at >5 Mt Zn, >500,000 t Cu, and >100,000 t Pb from ores averaging 21.4 wt.% Zn, 2.1 wt.% Cu and 0.88 wt.% Pb with additional trace metals of Cd (763 ppm), Co (100 ppm), Ge (68 ppm), Ag (28 ppm) and Re (3 ppm) (Cailteux 1986, 1994). Other rare metals include As, Ga, Mo, Bi, Hg, Ni, Sb, Se, Sn, Te and V.

The Kipushi deposit is hosted on the northern flank of a regional NW–SE trending anticline characterized by a faulted axial core filled with a transtratal megabreccia known as the "Axial Breccia" (Fig. 15.31a). The dip is 60–70° SW on the southern flank and 75–85° NE on the northern flank. The Axial Breccia is barren and consists of a heterogeneous layer-parallel breccia made up of highly strained and brecciated or rounded fragments of Roan and Nguba Group rocks as well as dolomites and meta-evaporites, and also includes arkosic sandstones and metabasic rocks along with white talcose dolomites (Table 15.9). Near identical Roan breccias underlie most Katangan thrusts and are interpreted as a rauhwacke, where much of the salt is long gone, leaving only pseudomorphs and patchy anhydrite (e.g., Jackson et al. 2003; Warren 1999, 2000b).

The ore is a discordant body, parallel to the former salt flow margin (transtratal) at the contact between a halokinetic breccia body and adjoining host rocks of the Upper Proterozoic Lower Kundelungu Group of the Katangan System (Fig. 15.31b; De Magnee and Francois 1988; Heijlen et al. 2008). It is currently exposed at the surface at the northeast margin of a large plunging anticline. The halokinetic breccia in the core of the anticline contains large blocks (up to 100 s of metres across) of Roan Supergroup rocks of several lithologies, as well as large blocks of gabbro. Much of the breccia at Kipushi is made up of fragments of white sparry dolomite, which are thought to have originally been derived from the halokinetic and solution induced break-up of the Dipeta Dolomite. The gabbro (now completely amphibitolised) is thought to have originally been emplaced as a sill in the Dipeta Dolomite within the Roan Supergroup (Fig. 15.31c).

Most workers accept there is an association with former evaporites and the Kipushi deposit breccias which host, or are adjacent to, mineralisation. Roan Supergroup sediment once contained several evaporite intervals (De Magnee and Francois 1988; Jackson et al. 2003; Heijlen et al. 2008). Regionally these former salt intervals are defined by evaporite dissolution breccias. Such solution breccias occur in the lower part of the Katangan System and are interlayered with alternating sparry dolostones, black shales, and chlorito-talcose dolomitic siltstones (Fig. 15.31). Prior to dissolution, the evaporites are thought to have acted as the mother salt bed for the Kipushi allochthon and other halokinetic features in the region. The upper part of the Katangan System is made up of the Lower and Upper Kundelungu Supergroup and is composed mostly of siliciclastics with some limestones, which are locally dolomitised.

Portions of the Katangan System are now intensely folded in the copper belt, with a disharmonic style reminiscent of the salt-cored European Jura. Cores of many anticlines in the copper belt are formed by megabreccias, containing blocks of Roan metasediment. Regionally, some of the larger clasts contain sufficient stratabound Cu-Co sulphides to be actively mined. The matrix between the blocks is a dolomitic metasiltstone, which also contains gypsum and anhydrite pseudomorphs (De Magnee and Francois 1988). Regionally, the megabreccias cut into the flanks of many megabreccia cored anticlines and reach into Upper Kundelungu strata. This is the case at Kipushi (Fig. 15.31a).

The megabreccia and its crosscutting relationships are very similar to outcropping halokinetic breccias in the Neoproterozoic Callanna Group megabreccias of the Flinders Ranges, South Australia (Chap. 7). There, many of the breccia geometries reflect the falling or deflation stage of diapir evolution and are located along regional extensional faults. Breccias in the Katangan System also follow major faults, which De Magnee and Francois (1988) called extrusion faults. If analogies to the Flinders Ranges are valid, some of these "extrusion faults" may be examples of outcropping fault welds. Once a basin undergoes inversion, such faults are often reactivated and can be easily misinterpreted as solely due to late-stage thrusting.

The Kipushi structure is interpreted as a salt diapir/allochthon that, after emplacement, was subject to ongoing dissolution of the more soluble salts, along with associated collapse brecciation. According to De Magnee and Francois (1988) and Chabu (1995), this dissolution process played an essential role in the base metal mineralisation, as it supplied an ongoing focus for the saline chloride-rich brines that leached and transported the heavy chalcophile metals. The matrix dolomites adjacent to the mineralising show little evidence of thermal effects and only the gangue dolomite indicate the elevation saline fluid temperatures associated with mineralisation (Fig. 15.32, Van Wilderode et al. 2013). De Magnee and Francois (1988) went on to argue that sulphur and organic matter must also be present to form a mineral deposit, as well as a high lateral thermal gradient to set up the circulation cells and an appropriate permeability structure to channel the ascending hydrothermal solutions.

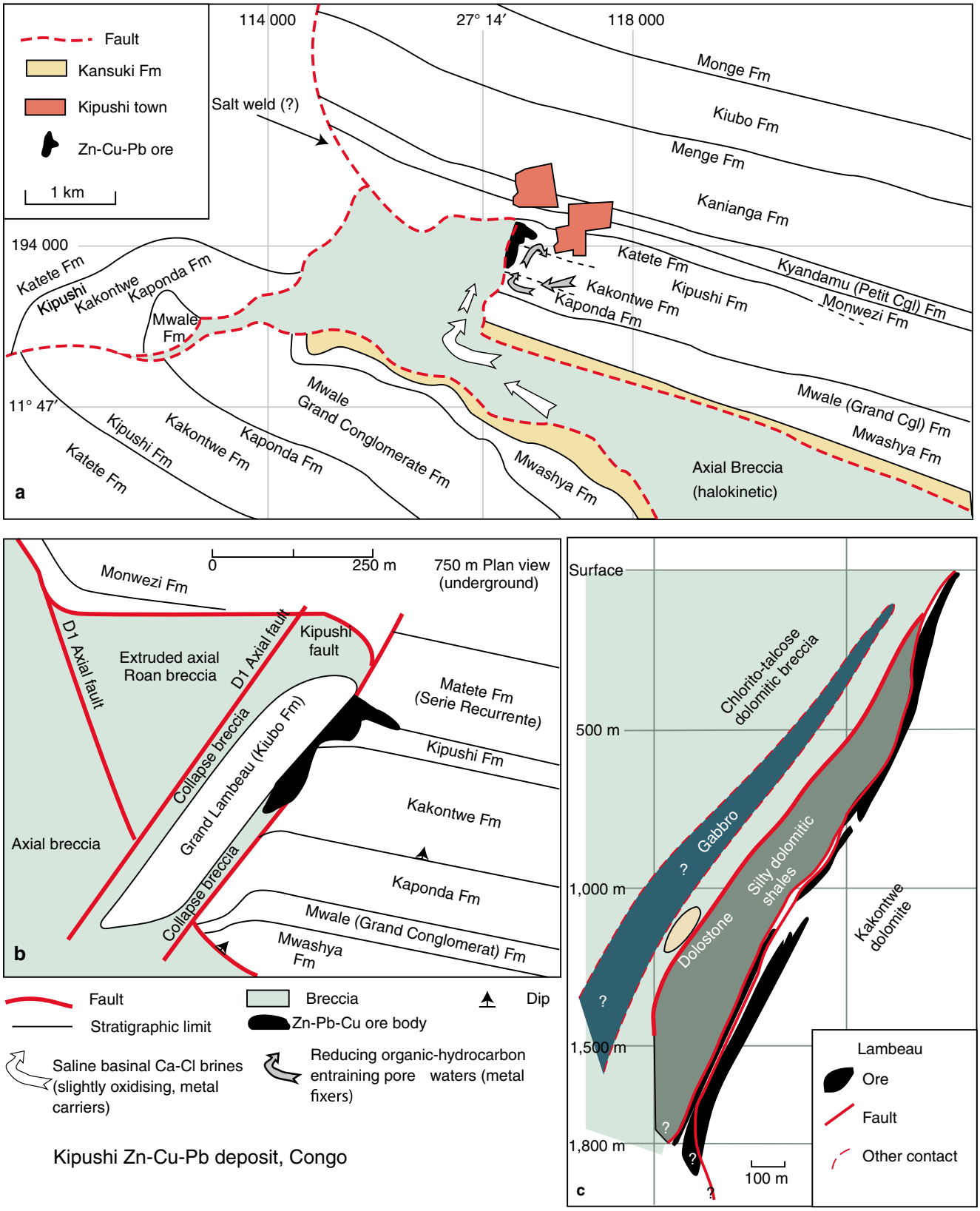

Fig. 15.31 Kipushi Zn-Cu-Pb deposit, Congo. (**a**) Geological map of the Kipushi area. (**b**) Generalised map (plan view) of underground structural features at the 750 m level in the Kipushi Mine. (**c**). Vertical section through the Kipushi ore zone (generalised in **a** and **b**). After Kampunzu et al. 2009, and de Magnee and Francois (1988)

Table 15.9 Stratigraphy of the Neoproterozoic Nguba Group at Kipushi and indication of the kinematic and sedimentological setting

		Formation	Lithology at Kipushi	Kinematic and sedimentological setting
Nguba Group	Bunkeya Subgroup	Monwezi	Dolomitic sandstones, siltstones and pelites	Transgressive clastic sequence prograding over the cap carbonates. Persistence of northern proximal facies and southern open basin
		Katete	"Serie Recurrente" Top (30–40 m): alternation green chloritic shales with nodules (e.g. gypsum) and white dolomites Middle (120–130 m): irregularly bedded greyish shales and white dolomites Bottom (60 m): grey dolomites and shales containing dolomite nodules	
	Muombe Subgroup	Kipushi	Black carbonaceous dolomite with oolites, cherts and shungite (100 m)	
		Kakontwe	Upper (20–50 m): irregular bedded and carbonaceous dolomite with black cherts. Middle (60–70 m): bedded dolomite with oolites and algal structures Lower (180–250 m): massive fine-grained grey dolomite	Cap carbonates. Proximal facies in the north, open basin towards the south
		Kaponda	Top (90 m): dolomites with cherts at the base, some shales Middle (30 m): lenticular or massive, limonitic dolomite Bottom (0–80 m): carbonaceous dolomitic shale – "Dolomie Tigree"	
		Mwale	Grand Conglomerat (300–500 m): green-grey, unsorted matrix supported conglomerate	Sturtian glaciation and transition from intracontinental rift into proto-oceanic basin with further basin widening

After van Wilderode et al. (2013)

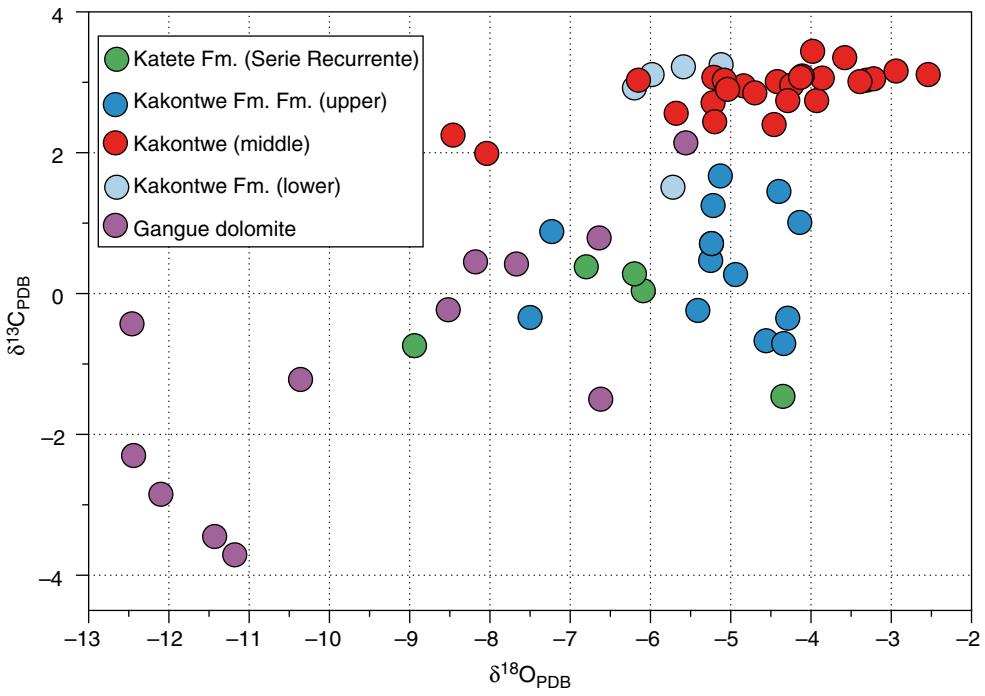

Fig. 15.32 Covariant carbon-oxygen stable isotope crossplot broken down by host formation dolomites using values extracted from Table 2 in Van Wilderode et al. (2013). Clearly illustrates the hotter fluid origin (indicated by more negative carbon and oxygen values of the gangue dolomites)

At Kipushi these conditions were created by a huge slab of silty dolomitic shale (Kundelungu Group), which lies alongside the wall of the halokinetic breccia and forms the current roof of the ore body. De Magnée and Francois go on to draw parallels with peridiapiric mineralised laminites in north Africa.

The genetic model of Heijlen et al. (2008) further refined their model and concluded that halite dissolution was an important process for generating the saline mineralizing fluids that formed Kipushi, as indicated by Cl–Br–Na systematics of fluid inclusions. The mineralising fluid of the main ore-forming phase had a salinity of ≈ 30–43 eq. wt.% NaCl and likely originated from formation waters or metamorphic fluids that were expelled late in the orogenic evolution. After dissolving evaporites and perhaps evolving scapolites, the resulting saline fluids were capable of leaching metals from upper crustal country rocks during their rise to the surface, as indicated by lead isotopes. The relatively high metal content (Ba, Zn, Fe, Pb) of the NaCl–KCl–$CaCl_2$ fluid suggests that the source rocks included felsic basement. The absence of baryte, despite the high Ba concentration in the fluid, indicates that the mineralisation occurred in reducing conditions and sulphur was locally available as sulphide.

$\delta^{34}S$ signatures of the main orebody demonstrate that the sulphide was derived from seawater sulphate through thermochemical sulphate reduction (TSR), simultaneously oxidising organic material and generating H_2S. Part of the sulphide in the concordant orebody along the contact of the Kipushi Formation and the Série Récurrente, however, was most likely derived from bacterial sulphate reduction (BSR) during diagenesis. They may have been preserved in the form of pyrites up to the time of ore formation. Heijlen et al. (2008) suggest that mineralisation took place when highly saline and metal-bearing fluids encountered an H_2S-rich hydrocarbon reservoir during fault-controlled expulsion. The Sr and Nd isotopic composition of the gangue dolomite and the metal content of fluid inclusions, indicate that the mineralising fluid interacted with rocks of both mafic and felsic affinities in the basement and possibly in the Roan. These rocks provided the metals for the Kipushi mineralisation (Van Wilderode et al. 2013).

For the purposes of "on ground" targeting of an analogous deposit an exact distinction in terms of fluid timing may be largely academic when defining greenfield sites for a preliminary sampling program. What is obvious from the relationship of mineralisation to the halokinetic breccia at Kipushi is that the breccia margin in contact with organic-rich sediments was the precipitational focus for the mineralising solutions. This occurred either as the residual salt was still dissolving, or once it had dissolved and scapolite transformations were supplying the metal-entraining volatiles (Fig. 15.31). An exact determination of the time of the mineralisation is not the fundamental control on the location of the deposit. The salt structure induced focus to fluid flow and its associated redox front is what is important. This relationship in a mineralised halokinetic province, even when metamorphosed, is predictable and mappable.

Interestingly' across the various documented SSC deposits, it seems that halokinetic associations constitute the larger deposits, rather than the bedded association we shall discuss next. This is because the dissolving edge of a flowing salt mass can maintain its position in earth space as more salt will flow in and replace the salt that is lost by dissolution, until the contact with the mother salt layer is lost via salt welding or the mother salt bed is depleted. In contrast, the redox front at the edge of a bedded salt mass is more likely to be a retreating front, and only the underside of a thick bedded mass is stable over long enough time frames to form an economic sulphide accumulation. We shall return to this discussion later in the chapter, after we have considered non-halokinetic examples.

Sediment-Hosted Cu in Bedded Evaporite Context

In this type of deposit the associated evaporite is typically bedded and the size of the resource in individual is typically less than in the halokinetic association. We shall start this discussion with the Corocoro ore district of Bolivia as it offers an interesting quandary as to the relative importance halokinesis played in its genesis. The other deposits discussed in this section have bedded evaporite not halokinetic redox associations

Corocoro and Other Sandstone-Hosted Deposits of the Central Andes

Stratabound deposits of copper (+Ag) hosted by variably-dipping continental clastic sedimentary rocks occur in Central Andean intermontane basins and are known to postdate compressive deformation/uplift events in the region (Flint 1986, 1989). The deposits are relatively small and include; Negra Huanusha, central Peru (Permo-Triassic); Caleta Coloso, northern Chile (Lower Cretaceous); Corocoro, northwestern Bolivia (Oligo-Miocene); San Bartolo, northern Chile (Oligo-Miocene); and Yasyamayo, northwestern Argentina (Miocene-Pliocene). The Corocoro area has produced the largest amount of copper in the Andean examples, something like 7.8 million tonnes of copper at a grade of 7.1 % (Cox et al. 2007). The location of mineralisation is controlled by structurally-focused redox fronts in bedded sediment hosts, which abut a steeply-dipping translatent fault (Fig. 15.33). Deposits are irregular, usually elongate lenses of native metal, sulphides, and their oxidation products. Typically, deposits are hosted in alluvial fan and playa sandstones or conglomerate facies that also contain abundant gypsum and lesser halite. The undersides of some copper sheets at Corocoro even preserve mud-crack polygons and bed-parallel burrow traces (Savrda et al.

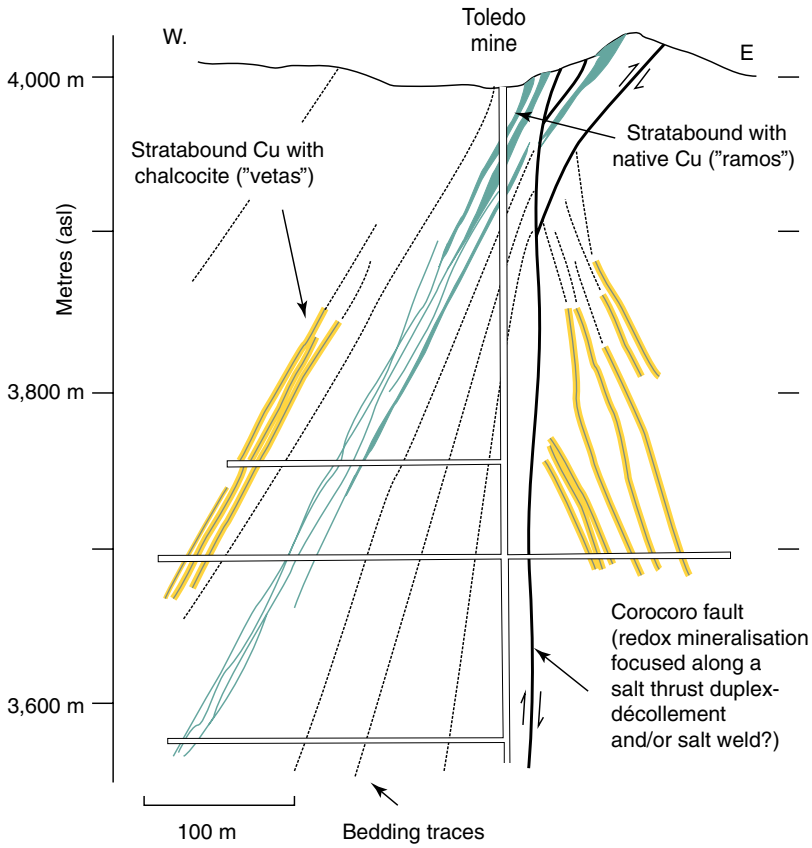

Fig. 15.33 Cross section of the Toledo mine in the Corocoro ore district (Adapted from Entwistle and Gouin 1955)

2006). Ore mimicry of mudcracks is not a feature controlled by on-for-one-replacement of organic material deposited in a sandstone, rather it is following preexisting permeability/redox contrasts.

The Corocoro deposits in Bolivia have been mined sporadically since they were first exploited by the local Indians, prior to the Spanish invasion in the sixteenth century and were largely exhausted in half a century of more intense mining operations beginning in 1873 (Fig. 15.33). Sandstone and conglomerate matrices show evidence of bleaching and leaching of the original redbed host with numerous red-greybed redox interfaces visible in the mined sequences. Ore minerals (dominantly native copper) are secondary fills within secondary intergranular pores created by the dissolution of earlier carbonate and sulphate masses and intergranular cements. Twelve grey sandstone beds, which were host to the long worked-out native copper ores, occur within a stratigraphic thickness of 60 m in a unit known as the Ramos Member which still hosts abundant $CaSO_4$ as gypsum.

Ores are stratabound, but not necessarily stratiform and the larger masses of native copper are typically present as vein fills. Sometimes the copper pseudomorphs large orthagonal-ended aragonite prisms that can be several centimetres across. There are two main styles of mineralization; (1) Ore minerals as a matrix to stratiform detrital silicates, typically low dipping and commonly highlighting primary sedimentary structures, such as cross stratification (2) Ores in stacked channelized bodies, that show steep dips in structurally complex and folded zones with local brecciation. Native copper commonly fills thin laterally extensive sheets in tectonic fractures in the limbs of such tight folds. Ljunggren and Meyer (1964) interpreted these folded diagenetic sheets of copper as a remobilization products precipitated during deformation of earlier matrix-pore filling copper.

Critical factors in Corocoro ore genesis include (Flint 1989): (1) Stratigraphic association of evaporites, organic-rich lacustrine mudstones, clastic reservoir rocks, and orogenic, igneous provenance areas for both basin-fill sediments and metals; and (2) Intrabasinal evolution of metal-mobilising saline brines derived from the buried and dissolving lacustrine evaporites that flush volcaniclastics, volcanics and feldspathic sediments. The same saline diagenetic fluids also caused the dissolution of early, framework supporting cement and large aragonite prisms, all now pseudomorphed by native copper.

The ore-hosting clastic horizons are consistently located in the highly gypsiferous Vetas Member of the Ramos Formation, which was deposited as redbeds in braidplains or fluviodeltaic playa margins centripetal to the edges of saline evaporitic lakes that were accumulating gypsum and halite (Fig. 15.34; Flint 1989). Abundant gypsum is still present in the Ramos Member as nodules and satinspar vein fills, both are secondary

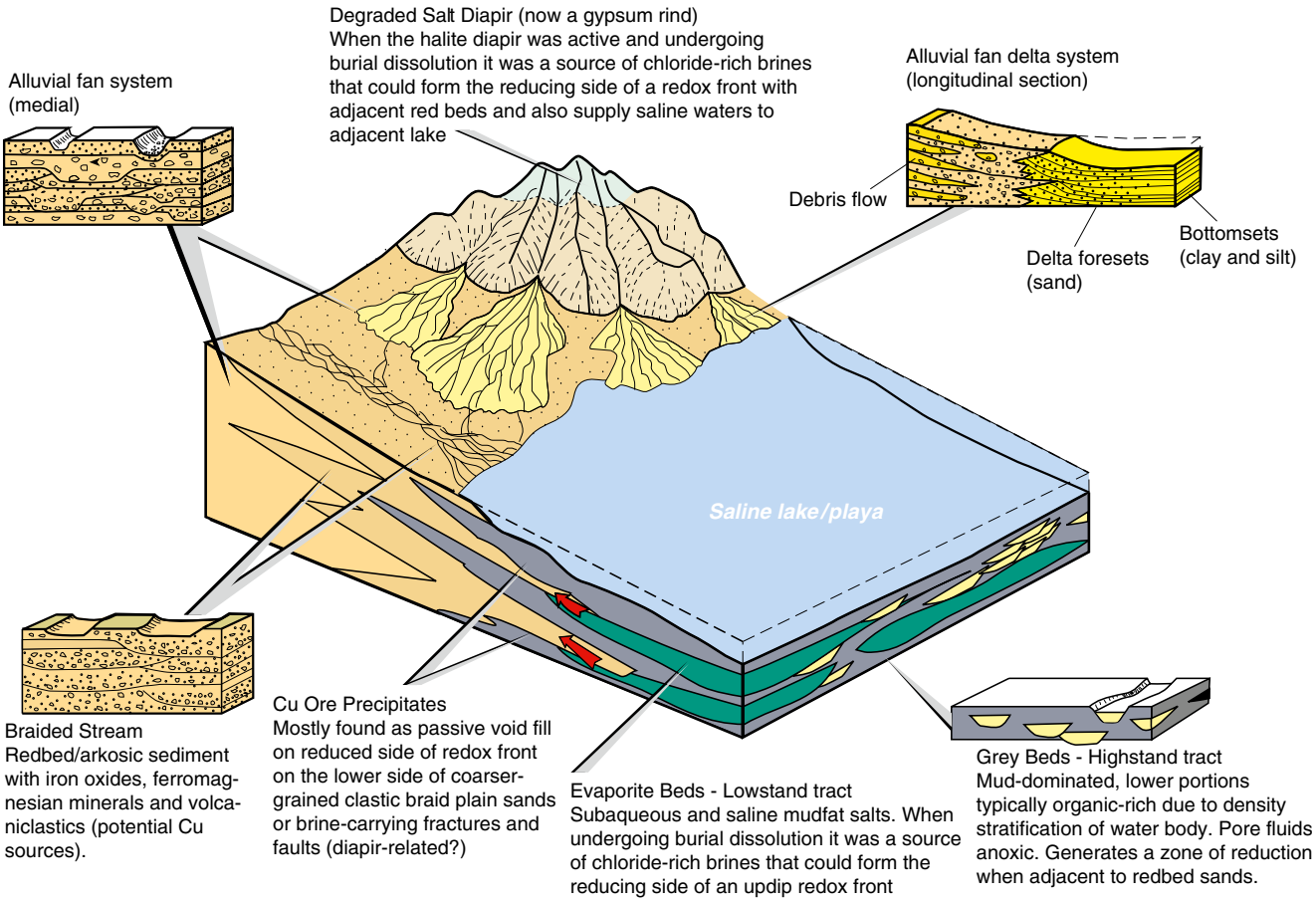

Fig. 15.34 Sedimentological model for precipitation of Corocoro ores showing source of metalliferous chloride brines by early burial dissolution of bedded evaporites or diapir or salt-décollement dissolution (or both) and the resultant setup of the Cu-precipitating redox front (In part after Flint 1989; Warren 2000b)

evaporite textures likely implying dissolution of previously more voluminous $CaSO_4$ and NaCl beds and masses. Gypsum along with celestite are the most common gangue minerals associated with native copper veins in all the Corocoro deposits (Singewald and Berry 1922). In the geological analysis of the first two decades of last century the copper-bearing beds of the westerly-dipping series were called "vetas" and those of the easterly-dipping beds "ramos" and, as a matter of convenience, the names became attached to the rocks themselves. The term "veta" is Spanish for vein and "ramo" the Spanish for branch (native copper). The 1922 paper by Singewald and Berry noted that the veta horizons were traceable continuously for over 5 km in outcrop, but there were no obvious primary trends related to ramos outcrops (Fig. 15.33).

Six mineralized layers of each kind were exploited in mining during the first two decades of last century, the thicknesses of which varied from a few centimetres to 7 m (Fig. 15.33). Sheets and masses of native copper, called charque, were up to 600 lb in weight, but larger volumes of copper were extracted from vetas sandstones where copper was found generally as diffuse minute grains, pellets, or granular masses of the native metal. Associated with the enriched copper zones were more oxidised minerals such as malachite, chrysocolla, azurite, domeykite, and chalcocite. Singewald and Berry (1922) noted gypsum and salt were the principal gangue minerals, while silver minerals were rare. The vetas sediment hosts tended to be coarser grained, often conglomeratic; whereas the ramos sediment hosts were finer-grained with copper present as smaller particles and masses.

The currently accepted interpretation of the Corocoro copper is that it formed during early diagenesis within a saline playa depositional environment, and in combination with dissolution of the adjacent bedded lacustrine evaporites (Fig. 15.34). This bedded combination is thought to have controlled the formation, transport and precipitation of the copper ore (Flint 1989). Playa sandstones, sealed between impervious evaporitic mudstones, created the plumbing for focused metalliferous fluid migration toward the basin margin. It is argued that the carbonaceous material at Corocoro was likely concentrated in the sandstones and conglomerates and not in the shalier members of the sedimentary sequence (Eugster 1989).

The organics were considered strata-entrained as primary plant matter (e.g. spores) preferentially in the sandstones, along with later possible catagenic/hydrothermally cracked products migrating as hydrocarbons out of the basin. This created locally reducing pore environments in the aquifers wherever these reduced fluids met with somewhat more oxidising updip pore waters. This updip migration of saline reducing waters, in combination with sulphur supplied as H_2S from the adjacent dissolving calcium sulphate beds and nodules, as well as from dissolving intergranular sulphate cements, precipitated copper in the newly created secondary porosity. The pore water chemistry and flow hydrology of this sandstone-hosted Cu system is thought to show many affinities with diagenetic uranium-redox precipitating systems, as defined by Shockey and Renfro (1974).

However there is, in my mind, a possible anomaly in this model, which assumes organics were deposited in fluvial sandstones at the time of deposition. It is highly unusual to have higher plant material accumulating in large volumes in a sandstone in a setting that is sufficiently arid and oxidising to precipitate ongoing interbeds of halite and gypsum. Such settings are typically too arid to allow abundant higher plant growth. Also, as we saw in Chaps. 2 and 9, groundwaters that are flowing basinward through bajada sandstones in Neogene sediments of the Andes are ephemeral or too oxidising to facilitate the longterm reducing conditions needed to preserve significant volumes of higher-plant remains in the sandstone aquifers.

What is also interesting in this sedimentological/diagenetic model of Tertiary age cupriferous redbeds deposits in the Andes, centred on Corocoro, but not considered in the published literature base, is the question…What controlled the folding, and the associated brecciation and perhaps even subsurface brine interfaces responsible for the Cu precipitation? All the stratabound Bolivian Cu deposits accumulated in sediment hosts that were deposited in fault-bound intermontane groundwater sumps. All are located in hydrologic lows in the crustal shortening tectonic scenario that typifies the Tertiary history of the Andes.

The variable ages of the host sediments and the predominance of evaporite indicators including gypsum in outcrop (often as diagenetic masses in fluvial hosts) and all intimately tied to the Corocoro ore forces the question...., "was the fluid focusing driving the Cu precipitation a response to compression-driven halokinesis in an evolving salt-lubricated thrust belt?" Did this on-ground scenario occur in a halokinetic hydrology, that was possibly related to a combination of thrust-driven telogenesis, redox setup, evaporite dissolution and aquifer focusing of brines with dissolution aiding local slumping? This, along with associated strike-slip prisms, could possibly better explain the stability of redox interfaces in sandstone aquifers across timeframes needed to accumulate significant native copper volumes. After all, most of the ore textures are passive precipitates, largely in pre-existing porosity. If so, perhaps these deposits are not a variation on a roll-front uranium theme, which is predicated on dispersed primary organic material in the host sandstones (Shockey and Renfro 1974).

Fig. 15.35 Corocoro district, Bolivia. Satellite image showing a gypsum-capped salt diapir that outcrops in a salt thrust décollement around a kilometer north of the main Corocoro deposits. Location is plotted using SaltWork version 1.6 mounted on the public version of the Bing® image base

When one plots the position of Corocoro using a GIS overlay of the region, the 1,000-lb gorilla that has been standing in the corner of the room for the past century becomes obvious. The Corocoro redbed copper is located on a fault system that is linked across less than a kilometre to an outcropping gypsum-capped remnant of a salt diapir that has intruded the anticlinal axis of a saline redbed/greybed Corocoro sequence (Fig. 15.35). The same diapir proximity is true of other nearby redbed copper deposits to the south-southeast, such as Veta Verde and Callapa. It is highly likely

that the saline fluid interfaces forming the redbed Cu deposits of Corocoro, Veta Verde and Callapa were halokinetically focused. A similar salt lubricated set of thrusts and strike-slip faults typifies halokinetic outcrops in Central Iran (Fig. 6.90). It is highly likely that much of the structuration that is controlling Corocoro ore positioning is a response to salt flow related uplift and fracture creation, probably in redox interfaces induced and controlled by regional salt-lubricated compressional tectonism and the associated salt-structure driven hydrology.

Work by Rutland (1966) did make an observation that the Corocoro ore deposits are related to an unconformity between the Ramos and Vetas Formations. Previously, the unconformity was interpreted as directly due to the outcrop of the Corocoro Fault. He noted that the fault and the unconformity were one and the same. In the 1960s there was no notion of a salt weld but it was nonetheless a highly astute observation by Roy Rutland. He went on to note a similar unconformity is tied to the growth of the Chuquichambi salt diapir, some 100 km southeast of Corocoro. Unfortunately, the halokinetic implications of Rutland's work were not considered 20 years later in Flint's key 1989 paper inferring a largely sedimentological origin for the Corocoro and other similar SSC deposits.

A possible halokinetic/weld association also leads to the question… Were the salt lakes, that are considered an integral part of the depositional and saline ore-precipitation systems at Corocoro by Flint, also a response to dissolution of the same nearby diapiric structures, when they were active in the mid to late Tertiary? This tie, between diapir/weld brines sourced in the drainage hinterland and bedded evaporite – lacustrine mud interbeds accumulating in the groundwater outflow sumps, is the case with groundwater inflow for the Salar de Atacama infill, as it is in other Quaternary salt lakes in the region. Figure 3.44 plots some of the many diapir remnants that typify the Andes region. It seems that the Corocoro style of Cu mineralisation is perhaps another example of suprasalt redox focusing in a halokinetic setting.

Whether the halokinetic scenario, or the currently accepted non-halokinetic bedded arid-lacustrine evaporite scenario, explains the Cu mineralisation Corocoro is yet to be tested. But in terms of future copper exploration for similar deposits, it probably requires an answer. A halokinetic association offers an exploration targeting mechanism, utilising satellite imagery and aerial/gravimetric data, prior to the acquisition of on-ground land positions and geochemical surveys.

Creta, Oklahoma

The Creta deposit occurs in the upper part of the Flowerpot Shale (Nippewala Group) within the Hollis-Hardeman Basin, Oklahoma. It is associated with the WNW-ESE trending Wichita basement high where the ore host strata overlie Cambrian bimodal igneous rocks. Similar cupriferous, but noneconomic, sediments occur in several other locations within Upper Permian strata in Oklahoma, Kansas, Texas and New Mexico. Regionally some 900–3,400 m of mixed clastic and chemical sediments of Ordovician to Permian age make up the Hollis-Hardeman basin fill, which, in turn, overlies a Precambrian to Cambrian basement made up of metasediments and metavolcanics. Locally, in the vicinity of the Creta deposit, sediment thickening is associated with movement on the Birch Fault, so that the sedimentary sequence is locally 3,200 m thick and dominated by fine-grained clastics that show a gradual upward increase in the proportion of evaporites in to the Upper Permian section.

Ore-grade material was mined, mostly as chalcocite, from the Creta copper-bearing shale in southwestern Oklahoma from October 1965 to February 1975, when a drop in the price of copper forced the mine to close. Production from Creta between 1965 and 1975 totalled around 1.8 Mt @ 2.3 % Cu, 5.5 g/t Ag. The nearby Magnum deposit is believed to have a sub-economic reserve of approximately 3.6 Mt @ 1 % Cu. This extracted volume makes Creta the second largest shale-hosted Cu deposit in the United States. Lead and zinc levels are negligible at Creta. At nearby Magnum, malachite [$CuCO_3Cu(OH)_2$] is the most abundant copper mineral, although chalcocite may be the dominant ore mineral in the subsurface.

According to Huyck and Chorey (1991), the mineralisation event at Creta was early diagenetic, as indicated by: (1) Copper sulphide replacing large spores and framboidal pyrite, (2) Lack of compaction of replaced spores relative to unreplaced spores, (3) Enclosure of uncompacted mud and copper sulphides by early "matrix gypsum", (4) Location of the ore bed within a thick sequence of fine-grained low permeability sediments.

Seven lithologic units occur in the upper 19 m of the Flowerpot Shale and include the Prewitt Shale member, which hosts the Creta deposit (Fig. 15.36). This interval is characterised by two common features: (a) Satinspar gypsum veins and (b) Variegated red-green layers. The veins both crosscut and parallel shale bedding and partings. They typically terminate within either nodular or massive gypsum beds or in gypsiferous green shale beds. In mineralised zones they usually encapsulate shale intraclasts and copper minerals. The variegated layers and lenses are composed of discontinuous silty (60–80 % silt) calcareous and gypsiferous red-brown layers. When the variegated layers are traced laterally they pass into adjacent gypsum, the layers obviously reflect dissolved gypsum or satinspar intervals.

The Prewitt Shale averages 2 % Cu in the mine area, with a matrix composed of illite and chlorite and as much as 20 % satinspar gypsum. It is made up of three layers: a lower blocky layer, a laminated layer and a discontinuous upper bed of impure gypsum (the "cap gypsum"). The lowest

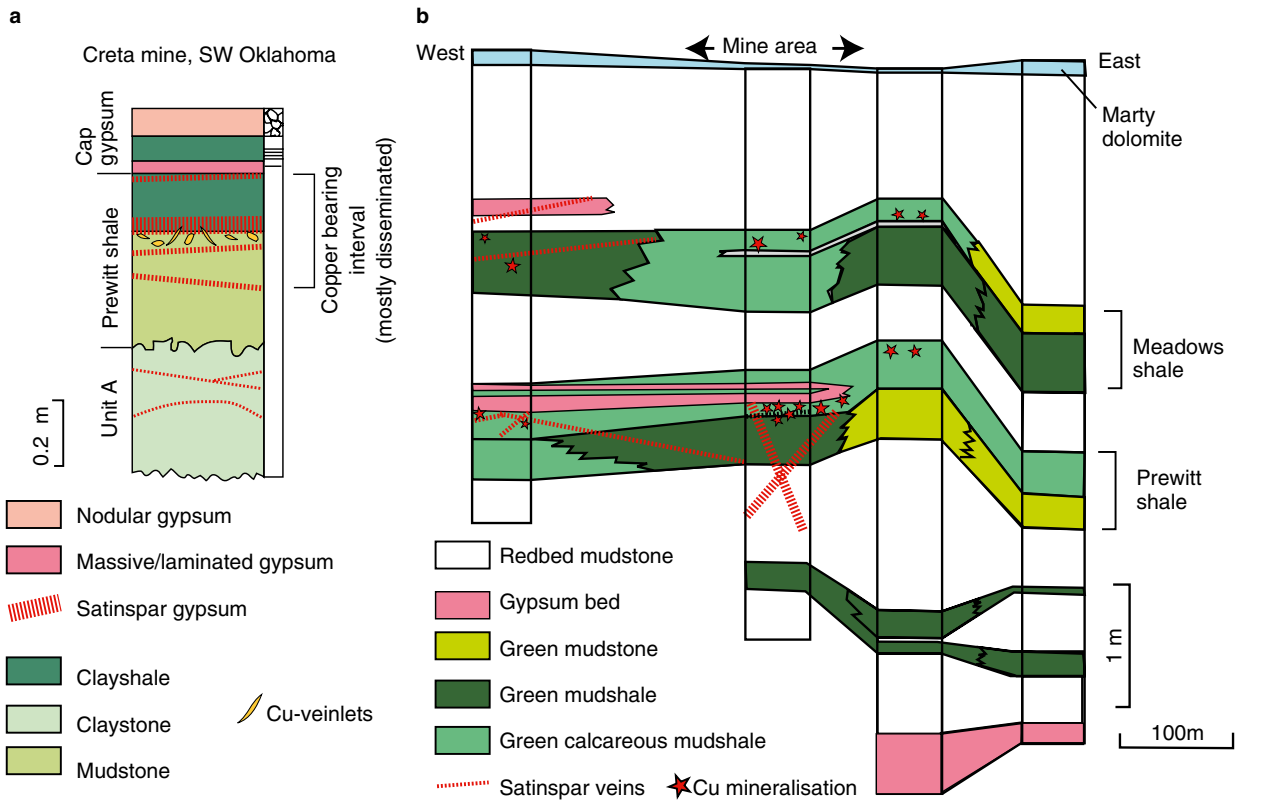

Fig. 15.36 Creta copper shale deposit, Oklahoma. (**a**) Mineralised stratigraphy in the Creta Mine. (**b**) Mine region stratigraphy showing intimate association between mineralisation and evaporite occurrence (After Huyck and Chorey 1991)

blocky layer is a claystone to mudstone; copper, when present, occurs only in the upper 10–13 cm and is concentrated in the mudstone (Fig. 15.36a). The overlying laminated shale, which contains as much as 4.5 % Cu, includes both gypsiferous and nongypsiferous clayshale. Copper is concentrated in the silty laminae both in outcrop (as malachite) and in thin section (as anilite). The cap gypsum bed directly overlies the laminated portion of the Prewitt Shale in the west, but pinches out in the east (Fig. 15.36b). Where fully developed the cap gypsum bed (10–25 cm thick) is made up of a lower gypsum, a thin green clayshale, and an upper gypsum.

Copper mineralisation only occurs in association with concentrations of pyrite and spores. The main ore mineral is anilite ($Cu_{1.75}S$) and is concentrated along silty or sulphide rich layers in the laminated unit. In gypsiferous shale the opaques are concentrated along the edge of the satinspar veins and within clay blebs in the matrix gypsum. Anilite is also weakly developed throughout the nongypsiferous portions of the Prewitt Shale. The association of Cu mineralisation with evaporite occurrence in the Prewitt Shale is obvious, and reflects a burial diagenetic mineralisation at a redox interface. In my opinion, it is associated with an anoxic reduction front (red-green transition) that was generated and maintained by the dissolving evaporites indicated by the satin-spar.

Most published work on this deposit documents satinspar gypsum as well as the cap gypsum, but none (including the most comprehensive work by Huyck and Chorey 1991) discuss its significance, nor do they mention the implications in terms of fluid focussing of a thick now variably-dissolved gypsum/anhydrite/halite units that dominate Blaine Formation and situated immediately above the mineralised portions of the Flowerpot Shale (Muir 1934; Askew 2013).

The presence of satinspar gypsum in the mineralised zone indicates a likely combination of halite solution-collapse and gypsum rehydration. As such, the current forms of $CaSO_4$ in the mine area are tertiary or telogenetic evaporites, a result of uplift and rehydration tied to salt dissolution (Chaps. 1 and 7). The current evaporites were not responsible for the precipitation of the sulphides as they postdate that event. They do, however, indicate the former presence of a more substantial, but now dissolved, evaporite unit composed either of anhydrite, or perhaps a combination of halite and anhydrite that focused mineralisation below it into the prepared ground in the Flowerpot shale. It was this former evaporite seal that was responsible for brine focusing and, through its dissolution (indicated by the cap and satinspar gypsum units), maintained a redox front that precipitated the copper sulphides. Creta is perhaps a smaller-scale subsalt example of a redox precipitation hydrology similar to the Kupferschiefer/Rudna Rote

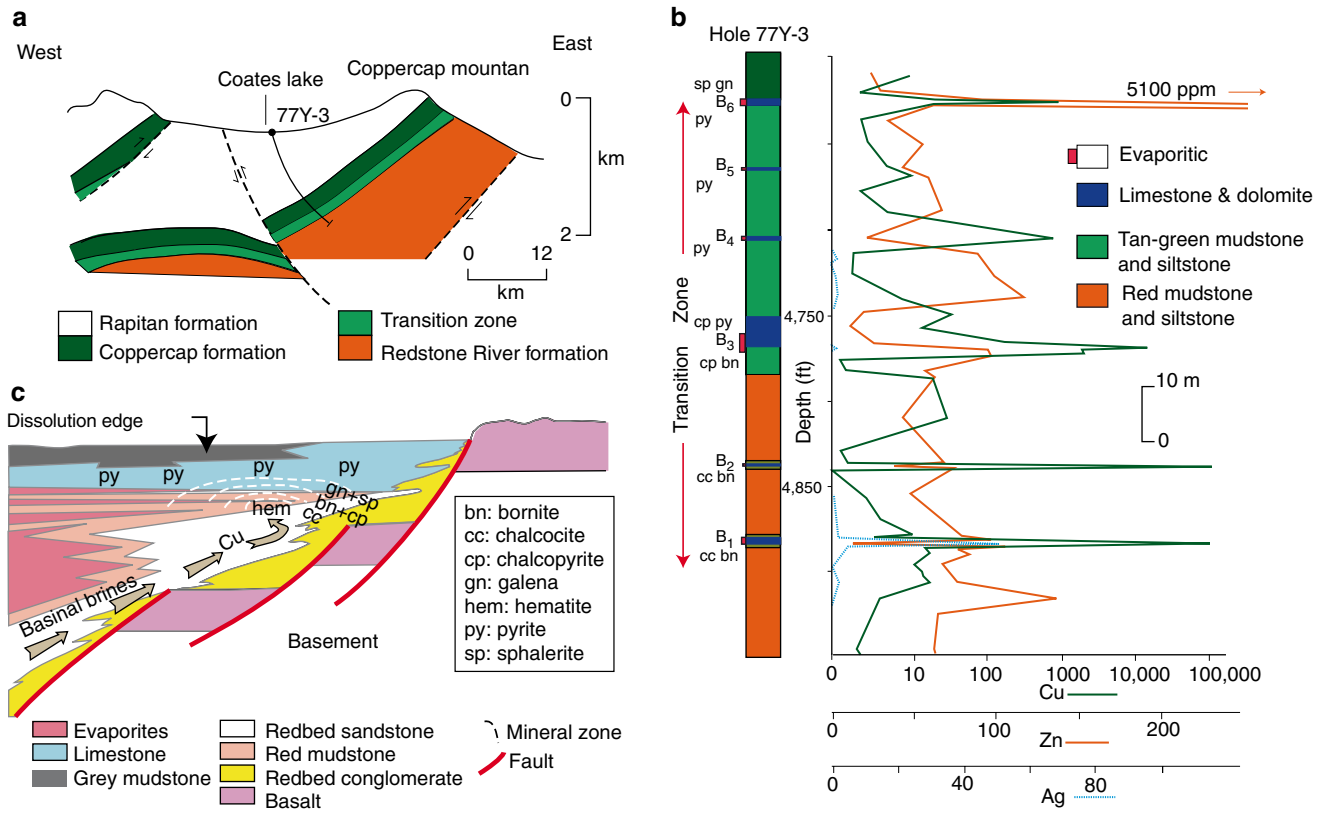

Fig. 15.37 Redstone Copper Belt, Canada. (**a**) E-W geological cross-section of Coates Lake region showing well 77Y-3. (**b**) Stratigraphy and metal content of well 77Y-3 (After Chartrand et al. 1989). (**c**) Diagrammatic section across a redbed-evaporite rift margin showing mineral zonation of precipitated sulphides. Modelled from Redstone Copper Belt, Northwest Territories, Canada (After Kirkham 1989)

Faule of Poland. Smaller perhaps, because the salt dissolution front was not maintained in a stable long-term position because of the lack of halokinetically driven salt resupply.

Redstone Copper Belt, Canada

Coates Lake is the largest stratiform redbed copper prospect in the Redstone Copper Belt, Northwest Territories, Canada. Associated with it are a number of smaller deposits (Hayhook, Keeles River), which all occur in a 250 km, northwest-trending, arcuate thrust belt made up of Neoproterozoic (Helikian) carbonates and redbeds. These sediments are part of the Mackenzie Mountain Supergroup (Fig. 15.37a and Table 15.10; Chartrand et al. 1989; Ruelle 1982; Brown 1997).

Coates Lake and the smaller various copper deposits occur at the contact (in the Transition Zone) between the continental alluvial redbeds of the Neoproterozoic (750 Ma) Redstone River Formation (0–1,220 m thick) and the shallow marine/ evaporitic rocks of the overlying Lower Coppercap Formation (≈250 m thick). The Transition Zone host strata are composed of several blanket-like variably-cupriferous units of dolomitic silty, evaporitic cryptalgal-laminated carbonates that were deposited atop the fault-bound Coates Lake, Hayhook Lake and Keele River embayments.

Sediments in the Transition Zone are made up of six shoaling peritidal cycles, deposited along arid shorelines with sabkha affinities (Chartrand et al. 1989). Higher levels of mineralisation are typically found within the evaporitic/ stromatolitic carbonate portion of each depositional cycle. At the base of a typical cycle, red siltstone and mudstone grade up over a few decimetres into tan and green-coloured siltstone, exhibiting the same sedimentary textures and structures as their underlying red counterparts (Fig. 15.37b). These terrigenous strata grade over a few centimetres into grey-green dolosiltite and dololutite overlain by microbial laminated carbonate, the principal host for the cupriferous sulphides. The dolosiltites and dololutites are capped by gypsum/ anhydrite-rich units that are decimetres thick. Evaporitic units are overlain by tan-green siltstone and mudstone and, finally, by red siltstone. Beds B4-B7 are dominated by tan-green colours with most of the entrained mudstone and siltstone intervals containing more calcite and/or dolomite than their counterparts in beds B1-B3 (Fig. 15.37b). The succession is crosscut by late-stage calcite and gypsum veins.

Beneath the Transition Zone sediments, in the Lower Redstone River Formation, Ruelle (1982) mentioned the presence of an unusual high Na-Mg Precambrian evaporite

Table 15.10 Stratigraphy of Redstone Copper belt

Unit		Description
Rapitan Formation (unconformable base)		Turbiditic, siliceous red siltstones, maroon and green debris flows and tillites, which lie with regional unconformity on the Coates Lake and Little Dal Groups.
Mackenzie Mountain Supergroup	Coppercap Formation (0–300 m)	Upper Unit (0–165 m) of well bedded, stromatolitic limestone and dolostone, Middle Unit (0–72 m) of argillaceous carbonate and calcareous shale, Lower Unit (0–63 m) of evaporitic limestone and dolostone, and laminated dolostone (Lower Middle and Upper Coppercap Formation carbonate sediments are all fetid and black).
	Transition Zone (40 to over 110 m)	Series of red, green, and tan coloured nearshore arid coastal deposits. Copper occurrences are hosted by up to eight fining-upwards, carbonate-evaporite beds, each composed of dolosiltite, dololutite, dolostone, gypsum, anhydrite and capped by a cryptalgal laminated carbonate bed.
	Redstone Formation (0–1,220 m)	A Lower "Evaporite" unit is composed of bedded and brecciated gypsum-anhydrite, which thins at basin margins and reaches thicknesses of over 215 m at basin centres. An Upper "Redbed" subunit is dominated by maroon mudstones with thin marginal fanglomerates.
	Thundercloud Formation (0–300 m)	Lower portion made up of basal volcaniclastics, alluvial fanglomerates, tidal arenites and paralic mudstones. These are overlain by rhythmically interbedded carbonate and dolostone locally containing evaporites, followed by cyclically interbedded sandstone and shale. Upper part of the formation is marked by evaporitic algal dolostones.
	Little Dal Formation contact	Contact with the underlying Little Dal Formation is marked by pillowed basaltic lava, or sandstone, dolomite, siltstone, and mudstone with local gypsum and conglomerate. Where basaltic lava is present the contact is conformable but the sedimentary units mark a distinct unconformity.

Based on Aitken (1981), Ruelle (1982), and Jefferson and Ruelle (1986)

assemblage now largely marked by collapse residues and breccias. Today, it is made up of 55 % glauberite [$Na_2Ca(SO_4)_2$], 20 % magnesite, 15 % talc and <10 % combined gypsum and anhydrite. Strauss (1993) consider these evaporites to be time-equivalent to the upper evaporite level, the Killian Formation, in the Amundsen Embayment At this time the significance of this sulphate-evaporite-rich residue assemblage in relation to the overlying sulphate evaporites and to focusing a redox front with any metal-transporting brines is neither well documented nor understood. At the time of mineralisation there may have been a much thicker, possibly halokinetic, halite mass. If so then the Transition Zone copper beds are suprasalt with affinities to the Lisbon Valley and possibly the Dzhezkazgan deposits. Without public domain detail beyond what was published in the 1980s, it is difficult to say. A map of the brecciation geometries in the Redstone Formation would be informative.

The largest and most economically promising Cu deposit in the Redstone Copper Belt is situated within the Coates Lake embayment and covers an area greater than 12 km^2. It occupies a bed 1 m thick and contains drill-indicated reserves of 37 million tonnes, averaging 3.92 % Cu and 0.33 oz. per tonne Ag (11.3 g/t). Mineralisation is best developed in the lower three carbonate units. For example, in drill hole 76Y-4, the richest Cu intersections are in bed 2a (0.15 m @ 5.5 % Cu) and bed 3 (1.16 m @ 1.18 % Cu), both occurrences are tied to preserved beds of nodular anhydrite (Ruelle 1982).

In well 77Y-3, the sulphide minerals are zoned vertically with bornite and chalcocite in the lower portion, passing up into a chalcopyrite-bornite interval, upwards into chalcopyrite-pyrite and finally into pyrite (Fig. 15.37b). Sphalerite and galena occur at the uppermost part of the Transition Zone in contact with the overlying carbonates of the Coppercap Fm (Chartrand et al. 1989). The relatively high silver content coincides with high copper contents in the base of the Transition Zone and, according to Ruelle (1982), indicates the silver is entrained within bornite.

Like the Kupferschiefer and Lisbon deposits, mineralisation in Redstone Copper Belt deposits show a pronounced mineral zonation, with the Cu:Fe ratio in the sulphides decreasing upsection through the Transition Zone and toward the embayment margins (Fig. 15.37c). The copper sulphides

occur as partial to complete diagenetic replacements of anhydrite nodules in the cryptalgal-laminated units and as disseminations of anhedral to euhedral grains in the intertidal mud flat facies. Bladelike anhydrite crystals are also partially to completely replaced by chalcopyrite. Preserved anhydrite nodules are ellipsoidal in cross section and up to several centimetres in diameter, although most are less than 1 cm. Mineralisation of these nodule layers creates a laminar fenestral fabric to the mineralisation. Further away from the Cu mineralisation front, pyrite with chert replaces the anhydrite nodules (Ruelle 1982).

Metals were leached and transported as metal-chloride complexes from volcaniclastic/redbeds that were derived from Cu-bearing mafic lavas in the Redstone River and Thundercloud formations (Fig. 15.37c). As slightly acidic and weakly oxidised basinal brines moved up and outward from the basin sediment pile, they were focused into the basin margins by the presence of overlying evaporite aquicludes. Near the margins, where the evaporite aquicludes were dissolved, had pinched out, or welded, the solutions seeped up section to encounter redox fronts associated with the organic-rich cryptalgalaminites of the Transition Zone. This interaction then fixed the metals on the reduced side of the redox front with a sulphide zonation identical to that found in the Kupferschiefer ore zones. In each of the cycles of the host stratigraphy the positions of oxidation reducing fronts are still preserved as the red to grey-green colour transition. Hematite is still visible in the red-coloured intervals and the proportion of Cu in the grey-green intervals is much higher (Rose et al. 1986).

Summary of SSC Deposits Tied to Evaporites

Clearly, stratabound copper accumulations in sediments can be related to redox fronts set up between saline, highly reducing pore waters and somewhat less saline, slightly acidic oxidising waters. The importance of the redox interface in diagenetic precipitation of copper was well known in the economic geology community since the 1970s (e.g. Rose 1976). and has been an integral part of the interpretive paradigm for redbed copper since that time. What is less appreciated is the role that evaporites both bedded and halokinetic can play in setting up and maintaining the position of the redox interface in earth space, so that substantial accumulations or copper can occur in a single buildups, such as in the Kupferschiefer-Lubin, or bed associated buildups as in the Dzhezkazgan district.

The redox interface is better maintained when the reducing side of the interface is supplied by dissolution of a halokinetic salt mass rather than an individual salt bed. This is because in a halokinetic system the salt is thick enough so that it will continue to flow into the site of dissolution until the conduit to the mother salt mass is lost either by salt welding or by the complete dissolution of the salt mass. Fractional dissolution of the halite also drives the enrichment of $CaSO_4$ at the site of dissolution. What is also obvious from the literature of SSC deposits is that salt residues are underappreciated or not even recognised. Yet they are indicators of former substantial salt masses which played significant roles as chloride brine sources and metal precipitation foci. We shall return to this notion of halokinesis supplying subsalt cupriferous brines and suprasalt/weld stability after we consider some of the larger Pb-Zn deposits in the same salty framework.

Stratiform Sediment Hosted Pb-Zn Deposits (Salt-Related)

Current economic geology literature typically considers SedEx (sedimentary exhalative) and MVT (Mississippi Valley Type) deposits as related responses to the flow of basinal fluids. SedEx deposits are typically a mineralised response to basinal fluid flow in deeper water mostly siliciclastic sediment hosts and MVT deposits the updip responses mostly hosted in carbonates (Fig. 15.38; Emsbo 2009; Leach et al. 2010).

Exact definitions of what constitutes a SedEx versus an MVT deposit vary, according to the syngenetic verses epigenetic inclination of the writer. For SedEx deposits, a good definition is that of Goodfellow and Lydon 2007. They define sedimentary exhalative (SedEx) deposits as typically tabular bodies, composed predominantly of Zn, Pb, and Ag, bound in sphalerite and galena, which occur interbedded with iron sulphides and basinal sedimentary rocks. Deposition was on the seafloor and associated with sub-seafloor vent complexes fed by hydrothermal fluids seeping into mostly reduced sedimentary basins in continental rifts. In the vicinity of the brine vent tract, SedEx deposits are typically zoned, with the proportion of Pb, baryte and Mn decreasing away from the feeder/vent zone, which is typically centred on one or more extensional faults (Fig. 15.74).

For MVT deposits a widely accepted definition is that of Leach and Sangster (1993). They define MVT deposits as a varied family of epigenetic ores, precipitated from dense basinal brines at temperatures ranging between 75° and 200 °C, typically in platform carbonate sequences and lacking genetic affinities to igneous activity. That is, in contrast to the basinal sediment host of SedEx deposits, MVT deposits tend to be hosted in dolomitised platform carbonates or more rarely in sandstone interbeds. Such mineralised systems are sometimes located at or near the high-energy fault-defined platform edge, as defined by the rock matrix character of the host (Fig. 15.38). And sometimes they are located adjacent to the dissolution edge of platform evaporites where the three features (fault, shelf edge, saltern edge) may coincide to focus ore precipitation,

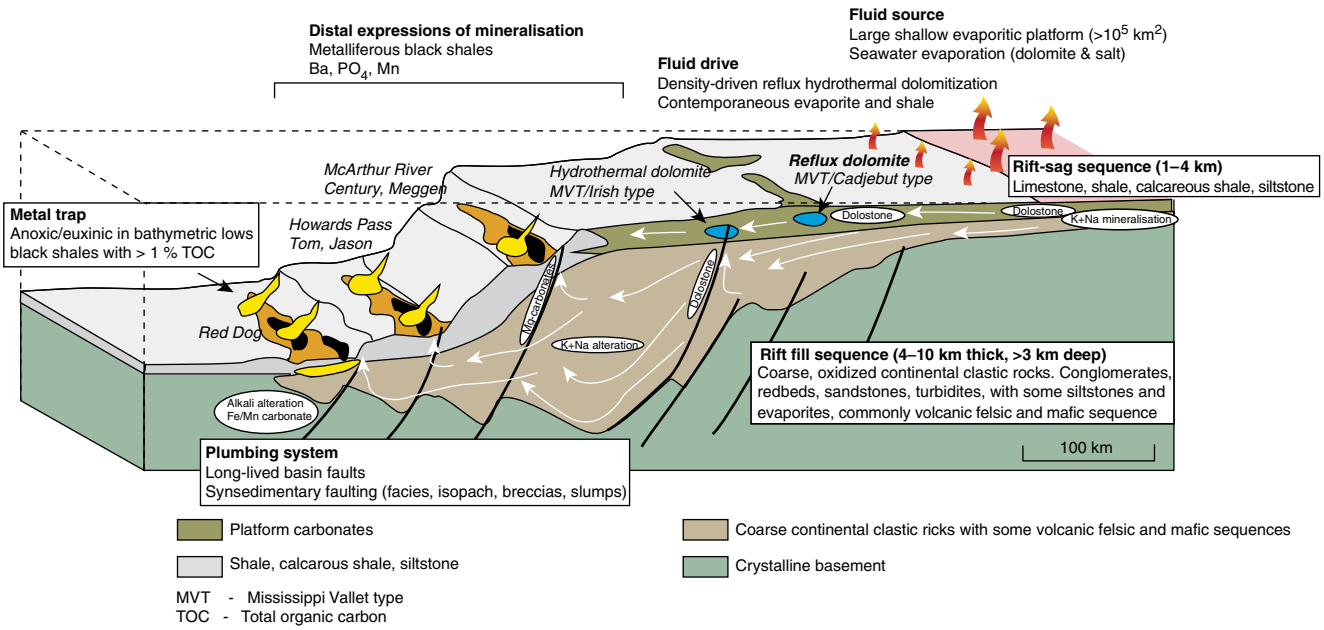

Fig. 15.38 Geologic setting and geologic assessment criteria for SedEx Zn-Pb-Ag deposits emphasising relationship between SedEx and MVT deposits as deduced by USGS worldwide synthesis (Emsbo 2009 and references therein). Likely locations of several important SedEx deposits relative to the shallow-water platform margin are indicated and may reflect the structural architecture of the basin or the maturity of the rift cycle (Figure based in part on Emsbo 2009)

as in the Cadjebut and San Vicente deposits. Other times they form in thrusted platform carbonates with a fluid flow system tied to evaporite-focused décollements, as in the Gays River/Ainslie deposit/prospects. MVT deposits often occur in fluid-defined clusters made up of a number of smaller deposits.

In contrast to the clustered nature within an ore district of MVT deposits, individual SedEx deposits tend to be larger stratiform deposits, spaced some distance apart. Russell et al. (1981) tied the larger separation of SedEx deposits to the size of convective fluid cells in thick sedimentary basin fills. As we shall see, whenever SedEx deposits can be tied syndepositionally to the presence of former evaporites they tend to be typified by orehosting sedimentary laminites deposited within deeper water anoxic seafloor lows filled with hypersaline brine (DHALs), with their seafloor positions controlled by a combination of halokinetic focusing of fluid flows and extensional feeder faults.

By the end of the chapter we will add an understanding of the importance of flowing and dissolving evaporites in a basin fills when SedEx and MVT deposits are forming. Once again, let me emphasise that evaporites do not form mineralised Pb-Zn deposits, rather as they dissolve and alter in the subsurface, evaporite masses focus and stabilise the position in earth-space of brine flow conduits and redox/thermal interfaces, within the diagenetic mineralising milieu of faults, vents and brine sumps that drives the creation of larger MVT districts and SedEx deposits.

Evaporite Associated MVT Deposits

Much like we have already seen in redbed Cu-evaporite associations, for MVT Pb-Zn deposits associated with evaporites, there are two fabric/structure styles: (1) Halokinetic edges, with the metalliferous brine interactions typically tied to fluid interfaces within the sulphate fringe (caprock or carapace), which defines the dissolutional periphery of a diapir crest or stem, a salt allochthon periphery, or below a salt-lubricated decollement plane, and; (2) Bedded sulphate interactions typically located where fault-controlled metalliferous fluids intersected with, and interacted with, one or more platform sulphate beds (salina or saltern). For SedEx deposits there is a third evaporite type, a suprasalt allochthon structuration that creates fault-fed, metal-prone, seafloor brine lakes. Thus we can target exploration in a predicative fashion for those MVT Pb-Zn deposits with an evaporite association: the targeting is based on identifying favourable intersections where fault structures (extensional faults or thrust planes) intersect units of dissolving bedded or halokinetic evaporites (now marked by residues and other "salt that was" textures, as detailed in Chap. 7).

Peridiapiric Diagenesis and Zn-Pb

For many years, the edges of diapirs or salt domes have been viewed as potential targets for petroleum, salt and sulphur accumulations. Lately, they have also come to be viewed as potential targets, or at least process analogs, for Pb and Zn

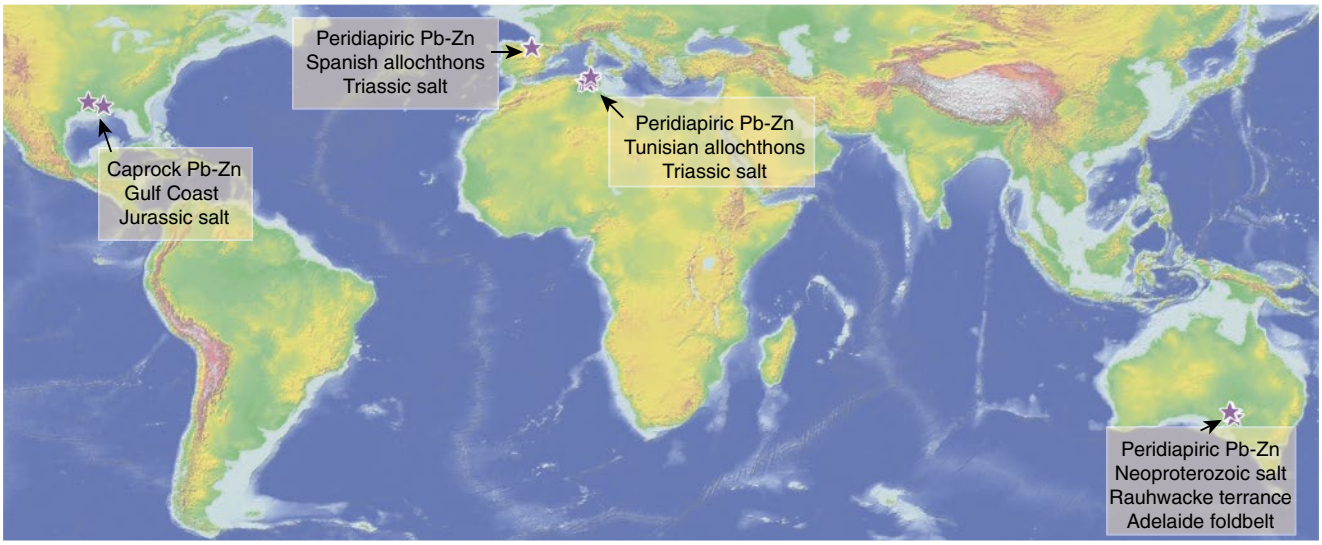

Fig. 15.39 Occurrences of documented MVT Pb-Zn occurrences related to diapirs or allochthons as discussed in text (Plot extracted from Saltwork GIS database version 1.6)

deposits (Wang et al. 1998a). Peridiapiric mineralised Pb-Zn systems can be divided into two types (Figs. 15.38 and 15.39): (1) Caprock/carapace hosted deposits, where the host rock consists of the anhydrite and bacteriogenic limestone carapace to the dissolving crest of a salt structure; (2) Diapir/allochthon proximal deposits, where the bulk of the mineralisation resides in laminar organic-rich sediment hosts, located adjacent to the diapir/allochthon or its residual carapace. Examples of both these deposit styles tend to be relatively small in volume and limited in extent.

Caprock-Hosted Pb-Zn, Gulf Coast & North Africa

Small deposits of Pb-Zn with a diapir association were recognised in northern Africa more than 100 years ago, but it was not until the geology of diapir-hosted subeconomic deposits in the Gulf of Mexico (Kyle 1991), and economic north African diapir- and peridiapir-hosted deposits, such as Bou Grine and Oued Jebs (Rouvier et al. 1985; Orgeval 1994; Bejaoui et al. 2013), were fully understood, that the significance of diapirism in controlling this style of small-scale Pb-Zn was fully appreciated (Fig. 15.39). Mineralogically, the diapir-associated mineral deposits are similar to many other carbonate and shale-hosted mineral deposits. They all contain pyrite, marcasite, sphalerite, galena and baryte; many deposits also contain high concentrations of pyrrhotite and celestite.

Caprock Pb-Zn Accumulations

Caprock sulphates and bacteriogenic limestones created during caprock formation are important ore hosts in this style of deposit. All that is required to form the anhydrite portion of a caprock is that the top of the diapiric salt stem or sheet be bathed in a solution that is undersaturated with respect to halite (see Chap. 6). To form the calcite portion from this anhydrite/gypsum precursor requires the presence of organics/hydrocarbons and sulphate-reducing bacteria in the region of the calcium sulphate cap (Fig. 15.40a). Such a situation exists subseafloor, as well as in zones of continental meteoric circulation. The anhydrite carapace that makes up the greater volume of a diapir caprock is not just a meteoric product, it is forming today on deep seafloor sites in zones of seawater driven fractional dissolution atop shallow salt diapirs and allochthonous salt sheets in the present day Gulf of Mexico (Kennicutt II et al. 1985; Roberts et al. 1990). These sites are coincident with petroleum seeps, so that the calcite cap, including that in entrained mollusc shells, has isotopic signatures indicating a crude petroleum source.

Pb-Zn sulphides begin forming as soon as an anhydrite cap rock carapace encrusts a developing salt structure. This can happen during the earliest phases of salt flow and continue, perhaps episodically, as long as the structure's crest is bathed in nearsurface halite-undersaturated waters and oil- or methane-bearing basinal fluids continue to circulate in the vicinity of the diapir. Some of the earliest minerals to form in the caprock are sulphides precipitated in equilibrium with anhydrite, where they often form laminar sulphide-anhydrite textures controlled by the morphology of the dissolution interface (Kyle and Posey 1991). Biogenic calcite forms as a byproduct of bacterial sulphate reduction as crude oil and thermogenic methane migrates up a diapir's margin to come into contact with anhydrite/gypsum in a low temperature environment (≈80 °C) (Fig. 15.40a). Sulphides, baryte and celestite can precipitate at the same time, or postdate, the calcite. Gypsum caprock continues to form after anhydrite and calcite caprock interfaces are well established, typically via the ongoing infiltration of undersaturated nearsurface

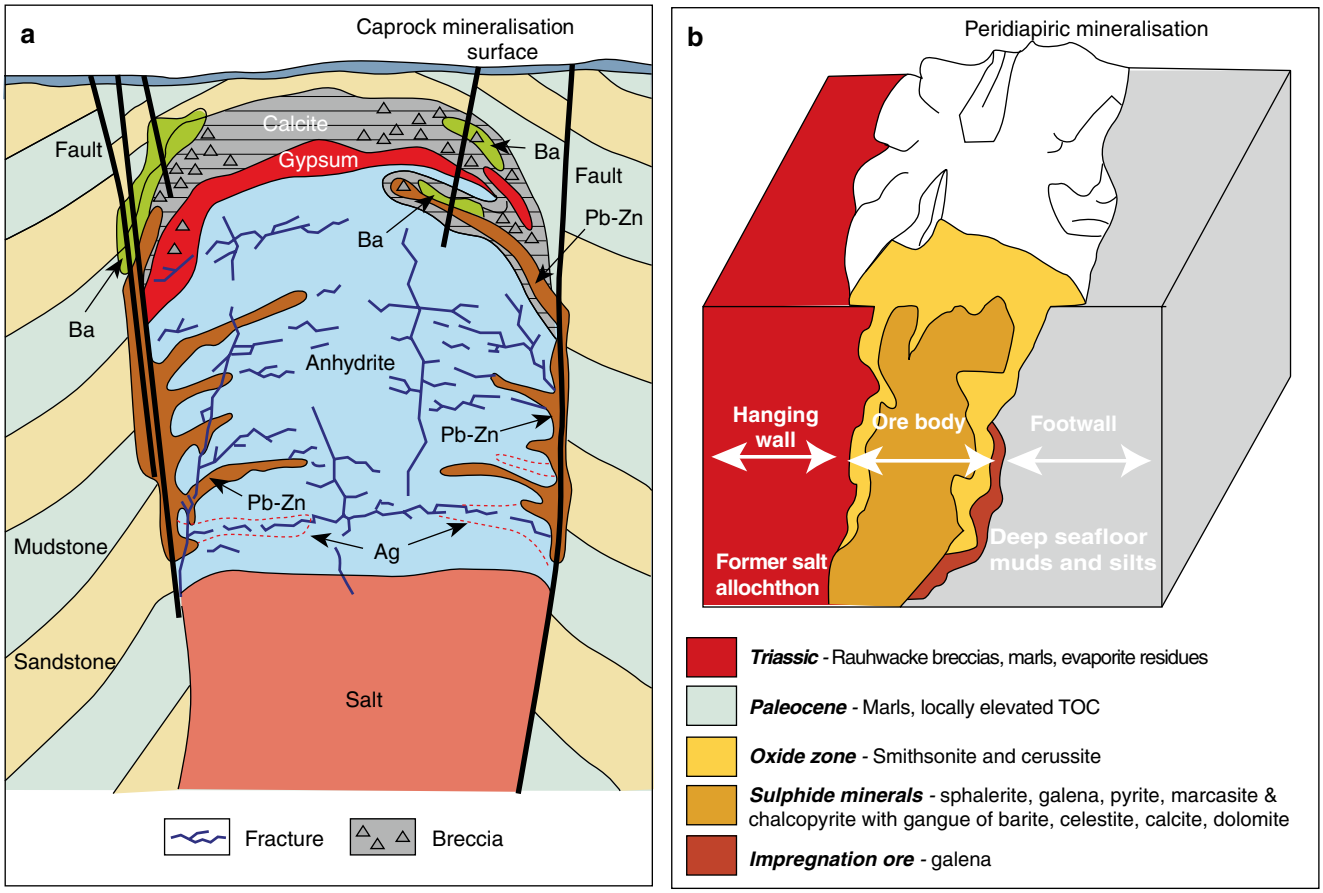

Fig. 15.40 Peridiapiric mineralisation. (**a**) Caprock rock -hosted model, based on the USA Gulf Coast as seen in the Winnfield, Hockley and Tatum salt diapir crests (After Kyle 1991). (**b**) Salt allochthon margin mineralisation, as seen in Ain Allega deposit, Tunisia (After Abidi et al. 2012)

waters that ultimately will rehydrate any remaining anhydrite (Werner et al. 1988).

Thus, iron sulphides typically form early at any particular site in a caprock/carapace deposit, even as the first laminar anhydrite residues accrue on the diapir periphery; galena and sphalerite form later; and baryte, celestite and sulphur are generally the last phases to precipitate. Banded or colloform textures, consisting of finely crystalline aggregates, are the most common textures exhibited by the iron sulphides and sphalerite. These base metal sulphides occur as; inter-anhydrite crystal cements, open-space fills in anhydrite, as carbonate/sulphate replacements, and as open-space (vug/cavity) fills. Most of the anhydrite-hosted mineralisation formed during anhydrite caprock accumulation, whereas most of the sulphides hosted in biogenic calcite formed prior to, or during, calcite precipitation, as seen in Hockley Dome caprock (Fig. 15.41; Kyle and Price 1986a, b).

In general, an anhydrite caprock accretes or thickens by growth along its underbelly by a process of underplating (Fig. 6.111). As diapiric salt dissolves from the uppermost portions of the underlying halite stem/sheet, it leaves behind the entrained anhydrite as a residue (Fig. 15.40a). Calcitic caprock also forms first at its bottom, but it does so via the progressive bacteriogenic replacement of the underlying calcium sulphate (Light and Posey 1992). Metal sulphides that precipitate syngenetically within either the anhydrite or the calcite cap rocks show isotopic compositions and major element compositions that vary with depth. This range in isotopic values may record chemical changes in upward migrating metal-bearing brines or changes in local chemical conditions relating to bacteriogenic overprints during sulphide precipitation (e.g. Fig. 9.72). The range in metal concentrations most likely reflects changes in brine composition due either to brine mixing or to evolution of brine composition.

A detailed record of episodic basin dewatering events is documented in mineralised anhydrite-rich cap rocks of two Gulf Coast salt domes: the Hockley Dome and the Winnfield Dome (Fig. 15.41; Kyle and Price 1986a, b; Hallager et al. 1990). There the majority of the highgrade mineralisation occurs as massive laminar sulphide lenses. The lenses are typically vuggy, fractured and brecciated. At Hockley, the highest sulphide concentrations occur in the periphery of the cap rock at depths ranging from 120 to 365 m (Fig. 15.41a). Elevated sulphide levels occur in both calcite and anhydrite

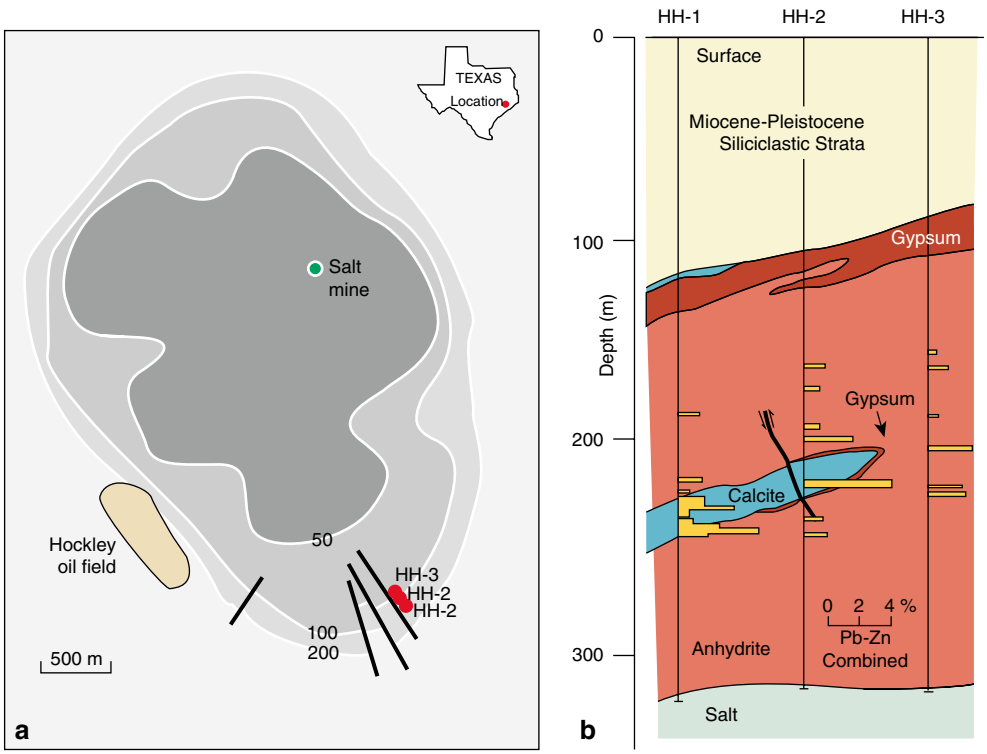

Fig. 15.41 Sulphides in caprock of Hockley Dome, Texas. (**a**) Structure contour map showing depth (metres) to top caprock. (**b**) Geologic cross-section in caprock based on wells HH-1 to HH-3. Intersections of Zn + Pb in wells are plotted on well trajectories (After Kyle and Price 1986a, Kyle 1991)

caprock hosts, are somewhat higher in the bacteriogenic calcite, with sulphide-rich zones between adjacent wells appearing laterally consistent in same-lithology units (Fig. 15.41b). Marcasite, pyrite, sphalerite, and galena range from trace components to local massive sulphide zones; significant Zn + Pb drill intercepts include 5.5 m of 7.1 % and 12 m of 4.2 %. Sphalerite is the dominant economic mineral, with an overall Zn/Pb ratio of about 3:1. Metal distribution studies suggest that there is a trend of increasing zinc/lead downward in the anhydrite cap rock (Kyle and Agee 1988).

The Winnfield Dome diapir is roughly circular in outline with a diameter of about 1.1 km at the −180 m structural elevation. The top of the salt is 76–80 m below sea level, is horizontal, and is directly overlain by anhydrite cap rock. The salt/anhydrite cap rock contact is marked by a brine cavity zone as much as a few meters thick. The anhydrite/calcite caprock interface at Winnfield is highly irregular and a gypsum zone as much as 12 m thick occurs locally. The calcite zone varies in areal extent and in thickness from about a meter to over 90 m. Sulphide layers in the caprock consist mostly of iron sulphides, with vugs and fractures lined with sphalerite, galena, baryte and calcite. The sulphide precipitates had their origins in deep metal-rich basinal brines that were intermittently expelled from geopressured zones deeper in the stratigraphic section. Brines were channelled upward along permeable escape structures bounding the diapir stems.

Sulphides at Winnfield mostly occur as laminar zones parallel to the tightly intergrown, layered anhydrite grains or as coarse euhedral crystals growing in open space within vugs in the anhydrite cap rock. Sulphide layers generally are less than one millimetre to several centimetres thick and can be traced laterally for tens of meters. The principal sulphide is monoclinic pyrrhotite, but sphalerite, galena, pyrite, and marcasite are abundant locally. A nearsurface overhanging caprock helped focus escaping metalliferous fluid into the zone of salt dissolution between the top of salt and the overlying residual anhydrite cap rock. Iron, lead, and zinc sulphides saturations were exceeded in this zone, possibly in response to H_2S generation related to periodic dissolution and biogenic reduction of the caprock sulphates.

In general, it seems that episodes when metalliferous brine entered accreting diapir caprocks are recorded as relatively thin bands of sulphide sandwiched between thicker bands of anhydrite. Continued dissolution of salt and underplating of residual anhydrite caused the sulphide bands to be displaced upward relative to the base of the cap, leading to an inverted stratigraphic record of basin dewatering events. Palaeomagnetic data from the Winnfield salt dome suggest that sulphide-producing basin dewatering events and anhydrite caprock accumulation occurred between 157 and 145 Ma, and that widespread sulphide precipitation in the cap is no longer active.

The paragenetic relationships among the metallic minerals and host caprocks at Hockley, Winnfield and other Gulf Coast salt domes are complex (Kyle 1991). Generally, iron sulphide minerals appear to have been the first sulphide precipitates, followed by sphalerite and galena, with the more oxidized sulphur species, such as elemental sulphur,

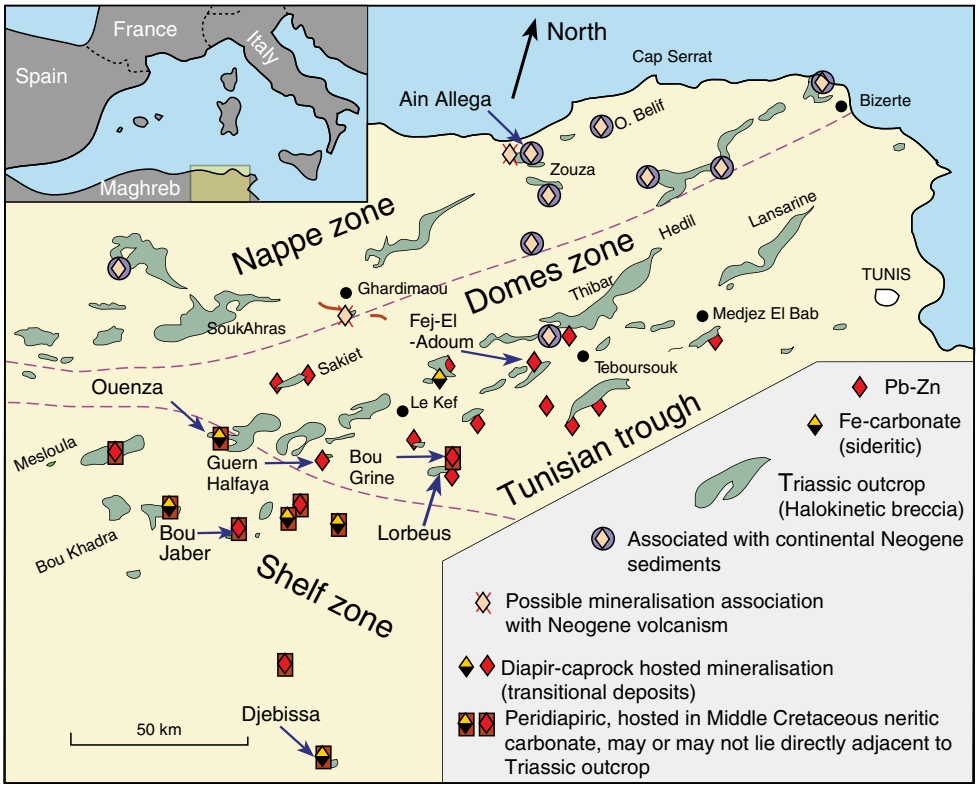

Fig. 15.42 Diapir-related mineralisation in the Triassic allochthon region known as Domes district in the Maghreb, Tunisia (After Rouvier et al. 1985)

manganese sulphides, and the sulphate minerals, forming later. This mineralisation sequence happened more than once in any dome cap.

Thus, stratiform laminar sulphide textures within the anhydrite cap rock are believed to represent mineralization at the salt/ cap rock interface (Ulrich et al. 1984) and are therefore syngenetic with regard to the enclosing host caprocks but epigenetic with respect to the encasing sediments. In addition, euhedral sulphide crystals can form simple open-space fillings of late fractures or vugs within the calcite cap rock; in other cases, earlier generations are brecciated and cemented by later sulphides or calcite (Kyle and Price 1986a). Calcite may also be intimately intergrown with sulphide minerals. Therefore, calcite precipitation, i.e. calcite cap rock formation, can pre-date, be contemporaneous with, or post-date local sulphide precipitation. The complex textural relationships among sulphide minerals and their host rocks is a function of an evolving geochemical system in which earlier mineral products are overprinted by pressurized fluids re-entering a zone of earlier sulphides with entry driven by later halokinetic and fluid events.

Allochthon-Edge Stratiform Pb-Zn (Sr-F)

As well as forming in the diapiric caprock, Pb-Zn deposits can be hosted in organic-rich pyritic and sideritic laminites located centripetal to salt sheets or halokinetic breccias, so making them stratiform peridiapiric ore deposits (Fig. 15.40b). The highly reduced, organic-rich, nature of laminated peridiapiric brine-pool sediments means that pyrite easily forms as a syndepositional precipitate in any adjacent DHAL laminite and its fault-fed surrounds (see Chap. 9). As this pyrite is buried deeper into the brine/ hydrothermal system it is bathed and altered by escaping metalliferous basinal brines. Examples of this brine pool or DHAL style of mineralisation are typically small to medium scale Pb-Zn accumulations, such as Bou Grine, Quern Halfaya and Ain Allegra in the Maghreb, North Africa and the Orduña and Murgía domes in Spain (Fig. 15.39; Bechtel et al. 1996; Jemmali et al. 2011, 2013; Grandia et al. 2003).

The eastern part of the Maghrebides fold–thrust belt in the southern Tunisian Atlas is perhaps the type area for outcrops of this style of deposit. The region is made up of the Nappe zone, which was formed by the stacking of Numidian flysch along south-verging Tellian thrust sheets and more importantly for this type of deposit, is the Domes region to the east and at the front of the Nappe zone (Fig. 15.42). This NE–SW trending, roughly 50-km-wide and 300-km-long zone comprises the Mejerda valley and is characterized by surface exposures of Triassic evaporitic lithologies related to the emergence of major thrusts and anticlines core with halokinetic salt and its associated breccias and residues (Perthuisot et al. 1999).

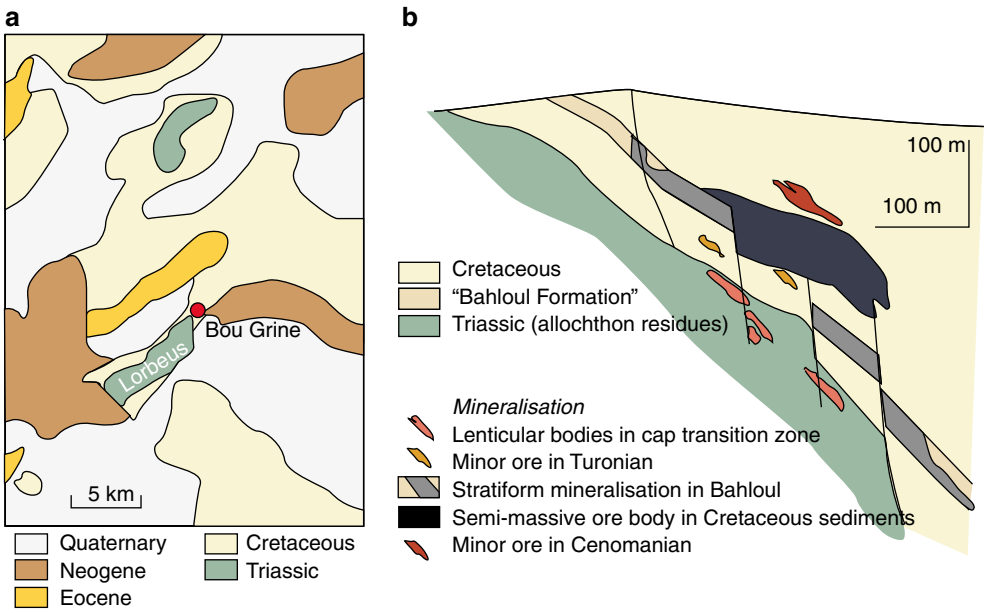

Fig. 15.43 Peridiapiric Bou Grine Pb-Zn deposit in plan (**a**) and section (**b**) views (After Bechtel et al. 1998)

The Domes region covers almost 8,000 km^2 with a large number of Triassic diapirs and allochthons piercing the Cretaceous cover rocks and aligned parallel to the regional folding. During the Early Cretaceous the area was a seafloor trough much like the modern slope and rise of the Gulf of Mexico and was then caught up in the subsequent Alpine Orogeny related to the collision of the African and Eurasian plates. Today remnants of the salt allochthon outcrops and subcrops are covered by pelagic Cretaceous sediments and in places are overlain by a variety of Tertiary sediments, including phosphates. All these postsalt sediments are variably pierced by diapirs and salt sheets, along with entrained sands, carbonate lenses and mottled clays with distributions controlled by highs and troughs related to salt flow. The Cretaceous cover includes a major discontinuity in the upper Albian strata that divides it into two megasequences: (1) an Early Cretaceous to Late Albian succession, and (2) a terminal Albian to Palaeocene sequence. There are strong facies and thickness variations in the Cretaceous sediments located close to the diapirs, indicating that halokinesis was active in the Aptian and continued into the Tertiary.

Pb-Zn (Ba, Sr, F) mineralisation in the Domes area occurs mainly in Cretaceous cover rocks near the edges of the Triassic diapirs in deposits such as Bou Grine, Oud Edeboua (Guern Halfaya), Jebel Hamra and Fej-el-Adoum. There are four main mineralisation types in these deposits: (1) Lenticular Pb-Zn-(Ba-Sr)-Fe bodies in the zone of transition from the Triassic to the Cretaceous host sediment (caprocks); (2) Stratiform Pb-Zn mineralisation in calcareous laminites, which are typically rich in organic matter (DHAL deposits in the Bahloul Formation); (3) Pb-Zn-Ba-F and Fe-Pb deposits, with vug-fill features similar to Mississippi Valley Type deposits, in the Aptian reef formations that formed atop seafloor highs created by diapir and salt allochthon emplacement; and (4) Vein-type deposits (Fig. 15.43).

The Bou Grine Zn-Pb deposit is situated at the edge of the Lorbeus diapir, in the Domes region of the Maghreb (Table 15.2 and Fig. 15.43a; Rouvier et al. 1985; Charef and Sheppard 1987, 1991; Orgeval 1991, 1994; Bechtel et al. 1996, 1998; Jemmali et al. 2013; Bejaoui et al. 2013; Masrouhi et al. 2014). Bou Grine mineralisation belongs mostly to the first and second groupings, that is, lenticular and stratiform (Fig. 15.43b). In this, the Bou Grine deposit differs from caprock sulphides in the Gulf of Mexico in that much of the Pb-Zn mineralisation resides not in diapir caprock but in the adjacent organic-rich limestone laminites of the DHAL successions in the Bahloul Fm adjacent to the diapir. As well, in Bou Grine a semi-massive ore body (hanging wall orebody) cuts the Cretaceous series in the second megasequence in the Cenomenian-Turonian Bahloul Formation. The geologic reserves, with a cutoff value of 4 % Pb+Zn, are estimated at 7.3 million tonnes of ore at 2.4 % Pb and 9.7 % Zn, equivalent to 880,000 tonnes of metal (Orgeval et al. 1989). Mining of Pb-Zn ore at Bou Grine ceased in September 2005.

The zinciferous laminites in the Bahloul Fm in the Bou Grine deposit are made up of mineralised bioclastic clayey-carbonaceous calcimicrites, whose major features are: (1) A regular, in places laminar, bedded structure implying low energy, subwavebase bottom conditions; (2) Numerous foraminifera and other bioclastic components showing open marine affinities; (3) Mineralisation that is in part affected by early diagenetic structures, especially ferroan and calcitic cements. Sphalerite is present as microcrystals disseminated along the bedding planes, or as coalescent flattened nodules; it also appears to have been remobilised as

concentrations along fissures and later fractures. Galena occurs in euhedral crystals along the bedding planes and as scattered crystals in later fractures associated with calcite and schalenblende[1]. Calcite is observed in fissures that were deformed during compaction, as well as in all the later fractures; it also pseudomorphs occasional sulphate crystals (baryte and anhydrite).

The early nature of mineralisation at Bou Grine is reflected in: (1) Convoluted mineralised laminar beds deformed by intraformational slip, with flow structures; (2) Compaction structures around rigid cores of pyrite nodules and galena crystals; (3) Deformed infilled fissures. Sphalerite developed as: (1) Early regularly disseminated microsphalerite crystals in a slightly compacted sediment; (2) As almost simultaneous concentrations along sedimentary structures, textures and discontinuities; (3) As later concentrations and deformations of the mineralisation due to compaction and subsequent fracturing; and (4) As diagenetic remobilised cements that were either passive infills or provoked by circulation of mineralising fluids.

Laminites of the Bou Grine region also show high total organic carbon contents (4–5 % TOC), low organic maturity (T_{max} = 423 °C) and a marine (Type II) phytoplankton origin (Bechtel et al. 1996). Hydrocarbon enrichment at particular levels suggests possible former hydrocarbon reservoirs in some of the sediments adjacent to the diapirs. Montacer et al. (1988) showed that sulphate reduction in the laminite facies was bacterially mediated, with evolution of the organic matter probably occurring by *in situ* maturation of the laminite source rock. Their isotope studies support the notion of a close relationship between the initial metal stock and the sedimentological/diagenetic setting. Sulphur isotopes also indicate development of mineralisation in a closed sulphur system. Along with Sr and Pb isotopes, they also show the deposit, and its aureole, formed under the influence of an organic-rich diagenetic paleocirculation, with Pb derived from a single source.

The Guern Halfaya deposit occurs comprises the perched Guern Halfaya syncline in the east and a tight anticline in the west (Figs. 15.42 and 15.44a, b; Jemmali et al. 2013). In the northwestern part, there are two longitudinal Triassic outcrops defining the Koudiat el Hamra–Jebel Oum Edeboua zone. The northern–northwestern parts are cut by NE–SW and N–S trending normal faults, which are at places invaded by Triassic evaporites. The lithologic succession at Guern Halfaya is composed of Mesozoic and Cenozoic sedimentary rocks.

The Triassic outcrop consist of chaotic gypsiferous clays, sandstones, black dolomitic-limestones, which are underlain in the subsurface by large amounts of anhydrite with a halite core (Hatira and Zouari 1997). Lower Cretaceous strata, which outcrop in the western part of the area, include Aptian–Lower Albian rocks, which encompass strongly iron-mineralized (oxidized siderite) micritic limestones and sandy clays overlain by thick *Orbitolina*-bearing limestones. Those limestones are covered by the Albian micrites and marls that can enclose lenses of coarse-grained platform limestones. The Upper Cretaceous is composed of Cenomanian marl–limestone alternations overlain by yellowish limestones. The Upper Cenomanian– Lower Turonian consists of laminated gray to black organic-rich limestones of the Bahloul Formation, with 3–7.5 % TOC. The while the overlying Turonian includes marls and banded limestones. The Upper Turonian–Eocene series are made up of the following formations, all of which outcrop in the SSW part of Jebel Oum Edeboua and form the vast syncline of Guern Halfaya. The Coniacian–Santonian Aleg Formation is primarily marly. The Upper Campanian–Lower Maastrichtian Abiod Formation consists of marl–limestones and limestones. The Paleocene–Lower Eocene El Haria Formation is a series of clays with marl, gypsum and rare limestone intercalations. The Ypresian Metlaoui Formation is a *nummulite-bearing* limestone forming the core of the Guern Halfaya syncline. The Miocene series starts with coarse conglomerates and carbonates and continues with micro-conglomerates, which are well represented at the northern foot of Koudiat el Hamra, and ends with sandstones and sandy clays. The Quaternary consists of alluvium and clayey sand aureoles on Miocene conglomerates.

The Guern Halfaya Pb-Zn deposit is composed of the Koudiat el Hamra Oum Edeboua orebodies, which are distributed around the periphery of NE–SW trending evaporite-bearing Triassic rocks and closely associated with the NE–SW and N–S trending normal faults (Fig. 15.44; Bejaoui et al. 2013). The deposits exhibit three styles of mineralization within the contact Triassic–Upper Cretaceous series, particularly in the Cenomanian marl–limestone alternations and in the Bahloul Formation and show strong affinites to mineralisation styles at Bou Grine, namely: (1) lenticular mineralization in the Cenomanian marl–limestone alternations consisting of abundant pyrite with marcasite, sphalerite, galena and celestite, hosted in halokinetically induced dolostone breccias as impregnations, substitutions and replacements of the clayey-dolostone matrix. (2) Stratiform mineralization in the Bahloul Formation consisting of framboidal and cubic pyrite, disseminated sphalerite and galena. (3) Veins, disseminations and stockworks in breccias of Cenomanian–Turonian limestones and of pyrite, galena and sphalerite.

Various workers in the Maghreb – Domes Pb-Zn deposits have found that sulphur isotope determinations in the host rocks and ores and gangues are consistently indicative of a

[1]Compact sphalerite and wurtzite masses of a pale brown colour, occurring in concentric layers with reniform surfaces, which also may contain pyrite and galena.

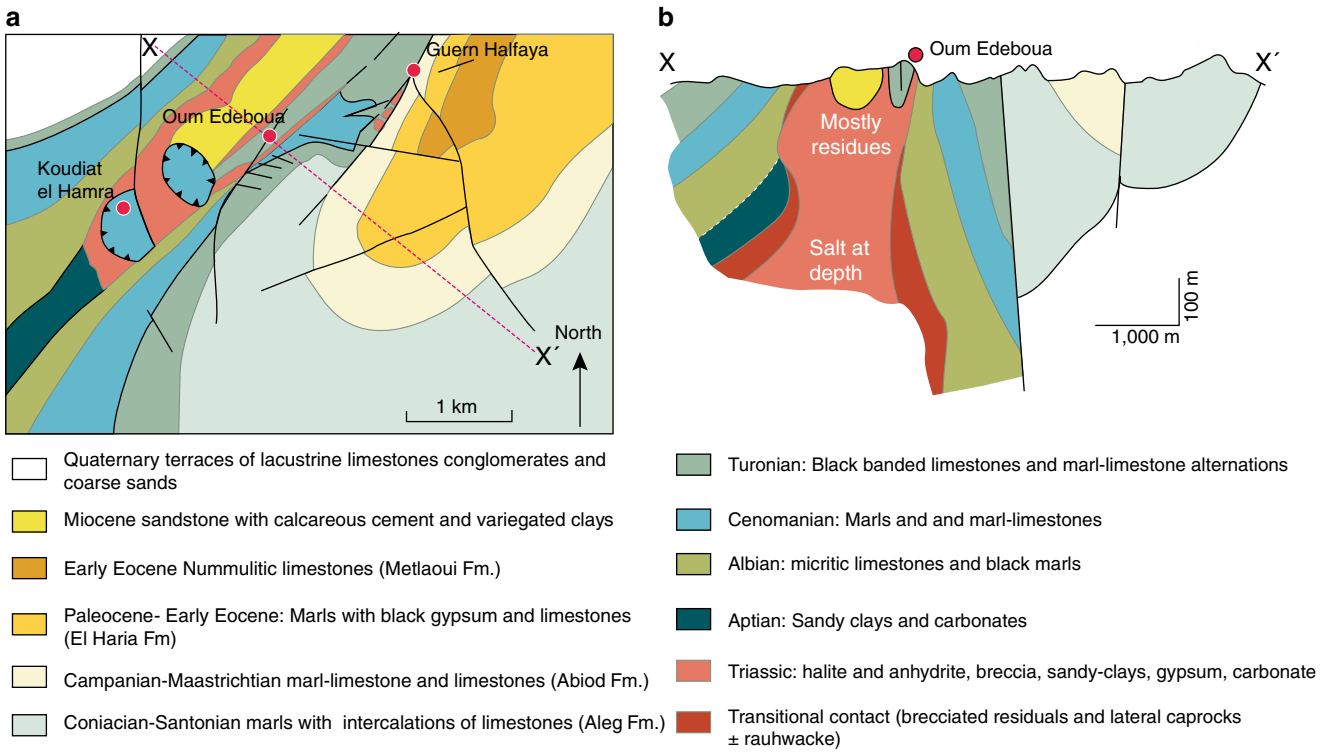

Fig. 15.44 Geological map (**a**) and schematic NW–SE cross-section (**b**) of the Guern Halfaya area where the Oum Edeboua mine and Jebel Guern Halfaya are located (After Jemmali et al. 2013)

bacterial sulphate reduction set of processes acting on sulphate evaporites, organics and hydrocarbons in the vicinity of the various Triassic salt structures (Jemmali et al. 2013; Bejaoui et al. 2013 and references therein) For example, gypsum, celestite and baryte in Triassic rocks at Oum Edeboua have $\delta^{34}S$ values ranging from 12.8 to 15.0‰, whereas anhydrite in Triassic evaporite (from drill core) at Tabbet Lahsan (Fej-el-Adoum district) yielded $\delta^{34}S$ values ranging from 14.2 to 15.6‰ (Fig. 15.45). These data are similar to typical $\delta^{34}S$ values of (a) about 16‰ obtained from anhydrite and celestite in Tunisian Triassic evaporite diapirs, (b) about 15‰ obtained from regional Tunisian sulphates and (c) 11–17‰ in Triassic marine sulphates (Fig. 15.45a). This consistency implies Triassic evaporites are likely sources of sulphur that can be associated with sulphate minerals in Triassic strata.

Galena in mineralized Triassic–Upper Cretaceous rocks at Oum Edeboua yielded $\delta^{34}S$ values of 3.3–9.5‰, whereas galena and sphalerite in mineralized Cenomanian–Turonian and Turonian rocks at Bou Grine yielded $\delta^{34}S$ values of 2.6–9.4‰. Such sulphur isotope compositions overlap sulphur isotope values of orebodies at Bou Grine (Fig. 15.45b). This implies the same or similar source of sulphur in the base-metal sulphide deposits in both the Oum Edeboua and Bou Grine with Triassic seawater brines and associated evaporites as likely ultimate sources of sulphur. In addition, diagenetic pyrite from the Bahloul Formation, with higher concentration in laminites, which were deposited in parts of the Bahloul deep seafloor that were Cretaceous DHALS.

More positive $\delta^{34}S$ values in base-metal sulphides from the Oum Edeboua and Bou Grine mines may suggest an additional sulphur input during abiotic thermally-driven sulphate reduction (TSR) of Triassic sulphates at depth. But, given the likelihood of lower temperatures at mineralisation, as documented in inclusion studies, it is less likely that TSR was a significant supplier of sulphur. TSR typically requires temperatures well in excess of 120–130 °C and produces sulphate–sulphide fractionations that typically range from ~0 to 10‰ (Chap. 9). Documented homogenization temperatures for mineralizations at Oum Edeboua and Bou Grine are 95–130 °C (Kassaa 1998) and 75–100 °C (Orgeval 1994). Bacterial sulphate reduction (BSR) typically occurs at temperatures lower than 110 °C and produce sulphate–sulphide fractionations that typically range from 15 to 60‰ with respect to seawater sulphur. Thus, both the sulphur isotope ranges and mineralisation temperatures favour BSR over TSR, with marine-derived sulphates and pyrite as the likely sulphur sources. The significance of BSR is further supported by the presence of bacterial relics in the Oum Edeboua mine (Kassaa 1998) and the Bou Grine mine (Orgeval 1994). In addition, pyrite associated with galena in the Oum Edeboua mine exhibits framboidal texture, which is

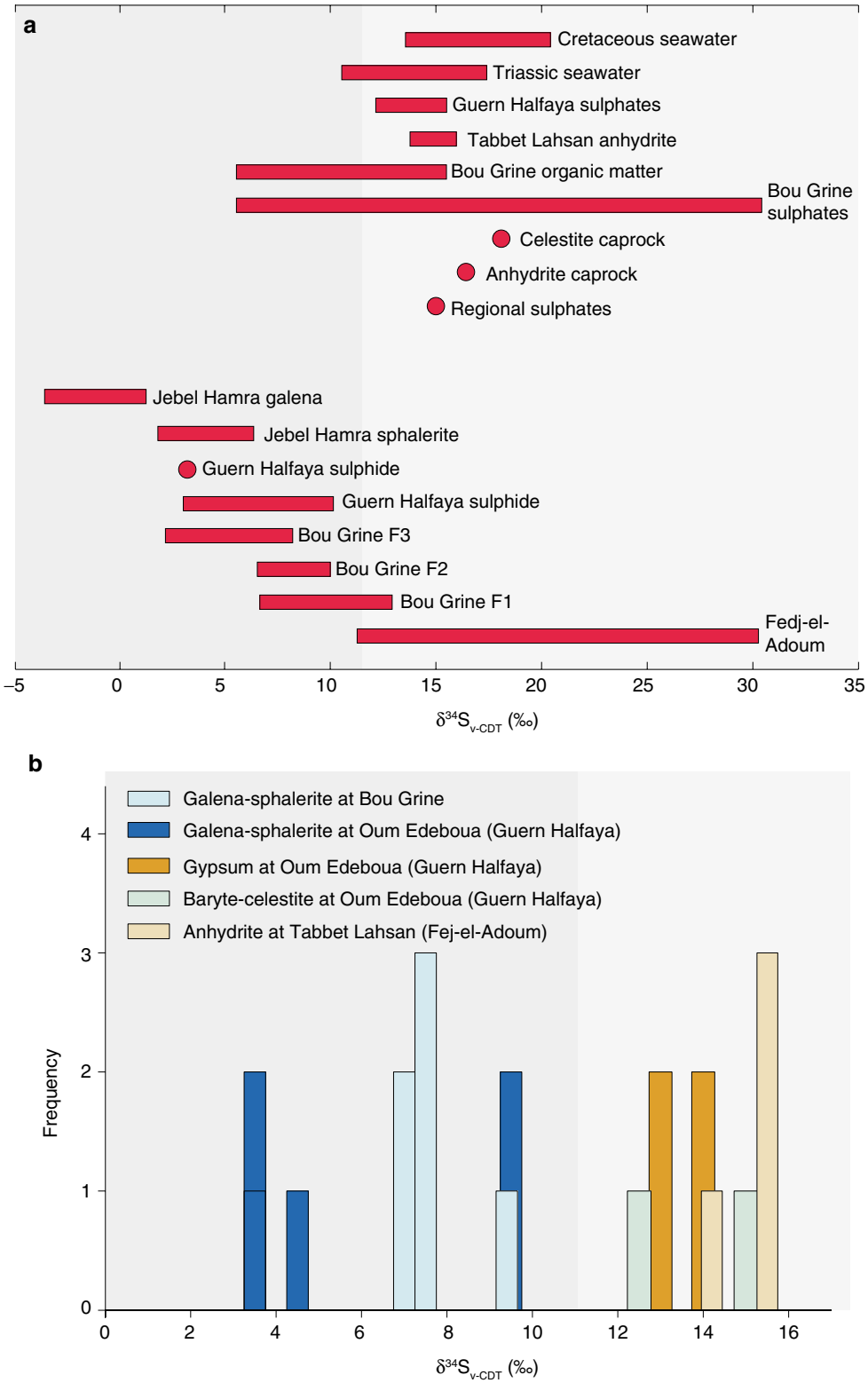

Fig. 15.45 Sulphur $\delta^{34}S$ isotope values in the Domes region of the Maghreb. (**a**) Spread of sample fields mostly collected from sites in Bou Brine, Guern Halfaya and Jebel Hamra regions. (**b**) Distribution (frequency) plot of site specific values of sulphides (galena + sphalerite) and sulphates (gypsum + baryte + celestite + anhydrite) from the Oum Edeboua, Bou Grine and Tabbet Lahsan deposits (After Jemmali et al. 2013 and Bejaoui et al. 2013)

characteristic of BSR-linked galena at several Pb–Zn deposits such as in Bleiberg, Austria and Navan, Ireland.

But, was the ultimate source of the metals local or more distal? The present Pb isotope data are homogeneous with $^{206}Pb/^{204}Pb$, $^{207}Pb/^{204}Pb$ and $^{208}Pb/^{204}Pb$ ratios of 18.723–18.783, 15.667–15.685 and 38.806–38.889, respectively (Jemmali et al. 2013). This suggests a single source reservoir of Pb at some depth in the upper crust. The syn-diagenetic mineralization in the Bahloul Formation and the calculated age from the Pb isotopic data suggest an Upper Cretaceous age for the Pb-Zn

deposits in the Guern Halfaya and Bou Grine areas. During this period, NE-SW to ENE-WSW trending regional extensional tectonic structures likely favoured migration of mineralizing fluids and eventual deposition at Guern Halfaya and Bou Grine in metal-rich brine conduits in redox positions controlled by a combination of salt focusing and associated faulting.

Across the Domes region a Pb-Zn deposit's locality and host rock geometry was controlled by a feedback between salt flow and the creation of Cretaceous deep seafloor brine sumps in response to synkinematic movement of the seafloor. Thus halokinesis and the associated allochthons controlled: (1) Local deposition of conglomerates and breccias adjacent to the highs atop the growing salt allochthons, (2) Local deposition of organic-rich pyritic laminites in areas of brine ponding (DHAL) on locally deepened seafloor, (3) Tilting of panels of sediments by listric faults activated by the emplacement of allochthons and diapirs, (4) Overlapping of sedimentary bodies by shoal/shelf progradation or truncation. Halokinesis also led to marked thickness variations of the various facies across the regions via the repetitious pulsing of the active diapir and its ongoing dissolution.

In addition to Pb and Zn, recent work by Dill et al. (2014) has related significant accumulations of Sr and F to the peripheries of salt structures in the Domes Region and their associated brines. Shallow halokinetic units create a basin-and-swell topography in any landscape and so provided the local and regional unconformities to which many of the Sr and F mineral deposits are related. Syndiapiric salt dissolution and welding also created carrier brines and focused their upwelling. Dill et al. argue that there are five mineralizing processes or stages, each with characteristic sedimentary ore textures related to subsurface salt movement and ore emplacement: (1 + 2) Early- and late-stage replacement ("zebra rocks"), (3) hydraulic fracturing ("fitting breccia"), (4) remobilization ("spinifex structures"), and (5) open-space filling ("caves and vein-like deposits"). All can be related to the coming and going of evaporite beds and flows.

Basinal brines from Mesozoic aquifers delivered Pb, Zn, Cd, REE, Y, Hg, and Se, while Sr, Cs, Be, Li, Cu and Co were perhaps derived from Cenozoic salinas across the Neo-Tethyan basin (Dill et al. 2014). Mixing of Mesozoic and Cenozoic brines between 28 and 19 Ma drove emplacement of Sr–F minerals at temperatures below 200 °C, under strongly alkaline conditions. Epigenetic polyphase Sr–F deposits bearing base-metals which are closely related to salt domes (Tunisian-Type) can also be traced into epigenetic monophase Sr deposits within bioherms (Cyprus-Type) largely devoid of Pb, Zn and F. Moving eastward in the Domes region, syndiagenetic monophase Sr deposits in biostromes (Gulf of Mexico-Type) herald the beginning of Sr concentration in Miocene sabkhas of the Neo-Tethys. Dill et al. (2014) argue their work bridges the knowledge gap between epigenetic carbonate-hosted MVT and syndiagenetic evaporite deposits.

The Domes region, at its halokinetic Cretaceous beginnings, was a submarine slope at the edge of a structural high. At that time, other than near a few local diapirs and salt allochthons, this area never seemed to have shoaled sufficiently for a true shallow water carbonate platform to have developed. The organic-rich sediments probably accumulated in this region only in the deeper areas of rim synclines about the active diapirs and salt sheets, hence the localisation of the mineralisation to laminites in the peridiapiric areas. Throughout the metal evolution history the salt was halokinetic, first in an extensional and then in a compressional (squeezed-diapir salt thrust) tectonic association. Only later with the withdrawal of the seaway did arid Cenozoic sabkha and salina deposition come to dominate.

Evaporite-Cored Thrusts and MVT's in the Maritimes Basin, Canada

Beyond the very obvious evaporite-related and Cretaceous hosted peridiapiric Pb-Zn deposits of the Domes region and the Tertiary-hosted Gulf of Mexico caprocks, there are a number of other older carbonate platform-hosted MVT accumulations in compressional traps, which are tied to salt allochthons or salt-cored thrust décollements. One of most obvious of these occurs in the Maritimes thrust belt of Canada, tied to the strike-slip system centred on the Minas Geofracture and subsidiary thrusts (Fig. 15.46; Waldron et al. 2013). These various metal accumulations include the well known Gays River and Jubilee/Ainslie and Walton deposits (Fig. 15.46a) Gays River and Jubilee in most current ore deposit classifications are typically pigeonholed as type examples of MVT (Mississippi Valley Type deposits; e.g. Paradis et al. 2007; Taylor et al. 2009). Siderites and barytes of the Walton-Magnet baryte deposit are also part of this halokinetic Maritimes association, but were discussed earlier as an examples of baryte accumulation in fault-related halokinetic alteration haloes (Fig. 7.95a) and so will not be considered in detail in this metals chapter.

Because this tie of the Pb-Zn mineralisation to an evaporite allochthon décollement is so obvious in Gays River and Jubilee (Fig. 15.46b), I now discuss them the current section dealing with undeniable peridiapiric-salt allochthon Pb-Zn associations. But, under all current definitions of MVT deposits, they definitively belong also to the MVT pigeonhole. We shall come back to classifications of various low-temperature ore deposits at the end of this chapter.

Gays River, Nova Scotia

The Gays River Zn-Pb deposit of southern Nova Scotia, Canada has reserves ca. 2.4 million tonnes at 14.3 % Zn and 6.3 % Pb of either massive or disseminated ore. The deposit

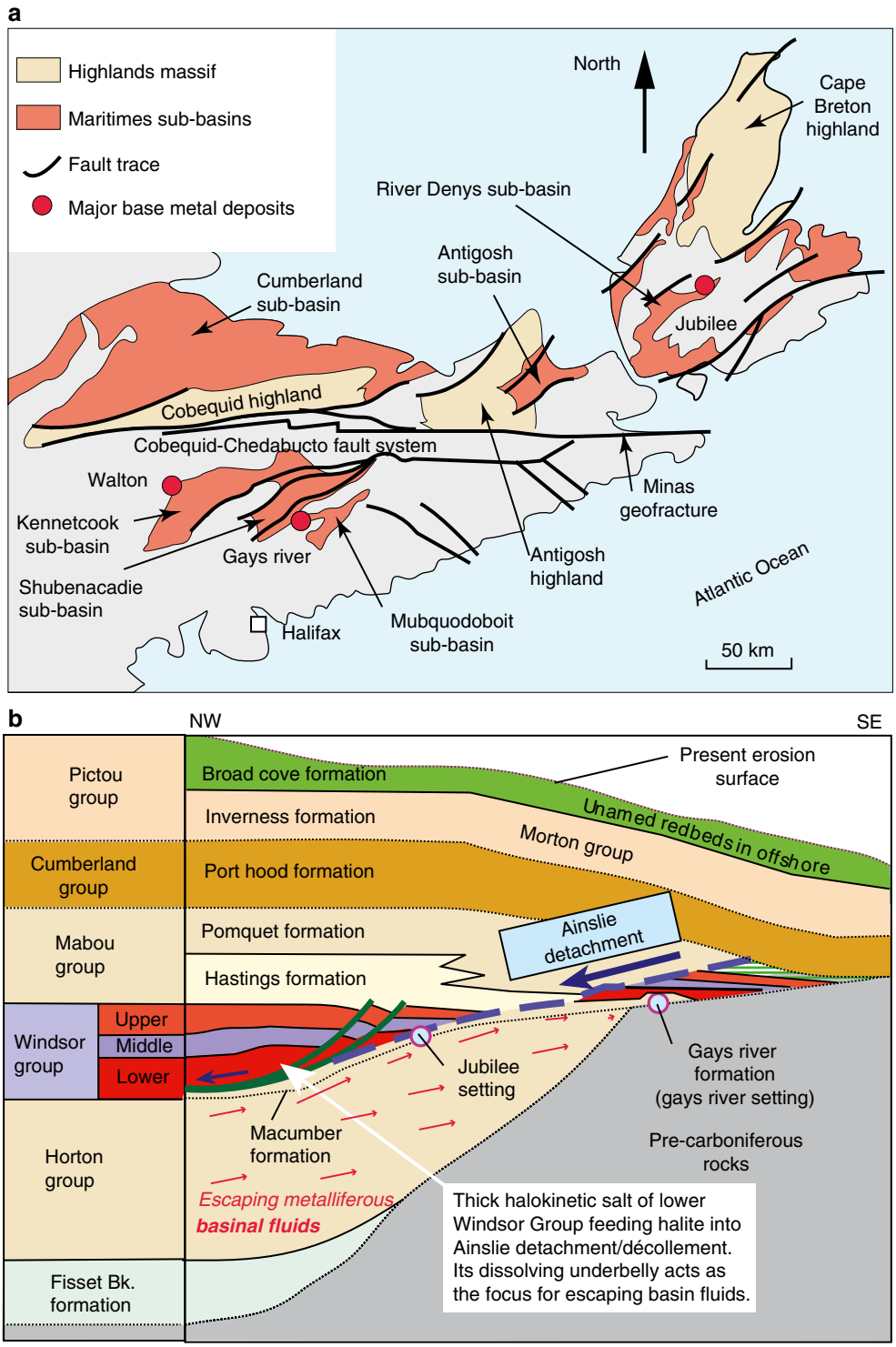

Fig. 15.46 Pb-Zn in the Maritimes Basin, Canada (**a**) Map of Nova Scotia showing Carboniferous sub-basins, major thrust fault traces and the Antigosh, Cape Breton and Cobequid highlands. (**b**) Schematic cross-section showing relationships between regional stratigraphy, mineralisation and the position of the Ainslie Detachment (After Lynch et al. 1998). Note that the timing of the detachment is indicated by a gap in the Windsor Group stratigraphy in the Gays River region created by the presence of a salt unit and salt flow. The thick salt, when it was formerly present at the level of the detachment, acted as a focus for the up-dip channelling of escaping basinal fluids

is located in the Meguma Terrane of southern Nova Scotia and is hosted by Windsor Group (Visean) carbonate/evaporites that were deposited in several sub-basins of the larger Maritimes Basin of eastern Canada (Fig. 15.46a; Kontak and Jackson 1995; Sangster et al. 1998a, b).

In terms of ore focusing, it was the adjacent dissolving and sealing evaporite units, along with associated entrapped hydrocarbons, and not the adjacent permeable dolomitised Carboniferous carbonate buildup, that controlled the locality and the process of mineralisation. The massive ore zone is directly adjacent to the sulphate evaporite bed and is made up of fine-grained, beige coloured sphalerite and medium to coarse-grained galena. The massive ore is only found along the carbonate-evaporite contact (Fig. 15.47a). Disseminated ore,

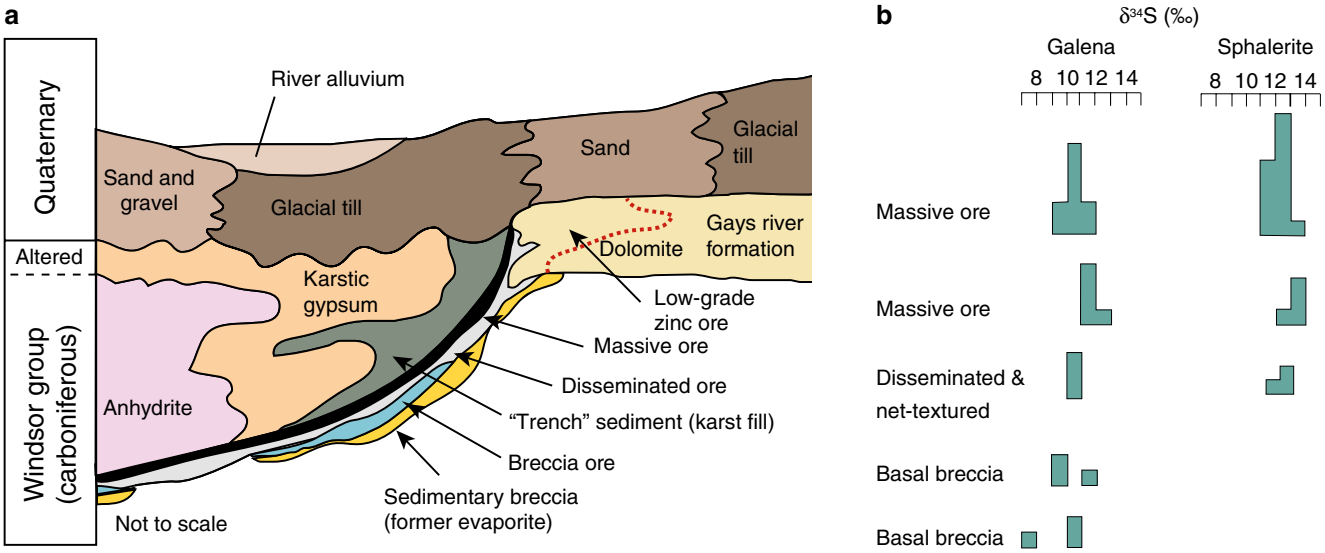

Fig. 15.47 Gays River Deposit, Nova Scotia (see Fig. 15.46a for location). (**a**) Schematic cross section showing intimate relationship between Pb-Zn mineralisation, ore textures, and the position of the gypsum-anhydrite residue as an indication of the position of former salt allochthon/décollement (in part after Kontak et al. 1994). (**b**) Sulphur isotopes classified using ore textures (After Sangster et al. 1998a, b)

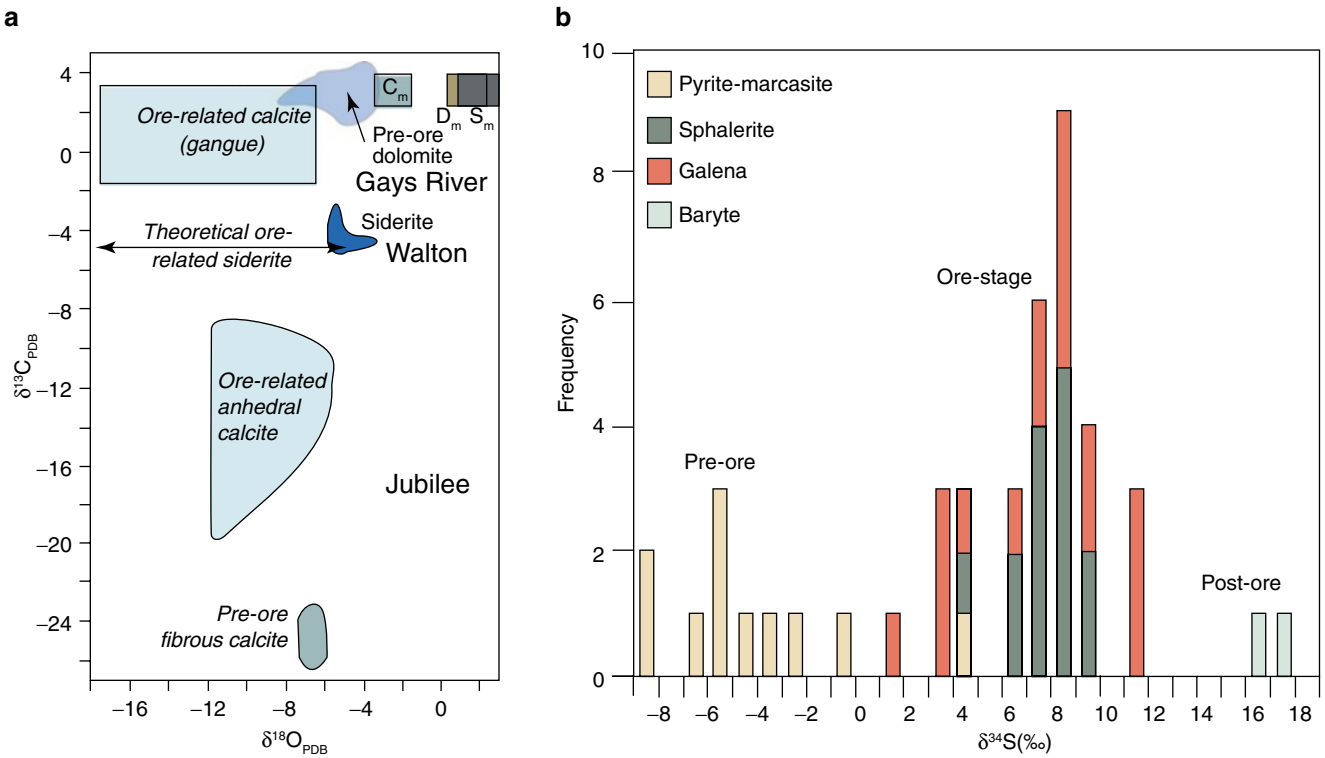

Fig. 15.48 Isotopes in selected Pb-Zn deposits of the Maritimes Basin (**a**) Carbon and oxygen plot-fields of pre-ore dolomite (*Dm*), calcite (*Cm*) and siderite (*Sm*) as well as ore-gangue calcites (more negative oxygen values indicate higher burial temperature). (**b**) Sulphur isotopes of pre-ore, ore and post-ore stage mineral precipitates in Gays River (After Sangster et al. 1998a, b)

adjacent to the massive ore and its evaporite seal, is hosted by Visean-age, dolomitised carbonate rocks that are part of a series of carbonate banks within the Gays River Formation. Both the galena and sphalerite show similar sulphur isotope values indicating they come from a similar, if not the same, sulphur source (Fig. 15.47b). When carbon oxygen values in the associated ore gangue calcite are plotted and compared with C-O plotfield of the earlier carbonate cements it is obvious that the fluids carrying the metals and gangue calcite are hotter and separate to the authigenic carbonate cements in the host dolomites (Fig. 15.48a).

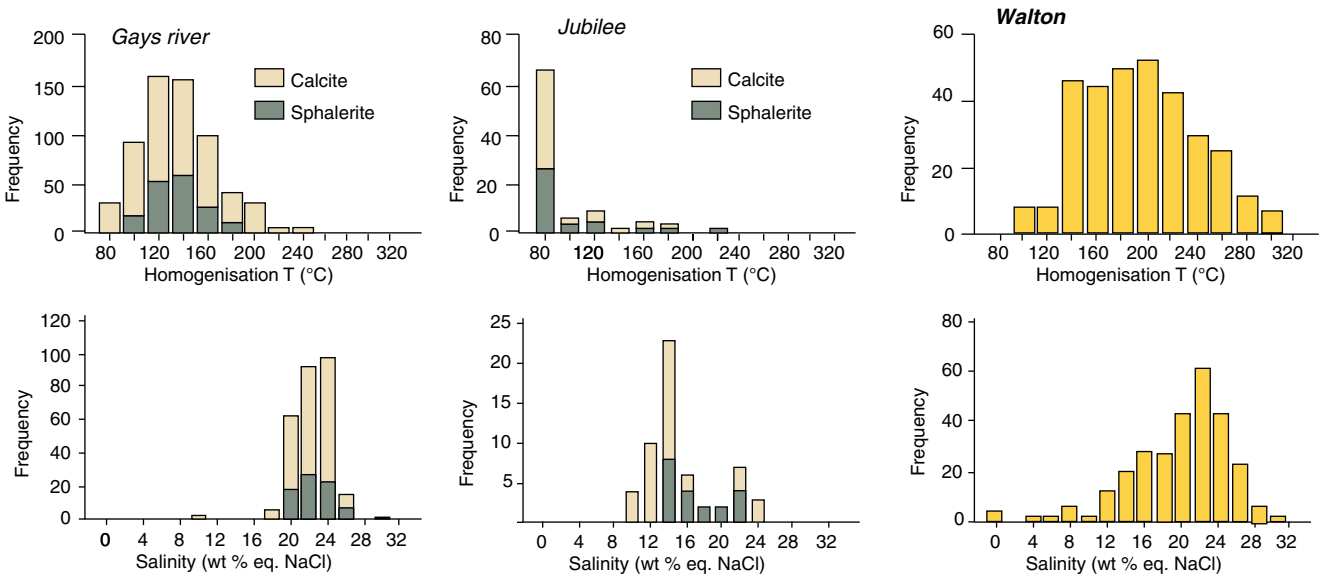

Fig. 15.49 Summary of fluid inclusion temperature and salinity in the three main deposits; Gays River, Jubilee and Walton (After Sangster et al. 1998a, b)

The Carboniferous sediments that host lower percentages of mineralisation than the evaporite contact initially grew on fault-controlled paleotopographic highs that were underlain by Lower Palaeozoic meta-turbidites of the Meguma Group, sometimes with local intervening breccia units (Horton Group). The breccias contain fragments (centimetre to metre scale) of Meguma Group lithologies within a dolostone matrix and are likely rauhwacke units (Figs. 15.46b and 15.47a). The disseminated, lower-grade mineralisation infilling porosity in the dolomitised carbonate banks consists of yellow to orange, millimetre-scale sphalerite and euhedral galena coating the walls of larger pores and cavities. Trace amounts of Fe and Cu sulphides as well as fluorite and baryte are also present.

To generate improved predictive exploration models based on a Gays River analog, requires that the evaporites at the mineralised contact are characterised in a basinal diagenetic context in as much, if not more, detail than the carbonates that host the lower ore grades in adjacent strata. Construction of surface plant and mill processing facilities commenced in 1978, and the mine was further developed to support an intended production rate of 1,350 t per day. Mill production commenced in October 1979, and by midsummer of 1981 a total of 554,000 t of ore and 272,000 t of waste had been mined. Throughout this period, efforts to achieve the full production rate, as well as efforts to mine areas of higher grade mineralization were continually thwarted by the combination of an extremely complex geological setting and severe hydrological problems. Throughout the life of the mine, water influx from karst piping tied to aquifers in the glacial overburden was an ongoing problem. Production operations at Gays River Mine were suspended indefinitely on August. 15, 1981, as a result of continuing problems with ore grade continuity and underground water. So today, the Gays River mine is now abandoned and flooded. The mine was only operational for 4 years from 1978 to 1981. This was more than three decades ago, in a time prior to our current understanding of diagenetic significance of various evaporite textures.

In the context of likely evaporite associations, the depositional setting of the carbonate banks hosting low-grade mineralisation and located adjacent to the main ore body is interesting. In the 1970s and 80s these banks were interpreted as shoalwater carbonate platform build-ups. But the abundance and perfection of preservation of filter-feeding brachiopods and bryozoans in many of the mounds was puzzling in a supposed shoal water photic community. The Gays River mounds were reinterpreted as vent-fed chemosynthetic mounds by von Bitter et al. (1992). Such an origin is more consistent with the distribution of the massive ore and with the obvious peridiapiric/allochthon distribution of the evaporite facies.

The main ore-hosting authigenic dolomite replaced its limestone precursor prior to the mineralisation event (pre-ore dolomite as seen in Fig. 15.48; Savard 1996). Dolomitization played a role in ground preparation, but was not directly tied to the Zn- and Pb-rich basinal fluids that mineralised the Gays River deposit. Stable isotopes show clearly that the main dolomite in carbonate buildups predates the mineralisation at Gays River (Fig. 15.48a). Fluid inclusion work on the coarse-grained sphalerites, and rare earth element profiles in late stage carbonate cements associated with the mineralisation, indicate that the mineralising fluids were warm (<120–140 °C), saline brines (>20–24 wt% NaCl)

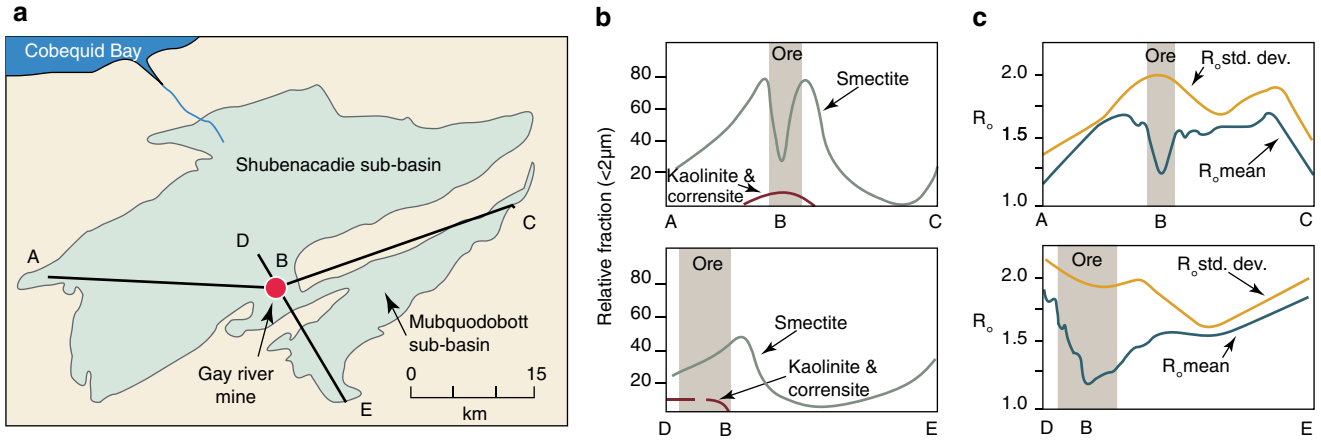

Fig. 15.50 Clay mineral and vitrinite reflectances as indicators of elevated temperatures associated with focused fluid flow in the Gays River Pb-Zn deposit. (**a**) Map showing position of sections *ABC* and *DBE*. (**b**) Relative abundance of authigenic kaolin±corrensite versus smectite in the vicinity of the orebody. (**c**) Variation in the mean reflectance and its standard deviation with respect to the orebody (After Heroux et al. 1996)

(Fig. 15.49; Akande and Zentilli 1984; Chi and Savard 1995; Kontak and Jackson 1995; Sangster et al. 1998a, b). $^{40}Ar/^{39}Ar$ dating places the mineralisation event at 300 Ma, while other isotopic data (Sr, C, O, Pb) indicate that the mineralising fluids were derived by fluid flushing of the underlying meta-turbidites of the Meguma Group or of the derived detritus that resides in the Devonian-Carboniferous Horton Group and carried to the sulphate-rich precipitation site by saline basinal brines (Kontak 1998; Kontak et al. 1994).

Heroux et al. (1994, 1996) found that the elevated temperatures and hydrocarbon contents of the mineralising brines also altered the clay mineralogy and organic maturity profiles of the adjacent carbonate/claystone matrix (Fig. 15.50a, b). The Gays River deposit is associated with smectite replacement of well crystallised detrital illite and chlorite. This forms a diagenetic halo around the main ore zone, while authigenic kaolinite and chlorite-corrensite typify the alteration halo in the immediate vicinity of the ore zone (Fig. 15.50b). Vitrinite reflectance (R_o) values and their absolute variability increase in the host rocks toward the ore zone (0.8–1.88 %) and show a relatively low R_o within the ore zone. That is, the R_o exhibits an anomalous suppressive effect with respect to depth of burial at the mine site, suggesting a chemical alteration of the organic matter in the mineralised zone.

Alternatively, as in other oil-generating basins in the world, vitrinite suppression can indicate overpressuring or the occurrence of H-enriched liptinites. The highest R_o values are associated with mosaic (recrystallised) textures in the host carbonates and outline a thermal anomaly in the region, probably related to the evaporite-focused escape of basinal brines. Heroux et al.'s work suggests that rock matrix relationships between clay mineralogies, organic anomalies and the mineralisation as defined at the Gay River Mine at the mine can be used as sedimentological guides in the exploration for base-metal sulphides in this area and elsewhere.

Inclusion studies in sphalerite and pre- and post-ore calcite also indicate that the mineralising fluids were hypersaline basinal brines with locally elevated temperatures (Fig. 15.49; Chi and Savard 1997, 1998). The $Na_{deficit}$- Ca_{excess} plot shows the mineralizing brines were not tied to meteoric waters, rather they were a product of mixing of halite-dissolution fluid and evaporated seawater (indicated by lines a and b in Fig. 15.51, respectively).

Rock matrix relationships, and the salt-décollement-adjacent position of the massive and disseminated ore zones in the Gays River deposit (Figs. 15.46b and 15.47) imply evaporite impermeability and the fractionated base-salt sulphate-dissolution residuum position controlled the precipitation position of the metal sulphides. That is, the presence of massive ore at the host-evaporite (anhydrite) contact is a response to the focusing effect of the impervious evaporites, and that the basal anhydrite along the underbelly of the thick evaporite package was probably the major source of sulphur. It is highly likely that halokinetic evaporites once covered the Gays River carbonate buildup and formed a regional focus and likely seal at the time of ore emplacement. The allochthonous salt mass stabilized the precipitation interface and allowed mineralising solutions to pond at the contact with the permeable dolomite host rocks beneath it (Fig. 15.47a).

Later the evaporite seal was breached by meteoric dissolution, perhaps in the Cretaceous, and the karst system is still active today (McKee and Hannon 1985). The effect of this breaching clearly has a surface expression in the present glacial landsurface in the presence of numerous collapse dolines in the tills and related lithofacies thicknesses and distribution above the deposit. These Pleistocene sediments infilled an evaporite karst landscape. Fluid temperatures in excess of 120 °C seen in the ore sphalerite and galena inclusions implies thermochemical sulphate reduction occurred much

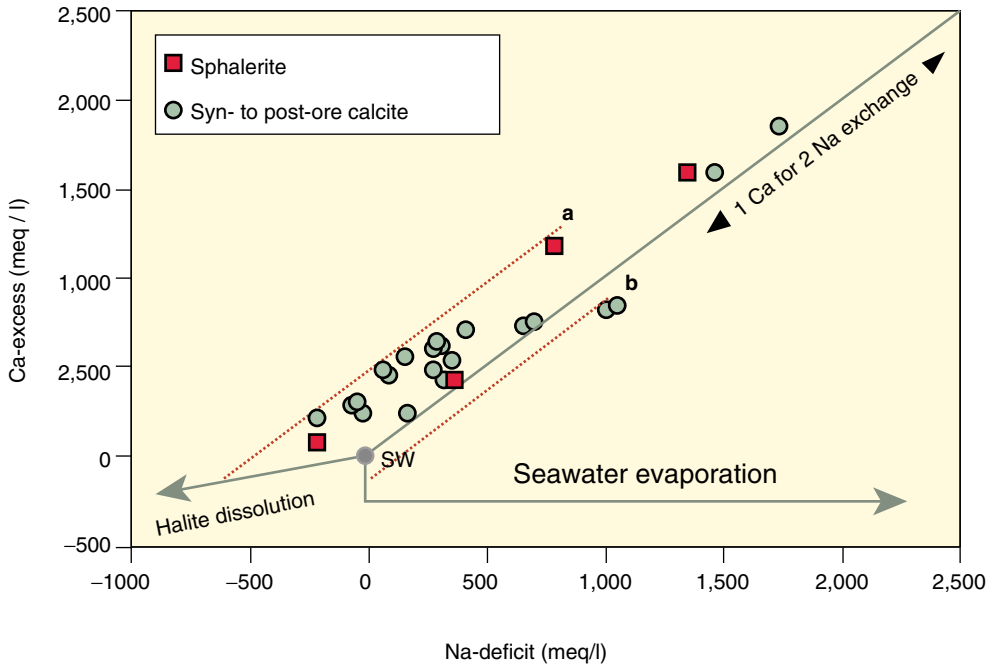

Fig. 15.51 $Na_{deficit}$ -Ca_{excess} plot of inclusion fluids from sphalerite and syn- to post-ore calcite in the Gays River MVT deposit (Data from Savard and Chi 1998; assumed salinity = 24 wt%). Lines *a* and *b* indicate the predicted position of a fluid with a [Cl] = 150 g/l originating from halite-dissolution and seawater evaporation, respectively

earlier than telogenesis, perhaps during or slightly later than the main thrust décollement and well prior to karst development. That is, all mineralisation and associated gangue calcite precipitation was mesogenetic and not telogenetic (Figs. 15.48a and 15.49). Ore was precipitated as a passive infill in whatever porosity was available at the time in the periodically overpressured subsurface TSR mixing zone (Chi et al. 1995; Heroux et al. 1996).

It was the evaporite-organic-sulphate TSR interface (not BSR) that focused the mineralising fluids. Pre-ore dolomitisation of the matrix was likely a response to the crossflow of the same evaporite-focused plumbing that later focused hotter mineralising hydrothermal brines. Dolomitisation is not a direct indicator of metal emplacement. The main economic role of dolomitised carbonate in the Gay's River deposit was that of passive host to the mixing of mineralising solutions, entrained hydrocarbons, and the thermochemically reduced sulphur derived from the dissolving evaporites. Prior dolomitisation events, likely related to less evolved escaping basinal brines, or even syndepositional brine reflux, may well have enhanced the aquifer properties of the ore host in the vicinity of the evaporite aquiclude.

Jubilee Zn-Pb Deposit, Nova Scotia

The Jubilee Zn-Pb prospect, Nova Scotia, is located 2 km southeast of Little Narrows village, near the quarry of the Little Narrows Gypsum Co. (Fallara et al. 1998). Like Gays River, it is one of many lead and zinc shows in Early Carboniferous limestones of the Maritime region, eastern Canada (Fig. 15.46a; Armstrong et al. 1993; Coron 1982). At Jubilee, a laminated limestone is overlain by transitional, interstratified limestone and anhydrite, with a massive anhydrite unit capping the sequence. The deposit extends over 2.75 km^2, and contains 0.9 million tonnes of 5.2 % Zn and 1.4 % Pb, and is hosted in the laminated limestones and breccias of Macumber Formation (basal Windsor Group). The Macumber Formation is the lateral equivalent to the Gays River Formation that hosts the Gays River deposit.

The Macumber Formation in the Jubilee deposit is made up of three main lithofacies: (1) A micritic lithofacies that locally contains ooids, oncolites and pellets, (2) A finely laminated lithofacies, and (3) A mineralised breccia facies (Fallara et al. 1998). The facies transition between the first two lithofacies is gradational and concordant, whereas the contact between the finely laminated lithofacies and the mineralised breccia is sharp. The breccia is conformable at the top of the Macumber Formation and never crosscuts it (Fig. 15.46b). The deposit is located near two faults interpreted as normal synsedimentary faults. Armstrong et al. (1993) suggested the mineralisation was a low temperature sulphide system related to the former presence of hydrocarbons.

Overlying the breccia at the base of the Carrols Corner Formation is a transitional zone of interbedded limestone and evaporite. Some of the limestone is replaced by anhydrite in the basal part of the transition zone. The overlying Carrols Corner Formation is a thick sequence of anhydrite and gypsum, up to 300 m thick. The breccia that hosts the ore has been variably interpreted as: (1) An evaporite solution collapse breccia, (2) A tectonic breccia that was the result of normal faulting and magmatic intrusions that created a horst structure, and (3) A collapse breccia produced by the

Table 15.11 Characteristics of the three breccia styles that constitute the various breccias that occur in the basal Windsor Formation, aka Pembroke Breccia sensu lato

	Early	Late	
	Early (synsedimentary)	Tectonic	Karstic
% clasts	60–95 %	40–75 %	40–90 %
Nature	Laminite	Laminite	Laminite, breccia, red mudstone, various siliciclastics (siderite in Walton)
Rounding	Some	None	Some for mudstone
Size	<1 mm–10 cm	>1 mm–5 cm	1 mm–50 cm
Matrix cement	Crushed fragments and lime mud	Crushed fragments and fibrous calcite cement	Carbonate fragments, red siliciclastics, lime mud, calcite cement
Sedimentary structures	Soft sediment deformation, concave upward shear failure planes, Cyclic pattern	Jig-saw puzzle like textures (crackle breccias)	Coarsening and fining upward, graded matrix
Diagenetic elements	Pre stylolite, prior to secondary dissolution	Post secondary dissolution	Dissolution surfaces on clasts. Oxidised rims and matrix. Post-stylolite (post siderite) and post sulphides
Timing of formation	Pre-burial and hydrocarbon migrations (Pre-Visean)	Syn-burial and hydrocarbon migration (locally) (Namurian Westphalian)	Post-burial and other breccias (Westphalian or younger?)
Unit	Macumber	Macumber	Pembroke *(sensu strictu)*

After Lavoie et al. (1995, 1998)

subsurface dissolution of evaporite during the circulation of the mineralising fluid.

Work on breccias in the lower part of the Windsor Group by Lavoie et al. (1995, 1998) and has shown that all three origins are correct. What previously was loosely called the Pembroke Breccia (*sensu lato*), and considered a single unit, does in part host the ore. The problem is that the Pembroke Breccia is a term that is used to describe all breccias in the region, when in reality it does not describe a single lithofacies or a formation specific unit. Rather, the term Pembroke Breccia has been applied to three temporally and genetically distinct breccia bodies (Table 15.11). There is a pre-ore syn-sedimentary carbonate slope breccia, a syn-ore tectonic breccia related to the Ainslie Detachment, and a modern karstic post-ore evaporite solution collapse breccia related to the modern groundwater system. The formation of the syn-ore breccia was aided by pressure buildup and hydrofracturing beneath the regional evaporite cap; processes which also facilitated the formation of the regional subsalt detachment (Ainslie Detachment) at the base of the Windsor Group (Fig. 15.46b).

The main ore host is this syntectonic hydraulic breccia; it is a mineralised-matrix breccia is that contains pyrite, marcasite, sphalerite, galena and baryte, in addition to burial calcite and siderite. Its clasts have been extensively recrystallised and commonly retain finely disseminated sulphides. Anhydrite is absent, as is true sedimentary interclast matrix. Instead, the recrystallised breccia fragments are cemented by equant sparry, or locally radiaxial fibrous calcite, together with sulphides. Liquid hydrocarbons and solid bitumens are abundant, particularly within sulphide-rich domains, and also occur as inclusions within sphalerite and baryte crystals. Stable isotope data clearly show the metals in the mineralised matrix breccia were derived from escaping basinal brines (Armstrong et al. 1993).

In contrast, the evaporite solution breccia that forms via surface related dissolution of the evaporites is a classic rock matrix collapse breccia; it contains clast-supported, chaotically distributed, centimetre-sized, subrounded to angular fragments of the Macumber Formation. Most of the clasts retain their original laminated texture and have not been extensively recrystallised. According to Hein et al. (1991), the clasts in the breccia fell into open spaces created by dissolving evaporite interbeds and interlaminae. The interclast matrix is made up of finely comminuted rock fragments of the overlying Macumber Formation. This rock matrix breccia can be present in cored intervals that also intersect mineralised intervals, hence the earlier confusion in separating the two styles of breccia.

The NNW-trending faults that cut the Jubilee deposit have been shown by Hein et al. (1991) to be synsedimentary and continued to be active solution conduits after they were overthrust by a thick evaporite seal. In the early stages, prior to the thrust emplacement of the evaporite, the faults supplied nutrient-rich waters that vented on to the sea floor. This allowed enhanced carbonate sedimentation on the deep sea

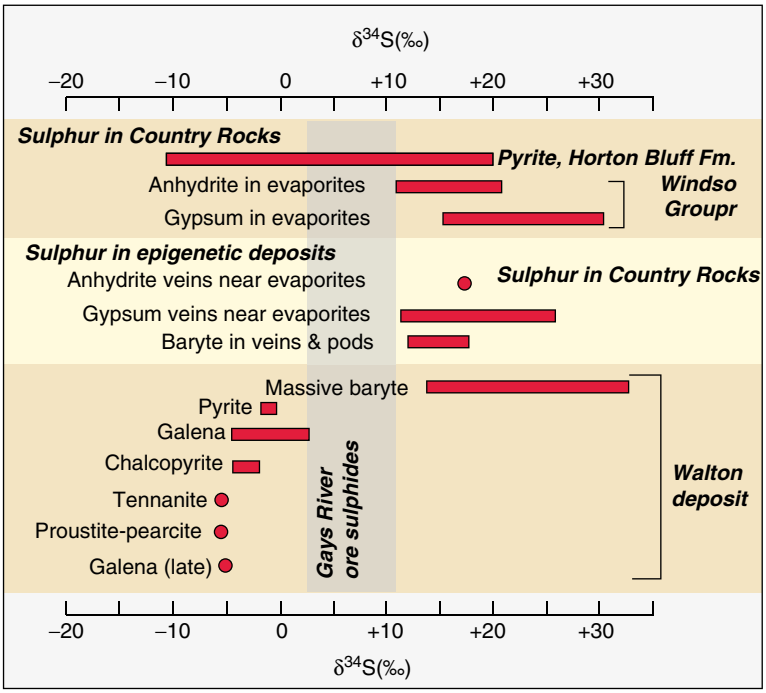

Fig. 15.52 Sulphur isotope ranges for various mineral phases in the Walton deposit and its evaporitic sulphate surrounds, shaded central panel shows sulphide range for the sphalerite and galena in the Gays River mine (After Sangster et al. 1998a, b)

floor in the vicinity of the vents, where chemosynthetic communities of fossil tubes, serpulid and spirorbid worms, conularids, brachiopods, bryozoa and ostracods flourished (von Bitter et al. 1990). Later, during burial diagenesis, and after thrust emplacement of the evaporite cap, the faults acted as conduits that carried metalliferous basinal fluids up into the base of the anhydrites where the sulphides then precipitated. This explains why, even though it is syn-ore tectonic breccia, the mineralised breccia unit is thickest and most heavily mineralised adjacent to the Jubilee Fault.

The Walton Ba-Cu-Pb-Zn-Ag deposit produced some 4.5 million metric tons (Mt) >90 % $BaSO_4$ and 412,850 t @ 0.52 % Cu, 4.28 % Pb, 1.29 % Zn, and 350 g/t Ag (Sangster et al. 1998a). It is hosted by Visean age carbonate rocks of the Macumber Formation and its associated breccia (Fig. 7.95a). The Macumber Formation in the Walton area is divided into two units, the lower Macumber, a laminated carbonate unit 9–12 m thick and the upper; Macumber, a synsedimentary carbonate breccia that forms two mounds up to 21 m thick.

Outside the immediate mine area the carbonate is either limestone or dolostone; the Macumber Formation surrounding the deposit has been altered to manganiferous siderite. Although three textural types of siderite are recognized, little variation in bulk chemical composition is evident among them. Minerals were deposited in the sequence: baryte, pyrite-marcasite, sphalerite, galena, tennantite, chalcopyrite, and (para)rammelsbergite. Each mineral replaces earlier minerals to varying degrees. Sulphur isotope data from the deposit are given in Fig. 15.52.

Based on baryte and metal content, two main ore types are defined (Sangster et al. 1998a). Type I, with a bulk composition of 0.3 % Cu, 2.5 % Pb, 0.2 % Zn, and 31.2 % $BaSO_4$, comprises baryte and variable sulfide contents. Type II, comprised of sulphides only, has a composition of 0.5 % Cu, 0.5 % Pb, 0.1 % Zn, 51 g/t Ag, and no baryte. Type I ore forms a roughly conformable sheet which straddles the upper Macumber-lower Macumber contact and contains lenses of Pb- and Cu-rich ore. Type II ore is most commonly associated with the upper Macumber mounds where it forms large pods which cut the type I ore zone. Type II ore also occurs within the underlying Horton Group sandstones but only where the upper Macumber mounds have developed. There is also a stratigraphic zonation in metal content in as much as all metals are higher, on average, in the lower Macumber relative to the upper Macumber.

The host stratigraphy is steeply dipping and faulted and both features are considered to be post-ore events. Karsting, which also postdates mineralization and probably folding, has removed portions of the stratigraphic upper parts of the deposit. The cavities produced by this process are now partially filled with sand and limestone breccia. This work by Sangster et al. considers the ore host breccias to be depositional carbonate slumps and did not consider the possibility that the prepared ground could have been a response to halokinesis and salt dissolution (Fig. 7.95a)

Gays River, Jubilee and Walton deposits are part of a larger regional scale Zn-Pb-baryte-evaporite association, with consistent sulphur isotope, carbon-oxygen isotope and fluid temperature ranges, related to evaporite focused outflow interfaces. These were active during dewatering and salt-lubricated thrusting as the various tectonic sub-basins of the Maritimes Basin of eastern Canada were created

(Lynch et al. 1998; Sangster et al. 1998a, b, Waldron et al. 2013). Throughout central Nova Scotia, Pb-Zn and baryte deposits are tied to faults and salt structures responding to compression of the once laterally continuous saline giant that defined the original salt distribution in the Maritimes Basin fill. Deposits are generally tied to features at the Touraisian-Visean (Mississippian) clastic carbonate-evaporite disconformity, and overlie Cambrian to Devonian metasedimentary and granitic rocks, which likely acted as sources for the metals.

In addition to Gays River and Jubilee, other significant deposits of this association include: the Southvale baryte occurrence, the Pembroke Pb deposit, the Smithfield Pb-Zn-Cu-Ba deposit, the middle Stewiacke baryte occurrence, the Brookfield baryte deposit, the Hilden baryte occurrence, the Walton-Magnet Cove Ba-Pb-Zn-Cu-Ag deposit and the Lake Fletcher baryte deposit. All these deposits occur on the southern margin of the >10 km thick Carboniferous Maritimes (Fundy-Magdalen) Basin. Regional isotope and inclusion studies show the deposits all formed from basinal brines, which were derived from >5 km depths in catabaric sediments that lay beneath the Visean evaporites (Figs. 15.47a, 15.48, and 15.52; Ravenhurst and Zentilli 1987). According to Sangster et al. 1998b, the isotopic evidence suggests that the Walton, Gays River and Jubilee deposits were derived from the same brine source, probably deeply circulating sulphate-rich brines, as noted by Boyle et al. (1976), these sulphur signatures in these brines are virtually identical to an evaporite source.

Regional salt-lubricated detachment surfaces such as the Ainslie Detachment, controlled and focused the escaping basinal fluids, were probably first created by lateral "into-the-basin" gravity sliding or displacements along the sole of the regional salt thick in a foreland basin setting not too dissimilar to the Maghreb. The remaining salt now resides in the lower Windsor Group and, away from the dissolution edges to the various tectonic sub-basins, is today made up of some 350 m+evaporites of the Carrols Corner Formation and its equivalents (Waldron et al. 2013). During regional compression, the impervious underside of the salt and its allochthons and detachments focused the flow and periodic trapping of escaping metalliferous brines. Prior to reaching the sulphates of the salt base, these same fluids had circulated through the Tournisian clastic rocks and the immediately adjacent tectonic breccias of the detachments. Rising metalliferous brines mixed with shallower basinal fluids across breach points in the evaporite aquiclude, which are now accessible for mining mostly about the basin margin (Fig. 15.46a). Thermochemical sulphate reduction was the main metal fixing reaction of the various deposits, with the sulphur/sulphate supplied by the adjacent evaporites and the organics from the migrating hydrocarbons (Savard et al. 1996; Sangster et al. 1998b; Lynch et al. 1998; Lynch and Keller 1998).

Mississippi Valley Type (MVT) Deposits and Bedded Platform Sulphates?

In addition to the relatively small evaporite focused Pb-Zn deposits discussed so far, many of the larger carbonate-hosted Pb-Zn deposits within the MVT group of deposits are associated with salt-sourced hypersaline ore fluids. The hypersaline affinity is based on fluid inclusion studies that indicate most MVT sulphides are precipitated from highly saline basinal fluids at temperatures within the normal range for diagenetic brines (80–150 °C; Anderson and MacQueen 1990). Many of the larger MVT examples listed are also tied to dissolving evaporites as a source of the chloride-rich basinal waters carrying the metals and many to sulphur sources that are either at or near the precipitation site as bedded platform sulphates or as H_2S in the pore waters derived by sulphate reduction (bacterial and thermogenic), typically from $CaSO_4$ sources. The setting is much like the deposits discussed so far but not a metal precipitation setting that is necessarily directly adjacent to thick current, or former, salt masses.

In what follows we shall focus on some of those MVT deposits located on the platform and tied to bedded calcium sulphate units (Fig. 15.53). In an accompanying plot of grade versus ore tonnage I have indicated some of the MVT deposits known to be associated with evaporites or derived brines (Fig. 15.54). This includes some very large deposits, such as Polaris and Admiral Bay, as well as the small Pb-Zn deposits discussed in the preceding sections. My approach in the remainder of section is not to attempt to define an all encompassing Pb-Zn/MVT model, this has been done in excellent papers by Leach et al. (2010) and Emsbo (2009). Rather, as in the preceding sections, I shall restrict my discussion to those Pb-Zn MVT deposits that have an intimate association with evaporite beds or their residues, so as to develop a specific understanding that can give predictive exploration paradigms for those MVT deposits created by their association with evaporites.

Cadjebut Region, Lennard Shelf, Australia

Bedded calcium sulphate evaporites, and their lateral dissolutional equivalents, have been cored in the area around the Cadjebut mine on the Lennard Shelf and they pass into mine sulphides in the mine and its immediate surrounds (Figs. 15.55 and 15.56). The details of Cadjebut Pb-Zn ore system and ore textures at the mine scale were discussed in detail in Chap. 7 as an example of hydrothermal karst development in a platform saltern and so are only mentioned here. Evaporite solution breccias (rock matrix breccias) are the lateral equivalents of the mineralised sequence in the Cadjebut mine The deposit undoubtedly represents one of the best documented examples of *in situ* burial replacement of a number of evaporite beds by Pb-Zn sulphides on a one

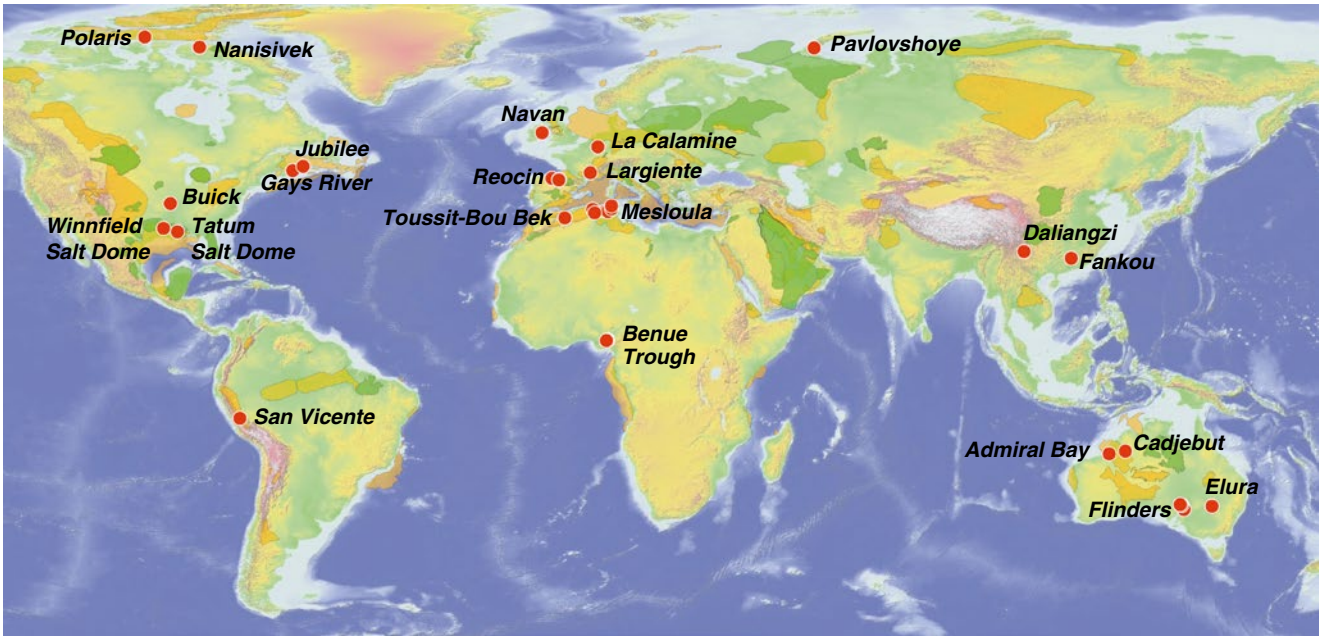

Fig. 15.53 Plot of some of the documented MVT deposits with known ties to evaporites, as detailed in the text

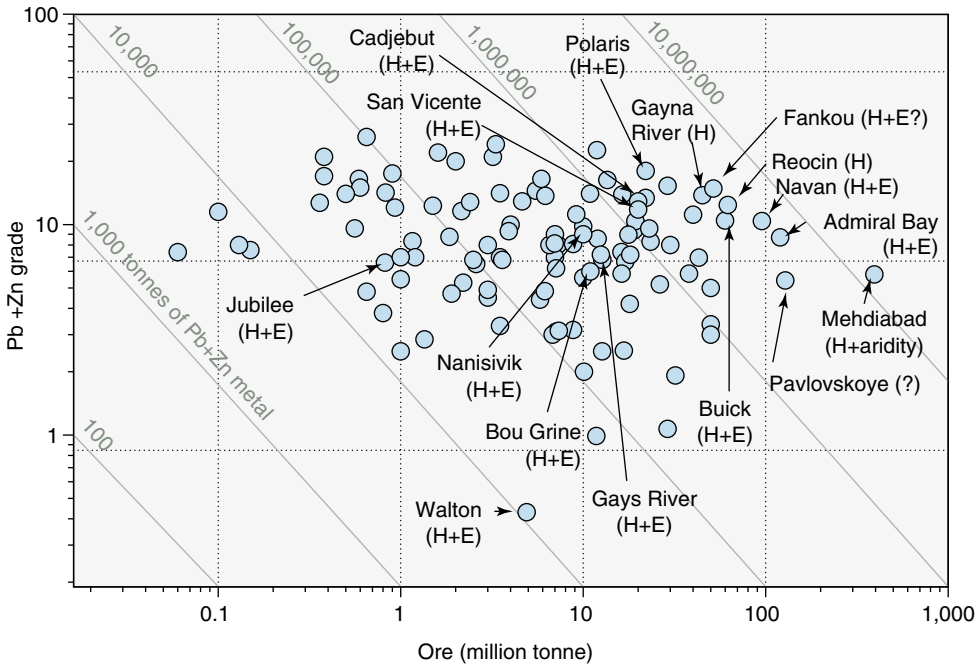

Fig. 15.54 Grade-tonnage plot of MVT deposits (Replotted from USGS data). *H* indicates hypersaline ore fluids, *E* indicates evaporites or indications of its former presence

for one basis (Tompkins et al. 1994a, b; Warren and Kempton 1997). That is, the pre-existing platform saltern beds are directly replaced by Pb-Zn sulphides and these saltern sulphates were the sulphur source. The sulphate to sulphide replacement process occurred across cm- to metre- sized cavities, and so the banded and breccia replacement textures are layered, sometimes forming "zebra" textures. This cavity infill replacement process means the ore textures are not necessarily a direct mimicry of the precursor laminar to nodular evaporite textures (Tompkins et al. 1994a, b versus Warren and Kempton 1997).

More broadly, the Cadjebut ore deposit is a Mississippi Valley Type (MVT) deposit hosted within the Givetian anhydrite entraining Lower Dolomite unit of the Cadjebut Fm. ramp. This sand-shoal-rimmed ramp was the depositional setting that immediately preceded the reef-rimmed Pillara Limestone platform, which defines the Lennard Shelf (Fig. 15.55). Regionally, the Givetian depositional setting

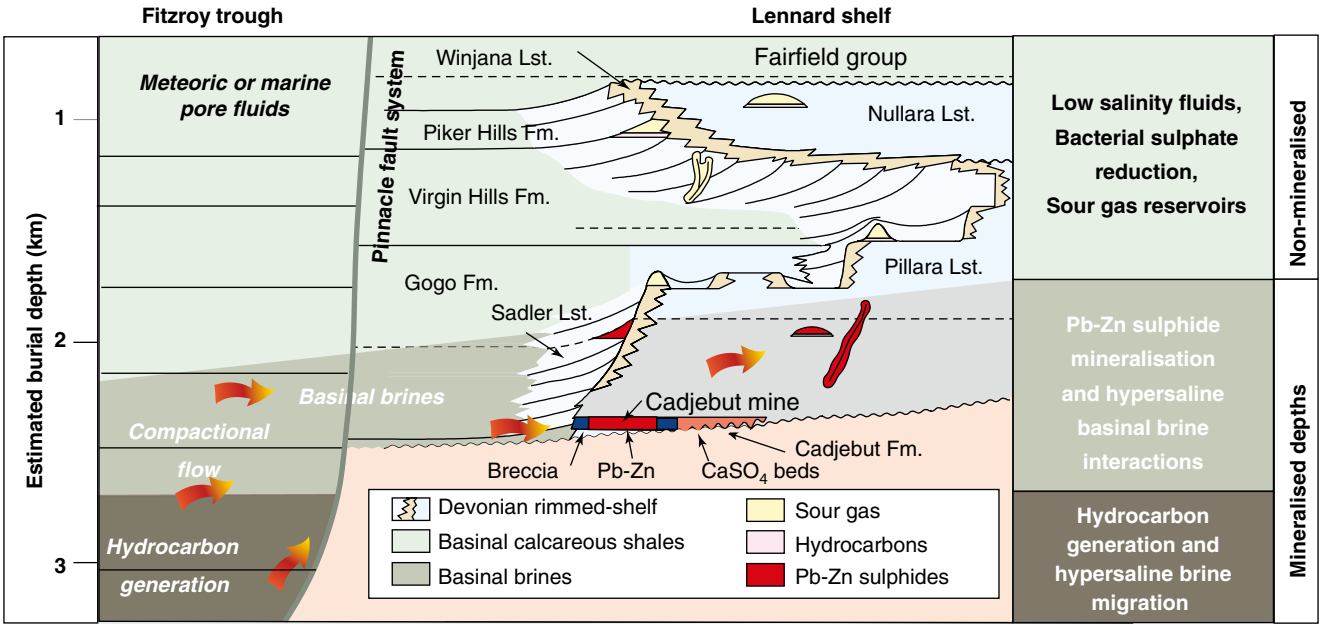

Fig. 15.55 Conceptual model for MVT sulphide precipitation on the eastern Lennard Shelf. At around 350 Ma, sediments of the Fitzroy Trough expelled metalliferous basinal brines and mature hydrocarbons by compactional flow. In shallow subsurface environments with low salinity and low temperature (60–70 °C) fluids, bacterial sulphate reduction occurred in and around saltern evaporite seals and hydrocarbon reservoirs within the Devonian platform. Sulphate reduction was largely fed by Givetian saltern $CaSO_4$ evaporites (Cadjebut Formation) and H_2S-rich reservoirs higher in the stratigraphy form in a variety of traps (faults, antiforms, and stratigraphic traps). Sulphides are precipitated when basinal brines interact directly with evaporites or invade intervals of trapped H_2S-rich (Modified from Playford and Wallace 2001; Wallace et al. 2002; Warren and Kempton 1997; Kerans and Harris 2008)

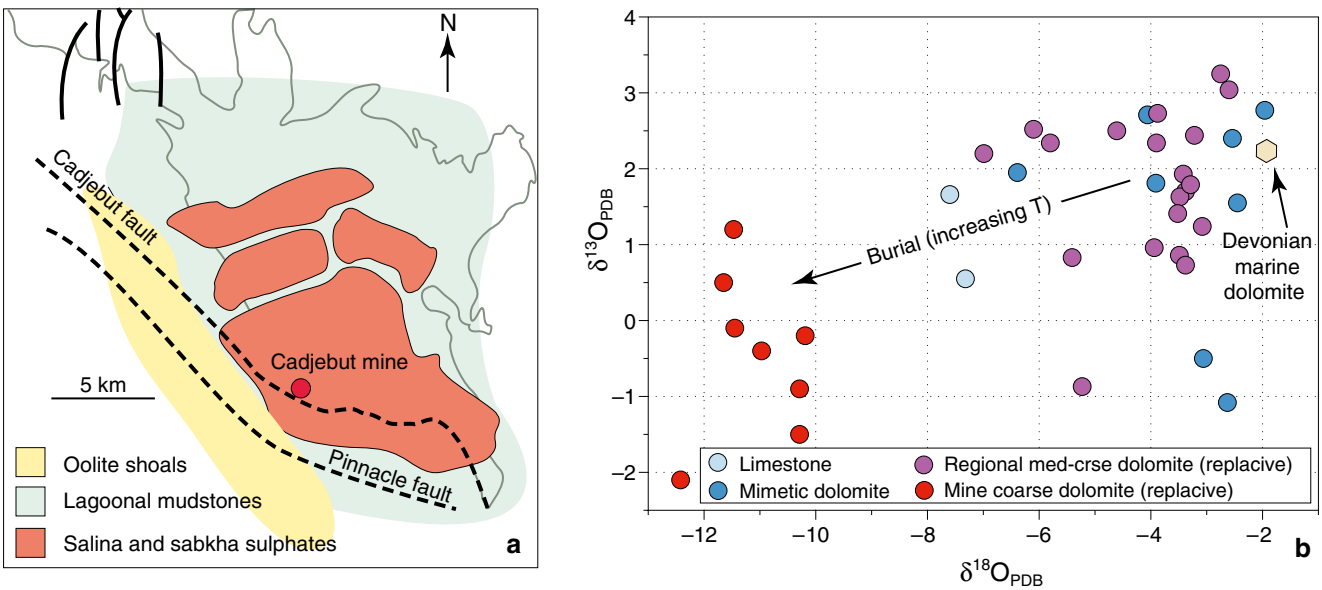

Fig. 15.56 Cadjebut Mine geological evolution. (**a**) Givetian paleogeographic reconstruction based on logged core intersections across the mine and its surrounds. *Grey line* defines the outline of the Emmanuel Ranges. Oolite shoals developed in vicinity of Cadjebut and Pinnacle faults, with dolomitised lagoonal wackestone and siltstone in back shoal area. A slight fall in relative sealevel created a sulphate mudflat complex in the vicinity of Cadjebut Mine. (**b**) Plot of $\delta^{18}O_{PDB}$ versus $\delta^{13}C_{PDB}$ for various dolomites in the Cadjebut mine and its surrounds (After Warren and Kempton 1997)

can be divided into two zones (Fig. 15.56a): (a) a higher energy shoal region in the vicinity of the mine and Cadjebut Fault and, (b) a landward more restricted, lower energy, at times evaporitic, lagoonal setting laid down in a series of shoaling carbonate cycles. The upper portion of each cycle is characterized by an evaporitic cap of laminar dolomitic

siltstone and mudstone with associated nodular anhydrite that formed a laterally extensive facies mosaic of sabkhas and salinas across an evaporitic mudflat. This originally shallow subaqueous or sabkha mudflat gypsum converted to nodular anhydrite during shallow burial and was subsequently replaced by Pb-Zn sulphides in the mine area.

Three petrographically distinct forms of dolomite occur in the lower dolomite unit across the Cadjebut region (Fig. 15.56b): (a) a regional finer-grained non ferroan mimetic form with $\delta^{18}O_{PDB}$ of −2 to −4‰ – this dolomite and (b) a ferroan medium to coarsely crystalline form with $\delta^{18}O_{PDB}$ -4 to −7‰ that is best developed about major growth faults. This dolomite overprints and replaces the finer grained stratabound mimetic dolomites as well as other carbonate facies. The finer grained ferroan dolomite formed by syndepositional brine reflux associated with the deposition of evaporites, while the coarser more ferroan dolomite formed during burial from escaping basinal fluids. These same fluids later carried metalliferous fluids from the Fitzroy Trough into sites of ore formation. Post-ore coarse replacement and saddle dolomites from the Cadjebut mine constitute the third dolomite type and are further depleted in $\delta^{18}O_{PDB}$ (−10 to −12‰) and likely indicate localized somewhat elevate thermal conditions related to sulphide mineralization.

Interaction of a metalliferous basinal brine with sulphate that was derived from the dissolving anhydrite beds precipitated the various ore lenses at Cadjebut mine. Sulphide-mineralised horizons in the Cadjebut mine can be correlated on a one to one basis with fine-rock matrix breccia horizons in the immediate area around the mine and with remnant bedded sulphate units well away from the mine. The precursor host lithology to the various ore horizons at Cadjebut are massive to bedded nodular anhydrite beds. The stratabound linear nature of the Cadjebut deposit reflects a time when metalliferous basinal fluids encountered bedded stratiform nodular anhydrites causing them to precipitate lead and zinc sulphides. This process locked in place a mineralization event at the stratigraphic position of each evaporite bed in the lower dolomite unit. Conduits for the metalliferous basinal fluids were the basin-margin-defining faults such as the Cadjebut and Pinnacle Faults (Fig. 7.71a). Fine-matrix breccias define subsurface evaporite dissolution both prior to and after the sulphide mineralization event. Today the remnant nodular anhydrite beds are rehydrating to satin-spar and poikilotopic gypsum as modern groundwaters seep into the units.

One of the problems with comparing nodular calcium sulphate and open-space filling zinc and lead sulphide textures in the Cadjebut region occurs when modern telogenetic effects go unrecognised. Much of the shallow anhydrite that was cored in the 1980's and 1990's is converting to porphyroblastic gypsum down to depths of hundreds of metres as it is flushed by modern meteoric waters (telogenetic alteration). Some workers (Tompkins et al. 1994a, b) did not realise that the current gypsum textures in relict anhydrite beds recovered in cores are replete with such telogenetic rehydration features (tertiary evaporites).

Such gypsum rose and cannonball textures should not be compared to possible primary depositional textures (erroneous assignment to a sabkha for massive sulphate units), nor to cavity fill and layered textures in the metal sulphides that formed in the mesogenetic realm. Ore evolution models that do not remove the effect of modern gypsum overprints, or any assumption that gypsum textures in recovered cored could be primary (has survived kilometres of burial and uplift) are erroneous. Respective precipitative processes for anhydrite rehydration and metal sulphide textures at Cadjebut are totally unrelated in terms of time and space (Warren and Kempton 1997).

The now depleted Cadjebut deposit is the largest and most concentrated of a number of MVT accumulations in the Lennard Shelf Pb-Zn province, mostly hosted in Devonian shelf carbonates, although the Cadjebut is deposited in ramp dolomites of the Givetian Cadjebut Fm, which immediately underlies the Frasnian-Famennian rimmed-margin dominated by the Willara and Pillara platforms (Fig. 15.55; Hocking et al. 1996). The rimmed-margin Frasnian-Famennian platform-hosted deposits include hydrothermal-karst dominated deposits (Goongewa and Bloodwood), and fault or fracture-hosted deposits (e.g. Pillara (aka Blendevale), Kapok, Fossil Downs). Fault and fracture hosted mineralization style dominates Frasnian and Famennian platform host across the Lennard Shelf (Wallace et al. 2002).

The Goongewa deposit is situated in the hanging wall of a normal fault (Cadjebut Fault). Stratigraphically, the mineralisation occurs around a Givetian platform margin and also occurs at the boundary between dolomitised and undolomitised carbonates. MVT sulphides there are largely present as cavity-filling cements within large hydrothermal karst caverns. The nearby Kutarta mineralisation (close to the old Price's Creek prospect) has a quite different style again, with much of the base-metal sulphide mineralisation being a replacement of dolomitised and brecciated back-reef carbonates (Pittari 1999).

The timing of MVT sulphide precipitation is well constrained by a number of techniques. Using carbonate cement stratigraphic relationships in host rock primary porosity, McManus and Wallace (1992) suggested that a single, widespread sulphide precipitation event (pyrite, sphalerite, galena, marcasite) occurred during early burial diagenesis during latest Devonian–earliest Carboniferous time (350 ± 15 Ma) within the reef complexes of the Lennard Shelf. This mineralisation age has since been confirmed by both Rb-Sr dating of sphalerite at Blendevale and U-Pb dating of ore-stage calcites from Goongewa (Wallace et al. 2002). Further south in the basin, the giant saltern

evaporite sealed Admiral Bay Pb-Zn deposit was discovered as part of an oil exploration program, but it is too deep to be exploited by conventional mining techniques McCracken et al. 1997).

Reinforcing the notion of ongoing fault focused fluid evolution controlling mineralisation in the Canning basin are the various stromatolite-baryte-sulphide mounds that constitute outcrops at a number of localities on the eastern Lennard Shelf. They are interpreted as fault-fed synsedimentary exhalative deposits on the Devonian deep basin-margin seafloor (Playford and Wallace 2001). For example, such stromatolite mounds occur near the Gogo Formation–base Virgin Hills Formation contact and are associated with extensive gossans in outcrop. In drill core, iron sulphides (marcasite and pyrite) are dominant, with base-metal sulphides only occurring as later stage cross-cutting veins.

The varying ore style geometries reflect the simple fact that no bedded evaporites were deposited in the Frasnian-Famennian backreef, only in the Givetian back-shoal region. And so, when the basinal fluid pulses of metalliferous fluids moved up along faults at the basin margin and through the various carbonate hosts, it precipitated well bedded ore units where metal-carrying fault conduits intersected anhydrites in the Cadjebut Formation and fault/ hydrothermal karst geometries where faults encountered mixtures of hydrocarbons and other reductants in the Frasnian-Famennian platform hosts. Once again, dissolving evaporites do not necessarily make ore deposits, when they do, they tend to focus the precipitative process and so make a more concentrated accumulation.

Polaris Zn-Pb Mine, Nanavut, Canada

The Mine, near the coast of Little Cornwallis Island, is hosted by the Ordovician Thumb Mountain Formation and located on the northeast flank of a large NW–SE oriented salt-cored antiform that formed in the Ellesmerian Foldbelt, during the Late Silurian to the Middle Devonian (Figs. 15.57 and 15.58; Thorsteinsson and Uyeno 1980 Dewing and Copper, 1991). Based on paleomagnetism Rb-Sr and Re-Os dates from ore sphalerites and bitumens, respectively, the mineralisation is known to have occurred at 366 ± 15 Ma and so is co-occurrent with tilting and compression that formed the Ellesmerian (Parry Island) foldbelt and the Boothia Uplift (Symons and Sangster 1992; Selby et al. 2005; Jober et al. 2007). The mine commenced operation in 1981 and closed in July 2002, When in operation, the mine had a reserve of over 20 Mt of sphalerite (ZnS) and galena (PbS) and was hosted in brecciated and dolomitised carbonate rocks of the Upper Ordovician Thumb Mountain Formation. The now-depleted Polaris Mine exploited one of the largest single Mississippi Valley-type ore deposits in the world (Reid et al. 2013).

Dimensions of the Polaris deposit are: 800 m strike length, 300 m at its widest point and a thickness ranging from 20 m in the west to 100 m in the central portion (Dewing et al. 2005). The deposit is blind, with the topmost ore lying 50 m below surface on the west and up to 160 m below surface on the east side. It forms a continuous sulphide body broken down based on grade, position and textures into a number of units; P_1 -P_2 and K_1 to K_3 (Table 15.12; Dewing et al. 2005). Of the five ore types recognized: two occur in the upper Thumb Mountain and three in the lower Thumb Mountain Formation (Fig. 15.59).

P_1 ore was the economically most important and formed a 10–30 m thick, high grade Zn-Fe-Pb, tabular unit hosted in

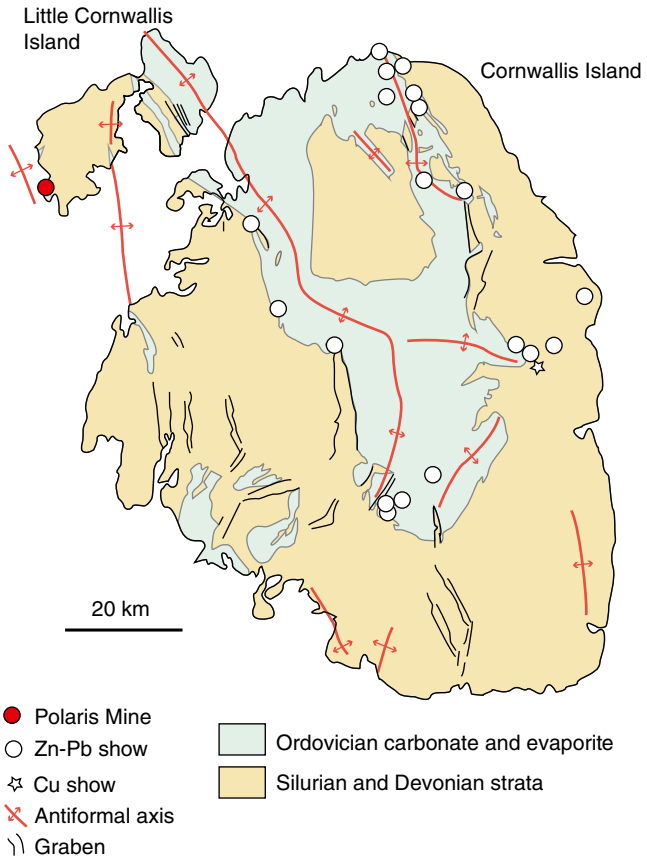

Fig. 15.57 Map of the Cornwallis Island region showing positions of salt-cored antiforms on the Boothia Uplift in the Ellesmerian foldbelt, the Polaris Mine on Little Cornwallis Island and a number of Zn-Pb and Cu shows (After Reid et al. 2013)

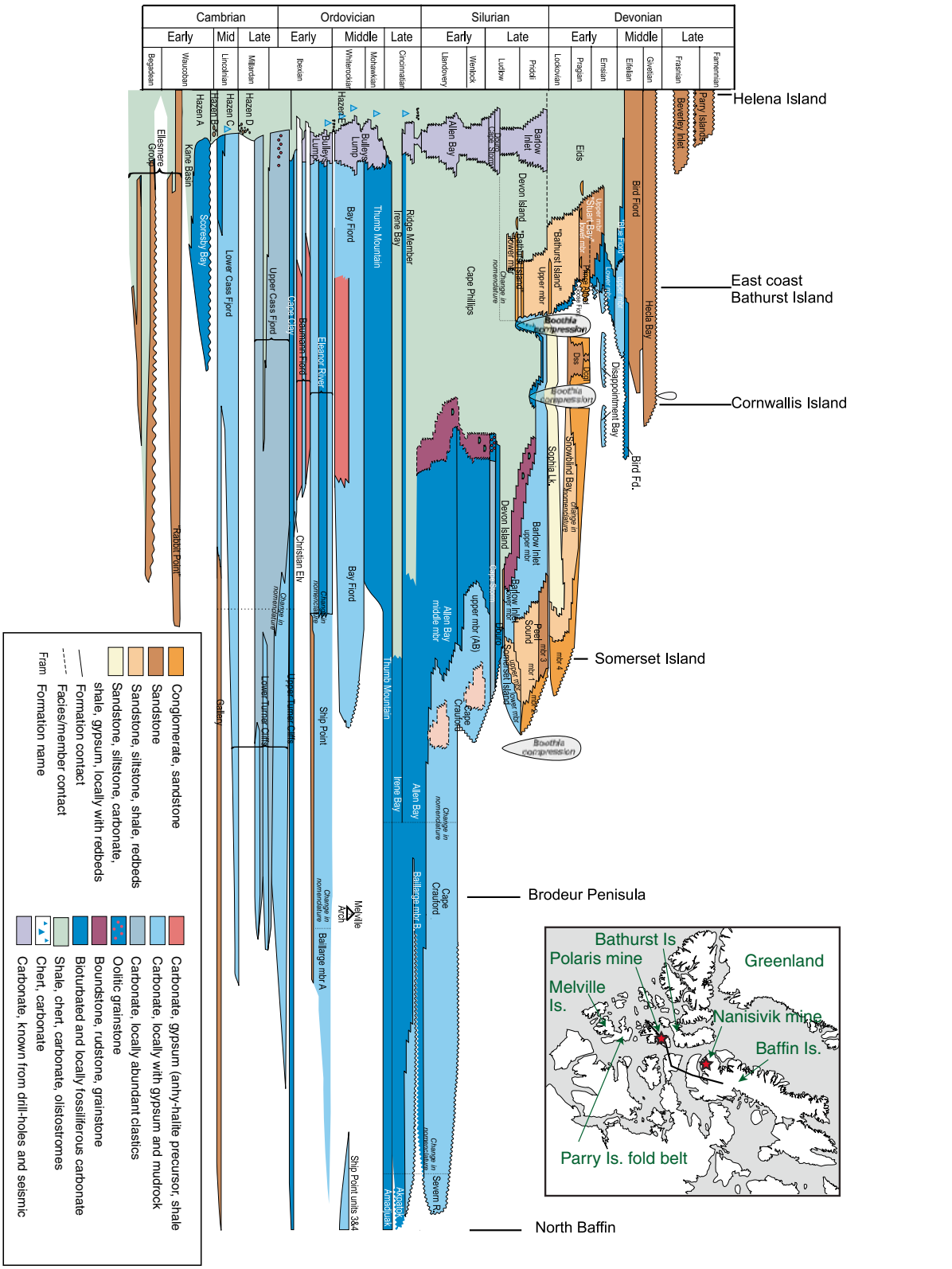

Fig. 15.58 Time-stratigraphic diagram showing a south to north transect from northwestern Baffin Island to northern Bathurst Island (see *inset*). The chart is after Dewing et al. 2005 and references therein. Importantly the cited chart is based on outcropping mineralogies and does not consider that textural evidence throughout the region indicates that much of the gypsum in outcrop is after halokinetically overprinted anhydrite and that this halite was once present in the region. It is still present in surface equivalents, for example, the *star* indicates gypsum/halite remnant breccias, in Bay Fiord Fm. as illustrated Fig. 15.59

the basal part of the upper Thumb Mountain Formation. P_1 ore consisted of massive, carbonate replacement, breccia-fill and vein sulphide averaging 4–5 % Fe with up to 30 % Fe (Table 15.12). Overlying the P_1 ore, above the major N-S structures defining the boundaries of the Keel graben, are blocks designated as P_2 ore. This ore is composed of numerous thin to 1 m thick veins of sphalerite, marcasite and galena oriented vertically, sub-perpendicular to bedding. Marcasite halos surround most P_2 veins. Directly underlying the P_1 tabular body is the high grade K_3 ore, composed of complex, cross-cutting veins along with massive to disseminated metal sulphides replacing *Tetradium* beds containing 3–5 % Fe (Fig. 15.59).

Differentiation between K_3 and P_1 ore was based mainly on lower iron contents of K_3 versus the P_1 ore. K_2 ore underlies the K_3 unit and is composed of fracture filling and vein sulphides with lesser replacement of carbonate, with local pods of mineralized brecciation carrying grades of 8–20 % Pb + Zn and 1–2 % Fe. The lowermost ore unit is K_1 ore composed of fracture-filling and vein sulphides, discontinuous and lower grade (10–15 % Pb + Zn, 1 % Fe). This ore unit follows either the N-S (mine grid) axis of mineralization or a NE-SW trend and is centred on lower stratigraphic horizons around a green marker bed in the lower Thumb Mountain Formation (Fig. 15.59). To the east and west of the orebody, sulphide mineralization dies out rapidly within 15 m of the ore boundaries. Sulphide feathers out into small, scattered lenses and sulphide vein systems to the north and south of the orebody and further out transitions into a breccia unit, called pseudobreccia, in the mine terminology

Diagenesis of the mine series is indicated by extensive hydrothermal alteration, including sequential dolomitisation, marcasite and baryte precipitation events (Figs. 15.60 and 15.61; Savard et al. 2000; Reid et al. 2013). There are three paragenetic stages: (1) Early replacement dolomites and marcasite; (2) Main stage sulphide and hydrothermal coarsely-crystalline (saddle) dolomite; and (3) Late calcite, marcasite and baryte. Ore mineral textures range from discrete crystals to massive crystal aggregates and formed as replacements of the dolomite host rock or as fracture- and open space-filling mineralization. Zinc concentration is highest in the core of the deposit where open-space fill and botryoidal aggregates predominate. Locally elevated T_h values $\approx$ 100 °C are associated with nearby organic-rich strata and bitumens, while the ore carries a geochemical signature that includes *in situ* sulphur fractionation. Detailed isotope

Table 15.12 Ore grade divisions in the Polaris Mine (Dewing et al. 2005)

Zone	Pb + Zn	Fe	Zn/Pb
P_2	16.5	4.6	3.1
P_1	22.4	4.5	3.5
K_3	19.1	3.1	5.6
K_2	17.3	1.7	4.3
K_1	15.5	0.8	8.1

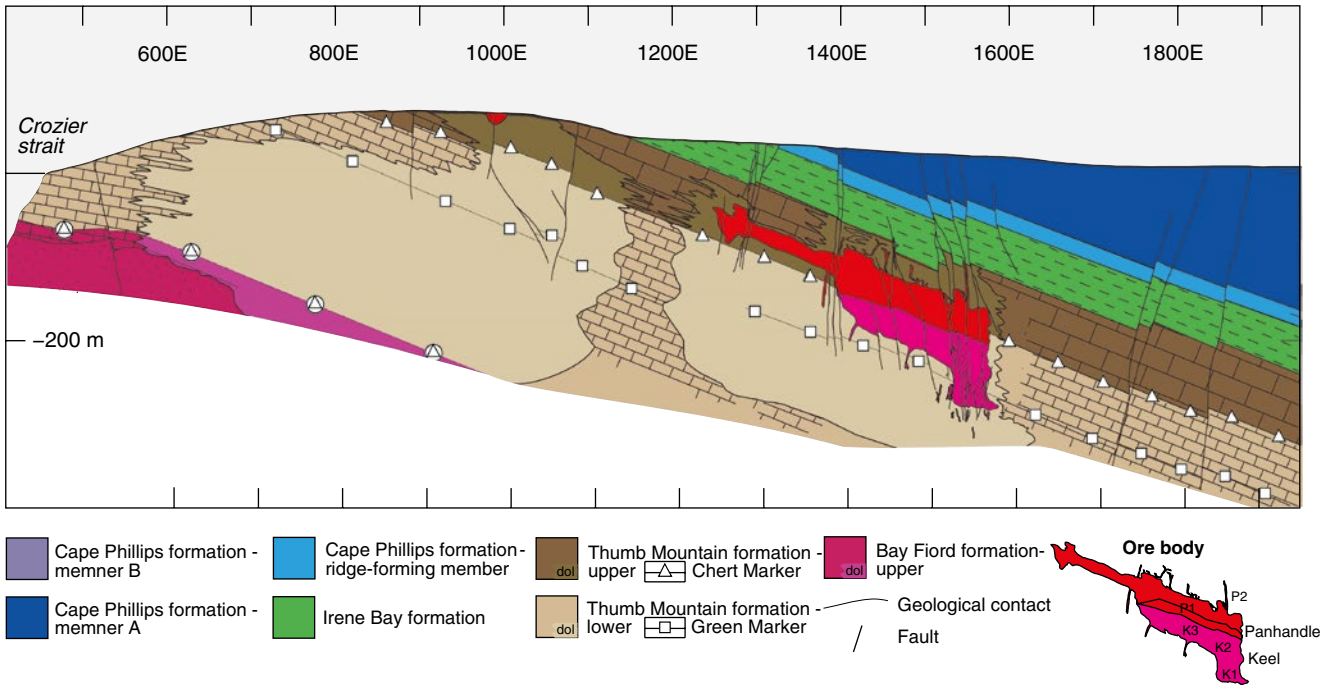

Fig. 15.59 Section through Polaris Mine on mine grid 2,100 N showing the outline of the ore and dolomitisation. *P* denotes Panhandle Zone ore, and *K* denotes Keel Zone ore; see text and Table 15.12 for descriptions and grades of the P_2, P_1, K_3, K_2, and K_1 ore types (After Dewing et al. 2005)

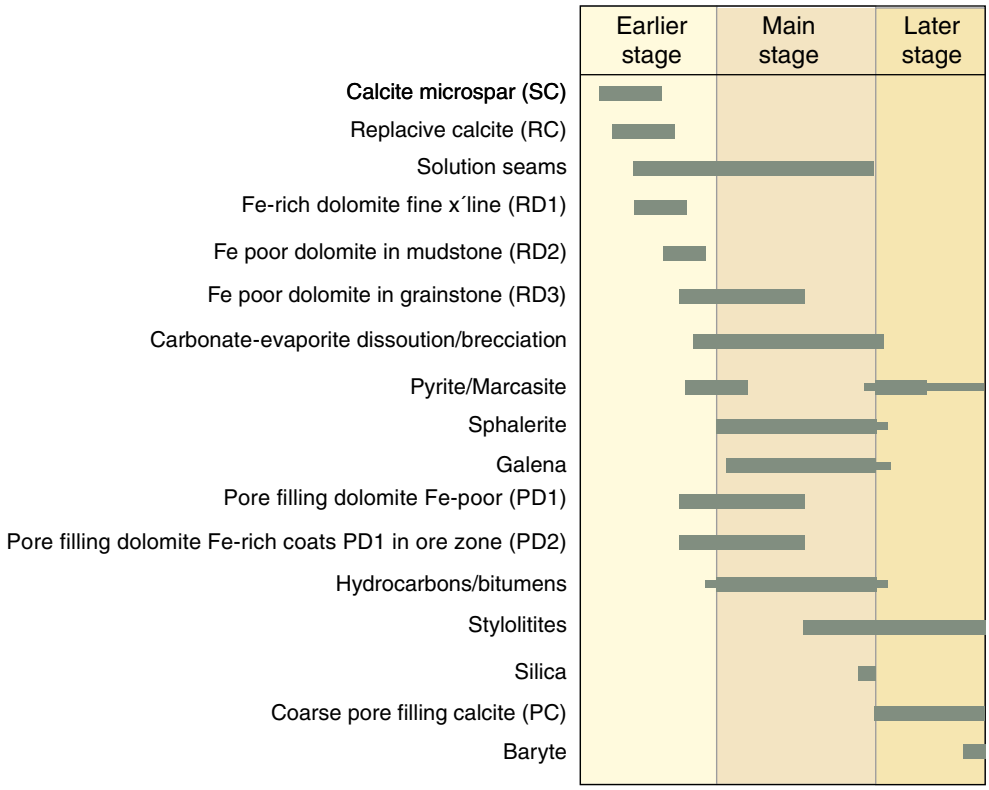

Fig. 15.60 Paragenetic-diagenetic sequence in the Polaris Mine (After Savard et al. 2000; Reid et al. 2013)

study tied to petrography clearly shows that replacive dolomite predates and is synchronous with ore emplacement. As in other MVT deposits so far, dolomitisation is associated with emplacement of sulphide minerals, but is not the controlling process for mineralisation.

Five types of dolomite were distinguished by Savard et al. (2000), including three replacement (RD) and two pore-filling dolomites (PD). The paragenetic order is RD1, RD2, RD3, PD1, and PD2. Pore-filling calcite (PC) postdates all other minerals. Baryte and silica are late-stage precipitates. In most cases, sulphides and dolomite did not co-precipitate, but sphalerite and galena largely overlap with RD3 and PD1. Various dolomites are dissolved or replaced by sulphide-precipitating fluids; sulphides in turn can be overgrown by dolomites. Colloform texture in sphalerite is widespread.

Early calcite, both microspar replacement (SC) and early replacive calcite spar (RC) have C-O stable isotope values closest to ambient seawater, as does early fine-grained dolomite (RD1). The isotopic values of RD2, RD3, PD1, and PD2 cluster tightly and form largely overlapping domains (Fig. 15.61a). With respect to the host limestone, they are depleted in ^{18}O, similar in $\delta^{13}C$, and slightly enriched in ^{87}Sr. Fluid inclusions were studied by Savard et al. (2000) in RD3, PD1, PD2, sphalerite, and PC. The overall ranges of homogenization temperatures (T_H) for non-stretched fluid inclusions in dolomites and sphalerites range from 67° to 110 °C, indicative of warm basinal brines with high salinities and elevated Ca/Na ratios (Fig. 15.61b). Gas chromatographic analysis of these same fluid inclusions indicates low concentrations of hydrocarbons (<0.06 mol%).

There are no regular spatial variations for fluid inclusion and isotope data during metal sulphide emplacement, indicating an overall geochemical homogeneity in the hydrothermal system at that time. Sulphur isotopes show slightly different groupings for galena and sphlarite, with sphalerite tending toward somewhat more negative $\delta^{34}S$ values (Fig. 15.61c). Some samples close to the fracture zones in the orebody show slightly elevated T_H and $^{87}Sr/^{86}Sr$ values and more depleted $\delta^{18}O$ values, suggesting that the fracture zone was the likely conduit for warm metalliferous brines.

Based on the geological and geochemical characteristics of the deposit, Savard et al. (2000) propose that sulphide precipitation at Polaris was caused by the mixing at the site of mineralization of a reduced, metal-rich, sulphur-poor fluid with a reduced, metal-poor, sulphur-rich fluid. The metal-carrying fluid ascended along fractures from below the deposit and was hotter than the host rocks, whereas the reduced sulphur-carrying fluid was delivered to the site of mineralization laterally from dissolving sulphate beds and was in thermal equilibrium with the host rocks (Savard et al. 2000). This model can explain the dissolution of dolomite/evaporite during sulphide precipitation and the abundance of colloform sphalerite, as well as the low concentrations of hydrocarbons in fluid inclusions.

An alternative model for the Polaris deposit is that sulphate was supplied by dissolution of anhydrites of the under-

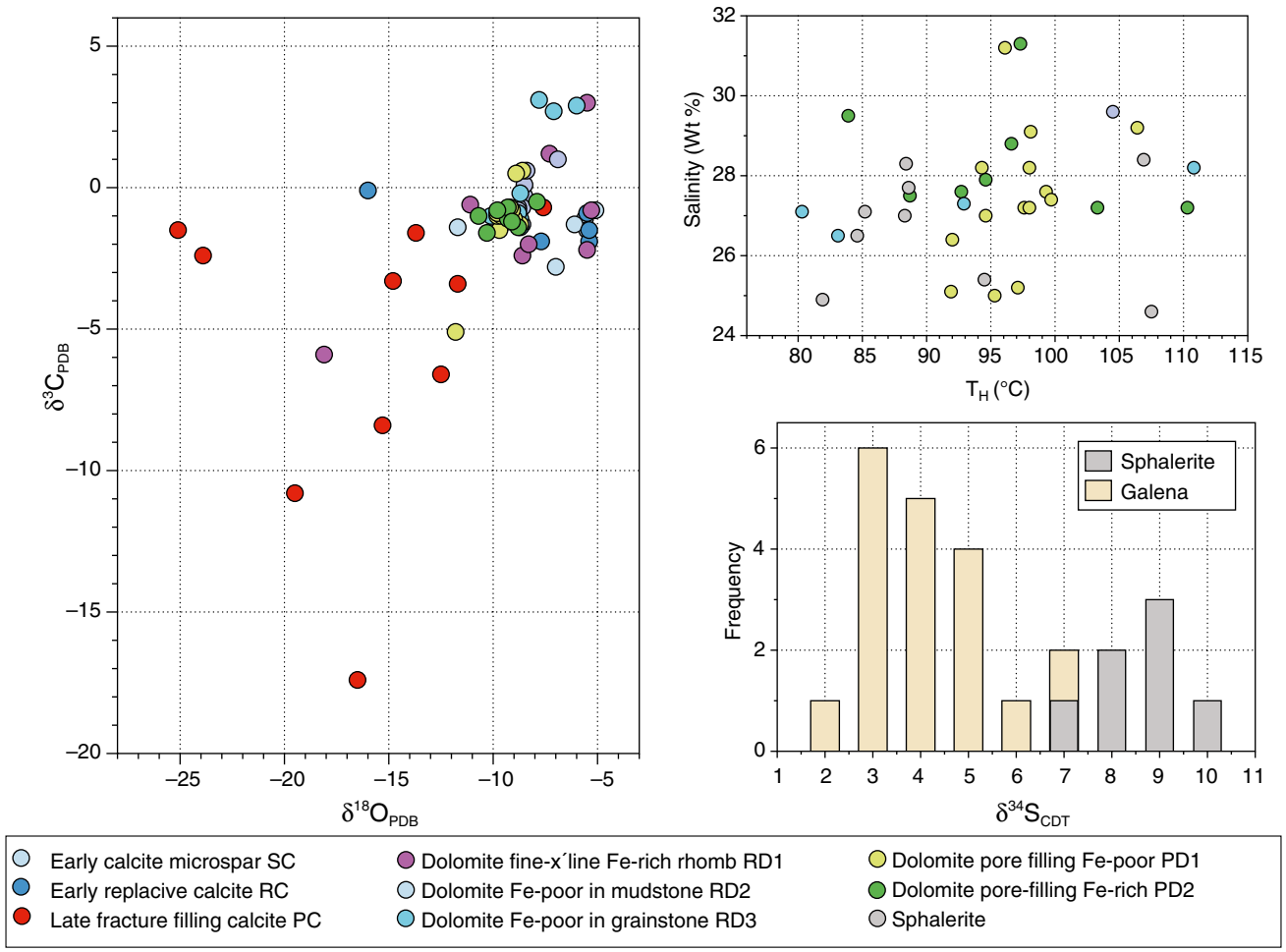

Fig. 15.61 Isotopes and temperatures in the Polaris Mine. (**a**) Carbon-oxygen isotope crossplot in various carbonate phases in the Polaris mine. (**b**) Salinities (wt%) and homogenisation temperatures (T_H) in inclusions of selected carbonate phases and sphalerite. (**c**) Sulphur isotope determinations in sphalerite and galena (From Savard et al. 2000; Reid et al. 2013)

lying Bay Fiord Formation, while the organic-rich shales of the Irene Bay formation acted as both seal and as a source of organics in the fault focused zone of sulphate reduction that drove the mineralisation (Fig. 15.62a; Reid et al. 2013; Dewing et al. 2005).

TSR is unlikely to have been the dominant precipitative mechanism in either model, since: (i) the temperatures are too low (>120 °C is needed), (ii) there is no blocky calcite with strongly negative $\delta^{13}C$ values that is typically produced during TSR, (iii) there is fractionation of the sulphur isotopes, a process that does not occur during TSR (Machel et al. 1995), and (iv) the $\delta^{34}S$ in individual sphalerite masses is inhomogeneous, typically showing a variation from 8‰ in the colloform centre of the sphalerite mass to 12‰ at the outer crystalline rim which is somewhat similar to the galena. Presumably this reflects pulses of fluid activity, with BSR producing a gas cap with strongly fractionated H_2S, followed by the introduction of metal-rich brine, rapid precipitation of amorphous colloform sphalerite, followed by slower precipitation of crystalline sphalerite as the gas cap is depleted and gas slowly produced by ongoing BSR.

Any model for the Polaris deposit (Fig. 15.61) must invoke a source of metal ions within the stratigraphic column, since strontium or lead isotopes show no indication of basement involvement. The likely metal source was units beneath the dissolving and deforming Bay Fiord salt seal where metals were convectively flushed by chloride-rich saline brines and were carried toward the basin edges through aquifers deep in the stratigraphic column. Driven by the Late Devonian Ellesmerian Orogeny, the fluids rose along faults until they encountered the organic-rich, permeable Thumb Mountain Formation limestone overlain by the impermeable Irene Bay Formation shale.

Bacterial sulphate reduction (BSR) likely reduced sulphate to H_2S utilising the abundant algal organic matter in the upper Thumb Mountain Formation as a reductant. The resulting H_2S explains a shift in $\delta^{34}S$ values of −15‰ (Fig. 15.62a). The H_2S reacts inorganically with zinc, lead,

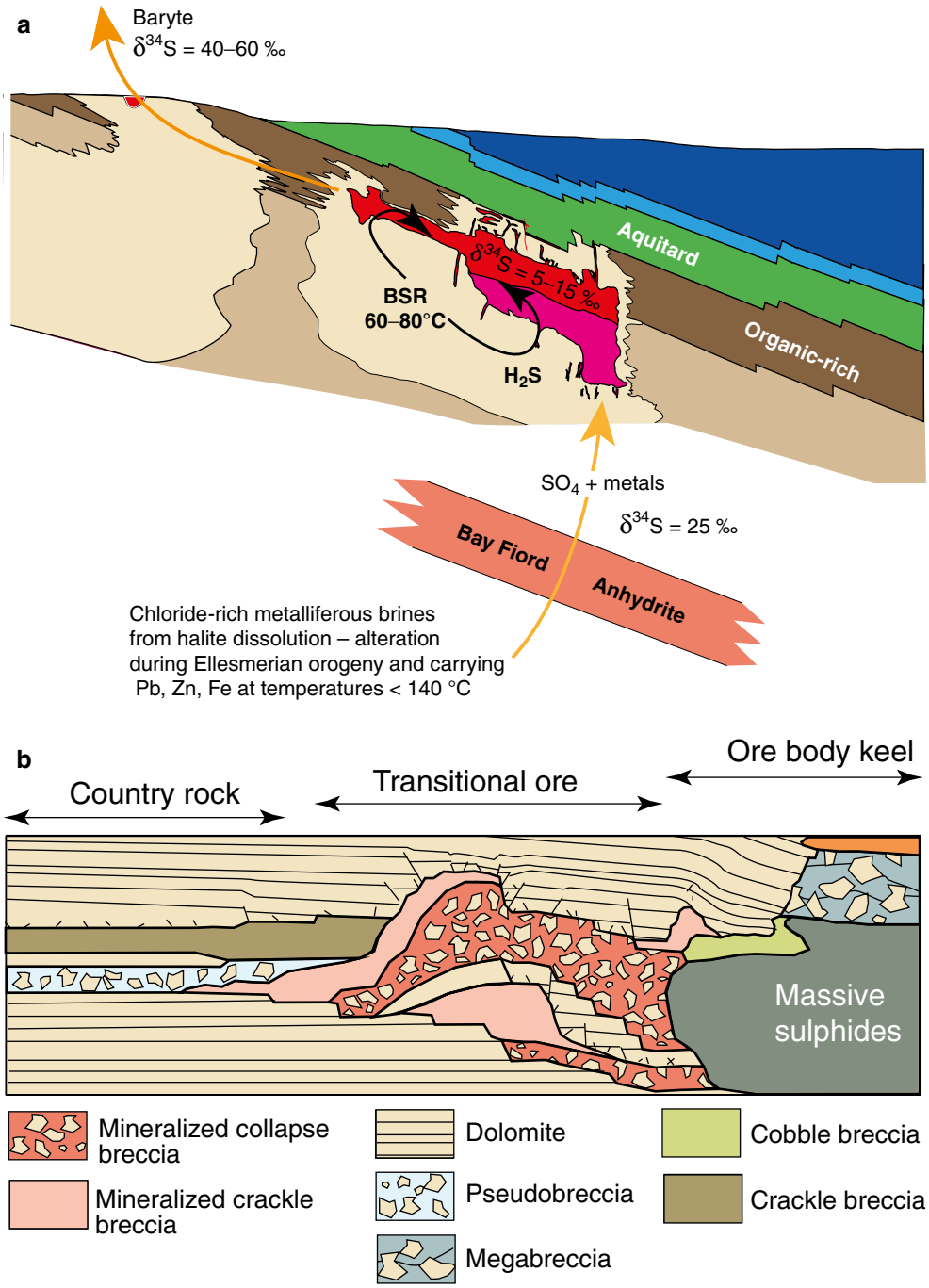

Fig. 15.62 Polaris Mine. (**a**) Mineralisation model showing the halite dissolution origin of metal and sulphate-rich fluids in the sedimentary pile. Transport was as a single saline fluid to site of ore precipitation, where reduction and fractionation was driven by bacterial sulphate reduction, in combination with isotopically light H_2S and metal ions to form ore and create acidic fluids that created hydrothermal karst cavities and associated open-space collapse textures. The expulsion of isotopically heavy sulphate produces a characteristic baryte halo. Refer to Fig. 15.59 for lithology legend (Adapted from Dewing et al. 2005). (**b**). Model of detailing the distribution of breccia types relative to massive sulphide mineralisation (After Reid et al. 2013)

and iron ions to produce sulphides with a $\delta^{34}S$ value of about 10‰. Released hydrogen ions dissolve carbonate resulting in dissolution breccias and other open-space dissolution fabrics. Excess sulphate was expelled from the system and produced a halo of baryte up to 10 km from the deposit, with $\delta^{34}S$ of +40 to +60‰ (Dewing et al. 2005). Evidence of a temporal link between baryte and ore is based on the following; (i) a sample from the 930–124 stope at Polaris that has sphalerite, which pre- and post-dates baryte, (ii) the proximity of baryte to Polaris (baryte is common on southern Little Cornwallis Island), (iii) the heavy sulphur isotope values, and iv) co-occurrence of baryte with late stage marcasite.

Temperatures measured from fluid inclusions in the sphalerite and inferred from the thermal maturity data from kerogens in the mine series indicate a range of 80–105 °C (Reid et al. 2013; Dewing et al. 2005). This is the appropriate range for bacterial sulphate reduction. Thermochemical sulphate reduction (TSR) is unlikely to have been active since; (1) The temperatures are too low (>140 °C is needed), (2) There is no blocky calcite with strongly negative $\delta^{13}C$ values that is

typically produced during TSR, (3) There is fractionation of the sulphur isotopes, a process that typically does not occur during TSR (Machel et al. 1995), and (4) the $\delta^{34}S$ in individual sphalerite masses is inhomogeneous, typically showing a variation from 8‰ in the colloform centre of the mass to 12‰ at the outer crystalline rim. Presumably this reflects pulses of fluid activity, with BSR producing a gas cap with strongly fractionated H_2S, followed by the introduction of metal-rich brine, rapid precipitation of amorphous colloform sphalerite, followed by slower precipitation of crystalline sphalerite as the gas cap is depleted and gas slowly produced by ongoing BSR.

Given this paragenesis, let us once again step away from the Polaris deposit look more broadly at its regional evaporite association. As Davies (1974) notes, there are two significant evaporite units that lie beneath the Thumb Mountain Formation, the Early Ordovician Baumann Fiord Formation and the Middle Ordovician Bay Fiord Formation (Figs. 15.58 and 15.62). The Baumann Fiord is exposed on eastern and southern Ellesmere Island, and extends southwestward to Cornwallis Island (Thorsteinsson and Kerr 1968), where it forms the exposed Ordovician core of a large central dome. The Baumann Fiord Formation is about 750 m thick in the type area on eastern Ellesmere Island; about 600 m of this current thickness is anhydrite with cyclically-interbedded carbonates, some stromatolitic (Mossop 1972, 1973). The anhydrite grades westward into shallow-water shelf carbonates, while to eastward it thins, becomes sandier, and may pass to an unconformity close to the shelf-craton margin. Mossop (1972) interprets the Baumann Fiord evaporite-carbonate units to be a succession of sabkha cycles. Halite in the Baumann Fiord is not exposed at the surface. I would interpret it as a series of stacked sulphate salterns in an intracratonic sag basin.

The next youngest and most extensive Ordovician evaporite unit is the Bay Fiord Formation (Kerr 1977) of Middle Ordovician age (Fig. 15.63). It lies immediately below the Thumb Mountain Formation and constitutes the basal formation of the Cornwallis Group. The Bay Fiord is exposed in eastern and southern Ellesmere Island, and can be traced southwestward to Cornwallis Island and Bathurst Island. In the type area on eastern Ellesmere Island (Kerr 1968), the Bay Fiord Formation contains gypsum and anhydrite in the lower part of a 500 m thick section of argillaceous and dolomitic limestone, siltstone and shale. The Bay Fiord are thought to lie within the carbonate-dominant shelf succession that extends southeastward of the Franklinian trough, approximately co-extensive with the older Baumann Fiord Formation. The thickness an purity of the sulphate units in the Bay Fiord once again indicates they are salterns within an intracratonic sag (Warren 2010). But more significantly away from their leached outcrop positions there are halite units in the Bay Fiord, and some are extensively thrusted and folded (Fig. 15.63; Chap. 6; Harrison 1995)

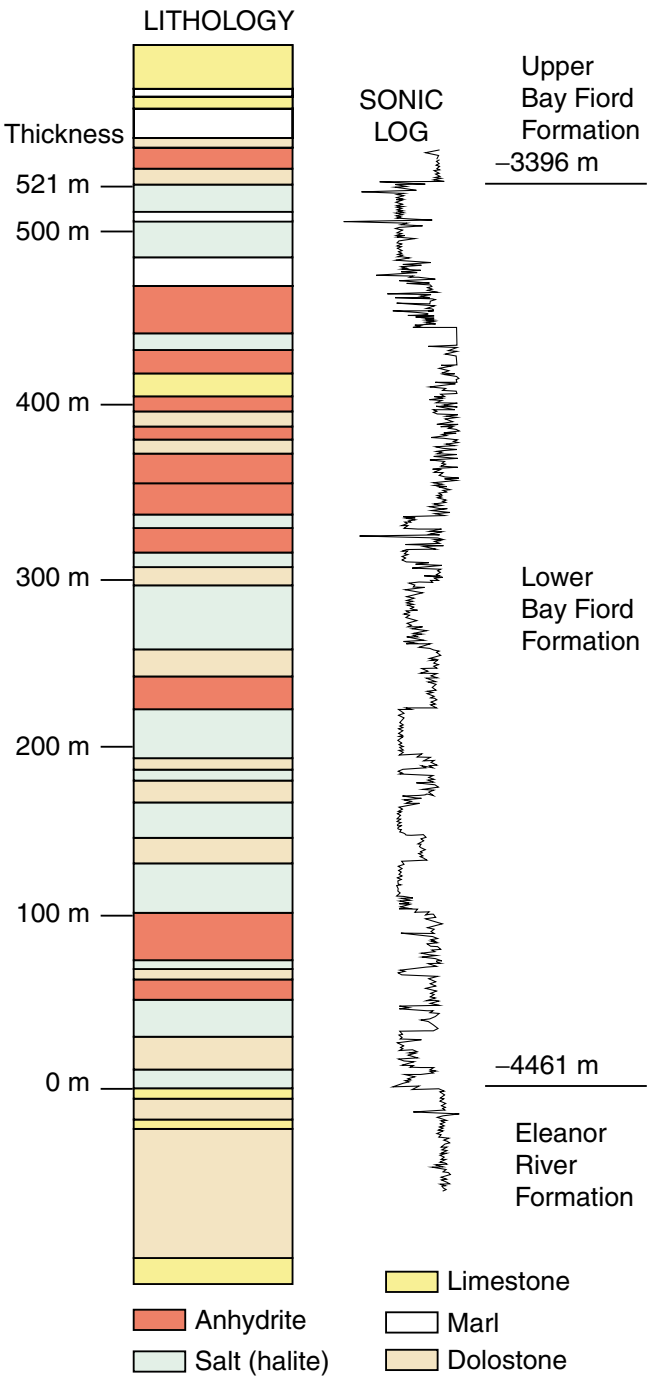

Fig. 15.63 Interpreted lithostratigraphy and sonic log trace showing the anhydrite – halite distribution in the Lower Bay Fiord Formation in Sabina Bay A-07 well on Melville Island (Harrison 1995) (See *inset* in Fig. 15.58 for location)

On Cornwallis Island, carbonate breccias in the Bay Fiord exposures are interpreted as solution-collapse breccias (Thorsteinsson and Kerr 1968) due to removal of halite. More than 1,000 m of halite apparently equivalent to the exposed Bay Fiord sulphate residues on Cornwallis Island occur in the subsurface of eastern Bathurst Island (Fig. 15.63;

Davies 1974; Harrison 1995); the km thickness on eastern Bathurst may be in part an expression of tectonic thickening and associated diapirism that occurred during the formation of the Ellesmerian foldbelt. The Bay Fiord is the key halokinetic stratum caught up in the Ellesmerian orogeny. Diapiric capstones to the Bay Fiord evaporites are exposed anhydrite carapaces on Bathurst Island. The Bay Fiord evaporites played an important role as a detachment zone and the creation of antiformal welts during mid-Palaeozoic Ellesmerian folding and the development of the Parry Island and Cornwallis Foldbelts structural junction (Harrison 1995).

The possibility of salt/thrust weld fluid focusing and a more localised anhydrite source is not considered in any of the current published models. In current Polaris models the Bay Fiord is typically offered as the sulphur source and that is the only evaporite association discussed (Fig. 15.62a). In the context I would like to note that there is anomalous clastic matrix dominant carbonate clast unit called the cobble conglomerate that is only found in the immediate mine area (Fig. 15.62b). "Cobbles" are 1 to 3 cm in size, usually of slightly elliptical shape, packed in a dark muddy terrigenous matrix that looks somewhat like a cobble-supported conglomerate (Randell and Anderson 1997). Earlier workers described this unit as "transported and re-deposited cobble conglomerate" as meteoric cave-fill and argued this jumble of cobble conglomerate clastics as completely incompatible with the environment of deposition of the Thumb Mountain Formation. It was attributed to the choking of meteoric karst by transgressive conglomerates advancing across the early Devonian unconformity.

But as noted by Randall and Anderson (1997) cobble conglomerate has gradational contacts with normal Upper Thumb Mountain Formation; occurs exclusively in Upper Thumb Mountain Formation; carries remnants of galena veinlets and dolomite veinlets exclusively in the cobbles, not in the "matrix"; is extensively riven by stylolites and, most tellingly, commonly exhibits whole fossils in place: many *Receptaculitids*, many *Cateniporids* and *Halysitids*, and the large solitary rugose coral *Bighornia.* Likewise, microfossils recovered from this rock match those of the usual Upper Thumb Mountain Formation. Cobble clasts preserved burrow structures, and the "matrix" an insoluble residue. "Cobble conglomerate" is not evidence for cave-fill, karsting or the exposure of Thumb Mountain cited by Kerr (1977). Randell and Anderson (1997) interpret the cobble conglomerate as a hydrothermal karst fill.

In my mind, I wonder if it and the other non-mineralised breccias could not be the remnants of a halokinetic salt tongue or salt lubricated thrusts with a now mineralized and replaced fault feeder sourced in the Bay Fiord (a remnant of a squeezed weld or diapir). In a key paper on salt-lubricated thrusting in the Parry Island foldbelt, located south of Polaris, Harrison and Bally (1988) noted that… "In the earliest phase of visible shortening (0–1 %), deformation is manifested by the buckling of the competent carbonate and black shale formations (upper Bay Fiord, Thumb Mountain, and Cape Phillips formations and age-equivalent strata). Evaporites in the lower Bay Fiord ductile zone, already weakened and buoyed up by the influence of high pore fluid pressures, simultaneously migrate into the axial region of each anticline. The shortening is redistributed through the upper ductile zone of the Cape de Bray Formation by thinning of shale over the crestal regions of the anticline." They go on to note that there are significant thrust detachment levels in the Thumb Mountain formation, as well as significant tectonic wedging of the upper Bay Fiord and Thumb Mountain formations (p. 318, Harrison and Bally 1988)

The various breccias at Polaris are still enigmatic mesogenetic units in their variably-thrusted platform carbonate host. The geological focus of most of the work at Polaris was on the ore and its paragenesis. A sedimentological study of "pseudo breccia" the "mega-breccia" and the "cobble conglomerate" (Fig. 15.62b) and an understanding of "the salt that was" would likely have improved our understanding of the deposit's diagenetic evolution. Whatever the origin of the various non-mineralised breccias, all workers agree that the sulphur source for Polaris was anhydrite, with BSR as the dominant precipitative mechanism (Reid et al. 2013). Halite/sulphate units of the Bay Fiord did not directly drive the formation of the Polaris MVT deposit. Rather, through their ongoing dissolution and deformation, they drove regional suprasalt structuration and hypersaline brine flows that supplied metalliferous brines and evaporite-derived sulphate to the structurally-focused trap configurations known as the Polaris deposit.

Nanisivik Baffin Island, Canada

The Zn-Pb-Ag ore at Nanisivek, near the north end of Baffin Island, consists of massive sulphides hosted in dolomite of the platform/ramp carbonates of Middle-Upper Proterozoic Society Cliffs Formation (Fig. 15.64a; Clayton and Thorpe 1982). The mine first opened on 15 October 1976 and permanently closed in September 2002. Textural and mineralogical variations divide the Main orebody into three vertical and four horizontal ore zones (Arne et al. 1991). The upper lens of the Main orebody can be further subdivided into six texturally distinct, laterally extensive mine units. Pyrite is the main sulphide mineral in the region, but in places sphalerite and galena are present in ore-grade proportions. Most of the known sulphides are in horizontal lenses about 10 m thick. The Main Ore Zone is 3,000 m long and, on average, about 100 m wide. This body is estimated to contain 11 million tonnes of sulphides, of which 6.5 million tonnes are ore-grade, averaging 12 % Zn, 1.5 % Pb and 50 g Ag/tonne (McNaughton and Smith 1986). There are also sulphides below the main lenses, either in horizontal lenses or in

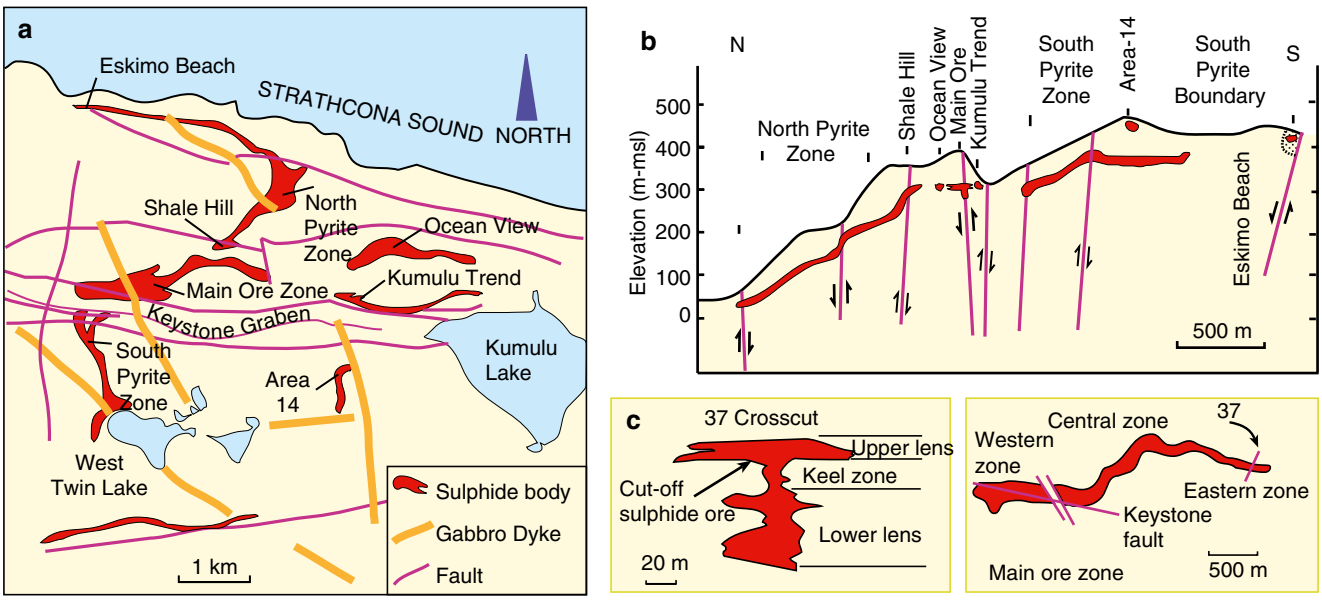

Fig. 15.64 Nanisivik region, Baffin Island. (**a**) Map of the major sulphide bodies and structural features in the Nanisivik Region. (**b**) Schematic N-S cross section howing major faults and sulphide bodies. (**c**) Cross section of Main Ore Zone showing upper and lower lenses connected by keel zone at crosscut 37 and the plan view of upper lens, Main ore zone (After Ghazban et al. 1990; Arne et al. 1991)

near-vertical vein-like structures. The host dolomite has been extensively block-faulted. Sulphide bodies pass laterally through some of these faults and appear to be confined to the upper half of the formation, which is mostly constructed of laminated algal dolomite that has been extensively brecciated and recrystallised. Crosscutting relationships shows the deposits are clearly diagenetic, not syngenetic.

The orebodies are characterised by well-banded ore textures, interpreted by Arne et al. (1991) as progressive replacement of the carbonate wall rock. In contrast, Ghazban (1988) noted the obvious knife-sharp contacts between the massive pyrite and the adjacent host dolostone, and the presence of unaltered relict "fins" of the host dolostone. Ghazban et al. (1992) use this relationship to argue for a more passive fill of hydrothermal karstic caves, with ore precipitating as the matrix was dissolving. There is a third possibility, namely the precipitation of ore in cavities adjacent to or within dissolving sulphate bodies, in a manner akin to that characterising the Cadjebut ores where similar "fins" and other equivalent ore textures are present (Warren and Kempton 1997). A study of the solution breccias in the Nanisivik deposit and listing of the presence or absence of evaporite indicators would help in resolving which of the three possible mechanisms is the most viable.

In this context, it is interesting to note that the sphalerite -galena body is dominantly stratabound and lies within the dolostones of the Society Cliffs Formation, which dips 10–20° to the north (Fig. 15.64b, c). Gypsum outcrops in the Society Cliffs Formation near Arctic Bay (25 km west of Nanisivik) and in the southeastern Borden Basin (Fig. 15.65;

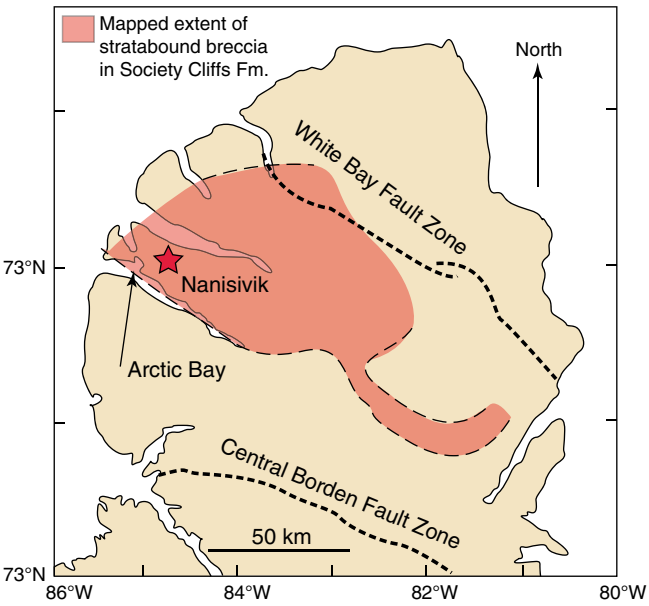

Fig. 15.65 Extent of brecciation mainly within the upper part of the Society Cliff Formation in the western Borden Peninsula (After Jackson et al. 1978)

Ghazban et al. 1990, 1992) Kah et al. (2001) noted that the 1.2 Ga Society Cliffs Formation (Bylot Supergroup, northern Baffin Island) today consists of some 720 m of peritidal carbonates, evaporites, and minor siliciclastic rocks. Evaporites occur predominantly in the lowermost 300 m of the Society Cliffs Formation, where gypsum beds (1–250 cm thick) constitute up to 15 % of the exposed strata. Stratigraphic and

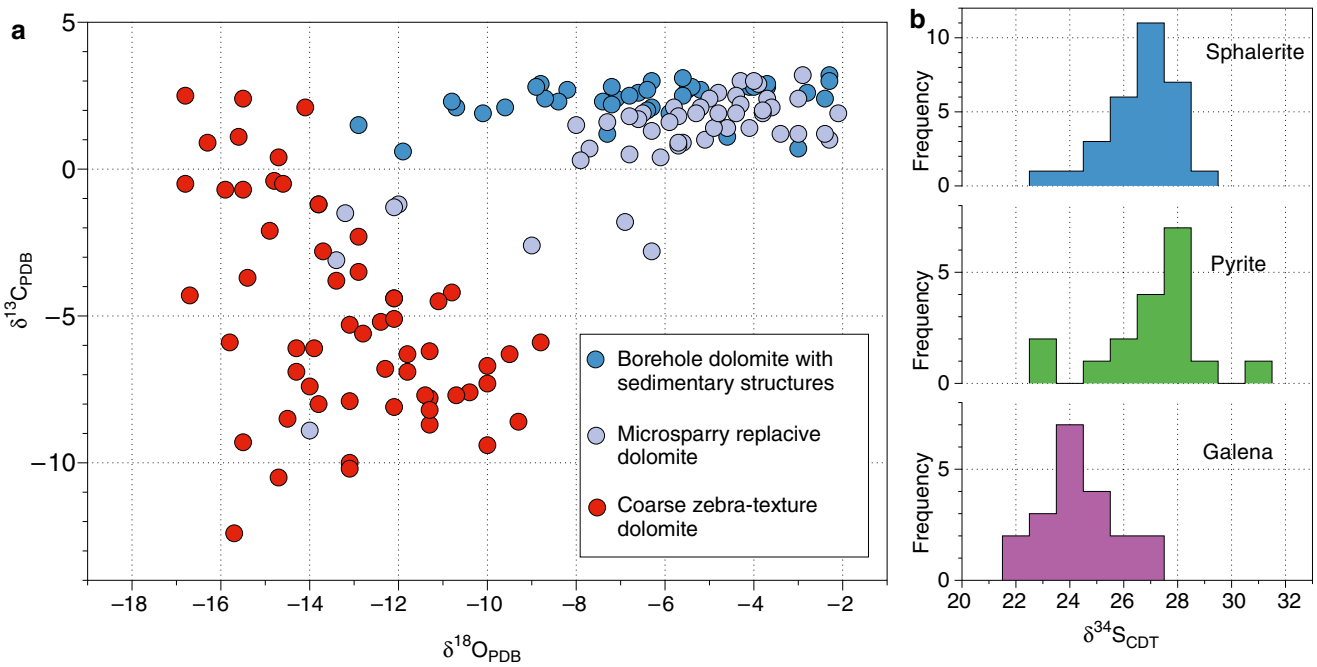

Fig. 15.66 Isotopes in the Nanisivik ore deposit. (**a**) Carbon-oxygen isotope crossplot of the various dolomites associated with the Nanisivik deposit. (**b**) Sulphur isotope values of metal sulphides in the Nanisivik deposit (Replotted from data tables in Ghazban 1988)

sedimentologic constraints, as well as isotopic (C, O, Sr) and elemental (Ca, Sr, Na, K, Ba) compositions of evaporites and associated carbonates, indicate a initial marine origin for Society Cliffs gypsum. However it must have experienced a significant degree of mineralogical alteration during its passage through the mesogenetic and telogenetic environments to where no more than relicts of the original beds outcrop today.

There are also red beds with halite casts and associated with gypsum-bearing mudflat sequences within the lower Society Cliffs Formation on Bylot Island, some 150 km east of Nanisivek (Jackson and Cumming 1981). Outcrops patterns on Bylot Island show high levels of deformation and evaporite-related folding in the Society Cliffs Formation (Jackson and Cumming 1981). The documented extent of such salty features in the Society Cliffs formation for may kilometres east and west of Nanisivik suggests that at least portions of the Society Cliff succession once contained a much greater volume of halite and that the unit, at least in some regions was halokinetic.

Closer to the Nanisivik deposit, a thin bed of relict gypsum (5–10 cm thick) was encountered at the same stratigraphic level as the ore zone in two boreholes immediately west of the main ore zone. In addition, gypsum (satin spar) commonly fills fractures in the dolostones surrounding the ore zones in the mine area. Much of the Society Cliffs Formation outcrop is extensively brecciated, particularly in the western Borden Peninsula, with interfragment spaces filled with sparry dolomite and less frequently with sulphide minerals (Fig. 15.65). The breccia zones are stratabound appear to be stratigraphically controlled, they bear no close or obvious relationships to faults and folds within the formation (Olson 1984). The association of secondary $CaSO_4$ and stratiform brecciation implies the karstic brecciation is associated with, and perhaps controlled by, evaporite solution collapse (Jackson et al. 1978).

Three distinct stages of dolomitisation can be distinguished by their petrographic, cathodoluminescence, and isotopic characteristics (Fig. 15.66): (1) Massive fine-medium crystalline dolomitisation of precursor carbonates preserving sedimentary features, and (2) Microsparry replacive dolomite, (3) Coarse latestage dolomite cementation forming "zebra" dolomites (Fig. 15.66a; Ghazban et al. 1992). The massive dolomites in the sulphate-bearing facies of the lower member of the Society Cliffs Formation and laminated algal stromatolitic to massive dolostones of the upper member are isotopically similar. Covariant C-O isotope signatures imply later dolomite cements was precipitated from warmer pore fluids, along with ongoing replacement and isotopic re-equilibration of some of the earlier dolomite precipitates. Such rock-fluid interactions with increasing fluid temperatures typify mesogenetic textures in fold and thrust belts worldwide (Warren et al. 2014). Dolomitising fluids responsible for later fracture and vug filling zebra dolomite cements may have been released by compaction of the underlying Arctic Bay Shale, which also appear to have been the source of the base metals (Ghazban et al. 1992).

Heavy $\delta^{34}S$ values of sulphides, ranging from 21.5 to 31.2‰, suggest complete reduction of marine evaporitic sulphate, with no isotopic difference between sulphate and sulphides. Isotopic temperatures from intersulphide fractionations range from 90 to 270 °C. Plots of fractionation versus $\delta^{34}S$ show that the sulphur source was heavy throughout sulphide precipitation, and was also consistent with total *in situ* thermochemical sulphate reduction (Fig. 15.66b; Ghazban et al. 1990). The likely reductant was organic matter, traces of which remain as pyrobitumen, although methane and volatile hydrocarbons may also have been involved. Striking evidence for the role of organic derivatives is found in $\delta^{13}C$ values of the white sparry ore dolomite, which varies between +6 and −12‰ (Fig. 15.66a; Ghazban et al. 1992).

Whatever the fine-scale paragenetic detail, overall ore formation at Nanisivik reflects processes involving *in situ* reduction of calcium sulphate in the presence of hydrocarbons and derived H_2S at the site of ore deposition. The location and configuration of the orebodies was probably controlled by the former position of near horizontal fluid redox interfaces. The question to be resolved by future matrix characterisation is: was that interface there because of a now-dissolved evaporite seals?

San Vicente, Peru

The San Vicente Zn-Pb deposit is the largest of a number of similar Pb-Zn-Ag accumulations hosted in the Upper Triassic Lower Jurassic Pucará Group in central Peru (Fig. 15.67) and situated 300 km east of Lima, in central Peru. It is part of an outcrop belt that defines the eastern part of the NNW-trending Pucará Basin at the margin of the Brazilian Shield. In the San Vicente district, evaporitic platform carbonates of the Pucará Group constitute a thrust prism that overlies magmatic and continental siliciclastic rocks of the Upper Permian – Lower Triassic Mitu Group. Phyllites of the Lower to Middle Palaeozoic Excelsior Group occur regionbelow the Mitu Group (Fig. 15.68; Badoux et al. 2001). During Late Permian – Early Triassic time, various intrusions were emplaced, such as the San Ramon granite and the Tarma granodiorite. In the San Vicente area, the Tarma granodiorite and Precambrian metamorphic basement rocks have been thrust over the Pucará carbonate rocks from west

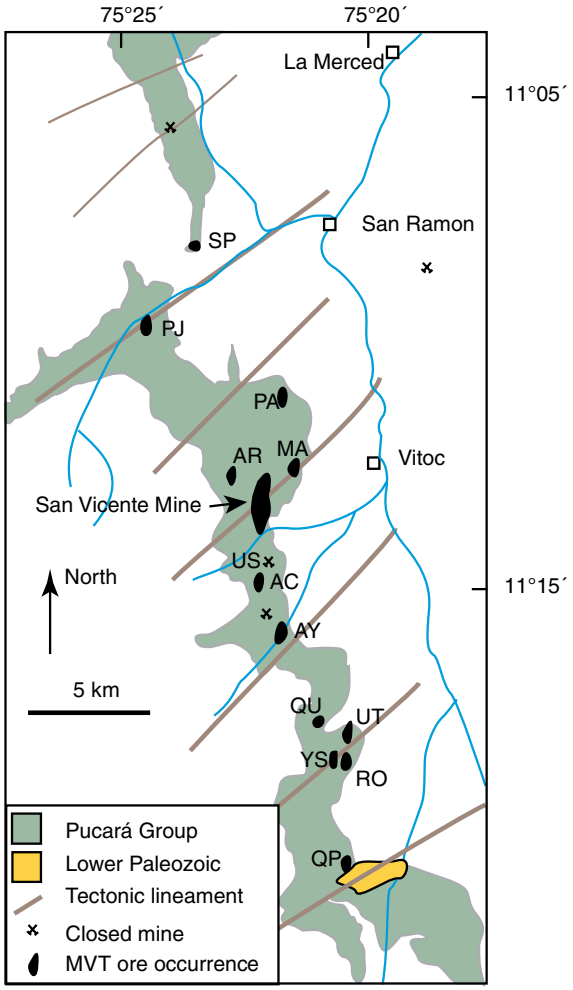

Fig. 15.67 San Vicente, Central Peru. (**a**) Map of San Vicente MVT district. *QP* Quebrada Pifion, *RO* Rondayacu, *YS* Yanachuro Sur, *UT* Utcuyacu, *QU* Quebrada Uteuyacu, *AY* Aynamayo, *CH* Chilpes, *US* Uncush Sur, *AC* Afloramiento Campana, *SV* San Vicente mine, *AR* Arcopunco, *MA* Machuyacu, *PA* Palmapata, *PJ* Puntayacu Junior, *PS* Pichita Sur

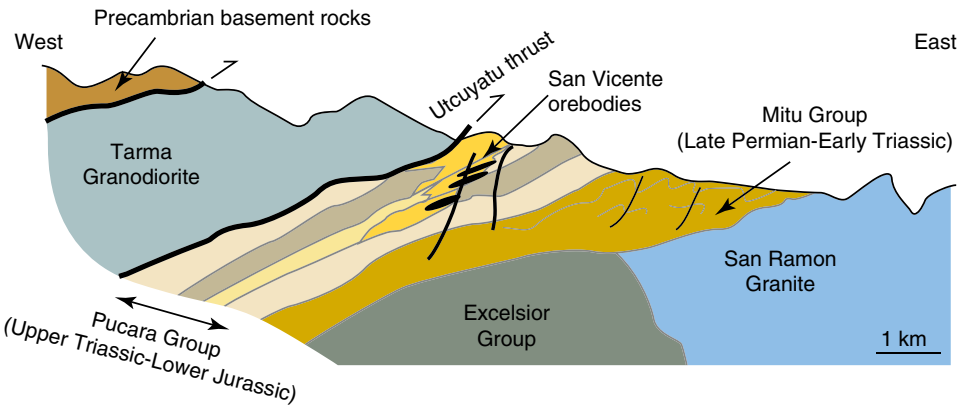

Fig. 15.68 Schematic cross-section of the San Vicente district, Bolivia. The Pucará Group has been overthrust by the Tarma Granodiorite along the Utcuyatu fault. The Pucará Group is a variably dolomitic and evaporitic sequence undergoing shearing along a westerly plane dipping ~25–30° (After Badoux et al. 2001)

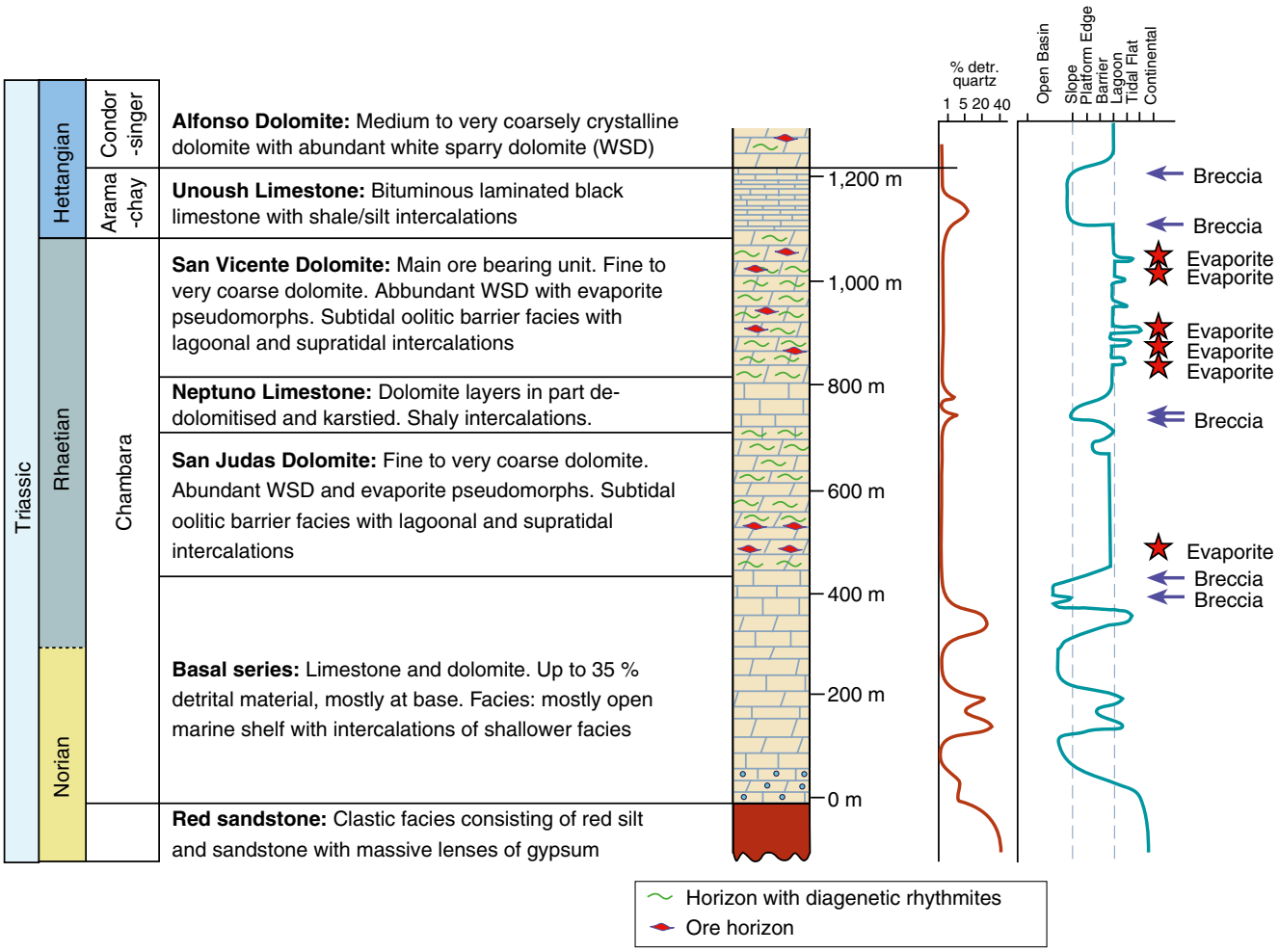

Fig. 15.69 Stratigraphy of part of the Pucará Group in the San Vicente Mine area (In part after Fontboté and Gorzawski 1990)

to east along the Utcuyacu thrust. Minor thrust zones also occur in the Pucará Group. The thrusts are located along a major Andean thrust zone, which is probably Miocene in age (Badoux et al. 2001).

The first written records of mining activity in the San Vicente region are from 1820, when the area was named the Guernica Mine. Various operations continued, at times sporadically, since then and operations continue today. Production during the past 20 years, plus present reserves, exceeds 12 million tonnes of ore assaying about 12 % Zn and 1%Pb. Sphalerite and galena, the only ore minerals, occur as lens-shaped bodies generally parallel to the bedding. There are three ore-bearing dolomites that lie within the 1,400 m thick Pucará sequence (Figs. 15.68 and 15.69). The San Vicente dolomite is the main ore-bearing unit and hosts the exploited part of the San Vicente mine. Other ore occurrences are located in the San Judas Dolomite and the Alfonso Dolomite. Individual ore lenses are hosted in dolomitised tidal flat and lagoon facies characterised by cryptalgal laminae and evaporite moulds after former sulphate evaporites (including gypsum).

Sphalerite and galena are the main ore minerals, with accessory pyrite and traces of marcasite, chalcopyrite and sulphosalts. The gangue consists predominantly of dolomite with accessory calcite. Different generations of hydrothermal carbonates can be distinguished: (1) early, dark replacement dolomite; (2) open-space filling, white sparry dolomite; (3) late stage void-filling dolomite and calcite; and (4) dolomite and calcite replacing sulphates in evaporitic units. Most of the sphalerite occurs in the same paragenetic position as the hydrothermal dolomite. Fine-grained, dark brown sphalerite accompanies early, dark replacement dolomite, and coarse-grained brown to yellow sphalerite is associated with white sparry dolomite. Galena precipitated mainly with late stage void-filling dolomite (Fontboté and Gorzawski 1990).

Three major types of gangue structures can be at the San Vicente mine (Fig. 15.69): (1) rhythmic, inter-layering of dark replacement and white sparry dolomite, defining typical zebra structures; (2) breccia with clasts of dark replacement dolomite in a matrix of white sparry dolomite; and (3) veins

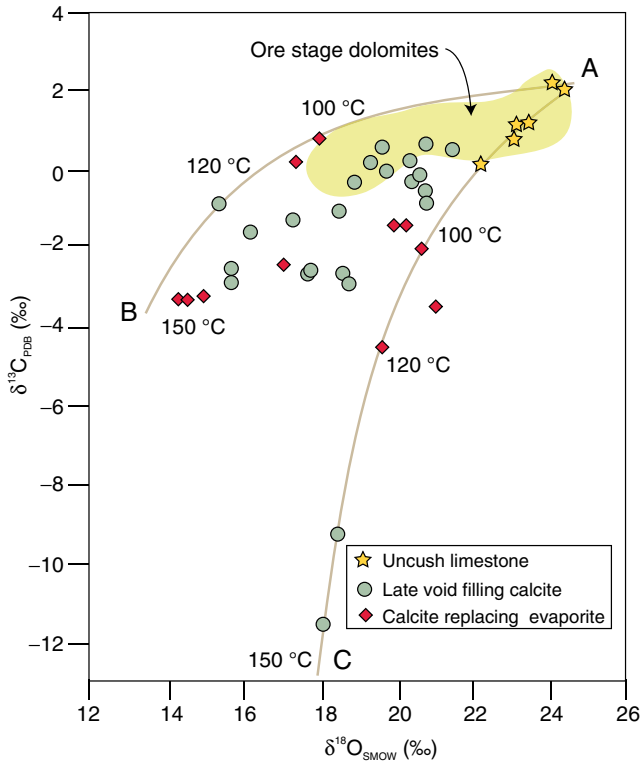

Fig. 15.70 $\delta^{13}C$ vs. $\delta^{18}O$ for various calcites from the San Vicente mine. Also plotted are theoretical temperature curves for calcites indicated by mixing of fluids (A, B, C). *Shaded field* indicates plot field occupied by ore-stage dolomites (Based on analyses listed and interpretation by Fontboté and Gorzawski 1990)

filled with white sparry dolomite. These structures are recognised in both economic and barren areas of the mine. In ore-bearing areas, brown to yellow sphalerite generally occurs between dark dolomite and white, sparry dolomite, whether it is zebra, breccia or vein-type ore (Fontboté and Gorzawski 1990). Ore lenses tend to occur as stratabound units adjacent to oolitic grainstones of former barrier-shoal facies. All three ore-hosting dolomite units were deposited in a peritidal carbonate platform that comprised: (1) the inner margin of the lagoon (tidal flat), (2) the lagoon sensu stricto and (3) the outer margin of the lagoon (barrier subenvironment).

Strontium, carbon, oxygen, and sulphur isotope geochemistry was carried out on consecutive crystallisation generations in the San Vicente region (Spangenberg et al. 1996; Moritz et al. 1996). The results obtained display systematic trends that all show San Vicente lead-zinc deposit formed during burial diagenesis via the mixing of incoming hot saline, slightly acidic, radiogenic (Pb, Sr) basinal fluids and local sulphate-rich formation waters derived from calcium sulphate beds. The temperatures indicated by sulphur isotope geothermometry and carbon and oxygen ore stage dolomites are consistent with temperatures of 75–92 °C (Fig. 15.70).

According to Fontboté and Gorzawski (1990), such burial temperatures would have been attained when sediments reached at a burial depth of ≈2–3 km and indicative of burial depths reached by the end of the Jurassic. However, the timing of the ore emplacement is controversial. Fontboté and Gorzawski (1990) suggested that brine circulation was related to uplift of the Marañon geoanticline at the end of the Jurassic, and Moritz et al. (1996) proposed that the San Vicente deposit was contemporaneous with the Incaic phase of the Andean orogeny at ~40 Ma. Underground mine extensions in recent years have revealed abundant ore-bearing structures suggestive of a syntectonic origin for the San Vicente deposit (Badoux et al. 2001). Thus, the deposit might be as young as the host thrust zone, which is probably Miocene in age.

Whatever the emplacement age, ores were emplaced by the thermochemical reduction of evaporite-derived sulphates at or near the ore site and the introduction of a zinc- and lead-bearing basinal brine (Fontboté and Gorzawski 1990). After the low temperature sulphide ore emplacement stage, the replacement of the evaporites continued with the precipitation of calcite replacing evaporites with isotope characteristics indicating fluid temperatures in excess of 150 °C (Fig. 15.70).

Interestingly, San Vicente ore zones are associated not just with sulphate evaporites, but with well developed stratabound breccia layers. Historically, these breccias were interpreted as depositional slope deposits by Fontboté and Gorzawski (1990). Their interpretation was done 25 years ago, before there was a widespread understanding of evaporite solution breccia textures. More broadly, the Pucará group was deposited in an extensive system of Traissic rift-to-drift grabens that constitute the Oriente-Ucayali-Ene Basin. In northeast Peru the Pucará Group depositional system contains thick halites at the level of the Mitu Group. This same salt level is now the mother salt horizon for a number of diapiric structures, such as the Huallaga diapirs, which have seen seismically imaged and drilled by the petroleum industry (Alemán an Marksteiner 1995, 1997). The same salt is also caught up in thrusts and other Andean deformation features. If the same halite level once extended as far south as the San Vicente area is not known, but the evaporitic conditions certainly did, as evidenced by the gypsum beds in the Alfonso dolomite, the San Vicente dolomite and the San Judas Dolomite.

Largentière, Ardèche, France

The Largentière Pb–Zn deposit is located at the boundary between the sedimentary cover and the Massif Central block and belongs to the Cévennes Pb–Zn MVT province (Fig. 15.71a; Aquilina et al. 2011; Leach et al. 2006; much of the following is based on these references). Since it is not in limestone, the sandstone-hosted Largentière deposit lies

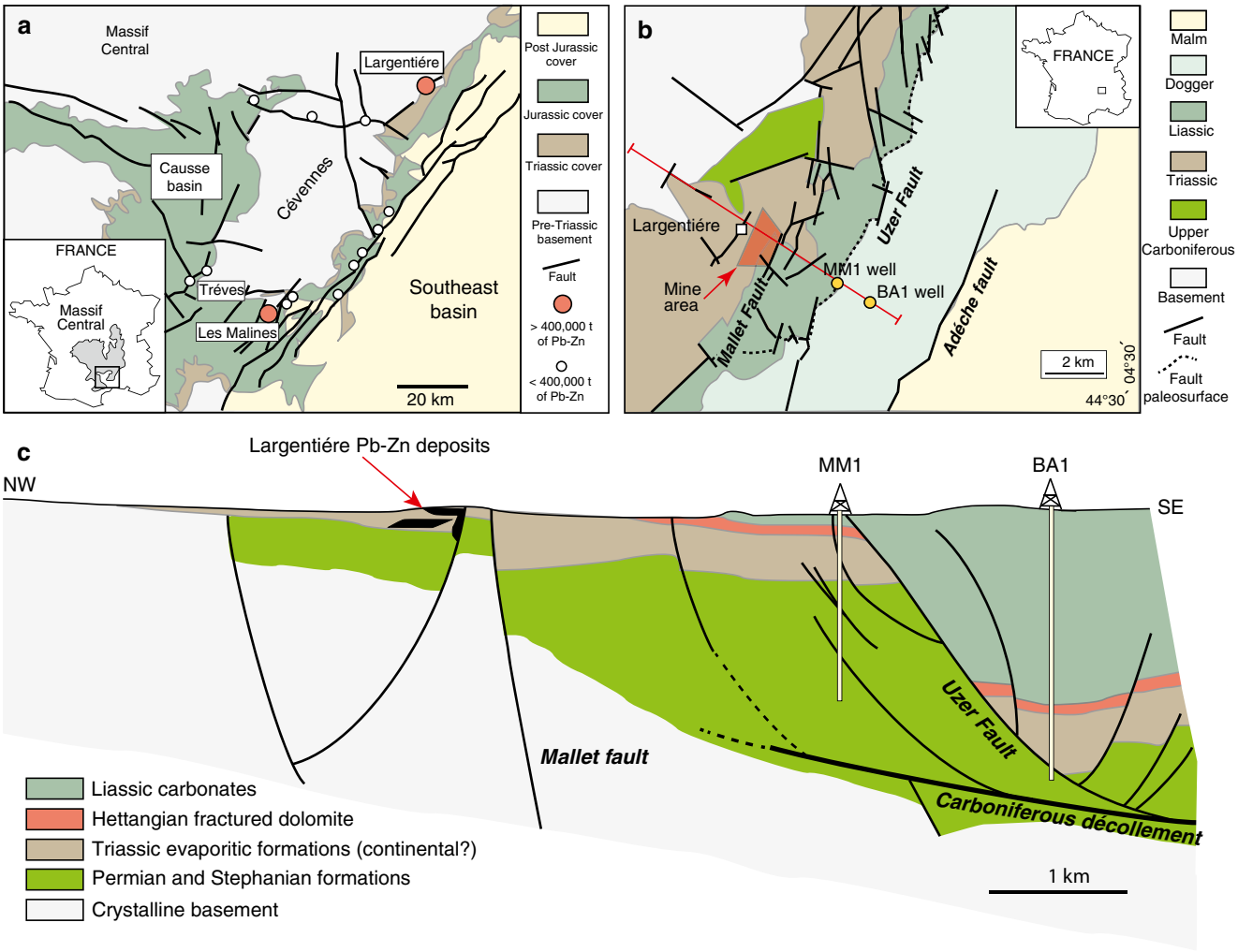

Fig. 15.71 Largentiére Pb-Zn, SW France. (**a**) Regional geological map showing Pb-Zn occurrences in the Cevenne District. (**b**) Local geology of the Largentiére region. (**c**) Cross section of the Largentiére region, position of section indicated on Fig. 15.71b (After Aquilina et al. 2011)

outside the typical carbonate platform host assumed for MVT Zn-Pb mineralisation deposit (Sverjensky 1986). Largentière is considered to be part of a broader sandstone-hosted Pb-Zn association, mostly related to saline basinal-brine metal carriers (Schrijver 1992). In addition, there are many Zn-Pb deposits along the same Cévennes margin, hosted in platform carbonates. Hence, the area is also considered an MVT district, made up of numerous small deposits, including those with sandstone ore hosts.

Independent of host lithology there is clearly a common genetic origin to the Pb-Zn deposits of the Cévennes district that ties them to a combination of chloride-rich fluids, structure and calcium sulphate. The Cévennes district is structurally related to the Mesozoic Southeast Basin to the east as well as the Triassic and Jurassic cover of the Causse basin to the west (Fig. 15.71a). The fact that the host is a sandstone is why I will describe these deposits in a fair degree of detail. I use Largentière to illustrate that Pb-Zn precipitation association is a fluid-driven set of processes tied to a chemistry and hydrology driven by dissolving evaporites; it is an precipitative interaction between evaporitic sulphate, chloride brines and hydrocarbons/ organic matter. "MVT" style precipitation can be independent of the ore matrix, although sulphate evaporites are more typically found in platform carbonates. In Largentiére, sulphates reside in redbed sandstones, not salterns or carbonate hosted evaporitic mudflats. Locally, the precipitation process (in this case TSR) can be independent of the matrix lithology (sandstone or carbonate). The commonality between the two matrices (carbonate versus siliciclastic) is in the presence of calcium sulphate on the reducing (greenbed) side of the redbed/greenbed diagenetic front.

Ores in the Cévennes MVT district occur in various geological contexts: Cambrian and Jurassic carbonates, fault-related or massive deposits, vug fillings in carbonates, etc. as well as in various types of mineralogical sequences (Aquilina et al. 2011). Most of the economic precipitates are

hosted in platform carbonate rocks and consist of sphalerite, galena, pyrite and baryte (and fluorite). On a larger scale, they can be related to the MVT deposits of Mesozoic sedimentary basins in western Europe associated with the break-up of Pangea (Heijlen et al. 2001; Muchez et al. 2005). There are numerous mining sites along the Cévennes chain (Fig. 15.71a). The deposits of Les Malines include massive sulphide bodies in Bathonian karst cavities (40 % of the total tonnage) and ore bodies within Triassic karstic infills of cavities developed in Cambrian dolomites (35 % of the total tonnage).

The Cévennes is one of the most important Pb–Zn districts in Europe, with a total metal content of 2 Mt of Pb and Zn (Aquilina et al. 2011). Largentière, the northernmost deposit, was estimated as hosting 350,000 t of Pb and 70,000 t of Zn (9.6 Mt of ore mined) and 710 t of Ag. The most recent mine at Largentiére operated as France's largest Pb mine from 1953 to 1984, but silver was mined in the region as early as the 14th and 15th centuries. The mine site at Largentiére is on the western edge of the Cévennes is Trèves, with an estimated 80,000 t of Zn and 20,000 t of Pb (3,600 t Zn and 817 t Pb produced, respectively) (Fig. 15.71b).

Largentière Pb-Zn mineralization covers an area some 1.5–3 km across, where precipitates include galena, sphalerite, pyrite and baryte (Fig. 15.71b). Mineralisation occurs mostly within Lower Triassic sandstones and arkoses (30–50 m thick), less frequently in about 20 m of overlying Middle Triassic dolomite, and rarely in Upper Triassic argillaceous sandstones (Bouladon 1984). Ore at Largentière occurs either as fracture fillings, as disseminated sulphides, or as fracture controlled massive sulphide ore. Whilst pyrite appears in the mineralized area associated with quartz, anhydrite is observed in the western part of the district. At the scale of the Southeast basin, the ore deposits always appear at the contact between the sandstone and the sedimentary anhydrite facies (Fig. 15.71b, c; Debrand-Passard 1984).

For example, Bed 5 ore at Largentiére formed as a cement within coarse-grained sandstones at the base of the Triassic section and is located less than 15 m above the Permian contact. There is not always a single mineralised horizon, but stratiform character is the rule at Largentiére. Local ore enrichments are related to shear zones, the general connection between mineralisation and faults in bed 5 ore is not always clear, but the tie to the redbed-green bed ($CaSO_4$) contact is. About 10 m above bed 5, the redbed sandstones change to dolomite-cemented greenbeds and green argillaceous, gypsum-bearing lagoonal siltstones appear (the reduced facies). The Pb-Zn mineralisation in beds 1, 2 and 3 (termed the "upper mineralised horizon") is consistently tied to the presence of gypsum within the mineralised intervals (Bouladon 1984). In this upper interval, mineralisation is associated with faults, and "fissure ore" dominates in dolomitic sandstones and marls. Gypsum has been reprecipitated in the Volpilliare region, along with galena in fibrous veins (satin-spar) crosscutting the marls. The possible significance of satinspar texture as a likely indicator of former more widespread halite is not considered in the existing literature.

The coincidence between sedimentary facies, faulting and the location of mineralization implies a lithologic/structural control to the ore deposit. Regionally Pb-Zn mineralization appears along the Hercynian faults of the Mallet horst but is also controlled by synsedimentary faults in some Triassic beds (Fig. 15.71c). Mixing of hot basinal chloride brines (high metal content) derived in part from dissolving downdip Permian evaporite masses and cooler meteoric fluids leaching of Triassic sulphates (high sulphur content) is proposed for the Trèves deposit located close to Largentière (Fig. 15.71a; Leach et al. 2006).

The key to the interpretation of the mineralisation paragenesis at Largentiére comes from placing the isotopic and petrographic signatures of this and other nearby Pb-Zn deposits in into a more regional diagenetic and structural context, as was done by Aquilina et al. 2011 (Fig. 15.72). Their synthesis shows that a major fluid circulation event occurred across the Alpine margin of Tethys during the Early Jurassic (Hettangian–Bathonian). It produced a general cementation of the rock porosity, through precipitation of dolomite, burial anhydrite and baryte. Fracture fillings yield isotopic signatures distinct from the matrix cements (Fig. 15.72; sedimentary sulphate versus fluid-related sulphate plot field). Matrix cements have particular characteristics, i.e. $\delta^{34}S$ and $\delta^{13}C$ values that indicate a marine-brine hypersaline source. The $\delta^{34}S$ values of Permo-Carboniferous to Triassic sulphides from fracture cements likely indicate thermo-chemical reduction of sulphates. Fracture sulphates in the same geological formations yield $\delta^{34}S$ values that define a relatively homogeneous end-member, with compositions similar to fluid-related calcium sulphates in the Largentière Pb–Zn ore deposit. The source of S and the metalliferous chloride-rich brines is attributed to dissolving evaporite masses in the Permo-Carboniferous succession. The extensional geometries so obvious in Fig. 15.71c show structural similarities it the updip salt-withdrawal basin-edge grabens in the Gulf of Mexico, onshore Texas.

The borehole fracture fillings are attributed to a major fluid circulation stage compatible with the Early Jurassic stage. The formation of the Largentière deposit is considered as resulting from the mixing of Early Jurassic fluids with hydrothermal fluids circulating in a basement horst, along the basement high that constitutes the up-dip margin of the sedimentary basin (Fig. 15.71c). Other nearby Pb–Zn deposits are also related to fluid migration along the basement/sedimentary cover interface in the eastern and western parts of the Massif Central. According to Aquilina et al. (2011), this regional fluid circulation event is a likely geodynamic marker of the Jurassic extensional phase.

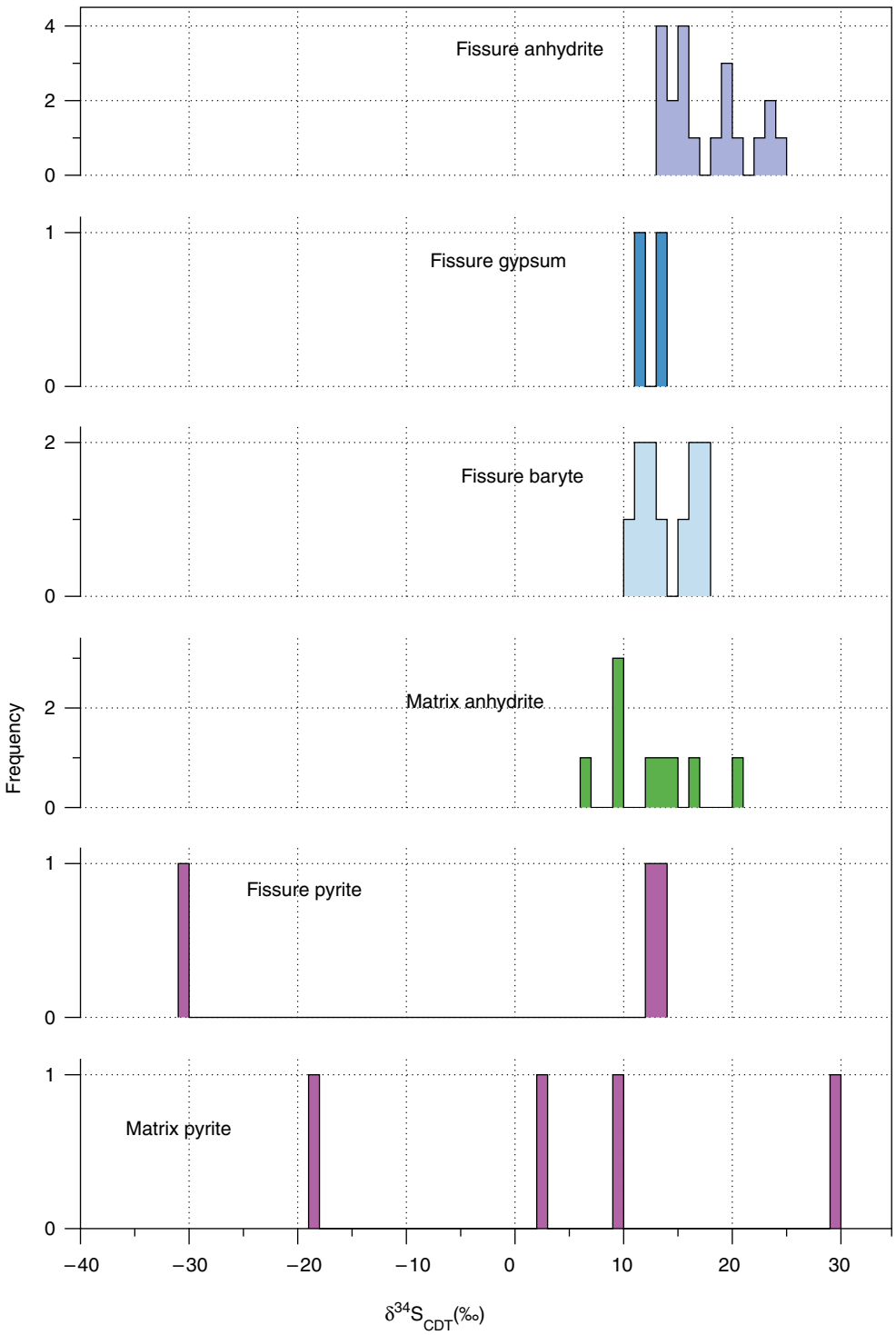

Fig. 15.72 Sulphur isotope frequency histograms from samples collected in the MM1 and BA boreholes. Largentiére region (Replotted for data tables in Aquilina et al. 2011)

In the Palaeozoic formations in the Largentiére region, sulphur from sulphates and sulphides shows a relatively narrow range of isotopic variation (−10‰ to +5‰, except for two pyrite values), similar to the Largentière Pb–Zn deposits (−10‰ to +6‰). Such values are different from the marine sedimentary signature (Fig. 15.72). They likely indicate the thermal sulphate reduction of calcium sulphates to sulphur or biological reduction of sulphate followed in both cases by precipitation of pyrite and other metal sulphide via interaction with H_2S. Both the TSR and BSR mechanisms lead to stable isotope fractionation plot fields of pyrite sulphur that can overlap (−20‰ to −10‰ at 200–100 °C and −15‰ to −30‰ at ambient temperature). Biological reduction is unlikely at Largentiére because (1) Excessively high

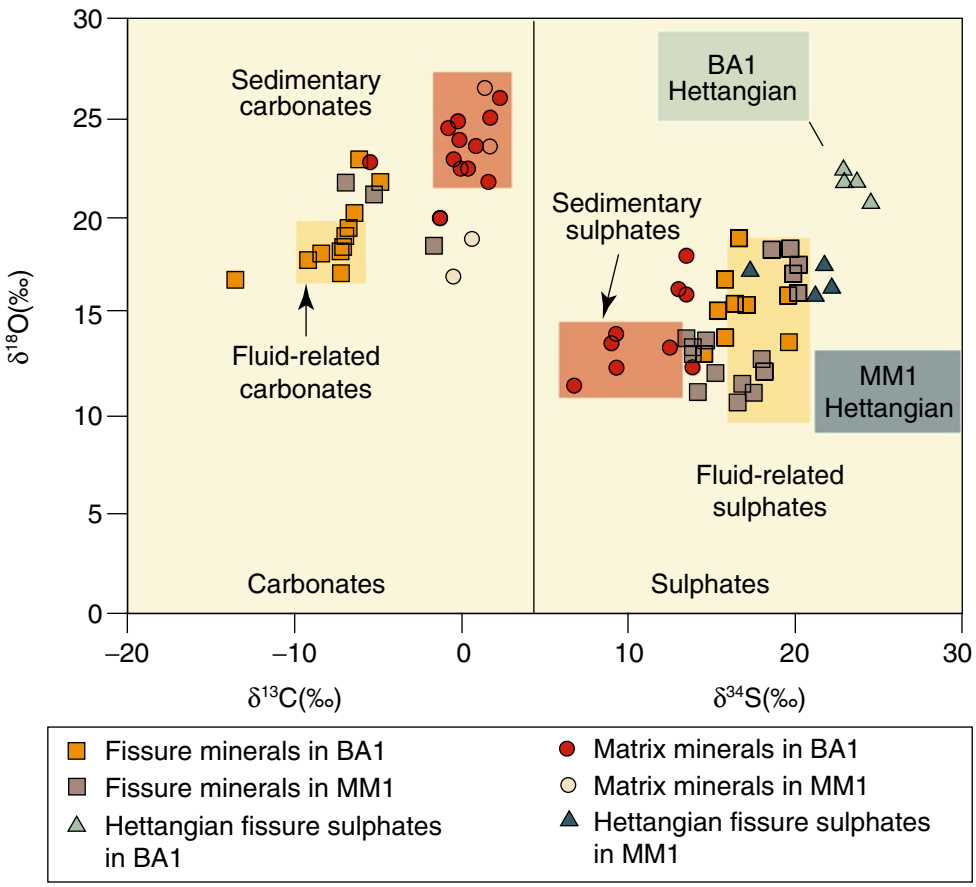

Fig. 15.73 Carbonate and Sulphate stable isotope plot fields indicating the diagenetic nature of the calcium sulphate in the BA 1 and MM wells in the Largentiére region. See Fig. 15.71b for location (After Aquilina et al. 2011)

temperatures are indicated in fissure cements in the Palaeozoic (about 100–200 °C), (2) $\delta^{34}S$ are higher (more positive) than the values found in matrix sulphides related to biological sulphate reduction and (3) lower fractionation differences at the relatively high temperatures produced by thermo-reduction, compared with biological reduction, fits better with the data (e.g., note the strong overlap between fluid-related sulphates and the sulphide pyrite values in Fig. 15.72).

The $\delta^{34}S$ values in the fissure sulphates from Palaeozoic and Triassic formations vary from +13‰ to +22‰ (Fig. 15.72). This is interpreted by Aquiliana et al. (2011) as the result of mixing between the sedimentary sulphate pool of the Triassic middle sulphate unit and sulphate with a higher $\delta^{34}S$ signature. The Triassic sulphate signature is particularly marked at the base of the middle calcium sulphate unit in the well MM1 and immediately below the equivalent unit in the BA1 well. The high $\delta^{34}S$ population observed in the calcium sulphates of the Triassic, and even more clearly in the Palaeozoic formations, is in the range +17‰ to +20‰. This range is similar to that observed in the Largentière Pb–Zn deposits (+17‰ to +22‰). This very narrow range of $\delta^{34}S$ for the sulphate deposits across the region in a sedimentary pile about 800 m thick, as seen in the two boreholes, requires a large-sized and homogeneous sulphate pool.

Three potential sulphur sources are considered by Aquilina et al. (2011): (1) Triassic evaporitic units: but, as already mentioned, the S isotope signature of the sedimentary anhydrites is too low to be a diagenetically unmodified calcium sulphate source. (2) Hypersaline brine migration from the eastern part of the basin: fluid migration related to Triassic diapirs has been identified from fluid inclusion studies in the deeper eastern part of the southeast basin, but similar fluid inclusions (NaCl type) were not identified in cements in the BA1 and MM1 boreholes. Furthermore, the isotopic signature of the calcium sulphates of these fluids should be similar to those of the Triassic evaporites in BA1 and MM1, since the evaporitic formations in the Southeast basin are contemporaneous. (3) Palaeozoic calcium sulphates: Permian and Carboniferous evaporitic formations attain a great thickness over the whole margin (about 1,000 m), representing a large source of S with a marine isotopic signature. Burial of these Permian formations to a depth close to 1,000 m at the end of the Triassic, and reaching 2,500–4,000 m during the Jurassic, along with ongoing dissolution of the Permian halites created early conditions for fluid expulsion.

The link of the Uzer fault with intra-Carboniferous décollement led to Permo-Carboniferous derived fluid moving up along the Uzer and other related extensional faults (Fig. 15.71c). As observed for the sulphate $\delta^{34}S$ values in the anhydrite cements, the $\delta^{13}C$ of the fissure carbonates is relatively homogeneous across the Palaeozoic and Triassic, with a narrow range of −5‰ to −10‰ (Fig. 15.73). Such values

do not represent marine sedimentary carbonates and cannot be attributed to simple C-isotope fractionation between calcite and CO_2 or HCO_3. This is because, at 100 °C, calcite is enriched in ^{13}C by about 1.5‰ compared with these fluid species. These low carbon isotope signatures imply the contribution of low-$\delta^{13}C$ organic carbon, a common feature that has already been observed under similar burial conditions in other Pb-Zn deposits (Aquilina et al. 2011). Indeed, organic matter is present in this context, as well as CO_2 accumulations with negative $\delta^{13}C$ (−2.7‰ to −3.2‰). Furthermore, this carbon signature represents a relatively homogeneous 'crustal' carbon, even though it originates from both a marine and an organic source. As such, it provides another indication of fluid transfer at the margin scale, including density and thermal-driven convective circulation within the margin basement (See Chap. 8).

The fissure sulphates in the Hettangian interval can have high $\delta^{34}S$ and high Sr isotope ratios in both the boreholes, which could indicate a different fluid circulation stage and/or slightly different source or conditions of evolution for higher value cements. However, as observed in Fig. 15.73, this mainly applies to cements the Hettangian in BA1, but is less clear for MM1, which yields $\delta^{34}S$ overlapping values than the Triassic fluid carried sulphates. Although affected by the same generalized fluid circulation event at a geological scale, the Hettangian hosted cements in well BA1 may represent a different regime with higher temperatures lower fluid/rock ratios and slightly different fluids. Such a difference between the two geological formations may be linked to the Uzer fault. The very high initial porosity of the Triassic upper sandstone unit (and, to a lesser extent, the lower sandstone unit) may have channelled the fluid circulation, whilst more limited fluid flow could have occurred in the Hettangian.

Largentiére and all the other Pb-Zn deposits discussed in this section illustrate what happens when metalliferous chloride-rich saline fluid climbs into basin margin sediments, where they precipitate Pb-Zn sulphides at a chemical interface, which is typically a redox front tied to either bacterial or thermogenic sulphate reduction. The sulphur that ends up in the metal sulphide is typically evaporite-derived; it may be locally sourced in saltern beds or nodule sulphate in evaporitic mudflats, it may be a burial anhydrite cement in a sandstone, or it may be a residual carapace or caprock to a salt structure. Alternatively sulphur may be carried to the final site of precipitation (trap) in solution as sulphate or as H_2S, depending on the chemical state of the carrier fluid. Much of the time the carrier bed geometries are tied to combinations of dissolving salt masses, permeable beds and fault foci. Much of the faulting, either suprasalt or updip is related to structural accommodation driven by flowing and dissolving downdip salt masses. Such fault and salt mass focused fluid flow and mixing can occur in either extensional or compressional tectonic settings.

We shall come back to this notion of regional salt-related controls to low temperature diagenetic ore deposits in a variety of tectonic settings, after we consider what happens to saline fluids from the haloes of halokinetic salt masses that pass vertically to seafloor rather than migrating to the basin margin. We touched on this type of ore deposit in the discussion of the Atlantis II Deep sulphides and brine pools at the edge of dissolving salt allochthons in a salt-covered rift-induced basinal brine sump, and so we come to a discussion of evaporite-associated SedEx deposits

Evaporite-Associated SedEx Deposits

Associated with a hydrothermal vent-related origin for various sediment-hosted exhalative (SedEx) deposits, most authors currently accept there are two laminite endmember models, namely, SedEx deposits that are; (1) Vent-proximal laminites formed by rain-out of a metalliferous plume spreading in the water column, considered by some to tied to VMS black-smoker or Cyprus-style vent deposits (see Chap. 16) versus, (2) Vent-distal laminites formed in a bottom-hugging saline pond in a sea-bottom brine sump or lake, much like the Atlantis II deep discussed earlier (Fig. 15.74). The matrix within many Pb-Zn laminite deposits typically contains little or no carbonate. Within this classification framework, additional subtypes, typically listed by economic geologists as SedEx in the broader sense can include; Broken Hill type (BHT) deposits and those Pb-Zn deposits that formed below, but near, a seafloor vent system (e.g., Irish-type Navan deposits; Goodfellow and Lydon 2007). The Irish type of SedEx deposit is hosted predominantly in carbonate rocks and these deposits, either individually or collectively (district-wide), may show characteristics of saline brines involved in both seafloor deposition (seep-related chemosynthetic communities) and in epigenetic/hydrothermal karst settings, which many geologists consider more typical of Mississippi Valley-type deposits.

Irish-type deposits are considered to have formed by ore-forming processes similar to those of seafloor SedEx deposits. But, because carbonate platforms are highly soluble in mildly acidic ore fluids, the ores were typically deposited subsurface rather than at-surface, as passive precipitates in open porosity in a carbonate host that commonly formed by hydrothermal karsting (e.g., mineralisation in hypogene dissolution voids, collapse breccias; stylolite replacements; Reed and Wallace 2004). Broken Hill Type deposits are characterized by higher metamorphic grade, elevated base metal to sulphur ratios, a spatial and temporal association with Fe-Si-Mn oxide exhalites, and bimodal felsic-mafic volcanic/intrusive and fine- to coarse-grained, mostly clastic sedimentary host rocks (Figs. 14.64 and 15.38; Conor and Preiss 2008).

A plethora of overlapping characteristics and poorly defined associations to particular analogs typifies the current state of classification of low temperature Pb-Zn SedEx

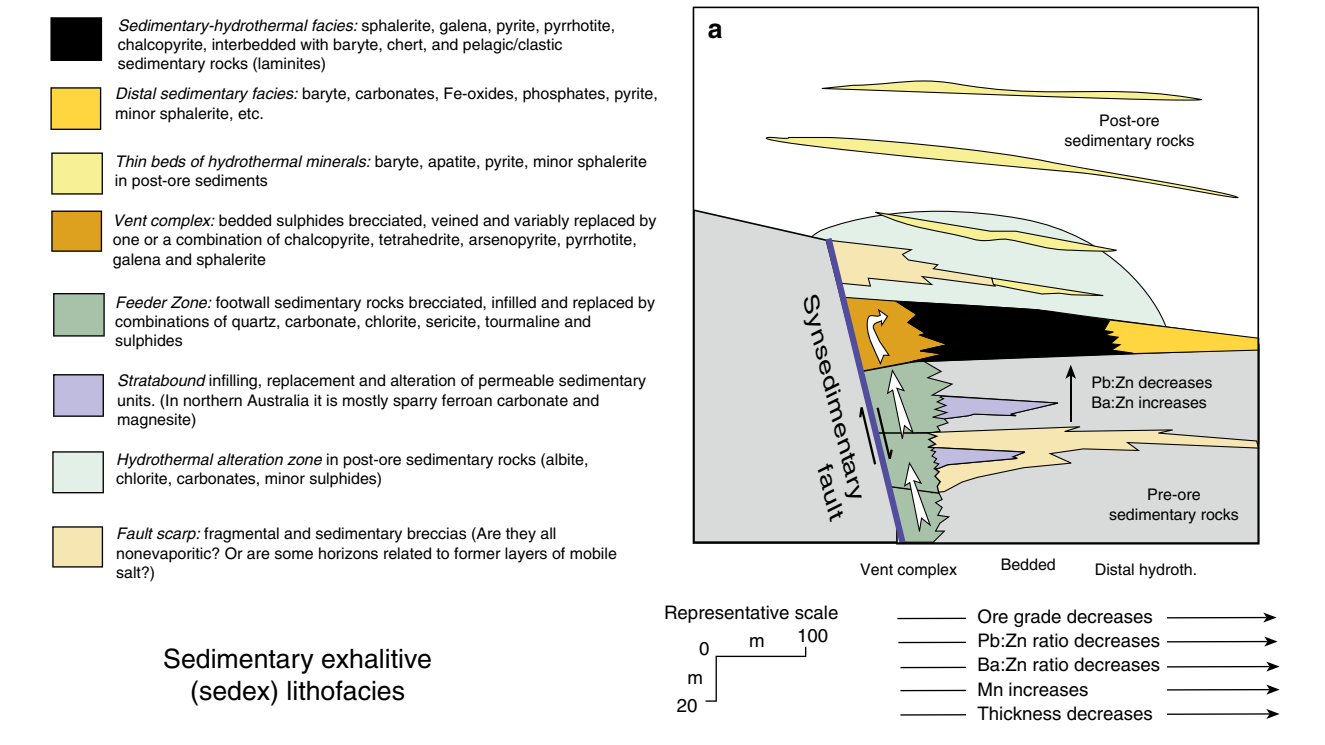

Fig. 15.74 Sedimentary exhalative (SedEx) deposit model. (**a**) Schematic cross section of SedEx mineralisation showing zonation and accompanying lithofacies. (**b**) SedEx in proximal position with brine plume dispersal. (**c**) Brine lake style with brines venting some distance from the brine lake. Venting brines are dense and hug the seafloor as they flow toward the deep-seafloor brine sump (After Goodfellow et al., 1993; Goodfellow and Lydon 2007; Warren 1999, 2000b)

deposits (as noted by Groves et al. 2005, 2010). In the economic geology literature it is generally argued, especially at the deposit scale, that, no matter what criteria are used to define a SedEx deposit, there is a continuum of characteristics between SedEx and VMS (volcanogenic massive sulphide) deposits on the one hand, and SedEx and MVT deposits on the other hand.

I disagree, the following sedimentologic/diagenetic/meta-evaporite criteria clearly separate the three deposit styles, namely; (1) the nature of the associated $CaSO_4$ (depositional beds versus burial diagenetic verses hydrothermal in an igneous-rich matrix), (2) tectonic settings that facilitate thick bedded halite deposits, thick halite cannot precipitate at open ocean basalt ridges. At continent -continent promixal young-oceanic ridges, the halite must be halokinetic – as in the thermal Atlantis II deep, (3) solution chemistry and characteristics of sulphide and non-sulphide cements in the associated breccias in the immediate vicinity of ore lenses [either warm as in diagenetic (<200–250 °C; versus hot >250–300 °C] in igneous VMS associations. The differences in these three factors are indicators of the specific ore system; as is the nature of the surrounding non-ore matrices, as well as the type and geometry of the alteration residues. In addition, differences in ionic proportions seen in the hydrochemical details, captured in fluid inclusions, are pointers to the ultimate brine source. In combination, all these factors can be used to separate the three deposit styles.

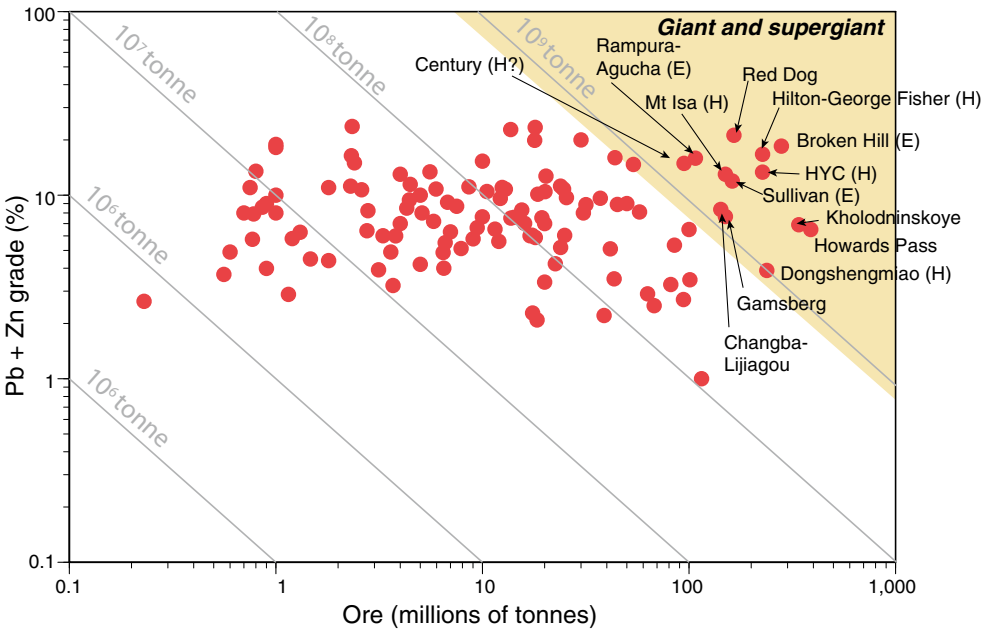

Fig. 15.75 Resource plot for sedimentary exhalative deposits. Halokinetic association indicated by *H*, bedded evaporite association by *B* and metamorphic evaporite association by *M* (Plotted data values were extracted from, integrated with the SedEx evaporite association GIS base and classification extracted from the SaltWork database version 1.6)

SedEx and MVT deposits tend to occur within slope deposits of thick sedimentary basin fills or in platform carbonates, respectively. Both are the result of the upward and lateral migration of slightly acidic basinal chloride-rich metalliferous somewhat lower-temperature saline fluids. Updip fluid movements often enhanced or focused by fault and fracture-related conduits, which are related to halite flow (diapirism and gravity gliding) and salt dissolution. And, as we shall see, the strength of the ore-depositing SedEx system can be enhanced by the dissolution of basinal or platform evaporites.

In contrast, VHMS deposits occur in submarine volcanic-sedimentary host sequences (associated with Kuroko-style anhydrites), which host hot convective hydrothermal flows of seawater and/or magmatic fluids, mostly through igneous basement, driven by the heatflow from a subvolcanic magma body. Typically, no sedimentary evaporites are involved in the metal transport or precipitative portions of a Volcanic Hosted Massive Sulphide (VHMS) deposit, although remnant textures from hydrothermal-seawater anhydrites can be a common gangue phase. VHMS deposits are discussed in the next chapter.

Using Goodfellow and Lydon's (2007) definition, SedEx deposits encompass a broad range of tonnages and grades (Fig. 15.75). They account for more than 50 % of the world's zinc and lead reserves and furnish more than 25 % of the world's production of these two metals (Emsbo 2009). More than 130 deposits of this type have been recognized in sedimentary basins around the world (Leach and others 2005; Goodfellow and Lydon 2007). A compilation based on Sangster and Hillary (2000) shows that the largest 65 deposits occur in 25 sedimentary basins, six of which contain more than 10 metric tons (Mt) combined Pb + Zn. In order of decreasing endowment these six are; Mt. Isa–McArthur basins (7 deposits totalling 112 Mt of Zn + Pb metal), Selwyn basin (17 deposits totalling 55 Mt), Brooks Range (3 deposits totalling 40 Mt), Rajasthan (5 deposits totalling 20 Mt), Belt-Purcell (1 deposit totalling 19 Mt), and the Rhenish Basin (2 deposits totalling 11 Mt) (Figs. 15.75 and 15.76).

Distribution of SedEx deposits is not equally spread across geological time (Fig. 15.77; Lyons et al. 2006). SedEx Zn-Pb-sulphide mineralization first occurred on a large scale during the late Paleoproterozoic with only a few small dubious set of examples in the Archaean, most of which are better pigeonholed in a VMS setting. Because free oceanic sulphate ions and resulting sulphate evaporites are produced mostly through weathering of the continents in the presence of oxygen, a lack of calcium sulphate beds in the Archaean and the beginnings of sulphate bedded deposits in the early Proterozoic implies a transition into more oxygeneated ocean surface waters. Sulphate (not H_2S) typified ocean waters at that time and since. This event was biogenically driven and is called the first "Great Oxidation Event." Colloquially, it is known as the time when the oceans rusted and widespread oceanic banded iron formation (BIF) precipitation largely ceased (Chap. 2). The subsequent period (≈1,800–800 Ma) was typified by relatively low oxygen concentrations, when atmospheric levels lay between the abundances of the Phanerozoic and the deficiencies of the Archaean, as indicated by the Precambrian sulphur isotope record (Chap. 2).

Given the limited availability of atmospheric oxygen, deepwater anoxia may have persisted well into the Proterozoic in the presence of a growing sulphate reservoir,

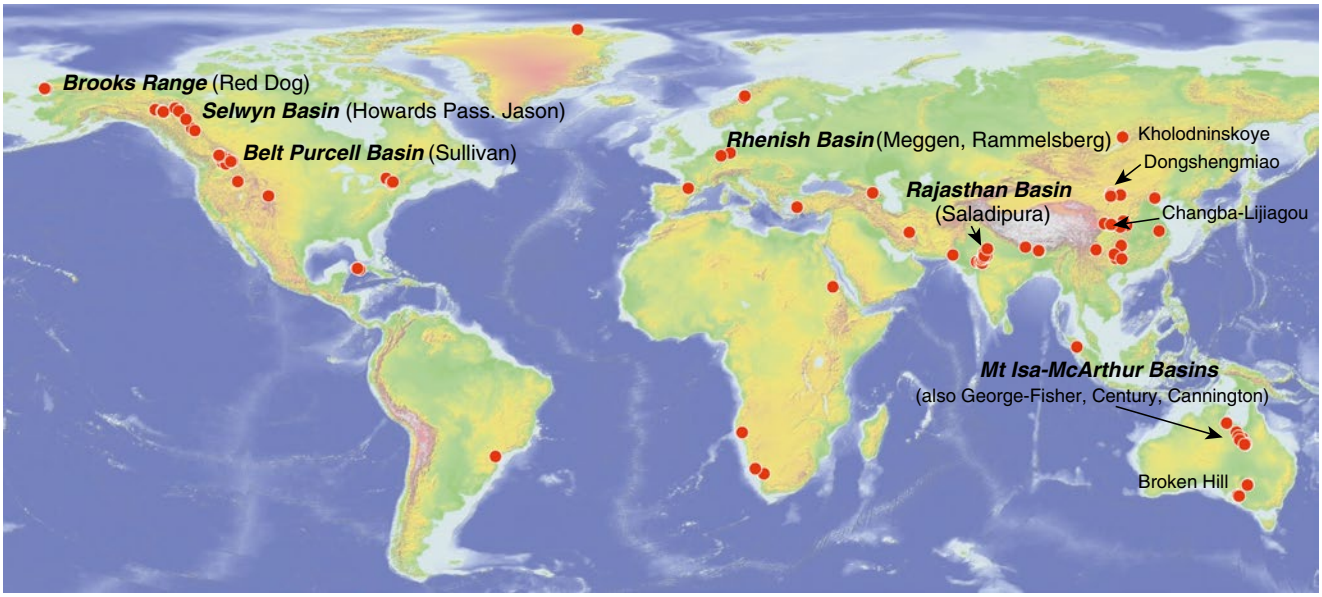

Fig. 15.76 Location of the world's larger SedEx deposits and the sedimentary basins in which they occur (Replotted from Pb-Zn module in SaltWork database, version 1.6)

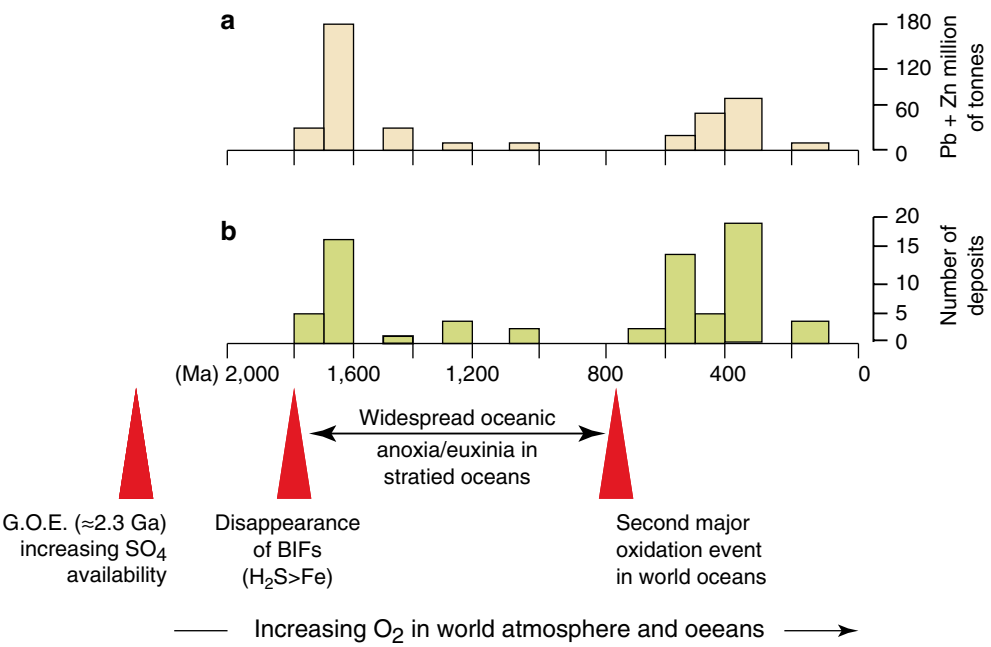

Fig. 15.77 Age distribution of SedEx mineralization as (**a**) tons of Zn and Pb per 100 m.y. interval and, (**b**) number of deposits per 100 m.y. interval (After Lyons et al. 2006)

which promoted prevalent euxinia. Collectively, these observations suggest that the mid-Proterozoic maximum in SedEx mineralization and the absence of Archaean deposits indicate a critical threshold in the accumulation of oceanic sulphate and thus sulphide within anoxic bottom waters and pore fluids—conditions that favoured both the production and preservation of sulphide mineralization at or just below the seafloor. Consistent with these evolving global conditions, the appearance of voluminous SedEx mineralization around 1,800 Ma coincides generally with the disappearance of banded iron formations—marking the transition from an early iron-dominated ocean to one more strongly influenced by sulphide availability. By contrast, the generally more oxygenated Phanerozoic ocean may have only locally and intermittently favoured the formation and preservation of exhalative mineralization in brine-floored sumps, and most Phanerozoic deposits formed from reduced fluids that carried some sulphide to the site of ore precipitation.

Within this worldscale breakdown it is also worthwhile noting the number of large SedEx deposits in the Proterozoic

and Phanerozoic that are located above, or lateral to, a present or former halite mass in the same sedimentary basin (indicated by E in Fig. 15.75). In my mind this regional association with a thick dissolving salt bed in the basin stratigraphy is more than fortuitous and once again illustrates the principle that evaporites do not form sulphide accumulations. Rather, ongoing salt flow and dissolution tends to stabilise the metal precipitation interface in a particular position in earthspace, so sediment-hosted deposits associated with disappearing evaporites tend to be larger and richer.

To illustrate the significance of this evaporite association I will focus on Proterozoic examples in Australia that I have worked during consultancy projects over the past 30 years. These and all the other examples I will discuss in this section are SedEx deposits tied to present or former dissolving halokinetic salt masses. They are chosen to illustrate how salt dissolution, and associated brine flow, can aid in the formation of sulphide precipitates in seafloor brine lakes (Fig. 15.74c). Broader SedEx compilations are published in excellent papers by Leach et al. (2010), Goodfellow and Lydon (2007) and Lyons et al. (2006).

We have already looked at the best documented active SedEx brine system in a metalliferous halokinetic association, namely the modern Atlantis II Deep. There metal sulphides are accumulating in a deep seafloor saline brine lake, mostly sourced from an adjacent basalt-volcaniclastic aquifer, with outflow focused about the thinned and faulted edges of a thick halokinetic salt mass. In the remainder of this chapter, we shall look at some older examples of a similar set of salt-dissolution brine focusing processes, but where the dissolution brines are partially suprasalt and have passed along leaky fault conduits through a substantial thickness of passive margin sediments. Unlike the Atlantis II deep, they do no sit atop or adjacent to seafloor basalts. Differences in source-feeder mineralogies explain why the Atlantis II Deep is a Cu-Pb association (leaching Cu from the subsalt basalt-redbed understory), while most SedEx deposit are Pb-Zn, largely leaching their metals from the suprasalt sediment pile (Sverjensky 1989).

To understand how the system operates we will also need to look through a veil of textural confusion in the economic geology community, especially what constitutes a replaced or altered evaporite association in Precambrian successions where the evaporites are typically long gone or represented by recrystallised anhydrites. There is also a widespread problem where some Proterozoic carbonate successions dominated by early marine cementstone textures on the floor of a CO_2 -saturated shallow ocean floor have been misinterpreted as evaporitic. I will do this in detail for the McArthur Basin where I have some experience of the geology, both in the field as well as in core study. A study of the literature base in other SedEx basins makes it clear that similar analysis and refinement of possible evaporite indicators is needed in many Precambrian basins worldwide.

McArthur River Basin and the HYC Deposit, Northern Territory

The McArthur River (aka HYC) zinc-lead deposit is one of the largest in the world and is one of a number of Proterozoic Pb-Zn deposits in northeastern Australia, south of the Gulf of Carpentaria (Figs. 15.78 and 15.79). Current mineral resources at the HYC McArthur River deposit are estimated at 157 Mt @ 11.3 % Zn, 4.9 % Pb and 49 g/t Ag. The ore is made up of laminites dominated by fine-grained galena and sphalerite, with pyrite and pyrrhotite. There is either a iron-manganese or a silicate alteration halo to the ore zones, which show combinations of synsedimentary and replacement ore textures. The McArthur River (HYC) deposit comprises 50 % of the world's current zinc and lead reserves and some 20–25 % of world zinc and lead production. The HYC ("Here's Your Chance") deposit occurs at or near the base of the HYC Pyritic Shale Member and the deposits proximity to feeder faults (e.g. Western and Emu faults) is regarded as being an important factor in understanding the genesis of HYC and nearby Ridge Cooley deposits (Fig. 15.80; Ireland et al. 2004; Large et al. 2005).

Current consensus is that the HYC deposit is a SedEx deposit, which accumulated in an anoxic seafloor brine basin, adjacent to a set of feeder faults that supplied brine and metals to the deep seafloor sump. Likely formative mechanisms are detailed in an excellent paper by Large et al. (2005) and associated papers by Davidson (1999), Bull (1998), Walker et al. (1977a, b). I will not repeat the details here other than to note the proximity of the deposit to the Western Fault, its alteration halo and the association of the Cooley Dolomite breccia unit to the deposit and the overlying HYC Pyritic Shale (Fig. 15.80a). The Western Fault and the adjacent Emu Fault acted as a source of the debris and hydrothermal fluids, as noted by Ireland et al. 2004 (Figs. 15.79 and 15.80b, c). The source of hypersaline fluids seeping into the basin sump appears to change from a more northerly source during the deposition of ore lenses 1–4, to a more easterly source for the upper ore lenses 5–8 (Fig. 15.80b). Throughout the time metalliferous laminites accumulated in the lower part of the HYC pyritic shale, the depositional setting was a deep seafloor sump where noncarbonate laminites accumulated, surrounded by shoal-water carbonate platform sediments and separated across a deep-basin bounding fault (Fig. 15.80c).

Beyond this consensus, which is also consistent with the brine pool model of Goodfellow and Lydon (Fig. 15.74c), there is the question of the deposit's regional significance with respect to future exploration and exploitation for similar SedEx laminites, both within the basin and elsewhere. That is, what drove and maintained the intraplatform sumps or lows where the metalliferous sediments accumulated? At the broad scale, the deposit sits in an intracontinental sag known as the Batten Fault zone (Fig. 15.78). But, more locally, what

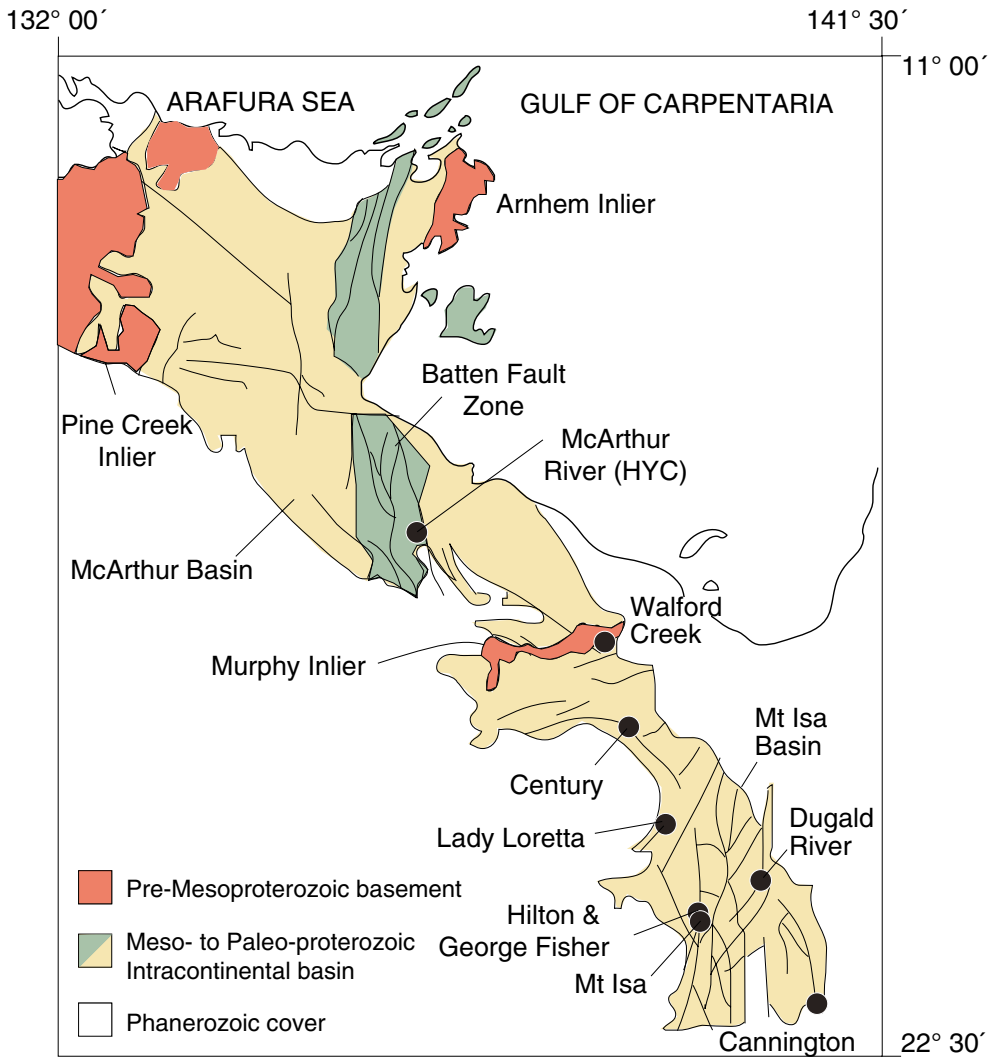

Fig. 15.78 Proterozoic Pb-Zn SedEx deposits in northeastern Australia

drove and maintained the anoxic brine ponds where the metalliferous sediment has accumulated? The lack of a pervasive metamorphic overprint makes the McArthur Basin a suitable place to study mineralising characteristics in syndepositional and early burial settings. These determinations can then be used to better understand other similar but more heavily metamorphosed SedEx successions, such as the Mt Isa, Dugald River, Hilton and Century deposits.

With this question of regional controls to mineralisation in mind, what I want to explore is the broader depositional association of the McArthur River (HYC) deposit, with ties to possible salt flow, withdrawal and related diagenesis, in a framework of evaporite indicator distribution in the basin stratigraphy. This has not been done before in the public realm, and to do so in a reliable way requires a relook at the nature and distribution of evaporites and their indicators in the McArthur Basin sediments. Table 15.13 and Fig. 15.81 list the distribution of evaporite indicators in the basin stratigraphy in the units that overlie and underlie the McArthur River (HYC) Zn-Pb deposit, which is hosted in the Barney Creek Formation. Table 15.14 lists the characteristics of evaporite occurrence in some other major "SedEx" deposits hosted in the Proterozoic sediments of northeastern Australia.

In studies conducted in the McArthur Basin across the 1960s through the 1980s, evaporites were interpreted as occurring throughout much of the Proterozoic stratigraphy in the McArthur Basin (see Walker et al. 1977a, b); Wells 1980 and Jackson et al. 1987b for a good summaries of this literature). The ubiquitous and pervasive nature of inferred evaporite indicators across large portions of the stratigraphic column, immediately arouses suspicions as to its validity. In all basins with significant evaporites, thick sequences of evaporite salts, especially halite, are typically confined to particular tectonically-controlled positions in the stratigraphy (see Chap. 5 and Warren 2010).

My field work, as part of a number of consultancy contracts, including walking out and mapping of contacts of key units in the McArthur Basin, shows that the "siderite marbles" of Jackson et al. (1987), one of the most ubiquitous indicators of former evaporites across the stratigraphy, were

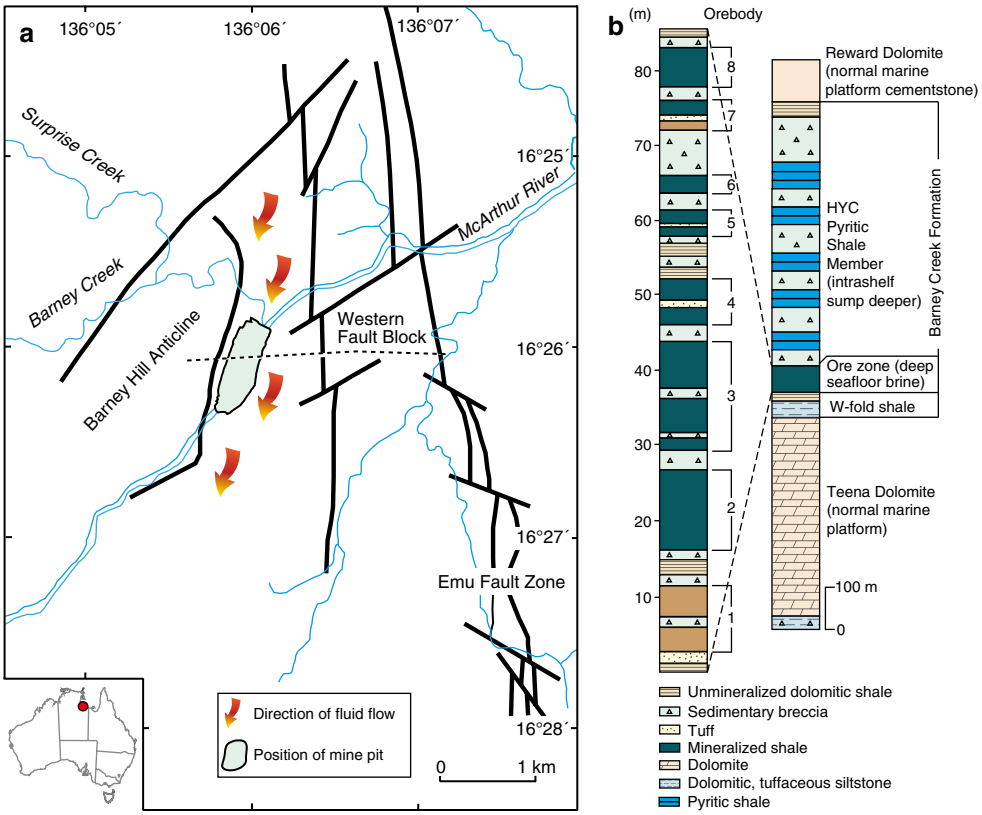

Fig. 15.79 McArthur River Mine (HYC Pb-Zn-Ag deposit), Northern Territory, Australia. (**a**) Deposit location within the Barney Creek graben and the position of metalliferous fluid flow in the graben. Dashed line indicates approximate position of schematic section in Fig. 15.80a. (**b**) McArthur Basin stratigraphy in the ore interval with an expanded view of the HYC deposit showing the eight ore bodies (Based on Williford et al. 2011). *Dashed line* indicates approximate position of schematic section in Fig. 15.80a

incorrectly interpreted as gypsum pseudomorphs (Fig. 15.82). Rather, "siderite marbles" are fault-controlled diagenetic brine haloes made up of sparry hydrothermal ferroan replacements in marine platform sediments (Warren 1999). "Siderite marbles" occur along and adjacent to faults, fractures, salt welds and joints that were fed by subsurface $FeCl_2$-rich basinal brines. Away from their transtratal feeder faults, the "siderite marbles" show a tendency to become bedding parallel and then pass laterally into non-replaced sediments. This reflects preferential fluid entry along beds that were more permeable at the time the Fe-Cl rich basinal brines were ascending the feeder faults. Thus, at the time of fluid crossflow, such coarser grained beds (grainstones and floatstones), along with joint planes, show a propensity to be replaced first and most effectively by ferroan carbonate. Less permeable micritic intervals tend not to be fully replaced and so retain less pervasive overprints of ferroan carbonate precipitates, such as cm-sized isolated lozenges of ferroan carbonate with pinolitic[2] textures (Fig. 15.82).

These sparry lozenge-shaped crystals originally formed as diagenetic replacements in dolomitic, open marine, intraclastic and peloidal wackestones, grainstones and rudstones. They do not, as reported in earlier work, define former beds composed of lenticular gypsum. A nonstratiform facies expression of the "siderite marbles" can be clearly seen when the edges, and not the permeability-parallel tops, of these stratiform ferroan bodies are walked out and mapped. The margins of the replaced regions are typically pinolitic and facies transgressive. The edges of a "sideritic marble" unit do not parallel bedding but, at the broad scale, follow faults or pass laterally into unaltered carbonate. These textures clearly do not indicate a replaced $CaSO_4$ bed.

At the mesoscale, replaced ferroan intervals can sometimes be seen to nucleate off joint planes (e.g. Figs. 74, 75 in Jackson et al. 1987 and Plate 1 in Pietsch et al. 1991). Similarly, bedding planes and chert nodule horizons in adjacent unaltered carbonates can be traced into the sparry ferroan carbonate replacement zones without any loss in vertical spacing of the bedding indicators. This clearly shows that the sparry replacement did not form as a replacement of a bedded evaporite unit, nor of its solution breccia. Likewise, the chert nodules that are encased in the "siderite marble" zones are smooth-walled nodules with normal marine affinities. There are no knobbly-surfaced cauliflower cherts after anhydrite, gypsum or trona in any of the "siderite marble" units in the McArthur Basin. Historically some these smooth-walled cherts, which internally retain uncompacted marine peloids and no evaporite pseudomorphs, have

[2]Pinolitic describes crystal splay textures made up of elongate lenticular crystals of ferroan to magnesian carbonate (siderite, ankerite, brunnerite, magnesite) with outlines in two dimensions that resemble the patterning along the outside of a closed or partially closed pine-cone (*Pinus pinea*).

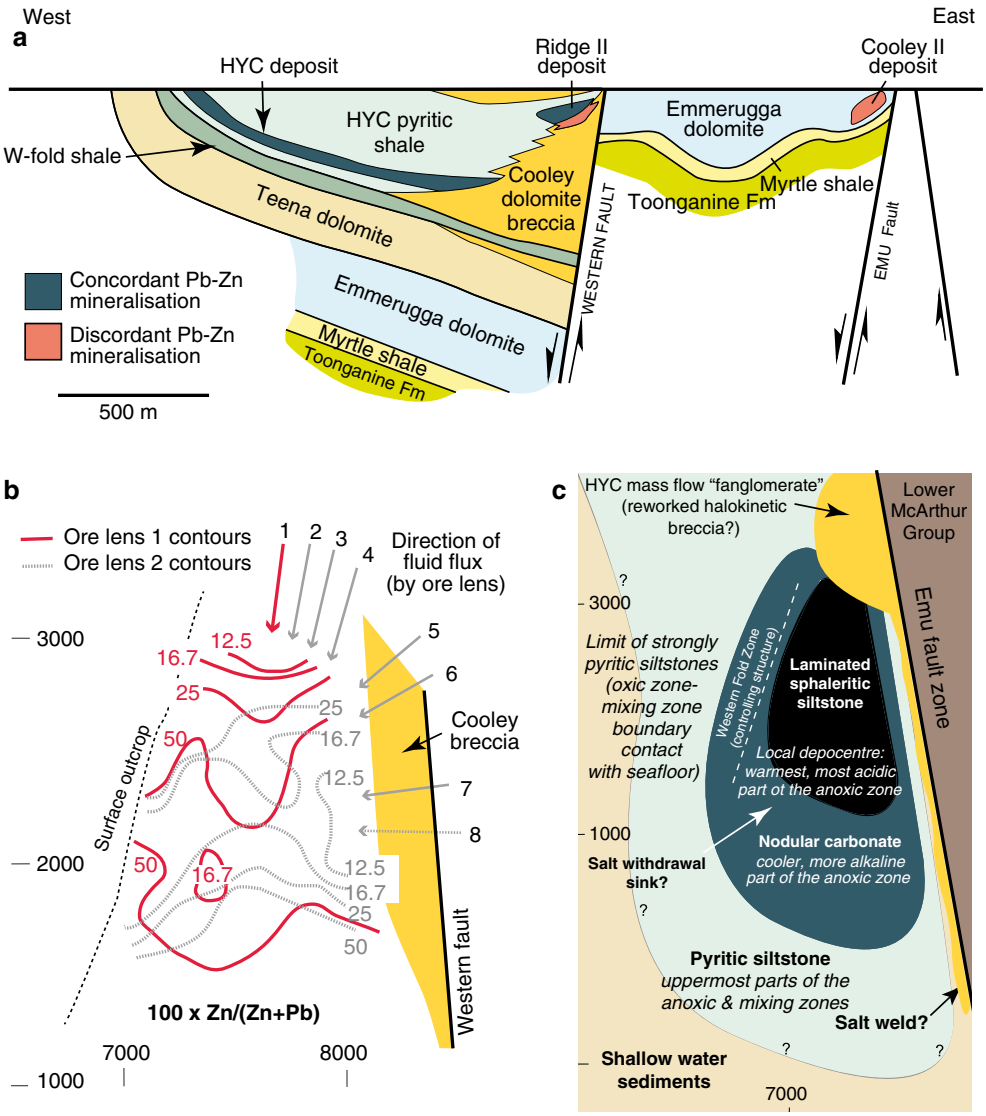

Fig. 15.80 HYC Geology. (**a**) Schematic E-W cross section see Fig. 15.79a for approximate position. (**b**) Combined plot showing up-section change in the orientation of metal zonation within the deposit, and the contours of the ratio 100×Zn/(Zn+Pb) for the lowermost and uppermost ore lenses. *Arrows* depict the interpreted direction of fluid flux through the mineralising system during formation of each ore lens (**c**) Schematic plan view showing likely synsedimentary spatial relationship between pyritic siltstones, nodular carbonates, and base metal-mineralized siltstones in the HYC subbasin. Fault control of the eastern basin margin and impingement of a fanglomerate wedge in the north (Adapted from Walker et al. 1977b; Ireland et al. 2004)

been misinterpreted as replacements of anhydrite nodules in gypsum beds.

XRD analysis shows "siderite marbles" of the McArthur Basin are not composed solely of siderite but of a range of ferroan carbonates dominated by sparry ferroan magnesites. In many sampled outcrops siderite was not present in the coarse spar facies. The mineralogy of the replacing sparry carbonates is in large part dependent on what lithology was replaced. Ferroan magnesites tend to dominate where platform dolomite was replaced. Siderite tends to occur where a calcitic precursor mineralogy dominated, or in more localised limestone regions that were flushed by large volumes of bathyphreatic $FeCl_2$ brine. In outcrop, ferroan carbonate phases ultimately weather to fine powdery to massive goethite/hematite, and so reliable analysis of the ferroan carbonate parent is best conducted on samples from core or in mine workings.

Thin sections of the "siderite marbles" retain poikilotopically enclosed ghost textures of peloidal carbonate grain fabrics, which were the dominant textures in the precursor open-marine platform carbonates and are not evaporite indicators. Likewise, the lenticular outlines of individual ferroan crystals (e.g. Fig. 74 in Jackson et al. 1987) do not mimic lenticular bird-beak gypsum or axe-head anhydrite (Chap. 1). Rather, the crystals show the characteristic blunt-ended or stubby lozenge-shaped outlines of pinolitic ferroan carbonates (especially, sparry ferroan magnesite and siderite; Fig. 15.82).

The notion of a "sideritic marble" being a replacement of a syndepositional gypsum mush bed, means the presence of siderite lozenges were used incorrectly by some authors to assign and evaporite depositional setting to outcrops of a number of formations in the McArthur Group cross cut by feeder faults, such as the Amelia Dolomite, Reward Dolomite, Teena Dolomite, Emmerugga Dolomite that were actually normal-salinity epeiric marine carbonates (Table 15.13). Elsewhere, in other Proterozoic basins of the Northern

Table 15.13 Re-interpreted evaporite occurrence chart in the McArthur Basin stratigraphy, emphasising the overinterpretation of evaporites in the stratigraphy by some earlier studies (e.g., Jackson et al. 1987 and references therein)

Formation	Member	Dominant lithologies	Thickness (m)	Evaporite indicators	Significance
Looking Glass Formation (Amos Fm)		Chert; chert breccia; minor dolomite	25–230	None noted	Coarse dolospar in the Caranbirini Member is a possible late stage dolomitisation overprint
Stretton Sandstone		Flaggy quartz sandstone	30–245	None noted	
Yalco Formation		Chert; chert breccia; minor dolomite	130	C, LD, DBH	Non-evaporitic shallow carbonate platform
Lynott Formation	Donnegan Member Hot Spring Member Caranbirini Member	Dolomitic siltstone; chert; chert breccia; minor dolomite	50–300	N, Co, DBH?	Non-evaporitic shallow carbonate platform
Reward Dolomite		Dolomite with chert pellets; minor dolomite	210–760	LD, C, DBH?	Non-evaporitic shallow carbonate platform
Barney Creek Formation	HYC Pyritic Shale Mbr (basinal) W-fold Shale Mbr. (basinal) Cooley Dolostone member (platform).	Pyritic carbonaceous dolomitic shale; dolomite, dolomitic breccia; HYC deposit	0–490	Non-noted; breccias are commonplace; possible DBH	Infill of deeper intraplatform depressions on a shallow carbonate platform. Tectonism possibly associated with halokinesis.
Teena Dolomite	Coxco Dolomite Member	Massive and laminated stromatolitic dolomite	57	H, N, Co, DBH, SM	Non-evaporitic shallow carbonate platform
Emmerugga Dolomite Massive and laminated	Mitchell Yard Dolomite Mara Dolomite Member	Massive and laminated stromatolitic dolomite	500	H, LD, N, Co, DBH, SM	Non-evaporitic shallow carbonate platform
Significant interstratal and transtratal evaporite dissolution breccia layer mostly at or near Mara/Myrtle contact; likely indicative of former allochthonolayer.					
Myrtle Shale		Thin evaporitic red bed unit	30–100	H, DBH	Transitional restricted terrigenous evaporitic platform (?lacustrine in part)
Leilia Sandstone		Coarse-grained and crossbedded dolomitic sandstone	20–30	None noted	
Tooganinie Formation		Stromatolitic dolomite; dolomitic shale; quartzarenite; dolomitic siltstone	800	H, LD, SM	Non-evaporitic marine dolomites and cherts overprinted by coarsely crystalline diagenetic magnesite (not primary evaporite).
Tatoola Sandstone		Quartz arenite; dolomitic siltstone	140	LD	
Amelia Dolomite		Laminated and stromatolitic dolomite, (passive gypsum pseudomorphs in beds)	90–240	H, LD, C, DBH, false SM	Ferro-magnesite haloes near fault zones that were incorrectly interpreted using SM. These are fault -fed diagenetic ferroan carbonate haloes that crosscut primary bed contacts

(continued)

Table 15.13 (continued)

Formation	Member	Dominant lithologies	Thickness (m)	Evaporite indicators	Significance
Mallapunyah Formation		Purple dolomitic siltstone; minor dolomite; quartz arenite	30–750	H, LD, C, DBH, SM	Diagenetic anhydrite nodules perhaps formed by post-depositional brine reflux (evaporites are possibly arid lacustrine, but not sabkha)
Masterson Sandstone		Coarse braided sandstone, ferruginous and siliceous cement sandstone	30–350	H, LD, in uppermost beds	Post-depositional halite growth in an alluvial fan/fluvial uppermost beds. Indicates reflux rather than evaporitic at deposition

KEY *H* Halite casts, *LD* Euhedral and discoidal gypsum and/or anhydrite pseudomorphs, not all are syndepositional, *N* Acicular gypsum pseudomorphs, *C* Cauliflower chert nodules, *SM* Sideritic "marble" (incorrectly interpreted as after bedded gypsum?), *DBH* Dissolution breccia horizon "Coxco" (cock's-comb) structures incorrectly interpreted as gypsum pseudomorphs, actually marine aragonite cement splays in cementstone units SM is not siderite but ferro-magnesite under XRD (brunnerite) and is a diagenetic hydrothermal precipitate. It is not a replacement of a primary gypsum bed (incorrect earlier interpretation). LD is mostly displacive and replacive late stage ferroan carbonate associated with "SM" haloes. N is a Proterozoic seafloor carbonate cement, no association with a gypsum precursor. Some DBH units are halokinetic residue layers

Territory, the same lenticular texture in sparry ferroan carbonates was applied inappropriately as an indicator of evaporite pseudomorphs. For example. Muir (1987) makes an early diagenetic lenticular gypsum interpretation of what are hydrothermal pinolitic structures in fault-fed metasomatic magnesites in the Pine Creek Inlier. Work by Bone (1983), and later by Aharon (1988), on the same Pine Creek magnesites correctly interprets them as indicators of epigenetic replacement of a dolomite precursor by throughflushing of hot basinal brines. Interestingly, Muir (p.8 *opp. cit.*) quotes the misinterpreted "sideritic marbles" of the Amelia Dolomite in the McArthur Basin as her main argument that the Pine Creek magnesites are low temperature replacements of an earlier evaporite bed and so erroneously concludes the marbles cannot be hydrothermal replacements.

Sideritic marbles in the McArthur Basin, and other similar fabrics worldwide, are not formation or precursor specific but process specific; they indicate diagenetic replacement of platform carbonates by ferruginous chloride-rich basinal waters, supplied via hydrothermal feeder zones, located near active faults or salt welds. The ultimate source of these chloride-rich waters was from convecting basinal brines, with their high levels of chloride supplied by thick dissolving halite units buried deeper in the basin. The dissolving and flowing salt mass focused leaching of iron as the brines circulated through subsalt sediments during passage to the salt edge and/or the basin margin.

The other major misinterpretation of an evaporite indicator, leading to inappropriate evaporite distribution maps in the McArthur Basin stratigraphy, was that of dolomite-replaced splays of aragonite cement as being indicators for replaced gypsum (Table 15.13). Terminations of many of the crystal outlines suggest the precursor was dominated by grasslike cementstone layers and botryoids of aragonite or Mg-calcite, which were subsequently dolomitised. The crystal splays, locally know as Coxcos[3], because of their resemblance in two-dimensions to a "cock's-comb," were used, like occurrences of siderite marbles, in studies in the 1960s through 90s, to indicate former evaporites. A predominance of replaced splays in one particular unit gave that formation its name, the Coxco Dolomite. But as with siderite marbles, "Coxcos" are a process indicator and so are not formation specific. Rather they indicate the predominance of aragonite cements in the carbonate-saturated tropical normal-marine seaways of the Proterozoic when CO_2 levels in the atmosphere and oceans was much higher than today (Grotzinger 1995). They define widespread cementstone layers and typify shallow marine hardgrounds in a number of formations in the basin, and are found numerous cores from wells in the basin, including the shoal water platforms that surround and underlie the mineralised zones of the Barney Creek formation (Table 15.13)

When occurrences of "siderite marbles" are plotted in the McArthur Group stratigraphy, the "siderite marbles" are not found deeper in the stratigraphy than the Wollogorang Formation, implying the ultimate source of the ascending chloride-rich brines was at this level in the stratigraphy. In the McArthur Basin the primary salt weld was probably at the level of the Wollogorang Formation (Fig. 15.81).

Multiple layers of evaporite dissolution breccias, as in the well DD91RC18 (Fig. 15.83), indicate the former presence of a number of thick intervals of now dissolved bedded halite within the Mesoproterozoic Wollogorang Formation. This

[3]The coxco features were correctly interpreted as marine aragonite splay pseudomorphs Brown et al. (1978), then misidentified as pseudomorphs after radiating gypsum splay in subsequent studies; e.g. Walker et al. 1977; Jackson et al. 1987)

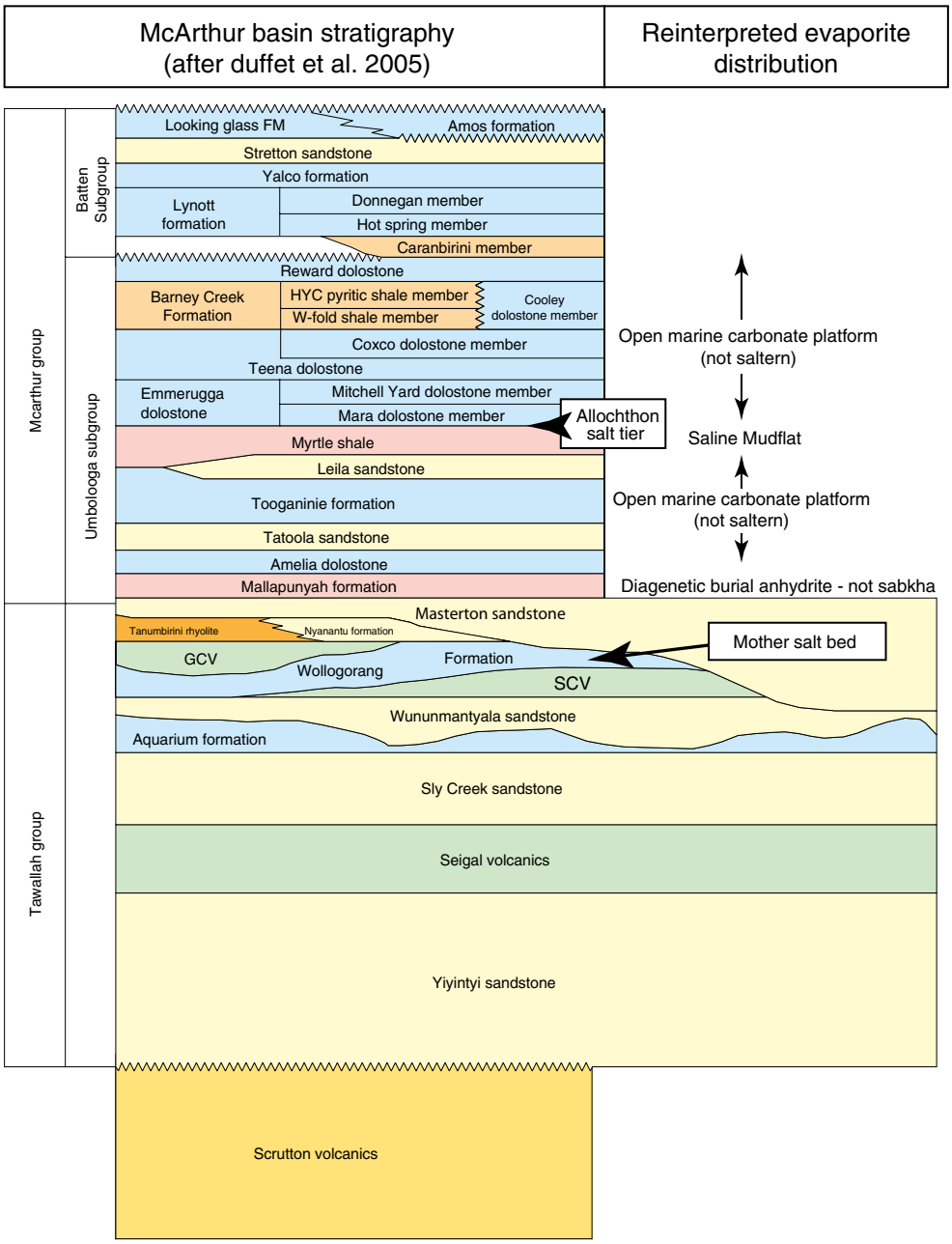

Fig. 15.81 Stratigraphy of the McArthur Basin in the vicinity of the McArthur (HYC) mine, Batten Trough, Northern Territory, Australia (After Duffett et al. 2005) and the interpreted evaporite distribution, based on discussion in this chapter

core, and many Wollogorang breccia outcrops, show characteristic salt dissolution features, such as smooth breccia bases that are overlain by thin beds of insoluble residues, along with commonplace radial quartz micronodules and length-slow quartz euhedra preserved within the breccia matrix. The breccia beds at each former halite level pass up through rubble breccia into mosaic to crackle-brecciated bed tops (see Chap. 4).

When public-domain base-metal data are replotted against same scale sedimentological log, the utility of an applied sedimentological approach in the economic geology of the region is obvious (Fig. 15.83). The plot clearly shows that the Pb and Zn anomalies are suprasalt and centred on dark organic-rich laminites (locally known as the "ovoid beds"), while the Cu peaks occur mostly in dissolution-effected breccia intervals. Cu migration through this sequence is clearly later diagenetic and postdates salt solution. In contrast, the Zn and Pb anomalies show an early diagenetic (possibly syngenetic) control.

Work by Williford et al. (2011) on organic signatures in extractable hydrocarbons from the mineralized shales of the HYC deposit further reinforces the importance of the evaporitic brines sourced at the Wollogorang level in the stratigraphy. δD of n-alkanes, branched alkanes and bulk aromatic fractions were measured, and $\delta^{13}C$ of n-alkanes, polynuclear aromatic hydrocarbons (PAHs) and bulk kerogen were measured to

Table 15.14 Characteristics of relatively low temperature (subgreenschist to greenschist grade) Proterozoic SedEx deposits, Australia

Deposit	Age (Ma)	Characteristics	Host, its age and depositional setting	Tonnes (Mt)	Grade	Ore	Metamorphic grade	Model	References
Mount Isa	1,653	30 stacked lenses, most of which occur in the upper 650 m of the Urquhart Shale; deposit is located to the east of the Mount Isa fault zone and in the hanging wall of the syn-extensional Paroo fault; intense overprinting during the Isan orogeny	Urquhart Shale (1,652 Ma): carbonaceous, pyritic, and dolomitic siltstones; tuffaceous horizons. Neudert and Russell (1981) and Neudert (1986) favour deposition in a sabhka setting, whereas Domagala et al. (2000) interpret the Urquhart Shale to be turbidite and/or tempestite sediments related to a submarine fan. A halokinetic association favors a deepwater interpretation.	150	7 %Zn 6 %Pb 150 g/t Ag (248Mt @ 3.3 % Cu)	Bedding-parallel bands of galena and sphalerite; fine grained pyrite, pyrrhotite, and minor chalcopyrite, arsenopyrite, and marcasite. At Mt Isa the orebodies are on one limb of a plunging anticline and are extensively faulted. Also in the Mt Isa mine is a Cu ore zone, hosted in the epigenetic silica-dolomite halokinetic unit (preserves a massive anhydrite unit)	Greenschist	Both sedimentary exhalative and diagenetic models; overprint during the Isan orogeny has resulted in remobilization of the Pb-Zn mineralization; remobilized ore has been used to argue for synorogenic epigenetic mineralization (Perkins and Bell 1998). Sulphur isotopes indicate sulphur source was local sulphate evaporites, pseudomorphs of which are present throughout the Urquhart Shale (i.e., gypsum, anhydrite, and baryte). Deep-burial diagenetic replacement of these evaporites resulted in sulphate-bearing basin waters which migrated parallel to bedding. Were the sulphates primary, or halokinetic dissolution residue layers sourced above or below the mineralisation level?	Neudert and Russell et al. (1981), McGoldrick and Keays (1990), Forrestal (1990), Painter et al. (1999), Wilde (2011)
Hilton	1,653	7 stacked ore lenses in the upper Urquhart Shale, complicated by intense shortening associated with the Isan orogeny		120	10.2 % Zn 5.5 % Zn 100 g/t Ag		Greenschist		Forrestal (1990), Valenta (1994)
George Fisher	1,653	11 stacked ore lenses in the upper Urquhart Shale		108	11.1 % Zn 5.4 % Pb 93 g/tAg		Sub- to lower greenschist		Chapman (2004)
Lady Loretta	1,650	Approximately 50-m-thick single ore horizon; the ore horizon is preserved within a regional syncline and is bounded to the north and west by inverted extensional faults	Lady Loretta Formation (1,647+ 4 Ma): carbonaceous pyritic, dolomitic, and sideritic, siltstone and shale. Deep water laminite	8.3	18.4 % Zn 8.5 % Pb 125 g/t Ag	Sphalerite, galena, and pyrite, baryte-chert-sulphide, minor chalcopyrite, quartz, siderite, tetrahedrite, and freibergite	Sub-greenschist	Interpreted as a combination of sedimentary exhalative and diagenetic processes in which hydrothermal brines were transported along extensional faults during the deposition of the Lady Loretta Formation	Hancock and Purvis (1990), McGoldrick et al. (1996), Domagala et al. (2000)

Century	1,575	Mineralized 40-m interval with 2 ore horizons; preserved in an open fault-bounded syncline; stylolitic layering in ore succession focused mineralization, mineralization transgresses bedding at deposit scale; deposit is proximal to intersection of the Termite Range fault and a buried normal fault. Mineralisation ≈ 1,558 ± 4 Ma	Lawn Hill Formation (1,595 + 6 Ma): siliciclastic, carbonaceous (TOC 1–5 %), sideritic, shale and siltstone, with tuffaceous horizons. Deposited in a deep water laminate setting (sea-bottom brine lake).	118	10.2 % Zn 1.5 % Pb 36 g/t Ag	Sphalerite dominated; bedding-parallel, finegrained sphalerite, galena, and pyrite; siderite is the main Fe gangue phase and is developed in siderite siltstone and siderite carbonaceous mudstone layers that separate the mineralized horizons	Sub-greenschist	Epigenetic mineralization in which hot basinal brines (120–180 °C) caused maturation of organic material (pyrobitumen) leading to sulphate reduction and base metal precipitation; deposit is interpreted to have formed at a depth between 800 and 3,000 m; fluid flow is interpreted to have been tectonically driven, occurring during basin inversion, and it has been compared with Mississippi Valley-type ore-forming environments	Broadbent et al. (1998), Large et al. (2005), Polito et al. (2006), Kawasaki et al. (2010)
HYC	1,640	8 ore lenses in 70-m interval; deposit located in unmetamorphosed successions and preserved in the hanging wall of inverted (strikeslip?) Emu fault near its intersection with a normal fault	Barney Creek Formation (1,640 + 3 Ma): dolomitic siltstone, coarse sedimentary breccias, tuffaceous horizons, pyritic shale; pyritic shale is organic rich (7 % TOC). Deposited in a deep water laminate setting (sea-bottom brine lake).	240	9.2 % Zn 4.1 % Pb ~41 g/tAg	Pyrite, galena, and sphalerite, finely disseminated throughout the siltstone interlayered with poorly mineralized siltstone, fine sandstone, breccia, and mudstone horizons	Sub-greenschist	Sedimentary exhalative (e.g., Large et al. 1998) vs. early diagenetic (e.g., Rye and Williams 1981; Eldridge et al. 1993; Hinman 1995; Logan et al. 2001) models proposed; in synsedimentary exhalative model the formation of numerous ore lenses when metalliferous brines were exhaled during several pulses of mineralization, related to episodic fault movements; in diagenetic model fewer pulses of mineralization are envisaged, with epigenetic mineralization occurring through lateral flow of metalliferous fluids via the Emu fault zone	Williams (1978), Eldridge et al. (1991, 1993), Hinman (1995, 1997), Bull (1998), Large et al. (1998, 2000), Logan et al. (2001)

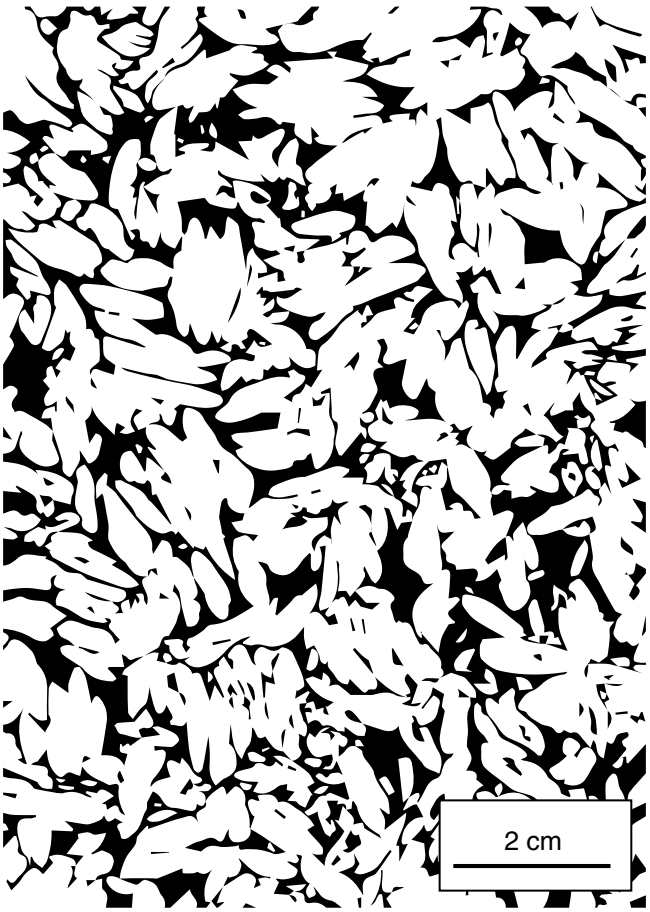

Fig. 15.82 Pinolitic texture from a scanned black and white field photograph of a siderite marble (brunnerite) halo. This texture was incorrectly interpreted in the 1960s and 70s as replaced gypsum beds, as were some baryte rosettes. A few hours of walking out contacts of this diagenetic units clearly shows that although it is locally stratiform, on the broader scale it is mostly transtratal and ties back to feeder-fault haloes

assess the isotopic effects of a varying degree of hydrothermal alteration on different components of HYC organic matter (Fig. 15.84a–c respectively). Relative to n-alkanes in Barney Creek Formation sediments that did not undergo mineralization, HYC n-alkanes are enriched in deuterium (D) by 50–60 ‰. This is likely to be a result of equilibrium hydrogen exchange during ore genesis with a highly D-enriched fluid that originated in an underlying evaporitic unit.

Trends with distance along the sample transect are ambiguous, but from the northernmost to southernmost point, n-alkanes are less D-enriched, and PAHs are less abundant and less ^{13}C-enriched (Fig. 15.84). This could be due to decreasing hydrothermal alteration effects, decreasing delivery of highly altered OM by the mineralizing fluid, or both, hence the fluid flow path illustrated in Fig. 15.79. The carbon isotopic composition of HYC PAHs is inconsistent with a Barney Creek Fm source, but consistent with an origin in the underlying Wollogorang Formation. PAHs are ^{13}C-depleted relative to n-alkanes, reflecting a kerogen source that was ^{13}C depleted compared to n-alkanes, typical for Precambrian sediments (Fig. 15.84b, c). PAHs are more ^{13}C-depleted with increasing molecular weight and aromaticity, strengthening the case for a negative isotopic effect associated with aromatization in ancient sediments. According to Williford et al. (2011) these data are consistent with an ore deposition model in which fluids originated in an evaporitic deposit lower in the basin and interacted with metals and organic matter in the Tawallah Group at temperatures above 250 °C and a depth of ~ 6 km, before ascending conduits associated with the Emu Fault and cooling to 200 ± 20 °C before reaching Barney Creek sediments.

In summary, if ancient fine-grained or sparry ferroan replacements in sedimentary hosts in the McArthur Basin are interpreted as possible palaeoplumbing indicators, rather than as ubiquitous pseudomorphed primary evaporite beds, they become useful indicators of fluid conduits, which typically can be traced back to extensional feeder faults. This reinterpretation of evaporite textures defines an evolving diagenetic hydrology where metalliferous $FeCl_2$ -rich basinal brines have ascended from depth. The lowest occurrence of the "siderite marbles" in the stratigraphy, at the Wollogorang Fm. level, likely defines the level of the former thick mother salt bed that, as it flowed and dissolved, supplied the high chloride content and metal carrying capacity to the basinal brine. Before the mother salt level and its allochthon tiers were halokinetically breached and evolved into welds, it also acted as an overpressured seal, facilitating hydrothermal convection and metal enrichment in density-fed brines flushing the underlying marine shales. The flow and breaching of the same mother salt also facilitated the formation of various structures that acted as conduits for the escape of the Fe-rich basinal brine. During their subsequent ascent along focused conduits (faults, fractures, joints and salt welds), the brines leaked into adjacent permeable sediments to form characteristic pinolitic and massive ferroan replacement fabrics.

When evaporite textures are correctly interpreted, then a depositional model for the McArthur River (HYC) deposit HYC becomes a fault-bound hydrographically closed intrashelf anoxic deep atop salt withdrawal seafloor sumps within a typical Proterozoic normal marine platform carbonate succession. Relogging of a number of relevant cores and mapping of the stratigraphy below the Pb-Zn laminites of the HYC mine region, from an evaporite-aware perspective, shows that feeder faults intersect underlying breccias that entrain indicators of former evaporite beds and allochthons. These feeder faults have hydrothermal haloes of diagenetic ferroan carbonate cements that replace adjacent platform carbonate.

The stratigraphy of most wells in the McArthur Basin that pass through the equivalents of the Barney Creek Formation, host to HYC deposit, clearly show a deepening (gradational) profile upward from the platform cementstones of the Teena and Coxco dolomites, and equivalents, into the deepened waters of the Barney Creek mass flows and laminites

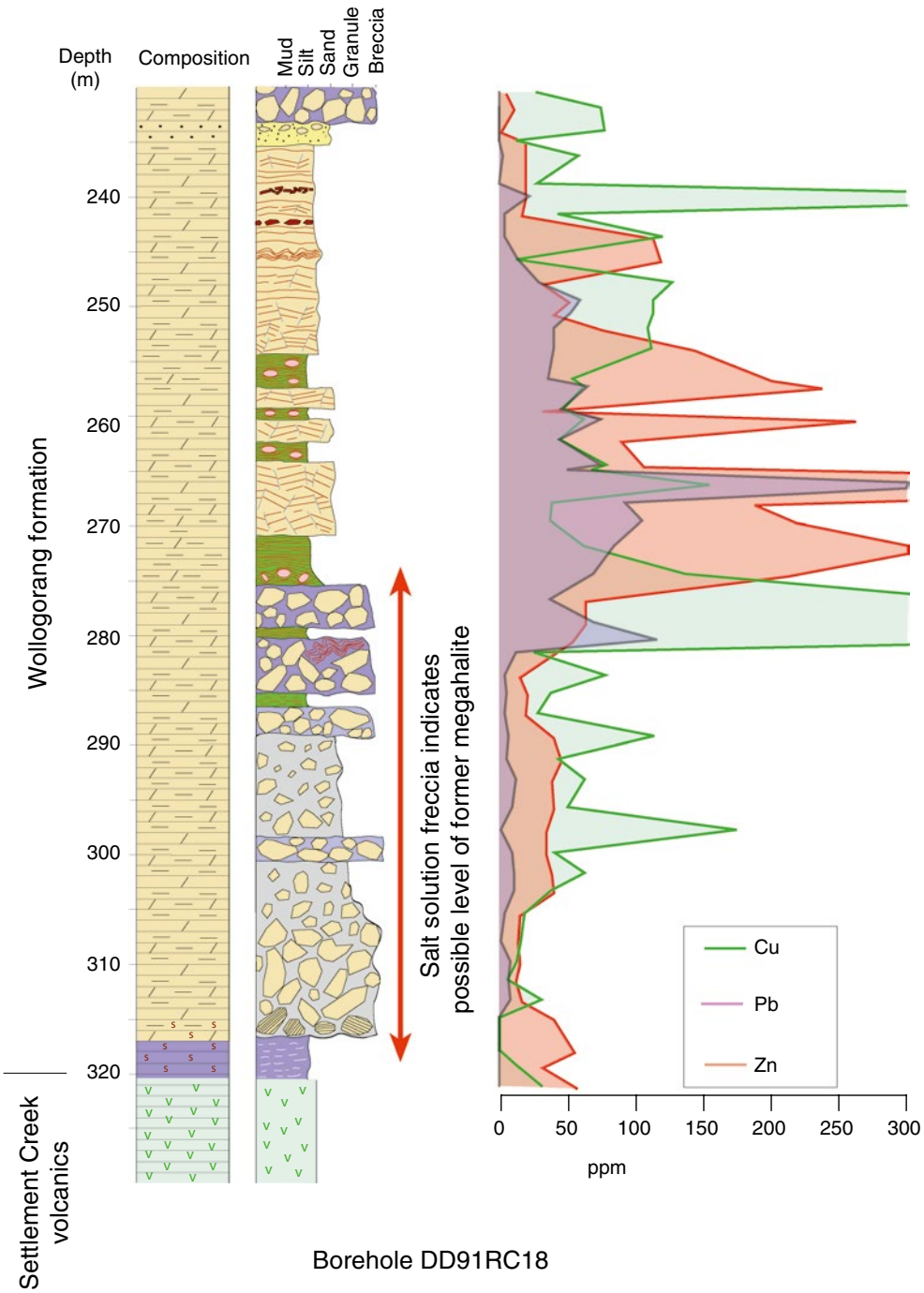

Fig. 15.83 Log of the mother salt level in the Wollogorang Formation in the DD91RC 18 borehole in the McArthur Basin. See text for detail

(Fig. 15.85). Units in almost all wells through the Barney Creek Formation and its equivalents can be broken down into three facies belts (A, B, C; Figs. 15.85 and 15.86).

Facies A is now dolomitised; it was originally deposited on the floor of a shallow normal-marine tropical ocean as cementstones interlayered with micritic intraclast packstones and rudstones. Terminations of many of the crystal outlines suggest it was dominated by grasslike cement layers and botryoids of aragonite and perhaps Mg-calcite that were subsequently dolomitised. This facies, with its abundant normal marine cements, is identical to other tropical carbonate platform sediments of the same age and is indicative of a CO_2-enriched Proterozoic atmosphere (e.g. Grotzinger 1995; Grotzinger and Knoll 1995).

Facies B is a layered to laminated dolomitised siltstone with interbedded packstones. It is usually slumped or cross-laminated and was deposited as some form of intrabasin slope deposit. Its lack of cementstone layers implies it was deposited in deeper, but still oxygenated, shelf waters. It too is now extensively dolomitised, although the occasional siliceous interval is still cemented by calcite not dolomite. The dolomitising mechanism for the region was relatively

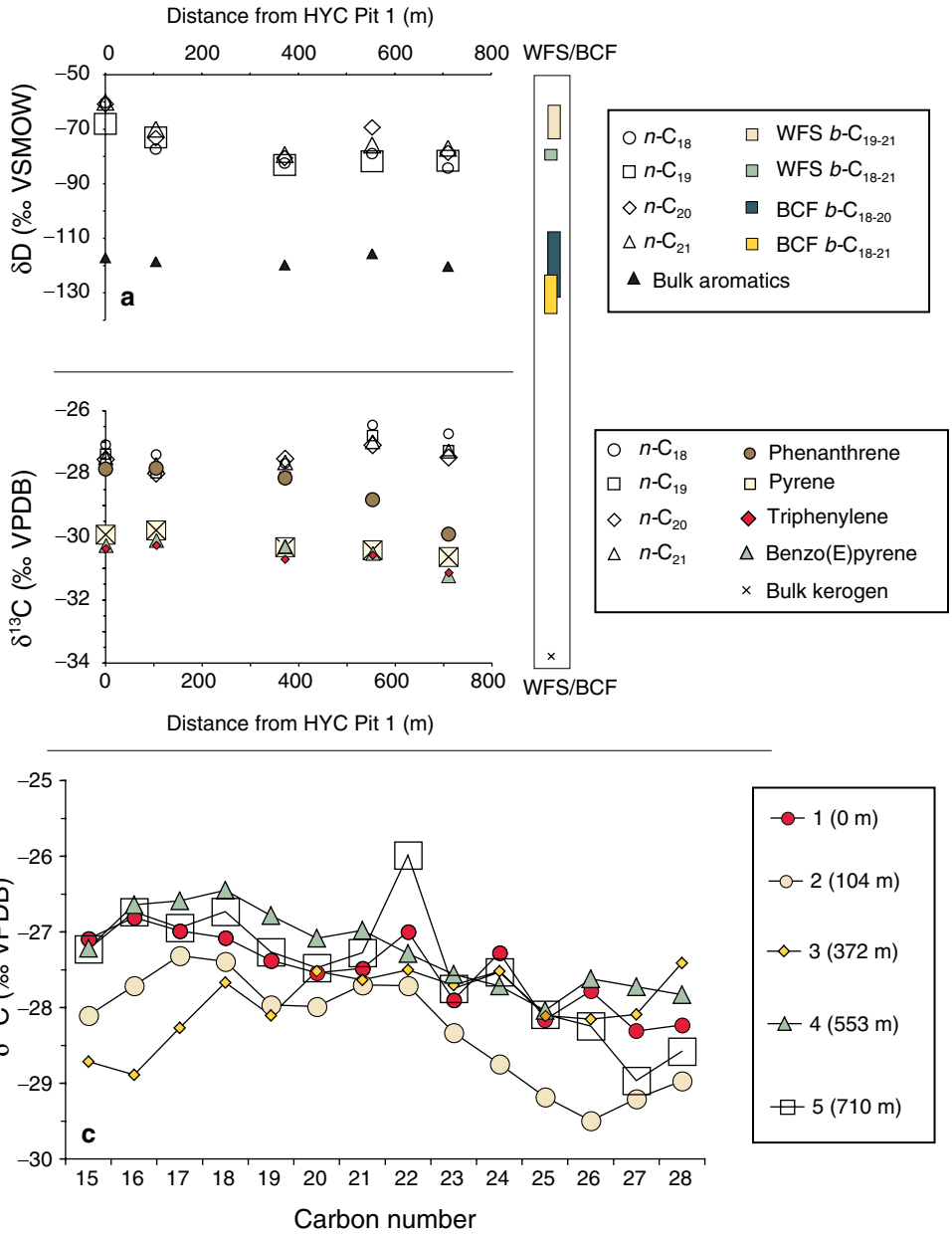

Fig. 15.84 Organic characteristics in the HYC deposit (After Williford et al. 2011). (**a**) δD of four n-alkanes and bulk aromatic fractions with distance from Pit 1 (S 16° 25′ 53.3742″ E 136° 6′ 1.0368″) along a northeast–southwest transect in the HYC deposit. Also plotted are n-alkane and branched (b-) alkane values for the W-Fold Shale (WFS) below the HYC deposit and previously reported n-alkane values for bitumen recovered from the Barney Creek Formation (BCF) (Sessions et al. 2004). (**b**) $\delta^{13}C_{PDB}$ for four n-alkanes and four PAHs with distance south from Pit 1. (**c**) $\delta^{13}C_{PDB}$ of n-alkanes recovered from five samples in the HYC deposit. Note; Size of data points in (**a**) and (**b**) and (**c**) indicates analytical uncertainty (±1σ) for replicate measurements of indicated compounds averaged across all samples

early and driven by hydrological processes that were most active in platform sediments (e. g. epeiric brine reflux).

Facies C is a finely laminated organic-rich siltstone. Its inherently higher levels of organics and framboidal pyrite imply it accumulated under anoxic bottom conditions. Of the three platform facies it was deposited in the deepest waters in intrashelf basins that were too anoxic and acidic on the bottom to accumulate significant carbonate, even hemipelagic carbonate mud did not survive on this H_2S-enriched deeper seafloor. This is the facies style that hosts the HYC ore.

The presence of an evaporite solution breccia (possible former allochthon tier) at the Myrtle-Mara contact immediately below the level of the Barney Creek Formation (Table 15.13), and evidence of a major thick regional mother salt bed at the level of the Wollogorang Formation (Fig. 15.81), suggests an alternative salt-floored halokinetic model of formation for SedEx deposits in the McArthur Basin and other SedEx entraining basins in Northern Australia. This model can only be applied to sedimentary basins with evidence of former thick salt units below the ore level, located regionally in an extensional passive margin tectonic setting at the time of mineralisation.

Analysis of underlying evaporite solution breccias and vertical changes in sedimentation style in the vicinity of the McArthur Deposit, and its equivalents in other nearby sediment thicks such as the Glyde sub-basin, suggests the various intraplatform deepwater pyritic thicks in the Barney Creek Formation where metalliferous basinal brines seeped

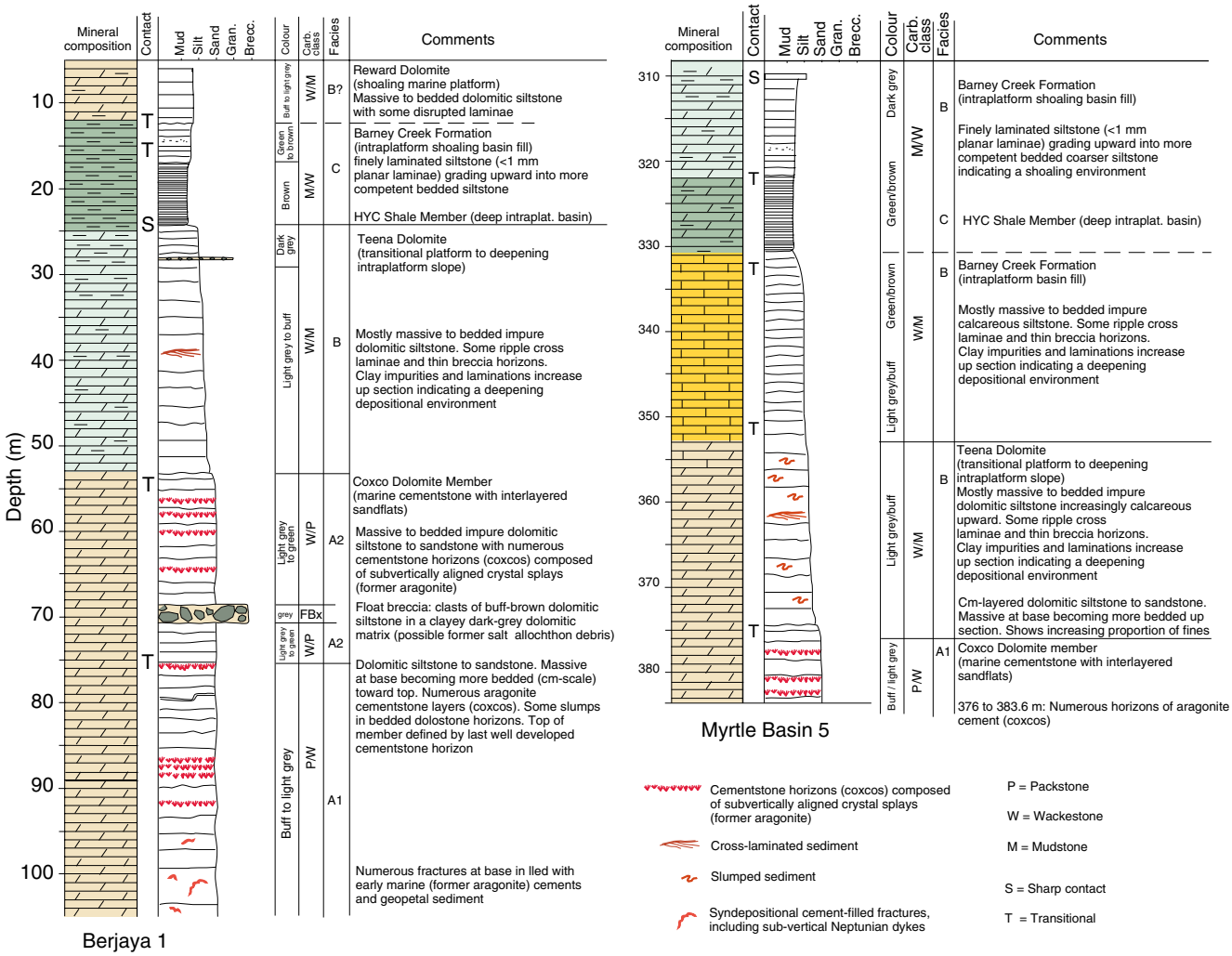

Fig. 15.85 Facies and depositional setting in the Berjaya 1 and Myrtle Basin 5 wells, McArthur Basin, Northern Territory, Australia. Facies belts are illustrated in Fig. 15.86

into local brine-filled anoxic deeps. The subsurface passage of the halite-dissolution-derived Fe-chloride rich brines that fed these pools is indicated by Fecarbonate haloes along faults and glide shears, such as portions of the Emu fault zone in the vicinity of the HYC deposit.

However, as in the peridiapiric North African deposits discussed earlier (Fig. 15.42), these ferroan carbonate haloes are not deposit or formation specific, and can be found over much wider areas than the immediate region of metalliferous laminites of the McArthur deposit. The accumulation of substantial sulphides, especially pyrite framboids formed in the early stages of sulphide accumulation, requires the presence of stable anoxic bottom brines in the deeper portions (brine sumps) of isolated depressions on the shelf floor.

Sedimentological analysis of public domain cores and well exposed outcrops in the vicinity of the HYC deposit suggests allochthonous salt sheets, such as those that define the Myrtle Mara contact (disconformity), played a role in controlling seafloor positions of ore-hosting pyritic shales. The halokinetic scenario outlined in Fig. 15.87 is one possible halokinetic scenario that can explain the regional setting of the HYC deposit. It uses a five stage model of a deforming salt allochthon in a salt entraining basin that is undergoing extensional deformation and is based upon a typical extensional margin undergoing raft tectonics (see Chaps. 6 and 9 for a full discussion of the relevant halokinetic and raft tectonics mechanisms that can form local organic-rich deeps and depopods). Salt flow settings, other than the salt-hinged platform-edge raft tectonic model given in Fig. 15.87, are also possible. Which of the various halokinetic deformation styles was the most likely requires a detailed sedimentological analysis of breccias, both beneath and within the ore deposit, to be tied to a back-stripped regional structural analysis. This requires access to proprietary company-held core and the permission to publish the results.

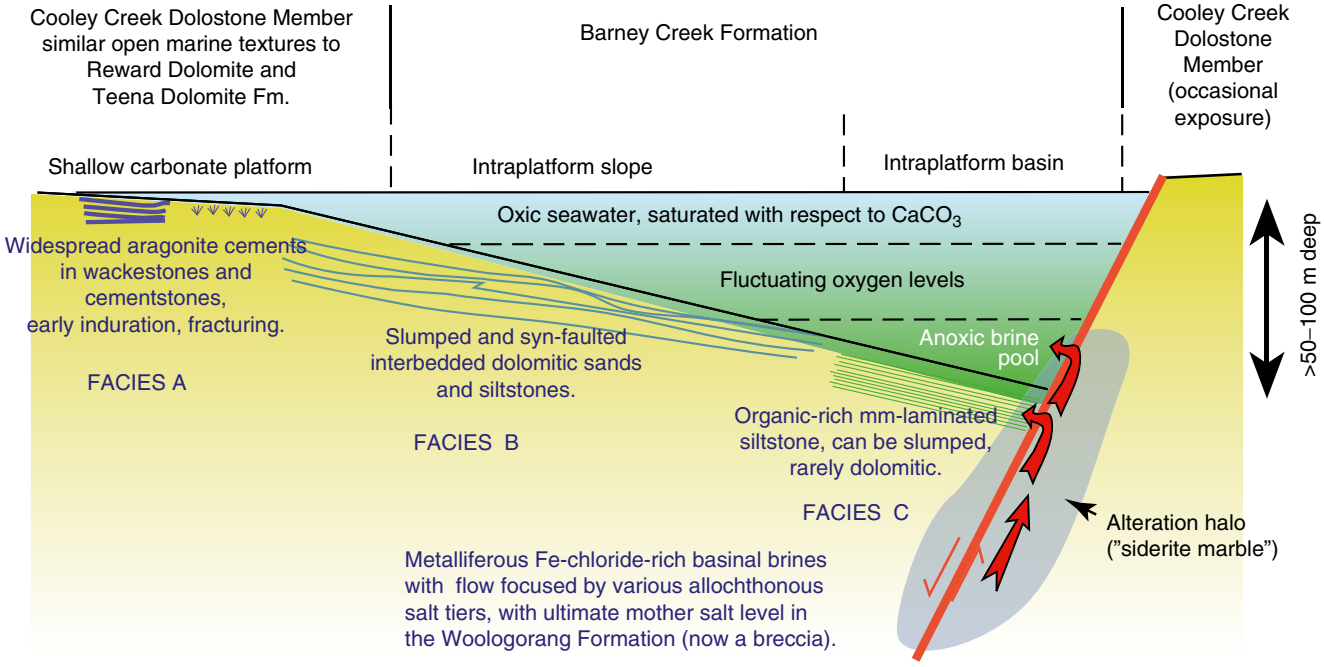

Fig. 15.86 Interpreted intra-platform deep setting for mineralised portions of the lower Barney Creek Formation. Seafloor low formed atop salt withdrawal sinks adjacent to active basin -edge fault (Based on author's work in the basin in the 1990s)

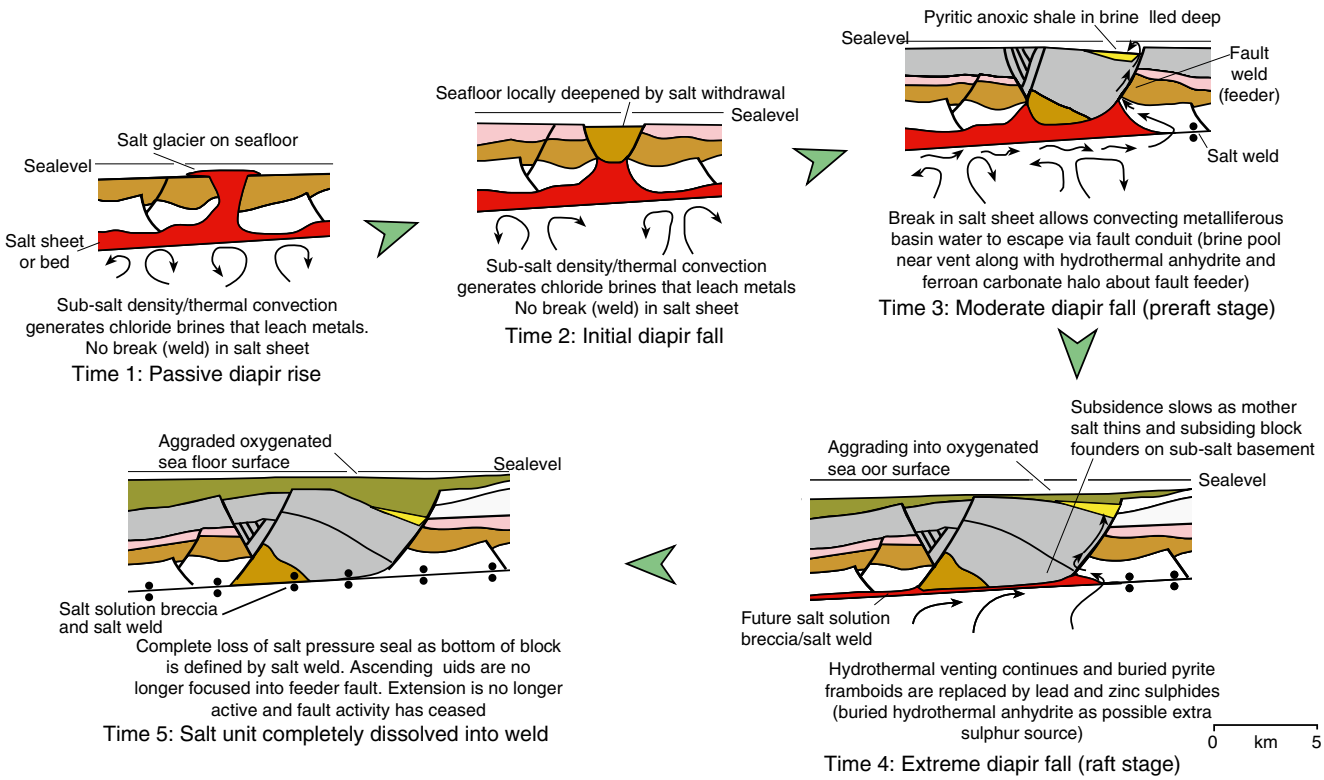

Fig. 15.87 Salt-floored extensional basin model explaining the formation of localised intraplatform brine-pool laminites in the HYC (McArthur River) deposit

For the purposes of this discussion, I will only use the salt tectonic style shown in Fig. 15.87, for the HYC deposit, it does explain:

- Underlying and syndeformational halokinetic solution breccias;
- Ongoing soft sediment extensional faulting, which breaks up the continuity of individual ore layers in the HYC deposit;
- Pyritic and organic-rich nature of the ore host;
- Localised syndepositional thickening of the Barney Creek Formation within an otherwise shallower water setting (compare Time 3 scenario with depositional setting based on sedimentological analysis shown in Fig. 15.86);
- Ferroan carbonate halo distribution about faults, especially along the intrashelf basin edge; and
- Syndepositional extensional graben structuring seen in the regional structure of HYC the deposit.

Time 1 encapsulates a typical passive diapir scenario, where the upper portion of the diapir is near, or at, the seafloor. The underlying source salt bed or allochthon is intact and acting as a pressure seal to deep basinal brines. Ongoing dissolution along its underbelly is continually supplying dense chloride-rich basinal brines into active hydrothermal convection cells. These convecting brines are leaching metals from sediments and volcanics below the salt sheet. At the surface, periodic dissolution and slumping of the allochthon carapace is creating monomict and occasional polymict sedimentary breccias atop the surrounding seafloor (facies A).

Time 2 is the falling diapir stage, where ongoing extension causes the diapir crest to fall, with the formation of a local deep atop the falling diapir crest (the bicuspidate diapir stage). The deepening of the seafloor is indicated in core by the transition from the shoal water platform carbonates of facies A to the deeper water carbonate slope deposits of facies B. Hydrothermal circulation continues unabated beneath the source salt unit (Fig. 15.86).

By time 3, ongoing basin extension has created a breach in the mother salt unit (a salt weld), which allows pressured hot Fe-rich basinal waters to escape across the weld. Their subsequent upward passage is focused into the still active zone of extension associated with the growth fault. The subsurface passage of these rising and cooling Fe-rich hydrothermal waters along the feeder fault creates replacement haloes of ferroan carbonate cement in the adjacent sediments. Cooling of these ascending waters means copper is not carried far above the level of the sealing salt bed and so does not make it to the seafloor at this early diagenetic stage of burial (see copper transport discussion in next chapter). Where these brines vent and pond as a seafloor brine pool it facilitates the formation of pyritic shales in anoxic closed deeps (facies C). The anoxic acidic bottom conditions mean that little or no carbonate matrix survives in the pelagic shale intervals.

By the end of time 3, the subsidence of the down-hinged structural block is slowing as the mother salt bed is thinning to where the bottom of the block begins to founder on the sub salt basement. Throughout time 3 and time 4, the dissolution feather-edge of the mother salt continues to focus the ascending hydrothermal brines into the main set of basin defining faults. The burial of the pyritic ore-host laminites means hotter ascending brines now have access to the pyritic laminites. The early diagenetic replacement of the pyrite and other early sulphides by coarser hotter Zn and Pb sulphides begins.

As long as the withdrawal edge of the mother salt bed continues to focus ascending hydrothermal brines, the feeder fault continues to act a focus for the ongoing subsurface influx of metalliferous basinal brine into the now shallow-buried pyritic laminites. The elevated burial temperatures associated with ongoing brine flushing facilitate the nearsurface replacement of earlier formed pyrite by Pb and Zn sulphides, driven by BSR at lower pore temperatures and TSR at higher temperatures. Any hydrothermal anhydrite initially formed near the brine vent will now redissolve and may act as an extra source of sulphur for newly forming metal sulphides. Once the mother salt mass is completely dissolved or drained from the system, then its focusing effect on fluid flow is lost and the mineralisation process becomes inactive (time 5).

At the surface, this cessation of salt-induced subsidence, or a lessening in the rate of supply of brine, means the brine pool sediment surface can now aggrade back into oxic settings (facies C to B in Figs. 15.85 and 15.86). Ultimately, pyrite accumulation on the seafloor ceases as shallower, oxygenated seafloor sediments cover pyrite-rich laminites for the last time (Time 5 in Fig. 15.87).

SedEx Deposits Within Fe-carbonate Haloes/ Hosts in the Mt Isa Inlier, Australia

In terms of zinc, lead, and silver metal endowment, the Proterozoic sedimentary basins of northern Australia, especially those in the Mt Isa Inlier, rank number one in the world (Fig. 15.75; Large et al. 2005; Murphy et al. 2011). In total the Mt. Isa-McArthur basin system hosts five supergiant, stratiform, sedimentary rock-hosted Zn-Pb-Ag deposits (McArthur River, Century, Mt. Isa, Hilton, and George Fisher) at or below greenschist grade and one supergiant strata-bound Ag-Pb-Zn deposit (Cannington) at amphibolite grade (Table 15.14). As well as some of the largest Pb–Zn stratiform deposits in the world (e.g., Mount Isa, HYC, Century), the Mount Isa Inlier hosts and also several IOCG (Iron Oxide Copper Gold) deposits (e.g., Ernest Henry, Eloise, Starra) that are discussed in the next chapter.

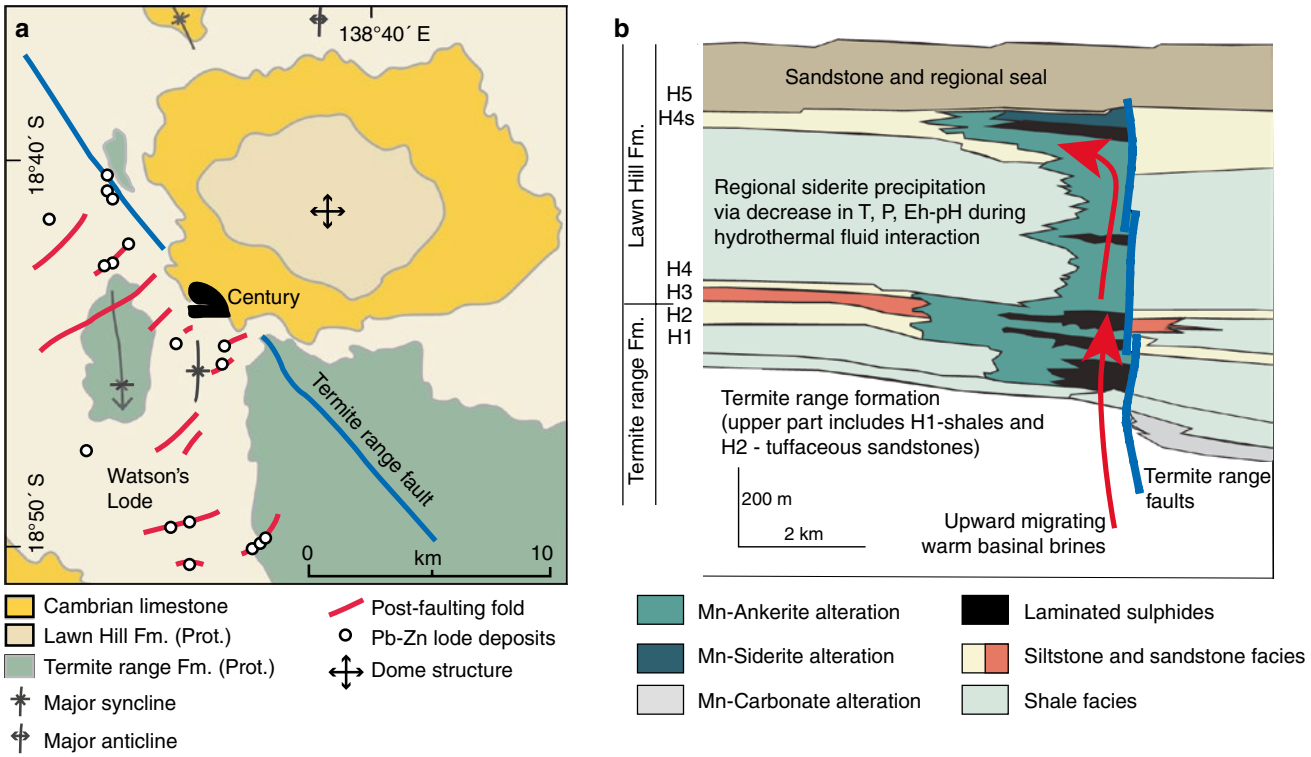

Fig. 15.88 Century deposit, Queensland. (**a**) Map view showing proximity to domal structure (interpreted as astrobleme or diapiric sag). (**b**) Model of mineralisation emphasizing fault focus to metalliferous fluid supply (After Kawasaki et al. 2010; Large et al. 2005; Pirajno 2009)

Common to almost all these economic deposits are: (1) ties to highly saline evaporitic brines, (2) the proximity of deposits and prospects to faults that were active during basin evolution (Neudert and McGeough 1996; Betts and Lister 2002) and, (3) a thick, now dissolved and altered halite unit that deformed halokinetically and gave a strong structural focus to the various mineralising events, both synsedimentary and syntectonic (see also Chap. 16 and Betts et al. 2004).

The Century deposit, Queensland, with its mineralisation hosted in deepwater sideritic siltstones, like the HYC deposit is a structurally and hydrothermally focused metal trap and like the HYC shows textures that have not been obliterated by subsequent metamorphism (Table 15.14; Waltho and Andrews 1993; Broadbent et al. 1998). It is located close to the Termite Range Fault, which was probably the major conduit for ore fluids.

Century Zn-Pb deposit is located on the west side of an interesting 20-km-diameter circular structure (Fig. 15.88a). This structure has been interpreted as a possible meteorite impact feature (Shoemaker and Shoemaker 1996; Salisbury et al. 2008) and is outlined by a brecciated Cambrian Thortonia Limestone fill. The notion of an impact crater has not been accepted by most geologists in the companies working the deposit (Salisbury et al. 2008). In my mind this circular feature, if it is an astrobleme, is unlikely to be associated with the mineralisation event as the Termite Range Fault and the mineralisation that is Century continues unabated across the edge of the circular structure. Likewise the widespread breccia textures are as easily interpreted as evaporite dissolution features as due to an astrobleme. If so, it is an indicator of the former presence of a salt-cored anticlinal dome, with the salt now dissolved. The co-occurrence of a domal feature and a fault intersection better explains the association with the mineralisation and the subsequent weathering also explains the Cambrian sag fill. Stewart (1999) discusses criteria that can be used to interpret various circular structures preserved in the rock record. A new look at how hydrothermally altered breccias formed in Century, starting with the capping breccia in the mine pit, perhaps as possible salt allochthon and rauhwacke residues, would help refine the deposit's genesis.

Century has a higher Zn:Pb ratio (6.8) than other major Australian SedEx deposits (1.2–2.9), with a geologic resource of 167.5 Mt (8.2 wt % Zn, 1.2 % Pb. and 33 g/t Ag), including a higher grade mining resource of 105 Mt (12.1 wt % Zn, 1.75 % Pb, and 46 g/t Ag; Large et al. 2005). Although the Century Deposit's hosting laminite has many depositional similarities to the synsedimentary McArthur River deposit, it's Zn-Pb mineralisation likely has a different, deeper diagenetic replacement origin, synchronous with fault-focused metalliferous fluid crossflows, perhaps driven by an episode of compression and basin inversion (Broadbent et al. 1998, 2002).

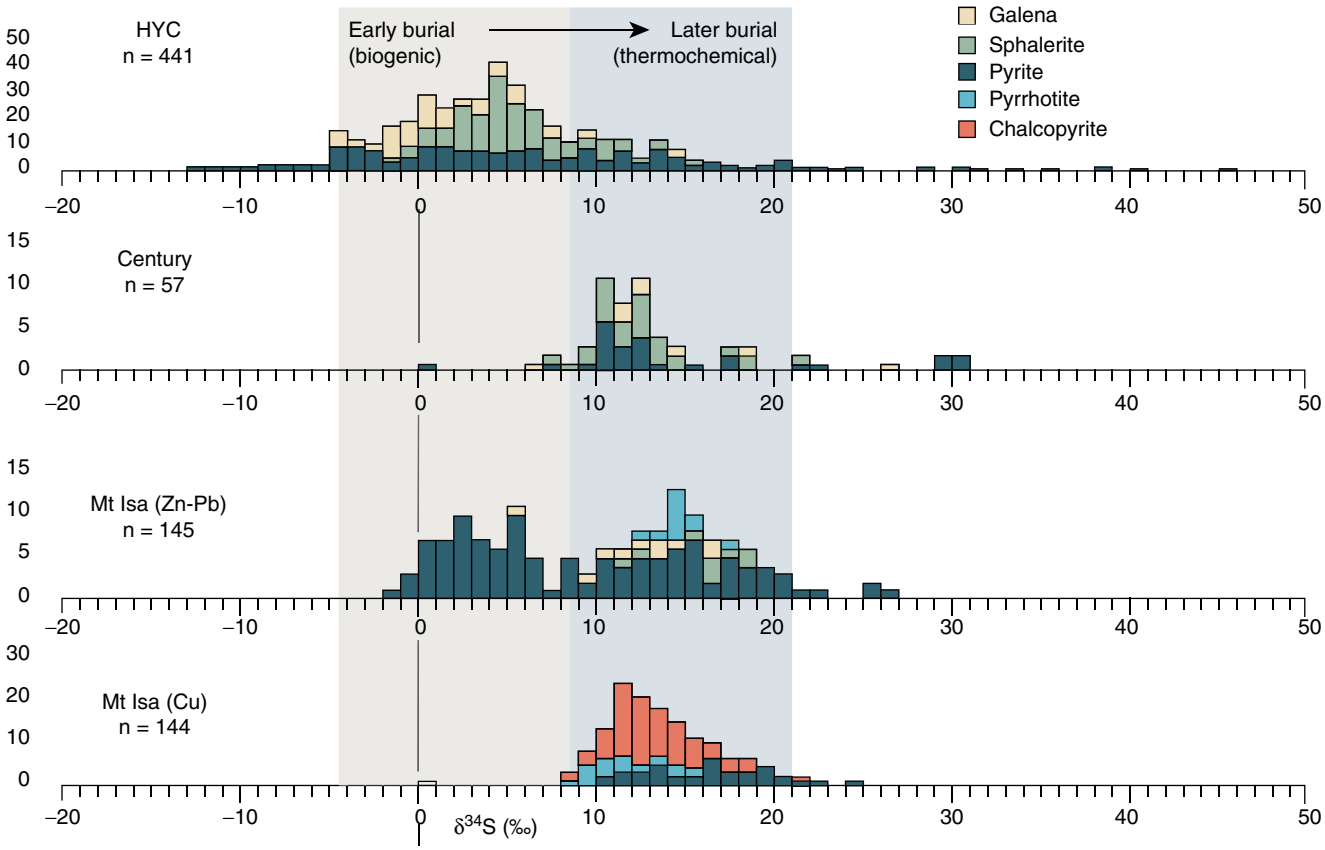

Fig. 15.89 $\delta^{34}S$ values for sulphide minerals from McArthur HYC, Century and Mount Isa Zn-Pb and Mt Isa Cu ores after Pirajno (2009) and references therein

Ore-hosting siderites were likely emplaced earlier via predominantly subsurface seepage during extension, followed by compression driven, fault-focused metalliferous basinal brine crossflows that were focused into anticline traps in their ferroan carbonate-rich deepwater sediment hosts (Fig. 15.88b; Broadbent et al. 1998; Large et al. 2005). That is, the Zn-Pb mineralisation at Century transgresses the stratigraphy, in that the higher grade zones are associated with thicker black shale host rocks (Fig. 15.88b). The deposit is spatially associated with regional-scale lode mineralisation, mainly veins and breccias within fault zones. The main ore mineral is sphalerite, of which two varieties are present: one porous and associated with abundant pyrobitumen, the other is non-porous and with a low pyrobitumen content. The intergrowth of the sphalerite with hydrocarbons, suggests that thermochemical sulphate reduction (reaction of deeper sulphate and metal-bearing fluids with liquid and gaseous hydrocarbons), took place in a burial setting and perhaps not syndepositionally (Fig. 15.88b; Pirajno 2009).

Broadbent et al. (1998) argues that the sulphate-bearing hydrothermal solutions originated from the deeper more saline parts of the basin stratigraphy and were channelled up along faults (Termite Range Fault system). The movement of fluids was driven by phases of basin inversion and regional compression. Hot fluids reacted with organic-rich sideritic shales, producing gas and liquid hydrocarbons. This led to the thermochemical reactions, which resulted in the precipitation of sulphides. Sulphur isotope systematics revealed progressively higher $\delta^{34}S$ values, from 5–10 % to 20–25 %, reflecting a closed-system hydrothermal reservoir with enrichment in heavy sulphur over the life of the mineralisation event reflecting the passage from biogenic to thermochemical sulphate reduction with increasing burial (Fig. 15.89). Illite and chlorite crystallinity variation across the Lawn Hill Platform suggest the southern part of the platform experienced higher temperatures (up to 300 °C) than similar stratigraphic horizons in the north. Much of the more intense thermal alteration is focused by fault conduits, which were active a number of times in their tectonic history (Golding et al. 2006).

There is also the obvious burial-related bimodal isotope signature of the Mt Isa Zn-Pb sulphides and the clear later burial origin of the copper sulphides there (Fig. 15.89). The sulphate bearing fluids in Century were likely derived from evaporitic rocks in the deeper parts of the basin (Broadbent et al. 1998, 2002; Pirajno 2009). What is not considered in

the existing literature in the origin of the various Proterozoic SedEx deposits of Australia is the strong likelihood of halokinetic focusing to the fluid flow from early to later burial and the importance of now dissolved salt in the extensional welds and décollements, similar to the various halokinetic examples discussed earlier in this chapter and also explains the ore distributions in SedEx deposits with host matrices now in the metamorphic realm (see Chap. 14 for a discussion of Mt Isa and the eastern foldbelt – Mary Kathleen meta-evaporite deposits).

Arid-Zone Diagenetic Uranium and Copper Associations

As well as the low temperature base metal evaporite associations that benefit from the presence of dissolving and flowing evaporites in their burial evolution there are other economic accumulations that benefit from the brine concentrating effects in near surface waters in arid evaporitic climates. They include low temperature secondary enrichment phases in uranium and porphyry copper deposits.

Duricrusts: Yilgarn Australia and Namibe, Africa

In the arid desert zone that is the northern Yilgarn of West Australia, U deposits occur in playa and paleochannel calcretes, with an intermediary third type occurring geomorphologically between the two settings, typically designated as platform or delta calcretes, often located where channel drainages enter playas (Table 15.15 and Fig. 15.90a; Noble et al. 2011). All deposits are at or near the land surface and have a similar capillary-driven genesis and ore mineralogy. They are responses to concentrative changes in shallow groundwater redox interfaces, with circulations driven by evaporation, and U-precipitates typically dominated by carnotite ($K_2(UO_2)_2(VO_4)_2 \cdot 3H_2O$). Uranium-rich secondary silica is also important locally in the mineralised zones (Fig. 15.90b). Carnotite deposits occur along the drainage systems throughout the Yilgarn region and include the world class Yeelirrie deposit (Fig. 15.91a). Other potential U-resources on the Yilgarn craton are the Lake Maitland, Centipede and Lake Way prospects (Table 15.15; Carlisle et al. 1978; Noble et al. 2011).

Uranium in the Yilgarn groundwater is sourced from granite weathering, and vanadium from greenstones and alluvial sediments (Mann and Deutscher 1978; Morgan 1993; Noble et al. 2011). Groundwater moves down gradient into the channels (Figs. 15.90 and 15.91a), where capillary evaporation occurs (both in channels and playas) and, as a result, carbonate and apatite (if PO_4 is present) precipitates. This is important for two reasons (Noble et al. 2011): (i) carbonate-rich zones will have a high-pH groundwater; and (ii) the formation of carbonate and apatite will result in the loss of P and HCO_3 from the groundwater. Both of these conditions force the reaction of the aqueous species of U, V and K and so form carnotite.

Although apatite precipitation could drive this reaction, it is a minor contributor to the carbonate formation in the Yilgarn. The role of PO_4 in the solubilisation of U is hypothesised by Noble et al. (2011) to be most important where groundwater pH is more acidic, such as the active weathering uplands (closer to the breakaway crests). Apatite precipitation is more likely near these zones and away from the carnotite mineralisation. This process will shift the pH to more alkaline and change the dominant U-bearing aqueous species from UO_2HPO_4 to $UO_2(CO_3)_2$. The arid association of the uraniferous calcretes in Australia means gypsum is often present as a gangue mineral and this can create processing problems (Pownceby and Johnson 2014). The presence of gypsum is a processing hindrance when an alkaline leach solution is used as it reacts to precipitate calcium carbonate and forms sodium sulphate in solution. A gypsum content of more than 4 % in a surficial calcrete uranium ore leads to excessive reagent consumption and sufficiently

Table 15.15 Size of major valley channel and playa calcretehosted U deposits in the Yilgarn area, including the worldclass Yeelirrie Deposit (After Noble et al. 2011). Delta deposits are transitional between channel and playa types

Deposit	Type	U_3O_8 t	Grade cutoff (ppm)	Grade U_3O_8 (ppm)
Yeelirrie	Channel	52,500	?	1,500
Lake Maitand	Playa	11,420	370	370
Lake Way	Delta	5,710	200	540
Centipede	Delta	5,355	200	550
Lake Austin	Playa	?	?	?
Lake Raeside	Playa	1,700	250	200
Lake Mason	Playa	2,700	?	350
Hillview	Channel	3,720	2,150	180
Little Well	Channel	?	?	350
Dawson Well	Channel	4,700	150	228

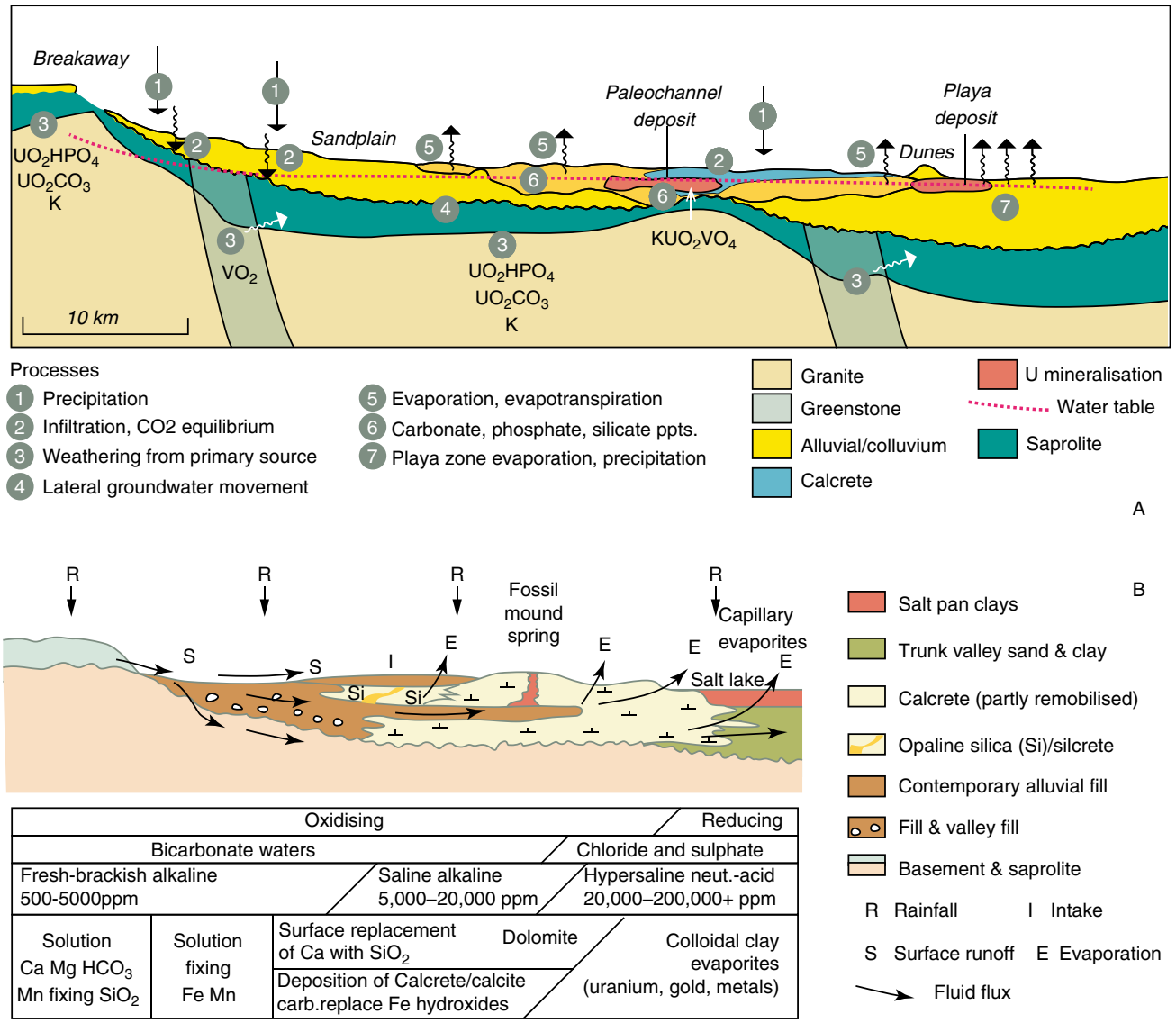

Fig. 15.90 Uraniferous calcrete. (**a**) Location and mechanisms involved in formation of channel and playa secondary U deposit formation in the northern Yilgarn Craton (Modified from Noble et al. 2011; Mann and Deutscher 1978). (**b**) General model of water–rock interaction, processes and hydrogeochemistry in regions of uraniferous calcrete (After Morgan 1993)

affects processing costs to rule out the use of relatively cheap sodium carbonate-based leach solutions.

As well as the Australian calcrete examples listed in Table 15.15, significant uraniferous calcrete accumulations have been identified at the northern margin of the Namibe Erg, south-west Africa and include Langer Heinrich, Tubas Grant, and Klein Spitkoppe (Carlisle et al. 1978). The Langer Heinrich deposit became an operational uranium mine in 2007 (Fig. 15.91b). Mineralisation at Langer Heinrich consists of sub-horizontal carnotite that has been precipitated within clastic valley-fill rock units, which vary from conglomerates through grits and sands to micaceous claystone. In a general way, ore becomes finer grained with depth and hence ore from beneath the watertable is mainly micaceous claystone (Princep and Hutson 2010). The mineralisation occurs as an undulating 1–30 m thick layer, which is shaped like a subterranean meandering river. At intervals down the valley, thick "pond-like" pods of higher-grade uranium have formed. These are generally located immediately upstream of a narrowing of the valley edges. Carnotite occurs preferentially in less cemented sections of the ore but shows no relationship to any rock type in the alluvial matrix. Nor does it occur within any of the detrital clasts, whether boulder, sand, or silt size.

The uraniferous calcrete and gypcrete-hosted deposits in Namibia differ from the Australian calcrete deposits in the following ways: (1) A likely Late Tertiary age with uplift-related erosion of the upper parts of some deposits, (2) An

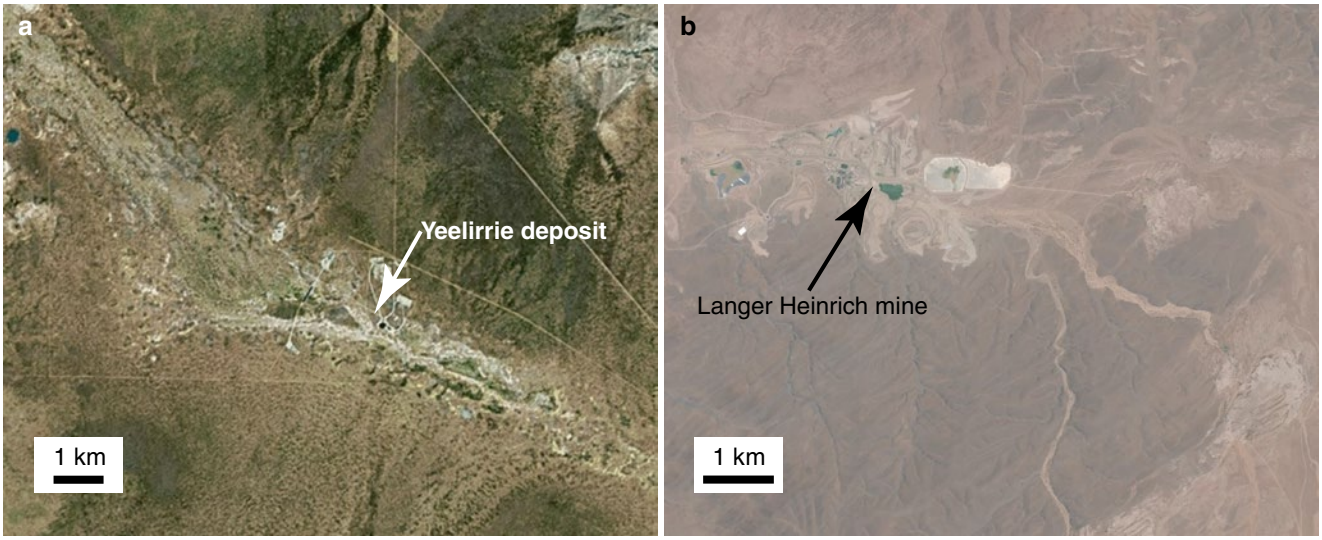

Fig. 15.91 Arid zone uraniferous calcretes. (**a**) Yeelirrie deposit, West Australia. (**b**) Langer Heinrich Mine, Namibia

abundance of coarse detrital fragments in a braidplain host, which constitute the skeletal framework of the uraniferous calcrete. Radiogenic carbonate cement typically making up around 15 % of the rock volume, (3) This carbonate cement is predominantly sparry calcite, with neither dolomite nor opaline silica as co-precipitates, (4) The presence of abundant gypsum in the upper parts of profile in occurrences within 60 km of the Atlantic and the gypsum is probably marine saltspray derived (Chap. 2), and (5) A vertical gradation upward into pedogenic sheet calcrete and gypcrete (perhaps indicative of the greater age compared to the Yilgarn deposits).

Reasons for the coarse detritus host in Namibe are: (1) the very appreciable relief between the Great Western Escarpment, with hinterland elevations in excess of 2,000 m in the Khomas Hochland, and the broad coastal platform (lowland) of the central Namib Desert and, (2) the relatively modest degree of chemical weathering in the basement compared to the deep sapropelic weathering in Australia. Namibian calcretes do not typically develop abundant dehydration or shrinkage cracks, and unlike the Australian calcrete hosts, the lack of current microporosity means they today are not as permeable aquifers, though locally there can be appreciable permeability. In several places, irregular open solution tubules and replacement bodies about the size of a finger, but sometimes much larger, have developed in the calcrete. Commonly, the tubules have a shell of impure calcite and a sandy porous filling, which, under some conditions, is richly mineralized with carnotite. Owing to the higher gradient setting of the local and regional hydrology draining toward the coast, Namibian uraniferous-calcretes do not seem to occur preferentially in playa or saline delta settings.

When comparing deposits between the two regions, the marked process similarities are obvious (Fig. 15.90). Interestingly, the Langer Heinrich mine, the richest of the various known Namib examples, is located in a definite valley constriction. First and foremost is the required combination of groundwater and aridity to drive capillary concentration of the uraniferous salts, and the co-precipitation of evaporitic capillary salts. Lateral transport of uranium in brackish to increasingly saline groundwater in the outflow sump is essential to ore deposition in both regions, as is the presence of bedrock barriers or constrictions in order to narrow the channel of subsurface flow, and act as sills. This forces the groundwater to pond and so move closer to the land surface, where it is subject to evaporation and loss of dissolved CO_2. In both regions the larger part of all valley calcretes and gypcretes are unmineralized. Ore-grade mineralization is roughly horizontal in attitude and related to capillary concentration of shallow past or present groundwater tables. Source rocks in both regions are weathered Proterozoic to Archaean migmatites, pegmatites, alaskites, and granites; many are "hot" sources, that is, they are already appreciably enriched in uranium. Lastly and most significantly, deposits in both areas could not form without evaporitic ground conditions. The uranium salts in both regions are true evaporite salts in the same way that capillary anhydrite and capillary halite are true evaporite salts.

Porphyry Copper, Supergene Enrichment and Aridity

Porphyry copper deposits are well developed in the in the Atacama Desert of northern Chile, where supergene enrichment is considered to be the principal factor in making this region the greatest producer of Cu in the world. Classic

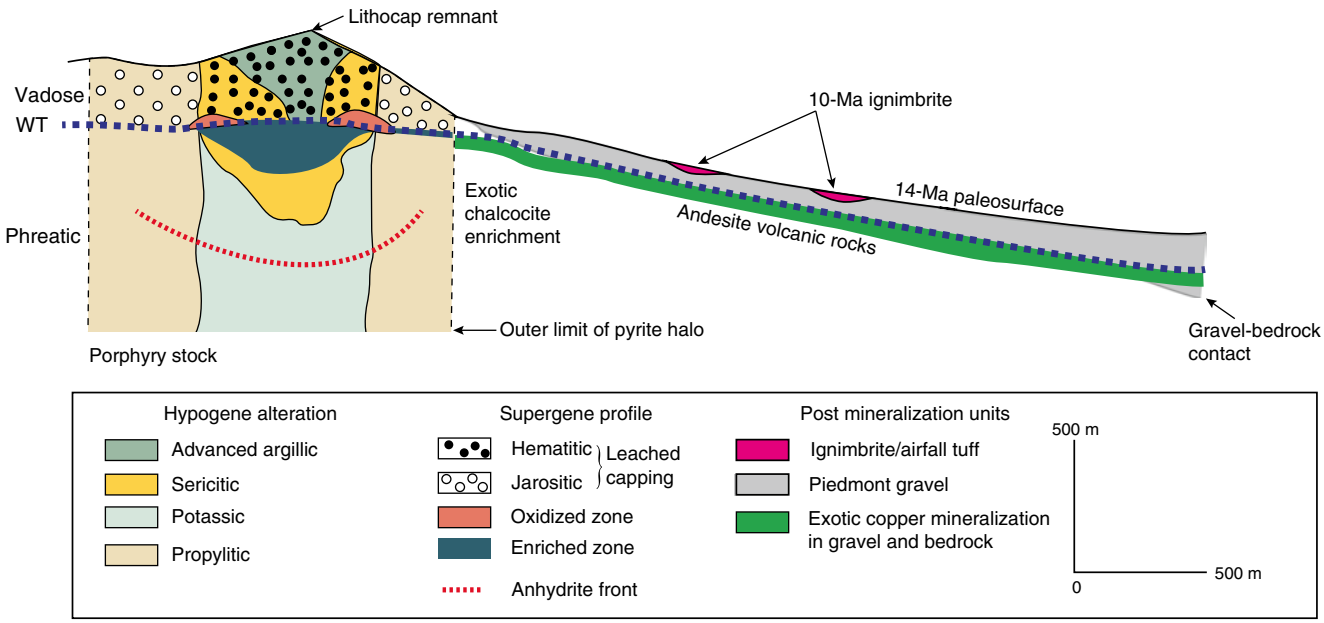

Fig. 15.92 Mature supergene profile based on porphyry copper deposits in northern Chile (After Sillitoe 2005). Position and configuration of leached capping (patterned) and the enriched sulphide ore zone (*dark green*) are controlled by relatively unreactive advanced argillic and sericitic alteration. Copper oxide ore is stabilized by higher pH fluid in outer potassic and inner propylitic alteration zones. Position and configuration of exotic chalcocite enrichment and exotic copper oxide mineralization in gravel and bedrock are controlled by the pyrite halo and paleo-watertable. Anhydrite front defines depth above which anhydrite has been leached

models argue that supergene enrichment was driven by the exposure of Cu sulphides to the effects of oxidative weathering during times of moderate precipitation (Fig. 15.92; Sillitoe 2005; Sillitoe and McKee 1996). Thus, the development of porphyry copper "giants" in the Atacama Desert is strongly coupled to climatic evolution. Isotopic dating of supergene minerals, principally alunite group minerals, has shown that supergene enrichment in the Atacama occurred over a long period from ~45 to 9–5 Ma, possibly reaching a maximum at 14–21 Ma (Reich et al. 2009).

Supergene enrichment is traditionally believed to have ceased when semi-arid conditions in the Atacama, with significant pluvial precipitation periods, changed to hyperarid. However, there is no consensus about the onset of hyperaridity, which may have commenced as early as 25 Ma and even extend back to the Triassic (Clarke 2006). If this is so, then Cu enrichment may not be driven solely by periods with relatively abundant fresh meteoric waters. There may be as aspect of Cu concentration in the Atacama that is associated with more saline groundwaters.

Recent geochemical and isotopic studies reveal that atacamite ($Cu_2Cl(OH)_3$), a major constituent of supergene Cu-oxide zones in Chilean deposits and co-associated with capillary gypsum, formed within the last few million years (Palacios et al. 2011; Reich et al. 2009). Atacamite is a product of the upward flow of saline basement waters through the pre-existing oxide zones, focused along active faults and has been preserved in the hyperarid climate prevailing since that time. If this is so then, as suggested by Clarke (2006), supergene enrichment is tied to periods of landscape uplift and dissection, not to landscape stability. Such periods of uplift in the Andes would drive a relative fall in the watertable and vadose (supergene) mineral cycling independent of the transition to hyperaridity.

It seems that in the hyperarid sediments of the Atacama desert the distribution of copper minerals is controlled by a combination of evaporatively driven "*per ascendum* and *per descendum*" hydrologies. The first stage of supergene oxidation peaked between 21 and 15 Ma as the result of percolating oxygenated meteoric waters in a semi-arid setting. This was followed by a second stage of supergene oxidation where atacamite formed from uprising basinal brines and subsequently preserved under hyper-arid conditions for at least the last 2 Ma.

Evaporitic high-altitude low-temperature conditions are not directly involved in the formation of porphyry copper accumulations, which are formed by a combination of igneous emplacement and hydrothermal circulation (John et al. 2010). But the transition from semi-arid to hyperarid climates in Chile were responsible, first for supergene enrichment and then for preservation of the resulting deposits, along with ongoing deposit enrichment. Understanding the history of Neogene aridity, responding to uplift/adiabatic climate is a significant component in understanding ore distribution in high-altitude arid-zone porphyry copper deposits (Fig. 15.92).

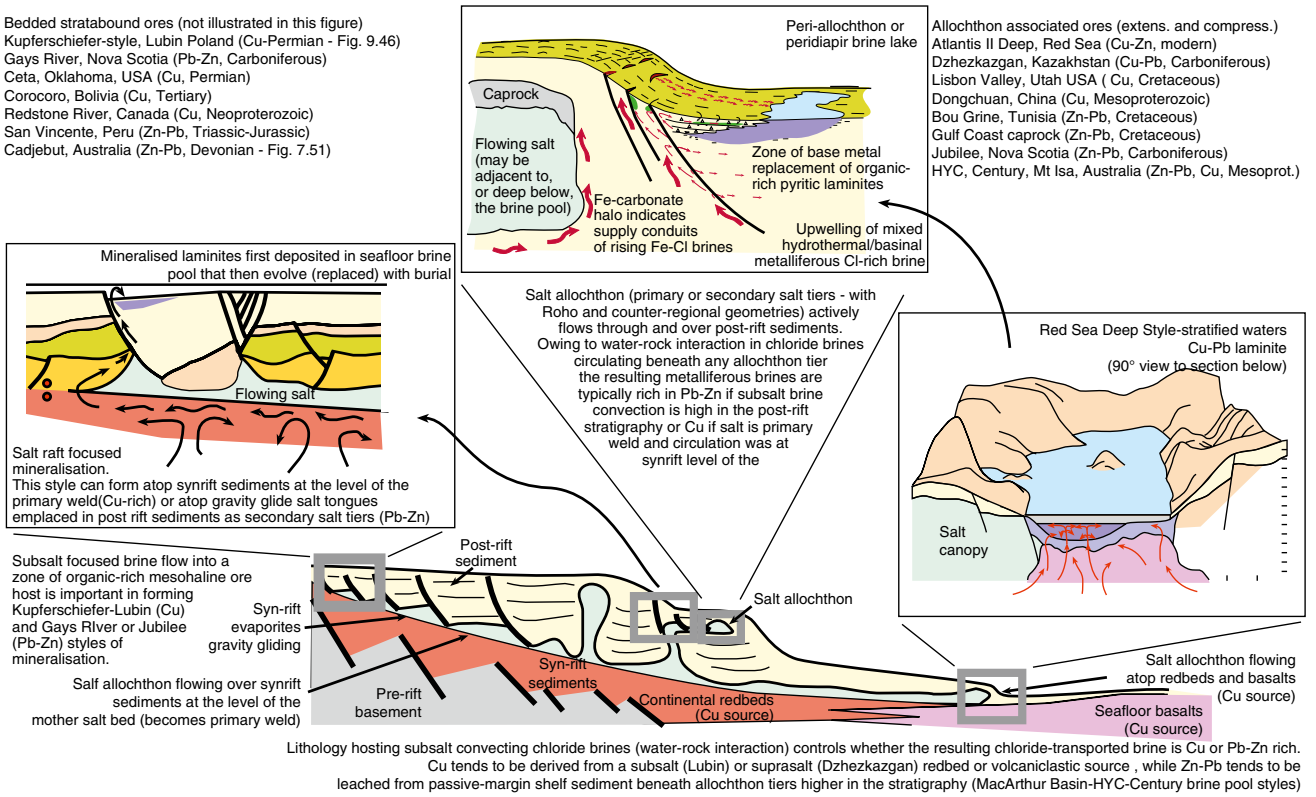

Fig. 15.93 Base metal associations in the context of a salt allochthon terrane (After Warren 2000b)

Base Metals, Evaporites and Diagenetic Accumulations: A Summary

Many low-temperature base metal deposits in evaporite entraining sedimentary basins can be related to the presence of preserved evaporites or indicators of the former presence of evaporites, such as bedded and halokinetic breccias, chert nodules and other indicators of "the evaporite that was" (Fig. 15.93). The link is either direct, with metal accumulation at the site of the present or former evaporites, especially calcium sulphate beds; or indirect, from ascending hypersaline fluids supplied from a dissolving mother salt bed via a single or a series of feeder faults. Thus mineralisation can be subsalt, intrasalt, or suprasalt and the salt, or its breccia, can be bedded or halokinetic. In many cases the H_2S that causes the ore to precipitate at the redox interface is derived from bacteriogenic or thermochemical reduction of nearby evaporitic sulphate in combination with organics supplied by hydrocarbons ponded beneath an evaporite seal (Table 15.2).

The diagenetic evaporite-base metal association includes world class Cu deposits, such as the Kupferschiefer-style Lubin deposits of Poland and the large accumulations in the Dzhezkazgan region of Kazakhstan. The Lubin deposits are subsalt and occur where longterm dissolution of salt in conjunction with upwelling metalliferous basin brines created a stable redox front, now indicated by the facies of the Rote Faule. The Dzhezkazgan deposits (as well as smaller scale Lisbon-Valley style deposits) are suprasalt and formed where a dissolving halite-dominated salt structure maintained a structural focus to a regional redox interface. It also drove the circulation system whereby metalliferous saline brines leached adjacent redbeds. In both scenarios the resulting sulphides are zoned and arranged in the order Cu, Pb, Zn as one moves away from the zone of salt-solution supplied brines. This redox zonation can be used as a regional pointer to both mineralisation and, more academically, to the position of a former salt bed. In the fault-fed suprasalt accumulations the feeder faults were typically created and maintained by the jiggling of brittle overburden blocks atop a moving and dissolving salt unit. A similar mechanism localises many of the caprock replacement haloes seen in the diapiric provinces of the Gulf of Mexico and Northern Africa.

Evaporite-associated Pb-Zn deposits, like Cu deposits, can be associated with both bedded and halokinetic salt units or their residues. Stratiform deposits such as Gays River, Cadjebut and Nanisivek, have formed immediately adjacent to or within the bedded salt body, with the bedded sulphate acting as a sulphur source. In diapiric deposits the Pb-Zn mineralisation can occur both within a caprock or adjacent to the salt structure as replacements of peridiapiric organic-rich

pyritic sediments. In the latter case the conditions of bottom anoxia that allowed the preservation of pyrite were created by the presence of brine springs and seeps fed from the dissolution of nearby salt sheets and diapirs. The deposits in the peridiapiric group tend to be widespread; but, in Phanerozoic strata, the individual deposits are relatively small and mostly subeconomic. However, the fluid flow and brine pool mechanisms, as well as models of replacement haloes in bottom brine sediments, can be used to model larger counterparts within Proterozoic settings for which there are no modern analogs. This notion is developed further in the next chapter.

In all the deposits discussed in this chapter there are four common factors that can be used to recognise suitably prepared ground and so improve exploration models:

- A dissolving evaporite bed acts either as a supplier of chloride-rich basinal brines capable of leaching metals, or as a supplier of sulphur and organics that can fix metals.
- Where the dissolving bed is acting as a supplier of chlochloride-rich brines, there is a suitable nearby source of metals that can be leached by these basinal brines.
- There is a redox interface where these metalliferous chloride rich waters mix with anoxic waters within a pore fluid environment that is rich in organics and sulphate/sulphide/H_2S.
- There is a salt-induced focusing mechanism that allows for a stable, longterm maintenance of the redox front, e.g. the underbelly of the salt bed (subsalt deposits), a dissolution or halokinetically maintained fault activity, the overburden (suprasalt deposits), a stratiform intrabed evaporite dissolution front (intrasalt deposits).

Most important is the notion that the sulphide orebodies that form at the redox interfaces can remain long after the actual salt units have dissolved or evolved into metaevaporites. To an explorationist trained in the recognition of former salts, the indicators remain visible and act as pointers to zones of structural or diagenetic foci for the mineral-depositing redox system. When such zones are recognised, and placed within the regional framework or basin architecture, then particular zones or lithologies of interest are quickly defined and suitable for more intense exploration.

Magma-Evaporite-Hydrothermal Metal Associations

16

Introduction

Metalliferous fluid indicators and ore deposits due to direct and indirect interactions between magma and evaporites at a regional scale are neither well documented, nor well understood. Mostly, this is because little or no actual salt remains once these high temperature interactions have run their course. On top of that, some hard-rock geologists with a career working in igneous and metamorphic terranes may not be well versed in sedimentary evaporites or their meta-evaporitic siblings. The term pyrometasomatic encompasses some, but not all, of the types of salt-magma interaction that are the focus of this chapter.

For the purpose of our discussion, styles of evaporites interacting with magma to form various economic metal accumulations are divided into two; (1) orthomagmatic (salt-assimilative and internal to the magma), and (2) paramagmatic (salt-interactive and external to the magma). Both outcomes, which include a variety of substantial ore deposits, are typically inferred not from the presence of evaporite salts, but from chemistry and mineralogy of the reaction products. Only where igneous sills and dykes have intruded salt masses, with contacts preserved, can direct effects of magma-salt interaction be documented.

Orthomagmatic and paramagmatic associations are distinct from occurrences of primary igneous/magmatic anhydrites, which precipitate from sulphate-saturated melts, as in the anhydrite crystals crystallised in trachyandesitic pumices erupted from El Chichón Volcano in 1982, dacitic pumices erupted from Mount Pinatubo in 1991 and acidic lavas in the Yanacocha district of northern Peru (Luhr 2008; Chambefort et al. 2008). They are also distinct from fumarolic anhydrite, which precipitates where groundwaters and sulphur-bearing magmatic fluids interact, as on Usu Volcano, Hokkaido, many central American and Andean volcanoes, including El Laco (Zimbelman et al. 2005). Likewise, they are distinct from the anhydrite precipitates (white smokers) in and below submarine vents across numerous mid-oceanic ridges (Humphris et al. 1995).

Fumarolic and vent (white-smoker) anhydrites can form significant anhydrite masses that in the subsurface can be confused with metasedimentary anhydrite, and so are discussed in some detail later in this chapter. Primary magmatic anhydrites are interesting in terms of defining particular magma chemistries, but do not form anhydrite in significant volumes and so are not discussed in detail. The maximum amount of sulphur (S) that can be dissolved in silicate melt is controlled by saturation of the melt with an S-bearing phase (Fig. 16.1a). At relatively low oxygen fugacities, this phase is either an immiscible iron-rich sulfide liquid (with as much as 10 % oxygen), which occurs in high-temperature basaltic melts, or crystalline pyrrhotite ($Fe_{1x}S$) in intermediate (andesitic) and silicic (rhyolitic) melts. A Cu-Fe sulfide mineral known as "intermediate solid solution," may also crystallize from andesitic to rhyolitic melts. At higher oxygen fugacities, anhydrite crystallizes from a wide range of melt compositions. Silicate melts at intermediate oxygen fugacities can crystallize both pyrrhotite and anhydrite, an assemblage that occurs in the trachyandesite tephra from the 1982 eruption of El Chicho'n in Mexico. The interested reader is referred to Luhr 2008 for a comprehensive discussion of primary igneous anhydrites and their chemistries.

Orthomagmatic ore deposits, tethered to the assimilation of evaporite masses into a magma, form prior to complete solidification of the igneous melt. That is, potential ore-forming liquid magmas assimilate salts and then fractionate/metasomatise *in situ* into ore segregations, before solidus. In contrast, paramagmatic-hydrothermal ore deposits form external to the melt. They are produced by country-rock/basinal brine interactions with magmatically-derived or thermally-driven super- or sub-critical fluid circulation under a general grouping sometimes called hydrothermal alteration.

Base metal sulphides (Ni, Cu) oxides (magnetite, ilmenite, chromite) and many ores of the precious metals (Au, Pt, Pd) are typical orthomagmatic ores in ultramafic and mafic igneous rocks (Pohl 2011). Less often, various magnetite-hosted ores occur in intermediate and silicate melts.

© Springer International Publishing Switzerland 2016

J.K. Warren, *Evaporites: A Geological Compendium*, DOI 10.1007/978-3-319-13512-0_16

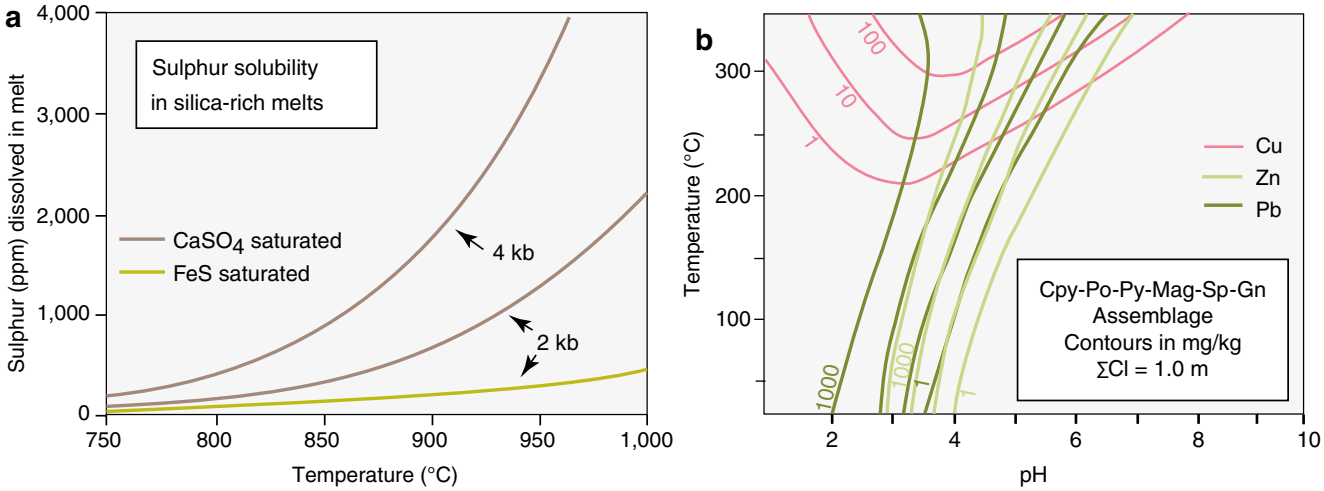

Fig. 16.1 Sulphur carrying capacity. (**a**) Experimental determinations of sulfur solubility versus temperature for hydrous silica-rich melts at different pressures and oxygen fugacities. (**b**) Sulphide solubility patterns due to chloride complexing. Calculated total metal concentrations (in $mg \cdot kg^{-1}$) in a 1 m solution in equilibrium with a chalcopyrite-pyrite-pyrrhotite-magnetite-sphalerite-galena assemblage. Note that the sulphur content of the solution ranges from <<1 $mg \cdot kg^{-1}$ at low pH and low temperature to >10,000 $mg \cdot kg^{-1}$ at high pH and high temperature. The isothermal decrease in chalcopyrite solubility with decreasing pH at low pH is due to the decrease in activity of Cl- as the relative proportion of chloride complexed with metals increases (After Lydon 1984)

Orthomagmatic deposits show ore textures that indicate precipitation at magmatic temperatures, while the adjacent melt was essentially liquid. These ores form as various types of fractionation segregates and cumulates, with fluctuating levels of "filter pressing" in the magma chamber. As such, many orthomagmatic ores are located within intrusive masses, but there are notable extrusive examples, like the Ni-Cu-Fe-sulphides of the Archaean Greenstone belts of the Yilgarn craton in SW Australia and the magnetite-haematite lavas and tuffs in andesitic-rhyolitic volcanoes in Chile, Mexico and Pakistan.

Paramagmatic deposits are related to solutions and gases segregated and generated by magmas containing more dissolved volatiles (H_2O, CO_2, S, B, F, Li, Cl etc.) than the proportion that can be accommodated by silicates during their crystallisation. These volatile-rich fluids tend to convectively circulate in the adjacent country-rock strata and can drive alteration haloes, as well as produce further heat-generated volatiles and mineral phases via heating and interacting with labile phases in the country rock. Mineralogies in the country rock are indicative of the chemistry of the interacting lithologies and the parent (including juvenile) fluids. Compared to ores tied to orthomagmatic deposits, this style of deposit is more subject to controversy in terms of genesis and the relative contributions of magmatic versus country-rock volatiles and/or basinal brines.

Worldwide, the majority of paramagmatic and orthomagmatic ore deposits are likely not tied to evaporite interactions; but once again, as in previous chapters, in this chapter we will focus on those that are (Table 16.1). The single most important point that comes out the various deposit analyses in this chapter, is that the presence of evaporites once again enhances ore volumes, not creates them. It does so by increasing metal transport efficiency and/or precipitative focusing, rather than directly spawning a metalliferous ore deposit. As in the previous chapter, the role of evaporites is to create and enhance the metal carrier system and to locally contribute reductants that can fix various metal sulphides and oxides. For example, such sulphate evaporite enhancement explains the large ore volumes in the orthomagmatic supergiant Noril'sk Ni-Cu deposit in Siberia and the paramagmatic supergiant Muruntau gold deposit of Uzbekistan (Li et al. 2009; Wilde et al. 2001)

In elucidating the igneous-ore-evaporite association, we shall use a framework of direct and indirect magma interactions with basinal fluids and sediments, with an emphasis on outcomes in systems where bedded or halokinetic evaporites were present. Purely orthomagmatic interactions (assimilations) of evaporites are discussed separately from paramagmatic interactions, but in the real world the two styles can be co-occurrent. From this, and observations of pervasive diagenetic iron mobility within halokinetic systems, as documented in the previous chapter, we shall attempt to define criteria indicative of former evaporite interactions in various evolving igneous-driven mineralised systems.

We already know from our discussions of meta-evaporites and low temperature stratabound mineralisation that, by the time a rock attains the elevated temperatures and pressures that define the igneous-emplacement realms, most sedimentary salts have been pervasively altered and transferred into basinal fluids or chloride-sulphate meta-evaporites. Before we consider the various economic deposits created by the

Table 16.1 Selected orthomagmatic examples that illustrate some of the many possible styles of evaporite-igneous interactions

Unit, location and age	Character	Reference
Crustal silicocarbonatites (515–504 Ma) in southern Madagascar	Pegmatites and associated syenites crystallised from immiscible silicocarbonatitic and peralkaline syenitic melts in the final extensional phase of the Panafrican continental collision and connected metamorphic/metasomatic events. The studied pegmatites and genetically associated syenitic rocks are very rare examples for crustal silicocarbonatitic melts generated in a Panafrican collisional setting. Model T-Nd ages suggest that the melts were produced by partial melting of 3.5 Ga partially evaporitic continental crust	Morteani et al. (2013)
Salts in southern Yakutian kimberlites, Siberia (≈360 Ma)	Alkali carbonates, sodalite, gypsum, anhydrite, halite and sylvite are present in the groundmass and matrix of many kimberlites in the southern part of the Yakutian kimberlite province. In the global context, southern Yakutian kimberlites are unprecedented in the amount of the crustal carbonate and evaporite material included in the pipes, as evidenced by the bulk major element chemistry and isotopic compositions of Sr, C, O, Cl and S. The kimberlites were emplaced through 2 km-thick section of evaporite-bearing carbonate sediments, saturated with hypersaline brines	Kopylova et al. (2013)
Cihai diabase in the Beishan region, NW China (128.5 Ma)	Diabase dykes in Cihai, Beishan region, NW China are spatially and temporally associated with Cornwall-type iron deposits. The iron-rich fluids were derived from deep sources, and the iron ores were concentrated through a convection cell driven by temperature gradients established by the intrusion of the diabase sills. The deposits are the result of the combined processes of subduction-related enrichment in the source, shallow depth of emplacement, and the involvement of large-scale circulation cells of basinal brines from an evaporitic source	Hou et al. (2013)
Gabbros of the Pasveh pluton, NW Iran (≈40 Ma)	Pasveh gabbros can be divided into two groups: free scapolite and scapolite-bearing gabbros. Two stages of metasomatism affected the primary composition of mafic rocks. Firstly, high temperature reactions inverted primary high-Ti clinopyroxene to low-Ti clinopyroxene + high-Ti amphibole. This reaction was extensive and included all gabbroic samples. Hydrothermal fluids involved in this process were derived by dehydration reactions of country rocks or from other magmas incorporated in the formation of Pasveh complex pluton. The second metasomatic stage relates to scapolitization of limited parts of gabbroic rocks. An external saline fluid, which is composed dominantly of NaCl and minor KCl and P2O5 components, impacted locally on Pasveh gabbros and formed the second metasomatic stage. Likely sources of Na and Cl were primary evaporites or hypersaline basinal brines, which were present in the host sediments of the gabbros. The carbonate-free nature of these hydrothermal fluids suggests that hydrothermal fluids responsible for the formation of scapolite in Pasveh gabbros are derived mostly from a marine evaporite parentage	Mazhari et al. (2011)

interactions of salts with magmas and related fluids, we need to define the basics of metal transport in higher temperature fluids associated with igneous emplacement, namely; hypothermal (300–700 °C), mesothermal (200–300 °C) and epithermal (50–200 °C).

Metal Transport in the High Temperature Saline Realm

In Chap. 15 we discussed the transport and precipitation of Pb, Zn and Cu in relatively low-temperature diagenetic hydrothermal settings, with a stratabound sediment host to the mineralisation at temperatures < 200–250 °C, encompassing the mesothermal and epithermal and the lower temperature portion of the hydrothermal range. A hydrothermal mineral deposit tends to form via precipitation of ore and gangue minerals in fractures, faults, breccia openings, or other permeable spaces. It is typified by replacement textures or open space fillings, fed by aqueous fluids ranging in temperature from 50 to 700 °C, but generally below 400 °C, under pressures in the range 1–3 kilobars. Parent fluids are of diverse origins and varying degrees of alteration in the host rock are common.

Once the metamorphic and igneous realms are entered, temperatures of subsurface/hydrothermal waters interacting with an evaporite mass can be well above 300 °C and cool into the mesothermal and epithermal range, either with distance from the molten mass, or with time. At these high temperatures and pressures, hypothermal fluids can be chloride-rich independent of the involvement of dissolving evaporites. But hydrothermal fluids are especially chloride-rich if the interacting country rock was originally halite-rich (Henley 1973; Yardley and Graham 2002). The resulting hot chloride brines are capable of transporting Fe, Cu, Au, Pb and Zn over considerable distances (Figs. 16.1b and 16.2)

Like Cu, Pb and Zn, the solubility of gold increases with temperature in both chloride and bisulphide complexes

(Fig. 16.2a; Williams-Jones et al. 2009). The relative importance of temperature change in gold transport and precipitation is poorly understood, as temperature interacts with other known transport parameters, such as pH and fO_2, either of which may exert a greater influence on precipitation than temperature or salinity fluctuations, especially in mesothermal and epithermal temperature ranges (Fig. 16.2b; Williams-Jones et al. 2009).

The relevant transport reaction equation for chloride complexes carrying gold at higher temperatures (>350 °C), and influenced by the presence of dissolved or altered halite is (Fig. 16.2a; Williams-Jones et al. 2009);

$$4AuCl^-_2 + 2H_2O = 4Au^{(0)}_{(s)} + 8Cl^- + 4H^+_{(aq)} + O_2$$

This reaction indicates gold precipitation within this part of the hydrothermal temperature range is from a chloride carrier. Precipitation is driven by a lowering of temperature, a decrease in salinity (lowering of aCl^-) or a decrease oxygen fugacity (fO_2); all of which can be tied to zones of fluid mixing (between less saline and more saline hydrothermal or basinal brines; Simon et al. 2005). At lower temperatures (mesothermal, epithermal), where bisulphide transport is more typical, gold is thought to precipitate via an increase in pH, which is often tied to boiling and the loss of volatiles (Fig. 16.2b).

When chloride-dominant hot basinal brines are part of the gold transport system, then changes in pH can also be related to changes in hydrocarbon levels in the pore fluids, as well as to more classic consideration of changes related to redox/pH interfaces. This the case in the fine-gold deposits in the shale-hosted Carlin-type gold deposits, such as those of the Alligator Ridge District, Nevada and other sediment-hosted orogenic gold deposits (Large et al. 2011). Precipitated gold at Alligator Ridge retains penecontemporaneous inclusions of hydrocarbons within a hydrothermally altered host rock, made up of the strongly decalcified, silicified, and collapse-brecciated Mississippian to Devonian Pilot Shale (Hulen and Collister 1999).

High temperature chloride transport has created a large group of Proterozoic Cu-Au deposits emplaced in igneous masses surrounded by meta-sediments in Australia, Scandinavia and elsewhere and sometimes classified under the broad umbrella of iron-oxide copper gold (IOCG) deposits. Many of the metasediments in these systems show evidence of the former presence of evaporites. All show inclusion and isotopic characteristics that indicate hydrothermal transport of Cu and Au via hot chloride-rich brines and, by association, their relative lack of pyrite. As such, this group of deposits can be distinguished from the more typical lower temperature sediment-hosted orogenic gold deposits and the pyritic epithermal and VHMS deposits of the Phanerozoic and Archaean.

Lower salinity mesothermal hydrothermal waters are capable of entraining abundant sulphur, and so typically transport and deposit gold in equilibrium with pyrite or pyrrhotite and arsenopyrite (Fig. 16.3). If nearby sedimentary or

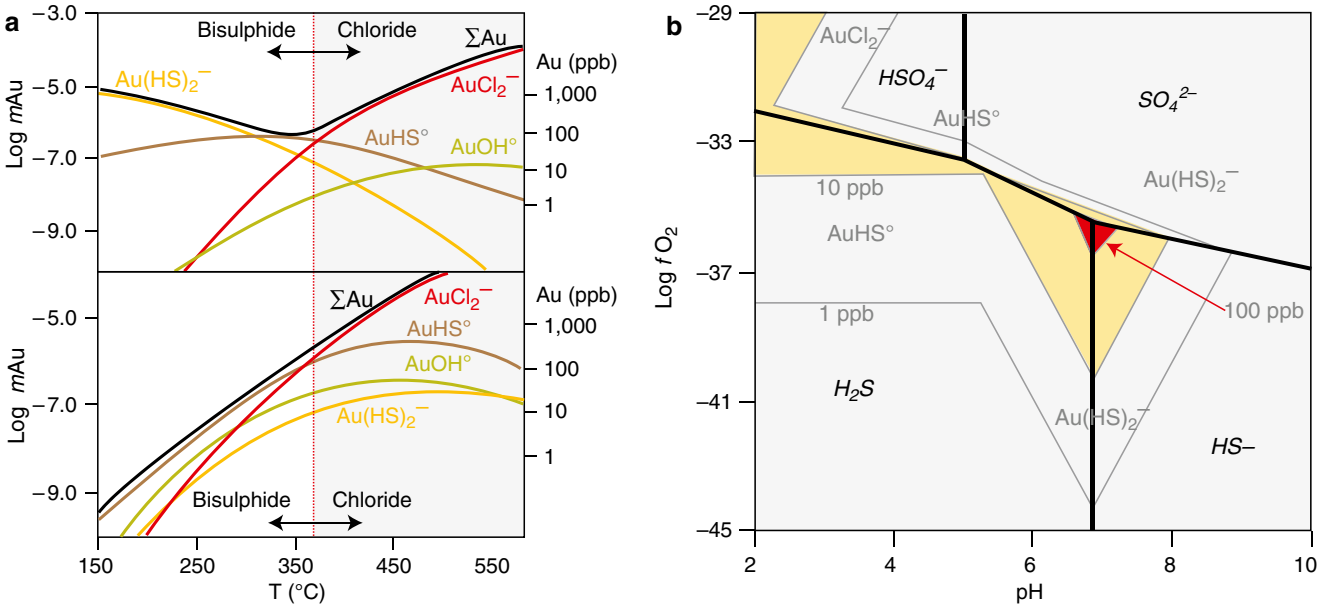

Fig. 16.2 Gold transport. (**a**) Gold solubility (in terms of molality, m, and parts per billion) and speciation at 1 kbar as a function of temperature for an aqueous solution containing 1.5 molal (m) NaCl and 0.5 m KCl, with pH buffered by the assemblage K-feldspar–muscovite–quartz. ∑S (total S) = 0.01 m and fO_2 (oxygen fugacity) is buffered by the assemblage hematite–magnetite. (**b**) ∑S and fO_2 are buffered by the assemblage pyrite–pyrrhotite–magnetite; the maximum value of ∑S is 0.1 m. The black line (∑Au) indicates the total solubility of gold. C) Gold solubility (in parts per billion; solid grey lines) and speciation at 500 bar and 250 °C as a function of log fO_2 and pH in a solution containing 1 m NaCl with ∑S = 0.01 m. The solid black lines separate regions of predominance of H_2S, HS^-, SO_4^{2-} and HSO_4^-. Regions of high solubility are highlighted in *yellow* and *red* (After Williams-Jones et al. 2009)

metasedimentary sulphate evaporites are bathed by these waters, then the dissolving evaporite can contribute sulphur to the transport complex. Gold in VHMS (volcanic-hosted massive sulphide) deposits typifies this sulphur system and Au is transported as lower temperature sulphidic ligand complexes (Davidson and Large 1994). Thermal waters supplying such pyritic mesothermal deposit styles typically have temperatures of 200–300 °C, are reduced H_2O-CO_2-CH_4 waters, with relatively low salinities and typically not associated with basinal brines. Rather, they are associated with prograde precipitation of somewhat ephemeral but massive hydrothermal anhydrite haloes (see later).

Iron Oxide Cu-Au (IOCG) systems are typified by initial temperatures at the upper end of the hydrothermal spectrum where chloride transport dominates (Fig. 16.3). They typically show a marked lack of iron sulphides; rather, they are associated with iron oxides and significant quantities of Cu, along with other chalcophile elements such as U, REE, Bi, Co and Mo, all metals that can be carried in high-salinity chloride brines (Davidson and Large 1994; Williams-Jones et al. 2005). Inclusion studies show these deposits generally precipitate from high salinity (15–35 wt. % NaCl equiv.), low total sulphur (a_{SS} = 10^{-3} to 10^{-2}), high fO_2 hydrothermal fluids (Fig. 16.3). But, as mentioned earlier, high salinity fluids in the igneous realm do not necessarily mean an evaporitic parent; we shall discuss this in more detail when we look at IOCG systems later in this chapter.

Regional Orthomagmatic- Evaporite Interactions

Fe-rich examples related to the assimilation of evaporites into a magma are numerous and well documented in the Phanerozoic, others, associated with Cu-Ni deposits, are more contentious. When substantial halite-rich masses are absorbed into a magma body, the response is a more sodic chemistry and the precipitation of a number of chloride daughter products. Likewise, a more sulphidic magma results, when substantial volumes of anhydrite are assimilated. For example, the

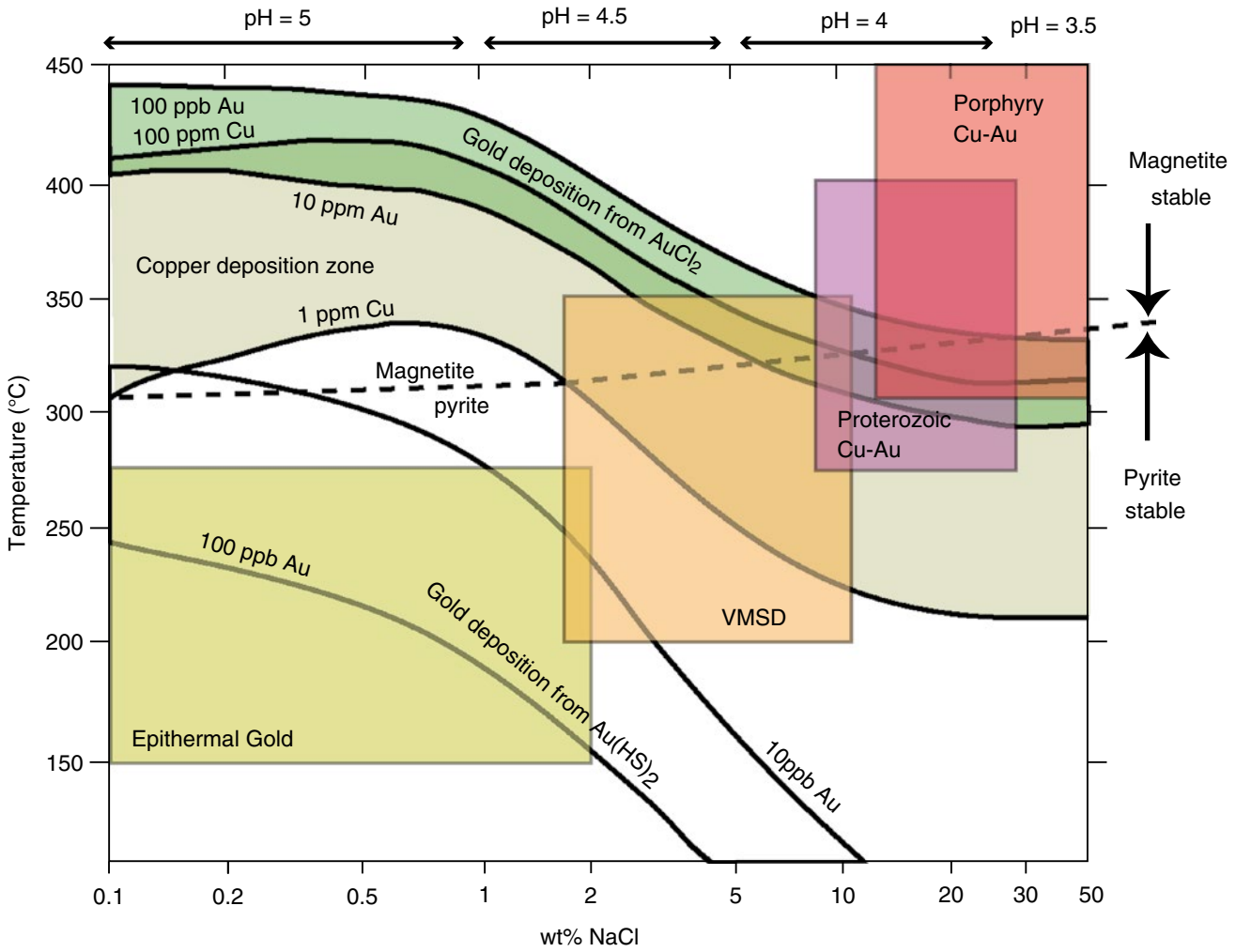

Fig. 16.3 Copper and gold controlled by temperature and NaCl content (After Davidson and Large 1994)

15 m thick alteration aureole off the main Kharaelakh shoot in the Noril'sk deposit contains; high-Ti (up to 10–11 wt.% TiO_2) biotite and phlogopite with significant contents of F and Cl, apatite (from F-containing to Cl-rich (5–7 wt.% Cl)), brown green hornblende (pargasite; an amphibole group mineral with formula $NaCa_2(Mg,Fe_2^+)_4Al(Si_6Al_2)O_{22}(OH)_2$), anhydrite, and Cl-containing alkaline sulphides such as djerfisherite $\{K_6Na(Fe^{2+},Cu,Ni)_{25}S_{26}C\}$ and bartonite $\{(K,Na)_{5.68}(Fe,Cu,Ni)_{20.27}S_{26}(S,Cl)_{0.93}\}$ (Spiridonov 2010)

But in terms of recognising a mineralogic outcome indicative of evaporite assimilation, it can difficult to unequivocally define the precursor to a final rock product alteration halo for high levels of sodium and sulphur and chloride can characterise many magmas, especially in the later stages of solidification (solidus) without any evaporite input to the magma chemistry. Published examples where evaporites have been recognised as playing a role in the final product include (Table 16.1): (1) the assimilation of salts or brines from Triassic evaporites in the polymetallic Sb-As-Au-W deposits hosted in granodiorites at Dubrava, in the Western Carpathians (Chovan et al. 1995); (2) Evaporite-derived solutions that played a significant role in forming the Saint-Salvy vein-hosted Zn (+Ge) deposit on the southern margin of the late Variscan Sidobre Granite (Munoz et al. 1994). (3) Creation of scapolite-bearing gabbros in the Pasveh gabbros of the northwest Sanandaj-Sirjab zone of Iran (Mazhari et al. 2011).

Wherever an intrusive magma body comes into contact with calcium sulphate-entraining sediments, the interaction can facilitate the precipitation of sulphide-associated metals, which may already be in solution within the pores of the adjacent sedimentary system. For example, when igneous trap intrusives interact with sediments containing hydrocarbon-water-sulphate-carbonate at temperatures of 100–700 °C, the sulphates and carbonates in a skarn typically decompose to form large volumes of hydrogen sulphide and carbon dioxide, respectively. At the same time mercaptans appear among the hydrocarbons (Kontorovich et al. 1996). A mercaptan is an organic compound containing the sulphydryl group (—SH), they are the sulphur analogs of the alcohols in that the oxygen in the alcohol group (—OH) is replaced by sulphur. The H_2S and mercaptans can then act as reductants to fix any metals that may be in solution within the adjacent hydrothermal system. Alteration aureoles, with mercaptans, about dolerite intrusives extend 1–10 m into the salt in the Werra Potash zone of Germany, in the Yesso Hills in New Mexico, in Castle Valley in Utah and in Permo-Carboniferous massive bedded salt sequences of the Amazon Basin (Sidle et al. 1985; Pavlov 1970; Szatmari et al. 1979).

Regionally, Permian igneous activity throughout much of the Siberian evaporite platform has driven the alteration and melting of masses of nearby salt and been responsible for two styles of ore mineralisation – (1) Noril'sk Ni-Cu deposits (deeper assimilative interactions with Permian sulphate evaporite and coals) versus (2) Korshunovskoye iron ores (shallower hydrothermals encompassing volatile interactions with bedded Cambrian halite and organic-rich muds). Likewise the kimberlite pipes in the Yakutian Kimberlite province of the Siberian Platform have assimilated Cambrian evaporite phases, so that they now contain elevated amounts of alkali carbonates, sodalite, gypsum, anhydrite, halite and sylvite (Kopylova et al. 2013). And yet ambiguity rather than certainty is the rule with many possibly evaporite-associated halo minerals. For example, precipitates of the late-stage chloride salts, hibbingite (γ-$Fe_2(OH)_3Cl$) and kempite ($Mn_2(OH)_3Cl$), which probably constitute a solution series, occur in a number of Ni-Cu and magnetite ore deposits (Fig. 16.4; Saini-Eidukat et al. 1998). Some metalliferous orthomagmatic occurrences, such as Noril'sk and Korshunovskoye, are likely associated with the assimilation of evaporites into the magma prior to solidus, others, like Sudbury and Duluth, are not. As we shall see in the following sections, isotopes, rather than mineralogies, are key in determining likely evaporite associations.

Orthomagmatic Ni-Cu Associations with Evaporites as a Sulphur Source

Assimilation of evaporites in a ferroan skarn typically forms smaller-scale magnetite and sulphide deposits in the immediate vicinity of the emplaced magma. This is the case in the stratiform Mesozoic Longqiao iron (magnetite and minor pyrite) ore deposit in its carbonate host in the Lu-Zong volcano-sedimentary rift basin, Middle-Lower Yangtze (Changjiang) River Valley, Eastern China. There the magnetite ore skarn passes laterally into evaporite-bearing sideritic carbonate beds of the Triassic Dongma'anshan Formation (Taofa et al. 2011).

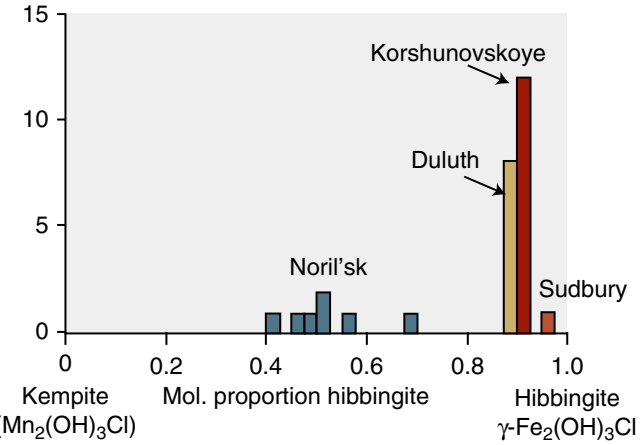

Fig. 16.4 Histogram showing compositional range of the chloride minerals hibbingite and kempite in major Ni-Cu deposits (Saini-Eidukat et al. 1998)

Some of the larger orthomagmatic metal accumulations, such as Noril'sk, have formed where substantial volumes of assimilated sulphate evaporites contributed significant volumes of sulphur into a sulphur-depleted magma and so gave rise to magmas rich in metal sulphide precipitates. Magma chemistry driving assimilation of the sedimentary sulphur to form magmatic sulphides tends to be picritic or komatiitic (sulphur-undersaturated). This is a different ore-forming mechanism to that created by halite salts contributing large volumes of chloride to the chemistry of the circulating hydrothermal basinal and metamorphic fluids, (and so forming a number of IOCG deposits).

The importance of komatiitic and picritic magmas in ore forming processes arises from the fact that they are among the few mafic/ultramafic magma types that are sulphur-undersaturated at the time of magma formation (Keays 1995). As a general rule, and independent of whether sulphate evaporites were involved, the magmatic ore forming process is controlled by the availability of S, not Ni or Cu. Sulphur-saturation of a magma as it forms leads to marked depletion in the chalcophile metals. Komatiitic and picritic magmas are S-undersaturated because they are high temperature magmas, produced by large degrees of partial melting in upper mantle source regions, which were already depleted in sulphur through earlier partial melting events.

Most mafic magmas, produced by less than 25 % partial melting, are S-saturated and hence depleted in the ore-forming chalcophile elements. In contrast, komatiitic and picritic magmas have their full complement of chalcophile metals. When they do become S-saturated, they form sulphide precipitates, which are strongly enriched in Ni, Cu, Au and PGEs (platinum group elements). The metals may accumulate to form ore deposits directly (e.g., magmatic Ni-Cu-PGE sulphides via "squeeze-filtering") or be dispersed in komatiitic/picritic rocks and their fractionation products, so making igneous source rocks for hydrothermal Au or VMS (volcanic massive sulphide) deposits.

Sudbury, Noril'sk and Jinchaun are three of the largest currently mined magmatic Ni-Cu deposits (Fig. 16.5; Naldrett 1999). Although of less tonnage, the higher grade of the Noril'sk ore (900 million tonnes of 2.7 wt.% Ni gives a reserve of 23.1 million tonnes) means that its Ni reserve is

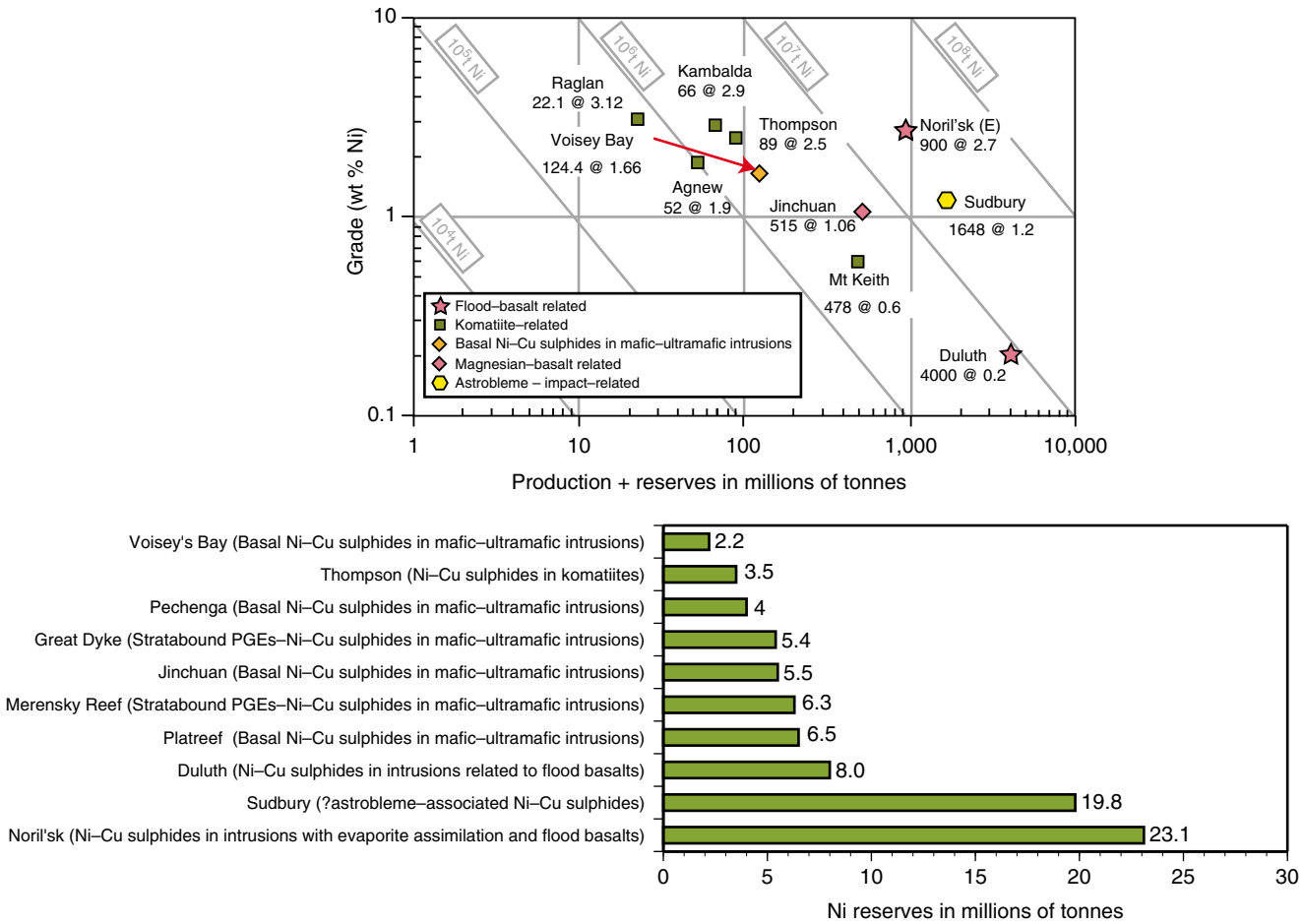

Fig. 16.5 Ore grade in wt.% Ni versus production and reserves in millions of tonnes for major Ni sulphide deposits of the world (Modified after Naldrett 1999). Lower figure ranks the deposits by their reserves

larger than Sudbury, which is considered the largest known Ni deposit in the world by nickel-hosting rock volume (1,648 million tons at 1.2 wt.% gives a Ni reserve of 19.8 million tonnes). The Noril'sk ore also contains 2 times as much Cu and 15 times as much platinum group elements as at Sudbury (Naldrett 1993). Jinchuan in China is the world's third largest Ni deposit with 515 Mt. at 1.06 wt.% of Ni (production + reserves) and forms the keel of a much larger body of magnesian basalt. The Noril'sk ore field contains ~75 % of the world's known Pd and 15 % of the world Pt resources, as well as a significant portion of the Russian Ag and Au resources (Spiridonov 2010).

Unlike Noril'sk, most worldclass Ni deposits are Precambrian, including the komatiitic lava-hosted deposits of the Archaean, and typically show no association with evaporites. Some Proterozoic Ni deposits (like Duluth) are associated with the assimilation of S-rich meta-sediments. Sudbury Ontario is unusual in the spectrum of Cu-Ni deposits, as it considered, at least in part, to be the result of a bolide impact, some 1.7 Ga (Reimold 1993). Most Australian Ni deposits in the Archaean Agnew-Wiluna greenstone belt of Western Australia formed as hot (1,600 °C+) thermally-erosive Archaean ultramafic lava rivers (komatiite), which when contaminated with sedimentary sulphide created the rich nickel ores of the district (Hill et al. 1989; Evans et al. 1989). Such mineralising systems are tied to the more active tectonics, thinner crust and strongly reducing atmosphere in the Archaean and not to evaporites.

Noril'sk Region Siberia

Noril'sk-Talnakh, like Sudbury, is an unusual Cu-Ni deposit. It did not form in the Archaean, and so is much younger than most Ni deposits. It formed at the end of the Palaeozoic, straddles the Permo-Triassic boundary, and crystallised outside the influence of a reducing planetary atmosphere that typifies Archaean Ni deposits. The high temperatures and near complete assimilation of sulphate evaporites within the Noril'sk magma mean that this is one of the more enigmatic ("salt is elsewhere") styles of evaporite-related ore deposit discussed in this chapter.

Notions of evaporite assimilation for these sorts of deposits are usually only one of multiple possible explanations, but in my opinion for Noril'sk this is the most likely. For the purposes of this chapter, I have chosen to emphasise the evaporite connection for the Noril'sk deposit in Siberia (Fig. 16.6a). Alternate nonevaporitic orthomagmatic explanations for the same deposit can be found in papers such as Wooden et al. (1992) and Lightfoot and Hawkesworth (1997).

In the vicinity of the Noril'sk Talnakh nickel deposits, lower Palaeozoic marine argillaceous sediments are overlain by thick extensive Devonian evaporite deposits, along with lower Carboniferous lagoonal and continental sediments, the Tungusskaya Series, that include a number of coal measures (Fig. 16.6b, c). An extremely large volume (approximately one million cubic kilometres) of Permo-Triassic flood basalts, known as the Siberian Traps, now covers this sedimentary sequence (Figs. 16.6a and 16.7a). Sill-like tholeiitic intrusions, varying in composition from subalkaline dolerite to gabbro-dolerite were emplaced into the sediment pile at the same time as the overlying flood basalts, and were part of the feeder system to the flood basalts. The ore-bearing gabbroic-dolerites can be differentiated, whereby picrite and picritic dolerite are overlain by more felsic differentiates. Individual sills may attain lengths of 12 km, widths of 2 km and thicknesses of 30–350 m. The Cu-Ni-platinoid mineralisation forms relatively persistent horizons of massive sulphides, which in the lower portions of the intrusions are made up of segregations and accumulations of pyrrhotite, pentlandite and chalcopyrite.

The regional structure of the Noril'sk district is dominated by NNE-NE Permo-Triassic block faulting, which was coeval with the magmatic activity. Individual faults may be over 500 km in length with throws of up to a kilometre (Naldrett 1997). Mineralised intrusions radiated outward and upward from intrusive centres as they penetrated the sedimentary sequence. Many of the intrusive centres are associated with prominent block faulting. The main Noril'sk-Kharaelakh fault occurs within the Siberian Platform, but is parallel to the main fault system that defines the boundary between the platform and the nearby Yenisei Trough. The Kharaelakh-Noril'sk fault guided the main upwelling magma body Fig. 16.6c).

The anomalous Phanerozoic age of the Noril'sk ore deposits, compared with the Precambrian ages of other magmatic Ni-Cu deposits, and its relative enrichment in Ni, Cu, Pt and Pd compared with Sudbury and Jinchuan, is thought to reflect the anomalously high volumes of sulphur contributed to the evolving magma chamber via assimilation of a thick bedded sulphate evaporite succession (Fig. 16.7a; Naldrett 1981, 1993, 1997; Pang et al. 2013). Its rich sulphur supply from assimilation of bedded sulphates contrasts with that of the Archaean Cu-Ni deposits, where the sedimentary sulphur supply came from more ubiquitous, less-focused sulphur sources entrained in widespread sedimentary pyrite. Such pyrite characterised a significant portion of the fine-grained Archaean sediments accumulating under an anoxic reducing atmosphere.

Abundant crystals of magmatic anhydrite today typify the olivine-bearing (picritic) gabbros in the Kharaelakh intrusion (Li et al. 2009; Spiridonov 2010). Along with disseminated sulphides, the anhydrite crystals are characterized by planar boundaries with co-associated olivine and augite. Dihedral angles of ~120°, characteristic of simultaneous crystallization, are common throughout the anhydrite-augite

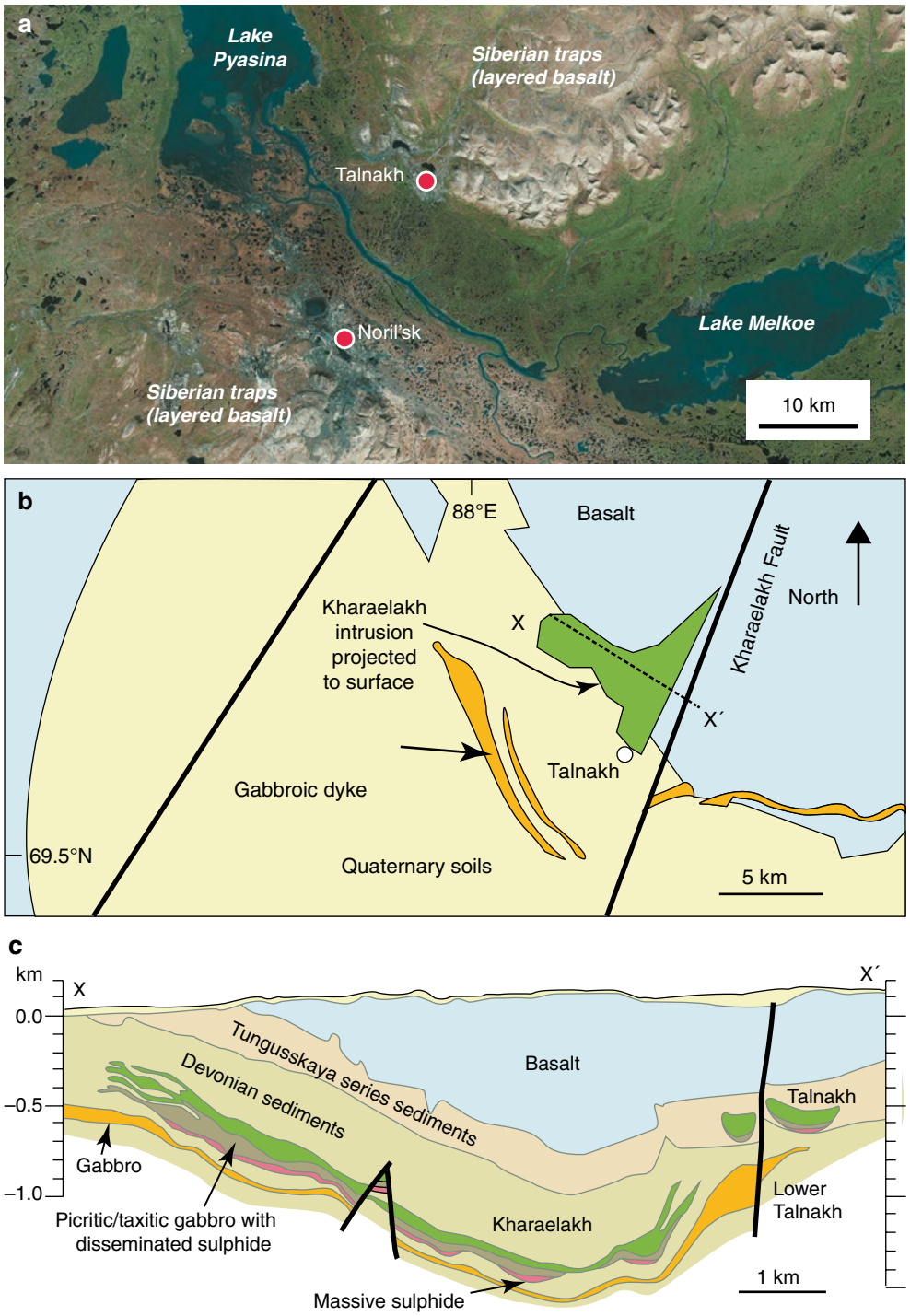

Fig. 16.6 Geology of the Talnakh-Noril'sk area. (**a**) Scaled satellite image showing relative positions of the Talnakh and Noril'sk mines. (**b**) Simplified geology map showing extent of the Kharaelakh intrusion when projected to the surface. (**c**) Cross section X-X' showing depth and relative positions of the Kharaelakh and Talnakh intrusions (After Ripley et al. 2010)

assemblages. Inclusions of anhydrite in augite and vice-versa are also typical. Rounded and subrounded sulphide inclusions composed of pyrrhotite, pentlandite, and chalcopyrite, that crystallized from immiscible sulphide liquid droplets in the magma, are commonplace within the magmatic anhydrite crystals. Visual estimates by Li et al. (2009), based on 5 polished thin sections indicate that the ratio of anhydrite to sulphide in the samples varies from 0.05 to 0.1.

Isotopic analysis of $\delta^{34}S$ in the magmatic anhydrites and associated metal sulphides in the Kharaelakh intrusives require the assimilation of externally-derived high-$\delta^{34}S$ sulphur from the adjacent country rock (Ripley and Li 2007, 2010).

Where complete sulphate reduction occurred, the $\delta^{34}S$ values require mixtures of some 60 % anhydrite-derived evaporitic marine sulphur ($\delta^{34}S$ values near 20‰), with 40 % mantle-derived sulphide ($\delta^{34}S$ of 0‰) to produce the required measured magmatic sulphide values ≈ 12‰ (Fig. 16.7b).

Intense intracontinental rifting in the Noril'sk region brought mafic magmas into contact with supracrustal sulphur from evaporitic sulphates. Noril'sk lies at the extreme northwestern margin of the Siberian Platform, an area that has been a stable cratonic block since the end of the Palaeozoic. To the north, the Khatanga Trough separates the Siberian Platform from a second stable platform (the Taymyr Peninsula). To the east, the Yenisei Trough separates the Siberian Platform from the East European-Urals cratonic block. Thus, the area is a classic rift aulacogen.

Naldrett and Macdonald (1980) noted that plate-scale triple junctions, in particular the aulacogens that may result, are areas where substantial thicknesses of evaporite and mafic magmatism are natural consequences of the tectonic development (Chap. 5). Thus, in arid latitudes in the Phanerozoic, such settings are likely regions for magmatic Ni-Cu sulphide ore formation, with the prerequisite sulphur supplied by the assimilation of bedded sulphate evaporites.

Sulphur isotope data show the mineralised intervals at Noril'sk are anomalously heavy in $\delta^{34}S$, as at Kharaelakh (Fig. 16.7b). These data are inconsistent with sulphur derived from the mantle ($\delta^{34}S$ values near zero), and are consistent with assimilation of an evaporitic sulphate source (Godlevski and Grinenko 1963; Grinenko 1985; Li et al. 2009; Pang et al. 2013). As the magma rose through the sedimentary

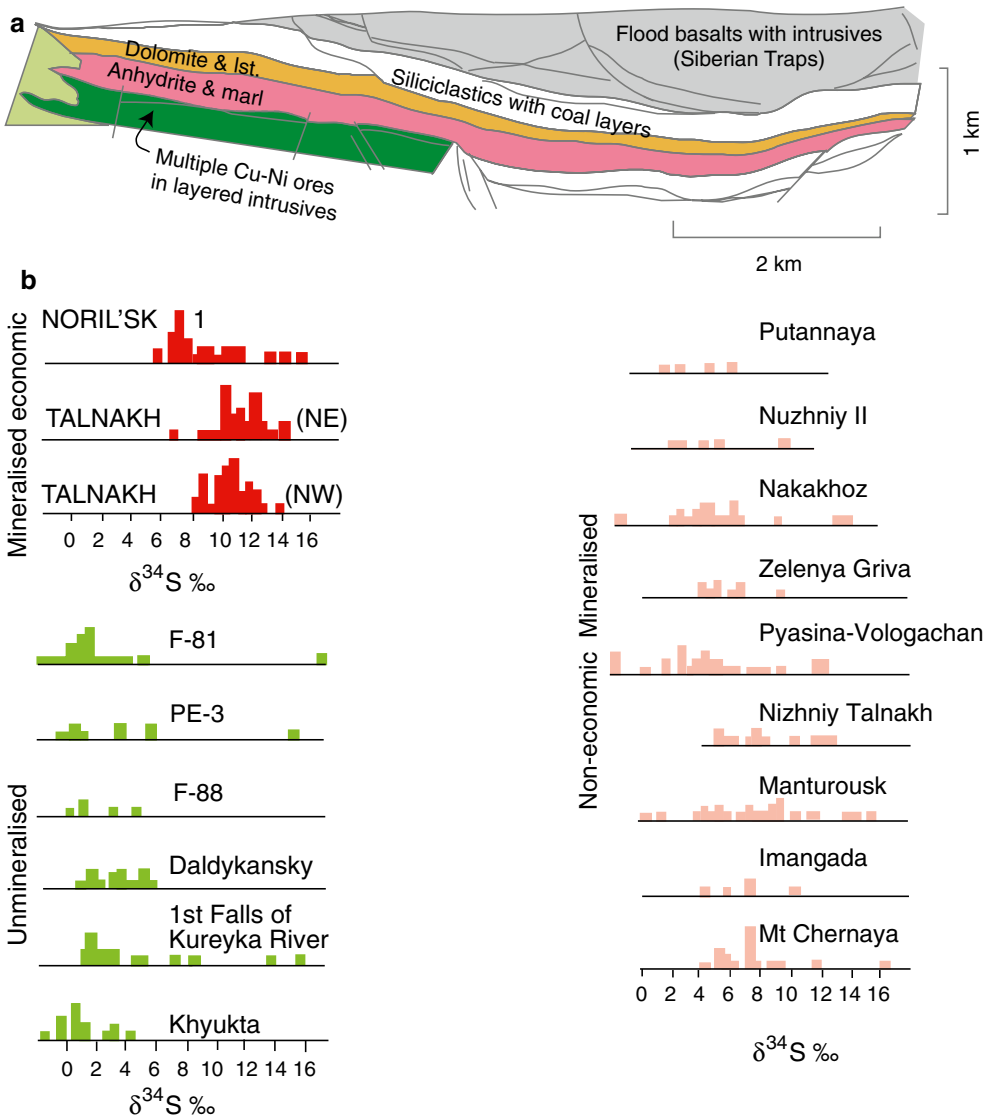

Fig. 16.7 Isotopic responses tied to intrusions Noril'sk-Talnakh region, Siberia. (**a**) Geological section through the northwestern part of the Talnakh ore field (Simplified from Naldrett 1993). (**b**) Isotopic composition of sulphur in unmineralised, mineralised economic and mineralised subeconomic intrusions of the Noril'sk – Talnakh region (After Grinenko 1985; Naldrett 1993, 1997)

cover, it penetrated and assimilated sulphur from extensive thick sedimentary evaporites (Fig. 16.7a). Sulphur in calcium sulphate was reduced to sulphide, CaO entered the magma, and iron from the magma reacted with reduced sulphur so that the end result was droplets of immiscible iron sulphide dispersed through the melt (Naldrett and Macdonald 1980). These droplets acted as collectors for Ni, Cu and the platinum group elements, which are now so enriched in the Noril'sk ores.

Naldrett (1993, 1997) suggested that prehnite + biotite + anhydrite + carbonate + zeolite + chlorite ± sulphide globules, which typify chromite agglomerations in the picrite of the Noril'sk intrusions, could represent remnants of partially assimilated sulphate-rich country rock. Assimilation of anhydrite-rich rocks, coupled with the reduction of sulphate to sulphide, would have introduced considerable oxygen into the silicate melt, which then drove precipitation of chrome-spinel minerals (chromite – $FeCr_2O_4$; mangnesiochromite – $MgCr_2O_4$). Inclusions of anhydrite-rich material, floating in the magma, would have served as loci for chromite crystallisation, thus giving rise to the association between the agglomerations and the globules. Tarasov (1970) pointed out that Middle Carboniferous coal measures were also assimilated and may have supplied organics that assisted in the reduction of calcium sulphate.

That is, during the magma chamber-driven assimilation and contact metamorphism with the anhydrite and the coals, huge amounts of high-temperature reduced gases were produced (methane, hydrogen, CO, etc.), which actively interacted with anhydrite in the Palaeozoic strata (Fig. 16.8; Spiridonov 2010). Thermochemical sulphate reduction in the country rocks resulted in sulphurous gases, sulphur, hydrogen sulphide, sulphur dioxide, carbon disulphide, etc. Ore sulphur has an anhydrite-parent-dominated isotopic composition and so is richer in the heavier isotope compared with mantle sulphur (Fig. 16.7b). These sediment-derived gaseous products penetrated into cooling and shrinking intrusions and so intensely interacted with Fe-containing minerals to produce fine sulphide disseminations in rocks and secondary sulphide melts.

Assimilation of sulphate via partial melting of a basaltic magma is difficult, owing to the high melting points of calcium sulphate minerals (typically ranging between 1,360 and 1,450 °C). Therefore, either a fluxing mechanism is envisioned, or hydrothermal leaching of sulphate followed by partial reduction, or a process involving the dissolution, rather than melting, of sulphate in mafic magma, hence the TSR mechanism outlined in the preceding paragraph (Ripley and Li 2007). The observation of abundant wollastonite in contact aureole rocks suggests that reactions such as $CaSO_4 + SiO_2 + H_2O = CaSiO_3 + H_2S + 2O_2$ occurred, and that sulphate was likely reduced to sulphide prior to incorporation into the magma.

Such igneous – sulphate sediment interaction explains, at least in part: (1) the huge amount of sulphide melt in the Noril'sk ore field; (2) the heavy quasi-anhydrite isotopic composition of

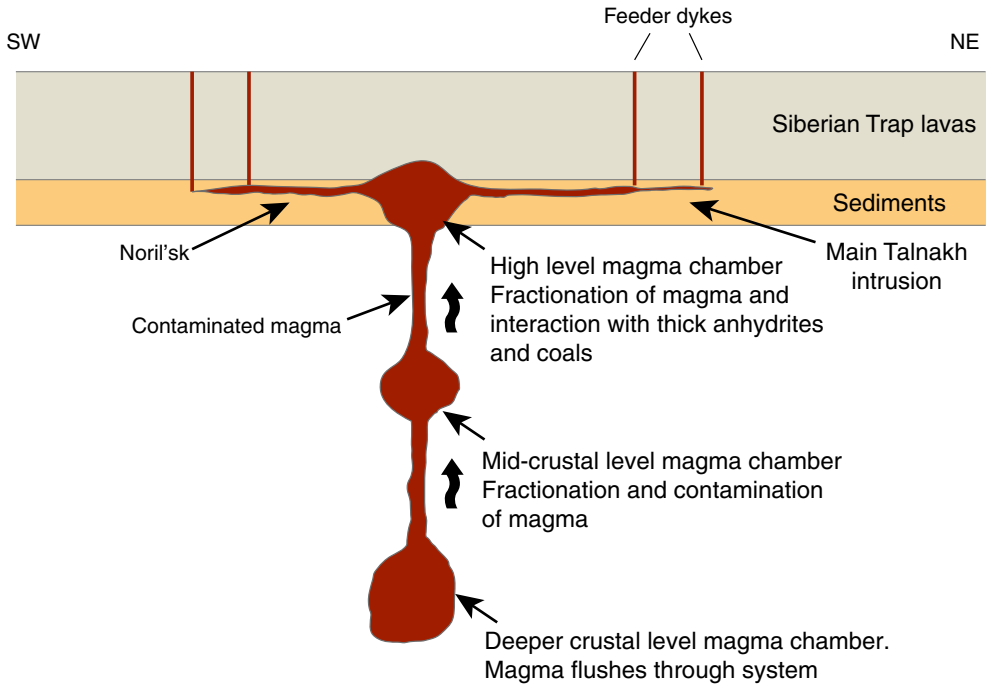

Fig. 16.8 Schematic of likely contamination and sulphur addition sites in the ascending magma pathway supplying the Ni-Cu Noril'sk and Talnalkh intrusions, Siberia (After Pirajno 2007; Naldrett 1997)

sulphur in sideronitic and massive ores; (3) the reduced contents of noble metals in these ores (compared with the drop sulphides that occur toward base of the intrusions and have a likely mantle sulphide source); and (4) the high contents of radiogenic (crustal) osmium in sideronitic and massive ores (Spiridonov 2010; Walker et al. 1994). In summary, this world class Ni-PGE deposit at Noril'sk, with its anomalous Mesozoic age, likely reflects a fortuitous occurrence of thick sulphate evaporites (ultimate sulphide source) atop an active later set of deep mantle-tapping rift grabens.

Evidence of the assimilation of large volumes of anhydrite and coaly organics into the magma mass has implications beyond the formation of the Noril'sk ore deposit. Li et al. (2009) identified magmatic anhydrite-sulphide assemblages in a subvolcanic intrusion associated with the Siberian Traps. The $\delta^{34}S$ values of anhydrite and coexisting sulphide crystals analysed by ion probing are 18‰–22‰ and 9‰–11‰, respectively, much higher than the anhydrite-contaminated ore values shown in Fig. 16.7b. To obtain this level of fractionation means more than 50 % of the total sulphur in the intrusion was derived from marine evaporites in the footwall strata. The contaminated magma was highly oxidized and able to dissolve up to one order of magnitude more sulphur than pure mantle-derived basaltic magma. Such sulphur-contaminated magma, if erupted, would have released far more SO_2 into the atmosphere than is generally appreciated (Black 2012). That is, the eruption of the evaporite-contaminated magma that is the Siberian Traps may help explain the intensity of the end-Permian extinction.

Paramagmatic Interactions

By definition, paramagmatic associations are external to the magma body, but with hydrologies and alteration haloes driven, or at least influenced, by the heating created by the emplacement of the magma. This influence can be as simple as the local heating effects of a sill or dyke extending out a few metres into the adjacent salt. Or, it can create unique salt/magmatic skarns such as the borosilicate skarns (datolite and danburite) near Dal'negor'sk in far-eastern Russia, which are cogenetic with Pb-Zn-Ag skarns and replacements in the same ore field (Chap. 13; Dubinina et al. 2011; Baskina 2008). Or, it can drive regional phreatomagmatic explosions, via heating of the high levels of volatiles trapped and stored as hydrocarbons in the lower parts of a thick evaporite succession.

Cooking the Salt: Dykes and Sills in Salt

At a local scale (measured in metres) with respect to an intrasalt-igneous interaction, there are a number of documented thermally-driven alteration styles, typically created by the intrusion of dolerite dykes and sills into cooler salt, or the outflow of extrusive igneous flows over cooler salt beds (Knipping and Herrmann 1985; Knipping 1989; Grishina et al. 1992, 1998; Gutsche 1988; Steinmann et al. 1999; Wall et al. 2010). Hot igneous material interacts with somewhat cooler anhydrous salt masses to create narrow but distinct heat and mobile fluid-release envelopes, also reflected in the resulting salt textures. At times, relatively rapid magma emplacement can lead to linear breakout trends outlined by phreatomagmatic explosion craters, as imaged in portions of the North Sea (Wall et al. 2010).

Based on studies of inclusion chemistry and homogenization temperatures in fluid inclusions in bedded halite near intrusives, it seems that the extent of the influence of a dolerite sill or dyke in bedded salt is marked by fluid-inclusion migration, evidenced by the disappearance of chevron structures and consequent formation of clear halite with a different set of higher-temperature inclusions. Such a migration envelope is well documented in bedded Cambrian halites intruded by end-Permian dolerite dykes in the Tengushka region of Siberia (Grishina et al. 1992). Defining h as the thickness of the dolerite intrusion in these salt beds, and d as the distance of the halite from the edge of the intrusion, then the disappearance of chevrons occurs at greater distances above than below the intrusive sill. For $d/h < 0.9$ below the intrusion, $CaCl_2$, $CaCl_2$, KCl and $n CaCl_2$, $m MgCl_2$ solids occur in association with water-free and liquid-CO_2 inclusions, with H_2S, SCO and orthorhombic or glassy S_8. For a d/h of 0.2–2 above the intrusion, H_2S-bearing liquid-CO_2 inclusions are typical, with various amounts of water. Thus, as a rule of thumb, an alteration halo extends up to twice the thickness of the dolerite sill above the sill and almost the thickness of the sill below (Fig. 16.9).

A similar situation occurs in the dyke-intruded halite levels exposed in the mines of the Werra-Fulda district of Germany (Steinmann et al. 1999). There, the Permian Zechstein salt series contains two important potash salt horizons (2–10 m thick), which are mined at a depths ≈ 800 m from within a 400 m thick halite host (Fig. 16.10a). In the late Tertiary, basaltic melts intruded these Zechstein evaporites, but only a few dykes reached the Miocene land surface. Basaltic melt production was related to regional volcanic activity some 10–25 Ma. Basalts exposed in the mine walls are typically subvertical dykes, rather than sills. These basaltic intervals can crosscut the salt over zones up to several kilometres wide (Fig. 16.10b). However, correlations of individual dyke swarms, between different mines, or between surface and subsurface outcrops is difficult.

The basalts are phonolitic tephrites, limburgites, basanites and olivine nephelinites. The dyke margins are usually vitrified, forming a microlitic limburgite glass along dyke edges in contact with salt (Knipping 1989). At the contact on the evaporite side of the glassy rim there is a cm-wide carapace of

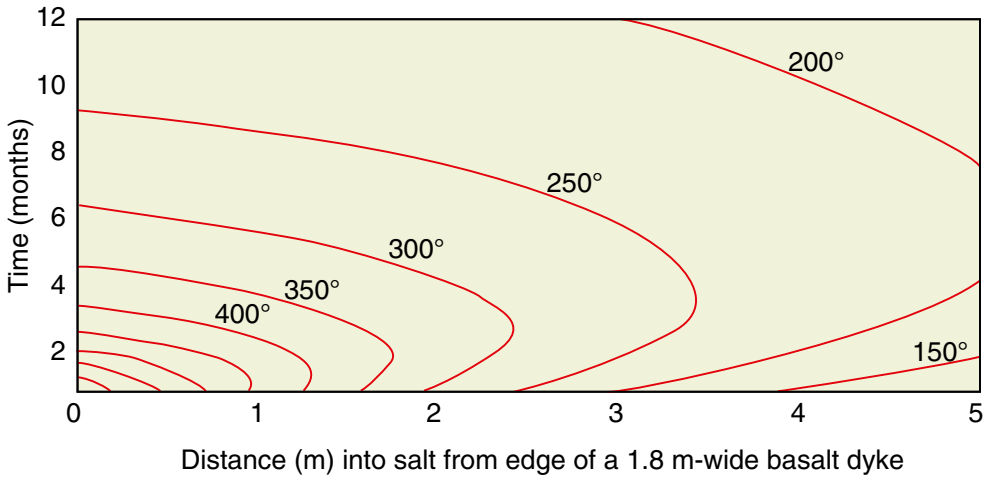

Fig. 16.9 Temperature effects in salt across time (1 year) and distance (m) from the edge of a 1.8 m-wide basalt intrusion into halite (After Knipping 1989)

high temperature salts (mostly anhydrite and ferroan carbonates). Further out, the effect of the high temperature envelope is denoted by transitions to clear halite, with higher temperature fluid inclusions (Knipping 1989). All of this metre-scale alteration is an anhydrous alteration halo, the salt did not melt (melting temperature of 804 °C), rather than migrating, the fluid driving recrystallisation was largely from entrained brine inclusions. The dolerite/basalt interior of the basaltic dyke is likewise altered and salt soaked, with clear, largely inclusion-free halite typically filling vesicles in the basalt.

Worldwide, dykes intersecting salt beds tend to widen to become sills in two zones: (1) along evaporite units within the halite mass that contain hydrated salts, such as carnallite or gypsum (Fig. 16.10d, e) and, (2) where rising magma has ponded and so created laccoliths at the upper or lower halite contact with the adjacent nonsalt strata or against a salt wall (Figs. 16.10 vs. 16.11). The first is a response to a pulse of released water as dyke-driven heating forces the dehydration of hydrated salt layers. The second is a response to the mechanical strength contrast at the salt-nonsalt contact.

Heating of hydrated salt layers, adjacent to a dyke or sill, tends to drive off the water of crystallisation (chemical or hydration thixotropy) at much lower temperatures than that at which anhydrous salts, such as halite or anhydrite, thermally melt (Table 16.2). For example, in the Fulda region the thermally-driven release of water of crystallisation within particular salt beds creates thixotropic or subsurface "peperite" textures in carnallitite ore layers, where heated water of crystallisation escaped from the hydrated-salt lattice. Dehydration-driven loss of mechanical strength focuses zones of magma entry into to particular horizons in the salt mass, wherever hydrated salt layers were present (Fig. 16.10c verses d). In contrast, dyke and sill margins are much sharper and narrower in zones of contact with anhydrous salt intervals (Fig. 16.10b; Schofield et al. 2014).

Accordingly, away from immediate vicinity of the direct thermal aureole, heated and overpressured dehydration waters can enter a former carnallite halite bed, and drive the creation of extensive soft sediment deformation and peperite[1] textures in the former hydrated layer (Fig. 16.10d, e). Mineralogically, sylvite and coarse recrystallised halite dominate the salt fraction in the peperite intervals. Sylvite in these altered zone is a form of dehydrated carnallite, not a primary-textured salt. In the Fulda region, such altered zones and deformed units can extend along former carnallite layer to tens or even a hundred or more metres from the dyke feeder. Ultimately, the deformed potash bed passes back out into the unaltered bed, which retains abundant inclusion-rich halite and carnallite (Fig. 16.10d versus e). That is, nearer the basalt dyke, the carnallite is largely transformed into inclusion-poor halite and sylvite, the result of incongruent flushing of warm saline fluids mobilized from the hydrated carnallite crystal lattice as it was heated by dyke emplacement. During Miocene salt alteration/thermal metamorphism in the Fulda region, NaCl-fluids were mixed with fluids originating from thermally-mobilised crystallisation water in the carnallite, as it converted to sylvite. This brine mixture altered the basalts during post-intrusive cooling, an event which numerical models suggest was quite rapid (Knipping 1989): a dyke of less than 0.5 m thickness probably cooled to temperatures less than 200 °C within 14 days of dyke emplacement.

The contrast in alteration extent between Fig. 16.10b, d shows alteration effects are minimal wherever the emplacement temperature of the magma is below that of the anhydrous salt body it is moving through. This is the case in the La Sal Mountain laccoliths of the Paradox basin, Utah (Ross

[1]Peperite is a sedimentary rock that contains fragments of igneous material and is formed when magma comes into contact with wet sediments.

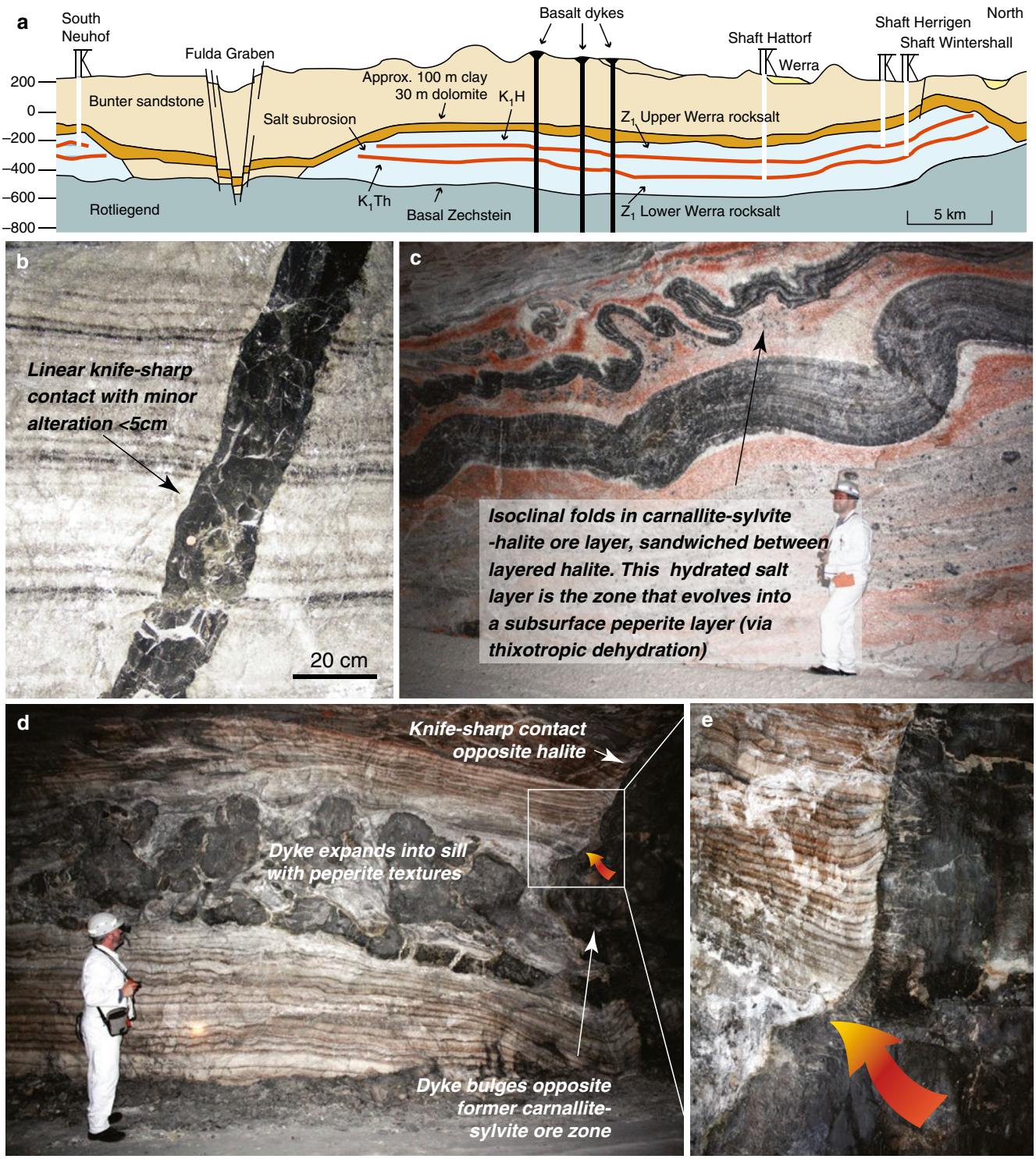

Fig. 16.10 Tertiary basalt dyke intrusions in Zechstein halite in the Fulda region, Germany. (**a**) Geological cross section. (**b**) Steeply inclined dyke in laminated halite showing knife-sharp contacts. (**c**) Carnallite-sylvite ore zone showing typical isoclinal folds sandwiched between layered halite units. (**d**) Near vertical dyke showing knife-sharp contacts opposite layered halite and bulges into level of former ore zone. (**e**) Close up of bulge zone (Schofield et al. 2014)

1998; Doelling 2001). There, the northern and southern intrusive centres, dominated by diorite porphyry, were emplaced some 25.1–27.9 Ma into pre-existing elongate salt anticlines (salt walls) composed of Permian Paradox salt that had largely stopped flowing in the Jurassic (Fig. 6.83; Ross 1998). The trachyte-dominated intrusions now form several laccoliths, plugs, and sills in a circular cluster arrangement (Fig. 16.11). Other than the elongation that parallels the salt

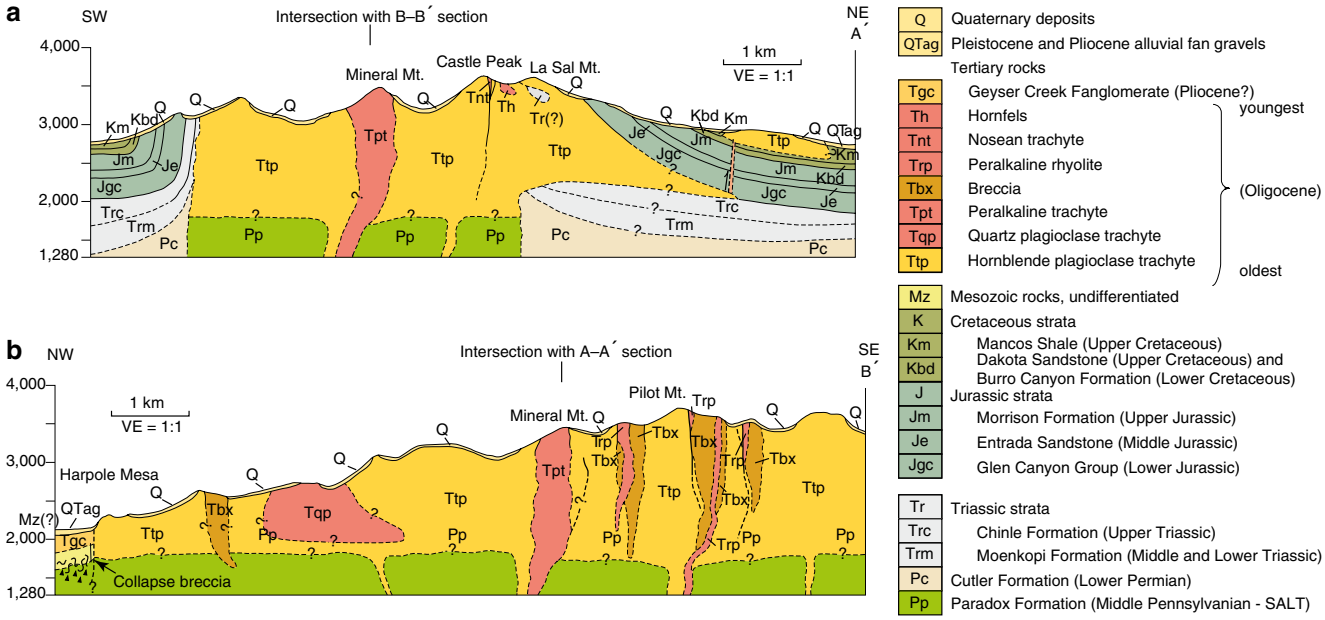

Fig. 16.11 La Sal Mountains, Utah. Interpretive cross sections through the Warner Lake and Mount Waas quadrangles showing laccolith position is focused by the pre-existing salt wall (See Fig. 6.83). Note the intensity of solution collapse in the section covered by sediment rather than laccolithic material (After Ross 1998)

Table 16.2 Decomposition and melting points of selected salts and typical ranges of magma temperatures

Salt	Formula	Decomposition/melt point (°C)
Halite	NaCl	804 anhydrous melt
Gypsum	$CaSO_4{\cdot}2H_2O$	100–150 loss of water
Anhydrite	$CaSO_4$	1,460 anhydrous melt
Carnallite	$KMgCl_3{\cdot}6H_2O$	110–120 loss of water
Sylvite	KCl	750–790 anhydrous melt
Bischofite	$MgCl_2{\cdot}6H_2O$	>118 loss of water
		712 anhydrous melt
Epsomite	$MgSO_4{\cdot}7H_2O$	>70–80 loss of water
Kieserite	$MgSO_4{\cdot}H_2O$	150–200 loss of water
		1,120–1,150 anhydrous melt
Trona	$Na_3H(CO_3)_2{\cdot}2H_2O$	>70 loss of water
Nahcolite	$NaHCO_3$	270 anhydrous melt
Typical magma/eruption temperatures		
Picritic		1,400–1,500
Basaltic		1,100–1,200
Rhyolitic		800–900
Natrocarbonatite		500–600

trend wall, the exact shape and size at depth of the hornblende plagioclase trachyte intrusions making up the main pluton (within the preexisting salt-cored anticline) are poorly understood.

According to Ross (1998) there appears to have been little interaction or contamination of the magma as it passed through the halite mass. However, little is published on the nature of the igneous material where it is in contact with the salt as this contact is covered bya dissolution debris-collapse apron about the edge of the deposit. Low levels of intrasalt alteration implies the temperature of magma emplacement was below that of the melting point of halite. Also, there is a lack of salt dissolution induced collapse features across the area covered by the emplaced magmas, implying a lack of dissolution beneath a relatively impervious magma mass. This is in stark contrast to the situation in adjacent areas, where salt lies beneath the sedimentary cover. One of the reasons for the contrast in salt karst intensity is that the emplacement of a laccolith dome would have elevated the Oligocene landscape in the vicinity of the emplacement by more than 1,500 m. This would ensure that the margins of the laccolith focused groundwater and surface runoff from

the newly formed supra-laccolith mountains into the area about the laccolith periphery wherever it was in contact with the adjacent permeable sediments.

A corollary to these contrasting examples of igneous emplacement in salt is that they offer accessible evidence of heated-halite containment over narrow zones across very large spatial domains and long time periods. As such, they offer real-world analogs for qualitative performance assessment arguments supporting complete containment of nuclear waste stored in halite cavities, even if heated (Chap. 13). But also in this context, a thorough knowledge of the possible distribution of hydrated salts in the halite mass is extremely important. An obvious rule of thumb is; keep the locale of any purpose-built nuclear waste cavity away from zones and layers of hydrated salts.

Molten Salts: Natrocarbonatite and Brine

In terms of its formative conditions, the carbonatite[2] group perhaps lies astride the orthomagmatic and paramagmatic association. Natrocarbonatites are highly alkaline igneous rocks, with the more sodic members exemplified by modern sodium carbonate lavas, which are extruded at Oldoinyo Lengai in Tanzania in the African Rift. Across the latter half of the twentieth century, carbonatite eruptions had filled the northern summit crater of Oldoinyo Lengai to the brim with mottled brown, white, gray and black lava flows, studded with spike-like spatter cones. However, the explosive summit eruption of 2007–2008, destroyed this fantastic landscape, leaving a gaping collapse pit in its place.

Oldoinyo Lengai lavas are unique in terms of their magmatic petrology (Keller and Zaitsev 2012). With eruption temperatures between 500 and 600 °C, about half that of an erupting basalt, they exhibit what are the lowest known magmatic eruption temperatures for modern lavas. When erupting, temperatures of carbonatite lavas are so low that they lack the red shimmering glow, which in daylight characterises most of the world's active lava bodies. In daylight, flowing lavas more resemble a runny black mud and move much more rapidly than silicate lavas, more like motor oil flowing over the ground and typically construct a fresh lava layer only a few centimetres thick. Fresh lava and spatter changes colour from black to white within a few hours of extrusion, due to alteration and hydration of highly labile anhydrous igneous minerals, dominated by nyerereite $(Na,K)_2Ca(CO_3)_2$ and gregoryite $(Na,K,Ca_x)_{2x}(CO_3)$.

[2]Carbonatites are igneous rocks made up of at least 50 % carbonate minerals. Although most carbonatites occur as plutonic rocks, there are well over forty localities with extrusive carbonatites, at nine of which there are lavas, mostly in the East African rift. Carbonatite masses can also take the form of hydrothermal and replacement bodies.

Carbonatite lavas are also highly fluid when moving over the landscape. They have viscosities around 0.5 pascal seconds (Pa.s), which is around 500 times the viscosity of water). This end of the viscosity range also encompasses most fluid endmembers of one of the most common magma types, namely the basalts. At the other end of the lava viscosity range are the silica-rich rhyolites; dry high-silica rhyolites can have viscosities that exceed 10^{12} Pa s. Because of their typically low viscosities, carbonatite flows tend to flow across the landscape in a way that is more akin to a spreading water sheet and, if extruded down slope, quickly move to the lowest part of the landscape to form laterally confined lava flows or "canali."

Natrocarbonatites at Oldoinyo Lengai are extremely alkali-rich, with Na_2O+K_2O generally about 40 wt.%, with high CaO contents of 14–18 wt.%. This initial alkaline composition is due the presence of phenocrysts of nyerereite and gregoryite dominating the highly porphyritic natrocarbonatite lavas, with sylvite and fluorite as main groundmass minerals. Mineralogy of the extruding Oldoinyo Lengai lava has fluctuated over two decades of sampling and study (Keller and Zaitsev 2012): (1) Silicate-bearing natrocarbonatites, characterized by the occurrence of nephelinite spheroids, typify the 1993 and 2006 lavas; (2) Residual melt compositions, as described from the 1988 eruptive period, are indicated by an aphyric filter-pressed interstitial melt of solidifying porphyritic lavas; (3) A separate interlude during the year 2000 when natrocarbonatites with sylvite and fluorite microcrysts were emitted. After 25 years of mostly mild activity, characterized by effusion and spattering of fluid natrocarbonatite lava, there was a paroxysmal ash eruption on September 4, 2007, which changed dramatically the crater morphology, eruptive dynamics and magma composition of Oldoinyo Lengai. This renewed burst of activity means fresh natrocarbonatites, if present at the bottom of the new deep crater pit that formed during the 2007–2008 explosive activity, will possibly remain inaccessible for decades.

Once emplaced the magmatic minerals of Oldoinyo Lengai natrocarbonatite lavas are unstable under atmospheric conditions (Zaitsev and Keller 2006; Keller and Zaitsev 2012). The subsolidus minerals in natrocarbonatites, as listed in Table 16.3, form; (i) Along cracks on the lava surface from hot gases escaping during cooling, (ii) As atmospheric alteration products via solution of water-soluble igneous salt minerals, in particular halides and gregoryite, and by hydration of nyerereite under the influence of meteoric water and, (iii) By reaction with fumarole gases. After solidification, the lavas are cut by a network of thin shrinkage cracks, the edges of which are covered by polymineralic encrustations.

Lava samples from Oldoinyo Lengai, collected 2–24 h after eruption, contain nahcolite, trona, sylvite, and halite with accessory kalicinite and villiaumite (Table 16.3). Atmospheric humidity results immediately (>2 h after

Table 16.3 Subsolidus minerals in Oldoinyo Lengai natrocarbonatites

Minerals	Minerals formed due to		
	Lava degassing during cooling	Atmospheric alteration and hydration by meteoric waters	Reaction with fumarole gases
Nahcolite, $NaHCO_3$	Major	Major	
Trona, $Na_3H(CO_3)_2 \cdot 2H_2O$	Major	Major	
Thermonatrite, $Na_2CO_3 \cdot H_2O$	Major	Major	
Halite, NaCl	Major		
Sylvite, KCl	Major		
Aphthitalite, $K_3Na(SO_4)_2$	Minor	Acc.	
Kalicinite, $KHCO_3$	Acc.		
Villiaumite, NaF	Acc.		
Pirssonite, $Na_2Ca(CO_3)_2 \cdot 2H_2O$		Major	
Gaylussite, $Na_2Ca(CO_3)_2 \cdot 5H_2O$		Major	
Shortite, Na_2Ca_2 $(CO_3)3$		Major	
Kogarkoite, Na_3 $(SO_4)F$		Acc.	
Calcite, $CaCO_3$		Major	Major
Sulphur, S			Major
Gypsum, $Ca(SO_4) \cdot 2H_2O$			Major
Anhydrite, $CaSO_4$			Minor
Monohydrocalcite, $Ca(CO_3) \cdot H_2O$			Minor
Fluorite, CaF_2		Acc.	Minor
Baryte, $BaSO_4$			Minor
Celestine, $SrSO_4$			Acc.

After Zaitsev and Keller (2006)

eruption) in hydroscopic alteration of black lavas, which is marked by the appearance of white powdery thermonatrite, along with nahcolite, on the lava surface. Subsequent reaction (weeks, months, years) of natrocarbonatite with meteoric water and the atmosphere results in the formation of hydrated sodic salts dominated by pirssonite, as well as gaylussite, shortite, trona, thermonatrite, nahcolite as well as calcite (Table 16.3). Generally, the first important step is the formation of pirssonite, along with other end-members including calcite carbonate rocks and loose nepheline-entraining volcanic aggregates and agglomerates. The carbonatite flows in nearby, now inactive, Kerimasi have somewhat higher carbonate contents than Oldoinyo Lengai; silicates are more undersaturated, with less feldspar and more nepheline ($Na_3KAl_4Si_4O_{16}$) and melilite $(Ca,Na)_2$ (Al,Mg,Fe^{2+}) $[(Al,Si)SiO_7]$. There is also strong evidence that calcite was a primary magmatic phase in some carbonatite flows at Kerimasi (Mariano and Roeder 1983).

Rapid post-extrusion changes in mineralogy of the natrocarbonatite drive substantial geochemical transformations in the lava mineral suites and the surrounds. Most obvious is the loss of Na, K, Cl and S to the groundwater system, combined with an increase in H_2O, Ca, Sr, Ba, F and Mn in the lava mineralogy. This is seen in the nearby but slightly older, now inactive, Kerimasi and Mount Homa volcanics, where the natrocarbonatite tephra is converted to supergene Ca-carbonatite that co-mingles with calcrete (Mariano and Roeder 1983).

The oxygen and carbon isotopic composition of altered natrocarbonatites shows a significant shift from the primary "Lengai Box" to high values of $\delta^{18}O$ and $\delta^{13}C$. Calcite exhibits $\delta^{13}C_{PDB}$ values between −2 and −4 ‰ and $\delta^{18}O_{SMOW}$ values of +23‰ to +26‰ (Fig. 16.12). The observed assemblages of secondary minerals formed by reaction with atmosphere and meteoric water, the changes in chemical composition of the natrocarbonatite and field observations suggest that alteration of natrocarbonatite is an open-system low-temperature process. It takes place at temperatures between 8° and 43 °C with the addition of H_2O to the system and the removal of Na, K, Cl and S from the carbonatites.

At Oldoinyo Lengai, Na_2O makes up 32 % of the lava chemistry and the Na_2O/K_2O ratios hover around 4. This, and proximity to the nearby trona deposits of Lake Natron and Lake Magadi, has led some authors to postulate that their unique sodic-rich igneous chemistry indicates an interaction/cycling between a silicate melt and either soda-rich subsurface trona beds (Milton 1968, 1989) or associated saline basinal brines (Eugster 1970, 1986). In this context, they can be considered at least partial paramagmatic deposits.

But any sedimentary influence in the magma chemistry is strongly contested by many in the igneous community, who interpret natrocarbonatites as the end result of a highly saline magmatic separation. For example, Bell and Dawson (1995)

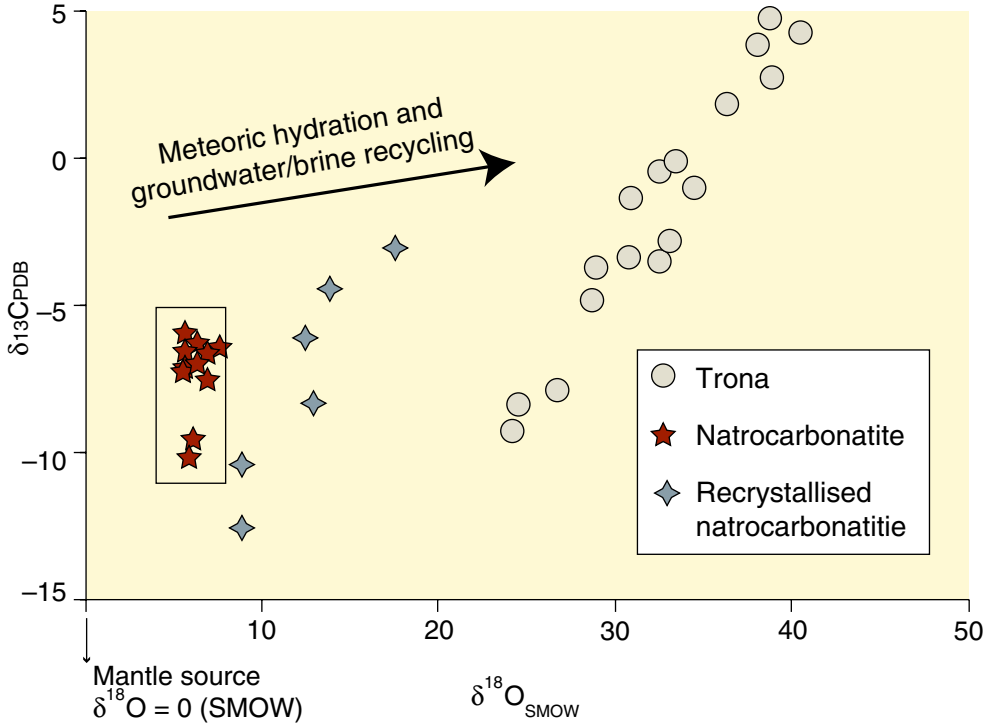

Fig. 16.12 Carbon-oxygen crossplot of natrocarbonatites from Oldoinyo Lengai and trona from Lake Magadi. Recrystallised natrocarbonatites are either altered or recrystallised in the presence of meteoric water (Plot compiled from Bell and Dawson (1995) and data sources therein)

conclude the stable and radiogenic isotopic signatures of natrocarbonatites of Oldoinyo Lengai are different to those of sedimentary trona and similar to other magmatic rocks, including young carbonatites, from elsewhere in east Africa (Fig. 16.12). Therein lies the problem; Bell and Dawson's isotopic data for trona comes from unaltered sedimentary trona, they ignore the highly reactive nature of buried evaporites within active hydrothermal hydrologies, which characterise rift systems (Chap. 2). Nor does their argument consider temperature related fractionation effects that typify evolving stable isotope signatures of oxygen-entraining minerals undergoing burial diagenesis. How much is the oxygen isotope signature of trona lightened as it is buried in settings where it undergoes dissolution/reprecipitation interactions with increasingly hotter throughflowing hydrothermal brines?

The fact that these sodium carbonate lavas at Oldoinyo Lengai, with their highly elevated sodium contents, are: (1) Unique amongst all the world's carbonatites; (2) erupting today; and, (3) Occur in proximity to one of the largest examples of modern endoheic trona accumulation (see Lake Magadi in Chap. 11); must at least argue for some subsurface interaction with trona-derived brines. This is the model proposed by Eugster (1970, 1986) who envisaged a deep actively-circulating saline groundwater reservoir in the Magadi Basin. He interprets the sodium carbonate lavas of Oldoinyo Lengai, not so much as remobilised sedimentary trona, but as the product of the interaction of an evaporite-influenced basinal brine with alkaline silicate magmas.

There can be no doubt that the sodium and bicarbonate ions now held in trona salt beds of the Magadi and Natron basins were derived, at least in large part, by surface weathering and groundwater leaching of the surrounding volcanic ashes and flows, including the natrocarbonatite lavas of Oldoinyo Lengai (Chaps. 2 and 13). Even today, this leachate is carried into perennial trona lakes that occupy the lowermost parts of the two basins. There it is concentrated by solar evaporation to deposit beds of sedimentary trona. Ongoing extension and subsidence within the rift then caries this evaporite into the subsurface, where it is leached by an active hydrothermal hydrology.

But, the carbonatites of this part of the African rift are unusual in the intimate relationship between these sodic-carbonate lava flows and the formation of nearby trona-natron bedded salts and relates to the adiabatic shadow and arid conditions that define this part of the rift. More generally, bedded trona deposits are not part of the association, then again most other carbonatites do not show such high levels of what are evaporite-like sodic mineralogies, rather the bulk of the world's carbonotites deposits are typified by combinations of; calcite, dolomite, phlogopite, biotite, quartz, aegerine, ankerite and K-spar, along with ore minerals such as apatite, pyrochlore, baryte, magnetite, pyrite, monzonite and fluorite. Carbonatites are also the world's main source of rare earth elements and so are of considerable economic import (Berger et al. 2009).

In a GIS-based compilation of known carbonatites, ranging in age from Archaean the modern, Woolley and Kjarsgaard (2008) concluded that the majority of carbonatite deposits are localized within stable continental tectonic units, such as shields, cratons, and crystalline blocks, with well-developed old Earth crust. Inside these large regional structures, carbonatites are confined to alkaline magmatic provinces controlled by intracontinental rift and fault systems. In the correct climatic and hydrologic setting, such sites also likely regions of evaporite accumulations. Carbonatites (but not natrocarbonatites) define an igneous lithological grouping across geologically broader ranges than Oldoinyo Lengai and the Gregory Rift (Morteani et al. 2013; Zaitsev et al. 2013). Some examples, such as the 500 Ma carbonatites of Madagascar, likely assimilated crustal evaporites to help attain their characteristic alkaline earth-rich magma chemistry

Phreatomagmatic Iron-Rich Associations

If the amount of produced volatiles is large when a magma body interacts with country rock sediments, then the result can be a mobile mixture of igneous and sedimentary material that moves rapidly and explosively to the surface in phreatomagmatic breccia pipes, typically with cratered tops (Mazurov et al. 2007; Svensen et al. 2009). When such phreatomagmatic breccia pipes transect salt layers, especially if there are beds of hydrated salts, then the breccias are typically halite-cemented and with a highly altered glassy matrix and numerous large angular volcanic clasts (Korshunovsky-style breccia pipes).

Anhydrite's melting point is much greater than halite, carnallite or sylvite, so rather than melt it tends to dissolve in the hydrothermal milieu generated by most magmas, except picritic, which have emplacement temperatures sufficient to melt anhydrite (Table 16.2). In the 10 m-wide alteration zone formed in lower Cambrian halite at Irkutsk/Nepa, the clear halite crystals adjacent to the dolerite sills are 4–6 cm across (Fig. 16.14). The anhydrite has been altered to rounded grains with characteristic fused edges, which indicate partial exsolution as the molten halite cooled (Pavlov 1970). Sylvite also appears as separate crystal segregations in the clear recrystallised salt, whereas prior to melting it was finely dispersed in brine inclusions throughout the chevron halite.

Korshunovsky (Korshunovskoye) Iron Ore Deposits, Siberia

This region, in the Irkutsk district, is the eighth largest iron ore producer in Russia, with an annual output of 5 Mt of iron ore concentrate. Ore is extracted from magmatic intrusions that completely penetrated a highly evaporitic Phanerozoic succession (Fig. 16.13; Mazurov et al. 2007). Early work on this intrusive magnetite style, which surrounds brecciated diatreme-like pipes, classified it as a skarn association forming a halo around a set of explosive pipes, accompanying regional trap magmatism (Ivashchenko and Korabel'nikova 1960). Some of the more texturally interesting examples of this dolerite/evaporite interaction are in contact-reaction magnesian skarns surrounding Angara-Ilim volcanics in the intracontinental paleorift zones of the Siberian Platform (Mazurov and Titov 1999). There characteristic spinel-forsterite magnesian skarns are confined to the overdome parts of large doleritic bodies and are the result of interactions of massive evaporitic and petroliferous dolomites with fluids released from liquid magma.

Magnesian skarns of the postmagmatic stage are localized in the marginal parts and on the front (outwedged portions) of doleritic sills, apophyses, and the branches of intrusive bodies hosted in Cambrian carbonate-evaporite successions (Fig. 16.13). The skarns have a banded or layered structure and resemble gravel conglomerates, with carbonate cements. The round fragments (pseudo-conglomerates) are composed of globules of disintegrated doleritic porphyrite, completely or partially substituted by zonal magnesian skarns. Their mesostasis is cryptocrystalline and early phenocrysts of olivine, plagioclase, and pyroxene have undergone dispersion and substitution. Unaltered cores of 'conglomerate' are in contact with a fassaite zone, which passes outward into a spinel-fassaite zone and then into a forsterite-magnetite and calciphyre zone (Fig. 16.13).

In typical nonevaporitic palaeo-island-arc and continental-margin regions elsewhere in the world, these skarns have no analogs, in either texture-structural peculiarities or formation mechanisms. They are the texture-specific result of intrusion and solidification of basic magma in a chemically active carbonate-evaporite country rock. Some of the conglomeratic appearance may be indicative of ongoing subsurface dissolution of evaporite salts that were originally part of the rock matrix. In my mind, a partial emplacement analog is seen in the interaction of basalts with hydrated salts in the Fulda region (Fig. 16.10d).

Magnetite pipes and the associated Siberian traps likely played a significant role in the end-Permian extinction event (Fig. 16.15; Svensen et al. 2009; Li et al. 2009). Emplacement of the Siberian Traps set up a life-threatening phreatomagmatic events tied to (1) magma interacting with high levels of hydrocarbon volatiles trapped in and below halites in the Tunguska Basin, and (2) SO_2 release, which was tied to massive Devonian anhydrite assimilation in the nearby Noril'sk region. Together these two styles of magma-evaporite-hydrocarbon interactions released huge volumes of toxic gases into the atmosphere.

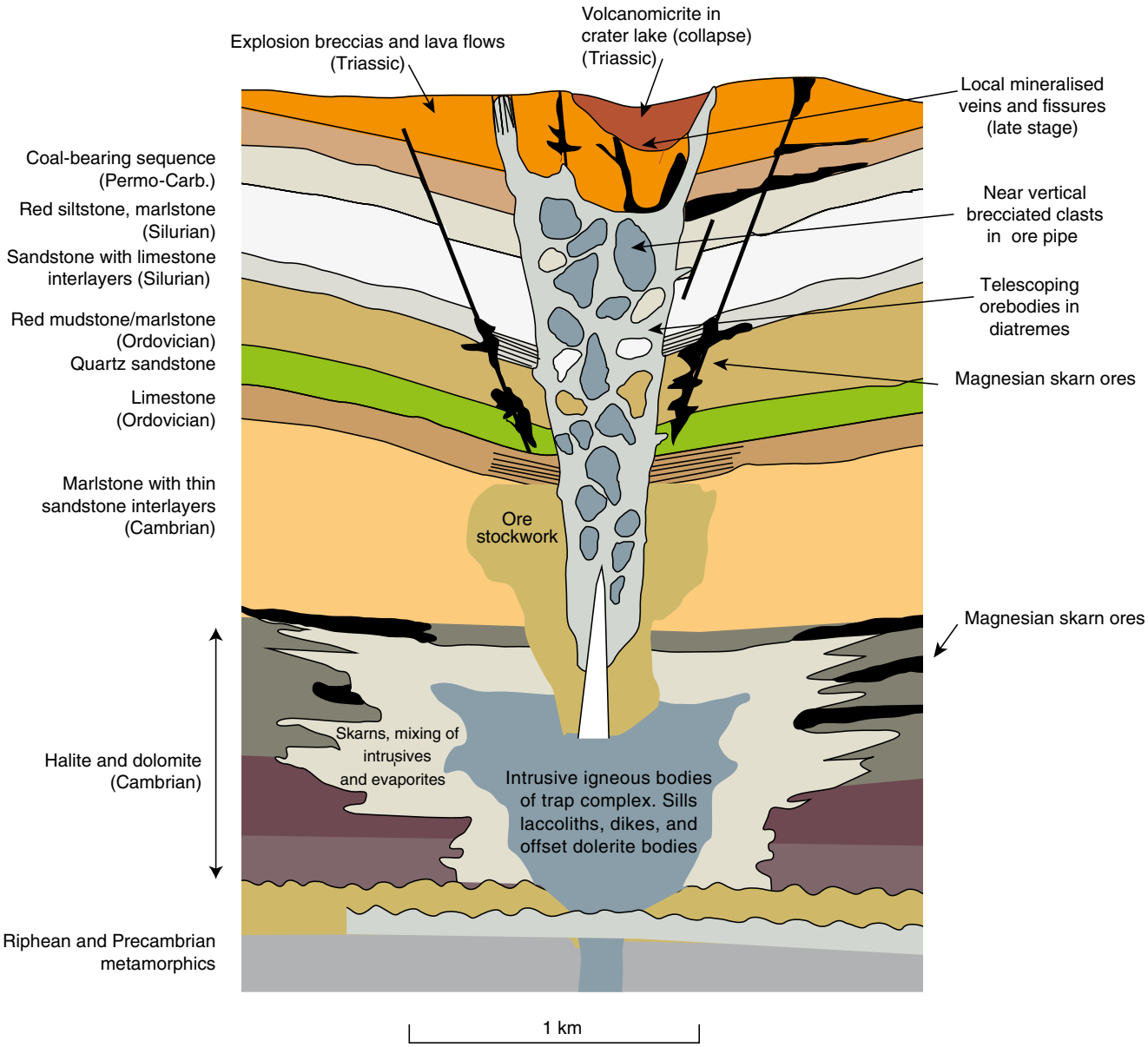

Fig. 16.13 Schematic cross section of an ore-magmatic system of the Angara–Ilim type (After Mazurov et al. 2007), see Fig. 16.14 for stratigraphic detail

As noted by Svensen et al. (2009), across earth history there are a number of large igneous provinces that are associated with significant extinction events and then there are others with similar emplacement volumes that are not. The key question becomes why some large igneous provinces are associated with extinctions, whereas others had apparently minor effects on the biosphere. Sediment composition around sill intrusions of large igneous provinces is perhaps the most important parameter in causing broader environmental change. Significant extinctions tend to occur when sedimentary basins with major evaporite and organic matter deposits are intruded by thick sills, typical of large igneous provinces (megaplume emplacement) or are caught up in a bolide impact (end-Cretaceous). That is, emplacement of widespread intrusions, which typify the Siberian Traps, led to huge outputs of toxins and likely led a mass extinction, whereas the formation of many other large igneous provinces did not: a few kilometre-thick interval of intruded evaporites, trapped hydrocarbons and coals, likely made the difference.

Paramagmatic Saline Haloes

So far, we have focused on orthmagmatic-evaporite interactions, where the magma body is in direct contact with, and is assimilating, evaporite salts or interacting with associated entrapped volatiles. But, there is a much larger spectrum of

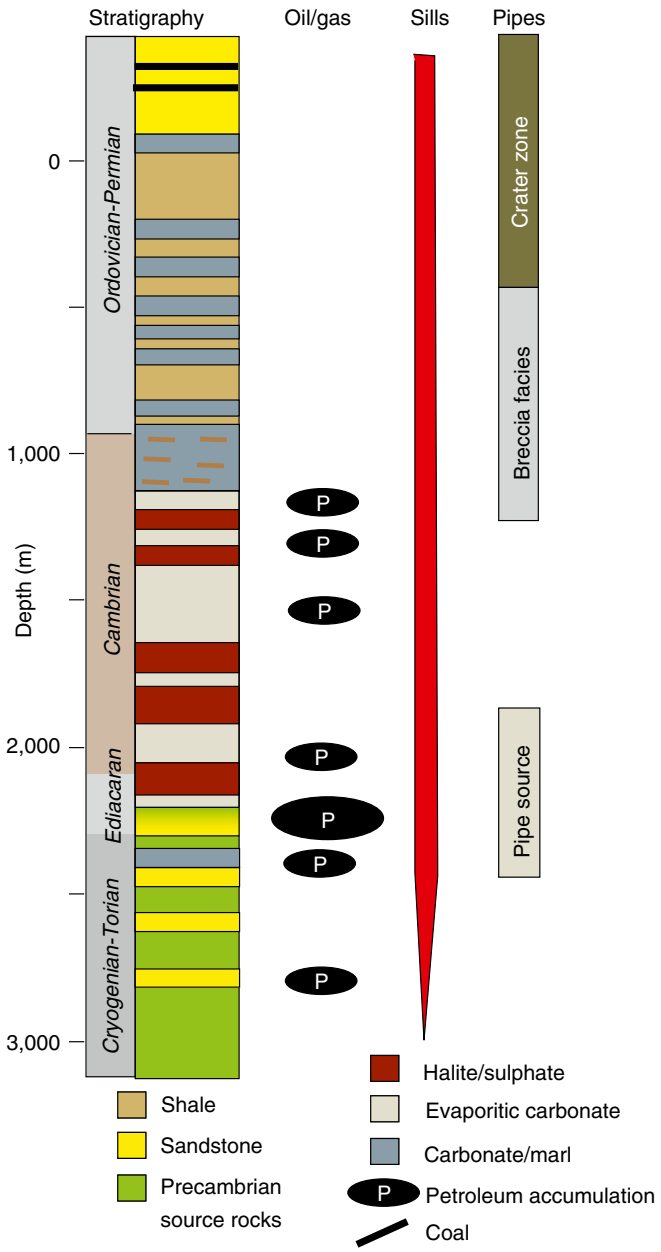

Fig. 16.14 Nepa district stratigraphy in the Tunguska Basin showing levels with petroleum occurrences (After Svensen et al. 2009). The stratigraphy is representative for the basin segment with outcropping or subcropping pipes. Thicknesses of the Precambrian strata vary considerably (1–10 km) but has not been drilled in the central parts of the basin. Sill intrusions are present throughout the basin stratigraphy. The pipes are rooted in the Cambrian evaporite or possibly deeper, but have only been drilled to Upper Cambrian levels, as at Nepa. The inferred source region of the pipes, where intense magma-sediment interactions took place, is likely within the lower Cambrian strata. Craters are filled with up to 750 m of crater-lake sediments

metal deposits where the ore body is largely the result of the mixing/cooling of hydrothermal fluids. In some cases the fluids are derived largely from the cooling magma (juvenile waters), while at the other end of the hydrothermal spectrum the magma acts as little more than a heat source driving the circulation and mixing of highly saline basinal brines. In yet other cases, the circulating brines are part of the burial/metamorphic milieu and may not require a magmatic heat source (Fig. 16.16). The resulting deposit styles range from successions best interpreted as skarns, to others best interpreted in the context of mineral haloes related to regional metamorphism (Chap. 13).

One of the keynote papers to summarise notions of ore deposits from evaporite-related paramagmatic hydrothermal haloes was that of Barton and Johnson (1996), followed by Barton and Johnson (2004). They explored the notion that hybrid evaporite/magmatic chloride-rich hydrothermal fluids play a significant role in the formation of some igneous ore

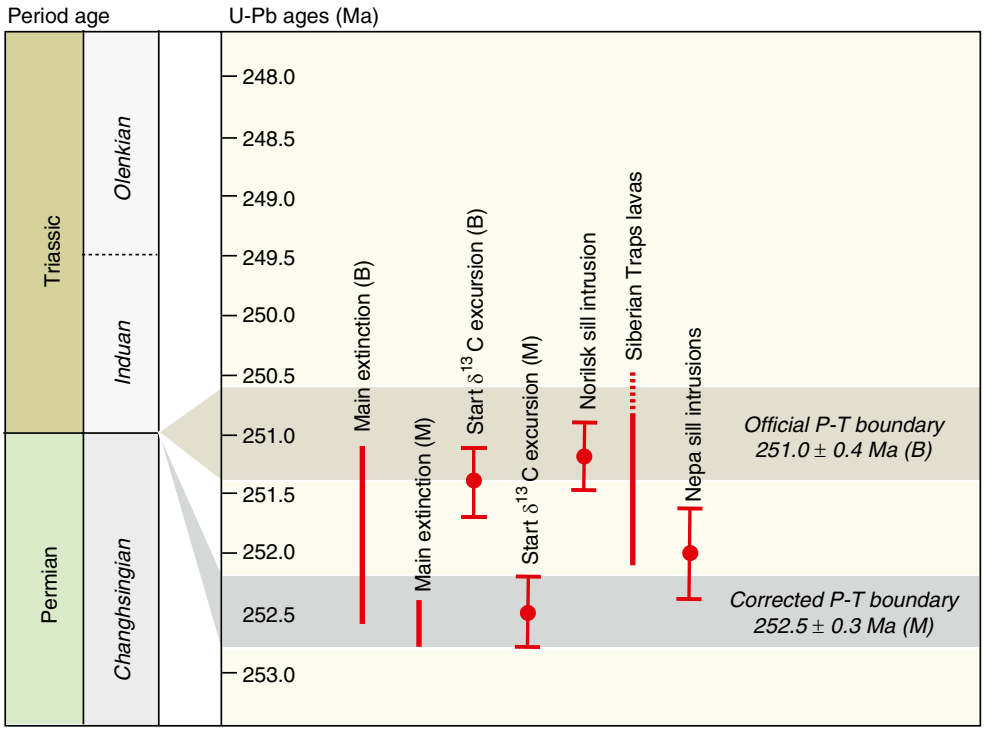

Fig. 16.15 Compilation of zircon U–Pb ages of key end-Permian events (After Svensen et al. 2009). The ages of the P–T boundary are from Gradstein et al. (2004) deduced from Bowring et al. (1998) (labelled "B"), and from a revised age by Mundil et al. (2001), (labelled "M"). The age of the sill emplacement at Nepa is synchronous with pipe formation and release of carbon gases and halocarbons to the atmosphere. The main phase of the extinction is dated to have occurred between 252.3 ± 0.3 and 251.4 ± 0.3 Ma by Bowring et al. (1998) (labelled "B") and 252.6 ± 0.2 Ma by Mundil et al. (2004) (labelled "M")

deposits, including many of major Fe-oxide-Au deposits or IOCG deposits (Table 16.4). Their conclusions encompassed evaporite/saline brine/aridity associations ranging from Proterozoic Cu-Au deposits, back to the Archaean and into the Neogene, in tectonic settings ranging form rifts to collision belts. In both papers, they concluded that variation in primary magmatic composition is a secondary control when compared to variations in the hydrothermal chemistries contributed by dissolving chloride-rich evaporite sediments and metasediments (Fig. 16.16). In other words defining the evaporitic origin and flow pathway indicators of chloride brines are key to understanding this type of ore distribution.

According to Barton and Johnson (2004), evaporite-associated hydrothermal deposits have abundant Fe oxides, as well as a characteristic suite of accessory elements, at least some sodic hydrothermal alteration, along with evidence for vigorous emplacement processes, and a genetic link to magmatic interactions in evaporitic terrains (Table 16.5; Fig. 16.16). The circulation systems are typified by large volumes of Ti-poor Fe oxides (commonly >10^6 tonnes magnetite or haematite) with lesser amounts of phosphates (apatite, REE phosphates), Cu-Fe sulphides and sporadic Au, U, Ag and Co minerals. Proximal and deeper mineralisation consists of early magnetite ± apatite rocks, commonly with abundant sodic (albite ± scapolite ± hornblende) wallrock alteration. Superimposed or distal mineralisation consists of haematite ± Cu-Fe sulphides ± REE minerals with ± potassic alteration. Variants include deposits with substantial sodic alteration and Cu or U mineralisation, but subordinate Fe-oxide. Sodic alteration occurs in nearly all districts, is typically voluminous, and a number of examples have local peralkaline assemblages containing Na-Fe^{3+} bearing amphibolites or pyroxenes. Calcareous host rocks contain calcic or magnesian skarn assemblages with hydrous distal assemblages (actinolite-chlorite-carbonate) that are superimposed on anhydrous assemblages (pyroxene + garnet). In shape, these deposits may consist of stratabound massive Fe-oxides hosted in volcanic and sedimentary rocks, although most commonly they are discordant, variably brecciated, tabular to irregular masses. The former have previously been interpreted by others as syngenetic replacement bodies, while the latter have been interpreted as veins, dykes and breccia fills associated with magmatism.

Igneous rocks can be closely linked to these deposits, but there appears to be little correlation of mineralisation to igneous composition or intrusive phases (Barton and Johnson 1996, 2004). The ions in the circulating hydrothermal fluids are, at least in part, derived by reflux/dissolution of coeval or older evaporitic sources. Circulation is usually driven by the thermal effects of the magmatism. Igneous rocks typically also serve as the source and host for mineralisation, making the total system a form of large-scale

Table 16.4 Characteristics of a selection of aridity/salinity associated Fe-Oxide(−REE-Cu-Au-U) bearing regions

Region and district	Age and setting	Size* and metals, sodic alteration	Comments	References
Red Sea region (Afar, Atlantis II)	Holocene - rift basaltic volcanism, abundant evaporites	>100? (>15?) FeOx + MnOx ± Zn-Cu-Pb sulphides seds; localised peralkaline alteration	Modern geothermal circulation through evaporitic beds	Zierenberg and Shanks (1983), Bonatti et al. (1972)
Chilean Andes (El Laco, Magnetita Pedernates)	Neogene – interm. Volcanic centres in closed basins	>1,000? (>500) FeOx in 2 districts; minor sodic ± peralk alt	Arid; volcanos adjacent to salars containing halite	Vivallo et al. (1994)
Mexican Altiplano (Cerro de Mercado, La Peria)	Mid-Tertiary - continental arc felsic volcanic centres	>300 (>100) FeOx ± REE, Cu in >20 locs; modest sodic ± peralk alt	Arid palaeoclimate, sulphates in volcanic basins, Jurassic salt	Lyons (1988)
Basin & Range, USA (Cortez Mtns., Humboldt complex)	Jurassic – back-arc mafic and felsic volcanic complexes	>1,000 (>75) FeOx ± REE, Cu; >40 locs; ext sodic ± peralk alt	Arid palaeoclimate, evaps in region; heavy S, saline fluids	Battles and Barton (1995), Barton et al. (1991)
Andean coastal belt, Peru & Chile (El Romeral, Raul, Candelaria, Monterrosas)	Jurassic-Cretaceous – extensional arc interm-mafic volcano-plutonic centres	>3,000 (350) FeOx ± major Cu(Au), minor Co, REE; >150 locs; ext sodic ± peralk(?) alt	Arid palaeoclimate, Jurassic evaps; variable S, saline fluids, VMS in same arc	Vidal et al. (1990)
Mid-Atlantic, USA (Cornwall, Grace)	Triassic-Jurassic – mafic sills in rift basins	>350 (>100) FeOx ± Cu, Co (± U); >50 locs; skarn & sodic alt	Redbeds ± evaps; geochem evidence for evap source	Rose et al. (1985)
Siberian Platform, Russia (Korshunovsk, Tagar)	Permo-Triassic - mafic intrusions with flood basalts	>3,000 (>650) FeOx + minor Cu, Co in >150 locs; skarn and sodic alt	Basalts interact with Cambrian salt, saline fluids, heavy S	Smirnov (1977), Vakhrushev et al. (1981), Zharkov (1984)
Turgai, Kazakhstan (Sarbat, Kachar)	Carboniferous – intermmafic arc volcanic centres	>4,000 (>1,500) FeOx + minor Cu, Co; ext sodic alt & skarn	Arid palaeoclimate, possible evaps	Smirnov (1977), Zharkov (1984)
Central Iran (Bafq, Gole Gohar, Hamadan)	Cambrian & younger -anorogenic felsic volcanic centres	>2,500 (>1,000) FeOx ± Cu, REE; >25 locs; sodic ± peralk alt	Extensive Cambrian & younger evaps; distal MnOx & Pb + Zn	Forster and Jafarzadeh (1994)
NW Canada (Great Bear, Wernecke Mtns.)	Proterozoic – interm arc volcano-plutonic centres	>50? (>10?) FeOx ± Cu, U, Ag, Co; >25 locs; regional sodic alt	No evaps reported; zoned from FeOx to distal Ag-Co-U	Hildebrand (1986), Hitzman et al. (1992)
South Australia (Acropolis, Olympic Dam, Emmie Bluff)	Mid-Proterozoic – anorogenic felsic-mafic(?) suite	>3,000 (>2,000) FeOx + major Cu, REE, U, Au; >5 deposits	High salinities, but no described Proterozoic evaps	Haynes et al. (1995), Gow et al. (1994)
Northern Sweden (Kiruna, Gallivare, Ekstromberg)	Mid-Proterozoic – maficfelsic volcanic suite, extensional(?)	>5,000 (>2,000) FeOx ± Cu, REE, Au, U; >20 locs; ext sodic ± peralk alt	Evidence for rifting with coeval evap source	Hitzman et al. (1992), Hauck (1990)
Northeastern USA (Benson mines, Mineville, Dover)	Mid-Proterozoic(?) – felsicinterm anorogenic suite	>1,000 (200) FeOx + REE ± Cu, U; >30 locs; ext sodic ± peralk & skarn	Evaps present; some interpret FeOx to be related to Grenville	Foose and McClelland (1995)

After Barton and Johnson (1996)
In millions of tonnes;* first number is total district resource, numbers in parentheses are tonnages for largest deposit within the district. Abbreviations; *peralk* peralkaline, *seds* sediments, *alt* alteration, *evaps* evaporites, *ext* extensive, *interm* intermediate, *locs* locations, ? indicates estimate

contact metamorphism. The dissolving evaporite or meta-evaporite provides much of the chloride necessary for metal transport, as well as the Na observed in the widespread sodic haloes that typify the dominant alteration in many of these deposits.

During extensional events, the downward penetration of surface/basinal pore fluids into basement rocks can occur along fault zones penetrating the basement (e.g., Fig. 14.57; Oliver et al. 2006). These fluids can leach metals from the basement and transport them, leading later to the formation of hydrothermal ore deposits in the basement and/or the overlying cover sequences. Indeed, many hydrothermal ore deposits in sedimentary basins have isotopic and geochemical signatures pointing to the involvement of basement rocks, particularly as a source of metals (e.g., Shelton et al. 1995; Piqué et al. 2008).

Products from the dissolution of thick halite beds generally are caught up in circulating basinal fluids. Owing to the chloride-rich nature of dissolving halite beds, sulphur levels tend to be relatively low in the brine. Reaction of these

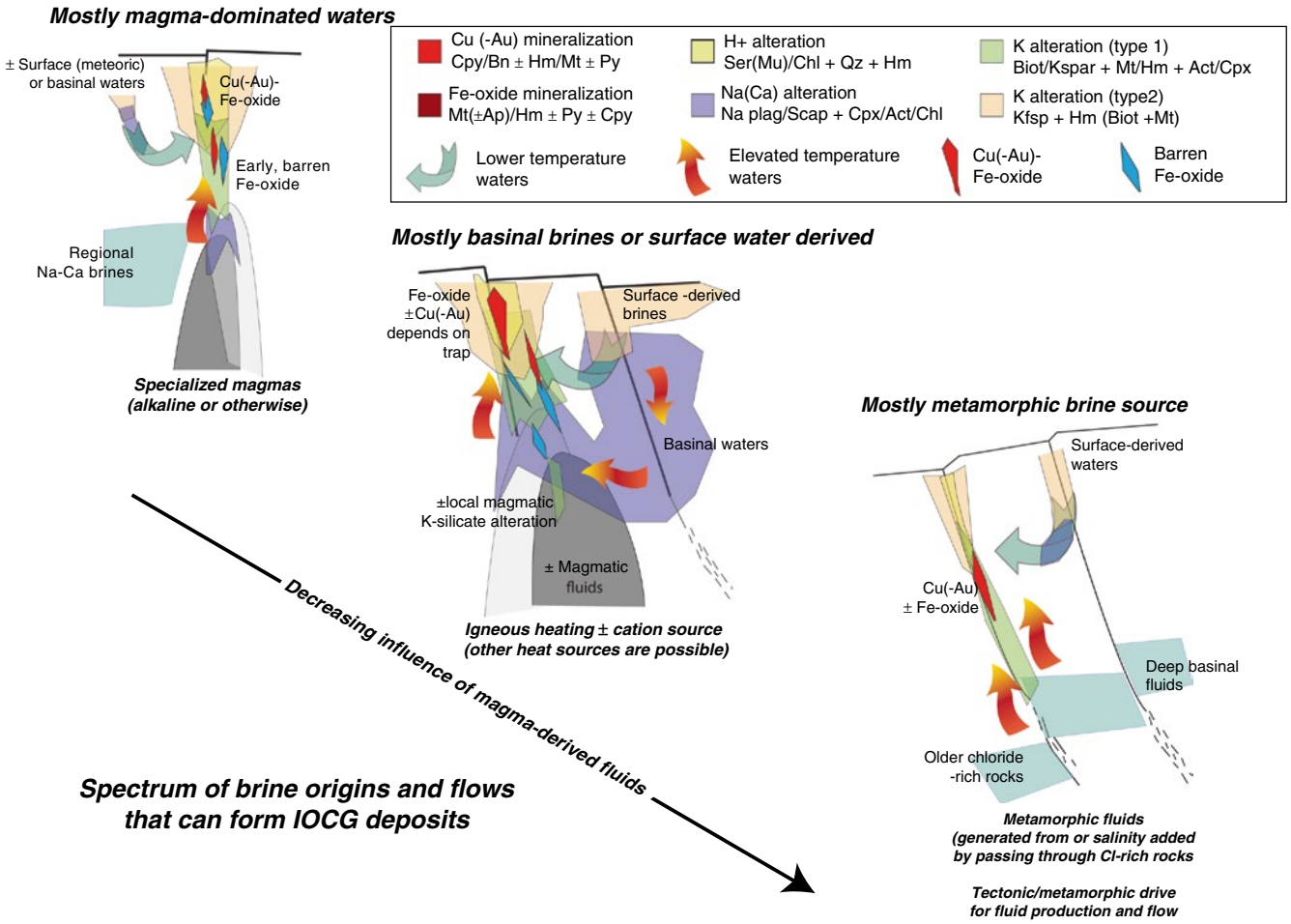

Fig. 16.16 Spectrum of brine origins and contributions of various hydrothermal brines and waters in IOCG deposits across the range of models from magma-dominated to basin-brine-dominated to deposits created by chloride-rich metamorphic fluids (Modified from Barton and Johnson 2004). See also Table 16.4

fluids along hydrothermally-driven circulation pathways produces predictable patterns of alteration and mineralisation (Fig. 16.16; Barton and Johnson 2004). Patterns can be similar to those created by nonevaporitic igneous-related hydrothermal circulation cells (e.g., metamorphosed porphyry deposits). However, there are diagnostic differences in the proportions of indicator minerals in the alteration haloes and nearby metaevaporites, such as scapolite and sodic amphiboles, along with characteristic solution breccia textures that distinguish these deposits. Voluminous sodic alteration typically dominates, independent of other factors of the magmatic history, and in far greater volumes than any potassic alteration that develops later in the circulation history.

On the downwelling limb, sodic alteration reflects the high Na contents in relatively low temperature fluids (Fig. 16.16). Alteration volumes are limited only by the amount of fluid that can circulate (heat balance), rather than by the S and Cl contents of causative intrusions, and so contrast with the typical situation in many porphyry-type systems. Coincident with sodic alteration, downwelling fluids can leach components in which it is undersaturated (Fe, K, Ca, reduced S, REEs, SiO_2; Barton et al. 1991; Dilles and Proffett 1995).

If temperatures are relatively high, marialitic scapolite (scp) + hornblende (hbl) dominate the alteration halo. However, the presence of scapolite and hornblende is, by itself, not diagnostic of an evaporitic source as both minerals can also form in nonevaporitic intermediate and mafic systems. It is the total association, its geometry and the recognition of a range of former evaporite/meta-evaporite textures and/or salt mass/halokinetic geometries in the country rock that are key to an interpretation of the relative importance of evaporite/basinal brine versus magmatic fluid inputs to the mineralizing system. However, many economic geologists, well versed in their understanding of rocks and processes formed or overprinted by high temperature fluids, do not promptly recognise indicators of the involvement of precursor saline mineral masses or beds (see Chaps. 7 and 13).

Table 16.5 Synopsis of likely evaporite indicators tied to IOCG styles and paramagmatic brine/hydrothermal associations, as defined by Barton and Johnson (2004)

Fluid source	Mostly magmatic waters	Mostly non-magmatic waters	
		Basinal and/or surface-derived	Metamorphic waters
Fundamental processes	Release of S-poor metal bearing brine from magma; fluids rise by buoyancy	Thermal/density convection of nonmagmatic brines; wall rock reaction provides metals	Metamorphic release of brine components by devolatilization or reaction with other aqueous fluids; rise by buoyancy
	Cooling, wall-rock reaction ± fluid mixing provide trap	Cooling, wall-rock reaction or fluid mixing provide trap; second fluid may provide metals	Cooling, wall-rock reaction ± fluid mixing provide trap
Igneous associations	High-K, oxidized suites ranging in composition from diorites to granites	Igneous rocks diverse (gabbro to granite); nonmagmatic examples known	No necessary connection, though commonly present
	Carbonatite and strongly alkaline connections proposed by some workers	Key heat source in most	Could be heat source in some settings
		Material source, diversity reflected in geochemistry	Can be material source
Hydrothermal alteration in feldspathic hosts	Na(Ca) and other types (K, H+) link to magmas	K (type I), $H^+ \pm$ Na(Ca) in upwelling zones	Primarily K and H^+ alteration associated with deposits
	Regional Na(Ca) coincident but not directly related to Cu(−Au)	Na(Ca) ± K (type II) in recharge zones	Regional Na(Ca) association reflects sources
Relationship of Fe-oxides to Cu(−Au)	Some Fe-oxides with Cu(− Au), may be deeper or higher-T equivalents	Mt-rich are deeper, earlier, higher temperature parts of ore-forming; Mt or Hm also typical with Cu	Fe-oxides present, but relatively minor (Bi or Chl common); Fe oxides commonly generated by breakdown of mafic minerals rather than Fe introduction
	Barren Fe oxides may form from distinct fluids and commonly in older hydrothermal systems in same area	Barren Fe oxides represent lack of S trap for Cu or lack of second Cu-bearing fluid	
Local setting: depth/structure	Shallow to mid crustal levels; commonly along regional structures but near causative intrusions	In (mainly) brittle upper crust; plumbing provided by regional or volcanotectonic structures	Mid- to shallow crustal levels near or on major structures; surface fluids require shallow levels
Global setting	Arcs or extensional environments that produce characteristic magmas (oxidized high-K or alkaline)	Regions with appropriate brine sources (arid settings or buried Cl-rich evaporitic materials), faultfocused plumbing systems, and thermal/density drives	Regions with Cl-rich low to intermediate-grade source rocks (typically meta-evaporites); compressional setting (e.g., basin-collapse) or prograde metamorphism
Possible evaporite indicators	Not typically noted, may be present if any interactions with nearsurface evaporites, saline waters and/or hypersaline brines have occurred	Salt beds, dissolution breccias, halokinetic geometries, alteration haloes can outline fault/salt welds, meta-evaporite indicators in more deeply-buried Cl sources	Meta-evaporite indicators, dissolution breccias, halokinetic geometries, alteration haloes can outline fault/salt welds

Albite (alb) + actinolite (act) + chlorite (chl) tend to form as co-precipitates in more mafic systems (Fig. 16.16). Such peralkalic assemblages are typically present in many evaporite-associated Fe-oxide occurrences. They are hard to rationalise by ordinary igneous or magmatic hydrothermal mechanisms (Barton and Johnson 2004). In contrast, the extremely high Na^+/H^+ levels of a dissolving evaporitic source can drive reactions such as:

$$2NaCl_{aq} + Fe_2O_3 + SiO_2 + H_2O \text{—} > 2NaFeSi_2O_6 + 2HCl$$

On the upwelling limb, cooling wallrock reaction and mixing of hot fluids with other basinal fluids creates distinctive mineral products, dependent on rock type and flow path. Sodic alteration persists where fluid-to-rock ratios are high. Hydrolytic alteration haloes [producing K-mica (sericite) + quartz in felsic rocks, chlorite in mafic rocks] form in response to cooling, along with precipitation of metals from chloride complexes. In rocks with moderate K_2O contents, potassic alteration (secondary biotite + K-feldspar) can form by alkali exchange (Hitzman et al. 1992).

Evaporitic brines sourced from dissolving thick halites have exceptionally high Cl/S ratios; thus metal content greatly exceeds the amount of sulphur available to precipitate them (Barton and Johnson 1996, 2004). Partial reduction and incorporation of sulphides may modify any original sulphate-bearing fluids, but they generally have too little sulphur to precipitate sulphide minerals at higher temperatures associated with circulation close to the intrusive. Consequently, only the least soluble chalcophile elements (e.g., Cu) form sulphides, along with the other elements that precipitate oxides or oxysalts (Fe, REEs, U) or the native elements (e.g., Au). Because adequate S is lacking, Pb and Zn will be removed from the system, and Fe-sulphides will be sparse. In some circumstances, reduction of these fluids

might precipitate distal Co-As-U. Early precipitation of magnetite/apatite is superseded by haematite ± copper-iron sulphides (Cp-Py) ± other REE minerals, as H-O(−Cl-S) fluids become more oxidising and sulphidising with decreasing temperatures (Barton et al. 1991). Barton and Johnson's (1996, 2004) broad grouping of igneous-evaporite/aridity related deposits includes the evaporite-associated IOCG deposits discussed next, but does not encompass the complete broad spectrum of styles and mechanisms inherent to the formation of all IOCG deposits.

Iron-Oxide Copper Gold (IOCG) Deposits

The discovery by Western Mining in the 1970s of the giant (2,320 Mt) Olympic Dam deposit near the edge of the Gawler Craton, South Australia, and the ensuing increase in exploration and research aimed at the discovery of similar low sulphidation ore deposits, led to the recognition of a new and what was first, and is still to many workers, a very broad deposit class, called iron oxide Cu-U-Au-rare earth elements (REE) deposits (e.g., Einaudi and Oreskes 1990; Gandhi and Bell 1990) and abbreviated to IOCG deposits (iron-oxide copper gold). The poorly defined class of ore deposits known as IOCG deposits, although better defined in recent years, still encompasses a diversity of formative settings that in earlier classifications of IOCG deposits grouped occurrences that ranged across orthomagmatic (intrusive and extrusive) to magmatic-hydrothermal deposits (Fig. 16.17). In the early days of IOCG studies, little space was given to defining the relative importance of magmatic versus basinal contributions to the ore forming hydrology. Many would say, including I, that the IOCG deposit class is still so broad, and still not tied to indicator chemistries and textures, that it is of little use as an on-ground exploration tool.

IOCG classification has been problematical at least since the definition of the Fe oxide–Cu–Au (IOCG) class of deposits by Hitzman et al. (1992). Subsequent research has refined the definition of this depositi style (Hitzman 2000; Williams et al. 2005; Groves et al. 2010), and suggested the Fe oxide-apatite (Kiruna-type) deposits likely are a separate, but related, type of ore deposit. A range of genetic models have also been proposed for IOCG deposits, many include the involvement of basinal brines, or fluids that have interacted with meta-evaporites, or surface-derived brines (e.g., Barton and Johnson 1996, 2002) and subsequent interactions with magmatic fluids.

Olympic Dam was, and is, considered to be the "type" IOCG deposit, and it is still the only supergiant ore deposit in this class. A comprehensive description of general characteristics across a range of IOCG deposits, published by Hitzman et al. (1992), was based largely on studies of iron-rich sulphide-poor deposits centred on Olympic Dam and prospects in the Stuart Shelf (Australia), along with deposits in the Cloncurry District of Queensland, the Kiruna district (Sweden), the southeast Missouri (Pea Ridge) iron district (USA), and the Wernecke Breccias (Canada). Within this IOCG classification, Hitzman (2000) identified 3 broad

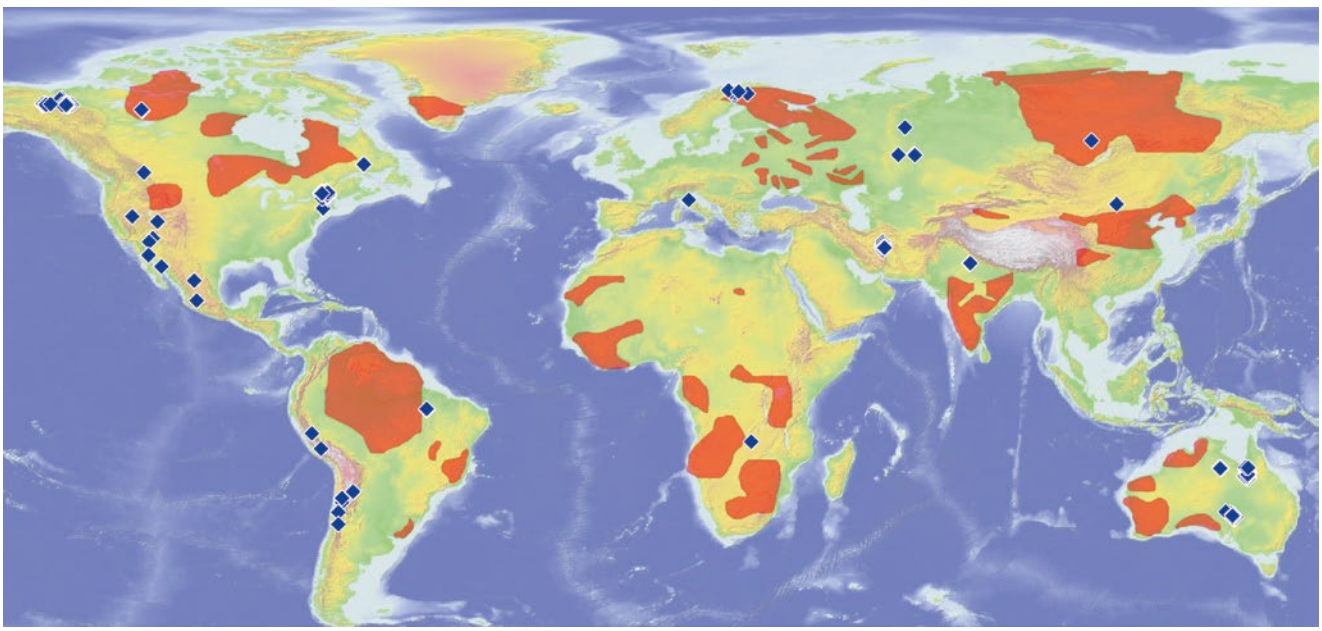

Fig. 16.17 IOCG deposits (*sensu lato*) with ties to basinal brine/evaporite fluids shown as *blue diamonds* on a world topographic base, also plotted are the larger Archaean craton blocks (*red areas*) (Plot compiled as GIS, using MapInfo® and SaltWorks IOCG version 1.6 data module as data source)

tectonic associations: (1) Intracontinental orogenic collapse (e.g., Cloncurry district), (2) Intracontinental anorogenic magmatism (e.g., Olympic Dam and Pea Ridge districts) and, (3) Extensional environments along a subduction-related continental margin (e.g., Chilean Iron Belt).

Some deposits previously classified as IOCG deposits and, often as not, associated with nearby evaporites, basinal brines and meta-evaporites, did not sit comfortably within the notion that IOCG deposits were the result of hydrothermal processes driving Cu-Au precipitation. Such *sensu lato* examples of IOCG deposits encompass the Proterozoic Kiruna iron ores of Scandinavia and the Pliocene magnetitic and extrusive iron ore bodies at El Laco, Chile. And so, as such *sensu lato* examples lacked elevated levels of Cu and Au, the definition of IOCG deposit was further refined by Hitzman (2000) in a reclassification that excluded Kiruna-type magnetite-apatite deposits. Instead, the magnetite-apatite deposits of Kiruna and iron extrusives such as El Laco were listed as likely endmembers in a spectrum of iron-rich deposits. Since then, most more recent classifications and listings, follow with this tenet, and tend to exclude the Kiruna and El Laco styles of deposits from the IOCG group (Groves et al. 2010).

The debate continues, but the consensus is that IOCG deposits are hydrothermally influenced and external to a magma body. There is a strongly-hydrothermal saline association in the country rock with variable levels of magmatic volatiles, rather than a purely orthomagmatic derivation. This is now the widely accepted mechanism for the larger economic examples of the IOCG group of deposits, including the "type" IOCG deposit at Olympic Dam in the Gawler Craton, South Australia (Gillen 2010; McPhie et al. 2011). For a comprehensive discussion of the geology of the broad range of Iron-Oxide Cu-Au deposits, the reader is referred to excellent reviews by Davidson and Large (1994) of the Australian deposits, while Frietsch et al. (1997) provide an excellent summary of the Scandinavian deposits. Williams et al. 2005, Pirajno et al. 2008, Groves et al. 2010 and Gillen (2010) provide comprehensive world overviews of the IOCG deposit class.

According to all these authors, the IOCG end of the hydrothermal iron-deposit spectrum is still very loosely defined. It encompasses copper ± gold (± uranium) deposits of Archaean to Tertiary age, which are linked primarily by the presence of abundant Ti-poor (<2 wt.% TiO_2) magnetite and/or haematite, and extensive alteration, particularly Fe-, Na-, and K-metasomatism (Hitzman et al. 1992; Hitzman 2002; Sillitoe 2003; Williams et al. 2005; Hunt et al. 2007; Gillen 2010). But, as recently noted by Groves et al. 2010, this still somewhat broad grouping encompasses numerous small iron-rich deposits that make the definition of an exploration-relevant tectonically-focused exploration model an impossible task.

Groves et al. (2010) suggests breaking out of this broad IOCG grouping, a tighter definition focused on characteristics of known economic associations. The resulting IOCG *sensu stricto* deposits are all: (1) magmatic-hydrothermal deposits that contain economic Cu and Au grades; (2) are structurally controlled, typically contain significant volumes of breccia; (3) are commonly associated with presulphide sodic or sodic-calcic alteration; (4) have alteration and/or brecciation zones at a broad, typically regional, scale relative to economic mineralization; (5) have abundant low Ti iron oxides and/or iron silicates intimately associated with, but generally paragenetically older than Au-Cu sulphides, with REE enrichment and low S sulphides (lack of abundant pyrite) and; (6) lack widespread quartz veins or silicification. Many of the IOCG deposits in this more narrowly defined group of IOCG deposits show a temporal, but not a close spatial, relationship to major magmatic intrusions and most encompass a range of evaporite associations (Table 16.6, Fig. 16.18).

This tighter definition excludes most porphyry and skarn deposits from the *sensu stricto* IOCG grouping. Intrusions, where identified, are typically alkaline to subalkaline, mixed mafic (even ultramafic) to felsic in composition, with evidence for mantle derivation of at least the mafic end members of the suite. According to Groves et al. (2010), the giant-size of many of the *sensu stricto* IOCG deposits and surrounding alteration zones, the highly saline ore fluids, and the available stable and radiogenic isotope data indicate likely release of deep, volatile-rich magmatic fluids through devolatization of causative, mantle-derived magmas and variable degrees of mixing of these magmatic fluids with other crustal fluids, especially basin brines, along regional-scale fluid flow paths.

Within such a *sensu strictu* classification, Precambrian IOCG deposits are the dominant members of the IOCG group in terms of both copper and gold resources. Within this *sensu stricto* grouping there are twelve IOCG deposits with >100 tonne resources that are located in intracratonic settings within some 100 km of the margins of Archaean or Paleoproterozoic cratons or other lithospheric boundaries. They tend to have formed 100–200 m.y. after supercontinent assembly (Fig. 16.18). Their tectonic setting at formation was mostly anorogenic[3], with magmatism and associated hydrothermal activity likely driven by mantle underplating and/or plume hot spots. According to Groves et al. (2010), limited amounts of partial melting of volatile-rich and possibly metal-enriched metasomatized early Precambrian sub-

[3] Anorogenic means not orogenic, and so such plutons were emplaced in periods lacking in, or unrelated to orogenic disturbance. A-type granitoids are emplaced in such periods in settings that typically encompass apparently stable cratons and intraplate (within-plate) extensional continental rifts, but can also include oceanic islands, generally near spreading ridges (Réunion, Ascension, Azores, Canary).

Table 16.6 Typical examples within the spectrum of Iron-Oxide-Copper-Gold (IOCG) deposits

Deposit	Tonnes ($\times 10^6$)	Commodity grade	Associated metals	Mineralization styles	Evaporite/fluids association
Non-Magmatic End-Member IOCG					
Wernecke Breccia, Yukon, Canada (ca 1,710 Ma) Hunt et al. (2005), Gillen (2010)	Slab: 20	Cu(%)0.35	U, Co, Mo	Disseminations, veins, breccia infill	Wernecke breccia is likely halokinetic. Mother salt was in Fairchild Lake Group, indicated by widespread evaporate solution breccias, deposits associated with abundant Naand Cl-rich (marialitic) scapolite and Mg-rich biotite.
Tennant Creek, Northern Territory, Australia ca. 1,860 Ma Williams and Pollard (2003)	W. Peko: 3.2 Eldorado: 0.0292	Cu (%) Au (g/t)4 20.8	Bi	Massive and vein mineralization overprinting ironstone	Small high-grade Cu-Au ironstone deposits hosted in fault-focused zones in deformed greenschist metasediments. Ironstones formed from hypersaline basinal brine with possible magmatic contribution
Redbank area, Queensland, Australia (<1,780–1,720 Ma) Knutson et al. (1979)	Bluff: 2 Sandy Flat: 1.5	Cu (%)1.6 Cu (5)6 2	Pb, Zn, REE	Breccia infill, veins, disseminations	50 breccia pipes located along a series of basement faults and source in halokinetic interval in Tallawallah Grp (pers. obs). Abundant K feldspar, hematite, and chlorite in breccias and host strata. Mostly from heated connate brines and/or marine waters rather than magmatic-hydrothermal fluids
Hybrid Magmatic-Non-Magmatic IOCG					
Olympic Dam, Gawler Craton, South Australia (ca. 1,590 Ma) McPhie et al. (2011)	2320	Cu (%)1.3 Au (g/t)0.5 Ag (g/t)2.9 U308 (kg/t) 0.4	Co, REE (dominantly La and Ce), Ni, As	Disseminations, veinlets, and fragments within breccias zones, primarily within breccia matrix with sedimentary clasts in breccia. Historically interpreted as diatreme.	Red-beds (possibly evaporitic) of the Pandurra Formation etc. lie beneath the younger cover sequence and pinch out against a crystalline basement high of predominantly foliated Donnington Suite granite. Strong intraclast breccias evidence for involvement of overlying (now eroded) sedimentary system in mineralisation.
Aitik. Northern Fennoscandia (ca 1870 Ma) Wanhainen et al. (2003), Frietsch et al. (1997)	800	Cu (%)0.3 Au (g/t)0.2 2	Mo	Disseminations and veins	Main ore was deposited from an aqueous, highly saline (31–37 eq. wt% NaCl + CaCl2) fluid. There was a contribution from dissolving evaporitic rocks to the salinity of mainly magmatic-hydrothermal fluids.
Candelaria, Chilean Coastal Belt (Early Cretaceous) Chiaradia et al. (2006)	470	Cu (%).95 Au (g/t).22 Ag (g/t)3.1	Zn, Mo, As, LREE	Vein, breccia- hosted, mantos, overprints magnetite replacement bodies	Inclusion studies indicate mixing of a high ^{37}Cl magmatic fluid with near zero values from ^{37}Cl basinal brines. That is early fluids were magmatic followed by mixing with likely evaporite-dissolution sourced basinal brine
Salobo, Carajas district, Brazil (2,580 Ma) Xavier et al. (2008)	450	Cu (%)1.15 Au (g/t)0.5	Ag, U, Co, Mo, F, LREE	Lenses, veins, pipelike or ringlike bodies of mineralisation	$\delta^{11}B$ values from 14 to 26.5‰ in the associated tourmalinites confirm marine evaporite-derived brines were present in the ore fluids
Ernest Henry, Cloncurry IOCG district, Australia (ca 1780–1720 Ma) Marshall and Oliver (2008); Foster et al. (2007)	166	Cu (%)1.1 Au (g/t)0.54	Co, Mo, U, REE, F, Mn, As, Ba	In isolated breccias pipes	Mixing of hypersaline basinal brines (mostly from evaporite-dissolution, e.g., meta-evaporite remnants of halokinetic scapolitic Corella Fm.) mixed with evolved magmatic-derived fluids
Magmatic End-Member IOCG					
Lightning Creek, Cloncurry IOCG district, Australia (≈1,540 to 1,500 Ma) Perring et al. (2000)	–	Cu (%) minor Au (g/t) minor	–	Qz-Mt ± Py ± chalcopyrite veins	Hosted by intrusives, largely made up of sodic-calcicaltered quartz monzodiorite. Sills are interpreted to be late-stage differentiates that crystallized under hydrous conditions with the episodic release of a fluid phase that underwent phase separation resulting in CO_2–rich vapour and a hypersaline (33–55 wt.% NaCl eq.) aqueous phase

Table 16.6 (continued)

Deposit	Tonnes (× 10^6)	Commodity grade	Associated metals	Mineralization styles	Evaporite/fluids association
Eloise, Cloncurry IOCG district, Australia (≈1,540 to 1,500 Ma) Baker et al. (2001b)	3.2	Cu (%)5.8 Au (g/t)1.5 Ag (g/t)19	Co, Ni, Zn, As, Bi	Veins, stockwork veins, massive sulphide	Fluids of pervasive pre-mineralization albite and hornblende-biotite assemblages were high-temperature (400–600 °C), highly saline (≥26–68 wt.% total salts) brines. Copper-gold-bearing assemblages were precipitated from lower temperature (200°–450 °C), lower salinity (30–47 wt.% total salts) fluids. Source of fluids is interpreted to be magmatic based on the high salinity of the fluids and the magmatic signature of the isotope data

After Hunt et al. (2007) and Saltwork IOCG GIS database, Version 1.6

Compare this table with the models illustrated in Fig. 16.15

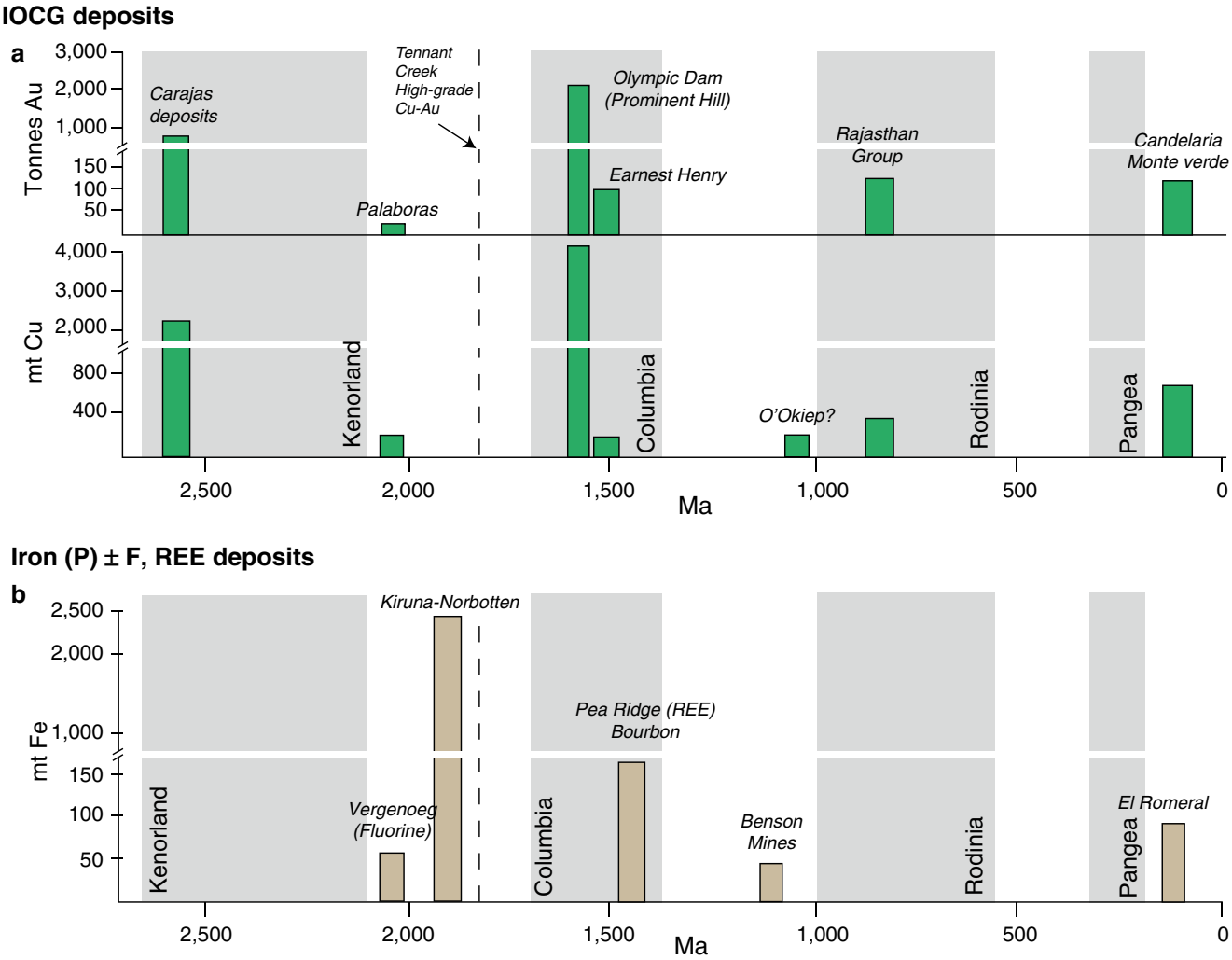

Fig. 16.18 IOCG deposits, tonnages and occurrences across geological time. (**a**) *Sensu strictu* IOCG deposits. (**b**) Fe (Ap) – Kiruna style (After Groves et al. 2010)

continental lithospheric mantle (SCLM), fertilized during earlier subduction, likely produced basic to ultrabasic magmas, which melted overlying continental crust. This mixed with felsic melts, along with devolatilization and some pene-contemporaneous incorporation of other lower to middle crustal fluids, combined to produce the larger IOCG deposits. Others of a more hydrothermal bent, would argue the metal source was largely in basinal waters flushing sediments

deposited under a less oxic Precambrian atmosphere. Preservation of near-surface deposits, such as Olympic Dam, is possibly due to their formation above buoyant and refractory SCLM, which resisted delamination and associated uplift from the time of formation until now (see Chap. 13).

Most other Precambrian iron oxide (P-rich) or magnetite-apatite (Kiruna-type) deposits (IOCG *sensu lato*) have a different temporal distribution, apparently forming in convergent margin settings prior to or following supercontinent assembly. It is only in the Phanerozoic that IOCG (*sensu lato*) and magnetite-apatite deposits are roughly penecontemporaneous within convergent margin settings (Fig. 16.18; Groves et al. 2010). Economically significant Phanerozoic IOCG deposits, such as Candelaria in Chile, occur in anomalous extensional to transtensional zones in the Coastal Cordillera, which are also the sites of mantle-derived mafic to felsic intrusions that are anomalous in a regional Andean context. This implies that special conditions, possibly detached slabs of metasomatized SCLM, may be required in convergent margin settings to generate worldclass IOCG deposits. It is highly likely that formation of giant IOCG deposits was mainly a Precambrian phenomenon related to the extensive mantle underplating that impacted on buoyant metasomatized SCLM (see Chap. 13). Generally, smaller and rarer Phanerozoic IOCG deposits formed in tectonic settings where conditions similar to those in the Precambrian were locally replicated.

Within the *sensu lato* set of IOCG deposits there is a general consensus that the formation of an IOCG deposit requires hypersaline CO_2- and $CaCl_2$-rich and S-poor fluids, active at shallow to mid-crustal levels, typically within cratonic or crustal-margin settings. Although IOCG deposits are often hosted by magmatic rocks, the fluids are not always clearly related to igneous activity. As noted by Hunt et al. (2007) and Chiaradia et al. (2006), there are noteworthy differences, both between deposits within an IOCG district and between districts, leading to a number of contrasting genetic models for IOCG deposits.

Some authors propose IOCG deposits developed from dominantly magmatic fluids – that is, dominantly orthomagmatic deposits (e.g., Hitzman et al. 1992; Pollard et al. 1998; Wyborn 1998; Skirrow 1999; Perring et al. 2000; Pollard 2001, 2002). Others propose a strongly magmatic fluid was the main source of metals (and sulphur), but invoke mixing with different fluids, usually cooler, less saline and more oxidizing, as the mechanism responsible for metal precipitation-i.e., paramagmatic deposits (e.g., Reeve et al. 1990; Baker 1998; Marschik and Fontbote 2001). Yet others propose that hydrothermal circulation of basinal fluid is a necessary requirement to form the larger IOCG deposits (Barton and Johnson 2004). The relative contribution made to the metal budget by these additional fluids is not clear, although there is a growing body of evidence that saline nonmagmatic waters are involved in most IOCG deposits, even in the formation of Olympic Dam (McPhie et al. 2011). Several authors suggest large volumes of saline non-magmatic fluids, that are perhaps evaporite-derived, are necessary for the formation of significant volumes of IOCG mineralization (e.g., Haynes et al. 1995; Barton and Johnson 1996, 2002; Haynes 2002; Hitzman 2002, McPhie et al. 2011). The corollary is that magmatism is important primarily as a source of heat to drive hydrothermal convection, but not necessarily as a source of the actual metals (Barton and Johnson 1996, 2002; Rhodes and Oreskes 1999). Figure 16.19 illustrates an example of the isotopic evidence that can be useful as indicators of fluid mixing during the formation of typical Phanerozoic IOCG deposits (*sensu lato*), as well as in interpreting batholith-driven hydrothermal fluid mixing with evaporite-influenced basinal brines

Much of the following geological detail on IOCG deposits is drawn from the preceding references but, as in previous sections on the metal-evaporite association, I divide my discussion of IOCG into a simple two-part classification, based on whether or not salts or their indicators are present or can be inferred from textural and mineralogic evidence in the ore forming system. I focus on the evaporite-associated class of IOCG deposits and deal more generally with those deposits that are not (Table 16.6). If I didn't, then the length of this chapter would have doubled. However, even in the following examples I give of the evaporite-IOCG association, the intrinsically high degree of sodic alteration and pervasive hydrothermal flushing that forms these deposits, means that undeniable evidence for a former salt masses supplying chloride to the transport system and/or focusing the precipitating system can at times be somewhat equivocal or enigmatic. So, the reader should be familiar with the material in Chaps. 7 and 13 in order to make best use of the following discussion.

Interestingly, when 12 of the larger IOCG deposits (*sensu strictu* of Groves et al. 2010) are placed in this evaporite spectrum, all show an affinity with hypersaline basinal fluids, evaporites or both (Table 16.5; Fig. 16.17). In general, deposits associated with either former evaporites or saline basinal brines show a broad tonnage range from high grade-low tonnage such as Juno and Peko in the Tennant Creek region to low grade-high tonnage such as Olympic Dam, Carapateena and Salabo (Fig. 16.20). Other than the supergiant Olympic Dam deposit, most of the known IOCG deposits are higher grade and lower tonnage than porphyry Cu deposits and related skarns, although the overall metal content of the two deposit styles is similar, falling in the range 10–100 tonnes Au-equivalent (Davidson and Large 1998).

IOCG in an Evaporite/Basinal Brine Milieu

Because evaporites are best preserved in Phanerozoic successions, we shall start our evaporite-IOCG deposit discussion there; first, with a discussion on iron oxide deposits

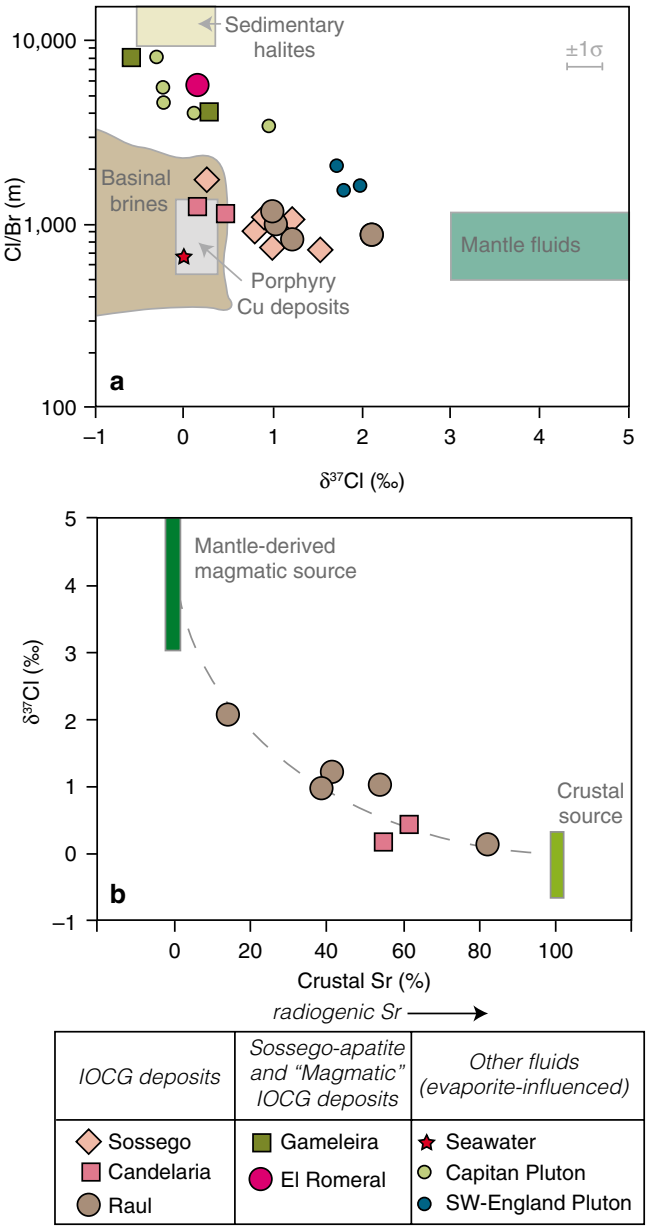

Fig. 16.19 Fluid chemistry from various South American IOCG deposits (After Chiaradia et al. 2006). (**a**) Cl/Br (molar) vs $\delta^{37}Cl$ diagram of fluids and relevant summary brine fields from various settings. (**b**) $\delta^{37}Cl$ vs crustal Sr(%) diagram for the fluids of the Candelaria, Raúl–Condestable, and El Romeral deposits. The crustal Sr (%) contribution was calculated using the mixing equations; $X_{magmatic} \times R_{magmatic} + X_{crustal} \times R_{crustal} = R_{measured}$ and $X_{magmatic} + X_{crustal} = 1.0$. X represents the percentage of contribution from the mantle-derived magmatic or crustal source, $R_{magmatic}$ is the $^{87}Sr/^{86}Sr$ values reported from the magmatic rocks associated with the various deposits, and $R_{crustal}$ is $^{87}Sr/^{86}Sr = 0.7073$ taken as the average value of an evaporitic source during the Cretaceous–Jurassic

formed where a magma mass may be the dominant driver for the hydrothermal fluid system. The most striking examples are magnetite bodies in the El Laco volcanic district of Chile that include magnetite lavas, as well as magnetite intrusives. Many of the Phanerozoic magma-fluid dominant Fe-oxide deposits are classified as IOCG deposits only under a *sensu lato* definition. They are excluded in deposit classifications using stricter definitions of IOCG deposits requiring the presence of economic levels of Cu-Au.

Phanerozoic Fe-Oxide Deposits

Phanerozoic magmatic IOCG (*sensu lato*) deposits are exemplified by Late Tertiary magnetite intrusive/extrusive volcanic complexes centred on El Laco, Chile and the Late Mesozoic (110 Ma) manto and Kiruna-style deposits of the Chilean Iron Belt. This latter grouping includes the large Fe-oxide accumulations at Marcona, El Romeral and El Soldado in the Andean subduction belt. In some ways these dominantly magmatic Fe-oxide deposits overlap nearby Cu-porphyry styles (Tornos et al. 2010). Like Cu-porphyry deposits, many of the exploited magnetite examples are tied to subduction, while those with noticeable Cu-Au mineralization show evidence of an early magmatic-fluid episode, which was dominantly characterised by hotter barren Fe-oxide (magnetite) styles, and later economic (Cu-Au precipitative) interactions with cooler nearsurface and saline basinal brines.

Interestingly, Carrillo-Rosúa et al. (2014) document extremely negative and inhomogeneous sulphur isotope signatures in Cretaceous Chilean manto-typeCu-(Ag) deposits in the Coastal Range of central Chile. For example, values in the MelipellaNaltahua deposit are as negative as $\delta^{34}S$ −50.4‰, which are among the lowest values found in any magma-associated ore deposit, worldwide. The ore precipitates are thought to be tied to bacterial sulphate reduction of basinal brines, relayed to the precipitation site by saline subsurface waters carrying hydrocarbons and sulphates from dissolved continental evaporites.

The El Laco volcano in the Andean Cordillera of northern Chile, contains the youngest, least altered, and best preserved magnetite-apatite ores known (Fig. 16.21). It was first described by Park (1961), who reported iron oxide ore bodies that resembled lava flows, and he suggested that the deposit was a result of a volatile-rich, iron-rich magma, which intruded the local volcanic sequence at shallow depth and in places erupted. This extrusive interpretation was assumed by many subsequent investigators focusing on the geochemical specifics of the deposit (Naslund, et al. 1997, 1998, 2002, 2003; Henriquez et al. 2003). However, others have suggested that the El Laco iron-oxide deposit has a hydrothermal origin (Hitzman 2000; Sillitoe and Burrows 2002).

The El Laco iron deposits are exposed at elevations between 4,700 to 5,300 m on the flanks of El Laco, a calc-alkaline volcanic complex in the Central Andes of northern Chile (23°48'S, 67°30'W). Within an area of 30 km^2 there are seven Fe-oxide deposits, with total resources on the order of 500 million tons of high-grade iron ore (Nystrom and Henriquez 1994). The ore bodies are not just rich in

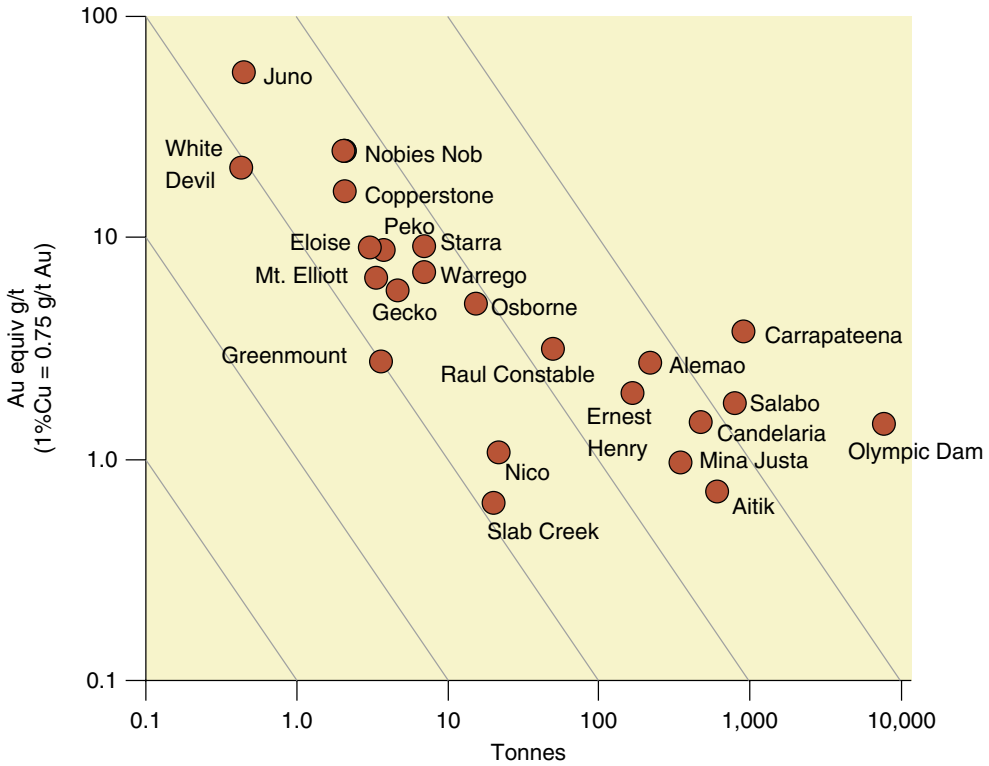

Fig. 16.20 Tonnage grade plot of selected IOCG deposits (sensu stricto due to elevated Cu ± Au levels) See Table 16.5 and text for details

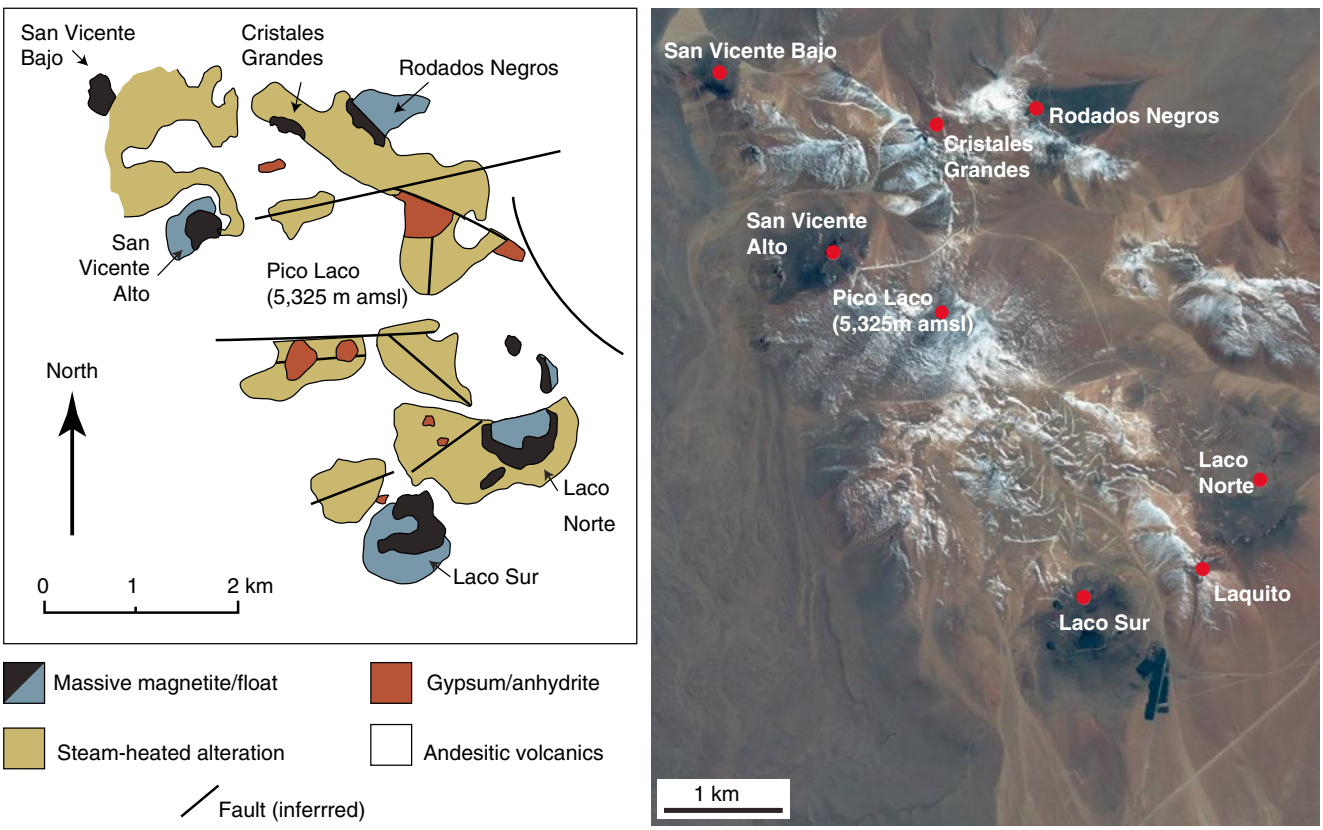

Fig. 16.21 Map of the El Laco magnetite deposits (After Vivallo et al. 1991. Laco Sur is the only one that has been extensively mined)

iron oxide, they are extremely rich in iron oxide, with many samples > 98 % iron-oxide; such rocks could be called "magnetitites."

Magnetite units at El Laco are porous, with high internal surface areas. Although composed primarily of magnetite and haematite, some samples have densities less than 2.0 and densities less than 3.0 are quite common. Open, unfilled void spaces in these samples can be described as pore-spaces and interpreted by some as the product of degassing during the eruption and crystallization of volatile-rich, Fe-rich magmas. Other investigators have suggested that some pore spaces are formed by the replacement of original vesicular silicate material by magnetite derived from Fe-rich hydrothermal fluids, and that other pore spaces were formed during the replacement process and represent open spaces leached out of the original protoliths by the removal of pre-existing material.

With the exception of the magnetite ore bodies, the El Laco district is similar to other volcanic complexes in the area in terms of silicate lava compositions, phenocryst assemblages, general eruptive history, and degree and distribution of alteration (Fig. 16.21). The ore deposits are dated by apatite fission track analysis at 2.1 ± 0.1 Ma and the overlying silicate lavas have been dated at 2.0 ± 0.3 by K/Ar. Andesitic to dacitic lavas predate and postdate ore deposition. Fumarolic activity continues at El Laco to the present day and is responsible for a number of sulphate (gypsum/anhydrite) accumulations in the region, as well as saline groundwater runoff into the intervolcanic salinas and salars (Chaps. 2 and 4).

El Laco is located slightly behind an active volcanic arc, as defined by the volcanoes Láscar, Licancabur, and Putana to the north, and Socompa, Lastarria, and Antofalla to the south. Crustal thickness beneath El Laco is ≈ 60 km, and the depth to the well-defined Benioff zone beneath the volcano is approximately 125 km (Frutos 1990). Tectonic reconstructions suggest that the crustal section below El Laco contains a Lower Palaeozoic basement of marine sedimentary rocks, unconformably overlain by Mesozoic and Lower Tertiary continental sediments and Upper Tertiary volcanic rocks (Frutos 1990).

A recent core-based study of the effects of magmatic metasomatism showed that even in these young volcanics (≈2 Ma) the effects of extensive subvolcanic contact-metasomatism is significant (Naranjo et al. 2010). This reflects the shallow-level emplacement of a volatile-rich iron-oxide magma, with associated fluid discharge and fracturing of overlying volcanic rocks. The brecciated rocks were altered by hot magmatic fluids emitted from the cooling intrusion (mainly extensive scapolitization and formation of pyroxene), and were accompanied by magnetite deposition. With time and decreasing temperature, the metasomatic fluids evolved to hydrothermal fluids, with a final recent geothermal pulse that deposited superficial gypsum over a large part of the El Laco Volcanic Complex (Fig. 16.21).

The extensive preservation of high-level extrusives in the El Laco deposit is unusual. More typical of the IOCG deposits within the *sensu strictu* members of the IOCG class are a number of intrusive members in the Mesozoic Chilean Iron belt; they include La Candelaria-Punta del Cobre, Mantoverde, Raul-Condestable, and Mina Justa. There are other members, also Mesozoic intrusives, in the same iron belt that contain lower levels of Cu-Au and only belong to the *sensu lato* IOCG grouping. A recent study of Marcona, one of the larger IOCG *sensu lato* deposits, by Chen et al. (2010) focused on the nature of the Fe oxide and Cu (−Zn-Pb) distributions across this deposit. Marcona, is a pre-eminent Mesozoic Andean magnetite deposit (1.9 Gt @ 55.4 % Fe and 0.12 % Cu) located in the IOCG subprovince of littoral south-central Peru. Chen et al. found that mineralization was controlled by northeast-striking faults transecting a Middle Jurassic (Aalenian-to-Oxfordian) andesitic, shallow-marine arc.

The mineralisation penetrates a succession of contiguous, plate-boundary-parallel, Late Jurassic to mid-Cretaceous volcanosedimentary basins. At Marcona, hydrothermal activity was initiated in the earliest Middle Jurassic (161–177 Ma) by high-temperature Mg-Fe metasomatism represented by cummingtonite and phlogopite-magnetite assemblages. Subsequently, during the terminal eruptions (156–162 Ma) of the arc, widespread albite-marialite alteration (Na-Cl metasomatism) was followed by the emplacement of an en echelon swarm of massive magnetite ore-bodies with subordinate, overprinted magnetite-sulphide assemblages, hosted largely by Palaeozoic meta-siliciclastics. As such, the hydrothermal evolution of this Cretaceous iron belt is not dissimilar to the smaller scale hydrothermal Fe-system driven by intrusive processes and sequences at El Laco.

The various magnetite orebodies exhibit abrupt, smoothly curving contacts, dyke-like to tubular apophyses, and intricate, amoeboid interfingering with dacite porphyry intrusions. There is no convincing megascopic or microscopic evidence for large-scale Fe-metasomatism associated with the main, sulphide-poor mineralization. The largest example in the district, the 400 Mt Minas 2-3-4 orebody, is interpreted as a bimodal magnetite-dacite intrusion, comprising commingled immiscible melts generated through the dissolution of metasedimentary quartz in parental andesitic magma. Oxygen and sulphur stable-isotope geothermometry indicates that, at ≈ 159 Ma, the evolution from magnetite-biotite-calcic amphibole ± phlogopite ± fluorapatite to magnetite-phlogopite-calcic amphibole-pyrrhotite-pyrite assemblages, coincided with quenching from above 800 °C to below 450 °C and the concomitant exsolution of dilute aqueous magmatic brines.

Subsequently, chalcopyrite-pyrite-calcite ± pyrrhotite ± sphalerite ± galena assemblages, in part metasomatic, were

deposited from lower temperature (≈360 °C) brines. The Cu-poor Marcona (Kiruna-type, Cu-Au barren magnetite phase) and the Cu-rich IOCG deposits in the same region, therefore, although spatially contiguous, represent contrasting ore deposit types. The former are mostly barren in terms of economic metals, other than iron, and are interpreted as the product of Fe-oxide melt coexisting with dacite magma, within an andesitic arc that failed (collapsed) during the closure of a back-arc basin. The weak associated magmatic-hydrothermal Cu-sulphide mineralization at Marcona was generated through melt vesiculation and was a localised product.

This stands in stark contrast with later considerably higher grade Cu- and Ag-rich orebodies of the major Cu-rich IOCG deposits in the Central Andes, e.g., La Candelaria-Punta del Cobre, Mantoverde, Raul-Condestable, and Mina Justa, which were the products of cooler, oxidized, hydrothermal and saline fluids, likely expelled from the adjacent evaporite-entraining basins during tectonic inversion (Fig. 16.19; Chiaradia et al. 2006; Chen et al. 2010). If we look at the Cu-Au grouping in the Phanerozoic deposits centred on the Andes, then hydrothermal processes and saline basinal waters (often evaporite-dissolution associated) are a significant component in the formation of the majority of larger *sensu-strictu* IOCG deposits.

Next, we consider whether the same external process set, i.e., hydrothermal and basinal brines, rather than purely orthomagmatic waters, also influences Proterozoic IOCG deposits. This next section focuses on Australia, where most of the larger known economic IOCG deposits (*sensu strictu*) occur, including the supergiant Olympic Dam deposit.

Proterozoic Iron-Oxide Deposits in Australia

Davidson and Large (1994) noted there are four styles of Proterozoic, iron-oxide, gold-producing deposits in Australia and all accumulated some 1.55–2.00 Ga (Fig. 16.18). The Australian IOCG groupings are (Fig. 16.22):

- *Type 1:* Stratabound Au +/− Cu-bearing iron formations (152.4 t Au) – exemplified by the Starra deposit.
- *Type 2:* Unconformity-style U +/− Cu/PGM/Au deposits (53 t Au) – exemplified by the Jabiluka and Coronation Hill deposits.
- *Type 3:* Iron oxide-dominated Au+Cu mineralisation hosted within elements of ductile deformation (146.7 t Au) – exempli-fied by the Tennant Creek deposits.
- *Type 4:* Iron oxide-dominated, breccia-hosted, Cu-U +/− Au hydrothermal replacement deposits spatially associated with felsic intrusions (273 t Au) – exemplified by the Olympic Dam deposit.

A key point is that in all examples discussed, with the possible exception of Olympic Dam, the mineralisation is hosted in sedimentary or metasedimentary hosts, not in a granite; so hydrothermal circulation must be a significant part of the emplacement process. Davidson and Large (op. cit.) go on to postulate that the most effective method of metal fixing in all four types is via subsurface fluid mixing. This hydrothermal process set achieves a synchronous decrease in fO_2 and temperature. In some IOCG deposits outside Australia, especially those in Scandinavia, the redox barrier that regulated the deposition of copper and gold is tied to the presence of graphite, typically in graphitic schists.

In Australia, Type 1 through 3 deposits usually occur in association with well developed, stratabound, ironstone units, suggesting the same reducing environment that formed the ironstones was also capable of fixing the Cu and Au. Davidson et al. (1989) interpret the ironstones of the Starra deposit as syngenetic exhalites (their 'magnetite-rich VHMS deposits').

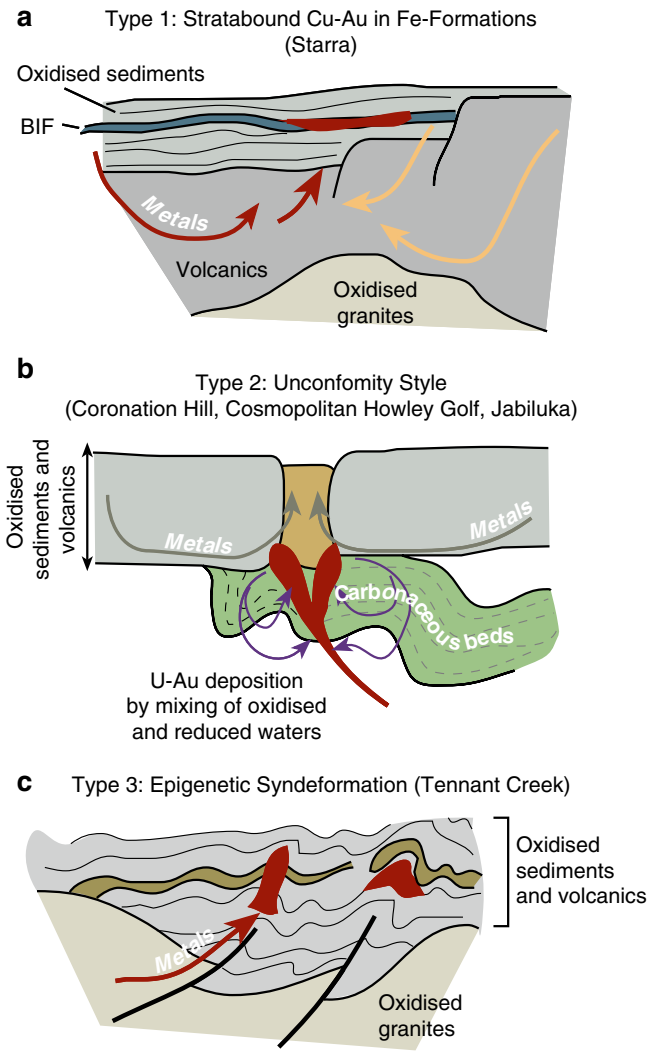

Fig. 16.22 Models of Proterozoic gold (±Cu) deposition (Types 1–3 indicated by **a**–**c** and discussed in detail in text). All involve chloride brines, high temperatures and evaporites (Modified from Davidson and Large 1994). One of the key points to be noted is that the mineralisation is in a sedimentary or metasedimentary host not in a granite or granite carapace, unlike Olympic Dam (Type 4; see Fig. 16.23)

Williams (1994) argues that different modes of occurrence of various ironstones indicate an epigenetic origin, whereby late hypersaline fluids generate magnetite replacement bodies. In my opinion, both styles of formation can be encapsulated in the notion of FeCl-rich brines supplied by sequences flushed by brines that are fed by dissolving and altering halite-dominated halokinetic evaporites (Fig. 15.80).

Type 1, stratabound Au +/− Cu-bearing iron formation deposits, are exemplified by the Starra deposit, Queensland (Fig. 16.22a; Davidson 1994). The Starra ore bodies are hosted by the meta-evaporitic Staveley Formation (1,720 Ma) of the Mary Kathleen Group, Mt Isa Eastern Succession (Chap. 14). Starra is the major mine of the Selwyn Cu-Au Project, consisting of 4 geographically separate outcropping ironstone hosted lodes, totalling 5.3 million tonnes at 5.0 g/t Au and 1.98 % Cu. Stratabound Cu-Au mineralisation occurs in a series of massive ironstone ridges, known as the Western Hematites, with a strike length of 6.5 km near the base of the Staveley Formation (Fig. 14.60). The ironstones strike north-south and occur as discontinuous lenses, that in places cross-cut the host rock. Unmineralised varieties of ironstones crop out over a much larger area.

Within the ironstones, the Cu-Au mineralisation occurs at the lithological contact of a metamorphosed sandstone/siltstone sequence with a succession of foliated chlorite-biotite-magnetite schists (Fig. 16.22a; Rotherham 1997; Davidson 1994). Ore lenses are immediately underlain by variably sheared albite-magnetite-haematite-pyrite-bearing rocks, and overlain by mainly unaltered, less-sheared, metasediments. Evidence indicating that albite was abundant prior to deformation, and also prior to the main hydrothermal addition of Fe, S, Cu and Au, includes; (1) regional albite development at this stratigraphic level; (2) alteration of albite by ore-related sericite; and (3) inclusion of unfoliated inclusions of albite and haematite in ore-related pyrite. Nevertheless, albite also developed around dolerites and within hanging wall shears during ongoing metamorphism and deformation.

Magnetite ironstone textures are generally massive in appearance, but relict deformed breccia and foliation textures are locally preserved. Sulphide ore textures are more brittle and consist mostly of fine, pervasive breccias in the ironstones and host rocks. Isotopically the vein gangue-calcites in the mineralised ironstones indicate a more reducing setting at the time of mineralisation, compared to other non-ironstone hosted IOCG deposits in the region, which show the effects of meteoric mixing and mantle sources (Fig. 16.23b; Marshall et al. 2006).

Davidson (1994) interprets the sodic metasomatism that formed the albite as a metasomatic halo fed by the metamorphic evolution of pre-existing halite-dominated evaporites. Regionally, the sodic rocks in the Proterozoic Mt Isa Eastern Succession are increasingly being recognised as the legacy of volatile-derived fluids fed, at least in part, by evolving meta-evaporites. There were several episodes of sodium introduction prior to, during, and following the major deformation. They were in part driven by hydrothermal fluid flow associated with granite intrusions and by halite/scapolite metamorphic evolution (Oliver and Wall 1987; Oliver et al. 1992; Williams et al. 1993; Williams 1994; Marshall et al. 2006).

Rotherham's et al. (1998) petrological and textural observations support a hydrothermal origin for both ironstone and mineralisation in the Eastern Succession. He recognised three dominant post-peak metamorphic paragenetic stages of alteration and mineralisation: (1) Early widespread Na-Ca metasomatism consisting of albite-quartz-actinolite-scapolite, (2) Localised K-Fe metasomatism consisting of biotite-magnetite-hematite-quartzpyrite and, (3) The mineralising stage, consisting of anhydrite-calcite-haematisation of magnetite-pyrite-chalcopyrite-gold and extreme chloritisation of biotite. The Na-dominant alteration occurs throughout the Eastern Foldbelt and for at least 50 km to the east and 150 km to the north of Starra (Fig. 16.23a). The ironstones that host the ore are interpreted as products of localised Fe-metasomatism associated with shearing and brecciation of previously Na-metasomatised host rocks. Gold and copper mineralisation resulted from the interaction of magnetite, a late oxidising fluid, and an increase in pH. This produced variable haematisation of magnetite and caused the solubility of chloride-complexed gold to decrease dramatically.

Albite was abundant prior to deformation in the Starra deposit, and also prior to the main hydrothermal addition of Fe, S, Cu and Au (Davidson 1994; Davidson and Large 1994; Rotherham et al. 1998). Davidson (1994) goes on to conclude that the fluids responsible for the sodic alteration at Starra, and for ore deposition, were saline, acidic (pH = 3.9–6.0) and high temperature, with relatively low levels of sulphur, with the gold carried as chloride complexes (Fig. 16.3). This, and the association with abundant meta-evaporite indicators in the region (mostly a NaCl, not $CaSO_4$, protolith), suggests that dissolving halite at high temperatures (or chloride released during the pressure-induced lattice collapse of marialitic-scapolitic daughter products – see Chap. 14) were responsible for the chloride transport and perhaps focusing of the gold precipitates into the deposit shear zones.

Albite in the Starra region also shows protolith and structural controls. As well as being preserved as bedding parallel units, it is often developed around dolerites and within hangingwall shears. Davidson saw this as a possible problem in interpreting the sodic metasomatism as being related solely to an evaporite precursor. In my opinion, the nonstratiform fault- and dolerite-related geometries of some of the sodic metasomatism is not a problem when invoking a metaevaporite fluid genesis. All it is reflecting is the typical reality that deforming salt is non stratiform. Once a salt body flows, it

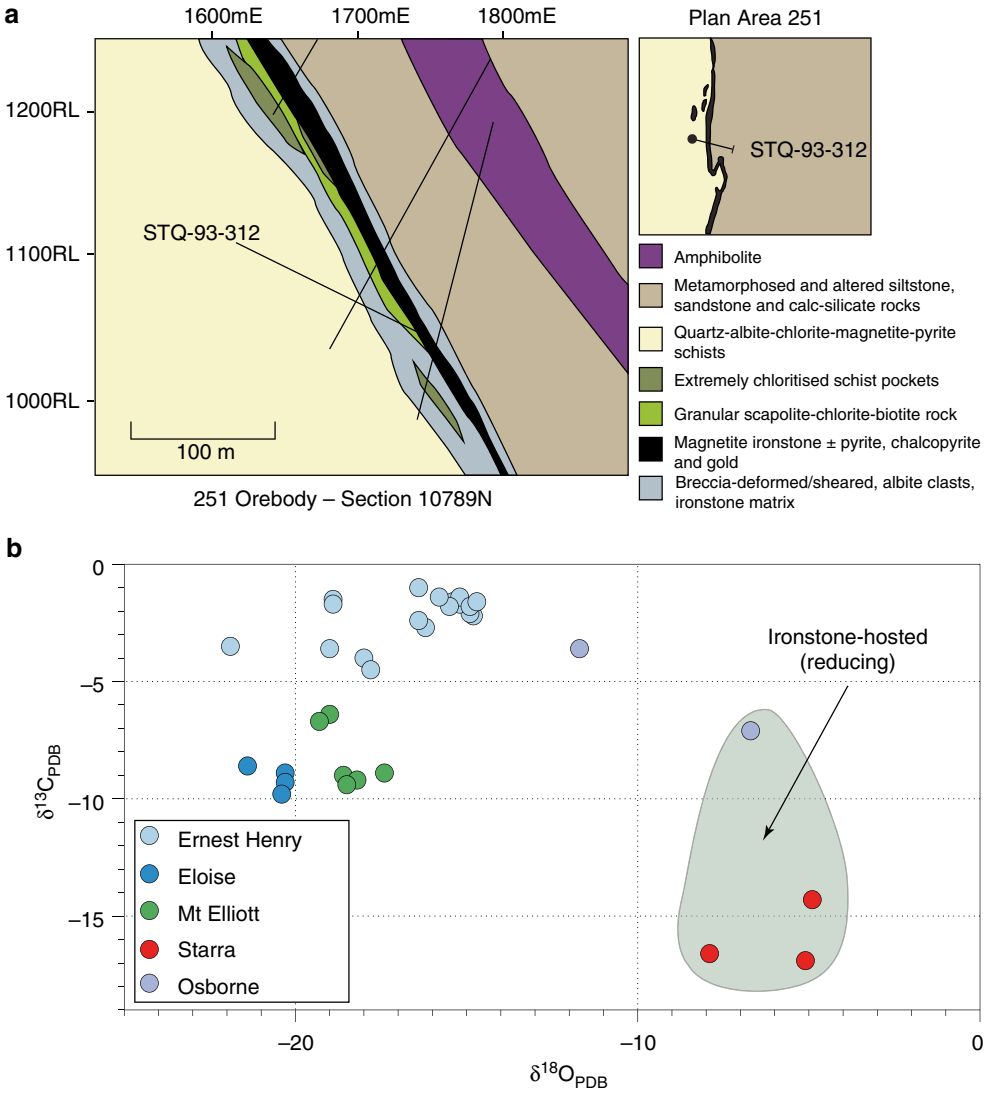

Fig. 16.23 Starra deposits. (**a**) Local geology (cross-section and plan the 251 ore body (After Rotherham et al. 1998). (**b**) Isotopic signature of ore-associated vein calcites in the ironstones of Starra and Osborne deposits define a separate plot field indicative of reducing conditions compared to warmer, more burial related signatures in the gangue vein calcites of the Ernest Henry, Eloise and Mt Elliott deposits (After Marshall et al. 2006)

and its brine products will have climbed the stratigraphy as a number of salt slugs and tiers that generate both salt and fault welds. These features can evolve from salt welds to fault welds and continues to act as ongoing planes of weakness (shears) and as fluid conduits in the metamorphic realm. They can be reactivated whenever the succession undergoes renewed extension, compression or even igneous intrusion. With ongoing metasomatism the fault/shears will gain sodic haloes, supplied by the evolving salt or metamorphic fluids from its daughter products. Even in the metamorphic realm, sodic alteration, which is commonly associated with meta-evaporites, will show nonstratabound trends that can be related to the deformation of a flowing salt body as it is squeezed through the subsurface (e.g., Wang et al. 1998a).

Type 2: Unconformity-style, U ± Cu/PGM/Au deposits are exemplified by two provinces in Northern Australia; the South Alligator Valley minerals field in the Pine Creek Inlier and the Alligator Rivers mineral field, both within the Pine Creek Orogen (Figs. 16.22b and 16.24; Davidson and Large 1994; Ahmad et al. 2009). Mineralisation in both provinces is localised at an unconformity between overlying relatively undeformed oxidised siliciclastic sediments and strongly deformed carbonaceous graphitic units. Coronation Hill is a viable, South Alligator Valley deposit, but legally unmineable due to its proximity to Jabiluka (Mernagh et al. 1994; Needham and De Ross 1990), while exploited uranium deposits like Jabiluka are well documented in the Alligator River minerals field (Fig. 16.24). Similar evaporite-related

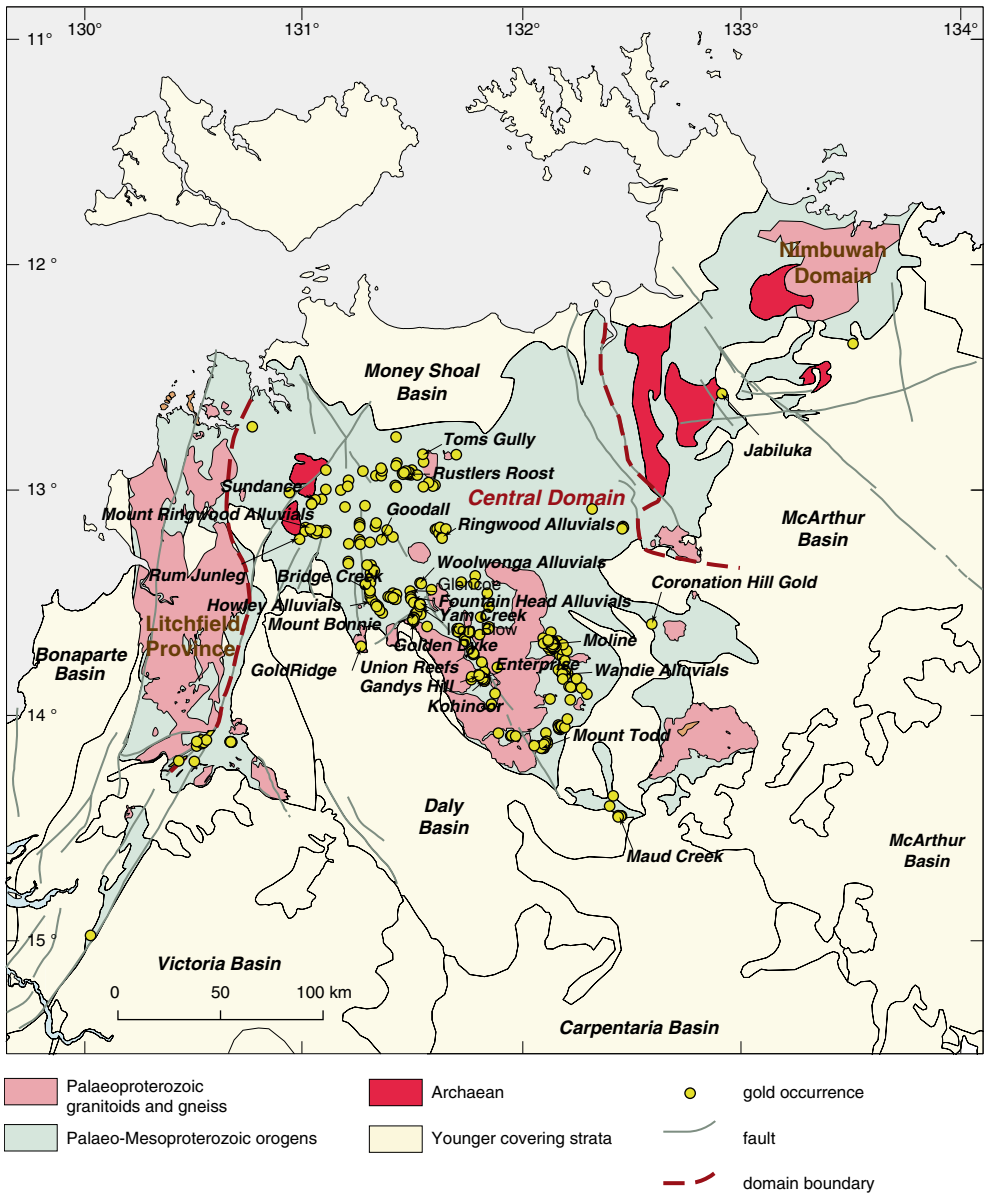

Fig. 16.24 Regional geology also showing gold occurrences in the Pine Creek Orogen (After Ahmad et al. 2009)

uranium distributions, tied to high-grade metamorphism of evaporites, occur in the Western Zambian Copperbelt of Africa (Eglinger et al. 2014)

From west to east, the Pine Creek Orogen is divided into three domains (Fig. 16.24: the Litchfield Province, Central Domain, and Nimbuwah Domain (Ahmad et al. 2009 and references therein). The Litchfield Province encompasses an area of high-temperature, low-pressure greenschist to granulite facies, meta-sedimentary and meta-igneous rocks. The Central Domain contains greenschist facies metasedimentary rocks and simple structures dominated by upright northwest- and north-trending folds. The Nimbuwah Domain is characterised by amphibolite facies Palaeoproterozoic metasedimentary rocks and granite, with widespread gneissic Archaean basement and upright to recumbent folds. The Pine Creek Orogen succession unconformably overlies Neoarchaean (≈2,670–2,500 Ma) granitic basement, which is exposed in the Rum Jungle Complex of the Central Domain, and the Nanambu Complex and Kukalak gneiss in the Nimbuwah Domain. Pine Creek Orogen is made up of an alternating succession of sandstone and shale, with minor carbonate and volcanic rocks. Dolerite sills (Zamu Dolerite and equivalents) intruded the succession prior to deformation and metamorphism.

The timing of deposition of the Pine Creek Orogen succession is constrained between 2,470 and 1,860 Ma and the succession is divided into two supergroups. The older Woodcutters Supergroup includes the Manton and Mount

Partridge groups and equivalent strata. This supergroup unconformably overlies the Archaean basement and consists of current-bedded and ripple-marked fluvial to shallow-marine sandstone, intertidal stromatolitic-evaporitic carbonates and shale, including carbonaceous and pyritic shale. Tuffaceous sediments from the Mount Partridge Group give ages of ≈2,020 Ma. The younger Cosmo Supergroup is made up of the South Alligator and Finniss River groups and equivalent strata. This succession is more widespread than the unconformably underlying Woodcutters Supergroup and comprises BIF, mudstone and tuff, succeeded by a monotonous flysch succession.

Tuffaceous sedimentary rocks in the Gerowie Tuff of the South Alligator Group give zircon ages of 1,861 ± 3 Ma and 1,863 ± 3 Ma (Worden et al. 2008), while zircon from the Warrs Volcanics in the Finniss River Group yield an age of 1,862 Ma ± 3 Ma. There thus appears to be a major depositional break between the Woodcutters and Cosmo supergroups, extending over a period of about 150 My. Recent detrital zircon geochronology across the Pine Creek Orogen suggests that the metamorphosed successions in the Litchfield Province represent stratigraphic equivalents of the Woodcutters and Cosmo Supergroups. In comparison, the Palaeoproterozoic succession in the Nimbuwah Domain (Nourlangie Schist and Cahill Formation) has a different provenance to sedimentary rocks in the central Pine Creek Orogen, and was deposited earlier, in the interval 1,900–1,870 Ma.

Regional deformation and metamorphism occurred across the Pine Creek Orogen in the interval 1,865–1,850 Ma. In the Nimbuwah Domain in the east, high-pressure mid- to upper amphibolite-facies metamorphism occurred at 1,865–1,860 Ma, accompanying intrusion of granites of the Nimbuwah Complex and regional west-directed compressional deformation. In the Litchfield Province in the west, high-temperature low-pressure metamorphism occurred at ≈1,853 Ma, probably in an extensional environment. The timing of upright deformation and low-grade metamorphism of the Central Domain is less well constrained, but must postdate the deposition of the Finniss River Group at ≈1,860 Ma.

In the Central Domain, the earliest deformation, D_1, caused north-trending monoclinal warping, recumbent north-trending isoclinal folding and shear zones. D_2 deformation is represented by thrusting and recumbent folding. The D_3 deformation event was more widespread and is indicated by north- to northwest-trending non-cylindrical, closed to tight folds. These folds are an important structural control for vein-type mineralisation in the Central Region. D_4 deformation was associated with granitic intrusions and produced open, small-amplitude regional folds, which are responsible for the formation of elongated basins and domes. D_5 deformation produced steeply plunging polyclinal kinks and drag folds associated with dextral movements along major faults.

A major period of igneous activity, minor deformation and rift-related sedimentation occurred in the Central Domain at 1,835–1,800 Ma and this is termed the Cullen Event (Ahmad et al. 2009). Albite-epidote hornfels is present in all contact aureoles, commonly with a narrow, inner continuous zone of hornblende-hornfels. Effects of contact metamorphism are seen up to 10 km away from granite contacts. The Central Domain, where I-type[4] granites dominate, contains the majority of the gold, base metal and tin deposits, as well as stratabound gold and polymetallic deposits. The Litchfield Province S-type granites are related to Sn-Ta bearing pegmatites (Ahmad et al. 2009).

Coronation Hill in the Central Domain, is a typical unconformity-style deposit (Fig. 16.24; Mernagh et al. 1994; Ahmad et al. 2009). Pd–Pt–Au mineralization at Coronation Hill occurs in structurally-controlled lenses in Proterozoic metasediments and in altered volcanics near the unconformity with overlying sediments (5.4 Mt grading 4.31 g/t Au, 0.65 g/t Pd and 0.19 g/t Pt (Fig. 16.25; Carville et al. 1990). Although economic, it will not be mined due to the deposit's proximity to Kakadu National Park. The sub-unconformity mineralisation separates a deformed and metamorphosed basement (composed of igneous intrusions, volcaniclastic rocks, and calcareous and carbonaceous meta-sedimentary units, including sparry magnesites and tourmalinites) from a cover sequence (Kombolgie Group) of little-deformed haematitic quartz sandstones, organic shales and sedimentary breccias. Uranium ore is located in semi-brittle shears and breccias that are subparallel to the units in the Nanambu Complex and typically developed at the hinge zones of fault-related folds. Uraninite veins are intimately associated with chlorite, sericite, haematite, quartz, and illite veins, which extend in to the basal 2 m of the Kombolgie Formation

Geologic, fluid inclusion, stable isotope, and thermodynamic data indicate mineralization at Coronation Hill was driven by reaction of oxidised and acid hypersaline basin brines (originating from the supra-unconformity Palaeoproterozoic cover sequence and its hydrosphere), with feldspathic and reducing rocks and fluids supplied by sub-unconformity crystalline Archaean basement (Mernagh

[4]I-type granite is metaluminous to weakly peraluminous, relatively sodic, and has a wide range of silica content (56–77 wt% SiO_2). It was inferred to have formed from a mafic, meta-igneous source. The other dominant granite type is strongly peraluminous, relatively potassic and restricted to higher silica compositions (64–77 wt % SiO_2). Chappell & White in a widely distributed 1974 abstract called these S-type granitoids because these they are inferred to have formed from melting of metasedimentary rocks. This scheme received instant popularity and has been applied worldwide (Chappell and White 2001). It is based upon the assumption that one can easily distinguish the origin of the granitoid precursor utilising whole rock geochemistry. However, similar granitic compositions can be produced by partial melting and/or assimilation of a variety of sources including highly sodic evaporites and meta-evaporites.

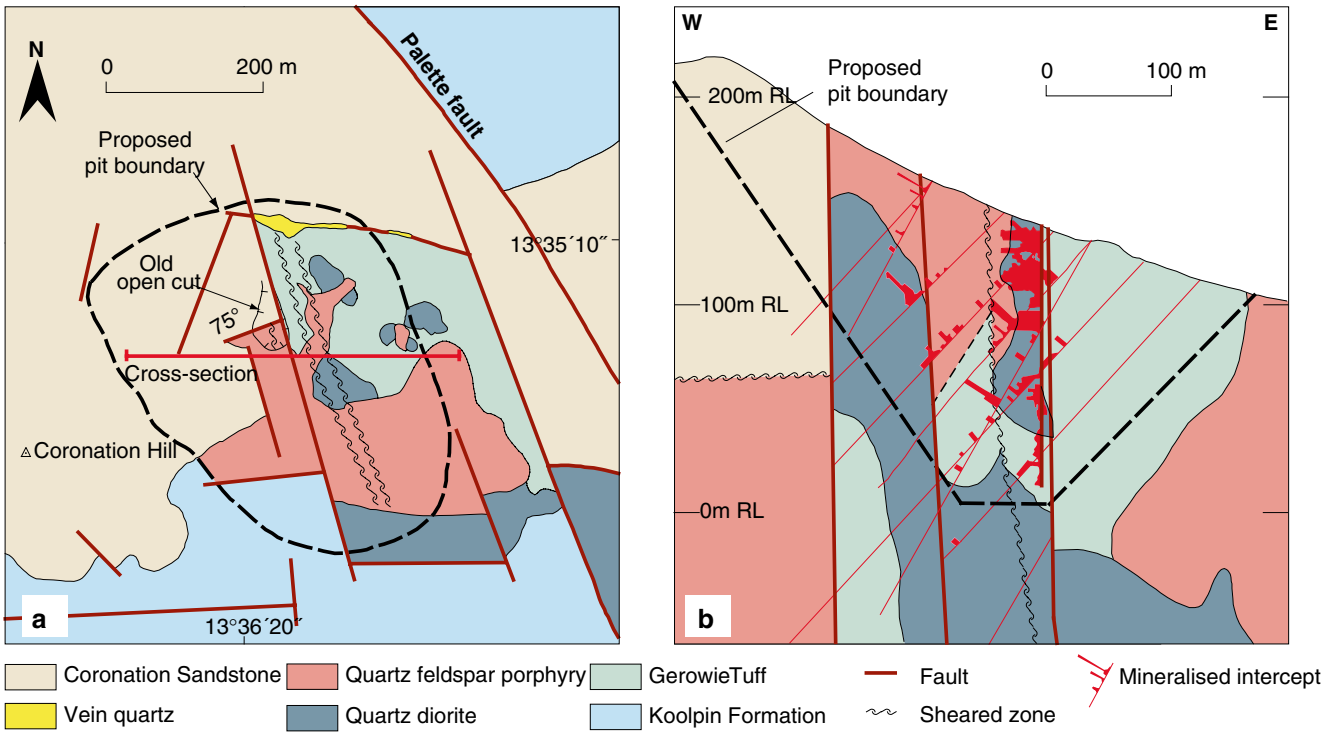

Fig. 16.25 Coronation Hill, Northern Territory, Australia (After Carville et al. 1990). (**a**) Plan view. (**b**) Cross section. Note higher mineralised section is associated with quartz feldspar porphyry quartz diorite intersection, adjacent to unconformity

et al. 1994). Inclusion analysis shows the ore fluids were hypersaline and calcium-chloride dominated (≈26 wt% $CaCl_2$ equiv.) and that mineralization occurred at around 140 °C. These are the characteristics of hydrothermal basinal brines in evaporite-entraining basins (Chaps. 2 and 8) and similar marine evaporite-derived brines played a similar role in the formation of the 1.8 Ga unconformity-related U deposits of the Athabasca Basin, Canada (Richard et al. 2011; Mercadier et al. 2012).

The lowest member of the Palaeoproterozoic cover sequence at Coronation Hill is the Koolpin Formation. It was deposited in a terrigenous-dominated arid peritidal setting in an opening rift depression (Matthai and Henley 1996). Further south, the unit hosts the Cosmo Howley Au deposit. The Cosmo Howley deposit straddles the axis of the Howley Anticline, a regionally continuous 30 km long structure. In the mine area the fold axis plunges at 50° towards 325°, with a well-developed consistent slaty cleavage (Fig. 16.26). The global resource, including underground ores centred on the mine, was stated in 1995 at 10 Mt @ 2.75 g/t Au (Matthai et al. 1995). Intense faulting, sometimes with associated brecciation, parallels the cleavage through the axial zone and east limb in zones from 1 to 10 m wide.

The Koolpin Formation, the main host to the Au ore is divided into three members: (1) 250 m thick Lower Member of carbonaceous and micaceous mudstone and siltstone. (2) Middle Member, which is up to 100 m thick and mainly composed of interbedded iron formation (10–15 % Fe as oxide and sulphide), carbonaceous mudstone and mudstone, and (3) 50–150 m thick Upper Member of carbonaceous mudstone. Significant gold ore is developed at a number of levels within the Middle Member, although substantial economic mineralisation is also found in ironstones and mudstones in both the Upper and Lower Members. Some 40 % of the reserves are in the Lower Member.

The dominant ore host in the Cosmo Howley Au deposit consists of quartz veins along steeply dipping limbs and across the hinge of the Howley Anticline, perhaps located regionally in what was the high-temperature aureole of the Cullen Batholith. Veins are hosted by upper greenschist to lower amphibolite facies comprised of carbonaceous pelites, metasiltstones, and ironstones of the Koolpin Fm., which also contains recrystallised chert nodules and bands, metadolerite sills, along with scapolite (Fig. 16.26; Ahmad et al. 2009). Gold is concentrated in structurally controlled sites developed at or near the contact between ironstone and carbonaceous units and it forms inclusions in arsenopyrite and pyrite, hosted by both concordant and discordant quartz veins. Associated ore minerals include chalcopyrite, pyrrhotite, galena, and sphalerite (Ahmad et al. 2009). Matthai et al. (1995) suggested that reduction of late magmatic brine by mixing with saline metamorphic fluids near the carbonaceous pelite was responsible for localization of gold. Heat from the prolonged intrusive and cooling history of

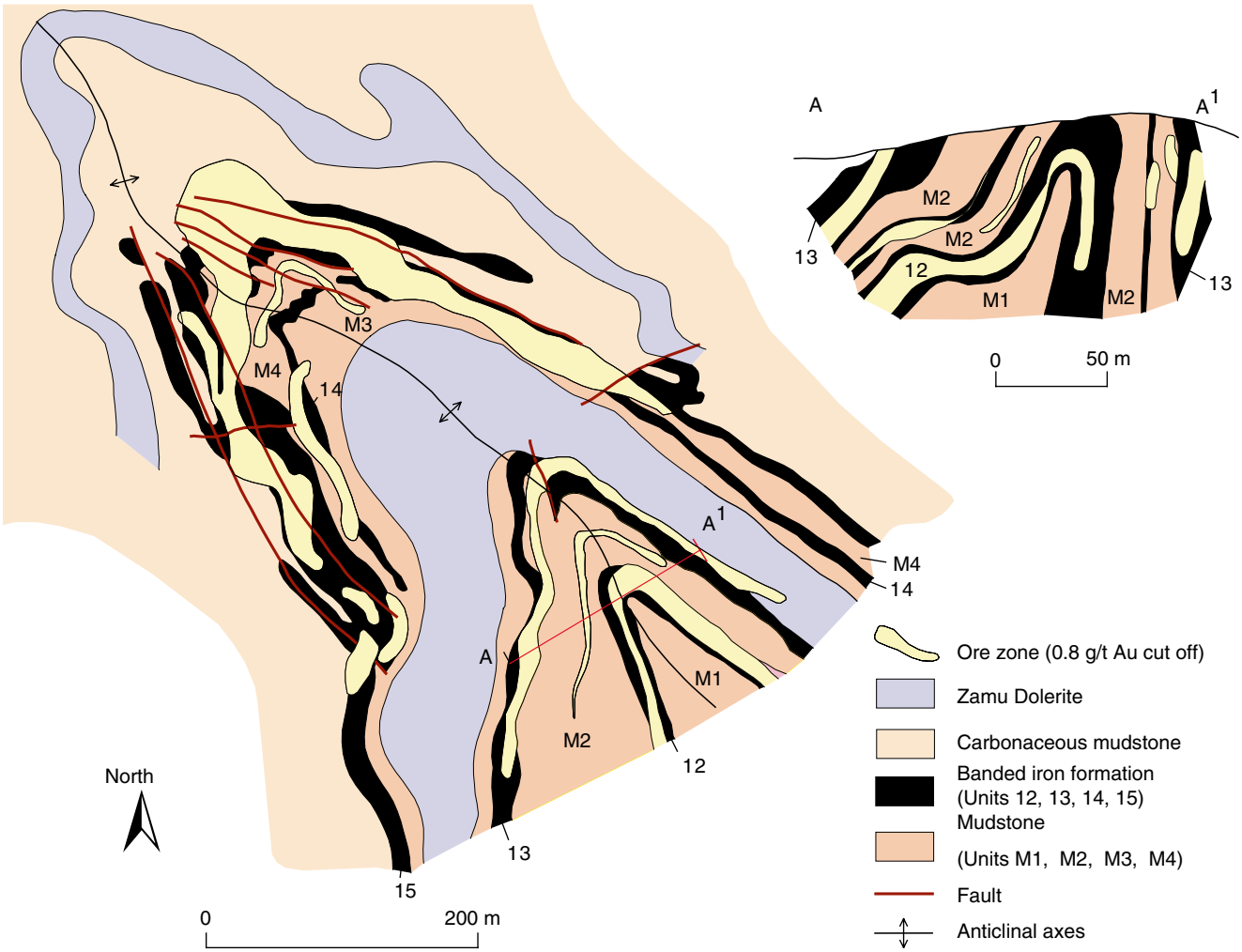

Fig. 16.26 Cosmo Howley Mine, Northern Territory, Australia, showing plan view and cross section A–A' (After Ahmad et al. 2009)

younger ≈ 1,800 Ma granites in the Cullen Batholith, coupled with pre-existing faults and shears, allowed long-lived hydro-thermal systems to channel fluids from granite and metamorphic sources (Kominsky et al. 1996).

Some outcrops of the Koolpin Formation contains textures indicating the former presence of evaporites, as does sodic scapolite, suggesting metal transport as chloride complexes (J. Stewart, pers. comm.). It would be an interesting exercise to test, via matrix characterisation, if some of the "sedimentary breccias and chert breccias" along the unconformity are possible evaporite solution breccias, including those in portions of the Kombolgie Unconformity that regionally host the gold and U ores. That is, did a now-dissolved, once clean thick salt unit reside atop this unconformity, and prior to and during its dissolution act as a focus for mineralising fluids? Under this scenario, any improved exploration targeting requires better definition of mineralised relationships to alteration haloes with respect to faults, which would also intersect or sole out into synkinematic breccias. Sparry carbonate replacement haloes, which occur around some feeder faults to the mineralisation in the region, should be redefined and mapped with a possible halokinetic perspective. This would test any regional mineralisation/lithological/salt solution relationships.

Regionally, in the Alligator Rivers mineral field, a structural control to the mineralisation is less obvious than at Coronation Hill, although mineralised reverse (thrust) faults are present and several deposits are fault displaced. Regionally, the massive haematitic Kombolgie Sandstone (1,648 ± 219 Ma) and mafic Nungbalgarri Volcanics unconformably overlie polydeformed semipelitic to graphitic schists and amphibolites of the Lower Proterozoic Cahill Formation and the Myra Falls Metamorphics (Davidson and Large 1994). A thick (up to 1,800 m presently preserved) unmetamorphosed detrital sequence, composed of fluvial and aeolian sandstones (the 'Kombolgie Sub-Group'), unconformably overlies the crystalline and metamorphic basement and is dated at 1,822 and 1,720 Ma (Boiron et al.

2010). The youngest members of the Kombolgie Sub-group were deposited in marine conditions, as suggested by the occurrence of glauconite and halite crystal casts (Kyser et al. 2000) and by stromatolitic and evaporitic dolostones-sandstones in the McKay formation (Rawlings 1999). The deepest mineralisation (mostly U) occurs as much as 500 m below the unconformity. Primary ore at Jabiluka occurs as uraninite-filled veins, cements and disseminations in which gold and tellurides are present as inclusions and veins, along with magnesian chlorite and anhydrite (Binns et al. 1980).

Sparry ferroan magnesite occurs in the Coomalie and Celia dolomites in the nearby Rum Jungle area. Disparate interpretations of halite and gypsum pseudomorphs (Crick and Muir 1980), versus high temperature recrystallised magnesite (Bone 1983), versus hydrothermal replacement of precursor dolomite (Aharon 1988) were discussed in Chap. 14. These, at first, disparate explanations, can be drawn into a much more coherent escaping-basinal-water model, centred on fluids derived as host strata pass from the diagenetic into the metamorphic realm. All it requires is that protolith analogies are drawn with fault-fed hydrothermal sparry replacements, which occur atop halokinetic provinces in northern Africa and the McArthur Basin. Such intervals show fluids capable of carrying metals have been focused along faults carrying hypersaline brines outlined by sparry ferroan replacement haloes.

Type 3 deposits are exemplified by Tennant Creek style deposits, where iron-oxide -bearing Cu-Au pipes are the main ore bodies (Fig. 16.22c; Davidson and Large 1994; Rattenbury 1994). Since 1932, the Tennant Creek mineral field has produced 130.2 t Au, 345 000 t Cu, 14 000 t Bi, 220 t Se and 56 t Ag from over a hundred small- to medium-sized mines (Fig. 16.27). To the south, in the Davenport Province, there are several minor gold occurrences in quartz veins and stringers that have contributed 75 kg Au. The bulk of historical gold production was in the period 1960–1980, during which the Tennant Creek mines produced about 64 t Au. Most production was derived from 12 main deposits, with Warrego, Nobles Nob and Juno providing over 96 t Au (Fig. 16.28)

The Tennant Creek goldfield is characterised by large massive haematite/magnetite + quartz + chlorite "ironstones", which host gold, copper and bismuth ores in metasediments of the rift-fill Warramunga Group (Figs. 16.27 and 16.28). Once again, the dominance of gold occurrence in metasediment, not igneous apophyses, implies that the igneous suite did not directly control the precipitative positions of the gold mineralisation (Fig. 16.27). Rather, the juxtaposition of ironstone and faults/shears is the dominant control. The ironstone bodies are irregular, flattened, ellipsoidal and pipe shaped, and range in mass from a few tonnes to over 15 Mt. Over 700 ironstone bodies have been recorded throughout the Tennant Creek ore field, but fewer than 200 are known to contain significant mineralisation, and only 25 have produced more than 100 kg Au (Ahmad et al. 2009)

The ironstones formed during east-west folding, initially from crossflows of high salinity basinal brines, which later mixed with magmatic brines to form the Cu-Au-Bi mineralisation stage. Rattenbury (1994) interprets the folding as derived from a relatively thin skinned thrust system that deformed the Warramunga Group, thrusting mostly metasedimentary rocks up and over from the south toward the north resulting in a series of steep listric reverse fault splays and folds. The hypersaline ironstone-forming fluids used the thrust faults as major conduits as well as the developing cleavage planes in the turbidites and other deepwater sediments of the Warramunga Group. Ironstones then formed mineralised zones where the cleavage-parallel conduits intersected iron-rich parts of the stratigraphy, and in numerous instances show a close spatial association with stratiform quartz-feldspar porphyries. The latter has been interpreted as being emplaced into the sediments of the Warramunga group while they were still unconsolidated and water-saturated (McPhie 1993). Thus the ironstones formed early in the burial history of the basin sediment pile. It is tempting to argue such a mechanism may well be tied to ascending FeCl-rich evaporite-associated basinal waters.

Based on fluid inclusion work, Zaw et al. (1994) favour a mostly basinal brine genesis for the chloride-rich solutions that first created the ironstones and then mineralised them. They also acknowledge that some magmatic contribution cannot be ruled out. Fluid inclusions in the ironstones have a salinity range of 10–30 NaCl equiv. wt % and homogenization temperatures of 100–350 °C, with a mode at 200–250 °C. Salinity measurements on fluid inclusions in the mineralised ironstones gives a range of 10–50 NaCl equiv. wt %, with a mode of 35 NaCl equiv. wt%; while homogenization temperatures range from 250 to 600 °C, with a mode of 350 °C. Similar elevated salinities in basinal brines are typically found in modern basins where evaporite beds are dissolving (Chap. 8).

No evaporite solution breccias have yet been recognised associated with the sediments of the mineralised Tennant succession. If they are present, there are two likely positions in the stratigraphy for the primary weld. One likely position is near the base of that portion of the Warramunga sediments that indicates the first incursion of marine waters into the opening rift. Given the deepwater setting of the ore-host sequence, this tectonic setting means the dissolution breccia would likely lie below the mineralised part of the stratigraphy. The other setting likely to deposit widespread evaporites, which could have supplied ions and high salinity to the basinal brines, would be at or near the time of the collision event that created the thrust faulting. These beds would tend to lie stratigraphically above the mineralised intervals.

Type 4 deposits are exemplified by the Olympic Dam Breccia Complex, in the northeast part of the Gawler Craton,

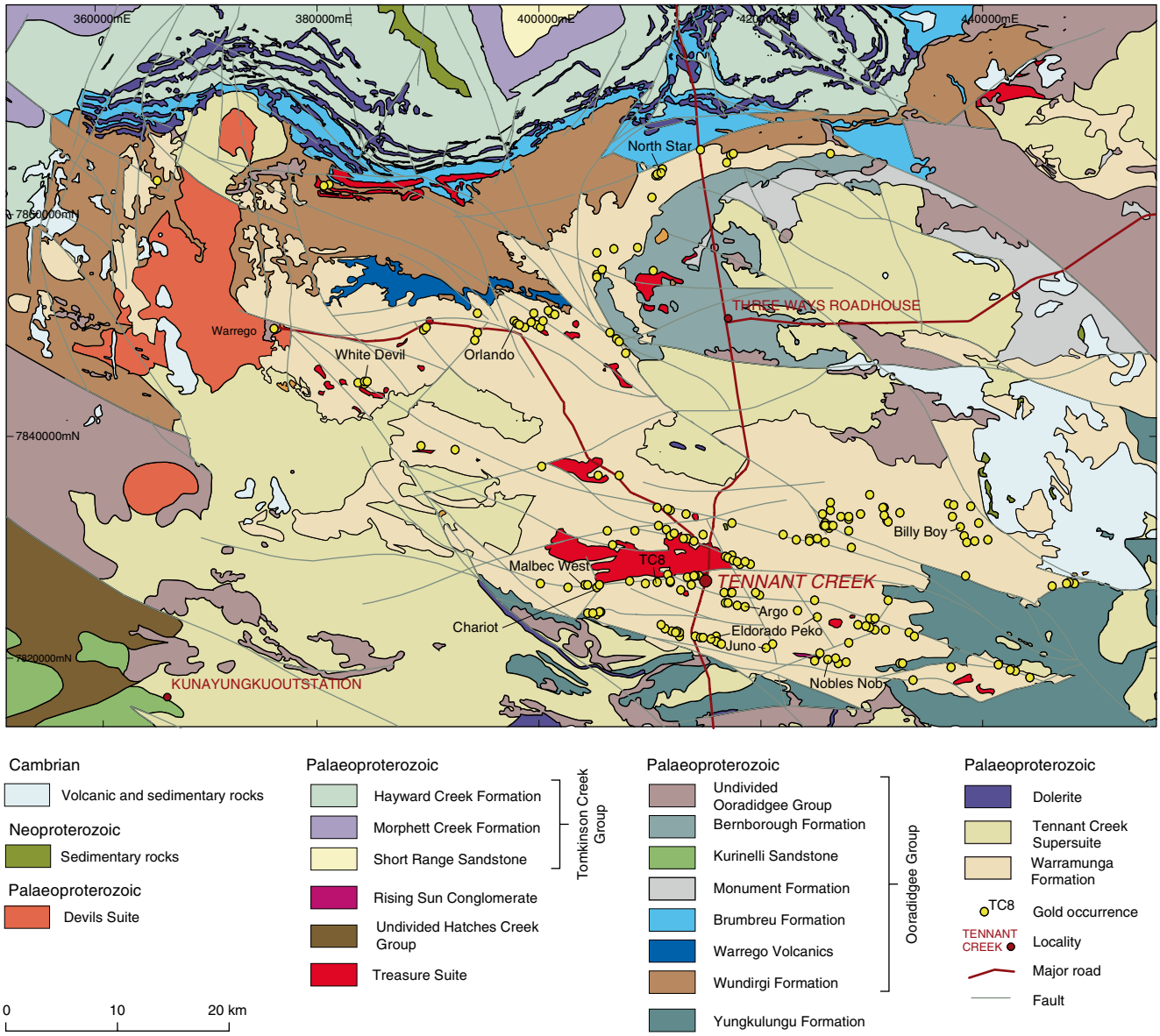

Fig. 16.27 Regional geology and gold deposits of Warramunga Province, Tennant Creek Region (After Donnellan et al. 1999; Ahmad et al. 2009)

South Australia (Haynes et al. 1995). The geologic setting of this world-class ore body is poorly defined as the breccia complex is buried beneath approximately 300 m of Stuart Shelf cover rocks, and the nearest exposed rocks of the Gawler Craton are more than 100 km distant (Fig. 16.29). The upper parts of the deposit and the surrounding rocks have long since been removed by Precambrian erosion. Any local geologic setting at the time of mineralisation must be inferred from the remnants of the upper parts of the complex, now preserved within the breccia complex, and from coeval rocks preserved elsewhere in the northeast part of the Gawler Craton. The geological setting that drove the mineralising system at Olympic Dam is even more enigmatic than the other three types, with divergent opinions as to its ultimate origin. Interpretation is further complicated by multiple brecciation and alteration events within the breccia body. Of prime importance to the genesis of this deposit is the relative significance of direct magmatic versus hypogene hydrothermal processes, and the relative levels of fluid mixing with nearsurface and basinal brines, generated via dissolving evaporite units.

A two-fluid mixing hypothesis for ore formation at Olympic Dam was first proposed by D. W. Haynes (in Roberts and Hudson 1983) and was based on the sulphide-pitchblende-haematite association of the ore body, as well as the ore textures and the overall sulphide zonation pattern. Reed and Haynes (in Haynes et al. 1995) numerically modelled a hypothetical Olympic Dam system where an oxidised 150 °C water, derived from a synthetic arkose, interacted with a proto-ore assemblage consisting of siderite,

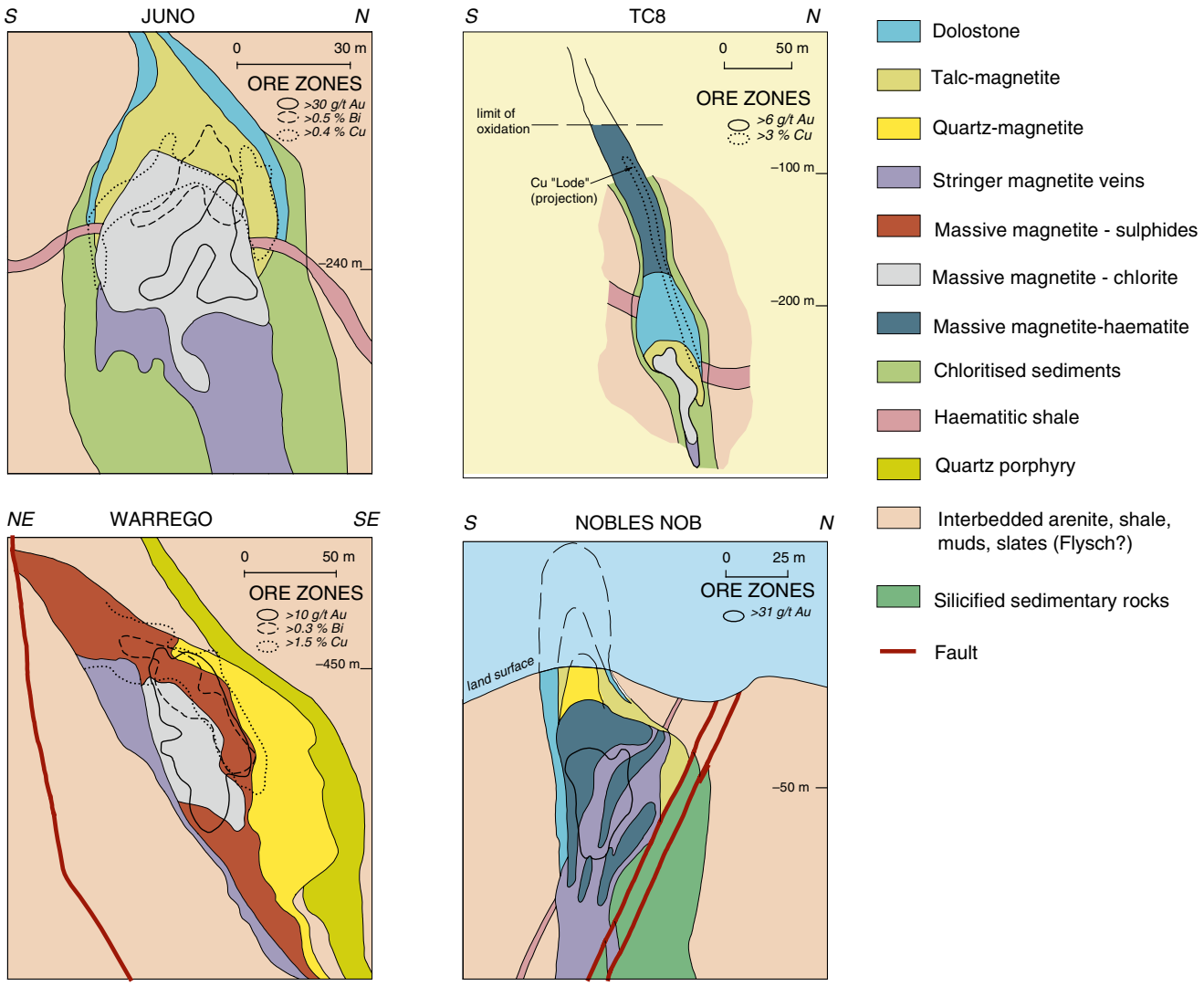

Fig. 16.28 Tennant Creek gold district Northern Territory, Australia. Show relationships between ironstone zones and ore grades (After Ahmad et al. 2009). See Fig. 16.27 for locations

pyrite, magnetite and chlorite. Wall and Valenta (1990) speculated that an analogous, but two-stage, mechanism was responsible for the genesis of both the Olympic Dam and the Tennant Creek orebodies. The modelling of Reed and Haynes implied that such a two stage mechanism was unlikely to result in ore formation at Olympic Dam, and was not consistent with textural and mineralogical characterisation of the orebody (Reeve et al. 1990) nor with its Sm/Nd and U/Pb isotopic signatures (Johnson and Cross 1991).

Einaudi and Oreskes (1990) and Oreskes and Einaudi (1990) also presented a multistage mechanism for the development of the deposit. They proposed a primary hypogene origin for the iron and some of the copper and uranium in the deposit, but suggested that much of the ore-grade mineralisation was produced by a discrete (up to 200 My younger) second stage Cu-U overprint. They argued that the orebody had undergone a low temperature secondary enrichment as a result of uplift, unroofing and weathering at the Proterozoic landsurface. Reeve et al. (1990) described a model involving nearsurface cyclic interaction of hot ascending saline magmatic waters and cooler, more oxidised saline waters. They argued against the notion that the orebody had been extensively upgraded by any distinct low temperature weathering event, and supported a two fluid mixing model first presented in Roberts and Hudson (1983).

Oreskes and Einaudi (1992), with reference to fluid inclusion and isotopic data, refined their earlier hypothesis noting that two fluids were likely involved in ore genesis. They concluded that a deep-seated or magmatic fluid was responsible for the genesis of the magnetite-rich proto-ore. Water of surficial origin was then involved in the later stages of hydrothermal activity, which in turn formed the haematite breccias, and that sulphide deposition mainly occurred late relative to brecciation and deposition of haematite. They speculated

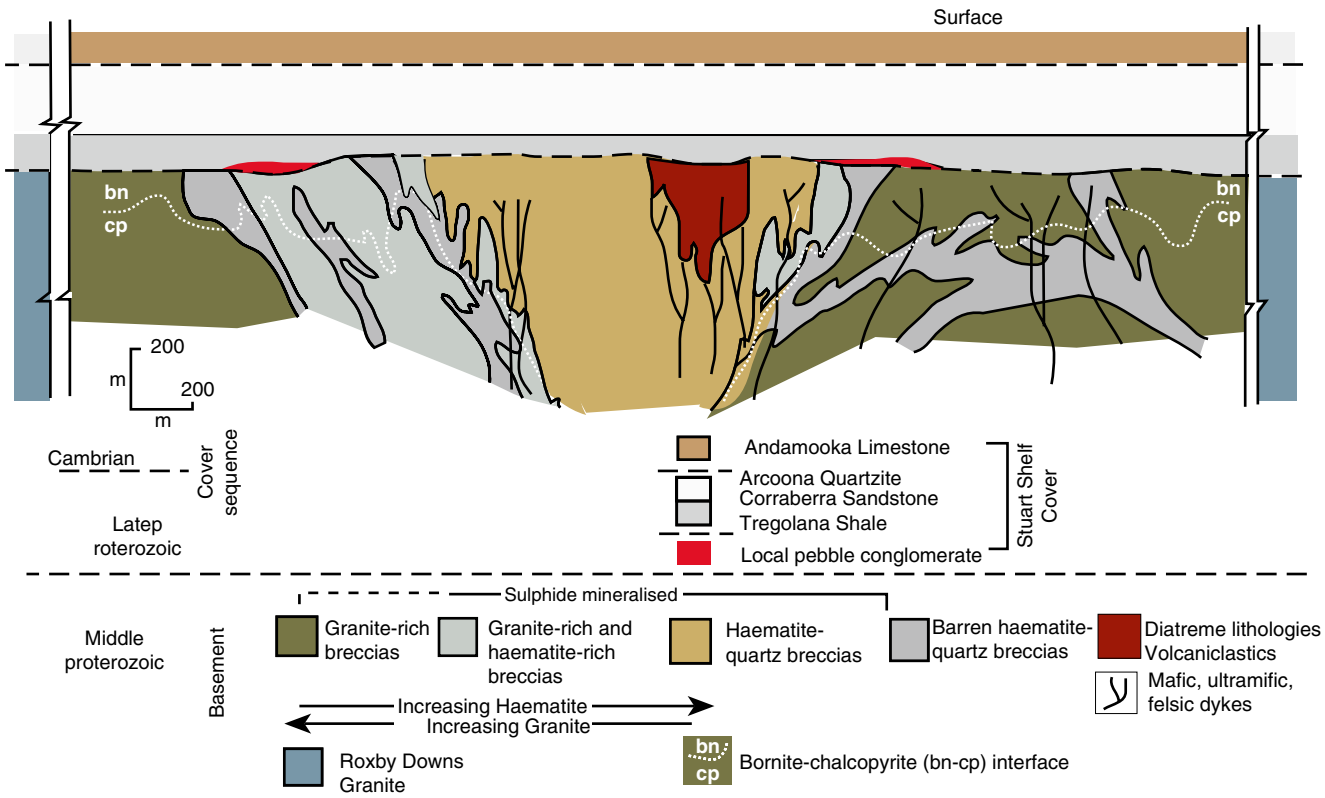

Fig. 16.29 Simplified geological section of the Olympic Dam Breccia Complex (After Haynes et al. 1995)

that the magnetite deposition may have preceded haematite deposition by some 150 My. In contrast, Haynes et al. (1995) concluded that their two-fluid fluid mixing model best explains the precipitation of the sulphides, magnetite and haematite and many associated minerals. They do not think the data support a discrete episode of sulphide enrichment related to later hypogene hydrothermal events, or to later weathering of the upper part of the orebody. The debate continues.

If both Haynes et al. and Reeve et al. are correct in their assertion of the presence of a saline water body in the caldera, which mixed with deeper magmatic water to form the deposit, then there may well be indications of former saline minerals and burial salts still preserved in the locally preserved pods of slumped and deformed caldera sediment fill. To my knowledge these textures have yet to be documented in any published literature base.

However, in support of the significance of a nonmagmatic pore fluids in the generation of this supergiant, McPhie et al. 2011, note the presence of sedimentary fragments in the main breccia, now enclosed by granites (Fig. 16.30). The breccia is composed mainly of granite clasts and minor amounts of Mesoproterozoic volcanic clasts. Very thick (>350 m) sections of bedded sedimentary facies that occur in the breccia complex include laminated to very thin planar mudstone beds, thin to medium internally-graded sandstone beds, and thick conglomerate beds. The bedded sedimentary facies extend continuously across a 1.5 km by 0.9 km area and are not limited to small separate maar craters, as previously thought. Detrital chromite and volcanic quartz in the bedded sedimentary facies cannot be matched with local sources, and imply that the provenance extended beyond the area of Olympic Dam. The lateral continuity, provenance characteristics, great thickness, below-wave-base lithofacies, and intracontinental setting suggest that the bedded sedimentary facies are remnants of a sedimentary basin that was present at Olympic Dam prior to formation of the breccia complex. McPhie et al. (2011) conclude that the Olympic Dam hydrothermal system operated beneath and partly within an active sedimentary basin, was not confined to maar craters, and did not vent. This new view of the setting raises the possibility that sedimentary processes, as well as actively circulating basinal fluids, were involved in ore genesis (Fig. 16.30).

Candaleria As a Younger Analog?

The Lower Cretaceous Candelaria Cu-Au skarn deposit (IOCG) of Mexico is a more recent example of ferroan/evaporite hydrothermal circulation, with many of its early fluid system features comparable to Olympic Dam style circulation (Fig. 16.31; Ullrich et al. 2001). Its andesite-hosted mineralization (470 Mt @ 0.95 % Cu, 0.22 g/t Au) was largely

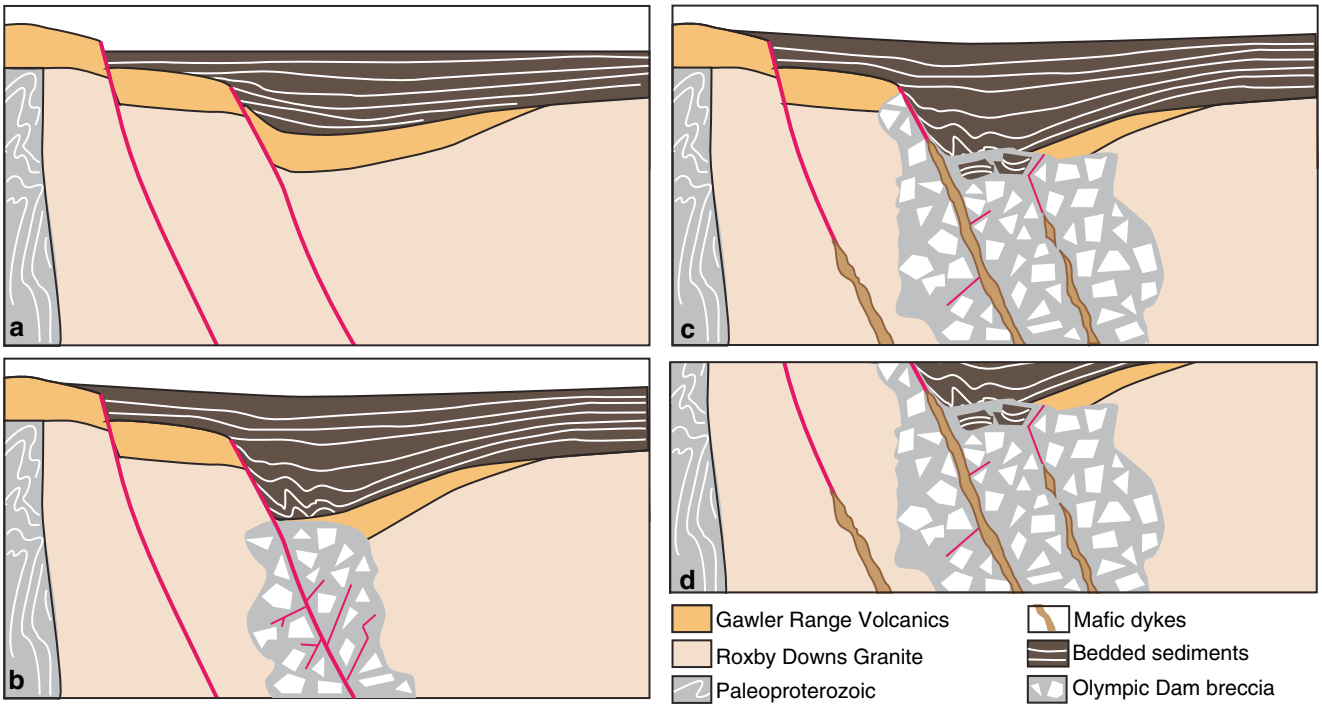

Fig. 16.30 Evolution of Olympic Dam facies. (**a**) Bedded sedimentary facies accumulated in fault-bound basin above Meso-proterozoic granite and lavas. (**b**) Fault-controlled subsurface fragmentation of Roxby Downs Granite, Gawler Range Volcanics lavas, and bedded sedimentary facies to form the Olympic Dam breccia complex. (**c**) Mafic dykes intruded granite and breccia complex along faults. (**d**) Erosion unroofed the breccia complex, removing almost all traces of bedded sedimentary facies (After McPhie et al. 2011)

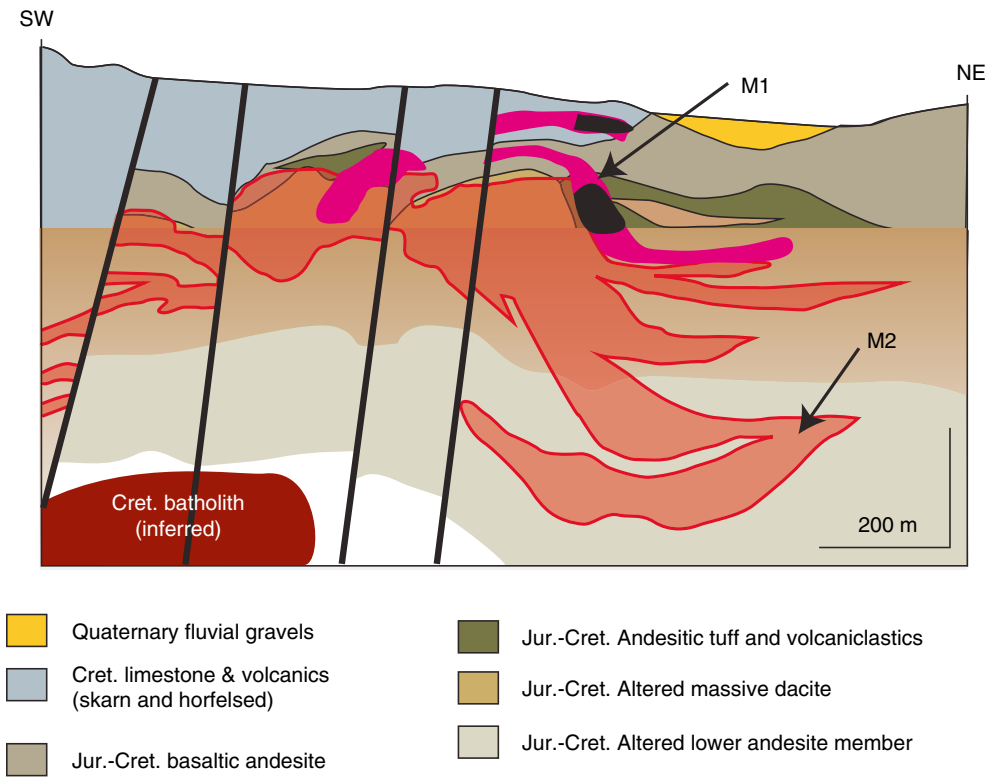

Fig. 16.31 Cross section of Candelaria Cu-Au deposit, Tierra Amarilla, Chile. M1 Marginal Cu ore replacing metasediments (*solid black* indicates massive pyrrhotite). M2 Main orebodies, Chalcopyrite with magnetite "mantos" in early K-silicate (mainly biotite) altered andesite, overprinted by Ca-Na alteration synchronous with Cu emplacement

associated with Ca-amphibole (^{40}Ar-^{39}Ar plateau at 111.7 ± 0.8 Ma), albite, microcline, magnetite and green biotite emplacement (112.8 ± 0.7 Ma), followed by subordinate chalcopyrite-epidote-chlorite and, finally, chalcopyrite-haematite-calcite-chlorite stages.

The hydrothermal system, which was hypersaline and CO_2-rich throughout, cooled from over 400 °C to below 275 °C. Ore deposition and Ca-metasomatism, simultaneously generated Cu-poor andradite-diopside-scapolite "skarns" in the andesitic hangingwall of the orebody. They were preceded at 114.1 ± 0.7 Ma by a large-scale and locally intense Fe- and K-metasomatism event, which generated magnetite and brown biotite, respectively. This process was contemporaneous with ductile deformation along major faults in the deposit. It was a barren precursor alteration stage to ore deposition and was superimposed on a wider zone of quasi-pervasive albitization of the andesites and, locally, of adjacent granitoids.

O and S isotopic compositions of ore and alteration minerals predicate progressive changes in fluid chemistry during hydrothermal activity (Ullrich et al. 2001). Thus, $\delta^{18}O_{fluid}$ evolved from around +7.0‰ for pre-ore K-metasomatism, similar to values for contiguous granitoids (+5.4 to +9.6‰), to ≈ −0.2‰ in the late "Olympic Dam-like" stage. $\delta^{34}S$ fluid simultaneously increased from "magmatic" values of +5.7‰ in the earliest Cu (−Mo, Zn, Au, Ag) ore sub-stage to +12.0 < × < +20.2‰ during precipitation of late-stage chalcopyrite-haematite and terminal-stage anhydrite. Hydrothermal activity was focused at the western margin of a defunct Valanginian-to-Barremian (ca. 138–119 Ma) back-arc, shallow-marine basin, which incorporated significant evaporites. The isotopic data record a progressive mixing of magmatic-hydrothermal waters with non-magmatic, plausibly evaporite-sourced waters. Mineralization overlapped temporally with the intrusion of the medium-K calc-alkaline Ojancos Plutonic Complex from 117.2 ± 1.0 to 110.5 ± 1.7 Ma, a probable source of ore-metals and juvenile fluids, and also with the uplift and recycling in basinal waters of the nearby evaporites.

Other Proterozoic Cu-Au Fe-Oxide/Evaporite Associations

As well as Australian examples, there are numerous other Proterozoic IOCG (*sensu lato*) deposits that show strong affinities with hypersaline basinal waters and possibly with chloride-rich brines, derived from dissolving evaporites (Table 16.5). Some of the best documented Proterozoic Cu-Au meta-evaporite/volcanic associations (IOCG *sensu lato*) are to be found in the Cu or Cu-Au deposits of Scandinavia. In the Kiruna-Tjåmotis-Arjeplog district of Northern Sweden, the iron oxide deposits and associated greenstone lithologies are extensively scapolitised (Parák 1991). These Kiruna greenstones were formed close to 1.9 Ga. Magma eruption and emplacement, along with associated evaporitic rift sedimentation, was closely followed by metamorphism and hydrothermal circulation driven by the volcanism.

Scapolitisation can often be seen around lava pillows as well as in syenite, gabbro and diabase. Scapolite is commonplace in the copper mineralised areas at Svappavaara and Nautanen where it is accompanied by apatite, tourmaline, magnetite and skarn. At Ultevis it occurs as well developed crystals up to several centimetres in size in coarse-grained skarn and as pegmatite in a rusty, graphite-bearing rock. The most impressive scapolite occurrences occur in the metasedimentary pile, where it forms almost pure bands or layers in skarn, biotite-bearing limestone, biotite-bearing schist, and graphite bearing schist. In some cases, scapolite in the metasediments makes up more than 50 % of the rock volume. The strongly stratiform distribution of scapolites in the Kiruna district implies a sedimentary sodic precursor (Parák 1991).

The nearby (now depleted) Viscaria copper deposit reflects a strongly evaporitic protolith with mineralisation occurring in Proterozoic playa metasediments in a mafic volcanic terrane (Godin and Lager 1986). Within a 700-m section of predominantly tholeiitic basalts there are four mineralised horizons. The highest concentration of sulphide minerals occurs within graphitic schists and calcsilicates lenses and layers within the meta-basalts. The graphitic units are interpreted as original organic-rich sediments deposited in the deeper parts of a fault-bounded anoxic lake and were the units that likely acted as reductants to the Cu carrying chloride brines (see Chap. 15 for a discussion of organic-associted redox mechanisms in the diagenetic realm). The calcsilicates were originally limestones deposited as shallower nearshore deposits. The original shallow water setting is also reflected in locally preserved sedimentary structures: mud cracks, ripple marks, shallow-water crossbeds, erosion surfaces, and breccia beds.

Evaporite mineral pseudomorphs suggest the chert-albite units were formed in a saline lake as magadiite chert replacements of sodium silicate precursors (Godin and Lager 1986). Some of the aligned growth fabrics, still preserved in the albite-chert layers, are reminiscent of bottom-nucleated and splayed trona precursors (pers. obs, 1986). Areas of more intense scapolite and albite alteration may represent metamorphosed endproducts of authigenic reaction haloes in the volcaniclastics that surrounded the lake. Sulphide minerals appear to have begun to replace the organics relatively early in the diagenetic history of the lacustrine sediments. Parák (1991) suggests that the hydrothermal system of this greenstone belt, which was driving alteration in the subsurface, may also have supplied the ionic components to the depositing primary evaporites at much shallower burial depths.

The likelihood of an evaporite protolith for the Swedish Cu deposits is further reinforced by the presence of anhydrite

lenses in the Kiirunavaara deposit, where re-examination of drill core from the deposit showed anhydrite in 26 holes, partly as lenses and partly as secondary fissure-filling (Parák 1991). Tuisku (1985) discussed the origin of scapolites in the schists of nearby central Finland; as in Kiruna, he concluded the chlorine for the scapolitisation was provided by dissolving precursor evaporites. "…The chlorine of the basic igneous rocks was either introduced directly into the magma from evaporites or brines or into the cooling igneous rocks from later circulating brines" (p.169).

Evaporite-associated Au-Cu deposits also occur at Pahtohavare and Bidjovagge in the greenstone terranes of Norway (Lindblom et al. 1996; Ettner et al. 1994). The Pahtohavare deposit is located some 10 km south of the Viscaria Cu deposit, while Bidjovagge is located in greenstones some 200 km to the northeast. At Pahtohavare the gold mineralisation occurs as impregnations, epigenetic quartz-rich breccias and fracture fillings, along with pyrite, chalcopyrite and pyrrhotite. It is hosted in zones of fine-grained albitised rocks within tuffite, black graphitic schists and mafic sills (Fig. 16.32). The graphite horizons in the albite-altered blackschist have been replaced completely by albite in the most mineralised sections. Albite-altered zones are surrounded symmetrically with barren biotite-scapolite-altered rocks. The scapolite is marialitic and occurs as porphyroblasts and irregular veinlets or networks. Coarse-grained carbonate veins are common both in the ores and surrounding altered rocks. Syngenetic magnetite occurs at several stratigraphic levels within the tuffite (Lindblom et al. 1996).

At Bidjovagge the deposit is hosted in the metavolcanic and metasedimentary Cas'kejas Formation, which is composed of amphibolites and mafic metavolcanics, interbedded with minor thin beds of carbonate, graphitic schist, albitic felsite and metatuffite (Ettner et al. 1994). Originally, the host sequence is thought to have been a sequence of lava flows, ash deposits, black shales, limestones and evaporitic shales deposited in a shallow early rift basin. A series of thick diabase sills intrude the Cas'kejas Formation and a zone of albitic felsite has developed between the contact of the diabase sills and graphitic schists. Mineralisation is of two types (Au-rich and Cu-rich), hosted in a series of mineralised lenses along a shear zone some 2.5 km long. This mineralised shear zone lies in an albitic felsite made up very fine-grained albite with impurities of rutile and carbonate. It is a product of sodic metasomatism of black shales, driven by the intrusion of the diabase sills and associated circulation of hot saline brines. The gold-rich ore is hosted within ductile to brittle structures in the shear, while the copper-rich ores occur within brittle structures in shears that crosscut the ductile fabric. A series of syenodioritic intrusions crosscut the shear texture in the albitic felsite and are cross cut by quartz-carbonate chalcopyrite veins. Based on crosscutting relationships these dykes probably intruded during the period between the gold-rich and copper-rich mineralisations.

Inclusion studies in both Pahtohavare and Bidjovagge show gold transport can be tied to highly saline NaCl fluids (30–45 wt%) that carried CO_2 and CH_4 at temperatures near 350 °C. This is consistent with the broader highly saline character of fluid inclusions in quartz across the range of

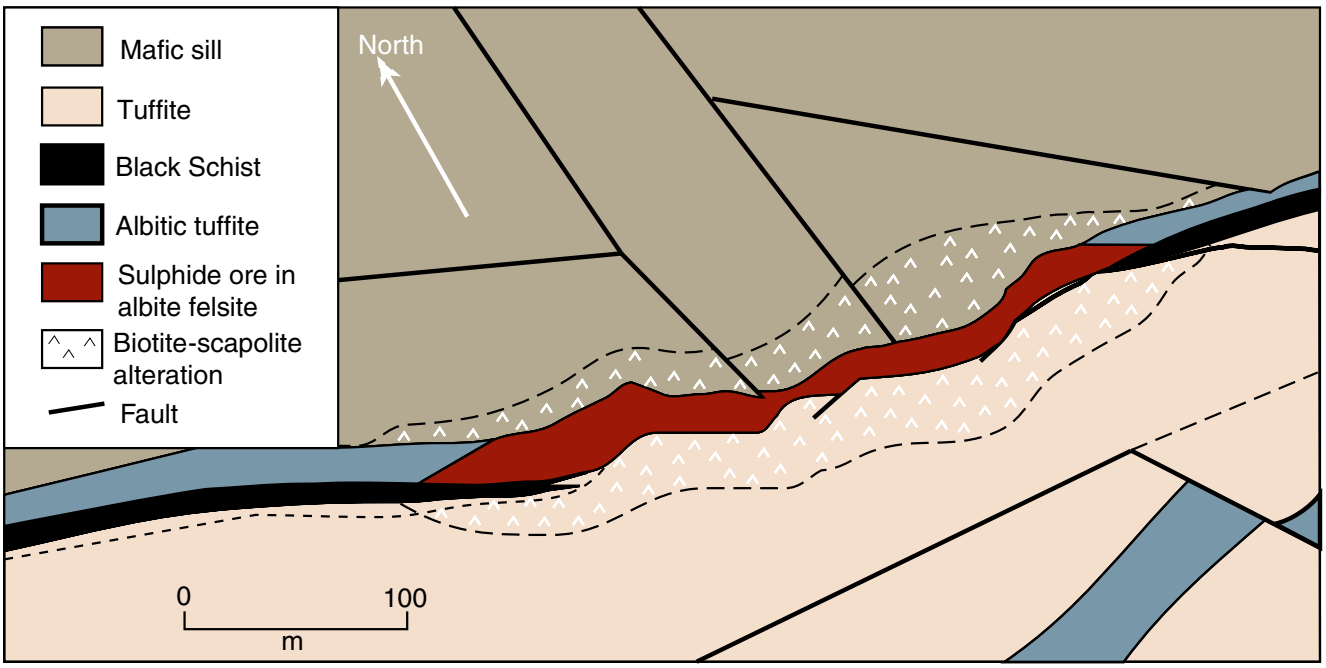

Fig. 16.32 Geology of the Pahtohavare copper deposit, Norway (After Ettner et al. 1994)

IOCG deposits in the Kiruna district of Sweden (Fig. 16.33; Smith et al. 2013). Fluid inclusions in quartz veins cutting Fe oxide-apatite of these deposits range in salinity from 33 to 37 wt.% NaCl eq., and those in IOCG-type deposits from 41 to 54 wt.% NaCl eq. (Fig. 16.33a). According to Smith et al. 2013 the minimum trapping conditions for these inclusions are ≈200–300 MPa and 200–300 °C in the Fe oxide-apatite bodies, and 250–300 MPa and 300–500 °C in the IOCG deposits. Deformed Cu-Au deposits have similar early fluid characteristics, but contain complex secondary fluid inclusion assemblages including halite-saturated (20–30 wt.% NaCl eq.), aqueous-carbonic (3–13 wt.% NaCl eq.; $X(CO_2) \approx 0.17–0.29$) and CO_2-rich fluids. The aqueous-carbonic and carbonic inclusions are consistent with aqueous-carbonic fluid immiscibility at ≈150 MPa. A secondary inclusion population, with a high Ca-content occurs in all deposit types.

Halogen contents in the Kiruna district indicate a range of salinity sources with possible inputs from both magmatic and halite-dissolution brines (Smith et al. 2013). Although some samples have Cl/Br ratios consistent with a magmatic source for the halogens, the Cl-enrichment apparent in the total dataset is a strong indicator of interaction of fluids with (meta-) evaporites and consequent halite dissolution (Fig. 16.33a, b), followed by extensive water–rock interaction. No single group of inclusions or sample type shows a range of ratios consistent with a single fluid source, nor do all higher Cl/Br ratios correlate with the highest salinity fluids (Fig. 16.33a), implying that halite dissolution was not the only mechanism that generated highly saline brines. Typical magmatic-hydrothermal fluids are expected to have low salinities and salinities of 6 wt.% NaCl eq. were used by Barton and Johnson (2002) for mass balance models of IOCG deposit formation. In this situation, however, highly saline magmatic brines could be produced by aqueous–carbonic fluid exsolution from magmas at relatively high pressure. In general the geological distributions and inclusion chemistry favours the involvement of evaporite-derived brines and daughter products such as scapolite, but it does not exclude magmatic influences.

Element ratios suggest the alkali content of the fluid exceeded the buffer capacity of the host rocks. Iron and other transition metal contents correlate strongly with Cl concentrations, with secondary controls on solubility from pH, redox and temperature. Copper and Ag contents are higher in lower salinity aqueous-carbonic brines (up to 5,000 ppm Cu, 900 ppm Ag) than in the most saline brines (up to 2,297 ppm Cu, 837 ppm Ag). This may reflect differences in metal source between deposit types, but is also consistent with the complexation of Cu by bisulphide in the lower salinity fluids. Late stage aqueous-carbonic fluid flux through the deformed deposits either introduced additional

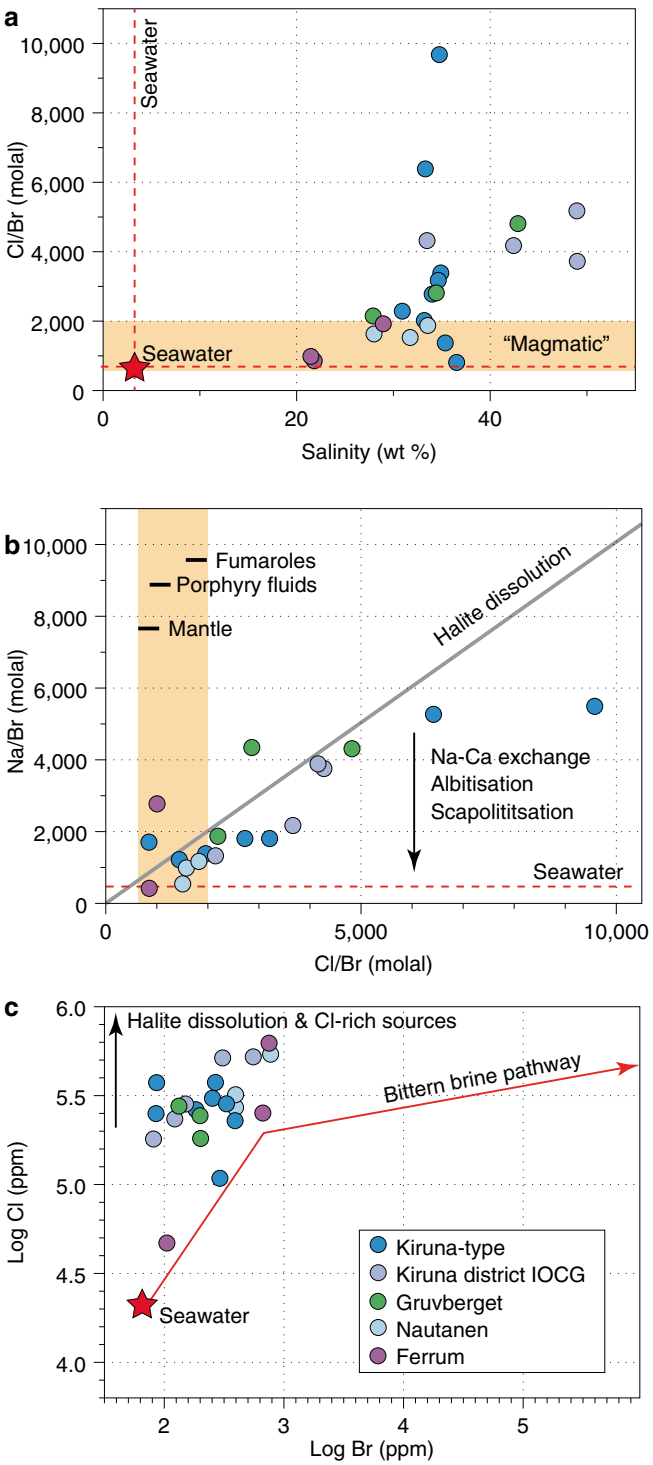

Fig. 16.33 Halogen geochemistry of fluid inclusions in quartz veins from the Norrbotten district (Replotted from Smith et al. (2013)). (**a**) Plot of molal Cl/Br ratio against fluid inclusion salinity determined from microthermometry. (**b**) Molal Na/Br and Cl/Br ratios compared with the ranges of ratios from seawater and 'magmatic' fluids, and the halite dissolution trend. (**c**) Comparison of Cl and Br concentrations in reconstructed inclusion fluids with the seawater brine evolution trend (*red arrow*)

copper to the deposits, remobilised pre-existing copper or both (Smith et al. 2013)

These fluid characteristics are very similar to those associated with the emplacement of the higher temperature Australian Cu-Au deposits. Ettner et al. (1994) relate gold precipitation at Bidjovagge to redox reactions between the fluid and the graphitic schists. Lindblom et al. (1996) suggest gold precipitation at Pahtohavare was the result of cooling of a chloride brine as it mixed with a lower salinity fluid during tectonic fracturing along with associated pressure fluctuations and CO_2 mixing. They go on to suggest, by comparison with Olympic Dam (as per Oreskes and Einaudi 1992), that the saline ore fluids were magmatically derived. Subsequent work of Haynes et al. (1995) showed that magmatic fluids at Olympic Dam may have mixed with saline evaporite-derived subsurface waters. They also ignore the possibility that the source of the chlorine and sodium in the inclusions, and the marialitic scapolites, and the albitites, could reflect a meta-evaporite association. This in a deposit located less than 10 km from the Viscaria Copper deposit and along the same greenstone trend as the classic meta-evaporite Viscaria locality of Godin and Lager (1986). Ettner et al. (1994) are a little more circumspect in their interpretation of the origin of the Na-Cl brine, and suggest these highly saline chloride brines may have had either an igneous or a metasedimentary source, as does subsequent work by Smith et al. (2013).

Non-IOCG Gold- Evaporite Associations

The Santa Rita gold deposit in the Middle to Upper Proterozoic Paranoá Group in Goiás, Brazil, is another example of a possible evaporite/brine formed gold deposit. But, in this case, the solutions were at times also capable of precipitating pyrite within the quartz-carbonate veins that host the ore (Giuliani et al. 1993). Fluid inclusion studies of quartz from these veins identifies two fluids: (1) a highly saline CO_2-N_2-rich aqueous fluid with halite ± sylvite daughter minerals, and (2) a CO_2-N_2-rich aqueous fluid with moderate salinity. The two fluid types can occur in the same quartz domain and display great variation in the degree of filling, as well as notable dispersion of the microthermometric data. On heating, all the inclusions decrepitate between 200 and 300 °C. The simultaneous entrapment of compositionally variable fluids in the system H_2O-CO_2-N_2-NaCl-KCl is interpreted as heterogeneous trapping resulting from the mixing of high-salinity fluids (H_2O-NaCl-KCl system) with carbonic fluids (H_2O-CO_2 system). The latter moderate-salinity fluids were produced by devolatilisation of carbonate and phyllitic host rocks. The former, the high salinity brines, were derived by leaching of the evaporites that characterised the lower part of the Paranoá Group (Giuliani et al. 1993).

Gold was initially transported as an $AuCl_2$-complex ($T > 300$ °C, low pH, moderate *fO2*) much like the Proterozoic Cu-Au deposits of Australia. When temperatures fell below 290 °C, the "switch-over" process (Large et al. 1989 – see Fig. 16.3) lead to a predominance of $Au(HS)_2$ in the carrier fluid, so that pyrite was a coprecipitate at these lower temperatures. The oscillatory zoning in the As-Co-Ni-bearing pyrites also indicates episodic fluctuation of the fluid composition. Such changes in fluid character typify fluid-mixing systems subject to fluctuating levels of feed waters within an active hydrothermal system. The model proposed by Giuliani et al. encompasses a Proterozoic geothermal system that was characterised by a heated fluid flow regime along fault feeder structures that also crosscut the dissolving Paranoá evaporites. Today, the preserved equivalents of such brine-fed systems are likely to be represented by dissolution breccias and salt welds intersecting the faults rather than actual salt beds that have long since dissolved.

A similar fluid mixing system, involving highly saline evaporite-derived basinal brines and magmatic waters, is also suggested as the mechanism for mesothermal gold mineralisation in the Transvaal Sequence in South Africa (Anderson et al. 1992). In this case, mixing occurred between a deep-seated homogenous CO_2-rich fluid of magmatic/metamorphic origin and a saline (subsurface/intraformational) basinal brine derived by the dissolution of evaporites in the sediments of the Chuniespoort and Pretoria groups of the Transvaal sequence, where Tyler (1986) documented widespread salt casts.

Another evaporite-associated gold setting is the Cu-Co-Au deposits of the Idaho Cobalt Belt, USA (Nash and Connor 1993). These deposits are stratabound and, in the Blackbird Mine, the mineralisation is locally stratiform. The ore host is the Mesoproterozoic Yellowjacket Formation, composed of dark-coloured, thin-bedded to laminated argillites and siltites, quartzites and minor marbles. These units have equivalents in the Belt Supergroup that are known to be meta-evaporitic. The mineralised Blackbird Member shows anomalously high levels of Cl, K and Fe in the biotites, as well as the presence of stratiform scapolite and tourmalinites (Trumbull et al. 2011). Locally, Fe-enriched sediments become ironstones. The Blackbird Member is also characterised by crosscutting growth faults, soft sediment disruption zones and likely hydrothermal seafloor vents. Nash and Connor (op. cit.) underline similarities in the mineralising system with the evaporite-associated Red Sea deeps and the Salton Sea hydrothermal sulphides, while Trumbull et al. (2011) utilise boron isotopes to argue for a marine meta-evaporitic origin for some of the tourmalines.

The most impressive evaporite-associated gold system is probably Muruntau in Uzbekistan, which is one of the biggest gold deposits in the world, with 5,200 t of contained Au (Fig. 16.34a, b; Wilde et al. 2001; Bierlein and Wilde 2010). The origin and genesis of gold mineralisation at Muruntau

remain highly contentious. Based on strong structural control and its overall tectonic setting, it has been interpreted as a typical shear zone-related, Au-bearing quartz-vein association, perhaps in a metamorphic belt-hosted orogenic-gold system. Others propose a thermal-aureole gold origin for the deposit, with the ore fluid inferred to have been largely derived from the Murunski Granite, which has been intersected in diamond drillcore at 4 km depth beneath the deposit. Opposing schools argue over the relative import of magmatism versus basinal waters in its genesis. Magmatists emphasise the close spatial association of gold with post-tectonic Permian felsic intrusions and superimposition of hydrothermal alteration upon a contact metamorphic aureole as indicating a magmatic origin for metals, heat, and ore-forming fluids.

The $^{40}Ar/^{39}Ar$ ages of hydrothermal sericite suggest that ore formation occurred in at least two pulses at about 245 and 220 Ma (during the Triassic period), some 30 m.y. after intrusion. However, the intrusion age is poorly constrained. Orebody genesis via regional metamorphic devolatilization is implausible, because basement rocks would have been substantially devolatilized during the Caledonian deformation about 200 m.y. prior to intrusion. Detectable H_2S in fluid inclusions raises a distinct likelihood that gold was transported into the deposit as a bisulphide complex and offers a somewhat distinct set of precipitative processes for this supergiant gold deposit (Wilde et al. 2001).

If bisulphide transport was the case, then a likely explanation of the huge gold endowment is that an unusually large reservoir of reduced sulphur was available to the ore-forming fluids. Furthermore, if fluids were able to scavenge gold from a particularly large source area, then the probability of generating a giant deposit would have been increased. Wilde et al. (2001) suggest, therefore, that a possible source of fluid and metal for the Muruntau deposit was the anhydrite-rich evaporitic sediments in cover sequences 1 and 2.

This setting would have provided large volumes of H_2S, via thermochemical sulphate reduction. Anhydrite begins to break down in the presence of methane at temperatures of about 140 °C to yield calcite and H_2S, via a reaction such as; $CaSO_4 + CH_4 = CaCO_3 + H_2S + H_2O$ (thermochemical sulphate reduction; Worden et al. 1995). High H_2 S gas activity would favour gold transport by increasing the dissolved reduced sulphur activity of a coexisting aqueous fluid phase.

The $^{40}Ar/^{39}Ar$ and Rb-Sr ages suggest that deposition of auriferous quartz veins and associated sericitic alteration occurred in the same frame time as deposition of cover sequence 2 sediments and volcanic rocks in the adjacent rift. Petroleum studies show that this cover succession loaded and buried the basal Devonian sedimentary rocks (with their significant entrained volumes of $CaSO_4$) to depths of more than 7 km (this is the maximum known thickness of cover sequences 1 and 2). At such depths large volumes of $CaSO_4$ experienced temperatures of 140 °C and so TSR volatilisation was highly likely. Cover sediments were then uplifted during a number of superimposed compressional events (Fig. 16.34b, c)

Fluid inclusion data suggest that hydrothermal fluids at Muruntau evolved from a relatively reduced (CH_4-rich) to a more oxidized (CO_2-rich) content during gold deposition (Fig. 16.34c; Wilde et al. 2001). Thus, oxidation of evaporite-derived gold bisulphide complexes is a possible precipitative mechanism. The origin of oxidized fluid is uncertain. Source options include meteoric, magmatic water or a more oxidized saline connate water from the adjacent evaporite-entraining rift sequence. At this time, the ultimate fluid source is still contentious.

So What Is a IOCG Deposit and Is Mineralisation Evaporite/Brine Related?

Interestingly, Chen (2013) argues that the sulphur source for many Cu-rich IOCG deposits worldwide is external and the result of mixing of multiple fluids and can be used to classify (Fig. 16.35; Table 16.7). Some deposits are derived from mixing of magmatic and saline basinal brines or refluxing seawater-derived brines (e.g., Central Andean and Carajás deposits), or from formation water and metamorphic fluids (e.g., the Cloncurry deposits), or introduced by magmatic assimilation of metasedimentary units (e.g., Phalaborwa),. However, only the evaporite-sourced fluids yield diagnostically high $\delta^{34}S$ values (i.e., >10‰), while sedimentary formation waters or metamorphic fluids commonly have lower values and are less clearly distinguishable from magmatic fluids, as in the Cloncurry deposits. There the involvement of external fluids is revealed by other evidence, such as noble gas isotopes,

A common theme in the various Proterozoic Cu-Au deposits is transport of copper and/or gold at relatively high temperatures within saline chloride complexes, often derived from the dissolution of deeply buried salt units or their metamorphosed successors. Precipitation was typically either at some sort of redox front associated with graphitic schists, to give a stratabound style of precipitation, or at some form of subsurface groundwater/fluid mixing zone, often with a more structurally focused mode of precipitation associated with ironstone precipitation or replacement. Those cases showing a strong structural control to the mixing zone, imply precipitation was coincident with, or later than, a major deformation event that had facilitated the formation of a more permeable pathway. Precipitation was often associated with some form of tectonic pressure shadow. In most cases a strong argument can be made that the high-temperature metal-carrying brine was derived by dissolving chloride-rich evaporites or pressure-driven escape of chloride-rich volatiles from subsequent meta-evaporites. In some cases, a strong argument can be made for an evaporitic association in

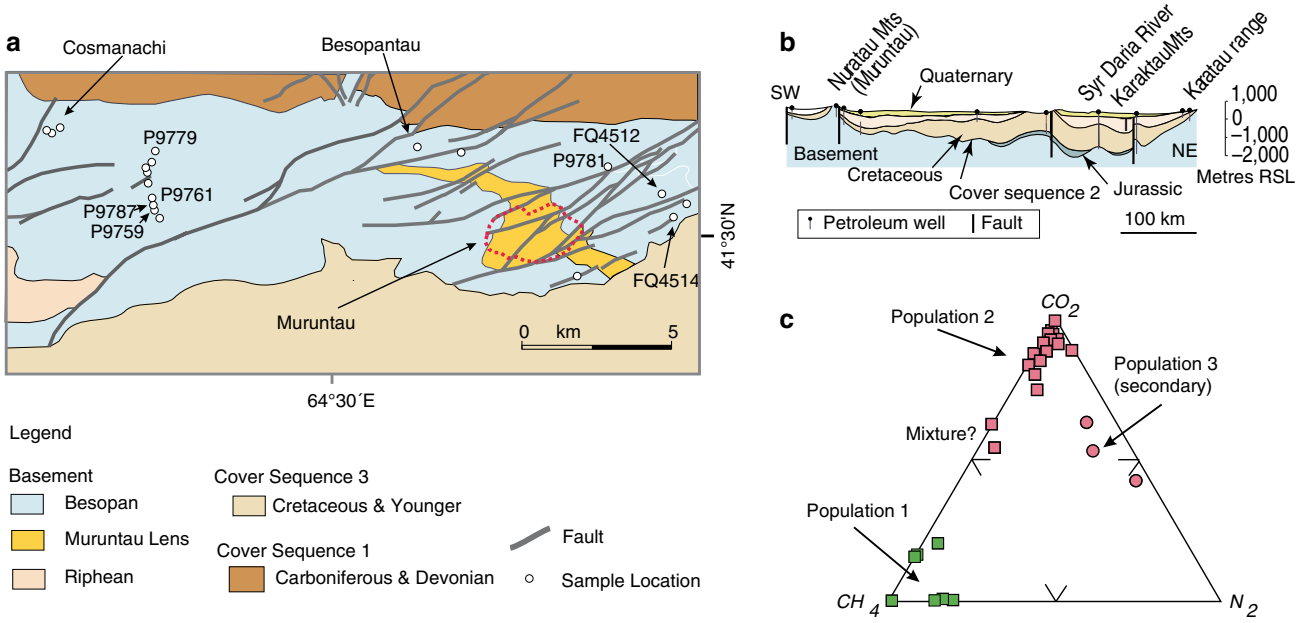

Fig. 16.34 Supergiant Muruntau gold deposit, Uzbekistan, (**a**) Geology of the Muruntau mine areas howing the contact between the deformed basement and overlying Devonian and Carboniferous rocks is a low-angle fault, which dips to the north. (**b**) Idealised SW NE section in the Muruntau area based on Soviet-era petroleum wells. (**c**) Ternary diagram illustrating the measured gas content of primary fluid inclusions. The data have been interpreted to indicate two discrete fluids (After Wilde et al. 2001)

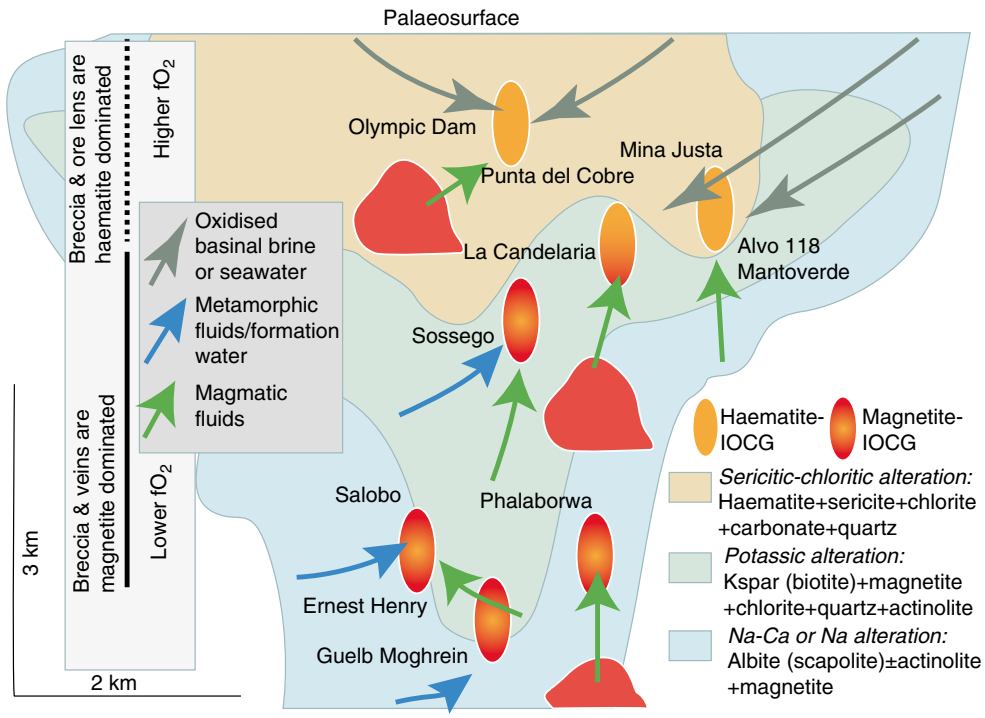

Fig. 16.35 Fluid-related settings of various IOCG deposits (After Chen 2013). Regional Na\Ca or Na alteration commonly precedes mineralization, while potassic alteration and hydrolytic (sericite–chlorite) alteration are usually mineralization-related. (1) Ca-metasomatism dominates the La Candelaria-Punta del Cobre district. (2) Na\Ca alteration widespread in the Cloncurry district, whereas Na-alteration dominates the Central Andean IOCG centres. Under conditions of high thermal gradient/heat-flow, the Y-axis will be compressed. Basinal brines or seawater are probably more oxidized than magmatic and metamorphic fluids. With the exception of Phalaborwa, the other IOCG deposits are the result of more than one fluid source

Table 16.7 Classification of IOCG deposit as proposed by Chen (2013)

Deposit types	Iron oxide (IO)[a]	IOCG	
Subtype	Magnetite	Magnetite subclan	Hematite subclan
Ore-forming fluids	Magmatic[b]	Magmatic[c] and hybrid magmatic — nonmagmatic	Hybrid magmatic — non-magmatic and non-magmatic
Examples	Lightning Creek, Acropolis (Australia); Acari, Morritos, part of CIB[d] (Central Andes); Benson, Cornwall (USA); Esfordi (Iran); and "ironstone" in IOCG	Sossego, Salobo (Carajas); Ernest Henry, Eloise (Cloncurry); West Peko (Tennant Creek); La Candelaria-Punta del Cobre, Raul-Condestable (Central Andes); Tjarrojakka, Aitik[e] (Norbotten); Khetri (NW India); Boss-Bixby (SW Missouri); Wernecke, Nico (Canada); Guelb Moghrein (Akjoujt); Ossa Morena (Spain); Phalaborwa (South Africa)	Olympic Dam, Prominent Hill, Redbank (South Australia); Mantoverde, Mina Justa, Mantos Blancos (Central Andes); Alvo 118 (Carajas); Mont-de-1'Aigle, Sue-Dianne (Canada); Salton Sea (USA); Malundae (Lufilian arc); Boleo (Mexico)
Economic elements	Fe (±P)	Cu-Au (±Co ± Bi ± U ± REE ± Ni)(P-Mg: Phalaborwa)	Cu ± Ag ± Au ± Co ± Zn (U-REE: Olympic Dam)
Ore assemblages	mt-act-apt-qtz±ab±cpx±bt±K-feldspar ± py ± cpy	Commonly: mt-cpy-py ± po ± hem Locally: mt-cpy-bn-cc (Salobo, Phalaborwa)	hem-cpy-bn-cc and hem-cpy-py
Hydro thermal alteration	Regional: Na-Ca ± Cl ± B Mineralization-related: Fe-K-Ca	Regional: Na ± Ca Mineralization-related: K ± Fe ± Ca ± CI ± Na	Regional: weak Na ± CI ± Ca Mineralization-related: K-Cl ± Na ± Ca
Ore morphology	Veins, stockwork; local breccias	Veins and breccias; local lenses (Salobo)	Breccias, lenses (manto) and veins
Ore precipitation mechanism	Cooling	Fluid mixing and cooling	Fluid mixing and fluid reduction
Non-magmatic fluids	No	Basinal brine/seawater (Candelaria); $\delta^{34}S_{fluids} > 10‰$; Metamorphic fluids/formation water (Ernest Henry; Guelb Moghrein): $\delta^{34}S_{fluids} < 10‰$	Basinal brine/seawater: $S^{34}S_{fluids}$ commonly >10‰
Characteristics of oreforming fluids	High T (>450 °C) and salinity (>25 wt.% NaCl eq.); CO_2-rich or CO_2-bearing[f]	High-T (Ernest Henry: >350 °C) or wide range of T (Salobo: 100–500 °C); moderate-high salinity (15–50 wt% NaCl eq.); Na-Ca dominant and Na > Ca; CO_2-rich or CO_2-bearing	Moderate-low T (<300 °C), and moderate-high salinity (>15 wt% NaCl eq.); Ca-Na dominant and Ca > Na; CO_2-bearing or CO_2-poor
Mineralization level	Deep (>3 km) to shallow	Deep (>6 km, Ernest Henry) to shallow (<3 km, Candelaria)	Shallow (generally <3 km)
Ore-controlling structure	Shear zone, local rift	Shear zone	Normal fault-detachement-dilational zone/Shear zone
Subtype	Magnetite	Magnetite subclan IOCG	Hematite subclan IOCG
Host rocks	Sedimentary and volcanic rocks and intrusions	Sedimentary and volcanic rocks and intrusions	Sedimentary and volcanic rocks and intrusions
Distance to syn-mineralization magmatism	Close (<3 km)	Close (<3 km) — Sossego, Eloise, La Candelaria; Far (>3 km) — Ernest Henry, Wernecke	Close (<3 km) — Olympic Dam; Mantos Blancos Far (>3 km) — Mina Justa, Mantoverde[g]
Mineralization age	Mesoproterozoic to tertiary	Archean to tertiary	Mesoproterozoic to pleistocene
Tectonomagmatic setting	(A) (Acropolis) (B) (Central Andean deposits) (C) (Lightning Creek)	(A) Precambrian intracratonic basins, anorogenic; A-type magmatism (Carajas, Norbotten, SW Missouri, Phalaborwa) (B) Inversion of basins in extensional arc on subduction-related continental margin; calc-alkaline arc magmatism (Central Andes) (C) Inversion of post-collisional orogenic basins; calc-alkaline magmatism postdating metamorphic peak (Cloncurry) (D) extension following retrograde metamorphism (Guelb Moghrein, Wernecke)	(A) (Olympic Dam, Prominent Hill) (B) (Central Andean deposits) (C) (Mont-de-1'Aigle)

[a]Melt-origin "Kiruna-type" magnetite-apatite deposits not included
[b]Magmatic fluids without external sulphur
[c]Magmatic fluids with external sulphur, e.g., Phalaborwa
[d]CIB-Chilean Iron Belt
[e]Late IOCG-like magnetite-bornite-chalcopyrite stage
[f]Defined in this table: CO_2-rich — fluid inclusions containing $CO_2 > 20$ %; CO_2-bearing: a few fluid inclusions (<20 %) contain CO_2; CO_2-poor: no CO_2 identified in fluid inclusions
[g]Intra-mineralization dykes locally developed

the organic-rich-shale precursor of the graphitic schists, which later set up a metal-precipitating redox interface.

Most published papers to date have not considered an evaporite associated protolith to any of the ore-hosting ironstones. And yet, as was documented in Chap. 15, refluxing brines associated with dissolving evaporites can build up high metal contents and then release ferroan chloride-rich basinal brines along structurally focused paths (salt welds and fault welds). As the ferroan chloride brines seep upward or laterally they precipitate ferroan carbonate haloes along the fault or thrust conduits, or in structurally focused traps or as parts of widespread stratiform iron-hydroxide and iron-sulphide rich sediments about the brine outflow zones. Could these diagenetic ferroan replacements and structurally controlled ferroan haloes along regional basinal faults be the precursors ("prepared ground") to some of the stratiform and structurally aligned ironstones in strongly sodic metasedimentary terranes? Only when the rock matrix is characterised by geologists who understand possible evaporite and metal precursors, as well as high temperature magmatic systems, can exploration paradigms based on hybrid fluids from magmatic and meta-evaporite sources be considered.

In summary, evidence of former evaporite influence and associated basinal brines and hypersaline hydrothermal waters in IOCG deposits is subtle and unless one seeks it out, will be largely lost in a broader milieu of hydrothermal alteration. Criteria for upgrading the possibility of an evaporite association in an Fe-oxide Cu-Au deposit include: (1) abundant sodic alteration, often combined with widespread elevated Cl content in some minerals (e.g., abundant marialitic scapolite, and increased Cl content in amphiboles and biotites); (2) laterally equivalent metasediments or sedimentary remnants that retain evaporite pseudomorphs or dissolution breccias; (3) sediment systems that were deposited under arid/redbed conditions; (4) an abundance of transported iron with little evidence of sulphur in the transport system. As mentioned earlier, IOCG deposit comparisons across the Precambrian to Phanerozoic time scale shows the larger *sensu strictu* IOCG examples are Paleoproterozoic (Fig. 16.18). This time period may be related a unique set of world-scale underplating conditions related to the long term cooling and slowing of the asthenosphere (Groves et al. 2010).

Hydrothermal (Non-evaporitic) Salts and Metalliferous VHMS Deposits

Volcanogenic-hosted massive sulphide (VHMS) deposits are distinctive in that they formed in close temporal association with submarine volcanism and associated hydrothermal circulation and exhalation of sulphides, which are largely independent of sedimentary processes. This sets VHMS deposits apart from sedimentary exhalative (SedEx) and most IOCG deposits. However, anhydrite is a widespread mineral precipitate in VHMS deposits formed at or just below the seafloor. This anhydrite is hydrothermal not sedimentary.

Anhydrite's retrograde solubility means the solubility of anhydrite decreases rapidly with increasing temperature (Fig. 16.36a; Blount and Dickson 1969, 1973). Hydrothermal anhydrite precipitates within submarine volcanics and volcaniclastics during the heating of seawater caught up in submarine hydrothermal circulation cells (Fig. 16.36b). Retrograde solubility also ex- explains why anhydrite is most obvious in the upper portions of vent mounds and in black and white "smokers". Its heating behaviour is the opposite of baryte, another common hydrothermal sulphate precipitate. Simple heating of seawater adjacent to seafloor vents, even without fluid mixing, will precipitate anhydrite, while simple cooling of hydrothermal waters will precipitate baryte. Once buried, hydrothermal calcium sulphate, in the presence of organic matter or hydrocarbons and circulating hydrothermal brines, acts as a sulphur source to create H_2S, which then interacts with metal-carrying pore waters to precipitate metal sulphides. Although hydrothermal forms of $CaSO_4$ are not "true" evaporites, it needs to be discussed in the metals context of this chapter. Hydrothermal anhydrite, or indicators of its former presence, are commonplace within volca-plains why anhydrite is most obvious in the upper portions of ventnogenic hosted massive sulphide (VHMS) deposits. VHMS deposits typically form in submarine depressions as circulating seawater becomes an ore-forming hydrothermal fluid through interaction with the heated upper crustal rocks. Submarine depressions, especially those created by submarine calderas and/or by large-scale tectonic activity (median rift valleys), are favourable sites.

Fundamental processes leading to the formation of VHMS deposits include Ohmoto (1996):

- Intrusion of a heat source (typically $\approx 10^3$ km size pluton) into an oceanic crust or a submarine continental crust, which causes deep convective circulation of seawater around the pluton (Fig. 16.42). The radius of a circulation cell is ≈ 5 km. The temperatures of fluids that discharge on the seafloor increase with time from the ambient seafloor temperature to a typical maximum of ≈ 350 ° C, and then decrease gradually once more to ambient temperatures on a time scale of $\approx$ 100–10,000 years. The majority of subsurface sulphide and sulphate mineralization occurs during the waxing stage of hydrothermal activity,
- Reactions between warm country rocks and downward percolating seawater cause seawater SO_4^{2-} to precipitate as disseminated and fracture-fill hydrothermal anhydrite in the country rock in areas where internal temperatures are greater than 150 °C.
- Reactions of "modified" seawater with higher-temperature rocks during the waning stages of hydrothermal circulation transform this sulphate-depleted "seawater" into

metal-rich or H_2S-rich ore-forming fluids. Metals are leached from the country rocks, while previously formed hydrothermal $CaSO_4$ is reduced by Fe^{2+}-bearing minerals and organic matter to provide H_2S. The combined mass of high temperature rocks that provide the metals and reduced sulphur in each VHMS marine deposit is typically $\approx 10^{11}$ tonnes ($\approx$40 km^3 in volume). Except for SO_2, which produces acid-type alteration in some systems, the roles of magmatic fluids or gases are minor in most massive sulphide systems.

- Reactions between the ore-forming fluids and cooler rocks in the discharge zone cause alteration of the rocks and precipitation of ore minerals in the stockwork ores.
- Mixing of the ore-forming fluids with local seawater within unconsolidated sediments and/or on the seafloor can cause precipitation of "primitive ores" with the black ore mineralogy (sphalerite + galena + pyrite + baryte + anhydrite).
- Reactions between the "primitive ores" with later and hotter hydrothermal fluids beneath a sulphate-rich thermal blanket causes transformation of "primitive ores" to "matured ores" that are enriched in chalcopyrite and pyrite.

Hydrothermal anhydrite distribution in VHMS deposits is reflected by REE distributions in mid-oceanic ridges. For example, anhydrite is co-associated in hydrothermal/marine solutions, hotter than 400 °C, emanating from various white smokers in two submarine hydrothermal vent fields at 5°S on

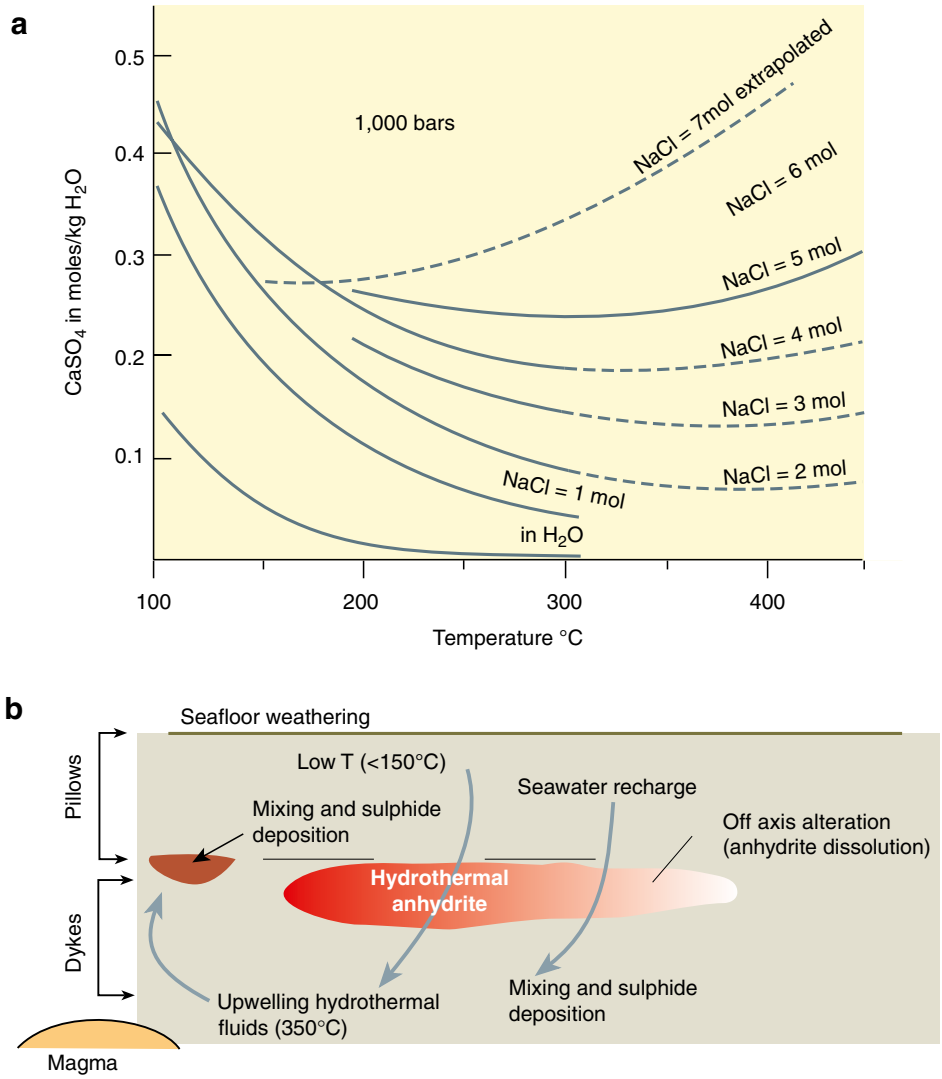

Fig. 16.36 Hydrothermal anhydrite. (**a**) Anhydrite solubility as a function of temperature at 1,000 bars in H_2O and NaCl-H_2O solutions of various concentrations. *Dashed lines* indicate extrapolated values (After Blount and Dickson 1969, 1973). (**b**) Formation of hydrothermal anhydrite from heated seawater in oceanic crust

the Mid-Atlantic Ridge (MAR) – Turtle Pits and Comfortless Cove. There, the distribution of anhydrite controls the distribution of the rare earth elements (REE) and yttrium (Fig. 16.37; Schmidt et al. 2010). The emanating brines define vapour-phase fluids at conditions close to the critical point of seawater (407 °C, 298 bars). According to the authors, the positive correlation of total REE, Ca, and Sr concentrations in Turtle Pits and Comfortless Cove fluids, indicates that precipitation/dissolution of hydrothermal anhydrite controls the variability in REE concentrations and distributions in these fluids and the transformation of one fluid type to the other. They note that the variable distribution of REE can be explained by the accumulation of particulate anhydrite (with concave-downward REE distribution and negative Eu anomaly) into a fluid with a more common REE distribution (type I), followed by the modification of the REE fluid signature due to subsequent dissolution of the incorporated anhydrite.

In order to form VHMS deposits on the seafloor, through-flushing hydrothermal fluids must transport sufficient amounts of metals and reduced sulphur, each at concentration levels > 1 ppm Ohmoto (1996). For a hydrothermal fluid with the salinity of normal seawater (≈0.7 m $\sum$Cl) to be capable of transporting this amount of Cu and other base metals, it must be heated to temperatures > 300 °C. Fluids with temperatures in excess of 300 °C will boil at pressures >200 bars. Under such conditions the resulting vapour cannot carry sufficient quantities of metals to form a VHMS deposit. Boiling of a metalliferous hydrothermal brine outflow is prevented when the fluid vents into water that is deep enough to generate a sufficient confining pressure. At 350 °C, a minimum seawater depth of 1,550 m is necessary to prevent boiling. If the fluid passes through a sedimentary package where it loses temperature and metals (Cu, Ba) before emanating, the water depth beneath which boiling is prevented is less (≈1,375 m). Once vented, the turbulent mixing of hot hydrothermal waters with cooler seawater causes rapid precipitation of sulphides and calcium and barium sulphate, which produces the familiar black and white smokers (Blum and Puchelt 1991).

VHMS deposit styles of mineralisation are always related to submarine volcanism and hydrothermally-driven circulation within adjacent deepwater sediments, but typify a variety of tectonic settings and sediment types:

- VHMS deposits formed in subduction-related island-arc settings (Kuroko-type deposits);
- VHMS deposits formed at mid-oceanic or back-arc spreading centres (Cyprus or TAG mound type deposits);
- VHMS deposits formed at spreading centres, but, due to the proximity of one or more landmasses, the deposit is

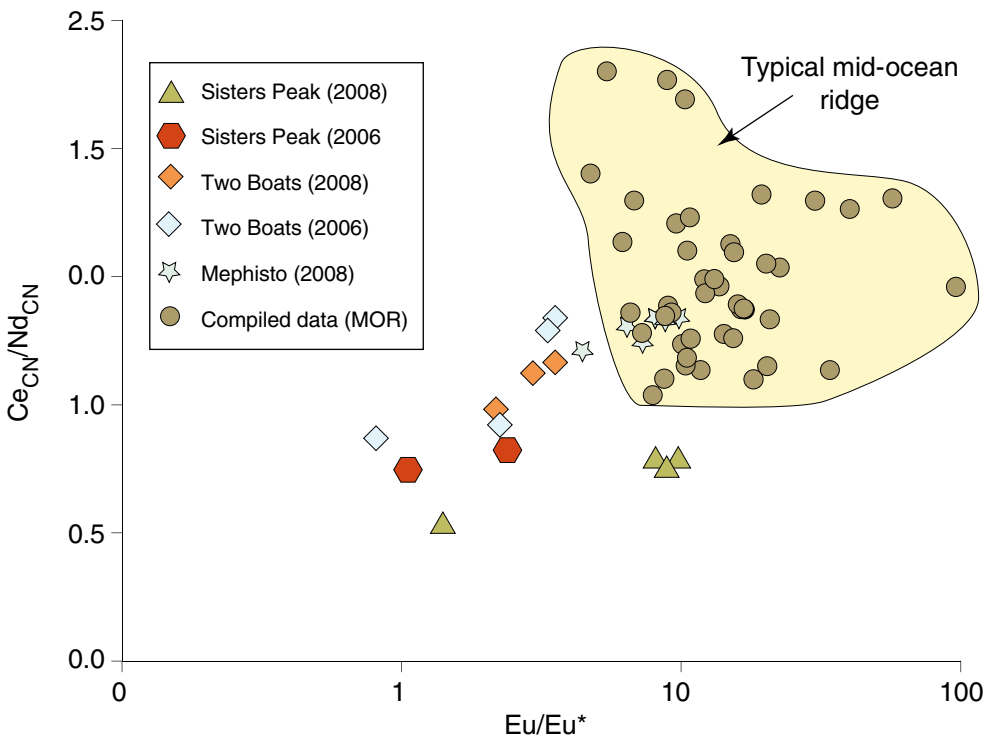

Fig. 16.37 Plot field of Eu anomaly (Eu/Eu*) as function of LREE fractionation (Ce_{CN}/Nd_{CN}) comparing typical values of mid-ocean ridge hydrothermal fluid compared to anhydrite emanations (>400 °C). Plots from various sites and times define the distinct REE signature associated with hydrothermal anhydrite as seen at Two Boats and Sisters Peak. Note the positive correlation of both parameters for each sampling campaign, although the determinations are 2 years apart (After Schmidt et al. 2010)

sediment-hosted (Besshi-type deposits). This style of deposit shows some affinities with SedEx deposits, but unlike a SedEx deposit the hydrological drive is always tied to igneous intrusion

For brevity and relevance, the emphasis in the following discussion of VHMS deposits is on the location and significance of the hydrothermal salts in the VHMS deposit, especially anhydrite and gypsum, rather than on a general discussion of mineralisation style. For excellent summaries of the relevant economic mineralisation literature, the interested reader is referred to Pirajno (1992), Ohmoto (1996), Shikazono et al. (2012).

VHMS Deposits in Subduction-Related Island-Arc Settings: Kuroko-Style Deposits

Kuroko-style deposits are composed of copper-and zinc-bearing massive sulphide deposits and typically hosted in felsic to intermediate volcanics (Fig. 16.38; Ohmoto and Skinner 1983; Ogawa et al. 2007). Deposits tend to occur near felsic domes and toward the stratigraphic top of the volcanic or volcano-sedimentary sequences. Host strata can be marine rhyolites, dacites, subordinate basal and organic-rich mudstones and shale. Often the host strata are brecciated or made up of volcanic flows, tuffs, or, in some cases, are actually part of a preserved felsic dome. Pyritic siliceous rock (exhalite) may mark the horizon at which the deposit occurs, and proximity to a deposit is often indicated by sulphide clasts in a volcanic breccia. Some deposits appear to be gravity transported. Ancient examples range in age from Archaean to Cenozoic and the type example of this Kuroko-style of mineralisation is located in Miocene volcanics of northern Japan.

There, hydrothermal $CaSO_4$ is widespread in the type region in the Miocene Hokuroko Basin, where it forms an integral part of the Kuroko-type ore association (Figs. 16.38 and 16.39; Ogawa et al. 2007). Kuroko polymetallic massive sulphide deposits form at discharge sites of submarine hydrothermal systems, associated with caldera structures (Ohmoto 1996). Calderas create depressions, such as the Hokuroko Basin, which become loci for discharging and ponding hydrothermal metalliferous solutions. Faulting associated with caldera formation provides permeable channel-ways for the circulating hydrothermal fluids. Type localities are in the Miocene Green Tuff Belt on Honshu and Hokkaido Islands (Fig. 16.39a). There the metal production is dominated by ore clusters centred around caldera structures, such as the Hokuroko Basin (Fig. 16.39b). Similar base metal deposits, in terranes characterised by submarine felsic volcanics and secondary ores containing varying amounts of hydrothermal anhydrite, have now been identified around the entire Pacific Rim (Sawkins 1990; Shikazono et al. 1983; Kusakabe and Chiba 1983; Chen 2013). The isotopic signature of anhydrite and baryte in most Kuroko-style deposits is intermediate between that of Miocene seawater and sulphate in hydrothermal fluids, suggesting that both types of sulphate precipitated from mixtures of hydrothermal fluids and local unaltered seawater (Ohmoto 1996).

The Japanese Kuroko deposits are, in general, characterised by a common stratigraphic mineral zonation (Figs. 16.39 and 16.40; Table 16.8) from the lowermost siliceous ore zone (keiko), through the overlying yellow ore zone (oko), to the upper black ore zone (kuroko). Baryte occurs mainly in the black ore zone and the overlying bedded baryte zone (Figs. 16.40 and 16.41). Keiko (siliceous) ores indicate the highest fluid temperatures (>300 °C) and were the feeder zone to the yellow and black ore systems. Most ores are compact, and massive but bedded, brecciated, or colloform textures dominate locally and graded sedimentary bedding and other sedimentary features, such as slumps, can be seen in the black ore.

Each of the major mines is centred on a cluster of ore lenses that range in size from less than 0.1 million tonnes to ≈ 10 million tonnes (Fig. 16.39b and 16.40). The stratabound lenses are typically elongate, with sharp upper boundaries and more diffuse lower boundaries that grade downward through lower grade stockworks into unmineralised footwall volcanics and tuffs. In many cases, hydrothermal anhydrite, with gypsum, occurs at the periphery of the black ore zone, either as near-monomineralogic aggregates or as units containing sulphide minerals (sekko ore). Anhydrite is rare in the central part of the sericite-chlorite alteration zone where temperatures were >300 °C, but is increasingly common in the more peripheral montmorillonite and zeolite alteration zones (T < 300 °C). Calcium sulphate underlies black ore in almost all mines in the Kuroko region and forms a mineable horizon of sekko ore; between 10^5 and 10^6 tonnes of sekko ore have been removed from individual deposits. Sekko ore can be further subdivided into sekko-kuroko and sekko-oko ores (Table 16.8).

There are four types of hydrothermal anhydrite in sekko ores: (1) nodular anhydrite, (2) anhydrite associated with sulphide minerals, (3) anhydrite in sulphide ore, and (4) vein anhydrite (Fig. 16.40). Type 1, or nodular anhydrite, is the most abundant and typically constitutes more than 90 % of the anhydrite in individual deposits. It occurs within dacitic tuff breccias and in tuff hosts, and changes up section into type 2 massive nodular anhydrite at the uppermost part of the sekko ore horizon. The diameters of the anhydrite nodules in sekko ore increase upward from a few mm to several metres. The thickness of the sekko ore varies within and between different deposits. The maximum thickness of sekko in the

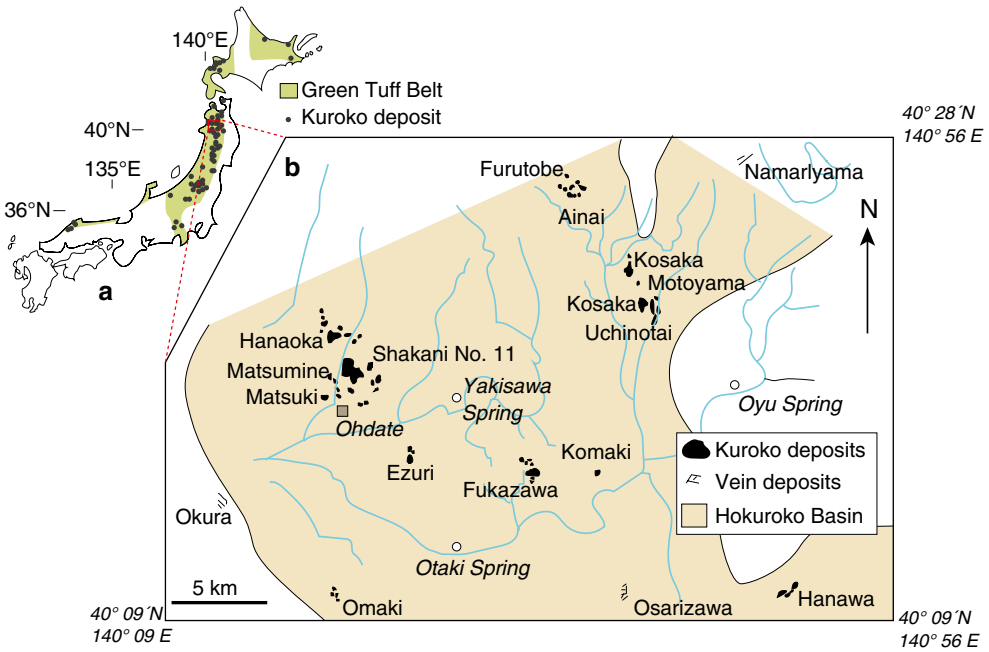

Fig. 16.38 Distribution of the Kuroko deposits in Japan. (**a**) Green Tuff region and dis-tribution of the Kuroko deposits. (**b**) Location of study area; Hokuroku district, Akita Pref., Northern Japan (After Ogawa et al. 2007)

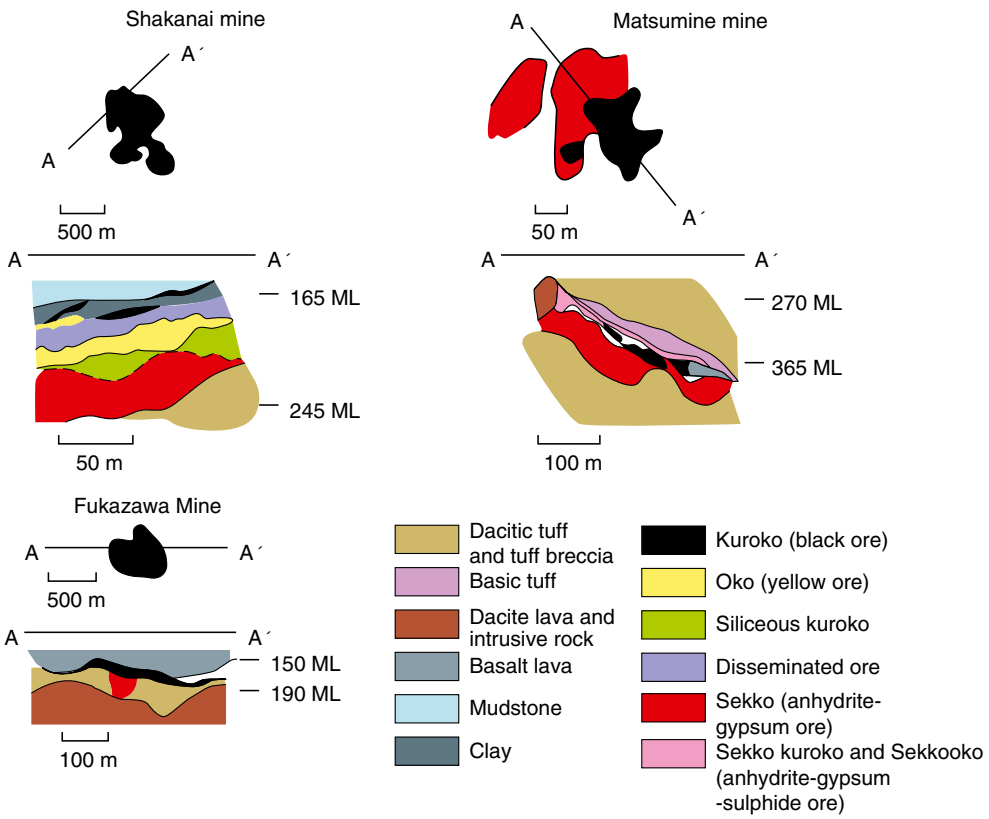

Fig. 16.39 Geology of selected mines in the Kuroko region, Japan (see Fig. 16.38 for locations). Note the common association of ore zones with hydrothermal calcium sulphate (After Shikazono et al. 1983)

Matsumine and Shakanai mines is more than 100 m, but is less than 50 m in the Fukazawa Mine (Fig. 16.39). Thicknesses of sekko-kuroko or sekko-oko are generally less than 10 m.

That is, anhydrite typically occurs in sekko ore together with local near-surface gypsum, which is a secondary mineral. Much of the gypsum that outcrops or subcrops in the region (Fig. 16.39) is a secondary rehydration product from original hydrothermal anhydrite (Kuroda 1983; Shikazono et al. 1983). The proportion of gypsum to anhydrite in the sekko ores probably reflects the rate of penetration of the modern meteoric groundwater system into the massive stratiform anhydrite units.

For example, gypsum/anhydrite and small amounts of sulphides (e.g., chalcopyrite, sphalerite, fukuchiite) and baryte are found at the marginal zone (upper horizon) of the anhydrite zone in the centre of the sekko ore in the Motoyama deposits of the Hanawa mine. The minerals associated with anhydrite are Mg-bearing minerals (Mg-chlorite, talc, Mg-chlorite/saponite mixed layer clay mineral, dolomite). Based on observations from the Shakanai and Matsumine Kuroko deposits, sekko ore consisting of anhydrite, gypsum, Mg-chlorite, sericite/montmorillonite mixed-layer clay minerals, changes gradually in ascending order to sekko-rich yellow ore, to sekko-rich black ore to yellow ore and rich black ore, (Fig. 16.40). In the sekko-rich black ore and sekko-rich yellow ore, sulphide minerals such as pyrite, chalcopyrite, sphalerite, and galena and baryte occur and are associated with nodular anhydrite.

Shikazono et al. (1983, 2012) concluded the anhydrite in the Kuroko ores formed by the mixing of a connate hydrothermal solution (containing high concentrations of Ca^{2+} and very little Sr^{2+} or SO_4^{2-}), with seawater. This took place at shallow depths, just slightly below the seafloor and was accompanied by hydrothermal/zeolite interactions with labile volcanic rocks (dacitic tuff breccia) under seawater-

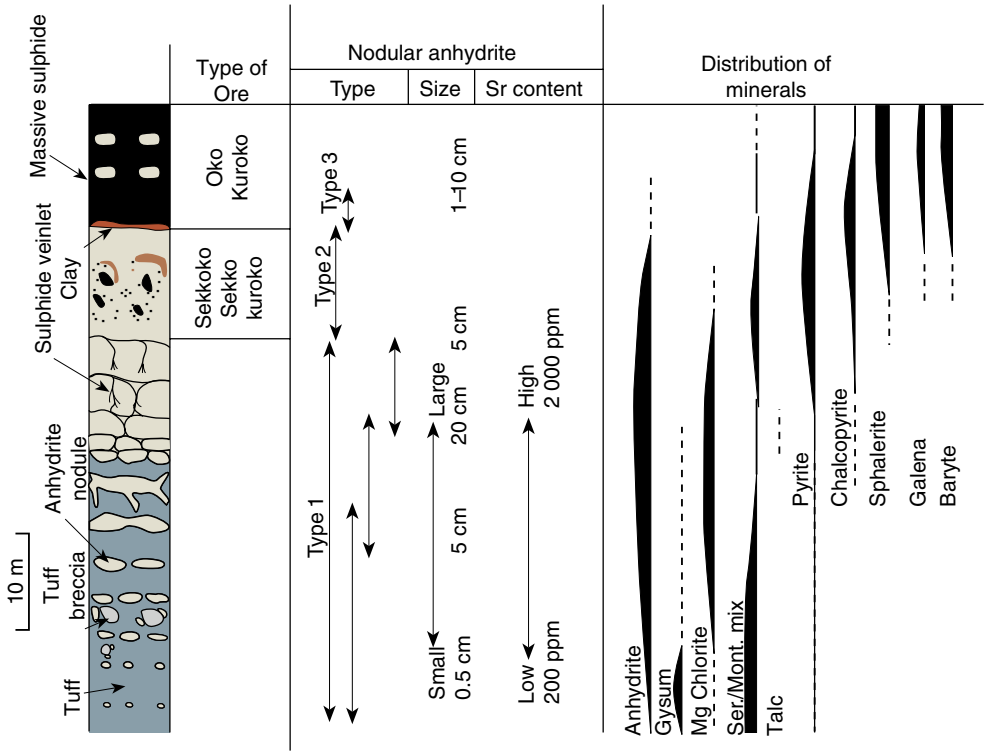

Fig. 16.40 Vertical zonation of anhydrite in Kuroko ore, see text for discussion of the anhydrite types (After Shikazono et al. 1983)

Table 16.8 Mineralogy of mineralised zones in classic Kuroko deposits

Name	Mineral phase
Kuroko Ore	Sphalerite + galena + baryte
Oko ore	Chalcopyrite + pyrite
Sekko	Anhydrite + gypsum
	Anhydrite + gypsum + sphalerite + galena + baryte
	Anhydrite + gypsum + chalcopyrite + baryte
Keiko Ore	Quartz + pyrite + chalcopyrite

dominated conditions. Thus, most of the anhydrite formed during the early stages of Kuroko mineralization, accompanied by precipitation of authigenic/hydrothermal Mg-bearing minerals (Mg-chlorite etc.) from a seawater-dominated Mg- and SO_4 -rich fluid. Reactions between warmer country rocks (T > 150 ° C) and percolating seawater precipitated seawater sulphate as disseminated hydrothermal anhydrite. Kuroda (1983) in an inclusion-based study of the Furutobe and Matsuki deposits showed how convecting seawater was heated as it approached the high temperature zone nearer the ore deposit core and so precipitated anhydrite along the way, mostly in the interstices of dacitic pyroclastic rocks and fine grained tuffs and in occas-sional fractures and fissures. This is the texture that is illustrated in the lower two-thirds of the type 1 texture in Fig. 16.40.

The Kuroko ore funnel from the Hanaoka mine is divided into four zones (Shimazaki and Horikoshi 1990), and baryte is abundant in all four, including the outermost zone. In contrast, quartz precipitates only in the interior zone. This indicates that baryte formed at lower temperatures in the precipitation series than quartz. Figure 16.41 shows the relationship between the content of baryte and quartz in the Kuroko ore samples studied; no positive or negative correlation was found to exist. From the figure, it is seen that the Kuroko ore can also be divided into either baryte-rich or quartz-rich ores. The black ore (kuroko) samples are baryte-rich whereas the siliceous (keiko) ore samples are quartz-rich. Most of the yellow ores contain quartz but not baryte, although some are locally baryte-rich.

In many Kuroko deposits, the nature of the up section increase in anhydrite nodule size and purity, along with an associated upsection increase in Sr content, is still not completely understood (Shikazono and Holland 1983; Ogawa et al. 2007). Given the hot hydrothermal nature of the precipitating setting and the deep seafloor setting of adjacent sediments, the zones of coalesced anhydrite nodules (upper part of type 1 and type 2) cannot reflect ghosting of a gypsum precursor. Changes in nodule size and purity are more likely to reflect rates of hydrothermal anhydrite crystallisation/replacement or the stability of the anhydrite-precipitating environment (larger nodules probably indicate slower, more stable, growth settings). At the time of anhydrite precipitation the host sediment was at times a thixotropic slurry, which passed laterally, away from the ore sites, into normal deepwater bottom sediment (diatomaceous fine-grained volcaniclastics and ash)

The ongoing preservation of widespread anhydrite, adjacent to, and beneath the massive sulphide bodies in the Hokuroko district requires more than the accumulation of anhydrite derived from chimney vent (smoker) remains (Ogawa et al. 2007). It supports the notion of a characteristic zone of widespread subsurface anhydrite precipitation in this type of deposit and, as well shall see in the next section, this is also true in many other hydrothermal seafloor deposits (Fig. 16.42; Shikazono et al. 2012). But anhydrite quickly dissolves beneath the shallow seafloor once heated pore brines are replaced by cooler waters with temperatures below 150 °C. That is, once active hot hydrothermal circulation ceases, hy-drothermal anhydrite is susceptible to flushing and leaching by cooler seawater. On uplift, it also converts to gypsum when anhydrite's widespread occurrence and preservation in the Kuroko ores implies hydrologic isolation of Kuroko anhydrite from cold seawater, perhaps because it tended to form a cemented zone in volcanic breccias rather than as piles of more porous vent precipitates. Its partial conversion to gypsum during post-Miocene

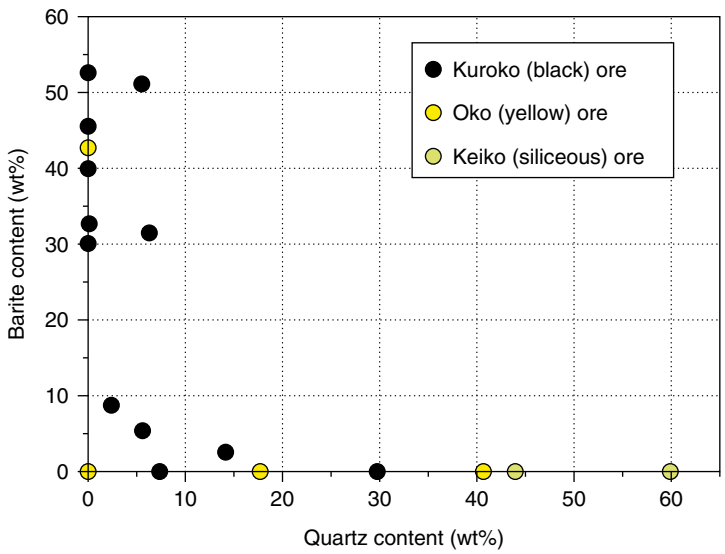

Fig. 16.41 Baryte and quartz contents of the Kuroko ore (Replotted from Shikazono et al. 2012)

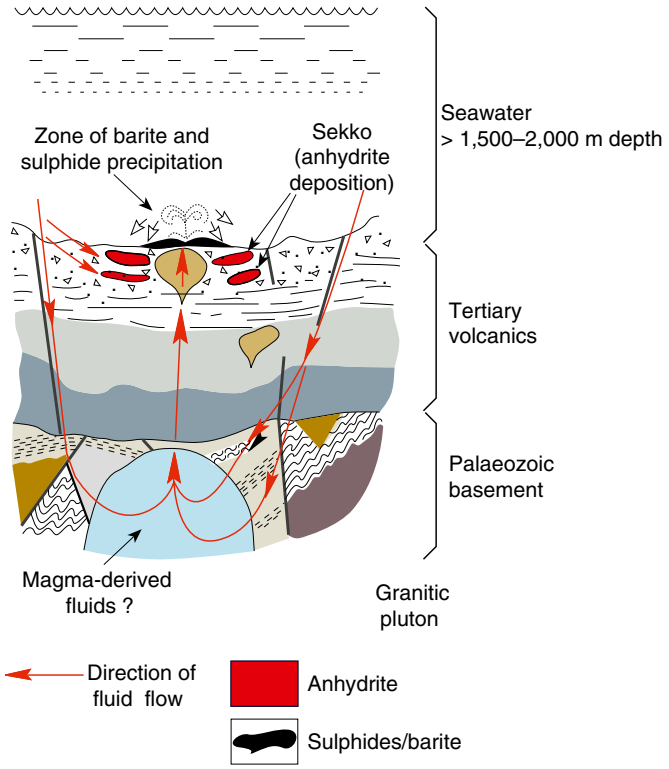

Fig. 16.42 Hydrothermal circulation that characterises Kuroko deposits (After Shikazono et al. 1983)

uplift indicates subsequent meteoric flushing. Anhydrite's solubility in cool seawater pore brines (<150 °C) also explains the lack of abundant $CaSO_4$ in massive sulphide bodies from older Kuroko-style deposits outside of Japan. There are, however, some intriguing breccias in these older Kurokostyle VHMS deposits. Table 16.9 compares the character of hydrothermal anhydrites in active Kuroko-style deposits and deep seafloor spreading centres, which are discussed next.

VHMS Deposits with Thermal Anhydrites at mid Ocean and Back-Arc Spreading Centres

Hydrothermal anhydrite is common also in extensional active back-arc basin and mid-oceanic ridge hydrothermal systems (Shikazono et al. 2012). The rare earth element (REE) content, strontium content, and the isotopic composition of strontium, oxygen, and sulphur indicates that most of this anhydrite also precipitated due to the mixing of ascending hydrothermal solutions an heating of ambient cold seawater, as in the Kuroko ores just discussed (Table 16.9). However, unlike the onshore Kuroko deposits just discussed, the formation mechanism of anhydrite below the seafloor in these extensional mid-ocean ridge settings has not been well studied, and is to date only well documented in the TAG mound region (Humphris et al. 1995).

TAG mound is an active hydrothermal mound, located 2.4 km east of the neovolcanic zone at 26° N, Mid-Atlantic Ridge. It is 200 m in diameter, exhibits 50 m of relief, and is covered entirely by hydrothermal precipitates. It made up of two superposed platforms representing different phases of active growth (Fig. 16.43: Humphris et al. 1995; Robert 2009) The larger lower platform shows evidence of mass wasting and supports a complex of white smokers venting fluids at temperatures of 260–300 °C. The narrower upper platform is characterised by black smoker complex of high temperature fluid discharge. The white smoker fluids (which principally precipitate anhydrite and low-Fe sphalerite, with minor marcasite and amorphous silica) are believed to be derived from the black smoker fluid (which principally precipitate pyrite, chalcopyrite and lesser anhydrite).

Smokers are the result of fluid cooling, mixing with seawater and precipitation of sulphides within the mound. Flanks of the mound are relatively steep and in part covered by aprons of sulphide debris, as well as fine-grained oxides eroded from the weathered slopes, which grade outward into biogenic oozes. The surrounding seafloor sediments are locally silicified (red chert). It is thought that the growth and collapse of sulphide chimneys in TAG Mound progressively built accumulations of brecciated sulphide deposits during the Late Pleistocene and the Holocene.

Surface samples were recovered from TAG mound by the submersibles "Alvin" and "Mir" in 1986, 1990, and 1991. In

Table 16.9 Characteristic features of anhydrite and hydrothermal solutions responsible for the hydrothermal anhydrite in East Pacific Rise N21°N and Kuroko deposits

	Kuroko-type deposits	East Pacific Rise N21° sulphide deposits
Occurrence	Nodular, massive in tuff under the sulphides with silicates 0.0n mm-n cm in diameter Rectangular crystals	White smoker, white chimney, white snow balls, black smoker with sulphides and silicates 0.00n-n mm in diameter Acicular and rectangular
Sr content	150–2,000 ppm (av. 700 ppm) (100 samples)	2,000–3,500 ppm (6 samples)
$^{87}Sr/^{86}Sr$	0.7075–0.7083 (anhydrite) 0.7070–0.7084 (gypsum) 0.704 (dacite and basalt) 0.7100–0.7400 (Palaeozoic basements) 0.7050–0.7084 (hydrothermal solution + seawater) 0.7050–0.7070 (hydrothermal solution)	0.7055–0.7085 (anhydrite) 0.70224–0.70240 (basalt) 0.70385–0.70796 (hydrothermal solution + seawater) 0.7030 (hydrothermal solution)
Partition coefficient		0.74 (coarse grained) 1.1 (fine grained)
$\delta^{34}S$	+22 to +27‰	+19.6 to +20.8‰
$\delta^{18}O$	+7.5 to +17‰ (anhydrite) 0 to +5‰ (hydrothermal solution)	+1.5 ‰ (hydrothermal solution)
Temperature	250–330 °C	260–350 °C
Concentrations of Ca and Sr	500–1,000 ppm (Ca) 1–5 ppm (Sr)	1,000 ppm (Ca) 8–9 ppm (Sr)
Water/Rock ratio	4–20 (?)	1–5 (?)
Depositional mechanism	Mixing of hydrothermal solution with seawater under seawater/rock interface	Mixing of hydrothermal solution with seawater above seawater/rock interface
Origin of hydrothermal solution	Country rock/seawater interaction	Basalt/seawater interaction

After Shikazono et al. (2012)
? indicates estimate

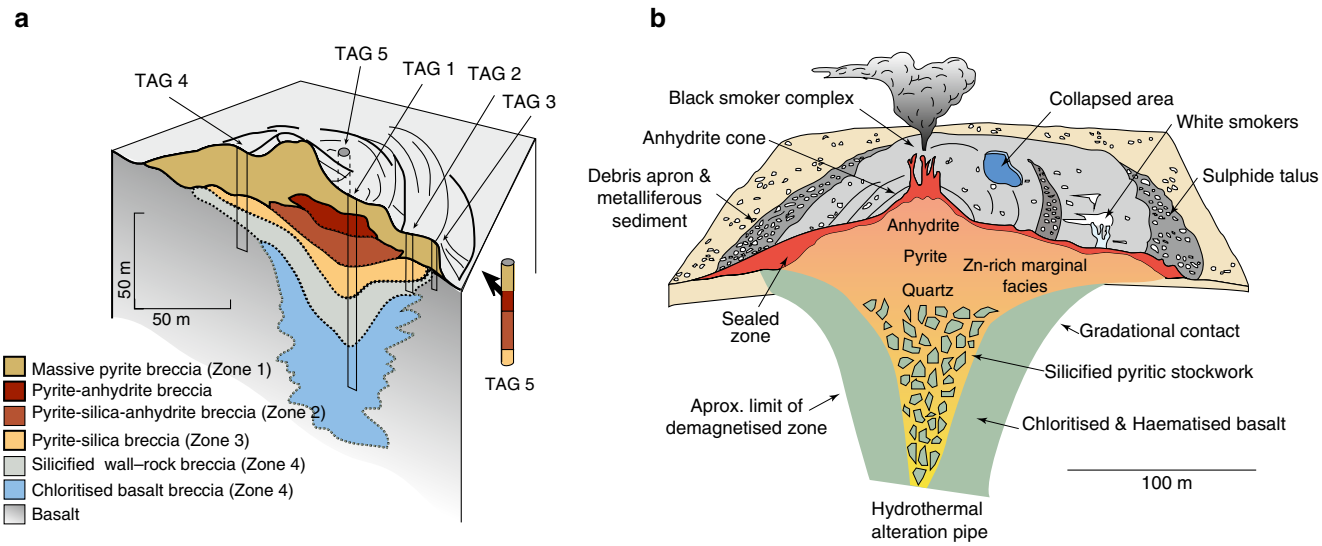

Fig. 16.43 Volcanic Hosted Massive Sulphides. (**a**) Hydrothermal anhydrite distribution within the internal mineral zonation of Tag mound. Note the importance of hydrothermal anhydrite in the internal structure of the mound. Well Tag 5 is out of the plane of section (After Humphris et al. 1995). (**b**) Cross section of a typical VHMS deposit showing accumulations of massive sulphides on the seafloor are related to and underlying zoned succession of anhydritic zone of stockwork mineralisation (After Hannington et al. 1998)

September-November 1994, the Ocean Drilling Program Leg 158 drilled a series of holes into the active mound to reveal unexpected high volumes of hydrothermal anhydrite within the sulphide mound. In fact, anhydrite occurs in breccias and as late-stage veins throughout most of the mound and its stockwork, down to at least 125 m below sea floor. As stated by Humphris et al. (1995): "These observations demonstrate the role of anhydrite in the growth of massive sulphide deposits, despite its absence in those preserved on land". Similar significant volumes of hydrothermal anhydrite have since been confirmed in other mounds, such as Manus mound, in a back-arc basin, offshore Papua New Guinea (Craddock and Bach 2010).

Modern hydrothermal activity on the TAG mound surface includes highly focused outflow of a 363 °C fluid from a chimney cluster on the top of the mound and deposition of a high S_2-O_2 mineral assemblage, reflected in low concentrations of H_2S in the black smoker fluid (Tivey et al. 1995). Blocks of sulphide and white smoker chimneys (enriched in Zn, Au, Ag, Sb, Cd, and Pb) are accumulating atop the mound as settleout and precipitates from venting black smoker fluids. The outflow fluid chemistries are modified by mixing with entrained seawater, so precipitating metal sulphides and anhydrite. The amount of anhydrite precipitating from the venting fluids of TAG mound is estimated at $5–15 \times 10^7$ kg/yr (James and Elderfield 1996). This is an order of magnitude greater than that of the Cu and Zn sulphides (10^6–10^7 kg/yr), clearly illustrating that much of the anhydrite forming on the mound surface is rapidly redissolved into the ambient seawater, leaving behind the sulphides.

Away from the active smoker vents, the bathing of the mound surface in normal seawater dissolves the anhydrite and oxidizes the sulphides to leave behind a carapace of ochreous and iron oxide-rich material. Such outer red-oxide layers, which formed during previous hydrothermal episodes, are now exposed on the steep outer walls of the lower part of mound. These flank deposits include a novel form of moss agate dominated by ferric iron oxyhydroxides (Hopkinson et al. 1998). The agate has an isopachous concentric laminar texture that formed during a series of rapid irreversible fluid changes as cooling fluid passed across a redox and pH front that separated oxidizing highly viscous siliceous gels from a mixed pyrite-iron oxide sediment. The laminar texture is a totally inorganic construct, and yet, based on its laminar accretionary texture, the agate could easily be confused with a biogenic structure. If such features are also present in ancient vent mounds they may easily be confused with stromatolitic features (e.g., see discussion of North Pole, Pilbara, in Chap. 2).

Beneath the mound surface lies a complex assemblage of sulphide-anhydrite-silica breccias (Fig. 16.32a; Humphris et al. 1995). Drilling has shown that sulphide seafloor mounds grow largely as an *in situ* accretionary breccia pile, driven by ongoing episodes of hydrothermal activity, with thermallydriven seafloor hydrologies, not too dissimilar from Kuroko-style deposits. Ridge mounds do not grow simply by the accumulation of sulphide fallout onto the sea floor. During times of active hydrothermal circulation the internal mixing of black smoker fluids and heated seawater precipitates widespread sulphides and anhydrites. Inactive periods are marked by dissolution of anhydrite and collapse and brecciation of the mound interior. Subsequent episodes of hydrothermal activity form new hydrothermal precipitates, as well as cementing earlier breccias.

Breccia in the mound can be broken down into 4 zones (Fig. 16.43a; Humphris et al. 1995). Zone 1 is dominated by clastsupported massive pyrite breccias that dominate in the upper 10–20 m of the mound. These are underlain by the anhydritic zone 2 in the central part of the mound. Pyrite-anhydrite breccias are present down to 30 m below sea floor and are underlain by pyrite-silica-anhydrite breccias that extend to the bottom of the anhydrite-rich zone 2 at about 45 m below the seafloor. Anhydrite veining is extremely well developed throughout zone 2, where composite anhydrite veins up to 45 cm thick are present. They comprise multistage fracture fillings and linings some of which include disseminated, fine-grained pyrite and chalcopyrite, as well as trace amounts of haematite. Zone 3 consists of intensely silicified and brecciated wall rock, which comprises the upper part of the upflow zone beneath the mound. Pyrite-silica breccias occur in the upper part of this zone and are underlain by silicified wallrock breccias. Below about 100 m below the seafloor the silicified wall rock breccia grades into a chloritised basalt breccia (zone 4), where chloritised and weakly mineralised basalt fragments (1–5 cm diam) are cemented and veined by quartz ± pyrite.

Dating of the sulphides and anhydrites within the mound breccias clearly shows that sulphide accumulation and mound growth is not a continuous process (You and Bickle 1998). The oldest material (11,000 to 37,000 years old) forms a layer across the centre of the mound stratigraphy, with younger material (2,300 to 7,800 years old) both above and below. This age distribution implies that TAG mound accreted via episodic activity of the hydrothermal system, with growth recurring at intervals of up to 2,000 years.

Extensive precipitation of anhydrite within the TAG mound indicates extensive entrainment and heating of seawater. Teagle et al. (1998) found that the $^{87}Sr/^{86}Sr$ ratios indicate that most of the anhydrite formed from ≈2:1 mixture of seawater and black smoker fluids (65 % ± 15 % seawater). The oxygen-isotopic compositions imply that anhydrite precipitated at temperatures between 147 and 270 °C (Table 16.9). This means the circulating seawater must have been conductively heated to between 100 and 180 °C, before mixing and precipitation occurred. Precipitation of anhydrite within the TAG mound is also the major mechanism for removal of REE during mound circulation. Something like 0.15–0.35 g of anhydrite is inferred to precipitate from every kg of fluid venting from the white smoker chimneys (Mills and Elderfield 1995).

Collapse and mass wasting of the porous sulphide in TAG mound during burial was followed by recrystallisation of most sulphide minerals into pyrite. There is textural evidence that the anhydrite matrix in the pyrite-anhydrite breccias did not replace a pre-existing matrix and did not fill pre-existing cavities. It is probable that in situ precipitation of anhydrite was made possible because of high fluid pressure compensating for burial and fluid percolation through displaced sulphide clasts. This process probably led to significant internal expan-

sion and fracturing of the TAG mound (Robert 2009). Variations of hydrothermal activity during the Late Pleistocene and the Holocene likely resulted in a succession of internal collapses (anhydrite dissolution) and reactivations (anhydrite precipitation) leading to disruption of the breccias and uplift of older fragments of breccia and altered basalt. However, anhydrite veins seem to have formed through filling of fissures and fractures which developed within the mound and acted as pathways for hydrothermal fluids. The pyrite-silica breccia evolved from pre-existing pyrite-anhydrite breccia through progressive replacement of the anhydrite matrix by quartz aggregates. It is probable that initial deposition of amorphous silica and/or cryptocrystalline quartz was followed by hydrothermal recrystallization and a related minor decrease in volume. The relationships between pyrite and quartz are confused by mutual intergrowth and replacement.

The upper pyrite-silica breccia corresponds to the inferred depth of the oceanic crust, and the presence of altered basaltic clasts increasing with depth suggests that for a large part this unit was initially oceanic basalt. This is reflected in the general model of zonation in a VHMS deposit (Fig. 16.43b; Hannington et al. 1998). The hydrothermal alteration of the oceanic crust started with the chloritization of the basalts through interaction with Mg-bearing hydrothermal solutions. Chloritization was especially intense below the currently active hydrothermal mound, decreasing in importance at the periphery. As alteration progressed, most of the previously altered and relict minerals were replaced by paragonite, quartz and pyrite. The presence of pyrite crystals with quartz corona and zoned quartz with pyrite veins suggest that recurrent intervals of silicification and pyritization deeply altered the basaltic stockwork. Anhydrite locally precipitated as veins in open spaces, as in the upper parts and surrounds of the mound, as a consequence of significant infiltration of seawater into the active hydrothermal system.

Another seafloor ridge region with significant documented volumes of anhydrite is in the sediment-hosted Grimsey hydrothermal field in the Tjörnes fracture zone on the seafloor, north of Iceland (Fig. 16.44a: Kuhn et al. 2003). There the fracture zone is located at a ridge jump of 75 km, which caused widespread extension of the oceanic crust in this area. Hydrothermal activity occurs in Grimsey field over a 300 m by 1,000 m area, at a water depth of 400 m. Active and inactive anhydrite chimneys up to 3 m high and hydrothermal anhydrite mounds are typical of the seafloor in this are. Clear, metal-depleted, up to 250 °C hydrothermal fluids are venting from active chimneys and fluid inclusion in the precipitated anhydrites show the same homogenisation temperature range (Fig. 16.44b).

Anhydrite samples collected from Grimsey field average 21.6 wt.% Ca, 1,475 ppm Sr and 3.47 wt.% Mg. The average molar Sr/Ca ratio is 3.3×10^{-3}. Sulphur isotopes from anhydrites have typical $\delta^{34}S$ seawater values of $22 \pm 0.7‰$,

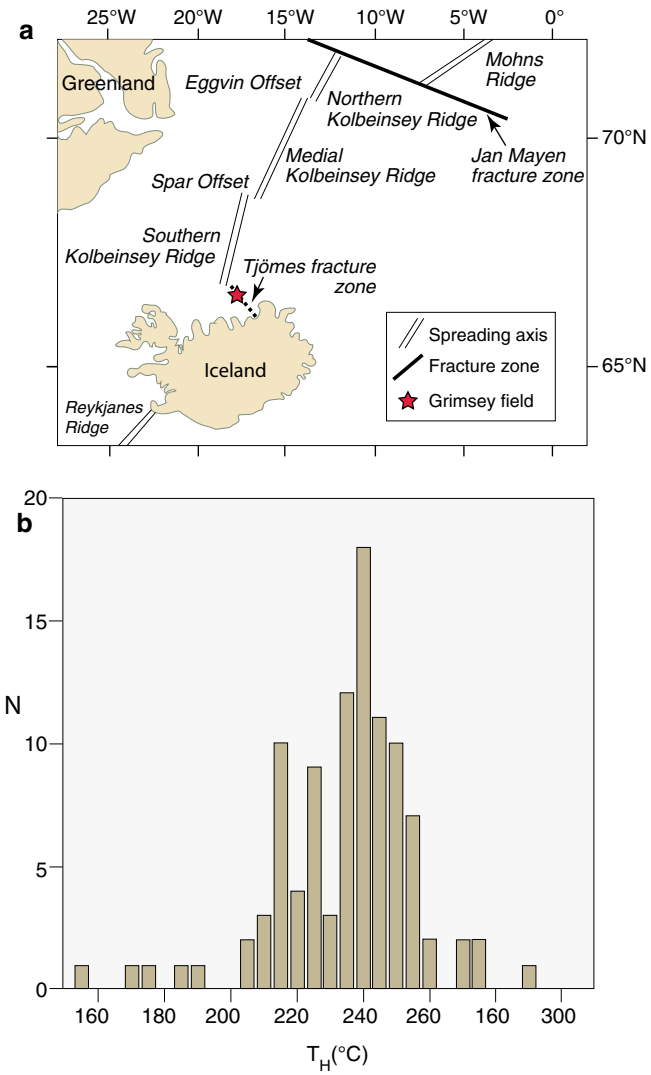

Fig. 16.44 Grimsey hydrothermal field, offshore Iceland. (**a**) Location map. (**b**) homogenization temperatures of fluid inclusions in anhydrite. Most of the temperatures range between 200 and 280 °C and therefore, are consistent with the *in situ* temperature of the venting fluids of 248–250 °C (After Kuhn et al. 2003)

indicating a seawater source for SO_4^{2-}. Strontium isotopic ratios average 0.70662 ± 0.00033, suggesting precipitation of anhydrite from a hydrothermal-seawater mixture. The endmember of the venting hydrothermal fluids, calculated on a Mg-zero basis, contains 59.8 µmol/kg Sr, 13.2 mmol/kg Ca and a $^{87}Sr/^{86}Sr$ ratio of 0.70634. The average Sr/Ca partition coefficient between the hydrothermal fluids and anhydrite is about 0.67, implying precipitation from a non-evolved fluid. In combination, this suggests anhydrite forms in a zone of mixing between upwelling hydrothermal fluids and shallowly circulating seawater. Before and during mixing, seawater is heated to 200–250 °C, which drives anhydrite precipitation and the likely formation of an extensive anhydrite-rich zone beneath the seafloor, as in Tag Mound and the Hokuroko Basin.

Once hydrothermal circulation slows or stops on a ridge or mound, and the "in-mound" temperature falls below 150 °C, anhydrite in that region is likely to dissolve. During such inactive periods, the collapse of sulphide chimneys, the internal dissolution of mound anhydrite, and ongoing disruption by faulting will all cause an internal brecciation of the deposit. Through dissolution, former zones of hydrothermal anhydrite create intervals of enhanced porosity and cavities in the mound. Such intervals initiate fracture and collapse in the adjacent lithologies, which become permeable pathways during later renewed fluid circulation episodes. The alternating "coming and going" role of hydrothermal anhydrite creating preciptation space within the mound hydrology is similar to that of sedimentary evaporites in the sedimentary mineralising systems.

TAG mound, along with other active seafloor mounds (smokers), are considered to be modern analogs for Cyprus-style ore deposits. Prior to the drilling of the TAG mound, the importance of widespread hydrothermal anhydrite in modern and ancient seafloor ridge mounds, both as a sulphur source and as an integral mechanism for internal brecciation and pore space creation, was not well understood. Take away the anhydrite, and the internal structure of the TAG mound bears a striking resemblance to ancient volcanic-hosted massive sulphide exposed in ophiolite terranes (Cyprus-type deposits). Or, if we mentally replace the sea floor basalt with dacite, the zonation and distribution of the anhydrite and mineralisation is near identical to that in a Kuroko-style deposit. This underlies the significance of seawater-fed hydrothermal circulation cells, rather than the mineralogy of the host matrix, in controlling both sulphide mineralisation and the precipitation of anhydrite.

Although hydrothermal anhydrite ultimately dissolves it can, while the mound is active, act as a concentrated subsurface sulphur source, which plays an fundamental role in the growth and maturation of sulphide mineralisation in the mound (Ohmoto 1996). The question that have yet to be addressed in this and other styles of VHMS deposits are: "What are the indicators of the hydrothermal salt that was?" Are they similar to those of dissolved low temperature evaporites (Chap. 7) or is there a whole new and distinctive suite of indicators and breccias that, once fully documented, will be used to refine predictive models of hydrothermal deposits?

VHMS Deposits with Hydrothermal Anhydrite at Sediment-Covered Spreading Centres: Besshi-Style and the Guaymas Basin

The type Besshi deposit is in Japan, it is metamorphosed, with a Precambrian age. This and other ancient Besshi-style deposits typically form stratiform lenses and sheetlike accumulations of semi-massive to massive sulphides, which lack any preserved calcium sulphate but show evidence of being dominated by seafloor sediments at the time of ore formation. Given the Precambrian age of most examples of this deposit style and its seafloor genesis, a lack of preserved hydrothermal anhydrite is not surprising, even if precipitation of prograde thermal anhydrite was a fundamental part of its formation. Besshi ore minerals are dominantly pyrite and/or pyrrhotite with variable amounts of chalcopyrite and sphalerite and minor to trace galena, arsenopyrite, and gold or electrum; baryte is generally absent (Slack 1993). Many deposits have significant cobalt and high cobalt/nickel ratios. Typically associated with the deposits are a variety of wall rocks, including metachert, magnetite iron formation, sericite- and chlorite-rich schist, tourmalinite and albitite. According to Slack (1993), these wallrock lithologic units formed by pre-metamorphic hydrothermal alteration and/or by chemical sedimentation coeval with massive sulphide deposition.

Besshi-type deposits typically form where a hydrothermal ridge or axis is proximal to a source of terrigenous sediment, so that the axial ridge is covered by beds of finer-grained deep sea sediment (Fox 1984). In this situation the ascending magmas do not make it to the seafloor, but form sills and dykes in sedimentary hosts. These features then act as a heat source driving hydrothermal circulation cells within the sediments. The presence of ubiquitous host sediment between ore layers distinguishes this type of deposit from the more open-marine sediment-free Cyprus-style of marine rift deposit exemplified by the modern TAG mound and from the sediment-starved style of rift deposit exemplified by the metalliferous deeps of the Red Sea.

A modern day counterpart to Besshi-style ores is located in the Guaymas Basin of the Gulf of California (Fig. 16.45a). There muddy biogenic and turbiditic sediments, up to 500 m thick, cover a series of spreading ridges and transform faults. In Chap. 9 this region was discussed in terms of hydrothermal cracking creating hydrocarbons from the rapid heating of organic-rich diatomaceous ooze (Fig. 9.73). The shallower intrusions lie some 400 m below the sediment surface beneath waters more than 1,800 m. There a section extending over a little more than 120 km long, encompassed more than 120 hydrothermal vent sites, all with mineral deposits. The same side scan sonar deep-tow vehicle passed through 20 thermal plumes along the same trackway (Lonsdale and Becker 1985; Peter and Scott 1991a, b). Temperatures as high as 315 °C were measured at some vent exits. A dredge sample from one of these sites – the Seacliff hydrothermal site – contained sulphates (anhydrite and baryte), as well as talc, calcite, pyrrhotite, sphalerite, wurtzite, marcasite, chalcopyrite and galena, all soaked in hydrothermal petroleum condensates.

The isotope signatures of the anhydrite, as well as the hydrothermal baryte and metal sulphide phases show sulphur signatures reflecting their genesis from hydrothermally

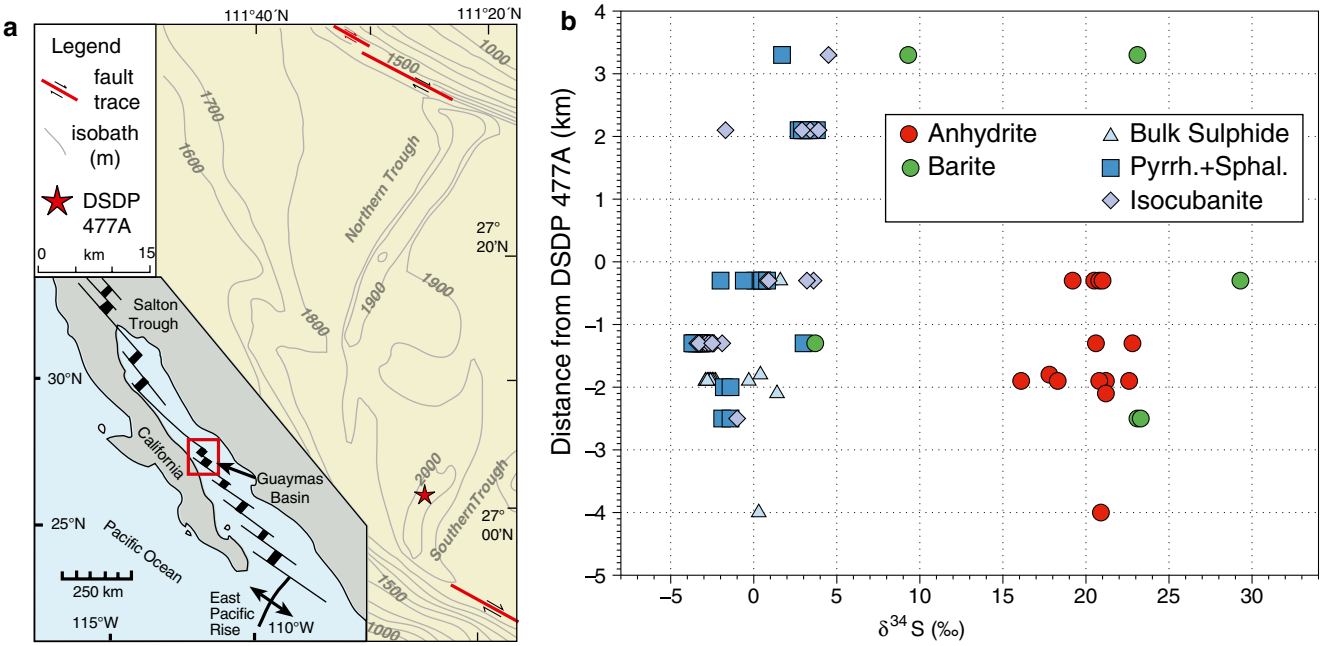

Fig. 16.45 Guaymas Basin. (**a**) Location of DSDP drill hole 477A. (**b**) Sulphur isotopes from hydrothermal anhydrite and baryte and various sulphide phases in seafloor samples from the Southern Trough in the vicinity of DSDP 477A (Replotted from isotope data in Peter and Shanks 1992)

heated seawater. Notably, the sulphur isotope field of this hydrothermal anhydrite is the same as that of evaporitic anhydrite and gypsum. Also of some interest, but not as yet considered a feature incorporated in fluid evolution models for this type of hydrocarbon genesis, is the recently-documented presence of a 2-km thick, 50×100 km long evaporite body, which defines the eastern margin of the Guaymas Basin (Miller and Lizarralde 2013). This halokinetic body of salt lies to the immediate west of the portion of the Guaymas Trough where the documented hydrothermal hydrocarbons occur and likely exerted some influence on the basin's brine chemistry.

Cooling hydrothermal outflow waters construct anhydritic chimneys, mounds and spires, with local clogging by worm tubes. The mineral chimneys and other constructs can rise up to 5 m on mounds that in turn rise 5–25 m above the surrounding seafloor. Chimneys are dominated by mixtures of anhydrite and pyrrhotite with lesser amounts of the other metal sulphides. The mounds can grow upwards, sideways and downward depending on how the mineral precipitates clog the outflow vents. The resulting vent shapes range from simple conical chimneys to multi-tiered pagoda-like spires with multiple horizontal eaves. Ultimately, the chimneys become unstable and collapse, causing the broken vent base to reopen and chimney growth to begin anew.

Web-like mats of the filamentous sulphide-oxidising eubacterium *Beggiatoa sp.* occur among the chimneys and worm tubes and on the surface of zones of nearby anoxic bottom sediment (Jannasch et al. 1989; Gundersen et al. 1992). This monospecific bacterial buildup constructs mats up to 30 cm thick in areas between the wormtubes, while thicknesses of up to 3 cm are common as bright yellow and orange mats on the seafloor adjacent to hydrothermal vents. Individual bacteria are gigantic, made up of cell filaments up to 120 µm in diameter. They are so large that individual filaments can be seen with the unaided human eye and resemble glass fibres in the lights of a submersible.

Because hydrothermal anhydrite dissolves under open seafloor conditions, it is usually absent in the material that covers inactive vents in the Guaymas Basin. It does, however, convert to gypsum which can be found in sediment cores from areas where the vents are no longer active (Sturz et al. 1996) $\delta^{34}S$ values for the sulphate minerals in the mounds range from 16.1‰ to 23.1‰ for the anhydrite, and from 23.1‰ to 215.3‰ for the baryte (Fig. 16.45b; Peter and Shanks 1992). Sulphur-isotopic composition indicates an unfractionated seawater sulphate source, although some samples from within the chimneys have more negative values, which suggest local sulphate reduction and sulphide oxidation related to bacterial processes. Differences in $\delta^{34}S$ between coexisting sulphide minerals from the mounds are generally small, suggesting sequential deposition of copper, zinc and iron sulphide minerals from a hydrothermal fluid of nearly constant $\delta^{34}S_{H2S}$ composition. During mineral replacement processes, which are common in the chimneys, secondary sulphides undoubtedly inherit some of their sulphur from precursor sulphide minerals (Peter and Scott 1991a, b).

Overall, the hydrothermal circulation processes involving anhydrite precipitating in Guaymas vent regions are similar to those acting in Kuroko and TAG mound settings. That is the precipitation of hydrothermal anhydrite is a response ot the heating of circulation seawater pore brines and is largely independent of host lithology. The host tends to be an acidic volcanic in a Kuroko (arc) setting, a mafic or ultramafic/basaltic host in an mid oceanic and ridge setting, and fine-grained diatomaceous/siliciclastic sediments in a Besshi/Guaymas setting. The relative volumes and significance of high-temperature anhydrite preserved within and below the mineralised mound features across all three styles cannot be quantified without more detailed drilling of all three styles. Suffice it to say that anhydrite is a supplier of sulphur to the mineralisation in all settings (Fig. 16.46). It would not be surprising if subsurface hydrothermal anhydrite made up a large proportion of the hydrothermal precipitates in zones of actively circulating hydrothermal seawater, in all as more detailed drilling and mining has shown in TAG mound and the Kuroko-style deposits. One possible difference between vent deposits of the Guaymas Basin compared with other VHMS deposits may well be the volume of entrained organics in sediment-covered hydrothermal cells. These organics are hydrothermally cracked and so have distinctive organic signatures (Fig. 9.73).

Evaporites and Metalliferous Deposits

What our discussions in this and the previous few chapters clearly show is that evaporites do not directly create base and precious metal accumulations, nor are they direct indicators of gemstone occurrence. Rather, what evaporites tend to do in the diagenetic or metamorphic/igneous realm is to enhance conditions likely to lead to an economic accumulation of base and precious metals.

They can act as a source of chloride-rich brines, which are capable base metal carriers, even of gold at higher temperatures. They do this via dissolution and metamorphic evolution. In the lower temperatures of the diagenetic realm they do this via dissolution of chloride salts, mostly halite, which is an ongoing process deep into the subsurface. In the high temperature metamorphic realms they do this as suppliers of ionic components to metamorphic and hydrothermal waters, or via daughter products, such as scapolite, which continue to release chloride as the scapolite lattice cage is compressed in response to increasing temperature and pressure. In basins with thick buried halites passing into the metamorphic realm, there is a pulse of chloride-rich brine released at the onset of greenschist conditions. It is the result of the change in the polyhedral lattice structure of salt, which turns a halite aquitard/aquiclude into a warm halite aquifer undergoing self cannibalisation.

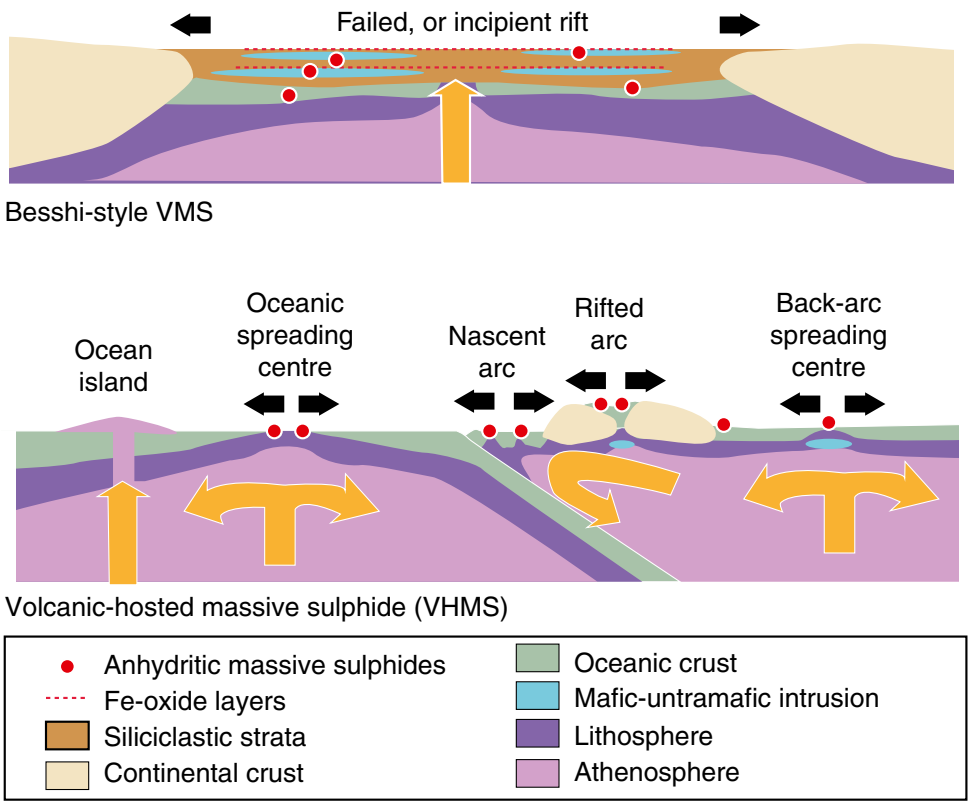

Fig. 16.46 Typical plate tectonic settings where hydrothermal anhydrite precipitates in VHMS and Beshi-style deposits

Sulphate evaporites, as they dissolve, can also act as sulphur sources and hence can help fix metals via biochemical sulphate reduction in lower temperatures (<110 °C) of the diagenetic realm or by thermochemical reduction at the upper end of the diagenetic realm and into the metamorphic realm. Thick calcium sulphate beds can also be assimilated into magma and so introduce addition sulphur to the igneous system, as they did in helping form the Phanerozoic nickel and iron deposits of Siberia and the supergiant Muruntau gold deposit in Uzbekistan.

Thick salt beds not only dissolve but also tend to flow. Halokinesis can thus stabilise a redox front and so lead to significant increases in size and purity of metal deposits both at precipitative sites. This is true in the subsurface, as was the case in the Permian-hosted sub-salt stratiform copper deposits in the Lubin region Poland and the late Palaeozoic supra-salt copper deposits of the Dzhezkazgan region in Kazakhstan. Brine outflow, associated with shallow halokinesis, can also focus and stabilise brines venting onto the deep seafloor and so stabilise brine lakes in deep sea floor settings where the sumps accumulating the brines are often a result of halokinetic structuration of the seafloor. This creates longterm anoxic interfaces and reducing settings where significant volumes of base metal laminites can accumulate. This was the case in the McArthur River, Mt Isa, Cloncurry deposits of Australia and the Atlantis II deep in the Red Sea.

What is common to all economic examples is that the role of evaporites and hydrothermal salts becomes significant in mineralisation only when the salts and their daughter products convert to brines. This is why the role of evaporites in forming metal accumulations is not well understood. The evaporite beds and masses must go, in order to form metal accumulations. If you have a metal accumulation where evaporites played a role in focusing and concentrating precipitation, the actual evaporite salts are typically long gone and all that remains are subtle indicators of "the salt that was."

The influence of "the evaporite that was", is also seen in the many igneous economic accumulations associated with the disappearance of evaporite salts as discussed in this chapter. The fact that the evaporites dissolve in circulating waters or are assimilated in magmas makes recognition of the associations in this chapter even more enigmatic and difficult. Identifying the presence of hydrothermal salts such as some forms of anhydrite, which are commonplace precipitates in volcanogenic massive sulphide deposits is very difficult once the salts dissolve from their igneous matrix. Yet, both metasedimentary and hydrothermal $CaSO_4$ play important roles in the formation of many high temperature metal accumulations. Hydrothermal anhydrite in a VHMS deposit is retrograde salt, which like most calcium sulphate in evaporite beds is sourced in seawater, but as was first pointed out in Chap. 1, it is not a "true" evaporite salt formed by solar evaporation of a brine. In contrast, the greenschist calcium sulphate that dissolved to create the bisulphide carrier for Au in the supergiant Muruntau gold deposit has a sedimentary source. Defining and separating origins of the major ions in metalliferous fluids, which precipitate high temperature precious and base metal accumulations, is one of the most difficult aspects of the broader field of evaporite studies.

References

Aagaard, P., P. K. Egeberg, G. C. Saigal, S. Morad, and K. Bjorlykke, 1990, Diagenetic albitization of detrital K-feldspars in Jurassic, Lower Cretaceous and Tertiary clastic reservoir rocks from offshore Norway; II, Formation water chemistry and kinetic considerations: Journal of Sedimentary Research, v. 60, p. 575–581.

Aal, A., A. El Barkooky, M. Gerrits, H. Meyer, M. Schwander, and H. Zaki, 2000, Tectonic evolution of the Eastern Mediterranean Basin and its significance for hydrocarbon prospectivity in the ultradeepwater of the Nile Delta: The Leading Edge, v. 19, p. 1086–1102.

Aamir, M., and M. M. Siddiqui, 2006, Interpretation and visualization of thrust sheets in a triangle zone in eastern Potwar, Pakistan: The Leading Edge, v. 25, p. 24–37.

Abalos, B., A. Alkorta, and V. Iribar, 2008, Geological and isotopic constraints on the structure of the Bilbao anticlinorium (Basque-Cantabrian basin, North Spain): Journal of Structural Geology, v. 30, p. 1354–1367.

Abboud, M., R. P. Philp, and J. Allen, 2005, Geochemical correlation of oils and source rocks from central and NE Syria: Journal of Petroleum Geology, v. 28, p. 203–217.

Abed, A. M., and R. Yaghan, 2000, On the paleoclimate of Jordan during the last glacial maximum: Palaeogeography Palaeoclimatology Palaeoecology, v. 160, p. 23–33.

Abidi, R., N. Slim-Shimi, C. Marignac, N. Hatira, D. Gasquet, C. Renac, A. Soumarin, and S. Gleeson, 2012, The origin of sulfate mineralization and the nature of the $BaSO_4$ -$SrSO_4$ solid-solution series in the Ain Allega and El Aguiba ore deposits, Northern Tunisia: Ore Geology Reviews, v. 48, p. 165–179.

Abraham, K., H. Mielke, and P. Povondra, 1972, On the enrichment of tourmaline in metamorphic sediments in metamorphic sediments of the Arzberg Series, W. Germany (N.E. Bavaria): Neues Jahrbuch für Mineralogie Monatschefte, p. 209–219.

Abu-Hamatteh, Z. S. H., and A. M. Al-Amr, 2008, Carnallite froth flotation optimization and cell efficiency in the Arab Potash Company, Dead Sea, Jordan: Mineral Processing and Extractive Metallurgy Review: An International Journal, v. 29, p. 232–257.

Abu-Jaber, N. S., 1998, A new look at the chemical and hydrological evolution of the Dead Sea: Geochimica et Cosmochimica Acta, v. 62, p. 1471–1479.

Abu-Zeid, M. M., A. R. Baghdady, and H. A. El-Etr, 2001, Textural attributes, mineralogy and provenance of sand dune fields in the greater Al Ain area, United Arab Emirates: Journal of Arid Environments, v. 48, p. 475–499.

Achauer, C. W., 1982, Sabkha anhydrite; the supratidal facies of cyclic deposition in the Upper Minnelusa Formation (Permian), Rozet Fields area, Powder River basin, Wyoming, in C. R. Handford, Loucks, R. G., Davies, G. R., ed., Depositional and diagenetic spectra of evaporites; a core workshop., v. 3: Tulsa, OK, SEPM Core Workshop, p. 193–209.

Achauer, C. W., 1985, Facies morphology and major reservoir controls, James Atoll Reef, Fairway Field, Texas, in P. Roehl, and P. Choquette, eds., Carbonate petroleum reservoirs – a casebook: New York, Springer–Verlag, p. 485–494.

Ackermann, R. V., P. W. Schlische, and P. E. Olsen, 1995, Synsedimentary collapse of portions of the Lower Blomidon Formation (Late Triassic), Fundy Rift Basin, Nova Scotia: Canadian Journal of Earth Sciences, v. 32, p. 1965–1976.

Adams, G. C., 1993, Gypsum and anhydrite resources in Nova Scotia: Economic Geology Series (Halifax), Nova Scotia Department of Natural Resources Information Circular, 15 p.

Adams, J. B., A. R. Gillespie, M. P. A. Jackson, D. R. Montgomery, T. P. Dooley, J. P. Combe, and B. C. Schreiber, 2009, Salt tectonics and collapse of Hebes Chasma, Valles Marineris, Mars: Geology, v. 37, p. 691–694.

Adams, J. E., and H. N. Frenzel, 1950, Capitan barrier reef, Texas and New Mexico: Journal of Geology, v. 58, p. 289–312.

Adams, J. F., and M. L. Rhodes, 1960, Dolomitisation by seepage refluxion: American Association of Petroleum Geologists Bulletin, v. 44, p. 1912–1920.

Adams, S. S., 1970, Ore controls, Carlsbad potash district, southeast New Mexico, in J. L. Rau, and L. F. Dellwig, eds., Third Symposium on Salt, v. 1: Cleveland, Northern Ohio Geological Society, p. 246–257.

Adams, S. S., and R. J. Hite, 1983, Potash, in S. J. LeFond, ed., Industrial minerals and rocks (nonmetallics other than fuels): New York, AIME, p. 1049–1077.

Adams, T. C., 1938, Recent Deposition of Salts from the Great Salt Lake: Journal of Geology, v. 46, p. 637–646.

Addy, K. S., and E. W. Behrens, 1980, Time of accumulation of hypersaline anoxic brine in Orca basin (Gulf of Mexico): Marine Geology, v. 37, p. 241–252.

Agarwal, B., H. Hermansen, J. Sylte, and T. L., 2000, Reservoir Characterization of Ekofisk Field: A Giant, Fractured Chalk Reservoir in the Norwegian North Sea?: SPE Reservoir Evaluation & Engineering (SPE-68096-P), v. 6, p. 534–543.

Aghashahi, E., and H. Zomorodian, 1981, Gravity study of Qum salt dome in Iran: Journal of Earth and Space Physics, v. 10, p. 21–24.

Aharon, P., 1988, A stable isotope study of magnesites from the Rum Jungle Uranium field. Australia: Implications for the origin of massive stratabound massive magnesites: Chemical Geology, v. 69, p. 127–145.

Aharon, P., Y. Kolodny, and E. Sass, 1977, Recent hot brine dolomitization in the "Solar Lake," Gulf of Elat; isotopic, chemical, and mineralogical study: Journal of Geology, v. 85, p. 27–48.

Aharon, P., H. H. Roberts, and R. Snelling, 1992, Submarine venting of brines in the deep Gulf of Mexico: observations and geochemistry: Geology, v. 20, p. 483–486.

Ahlfeld, F., and J. Muñoz Reyes, 1955, Las especies minerales de Bolivia, Bilbao, 180 p.

Ahmad, M., ., A. S. Wygralak, and P. A. Ferenczi, 2009, Gold deposits of the Northern Territory (updated from 1989 version): Northern Territory Geological Survey, Report v. 11.

© Springer International Publishing Switzerland 2016

J.K. Warren, *Evaporites: A Geological Compendium*, DOI 10.1007/978-3-319-13512-0

Ahr, W. M., 1973, The carbonate ramp: an alternative to the shelf model: Transactions of Gulf Coast Association of Geological Societies, v. 23, p. 221–225.

Ahr, W. M., 2008, Geology of carbonate reservoirs: the identification, description, and characterization of hydrocarbon reservoirs in carbonate rocks: Hoboken, N.J., Wiley InterScience, 277 p.

Ahr, W. M., and G. J. Palko, 1981, Depositional and diagenetic cycles in Smackover limestone-sandstone sequences, Lincoln Parish, Louisiana: Transactions of Gulf Coast Association of Geological Societies, v. 31, p. 7–17.

Ainsworth, R. B., S. T. Hasiotis, K. J. Amos, C. B. E. Krapf, T. H. D. Payenberg, M. L. Sandstrom, B. K. Vakarelov, and S. C. Lang, 2012, Tidal signatures in an intracratonic playa lake: Geology, v. 40, p. 607–610.

Aitken, B. G., 1983, T-CO_2 stability relations and phase equilibria of a calcic carbonate scapolite.: Geochimica et Cosmochimica Acta, v. 47, p. 351–362.

Aitken, J. D., 1981, Stratigraphy and sedimentology of the upper Proterozoic Little Dal Group, Mackenzie Mountains, Northwest Territories: Campbell, F. H. A. Proterozoic basins of Canada. Paper Geological Survey of Canada, v. 10, p. 47–71.

Aitken, J. D., and D. G. Cook, 1969, Geology, Lake Belot, District of Mackenzie: Geological Survey of Canada Map 6.

Aizenshtat, Z., I. Miloslavski, D. Aschengrau, and A. Oren, 1998, Chapter 8: Hypersaline depositional environments and their relation to oil generation, in A. Oren, ed., Microbiology and biogeochemistry of hypersaline environments, CRC Press, p. 89–108.

Akande, S. O., and M. Zentilli, 1984, Geologic, fluid inclusion, and stable isotope studies of the Gays River lead-zinc deposit, Nova Scotia, Canada: Economic Geology, v. 79, p. 1187–1211.

Aktas, G., and J. D. Cocker, 1995, Diagenetic and depositional controls on reservoir quality in Khuff and Unayzah sandstones, Hawtah trend, central Saudi Arabia: Middle East Petroleum Geosciences Conference: Geo-94, v. 1: Manama, Bahrain, Gulf Petrolink, 44–52 p.

Al Eid, G. A., and A. A. Al Tawil, 2009, Depositional Anhydrite Types and Controls from Anhydrite Cementation within a High-Resolution Sequence Stratigraphic Framework of the Khuff C, Hawiyah Area; Saudi Arabia (Abs.): American Association Petroleum Geologists Search and Discovery Article #90090 ©2009 American Association Petroleum Geologists Annual Convention and Exhibition, Denver, Colorado, June 7–10, 2009

Al Silwadi, M. S., A. Kirkham, M. D. Simmons, and B. N. Twombley, 1996, New insights into regional correlation and sedimentology, Arab Formation (Upper Jurassic), offshore Abu Dhabi: GeoArabia, v. 1, p. 6–27.

Al-Awwad, S. F., and L. B. Collins, 2013, Carbonate-platform scale correlation of stacked high-frequency sequences in the Arab-D reservoir, Saudi Arabia: Sedimentary Geology, v. 294, p. 205–218.

Al-Bakri, D. H., F. I. Khalaf, and Al-Ghadban, 1984, Mineralogy, genesis, and sources of surficial sediments in the Kuwait marine environment, northern Arabian Gulf: Journal of Sedimentary Petrology, v. 54, p. 1266–1279.

Al-Barwani, B., and K. McClay, 2008, Salt tectonics in the Thumrait area, in the southern part of the South Oman Salt Basin: Implications for mini-basin evolution: GeoArabia, v. 13, p. 77–108.

Al-Farraj, A., 2005, An evolutionary model for sabkha development on the north coast of the UAE: Journal of Arid Environments, v. 63, p. 740–755.

Al-Helal, A. B., F. F. Whitaker, and Y. Xiao, 2012, Reactive transport modeling of brine reflux: dolomitization, anhydrite precipitation, and porosity evolution: Journal of Sedimentary Research, v. 82, p. 196–215.

Al-Hurban, A., and I. Gharib, 2004, Geomorphological and sedimentological characteristics of coastal and inland sabkhas, Southern Kuwait: Journal of Arid Environments, v. 5 8, p. 59–85.

Al-Husseini, M., J. E. Amthor, J. P. Grotzinger, and J. Mattner, 2003, Arabian Plate Precambrian-Cambrian Boundary interpreted in Oman's Ara Group: GeoArabia, v. 8, p. 578–580.

Al-Husseini, M. I., 1997, Jurassic sequence stratigraphy of the western and southern Arabian Gulf: GeoArabia, v. 3, p. 361–382.

Al-Jallal, I. A., 1991, Depositional Environments, Lithofacies Types, and Reservoir Development of the Permian Khuff Formation in Eastern Saudi Arabia: American Association Petroleum Geologists – Bulletin, v. 75, p. 1401.

Al-Jallal, I. A., 1995, The Khuff Formation: its regional reservoir potential in Saudi Arabia and other Gulf countries: depositional and stratigraphic approach, in M. I. Al-Husseini, ed., Middle East Petroleum Geosciences Conference, GEO'94: v. 1: Manama, Bahrain, Gulf PetroLink, Bahrain, p. 103–119.

Al-Juboury, A. I., and T. McCann, 2008, The Middle Miocene Fatha (Lower Fars) Formation, Iraq: Geoarabia, v. 13, p. 141–174.

Al-Murani, G. S. G., 1986, Sedimentology and petrophysical aspects of the middle Miocene Jeribe Formation, East Baghdad field, Iraq: doctoral thesis, University of Oxford, Oxford, 256 p.

Al-Rawashdeh, R., and P. Maxwell, 2014, Analysing the world potash industry: Resources Policy, v. 41, p. 143–151.

Al-Saad, H., 2003, Facies analysis, cyclic sedimentation and paleoenvironment of the Middle Eocene Rus Formation in Qatar and adjoining areas: Carbonates and Evaporites, v. 18, p. 41–50.

Al-Saad, H., and F. N. Sadooni, 2001, A new depositional model and sequence stratigraphic interpretation for the Upper Jurassic Arab "D" reservoir in Qatar: Journal of Petroleum Geology, v. 24, p. 243-264.

Al-Saeedi, M. J., D. Al-Enezi, and M. Sounderrajan, 2013, Drilling Fluids Challenges in Successful Drilling of Gotnia Formation in the State of Kuwait: IPTC 2013: International Petroleum Technology Conference; Well construction: Cementing and drilling fluids, 26 March, 2013.

Al-Sarawi, A. M., 1988, Morphology and facies of alluvial fans in Kadmah Bay, Kuwait: Journal of Sedimentary Petrology, v. 58, p. 902–907.

Al-Sarawi, M., A. Al Zamel, and I. A. Alrifaiy, 1993, Late Pleistocene and Holocene sediments of the Khiran area (south Kuwait): Journal of the University of Kuwait-Science, p. 145–157.

Al-Siyabi, H. A., 2005, Exploration history of the Ara intrasalt carbonate stringers in the South Oman Salt Basin: GeoArabia, v. 10, p. 39–72.

Al-Zamel, A., and M. Al-Sarawi, 1998, Late Quaternary Sabkha sedimentation along Kadhmah B ay Coast, Kuwait, Arabian Gulf: Arab Gulf Journal of Scientific Research, v. 16, p. 471–495.

Ala, M. A., 1982, Chronology of trap formation and migration of hydrocarbons in Zagros Sector of Southwest Iran: American Association Petroleum Geologists – Bulletin, v. 66, p. 1535–1541.

Alam, S., and W. Ahmed, 2008, Distribution and source rock potential assessment of Paleozoic source rocks of Punjab platform (Middle Indus basin) Pakistan (Goldschmidt Conference Abstracts): Geochimica et Cosmochimica Acta, v. 72, p. A13.

Alavi, M., 2004, Regional stratigraphy of the Zagros fold-thrust belt of Iran and its proforeland evolution: American Journal of Science, v. 304, p. 1–20.

Alavi, M., 2007, Structures of the Zagros fold-thrust belt in Iran: American Journal of Science, v. 307, p. 1064–1095.

Alberto, W., F. Carraro, M. Giardino, and D. Tiranti, 2007, Genesis and evolution of 'pseudocamiole': preliminary observations from the Susa Valley (Western Alps): Geological Society, London, Special Publications, v. 285, p. 155–168.

Alberto, W., M. Giardino, G. Martinotti, and D. Tiranti, 2008, Geomorphological hazards related to deep dissolution phenomena in the Western Italian Alps: Distribution, assessment and interaction with human activities: Engineering Geology, v. 99, p. 147–159.

Albuquerque, L., M. Taborda, V. La Cono, M. Yakimov, and M. S. da Costa, 2012, Natrinema salaciae sp. nov., a halophilic archaeon isolated from the deep, hypersaline anoxic Lake Medee in the Eastern

Mediterranean Sea: Systematic and Applied Microbiology, v. 35, p. 368–373.
Alçiçek, H., 2009, Late Miocene nonmarine sedimentation and formation of magnesites in the Acigöl Basin, southwestern Anatolia, Turkey: Sedimentary Geology, v. 219, p. 115–135.
Alcocer, J., and W. D. Williams, 1996, Historical and recent changes in Lake Texcoco, a saline lake in Mexico: International Journal of Salt Lake Research, v. 5, p. 45–51.
Alderman, A. R., and H. C. W. Skinner, 1957, Dolomite sedimentation in the southeast of South Australia: American Journal of Science, v. 255, p. 561–567.
Alderman, A. R., and C. C. von der Borch, 1963, Dolomite reaction series: Nature, v. 198, p. 465–466.
Alderman, S. S. J., 1985, Geology of the Owens Lake evaporite deposit, in B. C. Schreiber, and H. L. Harner, eds., Sixth international symposium on salt, v. 1, Salt Institute, VA, p. 75–83.
Aldrich, T. W., and D. S. Paul, 2002, Avian ecology of Great Salt Lake, in J. W. Gwynn, ed., Great Salt Lake, An Overview of Change, Special Publication of the Utah Department of Natural Resources, Salt Lake City, Utah, p. 343–374.
Aleali, M., H. Rahimpour-Bonab, R. Moussavi-Harami, and D. Jahani, 2013, Environmental and sequence stratigraphic implications of anhydrite textures: A case from the Lower Triassic of the Central Persian Gulf: Journal of Asian Earth Sciences, v. 75, p. 110–125.
Aleksandrov, S., and V. Senin, 2006, Genesis and composition of lazurite in magnesian skarns: Geochemistry International, v. 44, p. 976–988.
Alemán, A. M., and R. Marksteiner, 1995, Structural Styles in the Santiago Fold and Thrust Belt: A Salt Related Orogenic Belt, Secon ISAG, Oxford, UK, 21–23 September 1993, p. 147–153.
Alemán, A. M., and R. Marksteiner, 1997, Petroleum Systems and Structural Styles in the Santiago Fold and Thrust Belt: A Salt Related Orogenic Belt, Asociación Colombiana de Geólogos y Geofisicos del Petróleo (ACGGP) VI° Simposio Bolivariano, Bogotá, 1997, Petroleum Exploration in the Subandean Basins, pt. 2, p. 171–186.
Alexander, L. L., and P. B. Flemings, 1995, Geologic evolution of a Pliocene-Pleistocene salt-withdrawal minibasin – Eugene Island Block 330, offshore Louisiana: American Association Petroleum Geologists Bulletin, v. 79, p. 1737–1756.
Ali, Y. A., and I. West, 1983, Relationships of modern gypsum nodules in sabkhas of loess to compositions of brines and sediments in northern Egypt: Journal of Sedimentary Petrology, v. 53, p. 1151–1168.
Aljubouri, Z. A., and S. Alddabbagh, M., 1980, Sinjarite, a new mineral from Iraq: Mineralogical Magazine, v. 43, p. 643–645.
Allan, R. J., J. A. T. Bye, and P. Hutton, 1986, The 1984 filling of Lake Eyre, South Australia: Transactions Royal Society South Australia, v. 110, p. 81–87.
Allen, B. D., and R. Y. Anderson, 2000, A continuous, high-resolution record of late Pleistocene climate variability from the Estancia basin, New Mexico: Geological Society of America Bulletin, v. 112, p. 1444–1458.
Allen, D. E., B. R. Strazisar, Y. Soong, and S. W. Hedges, 2005, Modeling carbon dioxide sequestration in saline aquifers: Significance of elevated pressures and salinities: Fuel Processing Technology, v. 86, p. 1569–1580.
Allen, J. S., W. S. Thomas, and D. Lavoie, 2010, The Laurentian margin of northeastern North America, in R. P. Tollio, M. J. Bartholomew, J. P. Hibbard, and P. M. Karabinos, eds., From Rodinia to Pangea: The Lithotectonic Record of the Appalachian Region, Geological Society of America, Memoir 206, p. 71–90.
Allen, M. A., F. Goh, B. P. Burns, and B. A. Neilan, 2009, Bacterial, archaeal and eukaryotic diversity of smooth and pustular microbial mat communities in the hypersaline lagoon of Shark Bay: Geobiology, v. 7, p. 82–96.
Allen, P. A., and P. F. Hoffman, 2005, Extreme winds and waves in the aftermath of a Neoproterozoic glaciation: Nature, v. 433, p. 123–127.
Alley, N. F., 1998, Cainozoic stratigraphy, palaeoenvironments and geological evolution of the Lake Eyre Basin: Palaeogeography Palaeoclimatology Palaeoecology, v. 144, p. 239–263.
Allison, G. B., and C. J. Barnes, 1985, Estimation of evaporation from the normally 'dry' Lake Frome in South Australia: Journal of Hydrology, v. 78, p. 229–242.
Allison, M. L., 2001, The Hutchinson Gas Explosions: Unraveling a Geologic Mystery: Kansas Bar Association, 26th Annual KBA/KIOGA Oil and Gas Law Conference, v. 1, p. 3.1-3.29.
Allwood, A. C., M. R. Walter, I. W. Burch, and B. S. Kamber, 2007, 3.43 billion-year-old stromatolite reef from the Pilbara Craton of Western Australia: Ecosystem-scale insights to early life on Earth: Precambrian Research, v. 158, p. 198–227.
Almogi-Labin, A., R. Simantov, A. Rosenfeld, and E. Debard, 1995, Occurrence and distribution of the foraminifer *Ammonia Beccarii Tepida* (Cushman) in water bodies, Recent and Quaternary of the Dead Sea rift, Israel: Marine Micropaleontology, v. 26, p. 153–159.
Aloisi, G., M. Baudrand, C. Lécuyer, J. M. Rouchy, R. D. Pancost, M. A. M. Aref, and V. Grossi, 2013, Biomarker and isotope evidence for microbially-mediated carbonate formation from gypsum and petroleum hydrocarbons: Chemical Geology, v. 347, p. 199–207.
Alonso, H., and F. Risacher, 1996, Geochemistry of the Salar de Atacama. 1. Origin of components and salt balance [Spanish]: Revista Geologica de Chile, v. 23, p. 113–122.
Alonso, R., 1991, Evaporitas neógenas de los Andes Centrales, in J. J. Pueyo, ed., Génesis de Formaciones Evaporíticas. Modelos Andinos e Ibéricos, Universitat de Barcelona. Estudi General, v. 2, p. 267–329.
Alonso, R. N., 1986, Ocurrencia, posición estratigráfica y génesis de los depósitos de boratos de la Puna Argentina: Doctoral thesis, Universidad Nacional de Salta, Argentina, 196 p.
Alonso, R. N., C. Helvaci, R. J. Sureda, and J. G. Viramonte, 1988, A new Tertiary borax deposit in the Andes: Mineralium Deposita, v. 23, p. 299–305.
Alonso, R. N., T. E. Jordan, K. T. Tabbutt, and D. S. Vandervoort, 1991, Giant evaporite belts of the Neogene central Andes: Geology, v. 19, p. 401–404.
Alonso-Azcarate, J., S. H. Bottrell, and J. Tritlla, 2001, Sulfur redox reactions and formation of native sulfur veins during low grade metamorphism of gypsum evaporites, Cameros Basin (NE Spain): Chemical Geology, v. 174, p. 389–402.
Alonso-Zarza, A. M., Y. Sánchez-Moya, M. A. Bustillo, A. Sopeña, and A. Delgado, 2002, Silicification and dolomitization of anhydrite nodules in argillaceous terrestrial deposits: an example of meteoric-dominated diagenesis from the Triassic of central Spain: Sedimentology, v. 49, p. 303–317.
Alpers, C. N., R. O. Rye, D. K. Nordstrom, L. D. White, and B.-S. King, 1992, Chemical, crystallographic and stable isotopic properties of alunite and jarosite from acid-hypersaline Australian lakes: Chemical Geology, v. 92, p. 203–226.
Alsharhan, A. S., 1993, Facies and sedimentary environment of the Permian carbonate (Khuff Formation) in the United Arab Emirates: Sedimentary Geology, v. 84, p. 89–99.
Alsharhan, A. S., 2003, Petroleum geology and potential hydrocarbon plays in the Gulf of Suez rift basin, Egypt: American Association Petroleum Geologists – Bulletin, v. 87, p. 143–180.
Alsharhan, A. S., 2006, Sedimentological character and hydrocarbon parameters of the Middle Permian to Early Triassic Khuff Formation, United Arab Emirates: Geoarabia, v. 11, p. 121–158.
Alsharhan, A. S., and C. G. S. Kendall, 2003, Holocene coastal carbonates and evaporites of the southern Arabian Gulf and their ancient analogues: Earth Science Reviews, v. 61, p. 191–243.

Alsharhan, A. S., and C. G. S. C. Kendall, 1994, Depositional setting of the Upper Jurassic Hith Anhydrite of the Arabian Gulf; an analog to Holocene evaporites of the United Arab Emirates and Lake MacLeod of Western Australia: American Association Petroleum Geologists – Bulletin, v. 78, p. 1075–1096.

Alsharhan, A. S., and A. E. M. Nairn, 1993, Geology and hydrocarbon habitat in the Arabian Basin – the Mesozoic of the State of Qatar: Geologie en Mijnbouw, v. 71, p. 265–294.

Alsharhan, A. S., and A. E. M. Nairn, 1997, Sedimentary Basins and Petroleum Geology of the Middle East: Amsterdam, The Netherlands, Elsevier Science B. V., 942 p.

Alshuaibi, A., M. J. Duane, and H. Mahmoud, 2012, Microbial-Activated Sediment Traps Associated with Oncolite Formation Along a Peritidal Beach, Northern Arabian (Persian) Gulf, Kuwait: Geomicrobiology Journal, v. 29, p. 679–696.

Alsop, G. I., D. J. Blundell, and I. Davison, 1996, Salt Tectonics: Special Publication, v. 100: London, Geological Society, 310 p.

Alsop, G. I., J. P. Brown, I. Davison, and M. R. Gibling, 2000, The geometry of drag zones adjacent to salt diapirs: Journal of the Geological Society, v. 157, p. 1019–1029.

Alsouki, M., M. A. Riahi, and A. Yassaghi, 2011, Seismic imaging of sub-circular salt-related structures: evidence for passive diapirism in the Straits of Hormuz, Persian Gulf: Petroleum Geoscience, p. 1.

Amadi, F. O., R. P. Major, and L. R. Baria, 2012, Origins of gypsum in deep carbonate reservoirs: Implications for hydrocarbon exploration and production: American Association Petroleum Geologists – Bulletin, v. 96, p. 375–390.

Amery, G. B., 1969, Structure of Sigsbee Scarp, Gulf of Mexico: American Association of Petroleum Geology Bulletin, v. 53, p. 2480–2482.

Amery, G. B., 1978, Structure of continental slope, northern Gulf of Mexico, in A. H. Bouma, C. T. Moore, and J. M. Coleman, eds., Framework, facies, and oil-trapping characteristics of the upper continental margin, American Association Petroleum Geologists Studies in Geology, v. 7, p. 141–153.

Amiel, A. J., and G. M. Friedman, 1971, Continental sabkha in Arava Valley between Dead Sea and Red Sea: Significance for origin of evaporites: American Association Petroleum Geologists – Bulletin, v. 55, p. 581–592.

Amieux, P., 1980, Exemple d'un passage des 'black shales' aux evaporites dans le Ludien (Oligocene inferieur) du bassin de Mormoiron (Vaucluse, Sud- Est de la France). (Example of a transition of black shales to evaporites in the Ludian (Lower Oligocene) of the Mormoiron Basin, Vaucluse, south- eastern France): Bulletin, Centres de Recherches Exploration-Production Elf- Aquitaine, v. 4, p. 281–307.

Amin, A., and K. Bankher, 1997b, Causes of land subsidence in the Kingdom of Saudi Arabia: Natural Hazards, v. 16, p. 57–63.

Amin, A. A., and K. A. Bankher, 1997a, Karst hazard assessment of eastern Saudi Arabia: Natural Hazards, v. 15, p. 21–30.

Amit, R., E. Zilberman, N. Porat, and Y. Enzel, 1999, Relief inversion in the Avrona Playa as evidence of large-magnitude historical earthquakes, southern Arava Valley, Dead Sea Rift: Quaternary Research, v. 52, p. 76–91.

Amrani, A., A. Deev, A. L. Sessions, Y. Tang, J. F. Adkins, R. J. Hill, J. M. Moldowan, and Z. Wei, 2012, The sulfur-isotopic compositions of benzothiophenes and dibenzothiophenes as a proxy for thermochemical sulfate reduction: Geochimica et Cosmochimica Acta, v. 84, p. 152–164.

Amthor, J., and J. Okkerman, 1998, Influence of early diagenesis on reservoir quality of Rotliegende sandstones, northern Netherlands: American Association Petroleum Geologists – Bulletin, v. 82, p. 2246–2265.

Amthor, J. E., 2000, Precambrian carbonates of Oman: A regional perspective (abs): GeoArabia, v. 5, p. 47.

Amthor, J. E., and N. L. Frewin, 1999, Enigmatic Origin of a Late Pre-Cambrian Laminated Chert: Have Bacteria Done It?: Bulletin American Association of Petroleum Geologists American Association Petroleum Geologists Annual Meeting San Antonio, Texas, April 11–14, 1999, v. 83.

Amthor, J. E., J. Ramezani, M. W. Martin, A. Matter, J. P. Grotzinger, S. Schröder, and S. A. Bowring, 2003, Extinction of Cloudina and Namacalathus at the Precambrian-Cambrian boundary in Oman: Geology, v. 31, p. 431–434.

Amthor, J. E., K. Ramseyer, T. Faulkner, and P. Lucas, 2005, Stratigraphy and sedimentology of a chert reservoir at the Precambrian-Cambrian boundary: the Al Shomou Silicilyte, South Oman Salt Basin: Geoarabia, v. 10, p. 89–122.

Amthor, J. E., W. Smits, and P. Nederlof, 1998, Prolific Oil Production from a Source Rock- The Athel Silicilyte Source-Rock Play in South Oman (abs.): American Association Petroleum Geologists – Bulletin, American Association Petroleum Geologists Annual Meeting, Salt Lake City, Utah, May 17–20, 1998, v. 82 (13).

An, F., H. Ma, H. Wei, and Z. Lai, 2012, Distinguishing aeolian signature from lacustrine sediments of the Qaidam Basin in northeastern Qinghai-Tibetan Plateau and its palaeoclimatic implications: Aeolian Research, v. 4, p. 17–30.

Anati, D. A., 1998, Dead Sea water trajectories in the T–S space: Hydrobiologia, v. 381, p. 43–49.

Anati, D. A., 1999, The salinity of hypersaline brines: concepts and misconceptions: International Journal of Salt Research, v. 8, p. 1–16.

Anati, D. A., Gavrieli, and A. Oren, 1995, The residual effect of the 1991–93 rainy winter on the Dead sea stratification: Israel Journal of Science, v. 44, p. 63–70.

Anbar, A. D., 2008, Elements and Evolution: Science, v. 322, p. 1481–1483.

Anderle, J. P., K. S. Crosby, and D. C. E. Waugh, 1979, Potash at Salt Springs, New Brunswick: Economic Geology, v. 74, p. 389–396.

Andersen, D. T., D. Y. Sumner, I. Hawes, J. Webster-Brown, and C. P. McKay, 2011, Discovery of large conical stromatolites in Lake Untersee, Antarctica: Geobiology, v. 9, p. 280–293.

Anderson, E. G., 1979, Basic Mesozoic study in Louisiana: The northern coastal region and the Gulf Basin Province: Louisiana Geological Series Folio Series 3, 58 p.

Anderson, E. J., 1981, Deep-seated salt dissolution in the Delaware Basin, Texas and New Mexico: in Wells, S.G., Lamber, W., and Callender, J.F., eds., Environmental geology and hydrology in New Mexico: Special Publication 10, New Mexico Geological Society, p. 133–145.

Anderson, G. M., 1973, The hydrothermal transport and deposition of galena and sphalerite near 100 °C: Economic Geology, v. 68, p. 480–492.

Anderson, G. M., 1975, Precipitation of Mississippi Valley-type ores: Economic Geology, v. 70, p. 937–942.

Anderson, G. M., 1983, Some geochemical aspects of sulphide precipitation in carbonate rock, in G. Kisvarsanyi, S. K. Grant, W. P. Pratt, and J. W. Koenig, eds., International Conference on Mississippi Valley Type Lead-Zinc Deposits, Proceedings Volume, University of Missouri, Rolla, p. 61–76.

Anderson, G. M., and R. W. Macqueen, 1988, Ore deposit models — 6. Mississippi Valley-type lead-zinc deposits: Geoscience Canada Reprint Series, v. 3, p. 79–90.

Anderson, G. M., and R. W. MacQueen, 1990, Mississippi valley-type lead-zinc deposits, in R. G. Roberts, and P. A. Sheahan, eds., Ore Deposit Models, v. 3: St. John's, Geoscience Canada Reprint Series, p. 79–90.

Anderson, J. E., J. Cartwright, S. J. Drysdall, and N. Vivian, 2000, Controls on turbidite sand deposition during gravity-driven extension of a passive margin: examples from Miocene sediments in

Block 4, Angola: Marine & Petroleum Geology, v. 17, p. 1165–1203.
Anderson, M. R., A. H. Rankin, and B. Spiro, 1992, Fluid mixing in the generation of mesothermal gold mineralisation in the Transvaal Sequence, Transvaal, South Africa: European Journal of Mineralogy, v. 4, p. 933–948.
Anderson, N. L., R. J. Brown, and R. C. Hinds, 1988, Geophysical aspects of Wabamun salt distribution in southern Alberta: Can. Jour. Expl. Geophys., v. 24, p. 166–178.
Anderson, N. L., and D. A. Cederwall, 1993, Westhazel General Petroleums Pool; case history of a salt-dissolution trap in west-central Saskatchewan, Canada: Geophysics, v. 58, p. 889–897.
Anderson, N. L., J. Hopkins, A. Martinez, R. W. Knapp, P. A. Macfarlane, W. L. Watney, and R. Black, 1994, Dissolution of bedded rock salt; a seismic profile across the active eastern margin of the Hutchinson Salt Member, central Kansas: Computers and Geosciences, v. 20, p. 889–903.
Anderson, N. L., and R. Knapp, 1993, An overview of some of the larger scale mechanisms of salt dissolution in Western Canada: Geophysics, v. 58, p. 1375–1387.
Anderson, N. L., A. Martinez, J. F. Hopkins, and T. R. Carr, 1998, Salt dissolution and surface subsidence in central Kansas – A seismic investigation of the anthropogenic and natural origin models: Geophysics, v. 63, p. 366–378.
Anderson, R. N., L. M. Cathles III, and H. R. Nelson, 1991, "Data Cube" depicting fluid flow history in Gulf Coast sediments: Oil and Gas Journal, v. 89, p. 50–55.
Anderson, R. N., P. Flemings, S. Losh, and J. A. Austin, 1994, Gulf of Mexico growth fault drilled, seen as oil, gas migration pathway: Oil and Gas Journal, June 6, 1994, p. 97 & ff.
Anderson, R. Y., W. E. J. Dean, D. W. Kirkland, and H. I. Snider, 1972, Permian Castile Varved Evaporite Sequence, West Texas and New Mexico: Geological Society of America Bulletin, v. 83, p. 59–85.
Anderson, S. B., and J. B. Hunt, 1964, Devonian salt solution in north central North Dakota: Third International Williston Basin Symposium Proceedings, p. 93–104.
Andreason, M.W., 1992, Coastal siliciclastic sabkhas and related evaporative environments of the Permian Yates Formation, North Ward-Estes field, Ward County, Texas: American Association of Petroleum Geologists Bulletin, v. 76, p. 1735–1759.
Andreev, R. Y., V. N. Apollonov, G. A. Galkin, G. M. Drugov, M. A. Zharkov, Y. G. Mashovich, A. L. Protopopov, V. F. Sadovyi, and K. S. Khechoyan, 1986, The Potassium-Containing Horizons of the Nepa Basin: Soviet Geology and Geophysics, v. 27, p. 38–45.
Andrejchuk, V., 2002, Collapse above the world's largest potash mine, Ural, Russia: International Journal Speleology, v. 31, p. 137–158.
Andrejchuk, V., A. Eraso, and M. Domínguez, 2000, A large sinkhole in the Verchnekamsky potash basin in the Urals: Mine Water and the Environment, v. 19, p. 2–18.
Andrejchuk, V. N., and A. B. Klimchouk, 2001, Geomicrobiology and redox geochemistry of the karstified Miocene gypsum aquifer, western Ukraine: The study from Zoloushka Cave: Geomicrobiology Journal, v. 18, p. 275–295.
Andrejchuk, V. N., and A. B. Klimchouk, 2004, Mechanisms of karst breakdown formation in the gypsum karst of the fore-Ural region, Russia (from observations in the Kungurskaja Cave): Speleogenesis and Evolution of Karst Aquifers 2 (2), available at www.speleogenesis.info, (online journal).
Angulo, M. A., 2011, Iodine: U.S. Geological Survey, 2010 Minerals Yearbook, (Advanced release – Sept 2011)
Anissimov, L., E. Postnova, and O. Merkulov, 2000, Tengiz oilfield: geological model based on hydrodynamic data: Petroleum Geoscience, v. 6, p. 59–65.
Anonymous, 2007, Sulfur, Kirk-Othmer Encyclopedia of Chemical Technology, v. 23, John Wiley & Sons, Inc., p. 1–37.
Anschutz, P., and G. Blanc, 1995, Geochemical dynamics of the Atlantis II Deep (Red Sea) – silica behaviour: Marine Geology, v. 128, p. 25–36.
Anschutz, P., and G. Blanc, 1996, Heat and salt fluxes in the Atlantis II Deep (Red Sea): Earth and Planetary Science Letters, v. 142, p. 147–159.
Antrett, P., A. A. Vackiner, P. Kukla, N. Klitzsch, and H. Stollhofen, 2012, Impact of arid surface megacracks on hydrocarbon reservoir properties: Bulletin American Association Petroleum Geologists, v. 96, p. 1279–1299.
Antunes, A., D. K. Ngugi, and U. Stingl, 2011, Microbiology of the Red Sea (and other) deep-sea anoxic brine lakes: Environmental Microbiology Reports, v. 3, p. 416–433.
Apak, S. N., K. A. R. Ghori, G. M. Carlsen, and M. K. Stevens, 2002, Basin Development with implications for Petroleum Trap Styles of the Neoproterozoic Officer Basin, Western Australia: The sedimentary basins of Western Australia 3. Proceedings of the West Australian basins Symposium: Perth, Petroleum Exploration Society of Australia, p. 913–927.
API, 1994, Design of solution-mined underground storage practices: Washington, DC, American Petroleum Institute, Recommended practice No. 1114
Apodaca, L. E., 2012, Sulfur Mining Engineering, v. 64, p. 91–92.
Appel, P. W. U., 1984, Tourmaline in the Early Archaean Isua Supracrustal Belt, West Greenland: The Journal of Geology, v. 92, p. 599–605.
Appel, P. W. U., 1994, Stratabound scheelite in altered Archaean komatiites, west Greenland: Mineralium Deposita, v. 29, p. 341–352.
Appel, P. W. U., 1995, Tourmalinites in the 3800 Ma old Isua supracrustal belt, West Greenland: Precambrian Research, v. 72, p. 227–234.
Aqrawi, A. A. M., and G. Evans, 1994, Sedimentation in the lakes and marshes (Ahwar) of the Tigris Euphrates delta, southern Mesopotamia: Sedimentology, v. 41, p. 755–776.
Aqrawi, A. A. M., M. Keramati, S. N. Ehrenberg, N. Pickard, A. Moallemi, T. Svana, G. Darke, J. A. D. Dickson, and N. H. Oxtoby, 2006, The origin of dolomite in the Asmari Formation (Oligocene-Lower Miocene), Dezful Embayment, SW Iran: Journal of Petroleum Geology, v. 29, p. 381–401.
Aquilina, L., A. N. Dia, J. Boulegue, J. Bourgois, and A. M. Fouillac, 1997, Massive barite deposits in the convergent margin off Peru: Implications for fluid circulation within subduction zones: Geochimica et Cosmochimica Acta, v. 61, p. 1233–1245.
Aquilina, L., P. Boulvais, and J.-R. Mossmann, 2011, Fluid migration at the basement/sediment interface along the margin of the Southeast basin (France): implications for Pb-Zn ore formation: Mineralium Deposita, v. 46, p. 959–979.
Arakel, A. V., 1980, Genesis and diagenesis of Holocene evaporitic sediments in Hutt and Leeman lagoons, Western Australia: Journal of Sedimentary Petrology, v. 50, p. 1305–1326.
Arakel, A. V., and T. Hong Jun, 1994, Seasonal evaporite sedimentation in desert playa lakes of the Karinga Creek drainage system, central Australia, in R. W. Renaut, and W. M. Last, eds., Sedimentology and geochemistry of modern and ancient saline lakes: Tulsa, OK, Society for Sedimentary Geology; Special Publication, v. 50, p. 91–100.
Arakel, A. V., G. Jacobson, and W. B. Lyons, 1990, Sediment-water interaction as a control on geochemical evolution of playa lake systems in the Australian arid interior: Hydrobiologia, v. 197, p. 1–12.
Arbey, N., 1980, Silicification des évaporites: Bulletin, Centres de Recherches Exploration-Production Elf- Aquitaine, v. 4, p. 309–365.
Aref, M. A. M., 1998a, Holocene stromatolites and microbial laminites associated with lenticular gypsum in a marine-dominated environ-

ment, Ras el Shetan area, Gulf of Aqaba, Egypt: Sedimentology, v. 45, p. 245–262.

Aref, M. A. M., 1998b, Biogenic carbonates – are they a criterion for underlying hydrocarbon accumulations – an example from the Gulf of Suez region: American Association Petroleum Geologists – Bulletin, v. 82, p. 336–352.

Aref, M. A. M., 2003, Classification and depositional environments of Quaternary pedogenic gypsum crusts (gypcrete) from east of the Fayum Depression, Egypt: Sedimentary Geology, v. 155, p. 87–108.

Aref, M. A. M., O. E. A. Attia, and A. M. A. Wali, 1997, Facies and depositional environment of the Holocene evaporites in the Ras Shukeir area, Gulf of Suez, Egypt: Sedimentary Geology, v. 110, p. 123–145.

Arenas, C., and G. Pardo, 1999, Latest Oligocene-Late Miocene lacustrine systems of the north-central part of the Ebro Basin (Spain): sedimentary facies model and palaeogeographic synthesis: Palaeogeography Palaeoclimatology Palaeoecology, v. 151, p. 127–148.

Arenas, C., A. M. A. Zarza, and G. Pardo, 1999, Dedolomitization and other early diagenetic processes in Miocene lacustrine deposits, Ebro Basin (Spain): Sedimentary Geology, v. 125, p. 23–45.

Arkin, Y., and A. Gilat, 2000, Dead Sea sinkholes – an ever-developing hazard: Environmental Geology, v. 39, p. 711–722.

Armenteros, I., 2010, Chapter 2 Diagenesis of Carbonates in Continental Settings, in A. M. Alonso-Zarza, and L. H. Tanner, eds., Developments in Sedimentology, v. Volume 62, Elsevier, p. 61–151.

Armenteros, I., B. Daley, and E. Garcia, 1997, Lacustrine and palustrine facies in the Bembridge Limestone (Late Eocene, Hampshire Basin) of the Isle of Wight, Southern England: Palaeogeography Palaeoclimatology Palaeoecology, v. 128, p. 111–132.

Armstrong, A. K., 1995, Facies, diagenesis, and mineralogy of the Jurassic Todilto Limestone Member, Grants uranium district, New Mexico, v. 153, New Mexico Bureau of Mines Bulletin, 41 p.

Armstrong, J. P., F. J. Longstaffe, and F. J. Hein, 1993, Carbon and oxygen isotope geochemistry of calcite from the Jubilee Zn-Pb deposit, Breton Island: Canadian Mineralogist, v. 31, p. 755–766.

Armstrong, L. A., A. Ten Have, and H. D. Johnson, 1987, The geology of the Gannet fields, central North Sea, in J. Brooks, and K. W. Glennie, eds., Petroleum Geology of NW Europe: London, Graham and Trotman, p. 533–548.

Arne, D. C., L. W. Curtis, and S. A. Kissin, 1991, Internal zonation in a carbonate-hosted Zn-Pb-Ag deposit. Nanisivik, Baffin Island, Canada: Economic Geology, v. 86, p. 699–717.

Arnow, T., and D. Stephens, 1990, Hydrologic characteristics of the Great Salt Lake, Utah, 1847–1986: US Geological Survey Water-Supply Paper 2332, 32p.

Arp, G., 1995, Lacustrine bioherms, spring mounds, and marginal carbonates of the Ries-impact-crater (Miocene, southern Germany): Facies, v. 33, p. 35–89.

Arp, G., C. Ostertag-Henning, S. Yücekent, J. Reitner, and V. Thiel, 2008, Methane-related microbial gypsum calcitization in stromatolites of a marine evaporative setting (Münder Formation, Upper Jurassic, Hils Syncline, north Germany): Sedimentology, v. 55, p. 1227–1251.

Arp, G., A. Reimer, and J. Reitner, 2001, Photosynthesis-induced biofilm calcification and calcium concentrations in Phanerozoic oceans: Science, v. 292, p. 1701–1704.

Arthurton, R. S., 1973, Experimentally produced halite compared with Triassic layered halite-rock from Cheshire, England: Sedimentology, v. 20, p. 145–160.

Artieda, O., 2013, Morphology and micro-fabrics of weathering features on gyprock exposures in a semiarid environment (Ebro Tertiary Basin, NE Spain): Geomorphology, v. 196, p. 198–210.

Arzaghi, S., K. Khosrow-Tehrani, and M. Afghah, 2012, Sedimentology and petrography of Paleocene-Eocene evaporites: the Sachun Formation, Zagros Basin, Iran: Carbonates and Evaporites, v. 27, p. 43–53.

Asael, D., A. Matthews, S. Oszczepalski, M. Bar-Matthews, and L. Halicz, 2009, Fluid speciation controls of low temperature copper isotope fractionation applied to the Kupferschiefer and Timna ore deposits: Chemical Geology, v. 262, p. 147–158.

Askew, R. L., 2013, Distribution of the Permian Blaine Formation Salt in the Subsurface of the Hugoton Embayment Area of Baca County, Southeast Colorado: The Mountain Geologist, v. 50, p. 65–75.

Asmar, B. N., and P. Ergenzinger, 1999, Estimation of evaporation from the Dead Sea: Hydrological Processes, v. 13, p. 2743–2750.

Asmar, B. N., and P. Ergenzinger, 2002, Dynamic simulation of the Dead Sea: Advances in Water Resources, v. 25, p. 263–277.

Assereto, R. C., and R. L. Folk, 1976, Brick-like texture and radial rays in Triassic pisolites of Lombardy, Italy: A clue to distinguish ancient aragonitic pisolites: Sedimentary Geology, v. 16, p. 205–222.

Assereto, R. I. A. M., and C. G. S. C. Kendall, 1977, Nature, origin, and classification of peritidal teepee structures and related breccias,: Sedimentology, v. 24, p. 153–210.

Astin, T. R., and D. A. Rogers, 1991, "Subaqueous shrinkage cracks" in the Devonian of Scotland reinterpreted: Journal of Sedimentary Petrology, v. 61, p. 850–859.

Aswasereelert, W., S. R. Meyers, A. R. Carroll, S. E. Peters, M. Smith, and K. L. Feigl, 2013, Basin-scale cyclostratigraphy of the Green River Formation, Wyoming: Geological Society of America Bulletin, v. 125, p. 216–228.

Atia, A. K. M., E. E. Hilmy, and S. M. Bolous, 1970, Mineralogy of the Salt Deposits of Wadi El Natrun: Arab Republic of Egypt, Desert Institute Bulletin, v. 20, p. 49–74.

Attia, O. E. A., 2013, Sedimentological characteristics and geochemical evolution of Nabq sabkha, Gulf of Aqaba, Sinai, Egypt: Arabian Journal of Geosciences, v. 6, p. 2045–2059.

Aufderheide, A. C., 2011, The Scientific Study of Mummies, Cambridge University Press, 634 p.

Augustin, N., C. W. Devey, F. M. van der Zwan, P. Feldens, M. Tominaga, R. A. Bantan, and T. Kwasnitschka, 2014, The rifting to spreading transition in the Red Sea: Earth and Planetary Science Letters, v. 395, p. 217–230.

Augustithis, S. S., 1980, On the textures and treatment of the sylvinite ore from the Danakili Depression, Salt Plain (Piano del Sale), Tigre, Ethiopia: Chem. Erde., v. 39, p. 91–95.

Aulstead, K. L., and R. J. Spencer, 1985, Diagenesis of Keg River Formation, northwestern Alberta; fluid inclusion evidence: Bulletin of Canadian Petroleum Geology, v. 33, p. 167–183.

Austin, G. S., and B. Humphrey, 2006, Sodium sulfate resources, in J. E. Kogel, N. C. Trivedi, J. M. Barker, and S. T. Krukowski, eds., Industrial Minerals and Rocks, SME (Soc. Mining Metallurgy and Exploration), p. 879–892.

Autin, W. J., 2002, Landscape evolution of the Five Islands of south Louisiana: scientific policy and salt dome utilization and management: Geomorphology, v. 47, p. 227–244.

Autin, W. J., and R. P. McCulloh, 1995, Quaternary geology of the Weeks and Cote Blanche islands salt domes: Gulf Coast Association of Geological Societies Transactions, v. XLV, p. 39–46.

Awramik, S. M., and H. P. Buchheim, 2009, A giant, Late Archean lake system: The Meentheena Member (Tumbiana Formation; Fortescue Group), Western Australia: Precambrian Research, v. 174, p. 215–240.

Awramik, S. M., and J. Sprinkle, 1999, Proterozoic stromatolites: the first marine evolutionary biota: Historical Biology, v. 13, p. 241–253.

Aydemir, A., 2008, Hydrocarbon potential of the Tuzgolu (Salt Lake) Basin, Central Anatolia, Turkey: A comparison of geophysical investigation results with the geochemical data: Journal of Petroleum Science and Engineering, v. 61, p. 33–47.

Ayenew, T., 2008, The distribution and hydrogeological controls of fluoride in the groundwater of central Ethiopian rift and adjacent highlands: Environmental Geology, v. 54, p. 1313–1324.

Ayora, C., 1999, Modelo de dedolomitización, in I. Armenteros, J. A. Blanco Sañchez, and E. Merino, eds., Dinámica de las interacciones entre aguay minerales en medios de baja temperatura (meteorización, diagénesis, metasomatismo), Reunión Científica y Curso Extraordinario, Salamanca, Spain, p. 197–207.

Ayora, C., D. I. Cendon, C. Taberner, and J. J. Pueyo, 2001, Brine-mineral reactions in evaporite basins: Implications for the composition of ancient oceans: Geology, v. 29, p. 251–254.

Ayora, C., J. Garciaveigas, and J. Pueyo, 1994, The chemical and hydrological evolution of an ancient potash-forming evaporite basin as constrained by mineral sequence, fluid inclusion composition, and numerical simulation: Geochimica et Cosmochimica Acta, v. 58, p. 3379–3394.

Ayres, M. G., M. Bilal, R. W. Jones, L. W. Slenz, M. Tartir, and A. O. Wilson, 1982, Hydrocarbon Habitat in Main Producing Areas, Saudi Arabia: American Association of Petroleum Geologists Bulletin, v. 66, p. 1–9.

Ayuso, R. A., and C. E. Brown, 1984, Manganese-rich red tourmaline from the Fowler talc belt, New York: Canadian Mineralogist, v. 22, p. 327–331.

Azam, S., 2007, Study on the geological and engineering aspects of anhydrite/gypsum transition in the Arabian Gulf coastal deposits: Bulletin of Engineering Geology and the Environment, v. 66, p. 177–185.

Azer, M., R. Stern, and J.-I. Kimura, 2010, Origin of a late Neoproterozoic (605 ± 13 Ma) intrusive carbonate-albitite complex in Southern Sinai, Egypt: International Journal of Earth Sciences, v. 99, p. 245–267.

Azer, S. R., and R. G. Peebles, 1998, Sequence stratigraphy of the Arab A to C members and Hith Formation, offshore Abu Dhabi: GeoArabia, v. 3, p. 251–268.

Aziz, H. A., E. Sanz-Rubio, J. P. Jose P. Calvo, F. J. Hilgen, and W. Krijgsman, 2003, Palaeoenvironmental reconstruction of a middle Miocene alluvial fan to cyclic shallow lacustrine depositional system in the Calatayud Basin (NE Spain): Sedimentology, v. 50, p. 211–236.

Baadsgaard, H., 1987, Rb-Sr and K-Ca isotope systematics in minerals from potassium horizons in the Prairie Evaporite Formation, Saskatchewan, Canada: Chemical Geology, v. 66, p. 1–15.

Baar, C. A., 1974, Geological problems in Saskatchewan potash mining due to peculiar conditions during deposition of Potash Beds, in A. H. Coogan, ed., Fourth Symposium on Salt, v. 1: Cleveland, North Ohio Geological Society, p. 101–118.

Babel, M., 1990, Crystallography and genesis of the giant intergrowths of gypsum from the middle Miocene evaporites of southern Poland: Archiwum Mineralogizne, v. 44, p. 103–35.

Babel, M., 1991, Dissolution of halite within the middle Miocene (Badenian) laminated gypsum of southern Poland: Acta Geologica Polonica, v. 41, p. 165–182.

Babel, M., 2007, Depositional environments of a salina-type evaporite basin recorded in the Badenian gypsum facies in the northern Carpathian Foredeep: Geological Society, London, Special Publications, v. 285, p. 107–142.

Babieri, M., and U. Masi, 1984, Sr geochemical evidence on the origin of celestite-barite deposits at Pian dell'Organo in the Tolfa Mountains area (Latium, central Italy): Mineralogy and Petrology, v. 28, p. 33–37.

Bach, J., I. Fitz, N. Gueschow, V. Rentjes, H. J. Kretzchmar, and M. Krafki, 1985, Recovery of carnallite by isothermal solution mining, German (East) patent DD221235A1,VEB Kombinat Kali,, p. 8.

Bache, F., S.-M. Popescu, M. Rabineau, C. Gorini, J.-P. Suc, Clauzon, J.-L. Olivet, J.-L. Rubino, M. C. Melinte-Dobrinescu, F. Estrada, L. Londeix, R. Armijo, B. Meyer, L. Jolivet, G. Jouannic, E. Leroux, D. Aslanian, A. T. D. Reis, L. Mocochain, N. Dumurdžanov, I. Zagorchev, V. Lesi, D. Tomi, M. Namik Ça atay, J.-P. Brun, D. Sokoutis, I. Csato, G. Ucarkus, and Z. Çakir, 2012, A two-step process for the reflooding of the Mediterranean after the Messinian Salinity Crisis: Basin Research, v. 24, p. 125–153.

Bachman, G., and R. B. Johnson, 1973, Stability of Salt in the Permian Salt Basin of Kansas, Oklahoma, Texas and New Mexico: U. S. Geol. Surv. Open-File Rept.. v. 4339–4.

Bachman, G. O., 1981, Geology of Nash Draw, Eddy County, New Mexico.: U. S. Geol. Surv. Open-File Rept. 81–3.

Bachman, G. O., 1984, Regional geology of Ochoan evaporites, northern part of Delaware Basin: New Mexico Bureau of Mines and Mineral Resources, Circular, v. 184, p. 22.

Bachman, G. O., 1990, Evaporite karst in the Pecos River Drainage, southeastern New Mexico. In: Geological and Hydrogeological Studies of Evaporites in the Northern Delaware Basin for the Waste Isolation Pilot Plant (WIPP), New Mexico, Geological Society of America Annual Meeting, November Geological Society of America Annual Meeting, November 1–4, 1990, Field Trip #14, Guidebook, p. 181–186.

Bacik, P., P. Uher, J. Cempirek, and T. Vaculovic, 2012, Magnesian tourmalines from plagioclase-muscovite-scapolite metaevaporite layers in dolomite marble near Prosetin (Olesnice Unit, Moravicum, Czech Republic): Journal of Geosciences, v. 57, p. 143–153.

Bacik, P., P. Uher, M. Sykora, and J. Lipka, 2008, Low-Al tourmalines of the schorl-dravite-povondraite series in redeposited tourmalines from the Western Carpathians, Slovakia: Canadian Mineralogist, v. 46, p. 1117–1129.

Backé, G., G. Baines, D. Giles, W. Preiss, and A. Alesci, 2010, Basin geometry and salt diapirs in the Flinders Ranges, South Australia: Insights gained from geologically-constrained modelling of potential field data: Marine and Petroleum Geology, v. 27, p. 650–665.

Backer, H., and K. Lange, 1987, Recent hydrothermal metal accumulation, products and conditions of formation, in P. G. Telecki, M. R. Dobson, J. R. Moore, and U. von Stackelberg, eds., Marine Minerals: Dordrecht, Reidel, p. 317–337.

Badaut, D., and F. Risacher, 1983, Authigenic smectite on diatom frustules in Bolivian saline lakes: Geochemica et Cosmochimica Acta, v. 47, p. 363–375.

Badoux, V., R. Moritz, and L. Fontboté, 2001, The Mississippi Valley-type Zn-Pb deposit of San Vicente, central Peru: An Andean syntectonic deposit.: In Mineral Deposits at the Beginning of the 21st Century, Proceedings of the 6th Biennial SGA Meeting, Krakow, Poland, p. 26–29.

Bahroudi, A., and H. A. Koyi, 2003, Effect of spatial distribution of Hormuz salt on deformation style in the Zagros fold and thrust belt: An analogue modelling approach: Journal of the Geological Society, v. 160, p. 719–733.

Bai, G., and Y. Xu, 2014, Giant fields retain dominance in reserves growth: Oil & Gas Journal, v. 112, p. 44h.

Bailey, R. K., 1949, Talc in the salines of the potash field near Carlsbad, Eddy County, New Mexico: American Mineralogist., v. 34, p. 9–10.

Bain, R. J., 1990, Diagenetic, nonevaporative origin for gypsum: Geology, v. 18, p. 447–450.

Baker, B. H., 1958, Geology of the Magadi Area: Geological Survey of Kenya Report, v. 42, p. 81 p.

Baker, D. M., R. J. Lillie, R. S. Yeats, G. D. Johnson, M. Yousuf, and A. S. H. Zamin, 1988, Development of the Himalayan frontal thrust zone: Salt Range, Pakistan: Geology, v. 16, p. 3–7.

Baker, P. A., and S. H. Bloomer, 1988, The origin of celestite in deep water carbonate sediments: Geochim. Cosmochim. Acta, v. 52, p. 335–339.

Baker, P. A., and M. Kastner, 1981, Constraints on the formation of sedimentary dolomite.: Science, v. 213, p. 214–216.

Baker, P. A., C. A. Rigsby, G. O. Seltzer, S. C. Fritz, T. K. Lowenstein, N. P. Bacher, and C. Veliz, 2001, Tropical climate changes at

millennial and orbital timescales on the Bolivian Altiplano: Nature, v. 409, p. 698–701.
Baker, T., 1998, Alteration, mineralization, and fluid evolution at the Eloise Cu-Au deposit, Cloncurry District, Northwest Queensland, Australia: Economic Geology, v. 93, p. 1213–1236.
Baker, T., C. Perkins, K. L. Blake, and P. J. Williams, 2001, Radiogenic and Stable Isotope Constraints on the Genesis of the Eloise Cu-Au Deposit, Cloncurry District, Northwest Queensland: Economic Geology, v. 96, p. 723–742.
Bakr, M. M. Y., and H. Wilkes, 2002, The influence of facies and depositional environment on the occurrence and distribution of carbazoles and benzocarbazoles in crude oils: a case study from the Gulf of Suez, Egypt: Organic Geochemistry, v. 33, p. 561–580.
Balch, D. P., A. S. Cohen, D. W. Schnurrenberger, B. J. Haskell, B. Valero-Garces, J. W. Beck, H. Cheng, and R. L. Edwards, 2005, Ecosystem and paleohydrological response to Quaternary climate change in the Bonneville Basin, Utah: Palaeogeography, Palaeoclimatology, Palaeoecology, v. 221, p. 99–122.
Baldschuhn, R., F. Binot, U. Frisch, and F. Kockel, 2001, Atlas von Nordwest-Deutschland un dem deutschen Nordsee-Sektor (Tectonic atlas of Northwest Germany and the German North Sea sector): Geologisches Jahrbuch, v A153:3 CD-ROM, 88 p.
Balk, R., 1953, Salt Structure of Jefferson Island Salt Dome, Iberia and Vermilion Parishes, Louisiana: Bulletin American Association Petroleum Geologists, v. 37, p. 2455–2474.
Balkwill, H. R., 1978, Evolution of Sverdrup Basin, Arctic Canada: Bulletin American Association Petroleum Geologists, v. 62, p. 1004–1028.
Ballot, A., 2004, Cyanobacteria in Kenyan Rift Valley lakes: A biological and toxicological study: Doctoral thesis, Fachbereich Biologie, Chemie, Pharmazie der Freien Universität Berlin.
Banat, K. M., F. M. Howari, and M. B. Abdullah, 2006, Mineralogy and hydrochemical characteristics of the late marshes and swamps of Hor Al Hammar, Southern Iraq: Journal of Arid Environments, v. 65, p. 400–419.
Banerjee, D. M., H. Strauss, S. K. Bhattacharya, V. Kumar, and A. Mazumdar, 1998, Isotopic composition of carbonate and sulphates, potash mineralisation and basin architecture of the Nagaur-Ganganagar evaporite basin (north-western India) and their implications on the Neoproterozoic exogenic cycle: Mineralogical Magazine (India), v. 62a, p. 106–107.
Banham, S. G., and N. P. Mountney, 2014, Climatic versus halokinetic control on sedimentation in a dryland fluvial succession: Sedimentology, v. 61, p. 570–608.
Banin, A., 2002, Mars soil formation and properties: The 'Acid Fog' hypothesis in view of recent evidence (abstract): Second Astrobiology Science Conference; NASA AMES Research Center – April 7–11, 200.
Banks, D. A., G. Giuliani, B. W. D. Yardley, and A. Cheilletz, 2000, Emerald mineralisation in Colombia: fluid chemistry and the role of brine mixing: Mineralium Deposita, v. 35, p. 699–713.
Barbé, A., J. O. Grimalt, and J. Albaigés, 1988, Novel cyclohexyl isoprenoid hydrocarbons in carbonate-evaporite crude oils: Naturwissenschaften, v. 75, p. 624–625.
Barbé, A., J. O. Grimalt, J. J. Pueyo, and J. Albaiges, 1990, Characterization of model evaporitic environments through the study of lipid components: Organic Geochemistry, v. 16, p. 815–828.
Barbeau, D. L., 1999, A Flexural Model for the Paradox Basin: Bulletin American Association Petroleum Geologists, v. 83, p. 1881–1882.
Barbieri, R., and N. Stivaletta, 2011, Continental evaporites and the search for evidence of life on Mars: Geological Journal, v. 46, p. 513–524.
Barbieri, R., N. Stivaletta, L. Marinangeli, and G. G. Ori, 2006, Microbial signatures in sabkha evaporite deposits of Chott el Gharsa (Tunisia) and their astrobiological implications: Planetary and Space Science, v. 54, p. 726–736.
Baria, L. R., D. I. Stoudt, P. M. Harris, and P. D. Crevello, 1982, Upper Jurassic reefs of Smackover Formation, United States GulfCoast: American Association Petroleum Geologists Bulletin, v. 66, p. 1449–1482.
Barkan, E., B. Luz, and B. Lazar, 2001, Dynamics of the carbon dioxide system in the Dead Sea: Geochimica et Cosmochimica Acta, v. 65, p. 1.
Barker, J. M., D. E. Cochran, and R. Semrad, 1979, Economic geology of the Mishraq native sulfur deposit, northern Iraq: Economic Geology, v. 74, p. 484–495.
Barker, R. A., P. W. Bush, and E. T. Baker, 1994, Geologic history and hydrogeologic setting of the Edwards-Trinity aquifer system, West-Central Texas: US Geological Survey Water-Resources Investigation Report 94–4039, 51 p.
Barley, M. E., J. S. R. Dunlop, J. E. Glover, and D. I. Groves, 1979, Sedimentary evidence for an Archaean shallow-water volcanic-sedimentary facies, eastern Pilbara Block, Western Australia: Earth and Planetary Science Letters, v. 43, p. 74–84.
Barnard, R. M., and R. B. Kistler, 1966, Stratigraphic and Structural Evolution of the Kramer Sodium Borate Body, Boron, California: Second Symposium on Salt, Northern Ohio Geological Society, Cleveland, OH, v. 1, p. 133–150.
Barnes, F. S., and J. G. Levine, 2011, "Natural Gas Storage." Large Energy Storage Systems CRC Publishing, 213 p.
Barnes, J. W., J. Bow, J. Schwartz, R. H. Brown, J. M. Soderblom, A. G. Hayes, G. Vixie, S. Le Mouélic, S. Rodriguez, C. Sotin, R. Jaumann, K. Stephan, L. A. Soderblom, R. N. Clark, B. J. Buratti, K. H. Baines, and P. D. Nicholson, 2011, Organic sedimentary deposits in Titan-dry lakebeds: Probable evaporite: Icarus, v. 216, p. 136–140.
Barovich, K., and M. Hand, 2008, Tectonic setting and provenance of the Paleoproterozoic Willyama Supergroup, Curnamona Province, Australia: Geochemical and Nd isotopic constraints on contrasting source terrain components: Precambrian Research, v. 166, p. 318–337.
Barrat, J. A., J. Boulegue, J. J. Tiercelin, and M. Lesourd, 2000, Strontium isotopes and rare-earth element geochemistry of hydrothermal carbonate deposits from Lake Tanganyika, East Africa: Geochimica et Cosmochimica Acta, v. 64, p. 287–298.
Barrett, M. L., 1986, Replacement geometry and fabrics of the Smackover (Jurassic) Dolomite, southern Alabama: GulfCoast Association of Geological Societies Transactions, v. 36, p. 9–18.
Barrett, T. J., and G. M. Anderson, 1988, The solubility of sphalerite and galena in 1–5 m NaCl solutions to 300°C: Geochimica et Cosmochimica Acta, v. 52, p. 813–820.
Barth, H. J., and B. Böer, 2002, Sabkha Ecosystems: Volume 1: The Arabian Peninsula: Berlin, Springer, 368 p.
Barton, D. C., 1933, Mechanics of formation of salt domes with special reference to Gulf Coast salt domes of Texas and Louisiana: American Association Petroleum Geologists Bulletin, v. 17, p. 1025–1083.
Barton Jr, J. M., 1996, The Messina layered intrusion, Limpopo Belt, South Africa: an example of in-situ contamination of an Archean anorthosite complex by continental crust: Precambrian Research, v. 78, p. 139–150.
Barton Jr, J. M., R. Klem, C. L. Byron, and M. Beattie, 1990, Albitization and the gold-bearing Roodepoort pluton, Pietersburg granite-greenstone terrane, South Africa: South African Journal of Geology, v. 93, p. 776–784.
Barton, M. D., R. P. Ilchik, and M. A. Marikos, 1991, Metasomatism, in D. M. Kerrick, ed., Contact Metamorphism, Mineralogical Society of America, Reviews in Mineralogy, 26, p. 321–350.
Barton, M. D., and D. A. Johnson, 1996, Evaporitic-source model for igneous-related Fe-oxide—(REE-Cu-Au-Au) mineralisation: Geology, v. 24, p. 259–262.
Barton, M. D., and D. A. Johnson, 2002, Alternative Brine Sources for Fe-Oxide (-Cu-Au) Systems: Implications for Hydrothermal

Alteration and Metals, in T. M. Porter, ed., Hydrothermal Iron Oxide Copper-Gold and Related Deposits: A Global Perspective, v. 1, PGC Publishing, Adelaide, p. 27–41.

Barton, M. D., and D. A. Johnson, 2004, Footprints of Fe-oxide(-Cu-Au) systems: Centre for Global Metallogeny, Spec. Pub. 33, The University of Western Australia, p. 112–116.

Bartov, Y., M. Stein, Y. Enzel, A. Agnon, and Z. Reches, 2002, Lake Levels and Sequence Stratigraphy of Lake Lisan, the Late Pleistocene Precursor of the Dead Sea: Quaternary Research, v. 57, p. 9–21.

Baskina, V. A., 2008, Sources of boron from the Dal'negorsk borosilicate deposit: Doklady Earth Sciences, v. 423, p. 1308–1311.

Bass-Becking, L. G. M., 1928, On organisms living in concentrated brines: Tijdsch. Ned. Dierk. Ver., v. Series 3, p. 6–9.

Bassot, J. P., 1997, Albitisation of the Paleoproterozic of eastern Senegal: Relation to iron ore along the left bank of Faleme (French): Journal of African Earth Sciences, v. 25, p. 353–367.

Bates, R. L., 1969, Potash Minerals: Geology of the industrial rocks and minerals: New York, Dover Publ., 370–385 and 439–440 p.

Bathurst, R. G. C., 1980, Deep crustal diagenesis in limestones: Revista Instituto Investaciones Geologicas, University of Barcelona, v. 34, p. 89–100.

Battles, D. A., and M. D. Barton, 1995, Arc-related sodic hydrothermal alteration in the western United States: Geology, v. 23, p. 913–916.

Baud, A., and J. L. Haglund, 1996, Enhanced subsalt exploration utilzing the basal salt shear model: Transactions of Gulf Coast Association of Geological Societies, v. XLVI, p. 9–14.

Baudrand, M., V. Grossi, R. Pancost, and G. Aloisi, 2010, Non-isoprenoid macrocyclic glycerol diethers associated with authigenic carbonates: Organic Geochemistry, v. 41, p. 1341–1344.

Bauer, S., 1999, Analysis of subsidence data for the Bryan Mound site, Texas: Sandia Report, SAND99-1739, Sandia National Laboratories.

Bauer, S. J., B. L. Ehgartner, and J. T. Dale, 2000, Geotechnical studies associated with decommissioning the Strategic Petroleum Reserve facility at Weeks Island, Louisiana: a case history: Proc. Solution Mining Research Institute (S.M.R.I.) Fall Meeting Technical Session, San Antonio, p. 146–156.

Bäuerle, G., O. Bornemann, F. Mauthe, and D. Michalzik, 2000, Origin of stylolites in Upper Permian Zechstein Anhydrite (Gorleben Salt Dome, Germany): Journal of Sedimentary Research, v. 70, p. 726–737.

Baumgardner, R. W., A. D. Hoadley, and A. G. Goldstein, 1982, The Wink Sink; a case history of evaporite dissolution and catastrophic subsidence: Formation of the Wink Sink, a salt dissolution and collapse feature, Winkler County, Texas: . v. Bureau of Economic Geology, The University of Texas at Austin, Report of Investigations No. 114, 38p.

Baumgartner, L. K., R. P. Reid, C. Dupraz, A. W. Decho, D. H. Buckley, J. R. Spear, K. M. Przekop, and P. T. Visscher, 2006, Sulfate reducing bacteria in microbial mats: Changing paradigms, new discoveries: Sedimentary Geology, v. 185, p. 131–145.

Baur, F., R. Littke, H. Wielens, C. Lampe, and T. Fuchs, 2010, Basin modeling meets rift analysis – A numerical modeling study from the Jeanne d'Arc basin, offshore Newfoundland, Canada: Marine and Petroleum Geology, v. 27, p. 585–599.

Bäurle, G., O. Bornemann, F. Mauthe, and D. Michalzik, 2000, Origin of stylolites in Upper Permian Zechstein Anhydrite (Gorleben Salt Dome, Germany): Journal of Sedimentary Research, v. 70, p. 726–737.

Bayari, C. S., E. Pekkan, and N. N. Ozyurt, 2009, Obruks, as giant collapse dolines caused by hypogenic karstification in central Anatolia, Turkey: Analysis of likely formation processes: Hydrogeology Journal, v. 17, p. 327–345.

Bayly, I. A. E., and W. E. Williams, 1973, Inland waters and their ecology: Hawthorn, Vic., Longman Australia.

Bazargani-Guilani, K., and M. A. N. Tak, 2008, Celestite Ore Deposit and Occurrences of the Qom Formation, Oligo-Miocene, Central Iran: 2nd IASME / WSEAS International Conference on GEOLOGY and SEISMOLOGY (GES '08), Cambridge, UK, February 23–25, 2008.

Beach, D. K., and J. W. Giffin, 1992, Stanley Field, USA Williston Basin, North Dakota, in N. H. Foster, and E. A. Beaumont, eds., Treatise of Petroleum Geology; Atlas of Oil and Gas Fields: Stratigraphic Traps III: Tulsa, OK, American Association Petroleum Geologists, p. 389–420.

Beadle, L. C., 1974, Inland waters of tropical Africa: London, Longman, 365 p.

Beales, F. W., and S. A. Jackson, 1966, Precipitation of lead-zinc ores in carbonate reservoirs as illustrated by Pine Point ore field, Canada: Trans. – Inst. Min. Metall., Sect. B, v. 75, p. 278–285.

Beales, F. W., and A. E. Oldershaw, 1969, Evaporite-solution brecciation and Devonian carbonate reservoir porosity in western Canada: Am. Assoc. Petroleum Geologists Bull, v. 53, p. 503–512.

Beauheim, R. L., and R. M. Roberts, 2002, Hydrology and hydraulic properties of a bedded evaporite formation: Journal of Hydrology, v. 259, p. 66–88.

Becher, J. W., and C. H. Moore, 1976, The Walker Creek Field – A Smackover diagenetic trap: Transactions of Gulf Coast Association of Geological Societies, v. 26, p. 34–56.

Bechtel, A., A. Gratzer, W. Puttmann, and S. Oszczepalski, 2002, Geochemical characteristics across the oxic/anoxic interface (Rote Fäule front) within the Kupferschiefer of the Lubin-Sieroszowice mining district (SW Poland): Chemical Geology, v. 185, p. 9–31.

Bechtel, A., and S. Hoernes, 1993, Stable isotopic variations of clay minerals: a key to the understanding of Kupferschiefer-type mineralization, Germany: Geochimica et Cosmochimica Acta, v. 57, p. 1799–1816.

Bechtel, A., M. Pervaz, and W. Puttmann, 1998, Role of organic matter and sulphate-reducing bacteria for metal sulphide precipitation in the Bahloul Formation at the Bou Grine Zn/Pb deposit (Tunisia): Chemical Geology, v. 144, p. 1–21.

Bechtel, A., and W. Puttmann, 1997, Palaeoceanography of the early Zechstein Sea during Kupferschiefer deposition in the Lower Rhone Basin (Germany) – A reappraisal from stable isotope and organic geochemical investigations: Palaeogeography Palaeoclimatology Palaeoecology, v. 136, p. 331–358.

Bechtel, A., W. Puttmann, and S. Hoernes, 1995, Reconstruction of the thermal history of the Kupferschiefer within the Zechstein Basin of Central Europe: a stable isotope and organic geochemical approach: Ore Geology Reviews, v. 9, p. 371–389.

Bechtel, A., S. M. Savin, and S. Hoernes, 1999, Oxygen and hydrogen isotopic composition of clay minerals of the Bahloul Formation in the region of the Bou Grine zinc-lead ore deposit (Tunisia): evidence for fluid-rock interaction in the vicinity of salt dome cap rock: Chemical Geology, v. 156, p. 191–207.

Bechtel, A., Y. N. Shieh, M. Pervaz, and W. Puttmann, 1996, Biodegradation of hydrocarbons and biogeochemical sulfur cycling in the salt dome environment – inferences from sulfur isotope and organic geochemical investigations of the Bahloul Formation at the Bou Grine Zn/Pb ore deposit, Tunisia: Geochimica et Cosmochimica Acta, v. 60, p. 2833–2855.

Becker, F., and T. Bechstadt, 2006, Sequence stratigraphy of a carbonate-evaporite succession (Zechstein 1, Hessian Basin, Germany): Sedimentology, v. 53, p. 1083–1120.

Beckman, J., 1999, Study reveals overpressure sources in deep-lying formations: Oil and Gas Journal, v. September, p. 137.

Beeby, D. J., 2002, Borate deposits in California: past, present and future, in P. W. Scott, and C. M. Bristow, eds., Industrial minerals and Extractive Industry Geology, v. Geological Society of London Miscellaneous Titles, p. 87–92.

Begin, Z. B., W. Broecker, B. Buchbinder, Y. Druckman, A. Kaufman, M. Magaritz, and D. Neev, 1985, Dead Sea and Lake Lisan levels in the past 30,000 years: Geological Survey of Israel, Preliminary report, v. GSE29.8, p. 18 p.

Begin, Z. B., A. Ehrlich, and Y. Nathan, 1974, Lake Lisan, the Pleistocene precursor of the Dead Sea: Bulletin Geological Survey Israel, v. 63, p. 30.

Beglinger, S. E., H. Doust, and S. Cloetingh, 2012, Relating petroleum system and play development to basin evolution: West African South Atlantic basins: Marine and Petroleum Geology, v. 30, p. 1–25.

Behr, H.-J., and C. Röhricht, 2000, Record of seismotectonic events in siliceous cyanobacterial sediments (Magadi cherts), Lake Magadi, Kenya: International Journal of Earth Sciences, v. 89, p. 268–283.

Behr, H. J., H. Ahrendt, H. Martin, H. Porada, J. Rohrs, and K. Weber, 1983, Sedimentology and mineralogy of Upper Proterozoic playa-lake deposits in the Damara orogen, in H. Martin, and F. W. Eder, eds., Intracontinental Fold Belts: Berlin, Springer-Verlag, p. 577–610.

Behr, H. J., and E. E. Horn, 1982, Fluid inclusion systems in metaplaya deposits and their relationships to mineralization and tectonics: Chemical Geology, v. 37, p. 173–189.

Bein, A., and A. R. Dutton, 1993, Origin, distribution, and movement of brine in the Permian Basin (USA) – A model for displacement of connate brine: Geological Society of America Bulletin, v. 105, p. 695–707.

Bein, A., S. D. Hovorka, R. S. Fisher, and E. Roedder, 1991, Fluid inclusions in bedded Permian halite, Palo Duro Basin, Texas; evidence for modification of seawater in evaporite brine-pools and subsequent early diagenesis: Journal of Sedimentary Petrology, v. 61, p. 1–14.

Bein, A., and L. S. Land, 1982, San Andres carbonates in the Texas Panhandle: sedimentation and diagenesis associated with magnesium- calcium-chloride brines: Bureau of Economic Geology, University of Texas, Report of Investigation, v. 121, p. 48 pp.

Bein, A., and L. S. Land, 1983, Carbonate sedimentation and diagenesis associated with Mg-Ca-Chloride brines: The Permian San Andres Formation in the Texas Panhandle: Journal of Sedimentary Petrology, v. 53, p. 243–260.

Bejaoui, J., S. Bouhlel, E. Cardellach, Á. Canals, J. Perona, and Á. Piqué, 2013, Mineralization and fluid inclusion studies of the Aptian carbonate-hosted PbZnBa ore deposits at Jebel Hamra, Central Tunisia: Journal of Geochemical Exploration, v. 128, p. 136–146.

Bekker, A., and H. D. Holland, 2012, Oxygen overshoot and recovery during the early Paleoproterozoic: Earth and Planetary Science Letters, v. 317-318, p. 295–304.

Bell, C. M., 1989, Saline lake carbonates within an Upper Jurassic-Lower Cretaceous continental red bed sequence in the Atacama region of northern Chile: Sedimentology, p. 4.

Bell, C. M., 1997, Saline lake turbidites in the La Coipa area, Northern Chile: Revista Geologica de Chile, v. 24, p. 259–267.

Bell, C. M., and M. Suarez, 1993, The depositional environments and tectonic development of a Mesozoic intra-arc basin, Atacama region, Chile: Geological Magazine, p. 417–430.

Bell, K., and J. B. Dawson, 1995, An assessment of the alleged role of evaporites and saline brines in the origin of natrocarbonatite, in K. Bell, and J. Keller, eds., Carbonatite volcanism: Oldoinyo Lengai and the petrogenesis of natrocarbonatites: Berlin, Springer-Verlag, p. 137–147.

Bellah, A. M., and H. Hassouba, 1995, Quaternary sediments from the coastal plain of northwestern Egypt (from Alexandria to el Omayid): Carbonates & Evaporites, v. 10, p. 8–44.

Bellanca, A., J. P. Calvo, P. Censi, R. Neri, and M. Pozo, 1992, Recognition of lake-level changes in Miocene lacustrine units, Madrid Basin, Spain. Evidence from facies analysis, isotope geochemistry and clay mineralogy: Sedimentary Geology, v. 76, p. 135–153.

Bellanca, A., and R. Neri, 1986, Evaporite carbonate cycles of the Messinian, Sicily; stable isotopes, mineralogy, textural features, and environmental implications: Journal of Sedimentary Petrology, v. 56, p. 614–621.

Belloni, S., B. Martins, and G. Orombelli, 1972, Karst of Italy, in M. Herak, and V. T. Springfield, eds., Karst: Important karst regions of the Northern Hemisphere: Amsterdam, Elsevier, p. 85–128.

Belous, I. R., S. I. Kirikilitsa, M. L. Levenshteyn, E. K. Rodina, and V. N. Florinskaya, 1984, Occurrences of mercury in northeastern Donbass salt dome: Internat. Geol. Rev., v. 26, p. 573–582.

Belperio, A. P., and D. G. Fotheringham, 1990, Geological setting of two Quaternary footprint sites, western South Australia: Australian Journal of Earth Sciences, v. 37, p. 37–42.

Ben Baccar, M., B. Fritz, and B. Made, 1993, Diagenetic albitization of K-feldspar and plagioclase in sandstone reservoirs; thermodynamic and kinetic modeling: Journal of Sedimentary Research, v. 63, p. 1100–1109.

Ben-Avraham, Z., T. Niemi, C. Heim, J. Negendank, and A. Nur, 1999, Holocene stratigraphy of the Dead Sea: Correlation of high-resolution seismic reflection profiles to sediment cores: Journal of Geophysical Research-Solid Earth, v. 104, p. 17617–17625.

Ben-Avraham, Z., T. M. Niemi, D. Neev, J. K. Hall, and Y. Levy, 1993, Distribution of Holocene sediments and neotectonics in the deep north basin of the Dead Sea: Marine Geology, v. 113, p. 219–231.

Benali, S., B. C. Schreiber, M. L. Helman, and R. P. Philp, 1995, Characterisation of organic matter from a restricted/ evaporative sedimentary environment – Late Miocene of Lorca Basin, south-eastern Spain: American Association of Petroleum Geologists – Bulletin, v. 79, p. 816–830.

Benan, C. A. A., and G. Kocurek, 2000, Catastrophic flooding of an aeolian dune field: Jurassic Entrada and Todilto Formations, Ghost Ranch, New Mexico, USA: Sedimentology, v. 47, p. 1069–1080.

Benison, K. C., 2006, A Martian analog in Kansas: Comparing Martian strata with Permian acid saline lake deposits: Geology, v. 34, p. 385–388.

Benison, K. C., and B. B. Bowen, 2013, Extreme sulfur-cycling in acid brine lake environments of Western Australia: Chemical Geology, v. 351, p. 154–167.

Benison, K. C., and R. H. Goldstein, 1999, Permian paleoclimate data from fluid inclusions in halite: Chemical Geology, v. 154, p. 113–132.

Benison, K. C., and R. H. Goldstein, 2000, Sedimentology of ancient saline pans: An example from the Permian Opeche Shale, Williston Basin, North Dakota, USA: Journal of Sedimentary Research Section A-Sedimentary Petrology & Processes, v. 70, p. 159–169.

Benison, K. C., and R. H. Goldstein, 2001, Evaporites and siliciclastics of the Permian Nippewalla Group of Kansas, USA: a case for non-marine deposition in saline lakes and saline pans: Sedimentology, v. 48, p. 165–188.

Benison, K. C., and R. H. Goldstein, 2002, Recognizing acid lakes and groundwaters in the rock record: Sedimentary Geology, v. 151, p. 177–185.

Benito, G., F. Gutierrez, A. Perez-Gonzalez, and M. Machado, 2000, Geomorphological and sedimentological features in Quaternary fluvial systems affected by solution-induced subsidence (Ebro Basin, NE-Spain): Geomorphology, v. 33, p. 209–224.

Benito, G., A. Perezgonzalez, F. Gutierrez, and M. J. Machado, 1998, River response to Quaternary subsidence due to evaporite solution (Gallego River, Ebro Basin, Spain): Geomorphology, v. 22, p. 243–263.

Bennett, S. S., and J. S. Hanor, 1987, Dynamics of subsurface salt dissolution at the Welsh Dome, Louisiana Gulf Coast, in I. Lerch, and J. J. O'Brien, eds., Dynamical geology of salt and related structures: New York, Academic Press Inc, p. 653–677.

Benson, J., L. M. Pultz, and D. D. Bruner, 1996, Paleotopographic Vs Eustatic Controls on Deposition of the Smackover Formation,

Appleton Field, Escambia County, Alabama (Abs.): American Association Petroleum Geologists – Bulletin, v. 80, p. 1495.
Benson, L., B. Linsley, J. Smoot, S. Mensing, S. Lund, S. Stine, and A. Sarna-Wojcickig, 2003, Influence of Pacific Decadal Oscillation on the climate of Sierra Nevada, California and Nevada: Quaternary Research, v. 59, p. 151–159.
Benson, R. H., K. Rakic-El Bied, and L. W. McKenna, 1997, Eustatic implications of late Miocene depositional sequences in the Melilla Basin, northeastern Morocco: Sedimentary Geology, v. 107, p. 147–165.
Bentz, L. M., 1992, Pecos Slope Field – USA, Permian Basin, New Mexico, in N. H. Foster, and E. A. Beaumont, eds., Treatise of Petroleum Geology; Atlas of Oil and Gas Fields: Stratigraphic Traps III: Tulsa, OK, American Association Petroleum Geologists, p. 129–153.
Berastegui, X., C. J. Banks, C. Puig, C. Taberner, D. Waltham, and M. Fernandez, 1998, Lateral diapiric emplacement of Triassic evaporites at the southern margin of the Guadalquivir Basin, Spain: Geological Society, London, Special Publications, v. 134, p. 49–68.
Bérest, P., J. Bergues, and B. Brouard, 1999, Static and dynamic compressibility of deep underground caverns: Int. J. Rock Mech. & Mining Sci., v. 36, p. 1031–1049.
Bérest, P., and B. Brouard, 2001, Storage of tritiated water in salt caverns: In Proc. KIWIR 6th International Workshop on Key Issues in Waste Isolation Research, ENPC, P. Delage ed., Presses de l'Ecole Nationale des Ponts et Chaussées, Paris, p. 497–511.
Bérest, P., and B. Brouard, 2002, Safety of salt caverns used for underground storage: Proc. 8th Portuguese Congress for Geotechnique, 15–18 April 2002, Lisbon, Portugal.
Bérest, P., and B. Brouard, 2003, Safety of salt caverns used for underground storage: Oil and Gas Science and Technology – Rev. IFP, v. 58, p. 361–384.
Bérest, P., B. Brouard, and G. Hévin, 2011, Twelve-year monitoring of the idle Etrez salt cavern: International Journal of Rock Mechanics and Mining Sciences, v. 48, p. 168–173.
Berger, A., 1992, Orbital variations and insolation database: IGBP PAGES (International Geosphere-Biosphere Programme Past Global Changes)/World Data Center for Paleoclimatology Data Contribution Series 92-007:: Boulder, Colorado, National Oceanic and Atmospheric Administration/ National Geophysical Data Center, World Data Center for Paleoclimatology Data, http://gcmd.nasa.gov/records/GCMD_EARTH_LAND_NGDC_PALEOCLIM_INSOL.html.
Berger, V. I., D. A. Singer, and G. J. Orris, 2009, Carbonatites of the World, Explored Deposits of Nb and REE—Database and Grade and Tonnage Models, US Geological Survey Open-File Report 2009–1139, 17 p.
Bergquist, D. C., T. Ward, E. E. Cordes, T. McNelis, S. Howlett, R. Kosoff, S. Hourdez, R. Carney, and C. R. Fisher, 2003, Community structure of vestimentiferan-generated habitat islands from Gulf of Mexico cold seeps: Journal of Experimental Marine Biology and Ecology, v. 289, p. 197–222.
Bergquist, D. C., F. M. Williams, and C. R. Fisher, 2000, Longevity record for deep-sea invertebrate: Nature, v. 403, p. 499–500.
Berner, R. A., 1980, Early Diagenesis – A theoretical approach: Princeton NJ, Princeton University Press, 241 p.
Berner, R. A., 1999, A new look at the long-term carbon cycle: GSA Today, v. 9, p. 1–6.
Berry, P. F., and P. E. Playford, 2002, Biology of modern *Fragum erugatum* (Mollusca, Bivalvia, Cardiidae) in relation to deposition of the Hamelin Coquina, Shark Bay, Western Australia: Marine and Freshwater Research, v. 48, p. 415–420.
Berry, R. F., R. B. Flint, and A. E. Grady, 1978, Deformation history of the Outalpa area and its application to the Olary Province, South Australia: Transactions Royal Society of South Australia, Adelaide, South Aust., Australia, v. 102, p. 43–53.
Bertoni, C., J. Cartwright, and C. Hermanrud, 2013, Evidence for large-scale methane venting due to rapid drawdown of sea level during the Messinian Salinity Crisis: Geology, v. 41, p. 371–374.
Betancourt, J. L., C. Latorre, J. A. Rech, J. Quade, and K. A. Rylander, 2000, A 22,000-Year Record of Monsoonal Precipitation from Northern Chile's Atacama Desert: Science, v. 289, p. 1542–1546.
Bethke, C., and S. Marshak, 1990, Brine migration across North America: the plate tectonics of groundwater hydrology: Ann. Rev. Earth Planet. Science, v. 18, p. 287–315.
Betts, P. G., D. Giles, and G. S. Lister, 2004, Aeromagnetic patterns of half-graben and basin inversion: implications for sediment-hosted massive sulfide Pb-Zn-Ag exploration: Journal of Structural Geology, v. 26, p. 1137–1156.
Betts, P. G., and G. S. Lister, 2002, Geodynamically indicated targeting strategy for shale-hosted massive sulfide Pb-Zn-Ag mineralisation in the Western Fold Belt, Mt Isa terrane: Australian Journal of Earth Sciences, v. 49, p. 985–1010.
Beydoun, Z. R., 1993, Evolution of the northeastern Arabian plate margin and shelf – Hydrocarbon habitat and conceptual future potential: Revue de l' Institut Francais du Petrole, v. 48, p. 311–345.
Beydoun, Z. R., 1998, Arabian Plate oil and gas: why so rich and prolific?: Episodes, v. 21, p. 74–81.
Beydoun, Z. R., M. W. Hughes Clark, and R. Stoneley, 1992, Petroleum in the Zagros Basin: A Late Tertiary foreland basin overprinted onto the outer edge of a vast hydrocarbon-rich Palaeozoic-Mesozoic passive-margin shelf, in R. W. Macqueen, and D. A. Leckie, eds., Foleland basins and fold belts: Tulsa. OK, American Association of Petroleum Geologists Memoir 55, p. 309–339.
Biddle, P. G., 1983, Patterns of drying and moisture deficit in the vicinity of trees on clay soils: Geotechnique, v. 33, p. 107–126.
Bierlein, F. P., 1995, Rare-earth element geochemistry of elastic and chemical metasedimentary rocks associated with hydrothermal sulphide mineralisation in the Olary Block, South Australia: Chemical Geology, v. 122, p. 77–98.
Bierlein, F. P., P. M. Ashley, and P. K. Seccombe, 1996, Origin of hydrothermal Cu-Zn-Pb mineralisation in the Olary Block, South Australia: evidence from fluid inclusions and sulphur isotopes: Precambrian Research, v. 79, p. 281–305.
Bierlein, F. P., and A. R. Wilde, 2010, New constraints on the polychronous nature of the giant Muruntau gold deposit from wall-rock alteration and ore paragenetic studies: Australian Journal of Earth Sciences: An International Geoscience Journal of the Geological Society of Australia, v. 57, p. 839–854.
Bigham, J. M., and D. K. Nordstrom, 2000, Ion and aluminum hydroxysulfates from acid surface waters, in C. N. Alpers, J. L. Jambor, and D. K. Nordstrom, eds., Sulfate Minerals: Crystallography, Geochemistry, and Environmental Significance, Mineralogical Society of America, Reviews in Mineralogy and Geochemistry, No. 40, p. 351–403.
Bildstein, K. L., C. B. Golden, B. J. McCraith, and B. W. Bohmke, 1993, Feeding Behavior, Aggression, and the Conservation Biology of Flamingos: Integrating Studies of Captive and Free-ranging Birds: American Zoologist, v. 33, p. 117–125.
Billo, S. M., 1986, Petrology and kinetics of gypsum-anhydrite transitions: Journal of Petroleum Geology, v. 10, p. 73–86.
Billo, S. M., 1996, Geology of marine evaporites favorable for oil, gas exploration: Oil & Gas Journal, v. 94, p. 69–73.
Bills, B. G., S. L. de Silva, D. R. Currey, R. S. Emenger, K. D. Lillquist, and B. Don, 1994, Hydro-isostatic deflection and tectonic tilting in the central Andes: initial results of a GPS survey of Lake Minchin shorelines: Geophysical Research Letters, v. 21.
Bingham, C. P., 1980, Solar production of potash from brines of the Bonneville Salt Flats, in J. W. Gwynn, ed., Great Salt Lake; a scientific, history and economic overview. , v. 116, Bulletin Utah Geological and Mineral Survey, p. 229–242.
Binns, R. A., J. McAndrew, and S. Sun, 1980, Origin of uranium mineralisation in Jabiluka, in J. Ferguson, and A. Goleby, eds., Uranium

in the Pine Creek Geosyncline: Vienna, International Atomic Energy Agency, p. 543–562.
Birnbaum, S. J., and J. W. Wireman, 1985, Sulfate-reducing bacteria and silica solubility; a possible mechanism for evaporite diagenesis and silica precipitation in banded iron formations: Canadian Journal of Earth Sciences, v. 22, p. 1904–1909.
Birsoy, R., and Ü. Özbaz, 2012, Activity diagrams of borates: implications on common deposits: Carbonates and Evaporites, v. 27, p. 71–85.
Bischoff, J. L., J. P. Fitts, and K. M. Menking, 1993, Sediment pore waters of Owens Lake Drill Hole OL-92, in I. S. Smith, and J. L. Bischoff, eds., Core OL-92 from Owens Lake, southeast California, U.S. Geological Survey Open-File Report 93–683 (available online at http://pubs.usgs.gov/of/of93-683/report.html).
Bischoff, J. L., R. Julia, W. E. C. I. Shanks, and R. J. Rosenbauer, 1994, Karstification without carbonic acid; bedrock dissolution by gypsum-driven dedolomitization: Geology, v. 22, p. 995–998.
Bischoff, J. L., S. Stine, R. J. Rosenbauer, J. A. Fitzpatrick, and T. W. Stafford Jr, 1993, Ikaite precipitation by mixing of shoreline springs and lake water, Mono Lake, California, USA: Geochimica et Cosmochimica Acta, v. 57, p. 3855–3865.
Bissell, H. J., and G. V. Chilingar, 1962, Evaporite type dolomite in salt flats of western Utah: Sedimentology, p. 200–210.
Bitzer, K., A. Travé, J. M. Carmona, and F. Calvert, 1998, Fluid flow in foreland basins during emplacement of thrust sheets: modelling the south-Pyrenean Ainsa basin: Bull. Soc. Geol. France, v. 169, p. 627–634.
Bjørlykke, K., and K. Gran, 1994, Salinity variations in North Sea formation waters; implications for large scale fluid movements: Marine & Petroleum Geology, v. 11, p. 5–9.
Black, M., 1933, The Algal Sediments of Andros Island, Bahamas: Philosophical Transactions of the Royal Society of London. Series B, Containing Papers of a Biological Character, v. 222, p. 165–192.
Black, T. J., 1997, Evaporite karst of northern lower Michigan: Carbonates & Evaporites, p. 81–83.
Black, T. J., 2012, Deep karst system research, Michigan, USA: Carbonates and Evaporites, v. 27, p. 119–122.
Blake, D. H., and A. J. Stewart, 1992, Stratigraphic and Tectonic Framework, Mount Isa Inlier: Australian Geological Survey Organization Bulletin, v. 243, p. 1–11.
Blanc, G., and P. Anschutz, 1995, New stratification in the hydrothermal brine system of the Atlantis II Deep, Red Sea: Geology, v. 23, p. 543–546.
Blanc-Valleron, M.-M., and M. Schuler, 1997, The Salt Basins of Alsace (Southern Rhine Graben), in G. Busson, and B. C. Schreiber, eds., Sedimentary Deposition in Rift and Foreland Basins in France and Spain (Paleogene and Lower Neogene): New York, Columbia University Press, p. 95–135.
Blanc-Valleron, M. M., 1991, Les formations paléogènes évaporitiques du bassin potassique de Mulhouse et des bassins plus septentrion aux d'Alsace (Document BRGM, 204), Université Louis Pasteur, Paris, 350 p.
Blanc-Valleron, M. M., C. Pierre, P. Caulet, A. Caruso, J. M. Rouchy, R. Cespuglio, M. Sprovieri, S. Pestrea, and E. Di Stefano, 2002, Sedimentary, stable isotope and micropaleontological records of paleoceanographic change in the Messinian Tripoli Formation (Sicily, Italy): Palaeogeography, Palaeoclimatology, Palaeoecology, v. 185, p. 255–286.
Blättler, C. L., and J. A. Higgins, 2014, Calcium isotopes in evaporites record variations in Phanerozoic seawater SO_4 and Ca: Geology, v. 42, p. 711–714.
Blenkinsop, T. G., C. R. Huddlestone-Holmes, D. R. W. Foster, M. A. Edmiston, P. Lepong, G. Mark, J. R. Austin, F. Murphy, A. Ford, and M. J. Rubenach, 2008, The crustal scale architecture of the Eastern Succession, Mount Isa: The influence of inversion: Precambrian Research, v. 163, p. 31–49.
Blount, C. W., and F. W. Dickson, 1969, The solubility of anhydrite ($CaSO_4$) in NaCl-H_2O from 100 to 450° C and 1 to 1000 bars: Geochimica et Cosmochimica Acta, v. 33, p. 227–245.
Blum, M., G. Kocurek, M. Deynoux, C. Swezey, N. Lancaster, D. M. Price, and J. C. Pion, 1998, Quaternary wadi lacustrine aeolian depositional cycles and sequences, Chott Rharsa basin, Southern Tunisia, in A. S. Alsharan, K. W. Glennie, G. L. Whittle, and G. C. S. C. Kendall, eds., Quaternary Deserts and Climate Change: Rotterdam, A. A. Balkema, p. 539–552.
Blum, N., and H. Puchelt, 1991, Sedimentary-hosted polymetallic massive sulphide deposits of the Kebrit and Shaban Deeps, Red Sea.: Mineralium Deposita, v. 26, p. 217–227.
Bobst, A. L., T. K. Lowenstein, T. E. Jordan, L. V. Godfrey, T. L. Ku, and S. D. Luo, 2001, A 106 ka paleoclimate record from drill core of the Salar de Atacama, northern Chile: Palaeogeography Palaeoclimatology Palaeoecology, v. 173, p. 21–42.
Bodine Jr, M. W., 1983, Trioctahedral clay mineral assemblages in Paleozoic marine evaporite rocks: Sixth international symposium on salt, v. 1, p. 267–284.
Bogoch, R., B. Buchbinder, and M. Magaritz, 1994, Sedimentology and geochemistry of lowstand peritidal lithofacies at the Cenomanian-Turonian boundary in the Cretaceous carbonate platform of Israel: Journal of Sedimentary Research Section A-Sedimentary Petrology & Processes, v. 64, p. 733–740.
Bohacs, K. M., A. R. Carroll, and J. E. Neal, 2003, Lessons from large lake systems 2; Thresholds, nonlinearity, and strange attractors, in M. A. Chan, and A. W. Archer, eds., Extreme Depositional Environments: Mega End Members in Geologic Time: Geological Society of America, Special Paper 370, p. 75–90.
Bohacs, K. M., A. R. Carroll, J. E. Neal, and P. J. Mankiewicz, 2000, Lake-basin type, source potential, and hydrocarbon character: An integrated sequence-stratigraphic – geochemical framework, in E. H. Gierlowski-Kodesch, and K. Kelts, eds., Lake basins through space and time, v. 46: Tulsa, American Association Petroleum Geologists Studies in Geology, p. 3–34.
Böhlke, J. K., G. E. Ericksen, and K. Revesz, 1997, Stable isotope evidence for an atmospheric origin of desert nitrate deposits in northern Chile and southern California, U.S.A: Chemical Geology, v. 136, p. 135–152.
Boiron, M.-C., M. Cathelineau, and A. Richard, 2010, Fluid flows and metal deposition near basement /cover unconformity: lessons and analogies from Pb-Zn-F-Ba systems for the understanding of Proterozoic U deposits: Geofluids, v. 10, p. 270–292.
Boles, J. R., 1982, Active albitization of plagioclase, Gulf Coast Tertiary: American Journal of Science, v. 282, p. 165–180.
Bonatti, E., D. E. Fisher, O. Joensuu, H. S. Rydell, and M. Beyth, 1972, Iron-manganese-barium deposit from the north Afar rift (Ethiopia): Economic Geology, v. 67, p. 717–730.
Bonch-Osmolovskaya, E. A., M. L. Miroshnichenko, A. V. Lebedinsky, N. A. Chernyh, T. N. Nazina, V. S. Ivoilov, S. S. Belyaev, E. S. Boulygina, Y. P. Lysov, A. N. Perov, A. D. Mirzabekov, H. Hippe, E. Stackebrandt, S. L'Haridon, and C. Jeanthon, 2003, Radioisotopic, Culture-Based, and Oligonucleotide Microchip Analyses of Thermophilic Microbial Communities in a Continental High-Temperature Petroleum Reservoir: Applied and Environmental Microbiology, v. 69, p. 6143–6151.
Bone, Y., 1983, Interpretation of magnesites at Rum Jungle, N. T. using fluid inclusions: Journal of the Geological Society of Australia, v. 30, p. 375–381.
Bone, Y., 1988, The geological setting of tourmalinite at Rum Jungle, N.T., Australia — genetic and economic implications: Mineralium Deposita, v. 23, p. 34–41.
Bonhomme, M., J. C. Baubron, and M. Jebrak, 1987, Minéralogie, géochimie, terres rares et age K-Ar des argiles associés aux minéralisations filoniennes: Chemical Geology, v. 65, p. 321–339.
Bonhomme, M. G., R. P. Dossantos, and C. Renac, 1995, K/Ar ating of clay minerals – The present state of the art (French): Bulletin des

Centres de Recherches Exploration-Production Elf Aquitaine., v. 19, p. 197–223.

Bonny, S. M., and B. Jones, 2008, Experimental Precipitation of Barite ($BaSO_4$) Among Streamers of Sulfur-Oxidizing Bacteria: Journal of Sedimentary Research, v. 78, p. 357–365.

Bontognali, T. R. R., C. Vasconcelos, R. J. Warthmann, S. M. Bemasconi, C. Dupraz, C. J. Strohmenger, and J. A. McKenzie, 2010, Dolomite formation within microbial mats in the coastal sabkha of Abu Dhabi (United Arab Emirates): Sedimentology, v. 57, p. 824–844.

Bontognali, T. R. R., C. Vasconcelos, R. J. Warthmann, R. Lundberg, and J. A. McKenzie, 2012, Dolomite-mediating bacterium isolated from the sabkha of Abu Dhabi (UAE): Terra Nova, p. no-no.

Bonython, C. W., 1966, Factors determining the rate of solar evaporation in the production of salt, Second Symposium on Salt, North Ohio Geol. Soc,, p. 152–167.

Bookman, R., Y. Enzel, A. Agnon, and M. Stein, 2004, Late Holocene lake levels of the Dead Sea: Geological Society of America Bulletin, v. 116, p. 555–571.

Booth, J., and N. Sattayarak, 2000, Multiple inversion of the Khorat Plateau Basin, NE Thailand, with the formation and preservation of a productive gas play (abs): 2000 American Association Petroleum Geologists International Conference and Exhibition, October 15–18, Bah, Indonesia.

Booth, J., and N. Sattayarak, 2011, Carboniferous-Cretaceous Geology of NE Thailand, in M. F. Ridd, A. J. Barber, and M. J. Crow, eds., The Geology of Thailand, The Geological Society, London, p. 185–222.

Borchert, H., 1977, On the formation of Lower Cretaceous potassium salts and tachyhydrite in the Sergipe Basin (Brazil) with some remarks on similar occurrences in West Africa (Gabon, Angola etc.), in D. D. Klemm, and H. J. Schneider, eds., Time and strata-bound ore deposits.: Berlin, Germany, Springer-Verlag, p. 94–111.

Borchert, H., and R. O. Muir, 1964, Salt deposits--The origin, metamorphism and deformation of evaporites: London, D. Van Nostrand Co., Ltd., 338 p.

Borchert, R., D. Fischer, R. Johnson, and L. C. Gerhard, 1990, Glenburn Field – USA, Williston Basin, North Dakota, in E. A. Beaumont, and N. H. Foster, eds., Treatise of Petroleum Geology; Atlas of Oil and Gas Fields: Stratigraphic Traps I: Tulsa, OK, American Association Petroleum Geologists, p. 91–106.

Borer, J. M., and P. M. Harris, 1991, Lithofacies and cyclicity of the Yates Formation, Permina Basin: Implications for reservoir heterogeneity: American Association Petroleum Geologists Bulletin, v. 75, p. 726–779.

Borin, S., L. Brusetti, F. Mapelli, G. D'Auria, T. Brusa, M. Marzorati, A. Rizzi, M. Yakimov, D. Marty, G. J. De Lange, P. Van der Wielen, H. Bolhuis, T. J. McGenity, P. N. Polymenakou, E. Malinverno, L. Giuliano, C. Corselli, and D. Daffonchio, 2009, Sulfur cycling and methanogenesis primarily drive microbial colonization of the highly sulfidic Urania deep hypersaline basin: Proceedings of the National Academy of Sciences, v. 106, p. 9151–9156.

Bornemann, O., R. Fischbeck, and G. Baüerle, 2000, Investigation of deformation textures of salt rock from various Zechstein units and their relationship to the formation of salt diapirs in NW Germany, in R. M. Geertman, ed., 8th World Salt Symposium: Amsterdam, Elsevier, p. 89–94.

Bosak, P., J. I. Bruthans, M. Fillippi, T. Svoboda, and J. Smid, 1999, Karst and salt caves in salt diapirs, SE Zagros Mountains (Iran): Acta Carsologica, v. 28, p. 41–75.

Boschetti, T., G. Cortecci, M. Barbieri, and M. Mussi, 2007, New and past geochemical data on fresh to brine waters of the Salar de Atacama and Andean Altiplano, northern Chile: Geofluids, v. 7, p. 33–50.

Bose, P. K., P. G. Eriksson, S. Sarkar, D. T. Wright, P. Samanta, S. Mukhopadhyay, S. Mandal, S. Banerjee, and W. Altermann, 2012, Sedimentation patterns during the Precambrian: A unique record?: Marine and Petroleum Geology, v. 33, p. 34–68.

Bosence, D., 2012, Carbonate-dominated marine rifts, in D. G. Roberts, and A. W. Bally, eds., Phanerozoic Rift systems and Sedimentary Basins, Elsevier, p. 105–130.

Bosworth, W., 2006, North Africa-Mediterranean present day stress field transition and implications for fractured reservoir production in the eastern Libyan basins: Proceedings of the Sedimentary Basins of Libya Third Symposium—Geology of East Libya, 17 p.

Bosworth, W., P. Huchon, and K. McClay, 2005, The Red Sea and Gulf of Aden Basins: Journal of African Earth Sciences, v. 43, p. 334–378.

Bots, P., L. G. Benning, R. E. M. Rickaby, and S. Shaw, 2011, The role of SO_4 in the switch from calcite to aragonite seas: Geology, v. 39, p. 331–334.

Bottinga, Y., 1969, Calculated fractionation factors for carbon and hydrogen isotope exchange in the system calcite-carbon dioxide-graphite-methane-hydrogen-water vapor: Geochimica et Cosmochimica Act, v. 33, p. 49–64.

Bottomley, D. J., D. C. Gregoire, and K. G. Raven, 1994, Saline groundwaters and brines in the Canadian Shield; geochemical and isotopic evidence for a residual evaporite brine component: Geochimica et Cosmochimica Acta, v. 58, p. 1483–1498.

Bottomley, D. J., A. Katz, L. H. Chan, A. Starinsky, M. Douglas, I. D. Clark, and K. G. Raven, 1999, The origin and evolution of Canadian Shield brines: evaporation or freezing of seawater? New lithium isotope and geochemical evidence from the Slave craton: Chemical Geology, v. 155, p. 295–320.

Bottomley, D. J., R. Renaud, Z. T. Kotzer, and I. D. Clark, 2002, Iodine-129 constraints on residence times of deep marine brines in the Canadian Shield: Geology, v. 30, p. 587–590.

Bottomley, N., 1996, Recent climate in Abu Dhabi, in P. E. Osborne, ed., Desert ecology of Abu Dhabi: Newbury, UK, Pisces Publications, p. 236.

Bottrell, S. H., S. Crowley, and C. Self, 2001, Invasion of a karst aquifer by hydrothermal fluids: evidence from stable isotopic compositions of cave mineralization: Geofluids, v. 1, p. 103–121.

Botz, R., M. Schmidt, H. Wehner, H. Hufnagel, and P. Stoffers, 2007, Organic-rich sediments in brine-filled Shaban- and Kebrit deeps, northern Red Sea: Chemical Geology, v. 244, p. 520–553.

Boucot, A. J., and J. Gray, 2001, A critique of Phanerozoic climatic models involving changes in the CO_2 content of the atmosphere: Earth-Science Reviews, v. 56, p. 1–159.

Bouladon, J., 1984, Syngenesis and epigenesis at the Largentiere (Ardeche, France) Pb- Zn-Ag deposit, in A. Wauschkuh, ed., Syngenesis and Epigenesis in the Formation of Mineral Deposits, Springer-Verlag, p. 422–430.

Boulter, C. A., and J. E. Glover, 1986, Chert with relict hopper moulds from Rocklea Dome, Pilbara Craton, Western Australia; an Archean halite-bearing evaporite: Geology, v. 14, p. 128–131.

Bouougri, E., G. Gerdes, and H. Porada, 2007, Inherent problems of terminology: definition of terms frequently used in connection with microbial mats, in J. Schieber, P. K. Bose, P. G. Eriksson, S. Banerjee, S. Sarkar, W. Altermann, and C. O, eds., Atlas of Microbial Mat Features Preserved within the Siliciclastic Rock Record: Amsterdam, Elsevier, p. 145–151.

Bouraoui, S., Z. Cakir, R. Bougdal, and M. Meghraoui, 2012, MT-InSAR monitoring of ground deformation around the Haoud Berkaoui sinkhole (SE Algeria): Geophysical Research Abstracts, EGU General Assembly 2012, held 22–27 April, 2012 in Vienna, Austria, v. 14, EGU2012-3344.

Bourrouilh, L.-J. F., J. L. Carsin, P. M. Niasussat, and Y. Thommeret, 1985, Sédimentation phosphatée actuelle dans le lagon confiné de I'lle de Clipperton (Océan Pacifique). Datations, sédimentologie et géochimie: Sciences géologiques, Mémoire, Strasbourg,, v. 77, p. 109–124.

Boutaiba, S., H. Hacene, K. A. Bidle, and J. A. Maupin-Furlow, 2011, Microbial diversity of the hypersaline Sidi Ameur and Himalatt Salt

Lakes of the Algerian Sahara: Journal of Arid Environments, v. 75, p. 909–916.
Bowen, B. B., and K. C. Benison, 2009, Geochemical characteristics of naturally acid and alkaline saline lakes in southern Western Australia: Applied Geochemistry, v. 24, p. 268–284.
Bowler, J. M., 1973, Clay dunes: their occurrence, formation and environmental significance: Earth-Science Reviews, v. 9, p. 315–338.
Bowler, J. M., 1983, Lunettes as indices of hydrologic change; a review of Australian evidence: Proceedings of the Royal Society of Victoria, v. 95, p. 147–168.
Bowler, J. M., 1986, Spatial variability and hydrologic evolution of Australian lake basins; analogue for Pleistocene hydrologic change and evaporite formation: Palaeogeography, Palaeoclimatology, Palaeoecology, v. 54, p. 21–41.
Bowlin, E. M., J. S. Klaus, J. S. Foster, M. S. Andres, L. Custals, and R. P. Reid, 2012, Environmental controls on microbial community cycling in modern marine stromatolites: Sedimentary Geology, v. 263-264, p. 45–55.
Bowman, J. P., S. A. McCammon, S. M. Rea, and T. A. Mc-Meekin, 2000, The microbial composition of three limnologically disparate hypersaline Antarctic lakes: FEMS Microbiology Letters, v. 183, p. 81–88.
Bowring, S. A., D. H. Erwin, Y. G. Jin, M. W. Martin, K. Davidek, and W. Wang, 1998, U/Pb zircon geochronology and tempo of the end-Permian mass extinction: Science, v. 280, p. 1039–1045.
Bowser, C. J., and F. W. Dickson, 1966, Chemical zonation of the borates at Kramer, California: Second Symposium on Salt, Northern Ohio Geological Society, Cleveland, OH, v. 1, p. 122–132.
Bowser, C. J., T. A. Rafter, and R. F. Black, 1970, Geochemical evidence for the origin of mirabilite deposits near Hobbs Glacier, Victoria Land, Antarctica: Mineralogical Society America Special Paper, v. 3, p. 261–272.
Boyer, B. W., 1982, Green River laminites: Does the playa-lake model really invalidate the stratified lake model?: Geology, v. 10, p. 321–324.
Boyle, R. W., 1962, Geology and Geochemistry of the Magnet Cove Barium-Lead-Zinc-Silver Deposit, Walton, Nova Scotia: Canadian Mining Journal, v. 83, p. 104–110.
Boyle, R. W., R. K. Wanless, and R. D. Stevens, 1976, Sulfur isotope investigation of the barite, manganese, and lead-zinc-copper-silver deposits of the Walton-Cheverie area, Nova Scotia, Canada: Economic Geology, v. 71, p. 749–762.
Boys, C., 1990, The geology of potash deposits at PCS Cory Mine, Saskatchewan: Master's thesis, University of Saskatchewan; Saskatoon, SK; Canada.
Boys, C., 1993, A geological approach to potash mining problems in Saskatchewan, Canada: Exploration & Mining Geology, v. 2, p. 129–138.
Bozeman, J., and S. Bozeman, 2002, Speleology of gypsum caves in Oklahoma: Carbonates and Evaporites, v. 17, p. 107–113.
Bozkurt, U., 1989, A fluid inclusion study of selected boreholes, Salton Sea geothermal system, Imperial Valley, California: Master's thesis, University of California, Riverside; Riverside, CA; United States.
Bradley, D., L. Munk, H. Jochens, S. Hynek, and K. Labay, 2013, A Preliminary Deposit Model for Lithium Brines: USGS Open-File Report 2013–1006.
Bradley, D. C., 2011, Secular trends in the geologic record and the supercontinent cycle: Earth-Science Reviews, v. 108, p. 16–33.
Bradley, W. H., and H. P. Eugster, 1969, Geochemistry and paleolimnology of the trona deposits and associated authigenic minerals of the Green River Formation of Wyoming: U. S. Geological Survey Professional Paper, v. 469B, p. 71p.
Bradshaw, J., 1988, The depositional, diagenetic and structural history of the Chandler Formation and related units, Amadeus Basin, central Australia: PhD thesis, University of New South Wales (Australia).
Bradshaw, J., 1991, Description and depositional model of the Chandler Formation; a Lower Cambrian evaporite and carbonate sequence, Amadeus Basin, central Australia: Bulletin – Australia, Bureau of Mineral Resources, Geology and Geophysics, v. 236, p. 227–244.
Brady, H. T., and B. Batts, 1981, Large salt beds on the surface of the Ross ice shelf near Black Island, Antarctica: Journal of Glaciology, v. 27, p. 11–18.
Braga, J. C., J. M. Martîn, and R. Riding, 1995, Controls on microbial dome fabric development along a carbonate-siliciclastic shelf-basin transect, Miocene, SE Spain: Palaios, v. 10, p. 347–361.
Braithwaite, C. J. R., and V. Zedef, 1994, Living hydromagnesite stromatolites from Turkey: Sedimentary Geology, v. 92, p. 1–5.
Braithwaite, C. J. R., and V. Zedef, 1996, Hydromagnesite stromatolites and sediments in an alkaline lake, Salda Golu, Turkey: Journal of Sedimentary Research A: Sedimentary Petrology and Processes, v. 66, p. 991–1002.
Braitsch, O., 1964, The temperature of evaporite formation, in A. E. M. Nairn, ed., Problems in palaeoclimatology: New York, Wiley, p. 479–490.
Braitsch, O., 1971, Salt Deposits: Their Origin and Compositions: New York, Springer-Verlag, 297 p.
Brandes, C., C. Schmidt, D. Tanner, and J. Winsemann, 2013, Paleostress pattern and salt tectonics within a developing foreland basin (north-western Subhercynian Basin, northern Germany): International Journal of Earth Sciences, v. 102, p. 2239–2254.
Brandt, K. K., and K. Ingvorsen, 1997, Desulfobacter halotolerans sp nov, a halotolerant acetate- oxidizing sulfate-reducing bacterium isolated from sediments of Great Salt Lake, Utah: Systematic and Applied Microbiology, v. 20, p. 366–373.
Branquet, Y., B. Laumonier, A. Cheilletz, and G. Giuliani, 1999, Emeralds in the Eastern Cordillera of Colombia: Two tectonic settings for on mineralization: Geology, v. 27, p. 597–600.
Brasier, A. T., 2011, Searching for travertines, calcretes and speleothems in deep time: Processes, appearances, predictions and the impact of plants: Earth-Science Reviews, v. 104, p. 213–239.
Brasier, A. T., A. E. Fallick, A. R. Prave, V. A. Melezhik, and A. Lepland, 2011, Coastal sabkha dolomites and calcitised sulphates preserving the Lomagundi-Jatuli carbon isotope signal: Precambrian Research, v. 189, p. 193–211.
Bray, R. B., and J. S. Hanor, 1990, Spatial variations in the subsurface pore fluid properties in a portion of southern Louisiana: implications for regional fluid flow and solute transport: Trans. Gulf Coast Assoc. Geol. Soc., v. 40, p. 53–64.
Breck, D. W., 1974, Zeolite Molecular Sieves: New York, Wiley-Interscience, 771 p.
Bregant, D., G. Catalano, G. Civitarese, and A. Luchetta, 1990, Some chemical characteristics of the brines in Bannock and Tyro Basins: salinity, sulphur compounds, Ca, F, pH, At, PO_4, SiO_2, NH_3: Marine Chemistry, v. 31, p. 35–62.
Breit, G. N., M. B. Goldhaber, D. R. Shawe, and E. C. Simmons, 1990, Authigenic barite as an indicator of fluid movement through sandstones within the Colorado Plateau: Journal of Sedimentary Petrology, v. 60, p. 884–896.
Breitbart, M., A. Hoare, A. Nitti, J. Siefert, M. Haynes, E. Dinsdale, R. Edwards, V. Souza, F. Rohwer, and D. Hollander, 2009, Metagenomic and stable isotopic analyses of modern freshwater microbialites in Cuatro Ciénegas, Mexico: Environmental Microbiology, v. 11, p. 16–34.
Brenchley, P. J., J. D. Marshall, G. A. F. Carden, D. B. R. Robertson, D. G. F. Long, T. Meidla, L. Hints, and T. F. Anderson, 1994, Bathymetric and isotopic evidence for a short-lived Late Ordovician glaciation in a greenhouse period: Geology, v. 22, p. 295–298.
Brennan, S. T., and T. K. Lowenstein, 2002, The major-ion composition of Silurian seawater: Geochimica et Cosmochimica Acta, v. 66, p. 2683–2700.

Brennan, S. T., T. K. Lowenstein, and J. Horita, 2004, Seawater chemistry and the advent of biocalcification: Geology, v. 32, p. 473–476.

Brett, R., 1992, The Cretaceous-Tertiary extinction; a lethal mechanism involving anhydrite target rocks: Geochimica et Cosmochimica Acta, v. 56, p. 3603–3606.

Bretz, J. H., 1952, A solution cave in gypsum: Journal of Geology, v. 6-, p. 279–283.

Briand, F. e., 2008, The Messinian Salinity Crisis from mega-deposits to microbiology – A Consensus report: CIESM Workshop Monographs v. 33, 168 p.

Bridges, J. C., and M. M. Grady, 1999, A halite-siderite-anhydrite-chlarapatite assemblage in Nakhla: Mineralogical evidence for evaporites on Mars: Meteoritics, v. 34, p. 407–415.

Bridges, J. C., and M. M. Grady, 2000, Evaporite mineral assemblages in the nakhlite (martian) meteorites: Earth & Planetary Science Letters, v. 176, p. 267–279.

Briere, P. R., 2000, Playa, playa lake, sabkha: Proposed definitions for old terms: Journal of Arid Environments, v. 45, p. 1–7.

Briggs, L. I., 1958, Evaporite facies: Journal of Sedimentary Petrology, v. 28, p. 46–56.

Briggs, L. I., D. Gill, D. Z. Briggs, and R. D. Elmore, 1980, Transition from open marine to evaporite deposition in the Silurian Michigan Basin, in A. Nissenbaum, ed., Hypersaline brines and evaporitic environments: Developments in Sedimentology, v. 28: Amsterdam, Elsevier, p. 253–270.

Briggs, M., 2007, Boron Oxides, Boric acid and Borates, Kirk-Othmer Encyclopedia of Chemical Technology, v. 4, John Wiley & Sons, Inc., p. 241–294.

Broadbent, G.C., S. J. Andrews, and I. J. Kelso, 2002, A decade of new ideas: Geology and exploration history of the Century Zn-Pb-Ag deposit, northwestern Queensland, Australia: Society of Economic Geologists Special Publication Series – Australasian Institute of Mining and Metallurgy, v. 9, p. 119–140.

Broadbent, G. C., R. E. Myers, and J. V. Wright, 1998, Geology and origin of shale-hosted Zn-Pb-Ag mineralization at the Century Deposit, Northwest Queensland, Australia: Economic Geology, v. 93, p. 1264–1294.

Brock, M. A., 1982a, Biology of the Salinity Tolerant Genus Ruppia L in Saline Lakes in South-Australia .1. Morphological Variation within and between Species and Ecophysiology: Aquatic Botany, v. 13, p. 219–248.

Brock, M. A., 1982b, Biology of the Salinity Tolerant Genus Ruppia L in Saline Lakes in South-Australia .2. Population Ecology and Reproductive- Biology: Aquatic Botany, v. 13, p. 249–268.

Brockamp, O., M. Zuther, and N. Clauer, 1994, K-Ar dating of episodic Mesozoic fluid migrations along the fault system of Gernsbach between the Moldanubian and Saxothuringian (Northern Black Forest, Germany): Geologische Rundschau, v. 83, p. 180–185.

Brocks, J. J., G. D. Love, R. E. Summons, A. H. Knoll, G. A. Logan, and S. A. Bowden, 2005, Biomarker evidence for green and purple sulphur bacteria in a stratified Palaeoproterozoic sea: Nature, v. 437, p. 866–870.

Brocks, J. J., and P. Schaeffer, 2008, Okenane, a biomarker for purple sulfur bacteria (Chromatiaceae), and other new carotenoid derivatives from the 1640†Ma Barney Creek Formation: Geochimica et Cosmochimica Acta, v. 72, p. 1396–1414.

Brocks, J. J., and R. E. Summons, 2003, Chapter 8.03: Sedimentary hydrocarbons, biomarkers for early life, in W. Schlesinger, ed., Treatise in Geochemistry, v. 8: Amsterdam, Elsevier, p. 53.

Brodylo, L. A., and R. J. Spencer, 1987, Depositional environment of the Middle Devonian Telegraph Salts, Alberta, Canada: Bulletin Canadian Petroleum Geology, v. 35, p. 186–196.

Brongersma-Sanders, M., 1972, Hydrological conditions leading to the development of bituminous sediments in the pre-evaporite phase [with discussion]: in Geology of saline deposits; Geologie des depots salins. Unesco Earth Sci. Ser. No.

Brookfield, M. E., 2003, The enigma of fine-grained alluvial basin fills: the Permo-Triassic (Cumbrian Coastal and Sherwood Sandstone Groups) of the Solway Basin, NW England and SW Scotland: Int J Earth Sci (Geol Rundsch), v. 93, p. 282–296.

Brookfield, M. E., 2008, Palaeoenvironments and palaeotectonics of the arid to hyperarid intracontinental latest Permian- late Triassic Solway basin (U.K.): Sedimentary Geology, v. 210, p. 27–47.

Broughton, P. L., 2013, Devonian salt dissolution-collapse breccias flooring the Cretaceous Athabasca oil sands deposit and development of lower McMurray Formation sinkholes, northern Alberta Basin, Western Canada: Sedimentary Geology, v. 283, p. 57–82.

Brown, A. A., and R. G. Loucks, 2001, Evaluation of Anhydrite Seals through Depositional, Structural, and Lithological Analysis; Example from the Jurassic Arab Formation, Al Rayyan Field, Qatar (abs.): American Association Petroleum Geologists – Bulletin, v. 85(13).

Brown, A. C., 1997, World-class sediment-hosted stratiform copper deposits – Characteristics, genetic concepts and metal-lotects: Australian Journal of Earth Sciences, v. 44, p. 317–328.

Brown, A. C., 2005, Iron transport in redbeds during the genesis of sediment-hosted stratiform copper deposits, in J. Mao, and F. P. Bierlein, eds., Mineral Deposit Research: Meeting the Global Challenge: Berlin, Springer, p. 83–86.

Brown, A. C., 2006, Close linkage of copper (and uranium) transport to diagenetic reddening of "upstream" basin sediments for sediment-hosted stratiform copper (and roll-type uranium) mineralization: Journal of Geochemical Exploration, v. 89, p. 23–26.

Brown, M. C, C. W. Claxton, and K. A. Plumb, 1978, The Proterozoic Barney Creek Formation and some associated units of the McArthur Group, Northern Territory, Australia: Bureau of Mineral Resources, Canberra, Record, v. 1969/145, p. 59.

Brown, C. E., and R. A. Ayuso, 1985, Significance of tourmaline-rich rocks in the Grenville Complex of St. Lawrence County, New York (USA). US Geological Survey Bulletin, v. 1626-C, 33 pp.

Brun, J.-P., and X. Fort, 2004, Compressional salt tectonics (Angolan margin): Tectonophysics, v. 382, p. 129–150.

Brun, J.-P., and X. Fort, 2011, Salt tectonics at passive margins: Geology versus models: Marine and Petroleum Geology, v. 28, p. 1123–1145.

Bruno, R. S., and J. S. Hanor, 2003, Large-scale fluid migration driven by salt dissolution, Bay Marchand Dome, offshore Louisiana: Gulf Coast Association of Geological Societies Transaction, v. 53, p. 97–107.

Bruthans, J., M. Filippi, N. Asadi, M. Zare, S. Slechta, and Z. Churckov, 2009, Surficial deposits on salt diapirs (Zagros Mountains and Persian Gulf Platform, Iran): Characterization, evolution, erosion and the influence on landscape morphology: Geomorphology, v. 107, p. 195–209.

Bruthans, J., M. Filippi, J. Smíd, and L. Palatinus, 2002, Trí Naháca (Three Nudes) and Ghar-e Daneshyu caves – The world's second and fifth longest salt caves: The International Caver 2002, Swindon, U.K., p. 27–36.

Bruthans, J., M. Filippi, M. Zare, Z. Churackova, N. Asadi, M. Fuchs, and J. Adamovic, 2010, Evolution of salt diapir and karst morphology during the last glacial cycle: Effects of sea-level oscillation, diapir and regional uplift, and erosion (Persian Gulf, Iran): Geomorphology, v. 121, p. 291–304.

Bruthans, J., J. Smid, M. Filippi, and O. Zeman, 2000, Thickness of cap rock and other important factors affecting the morphogenesis of salt karst: Acta Carsologica, v. 29, p. 51–64.

Bruthans, J., and O. Zeman, 2003, Factors controlling exokarst morphology and sediment transport through caves: Comparison of carbonate and salt karst: Acta Carsologica, v. 32, p. 83–99.

Bryant, R. G., 1999, Application of AVHRR to monitoring a climatically sensitive playa. Case study: Chott el Djerid, southern Tunisia.: Earth Surface Processes & Landforms, v. 24, p. 283–302.

Bryant, R. G., N. A. Drake, A. C. Millington, and B. W. Sellwood, 1994a, The chemical evolution of the brines on Chott el Djerid, southern Tunisia after an exceptional rainfall event in January 1990, in R. W. Renaut, and W. M. Last, eds., Sedimentology and geochemistry of modern and ancient saline lakes, v. 50: Tulsa, Okl, SEPM/Society for Sedimentary Geology; Special Publication, p. 3–12.

Bryant, R. G., B. W. Sellwood, A. C. Millington, and N. A. Drake, 1994b, Marine-like potash evaporite formation on a continental playa; case study from Chott el Djerid, southern Tunisia: Sedimentary Geology, v. 90, p. 269–291.

Buchardt, B., C. Israelson, P. Seaman, and G. Stockmann, 2001, Ikaite tufa towers in Ikka Fjord, southwest Greenland: Their formation by mixing of seawater and alkaline spring water: Journal of Sedimentary Research Section A-Sedimentary Petrology & Processes, v. 71A, p. 176–189.

Buchbinder, B., 1996, Miocene carbonates of the eastern Mediterranean, the Red Sea and the Mesopotamian Basin: geodynamic and eustatic controls, in E. K. e. a. Franseen, ed., Models for carbonate stratigraphy from Miocene reef complexes of Mediterranean regions, SEPM/Society for Sedimentary Geology; Concepts in Sedimentology and Paleontology, v. 5, p. 89–96.

Buck, B. J., T. F. Lawton, and A. L. Brock, 2010, Evaporitic paleosols in continental strata of the Carroza Formation, La Popa Basin, Mexico: Record of Paleogene climate and salt tectonics: Geological Society of America Bulletin, v. 122, p. 1011–1026.

Buck, M. J., D. C. Ford, and H. P. Schwarcz, 1994, Classification of cave gypsum deposits derived from oxidation of H2S, in I. Sasowsky, and M. V. Palmer, eds., Breakthroughs in Karst Geomicrobiology: Colorado Springs, Colorado, Karst Waters Institute, p. 5–9.

Budai, J. M., K. C. Lohmann, and R. M. Owen, 1984, Burial dedolomite in the Mississippian Madison Limestone, Wyoming and Utah thrust belt: Journal of Sedimentary Petrology, v. 54, p. 276–288.

Budd, D. A., A. H. Saller, and P. M. Harris, 1995, Unconformities and porosity in carbonate strata, v. American Association of Petroleum Geologists Memoir 63: Tulsa, Okla, American Association of Petroleum Geologists.

Buffet, A., 1998, The collapse of Compagnie des Salins SG4 and SG5 drilling: Proc. Solution Mining Research Institute Fall Meeting, Rome,, p. 79–105.

Buick, R., 1992, The antiquity of oxygenic photosynthesis; evidence from stromatolites in sulphate-deficient Archaean lakes: Science, v. 255, p. 74–77.

Buick, R., and J. S. R. Dunlop, 1990, Evaporitic sediments of early Archaean age from the Warrawoona Group, North Pole, Western Australia: Sedimentology, v. 37, p. 247–277.

Bull, S. W., 1998, Sedimentology of the Palaeoproterozoic Barney Creek formation in DDH BMR McArthur 2, southern McArthur basin, northern territory: Australian Journal of Earth Sciences: An International Geoscience Journal of the Geological Society of Australia, v. 45, p. 21–31.

Burban, B., 1990, Kunwarara magnesite deposit, in F. E. Hughes, ed., Geology of the mineral deposits of Australia and Papua New Guinea, Australasian Institute of Mining and Metallurgy Monograph Series, Volume 14 (2), p. 1675–1677.

Burchette, T. P., and V. P. Wright, 1992, Carbonate ramp depositional systems: Sedimentary Geology, v. 79, p. 3–57.

Burk, C. A., M. Ewing, J. L. Worzel, A. O. J. Beall, W. A. Berggren, D. Bukry, A. G. Fischer, and E. A. J. Pessagno, 1969, Deep-sea drilling into the Challenger knoll, central Gulf of Mexico: Bulletin American Association Petroleum Geologists, v. 53, p. 1338–1347.

Burke, C. M., 1995, Benthic microbial production of oxygen supersaturates the bottom water of a stratified hypersaline lake: Microbial Ecology, v. 29, p. 163–171.

Burke, C. M., and B. Knott, 1997, Homeostatic interactions between the benthic microbial communities and the waters of a saline lake: Marine & Freshwater Research, v. 48, p. 623–631.

Burkova, V. N., E. A. Kurakolova, N. S. Vorob'eva, M. L. Kondakova, and O. K. Bazhenova, 2000, Hydrocarbons of the hypersaline environment of the Tyro deep-sea depression (eastern Mediterranean): Geochemistry International, v. 38, p. 883–894.

Burliga, S., 1996, Kinematics within the Klodawa salt diapir, central Poland, in G. I. Alsop, D. J. Blundell, and I. Davison, eds., Salt tectonics: London, United Kingdom, Geological Society of London Special Publication, v. 100, p. 11–21.

Burne, R., and L. Moore, 1993, Microatoll microbialites of Lake Clifton, Western Australia: Morphological analogues of Cryptozoön proliferum Hall, the first formally-named stromatolite: Facies, v. 29, p. 149–168.

Burne, R. V., J. Bauld, and P. De Deckker, 1980, Saline lake charophytes and their geological significance: Journal of Sedimentary Petrology, v. 50, p. 281–293.

Burne, R. V., and L. S. Moore, 1987, Microbialites; organosedimentary deposits of benthic microbial communities: Palaios, v. 2, p. 241–254.

Burne, R. V., L. S. Moore, A. G. Christy, U. Troitzsch, P. L. King, A. M. Carnerup, and P. J. Hamilton, 2014, Stevensite in the modern thrombolites of Lake Clifton, Western Australia: A missing link in microbialite mineralization?: Geology, v. 42, p. 575–578.

Burns, K. L., O. Stephansson, and A. J. R. White, 1977, The Flinders Ranges breccias of South Australia — diapirs or decollement ?: Quarterly Journal Geological Soc. London, v. 134, p. 363–384.

Burri, E., 1986, Various aspects of karstic phenomena in the urbanised area of Gissi and neighbouring areas (southern Abruzzo, Italy): Le Grotte d'Italia, v. 4, p. 143–161.

Burri, P., R. du Dresnay, and C. W. Wagner, 1973, Tepee structures and associated diagenetic features in intertidal carbonate sands (lower Jurassic, Morocco): Sedimentary Geology, v. 9, p. 221–228.

Burrough, S. L., D. S. G. Thomas, and R. M. Bailey, 2009, Mega-Lake in the Kalahari: A Late Pleistocene record of the Palaeolake Makgadikgadi system: Quaternary Science Reviews, v. 28, p. 1392–1411.

Burrus, J., and F. Audebert, 1990, Thermal and compaction processes in a young rifted basin containing evaporites; Gulf of Lions, France: American Association Petroleum Geologists – Bulletin, v. 74, p. 1420–1440.

Burt, J., S. Al-Harthi, and A. Al-Cibahy, 2011, Long-term impacts of coral bleaching events on the world's warmest reefs: Marine Environmental Research, v. 72, p. 225–229.

Burwood, R., 1984, Carbonate source rocks for six million barrels of oil per day – Zagros fold belt, southwestern Iran, in J. G. Palacas, ed., Petroleum geochemistry and source rock potential of carbonate rocks, American Association of Petroleum Geologists Studies in Geology 18, p. 206.

Burwood, R., 1999, Angola: source rock control for Lower Congo Coastal and Kwanza Basin petroleum systems: Geological Society, London, Special Publications, v. 153, p. 181–194.

Burwood, R., S. M. De Witte, B. Mycke, and J. Paulet, 1995, Petroleum geochemical characterisation of the lower Congo Coastal basin Bucomazi Formation, in B. Katz, ed., Petroleum source rocks: Berlin, Springer Verlag, p. 235–263.

Burwood, R., P. Leplat, B. Mycke, and J. Paulet, 1992, Rifted Margin Source Rock Deposition – a Carbon Isotope and Biomarker Study of a West African Lower Cretaceous Lacustrine Section: Organic Geochemistry, v. 19, p. 41–52.

Burwood, R., and B. Mycke, 1996, Coastal Angola and Zaire; a geochemical contrast of the lower Congo and Kwanza Basin hydrocarbon habitats (abs): American Association Petroleum Geologists – Bulletin, v. 80, p. 1277.

Bush, P., 1973, Some aspects of the diagenetic history of the sabkha in Abu Dhabi, Persian Gulf, in B. H. Purser, ed., The Persian Gulf: Holocene carbonate sedimentation and diagenesis in a shallow epicontinental sea: New York, Springer Verlag, p. 395–407.

Busson, G., 1980, Evaporite deposits; illustration and interpretation of some environmental sequences: Paris, France, Ed. Technip, 266 p.

Busson, G., 1991, Relationship between different types of evaporitic deposits, and the occurrence of organic-rich layers (potential source-rocks): Carbonates and Evaporites, v. 6, p. 177–192.

Busson, G., 1992, Bassins paleogenes saliferes de 1' Est de la France (Valence, Bresse et Haute-Alsace) Translated Title: Paleogene salt basins of eastern France, Valence, Bresse and Haute-Alsace: Geologie de la France, v. 1, p. 15–64.

Bustillo, M. A., J. Garcia-Guinea, J. Martinez-Frias, and A. Delgado, 1999, Unusual sedimentary geodes filled by gold-bearing hematite laths: Geological Magazine, v. 136, p. 671–679.

Butchins, C. S., and R. Mason, 1973, Metamorphic anhydrite in a kyanite-bearing schist from Churchill Falls, Labrador: Mineralogical Magazine, v. 39, p. 488–490.

Butler, G. P., 1966, Early diagenesis in the recent sediments of the Trucial Coast of the Persian Gulf: Doctoral thesis, University of London, 251 p.

Butler, G. P., 1969, Modern evaporite deposition and geochemistry of coexisting brines, the sabkha, Trucial coast, Arabian gulf: Journal of Sedimentary Petrology, v. 39, p. 70–89.

Butler, G. P., 1970, Holocene gypsum and anhydrite of the Abu Dhabi sabkha, Trucial Coast; an alternative explanation of origin: 3rd Symposium on Salt, Northern Ohio Geological Society, v. 1, p. 120–152.

Butler, G. P., 1973, Modern evaporite deposition and geochemistry of coexisting brines, the sabkha, Trucial Coast, Arabian Gulf [with comment]: in Marine Evaporites; Origin, Diagenesis, and Geochemistry, p.

Butler, G. P., P. M. Harris, and C. G. S. C. Kendall, 1982, Recent evaporites from the Abu Dhabi coastal flats, in C. R. Handford, R. G. Loucks, and G. R. Davies, eds., Depositional and diagenetic spectra of evaporites; a core workshop., v. 3, SEPM Core Workshop, p. 33–64.

Butler, G. P., R. H. Krouse, and R. Mitchell, 1973, Sulphur-Iso- tope Geochemistry of an Arid, Supratidal Evaporite Environment, Trucial Coast, in B. Purser, ed., The Persian Gulf: Berlin Heidelberg, New York, Springer Verlag, p. 452–462.

Butler, R. W. H., W. H. Lickorish, M. Grasso, H. M. Pedley, and L. Ramberti, 1995, Tectonics and sequence stratigraphy in Messinian basins, Sicily; constraints on the initiation and termination of the Mediterranean salinity crisis: Geological Society of America Bulletin, v. 107, p. 425–439.

Butts, D., 2007, Chemicals from Brines, Kirk-Othmer Encyclopedia of Chemical Technology, John Wiley & Sons, Inc., p. 784–803.

Butts, D., and D. R. Bush, 2007, Sodium sulfates and sulfides, Kirk-Othmer Encyclopedia of Chemical Technology, v. 20, John Wiley & Sons, Inc., p. 1–15.

Byerly, G. R., and M. R. Palmer, 1991, Tourmaline mineralization in the Barberton greenstone belt, South Africa; early Archean metasomatism by evaporite-derived boron: Contributions to Mineralogy and Petrology, v. 107, p. 387–402.

Cabral, A., M. Wiedenbeck, F. Rios, A. Seabra Gomes, Jr., O. Rocha Filho, and R. Jones, 2012, Talc mineralisation associated with soft hematite ore, Gongo Soco deposit, Minas Gerais, Brazil: petrography, mineral chemistry and boron-isotope composition of tourmaline: Mineralium Deposita, v. 47, p. 411–424.

Cailteux, J., 1986, Diagenetic sulphide mineralization within the stratiform copper- cobalt deposit of West Kambove (Shaba-Zaire). Sequence of mineralization in sediment-hosted copper deposits (Part 2), in G. H. Friedr, ed., Geology and Metallogeny of Copper Deposits, v. 4, Springer-Verlag; Special Publ. of the Society for Geology Applied to Mineral Deposits, p. 398–411.

Cailteux, J., 1994, Lithostratigraphy of the Neoproterozoic Shaba-type (Zaire) Roan Supergroup and metallogenesis of associated stratiform mineralization: Journal of African Earth Sciences, v. 19, p. 279–301.

Caja, M. K., I. S. Al-Aasm, R. Marfil, M. Tsige, T. Martin-Crespo, and R. Salas, 2003, Multiphase carbonate cementation related to fractures in the Upper Jurassic limestones, Maestrat Basin (Iberian Range, Spain): Journal of Geochemical Exploration, v. 78-9, p. 33–38.

Calaforra, J. M., and A. Pulido-Bosch, 1999, Gypsum karst features as evidence of diapiric processes in the Betic Cordillera, Southern Spain: Geomorphology, v. 29, p. 251–264.

Calaforra, J. M., and A. Pulido-Bosch, 2003, Evolution of the gypsum karst of Sorbas (SE Spain): Geomorphology, v. 50, p. 173–180.

Calder, I. R., and C. Neal, 1984, Evaporation from saline lakes: a combination equation approach: Hydrological Sciences Journal, v. 29, p. 89–97.

Callao, S., E. Arce, and A. Andia, 2002, Mineralogia, quimica e inclsiones fluidas en lo depositos de nitratos de Maria elena, Lla region, Chile: Bol. Soc. Chil. Quím., v. 47, p. 181–190.

Callot, J.-P., V. Trocmé, J. Letouzey, E. Albouy, S. Jahani, and S. Sherkati, 2012, Pre-existing salt structures and the folding of the Zagros Mountains: Geological Society, London, Special Publications, v. 363, p. 545–561.

Calon, T. J., A. E. Aksu, and J. Hall, 2005, The Oligocene-Recent evolution of the Mesaoria Basin (Cyprus) and its western marine extension, Eastern Mediterranean: Marine Geology, v. 221, p. 95–120.

Calvo, J., B. Jones, M. Bustillo, R. Fort, A. Zarza, and C. Kendall, 1995, Sedimentology and geochemistry of carbonates from lacustrine sequences in the Madrid Basin, Spain: Chemical Geology, v. 123, p. 173–191.

Calvo, J. P., M. M. Blanc-Valleron, J. P. Rodriguez Arandia, J. M. Rouchy, and M. E. Sanz, 1999, Authigenic clay minerals in continental evaporitic environments: International Association Sedimentologists Special Publication, No. 27, p. 129–151.

Camerlenghi, A., 1990, Anoxic Basins of the eastern Mediterranean: geological framework: Marine Chemistry, v. 31, p. 1–19.

Camerlenghi, A., D. Accettella, S. Costa, G. Lastras, J. Acosta, M. Canals, and N. Wardell, 2009, Morphogenesis of the SW Balearic continental slope and adjacent abyssal plain, Western Mediterranean Sea: International Journal of Earth Sciences, v. 98, p. 735–750.

Camerlo, R. H., and E. F. Benson, 2006, Geometric and seismic interpretation of the Perdido fold belt: Northwestern deep-water Gulf of Mexico: Bulletin American Association Petroleum Geologists, v. 90, p. 363–386.

Camoin, G., J. Casanova, J. M. Rouchy, M. M. Blancvalleron, and J. F. Deconinck, 1997, Environmental controls on perennial and ephemeral carbonate lakes – the central Paleo-Andean basin of Bolivia during Late Cretaceous to Early Tertiary times: Sedimentary Geology, v. 113, p. 1–26.

Campos, P. G., J. O. Grimalt, L. Berdie, J. O. Lopez-Quintero, and L. E. Navarrete-Reyes, 1996, Organic geochemistry of Cuban oils--I. The northern geological province: Organic Geochemistry, v. 25, p. 475–488.

Camur, M. Z., and H. Mutlu, 1996, Major-ion geochemistry and mineralogy of the Salt Lake (Tuz Golu) basin, Turkey: Chemical Geology, v. 127, p. 313–329.

Cañaveras, J. C., S. Sanchezmoral, J. P. Calvo, M. Hoyos, and O. S., 1996, Dedolomites associated with karstification – an example of early dedolomitisation in lacustrine sequences from the Tertiary Madrid basin, central Spain: Carbonates & Evaporites, v. 11, p. 85–103.

Cañaveras, J. C., S. Sanchezmoral, E. Sanzrubio, and M. Hoyos, 1998, Meteoric calcitization of magnesite in Miocene lacustrine deposits (Calatayud basin, NE Spain): Sedimentary Geology, v. 119, p. 183–194.

Canet, C., R. M. Prol-Ledesma, E. Escobar-Briones, C. Mortera-Gutierrez, R. Lozano-Santa Cruz, C. Linares, E. Cienfuegos, and P. Morales-Puente, 2006, Mineralogical and geochemical characterization of hydrocarbon seep sediments from the Gulf of Mexico: Marine and Petroleum Geology, v. 23, p. 605–619.

Canfield, D. E., and D. J. Des Marais, 1991, Aerobic sulfate reduction in microbial mats: Science, v. 251, p. 1471–1473.

Canfield, D. E., K. B. SØRensen, and A. Oren, 2004, Biogeochemistry of a gypsum-encrusted microbial ecosystem: Geobiology, v. 2, p. 133–150.

Cann, J. H., and P. De Deckker, 1981, Fossil Quaternary and Living Foraminifera from Athalassic (Non – Marine) Saline Lakes, Southern Australia: Journal of Palaeontology, v. 55, p. 660–670.

Cantrell, D. L., and R. M. Hagerty, 1999, Microporosity in the Arab Formation Carbonates, Saudi Arabia: GeoArabia, v. 4, p. 129–154.

Cantrell, D. L., and R. M. Hagerty, 2003, Reservoir rock classification, Arab-D reservoir, Ghawar field, Saudi Arabia: GeoArabia, v. 8, p. 129–154.

Cantrell, D. L., P. K. Swart, C. R. Handford, C. G. S. C. Kendall, and H. Westphal, 2001, Geology and production significance of dolomite, Arab D reservoir, Ghawar Field, Saudi Arabia: GeoArabia, v. 6, p. 45–60.

Carlisle, D., P. M. Merifield, A. R. Orme, M. S. Kohl, O. Kolker, and O. R. Lunt, 1978, Distribution of calcretes and gypcretes in southwestern United States and their uranium favorability, based on a study of deposits in Western Australia and South West Africa (Namibia): US DOE Report GJBX-29(78), 274 p.

Carlson, C. A., F. M. Phillips, D. Elmore, and H. W. Bentley, 1990, Chlorine-36 tracing of salinity sources in the Dry Valleys of Victoria Land, Antarctica: Geochimica et Cosmochimica Acta, v. 54, p. 311–318.

Carlson, E. H., 1983, The occurrence of Mississippi Valley-type Mineralization in northwestern Ohio, in G. Kisvarsanyi, S. K. Grant, W. P. Pratt, and J. W. Koenig, eds., International Conference on Mississippi Valley Type lead-zinc deposits; Proceedings, University of Missouri Rolla, Mo, p. 424–435.

Carlson, E. H., 1987, Celestite replacements of evaporites in the Salina Group: Sedimentary Geology, v. 54, p. 93–112.

Carlson, E. H., 1992, Reactivated interstratal karst – example from the late Silurian rocks of western Lake Erie (USA): Sedimentary Geology, v. 76, p. 273–283.

Carmona, V., J. J. Pueyo, C. Taberner, G. Chong, and M. Thirl-wall, 2000, Solute inputs in the Salar de Atacama (N. Chile): Journal of Geochemical Exploration, v. 69, p. 449–452.

Carniel, R., E. M. o. Jolis, and J. Jones, 2010, A geophysical multiparametric analysis of hydrothermal activity at Dallol, Ethiopia: Journal of African Earth Sciences, v. 58, p. 812–819.

Carozzi, A. V., I. A. Orchuela, and M. L. R. Schelotto, 1993, Depositional models of the Lower Cretaceous Quintuco-Loma Montosa Formation, Neuquen Basin, Argentina: Journal of Petroleum Geology, p. 421–450.

Carpenter, A. B., 1978, Origin and chemical evolution of brines in sedimentary basins: Oklahoma Geological Survey Circular, v. 79, p. 60–77.

Carpenter, A. B., M. L. Trout, and E. E. Pickett, 1974, Preliminary report on the origin and chemical evolution of oil field brines in central Mississippi: Economic Geology, v. 69, p. 1191–1206.

Carpenter, S. B., and R. B. Kistler, 2006, Boron and borates, in J. E. Kogel, N. C. Trivedi, J. M. Barker, and S. T. Krukowski, eds., Industrial Minerals and Rocks, SME (Soc. Mining Metallurgy and Exploration), p. 275–284.

Carrigan, W. J., G. A. Cole, E. L. Colling, and P. J. Jones, 1995, Geochemistry of the Upper Jurassic Tuwaiq Mountain and Hanifa Formation petroleum source rocks of eastern Saudi Arabia, in B. Katz, ed., Petroleum source rocks: Berlin, Springer Verlag, p. 67–87.

Carrillo-Rosúa, J., A. J. Boyce, S. Morales-Ruano, D. Morata, S. Roberts, F. Munizaga, and V. Moreno-Rodríguez, 2014, Extremely negative and inhomogeneous sulfur isotope signatures in Cretaceous Chilean manto-type Cu-(Ag) deposits, Coastal Range of central Chile: Ore Geology Reviews, v. 56, p. 13–24.

Carroll, A. R., 1998, Upper Permian lacustrine organic facies evolution, southern Junggar basin, NW China: Organic Geochemistry, v. 28, p. 649–667.

Carroll, A. R., and K. M. Bohacs, 1999, Stratigraphic classification of ancient lakes: Balancing tectonic and climatic controls: Geology, v. 27, p. 99–102.

Carroll, A. R., S. C. Brasell, and S. A. Graham, 1992, Upper Permian lacustrine oil shales, southern Junggar Basin, Northwest China: American Association Petroleum Geologists – Bulletin, v. 76, p. 1874–1902.

Carter, N. L., 1976, Steady-state flow of rocks: Review of Geophysics and Space Physics, v. 14, p. 301–360.

Carter, N. L., and F. D. Hansen, 1983, Creep of rocksalt: Tectonophysics, v. 92, p. 275–333.

Carter, N. L., S. T. Horseman, J. E. Russell, and J. Handin, 1993, Rheology of rock salt: Journal of Structural Geology, v. 15, p. 1257–1271.

Cartwright, J., M. Huuse, and A. Aplin, 2007, Seal bypass systems: American Association Petroleum Geologists – Bulletin, v. 91, p. 1141–1166.

Cartwright, J. A., and D. N. Dewhurst, 1998, Layer-bound compaction faults in fine-grained sediments: Geological Society of America Bulletin, v. 110, p. 1242–1257.

Cartwright, J. A., and M. P. A. Jackson, 2008, Initiation of gravitational collapse of an evaporite basin margin: The Messinian saline giant, Levant Basin, eastern Mediterranean: Geological Society of America Bulletin, v. 120, p. 399–413.

Cartwright, M., M. McLaughlin, J. Ratigan, and D. Blankenship, 2000, A sinkhole at the EGP Fuels Company LPG storage terminal Mount Belvieu Texas: Proc. Solution Mining Research Institute Fall Meeting Technical Session, San Antonio, p. 128–143.

Carville, D. P., J. F. Leckie, C. F. Moorhead, J. G. Rayner, and A. A. Durbin, 1990, Coronation Hill gold platinum-palladium deposit: Australasian Institute of Mining and Metallurgy Monograph, v. 14, p. 759–762.

Casabianca, D., R. J. H. Jolly, and R. Pollard, 2007, The Machar Oil Field: waterflooding a fractured chalk reservoir: Geological Society, London, Special Publications, v. 270, p. 171–191.

Casanova, J., 1986, East African Rift stromatolites, in L. E. Frostick, R. W. Renaut, I. Reid, and J. J. Tiercelin, eds., Sedimentation in the African Rifts, Journal of the Geological Society of London, Special Publication No. 25, p. 201–210.

Casanova, J., and D. Nury, 1989, Biosédimentologie des stromatolites fluvio-lacustres du fossé oligocene de Marseille: Bull. Soc. Geol. Fr., v. 8, p. 1111–1128.

Casas, E., 1992, Modern carnallite mineralisation and Late Pleistocene to Holocene brine evolution in the nonmarine Qaidam Basin, China: Doctoral thesis, State University of New York at Binghampton.

Casas, E., and T. K. Lowenstein, 1989, Diagenesis of saline pan halite; comparison of petrographic features of modern, Quaternary and Permian halites: Journal of Sedimentary Petrology, v. 59, p. 724–739.

Casas, E., T. K. Lowenstein, R. J. Spencer, and P. Zhang, 1992, Carnallite mineralization in the nonmarine, Qaidam Basin, China; evidence for the early diagenetic origin of potash evaporites: Journal of Sedimentary Petrology, v. 62, p. 881–898.

Casey, W. H., and B. Bunker, 1990, Leaching of mineral and glass surfaces during, in M. F. Hochella, and A. F. White, eds., Mineral–Water Interface Geochemistry, Reviews in Mineralogy, v. 23, p. 397–426.

Cassidy, D. P., and V. Ranganathan, 1992, Groundwater Upwelling, Near Bay St. Elaine Salt Dome in Southeastern Louisiana, as Inferred from Fluid Property Variations: American Association Petroleum Geologists – Bulletin, v. 76, p. 1560–1568.

Castañeda, C., F. Gutiérrez, M. Manunta, and J. P. Galve, 2009, DInSAR measurements of ground deformation by sinkholes, mining subsidence, and landslides, Ebro River, Spain: Earth Surface Processes and Landforms, v. 34, p. 1562–1574.

Castanier, S., J.-P. Perthuisot, J.-M. Rouchy, A. Maurin, and O. Guelorget, 1992, Halite ooids in Lake Asal, Djibouti: Biocrystalline build-UPS: Geobios, v. 25, p. 811–821.

Castanier, S., J. P. Perthuisot, M. Matrat, and J. Y. Morvan, 1999, The salt ooids of Berre salt works (Bouches du Rhone, France): the role of bacteria in salt crystallisation: Sedimentary Geology, v. 125, p. 9–21.

Castellini, D. G., G. R. Dickens, G. T. Snyder, and C. D. Ruppel, 2006, Barium cycling in shallow sediment above active mud volcanoes in the Gulf of Mexico: Chemical Geology, v. 226, p. 1–30.

Castorina, F., U. Masi, G. Padalino, and M. Palomba, 2006, Constraints from geochemistry and Sr-Nd isotopes for the origin of albitite deposits from Central Sardinia (Italy): Mineralium Deposita, v. 41, p. 323–338.

Cathro, D. L., J. K. Warren, and G. E. Williams, 1992, Halite saltern in the Canning Basin, Western Australia; a sedimentological analysis of drill core from the Ordovician-Silurian Mallowa Salt: Sedimentology, v. 39, p. 983–1002.

Caumette, P., 1993, Ecology and physiology of phototropic bacteria and sulphate-reducing bacteria in marine salterns: Experientia, v. 49, p. 473–481.

Cavicchioli, R., 2006, Cold-adapted archaea: Nature Reviews, Microbiology, v. 4, p. 331–343.

Cayol, J. L., B. Ollivier, B. K. C. Patel, G. Prensier, J. Guezennec, and J.-L. Garcia, 1994, Isolation and characterization of Halothermothrix orenii gen. nov., sp. nov., a halophilic, thermophilic, fermentative strictly anaerobic bacterium: Int. J. Syst. Bacteriol., v. 44, p. 534–540.

Cendón, D., J. J. Pueyo, C. Ayora, J. G. Veigas, and M.-M. Blanc-Valleron, 2010, Exploring the hydrochemical evolution of brines leading to sylvite precipitation in ancient evaporite basins (abs.): Geophysical Research Abstracts, v. 12, EGU2010- 3807-1.

Cendon, D. I., C. Ayora, J. J. Pueyo, and C. Taberner, 2003, The geochemical evolution of the Catalan potash subbasin, South Pyrenean foreland basin (Spain): Chemical Geology, v. 200, p. 339–357.

Cendon, D. I., C. Ayora, J. J. Pueyo, C. Taberner, and M. M. Blanc-Valleron, 2008, The chemical and hydrological evolution of the Mulhouse potash basin (France): Are "marine" ancient evaporites always representative of synchronous seawater chemistry?: Chemical Geology, v. 252, p. 109–124.

Cendon, D. I., C. Ayora, and J. P. Pueyo, 1998, The origin of barren bodies in the Subiza potash deposit, Navarra, Spain – Implications for sylvite formation: Journal of Sedimentary Research Section A-Sedimentary Petrology & Processes, v. 68, p. 43–52.

Cercone, K. R., 1988, Evaporative sea level drawdown in the Michigan Basin: Geology, v. 16, p. 387–390.

Cercone, K. R., and K. C. Lohmann, 1986, Diagenetic history of the Union 8 pinnacle reef (Middle Silurian), northern Michigan, USA, in B. Purser, and J. Schroeder, eds., Reef diagenesis.: Berlin, Germany, Elsevier, p. 381–398.

Ceriani, a., A. Di Giulo, H. Goldstein, and C. Rossi, 2002, Diagenesis associated with cooling during burial: An example from Lower Cretaceous reservoir sandstones (Sirt basin, Libya): Bulletin American Association Petroleum Geologists, v. 86, p. 1573–1591.

Cesaretti, N. N., J. Parnell, and E. A. Dominguez, 2000, Pore fluid evolution within a hydrocarbon reservoir: Yacoraite Formation, (Upper Cretaceous), Northwest Basin, Argentina: Journal of Petroleum Geology, v. 23, p. 375–398.

Chabert, C., and P. Courbon, 1997, Atlas de cavités non calcaires du monde: Union Int. Spéléol. au prés Madame Carle, Paris, p. 1–120.

Chabiron, A., M. Cuney, and B. Poty, 2003, Possible uranium sources for the largest uranium district associated with volcanism: the Streltsovka caldera (Transbaikalia, Russia): Mineralium Deposita, v. 38, p. 127–140.

Chabou-Mostafai, S., J. J. DeVolce, Y. Fuchs, G. Memant, and M. Riviere, 1978, Sur les niveaux a celestite de Tunisie centrale et du sud-Constantinois: Sciences de la Terre, v. 22, p. 293–300.

Chabu, M., 1995, The geochemistry of phlogopite and chlorite from the Kipushi Zn-Pb-Cu deposit, Zaire: Canadian Mineralogist, v. 33, p. 547–558.

Chafetz, H. S., and R. L. Folk, 1984, Travertines: depositional morphology and the bacterially constructed constituents: Journal of Sedimentary Petrology, v. 54, p. 289–316.

Chafetz, H. S., and J. L. Zhang, 1998, Authigenic euhedral megaquartz crystals in a Quaternary dolomite: Journal of Sedimentary Research Section A-Sedimentary Petrology & Processes, v. 68, p. 994–1000.

Chakhmakhchev, A., and N. Suzuki, 1995, Saturate biomarkers and aromatic sulfur compounds in oils and condensates from different source rock lithologies of Kazakhstan, Japan and Russia: Organic Geochemistry, v. 23, p. 289–299.

Chambefort, I., J. H. Dilles, and A. J. R. Kent, 2008, Anhydrite-bearing andesite and dacite as a source for sulfur in magmatic-hydrothermal mineral deposits: Geology, v. 36, p. 719–722.

Channer, D. M. D., C. E. J. de Ronde, and E. T. C. Spooner, 1997, The Cl-Br-I composition of ≈3.23 Ga seawater: Implications for the geological evolution of ocean halide chemistry: Earth and Planetary Science Letters, v. 150, p. 325–335.

Chao, L., P. Zicheng, Y. Dong, L. Weiguo, Z. Zhaofeng, H. Jianfeng, and C. Chenlin, 2009, A lacustrine record from Lop Nur, Xinjiang, China: Implications for paleoclimate change during Late Pleistocene: Journal of Asian Earth Sciences, v. 34, p. 38–45.

Chapman, L. H., 2004, Geology and Mineralization Styles of the George Fisher Zn-Pb-Ag Deposit, Mount Isa, Australia: Economic Geology, v. 99, p. 233–255.

Chappell, B. W., and A. H. White, 2001, Two contrasting granite types: 25 years later: Australian Journal of Earth Sciences, v. 48, p. 489–499.

Charef, A., and S. M. F. Sheppard, 1987, Pb-Znmineralization associated with diapirism: fluid inclusion and stable isotope (H, C, O) evidence for the origin and evolution of the fluids at Fedj-el-Adoum, Tunisia.: Chemical Geology, v. 61, p. 113–134.

Charef, A., and S. M. F. Sheppard, 1991, The diapir related Bou Grine Pb-Zn deposit (Tunisia); evidence for role of hot sedimentary basin brines, in M. Pagel, and J. L. Leroy, eds., Source, transport and deposition of metals; Proceedings of the 25 years SGA Anniversary Meeting, A. A. B alkema, Rotterdam, Netherlands, p. 269–272.

Charrach, J., 1986, Genesis of halite islands in the southern basin of the Dead Sea: Israel Geological Society, Annual Meeting, v. 1986, p. 26–27.

Chartrand, F. M., A. C. Brown, and R. V. Kirkham, 1989, Diagenesis, sulphides, and metal zoning in the Redstone copper deposit, Northwest Territories: Geological Association of Canada Special Paper, v. 36, p. 189–206.

Chavdarian, G. V., and D. Y. Sumner, 2011, Origin and evolution of polygonal cracks in hydrous sulphate sands, White Sands National Monument, New Mexico: Sedimentology, v. 58, p. 407–423.

Cheilletz, A., and G. Giuliani, 1996, The genesis of Colombian emeralds: are statement: Mineralium Deposita, v. 31, p. 359–364.

Chekunov, A. V., V. K. Garvish, R. I. Kutas, and L. I. Ryabchun, 1992, Dnieper-Donets palaeorift: Tectonophysics, v. 208, p. 257–272.

Chen, H., 2013, External sulphur in IOCG mineralization: Implications on definition and classification of the IOCG clan: Ore Geology Reviews, v. 51, p. 74–78.

Chen, H., A. H. Clark, and T. K. Kyser, 2010, The Marcona Magnetite Deposit, Ica, South-Central Peru: A Product of Hydrous, Iron Oxide-Rich Melts?: Economic Geology, v. 105, p. 1441–1456.

Chen, J., M. R. Walter, G. A. Logan, M. C. Hinman, and R. E. Summons, 2003, The Paleoproterozoic McArthur River (HYC) Pb/Zn/Ag deposit of northern Australia: organic geochemistry and ore genesis: Earth and Planetary Science Letters, v. 210, p. 467–479.

Chen, J. Y., Y. P. Bi, J. G. Zhang, and S. F. Li, 1996, Oil-source correlation in the Fulin basin, Shengli petroleum province, East China: Organic Geochemistry, v. 24, p. 931–940.

Chen, K., and J. M. Bowler, 1986, Late Pleistocene evolution of salt lakes in the Qaidam Basin, Qinghai Province, China: Palaeogeography, Palaeoclimatology, Palaeoecology, v. 54, p. 87–104.

Chen, S., X. Wang, X. Yin, and G. Zhang, 2013, Genesis of anhydrite in hydrothermally altered basalt from the East Pacific Rise near 13°N: Acta Oceanologica Sinica, v. 32, p. 12–17.

Chen, X. Y., J. R. Prescott, and J. T. Hutton, 1990, Thermoluminescence dating on gypseous dunes of Lake Amadeus, central Australia: Australian Journal of Earth Sciences, v. 37, p. 93–101.

Chen, Y., 1986, Hydrochemistry and evolution of interstitial brine in the Zhabuye saline lake of Tibet. (Chinese): Bulletin of the Institute of Mineral Deposits, Chinese Academy of Geological Sciences, v. 18, p. 176–184.

Cheng, A., and J. T. Kwan, 2012, Optimal Injection Design Utilizing Tracer and Simulation in a Surfactant Pilot for a Fractured Carbonate Yates Field, Society of Petroleum Engineers.

Chengzao, J., and L. Qiming, 2008, Petroleum geology of Kela-2, the most productive gas field in China: Marine and Petroleum Geology, v. 25, p. 335–343.

Chetty, D., and H. E. Frimmel, 2000, The role of evaporites in the genesis of base metal sulphide mineralisation in the Northern Platform of the Pan-African Damara Belt, Namibia: geochemical and fluid inclusion evidence from carbonate wall rock alteration: Mineralium Deposita, v. 35, p. 364–376.

Chi, G., M. M. Savard, and Y. Héroux, 1995, Constraints from fluid inclusion data on the origin of the Jubilee carbonate-hosted Zn-Pb deposit, Cape Breton, Nova Scotia: The Canadian Mineralogist, v. 33, p. 709–721.

Chi, G. X., and M. M. Savard, 1995, Fluid evolution and mixing in the Gays River Carbonate-hosted Zn-Pb deposit and its surrounding barren areas, Nova Scotia: Atlantic Geology, v. 31, p. 141–152.

Chi, G., M. M. Savard, and Y. Héroux, 1995, Constraints from fluid inclusion data on the origin of the Jubilee carbonate-hosted Zn-Pb deposit, Cape Breton, Nova Scotia: The Canadian Mineralogist, v. 33, p. 709–721.

Chi, G. X., and M. M. Savard, 1997, Sources of basinal and Mississippi Valley-Type mineralizing brines – Mixing of evaporated seawater and halite dissolution brine: Chemical Geology, v. 143, p. 121–125.

Chi, G. X., and M. M. Savard, 1998, Basinal fluid flow models related to Zn-Pb mineralisation in the southern margin of the Maritimes basin, eastern Canada: Economic Geology, v. 93, p. 896–910.

Chiaradia, M., D. Banks, R. Cliff, R. Marschik, and A. Haller, 2006, Origin of fluids in iron oxide-copper-gold deposits: Constraints from ^{37}Cl, $^{87}Sr/^{86}Sr$ and Cl/Br: Mineralium Deposita, v. 41, p. 565–573.

Childress, B., S. Nagy, and B. Hughes, 2008, International Single Species Action Plan for Conservation of the Lesser Flamingo (Phoenicopterus minor): CMS Technical Series No. 18, AEWA Technical Series No. 34, Bonn, Germany, 59 pp.

Chimene, C. A., 1991, Walker Creek Field – USA, Gulf of Mexico Basin, Arkansas, in E. A. Beaumont, and N. H. Foster, eds., Treatise of Petroleum Geology; Atlas of Oil and Gas Fields: Stratigraphic Traps II: Tulsa, OK, American Association Petroleum Geologists, p. 55–117.

Chipley, D. B. L., 1995, Fluid history of the Saskatchewan sub-basin of the western Canada sedimentary basin: Evidence from the geochemistry of evaporites: Doctoral thesis, University of Saskatchewan.

Chipley, D. B. L., and T. K. Kyser, 1989, Fluid inclusion evidence for the deposition and diagenesis of the Patience Lake Member of the Devonian Prairie Evaporite Formation, Saskatchewan, Canada: Sedimentary Geology, v. 64, p. 287–295.

Chivas, A. R., A. S. Andrew, W. B. Lyons, M. I. Bird, and T. H. Donnelly, 1991, Isotopic constraints on the origin of salts in Australian playas; I, Sulphur: Palaeogeography, Palaeoclimatology, Palaeoecology, v. 84, p. 309–322.

Chong Diaz, G., J. J. Pueyo, P. Turner, M. Mendoza, and J. Garcia-Veigas, 1999, Evolution and geochemical signatures in a Neogene fore arc evaporitic basin: The Salar Grande (Central Andes of Chile): Palaeogeography, Palaeoclimatology, Palaeoecology, v. 151, p. 39–54.

Chong, G., J. J. Pueyo, and C. Demergasso, 2000, The borate deposits in Chile. [Spanish]: Revista Geologica de Chile, v. 27, p. 99–119.

Choquette, P. W., and L. C. Pray, 1970, Geologic Nomenclature and Classification of Porosity in Sedimentary Carbonates: Bulletin American Association Petroleum Geologists, v. 54, p. 207–250.

Chough, S. K., S. B. Kim, and S. S. Chun, 1996, Sandstone/chert and laminated chert/black shale couplets, Creataceous Uhangri Formation (southwest Korea): depositional events in alkaline lake environments: Sedimentary Geology, v. 104, p. 227–242.

Chovan, M., V. Hurai, H. K. Sachan, and J. Kantor, 1995, Origin of the fluids associated with granodiorite-hosted, Sb-As-Au-W mineralisation at Dubrava (Nizke Tatry Mts., Western Carpathians): Mineralium Deposita, v. 30, p. 48–54.

Chow, N., and A. D. George, 2004, Tepee-shaped agglutinated microbialites: an example from a Famennian carbonate platform on the Lennard Shelf, northern Canning Basin, Western Australia: Sedimentology, v. 51, p. 253–265.

Chowksey, V., D. M. Maurya, N. Khonde, and L. S. Chamyal, 2010, Tectonic geomorphology and evidence for active tilting of the Bela, Khadir and Bhanjada islands in the seismically active Kachchh palaeorift graben, Western India: Zeitschrift fiir Geomorphologie, NF, v. 54, p. 467–490.

Chown, E. H., 1987, Tourmalinites in the Aphebian Mistassini Group, Quebec: Canadian Journal Earth Science, v. 24, p. 826–830.

Chowns, T. M., and J. E. Elkins, 1974, The origin of quartz geodes and cauliflower cherts through the silicification of anhydrite nodules: J. Sediment. Petrol., v. 44, p. 885–903.

Christ, C. L., and R. M. Garrels, 1959, Relations among sodium borate hydrates at the Kramer deposit, Boron, California: American Journal of Science, v. 257, p. 516–528.

Christ, N., A. Immenhauser, F. Amour, M. Mutti, R. Preston, F. F. Whitaker, A. Peterhänsel, S. O. Egenhoff, P. A. Dunn, and S. M. Agar, 2012, Triassic Latemar cycle tops- Subaerial exposure of platform carbonates under tropical arid climate: Sedimentary Geology, v. 265-266, p. 1–29.

Christiansen, F. G., S. Piasecki, L. Stemmerik, and N. Telnaes, 1993, Depositional environment and organic geochemistry of the Upper Permian Ravnjeld Formation source rock in East Greenland: American Association Petroleum Geologists – Bulletin, v. 77, p. 1519–1537.

Chuber, S., and W. C. Pusey, 1985, Productive Permian carbonate cycles, San Andres Formation, Reeves field, West Texas, in P. O. Roehl, and P. W. Choquette, eds., Carbonate petroleum reservoirs: New York, Springer-Verlag, p. 289–307.

Cita, M. B., 1983, The Messinian salinity crisis in the Mediterranean: A review, in H. Berckhemer, and K. J. Hsu, eds., Alpine Mediterranean Geodynamics Review, v. 8, American Geophysical Union; Geodynamics Series, p. 113–140.

Cita, M. B., 2006, Exhumation of Messinian evaporites in the deep-sea and creation of deep anoxic brine-filled collapsed basins: Sedimentary Geology, v. 188-189, p. 357–378.

Cita, M. B., G. Grecchi, and F. Roegl, 1978, Intragypsifeous marls of the San Miguel de Salinas Basin (Spain); paleogeographic implications of a quantitative study: Cita, M. B. International meeting on

geodynamic and biodynamic effects of Messinian salinity crisis in the Mediterranean. Messinian Semin.

Clark, C., A. S. Mumm, and K. Faure, 2005, Timing and nature of fluid flow and alteration during Mesoproterozoic shear zone formation, Olary Domain, South Australia: Journal Of Metamorphic Geology, v. 23, p. 147–164.

Clark, D., J. Heaviside, and K. Habib, 2003, Reservoir properties of Arab carbonates, Al Rayyan field, offshore Qatar, in C. J. R. Braithwaite, G. Rizzi, and G. Darke, eds., The geometry and petrogenesis of dolomite hydrocarbon reservoirs, v. 235, Geological Society (London) Special Publication, p. 193–232.

Clark, D. N., 1980a, The sedimentology of the Zechstein 2 Carbonate Formation of eastern Drenthe, the Netherlands, in H. Fuchtbauer, and T. Peryt, eds., The Zechstein basin with emphasis on carbonate sequences, E. Schweizerbart'sche VbH: Contributions to Sedimentology 9, p. 131–165.

Clark, D. N., 1980b, The diagenesis of Zechstein carbonate sediments, in H. Fuchtbauer, and T. Peryt, eds., The Zechstein basin with emphasis on carbonate sequences, E. Schweizerbart'sche VbH: Contributions to Sedimentology 9, p. 167–203.

Clark, I. D., T. Al, M. Jensen, L. Kennell, M. Mazurek, R. Mohapatra, and K. G. Raven, 2013, Paleozoic-aged brine and authigenic helium preserved in an Ordovician shale aquiclude: Geology, v. 41, p. 951–954.

Clark, J. A., J. A. Cartwright, and S. A. Stewart, 1999, Mesozoic dissolution tectonics on the West Central Shelf, UK Central North Sea: Marine & Petroleum Geology, v. 16, p. 283–300.

Clark, J. A., S. A. Stewart, and J. A. Cartwright, 1998, Evolution of the NW margin of the North Permian Basin, UK North Sea: Journal of the Geological Society, v. 155, p. 663–676.

Clark, J. P., and R. P. Philp, 1989, Geochemical characterization of evaporite and carbonate depositional environments and correlation of associated crude oils in the Black Creek basin, Alberta: Bulletin of Canadian Petroleum Geology, v. 37, p. 401–416.

Clark, R. N., J. M. Curchin, J. W. Barnes, R. Jaumann, L. Soderblom, D. P. Craikshank, R. H. Brown, S. Rodriguez, J. Lunine, K. Stephan, T. M. Hoefen, S. Le Mouélic, C. Sotin, K. H. Baines, B. J. Buratti, and P. D. Nicholson, 2010, Detection and mapping of hydrocarbon deposits on Titan: Journal of Geophysical Research: Planets, v. 115, E10005, doi:10.1029/2009JE003369

Clarke, G. L., M. Guiraud, R. Powell, and J. P. Burg, 1987, Metamorphism in the Olary Block, South Australia; compression with cooling in a Proterozoic fold belt: Journal of Metamorphic Geology, v. 5, p. 291–306.

Clarke, J. D. A., 1994, Evolution of the Lefroy and Cowan palaeodrainage channels, Western Australia: Australian Journal of Earth Sciences,, v. 41, p. 55–68.

Clarke, J. D. A., 2006, Antiquity of aridity in the Chilean Atacama Desert: Geomorphology, v. 73, p. 101–114.

Clarke, P., and J. Parnell, 1999, Facies analysis of a back-tilted lacustrine basin in a strike-slip zone, Lower Devonian, Scotland: Palaeogeography Palaeoclimatology Palaeoecology. v. 151, p. 167–190.

Clauzon, G., J. P. Suc, F. Gautier, A. Berger, and M. F. Loutre, 1996, Alternate interpretation of the Messinian salinity crisis: controversy resolved?: Geology, v. 24, p. 363–366.

Clavero, E., M. Hernandez-Marine, J. O. Grimalt, and F. Garcia-Pichel, 2000, Salinity tolerance of diatoms from thalassic hypersaline environments: Journal of Phycology, v. 36, p. 1021–1034.

Clayton, R. H., and L. Thorpe, 1982, Geology of the Nanisivik zinc-lead deposit: Geological Association of Canada, Special Paper, v. 25, p. 739–758.

Clement, G. P., and W. T. Holser, 1988, Geochemistry of Moroccan evaporites in the setting of the North Atlantic Rift.: Journal of African Earth Sciences, v. 7, p. 375–382.

Clement, J. H., 1985, Depositional sequences and characteristics of Ordovician Red River Reservoirs, Pennel Field, Williston Basin, in P. O. Roehl, and P. W. Choquette, eds., Carbonate petroleum reservoirs: a case book: New York, Springer Verlag, p. 71–84.

Clemmensen, L. B., 1978, Alternating aeolian, sabkha and shallow-lake deposits from the Middle Triassic Gipsdalen Formation, Scoresby Land, East Greenland: Palaeogeography, Palaeoclimatology, Palaeoecology, v. 24, p. 111–135.

Clemmensen, L. B., W. T. Holser, and D. Winter, 1984, Stable isotope study through Permain Triassic boundary: Bull. Geol. Soc. Denmark, v. 33, p. 253–260.

Clemmey, H., and N. Badham, 1982, Oxygen in the Precambrian atmosphere; an evaluation of the geological evidence: Geology, v. 10, p. 141–146.

Closson, D., 2005, Structural control of sinkholes and subsidence hazards along the Jordanian Dead Sea coast: Environmental Geology, v. 47, p. 290–301.

Closson, D., and N. Abou Karaki, 2009, Human-induced geological hazards along the Dead Sea coast: Environmental Geology, v. 58, p. 371–380.

Closson, D., N. Abou Karaki, and F. Hallot, 2010, Landslides along the Jordanian Dead Sea coast triggered by the lake level lowering: Environmental Earth Sciences, v. 59, p. 1417–1430.

Closson, D., P. LaMoreaux, N. Abou Karaki, and H. al-Fugha, 2007, Karst system developed in salt layers of the Lisan Peninsula, Dead Sea, Jordan: Environmental Geology, v. 52, p. 155–172.

Cloud, P. E., 1972, A working model of the primitive earth: Am. J. Sci., v. 272, p. 537–548.

Cobbold, P. R., K. E. Meisling, and V. S. Mount, 2001, Reactivation of an obliquely rifted margin, Campos and Santos basins, southeastern Brazil: Bulletin American Association Petroleum Geologists, v. 85, p. 1925–1944.

Cobbold, P. R., P. Szatmari, L. S. Demercian, D. Coelho, and E. A. Rossello, 1995, Seismic and experimental evidence for thin-skinned horizontal shortening by convergent radial gliding on evaporites, deepwater Santos Basin, Brazil, in M. P. A. Jackson, D. G. Roberts, and S. Snelson, eds., Salt tectonics: a global perspective, American Association Petroleum Geologists Memoir, v.65, p. 305–322.

Cocherie, A., J. Y. Calvez, and E. Oudin-Dunlop, 1994, Hydrothermal activity as recorded by Red Sea sediments; Sr-Nd isotopes and REE signatures: Marine Geology, v. 118, p. 291–302.

Cocker, M. D., G. J. Orris, C. Yang, and P. Dunlap, 2010, The U.S. Geological Survey's assessment of potash resources in the Prairie Evaporite Formation, Elk Point Basin, Canada and the United States: Open House 2010 Abstract Volume, Saskatchewan Geological Survey, p42.

Cody, R. D., 1976, Growth and early diagenetic changes in artificial gypsum crystals grown within bentonite muds and gels: Geological Society America Bulletin, v. 87, p. 1163–1168.

Cody, R. D., and A. M. Cody, 1988, Gypsum nucleation and crystal morphology in analog saline terrestrial environments: Journal of Sedimentary Petrology, v. 58, p. 247–255.

Coenraads, R., and C. C. de Bon, 2000, Lapis Lazuli from the Coquimbo Region, Chile: Gems & Gemology, v. 36, p. 28–41.

Cogley, J. G., 1984, Continental margins and the extent and number of the continents (Paper 4R0215): Reviews Geophysics Space Physics, v. 22, p. 101–122.

Cohen (ed), P., 1989, ASME Handbook on Water Technology for Thermal Power Systems, American Society of Mechanical Engineers, 1900 p.

Cohen, A. S., 1989, Facies relationships and sedimentation in large rift lakes and implications for hydrocarbon exploration: Examples from Lake Turkana and Tanganyika: Palaeogeography Palaeoclimatology Palaeoecology, v. 70, p. 65–80.

Cohen, A. S., and A. L. Coe, 2007, The impact of the Central Atlantic Magmatic Province on climate and on the Sr- and Os-isotope evolution of seawater: Palaeogeography Palaeoclimatology Palaeoecology, v. 244, p. 374–390.

Cohen, A. S., and C. Thouin, 1987, Nearshore carbonate deposits in Lake Tanganyika: Geology, v. 15, p. 414–418.

Cohen, T. J., G. C. Nanson, J. D. Jansen, B. G. Jones, Z. Jacobs, J. R. Larsen, J. H. May, P. Treble, D. M. Price, and A. M. Smith, 2012,

Late Quaternary mega-lakes fed by the northern and southern river systems of central Australia: Varying moisture sources and increased continental aridity: Palaeogeography, Palaeoclimatology, Palaeoecology, v. 356-357, p. 89–108.

Cohen, T. J., G. C. Nanson, J. D. Jansen, B. G. Jones, Z. Jacobs, P. Treble, D. M. Price, J.-H. May, A. M. Smith, L. K. Ayliffe, and J. C. Hellstrom, 2011, Continental aridification and the vanishing of Australia's megalakes: Geology, v. 39, p. 167–170.

Cole, G. A., M. A. Abuali, E. L. Colling, H. I. Halpem, W. J. Carrigan, G. R. Savage, R. J. Scolaro, and S. H. Aisharidi, 1995, Petroleum geochemistry of the Midyan and Jaizan basins of the Red Sea, Saudi Arabia: Marine and Petroleum Geology, v. 12, p. 597–614.

Cole, L.H., 1926, Pages 26–27, 74–78, 113 in Sodium Sulphate of Western Canada. Number 646. Ottawa: Canada Department of Mines.

Cole, R. D., 1985, Depositional environment of oil shale in the Green River Formation, Douglas Creek Arch, Colorado and Utah, in M. D. Picard, ed., Geology and Energy Resources, Uinta Basin of Utah: Salt Lake City, Utah, Utah Geological Association, p. 211–224.

Collenette, P., and D. J. Grainger, 1994, Mineral Resources of Saudi Arabia (not including oil, natural gas and sulfur): DGMR Special Publication, v. SP-2, p. 322.

Collett, T. S., A. H. Johnson, C. C. Knapp, and R. Boswell, 2009, Natural Gas Hydrates: A Review, in T. Collett, A. Johnson, C. Knapp, and R. Boswell, eds., Natural gas hydrates—Energy resource potential and associated geologic hazards: American Association of Petroleum Geologists Memoir, v. 89, p. 146–219.

Collins, A. G., 1975, Geochemistry of oil field waters: Developments in Petroleum Science, 1: Amsterdam, Elsevier, 496 p.

Collins, A. G., J. H. Bennett, and O. K. Manuel, 1971, Iodine and Algae in Sedimentary Rocks Associated with Iodine-Rich Brines: Geological Society of America Bulletin, v. 82, p. 2607–2610.

Collins, D., D. Briggs, and S. C. Morris, 1983, New Burgess Shale Fossil Sites Reveal Middle Cambrian Faunal Complex: Science, v. 222, p. 163–167.

Collins, J. F., J. A. M. Kenter, P. M. Harris, G. Kuanysheva, D. J. Fischer, and K. L. Steffen, 2006, Facies and reservoir-quality variations in the late Visean to Bashkirian outer platform, rim, and flank of the Tengiz buildup, Precaspian Basin, Kazakhstan, in P. M. Harris, and L. J. Weber, eds., Giant hydrocarbon reservoirs of the world: From rocks to reservoir characterization and modeling, American Association Petroleum Geologists Memoir 88/SEPM Special Publication, p. 55–95.

Colman, S. M., K. Kelts, and D. A. Dinter, 2002, Depositional history and neotectonics in Great Salt Lake, Utah, from high-resolution seismic stratigraphy: Sedimentary Geology, v. 148, p. 61–78.

Colson, J., and I. Cojan, 1996, Groundwater dolocretes in a lake-marginal environment – An alternative model for dolocrete formation in continental settings (Danian of the Provence Basin, France): Sedimentology, v. 43, p. 175–188.

Comer, J. B., 2012, Woodford Shale and the evaporite connection – The significance of aridity an hypersalinity in organic matter productivity and preservation (abs.): Geological Society of America- North-Central Section – 46th Annual Meeting (23–24 April 2012)

Comodi, P., M. Mellini, and P. F. Zanazzi, 1990, Scapolites: variation of structure with pressure and possible role in the storage of fluids: European Journal of Mineralogy, v. 2, p. 195–202.

Condie, K. C., 2004, Supercontinents and superplume events: distinguishing signals in the geologic record: Physics of the Earth and Planetary Interiors, v. 146, p. 319–332.

Condie, K. C., and A. Kröner, 2008, When did plate tectonics begin? Evidence from the geologic record: Geological Society of America Special Papers, v. 440, p. 281–294.

Conklin, J., 1974, Structural geology of the Huizachal-Peregrina Anticlinorium: Pan American Geological Society, Geology of Huizachal-Peregrina Anticlinorium, p. 21–31.

Conly, A. G., 1995, Geological setting and genesis of the hanging wall sulphide zones, Sullivan Zn-Pb Deposit, southeastern British Columbia: Masters thesis, Carleton University, Ottawa, ON, Canada.

Connan, J., and D. Dessort, 1987, Novel family of hexacyclic hopanoid alkanes (C32---C35) occurring in sediments and oils from anoxic paleoenvironments: Organic Geochemistry, v. 11, p. 103–113.

Conor, C. H. H., and W. V. Preiss, 2008, Understanding the 1720–1640 Ma Palaeoproterozoic Willyama Supergroup, Curnamona Province, Southeastern Australia: Implications for tectonics, basin evolution and ore genesis: Precambrian Research, v. 166, p. 297–317.

Converse, D. R., P. H. Nicholson, R. J. Pottorf, and T. W. Miller, 2000, Controls on Overpressure in Rapidly Subsiding Basins and Implications for Failure of Top Seal (Chapter 11), in M. R. Mello, and B. J. Katz, eds., Petroleum Systems of South Atlantic Margins, v. 73, American Association Petroleum Geologists Memoir p. 133–150.

Cook, D. J., A. F. Randazzo, and C. L. Sprinkle, 1985, Authigenic fluorite in dolomitic rocks of the Floridan Aquifer: Geology, v. 13, p. 390–391.

Cook, F. S., and P. S. J. Coleman, 2007, Benthic diatoms in the salinas of the Dry Creek saltfields, South Australia: Hydrobiologia, v. 576, p. 61–68.

Cook, N., 1992, Geology of metamorphosed Proterozoic playa lake deposits, Olary Block, South Australia: PhD thesis, University of New England.

Cook, N., 1993, Composition and source of fluids in metamorphosed non-marine evaporites, Olary Block, South Australia: Conference: Mid- to lower-crustal metamorphism and fluids conference, Mount Isa, Mount Isa, Queensland, Australia, July 26-Aug. 1, 1993, p. 42.

Cook, N. D. J., and P. M. Ashley, 1992, Meta-evaporite sequence, exhalative chemical sediments and associated rocks in the Proterozoic Willyama Supergroup, South Australia: implications for metallogenesis: Precambrian Research, v. 56, p. 211–226.

Cooke, D. R., S. W. Bull, R. R. Large, and P. J. McGoldrick, 2000, The importance of oxidized brines for the formation of Australian Proterozoic stratiform sediment-hosted Pb-Zn (sedex) deposits: Economic Geology, v. 95, p. 1–17.

Cooke, R. U., A. Warren, and A. S. Goudie, 1993, Desert Geomorphology: London, Butler and Tanner, 526 p.

Cooper, A. H., 1986, Subsidence and foundering of strata caused by the dissolution of Permian gypsum in the Ripon and Bedale areas, North Yorkshire: Harwood, Gill M., Smith, Denys B. The English Zechstein and related topics. Univ. Newcastle upon Tyne, Newcastle upon Tyne, United Kingdom. Geological Society Special Publications, v. 22, p. 127–139.

Cooper, A. H., 1995, Subsidence hazards due to the dissolution of Permian gypsum in England: Investigation and remediation, in B. F. Beck, ed., Karst Geohazards – Engineering and Environmental Problems in Karst Terrane. Proceedings of the fifth multidisciplinary conference on sinkholes and the environmental impacts of karst, Gatlinburg, Tennessee: Rotterdam, A.A. Balkema, p. 23–29.

Cooper, A. H., 1998, Subsidence hazards caused by the dissolution of Permian gypsum in England: geology, investigation and remediation, in J. G. Maund, and M. Eddleston, eds., Geohazards in Engineering Geology, v. 15: London, Geological Society, London, p. 265–275.

Cooper, A. H., and F. Gutiérrez, 2013, Dealing with gypsum karst problems: hazards, environmental issues, and planning, in J. F. Shroder, ed., Treatise on geomorphology, Elsevier, p. 451–462.

Cooper, A. H., and J. M. Saunders, 2002, Road and bridge construction across gypsum karst in England: Engineering Geology, v. 65, p. 217–233.

Cooper, A. H., and A. C. Waltham, 1999, Subsidence caused by gypsum dissolution at Ripon, North Yorkshire: Quarterly Journal of Engineering Geology, v. 32, p. 305–310.
Cooper, A. M., 1991, Late Proterozoic hydrocarbon potential and its association with diapirism in Blinman #2, Central Flinders Ranges.: Honours thesis, University of Adelaide – National Centre Petroleum Geology and Geophysics.
Cooper, B. S., P. C. Barnard, and N. Telnaes, 1995, The Kimmeridge Clay Formation of the North Sea, in B. Katz, ed., Petroleum source rocks: Berlin, Springer Verlag, p. 89–110.
Cordell, R. J., 1992, Carbonates as hydrocarbon source rocks, in G. V. Chilingarian, S. J. Mazzullo, and H. H. Rieke, eds., Carbonate reservoir characterisation: a geologic-engineering analysis, part 1: Developments in Petroleum Science, v. 30: Amsterdam, Elsevier, p. 271–329.
Cordes, E. E., D. C. Bergquist, and C. R. Fisher, 2009, Macro-Ecology of Gulf of Mexico Cold Seeps, Annual Review of Marine Science: 1, p. 143–168.
Cordier, D., J. W. Barnes, and A. G. Ferreira, 2013, On the chemical composition of Titan's dry lakebed evaporites: Icarus, v. 226, p. 1431–1437.
Cornford, C., 2005, The Petroleum System, in R. C. Selley, L. R. M. Cocks, and I. R. Plimer, eds., Encyclopedia of Geology, Elsevier Academic Press, p. 268–294.
Coron, C. R., 1982, Facies relations and ore genesis of the Newfoundland Zinc mines deposit, Daniel's Harbour, western Newfoundland: Doctoral thesis, University of Toronto (Canada).
Corriveau, L., 2007, Iron Oxide Copper-Gold (±Ag, ±Nb, ±REE, ±U) Deposits: A Canadian Perspective, in W. D. Goodfellow, ed., Mineral Deposits of Canada: A Synthesis of Major Deposit Types, District Metallogeny, the Evolution of Geological Provinces, and Exploration Methods, Geological Association of Canada, Mineral Deposits Division, Special Publication, Vol. 5, p. 1–23.
Corriveau, L., S. Perreault, and A. Davidson, 2007, Prospective metallogenic settings of the Grenville Province, in W. D. Goodfellow, ed., Mineral Deposits of Canada: A Synthesis of Major Deposit-Types, District Metallogeny, the Evolution of Geological Provinces, and Exploration Methods, Geological Association of Canada, Mineral Deposits Division, Special Publication No. 5, p. 814–847.
Corriveau, L., P. J. Williams, and H. Mumin, 2009, Alteration vectors to IOCG mineralization – from uncharted terranes to deposits. , in L. Corriveau, and H. Mumin, eds., Exploring for Iron Oxide Copper-Gold Deposits: Canada and Global Analogues, Geological Association of Canada Mineral Deposits Division Short Course Volume 19, p. 87–106.
Corselli, C., and F. S. Aghib, 1987, Brine formation and gypsum precipitation in the Bannock Basin (eastern Mediterranean): Marine Geology, v. 75, p. 185–199.
Corsetti, F. A., and N. J. Lorentz, 2006, On Neoproterozoic cap carbonates as chronostratigraphic markers, in S. Xiao, and A. J. Kaufman, eds., Neoproterozoic Geobiology and Paleobiology: Berlin, Springer Scientific Publishing, p. 273–294.
Cortecci, G., T. Boschetti, M. Mussi, C. Herrera Lameli, C. Mucchino, and M. Barbieri, 2005, New chemical and original isotopic data on waters from El Tatio geothermal field, northern Chile: Geochemical Journal, v. 39, p. 547–571.
Cosgrove, J. W., 2001, Hydraulic fracturing during the formation and deformation of a basin: A factor in the dewatering of low-permeability sediments: American Association Petroleum Geologists – Bulletin, v. 85, p. 737–748.
Cosgrove, J. W., C. J. Talbot, and P. Aftabi, 2009, A train of kink folds in the surficial salt of Qom Kuh, Central Iran: Journal of Structural Geology, v. 31, p. 1212–1222.
Coshell, L., and M. R. Rosen, 1994, Stratigraphy and Holocene history of Lake Hayward, Swan Coastal Plain, Western Australia, in R. Renaut, and W. Last, eds., Sedimentology and Geochemistry of Modern and Ancient Lakes, v. 50: Tulsa OK, SEPM Special Publ., p. 173–188.
Coshell, L., M. R. Rosen, and K. J. McNamara, 1998, Hydromagnesite replacement of biomineralized aragonite in a new location of Holocene stromatolites, Lake Walyungup, Western Australia: Sedimentology, v. 45, p. 1005–1018.
Cossey, S. P., 2004, Celebrations began with cognac: American Association Petroleum Geologists Explorer, September 2004.
Cota, L., and G. Baric, 1998, Petroleum potential of the Adriatic offshore, Croatia: Organic Geochemistry, v. 29, p. 559–570.
Cotton, J. T., and H. A. Koyi, 2000, Modeling of thrust fronts above ductile and frictional detachments: Application to structures in the Salt Range and Potwar Plateau, Pakistan: Geological Society of America Bulletin, v. 112, p. 351–363.
Council, T. C., and P. C. Bennett, 1993, Geochemistry of ikaite formation at Mono Lake, California: implications for the origin of tufa mounds: Geology, v. 21, p. 971–974.
Courel, L., B. Fekirine, M. Oujidi, M. Soussi, A. Tourani, H. Aît Salem, N. Benaouiss, and M. Et-Touhami, 2003, Mid-Triassic to Early Liassic clastic/evaporitic deposits over the Maghreb Platform: Palaeogeography, Palaeoclimatology, Palaeoecology, v. 196, p. 157–176.
Coveney, R. M., 1989, A review of the origins of metal-rich Pennsylvanian black shales, central USA, with an inferred role for basinal brines: Applied Geochemistry, v. 4, p. 347–367.
Cowan, G., 1993, Identification and significance of aeolian deposits within the dominantly fluvial Sherwood Sandstone Group of the East Irish Sea Basin, UK., in C. P. North, and D. J. Prosser, eds., Characterization of Fluvial and Aeolian Reservoirs: London, Geological Society of London Special Publication 73, p. 231–245.
Coward, M., and S. Stewart, 1995, Salt-influenced structures in the Mesozoic-Tertiary cover of the southern North Sea , U.K, in M. P. A. Jackson, D. G. Roberts, and S. Snelson, eds., Salt Tectonics: A Global Perspective, v. 65, American Association of Petroleum Geologists Memoir, p. 229–250.
Cox, D. P., D. A. Lindsey, D. A. Singer, B. C. Moring, and M. F. Diggles, 2007, Sediment-Hosted Copper Deposits of the World: Deposit Models and Database: USGS Open File Report 03-107, Version 1.3 (Available online at http://pubs.usgs.gov/of/2003/of03-107/).
Cox, D. P., and D. A. Singer, 2007, Descriptive and Grade-tonnage models for Iron-oxide Cu-Au deposits: USGS Open File Report 2006–1155, 13 p.
Crabaugh, M., and G. Kocurek, 1993, Entrada Sandstone – example of a wet eolian system, in K. Pye, ed., The Dynamics and Environmental Context of Aeolian Sedimentary Systems, Geological Society London, Special Publication No. 72, p. 103–126.
Craddock, P. R., and W. Bach, 2010, Insights to magmatic-hydrothermal processes in the Manus back-arc basin as recorded by anhydrite: Geochimica et Cosmochimica Acta, v. 74, p. 5514–5536.
Craig, D. H., 1988, Caves and other features of Permian karst in San Andres dolomite, Yates field reservoirs, west Texas, in N. P. James, and P. W. Choquette, eds., Paleokarst: New York, Springer-Verlag, p. 342–363.
Craig, J., U. Biffi, R. F. Galimberti, K. A. R. Ghori, J. D. Gorter, N. Hakhoo, D. P. Le Heron, J. Thurow, and M. Vecoli, 2013, The palaeobiology and geochemistry of Precambrian hydrocarbon source rocks: Marine and Petroleum Geology, v. 40, p. 1–47.
Craig, J., J. W. Downey, A. D. Gibbs, and J. R. Russell, 1984, Possible major diapiric structures in the southern Canning and northern Officer basins, in P. G. Purcell, ed., The Canning Basin.: Perth, Petroleum Exploration Society of Australia; WA Branch.
Craig, J. R., R. D. Fortner, and B. L. Weand, 1974, Halite and Hydrohalite from Lake Bonney, Taylor Valley, Antarctica: Geology, v. 2, p. 389–390.

Cramer, B. S., J. R. Toggweiler, J. D. Wright, M. E. Katz, and K. G. Miller, 2009, Ocean overturning since the Late Cretaceous: Inferences from a new benthic foraminiferal isotope compilation: Paleoceanography, v. 24, p. PA 4216.

Cramez, C., and M. P. A. Jackson, 2000, Superposed deformation straddling the continental-oceanic transition in deep-water Angola: Marine and Petroleum Geology, v. 17, p. 1095–1109. Crangle Jnr., R. D., 2011, Gypsum 2009: US Geological Survey Minerals yearbook.

Crangle Jr., R. D., 2011, Gypsum 2009: US Geological Survey Minerals yearbook.

Crawford, A. J., and D. Hilyard, 1990, Geochemistry of Late Proterozoic tholeiitic flood basalts, Adelaide Geosyncline, South Australia: Geological Society of Australia Special Publication, v. 16, p. 49–67.

Crétaux, J. F., W. Jelinski, S. Calmant, A. Kouraev, V. Vuglinski, M. Bergé-Nguyen, M. C. Gennero, F. Nino, R. Abarca Del Rio, A. Cazenave, and P. Maisongrande, 2011, SOLS: A lake database to monitor in the Near Real Time water level and storage variations from remote sensing data: Advances in Space Research, v. 47, p. 1497–1507.

Crick, I. H., and M. D. Muir, 1980, Evaporites and uranium mineralization in the Pine Creek Geosyncline: Symposium on the Pine Creek Geosyncline, jointly sponsored by the Bureau of Mineral Resources, Geology and Geophysics and the CSIRO Institute of Earth Resources, in cooperation with the International Atomic Energy Agency,, p. 531–542.

Crocker, I. T., 1979, Fluorite mineralisation in the dolomite of the Transvaal Supergroup, South Africa: Geological Society of South Africa, Special Publication, v. 6, p. 73–82.

Crossley, N. G., 1997, Downhole probes evaluate cavern integrity: Oil and Gas Journal, March 3, 1997, p. 74–79.

Crossley, N. G., 1998, Sonar surveys used in gas-storage cavern analysis: Oil & Gas Journal, May 4, 1998, p. 98–108.

Crowley, J. K., 1993, Mapping playa evaporite minerals with AVIRIS data; a first report from Death Valley, California: Remote Sensing of Environment, v. 44, p. 337–356.

Crowley, S. F., S. H. Bottrell, M. D. B. McCarthy, J. Ward, and B. Young, 1997, Delta-S-34 of Lower Carboniferous anhydrite, Cumbria and its implications for barite mineralisation in Northern Pennines: Journal of the Geological Society, v. 154, p. 597–600.

Croxton, N. M., 2003, Subsidence on Interstate 70 in Russell County, Kansas, related to salt dissolution – A history, in K. S. Johnson, and J. T. Neal, eds., Evaporite karst and engineering/environmental problems in the United States, v. 109, Oklahoma Geological Survey Circular, p. 149–155.

Cucchi, F., and L. Zini, 2003, Gypsum karst of Zagros Mountains (I.R. Iran): Acta Carsologica, v. XXXII, p. 69–82.

Culbertson, W. C., 1966, Trona in the Wilkins Peak Member of the Green River Formation, southwestern Wyoming: US Geological Survey Professional Paper, v. 424-D, p. 170–173.

Cunningham, K. I., and K. I. Takahashi, 1992, Evidence for petroleum-assisted speleogenesis, Lechuguilla Cave, Carlsbad Caverns National Park, New Mexico: in Carter, L. M. H., ed., U.S. Geological Survey Research on Energy Resources – 1992 Program and Abstracts Eighth V.E. McKelvey Forum on Mineral and Energy Resources, Houston, TX, February 17–20, 1992: U.S. Geological Survey Circular 1074, p. 16–17.

Cunningham, K. J., R. H. Benson, K. Rakicelbied, and L. W. Mckenna, 1997, Eustatic implications of Late Miocene depositional sequences in the Melilla Basin, Northeastern Morocco: Sedimentary Geology, v. 107, p. 147–165.

Curial, A., D. Dumas, and G. Dromart, 1990, Organic matter and evaporites in the Paleogene West European Rift: The Bresse and Valence salt basins (France), in A. Y. Huc, ed., Deposition of Organic Facies, v. 30: Tulsa, OK, American Association Petroleum Geologists, Studies in Geology.

Currie, P. K., and J. V. Walters, 1985, Finite element modelling of cavity behaviour in the solution mining of magnesium salts, in W. J. Schlitt, ed., Salt and Brines '85: New York, Amer. Inst. Min. Met. Petr. Eng., p. 87–96.

Curtis, R., G. Evans, D. J. J. Kinsman, and D. J. Shearman, 1963, Association of dolomite and anhydrite in the Recent sediments of the Persian Gulf: Nature, p. 679–680.

Cytryn, E., D. Minz, R. S. Oremland, and Y. Cohen, 2000, Distribution and Diversity of Archaea Corresponding to the Limnological Cycle of a Hypersaline Stratified Lake (Solar Lake, Sinai, Egypt): Applied & Environmental Microbiology, v. 66, p. 3269–3276.

Czapowski, G., 1987, Sedimentary facies in the oldest rock salt (Na 1) of the Leba elevation (northern Poland), in T. M. Peryt, ed., The Zechstein Facies in Europe, v. 10: Berlin, Springer-Verlag Lecture Notes in Earth Sciences, p. 207–224.

D'Amore, F., D. Giusti, and A. Abdallah, 1998, Geothermics of the high-salinity geothermal field of Asal, Republic of Djibouti, Africa: Geothermics, v. 27, p. 197–210.

D'Ans, J., 1961, Uber die Bildungsmöglichkeiten des Tachhydrits in Kalisalzlagerstàtten: Kali and Steinsalz, v. 3, p. 119.

D'Heur, M., 1990a, West Ekofisk Field--Norway Central Graben, North Sea, Structural Traps IV: Tectonic and Nontectonic Fold Traps, American Association Petroleum Geologists, Special Publication, p. 57–83.

D'Heur, M., 1990b, Eldfisk Field--Norway Central Graben, North Sea, Structural Traps IV: Tectonic and Nontectonic Fold Traps, American Association Petroleum Geologists, Special Publication, p. 27–56.

D'Onfro, P., 1988, Mechanics of salt tongue formation with examples from Louisiana slope (abs): American Association of Petroleum Geology, Bulletin, v. 72, p. 175.

Dahl, J., J. M. Moldowan, and P. Sundararaman, 1993, Relationship of biomarker distribution to depositional environment – Phosphoria Formation, Montana, USA: Organic Geochemistry, v. 20, p. 1001–1017.

Dahl, J. E., J. M. Moldowan, S. C. Teerman, M. A. McCaffrey, P. Sundararaman, M. Pena, and C. E. Stelting, 1994, Source rock quality determination from oil biomarkers I. – An example from the Aspen Shale, Scully's Gap, Wyoming: Bulletin American Association Petroleum Geologists, v. 78, p. 1507–1026.

Dahl, L. J., 1985, Solution Mining Bibliography, in W. J. Schlitt, ed., Salt and Brines '85, Amer. Inst. Min. Met. Petr. Eng., p. 169–174.

Dahlkamp, F. J., 1993, Uranium Ore Deposits, Springer-Verlag, Berlin & Heidelberg, 460 p.

Dahm, T., S. Heimann, and W. Bialowons, 2011, A seismological study of shallow weak micro-earthquakes in the urban area of Hamburg city, Germany, and its possible relation to salt dissolution: Natural Hazards, v. 58, p. 1111–1134.

Dailly, G. C., 1976, A possible mechanism relating progradation, growth faulting, clay diapirism and overthrusting in a regressive sequence of sediments: Canadian Petroleum Geology Bulletin, v. 24, p. 92–116.

Dalgarno, C. R., and J. E. Johnson, 1966, Parachilna Sheet, South Australia. Geological Survey of South Australia, Map Series.

Dalgarno, C. R., and J. E. Johnson, 1968, Diapiric structures and late Precambrian-early Cambrian sedimentation in Flinders ranges, South Australia: American Association Petroleum Geologists, Memoir, v. 8, p. 301–314.

Dalthorp, M., and T. H. Naehr, 2011, Structural and Stratigraphic Relationships of Hydrocarbon Seeps in the Northern Gulf of Mexico and Geological Factors Contributing to Migration Variations: Gulf Coast Association of Geological Societies Transactions, v. 61, p. 105–122.

Damnati, B., and M. Taieb, 1995, Solar and ENSO signatures in laminated deposits from Lake Magadi (Kenya) during the Pleistocene/Holocene transition: Journal of African Earth Sciences, v. 21, p. 373–382.

Damste, J. S. S., J. W. De Leeuw, S. Betts, Yue Ling, and P. M. Hofmann, 1993, Hydrocarbon biomarkers of different lithofacies of the Salt IV Formation of the Mulhouse Basin, France: Organic Geochemistry, v. 20, p. 1187–1200.

Damste, J. S. S., N. L. Frewin, F. Kenig, and J. W. Deleeuw, 1995, Molecular indicators or palaeoenvironmental change in a Messinian evaporitic sequence (Vena del Gesso, Italy) .1. Variations in extractable organic matter of ten cyclically deposited marl beds: Organic Geochemistry, v. 23, p. 471–483.

Dardeau, G., and P. C. Graciansky, 1990, Halokinesis and alpine rifting in the Alpes-Maritimes (France): Bull. Centres Rech. Explr.-Prod. Elf Aquitaine, v. 14, p. 443–464.

Darragi, F., M. Gueddari, and B. Fritz, 1983, Mise en evidence d'un fluoro-sulfate de sodium, la kogarkoite, dans les croutes salines du Lac Natron en Tanzanie (Presence of Kogarkoite (Na_3SO_4F) in the salt paragenesis of Lake Natron in Tanzania: Comptes-Rendus des Seances de l'Academie des Sciences, Serie 2: Mecanique-Physique, Chimie, Sciences de l'Univers, Sciences de la Terre, v. 297, p. 141–144.

Darragi, F., and Y. Tardy, 1987, Authigenic trioctohedral smectites controlling pH, alkalinity silica and magnesium concentrations in alkaline lakes: Chemical Geology, v. 63, p. 59–72.

Das, N., J. Horita, and H. D. Holland, 1990, Chemistry of fluid inclusions in halite from the Salina Group of the Michigan Basin; implications for Late Silurian seawater and the origin of sedimentary brines: Geochimica et Cosmochimica Acta, v. 54, p. 319–327.

Dasgupta, S., M. R. Hong, and I. A. Al-Jallal, 2002, Accurate reservoir characterization to reduce drilling risk in Khuff-C carbonate, Ghawar field, Saudi Arabia: GeoArabia, v. 7, p. 81–100.

Dasgupta, S. P., K. V. Ramachandra, and M. S. Jairam, 1998, A framework analysis of Nagaur Ganganagar evaporite basin, Rajasthan: Indian Minerals, v. 42, p. 57–64.

DasSarma, S., and P. Arora, 2001, Halophiles: Encyclopedia of Life Sciences (Nature Publishishing Group www.els.net), p. 1–9.

Davidson, G. J., 1994, Hostrocks to the stratabound iron-formation-hosted Starra gold-copper deposit, Australia: Mineralium Deposita, v. 29, p. 237–249.

Davidson, G. J., 1998, Alkali alteration styles and mechanisms, and their implications for a brine factory source of base metals in the rift-related McArthurGroup, Australia: Australian Journal of Earth Sciences, v. 45, p. 33–49.

Davidson, G. J., 1999, Feldspar metasomatism along a Proterozoic rift-basin margin – "Smoke" around a base-metal "fire" (HYC deposit, Australia) or a product of background diagenesis?: Geological Society of America Bulletin, v. III, p. 663–673.

Davidson, G. J., and R. R. Large, 1994, Gold metallogeny and the copper-gold association of the Australian Proterozoic: Mineralium Deposita, v. 29, p. 208–223.

Davidson, G. J., and R. R. Large, 1998, Proterozoic copper-gold deposits: AGSO Journal of Australian Geology and Geophysics, v. 17, p. 105–113.

Davidson, G. J., R. R. Large, G. L. Kary, and R. Osborne, 1989, The deformed iron formation-hosted Starra and Trough Tank Au-Cu mineralisation: a new association from the Proterozoic Eastern Succession of Mount Isa, Australia: Econ. Geol. Monograph, v. 6, p. 135–150.

Davidson, G. J., H. Paterson, S. Meffre, and R. Berry, 2008, Constraints on uranium introduction into a hematitic breccia (Oak Dam IOCG Prospect, Olympic Dam region); can we take a leaf out of the unconformity-U page?: International Geological Congress, Abstracts = Congres Geologique International, Resumes, v. 33.

Davies, G. R., 1970, Carbonate bank sedimentation, eastern Shark Bay, Western Australia, in B. W. Logan, G. R. Davies, J. F. Read, and D. E. Cebulski, eds., Carbonate Sedimentation and Environments, Shark Bay, Western Australia, American Association of Petroleum Geologists Memoir, v. 13, p. 85–168.

Davies, G. R., 1974, Paleozoic evaporites of the Canadian Arctic Archipelago, in A. H. Coogan, ed., Fourth International Symposium on Salt, Northern Ohio Geological Society, p. 119–125.

Davies, G. R., and L. B. Smith, 2006, Structurally controlled hydrothermal dolomite reservoir facies: An overview: Bulletin American Association Petroleum Geologists, v. 90, p. 1641–1690.

Davies, P. B., 1984a, Deep-Seated Dissolution and Subsidence in Bedded Salt Deposits: Doctoral thesis, Stanford University.

Davies, P. B., 1984b, Structural analysis of a deep seated salt dissolution collapse chimney; implications for nuclear waste disposal: Neues Jahrbuch fuer Mineralogie, Abhandlungen, v. 149, p. 163–175.

Davila, A. F., I. Hawes, C. Ascaso, and J. Wierzchos, 2013, Salt deliquescence drives photosynthesis in the hyperarid Atacama Desert: Environmental Microbiology Reports, v. 5, p. 583–587.

Davis, A., and P. Rahn, 1997, Karstic gypsum problems at wastewater stabilization sites in the Black Hills of South Dakota: Carbonates and Evaporites, v. 12, p. 73–80.

Davis, D. G., 1980, Cave development in the Guadalupe Mountains. A critical review of recent hypotheses: Natl. Speleol. Soc. Bull., v. 42, p. 42–48.

Davis, D. M., and T. Engelder, 1985, The role of salt in fold and thrust belts: Tectonophysics, v. 19, p. 67–88.

Davis, D. M., and T. Engelder, 1987, Thin-skinned deformation over salt, in I. Lerche, and J. J. O'Brien, eds., Dynamical geology of salt and related structures: New York, Academic Press, p. 301–337.

Davis, J. B., and D. W. Kirkland, 1970, Native sulfur deposition in the Castile formation, Culberson county, Texas: Econ. Geol., v. 65, p. 107–121.

Davis, J. B., and D. W. Kirkland, 1979, Bioepigenetic sulfur deposits: Economic Geology, v. 74, p. 462–468.

Davis, J. R., I. Friedman, and J. D. Gleason, 1986, Origin of the lithium-rich brine, Clayton Valley, Nevada: US Geological Survey Bulletin, v. 1622, p. 131–138.

Davis, T. B., 2004, Mine-Scale Structural Controls on the Mount Isa Zn-Pb-Ag and Cu Orebodies: Economic Geology, v. 99, p. 543–559.

Davison, I., 2007, Geology and tectonics of the South Atlantic Brazilian salt basins: Geological Society, London, Special Publications, v. 272, p. 345–359.

Davison, I., 2009, Faulting and fluid flow through salt: Journal of the Geological Society, v. 166, p. 205–216.

Davison, I., 2013, Keynote 1: Review of the Geology of Deformed Salt Bodies and the Implications for Seismic Imaging: 75th EAGE Conference & Exhibition – Workshops, Session: Ws11 – Interpreting the Imperfect Image, London, 10 June 2013

Davison, I., G. Alsop, N. Evans, and M. Safaricz, 2000a, Overburden deformation patterns and mechanisms of salt diapir penetration in the Central Graben, North Sea: Marine & Petroleum Geology, v. 17, p. 601–618.

Davison, I., G. I. Alsop, and D. J. Blundell, 1996a, Salt tectonics: some aspects of deformation mechanics, in G. I. Alsop, D. J. Blundell, and I. Davison, eds., Salt tectonics, Geological Society, London; Special Publication, v. 100, p. 1–10.

Davison, I., I. Alsop, P. Birch, C. Elders, N. Evans, H. Nicholson, P. Rorison, D. Wade, J. Woodward, and M. Young, 2000b, Geometry and late-stage structural evolution of Central Graben salt diapirs, North Sea: Marine & Petroleum Geology, v. 17, p. 499–522.

Davison, I., L. Anderson, and P. Nuttall, 2012, Salt deposition, loading and gravity drainage in the Campos and Santos salt basins: Geological Society, London, Special Publications, v. 363, p. 159–174.

Davison, I., D. Bosence, G. I. Alsop, and M. H. Al-Aawah, 1996b, Deformation and sedimentation around active Miocene salt diapirs on the Tihama Plain, northwest Yemen, in G. I. Alsop, D. J. Blundell, and I. Davison, eds., Salt tectonics, v. 100, Geological Society, London; Special Publication, p. 23–39.

Davison, I., D. Bosence, I. Alsop, and M. A. H. Al Aawah, 1995, Deformation and sedimentation above and below Miocene salt diapirs and their overhangs, NW Yemen: Proceedings of GCCSEPM Foundation 16th Annual Research Conference, Salt Sediment and Hydrocarbons, Dec 3–6, 1995, p. 33–40.

Davison, I., M. Insley, M. Harper, P. Weston, D. Blundell, K. McClay, and A. Quallington, 1993, Physical modelling of overburden deformation around salt diapirs: Tectonophysics, v. 228, p. 255–274.

Day, R., 1974, White River Nahcolite Solution Mine: Proceedings of the SME Annual Meeting, Albuquerque, NM, February, 14–17.

Day, R. W., 1967, Solution mining of carnallite, US Patent 3,555,212, Reynolds Metals, p. 5.

De Araújo, C. C., J. K. Yamamoto, S. P. Rostirolla, V. Madrucci, and A. Tankard, 2005, Tar sandstones in the Paraná Basin of Brazil: structural and magmatic controls of hydrocarbon charge: Marine and Petroleum Geology, v. 22, p. 671–685.

De Brodtkorb, M. K., V. Ramos, M. Barbieri, and S. Ametrano, 1982, The evaporitic celestite-barite deposits of Neuquen, Argentina: Mineralium Deposita, v. 17, p. 423–436.

De Celles, P. G., and G. Mitra, 1995, History of the Sevier orogenic wedge in terms of critical taper models, Northeast Utah and Southwest Wyoming: Geological Society of America Bulletin, v. 107, p. 454–462.

De Cort, G., I. Bessems, E. Keppens, F. Mees, B. Cumming, and D. Verschuren, 2013, Late-Holocene and recent hydroclimatic variability in the central Kenya Rift Valley: The sediment record of hypersaline lakes Bogoria, Nakuru and Elementeita: Palaeogeography, Palaeoclimatology, Palaeoecology, v. 388, p. 69–80.

De Deckker, P., 1981, Ostracods of Athalassic Saline Lakes – a Review: Hydrobiologia, v. 81-2, p. 131–144.

De Deckker, P., 1982, Holocene Ostracods, Other Invertebrates and Fish Remains from Cores of Four Maar Lakes in Southern Australia: Proc. R. Soc. Viet, v. 94, p. 183–220.

De Deckker, P., and M. C. Geddes, 1980, Seasonal fauna of ephemeral saline lakes near the Coorong Lagoon, South Australia: Australian Journal of Marine and Freshwater Research, v. 31, p. 677–699.

de Jager, J., 2003, Inverted basins in the Netherlands, similarities and differences: Geologie en Mijnbouw/Netherlands Journal of Geosciences, v. 82, p. 355–366.

de Jong, G., and P. J. Williams, 1995, Giant metasomatic system formed during exhumation of mid-crustal Proterozoic rocks in the vicinity of the Cloncurry Fault, northwest Queensland: Australian Journal of Earth Sciences, v. 42, p. 281–290.

de Lange, G. J., and W. Krijgsman, 2010, Messinian salinity crisis: A novel unifying shallow gypsum/deep dolomite formation mechanism: Marine Geology, v. 275, p. 273–277.

de Lange, G. J., J. J. Middleburg, C. H. van der Weijden, G. Catalano, G. W. Luther, III, D. J. Hydes, J. R. W. Woittiez, and G. P. Klinkhammer, 1990, Composition of anoxic hypersaline brines in the Tyro and Bannock Basins, eastern Mediterranean: Marine Chemistry, v. 31, p. 63–88.

de Leeuw, A., K. Bukowski, W. Krijgsman, and K. F. Kuiper, 2010, Age of the Badenian salinity crisis; impact of Miocene climate variability on the circum-Mediterranean region: Geology, v. 38, p. 715–718.

de Lorraine, W. F., 2001, Metamorphism, polydeformation, and extensive remobilization of the Balmat zinc orebodies, northwest Adirondacks, New York: Society of Economic Geologists, Guidebook Series, v. 5, p. 25–54.

de Magnee, I., and A. Francois, 1988, The origin of the Kipushi (Cu,Zn,Pb) Deposit in direct relation with a Proterozoic salt diapir; Copperbelt of Central Africa, Shaba, Republic of Zaire, in G. H. Friedrich, and P. M. Herzig, eds., Base metal sulfide deposits in sedimentary and volcanic environments: Berlin, Springer Verlag, p. 74–93.

de Meer, S., and C. J. Spiers, 1999, Influence of pore-fluid salinity on pressure solution creep in gypsum: Tectonophysics, v. 308, p. 311–330.

De Paola, N., C. Collettini, F. Trippetta, M. R. Barchi, and G. Minelli, 2007, A mechanical model for complex fault patterns induced by evaporite dehydration and cyclic changes in fluid pressure: Journal of Structural Geology, v. 29, p. 1573–1584.

De Putter, T., J. M. Rouchy, A. Herbosch, E. Keppens, C. Pierre, and E. Groessens, 1994, Sedimentology and palaeo-environment of the upper Visean anhydrite of the Franco-Belgian Carboniferous basin (Saint-Ghislain borehole, southern Belgium): Sedimentary Geology, v. 90, p. 77–93.

De Ronde, C. E. J., M. J. Dewit, and E. T. C. Spooner, 1994, Early Archean (>3.2 Ga) Fe-oxide rich, hydrothermal discharge vents in the Barberton Greenstone belt, South Africa: Geological Society of America Bulletin, v. 106, p. 86–104.

de Ronde, C. E. J., and T. W. Ebbesen, 1996, 3.3 BY age of organic compound formation near sea-floor hot springs: Geology, v. 24, p. 791–794.

de Ruiter, P. A. C., 1979, The Gabon and Congo basins salt deposits: Economic Geology, v. 74, p. 419–431.

De Vogel, S. B., J. W. Magee, W. F. Manley, and G. H. Miller, 2004, A GIS-based reconstruction of late Quaternary paleohydrology: Lake Eyre, arid central Australia: Palaeogeography, Palaeoclimatology, Palaeoecology, v. 204, p. 1–13.

Dean, W. E., 1978, Trace and minor elements in evaporites, in W. Dean, and B. C. Schreiber, eds., Marine evaporites, Society of Economic Paleontologists and Mineralogists, Short course notes, v. 4,, p. 86–104.

Dean, W. E., and R. Y. Anderson, 1982, Continuous subaqueous deposition of the Permian Castile evaporites, Delaware Basin, Texas and New Mexico: Handford, C. R., Loucks, R. G., Davies, G. R. Depositional and diagenetic spectra of evaporites; a core workshop. Society of Economic Paleontologists and Mineralogists Core Workshop, v. 3, p. 324–353.

Dean, W. E., and T. D. Fouch, 1983, Lacustrine Environment, in P. A. Scholle, D. G. Bebout, and C. H. Moore, eds., Carbonate Depositional Environments, v. 33: Tulsa, OK, American Assoc. Petroleum Geologists Memoir, p. 96–130.

Debrand-Passard, S., 1984, Synthèse géologique du sud-est de la France: Mémoires du BRGM, v. 125, 615 p.

Decima, A., J. A. McKenzie, and B. C. Schreiber, 1988, The origin of "evaporative" limestones: An Example from the Messinian of Sicily: Journal of Sedimentary Petrology, v. 58, p. 256–272.

Decima, A., and F. C. Wezel, 1971, Osservazioni sulle evaporiti messiniane della Sicilia centromeridionale: Rivista Mineraria Siciliana, v. 130–132, p. 172–187.

Deelman, J. C., 2011, Low-temperature formation of dolomite and magnesite * A comprehensive revision*: Compact Disc Publications, Geology Series, version 2.3 Compact Disc Publications, Eindhoven, The Netherlands. http://www.jcdeelman.demon.nl/dolomite/book-prospectus.html.

Deer, A., R. Howie, W. S. Wise, and J. Zussman, 2004, Rock Forming Minerals, vol. 4B. Framework Silicates: Silica Minerals, Feldspathoids and the Zeolites: London, The Geological Society.

Deffeyes, K. S., F. J. Lucia, and P. K. Weyl, 1965, Dolomitization of Recent and Plio-Pleistocene sediments by marine evaporite waters on Bonaire, Netherlands Antilles, in L. C. Pray, and R. C. Murray, eds., Dolomitization and limestone diagenesis A symposium. Soc. Econ. Paleontologists and Mineralogists Spec. Pub., v. 13, p. 71–88.

Degens, E. T., and D. A. Ross, 1969, Hot Brines and recent heavy metal deposits in the Red Sea: New York, N.Y., Springer Verlag, 600 p.

Degens, E. T., H. K. Wong, S. Kempe, and F. Kurtman, 1984, A Geological Study of Lake Van, Eastern Turkey: Geologische Rundschau, v. 73, p. 701–734.

Dejonghe, L., 1990, The sedimentary structures of barite: examples from the Chaudfontaine ore deposit, Belgium: Sedimentology, v. 37, p. 303–323.

Dela Pierre, F., E. Bernardi, S. Cavagna, P. Clari, R. Gennari, A. Irace, F. Lozar, S. Lugli, V. Manzi, M. Natalicchio, M. Roveri, and D. Violanti, 2011, The record of the Messinian salinity crisis in the Tertiary Piedmont Basin (NW Italy): The Alba section revisited: Palaeogeography, Palaeoclimatology, Palaeoecology, v. 310, p. 238–255.

Dela Pierre, F., P. Clari, E. Bernardi, M. Natalicchio, E. Costa, S. Cavagna, F. Lozar, S. Lugli, V. Manzi, M. Roveri, and D. Violanti, 2012, Messinian carbonate-rich beds of the Tertiary Piedmont Basin (NW Italy): Microbially-mediated products straddling the onset of the salinity crisis: Palaeogeography, Palaeoclimatology, Palaeoecology, v. 344–345, p. 78–93.

Dela Pierre, F., A. Festa, and A. Irace, 2007, Interaction of tectonic, sedimentary, and diapiric processes in the origin of chaotic sediments: An example from the Messinian of Torino Hill (Tertiary Piedmont Basin, northwestern Italy): Geological Society of America Bulletin, v. 119, p. 1107–1119.

Delfino, D. O., M. D. Wanderley, L. H. Silva e Silva, F. Feder, and F. A. S. Lopes, 2012, Sedimentology and temporal distribution of microbial mats from Brejo do Espinho, Rio de Janeiro, Brazil: Sedimentary Geology, v. 263–264, p. 85–95.

Dellwig, L. F., 1955, Origin of the Salina Salt of Michigan: Journal Sedimentary Petrology, v. 25, p. 83–110.

Dellwig, L. F., and R. Evans, 1969, Depositional processes in Salina salt of Michigan, Ohio, and New York: American Association Petroleum Geologists – Bulletin, v. 53, p. 949–956.

DeLuca, M., 1999, Forty-six wells designated subsalt in the Gulf of Mexico: Offshore, v. January Issue, p. 50.

Demaison, G. J., and B. J. Huizinga, 1991, Genetic classification of petroleum systems: American Association Petroleum Geologists – Bulletin, v. 75, p. 1626–1643.

Demaison, G. J., and G. T. Moore, 1980, Anoxic environments and oil source bed genesis: American Association of Petroleum Geologists Bulletin, v. 64, p. 1179–1209.

Demange, J., G. M. di Paola, J. Lavigne, M. Lopoukhine, and L. Stieljes, 1971, Etudé géothermique de Territore Francais des Afars et des Issas: Nov. 70, Avr. 71, Rapp. 71, SGN 262 GTM Bureau de Recherches Géoliques et Miniéres, Orléans.

Dembicki, H. J., W. G. Meinschein, and D. E. Hattin, 1976, Possible ecological and environmental significance of the predominance of even carbon number C20 – C30 n-alkanes: Geochimica et Cosmochimica Acta, v. 40, p. 203–208.

Demercian, S., P. Szatmari, and P. R. Cobbold, 1993, Style and pattern of salt diapirs due to thin-skinned gravitational gliding, Campos and Santos basins, offshore Brazil: Tectonophysics, v. 228, p. 393–423.

Demicco, R. V., T. K. Lowenstein, L. A. Hardie, and R. J. Spencer, 2005, Model of seawater composition for the Phanerozoic: Geology, v. 33, p. 877–880.

DeMille, G., J. R. Shouldice, and H. W. Nelson, 1964, Collapse structures related to evaporites of the Prairie Formation, Saskatchewan: Geological Society America Bulletin, v. 75, p. 307–316.

Deming, D., J. A. Nunn, and D. G. Evans, 1990, Thermal effects of compaction-driven groundwater flow from overthrust belts: J. Geophys. Research, v. 96, p. 2485–2499.

Demir, I., and B. Seyler, 1999, Chemical composition and geologic history of saline waters in Aux Vases and Cypress Formations, Illinois Basin: Aquatic Geochemistry, v. 5, p. 281–311.

DeMis, W. D., 1992, Elkhorn Ranch Field -USA, Williston Basin, North Dakota, in N. H. Foster, and E. A. Beaumont, eds., Treatise of Petroleum Geology; Atlas of Oil and Gas Fields: Stratigraphic Traps III: Tulsa, OK, American Association Petroleum Geologists, p. 369–388.

Denison, R. E., D. W. Kirkland, and R. Evans, 1998, Using strontium isotopes to determine the age and origin of gypsum and anhydrite beds: Journal of Geology, v. 106, p. 1–17.

Deniz, O., and M. Z. Yildiz, 2007, The ecological consequences of level changes in Lake Van: Water Resources, v. 34, p. 707–711.

Deocampo, D. M., 2002, Sedimentary structures generated by Hippopotamus amphibius in a lake-margin wetland, Ngorongoro Crater, Tanzania: Palaios, v. 17, p. 212–217.

Depowski, S., and T. Peryt, 1985, Carbonate petroleum reservoirs in the Permian dolomites of the Zechstein, Fore-Sudetic area, western Poland, in P. O. Roehl, and P. W. Choquette, eds., Carbonate petroleum reservoirs: New York, Springer-Verlag, p. 251–264.

Des Marais, D. J., 2003, Biogeochemistry of Hypersaline Microbial Mats Illustrates the Dynamics of Modern Microbial Ecosystems and the Early Evolution of the Biosphere: Biological Bulletin, v. 204, p. 160–167.

Desborough, G. A., 1978, A biogenic-chemical stratified lake model for the origin of oil shale of the Green River Formation: an alternative to the playa lake model: Bulletin Geological Society of America, v. 89, p. 961–971.

Deuser, W. G., 1971, Organic carbon budget of the Black Sea: Deep Sea Research, v. 18, p. 995–1004.

Deutsch, Z. G., 1978, Brine wells and pipelines, in D. W. Kuafmann, ed., Sodium Chloride: The production and properties of salt and brine: Washington DC, American Chemical Society, p. 142–185.

Dewing, K., and P. Copper, 1991, Upper Ordovician stratigraphy of Southampton Island, Northwest Territories: Canadian Journal of Earth Sciences, v. 28, p. 283–291.

Dewing, K., R. J. Sharp, and E. Turner, 2005, Regional Metallogeny Synopsis Of The Polaris Zn-Pb-Cu District, Canadian Arctic Islands, Nunavut: Electronic publication (pdf) available from http://gsc.nrcan.gc.ca/mindep/metallogeny/mvt/polaris/index_e.php.

Diaz, G. C., M. Mendoza, J. Garcia-Veigas, J. Pueyo, and P. Turner, 1999, Evolution and geochemical signatures in a Neogene forearc evaporitic basin: the Salar Grande (Central Andes of Chile): Palaeogeography Palaeoclimatology Palaeoecology, v. 151, p. 39–54.

Dickerson, R., R. Rupp, and J. Ford, 2014, Triassic Stratigraphy and Syndepositional Basin Development in the Central Panhandle, Carson County, Texas: The Mountain Geologist, v. 51, p. 223–240.

Dickey, P. A., 1979, Petroleum Development Geology: Tulsa, OK, PPC Books Division of the Petroleum Publishing Company, 398 p.

Dickinson, W. R., and T. F. Lawton, 2001, Tectonic setting and sandstone petrofacies of the Bisbee basin (USA-Mexico): Journal of South American Earth Sciences, v. 14, p. 475–504.

Dickson, J. A. D., I. P. Montanez, and A. H. Saller, 2001, Hypersaline burial diagenesis delineated by component isotopic analysis, Late Paleozoic limestones, west Texas: Journal of Sedimentary Research, v. 71, p. 372–379.

Didyk, B. M., and B. R. T. Simoneit, 1989, Hydrothermal oil of the Guaymas Basin and implications for petroleum formation mechanisms: Nature, v. 342, p. 65–69.

Diegel, F. A., J. F. Karlo, D. C. Schuster, R. C. Shoup, and P. R. Tauvers, 1995, Cenozoic structural evolution and tectono-stratigraphic framework of the northern Gulf Coast continental margin, in M. P. A. Jackson, D. G. Roberts, and S. Snelson, eds., Salt tectonics: a global perspective, v. 65, American Association Petroleum Geologists Memoir, p. 109–151.

Diehl, S. F., A. H. Hofstra, A. E. Koenig, P. Emsbo, W. Christiansen, and C. Johnson, 2010, Hydrothermal Zebra Dolomite in the Great Basin, Nevada – Attributes and Relation to Paleozoic Stratigraphy, Tectonics, and Ore Deposits: Geosphere, v. 6, p. 663–690.

Dietzel, M., and I. Letofsky-Papst, 2002, Stability of magadiite between 20 and 100°C: Clays and Clay Minerals, v. 50, p. 657–666.

Dill, H. G., A. Bechtel, Z. Berner, R. Botz, J. Kus, C. Heunisch, and A. M. B. Abu Hamad, 2012, The evaporite-coal transition:

Chemical, mineralogical and organic composition of the Late Triassic Abu Ruweis Formation, NW Jordan -Reference type of the Arabian Keuper: Chemical Geology, v. 298–299, p. 20–40.

Dill, H. G., R. Botz, Z. Berner, D. Stüben, S. Nasir, and H. Al-Saad, 2005, Sedimentary facies, mineralogy, and geochemistry of the sulphate-bearing Miocene Dam Formation in Qatar: Sedimentary Geology, v. 174, p. 63–96.

Dill, H. G., F. Henjes-Kunst, Z. Berner, and D. Stüben, 2009, Miocene diagenetic and epigenetic strontium mineralization in calcareous series from Cyprus and the Arabian Gulf: Metallogenic perspective on sub- and suprasalt redox-controlled base metal deposits: Journal of Asian Earth Sciences, v. 34, p. 557–576.

Dill, H. G., S. Nasir, and H. Al-Saad, 2003, Lithological and structural evolution of the northern sector of Dukhan anticline, Qatar, during the early Tertiary: with special reference to sequence stratigraphic bounding surfaces: GeoArabia, v. 8, p. 201–226.

Dill, H. G., N. Nolte, and B. T. Hansen, 2014, Lithology, mineralogy and geochemical characterizations of sediment-hosted Sr-F deposits in the eastern Neo-Tethyan region – With special reference to evaporation and halokinesis in Tunisia: Journal of African Earth Sciences, v. 92, p. 76–96.

Dillard, D. S., J. G. Davis, and R. L. Every, 1975, Solution mining potassium chloride from subterranean deposits, Canada Patent 961,408, p. 18.

Dilles, J. H., and J. M. Proffett, 1995, Metallogenesis of the Yerington Batholith, Nevada: Arizona Geological Society Digest, v. 20, p. 306–315.

Dimroth, E., and M. M. Kimberley, 1975, Precambrian atmospheric oxygen; evidence in the sedimentary distributions of carbon, sulfur, uranium, and iron: Canadian Journal of Earth Sciences, v. 13, p. 1161–1185.

Dischinger, J. D., and S. Mitra, 2006, Three-dimensional structural model of the Painter and East Painter reservoir structures, Wyoming fold and thrust belt: Bulletin American Association Petroleum Geologists, v. 90, p. 1171–1185.

Dissanayake, C. B., and R. Chandrajith, 1999, SriLanka-Madagascar Gondwana Linkage: Evidence for a Pan-African Mineral Belt: The Journal of Geology, v. 107, p. 223–235.

Dix, G. R., and G. W. Robinson, 2003, The geochemical record of hydrothermal mineralization and tectonism inboard of the Appalachian Orogen: The Ottawa Embayment: Chemical Geology, v. 197, p. 29–53.

Doe, B. R., 1960, The distribution and composition of sulfide minerals at Balmat, New York.: doctoral thesis, California Institute of Technology, Pasedena.

Doelling, H. H., 2001, Geologic map of the Moab and eastern part of the San Rafael Desert 30' × 60' quadrangles, Grand and Emery Counties, Utah, and Mesa County, Colorado: Utah Geological Survey Map 180.

Doelling, H. H., and T. C. Chidsey Jr., 2000, Dead Horse State Park and Vicinity, Geologic Road Logs, Gran and San Juan Counties, Utah, in P. B. Anderson, and D. A. Sprinkel, eds., Geologic Road, Trail, and Lake Guides to Utah's Parks and Monuments, 2000 Utah Geological Association Publication 29, p. 1–38.

Dogan, U., and S. Ozel, 2005, Gypsum karst and its evolution east of Hafik (Sivas, Turkey): Geomorphology, v. 71, p. 373–388.

Dolson, J. C., R. M. Rashed, M. V. Shann, S. I. Matbouly, and H. Hammouda, 2001, Egypt in the twenty-first century: Petroleum potential in offshore trends: GeoArabia, v. 6, p. 211–230.

Domagala, J., P. N. Southgate, B. A. McConachie, and B. A. Pidgeon, 2000, Evolution of the Palaeoproterozoic Prize, Gun and Lower Loretta Supersequences of the Surprise Creek Formation and MtIsa Group: Australian Journal of Earth Sciences, v. 47, p. 485–507.

Dommanget, A., J. P. Milesi, and D. M., 1993, The Loulo gold and tourmaline-bearing deposit- A polymorph type in the Early Proterozoic of Mali (West Africa): Mineralium Deposita, v. 28, p. 253–263.

Dong, Z., P. Lv, G. Qian, X. Xia, Y. Zhao, and G. Mu, 2012, Research progress in China's Lop Nur: Earth-Science Reviews, v. 111, p. 142–153.

Dongyan, W., L. Zhenmin, D. Xiaolin, and X. Shaokang, 1998, Biomineralization of mirabilite deposits of Barkol Lake, China: Carbonates and Evaporites, v. 13, p. 86–89.

Donnellan, N., K. J. Hussey, P. D. Kruse, and P. A. Ferenczi, 1999, Tennant Creek, Northern Territory (Second Edition). 1:250 000 geological map series explanatory notes, SE 53 -14. Northern Territory Geological Survey, Darwin.

Donovan, R. N., 1993, Evaporites in the Middle Devonian of the Orcadian Basin near Berriedale, Caithness: Scottish Journal of Geology, v. 29, p. 45–54.

Dooley, T. P., M. R. Hudec, and M. P. A. Jackson, 2012, The structure and evolution of sutures in allochthonous salt: Bulletin American Association Petroleum Geologists, v. 96, p. 1045–1070.

Dooley, T. P., M. P. A. Jackson, and M. R. Hudec, 2009, Inflation and deflation of deeply buried salt stocks during lateral shortening: Journal of Structural Geology, v. 31, p. 582–600.

Doran, H., R. S. Haszeldine, C. Taberner, and A. E. Fallick, 2004, Fluid Migration around the Machar Salt Diapir UK Central North Sea: Impact on Porosity and Permeability of a Fractured Carbonate Reservoir (abs) presented at American Association Petroleum Geologists Annual Meeting, Dallas, Texas, April 18–21, 2004: Bulletin American Association Petroleum Geologists, v. 88 (13).

Dostal, J., J. Keppie, H. Macdonald, and F. Ortega-Gutiérrez, 2004, Sedimentary origin of calcareous intrusions in the ~1 Ga oaxacan complex, Southern Mexico: tectonic implications: International Geology Review, v. 46, p. 528–541.

Dotsika, E., D. Poutoukis, I. Tzavidopoulos, Y. Maniatis, D. Ignatiadou, and B. Raco, 2009, A natron source at Pikrolimni Lake in Greece? Geochemical evidence: Journal of Geochemical Exploration, v. 103, p. 133–143.

Douglas, J. L., and S. A. Members of the 'Ain Dar/Shedgum Modeling Team, 1996, Geostatistical Model for the Arab-D Reservoir, North 'Ain Dar Pilot, Ghawar Field, Saudi Arabia: An Improved Reservoir Simulation Model: GeoArabia, v. 1, p. 267–284.

Douglas, S., 2002, ESEM-EDS and XRD study of micro-mineralogical layering in a microbial mat from a hypersaline pond on Lee Stocking Island, Bahamas: formation of celestite in microbial exopolymers: Annual meeting of the Geological Society of America. Abstracts.

Douglas, S., 2005, Mineralogical footprints of microbial life: American Journal of Science, v. 305, p. 503–525.

Douglas, S., and H. X. Yang, 2002, Mineral biosignatures in evaporites: Presence of rosickyite in an endoevaporitic microbial community from Death Valley, California: Geology, v. 30, p. 1075–1078.

Downey, M. W., 1984, Evaluating seals for hydrocarbon accumulations: American Association Petroleum Geologists – Bulletin, v. 68, p. 1752–1763.

Drake, N. A., 1997, Recent aeolian origin of surficial gypsum crusts in southern Tunisia: Geomorphological, archaeological and remote sensing evidence: Earth Surface Processes and Landforms, v. 22, p. 641–656.

Drake, N. A., F. D. Eckardt, and K. H. White, 2004, Sources of sulphur in gypsiferous sediments and crusts and pathways of gypsum redistribution in southern Tunisia: Earth Surface Processes And Landforms, v. 29, p. 1459–1471.

Draper, J. J., and A. R. Jensen, 1976, The geochemistry of Lake Frome, a playa lake in South Australia: Bureau of Mineral Resources Journal of Australian Geology Geophysics, v. 1, p. 83–104.

Dreher, A., R. Xavier, B. Taylor, and S. Martini, 2008, New geologic, fluid inclusion and stable isotope studies on the controversial

Igarapé Bahia Cu-Au deposit, Carajas Province, Brazil: Mineralium Deposita, v. 43, p. 161–184.

Dribus, J. R., M. P. A. Jackson, J. Kapoor, and M. F. Smith, 2008, The Prize Beneath the Salt: Oil Field Review (Schlumberger), v. 20, p. 4–17.

Driese, S. G., 1985, Interdune pond carbonates, Weber sandstone (Pennsylvanian-Permian) Northern Utah and Colorado: Journal of Sedimentary Petrology, v. 55, p. 187–195.

Drijkoningen, G., G. van Noort, R. Arts, J. Bullen, and J. Thorbecke, 2012, Seismic time-lapse effects of solution salt mining – a feasibility study: Geophysical Prospecting, v. 60, p. 239–254.

Driscoll, R., 1983, The influence of vegetation on the swelling and shrinking of clay soils in Britain: Geotechnique, v. 33, p. 93–105.

Dronkert, H., 1985, Evaporite models and sedimentology of Messinian and Recent evaporites: GUA Papers of Geology, Series 1, v. 24, p. 283 pp.

Droste, H., 1990, Depositional cycles and source rock development in an epeiric intra-platform basin; the Hanifa Formation of the Arabian Peninsula: Sedimentary Geology, v. 69, p. 281–296.

Droste, J. B., and R. H. Shaver, 1985, Comparative stratigraphic framework for Silurian reefs: Michigan Basin to surrounding platforms, in K. R. Cercone, and J. M. Budai, eds., Ordovician and Silurian Rocks of the Michigan Basin and its Margins, Michigan Basin Geological Society Special Paper No. 4, p. 79–94.

Druckman, Y., 1981, Sub-recent manganese-bearing stromatolites along shorelines of the Dead Sea, in C. Monty, ed., Phanerozoic stromatolites; case histories: Berlin, Federal Republic of Germany, Springer-Verlag, p. 197–208.

Druckman, Y., and C. H. Moore, 1985, Late subsurface secondary porosity in a Jurassic grainstone reservoir, Smackover formation, Mt Vernon Field, Southern Arkansas, in P. O. Roehl, and P. W. Choquette, eds., Carbonate petroleum reservoirs: New York, Springer-Verlag, p. 369–383.

Drury, M. R., 1999, Stepping stones; The making of our home world, Oxford University Press, 409 p.

Drury, M. R., and J. L. Urai, 1990, Deformation-related recrystallization processes: Tectonophysics, v. 172, p. 235–253.

Du Plessis, P. I., and J. P. Leroux, 1995, Late Cretaceous alkaline saline lake complexes of the Kalahari Group in northern Botswana: Journal of African Earth Sciences, v. 20, p. 7–15.

Duan, Z., and R. Sun, 2003, An improved model calculating CO_2 solubility in pure water and aqueous NaCl solutions from 273 to 533 K and from 0 to 2000 bar: Chemical Geology, v. 193, p. 257–271.

Duan, Z. H., and W. X. Hu, 2001, The accumulation of potash in a continental basin: the example of the Qarhan Saline Lake, Qaidam Basin, West China: European Journal of Mineralogy, v. 13, p. 1223–1233.

Duane, M. J., A. Al-Zamel, and C. J. Eastoe, 2004, Stable isotope (chlorine, hydrogen and oxygen), geochemical and field evidence for continental fluid flow vectors in the Al-Khiran sabkha (Kuwait): Journal of African Earth Sciences, v. 40, p. 49–60.

Duane, M. J., and A. Z. Al-Zamel, 1999, Syngenetic textural evolution of modern sabkha stromatolites (Kuwait): Sedimentary Geology, v. 127, p. 237–245.

Dubinina, E. O., V. A. Baskina, and A. S. Avdeenko, 2011, Nature of ore-forming fluids of the Dal'negorsk deposit: Isotopic and geochemical parameters of the altered host rocks: Geology of Ore Deposits, v. 53, p. 58–73.

Duffett, M. L., M. Roach, and D. E. Leaman, 2005, Inferring central McArthur Basin shape at HYC time: Integration of geophysical interpretation and geology using GIS, in T. J. Munson, and G. J. Ambrose, eds., Proceedings Central Australian Basins Symposium; Alice Springs 16–18 August, 2005, Northern Territory Geological Survey, Special Publication 2, p. 1–22.

Duffy, O. B., R. L. Gawthorpe, M. Docherty, and S. H. Brocklehurst, 2013, Mobile evaporite controls on the structural style and evolution of rift basins: Danish Central Graben, North Sea: Basin Research, v. 25, p. 310–330.

Dufour, M., A. Kol'tsov, A. Zolotarev, and A. Kuznetsov, 2007, Corundum-bearing metasomatic rocks in the Central Pamirs: Petrology, v. 15, p. 151–167.

Duggan, J. P., E. W. Mountjoy, and L. D. Stasiuk, 2001, Fault-controlled dolomitization at Swan Hills Simonette oil field (Devonian), deep basin west-central Alberta, Canada: Sedimentology, v. 48, p. 301–323.

Duguid, C., and J. R. Underhill, 2010, Geological controls on Upper Permian Plattendolomit Formation reservoir prospectivity, Wissey Field, UK Southern North Sea: Petroleum Geoscience, v. 16, p. 331–348.

Dulhunty, J. A., 1977, Salt crust solution during fillings of Lake Eyre: Transactions Royal Society South Australia, v. 101, p. 147–151.

Duncan, W. I., and N. W. K. Buxton, 1995, New evidence for evaporitic Middle Devonian Lacustrine sediments with hydrocarbon source potential on the East Shetland Platform, North Sea: Journal of the Geological Society, v. 152, p. 251–258.

Dunham, R. J., 1972, Capitan Reef, New Mexico and Texas: Facts and questions to aid interpretation and group discussion, v. 72–14: Midland, Texas, Permian Basin Section SEPM Publication.

Dunning, G. E., and J. F. J. Cooper, 1969, A second occurrence of antarcticite, from Bristol Dry Lake, California: American Mineralogist, v. 54, p. 1018–1025.

Dunrud, C. R., and B. B. Nevins, 1981, Solution mining and subsidence in evaporite rocks in the United States: U.S. Geological Survey Miscellaneous Investigation Series Map 1-1298, 2 sheets.

Dupraz, C., R. P. Reid, O. Braissant, A. W. Decho, R. S. Norman, and P. T. Visscher, 2009, Processes of carbonate precipitation in modern microbial mats: Earth-Science Reviews, v. 96, p. 141–162.

Dupraz, C., and A. Strasser, 1999, Microbialites and micro-encrusters in shallow coral bioherms (Middle to Late Oxfordian, Swiss Jura Mountains): Facies, v. 40, p. 101–130.

Dupraz, C., P. T. Visscher, L. K. Baumgartner, and R. P. Reid, 2004, Microbe-mineral interactions: early carbonate precipitation in a hypersaline lake (Eleuthera Island, Bahamas): Sedimentology, v. 51, p. 745–765.

Dupre, B., G. Blanc, J. Boulegue, and C. J. Allegre, 1988, Metal remobilization at a spreading centre studied using lead isotopes: Nature, v. 333, p. 165–167.

Durup, J. G., 1991, Relationship between subsidence and cavern convergence at Tersanne (France): Proc. Solution Mining Research Institute Spring Meeting, Atlanta.

Dusseault, M. B., and B. C. Davidson, 1999, Design and management of salt solution caverns for toxic waste disposal: Journal of Canadian Petroleum Technology, v. 38, p. 56–61.

Dusseault, M. B., V. Maury, F. Sanfilippo, and F. J. Santarelli, 2004, Drilling Through Salt: Constitutive Behavior And Drilling Strategies: Proceedings – Gulf Rocks 2004, the 6th North America Rock Mechanics Symposium (NARMS), June 5–9, 2004 , Houston, Texas.

Dutkiewicz, A., A. L. Herczeg, and J. C. Dighton, 2000, Past changes to isotopic and solute balances in a continental playa: clues from stable isotopes of lacustrine carbonates: Chemical Geology, v. 165, p. 309–329.

Dutkiewicz, A., and C. C. von der Borch, 1995, Lake Greenly, Eyre Peninsula, South Australia; sedimentology, palaeoclimatic and palaeohydrologic cycles: Palaeogeography, Palaeoclimatology, Palaeoecology, v. 113, p. 43–56.

Dutkiewicz, A., C. C. Von der Borch, and J. R. Prescott, 2002, Geomorphology of the Lake Malata-Lake Greenly complex, South Australia, and its implications for Late Quaternary Palaeoclimate: Transactions of the Royal Society of South Australia, v. 126, p. 103–115.

Dutton, D. M., and B. D. Trudgill, 2009, Four-dimensional analysis of the Sembo relay system, offshore Angola: Implications for fault

growth in salt-detached settings: Bulletin American Association Petroleum Geologists, v. 93, p. 763–794.

Duval, B., C. Cramez, and M. P. A. Jackson, 1992, Raft tectonics in the Kwanza Basin, Angola: Marine and Petroleum Geology, v. 9, p. 389–404.

Dworkin, S. I., and L. S. Land, 1994, Petrographic and geochemical constraints on the formation and diagenesis of anhydrite cements, Smackover sandstones, Gulf of Mexico: Journal of Sedimentary Research, Section A: Sedimentary Petrology and Processes, v. 64, p. 339–348.

Dworkin, S. I., and L. S. Land, 1996, The origin of aqueous sulfate in Frio pore fluids and its implication for the origin of oil field brines Source: 11, no.3 (1996) p. 403–408: Applied Geochemistry, v. 11, p. 403–408.

Dyni, J. R., 1981, Geology of the nahcolite deposits and oil shales of the Green River Formation in the Piceance Creek Basin, Colorado: Doctoral thesis, University of Colorado, Boulder, 182 p.

Dyni, J. R., 1996, Sodium carbonate resources of the Green River Formation: United States Geological Survey, Open File Report, v. 96–729, p. 39 p.

Dyni, J. R., 1998, Prospecting for Green River-type sodium carbonate deposits: Wyoming State Geological Survey Public Information Circular v. 40, p. 37–47.

Dyni, R. C., 1986, Subsidence investigations over salt-solution mines, Hutchinson, Kansas: United States Bureau of Mines Information Circular 9083.

Dyson, I. A., 1998, The Christmas tree diapir and salt glacier at Pinda Springs, central Flinders Ranges: MESA Journal, v. 10.

Dyson, I. A., 1999, The Beltana Diapir — a salt withdrawal minibasin in the northern Flinders Ranges: MESA Journal, v. 15, p. 40–46.

Dyson, I. A., 2004, Christmas tree diapirs and the development of hydrocarbon reservoirs; A model from the Adelaide Geosyncline, South Australia: In: Salt-sediment interactions and hydrocarbon prospectivity: concepts, applications and case studies for the 21st Century. Papers presented at the 24th Annual Gulf Coast Section SEPM Foundation Bob F. Perkins Research Conference, Houston Tx, December 5–8, 2004 (CD publication), p. 79–96.

Dyson, I. A., and M. G. Rowan, 2004, Geology of a welded diapir and flanking minibasins in the Flinders Ranges of South Australia, in P. J. Post, ed., Salt-sediment interactions and hydrocarbon prospectivity: concepts, applications and case studies for the 21st Century. Papers presented at the 24th Annual Gulf Coast Section SEPM Foundation Bob F. Perkins Research Conference, Houston Tx, December 5–8, 2004 (CD publication), p. 69–89.

Eardley, A. J., 1938, Sediments of Great Salt Lake, Utah: American Association Petroleum Geologists – Bulletin, v. 22, p. 1305–1411.

Eardley, A. J., 1962, Gypsum dunes and evaporite history of the Great Salt Lake Desert: Utah Geol. and Mineralog. Survey Spec. Studies vol. 2, 27 p.

Eastoe, C. J., A. Long, and L. P. Knauth, 1999, Stable chlorine isotopes in the Palo Duro Basin, Texas: Evidence for preservation of Permian evaporite brines: Geochimica et Cosmochimica Acta, v. 63, p. 1375–1382.

Eastoe, C. J., A. Long, L. S. Land, and J. R. Kyle, 2001, Stable chlorine isotopes in halite and brine from the Gulf Coast Basin: brine genesis and evolution: Chemical Geology, v. 176, p. 343–360.

Eastoe, C. J., and T. Peryt, 1999, Stable chlorine isotope evidence for non-marine chloride in Badenian evaporites, Carpathian mountain region: Terra Nova, v. 11, p. 118–123.

Eastoe, C. J., T. M. Peryt, O. Y. Petrychenko, and D. Geisler-Cussey, 2007, Stable chlorine isotopes in Phanerozoic evaporites: Applied Geochemistry, v. 22, p. 575–588.

Eatock, W. H., 1987, The Big Quill Lake sulphate of potash project, in C. F. Gilboy, and L. W. Vigrass, eds., Economic Minerals of Saskatchewan, Proceedings of a Symposium Held in Regina, Saskatchewan 17 & 18 November 1986, Saskatchewan Geological Society Special Publication Number 8, p. 206–210.

Ece, O. I., 1998, Diagenetic transformation of magnesite pebbles and cobbles to sepiolite (Meerschaum) in the Miocene Eskisehir lacustrine basin, Turkey: Clays & Clay Minerals, v. 46, p. 436–445.

Ece, O. I., and F. Coban, 1994, Geology, occurrence and genesis of Eskisesehir Sepiolites, Turkey: Clay and Clay Minerals, v. 42, p. 81–92.

Eckardt, F. D., R. G. Bryant, G. McCulloch, B. Spiro, and W. W. Wood, 2008, The hydrochemistry of a semi-arid pan basin case study: Sua Pan, Makgadikgadi, Botswana: Applied Geochemistry, v. 23, p. 1563–1580.

Eckardt, F. D., and B. Spiro, 1999, The origin of sulphur in gypsum and dissolved sulphate in the Central Namib Desert, Namibia: Sedimentary Geology, v. 123, p. 255–273.

Eckardt, F. D., H. Viles, N. Drake, G. A. S., and K. White, 2001, The role of playas in pedogenic gypsum crust formation in the Central Namib Desert: A theoretical model: Earth Surface Processes and Landforms, v. 26, p. 1177–1193.

Eder, W., L. L. Jahnke, M. Schmidt, and R. Huber, 2001, Microbial diversity of the brine-seawater interface of the Kebrit Deep, Red Sea, studied via 16S rRNA gene sequences and cultivation methods: Applied & Environmental Microbiology, v. 67, p. 3077–3085.

Edgcomb, V., W. Orsi, C. Leslin, S. Epstein, J. Bunge, S. Jeon, M. Yakimov, A. Behnke, and T. Stoeck, 2009, Protistan community patterns within the brine and halocline of deep hypersaline anoxic basins in the eastern Mediterranean Sea: Extremophiles, v. 13, p. 151–167.

Edgell, H. S., 1991, Proterozoic salt basins of the Persian Gulf area and their role in hydrocarbon generation: Precambrian Research, v. 54, p. 1–14.

Edgell, H. S., 1996, Salt tectonism in the Persian Gulf Basin, in G. I. Alsop, D. J. Blundell, and I. Davison, eds., Salt tectonics, v. 100: London, United Kingdom, Geological Society of London Special Publication, p. London, United Kingdom.

Edgett, K. S., and T. J. Parker, 1997, Water on early Mars – Possible subaqueous sedimentary deposits covering ancient cratered terrain in western Arabia and Sinus Meridiani: Geophysical Research Letters, v. 24, p. 2897–2900.

Edmunds, W. M., and P. Smedley, 2013, Fluoride in Natural Waters, in O. Selinus, ed., Essentials of Medical Geology, Springer Netherlands, p. 311–336.

Edwards, H., K. Currie, H. Ali, S. Jorge Villar, A. David, and J. Denton, 2007, Raman spectroscopy of natron: shedding light on ancient Egyptian mummification: Analytical And Bioanalytical Chemistry, v. 388, p. 683–689.

Edwards, S., D. McKirdy, Y. Bone, P. Gell, and V. Gostin, 2006, Diatoms and ostracods as mid-Holocene palaeoenvironmental indicators, North Stromatolite Lake, Coorong National Park, South Australia *: Australian Journal of Earth Sciences, v. 53, p. 651–663.

Egeberg, P. K., and P. Aagaard, 1989, Origin and evolution of formation waters from oil fields on the Norwegian Shelf: Applied Geochemistry, v. 4, p. 131–142.

Egemeier, S. J., 1981, Cavern development by thermal waters: National Spelological Society Bulletin, v. 43, p. 31–51.

Egenhoff, S. O., A. Peterhansel, T. Bechstadt, R. Zuhlke, and J. Grotsch, 1999, Facies architecture of an isolated carbonate platform: tracing the cycles of the Latemar (Middle Triassic, northern Italy): Sedimentology, v. 46, p. 893–912.

Eggenkamp, H. G. M., R. Kreulen, and A. F. K. Van Groos, 1995, Chlorine stable isotope fractionation in evaporites: Geochimica et Cosmochimica Acta, v. 59, p. 5169–5175.

Eggermont, H., O. Heiri, and D. Verschuren, 2006, Fossil Chironomidae (Insecta: Diptera) as quantitative indicators of past salinity in African lakes: Quaternary Science Reviews, v. 25, p. 1966–1994.

Eggink, J. W., D. E. Riegstra, and P. Suzanne, 1996, Using 3D seismic to understand the structural evolution of the UK Central North Sea: Petroleum Geoscience, v. 2, p. 83–96.

Eglinger, A., C. Ferraina, A. Tarantola, A.-S. André-Mayer, O. Vanderhaeghe, M.-C. Boiron, J. Dubessy, A. Richard, and M. Brouand, 2014, Hypersaline fluids generated by high-grade metamorphism of evaporites: fluid inclusion study of uranium occurrences in the Western Zambian Copperbelt: Contributions to Mineralogy and Petrology, v. 167, p. 1–28.

Ehgartner, B. L., J. T. Neal, and T. E. Hinkebein, 1998, Gas Releases from Salt: SAND98-1354, Sandia National Laboratories, Albuquerque, NM, June 1998.

Ehrenberg, S. N., P. H. Nadeau, and A. A. M. Aqrawi, 2007, A comparison of Khuff and Arab reservoir potential throughout the Middle East: Bulletin American Association Petroleum Geologists, v. 91, p. 275–286.

Ehrhardt, A., C. Hübscher, and D. Gajewski, 2005, Conrad Deep, Northern Red Sea: Development of an early stage ocean deep within the axial depression: Tectonophysics, v. 411, p. 19–40.

Eichenseer, H. T., F. R. Walgenwitz, and P. J. Biondi, 1999, Stratigraphic Control on Facies and Diagenesis of Dolomitized Oolitic Siliciclastic Ramp Sequences (Pinda Group, Albian, Offshore Angola): Bulletin American Association Petroleum Geologists, v. 83, p. 1729–1758.

Eilu, P., E. J. Mikucki, and A. L. Dugdale, 2001, Alteration zoning and primary geochemical dispersion at the Bronzewing lode-gold deposit, Western Australia: Mineralium Deposita, v. 36, p. 13–31.

Eimanifar, A., and F. Mohebbi, 2007, Urmia Lake (Northwest Iran): a brief review: Saline Systems, v. 3, p. 1–8.

Einaudi, M. T., and N. Oreskes, 1990, Progress toward an occurrence model for Proterozoic iron oxide deposits – a comparison between the ore provinces of South Australia and southeast Missouri: US Geological Survey Bulletin, v. 1932, p. 58–69.

Einsele, G., 2000, Sedimentary basins: evolution, facies and sediment budget: Berlin, Springer, 792 p.

Eisenberg, L., 2003, Giant stromatolites and a supersurface in the Navajo Sandstone, Capitol Reef National Park, Utah: Geology, v. 31, p. 111–114.

El Anbaawy, M. I. H., M. A. H. Al Aawah, K. A. Al Thour, and M. E. Tucker, 1992, Miocene evaporites of the Red Sea Rift, Yemen Republic; sedimentology of the Salif halite: Sedimentary Geology, v. 81, p. 61–71.

El Desouky, H. A., P. Muchez, and J. Cailteux, 2009, Two Cu-Co sulfide phases and contrasting fluid systems in the Katanga Copperbelt, Democratic Republic of Congo: Ore Geology Reviews, v. 36, p. 315–332.

El Tabakh, M., K. Grey, F. Pirajno, and B. C. Schreiber, 1999, Pseudomorphs after evaporitic minerals interbedded with 2.2 Ga stromatolites of the Yerrida basin, Western Australia: Origin and significance: Geology, v. 27, p. 871–874.

El Tabakh, M., A. Mory, B. C. Schreiber, and R. Yasin, 2004, Anhydrite cements after dolomitization of shallow marine Silurian carbonates of the Gascoyne Platform, Southern Carnarvon Basin, Western Australia: Sedimentary Geology, v. 164, p. 75–87.

El Tabakh, M., R. Riccioni, and B. C. Schreiber, 1997, Evolution of Late Triassic rift basin evaporites (Passaic Formation) – Newark Basin, eastern North America: Sedimentology, v. 44, p. 767–790.

El Tabakh, M., B. C. Schreiber, C. Uthaaroon, L. Coshell, and J. K. Warren, 1998a, Diagenetic origin of Basal Anhydrite in the Cretaceous Maha Sarakham Salt – Khorat Plateau, NE Thailand: Sedimentology, v. 45, p. 579–594.

El Tabakh, M., B. C. Schreiber, and J. K. Warren, 1998b, Origin of fibrous gypsum in the Newark rift basin, eastern North America: Journal of Sedimentary Research Section A-Sedimentary Petrology & Processes, v. 68, p. 88–99.

El Tabakh, M., C. Utha-aroon, L. Coshell, and J. K. Warren, 1995, Cretaceous saline deposits of the Maha Sarakham Formation in the Khorat BAsin, Northeastern Thailand: International Conference on Geology, Geochronoilogy and Mineral Resources of Indochina 22–25 November 1995, Khon Kaen, Thailand, v. Core Workshop Notes, p. 20 pp.

El Tabakh, M., C. Utha-Aroon, and B. C. Schreiber, 1999, Sedimentology of the Cretaceous Maha Sarakham evaporites in the Khorat Plateau of northeastern Thailand: Sedimentary Geology, v. 123, p. 31–62.

El Tabakh, M., C. Utha-Aroon, J. K. Warren, and B. C. Schreiber, 2003, Origin of dolomites in the Cretaceous Maha Sarakham evaporites of the Khorat Plateau, northeast Thailand: Sedimentary Geology, v. 157, p. 235–252.

El Taki, H., and B. R. Pratt, 2010, Syndepositional tectonic activity in an epicontinental basin revealed by deformation of subaqueous carbonate laminites and evaporites : RedRiver strata (Upper Ordovician) of Southern Saskatchewan, Canada: Bulletin Canadian Petroleum Geology, v. 60, p. 37–58.

El-Sayed, M. I., 1993, Gypcrete of Kuwait: field investigation, petrography and genesis: Journal of Arid Environment, v. 25, p. 199–203.

Eldridge, C. S., N. Williams, W. Compston, and J. L. Walshe, 1991, The HYC deposit at McArthur River Northern Territory, Australia: a non-exhalative model: SGEG Ore Fluids Conf., p. 15–16.

Eldridge, C. S., N. Williams, and J. L. Walshe, 1993, Sulfur isotope variability in sediment-hosted massive sulfide deposits as determined using the ion microprobe SHRIMP: II. A study of the H.Y.C. deposit at McArthur River, Northern Territory, Australia: Economic Geology, v. 88, p. 1–26.

Elias, A. R. D., L. F. De Ros, A. M. P. Mizusaki, and S. M. C. Anjos, 2004, Diagenetic patterns in eolian/coastal sabkha reservoirs of the Solimões Basin, Northern Brazil: Sedimentary Geology, v. 169, p. 191–217.

Eliassen, A., and M. R. Talbot, 2005, Solution-collapse breccias of the Minkinfjellet and Wordiekammen Formations, Central Spitsbergen, Svalbard: a large gypsum palaeokarst system: Sedimentology, v. 52, p. 775–794.

Elliott, L. A., and J. K. Warren, 1989, Stratigraphy and depositional environment of lower San Andres Formation in subsurface and equivalent outcrops; Chaves, Lincoln, and Roosevelt counties, New Mexico: American Association Petroleum Geologists – Bulletin, v. 73, p. 1307–1325.

Ellis, A. J., 1968, Natural hydrothermal systems and experimental hot-water/rock interaction; reactions with NaCl solutions and trace metal extraction: Geochimica et Cosmochimica Acta, v. 32, p. 1356–1363.

Ellis, D. M., 1978, Stability and phase equilibra of chloride-bearing scapolites at 750°C and 4000 bar: Geochimica et Cosmochimica Acta, v. 42, p. 1271–1281.

Ellis, P. M., 1985, Diagenesis of the Lower Cretaceous Edwards Group in the Balcones Fault Zone Area, South-Central Texas: Doctoral thesis, University of Texas – Austin, 652 p.

Ellis, P. M., 1986, Post-Miocene carbonate diagenesis of the Lower Cretaceous Edwards Group in the Balcones fault zone area, south-central Texa, in P. L. Abbott, and C. M. Woodruff, eds., The Balcones escarpment, geology, hydrology, ecology and social development in central Texas, Geological Society of America, p. 101–114.

Ellison, J. C., and S. Simmonds, 2003, Structure and productivity of inland mangrove stands at Lake MacLeod, Western Australia: Journal Royal Society of West Australia, v. 86, p. 21–26.

Elloumi, J., J.-F. Carrias, H. Ayadi, T. Sime-Ngando, M. Boukhris, and A. Bouain, 2006, Composition and distribution of planktonic ciliates from ponds of different salinity in the solar saltwork of Sfax, Tunisia: Estuarine, Coastal and Shelf Science, v. 67, p. 21–29.

Elorza, M. G., and F. G. Santolalla, 1998, Geomorphology of the Tertiary gypsum formations in the Ebro Depression (Spain): Geoderma, v. 87, p. 1–29.

Emami, M. H., and J. Hajian, 1980, 1:250,000 Geological Map of Qom. Geological Survey of Iran, E6.

Emery, D., and A. Robinson, 1993, Inorganic Chemistry: Applications to Petroleum Geology: Oxford, Blackwell Scientific Publications, 254 p.

Emsbo, P., 2009, Geologic Criteria for the Assessment of Sedimentary Exhalative (Sedex) Zn-Pb-Ag Deposits: USGS Report OF09-1209.

Enami, M., J. G. Liou, and D. K. Bird, 1992, Cl-bearing amphibole in the Salton Sea geothermal system, California: Canadian Mineralogist, v. 30, p. 1077–1092.

Engel, A. S., M. L. Porter, B. K. Kinkle, and T. C. Kane, 2001, Ecological assessment and geological significance of microbial communities from Cesspool Cave, Virginia: Geomicrobiology Journal, v. 18, p. 259–274.

Enger, S., and A. Logan, 2001, Ultradeepwater play paces gulf, North America: Oil & Gas Journal, v. 99, p. 80–85.

English, P. M., 2001, Formation of analcime and moganite at Lake Lewis, central Australia: significance of groundwater evolution in diagenesis: Sedimentary Geology, v. 143, p. 219–244.

Engvik, A. K., K. Mezger, S. Wortelkamp, R. Bast, F. Corfu, A. Korneliussen, P. Ihlen, B. Bingen, and H. Austrheim, 2011, Metasomatism of gabbro – mineral replacement and element mobilization during the Sveconorwegian metamorphic event: Journal of Metamorphic Geology, v. 29, p. 399–423.

Enick, R., and S. Klara, 1990, CO_2 solubility in water and brine under reservoir conditions: Chem. Eng. Commun., v. 90, p. 23–33.

Enos, J. S., and J. R. Kyle, 2002, Diagenesis of the Carrizo Sandstone at Butler Salt Dome, East Texas Basin, U.S.A.: Evidence for Fluid-Sediment Interaction Near Halokinetic Structures: Journal of Sedimentary Research, v. 72, p. 68–81.

Entwistle, L. P., and L. O. Gouin, 1955, The chalcocite-ore deposits at Corocoro, Bolivia: Economic Geology, v. 50, p. 555–570.

Enzel, Y., R. Bookman, D. Sharon, H. Gvirtzman, U. Dayan, B. Ziv, and M. Stein, 2003, Late Holocene climates of the Near East deduced from Dead Sea level variations and modern regional winter rainfall: Quaternary Research, v. 60, p. 263–273.

Epstein, J. A., B. Zelvianski, and G. Ron, 1975, Manganese in sodium chloride precipitating for mixing Dead Sea brines: Israel J. Earth Sci., v. 24, p. 112–113.

Epstein, J. B., 2001, Hydrology, Hazards, and Geomorphic Development of Gypsum Karst in the Northern Black Hills, South Dakota and Wyoming, in E. L. Kuniansky, ed., U.S. Geological Survey Karst Interest Group Proceedings, St. Petersburg, Florida February 13–16, 2001: Denver, Co, U.S. Geological Survey, Water-Resources Investigations Report 01–4011, p. 30–37.

Erba, E., 1991, Deep mid-water bacterial mats from anoxic basins of the eastern Mediterranean: Marine Geology, v. 100, p. 83–101.

ERCOSPLAN, 2007, Resource Estimate for the Makola Exploration Permit Area, Kouilou Region, Republic of Congo, Technical report for MagMinerals Inc; Project Reference: EGB 04–037, p. 102.

ERCOSPLAN, 2010, Technical report and current resource estimate: Danakhil Potash Deposit, Afar State, Ethiopia: Project Reference: EGB 08–024.

ERCOSPLAN, 2011, Resource Report for the Danakhil Potash Deposit, Afar State Ethiopia, commissioned by Allana Potash. Document EGB 11–008.

ERCOSPLAN, 2011, Rio Verde's Mineral Properties in the Segipe Basin, Brazil, Technical report; Project Reference: EGB 09–045. N02, p. 102.

Ericksen, G. E., 1981, Geology and origin of the Chilean nitrate deposits: US Geological Survey Prof. Paper, v. 1188, p. 37 pp.

Ericksen, G. E., 1983, The Chilean nitrate deposits: American Scientist, v. 71, p. 366–374.

Ericksen, G. E., 1993, Upper Tertiary and Quaternary continental saline deposits in the central Andean region: Geological Association of Canada Special Paper, v. 40, p. 89–102.

Ericksen, G. E., and M. E. Mrose, 1972, High-purity veins of soda-niter, NaN03, and associated saline minerals in the Chilean nitrate deposits: USGS Professional Paper 800-B, p. B43-B50.

Ericksen, G. E., and R. Salas, 1989, Geology and resources of salars in the central Andes, in G. E. Ericksen, M. T. Cañas Pinochet, and J. A. TReinemund, eds., Geology of the Andes and its relation to hydrocarbon and mineral resources. Earth Science Series 11: Houston, TX, Circum Pacific Council for Energy and Mineral Resources, p. 151–164.

Ericksen, G. E., J. D. Vine, and R. Ballon, 1978, Chemical composition and distribution of lithium-rich brines in salar de Uyuni and nearby salars in southwestern Bolivia: Energy, v. 3, p. 355–363.

Eriksson, K. A., E. L. Simpson, S. Master, and G. Henry, 2005, Neoarchaean (c.2.58 Ga) halite casts: implications for palaeoceanic chemistry: Journal of the Geological Society, v. 162, p. 789–799.

Eriksson, P. G., W. Altermann, D. R. Nelson, W. U. Mueller, and O. Catuneanu, 2004, The Precambrian Earth – Tempos and Events: Developments in Precambrian Geology, Elsevier, 941 p.

Eriksson, P. G., S. Banerjee, O. Catuneanu, P. L. Corcoran, K. A. Eriksson, E. E. Hiatt, M. Laflamme, N. Lenhardt, D. G. F. Long, A. D. Miall, M. V. Mints, P. K. Pufahl, S. Sarkar, E. L. Simpson, and G. E. Williams, 2013, Secular changes in sedimentation systems and sequence stratigraphy: Gondwana Research, v. 24, p. 468–489.

Ernst, W. G., 2009, Archean plate tectonics, rise of Proterozoic supercontinentality and onset of regional, episodic stagnant-lid behavior: Gondwana Research, v. 15, p. 243–253.

Erol, O., 1978, The Quaternary history of the lake basins of central southern Anatolia, in W. C. Brice, ed., The Environmental History of the Near and Middle East Since the Last Ice Age: London, Academic Press, p. 111–139.

Esch, W. L., and J. S. Hanor, 1995, Fault and fracture control of fluid flow and diagenesis around the Iberia salt dome, Iberia Parish, Louisiana: Gulf Coast Association of Geological Societies Transactions, v. 45, p. 181–187.

Eschner, T. B., and G. Kocurek, 1988, Origins of relief contacts between eolian sandstones and overlying marine strata: Bulletin American Association Petroleum Geologists, v. 72, p. 932–943.

Espitalie, J., M. Madee, and B. Tissot, 1980, Role of mineral matrix in kerogen pyrolysis: influence on petroleum generation and migration: American Association Petroleum Geologists – Bulletin, v. 64, p. 59–66.

Esteban, M., 1980, Significance of upper Miocene coral reefs of the Western Mediterranean: Palaeogeography Palaeoclimatology Palaeoecology, v. 29, p. 169–188.

Esteban, M., 1996, An overview of Miocene reefs from Mediterranean areas: general trends and facies models, in E. K. e. a. Franseen, ed., Models for carbonate stratigraphy from Miocene reef complexes of Mediterranean regions, v. 5, SEPM/Society for Sedimentary Geology; Concepts in Sedimentology and Paleontology, p. 3–53.

Esteban, M., and L. C. Pray, 1983, Pisoids and pisolite facies (Permian), Guadalupe Mountains, New Mexico and West Texas, in T. M. Peryt, ed., Coated Grains: Berlin, Springer-Verlag, p. 503–537.

Et-Touhami, M., 1996, L'origine des accumulations saliferes du Trias marocain: apport de la geochimie du brome du sel du bassin de Khemisset (Maroc central) The origin of Moroccan Triassic salt deposits: contribution of Br geochemistry in the halite-rock from the Khemisset Basin (central Morocco) [French]: Comptes Rendus de l Academie des Sciences Serie II Fascicule A-Sciences de la Terre et des Planetes, v. 323, p. 591–598.

Ettner, D. C., A. Bjorlykke, and T. Andersen, 1994, A fluid inclusion and stable isotope study of the Proterozoic Bidjovagge Au-Cu deposit, Finnmark, northern Norway: Mineralium Deposita, v. 29, p. 16–29.

Eugster, H. P., 1967, Hydrous sodium silicate from Lake Magadi, Kenya: precursors of bedded chert: Science, v. 157, p. 1177–1180.

Eugster, H. P., 1969, Inorganic bedded cherts from the Magadi area, Kenya: Contributions Mineralogy and Petrology, v. 22, p. 1–31.
Eugster, H. P., 1970, Chemistry and origin of the brines of Lake Magadi, Kenya: Special Publ. Geol. Soc., v. 3, p. 215–235.
Eugster, H. P., 1971a, The Beginnings of Experimental Petrology: Science, v. 173, p. 481–489.
Eugster, H. P., 1971b, Origin and deposition of trona: Contribution to Geology (Trona issue), v. 10, p. 49–55.
Eugster, H. P., 1980a, Geochemistry of Evaporitic Lacustrine Deposits: Annual Review of Earth and Planetary Sciences, v. 8, p. 35–63.
Eugster, H. P., 1980b, Lake Magadi, Kenya, and its precursors, in A. Nissenbaum, ed., Hypersaline brines and evaporitic environments, Elsevier Developments in Sedimentology 28, p. 195–232.
Eugster, H. P., 1985, Oil shales, evaporites and ore deposits: Geochimica et Cosmochimica Acta, v. 49, p. 619–635.
Eugster, H. P., 1986, Lake Magadi, Kenya; a model for rift valley hydrochemistry and sedimentation?, in L. E. Frostick, R. W. Renaut, I. Reid, and J. J. Tiercelin, eds., Sedimentation in the African rifts, Geological Society Special Publication 25, p. 177–189.
Eugster, H. P., 1989, Geochemical environments of sediment-hosted Cu-Pb-Zn deposits, in R. W. Boyle, A. C. Brown, C. W. Jefferson, and E. C. Jowett, eds., Sediment hosted stratiform copper deposits, v. 36, Geological Association of Canada, Special Paper, p. 111–126.
Eugster, H. P., and L. A. Hardie, 1978, Saline Lakes, in A. Lerman, ed., Lakes; chemistry, geology, physics: New York, NY, Springer-Verlag, p. 237–293.
Eugster, H. P., and B. F. Jones, 1978, Behavior of major solutes during closed-basin brine evolution: American Journal of Science, v. 279, p. 609–631.
Eugster, H. P., and G. Maglione, 1979, Brines and evaporites of the Lake Chad basin, Africa: Geochim. Cosmochim. Acta., v. 43, p. 973–982.
Eugster, H. P., and R. Surdam, 1973, Depositional environment of the Green River Formation of Wyoming: A preliminary report: Bulletin Geological Society of America, v. 84, p. 1115–1120.
Evans, A. M., 1993, Ore Geology and Industrial Minerals: An Introduction, 3rd Edition, Wiley-Blackwell, 400 p.
Evans, D., M. Stephenson, and R. Shaw, 2009, The present and future use of "land" below ground: Land Use Policy, v. 26, Supplement 1, p. S302-S316.
Evans, D. A. D., 2006, Proterozoic low orbital obliquity and axial-dipolar geomagnetic field from evaporite palaeolatitudes: Nature, v. 444, p. 51–55.
Evans, D. G., and J. A. Nunn, 1989, Free thermohaline convection in sediments surrounding a salt column: Journal of Geophysical Research-Atmospheres, v. 94, p. 12,413–12,422.
Evans, D. M., A. Cowden, and R. M. Barratt, 1989, Deformation and thermal erosion at the Foster nickel deposit, Kambalda-St. Ives, Western Australia, in M. S. Prendergast, and M. J. Jones, eds., Magmatic sulfides; the Zimbabwe volume; Fifth magmatic sulfide field conference, Zimbabwe,1987: London, United Kingdom, Inst. Min. and Metall., p. 215–219.
Evans, G., 1995, The Arabian Gulf: A modern carbonate-evaporite factory, a review: Cuadernos de Geologia Ibérica, v. 19, p. 61–96.
Evans, G., 2010, An historical review of the Quaternary sedimentology of the Gulf (Arabian/Persian Gulf) and its geological impact, Quaternary carbonate and evaporite sedimentary facies and their ancient analogues, IAS Special Publication: John Wiley & Sons Ltd., p. 11–44.
Evans, G., V. Schmidt, P. Bush, and H. Nelson, 1969, Stratigraphy and geologic history of the sabkha, Abu Dhabi, Persian Gulf: Sedimentology, v. 12, p. 145–159.
Evans, R., 1967, The structure of the Mississippian evaporite deposit at Pugwash, Cumberland County, Nova Scotia: Economic Geology, v. 62, p. 262–273.
Evans, R., 1978, Origin and significance of evaporites in basins around Atlantic margin: Bulletin American Association Petroleum Geologists, v. 62, p. 223–234.
Evans, R., and D. W. Kirkland, 1988, Evaporitic environments as a source of petroleum, in B. C. Schreiber, ed., Evaporites and hydrocarbons: New York, NY, United States, Columbia Univ. Press, p. 256–299.
Evans, R., and K. O. Linn, 1970, Fold relationships within evaporites of the Cane Creek Anticline: Third Symp. on Salt: North Ohio Geol. Soc., v. 1, p. 286–297.
Evans, W. B., 1970, The Triassic salt deposits of north-western England: Quarterly Journal of the Geological Society, v. 126, p. 103–123.
Ewing, M., and J. Antoine, 1966, New seismic data concerning sediments and diapiric structures in Sigsbee Deep and upper continental slope, Gulf of Mexico: American Association Petroleum Geologists Bulletin, v. 50, p. 470–504.
Eyde, T. H., and D. T. Eyde, 1987, The Bowie chabazite deposit, in H. W. Peirce, ed., 21st Forum on the Geology of Industrial Minerals, v. 4, Arizona Bur. Geol. and Min. Tech Spec. Paper., p. 133.
Ezersky, M., and A. Frumkin, 2013, Fault – Dissolution front relations and the Dead Sea sinkhole problem: Geomorphology, v. 201, p. 35–44.
Fabricius, I. L., B. Røgen, and L. Gommesen, 2007, How depositional texture and diagenesis control petrophysical and elastic properties of samples from five North Sea chalk fields: Petroleum Geoscience, v. 13, p. 81–95.
Fallara, F., M. M. Savard, and S. Paradis, 1998, A structural, petrographic, and geochemical study of the Jubilee Zn-Pb deposit, Nova Scotia, Canada and a new metallogenic model: Economic Geology, v. 93, p. 757–778.
Fard, A., M. Sepehr, and S. Sherkati, 2011, Neogene salt in SW Iran and its interaction with Zagros folding: Geological Magazine, v. 148, p. 854–867.
Fareeduddin, I. R. Kirmani, and S. Gupta, 2010, Low-Al tourmalines of 'oxy-dravite'-povondraite series from Cu-Au deposit of Ghagri area, Salumber-Ghatol belt, Aravalli Supergroup, Rajasthan: Current Science, v. 99, p. 933–938.
Farias, M. E., 2011, Modern Stromatolite Ecosystems at Alkaline and Hypersaline High Altitude Lakes at the Argentinian Puna, in V. Tewari, and J. Seckbach, eds., Stromatolites: Interaction of Microbes with Sediments: New York, Springer, p. 431–440.
Farley, T., 2005, Salt Withdrawal and Depositional Trends at the Pliocene/Miocene Boundary, Central Eugene Island and Ship Shoal Areas, Offshore Louisiana, USA: Gulf Coast Association of Geological Societies Transactions, v. 55, p. 163–183.
Farmer, P., D. Miller, and A. Pieprzak, 1996, Exploring the subsalt: Oilfield Review, Spring 1996, p. 50–64.
Farrimond, P., H. M. Talbot, D. F. Watson, L. K. Schulz, and A. Wilhelms, 2004, Methylhopanoids: Molecular indicators of ancient bacteria and a petroleum correlation tool: Geochimica et Cosmochimica Acta, v. 68, p. 3873–3882.
Faryad, S. W., 2002, Metamorphic Conditions and Fluid Compositions of Scapolite-Bearing Rocks from the Lapis Lazuli Deposit at Sare Sang, Afghanistan: Journal of Petrology, v. 43, p. 725–747.
Faulds, J. E., B. C. Schreiber, S. J. Reynolds, L. A. Gonzalez, and D. Okaya, 1997, Origin and paleogeography of an immense, non-marine Miocene salt deposit in the basin and range (Western USA): Journal of Geology, v. 105, p. 19–36.
Faure, G., and R. P. Felder, 1981, Isotopic composition of strontium and sulfur in secondary gypsum crystals, Brown Hills, Transantarctic Mountains: Journal of Geochemical Exploration, v. 14, p. 265–270.
Fay, R. O., and D. L. J. Hart, 1978, Geology and mineral resources (exclusive of petroleum) of Custer County, Oklahoma: Bull. Okla. Geol. Surv, v. 114.
Feazel, C. T., 1985, Diagenesis of Jurassic grainstone reservoirs in the Smackover Formation, Chatom Field, Alabama, in P. O. Roehl, and

P. W. Choquette, eds., Carbonate petroleum reservoirs: New York, Springer-Verlag, p. 357–367.

Feldens, P., M. Schmidt, N. Mitchell, and A. S. Basaham, 2012, Subsea salt flows in the Atlantis II Deep and Thetis Deep, Red Sea: Proceedings – EGU General Assembly 2012, 22–27 April, 2012 in Vienna, Austria., p.11261.

Feldmann, M., and J. A. McKenzie, 1997, Messinian stromatolite-thrombolite associations, Santa Pola, SE Spain: an analogue for the Palaeozoic?: Sedimentology, v. 44, p. 893–914.

Feldmann, M., and J. A. McKenzie, 1998, Stromatolite-thrombolite associations in a modern environment, Lee Stocking Island, Bahamas: Palaios, v. 13, p. 201–212.

Fendrihan, S., A. Legat, C. Gruber, M. Pfaffenhuemer, G. Weidler, F. Gerbl, and H. Stan-Lotter, 2006, Extremely halophilic archaea and the issue of long term microbial survival: Reviews in Environmental Science and Biotechnology, v. 5, p. 1569–1605.

Feneyrol, J., G. Giuliani, D. Ohnenstetter, A. E. Fallick, J. E. Martelat, P. Monié, J. Dubessy, C. Rollion-Bard, E. Le Goff, E. Malisa, A. F. M. Rakotondrazafy, V. Pardieu, T. Kahn, D. Ichang'i, E. Venance, N. R. Voarintsoa, M. M. Ranatsenho, C. Simonet, E. Omito, C. Nyamai, and M. Saul, 2013, New aspects and perspectives on tsavorite deposits: Ore Geology Reviews, v. 53, p. 1–25.

Feneyrol, J., D. Ohnenstetter, G. Giuliani, A. E. Fallick, C. Rollion-Bard, J.-L. Robert, and E. P. Malisa, 2012, Evidence of evaporites in the genesis of the vanadian grossular tsavorite deposit in Namalulu, Tanzania: The Canadian Mineralogist, v. 50, p. 745–769.

Feng, D., D. Chen, and J. Peckmann, 2009, Rare earth elements in seep carbonates as tracers of variable redox conditions at ancient hydrocarbon seeps: Terra Nova, v. 21, p. 49–56.

Feng, D., and H. H. Roberts, 2010, Massive barite deposits on the northern Gulf of Mexico continental slope: Precipitation processes: Gulf Coast Association of Geological Societies Transactions, v. 60, p. 261–270.

Feng, Z., Y. S. Zhang, and Z. K. Jin, 1998, Type, origin, and reservoir characteristics of dolostones of the Ordovician Majiagou Group, Ordos, North China platform: Sedimentary Geology, v. 118, p. 127–140.

Ferguson, J., 1980, Metamorphism in the Pine Creek Geosyncline and its bearing on stratigraphic correlations: International Uranium Symposium on the Pine Creek Geosyncline, Australia, 1979, Proceedings of the International Atomic Energy Agency, Vienna, p. 91–100.

Ferguson, J., H. Etminan, and F. Ghassemi, 1993, Geochemistry of deep formation waters in the Canning Basin, Western Australia, and their relationship to Zn-Pb mineralization: Australian Journal of Earth Sciences, v. 40, p. 471–483.

Ferguson, J., G. Jacobsen, W. R. Evans, R. A. Wooding, C. J. Barnes, and S. W. Tyler, 1992, Advection and diffusion of groundwater brines in modern and ancient salt lakes, Nulla groundwater discharge complex, Murray Basin, southeast Australia, in J. Kharaka, and A. S. Maest, eds., Rock-Water Interactions Proceedings: Balkema, Rotterdam, p. 643–647.

Ferrarase, F., T. Macaluso, G. Madonia, P. A., and U. Sauro, 2002, Solution and recrystallisation processes and associated landforms in gypsum outcrops of Sicily: Geomorphology, v. 49, p. 25–453.

Ferrer, M., J. Werner, T. N. Chernikova, R. Bargiela, L. Fernández, V. La Cono, J. Waldmann, H. Teeling, O. V. Golyshina, F. O. Glöckner, M. M. Yakimov, P. N. Golyshin, and M. S. C. The, 2012, Unveiling microbial life in the new deep-sea hypersaline Lake Thetis. Part II: a metagenomic study: Environmental Microbiology, v. 14, p. 268–281.

Ferrero, M., Farías, M. E., & Siñeriz, F., 2004, Preliminary characterization of microbial communities in High Altitude Wetlands of Northwestern Argentina by determining terminal restriction fragment length polymorphisms: Revista Latino-americana de Microbiologia, v. 46, p. 72–80.

Fertl, W. H., 1976, Abnormal Formation Pressures: Amsterdam, Elsevier Scientific, 382 p.

Fiduk, J. C., E. R. Brush, L. E. Anderson, P. B. Gibbs, and M. G. Rowan, 2004, Salt deformation, magmatism and hydrocarbon prospectivity in the Espirito Santo Basin, offshore Brazil, in P. J. Post, ed., Salt-sediment interactions and hydrocarbon prospectivity: concepts, applications and case studies for the 21st Century. Papers presented at the 24th Annual Gulf Coast Section SEPM Foundation Bob F. Perkins Research Conference, Houston Tx, December 5–8, 2004 (CD publication), p. 640–668.

Fike, D. A., J. P. Grotzinger, L. M. Pratt, and R. E. Summons, 2006, Oxidation of the Ediacaran Ocean: Nature, v. 444, p. 744–747.

Filippi, M., J. Bruthans, L. Palatinus, M. Zare, and N. Asadi, 2011, Secondary halite deposits in the Iranian salt karst: general description and origin: International Journal of Speleology, v. 40, p. 141–162.

Finkelstein, D. B., R. L. Hay, and S. P. Altaner, 1999, Origin and diagenesis of lacustrine sediments, upper Oligocene Creede Formation, southwestern Colorado: Geological Society of America Bulletin, v. 111, p. 1175–1191.

Finnie, A. B., 2001, A Case Study of High Pressure Brine Flows within the Zechstein Supergroup of the Southern North Sea: SPE Paper 67781 Presented at the SPE/IADC Drilling Conference held in Amsterdam, The Netherlands, 27 February-1 March 2001.

Fiori, M., and S. M. Grillo, 2002, Albite-chlorite and talc-chlorite deposits in metasedimantary andgranitoid rocks of central Sardinia (Italy): Boletim Paranaense de Geociências, v. 50, p. 51–57.

Fischer, A. G., 1981, Climatic oscillations in the biosphere, in M. Nitecki, ed., Biotic crises in ecological and evolutionary time: New York, Academic Press, p. 103–131.

Fischer, A. G., and L. T. Roberts, 1991, Cyclicity in the Green River Formation (lacustrine Eocene) of Wyoming: Journal of Sedimentary Petrology, v. 61, p. 1146–1154.

Fischer, A. G., and M. Sarnthein, 1988, Airborne silts and dune-derived sands in the Permian of the Delaware Basin: Journal of Sedimentary Petrology, v. 58, p. 637–643.

Fischer, D., T. Heck, and L. C. Gerhard, 1990, Medicine Pole Hills Field, Williston Basin, North Dakota, in E. A. Beaumont, and N. H. Foster, eds., Treatise of Petroleum Geology; Atlas of Oil and Gas Fields: Stratigraphic Traps I: Tulsa, OK, American Association Petroleum Geologists, p. 229–255.

Fisher, A. G., 1981, Climatic oscillations in the biosphere, in M. Nitecki, ed., Biotic crises in ecological and evolutionary times, New York Academy press, p. 103–131.

Fisher, C. R., I. R. MacDonald, R. Sassen, C. M. Young, S. A. Macko, S. Hourdez, R. S. Carney, S. Joye, and E. McMullin, 2000, Methane Ice Worms: Hesiocaeca methanicola Colonizing Fossil Fuel Reserves: Naturwissenschaften, v. 87, p. 184–187.

Fisher, R. S., 1988, Clay minerals in evaporite host rocks, Palo Duro Basin, Texas Panhandle: Journal of Sedimentary Petrology, v. 58, p. 836–844.

Fisher, W. L., and P. U. Rodda, 1969, Edwards Formation (Lower Cretaceous), Texas: Dolomitization in a Carbonate Platform System: Bulletin American Association Petroleum Geologists, v. 53, p. 55–72.

Fitzgerald, T. A., 1980, Giant oil field discoveries 1968–1978; An overview, in M. T. Halbouty, ed., Giant oil and gas fields of the decade 1968–1978: Tulsa, OK, American Association of Petroleum Geologists Memoir 30.

Flad, R., J. Zhu, C. Wang, P. Chen, L. von Falkenhausen, Z. Sun, and S. Li, 2005, Archaeological and chemical evidence for early salt production in China: Proceedings of the National Academy of Sciences of the United States of America, v. 102, p. 12618–12622.

Flament, N., N. Coltice, and P. F. Rey, 2008, A case for late-Archaean continental emergence from thermal evolution models and hypsometry: Earth and Planetary Science Letters, v. 275, p. 326–336.

Fletcher, R. C., M. R. Hudec, and I. A. Watson, 1995, Salt glacier and composite sediment-salt glacier models for the emplacement and early burial of allochthonous salt sheets, in M. P. A. Jackson, D. G. Roberts, and S. Snelson, eds., Salt tectonics: a global perspective, American Association Petroleum Geologists Memoir, v. 65, p. 77–108.

Flinch, J. F., A. W. Bally, and S. G. Wu, 1996, Emplacement of a passive-margin evaporitic allochthon in the Betic Cordillera of Spain: Geology, v. 24, p. 67–70.

Flint, S., 1986, Sedimentary and diagenetic controls on red-bed ore genesis; the middle Tertiary San Bartolo copper deposit, Antofagasta Province, Chile: Economic Geology, v. 81, p. 761–778.

Flint, S. S., 1989, Sediment-hosted stratabound copper deposits of the Central Andes: Geological Association of Canada Special Paper, v. 36, p. 371–398.

Fokker, P. A., 1995, The behaviour of salt and salt caverns: Doctoral thesis, Delft University of Technology, Delft, Netherlands, 143 p.

Folk, R., and E. Rasbury, 2007, Nanostructure of palygorskite/sepiolite in Texas caliche: Possible bacterial origin: Carbonates and Evaporites, v. 22, p. 113–122.

Folk, R. L., 1993, SEM imaging of bacteria and nannobacteria in carbonate sediments and rocks: Journal Sedimentary Petrology, v. 63, p. 990–999.

Folk, R. L., 1999, Nannobacteria and the precipitation of carbonate in unusual environments: Sedimentary Geology, v. 126, p. 47–55.

Folk, R. L., and J. S. Pittman, 1971, Length-slow chalcedony; a new testament for vanished evaporites: Journal Sedimentary Petrology, v. 41, p. 1045–1058.

Folk, R. L., and A. Siedlecka, 1974, The "schizohaline" environment: its sedimentary and diagenetic fabrics as exemplified by late Paleozoic rocks of Bear Island, Svalbard: Sedimentary Geology, v. 11, p. 1–15.

Fontboté, L., and H. Gorzawski, 1990, Genesis of the Mississippi Valley-type Zn-Pb deposit of San Vicente, Central Peru: Geologic and isotopic (Sr, O, C, S, Pb) evidence: Economic Geology, v. 85, p. 1402–1437.

Fontes, J. C., and R. Letolle, 1976, ^{18}O and ^{34}S in the upper Bartonian gypsum deposits of the Paris Basin: Chem. Geol., v. 18, p. 285–295.

Fontes, J. C., P. Pouchan, J. F. Saliege, and G. M. Zuppi, 1980, Environmental isotope study of groundwater system in Republic of Djibouti: Arid Zone Hydrology – Proceedings of Advisory Group Meeting, p. 237–267.

Food and Agriculture Organization of the United Nations (FAO), 2010, Current world fertiliser trends and outlook to 2014: Report published by Electronic Publishing Policy and Support Branch, Communication Division, FAO, Viale delle Terme di Caracalla, 00153 Rome, Italy.

Foose, M. P., and J. M. McLelland, 1995, Proterozoic low-Ti iron-oxide deposits in New York and New Jersey: relation to Fe-oxide (Cu-U-Au-rare earth element) deposits and tectonic implications: Geology, v. 23, p. 665–668.

Forbes, B. G., 1991, Olary, South Australia; Sheet SI 54–2; Explanatory Notes: Geological Survey of South Australia.

Ford, D., and P. Williams, 1989, Karst geomorphology and geology: London, Chapman and Hall.

Ford, D., and P. D. Williams, 2007, Karst hydrology and Geomorphology: New York, John Wiley and Sons, Ltd, 562 p.

Ford, D. C., 1997, Principal features of evaporite karst in Canada: Carbonates & Evaporites, v. 12, p. 15–23.

Ford, M., 2004, Depositional wedge tops: interaction between low basal friction external orogenic wedges and flexural foreland basins: Basin Research, v. 16, p. 361–375.

Forrestal, P. J., 1990, Mount Isa and Hilton silver-lead-zinc deposits, in F. E. Hughes, ed., The Mineral Deposits of Australia and Papua New Guinea: Volume 1, v. 14, Australasian Institute of Mining & Metallurgy: Monograph, p. 927–934.

Forster, H., and A. Jafarzadeh, 1994, The Bafq mining district in central Iran – a highly mineralized Infracambrian volcanic field: Economic Geology, v. 89, p. 16978–1721.

Forsythe, R. D., and J. R. Zimbelman, 1995, A case for ancient evaporite basins on Mars: Journal of Geophysical Research-Planets, v. 100, p. 5553–5563.

Fort, R., and M. Bustillo, 1986, Estudio geológico de los yesos miocenos de la zona este de la cuenca de Madrid: Est. Geol. Sect, v. 42, p. 387–395.

Fort, X., J.-P. Brun, and F. Chauvel, 2004, Salt tectonics on the Angolan margin, synsedimentary deformation processes: American Association Petroleum Geologists – Bulletin, v. 88, p. 1523–1544.

Forti, P., S. Galdenzi, and S. M. Sarbu, 2002, The hypogenic caves: a powerful tool for the study of seeps and their environmental effects: Continental Shelf Research, v. 22, p. 2373–2386.

Forti, P., E. Galli, and A. Rossi, 2004 Los mecanismos minerogenéticos activos en las Pozas, in G. Badino, T. Bernabei, A. de Vivo, I. Giulivo, and G. Savino, eds., Bajo el desierto, el misterio de las aguas de Cuatro Cíenegas, La Venta Esplorazioni Geografiche, Instituto Coahuilense de Ecología, Gobierno del Estado de Coahuila & Tintoretto Edizioni, p. 122–125.

Foshag, W., 1921, The origin of the colemanite deposits of California: Economic Geology, v. 16, p. 194–214.

Fossen, H., 2010, Structural Geology, Cambridge University Press, 463 p.

Foster, A. R., P. J. Williams, and C. G. Ryan, 2007, Distribution of Gold in Hypogene Ore at the Ernest Henry Iron Oxide Copper-Gold Deposit, Cloncurry District, NW Queensland: Exploration and Mining Geology, v. 16, p. 125–143.

Foster, D. R. W., and J. R. Austin, 2008, The 1800–1610 Ma stratigraphic and magmatic history of the Eastern Succession, Mount Isa Inlier, and correlations with adjacent Paleoproterozoic terranes: Precambrian Research, v. 163, p. 7–30.

Foster, P. T., and P. R. Rattey, 1993, The evolution of fractured chalk reservoir: Machar oilfield, UK, North Sea: Petroleum Geology of Northwest Europe, Barbican Conference Proceedings, Geological Society of London, v. 2, p. 1445–1452.

Fouke, B. W., C. J. Beets, W. J. Meyers, G. N. Hanson, and A. J. Melillo, 1996, Sr-87/Sr-86 chronostratigraphy and dolomitization history of the Seroe Domi Formation, Curacao (Netherlands Antilles): Facies, v. 35, p. 293–320.

Fowler, M. G., A. P. Hamblin, D. J. MacDonald, and P. G. McMahon, 1993, Geological occurrence and geochemistry of some oil shows in Nova Scotia: Bulletin of Canadian Petroleum Geology, v. 41, p. 422–436.

Fox, J. E., and T. S. Ahlbrandt, 2001, Petroleum Geology and Total Petroleum Systems of the Widyan Basin and Interior Platform of Saudi Arabia and Iraq: U.S. Geological Survey Bulletin 2202–E.

Fox, J. S., 1984, Besshi-type volcanogenic sulphide deposits a review: Canadian Mining & Metallurgical Bulletin, v. 77, p. 57–68.

Frakes, L. A., J. E. Francis, and J. I. Syktus, 1992, Climate modes of the Phanerozoic: the history of the earth's climate over the past 600 million years: New York, Cambridge University Press, 274 p.

Franchini, M. B., R. E. De Barrio, M. J. Pons, I. B. Schalamuk, F. J. Rios, and L. Meinert, 2007, Fe skarn, iron oxide Cu-Au, and manto Cu-(Ag) deposits in the Andes Cordillera of southwest Mendoza Province (34 degrees −36 degrees s), Argentina: Exploration and Mining Geology, v. 16, p. 233–265.

Frank, T. D., and C. R. Fielding, 2003, Marine origin for Precambrian, carbonate-hosted magnesite?: Geology, v. 31, p. 1101–1104.

Frank, T. D., Z. Gui, and t. A. S. M. S. S. Team, 2010, Cryogenic origin for brine in the subsurface of southern McMurdo Sound, Antarctica: Geology, v. 38, p. 587–590.

Franz, L., R. L. Romer, and C. Capitani, 2013, Protoliths and phase petrology of whiteschists: Contributions to Mineralogy and Petrology, v. 166, p. 255–274.

Franzmann, P. D., E. Stackebrandt, K. Sanderson, J. K. Volkman, D. E. Cameron, P. L. Stevenson, T. A. McMeekin, and H. R. Burton, 1988, Halobacterium lacusprofundi sp. nov., a halophilic bacterium isolated from Deep Lake, Antarctica: Syst. Appl. Microbiol., v. 11, p. 20–27.

Frape, S. K., P. Fritz, and R. H. McNutt, 1984, The role of water-rock interactions in the chemical evolution of groundwaters from the Canadian Shield: Geochimica et Cosmochimica Acta, v. 48, p. 1617–1627.

Frazier, W. J., 1975, Celestite in the Mississippian Pennington Formation, central Tennessee: Southeast. Geol., v. 16, p. 241–248.

Fredrich, J. T., D. D. Coblentz, A. F. Fossum, and B. J. Thorne, 2003, Stress perturbations adjacent to salt bodies in the deepwater Gulf of Mexico: SPE 84554. SPE Annual Technical Conference and Exhibition, Denver, CO, Society of Petroleum Engineers.

Fredrickson, J. K., and T. C. Onstott, 1996, Microbes deep inside the Earth: Scientific American, v. Oct. 1996, p. 68–73.

Frey, M. G., and W. H. Grimes, 1970, Bay Marchand—Timbalier Bay—Caillou Island Salt Complex, Louisiana: American Association Petroleum Geologists – Memoir, v. 14, p. 277–291.

Freytag, J. K., P. R. Girguis, D. C. Bergquist, J. P. Andras, J. J. Childress, and C. R. Fisher, 2001, A paradox resolved: Sulfide acquisition by roots of seep tubeworms sustains net chemoautotrophy: Proceedings of the National Academy of Sciences of the United States of America, v. 98, p. 13408–13413.

Friedman, G. M., A. J. Amiel, M. Braun, and D. S. Miller, 1973, Generation of carbonate particles and laminites in algal mats – Examples from sea-marginal hypersaline pool, Gulf of Aqaba, Red Sea: American Association Petroleum Geologists – Bulletin, v. 57, p. 541–557.

Friedman, G. M., and V. Shukla, 1980, Significance of quartz euhedra after sulphates; example from the Lockport Formation (Middle Silurian) of New York: Journal of Sedimentary Petrology, v. 50, p. 1299–1304.

Frietsch, R., P. Tuisku, O. Martinsson, and J. Perdahl, 1997, Early Proterozoic Cu-(Au) and Fe ore deposits associated with regional NaCl metasomatism in northern Fennoscandinavia: Ore Geology Reviews, v. 12, p. 1–34.

Frimmel, H. E., M. S. Basei, and C. Gaucher, 2011, Neoproterozoic geodynamic evolution of SW-Gondwana: a southern African perspective: International Journal of Earth Sciences, v. 100, p. 323–354.

Frimmel, H. E., and S. Y. Jiang, 2001, Marine evaporites from an oceanic island in the Neoproterozoic Adamastor ocean: Precambrian Research, v. 105, p. 57–71.

Frimmel, H. E., and W. Papesch, 1990, Sr, O and C isotope study of the Brixlegg barite deposit, Tyrol (Austria): Economic Geology, v. 85, p. 1162–1171.

Frumkin, A., 1994a, Hydrology and denudation rates of halite karst: Journal of Hydrology, v. 162.

Frumkin, A., 1994b, Morphology and development of salt caves: National Speleological Society, Bulletin, v. 56, p. 82–95.

Frumkin, A., 1996, Determining the exposure age of a karst landscape: Quaternary Research, v. 46, p. 99–106.

Frumkin, A., 1998, Salt cave cross-sections and their paleoenvironmental implications: Geomorphology, v. 23, p. 183–191.

Frumkin, A., 2000, Speleogenesis in salt – the mount Sedom area, Israel, in A. V. Klimchouk, D. C. Ford, A. N. Palmer, and W. Dreybrodt, eds., Speleogenesis; Evolution of Karst Aquifers, Speleological Society of America, Huntsville, AL, p. 443–451.

Frumkin, A., 2009, Formation and dating of a salt pillar in Mt Sedom diapir, Israel: Geological Society America Bulletin, v. 121, p. 286–293.

Frumkin, A., and Y. Elitzur, 2002, Historic Dead Sea Level Fluctuations Calibrated with Geological and Archaeological Evidence: Quaternary Research, v. 57, p. 334–342.

Frumkin, A., M. Ezersky, A. Al-Zoubi, E. Akkawi, and A.-R. Abueladas, 2011, The Dead Sea sinkhole hazard: Geophysical assessment of salt dissolution and collapse: Geomorphology, v. 134, p. 102–117.

Frumkin, A., and D. C. Ford, 1995, Rapid entrenchment of stream profiles in the salt caves of Mount Sedom, Israel: Earth Surface Processes & Landforms, v. 20, p. 139–152.

Frumkin, A., and E. Raz, 2001, Collapse and subsidence associated with salt karstification along the Dead Sea: Carbonates & Evaporites, v. 16, p. 117–130.

Frutos, J., 1990, The Andes Cordillera: A synthesis of the geologic evolution, in L. Fontboté, G. C. Amstrutz, M. Cardozo, E. Cedillo, and J. Frutos, eds., Stratabound ore deposits in the Andes: Berlin, Springer-Verlag, p. 3–35.

Frutos, J., and M. Cisternas, 2003, Isotopic Differentiation in Volcanic-Epithermal Surface Sulfur Deposits of Northern Chile: $\delta^{34}S < 0$ in "Fertile" Systems (Au-Ag-Cu Ore Deposits below), versus $\delta^{34}S > 0$ & for "Barren" Systems: Short Papers IV South American Symposium on Isotope Geology (Salvador, Brazil, 2003), p. 733–735.

Fry, J. C., R. J. Parkes, B. A. Cragg, A. J. Weightman, and G. Webster, 2008, Prokaryotic biodiversity and activity in the deep subseafloor biosphere: FEMS Microbiology Ecology, v. 66, p. 181–196.

Fryberger, S. G., 1986, Stratigraphic traps for petroleum in wind-laid rocks: American Association Petroleum Geologists – Bulletin, v. 70, p. 1765–1776.

Fryberger, S. G., T. S. Ahlbrandt, and A. S, 1979, Origin, sedimentary features and significance of low-angle eolian "sand sheet" deposits, Great Sand Dunes National Monument and vicinity, Colorado: Journal of Sedimentary Petrology, v. 49, p. 733–746.

Fryberger, S. G., A. M. Al Sari, and T. J. Clisham, 1983, Eolian dune, interdune, sand sheet, and siliciclastic sabkha sediments of an offshore prograding sand sea, Dhahran area, Saudi Arabia: American Association Petroleum Geologists – Bulletin, v. 67, p. 280–312.

Fryberger, S. G., A. M. Al Sari, T. J. Clisham, A. R. R. Syed, and G. A. H. Khattab, 1984, Wind sedimentation in the Jafurah sand sea, Saudi Arabia: Sedimentology, v. 31, p. 413–431.

Fryer, S., 2005, Halite caves of the Atacama: National Speleological Society, The NSS news, v. 63, p. 4–19.

Fu, B., P. Aharon, G. R. Byerly, and H. H. Roberts, 1994, Barite chimneys on the Gulf of Mexico slope. Initial reports on their petrography and geochemistry: Geo-Marine Letters, v. 14, p. 81–87.

Fu Chen, D., Q. Liu, Z. Zhang, L. M. Cathles Iii, and H. H. Roberts, 2007, Biogenic fabrics in seep carbonates from an active gas vent site in Green Canyon Block 238, Gulf of Mexico: Marine and Petroleum Geology, v. 24, p. 313–320.

Fu, Q. L., H. R. Qing, K. M. Bergman, and C. Yang, 2008, Dedolomitization and calcite cementation in the Middle Devonian Winnipegosis Formation in Central Saskatchewan, Canada: Sedimentology, v. 55, p. 1623–1642.

Fudral, S., C. Yu Lu, and A. Paillet, 2010, Dykes and Pipes of Remobilized Cornieules within the Cornieule Evaporitic-Complex of the Mont Jovet Area (Northwestern French Alps): Geodinamica Acta, v. 23, p. 195–205.

Fuersich, F. T., S. Freytag, J. Roehl, and A. Schmid, 1995, Palaeoecology of benthic associations in salinity-controlled marginal marine environments; examples from the lower Bathonian (Jurassic) of the Causses (southern France): Palaeogeography, Palaeoclimatology, Palaeoecology, v. 113, p. 135–172.

Fürst, M., 1976, Tektonik und Diapirismus der östlichen Zagrosketten: Z. dtsch. geol. Ges., v. 127, p. 183–225.

Fusswinkel, T., T. Wagner, M. Wälle, T. Wenzel, C. A. Heinrich, and G. Markl, 2013, Fluid mixing forms basement-hosted Pb-Zn deposits: Insight from metal and halogen geochemistry of individual fluid inclusions: Geology, v. 41, p. 679–682.

Fuzesy, A., 1982, Potash in Saskatchewan: Report Saskatchewan, Department of Mineral Resources v. 181, 44 p.

Gablina, I. F., 1981, New data on the formation conditions of the Dzhezkazgan copper deposit: International Geology Review, v. 23, p. 1313–1311.

Gabriel, A. K., R. M. Goldstein, and H. A. Zebcker, 1989, Mapping small elevation changes over large areas: differential radar interferometry: Journal Geophysical Research, v. 94, p. 9183–9191.

Gac, J. Y., 1980, Géochimie du bassin du Lac Tchad: Travaux et Documents ORSTOM, v. 123, p. 54 pp.

Gac, J. Y., A. Al-Droubi, H. Paquet, B. Fritz, and Y. Tardy, 1977, Chemical model for origin and distribution of elements in salts and brines during evaporation of waters. Application to some saline lakes of Tibesti, Chad: Physics and Chemistry of the Earth, New York, v. 11, p. 149–158.

Galdenzi, S., 1990, Un modello genetico per la Grotta Grande del Vento: Mem. 1st. It. Speleol., v. II.

Galdenzi, S., and T. Maruoka, 2003, Gypsum deposits in the Frasassi Caves, central Italy: Journal of Cave and Karst Studies, v. 65, p. 111–125.

Galdenzi, S., and M. Menichetti, 1995, Occurrence of hypogenic caves in a karst region: Examples from central Italy: Environmental Geology, v. 26, p. 39–47.

Galloway, W. E., T. E. Ewing, C. M. Garret, N. Tyler, and D. G. Bebout, 1983, Atlas of major Texas oil reservoirs: The University of Texas at Austin, Bureau of Economic Geology special publication, 139 p.

Galve, J. P., F. Gutierrez, P. Lucha, J. Bonachea, J. Remondo, A. Cendrero, M. Gutierrez, M. J. Gimeno, G. Pardo, and J. A. Sanchez, 2009, Sinkholes in the salt-bearing evaporite karst of the Ebro River valley upstream of Zaragoza city (NE Spain) Geomorphological mapping and analysis as a basis for risk management: Geomorphology, v. 108, p. 145–158.

Gammon, P. R., D. M. McKirdy, and H. D. Smith, 2005, The timing and environment of tepee formation in a Marinoan cap carbonate: Sedimentary Geology, v. 177, p. 195–208.

Gammon, P. R., D. M. McKirdy, and H. D. Smith, 2012, The paragenetic history of a Marinoan cap carbonate: Sedimentary Geology, v. 243–244, p. 1–16.

Gandhi, S. S., and R. T. Bell, 1990, Metallogenic concepts to aid exploration for the giant Olympic Dam-type deposits and their derivatives [abs.]: 8th IAGOD Symposium, Ottawa, Canada, August 1990, Program with abstracts, p. A7.

Gandin, A., and D. T. Wright, 2007, Evidence of vanished evaporites in Neoarchaean carbonates of South Africa: Geological Society, London, Special Publications, v. 285, p. 285–308.

Gansser, A., 1957, Die geologische Erforschung der Qum Gegend, Iran: Ver. Schweiz. Petrol. Geol. u. Ing., B., v. 23 (65), p. 1–16.

Gao, G., S. D. Hovorka, and H. H. Posey, 1990, Limpid dolomite in Permian San Andres halite rocks, Palo Duro Basin, Texas Panhandle; characteristics, possible origin, and implications for brine evolution: Journal of Sedimentary Petrology, v. 60, p. 118–124.

Gao, G., and L. S. Land, 1991, Nodular chert from the Arbuckle Group, Slick Hills, SW Oklahoma: a combined field, petrographic and isotopic study: Sedimentology, v. 38, p. 857–870.

Garber, R. A., 1980, The sedimentology of the Dead Sea: Doctoral thesis, Rennsaler Polytechnic, 170 p.

Garber, R. A., and G. M. Friedman, 1983, Coated grains along the Dead Sea shore, in T. Peryt, ed., Coated Grains: New York, Springer Verlag, p. 163–168.

Garber, R. A., G. M. Friedman, and A. Nissenbaum, 1981, Concentric aragonitic ooids from the Dead Sea: Journal of Sedimentary Petrology, v. 51, p. 455–458.

Garber, R. A., P. M. Harris, and J. M. Borer, 1990, Occurrence and significance of magnesite in Upper Permian (Guadalupian) Tansill and Yates formations, Delaware Basin, New Mexico: American Association Petroleum Geologists Bulletin, v. 74, p. 119–134.

Garber, R. A., Y. Levy, and G. M. Friedman, 1987, The sedimentology of the Dead Sea: Carbonates and Evaporites, v. 2, p. 43–57.

García, A., and A. R. Chivas, 2004, Quaternary and extant euryhaline Lamprothamnium; Groves (Charales) from Australia: Gyrogonite morphology and paleolimnological significance: Journal of Paleolimnology, v. 31, p. 321–341.

Garcia, C. M., and F. X. Niell, 1993, Seasonal Change in a Saline Temporary Lake (Fuente-De-Piedra, Southern Spain): Hydrobiologia, v. 267, p. 211–223.

García-Del-Cura, M. Á., M. E. Sanz-Montero, M. A. De-los-Ríos, and C. Ascaso, 2014, Microbial dolomite in fresh water carbonate deposits: Sedimentology, v. 61, p. 41–45.

Garcia-Guinea, J., S. Morales, A. Delgado, C. Recio, and J. M. Calaforra, 2002, Formation of gigantic gypsum crystals: Journal of the Geological Society, v. 159, p. 347–350.

García-Ruiz, J. M., R. Villasuso, C. Ayora, A. Canals, and F. Otálora, 2007, Formation of natural gypsum megacrystals in Naica, Mexico: Geology, v. 35, p. 327–330.

Garcia-Veigas, J., D. I. Cendon, J. J. Pueyo, and T. M. Peryt, 2011a, Zechstein saline brines in Poland, evidence of overturned anoxic ocean during the Late Permian mass extinction event: Chemical Geology, v. 290, p. 189–201.

Garcia-Veigas, J., G. Chong, and J. J. Pueyo, 1996, Mineralogy and geochemistry of the Salar Grande salt rock: Third ISAG, St Malo (France), 17-19/9/1996, p. 679–682.

García-Veigas, J., Gündo an, C. Helvaci, and E. Prats, 2013, A genetic model for Na-carbonate mineral precipitation in the Miocene Beypazan trona deposit, Ankara province, Turkey: Sedimentary Geology, v. 294, p. 315–327.

García-Veigas, J., and C. Helvacı, 2013, Mineralogy and sedimentology of the Miocene Göcenoluk borate deposit, Kırka district, western Anatolia, Turkey: Sedimentary Geology, v. 290, p. 85–96.

García-Veigas, J., L. Rosell, F. Ortí, I. Gundogan, and C. Helvaci, 201lb, Mineralogy, diagenesis and hydrochemical evolution in a probertite-glauberite-halite saline lake (Miocene, Emet Basin, Turkey): Chemical Geology, v. 280, p. 352–364.

GarcÌa-Veigas, J., L. Rosell, I. Zak, E. Play‡, C. Ayora, and A. Starinsky, 2009, Evidence of potash salt formation in the Pliocene Sedom Lagoon (Dead Sea Rift, Israel): Chemical Geology, v. 265, p. 499–511.

Gardner, W. C., and E. E. Bray, 1984, Oil and source rocks of the Niagaran Reefs (Silurian) in the Michigan Basin, in J. G. Palacas, ed., Petroleum geochemistry and source rock potential of carbonate rocks, v. 18: Tulsa, Ok, American Association of Petroleum Geologists, Studies in Geology, p. 33–44.

Garea, B. B., and C. J. R. Braithwaite, 1996, Geochemistry, isotopic composition and origin of the Beda dolomites, block NC74F, SW Sirt Basin, Libya: Journal of Petroleum Geology, v. 19, p. 289–304.

Garfunkel, Z., and Z. Ben-Avraham, 1996, The structure of the Dead Sea: Tectonophysics, v. 266, p. 155–176.

Garfunkel, Z., I. Zak, and R. Freund, 1981, Active faulting in the Dead Sea Rift: Tectonophysics, v. 62, p. 37–52.

Garleff, K., H. Kugler, A. V. Poschinger, H. Sterr, H. Strunk, and G. Villwock, 1997, Germany, in C. Embleton, and C. Embleton, eds., Geomorphological hazards of Europe, Vol. 5. Developments in Earth Surface Processes, v. 5, p. 147–177.

Garlicki, A., 1993, Solution mining of Miocene salts in Poland and its environmental impact, in H. a. T. Hoshi Kakihana, ed., Proc. 7th Symp. on Salt, Kyoto, Japan, April 1992: Amsterdam, Elsevier Science, p. 419–424.

Garlicki, A., M. Pulina, and J. Rozkowski, 1996, Karst phenomena and their influence on the ground-waters threat in the Wieliczka salt mine (in Polish): Przeglad Geologiczny, v. 44, p. 1032–1038.

Garlicki, A., and Z. Wilk, 1993, Geological and hydrogeological background of the recent water damage in Wieliczka Salt Mine (in Polish): Przegla¸ d Geologiczny, v. 3, p. 183–192.

Garnier, V., G. Giuliani, D. Ohnenstetter, A. E. Fallick, J. Dubessy, D. Banks, H. Q. Vinh, T. Lhomme, H. Maluski, A. Pecher, K. A. Bakhsh, P. Van Long, P. T. Trinh, and D. Schwarz, 2008, Marble-hosted ruby deposits from Central and Southeast Asia: Towards a new genetic model: Ore Geology Reviews, v. 34, p. 169–191.

Garnier, V., D. Ohnenstetter, and G. Giuliani, 2004, Fluor-rich aspidolite: a witness of evaporite implication in the genesis of ruby Nangimali (Azad-Kashmir, Pakistan) marbles (in French). Comptes Rendus Geosciences, v. 336, p. 1245–1253.

Garnier, V., D. Ohnenstetter, and G. Giuliani, 2005, Fluor-rich aspidolite: a witness of evaporite implication in the genesis of ruby Nangimali (Azad-Kashmir, Pakistan) marbles (in French). Comptes Rendus Geosciences, v. 336, p. 1245–1253.

Garofalo, P. S., M. B. Fricker, D. Günther, P. Forti, A.-M. Mercuri, M. Loreti, and B. Capaccioni, 2010, Climatic control on the growth of gigantic gypsum crystals within hypogenic caves (Naica mine, Mexico)?: Earth and Planetary Science Letters, v. 289, p. 560–569.

Garrels, R. M., and C. L. Christ, 1965, Solutions, minerals, and equilibria: San Francisco, W. H. Freeman, 450 p.

Garrels, R. M., and F. T. Mackenzie, 1981, Evolution of sedimentary rocks: New York, W. W. Norton and Co.

Garrett, D., 2004, Handbook of lithium and natural calcium chloride, Elsevier Academic Press, 460 p.

Garrett, D. E., 1970a, The chemistry and origin of potash deposits, Third International Symposium on Salt, v. 1: Cleveland, Northern Ohio Geological Society, p. 211–222.

Garrett, D. E., 1985, Chemistry and origin of the Chilean nitrate deposits: Sixth international symposium on salt, v. 1, p. 285–302.

Garrett, D. E., 1995, Potash: Deposits, processing, properties and uses: Berlin, Springer, 752 p.

Garrett, D. E., 1998, Borates: Deposits, processing, properties and use: Amsterdam, Elsevier.

Garrett, D. E., 2001, Sodium sulfate: Handbook of deposits, processing, properties and uses: Amsterdam, Elsevier, 384 p.

Garrett, D. E., 2002, Sodium sulfate – 5,000 years of mining and production of salt cake: Mining Engineering, v. February, 2002, p. 17–22.

Garrett, D. E., 2004, Handbook of Lithium and natural Calcium Chloride; Their deposits, processing, uses and properties Amsterdam, Elsevier Academic Press, 476 p.

Garrett, P., 1970b, Phanerozoic stromatolites: noncompetitive ecologic restriction by grazing and burrowing animals: Science, v. 169, p. 171–173.

Garrison, R. E., and N. J. McMillan, 1999, Evidence for Jurassic continental rift magmatism in northeast Mexico: Allogenic meta-igneous blocks in El Papalote diapir, La Popa Basin, Nuevo Leon, Mexico, in C. Bartolini, J. L. Wilson, and T. F. Lawton, eds., Mesozoic sedimentary and tectonic history of north-central Mexico, Geological Society America Special Paper 340, p. 319–332.

Garven, G., 1995, Continental-scale groundwater flow and geologic processes: Annu. Rev. Earth Planet. Sci., v. 23, p. 89–117.

Gasiewicz, A., 2000, Comparative study of major element geochemistry of gypsum-ghost limestones and selenite lithofacies from the Miocene of northern Carpathian Foredeep: implication to the model of massive replacement of solid sulphates by calcium carbonates: Chemical Geology, v. 164, p. 183–218.

Gasse, F., and J. C. Fontes, 1989, Palaeoenvironments and palaeohydrology of a tropical closed lake (Lake Asal, Djibouti) since 10,000 yr B.P: Palaeogeography, Palaeoclimatology, Palaeoecology, v. 69, p. 67–102.

Gaullier, V., and B. C. Vendeville, 2005, Salt tectonics driven by sediment progradation: Part II – Radial spreading of sedimentary lobes prograding above salt: Bulletin American Association Petroleum Geologists, v. 89, p. 1081–1089.

Gaupp, R., A. Matter, J. Platt, K. Ramseyer, and J. Walzebuck, 1993, Diagenesis and fluid evolution of deeply buried Permian (Rotliegende) gas reservoirs, northwest Germany: Bulletin-American Association of Petroleum Geologists, v. 77, p. 1111–1128.

Gauthier, B. D. M., R. C. W. M. Franssen, and S. Drei, 2000, Fracture networks in Rotliegend gas reservoirs of the Dutch offshore: implications for reservoir behaviour: Geologie en Mijnbouw/Netherlands Journal of Geoscience, v. 79, p. 45–57.

Gauthier, M., F. Chartrand, A. Cayer, and J. David, 2004, The Kwyjibo Cu-REE-U-Au-Mo-F Property, Quebec: A Mesoproterozoic Polymetallic Iron Oxide Deposit in the Northeastern Grenville Province: Economic Geology, v. 99, p. 1177–1196.

Gautier, F., G. Clauzon, J. P. Suc, J. Cravette, and D. Violant, 1994, Age et durée de la crise de salinité messinienne: C. R. Acad. Sci. Paris Ser. 2, v. 318, p. 1103–1109.

Gavish, E., 1974, Geochemistry and mineralogy of a Recent sabkha along the coast of Sinai, Gulf of Suez: Sedimentology, v. 21, p. 397–414.

Gavish, E., 1980, Recent sabkhas marginal to the southern coasts of Sinai, Red Sea, in A. Nissenbaum, ed., Hypersaline brines and evaporitic environments, Elsevier, Amsterdam, p. 233–251.

Gavish, E., W. E. Krumbein, and J. Halevy, 1985, Geomorphology, mineralogy and groundwater geochemistry as factors of the hydrodynamic system of the Gavish Sabkha, in G. M. Friedman, and W. E. Krumbein, eds., Hypersaline ecosystems; the Gavish Sabkha, v. Ecological Studies Vol. 53: New York, Springer, p. 186–217.

Gavrieli, 1997, Halite deposition in the Dead Sea: 1960–1993, in T. Neimi, Z. Ben-Avraham, and J. R. Gat, eds., The Dead Sea, Oxford University Press, p. 161–171.

Ge, H. X., M. P. A. Jackson, and B. C. Vendeville, 1997, Kinematics and dynamics of salt tectonics driven by progradation: American Association Petroleum Geologists Bulletin-American Association of Petroleum Geologists, v. 81, p. 398–423.

Gebauer, D., H. P. Schertl, M. Brix, and W. Schreyer, 1997, 35 Ma old ultrahigh-pressure metamorphism and evidence for very rapid exhumation in the Dora Maira Massif, Western Alps: Lithos, v. 41, p. 5–24.

Gebhardt, F., D. Eby, and D. Barnette, 2001, Utilizing coiled tubing technology to control a liquid propane storage well fire, A case history: Proc. Solution Mining Research Institute Spring Meeting, Orlando, p. 301–308.

Geddes, M. C., 1975a, Studies on an Australian brine shrimp, Parartemia zeitziana Sayce (Crustacea: Anostraca). I. Salinity tolerance: Comp. Biochem. Physiol, v. 51A, p. 553–559.

Geddes, M. C., 1975b, Studies on an Australian brine shrimp, Parartemia zeitziana Sayce (Crustacea: Anostraca). II. Osmotic and ionic regulation: Comp. Biochem. Physiol., v. 51A, p. 561–571.

Geddes, M. C., 1975c, Studies on an Australian brine shrimp, Parartemia zeitziana Sayce (Crustacea: Anostraca). III. The mechanisms of osmotic and ionic regulation: Comp. Biochem. Physiol., v. 51A, p. 573–578.

Geddes, M. C., 1981, The Brine Shrimps Artemia and Parartemia – Comparative Physiology and Distribution in Australia: Hydrobiologia, v. 81–2, p. 169–179.

Geddes, M. C., P. De Deckker, and W. C. Williams, 1981, On the chemistry and biota of some saline lakes in Western Australia: Hydrobiologia, v. 81, p. 201–222.

Gee, M. J. R., H. S. Uy, J. Warren, C. K. Morley, and J. J. Lambiase, 2007, The Brunei slide: A giant submarine landslide on the North West Borneo Margin revealed by 3D seismic data: Marine Geology, v. 246, p. 9–23.

Geeslin, J. H., and H. S. Chafetz, 1982, Ordovician Aleman ribbon cherts; an example of silicification prior to carbonate lithification: Journal of Sedimentary Petrology, v. 52, p. 1283–1293.

Geisler-Cussey, D., 1987, Middle Muschelkalk Evaporitic deposits in the eastern Paris Basin, in T. M. Peryt, ed., Lecture Notes in Earth Sciences, v. 13: Berlin; New York, Springer-Verlag, p. 89–121.

Geletti, R., A. Del Ben, M. Busetti, R. Ramella, and V. Volpi, 2008, Gas seeps linked to salt structures in the Central Adriatic Sea: Basin Research, v. 20, p. 473–487.

Geluk, M., 1999, Late Permian (Zechstein) rifting in the Netherlands: models and implications for petroleum geology: Petroleum Geoscience, v. 5, p. 189–199.

Geluk, M. C., 1998, Internal tectonics of salt structures: Journal of Seismic Exploration, v. 7, p. 237–250.

Geluk, M. C., 2000, Late Permian (Zechstein) carbonate-facies maps, the Netherlands: Geologie en Mijnbouw, v. 79, p. 17–27.

Geluk, M. C, W. A. Paar, and P. A. Fokker, 2007, Salt, in T. E. Wong, D. A. J. Batjes, and J. de Jager, eds., Geology of the Netherlands, Royal Netherlands Academy of Arts and Sciences, p. 283–294.

Gely, J. P., V. M. M. Blanc, D. F. Fache, M. Schuler, and M. Ansart, 1993, Characterization of organic-rich material in an evaporitic environment; the lower Oligocene of the Mulhouse Basin (Alsace, France): Geologische Rundschau, v. 82, p. 718–725.

Gendzwill, D., and N. Martin, 1996, Flooding and loss of the Patience Lake potash mine: CIM Bulletin, v. 89, p. 62–73.

Gendzwill, D., and J. Unrau, 1996, Ground control and seismicity at International Minerals and Chemical (Canada) Global Ltd: CIM Bulletin, v. 89, p. 52–61.

Gendzwill, D. J., 1978, Winnipegosis mounds and Prairie Evaporite Formation of Saskatchewan – seismic study: American Association Petroleum Geologists – Bulletin, v. 62, p. 73–86.

Gerdes, G., K. Dunajtschik-Piewak, H. Riege, A. G. Taher, W. Krumbein, and H.-E. Reineck, 1994, Structural diversity of biogenic carbonate particles in microbial mats: Sedimentology, v. 41, p. 1273–1294.

Gerdes, G., T. Klenke, and N. Noffke, 2000a, Microbial signatures in peritidal siliciclastic sediments: a catalogue: Sedimentology, v. 47, p. 279–308.

Gerdes, G., W. E. Krumbein, and N. Noffke, 2000b, Evaporite Microbial Sediment, in R. E. Riding, and S. M. Awramik, eds., Microbial Sediments: Berlin Heidelberg, Springer-Verlag, p. 196–208.

Gerdes, G., H. Porada, and E. Bouougri, 2008, Bio-sedimentary structures evolving from the interaction of microbial mats, burrowing beetles and the physical environment of Tunisian coastal sabkhas: Senckenbergiana maritima, v. 38, p. 45–58.

Gerdes, K. D., P. Winefield, M. D. Simmons, and C. Van Oosterhout, 2010, The influence of basin architecture and eustacy on the evolution of Tethyan Mesozoic and Cenozoic carbonate sequences: Geological Society, London, Special Publications, v. 329, p. 9–41.

Gerhard, L. C., 1985, Porosity development in the Mississippian pisolitic limestones of the Mission Canyon formation, Glenburn field, Williston basin, North Dakota., in P. O. Roehl, and P. W. Choquette, eds., Carbonate Petroleum Reservoirs, Springer-Verlag, p. 191–205.

Gertman, I., and A. Hecht, 2002, The Dead Sea hydrography from 1992 to 2000: Journal of Marine Systems, v. 35, p. 169–181.

Ghai, R., L. Pasic, A. B. Fernandez, A.-B. Martin-Cuadrado, C. M. Mizuno, K. D. McMahon, R. T. Papke, R. Stepanauskas, B. Rodriguez-Brito, F. Rohwer, C. Sanchez-Porro, A. Ventosa, and F. Rodriguez-Valera, 2011, New Abundant Microbial Groups in Aquatic Hypersaline Environments: Scientific reports.

Ghazban, F., 1988, Geological and stable isotope studies of carbonate-hosted lead zinc deposits in Nanisivik, northern Baffin Island, NWT, Canada.: Open Access Dissertations and Theses. Paper 3989. http://digitalcommons.mcmaster.ca/opendis sertations/3989.

Ghazban, F., H. P. Schwarcz, and D. C. Ford, 1990, Carbon and sulfur isotope evidence for in situ reduction of sulfate, Nanisivik lead-zinc deposits, Northwest Territories, Baffin Island, Canada: Economic Geology, v. 85.

Ghazban, F., H. P. Schwarcz, and D. C. Ford, 1992, Multistage dolomitization in the Society Cliffs Formation, northern Baffin Island, Northwest Territories, Canada: Canadian Journal of Earth Sciences, v. 29, p. 1459–1473.

Ghori, K. A. R., 2002, Modelling the hydrocarbon generative history of the Officer Basin, Western Australia: PESA Journal, v. 29, p. 29–43.

Gibert, J. M. D., and A. A. Ekdale, 1999, Trace Fossil Assemblages Reflecting Stressed Environments in the Middle Jurassic Carmel Seaway of Central Utah: Journal of Paleontology, v. 73, p. 711–720.

Gibert, L., G. R. Scott, P. Montoya, F. J. Ruiz-Sánchez, J. Morales, L. Luque, J. Abella, and M. Lería, 2013, Evidence for an African-Iberian mammal dispersal during the pre-evaporitic Messinian: Geology, v. 41, p. 691–694.

Giblin, A. M., and E. C. Appleyard, 1987, Uranium mobility in non-oxidizing brines: field and experimental evidence: Applied Geochemistry, v. 2, p. 285–295.

Gibling, M. R., G. C. Nanson, and J. C. Maroulis, 1998, Anastomosing river sedimentation in the Channel Country of central Australia: Sedimentology, v. 45, p. 595–619.

Gibson, G. M., M. J. Rubenach, N. L. Neumann, P. N. Southgate, and L. J. Hutton, 2008, Syn- and post-extensional tectonic activity in the Palaeoproterozoic sequences of Broken Hill and Mount Isa and its bearing on reconstructions of Rodinia: Precambrian Research, v. 166, p. 350–369.

Gibson, J. A. E., 1999, The meromictic lakes and stratified marine basins of the Vestfold Hills, East Antarctica: Antarctic Science, v. 11, p. 175–192.

Gierlowski-Kordesch, E., and K. Kelts, 1994, The global geological record of lake basins: Cambridge, Cambridge University Press.

Gierlowski-Kordesch, E. H., 2010, Chapter 1 Lacustrine Carbonates, in A. M. Alonso-Zarza, and L. H. Tanner, eds., Developments in Sedimentology, v. Volume 61, Elsevier, p. 1–101.

Giles, K., T. Lawton, A. Shock, R. Kernen, T. Hearon, and M. Rowan, 2012, A Halokinetic Drape-Fold Model for Caprock in Diapir-Flanking and Subsalt Positions (abst.): American Association Petroleum Geologists Search and Discovery Article #90142 © 2012; American Association Petroleum Geologists Annual Convention and Exhibition, April 22–25, 2012, Long Beach, California.

Giles, K. A., and R. K. Goldhammer, 2002, Isolated to Coalesced Carbonate Buildups Developed on Passive Salt Diapir Bathymetry, La Popa Basin, NE Mexico: American Association Petroleum Geologists – Bulletin, v. 86.

Giles, K. A., and T. F. Lawton, 1999, Attributes and evolution of an exhumed salt weld, La Popa basin, northeastern Mexico: Geology, v. 27, p. 323–326.

Giles, K. A., and T. F. Lawton, 2002, Halokinetic sequence stratigraphy adjacent to the El Papalote diapir, northeastern Mexico: Bulletin American Association Petroleum Geologists, v. 86, p. 823–840.

Gilhooly III, W. P., R. S. Carney, and S. A. Macko, 2007, Relationships between sulfide-oxidizing bacterial mats and their carbon sources in northern Gulf of Mexico cold seeps: Organic Geochemistry, v. 38, p. 380–393.

Gill, B. A., and S. Akhtar, 1982, The rock mechanics and ground control methods associated with Saskatchewan potash mining; an overview: The Geological Bulletin of the Punjab University, v. 17, p. 33–36.

Gill, D., 1977, Salina A-1 sabkha cycles and the Late Silurian paleogeography of the Michigan Basin: Journal of Sedimentary Petrology, v. 47, p. 979–1017.

Gill, D., 1979, Differential Entrapment of Oil and Gas in Niagaran Pinnacle-Reef Belt of Northern Michigan: Bulletin American Association Petroleum Geologists, v. 63, p. 680–620.

Gill, D., 1985, Depositional facies of Middle Silurian (Niagaran) pinnacle reefs, Belle River Mills gas field, Michigan Basin, SE Michigan, in P. O. Roehl, and P. W. Choquette, eds., Carbonate

petroleum reservoirs: a case book: New York, Springer Verlag, p. 123–139.
Gill, D., 1994, Niagaran reefs of Northern Michigan. 1. Exploration portrait: Journal of Petroleum Geology, v. 17, p. 99–110.
Gill, W. D., and M. A. Ala, 1972, Sedimentology of the Gachsaran Formation (Lower Fars Series), Southwest Iran: American Association Petroleum Geologists – Bulletin, v. 56, p. 1965–1974.
Gillen, D., 2010, A study of IOCG-related hydrothermal fluids in the Wernecke Mountains, Yukon Territory, Canada: Doctoral thesis, James Cook University, Townsville, Australia.
Gillespie, R., J. W. Magee, J. G. Luly, E. Dlugokencky, R. J. Sparks, and G. Wallace, 1991, AMS radiocarbon dating in the study of arid environments: examples from Lake Eyre, South Australia: Palaeogeography Palaeoclimatology Palaeoecology, v. 84, p. 333–338.
Ginau, A., M. Engel, and H. Bruckner, 2012, Holocene chemical precipitates in the continental sabkha of Tayma (NW Saudi Arabia): Journal of Arid Environments, v. 84, p. 26–37.
Gindre-Chanu, L., J. K. Warren, C. Puigdefabregas, I. R. Sharp, D. C. P. Peacock, R. Swart, R. Poulsen, H. Ferreira, and L. Henrique, 2014, Diagenetic evolution of Aptian evaporites in the Namibe Basin (south-west Angola): Sedimentology, p. n/a-n/a
Gingras, M. K., S. G. Pemberton, K. Muelenbachs, and H. G. Machel, 2004, Conceptual models for burrow-related, selective dolomitization with textural and isotopic evidence from the Tyndall Stone, Canada: Geobiology, v. 2, p. 21–30.
Giordano, T., H., 2002, Transport of Pb and Zn by carboxylate complexes in basinal ore fluids and related petroleum-field brines at 100°C: the influence of pH and oxygen fugacity: Geochemical Transactions, v. 3, p. 56–56.
Giordano, T. H., 1985, A preliminary evaluation of organic ligands and metal-organic complexing in Mississippi Valley-Type ore solutions: Economic Geology, v. 80, p. 96–106.
Giordano, T. H., and Y. K. Kharaka, 1994, Organic ligand distribution and speciation in sedimentary basin brines, diagenetic fluids and related ore solutions: Geological Society, London, Special Publications, v. 78, p. 175–202.
Giralt, S., R. Julià, S. Leroy, and F. Gasse, 2003, Cyclic water level oscillations of the KaraBogazGol-Caspian Sea system: Earth and Planetary Science Letters, v. 212, p. 225–239.
Gischler, E., M. A. Gibson, and W. Oschmann, 2008, Giant Holocene Freshwater Microbialites, Laguna Bacalar, Quintana Roo, Mexico: Sedimentology, v. 55, p. 1293–1309.
Gisotti, G., 1991, A Case of Induced Subsidence for Extraction of Salt by Hydrosolution, Proceedings 4th International Symposium on Land Subsidence, v. 200, IAHL, p. 235–245.
Giuliani, G., A. Cheilletz, C. Arboleda, V. Carrillo, F. Rueda, and J. H. Baker, 1995, An evaporitic origin of the parent brines of Colombian emeralds; fluid inclusion and sulphur isotope evidence: European Journal of Mineralogy, v. 7, p. 151–165.
Giuliani, G., C. France-Lanord, A. Cheilletz, P. Coget, Y. Branquet, and B. Laumomnier, 2000, Sulfate reduction by organic matter in Colombian emerald deposits: Chemical and stable isotope (C, O, H) evidence: Economic Geology and the Bulletin of the Society of Economic Geologists, v. 95, p. 1129–1153.
Giuliani, G., G. R. Olivo, O. J. Marini, and D. Michel, 1993, The Santa Rita gold deposit in the Proterozoic Paranoa Group, Goias, Brazil; an example of fluid mixing during ore deposition: Ore Geology Reviews, v. 8, p. 503–523.
Giurgiu, I., 2005, Muntele recoldului mondial (in Romanian). Invitatie in Carpati v. 51, p. 3–16.
Gize, A. P., H. L. Barnes, and J. S. Bell, 1991, A critical evaluation of organic processes in Mississippi valley-type genesis, in M. Pagel, and J. L. Leroy, eds., Source, transport and deposition of metals: 25th anniversary meeting of the Society for Geology Applied to Mineral Deposits, Nancy, France, Aug. 30-Sept. 3, 1991, A. A. Balkema, Rotterdam, p. 527–530.
Glassley, W. E., J. A. Korstgård, and K. Sørensen, 2010, K-rich brine and chemical modification of the crust during continent-continent collision, Nagssugtoqidian Orogen, West Greenland: Precambrian Research, v. 180, p. 47–62.
Gleeson, S. A., B. W. Dyardley, I. A. Munz, and A. J. Boyce, 2003, Infiltration of basinal fluids into high-grade basement, South Norway: Sources and behaviour of waters and brines: Geofluids, v. 3, p. 33–48.
Gleeson, S. A., and M. P. Smith, 2009, The sources and evolution of mineralising fluids in iron oxide-copper-gold systems, Norrbotten, Sweden: Constraints from Br/Cl ratios and stable Cl isotopes of fluid inclusion leachates: Geochimica et Cosmochimica Acta, v. 73, p. 5658–5672.
Gleeson, S. A., J. J. F. M. Wilkinson, F. M. Stuart, and D. A. Banks, 2001, The origin and evolution of base metal mineralising brines and hydrothermal fluids, South Cornwall, UK: Geochimica et Cosmochimica Acta, v. 65, p. 2067–2079.
Glennie, K., and A. Hurst, 2007, Chapter 22: Fluidization and associated soft-sediment deformation in eolian sandstones: Hopeman Sandstone (Permian), Scotland, and Rotliegend, North Sea,, in A. Hurst, and J. Cartwright, eds., Sand injectites: Implications for hydrocarbon exploration and production, American Association Petroleum Geologists Memoir 87, p. 245–252.
Glennie, K. W., 1989a, A summary of tropical desert sedimentary environments, present and past: Geological Association of Canada Special Paper, v. 36, p. 67–84.
Glennie, K. W., 1989b, Some effects of the Late Permian Zechstein transgression in northwestern Europe: Geological Association of Canada Special Paper, v. 36, p. 557–565.
Glennie, K. W., 1990, Outline of North Sea history and structural framework, in K. W. Glennie, ed., Introduction to the petroleum geology of the North Sea (3rd edition): Oxford, Blackwell Scientific Publications, p. 34–77.
Glennie, K. W., 1998, The desert of southeast Arabia: a product of Quaternary climatic change, in A. S. Alsharhan, K. W. Glennie, G. L. Whittle, and C. G. S. C. Kendall, eds., Quaternary Deserts and Climatic Change: Rotterdam, A. A. Balkema, p. 279–291.
Glennie, K. W., and A. T. Buller, 1983, The Permian Weissliegend of NW Europe: the partial deformation of eolian sands caused by the Zechstein transgression: Sedimentary Geology, v. 35, p. 43–81.
Glennie, K. W., and G. Evans, 1976, A reconnaissance of the Recent sediments of the Ranns of Kutch, India: Sedimentology, v. 23, p. 625–647.
Glover, A. G., A. J. Gooday, D. M. Bailey, D. S. M. Billett, P. Chevaldonne, A. Colaco, J. Copley, D. Cuvelier, D. Desbruyeres, V. Kalogeropoulou, M. Klages, N. Lampadariou, C. Lejeusne, N. Mestre, G. L. J. Paterson, T. Perez, H. Ruhl, J. Sarrazin, T. Soltwedel, E. H. Soto, S. Thatje, A. Tselepides, S. Van Gaever, and A. Vanreusel, 2010, Temporal change in deep-sea benthic ecosystems: a review of the evidence from recent time-series studies: Advances In Marine Biology, v. 58, p. 1–95.
Godfrey, L. V., L. H. Chan, R. N. Alonso, T. K. Lowenstein, W. F. McDonough, J. Houston, J. Li, A. Bobst, and T. E. Jordan, 2013, The role of climate in the accumulation of lithium-rich brine in the Central Andes: Applied Geochemistry, v. 38, p. 92–102.
Godin, L., and I. Lager, 1986, Viscaria— a copper deposit in a Proterozoic playa-lake complex (abs): IAGOD Symposium 7th. Luleå, Sweden.
Godlevski, M. N., and L. N. Grinenko, 1963, Some data on the isotopic composition of sulphur in the sulphides of the Noril'sk deposit: Geochemica, v. 1, p. 335–341.
Goede, A., T. C. Atkinson, and P. J. Rowe, 1992, A giant late Pleistocene halite speleothem from Webbs Cave, Nullarbor Plain, southeastern Western Australia: Helictite, v. 30, p. 3–7.
Goff, J. C., 2005, Origin and Potential of Unconventional Jurassic oil reservoirs on the northern Arabian Plate: SPE Paper 3505-MS.

Golabian, H., 2011, Urmia Lake: Hydro-Ecological Stabilization and Permanence Macro-engineering Seawater in Unique Environments (pp. 365–397). Berlin: Springer-Verlag. doi 10.1007/978-3-642-14779-1_1.

Golani, P. R., M. K. Pandit, A. N. Sial, A. E. Fallick, V. P. Ferreira, and A. B. Roy, 2002, B-Na rich Palaeoproterozoic Aravalli metasediments of evaporitic association, NW India: a new repository of gold mineralization: Precambrian Research, v. 116, p. 183–98.

Golani, P. R., R. S. Rajawat, N. C. Pant, and M. S. Rao, 1999, Mineralogy of gold and associated alloys in sulfides of Bhukia Gold Prospect in southeastern Rajasthan, western India: J. Geol. Soc. India, v. 64, p. 121–128.

Goldberg, K., S. Morad, I. S. Al-Aasm, and L. F. De Ros, 2011, Diagenesis of Paleozoic playa-lake and ephemeral-stream deposits from the Pimenta Bueno Formation, Siluro-Devonian (?) of the Parecis Basin, central Brazil: Journal of South American Earth Sciences, v. 32, p. 58–74.

Golding, S. D., I. T. Uysal, M. Glikson, K. A. Baublys, and P. N. Southgate, 2006, Timing and Chemistry of Fluid-Flow Events in the Lawn Hill Platform, Northern Australia: Economic Geology, v. 101, p. 1231–1250.

Goldstein, R. H., 2001, Fluid inclusions in sedimentary and diagenetic systems: Lithos, v. 55, p. 159–193.

Gómez-Alday, J. J., F. Garcia-Garmilla, and J. Elorza, 2002, Origin of quartz geodes from Lano and Tubilla del Agua sections (middle-upper Campanian, Basque-Cantabrian Basin, northern Spain): isotopic differences during diagenetic processes: Geological Journal, v. 37, p. 117–134.

Gómez-Pugnaire, M. T., G. Franz, and V. L. Sanchez-Vizcaino, 1994, Retrograde formation of NaCl-scapolite in high pressure metaevaporites from the Cordilleras-Beticas (Spain): Contributions to Mineralogy & Petrology, v. 116, p. 448–461.

Gomis-Yagues, V., N. Boluda-Botella, and F. Ruiz-Bevia, 2000, Gypsum precipitation/dissolution as an explanation of the decrease of sulphate concentration during seawater intrusion: Journal of Hydrology, v. 228, p. 48–55.

Gonzaga, F. G., F. T. T. Gonçalves, and L. F. C. Coutinho, 2000, Petroleum geology of the Amazonas Basin, Brazil: modeling of hydrocarbon generation and migration (Chapter 13), in M. R. Mello, and B. J. Katz, eds., Petroleum systems of South Atlantic margins, American Association Petroleum Geologists Memoir 73, p. 159–178.

Gonzalez, R., 2012, The physiology of hyper-salinity tolerance in teleost fish: a review: Journal of Comparative Physiology B: Biochemical, Systemic, and Environmental Physiology, v. 182, p. 321–329.

González-Partida, E., A. Carrillo-Chávez, J. O. W. Grimmer, J. Pironon, J. Mutterer, and G. Levresse, 2003, Fluorite deposits at Encantada-Buenavista, Mexico: products of Mississippi Valley type processes: Ore Geology Reviews, v. 23, p. 107–124.

González-Sánchez, F., A. Camprubí, E. González-Partida, R. Puente-Solís, C. Canet, E. Centeno-García, and V. Atudorei, 2009, Regional stratigraphy and distribution of epigenetic stratabound celestine, fluorite, barite and Pb-Zn deposits in the MVT province of northeastern Mexico: Mineralium Deposita, v. 44, p. 343–361.

Goodall, I. G., G. M. Harwood, A. C. Kendall, T. McKie, and M. E. Tucker, 1992, Discussion on sequence stratigraphy of carbonate-evaporite basins; models and application to the Upper Permian (Zechstein) of Northeast England and adjoining North Sea: Journal of the Geological Society of London, v. 149, p. 1050–1054.

Goodall, T. M., 1995, The Geology and Geomorphology of the Sabkhat Matti Region (United Arab Emirates): a Modern Analogue for Ancient Desert Sediments from North-west Europe: Doctoral thesis, University of Aberdeen, Aberdeen, Scotland, 433 p.

Goodall, T. M., C. P. North, and K. W. Glennie, 2000, Surface and subsurface sedimentary structures produced by salt crusts: Sedimentology, v. 47, p. 99–118.

Goodfellow, W. D., and I. R. Jonasson, 1984, Ocean stagnation and ventilation defined by $\delta^{34}S$ secular trends in pyrite and barite, Selwyn Basin, Yukon: Geology, v. 12, p. 583–586.

Goodfellow, W. D., and J. W. Lydon, 2007, Sedimentary exhalative (SEDEX) deposits, in W. D. Goodfellow, ed., Mineral Deposits of Canada: A Synthesis of Major Deposit Types, District Metallogeny, the Evolution of Geological Provinces, and Exploration Methods, Geological Association of Canada, Mineral Deposits Division, Special Publication, Vol. 5, p. 163–183.

Goodfellow, W. D., J. W. Lydon, and R. J. W. Turner, 1993, Geology and genesis of stratiform sediment-hosted (SEDEX) zinc-lead-silver sulphide deposits: Geological Association of Canada Special Paper, v. 40, p. 201–251.

Goodman, W. M., J. M. Schneider, D. J. Gnage, D. A. Henard, and L. L. Van Sambeek, 2009, Two-dimensional seismic evaluation of the I&W brine cavern, Carlsbad, New Mexico:: RESPEC Topical Report RSI-2083.

Gorbunova, K. A., 1977, Morphology of a gypsum karst: Proc. 7th Int. Spel. Cong. (Sheffield), p. 221–222.

Gorbunova, K. A., 1979, Morphology and hydrogeology of gypsum karst (in Russian): Univ. Perm. All Union Karst and Speology Inst., p. 222–223.

Gordon, D. S., and P. B. Flemings, 1998, Generation of overpressure and compaction-driven fluid flow in a Plio-Pleistocene growth-faulted basin, Eugene Island 330, offshore Louisiana: Basin Research, v. 10, p. 177–196.

Gore, D. B., D. C. Creagh, J. S. Burgess, E. A. Colhoun, A. P. Spate, and A. S. Baird, 1996, Composition, distribution and origin of surficial salts in the Vestfold Hills, East Antarctica: Antarctic Science, v. 8, p. 73–84.

Gorin, G. E., L. G. Racz, and M. R. Walter, 1982, Late Precambrian – Cambrian Sediments of Huqf Group, Sultanate of Oman. American Association Petroleum Geologists Bulletin 66: 2609–2627: American Association Petroleum Geologists – Bulletin, v. 66, p. 2609–2627.

Gornitz, V. M., and B. C. Schreiber, 1981, Displacive halite hoppers from the Dead Sea; some implications for ancient evaporite deposits: Journal of Sedimentary Petrology, v. 51, p. 787–794.

Gorski, M., Z. Wojtkowiak, and S. Radecki, 1999, Barnowko-Mostno-Buszewo (BMB): the largest crude oil deposit in Poland: Petroleum Geoscience, v. 5, p. 5–15.

Gostincar, C., M. Lenassi, N. Gunde-Cinerman, and A. Plemenitas, 2011, Fungal adaption to extremely high salt conditions, in A. I. Laskin, G. M. Gadd, and S. Sariaslani, eds., Advances in Applied Microbiology, V. 77, p. 71–91: Burlington, Elsevier Science.

Gott, G. B., D. F. Wolcott, and C. G. Bowles, 1974, Stratigraphy of the Inyan Kara Group and localisation of Uranium deposits, Southern Black Hills, South Dakota and Wyoming: US Geol Surv. Prof. Paper, v. 763, p. 1–57.

Götzinger, M. A., and W. Grum, 1992, Die Pb-Zn-F Mineralisationen in der Umgebung von Evaporiten der Nördlichen Kalkalpen Österreich – Herkunft und Zusammensetzung der fluiden Phase: Mitt. Ges. Geol. Bergbaustud Österr (Vienna), v. 38, p. 47–56.

Govers, R., P. Meijer, and W. Krijgsman, 2009, Regional isostatic response to Messinian Salinity Crisis events: Tectonophysics, v. 463, p. 109–129.

Gow, P. A., V. J. Wall, N. H. S. Oliver, and R. K. Valenta, 1994, Proterozoic iron oxide (Cu-U-Au-REE) deposits: further evidence of hydrothermal origins: Geology, v. 22, p. 633–636.

Gowan, S. W., and S. M. Trader, 1999, Mine failure associated with a pressurized brine horizon: Retsof Salt Mine, western New York: Applications & Environmental & Engineer, v. 6, p. 57–70.

Gowariker, V., V. N. Krishnamurthy, S. Gowariker, M. Dhanorkar, and K. Paranjape, 2009, The Fertilizer Encyclopedia, Wiley, 880 p.

Gradmann, S., C. Beaumont, and S. J. Ings, 2012, Coupled fluid flow and sediment deformation in margin-scale salt-tectonic systems: 1.

Development and application of simple, single-lithology models: Tectonics, v. 31, p. TC4010.
Gradstein, F. M., J. G. Ogg, A. G. Smith, W. Bleeker, and L. J. Lourens, 2004, A new Geologic Time Scale, with special reference to Precambrian and Neogene: Episodes, v. 27, p. 83–100.
Graf, D. L., 1982, Chemical osmosis, reverse chemical osmosis, and the origin of subsurface brines: Geochimica et Cosmochimica Acta, v. 46, p. 1431–1448.
Graf, D. L., A. J. Eardley, and N. F. Shimp, 1961, A preliminary report on magnesium carbonate formation in Glacial Lake Bonneville: Journal of Geology.
Graham, B., W. K. Reilly, F. Beinecke, D. F. Boesch, T. D. Garcia, C. A. Murray, and F. Ulmer, 2011, Deep Water; The Gulf Oil Disaster and the Future of Offshore Drilling; Report to the President, National Commission on the BP Deepwater Horizon Oil Spill and Offshore Drilling, January 2011.
Graham, R., M. Jackson, R. Pilcher, and B. Kilsdonk, 2012, Allochthonous salt in the sub-Alpine fold-thrust belt of Haute Provence, France: Geological Society, London, Special Publications, v. 363, p. 595–615.
Graham Wall, B. R., R. Girbacea, A. Mesonjesi, and A. Aydin, 2006, Evolution of fracture and fault-controlled fluid pathways in carbonates of the Albanides fold-thrust belt: American Association of Petroleum Geologists Bulletin, v. 90, p. 1227–1249.
Grajales-Nishimura, J. M., E. Cedillo-Pardo, C. Rosales-Dominguez, D. J. Morán-Zenteno, D. J. Alverez, P. Claeys, J. Ruíz-Morales, J. GArcía-Hernández, P. Padilla-Avila, and A. Sánchez-Ríos, 2000, Chicxulub impact: The origin of reservoir and seal facies in the southeastern Mexico oil fields: Geology, v. 28, p. 307–310.
Gran, K., K. Bjørlykke, and P. Aagaard, 1992, Fluid salinity and dynamics in the North Sea and Haltenbanken derived from well log data, in A. Hurst, C. M. Griffiths, and P. F. Worthington, eds., Geological Application of Wireline Logs II, Geological Society London Special Publication, 65, p. 327–328.
Grande, L., 1980, Paleontology of the Green River Formation, with a review of the fish fauna: Bull. Univ. Geol. Surv. Wyoming, v. 63, p. 333p.
Grandia, F., A. Canals, E. Cardellach, D. A. Banks, and J. Perona, 2003, Origin of Ore-Forming Brines in Sediment-Hosted Zn-Pb Deposits of the Basque-Cantabrian Basin, Northern Spain: Economic Geology, v. 98, p. 1397–1411.
Grando, G., and K. McClay, 2004, Structural evolution of the Frampton growth fold system, Atwater Valley-Southern Green Canyon area, deep water Gulf of Mexico: Marine and Petroleum Geology, v. 21, p. 889–910.
Grant, S., W. D. Grant, B. E. Jones, C. Kato, and L. Li, 1999, Novel archaeal phylotypes from an East African alkaline saltern: Extremophiles, v. 3, p. 139–145.
Grantham, P. J., G. W. M. Lijmbach, J. Posthuma, M. W. Hughes Clarke, and R. J. Willink, 1988, Origin of crude oils in Oman: Journal of Petroleum Geology, v. 11, p. 61–80.
Grappe, J., 2000, Alternative uses of underground caverns: An introduction to the technology of solution mining; Spring 2000 Technical Class, Solution Mining Reseach Institute, Hague, Netherlands, p. 154–178.
Grasby, S. E., and R. Betcher, 2000, Pleistocene recharge and flow reversal in the Williston basin, central North America: Journal of Geochemical Exploration, v. 69–70, p. 403–407.
Grasby, S. E., and Z. Chen, 2005, Subglacial recharge into the Western Canada Sedimentary Basin; Impact of Pleistocene glaciation on basin hydrodynamics: Geological Society of America Bulletin, v. 117, p. 500–514.
Grasby, S. E., Z. Chen, and K. Dewing, 2012, Formation water geochemistry of the Sverdrup Basin: Implications for hydrocarbon development in the High Arctic: Applied Geochemistry, v. 27, p. 1623–1632.
Grasby, S. E., I. Rod Smith, T. Bell, and D. L. Forbes, 2013, Cryogenic formation of brine and sedimentary mirabilite in submergent coastal lake basins, Canadian Arctic: Geochimica et Cosmochimica Acta, v. 110, p. 13–28.
Gregory, G., C. Killey, and S. Stewart, 2002, Dahl Hit, Saudi Arabia, Cave Survey map; Last accessed on September 15, 2005, http://www.saudicaves.com/ainhit/17ain.jpg.
Gregory-Wodzicki, K. M., 2000, Uplift history of the central and northern Andes: A review: Geological Society of America Bulletin, v. 112, p. 1091–1105.
Greinert, J., and A. Derkachev, 2004, Glendonites and methane-derived Mg-calcites in the Sea of Okhotsk, Eastern Siberia: implications of a venting-related ikaite/glendonite formation: Marine Geology, v. 204, p. 129–144.
Gresens, R. L., 1978, Evaporites as precursors of massif anorthosite: Geology, v. 6, p. 46–50.
Gretener, P. E., 1982, Another look at Alborz nr. 5 in Central Iran: Vereinigung Schweizerischer Petroleum-Geologen und Ingenieure Bulletin, v. 48, p. 1–8.
Grew, E., J. Bada, and R. Hazen, 2011, Borate Minerals and Origin of the RNA World: Origins of Life and Evolution of Biospheres, v. 41, p. 307–316.
Grew, E. S., 1988, Kornerupine at the Sare Sang, Afghanistan, whiteschist locality: implications for tourmaline-kornerupine distribution in metamorphic rocks: American Mineralogist, v. 73, p. 345–357.
Grey, K., L. S. Moore, R. V. Burne, B. K. Pierson, and J. Bauld, 1990, Lake Thetis, Western Australia: an example of Saline Lake Sedimentation dominated by Benthic Microbial Processes: Marine and Freshwater Research, v. 41, p. 275–300.
Grice, K., S. Schouten, A. Nissenbaum, J. Charrach, and J. S. S. Damste, 1998, Isotopically heavy carbon in the C-21 to C-25 regular isoprenoids in halite-rich deposits from the Sedom Formation, Dead Sea basin, Israel: Organic geochemistry, v. 28, p. 349–359.
Griffin, D. L., 1999, The late Miocene climate of northeastern Africa: Unravelling the signals in the sedimentary succession: Journal of the Geological Society, v. 156, p. 817–826.
Griffin, D. L., 2002, Aridity and humidity: two aspects of the late Miocene climate of North Africa and the Mediterranean: Palaeogeography, Palaeoclimatology, Palaeoecology, v. 182, p. 65–91.
Griffith, E. M., and A. Paytan, 2012, Barite in the ocean – occurrence, geochemistry and palaeoceanographic applications: Sedimentology, v. 59, p. 1817–1835.
Grimalt, J. O., R. De Wit, P. Teixidor, and J. Albaiges, 1992, Lipid biogeochemistry of Phormidium and Microcoleus mats: Organic Geochemistry, v. 19, p. 509–530.
Grimalt, J. O., M. Grifoll, A. M. Solanas, and J. Albaigés, 1991, Microbial degradation of marine evaporitic crude oils: Geochimica et Cosmochimica Acta, v. 55, p. 1903–1913.
Grinenko, L. N., 1985, Sources of sulphur of the nickeliferous and barren gabbro-dolerite intrusions of the northwest Siberian platform: International Geology Review, p. 695–708.
Grishina, S., J. Dubessy, A. Kontorovich, and J. Pironon, 1992, Inclusions in salt beds resulting from thermal metamorphism by dolerite sills (eastern Siberia, Russia): European Journal of Mineralogy, v. 4, p. 1187–1202.
Grishina, S., J. Pironon, M. Mazurov, S. Goryainov, A. Pustilnikov, G. Fonderflaas, and A. Guerci, 1998, Organic inclusions in salt – Part 3 – Oil and gas inclusions in Cambrian evaporite deposits from east Siberia – A contribution to the understanding of nitrogen generation in evaporite: Organic Geochemistry, v. 28, p. 297–310.
Griswold, G. B., 1982, Geologic overview of the Carlsbad potash-mining district: Circular New Mexico Bureau of Mines and Mineral Resources, v. 182, p. 17–22.
Groat, L. A., G. Giuliani, D. D. Marshall, and D. Turner, 2008, Emerald deposits and occurrences: A review: Ore Geology Reviews, v. 34, p. 87–112.

Groat, L. A., and B. M. Laurs, 2009, Gem formation, production, and exploration: Why gem deposits are rare, and what is being done to find them: Elements, v. 5, p. 153–158.

Groeneveld, D. P., J. L. Huntington, and D. D. Barz, 2010, Floating brine crusts, reduction of evaporation and possible replacement of fresh water to control dust from Owens Lake bed, California: Journal of Hydrology, v. 392, p. 211–218.

Grosjean, E., G. D. Love, A. E. Kelly, P. N. Taylor, and R. E. Summons, 2012, Geochemical evidence for an Early Cambrian origin of the "Q"oils and some condensates from north Oman: Organic geochemistry, v. 45, p. 77–90.

Grosjean, E., G. D. Love, C. Stalvies, D. A. Fike, and R. E. Summons, 2009, Origin of petroleum in the Neoproterozoic-Cambrian South Oman Salt Basin: Organic Geochemistry, v. 40, p. 87–110.

Grossman, I. G., 1968, Origin of the sodium sulphate deposits of the northern Great Plains of Canada and the United States: U. S. Geol. Surv. Prof. Pap., v. 600-B, p. 104–109.

Grötsch, J., R. El-Khassawneh, S. Lokier, G. Coy, E. van der Weerd, S. Masalmeh, J. van Dorp, O. Suwaina, G. Ajlani, and A. Taher, 2003, The Arab Formation in central Abu Dhabi: 3-D reservoir architecture and static and dynamic modeling: GeoArabia, v. 8, p. 47–86.

Grotzinger, J., E. W. Adams, and S. Schroder, 2005, Microbial-metazoan reefs of the terminal Proterozoic Nama Group (c. 550–543 Ma), Namibia: Geological Magazine, v. 142, p. 499–517.

Grotzinger, J. P., 1986a, Cyclicity and paleoenvironmental dynamics, Rocknest Platform, northwest Canada: Geological Society America Bulletin, v. 97, p. 1208–1231.

Grotzinger, J. P., 1986b, Shallowing upward cycles of the Wallace Formation, Belt Supergroup, northwestern Montana and northern Idaho: Montana Bureau of Mines Geol. Spec. Pub., v. 94, p. 143–160.

Grotzinger, J. P., 1990, Geochemical model for Proterozoic stromatolite decline: American Journal of Science, v. 290-A, p. 80–103.

Grotzinger, J. P., 1995, Trends in Precambrian carbonate sediments and their implication for understanding evolution, in S. Bengtson, ed., Early Life on Earth: Nobel Symposium No. 84: New York, Columbia Univ. Press, p. 245–258.

Grotzinger, J. P., and J. F. Kasting, 1993, New constraints on Precambrian ocean composition: Journal of Geology, v. 101, p. 235–243.

Grotzinger, J. P., and A. H. Knoll, 1995, Anomalous carbonate precipitates – Is the Precambrian the key to the Permian: Palaios, v. 10, p. 578–596.

Grotzinger, J. P., and A. H. Knoll, 1999, Stromatolites in Precambrian carbonates: Evolutionary mileposts or environmental dipsticks?: Annual Review of Earth & Planetary Sciences, v. 27, p. 313–358.

Grotzinger, J. P., and J. F. Read, 1983, Evidence for primary aragonite precipitation, lower Proterozoic (1.9 Ga) Rocknest dolomite, Wopmay orogen, northwest Canada: Geology, v. 11, p. 710–713.

Grotzinger, J. P., and D. H. Rothman, 1996, An abiotic model for stromatolitic morphogenesis: Nature, v. 383, p. 423–425.

Groves, D., I. , and F. Bierlein, P. , 2007, Geodynamic settings of mineral deposit systems: Journal of the Geological Society, v. 164, p. 19–30.

Groves, D. I., F. P. Bierlein, L. D. Meinert, and M. W. Hitzman, 2010, Iron Oxide Copper-Gold (IOCG) Deposits through Earth History: Implications for Origin, Lithospheric Setting, and Distinction from Other Epigenetic Iron Oxide Deposits: Economic Geology, v. 105, p. 641–654.

Groves, D. I., K. C. Condie, R. J. Goldfarb, J. M. A. Hronsky, and R. M. Vielreicher, 2005, Secular changes in global tectonic processes and their influence on the temporal distribution of gold-bearing mineral deposits: Economic Geology, v. 100, p. 203–224.

Groves, D. I., S. D. Golding, N. M. S. Rock, M. E. Barley, and N. J. McNaughton, 1988, Archaean carbon reservoirs and their relevance to the fluid source for gold deposits: Nature, v. 331, p. 254–257.

Groves, I. M., C. E. Carman, and W. J. Dunlap, 2003, Geology of the Beltana Willemite Deposit, Flinders Ranges, South Australia: Economic Geology, v. 98, p. 797–818.

Gruber, P., W., P. Medino, A., G. Keoleian, A., S. E. Kesler, M. P. Everson, and T. J. Wallington, 2011, Global Lithium Availability: Journal of Industrial Ecology, v. 15, p. 760–775.

Grunau, H. R., 1987, A worldwide look at the cap-rock problem: Journal of Petroleum Geology, v. 103, p. 245–266.

Guarascio, M., G. Fernandez, and R. L. Thoms, 1995, Updated evaluation of sinkhole potential at the Belvedere Spinello Brinefield: Solution Mining Research Institute Fall Meeting, Sept 25 – Oct 1, Hanover, Germany, p. 43 p.

Gueddari, M., 1984, Geochimie et thermodynamique des evaporites continentales: etude de lac Natron en Tanzanie et du Chott el Jerid en Tunisie. (Geochemistry and thermodynamics of continental evaporites: a study of Lake Natron in Tanzania and the Chott el Djerid in Tunisia). Sciences Geologiques Memoire, v. 76, p. 143 pp.

Guerrero, J., F. Gutiérrez, and J. P. Galve, 2013, Large depressions, thickened terraces, and gravitational deformation in the Ebro River valley (Zaragoza area, NE Spain): Evidence of glauberite and halite interstratal karstification: Geomorphology, v. 196, p. 162–176.

Guglielmo, G., B. C. Vendville, and M. P. A. Jackson, 2000, 3-D Visualization and Isochore Analysis of Extensional Diapirs Overprinted by Compression: American Association Petroleum Geologists – Bulletin, v. 84, p. 1095–1108.

Guilhaumou, N., N. Ellouz, T. M. Jaswal, and P. Mougin, 2000, Genesis and evolution of hydrocarbons entrapped in the fluorite deposit of Koh-i-Maran, (North Kirthar Range, Pakistan): Marine and Petroleum Geology, v. 17, p. 1151–1164.

Guiraud, R., 1965, Geologie et hydrogeologie du bassin versant du Chott el Hodna; resume des connaissances actuelles: Algeria, Serv. Geol., Bull. No., v. 33, p. 51–66.

Gunatilaka, A., 1990, Anhydrite diagenesis in a vegetated sabkha, Al-Khiran, Kuwait, Arabian Gulf: Sedimentary Geology, v. 69, p. 95–116.

Gunatilaka, A., and S. Mwango, 1987, Continental sabkha pans and associated nebkhas in southern Kuwait, Arabian Gulf: Geophysical Society London, Special Publications, v. 35, p. 187–203.

Gunatilaka, A., A. Saleh, and A. Al-Temeemi, 1980, Plant-controlled supratidal anhydrite from Al-Khiran, Kuwait: Nature, v. 288, p. 257–260.

Gunatilaka, A., A. Saleh, A. Al-Temeemi, and N. Nassar, 1987, Calcium-poor dolomite from the sabkhas of Kuwait: Sedimentology, v. 34, p. 999–1006.

Gunde-Cimerman, N., J. C. Frisvad, P. Zalar, and A. Plemenitas, 2005, Halotolerant and halophilic fungi, in S. K. Deshmukh, and M. K. Rai, eds., Biodiversity of Fungi – Their Role in Human Life: New Delhi, Oxford & IBH Publishing Co. Pvt. Ltd, p. 69–128.

Gunde-Cimerman, N., J. Ramos, and A. Plemenitaš, 2009, Halotolerant and halophilic fungi: Mycological Research, v. 113, p. 1231–1241.

Gunde-Cimerman, N., P. Zalar, S. de Hoog, and A. Plemenita, 2000, Hypersaline waters in salterns – natural ecological niches for halophilic black yeasts: FEMS Microbiology Ecology, v. 32, p. 235–240.

Gundersen, J. K., B. B. Jorgensen, E. Larsen, and H. W. Jannasch, 1992, Mats of giant sulphur bacteria on deep-sea sediments due to fluctuating hydrothermal flow: Nature, v. 360, p. 454–456.

Gundogan, I., and C. Helvaci, 2001, Sedimentological and petrographical aspects of Upper Miocene evaporites in the Beypazari and Cankiri-Corum basins, central Anatolia, Turkey: International Geology Review, v. 43, p. 818–829.

Gundogdu, M. N., H. Yalcin, A. Temel, and N. Clauer, 1996, Geological, mineralogical and geochemical characteristics of zeolite deposits associated with borates in the Bigadic, Emet and Kirka Neogene lacustrine basins, western Turkey: Mineralium Deposita, v. 31, p. 492–513.

Guo, X., and H. S. Chafetz, 2012, Large tufa mounds, Searles Lake, California: Sedimentology, v. 59, p. 1509–1535.

Gupta, I., A. M. Wilson, and B. J. Rostron, 2012, Cl/Br compositions as indicators of the origin of brines: Hydrogeologic simulations of the Alberta Basin, Canada: Geological Society of America Bulletin, v. 124, p. 200–212.

Gurer, O. F., and A. Gurer, 1999, Development of evaporites and the counterclockwise rotation of Anatolia, Turkey: International Geology Review, v. 41, p. 607–622.

Gürgey, K., 2002, An attempt to recognise oil populations and potential source rock types in Paleozoic sub- and Mesozoic-Cenozoic supra-salt strata in the southern margin of the Pre-Caspian Basin, Kazakhstan Republic: Organic Geochemistry, v. 33, p. 723–741.

Gussow, W. C., 1968, Salt diapirism: importance of temperature, and energy source of emplacement, in J. Braunstein, and G. D. O'Brien, eds., Diapirism and diapirs: Tulsa OK, American Association of Petroleum Geologists Memoir 8, p. 16–52.

Gustavson, T. C., S. D. Hovorka, and A. R. Dutton, 1994, Origin of satin spar veins in evaporite basins: Journal of Sedimentary Research, Section A: Sedimentary Petrology and Processes, v. 64, p. 88–94.

Gustavson, T. C., W. W. Simpkins, A. Alhades, and A. D. Hoadley, 1982, Evaporite dissolution and development of karst features on the Rolling Plains of the Texas Panhandle: Earth Surface Processes and Landforms, v. 7, p. 545–563.

Gutierrez, F., 2010, Hazards associated to karst (Chapter 13), in I. Alcántara-Ayala, and A. S. Goudie, eds., Geomorphological Hazards and Disaster Prevention, Cambridge University Press, p. 161–176.

Gutiérrez, F., 1996, Gypsum karstification induced subsidence – effects on alluvial systems and derived geohazards (Calatayud Graben, Iberian Range, Spain): Geomorphology, v. 16, p. 277–293.

Gutiérrez, F., 2004, Origin of the salt valleys in the Canyonlands section of the Colorado Plateau; Evaporite-dissolution collapse versus tectonic subsidence: Geomorphology, v. 57, p. 423–435.

Gutiérrez, F., J. Calaforra, F. Cardona, F. Ortí, J. Durán, and P. Garay, 2008, Geological and environmental implications of the evaporite karst in Spain: Environmental Geology, v. 53, p. 951–965.

Gutierrez, F., D. Carbonel, J. Guerrero, J. P. McCalpin, R. Linares, C. Roque, and M. Zarroca, 2012, Late Holocene episodic displacement on fault scarps related to interstratal dissolution of evaporites (Teruel Neogene Graben, NE Spain): Journal of Structural Geology, v. 34, p. 2–19.

Gutiérrez, F., and A. H. Cooper, 2002, Evaporite dissolution subsidence in the historical city of Catalayud, Spain: Damage appraisal and prevention: Natural Hazards, v. 25, p. 259–288.

Gutierrez, M., N. Braunsdor, and B. Couzens, 2006, Calibration and ranking of pore-pressure prediction models: The Leading Edge, v. 25, p. 1516–1523.

Gutsche, A., 1988, Mineralreaktionen und Stotransporte an einem Kontakt Basalt-Hartsalz in der Werra-Folge des Werkes Hattorf: Unpubl. diploma thesis, thesis, Georg-August-Universita, Gottingen.

Gvirtzman, H., and E. Stanislavsky, 2000, Palaeohydrology of hydrocarbon maturation, migration and accumulation in the Dead Sea Rift: Basin Research, v. 12, p. 79–93.

Gwynn, J. W., 1984, Mining conditions and problems encountered within the TexasGulf-Cane Creek potash Mine near Moab, Utah: and potential mining conditions at Gibson Dome, Utah: Utah Geological and Mineral Survey Report of Investigation, No. 184, 12 p.

Gwynn, J. W., 2008, The Occurrence and Development of the Saline Resources of Western Utah: Geology and Geologic Resources and Issues of Western Utah, Utah Geological Assoc. 2009, p. 221–234.

Habermehl, M. A., 1980, The Great Artesian Basin: BMR Journal Australian Geology and Geophysics, v. 5, p. 9–38.

Habermehl, M. A., 1982, Springs in the Great Artesian Basin – Their Origin and Nature,. Bureau of Mineral Resources, Australia, Report 235, BMR Microfilm MF 179.

Habermehl, M. A., 1988, Springs of the Great Artesian Baisn: Aspects of Hydrogeologic, Hydrochemical, and Isotopic Characteristics: SLEADS Conference 88, Salt Lakes in Arid Lands, p. 30 pp.

Habermehl, M. A., 1996, Groundwater Movement and Hydrochemistry of the Great Artesian Basin, Australia: In Mesozoic Geology of the Eastern Australia Plate Conference, Geol. Society of Aust. Inc., Extended Abstracts, No. 43, pages 228–236.

Habicht, K. S., and D. E. Canfield, 1996, Sulphur isotope fractionation in modern microbial mats and the evolution of the sulphur cycle: Nature, v. 382, p. 342–343.

Haeri-Ardakani, O., I. Al-Aasm, and M. Coniglio, 2013, Fracture mineralization and fluid flow evolution: an example from Ordovician-Devonian carbonates, southwestern Ontario, Canada: Geofluids, v. 13, p. 1–20.

Haffert, L., M. Haeckel, V. Liebetrau, C. Berndt, C. Hensen, M. Nuzzo, A. Reitz, F. Scholz, J. Schönfeld, C. Perez-Garcia, and S. M. Weise, 2013, Fluid evolution and authigenic mineral paragenesis related to salt diapirism -The Mercator mud volcano in the Gulf of Cadiz: Geochimica et Cosmochimica Acta, v. 106, p. 261–286.

Hafid, M., 2000, Triassic-early Liassic extensional systems and their Tertiary inversion, Essaouira Basin (Morocco): Marine & Petroleum Geology, v. 17, p. 409–429.

Hahn, J., and P. Haug, 1986, Traces of Archaebacteria in ancient sediments: System. Appl. Microbiol., v. 7, p. 178–183.

Halbouty, M. T., 1979, Salt domes, Gulf region, United States and Mexico: Houston, Texas, Gulf Publishing, 561 p.

Halevy, I., S. E. Peters, and W. W. Fischer, 2012, Sulfate Burial Constraints on the Phanerozoic Sulfur Cycle: Science, v. 337, p. 331–334.

Haliva-Cohen, A., M. Stein, S. L. Goldstein, A. Sandler, and A. Starinsky, 2012, Sources and transport routes of fine detritus material to the Late Quaternary Dead Sea basin: Quaternary Science Reviews, v. 50, p. 55–70.

Hall, A., 1998, Zeolitization of volcaniclastic sediments: The role of temperature and pH: Journal of Sedimentary Research, v. 68, p. 739–745.

Hall, R., and C. K. Morley, 2004, Sundaland Basins, in P. Clift, P. Wang, W. Kuhnt, and D. E. Hayes, eds., Continent-Ocean Interactions within the East Asian Marginal Seas, AGU Geophysical Monograph, v. 149, p. 55–85.

Hall, S. H., 2002, The role of autochthonous salt inflation and deflation in the northern Gulf of Mexico: Marine and Petroleum Geology, v. 19, p. 649–682.

Hallager, W. S., M. R. Ulrich, J. R. Kyle, P. E. Price, and W. A. Gose, 1990, Evidence for episodic basin dewatering in salt-dome cap rocks: Geology, v. 18, p. 716–719.

Hallam, A., 1981, Facies interpretation and the stratigraphic record: San Francisco, W. H. Freeman and Co., 291 p.

Halley, R. B., 1976, Textural variation within Great Salt Lake algal mounds, in M. R. Walter, ed., Stromatolites: Developments in Sedimentology, v. 20: Amsterdam, Elsevier, p. 435–445.

Halley, R. B., 1977, Ooid fabric and structure in the Great Salt Lake and the Geologic record: Journal of Sedimentary Petrology, v. 47, p. 1099–1120.

Halley, R. B., 1985, Setting and geologic summary of the Lower Cretaceous, Sunniland field. Southern Florida, in P. O. Roehl, and P. W. Choquette, eds., Carbonate petroleum reservoirs: New York, Springer-Verlag, p. 443–454.

Hamilton, W. B., 1998, Archean magmatism and deformation were not products of plate tectonics: Precambrian Research, v. 91, p. 143–179.

Hammer, J., F. Junge, H. J. Rosler, S. Niese, B. Gleisberg, and G. Stiehl, 1990, Element and isotope geochemical investigations of the Kupferschiefer in the vicinity of 'Rote Faule', indicating copper mineralization (Sangerhausen Basin, G.D.R.): Chemical Geology, v. 85, p. 345–360.

Hammer, U. T., 1986, Saline lake ecosystems of the world (Monographiae Biologicae, Vol. 59): Dordrecht, Nederlands, Dr. W. Junk Publishers, 632 p.

Hammerli, J., C. Spandler, N. H. S. Oliver, and B. Rusk, 2014, Cl/Br of scapolite as a fluid tracer in the earth's crust: insights into fluid sources in the Mary Kathleen Fold Belt, Mt. Isa Inlier, Australia: Journal of Metamorphic Geology, v. 32, p. 93–112.

Hancock, M. C., and A. H. Purvis, 1990, Lady Loretta Silver-Lead-Zinc deposit, in F. E. Hughes, ed., Geology of the Mineral Deposits of Australia & Papua New Guinea, v. 14-1: Melbourne, AusIMM Monograph, p. 943–948.

Hand, M. P., A. J. Reid, M. A. Szpunar, N. Direen, B. Wade, J. Payne, and K. M. Barovich, 2008, Crustal architecture during the early Mesoproterozoic Hiltaba-related mineralisation event; are the Gawler Range Volcanics a foreland basin fill?: MESA Journal, v. 51, p. 19–24.

Handford, C. R., 1981, A process-sedimentary framework for characterizing Recent and ancient sabkhas: Sedimentary Geology, v. 30, p. 255–265.

Handford, C. R., 1982, Sedimentology and evaporite genesis in a Holocene continental sabkha playa basin – Bristol Dry Lake, California: Sedimentology, v. 29, p. 239–253.

Handford, C. R., 1990, Halite depositional facies in a solar salt pond: A key to interpreting physical energy and water depth in ancient deposits?: Geology, v. 18, p. 691–694.

Handford, C. R., 1991, Marginal marine halite; sabkhas and salinas, in J. L. Melvin, ed., Evaporites, petroleum and mineral resources, v. 50, Elsevier Developments in Sedimentology, p. 1–66.

Handford, C. R., A. C. Kendall, D. R. Prezbindowski, J. B. Dunham, and B. W. Logan, 1984, Salina-margin tepees, pisoliths and aragonite cements, Lake MacLeod, Western Australia; Their significance in interpreting ancient analogs: Geology, v. 12, p. 523–527.

Handford, C. R., and C. H. J. Moore, 1976, Diagenetic implications of calcite pseudomorphs after halite from the Joachim Dolomite (middle Ordovician), Arkansas: Journal of Sedimentary Petrology, v. 46, p. 387–392.

Handford, H. R., 1981, Coastal sabkha and salt pan deposition of the lower Clear Fork Formation (Permian), Texas: Journal of Sedimentary Petrology, v. 51, p. 761–778.

Hanna, M. A., 1953, Fracture Porosity in Gulf Coast: American Association Petroleum Geologists – Bulletin, v. 37, p. 266–281.

Hannington, M., J. Jamieson, T. Monecke, S. Petersen, and S. Beaulieu, 2011, The abundance of seafloor massive sulfide deposits: Geology, v. 39, p. 1155–1158.

Hannington, M. D., A. G. Galley, P. M. Herzig, and S. Petersen, 1998, Comparison of the TAG mound and stockwork complex with Cyprus-type massive sulfide deposits: Proceedings of the Ocean Drilling Program, Scientific Results, Volume 158, p. 389–415.

Hanor, J. S., 1987, Kilometer-scale thermohaline overturn of pore waters in the Louisiana Gulf Coast: Nature, v. 327, p. 501–503.

Hanor, J. S., 1988, Origin and migration of subsurface sedimentary brines: SEPM Short Course Notes, v. 21, 248 p.

Hanor, J. S., 1994a, Origin of saline fluids in sedimentary basins, in J. Parnell, ed., Geofluids; origin, migration and evolution of fluids in sedimentary basins: Geological Society Special Publications, v. 78: London, United Kingdom, Geological Society of London, p. 151–174.

Hanor, J. S., 1994b, Physical and chemical controls on the compositions of waters in sedimentary basins: Marine & Petroleum Geology, v. 11, p. 31–45.

Hanor, J. S., 1996, Controls on the solubilization of lead and zinc in basinal brines: Society of Economic Geologists, Special Publication, v. 4, p. 483–500.

Hanor, J. S., 2000, Barite-celestine geochemistry and environments of formation, in C. N. Alpers, J. L. Jambor, and D. K. Nordstrom, eds., Reviews in Mineralogy and Geochemistry – Sulfate Minerals: Crystallography, Geochemistry, and Environmental Significance, v. 40, Mineralogical Society of America, p. 193–263.

Hanor, J. S., 2004, A model for the origin of large carbonate and evaporite hosted celestine ($SrSO_4$) deposits: Journal Sedimentary Research, v. 74, p. 168–175.

Hanor, J. S., J. E. Bailey, M. C. Rogers, and L. R. Milner, 1986, Regional variations in physical and chemical properties of south Louisiana oil field brines: Gulf Coast Association Of Geological Societies, Transactions, v. 36, p. 143–149.

Hanor, J. S., and J. C. McIntosh, 2007, Diverse origins and timing of formation of basinal brines in the Gulf of Mexico sedimentary basin: Geofluids, v. 7, p. 227–237.

Hanor, J. S., and J. A. Mercer, 2010, Spatial variations in the salinity of pore waters in northern deep water Gulf of Mexico sediments: implications for pathways and mechanisms of solute transport: Geofluids, v. 10, p. 83–93.

Hanor, J. S., and R. Sassen, 1990, Evidence for large scale vertical and lateral migration of basinal waters, dissolved salt, and crude oil in the Louisiana Gulf Coast, in D. Schumacher, and B. F. Perkins, eds., Gulf Coast oils and gases: The characteristics, origin, distribution and exploration and production characteristics. Ninth Annual Research Conference Proceedings, GCSSEPM Foundation, October 1, Austin TX: Tulsa, SEPM, p. 283–296.

Hanshaw, B. B., and J. D. Bredehoeft, 1968, On the maintenance of anomalous fluid pressures; 2, Source layer at depth: Geol. Soc. Amer., Bull., v. 79, p. 1107–1122.

Hanson, A. D., 2014, A surprising asymmetric paleo-thermal anomaly around El Gordo diapir, La Popa basin, Mexico: Bulletin American Association Petroleum Geologists, v. 98, p. 213–226.

Hanson, A. D., B. D. Ritts, D. Zinniker, J. M. Moldowan, and U. Biffi, 2001, Upper Oligocene lacustrine source rocks and petroleum systems of the northern Qaidam basin, northwest China: American Association Petroleum Geologists Bulletin-American Association of Petroleum Geologists, v. 85, p. 601–619.

Hanson, R. E., T. J. Wilson, and H. Munyanyiwa, 1994, Geologic evolution of the Neoproterozoic Zambesi Orogenic belt in Zambia [Review]: Journal of African Earth Sciences & the Middle East., v. 18, p. 135–150.

Hao, F., S. T. Li, Y. C. Sun, and Q. M. Zhang, 1998a, Geology, compositional heterogeneities, and geochemical origin of the Yacheng gas field, Qiongdonggan Basin, South China Sea: American Association of Petroleum Geologists Bulletin, v. 82, p. 1372–1384.

Haq, B. U., and A. M. Al-Qahtani, 2005, Phanerozoic cycles of sea-level change on the Arabian Platform: GeoArabia, v. 10, p. 127–160.

Haq, B. U., J. Hardenbol, and P. R. Vail, 1987, Chronology of fluctuating sea levels since the Triassic: Science, v. 235, p. 1156–1167.

Haq, B. U., and F. W. B. van Eysinga, 1998, A geological time table. Elsevier Science Publishers. Amsterdam, The Netherlands. Wall chart.

Harben, P., and G. Edwards, 1998, Lithium: Times are Changing: Can. Inst. Mining and Metal., Special Volume, v. 50, p. 172–182.

Hardie, L. A., 1967, The gypsum-anhydrite equilibrium at one atmosphere pressure: American Mineralogist, v. 52, p. 172–200.

Hardie, L. A., 1968, The origin of the Recent non-marine evaporite deposit of Saline Valley, Inyo County, California: Geochimica et Cosmochimica Acta, v. 32, p. 1279–1301.

Hardie, L. A., 1984, Evaporites: Marine or non-marine?: American Journal of Science, v. 284, p. 193–240.

Hardie, L. A., 1990, The roles of rifting and hydrothermal $CaCl_2$ brines in the origin of potash evaporites: an hypothesis: American Journal of Science, v. 290, p. 43–106.

Hardie, L. A., 1991, On the significance of evaporites: Annual Review Earth and Planetary Science, v. 19, p. 131–168.

Hardie, L. A., 1996, Secular variation in seawater chemistry: an explanation for the coupled secular variation in the mineralogies of marine limestones and potash evaporites over the past 600 m.y.: Geology, v. 24, p. 279–283.

Hardie, L. A., A. Bosellini, and R. K. Goldhammer, 1986, Repeated subaerial exposure of subtidal carbonate platforms, Triassic, Northern Italy: evidence for high frequency sea level oscillations on a 10,000 year scale.: Paleoceanography, v. 1, p. 447–457.

Hardie, L. A., and H. P. Eugster, 1970, The evolution of closed-basin brines: Spec Pub. Mineral. Soc. Am., v. 3, p. 273–290.

Hardie, L. A., and H. P. Eugster, 1971, The depositional environment of marine evaporites: A case for shallow, clastic accumulation: Sedimentology, v. 16, p. 187–220.

Hardie, L. A., and T. K. Lowenstein, 2004, Did the Mediterranean Sea dry out during the Miocene? A reassessment of the evaporite evidence from DSDP Legs 13 and 42A cores: Journal of Sedimentary Research, v. 74, p. 453–461.

Hardie, L. A., J. P. Smoot, and H. P. Eugster, 1978, Saline lakes and their deposits: a sedimentological approach, in A. Matter, and M. E. Tucker, eds., Modern and Ancient Lake Sediments, v. 2, International Association Sedimentologists Special Publication, p. 7–41.

Harding, T. P., 1974, Petroleum traps associated with wrench faults: Bulletin American Association Petroleum Geologists, v. 58, p. 1290–1304.

Hardman, R. F. P., and W. J. Kennedy, 1980, Chalk reservoirs of the Hod Fields, Norway: The sedimentation of the North Sea reservoir rocks, Geilo: Norsk Petroleumforening, Section XI.

Harmer, R. E., 2002, Mineralisation of the Phalaborwa Complex and the carbonatite connection In Iron Oxide-Cu-Au-U-REE deposits, in T. M. Porter, ed., Hydrothermal Iron Oxide Copper-Gold and Related Deposits: A Global Perspective, v. 1, PGC Publishing, Adelaide, p. 331–340.

Harmon, R. S., T. C. Atkinson, and J. L. Atkinson, 1983, The mineralogy of Castleguard Cave, Columbia Icefields, Alberta, Canada: Arctic and Alpine Research, v. 15, p. 503–516.

Harraz, H. Z., and M. F. El-Sharkawy, 2001, Origin of tourmaline in the metamorphosed Sikait pelitic belt, south Eastern Desert, Egypt: Journal of African Earth Sciences, v. 33, p. 391–416.

Harris, P. M., and S. D. Walker, 1990, McElroy Field, Central Basin Platform, Permian Basin, Texas, in E. A. Beaumont, and N. H. Foster, eds., Treatise of Petroleum Geology; Atlas of Oil and Gas Fields: Stratigraphic Traps I: Tulsa, OK, American Association Petroleum Geologists, p. 195–227.

Harrison, H., and B. Patton, 1995, Translation of salt sheets by basal shear: Proceedings of GCCSEPM Foundation 16th Annual Research Conference, Salt Sediment and Hydrocarbons, Dec 3–6, 1995, p. 99–107.

Harrison, J. C., 1995, Tectonics and kinematics of a foreland fold belt influenced by salt, Arctic Canada, in M. P. A. Jackson, D. G. Roberts, and S. Snelson, eds., Salt tectonics: a global perspective, American Association Petroleum Geologists Memoir, v. 65, p. 379–412.

Harrison, J. C., and A. W. Bally, 1988, Cross-Sections of the Parry Islands Fold Belt on Melville Island, Canadian Arctic Islands: Implications for the Timing and Kinematic History of Some Thin-Skinned Decollement Systems: Bulletin of Canadian Petroleum Geology, v. 36, p. 311–332.

Harrison, W. J., and L. L. Summa, 1991, Paleohydrology of the Gulf of Mexico Basin: American Journal of Science, v. 291, p. 109–176.

Harrowfield, M., and M. Keep, 2005, Tectonic modification of the Australian North-West Shelf: episodic rejuvenation of long-lived basin divisions: Basin Research, v. 17, p. 225–239.

Hartig, K. A., G. S. Soreghan, R. H. Goldstein, and M. H. Engel, 2011, Dolomite in Permian paleosols of the Bravo Dome CO_2 field, U.S.A.; Permian reflux followed by late recrystallization at elevated temperature: Journal of Sedimentary Research, v. 81, p. 248–265.

Hartley, A., S. Flint, and P. Turner, 1991, Analcime: a characteristic authigenic phase of Andean alluvium, northern Chile: Geological Journal, v. 26, p. 189–202.

Hartley, A. J., and G. May, 1998, Miocene gypcretes from the Calama Basin, northern Chile: Sedimentology, v. 45, p. 351–364.

Hartmann, B. H., K. Ramseyer, and A. Matter, 2000, Diagenesis and pore-water evolution in Permian sandstones, Gharif Formation, Sultanate of Oman: Journal of Sedimentary Research Section A-Sedimentary Petrology & Processes, v. 70, p. 533–544.

Hartmann, M., J. C. Scholten, P. Stoffers, and K. F. Wehner, 1998, Hydrographic structure of the brine-filled deeps in the Red Sea – New results from the Shaban, Kebrit, Atlantis II, and Discovery deeps: Marine Geology, v. 144, p. 311–330.

Hartwig, A., R. di Primio, Z. Anka, and B. Horsfield, 2012, Source rock characteristics and compositional kinetic models of Cretaceous organic rich black shales offshore southwestern Africa: Organic Geochemistry, v. 51, p. 17–34.

Harvie, C. E., J. H. Weare, L. A. Hardie, and H. P. Eugster, 1980, Evaporation of sea water; calculated mineral sequences: Science, v. 208, p. 498–500.

Harville, D. G., and S. J. Fritz, 1986, Modes of diagenesis responsible for observed successions of potash evaporites in the Salado Formation, Delaware Basin, New Mexico: Journal Sedimentary Petrology, v. 56, p. 648–656.

Harwood, G. M., 1980, Calcitized anhydrite and associated sulphides in the English Zechstein First Cycle Carbonate (EZ1 Ca), in H. Fuechtbauer, Peryt, T. M., ed., The Zechstein Basin, with emphasis on carbonate sequences., E. Schweizerbart'sche VbH: Contributions to Sedimentology, v. 9, p. 61–72.

Hasegawa, H., S. Imsamut, P. Charusiri, R. Tada, Y. Horiuchi, and K.-I. Hisada, 2010, 'Thailand was a desert' during the mid-Cretaceous: Equatorward shift of the subtropical high-pressure belt indicated by eolian deposits (Phu Thok Formation) in the Khorat Basin, northeastern Thailand: Island Arc, v. 19, p. 605–621.

Hatira, N., and W. Zouari, 1997, Reconnaissance par sondages de la cible d'Oum Edheboua (region de Garn Halfaya, Tunisie Nord-Ouest), resultants et recommandations: Rapport Interne, Office National des Mines, Tunis.

Hauck, S. A., 1990, Petrogenesis and tectonic setting of Middle Proterozoic iron oxide- rich ore deposits – an ore deposit model for Olympic Dam-type mineralization: US Geological Survey Bulletin, v. 1932, p. 4–39.

Hauer, G., and A. Rogerson, 2005, Remarkable salinity tolerance of seven species of naked amoebae (gymnamoebae): Hydrobiologia, v. 549, p. 33–42.

Hauer, K. L., 1995, Protoliths, diagenesis, and depositional history of the Upper Marble, Adirondack Lowlands, New York: Doctoral thesis, Miami University.

Havholm, K. G., and G. Kocurek, 1994, Factors controlling eolian sequence stratigraphy: clues from super bounding surface features in the Middle Jurassic Page Sandstone: Sedimentology, v. 41, p. 913–934.

Hawas, and H. Takezaki, 1995, A Model for Migration and Accumulation of Hydrocarbons in the Thamama and Arab Reservoirs in Abu Dhabi, U.A.E. (abs.): American Association Petroleum Geologists – Bulletin, v. 79, p. 1221.

Hawtof, E. M., 1930, Results of deep well temperature measurements in Texas, in Earth temperature in oil fields: API Production Bulletin, v. 205, p. 62–108.

Hay, R. L., 1963, Zeolitic weathering in Olduvai Gorge, Tanganyika: Geological Society America Bulletin, v. 74, p. 1281–1286.

Hay, R. L., 1968, Chert and its sodium-silicate precursors in sodium-carbonate lakes of east Africa: Contributions to Mineralogy and Petrology, v. 17, p. 255–274.

Hay, R. L., 1970, Silicate reactions in three lithofacies of a semi arid basin, Olduvai Gorge, Tanzania: Mineralogical Society of America Special Paper, v. 3, p. 237–255.

Hay, R. L., 1981, Geology of zeolites in sedimentary rocks, in F. A. Mumpton, ed., Mineralogy and geology of natural zeolites, Min. Soc. America Reviews in Mineralogy, v. 4, p. 165–175.

Hay, R. L., S. G. Guldman, J. C. Matthews, R. H. Lander, M. E. Duffin, and T. K. Kyser, 1991, Clay mineral diagenesis in core KM-3 of Searles Lake, California: Clays & Clay Minerals, v. 39, p. 84–96.

Hay, R. L., R. E. Hughes, K. T. K., H. D. Glass, and J. Liu, 1995, Magnesium-rich clays of the Meerschaum Mines in the Amboseli, Tanzania and Kenya: Clays & Clay Minerals, v. 43, p. 455–466.

Hay, R. L., and T. K. Kayser, 2001, Chemical sedimentology and paleoenvironmental history of Lake Olduvai, a Pliocene lake in northern Tanzania: Geological Society of America Bulletin, v. 113, p. 1510–1521.

Hay, W. W., 1996, Tectonics and climate: Geologische Rundschau, v. 85, p. 409–437.

Hay, W. W., R. M. Deconto, and C. N. Wold, 1997, Climate – is the past the key to the future: Geologische Rundschau, v. 86, p. 471–491.

Hay, W. W., A. Migdisov, A. N. Balukhovsky, C. N. Wold, S. Flogel, and E. Soding, 2006, Evaporites and the salinity of the ocean during the Phanerozoic: Implications for climate, ocean circulation and life: Palaeogeography, Palaeoclimatology, Palaeoecology, v. 240, p. 3–46.

Haynes, D. W., 2002, Iron Oxide Copper (-Gold) Deposits: Their Position in the Ore Deposit Spectrum and Modes of Origin, in T. M. Porter, ed., Hydrothermal Iron Oxide Copper-Gold and Related Deposits: A Global Perspective, v. 1, PGC Publishing, Adelaide, p. 71–90.

Haynes, D. W., K. C. Cross, R. T. Bills, and M. H. Reed, 1995, Olympic Dam ore genesis; a fluid-mixing model: Economic Geology, v. 90, p. 281–307.

Haynes, H. W., 1997, Solution mining of trona: In Situ, v. 21, p. 357–394.

Hayward, A. B., and R. H. Graham, 1989, Some geometrical characteristics of inversion: Geological Society of London Special Publication, v. 44, p. 17–39.

Haywick, D. W., M. B. Hall-Brown, and L. Pfeiffer, 2000, Smackover Reservoir Diagenesis in the Appleton Oilfield, Escambia County, Alabama (abs): American Association Petroleum Geologists – Bulletin, v. 84, p. 1680.

Hazen, R. M., and C. M. Schiffries, 2013, Why Deep Carbon?: Reviews in Mineralogy and Geochemistry, v. 75, p. 1–6.

Heaney, P. J., 1995, Moganite as an indicator for vanished evaporites: a testament reborn?: Journal of Sedimentary Research A: Sedimentary Petrology & Processes, v. A65, p. 633–638.

Heard, H. C., and W. W. Rubey, 1966, Tectonic implications of gypsum dehydration: Geological Society America Bulletin, v. 77, p. 741–760.

Heathcote, J. A., and S. King, 1998, Umm as Samim: a sabkha with evidence for climate change, in A. S. Alsharhan, K. W. Glennie, G. L. Whittle, and C. G. S. C. Kendall, eds., Quaternary Deserts and Climatic Change: Rotterdam, A. A. Balkema, p. 141–153.

Heaton, R. C., M. P. A. Jackson, M. Bahahmoud, and A. S. O. Nani, 1995, Superposed Neogene extension, contraction, and salt canopy emplacement in the Yemeni Red Sea, in M. P. A. Jackson, D. G. Roberts, and S. Snelson, eds., Salt Tectonics: a global perspective: Tulsa, American Association Petroleum Geologists Memoir 65, p. 333–351.

Hedlund, F. H., 2012, The extreme carbon dioxide outburst at the Menzengraben potash mine, 7 July 1953: Safety Science, v. 50, p. 537–553.

Heggland, R., 2004, Hydrocarbon migration and accumulation above salt domes – Risking of prospects by the use, in P. J. Post, ed., Salt-sediment interactions and hydrocarbon prospectivity: concepts, applications and case studies for the 21st Century. Papers presented at the 24th Annual Gulf Coast Section SEPM Foundation Bob F. Perkins Research Conference, Houston Tx, December 5–8, 2004 (CD publication), p. 315–342.

Heijlen, W., D. A. Banks, P. Muchez, B. M. Stensgard, and B. W. D. Yardley, 2008, The Nature of Mineralizing Fluids of the Kipushi Zn-Cu Deposit, Katanga, Democratic Repubic of Congo: Quantitative Fluid Inclusion Analysis using Laser Ablation ICP-MS and Bulk Crush-Leach Methods: Economic Geology, v. 103, p. 1459–1482.

Heijlen, W., P. Muchez, and D. A. Banks, 2001, Origin and evolution of high-salinity, Zn-Pb mineralising fluids in the Variscides of Belgium: Mineralium Deposita, v. 36, p. 165–176.

Heimann, A., P. G. Spry, G. S. Teale, W. R. Leyh, C. H. H. Conor, G. Mora, and J. J. O'Brien, 2013, Geochemistry and genesis of low-grade metasediment-hosted Zn-Pb-Ag mineralization, southern Proterozoic Curnamona Province, Australia: Journal of Geochemical Exploration, v. 128, p. 97–116.

Hein, F. J., M. C. Graves., and A. Ruffman, 1991, The Jubilee zinc-lead deposit, Nova Scotia: the role of synsedimentary faults, in A. L. Sangster, ed., Mineral deposit studies in Nova Scotia, v. 90-8(2), Geol. Surv. Canada Paper.

Helfman, G., D. Facey, and B. Collette, 1997, The diversity of fishes: Oxford, UK, Blackwell Publishing, 1006 p.

Helgeson, H. C., 1969, Thermodynamics of hydrothermal systems at elevated temperatures and pressures: American Journal of Science, v. 267, p. 729–804.

Helgeson, H. C., 1970, A chemical and thermodynamic model of ore deposition in hydrothermal systems: Mineral. Soc. Am. Spec. Pap., 50th Anniv. Symp., ed. B. A. Morgan.

Helvaci, C., 1994, Mineral assemblages and formation of the Kestelek and Sultancayir borate deposits: 29th International Geological Congress, Proceedings Part A, Kyoto, Japan, 24 August – 3 September, 1992, p. 245–284.

Helvaci, C., 1995, Stratigraphy, mineralogy, and genesis of the Bigadic Borate deposits, Western Turkey: Economic Geology, v. 90, p. 1237–1260.

Helvaci, C., 1998, The Beypazari trona deposit, Ankara Province, Turkey., in J. R. Dyni, and R. W. Jones, eds., Proceedings of the first international soda ash conference; Volume II: Laramie, WY, Public Information Circular – Geological Survey of Wyoming, v. 40, p. 67–103.

Helvaci, C., and R. C. Alonso, 2000, Borate Deposits of Turkey and Argentina; A Summary and Geological Comparison: Turkish Journal of Earth Sciences, v. 9, p. 1–27.

Helvaci, C., H. Mordogan, M. Colak, and I. Gundogan, 2003, Presence and Distribution of Lithium in Borate Deposits and Some Recent Lake Waters of West-Central Turkey: International Geology Review, v. 46, p. 177–190.

Helvaci, C., and F. Orti, 1998, Sedimentology and diagenesis of Miocene colemanite-ulexite deposits (western Anatolia, Turkey): Journal of Sedimentary Research Section A-Sedimentary Petrology & Processes, v. 68A, p. 1021–1033.

Helvaci, C., and F. Orti, 2004, Zoning in the Kirka borate deposit, western Turkey: Primary evaporitic fractionation of diagenetic modifications?: Canadian Mineralogist, v. 42, p. 1221–1246.

Helvaci, C., F. Orti, J. Garcia-Veigas, L. Rosell, and I. Gungodan, 2012, Neogene Borate deposits: Mineralogy, Petrology and Sedimentology; A workshop with special emphasis on the Anatolian deposits International Earth Science Colloquium on the Aegean Region (IESCA- 2012, Izmir, Turkey) 64 pp.

Hemley, J. J., P. B. Hostetler, A. J. Gude, and W. T. Mountjoy, 1969, Some stability relations of alunite: Economic Geology, v. 64, p. 599–612.

Henchiri, M., and N. Slim-S'Himi, 2006, Silicification of sulphate evaporites and their carbonate replacements in Eocene marine sediments, Tunisia: two diagenetic trends: Sedimentology, v. 53, p. 1135–1159.

Henderson, K., 1974, Methods of joining two or more wells for brine production, in A. H. Coogan, ed., Fourth Symposium on Salt, v. 2: Cleveland, N. Ohio Geol. Soc., p. 211–218.

Hendron, A. J., and P. A. Lenzini, 1983, Subsidence investigation at Well #56, Carey Salt Brinefield, Hutchison Kansas: Solution Mining Research Institute Research Project Report, v. 83-0001-Solution Mining Research Institute, p. 67.

Henley, R. W., 1973, Solubility of gold in hydrothermal chloride solutions: Chemical Geology, v. 11, p. 73–87.

Henneke, E., G. W. Luther, G. J. Delange, and J. Hoefs, 1997, Sulphur speciation in anoxic hypersaline sediments from the Eastern Mediterranean Sea: Geochimica et Cosmochimica Acta, v. 61, p. 307–321.

Hennen, R. V., and R. J. Metcalf, 1929, Yates Oil Pool, Pecos County, Texas: American Association Petroleum Geologists -Bulletin, v. 13, p. 1509–1556.

Henriksen, S., and T. O. Vorren, 1996, Early Tertiary sedimentation and salt tectonics in the Nordkapp Basin, Southern Barents Sea: Norsk Geologisk Tidsskrift, v. 76, p. 33–44.

Henriquez, F., H. R. Naslund, J. O. Nystrom, W. Vivallo, R. Aguirre, F. M. Dobbs, and H. Lledo, 2003, New field evidence bearing on the origin of the El Laco magnetitie depositied, Northern Chile – A discussion: Economic Geology, v. 98, p. 1497–1500.

Henry, D. J., and B. L. Dutrow, 2012, Tourmaline at diagenetic to low-grade metamorphic conditions: Its petrologic applicability: Lithos, v. 154, p. 16–32.

Henry, D. J., and C. V. Guidotti, 1985, Tourmaline as a petrogenetic indicator mineral: an example from the staurolite grade metapelites of NW Maine: American Mineralogist, v. 70, p. 1–15.

Henry, D. J., B. L. Kirkland, and D. W. Kirkland, 1999, Sector-zoned tourmaline from the cap rock of a salt dome: European Journal of Mineralogy, v. 11, p. 263–280.

Henry, D. J., H. Sun, J. F. Slack, and B. L. Dutrow, 2008, Tourmaline in meta-evaporites and highly magnesian rocks: perspectives from Namibian tourmalinites: European Journal of Mineralogy, v. 20, p. 889–904.

Hentz, T. F., and C. D. Henry, 1989, Evaporite-hosted native sulfur in Trans-Pecos Texas; relation to late-phase Basin and Range deformation: Geology, v. 17, p. 400–403.

Heppenheimer, H., H. W. Hagemann, and W. Puttmann, 1995, A comparative study of the influence of organic matter on metal accumulation processes in the Kupferschiefer from the Hessian Depression and the north Sudetic Syncline: Ore Geology Reviews, v. 9, p. 391–409.

Herbst, D. B., and T. J. Bradley, 1988, Osmoregulation in Dolichopodid Larvae (*Hydrophorus-Plumbeus*) from a Saline Lake: Journal of Insect Physiology, v. 34, p. 369–372.

Herdendorf, C. E., 1984, Inventory of the morphometric and limnologic characteristics of the large lakes of the world: Ohio State University Sea grant Program Technical Bulletin, v. OHSU-TB-17, p. 78 p.

Heroux, Y., A. Chagnon, and M. Savard, 1996, Organic matter and clay anomalies associated with base-metal sulphide deposits: Ore Geology Reviews, v. 11, p. 157–173.

Heroux, Y., A. Chagnon, and M. M. Savard, 1994, Anomalies in properties of organic material as associated clay mineral assemblages – Pb-Zn of Gays River, Nova Scotia [French]: Exploration & Mining Geology, v. 3, p. 67–79.

Herrero, M. J., A. Martín-Pérez, A. M. Alonso-Zarza, I. Gil-Peña, A. Meléndez, and R. Martín-García, 2011, Petrography and geochemistry of the magnesites and dolostones of the Ediacaran Ibor Group (635 to 542Ma), Western Spain: Evidences of their hydrothermal origin: Sedimentary Geology, v. 240, p. 71–84.

Herries, R. D., and G. Cowan, 1997, Challenging the 'sheetflood' myth: the role of water-table-controlled sabkha deposits in redefining the depositional model for the Ormskirk Sandstone Formation (Lower Triassic), East Irish Sea Basin, in N. S. Meadows, S. Trueblood, M. Hardman, and G. Cowan, eds., Petroleum Geology of the Irish Sea and Adjacent Areas: London, Geological Society of London Special Publication 124, p. 253–276.

Herrmann, A. G., D. Knake, J. Schneider, and H. Peters, 1973, Geochemistry of Modern Seawater and Brines from Salt Pans; Main Components and Bromine Distribution: Contributions Mineralogy and Petrology, v. 40, p. 1–24.

Herut, B., I. Gavrieli, and L. Halicz, 1998, Coprecipitation of trace and minor elements in modern authigenic halites from the hypersaline Dead Sea brine: Geochimica et Cosmochimica Acta, v. 62, p. 1587–1598.

Herut, B., A. Starinsky, A. Katz, and A. Bein, 1990, The role of seawater freezing in the formation of subsurface brines: Geochemica et Cosmochimica Acta, v. 54, p. 13–21.

Hessami, K., F. Nilforoushan, and C. J. Talbot, 2006, Active deformation within the Zagros Mountains deduced from GPS measurements: Journal of the Geological Society, v. 163, p. 143–148.

Hesse, P. P., J. W. Magee, and S. van der Kaars, 2004, Late Quaternary climates of the Australian arid zone: a review: Quaternary International, v. 118–119, p. 87–102.

Hesse, R., 1986, Early diagenetic pore water/sediment interaction: Modern offshore basins: Geoscience Canada, v. 13, p. 165–197.

Hesse, R., 1989, Silica diagenesis: origin of inorganic and replacement cherts.: Earth Science Reviews, v. 26, p. 253–284.

Heward, A. P., 1990, Salt removal and sedimentation in southern Oman, in A. H. F. Robertson, M. P. Searle, and A. C. Ries, eds., The geology and tectonics of the Oman region, Geological Society of London, Special Publication, v. 49, p. 637–652.

Heward, A. P., S. Chuenbunchom, G. Makel, D. Marsland, and L. Spring, 2000, Nang Nuan oil field, B6/27, Gulf of Thailand: karst reservoirs of meteoric or deep-burial origin?: Petroleum Geoscience, v. 6, p. 15–27.

Heydari, E., 1997, The role of burial diagenesis in hydrocarbon destruction and H2S accumulation, Upper Jurassic Smackover Formation, Black Creek Field, Mississippi: American Association of Petroleum Geologists – Bulletin, v. 81, p. 26–45.

Heydari, E., 2000, Porosity Loss, Fluid Flow, and Mass Transfer in Limestone Reservoirs: Application to the Upper Jurassic Smackover Formation, Mississippi: American Association Petroleum Geologists – Bulletin, v. 84, p. 100–118.

Heydari, E., 2010, Dolomites of the Smackover and Buckner Formations in the Mississippi Salt Basin: A Key to Understanding the Dolomitization Process: Gulf Coast Association of Geological Societies Transactions, v. 60, p. 339–353.

Heydari, E., and L. Baria, 2006, A Microbial Smackover Formation and the Dual Reservoir–Seal System at the Little Cedar Creek Field in Conecuh County of Alabama: Transactions – Gulf Coast Association of Geological Societies, v. 55, p. 294–320.

Heydari, L. E., and C. H. Moore, 1989, Burial diagenesis and thermochemical sulfate reduction, Smackover Formation, Southeast Mississippi salt basin: Geology, v. 17, p. 1080–1084.

Hietanen, A. H., 1967, Scapolite in the Belt Series in the St. Joe-Clearwater Region, Idaho: Geol. Soc. Amer. Special Paper, v. 86, p. 56 pp.

Higgs, R., 2009, The vanishing Carib Halite Formation (Neocomian), Colombia-Venezuela-Trinidad prolific petroleum province: Geological Society, London, Special Publications, v. 328, p. 659–686.

Hilaire-Marcel, C., J. Casanova, and M. Taieb, 1987, Isotopic age and lacustrine environments during late Quaternary in the Tanzanian Rift (Lake Natron), in M. R. Rampino, J. E. Sanders, W. S. Newman, and L. K. Konigsson, eds., Climate; history, periodicity, and predictability: New York, NY, United States, Van Nostrand Reinhold Co., p. 117–123.

Hildebrand, R. S., 1986, Kiruna-type deposits; their origin and relationship to intermediate subvolcanic plutons in the Great Bear magmatic zone, Northwest Canada: Economic Geology, v. 81, p. 640–659.

Hilgen, F. J., and C. G. Langereis, 1988, The age of the Miocene-Pliocene boundary in the Capo Rossello area (Sicily): Earth and Planetary Science Letters, v. 91, p. 214–222.

Hill, B. F., 1993, Magnesite and magnesia production by Queensland Magnesia (Operations) Pty Ltd at Kunwarara and Rockhampton, Qld, in J. T. Woodcock, and J. K. Hamilton, eds., Australasian mining and metallurgy; the Sir Maurice Mawby Memorial volume: Melbourne, Victoria, Australia, Australasian Institute of Mining and Metallurgy, v. 19, p. 1388–1393.

Hill, C. A., 1990, Sulphuric acid speleogenesis of Carlsbad Caverns and its relationship to hydrocarbons, Delaware Basin, New Mexico and Texas: American Association of Petroleum Geologists Bulletin, v. 74, p. 1685–1694.

Hill, C. A., 1995, H_2S-related porosity and sulfuric acid oilfield karst, in D. A. Budd, A. H. Saller, and P. M. Harris, eds., Unconformities and porosity in carbonate strata, American Association Petroleum Geologists Memoir 63, p. 301–306.

Hill, C. A., 2000, Overview of the geologic history of cave development in the Guadalupe Mountains, New Mexico: Journal of Cave and Karst Studies, v. 62, p. 60–71.

Hill, C. A., 2003, Intrastratal karst at the Waste Isolation Pilot Plant site, southeastern New Mexico: Oklahoma Geological Survey Circular 109, p. 197–209.

Hill, C. A., and P. Forti, 1997, Cave Minerals of the World, 2nd edn: Huntsville, AL, National Speleological Society of America, 463 p.

Hill, R. E. T., M. J. Gole, and S. J. Barnes, 1989, Olivine adcumulates in the Norseman-Wiluna greenstone belt, Western Australia; implications for volcanology of komatiites, in M. S. Prendergast, and M. J. Jones, eds., Magmatic sulfides; the Zimbabwe volume; Fifth magmatic sulfide field conference, Zimbabwe,1987: London, United Kingdom, Inst. Min. and Metall., p. 189–206.

Hill, S. J., N. E. James-Rutledge, A. C. Canham, and J. Franques-Faixa, 2003, Paleozoic and Triassic Sandstones of North Africa and the Middle East: Diagenetic Controls on Reservoir Quality (abs.): American Association Petroleum Geologists Hedberg Conference "Paleozoic and Triassic Petroleum Systems in North Africa", February 18–20, 2003, Algiers, Algeria.

Hills, J. M., 1984, Sedimentation, tectonism, and hydrocarbon generation in Delaware Basin, West Texas and Southeastern New Mexico: American Association Petroleum Geologists -Bulletin, v. 68, p. 250–267.

Hindle, A. D., 1997, Petroleum migration pathways and charge concentration – a three-dimensional model: Bulletin-American Association of Petroleum Geologists, v. 81, p. 1451–1481.

Hinman, M., 1995, Base metal mineralisation at McArthur River: Stracture of the HYC-Cooley zone at McArthur River: AGSO – Record, v. 1995/5.

Hinman, M., 1997, The essential interplays between deformation, sedimentation, and fluid flow for the formation of the HYC-Deposit at McArthur River, Northern Territory: Abstracts – Geological Society of Australia, v. 47, p. 16–18.

Hinnov, L. A., and R. K. Goldhammer, 1991, Spectral analysis of the Middle Triassic Latemar Limestone: Journal of Sedimentary Petrology, v. 61, p. 1173–1193.

Hips, K., and G. B. Árgyelán, 2007, Controls on diagenesis of the Triassic Kurrachine Dolomite, Syria: GeoArabia, v. 12, p. 41–64.

Hite, R. J., 1961, Potash-bearing evaporite cycles in the salt anticlines of the Paradox Basin, Colorado and Utah; Article 337: U. S. Geological Survey Professional Paper. p. D323-D327.

Hite, R. J., and D. E. Anders, 1991, Petroleum and evaporites, in J. L. Melvin, ed., Evaporites, petroleum and mineral resources, v. 50: Amsterdam, Elsevier Developments in Sedimentology, p. 477–533.

Hite, R. J., D. E. Anders, and T. G. Jing, 1984, Organic-rich source rocks of Pennsylvanian age in the Paradox Basin of Utah and Colorado, in J. Woodward, F. F. Meissner, and J. L. Clayton, eds., Hydrocarbon source rocks of the Greater Rocky Mountain Region: Denver, Rocky Mountain Assoc. Geologists, p. 255–274.

Hite, R. J., and T. Japakasetr, 1979, Potash deposits of the Khorat Plateau, Thailand and Laos: Economic Geology, v. 74, p. 448–458.

Hite, R. J., and A. S. Wassef, 1983, Potential Potash Deposits in the Gulf of Suez, Egypt: Ann. Geol. Survey Egypt, v. 13, p. 39–54.

Hitzman, M., R. Kirkham, D. Broughton, J. Thorson, and D. Selley, 2005, The sediment-hosted stratiform copper ore system, Economic Geology; One hundredth anniversary volume, 1905–2005, Society of Economic Geologists, Littleton, CO, United States, p. 609–642.

Hitzman, M. W., 2000, Iron Oxide-Cu-Au deposits: What, where, when and why, in T. M. Porter, ed., Hydrothermal iron oxide copper-gold and related deposits a global perspective: Adelaide, Australian Mineral Foundation, p. 9–26.

Hitzman, M. W., 2002, Iron Oxide-Cu-Au Deposits: What, Where, When, and Why?, in T. M. Porter, ed., Hydrothermal Iron Oxide Copper-Gold and Related Deposits: A Global Perspective, v. 1, PGC Publishing, Adelaide, p. 9–25.

Hitzman, M. W., N. Oreskes, and M. T. Einaudi, 1992, Geological characteristics and tectonic setting of Proterozoic iron oxide (Cu-U-Au-REE) deposits.: Precambrian Research, v. 58, p. 241–287.

Hocking, R. M., I. A. Copp, P. E. Playford, and R. H. Kempton, 1996, The Cadjebut Formation: a Givetian evaporitic precursor to Devonian reef complexes of the Lennard Shelf, Canning Basin, Western Australia: Geological Survey of Western Australia, Annual Review, 1995–96, p. 48–55.

Hodell, D. A., J. H. Curtis, F. J. Sierro, and M. E. Raymo, 2001, Correlation of late Miocene to early Pliocene sequences between the Mediterranean and North Atlantic: Paleoceanography, v. 16, p. 164–178.

Hodge, B. L., 1986, Occurrence and exploitation of fluorite, in R. W. Nesbitt, and I. Nichol, eds., Geology in the real world – the Kingsley Dunham volume: London, Inst. Mining Metallurgy, p. p. 165.

Hodgkins, M., and M. J. O'Brien, 1994, Salt sill deformation and its implications for subsalt exploration: Leading Edge, v. August 1994, p. 849–851.

Hoeft, S. E., T. R. Kulp, J. F. Stolz, J. T. Hollibaugh, and R. S. Oremland, 2004, Dissimilatory arsenate reduction with sulfide as electron donor: experiments with Mono Lake water and isolation of strain MLMS-1, a chemoautotrophic arsenate respirer: Applied & Environmental Microbiology, v. 70, p. 2741–2745.

Hoffman, P. F., 2011, Strange bedfellows: glacial diamictite and cap carbonate from the Marinoan (635 Ma) glaciation in Namibia: Sedimentology, v. 58, p. 57–119.

Hoffman, P. F., A. J. Kaufman, G. P. Halverson, and D. P. Schrag, 1998, A Neoproterozoic Snowball Earth: Science, v. 281, p. 1342–1346.

Hofmann, H. J., K. Grey, A. H. Hickman, and R. I. Thorpe, 1999, Origin of 3.45 Ga coniform stromatolites in Warrawoona Group, Western Australia: Bulletin Geological Society of America, v. III, p. 1256–1262.

Hofmann, P., A. Y. Huc, B. Carpentier, P. Schaeffer, P. Albrecht, B. Keely, J. R. Maxwell, D. J. S. Sinninghe, L. J. W. de, and D. Leythaeuser, 1993a, Organic matter of the Mulhouse Basin, France; a synthesis: Organic Geochemistry, v. 20, p. 1105–1123.

Hofmann, P., D. Leythaeuser, and B. Carpentier, 1993b, Palaeoclimate controlled accumulation of organic matter in Oligocene evaporite sediments of the Mulhouse Basin: Organic Geochemistry, v. 20, p. 1125–1138.

Hogarth, D. D., 1979, Lapis lazuli from Edwards, New York; a possible metaevaporite: Geol. Assoc. Can. Mineral. Assoc. Can., Jt. Annu. Meet., Program Abstr.

Hogarth, D. D., and W. L. Griffin, 1978, Lapis lazuli from Baffin Island; a Precambrian meta-evaporite: Lithos, v. 11, p. 37–60.

Hogarth, D. D., and W. L. Griffin, 1980, Contact-metamorphic lapis lazuli; the Italian Mountain deposits, Colorado: Canadian Mineralogist, v. 18, p. 59–70.

Holail, H. H. M., M. M. N. Shaaban, A. S. Mansour, and I. Rifai, 2005, Diagenesis of the middle Eocene upper Dammam subformation, Qatar: Petrographic and isotopic evidence: Carbonates and Evaporites, v. 20, p. 72–81.

Holba, A. G., E. Tegelaar, L. Ellis, M. S. Singletary, and P. Albrecht, 2000, Tetracyclic polyprenoids: Indicators of freshwater (lacustrine) algal input: Geology, v. 28, p. 251–254.

Holcombe, R. J., P. I. Pearson, and N. H. S. Oliver, 1992, Structure of the Mary Kathleen Fold Belt, in A. I. Stewart, and D. H. Blake, eds., Detailed studies of the Mount Isa Inlier, Bureau of Mineral Resources, Australia, Bulletin 243, p. 257–287.

Holcombe, R. J., P. J. Pearson, and N. H. S. Oliver, 1991, Geometry of a middle Proterozoic extensional decollement in northeastern Australia: Tectonophysics, v. 191, p. 255–274.

Holland, H. D., 1972, Granites, solutions and base metal deposits: Economic Geology, v. 67, p. 281–301.

Holland, H. D., J. Horita, and W. Seyfried, 1996, On the secular variations in the composition of phanerozoic marine potash evaporites: Geology, v. 24, p. 993–996.

Holland, H. D., and H. Zimmermann, 2000, The Dolomite Problem Revisited: Int. Geol. Rev., v. 42, p. 481–490.

Hollander, D. J., A. Y. Huc, J. S. S. Damste, J. M. Hayes, and J. W. De Leeuw, 1993, Molecular and bulk isotopic analyses of organic matter in marls of the Mulhouse Basin (Tertiary, Alsace, France): Organic Geochemistry, v. 20, p. 1253–1263.

Holliday, D. W., 1970, The petrology of secondary gypsum rocks; a review: Journal of Sedimentary Petrology, v. 40, p. 734–744.

Hollis, J. A., and A. S. Wygralak, 2012, A review of the geology and uranium, gold and iron ore deposits of the Pine Creek Orogen: Episodes, v. 35, p. 264–272.

Holmes, R., 1991, Some aspects of the geology of the potash seam at Boulby mine: Journal of the Open University Geological Society, v. 12, p. 77–88.

Holness, M. B., 2003, Growth and albitization of K-feldspar in crystalline rocks in the shallow crust: a tracer for fluid circulation during exhumation?: Geofluids, v. 3, p. 89–102.

Holser, W. T., 1966, Bromide geochemistry of salt rocks: Second Symposium on Salt, Ohio Geological Society, p. 248–275.

Holser, W. T., 1977, Catastrophic chemical events in the history of the ocean: Nature, v. 267.

Holser, W. T., 1979, Mineralogy of evaporites, in R. G. Burns, ed., Marine Minerals, v. 6, Mineralogical Society America, Reviews in Mineralogy, p. 211–294.

Holser, W. T., 1984, Gradual and abrupt shifts in ocean chemistry during Phanerozoic time, in H. D. Holland, and A. F. Trendall, eds., Patterns of Change in Earth Evolution: Berlin, Springer-Verlag, p. 123–143.

Holser, W. T., G. P. Clement, L. F. Jansa, and J. A. Wade, 1988, Evaporite deposits of the North Atlantic Rift, in W. Manspeizer, ed., Triassic-Jurassic rifting: Continental breakup and the origin of the Atlantic Ocean and Passive margins, v. Developments in Geotectonics 22: Amsterdam, Elsevier, p. 525–556.

Holser, W. T., B. J. Javor, and C. Pierre, 1981, Geochemistry and Geology of Salt Pans at Guerrero Negro, Baja California: Field trip Guide No 1. Prepared for the Geological Society of America, Cordilleran Section, Annual Meeting, March 22–24, 1981.

Holser, W. T., M. Schidlowski, F. T. Mackenzie, and J. B. Maynard, 1988, Geochemical cycles of carbon and sulfur, in C. B. Gregor, R. M. Garrels, F. T. Mackenzie, and J. B. Maynard, eds., Chemical Cycles in the Evolution of the Earth: New York, Wiley, p. 107–173.

Holt, N. M., J. García-Veigas, T. K. Lowenstein, P. S. Giles, and S. Williams-Stroud, 2014, The major-ion composition of Carboniferous seawater: Geochimica et Cosmochimica Acta, v. 134, p. 317–334.

Holt, R. M., and D. W. Powers, 2010, Evaluation of halite dissolution at a radioactive waste disposal site, Andrews County, Texas: Geological Society of America Bulletin, v. 122, p. 1989–2004.

Holter, M., 1972, Geology of the Prairie Evaporite Formation of Saskatchewan, Canada, Geology of saline deposits (Geologie des depots salins), v. 7, UNESCO Earth Sci. Ser., p. 183–189.

Holwerda, J. G., and R. W. Hutchinson, 1968, Potash-bearing evaporites in the Danakil area, Ethiopia: Economic Geology, v. 63, p. 124–150.

Honarmand, J., and A. Amini, 2012, Diagenetic processes and reservoir properties in the ooid grainstones of the Asmari Formation, Cheshmeh Khush Oil Field, SW Iran: Journal of Petroleum Science and Engineering, v. 81, p. 70–79.

Honty, M., P. Uhlík, V. Sucha, M. Caplovicová, J. Francu, N. Clauer, and A. Biron, 2004, Smectite-to-illite alteration in salt-bearing bentonites (the East Slovak Basin) Clays and Clay Minerals, v. 52, p. 533–551.

Höök, M., B. Söderbergh, K. Jakobsson, and K. Aleklett, 2009, The Evolution of Giant Oil Field Production Behavior: Natural Resources Research, v. 18, p. 39–56.

Hooper, R. J., Leng Siang Goh, and F. Dewey, 1995, The inversion history of the northeastern margin of the Broad Fourteens Basin, in J. G. Buchanan, and P. G. Buchanan, eds., Basin inversion, Geological Society, London; Special Publication, 88, p. 307–317.

Hopkins, J. C., 1987, Contemporaneous subsidence and fluvial channel sedimentation: Upper Mannville C Pool, Berry Field, Lower Cretaceous of Alberta: American Association Petroleum Geologists – Bulletin, v. 71, p. 334–345.

Hopkinson, L., S. Roberts, R. Herrington, and J. Wilkinson, 1998, Self-organisation of submarine hydrothermal siliceous deposits – Evidence from the TAG hydrothermal mound, 26°N Mid-Atlantic Ridge: Geology, v. 26, p. 347–350.

Hopper, D., and A. Correa, 2000, The Panulcillo and Teresa de Colmo Copper Deposits; Two Contrasting Examples of Fe-Ox Cu-Au Mineralisation from the Coastal Cordillera of Chile, in T. M. Porter, ed., Hydrothermal Iron Oxide Copper-Gold and Related Deposits: A Global Perspective, v. 1, PGC Publishing, Adelaide, p. 177–189.

Horikoshi, K., G. Antranikian, A. T. Bull, F. T. Robb, and K. O. Stetter, 2011, Extremophiles Handbook, Springer, 1247 p.

Horita, J., 2009, Isotopic Evolution of Saline Lakes in the Low-Latitude and Polar Regions: Aquatic Geochemistry, v. 15, p. 43–69.

Horsfield, B., D. J. Curry, K. M. Bohacs, A. R. Carroll, R. Littke, U. Mann, M. Radke, R. G. Schaefer, G. H. Isaksen, H. G. Schenk, E. G. Witte, and J. Rulkotter, 1994, Organic geochemistry of freshwater and alkaline lacustrine environments, Green River Formation, Wyoming: Organic geochemistry, v. 22, p. 415–450.

Horsfield, B., and J. Rullkotter, 1994, Diagenesis, catagenesis, and metagenesis of organic matter, in L. B. Magoon, and W. G. Dow, eds., The petroleum system – from source to trap, v. 60, American Association Petroleum Geologists; Memoir, p. 189–199.

Hose, L., D., and J. A. Pisarowicz, 1999, Cueva de Villa Luz, Tabasco, Mexico: Reconnaissance study of an active sulfur spring cave and ecosystem: Journal of Cave and Karst Studies, v. 61, p. 13–21.

Hose, L. D., A. N. Palmer, M. V. Palmer, D. E. Northup, P. J. Boston, and H. R. DuChene, 2000, Microbiology and geochemistry in a hydrogen-sulphide-rich karst environment: Chemical Geology, v. 169, p. 399–423.

Hou, T., Z. Zhang, M. Santosh, J. Encarnacion, and M. Wang, 2013, The Cihai diabase in the Beishan region, NW China: Isotope geochronology, geochemistry and implications for Cornwall-style iron mineralization: Journal of Asian Earth Sciences, v. 70,Äì71, p. 231–249.

House, W. M., and J. A. Pritchett, 1995, Fluid migration and formation pressures associated with allochthonous salt sheets in the northern Gulf of Mexico: Gulf Coast Section SEPM Foundation Sixteenth Annual Research Conference, p. 121–124.

Houssein, D. E., and G. Axelsson, 2010, Geothermal resources in the Asal Region, Republic of Djibouti: An update with emphasis on reservoir engineering studies: Geothermics, v. 39, p. 220–227.

Houston, J., and D. Hart, 2004, Theoretical head decay in closed basin aquifers: an insight into fossil groundwater and recharge events in the Andes of northern Chile: Quarterly Journal of Engineering Geology and Hydrogeology, v. 37, p. 131–139.

Houston, S., C. Smalley, A. Laycock, and B. W. D. Yardley, 2011, The relative importance of buffering and brine inputs in controlling the abundance of Na and Ca in sedimentary formation waters: Marine and Petroleum Geology, v. 28, p. 1242–1251.

Hover, V. C., and G. M. Ashley, 2003, Geochemical signatures of paleodepositional and diagenetic environments: A STEM/AEM study of authigenic clay minerals from an arid rift basin, Oluvai Gorge, Tanzania: Clays and Clay Minerals, v. 51, p. 231–251.

Hovland, M., T. Kuznetsova, H. Rueslatten, B. Kvamme, H. K. Johnsen, G. E. Fladmark, and A. Hebach, 2006a, Sub-surface precipitation of salts in supercritical seawater: Basin Research, v. 18, p. 221–230.

Hovland, M., and H. Rueslatten, 2009, Origin and permeability of deep ocean salts: Geophysical Research Abstracts, v. 11.

Hovland, M., H. G. Rueslatten, H. K. Johnsen, B. Kvamme, and T. Kuznetsova, 2006b, Salt formation associated with sub-surface boiling and supercritical water: Marine and Petroleum Geology, v. 23, p. 855–869.

Hovorka, S., 1987, Depositional environments of marine-dominated bedded halite, Permian San Andres Formation, Texas: Sedimentology, v. 34, p. 1029–1054.

Hovorka, S. D., 1989, Depth evolution of the Delaware Basin-Castile/Salado transition, in P. M. Harris, and G. A. Grover, eds., Subsurface and Outcrop Examination of the Capitan Shelf Margin, Northern Delaware Basin, v. 13: Tulsa, Oklahoma, SEPM, Core Workshop, p. 441–450.

Hovorka, S. D., 1992, Halite pseudomorphs after gypsum in bedded anhydrite; clue to gypsum-anhydrite relationships: Journal of Sedimentary Petrology, v. 62, p. 1098–1111.

Hovorka, S. D., 2000, Understanding the processes of salt dissolution and subsidence: Solution Mining Research Institute Proceedings, p. 11–24 (PDF file); see also http://www.beg.utexas.edu/environqlty/salt/index.htm.

Hovorka, S. D., R. M. Holt, and D. W. Powers, 2007, Depth indicators in Permian Basin evaporites: Geological Society, London, Special Publications, v. 285, p. 335–364.

Howell, P., and A. W. Leibold III, 1992, Sequence Stratigraphy of the Silurian Carbonates and Evaporites in the Michigan Basin: American Association Petroleum Geologists – Bulletin, v. 76, p. 56–57.

Howell, P. D., and B. A. van der Pluijm, 1999, Structural sequences and styles of subsidence in the Michigan Basin: Geological Society America Bulletin, v. III, p. 974–991.

Hoy, R. B., R. M. Foose, and B. J. O'Neill Jr., 1962, Structure of Winnfield salt dome, Winn Parish, Louisiana: American Association Petroleum Geologists – Bulletin, v. 46, p. 1444–1459.

Hryniv, S., and T. M. Peryt, 2010, Strontium distribution and celestite occurrence in Zechstein (Upper Permian) anhydrites of West Poland: Chemie der Erde – Geochemistry, v. 70, p. 137–147.

Hryniv, S. P., B. V. Dolishniy, O. V. Khmelevska, A. V. Poberezhskyy, and S. V. Vovnyuk, 2007, Evaporites of Ukraine: a review: Geological Society, London, Special Publications, v. 285, p. 309–334.

Hryniv, S. P., and T. M. Peryt, 2003, Sulfate cavity filling in the Lower Werra Anhydrite (Zechstein, Permian), Zdrada area, northern Poland: Evidence for early diagenetic evaporite paleokarst formed under sedimentary cover: Journal Of Sedimentary Research, v. 73, p. 451–461.

Hsu, K. J., M. B. Cita, and W. B. F. Ryan, 1970, The origin of the Mediterranean evaporite: Ryan, W. B. F., Hsue, K. J., Cita, M. B., Dumitrica, P., Lort, J. M., Maync, W., Nesteroff, W. D., Pautot, G., Stradner, H., Wezel, F. C., Kaneps, A. G. Initial reports of the Deep Sea Drilling Project, covering Leg, v. 2, p. 1203–1231.

Hsu, K. J., W. B. F. Ryan, and M. B. Cita, 1973, Late Miocene Desiccation of the Mediterranean: Nature, v. 242, p. 240–244.

Hsu, K. J., and J. Schneider, 1973, Progress report on dolomitization of Abu Dhabi Sabkhas, Arabian Gulf, in B. H. Purser, ed., The Persian Gulf: Holocene carbonate sedimentation and diagenesis in a shallow epicontinental sea: New York, Springer-Verlag, p. 409–422.

Hsu, K. J., and C. Siegenthaler, 1969, Preliminary experiments on hydrodynamic movement induced by evaporation and their bearing on the dolomite problem: Sedimentology, v. 12, p. 448–453.

Hu, G., and N.-a. Wang, 2001, The sand wedge and mirabilite of the last ice age and their paleoclimatic significance in Hexi Corridor: Chinese Geographical Science, v. 11, p. 80–86.

Huang, X. Z., and H. S. Shao, 1993, Sedimentary characteristics and types of hydrocarbon source rocks in the Tertiary semiarid to arid lake basins of Northwest China: Palaeogeography Palaeoclimatology Palaeoecology, v. 105, p. 33–43.

Huber, R., M. Kurr, H. W. Jannasch, and K. O. Stetter, 1989, A novel group of methanogenic archaebacteria (Methanopyrus) growing at 110°C: Nature, v. 342, p. 833–834.

Hubert, J. F., and M. G. Hyde, 1982, Sheetflow deposits of graded beds and mudstones on an alluvial sandflat-playa system; the Upper Triassic Blomidon Redbeds, St Marys Bay, Nova Scotia: Sedimentology, v. 29, p. 457–474.

Hübscher, C., E. Tahchi, I. Klaucke, A. Maillard, and H. Sahling, 2009, Salt tectonics and mud volcanism in the Latakia and Cyprus Basins, eastern Mediterranean: Tectonophysics, v. 470, p. 173–182.

Huddart, D., and T. Stott, 2010, Earth Environments: Past, present and future: Oxford, Wiley and Sons, Inc.

Hudec, M. R., and M. P. A. Jackson, 2006, Advance of allochthonous salt sheets in passive margins and orogens: American Association Petroleum Geologists – Bulletin, v. 90, p. 1535–1564.

Hudec, M. R., and M. P. A. Jackson, 2007, Terra infirma: Understanding salt tectonics: Earth-Science Reviews, v. 82, p. 1–28.

Hudec, M. R., and M. P. A. Jackson, 2009, Interaction between spreading salt canopies and their peripheral thrust systems: Journal of Structural Geology, v. 31, p. 1114–1129.

Hudec, M. R., M. P. A. Jackson, and F. J. Peel, 2013b, Influence of deep Louann structure on the evolution of the northern Gulf of Mexico: Bulletin American Association Petroleum Geologists, v. 97, p. 1711–1735.

Hudec, M. R., I. O. Norton, M. P. A. Jackson, and F. J. Peel, 2013a, Jurassic evolution of the Gulf of Mexico salt basin: Bulletin American Association Petroleum Geologists, v. 97, p. 1683–1710.

Huichi, R., H. Renmin, and D. P. Cox, 1991, Copper deposition by fluid mixing in deformed strata adjacent to a salt diapir, Dongchuan

area, Yunnan Province, China: Economic Geology, v. 86, p. 1539–1545.
Huismans, R. S., and C. Beaumont, 2008, Complex rifted continental margins explained by dynamical models of depth-dependent lithospheric extension: Geology, v. 36, p. 163–166.
Hulen, J. B., and J. W. Collister, 1999, The oil-bearing, Carlintype gold deposits of Yankee Basin, Alligator Ridge District, Nevada: Economic Geology, v. 94, p. 1029–1049.
Hulme, M., and A. Trilsbach, 1989, The August 1988 storm over Khartoum: its climatology and impact: Weather, v. 44, p. 82–90.
Humphris, S. E., P. M. Herzig, D. J. Miller, J. C. Alt, K. Becker, D. Brown, G. Brugmann, H. Chiba, Y. Fouquet, J. B. Gemmell, G. G., M. D. Hannington, N. G. Holm, J. J. Honnorez, G. J. Iturrino, R. Knott, R. Ludwig, K. Nakamura, S. Petersen, A. L. Reysenbach, P. A. Rona, S. Smith, A. A. Sturz, M. K. Tivey, and X. Zhao, 1995, The internal structure of an active sea-floor massive sulphide deposit: Nature, v. 377, p. 713–716.
Hunt, D., and M. E. Tucker, 1992, Stranded parasequences and forced regressive wedge systems tract; deposition during base level fall: Sedimentary Geology, v. 81, p. 1–9.
Hunt, D. W., W. M. Fitchen, and E. Kosa, 2002, Syndepositional deformation of the Permian Capitan reef carbonate platform, Guadalupe Mountains, New Mexico, USA: Sedimentary Geology, v. 154, p. 89–126.
Hunt, J., T. Baker, and D. Thorkelson, 2005, Regional-scale Proterozoic IOCG-mineralized breccia systems: examples from the Wernecke Mountains, Yukon, Canada: Mineralium Deposita, v. 40, p. 492–514.
Hunt, J. A., T. Baker, and D. J. Thorkelson, 2007, A review of iron oxide copper-gold deposits, with focus on the Wernecke Breccias, Yukon, Canada, as an example of a non-magmatic end member and implications for IOCG genesis and classification: Exploration and Mining Geology, v. 16, p. 209–232.
Hunt, J. M., 1990, Generation and migration of petroleum from abnormally pressured fluid compartments: American Association Petroleum Geologists – Bulletin, v. 74, p. 1–12.
Hunt, J. M., 1996, Petroleum geochemistry and geology: New York, W. H. Freeman & Co., 743 p.
Hunt, J. M., J. K. Whelan, L. B. Eglinton, and L. M. Cathles III, 1998, Relation of shale porosities, gas generation, and compaction to deep overpressures in the US Gulf Coast, in B. E. Law, G. F. Ulmishek, and V. I. Slavin, eds., Abnormal pressures in hydrocarbon environments, v. 70: Tulsa, OK, American Association Petroleum Geologists Memoir, p. 87–104.
Huntington, E., 1907, Lop-Nor. A Chinese Lake. Part 1. The Unexplored Salt Desert of Lop: Bulletin of the American Geographical Society, v. 39, p. 65–77.
Hurford, A. J., H. R. Grunau, and J. Stöcklin, 1984, Fission track dating of an apatite crystal from Hormoz Island, Iran: Journal of Petroleum Geology, v. 7, p. 365–380.
Hurlbert, S. H., and C. C. Y. Chang, 1988, Distribution, structure, composition and thermal environment of ice deposits in Andean salt lakes: Hydrobiologia, v. 158, p. 271–299.
Hurley, N. F., and R. Budros, 1990, Albion-Scipio and Stoney Point fields, U.S.A., Michigan Basin, in E. A. Beaumont, and N. H. Foster, eds., Stratigraphic traps: I: Tulsa, OK, American Association Petroleum Geologists Treatise of Petroleum Geology, Atlas of Oil and Gas Fields, p. 1–37.
Hurtgen, M. T., 2012, The Marine Sulfur Cycle, Revisited: Science, v. 337, p. 305–306.
Husinec, A., and J. F. Read, 2006, Transgressive oversized radial ooid facies in the Late Jurassic Adriatic Platform interior: Low-energy precipitates from highly supersaturated hypersaline waters: Geological Society of America Bulletin, v. 118, p. 550–556.
Hussain, M., 2006, Recognizing attributes and oomoldic porosity development in eolianite in an arid setting: An example from the quaternary eolianite from the Arabian Gulf coastline, Saudi Arabia: Carbonates and Evaporites, v. 21, p. 124–132.
Hussain, M., and J. K. Warren, 1988, Dolomitization in a sulfate-rich environment; modern example from Salt Flat Sabkha (dried playa lake) in West Texas-New Mexico: Carbonates & Evaporites, v. 3, p. 165–173.
Hussain, M., and J. K. Warren, 1989, Nodular and enterolithic gypsum; the "sabkha-tization" of Salt Flat Playa, West Texas: Sedimentary Geology, v. 64, p. 13–24.
Husseini, M. I., 1989, Tectonic and deposition model of late Precambrian-Cambrian Arabian and adjoining plates: Bulletin American Association Petroleum Geologists, v. 73, p. 1117–1131.
Huston, D. L., and G. A. Logan, 2004, Barite, BIFs and bugs: evidence for the evolution of the Earth's early hydrosphere: Earth and Planetary Science Letters, v. 220, p. 41–45.
Hutchinson, R. W., and J. G. Holwerda, 1968, Potash-bearing evaporites, Danakil area, Ethiopia. Discussion: Economic Geology, v. 63, p. 978–979.
Hutchinson, R. W., and G. G. Engels, 1970, Tectonic significance of regional geology and evaporite lithofacies in northeastern Ethiopia: Philosophical Transactions of the Royal Society, v. A 267, p. 313–329.
Hutton, L. J., T. J. Denaro, C. Dhnaram, and G. M. Derrick, 2012, Mineral Systems in the Mount Isa Inlier: Episodes, v. 35, p. 120–130.
Huyck, H. L. O., and R. W. Chorey, 1991, Stratigraphic and petrographic comparison of the Creta and Kupferschiefer copper shale deposits: Mineralium Deposita, v. 26, p. 132–142.
Ibrahim, M. I. A., H. Al-Saad, and S. E. Kholeif, 2002, Chronostratigraphy, palynofacies, source-rock potential, and organic thermal maturity of Jurassic rocks from Qatar: GeoArabia, v. 7, p. 675–696.
Icole, M., J.-P. Masse, G. Perinet, and M. Taieb, 1990, Pleistocene lacustrine stromatolites, composed of calcium carbonate, fluorite, and dolomite, from Lake Natron, Tanzania; depositional and diagenetic processes and their paleoenvironmental significance: Sedimentary Geology, v. 69, p. 139–155.
Icole, M., and G. Perinet, 1984, Les silicates sodiques et les milieux evaporitiques carbonates bicarbonates sodiques: une revue: Revue de Geologie Dynamique et de Geographie Physique, v. 25, p. 167–176.
Iijama, A., 1980, Geology of natural zeolites and zeolitic rocks, in L. V. C. Rees, ed., Proceedings, 5th International conference on zeolites. Pure Applied Chemistry, v. 52, p. 2115–2130.
Illing, L. V., A. J. Wells, and J. C. M. Taylor, 1965, Penecontemporary dolomite in the Persian Gulf, in L. C. Pray, and R. C. Murray, eds., Dolomitization and limestone diagenesis, Society of Economic Paleontologists and Mineralogists Special Publication 13, p. 89–113.
Imhoff, J. F., H. G. Sahl, G. S. H. Soliman, and H. G. Trüper, 1979, The Wadi Natrun: Chemical composition and microbial mass developments in alkaline brines of eutrophic desert lakes: Geomicrobiology Journal, v. 1, p. 219–234.
Imhoff, J. F., 1988, Halophilic phototrophic bacteria, in F. Rodriguez-Valera, ed., Halophilic Bacteria, 1: Boca Raton Fl, CRC Press, p. 85-108.
Inan, K., A. C. Dunham, and J. Esson, 1973, Mineralogy, chemistry and origin of Kirka borate deposit, Eskishehir Province, Turkey: Trans. Inst. Mining Metall., Appl. Earth Sci., v. B-82, p. 114–123.
Ionescu, D., A. Lipski, K. Altendorf, and A. Oren, 2007, Characterization of the endoevaporitic microbial communities in a hypersaline gypsum crust by fatty acid analysis: Hydrobiologia Theme: Saline Waters and their Biota, v. 576, p. 15–26.
Iovine, G., M. Parise, and A. Trocino, 2010, Instability phenomena in the evaporite karst of Calabria, Southern Italy: Zeitschrift für Geomorphologie, v. 54, p. 153–178.

Ireland, T., S. W. Bull, and R. R. Large, 2004, Mass flow sedimentology within the HYC Zn-Pb-Ag deposit, Northern Territory, Australia: evidence for syn-sedimentary ore genesis: Mineralium Deposita, v. 39, p. 143–158.

Ireson, A. T., 1990, Review of the soluble salt process for in situ recovery of hydrocarbons from oil shale with emphasis on leaching [of nahcolite] and possible beneficiation, in J. H. Gary, ed., Twenty-third Oil Shale Symposium Proceedings: Colden, CO, Colorado Sch. Mines Press, p. 152–155.

Irion, G., and G. Mueller, 1968, Huntite, dolomite, magnesite and polyhalite of Recent age from Tuz Golu, Turkey: Nature, v. 220, p. 1309–1310.

Irwin, M. L., 1965, General theory of epeiric clear water sedimentation: American Association of Petroleum Geologists Bulletin, v. 49, p. 445–459.

Isik, V., C. Goncuoglu, and S. Demirel, 2004, Tourmalinite formation in the Yozgat Batholith, Central Anatolian core complex, Turkey; a case study for its structural setting: Abstracts with Programs – Geological Society of America, v. 36, p. 430.

Ivashchenko, M. A., Korabel'nikova, V.V., 1960, The Korshunovskoye deposit [In Russian] . In; Angaro-Ilimskie zhelezo-rudnie mestorozhdenia trappovoi formatsii yuzhnoi chasti sibirskoi platformy. Moscow. Pub. H. "Gosgeolthechizdat".

Jackson, C. A.-L., M. M. Lewis, and A. S. Mannie, 2013, Characterization and Origin of Anhydrite-Rich 'Lateral Caprock' Adjacent to Halite-Cored Salt Diapirs; Implications for Prospectivity in Salt Basins: Search and Discovery Article #41254. Adapted from oral presentation given at American Association Petroleum Geologists 2013 Annual Convention and Exhibition, Pittsburgh, Pennsylvania, May 19–22, 2013.

Jackson, C. A. L., and M. M. Lewis, 2012, Origin of an anhydrite sheath encircling a salt diapir and implications for the seismic imaging of steep-sided salt structures, Egersund Basin, Northern North Sea: Journal of the Geological Society, v. 169, p. 593–599.

Jackson, G. D., and L. M. Cumming, 1981, Evaporites and folding in the Neohelikian Society Cliffs Formation, northeastern Bylot Island, Arctic Canada: Current research, Part C. Paper Geological Survey of Canada.

Jackson, G. D., T. R. Iannelli, G. M. Narbonne, and P. J. Wallace, 1978, Upper Proterozoic sedimentary and volcanic rocks of the Northern Baffin Island, v. 78–17, Geological Survey Canada paper, 17 p.

Jackson, M. J., M. D. Muir, and K. A. Plumb, 1987, Geology of the southern McArthur Basin, Bureau Mineral Resources, Canberra, Australia, Bulletin 220, 173 p.

Jackson, M. P. A., and R. B. Cornelius, 1987, Stepwise centrifuge modelling of the effects of differential sediment loading on the formation of salt structures, in I. Lerche, and J. J. O'Brien, eds., Dynamical geology of salt and related structures: Orlando, Florida, Academic Press, p. 163–259.

Jackson, M. P. A., R. R. Cornelius, C. H. Craig, A. Gansser, J. Stocklin, and C. J. Talbot, 1990, Salt diapirs of the Great Kavir, central Iran: Memoir – Geological Society of America, v. 177, p. 139 pp.

Jackson, M. P. A., C. Cramez, and J. M. Fonck, 2000, Role of subaerial volcanic rocks and mantle plumes in creation of South Atlantic margins: implications for salt tectonics and source rocks: Marine and Petroleum Geology, v. 17, p. 477–498.

Jackson, M. P. A., and M. R. Hudec, 2004, A new mechanism for advance of allochthonous salt sheets, In: Salt-sediment interactions and hydrocarbon prospectivity: concepts, applications and case studies for the 21st Century. Papers presented at the 24th Annual Gulf Coast Section SEPM Foundation Bob F. Perkins Research Conference, Houston Tx, December 5–8, 2004 (CD publication), p. 220–242.

Jackson, M. P. A., M. R. Hudec, and D. C. Jennette, 2004, Insights from a gravity-driven linked system in deep-water Lower Congo Basin, Gabon, in P. J. Post, ed., Salt-sediment interactions and hydrocarbon prospectivity: concepts, applications and case studies for the 21st Century. Papers presented at the 24th Annual Gulf Coast Section SEPM Foundation Bob F. Perkins Research Conference, Houston Tx, December 5–8, 2004 (CD publication), p. 735–752.

Jackson, M. P. A., D. G. Roberts, and S. Snelson, 1995, Salt tectonics: American Association Petroleum Geologists Memoir, v. 65, American Society Petroleum Geologists, 454 p.

Jackson, M. P. A., D. D. Schultz-Ela, M. R. Hudec, I. A. Watson, and M. L. Porter, 1998, Structure and evolution of Upheaval Dome: A pinched-off salt diapir: Geological Society of America Bulletin, v. 110, p. 1547–1573.

Jackson, M. P. A., and C. J. Talbot, 1986, External shapes, strain rates, and dynamics of salt structures: Geological Society of America Bulletin, v. 97, p. 305–323.

Jackson, M. P. A., and C. J. Talbot, 1991, A glossary of salt tectonics: Geological Circular 91–4, Bureau of Economic Geology, University of Texas at Austin, 44 p.

Jackson, M. P. A., and C. J. Talbot, 1994, Advances in salt tectonics, in P. L. Hancock, ed., Continental deformation: Tarrytown, NY, Pergamon Press, p. 159–179.

Jackson, M. P. A., and B. C. Vendeville, 1994, Regional extension as a geologic trigger for diapirism: Geological Society of America Bulletin, v. 106, p. 57–73.

Jackson, M. P. A., B. C. Vendeville, and D. D. Shultz-Ela, 1994a, Structural dynamics of salt systems: Annual Review of Earth and Planetary Sciences, v. 22, p. 93–117.

Jackson, M. P. A., B. C. Vendeville, and D. D. Shultz-Ela, 1994b, Salt-related structures in the Gulf of Mexico: A field guide for geophysicists: The Leading Edge, v. August 1994, p. 837–842.

Jackson, M. P. A., O. N. Warin, G. M. Woad, and M. R. Hudec, 2003, Neoproterozoic allochthonous salt tectonics during the Lufilian orogeny in the Katangan Copperbelt, central Africa: Geological Society of America Bulletin, v. 115, p. 314–330.

Jacobson, G., 1988, Hydrology of Lake Amadeus, a groundwater-discharge playa in central Australia: BMR Journal of Australian Geology & Geophysics, v. 10, p. 301–308.

Jacobson, G., G. E. Calf, J. Jankowski, and P. S. McDonald, 1989, Groundwater chemistry and palaeorecharge in the Amadeus Basin, central Australia: Journal of Hydrology, v. 109, p. 237–266.

Jacobson, G., and J. Jankowski, 1989, Groundwater-discharge processes at a central Australian playa: Journal of Hydrology, v. 105, p. 275–295.

Jacoby, C. H., 1974, Solution mining of evaporites, in F. F. Aplan, ed., Solution Mining Symposium: New York, Am. Inst. Min. Met. Petrol. Eng., p. 165–171.

Jadoon, I. A. K., and W. Frisch, 1997, Hinterland-vergent tectonic wedge below the Riwat thrust, Himalayan foreland, Pakistan: implications for hydrocarbon exploration: American Association Petroleum Geologists – Bulletin, v. 81, p. 438–448.

Jagniecki, E. A., and K. C. Benison, 2010, Criteria for the recognition of acid-precipitated halite: Sedimentology, v. 57, p. 273–292.

Jagniecki, E. A., D. M. Jenkins, T. K. Lowenstein, and A. R. Carroll, 2013, Experimental study of shortite ($Na_2Ca_2(CO_3)_3$) formation and application to the burial history of the Wilkins Peak Member, Green River Basin, Wyoming, USA: Geochimica et Cosmochimica Acta, v. 115, p. 31–45.

Jagnow, D. H., C. A. Hill, D. G. Davis, H. R. DuChene, K. I. Cunningham, D. E. Northup, and J. M. Queen, 2000, History of sulfuric acid theory of speleogenesis in the Guadalupe Mountains, New Mexico. 62(2): 54-59.: Journal of Cave and Karst Studies, v. 62, p. 54–59.

Jahani, S., J.-P. Callot, D. Lamotte, J. Letouzey, and P. Leturmy, 2007, The Salt Diapirs of the Eastern Fars Province (Zagros, Iran): A Brief Outline of their Past and Present (Chapter 15), Thrust Belts and Foreland Basins, p. 289–308.

Jahnert, R., O. de Paula, L. Collins, E. Strobach, and R. Pevzner, 2012, Evolution of a coquina barrier in Shark Bay, Australia by GPR imaging: Architecture of a Holocene reservoir analog: Sedimentary Geology, v. 281, p. 59–74.

Jalili, S., I. Kirchner, D. Livingstone, and S. Morid, 2011, The influence of large-scale atmospheric circulation weather types on variations in the water level of Lake Urmia, Iran: International Journal of Climatology [10.1002/joc.2422].

James, N. P., and A. C. Kendall, 1992, Introduction to carbonate and evaporite facies models, in R. G. Walker, and N. P. James, eds., Facies Models: Responses to sea level change, Geological Association of Canada, p. 265–275.

James, N. P., G. M. Narbonne, R. W. Dalrymple, and T. K. Kyser, 2005, Glendonites in Neoproterozoic low-latitude, interglacial, sedimentary rocks, northwest Canada: Insights into the Cryogenian ocean and Precambrian cold-water carbonates Geology, v. 33, p. 9–12.

James, R. H., and H. Elderfield, 1996, Chemistry of the ore-forming fluids and mineral formation rates in an active hydrothermal sulphide deposit on the Mid-Atlantic ridge: Geology, v. 24, p. 1147–1150.

Jameson, J., D. D. Puls, and M. G. Kozar, 2009, Holocene Sabkha and Coastal Systems of Qatar: Process Models for the Interpretation of Ancient Arabian Plate Carbonate Evaporite Reservoirs (extended abstract): IPTC 2009: International Petroleum Technology Conference; Session: World Energy Challenges: Endurance and Commitment; Paper No. IPTC 13679, p. 1–8.

Jankowski, J., and G. Jacobson, 1989, Hydrochemical evolution of regional groundwaters to playa brines in central Australia: Journal of Hydrology, v. 108, p. 123–173.

Jankowski, J., and G. Jacobson, 1990, Hydrochemical processes in groundwater-discharge playas, central Australia: Hydrological Processes, v. 4, p. 59–70.

Janks, J. S., M. R. Yusas, and C. M. Hall, 1992, Clay mineralogy of an interbedded sandstone, dolomite, and anhydrite; The Permian Yates Formation, Winkler County, Texas, Origin, Diagenesis, and Petrophysics of Clay Minerals in Sandstones, v. 47, SEPM (Society for Sedimentary Geology), p. 145–157.

Jannasch, H. W., D. C. Nelson, and C. O. Wirsen, 1989, Massive natural occurrence of unusually large bacteria (Beggiatoa sp.) at a hydrothermal deep-sea vent site: Nature, v. 342, p. 834–836.

Jassim, S. Z., A. S. Jibril, and N. M. S. Numan, 1997, Gypsum karstification in the Middle Miocene Fatha Formation, Mosul area, Northern Iraq: Geomorphology, v. 18, p. 137–149.

Jassim, S. Z., R. Raiswell, and S. H. Bottrell, 1999, Genesis of the Middle Miocene stratabound sulphur deposits of northern Iraq: Journal of the Geological Society, v. 156, p. 25–39.

Javor, B. J., 2000, Biogeochemical models of solar salterns, in R. M. Geertmann, ed., 8th World Salt Symposium, v. 2: Amsterdam, Elsevier, p. 877–882.

Jaworska, J., 2010, An oxygen and sulfur isotopic study of gypsum from the Wapno Salt Dome cap-rock (Poland: Geological Quarterly (Warszawa), v. 54, p. 25–32.

Jeanbourquin, P., 1988, Nouvelles observations sur les cornieules en Suisse occidentale: Eclogae Geologicae Helvetiae, v. 81, p. 511–538.

Jeanbourquin, P., 1994, Early deformation of Ultrahelvetic mélanges in the Helvetic nappes (Western Swiss Alps): Journal of Structural Geology, v. 16, p. 1367–1383.

Jefferson, G. W., and J. C. L. Ruelle, 1986, The Late Proterozoic Redstone copper belt, Northwest Territories, in J. A. Morin, ed., Mineral deposits of the Northern Cordillera, v. 27, Canadian Institute Mining and Metallurgy Special Volume, p. 154–168.

Jellison, R., and J. M. Melack, 1993, Meromixis in hypersaline Mono Lake, California. 1. Stratification and vertical mixing during the onset, persistence, and breakdown of meromixis: Limnology & Oceanography, v. 38, p. 1008–1019.

Jellison, R., J. Romero, and J. M. Melack, 1998, The onset of meromixis during restoration of Mono Lake, California: Unintended consequences of reducing water diversions: Limnology and Oceanography, v. 43, p. 706–711.

Jemmali, N., F. Souissi, E. J. M. Carranza, and T. W. Vennemann, 2013, Sulfur and lead isotopes of Guern Halfaya and Bou Grine deposits (Domes zone, northern Tunisia): Implications for sources of metals and timing of mineralization: Ore Geology Reviews, v. 54, p. 17–28.

Jemmali, N., F. Souissi, I. M. Villa, and T. W. Vennemann, 2011, Ore genesis of Pb-Zn deposits in the Nappe zone of Northern Tunisia: Constraints from Pb-S-C-O isotopic systems: Ore Geology Reviews, v. 40, p. 41–53.

Jenkunawat, P., 2012, Drilling to study Salt Subsidence in Ban Nonsaaeng, Sakhon Nakhon, Thailand (abs.): Proceedings of the 12th Regional Congress on Geology, Mineral and Energy Resources of Southeast Asia, GEOSEA 2012, p. 47.

Jennings, J. N., 1985, Karst Geomorphology: London, Blackwell, 293 p.

Jenyon, M. K., 1986, Salt tectonics: New York, NY, USA, Elsevier Applied Science Publishers, 191 p.

Jenyon, M. K., and J. C. M. Taylor, 1983, Hydrocarbon indications associated with North Sea Zechstein shelf features: Oil and Gas Journal, v. 81, p. 155–160.

Jesse, G. D., M. Scott, B. Brad, H. Meredith, P. Nicolás, and A. S. David, 2009, Spatial and temporal variability in a stratified hypersaline microbial mat community: FEMS Microbiology Ecology, v. 68, p. 46–58.

Jiang, L., C. F. Cai, R. H. Worden, K. K. Li, and L. Xiang, 2013, Reflux dolomitization of the Upper Permian Changxing Formation and the Lower Triassic Feixianguan Formation, NE Sichuan Basin, China: Geofluids, v. 13, p. 232–245.

Jiang, L., R. H. Worden, and C. F. Cai, 2014, Thermochemical sulfate reduction and fluid evolution of the Lower Triassic Feixianguan Formation sour gas reservoirs, northeast Sichuan Basin, China: Bulletin American Association Petroleum Geologists, v. 98, p. 947–973.

Jiang, S.-Y., M. R. Palmer, J. F. Slack, and D. R. Shaw, 1999, Boron isotope systematics of tourmaline formation in the Sullivan Pb-Zn-Ag deposit, British Columbia, Canada: Chemical Geology, v. 158, p. 131–144.

Jiang, S.-Y., M. R. Palmer, and C. J. Yeats, 2002, Chemical and boron isotopic compositions of tourmaline from the Archean Big Bell and Mount Gibson gold deposits, Murchison Province, Yilgarn Craton, Western Australia: Chemical Geology, v. 188, p. 229–247.

Jiang, S. Y., M. R. Palmer, Q. M. Peng, and J. H. Yang, 1997, Chemical and stable isotopic compositions of Proterozoic metamorphosed evaporites and associated tourmalines from the Houxianyu borate deposit, Eastern Liaoning, China: Chemical Geology, v. 135, p. 189–211.

Jiang, S. Y., M. R. Palmer, C. J. Xue, and Y. H. Li, 1994, Halogen-rich scapolite-biotite rocks from the Tongmugou Pb-Zn Deposit, Qinling, Northwestern China – Implications for the ore-forming processes: Mineralogical Magazine, v. 58, p. 543–552.

Jiang, Z., and M. G. Fowler, 1986, Carentenoid-derived alkanes in oils derived from northwestern China: Organic Geochemistry, v. 10, p. 831–839.

Jin, Q., J. Wang, G. Song, L. Wang, L. Lin, and S. Bai, 2010, Interaction between source rock and evaporite: A case study of natural gas generation in the northern Dongying Depression: Chinese Journal of Geochemistry, v. 29, p. 75-81-81.

Jingwen, M., 1995, Tourmalinite from Northern Guangxi, China: Mineralium Deposita, v. 30, p. 235–245.

Jober, S.-A., K. Dewing, and J. C. White, 2007, Structural geology and Zn-Pb mineral occurrences of northeastern Cornwallis Island: implications for exploration of the Cornwallis Fold Belt, northern Nunavut: Bulletin of Canadian Petroleum Geology, v. 55, p. 138–159.

John, D. A., R. A. Ayuso, M. D. Barton, R. J. Blakely, R. J. Bodnar, J. H. Dilles, F. Gray, F. T. Graybeal, J. C. Mars, D. K. McPhee, R. R. Seal, R. D. Taylor, and P. G. Vikre, 2010, Porphyry copper deposit model, Chap. B of Mineral deposit models for resource assessment: : U.S. Geological Survey Scientific Investigations Report 2010–5070–B, 169 p.

Johns, R. K., 1968, Investigation of Lake Torrens and Gairdner: Geological Survey of South Australia, Report of Investigation, v. 31.

Johnson, C. A., P. Emsbo, F. G. Poole, and R. O. Rye, 2009, Sulfur- and oxygen-isotopes in sediment-hosted stratiform barite deposits: Geochimica et Cosmochimica Acta, v. 73, p. 133–147.

Johnson, J. P., and K. C. Cross, 1991, Geochronological and Sm-Nd isotopic constraints on the genesis of the Olympic Dam Cu-U-Au-Ag deposit, South Australia, in M. Pagel, and J. L. Leroy, eds., Source, transport and deposition of metals: Rotterdam, Netherlands, A. A. Balkema, p. 395–400.

Johnson, K., 2008a, Evaporite-karst problems and studies in the USA: Environmental Geology, v. 53, p. 937–943.

Johnson, K., 2008b, Gypsum-karst problems in constructing dams in the USA: Environmental Geology, v. 53, p. 945–950.

Johnson, K. J., 1996, Gypsum karst in the United States: International Journal of Speleology, v. 25, p. 183–193.

Johnson, K. S., 1987, Development of the Wink Sink in west Texas due to salt dissolution and collapse, Karst Hydrology: Proceedings of the Second Multidisciplinary Conference on Sinkholes and the Environmental Impacts of Karst, Orlando Florida, 9-11 October 1987: Rotterdam, A. A. Balkema, p. 127–136.

Johnson, K. S., 1989, Development of the Wink Sink in West Texas, USA, due to salt dissolution and collapse: Environmental Geology and Water Science, v. 14, p. 81–92.

Johnson, K. S., 2001, Sinkholes associated with petroleum boreholes drilled through salt deposits in the USA: Proc. Solution Mining Research Institute Fall Meeting, Albuquerque, p. 8–17.

Johnson, K. S., 2005, Subsidence hazards due to evaporite dissolution in the United States: Environmental Geology, v. 48, p. 395–409.

Johnston, P. A., K. J. Johnston, C. J. Collom, W. G. Powell, and R. J. Pollock, 2009, Palaeontology and depositional environments of ancient brine seeps in the Middle Cambrian Burgess Shale at The Monarch, British Columbia, Canada: Palaeogeography, Palaeoclimatology, Palaeoecology, v. 277, p. 86–105.

Jones, B., D. Naftz, R. Spencer, and C. Oviatt, 2009, Geochemical Evolution of Great Salt Lake, Utah, USA: Aquatic Geochemistry, v. 15, p. 95–121.

Jones, B., and R. W. Renaut, 1994, Crystal fabrics and microbiota in large pisoliths from Laguna Pastos Grandes, Boliva: Sedimentology, v. 41, p. 1171–1202.

Jones, B. E., W. D. Grant, A. W. Duckworth, and G. G. Owenson, 1998, Microbial diversity of soda lakes: Extremophiles, v. 2, p. 191–200.

Jones, B. F., 1965, The hydrology and mineralogy of Deep Springs Lake, Inyo County, California: U. S. Geological Survey Professional Paper, v. 502, p. A1-A56.

Jones, B. F., 1986, Clay mineral diagenesis in lacustrine sediments, in F. A. Mumpton, ed., Studies in diagenesis, v. 1578, US Geological Survey Bulletin, p. 291–300.

Jones, B. F., H. P. Eugster, and S. L. Rettig, 1977, Hydrogeochemistry of the Lake Magadi Basin, Kenya: Geochimica Cosmochimica Acta, v. 41, p. 53–72.

Jones, B. F., and E. Galán, 1988, Sepiolite and palygorskite, in S. W. Bailey, ed., Hydrous Phyllosilicates (Exclusive of Micas), v. 19: Washington, Mineralogical Society of America, Reviews in Mineralogy, p. 631–674.

Jones, B. F., J. S. Hanor, and W. R. Evans, 1994, Sources of dissolved salts in the central Murray Basin, Australia: Chemical Geology, v. III, p. 135–154.

Jones, B. F., S. L. Rettig, and H. P. Eugster, 1967, Silica in alkaline brines: Science, v. 158, p. 1310–1314.

Jones, C. E., and R. G. Blom, 2014, Bayou Corne, Louisiana, sinkhole: Precursory deformation measured by radar interferometry: Geology, v. 42, p. 111–114.

Jones, C. J. F. P., and A. H. Cooper, 2005, Road construction over voids caused by active gypsum dissolution, with an example from Ripon, North Yorkshire, England: Environmental Geology, v. 48, p. 384–394.

Jones, D. A., A. R. G. Price, and R. N. Hughs, 1978, Ecology of the high saline lagoons Dawhat as Sayh, Arabian Gulf, Saudi Arabia: Estuarine and Coastal Marine Science, v. 6, p. 253–262.

Jones, D. J., 1953, Gypsum-Oolite Dunes, Great Salt Lake Desert, Utah: Bulletin American Association Petroleum Geologists, v. 37, p. 2530–2538.

Jones, G. D., F. F. Whitaker, P. F. Smart, and W. E. Sanford, 2002, Fate of reflux brines in carbonate platforms: Geology, v. 30, p. 371–374.

Jones, G. D., and Y. Xiao, 2005, Dolomitization, anhydrite cementation, and porosity evolution in a reflux system: Insights from reactive transport models: Bulletin American Association Petroleum Geologists, v. 89, p. 577–601.

Jones, R. W., 1984, Comparison of carbonate and shale source rocks, in J. G. Palacas, ed., Petroleum geochemistry and source rock potential of carbonate rocks, v. 18: Tulsa, OK, American Association of Petroleum Geologists, Studies in Geology, p. 163–180.

Jordan, P., T. Noack, and T. Widmer, 1990, The evaporite shear zone of the Jura Boundary Thrust; new evidence from Wisen Well (Switzerland): Eclogae Geologicae Helvetiae, v. 83, p. 525–542.

Jordan, P., and R. Nuesch, 1989, Deformation structures in the Muschelkalk anhydrites of the Schafisheim Well (Jura Over-thrust, northern Switzerland): Eclogae Geologicae Helvetiae, v. 82, p. 429–454.

Jordan, T. E., C. Mpodozis, N. Munoz, N. Blanco, P. Pananont, and M. Gardeweg, 2007, Cenozoic subsurface stratigraphy and structure of the Salar de Atacama Basin, northern Chile: Journal of South American Earth Sciences, v. 23, p. 122–146.

Jordan, T. E., N. Muñoz, M. Hein, T. K. Lowenstein, L. Godfrey, and J. Yu, 2002, Active faulting and folding without topographic expression in an evaporite basin, Chile: Geological Society of America Bulletin, v. 114, p. 1406–1421.

Jørgensen, B. B., M. F. Isaksen, and H. W. Jannasch, 1992, Bacterial sulfate reduction above 100°C in deep-sea hydrothermal vent sediments: Science, v. 258, p. 1756–1757.

Jørgensen, N. O. G., P. Engel, R. Jellison, and J. T. Hollibaugh, 2008, Contribution of B acterial Cell Wall Components to DOM in Alkaline, Hypersaline Mono Lake, California: Geomicrobiology Journal, v. 25, p. 38–55.

Josephson, J., 1982, Supercritical fluids: Environmental Science and Technology, v. 16, p. 548A–551A.

Jowett, E. C., 1987, Formation of sulphide-calcite veinlets in the Kupferschiefer in Poland by natural hydrofracturing during basin subsidence: Journal of Geology, v. 95, p. 513–526.

Jowett, E. C., 1989, Effects of continental rifting on the location and genesis of stratiform copper-silver deposits: Geological Association of Canada Special Paper, v. 36, p. 53–66.

Jowett, E. C., 1992, Role of organics and methane in sulfide ore formation, exemplified by Kupferschiefer Cu-Ag deposits, Poland: Chemical Geology, v. 99, p. 51–63.

Jowett, E. C., L. M. Cathles III, and B. W. Davis, 1993, Predicting depths of gypsum dehydration in evaporitic sedimentary basins:

Bulletin American Association Petroleum Geologists, v. 77, p. 402–413.
Jowett, E. C., A. Rydzewski, and R. J. Jowett, 1987, The Kupferschiefer Cu-Ag ore deposits in Poland: a re-appraisal of the evidence of their origin and presentation of a new genetic model: Can Journ. Earth Sci., v. 24, p. 2016–2037.
Joye, S. B., V. A. Samarkin, B. N. Orcutt, I. R. MacDonald, K.-U. Hinrichs, M. Elvert, A. P. Teske, K. G. Lloyd, M. A. Lever, J. P. Montoya, and C. D. Meile, 2009, Metabolic variability in seafloor brines revealed by carbon and sulphur dynamics: Nature Geoscience, v. 2, p. 349–354.
Kabyshev, B., B. Krivchenkov, S. Stovba, and P. A. Ziegler, 1998, Hydrocarbon habitat of the Dniepr-Donets depression: Marine & Petroleum Geology, p. 177–190.
Kacaroglu, F., M. Degirmenci, and O. Cerit, 1997, Karstification in Miocene gypsum – An example from Sivas, Turkey: Environmental Geology, v. 30, p. 88–97.
Kadioglu, M., Z. Sen, and E. Batur, 1997, The greatest soda-water lake in the world and how it is influenced by climatic change: Ann. Geophysicae, v. 15, p. 1489–1497.
Kagya, M. L. N., 1996, Geochemical characterization of Triassic petroleum source rock in the Mandawa Basin, Tanzania: Journal of African Earth Sciences & the Middle East, v. 23, p. 73–88.
Kah, L. C., T. W. Lyons, and J. T. Chesley, 2001, Geochemistry of a 1.2 Ga carbonate-evaporite succession, northern Baffin and Bylot Islands: implications for Mesoproterozoic marine evolution: Precambrian Research, v. III, p. 203–234.
Kah, L. C., T. W. Lyons, and T. D. Frank, 2004, Low marine sulphate and protracted oxygenation of the Proterozoic biosphere: Nature, v. 431, p. 834–838.
Kalbskopf, S. P., and J. M. Barton, Jr., 2003, The Zandrivier Deposit, Pietersburg green belt, South Africa; an auriferous tour-malinite: South African Journal of Geology, v. 106, p. 361–374.
Kaldi, J., and J. Gidman, 1982, Early diagenetic dolomite cements; examples from the Permian Lower Magnesian Limestone of England and the Pleistocene carbonates of the Bahamas: Journal of Sedimentary Petrology, v. 52, p. 1073–1085.
Kalsbeek, F., 1992, Large-scale albitisation of siltstones on Qeqertakavsak island, northeast Disko Bugt, West Greenland: Chemical Geology, v. 95, p. 213–233.
Kamali, M. R., N. M. Lemon, and S. N. Apak, 1995, Porosity generation and reservoir potential of Ouldburra Formation carbonates, Officer Basin, South Australia: APEA Journal, v. 35, p. 106–120.
Kamona, A. F., and G. H. Friedrich, 2007, Geology, mineralogy and stable isotope geochemistry of the Kabwe carbonate-hosted Pb-Zn deposit, Central Zambia: Ore Geology Reviews, v. 30, p. 217–243.
Kampf, S. K., S. W. Tyler, C. A. Ortiz, J. F. Munoz, and P. L. Adkins, 2005, Evaporation and land surface energy budget at the Salar de Atacama, Northern Chile: Journal of Hydrology, v. 310, p. 236–252.
Kampunzu, A. B., J. L. H. Cailteux, A. F. Kamona, M. M. Intiomale, and F. Melcher, 2009, Sediment-hosted Zn-Pb-Cu deposits in the Central African Copperbelt: Ore Geology Reviews, v. 35, p. 263–297.
Karacan, E., and I. Yilmaz, 1997, Collapse dolines in Miocene gypsum – An example from SW Sivas (Turkey): Environmental Geology, v. 29, p. 263–266.
Karakitsios, V., and F. Pomonipapaioannou, 1998, Sedimentological study of the Triassic solution collapse breccias of the Ionian Zone (NW Greece): Carbonates & Evaporites, v. 13, p. 207–218.
Karakitsios, V., and N. Rigakis, 2007, Evolution and petroleum potential of western Greece: Journal of Petroleum Geology, v. 30, p. 197–218.
Karcz, I., and I. Zak, 1987, Bedforms in salt deposits of the Dead sea brines: Journal of Sedimentary Petrology, v. 57, p. 723–735.
Kargel, J. S., J. Z. Kaye, J. W. Head, G. M. Marion, R. Sassen, J. Crowley, O. Ballesteros, S. A. Grant, and D. L. Hogenboom, 2000, Europa's crust and ocean: Origin, composition, and the prospects for life: Icarus, v. 148, p. 226–265.
Kargel, J. S., R. L. Kirk, B. Fegley, and A. H. Treiman, 1994, Carbonate sulphate on Venus: Icarus, v. 112, p. 219–252.
Kargel, J. S., J. F. Schreiber, and C. P. Sonett, 1996, Mudcracks and dedolomitisation in the Wittenoom Dolomite, Hamersley Group, Western Australia: Global & Planetary Change, v. 14, p. 73–96.
Karlo, J. F., and R. C. Shoup, 2000, Classifications of Syndepositional Systems and Tectonic Provinces of the Northern Gulf of Mexico: Search and Discovery Article #30004 (2000), http://www.search-anddiscovery.net/documents/karlo/index.htm.
Karnin, W. D., E. Idiz, D. Merkel, and E. Ruprecht, 1996, The Zechstein Stassfurt carbonate hydrocarbon system of the Thuringian Basin, Germany: Petroleum Geoscience, v. 2, p. 53–58.
Karpychev, Y., 2007, Variations in the sedimentation in Kara Bogaz Gol Bay related to sea level fluctuations during the Novocaspian time: Oceanology, v. 47, p. 857–864.
Kashfi, M. S., 1983, Variations in tectonic styles in the Zagros geosyncline and their relation to the diapirism of salt in Southern Iran: Journal of Petroleum Geology, v. 6, p. 195–206.
Kashfi, M. S., 1985, The Pre-Zagros integrity of the Iranian Platform: Journal of Petroleum Geology, v. 8, p. 353–360.
Kashima, K., 2002, Environmental and climatic changes during the last 20,000 years at Lake Tuz, central Turkey: Catena, v. 48, p. 3–20.
Kasprzyk, A., 1994, Distribution of strontium in the Badenian (Middle Miocene) gypsum deposits of the Nida area, southern Poland: Geological Quarterly (Poland), v. 38, p. 497–512.
Kasprzyk, A., 2003, Sedimentological and diagenetic patterns of anhydrite deposits in the Badenian evaporite basin of the Carpathian Foredeep, southern Poland: Sedimentary Geology, v. 158, p. 167–194.
Kassaa, S., 1998, Pétrologie des matériaux carbonatés, sulfurés et strontianifères dans leur cadre stratigraphique, holocinétique et structural à Geurn Halfoya et au J. Boukhil (domaine des Diapirss et des Glaciers de sel Tunisie du Nord-Ouest), Tunis University, 373 p.
Kassler, P., 1979, Oil Generation and Migration in Lusitanian Basin, Portugal (abs.): Bulletin American Association Petroleum Geologists, v. 63, p. 477–478.
Kastner, M., 1984, Control of dolomite formation: Nature, v. 311, p. 410–411.
Kates, M., D. J. Kushner, and A. T. Matheson, 1993, The biochemistry of the Archaea: New Comprehensive Biochemistry, v. 26: Amsterdam, Elsevier, 582 p.
Katz, A., and A. Starinsky, 2009, Geochemical History of the Dead Sea: Aquatic Geochemistry, v. 15, p. 159–194.
Katz, B. J., 1990, Lacustrine Basin Exploration – Case studies and modern analogues, v. 50, American Association Petroleum Geologists Memoir, 340 p.
Katz, B. J., 1995, The Green River Oil Shale: An Eocene Carbonate Lacustrine Source Rock, in B. J. Katz, ed., Petroleum Source Rocks: Berlin, Springer-Verlag, p. 309–332.
Katz, B. J., 1995, A survey of rift basin source rocks: Geological Society, London, Special Publication, v. 80, p. 213–240.
Katz, B. J., 2005, Controlling factors on source rock development – A review of Productivity, preservation and sedimentation rate, The Deposition of Organic-Carbon-Rich Sediments: Models, Mechanisms, and Consequences, SEPM Special Publication No. 82, p. 7–16.
Katz, B. J., K. K. Bissada, and J. W. Wood, 1987, Factors limiting potential of evaporites as hydrocarbon source rocks (abs): American Association Petroleum Geologists Bulletin, v. 71, p. 575.

Kaufman, A. J., and S. Xiao, 2003, High CO_2 levels in the Proterozoic atmosphere estimated from analyses of individual microfossils: Nature, v. 425, p. 279–282.

Kaufmann, D. W., 1960, Sodium Chloride: New York, Reinhold.

Kautz, K., and H. Porada, 1976, Sepiolite formation in a pan of the Kalahari: Nues Jahrb. Mineral Monatsh., v. 12, p. 545–559.

Kawasaki, K., D. T. A. Symons, and T. Dawborn, 2010, Paleomagnetism of the world-class Century Zn-Pb_Ag deposits, Australia: Journal of Geochemical Exploration, v. 106, p. 137–145.

Kazakov, A. V., and E. I. Sokolova, 1950, Conditions of formation of fluorite in sedimentary rocks: Akad. Nauk SSSR Geologicheskiy Institut Trudy, v. 114, p. 22–64.

Kbir-Ariguib, N., D. B. H. Chehimi, and L. Zayani, 2001, Treatment of Tunisian salt lakes using solubility phase diagrams: Pure Appl. Chem., v. 73, p. 761–770.

Keays, R. R., 1995, The role of komatiitic and picritic magmatism and S-saturation in the formation of ore deposits: Lithos, v. 34, p. 1–18.

Kebede, S., 2012, Groundwater in Ethiopia: Features, numbers and opportunities, Springer.

Keeling, J., and A. Mauger, 1998, New airborne HyMap data aids assessment of magnesite resources: MESA Journal, v. 11, p. 7–11.

Keely, B. J., S. R. Blake, P. Schaeffer, and J. R. Maxwell, 1995, Distribution of pigments in the organic matter of marls from the Vena del Gesso evaporitic sequence: Organic Geochemistry, v. 23, p. 527–593.

Keely, B. J., J. W. De Leeuw, J. R. Maxwell, J. S. S. Damste, S. E. Betts, and Ling Yue, 1993, A molecular stratigraphic approach to palaeoenvironmental assessment and the recognition of changes in source inputs in marls of the Mulhouse Basin (Alsace, France): Organic Geochemistry, v. 20, p. 1165–1186.

Keene, J. B., 1983, Chalcedonic quartz and occurrence of quartzine (length-slow chalcedony) in pelagic sediments: Sedimentology, v. 30, p. 449–454.

Keheila, E., H. Khalifa, and A. El-Haddad, 1989, Holocene carbonate facies model, Ras Shukhier hypersaline pool and its surrounding sabkha, west Gulf of Suez, Egypt: Sedimentary Geology, v. 63, p. 155–169.

Keith, J., D., T. J. Thompson, and S. Ivers, 1996, The Uinta emerald and the emerald-bearing potential of the Red Pine Shale, Uinta Mountains, Utah: Abstracts with Programs – Geological Society of America, v. 28, p. 85.

Keller, E. A., and R. H. Blodgett, 2006, Natural Hazards: Earth's Processes as Hazards, Disasters, and Catastrophes (2nd edition): New Jersey, Pearson Prentice Hall.

Keller, J., and A. N. Zaitsev, 2012, Geochemistry and petrogenetic significance of natrocarbonatites at Oldoinyo Lengai, Tanzania: Composition of lavas from 1988 to 2007: Lithos, v. 148, p. 45–53.

Kelley, J. R., L. D. Wakeley, S. W. Broadfoot, M. L. Pearson, C. J. McGrath, T. E. McGill, J. D. Jorgeson, and C. A. Talbot, 2007, Geologic Setting of Mosul Dam and Its Engineering Implications: US Army Corps of Engineers; Engineer Research and Development Center Report ERDC TR-07-10.

Kelts, K., and M. Shahrabi, 1986, Holocene sedimentology of hypersaline Lake Urmia, northwestern Iran: Palaeogeography, Palaeoclimatology, Palaeoecology, v. 54, p. 105–130.

Kempe, S., 1972, Cave genesis in gypsum with particular reference to underwater conditions: Cave Science, v. 49, p. 1–6.

Kempe, S., and E. T. Degens, 1978, Lake Van varve record – the past 10,420 years, in E. T. Degens, and F. Kurtman, eds., Geology of Lake Van: Ankara, Turkey, MTA Press, p. 56–63.

Kempe, S., and E. T. Degens, 1985, An early soda ocean?: Chemical Geology, v. 53, p. 95–108.

Kempe, S., and J. Kazmierczak, 1994, The role of alkalinity in the evolution of ocean chemistry, organization of living systems, and biocalcification processes: Bulletin de la Institut Oceanographique (Monaco), v. 13, p. 61–117.

Kempe, S., J. Kazmierczak, G. Landmann, T. Konuk, A. Riemer, and A. Lipp, 1991, Largest known microbialites discovered in Lake Van, Turkey: Nature, v. 349, p. 605–608.

Kendall, A. C., 1983, Unconformity-associated replacement limestones after anhydrite in Mississippian of Williston Basin: American Association Petroleum Geologists Bulletin, v. 67, p. 494–495.

Kendall, A. C., 1988, Aspects of evaporite basin stratigraphy, in B. C. Schreiber, ed., Evaporites and hydrocarbons: New York, Columbia University Press, p. 11–65.

Kendall, A. C., 1989, Brine mixing in the Middle Devonian of Western Canada and its possible significance to regional dolomitization: Sedimentary Geology, v. 64, p. 271–285.

Kendall, A. C., 1992, Evaporites, in R. G. Walker, and N. P. James, eds., Facies Models: Responses to sea level change, Geological Association of Canada, p. 375–409.

Kendall, A. C., 2000, Compaction in halite-cemented carbonates – the Dawson Bay Formation (Middle Devonian) of Saskatchewan, Canada: Sedimentology, v. 47, p. 151–171.

Kendall, A. C., 2001, Late diagenetic calcitization of anhydrite from the Mississippian of Saskatchewan, western Canada: Sedimentology, v. 48, p. 29–55.

Kendall, A. C., and G. M. Harwood, 1989, Shallow water gypsum in the Castile Formation – significance and implications, in P. M. Harris, and G. A. Grover, eds., Subsurface and outcrop examination of the Capitan Shelf margin, northern Delaware Basin, v. 13, SEPM Core Workshop, p. 451–457.

Kendall, A. C., and K. L. Walters, 1978, The age of metasomatic anhydrite in Mississippian reservoir carbonates, southeastern Sasketchewan: Canadian Journal of Earth Sciences, v. 15, p. 424–430.

Kendall, C. G. S. C., and P. Skipwith, 1968a, Recent algal mats of a Persian Gulf lagoon: Journal of Sedimentary Petrology, v. 38, p. 1040–1058.

Kendall, C. G. S. C., and P. Skipwith, 1968b, Geomorphology of a recent shallow water carbonate province, Khor al Bazam, Trucial Coast, southwestern Arabian Gulf: Geological Society of America Bulletin, v. 80, p. 865–892.

Kendall, C. G. S. C., and S. P. A. D. E. Skipwith, 1969, Holocene shallow-water carbonate and evaporite sediments of Khor al Bazam, Abu Dhabi, southwest Persian Gulf: American Association Petroleum Geologists – Bulletin, v. 53, p. 841–869.

Kendall, C. G. S. C., and J. K. Warren, 1987, A review of the origin and setting of tepees and their associated fabrics: Sedimentology, v. 34, p. 1007–1027.

Kendall, C. G. S. C., and J. K. Warren, 1988, Peritidal evaporites and their sedimentary assemblages, in B. C. Schreiber, ed., Evaporites and hydrocarbons: New York, Columbia University Press, p. 66–138.

Kendall, H. W., and D. Pimental, 1994, Constraints on the Expansion of the Global Food Supply: Ambio, v. 23, p. 198–205.

Kendrick, M., and P. Burnard, 2013, Noble Gases and Halogens in Fluid Inclusions: A Journey Through the Earth's Crust, in P. Burnard, ed., The Noble Gases as Geochemical Tracers: Advances in Isotope Geochemistry, Springer Berlin Heidelberg, p. 319–369.

Kendrick, M. A., T. Baker, B. Fu, D. Phillips, and P. J. Williams, 2008, Noble gas and halogen constraints on regionally extensive mid-crustal Na-Ca metasomatism, the Proterozoic Eastern Mount Isa Block, Australia: Precambrian Research, v. 163, p. 131–150.

Kendrick, M. A., M. Honda, N. H. S. Oliver, and D. Phillips, 2011, The noble gas systematics of late-orogenic H_2O-CO_2 fluids, Mt Isa, Australia: Geochimica et Cosmochimica Acta, v. 75, p. 1428–1450.

Kenig, F., 2011, Distribution of organic matter in the transgressive and regressive Holocene sabkha sediments of Abu Dhabi, United Arab Emirates, in C. G. S. C. Kendall, and A. Abdulrahman, eds., Quaternary carbonate and evaporite sedimentary facies and their ancient analogues: A Tribute to Douglas James Shearman, Internation association of Sedimentologists, Special Publication 43, p. 277–298.

Kenig, F., A. Y. Huc, B. H. Purser, and J. L. Oudin, 1990, Sedimentation, distribution and diagenesis of organic matter in a recent carbonate environment, Abu Dhabi: Organic Geochemistry, v. 16, p. 735–747.

Kennedy, M., 1993, The Undoolya sequence – Late Proterozoic salt-influenced deposition, Amadeus Basin, central Australia: Australian Journal of Earth Sciences, v. 40, p. 217–228.

Kennet, J. P., 1982, The Terminal Miocene Event, Global Cooling and the Mediterranean Salinity Crisis, in J. P. Kennet, ed., Marine Geology: Englewood Cliffs, New Jersey, Prentice Hall, p. 738–742.

Kennicutt II, M. C., J. M. Brooks, R. R. Bidigare, R. R. Fay, T. L. Wade, and T. J. McDonald, 1985, Vent-type taxa in a hydrocarbon seep region on the Louisiana slope: Nature, v. 317, p. 351–353.

Kent, P. E., 1958, Recent studies of South Persian salt plugs: Bulletin American Association Petroleum Geologists, v. 42, p. 2951–2972.

Kent, P. E., 1970, The salt plugs of the Persian Gulf region: Trans. Leicester Lit. and Phil. Soc, v. 64, p. 56–88.

Kent, P. E., 1979, The emergent Hormuz salt plugs of southern Iran: Journal of Petroleum Geology, v. 2, p. 117–144.

Kent, P. E., 1987, Island salt plugs in the Middle East and their tectonic implications, in I. Lerche, and J. J. O'Brien, eds., Dynamical geology of salt and related structures, Academic Press, New York, p. 3–37.

Keppel, M. N., J. D. A. Clarke, T. Halihan, A. J. Love, and A. D. Werner, 2011, Mound springs in the arid Lake Eyre South region of South Australia: A new depositional tufa model and its controls: Sedimentary Geology, v. 240, p. 55–70.

Keppie, J. D., J. Dostal, K. L. Cameron, L. A. Solari, F. Ortega-GutiÈrrez, and R. Lopez, 2003, Geochronology and geochemistry of Grenvillian igneous suites in the northern Oaxacan Complex, southern Mexico: tectonic implications: Precambrian Research, v. 120, p. 365–389.

Kerans, C., and W. M. Fitchen, 1996, Sequence hierarchy and facies architecture of a carbonate-ramp system: San Andres Formation of Algerita escarpment and western Guadalupe Mountains, west Texas and New Mexico: Report of Investigation – Bureau of Economic Geology, Univ of Texas at Austin, v. 235, 86 p.

Kerans, C., W. M. Fitchen, W. C. Gardner, and B. R. Wardlow, 1993, New Mexico Geological Society Guidebook: 44th Field Conference, Carlsbad Region, New Mexico and West Texas, p. 175–184.

Kerans, C., and P. M. Harris, 2008, Devonian Reefal Platforms of the Canning Basin – Lessons Learned and Value as Analogs: American Association Petroleum Geologists Search and Discovery Article #40302 (2008) – Adapted from oral presentation at American Association Petroleum Geologists Annual Convention, Long Beach, CA, April 1–4, 2007.

Kerans, C., F. J. Lucia, and R. K. Senger, 1994, Integrated characterization of carbonate ramp reservoirs using Permian San Andres Formation outcrop analogs: American Association Petroleum Geologists – Bulletin, v. 78, p. 181–216.

Kernen, R. A., K. A. Giles, M. G. Rowan, T. F. Lawton, and T. E. Hearon, 2012, Depositional and halokinetic-sequence stratigraphy of the Neoproterozoic Wonoka Formation adjacent to Patawarta allochthonous salt sheet, Central Flinders Ranges, South Australia: Geological Society, London, Special Publications, v. 363, p. 81–105.

Kerr, J. W., 1968, Stratigraphy of central and eastern Ellesmere Island, Arctic Canada--Pt. 2, Ordovician: Canada Geol. Survey Paper.

Kerr, J. W., 1977, Cornwallis lead-zinc district; Mississippi Valley-type deposits controlled by stratigraphy and tectonics: Canadian Journal of Earth Sciences, v. 14, p. 1402–1426.

Kerr, S. D. J., and A. Thomson, 1963, Origin of nodular and bedded anhydrite in Permian shelf sediments, Texas and New Mexico: Bulletin American Association Petroleum Geologists, v. 47, p. 1726–1732.

Kesler, S. E., P. W. Gruber, P. A. Medina, G. A. Keoleian, M. P. Everson, and T. J. Wallington, 2012, Global lithium resources: Relative importance of pegmatite, brine and other deposits: Ore Geology Reviews, v. 48, p. 55–69.

Kesler, S. E., and L. M. Jones, 1981, Sulfur- and strontium-isotopic geochemistry of celestite, barite and gypsum from the Mesozoic basins of northeastern Mexico: Chemical Geology, v. 31, p. 211–224.

Kesler, S. E., J. Ruiz, and L. M. Jones, 1988, Strontium isotope geochemistry of the Galeana Barite District, Nuevo Leon, Mexico: Economic Geology, v. 83, p. 1907–1917.

Kevbrin, V. V., A. M. Lysenko, and T. N. Zhilina, 1997, Physiology of the alkaliphilic methanogen Z-7936, a new strain of Methanosalsus zhilinaeae isolated from Lake Magadi: Microbiology, v. 66, p. 261–266.

Kezao, C., and J. M. Bowler, 1985, Preliminary study on sedimentary characteristics and evolution of paleoclimate of Qarhan Salt Lake, Qaidam Basin: Scientia Sinica (series B), v. 28, p. 1218–1232.

Khalaf, F. I., and J. M. Al-Awadhi, 2012, Sedimentological and morphological characteristics of gypseous coastal nabkhas on Bubiyan Island, Kuwait, Arabian Gulf: Journal of Arid Environments, v. 82, p. 31–43.

Khalili, M., R. Beavers, and H. Torabi, 2007, Depositional environment of the evaporitic unit (D-member) of the Qom Formation (Central Iran): Carbonates and Evaporites, v. 22, p. 101–112.

Kharaka, Y. K., W. W. Carothers, L. M. Law, P. J. Lamonthe, and T. L. Fries, 1987, Geochemistry of metal-rich brines from the central Mississippi Salt Dome Basin, USA: Applied Geochemistry, v. 2, p. 543–562.

Kharaka, Y. K., and J. S. Hanor, 2003, Deep Fluids in the Continents: I. Sedimentary Basins, Treatise on Geochemistry: Oxford, Pergamon, p. 499–540.

Kharaka, Y. K., R. W. Hull, and W. W. Carothers, 1985, Water-rock interactions in sedimentary basins, in G. C. Gautier, Y. K. Kharaka, and R. Surdam, eds., Relationship of organic matter and mineral diagenesis: Tulsa OK, SEPM Short Course Notes, 17, p. 79–272.

Kharaka, Y. K., P. D. Lundegard, and T. H. Giordano, 2000, Distribution and origin of organic ligands in subsurface waters from sedimentary basins: Rev. Econ. Geol., v. 9, p. 119–131.

Kharaka, Y. K., and J. J. Thordsen, 1992, Stable isotope geochemistry and origin of water in sedimentary basins, in N. Clauer, and S. Chaudhuri, eds., Isotope Signatures and Sedimentary Records: Berlin, Springer, p. 411–466.

Kholief, M. M., and M. A. Barakat, 1986, New evidence for a petroleum source rock in a Miocene evaporite sequence, Gulf of Suez, Egypt: Journal of Petroleum Geology, v. 9, p. 217–226.

Khonde, N., D. M. Maurya, A. D. Singh, V. Chowksey, and L. S. Chamyal, 2011, Environmental significance of raised rann sediments along the margins of Khadir, Bhanjada and Kuar Bet islands in Great Rann of Kachchh, Western India: Current Science, v. 101, p. 1429–1434.

Khoriby, E. M., 2005, Origin of the gypsum-rich silica nodules, Moghra Formation, Northwest Qattara depression, Western Desert, Egypt: Sedimentary Geology, v. 177, p. 41–55.

Khutorskoi, M., E. Teveleva, L. Tsybulya, and G. Urban, 2010, Heat flow in salt-dome basins of Eurasia: A comparative study: Geotectonics, v. 44, p. 289–304.

Kiessling, W., E. Flugel, and J. Golonka, 1999, Paleoreef maps: Evaluation of a comprehensive database on Phanerozoic reefs:

American Association Petroleum Geologists Bulletin-American Association of Petroleum Geologists, v. 83, p. 1552–1587.
Kiessling, W., E. Flügel, and J. Golonka, 2003, Patterns of Phanerozoic carbonate platform sedimentation: Lethaia, v. 36, p. 195–226.
King, R. H., 1946, Carnallite-filled mud cracks in Salt Clay: Journal of Sedimentary Petrology, v. 16, p. 14.
Kinsman, David, J, and J, 1967, Huntite from a carbonate-evaporite environment: Amer. Mineral., v. 52, p. 9–10.
Kinsman, D. J. J., 1965, Gypsum and anhydrite of recent age, Trucial Coast, Persian Gulf: 2nd Symposium on Salt, Northern Ohio Geological Society, v. 1, p. 302–326.
Kinsman, D. J. J., 1969, Modes of formation, sedimentary associations, and diagnostic features of shallow-water and supratidal evaporites: American Association Petroleum Geologists Bulletin, v. 53, p. 830–840.
Kinsman, D. J. J., 1973, Evaporite Basins and the Availability of Oxygen in Natural Brines: Int. Symp. Salt, Tech. Program Abstr.
Kinsman, D. J. J., 1976, Evaporites; relative humidity control of primary mineral facies: Journal of Sedimentary Petrology, v. 46, p. 273–279.
Kipfer, R., W. Aeschbachhertig, H. Baur, M. Hofer, D. M. Imboden, and P. Signer, 1994, Injection of mantle type helium in Lake Van (Turkey) – the clue for quantifying deep water renewal: Earth & Planetary Science Letters, v. 125, p. 357–370.
Kirkham, A., 1997, Shoreline Evolution, Aeolian Deflation and Anhydrite Distribution of the Holocene, Abu Dhabi: GeoArabia, v. 2, p. 403–416.
Kirkham, A., 1998, Pleistocene Carbonate Seif Dunes and their Role in the Development of Complex Past and Present Coastlines of the U.A.E: GeoArabia, v. 3, p. 19–32.
Kirkham, A., 2011, Halite, sulphates, sabkhat and salinas of the coastal regions and Sabkha Matti of Abu Dhabi, United Arab Emirates, In Doug Shearman Memorial Volume – Quaternary carbonate and evaporite sedimentary facies and their ancient analogues, John Wiley & Sons Ltd., p. 265–276.
Kirkham, R. V., 1989, Distribution, settings, and genesis of sediment-hosted stratiform copper deposits: Geological Association of Canada Special Paper, v. 36, p. 3–38.
Kirkham, R. V., 2001, Sediment hosted stratiform copper (SSC). and other stratbound base metal deposits and the importance of basinal brines and/or evaporites, halotectonics and halokinesis, in P. A., ed., MIneral deposits at the beginning of the 21st Century (Proceedings of the Joint 6th Biennial SGA-SEG Meeting, Krakow, August 2001), Taylor and Francis, p. 15–18.
Kirkland, D. W., R. E. Denison, and W. E. Dean, 2000, Parent brine of the Castile evaporites (Upper Permian), Texas and New Mexico: Journal of Sedimentary Research Section A-Sedimentary Petrology & Processes, v. 70, p. 749–761.
Kirkland, D. W., and R. Evans, 1976, Origin of limestone buttes, Gypsum Plain, Culberson County, Texas: American Association of Petroleum Geologists, Bulletin, v. 60, p. 2005–2018.
Kirkland, D. W., and R. Evans, 1980, Origin of castiles on the Gypsum Plain of Texas and New Mexico: Guidebook New Mexico Geological Society, v. 31, p. 173–178.
Kirkland, D. W., and R. Evans, 1981, Source-rock potential of evaporitic environment: American Association Petroleum Geologists – Bulletin, v. 65, p. 181–190.
Kistler, R. B., and W. C. Smith, 1983, Boron and borates, in S. J. Lefond, ed., Industrial Minerals and Rocks: New York, AIME, p. 533–560.
Klemme, H. D., 1983, The geologic setting of giant gas fields: Laxemburg, Internation Institute for Applied Systems Analysis, p. 133–160.
Klemme, H. D., and G. F. Ulmishek, 1991, Effective petroleum source rocks of the world: Stratigraphic distribution and controlling depositional factors: American Association Petroleum Geologists – Bulletin, v. 75, p. 1809–1851.
Klepac-Ceraj, V., C. A. Hayes, W. P. Gilhooly, T. W. Lyons, R. Kolter, and A. Pearson, 2012, Microbial diversity under extreme euxinia: Mahoney Lake, Canada: Geobiology, v. 10, p. 223–235.
Klimchouk, A., 2007, Hypogene Speleogenesis: Hydrological and morphogenetic perspective: Carlsbad, New Mexico, National Cave and Karst Research Institute.
Klimchouk, A., 2012a, Speleogenesis, Hypogenic, in W. B. White, and D. C. Culver, eds., Encyclopedia of Caves (Second Edition): Amsterdam, Academic Press, p. 748–765.
Klimchouk, A., 2012b, Ukraine Giant Gypsum Caves, in W. B. White, and D. C. Culver, eds., Encyclopedia of Caves (Second Edition): Amsterdam, Academic Press, p. 827–833.
Klimchouk, A. B., 1992, Large gypsum caves in the western Ukraine and their genesis: Cave Science, v. 19, p. 3–11.
Klimchouk, A. B., 1996, Gypsum karst of the world: Journal of Speleology, v. 25.
Klimchouk, A. B., 2000, Speleogenesis of great gypsum mazes in the Western Ukraine, in A. B. Klimchouk, D. Ford, A. N. Palmer, and W. Dreybrodt, eds., Speleogenesis: Evolution of karst aquifers: Huntsville, Natl. Speleol. Soc., p. 261–273.
Klimchouk, A. B., 2003, Unconfined versus confined speleo-genetic settings: variations of solution porosity: Speleogenesis and Evolution of Karst Aquifers 1 (2), www.speleogenesis.info, 7 pages. (online journal).
Klimchouk, A. B., and S. D. Aksem, 2000, Gypsum karst in the western Ukraine, in G. Günay, K. S. Johnson, D. Ford , and A. I. Johnson, eds., Present State and Future Trends of Karst Studies, IHP-V, Technical Documents in Hydrology, 49(11), UNESCO, Paris, p. 67–80.
Klimchouk, A. B., and V. N. Andrejchuk, 2003, Karst breakdown mechanisms from observations in the gypsum caves of the Western Ukraine: Implications for Subsidence Hazard Assessment, Speleogenesis and Evolution of Karst Aquifers, The Virtual Scientific Journal: www.speleogenesis.info.
Klimchouk, A. B., G. V. Samokhin, and Y. M. Kasjan, 2008, The deepest cave in the word Krubera and its hydrogeological and paleogeographic significance (in Russian): Speleology and Karstology (Ukraine), v. 1, P- 100–104.
Klominsky, J., G. A. Partington, N. J. McNaughton, S. E. Ho, and D. I. Groves, 1996, Radiothermal granites of the Cullen Batholith and associated mineralisation (Australia): Czech Geological Survey, Prague, Czech Republic.
Knapp, R. W., D. W. Steeples, R. D. Miller, and C. D. McElwee, 1989, Seismic-reflection surveys at sinkholes in central Kansas, in D. W. Steeples, ed., Geophysics in Kansas, v. 226, Kansas Geological Survey, Bulletin, p. 95–116.
Knauth, L. P., 1998, Salinity history of the Earth's early ocean: Nature, v. 395, p. 554–555.
Knauth, L. P., and D. R. Lowe, 2003, High Archean climatic temperature inferred from oxygen isotope geochemistry of cherts in the 3.5 Ga Swaziland Supergroup, South Africa: Geological Society of America Bulletin, v. 115, p. 566–580.
Knight, J., J. Lowe, S. Joy, J. Cameron, J. Merrillees, S. Nag, N. Shah, G. Dua, and K. Jhala, 2002, The Khetri Copper Belt, Rajasthan: Iron Oxide Copper-Gold Terrane in the Proterozoic of NW India, in T. M. Porter, ed., Hydrothermal Iron Oxide Copper-Gold and Related Deposits: A Global Perspective, v. 2, PGC Publishing, Adelaide, p. 321–341.
Knipping, B., 1989, Basalt intrusions in evaporites: Lecture Notes in Earth Sciences (Springer-Verlag), v. 24, p. 132 pp.
Knipping, B., and A. G. Hermann, 1985, Mineralreaktionen und Stoff transporte an einem Kontakt Basalt-Carnallitit im Kalisalzhorizont Thüringen der Werra-Serie des Zechsteins: Kali und Steinsalz, v. 9, p. 111–124.

Knutson, J., J. Ferguson, W. M. B. Roberts, T. H. Donnelly, and I. B. Lambert, 1979, Petrogenesis of the copper-bearing breccia pipes, Redbank, Northern Territory, Australia: Economic Geology, v. 74, p. 814–826.

Ko, S. C., D. L. Olgaard, and B. Ueli, 1995, The transition from weakening to strengthening in dehydrating gypsum: Evolution of excess pore pressures: Geophys. Res. Lett., v. 22, p. 1009–1012.

Ko, S. C., D. L. Olgaard, and T. F. Wong, 1997, Generation and maintenance of pore pressure excess in a dehydrating system. 1. Experimental and microstructural observations: Journal of Geophysical Research-Solid Earth, v. 102, p. 825–839.

Kobluk, D. R., and D. R. Crawford, 1990, A modern hypersaline organic mud- and gypsum-dominated basin and associated microbialites: Palaios, v. 5, p. 134–148.

Koch, A., V. Mathur, R. Nagy, and F. Synder, 1998, Methodology for minibasin ranking in the deepwater Gulf of Mexico: Integration of Geologic Models for understanding risk in the Gulf of Mexico, American Association Petroleum Geologists Hedberg Research Conference, Galveston Texas.

Kocurek, G., M. Carr, R. Ewing, K. G. Havholm, Y. C. Nagar, and A. K. Singhvi, 2007, White Sands Dune Field, New Mexico: Age, dune dynamics and recent accumulations: Sedimentary Geology, v. 197, p. 313–331.

Kocurko, M. J., 1979, Dolomitization by spray-zone brine seepage, San Andres, Colombia: Journal of Sedimentary Petrology, v. 49, p. 209–214.

Koehler, G., T. K. Kyser, R. Enkin, and E. Irving, 1997, Paleomagnetic and isotopic evidence for the diagenesis and alteration of evaporites in the Paleozoic Elk Point Basin, Saskatchewan, Canada: Canadian Journal of Earth Sciences, v. 34, p. 1619–1629.

Koehler, G. D., T. K. Kyser, and T. Danyluk, 1990, Stable Isotope evidence for the petrogenesis of carnallite In the Middle Devonian Prairie Evaporite Formation, Saskatchewan: Summary of Investigations 1990, Saskatchewan Geological Survey; Saskatchewan Energy and Mines, Miscellaneous Report 90-04.

Kogel, J. E., N. C. Trivedi, J. M. Barker, and S. T. Krukowski, 2006, Industrial Minerals and Rocks, SME (Soc. Mining Metallurgy and Exploration), 1548 p.

Kokkalas, S., E. Kamberis, P. Xypolias, S. Sotiropoulos, and I. Koukouvelas, 2013, Coexistence of thin- and thick-skinned tectonics in Zakynthos area (western Greece): Insights from seismic sections and regional seismicity: Tectonophysics, v. 597–598, p. 73–84.

Kominz, M. A., J. V. Browning, K. G. Miller, P. J. Sugarman, S. Misintseva, and C. R. Scotese, 2008, Late Cretaceous to Miocene sea-level estimates from the New Jersey and Delaware coastal plain coreholes: An error analysis: Basin Research, v. 20, p. 211–226.

Konishi, Y., J. Prince, and B. Knott, 2001, The fauna of thrombolitic microbialites, Lake Clifton, Western Australia: Hydrobiologia, v. 457, p. 39–47.

Konrad, G., K. Sebe, A. Halasz, and E. Babinszki, 2010, Sedimentology of a Permian playa lake: the Boda Claystone Formation, Hungary: Geologos, v. 16, p. 27–41.

Kontak, D. J., 1998, A study of fluid inclusions in sulphide and nonsulphide mineral phases from a carbonate-hosted Zn-Pb deposit, Gays River, Nova Scotia, Canada: Economic Geology, v. 93, p. 793–816.

Kontak, D. J., E. Farrar, and S. L. McBride, 1994, Ar40-Ar39 dating of fluid migration in a Mississippi-Valley type deposit – The Gays River Zn-Pb deposit, Nova Scotia, Canada: Economic Geology, v. 89, p. 1501–1517.

Kontak, D. J., and S. Jackson, 1995, Laser-ablation ICP-MS microanalysis of calcite cement from a Mississippi-Valley type Zn-Pb deposit, Nova Scotia – Dramatic variability in REE content on macro- and micro-scales: Canadian Mineralogist, v. 33, p. 445–467.

Kontorovich, A. E., A. L. Pavlov, G. A. Tretyakov, and A. V. Khomenko, 1996, Physicochemical modelling of thermodynamic equilibria in a carbonate-evaporite sedimentary rocks water-hydrocarbons system during contact metamorphism and catagenesis (Russian): Geokhimiya, v. 7, p. 598–610.

Köppen, W., 1900, Versuch einer Klassification der Klimate, vorzsugsweise nach ihren Beziehungen zur Pflanzenwelt: Geographraphische Zeitschrift, v. 6, p. 593–611.

Kopylova, M. G., S. I. Kostrovitsky, and K. N. Egorov, 2013, Salts in southern Yakutian kimberlites and the problem of primary alkali kimberlite melts: Earth-Science Reviews, v. 119, p. 1–16.

Korotkov, A. N., 1974, Caves of the Pinego-Severodvinskaja karst (in Russain): Geog. Soc. USSR, Leningrad.

Kosarev, A., A. Kostianoy, and I. Zonn, 2009, Kara-Bogaz-Gol Bay: Physical and Chemical Evolution: Aquatic Geochemistry, v. 15, p. 223–236.

Kostick, D. S., 2011, Soda Ash: U.S. Geological Survey, 2010 Minerals Yearbook, (Advanced release – Sept 2011)

Kostick, D. S., 2012, Sodium Sulfate: U.S. Geological Survey, Mineral Commodity Summaries, January 2012.

Kosun, E., 2012, Facies characteristics and depositional environments of Quaternary tufa deposits, Antalya, SW Turkey: Carbonates and Evaporites, v. 27, p. 269–289.

Kottek, M., J. Grieser, C. Beck, B. Rudolf, and F. Rubel, 2006, World Map of the Köppen-Geiger climate classification updated: Meteorologische Zeitschrift, v. 15, p. 259–263.

Kotut, K., and L. Krienitz, 2011, Does the potentially toxic cyanobacterium *Microcystis* exist in the soda lakes of East Africa?: Hydrobiologia, v. 664, p. 219–225.

Kotwicki, V., 1986, Floods of Lake Eyre: Adelaide, Engineering and Water Supply Department, 99 p.

Kotwicki, V., and R. Allan, 1998, La Nina de Australia – contemporary and palaeo-hydrology of Lake Eyre: Paleogeography Paleoclimatology Paleoecology, v. 144, p. 265–280.

Kovalevich, V. M., 1975, Thermometric studies of inclusions in artificial crystals of halite: Fluid Inclusion Research, v. 8, p. 96.

Kovalevich, V. M., 1976, Halite of the salt deposits of Miocene age from the Forecarpathians: Fluid Inclusion Research, v. 9, p. 72.

Kovalevich, V. M., T. M. Peryt, and O. I. Petrichenko, 1998, Secular variation in seawater chemistry during the Phanerozoic as indicated by brine inclusions in halite.: Journal of Geology, v. 106, p. 695–712.

Kovalevych, V., J. Paul, and T. M. Peryt, 2009, Fluid inclusions in halite from the Rot (Lower Triassic) salt deposit in Central Germany: Evidence for seawater chemistry and conditions of salt deposition and recrystallisation: Carbonates and Evaporites, v. 24, p. 45–57.

Kovalevych, V., W. Zang, T. Peryt, O. Khmelevska, S. Halas, I. Iwasinska-Budzyk, P. Boult, and P. Heithersay, 2006a, Deposition and chemical composition of early Cambrian salt in the eastern Officer Basin, South Australia: Australian Journal of Earth Sciences, v. 53, p. 577–593.

Kovalevych, V. M., T. Marshall, T. M. Peryt, O. Y. Petrychenko, and S. A. Zhukova, 2006b, Chemical composition of seawater in Neoproterozoic: Results of fluid inclusion study of halite from Salt Range (Pakistan) and Amadeus Basin (Australia): Precambrian Research, v. 144, p. 39–51.

Kovalevych, V. M., T. M. Peryt, W. L. Zang, and S. V. Vovnyuk, 2006c, Composition of brines in halite-hosted fluid inclusions in the Upper Ordovician, Canning Basin, Western Australia: new data on seawater chemistry: Terra Nova, v. 18, p. 95–103.

Kovin, O., 2011, Mapping of evaporite deformation in a potash mine using ground penetrating radar: Upper Kama deposit, Russia: Journal of Applied Geophysics, v. 74, p. 131–141.

Koyi, H. A., 1991, Gravity overturns, extension, and basement fault activation: Journal of Petroleum Geology, v. 12, p. 117–242.

Koyi, H. A., 1998, The shaping of salt diapirs: Journal of Structural Geology, v. 20, p. 321–338.

Koyi, H. A., 2001, Modeling the influence of sinking anhydrite blocks on salt diapirs targeted for hazardous waste disposal: Geology, v. 29, p. 387–390.

Koyi, H. A., A. Ghasemi, K. Hessami, and C. Dietl, 2008, The mechanical relationship between strike-slip faults and salt diapirs in the Zagros fold-thrust belt: Journal of the Geological Society, v. 165, p. 1031–1044.

Koziy, L., S. Bull, R. Large, and D. Selley, 2009, Salt as a fluid driver, and basement as a metal source, for stratiform sediment-hosted copper deposits: Geology, v. 37, p. 1107–1110.

Kraemer, B., D. Adelmann, M. Alten, W. Schnurr, K. Erpenstein, E. Kiefer, P. van den Bogaard, and K. Gorler, 1999, Incorporation of the Paleogene foreland into the Neogene Puna plateau: The Salar de Antofalla area, NW Argentina: Journal of South American Earth Sciences, v. 12, p. 157–182.

Krainer, K., and C. Spotl, 1998, Abiogenic silica layers within a fluviolacustrine succession, Balzano volcanic complex, Northern Italy – A Permian analogue for Magadi-type cherts: Sedimentology, v. 45, p. 489–505.

Krauskopf, K. B., 1967, Introduction to Geochemistry, Mc-Graw-Hill, 721 p.

Krauss, J. B., and T. Rivers, 2004, High-pressure granulites in the Grenvillian Grand Lake thrust system, Labrador: Pres- suretemperature conditions and tectonic evolution: Geological Society of America Memoirs, v. 197, p. 105–133.

Krcmarov, R. L., and J. I. Stewart, 1998, Geology and mineralisation of the Greenmount Cu-Au-Co deposit, southeastern Marimo Basin, Queensland: Australian Journal of Earth Sciences: An International Geoscience Journal of the Geological Society of Australia, v. 45, p. 463 – 482.

Krekeler, D., A. Teske, and H. Cypionka, 1998, Strategies of sulfate-reducing bacteria to escape oxygen stress in a cyanobacterial mat: FEMS Microbiology Ecology, v. 25, p. 89–96.

Kribek, B., J. Hladikova, and D. Holeczy, 2002, Anhydrite-bearing rocks from the Rozna District (Moldanubian Zone, Czech Republic): high grade metamorphosed exhalites?: Mineralium Deposita, v. 37, p. 465–479.

Krienitz, L., A. Ballot, K. Kotut, C. Wiegand, S. Pütz, J. S. Metcalf, G. A. Codd, and S. Pflugmache, 2003, Contribution of hot spring cyanobacteria to the mysterious deaths of Lesser Flamingos at Lake Bogoria, Kenya: FEMS Microbiology Ecology, v. 43, p. 141–148.

Krienitz, L., and K. Kotut, 2010, Fluctuating algal food populations and the occurrence of Lesser Flamingoes (Phoeniconaias minor) in three Kenyan rift valley lakes: Journal of Phycology, v. 46, p. 1088–1096.

Kriens, B. J., E. M. Shoemaker, and K. E. Herkenhoff, 1999, Geology of the Upheaval Dome impact structure, southeast Utah: Journal of Geophysical Research-Planets, v. 104, p. 18867–18887.

Krijgsman, W., M. M. Blanc-Valleron, R. Flecker, F. J. Hilgen, T. J. Kouwenhoven, D. Merle, F. Orszag-Sperber, and J. M. Rouchy, 2002, The onset of the Messinian salinity crisis in the Eastern Mediterranean (Pissouri Basin, Cyprus): Earth & Planetary Science Letters, v. 194, p. 299–310.

Krijgsman, W., A. R. Fortuin, F. J. Hilgen, and F. J. Sierro, 2001, Astrochronology for the Messinian Sorbas basin (SE Spain) and orbital (precessional) forcing for evaporite cyclicity: Sedimentary Geology, v. 140, p. 43–60.

Krijgsman, W., F. J. Hilgen, I. Raffi, F. J. Sierro, and D. S. Wilson, 1999, Chronology, causes and progression of the Messinian salinity crisis: Nature, v. 400, p. 652–655.

Krijgsman, W., and P. T. Meijer, 2008, Depositional environments of the Mediterranean "Lower Evaporites" of the Messinian salinity crisis: Constraints from quantitative analyses: Marine Geology, v. 253, p. 73–81.

Kroeger, K. F., and W. Stinnesbeck, 2003, The Minas Viejas Formation (Oxfordian) in the Area of Galeana, Northeastern Mexico: Significance of Syndepositional Volcanism and Related Barite Genesis in the Sierra Madre Oriental: Chapter 23, in C. Bartolini, R. T. Buffler, and J. Blickwede, eds., The Circum-Gulf of Mexico and the Caribbean: Hydrocarbon habitats, basin formation, and plate tectonics, American Association Petroleum Geologists Memoir 79, p. 515–528.

Krull, E., D. Haynes, S. Lamontagne, P. Gell, D. McKirdy, G. Hancock, J. McGowan, and R. Smernik, 2009, Changes in the chemistry of sedimentary organic matter within the Coorong over space and time: Biogeochemistry, v. 92, p. 9–25.

Krumbein, W. E., 1975, Biogenic monohydrocalcite spherules in lake sediments of Lake Kivu (Africa) and the Solar Lake (Sinai): Sedimentology, v. 22, p. 631–634.

Krumbein, W. E., Y. Cohen, and M. Shilo, 1977, Solar Lake (Sinai) 4. Stromatolitic cyanobacterial mats: Limnology and Oceanography, v. 22, p. 635–656.

Krumbein, W. E., D. M. Paterson, and L. J. Stal, 1994, Biostabilization of Sediments, Oldenburg: BIS Verlag, 526 p.

Krumgalz, B. S., A. Hecht, A. Starinsky, and A. Katz, 2000, Thermodynamic constraints on Dead Sea evaporation: can the Dead Sea dry up?: Chemical Geology, v. 165, p. 1–11.

Krupp, R., T. Oberthür, and W. Hirdes, 1994, The early Precambrian atmosphere and hydrosphere: Thermodynamic constraints from mineral deposits: Economic Geology, v. 89, p. 1581–1598.

Krzywiec, P., 2004, Basement vs. salt tectonics and salt-sediment interaction – Case study of the Mesozoic evolution of the intracontinental Mid-Polish Trough, in P. J. Post, ed., Salt-sediment interactions and hydrocarbon prospectivity: concepts, applications and case studies for the 21st Century. Papers presented at the 24th Annual Gulf Coast Section SEPM Foundation Bob F. Perkins Research Conference, Houston Tx, December 5–8, 2004 (CD publication), p. 343–370.

Ku, T. L., S. D. Luo, T. K. Lowenstein, J. R. Li, and R. J. Spencer, 1998, U-series chronology of lacustrine deposits in Death Valley, California: Quaternary Research, v. 50, p. 261–275.

Kucha, H., 1990, Geochemistry of the Kupferschiefer, Poland: Geologische Rundschau, v. 79, p. 387–399.

Kucha, H., and M. Pawlikowski, 1986, Two-brine model of the genesis of strata-bound Zechstein deposits (Kupferschiefer type), Poland: Mineralium Deposita, v. 21, p. 70–80.

Kudryashov, A. I., 2001, Upper Kama Salt Deposit [in Russian]: Mining Institute, UrO RAN, Perm

Kudryashov, A. I., V. E. Vasyukov, G. S. Von-der-Flaass, E. A. Ikonnikov, V. A. Gershanok, L. A. Gershanok, and S. V. Glebov, 2004, Rupture Tectonics of the Upper Kama (Verkhnekamskoye) Salt Deposit (in Russian): Mining Institute of Ural Branch of the Russian Academy of Sciences & Perm State University, Perm.

Kuhn, O., 2004, Ancient Chinese drilling: Canadian Society of Exploration Geophysicists, Recorder, v. 29, p. 39–43.

Kuhn, T., P. M. Herzig, M. D. Hannington, D. Garbe-Schönberg, and P. Stoffers, 2003, Origin of fluids and anhydrite precipitation in the sediment-hosted Grimsey hydrothermal field north of Iceland: Chemical Geology, v. 202, p. 5–21.

Kukla, P., J. Urai, J. K. Warren, L. Reuning, S. Becker, J. Schoenherr, M. Mohr, H. van Gent, S. Abe, S. Li, Desbois, G. Zsolt Schléder, and M. de Keijzer, 2011a, An Integrated, Multiscale Approach to Salt Dynamics and Internal Dynamics of Salt Structures: American Association Petroleum Geologists Search and Discovery Article #40703 (2011).

Kukla, P. A., L. Reuning, S. Becker, J. L. Urai, and J. Schoenherr, 2011b, Distribution and mechanisms of overpressure generation and deflation in the late Neoproterozoic to early Cambrian South Oman Salt Basin: Geofluids, v. 11, p. 349–361.

Kulke, H., 1978, Tektonik und Petrographie einer Salinarformation am Beispiel der Trias des Atlassystems (NW-Afrika), in W. Zeil, ed., Geotektonische Forschungen, v. 55, p. 1–158.

Kunasz, I., 2006, Lithium Resources, in J. E. Kogel, N. C. Trivedi, J. M. Barker, and S. T. Krukowski, eds., Industrial Minerals and Rocks, SME (Soc. Mining Metallurgy and Exploration), p. 599–614.

Kunasz, I. A., 1983, Lithium raw materials, in S. J. Lefond, ed., Industrial minerals and rocks: New York, AIME, p. 869–880.

Kunstman, A., and M. M. Mazur, 2000, Cavern development and leaching simulation: An introduction to the technology of solution mining; Spring 2000 Technical Class, p. 60–80.

Kuntze, R. A., 2009, Gypsum: Connecting Science and Technology: West Conshohocken, PA, ASTM International, 114 p.

Kuo, L.-C., 1994, Lower Cretaceous lacustrine source rocks in northern Gabon: effect of organic facies and thermal maturity on crude oil quality: Organic Geochemistry, v. 22, p. 257–273.

Kupfer, D., 1976, Shear zones inside Gulf Coast salt stocks help to delineate spines of movement: American Association Petroleum Geologists – Bulletin, v. 60, p. 1434–1447.

Kurilenko, V. V., I. G. Ruday, and A. A. Shvarts, 1988, The origin and commercial exploitation of subsurface brines in the northern half of Kara-Bogaz-Gol: International Geology Reviews, v. 30, p. 1238–1245.

Kurlansky, M., 2002, Salt: A world history: New York, Walker & Co., 484 p.

Kuroda, H., 1983, Geologic characteristics and formation environments of the Furutobe and Matsuki kuroko deposits, Akita Prefecture, Northeast Japan: Economic Geology Monographs, v. 5, p. 149–156.

Kusakabe, M., and H. Chiba, 1983, Oxygen and sulfur isotope composition of barite and anhydrite from the Fukazawa Deposit, Japan: Economic Geology Monographs, v. 5, p. 292–301.

Kushnir, J., 1981, Formation and early diagenesis of varved evaporite sediments in a coastal hypersaline pool: Journal of Sedimentary Petrology, v. 51, p. 1193–1203.

Kushnir, J., 1982, The partitioning of seawater cations during the transformation of gypsum to anhydrite: Geochimica et Cosmochimica Acta, v. 46, p. 433–446.

Küster, Y., M. Schramm, O. Bornemann, and B. Leiss, 2009, Bromide distribution characteristics of different Zechstein 2 rock salt sequences of the Southern Permian Basin: a comparison between bedded and domal salts: Sedimentology, v. 56, p. 1368–1391.

Kuznetsov, S. I., 1957, A review of fundamental research on the microflora of petroleum deposits: Mikrobiologiya, v. 26, p. 651–658.

Kvenvolden, K. A., and B. R. T. Simoneit, 1990, Hydrothermally derived petroleum: examples from Guaymas Basin, Gulf of California, and Escanaba Trough, northeast Pacific Ocean: American Association of Petroleum Geologists Bulletin, v. 74, p. 223–237.

Kwak, T. A. P., 1977, Scapolite compositional change in a metamorphic gradient and its bearing on the identification of meta-evaporite sequences: Geological Magazine, v. 114, p. 343–354.

Kyle, J. R., 1991, Evaporites, evaporitic processes and mineral resources, in J. L. Melvin, ed., Evaporites, petroleum and mineral resources.: Developments in Sedimentology, v. 50: Amsterdam, Elsevier, p. 477–533.

Kyle, J. R., and W. N. Agee Jr, 1988, Evolution of metal ratios and delta (34)S composition of sulfide mineralization during anhydrite cap rock formation, Hockley Dome, Texas, U.S.A: Chemical Geology, v. 74, p. 37–55.

Kyle, J. R., and W. A. Gose, 1991, Paleomagnetic Dating of Sulfide Mineralization and Cap Rock Formation in Gulf Coast Salt Domes (abs): American Association Petroleum Geologists – Bulletin, v. 75, p. 615.

Kyle, J. R., and H. H. Posey, 1991, Halokinesis, Cap rock Development and salt dome mineral resources, in J. L. Melvin, ed., Evaporites, petroleum and mineral resources.: Developments in Sedimentology, v. 50: Amsterdam, Elsevier, p. 413–474.

Kyle, J. R., and P. E. Price, 1986, Metallic sulphide mineralization in salt-dome cap rocks, Gulf Coast, U.S.A: Institution of Mining and Metallurgy. Transactions, Section B: Applied Earth Sciences, v. 95, p. B6-B16.

Kyle, J. R., and P. E. Price, 1986, Sulfide mineralization in salt dome cap rocks of the Houston diapir province: Seni, Steven J., Kyle, J. Richard, Price, Peter E., Samuelson, Fairis. Comparison of cap rocks, mineral resources, and surface features of salt domes in the Houston diapir province. Univ. Tex. at Austin, Bur. Econ. Geol., Austin, Tx, United States. p.

Kyser, T. K., C. Renac, E. Hiatt, G. Holk, and K. Durocher, 2000, Comparison of Diagenetic Fluids in Proterozoic Basins, Canada and Australia: Implications for Long Protracted Fluid Histories in Stable Intracratonic Basins: GEOCANADA 2000, Calgary.

Laborde, M., 1983, Determination of Brine Evaporation Rates in Solar Ponds as a Function of Magnesium Chloride Concentration. t.: 6th Int Symposium on Salt. North Ohio Geological Society, v. 2, p. 407–416.

Lacazette, A., A. R. Thomas, and D. Kuhfal, 2007, Fracture Development in Salt Dome Caprock, Hardin County, Texas: Search and Discovery Article #50058: Extended abstract prepared for presentation at American Association Petroleum Geologists Annual Convention, Long Beach, California, April 1–4, 2007.

LaClair, D., and T. K. Lowenstein, 2009, Fluid inclusion microthermometry from halite in the Eocene Green River Formation, Piceance Creek basin, Colorado, USA: evidence for a perennial stratified saline lake. : Geol. Soc. Am. Annu. Meet., Abstracts with Programs, 41, 512.

Lacombe, O., J. Lavé, F. Roure, and J. Verges, eds., 2007, Thrust Belts and Foreland Basins: From Fold Kinematics to Hydrocarbon Systems, Springer-Verlag Berlin Heidelberg, 492 p.

Lakhdar, R., M. Soussi, M. H. Ben Ismail, and A. M'Rabet, 2006, A Mediterranean Holocene restricted coastal lagoon under arid climate: Case of the sedimentary record of Sabkha Boujmel (SE Tunisia): Palaeogeography, Palaeoclimatology, Palaeoecology, v. 241, p. 177–191.

Lamb, C. F., 1980, Painter reservoir field giant in Wyoming thrust belt: American Association Petroleum Geologists – Bulletin, v. 64, p. 638–644.

Lamb, M. P., W. W. Fischer, T. D. Raub, J. T. Perron, and P. M. Myrow, 2012, Origin of giant wave ripples in snowball Earth cap carbonate: Geology, v. 40, p. 827–830.

Lamba, V. J. S., and P. S. Agarkar, 1988, The tin potential of Precambrian rare-metal bearing pegmatites of Bastar district, M.P., India: Mineralium Deposita, v. 23, p. 218–221.

Lambert, S. J., 1983, Dissolution of Evaporites in and around the Delaware Basin, Southeastern New Mexico and West Texas: Sandia Nat'l. Labs. Report SAND82-0461, Albuquerque, NM, 96 pp.

Lambiase, J. J., 1990, A model for tectonic controls of lacustrine stratigraphic sequences in continental rift basins, in B. J. Katz, ed., Lacustrine Basin Exploration – Case studies and modern analogues, v. 50: Tulsa, OK, American Association Petroleum Geologists Memoir, p. 265–276.

Lamont-Black, J., P. L. Younger, R. A. Forth, A. H. Cooper, and J. P. Bonniface, 2002, A decision-logic framework for investigating subsidence problems potentially attributable to gypsum karstification: Engineering Geology, v. 65, p. 205–215.

Land, L., A., 2012, Electrical resistivity surveys of anthropogenic karst phenomena, southeastern New Mexico: New Mexico Geology, v. 34, p. 117–125.

Land, L., 2013, Geophysical records of anthropogenic sinkhole formation in the Delaware Basin region, Southeast New Mexico and West Texas, USA: Carbonates and Evaporites, v. 28, p. 183–190.

Land, L. S., 1985, The origin of massive dolomite: Journal of Geological Education, v. 33, p. 112–125.

Land, L. S., 1991, Evidence for vertical movements of fluids, Gulf Coast sedimentary basin: Geophysical Research Letters, v. 18, p. 919–922.
Land, L. S., 1995a, The role of saline formation water in crustal cycling: Aquatic Geochemistry, v. 1, p. 137–145.
Land, L. S., 1995b, Na-Ca-Cl saline formation waters, Frio Formation (Oligocene), south Texas, USA: Products of diagenesis: Geochimica et Cosmochimica Acta, v. 59, p. 2163–2174.
Land, L. S., R. A. Eustice, L. E. Mack, and J. Horita, 1995, Reactivity of evaporites during burial – An example from the Jurassic of Alabama: Geochimica et Cosmochimica Acta, v. 59, p. 3765–3778.
Land, L. S., J. A. Kupecz, and L. E. Mack, 1988, Louann Salt geochemistry (Gulf of Mexico sedimentary basin, U.S.A.); a preliminary synthesis: Chemical Geology, v. 74, p. 25–35.
Land, L. S., and K. L. Milliken, 1981, Feldspar diagenesis in the Frio Formation, Brazoria County, Texas Gulf Coast: Geology, v. 9, p. 314–318.
Land, L. S., and D. R. Prezbindowski, 1981, The origin and evolution of saline formation water, Lower Cretaceous carbonates, South-central Texas, U.S.A.: Journal of Hydrology, v. 54, p. 51–74.
Landes, K. K., and T. B. Piper, 1972, Effect upon environment of brine cavity subsidence at Grosse isla, Michigan 1971, Solution Mining Research Institute, Open-file Report, 812 Muriel St, Woodstock, Illinois, 52 p.
Landmann, G., G. M. Abu Qudaira, K. Shawabkeh, V. Wrede, and S. Kempe, 2002, Geochemistry of the Lisan and Damya Formations in Jordan, and implications for palaeoclimate: Quaternary International, v. 89, p. 45–57.
Landmann, G., and A. Reimer, 1996, Climatically induced lake level changes at Lake Van, Turkey, during the Pleistocene/Holocene transition: Global Biochemical Cycles, v. 10, p. 797–808.
Landmann, G., A. Reimer, G. Lemcke, and S. Kempe, 1996, Dating Late Glacial abrupt climate changes in the 14,570 yr long continuous varve record of Lake Van, Turkey: Palaeogeography Palaeoclimatology Palaeoecology, v. 122, p. 107–118.
Langdon, G. S., and J. K. Hall, 1994, Devonian-Carboniferous Tectonics and Basin Deformation in the Cabot Strait Area, Eastern Canada: Bulletin American Association Petroleum Geologists, v. 78, p. 1748–1774.
Langford, R. P., 2003, The Holocene history of the White Sands dune field and influences on eolian deflation and playa lakes: Quaternary International, v. 104, p. 31–39.
Large, D. J., and A. P. Gize, 1996, Pristane/phytane ratios in the mineralized Kupferschiefer of the Fore-Sudetic Monocline, southwest Poland: Ore Geology Reviews, v. 11, p. 89–103.
Large, D. J., J. Macquaker, D. J. Vaughan, Z. Sawlowicz, and A. P. Gize, 1995, Evidence for low temperature alteration of sulfides in the Kupferschiefer copper deposits of southwestern Poland: Economic Geology, v. 90, p. 2143–2155.
Large, R. R., S. W. Bull, D. R. Cooke, and P. J. McGoldrick, 1998, A genetic model for the HYC deposit, Australia: Based on regional sedimentology, geochemistry, and sulfide-sediment relationships: Economic Geology, v. 93, p. 1345–1368.
Large, R. R., S. W. Bull, and V. V. Maslennikov, 2011, A Carbonaceous Sedimentary Source-Rock Model for Carlin-Type and Orogenic Gold Deposits: Economic Geology, v. 106, p. 331–358.
Large, R. R., S. W. Bull, and P. J. McGoldrick, 2000, Lithogeochemical halos and geochemical vectors to stratiform sediment hosted Zn-Pb-Ag deposits Part 2. HYC deposit, McArthur River, Northern Territory: Journal of Geochemical Exploration, v. 68, p. 105–126.
Large, R. R., S. W. Bull, P. J. McGoldrick, S. Walters, G. M. Derrick, and G. R. Carr, 2005, Stratiform and stratabound Zn-Pb-Ag deposits in Proterozoic sedimentary basins, northern Australia: Economic Geology, v. 100th Anniversary, p. 931–963.
Larsen, B. D., Z. Ben-Avraham, and H. Shulman, 2002, Fault and salt tectonics in the southern Dead Sea basin: Tectonophysics, v. 346, p. 71–90.
Larsen, D., 1994, Origin and paleoenvironmental significance of calcite pseudomorphs after ikaite in the Oligocene Creede Formation, Colorado: Journal of Sedimentary Research A: Sedimentary Petrology & Processes, v. A64, p. 593–603.
Larsen, D., and L. J. Crossey, 1996, Depositional environments and paleolimnology of an ancient caldera lake – Oligocene Creede Formation, Colorado: Geological Society of America Bulletin, v. 108, p. 526–544.
Last, F. M., and W. M. Last, 2012, Lacustrine carbonates of the northern Great Plains of Canada: Sedimentary Geology, v. 277–278, p. 1–31.
Last, F. M., W. M. Last, and N. M. Halden, 2010, Carbonate microbialites and hardgrounds from Manito Lake, an alkaline, hypersaline lake in the northern Great Plains of Canada: Sedimentary Geology, v. 225, p. 34–49.
Last, W. M., 1989a, Continental brines and evaporites of the northern Great Plains of Canada: Sedimentary Geology, v. 64, p. 207–221.
Last, W. M., 1989b, Sedimentology of a saline playa in the northern Great Plains, Canada: Sedimentology, v. 36, p. 109–123.
Last, W. M., 1992, Petrology of carbonate hardgrounds from East Basin Lake, a saline maar lake, southern Australia: Sedimentary Geology, v. 81, p. 215–229.
Last, W. M., 1993, Salt dissolution features in saline lakes of the northern Great Plains, western Canada: Geomorphology, v. 8, p. 321–334.
Last, W. M., 1993a, Salt dissolution features in saline lakes of the northern Great Plains, western Canada: Geomorphology, v. 8, p. 321–334.
Last, W. M., 1994, Deep-water evaporite mineral formation in lakes of Western Canada, in R. W. Renaut, and W. M. Last, eds., Sedimentology and geochemistry of modern and ancient saline lakes, v. 50, SEPM Special Publication, p. 51–59.
Last, W. M., 2002, Geolimnology of salt lakes: Geosciences Journal, v. 6, p. 347–369.
Last, W. M., and F. M. Ginn, 2005, Saline systems of the Great Plains of western Canada: an overview of the limnogeology and paleolimnology: Saline Systems, v. 1, p. Article is available from http://www.salinesystems.org/content/1/1/10.
Last, W. M., and R. E. Vance, 1997, Bedding characteristics of Holocene sediments from salt lake of the Northern Great Plains, western Canada: Journal of Paleolimnology, v. 17, p. 297–318.
Lauterbach, A., 2007, Iodine and Iodine compounds, Kirk-Othmer Encyclopedia of Chemical Technology, v. 14, John Wiley & Sons, Inc., p. 1–30.
Laval, B., S. L. Cady, J. C. Pollack, C. P. McKay, J. S. Bird, J. P. Grotzinger, D. C. Ford, and H. R. Bohm, 2000, Modern freshwater microbialite analogues for ancient dendritic reef structures: Nature, v. 407, p. 626–629.
Lavoie, D., D. F. Sangster, M. M. Savard, and F. F., 1995, Multiple breccia events in the lower part of the Carboniferous Windsor Group, Nova Scotia: Atlantic Geology, v. 31, p. 197–207.
Lavoie, D., D. F. Sangster, M. M. Savard, and F. Fallara, 1998, Breccias in the lower part of the Mississippian Windsor Group and their relation to Pb-Zn mineralisation: a summary: Economic Geology, v. 93, p. 734–735.
Lawver, L. A., and L. M. Gahagan, 2003, Evolution of Cenozoic seaways in the circum-Antarctic region: Palaeogeography, Palaeoclimatology, Palaeoecology, v. 198, p. 11–37.
Lazar, B., and J. Erez, 1992, Carbon geochemisty of marine-derived brines. 1. C-13 depletions due to intense photosynthesis: Geochimica Cosmochimica Acta, v. 56, p. 335–345.
Laznicka, P., 1988, Breccias and coarse fragmentites: petrology, environments, associations, ores: Developments in Economic Geology, v. 25: New York, Elsevier, 832 p.

Lazo, D. G., M. Cichowolski, D. L. Rodriguez, and M. B. Aguirre-Urreta, 2005, Lithofacies, palaeoecology and palaeoenvironments of the Agrio Formation, Lower Cretaceous of the Neuquen Basin, Argentina: Geological Society, London, Special Publications, v. 252, p. 295–315.

Leach, D., J. C. Macquar, V. Lagneau, J. Leventhal, P. Emsbo, and W. Premo, 2006, Precipitation of lead-zinc ores in the Mississippi Valley-type deposit at Trèves, Cévennes region of southern France: Geofluids, v. 6, p. 24–44.

Leach, D., D. Sangster, K. Kelley, R. R. Large, G. Garven, C. Allen, J. Gutzmer, and S. Walters, 2005, Sediment-hosted lead-zinc deposits: A global perspective: Economic Geology 100th Anniversary edition, p. 561–607.

Leach, D. L., D. C. Bradley, D. Huston, S. A. Pisarevsky, R. D. Taylor, and S. J. Gardoll, 2010, Sediment-Hosted Lead-Zinc Deposits in Earth History: Economic Geology, v. 105, p. 593–625.

Leach, D. L., and D. F. Sangster, 1993, Mississippi Valley-type lead-zinc deposits: Geological Association of Canada Special Paper, v. 40, p. 289–314.

Leake, B. E., C. M. Farrow, and R. Townend, 1979, A pre-2,000 Myr old granulite facies metamorphosed evaporite from Caraiba, Brazil?: Nature, v. 277, p. 49–50.

Leary, D. A., and J. N. Vogt, 1986, Diagenesis of the San Andres Formation (Guadalupian), Central Basin Platform, Permian Basin, in D. G. Bebout, Harris, P. M., ed., Hydrocarbon Reservoir Studies San Andres/Grayburg Formations, Permian Basin, SEPM Special Publ. No. 26, p. 67–68.

Lebedev, L. M., 1972, Minerals of contemporary hydrotherms of Cheleken: Cheochemistry International, v. 9, p. 485–504.

Lebedeva, M., O. Lopukhina, and N. Kalinina, 2008, Specificity of the chemical and mineralogical composition of salts in solonchak playas and lakes of the Kulunda steppe: Eurasian Soil Science, v. 41, p. 416–428.

LeBlanc, L., 1994, Drilling, completion, workover challenges in subsalt formations: Offshore, v. 54, p. 21–22.

Lee, M. K., and D. D. Williams, 2000, Paleohydrology of the Delaware basin, western Texas: Overpressure development, hydrocarbon migration, and ore genesis: American Association Petroleum Geologists – Bulletin, v. 84, p. 961–974.

Lee, M. R., 1990, The sedimentology and diagenesis of the Raisby Formation (Z1 carbonate), northern England.: Masters thesis, University of Newcastle upon Tyne; Department of Geology.

Lee, M. R., 1994, Emplacement and diagenesis of gypsum and anhydrite in the late Permian Raisby Formation, north-east England: Proceedings – Yorkshire Geological Society, v. 50, p. 143–155.

Lee, M. R., 1995, Calcite concretions in carbonate rocks of the late Permian Raisby Formation, north-east England: Proceedings – Yorkshire Geological Society, v. 50, p. 245–253.

Lee, M. R., and G. M. Harwood, 1989, Dolomite calcitization and cement zonation related to uplift of the Raisby Formation (Zechstein carbonate), Northeast England: Sedimentary Geology, v. 65, p. 285–305.

Lee, R., and E. De Souza, 1998, The effect of brine on the creep behaviour and dissolution chemistry of evaporites: Canadian Geotechnical Journal, v. 35, p. 720–729.

Lee, R. V., 2001, Maladies, malaise, and modernization: health and development in Ladakh: Asian Affairs, v. 32, p. 300–306.

Lefond, S. J., and J. M. Barker, 1979, A borate and zeolite occurrence near Magdalena, Sonora, Mexico: Economic Geology, v. 74, p. 1883–1889.

Legler, B., J. W. Schneider, U. Gebhardt, D. Merten, and R. Gaupp, 2011, Lake deposits of moderate salinity as sensitive indicators of lake level fluctuations: Example from the Upper Rotliegend saline lake (Middle-Late Permian, Northeast Ger-many): Sedimentary Geology, v. 234, p. 56–69.

Lehmann, C., D. A. Osleger, and I. P. Montanez, 1998, Controls on cyclostratigraphy of Lower Cretaceous carbonates and evaporites, Cupido and Coahuila platforms, northeastern Journal of Sedimentary Research, v. 68, p. 1109–1130.

Lehner, P., 1969, Salt tectonics and Pleistocene stratrigraphy on continental slope of northern Gulf of Mexico: Bulletin American Association Petroleum Geologists, v. 53, p. 2431–2479.

Leibold, A. W., 1992, Sedimentological and geochemical constraints on Niagara/Salina deposition, Michigan Basin: Doctoral thesis, University of Michigan, 280 p.

Leibold, A. W., and P. D. Howell, 1991, Death of a carbonate basin; the Niagara-Salina transition in the Michigan Basin (abs): American Association Petroleum Geologists Bulletin, v. 75, p. 619.

Leitner, C., F. Neubauer, R. Marschallinger, J. Genser, and M. Bernroider, 2013, Origin of deformed halite hopper crystals, pseudomorphic anhydrite cubes and polyhalite in Alpine evaporites (Austria, Germany): International Journal of Earth Sciences, v. 102, p. 813–829.

Leitner, C., F. Neubauer, J. L. Urai, and J. Schoenherr, 2011, Structure and evolution of a rocksalt-mudrock-tectonite: The haselgebirge in the Northern Calcareous Alps: Journal of Structural Geology, v. 33, p. 970–984.

Leleu, S., and A. J. Hartley, 2010, Controls on the stratigraphic development of the Triassic Fundy Basin, Nova Scotia: implications for the tectonostratigraphic evolution of Triassic Atlantic rift basins: Journal of the Geological Society, v. 167, p. 437–454.

Lemon, N. M., 1985, Physical Modelling of Sedimentation Adjacent to Diapirs and Comparison with Late Precambrian Oratunga Breccia Body in Central Flinders Ranges, South Australia: American Association Petroleum Geologists Bulletin, v. 69, p. 1327–1328.

Lemon, N. M., 1988, Diapir recognition and modelling with examples from the Late Proterozoic Adelaide Geosyncline, Central Flinders Ranges, South Australia: Doctoral thesis, University of Adelaide.

Lemon, N. M., 2000, A Neoproterozoic fringing stromatolite reef complex, Flinders Ranges, South Australia: Precambrian Research, v. 100, p. 109–120.

Lerche, I., and K. Petersen, 1995, Salt and Sediment Dynamics: Boca Raton, CRC Press, 322 p.

Leroy, S. A. G., F. Marret, S. Giralt, and S. A. Bulatov, 2006, Natural and anthropogenic rapid changes in the Kara-Bogaz Gol over the last two centuries reconstructed from palynological analyses and a comparison to instrumental records: Impact of rapid environmental changes on humans and ecosystems, v. 150, p. 52.

Leslie, A. B., G. M. Harwood, and A. C. Kendall, 1997, Geochemical variations within a laminated evaporite deposit: Evidence for brine composition during formation of the Permian Castile Formation, Texas and New Mexico, USA: Sedimentary Geology, v. 110, p. 223–235.

Leslie, A. B., A. C. Kendall, G. M. Harwood, and D. W. Powers, 1996, Conflicting indicators of palaeoceanographic depth during deposition of the upper Permian Castile Formation, Texas and New Mexico, in A. E. S. Kemp, ed., Palaeoclimatology and Palaeoceanography from Laminated Sediments: London, Geological Society London Special Publication, No. 116, p. 111–124.

Letouzey, J., B. Colletta, R. Vially, and J. C. Chermette, 1995, Evolution of salt-related structures in compressional settings, in M. P. A. Jackson, D. G. Roberts, and S. Snelson, eds., Salt tectonics: a global perspective, American Association Petroleum Geologists Memoir, v. 65, p. 41–60.

Letouzey, J., P. Werner, and Y. Marty, 1990, Fault reactivation and structural inversion; backarc and intraplate compressive deformations; example of the eastern Sunda Shelf (Indonesia): Tectonophysics, v. 183, p. 341–362.

Levet, S., J. P. Toutain, M. Munoz, G. Berger, P. Negrel, N. Jendrzejewski, P. Agrinier, and F. Sortino, 2002, Geochemistry of the Bagneres-de-Bigorre thermal waters from the North Pyrenean Zone (France): Geofluids, v. 2, p. 25–40.

Levin, L. A., 2005, Ecology of cold seep sediments: Interactions of fauna with flow, chemistry and microbes, in R. N. Gibson, R. J. A. Atkinson, and J. D. M. Gordon, eds., Oceanography and Marine Biology: An Annual Review, v. 43, Taylor & Francis, p. 1–46.

Levy, Y., 1977a, Description and mode of formation of the supratidal evaporite facies in northern Sinai coastal plain: Journal of Sedimentary Petrology, v. 47, p. 463–474.

Levy, Y., 1977b, The origin and evolution of brine in coastal sabkhas, Northern Sinai: Journal of Sedimentary Petrology, v. 47, p. 451–462.

Levy, Y., 1980, Evaporitic environments in the Northern Sinai, in A. Nissenbaum, ed., Hypersaline brines and evaporitic environments, Elsevier, Amsterdam, p. 131–143.

Levy, Y., 1984, Halite from the bottom of the Dead Sea: Geolo. Surv. Israel Report GSE48/84.

Lewan, M. D., 1984, Factors controlling the proportionality of vanadium to nickel in crude oils: Geochimica et Cosmochimica Acta, v. 48, p. 2231–2238.

Lewis, M. M., C. A. L. Jackson, and R. L. Gawthorpe, 2013, Salt-influenced normal fault growth and forced folding: The Stavanger Fault System, North Sea: Journal of Structural Geology, v. 54, p. 156–173.

Lewis, S., and M. Holness, 1996, Equilibrium halite-H_2O dihedral angles: High rock salt permeability in the shallow crust: Geology, v. 24, p. 431–434.

Leyrer, K., C. Strohmenger, K. Rockenbauch, and T. Bechstaedt, 2001, High resolution forward stratigraphic modeling of Ca-2 carbonate platforms and off-platform highs (Upper Permian, Northern Germany), in J. Harff, W. Lemke, and K. Stattegger, eds., Computerised Modelling of Sedimentary Systems, Springer Verlag, p. 307-339.

Li, C., E. M. Ripley, A. J. Naldrett, A. K. Schmitt, and C. H. Moore, 2009, Magmatic anhydrite-sulfide assemblages in the plumbing system of the Siberian Traps: Geology (Boulder), v. 37, p. 259–262.

Li, J. R., T. K. Lowenstein, and I. R. Blackburn, 1997, Responses of evaporite mineralogy to inflow water sources and climate during the past 100 Ky in Death Valley California: Geological Society of America Bulletin, v. 109, p. 1361–1371.

Li, J. R., T. K. Lowenstein, C. B. Brown, T. L. Ku, and S. D. Luo, 1996, A 100 ka record of water tables and paleoclimates from salt cores, Death Valley, California: Palaeogeography Palaeoclimatology Palaeoecology, v. 123, p. 179–203.

Li, M., G. Ma, K. Guttikonda, S. Boyages, and C. Eastman, 2001, The re-emergence of iodine deficiency in Sydney, Australia: Asia Pacific J of Clin. Nutr., v. 10, p. 200–203.

Li, S., M. Dong, Z. Li, S. Huang, H. Qing, and E. Nickel, 2005, Gas breakthrough pressure for hydrocarbon reservoir seal rocks: implications for the security of long-term CO_2 storage in the Weyburn field: Geofluids, v. 5, p. 326–334.

Li, Z., H. Goldstein, and E. K. Franseen, 2013, Ascending fresh-water-mesohaline mixing; a new scenario for dolomitization: Journal of Sedimentary Research, v. 83, p. 277–283.

Li, Z. X., C. M. Powell, and R. Bowman, 1993, Timing and genesis of Hamersley iron-ore deposits: Exploration Geophysics, v. 24, p. 631–636.

Liang-Jie Tang, Cheng-Zao Jia, Zhi-Jun Jin, Shu-Ping Chen, Xue-Jun Pi, and H.-W. Xie, 2004, Salt tectonic evolution and hydrocarbon accumulation of Kuqa foreland fold belt, Tarim Basin, NW China: Journal of Petroleum Science and Engineering, v. 41, p. 97–108.

Lickorish, W. H., and M. Ford, 1998, Sequential restoration of the external Alpine Digne thrust system, SE France, constrained by kinematic data and synorogenic sediments: Geological Society, London, Special Publications, v. 134, p. 189–211.

Light, M. P. R., and H. H. Posey, 1992, Diagenesis and its relation to mineralisation and hydrocarbon reservoir development; Gulf Coast and North Sea Basins, in K. H. Chilingar, and G. V. Wolf, eds., Diagenesis III: Oxford-Amsterdam-New York, Elsevier, p. 511–541.

Lightfoot, P. C., and C. J. Hawkesworth, 1997, Flood basalts and magmatic Ni, Cu, and PGE sulphide mineralization: comparative geochemistry of the Noril'sk (Siberian Traps) and West Greenland sequences: Geophysical Monograph Series, v. 100, p. 357–380.

Likens, G. E., 2010, Plankton of Inland Waters, Elsevier.

Lindblom, S., C. Broman, and O. Martinsson, 1996, Magmatic-hydrothermal fluids in the Pahtohavare Cu-Au deposit in greenstone at Kiruna, Sweden: Mineralium Deposita, v. 31, p. 307–318.

Lindenmayer, Z. G., 1981, Evolucao geológica do Vale do Rio Curaca e dos corpos máfico-ultramáficos mineralizados a cobre, in H. A. V. lnda, M. M. Marinho, and F. B. Duarte, eds., Geologia e Recursos Minerais do Estado da Bahia, v. 4, Textos Basicos, p. 72–110.

Lindsay, J. F., 1987, Upper Proterozoic evaporites in the Amadeus Basin, central Australia, and their role in basin tectonics: Geological Society of America Bulletin, v. 99, p. 852–865.

Lindsay, R. F., D. L. Cantrell, G. W. Hughes, T. H. Keith, H. W. Mueller III, and S. D. Russell, 2006, Ghawar Arab-D reservoir: Widespread porosity in shoaling-upward carbonate cycles, Saudi Arabia in P. M. Harris, and L. J. Weber, eds., Giant hydrocarbon reservoirs of the world: From rocks to reservoir characterization and modeling, American Association Petroleum Geologists Memoir 88/SEPM Special Publication, p. 97–137.

Lindsay, R. F., and C. G. S. C. Kendall, 1985, Depositional facies, diagenesis, and reservoir character of Mississippian cyclic carbonates in the Mission Canyon Formation, Little Knife field, Williston Basin, North Dakota, in P. O. Roehl, and P. W. Choquette, eds., Carbonate petroleum reservoirs: New York, Springer-Verlag, p. 175–190.

Linn, J. K., and J. Culbert, 1999, Experience in underground storage of crude oil in salt: Special Publication 90, Geo-Inst. ASCE, p. 810 p.

Linn, K. O., and S. S. Adams, 1966, Barren halite zones in potash deposits, Carlsbad, New Mexico: Second Symposium on Salt, p. 59–68.

Liro, L. M., 1992, Distribution of shallow salt structures, lower slope of the northern Gulf of Mexico, USA: Marine and Petroleum Geology, v. 9, p. 433–451.

Lisk, M., M. M. Faiz, E. B. Bekele, and T. E. Ruble, 2000, Transient fluid flow in the Timor Sea, Australia: implications for prediction of fault seal integrity: Journal of Geochemical Exploration, v. 69, p. 607–613.

Littke, R., 1993, Depositional history of the Posidonia shale, Deposition, Diagenesis and Weathering of Organic Matter-Rich Sediments, v. 43, Springer Lecture Notes in Earth Sciences, p. 46–81.

Littke, R., H. J. Bayer, D. Gajewski, and S. Nelskamp, 2008, Dynamics of Complex Intracontinental Basins – The Central European Basin System: Berlin Heidelberg, Springer, 519 p.

Liu, C., M. Wang, P. Jiao, and Y. Chen, 2008, Characteristics and formation of the potash deposits in Lop Nur salt lake, Xinjiang, China (abs.): International Geological Congress, Oslo, August 6–14, 2008, Session MRB-01 General contributions to industrial mineral deposits

Liu, D., J. Tu, and K. Jin, 2003, Organic petrology of potential source rocks in the Tarim Basin, NW China: Journal of Petroleum Geology, v. 26, p. 105–124.

Liu, W. G., Y. K. Xiao, Z. C. Peng, Z. S. An, and X. X. He, 2000, Boron concentration and isotopic composition of halite from experiments and salt lakes in the Qaidam Basin: Geochimica et Cosmochimica Acta, v. 64, p. 2177–2183.

Ljunggren, P., and H. C. Meyer, 1964, The copper mineralization in the Corocoro basin, Bolivia: Economic Geology, v. 59, p. 110–125.

Lock, B. E., 2000, Geologic Mapping of Salt Mines in Salt Diapirs: Approaches and Examples from South Louisiana: Gulf Coast Association of Geological Societies Transactions, v. 50, p. 567–582.

Lock, B. E., W. F. Ashley, and E. Anderson, 2004, Bacteria-Petroleum Reactions; Salt Dome Cap Rock Genesis Compared with Similar Processes from Permian Outcrops in West Texas: Gulf Coast Association of Geological Societies Transactions, v. 54, p. 361–367.

Lock, B. E., and D. H. Kupfer, 2003, Salt Mines of South Louisiana, A field seminar for the Gulf Coast Association of Geological Societies 2003 Convention: Louisiana Geological Survey; Guidebook Series no. 7, Louisiana State University, Baton Rouge. 85 p.

Lock, D. E., 1986, The formation of modern epsomite deposits near Lake Eyre, and their significance for Early-Cainozoic weathering in central Australia: Sediments down under. 12th International Sedimentological Congress, sponsored by the International Association of Sedimentologists, Bureau of Mineral Resources, Geology and Geophysics, Geological Society of Australia and the Geological Society of New Zealand, Canberra, Australia, 24–30 August, 1986. Abstracts. Canberra: International Sedimentological Congress., p. 189.

Lofi, J., J. Déverchère, V. Gaullier, H. Gillet, C. Gorine, P. Guennoc, L. Loncke, A. Maillard, F. Sage, and I. Thinon, 2011, Atlas of the Messinian Seismic Markers in the Mediterranean and Black Seas: Mèmoires de la Société géologique de France, v. 179.

Lofi, J., C. Gorini, S. Berne, G. Clauzon, A. T. Dos Reis, W. F. Ryan, and M. S. Steckler, 2005, Erosional processes and paleo-environmental changes in the Western Gulf of Lions (SW France) during the Messinian Salinity Crisis: Marine Geology, v. 217, p. 1–30.

Logan, B. W., 1987, The MacLeod evaporite basin, western Australia; Holocene environments, sediments and geological evolution: Tulsa, OK, American Association of Petroleum Geologists Memoir 44, 140 p.

Logan, B. W., and R. G. Brown, 1976, Shark Bay, University of Western Australia, Excursion Guide, p. 63.

Logan, G. A., J. M. Hayes, G. B. Hieshima, and R. E. Summons, 1995, Terminal Proterozoic reorganisation of biogeochemical cycles: Nature, v. 376, p. 53–56.

Logan, G. A., M. C. Hinman, M. R. Walter, and R. E. Summons, 2001, Biogeochemistry of the 1640 Ma McArthur River (HYC) lead-zinc ore and host sediments, Northern Territory, Australia: Geochimica Cosmochimica Acta, v. 65, p. 2317–2336.

Lohmann, H. H., 1979, Seismic recognition of salt diapirs: American Association Petroleum Geologists – Bulletin, v. 63, p. 2097–2102.

Lokier, S., and T. Steuber, 2008, Quantification of carbonate-ramp sedimentation and progradation rates for the late Holocene Abu Dhabi shoreline: Journal of Sedimentary Research, v. 78, p. 423–431.

Lokier, S., and T. Steuber, 2009, Large-scale intertidal polygonal features of the Abu Dhabi coastline: Sedimentology, v. 56, p. 609–621.

Lokier, S. W., 2012, Development and evolution of subaerial halite crust morphologies in a coastal sabkha setting: Journal of Arid Environments, v. 79, p. 32–47.

Lomando, A. J., 1999, Structural influences on facies trends of carbonate inner ramp systems, examples from the Kuwait-Saudi Arabian coast of the Arabian Gulf and Northern Yucatan, Mexico: GeoArabia, v. 4, p. 339–360.

Lomando, A. J., T. P. Birdsall, and C. L. Goll, 1984, Deposition and porosity evolution of Rodessa (Lower Cretaceous) grainstone reservoirs, examples from West Purt and Bois D'Arc fields, Texas, in P. M. Harris, ed., Carbonate sands – a core workshop, v. 5, Society of Economic Paleontologists Mineralogists Core Workshop, p. 365–390.

Loncke, L., V. Gaullier, J. Mascle, B. Vendeville, and L. Camera, 2006, The Nile deep-sea fan: An example of interacting sedimentation, salt tectonics, and inherited subsalt paleotopographic features: Marine and Petroleum Geology, v. 23, p. 297–307.

Long, A., C. J. Eastoe, A. S. Kaufmann, J. G. Martin, L. Wirt, and J. B. Finley, 1993, High precision of chlorine stable isotope ratios: Geochemica et Cosmochimica Acta, v. 57, p. 2907–2912.

Long, D. T., N. E. Fegan, W. B. Lyons, M. E. Hines, P. G. Macumber, and A. M. Giblin, 1992a, Geochemistry of acid brines: Lake Tyrrell, Victoria, Australia.: Chemical Geology, v. 1–2.

Long, D. T., N. E. Fegan, J. D. McKee, W. B. Lyons, M. E. Hines, and P. G. Macumber, 1992b, Formation of alunite, jarosite and hydrous iron oxides in a hypersaline system: Lake Tyrrell, Victoria, Australia.: Chemical Geology, v. 96, p. 183–202.

Long, R. D., 2010, The Paroo Fault and the Mount Isa copper orebodies; a revised structural and evolutionary model, Mt Isa, Queensland, Australia: Doctoral thesis, James Cook University, 238 p.

Longman, M. W., T. G. Fertal, and J. S. Glennie, 1983, Origin and geometry of Red River Dolomite reservoirs, western Williston Basin: American Association Petroleum Geologists – Bulletin, v. 67, p. 744–771.

Lonnee, J., and H. G. Machel, 2006, Pervasive dolomitization with subsequent hydrothermal alteration in the Clarke Lake gas field, Middle Devonian Slave Point Formation, British Columbia, Canada: Bulletin American Association Petroleum Geologists, v. 90, p. 1739–1761.

Lonsdale, P., and K. Becker, 1985, Hydrothermal plumes, hot springs and conductive heat flow in the southern trough of the Guaymas Basin: Earth Planet. Sci. Lett., v. 73, p. 211–225.

Looff, K. M., 2000, Geologic and Microstructural Evidence of Differential Salt Movement at Weeks Island Salt Dome, Iberia Parish, Louisiana: Gulf Coast Association of Geological Societies Transactions, v. 50, p. 543–555.

Looff, K. M., 2001, Recent Salt Related Uplift and Subsidence at Sour Lake Salt Dome, Hardin County, Texas: Gulf Coast Association of Geological Societies Transactions, v. 51, p. 187–194.

Loope, D. B., 1984, Discussion: Origin of extensive bedding planes in aeolian sandstones: a defence of Stoke's hypothesis: Sedimentology, v. 31, p. 123–125.

Loope, D. B., and Z. E. Haverland, 1988, Giant desiccation fissures filled with calcareous eolian sand, Hermosa Formation (Pennsylvanian), southeastern Utah: Sedimentary Geology, v. 56, p. 403–413.

Loosveld, R. J. H., A. Bell, and J. J. M. Terken, 1996, The Tectonic Evolution of Interior Oman: GeoArabia, v. 1, p. 28–51.

Lopez-Cortes, A., J.-L. Ochoa, and R. Vazquez-Duhalt, 1994, Participation of halobacteria in crystal formation and the crystallization rate of NaCl Geomicrobiology Journal, v. 12, p. 69–80.

Loreau, J. P., and B. H. Purser, 1973, Distribution and ultrastructure of Holocene ooids in the Persian Gulf, in B. H. Purser, ed., The Persian Gulf: Holocene carbonate sedimentation, and diagenesis in a shallow epicontinental sea: Berlin, Springer-Verlag, p. 279 –328.

Lorentz, J. C., 2006, Assessment of the geological evidence for karst in the Rustler Formation at the WIPP Site, in L. Land, V. Lueth, B. Raatz, P. Boston, and D. Love, eds., Caves and Karst of Southeastern New Mexico, New Mexico Geological Society, Guidebook 57, p. 243–252.

Lorenz, J. C., 1988, Synthesis of late Paleozoic and Triassic redbed sedimentation in Morocco, in V. H. Jacobshagen, ed., The Atlas

system of Morocco; studies on its geodynamic evolution, v. 15: Berlin, Springer-Verlag, Berlin-Heidelberg-New York, Lecture Notes in Earth Sciences, p. 139–168.

Losh, S., E. Eglinton, M. Schoell, and J. Wood, 1999, Vertical and lateral fluid flow related to a large growth fault, South Eugene Island Block 330 field, offshore Louisiana: American Association Petroleum Geologists – Bulletin, v. 83, p. 244–276.

Losh, S., L. M. Walter, P. Meulbroek, A. Martini, L. M. Cathles III, and J. K. Whelan, 2002, Reservoir fluids and their migration into the South Eugene Island Block 330 reservoirs, offshore Louisiana: American Association Petroleum Geologists – Bulletin, v. 86, p. 1463–1488.

Lottermoser, B. G., 1988, A carbonatitic diatreme from Umberatana, South Australia: Journal of the Geological Society, London, v. 145, p. 505–513.

Lottermoser, B. G., and P. M. Ashley, 1996, Geochemistry and exploration significance of ironstones and barite-rich rocks in the Proterozoic Willyama Supergroup, Olary Block, South Australia: Journal of Geochemical Exploration, v. 57, p. 57–73.

Lotze, F., 1957, Steinsalz und Kalisalze: Berlin, Gebruder Borntraeger.

Loucks, R. G., and J. O. Crump, 1985, Vertical facies sequences of the Sunniland and Punta Gorda formations in the Lower Cretaceous South Florida Embayment; Natural Resource Management Corporation No. 31-2 Alico core: Bebout, D. G., Ratcliff, D. Lower Cretaceous depositional environments from shoreline to slope; a core workshop. Univ. Tex. at Austin, Bur. Econ. Geol., Austin, Tx, United States.

Loucks, R. G., and M. W. Longman, 1982, Lower Cretaceous Ferry Lake Anhydrite, Fairway Field, East Texas; product of shallow-subtidal deposition, in C. R. Handford, R. G. Loucks, and G. R. Davies, eds., Depositional and diagenetic spectra of evaporites; a core workshop., v. 3: Tulsa, OK, SEPM, p. 130–173.

Loucks, R. G., D. L. Richmann, and K. L. Milliken, 1979, Factors controlling porosity and permeability in geopressured Frio sandstone reservoirs, General Crude Oil-Dept. of Energy Pleasant Bayou Test Well, Brazoria County, Texas: Fourth Geopressured-Geothermal Energy Conf.

Loucks, R. G., and J. F. Sarg, 1993, Carbonate sequence stratigraphy : recent developments and applications, v. American Association of Petroleum Geologists Memoir 57: Tulsa, Oklahoma, U.S.A.

Lovatt Smith, P. F., R. B. Stokes, C. S. Bristow, and A. M. Carter, 1996, Mid-Cretaceous inversion in the Northern Khorat Plateau of Lao PDR and Thailand, in R. Hall, and D. Blundell, eds., Tectonic Evolution of Southeast Asia, v. 106: London, Geological Society Special Publication, p. 233–247.

Love, G. D., E. Grosjean, C. Stalvies, C. E. Snape, W. Meredith, D. A. Fike, J. P. Grotzinger, P. N. Taylor, M. J. Newall, and R. E. Summons, 2007, Self Sourcing of Ara Group Carbonate Stringer Oils in the Neoproterozoic-Cambrian South Oman Salt Basin from indigenous kerogen and bitumen (Abstract): American Association Petroleum Geologists Annual Meeting, April 1–4, 2007, Long Beach, California.

Love, S., 1992, Possible ages and origins of some rocks of the Willyama Supergroup, New South Wales: BSc Honours thesis, Australian National University, Canberra.

Low, R., D. M. Anderson, R. A. Boak, and G. Nkala, 2000, An Investigation of Solar Evaporation Pond Leakage and Possible Remedial Measures at Sua Pan, Botswana, in R. M. Geertmann, ed., Eighth World Salt Symposium; The Hague, Netherlands, 7–11 May 2000 v. 1: Amsterdam, Elsevier, p. 523–528.

Lowe, D. R., 1983, Restricted shallow-water sedimentation of early Archean stromatolitic and evaporitic strata of the Strelley Pool Chert, Pilbara Block, Western Australia: Precambrian Research, v. 19, p. 239–283.

Lowe, D. R., 1994, Archean greenstone-related sedimentary rocks, in K. C. Condie, ed., Archean Crustal Evolution: Amsterdam, Elsevier, p. 121–170.

Lowe, D. R., and M. M. Tice, 2004, Geologic evidence for Archean atmospheric and climatic evolution: Fluctuating levels of CO_2, CH_4, and O_2 with an overriding tectonic control: Geology, v. 32, p. 493–496.

Lowe, D. R., and G. F. Worrell, 1999, Sedimentology, mineralogy, and implications of silicified evaporites in the Kromberg Formation, Barberton greenstone belt, South Africa: Special Paper – Geological Society of America, v. 329, p. 167–188.

Lowenstein, T., and F. Risacher, 2009, Closed Basin Brine Evolution and the Influence of Ca-Cl Inflow Waters: Death Valley and Bristol Dry Lake California, Qaidam Basin, China, and Salar de Atacama, Chile: Aquatic Geochemistry, v. 15, p. 71–94.

Lowenstein, T. K., 1987a, Evaporite depositional fabrics in the deeply buried Jurassic Buckner Formation, Alabama: Journal of Sedimentary Petrology, v. 57, p. 108–116.

Lowenstein, T. K., 1987b, Origin of depositional cycles in a Permian "saline giant"; the Salado (McNutt Zone) evaporites of New Mexico and Texas: Geological Society of America Bulletin, v. 100, p. 592–608.

Lowenstein, T. K., 1988, Origin of depositional cycles in a Permian "saline giant"; the Salado (McNutt Zone) evaporites of New Mexico and Texas: Geological Society of America Bulletin, v. 100, p. 592–608.

Lowenstein, T. K., and R. V. Demicco, 2006, Elevated Eocene Atmospheric CO_2 and Its Subsequent Decline: Science, v. 313, p. 1928.

Lowenstein, T. K., and L. A. Hardie, 1985, Criteria for the recognition of salt-pan evaporites: Sedimentology, v. 32, p. 627–644.

Lowenstein, T. K., L. A. Hardie, M. N. Timofeeff, and R. V. Demicco, 2003a, Secular variation in seawater chemistry and the origin of calcium chloride basinal brines: Geology, v. 31, p. 857–860.

Lowenstein, T. K., J. R. Li, C. Brown, S. Roberts, M. , T. L. Ku, S. D. Luo, and W. B. Yang, 1999, 200 ky paleoclimate record from Death Valley salt core: Geology, v. 27, p. 3–6.

Lowenstein, T. K., B. A. Schubert, and M. N. Timofeeff, 2010, Microbial communities in fluid inclusions and long-term survival in halite: GSA Today, v. 21 (1), p. 4–9.

Lowenstein, T. K., and R. J. Spencer, 1990, Syndepositional origin of potash evaporites; petrographic and fluid inclusion evidence: American Journal of Science, v. 290, p. 43–106.

Lowenstein, T. K., and M. N. Timofeeff, 2008, Secular variations in seawater chemistry as a control on the chemistry of basinal brines: test of the hypothesis: Geofluids, v. 8, p. 77–92.

Lowenstein, T. K., M. N. Timofeeff, S. T. Brennan, H. L. A., and R. V. Demicco, 2001, Oscillations in Phanerozoic seawater chemistry: Evidence from fluid inclusions: Science, v. 294, p. 1086–1088.

Lowry, D. C., 1967, Halite speleothems from the Nullarbor Plain, Western Australia: Helicite, v. 6, p. 14–20.

Lu, F. H., and W. J. Meyers, 1998, Massive dolomitisation of a Late Miocene carbonate platform – A case of mixed evaporative brines with meteoric water, Nijar, Spain: Sedimentology, v. 45, p. 263–277.

Lu, F. H., and W. J. Meyers, 2003, Sr, S, and SO_4 Isotopes and the Depositional Environments of the Upper Miocene Evaporites, Spain: Journal of Sedimentary Research, v. 73, p. 444–450.

Lu, F. H., W. J. Meyers, and G. N. Hanson, 2002, Trace elements and environmental significance of Messinian gypsum deposits, the Nijar Basin, southeastern Spain: Chemical Geology, v. 192, p. 149–161.

Lu, F. H., W. J. Meyers, and M. A. Schoonen, 2001, S and $O(SO_4)$ isotopes, simultaneous modeling, and environmental significance of the Nijar messinian gypsum, Spain: Geochimica et Cosmochimica Acta, v. 65, p. 3081–3092.

Lu, F. H., W. J. Meyers, and M. A. A. Schoonen, 1997, Minor and trace element analyses on gypsum – An experimental study: Chemical Geology, v. 142, p. 1–10.

Lu, Y., and A. H. Cooper, 1997, Gypsum karst geohazards in China, in B. F. Beck, and J. B. Stephenson, eds., Engineering Geology and hydrogeology of Karst Terrains: Proceedings of the Sixth Multidisciplinary Conference on Sinkholes and the Engineering and Environmental Impacts of Karst Springfield, Missouri, 6-9 April 1997, Balkema, Rotterdam, p. 117–126.

Lucas, S. G., and O. R. Anderson, 1994, Ochoan (Upper Permian) stratigraphy and age determinations, southeastern New Mexico and West Texas: American Association Petroleum Geologists – Bulletin, v. 78, p. 496.

Lucha, P., F. Gutiérrez, and J. Guerrero, 2008, Environmental problems and geological implications derived from evaporite dissolution in the Barbastro salt anticline (NE Spain): Environmental Geology, v. 53, p. 1045–1055.

Lucia, F. J., 1961, Dedolomitization in the Tansill (Permian) formation: Geological Society America Bulletin, v. 72, p. 1107–1109.

Lucia, F. J., 1968, Recent sediments and diagenesis of south Bonaire, Netherlands Antilles: Journal of Sedimentary Petrology, v. 38, p. 845–858.

Lucia, F. J., 1972, Recognition of evaporite-carbonate shoreline sedimentation, in J. K. Rigby, and W. K. Hamblin, eds., Recognition of ancient sedimentary environments, v. 16, Soc. Econ. Paleontol. Mineral., Spec. Publ., p. 190–191.

Lucia, F. J., J. W. Jennings, and M. Rahnis, 2001, Permeability and rock fabric from wireline logs, Arab-D reservoir, Ghawar Field, Saudi Arabia: GeoArabia, v. 6, p. 619–646.

Lucia, F. J., and R. P. Major, 1994, Porosity evolution through hypersaline reflux dolomitization, in B. Purser, M. Tucker, and D. Zenger, eds., Dolomites – A Volume in Honour of Dolomieu, International Association of Sedimentologists Special Publication No. 21, p. 325–341.

Lucia, J. F., 1999, Carbonate reservoir characterisation: Berlin, Springer, 226 p.

Lucia, F. J., 2007, Carbonate Reservoir Characterization; An Integrated Approach (Second Edition), Springer Berlin Heidelberg, 336 p.

Luczaj, J. A., and R. H. Goldstein, 2000, Diagenesis of the lower Permian Krider member, southwest Kansas, USA: Fluid-inclusion, U-Pb, and fission-track evidence for reflux dolomitization during latest Permian time: Journal of Sedimentary Research Section A-Sedimentary Petrology & Processes, v. 70, p. 762–773.

Ludbrook, N. H., 1965, Occurrence of foraminifera in salt lakes.: Quarterly geological notes, Geological Survey of South Australia, v. 14, p. 6–7.

Lüders, V., B. Plessen, R. L. Romer, S. M. Weise, D. A. Banks, P. Hoth, P. Dulski, and G. Schettler, 2010, Chemistry and isotopic composition of Rotliegend and Upper Carboniferous formation waters from the North German Basin: Chemical Geology, v. 276, p. 198–208.

Luebking, G. A., M. W. Longman, and W. J. Carlisle, 2001, Unconformity-related chert/dolomite production in the Pennsylvanian Amsden Formation, Wolf Springs fields, Bull Mountains basin of central Montana: American Association of Petroleum Geologists Bulletin, v. 85, p. 131–148.

Lugli, S., 2001, Timing of post-depositional events in the Burano Formation of the Secchia valley (Upper Triassic, Northern Apennines), clues from gypsum-anhydrite transitions and carbonate metasomatism: Sedimentary Geology, v. 140, p. 107–122.

Lugli, S., R. Dominici, M. Barone, E. Costa, and C. Cavozzi, 2007, Messinian halite and residual facies in the Crotone basin (Calabria, Italy): Geological Society, London, Special Publications, v. 285, p. 169–178.

Lugli, S., V. Manzi, and M. Roveri, 2008, New facies interpretation of the Messinian evaporites in the Mediterranean, in F. e. Briand, ed., The Messinian Salinity Crisis from Mega-deposits to Microbiology—A Consensus Report: CIESM Workshop Monographs, Monaco, v. 33, p. 67–72.

Lugli, S., V. Manzi, M. Roveri, and C. B. Schreiber, 2010, The Primary Lower Gypsum in the Mediterranean: A new facies interpretation for the first stage of the Messinian salinity crisis: Palaeogeography, Palaeoclimatology, Palaeoecology, v. 297, p. 83–99.

Lugli, S., G. Morteani, and D. Blamart, 2002, Petrographic, REE, fluid inclusion and stable isotope study of magnesite from the Upper Triassic Burano Evaporites (Secchia Valley, northern Apennines): contributions from sedimentary, hydrothermal and metasomatic sources: Mineralium Deposita, v. 37, p. 480–494.

Lugli, S., B. C. Schreiber, Z. Gvirtzman, V. Manzi, and M. Roveri, 2012, Evidence of clastic evaporites in the canyons of the Levant basin (Israel): implications for the Messinian salinity crisis: EGU General Assembly 2013, held 7-12 April, 2013 in Vienna, Austria, id. EGU2013-6813.

Lugli, S., B. C. Schreiber, and B. Triberti, 1999, Giant polygons in the Realmonte mine (Agrigento, Sicily): Evidence for the desiccation of a Messinian halite basin: Journal of Sedimentary Research Section A-Sedimentary Petrology & Processes, v. 69, p. 764–771.

Luhr, J. F., 2008, Primary igneous anhydrite: Progress since its recognition in the 1982 El ChichÛn trachyandesite: Journal of Volcanology and Geothermal Research, v. 175, p. 394–407.

Luján, M., F. Storti, J. C. Balanya, A. Crespo-Blanc, and F. Rossetti, 2003, Role of decollement material with different rheological properties in the structure of the Aljibe thrust imbricate (Flysch Trough, Gibraltar Arc): an analogue modelling approach: Journal of Structural Geology, v. 25, p. 867–881.

Lund, K., R. G. Tysdal, K. V. Evans, M. J. Kunk, and R. M. Pillers, 2011, Structural Controls and Evolution of Gold-, Silver-, and REE-Bearing Copper-Cobalt Ore Deposits, Blackbird District, East-Central Idaho: Epigenetic Origins: Economic Geology, v. 106, p. 585–618.

Lundegard, P. D., and Y. K. Kharaka, 1994, Distribution and occurrence of organic acids in subsurface waters, in E. D. Pittman, and M. D. Lewan, eds., Organic Acids in Geologic Processes: New York, Springer-Verlag, p. 40–69.

Lydon, J. W., 1984, Ore Deposit Models #14. Volcanogenic Massive Sulphide Deposits Part 2: Genetic Models Geoscience Canada, v. 15, p. 43–65.

Lynch, G., and P. S. Giles, 1996, The Ainslie Detachment: a regional flat-lying extensional fault in the Carboniferous evaporitic Maritimes Basin of Nova Scotia, Canada: Canadian Journal of Earth Sciences, v. 33, p. 169–181.

Lynch, G., and J. V. A. Keller, 1998, Association between detachment faulting and salt diapirs in the Devonian-Carboniferous Maritimes Basin, Atlantic Canada: Bulletin of Canadian Petroleum Geology, v. 46, p. 189–209.

Lynch, G., J. V. A. Keller, and P. S. Giles, 1998, Influence of the Ainslie Detachment on the stratigraphy of the Maritimes Basin and mineralisation in the Windsor Group of Northern Nova Scotia, Canada: Economic Geology, v. 93, p. 703–718.

Lyons, J. I., 1988, Volcanogenic iron oxide deposits, Cerro de Mercado and vicinity, Durango, Mexico: Economic Geology, v. 83, p. 1886–1906.

Lyons, T. W., A. M. Gellatly, P. J. McGoldrick, and L. C. Kah, 2006, Proterozoic sedimentary exhalative (SEDEX) deposits and links to evolving global ocean chemistry, in S. E. Kesler, and H. Ohmoto, eds., Evolution of Early Earth's Atmosphere, Hydrosphere, and Biosphere—Constraints from Ore Deposits, v. 198, Geological Society of America Memoir, p. 169–184.

Lyons, W. B., H. E. Gaudette, and H. C. Gustafson, 1982, Dissolved organic carbon in pore waters from a hypersaline environment: Organic geochemistry, v. 3, p. 133–135.

Lyons, W. B., M. E. Hines, and H. E. Gaudette, 1984, Major and minor pore water geochemistry of modern marine sabkhas: the influence of cyanobacterial mats, in Y. Cohen, R. W. Castenholz, and H. O. Halvorsor, eds., Microbial Mats: Stromatolites: New York, A. R. Liss, p. 411–424.

Lyons, W. B., D. T. Long, M. E. Hines, H. E. Gaudette, and P. B. Armstrong, 1984, Calcification of cyanobacterial mats in Solar Lake, Sinai: Geology, v. 12, p. 623–626.

Lyons, W. B., S. W. Tyler, H. E. Gaudette, and D. T. Long, 1995, The use of strontium isotopes in determining groundwater mixing and brine fingering in a playa spring zone, Lake Tyrrell, Australia: Journal of Hydrology, v. 167, p. 225–239.

Ma, G., G. Beaudoin, S. Qi, and Y. Li, 2004, Geology and geochemistry of the Changba SEDEX Pb-Zn deposit, Qinling orogenic belt, China: Mineralium Deposita, v. 39, p. 380–395.

Ma, L., T. K. Lowenstein, B. Li, P. Jiang, C. Liu, J. Zhong, J. Sheng, H. Qiu, and H. Wu, 2010, Hydrochemical characteristics and brine evolution paths of Lop Nor Basin, Xinjiang Province, Western China: Applied Geochemistry, v. 25, p. 1770–1782.

Ma, L., T. K. Lowenstein, and J. M. Russell, 2011, A Brine Evolution Model and Mineralogy of Chemical Sediments in a Volcanic Crater, Lake Kitagata, Uganda: Aquatic Geochemistry, v. 17, p. 129–140.

Macaluso, T., and U. Sauro, 1996, Weathering and Karren on exposed gypsum surfaces: International Journal of Speleology, v. 25, p. 115–126.

MacDonald, G. J. F., 1953, Anhydrite-gypsum equilibrium relations: American Journal Science, p. 884–898.

MacDonald, I. R., 1992, Sea-floor brine pools affect behavior, mortality, and preservation of fishes in the Gulf of Mexico: lagerstatten in the making?: Palaios, v. 7, p. 383–387.

MacDonald, I. R., M. B. Peccini, and N. L. Guinasso Jr, 2000, Pulsed oil discharge from a mud volcano: Geology, v. 28, p. 907–910.

MacDonald, I. R., J. F. Reilly, N. L. Guinasso, J. M. Brooks, R. S. Carney, W. A. Bryant, and T. J. Bright, 1990, Chemosynthetic mussels at a brine-filled pockmark in the northern Gulf of Mexico: Science, v. 248, p. 1096–1099.

MacDonald, I. R., W. W. Sager, and M. B. Peccini, 2003, Gas hydrate and chemosynthetic biota in mounded bathymetry at mid-slope hydrocarbon seeps: Northern Gulf of Mexico: Marine Geology, v. 198, p. 133–158.

MacGowan, D. B., and R. C. Surdam, 1988, Difunctional carboxylic acid anions in oilfield waters: Organic Geochemistry, v. 12, p. 245–259.

Macgregor, D. S., 1996, Factors controlling the destruction or preservation of giant light oil fields: Petroleum Geoscience, v. 2, p. 197–217.

MacGregor, J., E. S. Grew, J. C. M. De Hoog, S. L. Harley, P. M. Kowalski, M. G. Yates, and C. J. Carson, 2013, Boron isotopic composition of tourmaline, prismatine, and grandidierite from granulite facies paragneisses in the Larsemann Hills, Prydz Bay, East Antarctica: Evidence for a non-marine evaporite source: Geochimica et Cosmochimica Acta, v. 123, p. 261–283.

Machel, H. G., 1987, Some aspects of diagenetic sulphate-hydrocarbon redox reactions, in J. D. Marshall, ed., Diagenesis of sedimentary sequences: Geological Society Special Publications, v. 36: London, Geological Society, p. 15–28.

Machel, H. G., 1989, Relationships between sulphate reduction and oxidation of organic compounds to carbonate diagenesis, hydrocarbon accumulations, salt domes, and metal sulphide deposits: Carbonates & Evaporites, v. 4, p. 137–151.

Machel, H. G., 1993, Anhydrite nodules formed during deep burial: Journal of Sedimentary Petrology, v. 63, p. 659–662.

Machel, H. G., 1998, Gas Souring by Thermochemical Sulfate Reduction at 140°C: A discussion: American Association Petroleum Geologists – Bulletin, v. 82, p. 1870–1873.

Machel, H. G., 2001, Bacterial and thermochemical sulfate reduction in diagenetic settings – old and new insights: Sedimentary Geology, v. 140, p. 143–175.

Machel, H. G., 2013, Secondary anhydrites in deeply buried Devonian carbonates of the Alberta Basin, Canada: Carbonates and Evaporites, p. 1–14.

Machel, H. G., and E. A. Burton, 1991, Burial-diagenetic sabkha-like gypsum and anhydrite nodules: Chemical Geology, v. 90, p. 211–231.

Machel, H. G., H. R. Krouse, and R. Sassen, 1995, Products and distinguishing criteria of bacterial and thermochemical sulfate reduction: Applied Geochemistry, v. 10, p. 373–389.

Mackintosh, A. D., and G. A. McVittie, 1983, Geological anomalies observed at the Cominco Ltd. Saskatchewan potash mine: Potash '83; Potash technology; mining, processing, maintenance, transportation, occupational health and safety, environment., p. 59–64.

Macnamara, S., and T. Furnell, 2009, Krubera-Voronja Cave – Towards the Centre of the Earth: Dublin, Speleological Union of Ireland, 58 p.

Macumber, P. G., 1992, Hydrological processes in the Tyrell Basin, southeastern Australia: Chemical Geology, v. 96, p. 1–18.

Madigan, M. T., J. M. Martinko, K. S. Bender, D. Buckley, H., and D. A. Stahl, 2015, Brock Biology of Microorganisms, Pearson Higher Education Publishing, 1006 p.

Magara, K., 1986, Geological models of petroleum entrapment: London, United Kingdom, Elsevier Appl. Sci. Publ.

Magaritz, M., 1987, A new explanation for cyclic deposition in marine evaporite basins; meteoric water input: Chemical Geology, v. 62, p. 239–250.

Magee, J., G. H. Miller, N. A. Spooner, and D. Questiaux, 2004, Continuous 150 k.y. monsoon record from Lake Eyre, Australia: Insolation-forcing implications and unexpected Holocene failure: Geology, v. 32, p. 885–888.

Magee, J. W., 1991, Late Quaternary lacustrine, groundwater, aeolian and pedogenic gypsum in the Prungle Lakes, southeastern Australia: Palaeogeography, Palaeoclimatology, Palaeoecology, v. 84, p. 229–257.

Magee, J. W., J. M. Bowler, G. H. Miller, and D. L. G. Williams, 1995, Stratigraphy, sedimentology, chronology and palaeohydrology of Quaternary lacustrine deposits at Madigan Gulf, Lake Eyre, South Australia: Palaeogeography Palaeoclimatology Palaeoecology, v. 113, p. 3–42.

Magee, J. W., and G. H. Miller, 1998, Lake Eyre palaeohydrology from 60 ka to the present: beach ridges and glacial maximum aridity: Palaeogeography Palaeoclimatology Palaeoecology, v. 144, p. 307–329.

Maglione, G., 1980, An example of Recent continental evaporitic sedimentation; the Chadian Basin (Africa), in G. Busson, ed., Evaporite deposits; illustration and interpretation of some environmental sequences: London, Editions Technip, marketed Graham & Trotman, p. 5–9 & 74–91(photos).

Magnier, C., I. Moretti, J. O. Lopez, F. Gaumet, J. G. Lopez, and J. Letouzey, 2004, Geochemical characterization of source rocks, crude oils and gases of Northwest Cuba: Marine and Petroleum Geology, v. 21, p. 195–214.

Magri, F., R. Littke, S. Rodon, U. Bayer, and J. L. Urai, 2008, Temperature fields, petroleum maturation and fluid flow in the vicinity of salt domes, in R. Littke, ed., Dynamics of Complex

Sedimentary Basins. The Example of the Central European Basin System, Springer-Verlag, Berlin-Heidelberg, p. 277–290.
Maiklem, W. R., 1971, Evaporative drawdown – a mechanism for water level lowering and diagenesis in the Elk Point Basin: Bulletin Canadian Petroleum Geology, v. 19, p. 487–503.
Mainguet, M., and C. Jacqueminet, 1984, Le Grand Erg Occidental et le Grand Erg Oriental. Classification des dunes, balance sédimentaire et dynamique d'ensemble. (Grand Erg Occidental and Grand Erg Oriental. Classification of the dunes, sediment balances and overall dynamics): Travaux de l'Institut de Géographie de Reims, 59–60:29–48. (in French).
Maisonneuve, J., 1982, The composition of the Precambrian ocean waters: Sedimentary Geology, v. 31, p. 1–11.
Majid, A. H., 1987, Exploration Strategy in Keg River Carbonates of Northwestern Alberta, Canada (abs.): American Association Petroleum Geologists – Bulletin, v. 71, p. 588.
Makhlouf, I. M., and A. A. El-Haddad, 2006, Depositional environments and facies of the Late Triassic Abu Ruweis Formation, Jordan: Journal of Asian Earth Sciences, v. 28, p. 372–384.
Malek, E., G. E. Bingham, and G. D. McCurdy, 1990, Evapotranspiration from the margin and moist playa of a closed desert valley: Journal of Hydrology, v. 120, p. 15–34.
Malek-Aslani, M., 1980, Environmental and diagenetic controls of carbonate and evaporite source rocks: Transactions Gulf Coast Association of Geological Societies, v. 30, p. 445–456.
Malenda, H. F., E. L. Simpson, M. J. Szajna, D. L. Fillmore, B. W. Hartline, E. A. Heness, E. R. Kraal, and J. L. Wilk, 2012, Taphonomy of lacustrine shoreline fish-part conglomerates in the Late Triassic age Lockatong Formation (Collegeville, Pennsylvania, USA): Toward the recognition of catastrophic fish kills in the rock record: Palaeogeography, Palaeoclimatology, Palaeoecology, v. 313–314, p. 234–245.
Malinski, E., A. Gasiewicz, A. Witkowski, J. Szafranek, K. Pihlaja, P. Oksman, and K. Wiinamaki, 2009, Biomarker features of sabkha-associated microbialites from the Zechstein Platy Dolomite (Upper Permian) of northern Poland: Palaeogeography, Palaeoclimatology, Palaeoecology, v. 273, p. 92–101.
Maliva, R. G., 1987, Quartz geodes; early diagenetic silicified anhydrite nodules related to dolomitization: Journal of Sedimentary Petrology, v. 57, p. 1054–1059.
Malovichko, A., D. Shulakov, R. Dyaguilev, R. Sabirov, and B. Ahmetov, 2001, Comprehensive Monitoring of the Large Mine-Collapse at the Upper Kama Potash Deposit in Western Ural: Rockbursts and Seismicity in Mines – RaSiM5, South African Institute of Mining and Metallurgy, p. 309–312.
Maltsev, V. A., and D. C. Ford, 1991, The influence of seasonal changes of cave microclimate upon the genesis of gypsum formations in caves: NSS Bulletin, v. 52, p. 99–103.
Maltsev, V. A., and D. I. Malishevsky, 1990, On hydrothermal phases during later stages of the evolution of Cup Coutunn Cave system, Turkmenia, USSR: NSS Bulletin, v. 52, p. 95–98.
Mancini, E. A., and D. J. Benson, 1980, Regional stratigraphy of the Upper Jurassic Smackover carbonates of southwest Alabama: Transactions of Gulf Coast Association of Geological Societies, v. 30, p. 151–165.
Mancini, E. A., J. Benson, B. S. Hart, R. S. Balch, W. C. Parcell, and B. J. Panetta, 2000, Appleton field case study (eastern Gulf coastal plain): Field development model for Upper Jurassic microbial reef reservoirs associated with paleotopographic basement structures (E & P Notes): American Association Petroleum Geologists – Bulletin, v. 84, p. 1699–1717.
Mancini, F., F. Stecchi, M. Zanni, and G. Gabbianelli, 2009, Monitoring ground subsidence induced by salt mining in the city of Tuzla (Bosnia and Herzegovina): Environmental Geology, v. 58, p. 381–389.
Manega, P. C., and S. Bieda, 1987, Modern sediments of Lake Natron, Tanzania: Sciences Geologiques – Bulletin, v. 40, p. 83–95.
Manheim, F. T., 1974, 33. Red Sea geochemistry: Woods Hole Oceanogr. Inst., Collect. Repr., v. 23, p. 975–998.
Mann, A. W., and R. L. Deutscher, 1978, Genesis principles for the precipitation of carnotite in calcrete drainages in Western Australia: Economic Geology, v. 73, p. 1724–1737.
Mann, C. J., and W. M. Nelson, 1989, Microbialitic structures in Storr's Lake, San Salvador Island, Bahamas Islands: Palaios, v. 4, p. 287–293.
Mann, S. D., 1988, Subaqueous Evaporites of the Buckner Member, Haynesville Formation, Northeastern Mobile County, Alabama: Gulf Coast Association of Geological Societies Transactions, v. 38, p. 187–196.
Mann, S. D., 1990, Depositional facies of saltern evaporites of the Buckner Anhydrite Member of the Haynesville Formation of southwestern Alabama: Geological Society of America, Southeastern Section, 39th annual meeting. Abstracts with Programs Geological Society of America, v. 22, p. 24.
Mann, S. D., and M. D. C. Kopaska, 1992, Depositional history of the Smackover-Buckner transition, eastern Mississippi interior salt basin: American Association Petroleum Geologists Bulletin, v. 76, p. 1463.
Mansour, A. R., and K. J. Takrouri, 2007, A new technology for the crystallization of Dead Sea potassium chloride: Chemical Engineering Communications, v. 194, p. 803–810.
Manspeizer, W., 1982, Triassic-Liassic basins and climate of the Atlantic passive margins: International Journal of Earth Sciences, v. 71, p. 895–917.
Manutchehr-Danai, M., 2005, Dictionary of Gems and Gemmology: Berlin, Springer, 879 p.
Manzi, V., S. Lugli, F. R. Lucchi, and M. Roveri, 2005, Deep-water clastic evaporites deposition in the Messinian Adriatic foredeep (northern Apennines, Italy): did the Mediterranean ever dry out?: Sedimentology, v. 52, p. 875–902.
Manzi, V., S. Lugli, M. Roveri, B. C. Schreiber, and R. Gennari, 2011, The Messinian "Calcare di Base" (Sicily, Italy) revisited: Geological Society of America Bulletin, v. 123, p. 347–370.
Manzo, E., E. Perri, and M. E. Tucker, 2012, Carbonate deposition in a fluvial tufa system: processes and products (Corvino Valley – southern Italy): Sedimentology, v. 59, p. 553–577.
Mao, J., Y. Chen, and J. Yu, 2008, The iron oxide-apatite deposits in the Ningwu Cretaceous Basin in the lower reach of the Yangtze River valley, China: International Geological Congress, Abstracts, v. 33.
Marco, S., R. Weinberger, and A. Agnon, 2002, Radial clastic dykes formed by a salt diapir in the Dead Sea Rift, Israel: Terra Nova, v. 14, p. 288–294.
Margulis, L., and M. F. Dolan, 2002, Early Life: Evolution on the Precambrian Earth, Jones and Bartlett, 224 p.
Mariano, A. N., and P. L. Roeder, 1983, Kerimasi: A Neglected Carbonatite Volcano: The Journal of Geology, v. 91, p. 449–455.
Mariner, R. H., and R. C. Surdam, 1970, Alkalinity and formation of zeolites in saline alkaline lakes: Science, v. 170, p. 977–980.
Marion, G. M., R. Farren, and A. Komrowski, 1999, Alternative pathways for seawater freezing: Cold Regions Science and Technology, v. 29, p. 259–266.
Markl, G., and K. Bucher, 1998, Composition of fluids in the lower crust inferred from metamorphic salt in lower crustal rocks: Nature, v. 391, p. 781–783.
Markl, G., and S. Piazolo, 1998, Halogen-bearing minerals in syenites and high-grade marbles of Dronning Maud Land, Antarctica – Monitors of fluid compositional changes during late-magmatic fluid-rock interaction processes: Contributions to Mineralogy & Petrology, v. 132, p. 246–248.

Marschik, R., and L. Fontbote, 2001, The Candelaria-Punta del Cobre iron-oxide Cu-Au(-Zn-Ag) deposits, Chile: Economic Geology, v. 96, p. 1799–1826.

Marschik, R., R. Spikings, and I. Kuscu, 2008, Geochronology and stable isotope signature of alteration related to hydrothermal magnetite ores in Central Anatolia, Turkey: Mineralium Deposita, v. 43, p. 111–124.

Marshak, S., and T. Flottmann, 1996, Structure and origin of the Fleurieu and Nackara arcs in the Adelaide fold-thrust belt, South Australia – Salient and recess development in the Delamerian Orogen: Journal of Structural Geology, v. 18, p. 891–908.

Marshall, A. T., P. Kyriakou, P. D. Cooper, P. Coy, and A. Wright, 1995, Osmolality of rectal fluid from two species of osmoregulating brine fly larvae (*Diptera: Ephyridae*): J. Insect Physiol., v. 41, p. 413–418.

Marshall, L., N. Oliver, and G. Davidson, 2006, Carbon and oxygen isotope constraints on fluid sources and fluid–wallrock interaction in regional alteration and iron-oxide–copper–gold mineralisation, eastern Mt Isa Block, Australia: Mineralium Deposita, v. 41, p. 429–452.

Marshall, L. J., and N. H. S. Oliver, 2008, Constraints on hydrothermal fluid pathways within Mary Kathleen Group stratigraphy of the Cloncurry iron-oxide-copper-gold District, Australia: Precambrian Research, v. 163, p. 151–158.

Marti-Cardona, B., T. E. Steissberg, S. G. Schladow, and S. J. Hook, 2008, Relating fish kills to upwellings and wind patterns in the Salton Sea: Hydrobiologia, v. 60, p. 85–95.

Martin, J. B., J. M. Gieskes, M. Torres, and M. Kastner, 1993a, Bromine and iodine in Peru Margin sediments and pore fluids – Implications for fluid origins: Geochimica et Cosmochimica Acta, v. 57, p. 4377–4389.

Martin, J. M., J. C. Braga, C. Betzler, and T. Brachert, 1996, Sedimentary model and high-frequency cyclicity in a Mediterranean, shallow-shelf, temperate-carbonate environment (uppermost Miocene, Agua Amarga Basin, southern Spain: Sedimentology, v. 43, p. 263–277.

Martin, J. M., J. C. Braga, and R. Riding, 1993b, Siliciclastic stromatolites and thrombolites, late Miocene, S.E. Spain: Journal of Sedimentary Petrology, v. 63, p. 131–139.

Martin, J. M., H. M. Ortega, and R. J. Torres, 1984, Genesis and evolution of strontium deposits of the Granada Basin (southeastern Spain): evidence of diagenetic replacement of a stromatolite belt: Sedimentary Geology, v. 39, p. 281–298.

Martinez, J. D., and R. Boehner, 1997, Sinkholes in glacial drift underlain by gypsum in Nova Scotia, Canada: Carbonates and Evaporites, v. 12, p. 84–90.

Martinez, J. D., K. S. Johnson, and J. T. Neal, 1998, Sinkholes in Evaporite Rocks: American Scientist, v. 86(1). DOI:10.1511/1998.17.909.

Martini, A. M., L. M. Walter, T. W. Lyons, V. C. Hover, and J. Hansen, 2002, Significance of early-diagenetic water-rock interactions in a modern marine siliciclastic/evaporite environment: Salina Ometepec, Baja California: Geological Society America Bulletin, v. 114, p. 1055–1069.

Martini, J. E. J., R. E. Wipplinger, and F. G. Moen, 1997, Mbobo Mkulu Cave, South Africa, in C. A. Hill, and R. Forti, eds., Cave Minerals of the World: Huntsville, Alabama, National Speleological Society, p. 336–339.

Martinsson, O., A. Allan, T. Niiranen, C. Wanhainen, R. Eilu, J. Ojala, V. Nykanen, and R. Weihed, 2008, Iron oxide-Cu-Au deposits in the northern part of the Fennoscandian Shield: International Geological Congress, Abstracts, v. 33.

Mascle, A., and R. Vially, 1999, The petroleum systems of the Southeast Basin and Gulf of Lion (France): Geological Society, London, Special Publications, v. 156, p. 121–140.

Masrouhi, A., O. Bellier, and H. Koyi, 2014, Geometry and structural evolution of Lorbeus diapir, northwestern Tunisia: polyphase diapirism of the North African inverted passive margin: International Journal of Earth Sciences, v. 103, p. 881–900.

Masse, M., O. Bourgeois, S. Le Mouelic, C. Verpoorter, A. Spiga, and L. Le Deit, 2012, Wide distribution and glacial origin of polar gypsum on Mars: Earth and Planetary Science Letters, v. 317–318, p. 44–55.

Matagi, S. V., 2004, A biodiversity assessment of the Flamingo Lakes of eastern Africa: Biodiversity and Conservation, v. 5, p. 13–26.

Mathalone, J. M. P., and M. Montoya R., 1995, Petroleum geology of the sub-Andean basins of Peru, in A. J. R. Tankard, S. Suárez, and H. J. Welsink, eds., Petroleum basins of South America, American Association Petroleum Geologist Memoir 62, p. 423–144.

Matias, H., P. Kress, P. Terrinha, W. Mohriak, P. T. L. Menezes, L. Matias, F. Santos, and F. Sandnes, 2011, Salt tectonics in the western Gulf of Cadiz, southwest Iberia: Bulletin American Association Petroleum Geologists, v. 95, p. 1667–1698.

Matsubara, S., A. Kato, and E. Hashimoto, 1992, Celestine from the Asaka gypsum mine, Koriyama City, Fukushima Prefecture, Japan: Min. J. (Japan), v. 16, p. 16–20.

Mattes, B. W., and S. Conway-Morris, 1990, Carbonate/ evaporite deposition in the Late Precambrian-Early Cambrian Ara Formation of southern Oman, in A. H. F. Robertson, M. P. Searle, and A. C. Ries, eds., The geology and tectonics of the Oman region, v. 49, Geological Society Special Publications, p. 617–636.

Matthai, S. K., and R. W. Henley, 1996, Geochemistry and depositional environment of the gold-mineralised Proterozoic Koolpin Formation, Pine Creek Inlier, Northern Australia, Northern Australia – A comparison with modern shale sequences: Precambrian Research, v. 78, p. 211–235.

Matthai, S. K., R. W. Henley, and C. A. Heinrich, 1995, Gold precipitation by fluid mixing in bedding-parallel fractures near Carbonaceous slates at the Cosmopolitan Howley gold deposit, northern Australia: Economic Geology, v. 90, p. 2123–2142.

Matthews, R. D., and G. C. Egleson, 1974, Origin and Implications of a Mid-Basin Potash Facies in the Salina Salt of Michigan, Fourth International Symposium on Salt, v. 1, Northern Ohio Geological Society, p. 15–34.

Matthews, W. J., G. J. Hampson, B. D. Trudgill, and J. R. Underhill, 2007, Controls on fluviolacustrine reservoir distribution and architecture in passive salt-diapir provinces: Insights from outcrop analogs: Bulletin American Association Petroleum Geologists, v. 91, p. 1367–1403.

Mauger, C. L., and J. S. Compton, 2011, Formation of modern dolomite in hypersaline pans of the Western Cape, South Africa: Sedimentology, v. 58, p. 1678–1692.

Mauger, R. L., 2007, Contact metamorphism-metasomatism associated with the latest Eocene northern Italian Mountain granite intrusion, Gunnison County, Colorado: Abstracts with Programs – Geological Society of America, v. 39, p. 394.

Mawson, S. D., 1929, Some South Australian limestones in process of formation: Quarterly Journal of the Geological Society, v. 85, p. 613–623.

Mayrhofer, H., 1985, World reserves of mineable potash salts based on structural analysis: Sixth international symposium on salt, v. 2, p. 141–160.

Mazhari, S. A., S. Amini, J. Ghalamghash, and F. Bea, 2011, Metasomatic stages and scapolitization effects on chemical composition of Pasveh pluton, NW Iran: Journal of Earth Science, v. 22, p. 619–631.

Mazurov, M., S. Grishina, V. Istomin, and A. Titov, 2007, Metasomatism and ore formation at contacts of dolerite with saliferous rocks in the sedimentary cover of the southern Siberian platform: Geology of Ore Deposits, v. 49, p. 271–284.

Mazurov, M. P., and A. T. Titov, 1999, Magnesian skarns from the sites of layer-by-layer injections of basic magma into the evaporites of

the platform's sedimentary cover [Russian]: Geologiya i Geofizika, v. 40, p. 82–89.

Mazzini, A., H. Svensen, G. Etiope, N. Onderdonk, and D. Banks, 2011, Fluid origin, gas fluxes and plumbing system in the sediment-hosted Salton Sea Geothermal System (California, USA): Journal of Volcanology and Geothermal Research, v. 205, p. 67–83.

Mazzoli, S., 1994, Early deformation features in syn-orogenic Messinian sediments of the northern Marchean Apennines (Italy): Annales Tectonicae, v. 8, p. 134–147.

Mazzullo, S. J., and B. A. Birdwell, 1989, Syngenetic formation of grainstones and pisolites from fenestral carbonates in peritidal settings: Journal of Sedimentary Petrology, v. 59, p. 605–611.

McArdle, P., M. Fitzell, M. G. Oosterom, P. J. O'Connor, and P. S. Kennan, 1989, Tourmalinite as a potential host rock for gold in the Caledonides of Southeast Ireland: Mineralium Deposita, v. 24, p. 154–159.

McArthur, J. M., J. Turner, W. B. Lyons, A. O. Osborn, and M. F. Thirlwall, 1991, Hydrochemistry on the Yilgarn Block, Western Australia: ferrolysis and mineralization in acidic brines: Geochimica et Cosmochimica Acta, v. 55, p. 1273–1288.

McArthur, J. M., J. Turner, W. B. Lyons, and M. F. Thirlwall, 1989, Salt sources and water-rock interaction on the Yilgarn Block, Australia: isotopic and major element tracers: Applied Geochemistry, v. 4, p. 79–92.

McBride, B. C., M. G. Rowan, and P. Weimer, 1998a, The evolution of allochthonous salt systems, northern Green Canyon and Ewing Bank (offshore Louisiana), northern Gulf of Mexico: American Association Petroleum Geologists – Bulletin, v. 82, p. 1013–1036.

McBride, B. C., P. Weimer, and M. G. Rowan, 1998b, The effect of allochthonous salt on the petroleum systems of northern Green Canyon and Ewing Bank (offshore Louisiana), Northern Gulf of Mexico: American Association of Petroleum Geologists Bulletin, v. 82, p. 1083–1112.

McBride, E. F., L. S. Land, and L. E. Mack, 1987, Diagenesis of aeolian and fluvial feldspathic sandstones, Norphlet Formation (Upper Jurassic), Rankin County, Mississippi, and Mobile County, Alabama.: American Association Petroleum Geologists Bulletin, v. 71, p. 1019–1034.

McCaffrey, M. A., B. Lazar, and H. D. Holland, 1987, The evaporation path of seawater and the coprecipitation of Br(-) and K(+) with halite: Journal of Sedimentary Petrology, v. 57, p. 928–937.

McCaig, A. M., J. Tritlla, and D. Banks, 2000, Fluid mixing and recycling during Pyrenean thrusting: Evidence from fluid inclusion halogen ratios: Geochimica et Cosmochimica Acta, v. 64, p. 3395–3412.

McCall, J., 2010, Lake Bogoria, Kenya: Hot and warm springs, geysers and Holocene stromatolites: Earth-Science Reviews, v. 103, p. 71–79.

McCammon, M. A., and J. S. Hanor, 2012, Spatial Variations in Pore Water Salinities above and below Allochthonous Salt in Offshore Gulf of Mexico Sediments—Implications for Mechanisms of Solute Transport and Timing of Salt Emplacement: Gulf Coast Association of Geological Societies Transactions, v. 62, p. 303–316.

McClay, K. R., 1990, Extensional fault systems in sedimentary basins: a review of analogue studies: Marine and Petroleum Geology, p. 206–233: Marine and Petroleum Geology, v. 7, p. 206–233.

McClay, K. R., 1992, Glossary of thrust tectonics terms, in K. R. McClay, ed., Thrust tectonics: London, Chapman and Hall, p. 419–433.

McClay, K. R., and D. G. Carlile, 1978, Mid-Proterozoic sulphate evaporites at Mount Isa Mine, Queensland, Australia: Nature, v. 274, p. 240–241.

McConachie, B. A., and J. N. Dunster, 1996, Sequence stratigraphy of the Bowthorn Block in the Northern Mt Isa Basin, Australia – Implications for the base metal mineralisation process: Geology, v. 24, p. 155–158.

McCord, T. B., G. B. Hansen, F. P. Fanale, R. Carlson, W. , D. L. Matson, T. V. Johnson, W. D. Smythe, J. K. Crowley, P. D. Martin, A. Ocampo, C. A. Hibbitts, and J. C. Granahan, 1998, Salts on Europa's surface detected by Galileo's near infrared mapping Spectrometer: Science, v. 280, p. 1242–1245.

McCord, T. B., P. Hayne, J.-P. Combe, G. B. Hansen, J. W. Barnes, S. b. Rodriguez, S. p. Le Mouélic, E. K. H. Baines, B. J. Buratti, C. Sotin, P. Nicholson, R. Jaumann, R. Nelson, and V. T. the Cassini, 2008, Titan's surface: Search for spectral diversity and composition using the Cassini VIMS investigation: Icarus, v. 194, p. 212–242.

McCracken, S. R., H. Etminan, A. G. Connor, and V. A. Williams, 1997, Geology of the Admiral Bay carbonate-hosted zinc-lead deposit, Canning Basin, Western Australia: Special Publication – Society of Economic Geologists, v. 4, p. 330–349.

McDougall, K., 2008, Late Neogene marine incursions and the ancestral Gulf of California: Special Paper – Geological Society of America, v. 439, p. 355–373.

McGlue, M. M., G. S. Ellis, A. S. Cohen, and P. W. Swarzenski, 2012, Playa-lake sedimentation and organic matter accumulation in an Andean piggyback basin: the recent record from the Cuenca de Pozuelos, North-west Argentina: Sedimentology, v. 59, p. 1237–1256.

McGoldrick, P J., Dunster, J., Cooke, D., and Aheimer, M., 1996, New observations from the Lady Loretta Zn-Pb-Ag deposit: Towards a genetic model: James Cook University, Economic Geology Research Unit Contribution, v. 55, p. 81–84.

McGoldrick, P. J., and R. R. Keays, 1990, Mount Isa copper and lead-zinc-silver ores; coincidence or cogenesis?: Economic Geology, v. 85, p. 641–650.

McGowan, R. R., S. Roberts, and A. J. Boyce, 2006, Origin of the Nchanga copper-cobalt deposits of the Zambian Copperbelt: Mineralium Deposita, v. 40, p. 617–638.

McGowran, B., G. Moss, and A. Beecroft, 1992, Late Eocene and early Oligocene in southern Australia: local neritic signals of global oceanic changes, in D. R. Prothero, and W. A. Berggren, eds., Late Eocene-Oligocene Climatic and Biotic Evolution: Princeton, NJ, Princeton University Press, p. 178–201.

McGregor, D. R., E. C. Pendery, and D. L. McGregor, 1963, Solution caves in gypsum, north central Texas: Journal of Geology, v. 71, p. 108–115.

McGuinness, D. B., and J. R. Hossack, 1993, The development of allochthonous salt sheets as controlled by the rates of extension, sedimentation, and salt supply, in J. M. Armentrout, R. Bloch, H. C. Olson, and B. F. Perkins, eds., Rates of Geologic Processes, Gulf Coast Section SEPM Foundation, 14th Annual Research Conference, Houston, Texas, p. 127–139.

McHague, T. R., 1990, Stratigraphic development of Proto-South Atlantic rifting in Cabinda, Angola – A petrolifeous lake basin, in B. J. Katz, ed., Lacustrine Basin Exploration-Case Studies and Modern Analogs, Am. Assoc. Petrol. Geol. Mem. 50, p. 307–326.

McIntosh, J. C., G. Garven, and J. S. Hanor, 2011, Impacts of Pleistocene glaciation on large-scale groundwater flow and salinity in the Michigan Basin: Geofluids, v. 11, p. 18–33.

McIntosh, R. A., and W. N. C., 1968, Barren halite bodies in the sylvinite mining zone at Esterhazy, Saskatchewan: Canadian Journal Earth Sciences, v. 5, p. 1221–1238.

McKay, C. P., 1996, Elemental composition, solubility, and optical properties of Titan's organic haze: Planetary & Space Science, v. 44, p. 741–747.

McKee, D. M., and P. J. Hannon, 1985, The hydrological environment at the Gays River Mine, Gays River, Nova Scotia, Canada: International Journal of Mine Water, v. 4, p. 13–34.

McKenzie, J. A., 1981, Holocene dolomitization of calcium carbonate sediments from the coastal sabkhas of Abu Dhabi, U.A.E.: Journal Geology, v. 89, p. 185–198.

McKenzie, J. A., K. J. Hsu, and J. F. Schneider, 1980, Movement of subsurface waters under the sabkha, Abu Dhabi, UAE and its relation to evaporative dolomite genesis, in D. H. Zenger, J. B. Dunham, and R. L. Ethington, eds., Concepts and Models of Dolomitization, SEPM Spec. Publ. 28, p. 11–30.

McKibben, M. A., J. P. Andes Jr, and A. E. Williams, 1988b, Active ore formation at a brine interface in metamorphosed deltaic lacustrine sediments: the Salton Sea geothermal system, California: Economic Geology, v. 83, p. 511–523.

McKibben, M. A., A. E. Williams, W. A. Elders, and C. S. Eldridge, 1987, Saline brines and metallogenesis in a modern sediment-filled rift; the Salton Sea geothermal system, California, U.S.A.: Applied Geochemistry, v. 2, p. 563–578.

McKibben, M. A., A. E. Williams, and S. Okubo, 1988a, Metamorphosed Plio-Pleistocene evaporites and the origins of hypersaline brines in the Salton Sea geothermal system, California; fluid inclusion evidence: Geochimica et Cosmochimica Acta, v. 52, p. 1047–1056.

McKirdy, D. M., A. J. Hayball, J. K. Warren, E. D., and C. C. von der Borch, 2010, Organic facies of Holocene carbonates in North Stromatolite Lake, Coorong region, South Australia: Cadernos Laboratorio Xeolóxico de Laxe, v. 35, p. 127–146.

McLaren, S., and M. W. Wallace, 2010, Plio-Pleistocene climate change and the onset of aridity in southeastern Australia: Global and Planetary Change, v. 71, p. 55–72.

McLaren, S., M. W. Wallace, and T. Reynolds, 2012, The Late Pleistocene evolution of palaeo megalake Bungunnia, southeastern Australia: A sedimentary record of fluctuating lake dynamics, climate change and the formation of the modern Murray River: Palaeogeography, Palaeoclimatology, Palaeoecology, v. 317,Äì318, p. 114–127.

McManus, A., and M. W. Wallace, 1992, Age of Mississippi Valley type sulfides determined using cathodoluminesence cement stratigraphy, Lennard Shelf, Canning Basin, Western Australia.: Economic Geology, v. 87, p. 189–193.

McManus, K. M., and J. S. Hanor, 1993, Diagenetic evidence for massive evaporite dissolution, fluid flow, and mass transfer in the Louisiana Gulf Coast: Geology, v. 21, p. 727–730.

McMillan, C., and F. N. Moseley, 1967, Salinity tolerances of five marine macrophytes of Redfish Bay, Texas: Ecology, v. 48, p. 503–506.

McMullin, E. R., K. Nelson, C. R. Fisher, and S. W. Schaeffer, 2010, Population structure of two deep sea tubeworms, *Lamellibrachia luymesi* and *Seepiophila jonesi*, from the hydrocarbon seeps of the Gulf of Mexico: Deep Sea Research Part I: Oceanographic Research Papers, v. 57, p. 1499–1509.

McNaughton, K., and T. E. Smith, 1986, A fluid inclusion study of sphalerite and dolomite from the Nanisivik lead- zinc deposit, Baffin Island, Northwest Territories, Canada: Economic Geology, v. 81, p. 713–720.

McNeal, R. P., and G. A. Hemenway, 1972, Geology of Fort Stockton Sulfur Mine, Pecos County, Texas: American Association Petroleum Geologists – Bulletin, v. 56, p. 26–37.

McNeil, B., H. F. Shaw, and A. H. Rankin, 1998, The timing of cementation in the Rotliegend sandstones of the southern North Sea – A petrological and fluid inclusion study of cements: Journal of Petroleum Geology, v. 21, p. 311–327.

McPhie, J., 1993, The Tennant Creek Porphyry revisited – A synsedimentary sill with peperite margins, Early Proterozoic, Northern Territory: Australian Journal of Earth Sciences, v. 40, p. 545–558.

McPhie, J., V. S. Kamenetsky, I. Chambefort, K. Ehrig, and N. Green, 2011, Origin of the supergiant Olympic Dam Cu-U-Au-Ag deposit, South Australia: Was a sedimentary basin involved?: Geology, v. 39, p. 795–798.

McQuillan, H., 1985, Fracture-controlled production from the Oligocene-Miocene Asmari Formation in Gachsaran and Bibi Hakimeh fields, Southwest Iran, in P. O. Roehl, and P. W. Choquette, eds., Carbonate petroleum reservoirs: New York, Springer-Verlag, p. 511–523.

McTavish, G. J., and L. W. Vigrass, 1987, Salt dissolution and tectonics, south-central Saskatchewan, in C. G. Carlson, and J. E. Christopher, eds., Proceedings of the fifth international Williston basin symposium, v. 9, Saskatchewan Geological Society, Special Publication, p. 157–168.

McWhae, J. R. H., 1953, The Carboniferous breccia of Bellefjordan: Geol. Mag., v. 90, p. 287–298.

Mees, F., C. CastaÒeda, J. Herrero, and E. Van Ranst, 2011, Bloedite sedimentation in a seasonally dry saline lake (Salada Mediana, Spain): Sedimentary Geology, v. 238, p. 106–115.

Mége, D., L. Le Deit, T. Rango, and T. Korme, 2013, Gravity tectonics of topographic ridges: Halokinesis and gravitational spreading in the western Ogaden, Ethiopia: Geomorphology, v. 193, p. 1–13.

Meier, R., 1979, Zum Problem praekambrischer Salinarvor-kommen: Z. Angew. Geol., v. 25, p. 1–9.

Meijer Drees, N. C., 1994, Chapter 10 – Devonian Elk Point Group of the Western Canada Sedimentary Basin, Atlas of the Western Canada Sedimentary Basin, Canadian Geological Survey, p. 129–147.

Meijer, P. T., 2012, Hydraulic theory of sea straits applied to the onset of the Messinian Salinity Crisis: Marine Geology, v. 326, Äì328, p. 131–139.

Meisling, K. E., P. R. Cobbold, and V. S. Mount, 2001, Segmentation of an obliquely rifted margin, Campos and Santos basins, southeastern Brazil: Bulletin-American Association of Petroleum Geologists, v. 85, p. 1903–1924.

Meister, F. M., and N. Aurich, 1972, Geologic outline and oil fields of Sergipe Basin, Brazil: American Assoc. Petrol. Geol. Bull., v. 56, p. 1034–1047.

Meister, P., C. Reyes, W. Beaumont, M. Rincon, L. Collins, W. Berelson, L. Stott, F. Corsetti, and K. H. Nealson, 2011, Calcium and magnesium-limited dolomite precipitation at Deep Springs Lake, California: Sedimentology, v. 58, p. 1810–1830.

Melack, J. M., and R. Jellison, 1998, Limnological conditions in Mono Lake: contrasting monomixis and meromixis in the 1990s: Hydrobiologia, v. 384, p. 21–39.

Melack, J. M., and P. Kilham, 1974, Photosynthetic rates of phytoplankton in East-African alkaline saline lakes: Limnology and Oceanography, v. 19, p. 743–755.

Melas, F. F., and G. M. Friedman, 1992, Petrophysical characteristics of the Jurassic Smackover Formation, Jay Field, Conecuh embayment, Alabama and Florida: American Association of Petroleum Geologists Bulletin, v. 76, p. 81–100.

Melchor, R. N., M. C. Cardonatto, and G. Visconti, 2012, Palaeonvironmental and palaeoecological significance of flamingo-like footprints in shallow-lacustrine rocks: An example from the Oligocene-Miocene Vinchina Formation, Argentina: Palaeogeography, Palaeoclimatology, Palaeoecology, v. 315–316, p. 181–198.

Melezhik, V. A., A. E. Fallick, P. V. Medvedev, and V. V. Makarikhin, 2001, Palaeoproterozoic magnesite: lithological and isotopic evidence for playa/sabkha environments: Sedimentology, v. 48, p. 379–397.

Melezhik, V. A., A. E. Fallick, D. V. Rychanchik, and A. B. Kuznetsov, 2005, Palaeoproterozoic evaporites in Fennoscandia: implications for seawater sulphate, the rise of atmospheric oxygen and local amplification of the delta C-13 excursion: Terra Nova, v. 17, p. 141–148.

Melgarejo, J. C., and R. M. Prol-Ledesma, 1999, Th and REE deposits in the Oaxaca Complex in southern Mexico, in C. J. Stanley, ed., Mineral deposits: Processes to processing: Rotterdam, Netherlands, Balkema, p. 389–392.

Melim, L. A., 1991, The origin of dolomite in the Permian (Guadalupian) Capitan Formation, Delaware Basin, west Texas and New Mexico:

implications for dolomitization models: Doctoral thesis, Southern Methodist University, Dallas, Texas, 200 p.

Melim, L. A., and P. A. Scholle, 2002, Dolomitization of the Capitan Formation forereef facies (Permian, west Texas and New Mexico): seepage reflux revisited: Sedimentology, v. 49, p. 1207–1227.

Mello, M. R., and J. R. Maxwell, 1991, Organic geochemical and biological marker characterization of source rocks and oils derived from lacustrine environments in the Brazilian continental margin, in B. J. Katz, ed., Lacustrine basin exploration case studies and modern analogs: Tulsa OK, American Association Petroleum Geologists Memoir, 50, p. 77–97.

Mello, U. T., G. D. Karner, and R. Anderson, 1995, Role of salt in restraining the maturation of sub-salt source rocks: Marine & Petroleum Geology, v. 12, p. 697–716.

Menduina, J., S. Ordonez, and M. A. Garcia del Cura, 1984, Geologia del yacimiento de glauberita de Cerezo del Rio Tiron (Provincia de Burgos): Boletin Geologico y Minero, Instituto Geologico y Minero de Espana, v. 95, p. 33–51.

Meng, F., P. Ni, J. D. Schiffbauer, X. Yuan, C. Zhou, Y. Wang, and M. Xia, 2011, Ediacaran seawater temperature: Evidence from inclusions of Sinian halite: Precambrian Research, v. 184, p. 63–69.

Menning, M., 1995, A numerical time scale for the Permian and Triassic periods: An integrative time analysis, in P. A. Scholle, T. Peryt, and D. S. Ulmer-Scholle, eds., The Permian of Northern Pangea, 1. Paleogeography, Paleoclimates, Stratigraphy: Berlin, Springer Verlag, p. 77–97.

Menzel, D. W., and J. H. Ryther, 1970, Distribution and recycling of organic matter in the oceans, in D. W. Hood, ed., Organic matter in natural waters, v. 1, University of Alaska, Institute of Marine Science, Occasional Publication, p. 31–53.

Merabet, O., and A. Popov, 1971, Les bassins saliferes de l'Algerie, in G. Richter-Bernberg, ed., Geology of saline deposits: Paris, UNESCO, p. 167–176.

Mercadier, J., A. Richard, and M. Cathelineau, 2012, Boronand magnesium-rich marine brines at the origin of giant unconformity-related uranium deposits: ^{11}B evidence from Mg-tourmalines: Geology, v. 40, p. 231–234.

Mernagh, T. P., C. A. Heinrich, J. F. Leckie, D. P. Carville, D. J. Gilbert, R. K. Valenta, and L. A. I. Wyborn, 1994, Chemistry of low-temperature hydrothermal gold, platinum, and palladium (+/- uranium) mineralization at Coronation Hill, Northern Territory, Australia: Economic Geology, v. 89, p. 1053–1073.

Merrell, M. P., P. B. Flemings, and G. L. Bowers, 2014, Subsalt Pressure Prediction in the Miocene Mad Dog Field, Gulf of Mexico Bulletin American Association Petroleum Geologists, v. 98, p. 315–340.

Meshref, W. M., 1990, Tectonic framework, in R. Said, ed., The Geology of Egypt: Rotterdam, A. A. BALKEMA, p. 113–156.

Mesolella, K. J., J. D. Robinson, L. M. McCormick, and A. R. Ormiston, 1974, Cyclic deposition of Silurian carbonates and evaporites in Michigan Basin: American Association Petroleum Geologists – Bulletin, v. 58, p. 34–62.

Messina, P., P. Stoffer, and W. C. Smith, 2005, Macropolygon morphology, development, and classification on North Panamint and Eureka playas, Death Valley National Park CA: Earth-Science Reviews, v. 73, p. 309–322.

Meyer, C., 1988, Proterozoic ore-forming habitats – Tectonic and chemical transitions, in G. Kisvarsanyi, and S. K. Grant, eds., Tectonic controls of ore deposits and vertical and horizontal extent of ore systems: Rolla, University of Missouri, October 6–8, 1987, Conference Proceedings, p. 217–235.

Meyer, D., L. Zarra, D. Rains, B. Meltz, and T. Hall, 2005, Emergence of the Lower Tertiary Wilcox Trend in the Deepwater Gulf of Mexico (May): World Oil, p. 72–77.

Meyer, D., L. Zarra, and J. Yun, 2007, From BAHA to Jack, Evolution of the Lower Tertiary Wilcox Trend in the Deepwater Gulf of Mexico: Sedimentary Record, v. 5, p. 4–9.

Meyer, F. O., R. C. Price, I. A. Al-Ghamdi, I. M. Al-Goba, S. M. Al-Raimi, and J. C. Cole, 1996, Sequential stratigraphy of outcropping strata equivalent to Arab-D Reservoir, Wadi Nisah, Saudi Arabia: GeoArabia, v. 1, p. 435–456.

Meyer, F. O., R. C. Price, and S. M. Al-Raimi, 2000, Stratigraphic and petrophysical characteristics of cored Arab-D super k intervals, Hawiyah area, Ghawar field, Saudi Arabia: GeoArabia, v. 5, p. 355–384.

Meyers, W. J., F. H. Lu, and J. K. Zachariah, 1997, Dolomitization by mixed evaporitic brines and freshwater, Upper Miocene carbonates, Nijar, Spain: Journal of Sedimentary Research Section A-Sedimentary Petrology & Processes, v. 67 A, p. 898–912.

Miall, A. D., 2010, The Geology of Stratigraphic Sequences: Berlin Heidelberg, Springer

Michael, K., H. G. Machel, and S. Bachu, 2003, New insights into the origin and migration of brines in deep Devonian aquifers, Alberta, Canada: Journal of Geochemical Exploration, v. 80, p. 193–219.

Michalski, J., and P. B. Niles, 2012, Atmospheric origin of Martian interior layered deposits: Links to climate change and the global sulfur cycle: Geology, v. 40, p. 419–422.

Michalzik, D., 1996, Lithofacies, diagenetic spectra and sedimentary cycles of Messinian (late Miocene) evaporites in SE Spain: Sedimentary Geology, v. 106, p. 203–222.

Middleton, G. V., 1961, Evaporite solution breccias from the Mississippian of southwest Montana: Journal of Sedimentary Petrology, v. 31, p. 189–195.

Middleton, H., and M. W. Wallace, 2003, The evolution of fluid flow systems prior to, during, and post MVT mineralization in the Givetian-Frasnian carbonates of the Emanuel Range, Western Australia: Journal of Geochemical Exploration, v. 78–79, p. 91–97.

Middleton, K., M. Coniglio, R. Sherlock, and S. K. Frape, 1993, Dolomitization of Middle Ordovician carbonate reservoirs, southwestern Ontario: Bulletin of Canadian Petroleum Geology,, v. 41, p. 150–163.

Milani, E. J., and P. V. Zalán, 1999, An outline of the geology and petroleum systems of the Paleozoic interior basins of South America: Episodes, v. 22, p. 199–205.

Milburn, D., and S. Wilcock, 1998, Kunwarara Magnesite Deposit, in D. A. Berkman, and D. H. MacKenzie, eds., Geology of Australian and Papua New Guinean Mineral Deposits, Australasian Institute of Mining and Metallurgy, Melbourne, p. 815–818.

Milesi, J. P., S. F. Toteu, Y. Deschamps, J. L. Feybesse, C. Lerouge, A. Cocherie, J. Penaye, R. Tchameni, G. Moloto-A-Kenguemba, H. A. B. Kampunzu, N. Nicol, E. Duguey, J. M. Leistel, M. Saint-Martin, F. Ralay, C. Heinry, V. Bouchot, J. C. Doumnang Mbaigane, V. Kanda Kula, F. Chene, J. Monthel, P. Boutin, and J. Cailteux, 2006, An overview of the geology and major ore deposits of Central Africa: Explanatory note for the 1:4,000,000 map "Geology and major ore deposits of Central Africa": Journal of African Earth Sciences, v. 44, p. 571–595.

Milkov, A. V., and R. Sassen, 2001, Estimate of gas hydrate resource, northwestern Gulf of Mexico, continental slope: Marine Geology, v. 179, p. 71–83.

Miller, C. F., and D. A. Wark, 2008, Supervolcanoes and their explosive supereruptions: Elements, v. 4, p. 11–16.

Miller, J. A., G. Viola, and N. S. Mancktelow, 2008, Oxygen, carbon and strontium isotope constraints on the mechanisms of nappe emplacement and fluid-rock interaction along the subhorizontal Naukluft Thrust, central Namibia: Journal of the Geological Society, v. 165, p. 739–753.

Miller, J. A., 1985, Depositional and reservoir facies of the Mississippian Leadville Formation, Northwest Lisbon Field, Utah, in P. O. Roehl,

and P. W. Choquette, eds., Carbonate petroleum reservoirs: New York, Springer-Verlag, p. 161–173.

Miller, K. G., G. S. Mountain, J. D. Wright, and J. V. Browning, 2011, A 180-million-year record of sea level and ice volume variations from continental margin and deep-sea isotopic records: Oceanography, v. 24, p. 40–53.

Miller, N. C., and D. Lizarralde, 2013, Thick evaporites and early rifting in the Guaymas Basin, Gulf of California: Geology, v. 41, p. 283–286.

Miller, R. G., 1990, A paleogeographic approach to Kimmeridge Shale formation, in A. Y. Huc, ed., Deposition of organic facies: Tulsa OK, American Association Petroleum Geologists Studies in Geology, 30, p. 13–26.

Milliken, K. L., 1979, The silicified evaporite syndrome; two aspects of silicification history of former evaporite nodules from southern Kentucky and northern Tennessee: Journal Sedimentary Petrology, v. 49, p. 245–256.

Mills, R., and H. Elderfield, 1995, Rare earth element geochemistry of hydrothermal deposits from the active TAG mound, 26 degrees N Mid-Atlantic Ridge: Geochimica et Cosmochimica Acta, v. 59, p. 3511–3524.

Milroy, P. G., and V. P. Wright, 2000, A highstand oolitic sequence and associated facies from a Late Triassic lake basin, southwest England: Sedimentology, v. 47, p. 187–209.

Milton, C., 1968, The "Natro-carbonatite Lava" of Oldoinyo Lengai, Tanzania: Geol. Soc. Amer. Program with Abstracts, p. 202.

Milton, C., 1989, Oldoinyo Lengai natrocarbonatite lava: its history (abs.): 28th International Geological Congress, Washington 1989, p. 2–441.

Minckley, W. L., 1969, Environments of the Bolsón of Cuatro Ciénegas, Coahuila, México: Texas Western Press, The University of Texas at El Paso, Science Series, Number 2, 65 pages.

Minckley, W. L., 1992, Three Decades near Cuatro Cienegas, Mexico: Photographic Documentation and a Plea for Area Conservation: Journal of the Arizona-Nevada Academy of Science, v. 26, p. 89–118.

Minckley, W. L., and G. A. Cole, 1968, Preliminary Limnologic Information on Waters of the Cuatro Cienegas Basin, Coahuila, Mexico: The Southwestern Naturalist, v. 13, p. 421–431.

Minter, N. J., K. Krainer, S. G. Lucas, S. J. Braddy, and A. P. Hunt, 2007, Palaeoecology of an Early Permian playa lake trace fossil assemblage from Castle Peak, Texas, USA: Palaeogeography, Palaeoclimatology, Palaeoecology, v. 246, p. 390–423.

Mirandagasca, M. A., J. A. Gomezcaballero, and C. J. Eastoe, 1998, Borate deposits of Northern Sonora, Mexico – Stratigraphy, tectonics, stable isotopes and fluid inclusions: Economic Geology, v. 93, p. 510–523.

Miser, D. E., J. S. Swinnea, and H. Steinfink, 1987, TEM observations and X-ray structure refinement of a twinned dolomite microstructure: American Mineralogist, v. 72, p. 188–193.

Mitchell, J. C., P. J. Lehmann, D. L. Cantrell, I. A. Al-Jallal, and M. A. R. Al Thagafy, 1988, Lithofacies, diagenesis and depositional sequence; Arab-D Member, Ghawar field, Saudi Arabia, in A. J. Lomando, and P. M. Harris, eds., Giant oil and gas fields – A core workshop: Tulsa, OK, SEPM core Workshop No. 12, p. 459–514.

Mitchell, N. C., M. Ligi, V. Ferrante, E. Bonatti, and E. Rutter, 2010, Submarine salt flows in the central Red Sea: Geological Society of America Bulletin, v. 122, p. 701–713.

Mitra, S., 2002, Structural models of faulted detachment folds: American Association Petroleum Geologists – Bulletin, v. 86, p. 1673–1694.

Mlynarski, M., and J. Zlotnicki, 2001, Fluid circulation in the active emerged Asal rift (east Africa, Djibouti) inferred from self potential and Telluric-Telluric prospecting: Tectonophysics, v. 339.

Moberg, E. G., D. M. Greenberg, R. Revelle, and E. C. Allen, 1932, The buffer mechanism of seawater: Scripps Inst. Oceanography Tech. Serv. Bull., v. 3, p. 231–278.

Moecher, D. P., E. J. Essene, and J. W. Valley, 1992, Stable isotopic and petrological constraints on scapolitization of the Whitestone metaanorthosite, Grenville Province, Ontario*: Journal Of Metamorphic Geology, v. 10, p. 745–762.

Mohammad, Y. O., H. Maekawa, and F. Ahmmad Lawa, 2007, Mineralogy and origin of Mlakawa albitite from Kurdistan region, northeastern Iraq: Geosphere, v. 3, p. 624–645.

Mohnot, J. K., V. V. R. Prasad, and H. K. Verma, 2005, Investment Opportunities for Potash Mining in India as an Import Substitute Mineral, 1st Indian Mineral Congress ISM, Dhanbad, Feb.28 – March 1, 2005.

Mohr, M., P. A. Kukla, J. L. Urai, and G. Bresser, 2004, New Insights to the evolution and mechanisms of salt tectonics in the Central European Basin system: An integrated modeling study from Northwest Germany, In: Salt-sediment interactions and hydrocarbon prospectivity: concepts, applications and case studies for the 21st Century. Papers presented at the 24th Annual Gulf Coast Section SEPM Foundation Bob F. Perkins Research Conference, Houston Tx, December 5–8, 2004 (CD publication), p. 90–118.

Mohr, M., J. K. Warren, P. A. Kukla, J. L. Urai, and A. Irmen, 2007, Subsurface seismic record of salt glaciers in an extensional intracontinental setting (Late Triassic of northwestern Germany): Geology, v. 35, p. 963–966.

Mohriak, W., M. Nemcok, and G. Enciso, 2008, South Atlantic divergent margin evolution: rift-border uplift and salt tectonics in the basins of SE Brazil: Geological Society, London, Special Publications, v. 294, p. 365–398.

Mohriak, W. U., P. Szatmari, and S. Anjos, 2012, Salt: geology and tectonics of selected Brazilian basins in their global context, in G. I. Alsop, S. G. Archer, A. J. Hartley, N. T. Grant, and R. Hodgkinson, eds., Salt Tectonics, Sediments and Prospectivity, v. 363, Geological Society, London, Special Publications, p. 131–158.

Moine, B., P. Sauvan, and J. Jarousse, 1981, Geochemistry of evaporite-bearing series; a tentative guide for the identification of meta-evaporites: Contributions to Mineralogy and Petrology, v. 76, p. 401–412.

Moiola, R. J., and E. D. Glover, 1965, Recent anhydrite from Clayton Playa, Nevada: Am. Mineralogist., p. 11–12.

Moldovanyi, E. P., and L. M. Walter, 1992, Regional trends in water chemistry, Smackover Formation, southwest Arkansas: geochemical and physical controls: American Association of Petroleum Geologists Bulletin, v. 76, p. 864–894.

Moldowan, J. M., J. Dahl, B. J. Huizinga, F. J. Fago, L. J. Hickey, T. M. Peakman, and D. W. Taylor, 1994, The molecular fossil record of oleanane and its relation to angiosperms: Science, v. 265., p. 768–771.

Moldowan, J. M., W. K. Seifert, and E. J. Gallegos, 1985, Relationship between petroleum composition and depositional environment of petroleum source rocks: American Association of Petroleum Geologists Bulletin, v. 69, p. 1255–1268.

Molenaar, N., and A. F. M. de Jong, 1987, Authigenic quartz and albite in Devonian limestones: origin and significance: Sedimentology, v. 34, p. 623–640.

Molinaro, M., S. A. Eshraghi, P. Leturmy, J. C. Guezou, and D. Frizon de Lamotte, 2005, The structure and kinematics of the southeastern Zagros fold-thrust belt, Iran: From thin-skinned to thick-skinned tectonics: Tectonics, v. 24, p. 1–19.

Monnin, C., and C. Ramboz, 1996, The anhydrite saturation index of the ponded brines and sediment pore waters of the Red Sea deeps: Chemical Geology, v. 127, p. 141–159.

Montacer, M., J. R. Disnar, J. J. Orgeval, and J. Trichet, 1988, Relationship between Zn-Pb ore and oil accumulation processes; example of the Bou Grine Deposit (Tunisia): Organic Geochemistry, v. 13, p. 423–431.

Montadert, L., J. Sancho, J. P. Fial, and J. Debysser, 1970, De 1' age tertiaire de la série salifére responsable des structu|res diapiriques en Méditerranee Occidentale (Nord-Est des Baléares): CRAS, v. 271, p. 812–815.

Montgomery, D. R., and A. Gillespie, 2005, Formation of Martian outflow channels by catastrophic dewatering of evaporite deposits: Geology, v. 33, p. 625–628.

Montgomery, D. R., S. M. Som, M. P. A. Jackson, B. C. Schreiber, A. R. Gillespie, and J. B. Adams, 2009, Continental-scale salt tectonics on Mars and the origin of Valles Marineris and associated outflow channels: Geological Society of America Bulletin, v. 121, p. 117–133.

Montgomery, S. L., 1997, Ordovician Red River "B" – Horizontal oil play in the southern Williston Basin: American Association Petroleum Geologists – Bulletin, v. 81, p. 519–532.

Montgomery, S. L., R. Karlewicz, and D. Ziegler, 1999b, Upper Jurassic "Reef" play, east Texas Basin: An updated overview: Part 2 – Inboard trend: American Association Petroleum Geologists – Bulletin, v. 83, p. 869–888.

Montgomery, S. L., and D. Moore, 1997, Subsalt play, Gulf of Mexico – A review: American Association Petroleum Geologists Bulletin-American Association of Petroleum Geologists, v. 81, p. 871–896.

Montgomery, S. L., T. H. Walker, P. Wahlman, R. C. Tobin, and D. Ziegler, 1999a, Upper Jurassic "Reef" play, east Texas Basin: An updated overview: Part 1 – Background and outboard trend: American Association Petroleum Geologists – Bulletin, v. 83, p. 707–728.

Montomoli, C., G. Ruggieri, R. Carosi, A. Dini, and M. Genovesi, 2005, Fluid source and pressure‚Äìtemperature conditions of high-salinity fluids in syn-tectonic veins from the Northeastern Apuan Alps (Northern Apennines, Italy): Physics and Chemistry of the Earth, Parts A/B/C, v. 30, p. 1005–1019.

Monty, C. L. V., 1976, The origin and development of cryptalgal fabrics, in M. R. Walter, ed., Stromatolites, v. 20: Amsterdam, Elsevier, p. 193–249.

Moody, J. D., 1959, Relationship of primary evaporites to oil accumulation: 5th World Petroleum Congress, New York, v. 1, p. 134–138.

Moore, C. H., 1984, The upper Smackover of the Gulf rim: depositional systems, diagenesis, porosity evolution and hydrocarbon production, in W. P. S. Ventress, B. M. Bebout, B. F. Perkins, and C. H. Moore, eds., The Jurassic of the Gulf rim, Gulf Coast Section, SEPM, p. 283–307.

Moore, C. H., 2001, Carbonate Reservoirs – Porosity Evolution and Diagenesis in a Sequence Stratigraphic Framework, v. 55, Elsevier, 444 p.

Moore, C. H., A. Chowdhury, and L. Chan, 1988, Upper Jurassic Smackover dolomitization, Gulf of Mexico; a tale of two waters, in V. Skula, and P. A. Baker, eds., Sedimentology and geochemistry of dolostones, SEPM Special Publication No. 43, p. 175–189.

Moore, C. H., and Y. Druckman, 1981, Burial diagenesis and porosity evolution, Upper Jurassic Smackover, Arkansas and Louisiana: American Association of Petroleum Geologists Bulletin, v. 65, p. 597–628.

Mora, C. I., and J. W. Valley, 1989, Halogen-rich scapolite and biotite: implications for metamorphic fluid-rock interaction: American Minealogist, v. 74, p. 721–737.

Mora, C. I., J. W. Valley, and F. Ortega-Gutiérrez, 1986, The temperature and pressure conditions of Grenville-age granulite facies in the Oaxacan Complex, southern Mexico: Instituto de Geología Revista, v. 5, p. 222–242.

Morad, S., M. Bergan, R. Knarud, and J. P. Nystuen, 1990, Albitization of detrital plagioclase in Triassic reservoir sandstones from the Snorre Field, Norwegian North Sea: Journal of Sedimentary Research, v. 60, p. 411–425.

Moragas, M., C. Martínez, V. Baqués, E. Playà, A. Travé, G. Alías, and I. Cantarero, 2013, Diagenetic evolution of a fractured evaporite deposit (Vilobí Gypsum Unit, Miocene, NE Spain): Geofluids, v. 13, p. 180–193.

Moran, J. E., 1996, Origin of iodine in the Anadarko Basin, Oklahoma: an 129I study: American Association of Petroleum Geologists Bulletin, v. 80, p. 685–694.

Moreira, N. F., L. M. Walter, C. Vasconcelos, J. McKenzie, and P. J. McCall, 2004, Role of sulfide oxidation in dolomitization: Sediment and pore-water geochemistry of a modern hypersaline lagoon system: Geology, v. 32, p. 701–704.

Morgan, K. H., 1993, Development, sedimentation and economic potential of palaeoriver systems of the Yilgarn Craton of Western Australia: Sedimentary Geology, v. 85, p. 637–656.

Morisseau, J. M., 2000, Uncontrolled leaching of salt layer in an oil field in Algeria: Proc. Solution Mining Research Institute Fall Meeting Technical Session, San Antonio, p. 330–333.

Moritz, R., L. Fontbote, J. Spangenberg, S. Rosas, Z. Sharp, and D. Fontignie, 1996, Sr, C and O isotope systematics in the Pucara Basin, central Peru: Comparison between Mississippi Valley-type deposits and barren areas: Mineralium Deposita, v. 31, p. 147–162.

Morley, C. K., 2004, Nested strike-slip duplexes and other evidence for Late Cretaceous-Paleogene transpressional tectonics before and during India-Eurasia collision, in Thailand, Myanmar and Malaysia: J. Geol. Soc. London, v. 161, p. 799–812.

Morley, C. K., 2007a, Interaction between critical wedge geometry and sediment supply in a deep-water fold belt: Geology, v. 35, p. 139–142.

Morley, C. K., 2007b, Development of crestal normal faults associated with deepwater fold growth: Journal of Structural Geology, v. 29, p. 1148–1163.

Morley, C. K., 2012, Late Cretaceous-Early Palaeogene tectonic development of SE Asia: Earth-Science Reviews, v. 115, p. 37–75.

Morley, C. K., and G. Guerin, 1996, Comparison of gravity-driven deformation styles and behaviour associated with mobile shales and salt: Tectonics, v. 15, p. 1154–1170.

Morley, C. K., R. King, R. Hillis, M. Tingay, and G. Backe, 2011, Deepwater fold and thrust belt classification, tectonics, structure and hydrocarbon prospectivity: A review: Earth-Science Reviews, v. 104, p. 41–91.

Morley, C. K., B. Kongwung, A. A. Julapour, M. Abdolghafourian, M. Hajian, D. Waples, J. Warren, H. Otterdoom, K. Srisuriyon, and H. Kazemi, 2009, Structural development of a major late Cenozoic basin and transpressional belt in central Iran: The Central Basin in the Qom-Saveh area: Geosphere, v. 5, p. 325–362.

Morley, C. K., J. Warren, M. Tingay, P. Boonyasaknanon, and A. Julapour, 2014, Comparison of modern fluid distribution, pressure and flow in sediments associated with anticlines growing in deepwater (Brunei) and continental environments (Iran): Marine and Petroleum Geology, v. 51, p. 210–229.

Morozov, A. F., B. N. Khakhaev, O. V. Petrov, V. I. Gorbachev, G. V. Tarkhanov, L. D. T svetkov, Y. M. Erinchek, A. M. Akhmedov, V. A. Krupenik, and K. Y. Sveshnikova, 2010, Rock salt mass in the Paleoproterozoic sequence of the Onega trough in Karelia (from the Onega parametric well data): Doklady Earth Sciences, v. 435, p. 1483–1486.

Morris, R. C., 1985, Genesis of iron ore in banded iron-formation by supergene and supergene metamorphic processes – a conceptual model, in W. K.H., ed., Handbook of strata-bound and stratiform ore deposits, v. 13, Elsevier, p. 73–235.

Morris, R. C., 1993, Genetic modelling for banded iron-formation of the Hamersley Group, Pilbara Craton, Western Australia: Precambrian Research, v. 60, p. 243–286.

Morrison, S. J., and W. T. Parry, 1986, Formation of carbonate-sulfate veins associated with copper ore deposits from saline basin brines, Lisbon Valley, Utah: fluid inclusion and isotopic evidence (USA): Economic Geology, v. 81, p. 1853–1866.

Morrow, D. W., 1982, Descriptive field classification of sedimentary and diagenetic breccia fabrics in carbonate rocks: Bulletin of Canadian Petroleum Geology, v. 30, p. 227–229.

Morrow, D. W., 2014, Zebra and boxwork fabrics in hydrothermal dolomites of northern Canada: Indicators for dilational fracturing, dissolution or in situ replacement?: Sedimentology, v. 61, p. 915–951.

Morrow, D. W., and B. D. Ricketts, 1988, Experimental investigation of sulfate inhibition of dolomite and its mineral analogues: Shukla, Vijai, Baker, Paul A. Sedimentology and geochemistry of dolostones, based on a symposium. Special Publication Society of Economic Paleontologists and Mineralogists, v. 43, p. 25–38.

Morrow, D. W., L. D. Stasiuk, and Mengwei Zhao, 2001, Dolomitisation and burial diagenesis of Devonian Slave Point and Keg River formations in the Cordova Embayment region of Northeast British Columbia (ext'd abs.): Canadian Society Petroleum Geologists, Rock the Foundation Convention, June 18–22, 2001, p. 026–1 to 026–5.

Morrow, D. W., M. Zhao, and L. D. Stasiuk, 2002, The gas-bearing Devonian Presqu'ile Dolomite of the Cordova embayment region of British Columbia, Canada: Dolomitization and the stratigraphic template: American Association Petroleum Geologists – Bulletin, v. 86, p. 1609–1638.

Morse, J. W., and F. Mackenzie, T., 1998, Hadean ocean carbonate geochemistry: Aquatic Geochemistry, v. 4, p. 301–319.

Morteani, G., Y. A. Kostitsyn, H. A. Gilg, C. Preinfalk, and T. Razakamanana, 2013, Geochemistry of phlogopite, diopside, calcite, anhydrite and apatite pegmatites and syenites of southern Madagascar: evidence for crustal silicocarbonatitic (CSC) melt formation in a Panafrican collisional tectonic setting: International Journal of Earth Sciences, v. 102, p. 627–645.

Morton, R. A., and L. S. Land, 1987, Regional variations in formation water chemistry, Frio Formation (Oligocene), Texas Gulf Coast: American Association Petroleum Geologists – Bulletin, v. 71, p. 191–206.

Morton, R. A., and J. R. Suter, 1996, Sequence Stratigraphy and Composition of Late Quaternary Shelf-Margin Deltas, Northern Gulf of Mexico: American Association Petroleum Geologists – Bulletin, v. 80, p. 505–530.

Mossadegh, Z. K., D. W. Haig, T. Allan, M. H. Adabi, and A. Sadeghi, 2009, Salinity changes during Late Oligocene to Early Miocene Asmari Formation deposition, Zagros Mountains, Iran: Palaeogeography, Palaeoclimatology, Palaeoecology, v. 272, p. 17–36.

Mossman, D. J., and M. J. Brown, 1986, Stratiform barite in sabkha sediments, Walton-Cheverie, Nova Scotia: Economic Geology, v. 81, p. 2016–2021.

Mossman, D. J., R. N. Delabio, and A. D. Mackintosh, 1982, Mineralogy of clay marker seams in some Saskatchewan potash mines: Canadian Journal of Earth Sciences, v. 19, p. 2126–2140.

Mossop, G., and I. Shetsen, 1994, Geological Atlas of the Western Canada Sedimentary Basin: Canadian Society of Petroleum Geologists and Alberta Research Council, 504 p.

Mossop, G. D., 1972, Lower Ordovician evaporites of the Baumann Fiord Formation, Ellesmere Island: In, Report of activities, Pt. B: November 1971 to March 1972. Geol. Surv. Canada, Paper 72-l, Pt. B, 129 pp., p. 86–90.

Mossop, G. D., 1973, Lower Ordovician evaporites of the Baumann Fiord Formation, Ellesmere Island,. I: In Report of activities, Pt. A: April to October 1972, Geol. Surv. Canada, Paper 73–1, Pt. A, 297 pp., p. 264–267.

Mostofi, B., and A. Gansser, 1957, The story behind the Alborz 5: Oil and Gas Journal, 21 January 1957, p. 78–85.

Moulton, T. P., and M. A. Burford, 1990, The mass culture of Dunaliella viridis (Volvocales, Chlorophyta) for oxygenated carotenoids: laboratory and pilot plant studies: Hydrobiologia, v. 204–205, p. 401–408.

Mount, T., 1975, Diapirs and diapirism in the Adelaide "Geosyncline": Doctoral thesis, University of Adelaide.

Mount, V. S., J. Suppe, and S. C. Hook, 1990, A Forward Modeling Strategy for Balancing Cross Sections: Bulletin American Association Petroleum Geologists, v. 74.

Mountney, N. P., and D. B. Thompson, 2002, Stratigraphic evolution and preservation of aeolian dune and damp/wet interdune strata: an example from the Triassic Helsby Sandstone Formation, Cheshire Basin, UK: Sedimentology, v. 49, p. 805–833.

Mouret, C., 1994, Geological history of NE Thailand since the Carboniferous: Relations with Indochina and the Carboniferous to early Cenozoic evolution model: Proc. Internat. Sympos. on Stratigraphic Correlation of Southeast Asia, Bangkok, p. 132–158.

Mouret, C., 1994, Geological history of northeastern Thailand since the Carboniferous. Relation with Indonesia and Carboniderous to Early Cenozoic evolution model, in P. Angsuwathana, T. Wongwanich, W. Tansathien, S. Wongsomsak, and J. Tulyatid, eds., Proceeding of the International Symposium on Stratigraphic Correlation of Southeast Asia, Bangkok, 15–20 November 1994, p. 132–158.

Mouret, C., H. Heggemann, J. Gouadain, and S. Krisadasima, 1993, Geological history of the siliciclastic Mesozoic strata of the Khorat Group in the Phu Phan Range area, Northeastern Thailand, in T. Thanasuthipitak, ed., Proceedings International Symposium on Biostratigraphy of Maninland SE Asia: Facies and Palaeontology, Chiang Mai, Thailand: Bangkok, p. 23–49.

Muchez, P., W. Heijlen, D. Banks, D. Blundell, M. Boni, and F. Grandia, 2005, 7: Extensional tectonics and the timing and formation of basin-hosted deposits in Europe: Ore Geology Reviews, v. 27, p. 241–267.

Muchez, P., C. Peeters, W. Viaene, and E. Keppens, 1992, Stable isotopic composition of an evaporite dissolution breccia in the Lower Viséan limestones of SE Belgium: Chemical Geology, v. 102, p. 119–127.

Muchez, P., P. Vanderhaeghen, H. El Desouky, J. Schneider, A. Boyce, S. Dewaele, and J. Cailteux, 2008, Anhydrite pseudomorphs and the origin of stratiform Cu-Co ores in the Katangan Copperbelt (Democratic Republic of Congo): Mineralium Deposita, v. 43, p. 575–589.

Mudd, G. M., 1998, The sustainability of mound springs in South Australia: Implications for Olympic Dam: Paper Presented at the Int'l Association of Hydrogeologists Meeting, Ballarat, Australia. Commission on Mineral and Thermal Waters Meeting, September 21 to 24, 1998, p. 1–13.

Mudd, G. M., 2000, Mound springs of the Great Artesian Basin in South Australia: a case study from Olympic Dam: Environmental Geology, v. 39, p. 463–476.

Mueller, G., and G. Irion, 1969, 'Salt-biscuits'; a special growth structure of NaCl in salt sediments of the Tuz Goelue ('Salt Lake'), Turkey: Journal of Sedimentary Research, v. 39, p. 1604–1607.

Muessig, S., 1958, First known occurrence of inyoite in a playa at Laguna Salinas: Am. Mineral., v. 43, p. 1144–1147.

Muessig, S. J., 1966, Recent South America Borate deposits: Proceedings – Second International Salt Symposium, Northern Ohio Geological Society, Cleveland, May 3–5, 1965, v. 1, p. 151–159.

Muir, I., and J. J. Dravis, 1992, Pool Entrapment in Devonian Keg River and Muskeg Dolomitized Sequences, Comet Platform, Western Canada(abs.): American Association Petroleum Geologists – Bulletin, v. 76, p. 93.

Muir, I. D., and J. J. Dravis, 1995, Incorporation of Core and Petrographic Data – Key to Improved Management and Exploitation of Middle Devonian Keg River Carbonate Pools in Rainbow Sub-Basin, Alberta, Western Canada (abs.): American Association Petroleum Geologists – Bulletin, v. 79, p. 69.

Muir, J. L., 1934, Anhydrite-Gypsum Problem of Blaine Formation, Oklahoma: Bulletin American Association Petroleum Geologists, v. 18, p. 1297–1312.

Muir, M. D., 1987, Facies models for Australian Precambrian evaporites, in T. M. Peryt, ed., Lecture Notes in Earth Sciences, v. 13: Berlin; New York, Springer-Verlag, p. 5–21.

Müller, D. W., and K. J. Hsu, 1987, Event stratigraphy and paleoceanography in the Fortuna Basin (Southeast Spain): a scenario for the Messinian Salinity Crisis: Paleoceanography, v. 2, p. 679–696.

Müller, D. W., J. A. McKenzie, and P. A. Mueller, 1990, Abu Dhabi sabkha, Persian Gulf, revisited; Application of strontium isotopes to test an early dolomitization model: Geology, v. 18, p. 618–621.

Müller, G., 1962, Zür Geochemie des Strontiums in Ozeanen Evaporiten unter besonderer Berücksichtigung der sedimentären Coelestinlagerstätten von Hemmelte-West (Süd-Oldenburg): Geologie, Supplement 35.

Müller, R. D., A. Dutkiewicz, M. Seton, and C. Gaina, 2013, Seawater chemistry driven by supercontinent assembly, breakup, and dispersal: Geology, v. 41, p. 907–910.

Müller, S., and G. Teitz, 1971, Dolomite replacing "cement A" in biocalcarenites from Fuerteventura, Canary Islands, Spain, in D. P. Bricker, ed., Carbonate Cements: Baltimore, John Hopkins Press, p. 376 p.

Mumpton, F. A., 1983, Commercial utilization of natural zeolites, in S. J. LeFond, ed., Industrial Minerals and Rocks: New York, American Institute of Mining, Metallurgical and Petroleum Engineers Inc., p. 1418–1431.

Mundil, R., K. R. Ludwig, I. Metcalfe, and P. R. Renne, 2004, Age and timing of the Permian mass extinctions: U/Pb dating of closed-system zircons: Science v. 305, p. 1760–1763.

Mundil, R., I. Metcalfe, K. R. Ludwig, P. R. Renne, F. Oberli, and R. S. Nicoll, 2001, Timing of the Permian-Triassic biotic crisis: implications from new zircon U/Pb age data (and their limitations): Earth & Planetary Science Letters, v. 187, p. 131–145.

Munoz, M., A. J. Boyce, P. Courjault-Rade, A. E. Fallick, and F. Tollon, 1999, Continental basinal origin of ore fluids from southwestern Massif central fluorite veins (Albigeois, France): evidence from fluid inclusion and stable isotope analyses: Applied Geochemistry, v. 14, p. 447–458.

Munoz, M., A. J. Boyce, P. Courjaultrade, A. E. Fallick, and F. Tollon, 1994, Multi-stage fluid incursion in the Palaeozoic basement-hosted San-Int-Salvy ore deposit (NW Montagne Noire, Southern France): Applied Geochemistry, v. 9, p. 609 ff.

Munson, D. E., 1997, Constitutive model of creep in rock salt applied to underground room closure: International Journal of Rock Mechanics & Mining Sciences & Geomechanics, v. 34, p. 233–247.

Munyanyiwa, H., 1990, Mineral assemblages in calc-silicates and marbles in the Zambezi Mobile Belt: their implications on mineral-forming reactions during metamorphism: Journal of African Earth Sciences, v. 10, p. 693–700.

Munz, I. A., B. W. D. Yardley, D. A. Banks, and D. Wayne, 1995, Deep penetration of sedimentary fluids in basement rocks from southern Norway: Evidence from hydrocarbon and brine inclusions in quartz veins: Geochimica et Cosmochimica Acta, v. 59, p. 239–254.

Munz, I. A., B. W. D. Yardley, and S. A. Gleeson, 2002, Petroleum infiltration of high-grade basement, South Norway: Pressure-Temperature-time-composition (P-T-t-X) constraints: Geofluids, v. 2, p. 41–53.

Murphy, F. C., L. J. Hutton, J. L. Walshe, J. S. Cleverley, M. A. Kendrick, J. Mclellan, M. J. Rubenach, N. H. S. Oliver, K. Gessner, F. P. Bierlein, B. Jupp, L. Aillères, C. Laukamp, I. G. Roy, J. M. Miller, D. Keys, and G. S. Nortje, 2011, Mineral system analysis of the Mt Isa–McArthur River region, Northern Australia: Australian Journal of Earth Sciences, v. 58, p. 849–873.

Murray, J. W., 1970, The foraminifera of the hypersaline Abu Dhabi lagoon, Persian Gulf: Lethaia, v. 3, p. 51–68.

Murray, R. C., 1964, Origin and diagenesis of gypsum and anhydrite: Journal of Sedimentary Petrology, v. 34, p. 512–523.

Murray, R. C., 1969, Hydrology of South Bonaire, Netherlands Antilles; a rock selective dolomitization model: Journal of Sedimentary Petrology, v. 39, p. 1007–1013.

Murrell, S. A. F., and I. A. H. Ismail, 1976, The effect of decomposition of hydrous minerals on the mechanical properties of rocks at high pressures and temperatures: Tectonophysics, v. 31, p. 207–258.

Murris, R. J., 1980, Middle East: Stratigraphic Evolution and Oil Habitat: American Association of Petroleum Geologists Bulletin, v. 64, p. 597–618.

Mutlu, H., S. Kadir, and A. Akbulut, 1999, Mineralogy and water chemistry of the Lake Acigol, Denizli, Turkey: Carbonates and Evaporites, v. 14, p. 191–199.

Mutti, M., 1994, Association of tepees and palaeokarst in the Ladinian Calcare Rosso (Southern Alps, Italy): Sedimentology, v. 41, p. 621–641.

Mutti, M., and J. A. T. Simo, 1993, Stratigraphic patterns and cycle-related diagenesis of upper Yates Formation, Permian, Guadalupe Mountains, in R. G. Loucks, and J. F. Sarg, eds., Carbonate sequence stratigraphy: recent developments and applications, v. 57, Memoir American Association Petroleum Geologists, p. 515–534.

Myers, A. J., 1962, A fossil sinkhole: Oklahoma Geological Notes, v. 22, p. 13–15.

Myers, D. M., and C. W. Bonython, 1958, The theory of recovering salt from sea water by solar evaporation: Journal of Applied Chemistry (Australia), v. 8, p. 207–219.

Nagy, Z. R., I. D. Somerville, J. M. Gregg, S. P. Becker, K. L. Shelton, and A. G. Sleeman, 2005, Sedimentation in an actively tilting half-graben: sedimentology and stratigraphy of Late Tournaisian-Viséan (Mississippian, Lower Carboniferous) carbonate rocks in south County Wexford, Ireland: Sedimentology, v. 52, p. 489–512.

Naiman, E. R., A. Bein, and R. L. Folk, 1983, Complex polyhedral crystals of limpid dolomite associated with halite, Permian upper Clear Fork and Glorieta formations, Texas: Journal of Sedimentary Petrology, v. 53, p. 549–555.

Nakla, F. M., and S. A. Saleh, 1985, Mineralogy, Chemistry and Paragenesis of the Beida Lake Thenardite Deposit at the Wadi El-Natrun: Applied Mineralogy (Metallurgical Society of AIME), v. l, p. 1001–1013.

Naldrett, A. J., 1981, Nickel sulfide deposits: classification, composition, and genesis: Economic Geology, v. Seventy-fifth Anniversary Volume (1905–1980), p. 628–685.

Naldrett, A. J., 1993, Ni-Cu-PGE ores of the Noril'sk region Siberia: a model for giant magmatic sulfide deposits associated with flood basalts: Society of Economic Geologists Special Publication, v. 2, p. 81–123.

Naldrett, A. J., 1997, Key factors in the genesis of Noril'sk, Sudbury, Jinchuan, Voiseys Bay and other worldclass Ni-Cu- PGE deposits – Implications for exploration: Australian Journal of Earth Sciences, v. 44, p. 283–315.

Naldrett, A. J., 1999, World-class Ni-Cu-PGE deposits: key factors in their genesis: Mineralium Deposita, v. 34, p. 227–240.

Naldrett, A. K., and A. J. Macdonald, 1980, Tectonic settings of Ni-Cu sulphide ores: their importance in genesis and exploration., in D. W. Strangway, ed., The Continental Crust and its Mineral Deposits. Proc. symposium held to honour J. Tuzo Wilson, Toronto, May 1979, Geological Association of Canada: Special Paper 20, p. 633–657.

Nalpas, T., and J. P. Brun, 1993, Salt flow and diapirism related to extension at crustal scale: Tectonophysics., v. 228, p. 349–362.

Nanson, G. C., R. A. Callen, and D. M. Price, 1998, Hydroclimatic interpretation of Quaternary shorelines on south Australian playas: Paleogeography Paleoclimatology Paleoecology, v. 144, p. 281–305.

Naranjo, J. A., F. Henriquez, and J. A. Nystrom, 2010, Subvolcanic contact metasomatism at El Laco Volcanic Complex, Central Andes: Andean Geology, v. 37, p. 110–120.

Nash, J. T., and J. J. Connor, 1993, Iron and chlorine as guides to stratiform Cu-Co-Au deposits, Idaho Cobalt Belt, USA: Mineralium Deposita, v. 28, p. 99–106.

Naslund, H. R., F. M. Dobbs, F. J. Henríquez, and J. O. Nyström, 1997, Irrefutable evidence for the eruption of iron-oxide magmas at El Laco volcano, Chile: EOS Tran. Amer. Geophys. Union 78, S333.

Naslund, H. R., F. M. Dobbs, F. J. Henríquez, and J. O. Nyström, 1998, Evidence for iron-oxide magmas at El Laco, Chile: Geol. Soc. Amer. Abstr. with Progr. 30, no 7, A-91.

Naslund, H. R., F. Henríquez, J. O. Nyström, R. Aguirre, and H. Lledó, 2003, El Laco, Chile: Evidence for the eruption of an immiscible Fe-O-S-P melt: Geol. Soc. Amer. Abstr. with Progr. 34, 394.

Naslund, H. R., F. Henríquez, J. O. Nyström, W. Vivallo, and F. M. Dobbs, 2002, Magmatic iron ores and associated mineralization: Examples from the Chilean High Andes and Coastal Cordillera, in T. M. Porter, ed., Hydrothermal iron oxide copper-gold & related deposits: A global perspective, v. 2: Adealide, PGC Publishing, p. 207–226.

Natalicchio, M., F. Dela Pierre, P. Clari, D. Birgel, S. Cavagna, L. Martire, and J. Peckmann, 2013, Hydrocarbon seepage during the Messinian salinity crisis in the Tertiary Piedmont Basin (NW Italy): Palaeogeography, Palaeoclimatology, Palaeoecology, v. 390, p. 68–80.

Ndiaye, P. M., and J. J. Guillou, 1997, Les tourmalinites stratiformes à dravite d'origine colloïdale du Paléoprotérozoïque sénégalo-malien: Journal of African Earth Sciences & the Middle East, v. 24, p. 215–226.

Neal, J. T., 1991, Prediction of Subsidence Resulting from Creep Closure of Solution-Mined Caverns in Salt Domes, in A. I. Johnson, ed., Land Subsidence: Proc. Fourth Inter. Symp. on Land Subsidence, IAHS Publ. No.200, p. 225.

Neal, J. T., 1994, Surface features indicative of subsurface evaporite dissolution: Implications for storage and mining: Solution Mining Research Institute, Meeting paper, 1994 Spring meeting, Houston Texas.

Neal, J. T., 1995, Supai salt karst features: Holbrook Basin, Arizona, in B. F. Beck, ed., Karst geohazards: engineering and environmental problems in karst terrane. Proc. 5th conference, Gatlinburg 1995, Balkema, p. 53–59.

Neal, J. T., S. Ballard, S. J. Bauer, B. L. Ehgartner, T. E. Hinkebein, E. L. Hoffman, J. K. Linn, M. A. Molecke, and A. R. Sattler, 1997, Mine-Induced Sinkholes Over the U.S. Strategic Petroleum Reserve (SPR) Storage Facility at Weeks Island, Louisiana: Geologic Mitigation Prior to and During Decommissioning, SAND96-2387A.: Presented at 6th Multidisciplinary Conference on Sinkholes and the Engineering & Environmental Impacts of Karst, Springfield, Missouri, April 6–9, 1997. Sandia National Laboratories, Albuquerque, NM.

Neal, J. T., S. J. Bauer, and B. L. Ehgartne, 1995, Sinkhole Progression at the Weeks Island, Louisiana, Strategic Petroleum Reserve (SPR) Site: Solution Mining Research Institute, Fall Meeting, San Antonio, Texas, October 1995. Sandia National Laboratories, Albuquerque, NM.

Neal, J. T., R. Colpitts, and K. S. Johnson, 1998, Evaporite Karst in the Holbrook Basin, Arizona, in J. Borchers, ed., Joseph F. Poland Symposium on Land Subsidence: Sudbury, MA, Assoc. Eng. Geologists Spec. Pub. 8, p. 373–384.

Neal, J. T., R. Colpitts, and K. S. Johnson, 2001, Evaporite Karst in the Holbrook Basin, Arizona: Solution Mining Research Institute (Solution Mining Research Institute) Report presented at the Fall 2001 Meeting 7–10 October 2001 Albuquerque, New Mexico, USA.

Neal, J. T., A. M. Langer, and P. F. Kerr, 1968, Giant desiccation polygons of Great Basin playas: Geological Society of America Bulletin, v. 79, p. 69–90.

Neal, J. T., and R. E. Myers, 1995, Salt dissolution sinkhole at the Weeks Island, Louisiana, strategic petroleum reserve storage site, in B. F. Beck, ed., Karst Geohazards: Engineering and environmental problems in karst terrane. Proc. 5th Conference, Gatlinburg 1995, Balkema, p. 61–65.

Neal, J. T., J. L. Todd, J. K. Linn, and T. R. Magorian, 1993, Threat of a sinkhole: A reevaluation of Cavern 4, Bayou Choctaw salt dome, Louisiana, Solution Mining Research Institute: paper presented at 1993 Fall Meeting, Oct. 24–28, Lafayette, Louisiana, 15 p.

Needham, R. S., 1988, Geology of the Alligator Rivers uranium field, Northern Territory: Bulletin – Bureau of Mineral Resources, Geology & Geophysics, Australia, v. 224, p. 96 pp.

Needham, R. S., and G. J. De Ross, 1990, Pine Creek Inlier – regional geology and mineralization, in F. E. Hughes, ed., The Mineral Deposits of Australia and Papua New Guinea: Volume 1, v. 14, Australasian Institute of Mining & Metallurgy: Monograph, p. 727–737.

Neev, D., and K. O. Emery, 1967, The Dead Sea: Depositional processes and environments of evaporites: Israel Mineral Development Geological Survey Bulletin, v. 41, p. 147 p.

Neev, D., and J. K. Hall, 1979, Geophysical investigations in the Dead Sea: Sedimentary Geology, v. 25, p. 209–238.

Neilson, J. E., and N. H. Oxtoby, 2008, The relationship between petroleum, exotic cements and reservoir quality in carbonates – A review: Marine and Petroleum Geology, v. 25, p. 778–790.

Nelson, K. H., and T. G. Thompson, 1954, Deposition of salts from seawater by frigid concentration: Journal Marine Research, v. 13, p. 166–182.

Nelson, T. H., 1991, Salt tectonics and listric normal faulting, in A. Salvador, ed., The Gulf of Mexico Basin: Boulder, Geol. Soc. America, p. 73–89.

Nelson, T. H., and L. H. Fairchild, 1989, Emplacement and evolution of salt sills in northern Gulf of Mexico (abs): American Association of Petroleum Geologists Bulletin, v. 73, p. 395.

Nesbitt, B. E., and K. Muehlenbachs, 1994, Paleohydrology of the Canadian Rockies and origins of brines, Pb-Zn deposits and dolomitization in the Western Canada Sedimentary Basin: Geology, v. 22, p. 243–246.

Nettleton, W. D., 1991, Occurrence, characteristics, and genesis of carbonate, gypsum, and silica accumulations in soils: Nettleton, W. D. Occurrence, characteristics, and genesis of carbonate, gypsum, and silica accumulations in soils. U. S. Dep. Agric., Natl. Soil Surv. Lab., Lincoln, NE, United States. SSSA Special Publication, v. 26, p. 1–16.

Neudert, M., 1986, A depositional model for the upper Mt Isa Group and implications for ore formation: PhD thesis, Research School of Earth Sciences, Australian National University, Canberra.

Neudert, M. K., and M. McGeough, 1996, A new tectonostratigraphic framework for the deposition of the upper McArthur Group, N.T, in T. Baker, J. F. Rotherham, J. M. Richmond, G. Mark, and P. J. Williams, eds., MIC 96, New developments in metallogenic research; the McArthur-Mount Isa-Cloncurry minerals province; extended abstracts., James Cook University of North Queensland, Geology Department, Townsville, Qld., Australia, p. 90–94.

Neudert, M. K., and R. E. Russell, 1981, Shallow water and hypersaline features from the Middle Proterozoic Mt Isa Sequence: Nature, v. 293, p. 284–286.

Neumann, C. A., B. M. Bedout, L. R. McNeese, C. K. Paull, and H. A. Paerl, 1988, Modern stromatolites and associated mats: San Salvador, Bahamas, in J. Mylroie, ed., Proceedings of the 4th Symposium on the geology of the Bahamas, Bahamas Field Station, 235–250, San Salvador.

Neumann, N. L., G. M. Gibson, and P. N. Southgate, 2009, New SHRIMP age constraints on the timing and duration of magmatism and sedimentation in the Mary Kathleen Fold Belt, Mt Isa Inlier, Australia.: Australian Journal Earth Scieces, v. 56, p. 965–983.

Newell, A. J., 2001, Bounding surfaces in a mixed eolian-fluvial system (Rotliegend, Wessex Basin, SW UK): Marine and Petroleum Geology, v. 18, p. 339–347.

Newell, A. J., M. J. Benton, T. Kearsey, G. Taylor, R. J. Twitchett, and V. P. Tverdokhlebov, 2012, Calcretes, fluviolacustrine sediments and subsidence patterns in Permo-Triassic salt-walled minibasins of the south Urals, Russia: Sedimentology, v. 59, p. 1659–1676.

Newson, T. A., and M. Fahey, 2003, Measurement of evaporation from saline tailings storages: Engineering Geology, v. 70, p. 217–233.

Newton, R. C., L. Y. Aranovich, E. C. Hansen, and B. A. Vandenheuvel, 1998, Hypersaline fluids in Precambrian deep-crustal metamorphism: Precambrian Research, v. 91, p. 41–63.

Nickless, E. F. P., S. J. Booth, and P. N. Mosley, 1975, Celestite deposits of the Bristol area: Inst. Min. Metall., Trans., Sect. B., v. 84, p. 62–63.

Nicolaides, S., 1995, Origin and modification of Cambrian dolomites (Red Heart Dolomite and Arthur Creek Formation), Georgina Basin, central Australia: Sedimentology, v. 42, p. 249–266.

Nie, Z., L. Bu, M. Zheng, and Y. Zhang, 2009, Crystallization Path of Salts from Brine in Zabuye Salt Lake, Tibet, During Isothermal Evaporation, in A. Oren, D. L. Naftz, P. Palacios, and W. A. Wurtsbaugh, eds., Natural Resources and Environmental Issues: Vol. 15, Article 1. Available at: http://digitalcommons.usu.edu/nrei/vol15/iss1/1 Berkley Electronic Press, p. 197–201.

Nielsen, P., R. Swennen, J. A. D. Dickson, A. E. Fallick, and E. Keppens, 1997, Spheroidal dolomites in a Visean karst system – bacterial induced origin?: Sedimentology, v. 44, p. 177–195.

Niemi, T., Z. Ben-Avraham, and J. R. Gat, 1997, The Dead Sea – The Lake and its setting, Oxford University Press, 336 p.

Nieto, A. S., and D. G. Russell, 1984, Sinkhole Development in Windsor-Detroit Solution Mines and the Role of Downward Mass Transfer in Subsidence: In-Situ, v. 8, p. 293–327.

Nigbor, M. T., 1982, State of the art of solution mining fo salt , potash, and soda ash: US Bureau of Mines, v. OFR 142–82, p. 90 pp.

Nijman, W., K. H. de Bruijne, and M. E. Valkering, 1999, Growth fault control of Early Archaean cherts, barite mounds and chert-barite veins, North Pole Dome, Eastern Pilbara, Western Australia: Precambrian Research, v. 95, p. 245-.

Nikolaevsky, A. P., 1938, The winter minerals of the Baskunchak salt lake: Priroda, v. 1, p. 86–93.

Nissen, S. E., W. L. Watney, and J. Xia, 2004, High-resolution seismic detection of shallow natural gas beneath Hutchinson, Kansas: Environmental Geosciences, v. 11, p. 129–142.

Nissenbaum, A., J. Rullkötter, and Y. Yechieli, 2002, Are the Curative Properties of 'Black Mud' from the Dead Sea Due to the Presence of Bitumen (Asphalt) or Other Types of Organic Matter?: Environmental Geochemistry and Health, v. 24, p. 327–335.

Nix, E. R., C. R. Fisher, J. Vodenichar, and K. M. Scott, 1995, Physiological ecology of a mussel with methanotrophic endosymbionts at three hydrocarbon seep sites in the Gulf of Mexico: Marine Biology, v. 122, p. 605–617.

Noble, R. R. P., D. J. Gray, and N. Reid, 2011, Regional exploration for channel and playa uranium deposits in Western Australia using groundwater: Applied Geochemistry, v. 26, p. 1956–1974.

Nof, R. N., G. Baer, A. Ziv, E. Raz, S. Atzori, and S. Salvi, 2013, Sinkhole precursors along the Dead Sea, Israel, revealed by SAR interferometry: Geology, v. 41, p. 1019–1022.

Noffke, N., G. Gerdes, and T. Klenke, 2003, Benthic cyanobacteria and their influence on the sedimentary dynamics of peritidal depositional systems (siliciclastic, evaporitic salty, and evaporitic carbonatic): Earth-Science Reviews, v. 62, p. 163–176.

Nollet, S., C. Hilgers, and J. Urai, 2005, Sealing of fluid pathways in overpressure cells: a case study from the Buntsandstein in the Lower Saxony Basin (NW Germany): International Journal of Earth Sciences, v. 94, p. 1039–1055.

Nordstrom, D. K., 1982a, The effect of sulfate on aluminum concentrations in natural waters: some stability relations in the system Al_2O_3-SO3-H_2O at 298 K: Geochimica et Cosmochimica Acta, v. 46, p. 681–692.

Nordstrom, D. K., 1982b, Aqueous pyrite oxidation and the consequent formation of secondary iron minerals, in J. A. Kittrick, D. S. Fanning, and L. R. Hossner, eds., Acid Sulfate Weathering, v. 10: Madison, WI, USA, Soil Science Society of America Special Publication, p. 37–56.

North, F. K., 1985, Petroleum Geology: Winchester, Mass, Unwin Hyman Ltd, 631 p.

North, F. K., 1990, Petroleum Geology. Second Ed.: Winchester, Mass, Unwin Hyman Ltd, 631 p.

Norton, C. F., and W. D. Grant, 1988, Survival of Halobacteria Within Fluid Inclusions in Salt Crystals: Journal of General Microbiology, v. 134, p. 1365–1373.

Notholt, A. J. G., 1983, Potash in Developing Countries, in R. M. McKercher, ed., Potash '83; Potash technology; mining, processing, maintenance, transportation, occupational health and safety, environment, p. 29–40.

Nunez, L., M. Grosjean, and I. Cartajena, 2002, Human Occupations and Climate Change in the Puna de Atacama, Chile: Science, v. 298, p. 821–824.

Nunn, J. A., 2013, Bubble, bubble, tremors and trouble: The Corne Bayou sinkhole [abs.]: Reflections (Southeastern Geophysical Society of New Orleans), no. 12, p. 2, http://www.nogs.org/Nunn-Abst&Bio-Sept'13.pdf.

Nunn, J. A., and N. B. Harris, 2007, Subsurface seepage of seawater across a barrier: A source of water and salt to peripheral salt basins: Geological Society of America Bulletin, v. 119, p. 1201–1217.

Nurmi, R. D., and G. M. Friedman, 1977, Sedimentology and depositional environments of basin-center evaporites, lower Salina Group (Upper Silurian), Michigan Basin, in J. H. Fisher, ed., Reefs and Evaporites—Concepts and Depositional Models American Association Petroleum Geologists Studies in Geology 5: Tulsa, OK, American Association of Petroleum Geologists, p. 23–52.

Nutman, A. P., and K. Ehlers, 1998, Archaean crust near Broken Hill: Australian Journal of Earth Sciences, v. 45, p. 687–694.

Nwe, Y. Y., and G. Morteani, 1993, Fluid evolution in the H_2O- CH_4 -CO_2 -NaCl system during emerald mineralization at Gravelotte, Murchison Greenstone Belt, Northeast Transvaal, South Africa: Geochimica et Cosmochimica Acta, v. 57, p. 89–103.

Nystrom, J. O., and F. Henriquez, 1994, Magmatic features of iron ores of the Kiruna type in Chile and Sweden: ore textures and magnetite geochemistry: Economic Geology, v. 89, p. 820–839.

Nystuen, J. P., A. Andresen, R. A. Kumpulainen, and A. Siedlecka, 2008, Neoproterozoic basin evolution in Fennoscandia, East Greenland and Svalbard: Episodes, v. 31, p. 35–42.

O'Brien, G. W., M. Lisk, I. R. Duddy, J. Hamilton, P. Woods, and R. Cowley, 1999, Plate convergence, foreland development and fault reactivation: primary controls on brine migration, thermal histories and trap breach in the Timor Sea, Australia: Marine & Petroleum Geology, v. 16, p. 533–560.

O'Brien, J., and I. Lerche, 1994, Understanding subsalt overpressure may reduce drilling risks: Oil and Gas Journal, v. 92, p. 28–29,32–34.

O'Connor, J. E., 1993, Hydrology, hydraulics, and geomorphology of the Bonneville flood: Geological Society of America Special Paper 274. 83 p.

O'Connor, J. E., and J. E. Costa, 2004, The World's Largest Floods, Past and Present: Their Causes and Magnitudes: U.S. Geological Survey Circular 1254, 3p.

O'Dell, P. M., 1998, The Athel: A Challenging Formation in South Oman: SPE 50981; presented at the 1997 SPE Middle East Oil Show held in Bahrain, 15–18 March.
O'Donoghue, M., 2006, Gems; Their Sources, Descriptions and Identification (6th Edition): Amsterdam, Elsevier, 873 p.
Ober, J. A., 2000, Sulfur in Minerals Commodity Summaries 2000: U.S. Geological Survey, p. 164–165.
Ober, J. A., 2011, Bromine: U.S. Geological Survey, 2010 Minerals Yearbook, (Advanced release – Sept 2011)
Obermajer, M., M. G. Fowler, and L. R. Snowdon, 1998, A geochemical characterization and a biomarker re-appraisal of the oil families from southwestern Ontario: Bulletin of Canadian Petroleum Geology, v. 46, p. 350–378.
Obermajer, M., M. G. Fowler, L. R. Snowdon, and R. W. Macqueen, 2000, Compositional variability of crude oils and source kerogen in the Silurian carbonate-evaporite sequences of the eastern Michigan Basin, Ontario, Canada: Bulletin of Canadian Petroleum Geology, v. 48, p. 307–322.
Obolenskiy, A. A., S. M. Rodionov, S. Ariunbileg, G. Dejidmaa, E. G. Distanov, D. Dorjgotov, O. Gerel, Duk Hwan Hwang, F. Sun, A. Gotovsuren, S. N. Letunov, Xujun Li, W. J. Nokleberg, M. Ogasawara, Z. V. Seminsky, A. P. Smelov, V. I. Sotnikov, A. A. Spiridonov, L. V. Zorina, and Hongquan Yan, 2007, Mineral Deposit Models for Northeast Asia, in W. J. Nokleberg, L. M. Parfenov, G. Badarch, N. A. Berzin, Duk Hwan Hwang, A. I. Khanchuk, M. I. Kuzmin, A. A. Obolenskiy, M. Ogasawara, A. V. Prokopiev, S. M. Rodionov, A. P. Smelov, Hongquan Yan, and M. F. Diggles, eds., Metallogenesis and Tectonics of Northeast Asia, U.S. Geological Survey, Reston Virginia, Open-File Report 2007–1183; Chapter C.
Odada, E. O., J. Raini, and R. Ndetei, 2006, Lake Nakuru – Experience and lessons learned; A Brief: Online report available at http://www.worldlakes.org.
Oehler, D. Z., J. H. Oehler, and A. J. Stewart, 1979, Algal fossils from a Late Precambrian, hypersaline lagoon: Science, v. 205, p. 338–340.
Oehler, J. H., 1984, Carbonate source rocks in the Jurassic Smackover trend of Mississippi, Alabama, and Florida, in J. G. Palacas, ed., Petroleum geochemistry and source rock potential of carbonate rocks: Tulsa, Oklahoma, American Association of Petroleum Geologists, Studies in Geology No. 18, p. 63–69.
Oesterhelt, D., and W. Marwan, 1993, Signal transduction in Halobacteria, in M. Kates, D. J. Kushner, and A. T. Matheson, eds., The Biochemistry of the Archaea, v. 26: Amsterdam, Elsevier, p. 173–187.
Ogawa, Y., N. Shikazono, D. Ishiyama, H. Sato, T. Mizuta, and T. Nakano, 2007, Mechanisms for anhydrite and gypsum formation in the Kuroko massive sulfide-sulfate deposits, north Japan: Mineralium Deposita, v. 42, p. 219–233.
Ogniben, L., 1957, Secondary gypsum of the sulphur series, Sicily, and the so-called integration: J. Sediment. Petrology., p. 64–79.
Ohmoto, H., 1996, Formation of volcanogenic massive sulphide deposits – The Kuroko perspective: Ore Geology Reviews, v. 10, p. 135–177.
Ohmoto, H., and B. J. Skinner, 1983, The Kuroko and related volcanogenic massive sulphide deposits: Economic Geology Monograph, v. 5, 605 p.
Okere, D., and S. Toothill, 2012, New insights into hydrocarbon plays in the Caspian Sea, Kazakhstan: Petroleum Geoscience, v. 18, p. 253–268.
Olaussen, S., 1981, Formation of celestite in the Wenlock, Oslo region Norway – evidence for evaporitic depositional environments: Journal of Sedimentary Petrology, v. 51, p. 37–46.
Oldham, D. W., 1893, Manual of the Geology of India: Calcutta, India, GSI Publications.
Olgaard, D. L., S. C. Ko, and T. F. Wong, 1995, Deformation and pore pressure in dehydrating gypsum under transiently drained conditions: Tectonophysics, v. 245, p. 237–248.
Olive, W. W., 1957, Solution-subsidence troughs, Castile Formation of Gypsum Plain, Texas and New Mexico: Geological Society of America, v. 68, p. 351–358.
Oliveira, E. P., and J. Tarney, 1995, Genesis of the Precambrian copper-rich Caraiba hypersthenite-norite complex, Brazil: Mineralium Deposita, v. 30, p. 351–373.
Oliver, J., 1986, Fluids expelled tectonically from orogenic belts; their role in hydrocarbon migration and other geologic phenomena: Geology, v. 14, p. 99–102.
Oliver, J. E., 2005, Encyclopedia of World Climatology: Dordrecht, Springer, 854 p.
Oliver, N. H. S., 1995, Hydrothermal history of the Mary Kathleen Fold belt, Mt Isa Block, Queensland: Australian Journal of Earth Sciences, v. 42, p. 267–279.
Oliver, N. H. S., J. S. Cleverley, G. Mark, P. J. Pollard, B. Fu, L. J. Marshall, M. J. Rubenach, P. J. Williams, and T. Baker, 2004, Modeling the Role of Sodic Alteration in the Genesis of Iron Oxide-Copper-Gold Deposits, Eastern Mount Isa Block, Australia: Economic Geology, v. 99, p. 1145–1176.
Oliver, N. H. S., T. J. Rawling, I. Cartwright, and P. J. Pearson, 1994, High temperature fluid-rock interaction and scapolitisation in an extension related hydrothermal system, Mary Kathleen, Australia: Journal of Petrology, v. 35, p. 1455–1491.
Oliver, N. H. S., M. J. Rubenach, B. Fu, T. Baker, B. T. G., J. S. Cleverley, L. J. Marshall, and P. V. Ridd, 2006, Granite-related overpressure and volatile release in the mid crust: fluidized breccias from the Cloncurry District, Australia: Geofluids, v. 6, p. 346–358.
Oliver, N. H. S., and V. J. Wall, 1987, Metamorphic plumbing system in Proterozoic calc-silicates, Queensland, Australia: Geology, v. 15, p. 793–796.
Oliver, N. H. S., V. J. Wall, and I. Cartwright, 1992, Internal control of fluid compositions in amphibolite-facies scapolitic calc-silicates, Mary Kathleen, Australia: Contributions to Mineralogy and Petrology, v. III, p. 94–112.
Oliveri, E., R. Neri, A. Bellanca, and R. Riding, 2010, Carbonate stromatolites from a Messinian hypersaline setting in the Caltanissetta Basin, Sicily: petrographic evidence of microbial activity and related stable isotope and rare earth element signatures: Sedimentology, v. 57, p. 142–161.
Oliveri, E., M. Sprovieri, D. S. Manta, L. Giaramita, V. La Cono, F. Lirer, P. Rumolo, N. Sabatino, G. Tranchida, M. Vallefuoco, M. M. Yakimov, and S. Mazzola, 2013, Sediment geochemistry of the Thetis hypersaline anoxic basin (eastern Mediterranean Sea): Sedimentary Geology, v. 296, p. 72–85.
Ollivier, B., P. Caumette, J. L. Garcia, and R. A. Mah, 1994, Anaerobic bacteria from hypersaline environments: Microbiological Reviews, v. 58, p. 27–38.
Olson, R. A., 1984, Genesis of paleokarst and strata-bound zinc-lead sulfide deposits in a Proterozoic dolostone, northern Baffin Island, Canada: Economic Geology, v. 79, p. 1056–1103.
Onac, B. P., 2005, Minerals, in D. C. Culver, and W. B. White, eds., Encyclopedia of Caves, Academic Press, New York, p. 371–378.
Opletal, V., J. Leichmann, and S. Houzar, 2007, Muscovite-plagioclase layers in dolomitic marble near Prosetin, Olesnice Unit, Moravicum; concordant injections of aplite or metaevaporites?: Acta Musei Moraviae. Scientiae Geologicae. Casopis Moravskeho Muzea, v. 92, p. 131–142.
Ordóñez, S., R. Fort, and M. Bustillo, 1989, Caracterización geoquímica de la ruptura sedimentaria entre los yesos de la unidad salina e intermedia de la cuenca de Madrid: Est. Geol. Sect, v. 45, p. 45–53.

Ordonez, S., and d. C. M. A. Garcia, 1988, The origin of sodium-calcium sulfate deposits of Madrid Basin (Spain): Water Resources Bulletin (Urbana), v. 24, p. 869–877.

Oremland, R. S., P. R. Dowdle, S. Hoeft, J. O. Sharp, J. K. Schaefer, L. G. Miller, J. S. Blum, R. L. Smith, N. S. Bloom, and D. Wallschlaeger, 2000, Bacterial dissimilatory reduction of arsenate and sulfate in meromictic Mono Lake. California Geochimica et Cosmochimica Acta, v. 64, p. 3073–3084.

Oren, A., 1993, The Dead Sea – Alive again: Experientia, v. 49, p. 518–522.

Oren, A., 1999, Microbiological studies in the Dead Sea: future challenges toward the understanding of life at the limit of salt concentrations: Hydrobiologia, v. 405, p. 1–9.

Oren, A., 2001, The bioenergetic basis for the decrease in metabolic diversity at increasing salt concentrations: implications for the functioning of salt lake ecosystems: Hydrobiologia, v. 466, p. 61–72.

Oren, A., 2002, Molecular ecology of extremely halophilic Archaea and Bacteria: FEMS Microbiology Ecology, v. 39, p. 1–7.

Oren, A., 2005, A century of Dunaliella research: 1905–2005, in N. Gunde-Cimerman, A. Oren, and A. Plemenitaš, eds., Adaptation to Life at High Salt Concentrations in Archaea, Bacteria, and Eukarya: Dordrecht, Netherlands, Springer, p. 491–502.

Oren, A., 2009, Microbial diversity and microbial abundance in salt-saturated brines: Why are the waters of hypersaline lakes red?: Natural Resources and Environmental Issues: Vol. 15, Article 49. Available at: http://digitalcommons.usu.edu/nrei/vol15/iss1/49

Oren, A., and N. Ben Yosef, 1997, Development and spatial distribution of an algal bloom in the Dead Sea: A remote sensing study: Aquatic Microbial Ecology, v. 13, p. 219–223.

Oren, A., G. Bratbak, and M. Heldal, 1997, Occurrence of virus-like particles in the Dead Sea: Extremophiles, v. 1, P- 143–149.

Oren, A., and P. Gurevich, 1995, Dynamics of a bloom of halophilic Archaea in the Dead Sea: Hydrobiologia, v. 315, p. 149–158.

Oren, A., P. Gurevich, D. A. Anati, E. Barkan, and B. Luz, 1995, A bloom of Dunaliella parva in the Dead Sea in 1992: biological and biogeochemical aspects: Hydrobiologia, v. 297, p. 173–185.

Oreskes, N., and M. T. Einaudi, 1990, Origin of rare earth element-enriched hematite breccias at the Olympic Dam Cu-U-Au-Ag deposit, Roxby Downs, South Australia: Economic Geology, v. 85, p. 1–28.

Oreskes, N., and M. T. Einaudi, 1992, Origin of hydrothermal fluids at Olympic Dam: preliminary results from fluid inclusions and stable isotopes.: Economic Geology, v. 87, p. 64–90.

Orgeval, J.-J., D. Giot, J. Karoui, J. Monthel, and R. Sahli, 1989, The discovery and investigations of the Bou Grine Pb-Zn deposit (Tunisian Atlas): Chronique de la Recherche Miniere, v. 57, p. 53–68.

Orgeval, J. J., 1991, A new type of Zn-Pb concentration related to salt dome activity: Example of the Bou Grine deposit (Tunisian Atlas), in M. Pagel, and J. L. Leroy, eds., Source, transport and deposition of metals., Balkema, p. 269–272.

Orgeval, J. J., 1994, Peridiapiric metal concentration: example of the Bou Grine deposit (Tunisian Atlas), in L. Fontboté, and M. Boni, eds., Sediment-hosted Zn-Pb ores, Society of Geology Applied to Mineral Deposits; Special Publication No. 10, p. 354–388.

Orozco, M., J. M. Molina, A. Crespo-Blanc, and F. M. Alonso-Chaves, 1999, Palaeokarst and rauhwacke development, mountain uplift and subaerial sliding of tectonic sheets (northern Sierra de los Filabres, Betic Cordilleras, Spain): Geologie en Mijnbouw, v. 78, p. 103–117.

Orszag-Sperber, F., 2006, Changing perspectives in the concept of "Lago-Mare" in Mediterranean Late Miocene evolution: Sedimentary Geology, v. 188–189, p. 259–277.

Orszag-Sperber, F., A. Caruso, M.-M. Blanc-Valleron, D. Merle, and J. M. Rouchy, 2009, The onset of the Messinian salinity crisis: Insights from Cyprus sections: Sedimentary Geology, v. 217, p. 52–64.

Orszag-Sperber, F., G. Harwood, A. Kendall, and B. H. Purser, 1998, A review of evaporites of the Red Sea – Gulf of Suez rift, in B. H. Purser, and D. W. J. Bosence, eds., Sedimentation and Tectonics of Rift Basins: Red Sea – Gulf of Aden: London, Chapman and Hall, p. 409–428.

Orszag-Sperber, F., J. Plaziat, F. Baltzer, and B. H. Purser, 2001, Gypsum salina-coral reef relationships during the Last Interglacial (Marine Isotopic Stage 5e) on the Egyptian Red Sea coast: a Quaternary analogue for Neogene marginal evaporites?: Sedimentary Geology, v. 140, p. 61–85.

Ortega-Gutierrez, F., 1984, Evidence of Precambrian evaporites in the Oaxacan granulite complex of southern Mexico: Precambrian Research, v. 23, p. 377–393.

Orti Cabo, F., M. J. J. Pueyo, and O. L. Rosell, 1985, Cartographic de subsurface du Salifere superieur du bassin potassique de Mulhouse (Oligocene, Alsace): Busson, G. Le sel; donnees geologiques en relation avec son exploitation et son utilisation; seance specialisee de la Societe Geologique de France. Salt; geologic data in relation to its exploitation and utilization; Special session of the Geological Society of France. Bulletin de la Societe Geologique de France, Huitieme Serie, v. l, p. 863–872.

Orti Cabo, F., and D. J. Shearman, 1977, Estructuras y fabricas deposicionales en las evaporitas del mioceno superior (Messiniense) de San Miguel de Salinas (Alicante, Espana): Instituto Investigaciones Geologicas Diputacion Provincial Universidad de Barcelone, v. 32, p. 5–54.

Orti, F., and B. Alonso, 2000, Gypsum-hydroboracite association in the Sijes Formation (Miocene, NW Argentina): implications for the genesis of Mg-bearing borates: Journal of Sedimentary Research, v. 70, p. 664–681.

Ortí, F., J. García-Veigas, L. Rosell, M. J. Jurado, and R. Utrilla, 1996, Formaciones salinas de las cuencas triásicas de la Península Ibérica: caracterización petrológica y geoquímica: Cuader. Geol. Ibér, v. 20, p. 13–35.

Orti, F., I. Gundogan, and C. Helvaci, 2002, Sodium sulphate deposits of Neogene age: the Kirmir Formation, Beypazari Basin, Turkey: Sedimentary Geology, v. 146, p. 305–355.

Orti, F., C. Helvaci, L. Rosell, and I. Gundogan, 1998, Sulphate-borate relations in an evaporitic lacustrine environment – the Sultancayir gypsum (Miocene, western Anatolia): Sedimentology, v. 45, p. 697–710.

Ortí, F., J. J. Pueyo, D. Geisler, and N. Dulau, 1984, Evaporitic sedimentation in the coastal salinas of Santa Pola (Alicante, Spain): Rev. Inst. Invest. Geol. Diput. Prov. Barc., v. 38–39, p. 169–220.

Orti, F., and L. Rosell, 2000, Evaporative systems and diagenetic patterns in the Calatayud Basin (Miocene, central Spain): Sedimentology, v. 47, p. 665–685.

Orti, F., L. Rosell, and P. Anadon, 2003, Deep to shallow lacustrine evaporites in the Libros Gypsum (southern Teruel Basin, Miocene, NE Spain): an occurrence of pelletal gypsum rhythmites: Sedimentology, v. 50, p. 361–386.

Orti, F., L. Rosell, and P. Anadon, 2010, Diagenetic gypsum related to sulfur deposits in evaporites (Libros Gypsum, Miocene, NE Spain): Sedimentary Geology, v. 228, p. 304–318.

Orti, F., L. Rosell, M. Inglés, and E. Playá, 2007, Depositional models of lacustrine evaporites in the SE margin of the Ebro Basin) Paleogene, SE Spain): Geologica Acta, v. 5, p. 19–34.

OrtÍ, F., L. Rosell, E. Playa, and J. M. Salvany, 2012, Meganodular anhydritization: a new mechanism of gypsum to anhydrite conversion (Palaeogene-Neogene, Ebro Basin, North-east Spain): Sedimentology, v. 59, p. 1257–1277.

Ortlieb, L., 1995, El Nino event and rainfall episodes in the Atacama Desert: the record of the last two centuries: Bull. Inst. Fr. Etud. Andin., v. 24, p. 519–537.

Orville, P. M., 1975, Stability of scapolite in the system Ab-An-NaCl-$CaCO_3$ at 4 kbar and 750°C: Geochimica et Cosmochimica Acta, v. 39, p. 1091–1105.

Osborn, W. L., 1989, Formation, diagenesis, and metamorphism of sulfate minerals in the Salton Sea geothermal system, California, U.S.A: Masters thesis, University of California, Riverside; Riverside, CA.

Osborne, R. H., G. R. Licari, and M. H. Link, 1982, Modern lacustrine stromatolites, Walker Lake, Nevada: Sedimentary Geology, v. 32, p. 39–61.

Oschmann, W., 2000, Microbes and Black Shales, in R. Riding, and S. Awramik, eds., Microbial Sediments, Springer Berlin Heidelberg, p. 137–148.

Oschmann, W., 2011, Black Shales, in J. Reitner, and V. Thiel, eds., Encyclopedia of Geobiology: Dordrecht, Netherlands, Springer, p. 201–206.

Oswald, E. J., 1992, Dolomitization of a Miocene reef complex; Mallorca, Spain: doctoral thesis, State University of New York at Stony Brook, 437 p.

Oszczepalski, S., 1989, Kupferschiefer in southwestern Poland: sedimentary environments, metal zoning, and ore controls: Geological Association of Canada Special Paper, v. 36, p. 571–600.

Oszczepalski, S., 1994, Oxidative alteration of the Kupferschiefer in Poland: oxide- sulphide parageneses and implications for ore-forming models: Kwartalnik Geologiczny, v. 38, p. 651–671.

Oszczepalski, S., and D. Blundell, 2005, 7–4: Kupferschiefer Copper Deposits of SW Poland: Lubin-Sieroszowice District: Lat. 51°35' N, Long. 16•6' E: Ore Geology Reviews, v. 27, p. 271–271.

Ottaway, T. L., F. J. Wicks, L. T. Bryndzia, T. K. Kyser, and E. T. C. Spooner, 1994, Formation of the Muzo hydrothermal emerald deposit in Colombia: Nature, v. 369, p. 552–554.

Ottes, W., P. Lambregts, and A. El-Barkooky, 2008, The Messinian salinity crisis in the Nile delta: chasing shallow marine reservoirs in a deep-water setting, in F. Briand, ed., The Messinian Salinity Crisis from Mega-deposits to Microbiology — A Consensus Report: CIESM workshop monograph, v. 33, p. 107–110.

Ovejero Toledo, A., R. N. Alonso, T. D. V. V Ruiz, and A. G. Quiroga, 2009, Evapofacies halitica en el Salar del Rincón: Rev. Asoc. Geol. Argent., v. 64, p. 4903–500.

Overmann, J., J. T. Beatty, and K. J. Hall, 1996, Purple sulfur bacteria control the growth of aerobic heterotrophic bacterioplankton in a meromictic salt lake: Applied and Environmental Microbiology, v. 62, p. 3251–3258.

Overmann, J., G. Sandmann, K. Hall, and T. Northcote, 1993, Fossil carotenoids and paleolimnology of meromictic Mahoney Lake, British Columbia, Canada: Aquatic Sciences, v. 55, p. 31–39.

Owen, J. V., and J. D. Greenough, 1999, Scapolite pegmatite from the Minas fault, Nova Scotia: tangible manifestation of Carboniferous, evaporite-derived hydrothermal fluids in the western Cobequid highlands?: Mineralogical Magazine, v. 63, p. 387–397.

Owen, J. V., F. J. Longstaffe, and J. D. Greenough, 2003, Petrology of sapphirine granulite and associated sodic gneisses from the Indian Head Range, Newfoundland: Lithos, v. 68, p. 91–114.

Owen, R. A., R. B. Owen, R. W. Renaut, J. J. Scott, B. Jones, and G. M. Ashley, 2008, Mineralogy and origin of rhizoliths on the margins of saline, alkaline Lake Bogoria, Kenya Rift Valley: Sedimentary Geology, v. 203, p. 143–163.

Owen, R. B., R. Crossley, T. C. Johnson, D. Tweddle, L. Kornfield, S. Davison, D. H. Eccles, and D. E. Engstrom, 1990, Major low levels of Lake Malawi and implications for speciation rates in cichlid fishes: Proc. Royal Soc. London Ser. B., p. 240–519.

Ozarslan, A., 2012, Large-scale hydrogen energy storage in salt caverns: International Journal of Hydrogen Energy, v. 37, p. 14265–14277.

Pache, M., J. Reitner, and G. Arp, 2001, Geochemical evidence for the formation of a large Miocene "travertine" mound at a sublacustrine spring in a soda lake (Wallerstein Castle rock, Nördlinger Ries, Germany): Facies, v. 45, p. 211–230.

Paik, I. S., and H. J. Kim, 1998, Subaerial lenticular cracks in Cretaceous lacustrine deposits, Korea: Journal of Sedimentary Research Section A-Sedimentary Petrology & Processes, v. 68, p. 80–87.

Paine, J. G., 1994, Subsidence beneath a playa basin on the Southern High Plains, U. S.A.; evidence from shallow seismic data: Geological Society of America Bulletin, v. 106, p. 233–242.

Painter, M. G. M., S. D. Golding, K. W. Hannan, and M. K. Neudert, 1999, Sedimentologic, petrographic, and sulfur isotope constraints on fine-grained pyrite formation at Mount Isa Mine and environs, Northwest Queensland, Australia: Economic Geology, v. 94, p. 883–912.

Pakzad, H., and R. Ajalloeian, 2004, Geochemistry of the Gavkhoni Playa Lake Brine: Carbonates and Evaporites, v. 19, p. 67–74.

Pal, D. C., R. B. Trumbull, and M. Wiedenbeck, 2010, Chemical and boron isotope compositions of tourmaline from the Jaduguda U (–Cu-Fe) deposit, Singhbhum shear zone, India: Implications for the sources and evolution of mineralizing fluids: Chemical Geology, v. 277, p. 245–260.

Palacas, J. G., 1984, Petroleum geochemistry and source rock potential of carbonate rocks, v. American Association Petroleum Geologists studies in geology No. 18: Tulsa, Okla., U.S.A, American Association of Petroleum Geologist, 208 p.

Palacas, J. G., D. E. Anders, and J. D. King, 1984, South Florida Basin – A prime example of carbonate source rocks of petroleum, in J. G. Palacas, ed., Petroleum geochemistry and source rock potential of carbonate rocks, v. 18: Tulsa, Oklahoma, American Association of Petroleum Geologists, Studies in Geology, p. 71–96.

Palacios, C., O. Rouxel, M. Reich, E. Cameron, and M. Ley-boume, 2011, Pleistocene recycling of copper at a porphyry system, Atacama Desert, Chile: Cu isotope evidence: Mineralium Deposita, v. 46, p. 1–7.

Palma, R. M., D. A. Kietzmann, G. S. Bressan, J. Martín-Chivelet, J. López-Gomez, M. E. Farias, and M. P. Iglesias Llanos, 2013, Peritidal cyclic sedimentation from La Manga Formation (Oxfordian), Neuquén Basin, Mendoza, Argentina: Journal of South American Earth Sciences, v. 47, p. 1–11.

Palmer, A. N., 2011, Distinction between epigenic and hypogenic maze caves: Geomorphology, v. 134, p. 9–22.

Palmer, A. N., and M. V. Palmer, 1995, The Kaskaskia paleokarst of the northern Rocky Mountains and Black Hills, northwestern U.S.A: Carbonates and Evaporites, v. 10, p. 148–160.

Palmer, A. N., and M. V. Palmer, 1998, Geochemistry of Cueva de Villa Luz, Mexico, an active H2S cave [abs.]. : Journal of Cave and Karst Studies, v. 60, p. 188.

Palmer, A. N., and M. V. Palmer, 2000, Hydrochemical interpretation of cave patterns in the Guadalupe Mountains, New Mexico: Journal of Cave and Karst Studies, v. 62, p. 91–108.

Palmer, M. R., and C. Helvaci, 1995, The boron isotope geochemistry of the Kirka borate deposit, western Turkey: Geochimica et Cosmochimica Acta, v. 59, p. 3599–3605.

Palmer, M. R., and C. Helvaci, 1997, The boron isotope geochemistry of the Neogene borate deposits of western Turkey: Geochimica et Cosmochimica Acta, v. 61, p. 3161–3169.

Palmer, M. R., and J. F. Slack, 1989, Boron isotopic composition of tourmaline from massive sulfide deposits and tourmalinites: Contributions to Mineralogy and Petrology, v. 103, p. 434–451.

Pan, Y., and P. Dong, 2003, Bromine in scapolite-group minerals and sodalite: XRF microprobe analysis, exchange experiments and application to skarn deposits: Canadian Mineralogist, v. 41, p. 529–540.

Pan, Y. M., M. E. Fleet, and G. E. Ray, 1994, Scapolite in two Canadian gold deposits – Nickel Plate, British Columbia and Hemlo, Ontario: Canadian Mineralogist, v. 32, p. 825–837.

Pancost, R. D., N. Crawford, and J. R. Maxwell, 2002, Molecular evidence for basin-scale photic zone euxinia in the Permian Zechstein Sea: Chemical Geology, v. 188, p. 217–227.

Pang, K.-N., N. Arndt, H. Svensen, S. Planke, A. Polozov, S. Polteau, Y. Iizuka, and S.-L. Chung, 2013, A petrologic, geochemical and Sr-Nd isotopic study on contact metamorphism and degassing of Devonian evaporites in the Norilsk aureoles, Siberia: Contributions to Mineralogy and Petrology, v. 165, p. 683–704.

Pape, H., C. Clauser, J. Iffland, R. Krug, and R. Wagner, 2005, Anhydrite cementation and compaction in geothermal reservoirs; interaction of pore-space structure with flow, transport, P-T conditions, and chemical reactions: International Journal of Rock Mechanics and Mining Sciences (1997), v. 42, p. 1056–1069.

Papioanou, F. P., and Z. Carotsieris, 1993, Dolomitization patterns in Jurassic-Cretaceous dissolution-collapse breccias of Mainalon Mountain (Tripolis Unit, Central Peloponnesus-Greece): Carbonates & Evaporites, v. 8, p. 9–22.

Pappalardo, R. T., and A. C. Barr, 2004, The origin of domes on Europa: The role of thermally induced compositional diapirism: Geophysical Research Letters, v. 31, p. L01701, doi:10.1029/2003GL019202, 2004.

Paquet, H., and G. Millot, 1972, Geochemical evolution of clay minerals in the weathered products of Mediterranean climate: Proceedings, International Clay Conference, Madrid, 21–24 June, 1972, p. 199–206.

Paradis, S., P. Hannigan, and K. Dewing, 2007, Mississippi Valley-type lead-zinc deposits, in W. D. Goodfellow, ed., Mineral Deposits of Canada: A Synthesis of Major Deposit Types, District Metallogeny, the Evolution of Geological Provinces, and Exploration Methods, Geological Association of Canada, Mineral Deposits Division, Special Publication, Vol. 5, p. 185–203.

Parafiniuk, J., 1989, Strontium and barium minerals in the sulfur deposits from the Tarnobrzeg region (SE Poland): Arch. Min., v. 43, p. 41–60.

Parák, T., 1991, Volcanic sedimentary rock-related metallogenesis in the Kiruna-Skellefte Belt of northern Sweden: Economic Geology Monograph, v. 8, p. 20–50.

Paraschiv, D., and G. Olteanu, 1970, Oil Fields in the Mid-Pliocene zone of the eastern Carpathians (District of Ploiesti, in M. T. Halbouty, ed., Geology of giant petroleum fields, American Association of Petroleum Geologists Memoir 14, p. 399–427.

Parcerisa, D., M. Thiry, and J. Schmitt, 2010, Albitisation related to the Triassic unconformity in igneous rocks of the Morvan Massif (France): International Journal of Earth Sciences, v. 99, p. 527–544.

Parente, C., L. Ronchi, A. Sial, J. Guillou, M. Arthaud, K. Fuzikawa, and C. Veríssimo, Ceara, 2004, Geology and geochemistry of Paleoproterozoic magnesite deposits (~1.8Ga), State of Ceará, Northeastern Brazil: Carbonates and Evaporites, v. 19, p. 28–50.

Paris, G., J. Gaillardet, and P. Louvat, 2010, Geological evolution of seawater boron isotopic composition recorded in evaporites: Geology, v. 38, p. 1035–1038.

Park, H., and W. H. Schlesinger, 2002, Global biogeochemical cycle of boron: Global Biogeochem. Cycles, v. 16, p. 1072.

Park Jr, C. F., 1961, A magnetite "flow" in northern Chile: Economic Geology, v. 56, p. 431–441.

Park, L. E., and K. F. Downing, 2001, Paleoecology of an exceptionally preserved arthropod fauna from lake deposits of the Miocene Barstow Formation, southern California, USA: Palaios, v. 16, p. 175–184.

Park, R. K., 1977, The preservation potential of some recent stromatolites: Sedimentology, v. 24, p. 485–506.

Parker, J. M., 1967, Salt solution and subsidence structures, Wyoming, North Dakota, and Montana: Bulletin American Association Petroleum Geologists, v. 51, p. 1929–1947.

Parkes, R. J., C. D. Linnane, G. Webster, H. Sass, A. J. Weightman, E. R. C. Hornibrook, and B. Horsfield, 2011, Prokaryotes stimulate mineral H2 formation for the deep biosphere and subsequent thermogenic activity: Geology, v. 39, p. 219–222.

Parnell, J., 1986, Devonian Magadi-type cherts in the Orcadian Basin, Scotland: Journal of Sedimentary Petrology, v. 56, p. 495–500.

Parnell, J., M. Baron, M. Davidson, D. Elmore, and M. Engel, 2000, Dolomitic breccia veins as evidence for extension and fluid flow in the Dalradian of Argyll: Geological Magazine, v. 137, p. 447–462.

Parnell, J., G. Earls, J. J. Wilkinson, D. H. W. Hutton, A. J. Boyce, A. E. Fallick, R. M. Ellam, S. A. Gleeson, N. R. Moles, P. F. Carey, and I. Legg, 2000, Regional Fluid Flow and Gold Mineralization in the Dalradian of the Sperrin Mountains, Northern Ireland: Economic Geology, v. 95, p. 1389–1416.

Pasteris, J. D., J. J. Freeman, B. Wopenka, K. Qi, Q. G. Ma, and K. L. Wooley, 2006, With a grain of salt: What halite has to offer to discussions on the origin of life: Astrobiology, v. 6, p. 625–643.

Patrick Muffler, L. J., and D. E. White, 1969, Active Metamorphism of Upper Cenozoic Sediments in the Salton Sea Geothermal Field and the Salton Trough, Southeastern California: Geological Society of America Bulletin, v. 80, p. 157–182.

Patterson, R. J., 1972, Hydrology and carbonate diagenesis of a coastal sabkha in the Persian Gulf: Doctoral thesis, Princeton University, 473 p.

Patterson, R. J., and D. J. J. Kinsman, 1981, Hydrologic framework of a sabkha along the Arabian Gulf: American Association Petroleum Geologists – Bulletin, v. 65, p. 1457–1475.

Patterson, R. J., and D. J. J. Kinsman, 1982, Formation of diagenetic dolomite in coastal sabkhas along the Arabian (Persian) Gulf: American Association of Petroleum Geologists Bulletin, v. 66, p. 28–43.

Paukstys, B., A. H. Cooper, and J. Arustiene, 1999, Planning for gypsum geohazards in Lithuania and England: Engineering Geology, v. 52, p. 93–103.

Paul, J., 1980, Upper Permian algal stromatolite reefs, Harz Mountains (F. R. Germany), in H. Fuchtbauer, and T. Peryt, eds., The Zechstein Basin with emphasis on carbonate sequences, E. Schweizerbart'sche Verlagsbuchhandlung, Stuttgart, West Germany, p. 253–268.

Paul, J., 1999, Evolution of a Permo-Carboniferous Basin: The Ilfeld Basin and its relationship to adjoining Permo-Carboniferous structures in Central Germany: Neues Jahrbuch fur Geologie und Palaontologie-Abhandlungen, v. 214, p. 211–236.

Paulick, H., and C. Breitkreuz, 2005, The Late Paleozoic felsic lava-dominated large igneous province in northeast Germany: volcanic facies analysis based on drill cores: International Journal of Earth Sciences, v. 94, p. 834–850.

Paull, C. K., J. R. Chanton, A. C. Neumann, J. A. Coston, and C. S. Martens, 1992, Indicators of methane-derived carbonates and chemosynthetic organic carbon deposits: examples from the Florida Escarpment: Palaios, v. 7, p. 361–375.

Pavlov, D. I., 1970, Halite anatectite and some of its less highly metamorphosed analogs: Acad. Sci. Ussr, Dokl., Earth Sci. Sect., v. 195, p. 171–173.

Pawlowski, S., K. Pawlowska, and B. Kubica, 1979, Geology and genesis of the Polish sulfur deposits: Economic Geology, v. 74, p. 475–483.

Payment, K. A., 2000, Loss of the Retsof salt mine: legal analysis of liability issues, in R. M. Geertmann, ed., Proc. 8th World Salt Symp., Salt 2000, The Hague, v. 1: Amsterdam, Elsevier, p. 399–404.

Paytan, A., and M. Kastner, 2002, Origin of marine barite deposits: Sr and S isotope characterization: Geology, v. 30, p. 747–750.

Peach, C., and C. J. Spiers, 1996, Influence of crystal plastic deformation on dilatancy and permeability development in synthetic salt rock: Tectonophysics, v. 256, p. 101–128.

Pearson, P. J., R. J. Holcombe, and R. W. Page, 1992, Synkinematic emplacement of the Middle Proterozoic Wonga Batholith into a mid-crustal extensional shear zone, Mount Isa Inlier, Queensland, Australia, in A. J. Stewart, and D. H. Blake, eds., Detailed studies of the Mount Isa Inlier, Bureau of Mineral Resources, Australia, Bulletin 243., p. 289–327.

PECAD, 2011, USDA/FAS/OGA and NASA Global Agriculture Monitoring (GLAM) Project. Lake and reservoir surface height variations from the USDA's Global Reservoir and Lake (GRLM) web site at: http://www.pecad.fas.usda.gov/cropexplorer/global_reservoir/. Altimetric lake level time-series variations from the Topex/Poseidon, Jason-1, Jason-2/OSTM, and Geosat Follow-On (GFO) missions.

Peck, W. H., and J. W. Valley, 2000, Large crustal input to high $\delta^{18}O$ anorthosite massifs of the southern Grenville Province: new evidence from the Morin Complex, Quebec: Contributions to Mineralogy and Petrology, v. 139, p. 402–417.

Peckmann, J., J. Paul, and V. Thiel, 1999, Bacterially mediated formation of diagenetic aragonite and native sulfur in Zechstein carbonates (Upper Permian, Central Germany): Sedimentary Geology, v. 126, p. 205–222.

Pedersen, K., 2000, Exploration of deep intraterrestrial microbial life: current perspectives: FEMS Microbiology Letters, v. 185, p. 9–16.

Pedley, M., J. A. G. Martín, S. O. Delgado, and D. Del Cura, 2003, Sedimentology of Quaternary perched springline and paludal tufas: criteria for recognition, with examples from Guadalajara Province, Spain.: Sedimentology, v. 50, p. 23–44.

Pedone, V. A., and J. A. D. Dickson, 2000, Replacement of Aragonite by Quasi-Rhombohedral Dolomite in a Late Pleistocene Tufa Mound, Great Salt Lake, Utah, U.S.A.: Journal of Sedimentary Research, Section A: Sedimentary Petrology and Processes, v. 70, p. 1152–1159.

Pedone, V. A., and R. L. Folk, 1996, Formation of aragonite cement by nannobacteria in the Great Salt Lake, Utah: Geology, v. 24, p. 763–765.

Peel, F. J., C. J. Travis, and J. R. Hossack, 1995, Genetic structural provinces and salt tectonics of the Cenozoic offshore U.S. Gulf of Mexico: a preliminary analysis, in M. P. A. Jackson, D. G. Roberts, and S. Snelson, eds., Salt tectonics: a global perspective: Tulsa OK, American Association Petroleum Geologists Memoir, v. 65, p. 153–175.

Pegrum, R. M., and N. Mounteney, 1978, Rift Basins Flanking North Atlantic Ocean and Their Relation to North Sea Area: Bulletin American Association Petroleum Geologists, v. 62, p. 419–441.

Peirce, H. W., 1981, Major Arizona salt deposits: Field Notes, Arizona Geological Survey, v. 11, p. 1–5.

Pell, S. D., A. R. Chivas, and I. S. Williams, 2000, The Simpson, Strzelecki and Tirari Deserts: development and sand provenance: Sedimentary Geology, v. 130, p. 107–130.

Peng, Q.-M., and M. R. Palmer, 2002, The Paleoproterozoic Mg and Mg-Fe Borate Deposits of Liaoning and Jilin Provinces, Northeast China: Economic Geology, v. 97, p. 93–108.

Peng, Q. M., and M. R. Palmer, 1995, The Palaeoproterozoic boron deposits in eastern Liaoning, China: a metamorphosed evaporite: Precambrian Research, v. 72, p. 185–197.

Peng, Q. M., M. R. Palmer, and J. W. Lu, 1998, Geology and geochemistry of the Paleoproterozoic borate deposits in Liaoning-Jilin, northeastern China: evidence of metaevaporites: Hydrobiologia, v. 381, p. 51–57.

Pérez-Asensio, J. N., J. Aguirre, G. Jiménez-Moreno, G. Schmiedl, and J. Civis, 2013, Glacioeustatic control on the origin and cessation of the Messinian salinity crisis: Global and Planetary Change, v. III, p. 1–8.

Pérez-Fodich, A., M. Reich, F. Álvarez, G. T. Snyder, R. Schoenberg, G. Vargas, Y. Muramatsu, and U. Fehn, 2014, Climate change and tectonic uplift triggered the formation of the Atacama Desert's giant nitrate deposits: Geology, v. 42, p. 251–254.

Perkins, R. D., 1991, Early and late diagenetic alteration of Ordovician Red River carbonates, Tioga Deep Field, Williston Basin, North Dakota: American Association Petroleum Geologists – Bulletin, v. 75, p. 652.

Perkins, W. G., and T. H. Bell, 1998, Stratiform replacement lead-zinc deposits: A comparison between Mount Isa, Hilton, and McArthur River: Economic Geology, v. 93, p. 1090–1212.

Perri, E., and A. Spadafora, 2011, Evidence of Microbial Biomineralization in Modern and Ancient Stromatolites, in V. Tewari, and J. Seckbach, eds., Stromatolites: Interaction of Microbes with Sediments: Cellular Origin, Life in Extreme Habitats and Astrobiology, v. 18, Springer Netherlands, p. 631–649.

Perri, E., M. E. Tucker, and A. Spadafora, 2012, Carbonate organo-mineral micro- and ultrastructures in sub-fossil stromatolites: Marion lake, South Australia: Geobiology, v. 10, p. 105–117.

Perring, C. S., P. J. Pollard, G. Dong, A. J. Nunn, and K. L. Blake, 2000, The Lightning Creek sill complex, Cloncurry district, northwest Queensland: A source of fluids for Fe oxide Cu-Au mineralization and sodic-calcic alteration: Economic Geology and the Bulletin of the Society of Economic Geologists, v. 95, p. 1067–1089.

Perski, Z., R. Hanssen, A. Wojcik, and T. Wojciechowski, 2009, InSAR analyses of terrain deformation near the Wieliczka Salt Mine, Poland: Engineering Geology, v. 106, p. 58–67.

Perthuisot, J.-P., 1975, La sebkha el Melah de Zarzis. Génese et évolution d'un bassin paralique: Travaux Laboratoire de Géologie, École Normale Supérieure, Paris.

Perthuisot, J. P., and S. Castanier, 2000, The role of extreme halophilic bacteria in the precipitation of salt, in R. M. Geertmann, ed., 8th World Salt Symposium, v. 1: Amsterdam, Elsevier, p. 173–180.

Perthuisot, J. P., S. Foridia, and A. Jauzein, 1972, Un modele recent de bassin cotier a sedimentation saline; la sebkha el Melah (Zarzis, Tunisie): Review Geographie Physical Geologie Dynamique, v. 14, p. 67–83.

Perthuisot, V., B. Henry, E. Laatar, A. Mansouri, H. Rouvier, A. Smati, J. Thibieroz, A. Bouzenoune, and N. Hatira, 1999, Les diapirs du Maghreb oriental: part des deformations alpines et des structures initiales cretacees et eocenes dans les formes actuelles Translated Title: Diapirs of the eastern Maghreb: the role of Alpine deformations and of initial Cretaceous and Eocene structures in the present architecture: Bulletin de la Societe Geologique de France, v. 170, p. 57–65.

Perucca, C. F., 2003, Potash processing in Saskatchewan – A review of process technologies: CIM Bulletin, v. 96, p. 61–65.

Peryt, T. M., 1989, Basal Zechstein in southwestern Poland: sedimentation, diagenesis, and gas accumulations: Geological Association of Canada Special Paper, v. 36, p. 601–625.

Peryt, T. M., 2000, Resedimentation of basin centre sulphate deposits: Middle Miocene Badenian of Carpathian Foredeep, southern Poland: Sedimentary Geology, v. 134, p. 331–342.

Peryt, T. M., and K. Dyjaczynski, 1991, An isolated carbonate bank in the Zechstein Main Dolomite Basin, western Poland: Journal of Petroleum Geology, v. 14, p. 445–458.

Peryt, T. M., and V. M. Kovalevich, 1997, Association of redeposited salt breccias and potash evaporites in the Lower Miocene of Stebnyk (Carpathian foredeep, West Ukraine): Journal of Sedimentary Research Section A-Sedimentary Petrology & Processes, v. 67 A, p. 913–922.

Peryt, T. M., A. A. Makhnach, S. Halas, O. Y. Petrychenko, L. F. Gulis, and S. M. Abravets, 2007, Sulfur isotopes in anhydrites from the Upper Devonian Prypiac and Dnipro-Donets basins (Belarus and Ukraine): Carbonates and Evaporites, v. 22, p. 43–54.

Peryt, T. M., F. Orti, and L. Rosell, 1993, Sulfate platform-basin transition of the lower Werra Anhydrite (Zechstein, Upper Permian),

western Poland; facies and petrography: Journal of Sedimentary Petrology, v. 63, p. 646–658.

Peryt, T. M., C. Pierre, and S. P. Gryniv, 1998, Origin of polyhalite deposits in the Zechstein (Upper Permian) Zdrada Platform (northern Poland): Sedimentology, v. 45, p. 565–578.

Peryt, T. M., and P. A. Scholle, 1996, Regional setting and role of meteoric water in dolomite formation and diagenesis in an evaporite basin – Studies in the Zechstein (Permian) of Poland: Sedimentology, v. 43, p. 1005–1023.

Peter, J. M., and S. D. Scott, 1991, Hydrothermal mineralization in the Guaymas Basin, Gulf of California, in J. P. Dauphin, and B. R. T. Simoneit, eds., The Gulf and Peninsula Province of the Californias, v. 47, American Association Petroleum Geologists Memoir, p. 721–741.

Peter, J. M., and S. D. Scott, 1991, Hydrothermal Mineralization in the Guaymas Basin, Gulf of California: Chapter 34: Part VI. Hydrothermal Processes: American Association Petroleum Geologists – Special Volume, v. 47, p. 721–741.

Peter, J. M., and W. C. Shanks III, 1992, Sulfur, carbon, and oxygen isotope variations in submarine hydrothermal deposits of Guaymas Basin, Gulf of California, USA: Geochimica et Cosmochimica Acta, v. 56, p. 2025–2040.

Peters, J. M., M. Shuster, H. A. Al-Siyabi, J. B. Filbrandt, J. P. Grotzinger, and M. J. Newall, 2003, Surface-piercing salt domes of interior North Oman, and their significance for the Ara carbonate 'stringer' hydrocarbon play: GeoArabia, v. 8, p. 231–270.

Peters, K. E., M. E. Clark, U. Dasgupta, M. A. Mccaffrey, and C. Y. Lee, 1995, Recognition of an Infracambrian source rock based on biomarkers in the Bahewala-1 oil, India: Bulletin American Association of Petroleum Geologists., v. 79, p. 1481–1494.

Peters, K. E., A. E. Cunningham, C. C. Walters, J. G. Jiang, and Z. A. Fan, 1996, Petroleum systems in the Jiangling-Dangyang area, Jianghan basin, China: Organic Geochemistry, v. 24, p. 1035–1060.

Peters, K. E., and J. M. Moldowan, 1993, The biomarker guide: Interpreting molecular fossils in petroleum and ancient sediments: Englewood Cliffs, NJ, Prentice Hall, 363 p.

Peters, K. E., J. M. Moldowan, and C. C. Walters, 2005, The Biomarker Guide: Volume 1, Biomarkers and isotopes in the environment and human history, Cambridge University Press, 490 p.

Peters, K. E., C. C. Walters, and J. M. Moldowan, 2005, The Biomarker Guide: Volume 2, Biomarkers and isotopes in petroleum systems and earth history, Cambridge University Press, 700 p.

Peters, S. E., and R. R. Gaines, 2012, Formation of the "Great Unconformity" as a trigger for the Cambrian explosion: Nature, v. 484, p. 363–366.

Petersen, K., and I. Lerche, 1995, Thermal Anomalies in Sediments near Evolving Salt Structures: Importance for Modeling the Timing of Oil Generation: Gulf Coast Association of Geological Societies Transactions, v. 44, p. 565–572.

Peterson, J. A., 1992, Aneth Field -USA, Paradox Basin, Utah, in N. H. Foster, and E. A. Beaumont, eds., Treatise of Petroleum Geology; Atlas of Oil and Gas Fields: Stratigraphic Traps III: Tulsa, OK, American Association Petroleum Geologists, p. 41–82.

Peterson, J. A., and R. J. Hite, 1969, Pennsylvanian evaporite-carbonate cycles and their relation to petroleum occurrence, southern Rocky Mountains: American Association Petroleum Geologists – Bulletin, v. 53, p. 884–908.

Peterson, M. N. A., G. S. Bien, and R. A. Berner, 1963, Radiocarbon studies of recent dolomite from Deep Spring Lake, California: Journal of Geophysical Research, v. 68, p. 6493–6505.

Peterson, M. N. A., and C. C. Von der Borch, 1965, Chert: modern inorganic deposition in a carbonate precipitating locality: Science, v. 149, p. 1501–1503.

Petrash, D. A., M. K. Gingras, S. V. Lalonde, F. Orange, E. Pecoits, and K. O. Konhauser, 2012, Dynamic controls on accretion and lithification of modern gypsum-dominated thrombolites, Los Roques, Venezuela: Sedimentary Geology, v. 245–246, p. 29–47.

Petrichenko, O. I., 1979, Translated title: Methods of inclusions in minerals of saline deposits: Fluid Inclusion Research, v. 12, p. 214–274.

Petrides, B., I. Cartwright, and T. Weaver, 2006, The evolution of groundwater in the Tyrrell catchment, south-central Murray Basin, Victoria, Australia: Hydrogeology Journal, v. 14, p. 1522–1543.

Petrychenko, O. Y., T. M. Peryt, and E. I. Chechel, 2005, Early Cambrian seawater chemistry from fluid inclusions in halite from Siberian evaporites: Chemical Geology, v. 219, p. 149–161.

Petryshyn, V. A., F. A. Corsetti, W. M. Berelson, W. Beaumont, and S. P. Lund, 2012, Stromatolite lamination frequency, Walker Lake, Nevada: Implications for stromatolites as biosignatures: Geology, v. 40, p. 499–502.

Petta, T. J., and S. D. Rapp, 1990, Appleton Field – USA, Gulf of Mexico Basin, Alabama, in E. A. Beaumont, and N. H. Foster, eds., Treatise of Petroleum Geology; Atlas of Oil and Gas Fields: Structural Traps IV – Tectonic and nontectonic fold traps: Tulsa, OK, American Association Petroleum Geologists, p. 299–318.

Petty, A. J., 1995, Ferry Lake, Rodessa, and Punta Gorda Anhydrite Bed Correlation, Lower Cretaceous, Offshore Eastern Gulf of Mexico: Gulf Coast Association of Geological Societies Transactions, v. 45, p. 487–495.

Pfeiffer, D., and J. Hahn, 1976, Karst of Germany, in M. Herak, and V. T. Stringfield, eds., Karst: Important karst regions of the Northern Hemisphere: Amsterdam, Elsevier, p. 189–223.

Philipp, S. L., 2008, Geometry and formation of gypsum veins in mudstones at Watchet, Somerset, SW England: Geological Magazine, v. 145, p. 831–844.

Philippe, Y., 1994, Transfer zone in the southern Jura thrust belt (eastern France): geometry, development and comparison with analogue modelling experiments, in A. Mascle, ed., Exploration and petroleum geology of France: Berlin, Springer Verlag, EAPG Memoir, v. 4, p. 327–346.

Phillips, G. N., P. J. Williams, and G. De Jong, 1994, The nature of metamorphic fluids and significance for metal exploration: Geological Society, London, Special Publications, v. 78, p. 55–68.

Philp, R. P., P. Fan, C. A. Lewis, J. Li, and H. Wang, 1991, Geochemical characteristics of oils from the Chaidamu, Shanganning and Jianghan basins, China: Journal of Southeast Asian Earth Sciences, v. 5, p. 351–358.

Philp, R. P., and C. A. Lewis, 1987, Organic geochemistry of biomarkers: Ann. Rev. Earth Planet. Science, v. 15, p. 363–395.

Phleger, F. B., 1969, A modern evaporite deposit in Mexico [with discussion]: American Association Petroleum Geologists – Bulletin, v. 53, p. 824–829.

Picard, L., 1943, Structures and evolution of Palestine with notes on neighbouring countries: Jerusalem Hebrew University Dept. Geol. Bulletin, v. 4, p. 1–134.

Picha, F., 1978, Depositional and diagenetic history of Pleistocene and Holocene oolitic sediments and sabkhas in Kuwait, Persian Gulf: Sedimentology, v. 25, p. 427–449.

Pierre, C., 1982, Teneurs en isotopes stables (^{18}O, ^{2}H, ^{13}C, ^{34}S) et conditions de genese des evaporites marines; application a quelques milieux actuels et au Messinien de la Mediterranee: Doctoral thesis, Orsay, Paris-Sud.

Pierre, C., 1985, Polyhalite replacement after gypsum at Ojo de Liebre Lagoon (Baja California, Mexico); an early diagenesis by mixing of marine brines and continental waters: Schreiber, B. Charlotte, Harner, H. Lincoln. Sixth international symposium on salt, v. 6, p. 257–265.

Pierre, C., 1988, Application of stable isotope geochemistry to the study of evaporites, in B. C. Schreiber, ed., Evaporites and hydrocarbons: New York, Columbia University Press, p. 300–344.

Pierre, C., and J. M. Rouchy, 1988, Carbonate replacements after sulphate evaporites in the Middle Miocene of Egypt: Journal of Sedimentary Petrology, v. 58, p. 446–456.

Pierret, M. C., N. Clauer, D. Bosch, and G. Blanc, 2010, Formation of Thetis Deep metal-rich sediments in the absence of brines, Red Sea: Journal of Geochemical Exploration, v. 104, p. 12–26.

Pietras, J. T., and A. R. Carroll, 2006, High-Resolution Stratigraphy of an Underfilled Lake Basin: Wilkins Peak Member, Eocene Green River Formation, Wyoming, U.S.A: Journal of Sedimentary Research, v. 76, p. 1197–1214.

Pietsch, B. A., D. J. Rawlings, P. M. Creaser, P. D. Kruse, M. Ahmad, P. A. Ferenczi, and T. L. R. Findhammer, 1991, Explanatory Notes-Bauhinia Downs SE53-3: Northern Territory Geological Survey.

Pilcher, R. S., B. Kilsdonk, and J. Trude, 2011, Primary basins and their boundaries in the deep-water northern Gulf of Mexico: Origin, trap types, and petroleum system implications: Bulletin American Association Petroleum Geologists, v. 95, p. 219–240.

Pinckney, J., H. W. Paerl, and B. M. Bebout, 1995, Salinity control of benthic microbial mat community production in a Bahamian hypersaline lagoon: Journal of Experimental Marine Biology & Ecology, v. 187, p. 223–237.

Piqué, A., A. Canals, F. Grandia, and D. A. Banks, 2008, Mesozoic fluorite veins in NE Spain record regional base metal-rich brine circulation through basin and basement during extensional events: Chemical Geology, v. 257, p. 139–152.

Pirajno, F., 1992, Hydrothermal Mineral Deposits: Berlin, Springer Verlag, 709 p.

Pirajno, F., 2007, Mantle plumes, associated intraplate tectonomagmatic processes and ore systems: Episodes, v. 30, p. 6–19.

Pirajno, F., 2009, Hydrothermal Processes and Mineral Systems: Berlin, Springer Science, 1252 p.

Pirajno, F., and L. Bagas, 2008, A review of Australia's Proterozoic mineral systems and genetic models: Precambrian Research, v. 166, p. 54–80.

Pirajno, F., R. Burlow, and A. Thorne, 2008, Magellan nonsulfide Pb and polymetallic Abra: Two stratabound giant deposits (abs): 33rd International Geological Congress, Oslo, August 6–14, 2008; MRD-04 Giant ore deposits.

Pirajno, F., and K. Grey, 2002, Chert in the Palaeoproterozoic Bartle Member, Killara Formation, Yerrida Basin, Western Australia: a rift-related playa lake and thermal spring environment?: Precambrian Research, v. 113, p. 169–192.

Pirlet, H., L. M. Wehrmann, B. Brunner, N. Frank, J. Dewanckele, D. van Rooij, A. Foubert, R. Swennen, L. Naudts, M. Boone, V. Cnudde, and J.-P. Henriet, 2010, Diagenetic formation of gypsum and dolomite in a cold-water coral mound in the Porcupine Seabight, off Ireland: Sedimentology, v. 57, p. 786–805.

Pittari, A., 1999, Geology of the Kutarta zinc-lead deposit, Lennard Shelf, Western Australia.: Honours Thesis, University of Melbourne, Department of Earth Sciences, unpublished.

Pittman, J. G., 1985, Correlation of beds within the Ferry Lake Anhydrite of the Gulf Coastal Plain: Transactions Gulf Coast Association of Geological Societies, v. 35, p. 251–260.

Playa, E., D. I. Cendon, A. Trave, A. R. Chivas, and A. Garcia, 2007, Non-marine evaporites with both inherited marine and continental signatures: The Gulf of Carpentaria, Australia, at ~ 70 ka: Sedimentary Geology, v. 201, p. 267–285.

Playa, E., F. Orti, and L. Rosell, 2000, Marine to non-marine sedimentation in the upper Miocene evaporites of the Eastern Betics, SE Spain: sedimentological and geochemical evidence: Sedimentary Geology, v. 133, p. 135–166.

Playa, E., and L. Rosell, 2005, The celestite problem in gypsum Sr geochemistry: An evaluation of purifying methods of gypsiferous samples: Chemical Geology, v. 221, p. 102–116.

Playford, P. E., and M. W. Wallace, 2001, Exhalative Mineralization in Devonian Reef Complexes of the Canning Basin, Western Australia: Economic Geology, v. 96, p. 1595–1610.

Plaziat, J. C., F. Baltzer, A. Choukri, O. Conchon, P. Freytet, F. Orszag-Sperber, B. Purser, A. Raguideau, and J. L. Reyss, 1995, Quaternary changes in the Egyptian shoreline of the northwestern Red Sea and Gulf of Suez: Quaternary International, v. 30, p. 11–22.

Plimer, I. R., 1977, The origin of the albite-rich rocks enclosing the cobaltian pyrite deposit at Thackaringa, NSW, Australia: Mineralium Deposita, v. 12, p. 175–187.

Plimer, I. R., 1984, The role of fluorine in submarine exhalative systems with special reference to Broken Hill, Australia: Mineralium Deposita, v. 19, p. 19–25.

Plimer, I. R., 1985, Broken Hill Pb-Zn-Ag deposit; a product of mantle metasomatism: Mineralium Deposita, v. 20, p. 147–153.

Plimer, I. R., 1986, Tourmalinites from the Golden Dyke Dome, Northern Australia: Mineralium Deposita, v. 21, p. 263–270.

Plimer, I. R., 1988, The association of tourmalinite with stratiform scheelite deposits; reply: Mineralium Deposita, v. 23, p. 314.

Plimer, I. R., 1994, Strata-bound scheelite in meta-evaporites, Broken Hill, Australia: Economic Geology, v. 89, p. 423–437.

Plimer, I. R., and T. C. Lees, 1988, Tourmaline-rich rocks associated with the submarine hydrothermal Rosebery Zn-Pb-Cu-Ag-Au deposit and granites in western Tasmania, Australia: Mineralogy & Petrology, v. 38, p. 81–103.

Pluta, I., and A. Zuber, 1995, Origin of brines in the Upper Silesian Coal basin (Poland) inferred from stable isotope and chemical data: Applied Geochemistry, p. 447–460.

Podladchikov, Y., C. Talbot, and A. N. B. Poliakov, 1993, Numerical models of complex diapirs: Tectonophysics., v. 228, p. 189–198.

Pohl, W., 1989, Comparative geology of magnesite and occurrences, Monograph Series on Mineral Deposits, v. 28, Gebruder Borntraeger, Berlin-Stuttgart, p. 1–13.

Pohl, W., 1990, Genesis of magnesite deposits – models and trends: Geologische Rundschau, v. 79, p. 291–299.

Pohl, W. L., 2011, Economic Geology: Principles and Practice: New York, Wiley-Blackwell, 680 p.

Poliakov, A. N. B., Y. Podladchikov, E. C. Dawson, and C. Talbot, 1996, Salt diapirism with simultaneous brittle faulting and viscous flow, in G. I. Alsop, D. J. Blundell, and I. Davison, eds., Salt tectonics, Geological Society, London; Special Publication, v. 100, p. 291–302.

Polito, P., T. Kyser, and C. Stanley, 2009, The Proterozoic, albitite-hosted, Valhalla uranium deposit, Queensland, Australia: a description of the alteration assemblage associated with uranium mineralisation in diamond drill hole V39: Mineralium Deposita, v. 44, p. 11-40-40.

Polito, P. A., T. K. Kyser, S. D. Golding, and P. N. Southgate, 2006, Zinc Deposits and Related Mineralization of the Burketown Mineral Field, Including the World-Class Century Deposit, Northern Australia: Fluid Inclusion and Stable Isotope Evidence for Basin Fluid Sources: Economic Geology, v. 101, p. 1251–1273.

Polkowski, G. R., 1997, Degradation of reservoir quality by clay content, Unayzah Formation, Central Saudi Arabia: Geo-Arabia, v. 2, p. 49–64.

Pollard, A. M., D. R. Brothwell, A. Aali, S. Buckley, H. Fazeli, M. H. Dehkordi, T. Holden, A. K. G. Jones, J. J. Shokouhi, R. Vatandoust, and A. S. Wilson, 2008, Below the salt: A Preliminary study of the dating and biology of five salt-preserved bodies from Zanjun Province, Iran: Iran, v. 46, p. 135–150.

Pollard, P. J., 2001, Sodic(-calcic) alteration in Fe-oxide– Cu–Au districts: an origin via unmixing of magmatic H_2O-CO_2-NaCl ± $CaCl_2$-KCl fluids: Mineralium Deposita, v. 36, p. 93–100.

Pollard, P. J., 2002, Evidence of a Magmatic Fluid Source for Iron Oxide-Cu-Au Mineralisation, in T. M. Porter, ed., Hydrothermal Iron Oxide Copper-Gold and Related Deposits: A Global Perspective, v. 1, PGC Publishing, Adelaide, p. 27–41.

Pollard, P. J., G. Mark, and L. C. Mitchell, 1998, Geochemistry of post-1540 Ma granites in the Cloncurry District, Northwest Queensland: Economic Geology, v. 93, p. 1330–1344.

Pollastro, R. M., 2003, Total Petroleum Systems of the Paleozoic and Jurassic, Greater Ghawar Uplift and Adjoining Provinces of Central Saudi Arabia and Northern Arabian-Persian Gulf: U.S. Geological Survey Bulletin 2202-H, 74 p.

Polyak, V. J., and N. Guven, 1996, Alunite, natroalunite and hydrated halloysite in Carlsbad Cavern and Lechuguilla Cave, New Mexico: Clays & Clay Minerals, v. 44, p. 843–850.

Polyak, V. J., W. C. Mcintosh, N. Guven, and P. Provencio, 1998, Age of Carlsbad cavern and related caves from Ar^{40}/Ar^{39} of alunite: Science, v. 279, p. 1919–1922.

Pomoni-Papaioannou, F., and V. Karakitsios, 2002, Facies analysis of the Trypali carbonate unit (Upper Triassic) in central-western Crete (Greece): an evaporite formation transformed into solution-collapse breccias: Sedimentology, v. 49, p. 1113–1132.

Ponder, W. F., 1986, Mound springs of the Great Artesian Basin, in P. De Decker, and W. D. Williams, eds., Limnology in Australia: Melbourne, Dr W. Junk, p. 403–420.

Pons, J. M., M. Franchini, L. Meinert, C. Recio, and R. Etcheverry, 2009, Iron skarns of the Vegas Peladas District, Mendoza, Argentina: Economic Geology, v. 104, p. 157–184.

Pope, K. O., K. H. Baines, A. C. Ocampo, and B. A. Ivanov, 1994, Impact winter and the Cretaceous/Tertiary extinctions: results of a Chicxulub asteroid impact model: Earth & Planetary Science Letters, v. 128, p. 719–725.

Pope, M. C., J. P. Grotzinger, and B. C. Schreiber, 2000, Evaporitic subtidal stromatolites produced by in situ precipitation: Textures, facies associations, and temporal significance: Journal of Sedimentary Research Section A-Sedimentary Petrology & Processes, v. 70, p. 1138–1151.

Porter, D., A. N. Roychoudhury, and D. Cowan, 2007, Dissimilatory sulfate reduction in hypersaline coastal pans: Activity across a salinity gradient: Geochimica et Cosmochimica Acta, v. 71, p. 5102–5116.

Porter GeoConsultancy, 2004, Dzhezkazgan (Jezkazgan, Zhezkazgan) Copper deposit, Kazakhstan: Porter GeoConsultancy database.

Porter, R. J., and R. W. Gallois, 2008, Identifying fluvio-lacustrine intervals in thick playa-lake successions; an integrated sedimentology and ichnology of arenaceous members in the Mid-Late Triassic Mercia Mudstone Group of South-West England, UK: Palaeogeography, Palaeoclimatology, Palaeoecology, v. 270, p. 381–398.

Posamentier, H. W., and D. P. James, 1993, An overview of sequence-stratigraphic concepts; uses and abuses, in H. W. Posamentier, C. P. Summerhayes, B. U. Haq, and G. P. Allen, eds., Sequence stratigraphy and facies associations, v. 18: Oxford, UK, Special Publication of the International Association of Sedimentologists, p. 3–18.

Post, F. J., and N. N. Youssef, 1977, A procaryotic intracellular symbiont of the Great Salt Lake brine shrimp Artemia salina (L.). Canadian Journal Microbiology, v. 23, p. 1232–1236.

Postgate, J. R., 1984, The sulphate-reducing bacteria, 2nd Edition, Cambridge University Press.

Pottorf, R. J., and H. L. Barnes, 1983, Mineralogy, geochemistry, and ore genesis of hydrothermal sediments from the Atlantis II Deep, Red Sea: Economic Geology Monographs, v. 5, p. 198–223.

Powell, C. M., N. H. S. Oliver, Z. X. Li, D. M. Martin, and J. Ronaszeki, 1999, Synorogenic hydrothermal origin for giant Hamersley iron oxide orebodies.: Geology, v. 27, p. 175–178.

Powell, C. M., W. V. Preiss, C. G. Gatehouse, B. Krapez, and Z. X. Li, 1994, South Australia record of a Rodinian epicontinental basin and its Mid-Proterozoic breakup (≈700 Ma) to form the Palaeopacific ocean: Tectonophysics, v. 237, p. 113–140.

Powell, T. G., and R. W. MacQueen, 1984, Precipitation of sulfide ores and organic matter: sulfate reactions at Pine Point, Canada: Science, v. 224, p. 63–66.

Powell, W. G., P. A. Johnston, C. J. Collom, and K. J. Johnston, 2006, Middle Cambrian brine seeps on the Kicking Horse Rim and their relationship to talc and magnesite mineralization and associated dolomitization, British Columbia, Canada: Economic Geology, v. 101, p. 431–451.

Power, I. M., S. A. Wilson, A. L. Harrison, G. M. Dipple, J. McCutcheon, G. Southam, and P. A. Kenward, 2014, A depositional model for hydromagnesite–magnesite playas near Atlin, British Columbia, Canada: Sedimentology, v. 61, p. 1701–1733.

Powers, D. W., 2000, Evaporites, casing requirements, water-floods, and out-of-formation waters: potential for sinkhole developments: Proc. Solution Mining Research Institute Fall Meeting Technical Session, San Antonio, p. 186–195.

Powers, D. W., R. L. Beauheim, R. M. Holt, and D. L. Hughes, 2006, Evaporite karst features and processes at Nash Draw, Eddy County, New Mexico, in L. Land, V. Lueth, B. Raatz, P. Boston, and D. Love, eds., Caves and Karst of Southeastern New Mexico: New Mexico Geological Society, Guidebook 57, p. 253–266.

Powers, D. W., and R. M. Holt, 2000, The salt that wasn't there: Mudflat facies equivalents to halite of the Permian Rustler Formation, southeastern New Mexico: Journal of Sedimentary Research Section A-Sedimentary Petrology & Processes, v. 70, p. 29–36.

Powers, R. W., 1962,Arabian Upper Jurassic carbonate reservoir rocks, in W. E. Ham, ed., Classification of carbonate rocks: a symposium, American Association of Petroleum Geologists Memoir, v. 1, p. 122–192.

Powley, D. E., 1980, Pressures, normal and abnormal:American Association Petroleum Geologists Advanced Exploration School, Unpublished Lecture Notes, 38 pp.

Pownceby, M. I., and C. Johnson, 2014, Geometallurgy of Australian uranium deposits: Ore Geology Reviews, v. 56, p. 25–44.

Prather, B. E., 1986, Diagenesis of Smackover Reservoir Rocks in Southeastern Gulf Coast (abs): American Association Petroleum Geologists – Bulletin, v. 70, p. 634.

Prather, B. E., 1992a, Origin of Dolostone Reservoir Rocks, Smackover Formation (Oxfordian), Northeastern Gulf Coast, U.S.A.: American Association Petroleum Geologists – Bulletin, v. 76, p. 133–163.

Prather, B. E., 1992b, Evolution of a Late Jurassic carbonate/evaporite platform, Conecuh Embayment, northeastern Gulf Coast, U.S.A: American Association Petroleum Geologists – Bulletin, v. 76, p. 164–190.

Pratt, B. R., 2002, Tepees in peritidal carbonates: origin via earthquake-induced deformation, with example from the Middle Cambrian of western Canada: Sedimentary Geology, v. 153, p. 57–64.

Préat, A., K. Kolo, J.-P. Prian, and F. Delpomdor, 2010, A peritidal evaporite environment in the Neoproterozoic of South Gabon (Schisto-Calcaire Subgroup, Nyanga Basin): Precambrian Research, v. 177, p. 253–265.

Preiss, W. V., 1987, The Adelaide Geosyncline, in W. V. Preiss, ed., The Adelaide Geosyncline – late Proterozoic stratigraphy, sedimentation, palaeontology and tectonics:, Geological Survey of South Australia, Bulletin No. 53, p. 255–282.

Presley, M. W., 1987, Evolution of Permian evaporite basin in Texas Panhandle: American Association Petroleum Geologists Bulletin, v. 71, p. 167–190.

Price, L. C., 1976, Aqueous solubility of petroleum as applied to its origins and primary migration: American Association Petroleum Geologists – Bulletin, v. 60, p. 213–244.

Price, L. C., 1981, Aqueous solubility of crude oil to 400°C and 2,000 bars pressure in the presence of gas: Journal of Petroleum Geology, v. 4, p. 195–223.

Price, L. C., and C. E. Barker, 1985, Suppression of vitrinite reflectance in amorphous rich kerogen – a major unrecognized problem: Journal of Petroleum Geology, v. 8, p. 59–84.

Prikryl, J. D., H. H. Posey, and J. R. Kyle, 1988, A petrographic and geochemical model for the origin of calcite cap rock at Damon Mound salt dome Texas: Chemical Geology, v. 74, p. 67–98.

Princep, D., and A. Hutson, 2010, Langer Heinrich, Namibia: Mineral Resource and Mineral Reserve Estimation: Paladin Energy Ltd.,Technical Report (Effective Date: 15th November 2010).

Prud'homme, M., and S. T. Krukowski, 2006, Potash, in J. E. Kogel, N. C. Trivedi, J. M. Barker, and S. T. Krukowski, eds., Industrial Minerals and Rocks, SME (Soc. Mining Metallurgy and Exploration), p. 723–742.

Prugger, F. F., and A. F. Prugger, 1991, Water problems in Saskatchewan potash mining—what can be learned from them?: CIM Bulletin, v. 84, p. 58–66.

Pu, R., and H. Qing, 2003, Pool characterization of Ordovician Midale field: Implication for Red River play in northern Williston basin, southeastern Saskatchewan, Canada: American Association Petroleum Geologists – Bulletin, v. 87, p. 1699–1715.

Pueyo, J. J., G. Chong, and A. Jensen, 2001, Neogene evaporites in desert volcanic environments: Atacama Desert, northern Chile: Sedimentology, v. 48, p. 1411–1431.

Pueyo, J. J., G. Chong, and M. Vega, 1998, Mineralogy and parental brine evolution in the Pedro de Valdivia nitrate deposit, Antofagasta, Chile (Spanish): Revista Geologica de Chile, v. 25, p. 3–15.

Pueyo-Mur, J. J., and M. Inglés-Urpinell, 1987, Magnesite formation in recent playa lakes, Los Monegros, Spain, in J. D. Marshall, ed., Diagenesis of Sedimentary Sequences, Geol. Soc. Lond. Spec. Publ. v. 36, p. 119–122.

Pulido-Bosch, A., J. M. Calaforra, P. Pulido-Leboeuf, and S. Torres-García, 2004, Impact of quarrying gypsum in a semidesert karstic area (Sorbas, SE Spain): Environmental Geology, v. 46, p. 583–590.

Purser, B. H., 1973, The Persian Gulf: Holocene carbonate sedimentation and diagenesis in a shallow epicontinental sea: New York, Springer-Verlag, 471 p.

Purser, B. H., 1973, Sedimentation around bathymetric highs in the southern Persian Gulf, in B. H. Purser, ed., The Persian Gulf: Holocene carbonate sedimentation and diagenesis in a shallow epicontinental sea: New York, Springer Verlag, p. 157–177.

Purser, B. H., and G. Evans, 1973, Regional sedimentation along the Trucial Coast, southeastern Persian Gulf, in B. H. Purser, ed., The Persian Gulf: Holocene carbonate sedimentation and diagenesis in a shallow epicontinental sea: New York, Springer Verlag, p. 199–210.

Purvis, K., 1989, Zoned authigenic magnesites in the Rotliegend Lower Permian, southern North Sea: Sedimentary Geology, v. 65, p. 307–318.

Putnis, A., and H. Austrheim, 2010, Fluid-induced processes: metasomatism and metamorphism: Geofluids, v. 10, p. 254–269.

Pysklywec, R. N., and J. X. Mitrovica, 2000, Mantle flow mechanisms of epeirogeny and their possible role in the evolution of the Western Canada Sedimentary Basin: Canadian J. Earth Science, v. 37.

Qing, H., and E. W. Mountjoy, 1994, Origin of dissolution vugs, caverns, and breccias in the Middle Devonian Presqu'ile barrier, host of Pine Point Mississippi Valley- type deposits: Economic Geology, v. 89, p. 858–876.

Qiusheng, Z., 1988, Early Proterozoic tectonic styles and associated mineral deposits of the North China Platform: Precambrian Research, v. 39, p. 1–29.

Quade, J., J. A. Rech, C. Latorre, J. L. Betancourt, E. Gleeson, and M. T. K. Kalin, 2007, Soils at the hyperarid margin: The isotopic composition of soil carbonate from the Atacama Desert, Northern Chile: Geochimica et Cosmochimica Acta, v. 71, p. 3772–3795.

Quadri, V. N., and S. M. G. J. Quadri, 2003, Oldest reservoirs of Cambrian, Permian lightly tested in Potwar basin, Pakistan: Oil and Gas Journal, v. 101, p. 32–36.

Queen, J. M., A. N. Palmer, and M. V. Palmer, 1979, Carbonate replacement of sulfate; new mechanism for porosity generation in carbonate rocks marginal to evaporite basins: American Association Petroleum Geologists – Bulletin, v. 63, p. 512–513.

Quijada, I. E., P. Suarez-Gonzalez, M. I. Benito, S. Lugli, and R. Mas, 2014, From carbonate-sulphate interbeds to carbonate breccias: The role of tectonic deformation and diagenetic processes (Cameros Basin, Lower Cretaceous, N Spain): Sedimentary Geology, v. 312, p. 76–93.

Quinlan, J. F., 1978, Types of karst, with emphasis on cover beds in their classification and development: Doctoral thesis, University of Texas at Austin.

Quinlan, J. F., R. O. Ewers, J. A. Raty, and K. S. Johnson, 1986, Gypsum karst and salt karst of the United States of America: Atti simposio internazionale sul carsismo nelle evaporiti; Le Grotte d'Italia, v. 12, p. 419–420.

Raab, M., G. M. Friedman, B. Spiro, A. Starinsky, and I. Zak, 2000, The geological history of Pliocene-Pleistocene evaporites in Mount Sedom (Israel) and how strontium and sulfur isotopes relate to their origin: Carbonates & Evaporites, v. 15, p. 93–114.

Rabbani, A. R., and M. R. Kamali, 2005, Source rock evaluation and petroleum geochemistry, Offshore SW Iran: Journal of Petroleum Geology, v. 28, p. 413–428.

Racey, A., 2009, Mesozoic red bed sequences from SE Asia and the significance of the Khorat Group of NE Thailand: Geological Society, London, Special Publications, v. 315, p. 41–67.

Rack, F. R., 1993, A geologic perspective on the Miocene evolution of the Antarctic Circumpolar Current system: Tectonophysics, v. 222, p. 397–415.

Rahimpour-Bonab, H., and Z. Kalantarzadeh, 2005, Origin of secondary potash deposits; a case from Miocene evaporites of NW Central Iran: Journal of Asian Earth Sciences, v. 25, p. 157–166.

Rahn, P. H., and A. D. Davis, 1996, Gypsum foundation problems in the Black Hills area, Dakota: Environmental and Engineering Geoscience, v. 2, p. 213–223.

Raines, M. A., and T. A. Dewers, 1997, Dedolomitization as a driving mechanism for karst generation in Permian Blaine Formation, southwest Oklahoma, USA: Carbonates & Evaporites, v. 12, p. 24–31.

Raiswell, R., and H. J. Al-Biatty, 1992, Depositional and diagenetic C-S-Fe signatures and the potential of shales to generate metal-rich fluids, in M. e. a. Schidlowski, ed., Early organic evolution: Implications for mineral and energy resources: Berlin- Heidelberg, Springer-Verlag, p. 415–425.

Raiswell, R., F. Buckley, R. A. Berner, and T. F. Anderson, 1988, Degree of pyritization of iron as a palaeoenvironmental indicator of bottom water oxygenation: Journal of Sedimentary Petrology, v. 58, p. 812–819.

Raith, J. G., 1988, Tourmaline rocks associated with Stratabound Scheelite Mineralization in the Austroalpine Crystalline Complex, Austria: Mineralogy and Petrology, v. 39, p. 265–288.

Rajendran, C. P., and K. Rajendran, 2001, Characteristics of Deformation and Past Seismicity Associated with the 1819 Kutch Earthquake, Northwestern India: Bulletin of the Seismological Society of America, v. 91, p. 407–426.

Rajendran, K., C. P. Rajendran, M. Thakkar, and M. P. Tuttle, 2001, The 2001 Kutch (Bhuj) earthquake: Coseismic surface features and their significance: Current Science, v. 80, p. 1397–1405.

Ram, E., A. Z. Ben, and Y. Kost, 1988, Halite bodies development in the evaporation pan No. 5 of Dead Sea Works: Israel Geological Society, annual meeting, v. 1988, p. 92–93.

Ramage, J. R., 1987, Lithofacies, regional stratigraphy, and depositional systems of the Clear Fork Group (Permian) Palo Duro Basin, Texas Panhandle: Masters thesis, University of Texas at Austin.

Ramboz, C., and M. Danis, 1990, Superheating in the Red Sea? The heat-mass balance of the Atlantis II Deep revisited: Earth & Planetary Science Letters, v. 97, p. 190–210.

Ramsay, C. R., and L. R. Davidson, 1970, The origin of scapolite in the regionally metamorphosed rocks of Mary Kathleen, Queensland: Contributions to Mineralogy & Petrology, v. 25, p. 41–51.

Ramsay, C. R., and J. Ridgway, 1977, Metamorphic patterns in Zambia and their bearing on problems of Zambia tectonic history: Precambrian Research, v. 4, p. 321–337.

Ramseyer, K., J. E. Amthor, A. Matter, T. Pettke, M. Wille, and A. E. Fallick, 2013, Primary silica precipitate at the Precambrian/Cambrian boundary in the South Oman Salt Basin, Sultanate of Oman: Marine and Petroleum Geology, v. 39, p. 187–197.

Ramseyer, K., J. R. Boles, and P. C. Lichtner, 1992, Mechanism of plagioclase albitization: Journal of Sedimentary Research, v. 62, p. 349–356.

Randell, R. N., and G. M. Anderson, 1997, Geology of the Polaris Zn-Pb deposit and surrounding area, Canadian Arctic Archipelago, in D. F. Sangster, ed., Carbonate-hosted lead-zinc deposits, Society of Economic Geologists Special Publication, No. 4, p. 307–319.

Ranganathan, V., 1991, Salt diffusion in interstitial waters and halite removal from sediments; examples from the Red Sea and Illinois basins: Geochimica et Cosmochimica Acta, v. 55, p. 1615–1625.

Ranganathan, V., and J. S. Hanor, 1988, Density-driven groundwater flow near salt domes: Chemical Geology, v. 74, p. 173–188.

Rango, T., G. Bianchini, L. Beccaluva, T. Ayenew, and N. Colombani, 2009, Hydrogeochemical study in the Main Ethiopian Rift: new insights to the source and enrichment mechanism of fluoride: Environmental Geology, v. 58, p. 109–118.

Rasmussen, B., and R. Buick, 2000, Oily old ores: Evidence for hydrothermal petroleum generation in an Archean volcanogenic massive sulfide deposit: Geology, v. 28, p. 731–734.

Rasmussen, L., and D. L. Rasmussen, 2009, Burial History Analysis of the Pennsylvanian Petroleum System in the Deep Paradox Basin Fold and Fault Belt, Colorado and Utah, in Houston et al., ed., The Paradox Basin Revisited-New Developments in Petroleum Systems and Basin Analysis, Rocky Mountains Association of Geologists Special Publication p. 24–94.

Rasmy, M., and S. F. Estefan, 1983, Geochemistry of saline minerals separated from Lake Qarun brine: Chemical Geology, v. 40, p. 269–277.

Rastogi, B. K., 2004, Damage due to the Mw 7.7 Kutch, India earthquake of 2001: Tectonophysics, v. 390, p. 85–103.

Ratcliff, D. W., and D. J. Weber, 1997, Geophysical imaging of subsalt geology: Leading Edge, Feb. 1997.

Ratigan, J., 2000, A status report on the Solution Mining Research Institute cavern sealing and abandonment program: Solution Mining Research Institute Report, 13 p.

Ratigan, J. L., 1991, Subsidence at Mont Belvieu, Texas, prepared by RE/SPEC Inc., Rapid City, SD, presented at the Spring Meeting of the Solution Mining Research Institute, Atlanta, GA.

Rattan, L., 2007, Anthropogenic Influences on World Soils and Implications to Global Food Security, in L. S. Donald, ed., Advances in Agronomy, v. Volume 93, Academic Press, p. 69–93.

Rattenbury, M. S., 1994, A linked fold-thrust model for the deformation of the Tennant Creek goldfield, northern Australia: Mineralium Deposita, v. 29, p. 301–308.

Raucoules, D., C. Maisons, C. Carnec, S. Le Mouelic, C. King, and S. Hosford, 2003, Monitoring of slow ground deformation by ERS radar interferometry on the Vauvert salt mine (France): Comparison with ground-based measurement: Remote Sensing Of Environment, v. 88, p. 468–478.

Raup, O. B., 1966, Bromine distribution in some halite rocks of the Paradox Member, Hermosa Formation, in Utah: Second Symposium on Salt; North Ohio Geol. Soc, Cleveland, p. 236–247.

Raup, O. B., 1970, Brine mixing – an additional mechanism for formation of basin evaporites: American Association Petroleum Geologists – Bulletin, v. 54, p. 2246–2259.

Raup, O. B., 1982, Gypsum precipitation by mixing seawater brines: American Association Petroleum Geologists – Bulletin, v. 66, p. 363–367.

Raup, O. B., and R. J. Hite, 1978, Bromine distribution in marine halite rocks: Dean, W. E., Schreiber, B. C. Marine evaporites. Soc. Econ. Paleontol. Mineral., Short Course Notes No. 3, p. 105–123.

Raup, O. B., and R. J. Hite, 1993, Preliminary data on the lithology, bromine distribution, and insoluble minerals from the A-1 Evaporite Formation, Salina Group, in the JEM Petroleum Corporation, Bruggers 3–7 Core, Missaukee County, Michigan: Open File Report U. S. Geological Survey, v. 93–236, p. 15 p.

Rausch, S., F. Böhm, W. Bach, A. Klügel, and A. Eisenhauer, 2013, Calcium carbonate veins in ocean crust record a threefold increase of seawater Mg/Ca in the past 30 million years: Earth and Planetary Science Letters, v. 362, p. 215–224.

Ravenhurst, C., and M. Zentilli, 1987, A model for the evolution of hot (>200°C) overpressured brines under and evaporite seal: The Fundy/Magdalen Carboniferous Basin of Atlantic Canada and its associated Pb-Zn-Ba deposits, in C. Beaumont, and A. J. Tankard, eds., Sedimentary Basins and Basin-Forming Mechanisms., Canadian Society of Petroleum Geologists, Memoir 12, p. 335–349.

Rawlings, D. J., 1999, Stratigraphic resolution of a multiphase intracratonic basin system: the McArthur Basin, northern Australia: Australian Journal of Earth Sciences, v. 46, p. 703–723.

Rayer, F. G., and O. L. Slind, 1999, Hydrocarbon potential of the East African Continental Margin – From Somalia to South Africa; an EARHS project of Canadian International Development Agency (CIDA) and NOCs.

Raymer, D. G., and J. M. Kendall, 1998, Seismic anisotropy in salt structures due to preferred crystal orientation: Revue de l Institut Francais du Petrole, v. 53, p. 585–594.

Raymer, D. G., A. Tommasi, and J. M. Kendall, 2000, Predicting the seismic implications of salt anisotropy using numerical simulations of halite deformation: Geophysics, v. 65, p. 1272–1280.

Read, J. F., 1985, Carbonate platform facies models.: American Association Petroleum Geologists – Bulletin, v. 69, p. 1–21.

Read, J. F., and A. D. Horbury, 1993, Eustatic and tectonic controls on porosity evolution beneath sequence-bounding unconformities and parasequence disconformities on carbonate platforms, in A. D. Horbury, and A. G. Robinson, eds., Diagenesis and basin development, v. 36, American Association Petroleum Geologists, Studies in Geology, p. 155–197.

Read, J. F., C. Kerans, L. J. Weber, J. F. Sarg, and F. M. Wright, 1995, Milankovitch sea-level changes, cycles, and reservoirs on carbonate platforms in greenhouse and ice-house worlds: SEPM/Society for Sedimentary Geology Short Course Notes, v. 35, 81 pp p.

Rech, J. A., J. Quade, and J. Betancourt, 2002, Late Quaternary paleohydrology of the central Atacama Desert (lat 22°–24°S), Chile: Geological Society of America Bulletin, v. 114, p. 334–348.

Rech, J. A., J. Quade, and W. S. Hart, 2003, Isotopic evidence for the source of Ca and S in soil gypsum, anhydrite and calcite in the Atacama Desert, Chile: Geochimica et Cosmochimica Acta, v. 67, p. 575–586.

Redfern, J., P. M. Shannon, B. P. J. Williams, S. Tyrrell, S. Leleu, I. Fabuel-Perez, C. Baudon, K. Stolfova, D. Hodgetts, X. Van Lanen, A. Speksnijder, P. D. W. Haughton, and J. S. Daly, 2010, An integrated study of Permo-Triassic basins along the North Atlantic passive margin: implication for future exploration, in B. A. Vining, and S. C. Pickering, eds., Petroleum Geology: From Mature Basins to New Frontiers – Proceedings of the 7th Petroleum Geology Conference: London, Geological Society, p. 921–936.

Reed, C. P., and M. W. Wallace, 2004, Zn-Pb mineralisation in the Silvermines district, Ireland: a product of burial diagenesis: Mineralium Deposita, v. 39, p. 87–102.

Reed, R. H., J. A. Chudek, R. Foster, and W. D. P. Stewart, 1984, Osmotic adjustment in cyanobacteria from hypersaline environments: Arch. Microbiol, v. 138, p. 333–33.

Reeve, J. S., K. C. Cross, R. N. Smith, and N. Oreskes, 1990, Olympic Dam copper-uranium-gold-silver deposit, in F. E. Hughes, ed., The Mineral Deposits of Australia and Papua New Guinea: Volume 2, Australian Institute of Mining and Metallurgy, p. 1009–1035.

Reich, M., C. Palacios, G. Vargas, S. Luo, E. Cameron, M. Leybourne, M. Parada, A. Zúñiga, and C.-F. You, 2009, Supergene enrichment of copper deposits since the onset of modern hyperaridity in the Atacama Desert, Chile: Mineralium Deposita, v. 44, p. 497–504.

Reid, P. R., N. P. James, I. G. Macintyre, C. P. Dupraz, and R. V. Burne, 2003, Shark Bay stromatolites: Microfabrics and reinterpretation of origins: Facies, v. 49, p. 299–324.

Reid, R. P., P. T. Visscher, A. W. Decho, J. F. Stolz, B. M. Beboutk, C. Dupraz, I. G. Macintyre, H. W. Paerl, J. L. Pinckney, L. Prufert-Beboutk, T. F. Steppe, and D. J. DesMaraisk, 2001, The role of microbes in accretion, lamination and early lithification of modern marine stromatolites: Nature, v. 406, p. 989–992.

Reid, S., K. Dewing, and R. Sharp, 2013, Polaris as a guide to northern exploration: Ore textures, paragenesis and the origin of the carbonate-hosted Polaris Zn-Pb Mine, Nunavut, Canada: Ore Geology Reviews, v. 51, p. 27–42.

Reilly, J. F., I. R. MacDonald, E. K. Biegert, and J. M. Brooks, 1996, Geologic controls on the distribution of chemosynthetic communities in the Gulf of Mexico, in D. Schumacher, and M. A. Abrams, eds., Hydrocarbon Migration and its Near-Surface Expression, American Association of Petroleum Geologists Memoir 66, p. 38–61.

Reimer, A., G. Landmann, and S. Kempe, 2009, Lake Van, Eastern Anatolia, Hydrochemistry and History: Aquatic Geochemistry, v. 15, p. 195–222.

Reimold, W. U., 1993, Further debate on the origin of the Sudbury structure -: South African Journal of Science, v. 89, p. 546–551.

Reinhardt, J., 1992, The Corella Formation of the Rosebud Syncline (central Mount Isa Inlier): deposition, deformation, and metamorphism: Australian Geological Survey Organisation (AGSO), Bulletin, v. 243, p. 229–255.

Reinhardt, J. W., J. E. Amthor, and F. Hoogendijk, 1999, Deep Oil Exploration in an Unconventional Reservoir – The Precambrian Intra-Salt Carbonate Play of Oman (abs): American Association Petroleum Geologists – Bulletin, v. 83.

Reinhardt, L., and W. Ricken, 2000, The stratigraphic and geochemical record of Playa Cycles: monitoring a Pangaean monsoon-like system: Palaeogeography, Palaeoclimatology, Palaeoecology, v. 161, p. 205–227.

Reith, F., 2011, Life in the deep subsurface: Geology, v. 39, p. 287–288.

Reitner, J., G. Arp, V. Thiel, G. P., G. U., and M. W., 1997, Organic matter in Great Salt Lake ooids (Utah, USA) – First approach to a formation via organic matrices: Facies, v. 36, p. 210–219.

Reitner, J., and V. Thiel, 2011, Encyclopedia of Geobiology: Dordrecht, Netherlands, Springer, 927 p.

Remmelts, G., 1995, Fault-related salt tectonics in the southern North Sea, The Netherlands, in M. P. A. Jackson, D. G. Roberts, and S. Snelson, eds., Salt Tectonics: A global perspective: Tulsa, American Association of Petroleum Geologists Memoir, v. 65, p. 261–272.

Remson, D. R., O. B. Dommers, and F. W. Jessen, 1966, Techniques for developing predetermined shaped cavities in solution mining, in J. L. Rau, ed., Second Symposium on Salt: Cleveland, OH, N. Ohio Geol. Soc., p. 297–310.

Renaut, R. W., 1993, Zeolitic Diagenesis of Late Quaternary Fluviolacustrine Sediments and Associated Calcrete Formation in the Lake Bogoria Basin, Kenya Rift-Valley: Sedimentology, v. 40, p. 271–301.

Renaut, R. W., 1993a, Morphology, distribution and preservation potential of microbial mats in the hydromagnesite-magnesite playas of the Cariboo Plateau, British Columbia, Canada: Hydrobiologia, v. 267, p. 75–98.

Renaut, R. W., 1993b, Zeolitic Diagenesis of Late Quaternary Fluviolacustrine Sediments and Associated Calcrete Formation in the Lake Bogoria Basin, Kenya Rift-Valley: Sedimentology, v. 40, p. 271–301.

Renaut, R. W., B. Jones, J. J. Tiercelin, and C. Tarits, 2002, Sublacustrine precipitation of hydrothermal silica in rift lakes: evidence from Lake Baringo, central Kenya Rift Valley: Sedimentary Geology, v. 148, p. 235–257.

Renaut, R. W., and P. R. Long, 1989, Sedimentology of the saline lakes of the Cariboo Plateau, Interior British Columbia, Canada: Sedimentary Geology, v. 64, p. 239–264.

Renne, P. R., W. D. Sharp, I. P. Montanez, T. A. Becker, and R. A. Zierenberg, 2001, Ar-40/Ar-39 dating of Late Permian evaporites, southeastern New Mexico, USA: Earth & Planetary Science Letters, v. 193, p. 539–547.

Rettig, S. L., B. F. Jones, and F. Risacher, 1980, Geochemical evolution of brines in the Salar of Uyuni, Bolivia: Chemical Geology, v. 30, p. 57–79.

Reuning, L., J. Schoenherr, A. Heimann, J. L. Urai, R. Littke, P. A. Kukla, and Z. Rawahi, 2009, Constraints on the diagenesis, stratigraphy and internal dynamics of the surface-piercing salt domes in the Ghaba Salt Basin (Oman): A comparison to the Ara Group in the South Oman Salt Basin: GeoArabia, v. 14, p. 83–120.

Reuschel, M., V. A. Melezhik, M. J. Whitehouse, A. Lepland, A. E. Fallick, and H. Strauss, 2012, Isotopic evidence for a sizeable seawater sulfate reservoir at 2.1 Ga: Precambrian Research, v. 192–195, p. 78–88.

Reutter, K.-J., R. Charrier, H.-J. Gotze, B. Schurr, P. Wigger, E. Scheuber, P. Giese, C.-D. Reuther, S. Schmidt, A. Rietbrock, G. Chong, and A. Belmonte-Pool, 2006, The Salar de Atacama Basin: a subsiding block within the western edge of the Altiplano-Puna Plateau, in O. Oncken, G. Chong, G. Franz, P. Giese, H.-J. Götze, V. A. Ramos, M. R. Strecker, and P. Wigger, eds., The Andes – Active Subduction Orogeny. Frontiers in Earth Science Series, Vol. 1. Berlin Heidelberg New York, Springer-Verlag, p. 303–326.

Reynolds, R. L., M. R. Hudson, N. S. Fishman, and J. A. Campbell, 1985, Paleomagnetic and petrologic evidence bearing on the age and origin of uranium deposits in the Permian Cutler Formation, Lisbon Valley, Utah: Geological Society of America Bulletin, v. 96, p. 719–730.

Rezak, R., 1985, Local carbonate production on a terrigenous shelf: Gulf Coast Association of Geological Societies Transactions, v. 35, p. 477–483.

Rezak, R., and T. J. Bright, 1981, Seafloor instability at the East Flower Garden Bank, northwest Gulf of Mexico: Geo-marine Letters, v. 1, p. 97–103.

Reznik, I. J., I. Gavrieli, and J. Ganor, 2009, Kinetics of gypsum nucleation and crystal growth from Dead Sea brine: Geochimica et Cosmochimica Acta, v. 73, p. 6218–6230.

Rhodes, A. L., and N. Oreskes, 1999, Oxygen isotope composition of magnetite deposits at El Laco, Chile: Evidence of formation from isotopically heavy fluids, in B. J. Skinner, ed., Geology and ore deposits of the Central Andes: Littleton, Co, Society of Economic Geologists Special Publication 7, p. 333–351.

Rhodes, M. E., S. T. Fitz-Gibbon, A. Oren, and C. H. House, 2010, Amino acid signatures of salinity on an environmental scale with a focus on the Dead Sea: Environmental Microbiology, v. 12, p. 2613–2623.

Riboulleau, A., J. Schnyder, L. Riquier, V. Lefebvre, F. Baudin, and J.-F. Deconinck, 2007, Environmental change during the Early Cretaceous in the Purbeck-type Durlston Bay section (Dorset, Southern England): A biomarker approach: Organic Geochemistry, v. 38, p. 1804–1823.

Riccioni, R. M., P. W. G. Brock, and B. C. Schreiber, 1996, Evidence for early aragonite in paleo-lacustrine sediments: Journal of Sedimentary Research Section A-Sedimentary Petrology & Processes, v. 66, p. 1003–1010.

Richard, A., D. A. Banks, J. Mercadier, M.-C. Boiron, M. Cuney, and M. Cathelineau, 2011, An evaporated seawater origin for the ore-forming brines in unconformity-related uranium deposits (Athabasca Basin, Canada): Cl/Br and δ37Cl analysis of fluid inclusions: Geochimica et Cosmochimica Acta, v. 75, p. 2792–2810.

Richardson, C., 1976, Phase relationships in sea ice as a function of temperature: Journal of Glaciology, v. 17, p. 507–519.

Richardson, C. K., and H. D. Holland, 1979, The solubility of fluorite in hydrothermal solutions, an experimental study: Geochim. Cosmochim. Acta, v. 43, p. 1313–1325.

Richardson, G. E., L. S. French, R. D. Baud, R. H. Peterson, C. D. Roark, T. M. Montgomery, E. G. Kazanis, G. M. Conner, and M. P. Gravois, 2004, Deepwater Gulf of Mexico 2004: America's Expanding Frontier, v. OCS Report Number MMS 2004–021: New Orleans, U.S. Department of the Interior, Minerals Management Service New Orleans, Gulf of Mexico OCS Region, 150 p.

Richmond, B. G., K. G. Hatala, H.-S. W. E. H., V. Rossi, A. Metallo, C. M. Liutkus, B. L. Pobiner, A. Gordon, H. Dingwall, D. G. Green, B. Zimmer, G. Olle Moita, and J. Brett, 2011, Early modern human footprint assemblage from Engare Sero, Tanzania (abs.): Paleoanthropology: A31.

Richner, D. R., D'Arcy Shock, J. K. Ahlness, D. R. Tweeton, W. C. Larson, D. J. Millenacker, and R. D. Schmidt, 1992, Solution Mining: In situ techniques, in H. L. Hartman, ed., SME Mining Engineering Handbook, v. 2: Liitleton, CO, Society for Mining, Metallurgy and Exploration, p. 1493–1528.

Richter-Bernburg, G., 1957, Isochrone Warven im Anhydrit des Zechstein 2: Germany, Geol. Landesanst., Geol. Jb. Bd.

Richter-Bernburg, G., 1980, Salt Tectonics, Interior structures of salt bodies: Bull. Cent. Rech. Explor.-Prod. Elf Aquitaine, v. 4, p. 373–393.

Richter-Bernburg, G., 1986, Zechstein 1 and 2 anhydrites; facts and problems of sedimentation, in G. M. Harwood, and D. B. Smith, eds., The English Zechstein and related topics: London, UK, Geological Society Special Publication No. 22, p. 157–163.

Riciputi, L. R., D. R. Cole, and H. G. Machel, 1996, Sulfide formation in reservoir carbonates of the Devonian Nisku Formation, Alberta, Canada – An ion microprobe study: Geochimica et Cosmochimica Acta, v. 60, p. 325–336.

Rickard, D. T., 1970, The origin of framboids: Lithos, v. 3, p. 269–293.

Riding, R., 1979, Origin and diagenesis of lacustrine algal bioherms at the margin of the Ries Crater, Upper Miocene, southern Germany: Sedimentology, v. 26, p. 645–680.

Riding, R., 1991, Classification of Microbial Carbonates, in R. Riding, ed., Calcareous Algae and Stromatolites: Berlin, Springer Verlag, p. 21–51.

Riding, R., 2000, Microbial carbonates: the geological record of calcified bacterial-algal mats and biofilms: Sedimentology, v. 47, p. 179–214.

Riding, R., 2002, Structure and composition of organic reefs and carbonate mud mounds: concepts and categories: Earth Science Reviews, v. 58, p. 163–231.

Riding, R., 2011, Microbialites, stromatolites and thrombolites, in J. Reitner, and V. Thiel, eds., Encyclopedia of Geobiology: Dordrecht, Netherlands, Springer, p. 635–654.

Riding, R., J. C. Braga, and J. M. Martin, 1999, Late Miocene Mediterranean desiccation: topography and significance of the 'Salinity Crisis' erosion surface on-land in southeast Spain: Sedimentary Geology, v. 123, p. 1–7.

Riding, R., J. C. Braga, J. M. Martin, and I. M. Sanchezalmazo, 1998, Mediterranean Messinian salinity crisis- Constraints from a coeval marginal basin, Sorbas, southeastern Spain: Marine Geology, v. 146, p. 1–20.

Riding, R., and L. Liang, 2005, Geobiology of microbial carbonates: metazoan and seawater saturation state influences on secular trends during the Phanerozoic: Palaeogeography, Palaeoclimatology, Palaeoecology, v. 219, p. 101–115.

Riding, R., J. M. Martin, and J. C. Braga, 1991, Coral-stromatolite reef framework, Upper Miocene, Almeria, Spain: Sedimentology, v. 38, p. 799–819.

Riegl, B., 2003, Climate change and coral reefs: Different effects in two high latitude areas (Arabian Gulf, South Africa): Coral Reefs, v. 22, p. 433–466.

Riegl, B., A. Poiriez, X. Janson, and K. Bergman, 2010, The Gulf: Facies Belts, Physical, Chemical, and Biological Parameters of Sedimentation on a Carbonate Ramp, in H. Westphal, B. Riegl, and G. P. Eberli, eds., Carbonate Depositional Systems: Assessing Dimensions and Controlling Parameters, Springer Netherlands, p. 145–213.

Rigakis, N., and V. Karakitsios, 1998, The source rock horizons of the Ionian Basin (NW Greece): Marine and Petroleum Geology, v. 15, p. 593–697.

Ripley, E. M., and C. Li, 2007, Applications of Stable and Radiogenic Isotopes to Magmatic Cu-Ni-PGE Deposits: Examples and Cautions: Earth Science Frontiers, v. 14, p. 124–131.

Ripley, E. M., C. Li, C. H. Moore, and A. K. Schmitt, 2010, Micro-scale S isotope studies of the Kharaelakh intrusion, Noril'sk region, Siberia: Constraints on the genesis of coexisting anhydrite and sulfide minerals: Geochimica et Cosmochimica Acta, v. 74, p. 634–644.

Risacher, F., B. Alonso, and C. Salazar, 2003, The origin of brines and salts in Chilean salars: a hydrochemical review: Earth-Science Reviews, v. 63, p. 249–293.

Risacher, F., and H. Alonso, 1996, Geochemistry of Salar de Atacama. 2. Water Evolution [Spanish]: Revista Geologica de Chile, v. 23, p. 123–134.

Risacher, F., and H. Alonso, 2001, Geochemistry of ash leachates from the 1993 Lascar eruption, northern Chile. Implication for recycling of ancient evaporites: Journal of Volcanology & Geothermal Research, v. 109, p. 319–337.

Risacher, F., H. Alonso, and C. Salazar, 2002, Hydrochemistry of two adjacent acid saline lakes in the Andes of northern Chile: Chemical Geology, v. 187, p. 39–57.

Risacher, F., and H. P. Eugster, 1979, Holocene pisoliths and encrustations associated with spring-fed surface pools, Pastos Grandes, Bolivia: Sedimentology, v. 26, p. 253–270.

Risacher, F., and B. Fritz, 1991, Geochemistry of Bolivian salars, Lipez, southern Altiplano: origin of solutes and brine evolution: Geochimica et Cosmochimica Acta, v. 55, p. 687–705.

Risacher, F., and B. Fritz, 1991, Quaternary geochemical evolution of the salars of Uyuni and Coipasa, central Altiplano, Bolivia: Chemical Geology, v. 90, p. 211–231.

Risacher, F., and B. Fritz, 2000, Bromine geochemistry of salar de Uyuni and deeper salt crusts, Central Altiplano, Bolivia: Chemical Geology, v. 167, p. 373–392.

Risacher, F., and B. Fritz, 2009, Origin of salts and brine evolution of bolivian and chilean salars: aquatic geochemistry, v. 15, p. 123–157.

Risacher, F., B. Fritz, and A. Hauser, 2011, Origin of components in Chilean thermal waters: Journal of South American Earth Sciences, v. 31, p. 153–170.

Risatti, J. B., W. C. Capman, and D. A. Stahl, 1994, Community structure of a microbial mat: the phylogenetic dimension: Proceedings National Academy of Science USA, v. 91, P- 10173–10177.

Rittenhouse, G., 1967, Bromine in oil-field waters and its use in determining possibilities of origin of these waters: American Association Petroleum Geologists – Bulletin, v. 51, p. 2430–2440.

Ritts, B. D., A. D. Hanson, D. Zinniker, and J. M. Moldowan, 1999, Lower-middle Jurassic nonmarine source rocks and petroleum

systems of the northern Qaidam basin, northwest China: American Association Petroleum Geologists – Bulletin, v. 83, p. 1980–2005.

Rivers, J. M., T. Kurt Kyser, and N. P. James, 2012, Salinity reflux and dolomitization of southern Australian slope sediments: the importance of low carbonate saturation levels: Sedimentology, v. 59, p. 445–465.

Rivers, J. M., T. K. Kyser, and N. P. James, 2009, Isotopic composition of a large photosymbiotic foraminifer: Evidence for hypersaline environments across the Great Australian Bight during the late Pleistocene: Sedimentary Geology, v. 213, p. 113–120.

Rivers, T., 2009, The Grenville Province as a large hot long-duration collisional orogen – insights from the spatial and thermal evolution of its orogenic fronts: Geological Society, London, Special Publications, v. 327, p. 405–444.

Robb, L., 2005, Introduction to Ore-Forming Processes: Oxford, Blackwell Publishing, 373 p.

Robert, C. M., 2009, Global Sedimentology of the Ocean: An Interplay Between Geodynamics and Paleoenvironment: Developments In Marine Geology (v. 3), Elsevier, 487 p.

Roberts, D. E., and G. R. T. Hudson, 1983, The Olympic Dam copper-uranium -gold deposit, Roxby Downs, South Australia: Economic Geology, v. 78, p. 799–822.

Roberts, G., and D. Peace, 2007, Hydrocarbon plays and prospectivity of the Levantine basin, offshore Lebanon and Syria from modern seismic data: GeoArabia, v. 12, p. 99–124.

Roberts, H. H., P. Aharon, R. Carney, J. Larkin, and R. Sassen, 1990, Sea floor responses to hydrocarbon seeps, Louisiana continental slope: Geo-Marine Letters, v. 10, p. 232–243.

Roberts, S. M., and R. J. Spencer, 1995, Paleotemperatures preserved in fluid inclusions in halite: Geochimica et Cosmochimica Acta., v. 59, p. 3929–3942.

Roberts, S. M., R. J. Spencer, W. B. Yang, and H. R. Krouse, 1997, Deciphering some unique paleotemperature indicators in halite-bearing saline lake deposits from Death Valley, California, USA: Journal of Paleolimnology, v. 17, p. 101–130.

Roberts, W., and P. F. Williams, 1993, Evidence for early Mesozoic extensional faulting in Carboniferous rocks, southern New Brunswick, Canada: Canadian Journal of Earth Science, v. 30, p. 1324–1331.

Robertson, A. H. F., S. Eaton, E. J. Follows, and A. S. Payne, 1995, Depositional processes and basin analysis of Messinian evaporites in Cyprus: Terra Nova, v. 7, p. 233–253.

Robertson, E., 1988, Thermal properties of Rocks: USGS Open File Report 88–441.

Robinson, B. W., and A. Gunatilaka, 1991, Stable isotope studies and the hydrological regime of sabkhas in southern Kuwait, Arabian Gulf: Sedimentary Geology, v. 73, p. 141–159.

Roca, E., P. Anadon, R. Utrilla, and A. Vazquez, 1996, Rise, closure and reactivation of the Bicorb-Quesa evaporite diapir, eastern Prebetics, Spain: Journal of the Geological Society, v. 153, p. 311–321.

Rodríguez-Aranda, J. P., 1995, Sedimentología de los Sistemas de Llanura Lutítica-lago Salino del Mioceno en la Zona Oriental de la Cuenca de Madrid (Tarancón-Auñon): Doctoral thesis, Universidad Complutense, Madrid, 474 p.

Rodríguez-Aranda, J. P., and J. P. Calvo, 1998, Trace fossils and rhizoliths as a tool for sedimentological and palaeoenvironmental analysis of ancient continental evaporite succesions: Palaeogeography Palaeoclimatology Palaeoecology, v. 140, p. 383–399.

Rodríguez-Aranda, J. P., J. P. Calvo, and M. E. Sanz-Montero, 2002, Lower Miocene gypsum palaeokarst in the Madrid Basin (central Spain): dissolution diagenesis, morphological relics and karst end-products: Sedimentology, v. 49, p. 1385–1400.

Rodríguez-Aranda, J. P., M. E. Sanz-Montero, F. Ayllón-Queve-do, and V. Souza-Egipsy, 2005, Formatión de celestina dentro de un contexto microbiano en ambiente lacustre salino. Mioceno Inferior de la Cuenca de Madrid: Macla, v. 3, p. 171–172.

Roedder, E., 1984a, The fluids in salt: American Mineralogist, v. 69, p. 413–439.

Roedder, E., 1984b, Fluid Inclusions: Mineralogical Society of America, Reviews in Mineralogy, v. 12, 646 p.

Roedder, E., and R. L. Bassett, 1981, Problems in determination of the water content of rock-salt samples and its significance in nuclear-waste storage siting: Geology, v. 9, p. 525–530.

Roedder, E., and B. J. Skinner, 1968, Experimental evidence that fluid inclusions do not leak: Economic Geology, v. 63, p. 715–730.

Roehler, H. W., 1993, Eocene climates, depositional environments, and geography, greater Green River Basin, Wyoming, Utah, and Colorado: U.S. Geological Survey Professional Paper, v. 1506-F, p. 74.

Roger, A. J., and A. G. B. Simpson, 2009, Evolution: Revisiting the Root of the Eukaryote Tree: Current biology : CB, v. 19, p. R165-R167.

Rogers, D. B., and S. J. Dreiss, 1995a, Saline groundwater in Mono basin, California .1. Distribution: Waters Resources Research, v. 31, p. 3131–3150.

Rogers, D. B., and S. J. Dreiss, 1995b, Saline groundwater in Mono basin, California .2. Long term control of lake salinity by groundwater: Water Resources Research., v. 31, p. 3151–3169.

Rokahr, R., K. Standtmeister, and D. Zander-Schiebenhofer, 1998, Mechanical determination of the maximum internal pressure for gas storage caverns in rock salt: Solution Mining Research Institute Fall Meeting, Oct. 4–7, Rome Italy, 455 p.

Rollet, N., P. E. O'Brien, A. T. Jones, M. Sexton, G. A. Logan, and J. M. Kennard, 2006, Characterisation and correlation of active hydrocarbon seepage using geophysical data sets: An example from the tropical, carbonate Yampi Shelf, Northwest Australia: Marine and Petroleum Geology, v. 23, p. 145–164.

Rollinson, H., 2007, When did plate tectonics begin?: Geology Today, v. 23, p. 186–191.

Romanovsky, V. E., S. Gruber, A. Instanes, H. Jin, S. S. Marchenko, S. L. Smith, D. Trombotto, and K. M. Walter, 2007, Global Outlook for Ice and Snow: Frozen Ground (Chpt. 7), Birkenland Trykkeri A/S, Norway.

Ronchi, P., F. Jadoul, A. Ceriani, A. Di Giulio, P. Scotti, A. Ortenzi, and E. Previde Massara, 2011, Multistage dolomitization and distribution of dolomitized bodies in Early Jurassic carbonate platforms (Southern Alps, Italy): Sedimentology, v. 58, p. 532–565.

Roney, H., G. Booth, and P. Cox, 2009, Competitive exclusion of cyanobacterial species in the Great Salt Lake: Extremophiles, v. 13, p. 355–361.

Rooney, T. P., B. F. Jones, and J. T. Neal, 1969, Magadiite from Alkali Lake, Oregon: American Mineralogist, v. 54, p. 1034–1043.

Root, K. G., 2001, Devonian Antler Fold and Thrust Belt and Foreland Basin Development in the Southern Canadian Cordillera: Implications for the Western Canada Sedimentary Basin: Bulletin of Canadian Petroleum Geology, v. 49, p. 7–36.

Rose, A. W., 1976, The effect of cuprous chloride complexes in the origin of red-bed copper and related deposits: Economic Geology, v. 71, p. 1036–1048.

Rose, A. W., D. C. Herrick, and P. Deines, 1985, An oxygen and sulfur isotope study of skarn-type magnetite deposits of the Cornwall type, southeastern Pennsylvania: Economic Geology, v. 80, p. 418–443.

Rose, A. W., A. T. Smith, R. L. Lustwerk, H. Ohmoto, and I. D. Hoy, 1986, Geochemical aspects of stratiform and red-bed copper deposits in the Catskill Formation (Pennsylvania, USA) and Redstone area (Canada). Sequence of mineralisation in sediment-hosted copper deposits (part 3), in G. H. Friedrich, A. D. Genkin, A. J. Naldrett, J. D. Ridge, R. H. Sillitoe, and F. M. Vokes, eds., Geology and Metallogeny of Copper Deposits: Berlin, Springer-Verlag, p. 412–421.

Rosell, L., and F. Ortí, 1981, The saline (potash) formation of the Navarra basin (Upper Eocene, Spain). Petrology: Revista Instituto Investigaciones Geologicas, v. 35, p. 71–121.

Rosell, L., and F. Ortí, 1992, Geochemical characteristics and facies analysis of a Miocene lacustrine gypsum deposit (Calatayud basin, Zaragoza, Spain) Abstract: IGCP-324 Glopals, Annual Meeting, p. 39–41.

Rosell, L., F. Orti, A. Kasprzyk, E. Playa, and T. M. Peryt, 1998, Strontium geochemistry of Miocene primary gypsum – Messinian of southeastern Spain and Badenian of Poland: Journal of Sedimentary Research Section A-Sedimentary Petrology & Processes, v. 68, p. 63–79.

Rosell, O. L., and C. F. Orti, 1980, Presencia de analcima y observaciones diageneticas en la anhidrita basal de la cuenca potasica de Navarra (Eocene superior, Cuenca del Ebro, Espana): Lectures and communications from the First symposium on diagenesis of sediments and sedimentary rocks. Univ. Barcelona, Dep. Petrol. y Geoquim., Barcelona, Spain. Revista del Instituto de Investigaciones Geologicas de la Diputacion Provincial de Barcelona, v. 34, p. 223–235.

Rosen, M. R., 1991, Sedimentologic and geochemical constraints on the evolution of Bristol Dry Lake Basin, California, U.S.A: Palaeogeography, Palaeoclimatology, Palaeoecology, v. 84, p. 309–332.

Rosen, M. R., 1994, The importance of groundwater in playas: A review of playa classifications and the sedimentology and hydrology of playas, in M. R. Rosen, ed., Paleoclimate and the Basin Evolution of Playa Systems, v. 289: Boulder, Co, Geological Society of America Special Paper, p. 1–18.

Rosen, M. R., G. B.Arehart, and M. S. Lico, 2004, Exceptionally fast growth rate of <100-yr-old tufa, Big Soda Lake, Nevada: Implications for using tufa as a paleoclimate proxy: Geology, v. 32, p. 409–412.

Rosen, M. R., L. Coshell, J. V. Turner, and R. J. Woodbury, 1996, Hydrochemistry and nutrient cycling in Yalgorup National Park, Western Australia: Journal of Hydrology, v. 185, p. 241–274.

Rosen, M. R., D. E. Miser, M. A. Starcher, and J. K. Warren, 1989, Formation of dolomite in the Coorong region, South Australia: Geochimica et Cosmochimica Acta, v. 53, p. 661–669.

Rosen, M. R., D. E. Miser, and J. K. Warren, 1988, Sedimentology, mineralogy and isotopic analysis of Pellet Lake, Coorong region, South Australia.: Sedimentology, v. 35, p. 105–122.

Rosen, M. R., J. V. Turner, L. Coshell, and V. Gailitis, 1995, The effects of water temperature, stratification, and biological activity on the stable isotopic composition and timing of carbonate precipitation in a hypersaline lake: Geochimica et Cosmochimica Acta, v. 59, p. 979–990.

Rosen, M. R., and J. K. Warren, 1990, The origin and significance of groundwater-seepage gypsum from Bristol Dry Lake, California, USA: Sedimentology, v. 37, p. 983–996.

Rosenfeld, L., 2000, Discovery and early uses of iodine: Journal of Chemical Education, v. 77, p. 984–987.

Rospondek, M. J., L. Marynowski, and M. Góra, 2007, Novel arylated polyaromatic thiophenes: Phenylnaphtho[b]thiophenes and naphthylbenzo[b]thiophenes as markers of organic matter diagenesis buffered by oxidising solutions: Organic geochemistry, v. 38, p. 1729–1756.

Ross, M. L., 1998, Geology of the Tertiary Intrusive Centers of the La Sal Mountains, Utah—Influence of Preexisting Structural Features on Emplacement and Morphology, in J. D. Friedman, and A. C. Huffman, Jr., eds., Laccolith Complexes of Southeastern Utah: Tectonic Control and Time of Emplacement--Workshop Proceedings, U.S. Geological Survey Bulletin 2158, p. 61–83.

Rossland, A., A. Escalona, and R. Rolfsen, 2013, Permian-Holocene tectonostratigraphic evolution of the Mandal High, Central Graben, North Sea: Bulletin American Association Petroleum Geologists, v. 97, p. 923–957.

Rotherham, J. F., 1997, A metasomatic origin for the iron-oxide Au-Cu Starra orebodies, Eastern Fold Belt, Mt Isa Inlier: Mineralium Deposita, v. 32, p. 205–218.

Rotherham, J. F., K. L. Blake, K. I. Cartwright, and P. J. Williams, 1998, Stable isotope evidence for the origin of the Mesoproterozoic Starra Au-Cu deposit, Cloncurry district, northwest Queensland: Economic Geology & the Bulletin of the Society of Economic Geologists, v. 93.

Rouchy, J. M., 1986, Sedimentologie des formations anhydritiques givetiennes et dinantiennes du segment varisque franco-belge: Bulletin de la Societe Belge de Geologie, v. 95, p. 111–127.

Rouchy, J. M., 1988, Relations évaporites-hydrocarbures:l'association laminites-récifes-évaporites dans le Messinien de Mediterranée et ses enseignements, in G. Busson, ed., Evaporites et hydrocarbures, v. 55, Mémoires du Muséum national d'Historie naturelle, (C), p. 15–18.

Rouchy, J. M., M. C. Bernet-Rollande, and A. F. Maurin, 1994, Descriptive petrography of evaporites:Applications in the field, subsurface and the laboratory, in T. c. French oil and gas industry association, ed., Evaporite sequences in petroleum exploration: 1. Geological Methods, Editions Technip, p. 70–123.

Rouchy, J. M., G. Camoin, J. Casanova, and J. F. Deconinck, 1993, The central palaeo-Andean basin of Bolivia (Potosi area) during the Late Cretaceous and early Tertiary: reconstruction of ancient saline lakes using sedimentological, paleoecological and stable isotope records: Palaeogeography, Palaeoclimatology, Palaeoecology, v. 105, p. 179–198.

Rouchy, J. M., and A. Caruso, 2006, The Messinian salinity crisis in the Mediterranean basin: Are assessment of the data and an integrated scenario: Sedimentary Geology, v. 188, p. 35–67.

Rouchy, J. M., A. Laumondais, and E. Groessens, 1987, The Lower Carboniferous (Visean) evaporites in northern France and Belgium; depositional, diagenetic and deformational guides to reconstruct a disrupted evaporitic basin: Peryt, Tadeusz M. (ed) Evaporite basins. Lecture Notes in Earth Sciences, v. 13, p. 31–67.

Rouchy, J. M., D. Noel, A. M. A. Wali, and M. A. M. Aref, 1995a, Evaporitic and biosiliceous cyclic sedimentation in the Miocene of the Gulf of Suez; depositional and diagenetic aspects: Sedimentary Geology, v. 94, p. 277–297.

Rouchy, J. M., F. Orszag-Sperbe, M. M. Blanc-Valleron, C. Pierre, M. Rivier, N. Combourieu-Nebout, and I. Panayides, 2001, Paleoenvironmental changes at the Messinian-Pliocene boundary in the eastern Mediterranean (southern Cyprus basins): significance of the Messinian Lago-Mare: Sedimentary Geology, v. 145, p. 93–117.

Rouchy, J. M., and C. Pierre, 1979, Donnees sedimentologiques et isotopiques sur les gypses des series evaporitiques messiniennes d'Espagne meridionale et de Chypre: Rev. Geogr. Phys. Geol. Dyn., v. 21, p. 267–280.

Rouchy, J. M., C. Pierre, and F. Sommer, 1995b, Deep-water resedimentation of anhydrite and gypsum deposits in the Middle Miocene (Belayim Formation) of the Red Sea: Sedimentology, v. 42, p. 267–282.

Rouchy, J. M., and J. P. Saint-Martin, 1992, Late Miocene events in the Mediterranean as recorded by carbonate-evaporite relations: Geology, v. 20, p. 629–632.

Rouchy, J. M., M. Servant, M. Fournier, and C. Causse, 1996, Extensive carbonate algal bioherms in Pleistocene saline lakes of the central Altiplano of Bolivia: Sedimentology, v. 43, p. 973–993.

Rouchy, J. M., C. Taberner, M. M. Blanc-Valleron, R. Sprovieri, M. Russell, C. Pierre, E. Di Stefano, J. J. Pueyo, A. Caruso, J. Dinares-Turell, E. Gomis-Coll, G. A. Wolff, G. Cespuglio, P. Ditchfield, S. Pestrea, N. Combourieu-Nebout, C. Santisteban, and J. O. Grimalt, 1998, Sedimentary and diagenetic markers of the

restriction in a marine basin: the Lorca Basin (SE Spain) during the Messinian: Sedimentary Geology, v. 121, p. 23–55.

Roulston, B. V., and D. C. E. Waugh, 1981, A borate mineral assemblage from the Penobsquis and Salt Springs evaporite deposits of southern New Brunswick: The Canadian Mineralogist, v. 19, p. 291–301.

Rouvier, H., V. Perthuisot, and A. Mansouri, 1985, Pb-Zn deposits and salt-bearing diapirs in southern Europe and North Africa: Economic Geology, v. 80, p. 666–687.

Roveri, M., S. Lugli, V. Manzi, and B. C. Schreiber, 2008, The Messinian Sicilian stratigraphy revisited: new insights for the Messinian salinity crisis: Terra Nova, v. 20, p. 483–488.

Roveri, M., V. Manzi, F. R. Lucchi, and S. Rogledi, 2003, Sedimentary and tectonic evolution of the Vena del Gesso basin (Northern Apennines, Italy): Implications for the onset of the Messinian salinity crisis: Geological Society of America Bulletin, v. 115, p. 387–405.

Roveri, M., V. Manzi, S. Lugli, C. B. Schreiber, A. Caruso, J.-M. Rouchy, S. M. Iaccarino, R. Gennari, F. P. Vitale, and F. Ricci Lucchi, 2006, Clastic vs. primary precipitated evaporites in the Messinian Sicilian basins: L'Ateneo parmense. Acta naturalia: organo della Società di medicina e scienze naturali di Parma 02/2013, v. 42, p. 125–199.

Rowan, M. G., 1995, Structural styles and evolution of allochthonous salt, central Louisiana outer shelf and upper slope, in M. P. A. Jackson, D. G. Roberts, and S. Snelson, eds., Salt tectonics; a global perspective: Tulsa, American Association Petroleum Geologists Memoir, v. 65, p. 199–228.

Rowan, M. G., 1997, Three dimensional geometry and evolution of a segmented detachment fold, Mississippi fan foldbelt, Gulf of Mexico: Journal of Structural Geology, v. 19, p. 463–480.

Rowan, M. G., 2014, Passive-margin salt basins: hyperextension, evaporite deposition, and salt tectonics: Basin Research, v. 26, p. 154–182.

Rowan, M. G., K. A. Giles, and T. F. Lawton, 2001, A Tale of Two Diapirs: The Effects of Shortening on Passive Growth (Abs): American Association Petroleum Geologists – Bulletin, v. 86 (13).

Rowan, M. G., M. P. A. Jackson, and B. D. Trudgill, 1999, Salt-related fault families and fault welds in the northern Gulf of Mexico: Bulletin-American Association of Petroleum Geologists, v. 83, p. 1454–1484.

Rowan, M. G., T. F. Lawton, and K. A. Giles, 2012, Anatomy of an exposed vertical salt weld and flanking strata, La Popa Basin, Mexico: Geological Society, London, Special Publications, v. 363, p. 33–57.

Rowan, M. G., T. F. Lawton, K. A. Giles, and R. A. Ratliff, 2003, Near-salt deformation in La Popa basin, Mexico, and the northern Gulf of Mexico: A general model for passive diapirism: Bulletin American Association Petroleum Geologists, v. 87, p. 733–756.

Rowan, M. G., F. J. Peel, and B. C. Vendeville, 2004, Gravity-driven Fold Belts on Passive Margins: Chapter 9, in K. McClay, ed., Thrust tectonics and hydrocarbon systems, v. 82, American Association Petroleum Geologists – Memoir, p. 157–182.

Rowan, M. G., F. J. Peel, B. C. Vendeville, and V. Gaullier, 2012, Salt tectonics at passive margins: Geology versus models – Discussion: Marine and Petroleum Geology, v. 37, p. 184–194.

Rowan, M. G., and B. C. Vendeville, 2006, Foldbelts with early salt withdrawal and diapirism: Physical model and examples from the northern Gulf of Mexico and the Flinders Ranges, Australia: Marine and Petroleum Geology, v. 23, p. 871–891.

Rowan, M. G., and P. Weimer, 1998, Salt-sediment interaction, Northern Green Canyon and Ewing Bank (offshore Louisiana), northern Gulf of Mexico: American Association of Petroleum Geologists Bulletin, v. 82, p. 1055–1082.

Royer, D. L., D. J. Beerling, R. A. Berner, I. P. Montanez, and N. J. Tabor, 2004, CO_2 as a primary driver of Phanerozoic climate: GSA Today, v. 14, p. 4–10.

Rozanova, E. P., and A. S. Khudyakova, 1974, New non-sporulating thermophilic organism Desulfovibrio thermophilus Sp. Nov. reducing sulphates: Mikrobiologiya, v. 43, p. 1069.

Rozen, O. M., 1979, Scapolite-plagioclase schists and the problem of Precambrian sulfate as illustrated by geochemical comparison of deposits of evaporite basins and metamorphic rocks of calcareous series: Doklady of the Academy of Sciences of the USSR, Earth Science Sections, v. 244, p. 138–141.

Rubenach, M., N. Oliver, L. Fisher, and M. Bertolli, 2008, The tectonothermal and metasomatic evolution of the Mount Isa Inlier and the formation of iron oxide Cu-Au deposits: International Geological Congress, Abstracts, v. 33.

Ruble, T. E., A. J. Bakel, and R. P. Philp, 1994, Compound-Specific Isotopic Variability in Uinta Basin Native Bitumens – Paleoenvironmental Implications: Organic Geochemistry, v. 21, p. 661–671.

Ruch, J., J. K. Warren, F. Risacher, T. R. Walter, and R. Lanari, 2012, Salt lake deformation detected from space: Earth and Planetary Science Letters, v. 331–332, p. 120–127.

Ruckmick, J. C., B. H. Wimberly, and A. F. Edwards, 1979, Classification and genesis of biogenic sulfur deposits: Economic Geology, v. 74, p. 469–474.

Ruegg, J. C., M. Kasser, J. C. Lepine, and A. Tarantola, 1979, Geodesic measurements of rifting associated with a seismo-volcanic crisis in Afar: Geophys. Res. Lett., v. 6, p. 817–820.

Ruelle, J. C. L., 1982, Depositional environments and genesis of stratiform copper deposits of the Redstone copper belt, Mackenzie Mountains, N. W. T., in R. W. Hutchison, C. D. Spence, and J. M. Franklin, eds., Precambrian Sulphide Deposits, v. 25, Geological Association of Canada Special Paper, p. 701–737.

Ruffell, A. H., N. R. Moles, and J. Parnell, 1998, Characterisation and prediction of sediment-hosted ore deposits using sequence stratigraphy: Ore Geology Reviews, v. 12, p. 207–223.

Rugless, C. S., and F. Pirajno, 1996, Geological and geochemistry of the Copperhead albitite "carbonatite" complex, East Kimberley, Western Australia: Australian Journal of Earth Sciences, v. 43, p. 311–322.

Ruilin, G., 1997, Advanced geodrilling techniques in China, in G. Huadong, V. Singhroy, and T. G. Farr, eds., New Technology for Geosciences, Proceedings 30th International Geological Congress, v. 10: Utrecht, Nederlands, VSP, p. 225–232.

Runnegar, B., W. Dollase, R. Ketcham, M. Colbert, and W. Carlson, 2001, Early Archean sulfates from Western Australia first formed as hydrothermal barites, not gypsum evaporites: Geological Society of America, Annual Meeting, November 5–8, 2001; Session No. 166.

Ruppel, S. C., and H. S. Cander, 1988, Dolomitization of shallow water carbonates by seawater and seawater-derived brines, San Andres Formation (Guadalupian), West Texas, in V. J. Shukla, and P. A. Baker, eds., Sedimentology and Geochemistry of Dolostones, v. 43: Tulsa Okla, SEPM Special Publ., p. 245–262.

Rush, J., and C. Kerans, 2010, Stratigraphic Response Across a Structurally Dynamic Shelf: The Latest Guadalupian Composite Sequence at Walnut Canyon, New Mexico, U.S.A: Journal of Sedimentary Research, v. 80, p. 808–828.

Russell, M., J. A. Grimalt, W. A. Hartgers, C. Taberner, and J. M. Rouchy, 1997, Bacterial and algal markers in sedimentary organic matter deposited under natural sulphurization conditions (Lorca Basin, Murcia, Spain): Organic Geochemistry, v. 26, p. 605–625.

Russell, M. J., J. K. Ingham, V. Zedef, D. Maktav, F. Sunar, A. J. Hall, and A. E. Fallick, 1999, Search for signs of ancient life on Mars: expectations from hydromagnesite microbialites, Salda Lake, Turkey: Journal of the Geological Society, v. 156, p. 869–888.

Russell, M. J., M. Solomon, and J. L. Walshe, 1981, The genesis of sediment-hosted, exhalative zinc + lead deposits: Mineralium Deposita, v. 16, p. 113–127.

Rutland, R. W. R. R., 1966, An unconformity in the Corocoro basin, Bolivia, and its relation to the copper mineralization: Economic Geology, v. 61, p. 962–964.

Ruzyla, K., and G. M. Friedman, 1985, Factors controlling porosity in dolomite reservoirs of the Ordovician Red River Formation, Cabin Creek field, Montana, in P. O. Roehl, and P. W. Choquette, eds., Carbonate petroleum reservoirs: A case book: New York, Springer Verlag, p. 39–58.

Ryan, B., D. Stanley, J. Hersey, D. Fahlquist, and T. Allan, 1970, The geology and tectonics of the Mediterranean Sea, in A. E. Maxwell, ed., The Sea: New York, Wiley, p. 387–491.

Ryan, M. J., and J. C. Escher, 1999, Albitised gneisses in the area between Paakitsoq and Kangerluarsuk, north-east Disko Bugt, West Greenland: Geology of Greenland Survey Bulletin, v. 181, p. 113–117.

Ryan, W., and W. Pitman, 1999, Noah's flood—The new scientific discoveries about the event that changed history: New York, Simon and Schuster, 310 p.

Rye, D. M., and N. Williams, 1981, Studies of base metal sulfide deposits at McArthur River, Northern Territory, Auatralia III: The stable isotope geochemistry of the HYC ridge and Cooley deposits: Economic Geology, v. 76, p. 1–26.

Sage, L., and J. Letouzey, 1990, Convergence of the African and Eurasian plates in the eastern Mediterranean, in J. Letouzey, ed., Petroleum and tectonics in mobile belts: Paris, Technips, p. 49–68.

Sahin, A., and S. Saner, 2001, Statistical distributions and correlations of petrophysical parameters in the Arab-D reservoir, Abqaiq oilfield, Eastern Saudi Arabia: Journal of Petroleum Geology, v. 24, p. 101–114.

Said, R., 1993, The River Nile: Geology, hydrology and utilization: Oxford, Pergamon Press.

Saigal, G. C., S. Morad, K. Bjorlykke, P. K. Egeberg, and P. Aagaard, 1988, Diagenetic albitization of detrital K-feldspar in Jurassic, Lower Cretaceous, and Tertiary clastic reservoir rocks from offshore Norway; I, Textures and origin: Journal of Sedimentary Research, v. 58, p. 1003–1013.

Saini-Eidukat, B., N. S. Rudashevsky, and A. G. Polozov, 1998, Evidence for hibbingite-kempite solid solution: Mineralogical Magazine, v. 62, p. 251–255.

Saintot, A., R. Stephenson, S. Stovba, and Y. Maystrenko, 2003, Structures associated with inversion of the Donbas Foldbelt (Ukraine and Russia): Tectonophysics, v. 373, p. 181–207.

Sajnovic, A., K. Stojanovic, B. Jovancivez, and O. Cvetkovic, 2008, Biomarker distributions as indicators for the depositional environment of lacustrine sediments in the Valjevo-Mionica basin (Serbia): Chemie der Erde – Geochemistry, v. 68, p. 395–411.

Salameh, E., and H. Bannayan, 1993, Water resources of Jordan: Present status and future potentials, Friedrich Ebert Stiftung.

Salameh, E., and H. El-Naser, 2000, The Interface Configuration of the Fresh-/Dead Sea Water – Theory and Measurements: Acta Hydrochim. Hydrobiol., v. 28, p. 323–328.

Salé, S. O., R. Gennari, S. Lugli, V. Manzi, and M. Roveri, 2012, Tectonic and climatic control on the Late Messinian sedimentary evolution of the Nijar Basin (Betic Cordillera, Southern Spain): Basin Research, v. 24, p. 314–337.

Saleh, A., F. Al-Ruwaih, A. Al-Reda, and A. Gunatilaka, 1999, A reconnaissance study of a clastic coastal sabkha in Northern Kuwait, Arabian Gulf: Journal of Arid Environments, v. 43, p. 1–19.

Salisbury, J. A., A. G. Tomkins, and B. F. Schaefer, 2008, New insights into the size and timing of the Lawn Hill impact structure: relationship to the Century Zn¬†-,Äì¬†Pb deposit: Australian Journal of Earth Sciences, v. 55, p. 587–603.

Saller, A. H., and J. A. T. D. Dickson, 2011, Partial dolomitization of a Pennsylvanian limestone buildup by hydrothermal fluids and its effect on reservoir quality and performance: Bulletin American Association Petroleum Geologists, v. 96, p. 1745–1762.

Saller, A. H., and N. Henderson, 1998, Distribution of porosity and permeability in platform dolomites – Insight from the Permian of west Texas: American Association Petroleum Geologists Bulletin-American Association of Petroleum Geologists, v. 82, p. 1528–1550.

Saller, A. H., and B. R. Moore, 1986, Dolomitization in the Smackover Formation, Escambia County, Alabama: Gulf Coast Association of Geological Societies Transactions, v. 36, p. 275–282.

Saller, A. H., D. Pollitt, and J. A. D. Dickson, 2014, Diagenesis and porosity development in the first Eocene reservoir at the Giant Wafra Field, partitioned zone (PZ), Saudi Arabia and Kuwait:American Association Petroleum Geologists – Bulletin, v. 98, p. 1185–1212.

Saller, M., and M. O'Driscoll, 2000, Lithium takes charge: Industrial Minerals, v. 390 (March), p. 37–47.

Salomon Mora, L. E., M. Cruz-Mercado, I. Alsop, and S. G. Archer, 2011, Tectonics, structure, and hydrocarbon potential of the Mexican Ridges Fold Belt, western Gulf of Mexico: Gulf Coast Association of Geological Societies Transactions, v. 61, p. 403–419.

Salter, D. I., and I. M. West, 1966, Calciostrontianite in the basal Purbeck Beds of Durlston Head, Dorset: Mineralogical Magazine, v. 35, p. 146–150.

Salvador, A., 1987, Late Triassic-Jurassic paleogeography and origin of the Gulf of Mexico basin: American Association Petroleum Geologists – Bulletin, v. 71, p. 419–451.

Salvan, H. M., 1972, Les niveaux salifers marocains, leurs caracteristques problemes, in G. Richter-bernburg, ed., Geology of Saline deposits: Paris, UNESCO, p. 147–168.

Salvany, J. M., 1989, Las formaciones evaporíticas del terciario continental de la cuenca del Ebro en Navarra y la Rioja: Litoestratigrafia, petrología y sedimentología: Doctoral thesis, Universitat de Barcelona.

Salvany, J. M., J. Garcia-Veigas, and F. Orti, 2007, Glauberite-halite association of the Zaragoza Gypsum Formation (Lower Miocene, Ebro Basin, NE Spain): Sedimentology, v. 54, p. 443–467.

Salvany, J. M., A. Munoz, and A. Perez, 1994, Nonmarine evaporitic sedimentation and associated diagenetic processes of the southwestern margin of the Ebro Basin (lower Miocene), Spain: Journal of Sedimentary Research, Section A: Sedimentary Petrology and Processes, v. 64, p. 190–203.

Salvany, J. M., and F. Orti, 1994, Miocene glauberite deposits of Alcanadre, Ebro Basin, Spain: sedimentary and diagenetic processes, in R. W. Renaut, and W. M. Last, eds., Sedimentology and geochemistry of modern and ancient saline lakes, SEPM/Society for Sedimentary Geology Special Publication, v. 50, p. 203–215.

Sánchez, J. A., P. Coloma, and A. Perez, 1999, Sedimentary processes related to the groundwater flows from the Mesozoic Carbonate Aquifer of the Iberian Chain in the Tertiary Ebro Basin, northeast Spain: Sedimentary Geology, v. 129, p. 201–213.

Sanchez-Mejorada, P., 1986, Evaporite Deposit of Laguna del Rey: Trans. Soc. Mining Eng., AIME, v. 280, p. 1923–1927.

Sanchez-Moral, S., J. C. Cañaveras, L. Laiz, C. Saiz-Jimenez, J. Bedoya, and L. Luque, 2003, Biomediated Precipitation of Calcium Carbonate Metastable Phases in Hypogean Environments: A Short Review: Geomicrobiology Journal, v. 20, p. 491–501.

Sanchez-Moral, S., S. Ordonez, M. A. G. Delcura, M. Hoyos, and J. C. Canaveras, 1998, Penecontemporaneous diagenesis in continental saline sediments – Bloeditization in Quero playa lake (La Mancha, Central Spain): Chemical Geology, v. 149, p. 189–204.

Sancho, C., J. L. Peña, R. Mikkan, C. Osácar, and Y. Quinif, 2004, Morphological and speleothemic development in Brujas Cave (Southern Andean Range,Argentine): palaeoenvironmental significance: Geomorphology, v. 57, p. 367–384.

Sandberg, P. A., 1975, New interpretations of Great Salt Lake ooids and of ancient non-skeletal carbonate mineralogy.: Sedimentology, v. 22, p. 497–537.

Sandler, A., Y. Harlavan, and G. Steinitz, 2004, Early formation of K-feldspar in shallow-marine sediments at near-surface temperatures (southern Israel): evidence from K-Ar dating: Sedimentology, v. 51, p. 323–338.

Saner, S., and A. Sahin, 1999, Lithological and zonal porosity-permeability distributions in the Arab-D reservoir, Uthmaniyah field, Saudi Arabia: American Association of Petroleum Geologists – BULLETIN, v. 83, p. 230–243.

Saner, S., and A. Sahin, 2000, Lithological and zonal porosity-permeability distributions in the Arab-D reservoir, Uthmaniyah field, Saudi Arabia: Reply: American Association Petroleum Geologists – Bulletin, v. 84, p. 1368–1370.

Sanford, W. E., and W. W. Wood, 1991, Brine evolution and mineral deposition in hydrologically open evaporite basins: American Journal of Science, v. 291, p. 687–710.

Sanford, W. E., and W. W. Wood, 2001, Hydrology of the coastal sabkhas of Abu Dhabi, United Arab Emirates: Hydrogeology Journal, v. 9, p. 358–366.

Sangster, D. F., M. D. Burtt, and D. J. Kontak, 1998, Geology of the B baseline Zone, Walton Cu-Pb-Zn-Ag-Ba deposit, Nova Scotia, Canada: Economic Geology, v. 93, p. 869–882.

Sangster, D. F., and E. M. Hillary, 2000, SEDEX lead-zinc deposits—Proposed subtypes and their characteristics: Exploration and Mining Geology, v. 7, p. 341–357.

Sangster, D. F., M. M. Savard, and D. J. Kontak, 1998, A genetic model for the mineralisation of Lower Windsor (Visean) carbonate rocks of Nova Scotia, Canada: Economic Geology, v. 93, p. 932–952.

Sanjuan, B., G. Michard, and A. Michard, 1990, Origine des substances dissoutes dans les eaux des sources thermales et des forages de la région Asal-Ghoubbet (République de Djibouti): Journal of Volcanology & Geothermal Research, v. 43, p. 333–353.

Sans, M., J. A. Munoz, and J. Verges, 1996b, Triangle zone and thrust wedge geometries related to evaporitic horizons (southern Pyrenees): Bulletin of Geological Petroleum Geology, v. 44, p. 375–384.

Sans, M., A. L. Sanchez, and P. Santanach, 1996a, Internal structure of a detachment horizon in the most external part of the Pyrenean fold and thrust belt (northern Spain), in G. I. Alsop, D. Blundell, and I. Davison, eds., Salt tectonics: London, Geological Society Special Publication, v. 100, p. 65–76.

SantamarÌa-Orozco, D., B. Horsfield, R. di Primio, and D. H. Welte, 1998, Influence of maturity on distributions of benzoand dibenzothiophenes in Tithonian source rocks and crude oils, Sonda de Campeche, Mexico: Organic Geochemistry, v. 28, p. 423–439.

Santini, K., T. Fastert, and R. Harris, 2006, Soda Ash, in J. E. Kogel, N. C. Trivedi, J. M. Barker, and S. T. Krukowski, eds., Industrial Minerals and Rocks, SME (Soc. Mining Metallurgy and Exploration), p. 859–878.

Santos, R. V., E. L. Dantas, C. G. de Oliveira, C. J. S. d. Alvarenga, C. W. D. d. Anjos, E. M. Guimarães, and F. B. Oliveira, 2009, Geochemical and thermal effects of a basic sill on black shales and limestones of the Permian Irati Formation: Journal of South American Earth Sciences, v. 28, p. 14–24.

Sanz-Montero, M. E., and J. P. Rodriguez-Aranda, 2012, Magnesite formation by microbial activity: Evidence from a Miocene hypersaline lake: Sedimentary Geology, v. 263-ì264, p. 6–15.

Sanz-Montero, M. E., J. P. Rodriguez-Aranda, and J. P. Calvo, 2006, Mediation of Endoevaporitic Microbial Communities in Early Replacement of Gypsum by Dolomite:A Case Study from Miocene Lake Deposits of the Madrid Basin, Spain: Journal of Sedimentary Research, v. 76, p. 1257–1266.

Sanz-Montero, M. E., J. P. RodrÌguez-Aranda, and M. A. GarcÌa del Cura, 2009, Bioinduced precipitation of barite and celestite in dolomite microbialites: Examples from Miocene lacustrine sequences in the Madrid and Duero Basins, Spain: Sedimentary Geology, v. 222, p. 138–148.

Sanz-Rubio, E., M. Hoyos, J. Calvo, and J. Rouchy, 1999, Nodular anhydrite growth controlled by pedogenic structures in evaporite lake formations: Sedimentary Geology, v. 125, p. 195–203.

Sanz-Rubio, E., S. Sanchez-Moral, J. C. Canaveras, J. P. Calvo, and J. M. Rouchy, 2001, Calcitization of Mg-Ca carbonate and Ca sulphate deposits in a continental Tertiary basin (Calatayud Basin, NE Spain): Sedimentary Geology, v. 140, p. 123–142.

Sarbu, S. M., T. C. Kane, and B. K. Kinkle, 1996, A chemoautotrophically based cave ecosystem: Science, v. 272, p. 1953–1955.

Sarbu, S. M., B. K. Kinkle, L. Vlasceanu, T. C. Kane, and R. Popa, 1994, Microbiological characterisation of a sulphide-rich groundwater system: Geomicrobiology Journal, v. 12, p. 175–182.

Sarg, J. F., 1981, Petrology of the carbonate-evaporite facies transition of the Seven Rivers Formation (Guadalupian, Permian), Southeast New Mexico: Journal of Sedimentary Petrology, v. 51, p. 73–96.

Sarg, J. F., 2001, The sequence stratigraphy, sedimentology, and economic importance of evaporite-carbonate transitions: a review: Sedimentary Geology, v. 140, p. 9–42.

Sarkar, A., J. A. Nunn, and J. S. Hanor, 1995, Free thermohaline convection beneath allochthonous salt sheets – An agent for salt dissolution and fluid flow in Gulf Coast sediments: Journal of Geophysical Research-Solid Earth, v. 100, p. 18085–18092.

Sarti, F., Y. Arkin, J. Chorowicz, A. Karnieli, and T. Cunh, 2003, Assessing pre- and post-deformation in the southern Arava Valley segment of the Dead Sea Transform, Israel by differential interferometry: Remote Sensing of Environment, v. 86, p. 141–149.

Sass, A. M., H. Sass, M. J. L. Coolen, H. Cypionka, and J. Overmann, 2001, Microbial communities in the chemocline of a hypersaline deep-sea basin (Urania basin, Mediterranean Sea): Applied and Environmental Microbiology, v. 67, p. 5392–5402.

Sass, E., and A. Bein, 1988, Dolomites and salinity; a comparative geochemical study: Shukla, Vijai, Baker, Paul A. Sedimentology and geochemistry of dolostones, based on a symposium. Special Publication Society of Economic Paleontologists and Mineralogists, v. 43, p. 223–233.

Sass, E., and Ben-Yaakov, 1977, The carbonate system in hypersaline solutions: The Dead Sea Brines: Marine Chemistry, v. 5, p. 83–109.

Sassen, R., D. A. DeFreitas, N. L. Eaker, H. H. Roberts, and C. Zhang, 2004, Brine vents on the Gulf of Mexico slope: Hydrocarbons, carbonate-barite-uranium mineralisation, red beds and life in an extreme environment: In, 24 Gulf Coast Section SEPM Foundation Bob F. Perkins Conference; Salt-sediment Interactions and Hydrocarbon productivity:Concepts, Applications and Casde Studies for the 21st Century, p. 444–63.

Sassen, R., I. R. MacDonald, A. G. Requejo, N. L. Guinasso, Jr., M. C. Kennicutt, II, S. T. Sweet, and J. M. Brooks, 1994, Organic geochemistry of sediments from chemosynthetic communities, Gulf of Mexico slope: Geo-Marine Letters, v. 14, p. 110–119.

Sassen, R., and P. Post, 2008, Enrichment of diamondoids and ^{13}C in condensate from Hudson Canyon, US Atlantic: Organic Geochemistry, v. 39, p. 147–151.

Satarugsa, P., 2011, The Lessons Learnt from Geophysical Investigation of Sinkholes in Rock Salt in Thailand.: Paper presented at International Conference on Geology, Geotechnology and Mineral Resources of Indochina (GEOINDO 2011) 1–3 December 2011, Khon Kaen, Thailand.

Satish-Kumar, M., J. Hermann, T. Tsunogae, and Y. Osanai, 2006, Carbonation of Cl-rich scapolite boudins in Skallen, East Antarctica: evidence for changing fluid condition in the continental crust: Journal Of Metamorphic Geology, v. 24, p. 241–261.

Sattayarak, N., S. Polachan, and R. Charusiriawad, 1991, Cretaceous rock salt in the NE part of Thailand (Abs.): GEOSEA VII, Bangkok 5–8 Nov., 1991, p. 96.

Saunders, J. A., and C. T. Swann, 1994, Mineralogy and geochemistry of a cap-rock Zn-Pb-Sr-Ba occurrence at the Hazlehurst salt dome, Mississippi: Economic Geology, v. 89, p. 381–390.

Saunders, J. A., and R. C. Thomas, 1996, Origin of exotic minerals in Mississippi salt dome cap rocks – Results of reaction path modeling: Applied Geochemistry, v. 11, p. 667–676.

Sauro, F., N. Tisato, J. De Waele, S. M. Bernasconi, T. R. R. Bontognali, and E. Galli, 2014, Source and genesis of sulphate and phosphate–sulphate minerals in a quartz-sandstone cave environment: Sedimentology, v. 61, p. 1433–1451.

Savage, A., and B. Knott, 1998, Artemia parthenogenetica in Lake Hayward, Western Australia. II. Feeding biology in a shallow seasonally stratified, hypersaline lake: International Journal of Salt Lake Research, v. 7, p. 13–24.

Savard, M., D. F. Sangster, and M. D. Burtt, 1998, Isotope geochemistry of sideritized host rocks, Walton Ba deposit, Kennetcook Sub-basin, Nova Scotia, Canada: Economic Geology, v. 93, p. 834–844.

Savard, M. M., 1996, Pre-ore burial dolomitization adjacent to the carbonate-hosted Gays River Zn-Pb deposit, Nova Scotia: Canadian Journal of Earth Sciences, v. 33, p. 302–315.

Savard, M. M., and G. Chi, 1998, Cation study of fluid inclusion decrepitates in the Jubilee and Gays River (Canada) Zn-Pb deposits; characterization of ore-forming brines: Economic Geology, v. 93, p. 920–931.

Savard, M. M., G. Chi, T. Sami, A. E. Williams-Jones, and K. Leigh, 2000, Fluid inclusion and carbon, oxygen, and strontium isotope study of the Polaris Mississippi Valley-type Zn–Pb deposit, Canadian Arctic Archipelago: implications for ore genesis: Mineralium Deposita, v. 35, p. 495–510.

Savard, M. M., G. Lynch, and F. Fallara, 1996, Burial diagenesis model for the Macumber Formation on Cape Breton Island – implications for the tectonic evolution of the Windsor Group: Atlantic Geology, v. 32, p. 53–64.

Savrda, C. E., R. B. Cook, and A. Petrov, 2006, Trace Fossil Preservation by Native Copper, Corocoro, Bolivia: Rocks & Minerals, v. 81, p. 362–363.

Sawkins, F. J., 1990, Metal deposits in relation to plate tectonics: New York, NY, Springer-Verlag, 461 p.

Sawlowicz, Z., 1992, Primary sulphide mineralization in Cu-Fe-S zones of Kupferschiefer, Fore-Sudetic monocline, Poland: Transactions – Institution of Mining & Metallurgy, Section B, v. 101, p. B1-B8.

Scares, D. R.,A. C. M. Ferreira, R. R. da Silva, and V. P. Ferreira, 2008, Alkali-Deficient elbaite from pegmatites of the Serido region, Borborema Province, NE Brazil: Brazilian Journal of Geology, v. 30, p. 293–296.

Schaad, W., 1995, The origin of Rauhwackes (Cornieules) by the karstification of gypsum [German]: Eclogae Geologicae Helvetiae, v. 88, p. 59–90.

Scheck, M., U. Bayer, and B. Leweren, 2003, Salt movements in the Northeast German Basin and its relation to major post-Permian tectonic phases—results from 3D structural modelling, backstripping and reflection seismic data: Tectonophysics, v. 361, p. 277–299.

Schelkes, K., P. Vogel, and H. Klinge, 2001, Density-Dependent Groundwater Movement in Sediments Overlying Salt Domes – The Gorleben Site Example: Phys. Chem. Earth (B), v. 26, p. 361–365.

Schenk, C. J., and S. G. Fryberger, 1988, Early diagenesis of eolian dune and interdune sands at White Sands, New Mexico: Sedimentary Geology, v. 55, p. 109–120.

Schenk, O., and J. L. Urai, 2004, Microstructural evolution and grain boundary structure during static recrystallization in synthetic polycrystals of sodium chloride containing saturated brine: Contributions to Mineralogy and Petrology, v. 146, p. 671–682.

Schenk, O., J. L. Urai, and S. Piazolo, 2006, Structure of grain boundaries in wet, synthetic polycrystalline, statically recrystallizing halite – evidence from cryo-SEM observations: Geofluids, v. 6, p. 93–104.

Schenk, P., and M. P. A. Jackson, 1993, Diapirism on Triton: A record of crustal layering and instability: Geology, v. 21, p. 299–302.

Schenk, P., P. Vonbitter, and R. Matsumoto, 1994, Deep-basin Deep-water carbonate-evaporite deposition of a saline giant – Loch Macumber (Visean), Atlantic Canada: Carbonates & Evaporites, v. 9, p. 187–210.

Scherf, A.-K., and J. Rullkötter, 2009, Biogeochemistry of high salinity microbial mats – Part 1: Lipid composition of microbial mats across intertidal flats of Abu Dhabi, United Arab Emirates: Organic Geochemistry, v. 40, p. 1018–1028.

Schidlowski, M., U. Matzeigkeit, W. G. Mook, and W. E. Kriumbein, 1985, Carbon isotope geochemistry and 14C ages of microbial mats from Gavish sabkha and Solar Lake, in G. M. Freiedman, and W. E. Krumbein, eds., Hypersalin ecosystems – The Gavish sabkha: New York, Springer-Verlag, p. 381–401.

Schieber, J., 2004, Microbial mats in the siliciclastic rock record: a summary of diagnostic features, in P. G. Eriksson, W. Altermann, D. Nelson, W. U. Mueller, O. Catuneanu, and K. Strand, eds., The Precambrian Earth: Tempos and Events: Developments in Precambrian Geology: Amsterdam, Elsevier, p. 663–672.

Schlager, W., and H. Bolz, 1977, Clastic accumulation of sulfate evaporites in deep water: Journal of Sedimentary Petrology, v. 47, p. 600–609.

Schleder, Z., and J. L. Urai, 2005, Microstructural evolution of deformation-modified primary halite from the Middle Triassic Rot Formation at Hengelo, The Netherlands: International Journal Of Earth Sciences, v. 94, p. 941–955.

Schlitt, W. J., 1982, Interfacing technologies in solution mining: Proc. of the Second SME-SPE Intl. Solution Mining Symp., Denver: New York, AIME, 370 p.

Schlüter, T., and R. Kohring, 2002, Palaeopathological fish bones from phosphorites of the Lake Manyara area, Northern Tanzania – Fossil evidence of a physiological response to survival in an extreme biocenosis: Environmental Geochemistry and Health, v. 24, p. 131–140.

Schmid, I. H., 1987, Turkey's Salda Lake: a genetic model for Australia's newly discovered magnesite deposits: Ind. Min., v. 239, p. 19–31.

Schmid, R. M., 1988a, Lake Torrrens Brine: Hydrobiologia, v. 158, p. 267–269.

Schmid, R. M., 1988b, Lake Torrens halite accumulation (South Australia): Zeitschrift der Deutschen Geologischen Gesellschaft, v. 139, p. 289–296.

Schmidt, K., D. Garbe-Schönberg, M. Bau, and A. Koschinsky, 2010, Rare earth element distribution in >400°C hot hydrothermal fluids from 5°S, MAR: The role of anhydrite in controlling highly variable distribution patterns: Geochimica et Cosmochimica Acta, v. 74, p. 4058–4077.

Schmidt Mumm, A., and C. H. H. Conor, 2008, Albitisation – from mineral grains to giant ore deposits (abs.): 33rd International Geological Congress, Oslo, Norway, August 6–14 2008. Session MPN-03 Mineral replacement and mass transfer in hydrothermal systems: From the nanoscale to the megascale.

Schmidt, V., I. A. McIlreath, and A. E. Budwill, 1985, Origin and diagenesis of Middle Devonian pinnacle reefs encased in evaporites, "A" and "E" pools, Rainbow field, Alberta, in P. O. Roehl, and P. W. Choquette, eds., Carbonate petroleum reservoirs: New York, Springer-Verlag, p. 141–160.

Schmidt-Mumm, A., H. J. Behr, and E. E. Horn, 1987, Fluid systems in metaplaya sequences in the Damara Orogen (Namibia): evidence for sulfur-rich brines-general evolution and first results: Chemical Geology, v. 61, p. 135–145.

Schnyder, J., F. Baudin, and J.-F. Deconinck, 2009, Occurrence of organic-matter-rich beds in Early Cretaceous coastal evaporitic setting (Dorset, UK): a link to long-term palaeoclimate changes?: Cretaceous Research, v. 30, p. 356–366.

Schoell, M., M. A. McCaffrey, F. J. Fago, and J. M. Moldowan, 1992, Carbon isotopic compositions of 28,30-bisnorhopanes and other biological markers in a Monterey crude oil: Geochimica et Cosmochimica Acta, v. 56, p. 1391–1399.

Schoellkopf, N. B., and B. A. Patterson, 2000, Chapter 25: Petroleum Systems of Offshore Cabinda, Angola, in M. R. Mello, and B. J. Katz, eds., Petroleum Systems of South Atlantic Margins, American Association Petroleum Geologists Memoir 73, p. 361–376.

Schoenherr, J., R. Littke, J. L. Urai, P. A. Kukla, and Z. Rawahi, 2007a, Polyphase thermal evolution in the Infra-Cambrian Ara Group (South Oman Salt Basin) as deduced by maturity of solid reservoir bitumen: Organic Geochemistry, v. 38, p. 1293–1318.

Schoenherr, J., L. Reuning, P. A. Kukla, R. Littke, J. L. Urai, M. G. Siemann, and Z. Rawahi, 2009, Halite cementation and carbonate diagenesis of intra-salt reservoirs from the Late Neoproterozoic to Early Cambrian Ara Group (South Oman Salt Basin): Sedimentology, v. 56, p. 567–589.

Schoenherr, J., Z. Schléder, J. L. Urai, P. A. Fokker, and O. Schulze, 2007c, Deformation mechanisms and rheology of Pre-cambrian rocksalt from the South Oman Salt Basin.- In (eds.), Hannover, Germany, in M. Wallner, K. Lux, W. Minkley, and H. Hardy Jr., eds., Proc. 6th Conference on the Mechanical Behavior of Salt (SaltMech6) – Understanding of THMC Processes in Salt Hannover, Germany, p. 167–173.

Schoenherr, J., J. L. Urai, P. A. Kukla, R. Littke, Z. Schleder, J.-M. Larroque, M. J. Newall, N. Al-Abry, H. A. Al-Siyabi, and Z. Rawahi, 2007b, Limits to the sealing capacity of rock salt: A case study of the infra-Cambrian Ara Salt from the South Oman salt basin: Bulletin American Association Petroleum Geologists, v. 91, p. 1541–1557.

Schofield, N., I. Alsop, J. Warren, J. R. Underhill, R. Lehné, W. Beer, and V. Lukas, 2014, Mobilizing salt: Magma-salt interactions: Geology, v. 42, p. 599–602.

Scholle, P. A., L. Stemmerik, and O. Harpoth, 1990, Origin of major karst-associated celestite mineralization in Karstryggen, central East Greenland: Journal of Sedimentary Petrology, v. 60, p. 397–410.

Scholle, P. A., L. Stemmerik, D. Ulmer-Scholle, G. Diliegro, and F. H. Henk, 1993, Palaeokarst-influenced depositional and diagenetic patterns in Upper Permian carbonates and evaporites, Karstryggen Area, Central East Greenland: Sedimentology, v. 40, p. 895–918.

Scholle, P. A., D. S. Ulmer, and L. A. Melin, 1992, Late-stage calcites in the Permian Capitan Formation and its equivalents, Delaware Basin margin, West Texas and New Mexico; evidence for replacement of precursor evaporites: Sedimentology, v. 39, p. 207–234.

Schorn, A., and F. Neubauer, 2014, The structure of the Hallstatt evaporite body (Northern Calcareous Alps, Austria): A compressive diapir superposed by strike-slip shear?: Journal of Structural Geology, v. 60, p. 70–84.

Schorn, A., F. Neubauer, and M. Bernroider, 2013b, Polyhalite microfabrics in an Alpine evaporite mélange: Hallstatt, Eastern Alps: Journal of Structural Geology, v. 46, p. 57–75.

Schorn, A., F. Neubauer, J. Genser, and M. Bernroider, 2013a, The Haselgebirge evaporitic melange in central Northern Calcareous Alps (Austria): Part of the Permian to Lower Triassic rift of the Meliata ocean?: Tectonophysics, v. 583, p. 28–48.

Schouten, S., W. A. Hartgers, J. F. López, J. O. Grimalt, and J. S. Sinninghe Damsté, 2001, A molecular isotopic study of ^{13}C-enriched organic matter in evaporitic deposits recognition of CO_2-limited ecosystems: Organic Geochemistry, v. 32, p. 277–286.

Schramm, J. M., 1991, The Permian–Triassic of the Gartnerkofel-1 Core (Carnic Alps, Austria): Illite crystallinity in shaly sediments and its comparison with pre-Variscan sequences: Abh Geol BA, v. 45, p. 69–77.

Schreiber, B. C., 1988, Subaqueous evaporite deposition, in B. C. Schreiber, ed., Evaporites and hydrocarbons: New York, Columbia University Press.

Schreiber, B. C., and M. El Tabakh, 2000, Deposition and early alteration of evaporites [Review]: Sedimentology, v. 47, p. 215–238.

Schreiber, B. C., and D. J. J. Kinsman, 1975, New observations on the Pleistocene evaporites of Montallegro, Sicily and a modern analog: Journal of Sedimentary Petrology, v. 45, p. 469–479.

Schreiber, B. C., R. P. Philp, S. Benali, M. L. Helman, J. A. de la Pena, R. Marfil, P. Landais, A. D. Cohen, and C. G. S. C. Kendall, 2001, Characterisation of organic matter formed in hypersaline carbonate/evaporite environments: Hydrocarbon potential and biomarkers obtained through artificial maturation studies: Journal of Petroleum Geology, v. 24, p. 309–338.

Schreiber, B. C., and E. Schreiber, 1977, The salt that was: Geology, v. 5, p. 527–528.

Schreiber, B. C., and D. Walker, 1992, Halite pseudomorphs after gypsum; a suggested mechanism: Journal of Sedimentary Petrology, v. 62, p. 61–70.

Schreiber, B. C., 1988b, Evaporites and hydrocarbons: New York, Columbia University Press, 475 p.

Schreyer, W., 1977, Whiteschists: Their compositions and pressure-temperature regimes based on experimental, field, and petrographic evidence: Tectonophysics, v. 43, p. 127–144.

Schreyer, W., and K. Abraham, 1976, Three-stage metamorphic history of a whiteschist from Sar e Sang, Afghanistan, as part of a former evaporite deposit: Contributions to Mineralogy & Petrology, v. 59, p. 111–130.

Schreyer, W., K. Abraham, and H. Kulke, 1980, Natural sodium phlogopite coexisting with potassium phlogopite and sodian aluminian talc in a metamorphic evaporite sequence from Derrag, Tell Atlas, Algeria: Contributions to Mineralogy & Petrology, v. 74, p. 223–233.

Schreyer, W., O. Medenbach, K. Abraham, W. Gebert, and W. D. Muller, 1982, Kulkeite, a new metamorphic phyllosilicate mineral: ordered 1:1 chlorite/talc mixed-layer.: Contributions to Mineralogy & Petrology, v. 80, p. 103–109.

Schrijver, K., 1992, Basinal brines and groundwaters as possible metal carriers in the formation of sandstone-hosted lead-zinc deposits: Mineralium Deposita, v. 27, p. 109–114.

Schröder, S., J. E. Amthor, and A. Matter, 2000b, Unusual hydrocarbon reservoirs in intrasalt carbonate stringers (Birba Area, Infracambrian Ara Group, S-Oman: GeoArabia, v. 5, p. 177.

Schroder, S., A. Bekker, N. J. Beukes, H. Strauss, and H. S. van Niekerk, 2008, Rise in seawater sulphate concentration associated with the Paleoproterozoic positive carbon isotope excursion: evidence from sulphate evaporites in the 2.2-2.1 Gyr shallow-marine Lucknow Formation, South Africa: Terra Nova, v. 20, p. 108–117.

Schroder, S., J. P. Grotzinger, J. E. Amthor, and A. Matter, 2005, Carbonate deposition and hydrocarbon reservoir development at the Precambrian-Cambrian boundary: The Ara Group in South Oman: Sedimentary Geology, v. 180, p. 1–28.

Schröder, S., B. C. Schreiber, J. E. Amthor, and A. Matter, 2000a, Evaporites of the Ara Group (South Oman): an essential element of stratigraphy in an Infracambrian salt basin: Geo Arabia, v. 5, p. 176–177.

Schröder, S., B. C. Schreiber, J. E. Amthor, and A. Matter, 2003, A depositional model for the terminal Neoproterozoic-Early Cambrian Ara Group evaporites in south Oman: Sedimentology, v. 50, p. 879–898.

Schroeder, W., S. Brooke, J. Olson, B. Phaneuf, J. McDonough, III, and P. Etnoyer, 2005, Occurrence of deep-water Lophelia pertusa and Madrepora oculata in the Gulf of Mexico, in A. Freiwald, and J. M. Roberts, eds., Cold-Water Corals and Ecosystems: Erlangen Earth Conference Series, Springer Berlin Heidelberg, p. 297–307.

Schubel, K. A., and T. K. Lowenstein, 1997, Criteria for the recognition of shallow-perennial-saline-lake halites based on Recent sediments from the Qaidam Basin, western China: Journal of Sedimentary Research Section A-Sedimentary Petrology & Processes, v. 67, p. 74–87.

Schubel, K. A., and B. M. Simonson, 1990, Petrography and diagenesis of cherts of Lake Magadi, Kenya: Journal of Sedimentary Petrology, v. 60, p. 761–776.
Schubert, C. J., 2011, Methane, Origin, in J. Reitner, and V. Thiel, eds., Encyclopedia of Geobiology: Dordrecht Netherlands, Springer, p. 578–586.
Schubert, J. K., and D. J. Bottjer, 1992, Early Triassic stromatolites as post-mass extinction disaster forms: Geology, v. 20, p. 883–886.
Schultz, H., G. Bauer, E. Schachl, F. Hagedorn, and P. Schmittinger, 2005, Potassium Compounds, John Wiley and Sons Inc., Ullmann's Encyclopedia of Industrial Chemistry 2005, Wiley-VCH, Weinheim., p. 1–68.
Schultz-Ela, D. D., 1992, Restoration of cross-sections to constrain deformation processes of extensional terranes: Marine and Petroleum Geology, v. 9, p. 372–388.
Schultz-Ela, D. D., 2003, Origin of "Drag" Folds Bordering Salt Diapirs: Bulletin American Association Petroleum Geologists, v. 87, p. 757–780.
Schultz-Ela, D. D., and M. P. A. Jackson, 1996, Relation of subsalt structures to suprasalt structures during extension: American Association of Petroleum Geologists Bulletin, v. 80, p. 1896–1924.
Schultz-Ela, D. D., M. P. A. Jackson, and B. C. Vendeville, 1993, Mechanics of active salt diapirism: Tectonophysics, v. 228, p. 275–312.
Schultze-Lam, S., and T. J. Beveridge, 1994, Nucleation of celestite and strontianite on a cyanobacterial S-layer: Applied and Environmental Microbiology, v. 60, p. 447–453.
Schulz, E., A. Abichou, T. Hachicha, S. Pomel, U. Salzmann, and K. Zouari, 2002, Sebkhas as ecological archives and the vegetation and landscape history of southeastern Tunisia during the last two millennia: Journal of African Earth Sciences, v. 34, p. 223–229.
Schuster, D. C., 1995, Deformation of allochthonous salt and evolution of related salt-structural systems, Eastern Louisiana Gulf Coast, in M. P. A. Jackson, D. G. Roberts, and S. Snelson, eds., Salt tectonics: a global perspective, American Association Petroleum Geologists Memoir, v. 65, p. 177–198.
Schwark, L., M. Vliex, and P. Schaeffer, 1998, Geochemical characterization of Malm Zeta laminated carbonates from the Franconian Alb, SW-Germany (II): Organic geochemistry, v. 29, p. 1921–1952.
Schwebel, D. A., 1983, Quaternary dune systems, in J. K. Ling, and J. W. Holmes, eds., Natural History of the South East: Adelaide, Royal Society of South Australia, p. 15–24.
Schwerdtner, W. M., 1964, Genesis of potash rocks in Middle Devonian Prairie Evaporite Formation of Saskatchewan: Am. Assoc. Petroleum Geologists Bull, p. 1108–1115.
Scott, J. J., R. W. Renaut, L. A. Buatois, and R. B. Owen, 2009, Biogenic structures in exhumed surfaces around saline lakes: An example from Lake Bogoria, Kenya Rift Valley: Palaeogeography, Palaeoclimatology, Palaeoecology, v. 272, p. 176–198.
Scott, J. J., R. W. Renaut, and R. B. Owen, 2012, Impacts of flamingos on saline lake margin and shallow lacustrine sediments in the Kenya Rift Valley: Sedimentary Geology, v. 277–278, p. 32–51.
Scrivener, R. C., and R. W. Sanderson, 1982, Talc and aragonite from the Triassic halite deposits of the Burton Row borehole, Brent Knoll, Somerset: United Kingdom, Inst. Geological Sciences, Report, v. 82, p. 58–60.
Seard, C., G. Camoin, J.-M. Rouchy, and A. Virgone, 2013, Composition, structure and evolution of a lacustrine carbonate margin dominated by microbialites: Case study from the Green River formation (Eocene; Wyoming, USA): Palaeogeography, Palaeoclimatology, Palaeoecology, v. 381–382, p. 128–144.
Searl, A., and S. Rankin, 1993,A preliminary petrographic study of the Chilean nitrates: Geological Magazine, v. 130, p. 319–333.
Sears, S. O., and F. J. Lucia, 1979, Reef growth model for Silurian pinnacle reefs, northern Michigan reef trend: Geology, v. 3, p. 299–302.
Sears, S. O., and F. J. Lucia, 1980, Dolomitization of Northern Michigan Niagara reefs by brine refluxion and fresh water/sea water mixing, in D. H. Zenger, J. B. Dunham, and R. L. Ethington, eds., Concepts and models of dolomitization, Society of Economic Paleontologists and Mineralogists, Special Publication 28, p. 215–235.
Sebag, D., E. P. Verrecchia, S. J. Lee, and A. Durand, 2001, The natural hydrous sodium silicates from the northern bank of Lake Chad: occurrence, petrology and genesis: Sedimentary Geology, v. 139, p. 15–31.
Seckbach, J., 2005, The Relevance of Halophiles and other Extremophiles to Martian and Extraterrestrial Environments, in N. Gunde-Cimerman, A. Oren, and A. Plemenitaš, eds., Adaptation to Life at High Salt Concentrations in Archaea, Bacteria, and Eukarya: Dordrecht, Netherlands, Springer, p. 123–136.
Seewald, J. S., 2003, Organic–inorganic interactions in petroleum-producing sedimentary basins: Nature, v. 426, p. 327–333.
Selby, D., R. A. Creaser, K. Dewing, and M. Fowler, 2005, Evaluation of bitumen as a 187Re–1870s geochronometer for hydrocarbon maturation and migration: A test case from the Polaris MVT deposit, Canada: Earth and Planetary Science Letters, v. 235, p. 1–15.
Sellwood, B. W., and R. E. Netherwood, 1984, Facies evolution in the Gulf of Suez area: Sedimentation history as an indicator of rift initiation and development: Modern Geology, v. 9, p. 43–69.
Senalp, M., and A. Al-Duaiji, 1995, Stratigraphy and sedimentation of the Unayzah reservoirs, Central Saudi Arabia, in M. I. Al-Husseini, ed., Middle East Petroleum Geosciences Conference, GEO'94, v. 1: Manama, Bahrain, Gulf Petrolink.
Sengupta, N., D. Mukhopadhyay, P. Sengupta, and R. Hoffbauer, 2005, Tourmaline-bearing rocks in the Singhbhum shear zone, eastern India; evidence of boron infiltration during regional metamorphism: American Mineralogist, v. 90, p. 1241–1255.
Seni, S. J., and M. P. A. Jackson, 1983a, Evolution of salt structures, East Texas diapir province; Part 1, Sedimentary record of halokinesis: American Association Petroleum Geologists – Bulletin, v. 67, p. 1219–1244.
Seni, S. J., and M. P. A. Jackson, 1983b, Evolution of salt structures, East Texas diapir province; Part 2, Patterns and rates of halokinesis: American Association Petroleum Geologists – Bulletin, v. 67, p. 1245–1274.
Senning, A., 2007, Elsevier's Dictionary of Chemoetymology: Amsterdam, Elsevier, 433 p.
Serdyuchenko, D. P., 1975, Some Precambrian scapolite bearing rocks evolved from evaporites: Lithos, v. 8, p. 1–7.
Sessions, A. L., S. P. Sylva, R. E. Summons, and J. M. Hayes, 2004, Isotopic exchange of carbon-bound hydrogen over geologic timescales: Geochimica Cosmochimica Acta, v. 68, p. 1545–1559.
Sessler, W., 1990, Influence of subrosion on three different types of salt deposits, in D. Heling, P. Rothe, U. Förstner, and P. Stoffers, eds., Sediments and Environmental Geochemistry: Berlin, Springer-Verlag, p. 179–196.
Seward, T. M., and H. L. Barnes, 1997, Metal transport by hydrothermal ore fluids, in H. L. Barnes, ed., Geochemistry of Hydrothermal Ore Deposits, John Wiley & Sons, p. 435–486.
Seymour, K. P., G. Rae, J. M. Peden, and K. Ormston, 1993, Drilling close to salt diapirs in the North Sea: SPE 26693, September 1993, p. 193–204.
Sha, Z., W. Huang, X.-k. Wang, and Y.-y. Zhao, 2009, Solubility and supersaturation of lithium carbonate in Zabuye Salt Lake Brine, Tibet: Natural Resources and Environmental Issues: Vol. 15, Article 41. Available at: http://digitalcommons.usu.edu/nrei/vol15/iss1/41.

Shackleton, N. J., J. Imbrie, and M. A. Hall, 1983, Oxygen and carbon isotope record of East Pacific core V19-3-1: implications for the formation of deep water in the late Pleistocene North Atlantic: Earth and Planetary Science Letters, v. 65, p. 233–244.

Shaker, S., 2008, The double edged sword: The impact of the interaction between salt and sediment on subsalt exploration risk in deep water: Gulf Coast Association of Geological Societies Transactions, v. 58, p. 759–769.

Shaker, S. S., 2004, Geopressure compartmentalization in salt basins: Their assessment for hydrocarbon entrapments in the Gulf of Mexico In: Salt-sediment interactions and hydrocarbon prospectivity: concepts, applications and case studies for the 21st Century. Papers presented at the 24th Annual Gulf Coast Section SEPM Foundation Bob F. Perkins Research Conference, Houston Tx, December 5–8, 2004 (CD publication), p. 421–433.

Shaker, S. S., and M. A. Smith, 2002, Pore Pressure Profile Predictions in the Challenging Supra/Sub-Salt Exploration Plays in Deep Water, Gulf of Mexico: American Association Petroleum Geologists Annual Meeting 2002.

Shakeri,A., J. Douraghinejad, and M. Moradpour, 2007, Microfacies and sedimentary environments of the late Oligocene-early Miocene Qom Formation of the Gooreh Berenji region (Jandaq area, central Iran): GeoArabia, v. 12, p. 41–60.

Shanks III, W. C., 1983, Economic and exploration significance of Red Sea metalliferous brine deposits, in W. C. Shank III, ed., Cameron Volume on Unconventional Mineral Deposits: New York, Society of Mining Engineers of the American Institute of Mining Engineering and Petroleum Engineers Monograph, p. 157–171.

Shanks III, W. C., and J. L. Bischoff, 1980, Geochemistry, sulfur isotope composition, and accumulation rates of Red Sea geothermal deposits: Economic Geology, v. 75, p. 445–459.

Sharland, P. R., R. Archer, D. M. Casey, R. B. Davies, S. H. Hall, A. P. Heward, A. D. Horbury, and M. D. Simmons, 2001, Arabian Plate Sequence Stratigraphy: GeoArabia Special Publication 2: Bahrain, Gulf Petrolink, 371 p.

Sharma, R. S., 1981, Mineralogy of a scapolite-bearing rock from Rajasthan, northwest peninsular India.: Lithos, v. 14, p. 165–172.

Sharp, J. M., T. R. Fenstemaker, C. T. Simmons, T. E. McKenna, and J. K. Dickinson, 2001, Potential salinity-driven free convection in a shale-rich sedimentary basin: Example from the Gulf of Mexico basin in south Texas: Bulletin American Association Petroleum Geologists, v. 85, p. 2089–2110.

Shaw, A. B., 1964, Time in Stratigraphy: New York, Mc-Graw-Hill, 365 p.

Shaw, A. B., 1977, A review of some aspects of evaporite deposition: Mountain Geologist, v. 14, p. 1–16.

Shearman, D. J., 1963, Recent anhydrite, gypsum, dolomite, and halite from the coastal flats of the Arabian shore of the Persian Gulf: Geological Society of London, Proceedings, v. 1607, p. 63–65.

Shearman, D. J., 1970, Recent halite rock, Baja California, Mexico: Inst. Min. Metall., Trans., Sect. B., v. 79, p. B155–B162.

Shearman, D. J., 1978, Evaporites of coastal sabkhas, in W. E. Dean, and B. C. Schreiber, eds., Marine evaporites.: Tulsa Ok., Soc. Econ. Paleontol. Mineral., Short Course Notes.

Shearman, D. J., and J. G. Fuller, 1969, Anhydrite diagenesis, calcitization, and organic laminites, Winnipegosis Formation, Middle Devonian, Saskatchewan: Bull. Can. Pet. Geol., v. 17, p. 496–525.

Shearman, D. J., J. Khouri, and S. Taha, 1961, On the replacement of dolomite by calcite in some Mesozoic limestones from the French Jura: Proceedings Geologists' Assoc., London, v. 72, p. 1–12.

Shearman, D. J., A. McGugan, C. Stein, and A. J. Smith, 1989, Ikaite, $CaCO_3$ $6H_2O$, precursor of the thinolites in the Quaternary tufas and tufa mounds of the Lahontan and Mono Lake Basins, western United States: Geological Society America Bulletin, v. 101, p. 913–917.

Shearman, D. J., G. Mossop, H. Dunsmore, and M. Martin, 1972, Origin of gypsum veins by hydraulic fracture: Inst. Min. Metall., Trans., Sect. B., v. 81, p. B149–B155.

Shearman, D. J., and A. J. Smith, 1985, Ikaite, the parent mineral of jarrowite-type pseudomorphs: Proceedings of the Geologists' Association, v. 96, p. 305–314.

Shelley, D. C., and T. F. Lawton, 2005, Sequence stratigraphy of tidally influenced deposits in a salt-withdrawal minibasin: Upper sandstone member of the Potrerillos Formation (Paleocene), La Popa basin, Mexico: Bulletin American Association Petroleum Geologists, v. 89, p. 1157–1179.

Shelton, J. S., R. P. Papson, and M. Womer, 1978, Aerial guide to geological features of southern California: Aeolian Features of Southern California: A Comparative Planetary Geology Guidebook, Office of Planetary Geology, National Aeronautics and Space Administration, U.S. Government Printing Office, Washington, D.C., p. 216–249.

Shelton, K. L., I. B. Burstein, R. D. Hagni, C. B. Vierrether, S. K. Grant, Q. T. Hennigh, M. F. Bradley, and R. T. Brandom, 1995, Sulfur isotope evidence for penetration of MVT fluids into igneous basement rocks, southeast Missouri, USA: Mineralium Deposita, v. 30, p. 339–350.

Shen, Y., J. Farquhar, A. Masterson, A. J. Kaufman, and R. Buick, 2009, Evaluating the role of microbial sulfate reduction in the early Archean using quadruple isotope systematics: Earth and Planetary Science Letters, v. 279, p. 383–391.

Sheppard, R. A., and A. J. Gude, 1968, Distribution and genesis of authigenic silicate minerals in tuffs of Pleistocene Lake Tecopa, Inyo County, Calif.: U.S. Geol. Surv. Prof. Paper, v. 597, p. 38 p.

Sheppard, R. A., A. J. Gude, and G. M. Elson, 1978, Bowie zeolite deposit, Cochise and Graham Counties, Arizona, in L. B. Sand, and F.A. Mumpton, eds., Natural Zeolites —Occurrence, Properties, Use, Pergamon, p. 319–328.

Sheppard, R. A., and F. A. Mumpton, 1984, Sedimentary fluorite in a lacustrine zeolitic tuff of the Gila Conglomerate near Buckhorn, Grant County, New Mexico: Journal of Sedimentary Petrology, v. 54, p. 853–860.

Sheu, D. D., 1987, Sulfur and organic carbon contents in sediment cores from the Tyro and Orca basins: Marine Geology, v. 75, p. 157–164.

Sheu, D. D., and B. J. Presley, 1986a, Formation of hematite in the euxinic Orca basin, northern Gulf of Mexico: Marine Geology, v. 69, p. 309–321.

Sheu, D. D., and B. J. Presley, 1986b, Variations of calcium carbonate, organic carbon and iron sulfides in anoxic sediment from the Orca Basin, Gulf of Mexico: Marine Geology, v. 70, p. 103–118.

Shi, T., Z. Chen, Z. Luo, S. Wang, and K. Wang, 2013, Mechanism of groundwater bursting in a deep rock salt mine region: a case study of the Anpeng trona and glauber mines, China: Environmental Earth Sciences, v. 68, p. 229–239.

Shiba, H., and K. Horikoshi, 1988, Isolation and characterization of novel anaerobic, halophilic eubacteria from hypersaline environments of western America and Kenya: In: Proceedings of the FEMS symposium—The microbiology of extreme environments and its biotechnological potential, Portugal, p. 371–373.

Shieh, Y. N., and H. P. Taylor, 1969, Oxygen and carbon isotope studies of contact metamorphism of carbonate rocks: Journal of Petrology, v. 10, p. 307–331.

Shields, G. A., 2002, 'Molar-tooth microspar': a chemical explanation for its disappearance 750 Ma: Terra Nova, v. 14, p. 108–113.

Shields, M. J., and P. V. Brady, 1995, Mass balance and fluid flow constraints on regional scale dolomitization, Late Devonian, Western Canada sedimentary basin: Bulletin of Canadian Petroleum Geology, v. 43, p. 371–392.

Shikazono, N., and H. D. Holland, 1983, The partitioning of strontium between anhydrite and aqueous solutions from 150 degrees to 250 degrees C: Economic Geology Monographs, v. 5, p. 320–328.

Shikazono, N., H. D. Holland, and R. F. Quirk, 1983, Anhydrite in kuroko deposits; mode of occurrence and depositional mechanisms: Economic Geology Monographs, v. 5, p. 329–344.

Shikazono, N., H. Kawabe, and Y. Ogawa, 2012, Interpretation of Mineral Zoning in Submarine Hydrothermal Ore Deposits in Terms of Coupled Fluid Flow-Precipitation Kinetics Model: Resource Geology, v. 62, p. 352–368.

Shimazaki, H., and E. Horikoshi, 1990, Black ore chimney from the Hanaoka Kuroko deposits, Japan: Mining Geology, v. 40.

Shinn, E. A., 1969, Submarine lithification of Holocene carbonate sediments in the Persian Gulf: Sedimentology, v. 12, p. 109–144.

Shinn, E. A., 1973, Carbonate coastal accretion in an area of longshore transport, NE Qatar, Persian Gulf, in P. B. H., ed., The Persian Gulf: Holocene carbonate sedimentation and diagenesis in a shallow epicontinental sea: New York, Springer-Verlag, p. 179–191.

Shinn, E. A., 1976, Coral recovery in Florida and the Persian Gulf: Environmental Geology, v. 1, p. 241–254.

Shinn, E. A., 1983, Birdseyes, fenestrae, shrinkage pores, and loferites; a reevaluation: Journal of Sedimentary Petrology, v. 53, p. 619–628.

Shirley, K., 2000, Gulf of Mexico deepwater and subsalt plays:The promise of the best of both worlds: American Association Petroleum Geologists Explorer, v. Oct. 2000.

Shirokova, L. S., V. Mavromatis, I. Bundeleva, O. S. Pokrovsky, P. Bénézeth, C. R. Pearce, E. Gérard, S. Balor, and E. H. Oelkers, 2011, Can Mg isotopes be used to trace cyanobacteria-mediated magnesium carbonate precipitation in alkaline lakes?: Biogeosciences Discussions, v. 4, p. 6473–6517.

Shirokova, L. S., V. Mavromatis, I. A. Bundeleva, O. S. Pokrovsky, P. Bénézeth, E. Gérard, C. R. Pearce, and E. H. Oelkers, 2013, Using Mg Isotopes to Trace Cyanobacterially Mediated Magnesium Carbonate Precipitation in Alkaline Lakes: Aquatic Geochemistry, v. 19, p. 1–24.

Shlichta, P. J., 1968, Growth, Deformation, and Defect Structure of Salt Crystals: Geological Society of America Special Papers, v. 88, p. 597–618.

Shock, D. A., 1985, Solution mining of soluble salts – its scope and its future, in W. J. Schlitt, ed., Salt and Brines '85: New York, Am. Inst. of Min. Met. and Pet. Eng., p. 1–10.

Shockey, P. N., and A. R. Renfro, 1974, Copper-silver solution fronts at Paoli, Oklahoma: Economic Geology, v. 69, p. 266–268.

Shoemaker, E. M., and C. S. Shoemaker, 1996, The Proterozoic impact record of Australia: AGSO Journal Geology & Geophysics, v. 16, p. 379–398.

Shortland, A., L. Schachner, I. Freestone, and M. Tite, 2006, Natron as a flux in the early vitreous materials industry: sources, beginnings and reasons for decline: Journal of Archaeological Science, v. 33, p. 521–530.

Shortland, A. J., 2004, Evaporites of the Wadi Natrun: Seasonal and annual variation and its implication for ancient exploration: Archaeometry, v. 46, p. 497–516.

Shternina, E. B., and J. V. Frolova, 1957, Rastvorimost' v sistemie $CaCO_3$-$CaSO_4$-NaCl-CO_2-H_2O: Zhurnal Neorganicheskoy Khimii, v. 2, p. 1648–1654.

Sibley, D. F., 1980, Climatic control of dolomitization, Seroe Doni formation (Pliocene), Bonaire, N. A., v. 28, SEPM Spec. Pub., p. 247–258.

Sibson, R., H., 2003, Brittle-failure controls on maximum sustainable overpressure in different tectonic regimes: American Association Petroleum Geologists – Bulletin, v. 87, p. 901–908.

Sibson, R. H., 1981, Fluid flow accompanying faulting: Field evidence and models, in W. Simpson, and G. Richards, eds., Earthquake Prediction: An International Review: Maurice Ewing Ser., v. 4: Washington, DC, American Geophysical Union, p. 593–603.

Sicree, A. A., and H. L. Barnes, 1996, Upper Mississippi Valley district ore fluid model: the role of organic complexes: Ore Geology Reviews, v. 11, p. 105–131.

Sidle, W. C., D. Sayala, and T. Steinborn, 1985, Natural analogues in evaporites for the interpretation of mineralogic and geochemical variations in a nuclear waste repository: EOS, v. 66, p. 1153.

Siedlecka, A., 1976, Silicified Precambrian evaporite nodules from northern Norway; a preliminary report: Sedimentary Geology, v. 16, p. 161–175.

Siefke, J. W., 1991, The Boron Open Pit Mine at the Kramer Borate Deposit, in M. A. McKibben, ed., The Diversity of Mineral and Energy Resources of Southern California, SEG Guidebook Series, v. 12, p. 4–15.

Sigalevich, P., and Y. Cohen, 2000, Oxygen dependent growth of the sulphate-reducing bacterium *Desulfovibrio oxyclinae* in coculture with *Marinobacter sp. strain MB* in a aerated sulphate-depleted chemostat: Applied Environmental Microbiology, v. 66, p. 5019–5023.

Sighinolfi, G. P., B. I. Kronberg, C. Gorgoni, and W. S. Fyfe, 1980, Geochemistry and genesis of sulphide-anhydrite-bearing Archean carbonate rocks from Bahia (Brazil): Chemical Geology, v. 29, p. 323–331.

Sillitoe, R., and H. McKee, 1996, Age of supergene oxidation and enrichment in the Chilean porphyry copper province: Economic Geology, v. 91, p. 164–179.

Sillitoe, R. H., 2003, Iron oxide-copper-gold deposits: an Andean view: Mineralium Deposita, v. 38, p. 787–812.

Sillitoe, R. H., 2005, Supergene oxidized and enriched porphyry copper and related deposits: Society of Economic Geologists, Economic Geology 100th Anniversary Volume, p. 723–768.

Sillitoe, R. H., and D. R. Burrows, 2002, New field evidence bearing on the origin of the El Laco Magnetite deposit, Northern Chile: Economic Geology, v. 97, p. 1101–1109.

Simeonova, A. P., and R. P. Iasky, 2005, Seismic mapping, salt deformation, and hydrocarbon potential of the central western Officer Basin, Western Basin: Geological Survey of Western Australia -Report 98, 50 pp.

Simkiss, K., 1977, Biomineralization and detoxification: Calcified Tissue Research, v. 24, p. 199–200.

Simkiss, K., 1989, Biomineralisation in the context of geological time: Royal Society of Edinburgh Transactions, Earth Sciences, v. 80, p. 193–199.

Simmons, R. E., 1995, Population declines, viable breeding areas and management options for flamingos in southern Africa: Conservation Biology, v. 10, p. 504–514.

Simon, A. C., M. R. Frank, T. Pettke, P. A. Candela, P. M. Piccoli, and C. A. Heinrich, 2005, Gold partitioning in meltvapor-brine systems: Geochimica et Cosmochimica Acta, v. 69, p. 3321–3335.

Simoneit, B. R. T., 1991, Hydrothermal Effects on Recent Diatomaceous Sediments in Guaymas Basin--Generation, Migration, and Deposition of Petroleum: Chapter 38: Part VI. Hydrothermal Processes: American Association Petroleum Geologists – Special Volume, v. 47, p. 793–825.

Simoneit, B. R. T., 1994, Organic matter alteration and fluid migration in hydrothermal systems, in J. Parnell, ed., Geofluids: Origin, Migration and Evolution of fluids in Sedimentary Basins, Geological Society London, Special Publication No. 78, p. 261–274.

Simoneit, B. R. T., T. A. T. Aboul-Kassim, and J. J. Tiercelin, 2000, Hydrothermal petroleum from lacustrine sedimentary organic matter in the East African Rift: Applied Geochemistry, v. 15, p. 355–368.

Simoneit, B. R. T., R. P. Philp, P. D. Jenden, and E. M. Galimol, 1984, Organic geochemistry of Deep Sea Drilling Project sediments from the Gulf of California-Hydrothermal effects on unconsolidated diatom ooze: Organic Geochemistry, v. 7, p. 173–205.

Simpson, A. G. B., and A. J. Roger, 2004, The real 'kingdoms' of eukaryotes: Current Biology, v. 14, p. R693–696.

Simpson, E. L., and K. A. Eriksson, 1993, Thin eolianites interbedded within a fluvial and marine succession: early Proterozoic Whitworth Formation, Mount Isa Inlier, Australia: Sedimentary Geology, v. 87, p. 39–62.

Simpson, F., 1988, Solution-generated collapse (SGC) structures associated with bedded evaporites; significance to base-metal and hydrocarbon localization: Geoscience Canada, v. 15, p. 89–93.

Singer, A., 1979, Palygorskite in sediments: detrital, diagenetic or neoformed – A critical review: Geologische Rundschau, v. 68, p. 996–1008.

Singer, A., K. Stahr, and M. Zarei, 1998, Characteristics and origin of sepiolite (Meerschaum) from central Somalia: Clay Minerals, v. 33, p. 349–362.

Singewald, J. T., and E. W. Berry, 1922, The geology of the Corocoro copper district of Bolivia: Johns Hopkins University studies in geology -- No. 1. 117 p.

Singh, S. P., and B. P. Singh, 2010, Geothermal evolution of the evaporite-bearing sequences of the Lesser Himalaya, India: International Journal of Earth Sciences, v. 99, p. 101–108.

Sinninghe Damste, J. S., J. Kenig, M. P. Koopmans, J. Koster, S. Schouten, J. M. Hayes, and J. W. De Leeuw, 1995, Evidence for gammacerane as an indicator of water column stratification: Geochimica et Cosmochimica, v. 59, p. 1895–1900.

Sinninghe Damsté, J. S., W. I. C. Rijpstra, J. W. de Leeuw, and P. A. Schenck, 1989, The occurrence and identification of series of organic sulphur compounds in oils and sediment extracts: II. Their presence in samples from hypersaline and non-hyper-saline palaeoenvironments and possible application as source, palaeoenvironmental and maturity indicators: Geochimica et Cosmochimica Acta, v. 53, p. 1323–1341.

Sissakian, V., N. Al-Ansari, and S. Knutsson, 2014, Karstification Effect on the Stability of Mosul Dam and Its Assessment, North Iraq. Engineering and Mining Journal, v. 6, p. 84–92.

Skippen, G., and V. Trommsdorff, 1986, The influence of NaCl and KCl on phase relations in metamorphosed carbonate rocks: American Journal of Science, v. 286, p. 81–104.

Skirrow, R. G., 1999, Proterozoic Cu-Au-Fe mineral systems in Australia: Filtering key components in exploration models, in C. J. Stanley, ed., Mineral deposits: Processes to processing: Rotterdam, Balkema, p. 1361–1364.

Slack, J. F., 1993, Descriptive and grade-tonnage models for Besshi-type massive sulphide deposits: Geological Association of Canada Special Paper, v. 40, p. 343–371.

Slack, J. F., M. R. Palmer, and B. P. J. Stevens, 1989, Boron isotope evidence for the involvement of non-marine evaporites in the origin of the Broken Hill ore deposits: Nature, v. 342, p. 913–916.

Slack, J. F., M. R. Palmer, B. P. J. Stevens, and R. G. Barnes, 1993, Origin and significance of tourmaline-rich rocks in the Broken-Hill District, Australia: Economic Geology, v. 88, p. 505–541.

Slater, B. E., and L. B. Smith Jr., 2012, Outcrop analog for Trenton-Black River hydrothermal dolomite reservoirs, Mohawk Valley, New York: Bulletin American Association Petroleum Geologists, v. 96, p. 1369–1388.

Sloss, L. L., 1953, The significance of evaporites: Journal of Sedimentary Petrology, v. 23, p. 143–161.

Slowakiewicz, M., and Z. Mikolajewski, 2009, Sequence stratigraphy of the Upper Permian Zechstein Main Dolomite carbonates in Western Poland: A new approach: Journal of Petroleum Geology, v. 32, p. 215–233.

Smirnov, V. I., 1977, Ore deposits of the U.S.S.R., Volumes I and III: London, Pitman Press, 491 p.

Smith, D. B., 1971, Possible displacive halite in the Permian Upper Evaporite Group of Northeast Yorkshire: Sedimentology, v. 17, p. 221–232.

Smith, D. B., 1972, Foundered strata, collapse breccias and subsidence features of the English Zechstein, in G. Richter-Bernberg, ed., Geology of saline deposits: Paris, UNESCO, p. 255–269.

Smith, D. B., 1996, Deformation in the Late Permian Boulby Halite (EZ3Na) in Teesside, NE England, in G. I. Alsop, D. J. Blundell, and I. Davison, eds., Salt tectonics: London, United Kingdom, Geological Society of London special Publication, v. 100, p. 77–88.

Smith, D. B., and A. Crosby, 1979, The regional and stratigraphical context of Zechstein 3 and 4 potash deposits in the British sector of the southern North Sea and adjoining land areas: Economic Geology, v. 74, p. 397–408.

Smith, D. G., and J. R. Pullen, 1967, Hummingbird structure of southeast Saskatchewan: Canadian Petroleum Geology Bulletin, v. 15, p. 468–482.

Smith, E. B., K. M. Scott, E. R. Nix, C. Korte, and C. R. Fisher, 2000, Growth and Condition of Seep Mussels (*Bathymodiolus childressi*) at a Gulf of Mexico Brine Pool: Ecology, v. 81, p. 2392–2403.

Smith, G. I., 1979, Subsurface stratigraphy and geochemistry of Late Quaternary evaporites, Searles Lake, California: US Geological Survey, Professional Paper, v. 1043, p. 130 pp.

Smith, G. I., and I. Friedman, 1998, Trona crystallisation processes-Observations at Owens Lake, California, 1970–1977, in J. R. Dyni, and R. W. Jones, eds., Proceedings of the First International Soda Ash Conference; Volume II, v. 40, Wyoming State Geological Survey Public Information Circular, p. 49–56.

Smith, L., 2006, Origin and reservoir characteristics of Upper Ordovician Trenton-Black River hydrothermal dolomite reservoirs in New York, U.S.A.: Bulletin American Association Petroleum Geologists, v. 90, p. 1691–1711.

Smith, M., and W. Chengyu, 2002, Geology and Genesis of the Bayan Obo Fe-Ree-Nb Deposit: A Review, in T. M. Porter, ed., Hydrothermal Iron Oxide Copper-Gold and Related Deposits: A Global Perspective, v. 1, PGC Publishing, Adelaide, p. 271–281.

Smith, M. E., A. R. Carroll, and B. S. Singer, 2008, Synoptic reconstruction of a major ancient lake system: Eocene Green River Formation, western United States: Geological Society of America Bulletin, v. 120, p. 54–84.

Smith, M. E., B. Singer, and A. Carroll, 2003, Ar-40/Ar-39 geochronology of the Eocene Green River Formation,Wyoming: Geological Society of America Bulletin, v. 115, p. 549–565.

Smith, M. P., S. A. Gleeson, and B. W. D. Yardley, 2013, Hydrothermal fluid evolution and metal transport in the Kiruna District, Sweden: Contrasting metal behaviour in aqueous and aqueous-carbonic brines: Geochimica et Cosmochimica Acta, v. 102, p. 89–112.

Smith, R. M. H., and T. R. Mason, 1998, Sedimentary environments and trace fossils of Tertiary oasis deposits in the central Namib desert, Namibia: Palaios, v. 13, p. 547–559.

Smoot, J. P., 1983, Depositional subenvironments in an arid closed basin; the Wilkins Peak Member of the Green River Formation (Eocene), Wyoming, USA: Sedimentology, v. 30, p. 801–827.

Smoot, J. P., 1991, Sedimentary facies and depositional environments of early Mesozoic Newark Group, Eastern North America: Paleogeography, Paleogeology and Paleoclimatology, v. 84, p. 369–423.

Smoot, J. P., and T. K. Lowenstein, 1991, Depositional environments of non-marine evaporites, in J. D. Melvin, ed., Evaporites, petroleum and mineral resources, v. 50, Elsevier Science, Developments in Sedimentology, p. 189–347.

Sneh, A., 1979, Fan deltas along the Dead Sea rift: Journal Sedimentary Petrology, v. 49, p. 541–552.

Sneider, R. M., 1995, Evaluation of Seals and Flow Barriers: Notes of a short course, sponsored by the New Orleans Geological Society, 160 p.

Sneider, R. M., J. S. Sneider, G. W. Bolger, and J. W. Neasham, 1997, Comparison of Seal Capacity Determinations: Conventional Cores

vs. Cuttings, in R. C. Surdam, ed., American Association Petroleum Geologists Memoir 67: Seals, Traps, and the Petroleum System.

Snyder, F. C., and J. A. Nugent, 1995, Teak – Testing a subsalt hydrocarbon trap geometry, South Timbalier Block 260, Gulf of Mexico: Proceedings of GCCSEPM Foundation 16th Annual Research Conference, Salt Sediment and Hydrocarbons, Dec 3–6, 1995, p. 257–267.

Sokolov, D. S., 1962, Osnovnyye usloviya razvitiya karsta: Moscow, Gosgeoltekhizdat, 322 p.

Solari, L. A., J. D. Keppie, F. Ortega-Gutiérrez, K. L. Cameron, R. Lopez, and W. E. Hames, 2003, 990 Ma and 1,100 Ma Grenvillian tectonothermal events in the northern Oaxacan Complex, southern Mexico: Roots of an orogen: Tectonophysics, v. 365, p. 257–282.

Sommaruga, A., 1999, Decollement tectonics in the Jura foreland fold-and-thrust belt: Marine and Petroleum Geology, v. 16, p. 111–134.

Sonnenfeld, P., 1985, Evaporites as oil and gas source rocks: Journal of Petroleum Geology, v. 8, p. 253–271.

Sonnenfeld, P., 1995, The color of rock salt; a review: Sedimentary Geology, v. 94, p. 267–276.

Sonnenfeld, P., and I. S. Al-Aasm, 1991, The Salina Group evaporites in the Michigan Basin, in P. A. Catacosinos, and P. A. Daniels, Jr., eds., Early sedimentary evolution of the Michigan Basin: Boulder, CO, Geological Society of America, Special Paper v. 256, p. 139–153.

Soriano, M. A., and J. L. Simon, 1995, Alluvial dolines in the central Ebro Basin, Spain – A spatial and developmental hazard analysis: Geomorphology, v. 11, p. 295–309.

Souissi, F., J. L. Dandurand, and J. P. Fortune, 1997, Thermal evolution of fluids during fluorite deposition in the Zaghouan Province, northeastern Tunisia: Mineralium Deposita, v. 32, p. 257–270.

Soulié-Marsche, I., 2008, Charophytes, indicators for low salinity phases in North African sebkhet: Journal of African Earth Sciences, v. 51, p. 69–76.

Southgate, P. N., 1982, Cambrian skeletal halite crystals and experimental analogues: Sedimentology, v. 29, p. 391–407.

Southgate, P. N., 1991, A sedimentological model for the Loves Creek Member of the Late Proterozoic Bitter Springs Formation, Australia: Bureau Mineral Resources (BMR), Geology and Geophysics, Bulletin, v. 236, p. 113–126.

Southgate, P. N., I. B. Lambert, T. H. Donnelly, R. Henry, H. Etminan, and G. Weste, 1989, Depositional environments and diagenesis in Lake Parakeelya: a Cambrian alkaline playa from the Officer Basin, South Australia: Sedimentology, v. 36, p. 1091–1112.

Southgate, P. N., N. L. Neumann, and G. M. Gibson, 2013, Depositional systems in the Mt Isa Inlier from 1800 Ma to 1640 Ma: Implications for Zn-Pb-Ag mineralisation:Australian Journal of Earth Sciences, v. 60, p. 157–173.

Spangenberg, J., L. Fontbote, Z. D. Sharp, and J. Hunziker, 1996, Carbon and oxygen isotope study of hydrothermal carbonates in the zinc-lead deposits of the San Vicente district, Central Peru – Quantitative modeling of mixing processes and CO_2 degassing: Chemical Geology, v. 133, p. 289–315.

Spathopoulos, F., 1996, An insight on salt tectonics in the Angola Basin, South Atlantic, in G. I. Alsop, D. J. Blundell, and I. Davison, eds., Salt tectonics, Geological Society, London; Special Publication, v. 100, p. 153–174.

Spear, F. S., 1993, Metamorphic phases equilibria and pressure-temperature-time paths, Mineralogical Society of America, 799 p.

Spear, N., H. D. Holland, J. Garcia-Veígas, T. K. Lowenstein, R. Giegengack, and H. Peters, 2014, Analyses of fluid inclusions in Neoproterozoic marine halite provide oldest measurement of seawater chemistry: Geology, v. 42, p. 103–106.

Speczik, S., 1995, The Kupferschiefer mineralization of Central Europe: new aspects and major areas of future research: Ore Geology Reviews, v. 9, p. 411–426.

Speed, R. C., 1974, Evaporite-Carbonate Rocks of the Jurassic Lovelock Formation, West Humboldt Range, Nevada: Geological Society America Bulletin, v. 85, p. 105–118.

Speed, R. C., 1975, Carbonate breccia (rauhwacke) nappes of the Carson Sink region, Nevada: Geological Society America Bulletin, v. 86, p. 473–486.

Speed, R. C., and R. N. Clayton, 1975, Origin of marble by replacement of gypsum in carbonate breccia nappes, Carson Sink region, Nevada: Journal of Geology, v. 83, p. 223–237.

Spencer, J. E., P. J. Patchett, P. A. Pearthree, P. K. House, A. M. Sarna-Wojcicki, E. Wan, J. A. Roskowski, and J. E. Faulds, 2013, Review and analysis of the age and origin of the Pliocene Bouse Formation, lower Colorado River Valley, southwestern USA: Geosphere, v. 9, p. 444–459.

Spencer, R. J., 1983, The geochemical evolution of Great Salt Lake, Utah: Doctoral thesis, Johns Hopkins University.

Spencer, R. J., H. P. Eugster, and B. F. Jones, 1985b, Geochemistry of Great Salt Lake, Utah II: Pleistocene-Holocene evolution: Geochimica et Cosmochimica Acta, v. 49, p. 739–747.

Spencer, R. J., H. P. Eugster, B. F. Jones, and S. L. Rettig, 1985a, Geochemistry of Great Salt Lake, Utah I: Hydrochemistry since 1850: Geochimica et Cosmochimica Acta, v. 49, p. 727–737.

Spencer, R. J., and L. A. Hardie, 1990, Control of seawater composition by mixing of river waters and mid-ocean ridge hydrothermal brines, in R. J. Spencer, and I. M. Chou, eds., Fluid Mineral Interactions: A Tribute to H. P. Eugster, v. 2: San Antonio, Geochem. Soc. Spec. Publ., p. 409–419.

Spencer, R. J., and T. K. Lowenstein, 1990, Evaporites: Geoscience Canada. Reprint Series, v. 4, p. 141–164.

Spiers, C. J., P. M. T. M. Schutjens, R. H. Brzesowsky, C. J. Peach, J. L. Liezenberg, and H. J. Zwart, 1990, Experimental determination of constitutive parameters governing creep of rocksalt by pressure solution, in R. J. Knipe, and E. H. Rutter, eds., Deformation mechanisms, rheology and tectonics., Geological Society Special Publication, v. 54, p. 215–227.

Spindler, W. M., 1977, Structure and stratigraphy of a small Plio-Pleistocene depocenter, Louisiana continental shelf: Gulf Coast Assoc. Geol. Soc. Trans, v. 27, p. 180–196.

Spiridonov, E. M., 2010, Ore-magmatic systems of the Noril'sk ore field: Russian Geology and Geophysics, v. 51, p. 1059–1077.

Spötl, C., 1989a, The Alpine Haselgebirge Formation, Northern Calcareous Alps (Austria): Permo-Scythian evaporites in an alpine thrust system: Sedimentary Geology, v. 65, p. 113–125.

Spötl, C., 1989b, Complex zoning and resorption in breunnerite from Hall in Tyrol, Austria: Evidence from back-scattered electron microscopy: Mineralogy and Petrology, v. 40, p. 225–233.

Spötl, C., 1992, Clay minerals in Upper Permian evaporites from the northern Calcareous Alps (Alpine Haselgebirge Formation, Austria): European Journal of Mineralogy, v. 4, p. 1407–1419.

Spötl, C., and S. Burns, 1994, Magnesite diagenesis in redbeds – A case study from the Permian of the Northern Calcareous Alps (Tyrol, Austria): Sedimentology, v. 41, p. 543–565.

Spötl, C., and C. Hasenhüttl, 1998, Thermal history of the evaporitic Haselgebirge mélange in the Northern Calcareous Alps (Austria): Geologische Rundschau, v. 87, p. 449–460.

Spötl, C., F. J. Longstaffe, K. Ramseyer, M. J. Kunk, and R. Wiesheu, 1998, Fluid-rock reactions in an evaporitic melange, Permian Haselgebirge, Austrian Alps: Sedimentology, v. 45, p. 1019–1044.

Spötl, C., and E. Pak, 1996, A strontium and sulfur isotopic study of Permo-Triassic evaporites in the Northern Calcareous Alps, Austria: Chemical Geology, v. 131, p. 219–234.

Sprynskyy, M., M. Lebedynets, and A. Sadurski, 2009, Gypsum karst intensification as a consequence of sulphur mining activity (Jaziv field, Western Ukraine): Environmental Geology, v. 57, p. 173–181.

St. John, J. W., and D. E. Eby, 1978, Peritidal carbonates and evidence for vanished evaporites in the Lower Ordovician Cool Creek

Formation; Arbuckle Mountains, Oklahoma: Gulf Coast Association of Geological Societies Transactions, v. 28, p. 589–599.
St. Peter, C., 2006, Geological relationship between the Cocagne Subbasin and Indian Mountain Deformed Zone, Maritimes Basin, New Brunswick.: New Brunswick Department of Natural Resources; Minerals, Policy, and Planning Division, Mineral Resource Report, v. 2006–3, p. 103–183.
Stafford, K. W., R. Nance, L. Rosales-Lagarde, and P. J. Boston, 2008a, Epigene and Hypogene Gypsum karst manifestations of the Castile formation: Eddy County, new Mexico and Culbesron County, Texas, USA: International Journal of Speleology, v. 37, p. 83–98.
Stafford, K. W., L. Rosales-Lagarde, and P. J. Boston, 2008b, Castile evaporite karst potential map of the Gypsum Plain, Eddy County, New Mexico and Culberson County, Texas: A GIS methodological comparison., v. 70, no. 1, p. 35–46.: Journal of Cave and Karst Studies, v. 70, p. 35–46.
Stamatakis, M. G., 1995, Occurrence and genesis of huntite-hydromagnesite assemblages, Kozani, Greece – important new white fillers and extenders: Transactions – Institution of Mining & Metallurgy, Section B, v. 104, p. 179–186.
Stan-Lotter, H., 2011, Halobacteria – Halophiles, in J. Reitner, and V. Thiel, eds., Encyclopedia of Geobiology: Dordrecht, Netherlands, Springer, p. 437–441.
Stanczuk, D. T., F. Tatom, W. Tolbert, J. Simmons, J. Vancil, R. L. Thoms, and C. G. Smith, 1976, The mechanisms and ecological impacts of the collapse of salt dome oil storage caverns: Project No. 5-210-00-567-04, Science Applications Inc. McLean Virginia.
Stanislavsky, E., and H. Gvirtzman, 1999, Basin-scale migration of continental-rift brines: Paleohydrologic modeling of the Dead Sea basin: Geology, v. 27, p. 791–794.
Stanley, D. J., and H. Sheng, 1979, Trona in Nile Cone Late Quaternary sediments: Probable redepositional origin: Marine Geology, v. 31, p. M21–M28.
Stanton Jr, R. J., 1966, The solution brecciation process: Geological Society of America Bulletin, v. 77, p. 843–847.
Stanworth, C. W., and J. P. N. Badham, 1984, Lower Proterozoic red beds, evaporites and secondary sedimentary uranium deposits from the East Arm, Great Slave Lake, Canada: Journal of the Geological Society, v. 141, p. 235–242.
Starinsky, A., and A. Katz, 2003, The formation of natural cryogenic brines: Geochimica et Cosmochimica Acta, v. 67, p. 1475–1484.
Stasiuk, L. D., 1994, Oil-prone alginite macerals from organic-rich Mesozoic and Paleozoic strata, Saskatchewan, Canada: Marine & Petroleum Geology, v. 11, p. 208–218.
Steen, A. K., J. A. Nunn, and J. S. Hanor, 2011, Indications of formation water flow and compartmentalization on the flank of a salt structure derived from salinity and seismic data: Geofluids, v. 11, p. 199–208.
Steenge, W. D., 1979, Solution mining at controlled production rate, Dutch patent, 7,905,287.
Stein, M., A. Starinsky, A. Katz, S. L. Goldstein, M. Machlus, and A. Schramm, 1997, Strontium isotopic, chemical, and sedimentological evidence for the evolution of Lake Lisan and the Dead Sea: Geochimica et Cosmochimica Acta, v. 61, p. 3975–3992.
Steinhauff, D. M., A. E. Gregory, and C. J. Heine, 2008, Eocene Rus anhydrite; limitations on exploration, production, and seismic interpretation (abs.): GeoArabia (Manama), v. 13, p. 237.
Steinhauff, D. M., C. J. Heine, and A. E. Gregory, 2007, The Eocene Rus Anhydrite: Important Arabian Seismic Reflector and Recorder of Cenozoic History: American Association Petroleum Geologists Search and Discovery Article #50480 © 2007 American Association Petroleum Geologists and American Association Petroleum Geologists European Region Conference, Athens, Greece.
Steinhoff, I., and C. Strohmenger, 1999, Facies differentiation and sequence stratigraphy in ancient evaporite basins – An example from the basal Zechstein (Upper Permian of Germany): Carbonates & Evaporites, v. 14, p. 146–181.
Steinhorn, I., 1983, In situ salt precipitation at the Dead Sea: Limnology and Oceanography, v. 28, p. 580–583.
Steinhorn, I., and J. R. Gat, 1983, The Dead Sea: Scientific American, v. 249, p. 102–109.
Steinmann, M., P. Stille, W. Bernotat, and B. Knipping, 1999, The corrosion of basaltic dykes in evaporites: Ar-Sr-Nd isotope and rare earth elements evidence: Chemical Geology, v. 153, p. 259–279.
Stengele, F., and W. Smykatz-Kloss, 1995, Mineralogical and geochemical study of Holocene sebkha sediments in southeastern Tunisia: Chemie der Erde-Geochemistry, v. 55, p. 241–256.
Stenger, B., T. Pham, N. Al-Araleg, and P. Lawrence, 2003, Tilted original oil/water contact in the Arab-D reservoir, Ghawar field, Saudi Arabia: GeoArabia, v. 8, p. 9–42.
Stenson, R. E., 1990, The morphometry and spatial distribution of surface depressions in gypsum, with examples from Nova Scotia, Newfoundland and Manitoba: MSc thesis, McMaster University, 134 p.
Stenson, R. E., and D. C. Ford, 1993, Rillenkarren on gypsum in Nova Scotia: Geographie Physique et Quaternaire, v. 47, p. 239–243.
Stephens, A. E., and J. H. Dilles, 2008, The Lights Creek District copper deposits; porphyry copper or evaporitic-source copper iron-oxide mineralization?: Abstracts with Programs – Geological Society of America, v. 40, p. 96.
Stephenson, R. A., J. T. van Berkel, and S. A. P. L. Cloetingh, 1992, Relation between salt diapirism and the tectonic history of the Sverdrup Basin, Arctic Canada: Canadian Journal of Earth Sciences, v. 29, p. 2695–2705.
Stern, R., 2007, When and how did plate tectonics begin? Theoretical and empirical considerations: Chinese Science Bulletin, v. 52, p. 578–591.
Stern, R. J., T. Tsujimori, G. Harlow, and L. A. Groat, 2013, Plate tectonic gemstones: Geology, v. 41, p. 723–726.
Stevens, B. P. J., R. G. Barnes, R. E. Brown, W. J. Stroud, and I. L. Willis, 1988, The Willyama Supergroup in the Broken Hill and Euriowie blocks, New South Wales: Precambrian Research, v. 40–41, p. 297–327.
Stevens, L. R., M. Djamali, V. Andrieu-Ponel, and J.-L. Beaulieu, 2012, Hydroclimatic variations over the last two glacial/interglacial cycles at Lake Urmia, Iran: Journal of Paleolimnology, v. 47, p. 645–660.
Stewart, A. J., and D. H. Blake, 1992, Detailed studies of the Mount Isa Inlier: Australian Geological Survey Organisation, Bulletin, v. 243.
Stewart, A. J., R. Q. Oaks Jr, J. A. Deckelman, and R. D. Shaw, 1991, 'Mesothrust' versus 'megathrust' interpretations of the structure of the northeastern Amadeus Basin, central Australia: Bulletin – Bureau of Mineral Resources, Geology &Geophysics, Australia, v. 236, p. 361–383.
Stewart, F. H., 1965, The mineralogy of the British Permian evaporites: Mineralogical Magazine, v. 34, p. 460–470.
Stewart, F. H., 1968, Geochemistry of marine evaporite deposits: Geological Society America Special Paper, v. 88, p. 539–540.
Stewart, J. I., 1991, Proterozoic geology and gold geochemistry of the Marimo Basin area, Cloncurry, NW Queensland: Masters thesis, James Cook University of Queensland.
Stewart, J. I., 1994, The role of evaporitic-shale sediment packages in the localisation of copper-gold deposits: Copper Canyon area, Cloncurry: Australian mining looks north – the challenges and choices, p. 207–214.
Stewart, J. I., 1994, The role of evaporitic-shale sediment packages in the localisation of copper-gold deposits; Copper Canyon area, Cloncurry: Publication Series – Australasian Institute of Mining and Metallurgy, v. 5/94, p. 207–214.
Stewart, J. R., S. Aspinall, M. Beech, P. Fenberg, P. Hellyer, N. Larkin, S. W. Lokier, F. G. Marx, M. Meyer, R. Miller, P. S. Rainbow, J. D.

Taylor, J. E. Whittaker, K. Al-Mehsin, and C. J. Strohmenger, 2011, Biotically constrained palaeoenvironmental conditions of a mid-Holocene intertidal lagoon on the southern shore of the Arabian Gulf: evidence associated with a whale skeleton at Musaffah, Abu Dhabi, UAE: Quaternary Science Reviews, v. 30, p. 3675–3690.

Stewart, S. A., 1999, Seismic interpretation of circular geological structures: Petroleum Geoscience, v. 5, p. 273–285.

Stewart, S. A., and M. P. Coward, 1995, Synthesis of salt tectonics in the southern North Sea, UK: Marine & Petroleum Geology, v. 12, p. 457–475.

Stewart, S. A., A. H. Ruffell, and M. J. Harvey, 1997, Relationship between basement-linked and gravity driven fault systems in the UKCS salt basins: Marine & Petroleum Geology, v. 14, p. 579–602.

Stieljes, L., 1973, Evolution tectonique récente du rift d'Asal: Review Geographie Physical Geologie Dynamique, v. 15, p. 425–436.

Stiller, M., and Y. C. Chung, 1984, Radium in the Dead Sea: A possible tracer for the duration of meromixis: Limnology and Oceanography, v. 29, p. 574–586.

Stiller, M., A. Nissenbaum, R. S. Kaufmann, and A. Long, 1998, Cl-37 in the Dead Sea system – preliminary results: Applied Geochemistry, v. 13, p. 953–960.

Stiller, M., J. M. Rosenbaum, and A. Nishri, 2009, The origin of brines underlying Lake Kinneret: Chemical Geology, v. 262, p. 293–309.

Stiller, M., and L. Sigg, 1990, Heavy metals in the Dead Sea and their coprecipitation with halite: Hydrobiologia, v. 197, p. 23–33.

Stine, S., 1990, Late Holocene fluctuations of Mono Lake, eastern California: Palaeogeography Palaeoclimatology Palaeoecology, v. 78, p. 333–381.

Stivaletta, N., 2011, Physicochemical Conditions and Microbial Diversity Associated with the Evaporite Deposits in the Laguna de la Piedra (Salar de Atacama, Chile): Geomicrobiology journal, v. 28, p. 83.

Stivaletta, N., and R. Barbieri, 2009, Endolithic microorganisms from spring mound evaporite deposits (southern Tunisia): Journal of Arid Environments, v. 73, p. 33–39.

Stivaletta, N., R. Barbieri, C. Picard, and M. Bosco, 2009, Astrobiological significance of the sabkha life and environments of southern Tunisia: Planetary and Space Science, v. 57, p. 597–605.

Stockhecke, M., M. Sturm, I. Brunner, H.-U. Schmincke, M. Sumita, R. Kipfer, D. Cukur, O. Kwiecien, and F. S. Anselmetti, 2014, Sedimentary evolution and environmental history of Lake Van (Turkey) over the past 600 000 years: Sedimentology, v. 61, p. 1830–1861.

Stoessell, R. K., and A. B. Carpenter, 1986, Stoichiometric saturation tests of NaCl1-xBrx and KCl1-xBrx: Geochimica et Cosmochimica Acta, v. 50, p. 1465–1474.

Stoessell, R. K., and C. H. Moore, 1983, Chemical constraints and origins of four groups of Gulf Coast reservoir fluids: Bulletin American Association Petroleum Geologists, v. 67, p. 896–906.

Stokes, W. L., 1968, Multiple parallel truncation bedding planes — a feature of wind-deposited sandstone formations: Journal of Sedimentary Petrology, v. 38, p. 510–515.

Stollhofen, H., S. Gerschutz, I. G. Stanistreet, and V. Lorenz, 1998, Tectonic and volcanic controls on Early Jurassic rift-valley lake deposition during emplacement of Karoo flood basalts, southern Namibia: Palaeogeography Palaeoclimatology Palaeoecology, v. 140, p. 185 ff.

Stovba, S. M., and R. A. Stephenson, 2003, Style and timing of salt tectonics in the Dniepr-Donets Basin (Ukraine): implications for triggering and driving mechanisms of salt movement in sedimentary basins: Marine and Petroleum Geology, v. 19, p. 1169–1189.

Strakhov, N. M., 1970, Principles of Lithogenesis (Reviews of USSR Sodium Sulfate Deposits): New York, Plenum Publishing.

Strauss, H., 1993, The sulfur isotopic record of Precambrian sulfates; new data and a critical evaluation of the existing record: Precambrian Research, v. 63, p. 225–246.

Strauss, H., 1997, The isotopic composition of sedimentary sulfur through time: Palaeogeography Palaeoclimatology Palaeoecology, v. 132, p. 97–118.

Strauss, H., D. M. Banerjee, and V. Kumar, 2001, The sulfur isotopic composition of Neoproterozoic to early Cambrian seawater – evidence from the cyclic Hanseran evaporites, NW India: Chemical Geology, v. 175, p. 17–28.

Strecker, M. R., R. N. Alonso, B. Bookhagen, B. Carrapa, G. E. Hilley, E. R. Sobel, and M. H. Trauth, 2007, Tectonics and climate of the southern central Andes, Annual Review of Earth and Planetary Sciences, p. 747–787.

Strohmenger, C., M. Antonini, G. Jager, K. Rockenbauch, and C. Strauss, 1996b, Zechstein 2 Carbonate reservoir facies distribution in relation to Zechstein sequence stratigraphy (upper Permain, northwest Germany) – an integrated approach: Bulletin des Centres de Recherches Exploration-Production Elf Aquitaine, v. 20, p. 1–35.

Strohmenger, C., E. Voigt, and J. Zimdars, 1996a, Sequence stratigraphy and cyclic development of Basal Zechstein carbonate-evaporite deposits with emphasis on Zechstein 2 off-platform carbonates (Upper Permian, Northeast Germany): Sedimentary Geology, v. 102, p. 33–54.

Strohmenger, C. J., R. H. S. Alway, R. W. Broomhall, R. F. Hulstrand, A. Al-Mansoori, A. A. Abdalla, and A. Al-Aidarous, 2002, Sequence stratigraphy of the Khuff Formation comparing subsurface and outcrop data (Arabian plate, U.A.E.): Society of Petroleum Engineers, SPE Paper 78535.

Strohmenger, C. J., H. Shebl, A. Al-Mansoori, K. Al-Mehsin, O. Al-Jeelani, I. Al-Hosani, A. Al-Shamry, and S. Al-Baker, 2011, Facies stacking patterns in a modern arid environment: a case study of the Abu Dhabi sabkha in the vicinity of Al- Qanatir Island, United Arab Emirates, in A. Alsharhan, and S. C. Kendall, C. G, eds., Quaternary Carbonate and Evaporite Sedimentary Facies and Their Ancient Analogues, v. 43, International Association of Sedimentologists, Special Publication, p. 149–182.

Strozyk, F., H. Van Gent, J. L. Urai, and P. A. Kukla, 2012, 3D seismic study of complex intra-salt deformation: An example from the Upper Permian Zechstein 3 stringer, western Dutch offshore: Geological Society, London, Special Publications, v. 363, p. 489–501.

Stueber, A. M., A. H. Saller, and H. Ishida, 1998, Origin, migration, and mixing of brines in the Permian Basin: geochemical evidence from the eastern Central Basin Platform, Texas:American Association of Petroleum Geologists Bulletin, v. 82, p. 1652–1672.

Sturz, A. A., A. E. Sturdivan, R. N. Leif, B. R. T. Simoneit, and J. Gieskes, 1996, Evidence for retrograde hydrothermal reactions in near surface sediments of the Guaymas Basin, Gulf of California: Applied Geochemistry, v. 11, p. 645 ff.

Sugitani, K., K. Mimura, K. Suzuki, K. Nagamine, and R. Sugisaki, 2003, Stratigraphy and sedimentary petrology of an Archean volcanic-sedimentary succession at Mt. Goldsworthy in the Pilbara Block, Western Australia: implications of evaporite (nahcolite) and barite deposition: Precambrian Research, v. 120, p. 55–79.

Sukanta, U., 1993, Sedimentology, sequence stratigraphy and palaeogeography of Marinoan sediments in the eastern Officer Basin, South Australia: Doctoral thesis, Flinders University (South Australia), Adelaide, 195 p.

Sullivan, L. A., and A. J. Koppi, 1993, Barite pseudomorphs after lenticular gypsum in a buried soil from central Australia: Australian Journal of Soil Research, v. 31, p. 393–396.

Sullivan, M. D., R. S. Haszeldine, A. J. Boyce, G. Rogers, and A. E. Fallick, 1994, Late anhydrite cements mark basin inversion; isotopic and formation water evidence, Rotliegend Sandstone, North Sea: Marine and Petroleum Geology, v. 11, p. 46–54.

Summons, R. E., J. M. Hope, R. Swart, and M. R. Walter, 2008, Origin of Nama Basin bitumen seeps: Petroleum derived from a Permian lacustrine source rock traversing southwestern Gondwana: Organic Geochemistry, v. 39, p. 589–607.

Summons, R. E., L. L. Jahnke, J. M. Hope, and G. A. Logan, 1999, 2-methylhopanoids as biomarkers for cyanobacterial oxygenic photosynthesis: Nature, v. 400, p. 554–557.

Summons, R. E., and T. G. Powell, 1987, Identification of arylisoprenoids in a source rock and crude oils: Biological markers for the green sulfur bacteria: Geochimica et Cosmochimica Acta, v. 51, p. 557–566.

Sumner, D. Y., and J. P. Grotzinger, 1996, Were kinetics of Archaean calcium carbonate precipitation related to oxygen concentration: Geology, v. 24, p. 119–122.

Sumner, D. Y., and J. P. Grotzinger, 2000, Late Archean Aragonite Precipitation: Petrography, Facies Associations, and Environmental Significance, in J. P. Grotzinger, and N. P. James, eds., Carbonate Sedimentation And Diagenesis In The Evolving Precambrian World, v. 67: Tulsa, SEPM Special Publication, p. 123–144.

Sumner, D. Y., and J. P. Grotzinger, 2004, Implications for Neoarchaean ocean chemistry from primary carbonate mineralogy of the Campbellrand Malmani Platform, South Africa: Sedimentology, v. 51, p. 1273–1299.

Sun, D., and B. Li, 1993, Origin of borates in the saline Lakes of China, Seventh International Symposium on Salt, v. 2, Elsevier, Amsterdam, p. 177–193.

Sun, H., 2007, Tourmalinites in Neoproterzoic Metaevaporitic Deposit of Duruchaus Formation, Damara Belt, Central Namibia: Doctoral thesis, Louisiana Stae University, New Orleans, 194 p.

Sun, S.-s., and N. C. Higgins, 1996, Neodymium and strontium isotope study of the Blue Tier Batholith, NE Tasmania, and its bearing on the origin of tin-bearing alkali feldspar granites: Ore Geology Reviews, v. 10, p. 339–365.

Sun, S. Q., 1992, Skeletal aragonite dissolution from hypersaline seawater: a hypothesis: Sedimentary Geology, v. 77, p. 249–257.

Sun, S. Q., 1995, Dolomite reservoirs; porosity evolution and reservoir characteristics: American Association of Petroleum Geologists Bulletin, v. 79, p. 186–204.

Sun, S. Q., and M. Esteban, 1994, Paleoclimatic controls on sedimentation, diagenesis, and reservoir quality – Lessons from Miocene carbonates: American Association Petroleum Geologists – Bulletin, v. 78, p. 519–543.

Sun, Y., and W. Püttmann, 1997, Metal accumulation during and after deposition of the Kupferschiefer from the Sangerhausen Basin, Germany: Applied Geochemistry, v. 12, p. 577–592.

Sun, Y., S. Xu, H. Lu, and P. Cuai, 2003, Source facies of the Paleozoic petroleum systems in the Tabei uplift, Tarim Basin, NW China: implications from aryl isoprenoids in crude oils: Organic Geochemistry, v. 34, p. 629–634.

Sun, Y. Z., W. Püttmann, and S. Speczik, 1995, Differences in the depositional environment of basal Zechstein in southwest Poland – Implications for base metal mineralization: Organic Geochemistry, v. 23, p. 819–835.

Suner, F., O. I. Ece, F. Coban, and F. Esenli, 2003, Occurrence and properties of natron in the Miocene lacustrine Beypazari basin, Turkey: Neues Jahrbuch Fur Mineralogie-Monatshefte, p. 31–48.

Supajanya, T., and M. C. Friederich, 1992, Salt tectonics of the Sakon Nakhon Basin, northeastern Thailand: Journal of Southeast Asian Earth Sciences, v. 7, p. 258–259.

Surdam, R. C., 1981, Zeolites in closed hydrologic systems, in F. A. Mumpton, ed., Mineralogy and Geology of Natural Zeolites, Mineralogical Society of America Reviews in Mineralogy, v. 4, p. 65–91.

Surdam, R. C., and H. P. Eugster, 1976, Mineral reactions in sedimentary deposits of Lake Magadi region, Kenya: Geological Society of America Bulletin, v. 87, p. 1739–1752.

Surdam, R. C., H. P. Eugster, and R. H. Mariner, 1972, Magadi-type chert in Jurassic and Eocene to Pleistocene rocks Wyoming: Geological Society America Bulletin, v. 83, p. 1739–1752.

Surdam, R. C., and R. A. Sheppard, 1978, Zeolites in saline alkaline lake deposits, in L. B. Sand, and F. A. Mumpton, eds., Natural Zeolites: Occurrence, properties, use: New York, Pergamon, p. 145–174.

Surdam, R. C., and C. A. Wolfbauer, 1975, Green River Formation, Wyoming: a playa lake complex: Geological Society of America Bulletin, v. 86, p. 335–345.

Susura, B. B., V. O. Glybovsky, and A. V. Kislitsin, 1986, Red-colored terrigenous sediments; specific copper-forming systems, in G. H. Friedrich, A. D. Genkin, A. J. Naldrett, J. D. Ridge, R. H. Sillitoe, and F. M. Vokes, eds., Geology and metallogeny of copper deposits; proceedings of the Copper symposium; 27th international geological congress, v. Special Publication of the Society for Geology Applied to Mineral Deposits, v. 4: Berlin, Springer-Verlag, p. 504–512.

Suwanich, P., 1986, Potash and Rock Salt in Thailand: Nonmetallic Minerals Bulletin No.2, Economic Geology Division, Department of Mineral Resources, Bangkok, Thailand.

Svendsen, J., H. Stollhofen, C. B. E. Krapf, and I. G. Stanistreet, 2003, Mass and hyperconcentrated flow deposits record dune damming and catastrophic breakthrough of ephemeral rivers, Skeleton Coast Erg, Namibia: Sedimentary Geology, v. 160, p. 7–31.

Svendsen, J. B., 2003, Parabolic halite dunes on the Salar de Uyuni, Bolivia: Sedimentary Geology, v. 155, p. 147–156.

Svengren, H., 2002, A study of the environmental conditions in Lake Nakuru, Kenya, using isotope dating and heavy metal analysis of sediments: Masters thesis, Dept. Structural Chemistry, University of Stockholm, Sweden.

Svenningsen, O. M., 1994, Tectonic significance of meta-evaporitic magnesite and scapolite deposits in the Seve-Nappes, Sarek Mountains, Swedish Caledonides: Tectonophysics, v. 231, p. 33–44.

Svenningsen, O. M., 1995, Extensional deformation along the Late Precambrian – Cambrian Baltoscandian passive margin: the Saektjåkkå Nappe, Swedish Caledonides: Geologische Rundschau, v. 84, p. 649–664.

Svenningsen, O. M., 2001, Onset of seafloor spreading in the Iapetus Ocean at 608 Ma: precise age of the Sarek Dyke Swarm, northern Swedish Caledonides: Precambrian Research, v. 110, p. 241–254.

Svensen, H., D. A. Karlsen, A. Sturz, K. Backer-Owe, D. A. Banks, and S. Planke, 2007, Processes controlling water and hydrocarbon composition in seeps from the Salton Sea geothermal system, California, USA: Geology, v. 35, p. 85–88.

Svensen, H., S. Planke, A. G. Polozov, N. Schmidbauer, F. Corfu, Y. Y. Podladchikov, and B. Jamtveit, 2009, Siberian gas venting and the end-Permian environmental crisis: Earth and Planetary Science Letters, v. 277, p. 490–500.

Sverjensky, D. A., 1986, Genesis of Mississippi Valley-type lead-zinc deposits: Annual Review of Earth and Planetary Sciences, v. 14, p. 177–199.

Sverjensky, D. A., 1989, Chemical evolution of basinal brines that formed sediment-hosted Cu-Pb-Zn deposits, in R. W. Boyle, A. C. Brown, C. W. Jefferson, and E. C. Jowett, eds., Sediment hosted stratiform copper deposits, v. 36, Geological Association of Canada, Special Paper, p. 127–134.

Swarbrick, R. E., M. J. Osborne, and G. S. Yardley, 2002, Comparison of overpressure magnitude resulting from the main generating mechanisms, in A. R. Huffman, and G. L. Bowers, eds., Pressure Regimes in Sedimentary Basins and their Prediction, v. 76: Tulsa, American Association of Petroleum Geologists Memoir, p. 1–12.

Swart, P. K., U. G. Wortmann, R. M. Mitterer, M. J. Malone, P. L. Smart, D. A. Feary, and A. C. Hine, 2000, Hydrogen sulfide-hydrates and saline fluids in the continental margin of South Australia: Geology, v. 28, p. 1039–1042.

Swarts, S. W., 1993, Global positioning system (GPS) and its application s for subsidence monitoring: Solution Mining Research Institute Spring Meeting, April 26, Syracuse, New York.

Sweet, A. C., G. S. Soreghan, D. E. Sweet, M. J. Soreghan, and A. S. Madden, 2013, Permian dust in Oklahoma: Source and origin for Middle Permian (Flowerpot-Blaine) redbeds in Western Tropical Pangaea: Sedimentary Geology, v. 284, Äì285, p. 181–196.

Sweet, M. L., 1999, Interaction between aeolian, fluvial and playa environments in the Permian Upper Rotliegend Group, UK southern North Sea: Sedimentology, v. 46, p. 171–187.

Swennen, R., W. Viaene, and C. Cornelissen, 1990, Petrography and geochemistry of the Belle Roche breccia (lower Visean, Belgium): evidence for brecciation by evaporite dissolution: Sedimentology, v. 37, p. 859–878.

Swennen, R., W. Viaene, L. Jacobs, and O. J. Van, 1981, Occurrence of calcite pseudomorphs after gypsum in the Lower Carboniferous of the Vesder region (Belgium): Bulletin de la Societe Belge de Geologie, v. 90, p. 231–247.

Swensen, R. E., 1967, Trap Mechanisms in Nisku Formation of northern Montana: American Association Petroleum Geologists – Bulletin, v. 51, p. 1948–1958.

Swett, K., and A. H. Knoll, 1989, Marine pisolites from Upper Proterozoic carbonates of East Greenland and Spitsbergen: Sedimentology, v. 36, p. 75–93.

Swezey, C., G. Kocurek, N. Lancaster, M. Deynoux, M. Blum, D. Price, and J.-C. Pion, 1999, Response of aeolian systems to Holocene climatic and hydrologic changes on the northern margin of the Sahara: a high-resolution record from the Chott Rharsa basin, Tunisia: Holocene, v. 9, p. 141–148.

Swezey, C. S., 2009, Cenozoic stratigraphy of the Sahara, Northern Africa: Journal of African Earth Sciences, v. 53, p. 89–121.

Swift, S. A., A. S. Bower, and R. W. Schmitt, 2012, Vertical, horizontal, and temporal changes in temperature in the Atlantis II and Discovery hot brine pools, Red Sea: Deep Sea Research Part I: Oceanographic Research Papers, v. 64, p. 118–128.

Swihart, G. H., P. B. Moore, and E. L. Callis, 1986, Boron isotopic composition of marine and nonmarine evaporite borates: Geochimica et Cosmochimica Acta, v. 50, p. 1297–1301.

Symons, D. T. A., and D. F. Sangster, 1992, Late Devonian paleomagnetic age for the Polaris Mississippi Valley-type Zn-Pb deposit, Canadian Arctic Archipelago: Canadian Journal of Earth Sciences, v. 29, p. 15–25.

Szatmari, P., 2000, Habitat of petroleum along the South Atlantic Margins, in M. R. Mello, and B. J. Katz, eds., Petroleum Systems of the South Atlantic Margins, v. 73: Tulsa, American Association of Petroleum Geologists Memoir, p. 69–75.

Szatmari, P., R. S. Carvalho, and I. A. Simoes, 1979, A comparison of evaporite facies in the late Paleozoic Amazon and the Middle Cretaceous South Atlantic salt basins: Economic Geology, v. 74, p. 432–447.

Szynkiewicz, A., R. C. Ewing, C. H. Moore, M. Glamoclija, D. Bustos, and L. M. Pratt, 2010, Origin of terrestrial gypsum dunes--Implications for Martian gypsum-rich dunes of Olympia Undae: Geomorphology, v. 121, p. 69–83.

Taberner, C., J. D. Marshall, J. P. Hendry, C. Pierre, and M. F. Thirlwall, 2002, Celestite formation, bacterial sulphate reduction and carbonate cementation of Eocene reefs and basinal sediments (Igualada, NE Spain): Sedimentology, v. 49, p. 171–190.

Tadesse, S., J.-P. Milesi, and Y. Deschamps, 2003, Geology and mineral potential of Ethiopia: a note on geology and mineral map of Ethiopia: Journal of African Earth Sciences, v. 36, p. 273–313.

Taimeh, A. Y., 1992, Formation of gypsic horizons in some arid regions soils of Jordan: Soil Science, v. 153, p. 486–498.

Takamatsu, N., N. Kato, G. I. Matsumoto, and T. Torii, 1998, The origin of salts in water bodies of the McMurdo Dry Valleys: Antarctic Science, v. 10, p. 439–448.

Talbot, C., P. Aftabi, and Z. Chemia, 2009b, Potash in a salt mushroom at Hormoz Island, Hormoz Strait, Iran: Ore Geology Reviews, v. 35, p. 317–332.

Talbot, C. J., 1978, Halokinesis and thermal convection: Nature, v. 273, p. 739–741.

Talbot, C. J., 1979, Fold trains in a glacier of salt in southern Iran: Journal of Structural Geology, v. 1, p. 5–18.

Talbot, C. J., 1992a, Quo vadis tectonophysics? With a pinch of salt!: Tectonophysics, v. 16, p. 1–20.

Talbot, C. J., 1992b, Centrifuged models of Gulf of Mexico profiles: Marine and Petroleum Geology, v. 9, p. 412–432.

Talbot, C. J., 1993, Spreading of salt structures in the Gulf of Mexico: Tectonophysics, v. 228, p. 151–166.

Talbot, C. J., 1998, Extrusions of Hormuz salt in Iran: Geological Society, London, Special Publications, v. 143, p. 315–334.

Talbot, C. J., 2008, Hydrothermal salt--but how much?: Marine and Petroleum Geology, v. 25, p. 191–202.

Talbot, C. J., and P. Aftabi, 2004, Geology and models of Qum Kuh central Iran: Journal of Geological Society of London, v. 161, p. 1–14.

Talbot, C. J., and M. Alavi, 1996, The past of a future syntaxis across the Zagros, in G. I. Alsop, D. J. Blundell, and I. Davison, eds., Salt tectonics, Geological Society, London; Special Publication, v. 100, p. 89–110.

Talbot, C. J., R. Farhadi, and P. Aftabi, 2009a, Potash in salt extruded at Sar Pohl diapir, Southern Iran: Ore Geology Reviews, v. 35, p. 352–366.

Talbot, C. J., and M. P. A. Jackson, 1987a, Internal kinematics of salt diapirs: American Association of Petroleum Geologists Bulletin, v. 71, p. 1068–1093.

Talbot, C. J., and M. P. A. Jackson, 1987b, Salt tectonics: Scientific American, v. 257, p. 70–79.

Talbot, C. J., and R. J. Jarvis, 1984, Age, budget and dynamics of an active salt extrusion in Iran: Journal of Structural Geology, v. 6, p. 521–533.

Talbot, C. J., S. Medvedev, M. Alavi, H. Shahrivar, and E. Heidari, 2000, Salt extrusion at Kuh-e-Jahani, Iran, from June 1994 to November 1997: Geological Society, London, Special Publications, v. 174, p. 93–110.

Talbot, C. J., W. Stanley, R. Soub, and N. Alsadoun, 1996, Epitaxial salt reefs and mushrooms in the southern Dead Sea: Sedimentology, v. 43, p. 1025–1047.

Talbot, C. J., C. P. Tully, and P. J. E. Woods, 1982, The structural geology of Boulby (potash) mine, Cleveland, United Kingdom: Tectonophysics, v. 85, p. 167–204.

Talbot, M. R., K. Holm, and M. A. J. Williams, 1994, Sedimentation in low-gradient desert margin systems; a comparison of the Late Triassic of Northwest Somerset (England) and the late Quaternary of east-central Australia, in M. R. Rosen, ed., Paleoclimate and basin evolution of playa systems, v. 289, Special Paper – Geological Society of America, p. 97–117.

Tan, H., H. Ma, B. Li, X. Zhang, and Y. Xiao, 2010, Strontium and boron isotopic constraint on the marine origin of the Khammuane potash deposits in southeastern Laos: Chinese Science Bulletin, v. 55, p. 3181–3188.

Tang, Z. H., J. Parnell, and F. J. Longstaffe, 1997, Diagenesis of analcime-bearing reservoir sandstones – the Upper Permian Pingdiquan Formation, Junggar Basin, Northwest China: Journal of Sedimentary Research Section A-Sedimentary Petrology & Processes, v. 67, p. 486–498.

Tanner, L. H., 2002, Borate formation in a perennial lacustrine setting: Miocene-Pliocene Furnace Creek Formation, Death Valley, California, USA: Sedimentary Geology, v. 148, p. 259–273.

Tanoli, S. K., R. Husain, and A. A. Sajer, 2008, Facies in the Unayzah Formation and the Basal Khuff Clastics in subsurface, northern Kuwait: Geoarabia, v. 13, p. 15–40.

Taofa, Z., W. Mingan, F. Yu, D. Chao, Y. Feng, Z. Lejun, L. Jun, Q. Bing, F. Pirajno, and D. R. Cooke, 2011, Geological, geochemical characteristics and isotope systematics of the Longqiao iron deposit in the Lu-Zong volcano-sedimentary basin, Middle-Lower Yangtze (Changjiang) River Valley, Eastern China: Ore Geology Reviews, v. 43, p. 154–169.

Taraschewski, H., and I. Paperna, 1981, Distribution of the snail Pirenella conica in Sinai and Israel and its infection by Heterophyidae and other Trematodes: Marine Ecology Progress Series, v. 5, p. 193–205.

Tarasov, A. V., 1970, Structural control of copper and nickel mineralization in Noril'sk I deposit: International Geol. Rev., v. 12, p. 933–941.

Tari, G., J. Molnar, and P. Ashton, 2003, Examples of salt tectonics from West Africa: A comparative approach: Geological Society Special Publication, v. 207, p. 85–104.

Taylor, C. D., Schulz, K.J., Doebrich, J.L., Orris, G.J., Denning, P.D., and Kirschbaum, M.J., 2009, Geology and nonfuel mineral deposits of Africa and the Middle East: U.S. Geological Survey Open-File Report 2005–1294-E, 246 p.

Taylor, D. G., 1970, Experiments on solution mining of borax at boron, California, in J. L. Rau, ed., Third Symposium on Salt, v. 1: Cleveland, N. Ohio Geol. Soc., p. 412–416.

Taylor, J., T. Fishburn, O. Djordjevic, and R. Sullivan, 2011, Velocity modeling workflows for sub-salt geopressure prediction: a case study from the Lower Tertiary trend, Gulf of Mexico: Geofluids, v. 11, p. 376–387.

Taylor, J., and E. Glover, 2009, New lucinid bivalves from hydrocarbon seeps of the Western Atlantic (Mollusca: Bivalvia: Lucinidae): Steenstrupia, v. 30, p. 111–124.

Taylor, J. C. M., 1990, Upper Permian-Zechstein, in K. W. Glennie, ed., Introduction to the Petroleum Geology of the North Sea (3rd Edition): Oxford, Blackwell, p. 153–190.

Taylor, K. G., and C. D. Curtis, 1995, Stability and facies association of early diagenetic mineral assemblages; an example from a Jurassic ironstone-mudstone succession, U.K.: Journal of Sedimentary Research, Section A: Sedimentary Petrology and Processes, v. 65, p. 358–368.

Taylor, P. M., and H. S. Chafetz, 2004, Floating rafts of calcite crystals in cave pools, central Texas, U.S.A; crystal habit vs. saturation state: Journal of Sedimentary Research, v. 74, p. 328–341.

Teagle, D. A. H., J. C. Alt, H. Chiba, S. E. Humphris, and A. Halliday, 1998, Strontium and oxygen isotopic constraints on fluid mixing, alteration and mineralisation in the TAG hydrothermal deposit: Chemical Geology, v. 149, p. 1–24.

Tekin, E., T. Ayyildiz, I. Gundogan, and F. Orti, 2007, Modern halolites (halite oolites) in the Tuz Golu, Turkey: Sedimentary Geology, v. 195, p. 101–112.

Tekin, E., B. Varol, and G. M. Friedman, 2001, A preliminary study: Celestite-bearing gypsum in the Tertiary Sivas basin, Central-Eastern Turkey: Carbonates & Evaporites, v. 16, p. 93–101.

Teller, J. T., J. M. Bowler, and P. G. Macumber, 1982, Modern sedimentation and hydrology in Lake Tyrrell, Victoria: Journal of the Geological Society of Australia, v. 29, p. 159–175.

Teller, J. T., K. W. Glennie, N. Lancaster, and A. K. Singhvi, 2000, Calcareous dunes of the United Arab Emirates and the Noah's flood: the post glacial reflooding of the Persia (Arabian Gulf): Quaternary International, v. 68–71, p. 297–308.

ten Haven, H. L., J. W. de Leeuw, J. W. Peakman, and T. M. Maxwell, 1986, Anomalies in steroid and hopanoid maturity indices: Geochimica et Cosmochimica Acta, v. 50, p. 853–855.

ten Haven, H. L., J. W. De Leeuw, J. Rullkötter, and J. S. Sinninghe Damste, 1987, Restricted utility of the pristane/phytane ratio as a paleoenvironmental indicator: Nature, v. 330, p. 641–643.

ten Haven, H. L., J. W. de Leeuw, and P. A. Schenk, 1985, Organic geochemical studies of a Messinian evaporite basin, northern Appennines (Italy), part 1: Hydrocarbon biological markers for a hypersaline environment: Geochimica et Cosmochimica Acta, v. 49, p. 2181–2191.

ten Haven, H. L., J. W. De Leeuw, J. S. Sinninghe Damsté, P. Schenk, S. E. Palmer, and J. E. Zumberge, 1988, Application of biological markers in the recognition of palaeo-hypersaline environments, v. 40: London, Blackwell, Geological Society London Special Publication, 123–130 p.

Tepper, D. H., W. H. Kappel, T. S. Miller, and J. H. WilliaMS, 1997, Hydrogeologic effects of flooding in the partially collapsed Retsof salt mine, Livingston County, New York: US Geol. Survey Open File Report, v. 97–47, p. 36–37.

Ter Heege, J. H., J. H. P. De Bresser, and C. J. Spiers, 2005, Rheological behaviour of synthetic rocksalt: the interplay between water, dynamic crystallisation and deformation mechanisms: Journal of Structural Geology, v. 27, p. 948–964.

Terken, J. M. J., N. L. Frewin, and S. L. Indrelid, 2001, Petroleum systems of Oman: Charge timing and risks: American Association Petroleum Geologists – Bulletin, v. 85, p. 1817–1845.

Terriere, R. T., 1976, Geology of Fairway Field, east Texas, North American oil and gas fields, American Association of Petroleum Geologists Memoir 24, p. 157–176.

Terzaghi, K., 1943, Theoretical soil mechanics: New York, John Wiley and Sons, Inc., 510 p.

Terzaghi, R. D., 1971, Brinefield subsidence at Windsor, Ontario, Third symposium on Salt, v. 2: Cleveland, Ohio, Northern Ohio Geological Society, p. 298–307.

Teske, A., A. Dhillon, and M. L. Sogin, 2003, Genomic Markers of Ancient Anaerobic Microbial Pathways: Sulfate Reduction, Methanogenesis, and Methane Oxidation: Biological Bulletin, v. 204, p. 186–191.

Testa, G., and S. Lugli, 2000, Gypsum-anhydrite transformations in Messinian evaporites of central Tuscany (Italy): Sedimentary Geology, v. 130, p. 249–268.

Thakur, N. K., and S. Rajput, 2011, Exploration of Gas Hydrates – Geophysical Techniques: Berlin, Springer, 281 p.

Thiede, D. S., and E. N. Cameron, 1978, Concentration of heavy metals in the Elk Point evaporite sequence, Saskatchewan: Economic Geology, v. 73, p. 405–415.

Thiel, V., A. Jenisch, G. Landmann, A. Reimer, and W. Michaelis, 1997, Unusual distributions of long-chain alkenones and tetrahymanol from the highly alkaline Lake Van, Turkey: Geochimica et Cosmochimica Acta, v. 61, p. 2053–2064.

Thierry, P., A. Prunier-Leparmentier, C. Lembezat, E. Vanoudheusden, and J. Vernoux, 2009, 3D geological modelling at urban scale and mapping of ground movement susceptibility from gypsum dissolution: The Paris example (France): Engineering Geology, v. 105, p. 51–64.

Thode, H. G., and J. Monster, 1973, Sulfur-isotope geochemistry of petroleum, evaporites, and ancient seas [with comment], in D. W. Kirkland, ed., Marine Evaporites; Origin, Diagenesis, and Geochemistry, Dowden, Hutchinson and Ross.

Thomas, D. W., and M. P. Coward, 1996, Mesozoic regional tectonics and South Viking Graben formation – Evidence for localized thin-skinned detachments during rift development and inversion: Marine & Petroleum Geology, v. 13, p. 149–177.

Thomeer, J. H. M. A., and J. A. Bottema, 1961, Increasing occurrence of abnormally high reservoir pressures in boreholes and drilling problems resulting therefrom: Bulletin American Association Petroleum Geologists, v. 45, p. 1721–1730.

Thoms, R. L., 2000, Subsidence and sinkhole development over salt caverns: An introduction to the technology of solution mining; Spring 2000 Technical Class, p. 127–141.

Thoms, R. L., and R. M. Gehle, 1994, The Jefferson Island mine flooding revisited: Proc. Solution Mining Research Institute Spring Meeting, Houston.

Thoms, R. L., and R. M. Gehle, 2000a, A brief history of salt cavern use, in R. M. Geertmann, ed., 8th World Salt Symposium, v. 1: Amsterdam, Elsevier, p. 207–214.

Thoms, R. L., and R. M. Gehle, 2000b, Winnfield mine flooding and collapse event of 1965: Proc. Solution Mining Research Institute Fall Meeting Technical Session, San Antonio, p. 262–274.

Thoms, R. L., and G. Kiddoo, 1998, Guidelines for safety assessment of salt caverns: Proc. Technical Class, Solution Mining Research Institute Fall Meeting, Roma, Texas, p. 113–140.

Thomson, A., P. D. Hine, J. R. Greig, and D. W. Peach, 1996, Assessment of subsidence arising from gypsum dissolution: Technical Report for the Department of the Environment. Symonds Group Ltd, East Grinstead. 288 p.

Thorsteinsson, R., and J. W. Kerr, 1968, Cornwallis Island and adjacent smaller islands, Canadian Arctic Archipelago, Geological Survey of Canada, Paper 67–64, 16 p.

Thorsteinsson, R., and T. T. Uyeno, 1980, Stratigraphy and conodonts of Upper Silurian and Lower Devonian rocks in the environs of the Boothia Uplift, Canadian Arctic Archipelago. Part I, Contributions to stratigraphy by R. Thorsteinsson with contributions by T.T. Uyeno; Part II, Systematic study of conodonts by T.T. Uyeno.: Geological Survey of Canada, Bulletin 292, 75 p.

Thrasher, J., A. J. Fleet, S. J. Hay, M. Hovland, and S. Düppenbecker, 1996, Understanding geology as the key to using seepage in exploration: the spectrum of seepage styles, in S. D., and M. A. Abrams, eds., Hydrocarbon migration and its near-surface expression: Tulsa, American Association Petroleum Geologists Memoir 66, p. 223–241.

Tiercelin, J.-J., C. Thouin, T. Kalala, and A. Mondeguer, 1989, Discovery of sublacustrine hydrothermal activity and associated massive sulfides and hydrocarbons in the north Tanganyika trough, East African Rift: Geology, v. 17, p. 1053–1056.

Tiercelin, J. J., and A. Mondeguer, 1991, The geology of the Tanganyika trough, in G. W. Coulter, ed., Lake Tanganyika and its life: London, Oxford University Press, p. 7–48.

Tiercelin, J. J., C. Pflumio, M. Castrec, J. Boulegue, P. Gente, J. Rolet, C. Coussement, K. O. Stetter, R. Huber, S. Buku, and W. Mifundu, 1993, Hydrothermal vents in Lake Tanganyika, East African Rift system: Geology, v. 21, p. 499–502.

Timms, B., 2009, A study of the salt lakes and salt springs of Eyre Peninsula, South Australia: Hydrobiologia, v. 626, p. 41–51.

Timms, B. V., 2005, Salt lakes in Australia: present problems and prognosis for the future: Hydrobiologia, v. 552, p. 1–15.

Timofeeff, M. N., T. Lowenstein, S. Brennan, R. Demicco, H. Zimmermann, J. Horita, and L. von Borstel, 2001, Evaluating seawater chemistry from fluid inclusions in halite: Examples from modern marine and nonmarine environments: Geochimica et Cosmochimica Acta, v. 65, p. 2293–2300.

Timofeeff, M. N., T. K. Lowenstein, M. A. M. da Silva, and N. B. Harris, 2006, Secular variation in the major-ion chemistry of seawater: Evidence from fluid inclusions in Cretaceous halites: Geochimica et Cosmochimica Acta, v. 70, p. 1977–1994.

Tingay, M., P. Bentham, A. De Feyter, and A. Kellner, 2011, Present-day stress-field rotations associated with evaporites in the offshore Nile Delta: Geological Society of America Bulletin, v. 123, p. 1171–1180.

Tinker, S. W., J. R. Ehrets, and M. D. Brondos, 1995, Multiple karst events related to stratigraphic cyclicity: San Andres Formation, Yates Field, west Texas, in D. A. Budd, A. H. Sailer, and P. M. Harris, eds., Unconformities and Porosity in Carbonate Strata Tulsa, Oklahoma, American Association Petrolem Geologists Memoir 63, p. 213–237.

Tinker, S. W., and K. C. Kirby, 1991, The Keg River/Winnipegosis Petroleum System--Source to Trap Part I (abs.): American Association Petroleum Geologists – Bulletin, v. 75, p. 682.

Tisato, N., F. Sauro, S. M. Bernasconi, R. H. C. Bruijn, and J. De Waele, 2012, Hypogenic contribution to speleogenesis in a predominant epigenic karst system: A case study from the Venetian Alps, Italy: Geomorphology, v. 151,Äì152, p. 156–163.

Tissot, B. P., and D. H. Welte, 1984, Petroleum formation and occurrence: Berlin, Springer, 699 p.

Tivey, M. K., S. E. Humphris, G. Thompson, M. D. Hannington, and P. A. Rona, 1995, Deducing patterns of fluid flow and mixing within the TAG active hydrothermal mound using mineralogical and geochemical data: Journal of Geophysical Research-Solid Earth, v. 100, p. 12527–12555.

Tleel, J. W., 1973, Surface geology of the Dammam Dome, Eastern Province, Saudi Arabia: American Association Petroleum Geologists – Bulletin, v. 57, p. 558–576.

Tolmachev, V.,A. Ilyin, B. Gantov, M. Leonenko, V. Khomenko, and I. A. Savarensky, 2003, The main results of engineering karstology research conducted in Dzerzhinsk, Russia (1952–2002), in B. Beck, ed., Sinkholes and the engineering and environmental impacts of karst: proceedings of the ninth multidisciplinary conference, September 6–10, 2003, Huntsville, Alabama, American Society of Civil Engineers, p. 502–516.

Tolmachev, V., and M. Leonenko, 2011, Experience in Collapse Risk Assessment of Building on Covered Karst Landscapes in Russia, in P. E. van Beynen, ed., Karst Management, Springer Netherlands, p. 75–102.

Tolmachev, V. V., S. E. Pidyashenko, and T. A. Balashova, 1999, The system of antikarst protection on railways of Russia, in B. F. Beck, A. J. Pettit, and J. G. Herring, eds., Hydrogeology and Engineering Geology of Sinkholes and Karst – 1999. Proceedings of the Seventh Multidisciplinary Conference on Sinkholes and the Engineering and Environmental Impacts of Karst. Harrisburg/Hershey, Pennsylvania, April 10–14, 1999: Rotterdam, A. A. Balkema., p. 423–429.

Tomascak, P. B., N. G. Hemming, and S. R. Hemming, 2003, The lithium isotopic composition of waters of the Mono Basin, California: Geochimica et Cosmochimica Acta, v. 67, p. 601–611.

Tomasko, D., 1985, A numerical model for predicting the thermal behaviour of caverns in the Strategic Petroleum Reserve: Doctoral thesis, University of New Mexico, Albuquerque.

Tompkins, L. A., V. A. Pedone, M. T. Roche, and D. I. Groves, 1994, The Cadjebut deposit as an example of Mississippi Valley-Type mineralization on the Lennard Shelf, Western Australia – Single episode or multiple events: Economic Geology, v. 89, p. 450–466.

Tompkins, L. A., M. J. Rayner, D. I. Groves, and M. T. Roche, 1994, Evaporites; in situ sulfur source for rhythmically banded ore in the Cadjebut Mississippi Valley-Type Zn-Pb deposit, Western Australia: Economic Geology, v. 89, p. 467–492.

Topper, R. P. M., and P. T. Meijer, 2013, A modeling perspective on spatial and temporal variations in Messinian evaporite deposits: Marine Geology, v. 336, p. 44–60.

Torabi-Kaveh, M., M. Heidari, and M. Miri, 2012, Karstic features in gypsum of Gachsaran Formation (case study; Chamshir Dam reservoir, Iran): Carbonates and Evaporites, v. 27, p. 291–297.

Torii, T., and J. Ossaka, 1965, A new mineral, calcium chloride hexahydrate, discovered in Antarctica: Science, v. 149, p. 975–977.

Tornos, F., and C. A. Heinrich, 2008, Shale basins, sulfur-deficient ore brines and the formation of exhalative base metal deposits: Chemical Geology, v. 247, p. 195–207.

Tornos, F., F. Velasco, F. Barra, and D. Morata, 2010, The Tropezón Cu-Mo-(Au) deposit, Northern Chile: the missing link between

IOCG and porphyry copper systems?: Mineralium Deposita, v. 45, p. 313–321.

Torrentera, L., and S. I. Dodson, 2004, Ecology of the brine shrimp Artemia in the Yucatan, Mexico, Salterns Journal of Plankton Research, v. 26, p. 617–624.

Torres-Roldan, R. L., 1978, Scapolite-bearing and related calc-silicate layers from the Alpujarride Series, (Betic Cordilleras of southern Spain); a discussion on their origin and some comments: Geologische Rundschau, v. 67, p. 342–355.

Torres-Ruiz, J., A. Pesquera, P. P. Gil-Crespo, and N. Velilla, 2003, Origin and petrogenetic implications of tourmaline-rich rocks in the Sierra Nevada (Betic Cordillera, southeastern Spain): Chemical Geology, v. 197, p. 55–86.

Torres-Ruiz, J., A. Pesquera, and V. Sánchez, V. L., 2003, Chromian tourmaline and associated Cr-bearing minerals from the Nevado-Filabride Complex (Betic Cordilleras, SE Spain): Mineralogical Magazine, v. 67, p. 517–533.

Torsvik, T. H., S. Rousse, C. Labails, and M. A. Smethurst, 2009, A new scheme for the opening of the South Atlantic Ocean and the dissection of an Aptian salt basin: Geophysical Journal International, v. 177, p. 1315–1333.

Tortochaux, F., 1968, Occurrence and structure of evaporites in north Africa: Geol. Soc. Amer., Spec. Paper, v. 88, p. 107–138.

Tosca, N. J., F. A. Macdonald, J. V. Strauss, D. T. Johnston, and A. H. Knoll, 2011, Sedimentary talc in Neoproterozoic carbonate successions: Earth and Planetary Science Letters, v. 306, p. 11–22.

Toulemont, M., 1984, Le karst gypseux du Lutetien superieur de la region parisienne; caracteristiques et impact sur le milieu urbain: Revue de Geologie Dynamique et de Geographie Physique, v. 25, p. 213–228.

Touret, J. L. R., 1985, Fluid regime in southern Norway, the record of fluid inclusions, in A. C. Tobi, and J. L. R. Touret, eds., The Deep Proterozoic Crust in the North Atlantic Provinces: Dordrecht, Reidel, p. 517–549.

Tourn, S. M., C. J. Herrmann, S. Ametrano, and M. K. de Brodtkorb, 2004, Tourmalinites from the Eastern Sierras Pampeanas, Argentina: Ore Geology Reviews, v. 24, p. 229–240.

Townson, W. G., 1985, The subsurface geology of the western Officer Basin – results of Shell's 1980–1984 petroleum exploration campaign: APEA Journal, v. 25, p. 34–51.

Tozer, R. S. J., A. P. Choi, J. T. Pietras, and D. J. Tanasichuk, 2014, Athabasca oil sands: mega-trap restoration and charge timing: Bulletin American Association Petroleum Geologists, v. 98, p. 429–447.

Trabelsi, R., K. Abid, and K. Zouari, 2012, Geochemistry processes of the Djeffara palaeogroundwater (Southeastern Tunisia): Quaternary International, v. 257, p. 43–55.

Trappe, J., 2000, Pangea: extravagant sedimentary resource formation during supercontinent configuration, an overview: Palaeogeography Palaeoclimatology Palaeoecology, v. 161, p. 35–48.

Trauth, M. H., A. Deino, and M. R. Strecker, 2001, Response of the East African climate to orbital forcing during the last interglacial (130–117 ka) and the early last glacial (117–60 ka): Geology, v. 29, p. 499–502.

Travé, A., F. Calvet, M. Sans, J. Verges, and M. Thirlwall, 2000, Fluid history related to the Alpine compression at the margin of the south-Pyrenean Foreland basin: the El Guix anticline: Tectonophysics, v. 321, p. 73–102.

Travé, A., P. Labaume, and J. Vergés, 2007, Fluid Systems in Foreland Fold-and-Thrust Belts:An Overview from the Southern Pyrenees, in O. Lacombe, J. Lavé, F. Roure, and J. Verges, eds., Thrust Belts and Foreland Basins: Frontiers in Earth Sciences, Springer Berlin Heidelberg, p. 93–115.

Trefry, J. H., B. J. Presley, W. L. Keeney-Kennicutt, and R. P. Trocine, 1984, Distribution and chemistry of manganese, iron, and suspended particulates in Orca Basin: Geomarine Lett., v. 4, p. 125–130.

Trendall, A. F., 1983, The Hamersley Basin, in A. F. Trendall, and R. C. Morris, eds., Iron Formations: Facts and Problems: Amsterdam, Elsevier, p. 69–129.

Tret'yakov, Y. A., 1974, Zones of impoverishment in the upper Kama potassium deposit (in Russian): Lithol. Miner. Resour., v. 9, p. 59–67.

Triantaphyllidis, G. V., T. J. Abatzopoulos, and P. Sorgeloos, 1998, Review of the Biogeography of the Genus Artemia (Crustacea, Anostraca): Journal of Biogeography, v. 252.

Trindade, L. A. F., J. L. Dias, and M. R. Mello, 1995, Sedimentological and geochemical characterisation of the Lagoa Feia Formation, rift phase of the Campos Basin, Brazil, in B. Katz, ed., Petroleum source rocks: Berlin, Springer Verlag, p. 149–165.

Trombotto, D., 2000, Survey of cryogenic processes, periglacial forms and permafrost conditions in South America: Rev. Inst. Geol., v. 21, p. 33–55.

Trombotto, D., and E. Borzotta, 2009, Indicators of present global warming through changes in active layer-thickness, estimation of thermal diffusivity and geomorphological observations in the Morenas Coloradas rockglacier, Central Andes of Mendoza, Argentina: Cold Regions Science and Technology, v. 55, p. 321–330

Trommsdorff, V., G. Skippen, and P. Ulmer, 1985, Halite and sylvite as solid inclusions in high-grade metamorphic rocks: Contributions to Mineralogy and Petrology, v. 89, p. 24–29.

Truc, G., 1978, Lacustrine sediments in an evaporitic environment: the Ludian (Palaeogene) of the Mormoiron Basin, SE France, in A. Matter, and M. E. Tucker, eds., Modern and ancient lake sediments, International Association Sedimentologists, Spec. Publ. 2, p. 187–202.

Trudgill, B. D., P. E. Gale, B. E. Korn, R. L. Phair, W. T. Gafford, G. R. Roberts, S. W. Dobbs, M. G. Rowan, J. C. Fiduk, and P. Weimer, 1999, The Perdido fold belt, northwestern deep Gulf of Mexico, Part 1: Structural geometry, evolution and regional implications: American Association of Petroleum Geologists Bulletin, v. 83, p. 88–113.

Trudinger, P. A., L. A. Chambers, and J. W. Smith, 1985, Low-temperature sulphate reduction; biological versus abiological: Canadian Journal of Earth Sciences, v. 22, p. 1910–1918.

Trumbull, R. B., J. F. Slack, M.-S. Krienitz, H. E. Belkin, and M. Wiedenbeck, 2011, Fluid sources and metallogenesis in the Blackbird Co-Cu-Au-Bi-Y-REE district, Idaho, U.S.A.: insights from major-element and boron isotopic compositions of tourmaline: The Canadian Mineralogist, v. 49, p. 225–244.

Trusheim, F., 1960, Mechanism of salt migration in Northern Germany: American Association Petroleum Geologists Bulletin, v. 44, p. 1519–1540.

Trzhtsinsky, Y., 2002, Human-induced activation of gypsum karst in the southern Priangaria (East Siberia, Russia): Carbonates and Evaporites, v. 17, p. 154–158.

Tsui, P. C., and D. M. Cruden, 1984, Deformation associated with gypsum karst in the Salt River Escarpment, northeastern Alberta: Canadian Journal of Earth Sciences, v. 21, p. 949–959.

Tucker, K. E., and R. G. Chalcraft, 1991, Cyclicity in the Permian Queen Formation – U.S .M. Queen Field, Pecos County, Texas (abs): SEPM (Society for Sedimentary Geology), Core Workshop, v. 15, p. 385–428.

Tucker, M. E., 1976a, Quartz replaced anhydrite nodules ('Bristol Diamonds') from the Triassic of the Bristol District: Geological Magazine, v. 113, p. 569–574.

Tucker, M. E., 1976b, Replaced evaporites from the late Precambrian of Finnmark, Arctic Norway: Sedimentary Geology, v. 16, p. 193–204.

Tucker, M. E., 1991, Sequence stratigraphy of carbonate-evaporite basins; models and application to the Upper Permian (Zechstein) of

Northeast England and adjoining North Sea: Journal of the Geological Society of London, v. 148, p. 1019–1036.

Tucker, M. E., 1993, Carbonate diagenesis and sequence stratigraphy: Sedimentology review, v. 1, p. 51–72.

Tucker, M. E., 1999, Sabkha cycles, stacking patterns and controls: Gachsaran (Lower Fars/Fatha) Formation, Miocene, Mesopotamian Basin, Iraq: Neues Jahrbuch fur Geologie und Palaontologie-Abhandlungen, v. 214, p. 45–69.

Tucker, R. M., 1981, Giant polygons in the Triassic salt of Cheshire, England: A thermal contraction model for their origin: Journal of Sedimentary Petrology, v. 51, p. 779–786.

Tuisku, P., 1985, The origin of scapolite in the central Lapland schist area, northern Finland: Preliminary results: Finland Geol. Surv. Bull., v. 331, p. 159–173.

Tuite, C. H., 2000, The Distribution and Density of Lesser Flamingos in East Africa in Relation to Food Availability and Productivity: Waterbirds: The International Journal of Waterbird Biology, v. 23, Special Publication 1: Conservation Biology of Flamingos, p. 52–63.

Turich, C., and K. H. Freeman, 2011, Archaeal lipids record paleosalinity in hypersaline systems: Organic Geochemistry, v. 42, p. 1147–1157.

Turk, L. J., 1973, Hydrogeology of the Bonneville Salt Flats, Utah: Utah Geological and Mineral Survey Water-Resources Bulletin 19, 81 p.

Turner, C. E., and N. S. Fishman, 1991, Jurassic Lake T'oo'dichi': A large alkaline, saline lake, Morrison Formation, eastern Colorado Plateau: Geological Society of America Bulletin, v. 103, p. 538–558.

Turner, P., D. Pilling, D. Walker, J. Exton, J. Binnie, and N. Sabaou, 2001, Sequence stratigraphy and sedimentology of the late Triassic TAG-I (Blocks 401/402, Berkine Basin, Algeria): Marine & Petroleum Geology, v. 18, p. 959–981.

Tyagi, A. K., A. D. Shukla, R. Bhushan, P. S. Thakker, M. G. Thakkar, and N. Juyal, 2012, Mid-Holocene sedimentation and landscape evolution in the western Great Rann of Kachchh, India: Geomorphology, v. 151,Äì152, p. 89–98.

Tyler, N., 1986, The origin of gold mineralization in the Pilgrim's Rest Goldfield, Eastern Transvaal, v. 179, Economic Geology Research Unit, Univ. Witwatersrand, Johannesburg, Information Circular 33 p.

Tyler, S. W., S. Kranz, M. B. Parlange, J. Albertson, G. G. Katul, G. F. Cochran, B. A. Lyles, and G. Holder, 1997, Estimation of groundwater evaporation and salt flux from Owens Lake, California, USA: Journal of Hydrology, p. 110–135.

Tyler, S. W., and R. A. Wooding, 1991, Experimental verification of convection of groundwater beneath salt lakes: EOS, v. 72, p. 216.

Tyson, R. V., P. Esherwood, and K. A. Pattison, 2005, Organic facies variations in the Valanginian-mid-Hauterivian interval of the Agrio Formation (Chos Malal Area, Neuquen, Argentina): local significance and global context: Geological Society, London, Special Publications, v. 252, p. 251–266.

Tyson, R. V., and T. H. Pearson, 1991, Modern and Ancient Continental Shelf Anoxia: Geological Society of London, Special Publications, v. 58, p. 1–24.

Uliana, M. A., and L. Legarreta, 1993, Hydrocarbon habitat in a Triassic to Cretaceous sub-Andean setting – Neuquen basin, Argentina: Journal of Petroleum Geology, v. 16, p. 397–420.

Ullman, W. J., 1995, The fate and accumulation of bromide during playa salt deposition: an example from Lake Frome, South Australia: Geochimica et Cosmochimica Acta, v. 59, p. 2175–2186.

Ullman, W. J., and K. D. Collerson, 1994, The Sr-isotope record of late Quaternary hydrologic changes around Lake Frome, South Australia: Australian Journal of Earth Sciences, v. 41, p. 37–45.

Ullrich, C. D.,A. H. Clark, and T. K. Kyser, 2001, The Candelaria Cu-Au deposit, III region, Chile: Product of longterm mixing of magmatic-hydrothermal and evaporite-sourced fluids: GSA Annual Meeting, November 5–8, 2001.

Ulmer-Scholle, D. S., and P. A. Scholle, 1994, Replacement of evaporites within the Permian Park City Formation, Bighorn Basin, Wyoming, USA: Sedimentology, v. 41, p. 1203–1222.

Ulmer-Scholle, D. S., P. A. Scholle, and P. V. Brady, 1993, Silicification of evaporites in Permian (Guadalupian) back- reef carbonates of the Delaware Basin, west Texas and New Mexico: Journal of Sedimentary Petrology, v. 63, p. 955–965.

Ulmishek, G. F., 2001a, Petroleum Geology and Resources of the Dnieper-Donets Basin, Ukraine and Russia: U.S. Geological Survey Bulletin, v. 2201-E.

Ulmishek, G. F., 2001b, Petroleum Geology and Resources of the North Caspian Basin, Kazakhstan and Russia: U.S. Geological Survey Bulletin 2201-B.

Ulmishek, G. F., V. A. Bogino, M. B. Keller, and Z. L. Poznyakevich, 1994, Structure, stratigraphy and petroleum geology of the Dnieper-Donets Basins, Byelarus and Ukraine, in S. M. Landon, ed., Interior Rift Basins, v. 59: Tulsa, OK, American Association Petroleum Geologists Memoir, p. 125–156.

Ulrich, M. R., J. R. Kyle, and P. E. Price, 1984, Metallic sulfide deposits in the Winnfield salt dome, Louisiana; evidence for episodic introduction of metalliferous brines during cap rock formation: Transactions Gulf Coast Association of Geological Societies, v. 34, p. 435–442.

Ulrich, M. R., J. R. Kyle, and P. E. Price, 1985, Textural evidence for origin of salt dome anhydrite cap rocks, Winnfield Dome, Louisiana (abs): American Association Petroleum Geologists – Bulletin, v. 69, p. 313.

UN Industrial Development Organization- Int'l Fertilizer Development Center (Eds.), 1998, Fertilizer Manual, UN Industrial Development Organization, 615 p.

Underhill, J. R., 2009, Role of intrusion-induced salt mobility in controlling the formation of the enigmatic Silverpit Crater, UK Southern North Sea: Petroleum Geoscience, v. 15, p. 197–216.

United Nations Environment Programme, 2012, The Drying of Iran's Lake Urmia and its Environmental Consequences:miller (Article reproduced from UNEP – Global Environmental Alert Service (GEAS): Environmental Development, v. 2, p. 128–137.

Uphoff, T. L., 2005, Subsalt (pre-Jurassic) exploration play in the northern Lusitanian basin of Portugal: Bulletin American Association Petroleum Geologists, v. 89, p. 699–714.

Urai, J. L., Z. Schléder, C. J. Spiers, and P. A. Kukla, 2008, Flow and Transport Properties of Salt Rocks, in R. Littke, ed., Dynamics of complex intracontinental basins: The Central European Basin System, Elsevier, p. 277–290.

Urai, J. L., C. J. Spiers, H. J. Zwart, and G. S. Lister, 1986, Weakening of rock salt by water during long-term creep: Nature, v. 324, p. 554–557.

Urien, C. M., and J. J. Zambrano, 1994, Petroleum Systems in the Neuquen Basin, Argentina: Chapter 32: Part V. Case Studies—Western Hemisphere, The Petroleum System—From Source to Trap, American Association Petroleum Geologists Memoir No. 60, p. 513–534.

Usdowski, E., and M. Dietzel, 1998, Atlas and data of solid-solution equilibria of marine evaporites: Berlin, Springer Verlag, 316 p.

Usiglio, M. J., 1849, Etudes sur la composition de l'eau de la Mediterranee et sur l'exploitation des sel quy'elle conteint: Ann. Chim. Phys., v. 27, p. 172–191.

Utha-aroon, C., 1993, Continental origin of the Maha-Sarakham evaporites, northeastern Thailand: Journal of Southeast Asian Earth Sciences, v. 8, p. 193–203.

Utha-aroon, C., L. Coshell, and J. K. Warren, 1995, Early and late dissolution in the Maha Sarakham Formation: Implications for basin stratigraphy: International Conference on Geology, Geochronoilogy and Mineral Resources of Indochina 22–25 November 1995, Khon Kaen, Thailand, p. 275–286.

Utrilla, R., 1985, Estudi sedimentológic i geoquímic de les salines de la Trinitat (Delta de l'Ebre) i San Pedro del Pinatar (Mar Menor): Masters thesis, Universitat de Barcelona.

Vakhrushev, V. A., G. S. Ripp, and M. S. Kaviladze, 1981, Isotope composition of sulfur from iron ore deposits of east Siberia: Soviet Geology and Geophysics, v. 22, p. 59–64.

Valenta, R., 1994, Syntectonic discordant copper mineralisation in the Hilton Mine, Mount Isa: Economic Geology, v. 89, p. 1031–1052.

Valero-Garces, B., C. Arenas, and A. Delgado-Huertas, 2001, Depositional environments of Quaternary lacustrine travertines and stromatolites from high-altitude Andean lakes, northwestern Argentina: Canadian Journal of Earth Sciences, v. 38, p. 1263–1283.

Valero-Garces, B. L., A. Delgado-Huertas, N. Ratto, and A. Navas, 1999, Large C-13 enrichment in primary carbonates from Andean Altiplano lakes, northwest Argentina: Earth & Planetary Science Letters, v. 171, p. 253–266.

Valyashko, M. G., 1956, Geokhimiya broma v protsessakh galogeneza i ispolzovanie soderzhaniya broma v kachestve geneticheskogo i poiskovogo kriteriya (Geochemistry of bromine in the processes of salt deposition and the use of bromine content as a genetic and prospecting criterion): Geokhimiya, v. 6, p. 570–589.

Valyashko, M. G., 1972, Playa lakes, a necessary stage in the development of a salt-bearing basin [with discussion]: Geology of saline deposits, Unesco Earth Sci. Ser., p. 41–51.

Van Alstine, R. E., 1976, Continental rifts and lineaments associated with major fluorospar districts: Economic Geology, v. 71, p. 977–987.

Van Breemen, N., 1982, Genesis, morphology, and classification of acid sulfate soils in coastal plains, in J. A. Kittrick, D. S. Fanning, and L. R. Hossner, eds., Acid Sulfate Weathering, v. 10: Madison, WI, Soil Science of America Special Publication, p. 95–108.

Van Buchem, F. S. P., T. L. Allan, G. V. Laursen, M. Lotfpour, A. Moallemi, S. Monibi, H. Motiei, N. A. H. Pickard, A. R. Tahmasbi, V. Vedrenne, and B. Vincent, 2010, Regional stratigraphic architecture and reservoir types of the Oligo-Miocene deposits in the Dezful Embayment (Asmari and Pabdeh Formations) SW Iran: Geological Society, London, Special Publications, v. 329, p. 219–263.

Van den Bark, E., and O. D. Thomas, 1980, Ekofisk: First of the Giant Oil Fields in Western Europe, Giant Oil and Gas Fields of the Decade 1968–1978, v. 30, American Association Petroleum Geologists Memoir, p. 195–224.

Van der Pluijm, B. A., and S. Marshak, 2004, Earth Structure: An introduction to structural geology and tectonics: New York, W. W. Norton & Company, Inc., 656 p.

Van der Sloot, H. A., D. Hoede, G. Hamburg, J. R. W. Woittiez, and C. H. Van der Weijden, 1990, Trace elements in suspended matter from the anoxic hypersaline Tyro and Bannock Basins (eastern Mediterranean): Marine Chemistry, v. 31, p. 187–203.

Van Driessche, A. E. S., L. G. Benning, J. D. Rodriguez-Blanco, M. Ossorio, P. Bots, and J. M. Garcia-Ruiz, 2012, The role and implications of bassanite as a stable precursor phase to gypsum precipitation: Science, v. 336, p. 69–72.

Van Gent, H., J. L. Urai, and M. de Keijzer, 2011, The internal geometry of salt structures – A first look using 3D seismic data from the Zechstein of the Netherlands: Journal of Structural Geology, v. 33, p. 292–311.

Van Houten, F. R., 1977, Triassic-Liassic deposits of Morocco and eastern North America; Comparison: American Association Petroleum Geologists Bulletin, v. 61, p. 79–99.

Van Kranendonk, M. J., R. Hugh Smithies, A. H. Hickman, and D. C. Champion, 2007, Review: secular tectonic evolution of Archean continental crust: interplay between horizontal and vertical processes in the formation of the Pilbara Craton, Australia: Terra Nova, v. 19, p. 1–38.

Van Lith, Y., C. Vasconcelos, R. Warthmann, J. C. F. Martins, and J. A. McKenzie, 2002, Bacterial sulfate reduction and salinity: two controls on dolomite precipitation in Lagoa Vermelha and Brejo do Espinho (Brazil): Hydrobiologia, v. 485, p. 35–49.

Van Lith,Y., R.Warthmann, C. Vasconcelos, and J.A. McKenzie, 2003, Microbial fossilization in carbonate sediments: a result of the bacterial surface involvement in dolomite precipitation: Sedimentology, v. 50, p. 237–245.

Van Rensbergen, P., R. R. Hillis, A. J. Maltman, and C. K. Morley, 2003, Subsurface sediment mobilization: Introduction, in P. Van Rensbergen, R. R. Hillis, A. J. Maltman, and C. K. Morley, eds., Subsurface Sediment Mobilization, v. 216: London, Geological Society of London Special Publication, p. 1–8.

Van Rensbergen, P., and C. K. Morley, 2000, 3D Seismic study of a shale expulsion syncline at the base of the Champion delta, offshore Brunei and its implications for the early structural evolution of large delta systems: Marine & Petroleum Geology, v. 17, p. 861–872.

Van Staal, C. R., N. Rogers, and B. E. Taylor, 2001, Formation of low-temperature mylonites and phyllonites by alkali-metasomatic weakening of felsic volcanic rocks during progressive, subduction-related deformation: Journal of Structural Geology, v. 23, p. 903–921.

Van Wagoner, J. C., R. M. Mitchum, K. M. Campion, and V. D. Rahmanian, 1990, Siliciclastic Sequence Stratigraphy in Well Logs, Cores and Outcrops, Amer. Assoc. Petrol. Geol. Methods in Exploration Series, No. 7: Tulsa.

Van Wagoner, J. C., H. W. Posamentier, R. M. Mitchum Jr., P. R. Vail, J. F. Sarg, T. S. Loutit, and J. Hardenbol, 1988, An overview of the fundamentals of sequence stratigraphy and key definitions, in C. K. Wilgus, B. S. Hastings, C. G. S. C. Kendall, H. W. Posamentier, C. A. Ross, and J. C. Van Wagoner, eds., Sea-Level Changes: An Integrated Approach, v. 42: Tulsa, Soc. Econ. Paleontol. Mineral. Spec. Publ., p. 39–45.

Van Wees, J. D., R. A. Stephenson, P. A. Ziegler, U. Bayer, T. McCann, R. Dadlez, R. Gaupp, M. Narkiewicz, F. Bitzer, and M. Scheck, 2000, On the origin of the Southern Permian Basin, Central Europe: Marine and Petroleum Geology, v. 17, p. 43–59.

Van Wilderode, J., W. Heijlen, D. De Muynck, J. Schneider, F. Vanhaecke, and P. Muchez, 2013, The Kipushi Cu-Zn deposit (DR Congo) and its host rocks: A petrographical, stable isotope (O, C) and radiogenic isotope (Sr, Nd) study: Journal of African Earth Sciences, v. 79, p. 143–156.

Vandervoort, D. S., 1997, Stratigraphic response to saline lake-level fluctuations and the origin of cyclic nonmarine evaporite deposits – The Pleistocene Blanca Lila Formation, Northwest Argentina: Geological Society of America Bulletin, v. 109, p. 210–224.

Vandervoot, D. S., T. E. Jordan, P. K. Zeitler, and R. N. Alonso, 1995, Chronology of internal drainage development and uplift, southern Puna Plateau, Argentine Central Andes: Geology, v. 23, p. 145–148.

Vanko, D. A., and F. C. Bishop, 1982, Occurrence and origin of marialitic scapolite in the Humboldt lopolith, N.W. Nevada.: Contributions to Mineralogy & Petrology, v. 81, p. 277–289.

Varela, C. L., and W. U. Mohriak, 2013, Halokinetic rotating faults, salt intrusions, and seismic pitfalls in the petroleum exploration of divergent margins: American Association of Petroleum Geologists Bulletin, v. 97, p. 1421–1446.

Vareschi, E., 1978, The ecology of Lake Nakuru (Kenya). I. Abundance and feeding of the lesser flamingo: Oecologia, v. 32, p. 11–35.

Vareschi, E., 1979, The ecology of Lake Nakuru (Kenya). II. Biomass and spatial distribution of fish: Oecologia, v. 37, p. 321–325.

Vareschi, E., 1982, The ecology of Lake Nakuru (Kenya). III. Abiotic factors and primary production: Oecologia, v. 55, p. 81–101.

Varol, B., H. Araz, L. Karadenizli, N. Kazanci, G. Seyitoglu, and S. Sen, 2002, Sedimentology of the Miocene evaporitic succession in the north of Cankiri-Corum basin, central Anatolia, Turkey: Carbonates and Evaporites, v. 17, p. 197–209.

Vasconcelos, C., and J.A. McKenzie, 1997, Microbial mediation of modern dolomite precipitation and diagenesis under anoxic conditions (Lagoa Vermelha, Rio de Janeiro, Brazil): Journal of Sedimentary Research Section A-Sedimentary Petrology & Processes, v. 67, p. 378–390.

Vasconcelos, C., R. Warthmann, J. A. McKenzie, P. T. Visscher, A. G. Bittermann, and Y. van Lith, 2006, Lithifying microbial mats in Lagoa Vermelba, Brazil: Modern Precambrian relics?: Sedimentary Geology, v. 185, p. 175–183.

Vasconcelos, C. O., J. A. McKenzie, S. Bernasconi, D. Grujic, and A. J. Tien, 1995, Microbial mediation as a possible mechanism for natural dolomite formation at low temperature: Nature, v. 337, p. 220–222.

Vaughan, D. J., M. Sweeney, G. Friedrich, R. Diedel, and C. Haranczyk, 1989, The Kupferschiefer: an overview with an appraisal of the different types of mineralization: Economic Geology, v. 84, p. 1003–1027.

Vearncombe, S., M. E. Barley, D. I. Groves, N. J. McNaughton, E. J. Mikucki, and J. R. Vearncombe, 1995, 3.26 Ga black smoker-type mineralization in the Strelley Belt, Pilbara Craton, Western Australia: Journal of the Geological Society of London, v. 152, p. 587–590.

Veevers, J. J., 2004, Gondwanaland from 650–500 Ma assembly through 320 Ma merger in Pangea to 185-100 Ma breakup: supercontinental tectonics via stratigraphy and radiometric dating: Earth Science Reviews, v. 68, p. 1–132.

Veil, J., D. Elcock, M. Raivel, D. Caudle, R. C. Ayers Jr., and B. Grunewald, 1996, Preliminary technical and legal evaluation of disposing of nonhazardous oil field waste into salt caverns, Washington, USA, Argonne National Laboratory, Report for US Department of Energy, Office of Fossil Energy under contract W-31-109-ENG-38.

Veizer, J., Y. Godderis, and L. M. Francois, 2000, Evidence for decoupling of atmospheric CO_2 and global climate during the Phanerozoic eon: Nature, v. 408, p. 698–701.

Velaj, T., 2002, Evaporites in Albania and their impact on the thrusting processes: Carbonates and Evaporites, v. 17, p. 68–78.

Velaj, T., I. Davison, A. Serjani, and I. Alsop, 1999, Thrust tectonics and the role of evaporites in the Ionian zone of the Albanides: American Association Petroleum Geologists Bulletin-American Association of Petroleum Geologists, v. 83, p. 1408–1425.

Vendeville, B. C., 2005, Salt tectonics driven by sediment progradation: Part I – Mechanics and Kinematics: Bulletin American Association Petroleum Geologists, v. 89, p. 1071–1079.

Vendeville, B. C., and M. P. A. Jackson, 1992a, The rise of diapirs during thin-skinned extension: Marine and Petroleum Geology, v. 9, p. 331–353.

Vendeville, B. C., and M. P. A. Jackson, 1992b, The fall of diapirs during thin-skinned extension: Marine and Petroleum Geology, v. 9, p. 354–371.

Vendeville, B. C., and M. P. A. Jackson, 1993, Some dogmas in salt tectonics challenged by modeling: American Association Petroleum Geologists Hedberg Research Conference on Salt tectonics, p. 163–165.

Vendeville, B. C., and K. T. Nilsen, 1995, Eposidic growth of salt diapirs driven by horizontal shortening: Gulf Coast Section Society of Economic Palaeontologists and Mineralogists Foundation. 16th Annual Research Conference, Salt Sediment and Hydrocarbons, p. 285–295.

Vengosh, A., A. R. Chivas, M. T. McCulloch, A. Starinsky, and Y. Kolodny, 1991, Boron isotope geochemistry of Australian salt lakes.: Geochimica et Cosmochimica Acta, v. 55, p. 2591–2606.

Vengosh, A., A. R. Chivas, A. Starinsky, Y. Kolodny, B. Zhang, and P. Zhang, 1995, Chemical and boron isotope compositions of nonmarine brines from the Qaidam Basin, Qinghai, China: Chemical Geology, v. 120, p. 135–154.

Vengosh, A., A. Starinsky, Y. Kolodny, A. R. Chivas, and M. Raab, 1992, Boron isotope variations during fractional evaporation of sea water: new constraints on the marine vs. nonmarine debate: Geology, v. 20, p. 799–802.

Ventisette, C. D., D. Montanari, M. Bonini, and F. Sani, 2005, Positive fault inversion triggering "intrusive diapirism": an analogue modelling perspective: Terra Nova, v. 17, p. 478–485.

Ventosa, A., J. J. Nieto, and A. Oren, 1998, Biology of moderately halophilic aerobic bacteria: Microbiology and Molecular Biology Reviews, v. 62, p. 504–544.

Verges, J., M. G. H. Goodarzi, H. Emami, R. Karpuz, J. Efstathiou, and P. Gillespie, 2011, Multiple detachment folding in Pusht-e Kuh arc, Zagros: Role of mechanical stratigraphy, in K. McClay, J. Shaw, and J. Suppe, eds., Thrust fault-related folding, v. 94: Tulsa, OK, American Association Petroleum Geologists Memoir, p. 69–94.

Vernon, R. H., and P. F. Williams, 1988, Distinction between intrusive and extrusive or sedimentary parentage of felsic gneisses; examples from the Broken Hill Block, NSW: Australian Journal of Earth Sciences, v. 35, p. 379–388.

Versfelt Jr., P. L., 2001, Major hydrocarbon potential in Iran, in M. W. Downey, J. C. Threet, and W. A. Morgan, eds., Petroleum provinces of the twenty-first century, American Association Petroleum Geologists Memoir 74, p. 417–427.

Verwer, K., G. D. Porta, O. Merino-Tom, and J. A. M. Kenter, 2009, Controls and predictability of carbonate facies architecture in a Lower Jurassic three-dimensional barrier-shoal complex (Djebel Bou Dahar, High Atlas, Morocco): Sedimentology, v. 56, p. 1801–1831.

Vially, R., J. Letouzey, F. Bénard, N. Haddadi, D. G., H. Askri, and A. Boudjema, 1994, Basin inversion along the North African margin, the Saharan Atlas (Algeria), in F. Roure, ed., Peritethyan Platforms: Paris, Technip, p. 79–118.

Vidal, C. E., E. J. Injoque, G. B. Sidder, and S. B. Mukasa, 1990, Amphibolitic Cu-Fe skarn deposits in the central coast of Peru: Economic Geology, v. 85, p. 1447–1461.

Vila, J.-M., F. Benkherouf, and A. Charriere, 1994, Interpretation du materiel triasique de la region de l'Ouenza (confins algero-tunisiens): un vaste "glacier de sel' sous-marin albien, a l'image des structures off-shore d'Aquitaine (Interpretation of the Triassic formations in the Ouenza area (Algerian-Tunisian confines): a large submarine Albian "salt-glacier', like the offshore structures of Aquitaine): Comptes Rendus – Academie des Sciences, Serie II: Sciences de la Terre et des Planete, v. 318, p. 109–116.

Vila, J. M., M. Ghanmi, M. B. Youssef, and M. Jouirou, 2002, The submarine "salt glaciers" of northeastern Maghreb (Algeria and Tunisia), and the US Gulf Coast passive continental margins: Comparisons, special look on the composite "salt glaciers" illustrated by the Fedj el Adoum structure (northwestern Tunisia), and global review: Eclogae Geologicae Helvetiae, v. 95, p. 347–380.

Ville, L., 1856, Notice geologique sur les salines des Zahrez et les gites de sel gemme de Rang el Melah et d' Ain Hadjera (Algerie): Annales de Mines, v. 13, p. 331–334.

Vinante, D., and R. N. Alonso, 2006, Evapofacies del Salar Hombre Muerto, Puna argentina: distribucion y genesis: Rev. Asoc. Geol. Argent., v. 61, p. 286–297.

Vincelette, R. R., and W. E. Chittum, 1981, Exploration for oil accumulation in Entrada Sandstone, San Juan Basin, New Mexico: American Association Petroleum Geologists – Bulletin, v. 65, p. 2546–2570.

Vinet, M. J., 1982, Stratigraphy and dolomitization of the Smackover and Buckner formation (Upper Jurassic) Jay-Big Escambia Creek field area, southern Alabama-western Florida (abs): Jurassic of the Gulf Coast rim; Gulf Coast Section SEPM, p. 110–113.

Viola, G., N. S. Mancktelow, and J. A. Miller, 2006, Cyclic frictional-viscous slip oscillations along the base of an advancing nappe complex: Insights into brittle-ductile nappe emplacement mechanisms from the Naukluft Nappe Complex, central Namibia: Tectonics, v. 25, p. TC3016.

Vishwakarma, R. K., 1996, 1.66 Ga old metamorphosed Pb-Cu deposit in Sargipali (Eastern India) – Manifestations of tidal flat environment and sedex type genesis: Precambrian Research, v. 77, p. 117–130.

Visscher, P. T., P. R. Reid, and B. M. Bebout, 2000, Microscale observations of sulfate reduction: Correlation of microbial activity with lithified micritic laminae in modern marine stromatolites: Geology, v. 28, p. 919–922.

Visscher, P. T., and J. F. Stolz, 2005, Microbial mats as bioreactors: populations, processes, and products: Palaeogeography, Palaeoclimatology, Palaeoecology, v. 219, p. 87–100.
Visser, D., T. G. Nijland, D. J. Lieftink, and K. J. Maiden, 1999, The occurrence of preiswerkite in a tourmalime scapolite rock from Blengsvatn, Norway: American Mineralogist, v. 84, p. 977–982.
Vitra, R. L., 2014, Zeolites (Natural): USGS Mineral commodity summaries. Available for download as pdf files at http://minerals.usgs.gov/minerals/pubs/commodity/zeolites/.
Vivallo, W., F. Henriquez, and S. Espinoza, 1994, Oxygen and sulfur isotopes in hydrothermally altered rocks and gypsum deposits at El Laco Mining District, northern Chile: Comuni-caciones, v. 45, p. 93–100.
Vivallo, W., F. Henríquez, and S. Espinoza, 1991, Alteración hidrotermal en el complejo volcánico El Laco, norte de Chile: VI Congreso Geológico Chileno, Actas 1, 44–47.
Vlasceanu, L., S. M. Sarbu, A. S. Engel, and B. K. Kinkle, 2000, Acidic, cave-wall biofilms located in the Frasassi Gorge, Italy: Geomicrobiology Journal, v. 17, p. 125–139.
Vogel, H. U., 1993, The Great Well of China: Scientific American, v. 268, p. 116–122.
Vogel, M. B., D. J. Des Marais, M. N. Parenteau, L. L. Jahnke, K. A. Turk, and M. D. Y. Kubo, 2010, Biological influences on modern sulfates: Textures and composition of gypsum deposits from Guerrero Negro, Baja California Sur, Mexico: Sedimentary Geology, v. 223, p. 265–280.
Vogel, M. B., D. J. Des Marais, K. A. Turk, M. N. Parenteau, L. L. Jahnke, and M. D. Y. Kubo, 2009, The Role of Biofilms in the Sedimentology of Actively Forming Gypsum Deposits at Guerrero Negro, Mexico: Astrobiology, v. 9, p. 875–893.
Volkova, N. I., 1998, Geochemistry of rare elements in waters and sediments of alkaline lakes in the Sasykkul' depressions, East Pamirs: Chemical Geology, v. 147, p. 265–277.
Volozh, Y., C. J. Talbot, and A. Ismail-Zadeh, 2003, Salt structures and hydrocarbons in the Pricaspian basin: Bulletin American Association Petroleum Geologists, v. 87, p. 313–334.
Volozh, Y. A., V. G. Groshev, and A. V. Sinelnikov, 1994, The overhangs of the southern Precaspian Basin (Khazakstan) [French]: Bulletin des Centres de Recherches Exploration-Production Elf Aquitaine, v. 18, p. 19–31.
Von Bitter, P., H., S. D. Scott, and P. E. Schenk, 1992, Chemosynthesis: An Alternate Hypothesis for Carboniferous Biotas in Bryozoan/Microbial Mounds, Newfoundland, Canada: Palaios, v. 7, p. 466–484.
von Bitter, P. H., S. D. Scott, and P. E. Schenk, 1990, Early C arboniferous lo w-temperature hydrothermal vent communities from Newfoundland: Nature, v. 344, p. 145–148.
Von der Borch, C. C., 1965, The distribution and preliminary geochemistry of modern carbonate sediments of the Coorong area, South Australia: Geochimica et Cosmochimica Acta, v. 29.
Von der Borch, C. C., 1976, Stratigraphy and formation of Holocene dolomitic carbonate deposits of the Coorong area, South Australia: Journal of Sedimentary Petrology, v. 46, p. 952–966.
Von der Borch, C. C., B. Bolton, and J. K. Warren, 1977, Environmental setting and microstructure of subfossil lithified stromatolites associated with evaporites, Marion Lake, South Australia: Sedimentology, v. 24, p. 693–708.
Von der Borch, C. C., and D. Lock, 1979, Geological significance of Coorong dolomites: Sedimentology, v. 26, p. 813–824.
Von der Haar, S. P., and D. S. Gorsline, 1977, Hypersaline lagoon deposits and processes in Baja California, Mexico, in H. J. Walker, ed., Research Techniques in Coastal Environments, Geoscience and Man, v. 18, p. 165–177.
Von Engelhardt, W. H., H. Fuchtbauer, and G. Muller, 1977, Sedimentary petrology, Halsted Press, New York.
Von Gehlen, K., H. Nielsen, and W. Ricke, 1962, S-Isotopen Verhaltnisse in Baryt und Sulfiden aus hydrothermalen Gangen im Schwarzwald und jüngeren Barytgangen in Suddeutschland und ihre genetische Bedeutung: Geochim Cosmochim. Acta, v. 26, p. 1189–1207.
Von Morlot, A., 1847, Ueber Dolomit und seine künstliche Darstellung aus Kalkstein: Naturwissenschaftliche Abhandlungen (Ed. W. Haidinger), Wien, 1, 305–315.
Von Rosen, L., 1990, Lapis lazuli in archaelogical contexts, in P. Aströms, ed., Studies in Mediterranean Archaeology and Literature, v. 93, Partille, Sweden.
Von Tryller, H., 2002, The Cavern Field No. 11 in Ocnele Mari – History, Present and Future: Solution Mining Research Institute Proceedings, Spring Meeting, 28 April 1 May, 2002, Banff, Canada, p. 10 pp.
Vonshak, A., 1997, Spirulina: Growth, physiology and biochemistry, in A. Vonshak, ed., Spirulina platensis (Arthrospina): Physiology, cell-biology and biotechnology: London, Taylor and Francis, p. 43–65.
Vovnyuk, S. V., and G. Czapowski, 2007, Generation of primary sylvite: the fluid inclusion data from the Upper Permian (Zechstein) evaporites, SW Poland: Geological Society, London, Special Publications, v. 285, p. 275–284.
Vreeland, R. H., W. D. Rosenzweig, and D. W. Powers, 2000, Isolation of a 250 million-year-old halotolerant bacterium from a primary salt crystal: Nature, v. 407, p. 897–900.
Vuhahula, E. A. M., J. R. P. Masalu, L. Mabelya, and W. B. C. Wandwi, 2009, Dental fluorosis in Tanzania Great Rift Valley in relation to fluoride levels in water and in "Magadi" (Trona): Desalination, v. 248, p. 610–615.
Wacey, D., 2009, Early Life on Earth: A Practical Guide: Topics in Geobiology, 31, Springer.
Wacey, D., D. T. Wright, and A. J. Boyce, 2007, A stable isotope study of microbial dolomite formation in the Coorong Region, South Australia: Chemical Geology, v. 244, p. 155–174.
Wade, W. J., J. S. Hanor, and R. Sassen, 1989, Controls on H2S concentration and hydrocarbon destruction in the eastern Smackover trend: Transactions – Gulf Coast Association of Geological Societies, v. 39, p. 309–320.
Wagner III, B. H., and M. P. A. Jackson, 2011, Viscous flow during salt welding: Tectonophysics, v. 510, p. 309–326.
Wagner, T., M. Okrusch, S. Weyer, J. Lorenz, Y. Lahaye, H. Taubald, and R. Schmitt, 2010, The role of the Kupferschiefer in the formation of hydrothermal base metal mineralization in the Spessart ore district, Germany: insight from detailed sulfur isotope studies: Mineralium Deposita, v. 45, p. 217–239.
Waldron, J. W. F., C. G. Roselli, J. Utting, and S. K. Johnston, 2010, Kennetcook thrust system: late Paleozoic transpression near the southern margin of the Maritimes Basin, Nova Scotia: Canadian Journal of Earth Sciences, v. 47, p. 137–159.
Waldron, J. W. F., and M. C. Rygel, 2005, Role of evaporite withdrawal in the preservation of a unique coal-bearing succession: Pennsylvanian Joggins Formation, Nova Scotia Geology, v. 33, p. 337–340.
Waldron, J. W. F., M. C. Rygel, M. R. Gibling, and J. H. Calder, 2013, Evaporite tectonics and the late Paleozoic stratigraphic development of the Cumberland basin, Appalachians of Atlantic Canada: Geological Society of America Bulletin, v. 125, p. 945–960.
Walker, R. J., J. W. Morgan, M. F. Horan, G. K. Czamanske, E. J. Krogstad, V. A. Fedorenko, and V. E. Kunilov, 1994, Re-Os isotopic evidence for an enriched-mantle source for the Noril'sk-type, ore-bearing intrusions, Siberia: Geochimica et Cosmochimica Acta, v. 58, p. 4179–4197.
Walker, R. N., R. G. Logan, and J. G. Binnekamp, 1977a, Recent geological advances concerning the H.Y.C. and associated deposits, McArthur river, N.Y: Journal of the Geological Society of Australia, v. 24, p. 365–380.
Walker, R. N., M. D. Muir, W. L. Diver, N. Williams, and N. Wilkins, 1977b, Evidence of major sulphate evaporite deposits in the

Proterozoic McArthur Group, Northern Territory,Australia: Nature, v. 265, p. 526–529.
Wall, M., J. Cartwright, R. Davies, and A. McGrandle, 2010, 3D seismic imaging of a Tertiary Dyke Swarm in the Southern North Sea, UK: Basin Research, v. 22, p. 181–194.
Wall, V. J., and R. K. Valenta, 1990, Ironstone-related gold-copper mineralisation: Tennant Creek and elsewhere: Pacific Rim '90 Congress Proceedings, v. III, p. 855–864.
Wallace, C. A., J. P. Thorson, J. V. Wright, and J. W. Keller, 2002, Metals and Brines of the Paradox Basin, Colorado and Utah: American Association Petroleum Geologists Search and Discovery Article #90012©2003; American Association Petroleum Geologists Hedberg Conference, Vail, Colorado, July 21–26, 2002.
Wallace, M. W., R. A. Both, S. M. Ruano, P. Fenoll Hach-Ali, and T. Lees, 1994, Zebra textures from carbonate-hosted sulfide deposits; sheet cavity networks produced by fracture and solution enlargement: Economic Geology, v. 89, p. 1183–1191.
Wallick, E. I., 1981, Chemical evolution of groundwater in a drainage basin of Holocene age, east central Alberta: Journal of Hydrology, v. 54, p. 245–283.
Wallmann, K., F. S. Aghi, D. Castradori, M. B. Cita, E. Suess, J. Greinert, and D. Rickert, 2002, Sedimentation and formation of secondary minerals in the hypersaline Discovery Basin, eastern Mediterranean: Marine Geology, v. 186, p. 9–28.
Walsh, P., and D. D. Schultz-Ela, 2003, Mechanics of graben evolution in the Canyonlands National Park, Utah: Geological Society America Bulletin, v. 115, p. 259–270.
Walter, M. R., S. Golubic, and W. V. Preiss, 1973, Recent stromatolites from hydromagnesite and aragonite depositing lakes near the Coorong Lagoon, South Australia: Journal of Sedimentary Petrology, v. 43, p. 1021–1030.
Walters, R. F., 1978, Land subsidence in central Kansas related to salt dissolution: Kansas Geological Survey Bulletin 214, p. 1–82.
Walters, R. F., 1991, Gorham Oil Field, Russell County, Kansas: Kansas Geological Survey Bulletin 228.
Waltham, D., 1997, Why does salt start to move?: Tectonophysics, v. 282, p. 117–128.
Waltham, T., F. Bell, and M. Culshaw, 2005, Sinkholes and Subsidence: Karst and Cavernous Rocks in Engineering and Construction: Berlin Heidelberg, Springer Praxis Books, 382 p.
Waltho, A. E., and S. J. Andrews, 1993, The Century zinc-lead deposit, northwest Queensland: Proc. Australasian Institute of Mining and Metallurgy conference, Adelaide, 1993, p. 41–61.
Walton, D., and B. E. Urband, 1997, Well design, casing challenges in Gulf of Mexico subsalt drilling: Offshore, April, 1997, p. 78–82.
Wang, A., Q. Peng, and M. R. Palmer, 1998, Salt dome-controlled sulfide precipitation of Paleoproterozoic Fe-Cu sulfide deposits, eastern Liaoning, northeastern China: Economic Geology, v. 93, p. 1–14.
Wang, G., T. G. Wang, B. R. T. Simoneit, L. Zhang, and X. Zhang, 2010, Sulfur rich petroleum derived from lacustrine carbonate source rocks in Bohai Bay Basin, East China: Organic Geochemistry, v. 41, p. 340–354.
Wang, G., G. You, and Y. Xu, 2008, Investigation on the Nanjing gypsum mine flooding, in H. Liu, A. Deng, and J. Chu, eds., Geotechnical Engineering for Disaster Mitigation and Rehabilitation: Berlin, Springer, p. 920–930.
Wang, J., 1987, A preliminary study of the characteristics and conditions for forming the Anpeng Trona deposit: Petrol Explor. Develop, v. 5, p. 93–99.
Wang, Q., and M. P. Coward, 1990, The Chaidam Basin (NW China): formation and hydrocarbon potential: Journal of Petroleum Geology, v. 13, p. 93–112.
Wang, R. L., 1998, Acyclic isoprenoids – molecular indicators of archaeal activity in contemporary and ancient Chinese saline/hypersaline environments: Hydrobiologia, v. 381, p. 59–76.
Wang, R. L., S. C. Brassell, J. M. Fu, and G. Y. Sheng, 1998, Molecular indicators of microbial contributions to recent and Tertiary hypersaline lacustrine sediments in China: Hydrobiologia, v. 381, p. 77–103.
Wang, S. L., S. C. Brassell, S. C. Scarpitta, M. P. Zheng, S. C. Zhang, P. R. Hayde, and L. M. Muench, 2004, Steroids in sediments from Zabuye Salt Lake, western Tibet: diagenetic, ecological or climatic signals?: Organic Geochemistry, v. 35, p. 157–168.
Wang, W., and M.-F. Zhou, 2014, Provenance and tectonic setting of the Paleo- to Mesoproterozoic Dongchuan Group in the southwestern Yangtze Block, South China: Implication for the breakup of the supercontinent Columbia: Tectonophysics, v. 610, p. 110–127.
Wani, M. R., and S. K. Al-Kabli, 2007, Reservoir characterization and stochastic modeling of the Second Eocene dolomite reservoir, Wafra field, Kuwait-Saudi Arabia Divided Zone (abstract). 7th Middle East Geosciences Conference, GEO 2006: GeoArabia, v. 12, p. 163.
Waples, D. W., P. Haug, and D. H. Welte, 1974, Occurrence of a regular C25 isoprenoid hydrocarbon in Tertiary sediments representing a lagoonal saline environment: Geochemica et Cosmochimica Acta, v. 38, p. 381–387.
Ward, R. F., C. G. S. C. Kendall, and P. M. Harris, 1986, Late Permian (Guadalupian) facies and their association with hydrocarbons: American Association Petroleum Geologists – Bulletin, v. 70, p. 239–262.
Wardlaw, N. C., 1968, Carnallite-sylvite relationships in the middle Devonian Prairie evaporite formation, Saskatchewan: Geological Society America Bulletin, v. 79, p. 1273–1294.
Wardlaw, N. C., 1972, Unusual marine evaporites with salts of calcium and magnesium chloride in Cretaceous basins of Sergipe, Brazil: Economic Geology, v. 67, p. 156–168.
Wardlaw, N. C., and G. D. Nicholls, 1972, Cretaceous evaporites of Brazil and West Africa and their bearing on the theory of continental separation: Internat. Geol. Congress, 24th, Section 6, p. 43–55.
Wardlaw, N. C., and W. M. Schwerdtner, 1966, Halite-anhydrite seasonal layers in the Middle Devonian Prairie Formation, Saskatchewan, Canada: Geological Society of America Bulletin, v. 77, p. 331–342.
Wardlaw, N. C., and D. W. Watson, 1966, Middle Devonian salt formations and their bromide content, Elk Point area, Alberta: Canadian Jour. Earth Sci, v. 3, p. 263–275.
Warrak, M., 1974, The petrography and origin of dedolomitized, veined or brecciated carbonate rock, the "cornieules" in the Frejus region, French Alps: Journ. Geol. Soc. Lond., v. 130, p. 229–247.
Warren, J., C. Morley, T. Charoentitirat, I. Cartwright, P. Ampaiwan, P. Khositchaisri, M. Mirzaloo, and J. Yingyuen, 2014, Structural and fluid evolution of Saraburi Group sedimentary carbonates, central Thailand: A tectonically driven fluid system: Marine and Petroleum Geology, v. 55, p. 100–121.
Warren, J. K., 1982a, The hydrological significance of Holocene tepees, stromatolites, and boxwork limestones in coastal salinas in South Australia: Journal of Sedimentary Petrology, v. 52, p. 1171–1201.
Warren, J. K., 1982b, Hydrologic setting, occurrence, and significance of gypsum in late Quaternary salt lakes, South Australia: Sedimentology, v. 29, p. 609–637.
Warren, J. K., 1983a, Tepees, modern (southern Australia) and ancient (Permian – Texas and New Mexico) – a comparison: Sedimentary Geology, v. 34, p. 1–19.
Warren, J. K., 1983b, Pedogenic calcrete as it occurs in Quaternary calcareous dunes in coastal South Australia: Journal of Sedimentary Petrology, v. 53, p. 787–796.
Warren, J. K., 1985, On the significance of evaporite lamination, in B. C. Schreiber, and H. L. Harner, eds., Sixth International Symposium on Salt, v. 6, p. 161–170.
Warren, J. K., 1986, Shallow water evaporitic environments and their source rock potential: Journal Sedimentary Petrology, v. 56, p. 442–454.

Warren, J. K., 1988, Sedimentology of Coorong dolomite in the Salt Creek region, South Australia: Carbonates and Evaporites, v. 3, p. 175–199.
Warren, J. K., 1989, Evaporite sedimentology: Importance in hydrocarbon accumulation: Englewood Clifs, Prentice-Hall, 285 p.
Warren, J. K., 1990, Sedimentology and mineralogy of dolomitic Coorong lakes, South Australia: Journal of Sedimentary Petrology, v. 60, p. 843–858.
Warren, J. K., 1991, Sulfate dominated sea-marginal and platform evaporative settings, in J. L. Melvin, ed., Evaporites, petroleum and mineral resources.: Developments in Sedimentology, v. 50: Amsterdam, Elsevier, p. 477–533.
Warren, J. K., 1992, Evaporites and Their Importance to Petroleum Exploration: Manual GL508 Petroleum Geology in the IHDRDC Video Library for Exploration and Production Specialists, p. 230 pp.
Warren, J. K., 1997, Evaporites, brines and base metals: brines, flow and "the evaporite that was": Australian Journal of Earth Sciences, v. 44, p. 149–183.
Warren, J. K., 1999, Evaporites: their evolution and economics: Oxford, UK, Blackwell Scientific, 438 p.
Warren, J. K., 2000a, Dolomite: Occurrence, evolution and economically important associations: Earth Science Reviews, v. 52, p. 1–81.
Warren, J. K., 2000b, Evaporites, brines and base metals: low-temperature ore emplacement controlled by evaporite diagenesis: Australian Journal of Earth Sciences, v. 47, p. 179–208.
Warren, J. K., 2000c, Geological controls on the quality of potash, in R. M. Geertmann, ed., 8th World Salt Symposium, v. 1: Amsterdam, Elsevier, p. 173–180.
Warren, J. K., 2006, Evaporites: Sediments, Resources and Hydrocarbons: Berlin, Springer, 1036 p.
Warren, J. K., 2008, Salt as sediment in the Central European Basin system as seen from a deep time perspective (Chapter 5.1), in R. Littke, ed., Dynamics of complex intracontinental basins: The Central European Basin System, Elsevier, p. 249–276.
Warren, J. K., 2010, Evaporites through time: Tectonic, climatic and eustatic controls in marine and nonmarine deposits: Earth-Science Reviews, v. 98, p. 217–268.
Warren, J. K., 2011, Evaporitic source rocks: mesohaline responses to cycles of "famine or feast" in layered brines, Doug Shearman Memorial Volume, (Wiley-Blackwell) IAS Special Publication Number 43, p. 315–392.
Warren, J. K., 2015a, Danakhil potash, Ethiopia: Modern hydrothermal KC1, (3 of 4): Salty Matters, published May 1, 2015, accessed at www.saltworkconsultants.com.
Warren, J. K., 2015b, Danakil potash: K_2SO_4 across the Neogene: Implications, Part 4 of 4: Salty Matters, published May 15, 2015, accessed at www.saltworkconsultants.com.
Warren, J. K., A. Cheung, and I. Cartwright, 2011, Organic Geochemical, Isotopic and Seismic Indicators of Fluid Flow in Pressurized Growth Anticlines and Mud Volcanoes in Modern Deepwater Slope and Rise Sediments of Offshore Brunei Darussalam; Implications for hydrocarbon exploration in other mud and salt diapir provinces (Chapter 10), in L. J. Wood, ed., Shale Tectonics, v. 93: Tulsa OK, American Association Petroleum Geologists Memoir 93 (Proceedings of Hedberg Conference), p. 163–196.
Warren, J. K., S. C. George, P. J. Hamilton, and P. Tingate, 1998, Proterozoic source rocks – Sedimentology and organic characteristics of the Velkerri Formation, Northern Territory, Australia: American Association of Petroleum Geologists Bulletin, v. 82, p. 442–463.
Warren, J. K., K. G. Havholm, M. R. Rosen, and M. J. Parsley, 1990, Evolution of gypsum karst in the Kirschberg Evaporite Member near Fredericksburg, Texas: Journal of Sedimentary Petrology, v. 60, p. 721–734.
Warren, J. K., and R. H. Kempton, 1997, Evaporite Sedimentology and the Origin of Evaporite-Associated Mississippi Valley-type Sulfides in the Cadjebut Mine Area, Lennard Shelf, Canning Basin, Western Australia., in I. P. Montanez, J. M. Gregg, and K. L. Shelton, eds., Basinwide diagenetic patterns: Integrated petrologic, geochemical, and hydrologic considerations: Tulsa OK, SEPM Special Publication, v. 57, p. 183–205.
Warren, J. K., and C. G. S. C. Kendall, 1985, Comparison of sequences formed in marine sabkha (subaerial) and salina (subaqueous) settings; modern and ancient: American Association Petroleum Geologists – Bulletin, v. 69, p. 1013–1023.
Warthmann, R., C. Vasconcelos, H. Sass, and J. A. McKenzie, 2005, Desulfovibrio brasiliensis sp. nov., a moderate halophilic sulfate-reducing bacterium from Lagoa Vermelha (Brazil) mediating dolomite formation: Extremophiles, v. 9, p. 255–261.
Wassmann, T. H., 1983, Cavity utilization in the Netherlands, Sixth International symposium on Salt, v. II, p. 191–201.
Watkins, J. S., G. MacRae, and G. R. Simmons, 1995, Bipolar simple-shear rifting responsible for distribution of mega-salt basins in Gulf of Mexico, in C. J. Travis, H. Harrison, M. R. Hudec, B. C. Vendeville, F. J. Peel, and B. F. Perkins, eds., Salt, sediment, and hydrocarbons, SEPM Foundation, Gulf Coast Section, 16th Annual Research Conference Program with Papers, p. 297–305.
Watney, W. L., S. E. Nissen, S. Bhattacharya, and D. Young, 2003, Evaluation of the Role of Evaporite Karst in the Hutchinson, Kansas, Gas Explosions, January 17 and 18, 2001, in K. S. Johnson, and J. T. Neal, eds., Evaporite karst and engineering/environmental problems in the United State, Oklahoma Geological Survey Circular 109, p. 119–147.
Watson, A., 1985, Structure, chemistry and origins of gypsum crusts in southern Tunisia and the central Namib Desert: Sedimentology, v. 32, p. 855–875.
Watts, R. A., 1991, Subsidence surveys: Solution Mining Research Institute Fall Meeting, Oct 29, Las Vegas Nevada, 23 p.
Webb, S., 2006, The First Boat People: Cambridge Studies in Biological and Evolutionary Anthropology v. 47, Cambridge University Press, 318 p.
Webb, S., 2009, Late Quaternary distribution and biogeography of the southern Lake Eyre basin (SLEB) megafauna, South Australia: Boreas, v. 38, p. 25–38.
Webb, T. C., 1977, Geology of the New Brunswick Glauberite Deposit: New Brunswick Dept. Natural Resources, Open File Rept. 77–15. 26pp.
Webster, D. M., and B. F. Jones, 1994, Paleoenvironmental implicationsof lacustrine clay minerals from the Double Lakes Formation, southern Great Plains, Texas., in R. W. Renaut, and W. M. Last, eds., Sedimentology and geochemistry of modern and ancient saline lakes, v. 50: Tulsa, Society Economic Paleontologists and Mineralogists Special Publication, p. 661–686.
Webster, R., 1975, Gems, their sources, descriptions and identification: London, Newnes, Butterworths.
Webster, R. E., 2004, Tropical versus Temperate Zone Lacustrine Source Rocks: Examples from Takutu Basin, Guyana, and General Levalle Basin, Argentina: American Association Petroleum Geologists Search and Discovery Article #10070 (Adapted from a poster presentation at American Association Petroleum Geologists Annual Convention, Dallas, Texas, April 18–21, 2004).
Wedepohl, K. H., 1964, Untersuchungen am Kupferschiefer in Nordwestdeutschland; ein Beitrag zur Deutung der Genese bitümino ser Sedimente: Geochimica Cosmochimica Acta, v. 28, p. 305–364.
Wedepohl, K. H., and J. Rentzsch, 2006, The composition of brines in the early diagenetic mineralization of the Permian Kupferschiefer in Germany: Contributions to Mineralogy and Petrology, v. 152, p. 323–333.
Weeks, L. G. e., 1958, Habitat of oil: AAPG symposium: Tulso, OK, American Association Petroleum Geologists, p. 1–16.

Weeks, L. G. e., 1961, Chapter 5, Origin, migration and occurrence of petroleum, in G. B. Moody, ed., Petroleum exploration handbook: New York, McGraw-Hill.

Weidlich, O., and M. Bernecker, 2004, Quantification of depositional changes and paleo-seismic activities from laminated sediments using outcrop data: Sedimentary Geology, v. 166, p. 11–20.

Weijermars, R., 1999, Surface Geology, Lithostratigraphy and Tertiary Growth of the Dammam Dome, Saudi Arabia: A New Field Guide: GeoArabia, v. 4, p. 199–226.

Weijermars, R., and M. P. A. Jackson, 2014, Predicting the depth of viscous stress peaks in moving salt sheets: Conceptual framework and implications for drilling: Bulletin American Association Petroleum Geologists, v. 98, p. 911–945.

Weijermars, R., M. P. A. Jackson, and B. Vendeville, 1993, Rheological and tectonic modeling of salt provinces: Tectonophysics, v. 217, p. 143–174.

Weimer, P., and R. T. Buffler, 1992, Structural geology and evolution of the Mississippi Fan fold belt, deep Gulf of Mexico: American Association of Petroleum Geologists Bulletin, v. 76, p. 225–251.

Weissberg, B. G., P. R. L. Browne, and T. M. Seward, 1979, Ore metals in active geothermal systems, in H. L. Barnes, ed., Geochemistry of hydrothermal ore deposits: New York, John Wiley & Sons, p. 738–780.

Wells, A. J., 1962, Recent dolomite in the Persian Gulf: Nature, v. 194, p. 274–275.

Wells, A. T., 1980, Evaporites in Australia: Australia Bureau of Mineral Resources Geology & Geophysics, Bulletin, v. 198, p. 104.

Wender, L. E., J. W. Bryant, M. F. Dickens, A. S. Neville, and A. M. Al-Moqbel, 1998, Paleozoic (Pre-Khuff) hydrocarbon geology of the Ghawar area, eastern Saudi Arabia: GeoArabia, v. 3, p. 272–302.

Wendte, J., I. Al-Aasm, G. Chi, and D. Sargent, 2009, Fault/Fracture Controlled Hydrothermal Dolomitization and Associated Diagenesis of the Upper Devonian Jean Marie Member (Redknife Formation) in the July Lake Area of Northeastern British Columbia: Bulletin of Canadian Petroleum Geology, v. 57, p. 275–322.

Wenkert, D., 1979, Flow of salt glaciers: Geophysical Research Letters, v. 6, p. 523–526.

Wentworth, S. J., E. K. Gibson, M. A. Velbel, and D. S. McKay, 2005, Antarctic Dry Valleys and indigenous weathering in Mars meteorites: Implications for water and life on Mars: Icarus, v. 174, p. 383–395.

Werner, M. L., M. D. Feldman, and L. P. Knauth, 1988, Petrography and geochemistry of water-rock interactions in Richton Dome cap rock (southeastern Mississippi, U.S.A.): Chemical Geology, v. 74, p. 113–135.

West, I. M., 1964, Evaporite diagenesis in the lower Purbeck beds of Dorset: Proceedings – Yorkshire Geological Society, v. 34, p. 315–330.

West, I. M., 1965, Macrocell structure and enterolithic veins in British Purbeck gypsum and anhydrite: Proceedings of Yorkshire Geological Society, v. 35, p. 47–58.

West, I. M., 1973, Vanished evaporites; significance of strontium minerals: Journal of Sedimentary Petrology, v. 43, p. 278–279.

West, I. M., 1979, Review of evaporite diagenesis in the Purbeck Formation of southern England, Symposium on: West European Jurassic Sedimentation – "Sedimentation Jurassique W. European", Association of French Sedimentologists Special Publication No. 1, p. 407–416.

West, I. M., Y. A. Ali, and M. E. Hilmy, 1979, Primary gypsum nodules in a modern sabkha on the Mediterranean coast of Egypt: Geology, v. 7, p. 354–358.

Westbrook, G. K., and T. J. Reston, 2002, The accretionary complex of the Mediterranean Ridge: tectonics, fluid flow and the formation of brine lakes – an introduction to the special issue of Marine Geology: Marine Geology, v. 186, p. 1–8.

Wezel, F. C., and D. Baioni, 2010, Evidence for subaqueously resedimented sulphate evaporites on Mars: Planetary & Space Science, v. 58, p. 1500–1505.

Wezel, F. C., and D. Baioni, 2014, Sulphate clastic injectites at Sinus Meridiani on Mars: Planetary and Space Science, v. 90, p. 106–112.

Wharton, D. A., 2002, Life at the limits; Organisms in extreme environments Cambridge, UK, Cambridge University Press, 307 p.

Wheeler, W. H., and D.A. Textoris, 1978, Triassic limestone and chert of playa origin in North Carolina: Journal of Sedimentary Petrology, v. 48, p. 765–776.

Whelan, J. F., R. O. Rye, W. de Lorraine, and H. Ohmoto, 1990, Isotopic geochemistry of the mid-Proterozoic evaporite basin; Balmat, New York: American Journal of Science, v. 290, p. 396–424.

White, A. H., and B. C. Youngs, 1980, Cambrian alkali playa-lacustrine sequence in the northeastern Officer Basin, South Australia.: Journal of Sedimentary Petrology, v. 50, p. 1279–1286.

White, D. E., 1981, Active geothermal systems and hydrothermal deposits: Economic Geology 75th Anniversary Volume, p. 392–423.

White, K., and N. Drake, 1993, Mapping the distribution and abundance of gypsum in south-central Tunisia from Landsat Thematic Mapper data: Zeitschrift fur Geomorphologie, v. 37, p. 309–325.

White, W. B., 1988, Geomorphology and hydrology of karst terrains: New York, Oxford University Press, 464 p.

Whiticar, M. J., and E. Suess, 1998, The cold carbonate connection between Mono Lake, California and the Bransfield Strait, Antarctica: Aquatic Geochemistry, v. 4, p. 419–454.

Whitney, P. R., and J. F. Olmsted, 1988, Geochemistry and origin of albite gneisses, northeastern Adirondack Mountains, New York: Contributions to Mineralogy and Petrology, v. 99, p. 476–484.

Whittaker, S. G., and E. W. Mountjoy, 1996, Diagenesis of an Upper Devonian carbonate-evaporite sequence: Birdbear Formation, southern Interior Plains, Canada: Journal of Sedimentary Research A: Sedimentary Petrology and Processes, v. 66, p. 965–975.

Whittig, L. D., A. E. Deyo, and K. K. Tanji, 1982, Evaporite mineral species in Mancos Shale and salt efflorescence, Upper Colorado River basin: Soil Science Society of America Journal, v. 46, p. 645–651.

Whittle, G. L., and A. S. Alsharhan, 1994, Dolomitization and certification of the Early Eocene Rus Formation in Abu Dhabi, United Arab Emirates: Sedimentary Geology, v. 92, p. 273–385.

Whittle, G. L., and A. S. Alsharhan, 1996, Diagenetic history and source rock potential of the Upper Jurassic Diyab Formation, offshore Abu Dhabi, United Arab Emirates: Carbonates and Evaporites, v. 11, p. 145–154.

Whyatt, J., and F. Varley, 2008, Catastrophic Failures of Underground Evaporite Mines: Proceedings of the 27th International Conference on Ground Control in Mining (ICGCM), July 29–31, 2008; Peng, S. S., Mark, C., Finfinger, G. L., Tadolini, S. C., Khair. A. W., Heasley, K.A., Luo-Y, eds., Morgantown, West Virginia University, p. 113–122.

Wiebe, N. S., N. Chow, and L. D. Stasiuk, 2013, Origin of source rocks in the Middle Devonian Keg River Formation, Rainbow and Zama sub-basins, Alberta: Sedimentological and organic petrological evidence: Bulletin of Canadian Petroleum Geology, v. 61, p. 187–210.

Wiggins, W. D., P. M. Harris, and R. C. Burruss, 1993, Geochemistry of post-uplift calcite in the Permian Basin of Texas and New Mexico: Geological Society of America Bulletin, v. 105, p. 779–790.

Wigley, T. M. L., J. J. Drake, J. F. Quinlan, and D. C. Ford, 1973, Geomorphology and geochemistry of a gypsum karst near Canal Flats, British Columbia: Canadian J. Earth Science, v. 10, p. 113–129.

Wiig, S. V., W. D. Grundy, and J. R. Dyni, 1995, Trona resources in the Green River Basin, southwest Wyoming, U.S. Geological Survey Open-File Report 95–476, 88 p.

Wilburn, D. R., T. Goonan, and D. Bleiwas, 2001, Technological Advancement -- A Factor in Increasing Resource Use: U.S. Geological Survey Open-File Report 01–197 (Version 1.03 Online Only – last updated 2005) accessed at http://pubs.usgs.gov/of/2001/of01-197 on April 29, 2012.

Wilde, A., M. Gregory, R. Duncan, K. Gessner, M. Kühn, and P. Jones, 2005, Geochemical process model for the Mt Isa Cu-Co-Ag deposits, in J. Mao, and F. P. Bierlein, eds., Mineral Deposit Research: Meeting the Global Challenge; Proceedings of the Eighth Biennial SGA Meeting Beijing, China, 18–21 August 2005 Berlin, Springer, p. 199–202.

Wilde, A. R., 2011, Mount Isa copper orebodies: improving predictive discovery: Australian Journal of Earth Sciences, v. 58, p. 937–952.

Wilde, A. R., P. A. Jones, K. Gessner, L. Ailleres, M. J. Gregory, and R. J. Duncan, 2006, A Geochemical Process Model for the Mount Isa Copper Orebodies: Economic Geology, v. 101, p. 1547–1567.

Wilde, A. R., P. Layer, T. Mernagh, and J. Foster, 2001, The giant Muruntau gold deposit geologic, geochronologic, and fluid inclusion constraints on ore genesis: Economic Geology, v. 96, p. 633–644.

Wilde, A. R., D. C. McPhail, J. Brugger, S. McKnight, and D. Garnett, 2005, Preliminary study of the source of base metals in MVT deposits of the Canning Basin, Western Australia, p. 195–198.

Wilgus, C. K., and W. T. Holser, 1984, Marine and Nonmarine Salts of Western Interior, United States: American Association Petroleum Geologists – Bulletin, v. 68, p. 765–767.

Wilke, A. R., C. Hellberg, and O. Bornemann, 2001, Geological interpretation of domal salt structures in the North European Zechstein Formation: Influence on cavern development: Solution Mining Research Institute Technical Paper Fall 2001 Meeting, 7–10 October, Albuquerque, New Mexico, p. 9 pp.

Wilkins, D. E., and D. R. Currey, 1999, Radiocarbon chronology and d13 C analysis of mid- to late-Holocene aeolian environments, Guadalupe Mountains National Park, Texas, USA : Holocene, v. 9, p. 363–372.

Wilkinson, J. J., B. Stoffell, C. C. Wilkinson, T. E. Jeffries, and M. S. Appold, 2009, Anomalously Metal-Rich Fluids Form Hydrothermal Ore Deposits: Science, v. 323, p. 764–767.

Williams, A. F., and J. W. Holmes, 1978, A novel method of estimating the discharge of water From the mound springs of the Great Artesian Basin, Central Australia: Journal of Hydrology, v. 38, p. 263–272.

Williams, D. F., and I. Lerche, 1987, Salt domes, organic-rich source beds and reservoirs in intraslope basins of the Gulf Coast region, in I. Lerche, and J. J. O'Brien, eds., Dynamical geology of salt and related structures: New York, Academic Press, p. 751–830.

Williams, G. K., 1984, Some musings on the Devonian Elk Point Basin, western Canada: Bulletin of Canadian Petroleum Geology, v. 32, p. 216–232.

Williams, J. B., M. J. Schwab, and A. Brauer, 2011, An early first-century earthquake in the Dead Sea: International Geology Review, v. 54, p. 1219–1228.

Williams, M. A. J., D. I. Dunkerley, P. De Deckker, A. P. Kershaw, and T. Stokes, 1993, Quaternary Environments: London, Edward Arnold, 330 p.

Williams, M. D., and V. Ranganathan, 1994, Ephemeral thermal and solute plumes formed by upwelling groundwaters near salt domes: Journal of Geophysical Research-Solid Earth, v. B8, p. 15667–15681.

Williams, N., 1978, Studies of base metal sulphide deposits at McArthur River, Northern Territory, Australia II. The sulphide-S and organic-C relationship of concordant deposits and their significance: Economic Geology, v. 73, p. 1036–1056.

Williams, P. J., 1994, Iron mobility during synmetamorphic alteration in the Selwyn Range area, NW Queensland – Implications for the origin of ironstone-hosted Au-Cu deposits: Mineralium Deposita, v. 29, p. 250–260.

Williams, P. J., M. D. Barton, D. A. Johnson, L. Fontboté, A. De Haller, G. Mark, N. H. S. Oliver, and R. Marschik, 2005, Iron oxide copper-gold deposits: geology, space-time distribution, and possible modes of origin: Economic Geology, v. 100th Anniversary Volume, p. 371–405.

Williams, P. J., and P. J. Pollard, 2003, Australian Proterozoic iron oxide-Cu-Au deposits: An overview with new metallogenic and exploration data from the Cloncurry district, northwest Queensland: Exploration and Mining Geology, v. 10, p. 191–213.

Williams, S. H., and J. R. Zimbelman, 1994, White Rock – An eroded Martian lacustrine deposit: Geology, v. 22, p. 107–110.

Williams, W. D., P. De Deckker, and R. J. Shiel, 1998, The limnology of Lake Torrens, an episodic salt lake of central Australia, with particular reference to unique events in 1989: Hydrobiologia, v. 384, p. 101–110.

Williams-Jones, A. E., R. J. Bowell, and A. A. Migdisov, 2009, Gold in Solution: Elements, v. 5, p. 281–287.

Williams-Stroud, S. C., 1994, The evolution of an inland sea of marine origin to a non-marine saline lake: the Pennsylvanian Paradox salt, in R. W. Renaut, and W. M. Last, eds., Sedimentology and geochemistry of modern and ancient saline lakes: Tulsa, OK, Society for Sedimentary Geology; Special Publication Volume 50, p. 293–306.

Williamson, B. M., 1987, Formation of authigenic silicate minerals in Miocene volcaniclastic rocks, Boron, California: Master of Science thesis, University of California, Santa Barbara.

Williamson, C. R., 1978, Depositional processes, diagenesis and reservoir properties of Permian Deep sea sandstones, Bell Canyon Formation, Texas – New Mexico: Doctoral thesis, University of Texas at Austin.

Williamson, C. R., and M. D. Picard, 1974, Petrology of carbonate rocks of the Green River Formation (Eocene): Journal of Sedimentary Petrology, v. 44, p. 738–759.

Williamson, D., M. Taieb, B. Damnati, M. Icole, and N. Thouveny, 1993, Equatorial extension of the younger Dryas event – Rock magnetic evidence from Lake Magadi (Kenya): Global & Planetary Change, v. 7, p. 235–242.

Williamson, M. D., S. J. Murray, W. S. Atkins, T. A. P. Hamilton, and M. A. Copland, 1997, A review of Zechstein Drilling Issues: SPE 38483, September 1997, p. 189–196.

Williford, K. H., K. Grice, G. A. Logan, J. Chen, and D. Huston, 2011, The molecular and isotopic effects of hydrothermal alteration of organic matter in the Paleoproterozoic McArthur River Pb/Zn/Ag ore deposit: Earth and Planetary Science Letters, v. 301, p. 382–392.

Willis, I. L., R. E. Brown, W. J. Stroud, and B. P. J. Stevens, 1983, The Early Proterozoic Willyama supergroup: stratigraphic subdivision and interpretation of high to low-grade metamorphic rocks in the Broken Hill block, New South Wales: Journal, Geological Society of Australia, v. 30, p. 195–224.

Willner, A. P., 1992, Tourmalinites from the stratiform peraluminous metamorphic suite of the Central Namaqua Mobile Belt (South Africa): Mineralium Deposita, v. 27, p. 304–313.

Wilson, A. A., and C. Ruppel, 2007, Salt tectonics and shallow subseafloor fluid convection: models of coupled fluid-heat-salt transport: Geofluids, v. 7, p. 377–386.

Wilson, A. H., and J. A. Versfeld, 1994, The early Archaean Nondweni greenstone belt, southern Kaapvaal Craton, South Africa; Part I, Stratigraphy, sedimentology, mineralization and depositional environment: Precambrian Research, v. 67, p. 243–276.

Wilson, A. O., 1985, Depositional and diagenetic facies in the Jurassic Arab-C and -D reservoirs, Qatif field, Saudi Arabia, in P. O. Roehl, and P. W. Choquette, eds., Carbonate petroleum reservoirs: New York, Springer-Verlag, p. 319–340.

Wilson, H. H., 1975, Sub Salt Origin of Exotic Blocks in Piercement Domes Reveals the Probability of Oligo-Miocene Salt in the Gulf of

Mexico Region: Gulf Coast Association of Geological Societies Transactions, v. 25, p. 109.

Wilson, J. T., 1966, Did the Atlantic close and then re-open?: Nature, v. 211, p. 676–681.

Wilson, M., S. Shahid, M.Abdelfattah, J. Kelley, and J. Thomas, 2013,Anhydrite Formation on the Coastal Sabkha of Abu Dhabi, United Arab Emirates, in S. A. Shahid, F. K. Taha, and M. A. Abdelfattah, eds., Developments in Soil Classification, Land Use Planning and Policy Implications, Springer Netherlands, p. 175–201.

Wilson, P., J. C. White, and B. V. Roulston, 2006, Structural geology of the Penobsquis salt structure: late Bashkirian inversion tectonics in the Moncton Basin, New Brunswick, eastern Canada: Canadian Journal of Earth Sciences, v. 43, p. 405.

Wilson, T. P., and D. T. Long, 1993, Geochemistry and isotope chemistry of Ca-Na-Cl brines in Silurian Strata, Michigan Basin, USA: Applied Geochemistry, v. 8, p. 507–524.

Wilson, W. E., 2002, Cuprian Elbaite from the Batalha Mine, Paraíba, Brazil: Mineralogical Record, v. 33, p. 127–137.

Winsborough, B. M., J. S. Seeler, S. Golubic, R. L. Folk, and B. Maguire, Jr., 1994, Recent fresh-water lacustrine stromatolites, stromatolitic mats and oncoids from northeastern Mexico, in J. Bertrand-Sarfati, and C. Monty, eds., Phanerozoic Stromatolites II: Amsterdam, Kluwer Academic Publishers, p. 71–100.

Winter, B., J. Valley, J. Simo, G. Nadon, and C. Johnson, 1995, Hydraulic seals and their origin – Evidence from the stable isotope geochemistry of dolomites in the Middle Ordovician St-Peter Sandstone, Michigan Basin: American Association Petroleum Geologists – Bulletin, v. 79, p. 30–48.

Withjack, M., and C. Scheiner, 1982, Fault patterns associated with domes—An experimental and analytical study: Bulletin American Association Petroleum Geologists, v. 66, p. 302–316.

Wittstrom, M. D., 1990, Little Knife Field – USA, Williston Basin, North Dakota, in E. A. Beaumont, and N. H. Foster, eds., Treatise of Petroleum Geology; Atlas of Oil and Gas Fields: Stratigraphic Traps I: Tulsa, OK, American Association Petroleum Geologists, p. 159–194.

Wodzicki, A., and A. Piestrzynski, 1994, An ore genetic model for the Lubin-Sieroszowice mining district: Mineralium Deposita, v. 29, p. 30–43.

Woese, C. R., 1993, Introduction. The archaea: their history and significance, in M. Kates, D. J. Kushner, and A. T. Matheson, eds., The Biochemistry of the Archaea, v. 26: Amsterdam, Elsevier, p. vii–xxix.

Woese, C. R., and G. E. Fox, 1977, Phylogenetic structure of the prokaryotic domain: the primary kingdoms: Proc. Natl. Acad. Sci. USA, v. 74, p. 5088–5090.

Woese, C. R., O. Kandler, and M. L. Wheelis, 1990, Towards a natural system of organisms: proposal for the domains Archaea, Bacteria, and Eucarya: Proc. Natl. Acad. Sci. USA, v. 87, p. 4576–4579.

Wolela, A., 2007, Source rock potential of the Blue Nile (Abay) Basin, Ethiopia: Journal of Petroleum Geology, v. 30, p. 389–402.

Wolfgramm, M., and A. Mumm, 2000, Spatial correlation of fluid inclusion generations: reconstructing fluid flow during basin evolution: Journal of Geochemical Exploration, v. 69, p. 397–402.

Wong, K. W., 1982, A manual on ground surveys for the detection and measurement of subsidence related to solution mining: Solution Mining Research Institute Research Project Report, v. 81-0003A-Solution Mining Research Institute.

Wong, S. W., P. M. O'Dell, C. J. de Pater, and J. Shaoul, 2000, FreshWater Injection Stimulation in a Deep Tight Oil Reservoir: SPE 62618: presented at the 2000 SPE/American Association Petroleum Geologists Western Regional Meeting held in Long Beach, California, 19–23 June 2000.

Wood, A. P., and D. P. Kelly, 1991, Isolation and characterisation of *Thiobacillus halophilus sp. nov.*, a sulphur-oxidising autotrophic eubacterium from a Western Australian hypersaline lake: Arch. Microbiol., v. 156, p. 277–280.

Wood, J., 1841, John Wood. A Personal Narrative of a Journey to the Source of the River Oxus by the Route of the Indus, Kabul, and Badakhshan, Performed under the Sanction of the Supreme Government of India, in the Years 1836, 1837, and 1838. Available as Elibron Classics, 2001, 458 pages. Replica of 1841 edition by John Murray, London.

Wood, M. W., and H. F. Shaw, 1976, The geochemistry of celestites from the Yates area near Bristol (U.K.): Chem. Geol., v. 17, p. 179–193.

Wood, S. A., and I. M. Samson, 1998, Solubility of ore minerals and complexation of ore metals in hydrothermal solutions: Reviews in Economic Geology, v. 10, p. 33–80.

Wood, W. W., and W. E. Sandford, 2002, Hydrology and solute chemistry of the coastal sabkha aquifer in the Emirate of Abu Dhabi, in H. J. Barth, and B. Böer, eds., Sabkha Ecosystems, v. 1: Dordrecht,, Kluwer Academic, p. 173–185.

Wood, W. W., W. E. Sanford, and A. R. S. Al Habshi, 2002, Source of solutes to the coastal sabkha of Abu Dhabi: Geological Society of America Bulletin, v. 114, p. 259–268.

Wood, W. W., W. E. Sanford, and S. K. Frape, 2005, Chemical openness and potential for misinterpretation of the solute environment of coastal sabkhat: Chemical Geology, v. 215, p. 361–372.

Wooden, J. L., G. K. Czamanske, R. M. Bouse, A. P. K. Likhachev, V. E., and V. Lyul'ko, 1992, Pb isotope data indicate a complex, mantle origin for the Noril'sk-Talnakh ores, Siberia: Economic Geology, v. 87, p. 1153–1165.

Wooding, R. A., 1960, Rayleigh instability of a thermal boundary layer in flow through a porous medium: Journal of Fluid Mechanics, v. 9, p. 183–192.

Woods, P. J. E., 1979, The geology of Boulby Mine: Economic Geology, v. 74, p. 409–418.

Woolley,A. R., and B.A. Kjarsgaard, 2008, Paragenetic types of carbonatite as indicated by the diversity and relative abundances of associated silicate rocks—evidence from global database: The Canadian Mineralogist, v. 46, p. 741–752.

Woolnough, W. G., 1937, Sedimentation in barred basins and source rocks of oil: American Association Petroleum Geologists – Bulletin, v. 29, p. 1101–1157.

Worden, K., C. Carson, I. Scrimgeour, J. Lally, and N. Doyle, 2008, A revised Palaeoproterozoic chronostratigraphy for the Pine Creek Orogen, northern Australia: Evidence from SHRIMP U-Pb zircon geochronology: Precambrian Research, v. 166, p. 122–144.

Worden, R. H., 1996, Controls on halogen concentrations in sedimentary formation waters: Mineralogical Magazine, v. 60, p. 259–274.

Worden, R. H., and P. C. Smalley, 1996, H2S-Producing reactions in deep carbonate gas reservoirs – Khuff Formation, Abu Dhabi: Chemical Geology, v. 133, p. 157–171.

Worden, R. H., P. C. Smalley, and M. M. Cross, 2000, The influence of rock fabric and mineralogy on thermochemical sulfate reduction: Khuff Formation, Abu Dhabi: Journal of Sedimentary Research Section A-Sedimentary Petrology & Processes, v. 70, p. 1210–1221.

Worden, R. H., P. C. Smalley, and A. E. Fallick, 1997, Sulfur cycle in buried evaporites: Geology, v. 25, p. 643–646.

Worden, R. H., P. C. Smalley, and N. H. Oxtoby, 1995, Gas souring by thermochemical sulfate reduction at 140° C: American Association Petroleum Geologists Bulletin-American Association of Petroleum Geologists., v. 79, p. 854–863.

Worden, R. H., P. C. Smalley, and N. H. Oxtoby, 1996, The effects of thermochemical sulphate reduction upon formation water salinity and oxygen isotopes in carbonate gas reservoirs: Geochimica et Cosmochimica Acta, v. 60, p. 3925–3931.

Woronick, R. E., and L. S. Land, 1985, Late burial diagenesis, Lower Cretaceous Pearsall and Lower Glen Rose Formations, south Texas (USA), in N. Schneidermann, and P. M. Harris, eds., Carbonate cements, SEPM, Tulsa; Special Publication 36, p. 265–275.

Worrall, D. M., and S. Snelson, 1989, Evolution of the northern Gulf of Mexico, with emphasis on Cenozoic growth faulting and the role of salt, in A. W. Bally, and A. R. Palmer, eds., Geology of North America _ An Overview: Boulder, CO, Geological Soc. America, p. 97–138.

Worrall, J. G., and J. K. Warren, 1986, Three-stage dolomitization of the Smackover Formation, SW Alabama; evidence for near-surface and burial-derived fluids: Society of Economic Paleontologists and Mineralogists Midyear Meeting Abstracts, v. 3, p. 118–119.

Worsley, N., and A. Fuzesy, 1979, The potash-bearing members of the Devonian Prairie Evaporite of southeastern Saskatchewan, south of the mining area: Economic Geology, v. 74, p. 377–388.

Wortmann, U. G., and A. Paytan, 2012, Rapid Variability of Seawater Chemistry Over the Past 130 Million Years: Science, v. 337, p. 334–336.

Wright, D. T., 1999, The role of sulphate-reducing bacteria and cyanobacteria in dolomite formation in distal ephemeral lakes of the Coorong region, South Australia: Sedimentary Geology, v. 126, p. 147–157.

Wu, C., 2008, Bayan Obo Controversy: Carbonatites versus Iron Oxide-Cu-Au-(REE-U): Resource Geology, v. 58, p. 348–354.

Wu Moude, and L. Xiji, 1981, Two types of diapiric structure of the Kunyang Group, Yunnan. (Chinese): Acta Geologica Sinica, v. 55, p. 105–117.

Wu, S., 1993, Salt and slope tectonics offshore Louisiana: Doctoral thesis, Rice Univ. Houston.

Wu, S., A. W. Bally, and C. Cramez, 1990b, Allochthonous salt, structure and stratigraphy of the north- eastern Gulf of Mexico. Part II: structure: Marine & Petroleum Geology, v. 7, p. 334–370.

Wu, S., P. R. Vail, and C. Cramez, 1990a, Allochthonous salt, structure and stratigraphy of the north-eastern Gulf of Mexico. Part I: stratigraphy: Marine & Petroleum Geology, v. 7, p. 318–333.

Wunder, B., A. Meixner, R. L. Romer, R. Wirth, and W. Heinrich, 2005, The geochemical cycle of boron: Constraints from boron isotope partitioning experiments between mica and fluid: Lithos, v. 84, p. 206–216.

Wünnemann, B., K. Hartmann, M. Janssen, and C. Zhang Hucai, 2007, Responses of Chinese desert lakes to climate instability during the past 45,000 years, Developments in Quaternary Science, v. Volume 9, Elsevier, p. 11–24.

Wyborn, L., 1998, Younger *ca* 1500 Ma granites of the Williams and Naraku Batholiths, Cloncurry district, eastern Mt Isa Inlier: Geochemistry, origin, metallogenic significance and exploration indicators: Australian Journal of Earth Sciences, v. 45, p. 397–411.

Wyborn, L. A. I., 1988, Petrology, Geochronology and Isotope – Geochemistry of the post-1820 Ma Granites of the Mount Isa Inlier: mechanisms for the generation of Proterozoic anorogenic granites: Precambrian Research, v. 40–41, p. 509–541.

Wylie, A. S., and J. R. Wood, 2005, Well-log tomography and 3-D imaging of core and log-curve amplitudes in a Niagaran reef, Belle River Mills field, St. Clair County, Michigan, United States: Bulletin American Association Petroleum Geologists, v. 89, p. 409–433.

Wyn Hughes, G., 1996, A New Bioevent Stratigraphy of Late Jurassic Arab-D Carbonates of Saudi Arabia: GeoArabia, v. 1, p. 417–434.

Wyn Hughes, G., 1997, The Great Pearl Bank Barrier of the Arabian Gulf as a Possible Shu'aiba Analogue: GeoArabia, v. 2, p. 279–304.

Xavier, R. P., M. Wiedenbeck, R. B. Trumbull, A. M. Dreher, L. V. S. Monteiro, D. Rhede, C. E. G. de Araujo, and I. Torresi, 2008, Tourmaline B-isotopes fingerprint marine evaporites as the source of high-salinity ore fluids in iron oxide copper-gold deposits, Carajas Mineral Province (Brazil): Geology, v. 36, p. 743–746.

Xiao, J., Y. K. Xiao, Z. D. Jin, M. Y. He, and C. Q. Liu, 2013, Boron isotope variations and its geochemical application in nature: Australian Journal of Earth Sciences, v. 60, p. 431–447.

Xiong, J., and C. E. Bauer, 2002, Complex evolution of photosynthesis: Ann Rev. Plant Physiol, v. 53, p. 503–521.

Xiyu, Z., 1984, Distribution characteristics of boron and lithium in brine of Zhacang Caka salt lake, Xizang (Tibet), China: Chinese Journal of Oceanology and Limnology, v. 2, p. 218–227.

Xu, G., 2000, Fluid inclusions with NaCl-CaCl2-H_2O composition from the Cloncurry hydrothermal system, NW Queensland, Australia: Lithos, v. 53, p. 21–35.

Xu, Z., and J. Parnell, 1993, Potash cement in modern and ancient halite beds: Carbonates and Evaporites, v. 8, p. 149–155.

Yagmurlu, F., and C. Helvaci, 1994, Sedimentological characteristics and facies of the evaporite-bearing Kirmir Formation (Neogene), Beypazari Basin, central Anatolia, Turkey: Sedimentology, v. 41, p. 847–860.

Yahi, N., R. G. Schaefer, and R. Littke, 2001, Petroleum generation and accumulation in the Berkine basin, eastern Algeria: Bulletin American Association Petroleum Geologists, v. 85, p. 1439–1467.

Yakimov, M. M., V. La Cono, R. Denaro, G. D'Auria, F. Decembrini, K. N. Timmis, P. N. Golyshin, and L. Giuliano, 2007, Primary producing prokaryotic communities of brine, interface and seawater above the halocline of deep anoxic lake L'Atalante, Eastern Mediterranean Sea: ISME J, v. 1, p. 743–755.

Yakimov, M. M., V. La Cono, V. Z. Slepak, G. La Spada, E. Arcadi, E. Messina, B. Mireno, L. S. Monticelli, D. Rojo, C. Barbas, O. V. Golyshina, M. Ferrer, P. N. Golyshin, and L. Giuliano, 2013, Microbial life in the Lake Medee, the largest deep-sea salt-saturated formation.: Scientific reports, 3; http://www.nature.com/srep/2013/131219/srep03554/full/srep03554.html.

Yan, S., G. Mu, Y. Xu, and Z. Zhao, 1998, Quaternary environmental evolution of the Lop Nur region, China: Acta Geographica Sinica, v. 53, p. 332–340.

Yang, C., I. Hutcheon, and H. R. Krouse, 2001, Fluid inclusion and stable isotope studies of thermochemical sulphate reduction from Burnt Timber and Crossfield East gas fields in Alberta, Canada: Bulletin of Canadian Petroleum Geology, v. 49, p. 149–164.

Yang, C., W. Jing, J. J. K. Daemen, G. Zhang, and C. Du, 2013, Analysis of major risks associated with hydrocarbon storage caverns in bedded salt rock: Reliability Engineering & System Safety, v. 113, p. 94–111.

Yang, W. B., and T. J. Ahrens, 1998, Shock vaporization of anhydrite and global effects of the K/T bolide: Earth & Planetary Science Letters, v. 156, p. 125–140.

Yang, W. B., R. J. Spencer, H. R. Krouse, T. K. Lowenstein, and D. Cases, 1995, Stable isotopes of lake and fluid inclusion brines, Dabusun Lake, Qaidam Basin, Western China – Hydrology and paleoclimatology in arid environments: Palaeogeography Palaeoclimatology Palaeoecology., v. 117, p. 279–290.

Yanosky, T. M., and W. M. Kappel, 1997, Effects of solution mining of salt on wetland hydrology as inferred from tree rings: Water Resources Research, v. 33, p. 457–470.

Yaoru, L., and A. H. Cooper, 1997, Gypsum karst geohazards in China, in B. F. Beck, and J. B. Stephenson, eds., The Engineering Geology and Hydrogeology of Karst Terranes. Proceedings of the 6th Multidisciplinary Conference on Sinkholes and the Engineering and Environmental Impacts of Karst, Springfield, MO, 6–9 April, 1997, p. 117–126.

Yardley, B. D., 1996, The Evolution of Fluids Through the Metamorphic Cycle, in B. r. Jamtveit, and B. D. Yardley, eds., Fluid Flow and Transport in Rocks, Springer Netherlands, p. 99–121.

Yardley, B. W. D., 2009, The role of water in the evolution of the continental crust: Journal of the Geological Society, London, v. 166, p. 585–600.

Yardley, B. W. D., 2013, The Chemical Composition of Metasomatic Fluids in the Crust, Metasomatism and the Chemical Transformation of Rock: Lecture Notes in Earth System Sciences, Springer Berlin Heidelberg, p. 17–51.

Yardley, B. W. D., and J. T. Graham, 2002, The origins of salinity in metamorphic fluids: Geofluids, v. 2, p. 249–256.

Yardley, B. W. D., and G. E. Lloyd, 1995, Why metasomatic fronts are really metasomatic sides: Geology, v. 23, p. 53–56.

Yassir, N. A., and J. S. Bell, 1994, Relationships between pore pressure, stresses, and present-day geodynamics in the Scotian Shelf, offshore eastern Canada: American Association Petroleum Geologists – Bulletin, v. 78, p. 1863–1880.

Yechieli, Y., M. Abelson,A. Bein, O. Crouvi, and V. Shtivelman, 2006, Sinkhole "swarms" along the Dead Sea coast: Reflection of disturbance of lake and adjacent groundwater systems: Geological Society of America Bulletin, v. 118, p. 1075–1087.

Yechieli, Y., I. Gavrieli, B. Berkowitz, and D. Ronen, 1998, Will the Dead Sea die?: Geology, v. 28, p. 755–758.

Yilmaz, I. ü. k., M. Marschalko, and M. Bednarik, 2011, Gypsum collapse hazards and importance of hazard mapping: Carbonates and Evaporites, v. 26, p. 193–209.

Yin, A., Y.-Q. Dang, L.-C. Wang, W.-M. Jiang, S.-P. Zhou, X.-F. Chen, G. E. Gehrels, and M. W. McRivette, 2008, Cenozoic tectonic evolution of Qaidam basin and its surrounding regions (Part 1): The southern Qilian Shan-Nan Shan thrust belt and northern Qaidam basin: Geological Society of America Bulletin, v. 120, p. 813–846.

Yoo, C. M., J. M. Gregg, and J. S. Shelton, 2000, Dolomitization and Dolomite Neomorphism: Trenton and Black River Limestones (Middle Ordovician) Northern Indiana, U.S.A.: Journal of Sedimentary Research, v. 70, p. 265–274.

Yoshida, T., 1992, Salt production techniques in ancient China: the Aobo tu (translated and revised by Hans Ulrich Vogel): Sinica Leidensia, v. 27: Leiden ; New York, E.J. Brill, 309 p.

You, C. F., and M. J. Bickle, 1998, Evolution of an active seafloor massive sulphide deposit: Nature, v. 394, p. 668–671.

Younes, M. A., and R. P. Philp, 2005, Source rock characterization based on biological marker distributions of crude oils in the southern Gulf of Suez, Egypt: Journal of Petroleum Geology, v. 28, p. 301–317.

Younker, L. W., P. W. Kasameyer, and J. D. Tewhey, 1982, Geological, geophysical, and thermal characteristics of the Salton Sea Geothermal Field, California: Journal of Volcanology and Geothermal Research, v. 12, p. 221–258.

Youssef, E. A. A., 1989, Geology and genesis of sulfur deposits at Ras Gemsa area, Red Sea coast, Egypt: Geology, v. 17, p. 797–801.

Youssef, E. S. A. A., 1998, Sequence stratigraphy of the Upper Jurassic evaporite-carbonate-sequence at the western area of Wadi Al-Jawf-Marib Basin, Yemen: Carbonates & Evaporites, v. 13, p. 168–173.

Youxun, Z., 1985, Geology of the Wucheng trona deposit in Henan, China: Schreiber, B. C., Warner, H. L. Sixth International Symposium on Salt, May 24–28, 1983, Toronto, Canada, Salt Institute, Alexandria, VA, v. 1, p. 67–73.

Yu, G., S. P. Harrison, and B. Xue, 2001, Lake status records from China: Data Base Documentation: MPI-BGC Technology Report, v. 4, p. 46–49.

Yu, J., C. Gao, A. Cheng, Y. Liu, L. Zhang, and X. He, 2013, Geomorphic, hydroclimatic and hydrothermal controls on the formation of lithium brine deposits in the Qaidam Basin, northern Tibetan Plateau, China: Ore Geology Reviews, v. 50, p. 171–183.

Yu, Y., Liangjie Tang, Wenjing Yang, Taizhu Huang, Nansheng Qiu, and Weiguo Li, 2014, Salt structures and hydrocarbon accumulations in the Tarim Basin, northwest China: Bulletin American Association Petroleum Geologists, v. 98, p. 135–159.

Yu, Z., I. Lerche, and A. Lowrie, 1992, Thermal impact of salt: Simulation of thermal anomalies in the gulf of Mexico: Pure and applied geophysics, v. 138, p. 181–192.

Yu, Z. H., and I. Lerche, 1996, Modelling abnormal pressure development in sandstone shale basins: Marine & Petroleum Geology, v. 13, p. 179–193.

Yuanxiong, L., and N. Chengxun, 1983, Technical development of solution mining of thinnly bedded rock salt deposits of Ziliujing, Sinchuan China, in B. C. Schreiber, ed., Proceedings 6th International Salt Symposium, v. 2: Alexandria VA, Salt Institute, p. 87–99.

Zacek, V., A. Petrov, and J. Hyrsl, 1998, Chemistry and origin of povondraite-bearing rocks from Alto Chapare, Cochabamba, Bolivia: Journal of the Czech Geological Society, v. 43, p. 59–68.

Zacharias, J., V. Zacek, M. Pudilova, and V. Machovic, 2005, Fluid inclusions and stable isotope study of quartz-tourmaline veins associated with beryl and emerald mineralization, Kafubu area, Zambia: Chemical Geology, v. 223, p. 136–152.

Zachos, J. C., M. Pagani, L. Sloan, E. Thomas, and K. Billups, 2001, Trends, rhythms, and aberrations in global climate 65 Ma to present: Science, v. 292, p. 686–693.

Zahid, M., and C. J. Moon, 1999, Genesis of tourmalinite from Chitral, northern Pakistan: Geological Bulletin, University of Peshawar, v. 32, p. 77–87.

Zahm, C., and R. G. Loucks, 2011, Fracture and non-matrix pore development related to evaporite paleokarst collapse, Lower Cretaceous Comanche Shelf, Texas: American Association Petroleum Geologists Search and Discovery Article #30215.

Zaikowski, A., B. J. Kosanke, and N. Hubbard, 1987, Noble gas composition of deep brines from the Palo Duro Basin, Texas: Geochimica et Cosmochimica Acta, v. 51, p. 73–84.

Zaitsev, A. N., and J. Keller, 2006, Mineralogical and chemical transformation of Oldoinyo Lengai natrocarbonatites, Tanzania: Lithos, v. 91, p. 191–207.

Zaitsev, A. N., T. Wenzel, T. Vennemann, and G. Markl, 2013, Tinderet volcano, Kenya: an altered natrocarbonatite locality?: Mineralogical Magazine, v. 77, p. 213–226.

Zak, I., 1997, Evolution of the Dead Sea brines, in T. M. Niemi, Z. Ben-Avraham, and J. R. Gat, eds., The Dead Sea, The Lake and Its Setting, v. 36: Oxford, Oxford University Press; Monographs on Geology and Geophysics, p. 133–144.

Zak, I., and R. Freund, 1980, Strain measurements in eastern marginal shear zone of Mount Sedom salt diapir, Israel: Bulletin American Association Petroleum Geologists, v. 64, p. 568–581.

Zak, I., and R. Freund, 1981, Asymmetry and basin migration in the Dead Sea rift: Tectonophysics, v. 80, p. 27–38.

Zambito, J. J., and K. C. Benison, 2013, Extremely high temperatures and paleoclimate trends recorded in Permian ephemeral lake halite: Geology, v. 41, p. 587–590.

Zamfirescu, F., M. Mocuta, T. Constantinecu, E. Medves, and A. Danchiv, 2003, The main causes of a geomechanical accident of brine caverns at field II of Ocnele Mari – Romania: RMZ – Materials and Geoenvironment, v. 50, p. 431–434.

Zampirro, D., 2004, Hydrology of the Clayton Valley brine deposits, Esmeralda County: Proceedings of the 39th Forum on the Geology of Industrial Minerals, Reno, Geological Society of Nevada, p. 271–280.

Zanor, G. A., E. L. Piovano, D. Ariztegui, and C. Vallet-Coulomb, 2012, A modern subtropical playa complex: Salina de Ambargasta, central Argentina: Journal of South American Earth Sciences, v. 35, p. 10–26.

Zappaterra, E., 1994, Source-Rock Distribution Model of the Periadriatic Region: Bulletin American Association Petroleum Geologists, v. 78, p. 333–354.

Zarei, M., E. Raeisi, and C. J. Talbot, 2012, Karst development on a mobile substrate: Konarsiah salt extrusion, Iran: Geological Magazine, v. 149, p. 412–422.

Zaritsky, P. V., 1961, Celestite from the Lower Permian deposits of the Donbas: Akademiya Nauk SSR, Doklady, v. 133, p. 801–804.

Zavialov, P., A. Ni, T. Kudyshkin, D. Ishniyazov, I. Tomashevskaya, and D. Mukhamedzhanova, 2009, Ongoing Changes of Ionic Composition and Dissolved Gases in the Aral Sea: Aquatic Geochemistry, v. 15, p. 263–275.

Zaw, K., D. L. Huston, R. R. Large, T. Mernagh, and C. F. Hoffmann, 1994, Microthermometry and geochemistry of fluid inclusions from the Tennant Creek Au-Cu deposits – Implications for ore deposition and exploration: Mineralium Deposita, v. 29, p. 288–300.

Zechner, E., M. Konz, A. Younes, and P. Huggenberger, 2011, Effects of tectonic structures, salt solution mining, and density-driven groundwater hydraulics on evaporite dissolution (Switzerland): Hydrogeology Journal, v. 19, p. 1323–1334.

Zegers, T. E., and P. E. van Keken, 2001, Middle Archean continent formation by crustal delamination: Geology, v. 29, p. 1083–1086.

Zen, E. A., 1965, Solubility measurements in the system Ca- SO_4-NaCl-H_2O at 35 degrees, 50 degrees, and 70 degrees C and one atmosphere pressure: J. Petrology, Oxford, p. 124–164.

Zeng, L., X. Tang, T. Wang, and L. Gong, 2012, The influence of fracture cements in tight Paleogene saline lacustrine carbonate reservoirs, western Qaidam Basin, northwest China: Bulletin American Association Petroleum Geologists, v. 96, p. 2003–2017.

Zhang, C., 1998, The natural soda deposits of China, in J. R. Dyni, and R. W. Jones, eds., Proceedings of the First International Soda Ash Conference; Volume II, v. 40, Wyoming State Geological Survey Public Information Circular, p. 57–66.

Zhang, X., H. Ma, Y. Ma, Q. Tang, and X. Yuan, 2013, Origin of the late Cretaceous potash-bearing evaporites in the Vientiane Basin of Laos: $\delta^{11}B$ evidence from borates: Journal of Asian Earth Sciences, v. 62, p. 812–818.

Zhao, X.-F., and M.-F. Zhou, 2011, Fe-Cu deposits in the Kangdian region, SW China: a Proterozoic IOCG (iron-oxide-copper-gold) metallogenic province: Mineralium Deposita, v. 46, p. 731–747.

Zhao, X.-F., M.-F. Zhou, J.-W. Li, and L. Qi, 2013, Late Paleoproterozoic sedimentary rock-hosted stratiform copper deposits in South China: their possible link to the supercontinent cycle: Mineralium Deposita, v. 48, p. 129–136.

Zhao, X.-F., M.-F. Zhou, J.-W. Li, M. Sun, J.-F. Gao, W.-H. Sun, and J.-H. Yang, 2010, Late Paleoproterozoic to early Mesoproterozoic Dongchuan Group in Yunnan, SW China: Implications for tectonic evolution of the Yangtze Block: Precambrian Research, v. 182, p. 57–69.

Zharkov, M. A., 1981, History of Paleozoic Salt Accumulation: Berlin, Springer Verlag, 308 pp p.

Zharkov, M. A., 1984, Paleozoic salt bearing formations of the world: Berlin, Springer Verlag, 427 p.

Zheng, H. B., C. M. A. Powell, and H. Zhao, 2002, Eolian and lacustrine evidence of late Quaternary palaeoenvironmental changes in southwestern Australia: Global and Planetary Change, v. 35, p. 75–92.

Zheng, J., and A. C. Palmer, 2009, Bamboo pipelines in Ancient China (and Now?): Journal of Pipeline Engineering, v. 8, p. 95–98.

Zheng, M., 1997, An introduction to saline lakes on the Qinghai-Tibet, Plateau: Monographiae Biologicae, v. 76, Springer, 328 p.

Zheng, M., and W. Liu, 1989, Translated title: Study of Zha Buye saline lake, Tibet: Maury, p. 1415–1424.

Zheng, M., and X. Liu, 2009, Hydrochemistry of Salt Lakes of the Qinghai-Tibet Plateau, China: Aquatic Geochemistry, v. 15, p. 293–320.

Zheng, X., 1987, Salt lakes and their origins in Xinjiang, China: Chinese Journal of Oceanology and Limnology = Zhongguo Haiyang Huzhao Xuebao, v. 5, p. 172–185.

Zhilina, T. N., and G. A. Zavarzin, 1994, Alkaliphilic anaerobic community at pH 10: Curr. Microbiol., v. 29, p. 109–112.

Zhilina, T. N., G. A. Zavarzin, F. Rainey, V. V. Kevbrin, N. A. Kostrikina, and A. M. Lysenko, 1996, *Spirochaeta alkalica sp nov, Spirochaeta africana sp nov,* and *Spirochaeta asiatica sp nov*, alkaliphilic anaerobes from the Continental soda lakes in Central Asia and the East African Rift: International Journal of Systematic Bacteriology, v. 46, p. 305–312.

Zhong, C., and J. Huang, 1997, Drilling and Gas Recovery Technology in Ancient China, Shell Companies in Greater China, 44 p.

Zhuang, G., J. K. Hourigan, P. L. Koch, B. D. Ritts, and M. L. Kent-Corson, 2011, Isotopic constraints on intensified aridity in Central Asia around 12Ma: Earth and Planetary Science Letters, v. 312, p. 152–163.

Ziegenbalg, S. B., D. Birgel, L. Hoffmann-Sell, C. Pierre, J. M. Rouchy, and J. Peckmann, 2012, Anaerobic oxidation of methane in hypersaline Messinian environments revealed by ^{13}C-depleted molecular fossils: Chemical Geology, v. 292–293, p. 140–148.

Ziegenbalg, S. B., B. Brunner, J. M. Rouchy, D. Birgel, C. Pierre, M. E. Bˆttcher, A. Caruso, A. Immenhauser, and J. Peckmann, 2010, Formation of secondary carbonates and native sulphur in sulphate-rich Messinian strata, Sicily: Sedimentary Geology, v. 227, p. 37–50.

Ziegler, A. M., 2001, Late Permian to Holocene paleofacies evolution of the Arabian Plate and its hydrocarbon occurrences: GeoArabia, v. 6, p. 445–504.

Ziegler, A. M., G. Eshel, P. M. Rees, T. A. Rothfus, D. B. Rowley, and D. Sunderlin, 2003, Tracing the tropics across land and sea: Permian to present: Lethaia, v. 36, p. 227–254.

Zierenberg, R. A., and W. C. Shanks III, 1983, Mineralogy and geochemistry of epigenetic features in metalliferous sediment, Atlantis II Deep, Red Sea: Economic Geology, v. 78, p. 57–72.

Zilberman, V. I., V. A. Serebryakov, M. V. Gorfunkel, and G. V. Chilingar, 2001, Prediction of Abnormally High Formation Pressures (AHFP) in petroliferous salt-bearing sections: Journal of Petroleum Science & Engineering, v. 29, p. 17–27.

Zimbelman, D. R., R. O. Rye, and G. N. Breit, 2005, Origin of secondary sulfate minerals on active andesitic stratovolcanoes: Chemical Geology, v. 215, p. 37–60.

Zimmer, B., C. Liutkus, S. Carmichael, B. Richmond, S. Hewitt, K. Hatala, W. E. H. Harcourt-Smith, A. Gordon, S. Mana, and J. Brett, 2012, A snapshot in time: Determining the age, environment and social structure of early Homo Sapiens, using trace fossils in the volcaniclastic rocks at the Engare Sero footprint site, Lake Natron, Tanzania (abs.): Geological Society America, Cordilleran Section – 108th Annual Meeting (29–31 March 2012).

Zimmer, P. W., 1947, Anhydrite and gypsum in the Lion Mountain magnetite deposit of the north, eastern Adirondacks: American Mineralogist, v. 32, p. 647–653.

Zimmerman, S. R. H., S. R. Hemming, N. G. Hemming, P. B. Tomascak, and C. Pearl, 2011, High-resolution chemostratigraphic record of late Pleistocene lake-level variability, Mono Lake, California: Geological Society of America Bulletin, v. 123, p. 2320–2334.

Zimmermann, H., 2000a, On the origin of fluid inclusions in ancient halite – basic interpretation strategies, in R. M. Geertmann, ed., Salt 2000 – 8th World Salt Symposium Volume 1: Amsterdam, Elsevier, p. 199–203.

Zimmermann, H., 2000b, Tertiary seawater chemistry – Implications from primary fluid inclusions in marine halite: American Journal of Science, v. 300, p. 723–767.

Zimmermann, H., 2001, On the origin of fluids included in Phanerozoic marine halite – basic interpretation strategies: Geochimica et Cosmochimica Acta, v. 65, p. 35–45.

Zimmermann, J. L., and R. Moretto, 1996, Release of water and gases from halite crystals: European Journal of Mineralogy, v. 8, p. 413–422.

Zobell, C., 1957, The ecology of sulphate-reducing bacteria.: Sulphate-Reducing Bacteria – their relation to the secondary recovery of oil, Symposium, St Bonaventure University, (Oct 23–24, 1957).

Zolotov, M. Y., B. Fegley, and K. Lodders, 1997, Hydrous silicates and water on Venus: Icarus, v. 130, p. 475–494.

Zouaghi, T., M. Bédir, and M. H. Inoubli, 2005, 2D seismic interpretation of strike-slip faulting, salt tectonics, and Cretaceous

unconformities,Atlas Mountains, central Tunisia: Journal of African Earth Sciences, v. 43, p. 464–486.

Zuber, A., J. Grabczak, and A. Garlicki, 2000, Catastrophic and dangerous inflows to salt mines in Poland as related to the origin of water determined by isotope methods: Environmental Geology, v. 39, p. 299–311.

Zubtsov, S., F. Renard, J.-P. Gratiera, R. Guiguet, D. K. Dysthe, and V. Traskine, 2004, Experimental pressure solution compaction of synthetic halite/calcite aggregates: Tectonophysics, v. 385, p. 45–57.

Zumberge, J. E., 1987, Prediction of source rock characteristics based on terpane biomarkers in crude oils: A multivariate statistical approach: Geochimica et Cosmochimica Acta, v. 51, p. 1625–1637.

Zverev, V. P., 1967, Otsenka nasyshchennosti podzemnykh vod sul'fatom kal'tsiya v diapazone temperature 0–40 degrees C: in Regional'naya geotermiya i rasprostraneniye termal'nykh vod, p. 308–313.

Index

A
Abu Dhabi sabkha
  hydrology of, 224
  intertidal facies (lagoon-edge muds), 220–222
  intertidal facies/strandline sands, 219–220
  island shoal and bank facies, 215–217
  subtidal facies, 217–219
  supratidal facies, 222–223
Acetate ligand, 1488
Acid saline lake system
  indicators, 128
  palaeodrainage fills, 128
  playa groundwater system, 130
  sedimentary minerals, 132
  sulphur cycling processes, 132
Aci Golu, Turkey, 342
Active diapir, 514–516
Active piercement conditions, of salt, 514, 515
Admiral Bay Pb-Zn deposit, 1555
Aerosols, 123–126
Aggrading/accreting systems, 177–178
Ainslie Detachment, 1551
Alabastrine gypsum, 75, 79
Alberta Basin Devonian formation, Canada, 787–788
Albite in Starra deposit, 1635
Albitisation, 1386
  albitites and, 1408–1412
  effects of, 1412
  feldspar and, 1410
  sodic alteration, 1408
Albitites
  and albitisation, 1408–1412
  distribution, 1411
  worldwide examples of, 1409
Alborz Anticline, 580
Algae
  organic productivity, 960
  salinity tolerance, 871–873
Algal mats. *See* Cyanobacteria
Alginites, 839
Alkanes, 867, 894
Al-Khiran sabkha, 237–240
Alligator Ridge, Nevada, 1604
Allochthon/allochthonous salt, 612, 972
  at basin scale, 550–553
  brine pools on sea floor, 923
  classification system, 547, 548
  distribution in Gulf of Mexico, 553
  fault families in, 547–550
  sheets, 523–527, 533, 543
  Sigsbee mass, 605
  structures, 494
Allochthon-edge stratiform Pb-Zn deposits
  Cretaceous cover, 1539
  galena crystals, 1540
  halokinetic units, 1543
  mineralisation, 1539–1540
  Nappe zone, 1538
  organic-rich sediments, 1543
  plan and section, 1539
  sulphur isotope, 1541, 1542
Alluvial fans
  alluvial fans-ephemeral saline lake, 256–277
  Early Pleistocene, 320
  Gulf of Suez sabkhas, 241
  Kadmah Bay Sabkhas, 234, 236
  Umm as Samim, 256
Alpine Foldbelt, Albania and Romania, 1073–1075
Al Salif diapir, Yemen, 589
Altiplano Puna plateau, remote sensing system, 177–178
Alunite in saline lacustrine, 82
Alunite-jarosite, 128
Amadeus Basin, Australia, 565, 583, 1139–1141
Ammonium chloride uses, 1193
Ammonium sulphate uses, 1193
Amphibolite
  to greenschist facies, 1439, 1448
  meta-evaporites in, 1445
    borates of Eastern Liaoning, China, 1445–1448
    Grenville complex, St Lawrence County, 1448–1450
    Mary Kathleen Fold Belt, 1453–1459
    Mount Isa Inlier, Northern Australia, 1450–1453
    Pine Creek Inlier, Northern Territory, 1466–1468
    Staveley Formation, 1459–1461
    Willyama Supergroup, 1461–1466
Anaerobic oxidation of methane (AOM), 939, 940
Anchizone, 1394
Ancient evaporites
  area contrasts, 389
  depositional settings, 395
  lacustrine deposits, 391
  palaeomagnetic latitudes, 391
  Phanerozoic evaporites in deep time, 392
  Phanerozoic marine-fed salts, 393
  potash (pre-quaternary)
    Canadian Maritimes (Mississippian of Nova Scotia and New Brunswick), 1165–1168
    Cretaceous Trans-Atlantic Potash, 1150–1153
    formation, mineable potash, 1177–1179
    German Potash (Z1, Z2 and Z3 Potash), 1154–1155
    Khorat Plateau, Thailand, 1144–1150
    Moroccan Meseta (Late Triassic), 1153–1154
    Nagaur-Ganganagar evaporite basin, India, 1175–1177
    New Mexico Potash, USA, 1159–1161

© Springer International Publishing Switzerland 2016
J.K. Warren, *Evaporites: A Geological Compendium*, DOI 10.1007/978-3-319-13512-0

Ancient evaporites (*cont.*)
Permian Potash, 1154
potash geology, WCSB, 1169–1173
Pripyat Basin (Devonian) Belarus, 1173–1175
quality control, 1179–1186
Upper Kama Potash Region, Cis-Urals Russia, 1161–1165
Upper Rhine Graben, France, 1141–1144
WCSB fluids, 1173
West Canadian Potash (Devonian), 1168–1169
Z3-Boulby Potash, UK, 1155–1159
salt accumulations, 389
salt beds, building blocks of
deepwater evaporites, 397–399
evaporitic mudflats, 394, 396
saltern, 396–397
tectonic and climatic conditions, 394
warmer climates, 394
Angara-Ilim volcanics, 1619, 1620
Anhydrite, 603
in Archaean carbonates, Brazil, 1473–1474
axe-head/ keg barrel, 61
burial, 5
calcitised, 728
chicken-wire, 61, 62
elongate anhydrite nodules, 61
enterolithic, 61, 62
in Greenschist Conditions, Salton Sea, 1437–1439
hydrothermal, 5
melting point, 1619
nodular, 70–74
texture**s,** 61
Anhydritization, 73, 482, 761
Anloo salt pillow, folded internal structure of, 506
Anpeng trona salt mine, China
solution mining, 1362–1363
Antarctica
evaporite accumulations, 87
microbes in modern salt lakes, 903
stratigraphic evolution, 386–387
Antarctic Circumpolar Current (ACC), 385
Anticlines, 607
Apennines, 461–469
Aptian-Lower Albian rocks, 1540
Aquathermal pressuring, by overpressure, 795
Arab Formation, Arabian Gulf, 985–990
Arabian (Persian) Gulf sabkhas
Eastern Saudi Arabia, 231–240
salt structures, 594
Southern Arabian Gulf, 212–231
Aragonian lacustrine gypsum, 682
Ara Group intrasalt reservoirs, Oman, 1055–1056
Ara Salt Group of Oman, 1086
Archaea
anaerobic methane-oxidising, 938, 939
biomarkers, 897, 898, 900
halophilic (haloarchaea), 889, 897, 898, 911, 912
hyperthermophilic, 945, 946
metabolic styles of prokaryotes on, 863
methane-oxidizing, 923, 937
methanogenic, 888
occurrence
Dead Sea, Middle East, 912, 916
Guaymas Basin, 959
Mediterrannean deeps, 930
Red Sea deeps, 932, 933
photoautotrophic mechanism, 890
salinity range, 900
Archaean salt allochthons, 589
Archaeoglobus, 875
Artemia
A. gracilis, 327
A. salina, 879
A. urmiana, 344
Arthrospira, 906–910
Asal, Republic of Djibouti, perennial saline lakes, 371–374
Atacama Desert, Chile
iodine, 1280–1281
minerals, 1281
nitrate salts, 1283–1287
Athabasca Tar Sands, Western Canada, 1082–1084
Athel (Al Shamou) silicilyte stringer reservoirs, 1064–1068
Atlantis II Deep, Red Sea
anhydrite‘s retrograde solubility, 1505
bathymetry, 1502
brine-filled deep, 1500–1501
brine pool stability, 1505
evaporite-specific exploration, 1500
Holocene sediments in, 1505
hydrothermal anhydrite, 1504
location, 1502
metalliferous laminite forming, 1499
mineralogical proportions, 1504
and Miocene evaporites, 1502
oceanographic and physical conditions, 1504
redox interface, 1503
salinity, 1502–1503
sulphide accumulation in, 1500
sulphide-rich layers, 1503
temperature, 1502–1503
Transition Zone, 1502
Upper Convective Layer, 1505
Atmospheric circulation, 87
Australia
acid saline lakes in, 128–132
coastal salinas
carbonate salinas, 306–312
gypsum salinas, 312–314
halite salinas, 314–316
playas, water composition in, 117
Authigenesis, 825
Authigenic anhydrite
dissolution-derived late burial anhydrite, 760
late stage anhydrite, 757–759
oxygen isotopic values, 759
sparry burial anhydrite, 757, 761
Authigenic salts, 82
Autochthonous salt
structures, 494
tectonics, 548–550
Autosutures
formation of, 543–544
identification of, 545, 546
Autotrophs, 860, 896

B

Back reactions, 121–123
Backstepping, 595
Bacteria
anoxic sulphur oxidising photosynthesizers, 873–874
chemosynthesizers, 874–875
sulphate reducers
alkalophiles, 877
archaeal sulphate reducers, 875

Baja California, Mexico, 876
halophilic and halotolerant bacterium, 877
metabolic character, 876
prokaryotes, 875
salinity range, 875
sulphur oxidisers, 875
Bacterial sulphate reduction (BSR). *See also* Thermochemical sulphate reduction (TSR)
activities of, 947
in aerobic/anaerobic interface, 946
Allochthon-edge stratiform deposits, 1541
bioepigenetic limestone, 946–947
cements and oil biodegradation, 948
Desulphovibrio and Desulphotomaculum, 945
diagenesis stage, 949
Kipushi deposit, 1525
metabolic process, 945
Polaris Zn-Pb Mine, 1559–1560
sulphate-reducing bacteria, 946
temperature, 945
Bacteriochlorophyll, 864, 899
Bacteriorhodopsins, 889–890
Bamboo drilling technology, in China, 1310, 1312
Barber‘s Hill salt dome, Texas, 1368–1369, 1375
Barney Creek formation, 1581
Barrovian metamorphism, 1384
Barycz site, Poland, 1337–1341
Baryte
cold-seep, 751–752
magnet cove deposit, 752
massive and vein-fill, 753
Morrison formation, 755
occurrence, 750
Olvido formation, 754–755
sand rosettes, 756
stratiform, 750
Basal anhydrite, 533, 607
Basal shear, 533–536
model, 533, 534
zones, 533–535
Base metals
concentrations, 1492
evaporites and diagenetic accumulations, 1597–1598
flushed matrix mineralogy, 1491
Lewis principles in transport, 1488
salt allochthon terrane, 1597
solubility, 1493
transportation and precipitation, 1497
Basin(s)
Alberta Devonian formation, Canada, 787–788
Amadeus Basin, Australia, 1139–1141
Canning Basin, West Australia, 1492
carbonate stringer reservoirs, South Oman Salt Basin, 1057–1064
Castile Formation, Delaware Basin, West Texas, 56
Central Basin Platform, West Texas, 1001–1002
Central Basin-Urumieh-Dokhtar zone, 579
continental subaqueous basins (*See* Perennial saline lakes)
Delaware Basin, West Texas, 56, 631–634
drawdown, 441–443
Elk Point Basin of Canada, 199–200
Emet Basin, Turkey, 1235
endorheic (internal drainage) basins, 85
epeiric basin, saline deposition in, 411
Green River Basin, Wyoming, 116, 1242–1245
Guaymas Basin, Gulf of California, 959, 1664–1666
Gulf of Mexico minibasin, 596
halite-entraining, 429
halokinetic, 812
hydrologically closed continental evaporite, 112
inverted salt, 565–566
Jurassic Louann Salt, Gulf of Mexico, 487–491
Kwanza Basin, Angola, 560, 561
La Popa Basin, Nuevo Leon, Mexico, 597–599
Libra oil fields in the Santos basin, 966
Lorca Basin, Spain, 914–916
Lower Clear Fork Formation, Palo Duro Basin, 416
Madrid Basin, Spain, 736, 737
margin sediments, 365–367
Maritimes Basin, Canada, 1543
metamorphism in evaporitic basins, 1385
Miocene Ebro Basin, Spain, 788–789
Miocene epikarst, Madrid Basin, Spain, 682–684
Mulhouse Basin (Oligocene), Europe, 921, 922
Nagaur-Ganganagar evaporite, India, 1175–1177
North Basin, of Dead Sea, 9
Palo Duro basin, Texas, 674–675, 785
Permian Basin, West Texas, 35
Permian Zechstein Basins, 479–483
Piceance Creek Basin, 1244–1247
Pripyat (Devonian) Belarus, 1173–1175
proterozoic basins, 666
Qaidam Basin in China, 1086, 1271–1273
Ramp, 541
and Range Playas, USA, continental sabkhas, 257
saline
degrading hydrology and playa capture, 175–176
dry mudflat/sandflat, 165–166
evaporitic saline mudflat, 163–165
fluctuating watertables indicators, 169
remote sensing, 177–185
stokes surfaces, 169–175
unconfined meteoric watertable, 168–169
salt basin
characterisations, 522–523
evolution, 595
evolution of, 595
in Gulf of Mexico, 489
salt basins in Gulf of Mexico, 489
San Andres Formation, Permian Basin, 416
Sicilian Basin, 466
Silurian evaporites, Michigan Basin, USA, 483–487
Silurian Pinnacle Reef Fields, Michigan Basin, 1014–1017
South Oman Salt Basin, 591
Subhercynian foreland basin-fill, 504
Sverdrup, 770–772
Syn-rift basins, 551
Tarim Basin, China, 1079
tertiary foreland basin, 564–565
Tertiary Piedmont Basin, 462
tertiary piedmont basin, 462
Vena del Gesso basin, 462–463
Welded-listric basins, 542
Williston Basin, 783
Basinal brines
chloride-rich, 1491, 1493, 1495
chlorine and bromine concentration, 1486
high-salinity, 1491
inorganic components in, 1485–1487
metal carrying capacity, 1489–1490
organics in, 1490
salinity of, 1485, 1486

Basin-scale burial hydrology
hydrotectonic flow patterns, 767–769
regional aquifers, 770
shallow and deeper aquifers, 770
Sverdrup basin, 770–772
tectonic process, 770
Basinward pinchout, 558, 559
Basinwide evaporites
anhydrite-halite evaporites, 477–483
basin edges, 439–440
deeper water-deep basin, 428
examples, 426–427
in greenhouse and icehouse periods, 453–455
gypsum-halite evaporites (*See* Messinian evaporites, of Mediterranean)
halite-dominated salt beds, 483–487
halite-entraining basins, 429
halokinetic terrain, 487–491
hypsometric analysis, 434
inappropriate scaling, 440
NaCl-dominant, 438
rapidity of deposition, 439
saltern textures, 427–428
sealevel and salt sequence, 447–448
sediment fill, 427
sequence stratigraphy, 444–447, 453–455
sequential plate restoration, 490–491
shallower water-deep basin, 428, 430
shallower water-shallow basin, 430
stratigraphic control, 439
stratigraphic relationships, 439
tectonic styles
continental sediments, 435
convergent, 430, 432
divergent, 430, 432
halokinesis, 438
intracratonic, 430, 432
Pangean supercontinent, 431
Rodinia/Gondwana supercontinent(s), 432– 433
synrift to postrift associations, 437
transform, 430, 432
Bathymodiolus childressi, 936, 941
Bathyphreatic karst, 678
Batten Fault zone, 1576
Baumann Fiord Formation, 1561
Bay Fiord Formation, 1561–1562
Bay Marchand dome, 815
Bayou Corne, Louisiana, solution mining, 1357–1358
Bedded evaporite, 971
basinwide, 1009–1010
salt seals, 976–979
seal type, 1021
Bedded solution-collapse breccias
Belle Roche breccia, 647
chalky dolomite, 644
clasts, 645
lower Visean Belle Roche breccia, 646
Beggiatoa sp., 1665
Belle Roche breccia, 647
Beneficiation, potash ore
alkali potassium hydroxide, 1105
carnallite ore processing method, 1103
conditioning, 1103
crushing process, 1101
desliming, 1101
electrostatic separation, 1103
flotation, 1102
frothers, 1102
insolubles separation, 1101
KCL use, 1105
langbeinite, 1104
Mannheim Process, 1103
media separation, 1103
occurrence, 1106–1109
particle size reduction, 1101
pulp separation, 1102
scrubbing, 1101
sylvite ores, 1101
thermal dissolution and crystallisation, 1103
Benzothiophenes (BTs), 951, 952
Bereznki mine collapses, Russia
solution mining, 1343–1344
Besshi-style deposits, Japan, 1664–1666
BHP-Billiton‘s Jansen project in Saskatchewan, 1095
Bidjovagge Au-Cu deposits, 1647–1649
Bioadaption
at cellular level, 888–891
high salt-in option, 891
to increasing salinity, 868
low salt-in option, 891
Biomarkers, 894–901
Bischofite, 1274, 1318
Black Hills, South Dakota, 636–637
Black salt, 508
Blanket management, solution mining, 1319, 1321
Bonneville saltflats, Utah, Eolian gypsum in, 52
Borate salts
with B_2O_3 equivalents, 1195
character and extraction history, 1192–1197
in China, 1213–1214
Death Valley area, 1210, 1211, 1212, 1213
definition, 1194
deposits of world, 1198–1202
Eastern Liaoning, China, 1445–1448
end uses, 1196
in North America, 1210–1214
production, 1194
Rio Tinto Borax Group, 1197, 1207
RNA World hydrochemistry, 1214
Saddleback Basalt, 1210
in South America, 1207–1210
textures, 1207
in Turkey, 1192, 1197, 1202–1207
uses, 1193
Borazon, 1197
Boron
distribution, 1418
isotopes as brine parenthood indicators, 139–141
Bou Grine Zn-Pb deposit, 1539–1540
Boulby mine UK, potash salts, 1094
Brain plain sediments and salt structures, 591
Breccia, 1463
bedded solution-collapse
Belle Roche breccia, 647
chalky dolomite, 644
clasts, 645
lower Visean Belle Roche breccia, 646
diapiric solution
Flinders Ranges, 655–657
Gulf Islands, 654
Hormuz formation, 655
outcropping and subcropoing areas, 653, 654
rock flour, 653
vs. salt ablation breccias, 657–659

evaporite dissolution
classification, 642–643
proto-conglomerates, 642
extent
hydrology and texture, 650–653
stratiform breccias, 649–650
pipes, 624
stages of, 1443
Brecciation, 685
Brenham explosion, salt caverns, 1365–1368
Brimstone. *See* Sulphur
Brine(s)
bittern evolution, 106
calcium chloride, 1273–1278
chemical divides, 148
curtain/reflux plume, 200
extraction methods, 1221–1225
flow regime, 773
flux, changing directions, 1035–1036
indicators of brine parenthood
boron isotopes, 139–141
bromine profiles, 132–135
chlorine isotopes, 141–144
fluid inclusions and brine temperatures, 144–147
sulphur and oxygen isotopes, 135–139
in Karabogazgol, 1225–1229
in Laguna Del Ray, Mexico, 1229–1231
lithium
geological setting of, 1267
production, 1261–1267
marine brines
bittern precipitates, 104
evolution of, 105
hydrogeochemistry of, 104
mineral to precipitate, 103
as penesaline waters, 104
salinity based classification, 104
mixed (marine/continental)
acid groundwater, 127–132
aerosols, 123–126
back reactions, 121–123
evaporite bedrock, 126–127
marine aerosols and continental gypsum, 123
mixing of brine, 110–112
natrocarbonatite and, 1616–1619
nonmarine brines
carbonate depletion in, 113–114
hydrologic classification and brine evolution, 113
mineral occurrences, 113
path I brines, 114–116
pool
in allochthon terrane, 923–927
ancient methanogenic seep carbonates, 939–942
in Bannock Basin, 928
hardgrounds precipitation, 937–939
iron (Fe) and sulphur in seafloor, 927–934
methane and hydrogen sulphide, seafloor in, 934–937
organic characteristics, 929
salt allochthon-associated *vs.* oxygenated seawater, 928, 929
potash evaporites from, 1129
reflux
dolomite, 190
dolomitisation, 190–194
gypsum replacement, 195
latent reflux, 192–193
Owens Lake, California, 196–197
Permian Capitan shelf, 193
seepage reflux, 191–192
salinity stratification controls texture, 185–190
salts behaviour in, 106
solution mining, production in, 1316
solution recovery in Utah, USA, potash evaporites, 1133–1137
stratification
bicarbonate in mixolimnion, 186
brine stability and evaporite textures, 188–190
monimolimnion, 186
Solar Lake, 187
trona-nahcolite-shortite chemistry, 114–116
Brine-rock burial evolution, 821–822
Bristol Dry Lake, California
continental sabkhas, 259–261
gypsum converts to burial anhydrite in, 70
Pleistocene evaporites, 70
Bromine
as brine parenthood indicators, 132–135
description, 1282
production, 1282–1283
uses, 1193
Browne Formation, 582–585
Bryan Mound salt dome, Texas
solution mining, 1374
BSR. *See* Bacterial sulphate reduction (BSR)
Buckner Anhydrite, 951
Bulk isotopic analyses, limestones, 825
Buoyancy forces, 795
Buoyancy forces, by overpressure, 795
Burial anhydrite
authigenic anhydrite, 757
dissolution-derived late, 760
Burial dewatering, hydrated salts
gypsum-anhydrite conversion, 817–819
gypsum dewatering and faulting, 820
mechanical model, 821
Triassic evaporites, 820–821
Burial hydrology
hydrotectonic flow patterns, 767–769
regional aquifers, 770
shallow and deeper aquifers, 770
Sverdrup basin, 770–772
tectonic process, 770
Buried diapirs, compressional reactivation of, 526–527

C

Cadibarrawirracanna, South Australia, bedrock component in, 124
Cadjebut Pb-Zn deposit, Australia
dolomites from, 1554
geological evolution, 1553
mineralisation, 1554–1555
ore evolution models, 1554
ore system and textures, 1551
saltern beds, 1552
Cadjebut zinc mine, 715–717
CAES. *See* Compressed air energy storage (CAES)
Calcined magnesia, 1287
Calcitisation
definition, 727
evaporites
aragonite inclusions, 731–732
bacterial calcitisation, 733
examples, 728–729
hydrological process, 729
meteoric flushing, 729
Mississippian sulphate, 732
Raisby formation, 729–730

Calcium carbonate and scapolite, 1402, 1405
Calcium chloride
  brines and minerals, 1273–1278
  occurrences, 1262
  uses, 1193
Calcium sulphate
  character and extraction history, 1251–1252
  production, 1252–1253
Calders reef, 743
Caltanisetta Basi, 468
Calyptogena
  clams, 880
  C. ponderosa, 936
Canadian Maritimes (Mississippian of Nova Scotia and New Brunswick)
  ancient (pre-quaternary) potash evaporites, 1165–1168
Candelaria, Chile
  Cu-Au deposit, 1644–1646
  Phanerozoic IOCG deposits, 1630
Canning Basin, West Australia
  base metal concentrations, 1492
  geochemical sampling, 1491
  Pb-Zn deposits, 1491
Canopies, 540–547
Canopy-margin thrust systems, 546
  types of, 547
Capillary evaporation
  displacive halite grows, 62
  halite grows by, 65
  mudflat aggradation, 168
  phreatic zone, 167
  in sabkha precipitates, 223
Capillary evaporites in Djerid, 1128
Caprock
  formation (diagenesis of salt), 602–607
  zonation, 602
Caprock carapace of Mt Sedom, Israel, 689
Caprock-hosted Pb-Zn deposit, Gulf Coast & North Africa
  bacteriogenic limestones, 1535
  biogenic calcite forms, 1535
  calcite precipitation, 1538
  iron sulphides, 1536
  metal sulphides, 1536
  peridiapiric mineralisation, 1536
  sulphides in, 1537
  Winnfield Dome diapir, 1537–1538
Carapace, 524
Carbonate, 603
  patterns, sediments, 592–595
  primary evaporitic
    Archaean, 38
    laminites, 13–14
    marine and hypersaline, 37–38
    microbialites and stromatolites, 15–32
    ooids and peloids, 34
    Palaeoproterozoic, 38
    Phanerozoic, 39
    pisolite, 32–34
    tepees, 35–37
  salinas
    bacteria, 312
    biomarker stratigraphy, 309
    dolomite precipitation, 307–308
    holocene lacustrine, 306
    packstone/mudstone, 309
    sapropel carbonates, 311
  stringer reservoirs, South Oman Salt Basin, 1057–1064
Carbonatite
  flows at Kerimas, 1617
  GIS-based compilation, 1619
Cargill saltworks, Kansas, 1346–1347
Carlsbad-Lechuguilla cavern system, 709–710
Carnallite
  ore processing method, 1103
  potash salts, 1087
  triaxial deformation experiments, 499–500
  viscosity, 497
Carrols Corner Formation, 1548–1549, 1551
Cas'kejas Formation, 1647
Castile(s)
  in gypsum karst terrain, 626
  mechanism of formation, 946
Castile Formation, Delaware Basin, West Texas, 56
Celestite
  barium in subsurface basinal brines, 746
  Eocene La Tossa and Calders reefs, 743, 744
  occurrence, 738, 739
  precipitation, 743
  replacements, 742, 743
  stratiform and layered celestine deposits, 745
  strontium levels, 740–742
Central Basin-Urumieh-Dokhtar zone, 579
Central Domain, iron-oxide deposits, 1637–1638
Centrifugal and centripetal flow, 783
Century deposit
  characteristics, 1584
  Zn-Pb deposit, 1591–1592
Chabazite, 1299, 1302, 1303
Chalky dolomite, 644
Chemotrophs, 860, 875
Chert nodules, 720
  disaggregated, 1460
  lutecite in, 727
Chilean saltpetre, 1284, 1285
Chloride salts, solubility of, 499
Chlorine isotopes, as brine parenthood indicators, 141–144
Chott el Djerid, chotts zone, 1124–1129
Christmas-tree diapirs, 538, 539, 659
CHS. *See* Composite halokinetic sequence (CHS)
Circum-diapir drag folds, 536
Circumsalt fluid flow, 815
Classic autochthon geometries, 613
Clayton Valley, Nevada, lithium in, 1269–1271
Climatic scales, local variations in
  humidity, 99
  salinity, 100
  salt crust formation, 99–100
  sediment type, 101
  surface brine, 99
  temperature, 99
Cluster well pads, solution mining, 1320–1322
Coble creep, 499
Colemanite, 1196
  formation, 1210
  nodules, 1204
  in Turkey, 1197, 1198
Collapse dolines, 622
Collapse-related traps, 1078
Collision margin burial realm, 767–769
Columbian emeralds
  formation model, 1430
  meta-evaporites, 1427–1431
  structural and regional geology of, 1428

Compactional drapes, 1080
Compactional fluids, 772
Composite halokinetic sequence (CHS), 606–607
Compressed air energy storage (CAES), 1326
Compressional salt tectonics, 553–554
  downbuilt *vs.* reactivated (mildly squeezed) diapirs, 568–573
  gravity glide shortening, 554–560
  inverted salt basins, 565–566
  mild shortening, 566–568
  thin-skinned fold and thrust belts, 560–565
Compression-driven salt-wing intrusion, 567, 569
Compressive deformation
  worldwide occurrences of, 554, 555
Conophyton, 27
Conrad Deep, 1501
Consolidation-related flow, 772
Contact metamorphism, 1384
  zones of, 1386
Continental evaporite basins, hydrologically closed, 112
Continental salt lakes, 116–120
Contractional faults, 547, 548
Contractional salt tectonism, 554
Conventional mining, potash salts
  active and projected solution mines, 1095–1097
  Boulby mine UK, 1094
  brownfield mine expansion, 1095
  extraction costs, 1095
  extraction techniques, 1094
  langbeinite mining, 1094
  production method, 1095
  provincial environmental regulations, 1095
  in quaternary saline lacustrine settings, 1098–1099
  room and pillar method, 1094
  Saskatchewan mines, 1094
  shaft excavation, 1095
  stress-relief mining, 1094
  sylvinite mining, 1094
  types, 1093
  underground ore transport, 1095
Coorong region, Australia
  Coorong-style, 725
  hypersaline chert-filled vugs in, 4
  lagoon, 307
  Lakes, dolomite precipitation, 307–308
Copper
  controlled by temperature and NaCl, 1605
  in Lisbon Valley, Utah, 1516–1518
Coral reefs, 589
Corella Formation, 1455–1459
Corocoro deposits, Central Andes
  bed-parallel burrow traces, 1525
  critical factors, 1526
  gypsum, 1527, 1528
  halokinetic/weld association, 1529
  mineralization, 1526
  mud-crack polygons, 1525–1526
  ore-hosting clastic horizons, 1526
  redbed copper, 1528–1529
  sedimentological model, 1527
  Toledo mine, 1526
  vetas sediment hosts, 1527
Coronation Hill, Australia, 1638–1640
Cosmo Howley Au deposit, 1639–1640
Couette flow, salt, 506
Counter-regional system, 540
Coxco Dolomite, 1581
Craton
  in Australia, 1390
  in Brazil, 1474
  definition, 1388
  mantle tomography, 1389
  Pilbara and Kaapvaal, 1393
  in Precambrian regions, 1388
  of southwestern Gondwana, 1441
Cretaceous Trans-Atlantic Potash, 1150–1153
Creta deposit, Oklahoma, 1529–1531
Crocodilus porosus, 287
Crustal cycling of brines, 829–835
Cryogenesis, 4
Cryogenic salts, 2, 95
Crystal-scale deformation, 499
Cyanobacteria
  adaption to increased salinity, 868, 871–873
  distribution in microbial mat, 860
  microbial mat, 892–894
  Microcoleus chthonoplastes, 892
  oil prone source rock, 840
  organic productivity, 960
  photosynthetic, 861
  phycobilisome pigments, 861
  salinity tolerance, 871–873

D
Dahl Hit at Ain Hit, 686–687
Damp salt, solution-transfer creep, 501
Danakil Depression, Ethiopia
  Holocene-Late Pleistocene perennial lake level, 44
  Pleistocene halite textures, 46
  quaternary potash evaporites, 1114
Dasht-e Kavir, salt desert, 299
Dasht-e Lut, sand and stone desert, 299
Dead-burned magnesite, 1287
Dead Sea, Middle East
  depression, 777–778
    halite caves, 688
    occurrence, 688
    Sedom cave, 689–690
  feast or famine in, 911–914
  green algae, 871
  haloarchaea, 916
  halophilic archaea, 912
  perennial saline lakes
    basin margin sediments, 365–367
    deepwater halite, 361–362
    deep water laminites, 362–365
    density stratification, 357–361
    geological settings, 353–355
    water level changes, 356–357
  potash
    area of concentration pans, 1129
    artificial salt ponds, 1130
    Dead Sea Salt Work‘s (DSW) production, 1133
    MOP manufacture, process stream, 1131
    production chemistries, 1132
    residual brine, crystallization process, 1132
Death Valley, California
  borate deposits, 1210, 1211, 1212, 1213
  continental sabkhas, 261–262

Dedolomitisation
definition, 727
dolomite matrix
evaporite-derived, 735
fracture-associated dedolomite, 738
Madrid Basin, Spain, 736, 737
textural variability, 735
Deepsea hypersaline anoxic lakes (DHALS), 924, 1500, 1501
Deep Springs Lake, California, continental sabkhas, 257–258
Deep structuring process, 551
Deepwater slope setting, 596
Deformation
Digne thrust sheet, 565
Northern Potwar deformation zone, 563
Degrading/deflating systems, 177–178
Delamination
in Middle Archaean, 1388
in Pilbara craton, 1388, 1390
Delaware Basin, West Texas, 56, 631–634
Delgado Sandstone Tongue, 598–599
Dense soda ash, 1242
Depopods, 540
Desert(s)
in Atacama, Chile
iodine, 1280–1281
minerals, 1281
nitrate salts, 1283–1287
causes of, 89
coastal upwelling, 91
continental distribution of, 86–89
earth-scale distribution, 89
high pressure belts, 89
Köppen climate classification, 92–94
Namib Desert, 125
quaternary, 86
rain shadow/adiabatic, 90–91
saline hydrologies, 92
strontium-isotopic composition, 89–90
Desulphohalobium retbaense, 875
Desulphotomaculum
characteristics, 945
D. nigrificans, 945
sulphate reducing bacteria, 945
Desulphovibrio, 876
D. brasiliensis, 222, 321
D. halophilus, 875
D. oxyclinae, 875
mesophilic isolates, 945
sulphate reducing bacteria, 945
Detroit-method wells, solution mining, 1315
Detroit River brinefield, USA, 1347–1348
Devonian carbonates of Canada, 1080
Dextral wrench zone, 563
Diagenetic trap, 1081
Diapir(s), 299–301
drag zones, 537
and extension, 514–516
fluviodeltaic sedimentation and, 590
piercement modes for, 514
sedimentation rate, 518–520
Diapiric solution breccias
Flinders Ranges, 655–657
Gulf Islands, 654
Hormuz formation, 655
outcropping and subcropoing areas, 653, 654
rock flour, 653
vs. salt ablation breccias, 657–659
Diapirism
and differential loading, 516–518
extensional faulting, 514
reactive, 514
Diatom
benthic, 873
Laguna de Pozuelos, 878
Dibenzothiophenes (DBTs), 951, 952
Dicarboxylate anions, brines in, 1489
Diffuse dissolution
basal anhydrite, Thailand
diagenetic basal anhydrite, 676
isotopic signatures, 677
Maha Sarakham formation, 675
Maha Sarakham salt, Thailand
landsurface, 674
nodular anhydrite residues, 672–673
subsurface structure, 671–672
Palo Duro basin, West Texas, 674–675
Diffusion creep, 499
Diffusion mechanism map, of damp rock salt, 497
Digne thrust sheet, 565
Diprotodon, 286–287
Dislocation creep, 499
Dissolution-derived late burial anhydrite, 675, 760
Dissolution, evaporites
breccia
classification, 642–643
proto-conglomerates, 642
hydrocarbons
Athabasca Tar Sands, Western Canada, 1082–1084
collapse-related traps, 1078
compactional drapes, 1080
Devonian carbonates of Canada, 1080
distribution, Tarim Basin, China, 1079
salt collapse depressions, 1078
stratigraphic traps, 1080
structural and diagenetic trap, 1081
trap styles, 1079
Westhazel General Petroleums Pool of west-central Saskatchewan, Canada, 1080
Wolf Springs fields, 1081
Djebel Friktia allochthon, Algeria, 532
Dolines
collapse, 622
solution, 622–623
suffosion, 622
Dolomite
composition, 1440–1441
drawdown basin, 441–443
scapolitic, 1441
Dolomitisation, 190–194, 1546
Dolomitised Limestones, Central Basin Platform, West Texas, 1001–1002
Dongchuan copper, China
chloride-rich brines, 1520
cu-sulphides, 1520
distribution, 1519
Fe-oxide ores, 1521
formations, 1518
geological map, 1520
stratigraphy, 1520
Don Juan Pond, 831

Downbuilt diapirs *vs.* reactivated (mildly squeezed) diapirs, 568–573
Downdip compressional terrain, 560, 561
Downdip space, 523
Dragon Breath cave on Hormuz Island, 691–692
Drag zones, 536–538
Drape-fold model of lateral caprock formation, 606
Drawdown basin, dolomite, 441–443
Drilling mud chemistry, 807–808
Dry lake valley, 635
Ductile flow, 499
Duricrusts, 1593–1595
Dykes in salt, 1612–1616
Dynamic metamorphism, 1384
  frictional heating, 1382–1383
  textures, 1382
  thrust belts, 1394–1401
Dzhezkazgan copper deposit, Kazakhstan
  hydrocarbons, 1516
  location, 1514
  mineralised system, 1514–1515
  paleo-environment, 1516
  reserves estimates for, 1514
  stratigraphic column, 1515

E
Eastern Liaoning, China, borates, 1445–1448
Eastern Mediterranean Coast, northern Sinai, 244–246
Eastern Saudi Arabia sabkhas, 231–240
East Mazyjan diapir, 658
Ebro Basin, Spain, Miocene lacustrine beds in, 4
Eclogite-delamination model, 1390
Edwards Mine, New York, lapis lazuli in, 1425
Ekofisk field, 809
Elk Point Basin of Canada
  evaporative drawdown, 199
  marine-fed platform evaporites, 199–200
El Laco iron deposits, Chile, 1631–1633
Elongate depressions. *See* Subsidence troughs
El Papalote diapir, 599–600
Emet Basin, Turkey, sodium sulphate from, 1235
Eminence, Mississippi, salt creep effect in, 1373
Endorheic (internal drainage) basins, 85
Enorama diapir, 594
Enorama reefs, 595
Enorama Shale, 594, 595
Eocene and Miocene Associations, Middle East, 1010–1014
Eocene Tay Sands, 592
Eolian gypsum, in Bonneville saltflats, Utah, 52
Eolian sabkhas
  salt-pans (marshes) and diapirs, 299–301
  sea-margin sabkha, 291–294
  sheets of eolian sabkhat, 294–299
Epeiric basin, saline deposition, 411
Epeiric ramps. *See* Ramp model, evaporitic epeiric
Epeirogenic movements, 794–795
Epeirogenic movements, and overpressure, 794–795
Etouchang Formation, 1518–1520
Eubacteria. *See* Bacteria
Euphotic, 864
Eustasy, icehouse and greenhouse
  basinwide evaporites, 453–455
  marine-margin platform evaporites, 448–451
  platform evaporites, 451
Evaporation, definition, 1
Evaporite(s)
  in Archaean distribution, 1390
  basic requirements, 8–12
  basinwide evaporites, 400 (*See also* Basinwide evaporites)
  bedrock, 126–127
  burial salt, 5
  continental playa/lacustrine deposits, 400
  cryogenic salts, 2, 4
  definition, 1
  depositional setting and texture, 8–11
  dissolution
    Athabasca Tar Sands, Western Canada, 1082–1084
    collapse-related traps, 1078
    compactional drapes, 1080
    Devonian carbonates of Canada, 1080
    distribution, Tarim Basin, China, 1079
    salt collapse depressions, 1078
    stratigraphic traps, 1080
    structural and diagenetic trap, 1081
    trap styles, 1079
    Westhazel General Petroleums Pool of west-central Saskatchewan, Canada, 1080
    Wolf Springs fields, 1081
  epeiric ramps, 414–425
  and hydrocarbons
    classification, 969
    dissolution, 1078–1084
    and hydrocarbon association, 966
    role in, 967
    seals to giant fields, 967
  hydrothermal salt, 5–8
  lacustrine evaporites (*See* Lacustrine evaporites)
  landforms, 621
  and metalliferous deposits, 1666–1667
  non-solar saline mechanisms, 4–5
  plate tectonic indicators and, 1387
  platform evaporites, 399–400
  pre-Quaternary/pre-Neogene, 11
  as pressure seals, 792–795
  primary (*See* Primary evaporite)
  saline clay authigenesis, 80–83
  salts, 498
  secondary (*See* Secondary evaporite)
  solar evaporation, 1–2
  tertiary (*See* Tertiary evaporite)
  textural synthesis, 83
Evaporite confining system (ECS), 785
Evaporite dissolution
  breccia
    classification, 642–643
    proto-conglomerates, 642
  indicators, 618–620
Evaporite karst
  changes in karst system, 707
  gypsum caves
    phreatic, 679–682
    Vadose
    Vadose: Miocene epikarst in Madrid Basin, Spain, 682–684
    Vadose: Modern Gypsum Karst in Saudi Arabia, 686–687
    Vadose: Modern Karst in Cretaceous Gypsum, Texas, 684–686
  halite caves
    Dead Sea depression, 688–691
    Diapiric Hormuz salt (Precambrian) in Arabian Gulf, 691–694
    solubility, 688

Evaporite karst (*cont.*)
hazards
collapse dolines or sinkholes, 696–697
groundwater drainage, 695
gypsum karst, 696
processes and mechanisms for hazard creation, 696
watertable level variation, 696
man-made structures atop salts
Badush dam, 706
Gachsaran formation, 704
Mosul dam, 705–706
St. Francis dam collapse, 703
Triassic Spearfish formation, 704
outcomes in, 708
problems in, 708
Miocene gypsum, Spain, 700–702
Mosul, Iraq, 702, 703
Ripon Area, UK, 697–700
speleothems in non-evaporite karstifid host, 694–695
Evaporite-sealed platform and reefs, Devonian, Canada, 1017–1021
Evaporitic mudflats. *See* Sabkhas
Exploration paradigms, bedded evaporite hydrocarbon association, 1030–1031
Extensional faults, 514, 547, 548
Extracellular polymeric substance (EPS), 20
Eyre Lake, Australia
brine chemistry, 280
ephemeral streams, 278
lacustral sedimentation, 282–283
lunette-cored islands, 282
monsoonal outbursts, 280
Quaternary evaporite, 92
salt-rich soils in, 117
sedimentation, 279
Warburton Channel, 279
western-fed flooding event, 281

F
Falling diapirs, 520–521
drive raft tectonics, 521–523
Fault-dominated minibasins, 613
Fault-segmented sheet (Roho), 539–540, 540
Fault welds, 547, 548
Feedback process, 540
Feldspar and albitisation, 1410
Feldspathoids, 1425
and lapis lazuli, 1426
Fe-oxide-Au deposits, 1622, 1623
Feoxide Cu-Au deposit, 1653
Ferroan dolomite, 1440
Filled vugs and nodules
baryte
cold-seep, 751–752
Magnet Cove deposit, 752
massive and vein-fill, 753
Morrison formation, 755
occurrence, 750
Olvido formation, 754–755
sand rosettes, 756
stratiform, 750
calcitisation (*see* Calcitisation)
celestite
barium in subsurface basinal brines, 746
Eocene La Tossa and Calders reefs, 743, 744
occurrence, 738, 739
precipitation, 743
replacements, 742, 743
stratiform and layered celestine deposits, 745
strontium levels, 740–742
composition, 719
fluorite
basinal fluid escape, 748
isotopic signature, 747
sedimentary, 749
silicified evaporites
abiological processes, 725
anhydite pseudomorphs, 722
bacterial degradation of organic matter, 725
chalcedony, 721
examples, 720–721
Italian cherts, 726
magadiite nodules, 725–726
moganite, 727
precipitation, 724
quartz nodules, 723, 724
silicified-calcitized anhydrite nodule texture, 722
Filter pressing, 1602
Five salt-dome crests, Gulf of Mexico, 638–639
Flamingo connection. *See* Organic matter
Flow edges, 533–536
Flower Garden Bank, 594
Flowing salt, sediments and, 585–587
Fluid flow
circumsalt, 815
in halokinetic basins, 812
hypersaline collision belts, 779, 780
lateral caprock model, 606
postorogenic, 769
suprasalt, 812–817
thermobaric, 773–777
Fluid inclusions, 953
Fluid inclusions-based salinities, 604–605
Fluid modelling, 536
Fluvial sand fairways, 592
Fluviodeltaic sedimentation and diapiris, 590
Fluviolacustrine sediments, 591
Focused rapid dissolution, 669–670
Fold belt structures, 555–556
Fold-thrust belts basal detachments in salt, 561, 562
Footwall shortcut thrusts, 565
Fracture pressure, 793
Fragum erugatum, 880
Free convection, 790
Free-flowing namakiers, 574
Friable alabastrine gypsum, 685
Frome Lake, South Australia, ephemeral stream floodplain, 284–287
Fulda region, hydrated salt layers, 1613, 1614
Fumarolic anhydrite, 1601
Furnace Creek Formation, 1211–1212
Fused magnesia, 1287

G
Galena, solubility of, 1487
Galkynysh (aka Yolotan/Osman) gas field, 966
Galynysh geology, 966
Gastropod
pellet production, 882
salinity tolerance, 883
Gays River Zn-Pb deposit, Nova Scotia
Carboniferous sediments, 1546
clay mineral and vitrinite reflectance, 1547
dolomitization, 1546
fluid inclusion temperature and salinity, 1546
isotopes, 1545
location, 1543–1544

massive ore zone, 1544
Pleistocene sediments, 1547–1548
TSR mixing zone, 1548
Gellenoncourt saltworks, France, 1341–1342
George Fisher deposit, 1583
German Potash (Z1, Z2 and Z3 Potash), 1154–1155
Geryonis, 287
Ghawar Field, Saudi Arabia, 990–998
Giant Russian gas fields, 964
Glauberite
and Glauber's salt, 1216
with gypsum/anhydrite, 1231
primary *vs.* secondary textured, 1232
in Spain, 1216, 1231–1233
transparent type, 1232
Glauber's salt. *See* Mirabilite
Gold deposit
at Alligator Ridge, 1604
bisulphide transport, 1650
controlled by temperature and NaCl, 1605
Muruntau, 1649–1651
non-IOCG, 1649–1650
in Pine Creek Orogen, 1637
precipitation, 1604
solubility of, 1603–1604
transport system, 1604
in VHMS deposits, 1605
Goongewa deposit, 1554
Gorham oil field, Kansas, 1355–1357
Gotnia formation, 807
Grain boundary
healing, 501
migration, 500
sliding, 499
Grand Saline sinkhole, Texas, 1358–1359
Granular flow, 499
Gravity glide shortening, 554–560
Gravity gliding *vs.* spreading, 513
Great Salt Lake, Utah
climate change, 329
geological settings, 325–326
mudstones, 327
perennial water body, 324–325
shorezone spits and bars, 327
sodium sulphate, 1237
water elevation, 329
Greenhouse climate mode, 383
Greenly complex, South Australia, lacustrine carbonates, 118, 119
Green River Basin, Wyoming
shortite in, 116
sodium carbonate, 1242–1245
Green River Formation, 1243, 1244, 1246
Greenschist Conditions, Salton Sea, anhydrite in, 1437–1439
Greenschist facies, 1386
amphibolite to, 1439, 1448
lower metamorphism, 1466
mineral assemblages, 1438
Greenschist realm, meta-evaporites in, 1437
Greenstone belts, 1391–1393, 1414, 1416
Grenville complex, St Lawrence County, meta-evaporites in amphibolite, 1448–1450
Grimsey hydrothermal field, 1663
Ground collapse, Tusla, solution mining, 1342–1343
Guaymas Basin, Gulf of California, 1664–1666
Guern Halfaya Pb-Zn deposit, 1540, 1541
Gulf of Mexico
minibasin, turbidite fill in, 596
reef system, 594
salt and allochthon distribution in, 553
Gulf of Suez, sabkhas, 240–241
Gypsum, 604
beds
Alabaster, 75, 79
aragonite pellets, 44
bird-beak, 40
crystal forms in, 40, 42
daisy gypsum, 75
fibrous, 76–79
pedogenic dominates in, 48–51
sand-sized lenticular gypsum, 41–42
satin-spar gypsum, 79
selenitic, 79
subaqueous form, 41
character and extraction history, 1251–1252
in China, 1252–1253
continental, 123
dissolution, 112
phreatic caves
bathyphreatic karst, 678
caprock sinkholes and vadose passages, Russia, 681, 682
maze cave, 679, 680
Optymistychna cave, western Ukraine, 679–681
plaster, 1251–1253
production, 1252–1253
salinas, 312–314
SSGS, 1439
synthetic, 1253–1254
uncalcined *vs.* calcined, 1253
in United States, 1254
uses, 1193
Vadose caves
Miocene epikarst, Madrid Basin, Spain, 682–684
Modern Gypsum Karst, Saudi Arabia, 686–687
modern karst in Cretaceous Gypsum, Texas, 684–686

H
Hadley Cells, 89
Haima pods, 591
Halite
in American Civil War, 1254
beds
access and rapidity, 45–46
capillary and freshwater flood textures, 47
chevron and raft growth, 44
coated grains, 48
crystals accumulations, 45
rafts and other cumulate, 47–48
subaqueous, 44, 45
caves
Dead Sea Depression, 688–691 (*see also* Sedom cave)
diapiric Hormuz salt (Precambrian) in Arabian Gulf, 688
Dragon Breath cave, 691–692
halokinetic salt cave ornamentation, 693
macrocrystalline skeletal deposits, 693–694
chevron, 144–146
in China, 1257, 1310
in Europe, 1255
metamorphism, 1397–1399
production, 1257–1261
salinas, 314–316
solution mining techniques, 1341
usage history, 1254–1256
uses, 1193
weight loss, 1399
in Yorkshire deposit, 1423
Haloarchaea. *See* Archaea
Halobacteria, 886

Halobiota
light dwellers and pigmentation, 860–864
metabolic pathways in producers and consumers, 858–860
non-photosynthesizers and layering, 864–868
salinity tolerance
bacteria (*see* Bacteria)
extremohiles, 884–888
heterotrophic consumers, 877
ingesters, grazers and pelletizers, 879–884
primary producers, 868–873
vertebrates, 877–879
Halodule uninervis, 219
Haloes, 789–792
Halogen
components in basinal brines, 1485–1487
geochemistry, 1648
Halokinetic basins, fluid flow in, 812
Halokinetic breccias, Flinders ranges, 655–657
Halokinetic deformation, 536
Halokinetic salt, 493
Halokinetic salt traps, 1036
Alpine Foldbelt, Albania and Romania, 1073–1075
Ara Group intrasalt reservoirs, Oman, 1055–1056
Athel (Al Shamou) silicilyte stringer reservoirs, 1064–1068
carbonate stringer reservoirs, South Oman Salt Basin, 1057–1064
intrasalt halokinetic plays, 1054–1055
limitations, 1037
Minibasin plays, 1052–1054
regionally-tiered salt plays, Gulf of Mexico, 1048–1051
Rocky Mountain Foldbelt, USA, 1075–1076
salt-related traps, Tarim Basin, China, 1076–1078
subsalt reservoirs, compressional evaporite provinces, 1068
supradiapiric traps, 1037–1043
tiered allochthon plays, deepwater realm, 1043–1048
Zagros Foldbelt, Iran, 1068–1073
Halokinetic sequence in marine shelf setting, 600, 601
Hanserian Evaporite Group (HEG) potash salt, 1086
Haoud Berkaoui oilfield, Algeria, 1359–1360
Harbour lake on Baffin Island, lapis lazuli in, 1425–1426
Harrison and Patton's notion of basal thrusting, 535
Haselgebirge breccias, 661–663
Hayward Lake, West Australia, brine stratification, 185, 186
Heiberg Formation, 770–772
Heishan Formation, 1518–1520
Heterotrophs, 877
High temperature saline realm, metal transport in, 1603–1605
Hilton deposit, 1583
Hockley Dome caprock, 603
Holbrook Anticline, Arizona, 634–636
Holomixis, 915
Homologous temperature scale (T_H), 499
Hook folds, 600
Howlite, 1205
Hutchison salt, Kansas, 630–631
explosion, salt caverns, 1370–1371
Hydrated salts
burial dewatering
gypsum-anhydrite conversion, 817–819
gypsum dewatering and faulting, 820
mechanical model, 821
Triassic evaporites, 820–821
layers, heating of, 1613
Hydroboracite, 1207
lamina, 1210
in Monte Amarillo, 1208
syndepositional formation, 1209
type I /II pseudomorphs, 1209–1210
Hydrocarbon(s), 536
ancient saltern and mudflat seals, 969
annual crude oil production, 965
dissolution, evaporite
Athabasca Tar Sands, Western Canada, 1082–1084
collapse-related traps, 1078
compactional drapes, 1080
Devonian carbonates of Canada, 1080
distribution, Tarim Basin, China, 1079
salt collapse depressions, 1078
stratigraphic traps, 1080
structural and diagenetic trap, 1081
trap styles, 1079
Westhazel General Petroleums Pool of west-central Saskatchewan, Canada, 1080
Wolf Springs fields, 1081
evaporite
classification, 969
dissolution, 1078–1084
and hydrocarbon association, 966
role in, 967
seals to giant fields, 967
Galkynysh (aka Yolotan/Osman) gas field, 966
Galynysh geology, 966
giant Russian gas fields, 964
halokinetic salt traps, 1036
Alpine Foldbelt, Albania and Romania, 1073–1075
Ara Group intrasalt reservoirs, Oman, 1055–1056
Athel (Al Shamou) silicilyte stringer reservoirs, 1064–1068
carbonate stringer reservoirs, South Oman Salt Basin, 1057–1064
intrasalt halokinetic plays, 1054–1055
limitations, 1037
Minibasin plays, 1052–1054
regionally-tiered salt plays, Gulf of Mexico, 1048–1051
Rocky Mountain Foldbelt, USA, 1075–1076
salt-related traps, Tarim Basin, China, 1076–1078
subsalt reservoirs, compressional evaporite provinces, 1068
supradiapiric traps, 1037–1043
tiered allochthon plays, deepwater realm, 1043–1048
Zagros Foldbelt, Iran, 1068–1073
International Energy Agency (IEA), 966
Kashagan oil field, 966
Kish 2 gas field, 966
Libra oil fields in the Santos basin, 966
reservoirs (bedded) and traps
bedded basinwide evaporites, 1009–1010
bedded salt seals, 976–979
brine flux, changing directions, 1035–1036
dolomitised limestones, Central Basin Platform, West Texas, 1001–1002
Eocene and Miocene Associations, Middle East, 1010–1014
evaporite-sealed platform and reefs, Devonian, Canada, 1017–1021
exploration paradigms, bedded evaporite hydrocarbon association, 1030–1031
Ghawar Field, Saudi Arabia, 990–998
Jurassic Arab Formation, Arabian Gulf, 985–990
Jurassic Smackover Fm., Gulf of Mexico, 1002–1009
North Ward-Estes Field, Texas, 1025–1028
peritidal muddy carbonates, evaporitic mudflat seals, 979–983
platform carbonates, bedded saltern seals, 983–985
quality tied to bedded evaporite seal type, 1021
recognising bed dissolution, 1034–1035
recognising depositional differences, 1031–1034
Rotliegende Sands of Northern Netherlands and North Sea, 1028–1030

Silurian Pinnacle Reef Fields, Michigan Basin, 1014–1017
Slaughter-Levelland Trend, West Texas and New Mexic, 998–1001
Yates Field, West Texas, 1021–1025
rock's inherent ductility, 969
in salt caverns, 1325–1327, 1366
Barber's Hill explosion and collapse, 1368–1369
Brenham explosion, 1365–1368
Hutchinson explosion, 1370–1371
Menzengraben potash mine, East Germany, 1371–1372
Mineola Propane fire, 1369–1370
Weeks Island, Louisiana, 1363–1365
West Hackberry explosion, 1365
seal capacity of evaporites
allochthons, 972
bedded evaporites, 971
biodegradation, 970
density/buoyancy, 970
environments favouring seal continuity, 973–976
hydrocarbon migration and trapping, south Oman salt basin, 975
marine carbonate reservoir, 975
oil re-entrapment, 970
salt permeability/brine permeation measurement, 970, 971
seal type and ultimate recoverable reserves, 965
Sulige gas field, China., 966
Hydrocarbon generation, by overpressure, 795
Hydrocarbon-related diagenetic zones (HRDZs), 780
Hydrocarbon-stained black salt, 800
Hydrographic isolation
brine curtain, 200
hydroseal, 201
Messinian salinity crisis, 199
Hydrohalite, 2
Hydrologically closed continental evaporite basins, 112
Hydrology. *See also* Brine(s)
active phreatic/vadose regime, 162–163
extraterrestrial salts, 200–205
saline basins
degrading hydrology and playa capture, 175–176
dry mudflat/sandflat, 165–166
evaporitic saline mudflat, 163–165
fluctuating watertables indicators, 169
remote sensing, 177–185
stokes surfaces, 169–175
unconfined meteoric watertable, 168–169
Hydrostatic pressure, 792
Hydrotectonic flow pattern, 766, 767
Hydrothermal mineral deposit, 1603
Hydrothermal ore deposits, 1621–1624
Hydrothermal salts, 1653–1656
alteration in, 1601
anhydrite
in sekko ore, 1656
cracking of organic matter, 956–959
fluids, convective circulation, 1384
metamorphism, 1384
VHMS deposits, anhydrite
chimneys, 1665
chloritization, 1663
distribution, 1654–1655
at mid ocean and back-arc spreading centres, 1660–1664
plate tectonic settings, 1666
at sediment-covered spreading centres, 1664–1666
sulphur isotopes, 1663
TAG mound, 1660–1664
Hypersaline fluid evolution
basin-scale burial hydrology
hydrotectonic flow patterns, 767–769
regional aquifers, 770
shallow and deeper aquifers, 770
Sverdrup basin, 770–772
tectonic process, 770
brine-rock burial evolution, 821–822
burial dewatering of hydrated salts
gypsum-anhydrite conversion, 817–819
gypsum dewatering and faulting, 820
mechanical model, 821
Triassic evaporites, 820–821
compactional fluids, 772–773
crustal cycling of brines
deep-basin brines, 831
Esker distribution, 831–833
evaporite derived Na-Cl brines, 833
Pyrenean collision zone, 833–835
seawater freezing, 830–831
deep flow in pull-apart basins, 777–778
drilling mud chemistry, 807–808
evaporites as pressure seals, 792–795
flow in collision belts
fractures, 781
inversion-related thrust faulting, 779
Miocene/Pliocene fluid flow, 779, 780
Pyrenean thrust belt, 782
squeegee effect, 779
flow in post-orogenic basins
Alberta Basin, 787–788
evaporite confining system, 785
gravitational pore-brine sinking, 783
lacustrine depression, 788
Palo Duro Basin, 785
Permian Basin of West Texas and Oklahoma, 787–785
Salado and Rustler evaporites, 785, 786
topography driven flow, 783
fluid flow in halokinetic basins, 812
haloes, convection and saltout, 789–792
Permian Gharif formation, 823, 824
salinity-driven convection, 789
salt-generated underpressure, 808–809
salt-maintained overpressure
allochthon basins, 802
Ara stringer, 800–801
black staining, 799, 800
hydrofracture, 798
Permian halite, 796
seismic valving and pumping, 802–803
stringers and rafts, 798, 799
Tengiz oil field, 796, 797
true pressure seal, 795
suprasalt fluid flow and alteration, 812–817
temperature anomalies and brine flow, 809–812
thermobaric-thermohaline fluids (*see* Thermobaric-thermohaline fluids)
unpredicted pressure change, 805–807
water-salt interactions, 827–829

I

Iberian Pyrite Belt, sulphide deposits, 1492
IC. *See* Illite crystallinity (IC)
Icehouse climate, 383
Idaho Cobalt Belt, USA, 1649

Ikaite, 763
Illite crystallinity (IC), 1394–1396
Illite, transformation character, 82–83
Imbricate wedge, 547
Incipient mud volcano, 608, 610, 612
Industrial salts, world production, 1194
Inland Chotts and Coastal Sabkhas in North Africa, potash evaporites
  Bayovar project, 1129
  capillary evaporites in Djerid, 1128
  deflationary, 1125
  ephemeral carnallite formation, 1128
  location, 1126
  pore brines, 1127
  rainfall and lake areas, 1127
  thenardite and carnallite, 1129
  Tunisian chott and sabkha brines, 1127
  Tunisian coast, near Zarzis, 1128
  zone of chotts, 1124
Inneston Lake, Southern Australia, gypsum beds in, 42
Inorganic components in basinal brines, 1485–1487
Intergranular pressure solution at grain contacts, 501
Intermediate solid solution, 1601
International Energy Agency (IEA), 966
Intrasalt halokinetic plays, 1054–1055
Intrasalt minibasins, 540–541
Intrasediment salts, 60–62
Inverted salt basins, 565–566
IOCG deposits. *See* Iron-oxide copper gold (IOCG) deposits
Iodine
  in Atacama Desert, Chile, 1280–1281
  in Australia, 1282
  costs, 1280
  description, 1278
  in optical polarising film, 1281
  production, 1279
  uses, 1193
Iron-oxide copper gold (IOCG) deposits
  basinal brine/evaporite fluid, 1626
  characteristics, 1622, 1623
  chloride transport, 1604, 1605
  classification, 1626, 1652
  Cu-rich deposits, 1634
  evaporite-associated class, 1630
  in evaporite/basinal brine milieu, 1630–1631
  fluid chemistry, 1631
  fluid-related settings, 1651
  hybrid magmatic-non-magmatic, 1628
  hydrothermal brines and waters, 1624–1626
  Kiruna-type deposits, 1626, 1627, 1629, 1630
  magmatic end-member, 1628–1629
  mineralisation, 1650–1653
  non-magmatic end-member, 1628
  precipitation, 1650
  sensu lato examples, 1627, 1630
  sensu stricto deposits, 1627, 1629
  tonnage grade plot, 1632
  Western Mining, 1626
Isachsen formation, 770–772
ISLA1 and ISLA2, 180
Isotopes, as brine parenthood indicator
  boron, 139–141
  chlorine, 141–144
  oxygen, 135–139
  sulphur, 135–139

J
Jabiluka, 1636, 1641
Jänecke plot, 107, 108
Jebel Dhanna diapirs, 593, 594
`J' hook folds, 600
Jinchaun, 1607
Jubilee Zn-Pb deposit, Nova Scotia
  Carrols Corner Formation, 1548–1549
  location, 1548
  Macumber Formation in, 1548
  NNW-trending faults, 1549
  sulphate-rich brines, 1551
  sulphur isotope, 1550
  thermochemical sulphate reduction, 1551
  Windsor Formation, 1549
Jurassic Arab Formation, Arabian Gulf, 985–990
Jurassic Louann Salt, Gulf of Mexico, 487–491
Jurassic Smackover Fm., Gulf of Mexico, 1002–1009
JWS sink, New Mexico, 1351–1354

K
Kadmah Bay/Kuwait Bay sabkha, 234–237
Karabogazgol
  brines in, 1225–1229
  sodium sulphate in, 1225–1229
  water salinity in, 1228
Karst domes, 624–626
Kashagan oil field, 966
Kebrit and Shaban Deeps, Red Sea
  bottom brine layers, 1506
  gypsum in, 1506–1507
  organic matter in, 1506
  piston core sampling, 1505–1506
  sulphide layering, 1506
  sulphur isotopes from gypsum, 1507
Keg River formation, 776
Kerimasi volcanics, 1617
Kernite, 1196–1198
Kerogen, 795, 852
  cracking, 839
  formation, 839
  long-chain hydrogens, 839–840
  oil and gas generating, 837, 838, 839
  sapropelic, 840–841
  type I-II hydrogen, 837
Keuper (Triassic) salt belts, 564
Keyes Field, 809
Khorat Plateau, Thailand, ancient potash evaporites, 1144–1150
Khuff Formation, Arabian Gulf, 416
Kiirunavaara deposit, 1647
Kipushi Zn-Cu-Pb deposit, Africa
  Axial Breccia, 1522
  bacterial sulphate reduction, 1525
  carbon-oxygen stable isotope, 1524
  geological map, 1523
  on ground targeting, 1525
  halokinetic breccia, 1522, 1525
  location, 1521–1522
  Neoproterozoic Nguba Group, 1521–1524
  salt diapir/allochthon, 1522
  thermochemical sulphate reduction, 1525
Kiruna-Tjåmotis-Arjeplog district, Sweden, iron oxide deposits, 1646
Kiruna-type deposits, 1626, 1627, 1629, 1630

Kish 2 gas field, 966
Komatiitic magmas, 1607
Koolpin Formation, Australia, 1639–1640
Kora Bogaz Gol, Caspian Sea, 292
Korshunovsky iron ore deposits, Siberia, 1606, 1619–1620
Kramer borate deposit, 1197, 1210–1211
Kuhe-Gach, Saveh, 580, 582
Kuh-e-Namak Qom, Iran, 579–581
  salt plug, 524
Kulkeite, 1421
Kupferschiefer copper deposits, Poland, 1485
  distribution, 1510
  mesohaline setting, 1512
  methanogenesis, 1512
  mineral content, 1512
  mineralisation, 1510–1512
  Rote Faule interval, 1511–1514
  Zechstein evaporites, 1513–1514
Kuroko-style deposits, Japan
  anhydrite vertical zonation, 1658
  baryte and quartz contents, 1659
  distribution, 1657
  geology of selected mines, 1657
  gypsum, 1658
  hydrothermal anhydrite, 1656, 1661
  hydrothermal circulation, 1660
  mineralised zones, 1658
Kuwait sabkhas
  Al-Khiran Sabkha, 237–240
  Kadmah Bay/Kuwait Bay, 234–237
Kwanza Basin, Angola, 560, 561

L
Lacustrine evaporites
  Eocene Lake Gosuite, USA, 403–405
  Mercia mudstone, 409
  model sabkhas
    depositional characteristics, 251–256
    groundwater transport, 253–254
    saline mudflat, 252–253
    saline pan, 254–256
  nodular beds of gypsum/anhydrite, 409
  Oligo-Miocene Lake, Calatayud Basin, Spain, 405–407
  Permian Lacustrine Redbeds, Kansas, 407–409
Lady Loretta deposit, 1583
Lagoa Vermelha, Brazil, dolomites, 321–323
Laguna Del Ray, Mexico, sodium sulphate brines, 1229–1231
Lake(s)
  acid saline lake, Australia, 128–132
  Antarctica microbes in modern salt lakes, 903
  brine processing and solution chemistry, 1101
  Bristol Dry Lake, California, 259–261
  continental salt lakes, 116–120
  Coorong Lakes, South Australia, 307–308
  East African saline lakes, 905–911
  Eocene Lake Gosuite, USA, 403–405
  Great Salt Lake, Utah (*see* Great Salt Lake, Utah)
  Harbour on Baffin Island, 1425–1426
  Holocene-Late Pleistocene perennial lake level, 44
  Lake Aci, Turkey, 342
  Lake Asal, Republic of Djibouti, 371–374
  Lake Cadibarrawirracanna, South Australia, 124
  Lake Eyre, Australia, 92, 278–283
  Lake Frome, South Australia, 284–287
  Lake Greenly complex, South Australia, 118, 119
  Lake Harbour on Baffin Island, 1425–1426
  Lake Hayward, Western Australia, 185, 186
  Lake Inneston, Southern Australia, 42
  Lake Lewis, Central Australia, 1304–1305
  Lake Lisan, Jordan Valley, 367–371
  Lake Macleod, Australia, 96
  Lake Magadi, East Africa, 115, 344–353
  Lake Natron, East Africa, 347–350
  Lake Peigneur, Louisiana, 1360–1362
  Lake Torrens, Australia, 881
  Lake Tuz, Turkey (Tuz Gölü), 340–342
  Lake Tyrell in Victoria, 128–129
  Lake Untersee, East Antarctica, 27
  Lake Urmia, NW Iran, 342–344
  Lake Van, Turkey, 335–338
  Lake Yaninee in South Australia, 128
  Lop Nur, 1137–1139
  Mahoney Lake, Canada, 916
  Mono Lake, California, 334
  North Stromatolite Lake, 309, 310
  Oligo-Miocene Lake, Calatayud Basin, Spain, 405–407
  oligotrophic lake, 916
  Owens Lake, California, 196–197
  Patience Lake-PCS solution mine, Saskatchewan, Canada, 1100
  perennial saline lakes (*See* Perennial saline lakes)
  Searles lake, California, 1212, 1213, 1219, 1236
  Soda Lakes, Nevada, 1243
  Solar Lake, Gulf of Aqaba, 187
  Solar Lake, Gulf of Elat, 316–318
  Storr's Lake, Bahamas, 912, 914
  Zabuye Lake, China, 1271–1273
Lamellibrachia luymesi, 936, 937
Laminae, 603
Laminar anhydrite caprock, development of, 603
Laminites
  carbonate systems, 13–14
  textural interlayering with, 57–58
LANDSAT satellite, 180
Langbeinite, 1104
  mining in Carlsbad, New Mexico, 1094
  ore, potash salts, 1087
Langer Heinrich deposit, 1594, 1595
Laoxue Formation, 1518–1520
Lapis lazuli
  in Edwards Mine, New York, 1425
  feldspathoids and, 1426
  geological setting, 1427
  in Lake Harbour on Baffin Island, 1425–1426
  meta-evaporites, 1425–1427
  in North Italian Mountains, Colorado, 1427
  Precambrian of Baffin Island, Canada, 1425
La Popa Basin, Nuevo Leon, Mexico, 597–599
La Popa weld, 533
Largentière Pb-Zn deposit, France
  biological reduction, 1570–1571
  calcium sulphate, 1571
  economic precipitates, 1568–1569
  fracture fillings, 1569
  geology, 1568
  location, 1567
  mineralization, 1569
  sulphates in, 1568
  sulphur isotope, 1570
  Uzer fault with, 1571–1572

La Sal Mountain laccoliths, Utah, 1613–1615
Late Pleistocene Salinas, Egyptian Red Sea Coast, 319–321
Lateral caprock, 603, 606, 607
  anhydritic, 607
  formation, drape-fold model of, 606
Late stage anhydrite in Leman Field, North Sea, 757–759
Lead and brines, 1488
Leptolyngbya spp., 27
Lewis acid, 1487, 1488
Lewis Lake, Central Australia, zeolites, 1304–1305
Lezkowice brinefield site, Poland, 1340
Libra oil fields in the Santos basin, 966
Life in saline subsurface, 960–961
Ligands and brines, 1487–1488
Light hydrocarbons, in salt caverns, 1324
Limestone, synthetic gypsum and, 1253
Liptinites, 838–839
Liquefied petroleum gas (LPG), salt caverns, 1325, 1327
Lisan Lake, Jordan Valley, perennial saline lakes, 367–371
Lisbon Valley, Utah, copper in, 1516–1518
Listric weld system, 539, 540
Litchfield Province, iron-oxide deposits, 1637–1638
Lithium
  brines
    geological setting of, 1267
    production, 1261–1267
    world in-situ resource, 1263
  in China, 1271–1273
  in Clayton Valley, Nevada, 1269–1271
  in Salar de Atacama, Chile, 1267–1269
Lithium carbonate
  brine resource, 1271
  costs of, 1264
  production, 1269
  solubility, 1272
Lithostatic pressure, 793
Local scale karst
  breccia chimneys and pipes, 624
  description, 621
  dolines
    collapse, 622
    solution, 622–623
    suffosion, 622
  evaporite expansion morphotypes, 626–627
  karst domes and castiles, 624–626
Local variations, in climatic scales. *See* Climatic scales, local variations in
Lomagundi Event (LE), 158
Lophelia pertusa, 937
Lop Nur Lake, 1137–1139
Lorca Basin, Spain, organic matter (Messinian) attributes, 914–916
Louann Salt, Gulf of Mexico, 487–491
Lower Clear Fork Formation, Palo Duro Basin, 416
Lower temperature ore deposits. *See also* Pb-Zn deposits
  anhydrite, 1479
  characteristics, 1583–1584
  classification, 1480, 1482–1483
  Creta, Oklahoma, 1529–1531
  dissolving salt beds, 1480
  Dongchuan Copper, China, 1518–1521
  Dzhezkazgan Region, Kazakhstan, 1514–1516
  geological time, 1479
  hypersaline ore deposits, 1481
  Kipushi Zn-Cu-Pb deposit, Africa, 1521–1525
  large-scale, 1478, 1479
  Lisbon Valley, Utah, 1516–1518
  metalliferous brines
    basinal brines, 1485–1487
    breach points, 1485
    buried evaporite unit, 1483, 1485
    carrier brines, 1493–1496
    composition, 1485
    grey-bed leaching, 1483
    ionic source, 1483
    metal carrying capacity, 1489–1490
    metal fixers, 1496–1499
    metals, ligands and salinity, 1487–1488
    organic components in, 1488–1489
    seal and trap, 1485
    sediments as metal sources, 1490–1493
  non-magmatic deposits, 1483, 1484
  orthomagmatic systems, 1481
  in plate-tectonic-time framework, 1481
  Red Sea (*see* Red Sea)
  Redstone Copper Belt, Canada, 1531–1533
  sediment-hosted deposits, 1481
  stratiform copper deposits, 1507–1509
Lucina carbonates, 941
Lucky Bay, Spencer Gulf, South Australia, 292
Lufilian halokinetic breccia, 667
Lye, potash salts, 1086

M
Macerals
  classification, 838
  definition, 838
  inertinite group, 839
  liptinites, 838–839
  measurements of, 837
  vitrinite, 839
Macleod Lake, Australia
  halite salinas, 314–315
  meteoric/halokinetic continental evaporite, 96
Macrocrystalline skeletal deposits, 693–694
Macrocyclic glycerol diethers (McGDs), 947
Macumber Formation
  in Jubilee deposit, 1548
  lower and upper, 1550
Madrepora oculata, 937
Magadi Lake, East Africa, 344–353
  trona evaporites in, 115
  trona in, 1250
Magma. *See also* Iron-oxide copper gold (IOCG) deposits
  decomposition and melting points, 1615
  intrasalt alteration, 1615
  orthomagmatic ore deposits, 1601
    evaporite-igneous interactions, 1603
    faulting, 1608
    filter pressing, 1602
    halite-rich masses, 1605
    mercaptan, 1606
    mineralogic outcome, 1606
    Ni-Cu deposits, 1606–1608
    Noril'sk Region Siberia, 1608–1612
  paramagmatic deposits, 1602
    basaltic melt production, 1612
    dykes and sills in salt, 1612–1616

Fe-oxide-Au deposits, 1622, 1623
hydrolytic alteration haloes, 1625
hydrothermal fluid circulation, 1621–1624
igneous rocks, 1622
IOCG deposits, 1622, 1623
iron-rich associations, 1619
Korshunovsky iron ore deposits, Siberia, 1619–1620
molten salts, 1616–1619
saline haloes, 1620–1626
Magnesites
Holocene occurrences of, 1289
Kunwarara deposits, 1289–1290
and magnesia salts, 1287–1292
in Rum Jungle Uranium Field, Northern Territory, 1467
Magnesium, 1287
in metasediments, 1435–1437
Maha Sarakham salt, Thailand
landsurface, 674
nodular anhydrite residues, 672–673
subsurface structure, 671–672
Mahoney Lake, Canada, biology and density stratification, 916
Malembo Group, 560
Mangarak fault zone, kinematics of, 576, 577
Marcona
Fe-oxide deposits, 1631, 1633
hydrothermal activity, 1633
Marine coastal sabkhas
beach-dune and fluvial sabkhat, 242–249
carbonate-hosted, 212–231
hydrology and hydrogeochemistry, 223–231
siliciclastic-hosted, 231–240
siliciclastic sediment, 212
Maritimes Basin, Canada, evaporite-cored thrusts and MVT in, 1543
Martian surface, hydrated salt minerals, 201–203
Mary Kathleen Fold Belt, meta-evaporites in amphibolite, 1453–1459
McArthur River (HYC) Pb-Zn deposit
brine-pool laminites in, 1589
characteristics, 1584
chloride-rich waters, 1581
Coxco Dolomite, 1581
depositional association, 1577
deposit location, 1578
facies, 1586–1588
geology, 1579
halokinetic deformation styles, 1588
hydrothermal circulation, 1590
lower Barney Creek Formation, 1589
mineral resources, 1576
mother salt level, 1585–1586
organic characteristics, 1587
pinolitic texture, 1585
re-interpreted evaporite occurrence chart, 1580–1581
sedimentological analysis, 1588
siderite marbles, 1578–1579, 1581
stratigraphy, 1577–1578, 1582, 1585–1586
sulphide minerals from, 1592
Wollogorang Formation, 1581–1582
McKay formation, 1641
Measurement while drilling (MWD) techniques, solution mining, 1322
Megalania prisca, 287
Megapolygonal desiccation cracks, 170–171
MelipellaNaltahua deposit, 1631
Menzengraben potash mine, East Germany, salt caverns, 1371–1372
Mercaptan, 1606
Mercator mud volcano (MMV), 613
Meromixis, 916, 918
Mesogenesis, 959
Messinian evaporites, of Mediterranean
Apennines, 461–469
basinwide drawdown, 457
Cyprus and Levantine basin, 469–472
deepest karst, 457
eustatic correlations, 475–476
Messinian salinity Crisis, 457
salinity crisis, 457–458
sicily, 466
Sorbas and Fortuna basins, Spain, 459–461
stratigraphy, 457–458, 472–471
tectonic setting, 456
Meta-evaporites, 1382
in amphibolite/granulite realm, 1445
borates of Eastern Liaoning, China, 1445–1448
Grenville complex, St Lawrence County, 1448–1450
Mary Kathleen Fold Belt, 1453–1459
Mount Isa Inlier, Northern Australia, 1450–1453
Pine Creek Inlier, Northern Territory, 1466–1468
Staveley Formation, 1459–1461
Willyama Supergroup, 1461–1466
description, 1382–1385
in greenschist conditions, Salton Sea, 1437–1439
implications, 1475
magnesium levels in metasediments, 1435–1437
metaplaya sequences, Damara Orogen, 1439–1445
mineral associations
albitites and albitization, 1408–1412
scapolite and scapolitization, 1401–1408
sodian phyllosilicates and talc, 1421–1424
tourmaline and tourmalinisation, 1412–1420
Naukluft Nappe Complex, 1444
Oaxacan Granulites, Mexico, 1470
occurrences, 1392
precious stones, 1424
Columbian emeralds, 1427–1431
lapis lazuli, 1425–1427
rubies in SE Asia, 1431–1433
pre-neoproterozoic, 1388–1391
processes and indicator minerals, 1387
protoliths, 1391–1394
regionally extensive, 1386
in Sar-e-Sang region, Afghanistan, 1423
scapolitic, Rajasthan, India, 1470–1473
Seve Nappe Complex, 1468–1470
sulphide-anhydrite Archaean carbonates, Brazil, 1473–1474
Swedish Caledonides, 1468–1470
tsavorite and tanzanite, 1433–1435
world-scale tectonism, 1386–1388
Metal
and brines, 1487–1488
transport
in high temperature saline realm, 1603–1605
precipitation models, 1496–1499

Metalliferous brines. *See also* Red Sea
acidification, 1495
basinal brines
chlorine and bromine concentration, 1486
inorganic components in, 1485–1487
metal carrying capacity, 1489–1490
salinity of, 1485, 1486
breach points, 1485
buried evaporite unit, 1483, 1485
carrier brines, 1493–1496
composition, 1485
Eh-pH and chlorinity/salinity, 1493–1496
evaporite brine mixing, 1497
grey-bed leaching, 1483
ionic source, 1483
metal fixers, 1496–1499
metals, ligands and salinity, 1487–1488
modern oil field, 1489
organic components in, 1488–1489
redox fronts, 1497–1499
seal and trap, 1485
sediments as metal sources, 1490–1493
in Tertiary-age basins, 1486
type II marine kerogen, 1486
Metalliferous deposits, evaporites and, 1666–1667
Metamorphic facies
depth *vs.* temperature, 1385
and mineral phases, 1383
regional metamorphism, 1386
Metamorphism
contact, 1384, 1386
dynamic (*see* Dynamic metamorphism)
in evaporitic basins, 1385
halite, 1397–1399
illite crystallinity and, 1394–1396
and metasomatism, 1408, 1425, 1433, 1459
regional (*see* Regional metamorphism)
world-scale tectonism, 1386–1388
Metasediments
in greenschist realm, 1437
magnesium levels in, 1435–1437
Mg-smectites, 82
$MgSO_4$ -depleted potash evaporites, 147
$MgSO_4$ -enriched potash evaporites, 148–149
Microbialites, 860, 867, 894, 961. *See also* Stromatolites
carbonate-precipitating, 24
classification of, 21
CO_2 degassing, 23
examples, 17–19
location and characteristics, 17–19
microfabrical classification, 16, 19
Precambrian, 27
sedimentology, 27–29
textures, 15–16
transition features, 30–32
travertine cement reefs, 23
Venn classification of, 16
Microcline, 1443
Microcoleus, 21
Middle Devonian evaporitic brine, 788
Middle East, coastal salinas
Late Pleistocene Salinas, Egyptian Red Sea Coast, 319–321
Ras Muhammad Pool, Southern Sinai, 318–319
Solar Lake, Gulf of Elat, 316–318
Mild shortening, 566–568
Mine of Mosaic, Saskatchewan (Canada), 1100
Mineola Propane fire, salt caverns, 1369–1370
Mineral conversion, by overpressure, 795
Minibasins, 540–547, 591
driving mechanisms for, 542–543
plays, 1052–1054
Miocene Ebro Basin, Spain, palaeohydrologic pattern, 788–789
Miocene epikarst, Madrid Basin, Spain, 682–684
Miocene evaporites, 1505
Miocene gypsum, Spain, gypsum-karst related subsidence, 700–702
Miocene redbeds, outcropping primary salt weld in, 532, 533
Mirabilite, 1237
Canadian production, 1222–1224
characteristics, 4
definition, 1216
extraction, 1224
in Great Salt Lake, USA, 1237
in Turkey, 1234, 1236
Mississippi Fan Fold Belt, 557
Mississippi Valley Type (MVT), 955
base metal deposits, 605
deposits, 1482
and bedded platform sulphates, 1551, 1552
grade-tonnage plot, 1552
in Maritimes Basin, Canada, 1543
Pb-Zn deposits, 1495–1496, 1534
SedEx deposit *vs.,* 1533–1534
sulphide precipitation, 1553, 1554
Mixolimnion, 916, 918
MMV. *See* Mercator mud volcano (MMV)
Moab Cane Creek Mine solution facility, Utah (USA), 1100
Mock-turtle anticline, 520
MODACON, 705
Modern Gypsum Karst, Saudi Arabia, 686–687
Molecular sieves, zeolites, 1297
geological controls on, 1299–1304
properties, 1298
usage and production, 1298–1299
Molten salts, 1616–1619
Mono Lake, California
hydrological and hydrogeochemical evolution, 334
lake levels and conditions, 331–332
tufa mound and pinnacles, 332–334
Monomixis, 918
Moroccan Meseta (Late Triassic), ancient potash evaporites, 1153–1154
Mosaic Potash Company in Belle Plaine, Saskatchewan, solution recovery brine, 1137
Mosul, Iraq
dam, catastrophic failure, 705–706
karst problems in, 702, 703
Motoyama deposits, 1658
Mount Homa volcanics, 1617
Mount Isa Inlier, Northern Australia
deposit characteristics, 1583
meta-evaporites in amphibolite, 1450–1453
SedEx deposits, 1590–1593
Zn-Pb sulphides, 1592
Mud diapirism
features of, 609–610
vs. salt diapirism, 607, 608
Mud diapirs, 607, 612, 613
Mulhouse Basin (Oligocene), Europe
organic matter, 921, 922
Mummification process, sodium carbonate, 1239–1240
Muriate of potash (MOP), 1088
lake brine processing and solution chemistry, 1101
Murunski Granite, 1650
Muruntau gold deposit, Uzbekistan, 1649–1651, 1667
Mussafah Channel, Abu Dhabi
CaSO4 occurrence in, 220
MVT deposits. *See* Mississippi Valley Type (MVT), deposits

N
Nabarro-Herring creep, 499
Nagaur-Ganganagar evaporite basin, India, ancient potash evaporites, 1175–1177
Nahcolite, Precambrian era, 157
Naica mine, Chihuahua, hydrothermal precipitation in, 7–8
Namakiers of Eastern Iran, 576
Namib Desert, pedogenic gypsum, 125
Namibe deposit, Africa, 1593–1595
Nanisivik Pb-Zn deposits, Canada, 1562–1565
Nash Draw, 632
Natrocarbonatite, 1616–1619
Natron
  definition, 1238
  use of, 1239
Natron Lake, East Africa
  brine chemistry, 347
  holocene sediments, 348–349
  late pleistocene sediments, 349–350
  magadiite and evaporitic chert, 350–353
Natural gas
  salt caverns, 1324–1325
  storage, salt caverns, 1321, 1325–1329, 1366, 1378
Natural hydrofracturing, 774
Near-diapir suprasalt shear (drag zones), 536–538
NedMag solution mining, Veendam, Netherlands, 1317–1318
Neogene evaporites, Spain, 462
Neoproterozoic Browne Formation, 584
Neoproterozoic halokinetic sediments, 582
Neoproterozoic salt allochthons, salt structure transition, 588–589
Nepa district stratigraphy, 1619, 1621
New Mexico Potash, USA, ancient potash evaporites, 1159–1161
Ni-Cu deposits
  chloride minerals hibbingite and kempite, 1606
  orthomagmatic metal accumulations, 1606–1608
  Sudbury, 1607–1608
Nile Delta sabkhas
  Eastern Mediterranean Coast, northern Sinai, 244–246
  Western Nile Delta Coast, Mediterranean, Egypt, 242–244
Nimbuwah Domain, iron-oxide deposits, 1637–1638
Nitrate
  in Atacama Desert, Chile, 1283–1287
  natural deposits, 1283
  in South America, 1284
  types of, 1284
Nitratite, 1283–1287
Nitre. *See* Saltpetre
Nodular daisy-head gypsum, 685
Non-evaporite indurated sediments, deformation mechanisms in, 498–499
Non-IOCG gold- evaporite associations, 1649–1650
Non-potash salts
  borate
    with B_2O_3 equivalents, 1195
    character and extraction history, 1192–1197
    in China, 1214–1215
    Death Valley area, 1210, 1211, 1212, 1213
    definition, 1194
    deposits of world, 1198–1202
    end uses, 1196
    in North America, 1210–1214
    production, 1194
    Rio Tinto Borax Group, 1197, 1207
    RNA World hydrochemistry, 1214
    in South America, 1207–1210
    textures, 1207
    in Turkey, 1192, 1197, 1202–1207
    uses, 1193
  bromine
    description, 1282
    production, 1282–1283
    in United States, 1282
    uses, 1193
  calcium chloride brines/minerals, 1273–1278
  gypsum
    character and extraction history, 1251–1252
    in China, 1252–1253
    plaster, 1251–1253
    in United States, 1254
  halite
    production, 1257–1261
    usage history, 1254–1256
  iodine
    in Atacama Desert, Chile, 1280–1281
    in Australia, 1282
    costs, 1280
    description, 1278
    in optical polarising film, 1281
    production, 1279
    uses, 1193
  lithium
    in Andean Salars, 1267–1269
    in China, 1271–1273
    in Clayton Valley, Nevada, 1269–1271
    geological setting of, 1267
    production, 1261–1267
  magnesite and magnesia salts, 1287–1292
  nitrate
    in Atacama Desert, Chile, 1283–1287
    natural deposits, 1283
    in South America, 1284
    types of, 1284
  sodium carbonate
    in African Rift, 1249–1251
    character and extraction history, 1238–1243
    in China, 1247–1249
    minerals, 1238
    in North America, 1243–1247
    uses, 1193
  sodium sulphate
    Canadian brine extraction, 1221–1225
    character and extraction history, 1214–1221
    chemistry, 1216
    in China, 1238
    deposits, 1217–1220
    exploited deposits, 1216
    Great Salt Lake, USA, 1237
    in Great Salt Lake, Utah, 1237
    in Karabogazgol, Kazakhstan, 1225–1229
    in Laguna Del Ray, Mexico, 1229–1231
    minerals, 1215
    Searles lake, California, 1219, 1236
    Spanish glauberite mines, 1231–1233
    in Turkey, 1233–1236
    uses, 1193
    US production of, 1236–1237
    world production of, 1220–1221
  sulphur
    biology of, 1295
    natural deposits, 1294–1295
    occurrences and textures, 1295–1297
    usage history and industry trends, 1292–1294
  zeolites, 1297
    properties, 1298
    in saline settings, 1299–1304
    usage and production, 1298–1299

Non-radioactive waste disposal, salt caverns, 1330
Noril'sk Region Siberia, 1607
  anhydrite crystals, 1608–1609, 1611
  faulting, 1608
  geology of, 1609
  intracontinental rifting, 1610
  Ni-PGE deposit at, 1612
  Phanerozoic age, 1608
  sulphate reduction, 1610
  sulphur isotope, 1609–1612
  thermochemical sulphate reduction, 1611
Norphlet formation, 759, 760
North America
  borate salts in, 1210–1214
  sodium carbonate in, 1243–1247
  trona in, 1243–1247
North Basin, of Dead Sea, 9
Northern Potwar deformation zone, 563
North Italian Mountains, Colorado, lapis lazuli in, 1427
North Stromatolite Lake, biomarker stratigraphy, 309, 310
North Ward-Estes Field, Texas, 1025–1028
Nullarbor's saline speleothems, 695

O
Oaxacan Granulites, Mexico, meta-evaporites, 1470
Ocnele Mari Brinefield, Romania, solution mining, 1332–1335
Offshore Brunei Darussalam, 607, 611
Oil and gas. *See* Hydrocarbon
Oil-base muds, 808
Old Belvedere Spinello brinefield, Italy, 1335–1337
Oldoinyo Lengai, African Rift
  carbonatite flow, 1617
  carbon-oxygen crossplot, 1618
  magmatic minerals, 1616
  natrocarbonatites at, 1616
  sodium carbonate lavas at, 1618
  subsolidus minerals in, 1617
Oligotrophic lake, 916
Olympic Dam deposit, South Australia, 1626, 1630
  evolution, 1645
  iron-oxide deposits, 1641–1644
Oncala breccias, 668
Ooids, 34
Open-toed sheet, 526, 529, 530
Optical polarising film (OPF), iodine in, 1281
Optymistychna cave, western Ukraine, 679–681
Ore
  potash evaporites, extraction technology
    conventional mining, 1093–1099
    lake brine processing and solution chemistry, 1101
    ore beneficiation, 1101–1105
    solution mining of potash, 1100–1101
  salts and contaminants, potash evaporites, 1087
Organic components in metalliferous brines, 1488–1489
Organic matter
  destruction, 902
  feast or famine cycle (*see also* Source rock)
    brines layered, biological responses to, 904
    in Dead Sea, 911–914
    Lorca Basin, Spain, 914–916
  flamingo connection, East African saline lakes
    African rift valley lakes, 905–906
    Arthrospira platensis, 906–910
    East African rift lakes, 905
    Lake Bogoria, 910, 911
    Lake Magadi, 911
    Lake Nakuru, 905, 908–910
    Lake Natron, 905
  organic productivity in saline waters, 903
  preservation, 902, 919–922
  production, 916–919
  sedimentation rate, 921, 922
  Storr's Lake, Bahamas, 912, 914
Orogenic belts
  continental, 1386
  definition, 1386
  in southwestern Africa, 1440
Orthomagmatic ore deposits, 1601. *See also* Iron-oxide copper gold (IOCG) deposits
  evaporite-igneous interactions, 1603
  faulting, 1608
  filter pressing, 1602
  halite-rich masses, 1605
  mercaptan, 1606
  mineralogic outcome, 1606
  Ni-Cu deposits, 1606–1608
  Noril'sk Region Siberia, 1608–1612
Osmotic pressure, 795
Osmotic stress, 868, 882, 888, 914
Ostracod
  halotolerant, 881, 882
  salinity tolerance, 868
Otto Fiord formation, 770, 771
Oulopholites, 694
Outcrop
  depositional patterns, potash evaporites, 1114–1119
  distribution and textures, 1117
Overburden pressure, 793
Overpressure
  aquathermal pressuring by, 795
  buoyancy forces by, 795
  causes of, 794–795
  epeirogenic movements by, 794–795
  hydrocarbon generation by, 795
  mineral conversion by, 795
  salt-maintained, 795–802
  seismic valving and pumping, 802–803
  stringers and rafts, 799
  in subsalt mud, 796
  Tengiz oil field, 796, 797
Overpressure in carbonate stringers, 799, 800
Owens Lake, California
  brine reflux, 196–197
  surface sediment in, 101
Oxygen isotopes as brine parenthood indicators, 135–139

P
Packbreccias, 643
Pahtohavare Au-Cu deposits, 1647–1649
PAJ1 and PAJ2, 180
Palaeohydrology, stokes surfaces and, 171–175
Palaeozoic evaporites, 779, 780
Paleocene-Lower Eocene El Haria Formation, 1540
Paleostress analysis, 604
Palimnarchos pollens, 287
Palo Duro basin, Texas, 674–675, 785
Paluxy sands, 590
Palygorskite, 82
Pangean supercontinent, assembly and disassembly, 431
Panning Sink, Kansas, 1355
Pans, saline, 254–256
Paradox Formation, 1316

Paramagmatic deposits, 1602
basaltic melt production, 1612
dykes and sills in salt, 1612–1616
Fe-oxide-Au deposits, 1622, 1623
hydrolytic alteration haloes, 1625
hydrothermal fluid circulation, 1621–1624
igneous rocks, 1622
IOCG deposits (*See* Iron-oxide copper gold (IOCG) deposits)
iron-rich associations, 1619
Korshunovsky iron ore deposits, Siberia, 1619–1620
molten salts, 1616–1619
saline haloes, 1620–1626
Parry Islands Foldbelt, Canada, 560
Partial salt dissolution
diffuse dissolution
basal anhydrite, Thailand, 675–677
Maha Sarakham Salt, Thailand, 671–674
Palo Duro Basin, West Texas, 674–675
focused rapid dissolution, 669–670
residue layer formation, 669
Parting muds, 1213
Passive diapirs
gross flow rate of salt, 518
shapes of, 515
Passive margin burial realm
brines, 768
characterization, 766
flow in, 767, 783–789
Patience Lake-PCS solution mine, Saskatchewan, Canada, 1100
Pb-Zn deposits
allochthon-edge stratiform, 1538–1543
Cadjebut Region, Australia, 1551–1555
caprock-hosted deposit, 1535–1538
Jubilee deposit, 1548–1551
Largentière deposit, 1567–1572
McArthur River (HYC) deposit, 1576–1590
modern oil field brines constituents, 1489
MVT deposits, 1534, 1535
Nanisivik Baffin Island, Canada, 1562–1565
peridiapiric diagenesis and, 1534–1535
Polaris Zn-Pb Mine, 1555–1562
San Vicente deposit, 1565–1567
stratiform sediment hosted, 1533–1534
PCS Patience Lake solution mine, Saskatchewan, Canada, 1100
Pearson's Principle, 1488
Peigneur Lake, Louisiana, solution mining, 1360–1362
Pekelmeer Lagoon, 191
Peloids, 34
Perdido foldbelt, 556–558
Perennial saline lakes
climate and scale, 377
Dead Sea, Middle East
basin margin sediments, 365–367
deepwater halite, 361–362
deep water laminites, 362–365
density stratification, 357–361
geological settings, 353–355
water level changes, 356–357
evaporite deposits variations, 374, 375
Great Salt Lake, Utah, 324–329
Lake Aci, Turkey, 342
Lake Asal, Republic of Djibouti, 371–374
Lake Lisan, Jordan Valley, 367–371
Lake Natron and Lake Magadi, East Africa, 344–353
Lake Tuz, Turkey (Tuz Gölü), 340–342
Lake Urmia, NW Iran, 342–344
Lake Van, Turkey, 335–338
Mono Lake, California
hydrological and hydrogeochemical evolution, 334
lake levels and conditions, 331–332
tufa mound and pinnacles, 332–334
physiography of, 375
and sabkhas, pans, 377–380
Salda Lake, Turkey, 338–340
Periodic salt breakout, 524–525
Peritidal muddy carbonates, evaporitic mudflat seals, 979–983
Permian Basin, West Texas
pisolites, 33
solution mining, 1349–1355
tepees, 35
Permian Capitan shelf, brine reflux, 193
Permian Cutler Formation, 1518
Permian Gharif Formation, 823, 824
Permian Potash, 1154
Permian Zechstein Basins
Ca2 carbonate, 482
carbonate platform, 480
mineralogy, 479
stacking patterns, 481
stratigraphic evolution, 477–483
Phanerozoic Fe-oxide deposits, 1631–1634
Phanerozoic IOCG deposits, 1630
Phanerozoic potash salt series, 1086
Phase chemistry, trona solution mining, 1322–1324
Phormidium spp., 27
Photosynthesis
cyanobacteria, 860
light dwellers and pigmentation, 860–864
Phreatic gypsum caves
bathyphreatic karst, 678
caprock sinkholes and vadose passages, Russia, 681, 682
maze cave, 679, 680
Optymistychna cave, western Ukraine, 679–681
Piceance Creek Basin, Colorado
Shell Oil in, 1322, 1323
sodium carbonate, 1244–1247
solution mining nahcolite in, 1324
trona solution mining, 1322–1324
Picritic magmas, 1607
Pinda Group, 560
Pine Creek Inlier, Northern Territory, meta-evaporites in amphibolite, 1466–1468
Pine Creek Orogen, iron-oxide deposits, 1637–1638
Pisolites
marine, 33
from Permian of West Texas, 33
vadose, 33–34
Plate tectonic
definition, 1389
development, 1385
indicators, 1387
paradigm, 1386, 1391
Proterozoic associations, 1411
Platform carbonates, bedded saltern seals, 983–985
Platform evaporites
broad-scale depositional models, 399–400
depositional styles, 414
epeiric/epicontinental seaways, 411
on epeiric shelves, 410–414
greenhouse eustasy, 413
holomictic salterns, 412
marine-fed mudflats, 412
megasulphate systems, 412

Playa
basin and range, 257
Death Valley, California, 261–262
degrading hydrology and, 175–176
groundwater system, 130
of Qaidam basin, 1105–1114
Saline Valley, California, 258–259
water composition, Australia, 117
Playas of Qaidam Basin, quaternary potash evaporites, 1105–1114
Plug-fed extrusion, 526–529
Plug-fed thrusts, 526, 528, 530
Poiseuille flow, salt, 506
Polaris Zn-Pb Mine, Canada
bacterial sulphate reduction, 1559–1560
Baumann Fiord Formation, 1561
Bay Fiord Formation, 1559, 1561–1562
dolomite, 1558
geological and geochemical characteristics, 1558
isotopes, 1559
location, 1555
mineralisation, 1560
ore grade divisions, 1557
paragenetic-diagenetic sequence, 1558
sedimentological study, 1562
temperatures, 1559–1561
Thumb Mountain Formation, 1555, 1557, 1562
time-stratigraphic diagram, 1555, 1556
Zinc concentration, 1557
Porphyry copper deposits, supergene enrichment, 1595–1597
Port Isabel fold belt, 557, 558
Post-induration interstratal breccia, 652
Post-kinematic layers, 587
Post-tectonic burial setting
brines, 768
characterisation, 766, 769
flow in, 767, 783–789
Potash salts, 1086
ancient (pre-quaternary)
Canadian Maritimes (Mississippian of Nova Scotia and New Brunswick), 1165–1168
Cretaceous Trans-Atlantic Potash, 1150–1153
formation, mineable potash, 1177–1179
German Potash (Z1, Z2 and Z3 Potash), 1154–1155
Khorat Plateau, Thailand, 1144–1150
Moroccan Meseta (Late Triassic), 1153–1154
Nagaur-Ganganagar evaporite basin, India, 1175–1177
New Mexico Potash, USA, 1159–1161
Permian Potash, 1154
potash geology, WCSB, 1169–1173
Pripyat Basin (Devonian) Belarus, 1173–1175
quality control, 1179–1186
Upper Kama Potash Region, Cis-Urals Russia, 1161–1165
Upper Rhine Graben, France, 1141–1144
WCSB fluids, 1173
West Canadian Potash (Devonian), 1168–1169
Z3 - Boulby Potash, UK, 1155–1159
from brine, 1129
carnallite, 1087
core-based geology, 1119–1124
Dead Sea Potash, Middle East, 1129–1133
depositional patterns, outcrop, 1114–1119
Inland Chotts and Coastal Sabkhas in North Africa, 1124–1129
MOP, 1088
occurrence and quality, at worldscale, 1106–1109, 1186–1190
operations, solution mining, 1316–1318
ore extraction technologies
conventional mining, 1093–1099
lake brine processing and solution chemistry, 1101
ore beneficiation, 1101–1105
solution mining of potash, 1100–1101
ore salts and contaminants, 1087
production and consumption
in Asia, 1092
in Canada, 1090
Permian potash, 1090
price, 1090, 1093
in United States, 1092
quaternary potash
Danakil Depression, Ethiopia, 1114
Playas of Qaidam Basin, 1105–1114
solution recovery brine in Utah, USA, 1133–1137
SOP, 1088 (*see also* Sulphate of potash (SOP))
sylvite, 1087
uses, 1193
world statistics, 1089
Potrerillos Formation, 598–599
Potwar Basin, 563
Power law behaviour, of dry rock salt, 497, 499
Precambrian
albitization, 1412
to Cambrian sulphur cycle, 160
diapiric hormuz salt, 691–694
IOCG deposits, 1627
magnesites, 1291
occurrences and mineralogies, 154
oceanic chemistry, 153–159
sedimentation, 389
sparry magnesites, 1291–1292
Precambrian-Cambrian transition, 159–162
Precambrian of Baffin Island, Canada, lapis lazuli, 1425
Pre-drill seismic techniques, 536
Prekinematic sediment layers, 587
Pre-Quaternary/pre-Neogene evaporite, 11. *See also* Ancient evaporites, potash (pre-quaternary)
Presqu'ile dolomite, 776
Pressure
cells and salinity-driven convection, 789
gradients, 794
osmotic, 795
seals, 792–795
unpredicted changes, 805–807
Pressure solution creep, 500
Primary evaporite
carbonate systems
Archaean, 38
laminites, 13–14
marine and hypersaline, 37–38
microbialites and stromatolites, 15–32
ooids and peloids, 34
Palaeoproterozoic, 38
Phanerozoic, 39
pisolite, 32–34
tepees, 35–37
depositional textures, 9
salts
gypsum beds, 39–44
halite beds, 44–48
laminites, 54–58
pedogenic and wind reworked, 48–54
reefs, 58–60

Pripyat Basin (Devonian) Belarus, ancient potash evaporites, 1173–1175
Problems in evaporite correlation
basin edges, 439–440
rapidity of deposition, 439
stratigraphic control, 439
stratigraphic relationships, 439
Proterozoic Cu-Au deposits, 1604
Proterozoic iron-oxide deposits, Australia
Candelaria Cu-Au deposit, 1644–1646
Coronation Hill, 1638–1640
Cosmo Howley Au deposit, 1639–1640
CuAu mineralisation, 1635
hydrothermal process, 1634
Kiirunavaara deposit, 1647
Koolpin Formation, 1639–1640
magnetite ironstone textures, 1635
Olympic Dam, 1634
Olympic Dam Breccia Complex, 1641–1644
Pine Creek Orogen, 1637–1638
scapolitisation, 1646
South Alligator Valley deposit, 1636
Starra deposit, 1635–1636
sulphide ore textures, 1635
Tennant Creek style deposits, 1641, 1643
two-fluid fluid mixing model, 1644
Proterozoic Ni deposits, 1608
Proterozoic salt allochthons, 589
Proto-conglomerates, 642
Protoliths, 1391–1394
Pseudomorphs
carbonate, 1464
copper, 1526
hydroboracite, 1209
Palaeo-evaporite, 1443
types, 1209–1210
Pull-apart burial realm, 766–768, 777–778
Pyrenees thrust belt, 782
Pyrite-silica-anhydrite breccias, 1662–1663

Q

Qaidam Basins, China
lithium, 1271–1273
potash evaporites, 1086
Qom Basin of central Iran, 578, 579
Qom Kuh, 579–581
Quaternary climate, 383–384
Quaternary deserts, 86
Quaternary evaporites, 91
continental-interior settings, 94–96
marine-margin settings, 96–98
playas of Qaidam Basin, potash
bedded and displacive salts, 1110
formation period, 1105
Lake Dabuxum, 1105
location, 1105, 1110
Qarhan Playa sump, 1110
Qarhan saltflat/lake, 1109
potash, Danakil Depression, Ethiopia, 1114

R

Radioactive waste disposal, salt caverns, 1330–1331
Raft tectonics
in Angola, 522
definition, 521
falling diapirs, 521–523
salt basin characterisations, 522–523
Ramos Formation, 1526
Ramp basins, 541
Ramp model, evaporitic epeiric
arid-zone carbonate ramps, 415
carbonate ramp, 414
Irwin's epicontinental-sea model, 415
Khuff Formation, 416, 417
Lower Clear Fork Formation, 416
marine *versus* nonmarine stages, 425
Permian Khuff Formation, 418
rimmed epeiric shelves, 419–425
San Andres Formation, 416
Ran El Melah, Algeria, 578
Rann of Kutch, sabkhas, 247–249
Rare earth elements (REE), concentrations and distributions, 1655
Ras Ghanada, UAE., 292
Ras Muhammad Pool, Southern Sinai, 318–319
Rauhwacke horizons
Burano formation, 663–665
definition, 659
deformation/lubrication, 660
Haselgebirge breccias, 661–663
Katangan Copper belt, 666
Muttlebury Nappe, 665
Oncala breccias, 668
proterozoic basins, 666
tectonite specific usage, 660
thermochemical sulphate reduction, 663
Rayleigh criteria, 130
Rayleigh number, 130
Rayleigh-Taylor instability, 497
Reactivated (mildly squeezed) diapirs, downbuilt diapirs *vs.,* 568–573
Reactive diapirism, 514, 549, 568, 585, 587
Reactive diapirs, 587–588
Red Sea
Atlantis II Deep (*see* Atlantis II Deep, Red Sea)
brine-filled deeps, 1501
Conrad Deep, 1501
Kebrit and Shaban Deeps, 1505–1507
metalliferous deep of, 1499–1500
sea floor depressions, 1507
seismic surveys, 1500
Redstone Copper Belt, Canada, 1531–1533
REE. *See* Rare earth elements (REE)
Reef system of Gulf of Mexico, 594
Regionally-tiered salt plays, Gulf of Mexico, 1048–1051
Regional metamorphism, 1384
metamorphic facies, 1386
thrust belts, 1394–1401
Regional-scale karst
subsidence and landscape in diapiric regions
Five Islands, Gulf of Mexico, 638–639
salt valleys, Moab region, 637–638
Zagros/Hormuz region, Arabian Gulf, 640–642
subsidence troughs
Black Hills, South Dakota, 636–637
creation, 628
Delaware Basin, West Texas, 631–634
Holbrook Anticline, Arizona, 634–636
Hutchison salt, Kansas, 630–631
subcrop salt dissolution, 628
Regional sediment starvation, 528
Rejuvenated diapirs, 571

Reservoirs and traps, hydrocarbons
bedded basinwide evaporites, 1009–1010
bedded salt seals, 976–979
brine flux, changing directions, 1035–1036
dolomitised limestones, Central Basin Platform, West Texas, 1001–1002
Eocene and Miocene Associations, Middle East, 1010–1014
evaporite-sealed platform and reefs, Devonian, Canada, 1017–1021
exploration paradigms, bedded evaporite hydrocarbon association, 1030–1031
Ghawar Field, Saudi Arabia, 990–998
Jurassic Arab Formation, Arabian Gulf, 985–990
Jurassic Smackover Fm., Gulf of Mexico, 1002–1009
North Ward-Estes Field, Texas, 1025–1028
peritidal muddy carbonates, evaporitic mudflat seals, 979–983
platform carbonates, bedded saltern seals, 983–985
quality tied to bedded evaporite seal type, 1021
recognising bed dissolution, 1034–1035
recognising depositional differences, 1031–1034
Rotliegende Sands of Northern Netherlands and North Sea, 1028–1030
Silurian Pinnacle Reef Fields, Michigan Basin, 1014–1017
Slaughter-Levelland Trend, West Texas and New Mexic, 998–1001
Yates Field, West Texas, 1021–1025
Retsof mine, USA, solution mining, 1344–1345
Riftia pachptila, 936
Rio Tinto Borax Group, 1197, 1207
Ripon Area, UK, gypsum-karst related subsidence
catastrophic collapse, 699
Edlington and Roxby formations, 699–700
groundwater pumping, 699
hydrogeological flow units, 699
sinkhole variation, 699–700
subsidence features, 697
Ure terrace, 700
watertable level fluctuations, 698–699
Rock salt. *See also* Halite
cycle, conceptual model of, 512
density, 496
diffusion mechanism map, 497
effective *vs.* differential stress diagram, 504
impurities effect, 501
level of neutral buoyancy, 496
micro and macro scale flow texturing, 509
microstructural domains, 511–512
microstructural process, 499, 500
physical properties, 496
power law behaviour, 497
seismic velocity, 512
thermal conductivity, 505
triaxial deformation experiments, 499–500
viscosity, 497
Rock's inherent ductility, hydrocarbon, 969
Rocky Mountain Foldbelt, USA, 1075–1076
Rodinia/Gondwana supercontinent(s), 432–433
Roho, 540
Roho/listric weld system, 540
Roho salt system, 550
Roof deposition/salt burial, 529–530
Roof-edge thrust, 547
Rotation recrystallization, 500
Rotliegende regional aquifer, 758
Rotliegende Sands of Northern Netherlands and North Sea, 1028–1030
Ruby, 1431
in SE Asia, 1431–1433
Rum Jungle
magnesites in, 1467
tourmalines, 1467–1468

S
Sabkha nodules and crystals, 62
Sabkhas
Abu Dhabi
intertidal facies (lagoon-edge muds), 220–222
intertidal facies/strandline sands, 219–220
island shoal and bank facies, 215–217
subtidal facies, 217–219
supratidal facies, 222–223
anhydrite nodules, 210
classification, 211
continental sabkhas
alluvial fan-ephemeral saline lake, 256–277
Basin and Range Playas, USA, 257
Bristol Dry Lake, California, 259–261
Death Valley Playa, California, 261–262
Deep Springs Lake, California, 257–258
ephemeral stream floodplain-dune field-saline lake, 277–289
perennial stream floodplain-perennial saline lake, 289
Sabkha Yotvata, Israel, 256–257
Saline Valley Playa, California, 258–259
definition and terminology, 210–211
Eastern Saudi Arabia, 231–240
eolian
salt-pans (marshes) and diapirs, 299–301
sea-margin sabkha, 291–294
sheets of eolian sabkhat, 294–299
Gulf of Suez, 240–241
holocene models, limitations of, 249–251
Kuwait
Al-Khiran Sabkha, 237–240
Kadmah Bay/Kuwait Bay, 234–237
lacustrine
depositional characteristics, 251–256
groundwater transport, 253–254
saline mudflat, 252–253
saline pan, 254–256
marine coastal
beach-dune and fluvial sabkhat, 242–249
carbonate-hosted, 212–231
hydrology and hydrogeochemistry, 223–231
siliciclastic-hosted, 231–240
siliciclastic sediment, 212
Nile Delta
Eastern Mediterranean Coast, northern Sinai, 244–246
Western Nile Delta Coast, Mediterranean, Egypt, 242–244
Rann of Kutch, 247–249
Shatt el Arab Estuarine Sabkha Iraq, 246–247
Southern Arabian Gulf, 212–231
subtidal sedimentation
open marine sedimentation, 217–218
restricted marine (khor) sedimentation, 218–219
world distribution, 207–209
Umm Ash Shurabyat, Saudi Arabia, 298
Yotvata, Israel, continental sabkhas, 256–257
Sagging, 623
St. Francis dam collapse, 703
Salada Mediana, Spain
sodium sulphate, 1234
Upper Miocene Kirmir Formation, 1233, 1234

Salado Formation, 1295–1297, 1349, 1351–1354
Salar de Atacama, Chile
  evaporation level in, 102
  lithium in, 1267–1269
Salar de Surire, Chile, borate deposits, 1207
Salar de Uyuni, Bolivia
  borate deposits, 1207
  lithium deposits, 1269
Salarium argentum, 1255
Salars of South America
  Salar de Atacama, Chile, 271–273
  Salar de Uyuni, Bolivian Altiplano, 267–271
  Salar Grande, Central Andes of Chile, 273–277
Salar surface, 178–180
Salda Lake, Turkey, perennial saline lakes, 338–340
Salina de Ambargasta, Central Argentina, 287–289
Salinas
  coasts of Australia
    carbonate salinas, 306–312
    gypsum salinas, 312–314
    halite salinas, 314–316
  coasts of Middle East
    Late Pleistocene Salinas, Egyptian Red Sea Coast, 319–321
    Ras Muhammad Pool, Southern Sinai, 318–319
    Solar Lake, Gulf of Elat, 316–318
  South American salinas and dolomite, 323–324
Saline basins
  degrading hydrology and playa capture, 175–176
  dry mudflat/sandflat, 165–166
  evaporitic saline mudflat, 163–165
  fluctuating watertables indicators, 169
  remote sensing, 177–185
  stokes surfaces, 169–175
  unconfined meteoric watertable, 168–169
Saline giants. *See* Basinwide evaporites
Saline pans
Saline realm, high temperature, 1603–1605
Saline Valley Playa, California
  continental sabkhas, 258–259
Salinity
  of basinal brines, 1485, 1486
  and brines, 1487–1488
Salinity-driven convection, 789
Salt
  advance mechanisms for salt canopies, 547
  allochthon, evolution of, 527
  basin, evolution of, 595
  basins in Gulf of Mexico, 489
  beds, building blocks of
    deepwater evaporites, 397–399
    evaporitic mudflats, 394, 396
    saltern, 396–397
  breakout, 524–525
  buoyancy, 572
  cake (*See* Sodium sulphate)
  collapse depressions, 1078
  creep
    in Eminence, Mississippi, 1373
    factors, 1372–1373
    ground subsidence, 1375–1376
    minimising subsidence from, 1377
    in Tersanne, France, 1373
  distribution in Gulf of Mexico, 553
  dykes and sills in, 1612–1616
  inflation, deflation, welds and basal (subsalt) shear zones, 526
  plug, 528
  primary evaporitic
    gypsum beds, 39–44
    halite beds, 44–48
    laminites, 54–58
    pedogenic and wind reworked, 48–54
    reefs, 58–60
  pumping, 525
  as sheets, allochthons and breakouts, 523–526
  sheets, emplacement of, 525, 526, 527, 528
  solution mining (*see* Solution mining)
  squeezing, 591
  stock canopy system, 550
  strength, 501, 502
  structures, 493, 494
    brain plain sediments and, 591
    description, 506
    diapir stage, 506–507
    evolution of, 516, 517
    internal complexity, 506–509
    landscape relief around active, 585
    in Moab area of southeast Utah, 573, 574
    sediments and, 587–589
  systems
    crystal size and stress-strain indicators, 509–511
    density, viscosity, strength & buoyancy, 496–505
    flow textures and rates, 506
    internal complexity, 506–509
    microstructural domains, 511–512
    thermal effects, 505
  temperature effects in, 1613
  welds, 531–533, 540–547
    classification of, 531
    formation of, 531–533
  welds, loading detachments and growth faults, 538–540
Salt caverns
  energy liquids/compressed air storage, 1324–1329
  gas storage, 1321, 1325, 1327–1329, 1366, 1378
  ground subsidence problems, 1375–1376
  hydrocarbon in, 1325–1327
  liquefied petroleum gas, 1325, 1327
  monitoring/minimizing collapse, 1377
  natural/anthropogenic subsidence, 1377–1378
  plugging, 1378–1379
  problems with hydrocarbons storage, 1366
    Barber's Hill explosion and collapse, 1368–1369
    Brenham explosion, 1365–1368
    Hutchinson explosion, 1370–1371
    Menzengraben potash mine, East Germany, 1371–1372
    Mineola Propane fire, 1369–1370
    Weeks Island, Louisiana, 1363–1365
    West Hackberry explosion, 1365
  salt creep, 1372–1374
  salt falls *vs.* roof collapses, 1374–1375
  and solution mining (*see* Solution mining)
  surface indicators of breached caverns, 1376–1377
  waste disposal, 1329
    nonradioactive, 1330
    radioactive, 1330–1331
  Winsford Mine, Cheshire, 1324
Salt deflation, 531–533
Salt deformation, representative strain rates and speeds of, 498
Salt-detached basins, 558, 559
Salt diapirism
  features of, 609–610
  mud diapirism *vs.,* 607, 608

Salt diapirs, 612–613
classification, 494
definition, 493
Salt dissolution
bedded solution-collapse breccias
Belle Roche breccia, 647
chalky dolomite, 644
clasts, 645
lower Visean Belle Roche breccia, 646
breccia extent
hydrology and texture, 650–653
stratiform breccias, 649–650
diapiric solution breccias
Flinders ranges, 655–657
Gulf Islands, 654
Hormuz formation, 655
outcropping and subcropoing areas, 653, 654
rock flour, 653
vs. salt ablation breccias, 657–659
evaporite dissolution breccia, 642–644
partial (*see* Partial salt dissolution)
Rauhwacke horizons (*see* Rauhwacke horizons)
Salt domains, 566
Salt extrusion, 526, 573–582
plug-fed extrusion, 526–529
Salt falls *vs.* roof collapses, 1374–1375
Salt-floored inverted basins, 565
Salt-floored minibasin, 540, 541, 542
Salt-floored rift basins, widening of, 560
Salt-generated underpressure, 808–809
Salt glaciers, 498
Salt hydraulics, 506
Salt inflation, types of, 526
Salt-lubricated extension, 520–521
Salt-maintained overpressure
allochthon basins, 802
Ara stringer, 800–801
black staining, 799, 800
convective heat flow, 804
hydrofracture, 798
Permian halite, 796
seismic valving and pumping, 802–803
stringers and rafts, 798, 799
Tengiz oil field, 796, 797
true pressure seal, 795
Salt-nappe system, 550
Salton Sea geothermal system (SSGS), 1437–1439
Salton Trough, 1437
Salt-pans (marshes) and diapirs, 299–301
Saltpetre, 1284, 1285
Salt Range region, Pakistan, 563
Salt-related traps, Tarim Basin, China, 1076–1078
Salt-roof thrust, 547
Salt tectonics
autochthonous, 548–550
contractional
downbuilt and reactivated diapirs, 568–573
gravity gliding, 554–560
inverted basins, 565–566
shortening, 566–568
thin-skinned fold and thrust, 560–565
geological principles, 493
in Northern Gulf of Mexico, 494, 495
style, 551
Salt-tongue systems, 550
Salt valleys, Moab region, 637–638
Salty gumbos, 533–536
San Andres Formation, Permian Basin, 416
Sandstone-hosted deposits, Central Andes, 1525–1529
Santa Rita gold deposit, Brazil, 1649
San Vicente Zn-Pb deposit, Peru
burial temperatures, 1567
calcites from, 1567
location, 1565
mining activity in, 1566
schematic cross-section, 1565
sphalerite and galena, 1566–1567
stratigraphy, 1566
Sar-e-Sang region, Afghanistan, meta-evaporites in, 1423
Satin-spar gypsum, 79
Scandinavian Caledonides, meta-evaporites, 1468–1470
Scapolite
Br/Cl ratios, 1407
calcium carbonate and, 1402, 1405
definition, 1401
distribution, 1401–1402
dolomite, 1441
meta-evaporites in Rajasthan, India, 1470–1473
minerals, 1405
and scapolitization, 1401–1408
sodium chloride and, 1402, 1405–1407
structure, 1401, 1402
worldwide examples, 1403–1404
Scapolitisation, 1646
scapolite and, 1401–1408
worldwide examples, 1403–1404
Schizohaline salinity cycles, 837, 961
SCLM. *See* Sub-continental lithospheric mantle (SCLM)
Seal capacity of evaporites
allochthons, 972
bedded evaporites, 971
biodegradation, 970
density/buoyancy, 970
environments favouring seal continuity, 973–976
hydrocarbon migration and trapping, south Oman salt basin, 975
marine carbonate reservoir, 975
oil re-entrapment, 970
salt permeability/brine permeation measurement, 970, 971
Seal type and ultimate recoverable reserves, 965
Searles lake, California
borate salts, 1212, 1213
bromine, 1282
sodium carbonate, 1242
sodium sulphate, 1219, 1236
Searles Valle Minerals, Inc., 1237
Seasalt production, 1257, 1260, 1261
Seawater chemistry
Phanerozoic dilemma
MgSO4 -depleted potash evaporites, 147
MgSO4 -enriched potash evaporites, 148–149
Precambrian
calcium sulphate textures, 158
evaporite occurrences and mineralogies, 154
gypsum, 156
nahcolite, 157
oxygen, sulphur and metal levels, 155
sulphate concentrations, 155–156
Precambrian-Cambrian transition, 159–162
Secondary evaporite
depositional textures, 11–12
intrasediment salts, 60–62
shallow mineralogic re-equilibration, 65–69
sulphate evaporites, 69–74
syndepositional karst, 62–65
Sediment(s)
caprock formation (diagenesis of salt), 602–607
carbonate patterns, 592–595
distribution of, 593

and evolving salt structures, 587–589
and flowing salt, 585–587
as metal sources, 1490–1493
salt basin evolution, 595
shale diapirism complications, 607–614
siliciclastic patterns, 589–592
subsalt sediments, 602
suprasalt carbonate sedimentation, 597–601
suprasalt clastic sedimentation, 596–597
Sedimentary Exhalative (SedEx) deposits, 1482, 1499. *See also* Pb-Zn deposits
age distribution, 1576
Atlantis II Deep, 1576
distribution, 1574
evaporite-associated, 1572–1576
in Fe-carbonate haloes/hosts, 1590–1593
Irish-type deposits, 1572
location, 1575
low temperature, 1583–1584
mid-Proterozoic maximum, 1576
model, 1573
vs. MVT deposit, 1533–1534
Proterozoic Pb-Zn deposits, 1576, 1577
resource plot for, 1574
Zn-Pb-Ag deposits, 1534
Sediment-hosted Cu, 1525
Sediment-hosted stratiform copper (SSC) deposits, 1507
classifications, 1508, 1509
halokinetic associations, 1510
Kupferschiefer copper deposits, 1510–1514
redox interface, 1533
resource plot, 1509
salt associations, 1509–1510
Sediment-loaded minibasin, 540
Sedom cave
caprock carapace, 689
mass balance calculation, 690
passage development, 690
sinkholes, 690
Seepiophila jonesi, 936, 937
Seismic valving, 802
Sekko ore, hydrothermal anhydrite in, 1656
Selenitic gypsum, 79
Self-convecting fluid system, 791
Sepiolite, 82
Sequence stratigraphy
basinwide evaporites, 452–455
chronostratigraphic correlation, 444–447
first and second order changes, 445–446
greenhouse earth, platform evaporites, 451–452
icehouse and greenhouse conditions, 446
icehouse and greenhouse eustasy, 448
marine-fed platform evaporites, 447
marine-margin platform evaporites, 448–451
sealevel and salt sequence, 447–448
sigmoidal/slug model, 445
in Silurian Salina Group, 483–491
in Zechstein, 477–483
Shale diapirism, complications of, 607–614
Shale sheaths, 505
Shallow allochthons, 612
Shallow drilling, 582–583
Shallow mineralogic re-equilibration
deeper burial, 68
limpid dolomite in mosaic halite, 68–69
porosity loss, 66–68
Shatt Al Arab delta, 212
Shatt el Arab Estuarine Sabkha, Iraq, 246–247
Shortite, 116
Siberian Traps, 1608
Sicilian Basin, 466
Sigsbee canopy, 551
Sigsbee Escarpment, 529, 530
Sigsbee Scarp, 523, 541, 542
Sijes Formation, 1207–1208
Siliciclastic patterns, sediments, 589–592
Silicified evaporites
abiological processes, 725
anhydite pseudomorphs, 722
bacterial degradation of organic matter, 725
chalcedony, 721
examples, 720–721
Italian cherts, 726
magadiite nodules, 725–726
moganite, 727
precipitation, 724
quartz nodules, 723, 724
silicified-calcitized anhydrite nodule texture, 722
Sills in salt, 1612–1616
Silurian evaporites, Michigan Basin, USA, 483–487
Silurian Pinnacle Reef Fields, Michigan Basin, 1014–1017
Single drill pads, solution mining, 1320–1322
Sinkholes. *See also* Dolines
Bayou Corne, Louisiana, 1357–1358
Cargill Saltworks, Kansas, 1346–1347
Detroit River brinefield, USA, 1347–1348
in Grand Saline, Texas, 1358–1359
in Hutchinson region, 1347
JWS, New Mexico, 1351–1354
Old Belvedere Spinello, Italy, 1335–1337
in Panning Sink, Kansas, 1355
Wink Sink, USA, 1349–1355
Slaughter-Levelland Trend, West Texas and New Mexic, 998–1001
Slave Point formation, 776
Sleaford Mere on Eyre Peninsula, algal tufas of, 307
Smackover Fm., Gulf of Mexico, 1002–1009
Snowball Earth model, 160
Society Cliffs Formation, 1563–1564
Soda ash. *See* Sodium carbonate
Soda Lakes, Nevada, 115
sodium carbonate deposit, 1243
Sodalite, 1425
Sodian phlogopite, 1421
Sodian phyllosilicates and talc, 1421–1424
Sodium carbonate
in African Rift, 1249–1251
in ancient Egypt, 1238
Chaganur lake deposit, 1248
character and extraction history, 1238–1243
in China, 1247–1249
Green River Basin, Wyoming, 1242–1245
in Lake Magadi, 1250
lavas at Oldoinyo Lengai, 1618
minerals, 1238
mummification process, 1239–1240
in North America, 1243–1247
occurrences of, 1240–1242
phase chemistry of, 114
Piceance Creek Basin, 1244–1247
production, 1250–1251
salts, 763
solution mining, 1322–1324
Solvay process, 1239–1240
in USA, 1242
uses, 1193
world production of, 1239–1240
Sodium chloride and scapolite, 1402, 1405–1407
Sodium hydroxide (Lye), 1086

Sodium, salinity, 1486
Sodium sulphate
  Canadian brine extraction, 1221–1225
  character and extraction history, 1214–1221
  chemistry, 1216
  in China, 1238
  deposits, 1216–1220
  Great Salt Lake, USA, 1237
  in Karabogazgol, Kazakhstan, 1225–1229
  in Laguna Del Ray, Mexico, 1229–1231
  minerals, 1215
  Searles lake, California, 1219, 1236
  Spanish glauberite mines, 1231–1233
  in Turkey, 1233–1236
  uses, 1193
  US production of, 1236–1237
  world production of, 1220–1221
Solar-heated brine concentration, 1–2
Solar Lake, Gulf of Aqaba, 187
Solar Lake, Gulf of Elat, 316–318
Solikamsk mine collapses, Russia, 1343–1344
Solubility, evaporite salts *vs.* limestone, 616–617
Solution dolines, 622–623
Solution mining
  advantage, 1310
  bamboo drilling technology, in China, 1310, 1312
  blanket management, 1319, 1321
  blinding and phase chemistry, 1322–1324
  Boies nahcolite bed, 1322
  Bryan Mound salt dome, Texas, 1374
  cluster well pads, 1320–1322
  disadvantage, 1310
  history, 1310–1312
  lithology effects cavity shape, 1318–1322
  MWD techniques, 1322
  NedMag, Veendam in Netherlands, 1317–1318
  potash operations, 1316–1318
  problems with cavities, 1333
    Anpeng trona salt mine, China, 1362–1363
    Barycz and Wieliczka site, Poland, 1337–1341
    Bayou Corne, Louisiana, 1357–1358
    Cargill saltworks, Kansas, 1346–1347
    Detroit River brinefield, USA, 1347–1348
    Gellenoncourt saltworks, France, 1341–1342
    Gorham oil field, Kansas, 1355–1357
    Grand Saline sinkhole, Texas, 1358–1359
    ground collapse, Tusla, 1342–1343
    Haoud Berkaoui oilfield, Algeria, 1359–1360
    Lake Peigneur, Louisiana, 1360–1362
    Ocnele Mari Brinefield, Romania, 1332–1335
    Old Belvedere Spinello brinefield, Italy, 1335–1337
    Panning Sink, Barton County, Kansas, 1355
    Permian Basin, USA, 1349–1355
    Retsof mine, USA, 1344–1345
    Solikamsk and Bereznki mine collapses, Russia, 1343–1344
    Windsor brinefield, Ontario, 1347
  process, 1313
  in reverse-circulation method, 1313
  salt caverns and (*see* Salt caverns)
  single well, 1316, 1320–1322
  Szechuan region, China, 1311
  trona, 1322–1324
  Tully method, 1315
  variable point injection, 1316
  waste components, 1310
  well and cavern design, 1312–1315
  well styles, 1315–1316
Solution mining of potash
  brine solution injection, 1100–1101
  Moose Jaw (Belle Plaine), 1100
  sylvite precipitation, 1100
  three-pipe-in-one-string solution method, 1100
Solution recovery brine in Utah, USA, potash evaporites, 1133–1137
  Cane Creek mine, 1136
  ditch water levels, 1134
  Moab Utah brine extraction operation, 1136
  Mosaic Potash Company in Belle Plaine, Saskatchewan, 1137
  natural brines, 1135
  solar pan concentration, 1133
  solution mining, 1136
  sylvite harvest ponds, 1134
Solution-reprecipitation creep, 500–501
Solution-transfer creep, 500
Solvay process, 1239–1240, 1257
Source-fed allochthonous fringes, 552
Source-fed thrusts, 528, 530–531
Source rock
  biomarkers indicating hypersalinity, 897–901
  catagenesis, 837
  definition, 837
  eogenesis, 837
  evaporitic
    accumulation, 842
    basin setting 1, 842, 852
    basin setting 2, 852–854
    basin setting 3, 854–855
    basin setting 4, 856
    basin setting 1a, 842, 856
    basin setting 1b, 852
    distribution of, 856
    dominant depositional styles, 851
    Phanerozoic time, 841–842
    selected, 843–850
  "feast or famine" style, 837, 904
  mesohaline, 838
  metagenesis, 837
  organic enrichment, 841, 902–903
South Alligator Valley deposit, Australia, 1636
South America
  borate salts in, 1207–1210
  Neogene borate-rich salar deposits in, 1207
  nitrates in, 1284
  Salinas and dolomite, 323–324
Southern Arabian Gulf sabkhas, 212–231
Southern North Sea
  extension and conversion structures, 567, 568
  salt structures in, 566, 567
South Oman Salt Basin, 591
Sparry burial anhydrite, 757, 761
Speleothemic sulphates, 712
Spika Formation, 1468–1469
Squeegee effect, 779
Squeeze mining method, 1318
SSC deposits. *See* Sediment-hosted stratiform copper (SSC) deposits
Stable isotope measurements, authigenic calcite cements, 780, 781
Starra deposit, Queensland, 1635–1636
Staveley Formation, meta-evaporites in amphibolite, 1459–1461
Stepped counter-regional system, 540, 550
Stevensite, 82
Strain
  and flow rates, 498
  markers, 509

Strategic Petroleum Reserve (SPR) program, 1325
ground subsidence, 1377
in Weeks Island, Louisiana, 1363–1364
Stratiform breccias, 649–650
Stratigraphic evolution
early Oligocene, 384
Matuyama magnetic chron, 388
Paleocene and Eocene, 385–387
Phanerozoic, 388
quaternary period, 384
Stratigraphic traps, 1080
Stratigraphy, 1621
Stress field, in Nile Delta, 503–504
Strike-slip faults, 547, 548
Stromatolites
cyanobacteria, 21–22
intertidal, 16
lacustrine, 16
laminae of, 27
microbial layers, 20–23
Subaerial salt glaciers, 589
Subaqueous salts. *See* Perennial saline lakes; Salinas
Sub-continental lithospheric mantle (SCLM), 1627, 1629–1630
Subgrains, 509
Subhercynian foreland basin-fill, 504
Submarine salt glaciers, 589
Subsalt reservoirs, compressional evaporite provinces, 1068
Subsalt sediments, 602
Subsidence troughs
Black Hills, South Dakota, 636–637
creation, 628
Delaware Basin, West Texas, 631–634
Holbrook Anticline, Arizona, 634–636
Hutchison salt, Kansas, 630–631
subcrop salt dissolution, 628
Subsurface non-evaporitic sediments, 498
Subsurface organic-sulphate reactions
bacterial sulphate reduction
activities of, 947
in aerobic/anaerobic interface, 946
bioepigenetic limestone, 946–947
cements and oil biodegradation, 948
Desulphovibrio and Desulphotomaculum, 945
diagenesis stage, 949
metabolic process, 945
sulphate-reducing bacteria, 946
temperature, 945
hydrogen sulphide (H_2S), 953–956
saline rift lakes, hydrothermal cracking in, 956–959
thermochemical sulphate reduction (*see* Thermochemical sulphate reduction (TSR))
Sudbury, 1607–1608
Suffosion dolines, 622
Sulige gas field, China., 966
Sulphate, assimilation of, 1611
Sulphate evaporites, 1667
nodular anhydrite and water loss, 70–74
nodules and stylolites, 74
Sulphate of potash (SOP), 1088
from brine
Amadeus Basin, Australia, 1139–1141
Lop Nur, 1137–1139
in Great Salt Lake, Utah, 1104
kainite/schoenite brine source, 1104
lake brine processing and solution chemistry, 1101
manufacture, processes and costs in 2012, 1103
Sulphate-reducing bacterium, 321
Sulphate reduction model, 1497–1498. *See also* Thermochemical sulphate reduction
Sulphate speleothems, 695
Sulphide deposits of Iberian Pyrite Belt, 1492
Sulphobus, 875
Sulphur
bacteriogenic production, 1294
biology of, 1295
carrying capacity, 1602
isotope at Noril'sk, 1609–1612
isotopes from gypsum, 1507
manufacturing process, 1294
metal solubility and fixation, 1493
natural deposits, 1294–1295
occurrences and textures, 1295–1297
production, 1293
usage history and industry trends, 1292–1294
Sulphuric acid speleogenesis
active and inactive sulphuric cavern systems, 708
bathyphreatic caves, 709
Carlsbad-Lechuguilla cavern system, 709–710
cave enlargement mechanisms, 713
H_2S-related karstification, 715
hypogenic caves, 709
inorganic models, 713
mineralised hypogene breccias
Cadjebut zinc mine, 715–717
infiltrated uranium mineralisation, 718
sulphur isotope value range, 712
tear drop cavern, 711
Sulphur isotopes as brine parenthood indicators, 135–139
Sulphur Point formation, 776
Supergene enrichment in Porphyry copper deposits, 1595–1597
Supradiapiric traps, 1037–1043
Suprasalt caprocks, 603
Suprasalt carbonate sedimentation, 597–601
Suprasalt clastic sedimentation, 596–597
Suprasalt deformation, 571
Surface casing, 1312
Sverdrup Basin, 770–772
Sylvinite mining in Carlsbad, New Mexico, 1094
Sylvite
potash salts, 1087
salt fraction, 1613
Syndepositional diapir, 595
Syndepositional karst, 62–65
Synkinematic layers, 587
Synkinematic sedimentation, 538
Syn-rift basins, 551
Szechuan region, China, solution mining, 1311

T

Tachyhydrite
carnallite and, 1274
description, 1276–1278
occurrences, 1274–1275
TAG mound type deposits, 1660–1664
Talc
meta-evaporitic mineralisation, 1424
sodian phyllosilicates and, 1421–1424
and tourmalines, 1423
Tank-track advance/frontal rolling, 524
Tanzanite, tsavorite and, 1433–1435
Tarim Basin, China, 1079
Tartus Basin, Troodos Larnaca Culmination, 469

Tata Chemicals Magadi Ltd, 1250
Tectonic stresses, 795
Tectonic stresses, by overpressure, 795
Tennant Creek style deposits, 1641, 1643
Tepees
  Permian Basin, West Texas, 35
  ridges, 36, 37
  saline-tepees, 36
  stacked sequence, 35
  Tansill formation, 35
Tersanne, France, salt creep effect in, 1373
Tertiary evaporite
  depositional textures, 10, 12
  fibrous gypsum and halite, 76–80
Tertiary foreland basin, 564–565
Tertiary Piedmont Basin, 462
Tertiary salt welds, 540
Textures
  borate salts, 1207
  dynamic metamorphism, 1382
  sulphur, 1295–1297
Thenardite, 1216
Thermal effects, salt flow, 505
Thermal maturation, 837
Thermobaric-thermohaline fluids
  fluid movement, 773–774
  natural hydrofracturing, 774
  thermal properties, 777
Thermochemical sulphate reduction (TSR), 1512, 1525
  BT *vs.* DBT values, 952, 953
  efficiency of, 949
  Jialingjiang Formation, 953, 954
  Khuff Formation, 950
  low salinity subsurface water, 950–951
  post-diagenesis, 953
  pre-diagenesis, 952–953
  reactants and sulphur generation product, 953
  Smackover Formation, 951, 952
Thermohaline suprasalt convection, 791
Thin-skinned fold, 560–565
Thrombolites
  biolithification of, 24
  Evolution and distribution of, 29
Thrust advance, 530
Thrust belts, 560–565
  décollement, 562
  dynamic/regional metamorphism, 1394–1401
  Lufilian foldbelt, Central Africa, 560
  taper angle, 560
Thumb Mountain Formation, 1555, 1557, 1562
Thylacoleo carnifex, 287
Thyroid-stimulating hormone (TSH), 1282
Tiered allochthon plays, deepwater realm, 1043–1048
Timor Sea, 779–781
Tincal. *See also* Borate salts
  definition, 1195–1196
  description, 1196
Tincalayu, Argentina, borate deposits, 1198, 1207
Tonalite, trondhjemite, and granodiorite (TTG) production, 1390
Topographic relief, 572, 589, 590
Torrens Lake, Australia, 881
Total dissolved solid (TDS) boundary, 1485–1486
Total Organic Carbon (TOC)
  and carbonate proportion, 918, 919
  modern saline settings, 857, 858
Tourmalines
  aluminium borosilicates, 1412
  boron isotopic composition, 1416, 1417, 1424, 1432
  characteristics, 1413
  composition, 1413
  dravite-uvite series, 1413
  lattice structure of, 1412
  with marine evaporites, 1414
  meta-evaporitic settings, 1413–1414
  mineralization characteristics, 1418
  Rum Jungle geochemistry, 1467–1468
  in Sullivan deposit, 1416, 1417
  talc and, 1423
  and tourmalinisation, 1412–1420
Tourmalinite, 1412
  mineral, 1412
  worldwide examples of, 1420
Transvaal Sequence, South Africa, 1649
Trap styles, 1079
Triassic Chinle Formation, 1518
Triassic evaporites, 781, 820–821, 833–834
Triassic extensional faults, 566–567
Triaxial deformation experiments
  carnallite, sylvite and rock salt, 499–500
Trona, 1238. *See also* Sodium carbonate
  in African Rift, 1249–1251
  deposits, 114–116
  evaporites in Lake Magadi, 115
  in North America, 1243–1247
  solution mining, 1322–1324
Trump method wells, solution mining, 1315
Truncations (unconformities), 587
Tsavorite
  genetic model, 1433
  nodules of, 1433–1434
  structure, 1434
  and tanzanite, 1433–1435
TSH. *See* Thyroid-stimulating hormone (TSH)
Tubeworm carbonates, 941
Tufa
  annual growth rates, 26
  Big Soda Lake, Nevada, 26
  mound and pinnacles, 332–334
  reef mounds, 307
Tully method wells, solution mining, 1315
Tumuli, 627
Turkey
  borate salts in, 1192, 1197, 1202–1207
  colemanite in, 1197, 1198
  mirabilite in, 1234, 1236
  sodium sulphate in, 1233–1236
Turtles, 520–521
Turtle-structure anticlines, 520
Tusanj site in Tuzla
  solution mining, 1342
Tuz Golu, Turkey, 340–342
Tuz Lake, Turkey (Tuz Gölü), perennial saline lakes, 340–342
Two Way Time (TWT) structure map, 583, 585
Tyrell Lake in Victoria, acid groundwater in saline, 128–129

U
Ukrainian Dniepr-Donets Basin (DDB), 572, 573
Ulexite, 1202
  nodules, 1204
  in Turkey, 1197, 1198
Umm Ash Shurabyat, Saudi Arabia, Sabkhat, 298
Umm as Samim sabkha, in Oman, 295
Underpressure, 794
Untersee Lake, East Antarctica, conical stromatolites in, 27
Upper Convective Layer (UCL) of Atlantis II Deep, 1505

Upper Kama Potash Region, Cis-Urals Russia, ancient potash evaporites, 1161–1165
Upper Mexican Ridges (UMR) unit, 556
Upper Red Formation, 578, 580
Upper Rhine Graben, France, ancient potash evaporites, 1141–1144
Uraniferous calcretes, 1593–1595
Uranium ore, 1638
Urmia Lake, NW Iran, perennial saline lakes, 342–344

V
Vadose caves
  Miocene epikarst, Madrid Basin, Spain, 682–684
  Modern Gypsum Karst, Saudi Arabia, 686–687
  modern karst in Cretaceous Gypsum, Texas, 684–686
Van Lake, Turkey, perennial saline lakes, 335–338
Van't Hoff plots, 106
Variable point injection, solution mining, 1316
Vein textures and inclusion studies, 779
Vena del Gesso basin, 462–463
Vent anhydrites, 1601
Vesicoya cordata, 936
VHMS deposits. *See* Volcanogenic-hosted massive sulphide (VHMS) deposits
Viscaria copper deposit, 1646, 1649
Visean Belle Roche breccia, 646
Vitrinite, 839
Vitrinite reflectance, 1547
Volcanogenic-hosted massive sulphide (VHMS) deposits, 1574
  formation, 1653–1654
  gold in, 1605
  hydrothermal anhydrite
    chimneys, 1665
    chloritization, 1663
    distribution, 1654–1655
    at mid ocean and back-arc spreading centres, 1660–1664
    plate tectonic settings, 1666
    at sediment-covered spreading centres, 1664–1666
    sulphur isotopes, 1663
    TAG mound, 1660–1664
  mineralisation, 1655–1656
  in subduction-related island-arc settings, 1656–1660
Vuggy carbonates, 940–941

W
Walton Ba-Cu-Pb-Zn-Ag deposit, 1550
Walton-Magnet baryte deposit, 1543
Warramunga Group sediments, Australia, 1641, 1642
Waste disposal, salt caverns, 1329
  nonradioactive, 1330
  radioactive, 1330–1331
Water-based drilling fluids, 807–808
Water level changes
  Dead Sea, 336, 356–357
  Great Salt Lake, USA, 325
  in Lake Urmia, Iran, 343
  Lake Van, Turkey, 336
  Mono Lake, USA, 331
Water-salt interactions, 827–829
Watt Mountain shale, 776
WCSB
  fluids, 1173
  potash geology, 1169–1173
Weeks Island, Louisiana, salt caverns, 1363–1365
Welded basins, 541, 542
Welded-listric basins, 542
Welded listric (Roho) basins, 541
West Canadian Potash (Devonian), ancient potash evaporites, 1168–1169
Western Hematites, 1635
Western Mining, 1626
Western Nile Delta Coast, Mediterranean, Egypt, 242–244
West Hackberry explosion, salt caverns, 1365
Westhazel General Petroleums Pool of west-central Saskatchewan, Canada, 1080
Wet salt
  creep and frictional strengths, 501
  specifics deformation of, 500
  weakness of, 502
Whiteschist, 1421–1423
Wieliczka site, Poland, solution mining, 1337–1341
Williston Basin, 783
Willyama Supergroup, meta-evaporites, 1461
  Broken Hill Block, 1464–1466
  Olary Block, 1462–1464
Windsor brinefield, Ontario, solution mining, 1347
Windsor Formation, 1549
Wink Sink, USA, solution mining, 1349–1355
Winsford Mine, Cheshire, salt caverns, 1324
Wolf Springs fields, 1081
Wollogorang Formation, 1581–1582
Wormy carbonate cement, 937
Wucheng, China, trona, 1247

Y
Yaninee Lake in South Australia, acid groundwater in saline, 128
Yas Island diapirs, 593, 594
Yates Field, West Texas, 1021–1025
Yilgarn Craton, West Australia, acid saline lake system, 130, 131
Yilgarn deposit, Australia, 1593–1595
Yinmin Formation, 1518–1520
Yorkshire deposit, halite in, 1423
Yudomski event, 159, 160

Z
Zabuye Lake, China
  lithium, 1271–1273
Zagros deformation front (ZDF), 582
Zagros Foldbelt, Iran, 1068–1073
Zagros front, 574–576
Zagros/Hormuz region, Arabian Gulf, 640–642
Z3 - Boulby Potash, UK, 1155–1159
ZDF. *See* Zagros deformation front (ZDF)
Zechstein evaporites, England
  potash from, 1154
  stratigraphic evolution in, 477–483
  transition depth, 74
Zechstein salt
  in Germany, 1319–1320
  potash salt horizons in, 1612
  structures, 496, 504
Zeolites, 1297
  in agriculture, 1299
  facies of, 1386
  geological occurrence, 1300
  Lake Lewis, Central Australia, 1304–1305
  properties, 1298
  in saline settings, 1299–1304
  usage and production, 1298–1299